



N-type Conductivity in Stabilized Zirconia Solid Electrolytes

T. H. Etsell* and S. N. Flengas**

Department of Metallurgy and Materials Science, University of Toronto, Toronto, Ontario, Canada

ABSTRACT

The n-type conductivity in commercially available stabilized zirconia electrolyte tubes was studied from 600° to 1400°C using three independent techniques: emf measurements on H₂-H₂O mixtures, coulometric titration of oxygen out of liquid silver or copper, and electrolyte breakdown in gas mixtures with low oxygen activities. From the coulometric titration results

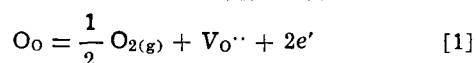
$$\log P_{\theta} = - \frac{54.5 \times 10^3}{T} + 14.0$$

where P_{θ} is the oxygen pressure at which the ionic and n-type conductivities are equal. Determinations of the electrolyte breakdown voltage permit reasonable estimates of P_{θ} to be made. Disagreement between the first two techniques was found which enabled discrepancies in the literature to be resolved.

Recent emf measurements on oxide electrolyte cells to determine thermodynamic properties have indicated that accuracies exceeding ± 1 mV (± 100 cal/mole O₂) can be realized (1, 2). In addition, accuracies exceeding ± 2 mV are often reported. Consequently, even small electronic transport numbers in the electrolyte can prove significant, emphasizing the importance of a knowledge of electronic conductivity in oxide electrolytes.

An increasing number of thermodynamic and kinetic studies using oxide electrolytes as well as almost all the investigations concerning either the determination of oxygen in metals or gases or the electrochemical control of oxygen in gas mixtures with oxide electrolyte cells (3) involve the use of commercially available calcia- or yttria-stabilized zirconia tubes (generally from the Zirconium Corporation of America). They are impervious and enable the electrode compartments to function independently. Nevertheless, electronic conductivity data are very limited for such tubes.

Previous work on electronic conductivity in stabilized zirconia samples exhibits marked disagreement. Since, from oxygen permeability measurements, $t_h \leq 10^{-3}$ at 600°-1200°C and $P_{O_2} = 1$ atm where t_h is the transport number of electron holes (4-6), p-type conductivity can be neglected. Nonetheless, it could become significant at higher temperatures since, for ZrO₂-CaO electrolytes, the activation energy for p-type conduction, 43.8 kcal/mole (6), is considerably higher than that for ionic conduction, 25-30 kcal/mole (3). However, n-type conductivity is appreciable at low oxygen pressures on account of the reaction



where O_O is an oxygen ion on a normal lattice site, $V_{O''}$ is a doubly ionized oxygen vacancy, and e' is an excess

* Electrochemical Society Student Associate Member.

** Electrochemical Society Active Member.

Key words: zirconia, solid electrolytes, n-type conductivity, mixed conduction, emf measurements, coulometric titration, electrolyte breakdown.

electron. The usual parameter to describe n-type conductivity is P_{θ} , the oxygen pressure at which $t_e = 0.5$ where t_e is the transport number of excess electrons (7). The widespread values of $\log P_{\theta}$ at 1000° and 1600°C which have been reported are listed in Table I. In this table, O symbolizes dissolved oxygen.

Regarding the techniques used to obtain these data, the measured emf, E_m , of an oxygen concentration cell having a stabilized zirconia electrolyte and oxygen pressures of P_{O_2}' and P_{O_2}'' at the anode and cathode, respectively, ($P_{O_2}'' > P_{O_2}'$) is given by

$$E_m = \frac{RT}{F} \ln \frac{P_{O_2}''^{1/4}}{P_{O_2}'^{1/4} + P_{\theta}^{1/4}} \quad [2]$$

providing that $P_{O_2}'' \gg P_{\theta}$ (7). It is assumed that the n-type conductivity, σ_n , follows the theoretical $P_{O_2}^{-1/4}$ dependence, predictable from Eq. [1]. If the oxygen activity at the anode is very low such that $P_{O_2}' \ll P_{\theta}$, a maximum emf, E_{max} , given by

$$E_{max} = \frac{RT}{4F} \ln \frac{P_{O_2}''}{P_{\theta}} \quad [3]$$

will be observed and P_{θ} can be calculated. In the maximum emf method, the low oxygen activity at the anode is achieved thermodynamically whereas, in the coulometric titration method, it is achieved by electrochemically removing oxygen from the anode chamber. In the latter case, if the applied potential is high enough and concentration overpotential only arises at the low oxygen-pressure side, E_{max} can be measured upon opening the circuit.

The thermodynamic emf, E_t , of the cell is

$$E_t = \frac{RT}{4F} \ln \frac{P_{O_2}''}{P_{O_2}'} \quad [4]$$

An average ionic transport number, \bar{t}_i , between the oxygen pressures imposed at the electrodes is defined as

$$\bar{t}_i = \frac{E_m}{E_t} \quad [5]$$

Table I. Reported $\log P_\theta$ values for stabilized zirconia electrolytes

Sample, mole per cent (m/o)	Technique	$\log P_\theta$, atm		Ref
		1000°C	1600°C	
ZrO ₂ -CaO-MgO tube	Maximum emf Ca-CaO vs. air	-24		(7)
ZrO ₂ + 10% Y ₂ O ₃ disk	Coulometric titration O ₂ out of H ₂ -H ₂ O	-27		(8)
ZrO ₂ + 15% CaO disk	Emf comparison NbO ₂ -Nb ₂ O _{5-x} vs. Fe-Fe ₂ O ₃	-31		(9)
ZrO ₂ + 15% CaO tube	Coulometric titration O ₂ out of air	-23		(10)
ZrO ₂ + 15% CaO tube	D-C polarization Fe-Fe ₂ O ₃ or Co-CoO vs. Au	-28	-13 ^(a)	(11)
ZrO ₂ + 15% CaO disk	A-C conductivity as function of P _{O₂}	-31		(11)
ZrO ₂ + 12% CaO + 4% MgO tube	Emf comparison H ₂ -H ₂ O vs. air		-15	(12)
ZrO ₂ + 15% CaO disk	Emf comparison CO-CO ₂ vs. air		-12	(13)
ZrO ₂ + 15% CaO tube	Coulometric titration	-27	-14	(14)
ZrO ₂ + 10% CaO tube	Maximum emf Al-Al ₂ O ₃ vs. O ₂	-23		(15)
ZrO ₂ + 14% MgO tube	Emf comparison O (in Fe-C) vs. O ₂		-13 ^(b)	(16)
ZrO ₂ + 7% Y ₂ O ₃ rod	Coulometric titration O out of Ag	-31 ^(c)	-16	(17)
ZrO ₂ + 15% CaO plate	D-C polarization N ₂ -O ₂ vs. N ₂ -O ₂	-37 ^(d)		(18)
ZrO ₂ + 10% Y ₂ O ₃ tube	D-C polarization N ₂ vs. air	-30 ^(e)		(19)

^(a) Extrapolated from 1227°C.

^(b) 1627°C.

^(c) Extrapolated from 1200°C.

^(d) Extrapolated from 727°C.

^(e) Log P_θ = -28 for ZrO₂ + 16% CaO.

The emf comparison method involves determining E_m for a cell which satisfies the requirement $P_{O_2}'' \gg P_{O_2}' \sim P_\theta$ and then calculating P_θ via Eq. [2], i.e., in effect, comparing E_m and E_t . Since only t_i values were reported in three papers (12-14), P_θ was found using, in turn, Eq. [4], [5], and [2].

In the d-c polarization technique, potentials are applied to a cell with one reversible electrode and one electrode, which is made the cathode, that prohibits the electrolyte from having access to oxygen because it is either irreversible (11, 19) or nonporous (18). Ionic current is blocked and a plot of log electronic current against applied potential can be used to obtain the n-type conductivity at the oxygen pressure defined by the reversible reference electrode (11, 18, 19). By consequence of the proportionality between σ_n and $P_{O_2}^{-1/4}$ and available ionic conductivity data (3), P_θ can be determined.

Lastly, a-c conductivity measurements as a function of oxygen pressure can be used to obtain σ_n and, therefore, P_θ directly if the required low oxygen activities can be reliably established.

The ionic transport number, t_i , can be readily shown to be

$$t_i = \frac{P_{O_2}^{1/4}}{P_{O_2}^{1/4} + P_\theta^{1/4}} \quad [6]$$

Accordingly, a knowledge of P_θ suffices for calculating the ionic transport number at any required oxygen pressure. Combining Eq. [2], [4], and [6] leads to

$$E_m = E_t + \frac{RT}{F} \ln (t_i) P_{O_2}' \quad [7]$$

Equation [7], in conjunction with Eq. [5], provides an important relationship between $(t_i) P_{O_2}'$ and t_i .

The purpose of this paper is threefold: first, to report P_θ values for commercially available stabilized zirconia tubes which were measured over a wide temperature range, second, to introduce an approximate electrolyte breakdown technique, and third, to compare the results obtained by several techniques so that reasons for the serious disagreement in Table I can be advanced thereby indicating which data are more reliable.

Experimental

The solid electrolytes were impervious ZrO₂ + 10 m/o CaO closed-end tubes supplied by the Zirconium Corporation of America. They were 24 in. long with an ID of 9.5 mm and OD of 13.5 mm and contained the following impurities in weight per cent (w/o): 0.62 SiO₂, 0.25 MgO, 0.10 Fe₂O₃, 0.18 Al₂O₃, and 0.11 TiO₂.

The tubes exhibited good thermal shock resistance and excellent stability during temperature cycling and were not destabilized after being partially reduced electrochemically.

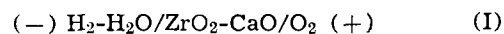
In all the experiments, the reference electrode consisted of oxygen at 1 atm pressure flowing through a piece of 45-mesh Pt gauze held firmly against the platinumized inside surface of the closed end of the electrolyte tube as previously illustrated (20). Either preanalyzed gas mixtures were passed at 1 atm pressure over a similar electrode on the outside surface of the closed end of the tube, which was held inside a quartz tube, or the electrolyte tube was dipped about 1/4 in. into liquid silver or copper of known oxygen content, which was controlled by bubbling preanalyzed gas mixtures (Ar-O₂ for silver and CO-CO₂ for copper) through the metal. Electrical contact with the liquid metals was established with Chromel A wire (80% Ni, 20% Cr) for silver and stainless steel wire (Type 314) for copper.

The measuring instruments have already been described (20).

Results and Discussion

The Pt, O₂ reference electrode is nonpolarizable from 700°-1200°C (20, 21) and hence any overpotential can be attributed to the Pt, gas mixture electrode or the liquid metal electrode.

Emf measurements.—The emf comparison technique was studied from 600°-1100°C with the cell



In an effort to make $P_{O_2}' \sim P_\theta$, ultrapure hydrogen (>99.999% on a helium-free basis) containing 4 ppm H₂O, 0.5 ppm O₂, ~50 ppm He, and <5 ppm N₂ was passed into the anode chamber. The equilibrium oxygen pressures or, more correctly, oxygen activities (22), measured emf's, and calculated P_θ values (Eq. [2] or Eq. [4], [7], and [6]) are given in Table II.

Table II. Results for the emf comparison technique

Temp, °C	log P_{O_2}' , atm	E_m , mV	log P_θ , atm
635	-33.33	1464	-34.2
800	-26.95	1466	-28.6
900	-26.89	1459	-25.8
1000	-25.14	1464	-23.9
1050	-24.37	1444	-22.5
1100	-23.65	1430	-21.4

Interchanging the gases in the electrode compartments did not affect the results.

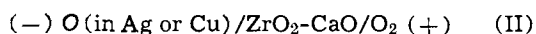
High gas flow rates were required to obtain these data. The emf increased markedly as the flow rate at the anode was increased and did not level off until the ultrapure hydrogen impinged on the electrode with room-temperature linear speeds of 80-100 cm/sec. On an average, flow rates of 2.2, 10, and 30 cm/sec at 25°C yielded emf's that were about 100, 50, and 10 mV lower than those listed in Table II. Because of electronic conductivity and, perhaps, slight porosity in the electrolyte, oxygen is continuously transferred (as ions and atoms or molecules, respectively) from the cathode to the anode chamber where it reacts with hydrogen. The resulting diffusion overpotential lowers the cell emf. High flow rates are needed so that the unwanted water molecules can be flushed away.

Unfortunately, experimental evidence indicates that the complete elimination of diffusion overpotential was impossible making the E_m values in Table II too low and the log P_θ values too high. This was suggested *a priori* by the severe flow rate dependence. The P_θ values are several orders of magnitude higher than those derived from the coulometric titration technique. Drying the H₂-H₂O mixture did not lead to any increase in E_m and its presence in the anode chamber did not produce any detectable changes in the conductivity of the electrolyte.

Oxygen permeability through the electrolyte arising from either electronic conductivity or porosity increases with temperature. From the results for cell (I) in Table II and Eq. [4] and [5], $\bar{t}_i = 0.98$ at 635°C and 0.89 at 1100°C. Interestingly, P_θ was not significantly affected by replacing oxygen in the reference compartment with a CO-CO₂ mixture containing 1.08% CO₂ [$P_{O_2}'' = 10^{-18}$ atm at 1000°C (22)] during the measurements at 1000°-1100°C. Although the driving force for open-circuit oxygen transfer is reduced, n-type conductivity in the electrolyte increases.

Less reducing H₂-H₂O mixtures were also passed into the anode chamber of cell (I). At 1000°C, measured emf's for mixtures containing 0.1% and 0.06% H₂O [$P_{O_2}' = 10^{-20.5}$ and $10^{-21.0}$ atm, respectively (22)] were about 10 and 15 mV too low, respectively. However, when $\bar{t}_i \sim 1$, calculation of P_θ using Eq. [2] is impractical which could, in part, account for the high P_θ values in Table II at the lower temperatures. Previously in H₂-H₂O mixtures, emf deviations from ideality were observed below oxygen pressures of only 10^{-18} - 10^{-19} atm at 1000°C (23, 24) and 10^{-8} - 10^{-9} atm at 1600°C (12, 23, 25) and have been attributed to both electronic conductivity (12) and porosity (24-26) in the ceramic electrolytes.

Coulometric titration.—Oxygen was electrochemically removed from liquid silver or copper containing 5×10^{-4} to 5×10^{-3} atomic per cent (a/o) O in the cell



Experiments were carried out from 1000°-1200°C for silver and from 1100°-1400°C for copper.

To appreciably lower the oxygen activity at the metal-electrolyte interface, the applied potential was held constant for 2 min prior to opening the circuit and immediately measuring the cell potential. Repeating this procedure at increasing applied potential (0.2V increments) led to maximum open-circuit cell potentials when the applied potential reached 2-3V. Subsequent

increases served only to further reduce the cathode side of the electrolyte. Substoichiometric ZrO₂, but never zirconium metal, was allowed to form. If reoxidation due to oxygen diffusion from the bulk of the liquid metal and oxygen migration through the electrolyte was prevented, the cathode side was observed to be a whitish-gray color, rather than white. If reoxidation was permitted, the original resistance of the electrolyte was generally restored within a few minutes indicating no detrimental structural changes had occurred.

In Fig. 1, E_{\max} is plotted against temperature. Comparable values were obtained by coulometrically titrating oxygen out of H₂-H₂O mixtures dilute in H₂O using cell (I). During current passage through cell (II), the only overpotential which appears is diffusion overpotential at the liquid metal electrode (21). Hence, equilibrium exists at the electrode-electrolyte interfaces and P_θ can be calculated from Eq. [3]. The results are presented in Fig. 2 and can be expressed as

$$\log P_\theta = -\frac{54.5 \times 10^3}{T} + 14.0 \quad [8]$$

The P_θ values are 5-6 orders of magnitude higher than the decomposition pressures of tetragonal ZrO₂ (22).

Such a dependence for P_θ can be predicted by noting that, for an oxide electrolyte

$$\sigma_i = A_i \exp(-\Delta H_i/RT) \quad [9]$$

$$\sigma_n = A_n P_{O_2}^{-1/4} \exp(-\Delta H_n/RT) \quad [10]$$

where σ_i and σ_n are the ionic and n-type conductivities, respectively, A_i and A_n are approximately constant, and ΔH_i and ΔH_n are apparent activation enthalpies for ionic and n-type conduction, respectively. When $\sigma_i = \sigma_n$, $P_{O_2} = P_\theta$ and, thus

$$P_\theta = (A_n/A_i)^4 \exp[-4(\Delta H_n - \Delta H_i)/RT] \quad [11]$$

meaning that

$$\log P_\theta = -\frac{A}{T} + B \quad [12]$$

where

$$A = \frac{1.7372(\Delta H_n - \Delta H_i)}{R} \quad [13]$$

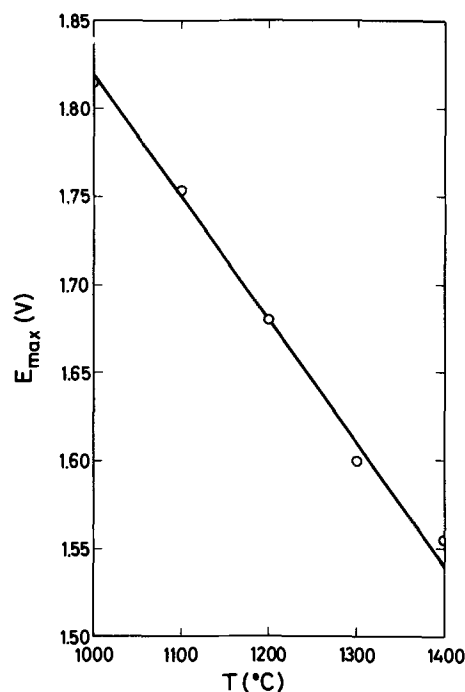


Fig. 1. Maximum cell potential resulting from coulometric titration of oxygen out of liquid silver or copper. Reference electrode was Pt, O₂ (1 atm).

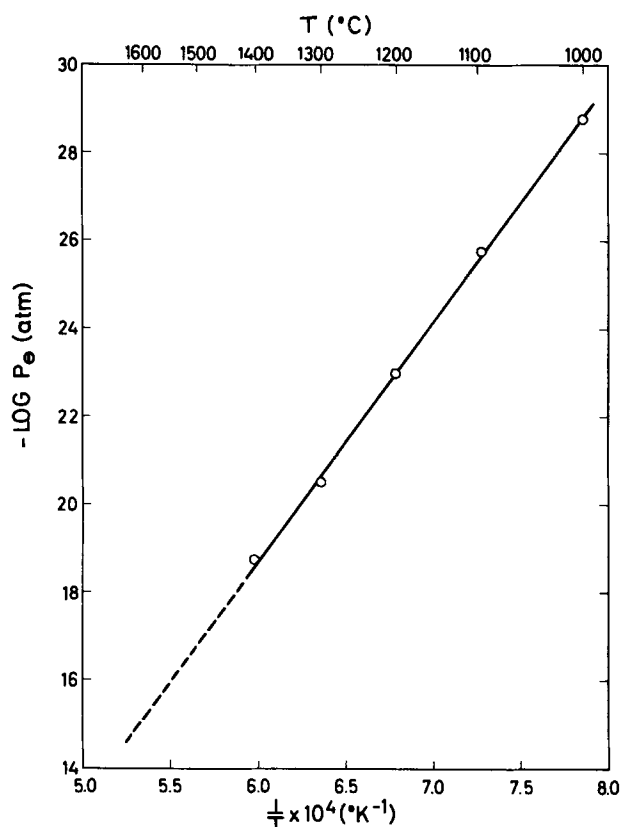


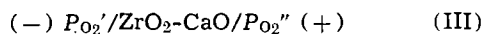
Fig. 2. Temperature dependence of P_θ for commercially available stabilized zirconia electrolytes.

and

$$B = 4 \log (A_n/A_i) \quad [14]$$

Possible changes in A_i or ΔH_i with temperature (3, 27) make lengthy extrapolations of Eq. [12] uncertain. Comparing Eq. [8], [12], and [13] gives $\Delta H_n - \Delta H_i = 62.3$ kcal/mole. Since ΔH_i was determined to be 25.3 kcal/mole, $\Delta H_n = 87.6$ kcal/mole. It will be associated with one half the enthalpy of reaction [1] and any enthalpy needed to release excess electrons from electron traps such as ionized oxygen vacancies, Zr^{4+} ions, and interstitial or easily reducible impurity cations.

Electrolyte breakdown.—In the electrolyte breakdown technique, a potential, E , is applied to the cell



as shown, making P_{O_2}' and P_{O_2}'' the oxygen pressures at the cathode and anode, respectively. The equilibrium concentration of electroactive species at the cathode (O , O_2 , CO_2 , H_2O , etc.) is kept low to essentially suppress ionic current and the anode is a nonpolarizable reference electrode. As the ionic IR drop and any transition overpotential will be negligible, concentration overpotential at the cathode accounts for the entire applied potential. Therefore

$$E = \frac{RT}{4F} \ln \frac{P_{O_2}''}{P_{O_2}'} \quad [15]$$

where P_{O_2}' is the oxygen pressure imposed at the cathode surface of the electrolyte by the applied potential (E is considered positive for convenience).

The n-type current density, i_n , obeys the equation

$$i_n = -\sigma_n \frac{dE}{dx} = \sigma_n \frac{E}{l} \quad [16]$$

where x is the distance across the electrolyte from the reference electrode, $\bar{\sigma}_n$ is the apparent average n-type conductivity, and l is the thickness of the electrolyte.

At any point inside the electrolyte under steady-state conditions

$$E = \frac{RT}{4F} \ln \frac{P_{O_2}}{P_{O_2}'}, \quad [17]$$

where P_{O_2} is the oxygen pressure corresponding to the local chemical potential. Differentiating Eq. [17] with respect to x , substituting into Eq. [16], and integrating across the electrolyte gives

$$i_n = \frac{RT}{4Fl} \int_{\ln P_{O_2}'}^{\ln P_{O_2}''} \sigma_n d \ln P_{O_2} \quad [18]$$

Equations of this type have been derived and discussed by Wagner (28).

Alternatively, at any point inside the electrolyte

$$i_n = \frac{\sigma_n}{F} \text{grad } \eta_{e'} \quad [19]$$

where $\eta_{e'}$ is the electrochemical potential of excess electrons and the absolute value of the vector $\text{grad } \eta_{e'} = d\eta_{e'}/dx$ (4). For reaction [1] in equilibrium

$$\text{grad } \mu_{O_0} = \frac{1}{2} \text{grad } \mu_{O_2} + \text{grad } \eta_{VO} + 2 \text{grad } \eta_{e'} \quad [20]$$

where μ is chemical potential. Since the ionic current is virtually zero, at steady state $\text{grad } \eta_{VO} = 0$. Also $\text{grad } \mu_{O_0} \sim 0$ meaning that

$$\text{grad } \eta_{e'} = -\frac{1}{4} \text{grad } \mu_{O_2} \quad [21]$$

Substitution of Eq. [21] into Eq. [19] followed again by integration across the electrolyte from $x = 0$ at the anode to $x = l$ at the cathode produces Eq. [18].

From Eq. [10]

$$\sigma_n = \sigma_i \left(\frac{P_{O_2}}{P_\theta} \right)^{-1/4} \quad [22]$$

Inserting Eq. [22] and $d \ln P_{O_2} = dP_{O_2}/P_{O_2}$ into Eq. [18] yields

$$i_n = \frac{RT}{Fl} \sigma_i P_\theta^{1/4} (-P_{O_2}''^{-1/4} + P_{O_2}'^{-1/4}) \quad [23]$$

Substitution of Eq. [15] into Eq. [23] leads to the final expression

$$i_n = \frac{RT}{Fl} \sigma_i P_\theta^{1/4} P_{O_2}''^{-1/4} [\exp(EF/RT) - 1] \quad [24]$$

This equation will only apply when E is low enough so that $\sigma_n \propto P_{O_2}'^{-1/4}$, i.e., at reasonably small deviations from stoichiometry in the electrolyte near the cathode.

In the case of significant ionic current

$$E = \frac{RT}{4F} \ln \frac{P_{O_2}''}{P_{O_2}'} + IR + \eta_t \quad [25]$$

where I is the ionic current, R is the ionic resistance of the electrolyte, η_t is transition overpotential, and, again, P_{O_2}' is the oxygen pressure at the cathode surface of the electrolyte. If $\eta_t \sim 0$ and P_{O_2}' is determined, i_n could be evaluated using Eq. [7] and [8] in a recent paper (29). For almost complete ion blocking, an approximate expression for i_n has been derived (18).

For the $ZrO_2 + 10$ m/o CaO electrolytes studied here

$$\sigma_i = 837 \exp(-25,300/RT) \quad [26]$$

and $l = 0.2$ cm. Theoretical electronic current density curves at 1000° and 1100°C for $P_{O_2}'' = 1$ atm, calculated from Eq. [24], are shown in Fig. 3. The P_θ data were obtained from Fig. 2. Applied potentials making $P_{O_2}' = P_\theta$ (Eq. [15]) cause considerable electrolyte breakdown, e.g., from Fig. 3, $i_n = 21$ and 47 mA/cm² at 1000° and 1100°C, respectively. According to Eq. [24], when $\exp(EF/RT) \gg 1$, P_θ could be quantitatively determined by extrapolating plots of $\ln i_n$ vs. E to $E = 0$.

To effect ion-blocking conditions, low oxygen activities at the cathode in cell (III) were established with either Ar-O₂ mixtures dilute in O₂, CO-CO₂ mixtures dilute in CO₂, or a H₂-H₂O mixture dilute in H₂O. High flow rates were required to eliminate or minimize open-circuit diffusion overpotential which

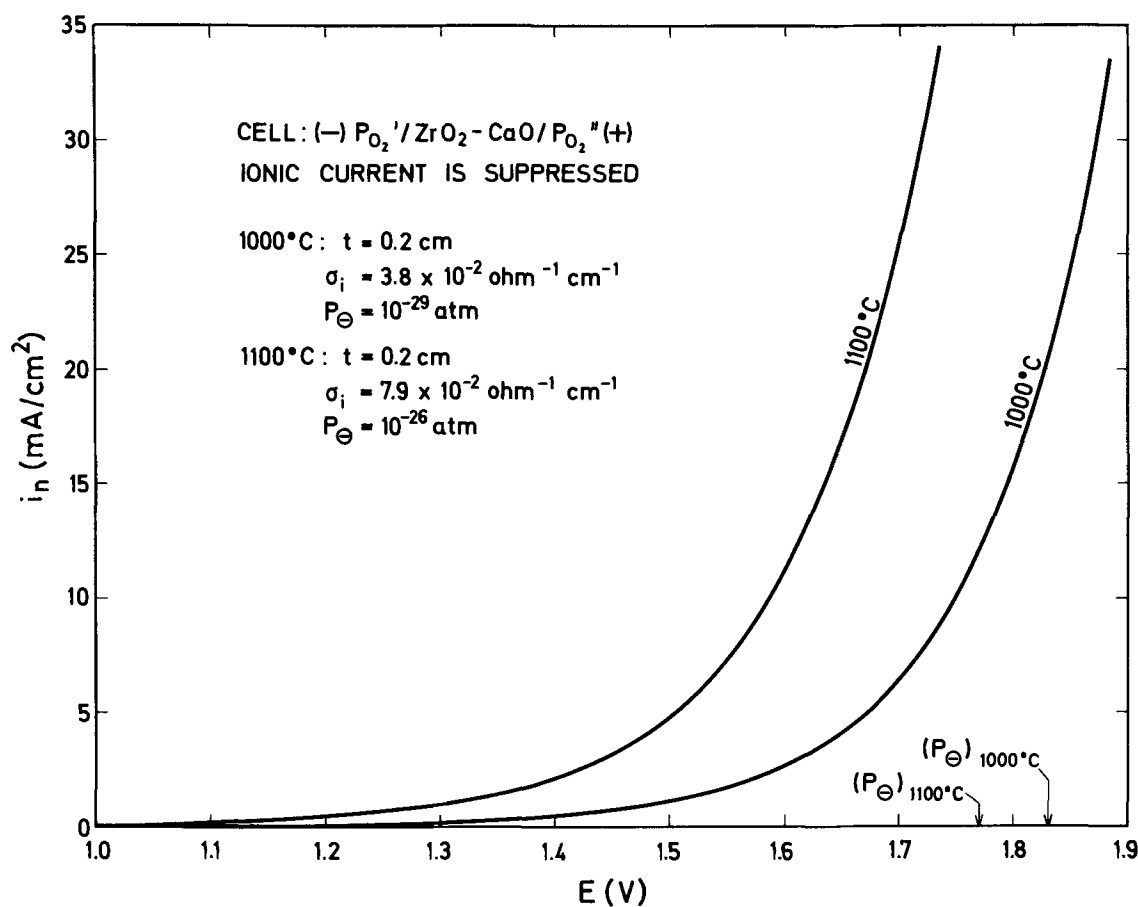


Fig. 3. Theoretical curves of n-type current density against applied potential at 1000° and 1100°C when ionic current is suppressed ($P_{O_2}'' = 1$ atm).

was discussed in the section on emf measurements. Prior to breakdown, the a-c resistance of the electrolyte measured at 3000 Hz was about 35 and 15 ohms at 1000° and 1100°C, respectively. Potential was applied to the cell allowing 20-30 min per 0.1V increment. Total current density *vs.* applied potential plots are shown for Ar-O₂ mixtures and for CO-CO₂ and H₂-H₂O mixtures in Fig. 4 and 5, respectively. The composition given for the H₂-H₂O mixture was calculated from the cell emf. Between 5 and 60 min were required to reoxidize the electrolyte by interrupting the current.

Comparing Fig. 4 and 5 with Fig. 3, it is evident that ionic current was not totally suppressed although ionic resistance polarization and transition overpoten-

tial, which is important in CO-CO₂ mixtures (20), are low. In addition, the surprisingly slow current increase at high applied potentials at 1000°C indicates that, at this temperature, the loading rate was too rapid for steady-state electronic currents to be fully realized. Lastly, the current densities are somewhat low since they are based on the geometric area of the cathode-electrolyte interface (1.0 cm²) rather than the actual area of contact between the Pt gauze and the electrolyte which was somewhat smaller. Nevertheless, currents were observed to increase significantly at potentials near those corresponding to P_θ (Fig. 1). Extrapolation of the steep portions of the curves to $i = 0$ gives breakdown voltages of 1.74 and 1.70V at 1000° and 1100°C, respectively, corresponding to oxygen

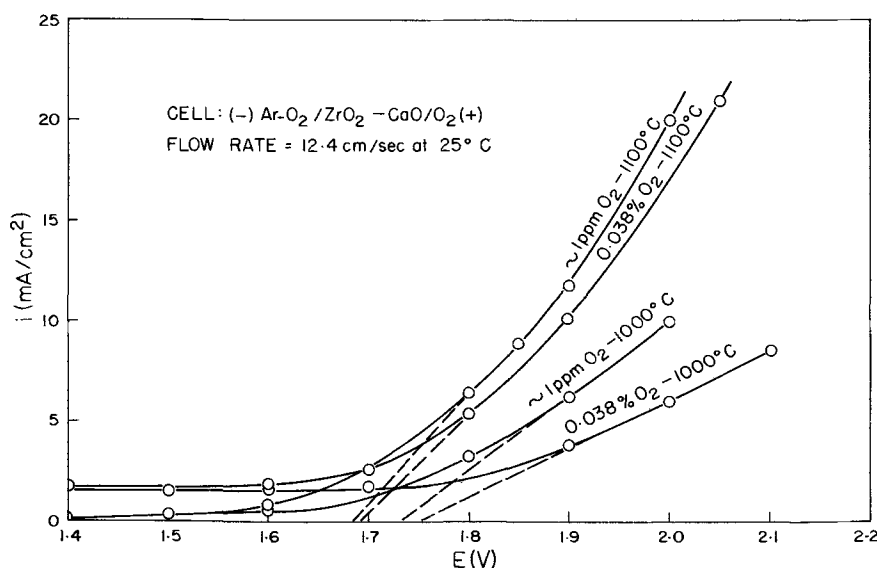


Fig. 4. Breakdown voltages in Ar-O₂ mixtures dilute in O₂.

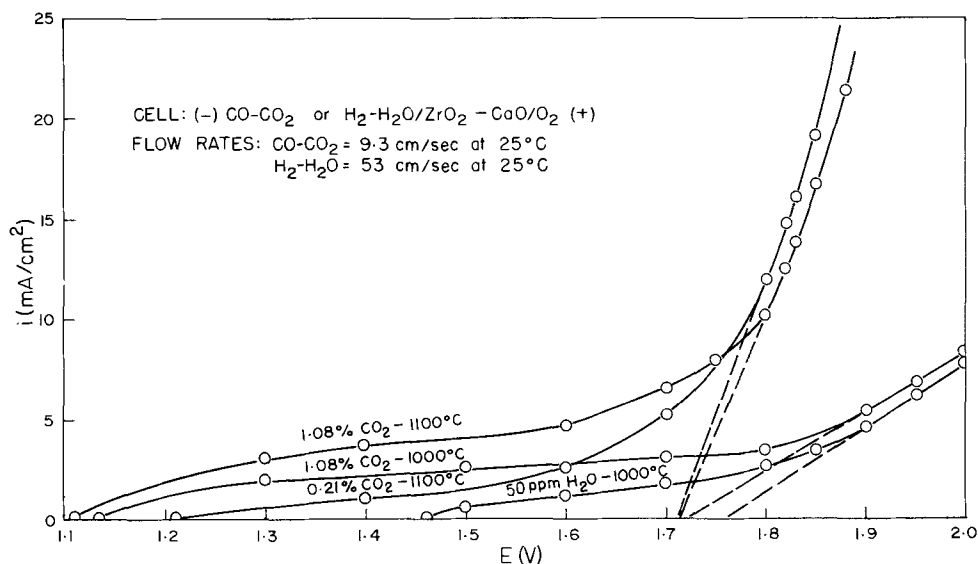


Fig. 5. Breakdown voltages in CO-CO₂ mixtures dilute in CO₂ and a H₂-H₂O mixture dilute in H₂O.

pressures about one order of magnitude higher than P_θ (Fig. 2).

Physically, electrolyte breakdown proceeds as follows. At applied potentials sufficiently high to make the oxygen activity at the cathode very low, the cathode surface of the electrolyte becomes electronically conducting via reaction [1]. The current increases since electrons can now be transferred directly from the cathode to the electrolyte forming F-centers (if they are trapped by oxygen vacancies) or Zr³⁺ ions and, as a consequence, more O⁼ ions initially migrate from the cathode side to the anode side of the electrolyte than are produced from oxygen-bearing species in the gas phase. Accordingly, the reduced zone spreads slowly towards the anode at a rate controlled by the electronic resistance of the electrolyte; this reduction causes large hysteresis in current-potential curves. Simultaneously, the electronic current continues to increase since the electronic conductivity of the electrolyte increases. Eventually, the equilibrium composition of the electrolyte, dictated by the oxygen activities at the anode and cathode, is reached and the current becomes constant. If the cathode region is markedly reduced ($t_i \sim 0$), oxygen-bearing species attempting to maintain the ionic current are obliged to diffuse through the reduced zone prior to electrochemical reaction. Severe reduction will result in the formation of either tetragonal ZrO₂ or α -zirconium (which may react with the electrode) in conjunction with a CaO-enriched cubic phase and simultaneous or subsequent cracking of the electrolyte (30, 31).

In general, care must be taken to ensure that oxygen-bearing species have limited access to the cathode surface of the electrolyte. The ionic current may increase at high applied potentials because, when the electrolyte can conduct electronically, direct oxygen transfer from the gas phase to the electrolyte does not necessitate the nearby presence of the electrode (18, 20, 32). Secondly, it may be impossible to decrease the oxygen activity in gas mixtures to very low levels because of either their buffer capacity or slow decomposition (15).

Comparison of the different techniques.—The P_θ results at 1000°–1100°C for the emf comparison technique, given in Table II, are 4–5 orders of magnitude higher than those shown for the coulometric titration technique in Fig. 2. Interestingly, using the 1000°C data in Table I, a parallel comparison can be drawn between previous studies involving emf measurements (7, 9, 15) and coulometric titration (8, 10, 14, 17).

In this work, a strong dependence of emf on flow rate for H₂-H₂O mixtures dilute in H₂O was found, which indicates that open-circuit oxygen transfer through the electrolyte leading to diffusion overpoten-

tial can seriously limit the accuracy of emf measurements at very low oxygen activities. Not surprisingly, as mentioned earlier, its influence was not eliminated. Its detrimental effect can be further appreciated by noting that P_θ calculated from available \bar{t}_i data (12) for cell (I) depends on the value of \bar{t}_i chosen, e.g., at 1600°C, $P_\theta = 10^{-15}$, 10^{-14} , and 10^{-13} atm using $\bar{t}_i = 0.99$, 0.98, and 0.95, respectively. Although oxygen transfer can be minimized by keeping $P_{O_2}' > P_\theta$ such that $t_i \sim 1$, the required calculation of P_θ from Eq. [2] becomes very sensitive to small errors in the measured emf. In some previous work, emf measurements were taken on cells having, as anodes, two-phase mixtures which only provide an invariant oxygen activity as long as both phases can be retained at the electrode-electrolyte interface. High P_θ values would be calculated if the anode were appreciably oxidized. However, to attribute the high values in Table I solely to concentration overpotential effects may be an oversimplification. For instance, Schmalzried (7) mentioned that his cell emf could be kept constant for hours. Other factors such as impurities in the electrolytes will be partly responsible.

The coulometric titration technique is rapid and should be accurate if very low oxygen activities can be established at the cathode. Failure to achieve this in N₂-O₂ mixtures at 600°–800°C might account for the inconsistently high coulometric titration P_θ data that has been reported (15). Disagreement can, at least in part, be traced to different electrolyte purities. In the electrolyte tubes used here, the ease of reduction of the Fe³⁺ and Ti⁴⁺ impurity ions could aid the onset of n-type conduction. The low P_θ values recently reported by Swinkels (17) are for high-purity electrolytes.

The d-c polarization technique is often inaccurate, especially when electronic transport numbers are low. Results achieved by this technique for ZrO₂-CaO electrolytes at low oxygen pressures and for ThO₂-Y₂O₃ electrolytes at high oxygen pressures disagreed markedly with a-c conductivity measurements (11). More recent values are entirely unrealistic since ionic current was insufficiently blocked. They are 2–3 orders of magnitude lower than the decomposition pressures of tetragonal ZrO₂ (22).

In summary, the coulometric titration results are preferable. Thermodynamic property measurements with stabilized zirconia cells support the P_θ data obtained by this technique (3).

Critical oxygen pressures for oxide electrolytes.—The results of this investigation are summarized in Table III. Results for the more stable ThO₂-Y₂O₃ electrolytes are included for comparison. The 1600°C values are based on the fact that ThO₂-Y₂O₃ electrolytes have been used

Table III. Critical oxygen pressures (activities) for solid oxide electrolytes

Electrolyte	Temp, °C	log P _{O₂} , atm				Ref
		$t_i = 0.50^{(a)}$	$t_i = 0.99$	$\bar{t}_i = 0.99^{(b)}$	$\bar{t}_i = 0.99^{(c)}$	
ZrO ₂ -CaO	1000	-29	-21	-26	-24	This work (9, 33)
	1600	-15 ^(d)	-7	-10	-13	
ThO ₂ -Y ₂ O ₃	1000	-33	-25	-30	-29	This work (34, 35)
	1600	-19	-11	-15	-13	

^(a) Log P_{O₂} = log P_θ.

^(b) In a cell with O₂ at 1 atm at the reference electrode (neglecting p-type conductivity in the case of ThO₂-Y₂O₃).

^(c) In a cell with an Fe-Fe₃O₄ reference electrode, i.e., oxygen pressures at the cathode of 10⁻¹⁵ and 10⁻⁸ atm at 1000° and 1600°C, respectively (22), neglecting mutual solubility of the liquid phases at 1600°C.

^(d) Extrapolated from 1400°C.

to obtain reliable free energy data for the Mn-MnO system at 1550°C (34) and the Si-SiO₂ system at 1600°C (35). The $t_i = 0.99$ data were calculated from Eq. [6] and the $\bar{t}_i = 0.99$ data were obtained by trial and error in Eq. [7] in conjunction with Eq. [6].

For ZrO₂-CaO electrolytes, the critical oxygen pressures are consistent with thermodynamic property measurements using stabilized zirconia cells. Results for the free energy of formation of Cr₂O₃, determined from emf measurements on the cell



at 700°-1200°C (10, 36, 37), are in excellent agreement with the literature (22). The Cr-Cr₂O₃ electrode exerts an oxygen pressure of 10^{-21.6} atm at 1000°C (22) and, from Table III and Eq. [2], [4], and [5], $\bar{t}_i = 0.999$ for cell (IV). Lower oxygen pressures at the anode generally introduce sufficient n-type conductivity to render accurate emf measurements impossible (3).

Evidence has been advanced to suggest that electronic conductivity is quite low at an oxygen pressure of 10⁻¹² atm at 1600°C (3). For cell (IV) at 1600°C, the anode oxygen pressure is 10^{-11.8} atm (22) and, from this work, $\bar{t}_i = 0.98$. The Cr-Cr₂O₃ electrode has been successfully used as a reference electrode in several recent studies at 1500°-1600°C (35, 38, 39).

Conclusions

Determination of n-type conductivity in oxide electrolytes via emf measurements at low oxygen activities is generally inaccurate on account of oxygen transfer through the electrolyte, an unavoidable consequence of electronic conductivity and porosity. Low oxygen activities are more reliably realized by coulometric titration. Following the breakdown of an oxide electrolyte can lead to reasonable estimates of the magnitude of n-type conductivity.

The oxygen activities imposed by the Cr-Cr₂O₃ system approximately define the lower limit of practical applicability of commercially available stabilized zirconia electrolytes.

Transport number determinations can only serve as a guide to the use of oxide electrolytes. Variables such as electrolyte purity and porosity, possible electrode-electrolyte interactions, and the cell arrangement render individual checks advisable whenever possible.

Acknowledgment

Financial assistance from the National Research Council of Canada is gratefully acknowledged.

Manuscript submitted June 4, 1971; revised manuscript received Sept. 13, 1971.

Any discussion of this paper will appear in a Discussion Section to be published in the December 1972 JOURNAL.

REFERENCES

- G. G. Charette and S. N. Flengas, *This Journal*, **115**, 796 (1968).
- U. V. Choudhary and A. Ghosh, *ibid.*, **117**, 1024 (1970).
- T. H. Etsell and S. N. Flengas, *Chem. Rev.*, **70**, 339 (1970).
- L. Heyne in "Mass Transport in Oxides," p. 149, J. B. Wachtman, Jr. and A. D. Franklin, Editors, NBS Special Publication 296, U.S. Government Printing Office, Washington (1968).
- R. Hartung and H.-H. Möbius, *Z. Phys. Chem.*, **243**, 133 (1970).
- L. Heyne and N. M. Beekmans, *Proc. Brit. Ceram. Soc.*, **19**, 229 (1971).
- H. Schmalzried, *Z. Elektrochem.*, **66**, 572 (1962).
- D. T. Bray and U. Merten, *This Journal*, **111**, 447 (1964).
- B. C. H. Steele and C. B. Alcock, *Trans. Met. Soc. AIME*, **233**, 1359 (1965).
- Yu. D. Tret'yakov, *Inorg. Mater.*, **2**, 432 (1966).
- J. W. Patterson, E. C. Bogren, and R. A. Rapp, *This Journal*, **114**, 752 (1967).
- W. A. Fischer and D. Janke, *Arch. Eisenhüttenw.*, **39**, 89 (1968).
- J. K. Pargeter, *J. Metals*, **20**(10), 27 (1968).
- Yu. D. Tret'yakov and A. Muan, *This Journal*, **116**, 331 (1969).
- D. Yuan and F. A. Kröger, *ibid.*, **116**, 594 (1969).
- K. Hirota, *Bull. Chem. Soc. Japan*, **42**, 1892 (1969).
- D. A. J. Swinkels, *This Journal*, **117**, 1267 (1970).
- R. J. Brook, W. L. Pelzmann, and F. A. Kröger, *ibid.*, **118**, 185 (1971).
- L. D. Burke, H. Rickert, and R. Steiner, *Z. Phys. Chem., N. F.*, **74**, 146 (1971).
- T. H. Etsell and S. N. Flengas, *This Journal*, **118**, 1890 (1971).
- T. H. Etsell and S. N. Flengas, *Met. Trans.*, **2**, 2829 (1971).
- O. Kubaschewski, E. Ll. Evans, and C. B. Alcock, "Metallurgical Thermochemistry," 4th ed., Pergamon Press, London (1967).
- H.-H. Möbius, *Z. Phys. Chem.*, **233**, 425 (1966).
- R. Hartung and H.-H. Möbius, *Chem. Ingr.-Tech.*, **40**, 592 (1968).
- W. A. Fischer and D. Janke, *Z. Phys. Chem., N. F.*, **69**, 11 (1970).
- H. Ullmann, D. Naumann, and W. Burk, *Z. Phys. Chem.*, **237**, 337 (1968).
- R. E. W. Casselton, *Phys. Status Solidi (a)*, **2**, 571 (1970).
- C. Wagner in "Proceedings of the 7th Meeting of the International Commission on Electrochemistry, Thermodynamics, and Kinetics, Lindau, 1955," p. 361, Butterworths, London (1957).
- N. S. Choudhury and J. W. Patterson, *This Journal*, **118**, 1398 (1971).
- R. E. W. Casselton, *Elec. MHD, Proc. Symp.*, Vol. V, p. 2951, International Atomic Energy Agency, Vienna (1968).
- R. E. W. Casselton, J. Penny, and M. J. Reynolds, *Trans. J. Brit. Ceram. Soc.*, **70**, 115 (1971).
- H. Yanagida, R. J. Brook, and F. A. Kröger, *This Journal*, **117**, 593 (1970).
- A. A. Vecher and D. V. Vecher, *Russ. J. Phys. Chem.*, **42**, 418 (1968).
- K. Schwerdtfeger, *Trans. Met. Soc. AIME*, **239**, 1276 (1967).
- R. J. Fruehan, L. J. Martonik, and E. T. Turkdogan, *ibid.*, **245**, 1501 (1969).
- Yu. D. Tret'yakov and H. Schmalzried, *Ber. Bunsenges. Phys. Chem.*, **69**, 396 (1965).
- L. A. Pugliese and G. R. Fitterer, *Met. Trans.*, **1**, 1997 (1970).
- R. J. Fruehan, *Trans. Met. Soc. AIME*, **245**, 1215 (1969).
- R. J. Fruehan, *Met. Trans.*, **1**, 865, 2083, 3403 (1970).

Mechanism of the Processes of Formation of Lead-Acid Battery Positive Plates

D. Pavlov, G. Papazov, and V. Iliev

*Institute of Physical Chemistry, Central Electrochemical Power Sources Division,
Bulgarian Academy of Sciences, Sofia 13, Bulgaria*

ABSTRACT

The processes involved in the formation of the positive lead-acid battery plate in H_2SO_4 with sp gr 1.15 and 1.05 and in 0.7M Na_2SO_4 were studied by x-ray diffraction, wet chemical analysis, and microscopic observations. It was found that formation takes place in two stages. During the first one, H_2SO_4 and H_2O penetrate from the bulk of the solution into the plate. As a result of chemical and electrochemical reactions tet-PbO and basic sulfates of lead are converted to PbSO_4 and $\alpha\text{-PbO}_2$. These compounds form zones which advance into the paste. Part of the hydrogen ions evolved during the reaction of formation of PbO_2 migrate from the plate in order for the latter to remain electroneutral. During the second period H_2O is consumed in the plate. Lead sulfate is oxidized to $\beta\text{-PbO}_2$. Sulfuric acid originates and diffuses in a direction opposed to that in the first period. Taking into account specific conditions of the chemical and electrochemical reactions in porous electrodes a mechanism is suggested for the formation processes of the positive plate. Ion diffusion and migration are considered to be the rate-limiting steps of the processes. The direction of advance of the PbO_2 and PbSO_4 zones is explained in terms of this mechanism as well as the $\alpha/\beta\text{-PbO}_2$ ratio during formation in the three solutions. The parameters which control the phase composition of the active material of the lead-acid battery positive plate are listed.

Formation is one stage of the technological process of lead-acid battery production. By mixing oxidized lead powder with sulfuric acid a paste is obtained which consists of lead monoxide and basic sulfates of lead. After pasting on a grid and curing, the paste is subjected to formation. During formation lead monoxide and the basic sulfates are converted by electrochemical reactions to active material, *i.e.* to lead at the negative plate and to lead dioxide at the positive one. Formation takes place in a sulfuric acid solution. Lead monoxide and basic sulfates of lead are unstable in sulfuric acid, and therefore the electrochemical reactions are accompanied by chemical sulfation processes. All this imparts a great complexity to the formation process. Until now attention has been mainly focused on the influence of paste, electrolyte and current density, of temperature, etc. on the processes at the positive plate (1-15). This interest may be explained by the fact that formed plates contain both the acidic β and the alkaline α polymorph of PbO_2 . On the other hand, the capacity and the life of the positive plate is determined by the ratio between the polymorphs in it. With the increase in the content of the beta polymorph in the active mass, the capacity increases but the life of the plate decreases.

Attempts at elucidating the formation processes of the positive plate were mainly concerned with determination of the mechanism of formation of $\alpha\text{-PbO}_2$. Two schools of thought are to be found in the literature. According to the first one, the solution in the pores is locally alkalized which leads to the formation of $\alpha\text{-PbO}_2$ (1, 5). According to the second one, $\alpha\text{-PbO}_2$ is a result of solid-state reactions within the basic lead sulfate crystals (2, 4). In order to elucidate the mechanism of the processes which take place upon formation of the positive plate, however, it is not enough to determine the causes which lead to the formation of $\alpha\text{-PbO}_2$.

In the present work the changes in phase and chemical composition occurring during formation of the positive plate in solutions of different pH were followed by x-ray diffraction and chemical analysis. This makes it

possible to determine the electrochemical and chemical processes of formation. In order to establish the chemical reactions between the solution and paste, the changes in phase composition upon leaving the plate in the solution at open circuit were followed by x-ray diffraction and chemical analysis. Since the products obtained contrast in color, it proved possible to determine the distribution of the processes within the plate by microscopic observations at low magnification. The suggested mechanisms of the processes of formation and of their dependence on the pH of the solution in which forming was carried out is based on these results.

Experimental

Plates of dimensions $143 \times 125 \times 1.8$ mm (14 A-hr) were formed. The paste was prepared by mixing lead powder with sulfuric acid [4.5 weight per cent (w/o) with respect to the lead powder]. The paste density was 3.60 g/cm^3 . The electroformation density current was 5 mA/cm^2 and the temperature 25°C . Formation was carried out in three kinds of solutions: H_2SO_4 sp gr 1.05 ($\text{pH} = 0.25$), and 1.15 ($\text{pH} = -0.20$) and 0.7M Na_2SO_4 ($\text{pH} = 7$). The phases in the dry paste were identified. Samples were taken close to the four corners and from the middle portion of the plate. The material was homogenized in a mortar and transferred to the sample holder of a TuR-M 61 x-ray diffractometer (filtered copper radiation).

Cells constituted by two positive and three negative plates were used in the investigation of the processes. The following parameters were measured every two hours during the formation process:

- (i) Potential of the positive plate under load ϕ_i .
- (ii) Potential of the positive plates at open circuit ϕ_o .
- (iii) Phase composition of the paste and of the active mass. One of the positive plates was removed and washed. Samples were taken as already described and x-rayed.
- (iv) Chemical composition of the paste and active mass. The following components were analytically determined: ($\alpha + \beta$) PbO_2 , total PbO (free PbO plus PbO in the basic sulfates), and total PbSO_4 (free PbSO_4 plus PbSO_4 bonded in the basic sulfates).
- (v) The distribution of the reaction products along the cross section of the plate. Under the binocular mi-

Key words: lead acid battery, lead acid battery technology, PbO_2 electrode, electrochemical reactions in a porous mass, electrochemical oxidation of lead oxide and basic sulfates.

roscope the distribution of the compounds was followed along the cross section of the plate. Color and black-and-white photographs were taken. After sampling the plate was returned into the cell, the current was adjusted, and the formation resumed.

Results

Formation in H₂SO₄ of sp gr 1.15.—Figure 1(a) shows the changes in the intensities of the characteristic diffraction lines of PbSO₄ $d = 3.00\text{\AA}$, 3PbO·PbSO₄·H₂O $d = 3.26\text{\AA}$, 2PbO·PbSO₄¹ $d = 2.95\text{\AA}$, tet-PbO and α -

¹The diffraction line with $d = 2.95\text{\AA}$ is common to PbO·PbSO₄ ($I = 100$) (16) and to 2PbO·PbSO₄ ($I = 100$) (16). The second strongest line of PbO·PbSO₄ has $d = 3.33\text{\AA}$ ($I = 100$) while for 2PbO·PbSO₄ it has $d = 2.87\text{\AA}$ ($I = 70$). In its x-ray diffraction pattern there is no line with $d = 3.33\text{\AA}$ whereas one with $d = 2.87\text{\AA}$ is observed. The intensity of the latter changes in a way similar to that of the 2.95Å line. This leads us to assume that the 2.95Å line belongs to 2PbO·PbSO₄.

PbO₂ $d = 3.12 - 3.13\text{\AA}$; β -PbO₂ $d = 2.79\text{\AA}$ measured on x-ray diffraction patterns during formation. Figure 1(b) illustrates the chemical analysis results for PbSO₄, PbO, and PbO₂.

From Fig. 1(a) it is seen that 3PbO·PbSO₄·H₂O and 2PbO·PbSO₄ disappear within the first two hours of formation while chemical analysis [Fig. 1(b)] shows that PbO reacts completely up to the sixth hour. Lead sulfate originates as a result of these reactions. This compound constitutes as much as half of all lead compounds in the plate during the first two hours of formation [Fig. 1(b)]. This amount of PbSO₄ begins to decrease after the fourth hour and after 18 hr forming only 10% of it remains. In addition Fig. 1(a) and 1(b) show that up to the fourth hour of formation only tet-PbO and the basic sulfates are electrochemically oxi-

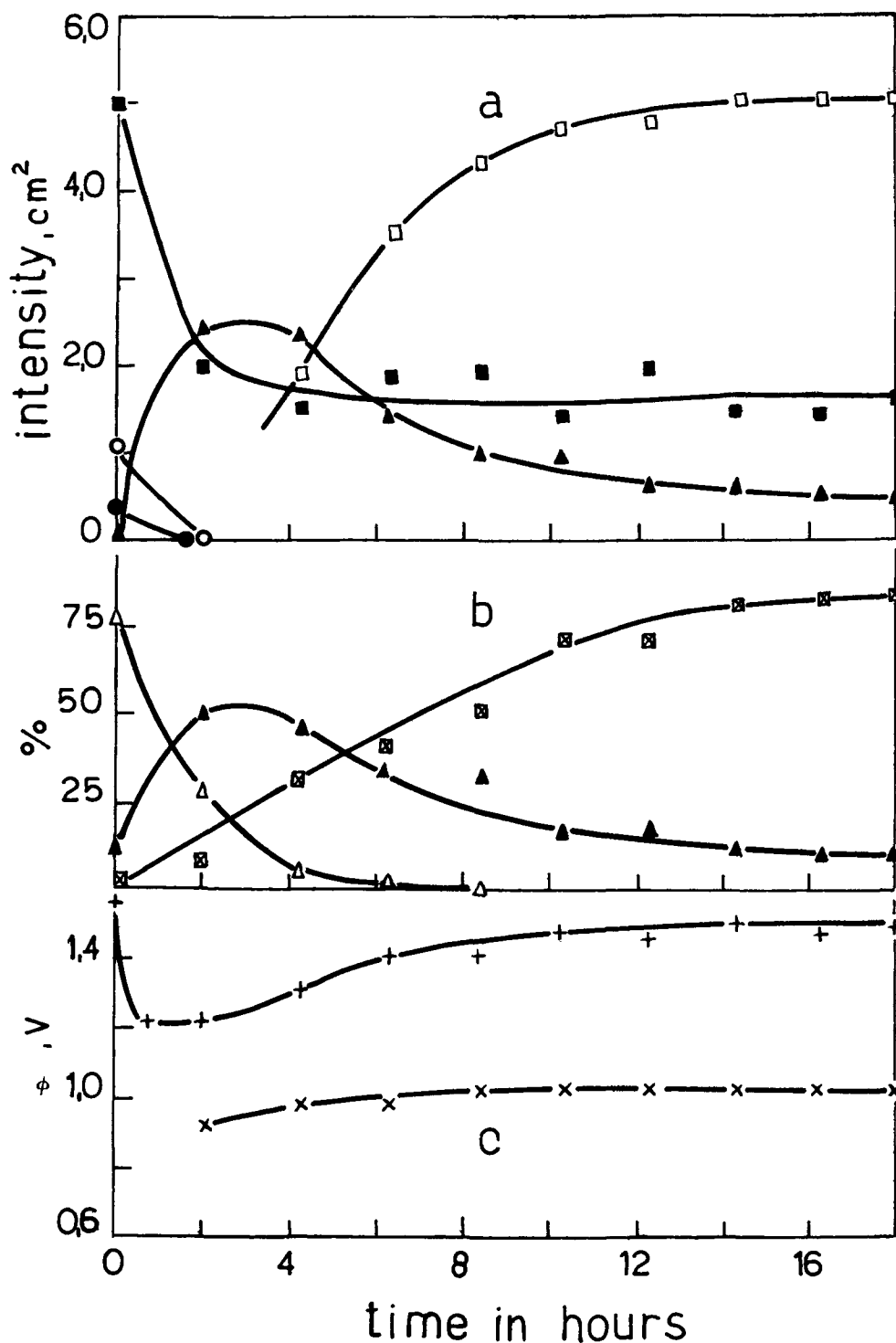


Fig. 1. (a). Intensity changes of the characteristic diffraction lines of 3PbO·PbSO₄·H₂O with $d = 3.26\text{\AA}$ (○), 2PbO·PbSO₄ with $d = 2.95\text{\AA}$ (●), PbSO₄ with $d = 3.00\text{\AA}$ (▲), β -PbO₂ with $d = 2.79\text{\AA}$ (□), tet-PbO + α -PbO₂ with $d = 3.12 - 3.13\text{\AA}$ (■) during formation in H₂SO₄ of sp gr 1.15. (b). Changes in the amounts of ($\alpha + \beta$)-PbO₂ (□), PbSO₄ (▲) and total PbO (△) in percentages during formation. (c). Change in plate potential (with respect to the Hg/Hg₂SO₄ electrode) under lead ϕ_i (+) and at open circuit ϕ_o (x) during formation.

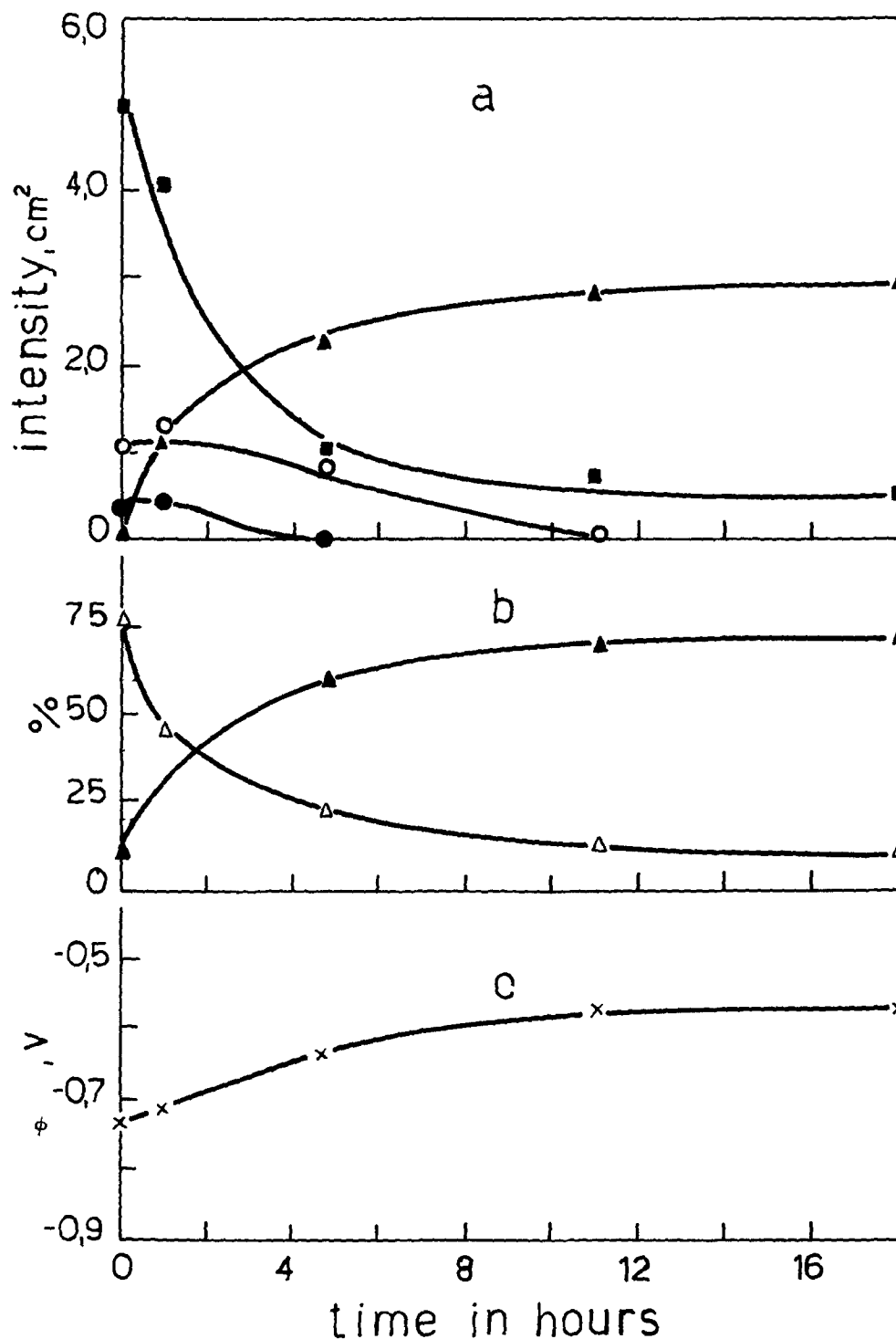


Fig. 2. (a). Intensity changes of the characteristic diffraction lines of $3\text{PbO}\cdot\text{PbSO}_4\cdot\text{H}_2\text{O}$ with $d = 3.26\text{\AA}$ (\circ), $2\text{PbO}\cdot\text{PbSO}_4$ with $d = 2.95\text{\AA}$ (\bullet), PbSO_4 with $d = 3.00\text{\AA}$ (\blacktriangle), tet-PbO with 3.12\AA (\blacksquare) upon leaving the plates in H_2SO_4 of sp gr 1.15. (b). Changes in the amounts of the total PbO (\triangle) and PbSO_4 (\blacktriangle) upon leaving the plate in H_2SO_4 of sp gr 1.15. (c). Change in the plate potential (with respect to the $\text{Hg}/\text{Hg}_2\text{SO}_4$ electrode) ϕ_0 (\times) upon exposure to H_2SO_4 of sp gr 1.15.

dized to PbO_2 . The 3.13\AA diffraction line of $\alpha\text{-PbO}_2$ coincides with the 3.12\AA line of tet-PbO. The intensity of this diffraction line common to both compounds abruptly decreases during the first four hours of the formation process after which it remains constant. This shows that $\alpha\text{-PbO}_2$ forms only during the first 2-4 hours. Similar results were also reported elsewhere (1, 2). Since during this period only tet-PbO and basic sulfates of lead are oxidized, it follows that $\alpha\text{-PbO}_2$ originates by electrochemical oxidation of these compounds. After 6 hr of formation the 3.13\AA diffraction line is diagnostic for $\alpha\text{-PbO}_2$. Beta lead dioxide forms intensively in the plate after the fourth hour. Lead sulfate is oxidized during this time interval. The moment at which the formation of $\beta\text{-PbO}_2$ begins can be assessed by x-ray diffraction only with great difficulty and uncertainty. This is due to the fact that the 2.79\AA

line of $\beta\text{-PbO}_2$ overlaps with the 2.80\AA line of tet-PbO, while the remaining strong lines of $\beta\text{-PbO}_2$ coincide either with those of PbSO_4 or of $\alpha\text{-PbO}_2$. At the end of the formation x-ray diffraction data show that the plate contains $\beta\text{-PbO}_2$ in an amount much larger than that of $\alpha\text{-PbO}_2$.

The values of the plate potential under polarization and at open circuit are plotted on Fig. 1(c). Prior to formation the grid is the only conducting element of the plate. At the beginning of the formation process the current density is large, owing to the small area of the grid. Therefore, the values of ϕ_i are high. With the formation of PbO_2 in the plate, the surface at which an electrochemical process may proceed increases and current density decreases, which leads to the decrease of ϕ_i . This occurs in the first 30 min after the start of formation. Subsequently, up to the fourth

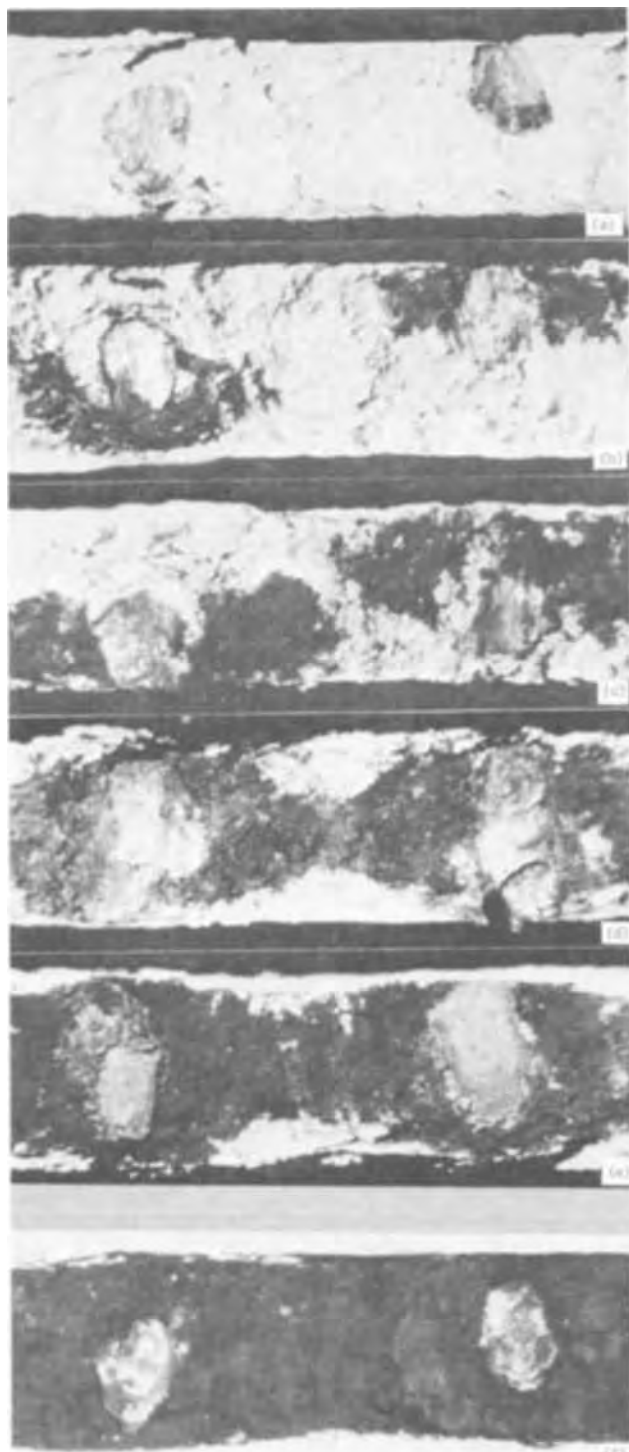


Fig. 3. Photomicrographs of cross sections of a portion of the plate between two grid bars at different stages of formation in H_2SO_4 of sp gr 1.15. (a). Unformed plate. (b-e). The dark portions are PbO_2 zones, while the light ones are zones of unformed divalent lead compounds. (f). Completely formed plate.

hour, the potential retains a comparatively constant value. This period is connected with the oxidation of tet-PbO and basic sulfates of lead to PbO_2 . When the amount of PbO becomes small, the potential increases, and $PbSO_4$ begins to oxidize to β - PbO_2 . At $\phi_i = 1460$ mV oxygen is evolved at the positive plate. This leads to a decrease in current efficiency for the formation of PbO_2 . The curve of PbO_2 in Fig. 1(b) rises more slowly.

Taking into account the changes in the above parameters, the process of formation can be divided into two stages:

First stage (prior to the fourth hour). Chemical reactions between H_2SO_4 and tet-PbO and basic sulfates with $PbSO_4$ as a result; electrochemical reaction during which tet-PbO and basic sulfates are oxidized mainly to α - PbO_2 and partially to β - PbO_2 .

Second stage (after the fourth hour). Lead sulfate is oxidized to β - PbO_2 . No α - PbO_2 forms. The electrochemical reaction takes place at high positive potentials at which OH^- oxidizes to O_2 . During this time interval a considerable part of the current is consumed for the evolution of O_2 .

In order to elucidate the reactions occurring between H_2SO_4 and the paste as well as the influence of the electrochemical reaction on the chemical reactions in the plate, the same number of positive and negative plates as in the formation experiment were assembled in a cell and soaked in H_2SO_4 of sp gr 1.15. At open circuit only chemical reactions take place in the paste. The results of phase and analytical investigations and of potential measurements are plotted in Fig. 2. Basic sulfates react completely with H_2SO_4 up to the tenth hour, while 12% tet-PbO remains in the plate even after staying 18 hr in H_2SO_4 . By comparing these results with those of Fig. 1, it becomes obvious that the rate of formation of $PbSO_4$ is accelerated by an electrochemical reaction.

The values of the electrode potential in H_2SO_4 of sp gr 1.15 are plotted in Fig. 2(c). These potential changes are due to chemical reactions, which occur in the paste at the surface of the grid. The $Pb/PbSO_4$ equilibrium potential is about 0.5V more negative than that of the Pb/PbO electrode in the same acid. From Fig. 2(a) it is seen that the amount of tet-PbO decreases, whereas that of $PbSO_4$ increases with time. Nevertheless, the plate potential becomes more positive. The electrochemical behavior of the plate is connected with passivation phenomena occurring at the lead grid, which were considered in some detail for the $Pb/PbSO_4$ electrode in a previous work (17).

Figure 3 shows photomicrographs of the plate cross section at the various stages of formation. It is seen that the formation proceeds by zones. The grid bars are alternately arranged with respect to the plate faces. Upon switching on the polarization those portions of the bar which are closest to the solution are covered first by a PbO_2 layer. An electrochemical reaction takes place at the PbO_2 surface as a result of which the paste is oxidized and a PbO_2 zone originates. The latter is located between the bar and the solution [Fig. 3(b)]. This zone grows subsequently inwards in the paste and is preceded by a bleached layer containing $PbSO_4$ crystals (this is seen on the color photographs). The PbO_2 zones from two neighboring bars advance one towards the other in the interior of the paste [Fig. 3(c)]. They include the $PbSO_4$ crystals obtained before them. This lasts until the PbO_2 zones join [Fig. 3(d)]. The chemical sulfation reactions begin with the soaking of the plate in the solution. The paste reacts with H_2SO_4 and $PbSO_4$ layers begin to grow in the paste from the two faces of the plate (color photographs). With the progress of formation a moment is reached in which tet-PbO and the basic sulfates disappear and the $PbSO_4$ zones cover the PbO_2 one [Fig. 3(d)]. Under the action of polarization PbO_2 now grows towards the bulk of the solution at the expense of the oxidation of the $PbSO_4$ zones. Beta lead dioxide is formed [Fig. 1(a), 3(e)]. The lead sulfate crystals included during the first stage in the PbO_2 zones are also oxidized to β - PbO_2 . At different heights and breadths the plate shows different stages of this most general course, followed by the motion of the processes throughout its cross section.

From this zonal course of the chemical and electrochemical reactions it follows that the phase composi-

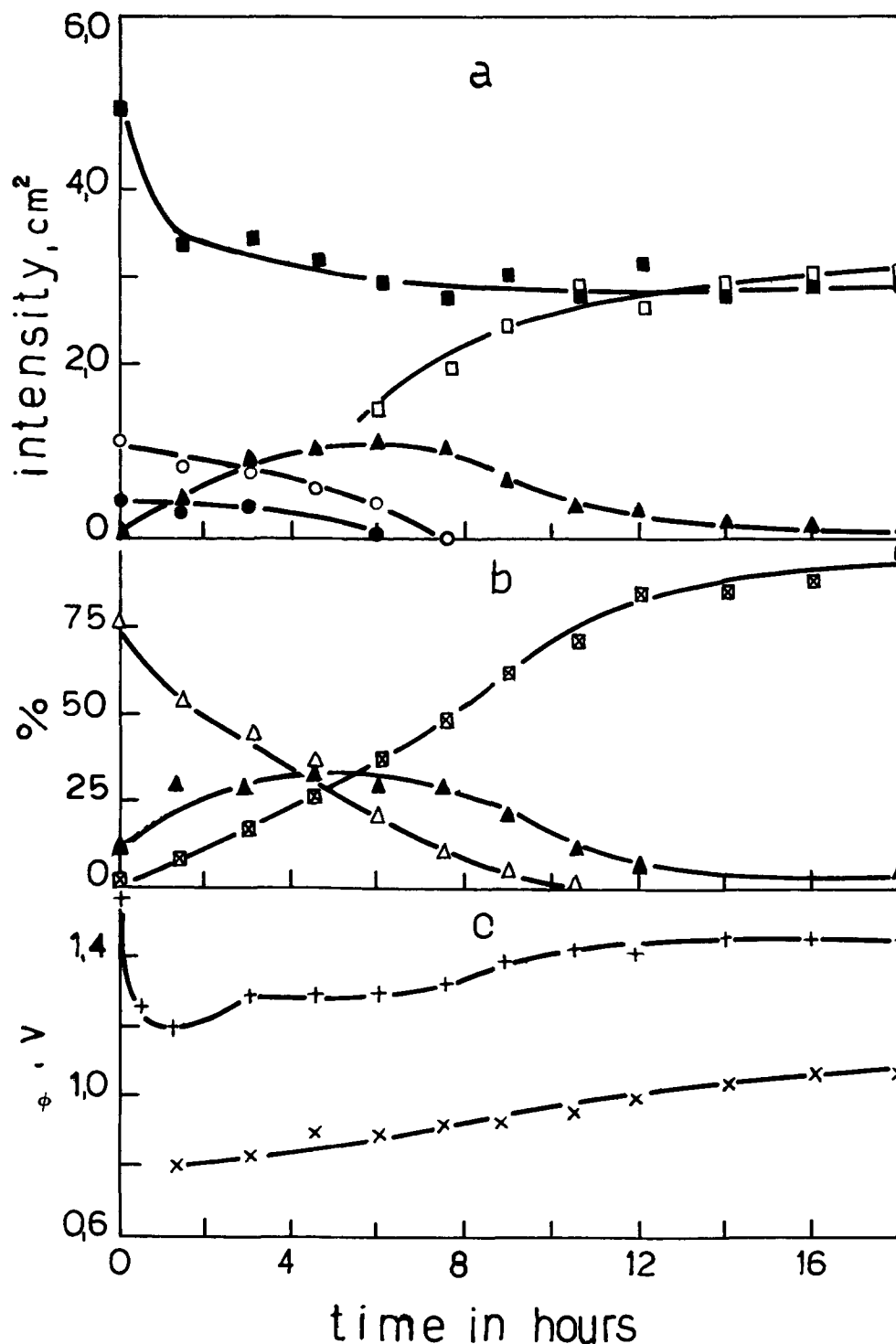


Fig. 4. (a). Intensity changes of the characteristic diffraction lines of $3\text{PbO}\cdot\text{PbSO}_4\cdot\text{H}_2\text{O}$ with $d = 3.26\text{\AA}$ (○), $2\text{PbO}\cdot\text{PbSO}_4$ with $d = 2.95\text{\AA}$ (●), PbSO_4 with $d = 3.00\text{\AA}$ (▲), $\beta\text{-PbO}_2$ with $d = 2.79\text{\AA}$ (□), tet-PbO + $\alpha\text{-PbO}_2$ with $d = 3.12\text{-}3.13\text{\AA}$ (■) during formation in H_2SO_4 of sp gr. 1.05. (b). Changes in the amounts of ($\alpha + \beta$) PbO_2 (⊠), PbSO_4 (▲), and total PbO (△) in percentages during formation. (c). Change in the plate potential (with respect to the Hg/Hg₂SO₄ electrode) under load ϕ_i (+) and at open circuit ϕ_o (x) during formation.

tion of the active material is different in the various portions of any plate segment. Such a difference in the phase composition was also observed by others (3). According to Fig. 1 and 3, around the grids and in a large internal portion of the plate the active material consists mainly of $\alpha\text{-PbO}_2$ while $\beta\text{-PbO}_2$ is to be found at the surface of the formed plate.

Formation in H_2SO_4 of sp gr 1.05.—Figure 4 gives the values of the parameters during formation. The pattern of the changes in phase and chemical composition is similar to that of Fig. 1. The decrease of H_2SO_4 in the formation solution lessens the role played by chemical sulfation reactions in the formation processes. As a result, the first stage of formation lasts about 8 hr. Basic sulfates react up to the sixth hour [Fig. 4(a)] and PbO up to the tenth hour [Fig. 4(b)]. The PbSO_4 content in the plate reaches about 30%. Only after the

eighth hour does PbSO_4 begin to oxidize to $\beta\text{-PbO}_2$. An analysis of the strong lines in the x-ray diffraction pattern of $\beta\text{-PbO}_2$ shows that the 2.79 and 3.51 \AA lines appear only at the sixth hour of formation. At the same time the plate contains considerable amounts of $\alpha\text{-PbO}_2$. Consequently, the time interval during which the α polymorph of PbO_2 originates upon formation in H_2SO_4 of sp gr 1.05 is longer than upon formation in H_2SO_4 of sp gr 1.15. In a completely formed positive plate the $\alpha\text{-PbO}_2$ content is approximately equal to that of $\beta\text{-PbO}_2$ [Fig. 4(a)]. The behavior of ϕ_i and ϕ_o follows the changes which take place in the phase composition [Fig. 4(c)] and confirms that the first formation stage lasts longer.

Figure 5 represents the changes in the phase and chemical composition of the plates soaked in H_2SO_4 of sp gr 1.05 at open circuit. At this sulfuric acid con-

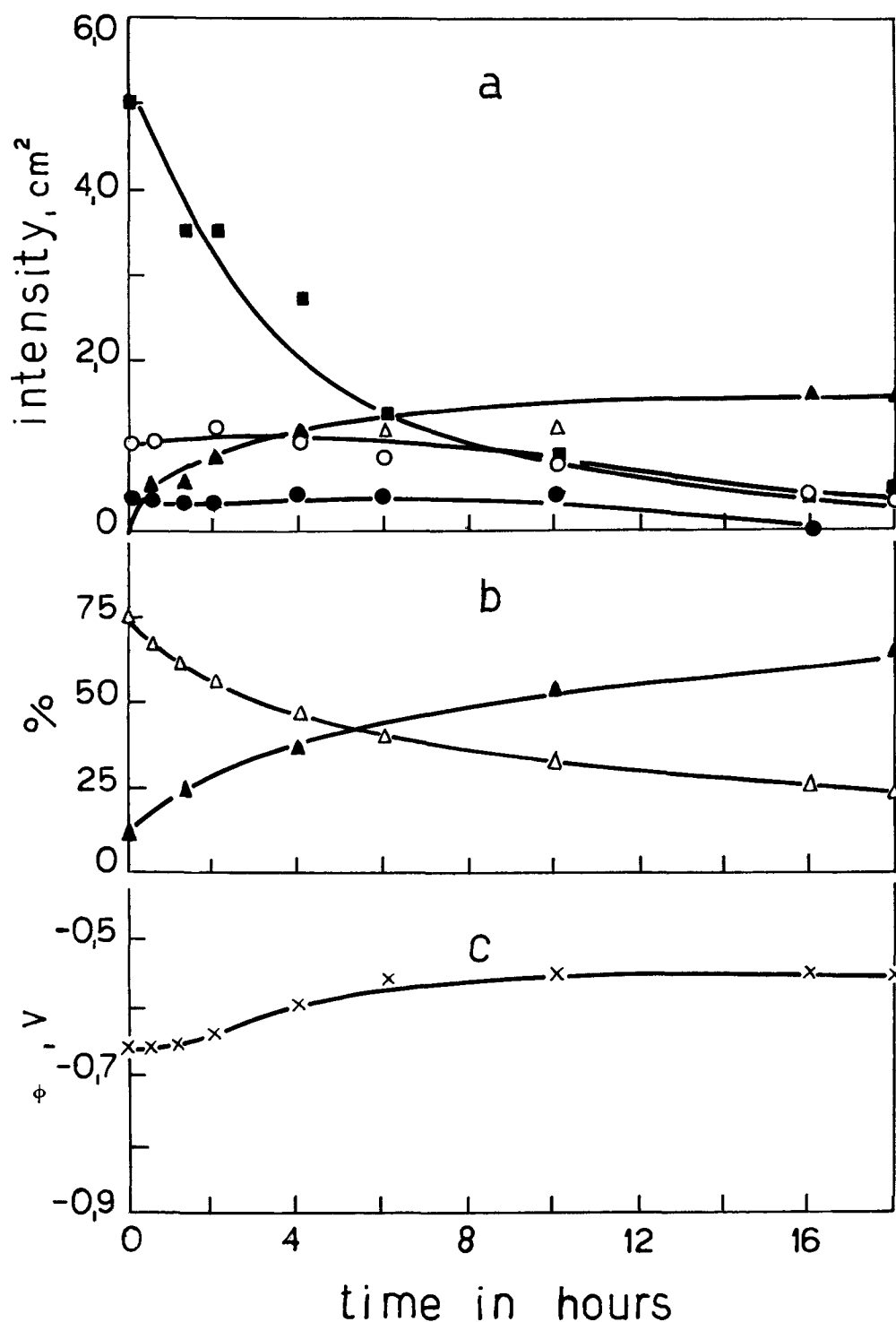


Fig. 5. (a). Intensity changes of the characteristic diffraction lines of $3\text{PbO}\cdot\text{PbSO}_4\cdot\text{H}_2\text{O}$ with $d = 3.26\text{\AA}$ (○), $2\text{PbO}\cdot\text{PbSO}_4$ with $d = 2.95\text{\AA}$ (●), PbSO_4 with $d = 3.00\text{\AA}$ (▲), tet-PbO with $d = 3.12\text{\AA}$ (■) upon leaving of the positive plates in H_2SO_4 of sp. gr 1.05. (b). Changes in the amounts of total PbO (△) and PbSO_4 (▲) upon leaving the plates in H_2SO_4 of sp gr 1.05. (c). Change in the plate potential (with respect to the $\text{Hg}/\text{Hg}_2\text{SO}_4$ electrode) ϕ_0 (x) upon exposure to H_2SO_4 of sp gr 1.05.

centration the rates of sulfation of tet-PbO and basic sulfates strongly decrease.

The microphotographs of the plate cross section at the various stages of formation indicate that the advance of the PbO_2 and PbSO_4 zones in the plate is similar to that observed during formation in H_2SO_4 of sp gr 1.15.

Formation in 0.7M Na_2SO_4 .—Figure 6 gives the values of the measured parameters during formation. The basic sulfates react up to the eighth hour [Fig. 6(a)] and PbO up to the tenth hour [Fig. 6(b)]. The formation of PbSO_4 is slow and its content reaches a maximum value only at the eighth hour [Fig. 6(a), (b)]. At the twelfth hour PbSO_4 begins to oxidize. From Fig. 6(a) it is seen that only $\alpha\text{-PbO}_2$ and PbSO_4 are formed during the first stage. The intensity of the 3.12\AA dif-

fraction line decreases up to the fifth hour owing to the decrease in the amount of tet-PbO. Subsequently the intensity of this particular diffraction line is controlled by $\alpha\text{-PbO}_2$ and therefore increases, reaching a constant value. After 10 hr the 3.12\AA line becomes characteristic for $\alpha\text{-PbO}_2$.

Between the eighth and the tenth hour of formation the amount of PbO in the plate is very small. The oxidation of this compound is unable to maintain a constant current. This is why the plate potential increases [Fig. 6(c)] and oxygen evolution begins. Starting from the twelfth hour of formation PbSO_4 is oxidized to $\beta\text{-PbO}_2$. During this time interval oxygen evolution is the second electrochemical reaction. A comparison of the intensities of the diffraction lines of $\alpha\text{-}$ and $\beta\text{-PbO}_2$ [Fig. 6(a)] shows that $\alpha\text{-PbO}_2$ is present in the formed plate in an amount larger than that of $\beta\text{-PbO}_2$.

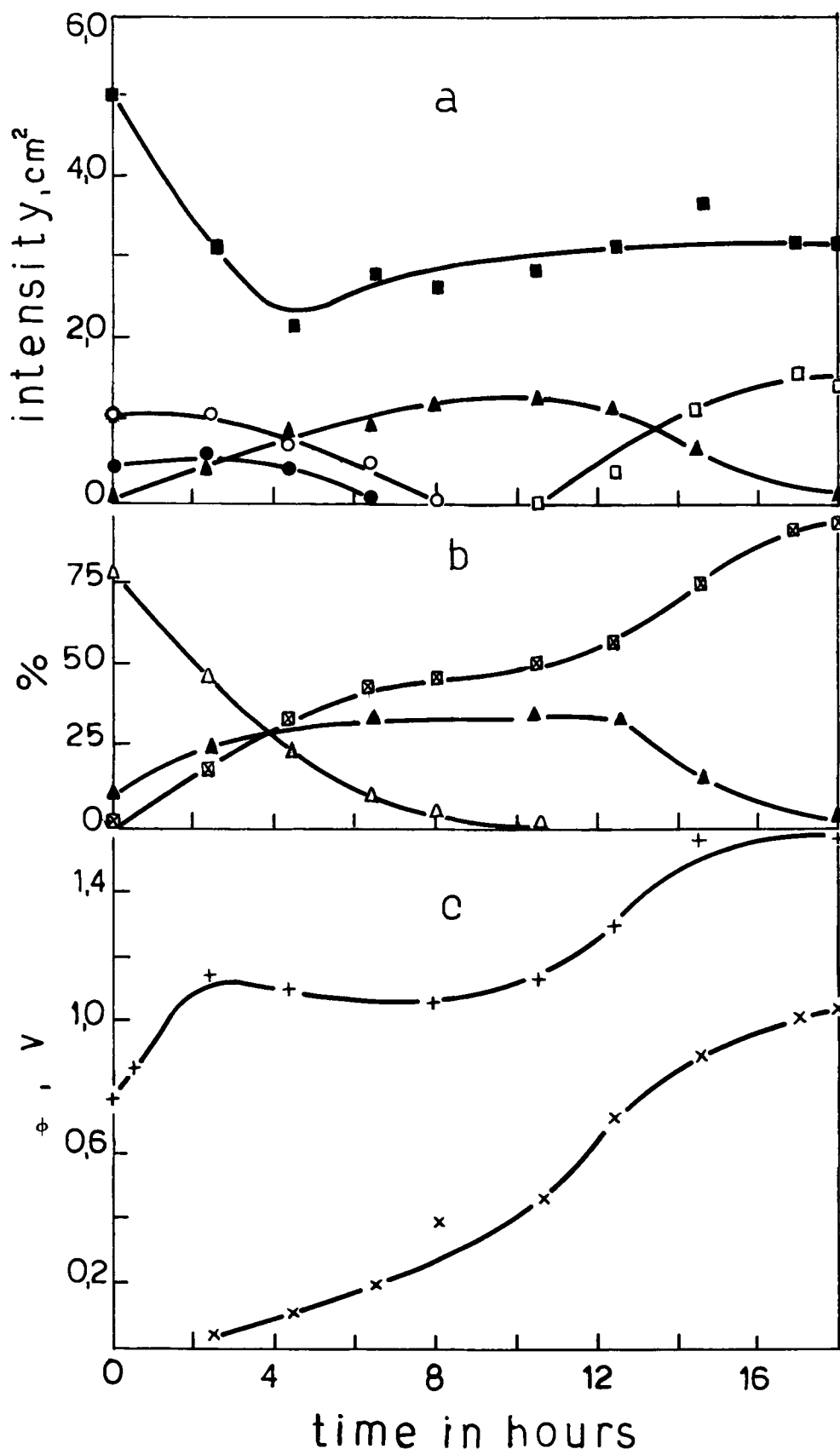


Fig. 6. (a). Intensity changes of the characteristic diffraction lines for $3\text{PbO}\cdot\text{PbSO}_4\cdot\text{H}_2\text{O}$ with $d = 3.26\text{\AA}$ (○), $2\text{PbO}\cdot\text{PbSO}_4$ with $d = 2.95\text{\AA}$ (●), PbSO_4 with $d = 3.00\text{\AA}$ (▲), $\beta\text{-PbO}_2$ with $d = 2.79\text{\AA}$ (□), tet-PbO + $\alpha\text{-PbO}_2$ with $d = 3.12\text{-}3.13\text{\AA}$ (■) during formation in $0.7\text{M Na}_2\text{SO}_4$. (b). Changes in the amounts of total PbO (△), PbSO_4 (▲) and ($\alpha + \beta$) PbO_2 (⊠) in percentages during formation. (c). Potential change in the plate potential (with respect to the $\text{Hg}/\text{Hg}_2\text{SO}_4$ electrode) under load ϕ_i (+) and open circuit ϕ_o (x) during formation.

Figure 6 indicates that the two formation stages are clearly separated. The first one ends at the eighth-ninth hour, while the second one begins at the eleventh-twelfth hour. During the first stage it was found that the pH of the solution is alkaline. The second stage begins only when the solution is acidified. This occurs after the tenth hour of formation when the pH

becomes less than 2. These changes in pH in the bulk of the solution are determined by the total balance of the ions which are consumed and originate at the positive and the negative plates. These phenomena will be studied in another paper.

An experiment was performed in which the pH of the formation solution was maintained between 10 and

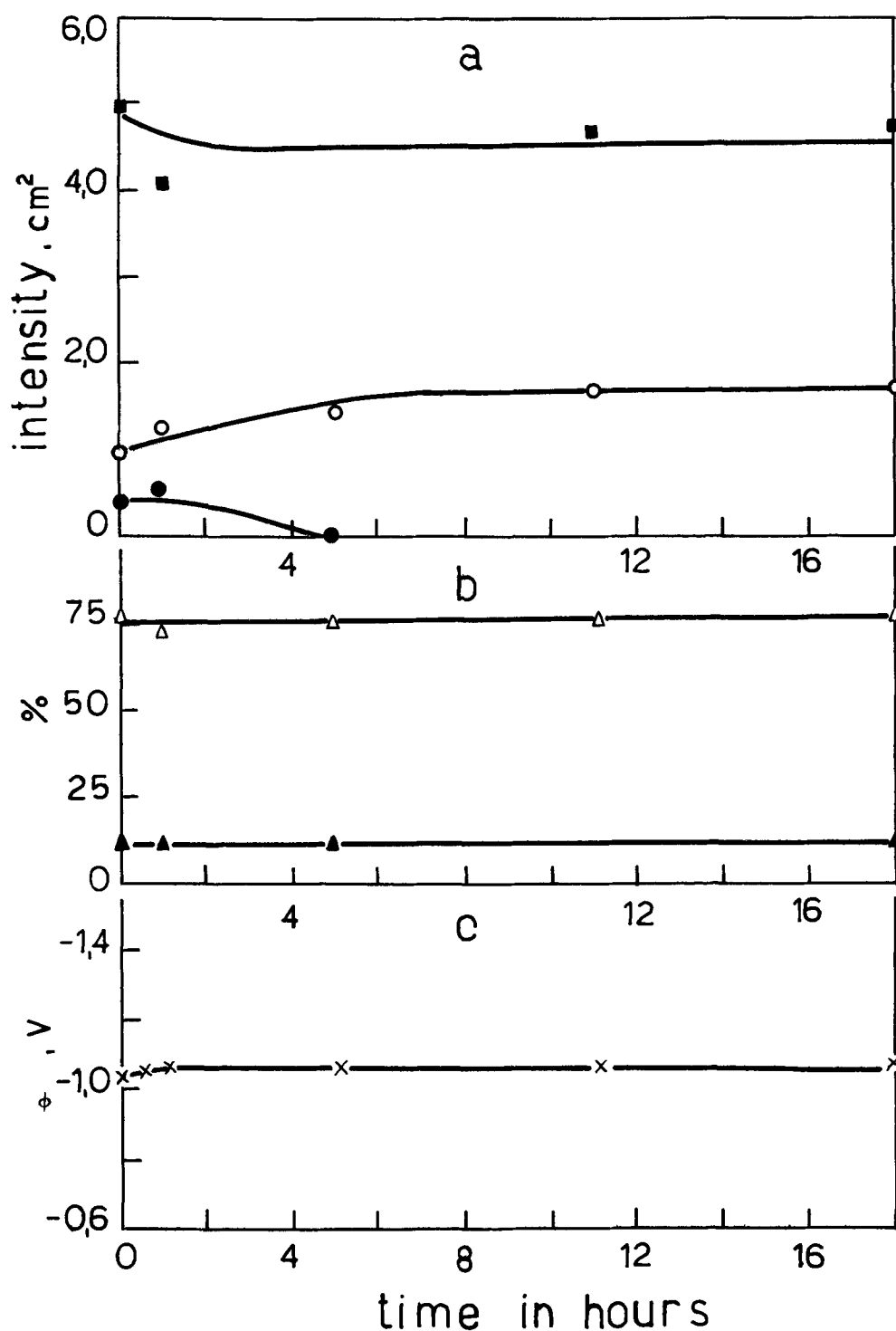


Fig. 7. (a). Intensity changes of the characteristic diffraction lines for $3\text{PbO}\cdot\text{PbSO}_4\cdot\text{H}_2\text{O}$ with $d = 3.26\text{\AA}$ (\circ), $2\text{PbO}\cdot\text{PbSO}_4$ with $d = 2.95\text{\AA}$ (\bullet), tet-PbO with $d = 3.12\text{\AA}$ (\blacksquare) upon leaving of the positive plates in a $0.7\text{M Na}_2\text{SO}_4$ solution. (b). Changes in the amounts of total PbO (Δ) and total PbSO_4 (\blacktriangle) upon leaving of the plates in a $0.7\text{M Na}_2\text{SO}_4$ solution. (c). Change in the plate potential (with respect to the $\text{Hg}/\text{Hg}_2\text{SO}_4$ electrode) ϕ (x) upon exposure to a $0.7\text{M Na}_2\text{SO}_4$ solution.

11 for 23 hr by means of NaOH. Up to the eighth hour PbO and the basic sulfates were converted to $\alpha\text{-PbO}_2$ and PbSO_4 . From the eighth to the twenty-third hour x-ray and chemical analyses revealed no change in the amounts of $\alpha\text{-PbO}_2$ and PbSO_4 . Oxygen was evolved at the positive plate during the period. At the twenty-third hour of formation the solution was acidified with H_2SO_4 and the pH adjusted to 2. For 4 hr the entire amount of PbSO_4 in the plate was oxidized to $\beta\text{-PbO}_2$. Thus the duration of the first stage and the start of the second one may be controlled by means of the pH of the solution.

Figure 7 gives the result of phase and chemical analyses of positive plates soaked in a $0.7\text{M Na}_2\text{SO}_4$ solution as a function of the time of exposure at open circuit. From Fig. 7(a) it is seen that $2\text{PbO}\cdot\text{PbSO}_4$ disappears after 4 hr from the plate. The amount of

tet-PbO decreases to a certain extent while that of $3\text{PbO}\cdot\text{PbSO}_4\cdot\text{H}_2\text{O}$ increases somewhat. This shows a conversion of $2\text{PbO}\cdot\text{PbSO}_4$ to $3\text{PbO}\cdot\text{PbSO}_4\cdot\text{H}_2\text{O}$. No diffraction lines of PbSO_4 were recorded in the x-ray patterns. Figure 7(b) shows that the amounts of total PbO and total PbSO_4 in the plate remain unchanged. This means that there are no reactions occurring between the compounds of the plate and Na_2SO_4 . If we compare these results with those of Fig. 6 it becomes clear that PbSO_4 [Fig. 6(a)] is produced during formation by a process induced by the electrochemical oxidation reaction of the basic sulfates present in the paste.

Figure 8 reproduces photomicrographs at the various stages of formation in $0.7\text{M Na}_2\text{SO}_4$. In this case, too, formation begins at those portions of the grid bars that are close to the plate surface [Fig. 8(b)]. How-

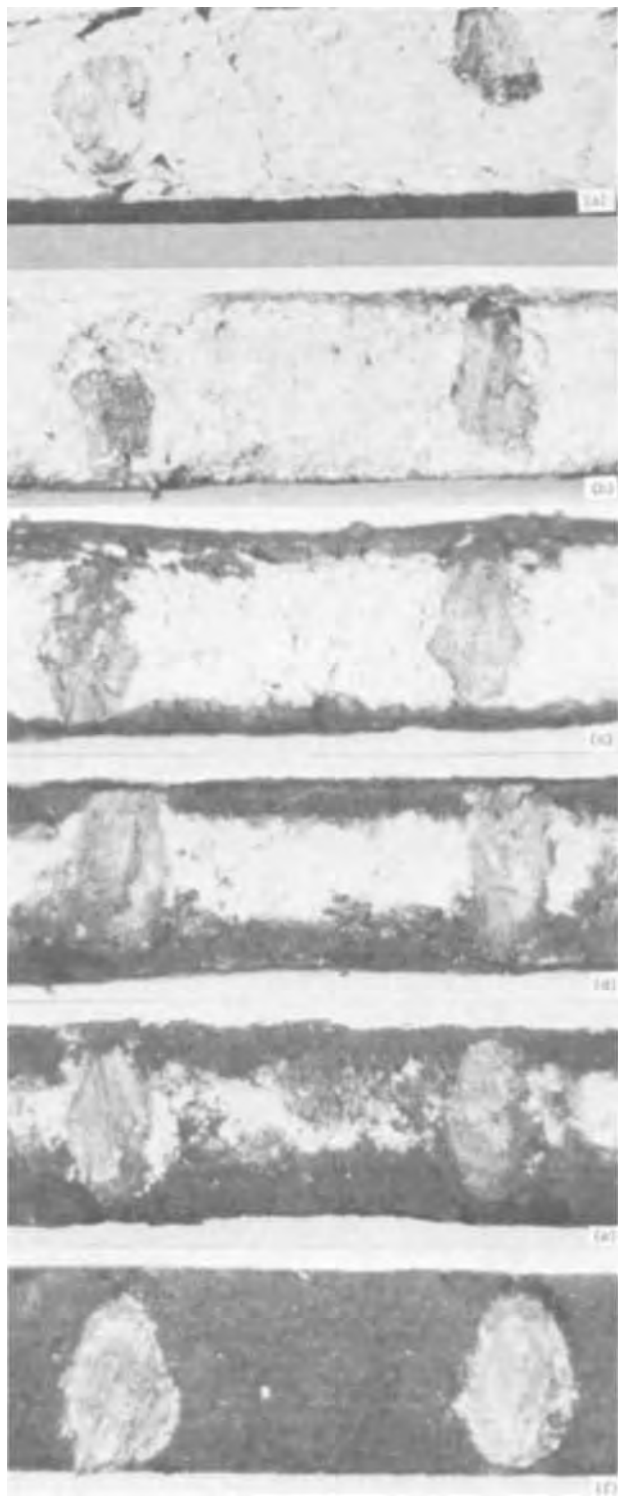


Fig. 8. Microphotograph of cross sections of a plate segment between two grid bars at different stages of formation in 0.7M Na_2SO_4 solution. (a). Unformed plate. (a-e). The dark portions in the section of the plate are PbO_2 zones while the light ones consist of unformed divalent lead compounds. (f). Completely formed plate.

ever, the distribution of the phases upon formation is different from that observed in an acid medium. First the PbO_2 zone grows along the plate surface. Soon the plate is covered with a thin brown layer of $\alpha\text{-PbO}_2$ [Fig. 8(c)]. Subsequently the PbO_2 layer continues to grow from the surface toward the interior of the paste [Fig. 8(d)]. Lead sulfate crystals originate before the PbO_2 zones (seen on color photographs). These crystals are included in the PbO_2 zones [Fig. 8(c), (d), (e)]. Thus the internal portions of the plate formed

during the first stage consist of $\alpha\text{-PbO}_2$ and PbSO_4 whereas the plate surface is constituted only by $\alpha\text{-PbO}_2$. After full conversion of PbO and basic sulfates to the above compounds and acidification of the solution, PbSO_4 oxidizes to $\beta\text{-PbO}_2$. The fully formed plate consists of $\alpha\text{-PbO}_2$ in which $\beta\text{-PbO}_2$ is precipitated [Fig. 8(f)].

Discussion of Results

Specific properties of electrochemical and chemical reactions in porous electrodes.—The electrochemical and chemical formation processes take place in a porous medium consisting of the starting and reaction end products. Therefore the number of occurring elementary processes (hydration, dissociation, dissolution, ion diffusion and migration, neutralization, charge transfer, nucleation, crystal growth, etc.) is considerable. Which one of these elementary processes plays a limiting role on electrochemical and chemical reaction rates depends on the specific conditions created by the porous electrode, which may be outlined in the following way.

First, the surface of the crystals is in contact with the solution in the pores. The volume of the solution in the pores is small compared to the surface of the crystals which inclose the pores. This is why under- and supersaturation of the solution in the pores is easily and rapidly achieved. This strongly favors the crystallization and dissolution processes of the crystals, as well as hydration and neutralization within the plate. These processes take place at very high rates.

Second, the pores in the unformed material electrically connect the grid or the PbO_2 zone with the bulk of the electrolyte. An equivalent electrical circuit of the plate would include parallel resistances, each corresponding to one pore. The formation process begins first at those locations in the plate where the length of the pores which connect the electrode surface with the bulk of the solution is smallest. There, the electrical resistance of the paste is smallest. Indeed, the formation begins at those portions of the grid bars which are closest to the bulk of the solution. The PbO_2 zone originates there [Fig. 3(b) and 8(b)]. With its appearance the current density decreases and the importance of other parameters which control the direction of motion of the PbO_2 zone in the paste increases. On the other hand, the pores have widely different electrical resistances. The large pores have a small resistance and favor ion transport between the bulk of the solution and the internal portions of the paste and active material. The small pores hinder this motion of ions. But, since the sum of the surfaces of the small pores is usually several times larger than that of the large pores it follows that the chemical and electrochemical processes are determined by the conditions prevailing in the small pores. The ratio between these two types of pores controls the limiting influence of diffusion and migration of ions on electrochemical and chemical reaction rates in the various portions of the plate.

Third, during the electrochemical process the positive charges of the lead ions increase from 2 to 4. In order for the solution in the pores to become electro-neutral, the excess positive charges must migrate from the interior of the plate into the bulk of the solution. The migration of the positive ions, if slowed down, hinders the electrochemical reaction at the given location in the plate. There, the growth of the PbO_2 zone is also slowed down. The participation of a given ionic species in the migration is controlled by its mobility and concentration. The H^+ ions possess a mobility several times higher than that of the remaining ones. Therefore, their participation in the migration process will be overriding. This imparts a considerable role to the pH of the solution on the processes occurring in the plate.

Mechanism of the formation processes.—The over-all chemical and electrochemical reactions which take place during formation of positive plate may be deter-

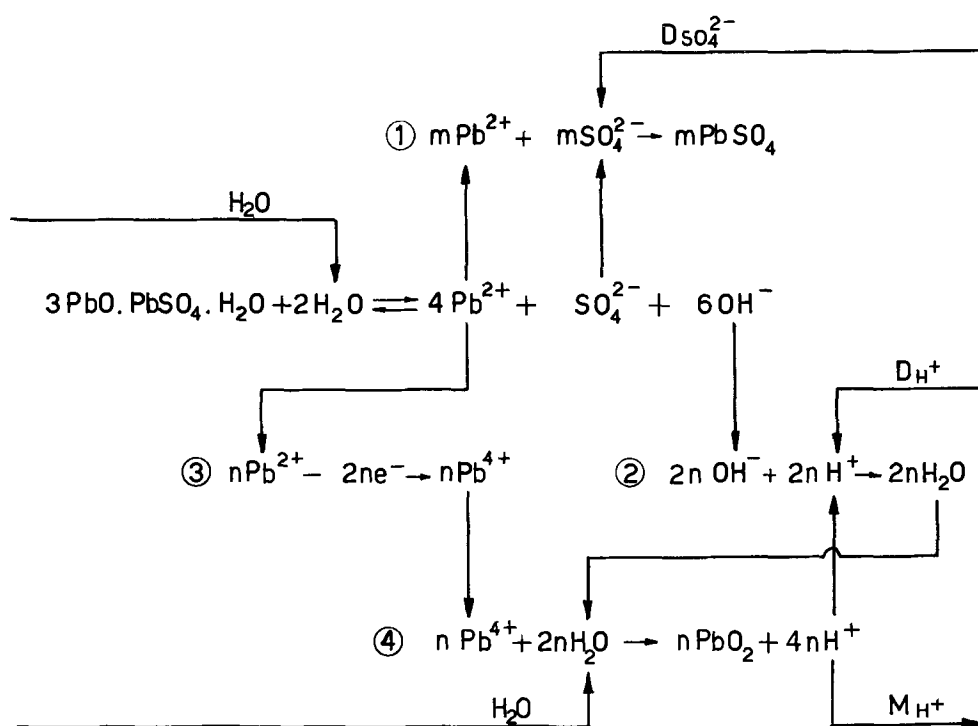
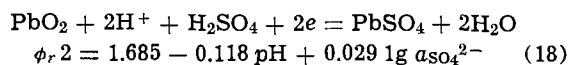
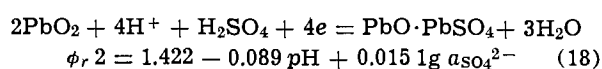
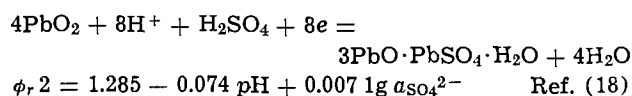
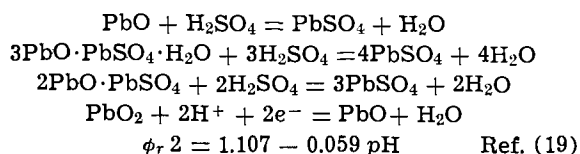


Fig. 9. Diagram of the elementary chemical and electrochemical processes during the first stage of formation.

mined from the $E/p\text{H}$ diagram of the lead-sulfuric acid-base system. A sufficiently complete $E/p\text{H}$ diagram was given by Ruetschi and Angstadt (18) from which it is seen that the following chemical and electrochemical reactions may take place during formation



The equations show that the reactions which occur during formation of the plate depend on the pH of the solution. In addition, the same starting compounds of the paste participate in two competing reactions: chemical and electrochemical. The chemical sulfation reaction is controlled by the concentrations of the ions in the solution in the pores. The electrochemical reactions of formation of PbO_2 depend not only on the ionic composition of the solution but also on the electrode surface potential.

In order to define the processes of formation two questions should be answered: First, what is the mechanism by which the alkaline α polymorph originates during formation in an acid medium and which factors affect the α/β - PbO_2 ratio. Second, what determines the direction of advance of the PbO_2 zone during formation. To this effect the over-all chemical and electrochemical reactions should be decomposed into elementary reactions. The relationships among the latter

within the pores should be established. On Fig. 9 this is done for the first stage of formation, $3\text{PbO} \cdot \text{PbSO}_4 \cdot \text{H}_2\text{O}$ being taken as example. After water has penetrated in the plate this compound is first hydrated, as a result of which certain Pb^{2+} , SO_4^{2-} , and OH^- concentrations are maintained in the pores. Besides water, H_2SO_4 diffuses in the plate ($D_{\text{SO}_4^{2-}}$ and D_{H^+}). After moving toward the interior of the paste it reacts according to reactions 1 and 2 and disappears. Generally speaking, as a result of these reactions tet- PbO and basic sulfate crystals contained in the paste are dissolved and yield PbSO_4 and H_2O . The reaction rates and the depth at which H_2SO_4 penetrates in the plate depend on the acid concentration in the formation solution. Our experiments showed that in H_2SO_4 of sp gr 1.15 the rate of formation of PbSO_4 is higher (Fig. 2) than that of H_2SO_4 of sp gr 1.05 (Fig. 5). In neutral solutions no PbSO_4 is formed, according to the $E/p\text{H}$ diagram. This is why reactions 1 and 2 do not take place when the plates are soaked at open circuit in a Na_2SO_4 solution (Fig. 7).

Microscopic examinations of the chemical reactions between the paste and H_2SO_4 showed that during a considerable time interval the internal portions of the plate remain unattacked by H_2SO_4 . Tribasic lead sulfate of such internal portions is in equilibrium with Pb^{2+} , SO_4^{2-} , and OH^- ions of the pore solution. When these pores contact with the PbO_2 surface, electrochemical reaction 3 and chemical reaction 4 will occur. In reaction 4, four H^+ ions are evolved for every lead ion. Two of these hydrogen ions must migrate out of the plate (M_{H^+}) in order to maintain the electroneutrality of the solution in the pores. The remaining two participate in the neutralization reaction 2. This reaction decreases the pH of the solution in the pores. The stability field of PbSO_4 is reached and PbSO_4 crystals are deposited in the pores before the PbO_2 zone. This may be observed on color photographs (which correspond to Fig. 3, 8). The changes in pH of the pore solution occur in the weakly alkaline, neutral, and weakly acidic pH range and yield the α polymorph of PbO_2 . Figures 1, 4, and 6 show that α - PbO_2 forms when the plate contains lead monoxide and basic sulfates. Therefore, the increase of PbSO_4 in the basic sulfates leads to a decrease in the OH^- ions in the pore solution. This diminishes the role of reaction 2 in the oxidation mechanism. The formation of α - PbO_2 decreases.

² The values are given with respect to the normal hydrogen electrode. The calculations do not take into account the two different polymorphs of PbO_2 . No equation is given in the quoted work for the equilibrium potential of $\text{PbO}_2/2\text{PbO} \cdot \text{PbSO}_4$.

Conversely, when the PbO content in the paste and in the basic sulfates is larger the role of reaction 2 is larger, and the amount of α -PbO₂ is larger. Consequently, the amount of α -PbO₂ in the active material is controlled by the PbO/PbSO₄ ratio in the paste, irrespective of whether these components are present as discrete phases or combined in basic sulfates. The PbO/PbSO₄ ratio changes in the paste when the amount of H₂SO₄ with respect to the lead powder during preparation of the paste is changed. In addition, this ratio changes during formation in H₂SO₄ as a consequence of chemical reactions 1 and 2 between the paste and the solution. Therefore, the α -PbO₂ amount in the active material depends on the concentration of sulfuric acid in the solution. In the case of sulfuric acid of sp gr 1.15 the active material contains less α -PbO₂ [Fig. 1(a)] than the active material obtained by formation in H₂SO₄ of sp gr 1.05 [Fig. 4(a)], since at this latter acid concentration less PbSO₄ has been produced during formation [Fig. 1(b), 4(b)].

The direction of motion of the PbO₂ zone in the paste constitutes the second important aspect of the mechanism of the processes taking place during formation. From the equations of the equilibrium potentials of the PbO₂/PbO, PbO₂/3PbO·PbSO₄·H₂O, PbO₂/PbO·PbSO₄, and PbO₂/PbSO₄ electrodes it is seen that at a given pH, the values of these potentials become more positive with the increase in the PbSO₄ content of divalent lead compounds. Therefore, by increasing the plate potential, the equilibrium potentials of PbO₂/PbO and of the basic sulfates are successively reached. The current density 5 mA/cm² is maintained constant by oxidation of these compounds. This explains why during the first stage the potential is low [Fig. 1(c), 4(c), 6(c)]. During formation in H₂SO₄ the surface of the plates is sulfated. Lead monoxide and basic sulfates of lead from the internal portions of the plate remain for a long time unattacked by the acid. This is why the PbO₂ zones advance in the plate, oxidizing the monoxide and the basic sulfates. Lead sulfate crystals formed as a result of the electrochemical reaction are included in the PbO₂ zone since the electrode potential is lower than that required for its oxidation. Figures 3(b), (c) show the advance of the PbO₂ zone at those locations of the paste where the PbO and basic sulfates content is largest. When the amount in the paste of these compounds reaches a small value, the potential increases, reaching values at which PbSO₄ is oxidized [Fig. 1(c), 4(c)]. The PbO₂ zone advances from the interior toward the surface of the plate [Fig. 3(d), (e)]. During formation in Na₂SO₄ the solution at the plate surface has a higher pH than that in the pores of the internal portion. This is why the PbO₂ zone advances first along the plate surface [Fig. 8(b), (c)].

The direction of motion of the PbO₂ zone is determined not only by these thermodynamic causes, but also by kinetic factors. Thus, the migration rate of the H⁺ ions obtained by reaction 4 may also control the direction of motion of the PbO₂ zone. If the migration is hindered the pore solution will be charged positively. This decreases the rate of electrochemical oxidation of Pb²⁺ since, as a result of this process the number of positive charges in the pore solution increases. Thus the rate of formation of PbO₂ decreases in those portions of the PbO₂ zone, where transport of H⁺ ions is hindered. The migration of H⁺ ions is favored in those pores which contain solution with the highest pH. In them the direction of diffusion of H⁺ coincides with the direction of their migration. During formation in H₂SO₄ the pores of the internal portions of the plate retain for the longest time the solution with the highest pH. The PbO₂ zone advances during the first stage toward the interior of the plate [Fig. 3(b), (c), (d)]. During formation in Na₂SO₄ or weakly alkaline solutions the migration of H⁺ ions is most favorable at the surface of the plate. This explains why the PbO₂ zone

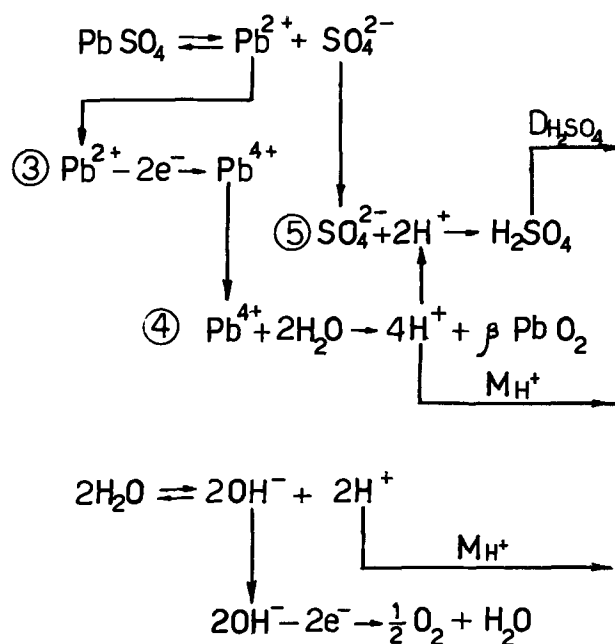


Fig. 10. Diagram of the elementary chemical and electrochemical processes during the second stage of formation.

first covers the plate surface and then advances within the plate [Fig. 8(b), (c)].

The x-ray data on the initial phase composition of the paste did not show the presence of unoxidized lead in it. In practice, however, the unformed paste frequently contains several per cent unoxidized lead. According to Ness (15) and Ruetschi and Cahen (14) upon formation lead powder is oxidized to α -PbO₂. The difference between the plate potential ϕ_i and the equilibrium potential of the Pb/PbO₂ electrode is largest, and, therefore, lead will be thermodynamically most unstable upon formation and the lead particles will be oxidized at the first stage of formation in which α -PbO₂ is obtained.

During the second period of formation PbSO₄ oxidizes to PbO₂ and OH⁻ to O₂. These processes are indicated in the diagram of Fig. 10. Oxidation of PbSO₄ takes place entirely in an acidic medium. Therefore, only β -PbO₂ is formed [Fig. 1(a), 4(a), 6(a)]. Sulfuric acid obtained as a result of reaction 5 diffuses from the plate into the bulk of the solution, as opposed to the first stage.

During the second period the electrode potential is more positive than the evolution potential of oxygen and oxygen is evolved at the PbO₂ surface.

At the end of the formation the H₂SO₄ concentration in the formation solution increases with respect to the initial one. The formation processes free the whole amount of H₂SO₄, used for producing basic sulfates during paste preparation.

Parameters which control the processes of formation of positive plates.—Starting from the mechanisms already outlined for the first and second formation stages it becomes possible to determine the parameters controlling the phase composition of the active material. According to them the ratio between α - and β -PbO₂ is determined by the equation

$$\alpha/\beta \text{ PbO}_2 = \frac{q^0_{\text{PbO}} - q'_{\text{PbSO}_4} - q'_{\text{PbO}}}{q^0_{\text{PbSO}_4} + q'_{\text{PbSO}_4} + q'_{\text{PbO}}}$$

q^0_{PbO} is the total starting amount of PbO occurring in the paste as a discrete phase or bonded in basic sulfates. Its value is determined by the ratio between the weight of the oxidized lead powder and that of the H₂SO₄ used in the preparation of the paste.

q_{PbO} is the amount of PbO converted to $\beta\text{-PbO}_2$. This process occurs between the first and the second stage oxidation. During this intermediate period the amount of unreacted PbO is relatively small. It is unable to maintain constant the formation current and the plate potential increases while PbSO_4 and OH^- begin to oxidize, thus acidifying the pore solution and leading to the formation of $\beta\text{-PbO}_2$ from PbO.

$q_{\text{PbSO}_4}^0$ is the initial amount of PbSO_4 combined in the basic sulfates. It is controlled by the amount of H_2SO_4 added to the lead powder during paste preparation.

q_{PbSO_4} is the amount of PbSO_4 produced during the first stage of formation. It depends on the following parameters:

(i) Amount of H_2SO_4 in the formation solution (H_2SO_4 concentration and its volume per plate). At equal volumes the larger the concentration of H_2SO_4 , the more $\beta\text{-PbO}_2$ will form. This is confirmed both by Dodson's experiments (1) and by the results obtained in the present work. During formation in diluted H_2SO_4 one should also take into account processes occurring at the negative plate. The products formed or consumed at this plate change the ionic composition of the formation solution.

(ii) Formation current density. This parameter determines the velocity of advance of the PbO_2 zones in the paste as well as the potential under current.

(iii) Paste density.

(iv) Exposure of the plates at open circuit to H_2SO_4 prior to formation. The longer this period, the larger the amount of PbSO_4 formed in the paste.

(v) Grid design. In thicker plates and in the case of smaller intergrid distances the amount of PbSO_4 during the first stage of formation should be less.

(vi) Temperature.

If the paste contains unoxidized lead an additional term, which takes into account the oxidation of Pb to $\alpha\text{-PbO}_2$, should be added to the above equation.

This considerable variety of parameters, which influence the formation processes, introduces serious difficulties in the production of plates having strictly defined characteristics. Determining the influence of each of the indicated parameters on the phase composition ($\alpha/\beta\text{-PbO}_2$) and also on the initial characteristics of the plate (capacity and start) will be the aim of our future investigations.

Manuscript submitted July 13, 1971; revised manuscript received ca. Sept. 22, 1971.

Any discussion of this paper will appear in a Discussion Section to be published in the December 1972 JOURNAL.

REFERENCES

1. V. H. Dodson, *This Journal*, **108**, 401 (1961).
2. A. C. Simon and E. L. Jones, *ibid.*, **109**, 760 (1962).
3. W. O. Butler, C. J. Venuto, and D. V. Wisler, *ibid.*, **117**, 1339 (1970).
4. J. R. Pierson, *Electrochem. Technol.*, **5**, 323 (1967).
5. J. Armstrong, I. Dugdale, and W. J. McCusker, "Power Sources 1966," pp. 163-176, Pergamon Press, Oxford (1967).
6. G. Sterr, *Electrochim. Acta*, **15**, 1221 (1970).
7. A. I. Rusin, M. A. Dasojan, and N. N. Fedorova, *Elektrotehnika*, **38**, 8, 4 (1967).
8. J. Burbank, *This Journal*, **113**, 10 (1966).
9. J. Burbank and E. J. Ritchie, *ibid.*, **116**, 125 (1969).
10. J. E. Buskirk, P. D. Boyd, and V. V. Smith, Paper 19, presented at Electrochem. Soc. Meeting, Houston, Oct. 9-13, 1960.
11. R. H. Greenburg and B. P. Caldwell, *Trans. Electrochem. Soc.*, **80**, 71 (1941).
12. J. E. Hatfield and O. W. Brown, *ibid.*, **72**, 361 (1937).
13. S. Ikari, S. Yoshizawa, and S. Okada, *J. Electrochem. Soc. Japan*, **27**, 426, 613 (1959).
14. P. Rüetschi and B. Cahan, *This Journal*, **105**, 376 (1958).
15. P. Ness, *Electrochim. Acta*, **12**, 161 (1967).
16. J. J. Lander, *This Journal*, **95**, 174 (1949).
17. D. Pavlov and R. Popova, *Electrochim. Acta*, **15**, 1483 (1970).
18. P. Rüetschi and R. Angstadt, *This Journal*, **111**, 1323 (1964).
19. J. Burbank, *ibid.*, **106**, 369 (1959).

Mechanism of the Formation of Blisters on the Lead Electrode of the Lead-Acid Battery

C. F. Yarnell*

Bell Telephone Laboratories, Incorporated, Murray Hill, New Jersey 07974

ABSTRACT

A constant current study of the reduction of tetrabasic lead sulfate to lead coupled with microscopic examination of the lead electrode showed that a solid layer of lead sulfate developed on the surface during formation. A fissure develops between the lead formed from the surface layer of lead sulfate and the lead in the center of the electrode. Hydrogen trapped in this fissure pushes the surface layer out to form a blister. A microscopic study of electrodes formed in decreasing concentrations of sulfuric acid showed that blistering is eliminated at lower concentrations.

The spongy-lead negative electrode of the lead-acid cell is made by electrochemical reduction in dilute sulfuric acid of a lead or lead alloy grid filled with a dried paste material. This paste material may be made in the conventional manner by mixing a leady oxide with water and sulfuric acid or by mixing tetrabasic lead sulfate with water (1). The reduction, which is known as formation, may take place either in a completely assembled cell containing unformed

positive and negative plates or the plates may be formed individually and subsequently assembled into cells. In the latter method, known as tank formation, the completely formed negative plates often have blistered surfaces. Since negative plates formed in assembled cells are rigidly held in place by the separators, the spongy lead is not free to expand and consequently blisters are not seen. Perhaps because most automobile batteries are made by this method, little attention has been given in the literature to the phenomenon of blistering during tank formation.

* Electrochemical Society Active Member.
Key words: lead sulfate, tetrabasic lead sulfate, negative lead electrode, hydrogen evolution.

Using optical microscopy, Simon and Jones have examined (2) plates that were tank formed in sulfuric acid of different specific gravities ranging from 1.05 to 1.45. They did not report the formation of blistered surfaces on their plates. It has been reported (2, 3) that the formation of lead started at the grid members and then a coating of lead rapidly formed on the outside of the plate which advanced inward toward the center of the plate. More recently Simon has reported (4) that in some plates the formation of lead started below the surface of the plate.

The modification of the lead crystals produced on formation of negative plates containing lignin and BaSO_4 in varying amounts was recently reported (5). Blisters were not observed since these negative plates were not tank formed, but formed in assembled cells containing 1.050 sp gr sulfuric acid. The surface layer of these negative plates was different and some plates contained large voids just below the surfaces. It was postulated (5) that the differences in crystal structure at the surface may be the result of surface sulfation.

The exact chemical composition of the unformed, cured plates used in the previous studies is not clear. The chemical composition of the plates undoubtedly affects their behavior during formation, and in fact we have observed that on tank formation, some commercial plates will form blistered surfaces, although others with a different formulation will not. In order to determine the mechanism of formation of the blisters, a study was undertaken using a pure compound, tetrabasic lead sulfate, as the negative paste material. Its performance in the negative plate has been previously reported (1).

Experimental Procedure

Lead-calcium alloy (0.05% Ca) negative grids ($7.6 \times 6.3 \times 0.4$ cm) were hand pasted with a water paste of tetrabasic lead sulfate plus 2% of an expander.¹ After air drying, each negative was placed in a Teflon holder between two formed positive (PbO_2) plates of the same size. The positive and unformed negative plates were 0.6 cm apart and microporous rubber separators were placed between them. Each three-plate cell was placed in a glass jar containing 2000 ml of sulfuric acid and allowed to soak for one-half hour. The specific gravity of the sulfuric acid was varied from cell to cell over a range of 1.005 to 1.210. The cells were then formed at a constant current of 0.35A for approximately 70 hr. This corresponds to a negative plate current density of about 0.35 A/dm² which is within the range recommended by Vinal (6).

During formation, the negative potential vs. a mercury/mercurous sulfate electrode and cell potential were recorded. In order to minimize the junction potential, mercury/mercurous sulfate reference electrodes were made with the same concentration of sul-

¹ National Lead Companies' KX expander.

furic acid as that used in the formation of the negative plate.

After formation, the negative plate was immediately washed in distilled water and dried in a heated vacuum desiccator. The dried negative plates were encapsulated in epoxy and examined under the microscope.

Results and Discussion

The number of blisters on a given plate varied from paste batch to batch and was probably dependent to some extent on the paste density. A negative plate which was severely blistered is shown in Fig. 1a. This negative plate was formed in 1.050 sp gr sulfuric acid. A cross-sectional view of a blister is shown at a magnification of 25 \times in Fig. 1b. Only a part of the blister is visible at this magnification. Porous lead has been lifted from the surface to form a dome-shaped blister.

Areas of the plate which did not contain blisters did contain a fissure which was at exactly the same depth as the thickness of the blister. This fissure is shown in Fig. 2 at a magnification of 25 \times . The porous lead on either side of the fissure had a different crystalline structure as shown at a magnification of 250 \times in Fig. 3 and 4. The lead in the center of the plate appeared to be made up of long dendritic crystals. The lead on the surface of the plate was in the form of many small needles radiating from a larger piece of lead. Only porous lead was found throughout the plate which indicates that the tetrabasic lead sulfate had been completely reduced to lead.

Figure 5 shows a typical plot of negative and positive plate potentials vs. $\text{Hg}/\text{Hg}_2\text{SO}_4$ as a function of time on formation at a constant current in 1.050 sp gr sulfuric acid. The positive potential remains constant throughout the formation since the positive plates were completely formed prior to use. Since the negative plate contains pure tetrabasic lead sulfate plus a known amount of expander, the time required to completely convert the plate to spongy lead may be calculated from Faraday's law. This time is plotted as the vertical line on the graph. The formation process is 100% efficient since the complete reduction to lead, as shown by the sudden increase of negative potential, occurs at the calculated theoretical end of formation time. To the right of the vertical line, hydrogen is being evolved at a potential which levels off at -1.55V .

In Fig. 5, three different potential steps or changes in slope are evident during the formation. They occur at 7-17 hr with a potential of -0.99V , at 20-26 hr with a potential of -1.02V , and at 32-37 hr with a potential of -1.105V . These steps could be due to reduction of lead compounds formed when tetrabasic lead sulfate is immersed in sulfuric acid.

Tetrabasic lead sulfate ($4\text{PbO}\cdot\text{PbSO}_4$) can react with sulfuric acid to yield $3\text{PbO}\cdot\text{PbSO}_4$, $\text{PbO}\cdot\text{PbSO}_4$, and PbSO_4 . $2\text{PbO}\cdot\text{PbSO}_4$ probably would not be formed since it is reported (7) to be unstable at

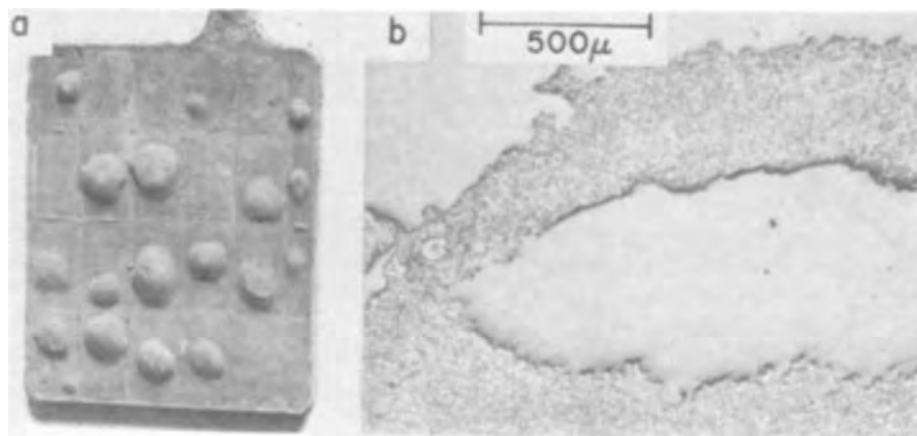


Fig. 1. Blistered negative plate. (a) View of a severely blistered plate. (b) Cross-section of part of a blister at 25X magnification. The base of the blister is to the left and the crest is at the right edge.

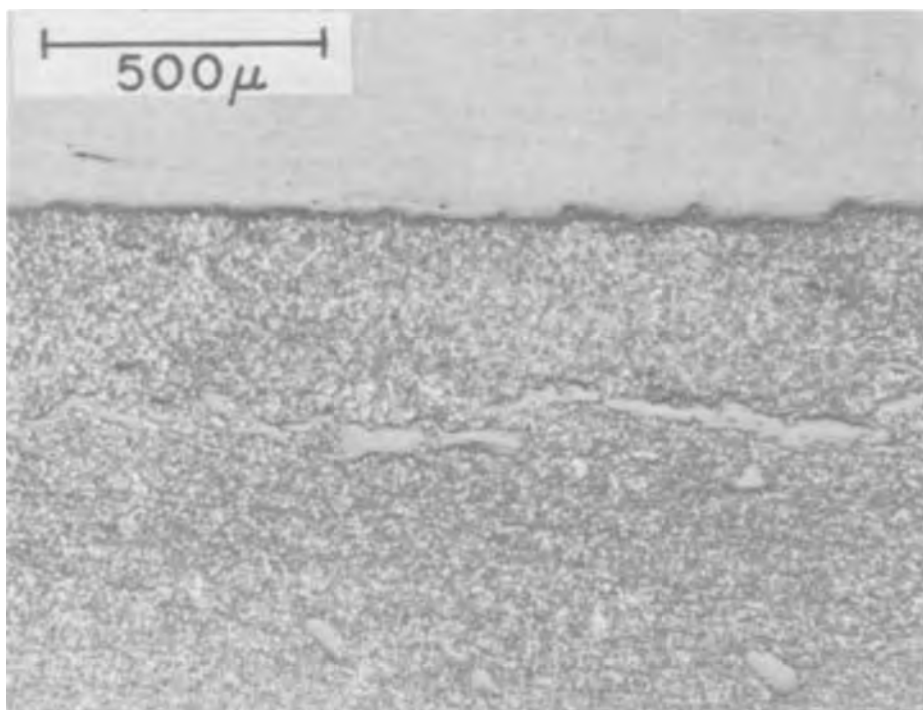


Fig. 2. Cross-sectional view of the surface of a formed negative plate showing the fissure that occurs just below the surface of the plate. Magnification 25X.

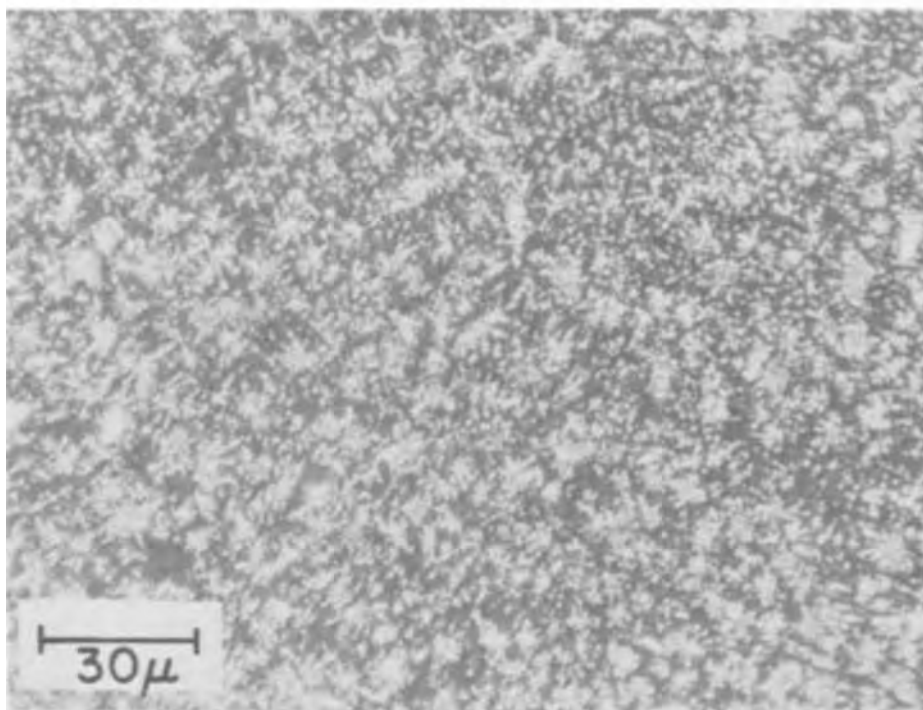


Fig. 3. Same as Fig. 2, cross-sectional view of lead above the fissure near the surface of the plate. Magnification 250X.

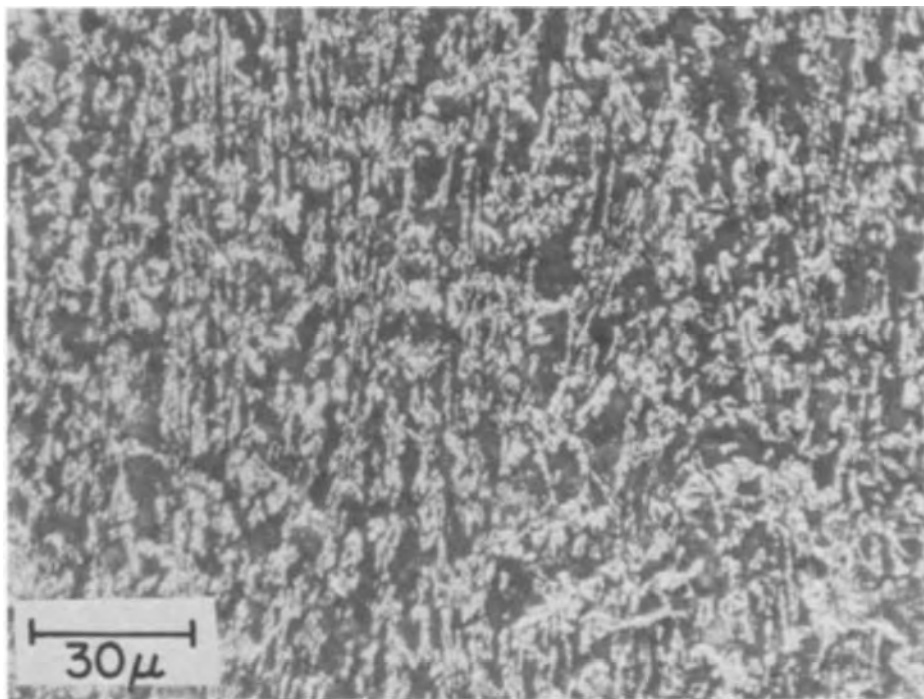
25°C. The extent and rate of the reactions that produce these compounds will of course depend upon the acid concentration. Calculations of the free energy of the reduction of each compound indicate that the order of reduction should be, in decreasing potential: $4\text{PbO}\cdot\text{PbSO}_4$, $3\text{PbO}\cdot\text{PbSO}_4$, $\text{PbO}\cdot\text{PbSO}_4$, and PbSO_4 . Since PbSO_4 would be the last compound to be reduced, one might expect the most prominent step occurring at -1.1V to be lead sulfate.

In order to determine whether or not lead sulfate was being reduced at -1.1V , a negative plate was removed from the formation jar after its negative potential *vs.* $\text{Hg}/\text{Hg}_2\text{SO}_4$ had reached -1.10V . A cross section of the surface of this incompletely formed negative plate is shown at a magnification of $25\times$ in Fig. 6. The negative plate contained only

spongy lead in the center, as in Fig. 4, and a layer of unformed material on the surface of the plate approximately the same thickness as the blisters. This unformed material contained no lead, but only a crystalline material surrounding very small pieces of tetrabasic lead sulfate. Some of this crystalline material was scraped off and analyzed. Chemical and x-ray diffraction analyses showed it to be lead sulfate. This suggests that the potential step occurring at -1.1V is due to reduction of lead sulfate to lead.

The thickness of this surface layer of lead sulfate corresponds exactly to the depth of the fissure (see Fig. 2) and the thickness of the blister (see Fig. 1b). As can be seen by comparing Fig. 3 with Fig. 4, the reduction of the lead sulfate in this surface layer produces spongy lead with a different structure from

Fig. 4. Same as Fig. 2, cross-sectional view of lead below the fissure, in the middle of the plate. Magnification 250X.



that in the center of the negative. The lead formed from the lead sulfate is more finely divided and consequently less porous than that formed in the center of the plate. The presence of spongy lead with a different structure on cycling on the surface of the negative plate has been previously reported (1).

The above observations suggest a plausible mechanism for blister formation. When a negative plate containing tetrabasic lead sulfate is immersed in 1.050 sp gr sulfuric acid, the surface of the plate reacts with the acid to form a layer of lead sulfate. Fissures develop between the lead sulfate and the material in the plate interior. The fissure is probably caused by the 50% increase in material volume associated with the conversion of tetrabasic lead sulfate to lead sulfate.

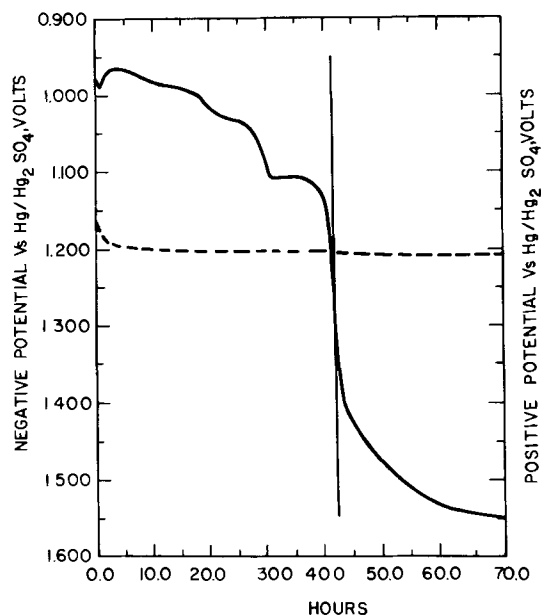


Fig. 5. Positive (dashed line) and negative (solid line) plate potentials vs. $\text{Hg}/\text{Hg}_2\text{SO}_4$ reference electrode as a function of time on formation in 1.050 sp gr sulfuric acid. The solid vertical line is the calculated end of formation time based on the weight of $4\text{PbO} \cdot \text{PbSO}_4$ contained in the plate.

This surface layer of lead sulfate is the last area of the negative plate to be reduced to lead. The lead formed from it has a different crystal morphology and is perhaps less porous than that in the center of the plate. Near the end of formation hydrogen gas is generated and becomes trapped in the fissure between the two differently structured spongy lead layers. Enough pressure is exerted to push the surface layer out to form a blister.

If the spongy lead contained trace metal impurities, the blistering could be disastrous. In this case, a metal impurity could lower the hydrogen overpotential causing generation of hydrogen before the plate is completely formed. This gas would very effectively be trapped behind the lead sulfate which forms a very nonporous (see Fig. 6) coating on the surface of the plate. Much of the gas generated would be trapped, causing the formation of many severe blisters. This latter phenomenon has been observed in paste batches that contained relatively high levels of metallic impurities.

The observations described previously were obtained with negative plates that were allowed to soak for one-half hour prior to the start of formation. However, a plate not soaked and one soaked for 20 hr prior to formation gave results which were identical to those for plates soaked for one-half hour. Therefore the length of the soak time does not appear to be a significant parameter in relation to the blistering phenomenon. The implications of this observation are being investigated as part of a more detailed study of the formation process.

The thickness of the blisters is directly related to the thickness of the solid layer of lead sulfate which develops on the surface of the plate. If the concentration of sulfuric acid available for reaction with tetra-

Table I. Thickness of outer lead layer in different concentrations of sulfuric acid

Specific gravity of acid	Measured range of thickness, cm	Thickness calculated from formation plot, cm
1.005	0.000-0.005	—
1.015	0.005-0.016	0.013
1.030	0.018-0.031	0.031
1.050	0.033-0.056	0.051
1.210	0.094-0.142	0.145

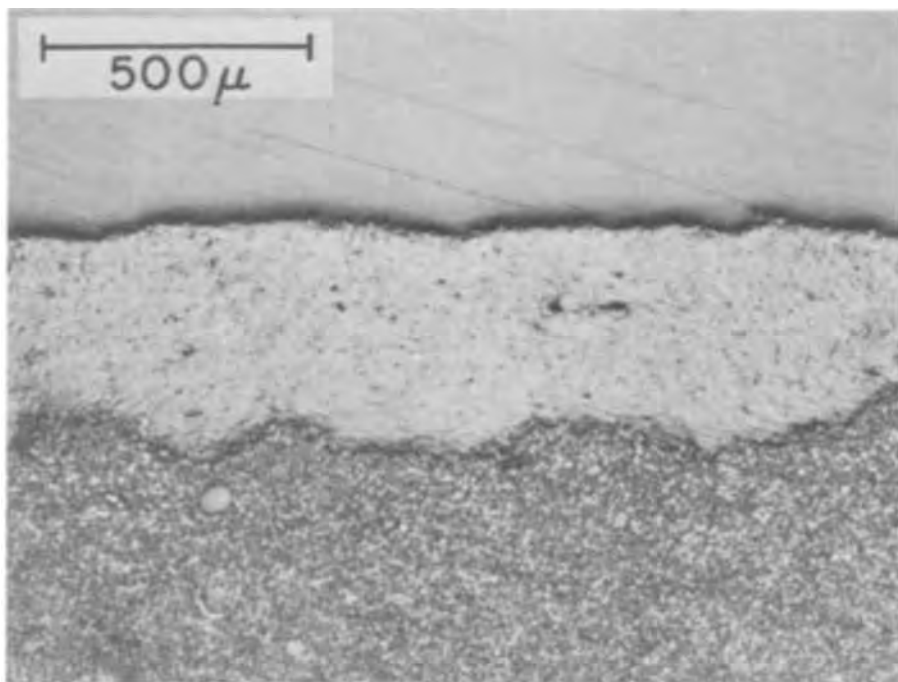


Fig. 6. Cross-sectional view of the surface of an incompletely formed negative plate which was removed after the negative plate potential vs. $\text{Hg}/\text{Hg}_2\text{SO}_4$ had reached -1.1V . Magnification 25X.

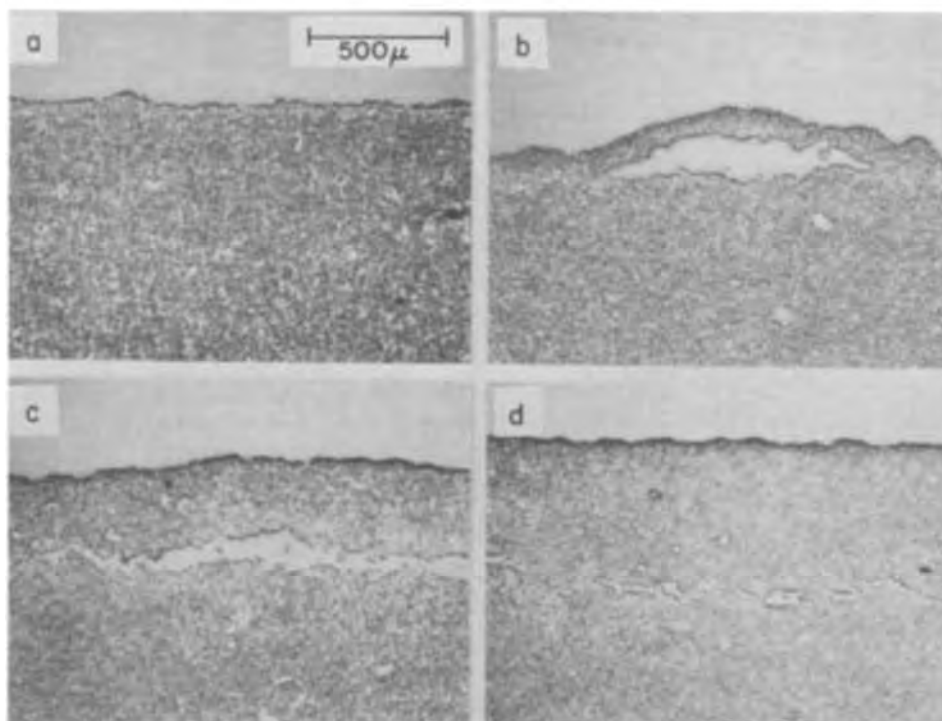


Fig. 7. Cross-sectional views of the surface of negative plates formed in (a) 1.005, (b) 1.015, (c) 1.030, and (d) 1.050 sp gr sulfuric acid. Magnification 25X.

basic lead sulfate is reduced, the thickness of the lead sulfate layer and lead formed from it should decrease. This is indeed what is observed as shown in Fig. 7 and Table I. The surface layer of lead due to surface sulfation on negatives formed in 1.005 sp gr acid is so thin that no blisters are observed. For negatives formed in 1.015 sp gr acid only tiny blisters were observed (Fig. 7b). As the specific gravity of the acid is increased, the blisters become larger and thicker until in 1.210 sp gr acid the blisters are so thick (see Table I) that they appear only as a humping of the pellets.

Formation plots of negatives in sulfuric acid of different specific gravities are shown in Fig. 8. For a specific gravity of 1.005, the step due to reduction of lead sulfate is not seen. At specific gravities greater than 1.015, the step increases in width until in 1.210 sp gr sulfuric acid it is the dominant feature of the plot.

The width of the lead sulfate step occurring in the formation plot is a measure of the thickness of the lead sulfate layer and consequently of the thickness of the lead resulting from its reduction. The thickness of the lead layer was estimated from the formation plots by taking the ratio of the width of the step to the theoretical end of formation time, multiplying by the thickness of the negative, and dividing by two. The results are given in Table I and it can be seen that the calculated results agree reasonably well with the measured results.

Conclusion

Blistering of negative plates has been shown to result from the reduction of a surface coating of lead sulfate which is produced by chemical reaction between the paste material and the forming acid. This phenomenon may be eliminated altogether by reducing the

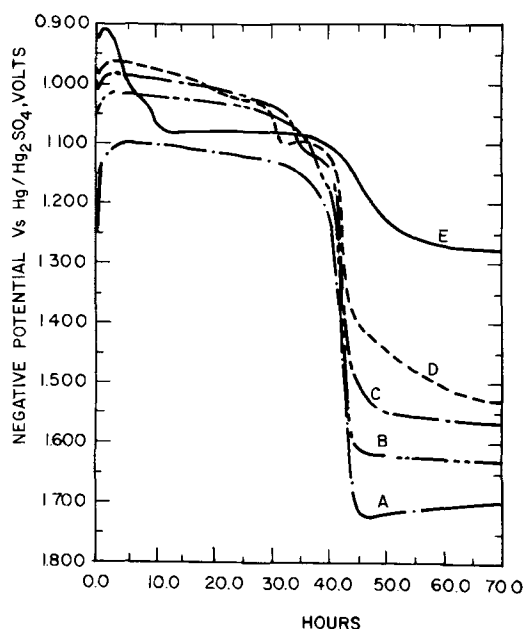


Fig. 8. Negative plate potentials vs. $\text{Hg}/\text{Hg}_2\text{SO}_4$ reference electrodes as a function of time on formation in (A) 1.005, (B) 1.015, (C) 1.030, (D) 1.050, and (E) 1.210 sp gr sulfuric acid.

concentration of the forming acid. In fact, negative plates without blisters have been formed in distilled water. However, by eliminating the blisters completely,

one sacrifices initial plate capacity. Blistering does increase the initial surface area of the plate as well as the amount of acid immediately available for discharge within the plate. However, after cycling a number of times, the capacity of plates without blisters does increase to that of the blistered plates. By choosing the proper concentration of forming acid, a balance may be obtained between the degree of blistering which can be tolerated and the initial capacity desired. Depending on the intended use for a particular battery, one may be willing to accept some blistering in order to obtain a higher initial capacity.

Manuscript received Aug. 25, 1971. This was Paper 20 presented at the Cleveland Meeting of the Society, Oct. 3-7, 1971.

Any discussion of this paper will appear in a Discussion Section to be published in the December 1972 JOURNAL.

REFERENCES

1. C. F. Yarnell, Abstr. 48, *Electrochem. Soc. Extended Abstracts, Fall Meeting, Atlantic City, Oct. 4-8, 1970*.
2. A. C. Simon and E. L. Jones, *This Journal*, **109**, 760 (1962).
3. N. E. Bagshaw and K. P. Wilson, *Electrochim. Acta*, **10**, 867 (1965).
4. A. C. Simon in "Proceedings of the Sixth International Symposium," D. H. Collins, Editor, p. 33, Pergamon Press, New York (1970).
5. J. R. Pierson, P. Gurlusky, A. C. Simon, and S. M. Caulder, *This Journal*, **117**, 1463 (1970).
6. G. W. Vinal, "Storage Batteries," p. 37-41, John Wiley and Sons, Inc., New York (1940).
7. J. J. Lander, *Trans. Electrochem. Soc.*, **95**, 174 (1949).

Impurity Distributions in Anodic Films on Tantalum

R. E. Pawel,^{*1} J. P. Pemsler,^{*2} and C. A. Evans, Jr.³

ABSTRACT

Anodization of tantalum in electrolytes containing phosphorus or fluorine ions resulted in the incorporation of a quantity of these elements into the anodic film. While phosphorus was concentrated in the outer portions of such films, fluorine was attracted to the oxide/metal interface. We employed an ion microprobe mass spectrometer to examine the concentration profiles of these elements in films formed by a variety of anodization procedures. These experiments demonstrated the usefulness of the IMMS as a tool for such work and, in addition, furnished information on the characteristics of both film growth and the distribution and movement of these impurities. The influence of fluorine-rich layers at the oxide/metal interface on the adherence of the anodic films was also shown.

During the anodization of tantalum (as well as several other valve metals), the inclusion in the product film of impurity atoms from the electrolyte is a common occurrence and impurity effects on both the characteristics of film formation and various film properties have been reported (1). In addition, it has been observed experimentally that the impurity distribution may not be uniform throughout the film and may, in fact, have an unusual variation with depth caused by the particular manner in which the anodization was accomplished. For example, the "two-layer" structure associated with films on tantalum anodized in sulfuric or phosphoric acid has been well documented (1-8). One can argue that important properties of these films

may be determined by both the amount and the distribution of the impurities within them.

Since the thickness of barrier-type anodic films on tantalum is generally limited to only a fraction of a micron, special techniques are required for their analysis. Most previous experiments concerning the direct determination of the impurity distribution within these films have involved radio-tracer methods combined with chemical sectioning. Chemical sectioning provides a surprisingly uniform removal of layers of the anodic oxide, although very careful experimental procedures are necessary to assure reproducible sectioning rates (1, 2, 4, 13).

We are examining the applicability of the Ion Microprobe Mass Spectrometer (GCA Technology Division, Bedford, Massachusetts) for the determination of impurity distributions in thin anodic oxide films. The details of the design and general operation of the IMMS have been described in detail previously (9). Basically, the instrument is a sputtering device in which the

* Electrochemical Society Active Member.

¹ Metals and Ceramics Division, Oak Ridge National Laboratory, Oak Ridge, Tennessee 37830.

² Ledgemont Laboratory, Kennecott Copper Corporation, Lexington, Massachusetts 02173.

³ Materials Research Laboratory, University of Illinois, Urbana, Illinois 61801.

Key words: ion microprobe, markers, microanalysis, microsectioning, thin films.

sputtered material is sampled by a mass spectrometer. Thus, for a constant sputtering rate, the output of the spectrometer furnishes a measure of the ion yield or concentration of a given material as a function of depth. Although, in principle, comparison of these ion intensities with appropriate standards would permit the determination of absolute concentrations, we have not yet attempted to use the IMMS as a tool for quantitative analysis. All of the profiles presented in this work are based on arbitrary ion intensity units, which may vary from experiment to experiment, and must be considered with this in mind.

In this paper we present results which test the sensitivity of the apparatus for various types of work with ultra-thin oxide films. These results concern the behavior of phosphorus and fluorine impurities incorporated during the anodization of tantalum and, in particular, the use of thin phosphorus-rich layers as "markers."

Experimental Procedure

Tantalum specimens⁴ were prepared from $1 \times 2 \times 0.05$ cm coupons. These were annealed in vacuum (10^{-6} Torr) for 2 hr at 1600°C , mechanically polished through 0.3μ -alumina, and electropolished in a 90% H_2SO_4 -10% HF solution. A short length of tantalum wire was spot-welded to each specimen to facilitate handling and to serve as electrical contact during anodization. The polished specimens were then washed carefully and boiled in distilled water for 1 hr to remove or counteract the effect of the residual fluoride from the electropolishing bath.

The specimens were anodized at room temperature to a given voltage in a simple cell in which the initially high currents were limited to about 10 mA/cm^2 by a variable series resistor. The resistance was reduced to zero and the specimen held at full voltage for a "standard" time of 2 min in order to be able to apply previously determined thickness calibrations (10) to the films: 16.5 A/V in dilute Na_2SO_4 and KF; 13.2 A/V in concentrated (14.7M) H_3PO_4 . The "duplex" and "sandwich" type films dealt with in this paper were produced by sequential anodization in the various electrolytes. It was assumed that the increment of thickness produced by an additional anodization depended only upon the voltage increment and the particular electrolyte.

Results and Discussion

Anodization in 0.035M (0.5%) Na_2SO_4 .—The anodization of tantalum in dilute sulfate solutions produces amorphous, essentially stoichiometric tantalum pentoxide films which have uniform properties over a range of formation conditions. We utilized such films in the preliminary stages of this study to observe the effect of instrument variables, particularly those which controlled the size, intensity, stability, and uniformity of the argon ion-beam used for sectioning.

As reported previously (9), some modifications in the ion lenses and ion current measuring devices proved very useful in increasing the reliability of the instrument for our purposes. With these changes, the uniformity of the beam was improved, resulting in a sectioning (crater) geometry which produced a depth resolution useful for work with anodic films. The geometry of material removal was checked by observing intermittently the uniformity of the interference color of the remaining film at the bottom of the $3 \text{ mm} \times 4 \text{ mm}$ elliptical crater produced by the beam. At a depth of 1000\AA , variations of the order of $\pm 50\text{\AA}$ across the crater were generally observed. Calibrations of the sputtering rates of these films as a function of the beam parameters were obtained by means of side-by-side color comparisons with a standard set of anodized specimens. Sputtering rates of 0.5 - $1\text{\AA}/\text{sec}$ used in this investigation could be reproduced from run-to-run to within $\pm 10\%$. By monitoring either the Ta or O ion intensities during sputtering of the films, the position

⁴ Nominal analysis is 99.7-99.8% Ta with Nb, Fe, W, and Si as major metallic impurities.

and effective "width" of the oxide/metal interface could be determined. Generally, a sigmoidal decrease of these intensities over a distance of about 200\AA was associated with the interface. This was viewed as a reasonable value, particularly since the surface of electropolished tantalum is not precisely planar on a fine scale (11).

Anodization in H_3PO_4 .—Anodic films formed on tantalum in H_3PO_4 solutions are known to contain significant quantities of phosphorus. Not unexpectedly, most of the properties of these films are significantly altered as a direct result of such incorporation. While a number of investigators have presented results which have been interpreted in terms of a nonuniform distribution of phosphorus, Randall *et al.* (4) were the first to include a quantitative description. These investigators found that all the phosphorus was concentrated in the outer half to two-thirds of the oxide, and that its concentration within this layer was uniform. Both the absolute concentration of phosphorus and the relative depth of the enriched layer depended upon the concentration of the electrolyte.

Typical phosphorus concentration profiles determined in the present investigation by the IMMS for films formed in concentrated (14.7M) H_3PO_4 are shown in Fig. 1. The phosphorus concentration drops off rapidly to a plateau which extends about two-thirds of the way through the film. The high apparent concentration at the electrolyte/film interface was also observed in earlier measurements (9) on films formed in both 14.7M and 0.9M H_3PO_4 . While the extent of the surface enrichment is reduced somewhat by ultrasonic cleaning of the specimens in detergent solution (used on the present specimens), its persistence suggests that more than simply a surface artifact or occlusion is involved. For the case of films formed in 0.9M H_3PO_4 , the phosphorus plateau extended about half way through the films; the high surface concentration was also observed. Thus, with the exception of our observation of phosphorus enrichment at the surface of the film, our profiles are in excellent agreement with those of Randall. Subject to the limitations discussed below, the phosphorus profile indicated that there is an apparent transport fraction for tantalum ions of about 0.65 for anodization in 14.7M H_3PO_4 .

"Sandwich" films and marker experiments.—The results that two distinct layers are formed when tantalum is anodized in H_3PO_4 solutions implies that both O and Ta ions are mobile. If additional oxide can only be formed at the electrolyte/oxide and oxide/metal interfaces and if the phosphorus itself is essentially immobile, it follows that sequential or multiple anodizations in concentrated and dilute electrolytes could establish zones rich in phosphorus entirely buried within

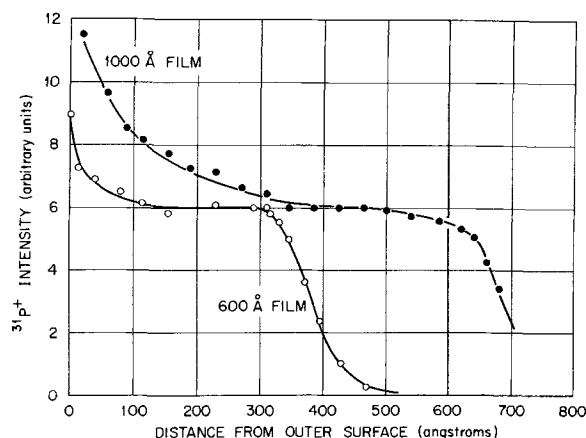


Fig. 1. Phosphorus concentration profiles in anodic films formed in concentrated (14.7M) H_3PO_4 to thickness of 600\AA , \circ , (45.5V) and 1000\AA , \bullet , (75.8V).

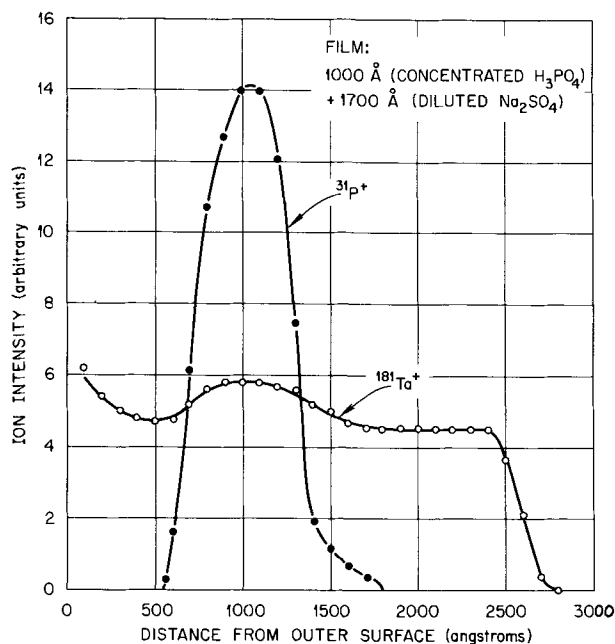


Fig. 2. Concentration profiles for tantalum and phosphorus across "sandwich" specimen formed by sequential anodization of tantalum in 14.7M H_3PO_4 (1000Å) and 0.035M Na_2SO_4 (+1700Å), ● phosphorus profile; ○ tantalum profile.

the layer. The existence of such zones would present interesting implications regarding the properties of these films.

The results of a duplex anodization are illustrated in Fig. 2. In this experiment, a 1000Å film was formed in concentrated (14.7M) H_3PO_4 ; the specimen was carefully washed and then reanodized in 0.035M Na_2SO_4 to a total film thickness of 2700Å. The Ta and P ion profiles shown in the figure confirm the fact that the phosphorus existed in an isolated region within the film. The thickness of the phosphorus-rich zone is consistent with its thickness prior to the second anodization, except that it does not exhibit the expected asymmetric distribution favoring the side toward the electrolyte. The variations in the Ta ion intensities are thought to be primarily the result of drifts in the sputtering beam currents.

A test of the resolving power of the IMMS for locating and describing thin, embedded layers in oxide films is shown in Fig. 3. In this set of specimens, phosphorus-rich layers having thicknesses of about 17, 35, and 65Å were sandwiched between layers of plain oxide by a three-step anodization in 0.035M Na_2SO_4 , 14.7M H_3PO_4 , and again in 0.035M Na_2SO_4 . All three layers were easily resolved by the IMMS, resulting in the Gaussian-type curves for relative phosphorus concentration shown. The measured widths at half-maximum intensity were 85, 115, and 150Å, respectively, for the three phosphorus layers. Even if we ignore the possibility that the final anodization step caused a slight spreading of the phosphorus layer, these values indicate that the technique is capable of locating an internal interface of this sort to within about 40Å. (Note that an infinitesimally thin layer would exhibit an apparent thickness of 60-80Å.) It therefore appears that the resolution of the instrument is entirely satisfactory for defining impurity distributions on this fine scale.

This method was used to study the systematic movement and broadening of a thin phosphorus-rich layer during subsequent anodization in dilute electrolytes. If the phosphorus is indeed immobile, as suggested by Randall (4), it would serve as an ideal "marker" and information relating to the mechanism of film formation could be obtained. We anodized a group of specimens in 14.7M H_3PO_4 to an apparent film thickness of

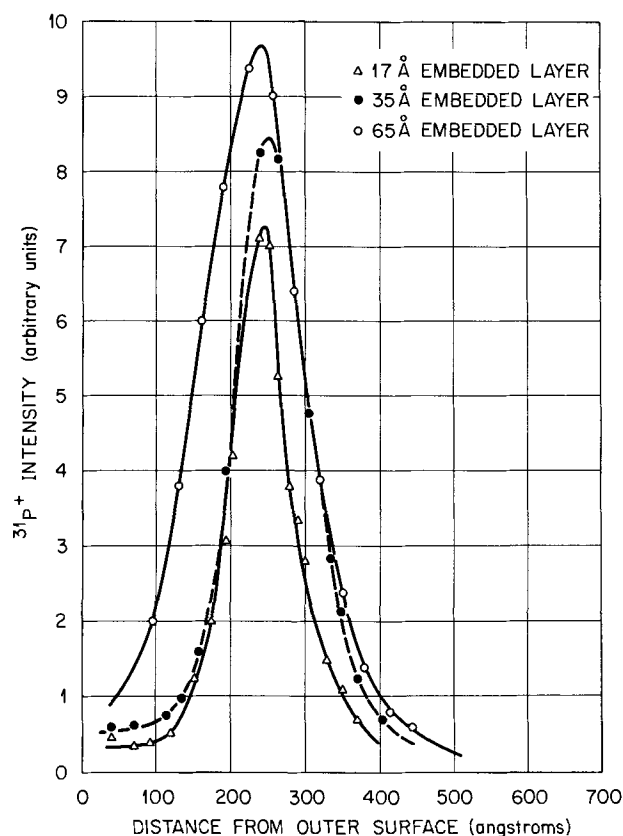


Fig. 3. Concentration profiles for thin phosphorus-rich layers embedded in anodic tantalum oxide film. The three specimens were prepared by (a) anodizing each to a film thickness of 500Å in 0.035M Na_2SO_4 , (b) reanodizing in 14.7M H_3PO_4 to add 25Å Δ , 50Å ●, and 100Å ○ of film, two thirds of which is phosphorus-rich, and finally, (c) anodizing again in 0.035M Na_2SO_4 to add 500Å more to the total film thickness.

25Å. If we neglect the effect of the pre-existing film and assume that the same phosphorus distribution exists here as in the thicker films of Fig. 1, the phosphorus-rich layer will be slightly less than 20Å thick, and its center will be located about 10Å from the outer surface. We then reanodized these specimens in 0.035M Na_2SO_4 to add increments of phosphorus-free oxide from 500-4000Å in thickness. The phosphorus profiles, determined by the IMMS and normalized to a constant peak intensity, are presented in Fig. 4. The final position of the marker layer is approximately in the center of the film for all specimens. Note also that the apparent thickness of the layer (defined as the width of

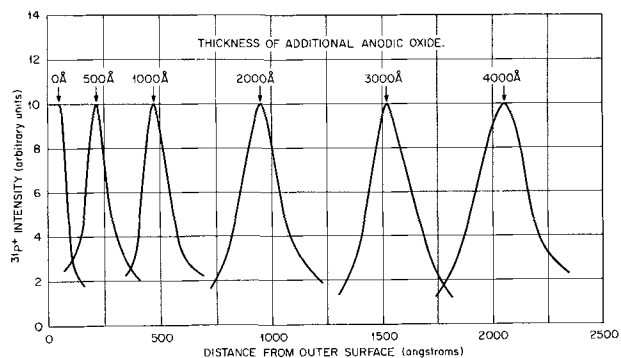


Fig. 4. "Marker" experiments with thin, phosphorus-rich layers. Concentration profiles exhibited by 17Å marker layer (25Å film formed directly on tantalum surface) after subsequent anodization in 0.035M Na_2SO_4 to 500, 1000, 2000, 3000, and 4000Å.

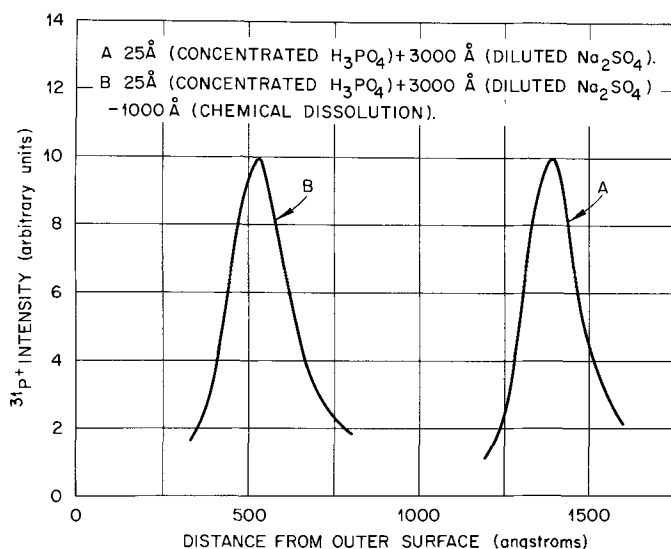


Fig. 5. Effect of marker layer depth on profile determination. Film 'A' contains a 17Å layer buried by subsequent anodization (3000Å) in 0.035M Na₂SO₄. Film 'B' is identical, except that approximately 1000Å of the outer film has been removed by chemical dissolution in NH₄F-HF solution.

the profile at half-maximum intensity), increases with the thickness of added oxide.

The final position of the marker is determined by the relative transport fractions of the ions across the film and also by the extent of its movement induced by the electric field and/or the ion flux. If the degree of the latter type of migration is directly proportional to the amount of anodization after the marker is placed, the transport fractions obtained from the data of Fig. 4 and similar experiments will be in error by a constant factor which relates this movement to the total amount of new oxide formed. The extent of this error cannot be determined from these experiments. However, the apparent spreading of the marker as a function of continued anodization implies at least some small degree of interaction with the ion flux or that some oxide is forming internally.

An apparent spreading of the marker layer would also be observed if the crater formed by the IMMS beam changed in shape or became roughened in proportion to the depth eroded. In order to check this possibility, we repeated the 3000Å film experiment employing chemical means to remove a portion of the outer oxide. Approximately 1000Å of oxide was removed from this specimen by partially dissolving the film in a solution of 25g NH₄F in 100 cc HF. Figure 5 indicates that the marker profiles obtained "before and after" are virtually identical. Thus, unless the chemical removal of the oxide produces an identical roughening of the surface, it appears reasonable to conclude that

the marker spreading is a real, albeit a comparatively small effect.

The results of our experiments which bear directly upon the mechanism of anodic oxidation of tantalum in the manner previously described in dilute aqueous solutions are listed in Table I. If it is assumed that the phosphorus-rich layer serves as an inert, immobile marker (i.e. that its changes in position are solely a result of the motion of the Ta and O ions), then the fractional burying of the marker, $\Delta X/\Delta W$, is a measure of the tantalum ion transport fraction. In this expression, ΔX is the observed change in marker depth relative to the oxide/electrolyte interface during the period in which the total thickness of the film is changing by ΔW . The tantalum ion transport fractions are listed in the last column of the table and are sensibly constant with a value of 0.46 ± 0.05 . Their constancy points out that if the phosphorus marker is indeed mobile, contrary to our above assumption, it moves in virtually direct proportion to the extent of subsequent anodization.

In excellent agreement with the above results, perhaps because phosphorus was also used as a marker, Randall (4) obtained a value of 0.48 for the corresponding transport fraction. However, Davies *et al.* (12) utilizing injected Xe¹²⁵ atoms as markers, and Whitton (14), using Kr⁸⁵, obtained values of about 0.3. In order to rationalize the two results on the basis of their face value, a difference in mobility of approximately 0.2 Å/Å must exist for the phosphorus and the inert gas markers during anodization. It may be pertinent to note that the mass of the marker species (13), as well as the charge (14), will determine its relative mobility and final position in the film. Obviously, marker behavior is complex and the categoric interpretation of such results is dangerous.

Anodization in 0.09M (0.5%) KF.—It is well known that anodization of tantalum specimens prepared by polishing in reagents containing HF produces anodic films that are poorly adherent. It has also been shown (15) that anodization even in dilute fluorine-containing electrolytes permits large numbers of such films to be stripped in sequence from a single specimen. This is the basis of a sensitive microsectioning technique which is applicable to both tantalum and niobium, as well as their alloys. A reasonable explanation for this behavior is that a fluorine-containing film—perhaps an oxy-fluoride—is formed at the oxide/metal interface and serves as an efficient parting agent between the metal and the film. The fact that this parting layer remains in position at the interface during anodizing has been used as evidence to support the idea that cation migration is the primary mechanism of anodic film formation (1).

Our application of the IMMS to the examination of fluorine profiles in anodic films furnishes an explanation for the effect which is consistent with the fact that both tantalum and oxygen ions are mobile. A fluorine concentration profile for a 2000Å anodic film formed in

Table I. Movement of thin, phosphorus-rich layers during anodization

Configuration ^(a)	Phos. peak position with respect to E/O interface, Å	Final width of P-rich zone (at ½ max. int.), Å	Fractional burying $\Delta X/\Delta W$	Apparent Ta transport fraction, τ_{Ta}
500/100P/500	240	150	210/500	0.42
1000/100P/1000	490	200	460/1000	0.46
25P/1000	450	200 (?)	440/1000	0.44
500/25P/500	240	85	230/500	0.46
500/25P/500	250	90	240/500	0.48
500/50P/500	255	115	238/500	0.48
25P/500	220	95	210/500	0.42
25P/1000	475	130	465/1000	0.47
25P/2000	950	180	940/2000	0.47
25P/3000	1520	190	1510/3000	0.50
25P/4000	2060	230	2050/4000	0.51
25P/3000	1400	180	1390/3000	0.46

^(a) "P" indicates a phosphorus-rich layer. For example, 500/100P/1000 means the first anodization was carried out in dilute Na₂SO₄ to 500Å; next, 100Å was formed in 14.7M H₃PO₄ (outer two-thirds is P-rich); finally, 1000Å were added by anodizing again in dilute Na₂SO₄.

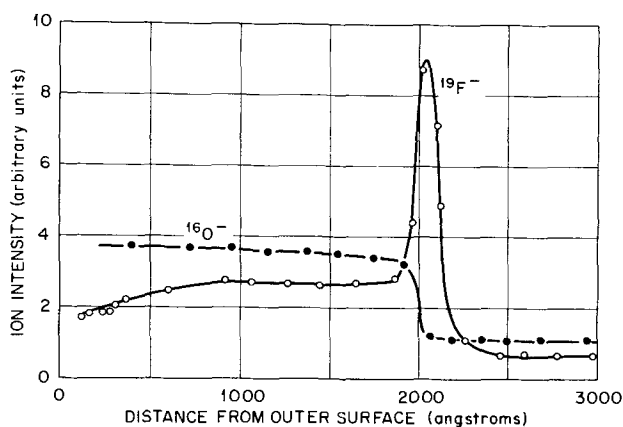


Fig. 6. Fluorine and oxygen concentration profiles in anodic film formed on tantalum in 0.09M (0.5%) KF. ○ Fluorine profile, ● oxygen profile.

a dilute KF solution is illustrated in Fig. 6. The concentration is essentially constant throughout the film, but rises abruptly at the oxide/metal interface. The oxygen profile, shown on a less sensitive scale, shows no such peak, but behaves in normal fashion through the interface. The presence of a fluorine-rich layer of some sort at the interface is evident. Furthermore, the width of the F peak at half-maximum intensity is only about 100Å and, taking into account the resolution limits of the IMMS for such interfaces, we estimate the thickness of this layer to be less than 50Å—perhaps much less.

In order to test the hypothesis that fluorine itself is mobile during anodization and may be driven through the film to the oxide/metal interface, we measured the fluorine profiles on a series of specimens which had been pre-anodized in a dilute sulfate solution to produce 500Å adherent layers of fluorine-free oxide and then reanodized in 0.09M KF to produce increments of fluorine-containing oxide with thicknesses of 250, 500, and 1000Å, respectively. If fluoride were immobile, none should be found within 500Å of the oxide/metal interface. The results of these experiments are presented in Fig. 7. Reanodization to add 250 and 500Å thickness to the oxide layer caused measurable amounts of fluorine to migrate into the formerly "plain" oxide layer as manifested by the considerable broadening of the F-distribution curves into this region. Reanodization to add 1000Å of film, however, resulted in the

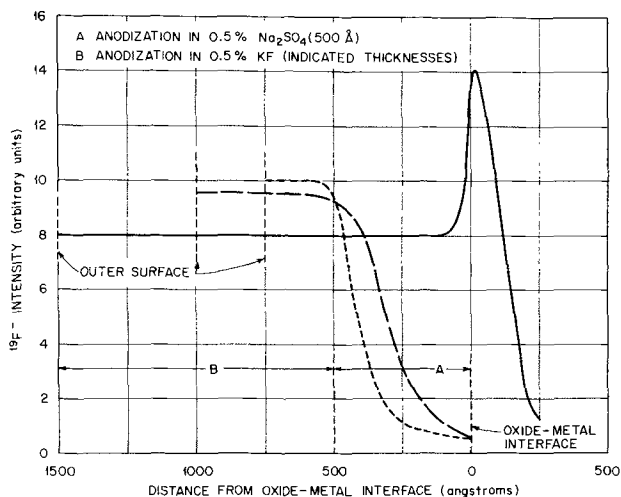


Fig. 7. Fluorine concentration profiles in anodic films formed stepwise on tantalum in dilute Na_2SO_4 and KF solutions. All three specimens were first anodized in 0.035M Na_2SO_4 to form 500Å of fluorine-free oxide. They were then reanodized in 0.09M KF to the indicated total thicknesses.

fluorine finally reaching and apparently being concentrated at the oxide/metal interface. This behavior is similar to that for anodization wholly in KF, and the eventual formation of a discrete F-rich layer shows that the fluorine migrated toward the oxide/metal interface to an extent which depended upon the amount of anodization. Thus, if a fluoride-rich layer does not already exist at the interface, sufficient fluorine can migrate to cause its formation and perhaps continued growth.

It is pertinent to point out that the films which have the fluoride layer at the interface easily strip from the specimen; the others do not. These results are useful in understanding the action of fluorine in determining the relative adherence of anodic films on tantalum. Only very small amounts of fluorine at the interface are required to decrease markedly the adherence of the film. For example, we have found that the fluorine in a 50Å film formed in dilute KF, when driven through an adherent anodic film to the interface, is sufficient to cause complete loss of adherence. Probably less than a monolayer of fluorine atoms is involved.

An estimate of the mobility of the fluorine was also obtained in these experiments. In order to drive fluorine from a "sandwich" through a given thickness of adherent film, it was necessary for additional oxide between two and three times this thickness to be formed. Holding the composite for extended periods of time under conditions where the electric field in the oxide was sufficient to maintain only very slow over-all growth rates did not cause appreciable fluorine movement. Apparently, gross ion movement, or the added field strength associated with it, was necessary to promote this effect.

Conclusions

The ion microprobe mass spectrometer has been shown to be a useful instrument for describing the distribution of impurities in thin anodic oxide films. The sputtering rates and crater shapes were controlled such that they varied very little with time and penetration depth (at least for several thousand angstroms). The effective resolution, in terms of the apparent thickness of a plane interface, was about 50Å. The inclusion and movement of phosphorus and fluorine in anodic tantalum oxide films during a variety of anodization procedures were studied. The specific conclusion are:

(i) When films are formed in concentrated H_3PO_4 , the phosphorus concentrates in the outer two-thirds of the film implying, if the phosphorus is immobile, a value of the tantalum ion transport fraction of about 0.65. This is different from the value of 0.46 found for anodization in the dilute sulfate solution. It may be significant in this respect to point out that the high-temperature oxygen permeation rates through anodic films containing phosphorus have been observed to be much less than those through the plain anodic oxide (10).

(ii) Thin, phosphorus-rich layers of known thickness may be positioned in otherwise normal anodic films.

(iii) Phosphorus-rich layers spread only slightly during continued anodization.

(iv) If phosphorus is itself mobile during anodization, it moves in virtually direct proportion to the amount of anodization and, thus no direct values could be determined concerning the extent of this movement. Assuming the phosphorus marker layer to be immobile, the apparent tantalum ion transport fraction is about 0.46 for anodization in dilute sulfate solutions. The corresponding transport fraction determined by previous investigators using inert gas atoms as markers is about 0.3. Thus, if these markers are immobile, phosphorus is drawn to the oxide/metal interface by approximately 0.2 Å/Å during anodization.

(v) During anodization, fluorine-rich marker layers or fluorine ions from the electrolyte may be driven comparatively large distances through the film toward the oxide/metal interface. Thus, fluorine cannot be

used effectively as a marker for ion transport studies.

(vi) The loss of adherence of the anodic films on tantalum occurs when a fluorine-rich layer forms at the oxide/metal interface. This "parting agent" can be produced by (a) anodizing specimens polished in fluoride-containing reagents, (b) anodizing specimens in fluoride solutions, or (c) driving a fluoride-rich layer through the anodic film by continued anodization.

Acknowledgments

The authors would like to thank N. A. Giardino, Kennecott Copper Corporation, for assistance in the use of the IMMS and J. V. Cathcart, Oak Ridge National Laboratory, for helpful discussions and comments concerning the manuscript.

Part of this research was sponsored by the U. S. Atomic Energy Commission under contract with the Union Carbide Corporation.

Manuscript submitted June 24, 1971; revised manuscript received Sept. 13, 1971. This was Paper 89 presented at the Cleveland, Ohio Meeting of the Society, Oct. 3-7, 1971.

Any discussion of this paper will appear in a Discus-

sion Section to be published in the December 1972 JOURNAL.

REFERENCES

1. See, for example, L. Young, "Anodic Oxide Films," Academic Press, New York (1961).
2. D. A. Vermilyea, *Acta Met.*, **2**, 482 (1954).
3. P. H. G. Draper, *Acta Met.*, **11**, 1061 (1963).
4. J. J. Randall, Jr., W. J. Bernard, and R. R. Wilkinson, *Electrochim. Acta*, **10**, 183 (1965).
5. D. M. Smyth, T. B. Tripp, and G. A. Shirn, *This Journal*, **113**, 100 (1966).
6. D. M. Smyth, *ibid.*, **113**, 1271 (1966).
7. G. Amsel, C. Cherki, G. Feuillade, and J. P. Nadai, *J. Phys. Chem. Solids*, **30**, 2117 (1969).
8. C. J. Dell'Oca and L. Young, *This Journal*, **113**, 1545 and 1548 (1970).
9. C. A. Evans and J. P. Pemsler, *Anal. Chem.*, **42**, 1060 (1970).
10. R. E. Pawel, *This Journal*, **114**, 1222 (1967).
11. J. V. Cathcart, R. Bakish, and D. R. Norton, *ibid.*, **107**, 668 (1960).
12. J. A. Davies, B. Domeij, J. P. S. Pringle, and F. Brown, *ibid.*, **112**, 675 (1965).
13. J. P. S. Pringle, Unpublished research, personal communication.
14. J. L. Whitton, *This Journal*, **115**, 58 (1968).
15. R. E. Pawel, *Rev. Sci. Instr.*, **35**, 1066 (1964).

The Effect of Fluoride Ion on the Anodic Behavior of Titanium in Sulfuric Acid

M. J. Mandry¹ and G. Rosenblatt^{*2}

Department of Metallurgical Engineering, Queen's University, Kingston, Ontario, Canada

ABSTRACT

The anodic behavior of titanium in the presence of fluoride ion and sulfuric acid has been studied. Fluoride ion accelerates active corrosion and results in more active, time-dependent corrosion potentials and greatly increased current requirements for passivation. The critical current density is found to be first order with respect to fluoride ion at low concentration and less than unity at higher fluoride levels. Corrosion in the passive region is also increased although to a lesser extent than in the active state.

Titanium offers many advantages over other materials when used in acid media, displaying excellent corrosion resistance. Recent literature (1-4) has been largely concerned with the anodic behavior of titanium in acid solutions. The effect of chloride ion on the corrosion resistance of titanium and its alloys has been recently outlined by Thomas and Nobe (2) for sulfuric acid solutions and by Levy (5) and Takamura (6) for concentrated chloride solutions. However, very little work (7-9) exists on the effect of fluoride ion on titanium corrosion, particularly in the small amounts encountered in industrial environments, despite the fact that fluoride ion has been found to be an extremely pernicious impurity with regard to titanium corrosion. The purpose of the following investigation was to determine the anodic behavior of titanium in the presence of fluoride ions.

Experimental Procedure

Titanium used in this study was commercially pure Ti75A (max % 0.08C, 0.05N, 0.015H, 0.20Fe) in the annealed condition. Samples cut from the slab of the as-received titanium were mounted in epoxy resin (Armstrong Activator W and C-4 resin) so that only one face was exposed to the test solution. Care was taken

to avoid crevices between the sample and the epoxy mount. Some titanium samples were machined into cylindrical electrodes and mounted using Teflon compression gaskets (10). Both methods gave the same results in the sulfuric acid-fluoride solutions used in the work. Samples were polished on metallographic abrasive paper, washed in detergent solution, mounted in an electrode holder (10), and degreased with acetone. They were finally rinsed with distilled water before immediate insertion into the cell. The cell and auxiliary platinized platinum electrodes were similar in design to those described earlier in the literature (4, 10), except that a Luggin probe-reference electrode assembly was employed which contained an isolating stopcock to avoid contamination by the chloride solution of the reference electrode. The stopcock was closed during the course of the experiment and ionic contact was maintained through a film of electrolyte on the stopcock. In all cases electrode potentials are reported vs. SCE, uncorrected for liquid junction potentials.

Anodic polarization was achieved by using an Anotrol potentiostat (Model 4100). Electrode potentials were measured with a high impedance electrometer (Wenking PPT-19) to an accuracy of 1 mV. The electrode potentials were set in steps of 25 mV into the passive region, after which 50 or 100 mV steps were taken in order to result in an over-all transfer rate of 0.3 V/hr. Solutions of 1N sulfuric acid were prepared from reagent-grade sulfuric acid and double-distilled water. Fluoride additions were made to the sulfuric

* Electrochemical Society Active Member.

¹ Present address: Consolidated Mining & Smelting Ltd., Kimberly, B.C., Canada.

² Present address: Canadian Porcelain Co. Ltd., P.O. Box 428, Hamilton, Ont., Canada.

Key words: anodic polarization, titanium corrosion, fluoride ion.

acid in the form of a concentrated solution of reagent-grade sodium fluoride. Purified hydrogen was bubbled through the solution during the test.

Titanium electrodes were self-activated (2) by immersion in 1N sulfuric acid solution through which purified hydrogen was passed for a period of 18 hr. Reproducible corrosion potentials were readily obtained using this procedure which was preferred to the activation treatment using HF (2) or cathodic pre-polarization (3). Anodic polarization was initiated only after a steady corrosion potential was attained (no change in potential of more than 2 mV for 30 min). Solutions containing fluoride required a further waiting period before this steady state was reached. The corrosion potential was found to be depressed by about 50 to 75 mV after immersion in the sulfuric acid-fluoride solution, but drifted in a positive direction to a steady potential after a 3-hr period.

Results

Anodic polarization of titanium.—The effect of fluoride ion on the anodic polarization characteristics of titanium are shown in Fig. 1. As can be seen from the data collected from these curves and summarized in Table I, small increases in fluoride ion concentration produce large increases in the critical current needed for passivation. The smallest NaF concentration examined (0.59×10^{-3} M) increased the current density for passivation by a factor of three over that of titanium in the absence of fluoride. Quantitative comparisons were difficult to make because earlier work studying the effect of fluoride ion on the corrosion of titanium involved larger fluoride concentrations and employed HF and various media with added NH_4F and HF. However, the trend observed previously (7-9) of increasing critical current densities with fluoride is in general agreement with our data. Although both the critical current and the passive current density (at 0.6V) show a rapid initial increase with increasing fluoride concentration, the form of the curves is different in each case (Fig. 2). At high fluoride concentrations (greater than 15×10^{-3} M), the passive current density is largely independent of fluoride concentration, while the critical current density required for passivation is found to continuously increase. A more active corrosion potential is also produced when NaF was added (greater than 1.2×10^{-3} M) (Table I) and the potential at which passivation is initiated (primary passivation potential) is also shifted to more active potentials. However, the primary passivation potential remains constant (-0.575V) between fluoride concentrations of 2.5×10^{-3} and $36 \times 10^{-3}\text{M}$.

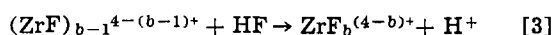
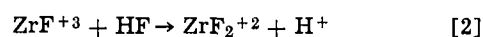
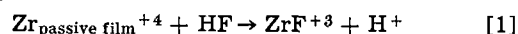
At this point it is interesting to compare the effects of fluoride ion with respect to chloride ion on titanium. Thomas and Nobe (2) reported that active titanium corrosion in H_2SO_4 was largely unaffected by additions of NaCl (up to 5.8%). A small decrease in the critical current required for passivation was recorded along with a decrease in the passive current density. Chloride ion therefore acts as a mild inhibitor in the passive

corrosion of titanium, but fluoride at much smaller concentrations is a very strong activator of both active and passive corrosion. Fluoride additions are extremely effective in preventing passivation by increasing the critical current and also the anodic current in the passive state and, therefore, reducing the effectiveness of the protective titanium oxide film.

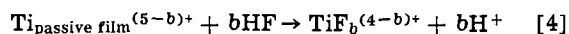
Effect of temperature.—Figure 3 shows the polarization behavior of titanium in 1N H_2SO_4 at different temperatures and fluoride concentrations. The active corrosion region for titanium is lengthened when the temperature is increased. Although current fluctuations around the corrosion potential and the narrowness of the active region before the onset of passivity prevented any accurate determination, the corrosion current was estimated to increase with temperature. Passivity was more difficult to attain as evidenced by the increased critical current density, but increased passive current density (at 0.6V vs. SCE) indicates that the passive state was less protective at higher temperatures. The potential at which passivation was initiated was found to be similar in all cases (-0.550V).

Discussion

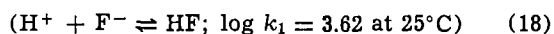
Fluoride ion provides a strong activating effect on the corrosion of titanium in both active and passive states. However, corrosion in the active state is more greatly accelerated by fluoride ion which results in the increased critical current densities and therefore increased charge requirements in order to reach the passive state. Taken together with the observation of a more active and time-dependent corrosion potential, this seems to indicate an adsorption process as part of the corrosion mechanism. However, the high hydration energy associated with the fluoride ion (11), as well as previous experimental work of fluoride adsorption on zirconium (12), seems to preclude any explanation requiring specific adsorption during anodic polarization. If the onset of passivity is delayed by the dissolution of existing film or consumption of the precursors for film formation, then a larger critical current density would be required. Previous mechanisms for zirconium dissolution in fluoride solutions proposed by Meyer (13, 14) and more recently by Rettig *et al.* (15) suggest that the passive film is dissolved by HF which diffuses to the electrode surface in the following reactions (14) involving fluoride complex ions



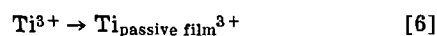
where $b = 2.5$ to 4.0 . A general equation can be formulated for titanium corrosion in the passive state



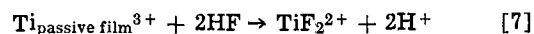
where $b = 1$ to 3 with HF being formed in solution



Further reactions are then possible with the fluoride complex ion according to the reaction scheme (Eq. [2] and [3]) proposed by Meyer (13, 14). Anodic dissolution studies on titanium in sulfuric acid (1) have indicated that titanium is oxidized to Ti^{3+} . If the same reaction can occur in the presence of fluoride then the passive film forming reactions



will occur in competition with the film dissolution reaction



During anodic polarization in the passive region, the film dissolution reaction becomes rate controlling and the increased local concentration of hydrogen ion pro-

Table I. Effect of fluoride ion on the anodic behavior of titanium in 1N sulfuric acid

Sodium fluoride concentration (10^{-3} molar)	Active corrosion potential (V vs. SCE)	Critical current density ($\mu\text{A}/\text{cm}^2$)	Passive current density at 0.600V vs. SCE ($\mu\text{A}/\text{cm}^2$)	Primary passivation potential (V vs. SCE)
0.0	-0.680	32	1.5	-0.500
0.6	-0.705	81	1.8	-0.550
1.2	-0.705	120	2.8	-0.550
2.4	-0.790	250	3.0	-0.575
4.5	-0.800	440	7.5	-0.575
6.9	-0.810	920	18.0	-0.570
8.9	-0.800	1185	32.0	-0.575
16.8	-0.780	1345	75.6	-0.575
24.0	-0.780	1700	81.2	-0.560
36.0	-0.795	2100	80.9	-0.575
120.0	-0.825	4580	259.0	-0.600

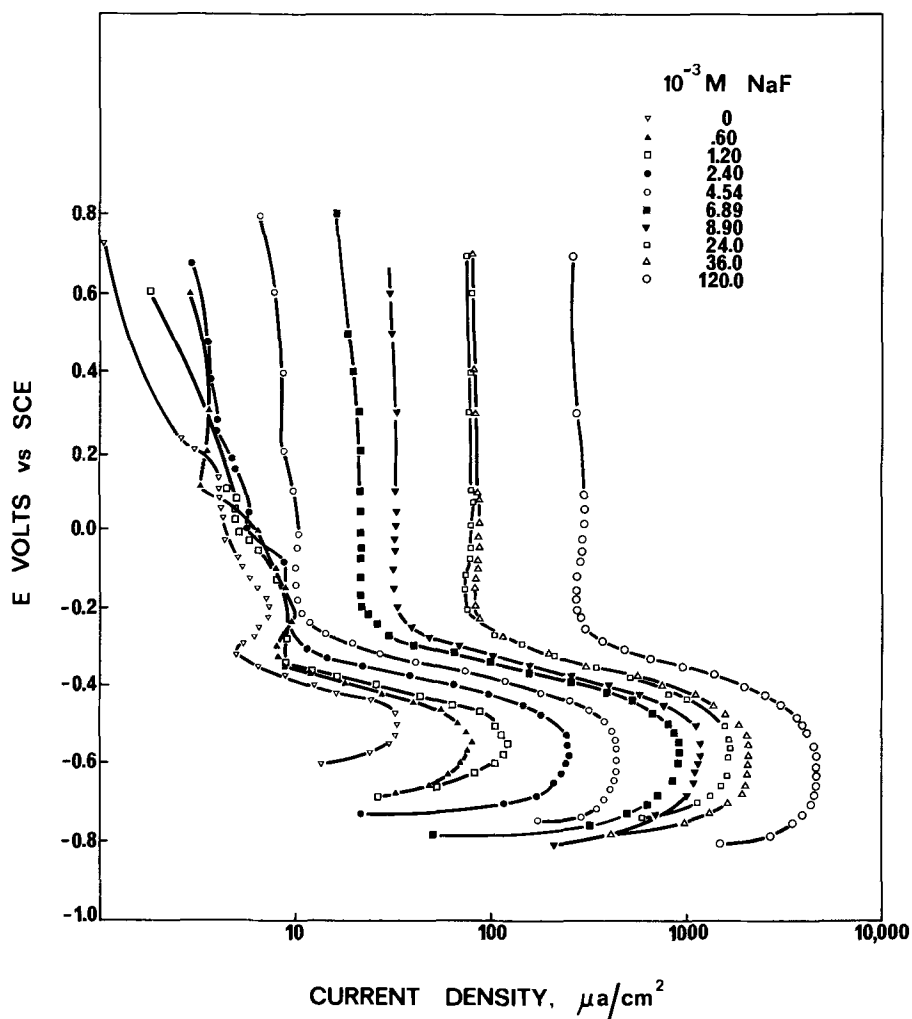


Fig. 1. Effect of fluoride ion on anodic polarization characteristics of titanium in 1N sulfuric acid.

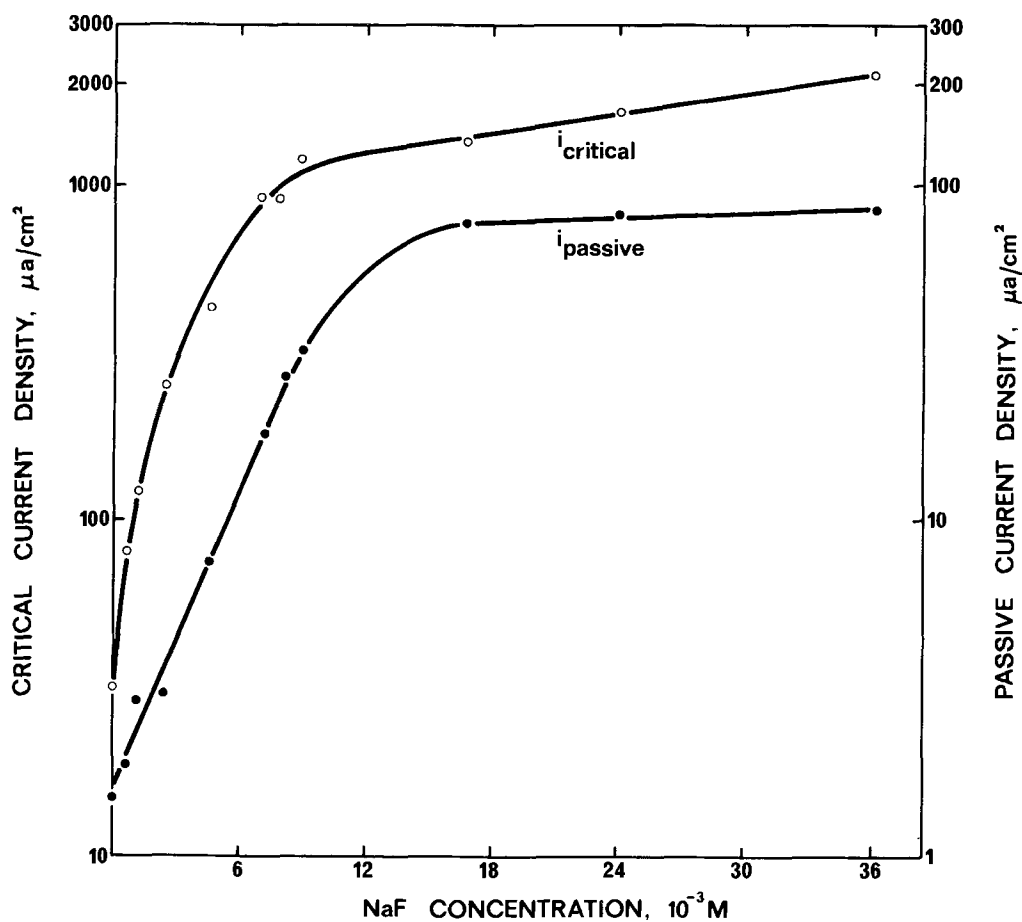


Fig. 2. Variation of critical current density and passive current density with fluoride concentration.

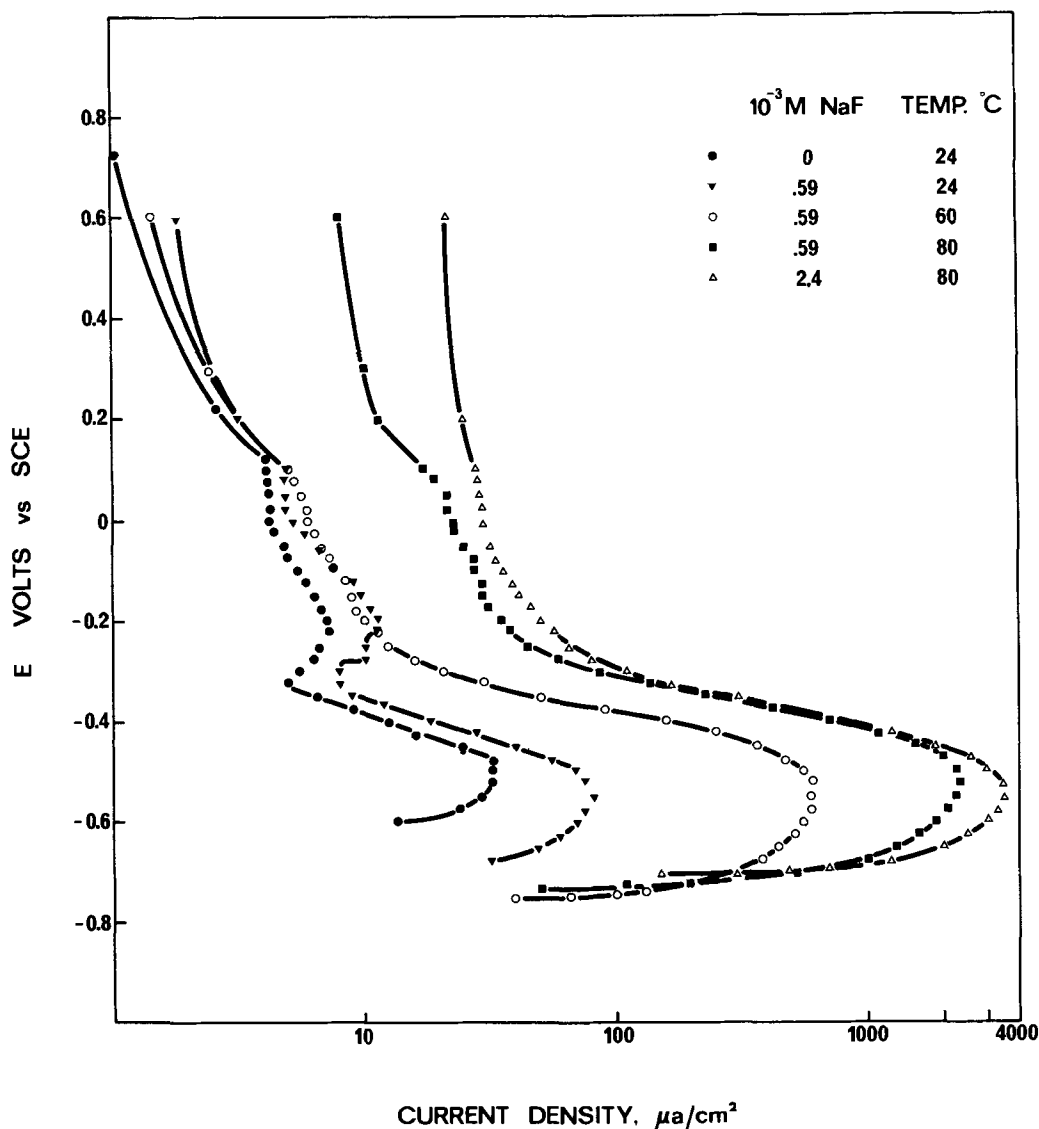


Fig. 3. The effect of temperature on the anodic polarization characteristics of titanium at different fluoride levels.

duced by the film dissolution reaction [7] results in the formation of HF near the titanium surface. The critical current density for passivation then becomes dependent on the local HF concentration. Etching on the tip of the Luggin probe situated near the surface was observed after completion of anodic polarization and confirmed the interfacial formation of HF. Meyer (14) also suggested that the order of the corrosion reaction for such a mechanism would be unity so that the rate would be given by an expression $r = k(\text{HF})$; where k is the rate constant of the reaction sequence. In our case an order slightly larger than unity was obtained for the dependence of critical current density on fluoride concentration (Fig. 4), although a fractional order (0.56) was obtained at higher fluoride concentrations. This change in reaction order indicates a different reaction mechanism from that at lower fluoride concentrations. To obtain an order of unity with respect to HF, a straightforward reaction scheme involving hydrogen ion is assumed. Above a critical concentration, reaction by way of an intermediate fluoride species, either as a surface film or complex ion situated at the surface, may occur and hence a fractional reaction order would then be possible.

In the region of active corrosion, fluoride produces a more active corrosion potential, decreases the anodic

and cathodic (hydrogen evolution) Tafel slopes, and results in an increased corrosion current (16). An important factor in the active corrosion of titanium in the presence of fluoride seems to be the increased hydrogen evolution rate brought about by the decreased Tafel slope for hydrogen. The mechanism by which fluoride alters this parameter is the subject of a future paper.

Within the passive region above the primary passivation potential, a fully consolidated oxide film exists, and the action of fluoride ion is difficult to describe without further measurements of oxide film thickness. Increased passive current density (Table I) could result from either the inhibiting action of fluoride ion on the oxide growth, incorporated within the oxide layer with a resultant weakening of the structure, or the increased dissolution of the oxide caused by HF produced within the solution. Potentiostatic pulse measurements (17) performed during the corrosion of titanium in fluoride solutions indicate the existence of a single porous oxide layer. The exact nature of this layer and changes with fluoride concentration remain undefined at present.

Manuscript submitted March 17, 1971; revised manuscript received Sept. 2, 1971.

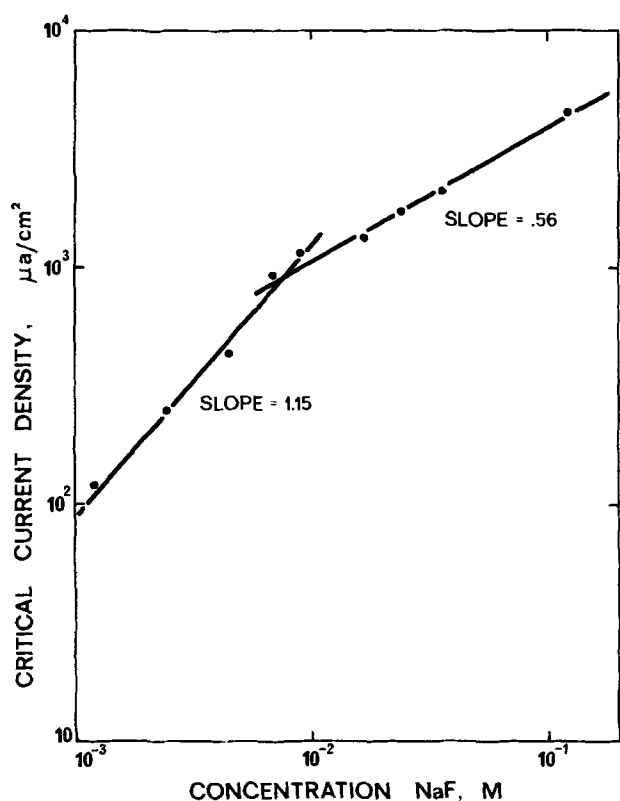


Fig. 4. Determination of the reaction order for the dissolution of titanium with respect to fluoride concentration.

Any discussion of this paper will appear in a Discussion Section to be published in the December 1972 JOURNAL.

REFERENCES

1. R. D. Armstrong, J. A. Harrison, H. R. Thirsk, and R. Whitfield, *This Journal*, **117**, 1003 (1970).
2. N. T. Thomas and K. Nobe, *ibid.*, **116**, 1748 (1969).
3. J. M. Peters and J. R. Myers, *Corrosion*, **23**, 326 (1967).
4. M. Levy, *ibid.*, **23**, 236 (1967).
5. M. Levy and G. N. Sklover, *This Journal*, **116**, 323 (1969).
6. A. Takamura, *Corrosion*, **23**, 306 (1967).
7. M. E. Straumanis and C. B. Gill, *This Journal*, **101**, 10 (1954).
8. M. Thompson, A. B. Scott, D. Chittick, and P. M. Gruzensky, *ibid.*, **106**, 737 (1959).
9. W. B. Fischer, *Werkstoffe Korrosion*, **10**, 597 (1961).
10. C. Bishop, Abs. 138, p. 339, Electrochem. Soc. Extended Abstracts, Fall Meeting, Atlantic City, Oct. 4-8, 1970.
11. J. O'M. Bockris, M. A. V. Devanathan, and K. Muller, *Proc. Roy. Soc. (London)*, **A274**, 55 (1963).
12. J. Dreyer and R. Dreyer, *Z. Phys. Chem.*, **231**, 315 (1966).
13. R. E. Meyer, *This Journal*, **111**, 147 (1964).
14. R. E. Meyer, *ibid.*, **112**, 684 (1965).
15. D. Rettig, C. Voigt, and K. Schwabe, *Corrosion Sci.*, **10**, 657 (1970).
16. G. Rosenblatt, To be published.
17. O. Radovici, S. Ciolac, and C. Vass, *Corrosion Sci.*, **7**, 209 (1967).
18. "Stability Constants of Metal-Ion Complexes," The Chemical Society, London (1964).

Effects of Alkyl Amine Surfactants on Mass Transfer Controlled Corrosion Reactions

G. Kar, I. Cornet,* and D. W. Fuerstenau

College of Engineering, University of California at Berkeley, Berkeley, California 94720

ABSTRACT

The cathodic polarization technique has been used to detect the specific role of concentration and chain length of alkyl amine surfactants on the corrosion reaction in a turbulent-flow system involving a rotating Monel cylinder-saline water interface. The mass transfer limiting current necessary for complete cathodic protection of Monel decreased with increased surfactant concentration and chain length. The phenomenon has been explained in terms of a "resistance barrier" due to the precipitate film of neutral amine molecules on the Monel surface. With the help of a simple "regression" analysis the relative significance of different variables and their interactions have been discussed.

Research on corrosion inhibition by adsorbed surface-active materials in turbulent-flow systems has been largely neglected despite the fact that corrosion and corrosion inhibition in numerous marine applications involve motion of a metal surface relative to a seawater environment. The interfacial region between the metal and the solution is the site for corrosion reaction, and the rate processes may be controlled by mass transfer of the reacting species through the interfacial film. This, in turn, is controlled by the dynamic shear conditions imposed by relative flow of metal and solution. There has been very little work reported on

the performance of corrosion inhibitors in such turbulent systems. However, there are several related areas of investigation that are significant to the study of such a system.

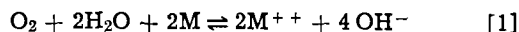
Several workers have considered the adsorption of simple organics (1-5) and long chain organic surfactants on polarized copper and nickel (6-8) surfaces and the mercury-water interface (9, 10). Hackerman (7, 8) has summarized the observed relationships between the inhibition process and surfactant molecular structure. Specific effects of organic inhibitors on the corrosion of mild steel in acid solution (11-13), and the effects of organic amine inhibitors on the corrosion of iron in acid solution (14), and in organic solvents (15) have also been reported. The analysis given in two

* Electrochemical Society Active Member.

Key words: Monel, rotating cylinder, cathodic protection, oxygen reduction, mass transfer limiting current, alkyl amines, adsorption, corrosion inhibition.

detailed reviews (7, 16) suggests that the effectiveness of organic and inorganic inhibitors for a given metal depends on the inhibitor concentration, the pH of the system, the velocity of the metal relative to the solution, time, surface preparation, surfactant chain length, temperature, cross-sectional area of the organic molecules, and the nature of the functional group on the inhibitor. Analysis of basic mass transfer-controlled reactions in turbulent systems, at the surface of rotating disks and cylinders and at static surfaces has received considerable attention (17-26). Reviews have also appeared on the suitability of several electrochemical techniques for analysis of the fundamental aspects of the adsorption of organic inhibitors on solid electrodes (27-30).

In the present investigation, the current required to protect a metal cylinder rotating in an aerated 4% NaCl (0.685M) solution has been investigated as part of the study of the effect of mass transfer on corrosion and corrosion prevention. In such a system, two major cathodic reactions can occur. At low negative potentials the reaction $O_2 + 2H_2O + 4e^- = 4OH^-$ ($E^\circ = -0.40V$) and at a slightly more negative potential the reaction $4H_2O + 4e^- = 4OH^- + 2H_{2(g)}$ ($E^\circ = -0.828V$) takes place. However, for the purpose of investigating the oxygen mass transfer to and reaction at the surface, the former cathodic reaction is usually considered as the primary one, and all experiments have been done in the potential range of this reaction. Subsequently, the corrosion of the metal can be considered to be governed by the redox reaction

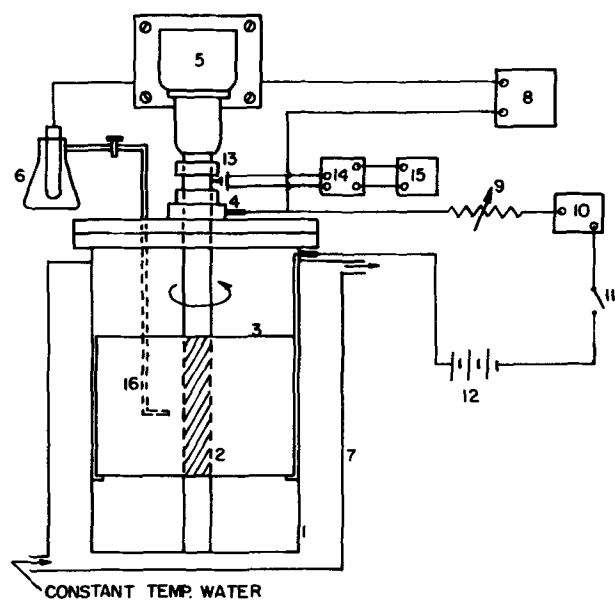


where M is a divalent metal. The metal, however, can be protected by cathodic polarization, whereby the oxygen reaching the metal surface is reduced by the external supply of electrons. The polarizing current necessary to protect the metal completely depends on the rate of convective diffusion and access of dissolved oxygen to the metal surface. This current is often termed "Mass Transfer Limiting Current" (MTLC). The MTLC can be reduced considerably by using cationic surfactants, which, when adsorbed from the solution phase onto the metal cathode, can form a barrier for oxygen diffusion.

The alkyl amine surfactants of various chain length were selected as model corrosion inhibitors in view of the key role of nitrogen centers discussed by Hackerman (7), Nakagawa *et al.* (14, 15), and of increasing chain length (8) in the action of corrosion inhibition. Furthermore, the quantitative hemimicelle model of surfactant adsorption at the solid-liquid interface developed by Fuerstenau *et al.* (31, 32), has been tested in detail for alkyl amines at negatively charged oxide surfaces. The extension to cathodically polarized metal surfaces is therefore well served by this earlier quantitative adsorption work. The results of this investigation have been summarized and discussed in terms of the mechanical and chemical variables affecting the process. An attempt has been made to understand the mechanism of corrosion inhibition and, particularly, its sensitivity to relative motion, inhibitor concentration, and surfactant chain length.

Experimental Method

In order to incorporate into polarization phenomena the effects due to mass transfer between the metal surface and the liquid, an apparatus with a vertically rotating cylindrical cathode was designed and constructed. The cylinder (19.2 cm long \times 1.91 cm diam) consisted of a 7.6 cm long test electrode made of Monel (67% Ni, 30% Cu, 1.4% Fe, 1.0% Si, 0.15% C, 0.01% S) alloy in the midsection and acrylic plastic at either end to avoid end effects. The test electrode, operated as a cathode, was rotated at the center of a concentric counterelectrode (7.6 cm long \times 14 cm diam) made of platinum strip on titanium. The cell containing the



- | | |
|------------------------------|--|
| 1. CELL | 10. MILLIAMMETER |
| 2. CATHODE (TEST ELECTRODE) | 11. SWITCH |
| 3. ANODE (PLATINUM-TITANIUM) | 12. 6V BATTERY |
| 4. MERCURY WELL CONTACT | 13. MAGNETIC PICK UP POINT FOR ELECTRODE RPM DETERMINATION |
| 5. MOTOR-VARIABLE SPEED | 14. AMPLIFIER |
| 6. REFERENCE ELECTRODE | 15. FREQUENCY COUNTER |
| 7. CONSTANT TEMPERATURE BATH | 16. CAPILLARY PROBE |
| 8. VACUUM TUBE VOLTMETER | |
| 9. VARIABLE DECADE RESISTOR | |

Fig. 1. Apparatus for polarization studies

electrolyte (4% NaCl aqueous solution) was made of Lucite and was partially open to the atmosphere at the top. The speed of the cylinder was varied using a variable-speed motor. Arrangements were made for a galvanostatic polarization study. The potential of the cathode was measured with reference to a saturated calomel reference electrode (SCE). The general layout of the experimental assembly and its electrical circuits is shown schematically in Fig. 1.

The Monel electrode was cleaned mechanically, etched with concentrated hydrochloric acid, and washed repeatedly before immersion in the 4% NaCl solution. This cleaning procedure yields a reproducible surface in that under a given set of solution conditions, the observed rest potential and limiting current are constant.

The alkyl amine surfactants were used as ammonium acetate salts. These were prepared by dissolving high-purity primary amines obtained from Armour Industrial Chemical Company in benzene and adding an equimolar quantity of glacial acetic acid. The acetate salt was recrystallized from benzene by cooling, and excess benzene was removed in a vacuum desiccator.

The oxygen content of the solution, which was analyzed for each run by the standard Winkler method, was varied by controlled exposure of air-saturated NaCl solution to helium gas for various time periods. In most experiments, the oxygen content was maintained reasonably constant by exposing the electrolyte solution to the atmosphere for a day to effect oxygen saturation. During the entire experiment, the electrolyte was left open to the atmosphere.

Considering the complexity arising out of temperature variations, which cause changes in oxygen solubility and its diffusivity, kinematic viscosity of the electrolyte, surfactant solubility, etc., all experiments were conducted at a fixed temperature of 20°C.

Results

Effect of speed of rotation.—In order to delineate the role of the mass transfer controlled process in rotating

Table I. The limiting current densities for a Monel cathode at various rotational speeds

Rotational speed (rpm)	Reynolds number	Oxygen conc., ppm	Limiting current density (A/cm^2) $\times 10^4$
60	1,130	6.40	0.77
73.5	1,390	6.45	0.99
151.2	2,860	6.32	1.42
200	3,780	5.98	1.82
380	7,180	6.40	2.96
800	15,210	5.60	4.40
900	17,010	6.40	5.26
1400	26,400	6.32	7.35
2000	37,800	6.18	8.77
2052	38,780	6.60	9.87
3330	62,940	6.06	12.06

Table II. The limiting current densities for a Monel cathode at 1400 rpm for various oxygen contents

Oxygen conc., ppm	Limiting current density (A/cm^2) $\times 10^4$
1.35	1.35
2.24	2.85
2.60	3.07
5.00	6.36
5.35	5.92
5.52	7.02
6.08	5.92
6.32	7.35

systems, the polarization behavior of Monel was determined as a function of the speed of rotation, in the absence of inhibitors in air-saturated 4% NaCl solution. From the polarization curve, the limiting current was taken as the point at which a slightly further increase in current resulted in a large increase in potential (virtually infinite slope of the polarization curve). The limiting current density values corresponding to particular rotational speed and oxygen concentrations are summarized in Table I. As the speed of rotation increases, the thickness of the diffusion boundary layer decreases, thereby increasing the oxygen concentration gradient and the limiting current density. Thus, in order to achieve protection of the metal surface, larger current density is required at higher rotational speed.

Effect of dissolved oxygen concentration.—Since oxygen is the primary species reduced at the cathode surface, its concentration in solution should control the MTLC. In order to verify this, the oxygen content

in solution was varied, keeping the speed of rotation constant at 1400 rpm, and the MTLC values were obtained from polarization measurements on the Monel cathode. These results are given in Table II.

Effect of surfactant concentration and surfactant chain length.—When alkyl amine acetates were added to the system, reduction in MTLC values were observed. A sample polarization curve for Monel in the presence of surfactant is shown in Fig. 2. This figure shows that at low concentrations of amine salt, (10^{-6} , $10^{-5}M$), the effect of surfactant on MTLC is hardly significant, while above $10^{-5}M$ there is a sharp decrease in MTLC. At concentrations exceeding $10^{-4}M$ a thin, white precipitate film appears to be coating the electrode uniformly. The film tends to grow with time. The film appears only towards the latter stages of the polarization experiment, and it dissolves into the electrolyte in a short time if the polarizing current is switched off. The electrode, which is usually hydrophilic before the start of the experiment, becomes hydrophobic after the experiment. The film is clearly a precipitate in that it is easily washable and soluble if the pH is lowered.

The effect of concentration of alkylammonium acetate on MTLC for protection of Monel was investigated at various rpm's of the electrode and various alkyl chain lengths of the surfactant. The results are presented in terms of limiting current density values that have been normalized with respect to oxygen concentration (which usually varied within $\pm 10\%$). In Fig. 3, the effect of the concentration of dodecylammonium acetate on the limiting current density is presented for several different rotational speeds of the electrode. Figure 4 presents the effect of the concentration of decyl (C_{10}), dodecyl (C_{12}), and tetradecyl (C_{14}) ammonium acetates on the limiting current density at an electrode rotational speed of 1400 rpm.

Effect of pH.—Most experiments were conducted with air-saturated 4% NaCl solution at a pH of about 5.3. Measurement of the pH of the bulk electrolyte during the experiment showed a definite upward trend of pH with the progress of the polarization experiment. When suitable buffers (sodium acetate and acetic acid for pH's below 7 and sodium borate and sodium hydroxide for pH's above 7) were used to fix the pH in both the acid and basic ranges below pH 8, there was no visible precipitate on the Monel surface, and MTLC values in each case coincided with that when no

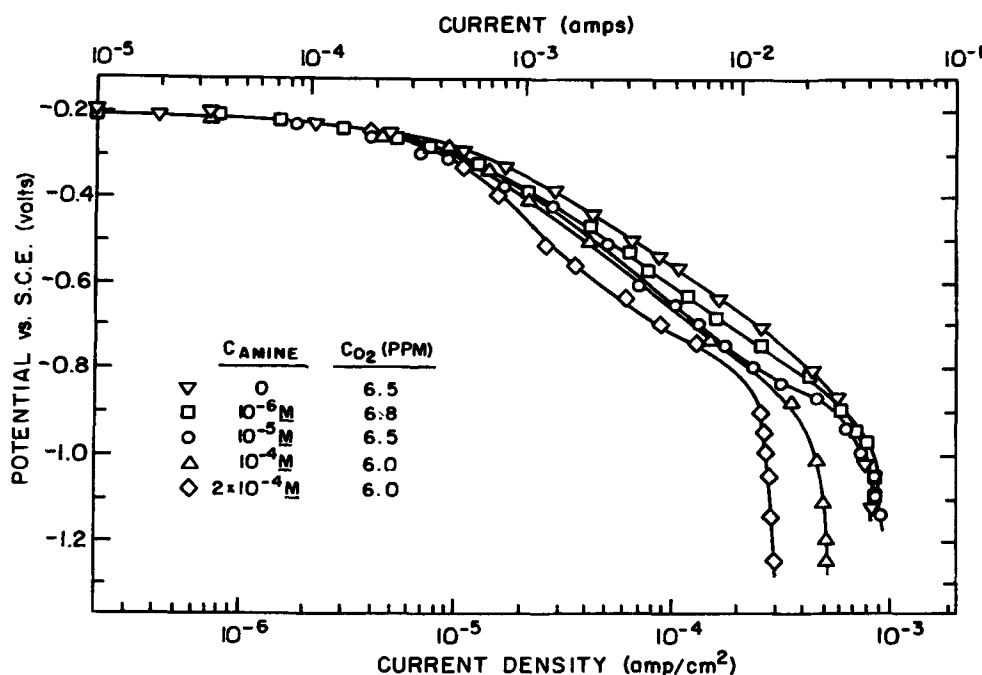


Fig. 2. A sample polarization curve for Monel in 4% NaCl (air-saturated) solution with dodecylammonium acetate at 20°C and 2000 rpm.

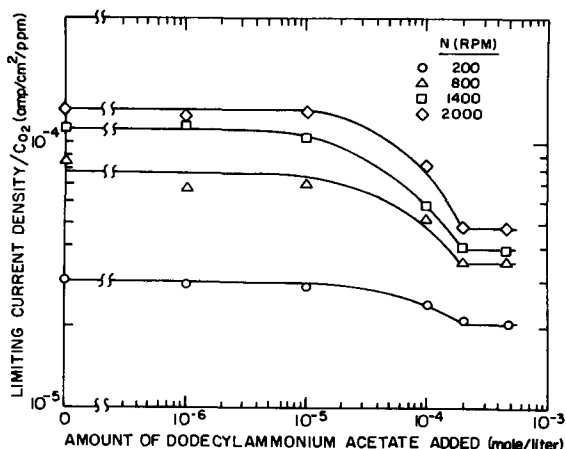


Fig. 3. Effect of the concentration of the added surfactant on the normalized limiting current density of Monel electrode in 4% NaCl (air-saturated) solution at 20°C and at different rotational speeds.

surfactant was present (Fig. 5).¹ In solutions buffered at pH 3.95, 5.15, 5.85, and 7.86, the limiting current densities were found to be 1.19×10^{-4} , 1.16×10^{-4} , 1.16×10^{-4} , and 1.23×10^{-4} A/cm²/ppm O_2 , respectively.

Discussion

MTLC in the absence of surfactants.—Since there is no general exact solution for diffusion of a species to and from a rotating cylinder in an infinite solution medium, the problem has been treated by considering different limiting cases separately. For turbulent flow cases, with a rotating cylinder, the use of dimensional analysis to correlate heat and mass transfer data has been found to be quite convenient. According to Ibl (17) and Eisenberg *et al.* (20, 21), mass transfer data for rotating cylinders can be correlated by the relationship

$$\text{Sh} = 0.079 \text{Re}^{0.7} \cdot \text{Sc}^{0.356} \quad [2]$$

where

$$\text{Sh (Sherwood number)} = \frac{i_L d}{nFD\Delta C}$$

¹Due to the swamping effect of high concentration of chloride ions in the 4% NaCl solution, the equivalent concentration of alkylammonium ions are largely governed by the chloride ion concentration. Therefore, the amount of acetate ions added for buffering would not affect the alkylammonium ion concentration very much.

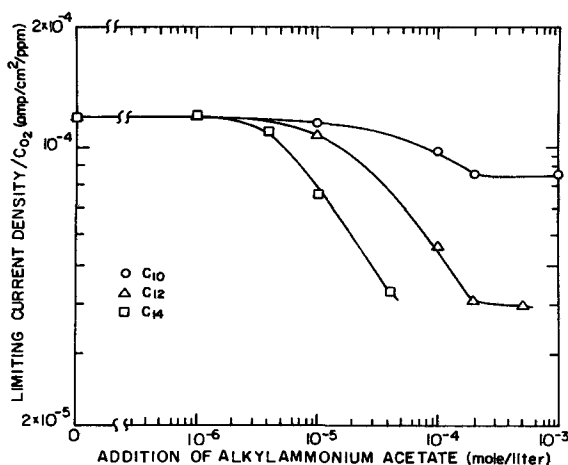


Fig. 4. Effect of the surfactant chain length on the normalized limiting current density of Monel electrode in 4% NaCl (air-saturated) solution at 20°C and 1400 rpm.

$$\text{Re (Reynolds number)} = \frac{ud}{\nu}$$

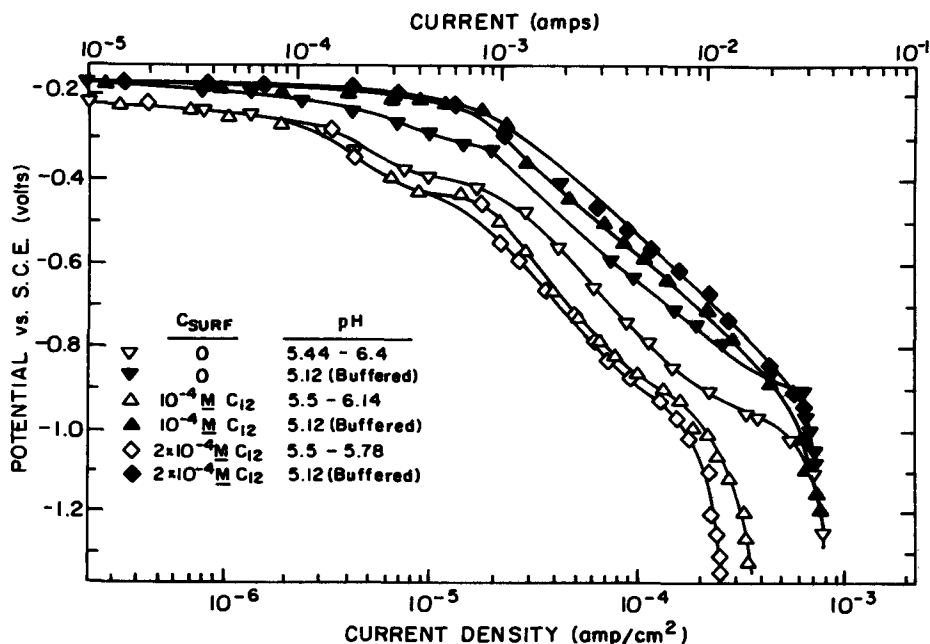
$$\text{Sc (Schmidt number)} = \frac{\nu}{D}$$

and

- i_L = mass transfer limiting current density (A·cm⁻²)
- d = characteristic length of cylinder (cm)
- n = number of electrons taking part in the reaction
- F = Faraday constant (A·sec·eqvt.⁻¹ mole⁻¹)
- D = diffusion coefficient for the diffusing species (cm²·sec⁻¹)
- ΔC = concentration gradient of the reacting species = bulk concentration, since at the MTLC, concentration of the reacting species at the metal surface is assumed to be zero (moles·cm⁻³)
- u = radial velocity of the cylinder (cm·sec⁻¹)
- ν = kinematic viscosity of the solution (cm²·sec⁻¹)

The results of our investigation in the absence of any surfactant have been analyzed in terms of the relationship given as Eq. [2] in order to confirm that oxy-

Fig. 5. The effect of buffered electrolyte on the polarization curve for Monel in 4% NaCl (air-saturated) solution with dodecylammonium acetate at 20°C and 1400 rpm.



gen reduction at the metal cathode is a typical mass transfer-limited reaction. In Eq. [2], using the experimental Sc value of 488, and reducing the other dimensionless numbers to measurable parameters, one arrives at the relationship

$$i_L = 7.41 \times 10^{-7} \cdot N^{0.7} [C_{O_2}] \quad [3]$$

where

$$N = \text{rotational speed of the electrode in rpm}$$

$$[C_{O_2}] = \text{bulk oxygen concentration at MTLC, in air-saturated 4\% NaCl solution at } 20^\circ\text{C (ppm)}$$

A linear regression analysis of the experimental data results in an equation of the form

$$i_L = 7.42 \times 10^{-7} \cdot N^{-(0.64 \pm 0.0333)} [C_{O_2}]^{(0.994 \pm 0.088)} \quad [4]$$

with t -values of 43.9 and 23.6 for N and $[C_{O_2}]$, respectively.

If a 95% confidence limit is assigned to the indices of N and $[C_{O_2}]$, Eq. [3] and [4] appear to be in excellent agreement. The results are plotted in Fig. 6 and 7. These results clearly indicate that oxygen reduction at the Monel surface, in a turbulent system, and in the absence of any surfactant, obeys the mass transfer correlation given in Eq. [2].

MTLC in the presence of surfactant.—When the surfactant is added to the electrolyte, various changes

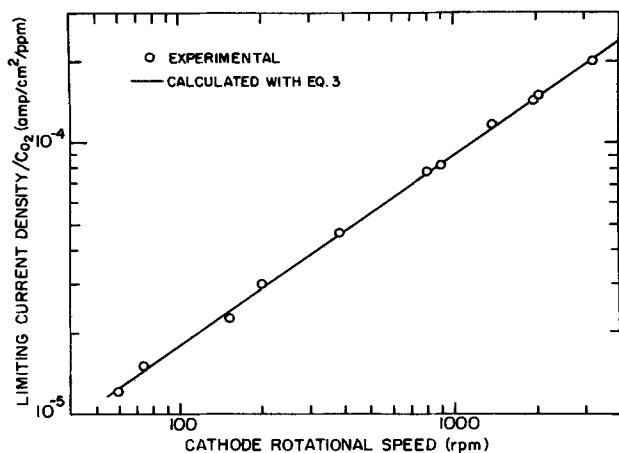


Fig. 6. Rotational speed vs. normalized limiting current density plot for Monel in 4% NaCl (air-saturated) aqueous solution at 20°C .

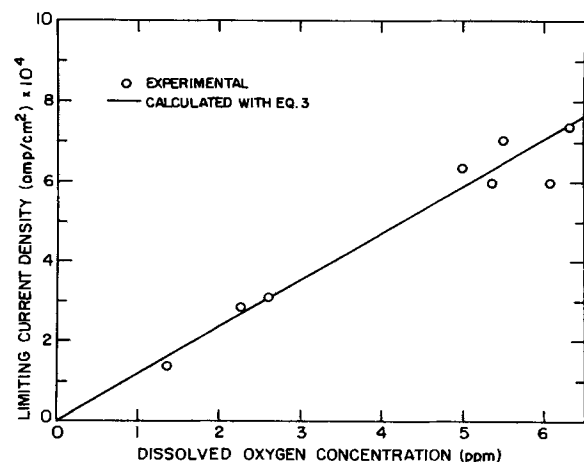


Fig. 7. Dissolved oxygen concentration vs. limiting current density plot for Monel in 4% NaCl (air-saturated) aqueous solution at 20°C and 1400 rpm.

may occur. Changes in oxygen solubility, viscosity of the electrolyte, diffusivity of oxygen molecules, etc., in addition to the adsorbed film at the electrode surface, result in over-all reduction in the MTLC. However, it may be assumed that the effect of changes in the solution properties due to the surfactant addition are minor at these low concentrations compared to the effect of the adsorbed film. The nature of the adsorbed film, on the other hand, may very well be a function of the speed of rotation, surfactant concentration and chain length, etc.

Figure 3, a plot of a logarithmic relation between the normalized limiting current density and concentration of added surfactant, has three clearly distinct regions. Up to a surfactant concentration of $1 \times 10^{-5}M$ there seems to be no effect of surfactant on the limiting current density. Between 1×10^{-5} and $2 \times 10^{-4}M$ concentration there is a rapid decrease of MTLC with increasing surfactant concentration. Above $2 \times 10^{-4}M$ concentration, there is no further reduction of MTLC. Presumably, below $1 \times 10^{-5}M$ concentration, there is very little adsorbed film to offer any resistance to the electron transfer process and thus there is no decrease in MTLC. A concentration of $2 \times 10^{-4}M$ behaves as a "critical concentration," above which there is no further reduction of MTLC. This is explained in the latter part of this section.

In the intermediate range where the surfactant addition causes significant change in MTLC, an attempt has been made with the help of a regression analysis to delineate the effects of different important variables. Based on the results shown in Fig. 3 and 4, the following functional relationship was used for the analysis

$$Y = \alpha X_1 + \beta X_2 + \gamma X_3 + \delta X_1 X_2 + \theta X_2 X_3 \quad [5]$$

where

$$Y = (i_L)_0 - (i_L)_{C_{\text{surf}}}$$

= the reduction in MTLC value due to the addition of surfactant

$(i_L)_0$ = limiting current density in the absence of the surfactant

$(i_L)_{C_{\text{surf}}}$ = limiting current density in the presence of a given concentration of the surfactant

$X_1 = \log N$

$X_2 = \log C_{\text{surf}}$ (C_{surf} = surfactant concentration)

$X_3 = \log e^m$ (m = number of carbon atoms in each chain; $14 \geq m \geq 8$)

$X_1 X_2, X_2 X_3, X_2 X_1$ are the first-order interaction terms

A test of the significance of the various terms in Eq. [5] showed that the rotational speed-surfactant interaction was not statistically significant at the 95% level. The reduced form of the regression equation written in terms of the "best fit" parameter values is as follows

$$(i_L)_{C_{\text{surf}}} = (i_L)_0 - 1.196 \times 10^{-14} N^{1.089} \cdot C_{\text{surf}}^{0.138m - 1.085} \cdot e^{1.784m} \quad [6]$$

The multiple correlation coefficient square was 0.9345, and t -values for α , β , γ , and θ were 10.3, 2.1, 4.1, and 3.2, respectively.

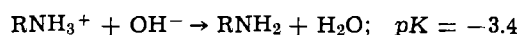
Although this is not a complete model and is limited to a small range, it is significant in the sense that it indicates the important variables which should be considered in case of any later development of a more complete model.

The pH effect on MTLC.—Thus far, the effect of rotational speed, oxygen concentration and alkylammonium acetate concentration and chain length on the MTLC of a Monel cathode has been discussed. However, another important variable such as the pH of the system should be considered here. As indicated

earlier, the pH of the bulk electrolyte continuously increases with the progress of the polarization experiment. A possible explanation for this is given in the following paragraphs.

The rotating cathode has a much thinner diffusion layer around it compared to that of the stationary anode. Although during the passage of the current, OH⁻ ions produced at the cathode and H⁺ ions produced at the anode are of equal quantity, the local amount of OH⁻ ions per unit volume is much greater than that of H⁺ ions because of a much smaller cathodic area compared to the anodic one. This higher concentration per unit volume combined with a thinner diffusion layer creates a higher driving force for OH⁻ ions than for H⁺ ions diffusing into the bulk solution. Since the entire system is a nonequilibrium one, the bulk pH increases with time during the polarization experiment. When the polarization is stopped, the bulk pH tends to assume the original pH value, after sufficient time is allowed for equilibration.

The nonequilibrium pH at the cathode surface is conceivably higher than that of the bulk electrolyte at any instant during the polarization measurement. The appearance of a white precipitate film on the Monel electrode is most likely due to the precipitation of neutral amine molecules according to the reaction



which occurs when the nonequilibrium surface pH reaches a value high enough for hydrolysis to become significant. An estimation of solubility constants indicate this reaction is more likely to occur than any other precipitation reaction. Also, infrared spectra of the dried precipitate confirmed that the film material is the amine and not an aminium salt. The bulk pH never attains a high enough value for hydrolysis, so the bulk solution remains clear. The reason that the precipitate film disappears shortly after the polarization current is switched off is that there is no further OH⁻ ion production at the surface and the bulk and surface attain an equilibrium pH value.

The above explanation can be justified by supplementing it with the evidence obtained from experiments with addition of a suitable buffer to the system. Figure 5 shows the effect of buffering. The buffering action extends up to the electrode surface and hence there is no local high pH with neutral amine molecule precipitation on the cathode. Therefore, no decrease in the MTLC values is observed, even in the presence of high surfactant concentration. Tests with trimethyldodecyl ammonium chloride which does not hydrolyze or precipitate at high pH showed no effect on the MTLC.

These results clearly indicate that the effect of alkyl amine surfactants on the reduction of MTLC is mainly due to a precipitate film of neutral amine molecules on the metal surface. The film, which may be formed by direct interaction with the metal surface and by association of these neutral molecules by van der Waals's forces, acts as a "resistance barrier" in addition to the diffusion layer resistance and affects the electron transfer process at the interface. The observation that the metal surface becomes hydrophobic in the presence of the surfactant indicates strong adsorption of alkylammonium ions on the metal surface. However, this initial adsorption alone does not reduce the MTLC. It is the subsequent formation of the precipitate film which affects this mass transfer controlled process.

As seen in Fig. 3 and 4, for all rotational speeds and chain lengths considered, $2 \times 10^{-4}M$ alkylammonium acetate concentration appears to be a critical value above which there is no further increase in the film thickness and reduction of the MTLC. This may result from the films being sufficiently thick when a concentration of $2 \times 10^{-4}M$ is reached so that the O₂ reduction is reduced sufficiently and the pH is insufficient

to cause any further hydrolysis. Except for the C₁₀ chain length case, no experiment could be done above $5 \times 10^{-4}M$ concentration because the surfactant solubility was limited in such concentrated NaCl solution.

Summary

The current requirements for the cathodic protection of a metal-saline water interface in a turbulent-flow system can be considerably reduced by using alkyl amine surfactants. The formation of a film of neutral amine molecules at the metal surface where the local nonequilibrium pH is quite high, causes a barrier to the oxygen diffusing to the metal surface. The current requirement is found to be sensitive to the relative velocity of the metal-electrolyte interface, surfactant concentration and chain length, and pH of the system. Considering the complex nature of the system, no rigorous physical model can be given at this stage to account for the variation of the film resistance with different variables. However, this study can eventually be applied to the problem of corrosion control by the use of cathodic protection and corrosion inhibitors in a variety of conditions in the marine environment.

Acknowledgments

The authors wish to acknowledge with appreciation the support of the Office of Naval Research, Contract No. N00014-69-A0200-1041. Extensive discussions with Dr. T. W. Healy are also acknowledged. Dr. R. R. Kappesser assisted in setting up some of the initial techniques used in this investigation.

Manuscript submitted May 28, 1971; revised manuscript received ca. Sept. 5, 1971.

Any discussion of this paper will appear in a Discussion Section to be published in the December 1972 JOURNAL.

REFERENCES

1. J. O'M. Bockris, M. Green, and D. A. J. Swinkels, *This Journal*, **111**, 743 (1964).
2. N. D. Tomashov, "Theory of Corrosion and Protection of Metals," The Macmillan Co., New York (1966).
3. G. Butler and H. C. K. Ison, "Corrosion and its Prevention in Waters," Reinhold Publishing Company, New York (1966).
4. P. F. Cox, L. Every, and O. L. Riggs, *Corrosion*, **20**, 299t (1964).
5. V. P. Grigorev and V. V. Ekilik, *J. Appl. Chem. USSR*, **41**, (12), 2542 (1968).
6. J. O'M. Bockris and D. A. J. Swinkels, *This Journal*, **111**, 736 (1964).
7. N. Hackerman, *Corrosion*, **18**, 332t (1962).
8. N. Hackerman and R. M. Hurd, 1st Int'l. Conference on Metallic Corrosion, London (1961), Butterworths, London (1962).
9. R. J. Meakins, *J. Appl. Chem.*, **15**, 416 (1965), *ibid.*, **17**, 157 (1967).
10. R. J. Meakins, M. G. Stevens, and R. J. Hunter, *J. Phys. Chem.*, **73**, 112 (1969).
11. G. Okamoto, M. Nagayama, J. Kato, and T. Baba, *Corrosion Sci.*, **2**, 21 (1962).
12. R. J. Meakins, *J. Appl. Chem.*, **13**, 339 (1963).
13. G. B. Hatch, *Corrosion*, **21**, 179 (1965).
14. N. Satoru and H. Genzo, *Denki Kagaku*, **36**(8) (1968).
15. N. Satoru and H. Genzo, *ibid.*, **36**(8) (1968).
16. L. L. Shreir, *Corrosion*, **2**, George Newness Ltd., London (1963).
17. N. Ibl, *Electrochim. Acta*, **1**, 117 (1959).
18. A. J. Arvia, J. S. W. Carrozza, and S. L. Marchianos, *ibid.*, **9**, 1483 (1964).
19. A. J. Arvia and J. S. W. Carrozza, *ibid.*, **7**, 65 (1962).
20. M. Eisenberg, C. W. Tobias, and C. R. Wilke, *Chem. Eng. Prog. Symp. Ser.*, **51**, 1 (1955).
21. M. Eisenberg, C. W. Tobias, and C. R. Wilke, *This Journal*, **101**, 306 (1954).
22. I. Cornet and R. Kappesser, *Trans. Inst. Chem. Engrs.*, **47**, T194 (1969).
23. I. Cornet, W. N. Lewis, and R. Kappesser, *Trans. Inst. Chem. Engrs.*, **47**, T222 (1969).
24. I. Cornet and V. Kaloo, Int Congr. Metal. Corros., 3rd, Moscow 1966 (1968).

25. T. K. Sherwood and J. M. Ryan, *Chem. Eng. Sci.*, **11**, 81 (1959).
 26. R. S. Rickard and M. C. Fuerstenau, *Trans. AIME*, **242** 1487 (1968).
 27. K. J. Vetter, "Electrochemical Kinetics, Theoretical and Experimental Aspects," Academic Press, New York (1967).
 28. E. Gileadi, *J. Electroanal. Chem.*, **11**, 137 (1966).
 29. B. B. Damaskin, "The Principles of Current Methods for the Study of Electrochemical Reactions," McGraw-Hill Book Co., New York (1967).
 30. A. C. Makrides, *Corrosion*, **18**, 338t (1962).
 31. P. Somasundaran and D. W. Fuerstenau, *J. Phys. Chem.*, **70**, 90 (1966).
 32. P. Somasundaran, T. W. Healy, and D. W. Fuerstenau, *ibid.*, **68**, 3652 (1964).

Passivation of Chromium-Containing Iron and Nickel-Base Alloys in Aqueous Solutions at 289°C

David A. Vermilyea* and Maurice E. Indig

Corporate Research and Development, General Electric Company, Schenectady, New York 12301

ABSTRACT

A system which allows electrochemical studies to be conducted in relatively uncontaminated aqueous solutions at 289°C, using a reference electrode which permits potentials to be referred to the standard hydrogen electrode scale, is described. Current-potential curves for Type 304 stainless steel, Inconel 600, and other iron and nickel-base alloys containing less than 14% Cr are presented. It is found that passivation in dilute H₂SO₄ is more difficult at 289°C than at 25°C because of the faster attack by the acid at the high temperature.

The advent of nuclear power has resulted in the use of some familiar materials in new environments and, as might be expected, a host of new corrosion problems have been encountered. In order to be able to understand corrosion processes in aqueous solutions at about 300°C it is necessary to have information about the electrochemical phenomena involved. During the last several years a few electrochemical studies under these conditions have been published (1-8). All of these previous studies have been difficult to interpret either because the electrical potential scale was not adequately defined or because the use of static autoclaves resulted in gradual contamination of the solutions with corrosion products.

In this paper we report studies conducted using an internal Ag/AgCl reference electrode, which permits potentials on the standard hydrogen electrode (SHE) scale to be determined. We have also used a refreshed autoclave system for part of our measurements to avoid contamination.

Experimental

The reference electrode used for studies in static autoclaves has already been described (9). That electrode is not suitable for a refreshed autoclave which is always completely full, and so the reference electrode shown in Fig. 1 was designed. The electrode itself is a silver wire onto one end of which a bead of AgCl is melted. The 0.035 in. diam wire passes through a standard high pressure electrical fitting (Conax Company) with a modified insulator. The insulator is made of Rulon for resistance to deformation at the operating temperature, has a hole drilled through it to permit passage of the silver wire, and is threaded at its outer end to accept a retaining nut in which a set screw clamps the silver wire. The retaining nut is required to prevent extrusion of the silver wire by the high internal pressure.

The electrode is insulated from the autoclave solution by means of a Teflon tube which is heat-shrunk onto the electrode. The Teflon tube also forms the salt bridge connecting the electrode to the autoclave solution, and contains an asbestos wick to assure a continuous electrical path. For assembly the Teflon tube containing the asbestos is shrunk onto the silver wire,

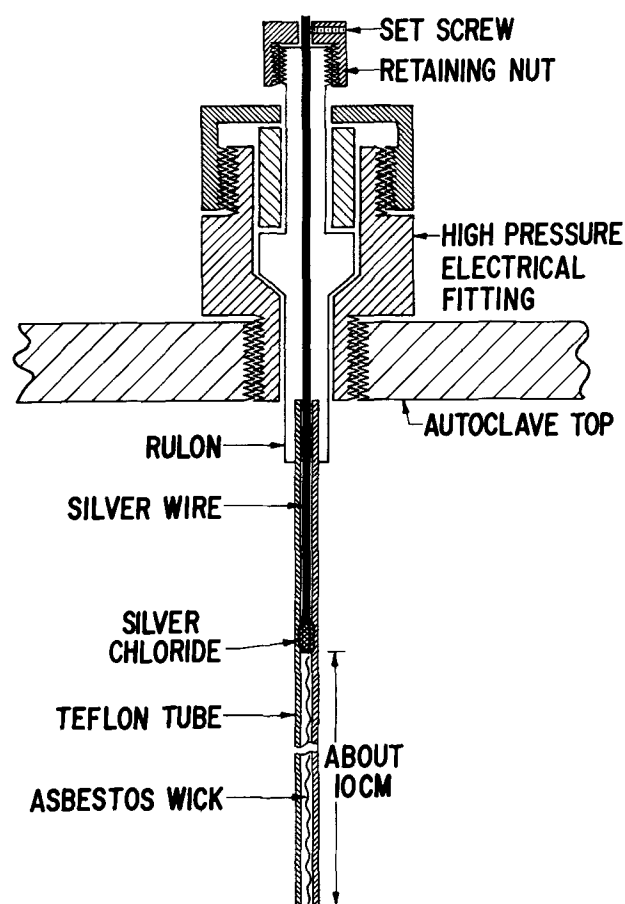


Fig. 1. Ag/AgCl reference electrode for use in refreshed autoclave system.

which is then inserted into the Rulon fitting so that the end of the Teflon tube is about ½ in. inside the Rulon. The salt bridge is filled with 10⁻²M KCl after evacuation of the air. The salt bridge is long enough (10 cm) so that about 10 days would be required for diffusion to alter the KCl concentration in the vicinity of the

* Electrochemical Society Active Member.

Key words: corrosion, polarization, electrochemical studies.

Ag/AgCl electrode. Contamination of the autoclave solution by the outward diffusion of chloride ions is small because of the small volume of the salt bridge and because of the continual refreshment of the autoclave solution.

We have found that electrodes of this design perform well, provided a pressure of about 200 psi above the vapor pressure of water is maintained on the system. At lower pressures the electrode tends to open circuit, probably because of bubble formation in the salt bridge. We have also found that the potentials developed by this electrode are less reliable than the potential maintained by the electrode used in the static system, and have observed deviations as large as 0.1V from electrode to electrode. We do not know the reason for these variations. Finally, these electrodes are entirely unsuitable for use in solutions containing hydrogen gas, which readily diffuses through the Teflon and reduces the silver chloride.

Specimen electrodes were mostly 0.030 in. wires, and were introduced via Conax fittings in the manner described for the reference electrode. The wires were usually electropolished using standard techniques, and no effort was made to remove the electropolishing residue. We have found that the friction between the wire and the Rulon is very low at 289°C, and that the retaining nut is essential to prevent extrusion of the electrode. The electropolishing residue may have an initial inhibitive action but is probably soon removed or altered by the corrosion process. Such a residue does represent an uncertainty in our experimental data.

Figure 2 shows a schematic diagram of the refreshed autoclave system used in these studies. Ion exchange columns are used to purify the make-up water, which is taken from the laboratory distilled water system. After purification the resistivity of the water is about 5×10^6 ohm-cm. The desired solution composition with

respect to acids, salts, and gases is produced in the holding tanks, from which the solution is pumped through a high pressure ion exchange column, to a regenerative heat exchanger and finally to the autoclave. After passing through the autoclave the solution is cooled, again ion exchanged to remove corrosion products in the effluent and depressurized prior to its return to the holding tank or discard. Pumping rates can be as high as 200 cc/min; we normally used 40 cc/min, giving a refreshment time of about 18 min for the 1 liter autoclaves. Autoclaves made from both 316 stainless steel and titanium alloy 6Al-4V were used.

We reported previously (9) that the open-circuit potentials of various electrodes such as stainless steel and Inconel 600 in solutions from pH 3 to pH 10 were close to that for a platinum electrode if the solution contained hydrogen or oxygen. We believe this behavior occurs because of the low corrosion rates of the electrodes and because hydrogen and oxygen react rapidly at 289°C; the electrodes behave as hydrogen or oxygen electrodes. In order to avoid such effects we used an argon atmosphere in all the tests to be reported here.

Potentiostatic polarization curves were obtained using standard equipment and techniques in the static and refreshed systems. The autoclave itself was grounded and used as the counterelectrode; and the potentiostat was connected to the a-c line through an isolation transformer. The resistances between the working electrodes and the autoclave were measured with an a-c bridge, and IR corrections (typically some tens of millivolts at 10^{-3} A/cm²) were made to the potentials. Since the resistance at a small cylindrical electrode is largely confined to the region very close to the electrode the errors involved in this procedure were small at the moderate current densities used.

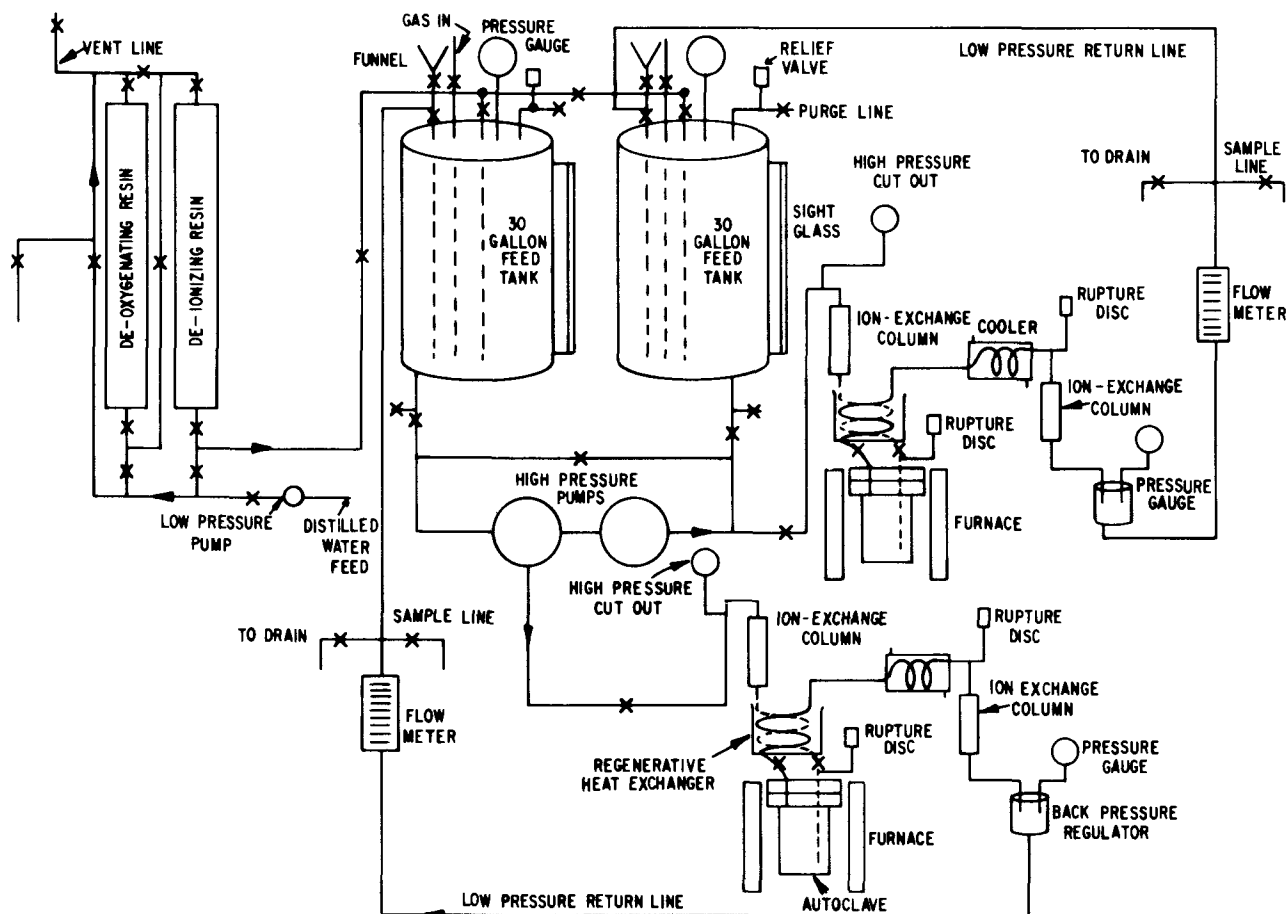


Fig. 2. The refreshed autoclave system

Results

Stainless steel.—A major problem with these passivation studies has been contamination of the solutions with iron dissolved from the specimens or system. The ferrous ions produced are readily oxidized to Fe_2O_3 , forming red dendritic deposits and contributing to the observed current. In static autoclaves in solutions of pH 3 the iron concentration may easily rise to about 3×10^{-4} M/L, and contribute a current of 3×10^{-4} A/cm². Figure 3 compares typical polarization curves for Type 304 stainless steel in pH 3 H_2SO_4 solutions in the static and refreshed autoclaves. It can be seen immediately that the curves do not coincide as far as potentials are concerned, with the curve for the refreshed system about 0.15V more positive than that for the static system. This shift represents an uncertainty in the reference electrode potential which we have not been able to resolve. It may result from poor control of the chloride ion concentration in the reference electrode used in the refreshed autoclave or from differences in the hydrogen or oxygen contents of the electrolytes in the two systems. It is believed that the potentials measured with the electrode used in the static system are more reliable. On that assumption, the oxidation of Fe^{+2} starts at about -0.2V . Even in the refreshed system Fe^{+2} and other impurities are not entirely excluded, and their oxidation contributed about 15×10^{-6} A/cm² in the passive region. The iron content of the solution after test was 7×10^{-6} M/L, which could account for most of the observed current. In the static system iron oxidation almost entirely obscures the passive corrosion of the metal, and causes a current density of about 250×10^{-6} A/cm² at potentials more positive than $+0.2\text{V}$. Contamination with iron and possibly other materials has so far prevented the

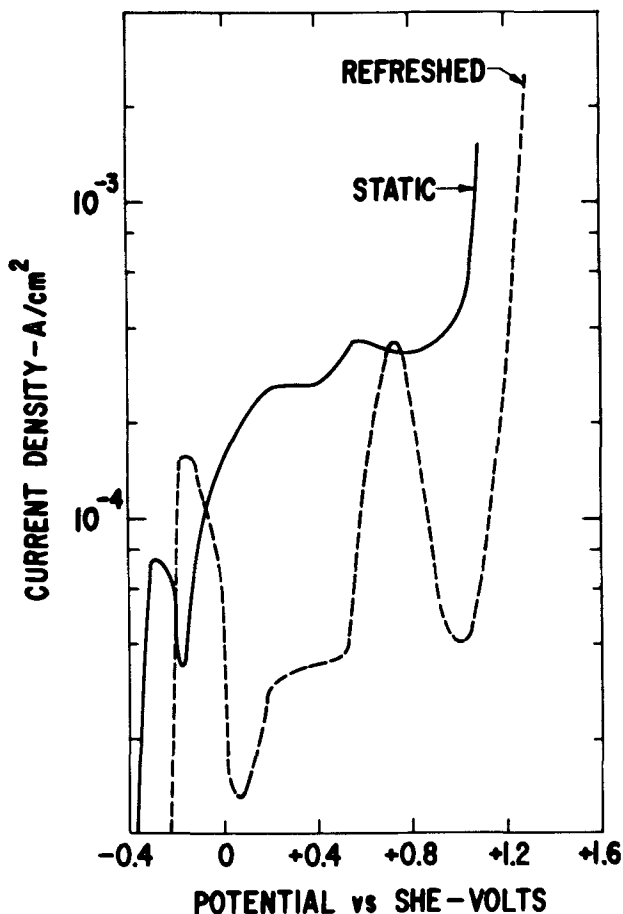


Fig. 3. Polarization curves for Type 304 stainless steel in pH 3 H_2SO_4 in static and refreshed autoclaves.

experimental determination of the true passive corrosion current in these acid solutions.

The general features of the passivation of stainless steel are readily visible in Fig. 3. At the open circuit potential stainless steel is "active;" upon polarization it becomes passive; at higher potentials the current increases presumably because of oxidation of Cr_2O_3 to chromate; secondary passivity then occurs; and finally oxygen evolution begins. Note that the current in the region of secondary passivity falls to about the same level as in the passive region, the current being determined by oxidation of Fe^{+2} and not by corrosion of the metal, which proceeds at a much slower pace.

In the "active" condition the metal is not "clean" but is covered with a corrosion product which reaches interference color thickness after hour-long exposures at pH 3-4 and grows to a thickness of about a few microns after a day. We suspect that this film is porous.

When a specimen is polarized into the passive region in dilute acid solutions an extremely thin, light tan film is formed in a day; it is probably less than 500Å thick. In a typical set of experiments a specimen polarized 54 hr in the passive region in an electrolyte containing pH 4 H_2SO_4 lost 1.64×10^{-4} g/cm² while a freely corroding specimen lost 2.34×10^{-3} g/cm²; passivation effected a great decrease in the corrosion rate.

The effect of pH on the polarization of stainless steel is shown in Fig. 4. As the pH increases the peak active current decreases, and at neutral (not shown) pH the material is observed to be passive at open circuit. Also as the pH increases the potential at which oxidation of Fe^{+2} starts decreases by 0.330 V/pH unit, while the potential at which Cr_2O_3 oxidation begins decreases by 0.183 V/pH unit. In neutral solutions, in which not much Fe^{+2} is soluble, the current in the passive region is quite low and decreases steadily with time as the passive film grows. In an experiment during which the specimen was polarized into the transpassive region the current fell in one day to about 9×10^{-6} A/cm², and the specimen remained bright. In other experiments in neutral water currents of about 10^{-6} A/cm² have been observed after polarization in the passive region for an hour or so. Probably spurious electrochemical effects contributed importantly to these currents.

Stainless steels depleted of chromium.—Special alloys containing Fe-10Ni-xCr where $x \approx 8, 10, 12.5,$ and 14% were vacuum arc melted and drawn to 0.030 in.

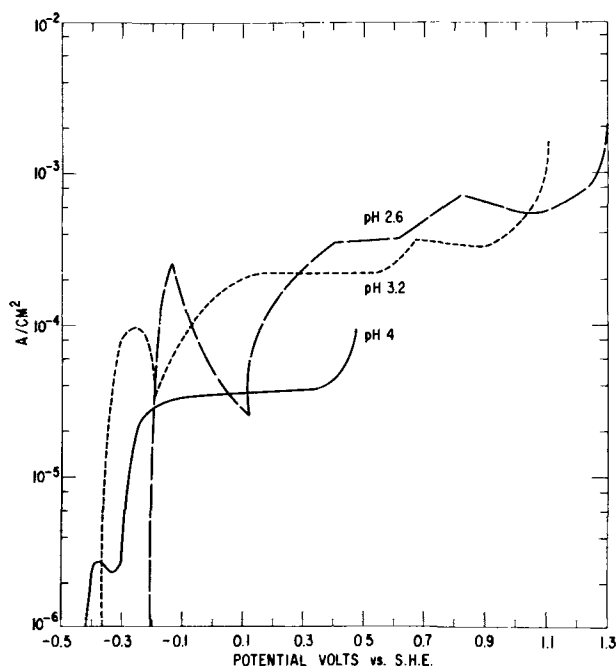


Fig. 4. The effect of pH on the polarization of Type 304 stainless steel in static autoclaves.

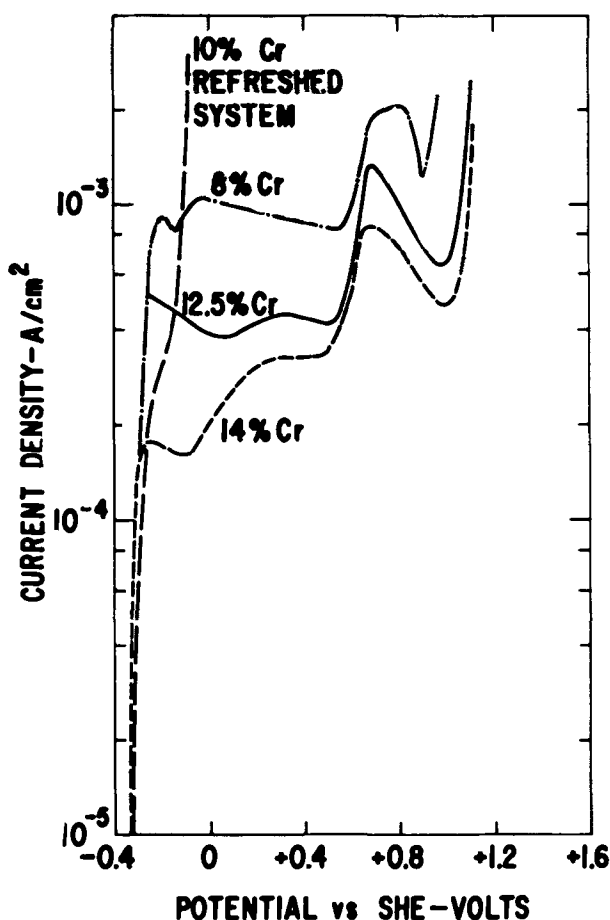


Fig. 5. Polarization curves for Fe-10Ni-xCr alloys in pH 3 H_2SO_4 in static (8%, 12.5%, and 14% Cr) and refreshed (10% Cr) autoclaves.

wires. These wires were annealed in hydrogen to produce a reasonably good surface and to remove cold work. Figure 5 shows several typical curves taken from runs made at pH 3 in static and refreshed autoclaves while Fig. 6 shows data obtained at pH 4 in a refreshed autoclave. A comparison of data for the 14% Cr alloy in Fig. 5 and 6 again demonstrates the effect of contamination with Fe^{+2} in the static autoclave. The data for the 8, 12.5, and 14% Cr alloys show that as the chromium content is reduced passivation becomes more difficult; the passive current for the 8% alloy is of the order of 10^{-3} A/cm² compared to about 10^{-5} A/cm² or less for Type 304 stainless steel. Surface condition and/or cold work was very important with these alloys; rough surfaces and heavy cold work greatly inhibited passivation.

The fact that the 10% Cr alloy did not passivate in the refreshed autoclave is an indication of another problem with static autoclaves, namely, that the pH increases with time as the protons are reduced in corrosion reactions. The actual pH in the static autoclaves for the experiments shown in Fig. 5 was greater than 3, and passivation was easier.

Inconel 600 and related alloys.—With one important exception Inconel 600 behaves in a manner very similar to that of 304 stainless steel. At low pH it is active at open circuit; it passivates readily upon polarization; and the current increases rapidly at about the potential at which Cr_2O_3 oxidation occurs. As shown in Fig. 7, however, the Inconel does not exhibit secondary passivity but instead corrodes at increasing rates at increasing potentials. Evidently the removal of chromium from the surface of the alloy results in a material which is not readily passivated.

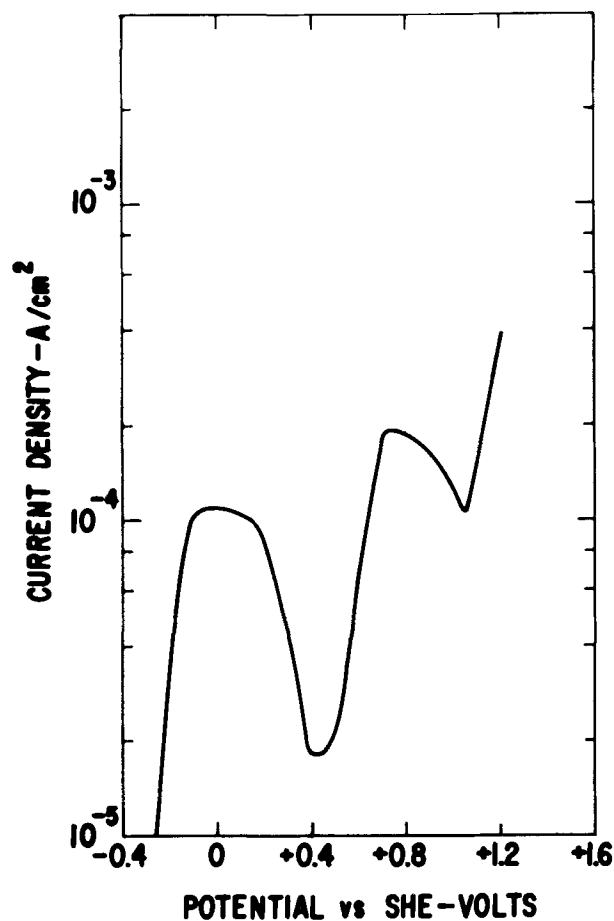


Fig. 6. Polarization curve for a Fe-10Ni-14Cr alloy in a refreshed autoclave.

Alloys containing Ni-8Fe-xCr, where $x = 5$ and 10 behave like depleted stainless steels, as shown in Fig. 8. The 5% alloy could not be passivated, while the 10% alloy could be polarized to high potentials but corroded at a high rate. The peculiar irregularities in the current potential curves for the 10% alloy have not yet been interpreted.

Discussion

It is interesting to contrast the behavior of the iron and nickel base alloys at 289°C and at 25°C. The curves for 304 and Inconel 600 in dilute acids at 289°C are similar to those obtained using 1N H_2SO_4 at 25°C, except that Inconel 600 does not show secondary passivity at 289°C. Evidently the attack by H_2SO_4 on the passive film is greatly accelerated at the high temperature so that dilute solutions cause high active currents and prevent secondary passivity of Inconel 600. The aggressive behavior of dilute sulfuric acid at 289°C is also shown by the fact that it is not possible to passivate nickel (or iron, for that matter) in such solutions.

A further interesting contrast is the observation of thick films on "active" materials at 289°C and the apparent absence of such films at 25°C. It is commonly thought that active metals are film-free; these experiments show that such is not always the case.

Acknowledgment

We are indebted for helpful advice and discussions to Mr. W. Nelson of General Electric's Atomic Power Equipment Department and to Dr. R. L. Cowan of the General Electric Nucleonics Laboratory.

Manuscript submitted June 7, 1971; revised manuscript received Sept. 9, 1971.

Any discussion of this paper will appear in a Discussion Section to be published in the December 1972 JOURNAL.

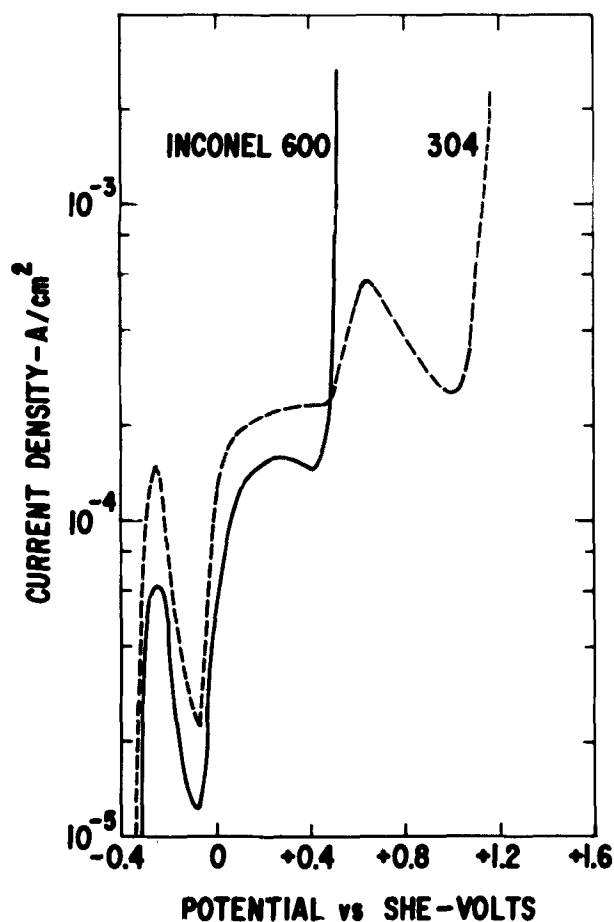


Fig. 7. Polarization curves for Type 304 stainless steel and Inconel 600 in pH 3 H_2SO_4 in refreshed autoclaves.

REFERENCES

1. A. L. Bacarella, *This Journal*, **108**, 331 (1961).
2. A. L. Bacarella and A. L. Sutton, *ibid.*, **112**, 546 (1965).
3. B. E. Wilde, *Corrosion*, **23**, 331 (1967).
4. A. H. Taylor and F. H. Cocks, *Brit. Corrosion J.*, **4**, 287 (1969).
5. J. Postlethwaite and R. A. Brierby, *Corrosion Sci.*, **10**, 885 (1970).
6. R. L. Cowan and R. W. Staehle, *This Journal*, **118**, 557 (1971).
7. T. Fujii, T. Kobayashi, and G. Ito, *Nippon Kinzoku Gakkaishi*, **35**, 41 (1971).

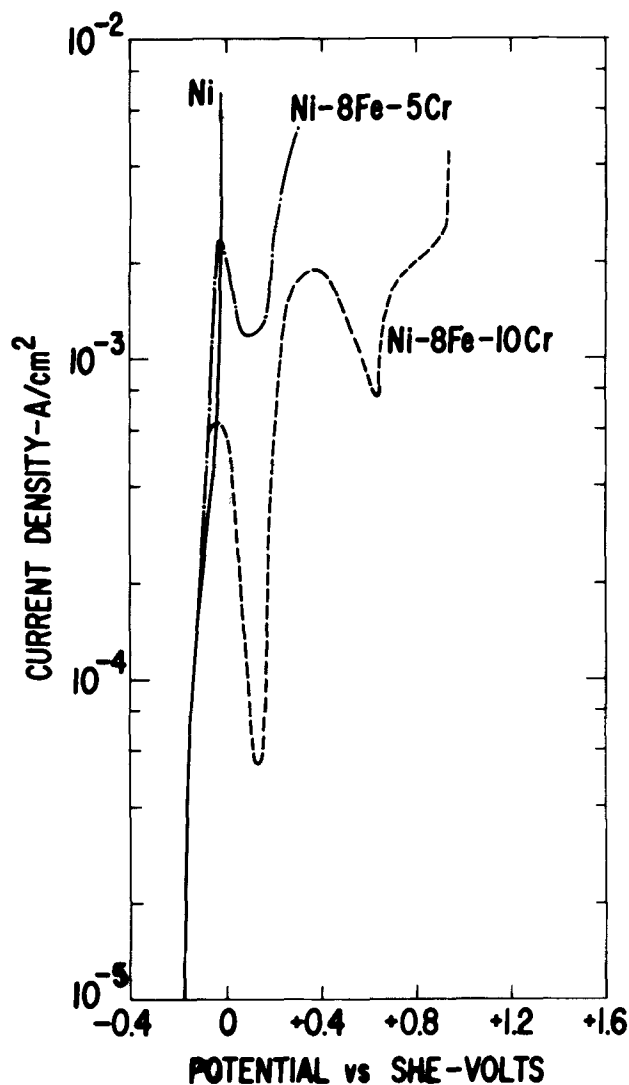


Fig. 8. Polarization curves for nickel and Ni-8Fe-xCr alloys in pH 3 H_2SO_4 in refreshed autoclaves.

8. T. Fujii, T. Kobayashi, and G. Ito, *ibid.*, **35**, 47 (1971).
9. M. Indig and D. A. Vermilyea, *Corrosion*, **27**, 312 (1971).

An Experimental Setup for Electroplating of Moving Wire

Aladar Tvarusko*

Engineering Research Center, Western Electric Company, Princeton, New Jersey 08540

ABSTRACT

A small experimental electroplating line was built to study under controlled laboratory conditions the metal electrodeposition process on wire moving up to 35 m/sec (7000 fpm). This paper describes in detail the wire electroplating line, the process instrumentation, and the computer/electroplating line interface, and briefly, the on-line digital data acquisition system. The electrodeposition of various metals can be studied potentiostatically or galvanostatically in steady-state or transient mode or potentiodynamically. The efficacy of the setup is illustrated by results on copper electrodeposition.

The electrodeposition of various metals has been extensively studied on stationary or rotating electrodes

* Electrochemical Society Active Member.

Key words: experimental electroplating line, moving wire, electrochemical instrumentation, digital data acquisition system, electrodeposition of copper.

but to much less extent on continuous substrates moving at high speeds.

The electroplating of rapidly moving steel sheets is widely used for the production of tinplate and has been the subject of numerous investigations (1). The elec-



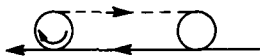
Fig. 1. View of the electroplating line

trodeposition of metals, especially magnetic alloys, on wire moving at slow speeds (up to 0.02 m/sec) has been studied because of its importance in the production of plated-wire memories (2). Electroplating of wire, especially electroplating of copper wire moving at high speed (up to 20 m/sec) is done commercially on a large scale. The few publications (3-10) on the electroplating of high-speed wire deal with commercial production lines.

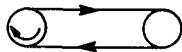
In view of the aforementioned, a small experimental electroplating line was built to study the metal electrodeposition process on moving wire under controlled laboratory conditions. This paper describes in detail the wire electroplating line, associated instrumentation, and briefly, the on-line digital data acquisition system. Results on copper electrodeposition are presented to illustrate the efficacy of this flexible setup.

Electroplating Line

In production, the wire continuously moves through a series of tanks without or with multipassing in the electroplating tank. This arrangement is not suitable



for laboratory investigation because of the need of large amounts of wire and heavy capstans. In the preferred loop arrangement, a kold-welded wire belt is



moved over two wheels, one of which is motor driven. The wire on the bottom level goes through the electroplating line.

The electroplating line, shown in Fig. 1-3, consists of electrocleaning, electroplating, rinsing, and air-wipe cells, wire transport and contact mechanism, solution transfer and storage, support frame with a jig plate, water, gas, and electricity supplies, and drain. The wire can be plated at speeds up to 35 m/sec (7000 fpm) or higher depending on the motor used.

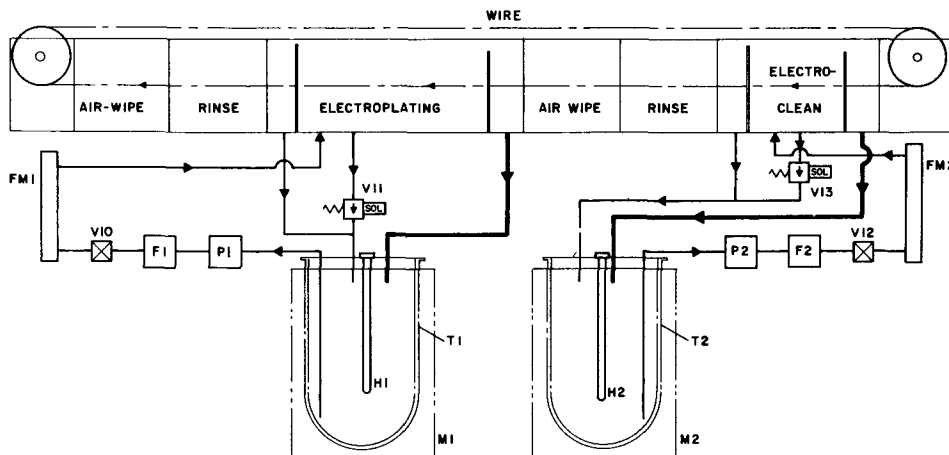
The various parts of the plating line are firmly fastened by stainless steel screws to a 2.5 cm thick aluminum jig plate top. This top is firmly screwed to the supporting frame made of steel square tubing (5 × 5 cm) which is firmly attached to the concrete floor to prevent its vibration and movement. The plating line rests at a convenient height of 90 cm. The compressed air, water, and drain pipes, and the support for the wire supply reel are firmly attached to the top plate from beneath. The connections to the various cells are made through three long and narrow slits in the top plate. Pumps, filters, flowmeters, and solution containers are located under the plating line. Polypropylene tubing and fittings are used.

Figure 2 shows the flow diagram of the electroplating and electrocleaning solutions which have similar paths. Therefore, only one of them will be described. The solution is stored in a 20 liter Teflon coated glass reaction flask T1 resting in the aluminum heating mantle M1. The magnetic coupled seal-less pump P1 forces the solution through the polypropylene filter. The flow rate is adjusted by the 14-turn stainless steel needle valve V10 and indicated on the flowmeter FM1. These are mounted onto a stainless steel bracket which is firmly screwed to the floor (Fig. 1). The solution enters the bottom of the inner compartment of cell near the wire exit and leaves it over the wall at the wire entrance. The solution flows back from the outer compartments of the cell to the container T1 by gravity and is recirculated by the pump. The solution from the inner compartment of the cell is released by turning off the pump and opening the Teflon solenoid valve.

Figure 3 shows the flow diagram of the water and gas supply lines and the drain. These services are connected to the central service droplines behind the plating line through appropriate, quickly disconnectable filters and shut-off valves (not shown). The temperature of the rinse water is adjusted by the valves in the hot and cold water droplines. Cold and hot water is available at the plating line through valves V1 and V8. The various supplies are turned on by actuating the proper solenoid valves from a central panel.

The compressed air to the air-wipe cells is adjusted by valve V3 to the desired rate of flow. Part of the air is taken from the air chamber of the air-wipe cell to the nozzles located in the electrocleaning and electroplating cells (Fig. 4); the purpose of these nozzles is to blow off most of the adhering solution before the wire enters the rinse cell. Another path from the compressed air dropline goes through solenoid valve V5 to

Fig. 2. Flow diagram of electroplating and electrocleaning solutions.



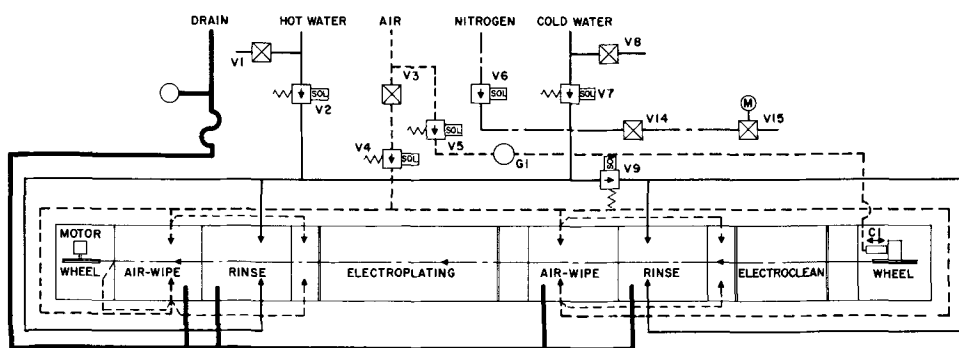


Fig. 3. Flow diagram of water and gas supply lines and drain.

the miniature air cylinder C1 and its rod is connected to the moving contact wheel assembly (Fig. 8). The pressure on the air cylinder is adjusted by regulator G1 to a desired value (0.3 to 1.7 atm) which assures a positive contact between the wire belt and the contact wheel. The tension on the wire, i.e., the pressure on air cylinder should be kept to an optimized minimum to avoid the stretching of the wire. Compressed air is taken from the air chamber of the left air-wipe cell to its last special wire guide (Fig. 5D); this setup significantly decreases the water drag-out by the moving wire.

The nitrogen is used to provide a positive inert atmosphere in the electroplating cell and reaction flask T1 if needed (e.g., in electroplating of tin).

The water from the Plexiglas rinse and air-wipe cells is discharged through PVC pipes into the central drain system without pretreatment.

The electrocleaning and electroplating cells are of similar construction but of various lengths as shown in Fig. 4. The polypropylene cells have three compart-

ments: two outer and a central. The solution is contained in the central, plating compartment by the two inner walls one of which is higher at the wire exit to prevent its escape over this wall. The solution is pumped into the central compartment through the left hole; when the central compartment is filled up, the solution flows over the right, lower inner wall onto the wire even at very high wire speeds and returns to the solution container through the large outlet. The overflowing solution is advantageous because (a) the wire is thoroughly wetted by the electrolyte before entering the inner plating compartment, and (b) the suction of air bubbles is thus eliminated. The solution is released from the inner compartment through the other hole by opening the solenoid valve. The contoured sheet metal anode is in the central compartment and is contacted through the back wall (not shown).

The press-fit Teflon wire guides in the walls (shown in Fig. 5): (a) guide the wire through the cells, (b) prevent excessive leakage of the solution owing to the small clearance around the wire, and (c) are easily replaceable to accommodate wires of various sizes. The 1/2 in. long Teflon wire guides are used in the inner walls. The 1 in. long guides (Fig. 5B), placed in the outer walls of the neighboring cells, help the alignment of the cells and prevent the dripping of the solution between two neighboring cells.

The electroplating cell has an attachment on the outside of the right inner wall (Fig. 4) for a reference electrode which is inserted through the two-piece Plexiglas cover (Fig. 1). The solution path from the wire to the reference cell is through small drill holes in a special, properly oriented Teflon wire guide (Fig. 5C), inner wall (subsequently plugged up), and the attachment to the inner wall. The overflowing solution and the solution dragged by the wire keeps this path filled. This solution path provides an isolated "capillary" to the wire allowing the measurement of the wire potential at the entrance. A similar arrangement can be added to the other inner wall and thus the potential could be measured at both ends of the wire.

The left outer compartment of both cells (Fig. 4) is equipped with two nozzles (Fig. 6) for high velocity gas which removes a large portion of the solution dragged out by the emerging wire. The solution droplets from this compartment flow back to the solution container through the bottom hole. The entire cell is covered by Plexiglas cover with lifting knobs to prevent the escape of liquid droplets into the air.

The nozzle can be rotated on the nozzle extension to an adequate degree and is tightened in this position by the nozzle clamp as shown in Fig. 6. This nozzle arrangement allows the fluid jet to strike the wire symmetrically. It is preferred to turn the nozzle into the moving wire and thus the fluid stream will hit the wire at less than a 90° angle.

The electroplating line contains two air-wipe and two water rinse cells made of Plexiglas which are similar except for some additional tappings in the air-wipe cells. Figure 7 shows a photo of the last air-wipe cell of the electroplating line. The fluid (air or water) enters

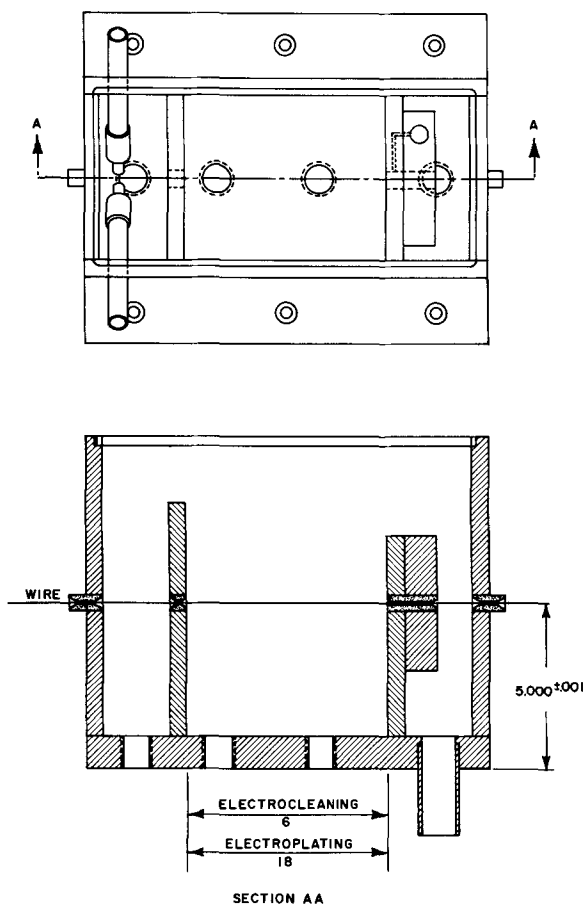


Fig. 4. Top view and cross section of electrocleaning and electroplating cells.

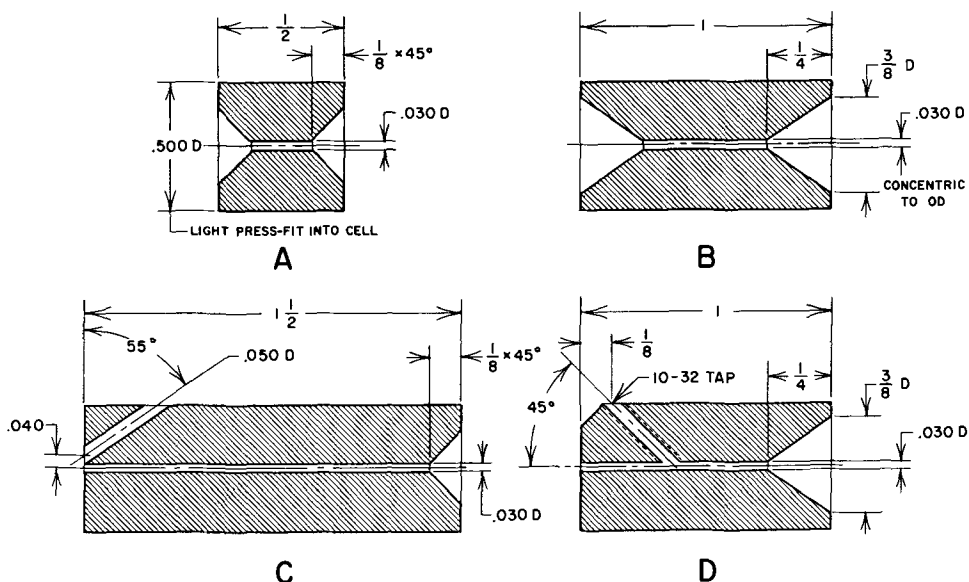


Fig. 5. Wire guides for 24 gauge wire used in inner cell walls (A), to connect outer walls of neighboring cells (B), for the reference electrode (C), and to decrease the water drag-out (D).

symmetrically on both sides of the cell through polypropylene fittings ($\frac{1}{2}$ in. NPT). The fluid leaving the chamber through the six nozzles impinges on the wire at six different locations from four different angles at high velocity and exits through the large tube glued into the bottom of the base plate. In order to prevent the escape of liquid droplets from these cells, they have slipfit covers.

Each air-wipe cell has additional polypropylene fittings ($\frac{1}{4}$ in. NPT, only one is shown in Fig. 7) to provide air to the two nozzles located in both electrolysis cells. The last air-wipe cell's right chamber has an additional brass hose fitting leading to the special wire guide (Fig. 5D).

The wire from the spool is threaded through the various cells, and pulled over the driving and contact wheels. The most frequently used copper wire is cut to the required length and the two ends are joined without a foreign material (by a "KOLDWELD" unit, Type KBM3-162, Division of Kelsey-Hayes Company, Utica, New York, shown in Fig. 1 before the plating line). The wire belt is tightened over the two wheels by activating the miniature air cylinder C1 (Fig. 3) to a predetermined pressure. The wire was found to move smoothly in the V-grooves of both wheels at all the speeds investigated.

The driving wheel assembly is located on the left side of the cells (Fig. 1). The phenolic driving wheel ($\frac{3}{8}$ in. thick) is fastened by two flanges and a key to the shaft of a d-c motor and has six 2-in. diameter equally spaced holes to make it lighter. The motor is

firmly screwed to the motor mounting. The vertical alignment of the wire is assured by the close tolerances in the motor mounting and the sideways alignment is made by moving and securing the phenolic wheel by the two flanges.

The sliding contact wheel and rotating contact unit is on the right side of the cells (Fig. 1) and is shown in detail in Fig. 8. The contact wheel assembly is electrically isolated from the metal frame by a thick phenolic base which is firmly screwed to the aluminum jig plate. The aluminum bracket provides a firm support for the sliding contact wheel and rotating contact unit.

The rotating mercury contact (ROTOCON, Model MSD-2, Meridian Laboratory, Inc., Madison, Wisconsin) provides a low resistance (~ 5 mohms) path from its stationary terminal post to the contact wheel for up to 20A continuous direct current; it can be rotated up to 4500 rpm. The stationary part of ROTOCON is electrically isolated from the stainless steel casing by a phenolic split spacer. The flange on ROTOCON's ro-

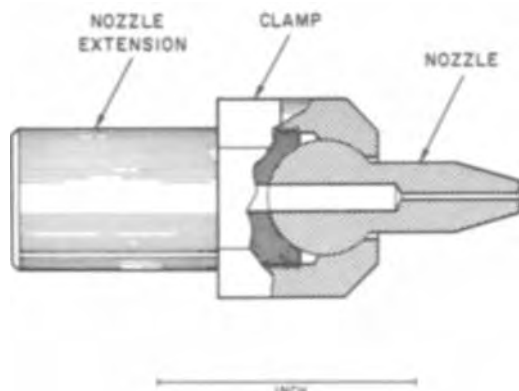


Fig. 6. Nozzle assembly used in rinsing and air-wiping of the wire.

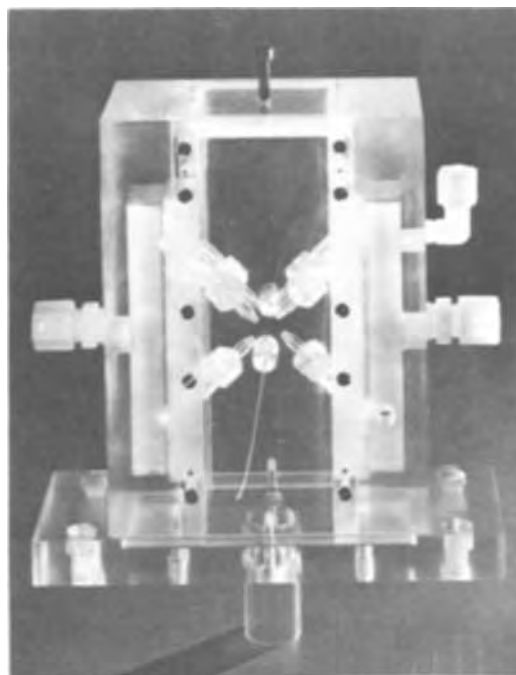


Fig. 7. View of an air-wipe cell

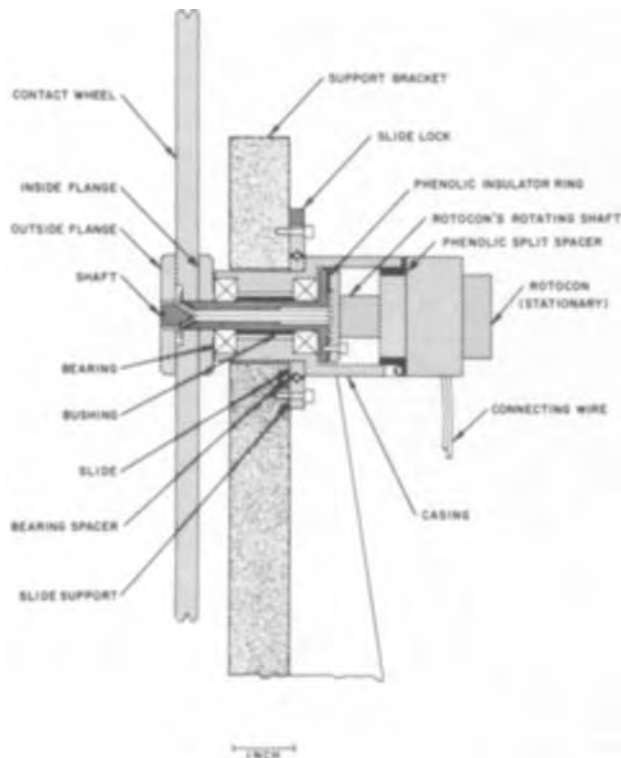


Fig. 8. Cross section of the sliding contact wheel and rotating contact unit.

tating shaft is electrically isolated by a phenolic insulator ring from the flange of the stainless steel shaft; these two flanges are firmly secured to each other by plastic screws. The shaft rotates in two bearings which are inserted into the casing and separated by a stainless steel bushing. The shaft is hollow to bring through the isolated contact wires from the rotating disks of the ROTOCON to the contact wheel. The inside flange and the contact wheel are press-fit onto the shaft and the aforementioned wires are soldered to the hard gold-plated contact wheel. The entire unit is tightened by the threaded outside flange.

The aforescribed rotating contact unit is firmly housed in the casing which moves on the slide supports. Two V-grooved, hardened tool steel slides are firmly screwed to the top and bottom of the casing. This unit moves on ten stainless steel balls whose equal spacings are ensured by two bearing spacers. These balls are contained by the V-grooved, hardened tool steel slide supports which are firmly screwed to the support bracket. The upper slide support is secured by a slide lock. The rotating contact wheel assembly is pushed away from cells by the air cylinder secured to the casing and thus the wire belt is tightened over the two wheels.

Rotating wheel and wire moving at high speed are potential safety hazards. Therefore, the two wheels are housed under tiltable safety covers. The sides of the cover are 1 in. thick Plexiglas sheets and the top is ¼ in. thick aluminum plate. The tubular Plexiglas wire guard forms a protective shield around the upper part of the wire belt between the two wheel covers and can be pushed back for easy access to the cells. The two halves of a Plexiglas tube are held together by three hinges on the rear side and can be opened by releasing push button fasteners in the front. These features can be seen in Fig. 1.

In order to eliminate the fumes and/or gases, an exhaust system with tiltable hood was added over the electroplating line and is connected to the ducts on the ceiling by a 10 in. diameter flexible hose (Fig. 10).

Instrumentation

The experimental wire electroplating setup is shown schematically for potentiostatic measurements in Fig. 9 and its view in Fig. 10. The wire is electrocleaned and electroplated on the plating line the process parameters of which are maintained constant by the various controllers. The electroplating of wire may be done potentiostatically or galvanostatically in steady-state or transient mode or potentiodynamically. The measured variable or variables are displayed on the various oscilloscopes and meters and collected by the digital data acquisition system through a suitable interface. The data are recorded on an IBM compatible magnetic tape which is hand-carried to an IBM 360/50 computer and the experimental data are stored on disks. The various experiments can be randomly retrieved from the disk and plotted on the plotter. The experimental data are reduced and correlated with the help of various computer programs.

Process controllers.—The various instruments are housed in standard electric racks and oscilloscope cart on both sides of the electroplating line (Fig. 10). The left rack next to the line contains the relay and solenoid panels for remote activation of the instruments and solenoid valves, motor speed control, heating man-

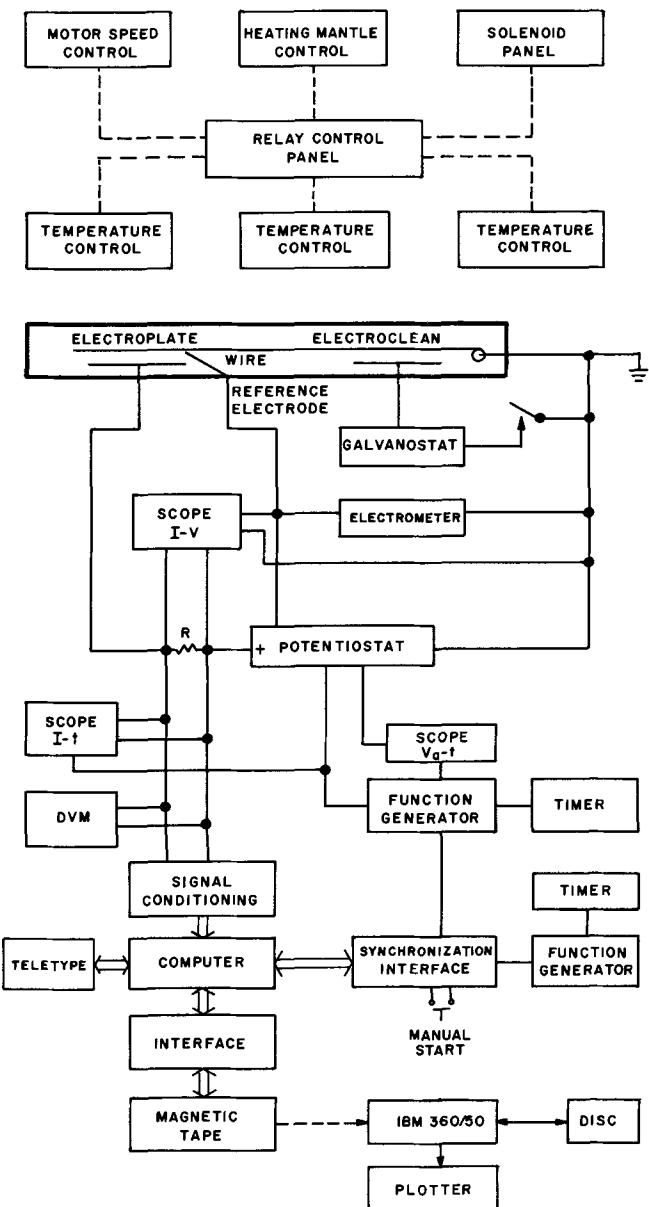


Fig. 9. Schematic of the experimental wire electroplating setup



Fig. 10. View of the experimental wire electroplating setup

tle control, three temperature controllers and temperature indicator for rinse water.

The solution temperatures are maintained at least within 0.2°C by temperature controllers of various ranges through the heating mantles, individual thermistor probes, and 500W immersion heaters.

The speed of the wire is maintained by controlling the speed of the $\frac{1}{4}$ hp d-c motor through its control unit and is adjusted by a ten-turn potentiometer which is paralleled by a diode for protection. A tachometer is mounted onto the shaft of the motor and its output is converted by a resistor network and displayed on a 4-digit digital voltmeter directly as motor speed in revolutions per minute or wire speed in feet per minute.

Instrumentation for electrochemical studies.—The wire, grounded at one place in the entire setup, is electrocleaned cathodically at constant current for a certain time by the galvanostat (Harrison Laboratories, a Division of Hewlett-Packard, Model 6438A). The lead between the stationary part of the ROTOCON contact and the negative pole of this power supply is opened by a relay after the electrocleaning. The anode is a stainless steel sheet and is connected inside the electrocleaning cell to a stainless steel terminal which is contacted by a tightly secured mechanical lug from the outside.

The potential of the wire in the electroplating solution is measured against the reference electrode (usually saturated calomel electrode) and continuously displayed on a battery-operated, solid-state electrometer with floating inputs (Keithley Instruments, Model 602).

There are two fast response potentiostats (~ 10 μsec rise time) (Tacussel, Lyon, France; J. P. Ryaby Associates, Passaic, New Jersey) available on the electroplating line. The first rack on the right of the electroplating line houses the 100A potentiostat (Type PRT20-100XZ), and the 10A potentiostat (Type PRT20-10XZ) is in the second rack. Both potentiostats are equipped with Zerostat and phase shift corrector plug-ins. The lead going to the working electrode receptacle of the potentiostat was interrupted by a relay to allow the correction of the signal's phase shift and set the pulse or sweep length and magnitude to the specified values in the absence of current flow [by a mercury-wetted relay (C. P. Clare & Company, Model HG2A-1007, 5A/pole) and a mercury power relay (C. P. Clare & Company, Model H-1) for the 10 and 100A potentiostat, respectively].

The current flowing through the electroplating cell is measured as a voltage drop on resistor R which is in series with the counterelectrode. The 10A potentiostat has two 0.1 ohm precision four-terminal wire wound current sensing resistors in parallel (5W, "Cur-

ristors," General Resistance Inc.) whereas the 100A potentiostat has three shunts mounted on a rear panel (Weston, 100A-100 mV, 50A-50 mV, 25A-50 mV). The voltage drop is fed to the various instruments through a BNC triaxial receptacle.

The potential of the working electrode can be maintained at a constant value for a certain period or varied linearly with the help of the function generator (Tacussel, Type GSTP2B). A single pulse or sweep is usually used and initiated by a manual trigger. There are two manual triggers in the setup. One is in the function generator and the other is connected to the synchronization interface. The manual start in the synchronization interface simultaneously triggers the function generator and associated instruments and the digital data acquisition system. The manual trigger in the function generator initiates the single pulse or sweep to the potentiostat and simultaneously triggers the various oscilloscopes and the timer.

The length of the pulse or sweep is measured by the timer with a microsecond resolution (Beckman Universal Eput[®] and Timer, Model 7360A). The input to this timer is taken from the synchronization output of the function generator.

The output of the function generator, ($V_a - t$) is displayed on the oscilloscope (Tektronix Readout, Type 567 with a digital unit, Type 6R1A, dual-trace amplifier plug-in, Type 3A2, and time base plug-in, Type 3B2). The magnitude of the superimposed signal is adjusted to the specified value and read on the digital unit of the readout scope. The shape of the signal taken from the function generator output is compared with the shape of the signal taken from the potentiostat output to the cell on the dual-trace plug-in. It is advantageous to make this visual comparison on repetitive signals. The signal taken from the reference electrode terminal is usually distorted and is corrected by adjusting the RC values of the potentiostat's phase-shift corrector plug-in until the two traces on the scope are closely similar.

The current-voltage curve ($I-V$) from the potential sweep measurement is displayed on a storage oscilloscope (Tektronix, Type 564 with two dual-trace differential amplifier plug-ins, Type 3A3). The current is displayed also as a function of time ($I-t$) on another storage oscilloscope (Tektronix, Type 564B with dual-trace differential amplifier plug-in, Type 3A3, and time base plug-in, Type 2B67). Polaroid oscillograms are taken with a trace recording camera and used for immediate qualitative evaluation of the experiment, filing, and comparison with the plots made subsequently by the plotter. The current is also displayed on an integrating digital voltmeter with a floating input (DVM, Weston Instruments, Model 1420). It is used to (a) establish the absence of current flow after the open-circuit potential of the cathode was compensated on the function generator, (b) display the current used for the frequent testing of the calibration of the signal conditioning amplifiers, and (c) display the current in digital form if it is changing slowly.

The experimental setup shown in Fig. 9 for a potentiostatic mode of operation, can be easily and speedily converted for galvanostatic or constant voltage measurements.

Digital Data Acquisition System

The voltage drop on the current measuring resistor R and other variables are available as analog signals. The tedious extraction of numerical data from the analog results for quantitative correlations can be eliminated if the data are collected in digital form in parallel to the analog display of the data.

In view of the aforementioned, a digital data acquisition system (Fig. 9 and 10) was added to the electroplating line which will be described separately in detail. Briefly, the analog signals are conditioned in the signal conditioning unit. The sampling rate of data acquisition, displayed on the timer (Itron, Model 651),

is variable from 36.7 μsec up depending on the computer program, function generator setting (Wavetek, Model 111), and number of channels (up to 5 with the presently available software). The synchronization interface contains a manual start which simultaneously initiates the experiment and the acquisition of data at a predetermined rate after the experimental conditions were entered via Teletype terminal. The maximum 2040 data points are stored in the memory of the computer (Digital Equipment Corporation, DEC, LINC-8) and automatically transferred at the end of the experiment to an IBM compatible 7-track magnetic tape through the magnetic tape interface. An incremental tape recorder (Precision Instrument, Palo Alto, California, Model PI-1167) is used to prepare digital magnetic tapes from low-speed pre-digitized data (coming from LINC-8) in IBM format.

The IBM compatible magnetic tape is carried by hand to an IBM 360/50 computer and the experimental data are transferred to a disk (IBM-2316 disk pack). The various experiments on the disk are randomly accessible and a software has been developed to manipulate, retrieve, and correlate the data and certain, specifically chosen points of the various experiments. The experimental data point and their correlations are plotted by a Cal-Comp plotter.

Signal conditioning.—The magnitudes of the analog signal inputs to the computer are not uniform. The input to the computer, on the other hand, must be $\pm 1.00\text{V}$ or less and one side of the input is near ground potential. In order to provide the optimum 1.00V input to the computer and to avoid ground loops in the entire experimental setup, an interface was built for maximum 10 channels. Its schematic diagram is shown in Fig. 11 for only two channels in view of their similarities.

The signal is fed to the differential input of a d-c operational amplifier which has a single-ended output with a slewing rate of 5 V/ μsec . These are commercially available amplifier boards (DEC, Type A201) which are plugged into DEC module sockets. These sockets with the d-c power supply (PS1, DEC, Type 2R1520-.400) are secured to a front panel which houses the fuses, lights, activating switch, and triaxial input signal receptacles. The front panel swings out from the rear of the module sockets so that their wire wrap connectors can be easily reached. The a-c power to this interface is taken from the computer to avoid unnecessary complications.

The feed-back resistors are chosen depending on the magnitude of the input signal. The output of the operational amplifier is fed to a 500 ohm, 15-turn trimpot

which is grounded at one end through the computer. This trimpot is adjusted so that the output is 1.00V for the maximum input. The amplifier input is protected by diodes.

Results

Some experimental data will be presented here to illustrate the efficacy of the aforescribed setup. The experimental results will be discussed in subsequent papers in more detail.

The current-voltage curves are frequently used for the investigation of electrochemical processes and can be obtained in steady-state or transient conditions. Figure 12 shows potentiodynamic *I-V* curves for the electrodeposition of copper from a flowing 0.024M CuSO_4 -0.24M H_2SO_4 solution onto copper wire (0.5 mm diameter, 24 gauge) at rest and moving at various speeds. It can be seen that the limiting current density, I_L , plateau is present at this slow sweep rate (0.1 V/sec) and I_L increases with increasing wire speed. The *I-V* curves shift toward higher potentials due to the lack of *IR* compensation.

Figure 13 shows the effect of sweep rate on the *I-V* curves for nonmoving copper wire (conditions similar to Fig. 12). The magnitude of *I* increases with increas-

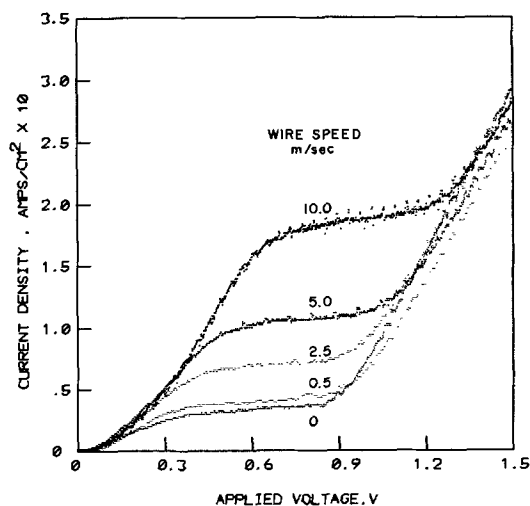


Fig. 12. Potentiodynamic *I-V* curves at various wire speeds and 0.1 V/sec sweep rate for the electrodeposition of copper from 0.024M CuSO_4 -0.24M H_2SO_4 solution on a 0.5 mm diameter copper wire.

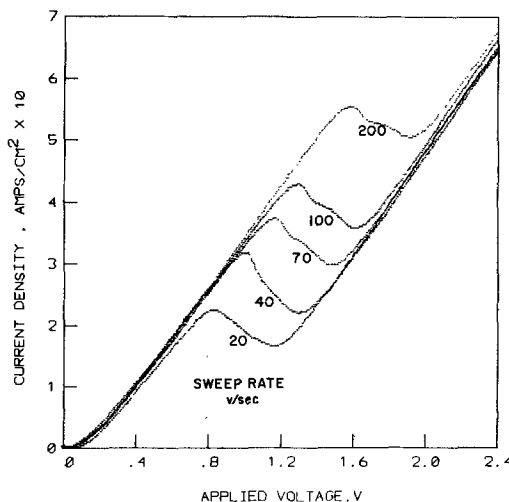


Fig. 13. Potentiodynamic *I-V* curves at various sweep rates for the electrodeposition of copper from 0.024M CuSO_4 -0.24M H_2SO_4 solution on a 0.5 mm diameter copper wire at rest.

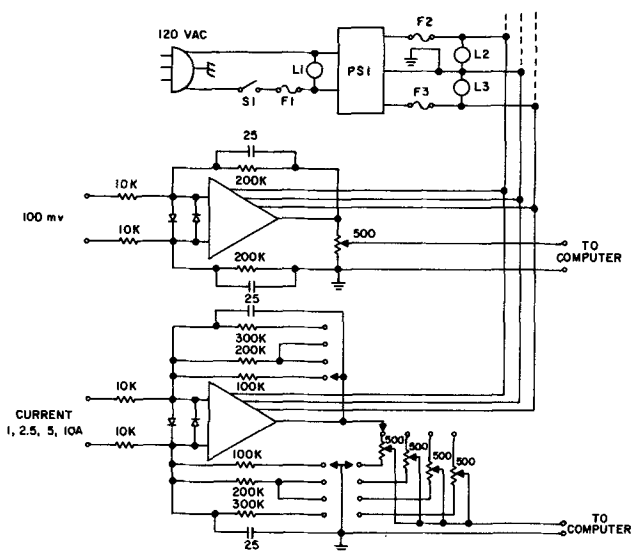


Fig. 11. Schematic diagram of the signal conditioning unit

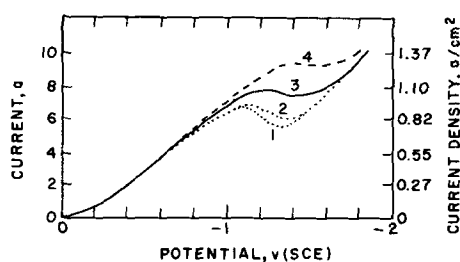


Fig. 14. Potentiodynamic I - V curves at various wire speeds, U and 50 V/sec sweep rate for the electrodeposition of copper from 0.24M CuSO_4 -2.36M H_2SO_4 flowing solution on a 0.5 mm diameter copper wire. Curve 1, $U = 3.30$ m/sec; curve 2, $U = 6.90$ m/sec; curve 3, $U = 10.52$ m/sec; curve 4, $U = 14.17$ m/sec.

ing sweep rate, as expected. The I_L plateau is absent at these sweep rates and I goes through a maximum and minimum before the start of H_2 evolution. It is to be noted that the sweep rate greatly influences the behavior of I between the maximum and minimum and a plateau appears at high sweep rates.

The instrumentation of this experimental setup provides parallel analog and digital data acquisition systems. Figures 12 and 13 are samples of the latter system and were plotted by the computer plotter. The data were not subjected to any smoothing. The analog signals are recorded as oscillograms on Polaroid films (Fig. 14 and 15). Thus, the experiment can be immediately evaluated and the data, obtained by the two acquisition systems, can be compared.

The wire speed significantly affects the I_L in the potentiodynamic I - V curves at low sweep rates (Fig. 12). At medium sweep rates, the magnitude of I increases also and the minimum in the I - V curves disappears gradually with increasing wire speed, as shown in Fig. 14 for a more concentrated solution (0.24M CuSO_4 -2.36M H_2SO_4).

Figure 15 shows the time dependence of I during a short potentiostatic pulse at various wire speeds in the aforementioned solution. The individual I - t curves are displaced by 2A (0.275 A/cm²) for clarity. The I - t curves were obtained in flowing solution except as noted. The fluid flow slightly increases the magnitude of I which decreases considerably with time in both cases; this decrease is especially large at longer times. The decrease of I with time becomes smaller with increasing wire speed and I remains nearly constant at the highest wire speeds.

As mentioned earlier, these results are described here to show the usefulness of this flexible wire electroplating setup. The interpretation and correlation of these and other results will be presented in future papers.

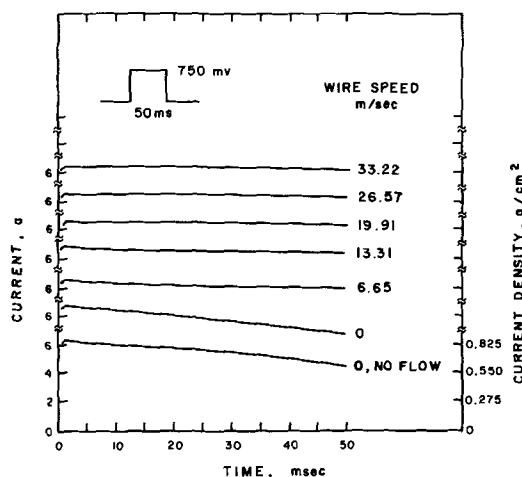


Fig. 15. Time dependence of current density at various wire speeds during potentiostatic pulses of 750 mV for the electrodeposition of copper from 0.24M CuSO_4 -2.36M H_2SO_4 flowing solution on a 0.5 mm diameter copper wire. The curves are displaced by 2A in the y direction for clarity.

Acknowledgment

The author wishes to thank Messrs. W. E. Wilson, Jr. and J. E. Comeau for their valuable assistance in the design, assembly, and building of the electroplating line and instrumentation.

Manuscript submitted March 8, 1971; revised manuscript received Sept. 7, 1971. This was Paper 203 presented at the Atlantic City Meeting of the Society, Oct. 4-8, 1970.

Any discussion of this paper will appear in a Discussion Section to be published in the December 1972 JOURNAL.

REFERENCES

1. W. E. Hoare, E. S. Hedges, and B. T. K. Barry, "The Technology of Tinplate," St. Martin's Press, New York (1965), and references therein.
2. J. S. Mathias and G. A. Fedde, *IEEE Trans. Magnetics*, **MAG-5**, 728 (1969).
3. F. A. Lowenheim, *Wire Wire Prod.*, **27**, 464, 506 (1952).
4. C. O. Bruestle, *ibid.*, **27**, 565, 632 (1952).
5. A. E. Carlson, *Plating*, **42**, 1149 (1955).
6. D. A. Pieszak, *Wire Wire Prod.*, **41**, 397, 400, 452 (1966).
7. E. Weber, *Draht*, **16**, 715 (1965).
8. W. Teller, *Draht-Welt (Düsseldorf)*, **52**, 715 (1966).
9. E. Weber, *Wire (Coburg)*, Issue 104, 331 (1969).
10. E. Weber, *Draht*, **20**, 600 (1969).

Electrothinning and Electrodeposition of Metals in Magnetic Fields

J. Dash and W. W. King

Physics Department, Portland State University, Portland, Oregon 97207

ABSTRACT

Experiments have shown that metals can be electrothinned and electrodeposited more uniformly if the electrolysis is performed in a magnetic field. In addition, the resistance of electrolytic cells is reduced in a magnetic field. These effects have been characterized for various orientations and strengths of the electric and magnetic fields.

In an earlier, preliminary report, some results were presented to show that the application of magnetic fields during electrolysis increases the uniformity of anodic dissolution of metals (1). These studies have been continued in order to investigate both anode and cathode processes for additional orientations and strengths of the electric fields (E) and magnetic fields (B) and other types of electrodes and electrolytes.

Experimental Methods and Results

Figure 1 shows a diagram of the circuit used for electrolysis. The constant current device was used to compensate automatically for changes in resistance of the electrolytic cell. In this way it was possible to maintain constant current during electrolysis and thus to follow the changes in cell resistance by means of the voltage-time recorder. The cell with the electrode arrangement used for the initial electrothinning experiments is shown in Fig. 2. Later experiments were performed with a plate disk cathode, shown in Fig. 3, which also shows the schematic positioning of the electrolytic cell between the polepieces of the 4 in. electromagnet, used for all experiments. Still other

experiments were performed with a 19 mm ID cylindrical cathode surrounding the sample (anode).

Experiments with the cell of Fig. 2 on Al-3.4 atomic per cent (a/o) Zn were performed at various applied magnetic field strengths in order to determine the minimum B required to produce relatively large electron-transparent films. As previously described (1), the 0.1 mm thick samples used for these experiments were in the solution-treated and air-cooled condition. The electrolyte consisted of 33 volume per cent (v/o) conc HNO_3 and 67 v/o methyl alcohol. This was cooled to -13°C prior to each experiment. Current was maintained at 0.075A during every experiment. Thus, the initial current density was approximately the same for all experiments (about 0.25 A/cm^2). No insulating lacquer was used for edge protection during electrolysis. After electrothinning, profiles were obtained by mounting the samples on clear glass in the object plane of a photographic enlarger and recording the patterns of transmitted light on printing paper.

The results obtained with B of increasing strength applied normal to the plane of the sample are shown in Fig. 4. Without an applied B , thinning is concentrated at the air-electrolyte interface, and perforation first occurs here. Application of B during the process lowers the air-electrolyte interface and causes the

Key words: electrothinning, electrodeposition, magnetic fields.

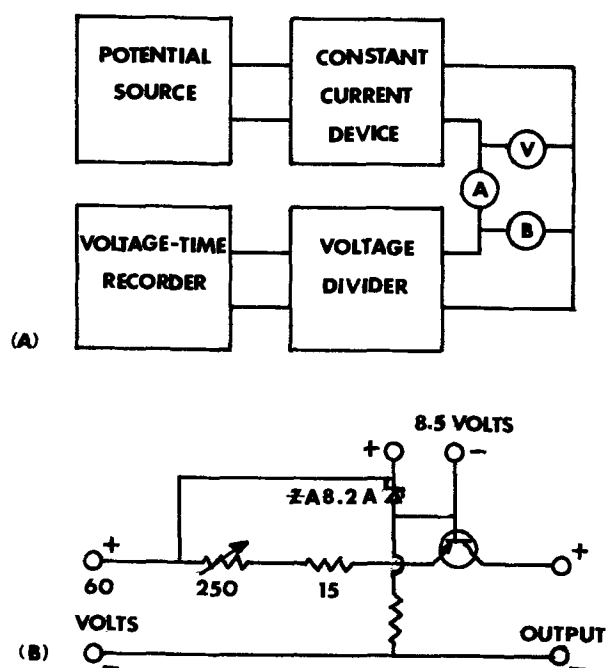


Fig. 1. (a) Schematic diagram of the circuit used for electrolysis. An ammeter is at A, the electrolytic cell at B, and a voltmeter at V. (b) Circuit of the constant-current device, which served to compensate automatically for changes in resistance of the electrolytic cell. Only direct current was used for these experiments.

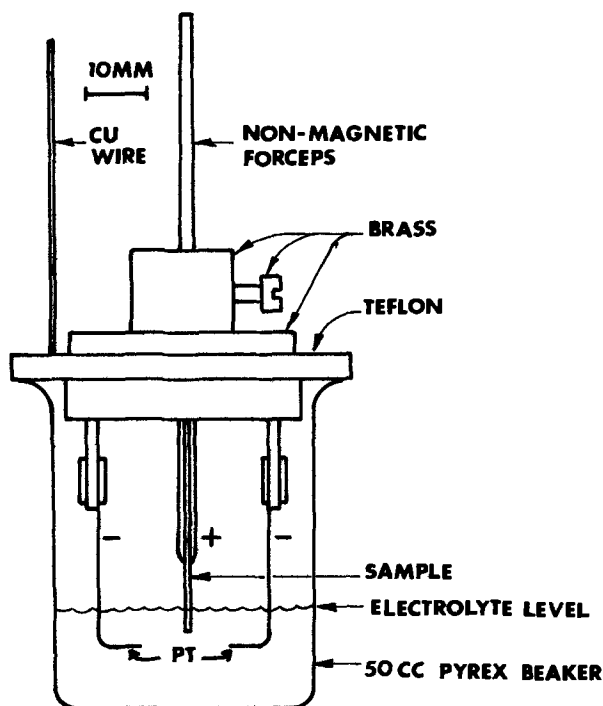


Fig. 2. Illustration of the electrode arrangement used for some of the electrothinning experiments.

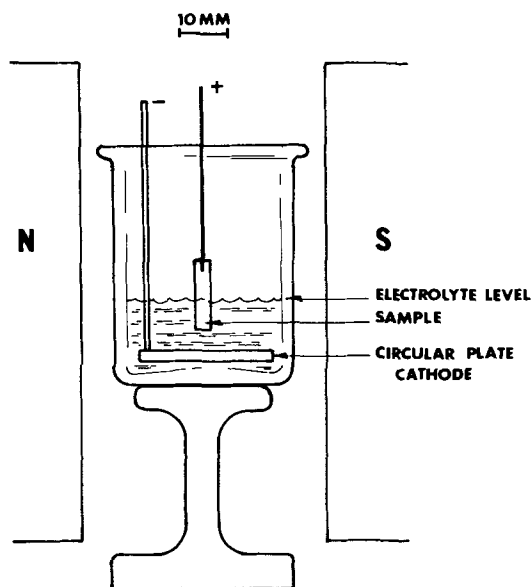


Fig. 3. Schematic arrangement of the electrolytic cell between the polepieces of an electromagnet. The plate-disk cathode, used for some of the experiments, is shown here.

process to occur more uniformly over the entire submerged portion of the sample. With $B = 4.5$ kG, preferential thinning at top of the electrolyte is no longer a limiting factor, and it is possible to continue electrolysis until the sample is fairly uniformly transparent to electrons over the entire remaining area. Electron micrographs taken from a sample thinned with B of 9 kG normal to the sample plane are shown in Fig. 5.

In Fig. 4 it is also apparent that the left edge of each sample thinned in the presence of an applied B has been preferentially dissolved. The stirring pattern established in the electrolyte by this particular orientation of B probably causes enhanced mobility and therefore an increased rate of reaction at this edge.

By periodic reversal of B during the process, it is possible to alternate the preferential attack from the left to the right edge and thus to improve the over-all uniformity of thinning.

With B applied parallel to the sample plane in the horizontal direction (electrode arrangement of Fig. 2), the stirring pattern is altered such that thinning occurs most rapidly at the bottom of the sample (Fig. 6). Again, $B = 4.5$ kG is required to prevent the sample from breaking off prematurely at the air-electrolyte interface. Periodic reversal of B in this orientation is

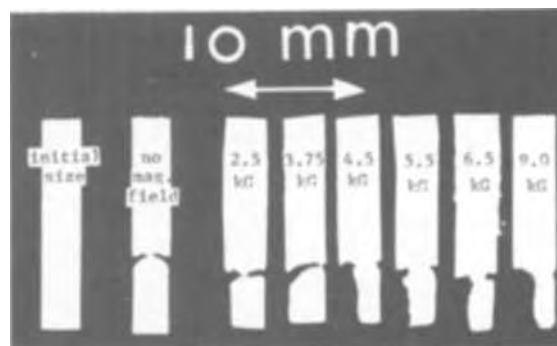


Fig. 4. Profiles of Al-3.4 a/o Zn samples thinned with B applied perpendicular to the sample plane in the cell of Fig. 2.

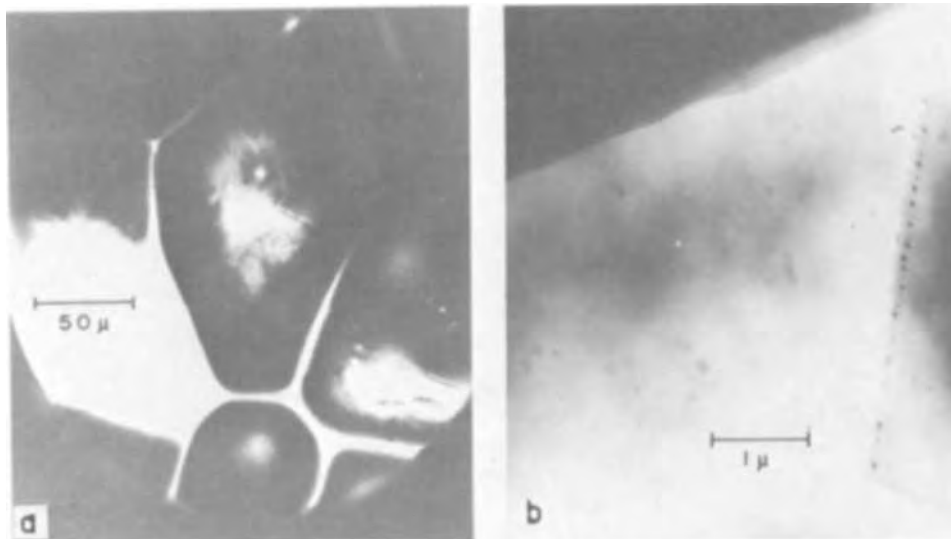
not as effective in increasing the uniformity of thinning as for the case of B normal to the sample plane.

The other electrode arrangements mentioned above helped to establish that it is the orientation of B with respect to the sample that primarily controls the final profile. The results in Fig. 7 and 8, obtained respectively with the cylindrical cathode and with the plate cathode, show that in both cases the profiles obtained with B normal to the sample plane are similar to those obtained for this case with the wire cathodes. This is also true for B parallel to the plane of the sample.

Of all the arrangements described above, perhaps the most practical for uniform thinning with minimum B strength is that shown in Fig. 3. It can be seen in Fig. 8 that B of 3 kG parallel to the sample plane was sufficient to prevent premature break-off at the air-electrolyte interface, whereas approximately 50% higher values of B were required to prevent break-off at this interface in all other arrangements.

Thinning in other metal-electrolyte systems with applied B has not yet been investigated extensively, but the studies which have been conducted indicate that the observations reported above are general. For example, some results of thinning pure, polycrystalline Cu in an electrolyte consisting of water saturated with CuSO_4 are shown in Fig. 9. The cell of Fig. 2 was used for these experiments, and the electrolyte temperature at the start of each experiment was 24°C . Constant current of 0.08A was maintained, and the initial current density was about 0.26 A/cm^2 . Although electrolytic polishing does not occur under these conditions, the profiles obtained without applied B and with B parallel to the sample plane (Fig. 9) are very similar to those obtained for the Al-Zn alloy under polishing conditions (Fig. 6). An obvious difference is the large number of tiny holes within the thinned regions of the

Fig. 5. Electron transmission photographs (50 kV) taken from Al-3.4 a/o Zn sample thinned with $B = 9$ kG normal to the plane of the sample. (a) Low magnification photograph to illustrate qualitatively the manner in which individual crystals dissolve during electrolysis in applied B . Though thinning occurs preferentially at grain boundaries and the edges of the grains are rounded, the centers of grains, where chemical composition is more uniform, thin much more uniformly. (b) High magnification photograph to show that relatively large areas are transparent to electrons of moderate energy.



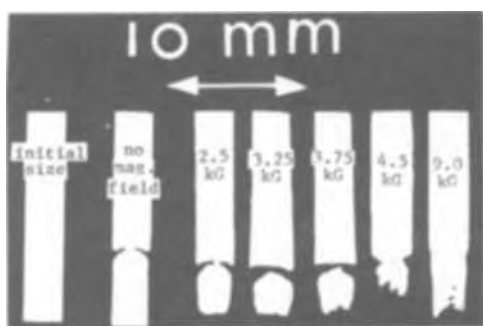


Fig. 6. Profiles of Al-3.4 a/o Zn samples thinned with *B* applied parallel to the sample plane in the cell of Fig. 2.

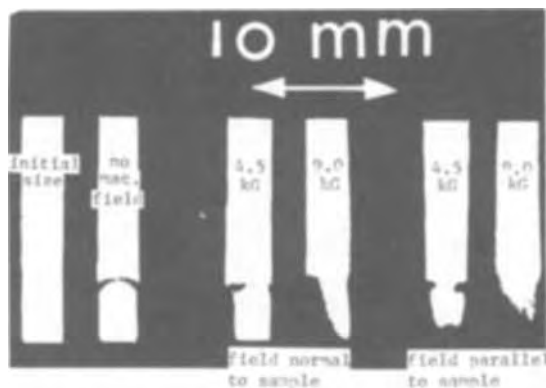


Fig. 7. Profiles obtained with cylindrical stainless steel cathode concentric with the samples (Al-3.4 a/o Zn).

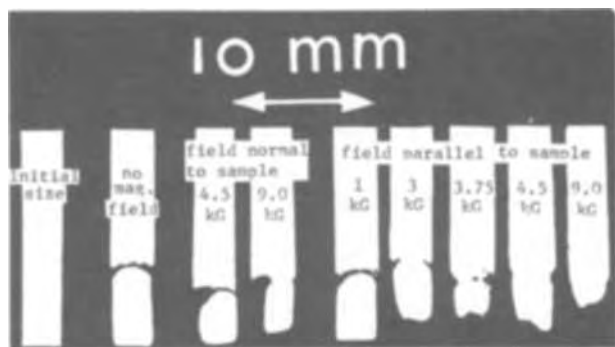


Fig. 8. Profiles of Al-3.4 a/o Zn samples obtained by thinning with the cell of Fig. 3.

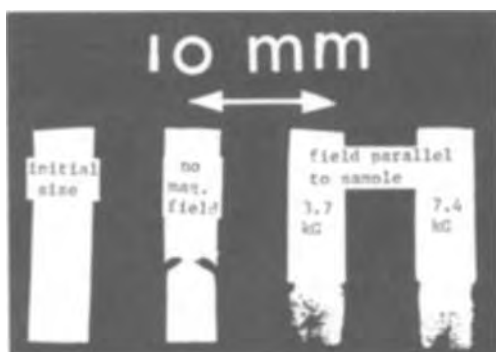


Fig. 9. Profiles of pure Cu obtained by thinning with $\text{CuSO}_4\text{-H}_2\text{O}$ electrolyte in cell of Fig. 2.

samples to which *B* was applied. These perforations were caused by preferential dissolution at grain boundaries. It should also be noted that the *B* strength required to prevent break-off at the air-electrolyte

interface is much less in this case than for electrothinning of Al-Zn with the HNO_3 -methyl alcohol electrolyte (Fig. 6). This suggests that a given *B* strength produces a greater degree of stirring in the CuSO_4 electrolyte than in the HNO_3 electrolyte. The main reason for this may be due to the greater degree of ionization of the CuSO_4 electrolyte and the resulting greater degree of interaction with the applied *B*.

Stirring effects observed at the cathodes of the cell during the electrothinning experiments with applied *B* suggested that there might be significant changes in the characteristics of electrodeposits, compared with deposits produced without applied *B*. This was investigated for the deposition of Cu from CuSO_4 -saturated H_2O solution with the cell shown in Fig. 10. The substrates used for deposition were double, 3 mm diam Cu grids used to "sandwich" thin specimens for electron microscope examination. These were spot-welded onto Pt wire leads and bent so that the plane of the lower grid was at 90° to the plane of the grid welded to the lead wire. In the electrolytic cell the lower grid was horizontal, as shown in Fig. 10. Profiles of a grid prior to electroplating are shown in Fig. 11(a1) and 11(b). The Cu anode strips were the same size as for the electrothinning experiments (Fig. 9).

Electrodeposition without applied *B* yielded the profile shown in Fig. 11(a2) [and at higher magnification in Fig. 11(c)] for the horizontal grid. Note that the originally square openings have become distorted to pin-cushion shapes. The corresponding photographs of a horizontal grid plated with the same cell current for the same time, but with *B* applied normal to the plane of the anode, are shown in Fig. 11(a3) and 11(d). In this case the shapes of the openings remain practically unchanged from the original.

Scanning electron microscope photographs of portions of the grids in Fig. 11(a1) and 11(a2) were taken to show the three-dimensional differences in morphology of the electrodeposits without and with applied *B*. These are shown in Fig. 12 and 13, respectively. The much greater degree of distortion of the original grid bar shapes resulting from deposition without applied *B* can be appreciated by comparing Fig. 12a with Fig. 13a. The enhanced uniformity of the electrodeposit with applied *B* is apparent from the comparison of Fig. 12b and 13b.

In addition to the morphology differences for both electrothinning and electrodeposition which result from the application of *B* during electrolysis, the electrical resistance of the cell is almost always less with applied

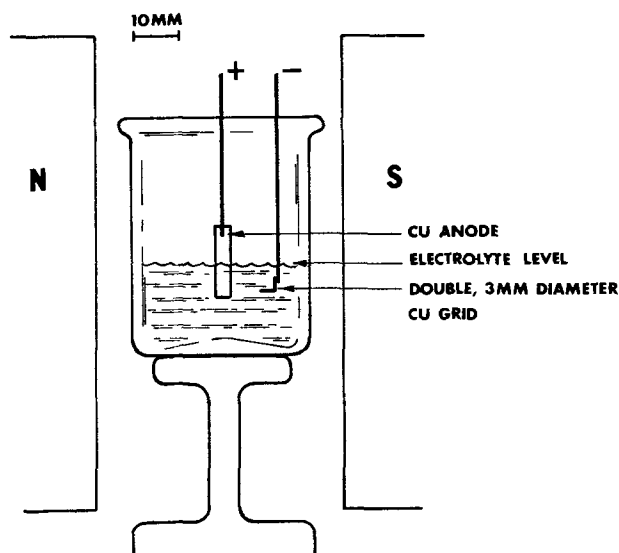
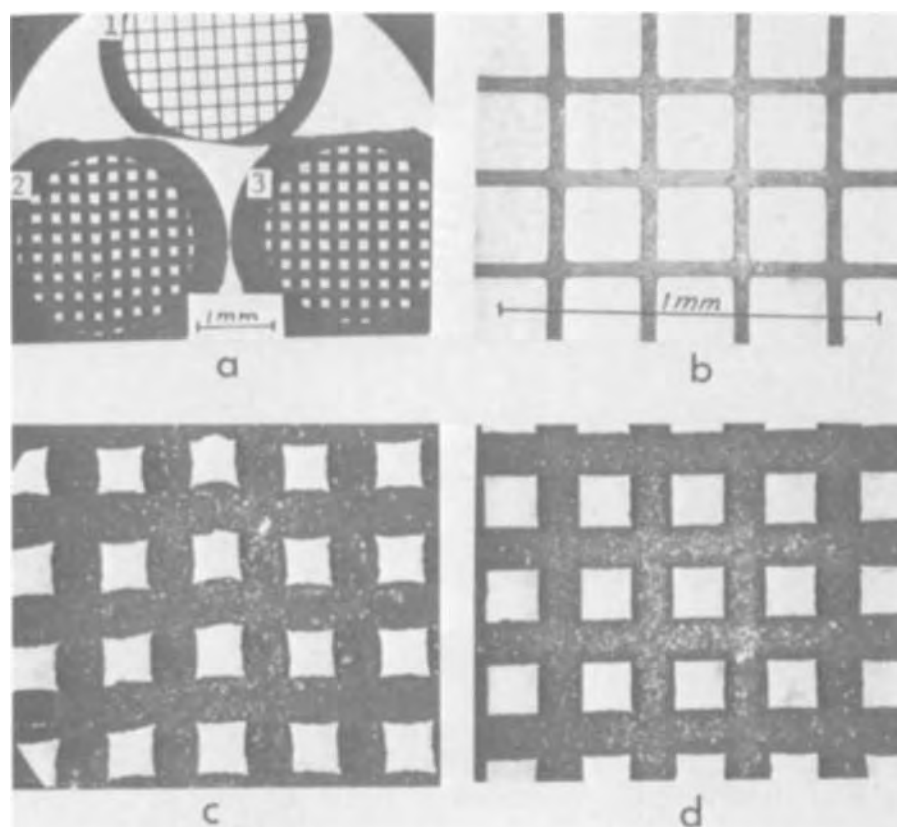


Fig. 10. Electrode arrangement used for deposition of Cu from $\text{CuSO}_4\text{-H}_2\text{O}$ electrolyte. The horizontal portion of the cathode was examined after deposition.

Fig. 11. Profiles of Cu grids electroplated with Cu from $\text{CuSO}_4\text{-H}_2\text{O}$ electrolyte: (a1, b) before electroplating; (a2, c) plated without applied B ; (a3, d) plated with $B = 7.4$ kG parallel to plane of the grid. The same deposition current (0.08A) and time (9.4 min) were used for (a2) and (a3).



B . For electrothinning of Al-Zn with the HNO_3 electrolyte, the cell resistance was lowered by about 20% with applied B of 9 kG. The original data for cell voltage at constant current for the electrodeposits of Fig. 11a2 and 11a3 are reproduced in Fig. 14a and 14b, respectively. These data show that the average cell resistance without applied B is at least 20% higher than when B is applied during the process. Furthermore, after about the first minute, deposition proceeds at almost constant cell resistance in the presence of applied B , whereas large fluctuations occur throughout the process without applied B . It is believed that most of this difference is due to changes in the anode processes, but no quantitative information is yet available.

The morphology of the Cu deposit is also dependent on the orientation of B with respect to the plane of the

cathode. This is shown by the results of deposition on double, 3 mm diam Cu electron microscope grids with hexagonal openings (Fig. 15). In this case the grids were suspended vertically in the electrolyte, parallel to the plane of the anode. The electrolyte and deposition conditions for these experiments are commonly used in standard plating practice (2). The results in Fig. 15 show that the deposit tends to build up parallel to the direction of B . The extent of closing of the holes is greatest for B parallel to the plane of the grid (Fig. 15d) and least for B normal to the plane of the grid (Fig. 15c). Even in these low magnification photographs, the deposits made with applied B (15c and d) appear more uniform than that made without B (15b). Microhardness tests, taken on comparable portions of the solid border of each grid, appear to confirm this.

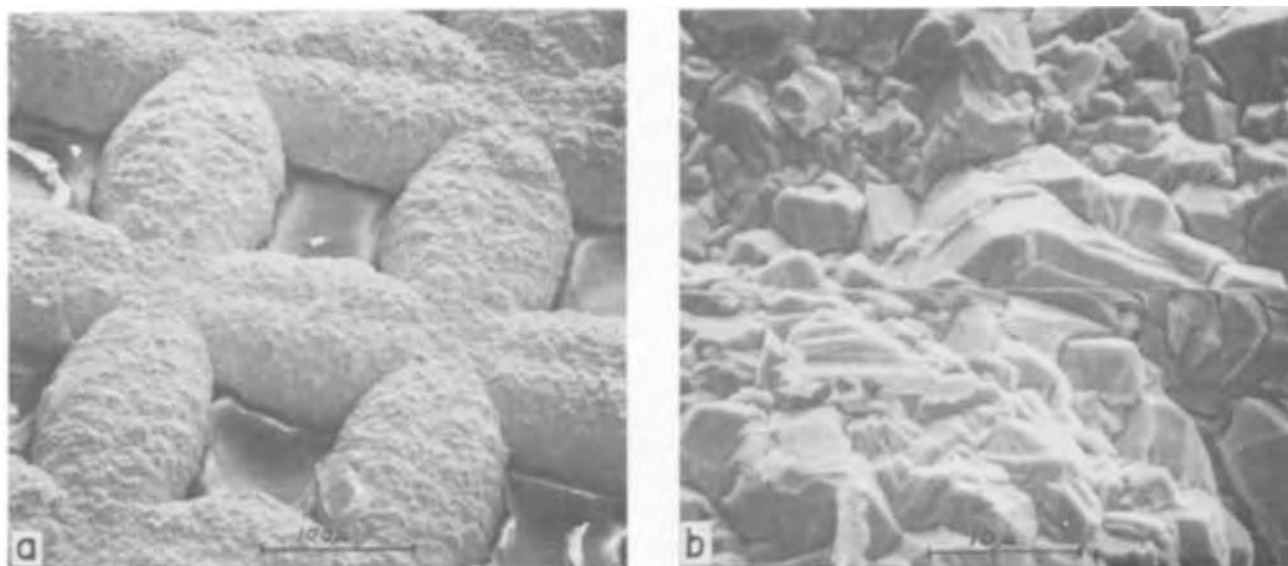


Fig. 12. Scanning electron micrographs of portions of the grid electroplated without applied B , shown in Fig. 11(a2): (a) low magnification; (b) a portion of a grid bar at high magnification.

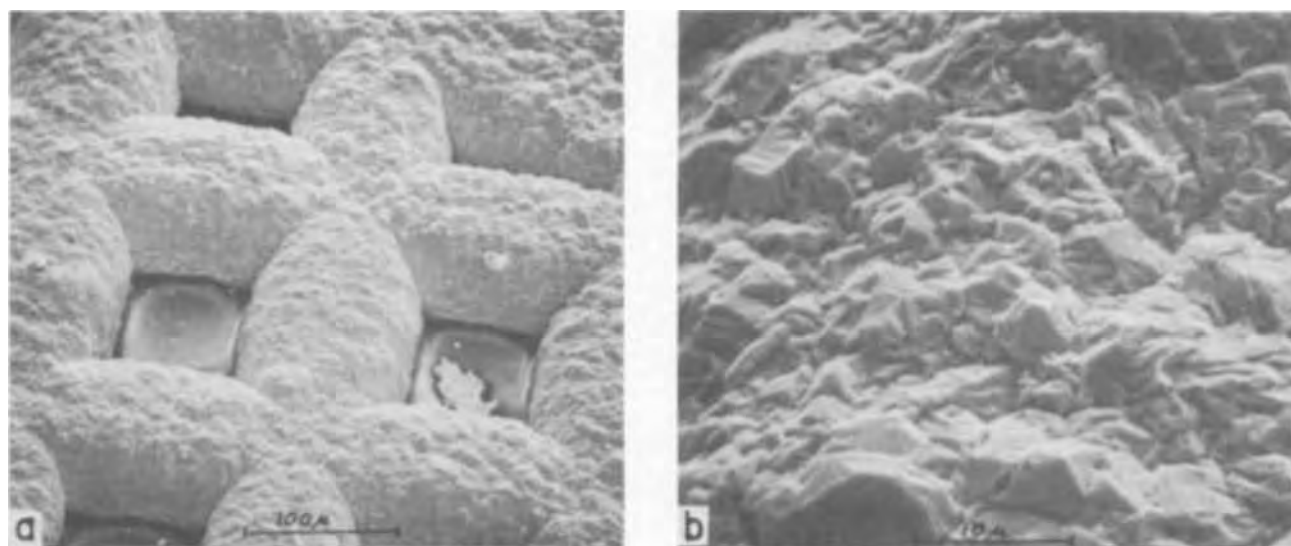


Fig. 13. Scanning electron micrographs of portions of the grid electroplated in the presence of applied B , shown in Fig. 11(a3): (a) low magnification; (b) a portion of a grid bar at high magnification.

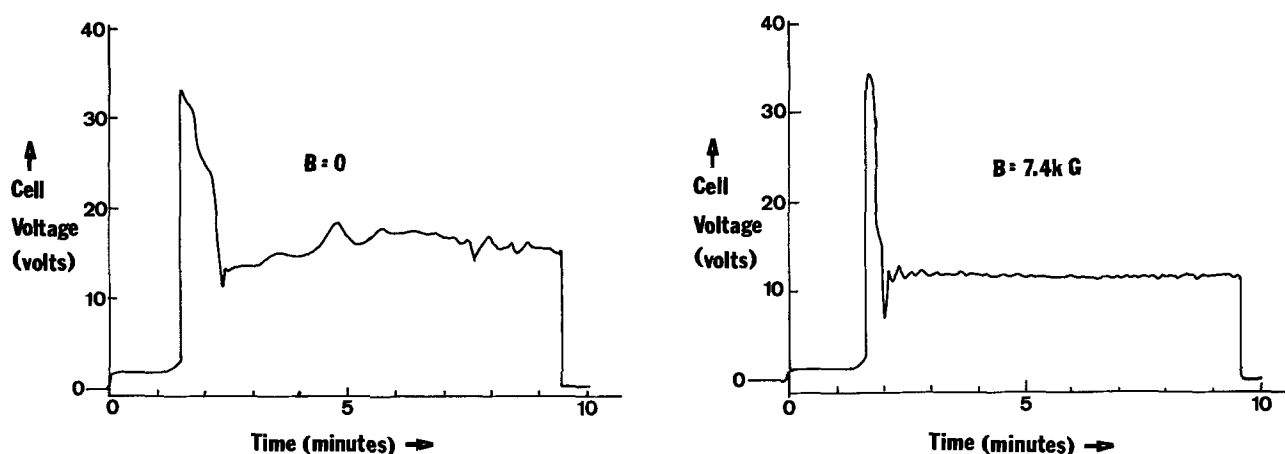


Fig. 14. Variation of cell voltage during deposition of Cu from $\text{CuSO}_4\text{-H}_2\text{O}$ electrolyte at constant current (0.08A). (a) Data for deposition on grid shown in Fig. 11(a2) (no applied B), (b) data for deposition on grid shown in Fig. 11(a3) (with $B = 7.4$ kG applied parallel to plane of the grid).

Photographs were taken of a group of 4 equally-spaced Knoop indentations on each grid (all made with a 100g load) by focusing on the roots of the indentations. The indentations in the electrodeposit made without applied B (Fig. 16b) are less well defined than either group of those made with applied B (Fig. 16c and d). The most probable cause of this difference is a rougher surface in the case of the deposit made without applied B . Further work is needed to assess the differences in hardness of these deposits.

To determine the effect of applied B on the cell resistance during deposition of Cu from the $\text{CuSO}_4\text{-H}_2\text{SO}_4$ electrolyte, B was varied both in strength and orientation during deposition on a double Cu grid suspended

vertically, parallel to the plane of the Cu anode. The results are given in Table I.

In this case the cell voltage (0.2-0.3V) is much lower than for the data of Fig. 14, due to the much lower cell current, higher temperature, and greater degree of ionization. The percentage reduction in the cell resistance was less in this case, but the magnitude of B was also less. The data of Table I show that a reduction in B from 5.5 kG to 3.0 kG increases the cell resistance by about 3%. Change in the orientation or direction of B with respect to the electrodes appears not to have any effect on the magnitude of the cell resistance.

Discussion of Results

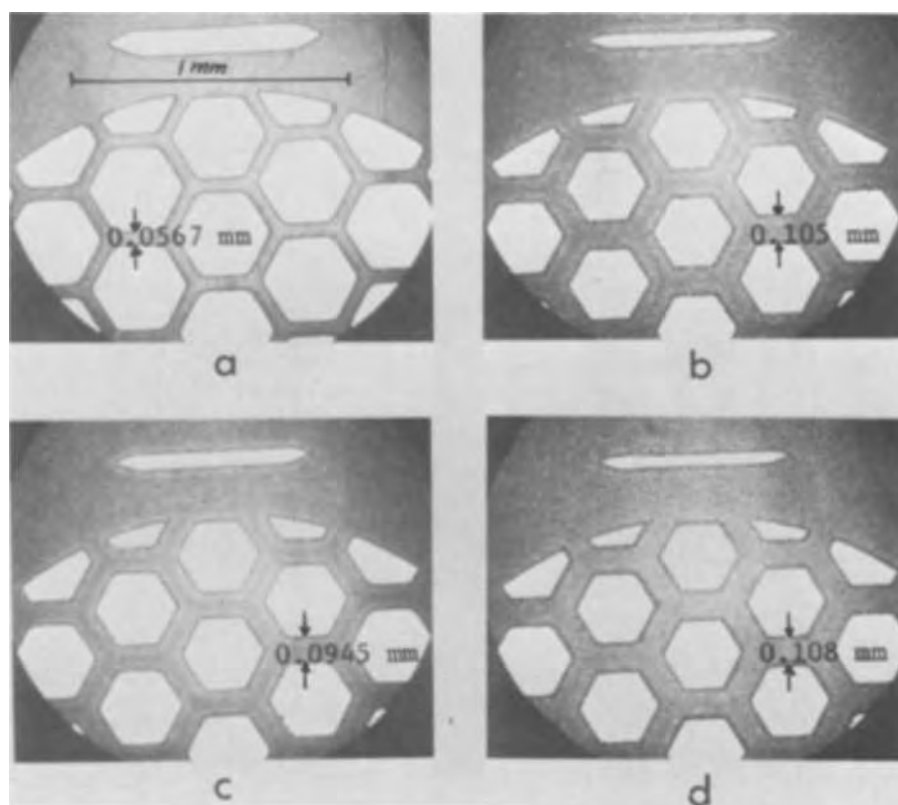
No previous reports of the effects of applied B on electrothinning processes have been found in the literature. Although there have been previous studies of electrodeposition under the influence of applied B (3-6), most of this work was concerned with deposition of the ferromagnetic elements, Fe, Co, and Ni. For deposition of Cu and Sb in applied B , no effect was observed (3). Yang (3) did observe that B applied normal to the cathode caused enhanced deposition of the ferromagnetic elements in this direction, but he reported no difference for the deposits obtained with B parallel to the cathode in comparison with those obtained without applied B .

Many of the effects of applied B on electrolytic processes described above appear to be similar to those

Table I. Electrolytic cell resistance as a function of magnitude and orientation of applied B

Strength (kG)	Applied B		Cell current (Amperes ± 0.0005)	Resistance lowering due to B (% ± 1)
	Orientation	Direction		
0	—	—	0.02	—
5.5	$B \perp$ cathode	Normal	0.02	10
5.5	$B \parallel$ cathode	Normal	0.02	10
3.0	$B \parallel$ cathode	Normal	0.02	7
3.0	$B \parallel$ cathode	Reversed	0.02	7

Fig. 15. Electrodeposition of Cu on Cu grids suspended vertically in electrolyte containing 0.22g CuSO₄ and 0.04 cc H₂SO₄ per cc H₂O. Electrolyte temperature was maintained at 50° ± 2°C, the current was constant at 0.02A, and the time of deposition was 740 sec for each of these experiments. (a) Profile of grid before deposition, (b) plated without applied *B*, (c) plated with *B* = 5.5 kG normal to the plane of the grid, (d) plated with *B* ≈ 5.5 kG parallel to the plane of the grid. The extent of deposition parallel to the plane of the grid is least for (c) and most for (d).



which occur due to ultrasonic vibration during electrolysis (7). The basic mechanisms by which the two types of field interact with electrolytes are quite different. Ultrasonic fields impart vibratory motion to all particles in the electrolyte, but magnetic fields interact only with moving charged particles. Through the Lorentz force, $\vec{F} = q(\vec{v} \times \vec{B})$, where q is the charge of a particle, \vec{v} its velocity, and \vec{B} the magnetic field strength, a moving charged particle is caused to spiral about its original path. The direction of spiraling is opposite for opposite charges. Other studies, using alternating current during electrolysis, have shown that the magnetic force decreases the mobility of moving charged particles in electrolytes (8). Thus our observation that applied *B* lowers electrolytic cell resistance in direct-current electrolysis (i.e. increases the mobility of charged particles) may be explainable by enhanced mobility at the solid-liquid interfaces due to intense mixing, which more than cancels the reduced mobility

in the bulk of the electrolyte. Similarly, the vibratory motion caused by ultrasonic fields may not increase mobility in the bulk of the electrolyte, but the reduction in polarization at the electrodes results in an overall reduction of cell resistance (7).

A fundamental difference between the ultrasonic and the magnetic interactions is that the former transfers energy to the electrolyte but the latter does not. Thus, if further research proves that magnetic fields are as effective as ultrasonic fields in improving electrodeposition and other important electrolytic processes, it would appear that the former have appreciable economic advantages. This is especially true if the necessary *B* can be supplied with permanent magnets.

Experimental and theoretical studies to improve the understanding of the results reported above are in progress.

Acknowledgments

We are grateful to R. W. Roeter for his assistance with some of the experiments. The scanning electron micrographs were taken through the courtesy of Perkin-Elmer Corporation on an SSM-2 microscope by Dr. R. Buchanan. This research was supported in part by a grant from Research Corporation.

Manuscript received July 23, 1971.

Any discussion of this paper will appear in a Discussion Section to be published in the December 1972 JOURNAL.

REFERENCES

1. J. Dash, R. W. Roeter, and W. W. King, "Proceedings 27th Annual Meeting of Electron Microscopy Society of America," p. 144, Claitor's Publishing Div., Baton Rouge (1969).
2. T. M. Rodgers, "Handbook of Practical Electroplating," p. 154, Macmillan, New York (1959).
3. L. Yang, *This Journal*, **101**, 456 (1954).
4. R. M. Bozorth, *Phys. Rev.*, **26**, 390 (1925).
5. A. Perrier and C. Mermod, *Helv. Phys. Acta*, **11**, 362 (1938).
6. A. Perrier, C. Mermod, and E. Besse-walter, *ibid.*, **26**, 1861 (1943).
7. S. M. Kochergin and G. Y. Vyaseleva, "Electrodeposition of Metals in Ultrasonic Fields," Consultants Bureau, New York (1966).
8. D. Laforgue-Kantzer, *Electrochim. Acta*, **10**, 585 (1965).

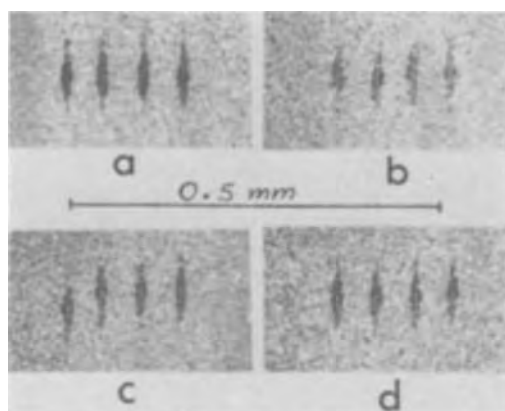


Fig. 16. Impressions from same locations in samples of Fig. 15 made with Knoop indenter under 100g load on Tukon microhardness tester. (a) Sample before deposition, (b) plated without applied *B*, (c) plated with *B* = 5.5 kG normal to plane of the grid, (d) plated with *B* = 5.5 kG parallel to plane of the grid.

Electrophoretic Deposition of Aluminide Coatings from Aqueous Suspensions

H. A. Fisch

TRW Inc., Equipment Group, Materials Technology Department, Cleveland, Ohio 44117

ABSTRACT

A process was developed on a laboratory scale for electrophoretic deposition of metals from aqueous suspensions formed by mixing metal powder or flake with an amine solubilized acrylic resin, glycerol, and a detergent wetting agent in deionized water. Electrophoretic deposition parameters are discussed in terms of deposits formed from aluminum flake on B-1900 alloy. From this basis, the process was extended to the deposition of bisque envelopes for the formation of aluminide coatings modified with additions of Cr, Si, and a Ti coating containing Al_2O_3 . Electrophoretically deposited Al, Al-Cr, and Al-Si coatings provided protection against dynamic hot corrosion (sulfidation) for times comparable to those observed for conventionally processed coatings.

Aluminide coatings are widely used in gas turbine power plants of military and commercial aircraft because they provide a reliable deterrent against oxidation, hot corrosion, and thermal fatigue damage of critical and expensive hardware. While much research has been and is currently being conducted to develop improved metallic coating systems, an aluminide coating on nickel- and cobalt-base superalloys has been demonstrated to be the most protective and economical system available for applications up to about 2000°F. Higher operating temperatures of advanced engines may require new substrates and coating alloys; however, in most cases internal cooling of blades and vanes will keep the temperature of some of these components within the protective range of the aluminides. Furthermore, while future turbine inlet temperature requirements may preclude the use of aluminides on first- and possibly second-stage blades and vanes, subsequent cooler stages which at present are uncoated will require protection within the temperature capability of the aluminide coatings.

Aluminide coatings for protecting nickel-base or cobalt-base superalloys against oxidation and hot corrosion are most commonly formed by pack cementation processes, or variations of this process such as pack-diffusion (1) or slurry-diffusion (2) and by slurry-fusion. A typical pack-diffusion process involves placing the article to be coated into a retort containing powdered metallic and nonmetallic coating material and, if required, an activator. This is followed by heating to a temperature sufficient to vaporize the powdered coating material thereby causing a solid-vapor interface reaction to occur between the article and the coating vapor. In a slurry-diffusion process, the analogous solid-vapor interface reaction is ordinarily achieved by applying a sprayed layer or bisque envelope of coating source materials onto the article to be coated, drying to form an adherent deposit, and forming the diffusion coating by heating. Slurry-fusion involves spraying to form a bisque on the surface then heating to melt and diffuse the source materials at the bisque-substrate interface. For each of these processes heating may be done in inert atmosphere, air, hydrogen, or vacuum.

Formation of coatings from a bisque is considered by many to be the most versatile process for producing coatings. In general, any coating formed by pack cementation can also be formed by slurry-diffusion and typical examples of this interchangeability have been described in the literature (1, 2). As modifications of the spray-pack process other means such as dipping, painting, or electrophoretic deposition can be used to form

the bisques. Among these methods, electrophoretic deposition has particular advantages. This method provides superior coverage to relatively inaccessible surfaces of the part being coated, better uniformity at edges, and reduced losses from over-spray and drag-out normally associated with spraying and dipping.

Present technology for the electrophoretic deposition of metals is based on using organic solvents as dispersants. Shyne *et al.* (3) discussed the deposition of nickel, nickel-chromium, and nickel-chromium-iron coatings as well as nonmetallic coatings onto base metals using alcohol as the suspending medium. Lamb and Reed (4) investigated the deposition of aluminum, silicon, germanium, GeO_2 , WO_3 , NiO, $BaTiO_3$ from water as well as organic liquids which were classed as nonpolar, including gasoline and cetane; slightly polar, such as ethers; and strongly polar comprising alcohols, nitroparaffins, and water. They were unable to obtain deposits from water, and the best deposits were obtained from liquids of intermediate polarity; *e.g.*, diethylene glycol dimethyl ether, and pyridine. The use of polar and nonpolar organic liquids for the deposition of aluminum flake on gold-plated Monel rods was investigated by Pearlstein *et al.* (5), who found that the best deposits were obtained from suspensions in butyl amine. Gutierrez *et al.* (6) used isopropanol and nitromethane as suspending media for depositing niobium, other refractory metals, carbides, and oxides on metal and graphite substrates. Ortner (7) deposited metals, oxides, and carbides on various metallic substrates using an isopropanol-nitromethane mixture. Fisch and Kmiecak (8) utilized this solution to deposit tungsten and tungsten-TiH₂ mixtures on a tantalum alloy. Aluminum has been deposited on steel strip and plate from organic suspensions containing water. The British Iron and Steel Institute (9) described the continuous aluminum coating of steel strip from a methanol-water solution containing a small amount of electrolyte and Yamada *et al.* (10, 11) discussed the use of alcohol-20% water, and pure alcohol as suspending media for depositing aluminum on steel plate.

Although electrophoretic deposition of metals from organic media is in an advanced state of development it has not been widely used as a means for applying coating bisques. This may be due in part to potential fire and health hazards associated with deposition from organic solvents. The use of water as the suspending medium would eliminate the fire hazard and to a great extent reduce the health and waste disposal problems associated with high concentrations of volatile organic solvents.

This paper discusses the use of water as the suspending medium for electrophoretic deposition of metals and mixtures of metals and oxides as bisques for the

Key words: aluminide coatings, sulfidation resistant coatings, aerospace coatings, electrophoretic deposition, electrocoating.

formation of aluminide coatings used for protecting aircraft gas turbine engine blades and vanes. Deposition of metallic bisques is analogous to commercial electrocoating processes (12-15) used to deposit resin and pigment mixtures. Each of these deposition processes utilizes suspensions of insoluble phases in water containing a soluble resin complex. Typically, a resin complex consists of a maleinized oil or organic solvent soluble polycarboxylic acid resin and an alkaline (KOH, amine, or ammonia) solubilizing agent. In a very simplified manner an electrocoating process may be described as a combination of three electrokinetic phenomena; electrophoresis, electroosmosis, electrolysis and electrodeposition. The presence of an electrical field produces electrophoretic migration of suspended particles to the anode where they are deposited and the deposit is concentrated and dewatered by electroosmosis. Simultaneously, electrolysis of water results in gas evolution; hydrogen at the cathode, and oxygen and H^+ at the anode. Electrodeposition occurs at the anode (18). At a metallic anode additional reactions may occur. Among these are: electrodisolution of the anode, the formation of organometallic complexes between ions resulting from this dissolution and the resin, and decarboxylation and cross-linking of the resin by reactions such as the Kolbe reaction. The formation of organometallic compounds, cross-linking of the resin and coagulation of the resin as a result of localized decreases in pH in the vicinity of the anode can lead to the deposition of resin on the anode (16-18). These various electrode reactions are schematically shown in Fig. 1 using an amine-solubilized resin as an example.

Procedures

Although electrophoretic deposition parameters were determined using aluminum flake having a particle size 7.5μ or less, deposits were also obtained using 4 to 44μ atomized powders. This flake together with various amounts of an amine-solubilized acrylic resin formulation containing 40% solids (No. 65137 Clear, Glidden-Durkee Division of SCM, Inc.), 4g glycerol, and 0.05g detergent wetting agent (Orvus AB, Procter and Gamble Company) were added to 70g deionized water having an initial resistivity of 1.2-2.0 megohm-cm. The over-all pH of the suspensions varied between 7.8 and 8.3.

The deposition cell was a 100 ml beaker and the aluminum flake was maintained in suspension by agitation with a Teflon-covered magnetic stirrer. The cathode of the deposition cell was a 20 mesh Monel screen having a hollow parallelepiped configuration 25 x 37 x 50 mm. Deposits (bisques) were formed on a centrally located anode which was a cast nickel-base superalloy (B-1900, composition; Ni, 8% Cr, 10% Co, 6% Mo, 6% Al, 1% Ti, 4% Ta, 0.1% C, 0.1% Zr, 0.015% B) coupon approximately 2 x 12 x 18 mm having an area about

5.3 cm^2 . Before deposition, coupon surfaces were prepared by degreasing in trichlorethylene followed by an acetone rinse. Bisques were formed from freshly prepared suspensions using 40 and 60V d.c. for times from 5 to 30 sec. After coating, the bisques were rinsed in water and air dried at 180°F . Coatings were formed by heating the bisques in a 1×10^{-4} Torr vacuum 4 hr at 1975°F .

Other aluminide coatings containing Cr, Si, and Ti plus Al_2O_3 modifiers were formed by substituting different coating source materials for the aluminum flake. In other respects the suspension compositions were essentially the same. However, for these coatings deposition times were as long as 5 min and deposition voltages up to 100V d.c. were used.

The hot corrosion (sulfidation) resistances of the simple aluminide coating and the Cr and Si modified coatings were evaluated using wedge-shaped simulated airfoil specimens in dynamic hot corrosion (sulfidation) rig tests and compared to the resistances of the corresponding conventionally formed coatings.

Electrophoretic Deposition of Aluminum Flake

Electrophoretic deposition of aluminum flake was investigated as a function of deposition voltage, time, and suspension composition.

Effect of suspension liquid composition.—The suspension liquid consisted of deionized water, an organic modifier, a wetting agent, and resin. Varying the composition and amounts of each of these materials had a significant effect on bisque formation.

The deionized water used for the suspensions had a specific resistance of 1.2-2.0 megohm-cm. However, bisque deposits could also be obtained using suspensions in ordinary tap water. Since decorative appearance was not a consideration, the presence of small amounts of impurities such as chloride or sulfate ions and soluble metal compounds¹ was relatively insignificant. However, because of its higher conductivity, the use of tap water may result in more gassing (electrolysis), less electrophoretic transfer of polymer and resin, and excessively pitted deposits.

Control of suspension pH was an important factor in electrophoretic deposition. As the pH increased thinner coatings resulted under equivalent conditions, possibly because an insulating film was formed more rapidly on the substrate as a result of enhanced coagulation of the resin due to the formation of metallic complexes resulting from increased anodic dissolution of the substrate or by cross-linking of the resin. At a bulk pH 10.5-11, the substrate surface under the bisque was etched and the bisque contained hemispherical pits. These observations are indicative of substrate dissolution and gas evolution accompanying bisque deposition. However, etching and gas evolution were not problems at pH 7.9-8.3 where usable bisques were deposited. Local variations in ion concentrations and suspension pH near the anode, and gas evolution at each electrode were not experimentally investigated. The lower usable suspension pH was determined either by the value at which the deposited bisques could not be sufficiently dewatered by electroosmosis, or the resin coagulated in the bulk of the suspension.

The organic modifiers contained one or more hydroxyl groups. Although the addition of glycerol provided the most uniform bisques, other modifiers such as methanol, isopropanol, and cyclohexanol could also be used. The concentration of modifier needed to produce an optimum deposit depended on both the chemical composition of the modifier and the bisque being deposited. In the absence of a modifier or at low concentrations, pitted and/or uneven nodular bisques were formed, while using too much modifier resulted in thin pitted bisques.

Addition of a detergent wetting agent improved bisque adherence and was also found to act as an anti-

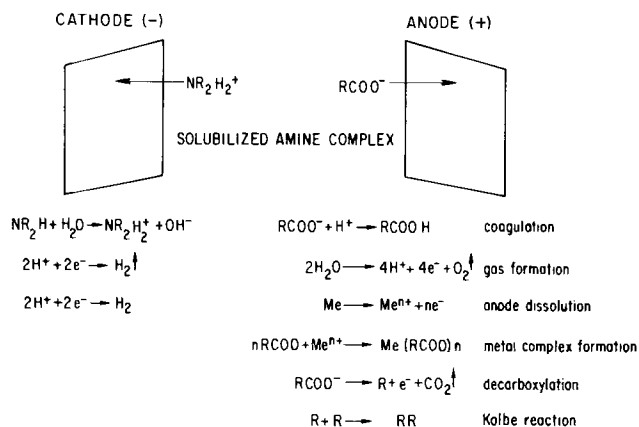


Fig. 1. Electrode reactions during electrocoating

¹ Typical analysis: 27 ppm Cl^- , 32 ppm SO_4^{2-} , 58 ppm metals, total hardness 125.

pitting agent. Virtually all of the work utilized an alkane sulfonate, "Orvus AB." A household detergent, "Trend," was also usable and other wetting agents compatible with the suspension could probably be substituted.

Effect of deposition temperature and voltage.—The electrophoretic bath was operated at room temperature with the maximum operating temperature being below a temperature (approximately 85°F) which would initiate thermal degradation of the resin-solubilizer complex. The deposition voltage was also critical. Below approximately 25V d.c. the bisque had poor adherence and contained too much water due to an insufficient potential gradient for proper electroosmosis. The upper voltage limit (above approximately 70V d.c.) was determined by a value which produced an unsatisfactory deposit because the bisque was too thin, it was excessively pitted or nodular rather than smooth and uniform or it was excessively thick at edges or corners. With other suspension constituents maintained constant, these limiting voltages varied with resin and aluminum concentrations.

Effect of resin and aluminum concentrations.—Bisques were formed from suspensions containing 0.014-0.086g Al/gram H₂O and solid resin to aluminum ratios 1:1.25, 1:2.5, and 1:5. Figure 2 shows typical variations of deposition current with time at 40V d.c. deposition potential. Similar relationships were observed at 60V d.c. At both voltages, the current decreased with time for all aluminum and resin concentrations. The decrease in current is attributed to progressively increasing resistance of the bisque as deposition progressed. At constant resin to aluminum ratios increasing aluminum concentrations led to a more nearly constant current *vs.* time relationship. The quantity of electricity passed during deposition $\int_0^t Idt$, was computed from these curves and effective currents were obtained by dividing values of this integral by deposition times. The relationship between the effective current at 40 and 60V d.c. and solid resin content of the suspension is shown in Fig. 3 and 4. In each of these figures the line represents the relationship determined in the absence of aluminum at pH 7.9-8.3. Between 0.01 and 0.02g resin/gram H₂O, the effective current changed rapidly and erratically with increasing resin concentration, but became essentially constant at concentrations greater than about 0.02g resin/gram

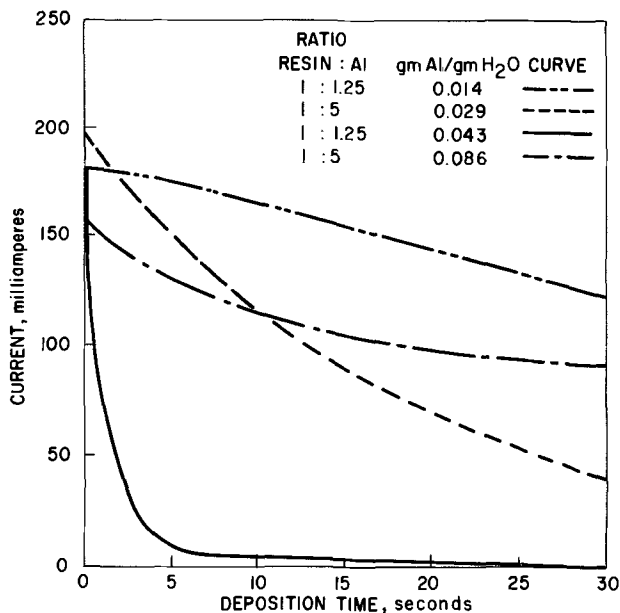


Fig. 2. Typical current-time relationships during electrophoretic deposition of aluminum at 40V.

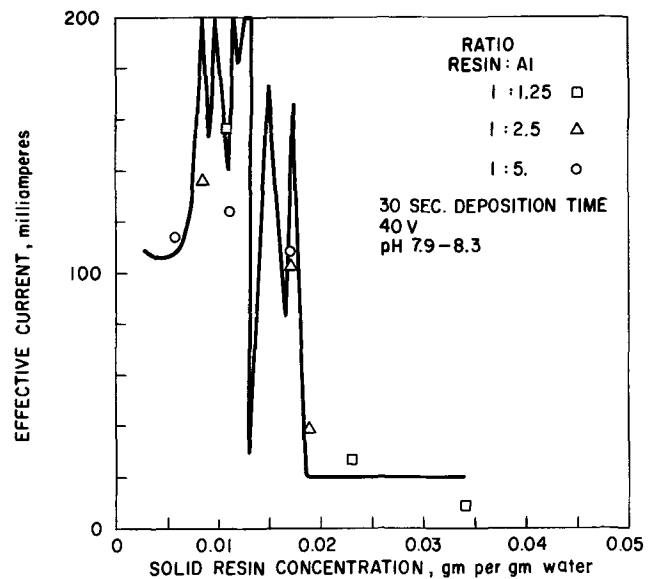


Fig. 3. Effective current at 40V as a function of resin concentration.

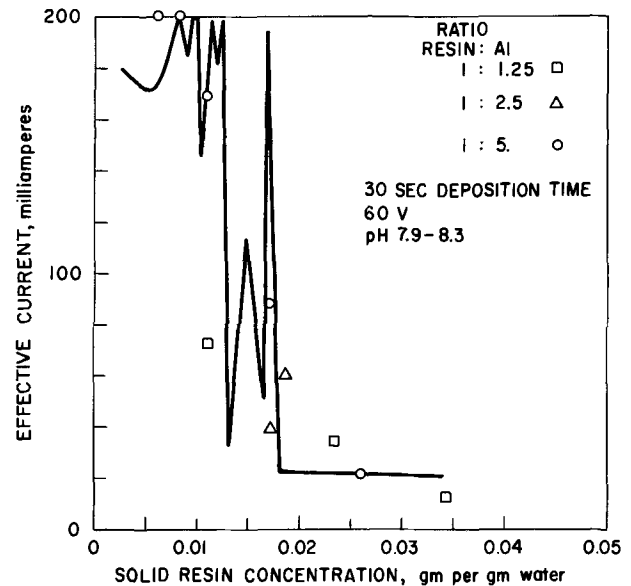


Fig. 4. Effective current at 60V as a function of resin concentration.

H₂O. The approximate correspondence between effective currents measured for suspensions with and without aluminum indicated that effective current depended principally on resin concentration. Similar relationships also were found at pH 7.2-7.6 and pH 8.6-8.8. Since these curves were determined using fresh suspensions, it was suspected that the erratic behavior was caused by incomplete hydrolysis of the resin; however, suspensions aged at room temperature for 4-24 hr provided essentially the same effective current relationships. Figure 5 shows a relationship between unit area bisque weight and coulombs. The slopes of the straight lines represent the coulombic yields of the depositions. Essentially equivalent yields were obtained at 40 and at 60V d.c. and the yields were independent of resin to aluminum ratios and aluminum concentrations up to 0.043 g/gram H₂O. However, at a higher aluminum concentration (0.086 g/gram H₂O) significantly higher yields were obtained.

The relationship between bisque weight and aluminum concentration is given in Fig. 6. Below about

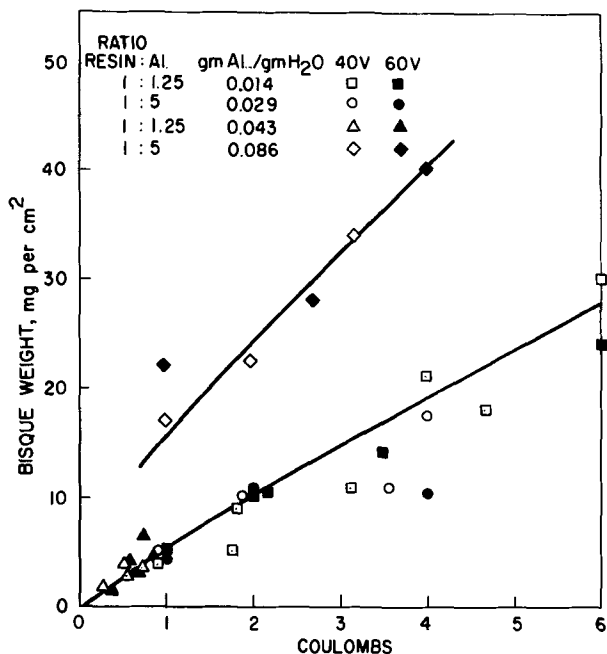


Fig. 5. Relationship between bisque weight and electric current

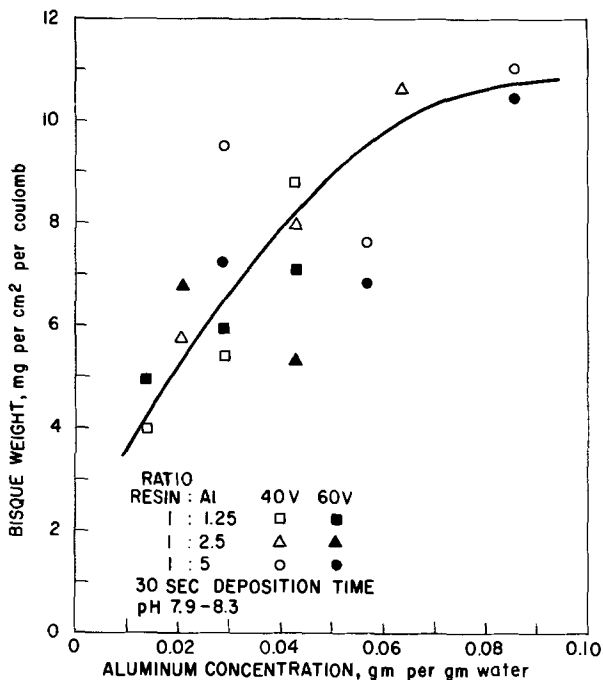


Fig. 6. Effect of aluminum concentration on bisque weight

0.04g Al/gram H₂O, the amount of bisque per coulomb increased in a nearly linear manner with aluminum concentration and appeared to level off above 0.06g Al/gram H₂O.

After vacuum firing to form coatings, the bisques were still intact and easily removed by lightly brushing the coupons. The surface appearances of the bisques and coatings are summarized in Table I. Based on appearance, the best over-all bisques and coatings were obtained from the following four suspensions:

Al conc, gram Al/gram H ₂ O	Ratio, resin: Al
0.014	1:1.25
0.029	1:5
0.043	1:1.25
0.086	1:5

Coating properties.—In the formation of a coating from a bisque having a specific composition, four physical characteristics are commonly used to evaluate the

Table I. Surface appearance of bisques and coatings

Ratio, resin:Al	Conc Al, g/g H ₂ O	Surface appearance			
		Bisque		Coating	
		40V	60V	40V	60V
1:1.25	0.014	U	Hp	U	S
	0.029	Sp	Hp	S	U
	0.043	Sp	U	U	U
1:2.5	0.021	U	U	U	U
	0.043	U	Hp	U	U
	0.064	Hp	Hp	S	U
1:5	0.029	U	U	U	S
	0.057	U	Sp	U	S
	0.086	U	Sp	U	S

U, uniform; Sp, slight pitting; Hp, heavy pitting; S, spotty.

coating and to control the coating formation process. These are: coating weight per unit area, thickness, build-up, and microstructure. For given bisque compositions and heat-treatment conditions, coating thickness is generally a function of bisque weight per unit area or of bisque thickness, and is essentially constant above a minimum bisque weight. For coating reproducibility, bisques are usually deposited at values above this minimum weight. Figure 7 shows curves for the relationship between coating weight and bisque weight using bisques formed at 40 and 60V d.c. from suspensions having resin to aluminum ratios of 1:1.25 and 1:5 with aluminum concentrations from 0.014 to 0.086g Al/gram H₂O. Essentially constant coating weights were obtained from bisques heavier than 10 mg/cm² for all of the conditions investigated up to an aluminum concentration of 0.043g Al/gram H₂O. At a higher aluminum concentration (0.086g Al/8m H₂O) heavier coatings were formed for the same bisque weight indicating an effect of aluminum concentration in the suspension on coating weight. These data illustrate the ranges over which suspension compositions may be varied while still producing an essentially constant coating weight.

As the aluminide coating was formed, the dimensions of the specimen also increased. The amount of this increase is defined as coating build-up, and is measured using a micrometer. Total coating thickness which also includes the aluminide found below the original surface, was determined metallographically on cross sections through the coating and substrate. Figure 8 shows that coating thickness increased linearly with coating weight while the relationship between coating build-up and coating thickness (Fig. 9) was similar to that observed between bisque and coating weight. A photomicrograph of a typical coating is shown in Fig. 10.

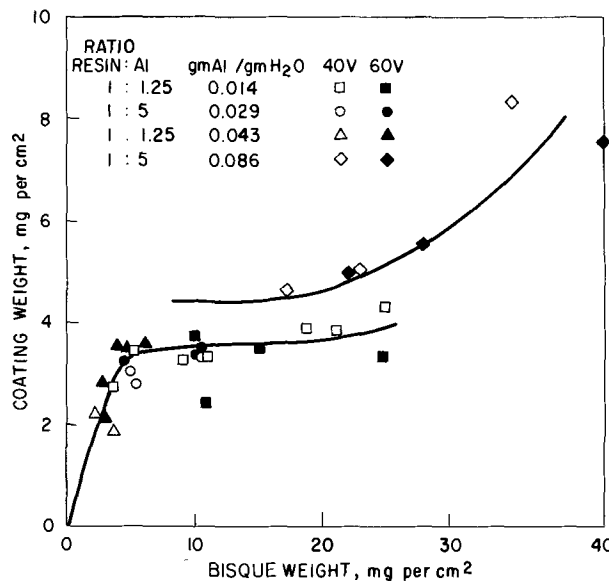


Fig. 7. Relationship between bisque weight and coating weight

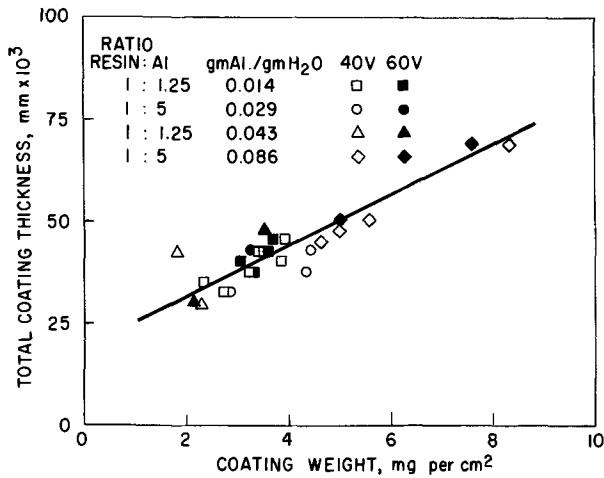


Fig. 8. Relationship between coating weight and coating thickness

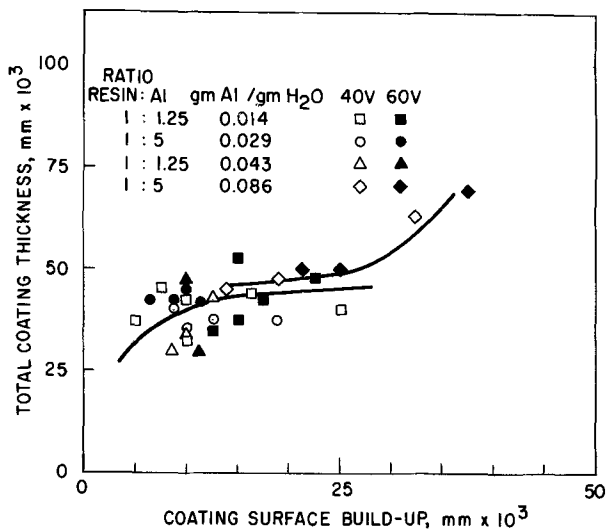


Fig. 9. Relationship between coating build-up and coating thickness.

Other coating properties such as chemical composition and composition gradients from the coating surface into the substrate were not investigated for this coating.

Formation of Other Aluminide Coatings

The electrophoretic deposition technique developed using flake aluminum was used to apply several aluminide coatings to B-1900 alloy coupons. These coatings comprised deposition from suspensions of alloys, mixtures of metals and nonmetals, and mixtures of alloys and oxides. Typical coating formation parameters and coating properties are summarized in Table II.

Deposition parameters such as time, current density, and voltage depended on factors such as the size of the

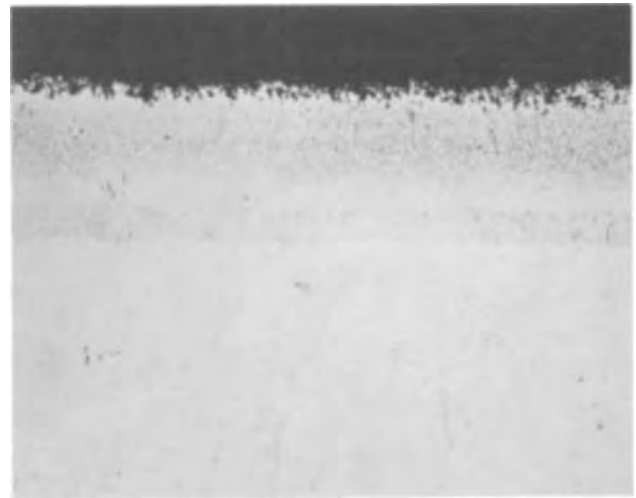


Fig. 10. Microstructure of a coating formed from aluminum flake (190X etched).

article to be coated and electrode spacing. The relative amounts of resin and coating source material depended on factors such as particle shape (granular or flake), particle size, size distribution, and chemical composition. There was an optimum solids to resin ratio and total solids concentration in the dispersion needed to avoid pitted bisques.

Cr modified coating.—In many pack-diffusion or slurry-diffusion processes, Cr-Al alloy powder source activated by inorganic halides is used as the aluminum source. However, these activation materials could not be used in electrophoretic deposition because they coagulated the suspension. Instead, a water insoluble chlorinated hydrocarbon, which did not produce coagulation, was used as an activator. Coating bisques were deposited from suspensions containing chlorinated hydrocarbon activator and -40μ prealloyed 56Cr-44Al powder. In addition, various bisques were deposited containing up to 50 w/o (weight per cent) -40μ Al_2O_3 . Two deposition voltages, 30 and 40V d.c. were used with deposition times up to 30 sec. Diffusion coatings were formed by heating the bisques 4 hr at 1900°F in argon at a pressure of 150 Torr.

The presence of Al_2O_3 in the bisques resulted in more friable bisques after heating but did not affect either the coating microstructure or coating weight gain relationships. The microstructure of a typical Al-Cr coating, Fig. 11, was essentially the same as for a coating formed by either diffusion-pack or spray-pack processes. Figure 12 shows the relationship between coating weight and the weight of 56Cr-44Al powder in the bisque. At the same pH and total solids in the suspension heavier deposits were obtained at 40V d.c. than were obtained at 30V d.c. As shown in Fig. 13, linear relationships were obtained between coating build-up and coating thickness as a function of coating weight.

Table II. Coatings formed using electrophoretic deposition from aqueous suspensions

Coating designation	Bisque composition, w/o	Electrophoretic bisque parameters			Heat treatment conditions			Coating properties		
		Volts, V d.c.	Time, sec	Weight, mg/cm ²	Time, hr	Temp, °F	Atm	Weight, mg/cm ²	Build-up, mm x 10 ³	Thickness, mm x 10 ³
Al-Cr	56Cr-44Al	40	30	133	4	1900	Ar*	10.3	38	75
Al-Si	Al + Si	30	10	21	4	1975	Vac.†	7.5	20	70
Al-Ti + Al ₂ O ₃	Al ₂ O ₃	50	1	15						
(2 step)	Al-Ti	40	240	160	6	1975	H ₂ ‡	4.1	12.5	44
Al-Ti + Al ₂ O ₃	(Al-Ti)-20Al ₂ O ₃	40	240	580	6	1975	H ₂ ‡	3.5	12.5	63
SermeTel J	Al + additives	40	300	80	2	1600	Ar*	4.7	28	70

* Argon at 150 Torr.
 † Vacuum of 1×10^{-4} Torr.
 ‡ Atmospheric pressure.

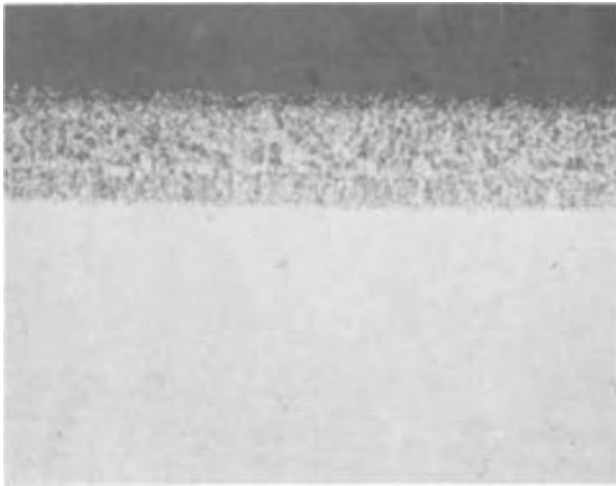


Fig. 11. Microstructure of an Al-Cr coating (190X etched)

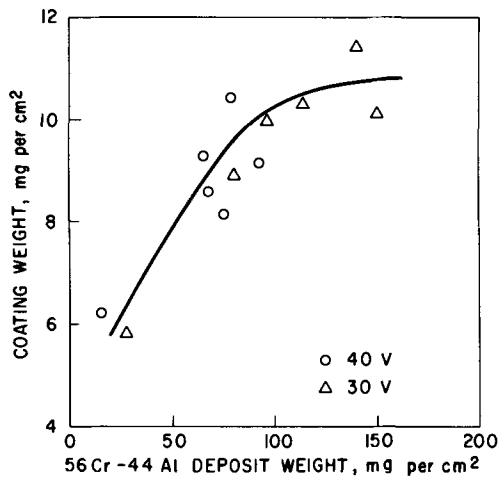


Fig. 12. Relationship between Al-Cr bisque weight and coating thickness for Al-Cr coatings.

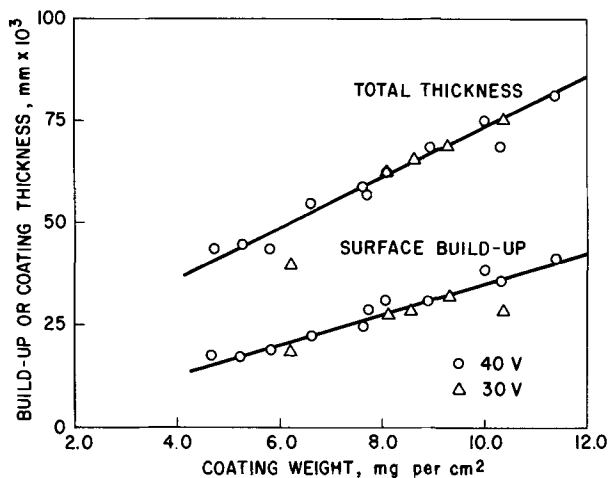


Fig. 13. Relationship between coating weight and coating surface and build-up thickness for Al-Cr coatings.

The relationship between coating build-up and coating thickness is shown in Fig. 14. These relationships are comparable to results obtained for Al-Cr coatings formed on B-1900 by a diffusion-pack process.

Si modified coatings.—Aluminide coatings containing silicon were formed from bisques which were deposited

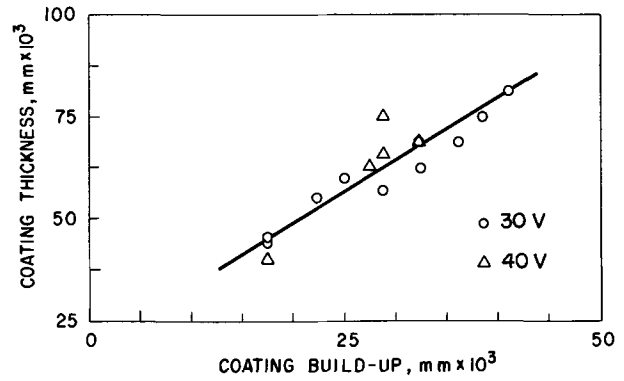


Fig. 14. Relationship between coating build-up and thickness for Al-Cr coatings.

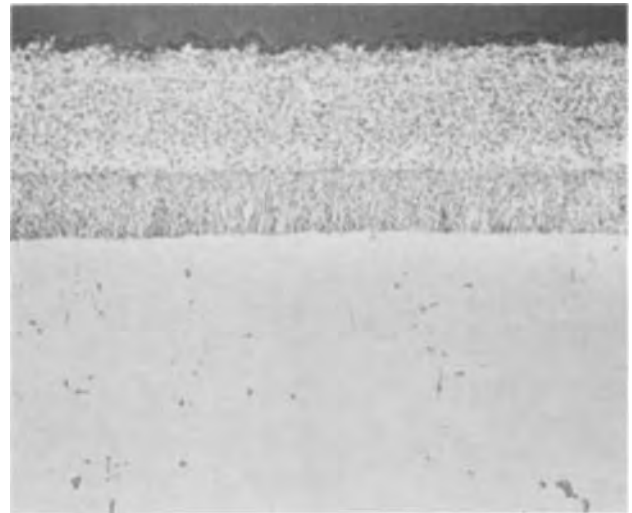


Fig. 15. Microstructure of an Al-Si coating (190X etched)

from suspensions containing either flake aluminum and -40μ powdered silicon or 3.5-6.0 atomized aluminum powder and -40μ silicon. Coatings were formed by heating the bisques at 1975°F for 4 hr in vacuum. Figure 15 shows the microstructure of a coating formed using an atomized powder bisque and comparable microstructures were obtained using bisques of flake aluminum. The presence of silicon in the coating was confirmed by electron microprobe examination.

Al-Ti modified coating containing Al₂O₃ particles.—Aluminide coatings were formed from bisques containing -40μ prealloyed Al-Ti powder, chlorinated hydrocarbon activator, and -40μ Al₂O₃. Coating bisques were applied in two ways: by electrophoretically depositing a layer of Al₂O₃ and subsequently depositing the Al-Ti bisque and by simultaneously depositing a bisque containing Al-Ti and Al₂O₃. Both types of bisques were fired in hydrogen for 6 hr at 1975°F. The microstructure of a coating formed by simultaneous deposition of Al-Ti and Al₂O₃, shown in Fig. 16, was comparable to those produced from sequentially deposited bisques.

SermeTel J coating.—The SermeTel J coating is ordinarily formed by spraying, painting, or dipping a proprietary composition (Teleflex, Incorporated) onto the part to be coated and firing at 1600°F in an inert atmosphere. Since the composition was supplied as a suspension in an organic media, and electrophoretic deposits have been obtained from organic liquids, initial, but unsuccessful, attempts were made to deposit bisques directly from that suspension. Also, it was not possible to form deposits from the as-received suspension either diluted with deionized water or diluted with resin and water.

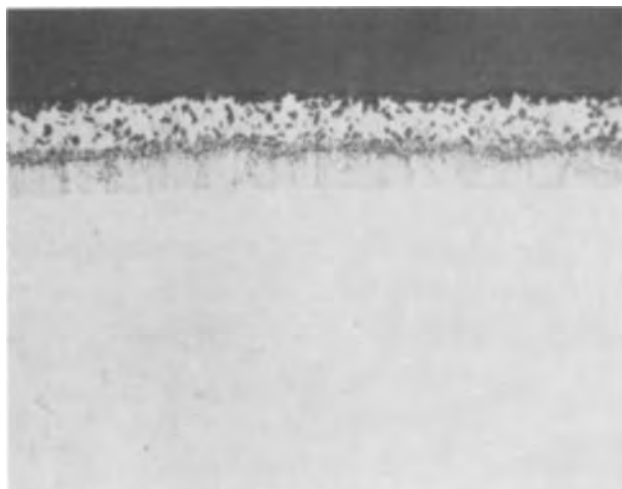


Fig. 16. Microstructure of an Al-Ti coating containing Al_2O_3 particles (190X etched).



Fig. 17. Microstructure of a SermeTel J coating (190X etched)

However, deposits were obtained by suspending the solid constituents of the SermeTel J in water to which resin had been added. The as-received organic suspension was evaporated to dryness, and residue ground and washed with water until the pH of the water increased from 2 to 6.5, then washed with isopropanol, and air dried. The dried powder was made into a suspension, deposits were formed and fired at 1600°F for 2 hr in argon at 150 Torr. A typical microstructure is shown in Fig. 17.

Hot Corrosion Resistance of Coatings

Aluminum, Al-Cr, and Al-Si coatings were formed on wedge-shaped B-1900 test bars approximately 12 mm diameter x 75 mm long (0.5 x 3 in.). These coat-

ings were subjected to a commonly used hot corrosion (sulfidation) test under dynamic conditions which simulate the exposure conditions in an aircraft jet engine. The test bars were rotated at 1750 rpm in a combusted gas stream having a velocity ratio of approximately 0.6 Mach. The apparatus burned Jet A fuel to which 0.4 w/o sulfur was added as ditertiary butyl disulfide and 35 ppm chloride was added as synthetic sea salt (16.6g $\text{MgO}_2 \cdot 6\text{H}_2\text{O}$, 1.9g CaCl_2 , 6.0g Na_2SO_4 , and 37.6g NaCl in 5 gal H_2O). Specimen temperatures were adjusted by varying the fuel/air ratio and temperatures were monitored using an optical pyrometer. The coated bars were exposed under the following temperature cycle:

- 1 min heat-up + 2 min at 1750°F
- 1 min heat-up + 1 min at 2050°F
- 2 min air cool.

The coating characteristics and the protective lives of the coatings are summarized in Table III. This table also gives the protective characteristics of Al-Cr coatings formed by the diffusion-pack process and tested simultaneously with the electrophoretically formed coatings, as well as independently measured protective lives for Al-Si and Al-Cr. These results show that coatings formed by electrophoretic deposition of the coating powders exhibited protective lives comparable to those obtained by the conventional procedures.

Summary and Conclusions

An electrophoretic deposition technique utilizing aqueous suspensions has been developed on a laboratory scale for forming coating bisques used in producing aluminide coatings on nickel-base superalloys. The process which is analogous to commercial electrocoating processes, utilizes a suspension of metallic particles in deionized water containing an amine-stabilized acrylic resin. Electrophoretic deposition parameters (suspension composition, deposition time, and voltage) were determined using aluminum flake. The process was extended to the formation of aluminide coatings modified with additions of Cr, Si, and a mixture of Ti and Al_2O_3 particles.

Chromium modified aluminide coatings were formed from bisques containing chlorinated hydrocarbon activator and prealloyed 56Cr-44Al powder. Silicon modified aluminide coatings were formed from bisques deposited using either aluminum flake or atomized aluminum powder and silicon powder. Titanium-modified aluminide coatings containing particulate Al_2O_3 and the "SermeTel J" coating were also formed from electrophoretically deposited bisques. Microstructures, thickness, and weight gains of these four coatings were comparable to the corresponding properties of coatings produced using vacuum-pack or spray-pack processes.

Simple aluminide, chromium-modified and silicon-modified aluminide coatings were formed on wedge shaped B-1900 test bars and hot-corrosion sulfidation tested under dynamic conditions which simulated conditions in a jet engine. The protective lives of coatings formed by electrophoretic deposition of bisques were comparable to those of the same coatings formed by diffusion-pack or spray-pack processes.

Table III. Hot corrosion resistance of aluminide coatings

Coating type	Bisque wt, mg/cm ²	Coating wt, mg/cm ²	Coating thickness		Protective life	
			mm x 10 ³	mils	hr/mil	Total hr
Electrophoretic						
Al	46	8.2	70	2.8	20	55
Al-Si	47	7.0	63	2.5	22	55
Al-Cr	140	8.0	63	2.5	33	82
Conventional						
Al-Si*	—	—	—	—	13-18	46-64
Al-Cr†	—	10.3	70	2.8	32	90

* Slurry coated.

† Diffusion-pack coated.

Because of its similarity to established electrocoating processes, electrophoretic deposition of metallic coating bisques has excellent potential for use in a continuous automated coating process for applying presently available commercial aluminide coatings to jet engine hardware. These coatings are typically formed using unalloyed metals, mixtures of metals, alloys or mixtures of metals and ceramics, and this work has shown that it is feasible to deposit bisques of these materials by electrophoretic deposition from water.

Manuscript submitted July 26, 1971; revised manuscript received Oct. 1, 1971.

Any discussion of this paper will appear in a Discussion Section to be published in the December 1972 JOURNAL.

REFERENCES

1. J. D. Gadd, H. A. Fisch, H. A. Kmiecik, and E. E. Jones, *Electrochem. Technol.*, **6**, 379 (1968).
2. J. D. Gadd, J. F. Nejedlik, and L. D. Graham, *ibid.*, **6**, 307 (1968).
3. J. J. Shyne, H. Barr, W. D. Fletcher, and H. G. Scheible, *Plating*, **42**, 1255 (1955).
4. V. A. Lamb and W. E. Reed, Jr., *ibid.*, **47**, 291 (1960).
5. F. Pearlstein, R. Wick, and A. Gallaccio, *This Journal*, **110**, 843 (1963).
6. C. P. Gutierrez, J. R. Moshey, and T. C. Wallace, *ibid.*, **109**, 923 (1962).
7. M. Ortner, *Plating*, **51**, 885 (1964).
8. H. A. Fisch, "Manufacturing Techniques for Application of a Duplex W/Si-W Coating on Tantalum Components", Report AFML-TR-70-164, June 1970.
9. "Aluminum Coating of Steel," *Metal Treat. Drop Forging*, **29**, 198, 117 (1962).
10. T. Yamada, M. Abe, and K. Kitabatake, *Light Metals*, **70**, 39 (1965).
11. T. Yamada, H. Kimata, and K. Sugimoto, *ibid.*, **70**, 46 (1965).
12. C. O. Hutchinson, *Plating*, **52**, 1133 (1965).
13. H. F. Reves, *Metal Finishing*, **63**, 2, 59 (1965).
14. H. L. Stein, *Metals Prog.*, **17**, 6, 75 (1970).
15. S. C. Warren, *Automation*, **17**, 4, 87 (April 1970).
16. S. Mercouris and W. F. Graydon, *This Journal*, **117**, 717 (1970).
17. J. P. Giboz and J. Hahaye, *J. Paint Tech.*, **42**, 545, 371 (1970).
18. L. R. LeBras, *J. Paint Technol.*, **38**, 493, 85 (1966).

Cell Design for Potentiostatic Measuring System

B. D. Cahan,¹ Z. Nagy,[†] and M. A. Genshaw^{*.2}

Electrochemistry Laboratory, University of Pennsylvania, Philadelphia, Pennsylvania 19104

ABSTRACT

Design criteria are examined for an electrochemical measuring system to be used for potentiostatic transient investigation of fast electrode reactions. The importance of codesign of the cell and electronics is emphasized. The cell design is examined in detail in this paper, while that of the potentiostat is treated in a separate paper. To obtain the desired characteristics of stability, good frequency response, accuracy in potential control, and uniform current distribution on the working electrode, the following features are required: small cell resistance, small reference electrode resistance, small interelectrode stray capacitances, small working electrode area, a small but variable solution resistance between the point of potential measurement and the working electrode, and a "symmetrical" electrode arrangement. A cell meeting these requirements was built. The main novel feature of the cell is the complete elimination of the troublesome "classical Luggin capillary."

In a potentiostatic system the cell is in the feedback of the control amplifier. The feedback fraction and phase shift in the feedback loop are determined by the cell, and therefore it can have a strong influence on the response characteristics of the system. When designing such a measuring apparatus it is, therefore, important to view the system as a single unit, to design the cell with the potentiostat in mind, and vice versa. The ideal potentiostatic setup is a physical impossibility. It would mean that the double layer capacitance is fully charged at $t = 0+$ time, that is, it would require a zero series resistance in the cell, and an infinite current capability of the potentiostat. A real system has finite response characteristics to a step input. These response characteristics can be determined by either the cell or the potentiostat. It is desirable for the experimenter to have control over these response characteristics and, therefore, they should be determined by the potentiostat. The cell characteristics are not under full control by the experimenter, since they depend on the electrode reaction; and even with the same electrode pro-

cess they are variable, depending on parameters like solution concentration and potential range investigated.³ It was the aim of the present work to design an apparatus for the investigation of fast electrode reactions with potentiostatic transient technique. The cell and the potentiostat were codesigned, and efforts were made to have the system controlled by the potentiostat at all times and under all experimental conditions. The cell design is described here. A later paper will treat the potentiostat (1).

Criteria of a Good Cell

The following properties of the system are used to establish design criteria for the cell: stability, frequency response, accuracy (including accuracy of potential control and accuracy of the point of potential control), and current distribution over the surface of the working electrode. Figure 1 gives a simplified schematic of a potentiostatic measuring system; both the reference and working electrodes are more complex than indicated, but this simple scheme will be sufficient for the present purpose.

Stability criteria.—The stability criteria of such systems have been treated in detail by Schroeder and

³ This treatment refers to a completely general case. In specific cases when the electrode reaction is already fairly well known the design problem is simplified.

* Electrochemical Society Active Member.

† Electrochemical Society Student Associate.

¹ Present address: Chemistry Department, Case-Western Reserve University, Cleveland, Ohio 44106.

² Present address: Ames Research Laboratory, Miles Laboratories, Inc., Elkhart, Indiana 46514.

Key words: low IR drop, low internal resistance, low stray capacitance reference, cell design, uniform current distribution, potentiostatic transients, fast electrochemical reactions.

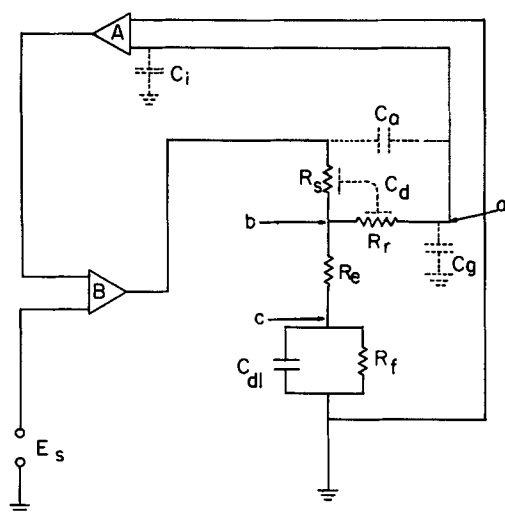


Fig. 1. Schematic for a potentiostatic system. R_s = solution resistance; R_r = resistance of reference electrode; R_e = error resistance; R_f = faradaic resistance; C_{dl} = double layer capacitance; C_g = stray capacitance between reference and ground; C_d = distributive capacitance between the cell solution and the electrolyte in Luggin capillary; C_a = stray capacitance between reference and auxiliary electrode; C_i = input capacitance of potentiostat; E_s = signal voltage; A = input stage of potentiostat; B = control and output stage of potentiostat.

Shain (2). It is required that the cell introduce only a small phase shift in the feedback to keep the system stable. Phase shifts are introduced by variation of the feedback ratio with frequency and by additional delays in the feedback loop, such as the complex impedance presented by the reference electrode capillary, shown as C_d in Fig. 1. The cell acts as a voltage divider and sets the feedback ratio as

$$B = \frac{Z_f + R_e}{Z_f + R_e + R_s}$$

Because Z_f (the electrode impedance)⁴ is frequency dependent, the phase shift and the feedback ratio also change with frequency. The worst phase shift occurs at the highest frequencies. Because of this, the stability and frequency response criteria are interconnected since stability can be obtained at a sacrifice in rise time by slowing down the potentiostat (1). This problem was treated in detail by Booman and Holbrook (3), who have shown that for optimum stability-rise time, the total cell impedance should be minimized, and R_e should be set to an optimum (nonzero) value which depends on the characteristics of the cell and the potentiostat. To avoid further signal delays in the feedback loop, the stray capacitance (C_g and C_d) should be kept to a minimum.

Response of system.—The response of the system to a voltage step is determined by the largest RC time constant in the system. It is desirable to keep all those associated with the cell [i.e., $R_e C_{dl}$, $R_r C_{dl}$, $R_r (C_g + C_i)$, and $R_r C_a$] at minimum value and set one in the potentiostat to control the rise (1).

It should be remembered here that the potential rise time can be defined at points a, b, and c (Fig. 1). In a practical cell, only that at "a" is measurable; on the other hand, we want to minimize the one at point "c." For example, the effect of $R_r C_a$ is to give a fast rise at "a" but a slow one at "c"; this is because C_a shunts the feedback divider, causing a unity feedback fraction at high frequencies and, therefore, making the potentiostat effectively inoperative at short times (C_d can also have a similar effect). $R_r C_{dl}$ is not directly

⁴ Z_f in this simple scheme is the parallel combination of R_f and C_{dl} , in reality it can be much more complex.

under the control of the experimenter, since it depends only on the electrode reaction being investigated. $R_e C_{dl}$ can be minimized by keeping R_e small. Decreasing the area of the electrode does not change $R_e C_{dl}$, since it causes opposite changes in R_e and C_{dl} . There is another reason, however, to keep the electrode small. The rise time of the system (when not controlled by an RC time constant in the cell) is determined by either the slew rate of the potentiostat or by i_{max}/C_{dl} , whichever is slower (where i_{max} is the maximum current of the potentiostat). For example, for a 1A potentiostat, the double layer charging takes 1 μ sec for every microfarad of double layer capacitance. Also, R_r , C_g , C_a , and C_d should be kept at minimum by cell design.

Accuracy criterion.—The accuracy criterion requires that, after the initial rise, the potential of the working electrode be kept exactly at the signal potential fed to the potentiostat. This criterion of potential control is twofold. The potentiostat controls the potential at point "a" (Fig. 1). Although the feedback fraction affects the gain and so the accuracy (at "a"), this effect is negligible for practical situations. The experimenter, however, wishes to control the potential at point "c"; and the error so introduced is iR_e , where i is the cell current. This can be minimized by keeping R_e small.

Uniform current distribution.—The fourth criterion of cell design is a uniform current distribution over the surface of the working electrode. The experimenter wishes to keep every point of the electrode at the preset potential, which requires that the equipotential lines in the vicinity of the electrode in the solution should run parallel to the electrode surface.

Summing up, then, the requirements: low total cell resistance, low-resistance reference electrode, small-area working electrode, low stray capacitances, and uniform current distribution over the working electrode surface. The requirements for R_e are contradictory: zero is required for precise potential control, but a finite resistance is required for stability; therefore a variable R_e is desired.

Previous Cell Designs

Among the above-listed requirements, those associated with the reference electrode are the most troublesome. The conventional Haber-Luggin capillaries (4) have several drawbacks. Barnartt (5) investigated the errors involved in different positionings of the capillary. When placed perpendicularly in front of the working electrode (the most usual arrangement), it has to be kept at a distance more than twice its outer diameter from the surface to avoid disturbing the equipotential lines; this introduces a considerable R_e . Placing it closer to the electrode will distort the current lines exactly at the point of control, causing most of the electrode surface to be at a potential different from that desired. In addition, the distorted current distribution may affect the nature of the electrode reaction itself. Vertical positioning at the side of the electrode, or backside placement (through a hole from the backside of the working electrode) does not avoid the current distortion problem. The high frequency characteristics of the Luggin capillary are also poor. It usually has a high ohmic resistance, since it is made thin to allow close placement; and it also has large coupling capacitance (C_d) between the cell solution and the electrolyte in the capillary. This question was investigated by Bewick *et al.* (6); they have found its electrical equivalent circuit to be very complex, best approximated by a transmission line. This line (represented by C_d in Fig. 1) cannot be represented by any simple RC time constant and can make the problem of correct compensation of potentiostat very difficult; it should therefore be eliminated.

Several efforts were made in the past to correct this situation. Piontelli *et al.* (7, 8) proposed a capillary shown in Fig. 2a. This is a flat-ended glass tube pressed

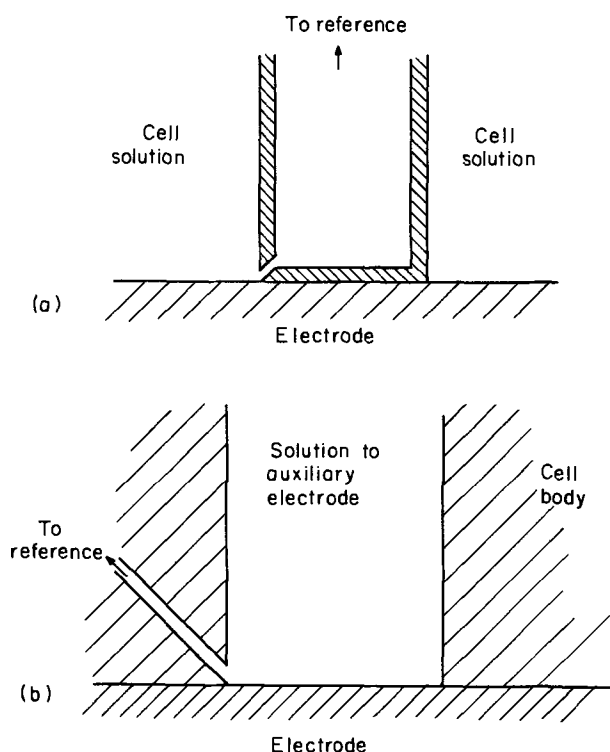


Fig. 2(a). Piontelli electrode; (b) sidehole electrode

against the electrode surface, with the electrical connection made through a small hole near the surface. This can produce low R_e , but the high-frequency characteristics are still poor. Cahan *et al.* (9) used a side-hole electrode, which is an inside-out version of the Piontelli capillary; this is shown in Fig. 2b. A flat working electrode is pressed against a glass or Teflon tube leading to the auxiliary electrode; a small capillary hole is drilled into the wall of this tube, close to the surface of the working electrode, which connects to the reference electrode. This arrangement provides low R_e , and the high-frequency characteristics are also improved. The stray capacitance is small because of the thick walls separating the reference from the other electrodes, and the ohmic resistance can also be made smaller than that of a conventional Luggin, since the capillary hole can be widened after a short distance. Fleischmann and Hiddleston (10) advocated the use of a very thin metal wire coated with organic resin on the sides, in place of the capillary. This also can give low R_e , but the high-frequency characteristics are not good for several reasons. The stray and distributive capacitances are large because of the thin resin coating. The resistance of such a reference electrode can also be high; the resistance of the metallic wire itself is negligible, but the faradaic resistance is high due to the small area exposed to the solution. Assuming that the potential-determining reaction has an exchange current density of 1 mA/cm², the faradaic resistance will be over 100 kohms for a 40 s.w.g. wire; if ($C_g + C_i$) is 50 pf (picofarad), a 5 μ sec rise time will result. In selection of such an electrode, therefore, the i_0 value of the electrode reaction becomes important, while this resistance term is negligible with usual reference electrodes. This type of reference is also limited to metal electrodes.

The other criteria, namely the low cell resistance and the uniform current distribution (neglecting distortion by the reference electrode), can be more easily met. The impedance of the counterelectrode can be made negligibly small by using a relatively large surface area, and it was completely neglected in the above discussion. The solution resistance can also be made small by using concentrated electrolytes and close

electrode spacing; the use of stopcocks between the electrode compartments of the cell should be avoided if possible.

Uniform current distribution can be achieved by a number of geometrical arrangements as given by Kasper (11). A spherical working electrode surrounded by a concentric counterelectrode sphere, or a cylindrical working electrode surrounded by a concentric counterelectrode cylinder with the solution limited to the height of the cylinders, are two possibilities. The counterelectrode does not have to follow exactly the shape of the working electrode if they are sufficiently far removed (12). These two arrangements also have the peculiarity that iR_e can be reduced, for a fixed position of the Luggin tip, by reducing the radius of the working electrode. In this case, R_e will increase with the inverse of the radius, while the area of the electrode will decrease as the square of the radius. Therefore the error, at a given current density, will decrease linearly with the radius. When the reference electrode is closer, and for the cylindrical case, the mathematics is somewhat more complicated, but the effect is in the same direction. An impractically small radius would be needed, however, for fast reactions.

Another way (11) to achieve uniform current distribution is to use parallel plate electrodes with the solution column between them having the same cross section, everywhere along its length, as the shape of the electrodes. Here again the counterelectrode can be of any shape as long as it is far enough removed from the working electrode. For example, if the solution column, having the same cross section as the working electrode, is at least three times as long as the diameter of the working electrode, the shape of the counterelectrode chamber, and the shape and position of the counterelectrode in it, have negligible effect on the current distribution.

Experimental

Cell design.—Among the above designs, the sidehole electrode satisfies best the requirements; but there are some remaining problems. To achieve low R_e , a very fine hole has to be drilled. This still can give considerable R_r , even if the capillary is short; it is not easy to fabricate; and there is possibility of gas bubble blocking, especially with Teflon. Also, it has been pointed out that very low R_e may not be desirable; and with this design, once the cell is assembled, R_e cannot be easily varied.

Extensions of the concept are shown in Fig. 3 and 4. In the first design (Fig. 3) the "sidehole" was extended 360° around to form a conical slot with the two Teflon pieces held apart by suitable spacers. This arrangement would considerably reduce R_r and any blockage problems. It can be used advantageously when a limited area of the large electrode is to be studied. Figure 4 shows the concept of the cell which was actually built. The cell consists of two fluorocarbon plastic pieces. The working electrode is press-fitted into the bottom piece, so as to provide a flush surface with the plastic. The top portion has a cylindrical hole corresponding exactly in position and dimension to the working electrode; this hole leads to the auxiliary electrode chamber. A thin gap between the two pieces, again 360° around, leads to the reference electrode.

A more detailed drawing of the design is shown in Fig. 5, and a photograph is given in Fig. 6. The working electrode (3 mm diameter) is press fitted into a slightly undersized hole to provide a good seal; a backup O-ring seal is also provided. The whole piece can be mechanically polished together to provide a perfectly flush surface, or the electrode can be prepared separately by any desired technique and adjusted flush with the Teflon surface under a microscope, with the adjusting

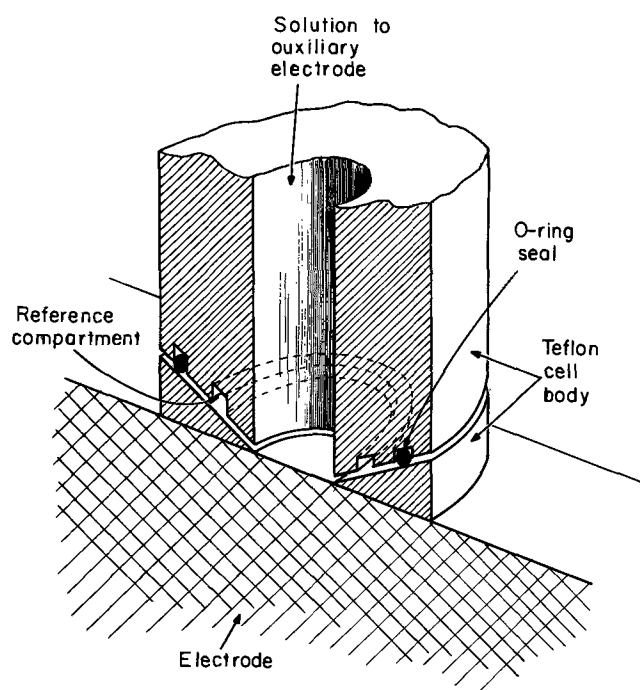


Fig. 3. Extension of the sidehole electrode concept, conical slot reference.

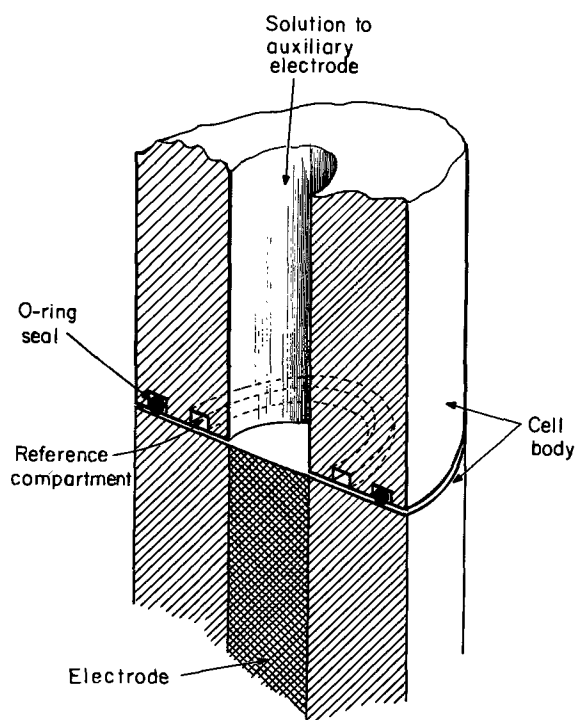


Fig. 4. Extension of the sidehole electrode concept, horizontal slot reference.

screw. Two electrical contacts are provided, one for the current source, the other for potential measurement. This arrangement serves two functions. First, it eliminates the contact resistance which was measured to be about 0.02 ohm, and the resistance of the current lead; these resistances could cause significant iR drop errors. Second, together with the differential input potentiostat (1), it reduces to a minimum the amount of common mode error signal introduced by the inductances of the current leads and by ground loop errors.

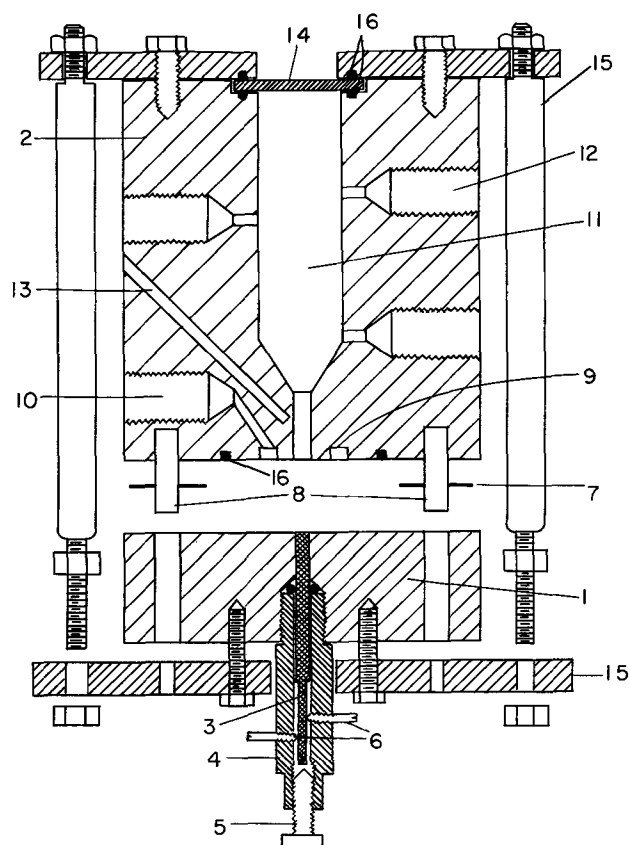


Fig. 5. Exploded cross sectional view of the cell. 1 = Teflon bottom piece; 2 = KEL-F top piece; 3 = working electrode; 4 = nylon bushing; 5 = adjusting screw; 6 = stainless steel contacts; 7 = stainless steel spacer; 8 = stainless steel locating pins; 9 = reference electrode groove; 10 = reference electrode connection, and to vacuum; 11 = auxiliary electrode chamber; 12 = connections for auxiliary electrode, solution inlet, etc.; 13 = hole for illuminating fiber light guide; 14 = observation window; 15 = part of stainless steel frame; 16 = Viton O-rings.

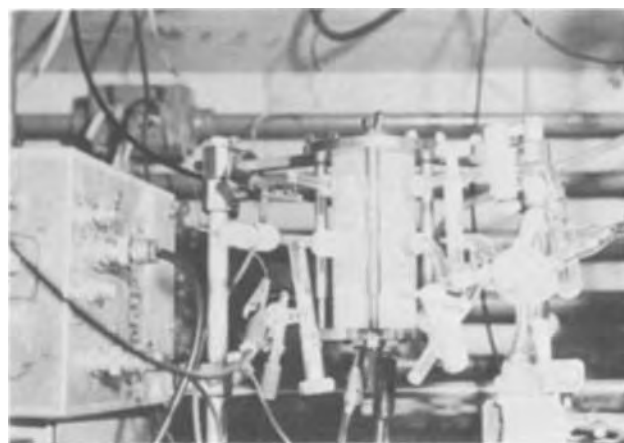


Fig. 6. Photograph of the cell with the potentiostat showing on the left.

The center hole in the top part is three times as long as the diameter of the working electrode. It is surrounded by two concentric grooves. The first one, which contains the reference electrode, is separated by a 1.5 mm wide gap from the center hole. The outside groove contains a Viton O-ring. The gap thickness between the two pieces is controlled by a stainless steel spacer available in thicknesses from 2.5×10^{-3} to 2.5×10^{-2} cm. The gap can also be continuously adjusted slightly

by loosening the nuts on the stainless steel frame holding the two parts together. The exact alignment of the upper and lower parts of the cell is assured by locating pins and by drilling the center hole at the same time in both parts. The auxiliary electrode is a platinum spiral located near the bottom of the auxiliary electrode chamber. The reference electrode in the present work was a metal wire ring in the inner groove. It must be noted here that the reference electrode does not have to form a full ring. As a matter of fact, not only metal wire reference electrodes but any type of reference electrode which can be prepared in micro form can be used (*e.g.*, mercury-coated gold wire for Hg/Hg₂O, Hg/Hg₂Cl₂, or Hg/Hg₂SO₄ electrodes; silver, or silver-coated platinum, for Ag/AgCl electrode; charged palladium, etc.).

The cell can be filled by evacuating it through the reference electrode connection and then sucking solution into the cell. Alternatively, filling with pressure while venting through the reference electrode connection can be used. In either case the solution is forced into the gap. Once the gap is filled, the internal tension will keep the solution in place, in spite of the hydrophobic nature of the surfaces.

Test results.—A set of tests were carried out to check whether the cell achieved the design criteria. The values of R_e , R_s , and R_r were measured and compared to calculated values. A platinum working electrode was polished with the cell bottom to provide a perfectly flush surface. The reference electrode was a zinc wire, and the electrolyte was potassium hydroxide solution. The conductivity of the electrolyte was separately determined. Galvanostatic pulses were applied, and from the resulting potential transient the value of R_e was determined. The values of R_s and R_r were measured with an a-c bridge. Measurements were carried out at a series of solution concentration, gap thickness, and current densities.

The results of R_e measurements are given in Table I. Two examples of the oscillograms are shown in Fig. 7. The value of R_s was measured in 1M KOH giving 70 ohms, the value calculated for the cylindrical channel alone is 60 ohms. The value of R_r was measured also in 1M KOH: 850, 75, and 40 ohms were found for 2.5, 12.5, and 25 $\times 10^{-3}$ cm gaps, respectively. The calculated figures were: 215, 43, and 22 ohms.

Discussion

The data presented above indicate that the design criteria have been met. The R_e value can be reduced to that equivalent to less than 0.0025 cm column of solution. This is much smaller than can be conveniently reached by normal Luggin (about 0.04 cm) (14), and about the same as claimed for the thin wire electrode (10). As can be seen in Table I, R_e is directly proportional to the solution conductivity, increases with gap thickness, and is independent of current density.

Table I. Results of R_e measurements

No.	KOH conc. (M)	d, spacer thickness (cm $\times 10^3$)	Current density (mA/cm ²)	R_e (ohm cm ²)	d_e , solution height equivalent to R_e (cm $\times 10^3$)	$(d_e - \frac{1}{2}d)$ (cm $\times 10^3$)
1	0.3	12.5	48	0.10	7.6	1.3
2	0.3	12.5	94	0.12	9.1	2.8
3	0.3	12.5	215	0.11	8.4	2.1
4	1	12.5	48	0.041	8.0	1.7
5	1	12.5	94	0.043	8.4	2.1
6	1	12.5	228	0.046	9.0	2.7
7	3	12.5	48	0.021	9.0	2.7
8	3	12.5	94	0.021	9.0	2.7
9	3	12.5	228	0.022	9.5	3.2
10	1	25.0	48	0.064	12.5	0.0
11	1	25.0	94	0.060	11.8	-0.7
12	1	25.0	228	0.062	12.3	-0.2
13	1	7.5	48	0.029	5.7	2.0
14	1	7.5	94	0.032	6.3	2.6
15	1	7.5	228	0.033	6.5	2.8
16	1	2.5	94	0.011	2.1	0.8
17	1	2.5	228	0.014	2.7	1.4

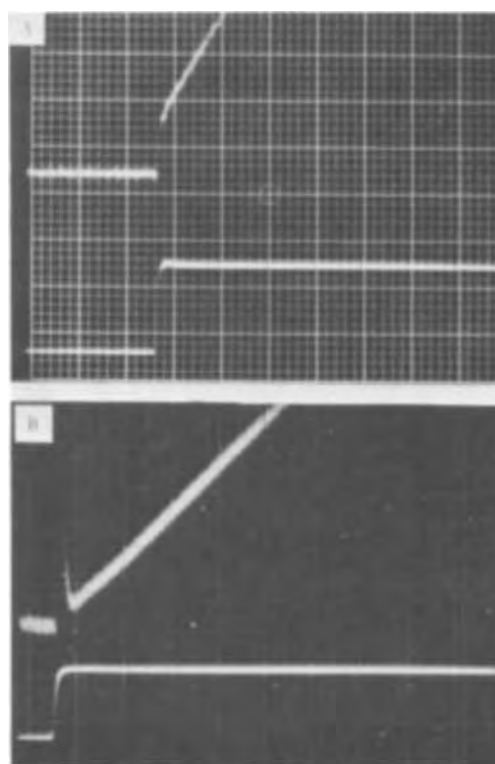


Fig. 7. Examples of R_e measurements. (a) Test No. 1, potential scale = 5 mV/cm; current scale = 2 mA/cm; horizontal = 5 μ sec/cm. (b) Test No. 16, potential scale = 10 mV/cm; current scale = 5 mA/cm; horizontal = 5 μ sec/cm.

From R_e values an equivalent solution column height was calculated, and compared to the half spacer thickness in Table I. Half of the spacer thickness was used because the reference electrode picks up an average potential over the gap, which should correspond to the midpoint since the current distribution is uniform. At the highest thickness the agreement is good, at the lower values there is an approximately constant error, 2.2×10^{-3} cm in average. This slight error is presumed to be caused by deformation of the plastic cell body under pressure. The frame is exerting a compressing stress on the cell at the edges which might result in a slight expansion of the middle portions, causing the gap to be larger than the spacer. In the examples shown on Fig. 7 a large spike can be seen at the beginning of the potential transient taken with the 0.0025 cm gap. This is due to stray capacitive pickup between the auxiliary and reference electrodes. When the gap is widened to 0.0125 cm this peak completely disappears, because the lowered R_r shunts this capacitive spike to ground.

The value of R_r is also small, in the few hundred ohms range. For a Luggin in the above-quoted (14) minimum thickness, using the same solution, it will be about 4 kohms for every millimeter length of the thinly drawn portion, which could then easily add up to many tens of kilo ohms. The measured gap resistance is about four times that of the calculated for 0.0025 cm gap, and about double for the 0.0125 and 0.025 cm gaps. This discrepancy may be due partially to incomplete filling of the gap by the electrolyte, and partially to the use of less than a full circle of reference wire (the reference wire was forming usually less than a half a circle). The stray capacitances are also reduced as compared to other types of references since heavy plastic blocks separate the electrodes. An important beneficial effect is that C_d is not of a transmission line nature any more but can be represented as a regular (and very small) stray capacitance.

With this cell geometry a compromise has to be reached regarding the requirements of low total cell resistance, and small electrode area. A 3 mm diameter seems reasonable, C_{dl} is then about 2 μ f, and since R_e can be lowered to about 0.1 ohm, the $R_e C_{dl}$ time constant is below the microsecond range. At the same time the total cell resistance is reasonably low at 70 ohms for a 1M solution of KOH.

The current distribution over the working electrode surface is uniform, in spite of the nonsymmetrical working-auxiliary arrangement, because of the long channel in front of the working electrode. Note that although the gap will cause some current distortion at the edges of the electrode, this will be very small because of the small thickness of the gap.

Observation of the working electrode is possible with a low power, long working distance, stereomicroscope through the quartz window. Illumination is provided through fiber light guide terminating close to the working electrode in the cell body. The slight transparency of the KEL-F plastic allows the passage of sufficient light.

Further testing of the cell under potentiostatic conditions is to be reported separately (1).

Some further improvements on the cell might be affected. The gap thickness could possibly be further reduced using thinner spacers. This, however, will raise R_e , which could be counteracted by using a less wide gap than the present 1.5 mm. The filling of the gap could be helped by sodium treatments of the gap surfaces to make them less hydrophobic, at the danger of possible introduction of impurities. Placing the reference groove in the lower part of the cell with outlet at the bottom would reduce inductive pickup. The inductive pickup is the function of the area of the loop formed by the reference electrode, working electrode, and connecting leads. When both electrode connections are at the bottom of the cell the loop can be minimized by closely spaced parallel leads. Placing a screen counterelectrode closer to the working electrode, within the channel, would cut down R_s at some sacrifice of current distribution uniformity.

Summary

A cell has been designed and built for potentiostatic transient study of fast electrode reactions which incorporates the following features. Low (and adjustable) error resistance between the point of potential control and the working electrode, a reference electrode having improved high-frequency characteristics, and uniform current distribution over the working electrode surface.

Acknowledgments

We wish to thank Professor J. O'M. Bockris, Dr. L. Nanis, and Mr. G. Razumney for helpful discussions. Financial assistance for this work was provided by the National Science Foundation under Grant No. GK-1724.

Manuscript submitted Nov. 9, 1970; revised manuscript received May 17, 1971.

Any discussion of this paper will appear in a Discussion Section to be published in the December 1972 JOURNAL.

REFERENCES

1. B. D. Cahan, Z. Nagy, and M. A. Genshaw, To be published.
2. R. Schroeder and I. Shain, *Chem. Instr.*, **1**, 233 (1969).
3. G. L. Booman and W. B. Holbrook, *Anal. Chem.*, **37**, 795 (1965).
4. F. Haber, *Z. Physik, Chem.*, **32**, 193 (1900).
5. S. Barnartt, *This Journal*, **99**, 549 (1952).
6. A. Bewick, A. Bewick, M. Fleischman, and M. Liler, *Electrochim. Acta*, **1**, 83 (1959).
7. R. Piontelli and G. Bianchi, *Gazz. Chim. Ital.*, **80**, 581 (1950).
8. R. Piontelli, G. Bianchi, and R. Aletti, *Z. Elektrochem.*, **56**, 86 (1952).
9. B. D. Cahan, J. B. Ockerman, R. F. Amlie, and P. Ruetschi, *This Journal*, **107**, 725 (1960).
10. M. Fleischmann and J. N. Hiddleston, *J. Sci. Instr.*, **1**, 667 (1968).
11. C. Kasper, *Trans. Electrochem. Soc.*, **77**, 353 (1940).
12. S. Barnartt, *This Journal*, **106**, 722 (1959).
13. K. J. Vetter, "Electrochemical Kinetics," pp. 394-395, Academic Press, New York (1967).
14. S. Barnartt, *This Journal*, **108**, 102 (1961).

Mass Transfer to a Rotating Sphere at High Schmidt Numbers

John Newman*

*Inorganic Materials Research Division, Lawrence Radiation Laboratory,
and Department of Chemical Engineering, University of California, Berkeley, California 94720*

ABSTRACT

The Lighthill transformation is used to calculate limiting rates of mass transfer to a rotating sphere on the basis of shear-stress calculations found in the literature.

Chin (1) has recently calculated rates of mass transfer to a rotating sphere on the basis of calculated velocity profiles from the literature. Near the poles of the sphere, the situation is essentially identical to a rotating disk. Chin has calculated also the next term in an expansion for small values of θ , the angle from the pole. He takes the Schmidt number to be large, a good approximation for electrolytic solutions.

This is an excellent situation in which to use the Lighthill transformation (2-4) to calculate the mass-transfer rate at angles θ which need not be small. For

high Schmidt numbers, the diffusion layer is much thinner than the hydrodynamic boundary layer, and the shear stress or the velocity derivative at the wall

$$\beta = \frac{\partial v_\theta}{\partial r} \Big|_{r=r_0} \quad [1]$$

provides sufficient information about the velocity profiles to permit the calculation of a first approximation to the mass-transfer rate. For axisymmetric bodies, this result takes the form (4)

$$i_n = \frac{nFD_1 c_s \sqrt{R\beta}}{s_1 \Gamma(4/3)} \Big/ \left[9D_1 \int_0^x R \sqrt{R\beta} dx \right]^{1/3} \quad [2]$$

* Electrochemical Society Active Member.
Key words: current distribution, limiting current.

where x is the distance along the electrode from its upstream end, $R(x)$ is the normal distance of the surface from the axis of symmetry, and s_i is the stoichiometric coefficient of the limiting reactant in the electrode reaction



This result applies at high Schmidt numbers to the limiting current density i_n when the effect of ionic migration on the limiting reactant can be ignored. Thus, the concentration of the limiting reactant is zero at the electrode surface and equal to c_∞ in the bulk solution outside the diffusion layer.

For a sphere

$$R = r_0 \sin \theta \text{ and } x = r_0 \theta \quad [4]$$

If we define a dimensionless shear-stress distribution $B(\theta)$ according to

$$B(\theta) = \beta \nu^{1/2} / r_0 \Omega^{3/2} \quad [5]$$

then Eq. [2] can be written as

$$\begin{aligned} \text{Nu}(\theta) &= \frac{2r_0 s_i i_n}{nFD_i c_\infty} \\ &= \frac{2\sqrt{B \sin \theta} \text{Re}^{1/2} \text{Sc}^{1/3}}{\Gamma\left(\frac{4}{3}\right) \left[9 \int_0^\theta \sqrt{B \sin \theta} \sin \theta d\theta\right]^{1/3}} \quad [6] \end{aligned}$$

where $\text{Nu}(\theta)$ is the local Nusselt number, $\text{Re} = r_0^2 \Omega / \nu$ is the Reynolds number, and $\text{Sc} = \nu / D_i$ is the Schmidt number. For an electrode extending from the pole to the angle θ , we can define the average Nusselt number Nu_{avg} analogously in terms of the average current density. Appropriate integration of Eq. [6] yields

$$\text{Nu}_{\text{avg}} = \frac{3^{1/3} \text{Re}^{1/2} \text{Sc}^{1/3}}{\Gamma(4/3) (1 - \cos \theta)} \left[\int_0^\theta \sqrt{B \sin \theta} \sin \theta d\theta \right]^{2/3} \quad [7]$$

Banks (5) has solved the boundary-layer equations for a rotating sphere and expresses the shear-stress distribution in an expansion for small θ

$$B(\theta) = 0.51023 \theta - 0.22129 \theta^3 + 0.02071 \theta^5 - 0.00189 \theta^7 \quad [8]$$

Manohar (6) has solved the boundary-layer equations numerically and gives a graph of the shear-stress distribution. His results should be better than those of Banks when the angle θ is not small.

On the basis of these results, we have expressed B as

$$B(\theta) = 0.51023 \theta - 0.1808819 \theta^3 - 0.040408 \sin^3 \theta \quad [9]$$

as shown in Fig. 1. For small values of θ , this reduces to

$$\begin{aligned} B(\theta) &= 0.51023 \theta - 0.22129 \theta^3 + 0.020204 \theta^5 \\ &\quad - 0.00438 \theta^7 + O(\theta^9) \quad [10] \end{aligned}$$

and approximates well Bank's expression 8 for the first three terms. Figure 1 can be compared with the graph given by Manohar (6).

The local and average Nusselt numbers are now obtained from Eq. [6] and [7] by carrying out the integration with $B(\theta)$ given by Eq. [9]. The results are shown in Fig. 2 along with Chin's result for the local Nusselt number. Chin obtained correctly the first two terms for the local Nusselt number in an expansion for small values of θ . However, he predicts too high a mass-transfer rate near the equator of the sphere. Thus, his value of 0.474 for $\text{Nu}_{\text{avg}} / 2\text{Re}^{1/2} \text{Sc}^{1/3}$ for a sphere or a hemisphere should be replaced by the value of 0.4508.

The boundary-layer results do not predict that the shear stress goes to zero at the equator, as it must. Thus, there must be a small region near the equator

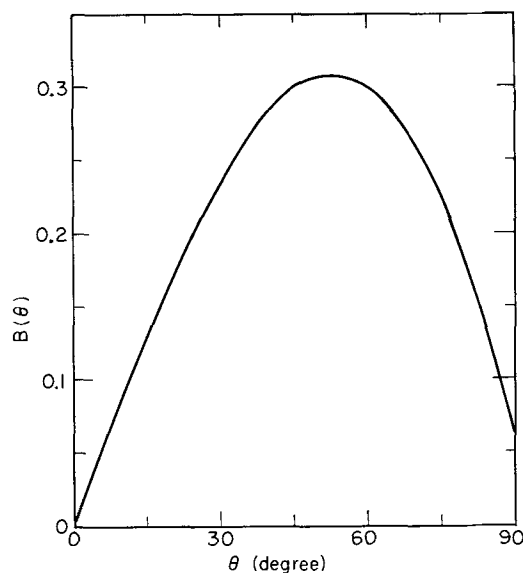


Fig. 1. Dimensionless velocity derivative on the surface of a rotating sphere.

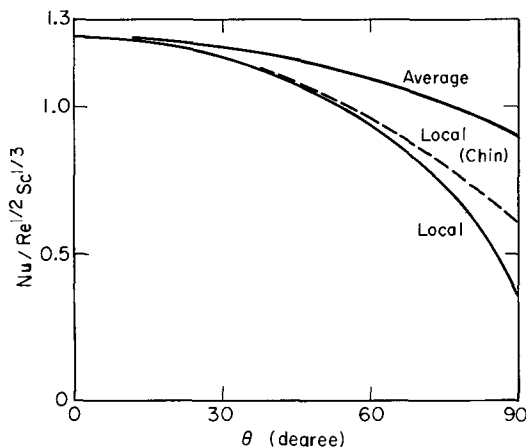


Fig. 2. Local and average Nusselt numbers for a rotating sphere at high Schmidt numbers, calculated from the shear stress results of Manohar. The local Nusselt numbers obtained from Chin's analysis are shown for comparison.

where B goes from the value predicted by boundary-layer theory to zero at the equator itself. This will lower the mass-transfer rates predicted for this region.

These results can be extended to metal deposition on a rotating sphere at the limiting current from a solution of a single electrolyte by redefining the local Nusselt number as

$$\text{Nu}(\theta) = \frac{(1 - t_+) 2r_0 i_n}{z_+ F D c_\infty} \quad [11]$$

and replacing the Schmidt number by $\text{Sc} = \nu / D$, where D is the diffusion coefficient of the electrolyte and z_+ and t_+ are the charge number and transference number of the reacting cation.

Acknowledgment

This work was supported by the United States Atomic Energy Commission.

SYMBOLS

B	dimensionless velocity derivative at the surface
c_∞	bulk concentration of the limiting reactant, mole/cm ³
D	diffusion coefficient of single electrolyte, cm ² /sec

D_i	diffusion coefficient of limiting reactant, cm ² /sec	z_i	charge number of species i
e^-	symbol for the electron	β	velocity derivative at the surface, sec ⁻¹
F	Faraday's constant, 96,487 coulombs/equiv	$\Gamma(4/3)$	0.89298, the gamma function of 4/3
i_n	limiting current density, A/cm ²	θ	angle from the pole of the sphere
M_i	symbol for the chemical formula of species i	ν	kinematic viscosity of the fluid, cm ² /sec
n	number of electrons transferred in the electrode reaction	Ω	rotation speed of sphere, radian/sec
$Nu(\theta)$	local Nusselt number		
Nu_{avg}	average Nusselt number		
r	radial distance, cm		
r_0	radius of sphere, cm		
Re	Reynolds number		
R	normal distance of surface from axis of symmetry, cm		
s_i	stoichiometric coefficient of species i in the electrode reaction		
Sc	Schmidt number		
t_+	cation transference number		
v_θ	velocity in the θ -direction, cm/sec		
x	distance along electrode from its upstream end, cm		

Manuscript received June 24, 1971.

Any discussion of this paper will appear in a Discussion Section to be published in the December 1972 JOURNAL.

REFERENCES

1. Der-Tau Chin, *This Journal*, **118**, 1434 (1971).
2. M. J. Lighthill, *Proc. Royal Soc.*, **A202**, 359 (1950).
3. Andreas Acrivos, *Phys. Fluids*, **3**, 657 (1960).
4. John Newman, *Ind. Eng. Chem.*, **60**, No. 4, 12-27 (April 1968).
5. W. H. H. Banks, *Quart. J. Mechanics and Applied Mathematics*, **18**, 443 (1965).
6. R. Manohar, *Z. Angew. Math. Phys.*, **18**, 320 (1967).

Technical Notes



Interstitial Silver Ions and Standard Potentials

Arnold Hoffman*

Research Laboratories of Polaroid Corporation, Cambridge, Massachusetts 02139

It has been suggested by Awad *et al.* (1) that the potential of a silver electrode is likely to vary with the activity of interstitial silver ions, Ag^+_i , in an adhering silver halide crystal in a manner analogous to the activity of silver ions, Ag^+ , in solution.

Subsequently, we had shown (2) that if it is assumed that the chemical potentials of silver lattice positions in silver halides can be equated and considered as a reference state, a relationship is obtained between the standard Gibbs-Stockholm potentials, E° , of a silver-silver halide electrode and the Ag^+_i composition in the silver halide crystal, *i.e.*

$$E^\circ = RT/nF \ln 1/X_i + B + C \quad [1]$$

where

$$RT/nF = 0.059V \text{ at room temperature}$$

$B = RT/2nF \ln \beta$ (β = number of available interstitial sites per silver ion lattice site). The range of values of X_i is relatively large compared to the small differences in the value of B . Therefore, B can be treated as a constant.

$C =$ Constant, assuming the energy of a silver ion lattice position can be taken as the reference state for all silver halides.

$$X_i = N_i/N_1$$

$N_i =$ Concentration of Ag^+_i , (number/cm³)

$N_1 =$ Concentration of silver ions at lattice positions; for all the silver halides $N_1 \gg N_i$ and the value of N_1 are approximately equal to each other, therefore X_i can be expressed as N_i .

or

$$E^\circ = RT/nF \ln 1/N_i + D \quad [2]$$

where

$$D = B + C + RT/nF \ln N_1 = \text{Constant}$$

* Electrochemical Society Active Member.

Key words: silver halides, interstitial silver ions, Frenkel defects, standard potentials.

Equation [2] predicts that a plot of the standard potentials, E° vs. the log of the concentration of interstitials, N_i , should give a straight line with a slope equal to -59 mV (at room temperature).

The standard potentials for the various silver halides are listed relative to NHE (3) in Table I. There exists two modifications of AgI at room temperature, a hexagonal β -phase and a cubic γ -phase (4). Ruby and Tremmel (5) using cathodic cyclic voltammetry with carbon paste silver halide electrodes obtain two current peaks for their AgI results. We have assumed that these two peaks reflect the reduction potential of the two modifications of AgI. These values differ from the value usually tabulated for an unspecified form of AgI [$-0.152V$ (3)].

Also listed in Table I are the concentration of interstitial silver ions obtained by several workers.

The data were obtained in the following ways:

(A) The slope of plot of ionic conductivity vs. the log $1/T$ which reflects, in part, the free-energy difference of a silver ion in a lattice and interstitial position (6).

(B) Applying a model of a diffuse space charge near the crystal surface to measurements of: (i) surface charge or zeta-potential of silver halide as a function of pAg using Grimley's theory (4), and (ii) dependence of latent-image distribution on an electric field as applied by Trautweiler (7).

A plot of E vs. $\log N_i$ is shown in Fig. 1. The straight line drawn through the points has a slope

Table I.

AgX	E (vs. NHE) volts	N_i	Reference
AgCl	+0.222	6×10^{10} - 6×10^{11}	(6)
AgBr	+0.071	5×10^{14} - 8×10^{14}	(6-9)
β -AgI	-0.099 ± 5	2.5×10^{10} - 2.5×10^{18}	(4)
γ -AgI	-0.189 ± 5	2×10^{10} - 3×10^{10}	(4)

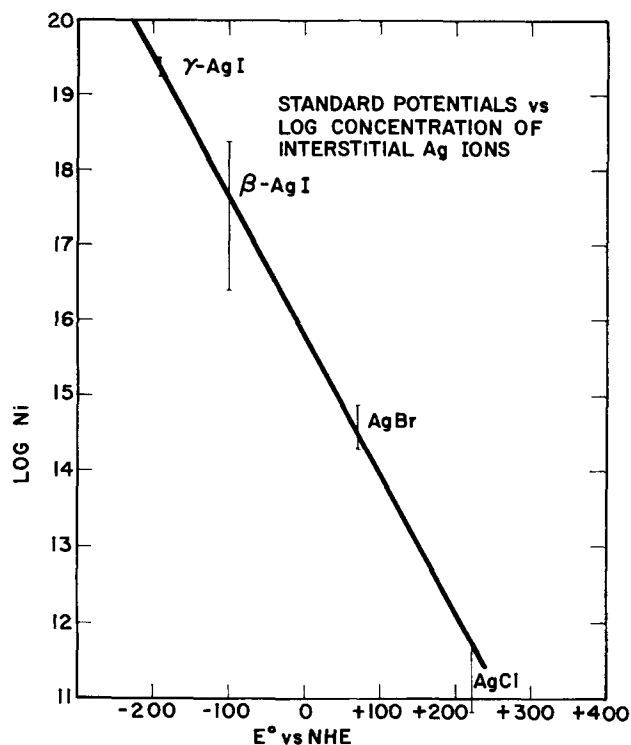


Fig. 1.

equal to about -55 mV, in good agreement with Eq. [2].

Thus, the model proposed by Honig *et al.*, that the silver halide lattice can be treated as a solvent, and the vacancies and interstitial ions as solute anions and cations, respectively, is justified.

The apparent validity of Eq. [2] suggests that any materials incorporated into a silver halide lattice that can change the concentration of interstitials should manifest a potential different from that of an undoped silver halide.

Teltow (10) has shown that the incorporation of small amounts of Cd^{++} [<0.01 mole per cent (m/o) CdBr_2] into AgBr decreased the ionic conductivity. An extrapolation of his data to room temperature indicates a reduction of Ag^+ by a factor of three to five at a concentration of 0.01 m/o CdBr_2 . Since the ionic conductivity of silver halides (in this range of impurity

concentration) is proportional to the concentration of interstitial silver ions, it may be concluded that in this range of concentration of Cd^{++} , the concentration of Ag^+ has been reduced by a factor of three to five.

It has been reported (11) that the cathodic characteristic potential of silver halides, formed in the presence of Cd^{++} (rinsed and reduced in KNO_3) were always more anodic (~ 30 mV for AgBr) compared to that obtained in the formation of the silver halide in the absence of Cd^{++} . (The actual amount of Cd^{++} incorporated into the silver halides was not measured.) This is equivalent to stating that the E° is more positive (~ 30 mV for AgBr) for the silver halide formed in the presence of Cd . The line in Fig. 1 predicts that a change of $+30$ mV for the E° of a silver halide (*e.g.* AgBr) should be accompanied by a reduction of the concentration of Ag^+ by a factor of 3.2. Thus, it would be expected that the level of Cd^{++} incorporated into the silver halide electrochemically is of the order of ≤ 0.01 m/o CdBr_2 . Quantitative data would be necessary to verify this.

Acknowledgments

The author expresses his grateful appreciation to Dr. P. van Heerden and Dr. L. Cerankowski for helpful discussions and encouragement.

Manuscript received Nov. 4, 1970.

Any discussion of this paper will appear in a Discussion Section to be published in the December 1972 JOURNAL.

REFERENCES

1. S. A. Awad, *J. Electroanal. Chem. Interfacial Electrochem.*, **21**, 483 (1969).
2. A. Hoffman, *This Journal*, In press.
3. A. J. deBethune, "Standard Electrode Potentials and Temperature Coefficients at 25°C ," Clifford A. Hampel, Editor, in "Encyclopedia of Electrochemistry," Rheinhold, New York (1964).
4. E. P. Honig, *Trans. Faraday Soc.*, **64**, 2248 (1969).
5. W. R. Ruby and C. G. Tremmel, *J. Electroanal. Chem. Interfacial Electrochem.*, **18**, 231 (1968).
6. H. C. Abbink and D. S. Martin, Jr., *J. Phys. Chem. Solids*, **27**, 205 (1965).
7. F. Trautweiler, *Phot. Sci. Eng.*, **12**, 98 (1968).
8. P. Muller, *Phys. Status Solidi*, **12**, 775 (1965).
9. E. P. Honig and J. J. Th. Hengst, *J. Colloid Interface Sci.*, **31**, 545 (1969).
10. J. Teltow, *Z. Physik. Chem.*, **195**, 197 (1950); *Ann. Physik.*, **5**, 63 (1949).
11. A. Hoffman, Thesis, "Chronopotentiometry of Silver Halides" p. 50, University Microfilms, Ann Arbor, Mich. (1966).

Interactions in Mixed Potential Systems

Francis M. Donahue*

Department of Chemical Engineering, The University of Michigan, Ann Arbor, Michigan 48104

Interactions between the anodic and cathodic partial processes in mixed potential systems, *e.g.* corrosion or electroless plating, can be ascertained from extensive studies of the electrode kinetics of the respective partial processes [*e.g.* see Ref. (1)]. During electroless plating studies, the author and co-workers (2,3) found that the interactions could be deduced without extensive electrode kinetic studies. Because of the general interest in mixed potential systems and a need for a relatively rapid method of deducing the magnitude of interactions among the reactants (if present), the pertinent relationships for this analysis are derived in this paper.

Consider the following generalized mixed potential system



To continue the generality, it will be assumed that both reactants of the mixed potential system interact in both of the partial processes. Thus, the respective rate laws may be written as

$$-r_a = k_a [\text{Red}]_a^\gamma [\text{Ox}]_c^{\delta_1} \quad [2]$$

and

$$-r_c = k_c [\text{Ox}]_c^\delta [\text{Red}]_a^{\gamma_1} \quad [3]$$

The mixed current density for such a system is

$$i_m = F n_a k_a^\circ [\text{Red}]_a^\gamma [\text{Ox}]_c^{\delta_1} \exp \left[\frac{\psi_o - \phi_a^\circ}{\beta_a} \right] \quad [4a]$$

$$i_m = F n_c k_c^\circ [\text{Ox}]_c^\delta [\text{Red}]_a^{\gamma_1} \exp \left[\frac{\phi_c^\circ - \psi_o}{\beta_c} \right] \quad [4b]$$

* Electrochemical Society Active Member.

Key words: corrosion, electrochemical reaction orders, electrode kinetics, electroless plating, rate equations.

Equating [4a] and [4b], taking logarithms and rearranging

$$\psi_0 = \frac{b_a b_c}{b_a + b_c} \left\{ \frac{\phi^{\circ c}}{b_c} + \frac{\phi^{\circ a}}{b_a} + \log \left[\frac{(n k^{\circ})_c}{(n k^{\circ})_a} \right] + (\delta - \delta_1) \log [\text{Ox}]_c - (\gamma - \gamma_1) \log [\text{Red}]_a \right\} \quad [5]$$

Partial differentiations of Eq. [5] yield

$$\left[\frac{\partial \psi_0}{\partial \log [\text{Ox}]_c} \right]_{[\text{Red}]_a, T} = (\delta - \delta_1) \frac{b_a b_c}{b_a + b_c} \quad [6]$$

and

$$\left[\frac{\partial \psi_0}{\partial \log [\text{Red}]_a} \right]_{[\text{Ox}]_c, T} = -(\gamma - \gamma_1) \frac{b_a b_c}{b_a + b_c} \quad [7]$$

Further useful relationships may be obtained by taking the logarithms of Eq. [4a] and [4b], solving for ψ_0 , equating the results and rearranging to obtain

$$\log i_m = \frac{1}{b_a + b_c} \left\{ \phi^{\circ c} - \phi^{\circ a} + b_c \log [\mathbf{F}(n k^{\circ})_c] + b_a \log [\mathbf{F}(n k^{\circ})_a] + (b_c \delta + b_a \delta_1) \log [\text{Ox}]_c + (b_a \gamma + b_c \gamma_1) \log [\text{Red}]_a \right\} \quad [8]$$

Partial differentiations of Eq. [8] yield

$$\left[\frac{\partial \log i_m}{\partial \log [\text{Ox}]_c} \right]_{[\text{Red}]_a, T} = \frac{b_c \delta + b_a \delta_1}{b_a + b_c} \quad [9]$$

and

$$\left[\frac{\partial \log i_m}{\partial \log [\text{Red}]_a} \right]_{[\text{Ox}]_c, T} = \frac{b_a \gamma + b_c \gamma_1}{b_a + b_c} \quad [10]$$

Finally, dividing Eq. [6] by [9] and Eq. [7] by [10] give the following

$$\left[\frac{\partial \psi_0}{\partial \log i_m} \right]_{[\text{Red}]_a, T} = \frac{b_a b_c (\delta - \delta_1)}{b_a \delta_1 + b_c \delta_1} \quad [11]$$

and

$$\left[\frac{\partial \psi_0}{\partial \log i_m} \right]_{[\text{Ox}]_c, T} = -\frac{b_a b_c (\gamma - \gamma_1)}{b_a \gamma + b_c \gamma_1} \quad [12]$$

Equations [6], [7], and [9]-[12] represent diagnostic criteria which can be used to evaluate the properties of mixed potential systems. In particular, these relationships permit the determination of the symbiotic effects of the partial processes.

Mathematically, the six equations noted above represent only four independent relationships. However, they do represent six "independent" combinations of experimental data points. Since there are six "unknowns" in the equations, *viz.* b_a , b_c , γ , γ_1 , δ , and δ_1 , it is more correct mathematically to evaluate two of the parameters independently of the mixed potential measurements. While the author does not wish to impose his bias on the reader, it is usually simpler to measure the Tafel slopes independently.

In order to demonstrate the utility of the technique two examples will be given. Kelly (1) studied the dissolution of iron in acidic solutions. From a separate study of the anodic partial process, he had ascertained that the rate law for iron dissolution was

$$-r_{\text{Fe}} = k_{\text{Fe}} [\text{H}^+]^{-1} \quad [13]$$

From Eq. [3], one deduces that $\delta_1 = -1$. His Eq. [22] is similar to Eq. [6] of this paper; likewise, Fig. 6 of his paper represents the data required for Eq. [6] of this paper. Solving Eq. [6] using the data in his figure and his observed Tafel slopes, one deduces that $\delta = 1$, which is consistent with all known data for hydrogen evolution on iron.¹

¹ Kelly clearly saw the potentiality of combining certain rate data with measurements at the mixed potential to deduce "unmeasured" reaction orders. However, his derived relationships, being specific to his system, lacked the appearance of generality.

Experiments in the author's laboratory (2-4) on electroless nickel plating led to the following conclusions: (i) nickel ions have no effect on the anodic partial process, and (ii) hypophosphite ions interact with the cathodic partial process with a calculated reaction order of 0.7. These conclusions were based upon determinations of the six diagnostic criteria derived above, the Tafel slope for nickel ion reported by Yeager and co-workers (5) and the assumption that $b_a > b_c$ [based on the "polarization curves" of Donahue and Yu (4)].

The foregoing analysis is general for all mixed potential systems. It is predicated upon (i) the commonly accepted principle that the rates of all electrochemical reactions at the mixed potential satisfy the requirement of charge conservation first enunciated by Wagner and Traud (6), and (ii) the commonly accepted principle that rate laws can be written for postulated chemical reactions in a general form using empirical reaction orders. A final assumption, which cannot be avoided in this analysis, is that the Tafel slopes for the respective partial processes in the mixed potential system are not different from those observed in separate electrokinetic studies. This assumption can be verified, however, by polarizing the mixed potential system and observing the respective Tafel slopes. More complex mixed potential systems, *e.g.* those involving more than two partial processes, reduce to equations similar in form to the equations derived here (7).

Manuscript received April 12, 1971.

Any discussion of this paper will appear in a Discussion Section to be published in the December 1972 JOURNAL.

LIST OF SYMBOLS

b_a	anodic Tafel slope ("base 10"), V
b_c	cathodic Tafel slope ("base 10"), V
\mathbf{F}	Faraday constant, 96,500 coulombs/g equiv.
$[\text{H}^+]$	concentration of hydrogen ions, M
i_m	mixed current density, A/cm ²
k_a	specific rate constant for the anodic partial process, units dependent upon reaction orders and concentration units
k_a°	specific rate constant for anodic partial process at the standard electrode potential, (see k_a for units)
k_c	specific rate constant for the cathodic partial process, (see k_a for units)
k_c°	specific rate constant for the cathodic partial process at the standard electrode potential, (see k_a for units)
k_{Fe}	specific rate constant for iron dissolution, g mole iron - g mole H ⁺ /cm ² l - sec
n_a	number of gram equivalents produced/g mole of anodic material reacted
n_c	number of gram equivalents produced/g mole of cathodic material reacted
Ox_a	product of the anodic partial process
Ox_c	reactant of the cathodic partial process
$[\text{Ox}]_c$	concentration of Ox_c , M
Red_a	reactant of the anodic partial process
Red_c	product of the cathodic partial process
$[\text{Red}]_a$	concentration of Red_a , M
$-r_a$	rate of the anodic partial process, g mole/cm ² sec
$-r_c$	rate of the cathodic partial process, g mole/cm ² sec
$-r_{\text{Fe}}$	rate of the iron reaction, g moles iron/cm ² sec
β_a	anodic Tafel slope ("base e"), V
β_c	cathodic Tafel slope ("base e"), V
γ	reaction order with respect to the anodic reactant in the anodic partial process, dimensionless
γ_1	reaction order with respect to the anodic reactant in the cathodic partial process, dimensionless
δ	reaction order with respect to the cathodic reactant in the cathodic partial process, dimensionless
δ_1	reaction order with respect to the cathodic reactant in the anodic partial process, dimensionless

- ϕ°_a standard electrode potential of the anodic partial process, V
 ϕ°_c standard electrode potential of the cathodic partial process, V
 ψ_0 mixed potential, V

REFERENCES

1. E. J. Kelly, *This Journal*, **112**, 124 (1965).
2. C. U. Yu and F. M. Donahue, Unpublished results.
3. F. L. Shippey and F. M. Donahue, To be published.
4. F. M. Donahue and C. U. Yu, *Electrochim. Acta*, **15**, 237 (1970).
5. J. Yeager, J. P. Cels, E. Yeager, and F. Hovorka, *This Journal*, **106**, 328 (1959).
6. C. Wagner and W. Traud, *Z. Elektrochem.*, **44**, 391 (1938).
7. F. M. Donahue, Unpublished results.

Brief Communications



The Carbon Cloth Electrode

R. Hand, A. K. Carpenter, C. J. O'Brien, and R. F. Nelson*¹

Department of Chemistry, Sacramento State College, Sacramento, California 95819

For some time, we have been using carbon cloth electrodes for coulometry and preparative scale electrolytic work. This is a woven graphite material that comes in large rolls from the Carbon Products Division of Union Carbide Corporation.

The carbon cloth appears generally to have the electrochemical properties of other carbon electrodes as far as working ranges in various solvents go. We have used it primarily for anodic work in aqueous and nonaqueous media; however, it functions well for cathodic work in the few systems that we have investigated. The electrochemical area is about 3 cm²/cm² geometrical area and the material stands up well under relatively high current densities. We have passed currents of 100 mA/cm² during controlled-potential preparative-scale electrolytic work with no apparent damage to the electrode. Filming does not appear to be any more of a problem with carbon cloth than with other electrodes; in fact, we have had somewhat better luck with it than with platinum with regard to filming by electrolysis products. A striking example of this is in the anodic oxidations of indole and tryptophan in aqueous buffer solution. At a platinum gauze electrode filming ensues from the start of the electrolysis and the currents obtained are very low, thus forcing a prolonged electrolysis. Upon substituting a carbon cloth electrode, however, much higher electrolysis currents were realized and the time of electrolysis was shortened dramatically.

The cloth is relatively inexpensive, so one can simply cut out a piece according to how much is needed and discard it after the electrolysis; alternately, the electrodes can be reused a number of times.

The major drawbacks to the cloth are that it is not readily suited for routine electrochemical work in chronoamperometry, cyclic voltammetry, etc., and it has poor mechanical strength. Because of its configuration, convection begins in acetonitrile after 2-3 sec and rapidly becomes a serious problem. In addition, the electrochemical area is relatively large for a small piece of cloth and this may lead to solution IR drop and amplifier limitation problems. In addition, at high cell currents of 5-20A, the resist-

ance of the cloth, normally just a few ohms/cm², leads to markedly uneven current distribution and poor potential control. However, at "ordinary" current levels, this is no problem at all.

Because it is a woven material, one needs a fairly large piece so that it will hold together. Contact can normally be made through an alligator clip, but it has to be firmly affixed. Because of the poor mechanical strength and the woven nature of the cloth, shredding occurs readily; this would obviously lead to problems in quantitative electrochemical work, since the area is changeable.

For precision coulometric studies the cloth electrode is more than satisfactory; background currents are negligible and the high surface area facilitates electrolysis. We had occasion to carry out low-concentration coulometric n-value studies on oxidations of a large series of substituted carbazoles using first platinum and then carbon cloth working electrodes. The n-value determinations were pretty much the same in both cases, but the pre-electrolysis background currents were considerably lower at the carbon cloth. The major use to which we have put the carbon cloth is for preparative-scale electrolyses. It is ideal for this type of work since one can readily vary the electrode configuration and surface area from one run to the next. Studies in both stirred solutions and flow systems have been very satisfactory.

Since the material is inexpensive (about \$35 per pound—and a pound makes a lot of electrodes!) and readily adaptable to a number of electrochemical applications, the carbon cloth electrode may be of considerable use to practical electrochemists.

Acknowledgment

It should be noted that to our knowledge the first use of carbon cloth for electrochemical work was in the laboratory of Dr. R. N. Adams at the University of Kansas. Financial support of this work through NSF grant No. GP-20606 is gratefully acknowledged. Special thanks are also due to Drs. R. N. Adams and D. E. Smith for their support and encouragement.

Manuscript submitted May 21, 1971; revised manuscript received ca. Sept. 24, 1971.

Any discussion of this paper will appear in a Discussion Section to be published in the December 1972 JOURNAL.

* Electrochemical Society Active Member.

¹ Present address: Department of Chemistry, University of Idaho, Moscow, Idaho 83843.

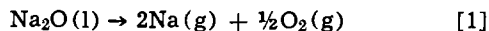
Key words: electrosynthesis, coulometry, graphite.

Torsion Effusion Determination of Sodium Partial Pressure Over Na₂O

V. Piacente, A. Desideri, and G. Bardi

Laboratorio di Chimica Fisica ed Elettrochimica, Università di Roma, Rome, Italy

The evaporation process of Na₂O has been investigated by several authors (1-5) who have shown that this oxide evaporates according to the scheme



Mass-spectrometric investigation have shown moreover that in the vapor phase NaO and Na₂O molecules are in the ratio $P_{\text{NaO}}/P_{\text{Na}_2\text{O}} \cong P_{\text{Na}}/P_{\text{Na}_2\text{O}} \cong 10^4$. No good agreement was noted between the Na partial vapor pressures from Brewer and Margrave (3) and Hildenbrand and Murad (4) and the ones measured by Kroger and Stratmann (5).

In order to utilize this oxide for a direct mass-spectrometric determination of sodium activity in an alloy utilizing a twin cell (6, 7), we were induced to carry out pressure measurement of the vapor over Na₂O(l) utilizing a torsion-effusion apparatus.

The torsion effusion method was originated by Volmer (8) and the principle of the method has been described elsewhere (9, 10).

Vapor pressures were calculated from the torsion effusion data by means of the equation

$$P = 2k\alpha / (a_1 d_1 f_1 + a_2 d_2 f_2) \quad [2]$$

where P is the pressure, α the deflection, k the torsion constant of the suspension, a_1 , a_2 , d_1 , and d_2 the orifice areas and distances from the axis of rotation and f_1 and f_2 the Freeman and Searcy (11) correction factors for orifice geometry.

In this experiment, cells of MgO, placed in a graphite container, were employed. The temperature was measured with a Pt, Pt-Rh 10% thermocouple inserted in a second container, similar to the one already mentioned and placed beneath it. The details of the effusion cell are given in Table I. Total vapor pressures from 1.2×10^{-5} to 2.0×10^{-4} atm obtained in the temperature range 1144°-1304°K are reported in Table II.

All calculated thermodynamic functions were based on the assumption that no significant number of gaseous oxide molecules were present in the vapor phase. The K_p values of reaction [1] have been calculated from $K_p = 0.286 P_{\text{tot}}^{5/2}$. Calculations of ΔH°_{298} for reaction [1], reported in Table II, are made from the equation

$$\Delta H^\circ_{298}/T = -R \ln K_p - \Delta[(G^\circ_T - H^\circ_{298})/T] \quad [3]$$

The free energy function values, $(G^\circ_T - H^\circ_{298})/T$, used for these calculations were taken from the JANAF tables (1967) (12) and are reported in Table II. An average third law value of $\Delta H^\circ_{298} = 149.2 \pm 0.4$ kcal/mole was obtained by this method (Table II).

Key words: vapor pressure, sodium vapor, sodium oxide.

Table I. Physical constants of the torsion effusion apparatus

Physical constant	Cell 1	Cell 2
Torsion constant k (dyne cm/rad) of W wire (length 34.2 ± 0.1 cm, diameter $30 \mu\text{m}$)	1.355	1.355
Orifice area of MgO cells (10^{-3} cm^2)	(1) 7.90 \pm 0.05	14.70 \pm 0.05
	(2) 9.15 \pm 0.05	12.30 \pm 0.05
Force correction factor (11)	(1) 0.80	0.85
	(2) 0.81	0.85
Moment arm (cm)	(1) 1.27 \pm 0.01	1.27 \pm 0.01
	(2) 1.29 \pm 0.01	1.29 \pm 0.01

Table II. Third law ΔH°_{298} values for the reaction: $\text{Na}_2\text{O}(l) \rightarrow 2\text{Na}(g) + \frac{1}{2}\text{O}_2(g)$

T (Kelvin)	$10^5 P_{\text{tot}}$ (atm)	$-R \ln K_p$ (eu)	$-\Delta[(G^\circ_T - H^\circ_{298})/T]$ (eu)	ΔH°_{298} (kcal/mole)
Cell 1				
1157	1.41	58.0	72.72	151.24
1163	1.86	58.6	71.80	149.34
1195	3.39	53.6	71.54	149.54
1205	4.27	52.5	71.46	149.61
1215	5.25	51.4	71.36	149.18
1219	5.76	51.0	71.34	149.13
1226	7.06	50.0	71.28	148.69
1246	9.32	48.6	71.12	149.17
1256	11.34	47.6	71.05	149.02
1269	13.64	46.7	70.95	149.30
1272	13.92	46.6	70.92	149.49
1285	16.90	45.6	70.82	149.60
1286	17.56	45.4	70.82	149.46
1304	20.32	44.7	70.68	150.46
Cell 2				
1144	1.21	58.7	71.95	149.46
1174	2.42	55.3	71.70	149.10
1184	3.24	53.8	71.62	148.50
1189	3.24	53.8	71.58	149.08
1206	4.84	51.8	71.46	148.65
1225	6.88	50.1	71.29	148.70
1234	7.25	49.8	71.23	149.35
1236	8.88	48.8	71.21	148.33
1246	9.33	48.6	71.12	149.17
1252	10.50	48.0	71.07	149.08
1259	11.81	47.4	71.03	149.10
1266	13.50	46.8	70.95	149.07
1271	14.13	46.5	70.93	148.11
1276	15.94	45.9	70.89	149.02
1280	17.00	45.6	70.86	149.07

Average 149.2 ± 0.4

A second law treatment of K_p for reaction [1] yields a ΔH°_T value at 1224°K of 136.4 ± 3.5 kcal/mole which corresponds to $\Delta H^\circ_{298} = 145.2 \pm 3.5$ kcal/mole calculated utilizing the $(H^\circ_T - H^\circ_{298})$ values reported in the JANAF tables (12).

A weighted average of the second law and third law values gives $\Delta H^\circ_{298} = 149 \pm 2$ kcal/mole, in agreement with the third law value of $\Delta H^\circ_{298} = 151.1 \pm 1.5$ kcal/mole obtained utilizing Hildenbrand and Murad's data (4).

The partial vapor pressure of sodium obtained from our total vapor pressures is somewhat less than the literature data (Fig. 1 open circles and squares), but does not show a very wide difference from Hildenbrand's value (black squares).

Considering the uncertainties associated with the applied measuring methods and with the instrumental sensitivity, for instance, the uncertainties in the Freeman factor or the effusion orifice area and with the relative cross section of Na(g) [about a factor 2 (13)] in Hildenbrand's data, we can conclude that our values are in good agreement with those proposed by this author.

In Fig. 1 a straight line which takes into account Hildenbrand's values and ours, is plotted. We propose this line as representative of the variation of the sodium partial vapor pressure with temperature over liquid Na₂O. The slope, 1.192×10^4 , was found by least-squares from our data, and is in good agreement with that obtained from the pressure values of Hildenbrand (1.178×10^4). Differences were found in the absolute values of the partial pressures of Na(g). However, considering the uncertainties of the measurements made by the two methods, the two sets should be considered as being in agreement, all the more so that Hildenbrand used a mass spectrometer which was not very

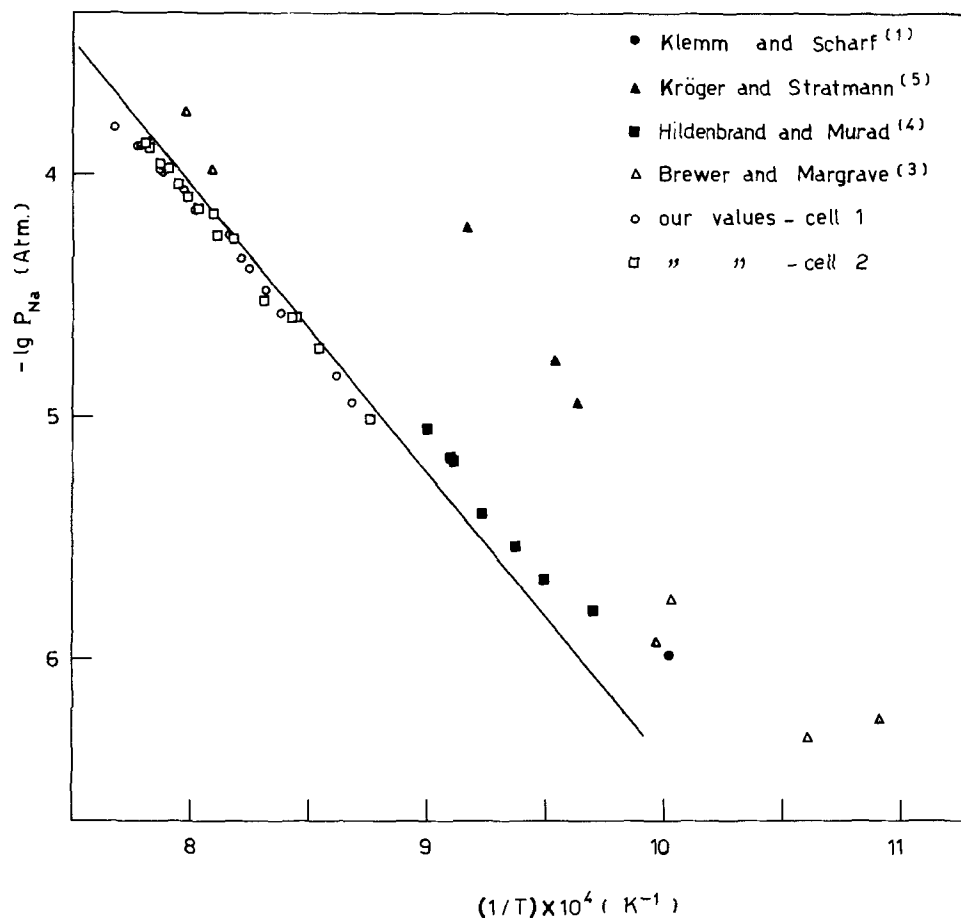


Fig. 1. Na (g) partial pressure over $\text{Na}_2\text{O}(c)$ between 1150° and 1300°K . The equation of the straight line is $\log P(\text{atm}) = 5.49 - 1.192 \times 10^4/T$.

sensitive for absolute measurements. Therefore Fig. 1 shows an intermediate line drawn with the same slope as the two experimental lines. The pressure values of the other observers are also shown for comparison; they were not considered in the selection of the line.

LIST OF SYMBOLS

α	Deflection angle, radiant
a	Orifice area, cm^2
d	Distance of the effusion orifice from the axis of rotation, cm
T	Absolute temperature, Kelvin
P	Partial pressure of gaseous species, atm
K_p	Equilibrium constant of reaction
ΔH°_{298}	Standard enthalpy of reaction at 298°K , kcal/mole
$\Delta[(G^\circ_T - H^\circ_{298})/T]$	Free energy function variation for the specified reaction, eu
$(H_T - H^\circ_{298})$	Enthalpy variation between 298°K and $T^\circ\text{K}$, kcal/mole

SUMMARY OF ΔH VALUES

"Second law"	Evaluation of ΔH°_T value of the specified reaction utilizing the van't Hoff equation in the investigated temperature range.
"Third law"	Evaluation of ΔH°_{298} value of the specified reaction utilizing the Gibbs-Helmholtz equation in the form

$$\Delta H^\circ_{298} = \Delta G^\circ_T - T[\Delta(G^\circ_T - H^\circ_{298})/T]$$

together with $[(G^\circ_T - H^\circ_{298})/T]$

values from the JANAF Tables (12).

Manuscript submitted March 30, 1971; revised manuscript received Sept. 9, 1971.

Any discussion of this paper will appear in a Discussion Section to be published in the December 1972 JOURNAL.

REFERENCES

1. W. Klemm and H. J. Scharf, *Z. Anorg. Allgem. Chem.*, **303**, 263 (1960).
2. J. H. Norman and P. Winchell, Final Report, General Atomic/General Dynamics, GA-7597, 1967.
3. L. Brewer and J. L. Margrave, *J. Phys. Chem.*, **59**, 421 (1955).
4. D. L. Hildenbrand and E. Murad, *J. Chem. Phys.*, **53**, 3403 (1970).
5. C. Kröger and J. Stratmann, *Glastech. Ber.*, **34**, 311 (1961).
6. G. G. Cameresi, G. De Maria, R. Gigli, and V. Piacente, *Ric. Sci.*, **37**, 1092 (1967).
7. G. De Maria and V. Piacente, *Bull. Soc. Chim. Belges*, In press.
8. M. Volmer, *Z. Physik. Chem.*, Bodenstein Festband, 863 (1931).
9. O. Kubaschewski and E. L. Evans, "Metallurgical Thermochemistry," pp. 140-158, Pergamon Press, New York (1958).
10. V. Piacente and G. De Maria, *Ric. Sci.*, **39**, 549-557 (1969).
11. R. D. Freeman and A. W. Searcy, *J. Chem. Phys.*, **22**, 762 (1954).
12. JANAF Thermochemical Tables. PB 370-371 (1967).
13. See Ref. (15), (16), (17), (22) of Hildenbrand and Murad.



Ionic Conduction and Oxygen Diffusion in Yellow Lead Oxide

L. Heyne, N. M. Beekmans, and A. de Beer¹

Philips Research Laboratories, N. V. Philips' Gloeilampenfabrieken, Eindhoven, Netherlands

ABSTRACT

Electrical conduction in yellow lead oxide has been studied between 500° and 800°C and ionic and electronic contributions separated by means of transport and EMF techniques. The electronic conductivity depends on oxygen partial pressure and on doping. Its dependence on the oxygen pressure is markedly different for samples doped with bismuth or with potassium. It increases with pressure in K-doped samples; approximately as $P^{1/n}$ with n between 4 and 6. In Bi-doped samples a decrease is found with n between -4 and -6 . Information on ionic conduction stems mainly from transport number determinations with the EMF technique. It was found that the ionic conduction, which is carried by oxygen, is independent of the oxygen pressure and increases on the addition of bismuth. Self-diffusion measurements of oxygen were carried out using the isotope exchange method. It was found that the exchange at the surface is too slow with oxygen gas, but a diffusion-controlled exchange rate could be obtained with a carbon dioxide gas. The results correspond well with those given by Thompson and Strong; the self-diffusion coefficient at 787°K amounts to about 10^{-10} cm²/sec. Doping with bismuth increases this value, whereas an influence of potassium dope is not so evident. No influence of the oxygen pressure could be found. Although doping with bismuth causes similar changes in the ionic conductivity and in the self-diffusion of oxygen, a quantitative comparison suggests that transport of oxygen in neutral form also makes a contribution to the diffusion.

Notwithstanding intensive research, the only good oxygen-ion conductors known are those with fluorite-type lattices like stabilized zirconia. The oxygen mobility in those structures is enhanced by doping with oxygen-vacancy generating ions.

It was suggested many years ago that oxygen is relatively mobile in orthorhombic lead oxide, the yellow, high-temperature modification. Self-diffusion studies by Lindner and Terem (1) showed that the lead mobility is too low to explain the observed oxidation rate of metallic lead and they concluded that fast oxygen diffusion must be possible. This idea was confirmed by measurement of the self-diffusion coefficient of oxygen by Thompson and Strong (2). The value of $7 \cdot 10^{-10}$ cm²/sec extrapolated from their data for 1000°K is comparable with the value of $2 \cdot 10^{-9}$ cm²/sec found for calcia stabilized zirconia at the same temperature (3).

Conductivity studies of orthorhombic lead oxide are scarce (4, 5). The only extensive investigations are those by Grünwald (6) and co-workers and by Ritschel and Schmidt, who summarized the results (7). However, although it was known from the above mentioned diffusion results and from direct observations (8) that ionic conduction must play a role, the conductivity data were interpreted by these authors entirely on the basis of electronic conduction. Moreover, the measurements were carried out at temperatures where the yellow modification is not stable and probably in an atmosphere where oxidation to a higher oxidation state takes place. Therefore, the value of the results and especially of the theoretical discussion seems doubtful.

With the aim of gaining insight into the defects present in the high-temperature phase of lead oxide a study of the electrical properties and of the oxygen self-diffusion was undertaken. The influence of oxygen partial pressure and of doping was investigated, and the ionic and electronic contributions separated by means of various solid electrolytic techniques. Preliminary results of this investigation were presented orally at a meeting of The Chemical Society (9).

Experimental

Sample preparation.—The starting material was very pure lead oxide, prepared at our laboratory by Kwes-troo and Huizing (10). The concentration of most impurities was at the ppm level or lower; no impurities could be detected with spectrographic analysis (10). The material was present in the red tetragonal form, the thermodynamic stable situation, which is also the only form in which high-purity lead monoxide can be kept at room temperature (11).

From this material, 3 mm thick pellets were pressed (compression force 6000 kg, diam 8 mm) in a steel die which was "cleaned" by carrying out several preliminary pressings. For contacting, platinum gauzes were pressed together with the material. The pellets were further densified by hydrostatic pressing at 30 kB. Analytical checks showed that with sufficient care contamination could be largely avoided.

Dopants were introduced in two steps using a 1% mixture obtained by sintering pressed pellets and subsequent powdering as an intermediate step. Bi and K-dopants were introduced as Bi₂O₃ and anhydrous K₂CO₃ of spectroscopic purity. The final compositions were checked analytically.

For the self-diffusion experiments single crystal plates and spheres were also used. Crystals were ob-

¹ Present address: N. V. Philips' Gloeilampenfabrieken, Information Systems and Automation, Eindhoven, Netherlands.

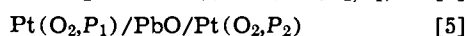
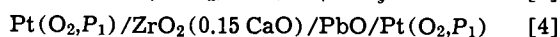
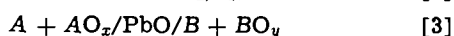
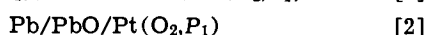
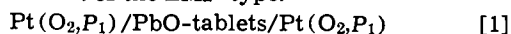
Key words: solid electrolyte, semiconductor, isotope exchange, lattice defects.

tained by pulling from a Pt-crucible or by slowly cooling a melt in a Pt-boat. They contained a variable amount of platinum of up to ½% depending on the oxygen partial pressure during melting, and they were only stable at room temperature if doped with Bi (12, 13). Spherical particles were obtained by melting the lower end of a strongly vibrating rod of sintered PbO and selecting the solidified drops which had sprinkled off according to size and perfection of shape.

Conductivity measurements.—Most electrical conductivity measurements were performed with low frequency a-c techniques. The sample was suspended between lightly pressed Pt-disks contacting the built-in Pt gauzes in such a way that no direct contact between the sample and the quartz glass or alumina sample holder existed. The latter was placed in a quartz glass furnace tube connected to a vacuum system. Stationary or flowing gases in the pressure range of about 10^{-4} to 10^{+3} Torr could be introduced. A special Pirani-type gauge was developed to cover this complete range (14); at a later stage also zirconia-type oxygen gauges (15) were used.

A difficulty arose because of the transformation of the initial low-temperature modification to the high-temperature modification studied. This led to a loss in packing density of the pellet, causing an increased intergrain resistance. If the sample was allowed to cool below the transformation point of about 500°C, often a complete disintegration accompanied the reversed phase transition. Thus the measurement program of a particular sample had to be carried out in one run without cooling. Because of the large intergrain resistances the absolute value of the resistance of the samples was not reproducible between samples. But, taking the precaution of allowing some time for sintering, the values for one sample were reproducible on pressure and temperature cycling in the range of 500°–750°C to within a few per cent and the characteristic pressure and temperature-dependence also reproduced between samples. Samples doped with Bi were stabilized in the yellow modification and consequently did not give rise to the above-mentioned difficulties.

Transport number determination.—Several types of galvanic cells were tried in order to obtain information about the transport numbers. They were of the current as well as of the EMF-type.



Tubandt's method of determining weight changes due to current flow in the tablets of cell [1] allows determination of the Pb-ion transport number (16, 17). The accuracy was found to be severely limited by pellet deformation, sintering together, and evaporation losses. The results suggest that about 1% of the current is transported by Pb-ions (air ambient, 700°C). This value was just above the limit of detectability; hence the influence of temperature, dopant and, oxygen partial pressure could not be studied.

The EMF of cell [2] yields an average ionic transport number, and from the slope of the EMF vs. oxygen pressure curve this transport number can in principle be found as a function of the oxygen pressure (18, 17). The difficulty of localizing the molten lead was solved by the use of a cup-shaped sample obtained by pressing with a suitably shaped die. However, the material to be used for the electrical contact with the lead droplet lying in the PbO-cup was a problem, because of alloying or the formation of an intermediate oxide layer. This, together with problems caused by the geometry and complicated by the poor wetting between Pb and PbO, had the result that no reliable data could be obtained with this cell.

Cells of type [3] are limited by the small choice of metal and metal-oxide mixtures that exhibit an oxygen partial pressure higher than that over Pb-PbO. In this respect Cu-Cu₂O and Bi-Bi₂O₃ are possible, but it appeared that they could not supply the oxygen current demanded by such a conductive, and at the same time "leaky," electrolyte like PbO without strong modification of the oxygen potential at the electrode-sample interface.

In cells of type [4] the electronic current in the PbO-sample is suppressed by the electrolyte tablet of stabilized zirconia, provided that no oxygen leak between the tablets takes place. At a first sight apparently trustworthy looking values for the ionic conductance of PbO could be derived from the slope of the current-voltage characteristics. A reproducible dependence on oxygen partial pressure, which was different for differently doped samples, was found. However, it appeared that the results were inconsistent with those obtained by means of cell [5]. Further investigation revealed that with the same oxygen partial pressure at both sides the results depended on the pressure of added inert gas, and that also a geometrical influence was present. It could be concluded that oxygen penetration by gas diffusion took place along the interface between the polished pellets; thereby partly removing the blocking action on the electronic current and causing an overestimate of the ionic transport number. Evidently, oxygen migrating between the pellets had occasionally to pass as ions through PbO and so an influence of the dopant concentration and deviation from stoichiometry of the samples was still present in the results. But, of course, a false law of dependence on oxygen pressure was suggested by this complicated and unpredictable mechanism. Attempts to block the gas diffusion, for instance by imbedding the cell in inert powder, were unsuccessful.

These negative results were quoted here primarily because they clearly illustrate the difficulties that may be encountered when applying to oxides the methods of Wagner (18), which were so fruitfully applied to halides.

The results presented below were all obtained by means of cells of type [5], where the sample is used as electrolyte and is arranged to separate two gas compartments. Figure 1 is a schematic drawing of the setup. The PbO-sample, with its platinum gauze contacts, was compressed inside an alumina tube. After inserting the latter in the rest of the equipment it was sintered for a few days and in many cases a reasonably gas-tight cell was obtained. As with the conductivity measurements, the temperature had to be kept above the transition temperature during the complete series of experiments with each sample. Often this took several weeks. Such cells are amenable to two types of measurement. Most direct is the quantitative determination with help of the pressure gauges of the amount of oxygen transported by a known current. In that case P_1 is chosen equal to P_2 . Calibration could be done easily by means of a current through the zirconia tube which also separated the two gas compartments. In this way residual leak-through was automatically compensated for. This method was only suitable in a narrow range of oxygen pressures where the differential sensitivity of the Pirani gauges was high.

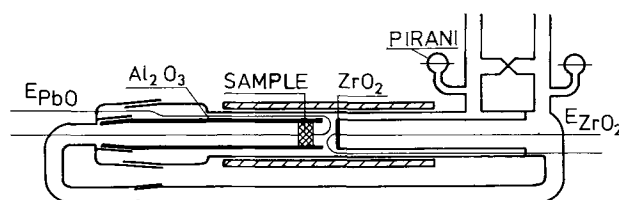


Fig. 1. Electrochemical cell with lead oxide separating two gas compartments. A zirconia cell is used as a reference.

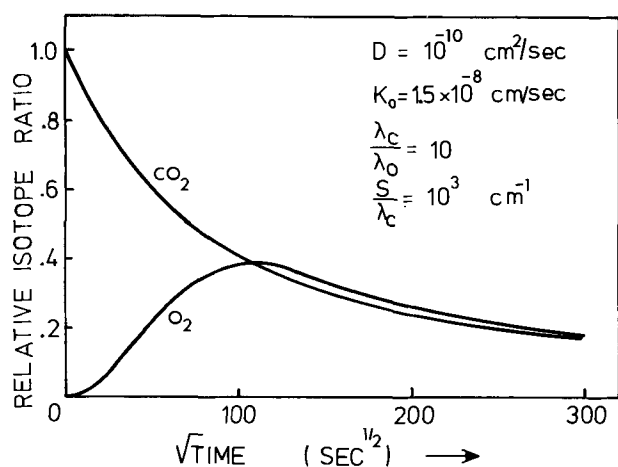


Fig. 2. Theoretical time dependence of the isotope ratio in originally enriched CO_2 -gas and initially natural O_2 -gas during exchange with natural lead oxide. The symbols used are explained in the appendix.

The method of measuring the EMF developed across the Pt-contacts when a small pressure difference was applied appeared to be applicable over a wider range of oxygen pressures. The ratio of the voltages over the PbO-sample and over the zirconia cell equals the ionic transport number in PbO. Several precautions had to be taken. First, only a relatively small pressure difference had to be used at each pressure in order to obtain a significant transport number, and also to minimize the effect of leak-through. Second, because of the small EMF's encountered, stray thermal EMF's have to be minimized by a very careful construction and positioning of the furnace to avoid thermal gradients. Nevertheless, correction for the residual thermal EMF was necessary. This could not be obtained by simply subtracting the voltage with no pressure difference since the thermoelectric force strongly depended on the average value of the oxygen pressure. However, corrections could be obtained by comparison of the EMF's obtained before and after reverting the high and low pressures. The difference between these voltages amounts to twice the significant EMF.

Oxygen self-diffusion measurements.—Use was made of the method of isotope exchange with a gas phase as introduced by Haul (19). It consists of following the isotope ratio of an O^{18} -enriched gas ambient during the establishment of equilibrium with the sample. For the analysis an Atlas type M86² mass spectrometer was used which is specially suited for the accurate determination of isotope concentration ratios because it is equipped with a double ion collector. The ratio of masses 34 and 32 was used. Equilibration of the molecular species in the gas mixture, which was obtained by heating with a platinum catalyst before the exchange experiment started. It was found that, in contrast to the experience of Thompson and Strong (2), the exchange rate was limited by a very slow surface reaction so that the self-diffusion coefficient could not be calculated from the results with any accuracy. However, O^{18} -exchange between lead oxide and carbon dioxide was very fast. So diffusion coefficients could be found from experiments with mixtures of carbon dioxide and oxygen, the latter being necessary to be able to control the deviation from stoichiometry.

Due to the very slow exchange rate of oxygen atoms between O_2 and CO_2 -molecules in the gas phase a very simple method appeared to be possible for the simultaneous determination of the rate constant for the exchange reaction between O_2 and PbO and the self-diffusion coefficient in the solid. It consisted of the use

for instance of natural O_2 mixed with enriched CO_2 and then following the O^{18} -content of both species during the diffusion experiment (masses 34 and 46). A theoretical time dependence of both isotope fractions during such an experiment is shown in Fig. 2.

The rate constant K_0 for the exchange reaction can be defined by the equation

$$\frac{dq}{dt} = -a K_0 (q - r_s) \quad [6]$$

where q is the O^{18} -isotope fraction in the oxygen gas and r_s that in the solid at the surface (19). If the constant a (dimension cm^{-1}) is defined as the ratio of the total number of O-atoms in a depth of 1 cm in the solid (calculated for the total reacting surface area) to the total number of O-atoms present in the oxygen gas, the proportionality factor K_0 attains the dimension of a velocity (dimension cm/sec). Since $r_s = r_{\text{CO}_2}$, because the CO_2 exchange reaction is very fast, K_0 can be calculated at every moment from the slope of the O_2 -curve and the separation between the two curves.

Of course, this holds good only if the exchange in the gas phase and at foreign surfaces is negligible. Blank experiments showed this to be the case provided no metals were present such as Pt or Au in the hot zone of the quartz-glass reactor. Furthermore, the PbO-sample had to be positioned in such a way that the slight amount of PbO that evaporates cannot condense on hot quartz surfaces near the temperature

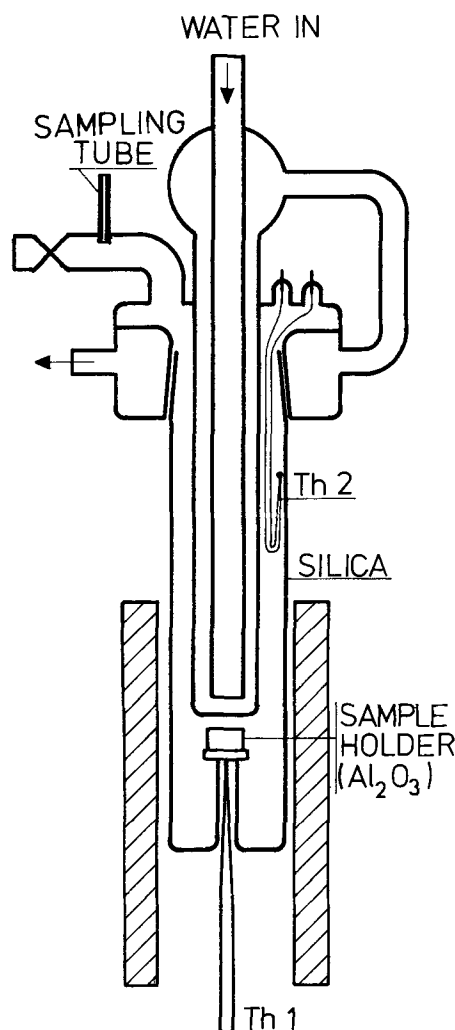


Fig. 3. Reactor vessel used for exchange experiments. A cooled finger screens the hot walls against evaporating lead oxide. The sample is contained in an alumina sample holder with a perforated lid.

² Marketed by Varian-MAT G.m.b.H., Bremen, West Germany.

transition zone. These conditions could be met with the setup shown in Fig. 3, in which a cool finger screened the transition zone from the sample holder. The required absence of metals made it necessary to determine the sample temperature in a separate run with the thermocouple Th 2 attached to the sample. It was afterwards bent back into the cool zone. The thermocouple Th 1, positioned in an intrusion of the reactor, served in the furnace-control unit.

Formulas used to calculate D and K_0 from experimental time dependence curves of the isotope ratios are given in the appendix. The data were analyzed by means of a digital computer.

Results

Measurement of total conductivity.—Figure 4 gives an impression of the temperature dependence of the total conductivity for different dopants at a fixed oxygen pressure. The slope of the curves for pure and for bismuth containing samples corresponds to an activation energy of 1.2 ± 0.05 eV independent of the dopant concentration and of the oxygen pressure. However, potassium containing samples exhibit a lower value of 0.9 ± 0.05 eV, which is again independent of the oxygen pressure, and which is the same for K-concentrations of 100 ppm and 1000 ppm.

Typical conductivity isotherms for differently doped samples are shown in Fig. 5 in a doubly logarithmic plot. Striking is the positive slope for potassium doped samples and the negative one for those containing bismuth. The slopes of straight line segments correspond to a $1/4$ to $1/6$ power dependence for K-doping and to the same values but with negative sign for Bi. Undoped samples show a shallow minimum and the curve for 10 ppm Bi illustrates the high sensitivity for contamination.

Isotherms taken at temperatures different from that in Fig. 5 have essentially the same shape; they show

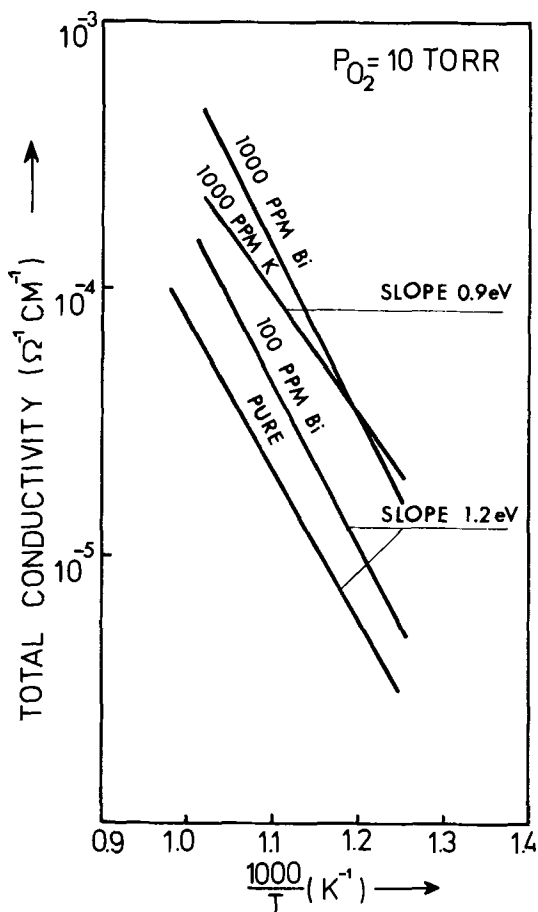


Fig. 4. Conductivity isobars for pure and doped lead oxide

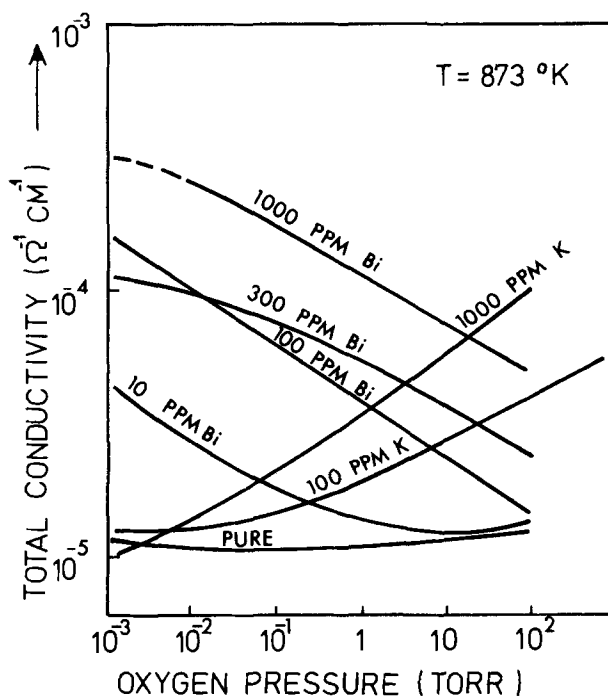


Fig. 5. Conductivity isotherms for pure and doped lead oxide

merely a shift corresponding to the temperature dependence depicted in Fig. 4. Because of this simple behavior of both the isotherms and the isobars, the information given in the figures is sufficient to derive the conductivity of a certain sample at any temperature and pressure in the ranges 800° – 1000° K and 10^{-3} to 760 Torr.

However, as mentioned before, the magnitude of the conductivity values did not reproduce well in the Bi-free samples. So there is some arbitrariness in the level on which the curves have been drawn corresponding to perhaps a factor of five. For the pure and the K-containing samples the curves represent the more conducting ones encountered. In the plot the minima in the low-doped sample curves fit reasonably well with that of the pure curve as should be expected if they correspond to intrinsic conductivity. But still, it may be possible that the complete set of curves should be shifted somewhat up to higher values. Of course these considerations do not affect the interesting pressure and dopant influences shown.

Ionic transport numbers.—Some typical transport number isotherms are shown in Fig. 6, while a summary of the results is given in Fig. 7. Again we encounter the slopes of Fig. 5, but now in the opposite direction. Because of the logarithmic scales curves representing the ionic conductivity, i.e. the product of total conductivity and transport number, can be obtained by simply adding the corresponding curves of Fig. 5 and 7. The opposite slopes then cancel and, to a first approximation, the ionic conductivity is found to be independent of oxygen pressure. For a special case this is shown in Fig. 8.

Since these transport numbers were derived directly from the EMF of cells of type [5], the values obtained were not influenced by intergrain contacts, as were those of the partial conductivities. In accordance with this the values were well reproducible between samples. Moreover, values derived from a direct comparison of the oxygen transported by a current through the PbO and the zirconia standard (see Fig. 1) fitted the curves well, as is illustrated by the triangles in Fig. 6. Only when the observed transport number comes out lower than about 1% are there indications that for some unknown reason the values are underestimated. Therefore, the full lines of Fig. 6 have not been extended to that region.

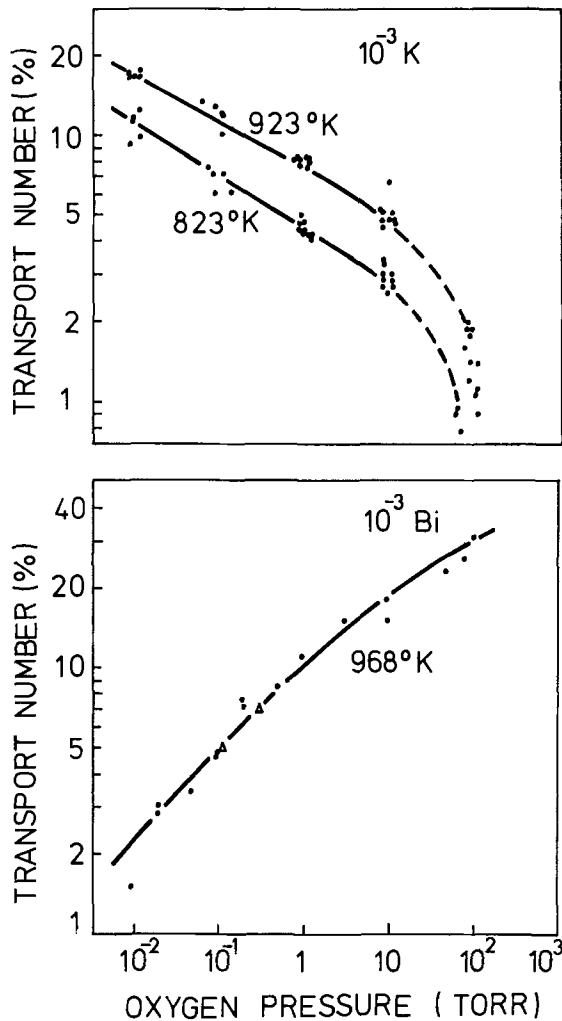


Fig. 6. Typical experimental results of transport number determinations. The triangles in the lower curve represent values obtained by measurement of the gas transported by a current.

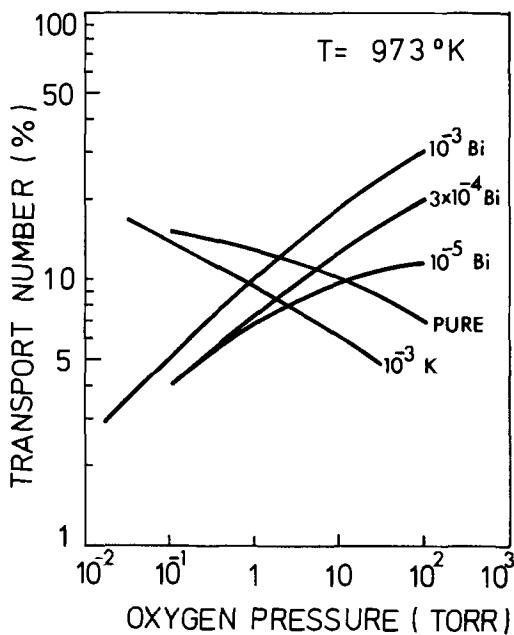


Fig. 7. Summary of transport-number isotherms for pure and doped lead oxide.

The transport numbers generally show a weak temperature dependence. For pure samples some increase is found for a temperature rise from 940° to 1000°K.

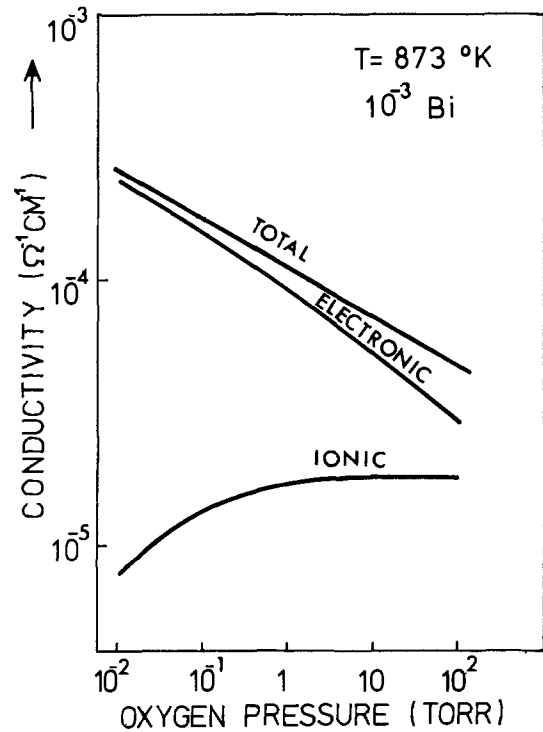


Fig. 8. Partial electronic and ionic conductivity isotherms for Bi-doped lead oxide.

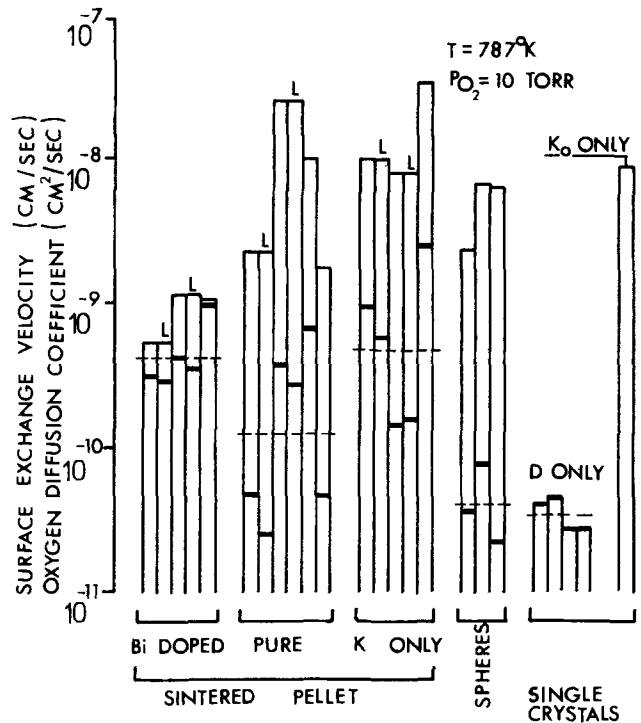


Fig. 9. Survey of results of exchange experiments. The upper levels indicate the rate constant K_0 for oxygen exchange with the surface. The intermediate levels give the self-diffusion coefficients D . The dashed horizontals indicate geometrical averages for D .

The increase with temperature for K-doped samples is apparent from Fig. 6. Moderately Bi-doped samples do not show any temperature dependence, while a very small decrease with temperature is found for the 100 ppm samples.

Self-diffusion coefficient of oxygen.—Since the temperature dependence of the oxygen self-diffusion is known from literature (2), most exchange experiments were performed at a fixed temperature of 787°K. An

influence of sample type, dopant or oxygen pressure was looked for. The results are presented in Fig. 9.

Every column represents an experiment, the upper level corresponds to the value K_0 found for the rate constant of the surface reaction with oxygen gas, the lower level gives the diffusion coefficient. The reaction rate constant was defined in Eq. [6].

The oxygen partial pressure was near 10 Torr for all points not marked with an L , and the K_0 -values given always correspond to that pressure. The L -marked columns show experiments with the left hand neighboring sample but performed in an oxygen-free CO_2 atmosphere. The doped samples contained 600 ppm Bi or K. The spheres had a radius of about 0.5 mm and were undoped. The single crystals contained up to 0.5% of platinum present as visible aggregates in the cleavage plane. Crystals were selected for absence of these visible defects.

The values show a considerable spread which is least for Bi-doped specimens as was the case in the conductivity experiments. For the pure and K-doped tablets there is a clear correlation between the values of D and K_0 . This can be seen in Fig. 9 from the lower spread in the distances between the D and K_0 levels, which correspond to the logarithms of their quotients. It seems therefore reasonable to assume that a significant part of the scatter stems from differences in effective surface area of different tablets. Consequently, the value of K_0 may be considered as a measure for this area, at least in comparable samples.

If the significantly lower values of K_0 for bismuth-doped samples also indicate a lower effective surface area with respect to pure tablets, the higher average D for these samples would be more pronounced than already suggested by the figure. A higher diffusion coefficient is consistent with the higher ionic conductivity found, and also with the better sinterability experienced with these samples leading to better reproducibility and possibly a smoother surface.

The values of the self-diffusion coefficient found for spheres and single crystals average at $4 \cdot 10^{-11}$ cm²/sec, which is in good agreement with the data of Thompson and Strong (2). It is somewhat lower than the average obtained with pure pellets.

Comparison of the diffusion values in L -marked columns, which were obtained at very low oxygen partial pressures with their left hand neighbors, shows that there is no significant pressure dependence on the part of the self-diffusion coefficient of oxygen.

Discussion

Electronic conductivity.—The electronic conductivity, which forms the main component of the total conductivity, shows a dependence on the oxygen pressure that suggests p-type conductivity in potassium and n-type in bismuth containing lead oxide. This is confirmed by the sign of the thermo EMF which was mentioned as a disturbing factor in the discussion of the cell experiments. A sign reversal of this thermo-force also occurred at the minimum of the conductivity isotherms of pure samples as could be expected for a transition from n to p-type. This behavior is consistent with elementary semiconductor theory where Bi is expected to be a donor and K an acceptor assuming them to substitute for Pb.

It is interesting to compare the experimental value for the intrinsic electronic conductivity σ_e obtained from Fig 5 ($\sigma_e = 10^{-5}$ ohm⁻¹ cm⁻¹ at 873°K) with a theoretical value that can be calculated from the optically determined bandgap value, the carrier mobility, and the effective mass. From the optical absorption spectrum we found indications of an indirect bandgap E at room temperature of 2.66 eV (20). Almost the same value is quoted by Ali Ben Hadj (21), while Iinuma, Seki, and Wada (13) give 2.75 eV at 300°K with a temperature coefficient of -1×10^{-3} eV/deg. Keezer, Bowman, and Becker (22, 23) determine the bandgap as 2.67 eV and find a value for the electron

mobility μ_n at room temperature of 50 cm²/V sec. If we assume the same mobility for holes and introduce a $T^{-3/2}$ dependence (24) we find with the formula

$$\sigma_e = 2 \left(\frac{2\pi mkT}{h^2} \right)^{3/2} \cdot \exp \left(-\frac{E}{2kT} \right) \cdot q(\mu_n + \mu_p) \quad [7]$$

a value of roughly 10^{-4} ohm⁻¹ cm⁻¹ for the intrinsic electronic conductivity at 873°K. This must be considered as consistent with the experimental value of 10^{-5} ohm⁻¹ cm⁻¹ remembering the use of the free electron mass m instead of the effective one and the nature of the sintered samples.

The corresponding free carrier concentration is of the order of magnitude of 10^{13} cm⁻³. This is several orders of magnitude lower than the dopant concentrations introduced in the doped samples, nevertheless we find only a moderate increase in the electronic conductivity on doping. So we must conclude that the dopant atoms do not act as simple donors or acceptors merely generating equivalent concentrations of free charge carriers but that the main charge compensation of the built-in ions of deviating valency is obtained by the simultaneous formation of charged lattice defects.

Ionic conductivity.—The same lattice defects could also determine the ionic conduction and the self-diffusion. The ionic conductivities as derived from the total conductivity curves (Fig. 5) and the transport numbers (Fig. 7) appear to be independent of the oxygen pressure irrespective of the impurities introduced. However, samples containing 1000 ppm of bismuth show a tenfold higher ionic conductivity than pure ones. Doping with potassium does not seem to give rise to a change in the ionic conductivity.

The activation energy of the ionic conductivity appears to have the same value of 1.2 eV for either bismuth or potassium doped lead oxide. It equals that of the electronic conductivity for Bi-containing samples (constant transport number) but exceeds the activation energy for the p-type conductivity of K-doped material. This results in the positive temperature coefficient of the transport number observed for this material.

The charged lattice defects formed by introduction of bismuth ions on lead ion lattice positions may be either lead vacancies or oxygen interstitials. The observed increase in the oxygen conduction leads us to conclude that interstitial oxygen ions are responsible for the ionic transport. This rather unusual mechanism may be connected with the crystal structure of orthorhombic lead oxide which is made up of sheets containing infinite Pb-O zigzag chains. The outer surfaces of such sheets contain only Pb-atoms, while all oxygen atoms are inside them (25-27). A weak bonding exists between these relatively widely spaced sheets.

Self diffusion.—If the same type of lattice defect is responsible for both ionic conductivity and self-diffusion both phenomena must be related by Einstein's relation, which for lead oxide can be written in the form

$$\sigma_{\text{ion}} = 2 \times 10^8 D/T \quad [8]$$

Here correlation effects are neglected and a charge of 2 is attributed to the mobile oxygen defects. Introducing the value of 10^{-10} cm²/sec for the diffusion coefficient at 787°K in pure samples, we find the value 2.5×10^{-5} ohm⁻¹ cm⁻¹ for the ionic conductivity carried by oxygen ions. This appears to be about 100 times greater than the value obtained from our experimental data for the ionic conductivity of those samples. For bismuth-doped lead oxide a higher D -value as well as higher ionic conduction was found, but here a large discrepancy factor exists too.

This could mean that some error was made in the interpretation of the experiments. It might be argued that the self-diffusion found is too high because of a fast grain boundary diffusion process. However, the insignificant D -difference found for poly and mono-

crystalline samples rules this out. Moreover, this process would also increase the ionic transport number obtained by both the EMF and the direct transport method.

It must be stated that the diffusion and conductivity measurements, although performed on comparable samples, did not pertain to the same region of the samples. The diffusion data come from experiments where the relevant part of the sample extends to only a few microns below the free surface. In the conductivity determinations the complete sample is involved. So a surface layer of a higher ionic conductivity could explain the results. However, experiments with electrode arrangements using a guard ring did not confirm the presence of such a layer.

Could then perhaps the conductivity measurement have led to much too low values? If grain boundary layers of lower electronic conductivity in the current path had led to underestimation of the conductivity, they would at the same time have caused a higher EMF because the oxygen potential gradient would have concentrated across these electron blocking layers especially. Thus a kind of compensation with regard to the ionic conductivity value would have occurred. Moreover, electronic barriers cannot exist in intrinsic material, since any band bending at the interface would lead to an increased surface conductivity. Furthermore, a nonuniform deviation from stoichiometry was not possible during the experiments, since the time constant for equilibration appeared to be of the order of a second, which value is consistent with the theory of chemical diffusion in a mixed conductor using the data for lead oxide.

There remains the possibility that very small contact areas between the grains are responsible for the loss of a factor of 100 in conductivity. In that case we should expect an impedance drop at higher measuring frequencies due to capacitive bridging of the narrow gaps. However, only a slight decrease in impedance was found at frequencies up to 5 MHz and this stood in no proportion to the factor looked for.

These considerations lead us to consider a fundamental reason for the relatively high diffusion constant, namely that oxygen transport in the neutral form should make the main contribution to it. The proposed predominant covalent character of the bonds in the oxides of lead (28) could be the origin of such behavior. However, the ionic conductivity must still be by oxygen in some charged form since, as we learned from the Tubandt type of transport experiments, the transport number of lead is too low to account for the observed ionic transport.

Defect model.—The relative insensitivity of both the self-diffusion and the ionic conductivity to doping indicates that a fair degree of natural atomic or ionic thermal disorder is present in lead oxide at the temperature of study. The threshold concentration where impurities begin to shift this intrinsic defect equilibrium must be of the order of 100 ppm since at about that concentration the self-diffusion and the ionic conductivity begin to change. As the experiments show, changes of this order of magnitude cannot be induced by pressure variations within our experimental range. Partial confirmation of this may be seen in some potentiometric titration experiments using a zirconia cell, which were not mentioned so far. It was aimed to determine the deviation from stoichiometry, but we could only deduce an upper limit of about 10^{-4} .

When we try to summarize the above-mentioned results in terms of a defect model, we encounter difficulties. The oxygen-pressure dependence of the electronic conductivity of doped samples is consistent with a situation where a concentration of doubly charged defects is fixed by the electroneutrality constraint. They were supposed to be interstitial oxygen ions for the case of Bi-doping. The experience that the ionic

conductivity is independent of the oxygen pressure and increases with Bi-content fits well into this picture.

Although the same qualitative behavior of the self-diffusion coefficient of oxygen was found, the quantitative disagreement led us to believe in neutral transport. However, the concentration of neutral interstitial oxygen atoms would certainly depend on the oxygen pressure, probably in proportion to the square root, and this would lead to the same pressure dependence of the coefficient of self-diffusion. This is not found.

This discrepancy is difficult to resolve. The supposition that the isotope diffusion goes by some associate of elementary defects would resolve the problem of the pressure dependence, but leaves the observed dopant dependence to explain. Perhaps more information on the dopant and pressure dependences of the lead-diffusion coefficient could provide a clue to unravel the mechanism in the future.

Conclusion

The conductivity of orthorhombic lead oxide is to an appreciable part ionic and carried by oxygen ions. This oxygen conductivity does not depend on the oxygen pressure. The variations in the ionic transport number with oxygen pressure are due to the changes induced in the electronic conductivity, which in turn depends on the type and concentration of impurities introduced.

Bi-doping results in n-type conductivity with an almost $-1/4$ power dependence on oxygen pressure. At the same time the ionic conductivity is increased; tenfold with 1000 ppm Bi. When in that case the electron conductivity is reduced by a high oxygen pressure, the maximum ionic transport number of about 50% is obtained.

Doping with potassium causes p-type conductivity with a near $+1/4$ power dependence on pressure. Consequently the maximum transport number occurs at the low pressure side with K-doped samples. The resulting electronic and ionic conductivities are somewhat lower than with bismuth as is the maximum transport number obtainable. The ionic conductivity is the same as in pure PbO.

From these results it is concluded that the incorporation of trivalent metal results in the formation of interstitial oxygen ions, which are responsible for the increase in ionic conductivity observed.

The self-diffusion experiments show that oxygen diffusion is also independent of oxygen pressure and increases upon doping with bismuth, just as does the oxygen ion conduction. However, there is a discrepancy because the self-diffusion coefficient appears to be about 100 times higher than would be expected on the basis of the ionic conductivity. It seems therefore that transport of oxygen in neutral form is responsible for the major part of the self-diffusion. However, the observed independence of oxygen diffusivity on oxygen pressure is difficult to understand in this light.

Acknowledgment

This work was started in close cooperation with Dr. Y. Haven who directed the initial self-diffusion studies. His initiatives in this difficult period of the work are gratefully acknowledged. Thanks are also due to Mr. A. T. Vink who built much of the electrical equipment and critically tested various electrochemical cells.

Manuscript submitted June 18, 1971; revised manuscript received Sept. 20, 1971. This was Paper 30 presented at the Atlantic City Meeting of the Society, Oct. 4-8, 1970.

Any discussion of this paper will appear in a Discussion Section to be published in the December 1972 JOURNAL.

APPENDIX

The diffusion results were compared with theoretical curves calculated with the formulas given below. They were derived along lines given by Haul, Dümgen, and Just (29) for the exchange with one gas species. It is assumed that the surface reaction velocity with CO_2 is very fast, while that with O_2 is described by a rate

constant K_0 . Separate formulas are given for a one dimensional geometry and for spherical samples. The error function type of solutions which holds good for relatively small penetration depths are given only. The following notations are used

p	the isotope fraction in CO_2
q	the isotope fraction in O_2
r	the isotope fraction in the solid
index _{t}	means at moment t
index _{0}	means initial value
λ_c	ratio of the total number of O-atoms in the CO_2 -gas to that in the solid
λ_0	ratio of the total number of O-atoms in the O_2 -gas to that in the solid
S	ratio of the exchanging surface area to the sample volume
D	the self-diffusion coefficient of oxygen
K_0	the surface reaction velocity of oxygen as defined by Eq. [6]
g	the quantity $(\lambda_c K_0)/(SD)$
$F(y)$	a function defined as $F(y) = y^3 + y^2 + (\lambda_c/\lambda_0 + 1)gy + g\lambda_c/\lambda_0$
y_i	the three roots of $F(y) = 0$ ($i = 1, 2, \text{ or } 3$)
$F'(y)$	the first derivative of $F(y)$
$G(y)$	a function defined as $G(y) = y^4 + y^3 + (g\lambda_c/\lambda_0 + g - \lambda_c/3)y^2 + gy\lambda_c/\lambda_0 - \lambda_c^2 g/(3\lambda_0)$
y_k	the four roots of $G(y) = 0$ ($k = 1, 2, 3, \text{ or } 4$)
$G'(y)$	the first derivative of $G(y)$
$\text{erfc}(x)$	the function $\exp(x^2) \text{erfc}(x)$
$\text{erfc}(x)$	the function $1 - \text{erf}(x)$
t	the time coordinate

For the initial conditions of an experiment starting with the natural isotope ratio in the oxide and in the oxygen gas and with enriched CO_2 we have: $q_0 = r_0$. The solutions for the CO_2 and the O_2 then become for one dimensional geometry

$$\frac{p_t - r_0}{p_0 - r_0} = \sum_{i=1}^3 \frac{y_i^2 + g\lambda_c/\lambda_0}{F'(y_i)} \text{erfc} \left(-\frac{S\sqrt{D}}{\lambda_c} y_i \sqrt{t} \right)$$

$$\frac{q_t - r_0}{p_0 - r_0} = \sum_{i=1}^3 \frac{g\lambda_c/\lambda_0}{F'(y_i)} \text{erfc} \left(-\frac{S\sqrt{D}}{\lambda_c} y_i \sqrt{t} \right)$$

for spherical geometry

$$\frac{p_t - r_0}{p_0 - r_0} = \sum_{k=1}^4 \frac{y_k^3 + g\lambda_c/\lambda_0}{G'(y_k)} \text{erfc} \left(-\frac{S\sqrt{D}}{\lambda_c} y_k \sqrt{t} \right)$$

$$\frac{q_t - r_0}{p_0 - r_0} = \sum_{k=1}^4 \frac{gy_k\lambda_c/\lambda_0}{G'(y_k)} \text{erfc} \left(-\frac{S\sqrt{D}}{\lambda_c} y_k \sqrt{t} \right)$$

REFERENCES

1. R. Lindner, *Arkiv Kemi*, **4**, 385 (1952); R. Lindner and H. N. Terem, *ibid.*, **7**, 273 (1954).
2. B. A. Thompson and R. L. Strong, *J. Phys. Chem.*, **67**, 594 (1963).
3. L. A. Simpson and R. E. Carter, *J. Am. Ceram. Soc.*, **49**, 139 (1966).
4. M. le Blanc and H. Sachse, *Phys. Z.*, **32**, 887 (1931).
5. O. A. Esin and V. L. Zyazev, *J. Inorg. Chem. (Moscow)*, **2**, 1998 (1957).
6. H. Grünwald and W. Neumann, *Z. Angew. Phys., Ann. Phys. Lpz.*, (7) **1**, 183 (1958); H. Grünwald and W. Neumann, *ibid.*, (7) **1**, 198, 344 (1958).
7. H. Ritschel and G. Schmidt, *Phys. Status Solidi*, **3**, 294, 303 (1963).
8. L. Heyne, *Philips Res. Rept. Suppl.*, **4**, 58 (1961).
9. A. de Beer, Y. Haven, and L. Heyne, Int. Symp. on Reaction Mechanisms of Inorganic Solids, Aberdeen, 11-16 July (1966). No proceedings issued.
10. W. Kwestroo and A. Huizing, *J. Inorg. Nucl. Chem.*, **27**, 1951 (1965).
11. W. Kwestroo, J. de Jonge, and P.H.G.M. Vromans, *ibid.*, **29**, 39 (1967).
12. See ref. 8, p. 2.
13. K. Iinuma, T. Seki, and M. Wada, *Mater. Res. Bull.*, **2**, 527 (1967).
14. L. Heyne and A. T. Vink, *Philips Tech. Rev.*, **30**, 166 (1969).
15. J. Weissbart and R. Ruka, *Rev. Sci. Instr.*, **32**, 593 (1961); H. Schmalzried, *Z. Elektrochem.*, **66**, 572 (1962); N. M. Beekmans and L. Heyne, *Philips Tech. Rev.*, **31**, 112 (1970).
16. C. Tubandt, in "Handbuch Experimentalphysik." W. Wien and F. Harms, Editors, **12**, Part 1, p. 394, Leipzig (1932).
17. L. Heyne, in "Mass Transport in Oxides," J. B. Wachtman, Editor, National Bureau of Standards Special Publication No. 296. Washington, 1968.
18. C. Wagner, Proc. 7th meeting Int. Comm. on Electrochem. Thermodynamics and Kinetics, Lindau (1955), p. 361, Butterworths, London (1957); C. Wagner, *Z. Elektrochem.*, **60**, 4 (1956).
19. R. Haul and D. Just, *ibid.*, **62**, 1124 (1958).
20. Referred to in: J. van den Broek, *Philips Res. Rept.*, **22**, 36 (1967).
21. A. Ben Hadj and P. Bergé, *Compt. Rend. Acad. Sci. (Paris)*, **266**, 714 (1968).
22. R. Keezer, D. Bowman, and J. Becker, *Bull. Am. Phys. Soc.*, Series 11, **10**, 534 (1965).
23. R. C. Keezer, D. L. Bowman, and J. H. Becker, *J. Appl. Phys.*, **39**, 2062 (1968).
24. See for instance C. Kittel, "Introduction to Solid State Physics," 2nd ed., p. 351, John Wiley & Sons, New York (1960).
25. A. Byström, *Arkiv Kemi Min. Geol.*, **25A**, No. 13, p. 1.
26. M. I. Kay, *Acta Cryst.*, **14**, 80 (1961).
27. J. Leciejewicz, *ibid.*, **14**, 86 (1961).
28. B. Dickens, *J. Inorg. Nucl. Chem.*, **27**, 1495 (1965).
29. R. Haul, G. Dümbgen, and D. Just, *Z. Physik. Chemie NF*, **31**, 309 (1962).

Optical Investigation of Cathodochromic Sodalite

C. Z. van Doorn, D. J. Schipper, and P. T. Bolwijn

Philips Research Laboratories, N. V. Philips' Gloeilampenfabrieken, Eindhoven, Netherlands

ABSTRACT

The fluorescence and reflection spectra are studied of sodalite doped with S^{--} , S_2^- , O_2^- , Mn^{2+} , Co^{2+} , Ni^{2+} , Cr^{3+} , or Fe^{3+} . New fluorescence emissions reported are an emission consisting of a number of peaks between 4500 and 7000 Å ascribed to O_2^- , an emission at 5420 Å ascribed to Mn^{2+} , and an emission at 6830 Å ascribed to Fe^{3+} . The transition metals appear to be incorporated preferentially at Al or Si sites. Electron irradiation causes irreversible changes in the uv reflection spectrum. These may be connected with the occurrence of a residual coloration after optical bleaching. A residual coloration appears to be connected also with the presence of O_2^- fluorescence under uv excitation.

Sodalite is a material which, because of its photochromic and cathodochromic properties, has been the subject of a number of investigations (1-8).

The chemical composition of the naturally occurring material is $Na_4Al_3Si_3O_{12}Cl$. Synthetic sodalites have been prepared in which the Cl is replaced by OH, Br, I, ClO_3 , ClO_4 , or BrO_3 , the Na by other alkalis, the Al by Ga, and the Si replaced by Ge. The cubic crystal structure ($a_0 = 8.870 \text{ \AA}$ for Cl-sodalite) was first elucidated by Pauling (9) and refined by Löns and Schulz (10).

Most of the work on the cathodochromism of sodalite concerns sulfur-doped halide sodalite. We found that doping with sulfur is not essential for cathodochromism to occur. This was also noted by Taylor *et al.* (5). Undoped sodalite samples, which are not at all or only slightly photochromic (for 2537 and 3650 Å radiation), may even show better cathodochromic properties than sulfur-doped samples. Since the presence of defect centers is essential in the process of coloring, one of the main objects of the present investigation is to try to understand the nature and the role of these defect centers in doped and "undoped" sodalite in order to achieve better control of its cathodochromic properties.

Fluorescence spectra and powder reflection spectra of sodalite samples are described and discussed.

Preparation of Sodalite Samples

Since a full account of the preparation of sodalite will appear in another publication (11), only a short description will be given here. Bromide sodalite is especially dealt with because it seems to show the best compromise between different properties such as sensitivity, bleaching rate, and color. The chloride and iodide sodalites result when sodium bromide in the following methods is replaced by sodium chloride or iodide.

Method 1.—One of the first known preparation methods for sodalite, due to Medved (12), was used by us in the early stages of the investigation. All our sulfur-doped samples were prepared by this method. The method consists in mixing the dry starting materials, *viz.* NaOH, Al_2O_3 , SiO_2 , NaBr, Na_2SO_4 , and Na_2CO_3 , and firing at 900°-1060°C in air. The resultant sodalite could be made photochromic by reduction in flowing hydrogen at 900°C. The reduced material often even developed a color in daylight and bleaching was poor. These properties could be improved by partial reoxidation by a short heating at 900°C in air.

Method 2.—This method was developed by Schuil and Holland of our company (13). It is also a "dry" method differing from the previous one in that a gel is first made of the starting materials ($NaAlO_2$, SiO_2 , and NaBr) in water and then evaporated to dry-

ness. This material is converted into sodalite by firing at 1100°C in air with extra NaBr.

Method 3.—The preparation of sodalite by low-temperature hydrothermal reaction was first applied by Barrer *et al.* (14), using kaolinite as a starting material. We used pure starting materials instead. An alkaline solution of sodium aluminate, silica, and sodium bromide was agitated for 5 days at 80°C in closed Teflon bottles. The sodalite formed was made cathodochromic by an "activation" consisting in firing for 15 min at 900°C in air. This was sometimes carried out with extra NaBr (75% by weight) added to increase the bromine content. Sodalites containing Ga instead of Al or Ge instead of Si were also made by this method by using the appropriate starting materials.

Method 4.—This is a modification of the previous method, using sodium bromate (or chlorate for Cl-sodalite) in the solution instead of the bromide (chloride). The activation procedure, which is the same as before, converts the halogenate sodalite into the corresponding halide sodalite.

Method 5.—Another modification of method 3 consists in leaving the halide out of the solution. This results in hydroxide sodalite being formed. The same activation procedure, using extra sodium halide, converts the hydroxide sodalite into the halide sodalite.

Measuring Equipment

Optical spectra were measured using a Hilger Monospek 1000 grating monochromator (focal length 1 m, dispersion 8 Å/mm) in conjunction with an 800 Hz chopper, photomultiplier, and lock-in amplifier. The (Philips) photomultipliers used were the 51 UVP (S 13 response) for the uv region and the XP 1002 (S 20 response) and XP 1005 (S 1 response) for the visible and near-infrared regions.

Reflection spectra of powder samples at room temperature were obtained by passing the chopped radiation from a deuterium or tungsten lamp through a monochromator and, after reflection by the sample, detecting it by a photomultiplier. Smoked MgO was used as a standard.

Fluorescence spectra were measured with the samples immersed in liquid nitrogen in a quartz Dewar vessel. Excitation was by radiation from a low-pressure mercury lamp (mainly 2537 Å), filtered by a liquid Bäckström filter (15) and a Schott UG 5 filter. In some cases 3650 Å radiation from a super-high-pressure mercury lamp (Philips SP 1000), filtered by liquid $CuSO_4$ and UG 1 filters, was used.

Mechanism of Coloring and Bleaching

There is no existing theory concerning defect centers in sodalite, and we will therefore give only a simple and qualitative description of the processes of coloring and bleaching.

Key words: reflection spectra, fluorescence spectra, sulfur, oxygen, transition metals.

 CONDUCTION BAND

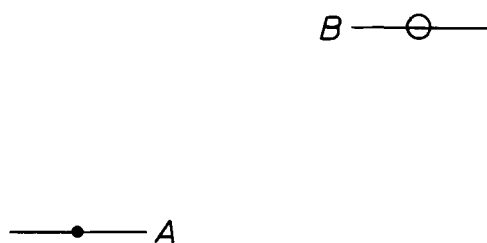


Fig. 1. Energy level diagram for defects in a crystal

We assume the presence in cathodochromic sodalite of two types of defect centers, the acceptor-like type A centers and the donor-like type B centers (see Fig. 1).

The coloration process can be described as the charge transfer from an electron-filled low-lying center A to an empty high-lying center B (see Fig. 1). The visible coloration is connected with the capability of the electron in B of being excited to the conduction band or to an excited state by absorption of a photon. In photochromism the charge transfer from A to B proceeds by photo-excitation of the electron in A to the conduction band and transfer via this band to B. In cathodochromism the final state of affairs is the same, but the primary process is the creation by electron excitation of a large number of free electrons in the conduction band and of free holes in the valence band, these electrons and holes then being captured by centers B and A, respectively.

Bleaching is the transfer of the electron at B back to A, induced by light or by heat. When the bleaching is by heat, the primary process may be the excitation of the electron from B to the conduction band or the excitation of the hole from A to the valence band. It is known from the theory of thermoluminescence (16) that, when a solid containing centers is heated at a constant rate, an approximately linear relation exists between the ionization energy of the centers and the absolute temperature at which the ionization rate reaches a maximum. The value of the proportionality factor for sodalite is not known but values for different materials are found to lie within the range of 1.9×10^{-3} to 2.8×10^{-3} eV/°K (16). It then follows from the temperature at which rapid bleaching occurs ($\approx 500^\circ\text{K}$) that the ionization energy must have a value of 0.95–1.4 eV. As shown by electron spin resonance (1) the B centers in sodalite are halogen vacancies which show an absorption band with a maximum at 2.3 eV. Their thermal ionization energy is not known but the value of 1.8 eV at the long-wavelength tail of the absorption band gives a reasonable estimate of this energy because optical absorption (involving the ground and ionized states) cannot occur for photon energies below the thermal ionization energy. This value is significantly higher than the values of 0.95–1.4 eV obtained from thermal bleaching, so that we conclude that A centers with ionization energies less than 1.4 eV ionize to cause the thermal bleaching rather than B centers.

A residual coloration, *i.e.* a coloration which cannot be bleached optically, can be explained if we assume a second type of A centers which may come into existence as a result of radiation damage and in which trapped holes have a negligible probability to recom-

bine with free electrons. The electrons will then be re-trapped by the B centers causing a permanent coloration.

The function of the type A centers can be twofold. In the uncolored state they can serve to compensate for the positive charge of the chlorine ion vacancies. In order to acquire the colored state they must be able to lose electrons to the chlorine vacancies and to bind the remaining holes so that the colored state may persist. Some type A centers may serve only one of these purposes. Type A centers in sodalite which fulfill both these functions can be, for example, S^{--} or O^{--} ions replacing Cl^- ions, Fe^{2+} ions replacing Al^{3+} ions, or sodium-ion vacancies.

Results and Discussion

Band gap of sodalite.—Since the band structure of sodalite is not known and accurate values of the absorption coefficient as a function of the wavelength cannot be obtained from powder reflection spectra, only rough estimates of the value of the bandgap can be made. The powder spectra show a steep drop of the reflection coefficient below a certain wavelength. The straight-line portions of the curve below and above the “knee” were linearly extrapolated and the intersection point was taken as the band edge. Bandgaps thus obtained were 6.1 eV for Cl-sodalite, 5.9 eV for Br-sodalite, and 5.2 eV for I-sodalite. Duncan *et al.* (7) mention a value of 5.2 eV but do not specify the type of sodalite.

Sulfur centers.—The effect of different treatments of sulfate-doped bromide sodalite on its uv reflection spectrum is shown in Fig. 2. The curve for an unreduced sample (curve 1) shows an absorption at 2600Å. This band is probably not characteristic for the SO_4^{--} ion because not all sulfate-doped samples show it. Irradiation by 2537Å uv does not give rise to coloration. These facts, together with the assumed acceptor-like character of the sulfate center, indicate an energy-level position close to the valence band, at a distance greater than 5 eV below the conduction band.

After reduction in hydrogen the uv reflection spectrum shows a strong absorption, with a tail extending up to 4000Å (see curve 2 in Fig. 2). We observed that excitation at 77°K by 3650Å radiation gives rise to a broad fluorescence band with a maximum at 9000Å. This emission was also observed by Taylor *et al.* (5) and was ascribed by them to S^{--} ions. We also ascribe the strong absorption to these ions.

A coloration is observed for radiation with wavelengths up to 4000Å. This fact indicates that the uv absorption must be due to the excitation of electrons from the S^{--} centers to the conduction band. We therefore locate the energy level of the S^{--} ion at a position about 3.1 eV below the conduction band (see Fig. 3), corresponding to the tail of the absorption. The fluorescence may be ascribed to the reverse process, possibly via an excited state.

If the assigned level position is correct, the distance to the valence band will be about 2.8 eV (see Fig. 3). Therefore, if empty S^{--} centers (*i.e.* S^- ions) are present, electrons from the valence band can be excited to the empty levels. Part of the observed uv absorption may be due to this process.

Partial reoxidation of the reduced sodalite samples by short heating to 900°C in air causes most of the strong absorption to disappear and a new absorption with a maximum at 3700Å to appear (see Fig. 2, curve 3). Excitation at 77°K with 3650Å radiation now gives rise to the characteristic fluorescence of the S_2^- molecule ion shown in Fig. 4. This emission is well known in sodalite (1, 5, 17) as well as in the alkali halides (18, 19). The emission peaks of some of our samples showed a fine structure (see Fig. 5) which was also reported by Rolfe (19) in alkali halides and ascribed to coupling with lattice phonons. Radiation of 2537Å wavelength gives rise to photochromism, whereas

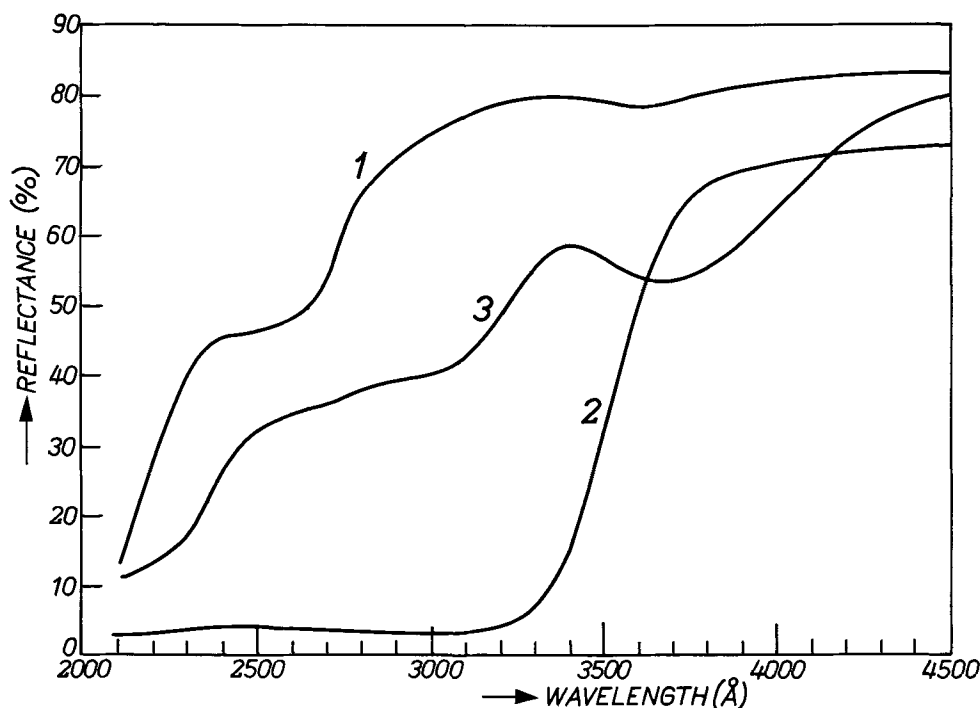


Fig. 2. UV reflection spectrum at 20°C of sulfate-doped bromide sodalite: curve 1, before reduction; curve 2, after reduction in H₂; and curve 3, after partial reoxidation in air.

3650Å radiation does not. These observations suggest an energy level scheme as shown in Fig. 6.

The partly reoxidized samples show a weaker photochromism than the reduced ones, whereas the bleaching properties are better. This may be the result of the different charge of the S^{•-} and S₂⁻ ions. In the uncolored state of the sodalites, S^{•-} has an effective negative charge of unity having a large capture cross section for holes, whereas S₂⁻ is effectively neutral, having a small capture cross section. In the colored state the empty S^{•-} center (i.e. the S⁻ ion) is effectively neutral and therefore has a small capture cross section for electrons in contrast to the empty S₂⁻ center (i.e. the S₂ molecule) which is effectively positive, resulting in a large capture cross section for electrons.

The above-mentioned partial reoxidation, converting S^{•-} centers into S₂⁻ centers, may be described by the reaction equation



In describing this chemical reaction we find it conven-

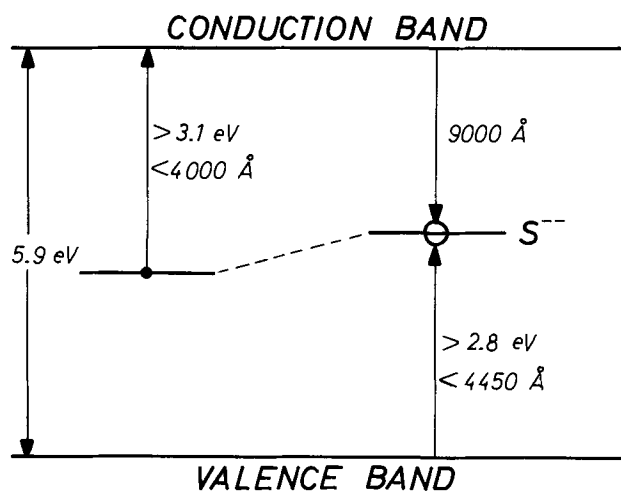
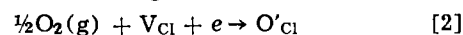


Fig. 3. Schematic energy level diagram of S^{•-} in bromide sodalite.

ient to use the notation of Kröger and Vink (20) for defect centers: S'_{Cl} is a S^{•-} ion on a Cl-site, S_{2Cl} is a S₂⁻ molecule-ion on a Cl-site, V_{Cl} is a chlorine-ion vacancy containing an electron, and e is an electron. The role of the oxidizing agent, i.e. the atmospheric oxygen, is to remove the electrons produced by Reaction [1], e.g. in the following way



where O'_{Cl} is an O^{•-} ion on a Cl-site.

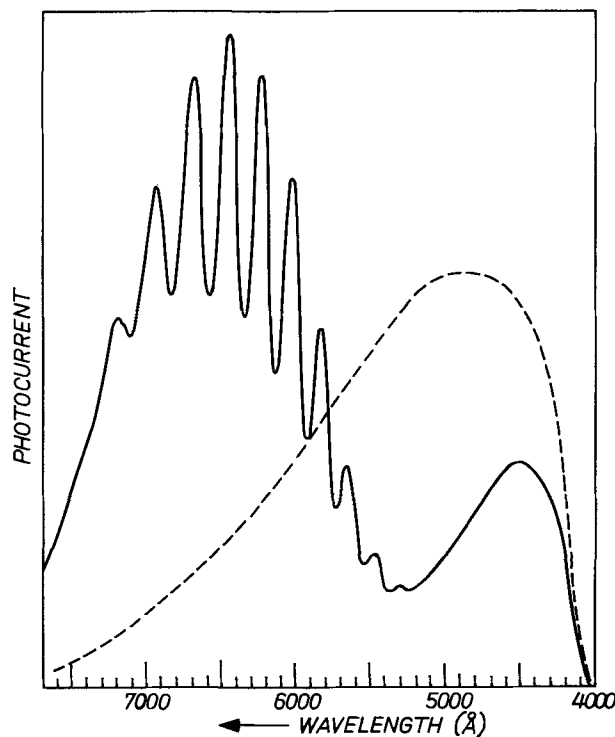
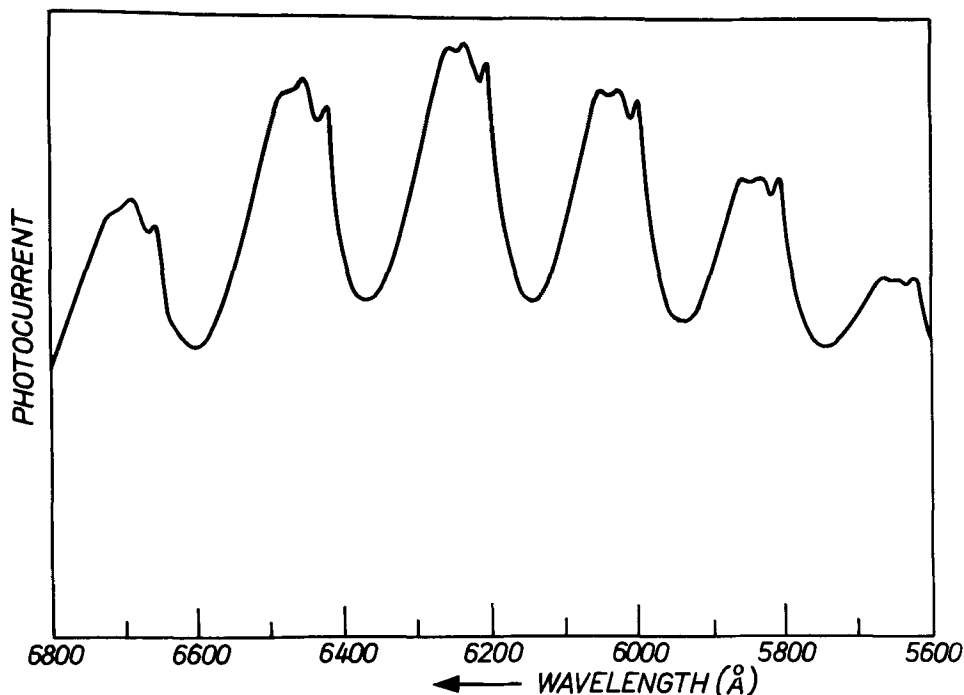


Fig. 4. Fluorescence of S₂⁻ in bromide sodalite at 77°K (solid curve). The spectral sensitivity of the equipment is shown by the dashed curve; the cutoff near 4000Å is due to a filter (Schott GG 15) used to suppress stray radiation.

Fig. 5. Fine structure on the S_2^- fluorescence peaks in bromide sodalite at 77°K.



It was found by Taylor *et al.* (5) that chloride sodalite doped with S^{--} showed a residual coloration after prolonged irradiation with electrons, *i.e.* the induced color could not be bleached optically. This was accompanied by the appearance of the S_2^- fluorescence under 3650Å radiation. Though there are probably many reasons for the residual coloration, we propose the following mechanism as a possible one. We assume that the sulfur is incorporated as S^{--} ions which may be excited or ionized by the electron bombardment and then may become mobile and combine with other sulfur ions, forming S_2^- molecule ions. This may again be described by the reaction Eq. [1]. In this case, however, we have no reaction like Eq. [2] to remove the electrons created by Reaction [1]. These electrons will then

fill empty chlorine vacancies causing a permanent coloration.

Oxygen centers.—Since oxygen is chemically related to sulfur it may be expected that oxygen centers exist that are analogous to the sulfur centers described in the previous section. These centers have been found in alkali halides (21-24) but, until recently, not in sodalite.

Some sodalite samples, when excited at 77°K with 2537Å radiation, show a weak, structured emission superimposed upon a broad background emission (see Fig. 7a) (25). The emission is relatively strong in chloride and bromide sodalite samples made by low-temperature hydrothermal synthesis (method 3) and has also been observed sometimes in samples made by method 4. We ascribe this emission to the O_2^- molecule ion because the general appearance and the peak spacings are similar to those of the O_2^- emission in the alkali halides.

No prominent absorption has been found which can be ascribed to the O_2^- center. Since 2537Å radiation excites the fluorescence while 3650Å radiation does not, the absorption spectrum may be similar to that in KCl with a maximum at 2500Å and almost no absorption at 3650Å (22). Photochromism is observed only for uv with wavelengths shorter than 2100Å. These observations agree with the energy level scheme in Fig. 8.

Sodalite samples exhibiting the O_2^- fluorescence often show a residual coloration. The cause may be the same as that proposed for the S_2^- centers.

We did not observe the O^{--} centers, either in absorption or in luminescence. The centers have been observed in alkali halides (24). We think that they are nevertheless present in sodalite and play an important role as type A centers. This has previously been suggested by Ballentyne and Bye (6).

Transition metals.—Sodalite samples doped with Co, Ni, Mn, Fe, and Cr show some interesting optical prop-

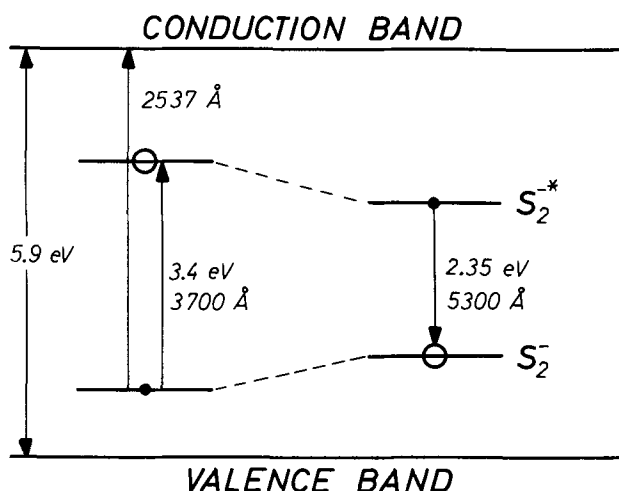


Fig. 6. Schematic energy level diagram of S_2^- in bromide sodalite; 3700Å radiation gives rise to fluorescence (zero-phonon wavelength 5300Å), 2537Å radiation gives rise to photochromism.

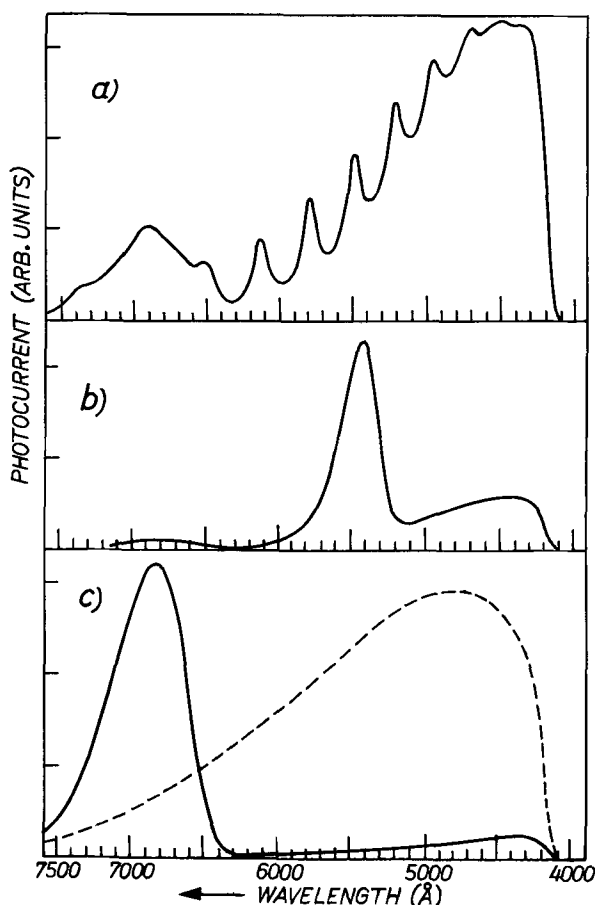


Fig. 7. Fluorescence of bromide sodalite at 77°K due to (a) O_2^- ions, (b) Mn^{2+} ions, and (c) Fe^{3+} ions. The dashed curve in (c) indicates the spectral sensitivity of the equipment (cf. Fig. 4).

erties. These samples were prepared by method 5. The doping was carried out by adding 2% by weight of the transition metal halides to the sodium halide used for the activation. The appearance of the doped powders was "cobalt blue" for Co, light purple for Ni, grayish

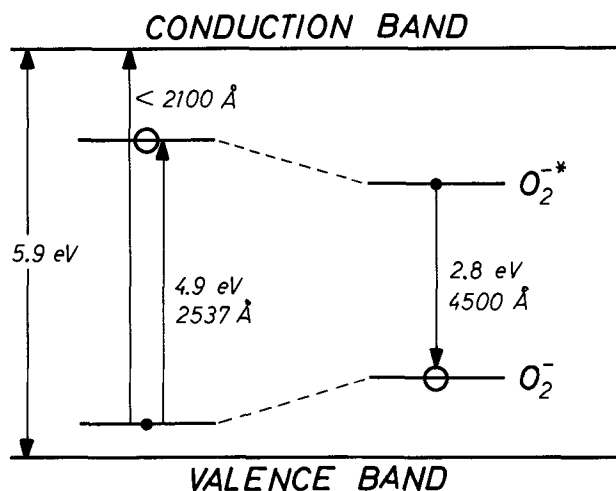


Fig. 8. Schematic energy level diagram of O_2^- in bromide sodalite; 2537Å radiation gives rise to fluorescence (zero-phonon wavelength 4500Å). Photochromism is observed for short-wavelength radiation ($< 2100\text{Å}$) only.

for Mn, and pure white for Fe and Cr. Some of the uv reflection spectra between 2000 and 4500Å are shown in Fig. 9. Fluorescence was observed in the Mn and Fe doped samples only. The green Mn fluorescence was weak, the red Fe fluorescence relatively strong (see Fig. 7b and c).

The incorporation of the transition metals in sodalite has several interesting aspects. First, the question whether the metal ions are incorporated in the aluminosilicate network, at chlorine or sodium sites, or interstitially; second, the coordination number of the ions; and third, their valency.

According to Linwood and Weyl (26), who studied the behavior of Ni, Co, and Mn in glasses, the blue color of the Co-doped samples, the purple color of the Ni-doped samples, and the green luminescence of the Mn-doped samples all point to a fourfold coordination of the divalent ions, which implies incorporation at Al

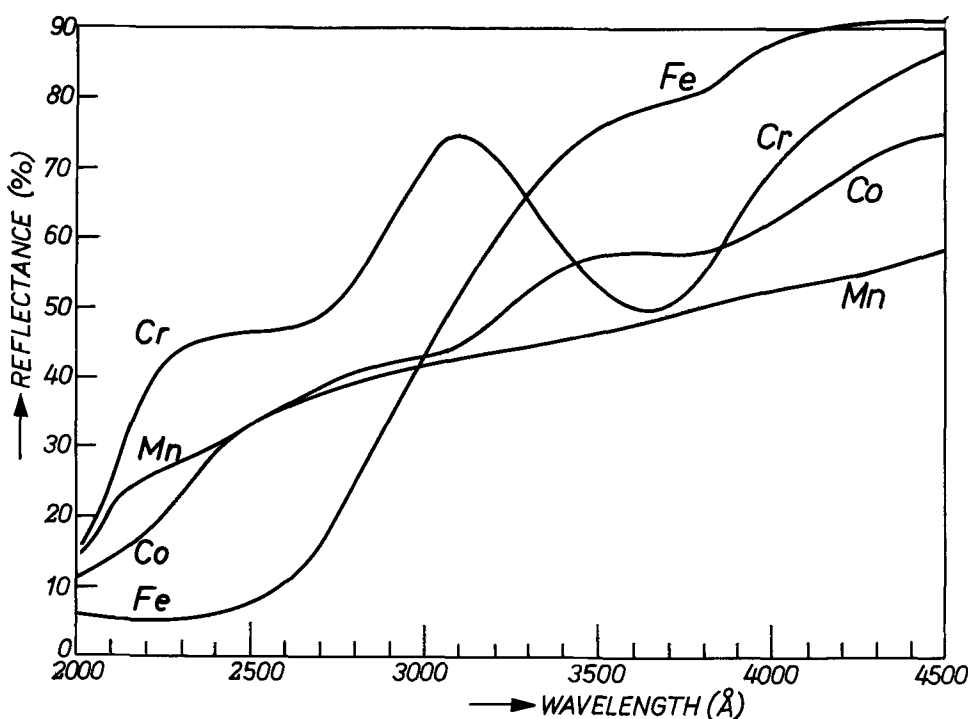


Fig. 9. UV reflection spectra at 20°C of bromide sodalite samples doped with Co, Cr, Fe, or Mn.

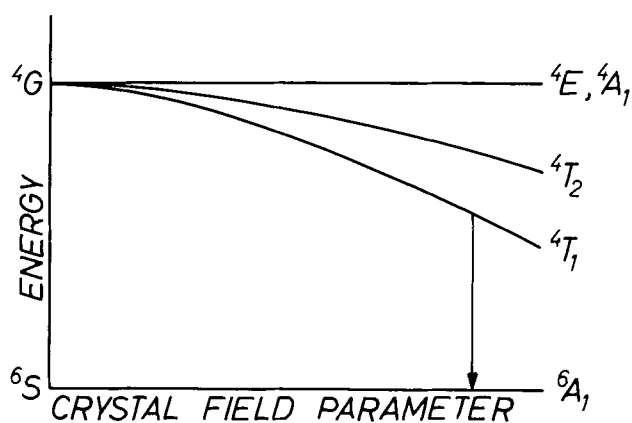


Fig. 10. Crystal-field splitting for the $3d^5$ configuration of Mn^{2+} and Fe^{3+} ions.

or Si sites. The luminescence of Mn^{2+} is connected with a transition from the lowest excited level (4T_1 split off from the 4G atomic level) to the ground level (6A_1 , atomic state 6S) (see Fig. 10).

Another argument for the fourfold coordination of Mn^{2+} is derived from its e.s.r. signal. An experimental relation between the hyperfine constant and the covalency divided by the coordination number for Mn^{2+} in various host crystals (27) gives a value for the hyperfine constant of $82 \times 10^{-4} \text{ cm}^{-1}$ for a sixfold coordination by oxygen and of $75 \times 10^{-4} \text{ cm}^{-1}$ for a fourfold coordination. The experimental value of $76 \times 10^{-4} \text{ cm}^{-1}$ (28) indicates a fourfold coordination.

For the case of iron we have to consider both the valency (2 or 3) and the coordination number (4 or higher). We can rule out divalent iron for the following reasons. The energy-level splitting of the divalent ion in a fourfold coordination is shown in Fig. 11. For a sixfold coordination the positions of the 5E and 5T_2 levels are reversed. The zero-phonon absorption of Fe^{2+} with a tetrahedral coordination of oxygen has been found at a phonon energy of 3595 cm^{-1} ($\lambda = 3.45\mu$) (29). The transition energy for an octahedral coordination is not known. In view of its linear crystal field dependence and the crystal field being 9/4 times as strong, it may be estimated to have a value of 8100 cm^{-1} or 1.235μ . Neither of these energies agrees with our experimental value of $15,900 \text{ cm}^{-1}$ or 6300\AA (the high-energy tail of the fluorescence band). The observation that iron-doped sodalite which has been reduced in flowing hydrogen at 900°C shows neither the fluorescence band at 6800\AA nor the absorption band at 2400\AA gives additional support to the conclusion that the iron is in the trivalent state.

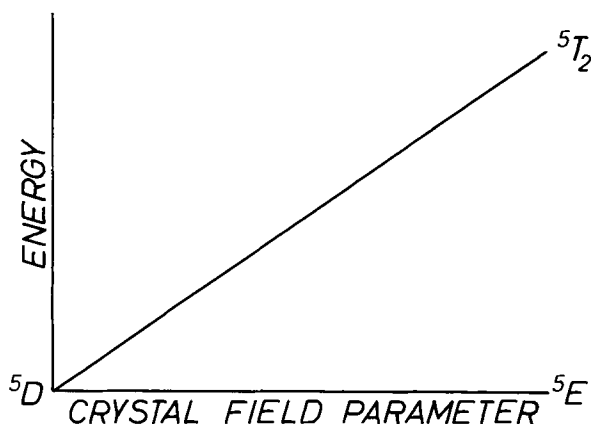


Fig. 11. Crystal-field splitting for the $3d^6$ configuration of Fe^{2+} with tetrahedral coordination.

The question of the coordination of the Fe^{3+} ion is more difficult to answer. Theoretically and experimentally, little is known about the crystal-field-split energy levels of Fe^{3+} . The electron configuration of Fe^{3+} is $3d^5$, the same as that of Mn^{2+} . The variation in the energy levels of Fe^{3+} and Mn^{2+} with the crystal field strength is qualitatively the same (see Fig. 10) but quantitatively different. The first excited level of the free Fe^{3+} ion is $32,000 \text{ cm}^{-1}$ above the ground state as compared to $26,859 \text{ cm}^{-1}$ in the case of Mn^{2+} . The crystal field splitting parameter is, however, larger for Fe^{3+} than for Mn^{2+} and the lowest transition energy of the Fe^{3+} ion in the crystal may therefore be lower than that of Mn^{2+} . Dvir and Low (30) find a value of $12,300 \text{ cm}^{-1}$ for the absorption corresponding to the lowest transition energy of octahedrally coordinated Fe^{3+} in beryl. Comparison of this value with that found above for the fluorescence ($15,900 \text{ cm}^{-1}$) indicates a fourfold coordination. Pott and McNicoll (31), however, observed blue and infrared emissions due to Fe^{3+} in γ -alumina which they ascribe to Fe^{3+} in fourfold and sixfold coordination, respectively. Melamed *et al.* (32) observed an emission band with a maximum at 6800\AA and a number of absorption bands due to Fe^{3+} in $LiAl_5O_8$. The emission band was ascribed to the 4T_1 (4G) \rightarrow 6A_1 (6S) transition of tetrahedrally coordinated Fe^{3+} . There was, however, some ambiguity in the band assignments, especially those of the absorption bands. We may conclude that the question of the coordination number has not yet been solved.

Doping with Fe, Ni, Mn, Co, or Cu in concentrations of 20-200 ppm causes an increase of the optical bleaching rate of electron-irradiated sodalite (33). This may be connected with the ability of these elements to act as recombination centers. Doping with Cr has little influence on the bleaching rate.

Radiation damage.—The coloring of sodalite by electron bombardment and the optical bleaching will be the subject of another paper (33). Here we will describe the effect of the electron bombardment on the reflection and fluorescence spectra, which was studied in connection with irreversible effects in coloring and bleaching.

The bombardment was carried out in a demountable tube. The duration of bombardment, the effects of bleaching by visible or uv radiation, the temperature, the storage time after the bombardment, and the composition of the material were varied.

A short irradiation (10 kV , $1 \mu\text{C}/\text{cm}^2$), giving a contrast of about 2:1, causes the appearance of two uv absorption bands at 2600 and 3500\AA (see curves 1 and 2 in Fig. 12). These bands are not directly connected with the visible coloration because bleaching of the latter has no effect on the uv bands. Irradiation with uv in one of the bands causes the bands to disappear simultaneously. This experiment has been performed using radiation of 3650\AA or 2537\AA , situated reasonably well within the absorption range of the bands. The bands always occur simultaneously and with the same intensity ratio. These facts indicate that the bands are associated with the same defect.

Irradiation for longer times (10 kV , $50 \mu\text{C}/\text{cm}^2$), causing saturation of the visible coloration, does not further increase the uv bands but produces a general absorption in the wavelength range of 2000 - 4000\AA (see curve 3 of Fig. 12). This is often accompanied by the appearance of a permanent color which cannot be bleached optically.

Heating to 200°C causes the complete disappearance of the two absorption bands but only partial disappearance of the diffuse absorption.

The uv absorption spectrum changes when the irradiated sodalite is stored at room temperature. Little change is observed for a couple of hours after irradiation but 24 hr later the absorption bands at 2600 and 3500\AA have disappeared and a new band shows up at

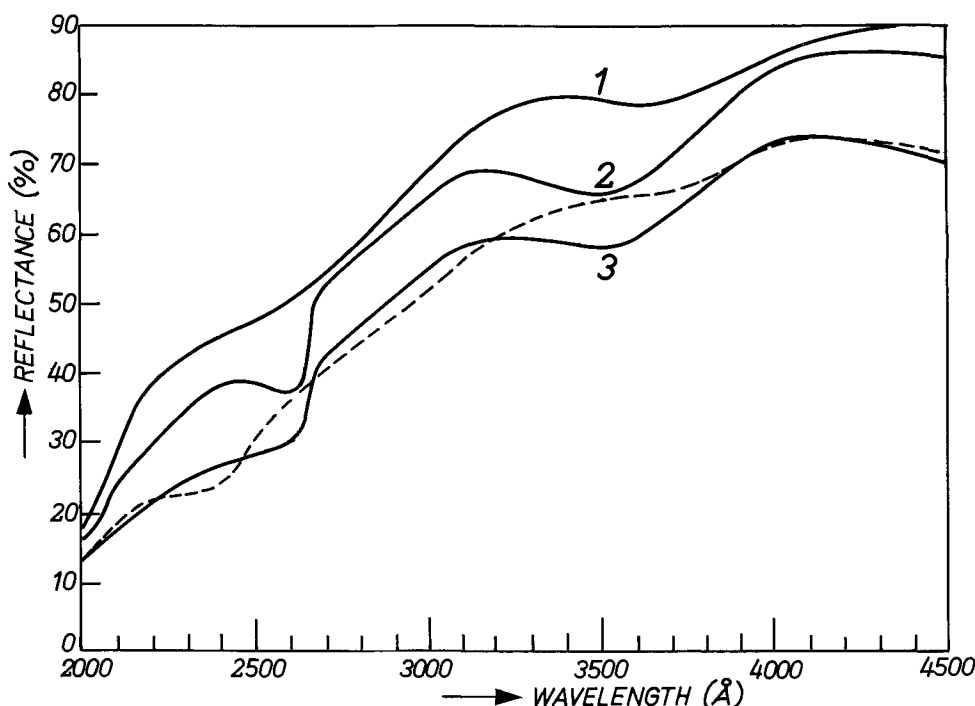


Fig. 12. UV reflection spectrum of bromide sodalite: curve 1, before electron irradiation and after electron irradiation with curve 2, a small dose ($1 \mu\text{C}/\text{cm}^2$, 10 kV), curve 3, a large dose ($50 \mu\text{C}/\text{cm}^2$, 10 kV), and dashed curve after 24 hr storage.

2400Å (see dashed curve in Fig. 12). Storage for longer periods does not change the spectrum any further. Preparation method 2 was used for the case illustrated but other methods were found to give similar results.

The effect of the following substitutions in the sodalite were studied: Br by OH, Cl, or I; Na by Li, K, or Rb; Si by Ge; and Al by Ga. In all cases the same absorption bands were observed. The sodalite structure also is not essential since nepheline, which has a different (hexagonal) structure likewise shows these bands.

In view of these observations we tentatively suggest that the defect is an oxygen radical ion, tied with one bond to a silicon or aluminum ion, or an oxygen ion that has been knocked completely free of the silicate network and is occupying some interstitial position.

The nature of the defect corresponding to the continuous absorption between 2000 and 4000Å is not yet known. Since this absorption develops simultaneously with a permanent coloration of the sodalite, there may be a connection between these two effects.

It is not yet certain whether the radiation damage in itself is harmful to the coloring and bleaching properties of sodalite.

The fluorescence spectrum of sodalite (at 77°K) is very sensitive to electron irradiation. A short irradiation (10 kV, $1 \mu\text{C}/\text{cm}^2$) causes the development of a broad emission band with a maximum in the near u.v. The origin of this band is not yet known. It vanishes again after prolonged irradiation. All other emissions (due to Fe^{3+} , Mn^{2+} , and O_2^-) are strongly quenched. These effects will be studied further.

Conclusion

Cathodochromic sodalite was prepared by high-temperature solid-state reaction and by low-temperature hydrothermal reaction.

Undoped samples were not photochromic but their cathodochromism was often superior to that of sulfur-doped ones. These "undoped" samples are assumed to contain O^{--} and O_2^- , acting as acceptor centers. Doping with Fe, Ni, Mn, Co, or Cu increases the optical bleaching rate of electron-irradiated sodalite. Cr has little effect, O_2^- causes a residual coloration. Mn^{2+} shows a green luminescence, Fe^{3+} a red luminescence, and O_2^- a luminescence with several peaks between 4500Å and 7000Å. The transition metals are probably incorporated at Al or Si sites of the sodalite. Permanent changes due to electron irradiation

were found in the uv reflection spectrum: one, after short irradiation, resulted in two absorption bands at 2600Å and 3500Å; the other, after prolonged irradiation, resulted in a general absorption between 2000Å and 4000Å. The interrelation between these phenomena and irreversible effects in cathodochromism is under study.

Acknowledgment

We wish to thank Th. W. Lathouwers for valuable assistance in the preparation of the sodalite samples and R. A. van Doorn for skillful assistance in the experiments on cathodochromism. We also acknowledge the contribution of J. Goorissen and J. A. M. Smets in the preparation of sodalite during the early stages of this work. Thanks are due to L. C. Bastings for the chemical analysis, to C. Langereis for the x-ray diffraction measurements, and to G. G. P. van Gorkom who kindly performed some e.s.r. experiments. We have further benefited from useful discussions with R. E. Schuil and A. M. B. M. Holland, who also put a number of sodalite samples at our disposal.

Manuscript submitted June 18, 1971; revised manuscript received ca. Sept. 13, 1971.

Any discussion of this paper will appear in a Discussion Section to be published in the December 1972 JOURNAL.

REFERENCES

1. W. G. Hodgson, J. S. Brinen, and E. F. Williams, *J. Chem. Phys.*, **47**, 3719 (1967).
2. F. W. Webster and E. A. D. White, Symposium on photochromism, London, May 25, 1967 (unpublished).
3. W. Phillips and Z. J. Kiss, *Proc. I.E.E.E.*, **56**, 2072 (1968).
4. E. F. Williams, W. G. Hodgson, and J. S. Brinen, *J. Am. Ceram. Soc.*, **52**, 139 (1969).
5. M. J. Taylor, D. J. Marshall, P. A. Forrester, and S. D. MacLaughlan, *Radio Electro. Eng.*, **40**, 17 (1970).
6. D. W. G. Ballentyne and K. L. Bye, *J. Phys. D. Appl. Phys.*, **3**, 1438 (1970).
7. R. C. Duncan, B. W. Faughnan, and W. Phillips, *Appl. Opt.*, **9**, 2236 (1970).
8. W. Phillips, *This Journal*, **117**, 1557 (1970).
9. L. Pauling, *Z. Krist.*, **74**, 213 (1930).
10. J. Löns and H. Schulz, *Acta Cryst.*, **23**, 434 (1967).
11. D. J. Schipper, C. Z. van Doorn, and P. T. Bolwijn, To be published.
12. D. B. Medved, U.S. Pat. 2,761,846 (1956).

13. R. E. Schuil and A. M. B. M. Holland, Private communication.
14. R. M. Barrer, J. F. Cole, and H. Sticher, *J. Chem. Soc. (A)* **1968**, 2475.
15. M. Kasha, *J. Opt. Soc. Am.*, **38**, 929 (1948).
16. J. T. Randall and M. H. F. Wilkins, *Proc. Roy. Soc.*, **A184**, 366 (1945); G. Curie and D. Curie, *J. Phys. Radium*, **11**, 199 (1955).
17. R. D. Kirk, *This Journal*, **101**, 461 (1954).
18. J. H. Schulman and R. D. Kirk, *Solid State Comm.*, **2**, 105 (1964).
19. J. Rolfe, *J. Chem. Phys.*, **49**, 4193 (1968).
20. F. A. Kröger and H. J. Vink, *Solid State Phys.*, **3**, 307 (1956).
21. F. Fischer, H. Grundig, and R. Hilsch, *Z. Phys.*, **189**, 79 (1966).
22. J. Rolfe, F. R. Lipsett, and W. J. King, *Phys. Rev.*, **123**, 447 (1961).
23. J. Rolfe, *J. Chem. Phys.*, **40**, 1664 (1964).
24. F. Fischer, *Naturwissenschaften*, **54**, 313 (1967).
25. C. Z. van Doorn and D. J. Schipper, *Phys. Letters*, **34A**, 139 (1971).
26. S. H. Linwood and W. A. Weyl, *J. Opt. Soc. Am.*, **32**, 443 (1942).
27. E. Simánek and K. A. Müller, *J. Phys. Chem. Solids*, **31**, 1027 (1970).
28. G. G. P. van Gorkom, Private communication.
29. G. A. Slack, F. S. Ham, and R. M. Chrenko, *Phys. Rev.*, **152**, 376 (1966).
30. M. Dvir and W. Low, *ibid.*, **119**, 1587 (1960).
31. G. T. Pott and B. D. McNicoll, *Chem. Phys. Letters*, **6**, 623 (1970).
32. N. T. Melamed, P. J. Vicarro, J. O. Artman, and F. de S. Barros, *J. Luminescence*, **1**, **2**, 348 (1970).
33. P. T. Bolwijn, D. J. Schipper, and C. Z. van Doorn, *J. Appl. Phys.*, To be published.

Characterization of a Gold-Copper Composite Surface for Plated Wire Memory

F. E. Luborsky, M. W. Breiter,* and B. J. Drummond

General Electric Corporate Research and Development, Schenectady, New York 12301

ABSTRACT

Gold electrodeposited at very low currents onto a coarse-grained copper surface was found to enhance nondestructive read-out (NDRO) memory performance when used as a substrate for the electrodeposition of Permalloy films. The structure of this Au layer is studied. Corrosion potential measurements are used to show that the Au covers about 0.4 of the surface when deposited on the coarse-grain Cu to produce optimum NDRO properties but the same quantity of Au deposited on fine-grain Cu covers ~0.7 of the surface. The average Au thickness, grain size, lattice parameter, and coverage all show a sharp change at the same current. This current occurs just beyond the deposition current used to produce the optimum surface for NDRO memory wire. It appears to correspond to the transition from a Au island structure to a continuous film structure and is close to the point at which the Au deposition efficiency rises sharply. Scanning electron micrographs indicate the presence of Au islands at the low currents but do not have sufficient resolution to show their detailed structure.

Wires plated with a thin film of NiFe are becoming increasingly important as elements for computer memories. The magnetic properties of the NiFe are critically dependent on the nature of the substrate. Copper has typically been used and control of its surface topography to achieve the desired characteristics has been discussed extensively. This area of work has been recently reviewed (1). More recently it has been shown (2, 3) that the presence of gold islands on the copper, particularly on rough coarse-grained Cu, results in greatly improved magnetic properties.

This paper describes the physical and metallurgical structures of these Au films deposited on Cu.

Sample Preparation

Wire samples were all prepared in a continuous plating system briefly described previously (2, 3). The substrate wire was either 2.2 mil diameter electroplated tungsten wire¹ plated with about 1 μ of Au or 2.2 mil CuBe wire² drawn to a smooth surface finish. A fine-grain smooth Cu layer with an average thickness of 2 μ was then deposited from a CuSO₄ electrolyte containing UBAC³ as a leveling agent. Some samples were then given a controlled roughness by depositing another layer of Cu from a CuSO₄

electrolyte at higher temperatures without any leveling agents. Finally Au was deposited from an Orosene 999 electrolyte⁴ at various currents using 30°C, 4.3 pH, and a constant flow across the wire from four perpendicular directions staggered along the length of the wire. All plating cells were 2 in. long.

Analytical Techniques and Results

Corrosion potential measurements.—Corrosion potentials on specimens consisting of two different metals have been shown (4-6) to be related to the proportion of the exposed areas of the two metals. It can be shown theoretically, assuming that both the anodic reaction of metal dissolution at exposed copper and the cathodic reaction of oxygen reduction at exposed gold are controlled by activation polarization, that

$$V_{\text{corr}} = K_1 - K_2 \log (A_{\text{Cu}}/A_{\text{Au}}) \quad [1]$$

where V_{corr} is the corrosion potential measured against a suitable reference electrode. K_1 and K_2 are constants which depend on the Tafel slopes of the individual electrode reactions, on the corrosion potential of the pure Cu, and on the exchange current densities. A_{Cu} designates the fraction of the total surface which is covered by copper, A_{Au} the fraction covered with gold. Calibration curves obtained on short-circuited Cu and Au electrodes are shown in Fig. 1 for a variety of conditions. As shown by the

* Electrochemical Society Active Member.
Key words: electrodeposited thin films, magnetic memory, film structure.
¹ General Electric Company, Lamp Metals and Components Department, Cleveland, Ohio 44117.
² Little Falls Alloys, Inc., Paterson, New Jersey 07501.
³ Udylite Corporation, Detroit, Michigan 48234.

⁴ Technic Inc., P.O. Box 965, Providence, Rhode Island 02901.

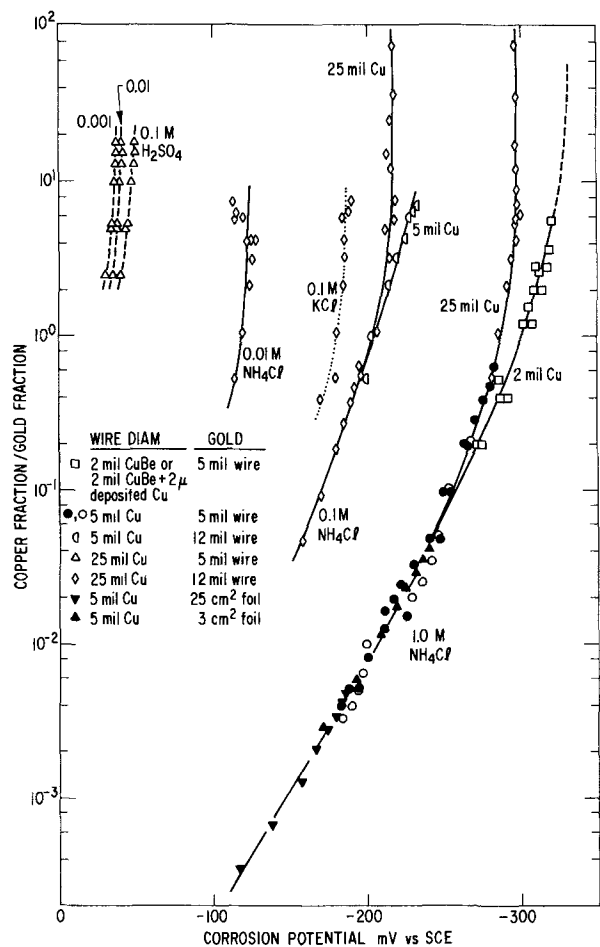


Fig. 1. Calibration for corrosion potentials of Cu-Au coupled samples of various geometries in different electrolytes. Electrolyte was air agitated at 1 ft³/hr for the open symbols or mildly stirred for the solid symbols.

results in 1M NH₄Cl, for A_{Cu}/A_{Au} less than ~ 0.05 the results follow the functional form of Eq. [1]. This has been demonstrated previously (5). In this range, the results were independent of the size and geometry of the coupled specimen of Cu and Au and independent of the degree of agitation.

For the investigation of small Au islands on Cu substrates in the present work, the region where A_{Cu}/A_{Au} is greater than 0.05 is important. As indicated in Fig. 1, in this range the potentials appear to be sensitive to electrode geometry, and to approach a limiting potential for each electrode geometry and for each of the electrolytes explored. Thus the results no longer follow the form of Eq. [1] at $A_{Cu}/A_{Au} > 0.05$. This suggests that the electrode reactions are at least in part diffusion controlled and that the exchange current for Au is very small compared to the Cu. Thus a steady-state mixed potential cannot be established. Nevertheless, empirical calibration curves can be established for a given set of experimental conditions.

In all cases, when the calibration samples were first immersed, the potentials showed an initial very rapid change with time, before stabilizing to a constant value. In the case of the samples of Au plated on Cu, after the initial rapid change in potential most samples slowly drifted in potential probably indicative of changes in the surface of the samples. Thus the potentials used were obtained by extrapolating this slowly changing portion of the curve back to zero time. Some typical examples of such curves are shown in Fig. 2 for samples prepared at different gold currents onto the rough Cu substrates. Similar curves were

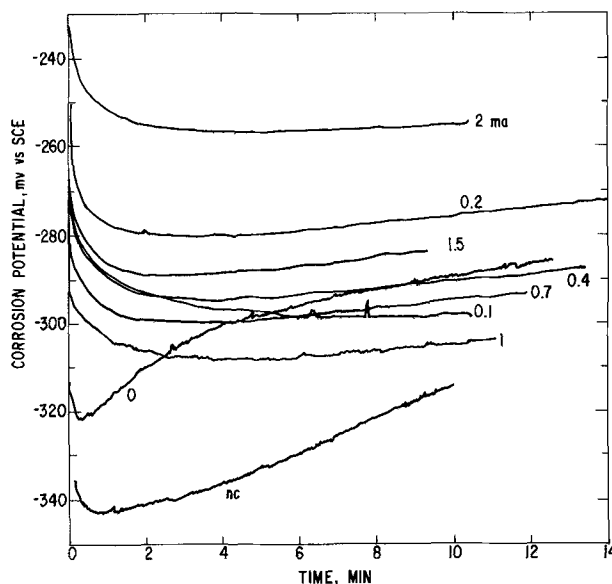


Fig. 2. Typical variation of corrosion potential with time after immersion in 1M NH₄Cl for samples prepared with no Au (nc) and with Au deposited at various currents in a 2 in. long cell onto the 2.2 mil diameter wire. Wire speed 14 in./min; Au electrolyte flow = 1.9 liters/min. Rough coarse-grain Cu substrate.

obtained for samples prepared on the smooth Cu substrates. The corrosion potentials obtained by extrapolation to $t = 0$ are shown in Fig. 3. On the right hand ordinate are the corresponding Cu area fractions obtained from the empirical calibration curve in Fig. 1 using the curve obtained with the 2-mil Cu-plated CuBe wire tested in 1M NH₄Cl. Note that at low Au deposition currents on the smooth Cu, the area fraction of exposed Cu is almost independent of current; $A_{Cu} = 0.3 \pm 0.1$ ($A_{Au} = 0.7 \pm 0.1$). For the rough Cu there is a pronounced minimum at 1.0 mA of the deposition current; $A_{Cu} = 0.55$ ($A_{Au} = 0.45$). For the thick Au films, the scatter indicates the random occurrence of pin holes or other flaws. Under

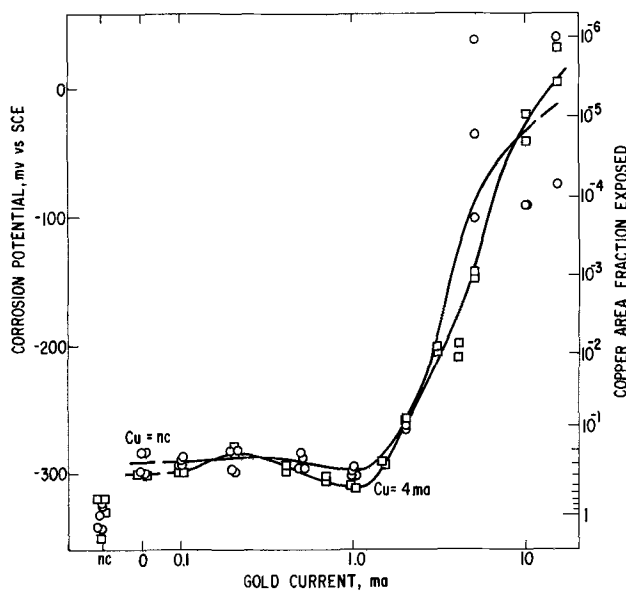


Fig. 3. Corrosion potentials obtained from curves in Fig. 2 by extrapolation from times > 4 min back to zero time, as a function of the current used to deposit the Au. The corresponding Cu area exposed is shown on the right hand ordinate as obtained from Fig. 1. \circ Smooth fine-grain substrate, \square rough coarse-grain substrate.

Table I. Area fractions of gold determined from corrosion potentials

Au current	On coarse-grained Cu	On fine-grained Cu	
		1st Test	2nd Test
nc	0	0	0
0.05	0.15 ± 0.1	0.6 ± 0.1	0.6 ± 0.1
0.2	0.35 ± 0.1	0.85 ± 0.05	0.80 ± 0.05
10	1.00000	1.00000	1.00000

Notes: Samples prepared at 21 in./min. Electrolyte flow = 0.3 liter/min in Au plating bath. Average value of two samples reported.

the Au plating conditions of Fig. 3, the memory characteristics, specifically the NDRO quality, show a pronounced optimum at a deposition current of 1 mA Au on the rough Cu, but little or no optimum on the smooth Cu. Thus the quality of the memory characteristics may be correlated in an empirical way to the shape of the curves in Fig. 3.

In another set of samples prepared at a lower electrolyte flow rate in the gold plating bath similar results (Table I) were obtained. However, the optimum magnetic properties for the data in Table I occurred at a gold deposition current of ~0.1 mA rather than at 1.0 mA for the data in Fig. 3. The difference is attributed to the different degree of agitation in the gold plating bath.

Cyclic voltammetry, in principle, could also give a quantitative measure of relative surface areas; but it was found in previous work (7) that for these Au-Cu surfaces the results could not be made quantitative because of interference of CuO_2^{--} .

Gold analysis.—Long lengths of CuBe wires plated with gold at various currents were analyzed for Au. A standard wet chemistry Au assay was used, good to $\pm 2 \mu\text{g}$. The results, converted to an average Au thickness, are shown in Fig. 4. The upper points were also obtained by calculation from the weight gain of the sample after the gold plating.

Since gold deposits are formed in the absence of a cathodic current, gold deposition occurs also by either a chemical reaction or a mixed potential process

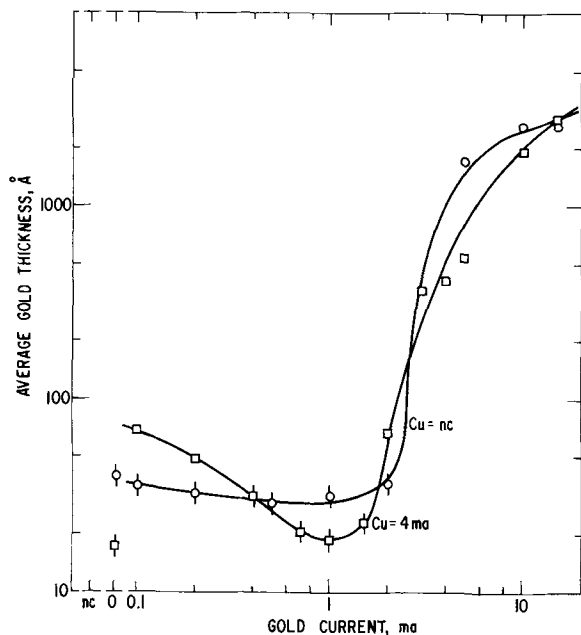


Fig. 4. Average Au thicknesses calculated from weight of Au found by chemical analysis on the same samples as in Fig. 2 and 3. Analytical error possible in the analysis is indicated by the vertical line.

at open circuit. During the deposition process the wires were in the plating bath for the same time (6 sec). Thus the abscissa in Fig. 4 represents also a measure of the number of coulombs consumed during the deposition. The data in Fig. 4 imply that the efficiency of gold plating (= average gold thickness/coulomb) decreases on both the smooth and the rough substrate with increasing current between 0.1 and 1 mA. After passing through a minimum at about 1 mA, the efficiency increases between 1 and about 5 mA; then it decreases again. The latter decrease of the efficiency is understandable. It results from the increase of the contribution of hydrogen evolution to the cathodic current. The decrease of the plating efficiency between 0.1 and 1 mA is more difficult to interpret because the composition of the commercial bath is not known. It is considered likely that the deposition at currents below 1 mA involves a complexed gold ion of a different valency than the deposition above 1 mA. Electrochemical conversion of the complexed ion, involved in the deposition process below 1 mA, to another complexed ion might account for the observed decrease of the plating efficiency between 0.1 and 1 mA.

X-ray diffraction.—In order to obtain x-ray diffraction results a thick film of Au was obtained by stopping the line. The lattice parameters and grain sizes obtained are shown in Fig. 5. The lattice parameters at low currents correspond to that of pure Au; at higher currents an alloy is indicated. The grain sizes were determined by line broadening using the average of several reflections. Corrections for strain broadening were not included. Thus the sizes are lower limits. Here also the change in properties occurs at the same Au current as in Fig. 3 and 4.

Scanning electron microscopy.—The same samples as in Fig. 2-5 were examined in a conventional scanning electron microscope using secondary electron detection. Typical pictures, on the smooth Cu substrate, are shown in Fig. 6, originally at 2000 magnification. The first picture (no contact with the plating bath) and the last two (prepared after gold deposition at 5 and 15 mA) show no fine structure. All the other samples show a fine structure which could not be clearly resolved even in pictures taken originally at 10,000 magnification (Fig. 7). The spots, assumed to be the Au islands, appear to be about $1000 \pm 500 \text{ \AA}$ in diameter and have a density of about $10^9\text{-}10^{10}/\text{cm}^2$ at a current of 1 mA.

Scanning micrographs of the Au deposits on the rough Cu substrates all looked alike. A typical example is shown in Fig. 8. The extreme roughness of the Cu masks any effects due to the Au.

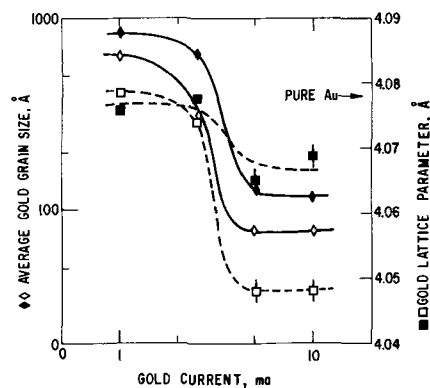


Fig. 5. The grain size and lattice parameter of the gold deposit for samples prepared as in Fig. 4 on a smooth fine-grain Cu surface but with the plating line stopped so as to form a thick enough film for x-ray diffraction. Open points for as deposited; solid points after annealing samples 1 hr at 250°C.

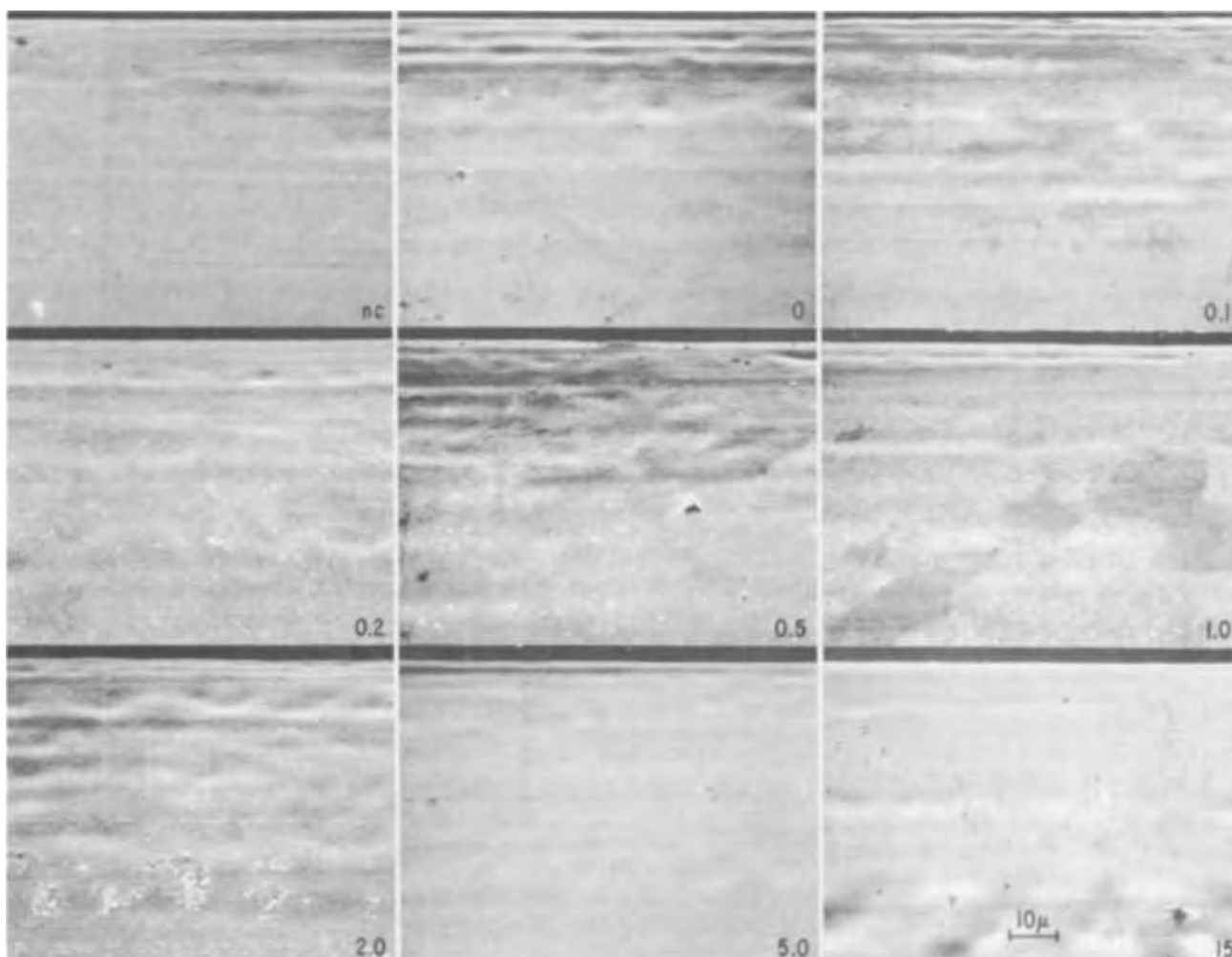


Fig. 6. Scanning electron micrographs of the samples prepared at different Au currents as indicated on the micrographs (nc = no contact with the Au electrolyte) using a smooth fine-grain Cu substrate.

Discussion

The magnetic properties developed in zero magnetostrictive Permalloy films electrodeposited on these substrates are discussed in detail elsewhere (2, 3). The optimum nondestructive read-out characteristics were obtained by deposition of the Permalloy onto a substrate of coarse-grained Cu with Au islands. The gold plating current necessary for the achievement of the optimum characteristics depended on the

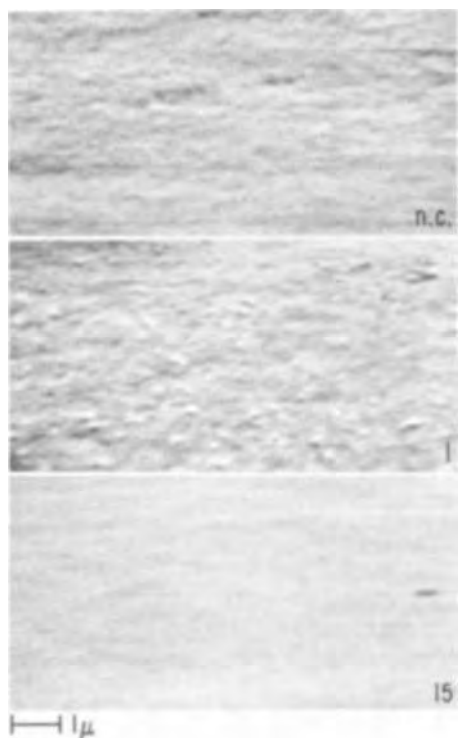


Fig. 7. Some samples from Fig. 6 at higher magnification

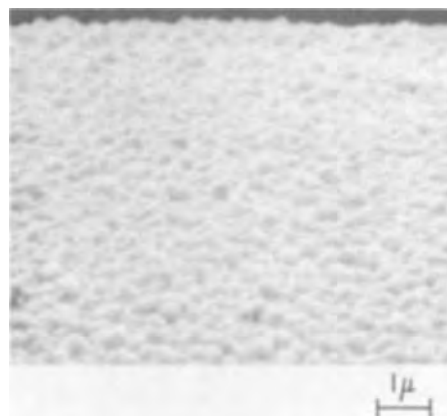


Fig. 8. A typical scanning electron micrograph of the rough Cu surface (Cu = 4 mA).

agitation around the wire as provided by the flow through the plating cell. The optimum current was ~ 0.1 mA for a flow of 0.3 liter/min and 1.0 mA for a flow of 1.9 liters/min. It was also shown (2, 3) that on fine-grained Cu substrates the presence of Au islands, prepared over the entire range of deposition currents, had little or no effect on the magnetic properties of the Permalloy. All of these results, obtained from the magnetic properties, are consistent with the results found in this work. For example, on the smooth Cu there was almost no change in the amount of Au deposited (Fig. 4) or in its coverage (Fig. 3) below the 1-2 mA range where Au islands form, but on the rough Cu there are significant changes.

One of the features of interest is the geometry of the Au islands. The average height, h , can be calculated assuming that the islands are cylindrical posts, by using the total weight of Au per square centimeter, W_{Au} , obtained from the chemical analysis and the fractional coverage A_{Au} from the corrosion potential measurements where

$$h = W_{Au}/19.3 A_{Au}$$

For the fine-grained substrates at the optimum plating current, $W_{Au} = 6.4 \times 10^{-6}$ g/cm² ($\approx 33\text{\AA}$ from Fig. 5) and $A_{Au} = 0.7 \pm 0.1$ (Fig. 4) giving

$$h = 48\text{\AA}$$

For the coarse-grained substrates, $W_{Au} = 3.7 \times 10^{-6}$ g/cm² ($\approx 19\text{\AA}$), $A_{Au} = 0.45 \pm 0.1$, and therefore

$$h = 43\text{\AA}$$

which is the same as on the fine-grain Cu.

The diameter D and number N of islands/square centimeter, were estimated from the high magnification scanning electron micrographs (Fig. 7) even though the poor resolution limited the accuracy of the measurements. The diameter on fine-grain Cu was estimated to be $1000\text{\AA} \pm 50\%$ and the number of islands as 10^9 to $10^{10}/\text{cm}^2$ at the optimum plating

current of 1 mA. The area fraction of Au, calculated from these estimates

$$A_{Au} = D^2N/4 = 0.08 \text{ to } 0.8 \pm 50\%$$

which is at least in the range of values obtained from the corrosion potential measurements.

It is suggested that the minimum in the curves of Au coverage vs. deposition current (Fig. 4) occurs because the quantity of Au deposited also goes through a minimum. The minimum is more pronounced for deposition of Au on the rough surface because of the selective deposition onto the high potential points, i.e., the high points on the surface.

Conclusions and Summary

The deposition of Au at low currents produces islands on the Cu. The production of optimum magnetic properties in a Permalloy film deposited on these substrates corresponds to a specific Au island structure which has been characterized by average thickness measurements, corrosion potential measurements, scanning electron micrographs, and x-ray diffraction results on two types of Cu surfaces. The application of the measurement of corrosion potential to determine the relative surface areas of Cu and Au was found to be especially useful.

Manuscript received May 28, 1971.

Any discussion of this paper will appear in a Discussion Section to be published in the December 1972 JOURNAL.

REFERENCES

1. J. S. Mathias and G. A. Fedde, *IEEE Trans. Magnetics*, **MAG-5**, 728 (1969).
2. F. E. Luborsky, R. E. Skoda, and W. D. Barber, *J. Appl. Phys.*, **42**, 1428 (1971).
3. F. E. Luborsky, W. D. Barber, and A. C. Chen, *IEEE Trans. Magnetics*, In press.
4. M. Stern, *Corrosion*, **14**, 329t (1958).
5. R. J. Morrissey, *This Journal*, **117**, 742 (1970).
6. F. E. Luborsky, M. W. Breiter, and B. J. Drummond, To be published.
7. M. W. Breiter and F. E. Luborsky, *This Journal*, **118**, 867 (1971).

Carrier and Zinc Concentrations for Zinc Diffusion in Gallium Arsenide

C. H. Ting

IBM Components Division, East Fishkill Facility, Hopewell Junction, New York 12533

and G. L. Pearson

Stanford Electronics Laboratories, Stanford University, Stanford, California 94305

ABSTRACT

The zinc and free carrier concentration profiles for zinc-diffused regions in GaAs were determined by means of radiotracer and Hall coefficient measurements, respectively. The carrier concentration is significantly lower than the total zinc concentration. The difference increases for longer diffusion times. This difference is attributed to zinc precipitates in the heavily damaged diffused region. The measurements indicate that about 20-35% of the zinc is precipitated in the samples studied. A novel method of making ohmic contacts for Hall measurements is described. These contacts are not destroyed by successive lapping, thus making the incremental Hall measurements possible. The sources of experimental error are discussed briefly.

Zinc is used extensively as an acceptor impurity in GaAs. It was reported that for melt-doped GaAs the free carrier concentration is essentially equal to the zinc concentration, even for heavily doped samples

Key words: radiotracer profiles, Hall measurement, precipitates, diffusion induced defects.

(1). However, for zinc-diffused samples the carrier concentration may be less than the zinc concentration since zinc diffusion is known to induce defects in GaAs (2, 3). Precipitates at these induced defects were revealed by infrared transmission microscopy and x-ray transmission microscopy. The precipitates

were found to be zinc rich by electron microprobe analysis (4). Goldstein (5) measured the free carrier concentration in zinc-diffused samples and found it to be approximately equal to the total zinc concentration. However, he did not give any experimental details so it is impossible to tell whether his samples were free of induced defects or to determine how accurately he could have measured a difference between the carrier and total zinc concentrations.

In this study both the carrier and zinc concentration profiles were measured on zinc-diffused GaAs samples. The zinc concentration profiles were determined by measuring the radioactivity of successively removed layers; the carrier concentration profiles were determined by Hall measurements on the same sample before and after the removal of each layer. A significant difference between the zinc and carrier concentrations was observed.

Experimental Procedure

The starting material was single-crystal, p-type GaAs oriented in the $\langle 111 \rangle$ direction. Pure Zn^{65} (245-day half-life) was used as a diffusion source. Two diffusion runs were carried out, one at 751°C for 3 hr and another at 755°C for 6 hr. After diffusion the samples were quenched quickly in water. Test samples of 0.200 in. diameter were cut out from the diffused samples with an ultrasonic cutter. The zinc concentration profiles were determined by a conventional radiotracer technique of lapping and counting; it will not be described in detail here. The carrier concentration profiles were determined by measuring sheet conductivity σ_s and sheet Hall coefficient R_{HS} before and after removal of small layers for radiotracer counting.

The experimental setup for Hall and conductivity measurements is similar to the four-point probe developed by Buehler and Pearson (6). This method requires a centered, square array of ohmic contacts on a circular sample, and is identical to the van der Pauw method (7) if the contacts are located on the periphery of the sample. Because edge contacts are difficult to make, the spacing of the square array, s , is usually smaller than the sample diameter, d , as illustrated in Fig. 1. The correction factors for nonperipheral contacts can be calculated for this case because of the simple symmetry of the square array centered on a circular sample; the values are given by Buehler (6).

Unlike point contacts on InAs (6), point contacts on GaAs generally do not yield good electrical contacts because an insulating layer always exists on the GaAs surface. Good ohmic contacts are necessary for the measurements. These contacts should be made to the entire depth of the diffused layer instead of just on the surface so they will not be destroyed by each lapping. This is accomplished by drilling ultrasonically a square array of small holes in the diffused sample; then alloy contacts are made inside these holes. The four-point probe can be used on these alloy contacts after successive lappings. The contact holes are 0.006 in. diameter and are spaced about 0.100 in. apart; the sample diameter is 0.200 in. Because the size of the drilled holes is very small compared to the sample size, these alloy contacts can be treated as point contacts. To carry out Hall measurements on the en-

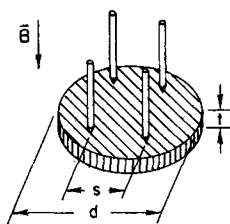


Fig. 1. Four-point Hall probe

tire diffused p layer, the holes for alloy contacts must be deeper than the diffused layer. In this case a hole depth of 0.005 in. was used.

The experimental results described here were obtained by diffusing zinc into p-type bulk with low carrier concentrations ($2 \times 10^{17} \text{ cm}^{-3}$), to avoid complicating the Hall measurements due to the p-n junction. With n-type bulk, meaningful measurements can be obtained only if the alloy makes good rectifying contacts to the n-type bulk so current flow is limited to the p layer. Good rectifying contacts cannot be obtained readily in the ultrasonically drilled holes and the resulting Hall measurements on n-type samples were unsatisfactory.

Experimental Results

The sheet conductivity σ_s and the sheet Hall coefficient R_{HS} obtained by successive measurements after removal of incremental layers parallel to the surface are shown in Fig. 2 for the 3-hr diffusion and in Fig. 3 for the 6-hr diffusion. The conductivity $\sigma(x)$ and carrier concentration $p(x)$ can be determined from the measured sheet coefficients by using the following relations (8, 9)

$$\sigma(x) = \frac{d}{dx} \sigma_s \quad [1]$$

$$p(x) = \frac{\left(\frac{d}{dx} \sigma_s\right)^2}{q \frac{d}{dx} (R_{HS} \cdot \sigma_s^2)} \quad [2]$$

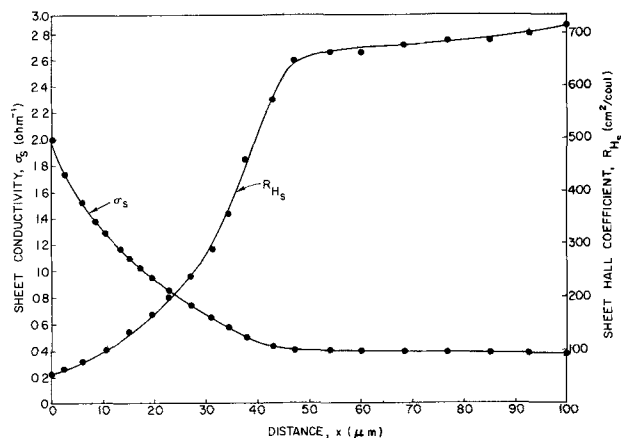


Fig. 2. Sheet conductivity and sheet Hall coefficient vs. distance from the surface for sample No. 1. Diffusion data: $T = 751^\circ\text{C}$, $t = 3 \text{ hr}$.

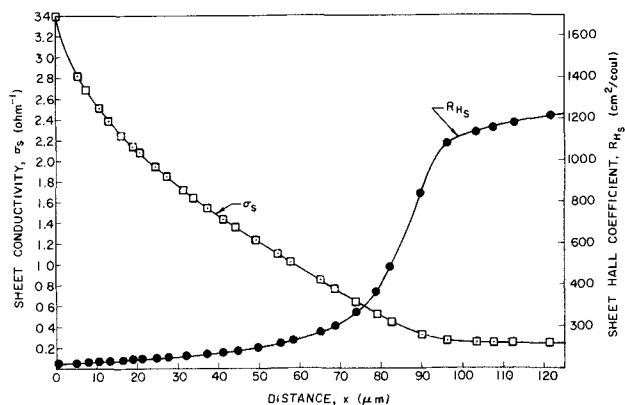


Fig. 3. σ_s and R_{HS} vs. distance from the surface for sample No. 2. Diffusion data: $T = 755^\circ\text{C}$, $t = 6 \text{ hr}$.

These equations and the data given in Fig. 2 were used to determine the conductivity $\sigma(x)$ and the hole concentration $p(x)$ for the 3-hr run, as shown in Fig. 4 and 5, respectively. The total zinc concentration obtained from radioactivity measurements is also shown in Fig. 5 for comparison. Two sets of data points, one obtained for the Hall measurement side and the other for the opposite side, were used to increase accuracy in constructing the zinc concentration profile. The conductivity and carrier concentration of the 6-hr run, obtained from the data given in Fig. 3, are shown in Fig. 6 and 7, respectively. The total zinc concentration profile obtained from the Hall measurement side is also given in Fig. 7 for comparison.

It should be pointed out that some precautions were taken to obtain reasonable accuracy. There are three major sources of experimental error.

1. *Noise*: The Hall voltage measured is rather small (a few microvolts) because of high carrier concentration and relatively low mobility; therefore, fluctuations caused by unavoidable external noise are important. To improve accuracy, the average of four readings obtained by reversing the current and magnetic field is taken, in the usual manner.

2. *Nonohmic contacts*: These will give superfluous voltages that will result in very large errors. Although alloyed ohmic contacts can be made on the diffused

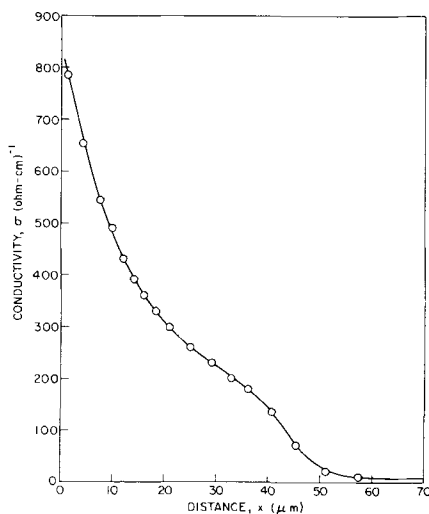


Fig. 4. Conductivity vs. distance from the surface for sample No. 1.

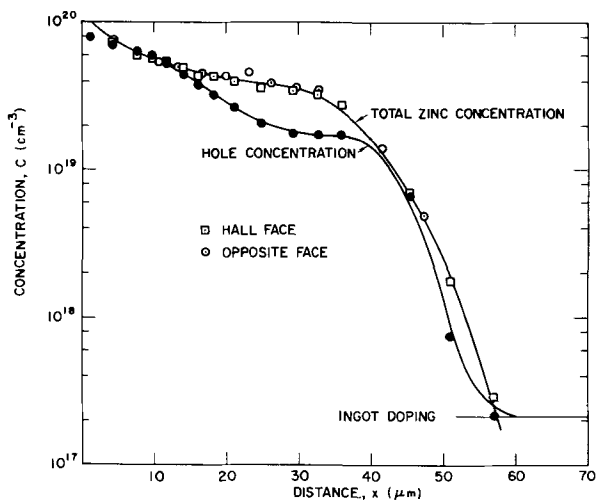


Fig. 5. Total zinc and hole concentration profiles for sample No. 1.

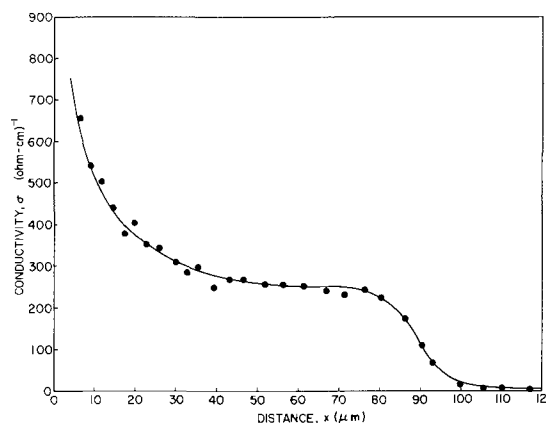


Fig. 6. Conductivity vs. distance from the surface for sample No. 2.

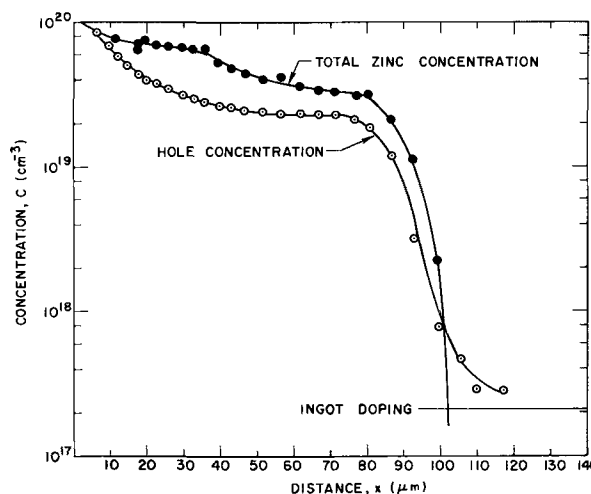


Fig. 7. Total zinc and hole concentration profiles for sample No. 2.

layer, their quality deteriorates as successive layers are removed, because it is more difficult to obtain ohmic contacts in the interior of the sample where carrier concentration is lower. This becomes a serious problem near the diffusion front where the concentration drops sharply.

3. *Nonparallel lapping*: The accuracy in determining diffusion depth is limited by the degree to which lapping is not parallel to the surface. This is particularly important for the first few layers.

Meaningful results can be obtained only when sufficient care is taken with the experiment. That this has been accomplished is evidenced by the small scatter in the experimental values of σ_s and R_{Hs} , as shown in Fig. 2 and 3. However, the final values of $\sigma(x)$ and $p(x)$ are not as accurate as the measured values of σ_s and R_{Hs} . This is because derivatives and the square of derivatives of the measured quantities are involved in the calculation of $\sigma(x)$ and $p(x)$; these derivatives tend to accentuate any experimental error. To increase accuracy, all derivatives obtained from experimental data are first plotted against distance to eliminate any dubious points, and only the smoothed values are used in subsequent calculations.

Discussion

It is clearly shown in Fig. 5 and 7 that the carrier concentration is less than the total zinc concentration in the diffused region. This difference can be attributed to zinc precipitation, since precipitates in the heavily damaged diffused layer have been identified as zinc rich

(4). Therefore, the results presented here verify quantitatively the existence of zinc precipitation in the diffused layer. This result should be compared with the measurements obtained from melt-doped samples, where a one-to-one correspondence between zinc and carrier concentration was reported for zinc at approximately 10^{19} cm^{-3} in the grown crystals (1). The difference could be due to the fact that the melt-doped samples have relatively small defect concentrations as compared to the diffused region.

It should be pointed out that in using Eq. [2] to calculate the carrier concentrations shown in Fig. 5 and 7, the Hall coefficient factor (10) has been taken as unity. It is well known in semiconductor theory that this factor is unity only for degenerate materials; in general its value lies between 1 and 2, depending on the scattering mechanism. In the case of p-type gallium arsenide, the material is degenerate for $p > \sim 10^{19} \text{ cm}^{-3}$ at room temperature (11). Therefore,

in Fig. 5 and 7, the calculated carrier concentrations are correct throughout the diffused region except at the sharp diffusion front where carrier concentration falls off rather sharply.

An estimate of the amount of zinc precipitation can be obtained from Fig. 5 and 7. The total zinc present in the diffused sample per unit surface area is given by the area under the concentration-distance curve; similarly, the total number of carriers is given by the area under the carrier-distance curve. Results obtained from Fig. 5 indicate that the number of free carriers is equal to approximately 78% of the total number of zinc atoms present; thus precipitation accounts for approximately 22% of the total zinc in the first sample. The results shown in Fig. 7 indicate that precipitation accounts for approximately 34% of the total zinc in the second sample.

It has been shown that for very shallow diffusions there are no significant induced defects (3). The shallow diffusion corresponds to the thin layer near the surface where defect concentrations should be

small; therefore, zinc precipitation should also be small. This is indeed the case since it is shown in Fig. 5 that the agreement between the carrier and zinc concentrations is quite good near the surface. The results presented here, therefore, are consistent with the observations made by Black (3). As diffusion time increases, induced defects will eventually propagate into the region near the surface and zinc precipitates will increase. This is illustrated by the significant difference between carrier and zinc concentrations in the region close to the surface shown in Fig. 7.

Acknowledgment

This work was supported by the Joint Services Electronics Program (United States Army, Navy, and Air Force) under Contract Nonr-225(83), and was performed at Stanford University, Stanford, California.

Manuscript submitted March 23, 1971; revised manuscript received ca. July 19, 1971.

Any discussion of this paper will appear in a Discussion Section to be published in the December 1972 JOURNAL.

REFERENCES

1. F. Ermanis and K. Wolfstirn, *J. Appl. Phys.*, **37**, 1963 (1966).
2. G. H. Schwuttke and H. Rupprecht, *ibid.*, **37**, 167 (1966).
3. J. F. Black and E. D. Jungbluth, *This Journal*, **114**, 181, 188 (1967).
4. J. F. Black, *ibid.*, **114**, 1292 (1967).
5. B. Goldstein, *Phys. Rev.*, **118**, 1024 (1960).
6. M. G. Buehler and G. L. Pearson, *Solid-State Electron.*, **9**, 395 (1966).
7. L. J. van der Pauw, *Philips Res. Rept.*, **13**, 1 (1958).
8. M. G. Buehler, Stanford Res. Rept. SEL-66-064 (1966).
9. R. Baron, G. A. Shifrin, and O. J. Marsh, *J. Appl. Phys.*, **40**, 3702 (1969).
10. E. H. Putley, "The Hall Effect and Related Phenomena," p. 105, Butterworths, London (1960).
11. O. V. Emelyanenko, T. S. Lagunova, and D. N. Nasledov, *Soviet Phys.—Solid State (English Transl.)*, **2**, 176 (1960).

Heteroepitaxial GaAs on Aluminum Oxide

The Formation and Electrical Properties of Zn- and Cd-Doped Films

H. M. Manasevit and A. C. Thorsen

Autonetics Division of North American Rockwell Corporation, Anaheim, California 92803

ABSTRACT

An all metalorganic-hydride chemical vapor deposition process has been used to produce p-type GaAs films on sapphire. Dimethylcadmium or diethylzinc have been combined with trimethylgallium and arsine to produce films with net acceptor concentrations as high as 5×10^{17} and $8 \times 10^{19} \text{ cm}^{-3}$, respectively. The doping concentrations are found to be an exponential function of growth temperature when other parameters remain fixed. The electrical properties of thick films are found to be equivalent to good quality bulk GaAs. Hole mobilities approximately 80-90% of the best thick-film values have been obtained for acceptor concentrations $\sim 10^{19} \text{ cm}^{-3}$ in thin ($\sim 1 \mu\text{m}$) films on sapphire and spinel.

In 1968 the first successful use of metalorganics in the preparation of epitaxial GaAs on sapphire (Al_2O_3) and other substrates was reported by our laboratories (1). Since that time, extensive studies of the properties of undoped GaAs/ Al_2O_3 films formed by the reaction of trimethylgallium (TMG) and arsine (AsH_3) have been carried out (2, 3). The process for producing p-type films by the addition of diethylzinc (DEZ) to

the reaction mixture containing TMG and AsH_3 (1) has been explored in more detail and has been extended to include dimethylcadmium (DMCd) as the dopant source. The electrical characteristics of these films have been investigated and related to the growth conditions.

Experimental

The apparatus, chemicals (except for DMCd), and experimental techniques used for the present work

Key words: chemical vapor deposition, metalorganics, trimethylgallium, arsine, spinel.

have been described previously (1-3). The DMCd was obtained from Orgmet, Inc., Hampstead, New Hampshire, and handled in a fashion similar to the DEZ.

The TMG was carried into the reactor by passing H_2 gas through the liquid, equilibrated at $0^\circ C$. AsH_3 diluted to 10% in H_2 was normally used as the source of As. The dopant gases were added by passing the carrier gas over the liquid (either DEZ or DMCd) maintained at $0^\circ C$, unless otherwise stated. In the data discussed in the following sections, a notation X-Y-Z describing a particular set of experimental conditions refers to X cm^3/min of the AsH_3-H_2 mixture passing into the reactor along with Y cm^3/min bubbled through TMG and Z cm^3/min of H_2 passed over the dopant liquid. These were mixed with the carrier gas flowing at 1-3 liters/min.

The dopant vapors were introduced into the reactor in three different ways in order to determine a preferred doping process: (i) with the TMG vapor after the introduction of AsH_3 into the reactor (pre- AsH_3 process); (ii) with the AsH_3 prior to the introduction of the TMG (pre- AsH_3 -DEZ process); and (iii) with all gases simultaneously introduced into the reactor.

Mechanically polished (0001) Al_2O_3 substrates were used exclusively for the studies reported.

Results and Discussion

Previous studies (1, 3) on the growth of undoped GaAs/ Al_2O_3 have led to considerable insight into the deposition conditions (such as gas flow rates and growth temperatures) necessary to produce good quality undoped epitaxial layers. The present work has extended this study with the objective of producing heavily doped 1 μm -thick p-type GaAs with acceptor concentrations greater than $10^{19} cm^{-3}$ for photocathode applications. Some results of photoemission measurements on these films have been described by Liu *et al.* (4). The over-all deposition conditions used for these doping studies have been those which yield good quality undoped films (3).

Doping Studies with Diethylzinc

Most of the studies of p^+ GaAs growth on Al_2O_3 involved the use of DEZ as the source of dopant. The results are discussed in detail in the following sections.

Effect of deposition conditions on carrier concentrations.—There are a number of growth parameters which can be varied in order to change the acceptor concentration in the GaAs films. An obvious one is the adjustment of the amount of dopant introduced into the reactor per unit time. This control has been achieved by two different means: (i) by adjusting the carrier gas flow over the dopant source; (ii) by controlling the bath temperature of the dopant source.

In Fig. 1, the effects are illustrated for Zn-doped GaAs films grown on Al_2O_3 for three different DEZ bath temperatures. For the DEZ bath at room temperature, the growth temperature was $725^\circ C$ with AsH_3 -TMG flows of 90-10; at the lower DEZ bath temperatures, a growth temperature of $700^\circ C$ was employed with AsH_3 -TMG settings of 175-65. The semilog plots indicate that higher flow rates produce increases in acceptor concentrations up to a point of saturation, after which the carrier concentration remains essentially constant. The higher carrier concentration obtained by increasing the DEZ bath temperature (and hence vapor pressure) indicate that the saturation in carrier concentrations at a given bath temperature is a consequence of the limited vaporization rate of the DEZ at the temperature of the bath and the depletion of the vapor over the DEZ caused by the high H_2 flow rates. The higher flows are believed to decrease the amount of DEZ vapor over the liquid below that which is expected for equilibrium conditions.

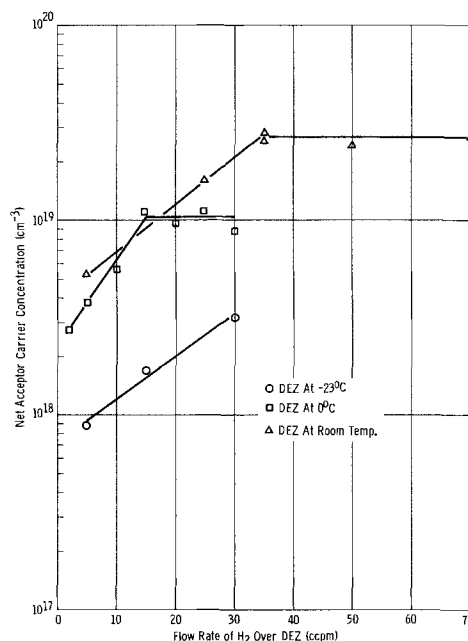


Fig. 1. Net acceptor concentration of Zn-doped GaAs/ Al_2O_3 films vs. flow rate of H_2 over DEZ. For DEZ at $0^\circ C$ and $-23^\circ C$: growth temperature = $700^\circ C$, film thickness $\approx 1 \mu m$, AsH_3 -TMG setting 175-65-Z; for DEZ at room temperature: growth temperature = $725^\circ C$, film thickness $\approx 7-10 \mu m$, AsH_3 -TMG setting 90-10-Z.

For a given set of growth conditions, the net acceptor concentration is also found to increase by lowering the growth temperature. A maximum net carrier concentration of $\sim 8 \times 10^{19} cm^{-3}$ was obtained in thick films at $650^\circ C$ for a DEZ bath temperature of $0^\circ C$. Films grown at temperatures of $625^\circ C$ did not appear, either electrically or visually, to be as good as those grown at higher temperatures.

A plot of the measured variation of acceptor concentration with reciprocal growth temperature is given in Fig. 2 for a series of thin ($\sim 1 \mu m$ -thick) Zn-doped samples grown under essentially identical conditions. It shows that an exponential relationship exists between the two variables. From the slope of the experimental line an activation energy of 2.1 eV can be

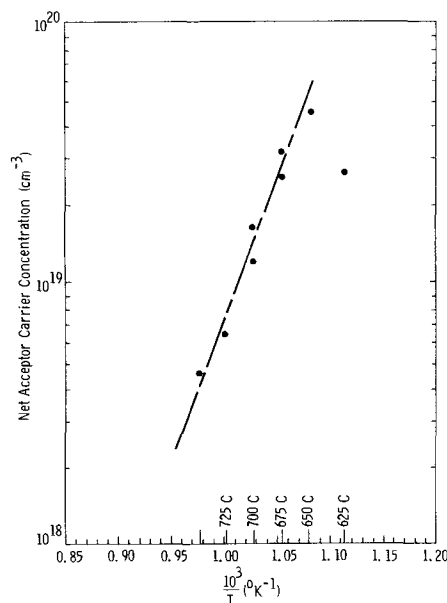


Fig. 2. Net acceptor concentration of $\sim 1 \mu m$ -thick Zn-doped GaAs/ Al_2O_3 film vs. reciprocal growth temperature.

Table I. Variation of mobility with film thickness for Zn-doped GaAs/Al₂O₃ films grown at 700°C

Thickness (μm)	Carrier concentration (10 ¹⁹ cm ⁻³)	Hole mobility (cm ² /V-sec)
0.4	2.5	59
0.6	2.3	63
1.0	2.5	66
4.1	2.4	72
5.7	2.5	75
7.9	2.6	77
17.3	2.4	77
21.1	2.4	75

deduced; however, the present data are insufficient to determine the mechanism responsible for this dependence.

Variation of electrical properties with film thickness.—As in the case of undoped GaAs/Al₂O₃ (3), there appears to be an improvement in film quality with film thickness. Table I illustrates the changes in hole mobility with thickness for the best films grown with a hole concentration of $\sim 2.5 \times 10^{19}$ cm⁻³. These films were grown either by the pre-AsH₃ process (with the DEZ mixed with the TMG) or by the pre-AsH₃-DEZ process (see Experimental section). The average mobilities increase with thickness and appear to reach a maximum at a thickness of about 4 μm. Thin films grown by the technique of premixing all gases were found to have consistently lower mobilities than those grown by the other two methods. Very little change was found in carrier concentration for films of different thicknesses grown under otherwise identical conditions. This indicates that a nearly uniform doping concentration profile exists in these heavily doped layers.

Hole mobility as a function of carrier concentration.—The electrical properties of many of the Zn-doped GaAs films on Al₂O₃ grown using the pre-AsH₃ and pre-AsH₃-DEZ processes are summarized in Fig. 3 and 4, where Hall mobility is plotted vs. acceptor concentration for thick and thin films, respectively. Growth rates of 0.6-1.0 μm/min and AsH₃-TMG flow rates which normally lead to good quality undoped films were used. The average hole mobilities characteristic of bulk GaAs (5) are shown for comparison (solid line), although the mobilities of many of the films are greater than these bulk values. For this reason a curve (dashed line) depicting the best mobilities in the thicker films is also plotted in both figures. It can be seen that the mobilities in the best thin films are typically from 80 to 90% of the best thick-film values where comparable data are available.

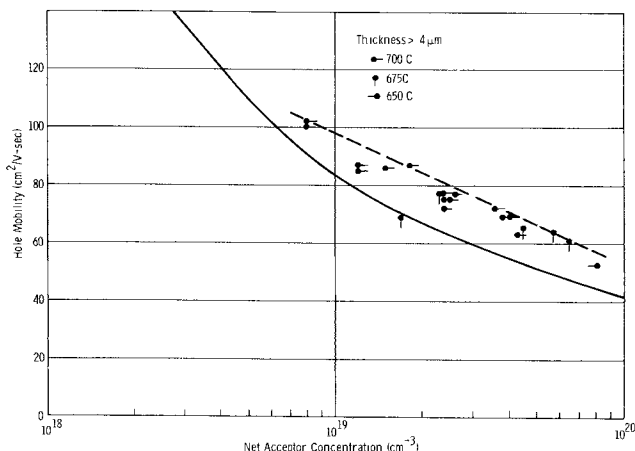


Fig. 3. Hole mobility vs. net acceptor concentration for thick (> 4 μm) Zn-doped GaAs/Al₂O₃ films grown at various temperatures. The solid line is an average bulk mobility from ref. (5).

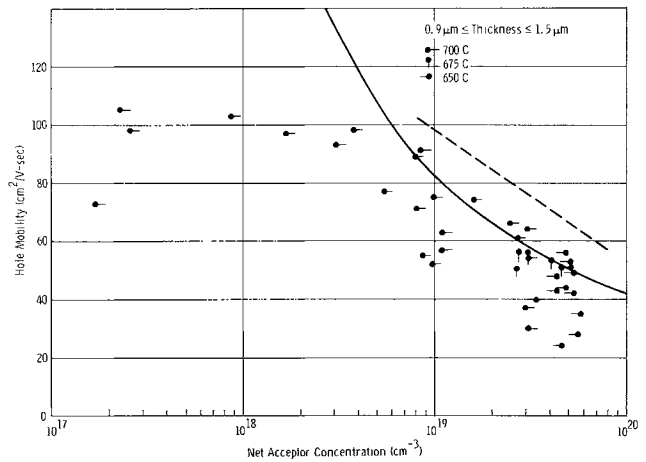


Fig. 4. Hole mobility vs. net acceptor concentration for thin (between 0.9 and 1.5 μm) Zn-doped GaAs/Al₂O₃ films grown at various temperatures. The solid line is an average bulk mobility from ref. (5), and the dashed line denotes the best thick-film mobilities from Fig. 3.

The mobilities in the thin films at carrier concentrations less than $\sim 5 \times 10^{18}$ cm⁻³ appear to saturate at a maximum value of about 100 cm²/V-sec. This behavior is probably due to the comparatively high defect structure found in thin layers (2).

Simultaneous growth studies of Zn-doped p⁺ GaAs on spinel and Al₂O₃.—Stoichiometric spinel (MgAl₂O₄) was also examined as a substrate for p⁺ GaAs epitaxy, with emphasis placed on the (110) orientation of MgAl₂O₄. A comparison of data compiled on a number of p⁺ Zn-doped GaAs films prepared simultaneously on (0001)Al₂O₃ and (110)MgAl₂O₄ substrates utilizing the pre-AsH₃-DEZ method and different doping levels is given in Table II for films grown at 625°-700°C. It would appear that p⁺ films grown on (110)MgAl₂O₄ [(100)-oriented growth of GaAs] are essentially equivalent electrically to those grown on (0001)Al₂O₃ [(111)-oriented growth of GaAs]. For both types of substrates, growth at 625°C (and to a lesser extent at 650°C) has not appeared to be as good as that obtained at higher temperatures.

When Al₂O₃ is used as a substrate, the growth and subsequent removal of a GaAs film is often found to condition the surface in such a way as to yield superior quality GaAs films on reuse. This behavior was not observed for (110)MgAl₂O₄ substrates. In all cases, GaAs films grown on reused but not repolished MgAl₂O₄ substrates have been found to be electrically inferior to those grown simultaneously on reused Al₂O₃ substrates.

Doping Studies with Dimethylcadmium

Dimethylcadmium (DMCd) was also examined as a possible dopant for the formation of p-type GaAs

Table II. Comparison of the electrical properties of p⁺ Zn-doped (111)GaAs/(0001)Al₂O₃ and (100)GaAs/(110)MgAl₂O₄ grown simultaneously by the pre-AsH₃-DEZ method at 625°-700°C

Growth temp (°C)	Thickness (μm)	Resistivity (ohm-cm)	Carrier conc (cm ⁻³)	Mobility (cm ² /V-sec)	Substrate
700	1.0	0.008	8.6×10^{18}	91	Sapphire
	1.0	0.010	7.4×10^{18}	84	Spinel
	20.8	0.008	8.0×10^{18}	102	Sapphire
	22.6	0.007	9.4×10^{18}	99	Spinel
675	1.0	0.0054	1.6×10^{19}	74	Sapphire
	1.0	0.0048	1.6×10^{19}	84	Spinel
	1.2	0.0029	4.1×10^{19}	54	Sapphire
	1.2	0.0027	3.6×10^{19}	66	Spinel
650	5.5	0.0016	6.6×10^{19}	60	Sapphire
	5.6	0.0025	3.6×10^{19}	69	Spinel
	1.1	0.0023	5.4×10^{19}	49	Sapphire
625	1.1	0.0020	5.2×10^{19}	59	Spinel
	19.1	0.0087	3.6×10^{19}	20	Sapphire
	18.9	0.0084	4.7×10^{19}	16	Spinel

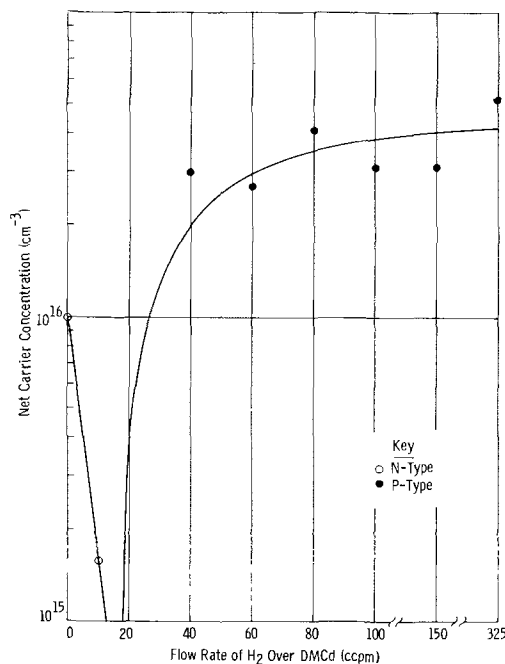


Fig. 5. Net carrier concentration vs. flow rate of H₂ over DMCd for thick (~20 μm) Cd-doped GaAs/Al₂O₃ films grown at settings of 175-65-Z.

films on (0001)Al₂O₃. The DMCd was maintained at a temperature of 0°C; gas flow conditions were used which had been satisfactory for Zn doping. The variation of net carrier concentration for a series of thick films grown at 700°C as a function of the flow rate of carrier gas over DMCd is shown in Fig. 5. When using gases which yield undoped films with net electron concentrations of ~10¹⁶ cm⁻³, the addition of a small amount of Cd results in a decrease in net electron concentration. With increases in Cd, the films become p-type, with the net hole concentration rising rapidly to ~3 × 10¹⁶ cm⁻³ and saturating at ~4-5 × 10¹⁶ cm⁻³. By changing the DMCd bath temperature to room temperature (from 0°C), and hence increasing the DMCd vapor pressure, the acceptor concentration in films grown at 700°C saturated at ~1 × 10¹⁷ cm⁻³ at a film growth rate of 1.2 μm/min. At a growth rate of 2 μm/min, the hole concentration increased to 1.6 × 10¹⁷ cm⁻³. This last effect, a slight increase in hole concentration with increasing growth rate, was also observed in the Zn-doping studies. The limiting value of carrier concentration appears to be determined by the temperature of the Cd source, as was found with Zn doping.

The net hole concentration in the Cd-doped films also increased exponentially with decreasing deposition temperature when other deposition conditions remain fixed. At 675°C the acceptor concentration increased to 2.2 × 10¹⁷ cm⁻³ at growth rates of 1.2 μm/min and to 5.2 × 10¹⁷ cm⁻³ at growth rates of 2 μm/min. At 725°C, a hole concentration of 4 × 10¹⁶ cm⁻³ was obtained. A plot of the acceptor concentration obtained for Cd doping (for a growth rate of ~1 μm/min) as a function of reciprocal growth temperature is shown in Fig. 6. The limited data available support an exponential relationship with an activation energy of ~2.8 eV, slightly larger than was found in the case of Zn-doped films.

The mobility carrier concentration data for Cd-doped GaAs films are shown in Fig. 7. The highest Hall mobilities for the thick films are slightly larger for a given hole concentration than those reported by Conrad and Haisty (6) for homoepitaxial GaAs films doped with Zn from DEZ, and compare favorably with the average hole mobilities of bulk GaAs taken

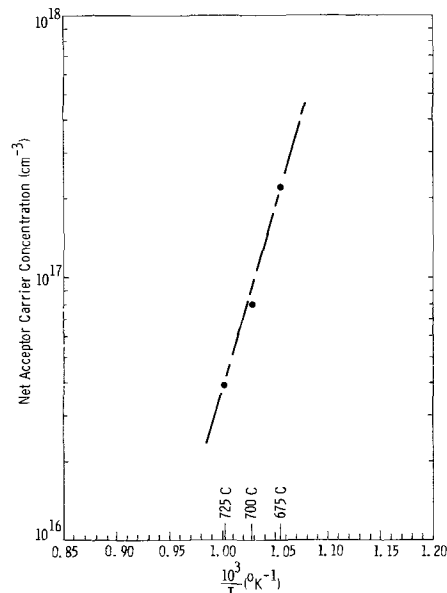


Fig. 6. Net acceptor concentration of thick (24-34 μm) Cd-doped GaAs/Al₂O₃ films vs. reciprocal growth temperature.

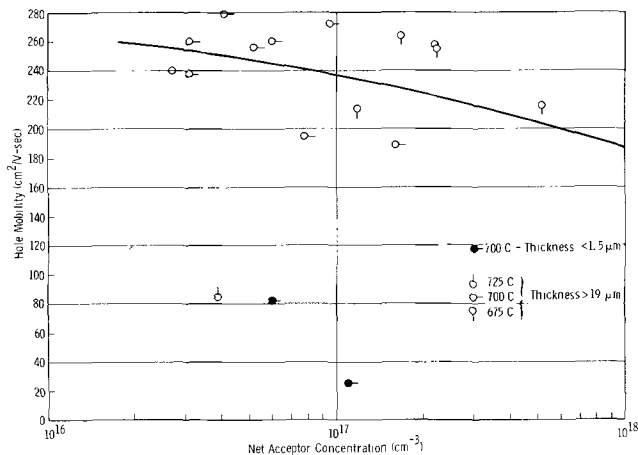


Fig. 7. Hole mobility vs. net acceptor concentration for Cd-doped GaAs/Al₂O₃ films grown at various temperatures. The solid line is an average bulk mobility from ref. (5).

from the data of Sze and Irvin (5)¹ (solid curve). The few thin Cd-doped samples that were measured, indicated by the solid circles in Fig. 7, exhibited much lower mobilities.

Conclusions

Diethylzinc and dimethylcadmium have been shown to be effective sources of dopant for the growth of p-type GaAs on insulating substrates by chemical vapor deposition techniques. It has been found that the acceptor concentrations obtained are an exponential function of growth temperature for a given set of growth conditions. The mechanism for this type of dependence cannot be deduced from the experimental data available. The maximum concentrations of Zn and Cd incorporated in the GaAs films in these experiments appear to be limited by the transport of sufficient dopant gas from the source.

Electrical measurements of the films grown in this study have shown that good quality GaAs may be grown over a wide range of acceptor concentration. Thick films are found to have hole mobilities typical

¹ The mobility (μ) vs. carrier concentration (n) data were calculated from Fig. 1 of (5) assuming μ = 1/neρ. There are some differences between these data and that in Fig. 2 of (5) at low carrier concentrations.

of the best bulk material for acceptor concentrations from $\sim 3 \times 10^{16}$ to $\sim 10^{19}$ cm $^{-3}$. At the highest doping concentrations the better Zn-doped thin (~ 1 μ m) films exhibited hole mobilities nearly as high as the best thick films. At concentrations less than 10^{19} cm $^{-3}$ the thin film mobilities appear to level off at values ~ 100 cm 2 /V-sec, although data are limited for these carrier concentrations. The fact that thick films can be grown with bulk mobilities indicates that lower-than-bulk mobilities in thin layers are probably due to a comparatively high defect structure in these films, rather than compensation from donor impurities in the gas sources.

Acknowledgments

The authors wish to acknowledge the assistance of W. I. Simpson in the preparation of the films used in this study, R. E. Johnson for the photolithographic processing of the bridge samples, and J. P. Wendt for carrying out many of the electrical measurements. We thank Dr. R. P. Ruth, Dr. A. J. Hughes, and Dr. J. L. Kenty for most helpful discussions of the subject matter.

This work was supported in part by the Night Vision Laboratory, USAECOM, Fort Belvoir, Virginia, under Contract No. DAAK02-69-C-0333.

Manuscript submitted March 26, 1971; revised manuscript received Sept. 21, 1971. This was Paper RNP 248 presented at the Atlantic City Meeting of the Society, Oct. 4-8, 1970.

Any discussion of this paper will appear in a Discussion Section to be published in the December 1972 JOURNAL.

REFERENCES

1. H. M. Manasevit and W. I. Simpson, *This Journal*, **116**, 1725 (1969).
2. H. M. Manasevit and A. C. Thorsen, *Met. Trans.*, **1**, 623 (1970).
3. A. C. Thorsen and H. M. Manasevit, *J. Appl. Phys.*, **42**, 2519 (1971).
4. Y. Z. Liu, J. L. Moll, and W. E. Spicer, *Appl. Phys. Letters*, **17**, 60 (1970).
5. S. M. Sze and J. C. Irvin, *Solid-State Electron.*, **11**, 599 (1968).
6. R. W. Conrad and R. W. Haisty, *This Journal*, **113**, 199 (1966).

Experiments and Calculation of the Ga-GaAs-GaP Ternary Phase Diagram

Kozo Osamura, Jun Inoue, and Yotaro Murakami

Department of Metallurgy, Faculty of Engineering, Kyoto University, Kyoto, Japan

ABSTRACT

A large part of the gallium rich side of the Ga-GaAs-GaP phase diagram has been determined using the DTA method and the powder x-ray method. The ternary phase diagram of Ga-GaAs-GaP has been calculated using two approaches, i.e. the quasi-chemical equilibrium model and the regular solution model. Both of these calculated ternary phase diagrams are found to agree with the experimental data.

Interest has increased recently in the semiconducting materials which are obtained when solid solution occurs between two compounds of the type A^{III}B^V. A number of the III-V ternary phase diagrams have been studied previously, because an understanding of the phase chemistry of these systems is particularly useful for the development of solution growth techniques. A considerable amount of work has been devoted to the study of the Ga-As-P ternary system. The liquidus curves in the parent Ga-As and Ga-P systems have been studied by many authors (1-4) and their thermodynamic properties have been discussed by Thurmond (5) and Arthur (6). The solidus line of the GaAs-GaP quasi-binary phase diagram has been determined by Osamura and Murakami (7). Panish (8) has determined the liquidus-solidus isotherms of the Ga-GaAs-GaP ternary system using the differential thermal analysis and an optical technique.

A method of calculating the ternary phase diagrams for III-V systems from the available thermodynamic data is extremely desirable because the experimental determination of the phase diagrams including liquidus curves and tie lines is a prohibitive task. Ternary phase diagrams of III-V compounds can be calculated using both the quasi-chemical equilibrium (QCE) and regular solution (RS) models which are based upon Ilegems and Pearson's (9) modifications of Vieland's equations (10) to ternary III-V systems. The QCE model has been applied by Stringfellow and Greene to several III-V systems, i.e. the In-Ga-As (11), In-As-Sb

(11), and Ga-In-P (12) systems. On the other hand, Antypas has used the RS model for the calculation of the In-Ga-As (13), Ga-As-Sb (14), and Ga-GaAs-GaP (15) ternary phase diagrams. However the QCE approach has not been applied to the Ga-GaAs-GaP system until now.

In the present paper, the determination of the liquidus-solidus isotherms in the Ga-GaAs-GaP ternary phase diagram has been performed in detail, especially in the region of the gallium-rich corner using the differential thermal analysis and the powder x-ray method. The ternary phase diagram of Ga-GaAs-GaP system is calculated using two approaches, i.e. the QCE and RS models. And both these calculated ternary phase diagrams are compared with the experimental data of this work and Panish's data.

Experimental Results

Differential thermal analysis was used for the determination of the liquidus-solidus isotherms. In this work, the materials used were semiconductor grade Ga, GaAs, and GaP. The DTA method used here is similar to that which was described earlier for the study (13) of the phase diagram of GaAs-GaSb compounds. In order to melt the constituents together completely, the DTA cell, placed in a large block inside a resistance furnace as shown in Fig. 1, was heated to 50°C above the expected temperature for the first appearance of solid. After holding at that temperature for 1 hr, the cell was slowly cooled with a constant cooling rate of 1.5°C/min. Thermal effects were noted by continuously

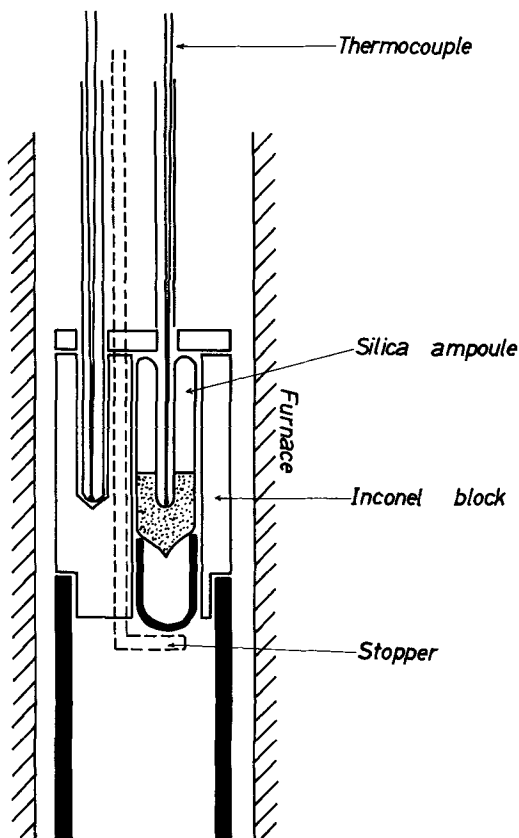


Fig. 1. Apparatus for differential thermal analysis

recording the emf of Pt-PtRh thermocouples. The determination of the transformation temperature seems to be reasonably accurate since the temperature difference between a specimen and the Inconel block was as small as several degrees centigrade. After the cell had been cooled to 50°C under the inflection point observed in the cooling curve, the cell was again heated with a constant heating rate of 1.5°C per minute; Fig. 2 shows a typical example of DTA curves. In both the cooling and heating curves the inflection point could be de-

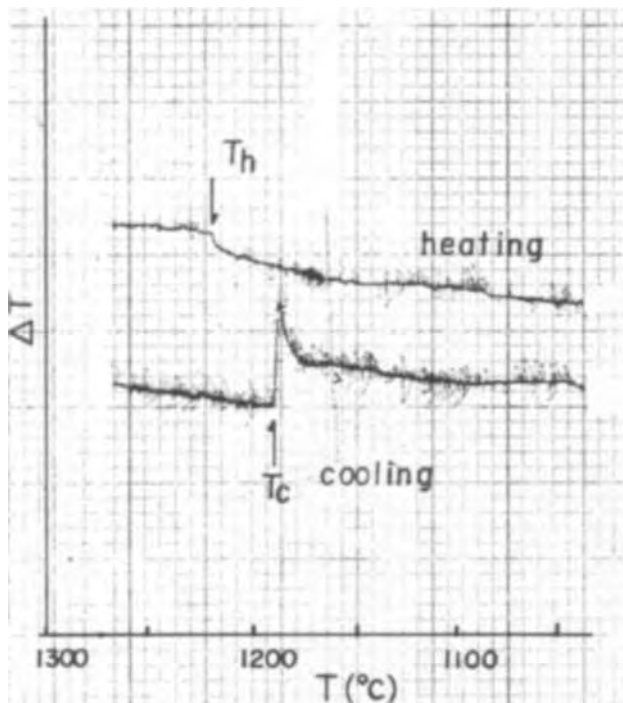


Fig. 2. Typical DTA curves

Table I. DTA determination of liquidus temperature and the corresponding measured solidus composition

N_{Ga}	(at %) N_{As}	N_P	T_c	(°C) T_h	T	X_{GaP}
90.00	8.00	2.00	1036	1067	1051.5	0.562
80.00	18.00	2.00	1118	1150	1134.0	0.311
75.00	23.00	2.00	1162	1186	1174.0	0.290
70.00	28.00	2.00	1188	1218	1203.0	0.158
60.00	38.00	2.00	1239	1248	1243.5	0.124
50.00	48.00	2.00	1250	1270	1260.0	0.110
90.00	6.00	4.00	1092	1120	1106.0	0.788
80.00	16.00	4.00	1151	1181	1166.0	0.556
75.00	21.00	4.00	1192	1220	1206.0	0.432
70.00	26.00	4.00	1216	1254	1235.0	0.402
60.00	36.00	4.00	1256	1266	1261.0	0.280
50.00	46.00	4.00	1260	1284	1272.0	0.206
90.00	4.00	6.00	1136	1162	1149.0	0.882
80.00	14.00	6.00	1197	1217	1207.0	0.670
75.00	19.00	6.00	1220	1250	1235.0	0.533
70.00	24.00	6.00	1248	1270	1259.0	0.523
90.00	2.00	8.00	1174	1198	1186.0	0.921
85.00	7.00	8.00	1195	1214	1204.5	0.833
80.00	12.00	8.00	1222	1240	1231.0	0.732
75.00	17.00	8.00	1246	1268	1257.0	0.650
75.00	25.00	—	1112	1152	1132.0	0.0
95.00	5.00	—	843	886	864.5	0.0
98.00	2.00	—	748	780	764.0	0.0

tected, where it is suggested that a primary crystal appears in the melt at the temperature, T_c , and the last solid completely dissolves at the temperature, T_h ; these temperatures are listed in Table I. It was found that T_c is about 20°–30°C lower than T_h . Panish (8) has pointed out that the supercooling effect leads to some discrepancy in DTA (cooling) and optical (heating) data. T_h may be higher than the correct transition temperature because the melting point of the solid which does not contact the equilibrated liquid is higher than the liquidus temperature, and therefore the complete dissolution will lag in the heating process. Therefore, in the present analysis, it seems that an average of T_c and T_h is a more reliable indication of the correct transition temperature.

The primary crystals were collected by the following technique. The same specimen used in the DTA was heated until it was completely liquid and then cooled slowly below its liquidus temperature (T_c) determined previously. After the inflection point was observed in a cooling curve, the ampul was quenched in water by removing the stopper shown in Fig. 1. After removal of the Ga by dissolution in hot HCl solution, the larger crystals were separated, and ground down to an average size of 10 μ .

Lattice parameters of the specimens were determined by the powder x-ray method, where the diffraction angle was calibrated by using the standard angles of Si powder. The average value of lattice parameter was calculated from the peaks corresponding to (440), (531), (620), (533), (444), and (511). Figure 3 shows typical x-ray diffraction patterns of (531), of which peaks for GaAs and GaP were measured at $2\theta = 107.42^\circ$ and 113.54° , respectively. Assuming that the change of lattice parameter in the solid solution with composition obeys Vegard's law (17), the alloy composition of specimens was estimated from the lattice parameter and listed in Table I.

Calculation of Phase Diagrams

The RS model assumes a completely random distribution of the constituent atoms and then a temperature independent interaction parameter. However, the interaction parameters in III-V binary solutions show a linear temperature dependence as pointed out by some authors (5, 6). It should be recognized that the RS model with $\Omega^R = a - bT$ is only an approximation for the QCE model as discussed by Stringfellow and Greene (18) for Ge-M, Si-M, and III-V systems. Therefore, the QCE calculation of the ternary phase diagram is mainly carried out and discussed, and the RS calculation is also performed in order to find the validity of the RS model as an approximate treatment of the QCE model in the Ga-As-P system.

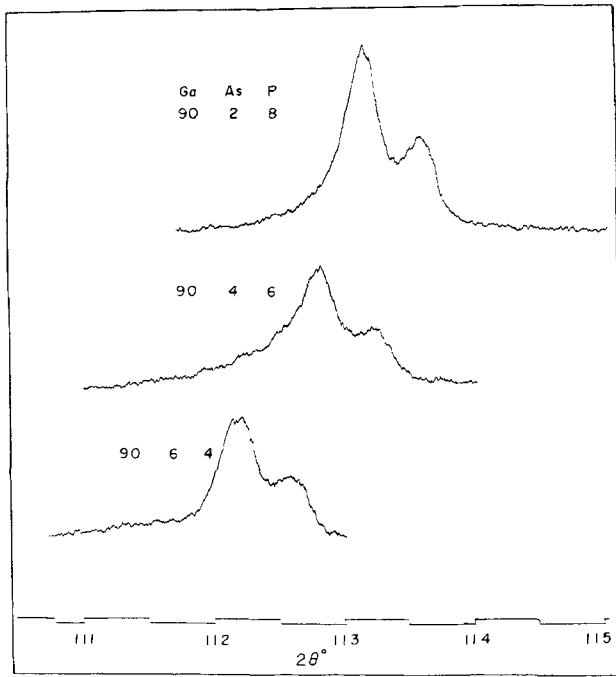


Fig. 3. Powder x-ray patterns of (531) plane for some $\text{GaAs}_{1-x}\text{P}_x$ solid solutions.

The binary liquidus line on the T - X phase diagram can be calculated using Vieland's expression (10) for the III-V compound-liquid equilibrium

$$\ln \left[\frac{1}{4X(1-X)} \right] + \ln \left[\frac{\gamma_A^{s.l.} \gamma_B^{s.l.}}{\gamma_A \gamma_B} \right] = \frac{\Delta S^F}{R} \left[\frac{T^F}{T} - 1 \right] \quad [1]$$

where A and B show the III group and V group component, respectively, and T^F is the melting point of AB compound and ΔS^F is the entropy of fusion per mole of compound and X is the atom fraction of A component in the liquid phase in equilibrium with solid AB at a temperature T , and γ_A and γ_B are activity coefficients, and $\gamma_A^{s.l.}$ and $\gamma_B^{s.l.}$ correspond to those of the stoichiometric liquid. These values may be expressed in terms of the interaction parameter by the two approaches, i.e. the QCE and RS models. The Ga-As and Ga-P interaction parameters were obtained by making a least squares fit of the calculated binary phase diagrams to the experimental data. In the present work, only the data of Köster and Thoma (3) for the Ga-As system and the data of Rubenstein (2) for the Ga-P system have been selected in order to link the ternary experimental data smoothly to the binary data in the region of temperatures where the experiments have been carried out. The temperatures of fusion of GaAs and GaP were extracted from the literature (5). An estimate of the entropy of fusion was obtained by a comparison with entropies of IV-group elements after Thurmond (5), but the values were employed from the table of Kubaschewski *et al.* (19). The interaction parameters in both of the QCE and RS models determined by fitting Eq. [1] to the experimental data are listed in Table II where it was found that the interaction pa-

Table II. List of thermodynamic parameters used in calculating the Ga-GaAs-GaP phase diagram

$T_{\text{GaP}}^F = 1465^\circ\text{C}$	$T_{\text{GaAs}}^F = 1238^\circ\text{C}$
$\Delta S_{\text{GaP}}^F = 16.25 \text{ e.u.}$	$\Delta S_{\text{GaAs}}^F = 15.45 \text{ e.u.}$
$\Omega_{\text{Ga-P}}^Q = -4170 \text{ cal/mole}$	$\Omega_{\text{Ga-As}}^Q = -6470 \text{ cal/mole}$
$\Omega_{\text{Ga-P}}^R = -3.0 \text{ T cal/mole}$	$\Omega_{\text{Ga-As}}^R = -5.2 \text{ T cal/mole}$
$\Omega_{\text{As-P}}^Q = \Omega_{\text{As-P}}^R = 0 \text{ cal/mole}$	
$\Omega_{\text{GaAs-GaP}}^Q = \Omega_{\text{GaAs-GaP}}^R = 0 \text{ cal/mole}$	

rameters for the Ga-As and Ga-P liquid system are constant from the QCE model and on the other hand are proportional to temperature from the RS model.

Ternary phase diagrams of III-V compounds have been calculated using the QCE and RS models. In both cases, as activity coefficients in the ternary system can be represented in terms of the interaction parameters in binary systems, ternary phase diagrams can be calculated without the aid of experiments. In computing the conditions for equilibrium between a ternary liquid solution A, B, C (Ga, As, P) and a quasi-binary solid solution AB - AC (GaAs-GaP), Stringfellow and Greene (11) derived the following equations

$$\ln \gamma_{AB} X = \ln \left[\frac{4\gamma_A \gamma_B N_A N_B}{\gamma_A^{s.l.} \gamma_B^{s.l.}} \right] + \frac{\Delta S_{AB}^F}{R} \left[\frac{T_{AB}^F}{T} - 1 \right] \quad [2a]$$

$$\ln \gamma_{AC} (1-X) = \ln \left[\frac{4\gamma_A \gamma_C N_A N_C}{\gamma_A^{s.l.} \gamma_C^{s.l.}} \right] + \frac{\Delta S_{AC}^F}{R} \left[\frac{T_{AC}^F}{T} - 1 \right] \quad [2b]$$

where γ_{AB} and γ_{AC} are the activity coefficients of AB and AC in the solid solution, X is the mole fraction of AB , N_i and γ_i ($i = A, B, C$) are the atom fractions and activity coefficients of i in the liquid solution, respectively. Equation [2] can be solved numerically on a computer to yield two sets of curves, one describing the liquidus isotherms and the other describing the solidus isoconcentration curves of the system.

First, the calculation of activity coefficients in the ternary system is based on the QCE model. The major assumptions necessary to calculate activity coefficients are:

(i) The distribution of constituent atoms is calculated using a mass action-like expression

$$N_{ij} N_{jj} / (N_{ij})^2 = \frac{1}{4} \exp [2\Omega_{ij}^Q / ZRT] \quad [3]$$

where i and j each represent either A, B , or C .

(ii) The molar heat of mixing is expressed as

$$\Delta H_m = [N_{AB} \Omega_{AB}^Q + N_{BC} \Omega_{BC}^Q + N_{AC} \Omega_{AC}^Q] / Z \quad [4]$$

and the excess free energy of mixing, ΔF^{XS} , is obtained from ΔH_m by integrating the Gibbs-Helmholtz equation. Therefore, the activity coefficients are derived from ΔF^{XS} using the general thermodynamic relation as follows

$$\ln \gamma_i = \Delta F^{XS} / RT + (1 - N_i) \left[\frac{\partial (\Delta F^{XS} / RT)}{\partial N_i} \right]_{N_j / N_k} \quad [5]$$

In the QCE model, the activity coefficient cannot be expressed analytically, but is computed numerically in terms of temperature and composition.

Second, using the RS model, activity coefficients in the ternary system can be analytically expressed in terms of the interaction parameters of the various binary systems as shown in the following

$$\ln \gamma_A = [\Omega_{AB}^R N_B (1 - N_A) - \Omega_{BC}^R N_B N_C + \Omega_{AC}^R N_C (1 - N_A)] / RT \quad [6a]$$

$$\ln \gamma_B = [\Omega_{AB}^R N_A (1 - N_B) + \Omega_{BC}^R N_C (1 - N_B) - \Omega_{AC}^R N_A N_C] / RT \quad [6b]$$

$$\ln \gamma_C = [-\Omega_{AB}^R N_A N_B + \Omega_{BC}^R N_B (1 - N_C) + \Omega_{AC}^R N_A (1 - N_C)] / RT \quad [6c]$$

This expression of ternary activity coefficients has been reported by Furukawa and Thurmond (20) and is consistent with Darken's quadratic representation (21) only in the case of the regular solution, where the parameter Ω_{ij}^R differs only by a factor of RT from α_{ij} of Darken.

The quasi-binary solid solution in equilibrium with the ternary liquid was assumed to be constituted of AB and AC chemical units (11). For the zincblende lattice, where AB - AC interactions are considered,

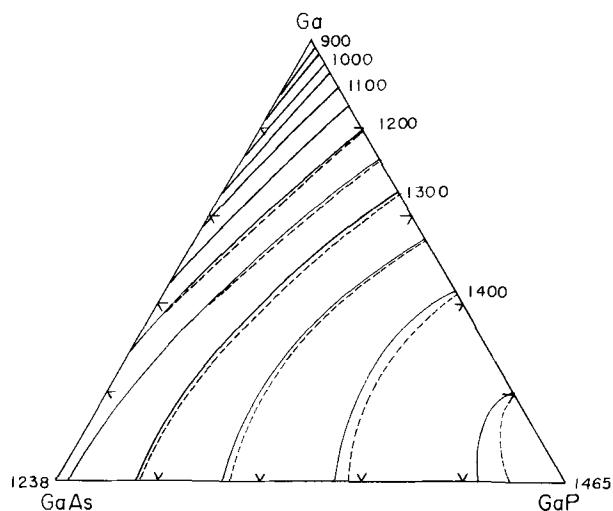


Fig. 4. Ga-GaAs-GaP liquidus isotherms. — QCE calculation; - - - RS calculation.

the appropriate value of Z is 12. The activity coefficients can be calculated similar to the case of the binary system based on the QCE and RS models. Therefore, substituting Eq. [5] or [6] in Eq. [2] the ternary phase diagram can be calculated numerically to yield the liquidus and solid distribution curves. Here the interaction parameter of the GaAs-GaP system was determined by fitting the solidus to experimental data (7) using the QCE model and the RS model. Both calculations were in good agreement for $\Omega_{\text{GaAs-GaP}} = 0$ cal/mole. The interaction parameter of the As-P system was also assumed to be zero cal/mole.

Figure 4 represents the calculated isothermal liquidus lines from 900° to 1450°C by 50°C increments. It is found that the solid lines obtained from the QCE model bend more steeply than the dotted lines from the RS model.

In Fig. 5-8, the experimental results reported by Thurmond for the Ga-As and Ga-P systems, and by Panish for the Ga-GaP-GaAs system from solution growth and solution epitaxy and our experimental results are compared with the computed diagrams. Figure 5 is a portion of Fig. 4, plotted in Cartesian coordinates, showing the equilibrium solubility of P as a function of the As concentration in the melt from 900° to 1300°C isotherms where the experimental points at each temperature are obtained by interpolation and extrapolation from Panish's data and from the data of this work. Figure 6 also shows a portion of the ternary phase diagram in greater detail, on which the solubility of As is plotted as a function of temperature at isophosphorous concentrations. Excellent agreement is obtained between calculated and experimental results. At the same time the liquidus curves calculated using the interaction parameters of the Ga-As and Ga-P binary systems presented in Ref. (15), are shown, where these parameters have been corrected with respect to the values of entropy and temperature of fusion. These liquidus curves are found to be higher than the experimental data on the side of the Ga-P binary system.

In Fig. 7, calculated GaP isoconcentration lines are plotted along with the experimental data, where each curve and point are labeled with X_{GaP} . Figure 8 shows a portion of the GaP isoconcentration lines as a function of As concentrations at isophosphorous concentrations. Although the primary crystals were obtained from the supercooled melts, the experimental results show generally good agreement with the calculated results. At low GaP concentration, experimental data deviate from the calculated isoconcentration lines. It should be pointed out that the liquidus in equilib-

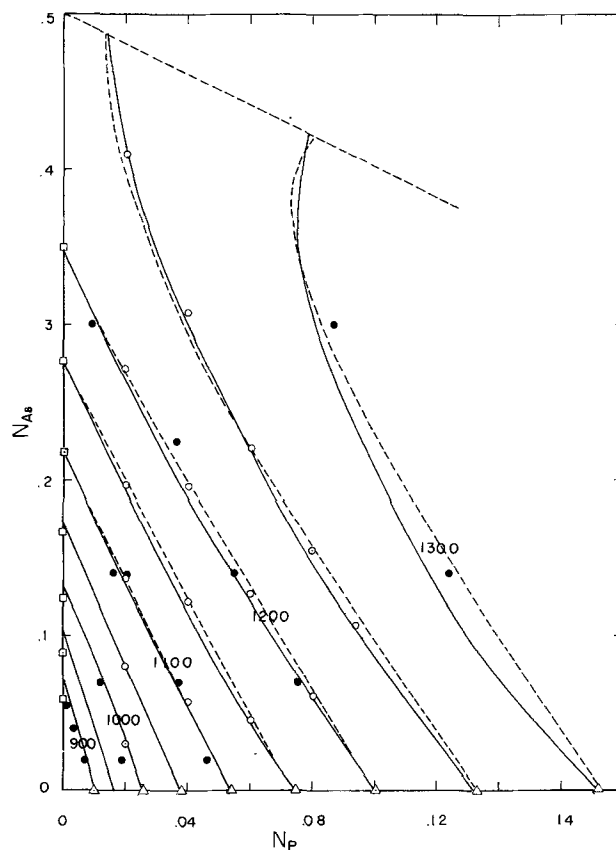


Fig. 5. Liquidus isotherms of the Ga-GaAs-GaP system. — QCE calculation; - - - RS calculation; \odot Present work; \bullet Panish (8); \square Köster and Thoma (3); \triangle Rubenstein (2) where these experimental points are obtained by interpolation and extrapolation.

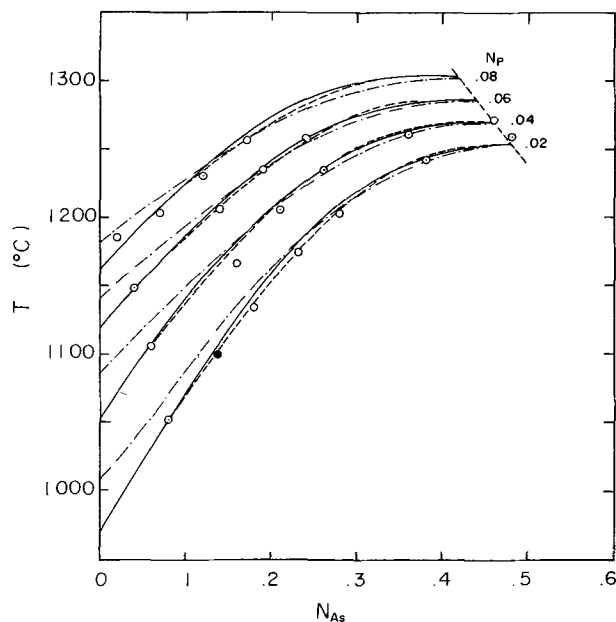


Fig. 6. Phosphorous isoconcentration curves plotted as a function of temperature and arsenic concentration in the melt. — QCE calculation; - - - RS calculation; - · - · - RS calculation using parameters that appeared in Ref. (15); \odot Present work; \bullet Panish (8).

rium with the quasi-binary solid solution falls rapidly over the binary liquidus and therefore the experimental inaccuracy with temperature is large.

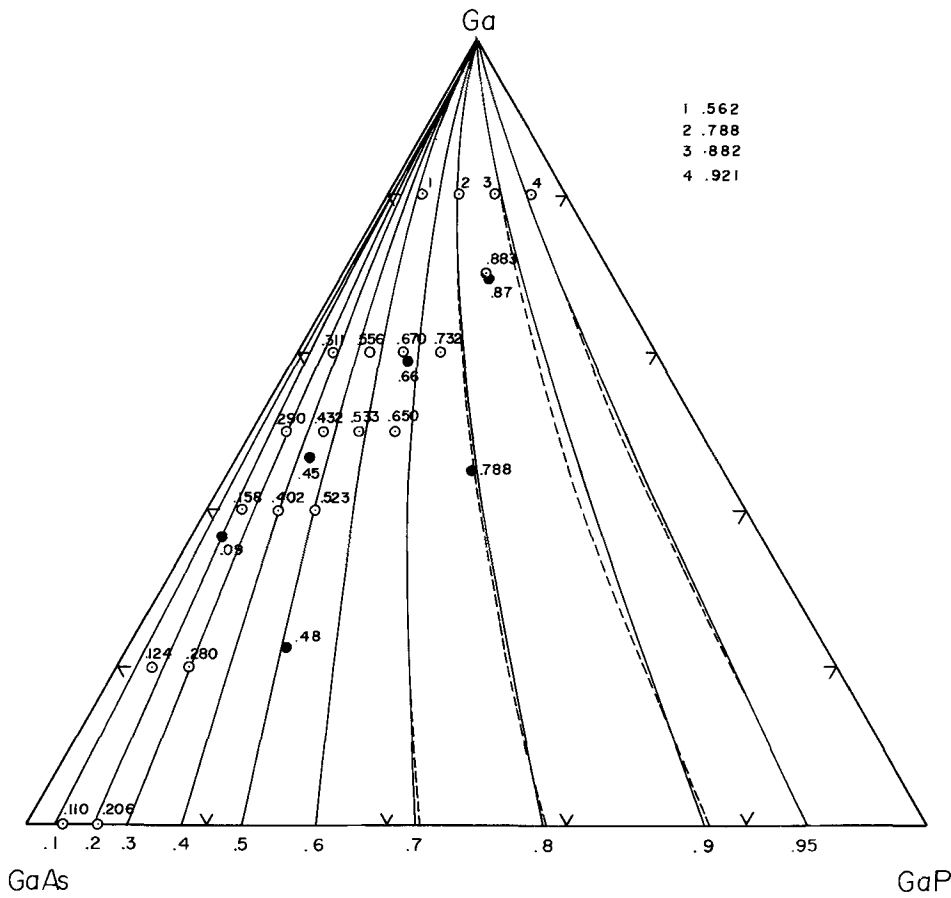


Fig. 7. GaP isoconcentration curves. — QCE calculation; - - - RS calculation; ○ Present work; ● Panish (8).

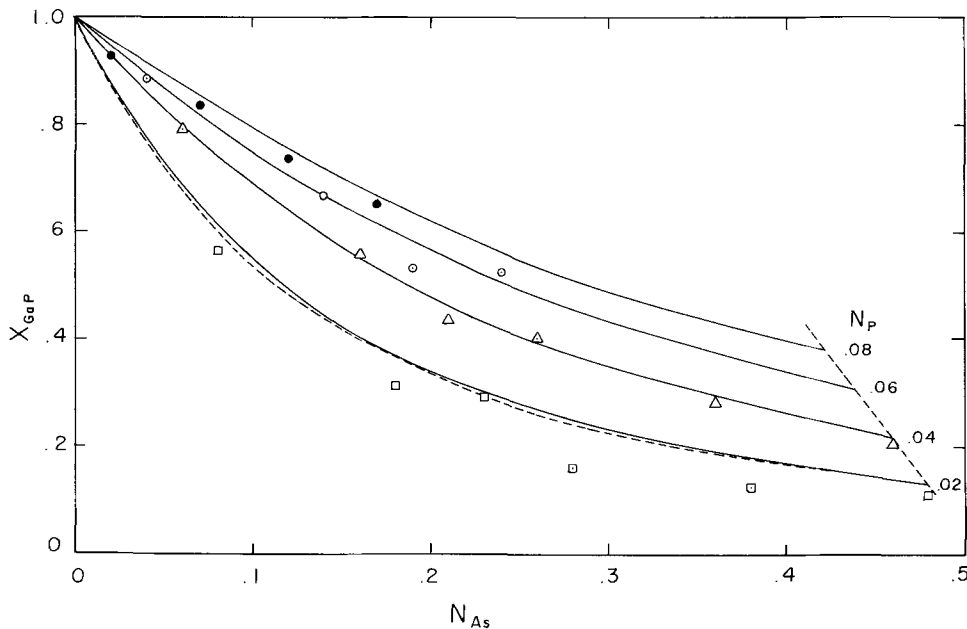


Fig. 8. GaP isoconcentration curves as a function of arsenic at isophosphorous concentrations. — QCE calculation; - - - RS calculation; ●, ○, △ and □ are $N_P = 0.08, 0.06, 0.04, \text{ and } 0.02$, respectively.

Discussions and Conclusions

The liquidus isotherms of the $\text{GaAs}_{1-x}\text{P}_x$ primary phase field of the Ga-GaAs-GaP system have been determined in detail over the Ga-rich part of the system using the DTA method, where the liquidus temperatures have been determined from the average of inflection points in heating and cooling curves. The liquidus isotherms were used to determine the liquidus compositions for the growth of $\text{GaAs}_{1-x}\text{P}_x$ crystals from the liquid. The primary crystals were obtained from supercooled melts and these compositions were determined using the powder x-ray method. Our experimental liquidus temperatures and solidus concen-

trations are generally in agreement with Panish's optical data.

The interaction parameters of Ga-As and Ga-P binary systems necessary to calculate the ternary phase diagram have been determined in the condition of a smooth linkage from the ternary liquidus curves to the binary data in the region of temperatures where experiments were carried out. It has also been shown that the calculated ternary phase diagram of the system Ga-GaAs-GaP based on the QCE model is in excellent agreement with experimental data. In addition, the ternary phase diagram obtained from the RS treatment is similar to that calculated by the QCE model and ex-

plains fairly the experimental results in the present region where experiments have been carried out. The interaction parameter Ω^Q in the QCE model is taken to be constant in the present work. In practice the temperature dependent interaction parameter should be chosen in order to fit the binary data in the wide range of composition up to $N_{Ga} = 1$, using both sets of data reported by Hall (1) and Köster and Thoma (3) for the Ga-As system

$$\Omega_{Ga-As}^Q = 5120 - 8.00T$$

and the data of Hall (1) and Rubenstein (2)

$$\Omega_{Ga-P}^Q = 5360 - 6.42T$$

for the Ga-P binary system. As pointed out by Stringfellow (12), it is, however, doubtful whether bending the model to fit the binary data improves the phase diagram calculation. The appropriate method of improving the calculation is to use a more sophisticated model which includes the physical processes which take into account that the interatomic interactions are temperature and composition dependent.

Acknowledgments

The authors wish to express their hearty thanks to the Research Laboratory of Sumitomo Electric Industries, Ltd. for a supply of the experimental materials. The works of Mr. Kazuo Nakajima in sample preparation and measurements are greatly appreciated.

Manuscript submitted May 18, 1971; revised manuscript received Aug. 23, 1971.

Any discussion of this paper will appear in a Discussion Section to be published in the December 1972 JOURNAL.

REFERENCES

1. R. N. Hall, *This Journal*, **110**, 385 (1963).
2. M. Rubenstein, Abs. 65, Vol. 11, No. 1, p. 129, Electrochem. Soc. Extended Abstracts, Spring Meeting, Los Angeles, May 6-10, 1962.
3. W. Köster and B. Thoma, *Z. Metallk.*, **46**, 291 (1955).
4. M. Rubenstein, Abs. 95, Vol. 13, No. 1, Electrochem. Soc. Extended Abstracts Spring Meeting, Toronto, Canada, May 3-7, 1964.
5. C. D. Thurmond, *J. Phys. Chem. Solids*, **26**, 785 (1965).
6. J. R. Arthur, *ibid.*, **28**, 2257 (1967).
7. K. Osamura and Y. Murakami, *Japan J. Appl. Phys.*, **8**, 967 (1969).
8. M. B. Panish, *J. Phys. Chem. Solids*, **30**, 1083 (1969).
9. M. Ilegems and G. L. Pearson, Proceeding of the 1968 Gallium Arsenide Symposium, p. 3.
10. L. J. Vieland, *Acta Metallk.*, **11**, 137 (1963).
11. G. B. Stringfellow and P. E. Greene, *J. Phys. Chem. Solids*, **30**, 1779 (1969).
12. G. B. Stringfellow, *This Journal*, **117**, 1301 (1970).
13. G. A. Antypas, *ibid.*, **117**, 1393 (1970).
14. G. A. Antypas and L. W. James, *J. Appl. Phys.*, **41**, 2165 (1970).
15. G. A. Antypas, *This Journal*, **117**, 700 (1970).
16. J. Inoue, K. Osamura, and Y. Murakami, *Trans. Japan Inst. Metals*, **12**, 13 (1971).
17. M. E. Straumanis and J.-P. Krumme, *This Journal*, **114**, 640 (1967).
18. G. B. Stringfellow and P. E. Greene, *ibid.*, **117**, 1075 (1970).
19. O. Kubaschewski and E. U. Evans, "Metallurgical Thermochemistry," p. 286, Pergamon Press, New York (1958).
20. Y. Furukawa and C. D. Thurmond, *J. Phys. Chem. Solids*, **26**, 1535 (1965).
21. L. S. Darken, *Trans. TMS-AIME*, **239**, 90 (1967).

Nondestructive Thickness Determination of Polycrystalline Silicon Deposited on Oxidized Silicon

Conrad J. Dell'Oca*

Research and Development Laboratory, Fairchild Camera and Instrument Corporation, Palo Alto, California 94304

ABSTRACT

Infrared interferometry is used to determine the thickness of polycrystalline silicon (polysilicon) deposited on oxidized silicon by the thermal decomposition of silane. The thickness is obtained by comparing the measured wavelength positions of the reflectivity extremes with those predicted theoretically and plotted against polysilicon thickness for a given underlying SiO₂ thickness. The infrared optical properties of polysilicon are found to be essentially the same as those of single-crystal silicon.

An accurate method is required for determining the thickness of polycrystalline silicon (polysilicon) films deposited on oxidized silicon substrates. Several non-destructive optical methods were considered because of their apparent advantages over destructive methods which have been used. Although the optical properties of polysilicon appear to depend on deposition and postdeposition conditions (1), it was assumed for the initial survey that these properties are essentially the same as those of single-crystal silicon.

Calculations and measurements indicate that ellipsometry would not be a convenient method except for very thin and smooth films. This is because (a) the ellipsometry curves cycle rapidly with polysilicon thickness, and thus this thickness must be known in

advance within rather narrow limits;¹ (b) the oxide thickness must be accurately known; and (c) the roughness of the polysilicon can be such that very large errors are introduced. Reflectance interferometry in the visible and near infrared has been used by several authors in measuring two dielectrics on silicon (2-4), but it has several drawbacks when applied to polysilicon. One is that the optical properties of the polysilicon and the substrate change rapidly over this spectral range. Another is that the polysilicon becomes absorbing, limiting the lower wavelength at which interference is observed. Conceivably a method (2) wherein the interference response is calibrated by an independent thickness measurement could be used

¹ For example, the polysilicon thickness must be known to within about 800Å when using a wavelength of 6328Å at an angle of incidence of 70°.

* Electrochemical Society Active Member.

Key words: infrared, interferometry, thin films, refractive index.

to overcome the first objection. Reflectance interferometry in the infrared suffers less than the other two methods in that: (a) above 1.5 μm wavelength both silicon and polysilicon can be considered to be nonabsorbing and nondispersive, and (b) the results are less affected by oxide thickness and surface roughness of the layer. There is, however, an increase in the minimum polysilicon thickness which can be measured. This paper describes the application of the last method to the measurement of polysilicon films.

Experimental Procedure

Silicon wafers [$\rho > 1.5$ ohm-cm, n- or p-type, and (111) orientation] which had their front sides mechanically-chemically polished were oxidized in dry oxygen at about 1200°C. The oxide thickness was measured with an ellipsometer. Polysilicon was then deposited on the front side of the oxidized wafer by the thermal decomposition of silane in a hydrogen carrier gas in a horizontal epitaxial reactor.²

The spectrophotometer used was a Beckman Model IR5A which has a wavelength range from 2 to 16 μm . Reflectivity measurements were made at an angle of incidence of 30° using a specular reflection attachment. Where computed and experimental reflectivity curves were compared, the spectrophotometer was calibrated by measuring the response of a bare silicon surface prior to and after measuring the response of the polysilicon film. The before and after calibration curves agreed in all cases within 1% intensity.

Calculations

The optical properties of the various materials considered (Fig. 1) are such that interference conditions are in error if calculated from approximations involving single reflection at the interfaces. The exact reflectivity equation must be used and for the reflection of unpolarized light, this equation is

$$\rho = (|R_p|^2 + |R_s|^2) / 2 \quad [1]$$

R_p and R_s are the amplitude reflectivity coefficients for light polarized respectively parallel and perpendicular to the plane of incidence, and for two layers on an infinite substrate each has the form (5)

$$R = \frac{r_1 + r_2 e^{-2j\delta_1} + r_3 e^{-2j(\delta_1 + \delta_2)} + r_1 r_2 r_3 e^{-2j\delta_2}}{1 + r_1 r_2 e^{-2j\delta_1} + r_1 r_3 e^{-2j(\delta_1 + \delta_2)} + r_2 r_3 e^{-2j\delta_2}} \quad [2]$$

where r_i is the Fresnel reflection coefficient of the i th interface, $\delta_i = 2\pi N_i d_i \cos \phi_i / \lambda$ is the phase retardation suffered by light of wavelength λ on crossing the i th film of refractive index $N_i = n_i - jk_i$ and thickness d_i , and ϕ_i is the refractive angle in the i th layer.

Fringe charts for determining polysilicon thickness were constructed by calculating from Eq. [1] the wavelength ($1.5 < \lambda < 12 \mu\text{m}$) at which the reflectivity reaches a maximum or minimum for various polysilicon and silicon dioxide thicknesses. In the calculation,

² Applied Materials Technology, Model AMH-620.

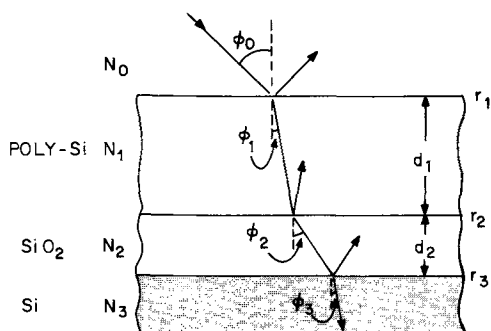


Fig. 1. Reflection of light from polysilicon on oxidized silicon

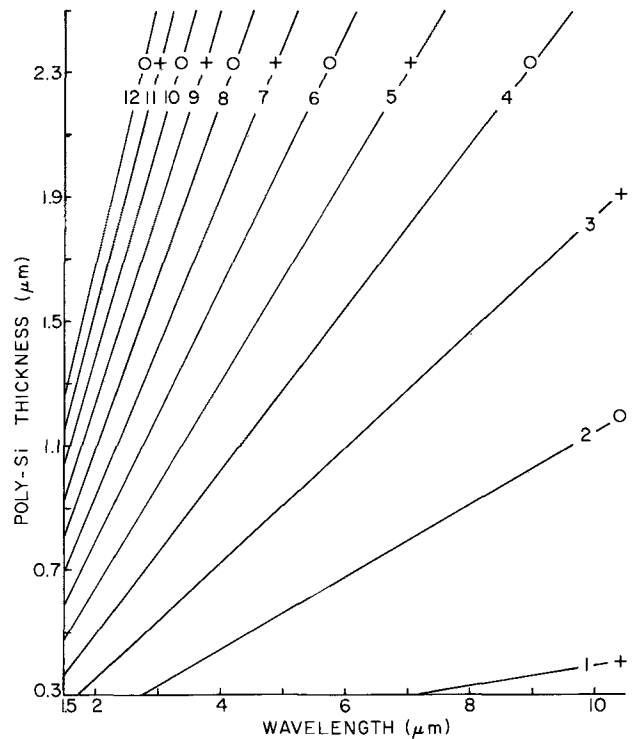


Fig. 2. Polysilicon thickness vs. wavelength position of extremes in intensity for 100 nm of SiO₂ on silicon (+, O, and numbers on lines denote, respectively, lines of minimum intensity, lines of maximum intensity, and the order in which they are encountered with decreasing wavelength).

the materials were assumed nondispersive and nonabsorbing. The index of refraction of polysilicon was assumed to be the same as that of the silicon substrate, which was taken to be 3.42 (6), and that of silicon dioxide was 1.46, the value found in the visible light range. Four charts were necessary to span the polysilicon thickness range of interest, which extended from less than 1 to 7.5 μm . A typical fringe chart, in this case for polysilicon on 100 nm of oxide, is shown in Fig. 2. Each line on this chart shows polysilicon thickness vs. wavelength position of a particular interference extreme. For the purpose of discussion, the lines are numbered with decreasing wavelength. Calculations indicate that extremes corresponding to lines 1 and 2 are too broad for their position to be determined accurately and are not useful in determining polysilicon thickness. Thus for the wavelengths considered, polysilicon thicknesses above 0.3 μm can be determined by using this chart.

The effect of oxide thickness on the fringe chart is as follows. Below 100Å, the variations in intensity diminish to a point where it becomes difficult to determine accurately the position of the extremes. Below about 600 nm, the fringe lines are linearly dependent on polysilicon thickness. A change in oxide thickness in this region displaces a given intensity extreme by an amount almost independent of polysilicon thickness. This is seen in Fig. 3, where fringe charts corresponding to 100, 300, and 500 nm of oxide are superimposed. Each interference order is represented by a set of three lines corresponding to the three oxide thicknesses. It is also evident from this figure that the wavelength of an extreme shifts much less (by about four times) for a change in oxide thickness than for the same change in polysilicon thickness. Oxides of 600 nm or more cause some of the fringe lines to become noticeably nonlinear. This is because conditions are being approached for interference at the polysilicon oxide interface. In this region, it is still possible

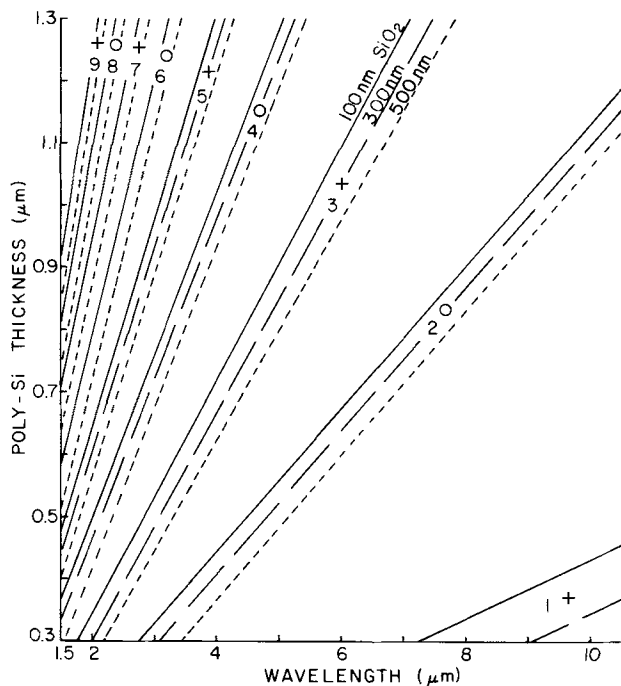


Fig. 3. Superposition of fringe charts for SiO_2 thicknesses of 100 nm (full line), 300 nm (dashed line), and 500 nm (dotted line). The 500 and 300 nm lines are, respectively, omitted from fringe 1 and 6 to 9. (Notation as in Fig. 2.)

to determine polysilicon thickness, but more expertise is required in interpreting the interference response.

Results

Test of assumptions.—Experimental and computed reflectivity curves were compared in order to test the assumptions made in the calculation of the charts. For the case of silicon covered only by thick silicon dioxide films, an index of refraction value of 1.46 for the silicon dioxide was found to hold out to 6 μm wavelength. Beyond this wavelength, deviation between calculated and experimental occurs, and eventually the SiO_2 structural response is observed. With thin polysilicon films (1 μm or less) or films deposited at low temperatures ($\sim 650^\circ\text{C}$) on oxidized silicon, agreement (within 2%) between calculated and experimental reflectivity curves is found out to 8 μm wavelengths (Fig. 4). Above this point, the SiO_2 structural response causes deviations. As the polysilicon thickness increases with respect to the oxide thickness, the effect of this response diminishes. With the thicker films, however, agreement between calculated and experimental results

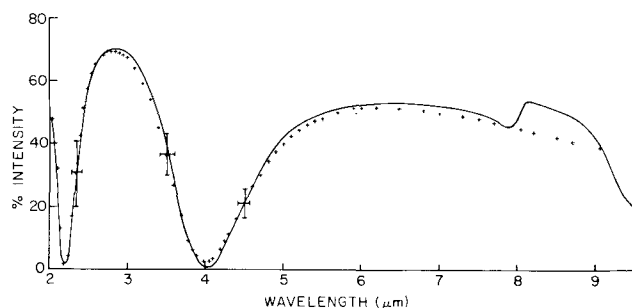


Fig. 4. Comparison of experimental reflectivity (solid line) response for polysilicon film on 240 nm of SiO_2 with the calculated reflectivity (points) using $N_1 = N_3 = 3.42$, $N_2 = 1.46$, and $\phi_0 = 30^\circ$ (cross bars indicate the calculated effect of $\pm 2\%$ variation in polysilicon thickness which is 680 nm, polysilicon deposited at 650°C).

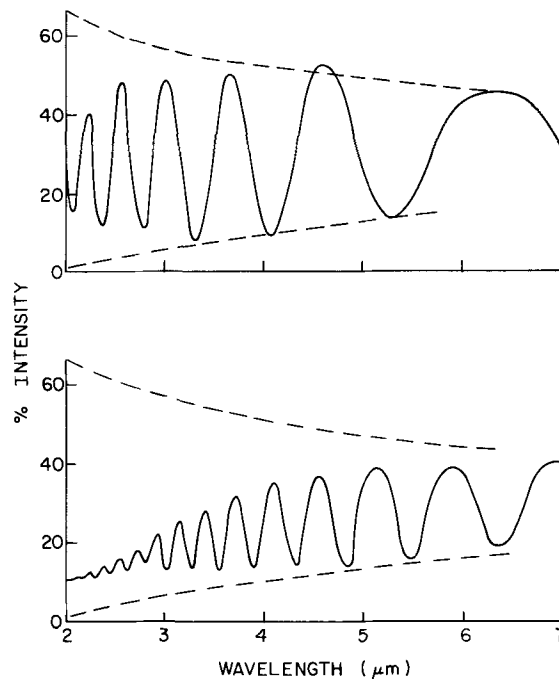


Fig. 5. Experimental reflectivity results yielding 2.45 μm (upper curve) and 5.86 μm (lower curve) of polysilicon on 140 nm of SiO_2 . The dashed lines indicate the expected calculated interference envelope. (Polysilicon deposited at 850°C .)

is no longer obtained as shown by the examples in Fig. 5 where the dashed lines represent the calculated reflectivity envelope. The diminished reflectivity response is caused by surface roughness of the polysilicon and not by absorption in the film. Infrared transmission studies of thick (175 μm), unsupported, polished polysilicon films indicate that although the polysilicon is more absorbing than silicon, the imaginary part of its index of refraction, which is about 0.001 at 2.5 μm and decreases with wavelength, is at least several orders too small to produce the observed decrease in the reflectivity.

Even more critical than the assumptions made about the optical properties is the assumption made in Eq. [2] that the silicon substrate is infinite when, in fact, it is transparent at these wavelengths. Nevertheless, the assumption may be used because it can be shown that interference occurring within the silicon substrate and the oxide layer covering its back side has little effect on the reflectivity response measured from the polysilicon. First, the thickness of the silicon substrate is such that interference within it will not be resolved by the IR-5A. This was confirmed by measurements made on unoxidized substrates. Second, any effect that interference in the substrate has on absolute intensity is eliminated by the spectrophotometer calibration. Finally, calculations indicate that the intensity reflected from the back side oxide-air interface is small, and interference occurring in this layer can be neglected. It was found that the wavelengths of the extremes remain, within experimental error, the same after the oxide is removed from the back of the substrate even in the case of thick oxides ($\sim 1 \mu\text{m}$).

Limitations and accuracy.—The polysilicon thickness was obtained by matching measured wavelengths of reflectivity extremes to those shown in the calculated fringe chart. Extremes occurring below 6 μm wavelength were used because the best agreement between experimental and calculated reflectivity occurs here. As the optical thickness of the polysilicon increases with respect to that of the oxide, the effect of the SiO_2 structural response on the interference response

diminishes, and the 6 μm upper wavelength limit can be relaxed. However, the 2 to 6 μm wavelength range is sufficient to measure polysilicon films from 0.3 to above 5 μm .

The accuracy is the sum of the theoretical and experimental accuracies. On the basis of the foregoing justification of assumptions, the theoretical accuracy is estimated to be 2% in determining polysilicon thickness using wavelengths from 2 to 6 μm . Experimentally, the wavelength of the reflectivity extremes obtained from thin polysilicon films can be measured to 1000Å or less except for extremes No. 1 and No. 2 which are not used. The position of the extremes can be determined more accurately as they get sharper; but the sharper extremes correspond to fringe lines of higher order which have steeper slopes. This results in an uncertainty of about 150Å in the polysilicon thickness determined from any of the extremes. For thicker polysilicon films this may be somewhat larger; for example, in the lower part of Fig. 5, the polysilicon thickness determined from each individual extreme is within 200Å of the mean thickness. Error in determining oxide thickness as was seen in the fringe chart contributes about one quarter of its value to the uncertainty, and this contribution can usually be neglected. Thus in the wavelength range from 2 to 6 μm , it is estimated that the over-all accuracy of the IR interference method is 2% + 150Å. The accuracy of relative measurements is less dependent on the correctness of the assumptions, and thickness variations corresponding to roughly twice the instrumental precision or about 75Å should be detectable for thin polysilicon films.

In comparing the IR interference technique with other methods of measuring film thickness, it must be kept in mind that this method gives an average thickness over the area covered by the IR beam (about 2 cm by 1 to 3 mm) while other methods measure local thickness. Table I presents a comparison of the thickness values for 15 polysilicon films determined from IR interference in the wavelength range from 2 to 6 μm with the values obtained by averaging two or more local measurements. The local measurements were made by either Nomarski or Tolanski interference techniques, or with a mechanical stylus (DEKTAC³). The nominal accuracy of these methods is estimated to be 0.25 and 0.1 fringes, or 750 and 300Å for the Nomarski and Tolanski techniques, respectively, and 4% for the DEKTAC. Within these accuracies agreement between IR and local measurements is found for all except three specimens of Table I. The discrepancy for these three specimens (DP2-1, C1, and C2) arises because they were much less uniform in thickness, as was indicated by local measurements.

Summary

An interference method is described for the thickness measurement of polycrystalline silicon deposited on

³ Manufactured by Sloan Instrument Corporation.

Table I. Thickness of polysilicon determined from infrared interference and from other methods

Specimen	SiO ₂ (nm)	Thickness of poly-Si (nm)	
		Other methods*	Infrared interference
P8-1	140	510 N	545
P8-2	140	420 N	448
DP2-1	240	655 T	700
DP2-2	240	625 T	645
DP2-3	240	660 T	680
DP1-2	240	810 T	780
C1	280	1350 T	1420
C2	280	1500 T	1600
P40-6	180	652 T	635
P40-20	180	630 T	630
P40-11	152	650 T	640
P20-14	210	820 T	625
P20-16	180	865 T	650
EY-1	140	2400 D	2450
TK-1	140	6000 D	5860

* Measurements made by: N-Nomarski interference, T-Tolanski interference, and D-mechanical stylus (DEKTAC).

thermally oxidized silicon. It provides a rapid nondestructive measurement of polysilicon thicknesses greater than 0.3 μm with an estimated accuracy of 2% + 150Å and a sensitivity of 75Å when the interference measurements are made in the 2 to 6 μm wavelength region. The method is developed for SiO₂ thicknesses of 0.5 μm or less but could be extended to larger thicknesses. The sensitivity to variation in thickness is four times greater for polysilicon than for silicon dioxide; thus, the method is particularly suitable for production control.

Acknowledgments

The author wishes to thank T. Kamins for his cooperation and for preparation of most of the polysilicon specimens; P. Fleming for aid in the Tolanski measurements; and M. Barry for discussions regarding this paper.

Manuscript submitted Feb. 19, 1971; revised manuscript received Sept. 2, 1971.

Any discussion of this paper will appear in a Discussion Section to be published in the December 1972 JOURNAL.

REFERENCES

1. M. H. Brodsky, R. S. Title, K. Weiser, and G. D. Pettit, *Phys. Rev. B*, **1**, 2632 (1970).
2. F. Reizman and W. Van Gelder, *Solid-State Electron.*, **10**, 625 (1967).
3. I. Franz and W. Langheinrich, *ibid.*, **13**, 807 (1969).
4. E. A. Corl and K. Kosanke, *ibid.*, **9**, 943 (1966).
5. O. S. Heavens, "Optical Properties of Thin Solid Films," p. 63, Butterworths, London (1955).
6. C. Salsberg and J. Villa, *J. Opt. Soc. Am.*, **47**, 244 (1957).

In-Process Thickness Monitor for Polycrystalline Silicon Deposition

T. I. Kamins* and C. J. Dell'Oca*

Research and Development Laboratory, Fairchild Camera and Instrument Corporation, Palo Alto, California 94304

ABSTRACT

An infrared interference method for monitoring the thickness of a film of polycrystalline silicon during its deposition on oxidized silicon is described. With this method, deposition can be terminated when the desired film thickness is obtained. Qualitative agreement has been found between the calculated and observed variations of the emitted intensity measured during deposition.

This paper describes an infrared interference method for monitoring the thickness of a layer of polycrystalline silicon during its deposition by the thermal decomposition of silane. A theoretical basis for the method is also given. The method is similar to one previously reported in the literature for the silicon-on-sapphire system (1), but in the present case the technique is applied to deposition on a two-layer substrate, such as is currently used in silicon technology.

Since the deposition rate is a strong function of the deposition temperature and the silane flow rate under normal operating conditions, accurate control of these two parameters is necessary. In general, poor control is detected only after the wafers are removed from the reactor and the thickness of the deposited layer is measured. The use of an in-line monitor allows the deposition to be terminated when the desired thickness is obtained. Since only one test wafer is monitored, however, good temperature and flow uniformity are still necessary in order to avoid wafer-to-wafer variations.

With this method of in-line monitoring, an infrared detector is used to observe the radiation emitted from an oxide-covered silicon wafer during the deposition of a polysilicon film on the oxide. As the thickness of the film increases, the intensity of the emitted radiation is modulated and passes through successive maxima and minima. The emitted intensity is also dependent on the optical properties of the materials and the thickness of the oxide layer.

The calculations involved in the preceding paper (2) and in the present paper are formally similar, but the variable monitored by the two methods differs. In the previous case, the intensity was observed as a function of wavelength after the deposition was completed, while the present method considers the intensity as a function of thickness during the deposition process.

Calculations

We show that, as the thickness of the polysilicon changes, interference effects modulate the emissivity and, hence, the radiation emitted from the wafer surface at a given angle.

The emissivity¹ of the wafer surface can be calculated indirectly by using the fundamental relationship that at a given temperature the emissivity and the absorptivity of a body are equal. The absorptivity, and hence the emissivity, can be calculated by considering the reflection of light from the polysilicon surface at an angle ϕ_0 from the normal. If we assume that the silicon substrate appears infinitely thick, then the incident intensity equals the absorbed intensity plus the reflected intensity; i.e., the absorptivity plus the reflectivity equals unity. Thus, the emissivity, ϵ , is re-

lated to the reflectivity, ρ , by the equation

$$\epsilon = 1 - \rho \quad [1]$$

where the reflectivity can be calculated for the polysilicon-oxide-silicon system as in the preceding paper (2).

Figure 2 shows the dependence of the emissivity on the polysilicon thickness for three oxide thicknesses as calculated using Eq. [1] for $\lambda = 2.4 \mu\text{m}$ and $\phi_0 = 36.4^\circ$ (Fig. 1). Since the optical properties of these materials are not well known at the temperatures and wavelengths under consideration, the room-temperature values of refractive index were used in this calculation. [At least for single-crystal silicon, there is some indication that the optical properties are not strongly dependent on temperature (3,4).] It was further assumed that the polysilicon was not absorbing and had the same refractive index as single-crystal silicon [3,42]. The refractive index of SiO_2 was taken to be 1.46. Figure 2 indicates that interference effects modulate the emissivity and the radiated intensity² as the thickness of the polysilicon layer changes.

According to the calculations, successive maxima or minima in the intensity are separated by a change in the polysilicon thickness, Δd , which causes a 180° change in the phase of the light traversing Δd ; that is

$$\begin{aligned} \Delta d &= \lambda(2n_1 \cos \phi_1)^{-1} \\ &= (\lambda/2) (n_1^2 - n_0^2 \sin^2 \phi_0)^{-1/2} \quad [2] \end{aligned}$$

where n is the refractive index and the subscripts 0 and 1 refer to the ambient and polysilicon, respectively. This equation indicates that Δd is independent of the oxide thickness and properties. Furthermore, since $n_1^2 \gg n_0^2$, Δd is also insensitive to the angle at which

² The total power radiated by the surface is the integral of the power radiated at all angles and wavelengths and should remain constant as the film thickness increases. Thus, the temperature of the surface will not reflect this modulation in emissivity.

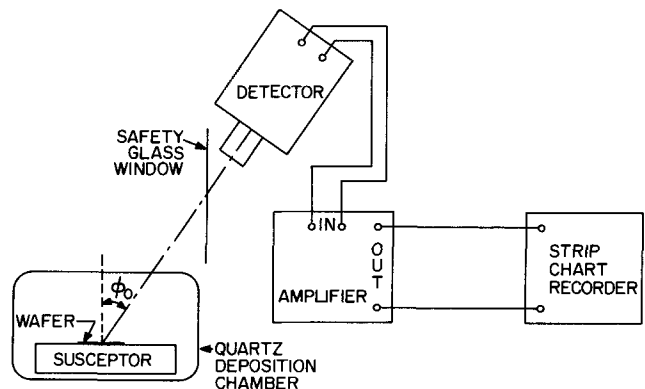


Fig. 1. Schematic representation of experimental arrangement

* Electrochemical Society Active Member.

Key words: infrared, interferometry, thin films.

¹ The emissivity is the ratio of the intensity radiated by a body to that radiated by a perfectly emitting body (a black body) at the same temperature.

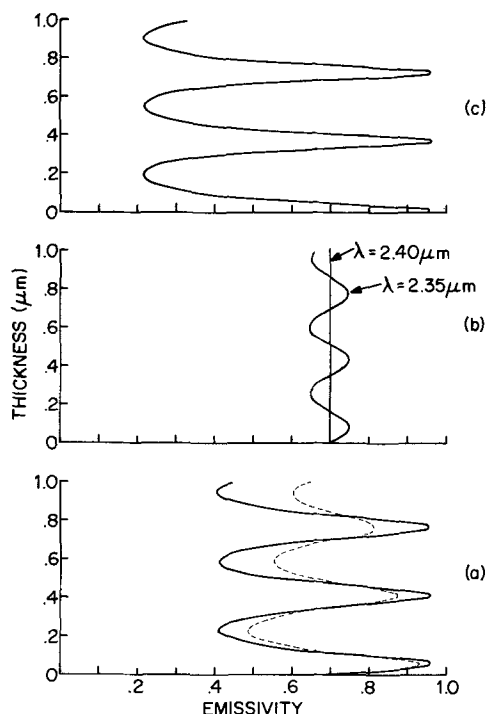


Fig. 2. Calculated dependence of the emissivity on the thickness of the polysilicon for three oxide thicknesses: (a) $0.13 \mu\text{m}$, (b) $0.90 \mu\text{m}$, and (c) $1.25 \mu\text{m}$. The dashed curve in (a) indicates the emissivity for a slightly absorbing polysilicon layer.

the radiation is intercepted so that some error in measuring the angle can be tolerated.

Figure 2 shows, however, that both the starting point and the amount of modulation of the emitted intensity during deposition will be functions of the oxide thickness. If the oxide thickness is such that the phase change, δ_2 , of the radiation crossing it is equal to $m\pi$, then the reflectivity and hence the emissivity will remain constant as the polysilicon thickness changes. For this condition, we obtain complete destructive interference between light reflected at the upper and lower surfaces of the oxide layer. Figure 2(b) shows the calculated emissivity for a $0.90 \mu\text{m}$ oxide film at two wavelengths; the curve for $\lambda = 2.40 \mu\text{m}$ represents destructive interference with $\delta_2 = \pi$.

If the polysilicon were to absorb some of the radiation, the amplitude of the emissivity modulation would decrease with increasing polysilicon thickness, so that the emissivity would eventually reach a constant value. This decrease in amplitude would set an upper limit on the polysilicon thickness which could be monitored. The dashed curve in Fig. 2(a) shows the emissivity calculated with the imaginary part of the refractive index of the polysilicon, k_1 , equal to 0.2.

Experimental Procedure

The thickness monitor has been used to observe the deposition of submicron films of polysilicon in an RF-heated, horizontal epitaxial reactor.³ An infrared pyrometer,⁴ which is sensitive in the wavelength range from 2.0 to $2.6 \mu\text{m}$, was used to detect the radiation being emitted from the growing film. Although only part of the radiation emitted from the wafer surface will reach the infrared detector, the wafer is expected to be the principal source of the radiation striking the detector. Once operating conditions are attained, the temperatures of the various surfaces in the reactor should remain essentially constant. Then, the intensity reaching the detector will be affected only by the changing thickness of the polysilicon film.

³ Applied Materials Technology, Model AMH-620.

⁴ IRCON, Model 300 T5C.

The experimental arrangement is shown in Fig. 1. The pyrometer was focused on the oxide-covered silicon wafer through the wall of the quartz deposition tube and a safety glass window; the light path between the heated wafer and the detector made an angle $\phi_0 \cong 37^\circ$ with the vertical. Radiation sensed by the detector originated from a spot less than 5 mm in diameter. The signal from the pyrometer was recorded on a strip-chart recorder. After the wafer was removed from the reactor, the polysilicon thickness was measured by infrared interferometry (2).

Experimental Results and Discussion

In order to study the usefulness of the method, the effects of deposit thickness, deposition temperature, and oxide thickness were considered.

In the first experiment polysilicon was deposited at 850°C on a silicon wafer covered by $0.13 \mu\text{m}$ of thermally grown SiO_2 . Figure 3(a) shows the recorder trace for an 8.18-min deposition with a flow consisting of 0.05% silane in a hydrogen carrier gas. The trace starts from a point determined by the thickness of the underlying oxide, increases to a maximum, and then goes through successive minima and maxima, in qualitative agreement with the calculated behavior shown in Fig. 2(a). The final film thickness was subsequently measured to be $0.90 \mu\text{m}$.

The decrease in amplitude as the film thickness increases can be attributed to three effects. These are dispersion, surface roughness, and absorption of radiation by the film. The first is perhaps the most important since the detector has a fairly large bandwidth. If the effect is solely one of absorption, which is unlikely, a k_1 of 0.2 would be required for the decrease. This value is roughly two orders of magnitude larger than that found at room temperature (2). Surface roughness is not a significant factor at these thicknesses as indicated by IR measurements (2). Five complete cycles have been observed during some depositions, at least four of which were useful for thickness monitoring. Therefore accurate control should be possible for films over $1 \mu\text{m}$ thick. The use of a narrower bandpass filter is expected to extend the use of this method to thicker films. Significantly longer wavelengths cannot easily be used because of the rapid decrease in the transmittance of quartz above $4 \mu\text{m}$.

Thickness corresponding to one cycle.—In order to find the thickness corresponding to one complete cycle, a series of films was deposited at 850°C on $0.13 \mu\text{m}$ of thermally grown SiO_2 . Each deposition was terminated at a maximum or minimum in the emitted inten-

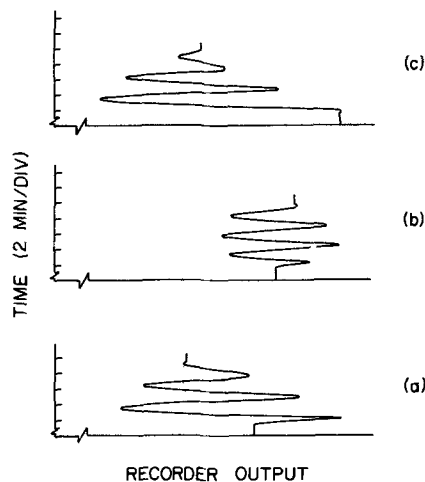


Fig. 3. Recorder traces observed during the deposition of polysilicon films on SiO_2 . The three parts of the figure correspond to oxide thicknesses of (a) $0.13 \mu\text{m}$, (b) $0.90 \mu\text{m}$, and (c) $1.2 \mu\text{m}$ and may be compared to the calculated curves shown in Fig. 2.

Table I. Deposition parameters for films deposited at 850°C with deposition terminated at an intensity extreme

Deposition time (min)	Cycles	Thickness (μm)	Thickness difference for half cycle (μm)
3.75	1.15	0.39	0.16
5.28	1.65	0.55	
6.78	2.15	0.73	
8.18	2.65	0.90	

sity. Table I shows the time and thickness of each deposit. The fractional part of the cycle corresponds to the trace from the starting point to the first peak and cannot be accurately determined. Therefore, the thickness per cycle was determined from the thickness differences between the successive depositions. We find one complete cycle for each 0.34 μm of deposited silicon. From Eq. [2], the equivalent wavelength is 2.4 μm when the room temperature value of the refractive index of silicon is used; this wavelength is near the center of the region of sensitivity of the detector. The trace [Fig. 2(a)] calculated by using this wavelength is in qualitative agreement with the experiment [Fig. 3(a)]. The agreement indicates that this method of compensating for the temperature variation of the refractive index by using the wavelength found from Eq. [2] leads to a self-consistent set of calculations.

Effect of temperature.—Films were deposited at 750°, 850°, and 950°C on 0.13 μm of thermally grown SiO_2 . Each deposition was terminated at the second minimum in the trace, and the thickness of the resulting deposit was measured after the wafer was removed from the reactor. The thickness of the three films was the same within experimental error ($0.56 \pm 0.01 \mu\text{m}$); the shape of the recorder trace was also the same for the three temperatures, confirming that the relation between emissivity and thickness is not a strong function of the deposition temperature. Therefore, slight errors in the temperature setting during the deposition will not be critically important. Of course, the

absolute magnitude of the emitted radiation changes with temperature.

Effect of oxide thickness.—In order to determine the effect of oxide thickness, films were also deposited on oxide layers 0.90 and 1.2 μm thick. Figures 3(b) and 3(c) show the experimental results, which may be qualitatively compared to the calculated behavior shown in Fig. 2(b) and 2(c). The thickness corresponding to one cycle is the same for the different oxide thicknesses, but the starting point and the magnitude of the intensity modulation vary. The trace for the deposit on the 1.2 μm oxide starts near a maximum and shows substantial intensity change, in agreement with the calculations [Fig. 2(c)]. The magnitude of the signal from the deposit on the 0.90 μm oxide is much weaker, as expected [Fig. 2(b)]. Successful use of the method requires avoiding oxide thicknesses close to those corresponding to $\delta_2 = m\pi$ since small experimental variations would lead to large errors in thickness. It should also be noted that the oxide thickness can be chosen so that the deposition of a given thickness of polysilicon will be terminated at a maximum or minimum for the best process control. In addition, best control will be achieved with an oxide thickness less than $\lambda/2n_2$ so that a given percentage uncertainty in oxide thickness will correspond to a small uncertainty in the phase.

Acknowledgments

The authors wish to thank M. Barry, R. Dyck, and R. Tucker for helpful discussions.

Manuscript submitted Feb. 19, 1971; revised manuscript received Sept. 2, 1971.

Any discussion of this paper will appear in a Discussion to be published in the December 1972 JOURNAL.

REFERENCES

1. D. J. Dumin, *Rev. Sci. Instr.*, **38**, 1107 (1967).
2. C. J. Dell'Oca, *This Journal*, **119**, 108 (1972).
3. M. Cardona, W. Paul, and H. Brooks, *J. Phys. Chem. Solids*, **8**, 204 (1959).
4. F. Lukes, *Czech. J. Phys.*, **B10**, 317 (1960).

Polymethonium-Silver Iodide Compounds as High-Conductivity Solid Electrolytes

M. L. Berardelli, C. Biondi, M. De Rossi,* G. Fonseca, and M. Giomini

Istituto di Elettrotecnica and Istituto di Chimica Generale, Università di Roma, Rome, Italy

ABSTRACT

Polyquaternaryalkylammonium iodide-silver iodide compounds with high ionic conductivity in the solid state have been prepared. The systems $(\text{R}_3\text{N}(\text{CH}_2)_n\text{-NR}_3)_2\text{I}_2 - \text{AgI}$, at 1:12 ratio, give specific conductivities of the order of 10^{-2} ($\text{ohm} \times \text{cm}$) $^{-1}$. For the system octamethyldiethyltriammonium iodide-silver iodide in the ratio 1:22, the specific conductivity reaches, at room temperature, a value of 5.8×10^{-2} ($\text{ohm} \times \text{cm}$) $^{-1}$.

Solid-state electrochemical generators are known to present some advantages over traditional ones widely employed in many fields of technique. Considerable further advantages could be attained, provided that the conductivity of a solid electrolyte becomes comparable with that of a strong electrolyte in aqueous solution. These reasons justify the interest in this field and the researches carried out, especially in recent years, on substances which may constitute high-conductivity solid electrolytes.

* Electrochemical Society Active Member.

Key words: electrical conductivity, silver iodide, solid-state electrochemistry.

Several promising results have recently been achieved, mainly as a consequence of work conducted by Takahashi and Yamamoto, Owens and Argue, Bradley and Greene, etc., as summarized in Table I.

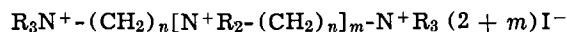
So far, the highest specific conductivity at room temperature has been measured with RbAg_4I_5 (10), which, in the best conditions, gives a value $\chi = 2.70 \times 10^{-1}$ ($\text{ohm} \times \text{cm}$) $^{-1}$. However, rubidium-containing compounds are quite expensive, so that it is of interest to look for other conducting materials of lower cost; moreover, still higher conductivities would be welcomed. Such compounds should also be thermodynamically

Table I.

Authors	Compound	Conductivity (ohm × cm) ⁻¹	Reference
Ives and Janz	AgCl	1 × 10 ⁻⁷	(1)
Miller and Maurer	AgBr	3 × 10 ⁻⁷	(2)
Lieser	β AgI	2 × 10 ⁻⁶	(3)
Mrgudich	AgI (amalg. el.)	1.5 × 10 ⁻⁴	(4)
Takahashi and Yamamoto	Ag ₃ SI	1 × 10 ⁻²	(5)
Bradley and Greene	RbAg ₄ I ₅	1.24 × 10 ⁻¹	(6)
Owens and Argue	RbAg ₄ I ₅	2.10 × 10 ⁻¹	(7)
De Rossi, Pistoia, and Scrosati	RbAg ₄ I ₅	2.50 × 10 ⁻¹	(8)
Takahashi and Yamamoto	RbAg ₄ I ₅	1.70 × 10 ⁻¹	(9)
Raleigh	RbAg ₄ I ₅	2.70 × 10 ⁻¹	(10)
Owens	Me ₂ NAg ₆ I ₇	4.0 × 10 ⁻²	(11, 12)
Owens	Me ₂ Et ₂ NAg ₇ I ₈	6.4 × 10 ⁻²	(11, 12)

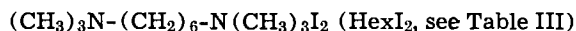
cally stable at low temperatures, while RbAg₄I₅ is not. These reasons have furthered studies on other compounds.

In recent papers, Owens (11, 12) extensively examined the behavior of a new series of solid electrolytes still based on AgI, in which rubidium iodide was replaced by a tetraalkylammonium iodide. Since promising results were so obtained (see Table I), the present study was carried out for a new series of compounds in which silver iodide is associated with alkylated polyammonium iodides of the general formula



where R is an alkyl radical: in particular, compounds in which $m = 0$ and $1 \leq n \leq 10$ have been examined.

Most of the experiments reported in this paper were carried out on hexamethonium iodide-silver iodide compounds, because the hexamethonium iodide is a low-cost, readily available material. It yields the intermediate value of $n = 6$. The chemical formula may be written as



Experimental

Among the products of the series under study, only three pentane-1,5-bis-trimethylammonium iodide (pentamethonium iodide), hexane-1,6-bis-trimethylammonium iodide (hexamethonium iodide) and decane-1,10-bis-trimethylammonium iodide (decamethonium iodide) could be found commercially as salts.

The other compounds were transformed into salts through two procedures (examples are reported below), method A for methyl derivatives of amines (1,1-bis-diethylamino-methane, 1,2-bis-dimethylamino-ethane, 1,3-bis-dimethylamino-propane, 1,4-bis-dimethylamino-butane), and method B for the free amine 1,9-diamino-nonane.

All the starting products employed were Fluka or Carlo Erba (analytical grade) and were used without further purification.

Method A.—5g (0.043 moles) of 1,2-bis-dimethylamino-ethane are dissolved in 50 ml of cyclohexane at a temperature of 0° to 5°C; 13g (0.091 moles—slight excess) of CH₃I, dissolved in 15 ml of cyclohexane, are slowly added to the solution, which is stirred for 2 hr, at 0° to 5°C. After filtering, the solid is dried at 140°C for 15 min: 15.5g of product (90% yield) are obtained.

Analysis $I_{th} = 63.5\%$ $I_{ex} = 63.1\%$

Method B (13).—4.74g (0.030 moles) of 1,9-diamino-nonane are slowly dissolved in 16.5g of 90% formic acid solution (0.320 moles—1:11 ratio) at a temperature not exceeding 5°C; then 13.5g of 35% formaldehyde solution (0.150 moles—1:5 ratio) are added. The mixture is first heated, until carbon dioxide evolution ceases and then is refluxed for 5 hr. After cooling, the solution is saturated with KOH whereupon, the resulting upper layer is extracted three times with ether; after washing with water, the ether is dried over Na₂SO₄.

A solution of 9g (0.063 moles—slight excess) of CH₃I, dissolved in 15 ml of ether, is slowly added (0°–5°C outside temperature—see method A) to the ethereal solution with stirring and then method A is followed through; 13.1g of product are obtained (88% yield).

Analysis $I_{th} = 51.0\%$ $I_{ex} = 50.9\%$

Octamethyldiethylentriammonium iodide (CH₃)₃N-(CH₂)₂-N(CH₃)₂-(CH₂)₂-N(CH₃)₃I₃ was prepared by method A from 10.9g of pentamethyldiethylentriamine and 28.4g of CH₃I: 34.2g of product were obtained (91% yield).

Analysis $I_{th} = 65.1\%$ $I_{ex} = 64.9\%$

The materials used for the conductance tests were prepared by melting the polymethonium iodides with silver iodide. Appropriate quantities of AgI and polymethonium iodide, powdered and intimately mixed, were heated under vacuum to a temperature approaching 250°C. The resulting compound, rapidly cooled to room temperature, was pelletized and annealed for approximately 20 hr at a temperature of 165°C.

The analytical composition of the samples was checked by the following method. A known quantity of the solid electrolyte, suspended in a known volume of a standard silver nitrate solution, was boiled for several hours to obtain the decomposition of the compound and the precipitation of I⁻ ions as AgI. After cooling, the excess of silver nitrate was titrated with a sodium chloride standard solution. The results of the above analysis show that the error on the indicated equivalent per cent of AgI (calculated as: 100 × AgI moles/AgI moles + 2 × polymethonium moles) does not exceed ±0.2%.

In order to try to achieve better conductivity results, a radiation test was carried out with some of the products under examination (HexI₂-AgI 1:12 and OdtI₃-AgI 1:22—see Table IV) and with RbAg₄I₅ and (CH₃)₄NAg₆I₇. A series of samples were exposed at room temperature to a 0.14 megarad/hr source of γ rays (⁶⁰Co) with an Atomic Canada Ltd. γ-cell. The radiation doses used ranged from a minimum of 7 megarad to a maximum of about 70 megarad. In no case were variations in electrical conductivity observed. However the color of the samples became reddish-brown, suggesting that, at least within the superficial layers, a decomposition of the iodides to elementary iodine should have occurred.

Differential thermal analyses (DTA) were operated with a 419-Type Netzsh instrument having the following characteristics: low-temperature apparatus, steel block, iron-constantan thermocouple protected against direct contact with the material under examination by suitably shaped platinum plates, calcined kaolin as reference material, heating rate 5° C/min.

X-ray diffraction experiments were performed with a PW 1050/25 Type Philips diffractometer, using nickel-filtered Cu_{Kα} radiation.

The specific conductivity of the samples was determined by using a cell (8) in which the electrolyte, pelletized under vacuum at 1100 kg/cm² pressure, was placed between two amalgamated silver electrodes. The measurements were carried out with a 4896 Type Tinsley conductivity bridge with oscillographic resetting (545 B Type Tektronix). The pressure of 1100 kg/cm² was selected since it gives the highest specific conductivity values for the examined electrolytes (see, for example, Table II).

Results and Discussion

DTA and x-rays.—DTA was carried out at temperatures ranging between room temperature and 230°C, i.e. up to a temperature just below melting, for different ratios of the HexI₂-AgI system (1:10, 1:11, 1:12, 1:13, 1:14). The results showed that each composition presents an endothermic peak at approx. 150°C, i.e. close to the AgI_β ⇌ AgI_α transformation temperature.

Table II. Specific conductivity of HexAg₁₂I₁₄ pellets as a function of applied pressure at room temperature (average value from 4 or 5 measurements)

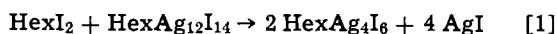
Applied pressure (kg/cm ²)	Specific conductivity χ (ohm \times cm) ⁻¹
400	0.025 \pm 0.001
800	0.027 \pm 0.001
1100	0.029 \pm 0.001
1500	0.027 \pm 0.001
2000	0.026 \pm 0.001

The quantity of heat involved in the transformation, per formula weight of compound, is a minimum for the 1:12 ratio. This seems to indicate that the thermal preparation, described in the experimental section, provides a substantially complete but not quantitative formation of the desired compounds (approx. 95% for the 1:12 ratio). This conclusion is supported by the x-ray diffraction spectra of the same materials.

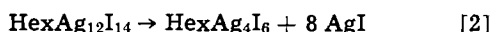
The AgI reflexes are always present, and their intensities as a function of composition follow the pattern of the areas under the DTA peaks, the 1:12 ratio giving the least AgI intensities.

Figure 1 shows the area of the DTA peaks obtained for the various ratios. The broken curve indicates the values corrected for excess of AgI added over the 1:12 ratio, on the basis of the area of the peak measured with pure AgI samples (average 88 mm²/mM AgI).

For ratios 1:12 and lower, it is observed that the corrected area (approx. 50 mm²/mM of the compound) is equivalent to 0.5-0.6 moles of AgI per formula weight, which may correspond to partial decomposition, or to incomplete formation of HexAg₁₂I₁₄. For compositions to the left of 1:12, i.e. an excess of HexI₂, the relative amount of free AgI is even higher, thus justifying the assumption that an excess of HexI₂ may decompose some of the conducting compound. The following may be a possible reaction



On the other hand, in the absence of HexI₂ in excess, the HexAg₁₂I₁₄ decomposition reaction could result



Both of these reactions could be responsible for the presence of free AgI in the range of compositions at the left of 1:12 in Fig. 1, while for other ratios only reaction [2] would apply. There is nothing, however, in the literature, to justify reactions [1] and [2], except the analogy with the RbAg₄I₅ decomposition reactions. As a matter of fact, the conductivity values calculated on these assumptions (taking into account the partial decomposition of HexAg₁₂I₁₄ to HexAg₄I₆ and AgI, which are both considered nonconducting compounds, and the relative dilution effects) give values that are substantially greater than the observed values above and below the 1:12 composition.

Conductivity.—The conductivity values obtained for the various compounds and compositions studied, are reported in Tables III and IV.

Figure 2 shows the specific conductivity as a function of the equivalent per cent of AgI for some of the systems studied. For comparison, the curves obtained by

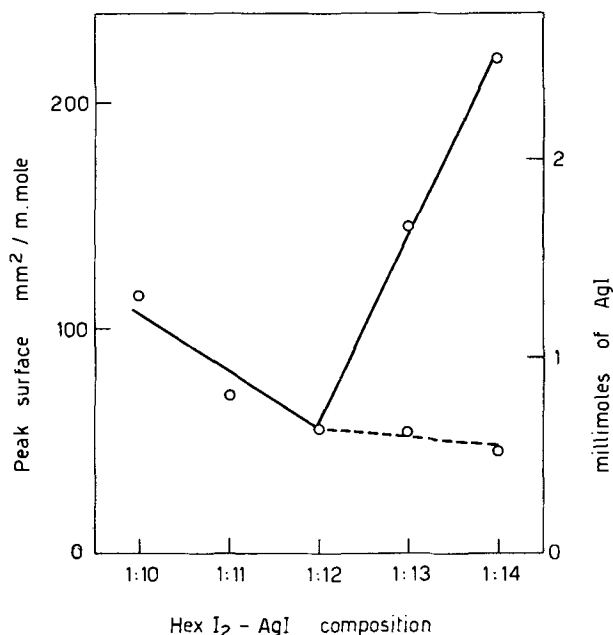


Fig. 1. DTA peak area as a function of molar composition for HexI₂-AgI system.

Owens for tetramethylammonium iodide-silver iodide and diethyldimethylammonium iodide-silver iodide systems are also shown. The maximum conductivity values indicate that, according to DTA and x-ray experiments, the formula of conducting polymethonium compounds is QAg₁₂I₁₄ (Q is the polymethonium cation).

For OdtI₃-AgI system the maximum conductivity value is obtained with a 1:22 ratio.

Table V reports the specific conductivity of HexAg₁₂I₁₄ at different temperatures. From these values, an Arrhenius activation energy of 2730 cal/mole can be calculated: the corresponding value for RbAg₄I₅ is about 2300 cal/mole, and for (CH₃)₄NAg₆I₇ about 4000 cal/mole.

It has been concluded, particularly on the basis of x-ray diffraction evidence, that the reason for the high ionic conductivity of crystals of silver iodide compounds with rubidium or tetraalkylammonium iodides may be ascribed to the high mobility of silver ions through channels made up of iodide ion tetrahedra (14, 15).

While there is the need for additional confirmatory studies, such as transference number measurements, d-c polarization measurements, and Hall effect, it may be assumed at this stage, on account of the similarity between the conductivity values reported in this work and those reported by Owens, and the analogy in the composition of these species that the cause for the high conductivity of our compounds is due to a similar mechanism.

The specific conductivity of AgI (α) at room temperature, obtained by extrapolating data at higher temperatures, is about 7×10^{-1} (ohm \times cm)⁻¹ (16). This value cannot be obtained directly because the

Table III. Specific conductivity of polymethonium iodide-silver iodide compounds in the ratio 1:12

Polymethonium iodide	χ (ohm \times cm) ⁻¹
1) (C ₂ H ₅) ₂ CH ₂ N-CH ₂ -N(CH ₂) ₂ (C ₂ H ₅) ₂ I ₂	(methane-1,1-bis-methyl-diethylammonium iodide) 0.045
2) (CH ₃) ₃ N-(CH ₂) ₂ -N(CH ₃) ₃ I ₂	(ethane-1,2-bis-trimethylammonium iodide) 0.027
3) (CH ₃) ₃ N-(CH ₂) ₃ -N(CH ₃) ₃ I ₂	(propane-1,3-bis-trimethylammonium iodide) 0.013
4) (CH ₃) ₃ N-(CH ₂) ₄ -N(CH ₃) ₃ I ₂	(butane-1,4-bis-trimethylammonium iodide) 0.027
5) (CH ₃) ₃ N-(CH ₂) ₅ -N(CH ₃) ₃ I ₂	(pentane-1,5-bis-trimethylammonium iodide) 0.012
6) (CH ₃) ₃ N-(CH ₂) ₆ -N(CH ₃) ₃ I ₂	(hexane-1,6-bis-trimethylammonium iodide) 0.029
7) (CH ₃) ₃ N-(CH ₂) ₈ -N(CH ₃) ₃ I ₂	(nonane-1,9-bis-trimethylammonium iodide) 0.014
8) (CH ₃) ₃ N-(CH ₂) ₁₀ -N(CH ₃) ₃ I ₂	(decane-1,10-bis-trimethylammonium iodide) 0.011

Table IV. Specific conductivity of pelletized $\text{HexI}_2\text{-AgI}$ and $\text{OdtI}_3\text{-AgI}$ systems as a function of equivalent per cent of AgI

Equiv. %, AgI	$\text{HexI}_2\text{-AgI}$, χ ($\text{ohm} \times \text{cm}$) ⁻¹	Equiv. %, AgI	$\text{OdtI}_3\text{-AgI}$, χ ($\text{ohm} \times \text{cm}$) ⁻¹
84.61	0.004	84.20	0.013
85.51	0.026	85.71	0.030
85.71	0.029	86.87	0.054
85.91	0.013	87.99	0.058
86.67	0.002	88.89	0.046
		90.70	0.024

* Odt = Octamethyldiethylentriammonium cation.

Table V. Temperature dependence of the specific conductivity of pelletized $\text{HexAg}_{12}\text{I}_{14}$

T (°K)	χ ($\text{ohm} \times \text{cm}$) ⁻¹
333.15	0.044
313.15	0.034
298.15	0.029
283.15	0.021
281.15	0.020
273.15	0.018
269.15	0.017
243.15	0.0095
237.15	0.0085
233.15	0.0075

alpha modification, $\text{AgI} (\alpha)$, is unstable below 146°C. The reaction of silver iodide with suitable salts, stabilizes a crystal lattice which possesses the high conductivity channels even at comparatively low temperatures. In a way, it can be thought as a perturbation, induced by the species introduced into the lattice, which, by hindering the close packing of the iodide

ions, characteristic of the nonconducting $\text{AgI} (\beta)$, makes it possible for a more open structure to persist at lower temperatures. Among the salts which stabilize such a structure (see Table I), silver sulfide can be mentioned. In a 1:1 molar ratio with silver iodide, Ag_2S induces a specific conductivity value of approx. 10^{-2} ($\text{ohm} \times \text{cm}$)⁻¹, and rubidium iodide which shows a specific conductivity of approx. 10^{-1} ($\text{ohm} \times \text{cm}$)⁻¹ in a 1:4 molar ratio.

Many quaternary ammonium compounds (Owens and this study) are also capable of modifying the AgI lattice, producing results approaching those obtained with RbI . The greater conductivity of RbAg_4I_5 with respect to the $\text{R}_4\text{NI-AgI}$ compounds is attributed (15) to the higher lattice symmetry of the former, to its higher holes- Ag^+ ratio, and to the lower volume of Rb^+ compared with organic cations.

Similar considerations can be made about the compounds studied in this work. In particular, it is possible to compare conductivities with respect to the size of the organic cations introduced in the lattice.

With reference to Owens' conclusion (11) that it is necessary to use alkylammonic cations of volumes ranging between 30 and 85 Å³ to obtain satisfactory results, it should be observed that in the case of the compounds reported in this study, it appears that it is not the total volume of each individual cationic particle present in the lattice that should be considered, but rather the volume of each stabilization cation, a term referring, in our case, to each individual alkylammonic group present in the organic cation introduced.

A sizable portion of the high conductivity channels are obstructed by the large organic cations. In this respect, perhaps better results would be obtained if a species could block a large number of AgI units in an open-structure lattice, while itself possessing a minimum molecular volume.

It appears that octamethyldiethylentriammonium iodide, whose compound with AgI presents the highest conductivity value among the species examined here, seems to follow this logical order, since in this case each alkylated nitrogen unit stabilizes slightly more than seven units of AgI , although its volume is less than half the volume of the polymethones. (This conclusion is also supported by the tendency of specific conductivity to decrease as the number of carbon atoms per stabilization cation.—See Table III).

In the case of methane-1,1-bis-methyldiethylenammonium iodide, the conductivity is greater than for other polymethones: a similar effect is reported by Owens, who finds the highest values in dimethyl-diethylammonium iodide. Further, a certain tendency for higher conductivity can be observed in polymethones containing an even number of intermediate $-\text{CH}_2-$ groups when compared to those with an odd number: this could be justified by the observation that the odd or even number of carbon atoms in normal saturated hydrocarbons determines conformational changes, which considerably affect their melting temperature and the relative enthalpy changes.

It appears then that the polymethonium cations with an even number of $-\text{CH}_2-$ intermediate groups tend to hinder less than the ones with an odd number the mobility of Ag^+ , as if they might be present in the lattice in a more "streamlined" position, thus obstructing a lower number of conduction channels.

From the above, it can be assumed that, at least for the compounds of the series mentioned here, the maximum specific conductivity limit which can be aimed at would be only slightly lower than the value that silver iodide would reach if it could be present at room temperature in a form with many holes available for each Ag^+ . This value, however, would be reasonably high, and could be considered as sufficient for many practical applications, once its ionic character is def-

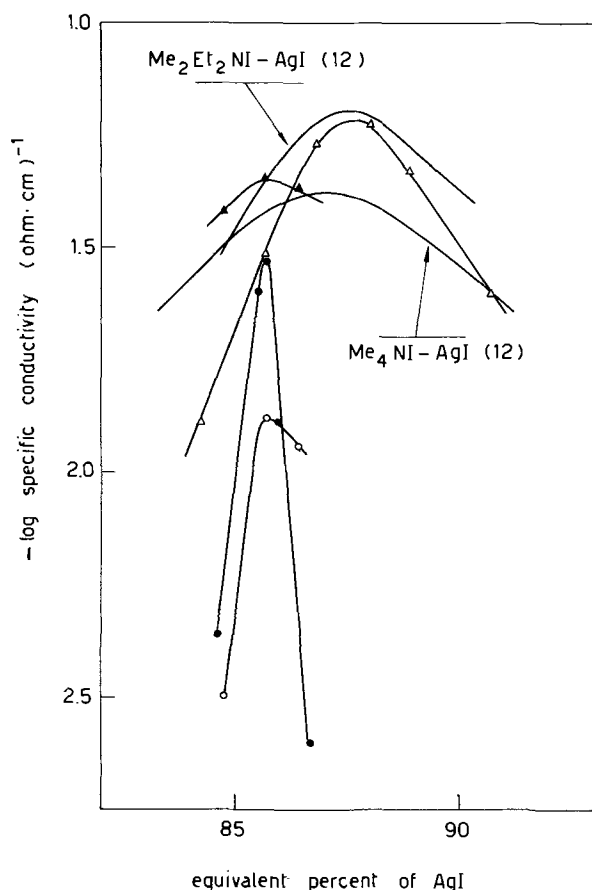


Fig. 2. Composition dependence of the specific conductivity of some binary solid electrolyte systems at room temperature. Δ , $\text{OdtI}_3\text{-AgI}$ (see Table IV); \blacksquare , No. 6 (see Table III); \square , No. 8 (see Table III); \blacktriangle , No. 1 (see Table III).

initely verified. Such studies are in progress and will be reported later. Cells of the type: Ag/HexAg₁₂I₁₄/HexI₂I₂C have been already put together and discharged for many hours with an initial emf of about 0.64V. Efforts in this direction should, therefore, be considered with interest.

Acknowledgment

This work was sponsored by the Consiglio Nazionale delle Ricerche under Contract CNR No. 70.00698/11 115.860.

Manuscript submitted July 20, 1971; revised manuscript received ca. Sept. 22, 1971.

Any discussion of this paper will appear in a Discussion Section to be published in the December 1972 JOURNAL.

REFERENCES

1. D. J. G. Ives and G. J. Janz, "Reference Electrodes," p. 185, Academic Press, New York (1961).

2. A. S. Miller and R. J. Maurer, *J. Phys. Chem. Solids*, **1**, 191 (1956).
3. K. H. Lieser, *Z. Physik. Chem., N.F.*, **B-9**, 302 (1956).
4. J. Mrgudich, *This Journal*, **107**, 475 (1960).
5. T. Takahashi and O. Yamamoto, *Electrochim. Acta*, **11**, 779 (1966).
6. J. N. Bradley and P. D. Greene, *Trans. Faraday Soc.*, **63**, 424 (1967).
7. B. B. Owens and G. R. Argue, *Science*, **157**, 308 (1967).
8. M. De Rossi, G. Pistoia, and B. Scrosati, *This Journal*, **116**, 1642 (1969).
9. T. Takahashi and O. Yamamoto, *This Journal*, **117**, 1 (1970).
10. D. O. Raleigh, *J. Appl. Phys.*, **41**, 1876 (1970).
11. B. B. Owens, U.S. Pat. 3476606 (1969).
12. B. B. Owens, *This Journal*, **117**, 1536 (1970).
13. B. Bobranski, T. Jakóbiec, and D. Prelicz, *Roczniki Chem.*, **30**, 623 (1956); C.A., **51**, 4272i (1957).
14. S. Geller, *Science*, **157**, 310 (1967).
15. S. Geller and M. D. Lind, *J. Chem. Phys.*, **52**, 5854 (1970).
16. A. W. Wells, "Structural Inorganic Chemistry," p. 174, Clarendon Press (1962).

Technical Notes



Washing Calcium Halophosphate Phosphors with Diethylenetriamine Pentaacetic Acid

E. A. Graff*

Westinghouse Electric Corporation, Bloomfield, New Jersey 07003

The calcium halophosphate phosphor having the formula $3\text{Ca}_3(\text{PO}_4)_2 \cdot \text{Ca}(\text{F}, \text{Cl})_2$ activated with antimony and manganese is generally prepared by firing a raw mix of the constituents required to satisfy the formulation. An inherent deficiency of the solid-state reaction is that the firing gives rise to local concentration excesses of constituents which are not entirely incorporated into the phosphor matrix. These unincorporated constituents, especially manganese and antimony, tend to absorb both ultraviolet and visible light thus reducing the phosphors response (1). In addition, if the antimony appears on the surface in a reduced state the phosphor may take on a gray body color which leads to an undesirable increase in absorption of visible light (2). Also the probability of mercury attachment to the phosphor arises if there are a number of free metal atoms present (3). This results in a grayish phosphor that yields poor performance in a fluorescent lamp.

Due to lamp output losses associated with the presence of the previously noted undesirable materials, it has long been the practice in the preparation of calcium halophosphate phosphors to employ inorganic and organic acids as washing aids (4, 5).

Martyny (6) showed that employing a sequestering agent, ethylenediamine tetraacetic acid (EDTA) as a washing agent would remove portions of those deleterious materials not previously removable with the organic and inorganic acids.

Though EDTA is an efficient sequestering agent, an even more efficient agent is diethylenetriamine pentaacetic acid (DTPA).

The DTPA is structurally similar to EDTA but it has the advantage of forming more stable complexes and of being able to complex two metal ions per mole. EDTA can only form 1:1 complexes. The structures of the two sequestering agents and the types of complexes formed are illustrated in Fig. 1.

Table I shows the significantly higher stability of the chelates formed with DTPA as compared with those formed employing EDTA.

Another factor in the greater stability of chelates formed with DTPA is its pH dependence in comparison to that of EDTA (7). The plots shown in Fig. 2 illustrate the difference between DTPA and EDTA where pM is a function of pH. pM is defined as the negative logarithm of the metal ion concentration (M^+). The data shown are typical of that obtained for many of the cations encountered in calcium halophosphate phosphors. From these data it is evident that DTPA is in many instances a better chelating agent than EDTA at both lower and higher pH values.

One last but quite important advantage in the use of DTPA is that it is more soluble than EDTA. At

Table I. Stability of DTPA and EDTA chelates

	Stability constants (Log K)	
	DTPA	EDTA
Manganese	15.11	13.47
Iron (II)	16.66	14.22
Iron (III)	28.6	25.1
Cadmium	18.93	16.48
Zinc	18.14	16.58
Lead	18.87	18.3
Calcium	10.11	10.97
Strontium	9.68	8.63
Magnesium	9.02	8.69

* Electrochemical Society Active Member.

Key words: phosphors, sequestering agents, ball milling, lumen output.

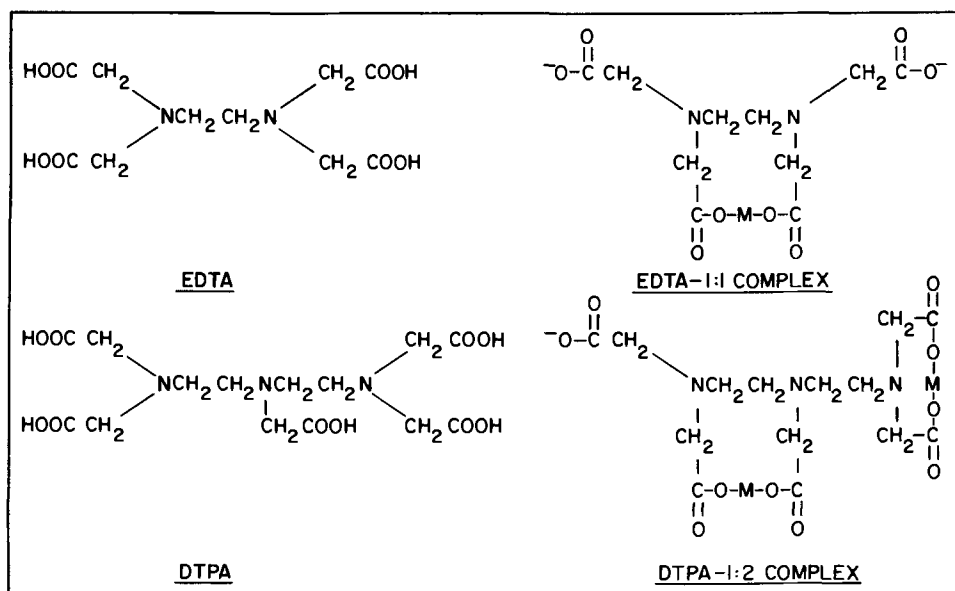


Fig. 1. EDTA and DTPA metal ion complexes.

room temperature the DTPA is 2½ times more soluble than EDTA, and at elevated temperatures the difference in the solubility of the two sequestering agents increases.

In this study I tried to determine if the apparent advantages of DTPA over EDTA could be translated into an improved treating or washing process for calcium halophosphate phosphors.

Initially, tests were run on standard Cool White halophosphate phosphor. This material was ball milled with different quantities of the sequestering agent. After milling, the slurry was washed several times by

decantation and then subjected to the normal lamp processing stages for this phosphor. All lamp results were obtained in 40W fluorescent lamps.

Figure 3 is a plot of lumen gain *vs.* weight per cent sequestering agent. As can be seen from the curves, for the weight per cents employed, the lumen improvement is significantly larger for the phosphors treated with DTPA than for those treated with EDTA. The improved output for the DTPA treated phosphors was only partially related to improved maintenance. Figure 4 is a plot of the 0-100 hr lumen drop *vs.* the weight per cent DTPA used. Data is only plotted for the apparently optimum range of 0.05-0.15 weight per cent (w/o) DTPA. As the quantity of the DTPA employed increased, the lamp maintenance degenerated. However, even at 0.15 w/o DTPA the lamp maintenance was somewhat better than for control lamps prepared with untreated phosphors. Figure 4 does show that maintenance improvements represent between 25 and 50% of the improvement obtained with the use of DTPA. The rest of the improvement is related to improved initial output. The data in Fig. 4 indicate the optimum DTPA content from the standpoint of maintenance to be at 0.05 w/o, however, the results plotted in Fig. 3 indicate that 100 hr output peaks at 0.10 w/o DTPA.

Figure 5 shows the effect of sequestering agents on the output of 40W fluorescent lamps over an extended burning period. The treated phosphors shown in the figure were processed with 0.10 w/o DTPA and EDTA based on the total weight of phosphor. After 2500 hr of burning, the lamps containing the DTPA treated phosphor have dropped 2% less in relation to their 100 hr output than the lamps containing the untreated phosphor. The maintenance of the DTPA treated phosphor is slightly better than that of the EDTA treated phosphor.

Analyses of wash water residues from phosphor slurries treated and not treated with DTPA show some marked differences. The level of impurities detected in the DTPA generated residue is generally greater than the level detected in the residue from the untreated phosphors. For some impurities such as manganese and cadmium the level of impurities differs by a factor of 10.

X-ray fluorescence measurements performed on phosphors treated and not treated with the DTPA show striking differences in the quantities of antimony and manganese present. Treated phosphors record 5-8% lower antimony and manganese levels than their untreated controls.

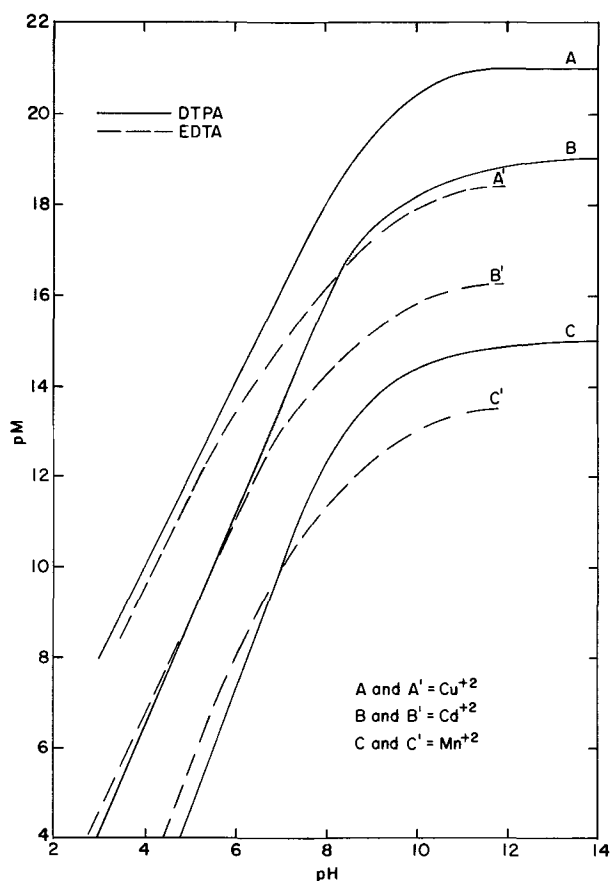
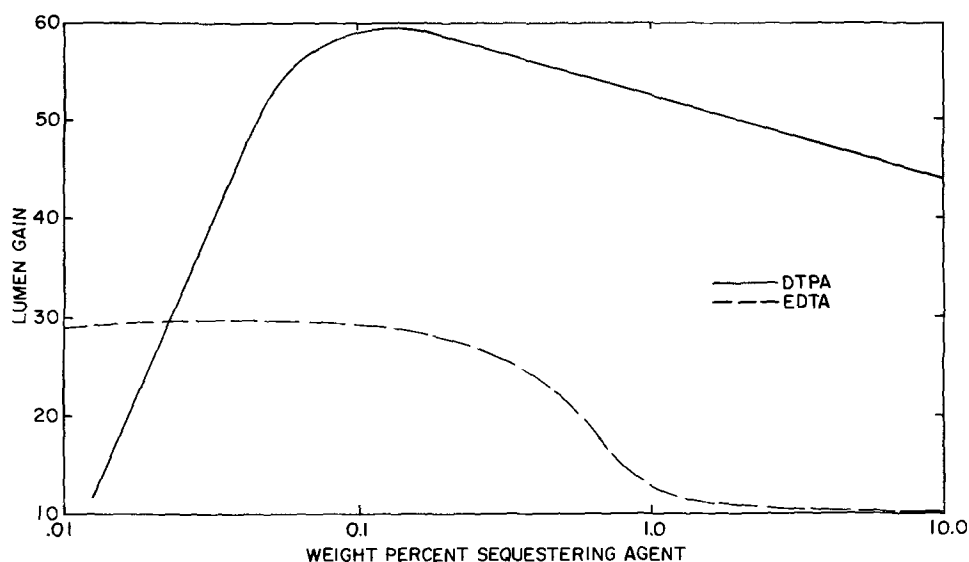


Fig. 2. Effect of pH on chelate formation

Fig. 3. Lumen gain at 100 hr vs. weight per cent sequestering agent.



From the work performed to date, several conclusions can be drawn.

(i) Diethylenetriamine pentaacetic acid is an effective aid in the processing of calcium halophosphate phosphors. Its use reduces the level of certain apparently unreacted phosphor constituents. This reduction in turn is related to both improved initial lamp performance and improved maintenance characteristics for the treated phosphors.

(ii) The intrinsic characteristics of diethylenetriamine pentaacetic acid make it a more suitable and effective sequestering agent than ethylenediamine tetraacetic acid for use in processing calcium halophosphate phosphors.

Acknowledgment

The author wishes to thank Mr. John F. Hall, Mr. John Chwan, and Mr. Matthew Wheelan for sample preparation and Mr. Eugene A. Wesley and Mr. Theodore A. Ellis for analytical measurements.

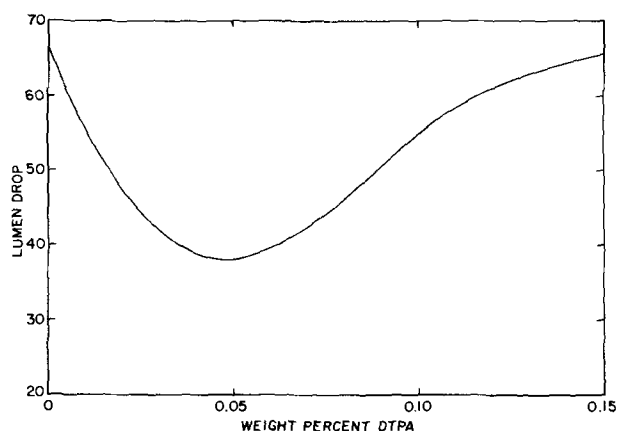


Fig. 4. 0-100 hr lumen drop vs. weight per cent DTPA

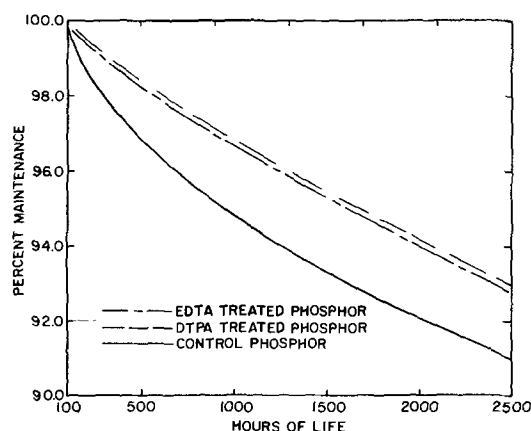


Fig. 5. Maintenance curves for phosphors treated and not treated with DTPA and EDTA.

Manuscript submitted Aug. 9, 1971; revised manuscript received ca. Sept. 10, 1971.

Any discussion of this paper will appear in a Discussion Section to be published in the December 1972 JOURNAL.

REFERENCES

1. J. L. Ouweltjes, "Modern Materials," Vol. 5, p. 207, B. Gonser, Editor, Academic Press, New York (1965).
2. W. L. Wanmaker and M. G. A. Tak, Paper 45 presented at Electrochem. Soc. Meeting, Washington, May 12-16, 1957.
3. H. C. Froelich, *J. Appl. Phys.*, **17**, 573 (1946).
4. K. H. Butler and H. H. Homer, U.S. Pat. 2,691,601 (1954).
5. F. M. Vodoklys, U.S. Pat. 3,023,339 (1962).
6. W. C. Martyny, U.S. Pat. 3,047,512 (1962).
7. E. J. Durham and D. P. Ryskiewich, *J. Am. Chem. Soc.*, **80**, 4812 (1958).

Dielectric Loss, Electrode Deterioration, and the Sodium Problem in MOS Structures

D. J. Silversmith

Bell Telephone Laboratories, Incorporated, Murray Hill, New Jersey 07974

Two reports of the high-temperature and low-frequency dielectric loss in MOS structures have purported to study ionic transport and space charge polarization effects. Using this data, the present note correlates the dielectric relaxation results to elevated temperature measurements of capacitance. The comparison indicates that above 300°C the metal electrode reacts with silicon dioxide to give a displacement current component similar to that associated with the "slow trapping instability." The solid-state electrolytic reactions indicated here make the precise ionic contribution to the displacement uncertain; therefore, voltage ramp measurements of ionic impurities above 350°C are problematic. Further evidence for a high-temperature solid-state electrolytic reaction is obtained from measurements performed alternately in N₂ and O₂ ambients.

Dielectric Loss Experiments

Using 3500Å thick steam oxides grown on 4-7 ohm-cm n-type silicon, Burkhardt (1) measured the frequency dependence of the dielectric loss in the oxide as a function of temperature (400°-525°C). From a plot of the frequency at which the dissipation factor, $\tan \delta$, peaked (at zero d-c bias) vs. the corresponding temperature, an activation energy of 0.438 eV was determined for the relaxation process. Burkhardt related the peak in $\tan \delta$ to an ionic space charge polarization; his inference is that a solid-state reaction between the aluminum electrode and the SiO₂ produces positively charged oxygen vacancies which can diffuse within the oxide under the influence of an electric field. Burkhardt eliminated the possibility that sodium ions were the source of space charge polarization by observing no change in the experimental results for intentionally contaminated devices. Measurements were also made on MOS devices with chrome field plates instead of aluminum, but these devices showed no structure in the dissipation factor at all.

Kriegler and Bartnikas (2) have reported on measurements of dielectric loss and capacitance as a function of temperature (300° to 425°C) and frequency (1.5 to 1000 Hz) in MOS structures. Gold-protected chrome was used for the field plate, and gold, for a back contact. Figure 1 gives the real and imaginary parts of the dielectric constant of a typical device at 400°C and is taken from the measured parallel capacitance and conductance data of Kriegler and Bartnikas. From the peak of the dissipation factor, $\tan \delta = \epsilon''/\epsilon'$, vs. measurement temperature, Kriegler and Bartnikas find activation energies ranging from 1.21 to 1.43 eV, depending on the extent of annealing. The relaxation phenomenon is ascribed to sodium contamination. Because the activation energy is close to the value of 1.39 eV found by Snow *et al.* (3) for sodium transport, Kriegler and Bartnikas inferred an indirect confirmation of an ionic model for dielectric loss.

Discussion of Dielectric Loss Data

Burkhardt's temperature range is significantly higher than that of Kriegler and Bartnikas, and different field plate metals were used. All Burkhardt's measurements were preceded by a 1-hr anneal at 490°C. Kriegler and Bartnikas have observed that the peak in the dis-

sipation factor and the structure of the real part of the dielectric constant decrease with time at elevated temperature. In fact, at 490°C a device with gold-protected chrome electrodes has all structure completely annealed out after 1 hr. Therefore, it is not surprising that Burkhardt found no discernable structure for chrome-metallized devices.

The case for Kriegler and Bartnikas' (2) determination of sodium as the source of structure in the frequency dependence of the dielectric constant is, however, tenuous. The apparent "annealing out" of sodium with time necessitates the inclusion of a deep trapping mechanism with a very high activation energy in the model. The work of Kuhn and Silversmith (4) suggests that at temperatures above 300°C the re-emission time for sodium traps is extremely small; no annealing out of ionic transport was observed. Experiments by Kuhn and Silversmith (4) on field-induced transport of alkali ions in MOS structures indicate that the analysis of diffusion of sodium ions in SiO₂ by Snow *et al.* (3) is, in fact, related to trap emission mechanisms at the metal-silica interface rather than to bulk diffusion.

Simultaneously and in substantial agreement with Kuhn and Silversmith (4), Chou (5) has made a study of the MOS current dependence as a function of temperature in terms of an electrochemical cell. He found it necessary to make mobile ion transport measurements in the range of 200° to 250°C to assure equilibrium conditions needed for consistent quasi-static or triangular voltage sweep measurements. Chou could not find any significant ionic current below 145°C; above 310°C there was evidence of a current contribution due to an electrolytic reaction at the electrode-

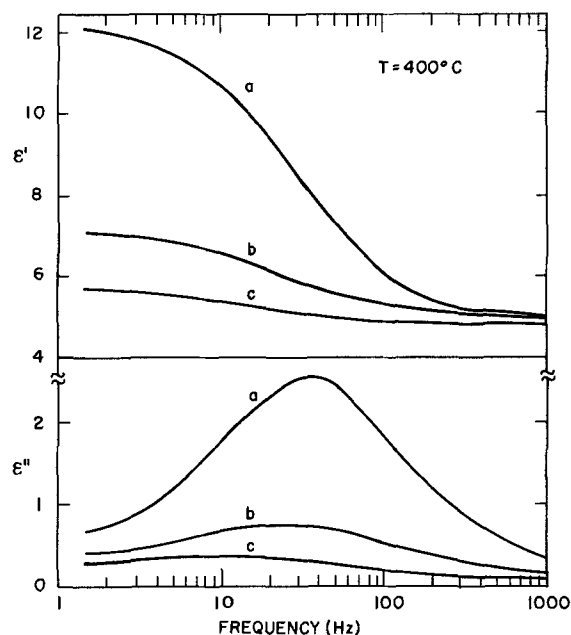


Fig. 1. Dielectric relaxation of a thermally grown SiO₂ film at 400°C from the work of Kriegler and Bartnikas (2). Time dependence of the relaxation spectrum: (a) initial measurement, (b) after 12 hr, and (c) after 6 days.

Key words: metal gate electrodes, ionic impurities, electrical instability in MOS devices, solid-state electrolytic reactions.

oxide interface. In addition, Chou and Eldridge (6) have observed that protracted, postmetallization annealing treatments (*viz.* 30 min at 500°C) can promote extensive low-field breakdown in MOS devices. Hofstein (7) and Yamin (8) have noted solid-state reactions between metal electrodes and silica at elevated temperatures of about 400°C. These reactions modify the apparent nature of the ionic drift instability. Kuhn and Silversmith (4) observed a temperature limit around 370°C, above which gross instabilities were evident. These instabilities appeared to be related to the deterioration of the aluminum or chrome field plate. These observations suggest that reactive metal electrodes can interact with silica to cause devitrification and growth of structural defects under the edge of the metal electrode.

Slow Trapping Instability

Negative bias aging of MOS devices at temperatures in excess of 200°C has been observed to shift the flat-band voltage negatively, as if positive charge drifted to the metal-oxide interface (9-11). This effect, which saturates in several hours at 300°C and within minutes at 400°C, has not been considered to be attributable to ionic transport. Deal *et al.* (10) suggested that silicon is injected from the bulk into the silica film under the influence of the negative electric field and that the excess silicon in silica is positively charged. Hofstein (11) has proposed that the effect is related to the trapping of holes by a level of donor-like states in the oxide close to the Si-SiO₂ interface with an energy level close to the Si valence band.

Although such discussions of the slow trapping instability have generally excluded electrode-insulator reactions, this note indicates that electrochemical effects are a likely source for this instability.

Electrolytic Dependence on Gaseous Ambient

In a recent piece of work, Chou (12) has observed displacement currents for triangular voltage sweep measurements on MOS devices at 390°C that were higher in a 10⁻³ Torr oxygen ambient than in 760 Torr oxygen. The present author has performed high-temperature quasistatic measurements alternatively in one atmosphere nitrogen and oxygen ambients. The oxides were prepared by the dry thermal process and were 2000Å thick. For oxides containing less than 10¹² mobile ions/cm² no significant differences in apparent ion current were observed below 300°C for measurements performed in nitrogen and oxygen. For either higher temperatures or much higher ion surface densities, a higher displacement current was seen for measurements in a nitrogen ambient than in an oxygen ambient.

A typical quasistatic I-V curve is given in Fig. 2 where nitrogen is denoted in solid line and oxygen in dashes. The measurements were made at 319°C on an oxide 2000Å thick. The peaks corresponding to the nitrogen ambient can be taken as a measure of alkali ion contamination if electrode reactions are disregarded. The peak corresponding to the decreasing voltage sweep is more sharply defined because there is, apparently, no trapping-release mechanism associated with the Si-SiO₂ interface; Kuhn and Silversmith (4) have noted, however, an ionic trapping mechanism at the metal-oxide interface. For the device analyzed in Fig. 2, the surface density of alkali (sodium) ions is $4.2 \times 10^{12}/\text{cm}^2$. The same measurement in an oxygen ambient indicates a slightly smaller displacement cur-

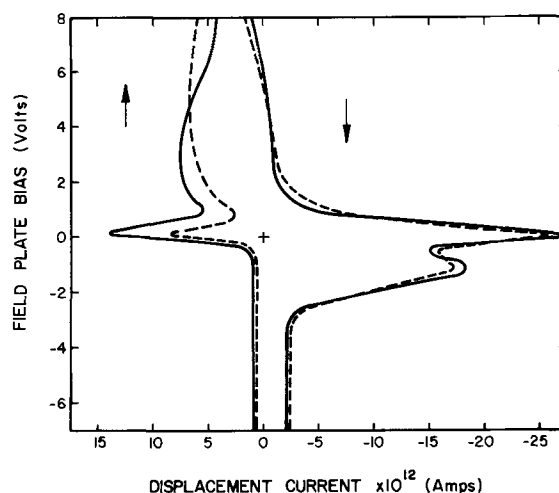


Fig. 2. Displacement current response of an MOS capacitor at 319°C. The substrate consisted of a P-type 10 ohm-cm (100) wafer. The oxide was 2000Å thick and was grown in a dry oxidation furnace at 1150°C. Fifteen-mil dots of 200Å Cr and 2000Å Au were deposited for field plates. The sweep rate of the d-c ramp was 44.8 mV/sec. The solid line measurement was made in a 760 Torr nitrogen ambient, and the dashed line measurement was made in 760 Torr oxygen.

rent. At temperatures somewhat higher than 319°C the differences between currents measured in nitrogen and oxygen can be as much as 20%. The problem with very high temperature measurements of the quasistatic I-V curve is that the repeatability is not good. Obviously the devices degrade with voltage cycling at high temperatures. The partial pressure dependences of ion current in MOS devices at temperatures above 300°C is explicable in terms of an electrochemical polarization process at the edge of the electrode-insulator interface, into which the ambient gas can diffuse. This dependence is *prima facie* evidence for the occurrence of a reaction at the electrode-insulator interface.

Manuscript submitted May 14, 1971; revised manuscript received Sept. 7, 1971.

Any discussion of this paper will appear in a Discussion Section to be published in the December 1972 JOURNAL.

REFERENCES

1. P. J. Burkhardt, *IEEE Trans. Electron Devices*, **ED-13**, 268 (1966).
2. R. J. Kriegler and R. Bartnikas, *ibid.*, **ED-17**, 1010 (1970).
3. E. H. Snow, A. S. Grove, B. E. Deal, and C. T. Sah, *J. Appl. Phys.*, **36**, 1664 (1965).
4. M. Kuhn and D. J. Silversmith, *This Journal*, **118**, 966 (1971).
5. N. J. Chou, *ibid.*, **118**, 601 (1971).
6. N. J. Chou and J. M. Eldridge, *ibid.*, **117**, 1287 (1970).
7. S. R. Hofstein, *IEEE Trans. Electron Devices*, **ED-13**, 222 (1966).
8. M. Yamin, *ibid.*, **ED-12**, 88 (1965).
9. A. Goetzberger and H. E. Nigh, *Proc. IEEE*, **54**, 1454 (1966).
10. B. Deal, M. Sklar, A. S. Grove, and E. H. Snow, *This Journal*, **114**, 266 (1967).
11. S. R. Hofstein, *Solid-State Electron.*, **10**, 657 (1967).
12. N. J. Chou, Abs. 171, p. 424, *Electrochem. Soc. Extended Abstracts*, Fall Meeting, Atlantic City, Oct. 4-8, 1970.

Activity Coefficients for a Regular Multicomponent Solution

A. S. Jordan

Bell Telephone Laboratories, Incorporated, Murray Hill, New Jersey 07974

The concept of a regular liquid or solid solution was first introduced by Hildebrand (1) and subsequently placed on a firm theoretical foundation by Guggenheim (2). Many applications of regular solution theory have been made in the field of semiconductor phase equilibria. In particular, in early work, Thurmond (3) and Thurmond and Kowalchik (4) analyzed the liquidus data for a large number of Si- and Ge-based binary systems by means of regular solution activity coefficients (2). More recently, the activity coefficients derived for regular binary (2) and ternary (5) solutions have been successfully applied to calculations of the binary liquidus curves and ternary liquidus isotherms in the Ga-As, Ga-P (6), Ga-As-Cu (7), Ga-As-Zn (8,9), Ga-P-Zn (9,10), and Ga-Al-As (11) systems.

Several semiconductor systems of current interest, such as the quaternary Ga-P-Zn-O and Ga-As-P-Zn systems, contain more than three components. Very recently, a schematic discussion of the main features of the Al-Ga-In-P, Ga-Sb-In-As, and Al-Ga-As-Sn quaternary systems have been presented by Panish and Ilegems (12). The eventual thermodynamic analysis of such complex systems would benefit from a knowledge of the activity coefficients for regular quaternary solutions. However, to the best of this author's knowledge, explicit formulas for the activity coefficients of regular solutions that contain more than three components are not available. It is the objective of this note to derive the activity coefficients for regular multicomponent solutions in a convenient form from the Gibbs free energy of mixing and to provide detailed expressions for the activity coefficients of quaternary mixtures.

The Gibbs free energy of mixing, G^M , of a regular binary solution containing n moles is given according to the statistical treatments of Guggenheim (2) and Prigogine (13) by

$$G^M = \frac{\alpha_{12}n_1n_2}{n} + R(n_1 \ln x_1 + n_2 \ln x_2) \quad [1]$$

where n_i and x_i , respectively, are the number of moles and mole fraction of component i ($i = 1$ or 2) and α_{12} is the so-called interchange energy related to the nearest neighbor pairwise interaction energies, u_{ij} , Avogadro's number, N_0 , and coordination number, Z , by $\alpha_{12} = N_0Z[u_{12} - (u_{11} + u_{22})/2]$. Phenomenologically, Eq. [1] states that the entropy of mixing of a regular solution is that of an ideal solution (second term) and that the heat of mixing is parabolic in n_1 and n_2 (first term).

It can be shown in a straightforward manner either by the generalization of the phenomenological definition or by an extension of the statistical work (2, 13) on binary solutions that for multicomponent systems Eq. [1] takes the form

$$G^M = \frac{1}{2} \sum_{k=1}^m \sum_{j=1}^m \frac{\alpha_{kj}n_kn_j}{n} + RT \sum_{k=1}^m n_k \ln x_k \quad [2]$$

where the summation extends to all of the m components and α_{kj} is the appropriate generalization of the interchange energy.

By an application of the well-known thermodynamic relationship

Key words: thermodynamics, phase diagrams, solution theory, compound semiconductors, liquidus surface calculations.

$$\frac{\partial G^M}{\partial n_i} = RT \ln a_i = RT \ln \gamma_i x_i \quad [3]$$

to Eq. [2],¹ where a_i and γ_i denote the activity and activity coefficient of component i , respectively, one finds

$$RT \ln a_i = RT \ln x_i + \frac{1}{2} \sum_{k=1}^m \sum_{j=1}^m \alpha_{kj} \frac{\partial}{\partial n_i} \left(\frac{n_k n_j}{n} \right) \quad [4]$$

Performing the indicated partial differentiation, the double sum in Eq. [4] separates into three sums. Then, after rearrangement, one can express $\ln \gamma_i$ as

$$RT \ln \gamma_i = \frac{1}{2} \sum_{j=1}^m \alpha_{ij} x_j + \frac{1}{2} \sum_{k=1}^m \alpha_{ki} x_k - \frac{1}{2} \sum_{k=1}^m \sum_{j=1}^m \alpha_{kj} x_k x_j \quad [5]$$

Since the indices k and j have identical limits and also $\alpha_{ki} = \alpha_{ik}$, the second single sum in Eq. [5] can be combined with the first one, so that $\ln \gamma_i$ reduces to

$$RT \ln \gamma_i = \sum_{j=1}^m \alpha_{ij} x_j - \frac{1}{2} \sum_{k=1}^m \sum_{j=1}^m \alpha_{kj} x_k x_j \quad [6]$$

By separating the quadratic terms present in Eq. [6] a more convenient expression for $\ln \gamma_i$ can be derived. Let us exclude the terms from the double sum in Eq. [6] for which $k = i$ and $j = i$ and absorb the resulting single sum

$$-\frac{1}{2} \sum_{j=1}^m \alpha_{ij} x_i x_j - \frac{1}{2} \sum_{k=1}^m \alpha_{ki} x_k x_i = - \sum_{j=1}^m \alpha_{ij} x_i x_j$$

in the single sum in Eq. [6]. Then, the single sum contains the term $1 - x_i$ which can be replaced by

$$1 - x_i = \sum_{k=1}^m \sum_{j=1}^m \alpha_{kj} x_k x_j$$

to yield for $\ln \gamma_i$

$$RT \ln \gamma_i = \sum_{j=1}^m \alpha_{ij} x_j^2 + \sum_{k=1}^m \sum_{j=1}^m \alpha_{kj} x_k x_j - \frac{1}{2} \sum_{k=1}^m \sum_{j=1}^m \alpha_{kj} x_k x_j \quad [7]$$

Contracting the double sums in Eq. [7] and restricting the values of k and j to $k < j$ gives the desired expression for the activity coefficient of component i in a regular multicomponent solution in the form

$$RT \ln \gamma_i = \sum_{j=1}^m \alpha_{ij} x_j^2 + \sum_{k=1}^m \sum_{j=1}^m x_k x_j (\alpha_{ij} + \alpha_{ik} - \alpha_{kj}) \quad [8]$$

¹ Note that to perform the partial differentiation with respect to n_i , one must rewrite x_k in Eq. [2] in terms of the number of moles as $n_k / \sum_{k=1}^m n_k$.

One can readily show that the set of Eq. [8] for $i = 1, 2, \dots, m$ satisfies the multicomponent Gibbs-Duhem equation.

It follows from Eq. [8] for $\ln \gamma_i$ that for an m -component system there are $(m - 1)$ quadratic terms and $[(m - 1)(m - 2)]/2$ cross-terms in the mole fractions x_j . In particular, taking $m = 2$ and $m = 3$, respectively, one has 1 and 2 quadratic terms and 0 and 1 cross-terms, in agreement with the well-known expressions for the activity coefficients of regular binary (2) and ternary solutions (5).

As an example, applying Eq. [8] to a quaternary regular solution (3 quadratic and 3 cross-terms) yields

$$\begin{aligned}
 RT \ln \gamma_1 &= \alpha_{12}x_2^2 + \alpha_{13}x_3^2 + \alpha_{14}x_4^2 + x_2x_3(\alpha_{12} + \alpha_{13} - \alpha_{23}) \\
 &\quad + x_2x_4(\alpha_{12} + \alpha_{14} - \alpha_{24}) + x_3x_4(\alpha_{13} + \alpha_{14} - \alpha_{34}) \\
 RT \ln \gamma_2 &= \alpha_{12}x_1^2 + \alpha_{23}x_3^2 + \alpha_{24}x_4^2 + x_1x_3(\alpha_{12} + \alpha_{23} - \alpha_{13}) \\
 &\quad + x_3x_4(\alpha_{23} + \alpha_{24} - \alpha_{34}) + x_1x_4(\alpha_{12} + \alpha_{24} - \alpha_{14}) \\
 RT \ln \gamma_3 &= \alpha_{13}x_1^2 + \alpha_{23}x_2^2 + \alpha_{34}x_4^2 + x_1x_2(\alpha_{13} + \alpha_{23} - \alpha_{12}) \\
 &\quad + x_2x_4(\alpha_{23} + \alpha_{34} - \alpha_{24}) + x_1x_4(\alpha_{13} + \alpha_{34} - \alpha_{14}) \\
 RT \ln \gamma_4 &= \alpha_{14}x_1^2 + \alpha_{24}x_2^2 + \alpha_{34}x_3^2 + x_1x_2(\alpha_{14} + \alpha_{24} - \alpha_{12}) \\
 &\quad + x_1x_3(\alpha_{14} + \alpha_{34} - \alpha_{13}) + x_2x_3(\alpha_{24} + \alpha_{34} - \alpha_{23})
 \end{aligned}$$

[9]

Obviously, if x_4 or x_3 and x_4 are equal to zero, the activity coefficients for ternary (5) or binary (2) regular solutions result from Eq. [9].

Manuscript submitted May 21, 1971; revised manuscript received ca. Oct. 6, 1971.

Any discussion of this paper will appear in a Discussion Section to be published in the December 1972 JOURNAL.

REFERENCES

1. J. H. Hildebrand and R. L. Scott, "The Solubility of Nonelectrolytes," 3rd Ed., Reinhold Publishing Corp., New York (1950).
2. E. A. Guggenheim, "Mixtures," Oxford University Press, London (1952).
3. C. D. Thurmond, *J. Phys. Chem.*, **57**, 827 (1953).
4. C. D. Thurmond and M. Kowalchik, *Bell System Tech. J.*, **39**, 169 (1960).
5. I. Prigogine and R. Defay, "Chemical Thermodynamics," Longmans Green and Co., London (1954).
6. C. D. Thurmond, *J. Phys. Chem. Solids*, **26**, 785 (1965).
7. Y. Furukawa and C. D. Thurmond, *J. Phys. Chem. Solids*, **26**, 1535 (1965).
8. M. B. Panish, *J. Phys. Chem. Solids*, **27**, 291 (1966).
9. A. S. Jordan, *Met. Trans.*, **2**, 1965 (1971).
10. M. B. Panish, *This Journal*, **113**, 224 (1966).
11. M. Ilegems and G. L. Pearson, "Proceedings of the Second International Symposium on GaAs, Dallas (1968)," Institute of Physics and the Physical Society, London (1969).
12. M. B. Panish and M. Ilegems, "Proceedings of the Third International Symposium on GaAs, Aachen (1970)," Institute of Physics, London and Bristol (1971).
13. I. Prigogine, "Molecular Theory of Solutions," North-Holland Publishing Co., Amsterdam (1957).



Lanthanum Trifluoride as a Membrane in a Reference Electrode for Use in Certain Molten Fluorides

H. R. Bronstein and D. L. Manning

*Chemistry Division and Analytical Chemistry Division,
 Oak Ridge National Laboratory, Oak Ridge, Tennessee 37830*

ABSTRACT

A reference electrode system which utilizes the unique properties of a single crystal lanthanum trifluoride membrane, namely, negligible solubility and virtually 100% current transport by fluoride ions, was successfully used both for electroanalytical measurements and for obtaining thermodynamic data in certain fluoride melts of interest to the Molten Salt Breeder Reactor.

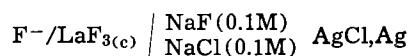
A knowledge of the chemical and thermodynamic properties of molten fluoride salt mixtures used or contemplated for use as fuel solvents or coolants in the Molten Salt Breeder Reactor (1) is necessary not only from the standpoint of operational suitability but also for the fuel reprocessing technology.

The measurement of equilibrium potentials of galvanic cells is in principle one of the most attractive and direct means of obtaining much of this information. As in all galvanic cells the half-cell of interest is coupled with a suitable reference electrode. However, difficulties are encountered in selecting a reference electrode for use in these fluoride melts. Of the few known reference electrodes each has certain inherent disadvantages. Our particular effort was to develop a simple, convenient, and stable reference electrode system useful for thermodynamic as well as electroanalytical measurements in fluoride melts of interest in connection with the Molten Salt Breeder Reactor.

The Ni/Ni(II) couple in fluoride salts shows Nernstian behavior (2). A nickel-nickel fluoride reference electrode contained in a thin-walled (1/32 in.) boron nitride (BN) thimble was previously developed for potential measurements in molten LiF-NaF-KF [42-11.5-46.5 mole per cent (m/o)] and LiF-BeF₂-ZrF₄ (65.6-29.0-5.4 m/o) at a working temperature of about 500°-550°C (2, 3). Boron nitride, normally an insulator in fluoride melts, is slowly impregnated by the melt to provide ionic contact. This wetting occurs in about 24 hr in molten LiF-NaF-KF while a longer period, 10-14 days, is usually required in LiF-BeF₂-ZrF₄ at 500°-550°C. At higher temperatures, however, the BN barrier appears to deteriorate permitting mixing of the melts.

Our modification of this electrode system was suggested by the successful use of single crystal membranes of CaF₂ at elevated temperatures in solid-state electrochemical cells such as Ni, NiF₂/CaF₂/MgF₂, Mg to obtain Gibbs energy data from measured emf values (4-6) and the fluoride ion electrode in aqueous media using a LaF₃ membrane (7)

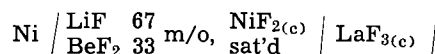
Key words: lanthanum trifluoride, membrane, emf measurements, reference electrode, electroanalytical, molten salts.



The successful operation of each system is basically due to the relatively "open" crystal structures of CaF₂ and LaF₃ which favor a mechanism of conduction virtually 100% by the mobile F⁻ ion (8, 9).

Experimental

Figure 1 illustrates the



reference electrode system. A CaF₂ crystal could not be used since its solubility is much too great in the fluoride melts of interest. Although no solubility data are available for LaF₃ in the fluoride melts used or contemplated for use in the Molten Salt Reactor Program, it was expected by analogy to CeF₃ (10) to be approximately 1 m/o at temperatures of interest 500°-600°C. The single crystals of LaF₃ 3/8 in. diam by 1 in. lengths were obtained from Optovac, Incorporated. The cup portion, 1/8 in. diam by 1/2 in. depth, was formed by drilling with a hollow diamond drill to the proper depth and then carefully breaking the center core loose from the main body. The cup contained the same fluoride salt mixture as the test melt except for the small quantity of NiF₂ necessary to saturate the melt, 10⁻³ mole fraction. Contact to the melt in the cup is achieved with the small nickel electrode. The LaF₃ crystal is contained inside the nickel sheath (some were of copper) but separated from the sheath by a form machined from solid boron nitride. The whole assembly is held firmly in place by the nickel nut. The purpose of the fine porosity nickel frit is to protect the crystal, as much as possible, from undue etching by the molten fluoride. Once the melt inside the frit and at the frit-crystal interface becomes saturated with LaF₃, further attack on the crystal is minimized due to the slow rate of diffusion of the melt in the pores of the frit.

Generally, electrical contact through the reference electrode was achieved within 5 min after dipping into the melt. A depth of 1/4 in. to 1/2 in. was usually main-

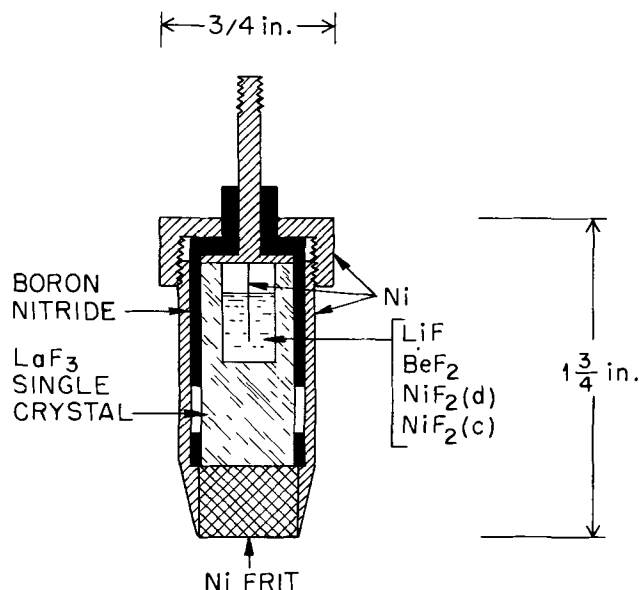


Fig. 1. Construction of the lanthanum trifluoride membrane reference electrode.

tained. Typical resistance of an electrode is of the order of 500 K ohms over the range 500°-600°C as indicated by a Keithley electrometer. The LaF_3 crystal showed insignificant attack from the molten fluorides when wetted through a fine porosity frit, approximately 10μ pore size. One crystal remained in excellent condition after contacting the melt approximately 50 days at 500°C. If care is exercised to heat and cool the crystals slowly to avoid cracking, they can be cleaned with water and reused. A model of an electrode system where a Ni-NiF₂ solid pellet (4) is press-fitted against one face of the solid LaF_3 crystal, the other face of the crystal against the nickel frit, was abandoned because of difficulties in maintaining good contact between the Ni-NiF₂ pellet and the LaF_3 crystal surface.

The experimental arrangement for voltammetric studies in molten fluorides has been described previously (11). The solvent used was LiF-BeF₂ (67-33 m/o). Uranium was added as LiF-UF₄ (73-27 m/o). Handling of the fluoride salts was carried out in a dry box. The controlled potential-controlled current cyclic voltammeter is described elsewhere (12). The voltammograms were displayed on a Moseley Model 2D-2A X-Y recorder or a Tektronix Type 549 storage oscilloscope. A dip-type platinum indicator electrode (area $\sim 0.1 \text{ cm}^2$) was used. The rate of voltage scan was 0.1 V/sec unless otherwise specified.

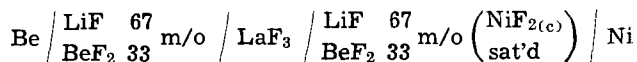
The LiF-BeF₂ (67-33 m/o) was prepared from optical grade single crystal LiF and doubly distilled BeF₂. For the galvanic cell measurements the melt was contained in a nickel cup, 2 1/2 in. diam by 3 in. high. The nickel cup was positioned within a stainless steel cylinder which in turn was set into a 3 in. diam \times 16 in. high Marshall furnace. The header closing the cylinder had provisions for raising and lowering the electrodes and the nickel thermocouple tube through Teflon vacuum-pressure seals. In addition, entry tubes in the header permitted evacuation and pressurization of the apparatus. The salt mixture was pretreated by slowly heating under vacuum. At the melting temperature the apparatus was pressurized with mass-spectrographically pure argon with an overpressure maintained at 3 psi greater than atmospheric as controlled by a nullmatic type of valve. The temperature of the melt was measured with a Chromel-Alumel thermocouple inserted into the nickel tube. Constant temperature $600^\circ \pm 2^\circ\text{C}$, was maintained by conven-

tional control devices. At temperature the electrodes were lowered into the melt to the required depths. The voltage of the cell was measured using a Potentiometric-Voltmeter bridge in conjunction with a Hewlett Packard Model 426 d-c micro voltammeter and recorder.

Results and Discussion

The LaF_3 membrane reference electrode was used to follow voltammetrically the half-wave potential of the U(IV)-U(III) reduction wave (11) in molten LiF-BeF₂-ZrF₄ (67-33 m/o) at 500°C. The melt contained approximately 0.2 m/o UF₄. The concentration of U(III) was varied by controlled reduction of U(IV) with zirconium metal (13). Of interest here was to observe if an increase in the concentration of U(III) (melt more reducing) would adversely affect the performance of the reference electrode which would be reflected in erratic half-wave potentials. The U(IV)/U(III) ratio was varied from $\sim 10:1$ to $> 10,000:1$. The $E_{1/2}$ of the U(IV) \rightarrow U(III) reduction wave vs. the reference electrode remained constant at $-1.352 \pm 0.024\text{V}$ over a period of 20 days and 62 determinations. The half-wave potential is the voltammetric equivalent of the standard electrode potential (E°), i.e. the potential at which the U(IV)/U(III) ratio is unity at the electrode surface. This potential occurs at 85% of the peak current (14). Since NiF_{2(c)} in the reference electrode is at unit activity, the measured potential is the standard potential of the cell (Ni, NiF_{2(c)})/U⁺³U⁺⁴). The value of E° was calculated to be -1.343V from the equation $\Delta G^\circ = -nFE^\circ$ and the free energy of formation of NiF₂ (15), and of UF₄, and UF₃ (15) in the solvent LiF-BeF₂ (67-33 m/o). The calculated E° is in good agreement with the voltammetric value.

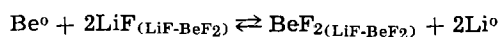
Since the activity coefficients are known for BeF₂ in LiF-BeF₂ melts (16) the galvanic cell



provides a means of ascertaining any deviation from ideal thermodynamic behavior of the reference electrode system.

With the fluoride activities in the melts on both sides of the LaF_3 crystal being essentially the same, and with the LaF_3 membrane conducting 100% by means of its mobile F⁻ ion, junction potentials should be virtually eliminated.

The measured voltage of this galvanic cell at 600°C should correspond to the voltage calculated by combining the data of the cell Be/LiF-BeF₂ (67-33 m/o)/Pt, H_{2(g)}, HF_(g) (16) and of the reaction NiF_{2(c)} + H_{2(g)} = 2HF_(g) + Ni (17) if asymmetry and junction potentials are negligible or nonexistent. The initial steady-state voltage was $2.045 \pm 0.003\text{V}$ in very good agreement with $2.041 \pm 0.003\text{V}$ obtained from combining data from Ref. (16, 17). Apparently asymmetry potentials at the LaF_3 crystal interfaces and liquid-solid junction potentials are negligible. However, after a period of initial stability, the potential began a slow decline. At the termination of the experiment it was found that the NiF₂ content of the reference cell had been converted to an equivalent amount of finely dispersed nickel metal. An impurity in the static atmosphere of purified argon or helium gas maintained in the quite limited volume of the apparatus could not be responsible for the consumption of NiF₂. Loss of NiF₂ due to beryllium metal transport in the vapor phase was ruled out since beryllium has no measurable vapor pressure at 600°C. Since this phenomenon did not occur in the U⁴⁺/U³⁺ experiment, some small intrinsic electronic conduction in the LaF_3 crystal was also ruled out. However, the possibility of the equilibrium reaction

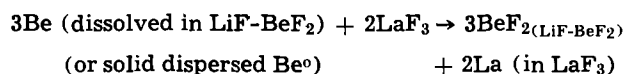


providing the source of reducing power via the gas phase must be considered. Pure Li at 600°C has a vapor pressure of approximately 10^{-4} atm. Since the activity of Li at equilibrium is approximately 10^{-10} from thermodynamic calculations (15, 18) and if the lithium is presumed to be soluble in the melt to that extent (19), it is safe to assume that its vapor pressure would be negligible. This assumption was proven valid by later experiments.

This almost negligible concentration of lithium would, however, provide the conditions under which certain ionic solids will start to conduct via electrons (20).



The lanthanum metal dissolving, or in other words, electrons substituting for fluoride ions, in the LaF_3 crystal would impart n-type conduction to the crystal (20). Alternatively, the same mechanism would occur if beryllium metal in some manner either by solution, perhaps as a subvalent ion Be^+ or Be_2^{2+} (21) or by the "chunking effect" (22, 23) reached the LaF_3 crystal.



From the equation $t_e = \frac{n^o \times \mu \times e}{\sigma \text{ ion}} a_{\text{La}}^{1/3}$, derived by

Wagner (20), one may readily calculate a value for the electronic transference number. Using the values $n^o = 10^{18}$, the number of electrons substituted for fluoride ions per cm^3 with the assumption that this value for Ca in CaF_2 at 600°C is a fair approximation of La in LaF_3 , $\mu = 10^{-4}$ $\text{cm}^2/\text{V}\cdot\text{sec}$, the mobility of the electron in the crystal (20), $e = 1.6 \times 10^{19}$ coulombs, the charge on the electron, $\sigma = 10^{-5}$ $\text{ohm}^{-1} \text{cm}^{-1}$ (9), the ionic conductivity of LaF_3 at 600°C, and $a = 10^{-9}$, the activity of the La obtained from the free energies of formation of LaF_3 (18) and of BeF_2 in $\text{LiF}\cdot\text{BeF}_2$ (67-33 m/o) (15), an electronic transference number, $t_e = 10^{-3}$ is obtained from the above equation. An electronic transference number of this magnitude is much too small to affect the initial measured voltage. However, the internal "short circuiting" resulting from this electronic conductivity (24), i.e. $\text{NiF}_2 + 2e^- \rightarrow \text{Ni}^o + 2\text{F}^-$, leads to the depletion of NiF_2 in the LaF_3 cup and ultimate failure of the electrode system as shown by the eventual decline in the voltage. This phenomenon does not occur with the $\text{U}^{4+}/\text{U}^{3+}$ melt as the formation of lanthanum by this couple is virtually nonexistent, $a_{\text{La}} = 10^{-29}$, as would be expected since the free energy per equivalent is much less negative than the Be/BeF_2 couple (15).

To differentiate between the "chunking effect" and solution of beryllium or of formation of dissolved Li the following experiments were performed. The beryllium electrode was immersed in a $\text{LiF}\cdot\text{BeF}_2$ (67-33 m/o) melt contained and separated from the main melt of $\text{LiF}\cdot\text{BeF}_2$ (67-33 m/o) by a BeO crucible whose porosity allowed ion migration. Since solid beryllium metal is less dense than the melt (25), any solid metal detached from the electrode by "chunking" would rise to, and be trapped at, the melt surface within the crucible. Dissolved metal, on the other hand, would still reach the LaF_3 crystal. The observation was that under these conditions the NiF_2 in the LaF_3 cup was still transformed into Ni metal. In another experiment, NiF_2 was added to the main melt as a "getter" for dissolved metal. The beryllium electrode was again encapsulated within the BeO crucible containing the pure $\text{LiF}\cdot\text{BeF}_2$ (67-33 m/o) melt. Any dissolved metal entering the main melt is immediately oxidized by the Ni^{++} ions. By this means the cell potential of $2.045 \pm 0.003\text{V}$ was maintained for a period of three days. Termination of the experiment was caused by the loss

of ion migration through the porous BeO crucible walls which had become plugged by the deposition of nickel. No metallic nickel was found in the cup, eliminating the vapor transport mechanism.¹

This value of $2.045 \pm 0.003\text{V}$ when combined with the data of Baes (16) and Blood (17) gives an $E_{600^\circ\text{C}}^o$ for NiF_2 , our standard, of $2.692 \pm 0.010\text{V}$. This value is in excellent agreement with $2.700 \pm 0.015\text{V}$ obtained from the following solid-state cells at 600°C

	emf (V) ²
$\text{Ni}, \text{NiF}_2/\text{CaF}_2/\text{AlF}_3, \text{Al}$	-1.720 ± 0.003 (5, 6)
$\text{Ni}, \text{NiF}_2/\text{CaF}_2/\text{MgF}_2, \text{Mg}$	-2.343 ± 0.003 (5, 6)
$\text{Mg}, \text{MgF}_2/\text{CaF}_2/\text{ThF}_4, \text{Th}$	$+0.310 \pm 0.005$ (4)
$\text{Th}, \text{ThF}_4/\text{CaF}_2/\text{AlF}_3, \text{Al}$	-0.310 ± 0.003 (4)

and the free energies of formation of MgF_2 ($\Delta G_{600^\circ\text{C}}^o = -232.4 \pm 0.6$ kg-cal) and AlF_3 ($\Delta G_{600^\circ\text{C}}^o = -306.5 \pm 0.7$ kg-cal) calculated from calorimetric data (27).

We have demonstrated the practicality of using single crystal LaF_3 with proper precautions as a bridging ionic conductor with certain high-temperature fluoride melts. Reference electrodes so constructed appear compatible with these molten fluorides for appreciable periods of time and afford a means of obtaining emf data of thermodynamic significance. Such a reference electrode is also useful for electroanalytical measurements, i.e. in a three-electrode configuration for voltammetry, chronopotentiometry, etc. The reference electrode couple, of course, is not restricted to nickel. We chose the $\text{Ni}/\text{Ni}(\text{II})$ couple in light of previous experience (2) which indicated its suitability as a reference electrode couple in molten fluorides.

Acknowledgments

The authors thank Prof. Gleb Mamantov and Fred R. Clayton of the University of Tennessee and M. A. Bredig and E. J. Kelly of ORNL for valuable discussions and assistance.

Research was sponsored by the U. S. Atomic Energy Commission under contract with the Union Carbide Corporation.

Manuscript submitted Aug. 27, 1971.

Any discussion of this paper will appear in a Discussion Section to be published in the December 1972 JOURNAL.

REFERENCES

- "A Review of Molten Salt Reactor Technology," *Nuclear Applications and Technology*, Vol. 8/No. 2, Feb. 1970.
- H. W. Jenkins, G. Mamantov, and D. L. Manning, *J. Electroanal. Chem.*, **19**, 385 (1968).
- H. W. Jenkins, G. Mamantov, and D. L. Manning, *This Journal*, **117**, 183 (1970).
- R. J. Heus and J. J. Egan, *Z. Phys. Chem.*, **49**, 38 (1966).
- N. F. Lofgren and E. J. McIver, U.K.A.E.A.-AERE-R-5169, 1966.
- T. L. Markin, R. J. Bones, and V. J. Wheeler, *Proc. British Ceramic Soc.*, **8**, 51 (1967); T. L. Markin, "Electromotive Force Measurement in High Temperature Systems," p. 91, "Proceedings of a Symposium," Imperial College, London, C. B. Alcock, Editor, April 1967.
- M. S. Frant and J. W. Ross, Jr., *Science*, **154**, 1553 (1966).
- R. W. Ure, *J. Chem. Phys.*, **26**, 1363 (1957).
- A. Sher, R. Solomon, K. Lee, and R. W. Muller, *Phys. Rev.*, **144**, 593 (1966).
- C. J. Barton, M. A. Bredig, L. O. Gilpatrick, and J. A. Fredricksen, *Inorg. Chem.*, **9**, 307 (1970).
- G. Mamantov and D. L. Manning, *Anal. Chem.*, **38**, 1494 (1966).

¹ In cooperation with Dr. J. P. Young of this Laboratory attempts were made to detect spectrally the presence of dissolved Li or Be present possibly as Be^+ or Be_2^{2+} in molten $\text{LiF}\cdot\text{BeF}_2$ (67-33 m/o). The experiments were performed with the melt in a molybdenum windowless cell (26). Both chemical, i.e. reaction of beryllium metal with the melt, and electrochemical, i.e. anodic dissolution of the beryllium, failed to show any evidence of the above species. It appears from these experiments that the concentrations of these species are too low to be seen spectrally.

² The sign convention conforms with the IUPAC, $\Delta G^o = -nFE^o$.

12. T. R. Mueller and H. C. Jones, *Chem. Ind.*, **2**, 65 (1969).
13. H. W. Jenkins, G. Mamantov, D. L. Manning, and J. P. Young, *This Journal*, **116**, 1712 (1969).
14. R. S. Nicholson and J. Shain, *Anal. Chem.*, **36**, 706 (1964).
15. C. F. Baes, Jr., Nuclear Metallurgy, Vol. 15, AIME Symposium on Reprocessing of Nuclear Fuels, pp. 615-644, 1969.
16. B. F. Hitch and C. F. Baes, Jr., *Inorg. Chem.*, **8**, 201 (1969).
17. C. M. Blood, Private communication, Oak Ridge National Laboratory, Sept. 1961.
18. W. J. Hamer, M. S. Malmberg, and B. Rubin, *This Journal*, **112**, 750 (1965).
19. A. S. Dworkin, H. R. Bronstein, and M. A. Bredig, *J. Phys. Chem.*, **66**, 572 (1962).
20. C. Wagner, *This Journal*, **115**, 933 (1968).
21. H. R. Bronstein, *J. Phys. Chem.*, **73**, 1320 (1969).
22. "The Encyclopedia of Electrochemistry," pp. 44-51, C. A. Hampel, Editor, Reinhold Publishing Corp., New York (1964).
23. H. Aida, J. Apelboin, and M. Garreau, *This Journal*, **118**, 243 (1971).
24. B. C. H. Steele, "Electromotive Force Measurements in High Temperature Systems," p. 1, "Proceedings of a Symposium," Imperial College, London, C. B. Alcock, Editor, April 1967.
25. S. Cantor, Private communication, Oak Ridge National Laboratory.
26. J. P. Young, *Anal. Chem.*, **36**, 390 (1964).
27. E. Rudzitis, H. M. Feder, and W. N. Hubbard, *J. Phys. Chem.*, **68**, 2978 (1964).

Electrochemical Properties of RbAg_4I_5 Solid Electrolyte

II. Study of Silver Electrode Reversibility

Bruno Scrosati*

Universita' di Roma, Rome, Italy

and A. Duane Butherus*

Bell Telephone Laboratories, Incorporated, Murray Hill, New Jersey 07974

ABSTRACT

The reversible behavior of silver electrodes in RbAg_4I_5 solid electrolyte has been tested by micropolarization studies. It has been found that while planar silver electrodes are reversible, the mixed silver-electrolyte electrodes most commonly used in solid-state batteries are not. The different behavior of the two electrodes has been related to the different physical aspects of their surfaces. In the case of the mixed electrolyte-silver electrodes, there are preferential points of silver deposition and depletion corresponding to areas of low IR drop through the electrolyte. This explanation has been confirmed by the observed dendritic growth of silver along the preferential deposition points on the $\text{Ag}(\text{RbAg}_4\text{I}_5)$ electrodes. Finally, it has been shown that even though planar silver electrodes behave reversibly at low current levels, they may also form dendritic growths at the current levels required for practical batteries. It appears that a practical rechargeable cell which uses RbAg_4I_5 electrolyte will require planar silver electrodes of very high surface area and the cell assembly will require a container which allows cell thickness change during cycling.

In recent years a considerable amount of research work has been reported on solid electrolytes, due to the technological advantages promised by solid-state batteries, such as long shelf life, extreme miniaturization, and a wide operating temperature range.

In particular, three types of batteries utilizing RbAg_4I_5 as solid electrolyte have been described in detail (1-3). Since the ionic conductivity of this electrolyte is solely due to Ag^+ ions, the above-mentioned three cells have silver as the main anodic material but use different cathodes as shown in Table I.

In both the cells described by Argue, Owens, and Groce (1) and by Takahashi and Yamamoto (3), an attempt to lower the polarization effects between the anodes and electrolyte (which must be minimized if practicable battery drain rates are to be achieved) was

made by mixing silver electrode material with the electrolyte itself, a procedure that enlarges the electrolyte/electrode interfacial area. The mixed electrolyte-silver electrode concept is analogous to the porous electrodes used in liquid electrolyte cells to increase the interfacial area and thus decrease the current density for a given discharge rate. A similar result has been obtained by DeRossi, Pistoia, and Scrosati (3) by amalgamation of the silver electrode according to the procedure recommended by Mrgudich (4). Amalgamated silver electrodes, however, are not usable as long-life anodes in solid-state batteries, since mercury slowly reacts with RbAg_4I_5 electrolyte, as was pointed out by Scrosati, Germano, and Pistoia (5).

The objective of these studies is an understanding of the $\text{Ag}/\text{RbAg}_4\text{I}_5$ electrode process on discharge and recharge. It is felt that such knowledge is needed before a practical secondary battery based on this elec-

* Electrochemical Society Active Member.
Key words: solid electrolyte, silver electrode reversibility.

Table I. RbAg_4I_5 solid electrolyte cells

Anode composition	Cathode composition	OCV (V)	Reference
Mixture of powdered carbon, silver and electrolyte	Mixture of carbon, RbI s and electrolyte	0.66	Argue, Owens, and Groce (1)
Amalgamated silver	Mixture of graphite, I_2 , and tetrabutyl ammonium iodide	0.58	DeRossi, Pistoia, and Scrosati (2)
Mixture of powdered silver and electrolyte	Mixture of Te , Ag_2Te , graphite, and electrolyte	0.22	Takahashi and Yamamoto (3)

trolyte can be developed, since the rechargeability of test cells has appeared to be limited by silver dendrites which are deposited at the silver electrode on recharge and which rapidly short the cell (2, 6). An understanding of the electrochemical reversibility of the silver electrode and the factors which influence the reversible behavior of the electrode are basic for the development of a rechargeable cell.

Experimental

The electrolyte was prepared by melting a stoichiometric mixture of AgI and RbI under a dry nitrogen atmosphere. The melt was quenched, crushed, and annealed for at least 24 hr at 160°C. Powder diffraction x-ray analysis showed the product identical to that reported by Bradley and Greene (7). The cells studied in this work were prepared by pressing the electrode materials and electrolyte into a single pellet. Pressures of about 2000 kg/cm² were used. The cell diameter was 1.27 cm and the electrolyte thickness of the order of 1-2 mm.

Micropolarization measurements have been shown to be useful tests for determination of electrode reversibility (8) and this technique, which is particularly suitable for the study of solid electrolyte systems, has been applied to the study of both silver and silver-electrolyte mixture electrodes.

Micropolarization behavior was examined by two different methods.

(i) *Dynamic*.—Small (± 1 mV) voltage excursions around zero cell potential were made by use of a Tacussel GSATP multifunction generator coupled to a Tacussel PRT 20-10x potentiostat, and the corresponding current-voltage curves were plotted on a Honey-

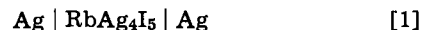
well Model 560 XY recorder. Times required for a complete voltage scan were varied from 10 sec to 3 hr. The potential was also monitored at the cell by a Cimron Model 6753 DVM. The DVM readings were used for the reported data.

(ii) *Static*.—Point by point voltage excursions were effected by use of a Kepco precision voltage source, and the currents monitored by use of the Cimron DVM and a precision resistor. After each new voltage setting, the current fell to a constant value after a few minutes, and these I-V points defined the micropolarization curves.

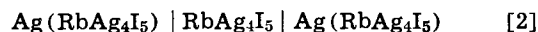
It was found that the results of both methods were identical for a given cell.

Results and Discussion

The micropolarization behavior of the cell



is shown in Fig. 1A. There is no evidence of hysteresis, and the anodic and cathodic lines being coincident, thus show that the electrodes prepared by pressing silver powder on the electrolyte so as to form a planar interface may be considered reversible. This is not the case for the electrodes usually used as anodes in solid-state batteries, i.e. the silver-electrolyte mixture. This is shown by the micropolarization behavior of the cell



reported in Fig. 1B. Gross hysteresis effects are present, and the lines related to the anodic and cathodic current are not coincident. The hysteresis effects were independent of whether the micropolarization measurements were made via voltage sweep methods or

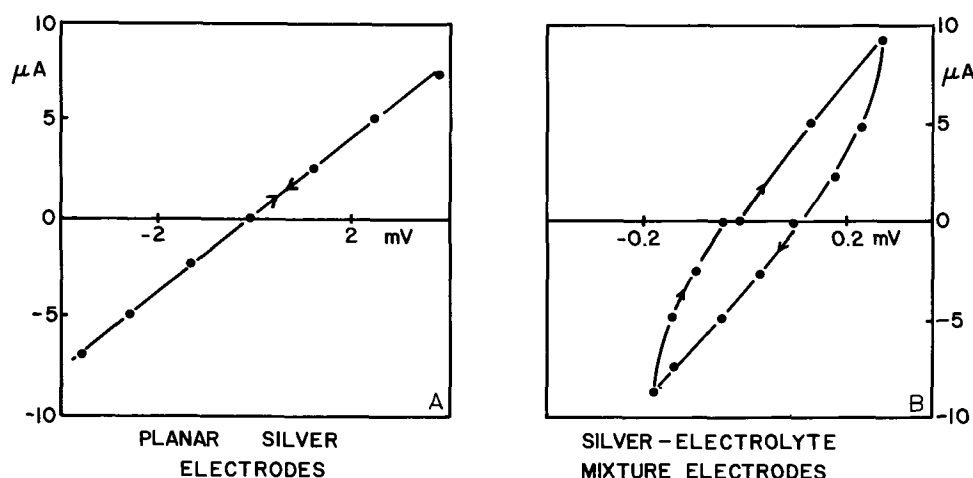


Fig. 1. Micropolarization test, electrode area 1.26 cm².

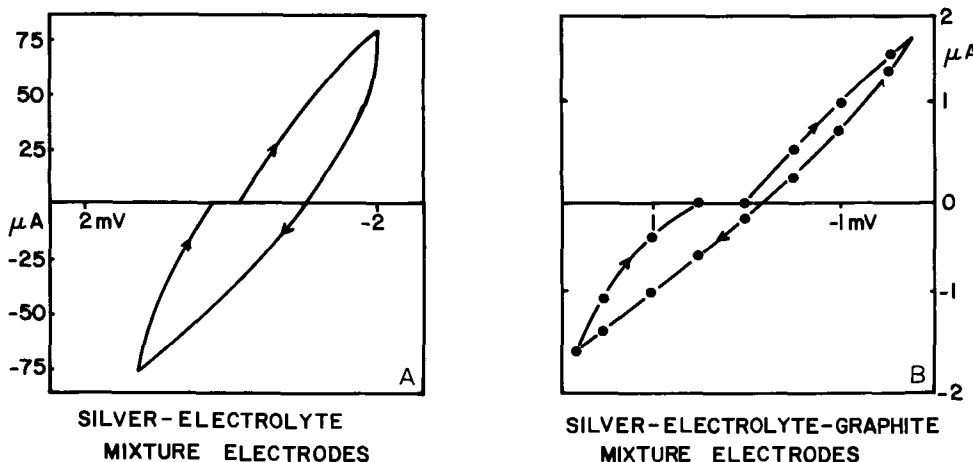


Fig. 2. Micropolarization tests

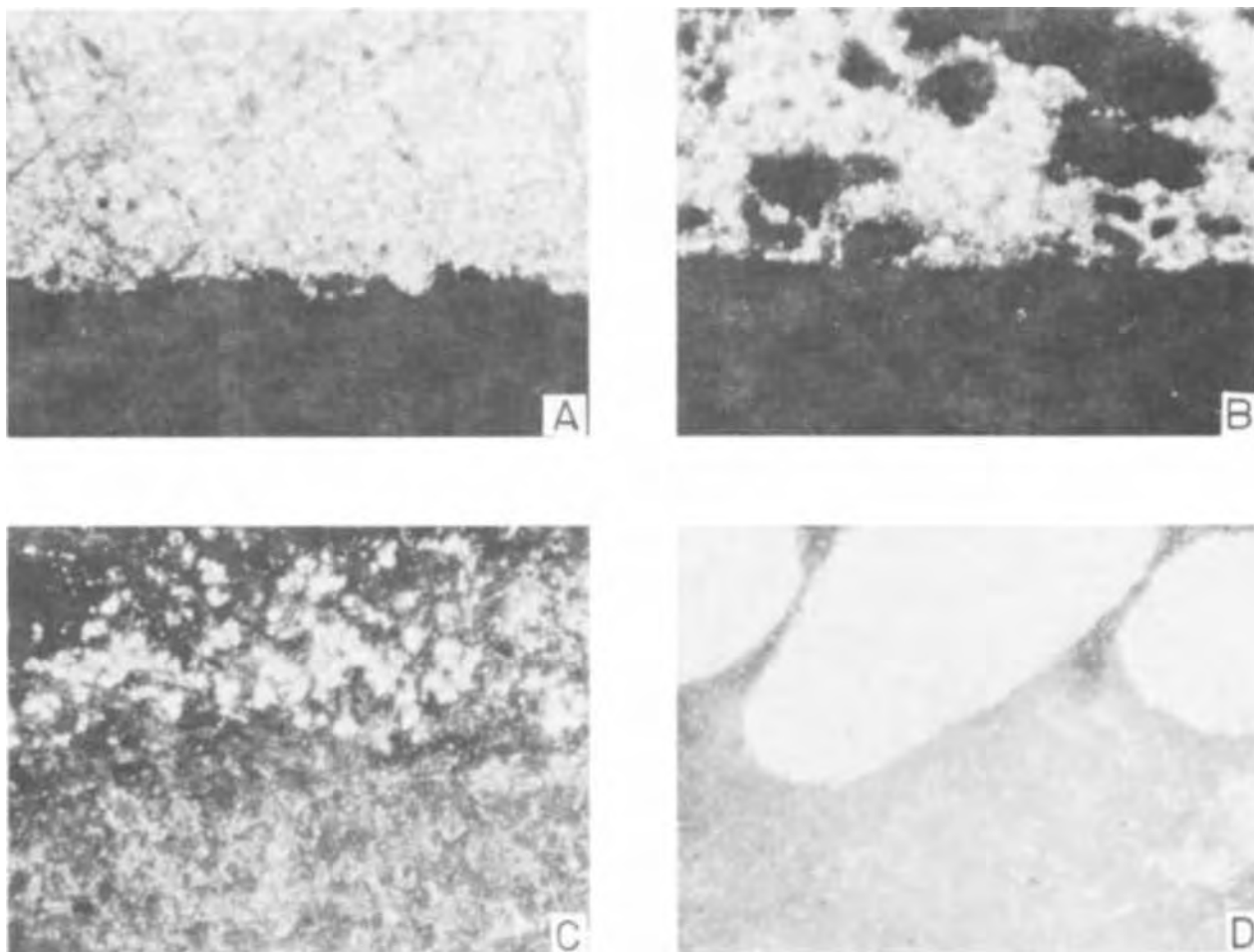


Fig. 3. Cross section of various electrodes. The electrolyte is the lower portion of the sample ($\times 100$). A, planar silver; B, silver-electrolyte mixture; C, silver-electrolyte graphite mixture; D, silver mesh.

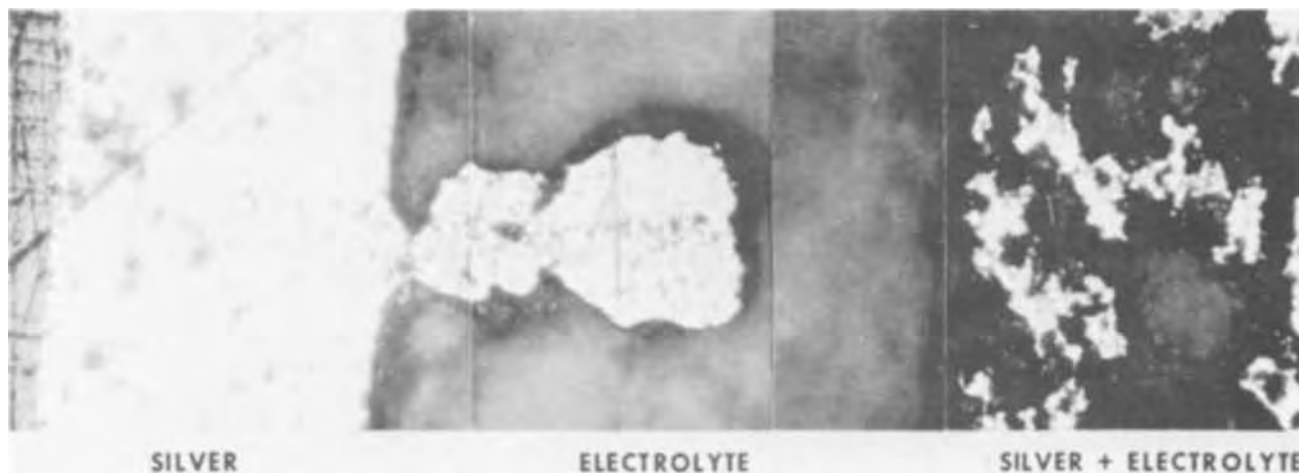


Fig. 4. Cross section of cell showing silver dendrite growth through the electrolyte ($\times 100$)

via point-by-point methods. Since polarization is proportional to current density, the micropolarization tests are compared on a current basis, even though for a given current the real current density for the high surface area mixed $\text{Ag-RbAg}_4\text{I}_5$ anode will be much lower than the corresponding planar cell. If the comparisons are made on a voltage basis, the hysteretic behavior of the mixed electrode is even more apparent, as shown in Fig. 2A. This increase in irreversibility with decreasing real current density (due to the increased surface area of the mixed electrode) is certainly an unexpected result.

The addition of graphite to the mixed $\text{Ag-RbAg}_4\text{I}_5$ anode has been done to prevent the electronic isolation of the silver particles in the electrode (9). Such an electrode shows the same type of hysteresis as the mixed electrode without the graphite, as shown in Fig. 2B. The explanation of the different behavior of the various electrodes may be related to the different physical aspects of their surfaces, as shown in the microphotographs reported in Fig. 3, which shows cross sections of the electrodes.

In the case of the mixed electrolyte-silver electrodes, the surfaces are strictly nonplanar, and thus there are

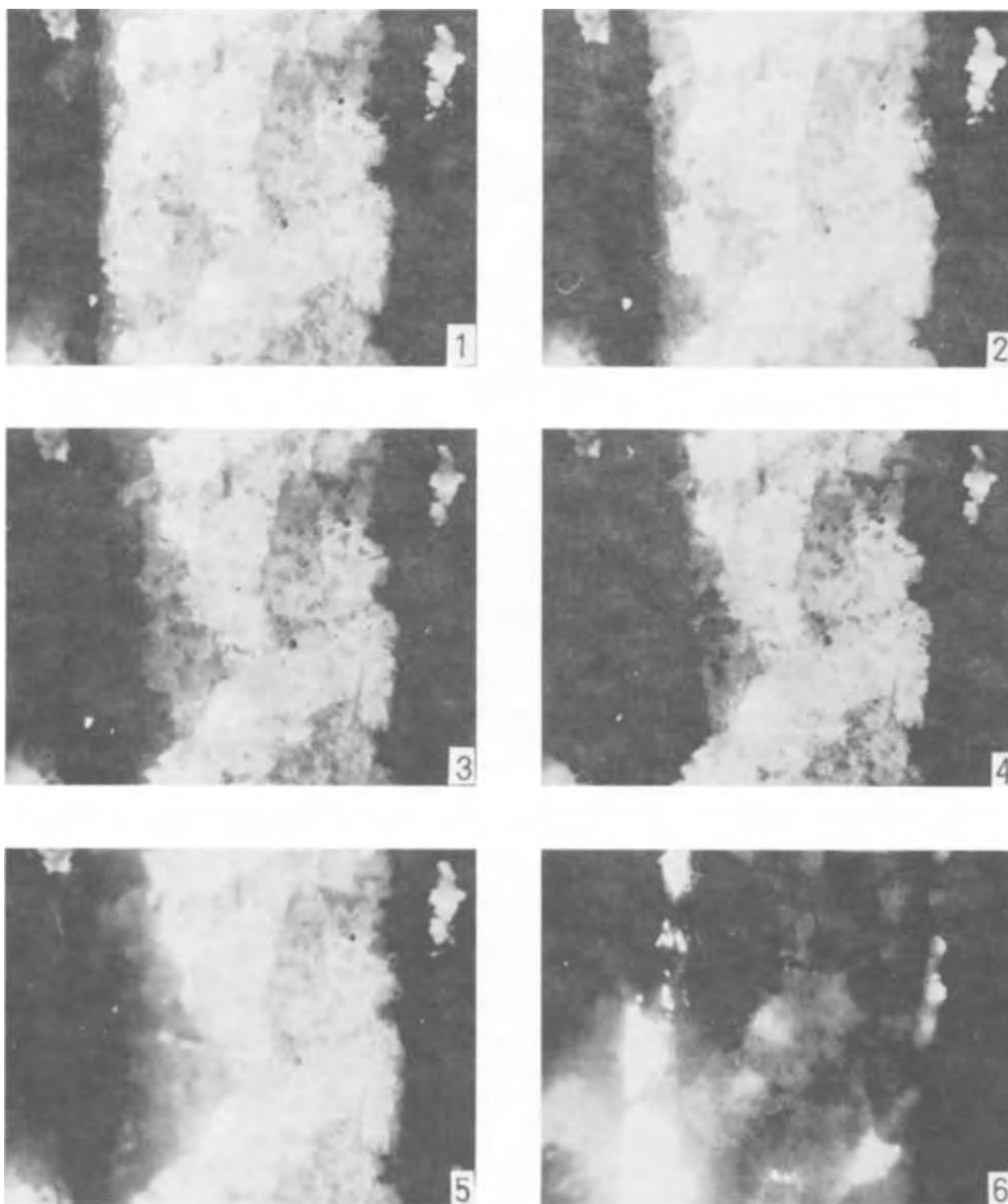


Fig. 5. Progressive dendrite growth and eventual electrolyte fracture. Pictures taken at 5 min intervals ($\times 30$).

preferential points of silver deposition and depletion corresponding to areas of low resistance through the electrolyte. At these points, the current density is very high, with consequent high polarization. On discharge (silver oxidation), a "leveling" process occurs; *i.e.* the silver at the projecting points is "dissolved" into the electrolyte, decreasing the height of the projection, with consequent increase of the resistance through the electrolyte at that point and thus a decreased current density.

On charge, however, there is no such "self-regulating" process, and the projections grow with preferential silver deposits. This lowers the resistance through the electrolyte at that point, increasing the current

density there with consequent shorting. Since the electrode surfaces continually change on charge and discharge, the current density across the "rough" electrode is therefore not only nonuniform but changes in a random, nonuniform manner. Additionally, the silver and electrolyte phases are noncontiguous, and many electronically isolated masses of electrolyte and silver exist in the electrode. These areas contribute further to the nonuniformity of the electrode and lack of reversibility found.

In an attempt to increase the surface area of the electrode and yet retain the reversible properties of the planar electrode, a silver mesh was pressed on the electrolyte. This electrode showed better micropolar-

Table II. Constant potential electrolysis data of Ag | RbAg₄I₅ | Ag cell

(1.26 cm² electrode surface)

Time (hr)	Current (mA)
0	0.50
26	0.40
80	0.23
100	0.19

ization behavior than the mixed electrode, but some hysteresis was apparent. An analysis of the effect of the dimensions of the roughness on the electrode reversibility may shed some light on this phenomenon. The concepts of micro- and macro-current distribution developed by Cheh (10) for deposition of gold on rough surfaces may be applicable here, and such a study is presently underway. A cross section of this electrode is shown in Fig. 3D.

The reversibility of the planar electrode is apparently due to the following:

i. Lower, more evenly distributed current density. No "Hot Spots."

ii. Minimized sites of preferential silver deposition.

If the explanation above is correct, there are strong possibilities of obtaining a dendritic growth of silver along the preferential deposition points on the Ag(RbAg₄I₅) electrodes. To test this possibility, a certain amount of charge (about 500 coulombs) has been passed through a Ag | RbAg₄I₅ | Ag(RbAg₄I₅) encapsulated cell. A cross section of the cell, reported in Fig. 4, shows gross dendritic growth through the electrolyte.

To test this further, a 2 mm thick cross section was cut from a test cell similar to [2]. Current was passed between the two electrodes at a current density of ≈ 20 mA/cm², and microphotographs were taken at 5-min intervals using light transmitted through the electrolyte. Figure 5 shows the cross section of the cell, with the cathode on the left in each microphotograph. The deposition of Ag shows as the shaded triangular area growing from the cathode into the electrolyte. Under the stated conditions a layer of about 1.8 mm of Ag was deposited during the electrolysis, a sufficient amount to cause the electrolyte fracture exhibited. The current decreased precipitously, of course, when the electrolyte fractured.

Though the planar electrodes showed reversible behavior at low current levels, they may also form den-

dritic growths at current levels required for practical batteries. About 150 coulombs were passed through the cell

Ag | RbAg₄I₅ | Ag [3]

at constant potential. The current remained steady for a time, then progressively fell off to lower values as shown in Table II. When removed from the cell holder, the anode was found disconnected from the cell, and gross silver deposits had separated the cathode from the electrolyte as shown in Fig. 6A. A cross section of the cell, Fig. 6B, shows that the anode surface had been eroded deeply, accounting for its detachment, and the cathode-electrolyte interface was opened up by the deposited silver. This behavior was also seen in a cell which used mixed silver-electrolyte electrodes.

The dendrite growth through the electrolyte always occurred when the cell was absolutely immobilized (i.e. encapsulated) and could not accommodate the thickness change due to the silver deposition on charge. In these latter two experiments, the cell was lightly loaded and accommodated the expansion.

Conclusion

The micropolarization results indicate that while mixing silver powder with electrolyte to increase the anode/electrolyte interfacial area may improve the discharge rate of a given cell, it certainly inhibits the reversibility of the silver anode in this system. The electrolysis study shows that there is probably an upper limit of the amount of charge which can be passed either to or from a silver electrode in contact with RbAg₄I₅ without seriously breaking the interfacial contact, and that a flexible rather than rigid packaging will prevent dendrite penetration of the electrolyte.

It thus appears that a practical rechargeable cell which uses RbAg₄I₅ electrolyte will require the following:

i. Planar Ag | RbAg₄I₅ interfaces of high surface area/electrode capacity. A thin-film multilayer sandwich construction appears suitable.

ii. Container which follows slight thickness change during cycling.

Cells which test these proposals are now under examination and the preliminary results appear to support these proposals. The fabrication, testing, and performance of these cells will be reported subsequently.

Manuscript submitted April 14, 1971; revised manuscript received Sept. 24, 1971.

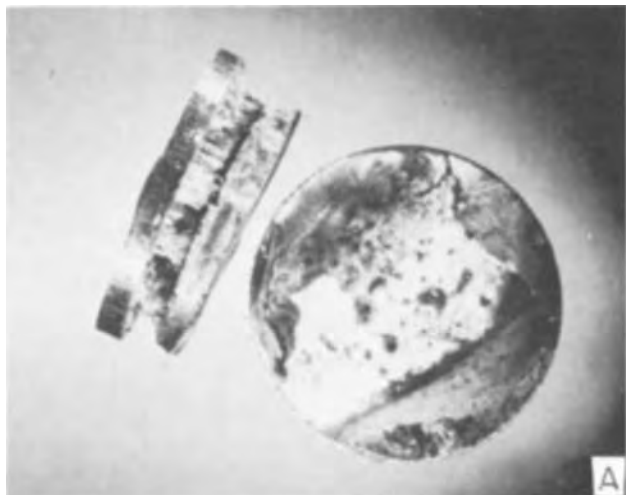


Fig. 6. Ag | RbAg₄I₅ | Ag cell after massive electrolysis. The positive electrode is on the right side in both photographs.



Any discussion of this paper will appear in a Discussion Section to be published in the December 1972 JOURNAL.

REFERENCES

1. G. R. Argue, I. J. Groce, and B. B. Owens, Proc. Power Source Conf. 103 (1968).
2. M. DeRossi, G. Pistoia, and B. Scrosati, *This Journal*, **116**, 1642 (1969).
3. T. Takahashi and O. Yamamoto, *ibid.*, **117**, 1 (1970).
4. J. N. Mrgudich, *ibid.*, **107**, 475 (1960).
5. B. Scrosati, G. Germano, and G. Pistoia, *ibid.*, **118**, 86 (1971).
6. J. N. Mrgudich, Solid Electrolyte batteries, in "Encyclopedia of Electrochemistry," p. 87, C. A. Hampel, Editor, Reinhold Publishing Corp., New York (1964).
7. J. N. Bradley and P. D. Greene, *Trans. Faraday Soc.*, **63**, 2516 (1967).
8. D. J. G. Ives and G. J. Janz, "Reference Electrodes," p. 18, Academic Press, New York (1961).
9. J. E. Oxley and B. B. Owens, *Power Sources 1970* Preprint Paper No. 32.
10. H. Y. Cheh, *This Journal*, **117**, 609 (1970).

Cathodic Discharge Controlled by Dissolution Kinetics

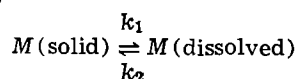
M. M. Nicholson* and M. L. Iverson

Atomics International, A Division of North American Rockwell Corporation, Canoga Park, California 91304

ABSTRACT

A theoretical analysis is presented for the constant-current discharge of a thin-layer cathode with control by dissolution and diffusion of the electroactive material. The treatment involves the solution of Fick's second law of diffusion for an electrolyte layer which is bounded on one side by a planar electrode of a metal to be electrodeposited and on the opposite side by a planar surface of a partially soluble compound of that metal. It is shown that the potential at the metal surface may reach a steady state within a few minutes after the current is applied in an initially saturated solution. There is a critical current density, however, at which a transition occurs and the potential approaches infinity. The dissolution rate constant and other parameters of the system may be determined by several procedures involving the use of transient data. This electrode configuration also provides a model of the inner structure of a porous battery cathode. Experimental results on cadmium fluoride in aqueous 4M KF indicated a dissolution rate constant of 8×10^{-9} mole/cm²-sec.

For a material M , with a surface area A , dissolving by the process



the rates of dissolution and crystallization may be expressed as

$$\text{Rate}_1 = k_1 A \quad [1]$$

and

$$\text{Rate}_2 = k_2 AC \quad [2]$$

where k_1 and k_2 are the respective rate constants on a unit area basis and C is the concentration of the dissolved material at the surface. At equilibrium, the dissolution and crystallization rates are equal. The exchange rate is then

$$k_1 = k_2 C^0 \quad [3]$$

where C^0 is the solubility of M in the liquid. At a surface concentration C , less than C^0 , the net dissolution rate is

$$\frac{dN}{dt} = k_1 A - k_2 AC \quad [4]$$

or

$$\frac{dN}{dt} = k_2 A (C^0 - C) \quad [5]$$

An equation in the form of [5] was given by Shchukarev in 1896 (1) and by Noyes and Whitney in 1897 (2), but k_2 was interpreted as a diffusion parameter. In 1904, Nernst introduced the diffusion boundary layer

concept, taking into account the concentration gradient near a dissolving surface by the relationship (3)

$$\frac{dN}{dt} = AD(C - C^0)/\delta \quad [6]$$

In Eq. [6], which approximates Fick's first law, D is the diffusion coefficient of the dissolved species, C is its concentration at the surface, C^0 is the concentration in the bulk of the solution, and δ is the effective thickness of the diffusion layer. For mixed kinetic and diffusion control, Eq. [5], as well as Fick's laws, must be satisfied. Most theoretical treatments of nonfaradaic dissolution rates since the time of Noyes and Nernst have emphasized mass transfer in the solution. Exceptions are the work of Jaenicke (4) and Vermilyea (5) on the potential-dependence of solution rates of salts.

Recent concern with battery electrode mechanisms has prompted further interest in this area. For example, the discharge of an insoluble cathode material will be very slow unless the process is assisted by electronic or ionic conductivity in the solid oxidizer phase (6). If the active material is sufficiently soluble in the electrolyte, however, it can be discharged by a solution mechanism involving dissolution of the solid, transport of the active species through the electrolyte, and subsequent electron transfer at the surface of an inert current collector. The dissolution rate of the oxidizer may then control the discharge process. A theoretical analysis of the solution mechanism is presented in the ensuing discussion, with the condition of constant current density. The results are applicable to battery electrode studies and to more general investigations of dissolution kinetics.

* Electrochemical Society Active Member.

Key words: battery electrodes, critical current density, rate constant, thin-layer.

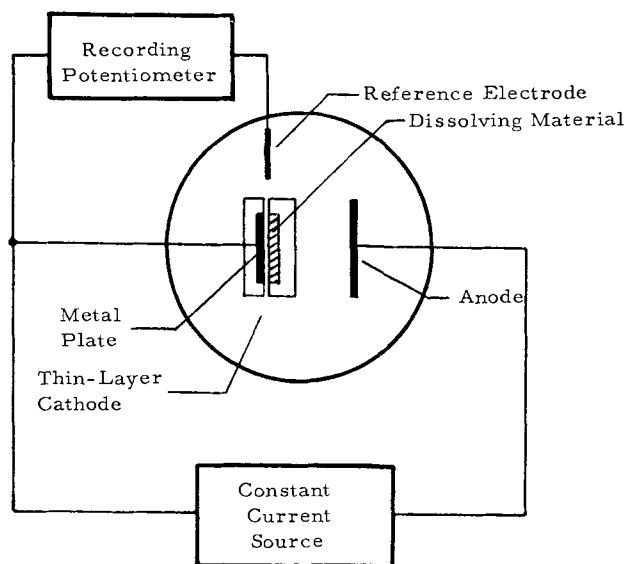


Fig. 1. Arrangement for galvanostatic measurements on thin-layer electrode.

Thin-Layer Electrode with Dissolving Reactant

The arrangement shown schematically in Fig. 1 includes a thin-layer cathode assembly with a smooth current-collector plate as one wall and a smooth non-porous plate of a reducible salt or oxide with significant solubility as the opposite wall. To simplify the analysis for metal ion reduction, the current collector is assumed to consist of the metal that is formed on cathodic discharge of the salt or oxide. The intervening space, of a small thickness l , is filled with an inert electrolyte of high concentration compared to that of the dissolved reactant. The influence of ohmic drop is therefore considered negligible. Discharge of the active material occurs when the metal plate is cathodically polarized. Connection through the electrolyte to the anode is established through the opening around the periphery of the parallel-plate structure. This arrangement is somewhat similar to the thin-layer electrode of Anson and co-workers (8), but the plate opposite the metal electrode now consists of the electroactive material, rather than an insulator.

It will be assumed in this discussion that Eq. [1] through [5] are valid. Generally, this will be true when the electrolyte and the dissolved reactant have a common anion; although k_2 may then depend on the electrolyte concentration, it will be essentially constant during an individual experiment. Variations of activity coefficients and diffusion coefficients with concentration are neglected in this analysis, as are changes in the layer thickness l due to dissolution and electrodeposition.

Analysis for Constant-Current Electrolysis

When a constant cathodic current density is applied to the metal plate, as shown in Fig. 1, the reactive cation will be depleted within the solution layer as the corresponding metal deposits on the electrode surface. Additional salt will dissolve to counteract this loss, and eventually, if the current is not too high, a steady state will be attained. Accordingly, the potential of the metal plate with respect to the reference electrode will change upon application of the current and finally reach a constant value which is a measure of the steady-state metal ion concentration at the plate surface. It will be shown that the rate constant k_1 may be determined from the steady-state potential or from the transient response of the electrode. Conversely, if k_1 and the solubility of the active material are known, the current-potential and potential-time curves may be estimated for a battery cathode with a given inner

spacing and a solution-controlled discharge mechanism.

To develop these relationships, it is necessary to solve Fick's second law of diffusion

$$\frac{\partial C}{\partial t} = D \frac{\partial^2 C}{\partial x^2} \quad [7]$$

for the appropriate initial and boundary conditions. In this problem, C represents the concentration of the active metal ion at any time t and distance x from the metal surface, and D is its diffusion coefficient in the supporting electrolyte. If the space between the electrode and the dissolving surface is saturated with the active material at the beginning of the experiment, the initial concentration is given by

$$C^0 = k_1/k_2 \quad (t=0) \quad (0 \leq x \leq l) \quad [8]$$

Under a constant current density I , the concentration gradient at the electrode surface ($x=0$) is given by

$$\left(\frac{\partial C}{\partial x} \right)_{x=0} = \frac{I}{nFD} \quad [9]$$

The flux of metal ion at the dissolving surface ($x=l$) is equal to the net dissolution rate

$$D \left(\frac{\partial C}{\partial x} \right)_{x=l} = k_1 - k_2 C_{x=l} \quad [10]$$

The corresponding heat transfer problem was solved by Newman and Green in 1934, using the principle of the heat balance integral (7). From their results, the metal ion concentration at any distance and time may be computed for both steady-state and transient conditions. The required transformations are facilitated by the following definitions of dimensionless quantities:

Concentration:	$nFD(C^0 - C)/(Il)$
Distance:	x/l
Time:	Dt/l^2
Dissolution rate parameter:	$k_1 l / (DC^0)$
Current density:	$Il / (nFDC^0)$

The data for concentration at the electrode surface are available as Table IV in Ref. (7), with the following changes of notation:

$$E = (C^0 - C_{x=0})nFD/Il \quad [11]$$

$$P = Dt/l^2 \quad [12]$$

$$Nu = k_1 l / (DC^0) \quad [13]$$

The steady state.—Although the transient solution requires a numerical presentation, conditions in the thin-layer electrode structure are quite simple at the steady state. It is apparent from Table IV of Ref. (7) that the dimensionless concentration variable at the metal electrode reaches a limiting value given by

$$\frac{nFD(C^0 - C_{x=0})}{Il} = \frac{1 + k_1 l / (DC^0)}{k_1 l / (DC^0)} \quad (t \rightarrow \infty) \quad [14]$$

Furthermore, at the dissolving surface

$$\frac{nFD(C^0 - C_{x=l})}{Il} = \frac{1}{k_1 l / (DC^0)} \quad (t \rightarrow \infty) \quad [15]$$

Since the concentration gradient at the steady state is uniform throughout the thickness of the electrolyte layer, Eq. [14] and [15] lead to the simple situation represented by Fig. 2.

Steady-state potential.—The concentration at the electrode surface is readily given in terms of the measured potential change ΔE if the metal/metal ion couple is assumed to be reversible

$$C_{x=0} = C^0 \exp(nF\Delta E/RT) \quad [16]$$

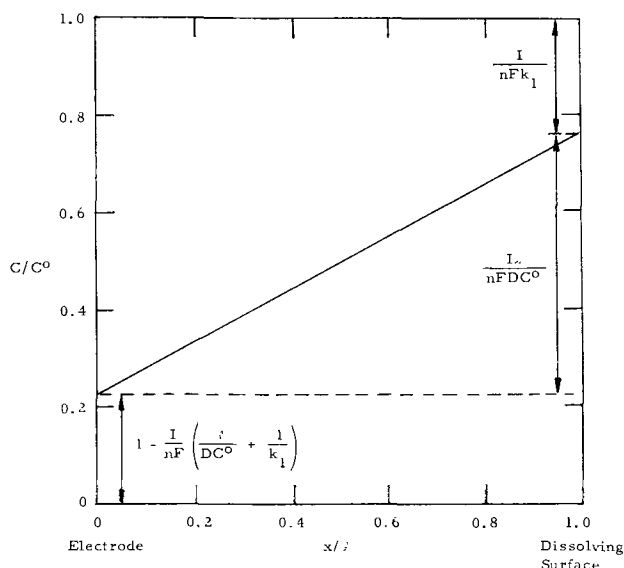


Fig. 2. Concentration profile at the steady state

The combination of Eq. [14] with Eq. [16] yields

$$1 - \exp(nF\Delta E_s/RT) = \frac{I}{nF} \left(\frac{l}{DC^0} + \frac{1}{k_1} \right) \quad [17]$$

from which the steady-state potential change ΔE_s may be calculated.

Critical current density.—It follows from Eq. [17] that $-\Delta E_s$ becomes infinite when

$$I = \frac{nF}{\left(\frac{l}{DC^0} + \frac{1}{k_1} \right)} \equiv I_c \quad [18]$$

The metal deposition process cannot sustain, indefinitely, a current density as high as the critical value I_c , defined by Eq. [18]. When the applied current meets or exceeds this condition, a transition is expected in the potential-time curve. The time at which this occurs is predictable as discussed below.

The transient response.—Figure 3 shows a set of potential-time curves calculated at several fractions of the critical current density. These transients were obtained from Table IV of Ref. (7), with Eq. [16], taking $l = 0.01$ cm, $D = 1 \times 10^{-5}$ cm²/sec, $T = 298^\circ\text{K}$, and $k_1l/(DC^0) = 1$. A rate parameter of unity corresponds to the condition

$$\frac{l}{DC^0} = \frac{1}{k_1} \quad [19]$$

in which the diffusion and dissolution terms contribute equally to the right side of Eq. [17]. The critical current density is then given by

$$\frac{I_c l}{nFDC^0} = \frac{1}{2} \quad \left(\frac{k_1 l}{DC^0} = 1 \right) \quad [20]$$

and the critical transient is the upper curve in Fig. 3. It is apparent from this group of curves that the transition occurs quite sharply at I_c . At a current density only 0.2% lower, for example, the potential shift reaches a steady-state value of 0.160V and, theoretically, will not exceed this limit.

Critical transition time.—The transition time $D\tau_c/l^2$ at the critical current density was determined by graphical interpolation of the data in Table I of Ref. (7). That table gives a function $F(O,P)$, which takes the form

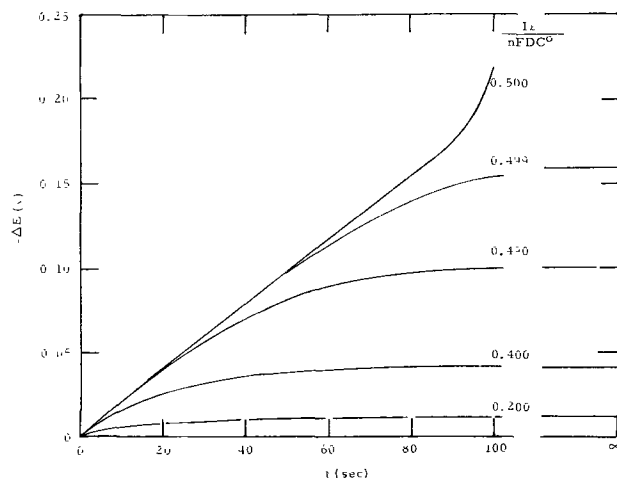


Fig. 3. Potential-time curves for dissolution-controlled electrode. $n = 1$; $k_1l/DC^0 = 1$; $l = 0.01$ cm; $D = 1 \times 10^{-5}$ cm²/sec; $T = 298^\circ\text{K}$.

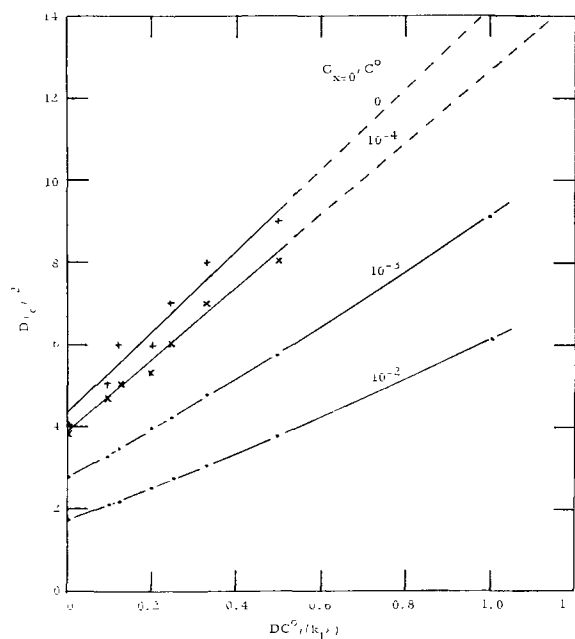


Fig. 4. Transition time function with different criteria for $C_{x=0}/C^0$.

$$F(O,P) = \left(1 + \frac{DC^0}{k_1 l} \right) \frac{C_{x=0}}{C^0} \quad (I = I_c) \quad [21]$$

$(P = Dt/l^2)$

for the critical condition in the electrochemical problem. Ideally, τ_c would correspond to the value of P , or Dt/l^2 , at which $C_{x=0}/C^0 = 0$ and $-\Delta E = \infty$. Since an infinite potential will not be reached experimentally, Dt/l^2 was evaluated for $C_{x=0}/C^0$ ratios of 10^{-2} , 10^{-3} , 10^{-4} , and $0 (< 5 \times 10^{-5})$. The respective values of $-\Delta E$, in volts at 25°C , are 0.118, 0.177, 0.236, and $\infty (> 0.254)$. These results are shown in Fig. 4, where $D\tau_c/l^2$ is plotted against the reciprocal of the rate parameter. The scattering of calculated points at the two lowest concentration ratios is due to loss of significant figures. It is clear from this analysis that the experimental transition time is better evaluated with reference to a selected $C_{x=0}/C^0$ ratio than by visual estimation on the shoulder of the potential-time curve. The condition $-\Delta E = 0.118\text{V}$ occurs before the transition (see Fig. 3), but the corresponding time is correlatable with k_1l/DC^0 . The plots in Fig. 4 are almost linear. In

Table I. Transition times for different electrode configurations^(a)

I ^(b) nC ^o (A × cm/ equiv)	Thin-layer electrode with dissolution				Thin-layer electrode without dissolution (8)	Unconfined electrode (9)
	k ₁ l DC ^o	C _{x=0} /C ^o			$\tau = \frac{nFlC^o}{I} - \frac{l^2}{3D}$ (sec)	$\tau = \frac{\pi n^2 F^2 DC^{o2}}{4I^2}$ (sec)
		10 ⁻³	10 ⁻⁴	0		
		τ _c (sec)				
8.76	0.1	—	—	—	107	955
32.1	0.5	—	—	—	27	71
48.2	1.0	91.4	125 ^(c)	143 ^(c)	17	31
64.3	2.0	57.5	81	93	12	18
80.4	5.0	39.5	55	63	—	11
87.6	10.0	32.8	47	54	—	9.5
96.5	∞	27.7	38	44	—	7.8

^(a) Conditions: $l = 0.01$ cm; $D = 1.0 \times 10^{-6}$ cm²/sec.

^(b) Chosen so that $I = I_c$ in the dissolving system.

^(c) Extrapolated; Fig. 4.

the limiting case, the dimensionless transition time is given by

$$\frac{D\tau_c}{l^2} = 9.8 \left(\frac{DC^o}{k_1 l} \right) + 4.4 \quad \left(\frac{k_1 l}{DC^o} \geq 2 \right)^1 \quad [22]$$

$(C_{x=0}/C^o = 0)$

over the indicated range of the rate parameter.

It is of interest to compare the critical transition time τ_c in the dissolving system with the chronopotentiometric transition time for a thin-layer electrode without dissolution (8) and for an unconfined planar electrode (9). The latter times are given by Eq. [23] and [24].

$$\tau = \frac{nFlC^o}{I} - \frac{l^2}{D} \quad \text{Thin-layer electrode without dissolution} \quad [23]$$

$(l^2 < \tau D)$

$$\tau = \frac{\pi n^2 F^2 DC^o}{4I^2} \quad \text{Unconfined electrode; semi-infinite linear diffusion} \quad [24]$$

Table I gives transition times calculated for the three electrode configurations at equal current densities. As expected, the transition is postponed in the dissolving system by the presence of a nearby source of reactive material. A small rate constant leads to a long critical transition time but corresponds to a small critical current density, according to Eq. [18]. When $k_1 = 0$, the problem of the dissolution-controlled electrode reduces to that of the earlier thin-layer electrode (8), and $I_c = 0$, i.e., a transition is no longer avoidable. In the opposite situation ($k_1 \rightarrow \infty$), the discharge is diffusion-controlled; $C_{x=l} = C^o$ at all times, and the dimensionless transition time reaches the limiting value

$$D\tau_c/l^2 = 4.4 \quad (k_1 = \infty) \quad [25]$$

$(C_{x=0}/C^o = 0)$

¹ This equation may be suitable for extrapolation to lower values of $k_1 l/DC^o$, but the direct numerical calculations have not been extended to that region.

Table II. Slope of the linear critical transient^(a)

k ₁ l/(DC ^o)	$-\frac{\partial(nF\Delta E/RT)}{\partial(Dt/l^2)}$
	Linear region
0	0
0.1	0.0967
0.5	0.427
1.0	0.741
2.0	1.160
3.0	1.423
4.0	1.599
5.0	1.725
8.0	1.955
10.0	2.045
∞	2.466

^(a) Reversible detector electrode.

Slope of the critical transient.—The critical transient for $k_1 l/(DC^o) = 1$ is seen in Fig. 3 to have a long linear section. The slope

$$\frac{-\partial(nF\Delta E/RT)}{\partial(Dt/l^2)}$$

was determined numerically from Table I of Ref. (7) for this and other values of the dissolution rate parameter. In each case, a region of constant slope was found for $Dt/l^2 > 0.5$, as shown in Fig. 5. Numerical values of the slope in the linear-transient region are given in Table II.

Evaluation of parameters.—The foregoing analysis provides several methods for the evaluation of k_1 if l , D , and C^o are known. Internal checks can thus be made on the interpretation of the data. The rate constant k_1 is available (i) from the steady-state potential, through Eq. [17], although this method is not very precise; (ii) from the critical current density, through Eq. [18]; (iii) from the critical transition time, according to Fig. 4 and Eq. [22]; and (iv) from the slope of the linear part of the critical transient, by means of Table II.

The kinetic and diffusion terms are conveniently resolved by the use of a variable-thickness cell. Equation [18] may be rearranged to the form

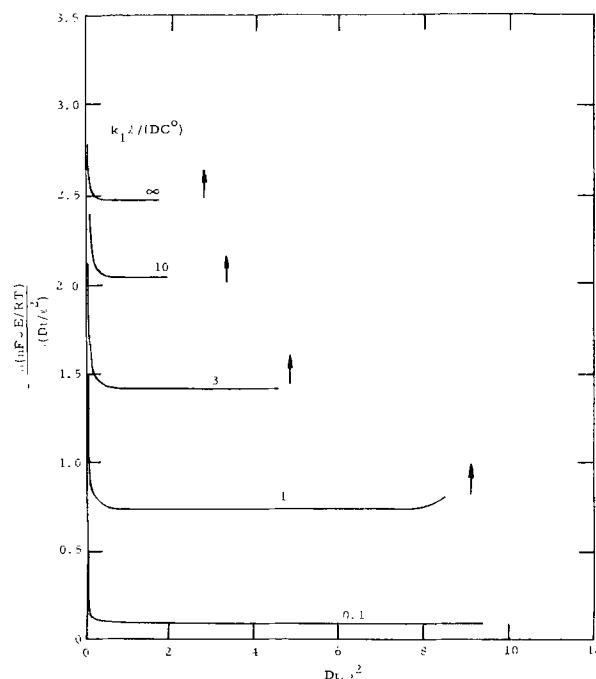


Fig. 5. Slope of the critical transient. Arrows indicate the times for $C_{x=0}/C^o = 10^{-3}$.

$$\frac{nF}{I_c} = \frac{l}{DC^0} + \frac{1}{k_1} \quad [26]$$

which is linear in l . Then if I_c is determined for several thicknesses of the electrolyte layer, and its reciprocal plotted as a function of l , the constant k_1 is found from the intercept at $l = 0$, and the product DC^0 is available from the slope. This is probably the most reliable procedure for determination of k_1 . The highest rate constant that can be measured in this way will depend on the relative magnitudes of k_1 and DC^0/l . In a typical situation, $D \approx 10^{-5}$ cm²/sec and $l \approx 10^{-3}$ cm. Then if C^0 is large, say 10^{-4} mole/cm³, the measurable k_1 might be as high as 5×10^{-6} mole/cm²-sec. When the dissolution is very slow, the critical current is independent of the electrode spacing, and k_1 is given simply by

$$k_1 = \frac{I_c}{nF} \left(\frac{DC^0}{l} \gg k_1 > 0 \right) \quad (27)$$

The smallest measurable k_1 will tend to be limited by extraneous faradaic current.

It is also possible, under favorable conditions, to determine D and C^0 separately from the dependence of τ_c on l . For this purpose, Eq. [22] may be written as

$$\frac{\tau_c}{l} = 9.8 \left(\frac{C^0}{k_1} \right) + 4.4 \left(\frac{l}{D} \right) \left(\frac{k_1 l}{DC^0} \approx 2 \right) \quad [28]$$

$(C_x=0/C^0=0)$

and the value of k_1 taken from the plot of $1/I_c$ vs. l . Present experience indicates that the critical transition time is more difficult to determine experimentally with satisfactory precision than is the critical current. It is significant, nevertheless, that all three parameters— k_1 , D , and C^0 —are obtainable, in principle, from thin-layer cell measurements.

Implications for Battery Electrode Processes

The thin-layer electrode discussed herein may be considered a model for the inner structure of a battery cathode containing a partially soluble reactant which is nonconductive in the solid state. Similarly, it may represent a discharged secondary anode with a slowly dissolving nonconductive solid reaction product. A more general application of this model to include dissolving materials with solid-state ionic or electronic conductivity would require external control of the potential at the dissolving interface. The potential dependence of k_1 , as discussed by Vermilyea, could then be taken into account (5). The thin-layer model is expected to find applications in organic-electrolyte batteries, where the solution-controlled cathode process may be a common occurrence (e.g., CuF_2). Some implications of the theory for battery electrode performance are as follows:

(i) The current density within the microstructure of a porous electrode must be less than that given by Eq. [18] if the discharge is to continue without extreme polarization.

(ii) As long as the critical current density region is avoided, a dissolution-controlled electrode will operate with a relatively low overvoltage ($\leq 0.2V$), attributable to concentration polarization, unless the faradaic process is irreversible.

(iii) With complete control by dissolution kinetics ($k_1 \ll DC^0/l$), the critical current density is proportional to the dissolution rate constant and independent of the spacing between the dissolving solid material and the current collector. With complete control by mass transport, the critical current density is inversely proportional to the spacing.

(iv) The number of coulombs obtainable per unit area of the current collector surface, at the critical current density, is given by

$$Q_c = I_c \tau_c \quad [29]$$

With I_c from Eq. [18] and τ_c from Eq. [22], this charge is found to be

$$Q_c = nFC^0 l \left[\frac{9.8 + 4.4 \left(\frac{k_1 l}{DC^0} \right)}{1 + \left(\frac{k_1 l}{DC^0} \right)} \right] \left(\frac{k_1 l}{DC^0} \approx 2 \right) \quad [30]$$

For very rapid dissolution, then

$$Q_c = 4.4 nFC^0 l \left(\frac{k_1 l}{DC^0} \gg 2 \right) \quad [31]$$

$$= 4.4 Q_1$$

where Q_1 is the electrical equivalent of the active material initially present in the solution layer at saturation. This limitation on the high-rate discharge depth may be avoided by keeping the current density below its critical value.

Dissolution Rate of CdF_2 in 4M KF

A brief investigation of cadmium fluoride dissolving in aqueous 4M KF was made to verify the thin-layer method for dissolution kinetics measurements. The procedures and results are reported below.

Experimental.—The thin-layer cell assembly, illustrated in Fig. 6, was mounted on a Starrett Model 2MARL micrometer caliper, readable to $\sim \pm 0.0001$ cm. The cadmium fluoride was a slice of a single crystal prepared in an earlier study (10). This material contained 0.01 mole per cent (m/o) Y(III) but was not cadmium-treated. The parallel plate, counter, and reference electrodes were all of cadmium metal. The area of the cadmium plate on which deposition occurred was 0.280 cm². The potential-time curves at constant currents were recorded at room temperature on a Princeton Applied Research Model 170 Electrochemistry System. The solubility of cadmium fluoride in 4M KF was estimated by a colorimetric method involving the comparison of cadmium sulfide suspensions (11).

Results and discussion.—The critical current effect predicted theoretically was observed for cadmium

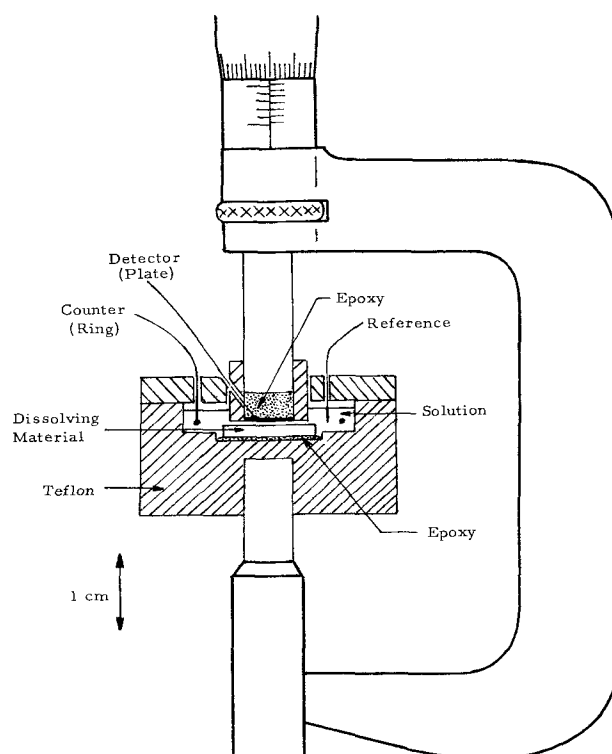


Fig. 6. Thin-layer cell assembly

Table III. Dissolution rate constant for cadmium fluoride in 4M KF

Evaluation method	$1/I_c$ vs. l Intercept	Linear slope	E vs. t	
			Transition time $C_{x=0}/C^0 = 10^{-3}$	$C_{x=0}/C^0 = 10^{-4}$
k_1 (mole/cm ² -sec)	8.1×10^{-9}	$2.3 \times 10^{-10(a)}$ $2.4 \times 10^{-9(b)}$	$4.5 \times 10^{-9(a)}$ $4.1 \times 10^{-9(b)}$	$5.4 \times 10^{-9(a)}$ $5.2 \times 10^{-9(b)}$

(a) $D = 9.5 \times 10^{-5}$ cm²/sec.(b) $D = 1.0 \times 10^{-5}$ cm²/sec.

fluoride, as in Fig. 7. Generally, it was possible to determine I_c within $\pm 10\%$, but an accurate τ_c proved somewhat more difficult to evaluate. The central curve in Fig. 7, for 7.9×10^{-4} A/cm², represented a close approach to the critical condition. The expected linear plot of $1/I_c$ vs. l was also obtained, as shown in Fig. 8. The dissolution rate constant k_1 , determined by several

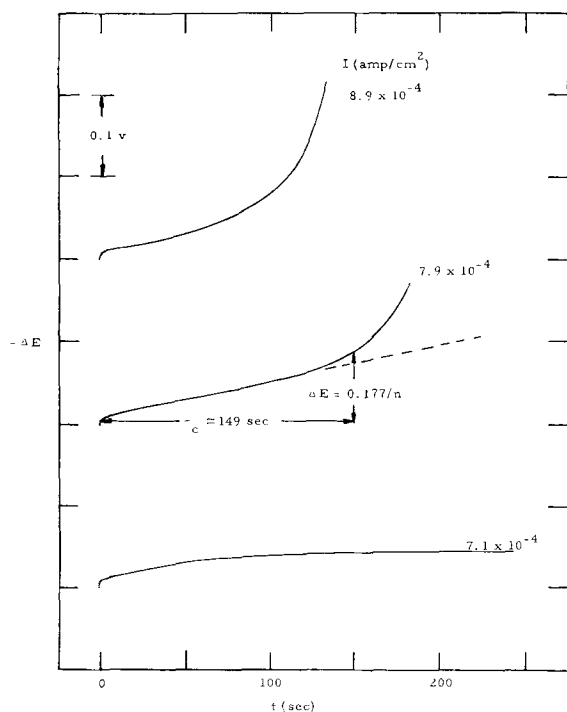


Fig. 7. Potential-time curves for CdF₂ dissolving in aqueous 4M KF. $l = 0.01$ cm.

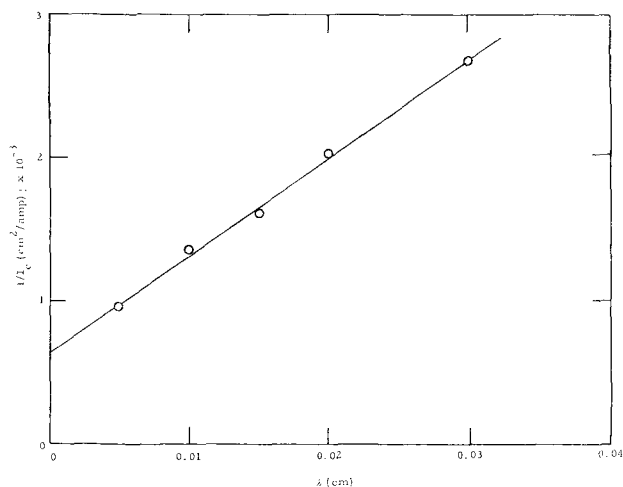


Fig. 8. Determination of k_1 for CdF₂ from critical current density in variable-thickness cell.

different procedures, is reported in Table III. The value of 8.1×10^{-9} mole/cm²-sec, from the intercept in Fig. 8, probably is the most accurate. A value of 7.6×10^{-11} mole/cm-sec was calculated for DC^0 from the slope of the same line. With the experimental C^0 of 8×10^{-7} mole/cm³, this result indicated a rather high diffusion coefficient of 9×10^{-5} cm²/sec for the cadmium-containing species in 4M KF. A solubility of 2.8×10^{-5} mole/cm³ is reported in the literature for CdF₂ in 4M KF at 20°C (12). However, this amount of CdF₂ did not dissolve, even on standing, in the present room-temperature experiments. The k_1 values for the E vs. t curves are therefore given on two bases in Table III: with $D = 9 \times 10^{-5}$, as calculated, and with $D = 1.0 \times 10^{-5}$, which is typical of metal ions in aqueous solutions. The smaller D yielded a more consistent result for k_1 from the linear slope.

These results show that the cadmium deposition process in the electrode system Cd/CdF₂(s)/4M KF was one of mixed control by dissolution kinetics and diffusion. The rate constant of 8×10^{-9} mole/cm²-sec corresponds to an equilibrium exchange rate of approximately 6 atomic layers/sec on the cadmium fluoride surface. Vermilyea (5) has estimated the maximum rate r_e for such an exchange from the relationship

$$r_e = DC^0/d \quad [32]$$

where d , the "jump distance," is of the order of 3×10^{-8} cm. With $DC^0 = 7.6 \times 10^{-11}$ mole/cm-sec, as found from the thin-layer measurements, the maximum exchange rate would be 2.5×10^{-3} mole/cm²-sec, or $\sim 10^5$ times as great as the observed k_1 .

Acknowledgment

This research was sponsored by the Air Force Cambridge Research Laboratories, Office of Aerospace Research, under Contract F19628-70-C-0086, but the report does not necessarily reflect endorsement by the sponsor.

Manuscript submitted July 6, 1971; revised manuscript received ca. Oct. 14, 1971.

Any discussion of this paper will appear in a Discussion Section to be published in the December 1972 JOURNAL.

REFERENCES

1. A. N. Shchukarev, *J. Russ. Phys. Chem. Soc.*, **28**, 604 (1896).
2. A. A. Noyes and W. R. Whitney, *Z. Physik. Chem.*, **23**, 689 (1897).
3. W. Nernst, *ibid.*, **47**, 52 (1904).
4. W. Jaenicke, *Z. Elektrochem.*, **56**, 473 (1952).
5. D. A. Vermilyea, *This Journal*, **113**, 1067 (1966).
6. M. M. Nicholson, *Proc. Power Sources Conf.*, **24**, 101 (1970).
7. A. B. Newman and L. Green, *Trans. Electrochem. Soc.*, **66**, 345 (1934).
8. C. R. Christensen and F. C. Anson, *Anal. Chem.*, **35**, 205 (1963).
9. P. Delahay, "New Instrumental Methods in Electrochemistry," Chap. 8, Interscience, New York (1954).
10. M. M. Nicholson, *This Journal*, In press.
11. F. D. Snell and C. T. Snell, "Colorimetric Methods of Analysis," 3rd ed., Vol. II, p. 148, Van Nostrand, New York (1949).
12. W. F. Linke and A. Seidell, "Solubilities," 4th ed., Vol. I, p. 731, Van Nostrand, New York (1958).

The Anodic Oxide of Iron: Its Component Layers and Their Properties

F. C. Ho* and J. L. Ord**

Department of Physics, University of Waterloo, Waterloo, Ontario, Canada

ABSTRACT

The anodic oxidation of an iron electrode in a neutral borate electrolyte is studied using a following ellipsometer. The oxide film is found to consist of two layers with different refractive indices: an outer layer of Fe_2O_3 and a thicker inner layer of Fe_3O_4 . A thin layer of Fe_3O_4 is grown on the electrode in the active state, and the electrode passivates when a partial monolayer of Fe_2O_3 is grown at the Fe_3O_4 -electrolyte interface. Passive state anodic oxidation causes simultaneous growth of the two layers, the inner layer growing approximately 80% faster than the outer layer. We conclude that the Fe_2O_3 layer inhibits anodic dissolution of the electrode, and that both the Fe_2O_3 layer and the portion of the Fe_3O_4 layer grown in the passive state act as the electrically limiting barrier across which the overpotential appears. The possibility that the two layers grow in a proportion dictated by the transport numbers of mobile defects (as has been proposed for the anodic oxide of tantalum) is discussed.

Iron has received considerable study as a passive electrode in acid electrolyte and as a battery electrode in basic electrolyte, but many recent studies (1-6) have been carried out in the neutral borate buffer made popular by Cohen and co-workers (7-10). This electrolyte offers many advantages for both electrochemical and ellipsometric measurements. At pH 8.4 iron has an active state which enables passivation to be studied, but the current density required to passivate the electrode (10^{-4} A/cm²) enables the electrode to be passivated readily without appreciable damage to the optical surface. In the passive state, there is negligible dissolution of the oxide, and the subsidiary layer of dissolution products which complicates optical measurements in acid electrolyte (3) is not present. In addition, the oxide layer can be removed from the surface at a controlled rate by cathodic reduction in the borate buffer, and the optical constants of the surface return to their initial values after reduction is complete.

There have been a number of optical studies of the anodic oxidation of iron in borate buffer (1, 3, 6), and although these studies have generally agreed on the thickness of the anodic oxide, they have disagreed on whether the anodic oxide consists of a single layer or two layers with different composition. The studies which favored two-layer models (1, 3) were unable to present optical evidence of the existence of more than one layer on the surface. The aim of this paper is to present direct optical evidence showing that the anodic oxide consists of two component layers.

Experimental

The following ellipsometer built in our laboratory, described in detail elsewhere (11), uses a helium-neon gas laser as a light source, and all of our measurements are carried out at a wavelength of 6328Å. The ellipsometer is driven by stepping motors geared to give the instrument a resolution of 0.01° and an average nulling time of 0.7 sec under the experimental conditions used in this study. In a typical experiment we record over 1000 data points with a range of 2° in polarizer reading, P , and 0.2° in analyzer reading, A , and a standard deviation of 0.005° as determined by least squares analysis. To simplify handling and displaying the data, we generally divide the points into groups at 0.1° increments in P and calculate an average value of A for the 15 to 30 points in each

group. These averaged points are then plotted in figures with the scale on the A -axis expanded fivefold over the scale on the P -axis. The averaged points generally exhibit a 0.003° standard deviation when fitted to straight lines using least squares. All of the measurements reported in this paper were made on a sample whose alignment was not disturbed throughout the series of experiments, and hence the data do not show the offset from experiment to experiment that generally characterizes ellipsometric data.

The cell used with the ellipsometer in this work is a hollow equilateral prism of 75 ml capacity into which a platinum counterelectrode, mercurous sulfate reference electrode with 0.1N K_2SO_4 salt bridge, gas dispersion tube, and sample holder can be inserted through standard-taper joints. The geometry of the cell requires that the ellipsometer be set for an angle of incidence of 60°. The cell has inlet and outlet connections enabling deaerated electrolyte to be added from a 2-liter reservoir, and electrolyte contaminated with ferrous ions to be flushed from the cell. The electrolyte used in all measurements is an equivolume mixture of 0.15N sodium borate and 0.15N boric acid of pH 8.4. All the experiments were carried out at room temperature (23°C).

The iron sample is a cylindrical single crystal 0.3 in. long by 0.2 in. in diam which is clamped between Teflon washers in the holder to expose a vertical surface of 1.2 cm² area to the electrolyte. The optical measurements are made on a flat on one side of the cylinder. Since variations in surface roughness can affect the optical data, the experiments were performed in a carefully chosen sequence. Several preliminary oxidation-reduction cycles were performed to smoothen the surface which had been chemically polished just prior to insertion in the cell. When the bare surface polarizer reading increased by no more than 0.01° after an oxidation-reduction cycle, the experiments were started, and no further change in surface roughness was detected until the final experiment in the series was performed. The linear potential sweep experiment was performed last because we expected the slow passivation to roughen the surface (which it did, introducing an offset of 0.06° in P).

The analog circuitry consists of three operational amplifiers which are used to supply the cell with constant currents, constant potentials, or linear potential sweeps, and two operational amplifiers which follow the potential and the current. The current source can provide an a-c current superimposed on the d-c en-

* Electrochemical Society Student Associate Member.

** Electrochemical Society Active Member.

Key words: anodic oxidation, iron oxide, passivity, ellipsometry.

abling a lock-in amplifier to detect the potential component 90° out of phase with the a-c current in order to monitor the capacitance of the electrode. All potentials quoted in this paper are measured relative to the mercurous sulfate reference electrode.

Results

When designing experiments for the following ellipsometer, we try to keep the layer growth rates reasonably slow and approximately constant so that the ellipsometer can achieve its optimum performance. Galvanostatic experiments usually provide the best conditions, and most of the experiments described here were performed at a constant $10 \mu\text{A}/\text{cm}^2$. This current density is not adequate to passivate the electrode, but a special passivation technique is required in any event in order to avoid the deposition of $\text{FeO}\cdot\text{OH}$ from ferrous ions in the electrolyte. Since our experiments are designed to look for a "fine structure" in the optical data, it is important to avoid deposition of even traces of $\text{FeO}\cdot\text{OH}$.

The effects of trace $\text{FeO}\cdot\text{OH}$ deposition show up clearly in a linear potential sweep experiment. This type of experiment provides good experimental conditions for the ellipsometer when the potential is swept in the anodic direction, and is better than a galvanostatic experiment for following passivation. Cathodic potential sweeps provide poor conditions for following layer removal because of the narrowness of the potential regions over which reduction takes place.

The data plotted in Fig. 1 were obtained from an experiment in which an anodic sweep at $10.8 \text{ mV}/\text{sec}$ was followed by galvanostatic reduction at $10 \mu\text{A}/\text{cm}^2$. The sweep begins at point A with the electrode under cathodic reduction in an unstirred electrolyte free of ferrous ions. (The argon flow was shut off for this experiment to provide reproducible conditions for an experiment in which diffusion plays a significant role.) The current density and polarizer null reading are plotted vs. potential in the lower part of the figure for the anodic sweep, and the optical data are displayed in a polarizer-analyzer plot in the upper portion of the figure.

The nature of the passivation process shows up clearly from the data in Fig. 1. The change in polari-

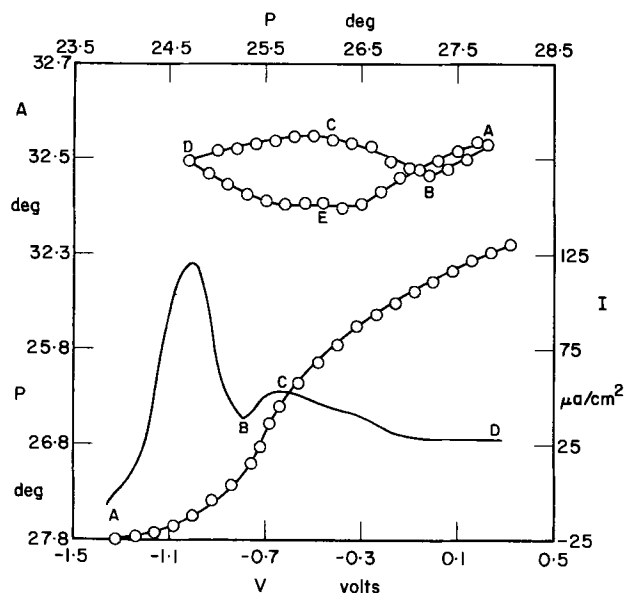


Fig. 1. Anodic potential sweep at $10.8 \text{ mV}/\text{sec}$ followed by cathodic reduction at $10 \mu\text{A}/\text{cm}^2$ for an iron electrode in borate buffer. The current density (solid curve, right scale) and polarizer readings (open circles, lower left scale) are plotted vs. potential in the lower portion of the figure for the anodic sweep ABCD. The optical data are plotted in the upper portion of the figure.

zer null position plotted in the figure is proportional to film thickness for thin films, and estimates of film thickness during passivation can be made using the approximate calibration factor of $15 \text{ \AA}/\text{deg}$ (see Appendix). Little film buildup is indicated until the current density approaches its peak value of $120 \mu\text{A}/\text{cm}^2$ at -0.990V , at which point about 4 \AA of film cover the surface. The layer thickens to 10 \AA as the current falls from its peak value to $35 \mu\text{A}/\text{cm}^2$ at -0.772V (point B in the figure).

As the linear sweep continues beyond point B, there are three experimental results which detect the deposition of $\text{FeO}\cdot\text{OH}$: the current density rises, the P - A plot inflects sharply upward, and the P - t slope increases. The deposition process has been studied in detail in this electrolyte by Markovac and Cohen (12, 13), and the optical properties of the deposited layer have been studied in our laboratory (14). The reason that even a small deposition partial current has a significant effect on optical measurements is twofold: the deposited $\text{FeO}\cdot\text{OH}$ has a real refractive index of 1.7 which differs significantly from the index of the anodic oxide, and deposition of one molecule of $\text{FeO}\cdot\text{OH}$ requires the transfer of only a single electron. Even though the concentration of ferrous ions in the electrolyte does not reach a significant level in this experiment, the critical factor determining the extent of deposition is the concentration of ferrous ions adjacent to the electrode as the potential crosses the value above which deposition takes place. The results presented in Fig. 1 are valid only for a vertical electrode in an unstirred electrolyte swept at $10.8 \text{ mV}/\text{sec}$, but any passivation process which takes the electrode through the active state directly to a potential above the deposition potential will show some of the effects of $\text{FeO}\cdot\text{OH}$ deposition. One very simple way to lessen the deposition effect is simply to pause at point B in Fig. 1 and increase the argon flow for a short time to allow the ferrous ions to diffuse into the bulk of the electrolyte. In the passivation technique we use, the electrode is passivated by connection to a potentiostat set at -0.825V , then, after the current density drops below $2 \mu\text{A}/\text{cm}^2$, the cell is drained and refilled with electrolyte three times before the electrode is taken to higher potentials in the passive region. This technique minimizes the total number of ferrous ions produced, and, after three changes of electrolyte, no traces of $\text{FeO}\cdot\text{OH}$ deposition can be detected optically.

Data obtained from a galvanostatic experiment performed in electrolyte free of ferrous ions are presented in Fig. 2. The electrode was first passivated by the technique described above, then the electrode was held at -0.825V until the current density reached $1.0 \mu\text{A}/\text{cm}^2$. At this point (point A in the figure) an anodic current of density $10 \mu\text{A}/\text{cm}^2$ was applied, and the growth of the film was followed to a potential of 0.3V (point B). The current was then reversed, and the reduction of the film proceeded through two potential plateaus with distinct optical data segments, BC and CD. At point D the optical data return to their initial values prior to passivation.

The plots of potential and polarizer null reading vs. time in the lower part of the figure show that a film builds up at a constant rate under anodic conditions, and is removed at a faster rate under cathodic conditions. In the upper part of the figure the optical data are shown on a polarizer vs. analyzer plot. The structure in the data is accentuated in the figure by the five-fold expansion of the analyzer scale over the polarizer scale. The oxidation data trace out a straight line from A to B, and on reduction the data fall on two distinct lines, BC and CD, both with slopes different from the slope of AB. The structure in this figure could not be resolved in the earlier work carried out in this laboratory with a manual ellipsometer (3).

As is always the case when very thin films are studied, unique refractive index and thickness values can-

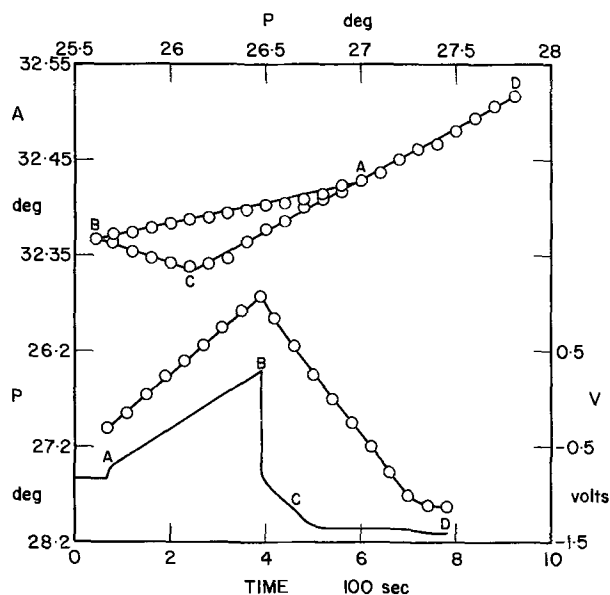


Fig. 2. Galvanostatic oxidation (AB) and reduction (BCD) at $10 \mu\text{A}/\text{cm}^2$ of an iron electrode in borate buffer. The optical data are displayed on a P - A plot in the upper portion of the figure (top and upper left scales), and potential (solid curve, right scale) and P (open circles, lower left scale) are plotted vs. time in the lower portion of the figure.

not be determined from the optical data. Calculations of possible refractive index values are given in the appendix, as are values for the thickness calibration factor (the number of angstroms of film which shift the polarizer null reading one degree).

It is possible, however, to interpret the structure in the optical data without detailed analysis. When a very thin film of constant refractive index builds up uniformly on a substrate, the optical data obtained with an ellipsometer during the growth of the film trace out a straight line on a P - A plot. The line starts at the bare substrate point and has a slope which depends on the value of the film refractive index. Of the three linear segments, AB, BC, and CD of the optical data in Fig. 2, only CD is a straight line passing through the bare substrate point, and hence only in this region can the surface be covered with a simple film of constant index and changing thickness. Both the passive growth segment, AB, and the first reduction segment, BC are linear, but neither extrapolates to the bare surface point, point D.

The two-plateau potential transient observed on cathodic reduction was interpreted by Nagayama and Cohen (7) as resulting from sequential removal of layers of $\gamma\text{-Fe}_2\text{O}_3$ and Fe_3O_4 from the surface. This interpretation of the process has met with wide, but not unanimous (6) agreement among workers in the field. It is the simplest interpretation which can be given the data presented in Fig. 2, and it is the only interpretation of the reduction process which is directly consistent with all our experimental results. We therefore conclude that segment BC of the optical data is generated as a constant-index layer of Fe_2O_3 is reduced in thickness until at point C the underlying layer of Fe_3O_4 is exposed to the electrolyte. Segment CD is then generated as this inner constant-index layer is reduced in thickness until at point D the bare substrate is exposed to the electrolyte. The difference between the slopes of segments BC and CD is due to the difference between the refractive indices of Fe_2O_3 and Fe_3O_4 . The sets of possible refractive indices for the two layers which fit the data in Fig. 2 are given in the appendix.

If the reduction process is identified as the sequential removal of layers of Fe_2O_3 and Fe_3O_4 , the passive-state

anodic oxidation process must result in the simultaneous growth of these two layers. (The active state oxidation data run parallel to CD indicating growth of Fe_3O_4 only.) The linearity of optical data segment AB shows that the two layers grow at rates whose ratio is a constant independent of potential. One can think of AB as a vector whose components along BC and CD are proportional to the thicknesses of the component layers grown during passive-state oxidation.

The constancy of the ratio of the layer growth rates and the linearity of the growth as a function of potential can be demonstrated by a series of experiments in which cathodic reduction is initiated at intermediate points along AB. In Fig. 3 the ABC data from Fig. 2 (for which the peak anodic potential was 0.3V) is replotted as A3-B3-C3, and data from experiments with peak potentials of 0.0 and -0.3V are plotted as A2-B2-C2 and A1-B1-C1, offset in the analyzer direction by 0.08° and 0.16° respectively. The offsets enable the data to be plotted without overlap, and construction lines are drawn through the triangle vertices to show the similarity of the triangles and the linear dependence of the lengths of their sides on the peak anodic potential. The lengths of the sides of the optical data triangles are directly proportional to the difference between the peak anodic potential and -0.97V .

The inflection at C in a P - A plot of the optical data can also be detected in plots of P or A vs. time. Since A has its minimum value at C, the detection of the inflection in an A - t plot is just as direct as it is in a P - A plot. The inflection in a P - t plot is less apparent, but even on the scale used for the P - t plot in Fig. 2 the inflection at C can be seen. The slope of the cathodic portion of the P - t plot is steeper than it is in the anodic portion.

If we were to choose specific values for the layer indices, we could, from the data presented to this point, calculate growth rates and thicknesses for the two component layers as a function of potential under anodic and cathodic conditions. In order to determine the electrochemical properties of the individual layers, however, we require additional data on the electrical behavior of the electrode. In galvanostatic experiments, the potential of the electrode is its most prominent electrical parameter. When a-c currents are super-

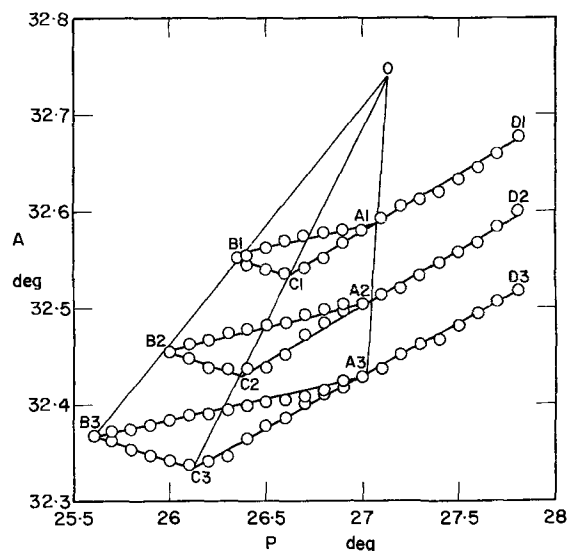


Fig. 3. P - A plot of the optical data obtained in galvanostatic experiments at $10 \mu\text{A}/\text{cm}^2$ with peak potentials of -0.3V (1), 0.0V (2), and 0.3V (3). The data from the 0.0V and -0.3V experiments are offset 0.08° and 0.16° respectively in the A direction to enable the construction lines to show the proportionality between the lengths of the triangle sides and the difference between the peak potential and -0.97V .

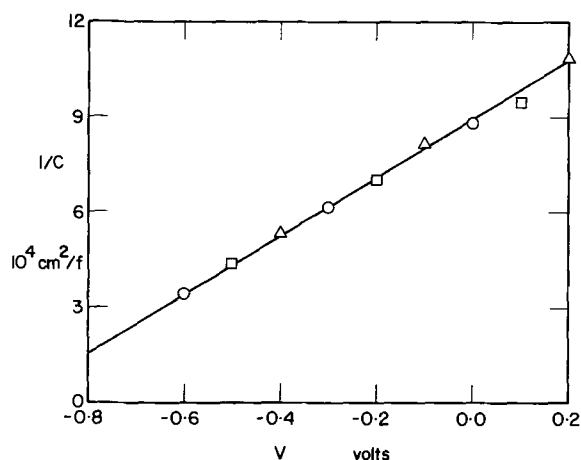


Fig. 4. Reciprocal capacitance as a function of potential during galvanostatic oxidation at $10 \mu\text{A}/\text{cm}^2$ with superimposed a-c currents of frequency 50 Hz (circles), 100 Hz (squares), and 200 Hz (triangles).

imposed in galvanostatic experiments, the a-c potential can be recorded along with the d-c potential. The capacitance of the electrode can be calculated from the component of the a-c potential 90° out of phase with the current, and conditions can be found for which this capacitance shows the reciprocal dependence on film thickness expected of the capacitance of an oxide film. In Fig. 4, values of reciprocal capacitance measured at frequencies of 50, 100, and 200 Hz are plotted vs. formation potential for galvanostatic oxidation at $10 \mu\text{A}/\text{cm}^2$. (We use the term formation potential to designate the potential of the electrode under galvanostatic oxidation at a specified formation current density.) The three sets of data all fall on a line which intersects the potential axis at -0.97V , the potential at which the optical data triangle extrapolates to zero. This is also the potential which was identified as the zero of overpotential of the passive iron electrode in this electrolyte in an earlier paper (3), in which open-circuit transients were used to determine both the Tafel slope and the reciprocal capacitance of the electrode. Hence the thickness of the passive layer, the electrically limiting layer across which the overpotential appears, has the same dependence on formation potential as have the lengths of the sides of the optical data triangle. The passive layer may correspond to any of the sides of the triangle, and thus it may consist of the outer layer of Fe_2O_3 , the inner Fe_3O_4 formed in the passive state, or both. The experiments described below are designed to enable us to decide among these three possibilities.

The key to the determination of the properties of the individual component layers is provided by the fact that they grow simultaneously but are removed sequentially. In principle, we can use cathodic reduction to "plane away" as much of the film as we wish from the side exposed to the electrolyte, then we can make the electrode anodic to determine the electrical properties of the portion of the film which remains. This experiment is complicated in practice by the necessity of sweeping ferrous ions produced on reduction from the electrolyte before the electrode is made anodic. We do this by opening the circuit and changing the electrolyte three times before reapplying the anodic current.

The first cycling experiments show the anodic behavior of the inner layer with the outer layer removed completely by cathodic reduction. The results of two such experiments are plotted in Fig. 5 with some of the finer detail plotted on an expanded scale in Fig. 6. The initial anodic cycles are the same as the one for the data plotted in Fig. 2. At point B the current is

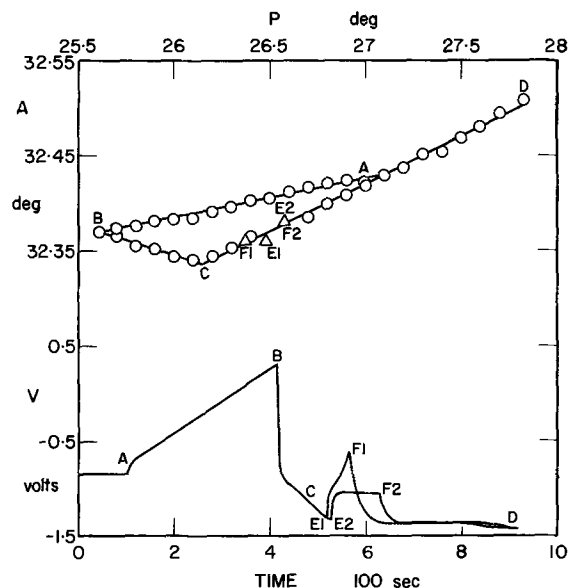


Fig. 5. Galvanostatic oxidation (AB), reduction (BCE), reoxidation (EF), and final cathodic reduction (FD) at $10 \mu\text{A}/\text{cm}^2$ of an iron electrode in borate buffer. The results of two experiments in which the initial reduction is taken to slightly different points are superimposed in the figure. The optical data are displayed in a P-A plot in the upper portion of the figure, and potential is plotted vs. time in the lower portion. The time required to change the electrolyte at point E is not shown in the figure.

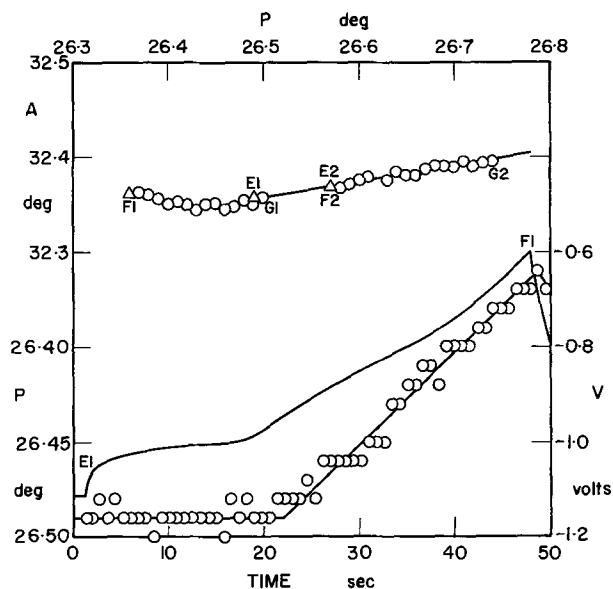


Fig. 6. Data from Fig. 5 plotted on expanded scales. Potential and polarizer reading are plotted vs. time in the lower portion of the figure for segment E1-F1, and the initial portions of the optical data obtained on reduction from F1 and F2 are plotted in the upper portion.

reversed and the electrode is reduced until all of the outer layer and about half of the inner layer formed in the passive state are removed from the electrode. The two experiments whose data are superimposed in the figure have the anodic current reapplied at slightly different points along the cathodic reduction transient. At point E1 in the first experiment and E2 in the second, the circuit is opened while the electrolyte is changed. The inner layer dissolves slowly during the minute or so required to change the electrolyte (not shown in the time plot in Fig. 5), and points E1 and

E2 are actually the optical readings recorded just prior to reapplying the anodic current. The anodic transients E1-F1 and E2-F2 differ considerably although their starting points are close together. E2-F2 is a typical active-state transient with the potential remaining in the active region and the optical data showing no change for a period of 100 sec at an anodic current density of $10 \mu\text{A}/\text{cm}^2$. E1-F1, plotted on an expanded scale in the lower part of Fig. 6, is a typical passivation transient with the potential staying in the active region for 20 sec before inflecting into the passive region. The polarizer reading shows no change until the potential reaches the passive region, then changes linearly with time at a rate similar to its rate during oxidation from A to B. The electrode is active at both E1 and E2, but at E1 it can be passivated at an anodic current density of $10 \mu\text{A}/\text{cm}^2$, whereas at E2 it cannot.

The final cathodic reductions from F1 and F2 to D are included in Fig. 5 and their initial portions are shown in an expanded P-A plot in the upper part of Fig. 6. Points E1 and F1 appear in the plot but the optical data obtained during oxidation from E1 to F1 are omitted in order not to obscure the structure in the reduction data. On reduction from F1 the data show the inflection characteristic of the presence of an outer layer, whereas on reduction from F2 the data all fall on the line characteristic of the inner layer.

The cycling data presented in Fig. 5 and Fig. 6 provide more information about the passivation process than they do about the potential profile in the passive state. They show that the inner layer is subject to anodic dissolution when exposed to the electrolyte, but they provide no information concerning the anodic behavior of the inner layer when covered by an outer layer which blocks the anodic dissolution reaction. In order to determine the electrical characteristics of the individual layers, we perform a cycling experiment in which we reapply the anodic current after reducing the outer layer until just sufficient of it to keep the electrode passive (less than one monolayer) remains covering the inner layer. The results of this experiment are plotted in Fig. 7.

The initial anodic cycle in Fig. 7 is the same as it is in Fig. 2 and Fig. 5. The reduction cycle is stopped at E by opening the circuit, and the electrolyte is changed

before reapplying the anodic current. As in Fig. 5, the time required to change the electrolyte is not shown in the time plot in the lower part of the figure. The open-circuit potential just before reapplying the $10 \mu\text{A}/\text{cm}^2$ anodic current is -0.92V , and hence the electrode is still passive. When the circuit is closed, the potential initially rises rapidly to point F, then takes on a slope more like the usual oxidation slope, until at point G the potential returns to 0.3V , its value at point B. The optical data show an inflection at point F, and when 0.3V is reached at point G the polarizer reading is significantly larger than it is at point B. The final cathodic reduction, GHD, enables the thicknesses of the component layers at G to be determined. The lengths of the optical data segments obtained on reduction indicate that point G the outer layer thickness is only 53% of its value at B, and that the inner layer grown in the passive state has increased its thickness by 12% at G over its thickness at B. The slope of the optical data segment GH is significantly greater than the slope of BE, hence the composition of the outer layer must be changed somewhat by the cycling process.

The reciprocal capacitance of the electrode was monitored during the cycling experiment, and the a-c potential recorded during segments AB and EFG of the experiment are plotted in Fig. 8. Along AB it is reasonable to take the a-c potential as a measure of the reciprocal capacitance of the oxide film (except in the region of point B where the curvature in the data is characteristic of the onset of oxygen evolution). On reoxidation, the a-c potential cannot be assumed proportional to the reciprocal capacitance of the film during the rapid rise in potential from E to F, but this assumption appears reasonable along FG. The data in Fig. 8 show that the reciprocal capacitance has lower values during reoxidation than it has at the same potential during oxidation.

Discussion

The difference between the indices of the component layers of the anodic oxide makes their direct experimental detection possible, and the proportionalities between layer thickness and formation potential follow directly from experimental results. The resulting conclusion that the passive-state overpotential must appear either across the outer layer, the inner layer formed in the passive state, or both, is not a definitive statement, but it is based directly on experimental results. In order to decide among these three possibilities we must use the cycling experiment data and draw conclusions concerning the electrochemical pro-

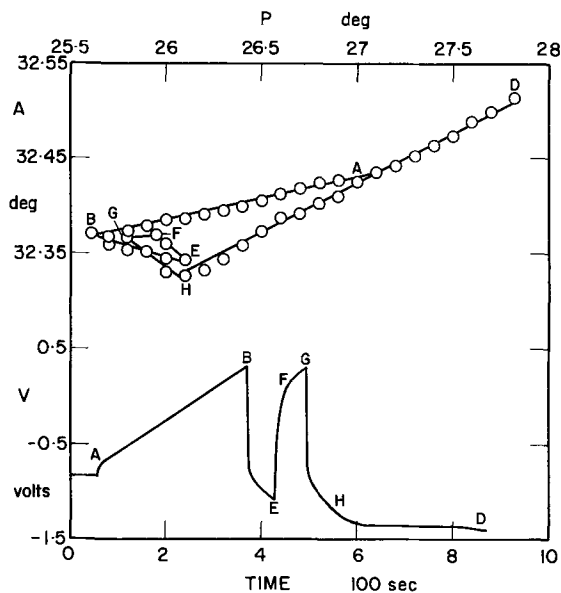


Fig. 7. Galvanostatic oxidation (AB), reduction (BE), reoxidation (EFG), and final reduction (GHD) at $10 \mu\text{A}/\text{cm}^2$ of an iron electrode in borate buffer. The optical data are displayed on a P-A plot in the upper portion of the figure, and potential is plotted vs. time in the lower portion. The time required to change the electrolyte at point E is not shown in the figure.

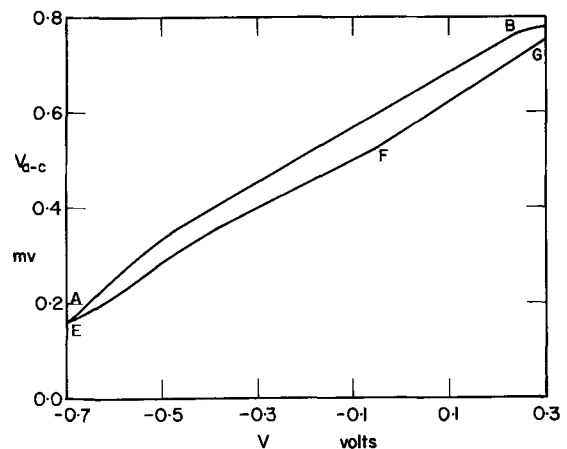


Fig. 8. The a-c potential 90° out of phase with a $10 \mu\text{A}/\text{cm}^2$ a-c current superimposed on a d-c current of $10 \mu\text{A}/\text{cm}^2$, plotted as a function of potential for segments AB and EFG of the cycling experiment plotted in Fig. 7.

erties of the individual layers. The way in which these conclusions are drawn requires some discussion.

The first cycling experiments show that the electrode is no longer passive once the outer layer is removed. This result can be interpreted in two ways: either the inner layer plays no role in passivity, or it can play a role only when it is protected from the electrolyte by the outer layer.

The final cycling experiment provides results which enable us to decide between these two possibilities. When the electrode is reoxidized with only a thin outer layer covering the lower layer, the potential rises rapidly to within 0.2V of its value at the end of the initial oxidation cycle, and when it does return to this peak potential, the outer layer has regained only 53% of its former thickness. If the overpotential appeared across the outer layer only, the reduction in its thickness would have resulted in a potential of $-0.30V$ rather than the observed $0.30V$ at point G. Hence the overpotential cannot appear across the outer layer alone; it must appear either across both it and the passive portion of the inner layer, or across the latter only.

Two results from the final cycling experiment show that the overpotential must appear across both the outer layer and the inner passive layer. When $0.3V$ is reached for the second time, the passive portion of the inner layer has increased in thickness by 12%, and if the potential appeared across this layer alone the potential at point G would have been $0.45V$ rather than the observed $0.3V$. In addition, the decrease in the reciprocal capacitance on cycling suggests that the two layers act as capacitors in series. A decrease in the thickness of the outer layer and an increase in the thickness of the inner layer can return the electrode to the same overpotential and lower reciprocal capacitance only if the overpotential appears across both the outer layer and the passive portion of the inner layer.

If we assume that a simple model of capacitors in series is valid, we can calculate the potentials across the component layers and their reciprocal capacitances at point B. The total potential and total capacitance can be expressed in terms of the individual layer capacitances and potentials at point B and G, yielding four equations. The proportionality between the thicknesses of the component layers at B and G is known from the optical data, and since all simple models have both reciprocal capacitance and potential proportional to thickness, the four equations can be written in terms of the four variables consisting of the component layer potentials and capacitances at point B. These equations can be solved to give $V_1 = 1.01V$ and $1/C_1 = 6.78 \times 10^4 \text{ cm}^2/\text{fd}$ for the passive inner layer, and $V_2 = 0.256V$ and $1/C_2 = 3.40 \times 10^4 \text{ cm}^2/\text{fd}$ for the outer layer.

With an additional assumption concerning the refractive indices of the layers, the fields in the component layers and their low frequency dielectric constants can be calculated. If we assume that the two layers differ little in index, and we take 2.0 for the real components of their indices, we calculate fields of 7.7 and $3.0 \times 10^6 \text{ V/cm}$ (at $10 \mu\text{A/cm}^2$), and dielectric constants of 22 and 27 for the inner and outer layers respectively. We present these values as typical of the numbers resulting from this line of reasoning, not as results following directly from experimental data. The optical evidence for a difference in the composition of the outer layer after cycling shows that these calculations are no more than a guess at quantitative values for the electrical parameters of the individual layers.

Although it is difficult to determine the individual layer parameters accurately, it is clear that both layers play important roles in passivity. The outer Fe_2O_3 layer inhibits the anodic dissolution process and drops some of the overpotential, but the bulk of the overpotential appears across the Fe_3O_4 formed in the passive

state, and hence it is the growth of this layer which is primarily responsible for the low currents characteristic of passivity. At the present time we can offer no explanation for the difference between the properties of the portions of the Fe_3O_4 layer formed in the active and passive states. We suspect that a slightly different layer is grown when Fe_3O_4 is exposed to the electrolyte, its growth competing with anodic dissolution, than when Fe_3O_4 is grown under a layer of Fe_2O_3 in the passive state. We could fit our optical data on reduction of Fe_3O_4 to two linear segments, but we doubt that this would be significant because the fit to a single line has a standard deviation of less than the resolution of the instrument.

Throughout this paper we have referred to the outer layer as Fe_2O_3 , and we have taken pains to point out that its refractive index differs from that of the FeOOH layer which can be deposited if ferrous ions are not removed from the electrolyte. We have taken care to remove ferrous ions from the electrolyte so that deposition of FeOOH does not take place except in the linear sweep experiment, but careful study of the structure in our data leads us to conclude that FeOOH can also be produced by direct anodic oxidation when Fe_3O_4 is exposed to the electrolyte. The buildup or removal of FeOOH can be detected by the slope of the data in a P - A plot, and we can distinguish between the two methods of its formation from a P - t plot because the deposition process involves only $1/3$ as much charge transfer as does direct oxidation, and begins at a higher potential. If we are correct in our conclusion that the hydrated ferric oxide (FeOOH or $\text{Fe}_2\text{O}_3 \cdot \text{H}_2\text{O}$) can be formed anodically when Fe_3O_4 is exposed to the electrolyte, whereas Fe_2O_3 is formed by anodic oxidation in the passive state, then passivation of the electrode must result from formation of a partial monolayer of FeOOH rather than Fe_3O_3 at the Fe_3O_4 surface. The rate of FeOOH formation indicates that the process is anodic oxidation in competition with anodic dissolution rather than dissolution-precipitation.

In most of our experiments the proportion of FeOOH in the outer layer is not significant. The most important exception occurs in the reoxidation segment of the final cycling experiment which was used to calculate the electrical parameters of the Fe_3O_4 and Fe_2O_3 layers. If we attempt to correct these calculations to take account of the presence of FeOOH , we obtain values of 8.8 and $2.2 \times 10^6 \text{ V/cm}$ for the fields at $10 \mu\text{A/cm}^2$, and 28 and 20 for the dielectric constants of the Fe_3O_4 and Fe_2O_3 layers respectively. The numbers should still be considered only rough estimates for the values of the parameters. The other experiment in which a significant proportion (if not all) of the outer layer is composed of FeOOH is the repassivation segment of the first cycling experiment. This is not readily apparent from inspection of Fig. 6 because an expanded polarizer scale is used in the figure.

The simultaneous growth of two layers requires that oxygen incorporated in the inner layer must be transported through the outer layer, and iron incorporated in the outer layer must be transported through the inner layer. With the possibility of iron being transported as ferrous and ferric vacancies or interstitials, and of oxygen perhaps being mobile in the form of vacancies, the problem is not so much one of proposing a model, but of finding sufficient experimental evidence to limit the number of models which can account for the data. The situation at the interface between the two layers is very complex, and no clear distinction can be drawn between growth and conversion processes. It is not surprising that our calculation of the layer parameters indicates that the electric displacement is not the same in the two layers, and hence the interface between them has a charge of density $1.6 \times 10^{-5} \text{ coulomb/cm}^2$ on it.

In this paper we have presented only the results of galvanostatic oxidation experiments carried out at a current density of $10 \mu\text{A/cm}^2$. Our aim in so doing has

been to present the results of measurements on this system under the simplest set of experimental conditions which show the important features of its behavior. We are currently involved in a more detailed study of this system under a wide variety of experimental conditions, and we will present our attempt at constructing a detailed model for the film growth process when the study is complete.

Acknowledgment

This work received partial support from the National Research Council of Canada under Grant No. A-1151.

Manuscript submitted May 8, 1971; revised manuscript received ca. Aug. 17, 1971.

Any discussion of this paper will appear in a Discussion Section to be published in the December 1971 JOURNAL.

APPENDIX

The optical data-analysis program is written in Hewlett-Packard's version of BASIC, and consists of approximately 110 statements. The program makes use of the matrix routines and is written to handle multiple-layer calculations. The substrate index calculated for iron at a wavelength of 6328 Å is 3.44-3.97i. Values of the layer index, $n-ik$, giving theoretical curves which fit the data, are obtained by plotting the locus traced out in the $P-A$ plane as k is varied for a layer of fixed n and thickness. This curve generally intersects the experimental data line at two points, one at a low value of k and one at a high value. These intersections give the values of k for which $n-ik$ is a possible value of the layer index, and enable thickness calibration factors, expressed as angstroms per degree change in P , to be calculated for each index value.

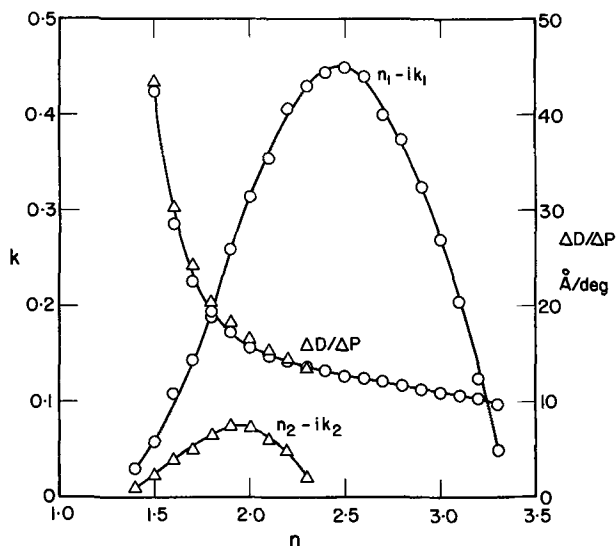


Fig. 9. The low k -value sets of possible refractive indices, plotted as curves in $n-k$ space, for the inner (n_1, k_1) and outer (n_2, k_2) layers, and the corresponding thickness calibration factors, $\Delta D/\Delta P$, plotted as a function of n .

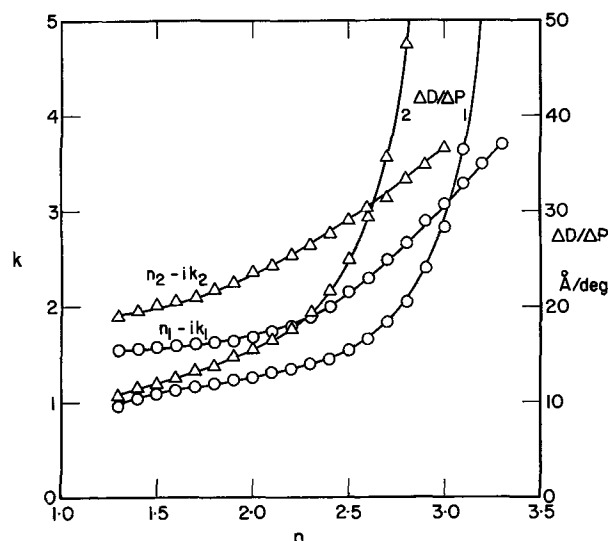


Fig. 10. The high k -value sets of possible refractive indices, plotted as curves in $n-k$ space, for the inner (n_1, k_1) and outer (n_2, k_2) layers, and the corresponding thickness calibration factors $\Delta D/\Delta P$, plotted as a function of n .

We display the results of these calculations as curves in $n-k$ space in Fig. 9 for low k values and in Fig. 10 for high k values. The values plotted for the outer layer index were calculated for an inner layer index of 2.5-0.45i, but the outer layer index calculation is not overly sensitive to the value chosen for the inner layer index. Each point on these curves gives a possible value of a layer index.

The thickness calibration factor corresponding to each index is plotted in the figures as a function of n . For low k values, the optical thickness calibration factor is not overly sensitive to k , and one curve is drawn for the two layers. If the low k indices plotted in Fig. 9 are taken as more reasonable on physical grounds, and if a value for n of 2 or a little greater is taken as reasonable for an oxide film, a "reasonable guess" at the thickness calibration factor of 15 Å/deg P is obtained.

REFERENCES

1. J. Kruger and J. P. Calvert, *This Journal*, **114**, 43 (1967).
2. J. L. Ord, *ibid.*, **113**, 213 (1966).
3. J. L. Ord and D. J. DeSmet, *ibid.*, **113**, 1258 (1966).
4. R. V. Moshtev, *Ber. Bunsenges.*, **71**, 1079 (1967).
5. R. V. Moshtev, *ibid.*, **72**, 452 (1968).
6. N. Sato, K. Kudo, and T. Noda, *Corrosion Sci.*, **10**, 785 (1970).
7. M. Nagayama and M. Cohen, *This Journal*, **109**, 781 (1962).
8. M. Nagayama and M. Cohen, *ibid.*, **110**, 670 (1963).
9. N. Sato and M. Cohen, *ibid.*, **111**, 512 (1964).
10. N. Sato and M. Cohen, *ibid.*, **111**, 519 (1964).
11. J. L. Ord, *Surface Sci.*, **16**, 155 (1969).
12. V. Markovac and M. Cohen, *This Journal*, **114**, 674 (1967).
13. V. Markovac and M. Cohen, *ibid.*, **114**, 678 (1967).
14. J. L. Ord and D. J. DeSmet, *ibid.*, **118**, 206 (1971).

Double Layer Capacitance of Iron and Corrosion Inhibition with Polymethylene Diamines

E. McCafferty¹ and Norman Hackerman^{*,2}

Department of Chemistry, The University of Texas, Austin, Texas 78712

ABSTRACT

The effect of α,ω -polymethylenediamines $\text{NH}_2\text{-(CH}_2)_n\text{-NH}_2$ ($n = 2-12$) on the corrosion of iron in deaerated 6*N* HCl at 25° was investigated by polarization measurements and colorimetric analysis of solution. The adsorption of these inhibitors at the metal/solution interface was monitored by measurement of the double layer capacitance using the single pulse method. 1,3-propanediamine was found to be a better inhibitor than ethylenediamine, but no further improvement in per cent inhibition resulted upon increasing the chain length from $n = 3$ to $n = 8$. Increased inhibitor efficiency for hydrocarbon chains longer than eight carbon atoms was attributed to the concomitant decreased solubility. On a relative solubility basis, the C_6 -diamine was more efficient than the C_{12} -diamine, although both inhibitors produced 90% inhibition at a reduced concentration of 0.1. The double layer capacitance was approximately constant at 21 $\mu\text{F}/\text{cm}^2$ for the C_2 - through C_8 -diamines, and alternated between 6 and 14 $\mu\text{F}/\text{cm}^2$ for the C_9 - through C_{12} -diamines. The constancy at 21 $\mu\text{F}/\text{cm}^2$ suggests that diamines with up to 8 carbon atoms are adsorbed in the same configuration, probably the flat position. The subsequent reduction and alternation in capacitance is believed due to a structuring of the adsorbate similar to that in the bulk where certain physical properties oscillate with carbon number. Colorimetric analysis of solutions with and without $\text{NH}_2\text{-(CH}_2)_4\text{-NH}_2$ additions showed the dissolution rates to be higher than those measured by the polarization technique, possibly due to the "chunk" effect, in which dislodged grains of metal contribute to the total but not faradaic corrosion.

Organic amines function as corrosion inhibitors in aqueous solutions by adsorption at the metal/solution interface so as to reduce the metal reactivity (1-3). The adsorption theory of corrosion inhibition (4, 5) postulating that adsorption is general over the entire surface was first proposed by Hackerman and Makrides (6). The first evidence for chemisorption of organic inhibitors was obtained in this laboratory (2, 7, 8), although the adsorption measurements were made separately in parallel noncorrosive environments, such as cyclohexane solutions. More recently, measurement of the double layer capacitance has proved promising in monitoring adsorption directly in the electrolyte of interest (9).

It has been clearly established that the molecular structure of the inhibitor has a major influence on corrosion inhibition (10, 11). Previous work by Annand, Hurd, and Hackerman (12) has shown that short repetitive chains $\text{-NH-(CH}_2)_2\text{-NH-}$ of polyethylene polyamines greatly improved inhibitor effectiveness on a per nitrogen basis compared to the monomeric species $\text{NH}_2\text{-(CH}_2)_2\text{-NH}_2$.

The present communication reports on the effect of increasing the hydrocarbon chain length between the end groups of α,ω -diamines of the homologous series $\text{NH}_2\text{-(CH}_2)_n\text{-NH}_2$, for $n = 2-12$.

These diamines were of interest due to the flexible hydrocarbon chains of the higher carbon numbers in the series. It was expected that the longer units would allow adsorption of both polar end groups connected by a buckled polymethylene chain so as to present hydrophobic "humps" to the corrodent solution. However, the shorter diamines proved to be the more efficient inhibitors on a relative concentration basis.

Corrosion rate measurements of iron in 6*N* HCl at 25°C were made by the polarization technique for several concentrations of each of the inhibitors. Adsorption

of the inhibitors was studied by measurement of the double layer capacitance using the single pulse technique developed in this laboratory (13). In separate experiments, the open-circuit corrosion rates with $\text{NH}_2\text{-(CH}_2)_4\text{-NH}_2$ as inhibitor were also determined colorimetrically by the mercaptoacetic acid method.

Experimental

Corrosion inhibitors.—Reagent grade ethylenediamine was used without purification. 1,12-dodecanediamine was analyzed by acidimetric titration with standard hydrochloric acid to be 99.4% pure and was also used without further purification. 1,6-hexanediamine was recrystallized from benzene at 10°C, and was titrated to be 99.1% pure. All other diamines were purified by distillation in air or under reduced pressure.

Inhibitor solutions were made by dissolving a known weight of inhibitor in 6*N* HCl, which was obtained by diluting the reagent grade acid with double distilled water prepared in a Barnstead still. All the inhibitors were completely soluble in the concentrations used; no suspensions were employed. Diamines with more than 12 methylene groups were not studied due to solubility problems. 6*N* HCl was used as the corrosion medium to minimize pH changes upon addition of the inhibitor.

Electrodes for corrosion studies.—Polarization measurements and colorimetric analyses of solutions of freely corroding iron utilized Mallinkrodt analytical grade iron wire (99.5% Fe, 0.01% C, 0.03% Mn, 0.001% P, <0.001% Si, 0.01% S). The wire was inserted through a close-fitting hole in a Teflon holder. The holder, in turn, was machined to fit into a standard tapered glass joint at the end of the electrode assembly. Electrical contact was made by means of mercury inside the tubing.

The wires were cut to a length of 2.0 cm to give a projected surface area of 0.227 cm^2 . Before use, an electrode was degreased with spectroscopic grade pentane and then electropolished at 85 mA/cm^2 for 2 min in a 4/1 mixture of $\text{HClO}_4\text{:CH}_3\text{COOH}$, a modification of the etch developed by Sewell, Stockbridge, and

* Electrochemical Society Active Member.

¹ Present address: Metallurgy Division, Naval Research Laboratory, Washington, D. C. 20390.

² Present address: Department of Chemistry, Rice University, Houston, Texas 77001.

Key words: corrosion, corrosion inhibition, electrical double layer, iron, adsorption, diamines.

Cohen (14). The electrode was then washed with double-distilled water and inserted into the polarization cell.

Polarization measurements.—Polarization measurements were made at 25°C using small glass cells (40 or 75 ml working volumes) in which anode and cathode compartments were separated by a fritted glass disk. Platinum foil of approximately 1 cm² area was used as the auxiliary electrode. Solutions were de-aerated for at least 8 hr with helium gas which passed through charcoal at liquid nitrogen temperature and then through a solution identical to that being studied to minimize vapor loss of solution in the polarization cell. The potential of the test electrode was measured vs. a saturated calomel electrode using a Keithley electrometer. A Luggin capillary was not necessary due to the high conductance of the solutions used. Steady open-circuit corrosion potentials were established in 1-8 hr, the longer times being required for the more concentrated inhibitor solutions. Polarization measurements were then made galvanostatically using a 90V battery with a series of variable resistors ($R_{\text{external}} \gg R_{\text{cell}}$). A second Keithley electrometer was used to measure the current. The cathodic branch was always determined first; the open-circuit potential was then re-established and the anodic curve determined. Potential values at a given current were generally steady within 1-5 min.

Colorimetric analysis.—Iron dissolution rates were also measured in separate experiments by colorimetric analysis of solution containing a freely corroding iron electrode. One milliliter samples were withdrawn periodically and analyzed for iron by the mercaptoacetic acid method (15). Absorbances were read at 526 m μ with a Beckman DU Spectrophotometer and were compared to a standard Lambert-Beer curve. The calibration factor for 1 ml of solution was either 3.29 μ moles Fe⁺⁺/adsorbance unit or 6.50 μ mole/absorbance unit, depending on the final dilution. The experimental conditions for these colorimetric runs were identical to the electrochemical polarization measurements in terms of electrode area, electrode preparation, solution volume (60-80 ml), and time of solution degassing.

Differential capacitance.—Electrical double layer capacitances were measured by the single current pulse technique using the pulse generator developed in this laboratory (13). The pulse duration was 10 μ sec with a $\frac{1}{2}$ μ sec rise time. Pulse amplitude and repetition rate were variable, but generally 800 μ A and 3 pulses/sec, respectively, were used. The double layer charging curves were displayed on a Tetrionix 531A oscilloscope with Type D plug-in unit and were photographed.

The double layer capacitance cell was similar to that used in previous work (16). It is essentially a 200 ml Pyrex glass cell which houses the working electrode and an auxiliary platinum electrode of ca. 400 cm² area. A side limb separated by fritted glass acted as an inlet port for the reference electrode. The solutions were de-aerated with helium as in the polarization measurements. No greases or lubricants were used to minimize solution contamination.

More reproducible capacitance data were obtained if a 99.99% iron rod was used in place of the 99.5% iron wire. The rod was enclosed in polyethylene to expose only the bottom face of 0.0108 cm² geometrical area. The electrode holder was fashioned so that the exposed portion of the electrode was vertical in the solution. Hydrogen bubbles tended to collect on horizontal electrodes initially used and lead to spurious data. Most capacitance data were taken in 6N HCl solutions, but a limited number of experiments were also made for 3N HCl.

Solubility determinations.—Because of the decreased inhibitor solubility with longer carbon chains, it was desired to compare the inhibitor efficiencies of the C₆- and C₁₂-diamines at the same relative concentrations,

C/C_{sat} , where C_{sat} is the saturation concentration. Saturated solutions of these two compounds were prepared by stirring excess diamine in 6N HCl for two months. The mixtures were filtered (or centrifuged) and the filtrate analyzed for diamine concentration.

The saturation concentration of the C₁₂-diamine was determined colorimetrically by the 2,4-dinitrofluorobenzene (DFB) method developed by Dubin (17). The main feature of this method is that colored side products of the DFB reagent are removed by dioxane prior to colorimetry. A standard Lambert-Beer plot was prepared from known solutions of NH₂-(CH₂)₁₂-NH₂ in 6N HCl. The method of Dubin was followed quite closely, except that all volumes were doubled, i.e., 0.1 ml of diamine solution was used. Absorbances were read at 350 m μ using a Cary 14 recording spectrophotometer. The saturated solution was treated in the same manner after dilution to a known appropriate volume so that the absorbance reading was within the region of the standard Lambert-Beer plot.

The saturated solution of NH₂-(CH₂)₆-NH₂ in 6N HCl was analyzed for amine concentration by back titration with standard hydrochloric acid. The amine concentration was given by the total number of equivalents titrated plus the equivalents required to neutralize the original 6N HCl.

Results

Polarization measurements.—Figure 1 shows polarization curves for iron in 6N HCl with and without additions of NH₂-(CH₂)₃-NH₂. These curves are representative of plots obtained for all inhibitors used in this study. The anodic Tafel region for both uninhibited and inhibited systems generally spanned less than a decade in current, but intersected with the cathodic Tafel line at the open-circuit corrosion potential. Anodic Tafel slopes were 70 \pm 10 mV/decade, in nominal agreement with the value of 60 mV/decade reported by Lorenz (18). Cathodic Tafel slopes were 130 \pm 20 mV/decade, in agreement with the usual value of 120 mV/decade (19).

Open-circuit corrosion rates determined from the polarization curves are shown in Fig. 2 as a function of inhibitor concentration for NH₂-(CH₂)₃-NH₂. The general decline in corrosion current density from the uninhibited rate of 1982 μ A/cm² to a limiting value of 150-200 μ A/cm² was observed for all inhibitors studied.

The various inhibitors in the series NH₂-(CH₂)_n-NH₂ are compared in Fig. 3. The inhibitor effectiveness is

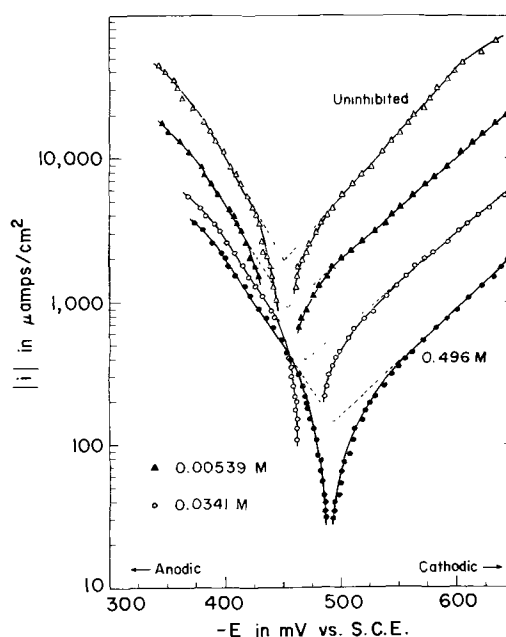


Fig. 1. Polarization curves for iron in deaerated 6N HCl at 25°C with NH₂-(CH₂)₃-NH₂ as inhibitor. (Molar concentrations of inhibitor are indicated).

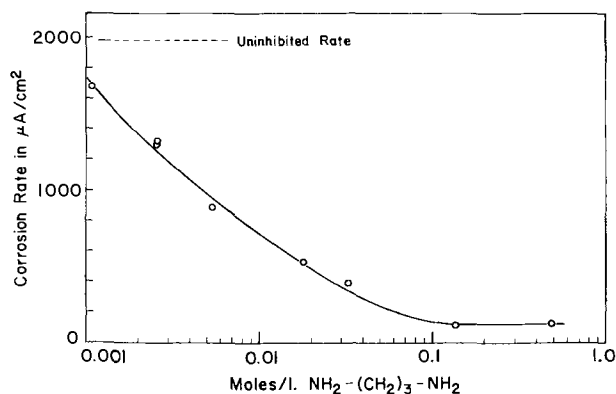


Fig. 2. Corrosion current densities for iron in deaerated 6N HCl with $\text{NH}_2\text{-(CH}_2\text{)}_3\text{-NH}_2$ inhibitor.

represented as the per cent inhibition, defined in the usual manner

$$\%I = \frac{i_0 - i}{i_0} \times 100 \quad [1]$$

where i_0 and i are the uninhibited and inhibited corrosion current densities, respectively. According to Fig. 3, $\text{NH}_2\text{-(CH}_2\text{)}_3\text{-NH}_2$ is a better inhibitor than ethylenediamine, in the sense that a lower concentration of amine is required to yield a given per cent inhibition. Increases in chain length up to C_8 have no further effect on the inhibitor efficiency. However, for longer carbon chains, the curves again shift to the left. Thus, the concentration of diamine needed to produce a given per cent inhibition follows the order: $\text{C}_{12} < \text{C}_{11} < (\text{C}_8 \text{ to } \text{C}_3) < \text{C}_2$.

From a practical standpoint, the C_{12} -diamine is the best inhibitor in terms of material requirement, but it also has the lowest solubility and dissolves with difficulty. In fact, the increase in per cent inhibition upon increasing the chain length from 6 to 12 carbon atoms is largely a solubility effect, as will be seen below. On a relative concentration basis, the C_6 -diamine is more efficient than the C_{12} -diamine.

Figure 4 shows the calibration curve developed to determine the solubility of $\text{NH}_2\text{-(CH}_2\text{)}_{12}\text{-NH}_2$ in 6N HCl by the 2,4-dinitrofluorobenzene (DFB) method. This Lambert-Beer plot was made by treating 0.1 ml samples of known concentration of $\text{NH}_2\text{-(CH}_2\text{)}_{12}\text{-NH}_2$ in 6N HCl. A 5 ml aliquot of the saturated solution, prepared as described earlier, was diluted to a known volume; and a 0.1 ml portion was analyzed by the DFB method. For two different dilution schemes, the results were: $C_{\text{sat}} = 9.3 \times 10^{-3}$ M/liter, and 8.6×10^{-3}

M/liter, respectively. Analysis of the saturated solution of $\text{NH}_2\text{-(CH}_2\text{)}_6\text{-NH}_2$ in 6N HCl by acid titration gave the result: $C_{\text{sat}} = 6.79$ M/liter.

Figure 5 shows per cent inhibition for the C_6 - and C_{12} -diamines as a function of reduced concentration C/C_{sat} . The C_6 -diamine is seen to be the more efficient inhibitor.

Double layer capacitance.—Figure 6 shows double layer capacitance curves for iron rod (99.99% purity) in 6N HCl with $\text{NH}_2\text{-(CH}_2\text{)}_{11}\text{-NH}_2$ as inhibitor. The effect of increased amine concentration is to decrease the double layer capacitance, due to adsorption of the surface active organic molecule (20, 21). In Fig. 6, as well as in all capacitance curves observed in this study, the double layer capacitance was a smooth function of electrode potential. No capacitance humps (9) were observed.

Figure 7 shows the double layer capacitance at open circuit potential as a function of $\text{NH}_2\text{-(CH}_2\text{)}_{11}\text{-NH}_2$ concentration. The values tend toward a limiting capacitance of $7 \mu\text{F/cm}^2$. Results for the C_{11} -diamine in 3N HCl are also shown in Fig. 7. The set of capacitance-potential curves for 3N HCl are very similar to the 6N curves, except that the initial uninhibited capacitance is somewhat lower for 3N HCl. However, the limiting capacitance is about the same.

Double layer capacitance curves for iron in 6N HCl with $\text{NH}_2\text{-(CH}_2\text{)}_{12}\text{-NH}_2$ are shown in Fig. 8. The limiting capacitance at open circuit potential is $15 \mu\text{F/cm}^2$.

As seen in Fig. 7, the double layer capacitance of the C_{12} -system attains its minimum at 5×10^{-4} moles $\text{NH}_2\text{-(CH}_2\text{)}_{12}\text{-NH}_2$ /liter: C_{dl} is then constant with further increases in inhibitor concentration. This value of 5×10^{-4} mole/liter is also that minimum concentration at which the system attains its maximum inhibition. Figure 3 shows the per cent inhibition to be essentially constant at 90% for $C \cong 5 \times 10^{-4}$ moles/liter. Similarly, comparison of Fig. 3 and 7 shows the C_{11} -system first exhibits minimum C_{dl} and 90% I at $C \cong 0.02$ moles/liter. Limiting double layer capacitances were thus measured for the various diamines at concentrations which yielded the maximum per cent inhibition (i.e., 90%). In the cases of the C_9 - and C_{10} -diamines, saturated solutions were used prepared by stirring excess diamine in 6N HCl for several days and then filtering. Several C-E curves are shown in Fig. 9 for various carbon numbers. Data for the limiting capacitances are summarized in Table I, and the trend is shown in Fig. 10.

The limiting values of the double layer capacitance are essentially constant at ca. $21 \mu\text{F/cm}^2$ for $n = 2-8$. The sharp drop at $n = 9$ is believed due to a change in inhibitor configuration at the metal/solution interface. The subsequent alternation in capacitance is thought to be another manifestation of the "even-odd effect" (22). These aspects will be discussed later.

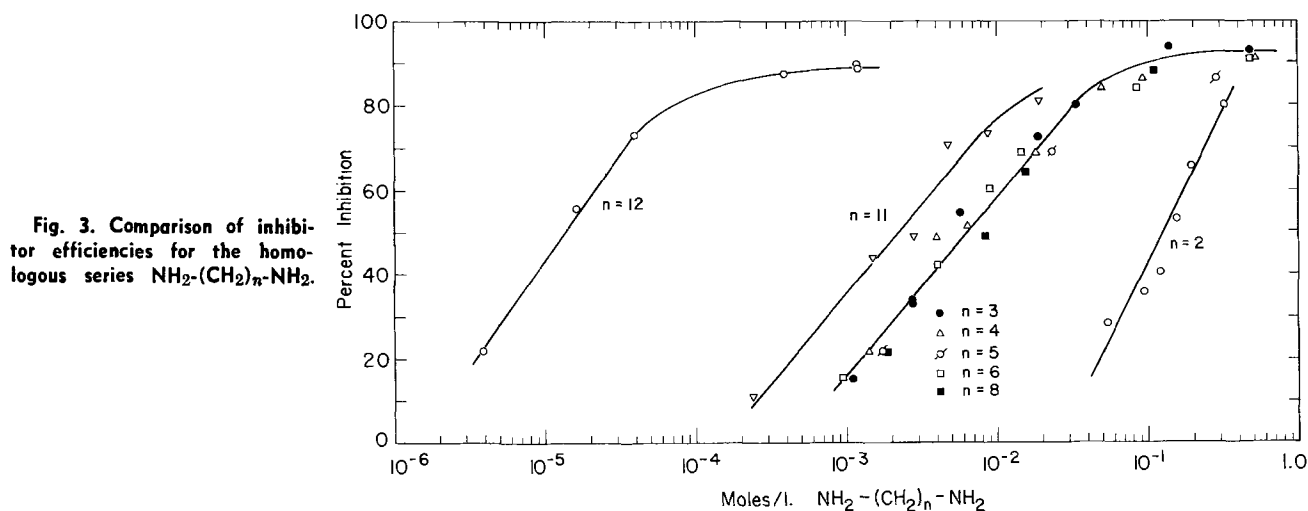


Fig. 3. Comparison of inhibitor efficiencies for the homologous series $\text{NH}_2\text{-(CH}_2\text{)}_n\text{-NH}_2$.

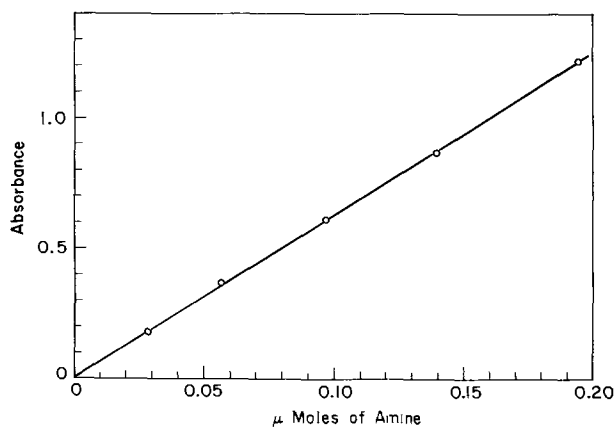


Fig. 4. Calibration curve for the determination of $\text{NH}_2\text{-(CH}_2\text{)}_{12}\text{-NH}_2$ by the 2,4-dinitrofluorobenzene method at 350 $m\mu$.

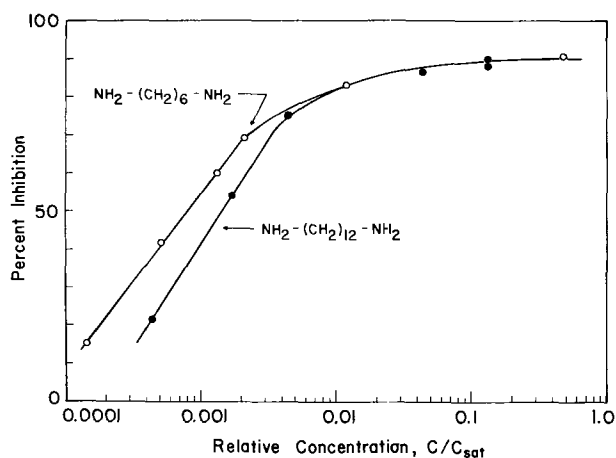


Fig. 5. Comparison of $\text{NH}_2\text{-(CH}_2\text{)}_6\text{-NH}_2$ and $\text{NH}_2\text{-(CH}_2\text{)}_{12}\text{-NH}_2$ inhibitors on a relative concentration basis.

Colorimetric analysis.—Figure 11 shows corrosion-time curves for iron wire (99.5% purity) at open-circuit potential in 6N HCl with $\text{NH}_2\text{-(CH}_2\text{)}_4\text{-NH}_2$ as in-

Table I. Limiting double layer capacitances of iron in $\text{NH}_2\text{-(CH}_2\text{)}_n\text{-NH}_2$ inhibited solutions of 6N HCl

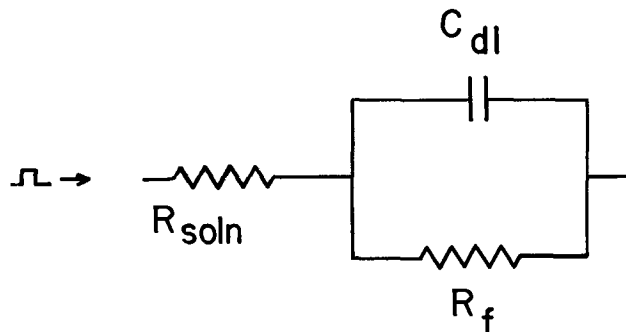
Carbon number	Conc. (M/liter)	C in $\mu\text{F/cm}^2$
2	0.409	22.3
3	0.400	18.7
4	0.507	20.7
5*	—	—
6	0.198	22.1
7	0.244	22.0
8	0.444	20.7
9	0.286	6.7
10	0.0620	16.1
11	0.0196	7.5
12	0.00137	14.2

* Data not taken for the C_8 -diamine.

hibitor. The concentration of Fe^{++} ions in solution was determined by the mercaptoacetic acid method. Equivalent corrosion current densities (based on $\text{Fe} \rightarrow \text{Fe}^{++} + 2e$) are compared with corrosion current densities determined from the polarization curves in Fig. 12. The two sets of rates do not agree, presumably due to the "chunk" effect (23), as will be discussed later.

Discussion

Double layer capacitance.—As is well known, the single pulse technique can separate double layer capacitance from coexistent faradaic effects by charging the double layer quickly relative to the duration of the chemical reaction. Using the Grahame model of the interface



the potential across the analog interface due to a cur-

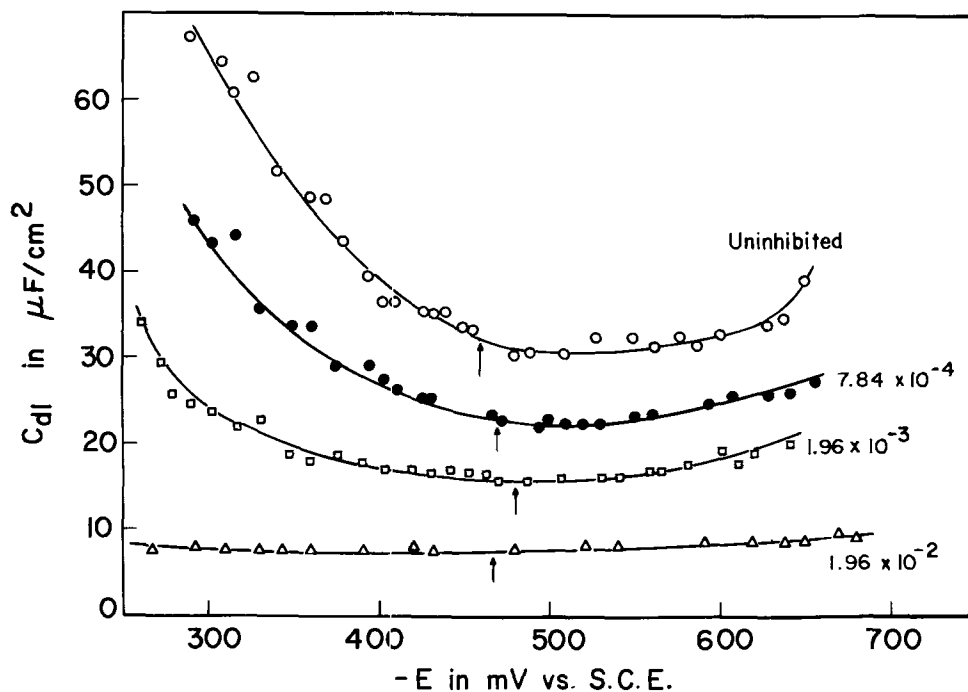


Fig. 6. Double layer capacitance for iron (99.99% purity) in 6N HCl with $\text{NH}_2\text{-(CH}_2\text{)}_{11}\text{-NH}_2$ inhibitor. (Inhibitor concentrations in mole/liter are given on the figure. Arrows indicate open-circuit potentials.)

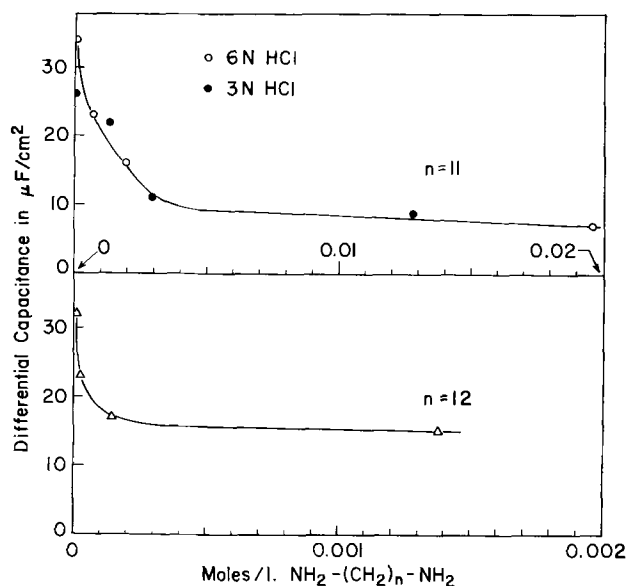


Fig. 7. Effect of inhibitor concentration on the open-circuit double layer capacitance of iron in 6N HCl at 25°.

rent pulse i is (24)

$$V = iR_f \left\{ 1 - \exp \left[-\frac{t}{C_{dl}} \left(\frac{1}{R_{std} + R_{soln}} + \frac{1}{R_f} \right) \right] \right\} \quad [2]$$

where C_{dl} is the double layer capacitance, R_f and R_{soln} the faradaic impedance and solution resistance, respectively, and R_{std} a standard resistance in the circuit used to fix the current pulse. For $(R_{std} + R_{soln}) \gg R_f$ ($R_{std} = 100 \text{ K}$ in this study) and for small t Eq. [2] reduces to

$$C_{dl} = i \frac{dt}{dV} \quad [3]$$

where dt/dV is the reciprocal slope of the charging curve. A typical trace is shown in Fig. 13.

As Lorenz and Fischer (25) have pointed out, minima in C-E curves for certain systems cannot prop-

erly be identified with the zero-point of charge of the metal due to specific adsorption of ions from solution. Thus, the minima in Fig. 6, 8, and 9 correspond to the potentials of the noncharged halide ion-covered surfaces (9). In most cases reported herein, the null point of the halide-covered surface is nearly identical with the open-circuit corrosion potential. In the cathodic direction, the double layer capacitance rises due to H^+ adsorption. In the anodic direction, the increase is due to adsorption of halide ions or possibly hydroxyl ions formed during the dissolution process (18, 19).

As seen in Fig. 6, 8, and 9, the addition of inhibitor leads to a general decrease in double layer capacitance over the entire C-E curve. This general decrease shows that the inhibitors are adsorbed on both anodic and cathodic sites, as was first proposed by Hackerman and Makrides in their adsorption theory of corrosion inhibition (6).

As mentioned earlier, double layer capacitances were measured using 99.99% iron instead of the 99.5% wire used in the polarization studies. The purer iron tended to give more reproducible capacitance data, presumably because of the diminished faradaic reaction. The hydrogen evolution reaction proved to be troublesome. Collection of bubbles on the iron electrode was initially a problem and resulted in spurious data until a vertical electrode was adopted.

Configuration of diamines.—The constant double layer capacitance at maximum coverage for $n = 2$ to $n = 8$ (Fig. 10) suggests that those diamines all adsorb at the Fe/HCl interface in the same configuration. The organic molecules are believed to lie flat with both end groups adsorbed. Reasons for this interpretation follow.

At the air/water interface, the surface tensions of short chain difunctional acids, alcohols, and amines are lower than the corresponding monofunctional compounds (26, 27) due to interaction of both polar end groups with the surface. At the metal/solution interface, the flat difunctional molecules exhibit the higher double layer capacitances due to a decreased distance between the "capacitor plates" (26, 27). In 1N Na_2SO_4 with 1N addition of ethylenediamine, double layer capacitances of $11.2 \mu\text{F}/\text{cm}^2$ have been reported for mercury (26) and *ca.* $15 \mu\text{F}/\text{cm}^2$ for lead (28). These values are of the same order reported herein, allowing for the differences in base solutions.

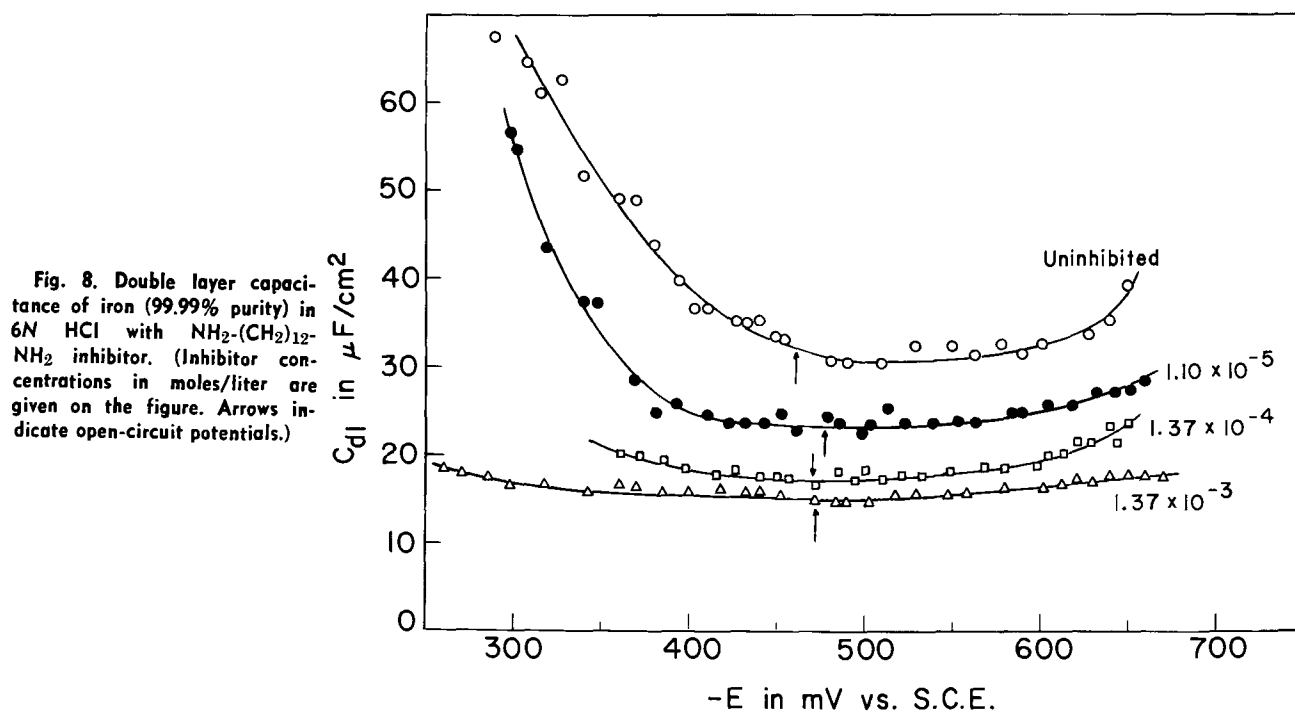


Fig. 8. Double layer capacitance of iron (99.99% purity) in 6N HCl with $\text{NH}_2-(\text{CH}_2)_{12}-\text{NH}_2$ inhibitor. (Inhibitor concentrations in moles/liter are given on the figure. Arrows indicate open-circuit potentials.)

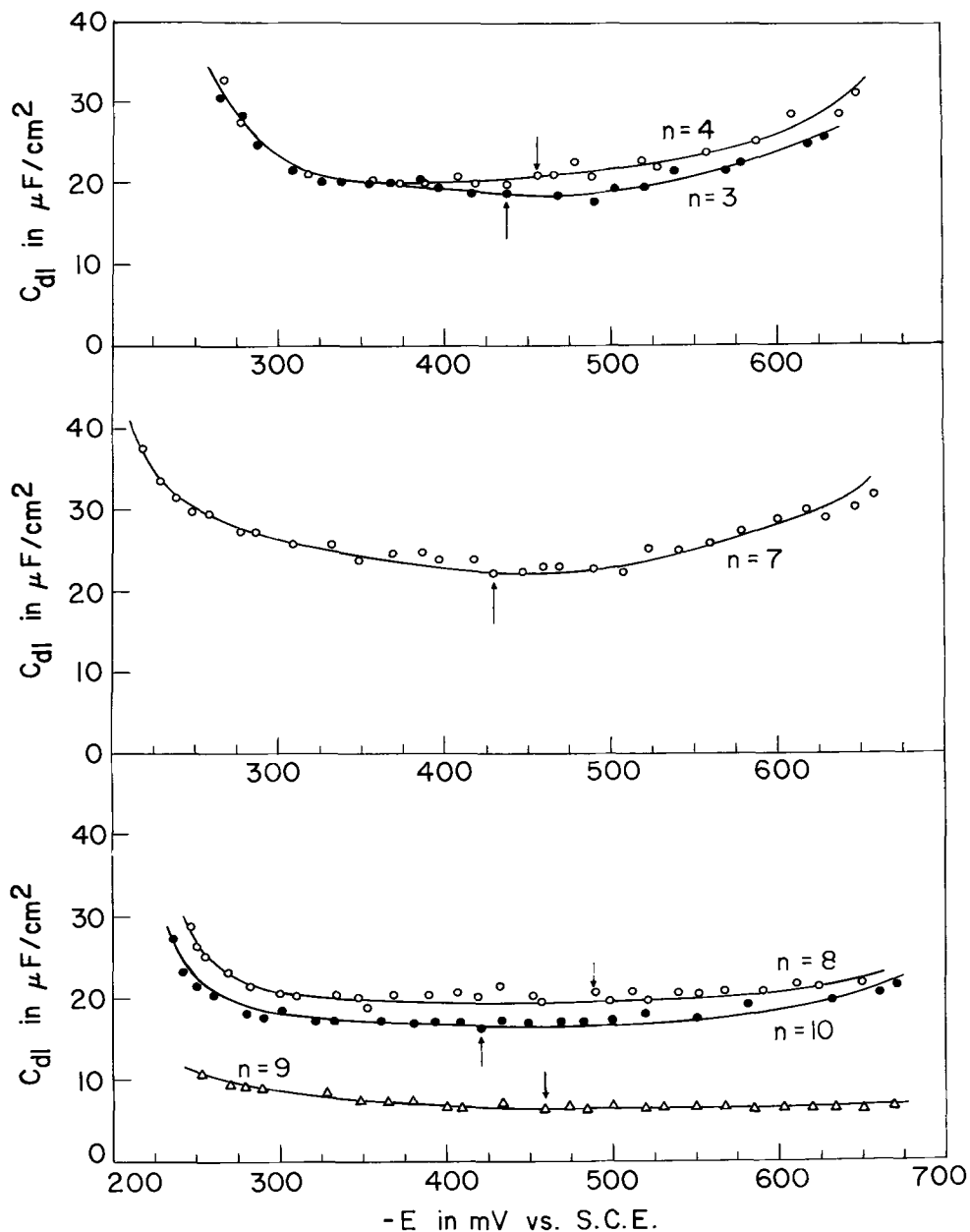


Fig. 9. Differential capacitance curves for several $\text{NH}_2\text{-(CH}_2)_n\text{-NH}_2$ inhibitors at concentrations of optimum corrosion inhibition. (Arrows indicate open-circuit potentials.)

Evidence that short linkages lie flat on the active iron electrode is provided in work by Annand, Hurd, and Hackerman (12), who found that short repetitive chains $\text{-NH-(CH}_2)_2\text{-NH-}$ of polyethylene polyamines

increased inhibitor effectiveness by orders of magnitude on a per nitrogen basis compared to the monomeric species. This effect was interpreted in terms

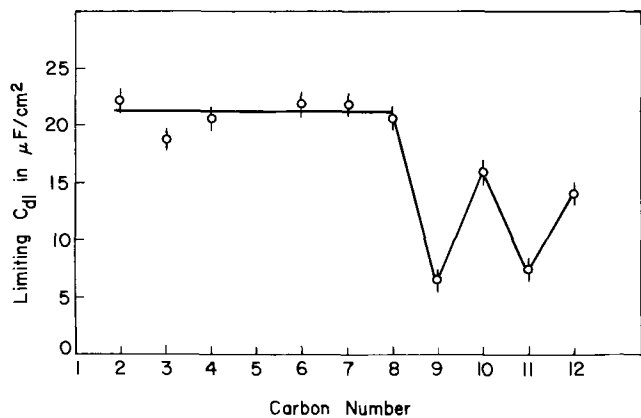


Fig. 10. Limiting double layer capacitances of the polymethylenediamines $\text{NH}_2\text{-(CH}_2)_n\text{-NH}_2$ at open-circuit potentials.

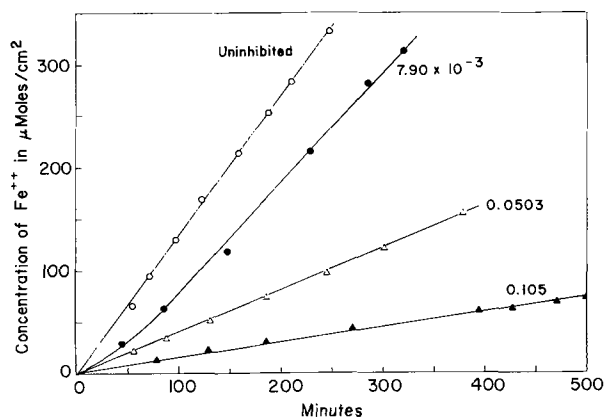


Fig. 11. Corrosion-time curves for iron (99.5% purity) in 6N HCl with $\text{NH}_2\text{-(CH}_2)_4\text{-NH}_2$ inhibitor. (Concentrations of amine are indicated on the figure.)

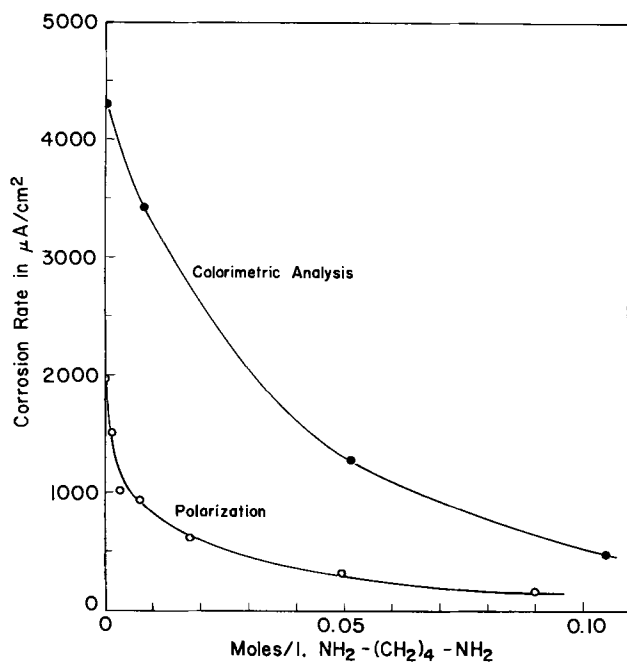


Fig. 12. Comparison of corrosion rates determined colorimetrically and by polarization curves for iron in 6N HCl with $\text{NH}_2\text{-(CH}_2\text{)}_4\text{-NH}_2$ inhibitor.

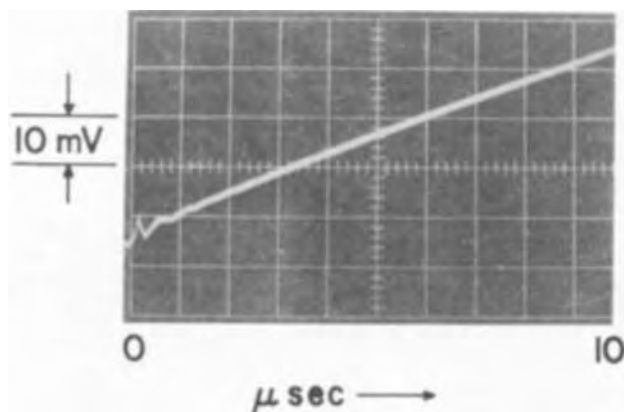


Fig. 13. Double layer charging curve for iron (99.99%) in 6N HCl with 0.0196 moles/liter $\text{NH}_2\text{-(CH}_2\text{)}_{11}\text{-NH}_2$ at open-circuit potential (-0.480V vs. SCE).

of increased adsorption, implying that the polymer units must adsorb at repeated distances along the surface.

The abrupt decrease in limiting differential capacitance in passing from $\text{NH}_2\text{-(CH}_2\text{)}_8\text{-NH}_2$ to $\text{NH}_2\text{-(CH}_2\text{)}_9\text{-NH}_2$ (Fig. 10) reflects a change in configuration and/or dielectric constant. With long enough polymethylene chains, repulsive interactions between amine end groups of adjacent flat molecules cause some of the molecules to reorient to the upright position. When additional metal surface is exposed due to this reorientation to the upright position, additional diamine molecules in solution adsorb end-on between vertical neighbors. The resulting capacitance is thus lower than for the $\text{C}_2\text{- to C}_8\text{-diamines}$ which are adsorbed in the flat position.

This change in conformation is probably a gradual one with coverage, passing through an intermediate stage in which the hydrocarbon chains are "buckled" between the adsorbed amine end groups. Direct determination of end-to-end distances in α,ω -dibromoalkanes has shown that folding of hydrocarbon chains becomes appreciable with 10 or more carbon atoms (29). Film balance studies at the air/water interface

with dicarboxylic acids of 12 or more methylene groups have shown considerable buckling of the hydrocarbon chain between the two hydrophilic end groups (30). In addition, based on interfacial tension data for $\text{NH}_2\text{-(CH}_2\text{)}_4\text{-NH}_2$ and $\text{NH}_2\text{-(CH}_2\text{)}_{10}\text{-NH}_2$ at the water/chloroform interface (31), the limiting cross-sectional molecular areas can be calculated from the Gibbs adsorption equation to be 151 and 58 square angstroms, respectively. The smaller area of the C_{10} -diamine must mean that the hydrocarbon chain is buckled in the organic phase, whereas the C_4 -diamine lies flat at the interface.

The reduction and ensuing alternation in differential capacitance for the $\text{C}_9\text{- to C}_{12}$ -diamines suggests that these adsorbates are structured similar to the bulk, where certain physical properties oscillate with carbon number. It is well known that the physical properties of α,ω -dicarboxylic acids in the solid state, e.g., melting point, refractive index, and solubility, show pronounced alternation with carbon number (32). These fluctuations in physical properties are caused by alternations in the crystal structures. In the zigzag arrangement of the methylene groups, the carbon chains of "even" acids lie in one plane; but the "odd" acids are twisted. This torsional effect imparts higher energies, and lower melting points for instance (33), to the odd acids.

Less is known about the physical properties of the corresponding α,ω -diamines. However, fluctuations in melting points (see Table II.) suggest that the homologous series of diamines also displays the "even-odd" bulk property effect. With regard to the surface, then, the regular oscillation in differential capacitance at saturation coverages can be attributed to alternations in the local dielectric constant, which in turn result from alternations in positioning of the polar end groups in the adsorbed monolayer. That is to say, the $\text{C}_9\text{- through C}_{12}$ -diamines are structured at the metal/solution interface with hydrocarbon chains in the vertical position. Structuring of polar adsorbates at the gas/solid and solid/liquid interfaces is well known in simpler systems (34, 35).

Comparison of inhibitors.—In comparing the relative efficiency of a homologous series of adsorption type corrosion inhibitors, account must be taken of the following molecular parameters (2-6, 10, 11): (i) the electron donating ability of the adsorbing inhibitor, (ii) molecular area, and (iii) inhibitor solubility.

The electron donating ability of the amines can be estimated from their base strengths (6). Table II lists acid dissociation constants pK_a taken from published literature (36, 37). Larger pK_a 's imply stronger bases and hence better electron donors. Table II shows ethylenediamine to be the weakest base. This fact explains the lower inhibition with ethylenediamine compared to propylenediamine (Fig. 3). The two inhibitors have comparable solubilities, and the differences in cross-sectional areas are too small to account for the differences in corrosion current densities. Based on liquid density calculations (38), these cross-sectional areas are 25.3\AA^2 for $\text{NH}_2\text{-(CH}_2\text{)}_2\text{-NH}_2$ and 29.4\AA^2 for $\text{NH}_2\text{-(CH}_2\text{)}_3\text{-NH}_2$. The former area is in agreement with the

Table II. Some properties of the diamines $\text{NH}_2\text{-(CH}_2\text{)}_n\text{-NH}_2$

n	Melting point, °C	pK_a		Ref.
		pK_1	pK_2	
2	8.5°	9.93-9.87	6.85-6.80	(36)
3	<0°	10.30-10.72	8.29-8.98	(36)
4	27°	10.19-10.82	8.78-9.61	(36)
5	12°	10.25	9.13	(36)
6	42°	10.93	9.83	(36)
7	28°	—	—	—
8	52°	11.0	10.1	(36)
9	37°	—	—	—
10	62°	11.2	10.7	(37)
11	58°	—	—	—
12	67°	—	—	—
13	51°	—	—	—

values 25.5–29.0A² observed for vapor phase adsorption of ethylenediamine on Al₂O₃ catalysts (39).

The agreement in the per cent inhibition *vs.* concentration curves for the C₃- to C₈-diamines (Fig. 3) was surprising in view of the increased basicity and molecular area (flat configuration) with increasing carbon number. Diamines with up to eight carbon atoms are readily soluble, so that solubility differences were minimal.

Two reasons can be given that the per cent inhibition curves coincide for the C₃-C₈ diamines. First, it is possible that the higher members within the C₃- to C₈-range do not stretch completely flat on the surface. X-ray determination of end-to-end distances in C₆- to C₁₈-polymethylene dihalides has shown that even the shorter chains display some buckling (29). This effect could reduce the differences between the effective cross-sectional areas of the C₃- to C₈-diamines. In addition, a given coverage of any of these inhibitors below the monolayer volume could serve to ennoble a much larger area of metal surface. Previous work, for instance, has shown that an absolute coverage of less than 0.1 monolayer of polypyridine produced 80% inhibition (12). Absolute adsorption isotherms were not determined in the present work, but Fig. 5 shows that a relative concentration of only 0.01 produced 80% inhibition for NH₂-(CH₂)₆-NH₂ or NH₂-(CH₂)₁₂-NH₂.

With increased chain length, the diamines become notably more insoluble, with lower concentrations required for protection. Here, the inhibitors must be compared on the basis of reduced concentration C/C_{sat} , in that the free energy of adsorption of the inhibitor is comprised in part of the term $RT \ln C/C_{\text{sat}}$ (40, 41).

At reduced concentrations of $C/C_{\text{sat}} \cong 0.01$, the C₆- and C₁₂-diamines yielded the same per cent inhibition, *i.e.*, 80% inhibition at $C/C_{\text{sat}} = 0.01$ and tending toward 90% at higher concentrations (see Fig. 5). For such efficiencies, the uptake of inhibitor is no doubt the maximum for each case, although the inhibitor configurations are different. As inferred from the double layer capacitances, the C₆-diamine lies flat but the C₁₂-diamine is vertical. Thus, at concentrations below maximum coverage, the C₆-diamine should cover more metal surface than the vertical C₁₂- and would be expected to be the more efficient inhibitor. Figure 5 shows that 1,6-hexanediamine is more efficient than 1,12-dodecanediamine at the lower reduced concentrations.

Other factors being equal, medium-sized hydrocarbon chains of NH₂-(CH₂)_{*n*}-NH₂ diamines are thus more efficient corrosion inhibitors than the longer hydrocarbon linkages.

Possibility of localized corrosion.—As shown in Fig. 12, open-circuit dissolution rates determined by polarization measurements are not in agreement with rates determined by colorimetric analysis of corroded solutions. The dissolution rate of uninhibited iron in 6N HCl was only half the rate determined by colorimetric analysis of the solution. This observation was reported a few years ago in this laboratory (10) and more recently by Oakes and West (42).

Oakes and West (42) following Florianovich, Kolotytkin, and Sokolova (43) attribute this disagreement between electrochemically and chemically determined rates to the operation of a separate, potential-independent "chemical dissolution" process (44), which is co-existent with the electrochemical process but not measured by the polarization curve.

Alternately, the observed effect could be due to localized corrosion. Before the appearance of the term "chemical dissolution," Marsh and Schaschl (23) had suggested that such effects could be explained by dissolution of metals in "chunks" or blocks of atoms. That is, preferential attack along grain boundaries can cause grains of metal to be dislodged from the metal surface. These dislodged grains would continue to produce Fe⁺⁺ ions, but would be disconnected from the elec-

trochemical circuit, so that the electrochemically measured rate would be too low.

Loose metallic particles collected from the surfaces of steel dissolving in HCl and H₂SO₄ have been identified by the optical microscope (45). Mechanical disintegration and spalling of various nonferrous metals is well known (46).

A limited number of experiments were also done with 3N HCl. Agreement was found between corrosion rates determined by the polarization method and by colorimetric analysis. For uninhibited iron, the two rates were 238 and 241 μA/cm² respectively. With 0.0105 M/liter of added NH₂-(CH₂)₄-NH₂, the rates were 101 μA/cm² by polarization and 119 μA/cm² by colorimetric analysis. Agreement between the two methods has also been reported for 1N HCl (1).

Figure 14 compares polarization data for NH₂-(CH₂)₄-NH₂ in 6N and 3N HCl. It is seen that the 3N data (where no "chunk" effect occurs) lie on the 6N curve (where there is an accompanying chemico-mechanical effect). Thus, the electrochemically determined per cent inhibition curves for 6N HCl accurately reflect the behavior of the inhibitor at lower acid concentrations. If the extent of localized corrosion is the same from diamine to diamine, the electrochemical rates also accurately evaluate the relative performances of the diamines in 6N HCl.

Conclusions

1. The double layer capacitance at the Fe/HCl interface decreases at all electrode potentials with additions of NH₂-(CH₂)_{*n*}-NH₂, for *n* = 2–12. This general decrease indicates that the inhibitors are adsorbed on the surface at both anodic and cathodic sites.

2. The limiting double layer capacitance at saturation coverage is approximately constant at 21 μF/cm² for *n* = 2–8. This constancy is interpreted on the basis that these diamines all assume flat configurations at the interface.

3. The limiting double layer capacitance for NH₂-(CH₂)₉-NH₂ drops to 6 μF/cm² and alternates with increasing carbon number between 6 and 14 μF/cm² for *n* = 9 → 12. The decrease in capacitance relative to *n* = 3 → 8 and subsequent alternation in value suggests that these monolayers are structured like the bulk solids with hydrocarbon chains outward.

4. 1,3-propanediamine is a better corrosion inhibitor than ethylenediamine, but no further increase in efficiency is obtained if up to eight methylene linkages are used.

5. On a relative solubility basis, NH₂-(CH₂)₆-NH₂ is more efficient inhibitor than NH₂-(CH₂)₁₂-NH₂, although both compounds produce 90% inhibition at $C/C_{\text{sat}} = 0.1$.

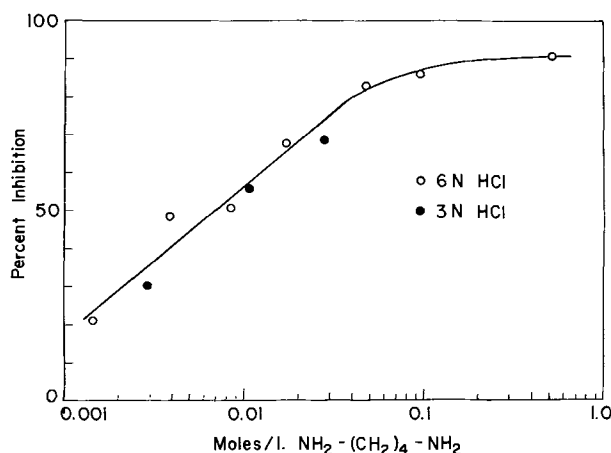


Fig. 14. Per cent inhibition with NH₂-(CH₂)₄-NH₂ in 6N HCl and 3N HCl.

Acknowledgments

The authors are grateful to the Robert A. Welch Foundation of Houston, Texas for financial support. E. Mc. wishes to acknowledge helpful discussions with other members of the laboratory, particularly Drs. D. Larkin and D. Justice.

Manuscript submitted June 8, 1971; revised manuscript received ca. Sept. 22, 1971. This was Paper 58 presented at the Cleveland, Ohio, Meeting of the Society, Oct. 3-7, 1971.

Any discussion of this paper will appear in a Discussion Section to be published in the December 1972 JOURNAL.

REFERENCES

- H. Kaesche and N. Hackerman, *This Journal*, **105**, 191 (1958).
- H. F. Finley and N. Hackerman, *ibid.*, **107**, 259 (1960).
- R. C. Ayers, Jr. and N. Hackerman, *ibid.*, **110**, 507 (1963).
- N. Hackerman, *Official Digest*, **36**, 1405 (1964).
- N. Hackerman, "Comptes Rendus Symposium Européen sur les Inhibiteurs de Corrosion," *Annali Univ. Ferrara, N.S., Sez. V, Suppl. n. 3*, p. 99 (1961).
- N. Hackerman and A. C. Makrides, *Ind. Eng. Chem.*, **46**, 523 (1954).
- E. L. Cook and N. Hackerman, *J. Phys. Chem.*, **56**, 524 (1952); *This Journal*, **97**, 1 (1950).
- N. Hackerman and A. H. Roebuck, *Ind. Eng. Chem.*, **46**, 1481 (1954).
- T. Murakawa, T. Kato, S. Nagaura, and N. Hackerman, *Corrosion Sci.*, **8**, 341, 483 (1968); also, references cited therein.
- N. Hackerman, R. M. Hurd, and R. R. Annand, *Corrosion*, **18**, 37t (1962).
- K. Aramaki and N. Hackerman, *This Journal*, **115**, 1007 (1968).
- R. R. Annand, R. M. Hurd, and N. Hackerman, *ibid.*, **112**, 144 (1965).
- J. S. Riney, G. M. Schmid, and N. Hackerman, *Rev. Sci. Instr.*, **32**, 558 (1961).
- P. B. Sewell, C. D. Stockbridge, and M. Cohen, *Can. J. Chem.*, **37**, 1813 (1959).
- E. B. Sandell, "Colorimetric Determination of Traces of Metals," Interscience Publishers, New York (1959).
- R. J. Brodd and N. Hackerman, *This Journal*, **104**, 704 (1957).
- D. T. Dubin, *J. Biol. Sci.*, **235**, 783 (1960).
- W. J. Lorenz, *Corrosion Sci.*, **5**, 121 (1965).
- E. J. Kelly, *This Journal*, **112**, 124 (1965).
- Z. A. Iofa, "Comptes Rendus de Qème Symposium Européen sur les Inhibiteurs de Corrosion," *Annali Univ. Ferrara, N.S., Sez V, Supp. n. 4*, p. 93 (1966); Z. A. Iofa, V. V. Batrakov, and Yu. A. Nikoforova, *Corrosion Sci.*, **8**, 573 (1968).
- B. Dus and Z. Szklarska-Smialowski, *Corrosion*, **25**, 69 (1969).
- N. D. Cheronis and J. B. Entekin, "Identification of Organic Compounds," p. 83, Interscience Publishers, New York (1963).
- G. A. Marsh and E. Schaschl, *This Journal*, **107**, 960 (1960).
- C. H. Presbrey, Jr. and S. Schuldiner, *ibid.*, **108**, 986 (1961).
- W. J. Lorenz and H. Fischer, *Electrochim. Acta*, **11**, 1597 (1966).
- R. I. Kaganovich, B. B. Damaskin, and M. M. Andrushev, *Soviet Electrochem.*, **5**, 696 (1969).
- R. I. Kaganovich, B. B. Damaskin, and I. M. Ganzhina, *ibid.*, **4**, 784 (1968).
- N. B. Grigor'ev and D. N. Machavariani, *ibid.*, **5**, 1270 (1969).
- G. W. Brady, E. Wasserman, and J. Wellendorf, *J. Chem. Phys.*, **47**, 855 (1967).
- P. M. Jeffers and J. Daen, *J. Phys. Chem.*, **69**, 2368 (1965); also: "Proceedings of the Fourth International Congress on Surface Active Substances," Brussels, 1964, Vol. II, p. 869, Gordon and Breach Science Publishers, New York (1967).
- V. Z. Nikonov and L. B. Sokolov, *Russ. J. Phys. Chem.*, **43**, 581 (1969).
- J. Oldham in "Rodd's Chemistry of Carbon Compounds," S. Coffey, Editor, Vol. I, Part D, p. 275, Elsevier Publishing Co., New York (1964).
- C. H. Mac Gillavry, G. Hoogschagen, and F. L. J. Sixma, *Rec. Trav. Chim.*, **67**, 869 (1948).
- E. McCafferty, V. Pravidic, and A. C. Zettlemoyer, *Trans. Faraday Soc.*, **66**, 1720 (1970).
- J. A. Kitchener, *Endeavour*, **22**, 118 (1963); also J. C. Henniker, *Rev. Mod. Phys.*, **21**, 322 (1949).
- D. D. Perrin, "Dissociation Constants of Organic Bases in Aqueous Solution," Butterworths, London (1965).
- G. Schill, *Acta. Pharm. Suecica*, **2**, 99 (1965).
- D. M. Young and A. D. Crowell, "Physical Adsorption of Gases," p. 226, Butterworths, Washington (1962).
- V. E. Vasserberg, A. A. Balandin, and M. P. Maksimova, *Russian J. Phys. Chem.*, **35**, 419 (1961).
- A. C. Makrides and N. Hackerman, *J. Phys. Chem.*, **59**, 707 (1955).
- J. O'M. Bockris and D. A. J. Swinkels, *This Journal*, **111**, 736 (1964).
- G. Oakes and J. M. West, *Br. Corrosion J.*, **4**, 66 (1969).
- G. M. Florianovich, Ya. M. Kolotytkin, and L. A. Sokolova, "Third International Conference on Metallic Corrosion," Moscow, 1966, Vol. I, p. 192.
- Ya. M. Kolotytkin and G. M. Florianovich, *Zashchita Metallov*, **1**, 7 (1965).
- M. E. Straumanis, G. E. Welch, and W. J. James, *This Journal*, **111**, 1292 (1961).
- W. J. James, M. E. Straumanis, and J. W. Johnson, *Corrosion*, **23**, 15 (1967). Also, see literature cited in Ref. (45).

Pitting and Deposits with an Organic Fluid by Electrolysis and by Fluid Flow

T. R. Beck,* D. W. Mahaffey, and J. H. Olsen

Boeing Scientific Research Laboratories, Seattle, Washington 98124

ABSTRACT

Electrolysis experiments were performed with iron electrodes in phosphate ester fluids. Pitting corrosion occurred and films were deposited on the electrodes. The effect of various additives was investigated and a model involving a threshold current density for pitting was formulated. The relationship of the results to corrosion by electrokinetic currents is studied. The occurrence of electrokinetically produced corrosion is discussed.

This paper describes some electrochemical experiments which were performed in phosphate-ester based hydraulic fluids. The experiments were associated with the discovery of a new wear mechanism in steel hydraulic-control valves. The wear mechanism is a corrosion reaction driven by electrokinetic currents associated with the flowing fluid and has been described in detail elsewhere (1). The present paper is concerned primarily with the associated electrochemistry of the phosphate ester fluids and its relationship to the wear mechanism.

Electrolysis Experiments

A primary objective of the experiments was to determine if corrosion could be produced by purely electrochemical means, without the fluid flow present in the hydraulic valves. The experiments were performed using phosphate ester fluids (2), whose properties are listed in Table I.

Parallel-Electrode Cells

An experiment was conducted with 2×12 cm parallel pure-iron sheet electrodes, separated by 0.3 cm, and immersed in 850 cc of continuously stirred phosphate ester fluid in a Pyrex beaker.

For an applied potential of 500V the initial current was 2 mA and decayed over the 313 hr of the test to 0.8 mA. This represented a range of current densities of 0.3-0.8 mA/cm² based on the facing areas. No corrosion of the electrodes was observed but deposited films were observed.

The electrodes were washed with acetone and films that had formed were scraped off. Upon returning the electrodes to the cell, the current was about 11% greater for a given potential than the current at the beginning of the run. In this and other experiments the anode film had the high resistance. Fluid conductivity, measured in a conductivity cell, was found to have increased slightly in this experiment although it decreased in other experiments.

* Electrochemical Society Active Member.

Key words: electrokinetics, streaming current, corrosion, phosphate ester, electrode films.

Table I. Properties of phosphate ester hydraulic fluid

Composition:	
Basestock—	approximately 90%—a mixture of phosphate esters
	$\begin{array}{c} R \\ \\ O \\ \\ RO-P-OR \\ \\ O \end{array}$
	with general formula RO-P-OR where R's may
	be alkyl or aryl groups.
Viscosity improver—	approximately 10%—polymethyl methacrylate
Corrosion inhibitors, dye, etc.—	minor constituents
Density—	1.05 g/cc
Viscosity—	12 centipoise
Vapor pressure at 25°C—	2-7 mm Hg
Electrical conductivity—	approx. 10^{-7} ohm ⁻¹ cm ⁻¹
Dielectric constant—	approx. 8

Current-potential curves both for clean and film-covered electrodes in the parallel-electrode cell are shown in Fig. 1. The slope of the curve for clean electrodes is consistent with the fluid conductivity and cell geometry. Extrapolation of the current-potential curve to zero current indicates a rather large polarization for the film-covered electrodes compared to the clean electrodes.

The light tan colored anode film cracked after washing with acetone and was easily removed with a Teflon scraper. The total weight was 0.135g and accounted for about 90% recovery of the anode film. The amount of the cathode film was only about 1-10% by volume of the anode film, and was very firmly adhering requiring a steel scalpel to remove it. Results of instrumental analyses of the films are presented in Table II. The anode film was amorphous and appeared to have a composition similar to the phosphate ester, although high in iron. Mass spectrographic analysis of the cathode film showed sodium, carbon, and oxygen as major components, suggesting that it was sodium carbonate.

An approximate current efficiency for formation of the anode film can be calculated assuming that the film is a polymer of phosphate ester formed by a one-electron/molecule process. This would be akin to

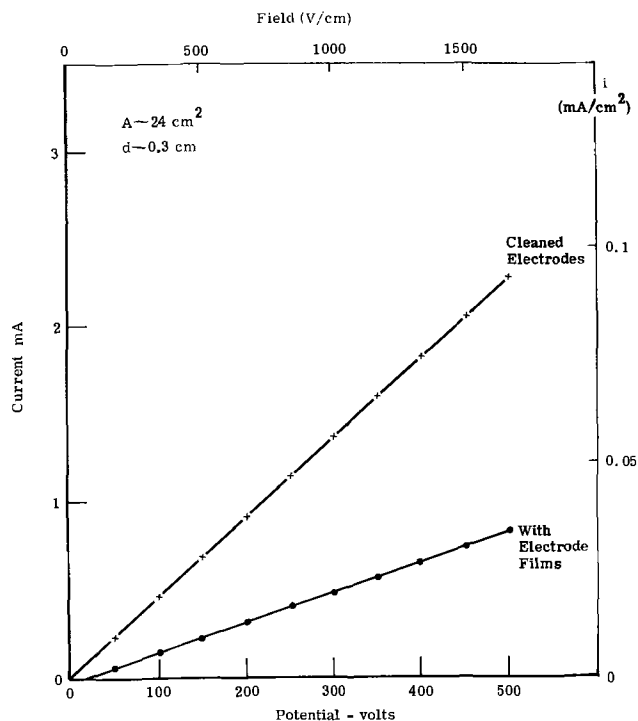


Fig. 1. Current-potential curves before and after electrolysis

Table II. Analyses of anode and cathode films from electrolysis of phosphate ester hydraulic fluid

Analysis	Anode film	Cathode film
X-ray diffraction	Amorphous	—
X-ray emission		
Major (>10%)	Organics	Na
Minor (~1-10%)	Fe, P	Ca, Fe, P, Mg
Lesser (~0.1-1%)		
Trace (<0.1%)	Mn, Mg, Cu, Al, Si, Cr	Cu, Al, Si
Mass spectrograph		
Major	C, O, organics	Na, C, O
Minor	Fe, P, H	
Lesser	Mn, Mg, Al, Si	P
Trace	Cu, Cr	Ca, Fe, Mg, Cu, Al, Si, H
Atomic absorption	10.7% Fe	

a Kolbe-type reaction in which free radicals are formed and subsequently polymerize. The calculation is based on tributyl phosphate with molecular weight 218, which was the dominant species in the fluid. The total charge passed in this experiment was 1100 coulombs which would give 2.5g of material for a one-electron reaction. Only 5.5% of this amount of material was collected. The reaction product was thus either quite soluble or other reactions giving soluble products occurred.

The conductivity of the anode film can be estimated from its thickness and the current-potential data of Fig. 1, to be about $10^{-9} \text{ ohm}^{-1}\text{cm}^{-1}$ which is about a factor of 100 less than that of the fluid.

Because of the absence of corrosion in the cell, a second parallel-electrode cell with much smaller, 0.025 cm, interelectrode spacing, illustrated in Fig. 2, was used to obtain higher current densities. The current-potential curves for it are given in Fig. 3. The current very rapidly decayed with time (in seconds) to a lower plateau when a constant potential was applied. The initial peak current was consistent with the conductivity of the fluid and the cell geometry. Replacement of the electrolyte in the cell, without cleaning the electrodes, gave the same current vs. time profile. Thus the limiting current was due to decreased electrolyte conductivity rather than the anode film which presumably could not form in the short time. At a potential of 400V or more across the thin cell, sparking occurred resulting in arc craters in the metal. The arc craters could be readily distinguished from corrosion by their contour and shiny appearance. A brownish or bluish coloration appeared on the electrodes but the film thickness was insignificant in these short runs as compared to the experiments in the beaker cell. No electrode corrosion was observed with either parallel-electrode cell.

Needle-to-Plane Cell

A small interelectrode distance was needed to obtain high current density to study pitting corrosion and a relatively large volume of electrolyte was required to avoid a decrease in conductivity. These requirements

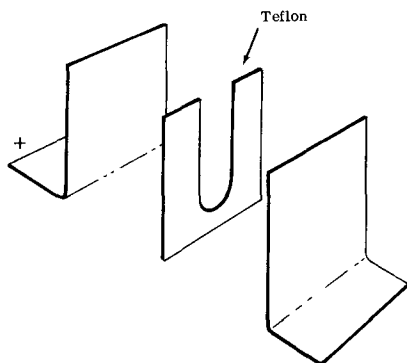


Fig. 2. Exploded view of thin cell

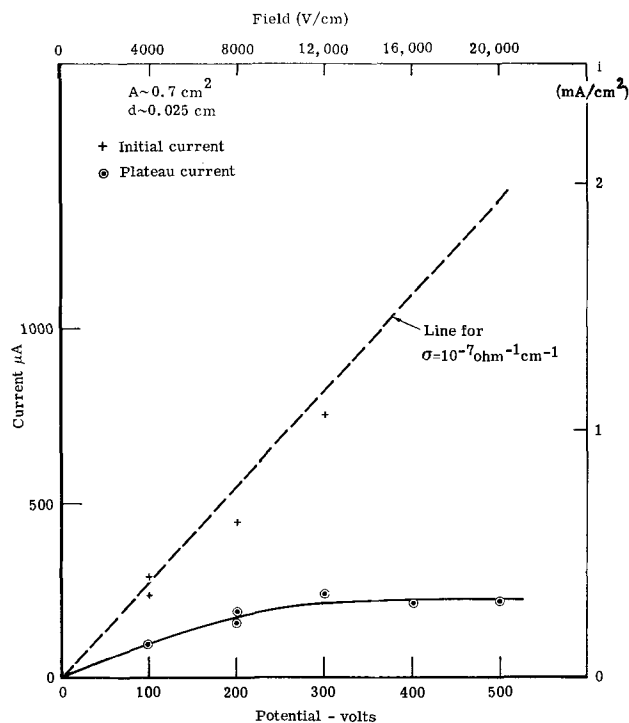


Fig. 3. Initial current and plateau current for thin electrolyte cell.

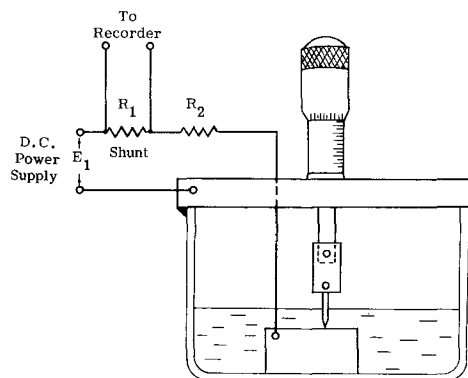


Fig. 4. Needle-to-plane cell

were met with the needle-to-plane cell illustrated in Fig. 4. One electrode was a steel phonograph needle with approximately a 25μ tip radius and the opposing electrode was a polished steel block. Interelectrode spacing could be adjusted with a micrometer head holding the needle. With a potential of about 1V across the cell, the needle was carefully moved until it touched the block as indicated by a sharp increase in current. It was then backed off to a suitable spacing, usually about 25μ .

Pitting corrosion was observed; it occurred only on the anodic electrode although deposits were formed on both. The polished block was anodic in most of the runs and photomicrographs were made of its surface. The effect of current density and various additives on the anodic pitting corrosion is summarized in Table III. Only relative measurements of the amount of pitting corrosion based on depth and areas of pitting corrosion were obtained.

A significant amount of pitting occurred in run 6. The maximum depth of the pitted area was about 4μ . The diameter of the continuously pitted area was about 150μ . The continuously pitted area was surrounded by a zone of individual pits.

Table III. Conditions and observations for needle-to-plane electrolysis experiments

Run	Electrolyte	ϕ (V)	I (μ A)	τ (min)	q (coulombs)	Cell conductance $\times 10^6$ (ohm $^{-1}$)	Relative amount of pitting (Scale of 10)
6	Phosphate ester	250	40	55	0.131	0.16	5
7	Phosphate ester	170	26	70	0.109	0.15	2
8	Phosphate ester + 1% CCl ₄	170	26	60	0.094	0.15	5
9	Phosphate ester + 2% H ₂ O	82	27	60	0.097	0.33	4
10	Phosphate ester + 1% CH ₃ NO ₂	170	15	95	0.085	0.09	Spark
11	Phosphate ester + 0.1% CH ₃ NO ₂	215	24	60	0.086	0.11	1
12	Phosphate ester	260	40	10	0.036	0.15	1
13	Phosphate ester	340	50	8	0.036	0.15	2
14	Phosphate ester	200	30	13.5	0.036	0.15	1
15	Phosphate ester	120	20	20	0.036	0.17	0
18	Phosphate ester + 1% hydroquinone	150	32	64	0.123	0.21	2
17	Phosphate ester + 11% hydroquinone	48	35	67	0.141	0.73	0
18	Phosphate ester + 1% CCl ₄	80	70	60	0.25	0.9*	10

Interelectrode spacing $d = 2.5 \times 10^{-3}$ cm in all runs.

* Solution had been in open beaker in laboratory atmosphere for several weeks.

Current efficiency of pitting corrosion in the center of the pitted area can be estimated by comparing the measured depth to the calculated depth based on maximum current density. The maximum current density in the center of the corroded area can be estimated from

$$i = \sigma \frac{\Delta\phi}{g} \quad [1]$$

A conductivity, $\sigma = 10^{-7}$ ohm $^{-1}$ cm $^{-1}$, an applied potential, $\Delta\phi = 250$ V, and a gap of 25μ gives a maximum current density of 1×10^{-2} A/cm 2 . The thickness of metal removed by this current density in 55 min, assuming the iron corrodes to valence 2, is 11μ from Faraday's law. Only 4μ were measured. The minimum current efficiency for corrosion in the center of the pitted area was therefore about 36%. The average current efficiency for corrosion for the whole surface based on the total volume of metal removed and the total charge was about 2%. Thus, most of the current passed was consumed in the film-forming and other oxidation reactions surrounding the pitted area. There appears to be a threshold current density for corrosion below which only the film-forming reaction or other oxidations occur.

Decreasing the current slightly, as in run 7, significantly decreased the amount of pitting. The deposit and the pitted area, before and after cleaning, is illustrated in Fig. 5 for run 7. The thickness of the deposit decreases with distance from the needle electrode. The center area was opaque while interference fringes are observed on the periphery (Fig. 5a).

Addition of carbon tetrachloride in run 8 markedly increased the amount of pitting as can be seen by

comparing Fig. 6 to Fig. 5 for runs having otherwise identical conditions. Addition of the 1% carbon tetrachloride did not change the conductivity of the electrolyte as can be seen by comparing the cell conductance of runs 6, 7, and 8 in Table III. In a second run with 1% carbon tetrachloride added, number 18, much higher conductance was observed. This solution was in an open beaker exposed to laboratory atmosphere for several weeks. Hydrolysis of CCl₄ or absorption of HCl from the laboratory atmosphere may have occurred. The current density was high in run 18, resulting in a relatively large amount of pitting.

Distillation-purified tributyl phosphate, reportedly containing 2 ppm chloride,¹ gave no measurable pitting with a needle-to-plane cell as compared to significant pitting with the unpurified fluid containing 21 ppm chloride for the same current and time. This behavior appears analogous to pitting of iron in aqueous solutions for which pitting is promoted by presence of halide ions. The hydraulic fluids used in the electrolysis experiments of Table III had residual chloride concentrations from the manufacturing process of 50-500 ppm.

Addition of 2% water in run 9 apparently doubled the conductivity and significantly increased the relative amount of pitting compared to run 7 for the same current. Addition of nitromethane, a possible corrosion inhibitor, in runs 10 and 11 caused a decrease in conductivity. Sparking occurred when it was attempted to run at the same current as in run 7. It is, therefore, not certain whether nitromethane acted as a corrosion inhibitor.

¹ Courtesy of Stauffer Chemical Company.

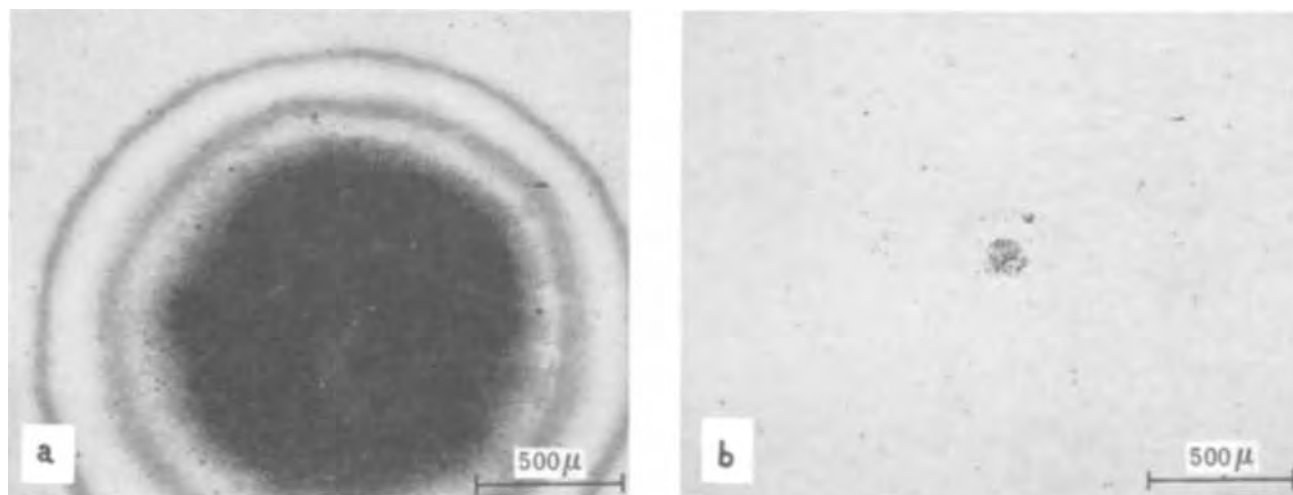


Fig. 5. Anode film and corroded area from run 7. a—Before cleaning, b—after cleaning

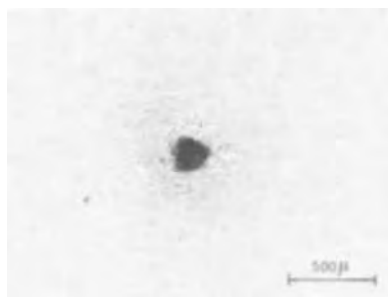


Fig. 6. Pitted area in run 8 with 1% CCl_4 after removal of the solid film.

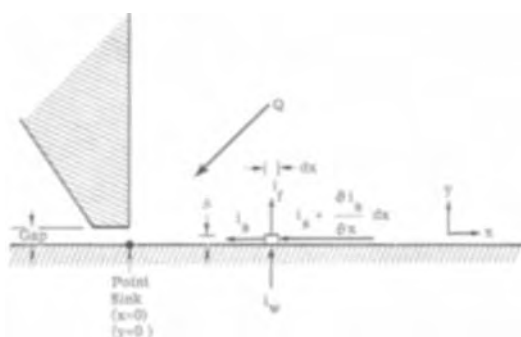


Fig. 7. Relation between streaming current and wall and fluid current densities in two-dimensional, unit-thickness converging channel.

Additions of hydroquinone were made in runs 16 and 17 to determine if an easily oxidizable material would consume current in preference to pitting corrosion. At the 11% level (approximately 1 mole/liter) in run 17, pitting was virtually eliminated for a condition of current density and time which would have otherwise produced a large amount of pitting. Addition of hydroquinone also increased the conductivity.

Flow Induced Pitting Corrosion

To understand the relationship of the electrochemistry of the phosphate esters to the flow induced wear mechanism, a brief description of that mechanism is given here. A detailed description has been published elsewhere (1).

The wear occurs upstream of small gaps at the end of 90° converging channels as shown in Fig. 7. The fluid is accelerated towards the gap and the streaming current i_s , produced by the flow, is a function of fluid velocity and must change with distance from the gap. Consideration of a differential volume element, δ by dx , and conservation of charge, requires the presence of the wall current density, i_w , and a fluid current density i_f , both normal to the wall. Using the assumptions listed in Table IV it has been shown (1) that

$$i_w + i_f = \frac{1.17e\zeta\nu}{x^3} \left(\frac{Q}{\nu} \right)^{3/2} \quad [2]$$

Table IV. Assumptions used in derivation of Eq. [2]

1. Equilibrium electrical double layer at walls of orifice, i.e., ζ does not change with velocity.
2. No local changes in fluid permittivity and viscosity.
3. Two-dimensional approximation for flow in orifice, i.e., radius of orifice, $R \gg$ gap (Fig. 8).
4. Diffuse double layer is thin compared to hydrodynamic boundary layer, therefore velocity is linear in y within double layer.
5. Jeffrey-Hamel solution of Navier-Stokes equations for flow into 90° -degree converging channel is applicable for $x \geq$ gap.
6. Reynolds number, $Q/\nu > 100$.
7. The wall current, i_w , is supplied by electrochemical reactions, e.g., oxidation of a fluid component or corrosion.

As a first approximation with phosphate ester fluids, i_f may be neglected with respect to i_w because resistance to current flow through the fluid is much greater than through the metal-fluid interface. Also, i_w is positive for phosphate ester fluids and results in anodic pitting corrosion of the upstream wall.

Many experiments were performed in tests of the above model. The experiment which is of most interest in connection with the electrochemistry used the apparatus shown diagrammatically in Fig. 8. All dimensions of the system were large compared with the gap width, so that the two-dimensional analysis represented by Fig. 7 and Eq. [2] is applicable. After fluid flow for a period of 28.5 hr both film deposits and pitting corrosion were found. The pitting looked identical in appearance to that produced in the needle-to-plane cell.

A photograph of the cleaned surface after the 28.5 hr experiment is shown in Fig. 9. The outer portion furthest from the center had no deposit and retained the polished appearance of the original surface. A worn ring located by the 0.25 cm marker averaged 6.35μ maximum depth directly under the inner edge of the orifice, i.e., at $x = 0$ in Fig. 7. An average profile of the corroded ring was determined from sixteen radial traverses using a Talysurf Model 3 instrument (1). The depth tapered off to zero at about 0.020 cm upstream from the inner edge of the orifice and about 0.005 cm downstream. A light-colored film covered the light-stained area both upstream and downstream of the worn ring. There was no measurable metal removal except within the worn ring. It

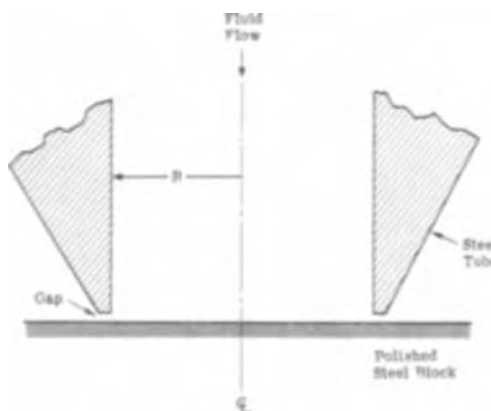


Fig. 8. Wear test apparatus

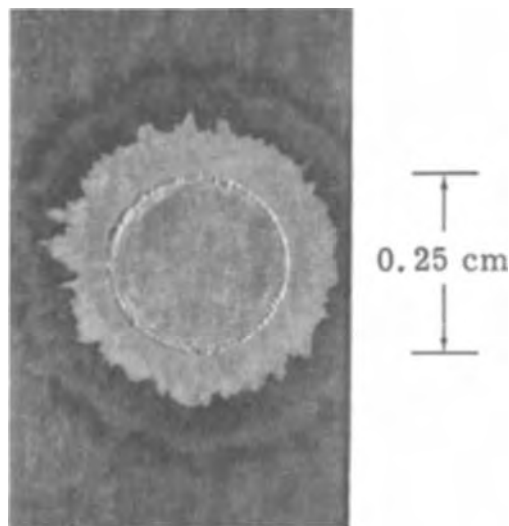


Fig. 9. Photograph of worn and stained areas on polished block

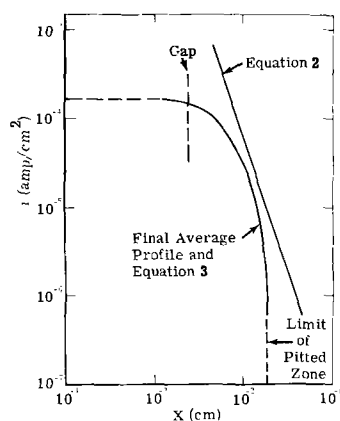


Fig. 10. Comparison of corrosion current density and model equation.

might be added that laminar flow obtains on the upstream side of the orifice so the wear and deposits there are not related to turbulence.

Corrosion current density was calculated from the average measured profile from Faraday's law

$$i_c = \frac{zF\rho_m t}{M\tau} \quad [3]$$

and is plotted as a function of position, x , upstream from the orifice in Fig. 10. Wall current density calculated from Eq. [2] is also plotted in Fig. 10. Values of the parameters used in Eq. [2] and [3] are given in Table V. There is a range of distance, x , for which there is a correlation between the model and the experiment. For values of x less than the gap width, Eq. [2] is not valid because the point-sink approximation used is invalid. No corrosion was observed for values of $x > 2 \times 10^{-2}$ cm.

Discussion

Relationship of Electrochemistry and Wear Mechanism

Formation of films on the electrodes at low current densities and corrosion plus film formation at high current densities observed in the electrolysis experiments with the needle-to-plane cell appears to have a direct analogy to the results obtained with the flow system. In Fig. 10 a sharp cut-off of the corroded zone at about 2×10^{-2} cm from the orifice was noted, and a film deposit on the surface at larger distances from the orifice is indicated by the light stained areas in Fig. 9. In Fig. 5 for the needle-to-plane cell it is seen that the anode film extends well beyond the pitted area. There is apparently a threshold potential or current density below which pitting does not occur. In both the electrolysis experiments and the flow experiments, the corrosion began as small discrete pits which grew in time and merged in the high-current-density zone.

Formation of a low-conductivity anode film may have a beneficial effect in decreasing corrosion by decreasing the wall current. Ohmic polarization of the anodic film can be calculated from Eq. [1]; a corrosion current density of 2×10^{-4} A/cm² under the film (Fig. 10), a film conductivity of 10^{-9} ohm⁻¹ cm⁻¹ and a film thickness of 2.5×10^{-4} cm (assuming 1/10 of the gap width) gives an ohmic polarization

Table V. Values of parameters used in Eq. [2] and [3]

ϵ	= 7.1×10^{-13} coulomb/V cm (dielectric constant = 8)
ζ	= 0.20V [determined with high-velocity, small gap streaming current instrument (1)]
ν	= 0.1 cm ² /sec
Q_{avg}	= 30.5 cm ² /sec
z	= 2 (assumed that Fe ²⁺ formed)
ρ_m	= 7.86 g/cm ³
M	= 55.8 g/mole
τ	= 28.5×3600 sec
t	determined as a function of x from average profile determined by Talysurf (1)
i_r	= 0

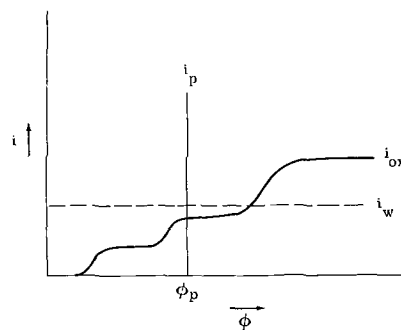


Fig. 11. Proposed relation of oxidation, pitting, and wall currents.

of the film of 50V. A corresponding potential drop would also occur in the fluid in the direction of flow. This is the same magnitude as the open-circuit potential measured with a stationary ring-disk electrode in the flow system (1). Conduction from the fluid may therefore explain the large deviations from theory in Fig. 10 at distances greater than the gap distance.

A proposed relationship between corrosion and oxidation of other species in phosphate ester fluids, illustrated in Fig. 11, is based on observations in the electrolysis experiments and flow experiments. It is perhaps an oversimplification but provides a basis for further experimentation. Direct experimental measurements of anodic overpotential in phosphate ester fluids have thus far been thwarted by the low conductivity. If there are several different species in the fluid that can be oxidized, the total current for oxidation of these species may be stepped as in a polarographic wave. It is proposed that there is a pitting potential, ϕ_p , as in aqueous solutions and that the current density for pitting rises steeply with potential above ϕ_p . For a wall current i_w , as shown in Fig. 11, pitting corrosion and oxidation of electrolyte species could occur simultaneously.

The amount of corrosion occurring at an orifice could be decreased in three ways according to Fig. 11.

Decrease i_w , e.g.: by decreasing zeta potential through control of surfactants present; by decreasing flow rate; by increasing conduction from fluid, with higher conductivity fluid or with high-resistance surface films on surface; by using a very-low conductivity (hydrocarbon) fluid.²

Increase i_{ox} , e.g.: by adding easily oxidized species.

Increase ϕ_p , e.g.: by removing species that promote pitting such as Cl⁻; by adding inhibitor.

Some of these techniques have been verified in practice, others remain to be tested.

Other Possible Occurrences of Wear Mechanism

At the completion of the work relating to the wear in the hydraulic valves, other possible technological applications of the theory were explored. A review of the literature and approximate calculations of wall current densities indicate conditions favorable to this mechanism may occur in cavitation, drop impingement and in ball and roller bearings. For example, collapse of a cavitation bubble adjacent to a wall according to the Rayleigh equation (4) can produce high current densities. Alternating currents would be generated at surfaces in these cases but corrosion may still occur, although at less than 100% current efficiency (5).

The review of bearing technology by Bisson and Anderson (6) in 1964, describes unexplained pitting and formation of films and sludges which should be examined in light of the new mechanism. Salomon

² Streaming current is observed to go through a maximum as a function of conductivity for hydrocarbons with added conducting species (3). It follows that wall current should exhibit similar behavior.

(7) found electrostatic effects in lubricated machinery and related these to wear but no adequate theory was presented. Furey (8) found interesting patterns of deposits in a rotating ball experiment suggestive of electrostatic fields being present. He also found voltage developed in these experiments although he did not have an explanation. Zaslavsky and Shor (9) observed that wear rate was related to the potential applied between two rubbing lubricated surfaces.

Investigations into relation of wear and deposit formation to wall currents generated during rolling and sliding contact could provide a new approach to understanding some old lubrication problems.

Conclusions

Electrolysis experiments were carried out with iron electrodes in phosphate ester hydraulic fluids having conductivities of 10^{-7} ohm $^{-1}$ cm $^{-1}$. It was found that:

- a. Film deposits with composition similar to the fluid formed on the anodes. The conductivity of these films was significantly lower than the parent fluid.
- b. Thinner deposits with composition approximating sodium carbonate formed on the cathodes.
- c. Pitting corrosion occurred on the anode at high current density. Pitting was promoted by addition of carbon tetrachloride and inhibited in low chloride fluids, analogous to effect of halide ions on pitting of iron in aqueous solutions.

d. The electrode films and corrosion were similar to films and corrosion observed in high velocity fluid flow systems in which electrokinetic currents are generated.

Manuscript received July 19, 1971; revised manuscript received ca. Aug. 29, 1971. This was Paper 84 presented at the Detroit Meeting of the Society, Oct. 5-9, 1969.

Any discussion of this paper will appear in a Discussion Section to be published in the December 1972 JOURNAL.

REFERENCES

1. T. R. Beck, D. W. Mahaffey, and J. H. Olsen, *J. Basic Eng.*, **92**, Ser. D, 782 (1970); and Document AD-695-492 available from Defense Documentation Center.
2. From hydraulic fluid vendors, Monsanto Co. and Stauffer Chemical Co.
3. A. Klinkenberg and J. Van der Minne, "Electrostatics in the Petroleum Industry," American Elsevier Publishing Co., Inc., New York (1958).
4. Lord Rayleigh, *Phil. Mag.*, **34**, 94 (1917).
5. e.g., T. Erdey-Gruz and J. Devay, *Electrochim. Acta*, **9**, 911 (1964).
6. E. E. Bisson and W. J. Anderson, "Advanced Bearing Technology," Chap. 11 and 12, NASA, Washington, D. C. (1964).
7. T. Salomon, *J. Inst. Petrol.*, **45**, No. 423 (1958).
8. M. J. Furey, *Wear*, **9**, 369 (1966).
9. Yu. S. Zaslavsky and G. I. Shor, *ibid.*, **10**, 223 (1967).

Sealing Studies of Anodic Oxides by Wide-Line NMR Spectroscopy

Bernard R. Baker and Robert M. Pearson

Kaiser Aluminum & Chemical Corporation, Center for Technology, Pleasanton, California 94566

ABSTRACT

Wide-line nmr measurements show that anodic coatings formed in 15% H₂SO₄ at 25°C and 12 A/ft² for 1 hr and sealed for 30 min in boiling water at pH 6 contain 11-13% H₂O as OH groups plus 1-4% physically adsorbed water. Nitrogen adsorption measurements show a surface area of about 20 m²/g for unsealed coatings and about 5 m²/g for sealed coatings. The unsealed coatings contain about 1.2×10^{11} pores/cm² of mean radius of 60Å. About 46% of the water contained in a sealed coating is on a surface. From this, and from nmr line widths, a surface area of 260 m²/g is estimated. The difference between the gas adsorption and nmr estimates of surface areas is explained by the model proposed for the coating structure, one consisting of an array of microcrystallites estimated to be about 25Å in radius. Gas adsorption analyzes only the major pore surfaces, but nmr analyzes the crystallite surfaces as well. Sealing is regarded to be primarily a surface reaction on the crystallites.

The porous anodic oxide films formed on aluminum by anodizing in sulfuric acid or other strongly acidic electrolytes are commonly sealed, usually by immersion in boiling water or dilute buffer solutions. The oxide becomes hydrated to a certain extent, the porosity decreases and susceptibility to staining or corrosive attack is minimized.

Because sealing is important in commercial anodizing, many investigators have expended considerable effort on studies of the mechanism of the reaction. Some of the more common techniques include electron microscopy, gas adsorption, x-ray and electron diffraction, x-ray emission spectroscopy, and infrared spectroscopy. Unfortunately, none of the techniques has yet produced a definitive answer to the fundamental problems of sealing, in particular, the mechanism by which the oxide adsorbs and binds water.

Key words: anodizing, aluminum, adsorption, hydration.

Several more or less plausible theories have arisen. We make no attempt here to correctly attribute all of these theories to their originators, partly because some of the ideas have almost assumed the status of folklore.

One of the more widely accepted concepts is that Al₂O₃ becomes hydrated to form boehmite (AlOOH) which, because of its greater specific volume, plugs the pores to a certain extent. Spooner and Forsyth (1) found boehmite patterns by x-ray diffraction, but nevertheless minimized the importance of boehmite as a sealing factor. They attempted to explain the apparent pore plugging by a dissolution and reprecipitation of an oxide hydrate. It is as difficult to argue with this concept as it is to prove it.

Another theory which may have considerable merit, at least in part, is the concept put forward by Murphy (2). He regards sealing as a surface effect rather than a pore plugging effect. Murphy postulated that re-

placement of surface sulfate ions by hydroxyl ions changes the surface from an active one that is receptive to dyes (and to stains or corrosive agents) to one that is more inert. This type of ion exchange must certainly occur to some extent, but it is not clear how it would affect coating properties.

O'Sullivan, Hockey, and Wood (3) proposed a model for unsealed coatings consisting of a relatively open array of alumina crystallites. During sealing, these crystallites agglomerate to some extent, forming hydroxylated surfaces and trapping molecular water in the intercrystallite voids.

Few workers have done more than to speculate on the nature of the water in sealed coatings although O'Sullivan, Hockey, and Wood made some reasonable estimates based on infrared spectra of ambient, evacuated, and deuterated films, both sealed and unsealed. They estimated that about 5-20% of the total hydroxylic species in sealed coatings is molecular water. The precise amount was indeterminate because of uncertainty in the extinction coefficient ratio necessary for the calculation. They were able to determine, however, that the relative amount of molecular water increased with an increase in sealing time.

In a preliminary report we discussed the adsorption of water vapor by dry, unsealed coatings formed at 25°C in 15% sulfuric acid on 99.99% aluminum anodized 1 hr at 12 amperes per square foot and 15V (4). We postulated a model similar to that of O'Sullivan, Hockey, and Wood in which the oxide was inferred to consist of submicrocrystallites of nearly anhydrous alumina. On exposure to water vapor, the crystallite surfaces adsorbed water converting it to surface hydroxyl groups which then physically adsorbed molecular water. In this paper, we present a method for analyzing anodic oxides for crystalline hydroxyl, surface hydroxyl, and physically adsorbed water by wide-line nmr. From these results and parallel gas adsorption studies we infer (i) a detailed model for unsealed as well as sealed coatings and (ii) a mechanism for the sealing reaction which contains several of the best features of previous models.

The analysis we use is based on techniques developed for the study of catalytic and desiccant aluminas (5). General references to the technique include a review by O'Reilly (6) and a paper by Saito and Hagewara (7).

Experimental

All coatings were formed on 99.99% aluminum foil, 3 mil thickness. The foil was partially slit prior to anodizing into 2 in. × 0.4 in. strips for nmr samples or 1 in. × 0.1 in. strips for gas adsorption samples. The end of each strip was left attached to a central bus strip for anodizing. The foil was mounted in a Lucite and aluminum rack, cleaned in Oakite inhibited

hydroxide. They were then placed either in tared 0.5 × 5 in. Pyrex nmr sample tubes sealed with rubber serum stoppers or in tared gas adsorption sample tubes. Oxide weights were obtained finally by stripping the oxide film from the substrate in a boiling solution containing 20 g/liter chromic acid and 35 ml/liter of 1.75 g/ml phosphoric acid leaving the "bare" metal.

Nitrogen adsorption and desorption isotherms were obtained on an Aminco Adsorptomat. Surface areas and pore radii distributions were obtained using the method of Barrett, Joyner, and Halenda (8). The nmr spectra were obtained as described earlier (4) except that data collection and reduction was performed using a Fabri-TEK Model 1074 instrument computer.

The spectra are a composite of a narrow line (ca. 0.2G) due to physically adsorbed water and a broad line (ca. 5.5-7.0G) due to chemisorbed water (hydroxyl or water coordinated to aluminum ions). If a narrow (0.125G) modulation is used the wide signal is minimized and the narrow signal is dominant. This allows quantitative determination of physically adsorbed water. To obtain a useful spectrum of the broad line species the physically adsorbed water must first be removed. This was accomplished either by heating to 90°C in a vacuum oven for several hours or by evacuating the sample at room temperature to about 10⁻⁴ mm Hg for several days. The two methods gave comparable results, however, each method also removes some broad line species as well, as shown by comparison of gravimetric and nmr results for the water loss. This difference was added to the nmr value for chemisorbed water as a correction.

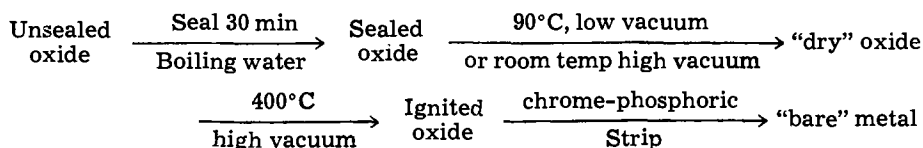
A sample of KA-201 (R) desiccant alumina (a Kaiser Aluminum & Chemical Corporation commercial transition alumina) containing a known concentration of physically adsorbed water was used as a standard for the narrow signal and a sample of gibbsite was used as a standard for the wide signal. The water content was calculated from the double integral of the spectrum using the relation

$$\begin{aligned} \% \text{ water} &= \% \text{ water (std)} \times \frac{\text{curve area (sample)}}{\text{curve area (std.)}} \\ &\times \frac{\text{oxide bulk density (std.)}}{\text{oxide bulk density (sample)}} \end{aligned}$$

The curve areas were corrected to a common instrument gain setting. The oxide densities were expressed as gram oxide/centimeter of sample tube.

Results

Water content of sealed coatings.—The analysis of the water content and distribution in sealed oxides is based on the following flow sheet



alkaline cleaning solution, given a 1 min caustic etch (45-57 g/liter sodium hydroxide, 1.5 g/liter sodium gluconate, 5-25 g/liter aluminum at 55°C), then desmuted in 35% nitric acid followed by a thorough distilled water rinse.

Coatings were made by anodizing at 14V, 12 A/ft², for 60 min in 15% H₂SO₄ at 25°C. After anodizing, the samples were rinsed thoroughly in distilled water and cut from the bus strip. They were then either sealed immediately for 30 min in boiling distilled water or blown dry in a stream of filtered air depending upon their purpose. The seal bath was prepared fresh for each sample by bringing boiling distilled water to pH 3 with acetic acid then adjusting to pH 6 with sodium

Weights were recorded at each stage. The nmr spectra were recorded for sealed oxide, dry oxide, and ignited oxide. Thus the water losses were observed by weight loss and by nmr. The spectra and water contents of unsealed oxides were discussed previously (4).

We assumed, initially, that gentle heating or strong evacuation would remove just the physically adsorbed water leaving the chemisorbed water intact. This assumption is not valid. The weight loss on heating to 90°C in a low vacuum or at room temperature in a high vacuum is always higher than the physically adsorbed water as determined from nmr (Table I). This is in accord with the thermogravimetric curve of Fig. 1 which shows a continuous water loss over the whole temperature range.

Table I. Comparison of gravimetric and nmr water determinations^{a,b}

Sample	Physically adsorbed water		Chemisorbed water		Total water loss		Residual water (nmr signal after 400°C ignition)
	wt. loss 90°C	nmr narrow signal	wt. loss 400°C	nmr (broad signal)	Gravimetric	nmr (corrected)	
1	6.3 ^(c)	3.6	5.5	7.1	12.1	13.4	1.7
2	4.8	1.1	6.1	6.0	10.9	10.8	1.3
3	4.6	2.4	6.4	8.7	11.0	13.3	1.6
4	3.8	1.8	6.7	7.6	10.5	11.4	1.8
5	5.3 ^(c)	3.3	9.3	9.4	14.6	14.7	0.93
6	4.4	2.3	7.2	9.1	11.6	13.5	1.7
7	5.3 ^(d)	3.0	10.0 ^(e)	9.1	15.3	14.4	0

^(a) All values are weight per cent based on sealed weights.

^(b) All samples sealed 30 min in boiling water at pH 6.0.

^(c) Weight loss in high vacuum at room temperature, all other losses in this column by heating to 90°C in low vacuum.

^(d) This coating was dried at 90°C before sealing. The residual water content after drying was 0.5%.

^(e) This sample ignited at 600°C.

We regard the nmr value for physically adsorbed water to be accurate to about $\pm 10\%$. The difference between the weight loss and the nmr value thus represents water, held as Al-OH₂ or Al-OH, which is lost easily, therefore not available for analysis as chemisorbed water in the next step. The difference is added to the nmr value for total water loss as a correction (column 7, Table I). It is, of course, not added to the gravimetric value since the total weight loss (column 6) already includes it. The values for chemisorbed water in columns 4 and 5 are the apparent water contents of the "dried" oxide.

The total water determined by nmr is always equal to or higher than the value obtained gravimetrically except for the sample ignited to 600°C. This difference appears also in columns 4 and 5 for chemisorbed water and probably results from reaction of water released from the oxide on the substrate, $2\text{Al} + 3\text{H}_2\text{O} \xrightarrow{400^\circ\text{C}} \text{Al}_2\text{O}_3 + 6\text{H}_2$. This reaction would result in a loss of protons without an appreciable accompanying weight loss.

We therefore regard the nmr values to be a better measure of water content and distribution than the gravimetric values but the nmr value for chemisorbed water must be corrected by gravimetric measurement in the first step of the analysis. The results are summarized in Table II which include the residual water content after ignition at 400°C. Table II also shows the line-widths of the chemisorbed water spectra which give information, discussed below, on the structure of the surface.

The relative water contents of about 1-4% physically adsorbed and 11-12% chemisorbed water are in

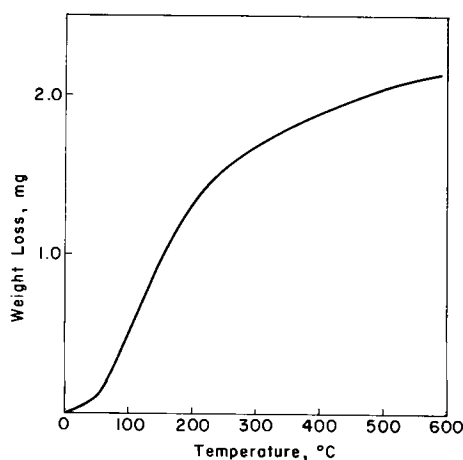


Fig. 1. Thermogravimetric analysis of 18.5 mg of sealed oxide heated at 10°C/min in a 30 cc/min H₂ purge.

Table II. Water contents of sealed anodic oxides^(a) (% of sealed weight)

Sample	Weight gain on sealing (% of sealed wt.)	Physically adsorbed water	Chemisorbed water	Total water	Line-width of signal of chemisorbed water (gauss)
1	10.8	3.6	11.5	15.1	7.0
2	8.8	1.1	11.0	12.1	7.0
3	—	2.4	12.5	14.9	7.0
4	—	1.8	11.4	13.2	7.0
5	—	3.3	12.3	15.6	7.0
6	10.2	2.3	12.9	15.2	6.7
7	12.0	3.0	11.4	14.4	5.9

^(a) Sealed 30 min boiling water, pH 6.0.

agreement with the estimates of O'Sullivan, Hockey, and Wood (3) on the relative amounts of free and bound water.

Gas adsorption.—Our analysis of the gas adsorption data follows standard procedures discussed by Barrett, Joyner, and Halenda (8); Lippens (9); and Brunauer, Emmett, and Teller (11). The adsorption isotherms permit two independent calculations of the surface area, S_{cum} and S_{BET} . Values of S_{cum} were determined by the Barrett, Joyner, and Halenda method. In principle, the mean pore radius is given by

$$\bar{r} = \frac{2V_P}{S}$$

where V_P is total pore volume and S is the surface area presented by the pores. This assumes uniform, cylindrical, nonintersecting pores. Such a pore will fill by capillary condensation when the pressure of the gas above the capillary reaches a pressure given by the Kelvin equation

$$\ln \frac{P}{P_0} = \frac{2\sigma V \cos \theta}{RT r_k}$$

where P/P_0 is the relative vapor pressure of the condensed gas, σ is the surface tension, θ is contact angle, V is the molar volume of the condensed gas, and r_k is the kelvin radius of the pore. In practice the pores are not all the same size and condensation will occur over a range of relative pressures. Thus r_k is obtained over each increment of pressure and

$$S = \frac{2V_P}{r_k}$$

is calculated for that increment.

Also in practice, as gas adsorbs on the pore walls the effective pore radius changes with each monolayer of gas adsorbed. This effect is accounted for in the Barrett, Joyner, and Halenda method by measuring the amount adsorbed at 64 standard values of the relative pressure, P/P_0 , for which corrections for the adsorbed thickness have been tabulated.

The value of S_{BET} is obtained from an analysis of the isotherm data using the BET equation

$$\frac{P}{X(P_0 - P)} = \frac{1}{X_m C} + \frac{(C - 1)P}{X_m C P_0}$$

where X is the weight (g) of adsorbant per gram of sample at pressure, P , and X_m is the weight of adsorbant per gram of sample at full monolayer coverage. C is a constant for a given gas and surface, containing, among other parameters, the energy of activation of adsorption and the vibration frequencies of the adsorbed molecules. If $P/X(P_0 - P)$ is plotted vs. P/P_0 , a straight line of slope $S = C - 1/X_m C$ and intercept $i = 1/X_m C$ is obtained. Solving the two equations simultaneously gives the values of the two unknowns, X_m and C . The value of S_{BET} is obtainable from X_m using a value of 16.2Å² as the area occupied by one adsorbed nitrogen molecule. Since the value of S_{cum}

Table III. Nitrogen absorption on anodic oxides

Sample	Median radius (Å)	Pore volume (cm ³ /g)	Surface area S _{cum} ^(a) (m ² /g)	S _{BET}
1 Unsealed	58	0.17	60.5	62.5
2 Unsealed	63.1	0.11	41.9	24.0
3 Unsealed	51.9	0.085	44.1	18.6
4 Unsealed	59.8	0.20	32.8	21.8
5 Sealed 2 weeks over room temp water vapor	19.8	0.04	33.7	5.1
6 Sealed 2 weeks over room temp water vapor	25.8	0.05	39.4	33.8
7 Sealed 2 weeks over room temp water vapor	64.4	0.02	12.9	5.0
8 Sealed 2 weeks over room temp water vapor	29.1	0.04	25.9	4.9
9 Sealed 1 min boiling water	15.2	0.007	9.0	—
10 Sealed 10 min boiling water	21.0	0.009	8.4	27.2
11 Sealed 30 min boiling water	18.9	0.0092	9.9	8.0
12 Model (Unsealed)	90 ^(a)	0.105	—	23.4
13 Model (Sealed)	20 ^(b)	0.052	—	5.2

(a) Model assumes 9.5×10^{10} pores/cm² and an apparent oxide density of 2.3 g/cm³. The pore radii are estimates based on electron photomicrographs of Ref. (16).

(b) Pore radius for model assumed to be 20Å according to gas adsorption data.

(c) From desorption data.

arises from specific assumptions concerning the shape of the pores and S_{BET} makes no assumptions of pore shapes, an agreement between S_{cum} and S_{BET} implies that the assumptions implicit in the value of S_{cum} (cylindrical, uniform, nonintersecting pores) are valid. It is seen from Table III that they are not equal. This implies, that in the equation

$$S = \frac{2V_P}{\bar{r}}$$

\bar{r} is too small, one interpretation of which is that the pores are bottle shaped or that each pore has a variable radius.

This interpretation would account for the hysteresis observed in the isotherm of Fig. 2 and in the different radius distribution curves for adsorption and desorption of Fig. 3. We choose not to belabor this interpretation, however. An equally plausible mechanism, described by Cohan (12), considers cylindrical pores to fill by adsorption on the pore walls presenting a cylindrical meniscus and to desorb by the Kelvin mechanism from a hemispherical meniscus.

In view of the rather poor reproducibility of the pore volumes (0.085-0.20 cm³/g) and surface areas (32.8-60.5 m²/g) for unsealed coatings it does not appear enlightening to pursue further the question of pore shapes. The poor reproducibility probably arises from (i) necessarily small oxide sample weights, (ii) relatively

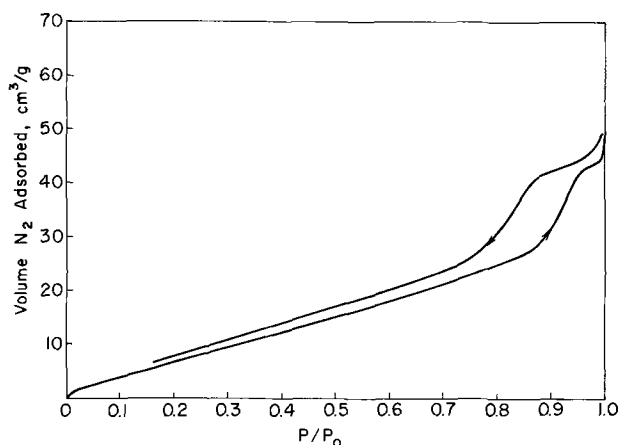


Fig. 2. Typical nitrogen adsorption-desorption isotherm of an unsealed oxide.

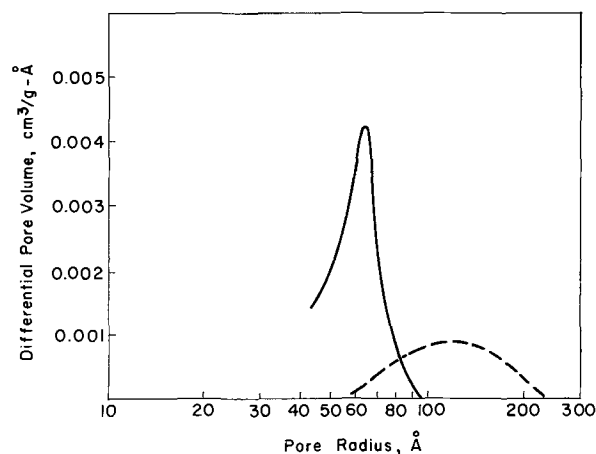


Fig. 3. Typical pore radius distribution curve for an unsealed oxide. The larger radius curve is from the adsorption leg, the smaller one from the desorption leg.

low porosity of the sample, and (iii) relatively poor reproducibility of the surface character. The results are good enough, however, to make comparisons to other results in the literature and to compare to current models of the coating structure.

The surface areas we obtain are roughly the same as those obtained by Burwell, Smudski, and May (13); Cosgrove (14); and Paolini, Masoero, Sacchi, and Paganelli (15), although direct comparison is difficult. Burwell *et al.* report 600 cm² real surface per cm² geometrical surface on coatings formed at about 14 A/ft² and 17V in 15% H₂SO₄ at 21°C. If we make a reasonable assumption of coating density, this converts to about 19 m²/g (for an apparent density of 2.5 g/cm³ and the density may be somewhat higher). They estimated a pore radius of 53Å and 1.55×10^{11} pores/cm². Cosgrove finds 81Å radii pores by n-butane adsorption and a surface area of 680 cm² per cm² of geometrical surface. This also converts to about 19 m²/g if the density is taken as 2.5 g/cm³. Cosgrove and Paolini *et al.* report isotherms that are somewhat steeper than ours in the capillary condensation region and they do not observe hysteresis.

Based on unpublished pore counts (9.5×10^{10}) from electron micrographs observed earlier in this laboratory for comparable coatings (16) and assuming 100Å radius cylindrical pores, we calculate a surface area of 26.0 m²/g for coatings having our experimental density (2.3 g/cm³). For 60Å radius pores, the calculated area is about 16 m²/g. Alternatively, using our experimental values of the radius (60Å) and surface area (20 m²/g), the calculated pore density is 1.2×10^{11} pores/cm².

In any event, the gas adsorption data is consistent with a pore model with pore counts and pore dimensions about the same as found by other workers from both gas adsorption and electron microscopy. The pore radii, volumes, and surface areas of sealed coatings are interesting. Sealing, either by boiling water or by vapor does not close the pores entirely (note radii of 15 to about 30Å, discounting the one value of 64.4Å). Boiling water seals result in a lower pore volume and surface area than vapor aging although there is not much difference in pore radii between vapor aged and boiling water sealed samples.

The nmr spectra also provide information on surface areas in two ways (5). The first method is an estimate of surface hydroxyl content from the width of the broad hydroxyl signal. It is based on the fact that motional narrowing of the signal occurs for surface protons to a greater extent than for protons bound to oxides on a crystallite interior. A silica gel having only surface hydroxyl groups has a width of 0.310G (6). Gibbsite with only interior hydroxyl groups has

a width of 12.75G. Using these two standards and assuming a linear relation between line width and relative surface concentration gives the equation $F = (12.75 - \Delta H)/12.44$ where F is the fraction of total protons residing on the surface.

The width of the hydroxyl signal on an unsealed coating containing 3% OH is 5.5G. The value of F is thus 0.58. The area covered by OH in the unsealed coating is $S = CFNS_0$, where C is moles of OH per gram of oxide, N is Avogadro's number, and S_0 is the area (in square meters) occupied by one OH group. Peri (17) gives a value of S_0 of 8\AA^2 . The value of S is thus $49\text{ m}^2/\text{g}$ which is about twice that obtained from nitrogen absorption. We conclude that the major pore surface is nearly completely covered by OH with the remainder of the hydroxyl groups distributed over crystallite surfaces in the pore walls and on the interior of crystallites.

A related empirical relation was developed from a comparison of aluminum-27 spectra with proton spectra for a series of nonanodic aluminas. This showed that the average line-width of hydroxyls in the first two layers of a crystallite is 2.5G. Comparison of this and gibbsite gives the relation $F_2 = (12.75 - \Delta H)/10.25$ where F_2 is the fraction of hydroxyl protons in the first two layers (5). For the unsealed coatings F_2 is 0.71.

The second estimate of surface area is based on an empirical inverse linear relationship observed between BET surface areas and line-widths for OH on the surface of desiccant aluminas (5). This relation, expressed as $\Delta H = 13.20 - 0.0243 S_{\text{BET}}$ gives a value of the surface area of the unsealed coatings of $317\text{ m}^2/\text{g}$. The obvious discrepancy between this value and the gas adsorption results can be rationalized easily by a model which assumes the coating to consist of submicrocrystallites penetrated by pores in the classical sense. Apparently, only the major pore surfaces are accessible to nitrogen in the times allowed for establishment of equilibrium in the isotherm experiments, but in the course of their formation or on long exposure to water vapor or shorter exposure to higher temperature water, water can penetrate into the pore walls. A possible mechanism of water penetration would be a hydroxyl migration from site to site across an oxide crystallite.

This model is supported by the water contents of sealed coatings. The line width of the hydroxyl signal is 7.0G which corresponds to $260\text{ m}^2/\text{g}$ where $F = 0.46$ as the fraction of total OH on the surface. Using 8\AA^2 surface per OH we calculate a surface capacity of 4.9% H_2O (as OH). If this represents 46% of the total, the total combined water content is 10.7%, in reasonable agreement with the experimental values of Table II.

Further support comes from an analysis of the water contents of coatings formed in an electrolyte of 5-sulfosalicylic acid and sulfuric acid. A preliminary analysis of two of these sealed films showed a hydroxyl line width of about 12G and a total water content of about 3%. The 12G line width corresponds to a surface area of $50\text{ m}^2/\text{g}$ which, compared to the sulfuric acid film, should have a capacity of $50/260 \times 11 = 2.1\%$.

We wish to compare the specific volume of the pore wall oxide to an oxide having no intercrystallite void volume in order to estimate the intercrystallite void volume of the pore wall oxide. Since we assume the crystallites in the pore wall to have a close-packed oxide structure, the best comparison is probably with $\alpha\text{Al}_2\text{O}_3$. The apparent coating density is $2.3\text{ g}/\text{cm}^3$ and the specific volume is $0.44\text{ cm}^3/\text{g}$. If the major pore volume of about $0.1\text{ cm}^3/\text{g}$ is subtracted from this the specific volume of pore wall oxide is $0.34\text{ cm}^3/\text{g}$. The single crystal density of $\alpha\text{Al}_2\text{O}_3$ is $3.97\text{ g}/\text{cm}^3$ and the specific volume is $0.252\text{ cm}^3/\text{g}$. The ratio $0.252/0.34 = 0.75$ gives an intercrystallite void volume of pore wall oxide of 25%.

It can be shown that each sphere in a collection of spheres in cubic close packing occupies a volume of about $5.6 r^3$ where r is the sphere radius. This volume includes the intercrystallite void volume associated with each sphere. The actual volume of the sphere is

$4/3 \pi r^3$ or $4.2r^3$. The ratio of actual volume to apparent volume is 0.75 in agreement with the experimental value. Thus, the oxide structure can be described in terms of a model consisting of close-packed oxide crystallites. If the volume of a model crystallite is $5.6r^3$, n crystallites has a volume, $V(n) = 5.6r^3n = 0.34\text{ cm}^3/\text{g}$. If the total crystallite area is $317\text{ m}^2/\text{g}$, the area of one crystallite is $3.17 \times 10^6/n = 4\pi r^2\text{ cm}^2/\text{g}$. From these two equations, the radius of the crystallite is calculated to be 24\AA , which is reasonable in view of the weak electron diffraction patterns obtained from anodic oxides (18).

Conclusions

Over half of the combined water in a sealed oxide resides within the first two oxide ion layers of a surface. In order to account for a surface area of this magnitude, capable of accommodating as much surface water as is observed, we postulate a sumicrocrystallite material penetrated by classical pores. The surface area and oxide density is consistent with a close-packed spherical crystallite model in which the crystallite diameter is about 40\AA . Only the major pore surfaces are accessible to nitrogen or other gaseous adsorbants but the crystallite surfaces are accessible to water in a reaction that is slow at room temperature. Coatings exposed to boiling water for 30 min absorb about the same quantity of water as similar coatings exposed to saturated water vapor at room temperature for two weeks (4). Furthermore, the relative amounts of physically and chemically adsorbed water are about the same; whether sealed in boiling water or by water vapor adsorption.

There is a difference, however, in porosity between films sealed by boiling water and by room temperature vapor. Boiling water sealing results in smaller pores, smaller pore volumes, and lower surface areas, even though the water contents of the films sealed by the two methods are the same. The partial pore closure observed for the vapor sealed films is probably the result of a swelling that must occur when the crystallite surfaces adsorb water. The additional pore closure for boiling water sealing may be the result of a dissolution and reprecipitation of oxide near the pore mouth as suggested by Spooner and Forsyth (1).

One of the somewhat surprising results of this study was the observation that some proton containing species other than physically adsorbed molecular water can be removed from the oxide relatively easily by gentle heating (90°C) or room temperature evacuation. Water (or, at least the elements of water) probably occur on the surface as $\text{Al}-\text{OH}^{(\text{I})}$, $\text{Al}-\text{OH}_2^{(\text{II})}$, and $\text{Al}-\text{O}-\text{H}-\text{OH}^{(\text{III})}$. The first two structures are responsible for the broad line (about 3-13G, depending on the relative concentration of surface to interior species). The last structure, physically adsorbed water is responsible for the narrow line (about 0.2G). Peri has described a model Al_2O_3 surface to account for differences in ease of dehydration of the oxide surface (17). According to his model adjacent hydroxyl groups combine to lose water randomly subject to the restriction that either adjacent O^{2-} pairs or adjacent exposed Al^{3+} pairs constitute higher energy sites, making H_2O removal from such sites more difficult. We postulate that coordinated water (structure II) should be removed more easily than water condensed from adjacent hydroxyl pairs and it is this form of water that is removed most easily, along with the physically adsorbed water.

One important practical consequence of the relative ease of removal of structural water is the possibility that a water loss-gain cycle is set up on anodized aluminum articles exposed to temperature and humidity changes. Such a cycle could have the effect over a period of time of loosening some of the oxide to form the powdery deposit called bloom or blush. This possibility is now under investigation.

Acknowledgments

We thank D. Przybycien for the gas adsorption measurements and Kaiser Aluminum & Chemical Corporation for permission to publish this work.

Manuscript submitted June 1, 1971; revised manuscript received Sept. 2, 1971.

Any discussion of this paper will appear in a Discussion Section to be published in the December 1972 JOURNAL.

Note added in proof: The broad-line species lost easily at low temperatures may result from condensation reactions occurring in gelatinous, hydrated alumina deposited in the pores and near the oxide surface, $-\text{Al}-\text{OH} + \text{HO}-\text{Al}- \rightarrow -\text{Al}-\text{O}-\text{Al}- + \text{H}_2\text{O}$. This type of reaction would break one Al—O bond but would establish another Al—O bond. On the other hand, a condensation of OH groups from two neighboring sites on a surface,

$$\begin{array}{c} \text{OH} \quad \text{OH} \quad \text{O} \\ | \quad | \quad | \\ \text{Al} \quad \text{Al} \quad \text{Al} \\ | \quad | \quad | \\ \text{Al} \quad \text{Al} \end{array} \rightarrow \begin{array}{c} \text{O} \\ | \\ \text{Al} \quad \text{Al} \\ | \quad | \\ \text{Al} \quad \text{Al} \end{array} + \text{H}_2\text{O} \text{ or}$$

$\text{Al} \quad \text{Al} \rightarrow \text{Al} \begin{array}{c} \diagup \quad \diagdown \\ \text{O} \end{array} \text{Al} + \text{H}_2\text{O}$, would break one Al—O bond and either leave a Lewis acid site or result in a change in Al coordination number. The condensation occurring in a gelatinous alumina should be more favorable energetically and could account for the easily lost broad-line species.

REFERENCES

1. R. C. Spooner and W. J. Forsyth, *Plating*, **55**, 336, 341, 463 (1968).

2. J. F. Murphy, Anodizing Symposium, Birmingham, April, 1967.
3. J. P. O'Sullivan, J. A. Hockey, and G. C. Wood, *Trans. Faraday Soc.*, **65**, 535 (1969).
4. B. R. Baker and R. M. Pearson, *This Journal*, **118**, 353 (1971).
5. R. M. Pearson, Presented at the Pacific Conference on Chemistry and Spectroscopy, San Francisco, October 6-9, 1970, *J. Catalysis*, To be published.
6. D. E. O'Reilly, *Advan. Catalysis*, **12**, 31 (1960).
7. T. Saito and J. Hagewara, *Bull. Chem. Soc., Japan*, **33**, 1463 (1960).
8. E. P. Barrett, L. G. Joyner, and P. P. Halenda, *J. Am. Chem. Soc.*, **73**, 373 (1951).
9. B. C. Lippens, Structure and Texture of Aluminas, Thesis, University of Delft (1961).
10. S. J. Gregg and K. S. Sing, "Adsorption, Surface Area and Porosity," Academic Press, New York (1967).
11. S. Brunauer, P. H. Emmett, and E. Teller, *J. Am. Chem. Soc.*, **60**, 309 (1938).
12. L. H. Cohan, *ibid.*, **60**, 433 (1938).
13. R. L. Burwell, Jr., P. A. Smudski, and T. P. May, *ibid.*, **69**, 1525 (1947).
14. L. A. Cosgrove, *J. Phys. Chem.*, **60**, 385 (1956).
15. G. Paolini, M. Masoero, F. Sacchi, and M. Paganelli, *This Journal*, **112**, 32 (1965).
16. Bruce E. Deal, Unpublished observations.
17. J. B. Peri, *J. Phys. Chem.*, **69**, 211 (1965).
18. S. Wernick and R. Pinner, "The Surface Treatment and Finishing of Aluminium and Its Alloys," p. 260, Robert Draper Ltd., Teddington (1969).

A Negative-Ion Type Instability in MOS Devices

Earl S. Schlegel*¹ and George L. Schnable*²

Philco-Ford Corporation, Blue Bell, Pennsylvania 19422

ABSTRACT

A hot-bias instability capable of shifting threshold voltages to positive values has been observed in the field oxide of MOS devices that have stable gate oxides. The instability is attributed to a contaminant that is introduced during thermal oxidation or other high-temperature processes, and is believed to be due to an immobile negative ion coexistent with a mobile positive ion. The activation energy and mobility of the mobile charge are similar to that of sodium in SiO₂. The effects of differences in processing are discussed.

The electrical properties of thermally grown SiO₂ and of its interface with silicon have been the subject of extensive studies designed to create and improve the technology for building planar diodes, transistors, and integrated circuits. These properties, to a large extent, control the performance, yield, and reliability of both bipolar and MOS devices.

A number of papers have been published that describe the electrical properties of thermally grown SiO₂ in detail (1, 2). This literature contains little information on negative charge in thermally grown SiO₂ layers. Kerr (3) found that net negative charge can be built up in lead-alumino-borosilicate or zinc-alumino-borosilicate that has been deposited by sedimentation techniques, if the structure is heated with an applied negative bias. Snow and Dumesnil (4) have shown that net negative charge can be developed in lead glass due to a combination of positive mobile lead ions and immobile negative ions. Snow and Deal (5) showed that net negative charge densities could be created in P₂O₅ (15 mole per cent) containing SiO₂ layers, due to dipolar polarization under negative bias at an elevated temperature. Kuper *et al.* (6, 7) reported that Br from NaBr partially neutralizes the effects

of positive ions in SiO₂ and that this Br diffuses much more slowly than sodium at 800°C. Gold is reported to be negatively ionized in SiO₂ (8-10). Chang and Tsao (11) reported that zinc behaves as a negative charge in SiO₂, but they did not show a net negative charge per unit area. Brotherton (12) has shown that platinum can create a large negative charge density in SiO₂ layers. Dunbar and Hauser (13) found a mobile negative ion that builds up large net negative charge densities in unannealed pyrolytic SiO₂ layers. Iwauchi and Tanaka (14) reported on a negative-ion type of instability in Si-SiO₂ structures that were formed by d-c reactive sputtering. They interpreted their observations in terms of a mobile negative ion and reported that it could be immobilized by phosphorus in a manner similar to that used widely in the industry to immobilize positive mobile ions such as sodium.

Many studies of thermally grown SiO₂ layers have shown that the as-formed condition (or the condition after the sample has been heated to 300°C with the metal electrode on the oxide shorted to the substrate) for mobile charge in the oxide is such that the flat-band voltage is near its least negative point. Radiochemical studies (6, 7) have shown that the mobile charge species in this case are alkali ions—most frequently sodium.

Two recent papers have described the existence of a negative-ion type of instability in thermally grown oxides. Reynolds *et al.* (15) showed a decrease in the

* Electrochemical Society Active Member.

¹ Present address: Westinghouse Research Laboratories, Beulah Road, Churchill Boro, Pittsburgh, Pennsylvania 15235.

² Present address: RCA Corporation, David Sarnoff Research Center, Princeton, New Jersey 08540.

Key words: SiO₂, MOS device instability, MOS device failure mechanism, negative ions in SiO₂, alkali ions in SiO₂.

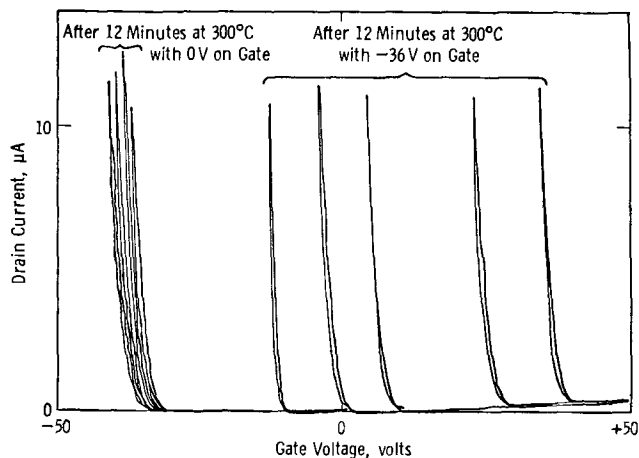


Fig. 1. Effect of Q_{neg} on the characteristics of p-channel MOS transistors located in different areas of a single wafer.

threshold voltage of thick oxide transistors designed for use as MOS test vehicles, due to step-stressing involving a negative bias. Deal (16) reported that negative ions, that are not mobile at 300°C, can contaminate oxides at temperatures of about 900°C and make silicon surfaces p-type.

In this paper, we report on the results of experimental studies of negative charge in thermally grown SiO_2 layers of the type used widely in the industry for field oxides in MOS microcircuits. The results of a study of the characteristics of this type of charge are reviewed and a model is proposed.

Experimental Findings

General.—The charge that is the subject of this paper is set apart from other mobile ion instabilities by a distinctive characteristic. This is that after the device has been fabricated or after it has been baked under shorted conditions, a bake with negative applied bias causes the capacitance-voltage characteristics of an MOS capacitor or the current-voltage characteristics of an MOS transistor to shift in the positive voltage direction. This shift sometimes changes the flat-band or inversion voltage to positive values; that is, the net effective charge density takes on negative values. Changes of this magnitude are shown in Fig. 1 for p-channel MOS transistors designed for use as test structures and fabricated in our laboratory. The oxide in the gate region was 15,000Å thick, and it was formed by the processes being used to form the field oxides in MOS microcircuits (thermal oxidation by a dry-wet-dry process, at 1200°C). The silicon was <111> orientation, phosphorus doped, with a resistivity of 5 ohm-cm. The metallization was e-gun evaporated aluminum.

In this paper we define Q_{neg} as the difference between the effective charge densities after a drift at 300°C under negative applied voltage and an anneal at 300°C under short-circuit conditions.

We have found significant amounts of Q_{neg} in samples from three other manufacturers, and we have found little to indicate that any manufacturer is free of this instability. (The problem is more readily uncovered in the samples from some manufacturers than from others because some microcircuit chips are made with discrete test structures and others are not.) Table I shows typical data taken from devices from three other manufacturers.

Spatial distribution.—This negative-ion type instability is almost never observed in the gate oxide, even in samples in which it occurs to a strong degree in the field oxide.

When Q_{neg} is found on a wafer, its distribution over the area of the wafer is nonuniform, as shown in Fig. 1. The data in Fig. 1 were taken from randomly chosen regions over the area of a single wafer. Each curve

Table I. Field inversion voltage instability in MOS IC's commercially available from three other manufacturers

Manufacturer	After bake under short-circuit conditions,* V	After bake with negative applied bias,* V
A	47	44
	47	47
	58	10
	44	27
	48	25
B	15	14.5
C	33	1
	34	4

* Drifting was performed at 300°C for 12 min with either 0 or -30V applied.

Table II. Data from etching experiment to determine location of negative charge

	Effective charge density calculated from the flatband voltage (10^{11} charges/cm ²)	
	After -36V drift	After 0V drift
Unetched layers (2µ thick)	-7.7 to +3.3	+3.4 to +4.0
Etched layers (1µ thick)	+1.7 to +2.6	+3.1 to +3.7

represents the current-voltage characteristics of a single transistor.

An etching experiment on an oxide sample that contained Q_{neg} showed both a reduction in the mobile and in the net negative charge when 1µ of the 2-µ thick oxide was etched away. The data in Table II show that most of the mobile charge and most of the negative charge were located in the outer half of the oxide.

Metallization effects.—The negative-ion type instability has been found in unmetallized samples that were drifted with a gold ball probe and under electrodes formed with a conductive paste.

Differences in the temperature or ambient composition during the alloying of the aluminum metal do not affect Q_{neg} . Experiments in which the aluminum was removed from metallized samples that were subsequently remetallized showed no significant change in the level of Q_{neg} .

High-temperature process effects.—The differences between the processes used to grow the gate and the field oxides that cause the difference in Q_{neg} in these oxides are believed to be the temperature and humidity levels used to grow the oxides. The field oxide is grown at 1200°C in oxygen bubbled through water at 95°C. The gate oxide, grown in regions from which

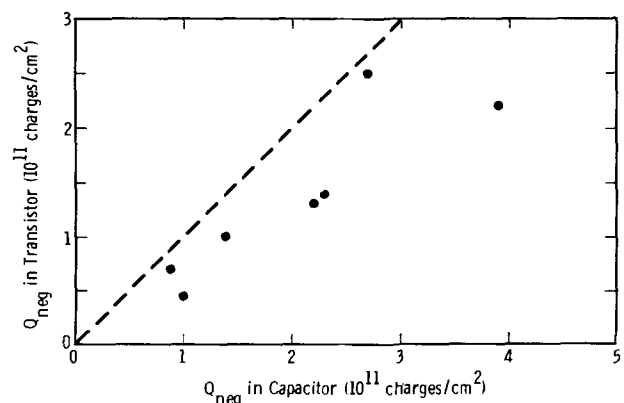


Fig. 2. Comparison of Q_{neg} in MOS capacitors and MOS transistors on the same wafer.

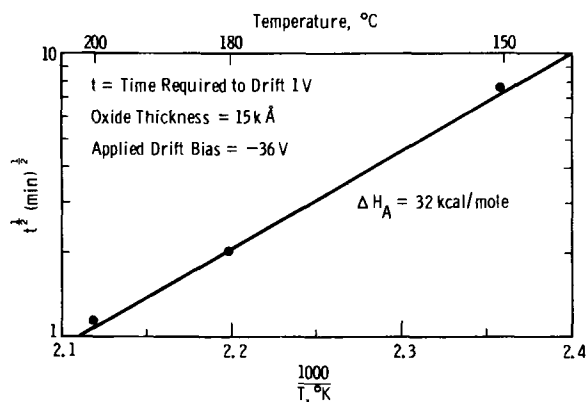


Fig. 3. Temperature dependence of the time required to drift Q_{neg} .

the field oxide was removed, is grown at 1000°C in dry oxygen.

Extensive studies lead to the conclusion that Q_{neg} is always dependent on conditions involved in processes performed above 600°C.

Gettering.—We find that Q_{neg} densities of 5×10^{11} cm^{-2} can be decreased to less than 1×10^{10} cm^{-2} by phosphorus or HCl treatments of the type known to immobilize sodium ions (17-20). The phosphorus was deposited from a $POCl_3$ source onto wafers at 1000°C for 5 min. The phosphorus glass was not stripped, and the phosphorus was driven in for 10 min at 1000°C. In the case of HCl, the sample was heated in 2% HCl in N_2 at 1000°C for 30 min.

We find that Q_{neg} is affected by the proximity of a pn junction, as shown in Fig. 2. This is similar to the effect of a pn junction on positive mobile ion densities (Q_0) reported in Ref. (21).

Kinetics of the instability.—There appears to be no difference between the drift rates for the initial drift and a subsequent recovery drift of Q_{neg} such as that usually found for positive mobile ions (22).

The Q_{neg} ions are nearly immobile at room temperature both before and after they have been drifted at 300°C, although shifts into the positive quadrant have been found after a bias of 10^5 V/cm was applied for 425 hr at room temperature. At 300°C a similar shift occurs in less than 12 min.

Measurements of the drift rate of Q_{neg} have been taken as a function of temperature, and an activation energy of 32 kcal/mole has been calculated. This value agrees very closely with that reported by Hofstein (22) and by Snow *et al.* (23) for sodium ions. Our data are shown in Fig. 3.

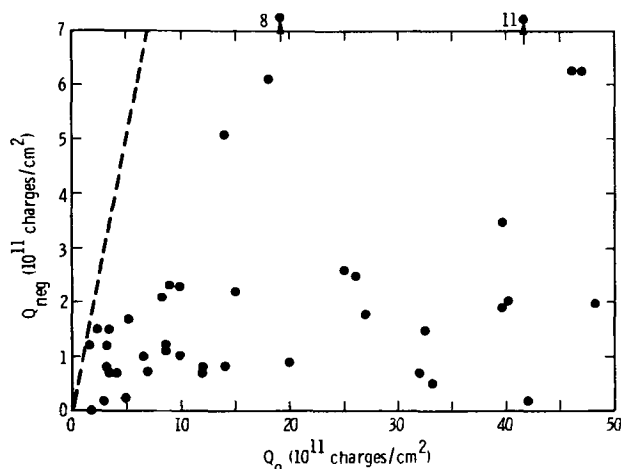


Fig. 4. Comparison between Q_{neg} and Q_0 (300°C) in MOS capacitors.

Comparison of Q_{neg} and Q_0 .—An effort to determine whether there is a correlation between Q_{neg} and the density of positive mobile ions (Q_0) in individual MOS capacitors yielded the results given in Fig. 4. The broken line shows the locus of points where the densities of the two types of charge would be equal. These data show that Q_{neg} is always less than Q_0 and that there is no clear correlation between these two types of charge.

Model

The negative-ion type instability must involve a mobile ion species rather than dipole polarization because the shift along the voltage axis is frequently found to be greater than the voltage that was used to induce the shift. Two possibilities exist: there could be (a) negative mobile ions or (b) negative immobile ions in combination with positive mobile ions.

Based on previously reported information (7) that anions are only mobile at temperatures of about 800°C or higher and on our observation that the instability appears to be introduced only during processes that involve temperatures above 600°C, we infer (24) that the instability is due to an immobile anion contaminant that is introduced during a high temperature process, in combination with a mobile cation believed to be sodium. The anion contaminant appears to be related to sodium, and sodium ions are typically found in samples that have the negative ion contamination. Apparently, the presence of the anion causes the sodium to be distributed to some extent through the thickness of the oxide layer, in contrast to the usual tendency for the sodium to lie near the metal-oxide interface.

Conclusions

An instability has been observed in the field oxide of MOS microcircuits that has been attributed to a combination of positive mobile ions, probably sodium, and negative immobile ions that are due to a contaminant that is introduced during a high-temperature processing step such as oxidation.

The inversion voltage under metal lines over field oxide of commercially available MOS-integrated circuits can be degraded to the point where the operating voltage causes channeling between two isolated p-regions and degrades or fails the circuit (25).

The instability is found only in field oxides and therefore a test of stability of only the gate oxide is an insufficient test for the prediction of microcircuit reliability.

The manufacture of reliable MOS microcircuits requires (a) an understanding of the possible effects of negative-ion type instability, (b) the use of fabrication techniques which avoid ionic contamination in field oxides or include gettering techniques, and (c) routine quality control techniques to insure the stability of field oxides in completed devices.

Manuscript submitted June 25, 1971; revised manuscript received ca. Oct. 21, 1971. This was Paper 26 presented at the Washington, D. C., Meeting of the Society, May 9-13, 1971.

Any discussion of this paper will appear in a Discussion Section to be published in the December 1972 JOURNAL.

REFERENCES

1. E. S. Schlegel, *IEEE (Inst. Elec. Electron. Engrs.) Trans. Electron Devices*, **ED-14**, 728 (1967).
2. E. S. Schlegel, *ibid.*, **ED-15**, 951 (1968).
3. D. R. Kerr, *IBM J. Res. Develop.*, **8**, 385 (1964).
4. E. H. Snow and M. E. Dumesnil, *J. Appl. Phys.*, **37**, 2123 (1966).
5. E. H. Snow and B. E. Deal, *This Journal*, **113**, 263 (1966).
6. A. B. Kuper, C. J. Slabinski, and E. Yon, in "Physics of Failure in Electronics," RADC Ser. in Reliability, **5**, 232 (1967).
7. A. B. Kuper, *Surface Sci.*, **13**, 172 (1969).
8. D. R. Collins, D. K. Schroder, and C. T. Sah, *Appl. Phys. Letters*, **8**, 323 (1966).
9. A. G. Nassibian, *Solid-State Electron.*, **10**, 879 (1967).

10. A. G. Nassibian, *ibid.*, **10**, 891 (1967).
11. C. Chang and K. Tsao, *ibid.*, **12**, 411 (1969).
12. S. D. Brotherton, *ibid.*, **13**, 1113 (1970).
13. P. M. Dunbar and J. R. Hauser, *This Journal*, **117**, 674 (1970).
14. S. Iwauchi and T. Tanaka, *Jap. J. Appl. Phys.*, **7**, 1193 (1968).
15. F. H. Reynolds, R. W. Parrott, and D. Braithwaite, *Proc. IEE (London)*, **118**, 475 (1971).
16. B. E. Deal, "Measurement and Control of Dielectric Film Properties During Semiconductor Device Processing," in Proceedings of the ASTM/NBS Symposium on Silicon Device Processing (held in Gaithersburg, Maryland, June 2-3, 1970) pp. 36-50 (Nov. 1970).
17. D. R. Kerr, J. S. Logan, P. J. Burkhardt, and W. A. Pliskin, *IBM J. Res. Develop.*, **8**, 376 (1964).
18. P. Balk and J. M. Eldridge, *Proc. IEEE (Inst. Elec. Electron. Engrs.)*, **57**, 1558 (1969).
19. E. MacKenna, V. Rodriguez, and P. Kodama, 1970 Fall Meeting of Electrochem. Soc., Atlantic City, N. J. (Abstract No. 146).
20. P. H. Robinson and F. P. Heiman, *This Journal*, **118**, 141 (1971).
21. E. S. Schlegel, *J. Appl. Phys.*, **42**, 425 (1971).
22. S. R. Hofstein, *IEEE (Inst. Elec. Electron. Engrs.) Trans. Electron Devices*, **ED-14**, 749 (1967).
23. E. H. Snow, A. S. Grove, B. E. Deal, and C. T. Sah, *J. Appl. Phys.*, **36**, 1664 (1965).
24. E. S. Schlegel and G. L. Schnable, Abs. 26, p. 69 in Electrochem. Soc. Extended Abstracts, Spring Meeting, Washington, D. C., May 9-13, 1971.
25. G. L. Schnable, H. J. Ewald, and E. S. Schlegel, "MOS Integrated Circuit Reliability," *IEEE Trans. Reliab.*, Feb. 1972.

Structure of Noncrystalline Co-25 a/o W Electrodeposit

T. Omi and H. Yamamoto*

College of Engineering, University of Osaka Prefecture, Sakai, Japan

and H. L. Glass¹

College of Engineering, Rutgers University, New Brunswick, New Jersey 08903

ABSTRACT

Noncrystalline electrodeposits of Co-25 atomic per cent (a/o) W prepared from ammoniacal alkaline tartrate electrolyte were studied by x-ray diffraction. A model for the structure of this alloy was developed. The principal assumptions involved in constructing the model are based mainly on requirements for the electrodeposition. The model requires that the alloy consist of distinct basic structural units in the form of tetrahedra, each composed of three cobalt atoms and one tungsten atom. The dimensions of this structural unit correspond to those of the intermetallic compound Co_3W . Certain criteria govern the bonding of the tetrahedra to form larger aggregates. The scattering function calculated from the model agrees quite well with the diffraction data. The model also accounts for differences in the composition of amorphous deposits prepared at different current densities. The electrochemical requirements for the formation of this structure by electrodeposition are discussed. The operation of similar processes in the electro- or chemical deposition of other alloys having stoichiometric composition is considered.

Solid amorphous binary and ternary alloys of various compositions (1-4) can be prepared by several different techniques (1, 2, 5, 6). Many of these alloys have x-ray diffraction patterns which are very similar to one another. This implies similarities in the atomic distributions of the respective alloys. A number of structural models have been considered to describe these distributions (2, 7). In a rather exhaustive study (7) it has been shown that these models generally do not give satisfactory agreement with x-ray diffraction data or that they conflict with physical parameters of the material.

Recently it has been shown (8) that for Ni-P amorphous deposit a model consisting of a dense random packing of hard spheres (9, 10) yields an atomic distribution function (11) which agrees quite well with the pair distribution function deduced from x-ray diffraction data. It is believed (8) that similar agreement should be found for other amorphous alloys possessing similar diffraction patterns.

The dense random packing model in its present form is monatomic and treats all the atoms in the alloy as identical. Its usefulness in the case of Ni-P appears to be related to the following properties of the Ni-P alloy examined: (i) the difference in Goldschmidt atomic radii of Ni and P is small; (ii) the contribution of P to the scattered x-ray intensity is relatively small. Thus, in so far as atomic arrangement and x-ray diffraction are concerned, the phosphorus may be con-

sidered as a perturbation in a pure nickel amorphous structure.

The present paper deals with the structure of Co-25 a/o W alloy which has a diffraction pattern similar to that of the Ni-P. This Co-W alloy does not appear to satisfy the conditions required for the usefulness of the monatomic model approximation. Furthermore, from electrochemical and crystallographic considerations to be described, Co-25 a/o W amorphous deposit is expected to possess a distinctive short range order. The dense random packing model, even in a binary form which explicitly recognizes the existence of the two atomic species, would not adequately treat this crucial feature of short range order. Instead, a model for the structure of this alloy is developed entirely from electrochemical and crystallographic considerations. The scattering function of this model is then calculated and is compared with the experimental results from x-ray diffraction measurement.

In a previous paper (12) the relationship between cathode potential and structure of deposits in the electrodeposition of Co-W alloys was reported. Since that paper was published in Japanese, the pertinent results will be summarized here.

Electrodeposition of Co-W alloy from the ammoniacal alkaline tartrate electrolyte has two main electrode reactions. One reaction produces a cathode deposit which is a close-packed hexagonal solid solution containing up to 17.9 a/o W. The second reaction produces a noncrystalline deposit having the stoichiometric composition of Co_3W . The occurrence of these two reactions is a function of the cathode potential. Within a certain range of cathode potential both reactions may be operative and the deposit will consist of a mixture

* Electrochemical Society Active Member.

¹ Visiting Researcher, University of Osaka Prefecture, supported by National Science Foundation Visiting Scientist Grant; present address: Physical Sciences Dept., Autonetics, Anaheim, California 92803.

Key words: amorphous alloy, induced electrodeposition, x-ray diffraction amorphous alloy, cobalt tungsten, alloy electrodeposition.

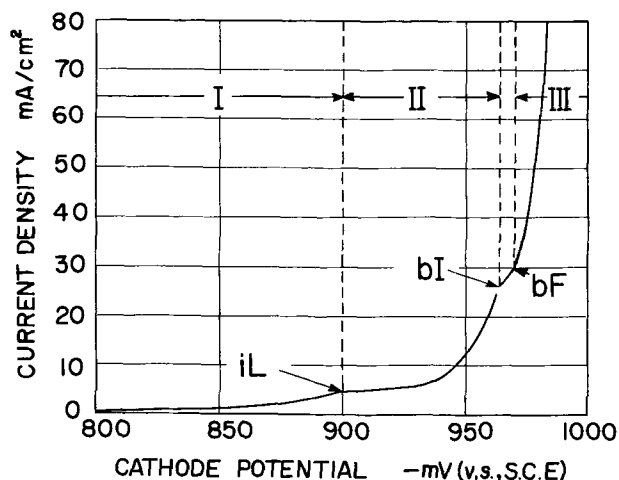


Fig. 1. Initial current density vs. cathode potential curve for deposition of Co-W alloy from ammoniacal alkaline tartrate electrolyte. $[(\text{NH}_4)_2\text{C}_4\text{O}_8\text{H}_4, 0.260 \text{ M/L}; \text{Na}_2\text{WO}_4, 0.247 \text{ M/L}; \text{CoSO}_4, 0.013 \text{ M/L}; \text{at } 80^\circ\text{C}, \text{pH } 8.7]$

of the two phases, *viz.*, noncrystalline phase and cph phase.

Figure 1 is the cathodic current density *vs.* potential curve for this system. There are three important ranges. In range I the cathode potential is less negative than at *iL* and the deposit consists only of the cph solid solution phase. In range II, from *iL* to *bI*, the deposit is a mixture of the cph and noncrystalline phases. Within range II the composition of the cph phase, as determined by gravimetric chemical analysis, remains constant at 17.9 a/o W. However, in going from *iL* to *bI* the fraction of noncrystalline phase in the deposit increases so that the total tungsten content of the deposit also increases; from 17.9 a/o W at *iL* to 22.2 a/o W at *bI*.

In ranges I and II the deposits are dense and can be electropolished to make thin foils for transmission electron microscopy. In deposits prepared at *bI* no crystalline phase is detectable by electron microscopy at higher magnifications or by selected area electron diffraction. (As will be explained in the Discussion, the deviation of the composition from that of Co_3W is probably due to excess cobalt rather than to the presence of cph phase.)

Deposits obtained in range III, where the cathode potential is more negative than *bF*, consist only of the noncrystalline phase having the stoichiometric composition of Co_3W . These deposits contain considerable amounts of hydrogen and, unlike the deposits of ranges I and II, are loose and cannot be prepared as thin foils.

It should be remarked that Fig. 1 is drawn for the particular case in which tungsten ions constitute 95% of the total metal ions in the solution, *i.e.*, $W/(W + \text{Co}) = 0.95$. The following deposition parameters were fixed in the experiment: ammonium tartrate 0.26 M/L; total metal concentration (sodium tungstate + cobalt sulfate) 0.26 M/L; $\text{pH} = 8.7$ as adjusted with ammonium hydroxide (all reagents were special grade); bath temperature $80.0^\circ \pm 0.2^\circ\text{C}$; no agitation. If the tungsten concentration is changed while keeping the total metal concentration fixed, the curve of Fig. 1 is displaced vertically; the current densities at *iL*, *bI*, and *bF* increase proportionally as the cobalt concentration increases. However, the values of cathode potential which define the boundaries of the three ranges are invariant. The three ranges with their respective deposit structures were observed to occur throughout a continuum of values of electrolyte tungsten concentration from 70-95%. Thus, the structure of the deposit depends chiefly on the cathode potential.

Deposits of various thicknesses ranging from about 10-50 μ were prepared. Neither the composition nor

x-ray scattering patterns showed any thickness dependence. Transmission electron diffraction patterns of deposits prepared at *bI* showed an essentially isotropic halo pattern characteristic of amorphous materials.

X-Ray Measurement and Results

For the present investigation noncrystalline deposits of about 20 μ thickness were electrodeposited onto mild steel substrates. The electrolyte had a molar metal ratio of $W/(W + \text{Co}) = 0.80$. The deposition parameters were the same as in the previous work (12). Specimens were prepared potentiostatically at *bI* in region II and galvanostatically at a current density far above *bF* in region III. The thickness of 20 μ was chosen so that the deposits would appear nearly infinite in thickness for the MoK_α radiation employed in the x-ray scattering measurements.

X-ray scattering data were measured at room temperature in air using a Rigaku Denki counter diffractometer equipped with the Type CN4133L generator. A rotating Mo target operated at a high output of 60 kV and 100 mA, a bent LiF monochromator in the diffracted beam, and a scintillation counter were used. Data were taken by a scanning at 1° of 2θ per min and reading the chart oscillations in steps of $0.2^\circ 2\theta$. The amplitude of random oscillations for all the scattering angles was less than 85 electron units before damping correction. Fixed time counts were made at $20^\circ 2\theta$ (near the position of the first maximum) and at $90^\circ 2\theta$. The ratio of these values compared well with the corresponding ratio taken from the chart.

Figure 2 shows experimental interference functions for two specimens; one prepared in region III (curve a) and the other prepared at *bI* in region II (curve b). These interference functions were extracted from the measured x-ray scattering data by the procedure described in the Appendix. The interference functions for the two specimens are very nearly the same in spite of the differences in over-all composition and occluded hydrogen. Therefore, all the deposits, those obtained at *bI* as well as those obtained in region III, may be considered to have essentially the same structure, *viz.*, amorphous Co_3W . Since the deposits have been found to be homogeneous and isotropic (12), the usual

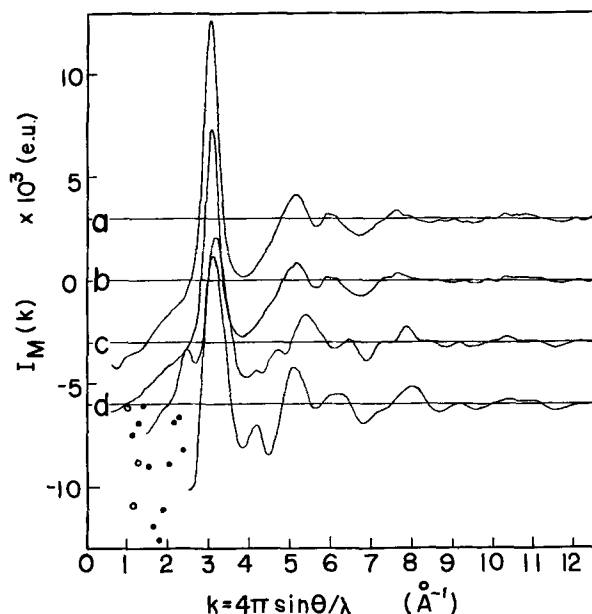


Fig. 2. Comparison of calculated model interference functions (curves c, d) with experimental interference functions (curves a, b). Zeros of intensity are displaced. a, Specimen prepared in region III; b, specimen prepared at *bI*; c, 276 atom model aggregate; d, 104 atom model aggregate. The circles are the scatterers at low angles for curve c (○) and d (●).

techniques for analysis of diffraction patterns of amorphous materials are applicable.

It should be noted that the loose nature of deposits prepared in region III prevents accurate correction for x-ray absorption. Thus, curve b is to be preferred for comparison between experimental and theoretical interference functions.

Theoretical Calculations and Results

Model: Basic Unit

The calculation of the interference function, the double summation term in Eq. [A1], begins with the selection of a model. As indicated above, the noncrystalline phase may be considered to consist only of Co₂₅ a/o W alloy. A simple model will have as its basic structural unit a group of four atoms; 3 Co and 1 W. These may be arranged in the form of a tetrahedron with interatomic distances 2.560Å for Co-Co and 2.545Å for Co-W. These are the interatomic distances in the Co₃W ordered cph alloy (19) and they should be a good approximation for the amorphous alloy. Pauling (20) or Goldschmidt (21) atomic sizes are not used since transition elements have marked electronic uncertainty, especially on alloying (22). This tetrahedral model is consistent with the observed homogeneity of the deposit (12) and with the location of the first maximum in the x-ray scattered intensity distribution.

An additional reason for the choice of a clustered arrangement comes from the fact that tungsten does not electrodeposit by itself from aqueous solutions (23) although cobalt and cobalt-tungsten alloys do. The tetrahedral basic unit permits each tungsten atom to be surrounded by cobalt atoms in the deposit.

Model: Aggregate

Having assumed a basic structural unit, the tetrahedron formed by three cobalt atoms and one tungsten atom, it is necessary to consider the conditions which govern the bonding of basic units to form larger aggregates. One condition, which shall be called Criterion I, is that for a given number of basic units the most stable of all possible aggregates will be the one having the maximum number of first nearest neighbor bonds. (If two or more possible aggregates have the maximum number of first nearest neighbor bonds, then the one with the maximum number of second nearest neighbor bonds will be the most stable.) Differences in atomic species are neglected. Criterion I has been shown to be valid for pairwise interactions involving Morse or Lennard-Jones potentials (24). Criterion I was implicitly applied in the choice of a tetrahedron as the basic unit.

According to Criterion I, when an additional basic unit is added to a pre-existing aggregate (which may consist only of one basic unit and which may include substrate atoms), one atom of the unit must bond to a tetrahedral site on the aggregate. Such tetrahedral sites are formed when three atoms on the aggregate surface are bonded in the form of a triangle. Keeping in mind the facts that tungsten cannot electrodeposit by itself from aqueous solutions and that the aggregate has the stoichiometric composition of Co₃W, Criterion II is introduced: deposition of a tungsten atom is preceded by the deposition of three cobalt atoms which form a triangular array to provide a tetrahedral site for the tungsten atom. Criterion II permits tungsten atoms to deposit only on tetrahedral sites formed by three cobalt atoms. Cobalt atoms, however, can deposit on any tetrahedral site. Although Criterion II is reasonable for small aggregates, it may be somewhat too restrictive when large aggregates are considered. Nevertheless, the criterion is expected to be satisfied most of the time and departures from the criterion in large aggregates should not greatly alter the scattered intensity distribution.

Figure 3 illustrates the way in which an additional basic unit may bond to a pre-existing aggregate. First one atom of the unit bonds to a tetrahedral site. Then

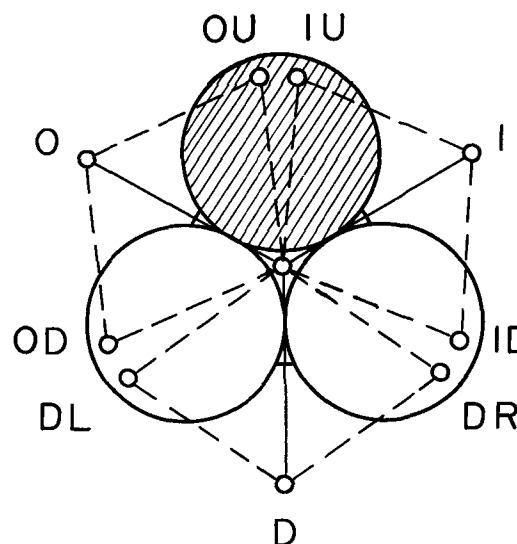


Fig. 3. Illustration of possible bonding sites on tetrahedron

the additional atoms of the unit take up positions so as to maximize the number of first nearest neighbor bonds. Thus, Criterion I is satisfied. In Fig. 3 the three large circles represent atoms on the aggregate surface which form a tetrahedral site. The shaded circle is a tungsten atom. The assumed growth sequence is that three cobalt atoms bond to the aggregate to form a new tetrahedral site which can be occupied by a tungsten atom (Criterion II). The first cobalt atom bonds to the tetrahedral site on the aggregate (center of figure). The second cobalt atom may bond to any of three possible sites; I, O, or D. Once the second atom is bound to one of these three sites, the third atom can bond to either of two sites. For example, if the second atom bonds to site I, the third atom can bond to site IU or to site ID. Although the order in which the three cobalt atoms bond is immaterial, a new tetrahedral site for the tungsten atom can be formed only if the three cobalt atoms take up one of six possible configurations indicated in Fig. 3.

Construction of model aggregate and the calculation of model interference function.—The assumed bond lengths in the basic structural unit were 2.560Å for Co-Co and 2.545Å for Co-W. The difference in these bond lengths, less than 1%, was neglected and a normalized bond length of 2.550Å was chosen for construction of model aggregates as well as for the calculation of model interference functions. This value for the bond length is an average arrived at by assigning the Co-W bond length twice the weight of the Co-Co. This weighing factor approximates the relative frequencies and relative scattering power of Co-W and Co-Co pairs.

The calculation of a model interference function $I_M(k)$ should be done using measured r_{ij} data obtained by selecting each atom in turn as an origin and measuring the distances to all the other atoms in the model. r_{ij} data thus obtained directly give the radial distribution function (RDF) if the model is large enough compared to the atomic size. The size of the model aggregate to be constructed is, however, limited. A significant distinction between small and large aggregates is that in the former the number of atoms lying at or near the surface of the aggregate is a large fraction of the total number of atoms. Therefore, the over-all shape of the model should be nearly spherical so that the environment of an interior atom of a very large aggregate can be represented with a minimum number of spheres.

To compute the model interference function, the atomic pair distribution function (PDF) of the model was measured. This was done by selecting one of the

interior spheres as an origin and measuring the distances to all the other spheres. These distances were normalized to give the actual interatomic dimensions. This procedure was repeated to obtain the PDF's with respect to four different interior atoms, three cobalt atoms, and one tungsten atom. The sum of the four PDF's, which should be approximately proportional to the RDF of a very large aggregate, was used to compute the model interference functions.

Two different model aggregates were constructed according to the prescription described in the preceding section and the model interference functions were computed. The calculations were performed with the aid of a TOSBAC 3400/41 computer.

The first model was built using 276 rigid spheres representing 207 cobalt atoms and 69 tungsten atoms. In constructing this model, the configurations between the pre-existing aggregate and additional basic units were chosen in a random manner within the restrictions of Criterion II. This procedure simulated the obstructive effects of the codepositing hydrogen on surface diffusion and choice of stable deposition sites for cobalts. Particular attention was paid to make the aggregate as dense as possible. Nevertheless, it was found to be impossible to prevent the formation of clearances or voids that could accommodate several atoms. In this model, Criterion II was strictly adhered to. Criterion I, however, was not rigidly maintained.

The second model was built using 104 rigid spheres representing 78 cobalt atoms and 26 tungsten atoms. It was intended to satisfy Criterion I. Certain restrictions were imposed in construction of this model. Three additional units were added to a unit (designated as the base) with the relation OU and satisfying Criterion II. To each of those three units further addition of three units was made with the same relation OU. Thirteen more units were added to make the aggregate as dense as possible and spherical. Criterion II was strictly adhered to. Though the occurrence of clearances was unavoidable, the resultant aggregate is believed to be the densest of numerous configurations examined.

The calculated model interference functions for the 276 and 104 atom aggregates are shown in Fig. 2 as curves c and d, respectively. In computing these functions, the measured PDF's were arbitrarily terminated at 12Å for the 276 atom model and at 9Å for the 104 atom model.

Discussion

The curves a and b in Fig. 2 are the experimental interference functions of specimens prepared in region III and at bI, respectively. As previously explained, absorption corrections for specimens prepared in region III are subject to some inaccuracy. Therefore, curve b is to be preferred for comparison with the calculated interference functions c and d. Such comparison shows that the 276 atom curve gives poor agreement with the experimental curve at lower scattering angles. At higher angles, however, the agreement is better and there is complete consistency of phase. The 104 atom curve gives quite good agreement over the entire angular range. The sharpness of the first maximum ($k = 3.1$) is reproduced quite well in both calculated curves. This serves to justify the choice of PDF used in the calculation. The additional small bumps at low angles in the calculated curves, where the contributions from the longer interatomic distances are significant, are probably termination effects.

For purposes of calculation it was assumed that the RDF of a very large aggregate could be represented by the sum of the PDF's with respect to four different interior atoms in the model aggregate. It should be mentioned that there were noticeable differences between those four PDF's. Thus, the sum may differ somewhat from the RDF of a very large aggregate. This may be responsible for some of the disagreement between the experimental and calculated interference functions.

The fundamental features of the model may be summarized as follows: (i) the alloy consists of basic structural units in the form of tetrahedra, each composed of one tungsten and three cobalt atoms; (ii) the deposition of a tungsten atom is preceded by the deposition of three cobalt atoms which form a triangular array to provide a tetrahedral site for the tungsten atom (Criterion II); (iii) the bonding energy of an aggregate should be minimized by maximizing the number of first nearest neighbor bonds (Criterion I) or by some other dense packing of the tetrahedra subject to the limitations imposed by (i) and (ii). These three assumptions seem reasonable in view of the justifying evidence already presented.

It should be noted that the aggregates constructed using the above rules exhibit neither crystal symmetry nor translational invariance. They do not correspond to the model of randomly stacked close-packed planes (ii).

As indicated above, the model was deduced from the existence of tetrahedra and from the rules that dominate the geometry during the coagulation of atoms of different species. These features of the model result in certain similarities to the model of dense random packing of hard spheres (11). The dense random packing model is the structure that rigid balls assume when they are poured into a vessel and vibrated to attain dense packing. This model was initially developed independently by Scott (10) and Bernal (11) for the structure of liquids.

The principal difference between the present model and the dense random packing model is that the present model deals explicitly with the existence of two atomic species with a distinct short-range order. The consequence of this is the existence in the present model of clearances and voids that can accommodate several atoms. This is impossible in Bernal's model. In contrast to the procedure of the present paper, Bernal extracted a statistical geometry describing the atomic arrangement in dense random packing. This statistical geometry consists of five polyhedral, arrays of atoms. Of these five Bernal polyhedra, the tetrahedron has the highest frequency of occurrence, 73%. In the present model the choice of basic structural unit (tetrahedron) and bonding rules (Criteria I and II) result in a preponderance of tetrahedrally arranged atoms. Some other polyhedra also form, such as at clearances and voids.

In view of the points that were mentioned here, the present model is new and different from the model of dense random packing. A short range order should also be considered in the case of the Ni-P system since evidence suggesting short-range order in Ni-P noncrystalline deposits has already been found (25, 26).

As previously mentioned, large aggregates will contain voids. These occur even when a conscientious effort is made to keep the aggregate as dense as possible. The voids are believed to contribute to the loose nature of deposits formed in region III (Fig. 1). Codepositing hydrogen is also expected to play a role in producing looseness at these higher current densities. The noncrystalline deposits formed at bI in region II are dense rather than loose. They also have an overall composition which is richer in cobalt, containing only 22.2 a/o W. These differences are attributed to excess cobalt filling in the voids of the deposits made in region II. Since individual voids are not expected to be large enough to accommodate more than a small number of cobalt atoms, the presence of the excess cobalt would not effect the observed scattered intensity distributions.

One must consider the character of the electrochemical processes for the formation of the homogeneous deposit at the stoichiometric composition Co₃W. Obviously, the basic unit composed of three cobalt atoms and one tungsten atom arranged in a tetrahedron is formed by the preferred deposition of tungsten on the tetrahedral site formed by the cobalt triangle. It should be noted that two features, (i) the deposition

sequence deduced from the empirical fact that cobalt can deposit by itself from aqueous solutions but tungsten cannot, and (ii) the specific site at which tungsten bonds, should both be strictly adhered to otherwise the tetrahedral structure and stoichiometric composition cannot exist.

The triangular array of three cobalts can form anywhere on the surface of the electrode by the diffusion of three deposited cobalts. Thus, for the formation of Co_3W , there must be a high probability that a tungsten bonds to the site formed by the cobalts regardless of where on the surface the triangle forms. This implies that everywhere near the surface the concentration of cobalt is nearly zero while the concentration of tungsten is finite. Such a situation will prevail if deposition of cobalt is a diffusion controlled process and if tungsten forms an adsorbed layer over the entire electrode surface. Since the basis supporting this electrochemical process (a diffusion controlled process and an adsorbed surface layer) is only geometrical, it should be independent of the following factors: (a) whether the process is electro- or chemical deposition; (b) whether the deposit is crystalline or noncrystalline; (c) what atomic species are involved; and (d) what the stoichiometric composition is. Thus an analysis of an electrochemical process will have a simplification if the deposit is found to have any fixed stoichiometric composition in the as-plated conditions.

It should be noted that the unquestionable existence of cobalt triangles to provide sites for the deposition of tungsten is in accordance with the recent (27) but classical (28) assumption that chemisorption, which should be required for catalytic action, involves more than one transitional metal-ion. Thus, the existence of the cobalt triangle is believed to give support for the catalytic interpretation of the deposition process of reluctant metals (29-31). There is no final agreement as to the mechanism by which the deposition of reluctant metals occurs, and the catalytic hypothesis is merely a restatement of the phenomenon with the unknown factors termed catalytic (32, 33). Though there is a basic problem of why the triangular array (34) of cobalt is stable in the electrodeposition of Co-W alloy, the explanation given here supports the concepts of catalytic action of freshly deposited iron group metals. Furthermore, the existence of an adsorbed layer, which was deduced here, is in accordance with considerations described elsewhere (29, 31, 35-37). The idea of cobalt deposition being diffusion controlled is not inconsistent with the formation of intermetallic compounds by electrodeposition at high current densities (38).

Acknowledgment

Thanks are due to the X-Ray Application Laboratory of Rigaku Denki Co., Tokyo, for x-ray diffraction measurements.

Manuscript submitted June 24, 1971; revised manuscript received ca. Oct. 18, 1971.

Any discussion of this paper will appear in a Discussion Section to be published in the December 1972 JOURNAL.

APPENDIX

Treatment of X-ray Scattering Data

As indicated, the samples are considered to be non-crystalline alloys formed by the units of three Co atoms and one W atom. The x-ray scattered intensity at $T = 0^\circ\text{K}$ is

$$I(k) = I_e \left\{ \sum_i f_i^2 + \sum_{i,j} \sum_{i \neq j} f_i f_j \frac{\sin(kr_{ij})}{kr_{ij}} + \sum_i S_i \right\} \quad [\text{A1}]$$

where $k = 4\pi \sin \theta/\lambda$; r_{ij} is the distance between atoms i and j ; f_i and S_i are, respectively, the scattering factor and inelastic scattering intensity of atom i ; and I_e is the intensity scattered by an isolated electron. The summations are carried out over all atoms in the diffracting volume. The first two terms on the right side of Eq. [A1] are the Debye formula (13).

Due to thermal agitation, the double summation term in [A1], which shall be called the model interference function $I_M(k)$, suffers Debye-Waller damping (14). At a temperature $T(^{\circ}\text{K})$, $I_M(k)$ may be expressed as $[I_M(k)]_T$

$$[I_M(k)]_T = \sum_i f_i^2 [1 - \exp(-2M)] + I_M(k) \exp(-2M) \quad [\text{A2}]$$

The value of B (15) involved in the Debye factor, $\exp(-2M) = \exp[-2B(\sin \theta/\lambda)^2]$, is a calculated mean value weighted by the alloy composition. At 300°K the value of B equals 0.44 for the alloy prepared at bI and 0.43 for the alloy prepared in region III.

The single summation terms in [A1] and the summation term in [A2] are the independent coherent, incoherent, and thermal diffuse scattering, respectively. These are determined by the alloy composition and are independent of the structure. The only term which is determined by the structure is the double summation term $I_M(k)$. The value of this term is determined by the atomic arrangement in the material, i.e., the values of r_{ij} which occur and their frequency of occurrence as well as the distribution of atomic species.

In this paper the interference functions $I_M(k)$ for two differently prepared samples are experimentally obtained by the procedure described below. The experimental interference functions are compared with the calculated model interference functions. No attempt is made to obtain an experimental radial distribution function (RDF).

The measured intensity data were corrected for air scattering, polarization, and absorption. The corrected intensities are proportional to $I(k)$ of [A1] in which $[I_M(k)]_T$ is involved in the double summation term. The intensity was normalized to electron units by assuming that at high scattering angles ($k > 10\text{\AA}^{-1}$)

$$I(k)/I_e \approx \sum_i \{f_i^2 + S_i + f_i^2 [1 - \exp(-2M)]\} \quad [\text{A3}]$$

Monochromator attenuation of Compton scattering at higher angles (16) was neglected. $I_M(k) \exp(-2M)$ was obtained from the normalized intensity by subtraction of all the single summation terms, viz., right side of [A3]. Multiplication by the inverse of the damping, $\exp(2M)$, gave the experimental interference function, $I_M(k)$.

In the treatment of the intensity data, linearly interpolated literature values were used for f_i (17) and S_i (18). The same values of f_i were used in the calculation of the model interference functions.

REFERENCES

- W. Klement, Jr., R. H. Willens, and Pol Duwez, *Nature*, **187**, 869 (1960).
- J. Dixmier and K. Doi, *Compt. Rend.*, **257**, 2451 (1963).
- Pol Duwez and S. C. H. Lin, *J. Appl. Phys.*, **38**, 4096 (1967).
- P. Maitrepierre, *ibid.*, **41**, 498 (1970).
- C. N. J. Wagner, T. B. Light, N. C. Halder, and W. E. Lukens, *ibid.*, **39**, 3690 (1968).
- B. G. Bagley and D. Turnbull, *ibid.*, **39**, 5681 (1968).
- G. S. Cargill III, *ibid.*, **41**, 12 (1970).
- G. S. Cargill III, *ibid.*, **41**, 2248 (1970).
- G. D. Scott, *Nature*, **194**, 956 (1962).
- J. D. Bernal, in *Liquids: "Structure, Properties, Solid Interactions,"* p. 25, T. J. Hugel, Editor, Elsevier Publishing Co., Inc., Amsterdam (1965).
- J. L. Finney, Ph.D. thesis, University of London, London, England (1968).
- S. Yoshioka, H. Yamamoto, and T. Omi, *J. Metal Finishing Soc. Japan*, **20**, 172 (1969).
- A. Guinier, "X-Ray Diffraction in Crystals, Imperfect Crystals, and Amorphous Bodies," p. 49, W. H. Freeman and Co., San Francisco (1963).
- A. Guinier, "X-Ray Diffraction in Crystals, Imperfect Crystals, and Amorphous Bodies," p. 186, W. H. Freeman and Co., San Francisco (1963).
- The International Union of Crystallography, "International Tables for X-Ray Crystallography," Vol. II, p. 241, Kynoch Pr., Birmingham, England (1959).
- W. Ruland, *Brit. J. Appl. Phys.*, **15**, 1301 (1964).

17. I. Nitta, Editor, "X-ray Crystallography," Vol. 1, p. 748, Maruzen Co., Tokyo (1968).
18. A. H. Compton and S. K. Allison, "X-Rays in Theory and Experiment," p. 781, D. Van Nostrand Co. Inc., New York (1936).
19. A. Magnelli and A. Westgren, *Z. Anorg. Chem.*, **238**, 268 (1938).
20. L. Pauling, "The Nature of the Chemical Bond," 3rd ed., p. 256, Cornell University Press, Ithaca, New York (1960).
21. R. P. Elliot, "Constitution of Binary Alloys, First Supplement," p. 872, McGraw-Hill Book Co., New York (1965).
22. W. Hume-Rothery, "Atomic Theory for Students of Metallurgy," p. 358, The Inst. of Metals, London (1962).
23. A. Brenner, "Electrodeposition of Alloys," Vol. 2, p. 347, Academic Press, New York (1963).
24. J. F. Nicholas, *Australian J. Phys.*, **21**, 21 (1968).
25. J. -P. Randin, P. A. Maire, and H. E. Hintermann, *This Journal*, **114**, 442 (1967).
26. J. -P. Randin and H. E. Hintermann, *ibid.*, **115**, 480 (1968).
27. L. Jansen, in "Molecular Processes on Solid Surfaces," p. 53, E. Drauglis *et al.* Editors, McGraw-Hill Book Co., New York (1969).
28. A. A. Balandin, *Advan. Catalysis*, **10**, 96 (1958).
29. M. L. Holt and L. E. Vaaler, *J. (and Trans.) Electrochem. Soc.*, **94**, 50 (1948).
30. T. L. Ramacher and K. I. Vasu, *Bull. India Sect., Electrochem. Soc.*, **11**, 34 (1961).
31. B. S. R. Sastry, *Metal Finishing*, 10-86 (1965).
32. I. A. Menzies, *Trans. Inst. Metal Finishing*, **39**, 172 (1962).
33. "Electrodeposition of Alloys," Vol. 2, p. 400, Academic Press, New York (1963).
34. D. Walton, *J. Chem. Phys.*, **37**, 2182 (1962).
35. W. E. Clark and M. H. Lietzke, *This Journal* **99**, 245 (1952).
36. D. W. Ernst and M. L. Holt, *This Journal*, **105**, 686 (1958).
37. J. M. West, "Electrodeposition and Corrosion Process," p. 121, D. Van Nostrand Co., London (1965).
38. K. M. Gorbunova and Yu. M. Polukarov, in "Electrodeposition of Metals and Alloys," N. E. Kholmotov, Editor, Issue 1, p. 28, Israel Program for Scientific Translations, Jerusalem (1969).

On the Uniformity of Phosphorus Emitter Concentration for Shallow Diffused Transistors

P. C. Parekh¹

Sylvania Electric Company, Woburn, Massachusetts 01801

ABSTRACT

The variables affecting the uniformity of sheet resistance for a two-step shallow phosphorus emitter diffusion were examined. The source used was POCl_3 . The uniformity of sheet resistance (and hence surface concentration) was predominantly dependent on the variables during the deposition process. These were oxygen and nitrogen flow, wet nitrogen flow and temperature of deposition. The latter ranged from 700° to 860°C. A comparison was made of the variables that affect phosphorus, boron, and arsenic depositions. The behavior of oxygen on the sheet resistance profile during phosphorus deposition was different from that observed for boron and arsenic depositions.

Recently considerable attention has been devoted to the fabrication of shallow diffused high-speed integrated circuits. Here the use of small components coupled with submicron diffusions places a considerable demand on the fabrication technology. In some recent work it has been shown that the uniformity of boron (1) and arsenic (2) diffusions is governed by the deposition variables. By optimizing these variables a desired control of surface concentration can be achieved. In this paper the variables controlling the uniformity of phosphorus emitter diffusion (using POCl_3 as a source) for shallow diffused transistors are investigated.

Experimental Conditions

The temperature of deposition was varied from 700° to 860°C. Drive-in was performed in dry oxygen at 1040°C. In all cases the time of deposition was 30 min while the time of drive-in was 10 min. The final junction depth was 0.8 μ .

Figure 1 shows the arrangement of the source bottle and the deposition furnace tube used in this experiment. A major portion of the nitrogen and oxygen gases (designated here as carrier gases) was introduced into the furnace tube at room temperature. In some cases wet nitrogen gas (designated as $\text{N}_2/\text{H}_2\text{O}$) was introduced by bubbling nitrogen gas through a water container maintained at 20°C. A fixed quantity of nitrogen gas (designated as N_2 /source, flow rate =

200 cm^3/min) flowing parallel to the surface of the POCl_3 liquid was used to introduce the POCl_3 vapor into the furnace tube at point A as shown in the figure. The temperature at position A varied from 500° to 680°C, the precise value was dependent on the temperature of the constant zone. The source bottle was maintained at 20°C.

The starting material was 2-in. diam n-type substrates of resistivity 0.2 ohm-cm and (111) orientation.

The wafers were diffused with a uniform shallow boron base diffusion with a surface sheet resistance of 300 ohm/sq. A flat boat 16 in. in length was loaded

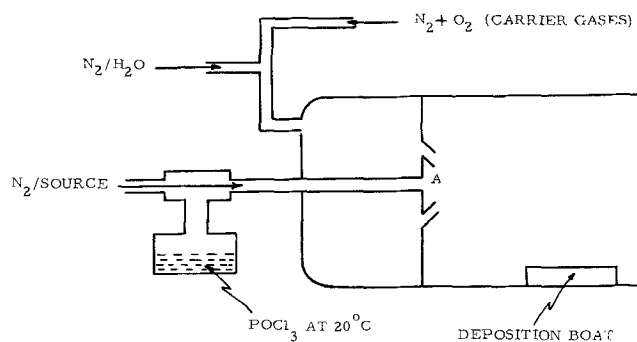


Fig. 1. Geometry of the source bottle and the deposition furnace tube.

¹ Present address: Raytheon Company, Microwave Transistor Group, Spencer Laboratory, Burlington, Massachusetts 01803.

Key words: silicon, sheet resistance, POCl_3 .

with these wafers and placed into a furnace tube for phosphorus deposition. The wafers were labeled to identify their position in the furnace tube. After 30 min of deposition, the wafers were driven at 1040°C for 10 min.

Some recent work has shown that the uniformity of diffusion is predominantly dependent on the variables during the deposition process (1, 2). Thus anomalous behavior during deposition can be detected after the drive-in diffusion by measuring sheet resistance, r_d , and junction depth, X_j . This was accomplished by the four-point probe method. The junction depth was measured using angle-lapping techniques and an interference microscope. From these measurements surface concentration, C_0 , (for a gaussian distribution) was obtained using Irvin's curves (3).

The uniformity of the diffusion is indicated by variations in surface concentration, C_0 , within a slice and from slice to slice. For a specific drive-in diffusion, the surface sheet resistance, r_d , is a good indication of the surface concentration involved. However, slight discrepancies may be observed for the following cases: (I) A nonuniform diffusion results in large variations in the concentration gradient within a slice and from slice to slice. This in turn causes variable junction depths, X_j . If a fixed value of X_j is chosen to evaluate C_0 , erroneous results are obtained. (II) When concentrations exceed the solid solubility limit in silicon at the diffusion temperature, sheet resistance measurements in general indicate a lower value of concentration than is actually present. This is due to the formation of phosphorus and silicon-phosphide precipitates. From the above cases uncertainty may exist in obtaining correct values of surface concentration in some instances. For most cases, however, the variation of r_d (after the drive-in diffusion) can be taken as a good indication of the surface concentration involved.

Results and Discussion

Factors Affecting the Uniformity of Diffusion

Recently, several workers (4-6) have considered the variables affecting the uniformity of phosphorus diffusion. Heynes and Wilkerson (4) used $POCl_3$ as a source and observed that the oxygen concentration was a critical parameter for deposition temperatures $\leq 1000^\circ C$. They also observed that in the absence of oxygen, etching of silicon occurred due to by-products formed by disassociation of $POCl_3$. In addition, this was accompanied by high sheet resistance values. Heynes and Van Loon (5) and Kesperis (6) observed that in a phosphine system, the presence of oxygen was essential in achieving good diffusion characteristics. In addition, increasing the oxygen concentration increased sheet resistance indicating that an increasing amount of SiO_2 was formed.

Also recently, in a two-step investigation of boron (1) for base diffusion (using BBr_3 as a source) and arsenic (2) for buried layer diffusion (using $AsCl_3$ and tetraethyl orthosilicate as the sources) three points were observed: (I) Increasing the oxygen concentration during deposition increased the rate of formation of B_2O_3 or As_2O_3 . This shifted the position of the zone of uniform sheet resistance toward the source end of the deposition tube. The "zone of uniform sheet resistance" is defined as that part of the furnace tube in which the rate of deposition of B_2O_3 or As_2O_3 on the wafers is maximum. This is indicated by the maximum glass thickness after deposition and the lowest value of r_d after the drive-in diffusion. (II) Increasing the deposition temperature increased the rate of formation of B_2O_3 or As_2O_3 , thus shifting the position of the zone of uniform sheet resistance toward the source end of the tube. (III) Increasing the nitrogen carrier flow shifted the position of the zone of uniform sheet resistance toward the open end of the tube.

From the above observations, the basic role of oxygen in the two systems is to change the rate of formation of B_2O_3 or As_2O_3 . No appreciable oxidation of

silicon, which could lead to high sheet resistance, was observed. In the subsequent discussion, it will be shown that oxygen did not influence the rate of formation of a phosphorus species in the furnace atmosphere. However, the presence of wet nitrogen considerably increased the rate of formation of such a species leading to lower sheet resistance.

The influence of oxygen flow on sheet resistance profile across the deposition boat.—Figure 2 shows the r_d profile across the deposition boat for a deposition temperature of 860°C. In one set of curves, the carrier gas was only oxygen with a flow rate of 1800 cm^3/min , while in the second set of curves, the carrier gas was only nitrogen with a similar flow rate. As indicated earlier, in both cases the N_2 /source flow rate was 200 cm^3/min . In the figure the zero reference of the boat is taken as that end nearest the gas inlet of the furnace tube (source end) while the numbers on the horizontal axis indicate the distance in inches from the zero reference to the center of a slice. From the figure, the following points may be observed: (I) Stripping glass prior to drive-in diffusion increases sheet resistance as expected. (II) Heynes and Wilkerson (4) observed that in the absence of O_2 and using $POCl_3$ as a source, a considerable amount of damage due to etching during deposition was observed. This was accompanied by shallow penetration of junctions and high sheet resistance. In this investigation, in the absence of O_2 , no surface damage such as etching of wafers was observed after deposition. In addition, the lowest value of r_d and the highest value of X_j were observed. The degradation of diffusion observed by Heynes and Wilkerson (4) may have been due to excessive $POCl_3$ present in the furnace atmosphere. From Fig. 1 it can be seen that N_2 gas carries vapor of $POCl_3$ into the furnace tube. This is unlike most $POCl_3$ systems used where N_2 gas is bubbled through $POCl_3$ liquid. This causes an excessive amount of $POCl_3$ to enter the furnace, resulting in the formation of large amounts of chlorine which leads to surface damage. The surface concentration (after the drive-in diffusion) in Fig. 2 in the absence of O_2 was 7×10^{20} atoms/ cm^3 when glass was not stripped (thickness $< 500\text{\AA}$) prior to the drive-in diffusion. (III) $POCl_3$ partially disassociates into its constituents. The disassociation products are

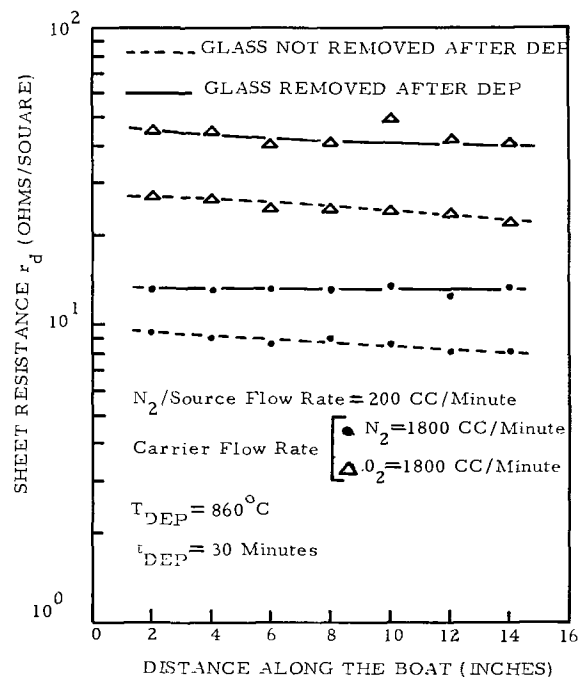
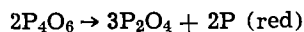


Fig. 2. Sheet resistance, r_d , profiles along the deposition boat with nitrogen and oxygen as the carrier gases. The drive-in temperature and time are 1040°C and 10 min, respectively.

P_4O_6 , PCl_3 , and Cl_2 . P_4O_6 in turn disassociates into P_2O_4 and red phosphorus by the following reaction (7)



The above compounds react with O_2 to form phosphorus pentoxide. Note that the point of contact between the phosphorus species and O_2 is at point A (temperature $680^\circ C$) as shown in Fig. 1.

The rate of formation of phosphorus pentoxide should be dependent on the O_2 concentration. Varying the O_2 flow rate should shift the position of the zone of uniform sheet resistance as in boron (1) and arsenic (2) diffusions. In the present work increasing the O_2 concentration increased sheet resistance uniformly on all slices across the boat while the position of the zone of uniform sheet resistance was insensitive to O_2 variations. In addition, the glass thickness on wafers after deposition remained constant (as observed visually, thickness $< 500\text{\AA}$) for different O_2 concentrations.

The influence of deposition temperature on sheet resistance profile across the deposition boat.—The rate of formation of phosphorus species (P_4O_6 , P_2O_4 , red phosphorus) in the furnace atmosphere is dependent on the temperature of deposition. This in turn profoundly affects the sheet resistance profile across the deposition boat, which was previously illustrated for boron (1) and arsenic (2) diffusions. Figure 3 shows the variation in sheet resistance profile across the deposition boat for phosphorus at deposition temperatures of 700° , 760° , and $860^\circ C$. Here no oxygen was used. From the figure, the following points can be observed: (I) toward the source end of the tube, sheet resistance is high for a deposition temperature of $700^\circ C$. As the gases proceed toward the open end of the tube, increasing amounts of phosphorus species are formed causing a reduction in sheet resistance. (II) For a deposition temperature of $860^\circ C$, the rate of formation of phosphorus species is enhanced, resulting in a low sheet resistance value across the deposition boat. The surface concentration here was calculated to be $\sim 10^{21}$ atoms/cm³ indicating that the solid solubility limit of phosphorus in silicon was reached. (III) In the boron (1) and arsenic (2) depositions, the sheet resistance

after the drive-in diffusion was correlated with the glass deposited after deposition. In Fig. 3, no glass was visually observed for a deposition temperature of $700^\circ C$, but for $860^\circ C$ the thickness was approximately 500\AA .

The influence of carrier gas velocity on sheet resistance profile across the deposition boat.—In the boron base system (1) increasing the carrier gas velocity shifted the position of the zone of uniform sheet resistance toward the open end of the tube. However, no increase in sheet resistance was observed due to dilution of B_2O_3 in the furnace atmosphere. This is a result of having a sufficient amount of B_2O_3 present even at the higher gas velocity. In the case of the arsenic deposition (2), the position of the zone of uniform sheet resistance shifted toward the open end of the tube upon increasing the N_2 carrier gas velocity. However, a decrease in surface concentration was obtained. This is thought to be due to an insufficient amount of As_2O_3 present when the gas velocity is increased. Similar behavior was observed here for the phosphorus system. Increasing the gas velocity shifted the position of the zone of uniform sheet resistance toward the open end of the tube. However, considerable dilution of phosphorus species in the furnace atmosphere was observed, thus increasing the sheet resistance. This is shown in Fig. 4 where r_d after the drive-in diffusion is plotted vs. nitrogen carrier flow rate for deposition temperatures of 760° and $860^\circ C$. For these two cases, approximately similar sheet resistances (solid solubility range) were observed for a nitrogen carrier flow rate of $300\text{ cm}^3/\text{min}$ when no glass was removed prior to drive-in diffusion. This indicates that the glass deposited at the lower deposition temperature was sufficiently doped for the surface concentration to attain the solid solubility limit. The decrease in the formation of the phosphorus species at the lower deposition temperature and at the higher nitrogen gas flow is apparent from the figure. When glass was stripped, prior to the drive-in diffusion, a higher sheet resistance was observed for both deposition temperatures as expected.

The influence of wet nitrogen flow on sheet resistance profile.—In the presence of a wet N_2 flow (with no

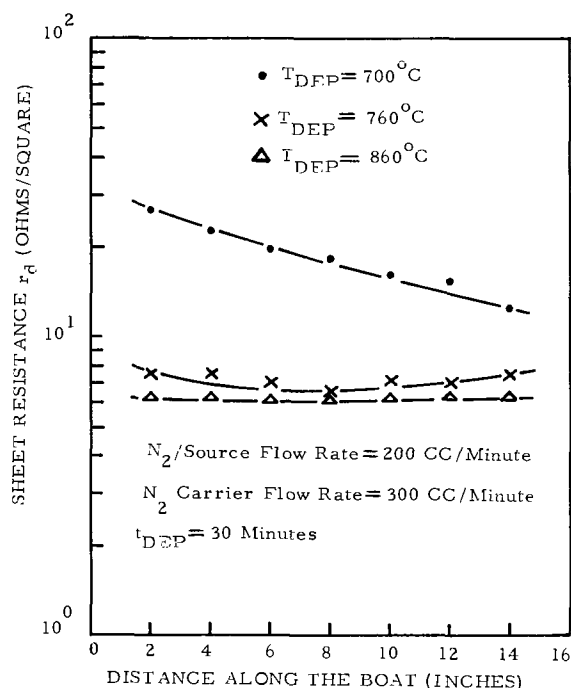


Fig. 3. Sheet resistance, r_d , profiles along the deposition boat for several deposition temperatures. The drive-in temperature and time are $1040^\circ C$ and 10 min, respectively.

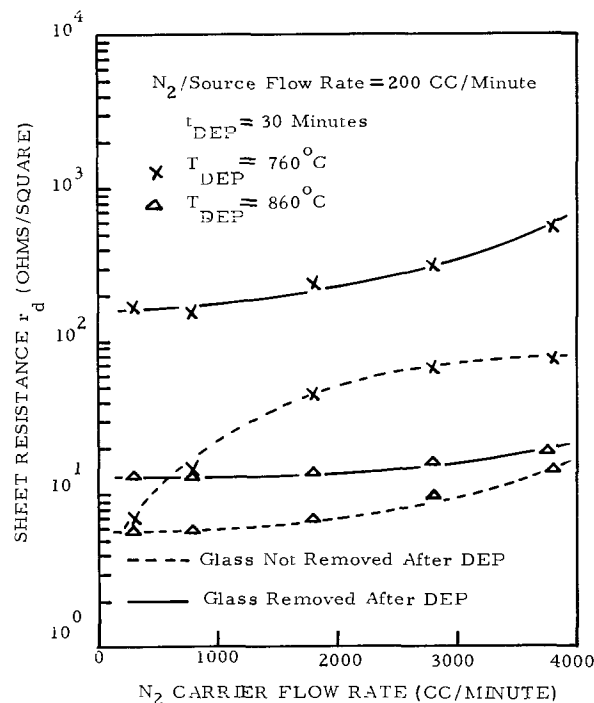
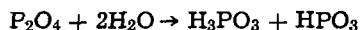


Fig. 4. Variation of r_d vs. N_2 carrier gas flow for deposition temperature of 760° and $860^\circ C$. The drive-in temperature and time are $1040^\circ C$ and 10 min, respectively.

O₂ present) the phosphorus specie formed by the disassociation of POCl₃ reacts with H₂O (7)



to form phosphorus and metaphosphoric acid. The former is immediately converted into orthophosphoric acid by the reaction



In general, the reaction of wet N₂ with P₂O₄ produces a series of mixtures such as orthophosphoric acid, present over the entire range of P₄O₁₀ · 6H₂O to P₄O₁₀ · 2H₂O; triphosphoric acid, H₅P₃O₁₀, likewise present over the entire range; pyrophosphoric acid, H₄P₂O₇, present up to 85% weight per cent (w/o) P₄O₁₀, and one or more polymers of metaphosphoric acid, (HPO₃)_n, present at P₄O₁₀ compositions above 83%.

Figure 5 shows the distribution of sheet resistance across the deposition boat in the presence and absence of wet nitrogen flow. In the former case, 150 cm³/min of nitrogen gas was bubbled through a water bath maintained at room temperature. The deposition temperature was 700°C and no oxygen was used. In the absence of wet nitrogen, no glass was visually observed after deposition. In the presence of wet nitrogen, the wafers toward the source end of the tube had a coating of 1300Å of glass, while on those toward the open end of the tube the coating was 600-700Å. The wafers were processed through the drive-in diffusion without stripping the glass. The effect of adding the wet nitrogen was to shift the position of the zone of uniform sheet resistance, r_d , toward the source end of the tube. Here, the glass formed consisted of complex compounds of the P₂O₅-H₂O system as described before. The concentration of these compounds deposited on the surface of the wafer was determined by their partial pressure in the gas. The partial pressure of the phosphorus specie formed in the presence of wet nitrogen far exceeds that formed when no wet nitrogen was added to the system.

Similar results, as indicated, were obtained when oxygen replaced nitrogen as the carrier gas. This is illustrated in Fig. 6 for a deposition temperature of 760°C. The addition of wet nitrogen decreased the

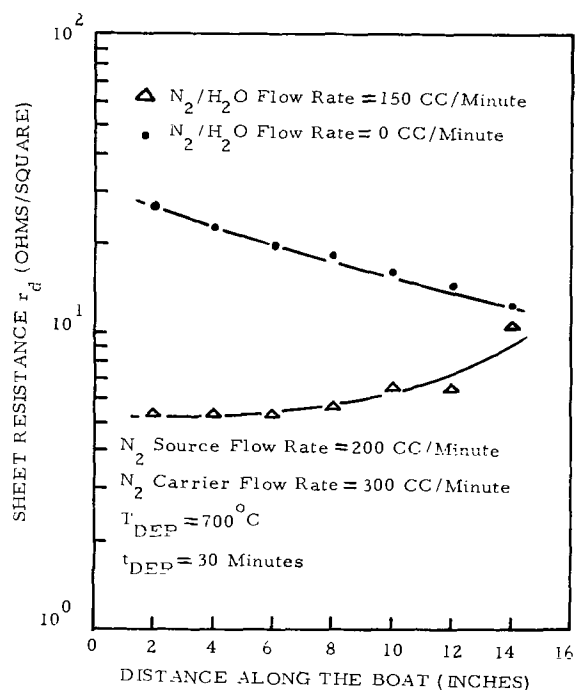


Fig. 5. Sheet resistance, r_d , profiles along the deposition boat with the presence and absence of N₂/H₂O flow using N₂ as the carrier gas. The drive-in temperature and time are 1040°C and 10 min, respectively.

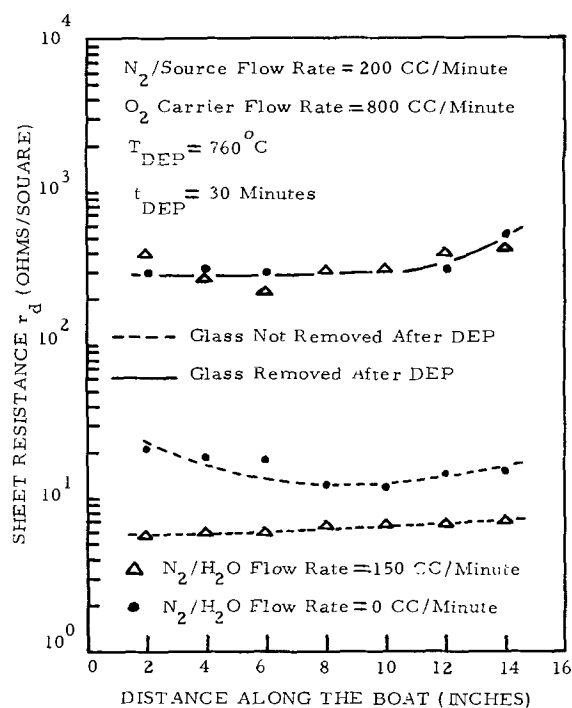


Fig. 6. Sheet resistance, r_d , profiles along the deposition boat with the presence and absence of N₂/H₂O flow using O₂ as the carrier gas. The drive-in temperature and time are 1040°C and 10 min, respectively.

sheet resistance considerably. No glass was detected in the absence of wet nitrogen; however, in the presence of wet nitrogen, the thickness of the deposited glass was approximately 1400Å. The dotted line in the figure shows the sheet resistance profile when glass was not removed prior to the drive-in diffusion. The solid line shows the case when glass was removed prior to drive-in diffusion. It can be seen that no difference in sheet resistance was recorded for the latter case between the absence and the presence of wet nitrogen. This indicates that at the temperature of deposition additional penetration of phosphorus into silicon did not occur when wet nitrogen was used. These results appear to contradict the predictions of Heynes and Van Loon (5) who indicated that phosphorus pentoxide and phosphoric acids are expected to be equally reactive with a silicon surface. However, a parallel analogy exists in the present work and Heynes' work on boron diffusion (8). The presence of water assisted in the distribution of doping through the formation of boric acids which are much more volatile than the B₂O₃ formed by the reaction of BBr₃ and O₂. The result was that higher surface concentrations were achieved when water was present.

Formation of Phosphorus Skin

The formation of arsenic (2) and boron (9) skins have been reported in the literature. Their occurrence is a result of the formation of a high rate of B₂O₃ or As₂O₃. In the present experiment under certain conditions the presence of a phosphorus skin (insoluble in HF) was observed. These conditions were low temperature of deposition, low carrier flow rate, and the presence of wet nitrogen.

Degradation of Device Parameter

The need for phosphorus emitter surface concentrations \leq the solid solubility has been emphasized by several workers. Lawrence (10) observed that the enhanced diffusion of base impurities (emitter dip effect) was attributed to excess vacancies in the base region generated by dislocations formed during the emitter diffusion. Recently, it was observed (11, 12) that degradation in Δh_{FE} [$\Delta h_{FE} = h_{FE}(T_2)/h_{FE}(T_1)$, $T_2 > T_1$] occurred as the phosphorus emitter concen-

tration increased. This has been attributed to a decrease in energy band gap in the emitter region upon increasing the phosphorus concentration. The formation of emitter edge dislocations due to high concentration phosphorus diffusion has been recently discussed (12-14). The increase in junction leakage current in the presence of these dislocations and the degradation of several transistor parameters clearly indicate the need for a well-controlled low concentration phosphorus emitter diffusion. The system presented in Fig. 1 is clearly capable of achieving a wide range of concentrations at and below the solid solubility limit.

Conclusion

For deposition temperature ranging from 700° to 860°C, the presence of O₂ increased sheet resistance while the deposited glass thickness was generally less than 500Å. In the presence of wet N₂, high surface concentrations resulted with a deposited glass thickness of 1300-1400Å. The position of the zone of uniform sheet resistance was affected by the introduction of moisture; however, it was insensitive to the presence of O₂. The position was also affected by varying the phosphorus deposition temperature when no O₂ or moisture were present.

It can be concluded that any reaction of O₂ with POCl₃ or its constituents appears to have no effect on surface concentration. The influence of O₂ is in masking the diffusion of phosphorus into silicon.

Manuscript submitted April 26, 1971; revised manuscript received Oct. 26, 1971.

Any discussion of this paper will appear in a Discussion Section to be published in the December 1972 JOURNAL.

REFERENCES

1. P. C. Parekh and D. M. Goldstein, *Proc. IEEE (Inst. Elec. Electron. Engrs.)*, **57**, 1507 (1969).
2. P. C. Parekh, D. M. Goldstein, and T. C. Chan, *Solid-State Electron.*, **14**, 281 (1971).
3. J. C. Irvin, *Bell System Tech. J.*, **41**, 387 (1962).
4. M. S. R. Heynes and J. T. Wilkerson, *Electrochem. Technol.*, **5**, 464 (1967).
5. M. S. R. Heynes and P. G. G. Van Loon, *This Journal*, **116**, 890 (1969).
6. J. S. Kesperis, *ibid.*, **117**, 554 (1970).
7. M. C. Sneed and R. C. Brasted, "Comprehensive Inorganic Chemistry," Vol. V, D. Van Nostrand Co., Inc., Princeton, N. J. (1956).
8. M. S. R. Heynes, *Electrochem. Technol.*, **5**, 25 (1967).
9. K. M. Busen, W. A. FitzGibbons, and W. K. Tsang, *This Journal*, **115**, 291 (1968).
10. J. E. Lawrence, *J. Appl. Phys.*, **37**, 4106 (1966).
11. D. Buhanan, *IEEE (Inst. Elec. Electron. Engrs.) Trans. Electron Devices*, **ED-16**, 117 (1969).
12. P. C. Parekh, E. Gavel, and V. Lyn, *Solid-State Electron.*, **13**, 707 (1970).
13. E. D. Jungbluth and P. C. Parekh, Paper 253 RNP presented at Electrochem. Soc. Meeting, Atlantic City, October 4-8, 1970.
14. J. M. Fairfield and G. H. Schwuttke, *This Journal*, **115**, 415 (1968).

Electrochemical Reduction of Benzofuroxan

I. Aqueous Solutions

C. D. Thompson* and R. T. Foley**

Chemistry Department, The American University, Washington, D.C. 20016

ABSTRACT

Constant potential reductions of benzofuroxan in acidic, neutral, and basic solutions over a stirred mercury pool electrode were followed by analysis of the products. The primary product was *o*-benzoquinone dioxime which was further reduced to 2,3-diaminophenazine and *o*-phenylenediamine in proportions which vary with the pH. Fast sweep voltammograms and data of other investigators suggest that the reduction of the dioxime proceeds through an *o*-benzoquinone diimine intermediate which further reduces or couples to yield the observed products.

Previous studies of the electrochemical reduction of benzofuroxan (BFO) include polarographic work at a dropping mercury electrode (DME) by Schindler (1) and Levin (2) and battery depolarizer work by Hardy (3) and Shaw (4). Schindler found that BFO reduced in two waves throughout the pH range from 1.24 to 9.90. The first wave corresponds to a two-electron reduction which was ascribed to formation of *o*-benzoquinone dioxime (ODI) on the basis of the spectrum and electrochemical behavior of the reduced solution. However, the height of the second wave was pH dependent. At pH's below about 4.5 or above 7.8, the height of the second wave indicated a further six-electron reduction, presumably to *o*-phenylenediamine (OPD). Between pH 4.5 and pH 7.8 the wave height indicated only a four-electron reduction, for which no explanation was given. The top line in Fig. 1 shows this relationship between polarographic current and pH from data extracted from Schindler's paper (1).

This paper presents data for constant potential reductions of aqueous BFO solutions over a stirred mer-

cury pool electrode at various pH values. Reductions performed at voltages more negative than the crest of the second polarographic wave resulted in an insoluble precipitate which was isolated and identified as 2,3-diaminophenazine (2,3-DAP). Analytical procedures were developed to measure quantitatively the concentrations of the various species in the reduced solutions and these are described in the experimental section.

The objective of this work has been to identify and measure quantitatively the major products resulting from the electrochemical reduction of benzofuroxan. The isolation of these products, fast sweep voltammograms, and the work of other researchers make possible a reasonable understanding of the pathway of the reduction.

Abbreviations and Structures

BFO	Benzofuroxan	
ODI	<i>o</i> -Benzoquinone dioxime	

* Electrochemical Society Student Associate.

** Electrochemical Society Active Member.

Key words: electro-organic, *o*-benzoquinone dioxime, *o*-phenylenediamine, *o*-benzoquinone diimine, cathode depolarizer.

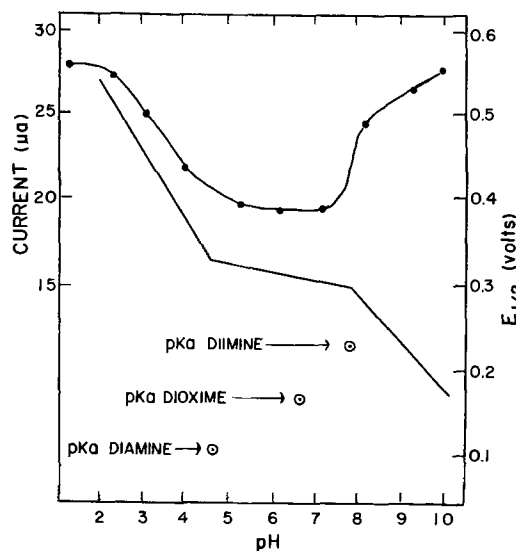
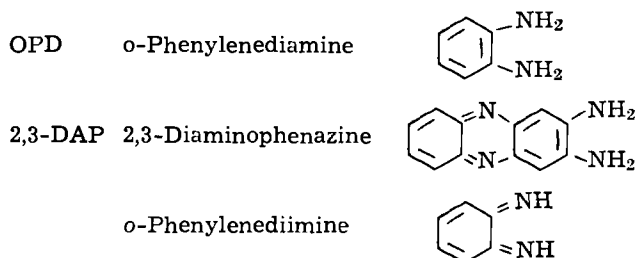


Fig. 1. Upper curve, left scale: maximum polarographic current vs. pH for the second reduction wave of benzofuroxan from Schindler's data (1). Lower curve, right scale: $E_{1/2}$ vs. pH for the oxidation of *o*-phenylenediamine from the data of Parker and Adams (13). This curve is a composite of 16 separate points.



Experimental

Reagents and Solutions

Electrolyte solutions at pH 2.12, 6.50, and 9.90 were made which contained 0.10N KCl as electrolyte. The pH 2.12 electrolyte was made by adding 7.5 ml H_3PO_4 to 1.0 liter water. KCl, 7.45g, was then added and the solution titrated to pH 2.12 by dropwise addition of 30% KOH. The pH 6.50 electrolyte was made by adding 403 ml 0.1N KOH to 900 ml 0.1M KH_2PO_4 containing 9.693g KCl. The pH 9.90 electrolyte was made by titrating a 1.0 liter solution containing 16.34g K_3PO_4 and 7.455g KCl to pH 9.90 with 6N HCl. Solutions of 1.0×10^{-3} M BFO were made by dissolving 0.0681g BFO (Eastman No. 10204) in 500 ml of the desired electrolyte.

o-Benzoquinone dioxime (ODI) was synthesized by the method of Pesin *et al.* (5) in which BFO is reacted with $H_2NOH \cdot HCl$. The product was recrystallized from ethanol and water two times and dried in a vacuum desiccator mp: 144.5°-145.0°C (uncorr.), literature 144° (5) and 149° (6).

2,3-DAP was synthesized by a method similar to that of Ullman and Mauthner (7) and Sawicki *et al.* (8) wherein OPD is reacted with $FeCl_3$ in acidic medium. After purification the product yielded yellow plates of 2,3-DAP mp: >320°. The visible and ultraviolet spectra showed peaks at 263, 280 (shoulder), 454, and 432 $m\mu$ (shoulder) which are in good agreement with those reported by Matsumura (9) of 265-285 and 454 $m\mu$. The IR spectrum was identical to that reported by Stammer and Taurins (10).

Analytical Procedures

ODI may be determined spectrophotometrically in the presence of BFO and OPD. In neutral solutions BFO absorbs at 356 $m\mu$ and interferes with the ODI

absorption at 397 $m\mu$. In 6N HCl or in dilute ammonia solution the ODI absorption is split into two peaks at 321 and 425 $m\mu$. The 425 $m\mu$ value is sufficiently high to prevent interference by BFO. Under these conditions, plots of ODI concentration vs. absorbance were made from which the ODI concentration in reduced solutions could be measured. 2,3-DAP interferes and the test cannot be used on solutions reduced at voltages more negative than the first polarographic wave.

2,3-DAP was also determined by a spectrophotometric procedure. Dechary *et al.* (11) determined glyoxal by condensing it with 2,3-DAP and measuring the blue color produced at 600 $m\mu$. For this work the determination was reversed: glyoxal was used to determine 2,3-DAP. For reasons of solubility, 2,3-DAP standard solutions were prepared in a 1:1 mixture of electrolyte solution and glacial acetic acid. Reduced solutions of BFO or ODI were also diluted with an equal volume of acetic acid and the test was then performed simultaneously on the standard and reduced solutions. Appropriate aliquots of samples and standards (0.5-3.0 ml) were diluted to 3.0 ml with a 1:1 mixture of electrolyte solution and acetic acid. To each of these solutions was added 1.0 ml conc H_2SO_4 and 50 μ l glyoxal. The tubes were placed in a boiling water bath and 50 μ l additional glyoxal was added. After 10-min heating, the tubes were removed, chilled in an ice bath until cold, and 1.0 ml KNO_2 solution (48 mg/200 ml H_2O) was added followed by 1.0 ml H_3PO_2 (50% aqueous Fisher A-154) and reheating for 30 min. On cooling, the tubes were diluted to 7.0 ml with 10N H_2SO_4 and absorbance of standards and samples read at 600 $m\mu$.

It was shown that BFO, ODI, and OPD do not interfere. The test performs less well in acidic electrolyte solutions where green rather than clear blue solutions are sometimes observed. In nonaqueous electrolyte solutions, *e.g.*, γ -butyrolactone-0.5M $LiClO_4$, the color fades on prolonged heating and the azo-forming step must be omitted.

OPD was determined by conversion of the OPD to 2,3-DAP followed by a second running of the 2,3-DAP test. Since the $FeCl_3$ oxidation does not go to completion, standard OPD solutions in the same electrolyte-acetic acid mixture were run concurrently with the reduced solutions and it was assumed that the same percentage oxidation was obtained in both cases. To 3.0 ml samples of reduced solutions or standards was added 1 drop 40% $FeCl_3 \cdot 6H_2O$ and 1 drop 10N H_2SO_4 . The solutions were heated in a boiling water bath for 10 min, cooled to room temperature, and diluted to 7.0 ml with distilled water. At this point, a white precipitate was sometimes observed due to formation of ferric phosphate from the phosphate buffer system in the electrolyte. If so, the tubes were centrifuged and aliquots used in the phenazine test. The normal conversion of OPD to 2,3-DAP was 70-80%.

Reductions

The polarograms and constant potential reductions were performed with a Beckman Electroscan-30 in a large H-cell constructed of two 100 ml beakers separated by a tube containing a glass frit. The working compartment contained a dropping mercury electrode, saturated calomel reference, mercury pool working electrode with an estimated area of 16.0 cm^2 , nitrogen bubbler, and a motor-driven glass rod which stirred the mercury pool. Electronic connection to the mercury pool was made through a platinum wire encased in a glass tube sealed at the lower end. The counterelectrode in the other cell compartment was a large platinum gauze. The stirred mercury pool arrangement was adopted as a result of preliminary studies at a stationary platinum electrode which resulted in insoluble film formation which made reductions difficult to perform.

An initial polarogram was made and the solution was reduced at the desired voltage. The coulombic data could be calculated from a chart of the current vs.

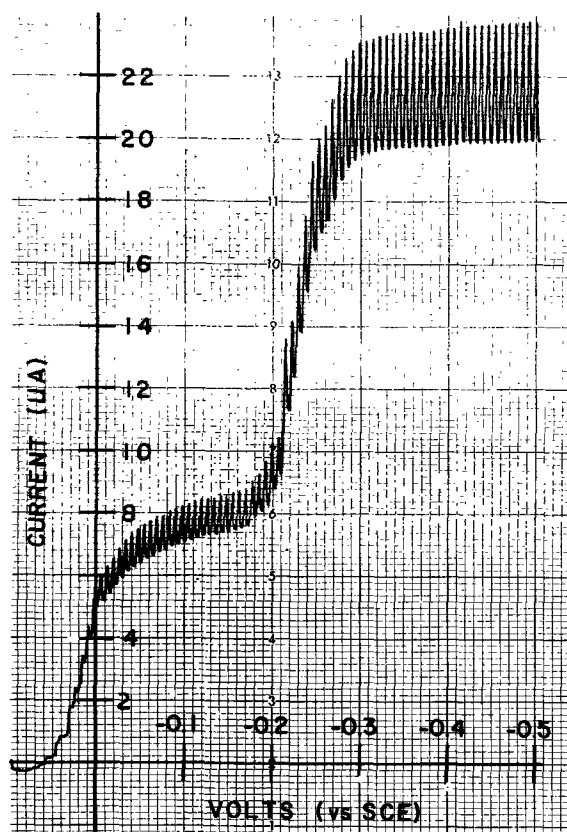


Fig. 2. Polarogram of 1.0×10^{-3} M benzofuroxan at pH 6.5

time. The reduction was interrupted periodically to run additional polarograms from which the BFO and ODI concentrations could be estimated. Figure 2 is a polarogram of 1.0×10^{-3} M BFO in pH 6.5 electrolyte. Two distinct waves can be seen that have $E_{1/2}$ values of -0.005 and -0.25 V, in substantial agreement with those reported by Schindler (1) of -0.00 and -0.26 V (SCE). The average diffusion currents measured at -0.10 and -0.40 V were 7.8 and $22.7 \mu\text{A}$, thus, the height of the second wave is $22.7 - 7.8 \mu\text{A}$, or $14.9 \mu\text{A}$. The ratio of the first and second waves at pH 6.5 is $7.8/14.9$, or very nearly one to two. Polarograms of ODI show only a single wave at the same $E_{1/2}$ value as the second reduction wave of BFO.

The polarographic current values for the various concentrations of BFO and ODI were measured in the three electrolyte solutions. Figure 3 shows a plot of average diffusion currents measured at -0.10 and -0.40 V vs. BFO and ODI concentration in pH 6.5 electrolyte from which the BFO and ODI concentrations in a reduced solution may be estimated. Similar plots were constructed at pH 2.12 and 9.90.

Fast sweep voltammograms at the DME were made with a Hewlett Packard Model 202-A triangle generator coupled with the Electroscan. The recorder of the Electroscan was disconnected and the cell current measured on a Tektronix Type 564B storage oscilloscope through terminals provided in the Electroscan. This arrangement results in the cell current being superimposed on the voltage sweep which makes absolute quantitative measurements of the current impossible. For this reason, current scales have been omitted from Fig. 5, 6, and 7. Since the sweep rate was fairly fast, 1 sec to 40 msec per cycle, compared to the drop time, 3.6 sec, it was felt that the growth of the drop during a single cycle would have a minimal effect.

Results

First reduction wave.— 85.0 ml 1.0×10^{-3} M BFO in pH 6.5 electrolyte was reduced at -0.10 V. The concentration of ODI after the passage of 3.86 coulombs was

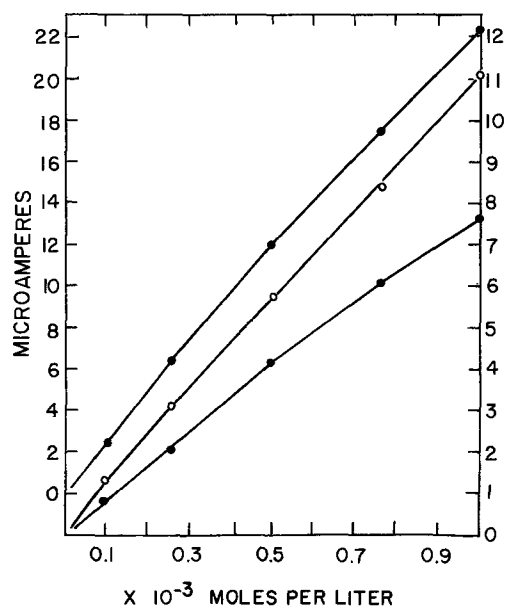


Fig. 3. Top curve, left scale: average polarographic current measured at -0.40 V (SCE) vs. concentration of benzofuroxan at pH 6.5. Bottom curve, right scale: average polarographic current measured at -0.10 V vs. concentration of benzofuroxan at pH 6.5. Middle curve, right scale: average polarographic current measured at -0.40 V vs. concentration of *o*-benzoquinone dioxime at pH 6.5.

measured as 0.26×10^{-3} M (acidic spectrophotometric test) and 0.30×10^{-3} M (basic spectrophotometric test). The theoretical coulombs necessary to produce the 0.26×10^{-3} M solution is 4.26 . Another reduction of 80.0 ml of the same solution at the same voltage yielded the results shown in Table I. In this case, the BFO and ODI concentrations were determined from the polarographic wave heights.

These results support the contention of Schindler (1) and Levin (2) that the product of the first wave is ODI resulting from a two-electron reduction of benzofuroxan.

Second reduction wave.—Reduction of 80.0 ml 1.0×10^{-3} M BFO in pH 6.5 electrolyte at -0.40 V, approximately -0.10 V beyond the crest of the second wave as seen in Fig. 2, resulted in the polarographic currents shown in Table II. After the passage of 12.8 coulombs, the BFO and ODI concentrations were 0.13×10^{-3} M and 0.90×10^{-3} M, respectively. The calculated coulombs necessary to reduce this much BFO to ODI is 13.4 . The implication is that reduction of BFO at potentials slightly more negative than the second wave does

Table I. Reduction of 80.0 ml 1.0×10^{-3} M BFO in pH 6.5 electrolyte at -0.10 V (SCE)

Coulombs passed	BFO conc $\times 10^3$ M	ODI conc $\times 10^3$ M	Theoretical coulombs for 2e- process
0.0	1.0	0.0	—
4.7	0.72	0.31	4.8
8.8	0.41	0.61	9.5
15.1	0.11	0.88	13.6

Table II. Reduction of 80.0 ml 1.0×10^{-3} M BFO in pH 6.5 electrolyte at -0.40 V (SCE)

Coulombs passed	Polarographic current (μA) at -0.10 V (SCE)	Polarographic current (μA) at -0.40 V (SCE)
0.0	7.6	21.9
12.8	2.1	12.1
59.4	0.0	2.5

Table III. Analytical and coulometric results obtained for the reduction of BFO and ODI at pH 9.9, 6.5 and 2.12

	Reduction of $1.0 \times 10^{-3}M$ benzofuroxan						Reduction of $1.0 \times 10^{-3}M$ o-benzoquinone dioxime					
	All concentrations times $10^{2}M$											
	1 Conc ODI	2* Conc 2,3-DAP	3 Conc OPD	4 Material accounted for, %	5 Coulombs to make 1, 2, 3	6 Measured coulombs	1 Conc ODI	2* Conc 2,3-DAP	3 Conc OPD	4 Material accounted for, %	5 Coulombs to make 1, 2, 3	6 Measured coulombs
pH 9.9	0.28	0.07 (0.14)	0.612	103	20.6	22.9	0.34	0.055 (0.11)	0.61	106	13.4	12.6
pH 6.5	0.075	0.17 (0.34)	0.202	61	16.2	24.2	0.13	0.17 (0.34)	0.23	70	8.1	16.6
pH 2.12	0.11	0.164 (0.33)	0.317	76	15.3	18.7	0.09	0.131 (0.26)	0.11	46	4.82	8.8

* 2,3-DAP values in () are as monomer.

not proceed directly to the fully reduced products but rather yields the dioxime which, after the BFO in solution is depleted, is then further reduced. The appearance of the solution during a reduction also supports this conclusion. Initially the solution is colorless. During the reduction, the solution becomes reddish-brown (the color of the dioxime at pH 6.5) until sufficient coulombs for a two-electron reduction have passed. Upon further reduction the solution clears to a yellowish color.

A small amount of brown precipitate was observed in the cell at the end of the reduction. The amount of this precipitate seemed to increase upon standing, even though the electrolytic reduction had been completed. Experiments were undertaken to determine the structure of this precipitate and the products remaining in solution.

Nine 80 ml solutions of $1.0 \times 10^{-3}M$ BFO in pH 6.5 electrolyte were reduced at $-0.40V$. The total coulombs passed were estimated at 600. After standing 4 to 6 hr, each solution was filtered, and the precipitate thoroughly rinsed with water. The total weight of this precipitate, referred to as "A," was 39.8 mg. The product remaining in solution was isolated by evaporation of the combined supernatant solutions and extraction with ethanol which was evaporated to yield "B."

The NMR, uv, IR, and visible spectra of B were identical with the spectra of synthetic 2,3-DAP. 2,3-DAP forms a green solution with concentrated H_2SO_4 which becomes brown upon dilution (12). Synthetic 2,3-DAP and product B gave positive results with this test.

The uv and visible spectra of A indicated that the product was, in part, also 2,3-DAP. However, the IR spectrum of A showed strong absorptions at 1340, 2850, and 2900 cm^{-1} which are not due to 2,3-DAP. A did not give nearly as strong a qualitative test with sulfuric acid as did synthetic 2,3-DAP or B. Because so little product was available, 40 mg, of which most had been used in qualitative tests and for IR, uv, and visible spectra, no further characterization was attempted.

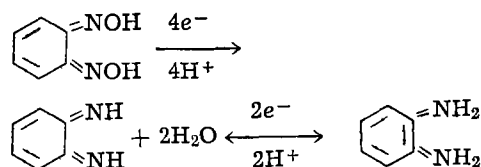
Since it was known that OPD air oxidizes to 2,3-DAP (13) and product B was isolated from evaporation of the reduced solutions, the 2,3-DAP and OPD determinations were developed which could be run directly on the solutions immediately following the reduction. Constant potential reductions at voltages slightly above the crest of the second wave were performed on BFO and ODI solutions at the three pH values. The coulombic, polarographic, and analytical data collected from these reduced solutions are given in Table III.

Discussion

The first two-electron polarographic wave in neutral and basic solutions results in the dioxime product. In acidic solutions the two waves cannot be distinguished as seen in Fig. 4, the polarogram of BFO in pH 2.12 electrolyte.

A satisfactory explanation of the processes involved with the second reduction wave, the two-electron

"dip" in the second reduction wave in the middle pH range as shown in Fig. 1 and the formation of the phenazine and diamine products can be made by assuming an o-benzoquinone diimine intermediate resulting from a four-electron reduction of the dioxime. This diimine may be further reduced to OPD or couple to produce 2,3-DAP. The over-all reaction for the formation of the imine and further reduction to OPD is shown in reaction I.



[I]

The argument in support of the diimine intermediate is summarized here followed by a more complete description of each line of evidence.

(a) Chemical and electrochemical oxidations of OPD in aqueous solutions are known to proceed through the diimine intermediate which couples to yield 2,3-DAP.

(b) The transition in the polarographic reduction wave of BFO and ODI from four to six electrons occurs at the same pH value, 7.8, as does the change in slope of the $E_{1/2}$ vs. pH curve for the oxidation of OPD. It has been shown that this pH is the same as the pK_a value for the diimine intermediate.

(c) The formation of the diimine intermediate, resulting from a four-electron reduction of ODI, ac-

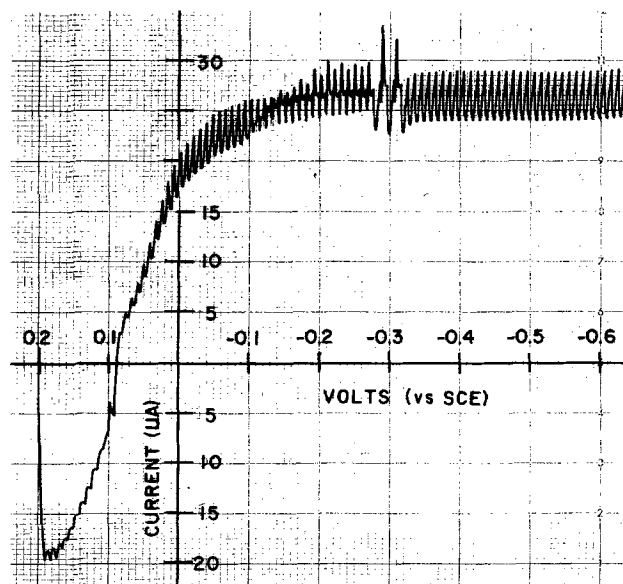


Fig. 4. Reduction polarogram of $1.0 \times 10^{-3}M$ benzofuroxan at pH 2.12.

counts for the four-electron polarographic wave observed in the middle pH range.

(d) Fast sweep voltammograms show a new peak for the reduction of BFO and ODI at pH 9.9. This is the expected result for an intermediate species in the reduction pathway between ODI and OPD.

The electrochemical oxidation of OPD has been studied in considerable detail in aqueous solutions throughout a wide range of pH values and at a variety of electrode surfaces (13-17). The unanimous consensus of these investigators is that the reaction proceeds through a two-electron oxidation of the diamine to diimine, and in middle or slightly acidic pH ranges the diimine couples with unreacted OPD to yield 2,3-DAP which is the observed product. This latter coupling reaction involves a further four-electron oxidation. Parker and Adams (14), who describe the initial two-electron wave as a redox couple, plotted $E_{1/2}$ values for the oxidation of OPD at a rotating platinum electrode and found sharp changes in the slope of the curve at pH 4.5 and 7.8. These data are shown in Fig. 1 along with a plot of the polarographic current of the second reduction wave from Schindler's data.

The correlation between the break in the $E_{1/2}$ curve at pH 7.8 and the transition between a four- and a six-electron reduction wave for BFO at the same pH is very striking. Parker and Adams (14) showed that this break is the pK_a value of the diimine intermediate. The other change in slope at pH 4.5 occurs at the pK_a value for OPD. Elving and Krivis (16, 17) found that at pH 5, in the region of the four-electron wave for the reduction of ODI, the oxidation of OPD gave two waves. The first wave is a two-electron oxidation to the diimine which then couples with unreacted OPD to form 2,3-DAP. This is followed by a second one-electron wave due to a free-radical reaction resulting in a polymeric film coating of the electrode. At pH 11 a single two-electron oxidation occurs but no further oxidation wave is seen, and the electrode is not fouled. Evidently, in solutions above pH 7.8 where the diimine is not protonated, it does not easily couple to form the phenazine. Consequently, when this intermediate is formed by the reduction of BFO or ODI above pH 7.8, the coupling does not occur, but rather the imine is further reduced to OPD. As a result a single six-electron wave is seen for the reduction of ODI above pH 7.8. This conclusion is supported by the data in Table III which show that OPD is the major reduction product at pH 9.9 and that very little phenazine is formed.

At pH values between about 4.5 and 7.8, where the imine is known to couple to form the phenazine, the reduction of ODI proceeds in only a four-electron process to the intermediate followed by coupling. Table III shows that the major reduction product in this pH range is 2,3-DAP.

Fast sweep voltammograms provide further evidence for the diimine intermediate. Figure 5 shows voltammograms of $1.0 \times 10^{-3}M$ BFO in pH 9.9 electrolyte solution at sweep rates of 1, 5, and 10 Hz. The initial voltage was 0.0 (SCE) and the sweep amplitude was $-1.05V$. At 1 Hz, peaks can be seen at -0.15 and $-0.52V$, with a very small peak at $-0.41V$ which is not present in the dropping mercury polarograms. As the frequency of the sweep is increased to 10 Hz the peak at $-0.41V$ becomes larger than the peak at $-0.52V$. This is the expected behavior if the reduction is proceeding through the diimine intermediate at this pH.

Voltammograms at pH 6.5 are shown in Fig. 6: The first wave is difficult to see. However, at 1 Hz there is a large wave at $-0.25V$ with a very small wave at $-0.73V$. At 10 and 25 Hz no change is seen which agrees with the polarographic behavior indicating only a four-electron reduction to the diimine in the middle pH ranges. It might be added that similar results are obtained from fast sweep voltammograms of ODI. This is expected since the initial BFO reduction yields the dioxime.

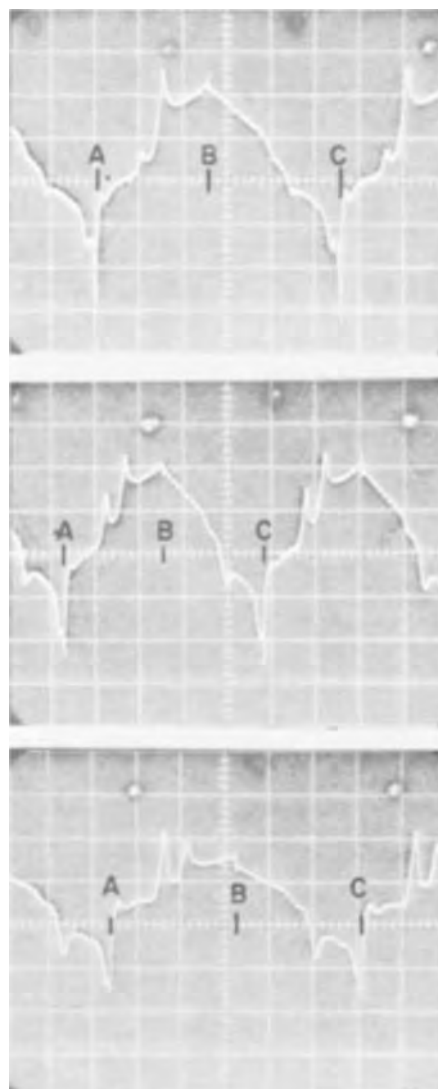


Fig. 5. Fast sweep voltammogram of $1.0 \times 10^{-3}M$ BFO at pH 9.9. For all three sweeps, point A marks the beginning of the cathodic sweep at 0.00V (SCE). Point B marks the end of the cathodic sweep and the beginning of the anodic sweep at $-1.05V$. Point C is the end of the anodic sweep, 0.00V. Upper sweep: 1 Hz, oscilloscope trace rate 0.2 sec and 0.41V/large division. Middle sweep: 5 Hz, 50 msec and 0.46V/large division. Lower sweep: 10 Hz, 20 msec and 0.37V/large division.

In acidic solutions below about pH 4.5 the situation is less clear. The polarographic wave for the reduction of BFO shifts from four to six electrons quite gradually as can be seen in Fig. 1. It is hard to correlate this shift with the change in the slope of $E_{1/2}$ vs. pH for the oxidation of OPD. However, one explanation seems possible. The papers of Elving and Krivis (17) and Parker and Adams (14) reported only a single two-electron oxidation wave for OPD to the diimine at pH's below 4.6. Nonetheless, an electrode coating or film was observed, which was attributed to a post-electrolytic reaction of the diimine in acidic solutions. There is evidence of such a process in the reduction of BFO. Figure 7 shows fast sweep voltammograms from $+0.20$ to $-0.88V$ for the reduction of BFO in pH 2.12 electrolyte. It was observed that there is an initial peak at $-0.04V$ followed by a large wave whose maxima is at $-0.55V$. Then, as the voltage decreases, another reduction wave is seen; an unusual occurrence. This may be interpreted as an electrochemical reduction followed by a chemical reaction which yields a product that may be further reduced. At 10 Hz the scan shows no second wave, perhaps because the scan is faster than

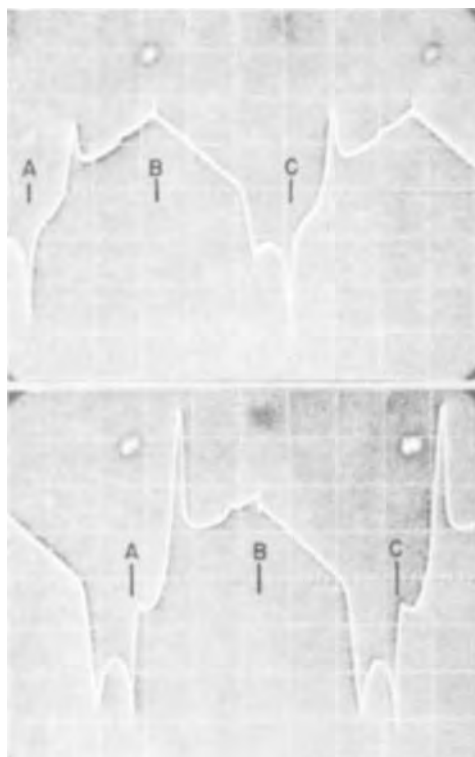


Fig. 6. Fast sweep voltammogram of 1.0×10^{-3} M BFO at pH 6.5. Cathodic sweep from A (+0.10V) to B (-0.98V). Anodic sweep from B to C (+0.10V). Upper sweep: 1 Hz, 0.2 sec and 0.40V/large division. Lower sweep: 10 Hz, 20 msec and 0.40V/large division.

the chemical reaction. Other explanations such as the production of an insoluble film on the electrode are also plausible.

The reduction of two molecules of ODI to 2,3-DAP requires six electrons over-all. This would account for the over-all six-electron reduction wave in acidic solutions. However, this explanation fails to account for the "missing" product noted in Table III for the reduction of ODI at pH 2.12. The fact that a film forms on the electrode during the oxidation of OPD and the same phenomenon is observed in the reduction of BFO (the odd behavior of the mercury electrode in Fig. 4 between -0.1 and -0.3V) indicates a polymer formation, perhaps due to successive coupling of diimine with phenazine molecules. The complexity of the reaction in acidic solutions is increased by the fact that BFO reacts with the mercury electrodes in acidic solutions. If a solution of BFO is allowed to stand over a mercury pool for several hours the solution darkens to reddish-brown. The uv and visible spectra indicate that this product is not the dioxime.

Conclusions

The general course of the reduction of benzofuroxan in aqueous solutions is clear. The BFO undergoes a two-electron reduction to *o*-benzoquinone dioxime which is further reduced to *o*-benzoquinone diimine by a four-electron process, reaction [II], below. The diimine is then reduced to *o*-phenylenediamine, reaction [III], or couples to form 2,3-diaminophenazine.

The details of the phenazine formation are not clear, but a number of possibilities must be considered. Condensation of ODI and OPD with loss of two molecules of water could lead to 2,3-DAP. However, in neutral or basic solutions, analysis of the reduction products showed that a considerable amount of these products can exist together without reaction, or with only very slow reaction. The more likely explanation is that the phenazine formation is electrochemical in nature and involves the imine intermediate. Reaction with BFO

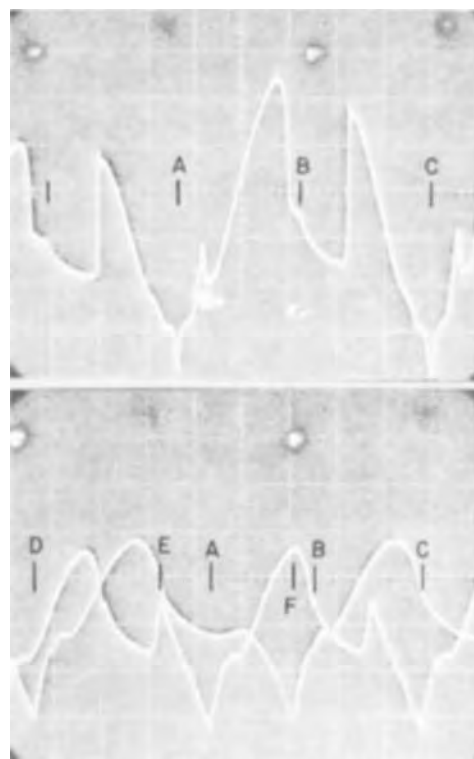
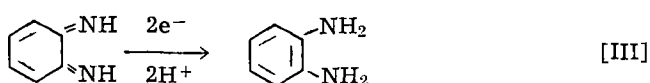
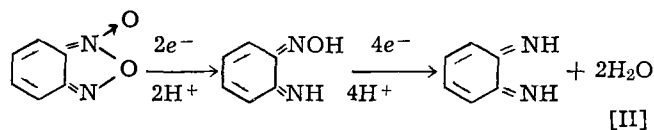


Fig. 7. Fast sweep voltammogram of 1.0×10^{-3} M BFO at pH 2.12. Cathodic sweeps from A (+0.20V) to B (-0.88V). Anodic sweep from B to C (+0.20V). Upper sweep: 1 Hz, 0.2 sec and 0.41V/large division. The lower sweep shows two traces. The sweep which includes the first major peak is at 5 Hz, 50 msec and 0.49V/large division. This sweep is marked by points A, B, and C. The trace of slightly larger amplitude is at 10 Hz and 0.40V/large division. The cathodic sweep is from D (+0.20V) to E (-0.88), and the anodic sweep is from E to F (+0.20V).

and subsequent reduction is ruled out because the first product of the reduction of BFO, even at voltages more negative than the second polarographic wave is ODI. That is, nearly all the BFO in solution is reduced to ODI before the ODI is further reduced to the imine. It is also possible that the phenazine formation results from a coupling of the diimine with ODI involving a two-electron reduction. This pathway is attractive except for the fact that no polarographic wave is seen to indicate this process. Also this would require six electrons over-all from the dioxime to the phenazine, whereas only a four-electron wave is observed in the middle pH range where the phenazine product is most abundant. This leaves coupling of the imine with itself or with OPD, there being precedent for the latter alternative (16, 17).



Acknowledgment

The authors are pleased to acknowledge the support of the United States Army Mobility Equipment Research and Development Center, Fort Belvoir, Virginia, under Contract No. DA 44-009-AMC-1386(T).

Manuscript submitted July 23, 1971; revised manuscript received ca. Sept. 1, 1971.

Any discussion of this paper will appear in a Discussion Section to be published in the December 1972 JOURNAL.

REFERENCES

1. R. Schindler, H. Will, and L. Holleck, *Z. Electrochem. Ber.*, **63**, 596 (1959).
2. E. S. Levin, Z. I. Fodiman, and Z. V. Todres, *Soviet Electrochemistry*, **2**, 175 (1966).
3. W. B. Hardy and R. A. Parent, U.S. Pat. 3, 163, 561, Dec. 29, 1964.
4. J. T. Shaw, J. D. Voorhies, and S. M. Davis, U.S. Pat. 3, 260, 621, July 12, 1966.
5. V. G. Pesin, A. M. Khaletskii, and T. Chou, *Z. Obshch. Khim.*, **28**, 2089 (1955); cf. *C.A.*, **53**, 2214i (1959).
6. J. H. Boyer and S. E. Ellzey, Jr., *J. Am. Chem. Soc.*, **82**, 2525 (1960).
7. F. Ullman and F. Mauthner, *Ber.*, **35**, 4302 (1902).
8. E. Sawicki, T. R. Hauser, and R. Wilson, *J. Anal. Chem.*, **34**, 505 (1962).
9. K. Matsumura, *J. Am. Chem. Soc.*, **52**, 3199 (1930).
10. C. Stammer and A. Taurins, *Spectrochim. Acta*, **19**, 1625 (1963).
11. J. M. Dechary, E. Kun, and H. C. Pitot, *J. Anal. Chem.*, **26**, 449 (1954).
12. O. Fisher and E. Happ, *Ber.*, **22**, 355 (1889).
13. R. N. Adams, "Electrochemistry at Solid Electrodes," p. 360, Marcel Dekker, Inc., New York (1969).
14. R. E. Parker and R. N. Adams, *J. Anal. Chem.*, **28**, (5), 828 (1956).
15. S. S. Lord, Jr. and L. B. Rogers, *ibid.*, **26**, (2), 284 (1954).
16. P. J. Elving and A. Krivis, *ibid.*, **30**, 1645 (1958).
17. P. J. Elving and A. Krivis, *ibid.*, **30**, 1648 (1958).

Interdependence of Parameters in Reactive Sputtering of Manganese in Oxygen

L. D. Locker,* R. W. Landorf, C. L. Naegele,¹ and F. Vratny*

Bell Telephone Laboratories, Incorporated, Murray Hill, New Jersey 07974

ABSTRACT

Manganese oxide thin films deposited over the Ta₂O₅ layer in tantalum capacitors are known to improve yield and reliability. In this investigation reactive sputtering is used to prepare manganese oxides. The results show that films with resistivities below 1 ohm-cm can be produced, but the interdependence of oxygen partial pressure, power input, and substrate temperature limits the deposition rates that can be obtained without producing oxide phases with higher resistivities.

With d-c sputtering at 4.0 kV, Mn₂O₃ is produced as the oxygen pressure increases from 3×10^{-2} to 4×10^{-2} Torr. This corresponds to a substrate temperature increase from 275° to 360°C and a 50% increase in deposition rate. The complexity of the interactions in both d-c and rf reactive sputtering is further illustrated by the maximum in substrate temperature obtained with argon-oxygen mixtures containing 0.5% O₂. For reactive sputtering of materials similar to Mn-O, where several phases and variable stoichiometry are possible, it is therefore necessary to determine experimentally the conditions of power density, pressure, and substrate temperature that give the maximum deposition rate for each phase.

Independent investigations (1-3) confirm the improvement in the yield and the reliability of tantalum thin-film capacitors obtained by adding a thin layer of MnO₂ over the Ta₂O₅ dielectric (e.g., Ta-Ta₂O₅-MnO₂-Au). The manganese dioxide films can be deposited by pyrolysis of Mn(NO₃)₂ sprayed onto the tantalum pentoxide, by reactive evaporation of manganese, or by reactive sputtering of manganese (4). Favorable capacitor performance has been obtained with d-c diode reactive sputtering in pure oxygen or in oxygen-argon mixtures when low resistivity (1-15 ohm-cm) MnO₂ is produced (2). RF sputtering of Mn in oxygen has produced manganese oxide films with resistivities as low as 5×10^{-3} ohm-cm (5). By using the technique of rf + d-c sputtering (6), deposition rates can be increased compared with the more conventional methods of diode sputtering. The plasma density is increased, and an insulating oxide layer that forms on the cathode can be sputtered. However, in reactive sputtering there is a complex interdependence among power input, substrate temperature, total pressure, and oxygen partial pressure, and the resultant deposition rate, composition, and electrical properties of the films. Especially for the Mn-O system, where several phases and variable stoichiometry can occur,

it is not usually possible to obtain the optimum electrical properties at high deposition rate.

Experimental

Sputtering was done in an oil-diffusion-pumped bell jar system with a liquid nitrogen baffle, capable of an ultimate pressure of 1×10^{-6} Torr. Corning 7059 glass substrates were mounted on a water-cooled support 3 in. above the cathode. The sputtering source consisted of electroplated manganese on stainless steel. The reactive gas was pure oxygen at pressures of 5×10^{-2} , 3×10^{-2} , 2×10^{-2} , 1×10^{-2} , and 5×10^{-3} Torr and oxygen-argon mixtures with different oxygen partial pressures between 2×10^{-5} and 2×10^{-2} Torr. In the oxygen-argon mixtures the total pressure was constant at 2×10^{-2} Torr. Cathode voltages with pure oxygen were either 1.5, 2.5, or 4.0 kV d.c., and 4.0 kV d.c. with the oxygen-argon mixtures. In separate experiments approximately 200W of rf power was combined with either 2.5 or 4.0 kV d.c. Film thicknesses were measured with the Talysurf, and resistivities were measured from the current-voltage characteristic between metal contacts evaporated on the sample surface. The substrate temperature was measured with a thermocouple imbedded in the substrate holder. Although this is a low estimate of the surface temperature, the heat flow conditions, and more recent measurements with thin film thermocouples that are cited below, indicate that the observed variations in tem-

* Electrochemical Society Active Member.

¹ Present address: Weston Components Company, Scranton, Pennsylvania 18501.

Key words: dielectric films, manganese oxides, sputtering, thin films.

perature are valid for the growing film. Crystallographic phase identification was done by x-ray diffraction.

Results

All of the phases Mn, MnO, Mn₃O₄, Mn₂O₃, and MnO₂ have been obtained in the course of the experiments, although the x-ray diffraction patterns are often difficult to interpret. The resistivities of the films cover the range from 10⁻² ohm-cm to 10⁷ ohm-cm. Deposition rates cover the range from 2.5 Å/min to 85 Å/min. The results are summarized in Fig. 1 and 2. In Fig. 1 the resistivity values in ohm-cm are marked next to the corresponding data points. The substrate tem-

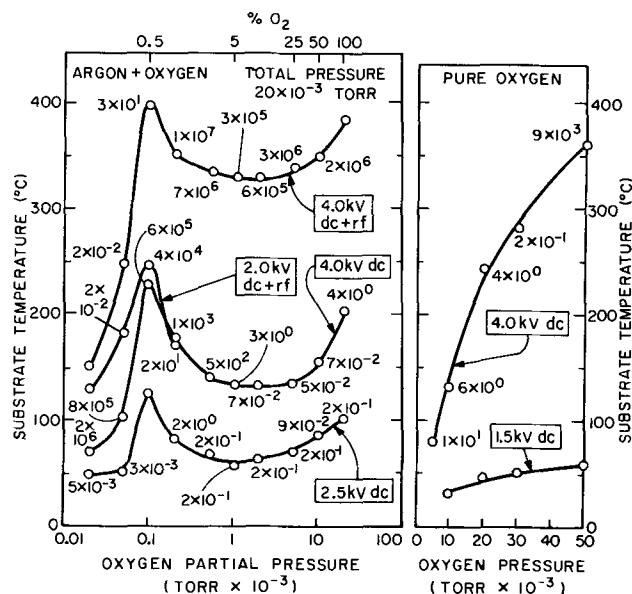


Fig. 1. Substrate temperature vs. oxygen pressure for different d.c. or d.c. and rf power levels. Numbers adjacent to data points are resistivity values (ohm-cm) for the manganese oxide films.

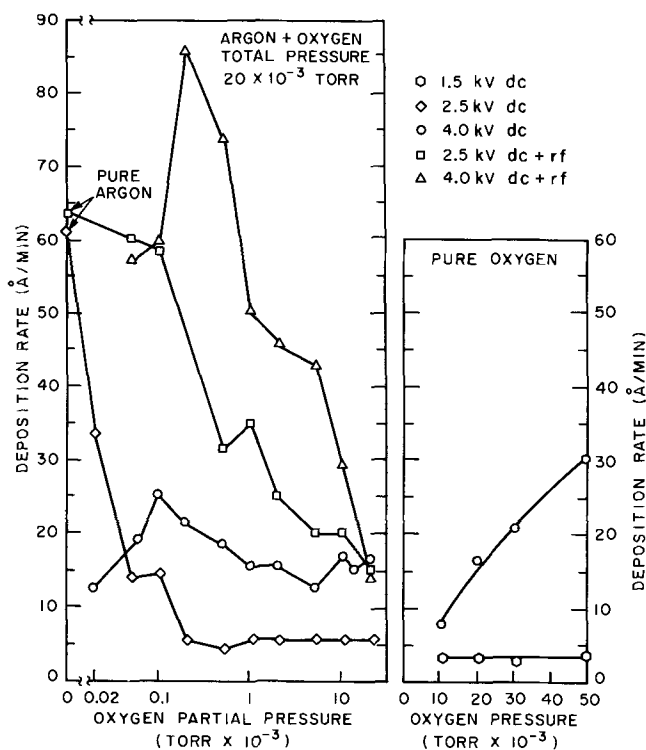


Fig. 2. Deposition rate vs. oxygen pressure for different d.c. or d.c. and rf power levels.

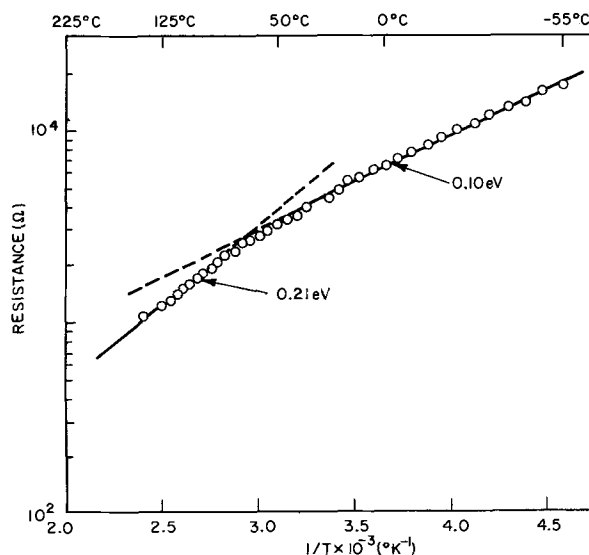


Fig. 3. Resistance vs. temperature typical of manganese oxides with resistivities between 0.1 and 10 ohm-cm.

perature maximum with approximately 0.5% O₂-95.5% A has been confirmed in an independent investigation (7), using a Pt/Pt-10% Rh thin film thermocouple on a glass substrate.

Films with resistivities between 0.1 and 10 ohm-cm are probably close in structure and composition to the MnO₂ prepared by pyrolysis of Mn(NO₃)₂ (8, 9). Only a few diffuse lines appear in the x-ray diffraction patterns of the sputtered films, so that a specific phase identification is not possible. However, for all the films in this resistivity range the temperature coefficient of resistance ($d \ln R/d(1/T)$) is approximately constant and is close to the values found with films produced by Mn(NO₃)₂ pyrolysis. The activation energy for the n-type conduction is indicated in Fig. 3. The apparent nonlinearity in the plot may be due to oxygen of water vapor evolution during heating. Upon recycling the sample temperature between -55° and 125°C, the 0.21 eV activation energy is removed and only the 0.10 eV value is obtained.

For d-c sputtering at 2.5 kV, the lowest oxygen partial pressure producing a resistivity in the 0.1 to 10 ohm-cm range is 2×10^{-4} Torr. In comparison, at 4.0 kV d.c. the lowest pressure is 1×10^{-3} Torr. The higher substrate temperatures in the latter case would favor transformation to Mn₂O₃ at a higher pressure than at 2.5 kV d.c. At 4.0 kV d.c. and an oxygen partial pressure of 5×10^{-4} Torr the x-ray diffraction pattern is clearly α -Mn₂O₃. Similarly, in pure oxygen at 4.0 kV d.c. there is a change to Mn₂O₃ between 3×10^{-2} and 5×10^{-2} Torr, when the substrate temperature increases from 275° to 360°C. In this case, the MnO₂ → Mn₂O₃ transition, which decreases the O:Mn ratio, occurs even as the oxygen pressure is increased. This is further evidence that the increase in substrate temperature and possibly the change in manganese sputtering rate from the cathode as the pressure is increased, are important in determining the phase that forms. The substrate temperature is also important in regard to the rate of film growth. When the substrate temperature is increased independently of power input and oxygen pressure (4.0 kV d.c., 5×10^{-2} Torr pure O₂), by resistance heating of the substrate holder, the film growth rate increases. The thermal activation energy is 4 ± 2 kcal/mole Mn₂O₃.

When rf power is added to the argon-oxygen discharge, the growth rates (Å/min), at corresponding pressures, increase in almost all cases. (An accurate comparison of rates in terms of mass/time must account for changes in film density.) The resistivity of the films also increases, and the x-ray diffraction pat-

terns show that a lower oxide than MnO_2 is produced. The results therefore indicate that the interdependence of the sputtering variables restricts the flexibility to obtain given film properties at high deposition rates.

Discussion

Valletta and Pliskin (10) have used the infrared spectra to characterize manganese oxides prepared by d-c reactive sputtering in oxygen at 5×10^{-2} Torr. They conclude that manganese dioxide is formed only when the substrate temperature is below $350^\circ C$. This is in agreement with the x-ray diffraction results presented above, where a definite transformation to Mn_2O_3 is observed between 275° and $360^\circ C$. The resistivity changes also indicate the phase transformation.

The metastable products formed in the thermal oxidation of manganese can be explained in terms of the rate-limiting transport reaction, producing concentration gradients and an electric field across the growing oxide film (11, 12). For example, thermal oxidation in 1 atm air at 350° - $450^\circ C$ produces Mn_3O_4 , and at pressures down to 10^{-4} Torr produces MnO and Mn_3O_4 (11). The situation is analogous in the oxidation of iron and copper. For copper, results on reactive sputtering have been obtained by Perny and Laville-St. Martin (13, 14). The Cu_2O phase is formed under conditions where equilibrium calculations predict CuO . Although the mechanism of reactive sputtering is unlikely to be the same as thermal oxidation, nonequilibrium conditions also exist during reactive sputtering since the oxide is deposited from species in an electric discharge.

Figures 1 and 2 suggest that the interactions in an argon-oxygen discharge are sensitive to the composition of the mixture. This is best illustrated by the maximum in substrate temperature observed with 0.5% O_2 . A complete explanation of the observed changes in substrate temperature and deposition rate require information on the concentrations of positively charged ions, secondary electrons, and reactive species in the discharge. The species in an argon rf glow discharge are A , A^+ , A^* , and e^- , where A^* denotes an excited argon atom. Lounsbury (15) has recently studied the effects of 1% O_2 added to the argon discharge at a total pressure of 4×10^{-2} Torr. The oxygen addition increases the A^+ concentration, decreases the A^* concentration, and probably causes a change in the electron energy distribution in the plasma. The increased ion concentration will cause an increase in secondary electron emission from the cathode. Secondary electron emission will also be affected if an

oxide layer is present on the cathode. These secondary electrons are responsible for the substrate heating (16, 17). Therefore, a combination of factors will have an effect on the substrate temperature and the sputtering rate from the cathode. Although the species in oxygen-argon mixtures have not been examined for compositions other than A-1% O_2 , this type of information is very important in general. When this is combined with information about the reaction processes on the substrate surface, a detailed mechanism of the reactive sputtering process can be proposed.

Acknowledgment

The authors wish to thank Mrs. M. H. Read for the x-ray diffraction studies.

Manuscript submitted May 20, 1971; revised manuscript received ca. Oct. 1, 1971. This was Paper 8 presented at the Washington, D.C., Meeting of the Society, May 9-13, 1971.

Any discussion of this paper will appear in a Discussion Section to be published in the December 1972 JOURNAL.

REFERENCES

1. D. A. McLean and F. E. Rosztochy, *Electrochem. Technol.*, **4**, 523 (1966).
2. J. H. Cash and R. S. Clark, *This Journal*, **113**, 58C (1966).
3. R. M. Valletta, J. S. Makris, and W. S. Pliskin, *Proc. 1966 Electron. Components Conf.* (May 1966).
4. R. W. Berry *et al.*, "Thin Film Technology," p. 387, D. Van Nostrand, Princeton, N. J. (1968).
5. R. L. Landorf, Unpublished data.
6. F. Vratny in "Thin Film Dielectrics," Frederick Vratny, Editor, p. 143, The Electrochemical Society Softbound Symposium Series, New York (1969).
7. C. D. Capio, Bell Telephone Laboratories, Private communication.
8. J. S. Wiley and H. T. Knight, *This Journal*, **111**, 656 (1964).
9. P. H. Klose, *ibid.*, **117**, 854 (1970).
10. R. M. Valletta and W. S. Pliskin, *ibid.*, **114**, 944 (1967).
11. A. Goswami, *Indian J. Chem.*, **3**, 285 (1965).
12. K. Hauffe, "Oxidation of Metals," p. 272, Plenum Press, New York (1965).
13. G. Perny *et al.*, *J. Phys.*, **25**, 5 (1964).
14. G. Perny and B. Laville-St. Martin, *ibid.*, **25**, 993 (1964).
15. J. B. Lounsbury, *J. Vacuum Sci. Technol.*, **6**, 838 (1969).
16. I. Brodie, L. T. Lamont, and D. O. Myers, *ibid.*, **6**, 124 (1969).
17. L. T. Lamont and A. Lang, *ibid.*, **7**, 198 (1970).

Growing Porous Layers

William Tiedemann*¹

Energy and Kinetics Department, School of Engineering and Applied Science,
University of California, Los Angeles, California 90024

and John Newman**

Inorganic Materials Research Division, Lawrence Radiation Laboratory, and
Department of Chemical Engineering, University of California, Berkeley, California 94720

ABSTRACT

The precipitation of ions generated at an electrode, operating at a constant current, with ions of the adjacent electrolytic solution has been modeled as a growing porous layer. The thickness of the layer as a function of time for short times is given by a power series expansion of time. The long-time solution was determined by a numerical calculation on a digital computer. A criterion for linear growth rate as a function of time is given.

Moving boundary problems, such as melting-freezing, evaporation-condensation, and purification of materials, involving heat and mass transfer have been treated in depth (1-7). A moving boundary problem is encountered in the field of electrochemistry when ions being generated at an electrode, operating at a constant current, form a precipitate with ions of the adjacent electrolytic solution. The resulting precipitate forms a growing porous layer on the electrode. Studies of anodic dissolution of various metals which form porous coatings (8) can be considered examples of growing porous layers. In the case of silver, a porous layer occurs only after a nonporous layer has been formed or when large currents are employed (9, 10). Jackson and Blomgren (11) studied the anodic dissolution of lithium in a 1M solution of AlCl_3 in propylene carbonate and observed a growing porous layer of LiCl . Other examples of growing porous layers are the oxidation of tungsten (12) and the scaling of metals (13). In the following analysis, the thickness of a growing porous layer as a function of time is determined, and a criterion for linear growth rate as a function of time is given.

Description of Model

The system under consideration consists of an electrode in contact with a binary electrolytic solution. The current density is assumed uniform over the surface of the electrode. Variation in concentration occurs only in the direction perpendicular to the electrode surface, and convection is assumed to be negligible. At time $t = 0$, a constant current is applied to the electrode. The metal ion which is being generated at the electrode surface combines with the anion of the binary electrolyte and precipitates at the electrode surface (the solution being initially at the saturation concentration, c_s). Further precipitation occurs at the interface between the advancing front of the porous layer and the electrolytic solution. The porous layer is assumed to have a homogeneous porosity. The saturation concentration inside the porous layer will be allowed to increase above the initial saturation value due to local resistance heating (10, 14). Dilute-solution theory (15) will be used to relate the derivative of the concentration at the electrode surface to the current density.

Mathematical Formulation

The equations necessary to describe the growing porous layer are (where c refers to the concentration inside the porous layer)

$$\frac{\partial c}{\partial t} = \bar{D} \frac{\partial^2 c}{\partial X^2} \quad 0 < X < \delta(t) \quad [1]$$

$$c|_{t=0} = c_s \quad [2]$$

$$c|_{X=\delta(t)} = c_s \quad [3]$$

$$\left. \frac{\partial c}{\partial X} \right|_{X=0} = - \frac{it}{nFD\epsilon} = - \frac{K}{e} \quad [4]$$

$$\frac{d\delta(t)}{dt} = - \frac{\bar{D}\epsilon}{(1-\epsilon)\rho_m} \left. \frac{\partial c}{\partial X} \right|_{X=\delta(t)} \quad [5]$$

Equation [1] is the species continuity equation with the rate of production in the porous layer equal to zero. Equations [2] and [3] give the initial and boundary value concentrations. Equation [4] relates the derivative of the concentration at the electrode surface to the applied current, transference number of anion, diffusion coefficient of the binary electrolyte in the porous layer, and porosity of the layer. Equation [5] is obtained from an over-all material balance and relates the rate of growth of the porous layer to the flux of precipitate in solution at $X = \delta$ (thickness of porous layer). The diffusion coefficients in these equations are assumed independent of concentration and equal to each other. The quantity $(1-\epsilon)\rho_m$, indicates the amount of precipitate present in the solid portion of the porous layer.

The following change of variables is made in order to immobilize the boundary (7)

$$\text{Let } x = X/\delta(t), \quad \tau = \bar{D}t(K/(1-\epsilon)\rho_m)^2 \\ \theta = (c - c_s)\epsilon/K\delta(t), \quad \Delta = \delta(t)K/(1-\epsilon)\rho_m \quad [6]$$

Equations [1-6] are now expressed as

$$\frac{\Delta^2 \partial \theta}{\partial \tau} + \frac{1}{2} \left(\theta - x \frac{\partial \theta}{\partial x} \right) \frac{d\Delta^2}{d\tau} = \frac{\partial^2 \theta}{\partial x^2} \quad 0 < x < 1 \quad [7]$$

$$\theta|_{\tau=0} = 1 - x \quad [8]$$

$$\theta|_{x=1} = 0 \quad [9]$$

$$\left. \frac{\partial \theta}{\partial x} \right|_{x=0} = -1 \quad [10]$$

$$\frac{d\Delta}{d\tau} = - \left. \frac{\partial \theta}{\partial x} \right|_{x=1} \quad [11]$$

$$\Delta|_{\tau=0} = 0 \quad [12]$$

The x domain has now been reduced to $0 < x < 1$. Equation [7] is slightly more complex than its counterpart (Eq. [1]), however, the dependence of Eq. [3] and [5] on $\delta(t)$ has been removed. The solution to Eq. [7-12] will first be examined for small τ by expressing Δ and θ as a power series in τ .

$$\Delta = \tau - a\tau^2 + b\tau^3 + c\tau^4 + d\tau^5 + 0(\tau^6) \quad [13]$$

* Electrochemical Society Student Associate Member.

** Electrochemical Society Active Member.

¹ Present address: Globe-Union Inc., Milwaukee, Wisconsin 53201.
Key words: porous layers, precipitation, growth rate.

$$\theta = 1 - x - A(x)\tau + B(x)\tau^2 - C(x)\tau^3 + D(x)\tau^4 + 0(\tau^5) \quad [14]$$

By substituting the above series into Eq. [7-12], the unknown coefficients can be determined. The result is given by

$$\Delta = \tau - \tau^2/2 + 5\tau^3/6 - 17\tau^4/8 + 827\tau^5/120 + 0(\tau^6) \quad [15]$$

$$\theta = (1-x) - (1-x^2)\tau/2 + 5(1-x^2)\tau^2/4 + [53(1-x^2)/12 - (1-x^4)/2]\tau^3 + [895(1-x^2)/48 - 17(1-x^4)/24]\tau^4 + 0(\tau^5) \quad [16]$$

Let us digress a moment and determine what a reasonable value for τ might be. For $i = 10^{-3}$ A/cm², $\epsilon = 0.1$, $D = 10^{-5}$ cm²/sec, $\rho_m = 4 \cdot 10^{-2}$ moles/cm³, $t = 5.4 \cdot 10^3$ sec one obtains $\tau \cong 0.001$. Therefore, as can be seen, the short-time solution can be used to describe the behavior of the porous layer for relatively long real times.

Let us now determine if $\Delta \sim \tau^{1/2}$ at long times, which would be characteristic of unrestricted semi-infinite diffusion from an electrode. The change of variables used to obtain Eq. [7-12] was useful in obtaining the short-time solution. For the development of the long-time solution, the following change of variables will be used in Eq. [1-6]

$$f(\eta, \tau) = \frac{(c - c_s) \epsilon}{(1 - \epsilon)\rho_m 2\sqrt{\tau}}$$

$$\eta = XK/2(1 - \epsilon)\rho_m\sqrt{\tau}$$

$$\Delta_1 = \delta(t)K/2(1 - \epsilon)\rho_m\sqrt{\tau}$$

$$\tau = \bar{D}t[K/(1 - \epsilon)\rho_m]^2$$

Equations [1-6] then become

$$4\tau \frac{\partial f}{\partial \tau} = \frac{\partial^2 f}{\partial \eta^2} + \eta \frac{\partial f}{\partial \eta} - 2f \quad [17]$$

$$f|_{\eta=\Delta_1} = 0 \quad [18]$$

$$\left. \frac{\partial f}{\partial \eta} \right|_{\eta=0} = -1 \quad [19]$$

$$\left. \frac{d\Delta_1}{d\sqrt{\tau}} + \frac{\Delta_1}{\sqrt{\tau}} = -\frac{\partial f}{\partial \eta} \right|_{\eta=\Delta_1} \quad [20]$$

$$\Delta_1|_{\tau=0} = 0 \quad [21]$$

Equations [14-19] can be transformed into the following to facilitate the computer computation

$$\frac{\Delta_1}{\sqrt{\tau}} + \frac{d\Delta_1}{d\sqrt{\tau}} \left[1 + \frac{\sqrt{\pi\tau} e^{\Delta_1^2}}{[\sqrt{\pi} \Delta_1 e^{\Delta_1^2} \text{erf} \Delta_1 + 1]^3} \right. \\ \left. \left[(\sqrt{\pi} \Delta_1 e^{\Delta_1^2} \text{erf} \Delta_1 + 1) \text{erf} \Delta_1 - \sqrt{\pi} \int_0^{\Delta_1} e^{\eta^2} (\text{erf} \eta)^2 d\eta \right] \right] = \frac{1}{[\sqrt{\pi} \Delta_1 e^{\Delta_1^2} \text{erf} \Delta_1 + 1]} \quad [22]$$

$$f = \eta + \frac{2\Delta_1 e^{\Delta_1^2} \left[\eta \int_0^{\eta} e^{-\eta^2} d\eta + e^{-\eta^2}/2 \right]}{[\Delta_1 \sqrt{\pi} e^{\Delta_1^2} \text{erf} \Delta_1 + 1]} \\ + \epsilon(\tau) \left[[e^{-\eta^2} - \sqrt{\pi} \eta \text{erfc} \eta] \int_0^{\eta} e^{\eta^2} \text{erf} \eta d\eta + \sqrt{\pi} \int_0^{\eta} e^{\eta^2} \text{erfc} \eta \text{erf} \eta d\eta \right] + B[\eta \text{erf} \eta + e^{-\eta^2}/\sqrt{\pi}] \quad [23]$$

where

$$\epsilon(\tau) = \frac{2\sqrt{\tau}}{\sqrt{\pi}} \frac{e^{-\Delta_1^2}}{\left[\Delta_1 \text{erf} \Delta_1 + \frac{e^{\Delta_1^2}}{\sqrt{\pi}} \right]^2} \frac{d\Delta_1}{d\sqrt{\tau}}$$

$$B = \frac{\epsilon(\tau)/2}{\left[\Delta_1 \text{erf} \Delta_1 + \frac{e^{-\Delta_1^2}}{\sqrt{\pi}} \right]} \left[[\sqrt{\pi} \Delta_1 e^{\Delta_1^2} \text{erfc} \Delta_1 - 1] e^{-\Delta_1^2} \int_0^{\Delta_1} e^{\eta^2} d\eta - [\sqrt{\pi} \Delta_1 \text{erfc} \Delta_1 + \sqrt{\pi} \Delta_1 \eta e^{-\Delta_1^2}] \int_0^{\Delta_1} e^{\eta^2} \text{erfc} \eta d\eta + \sqrt{\pi} \Delta_1 \int_0^{\Delta_1} e^{\eta^2} (\text{erfc} \eta)^2 d\eta \right]$$

Equations [22] and [23] were solved on the IBM 360 computer using a standard Runge-Kutta program. The short- and long-time solutions for Δ as a function of τ are given in Fig. 1.

Discussion

One can see from Fig. 1 that for $\tau < 0.01$ we have $\Delta \cong \tau$. As was shown earlier, this linear dependence can be used to characterize a growing porous layer for relatively long real times ($\sim 10^3$ - 10^4 sec). If for this region, $\Delta \cong \tau$, the resistance of the porous layer (small porosity) is the main factor in determining the potential difference between the metal electrode and a reference electrode located just outside the porous layer (at constant current), then one should observe a linear dependence of potential vs. time. Jackson and Blomgren (11) studied the anodic dissolution of lithium in a AlCl₃-propylene carbonate electrolyte solution and observed a growing porous layer of LiCl. Their model assumes a linear growth rate of the porous layer. Using the parameters suggested for their system, τ was found to be ~ 0.01 which justifies the use of the linear growth rate assumption. Using similar parameters for systems studied by Webb, Norton, and Wagner and Haycock, one obtains a value of $\tau < 0.01$ thus justifying their assumption of a linear growth rate of the porous layer.

As shown in Fig. 1, Δ does not become proportional to $\tau^{1/2}$ even for $\tau \sim 100$. Increasing the value of i in the previous example from 10^{-3} to 10^{-1} A/cm² gives $\tau = 10$. This value of τ corresponds to a concentration ~ 0.5 moles/cm³ at the electrode surface, a highly unrealistic number. We may therefore say that the physical properties of the solution are violated long before Δ becomes proportional to $\tau^{1/2}$.

In summary, while there are questions concerning the validity of some of the assumptions made in posing the growing porous model, it is believed that the qualitative description of the phenomena is correct and is in agreement with experimental results. Also a criterion for assuming a linear rate of growth of a porous layer is given by $\tau < 0.01$. The maximum value of τ for which Eq. [15] and [16] remain valid is ~ 0.1 .

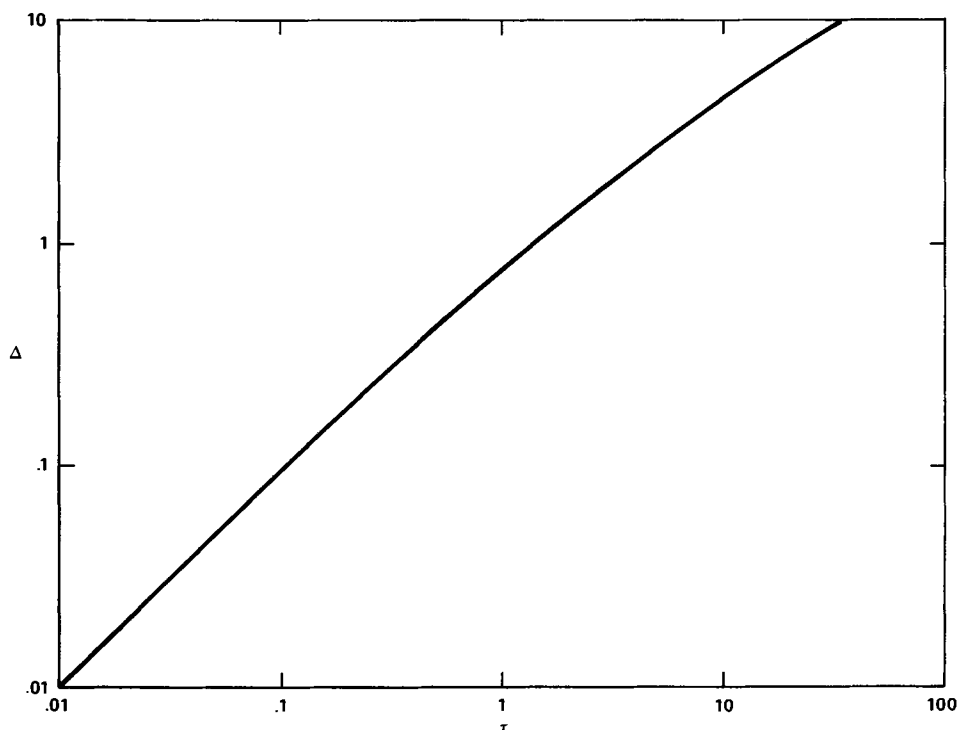
Manuscript submitted June 22, 1971; revised manuscript received ca. Oct. 14, 1971.

Any discussion of this paper will appear in a Discussion Section to be published in the December 1972 JOURNAL.

NOMENCLATURE

c	concentration of precipitate species in solution, moles/cm ³
c_s	saturation concentration of precipitate in solution, moles/cm ³
D	diffusion coefficient, cm ² /sec
\bar{D}	$= D\epsilon^{1.5}$, effective diffusion coefficient in porous medium, cm ² /sec
F	Faraday's constant, 96,493 coulombs/equiv
i	current density, A/cm ²
K	see Eq. [4]

Fig. 1. The dimensionless thickness of the porous layer as a function of dimensionless time.



n number of electrons involved in the electrode reaction
 t time, sec
 X distance from electrode surface, cm
 $x = X/\delta(t)$, dimensionless distance
 δ thickness of porous layer, cm
 $\Delta = \delta(t)K/(1-\epsilon)\rho_m$, dimensionless thickness
 ϵ porosity of porous layer
 $\theta = (c - c_s)\epsilon/K\delta(t)$, dimensionless concentration
 ρ_m density of crystalline precipitate, moles/cm³
 $\tau = \overline{Dt}(K/(1-\epsilon)\rho_m)^2$, dimensionless time
 t_- anion transference number

REFERENCES

- H. S. Carlaw and J. C. Jaeger, "Conduction of Heat in Solids," 2nd ed. Oxford Univ. Press, London and New York (1959).
- A. L. Ruoff, *Quart. Appl. Math.*, **16**, 197 (1958).
- E. L. Knuth, *Phys. Fluids*, **2**, 84 (1959).
- E. L. Knuth, *J. Am. Rocket Soc.*, **32**, 1424 (1962).
- G. T. Horvey, *J. Heat Transfer*, **82**, 37 (1960).
- H. G. Landau, *Quart. Appl. Math.*, **8**, 81 (1950).
- W. F. Ames, "Nonlinear Partial Differential Equations in Engineering," p. 159, Academic Press, New York (1965).
- Kurt Hubber, *This Journal*, **100**, 376 (1953).
- D. A. Vermilyea, *Advan. Electrochem. Electrochem. Eng.*, **3**, 270 (1963).
- M. S. Hunter and P. Fowle, *This Journal*, **101**, 514 (1954).
- G. W. Jackson and G. E. Blomgren, *ibid.*, **116**, 1483 (1969).
- Watt W. Webb, John T. Norton, and Carl Wagner, *ibid.*, 107 (1956).
- E. W. Haycock *ibid.*, **106**, 771 (1959).
- D. Landolt, R. H. Muller, and C. W. Tobias, *ibid.*, **116**, 1384 (1969).
- J. Newman, *Advan. Electrochem. Electrochem. Eng.*, **5**, 87 (1967).

Liquid Ammonia as a Nonaqueous Solvent: The Kinetics of the Pb/Pb²⁺ Exchange

D. Larkin,¹ N. Hackerman,^{*2} A. E. Buck,^{*3} and L. K. Thompson⁴

Department of Chemistry, The University of Texas at Austin, Austin, Texas 78712

ABSTRACT

The exchange reaction at polycrystalline lead electrodes in liquid ammonia at $-45^\circ \pm 1^\circ\text{C}$ has been investigated. At low overpotentials the reaction appears charge transfer controlled. At high overpotentials the reaction is more complex. It is suggested that this is due to the surface being blocked by $\text{Pb}(\text{NH}_3)_2(\text{NO}_3)_2$.

Liquid ammonia has considerable attraction for use as a nonaqueous solvent. It has a sizable temperature range in the liquid phase -33.3° to -77.7°C . It is interesting for electrochemists since its properties are analogous to those of water. Liquid ammonia dissociates in a similar manner to that of water



although its dissociation constant (1,2) $10^{-30 \pm 1}$ is considerably less than that of water 10^{-14} . Ammonium salts act as an equivalent to acids in water and amides as an equivalent to alkalis in water. Also, many common inorganic salts are soluble in liquid ammonia so that the problems of high electrolyte resistance and diffusion resistance are not frequently encountered in electrochemical studies as they frequently are in other nonaqueous solvents.

Liquid ammonia has been used extensively for the preparation of compounds which are either unstable at ambient temperatures or sensitive to water. These preparations have been carried out either electrochemically (3, 4) or chemically (5-7). We became interested in using an electrochemical technique to produce deprotonated species of the type $[\text{M}(\text{L} - \text{H})_x(\text{L})_{y-x}]\text{X}_z$ (where M = transition metal, L - H = deprotonated ligand, L = ligand, X = halide) which have previously been prepared by chemical methods (5-7).

Initial studies by us on the deprotonation of compounds of the above type were complicated by the lack of a suitable reference electrode for use in liquid ammonia. A literature search showed that few electrochemical studies have been made in this solvent. Pleskov and Monosohn (8) first described a Pb/Pb(NO₃)₂ half cell for use as a reference electrode in liquid ammonia. This has reportedly been used successfully by Laitinen and Shoemaker (9) and by Miles and Kellet (10). An electron reference electrode has been used by Hammer and Lagowski (11) while Watt and Sowards (12) describe the use of a Hg/HgCl₂ half cell as a reference electrode for potentiometric titrations. A hydrogen reference electrode has been described by Baldwin and Gill (13) though Herlem (1) indicated that such an electrode was not practical.

We have investigated all these reference electrodes with the exception of the electron electrode. We agree with the findings of Herlem (1) that the hydrogen electrode is not a practical reference electrode in liquid ammonia (the exchange current is too small) while investigations of the Hg/HgCl₂ electrode were incon-

clusive in that it appeared to operate for only a few minutes at a time. The Pb/Pb(NO₃)₂ electrode, however, appears to work well. Therefore it seemed useful to investigate it further and a kinetic study of this electrode is recorded in this paper.

Experimental

Vacuum line.—The vacuum line was evacuated using a rotary vacuum pump. Provision was made on the vacuum line for attaching an electrolytic cell and a cylinder of ammonia. A mercury manometer was used to monitor the pressure in the line. The electrolytic cell, cylinder of ammonia, and the vacuum pump could all be isolated individually from the vacuum line.

The cell.—The electrolytic cell consisted of a single compartment into which could be introduced, test, auxiliary, and reference electrodes. The cell was provided with a means to attach it to the vacuum line and a manometer for monitoring the pressure in the cell.

The electrodes.—The test, auxiliary, and reference electrodes were constructed from polycrystalline lead rod (99.999% supplied by Materials Research Corporation) sheathed in polyethylene. Electrical connections to the electrodes were via platinum wires fused to the lead rod.

The electrical circuit.—The experimental technique used in this study was that of linear sweep voltammetry. This was carried out using a potentiostat based on Philbrick Research K2W Operational amplifiers which were chopper stabilized by Philbrick Research K2PA amplifiers and used in a modified Philbrick Research Operational Manifold 6009. The sweep generator, current follower, and adder were of conventional chopper stabilized design. A Keithley 601B electrometer was used as a voltage follower. Current potential curves were recorded on a Mosley Autograf Model 2DR-2 X-Y recorder.

Experimental procedures.—A known quantity (analytical reagent grade) of lead nitrate and sodium nitrate [a constant concentration (2.0M NO₃⁻) in nitrate being maintained] were placed in the electrolytic cell together with a magnetic stirrer. The test electrodes were prepared by cutting a thin slice from the electrode, so exposing a new surface for every run. The cell and the electrodes were assembled together, connected to the vacuum line and then evacuated for a number of hours before use. During this time the cell was gently heated so as to drive off any water which may have been present. The cell and the vacuum line were then isolated from the vacuum pump and the combined system monitored for any leaks. This was accomplished by observing if there was any fall in the manometer attached to the vacuum line over a period of half an hour. The cell was then immersed in an isoproponyl/CO₂ bath at -70°C and allowed to cool. Ammonia gas was then introduced into the vacuum line from the cylinder of ammonia. The ammonia was twice distilled over potassium before use and condensed in the cell at a pressure of a few centi-

* Electrochemical Society Active Member.

¹ Present address: Department of Chemistry, Georgetown University, Washington, D.C. 20007.

² Present address: Department of Chemistry, Rice University, Houston, Texas 77011.

³ Present address: John Harrison Laboratory of Chemistry, University of Pennsylvania, Philadelphia, Pennsylvania 19104.

⁴ Present address: Department of Chemistry, Memorial University of Newfoundland, St. John's, Newfoundland, Canada.

Key words: liquid ammonia, lead, electrode kinetics.

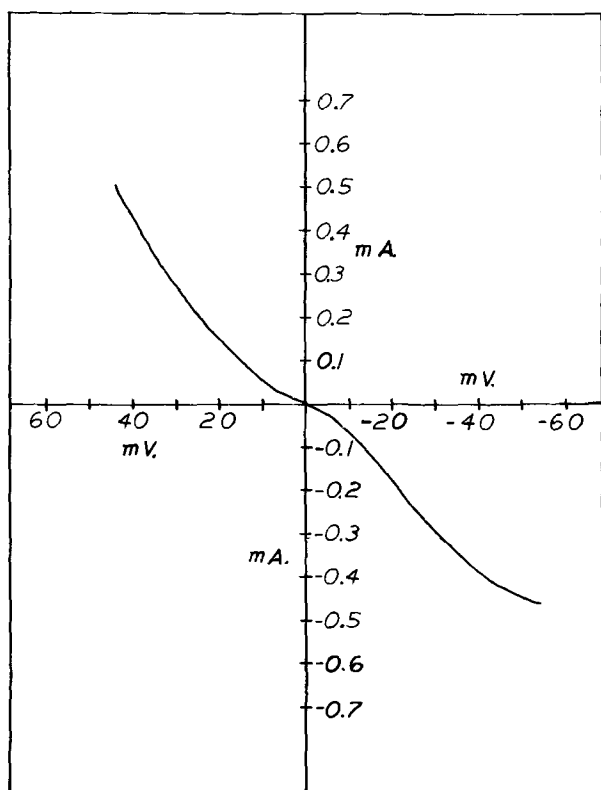


Fig. 1. A typical current density/overpotential curve, 0.5M Pb²⁺, 2.0M NO₃⁻, -45° ± 1°C.

meters less than atmospheric. The liquid ammonia was stirred continuously in the cell during condensation by means of the magnetic stirrer to help the dissolution of the salts. When the required volume of liquid ammonia had been condensed, the ammonia cylinder and the electrolytic cell were isolated from the vacuum system. The vacuum line was then evacuated, the small amount of ammonia left in the system being expelled into the atmosphere. The electrolytic cell was then removed from the vacuum line.

Ohmic resistance.—The contribution of R_E (the ohmic resistance) to the total resistive component of the electrode impedance was made negligible by the cell electrode geometry and could be neglected. Typical values of a few ohms were obtained from impedance measurements.

It was noticed that when the liquid ammonia reached its boiling point, -33.3°C, a white precipitate was obtained from the solution; this was collected and later analyzed.

Results

Figure 1 shows a typical current/voltage curve obtained at a polycrystalline lead electrode in sodium nitrate/lead nitrate/liquid ammonia electrolytes. A study was made of the kinetics of the exchange reaction at low and high overpotentials.

Low overpotentials.—Figure 2 shows a number of scans at different sweep rates. In Fig. 3 are shown a number of current/potential curves at varying lead ion concentrations. In Fig. 4 $\log \text{Pb}^{2+}$ has been plotted against i_0 ,⁵ the slope of the curve gives $\alpha = 0.50$.

High overpotentials.—Figure 5 shows typical anodic Tafel plots obtained at high overpotentials for two different lead concentrations. The slopes of the curves give $\alpha = 0.51 \pm 1$ assuming a two electron transfer. In general at lower lead ion concentrations the Tafel

⁵ i_0 is obtained from the reduced form of the Eyring-Gruz and Volmer equation which at low overpotentials reduces to $i = -i_0 \frac{zF\eta}{RT}$.

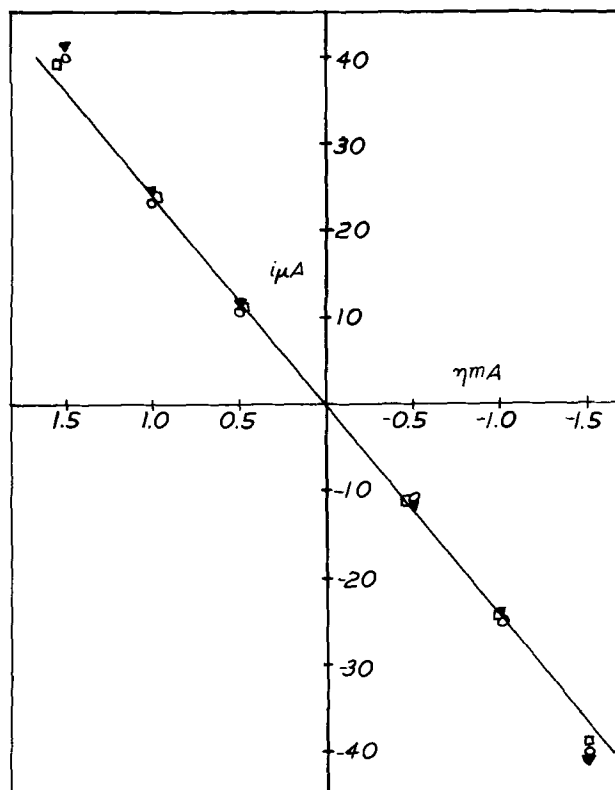


Fig. 2. Current density against overpotential curves at different sweep rates; ○ 0.02 V/min, ▼ 0.16 V/min, □ 0.8 V/min, 2.0M NO₃⁻, 0.7M Pb²⁺, -45° ± 1°C.

region became less distinct. Cathodic plots at high overpotentials did not show a distinct Tafel region. The electrode behaved as if the exchange reaction was slowly being blocked off.

Analysis of the white precipitate.—The white solid precipitated from solution when the temperature of the liquid ammonia reached its boiling point, -33.3°C, was analyzed and found to have the chemical formula Pb(NH₃)₂(NO₃)₂.

Discussion

At low overpotentials the rate-controlling step appears to be the charge transfer reaction



The value of $\alpha = 0.5$ indicates that at low overpotentials the reaction is not complicated by kinetically active adsorbed species (14). At high anodic overpotentials the reaction appears also to be charge transfer controlled. At high cathodic overpotentials (>40 mV from equilibrium) the current appeared to decrease with increasing cathodic potentials. If the electrode was maintained at a constant cathodic potential the current still decreased with time but did not become constant even after many hours. This behavior seems consistent with the electrode reaction being inhibited by some cathodic product blocking the electrode surface [tentatively identified as Pb(NH₃)₂(NO₃)₂, see later].

The exchange reaction at a polycrystalline lead electrode in aqueous solutions has been studied by a number of workers (15-17). They found that at low overpotentials the reaction was charge transfer controlled with an apparent exchange current of 100 mA cm⁻² (0.5M Pb²⁺), an activation energy of 12.6 ± 2 kJ mole⁻¹ and $\alpha = 0.68$. The high α value was attributed to the adsorption of Pb²⁺ ions on the electrode surface. As stated above, the value of $\alpha = 0.5$ obtained in liquid ammonia indicates that in this solvent such adsorption does not occur. If the apparent exchange cur-

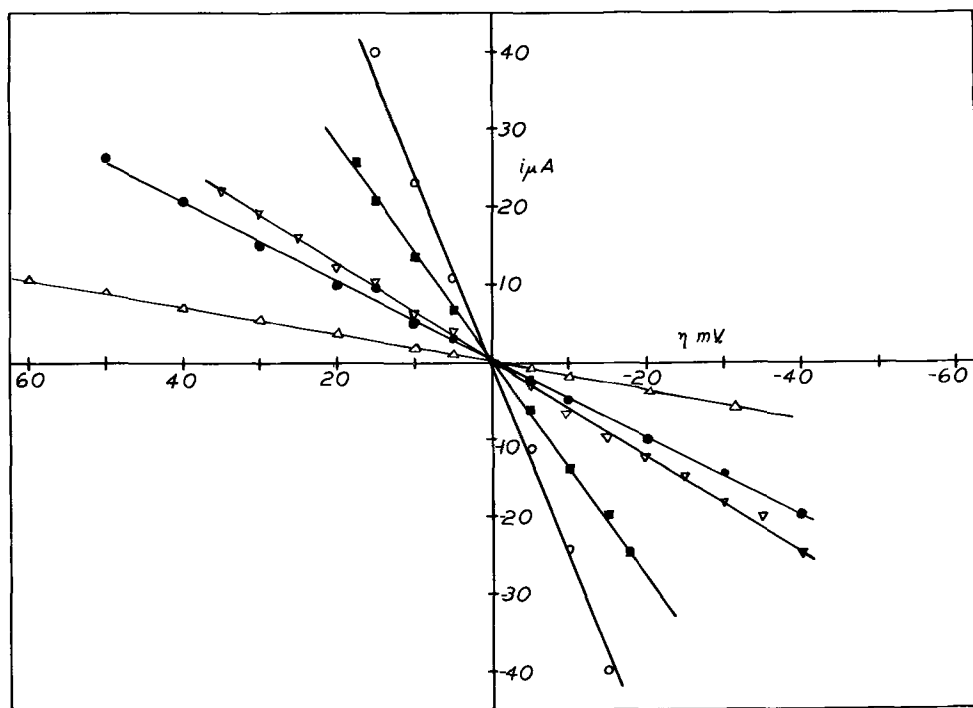


Fig. 3. Current density against overpotential curves at different Pb^{2+} concentrations; \circ 0.7M Pb^{2+} , \blacksquare 0.5M Pb^{2+} , ∇ 0.1M Pb^{2+} , \bullet 0.05M Pb^{2+} , \triangle 0.001M Pb^{2+} , 2.0M NO_3^- , $-45^\circ \pm 1^\circ C$.

rent in both solvents is calculated for the same temperature, a value of 31.0 mA cm^{-2} is obtained at $-45^\circ C$ for the exchange current in the aqueous system and 20.0 mA cm^{-2} for the exchange current in liquid ammonia. This seems to indicate that at low overpotentials the mechanism of the exchange reaction at a polycrystalline lead electrode is not primarily controlled by the solvent but by the surface of the electrode itself.

The white precipitate obtained from solution when the liquid ammonia is allowed to boil has been identified as $Pb(NH_3)_2(NO_3)_2$, showing that the species $Pb(NH_3)^{2+}$ leads to the production of this insoluble salt in liquid ammonia. As divalent lead tends to be either four or six coordinated, we can assume that in solution we have species of the type

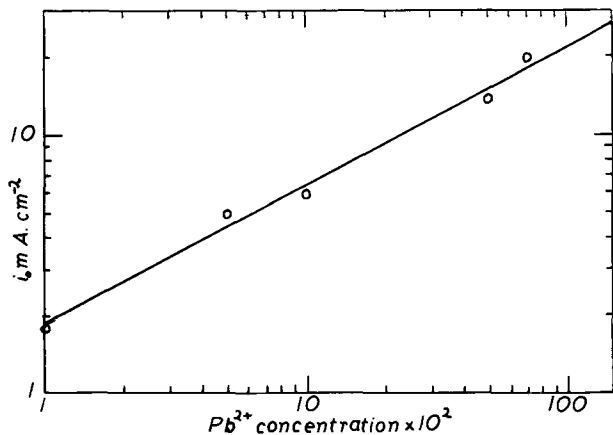
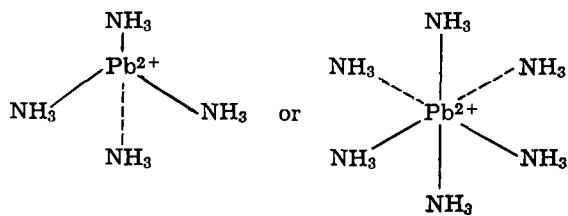


Fig. 4. The variation of exchange current with Pb^{2+} concentration; 2.0M NO_3^- , $-45^\circ \pm 1^\circ C$.

It is suggested that at low overpotentials the lead loses its ammonias of solvation simultaneously so that no species of the type $Pb(NH_3)^{2+}$ are produced while at high cathodic overpotentials the reduction goes via the $Pb(NH_3)^{2+}$ species, causing a solid to form on the electrode and so inhibiting the reaction. Therefore we can write

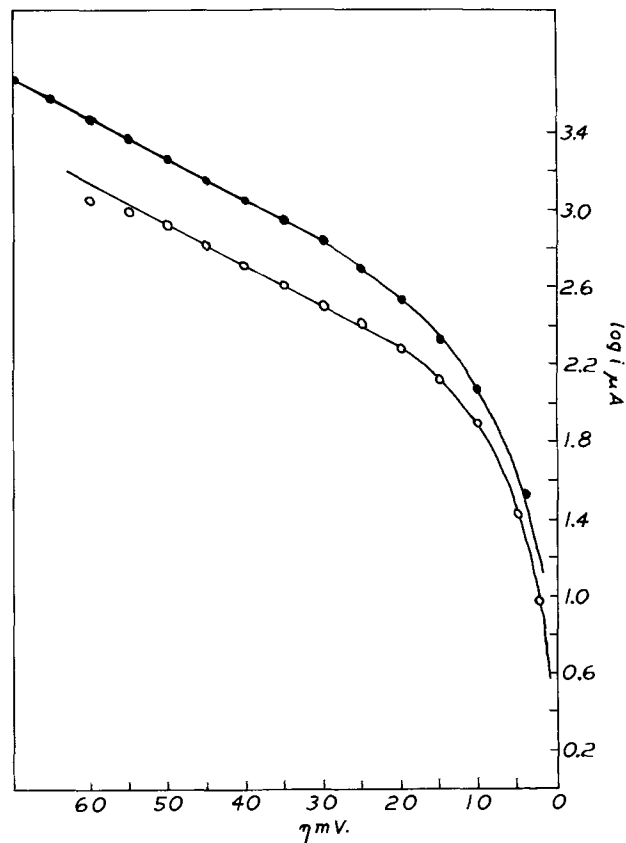
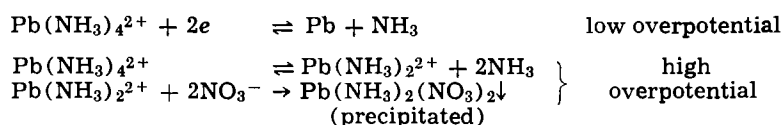


Fig. 5. Anodic Tafel plots obtained at different Pb^{2+} concentrations; \bullet 0.5M Pb^{2+} , \circ 0.05M Pb^{2+} , 2.0M NO_3^- , $-45^\circ \pm 1^\circ C$.



Acknowledgment

The authors wish to thank the Robert A. Welch Foundation of Houston, Texas, for their support of this work.

Manuscript submitted April 1, 1971; revised manuscript received ca. Oct. 4, 1971.

Any discussion of this paper will appear in a Discussion Section to be published in the December 1972 JOURNAL.

REFERENCES

- M. Herlem, *Bull. Soc. Chim.*, 1687 (1967).
- J. Cueilleron and M. Charret, *ibid.*, 802 (1956).
- C. A. Kraus, *J. Am. Chem. Soc.*, **35**, 1732 (1913).
- B. G. Gowenlock and J. Trotman, *J. Chem. Soc.*, 2114 (1957).
- G. W. Watt and P. W. Alexander, *Inorg. Chem.*, **1**, 537 (1968).
- G. W. Watt and D. G. Upchurch, *J. Am. Chem. Soc.*, **90**, 914 (1968).
- G. W. Watt and D. G. Upchurch, *Advan. Chem. Ser.*, **62** (1967).
- V. A. Pleskov and A. M. Monosohn, *Acta Physicochim., U.R.S.S.*, **1**, 871 (1935).
- H. A. Laitinen and C. E. Shoemaker, *J. Am. Chem. Soc.*, **72**, 663 (1950).
- M. H. Miles and P. M. Kellett, *This Journal*, **115**, 1225 (1968).
- R. N. Hammer and J. J. Lagowski, *Anal. Chem.*, **34**, 597 (1962).
- G. W. Watt and D. M. Sowards, *This Journal*, **102**, 545 (1955).
- J. Baldwin and J. B. Gill, *Chem. Comm.*, 1537 (1968).
- J. E. B. Randles, "Trans. Symp. Electrode Processes," 1959 ed., p. 213, Yeager (1961).
- W. Lorenz, *Z. Physik. Chem.*, **19**, 377 (1959).
- N. A. Hampson and D. Larkin, *Trans. Faraday Soc.*, **65**, 1660 (1969).
- S. Haruyama, *J. Electrochem. Soc. Japan*, **35**, 62 (1967).

The Temperature Dependence of Viscosity and Conductivity of Concentrated Aqueous Calcium Nitrate Solutions

J. H. Ambrus*

Naval Ordnance Laboratory, White Oak, Silver Spring, Maryland 20910

and C. T. Moynihan and P. B. Macedo

Vitreous State Laboratory, Catholic University of America, Washington, D. C. 20017

ABSTRACT

Shear viscosities have been measured as a function of temperature for aqueous calcium nitrate solutions in the composition range $R = 4$ -10 ($R =$ moles water/mole salt) over a temperature range from 25°C to as low as -83°C and over a viscosity range from 10^{-1} P to as high as 5×10^7 P. Conductivity measurements are also reported for the solution of composition $R = 8$ over the range 30° to -83°C. As is the case for a wide variety of other liquids, the Fulcher equation is found to give an inadequate description of the temperature dependence of the transport properties of these solutions when applied to data extending over many orders of magnitude, and the transport properties exhibit a tendency to return to Arrhenius behavior at high viscosities. Comparison of the conductivity and viscosity data for the $R = 8$ composition indicates that it is similar to other ionic liquids in that at low viscosities the time scales for viscous flow and for ionic conduction are comparable in magnitude, but that at high viscosities, in the vicinity of the glass transition temperature, the time scale for viscous flow is very much longer than that for conduction.

A characteristic feature of concentrated aqueous electrolyte solutions is their glass-forming ability. Angell and Sare (1) have recently reported glass-forming concentration ranges for a large number of these solutions, along with the corresponding glass transition temperatures, T_g , at which the solution viscosity approaches a value of around 10^{13} P. In some cases these solutions cannot only be quenched to the glassy state, but held in the supercooled state long enough to make physical measurements in the largely unexplored range between the thermodynamic liquidus temperature and the glass transition temperature. Reports of measurements of transport properties of concentrated electrolyte solutions at temperatures

well below room temperature are not uncommon [Garrett and co-workers (2) have carried out measurements as low as -75°C]. However, except for two recent reports (3, 4) on electrical relaxation phenomena near T_g , none of these studies have been carried to sufficiently low temperatures to allow observation of a significant fraction of the huge change in transport properties (as much as fifteen orders of magnitude for viscosity) which occurs between the temperature region of "normal" fluidities and the glass transition region.

As an initial effort in this direction, we report in this paper a study of the temperature dependence of the viscosity of concentrated aqueous calcium nitrate solutions in the glass-forming composition region over a viscosity range from 10^{-1} P to as high as 5×10^7 P. For purposes of comparison, the temperature depen-

* Electrochemical Society Active Member.
Key words: viscosity, conductivity, aqueous solutions, concentrated solutions, glass transition temperature, Fulcher equation.

Table I. Compositions, densities, and glass transition temperatures of calcium nitrate-water solutions

$R \left(\frac{\text{mole water}}{\text{mole salt}} \right)$	$m \left(\frac{\text{mole salt}}{\text{kg water}} \right)$	Density $\left(\frac{g}{\text{cm}^3} \right)$	T_g (K) *
4.018	13.815	$1.770-8.7 \times 10^{-4t}$ ($^{\circ}\text{C}$)	218
6.004	9.245	$1.635-8.6 \times 10^{-4t}$ ($^{\circ}\text{C}$)	195
8.035	6.908	$1.541-8.6 \times 10^{-4t}$ ($^{\circ}\text{C}$)	183
10.026	5.537	$1.480-8.0 \times 10^{-4t}$ ($^{\circ}\text{C}$)	175

* Data from Ref. (1).

dence of the conductivity has also been studied at one composition. Our choice of the calcium nitrate-water system for study was motivated by the relative ease with which these solutions can be supercooled and by their high glass transition temperatures, which lead to the development of high viscosities at temperatures not too greatly removed from ambient. In addition, considerable interest has been exhibited in the transport properties of this system over the past several years (1, 3, 5-13).

Experimental

Sample preparation.—Solutions were prepared from reagent grade calcium nitrate tetrahydrate (Mallinckrodt AR). To remove any insoluble matter capable of acting as nucleation centers for crystallization, the solutions were filtered in a recirculating system containing a Teflon filter of 5 μm pore size (Millipore Corporation). Water content was determined from the weight loss of samples dehydrated at 115 $^{\circ}\text{C}$ and then dried to constant weight at 190 $^{\circ}\text{C}$. Density measurements (see below) were used to cross check the composition of all samples. We will express solution compositions in terms of the molar water to salt ratio, R .

$$R = \text{moles water/mole salt}$$

The actual R values for the solutions studied are given in Table I along with the corresponding molalities. Since the R values are so close to integers, we will subsequently specify solution compositions by R values rounded off to the nearest integer ($R = 4, 6, 8, \text{ or } 10$). T_g values for these solutions taken from the paper of Angell and Sare (1) are also given in Table I.

Temperature control and measurement.—Samples were thermostated in a 4 liter Dewar flask containing either methanol or an ethanol-methanol mixture stirred with a mechanical stirrer. Temperature was controlled to within $\pm 0.01^{\circ}$ above -60°C and to within $\pm 0.05^{\circ}$ below -60°C by periodically adding small amounts of dry ice or liquid nitrogen to the bath. Temperatures were measured to an accuracy of $\pm 0.10^{\circ}\text{C}$ with a calibrated copper-constantan thermocouple whose measuring junction was situated in the bath just outside the sample container. Sufficient time for thermal equilibration was allowed at each temperature before measurements were started. The reproducibility of the data taken over a period of time at the same temperature was considered proof that thermal equilibrium with the bath had been reached.

Density measurements.—Densities of the solutions at 25 $^{\circ}\text{C}$ were measured in a pycnometer and agreed within 0.01% with the density data of Ewing and Mikovsky (14). Densities as a function of temperature were measured over the range -25° –25 $^{\circ}\text{C}$ by means of a calibrated dilatometer and agreed within 0.03% with densities extrapolated linearly from the Ewing and Mikovsky data (14) (measured over the range 25 $^{\circ}$ –60 $^{\circ}\text{C}$). Subsequently the density data were used both to check sample compositions and to calculate densities at temperatures below -25°C by linear extrapolation. Linear density vs. temperature equations for our solutions are given in Table I.

Viscosity measurements.—Viscosities below 200 P were determined with factory-calibrated Cannon-

Fenske capillary viscometers with an inherent accuracy of about $\pm 0.5\%$. Above $10^2 P$ viscosities were measured with a Brookfield Model RVT rotating cylinder viscometer using a 2.2 cm ID cylindrical glass sample container and a 0.32 cm OD stainless steel spindle immersed in the solution to a depth of 5.1 cm. The Brookfield viscometer was calibrated with NBS standard viscosity oils. In the range 10^2 – $10^4 P$ viscosities were measured with the Brookfield viscometer using the rotational method (inherent accuracy $\pm 1\%$). In the range 10^4 to $5 \times 10^7 P$ the decay method was used (inherent accuracy $\pm 2\%$). Weiler *et al.* (15) have described both methods in detail. The principal problem encountered in viscosity measurements at low temperatures was the limited amount of time the solutions could be kept in the supercooled state without crystallizing. With the $R = 8$ solution this problem necessitated frequent remelting of the sample, while with the $R = 4$ and $R = 10$ solutions the tendency of the solutions to crystallize prevented viscosity determinations above 10^4 and $10^1 P$, respectively.

Conductivity measurements.—Conductivities in the range 10^{-1} to $10^{-4} \text{ ohm}^{-1} \text{ cm}^{-1}$ were measured in the frequency region 1–30 kHz with a three-terminal transformer arm ratio bridge (inherent accuracy $\pm 0.5\%$) similar in design to that described by Cole and Gross (16). The conductivity cell used in this range was similar to one described previously (6, 17) and had a cell constant of 214.5 cm^{-1} . The conductivity cell, admittance bridges, and procedure used for measurements in the range 10^{-5} to $10^{-9} \text{ ohm}^{-1} \text{ cm}^{-1}$ have been described elsewhere (3). As is shown in Fig. 1, at the lower end of this range the measured conductivity of the sample exhibits a marked frequency dependence

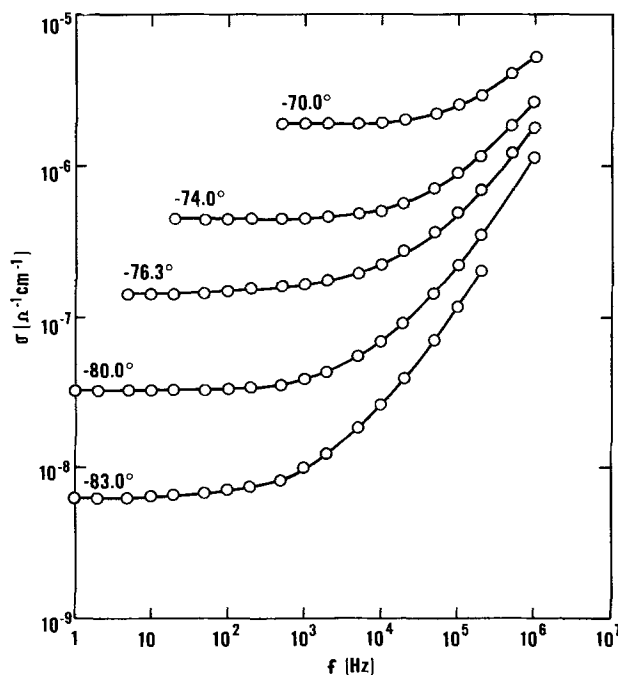


Fig. 1. Frequency dependence of measured conductivity of $\text{Ca}(\text{NO}_3)_2\text{-H}_2\text{O}$ solution, $R = 8$, at low temperatures.

Table II. Shear viscosity and conductivity as a function of temperature for $\text{Ca}(\text{NO}_3)_2\text{-H}_2\text{O}$ solutions

R = 4		R = 6		R = 8			R = 10		
t (°C)	η (P)	t (°C)	η (P)	t (°C)	η (P)	t (°C)	σ (ohm ⁻¹ cm ⁻¹)	t (°C)	η (°C)
-5.0	9.79×10^1	25.0	2.90×10^{-1}	22.6	1.120×10^{-1}	30.5	5.78×10^{-2}	10.0	1.004×10^{-1}
-10.0	2.32×10^2	20.0	3.61×10^{-1}	20.0	1.281×10^{-1}	24.5	5.16×10^{-2}	5.0	1.224×10^{-1}
-15.0	6.50×10^2	15.0	4.63×10^{-1}	10.0	1.907×10^{-1}	17.6	3.98×10^{-2}	0.0	1.512×10^{-1}
-20.0	2.31×10^3	5.0	8.54×10^{-1}	0.0	3.07×10^{-1}	8.3	2.90×10^{-2}	-5.0	1.902×10^{-1}
-25.0	8.4×10^3	0.0	1.198	-10.0	5.49×10^{-1}	0.0	2.02×10^{-2}	-10.0	2.46×10^{-1}
		-5.0	1.747	-15.0	7.87×10^{-1}	-5.0	1.58×10^{-2}	-15.0	3.29×10^{-1}
		-10.0	2.68	-20.0	1.155	-10.0	1.27×10^{-2}	-20.0	4.54×10^{-1}
		-15.0	4.39	-25.0	1.810	-15.0	9.34×10^{-3}	-25.0	6.50×10^{-1}
		-20.0	7.61	-30.0	3.01	-19.0	7.11×10^{-3}	-30.0	9.91×10^{-1}
		-25.0	1.516×10^1	-35.0	5.47	-25.0	4.46×10^{-3}	-35.0	1.592
		-30.0	3.27×10^1	-39.5	9.80	-30.0	2.91×10^{-3}	-40.0	2.79
		-35.0	8.23×10^1	-44.8	2.33×10^1	-35.0	1.77×10^{-3}	-50.0	1.074×10^1
		-40.0	2.47×10^2	-50.3	6.65×10^1	-40.0	9.97×10^{-4}		
		-45.0	6.81×10^2	-55.0	1.670×10^2	-45.0	5.10×10^{-4}		
		-50.0	3.05×10^3	-62.3	9.13×10^2	-50.0	2.35×10^{-4}		
		-55.0	1.77×10^4	-70.0	1.87×10^4	-66.0	6.3×10^{-6}		
		-57.5	5.2×10^4	-71.0	3.44×10^4	-70.0	1.92×10^{-8}		
		-60.6	1.60×10^5	-72.4	5.4×10^4	-74.0	4.5×10^{-7}		
		-61.0	2.64×10^5	-73.0	8.0×10^4	-76.3	1.44×10^{-7}		
		-62.0	4.28×10^5	-74.0	1.43×10^5	-80.0	3.3×10^{-8}		
		-63.0	7.4×10^5	-75.0	1.88×10^5	-83.0	6.3×10^{-9}		
		-64.0	1.27×10^6	-76.0	3.62×10^5				
		-65.0	2.25×10^6	-77.0	7.3×10^5				
		-66.0	3.92×10^6	-77.7	9.2×10^5				
		-67.0	7.8×10^6	-79.1	2.12×10^6				
		-68.0	1.52×10^7	-80.0	4.3×10^6				
		-69.0	2.77×10^7	-81.0	7.5×10^6				
		-70.0	5.5×10^7	-82.0	2.13×10^7				
				-82.7	3.45×10^7				

in the audio region due to relaxation processes in the solution (3,4), so that determination of the limiting low frequency conductivity at the lowest temperatures required measurements at frequencies as low as 1 Hz.

At all temperatures the over-all accuracy which may be claimed for our viscosity and conductivity measurements is primarily determined by the temperature dependence of the transport properties and the accuracy of the temperature determination (± 0.10). In the vicinity of room temperature, this temperature-induced uncertainty is in the range of 0.3-0.6%, but it rises to 5-8% in the vicinity of the lowest temperatures (around -80°C) at which measurements were performed.

Results and Discussion

Our experimental values for the shear viscosities, η , of solutions of composition $R = 4, 6, 8,$ and 10 and

specific conductances, σ , for the $R = 8$ composition are given in Table II.

In Fig. 2 and 3, Arrhenius plots are shown for the shear viscosities and the conductivity. As is the usual case for liquids in this viscosity range, these plots are curved in a direction corresponding to an increase in the apparent activation energy with decreasing temperature, where apparent activation energy, E , is defined by

$$E/R = \partial \ln w / \partial (1/T) \quad [1]$$

where w is a transport property such as η or $1/\sigma$, and R is the ideal gas constant. We have calculated apparent activation energies as a function of temperature for viscosity and conductivity from the slopes of least-squares fits of the data to equations cubic in $(1/T)$. These are plotted in Fig. 4. (The E vs. T plot for η at $R = 10$, which lies atop the E vs. T plot for $(1/\sigma)$

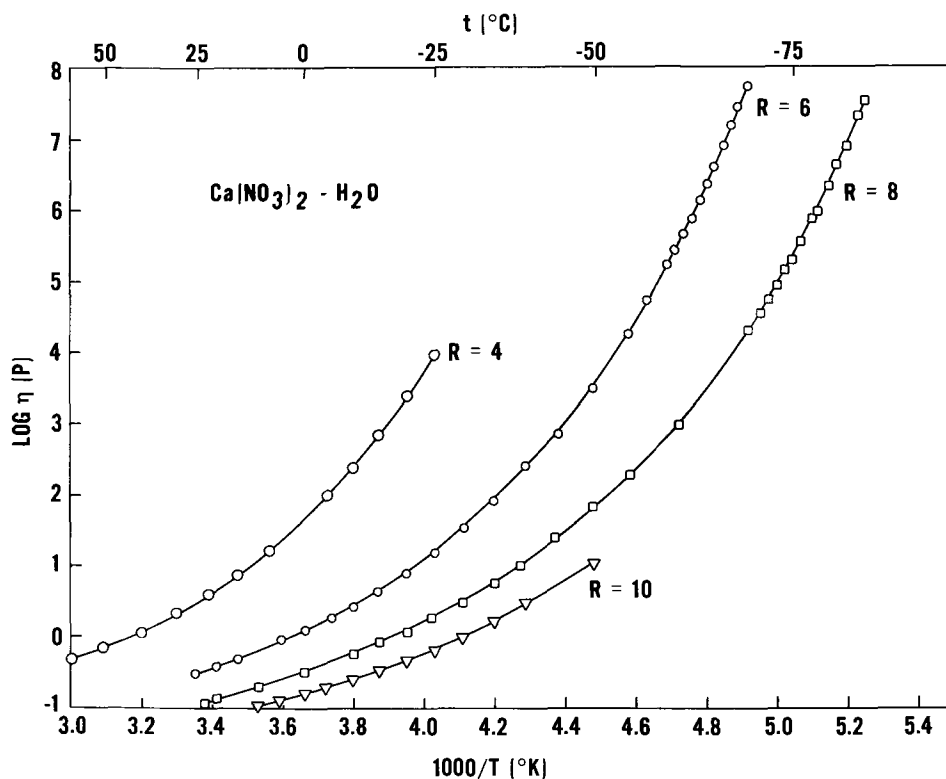


Fig. 2. Arrhenius plots of shear viscosity for aqueous calcium nitrate solutions.

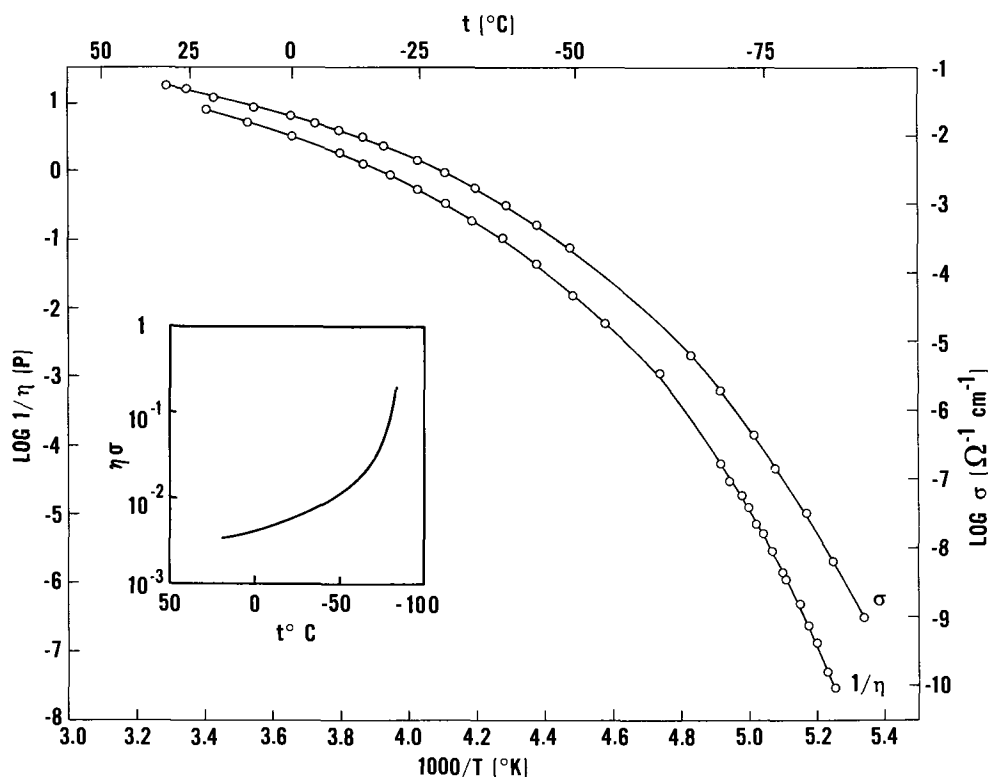


Fig. 3. Arrhenius plots of shear viscosity and conductivity for $\text{Ca}(\text{NO}_3)_2\text{-H}_2\text{O}$ solution, $R = 8$. Inset: Viscosity-conductivity product as a function of temperature.

at $R = 8$ has been omitted for clarity.) As may be seen from Fig. 2-4, the transport properties of these solutions become extremely temperature dependent at high viscosities so that at the highest viscosities for which measurements were performed the viscosity changes by an order of magnitude in only three to four degrees.

During the past several years the non-Arrhenius temperature dependence of concentrated aqueous electrolyte solutions in the viscosity range 10^{-1} to 10^1 P has frequently been accounted for in terms of the Fulcher equation (5-13)

$$\ln w = A + B/(T - T_0) \quad [2]$$

where A , B , and T_0 are empirical parameters. The T_0 has been interpreted as a zero-mobility temperature at which the free volume (18) or configurational entropy (19) of the liquid would vanish at equilibrium. In Table III are shown the Fulcher equation parameters obtained from least-squares fits of the viscosity or conductance data for each solution over the entire temperature range available. In the cases in which

the data cover an extensive range (η for $R = 6$ and 8 and $1/\sigma$ for $R = 8$), the standard deviations of $\ln w$ from the best-fit Fulcher equations lie outside the estimated uncertainties in the precision of our measurements. (Note that standard deviation $\ln w \approx |\Delta w/w| \text{ avg} \approx (1/100) \text{ avg \% error in } w$.) Hence the Fulcher equation does not give a good description of the transport properties of concentrated aqueous electrolyte solutions over extended ranges. To confirm this, we divided the data for each solution into subsets corresponding roughly to the viscosity ranges 10^{-1} to 10^1 , 10^1 to 10^4 , and 10^4 to 10^8 P and fit each subset to the Fulcher equation. These results are also shown in Table III and in all cases the standard deviations are consistent with the estimated precision of our data. Thus the Fulcher equation, as a smoothing function for transport property-temperature data, should not be applied over ranges covering more than about three orders of magnitude in the transport property.

It is noteworthy that for each solution, as one proceeds to higher and higher viscosity ranges, the T_0 value obtained from the Fulcher equation-fit in that range progressively decreases. The apparent activation

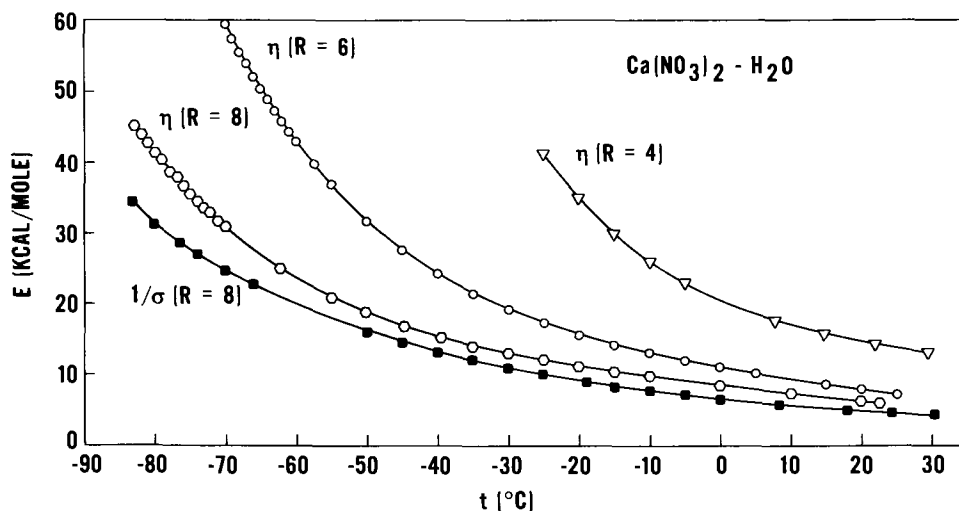


Fig. 4. Apparent activation energy as a function of temperature for transport properties of concentrated $\text{Ca}(\text{NO}_3)_2\text{-H}_2\text{O}$ solutions.

Table III. Best fit Fulcher equation parameters for $\text{Ca}(\text{NO}_3)_2\text{-H}_2\text{O}$ solutions over various viscosity and temperature ranges

Property w	R	Approx. range in η (P)	Temp. range ($^{\circ}\text{C}$)	A	B	T_0	Std. dev. in w
η (P)	4	$10^{-1}\text{-}10^{1*}$	7 to 70	-5.875	633.2	207	0.002
		$10^1\text{-}10^4$	-25 to 7	-9.507	1163.2	185.5	0.030
η (P)	6	$10^{-1}\text{-}10^1$	-25 to 70	-6.522	746.7	200.5	0.061
		$10^{-1}\text{-}10^1$	-25 to 25	-6.227	564.0	185	0.011
		$10^1\text{-}10^4$	-55 to -25	-8.541	881.2	170	0.052
η (P)	8	$10^4\text{-}10^8$	-70 to -55	-15.013	1516.3	157	0.025
		$10^{-1}\text{-}10^5$	-70 to 25	-8.073	845.0	170.8	0.108
		$10^{-1}\text{-}10^1$	-40 to 23	-6.558	541.1	172.5	0.011
		$10^1\text{-}10^1$	-70 to -40	-6.684	612.2	166	0.089
η (P)	10	$10^4\text{-}10^8$	-83 to -70	-7.201	722.4	161	0.095
		$10^{-1}\text{-}10^8$	-83 to 23	-7.805	738.3	161.2	0.116
		$10^{-1}\text{-}10^1$	-50 to 10	-6.809	496.0	168	0.008
$1/\sigma$ ($\text{ohm}^{-1}\text{ cm}^{-1}$)	4	$10^{-1}\text{-}10^{1*}$	5 to 70	-0.712	566.8	204	0.003
$1/\sigma$ ($\text{ohm}^{-1}\text{ cm}^{-1}$)	8	$10^{-1}\text{-}10^1$	-40 to 31	-0.625	449.8	173.5	0.016
		$10^1\text{-}10^1$	-70 to -40	-3.530	829.9	153.5	0.026
		$10^4\text{-}10^8$	-83 to -70	-12.275	1810.0	132	0.072
		$10^{-1}\text{-}10^8$	-83 to 31	-2.050	684.4	157.8	0.132

* Data from Ref. (6).

energy in terms of the Fulcher equation parameters is

$$E/R = BT^2/(T - T_0)^2$$

so that a decrease in T_0 indicates a reversion to Arrhenius behavior (constant E , corresponding to $T_0 = 0$) of the transport property in question. Hence these concentrated electrolyte solutions exhibit the same tendency to revert to Arrhenius behavior at very high viscosities that has been noted for a wide variety of other glass-forming liquids (20). In this respect it is also noteworthy that the rate of decrease of the apparent T_0 value with increasing viscosity is smaller for the less concentrated solutions, so that the more dilute solutions tend to revert to Arrhenius behavior at higher viscosities than do the more concentrated solutions.

Recently Tweer *et al.* (20) have proposed a theory (the "environmental relaxation model") for the temperature dependence of liquid transport properties over extensive viscosity ranges. The theory successfully predicts the occurrence of Arrhenius behavior at the high and low temperature viscosity extremes, along with an intermediate region of varying activation energy, by relating the temperature dependence of the apparent activation energy to the temperature dependence of the range of the local liquid microstructure. Tweer *et al.* (20) have also derived from the environmental relaxation model a semiempirical equation containing five adjustable parameters for the temperature dependence of liquid transport properties. Our present data do not cover a sufficient range to allow an unambiguous determination of these five parameters, which are highly interdependent. Hence we will not attempt at present any quantitative expression of our results in terms of the environmental relaxation model, but rather merely point out their qualitative accord with this theory.

Figure 5 shows isothermal logarithmic plots of viscosity *vs.* mole per cent salt. The large composition dependence of transport properties of these solutions and the increase in composition dependence with decreasing temperature has been noted previously by Angell (7, 8). Angell also noted that the isothermal composition dependence of the transport properties at temperatures above 0°C may be expressed simply in terms of the apparent composition dependence of the Fulcher equation T_0 parameter. In support of this correlation Angell and co-workers (9, 12) have noted that the measured T_0 and the Fulcher equation T_0 derived from data in the 10^{-1} to 10^1 P viscosity range show identical composition dependences. Our present measurements are in accord with this finding, the T_g/T_0 ratio being constant at 1.05 ± 0.01 over the composition range $R = 4\text{-}10$ for T_0 values extracted from data in the lowest viscosity region. For the higher viscosity ranges, however, the T_g/T_0 ratio is

no longer composition independent, so that it seems unlikely that Angell's treatment of the composition dependence of the transport properties of these solutions will be valid in these regions.

In the inset of Fig. 3 the $\eta\sigma$ product for the $R = 8$ solution has been plotted *vs.* temperature. The remarkable feature of this plot is the sharp upward bend in the $\eta\sigma$ curve at the lowest temperatures. This feature is also revealed in Fig. 4 in terms of the large differences in the viscosity and conductivity apparent activation energies at the lowest temperatures and in Table III in the more rapid decrease (with increasing viscosity) of the apparent T_0 value for conductivity relative to that for viscosity. In this respect, the $R = 8$ calcium nitrate-water solution is strikingly similar to the fused nitrate system $0.4\text{ Ca}(\text{NO}_3)_2\text{-}0.6\text{ KNO}_3$ (20, 21), in which the viscosity to conductivity apparent activation energy ratio, E_η/E_σ , was constant at about 1.29 up to a viscosity of about 10^4 P, then rose gradually with decreasing temperature, finally leveling off at a value of about 1.85 near T_0 . In the present case of the $R = 8$ calcium nitrate solution, E_η/E_σ is roughly constant at about 1.18 at higher temperatures, but, like the fused salt, begins to increase with decreasing temperature at a viscosity of about 10^4 P. Tweer *et al.* (20) have shown that in terms of the environmental relaxation model the observed temperature dependence of the E_η/E_σ ratio for the above mentioned nitrate melt (and hence also for the $\text{Ca}(\text{NO}_3)_2$

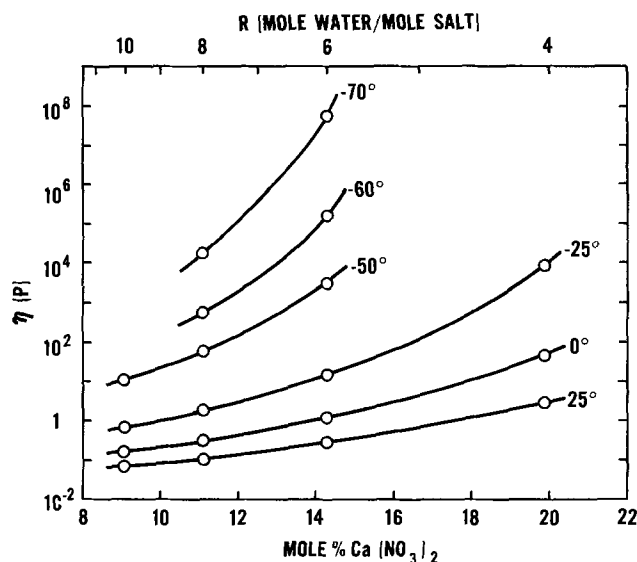


Fig. 5. Composition dependence of shear viscosity of $\text{Ca}(\text{NO}_3)_2\text{-H}_2\text{O}$ solutions.

$R = 8$ solution) may be interpreted in terms of differences in the ranges or distances over which the ionic conductivity and viscous flow processes are affected by the local liquid microstructure.

Both viscous flow and ionic conduction may be described in terms of characteristic relaxation times. For viscous flow the appropriate relation is (22)

$$\eta = G_{\infty} \langle \tau_s \rangle$$

where $\langle \tau_s \rangle$ is the average shear relaxation time and G_{∞} the limiting high frequency or "solid-like" shear modulus of the liquid. For ionic conductivity the relation is (3, 4, 23)

$$\sigma = \epsilon_0 \epsilon_s / \langle \tau_{\sigma} \rangle$$

where $\langle \tau_{\sigma} \rangle$ is the average conductivity relaxation time, ϵ_0 is the permittivity of free space ($8.854 \times 10^{-14} F cm^{-1}$), and ϵ_s is the relative permittivity or dielectric "constant" of the liquid arising from polarization processes not involved in long range charge transport. While G_{∞} and ϵ_s are in general temperature dependent, their variations with temperature are expected to be negligible compared to the order-of-magnitude changes encountered in σ and η . Reasonable "figure-of-merit" values for G_{∞} and ϵ_s are

$$G_{\infty} \sim 2 \times 10^{10} \text{ dyne cm}^{-2}$$

$$\epsilon_s \sim 10$$

so that to estimate the shear to conductivity relaxation time ratio we may use

$$\langle \tau_s \rangle / \langle \tau_{\sigma} \rangle = \eta \sigma / (G_{\infty} \epsilon_0 \epsilon_s) \sim 5 \times 10^1 \eta \sigma$$

In the temperature interval 25° to $-60^{\circ}C$ for the $Ca(NO_3)_2$ $R = 8$ solution, the $\eta \sigma$ product is (within a factor of two about 1×10^{-2} , which gives a $\langle \tau_s \rangle / \langle \tau_{\sigma} \rangle$ ratio of 0.5, i.e., approximately unity. Hence at high temperatures and low viscosities the time scales for the ionic conduction process and for the structural rearrangements involved in the viscous flow process are of similar magnitude, which is in turn the basis for the approximate validity of the Stokes-Einstein and the Nernst-Einstein relations in the highly fluid region of the liquid. As indicated in the inset of Fig. 3, however, the $\eta \sigma$ product begins to increase rapidly with decreasing temperature at viscosities above $10^4 P$, leading to a similar marked rise in the $\langle \tau_s \rangle / \langle \tau_{\sigma} \rangle$ ratio. At the lowest temperature for which data are available for the $Ca(NO_3)_2$ $R = 8$ solution the estimated $\langle \tau_s \rangle / \langle \tau_{\sigma} \rangle$ ratio has risen to about 15 and, judging from the temperature dependences of η and σ in this region, probably attains a value of at least 10^4 at T_g . The $\langle \tau_s \rangle / \langle \tau_{\sigma} \rangle$ ratio at T_g for the fused calcium-potassium nitrate mixture (21) is also around 10^4 . Hence near T_g ionic conduction in these liquids does not require simultaneous structural rearrangements of the liquid quasi-lattice. Such a phenomenon could be explained if the cations were considerably more mobile than the anions or *vice versa*, since viscous flow would require motion of both types of ions, while conduction would presumably involve primarily displacement of the more mobile ionic species. Thus a $\langle \tau_s \rangle / \langle \tau_{\sigma} \rangle$ ratio much greater than unity would be expected for alkali silicate melts, where charge would be transported by the alkali ion moving through a network formed by the large, multiply charged silicate ions. It is somewhat surprising, however, to find this in simpler ionic liquids, such as $Ca(NO_3)_2$ - H_2O solutions or $Ca(NO_3)_2$ - KNO_3 melts, where neither the cation nor the anion is incorporated into a covalently bonded network. Nonetheless on the basis of the two systems which have been investigated so far, we speculate that the occurrence of a $\langle \tau_s \rangle / \langle \tau_{\sigma} \rangle$ ratio near T_g which is substantially greater than unity is probably a general feature of all highly concentrated ionic conductors.

Previous interpretation of the Fulcher equation T_o parameter as an equilibrium property of a liquid had led Moynihan, Angell, and their co-workers (6, 12, 13,

24) to suggest that the T_o parameter should be the same for all transport properties of the same liquid. As may be seen from the T_o parameters for η and $(1/\sigma)$ for the $R = 4$ and 8 solutions in Table III, this is true within experimental uncertainty for the viscosity range 10^{-1} to $10^1 P$, but, as is shown for the $R = 8$ solution, ceases to hold true at higher viscosities. Results of the same sort were obtained from a comparison of viscosity and conductance for the nitrate melt $0.4 Ca(NO_3)_2$ - $0.6 KNO_3$ (21).

Conclusion

The present results for transport properties of concentrated aqueous $Ca(NO_3)_2$ solutions indicate the failure of the Fulcher equation to adequately account for the data over extensive ranges in viscosity, as has recently been found to be the case for a wide variety of other liquids (15, 20, 21, 25). These solutions also exhibit the general tendency to revert to Arrhenius behavior at high viscosities. At temperatures near T_g the large differences in the temperature dependences of the viscosity and conductivity lead to the conclusion that in the glass transition region there must be a large difference between the time scales for ionic conduction and for viscous flow. In the future we hope to report extensive results of ultrasonic and electrical relaxation experiments for these solutions to provide a quantitative comparison of the structural and electrical relaxation times.

Acknowledgments

The authors wish to thank Mr. K. Strom for assistance with the viscosity measurements and Mr. J. Costa and Mr. V. Provenzano for assistance with the conductivity measurements. This research was supported by the Naval Ordnance Laboratory's Independent Research Program and by a Themis Grant from the Office of Naval Research.

Manuscript submitted May 28, 1971; revised manuscript received ca. Oct. 8, 1971.

Any discussion of this paper will appear in a Discussion Section to be published in the December 1972 JOURNAL.

REFERENCES

1. C. A. Angell and E. J. Sare, *J. Chem. Phys.*, **52**, 1058 (1970).
2. A. B. Garrett, J. Welsh, S. Woodruff, R. Cooper, and J. Heiks, *J. Phys. Chem.*, **53**, 505 (1949); A. B. Garrett and S. A. Woodruff, *ibid.*, **55**, 477 (1951); F. Rakowsky and A. B. Garrett, *This Journal*, **101**, 117 (1954).
3. J. H. Ambrus, C. T. Moynihan, and P. B. Macedo, *J. Phys. Chem.*, In press.
4. C. T. Moynihan, R. D. Bressel, and C. A. Angell, *J. Chem. Phys.*, In press.
5. C. A. Angell, *This Journal*, **112**, 1224 (1965).
6. C. T. Moynihan, *J. Phys. Chem.*, **70**, 3399 (1966).
7. C. A. Angell, *ibid.*, **70**, 3988 (1966).
8. C. A. Angell, *J. Chem. Phys.*, **46**, 4673 (1967).
9. C. A. Angell, E. J. Sare, and R. D. Bressel, *J. Phys. Chem.*, **71**, 2759 (1967).
10. J. Braunstein, L. Orr, A. R. Alvarez-Funes, and H. Braunstein, *J. Electroanal. Chem.*, **15**, 337 (1968).
11. G. S. Darbari and S. Petrucci, *J. Phys. Chem.*, **73**, 921 (1969).
12. C. T. Moynihan, C. R. Smalley, C. A. Angell, and E. J. Sare, *ibid.*, **73**, 2287 (1969).
13. C. T. Moynihan and C. A. Angell, *ibid.*, **74**, 736 (1970).
14. W. W. Ewing and R. J. Mikovsky, *J. Am. Chem. Soc.*, **72**, 1390 (1950).
15. R. Weiler, S. Blaser, and P. B. Macedo, *J. Phys. Chem.*, **73**, 4147 (1969).
16. R. H. Cole and P. M. Gross, *Rev. Sci. Instr.*, **20**, 252 (1949).
17. C. T. Moynihan, *J. Chem. Educ.*, **44**, 531 (1967).
18. M. H. Cohen and D. Turnbull, *J. Chem. Phys.*, **31**, 1164 (1959).
19. G. Adam and J. H. Gibbs, *ibid.*, **43**, 139 (1965).
20. H. Tweer, J. H. Simmons, and P. B. Macedo, *ibid.*, **54**, 1952 (1971).
21. R. Bose, R. Weiler, and P. B. Macedo, *Phys. Chem. Glasses*, **11**, 117 (1970).

22. T. A. Litovitz and C. M. Davis, in "Physical Acoustics," Vol. IIA, pp. 281-349, W. P. Mason, Editor, Academic Press, New York (1965).
23. P. B. Macedo, R. Bose, and T. A. Litovitz, *J. Chem. Phys.*, Submitted for publication.
24. C. A. Angell and C. T. Moynihan, in "Molten Salts: Characterization and Analysis," pp. 315-375, G. Mamantov, Editor, Marcel Dekker, Inc., New York (1969).
25. P. B. Macedo and A. Napolitano, *J. Chem. Phys.*, **49**, 1887 (1968).

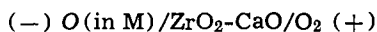
Voltammetric Determination of Oxygen in Liquid Metals Using Solid Oxide Electrolytes

T. H. Etsell* and S. N. Flengas*

Department of Metallurgy and Materials Science, University of Toronto, Toronto, Ontario, Canada

ABSTRACT

Dissolved oxygen was electrochemically reduced in cells of the type

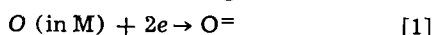


where *M* was either silver or copper. Impervious $\text{ZrO}_2 + 10$ m/o (mole per cent) CaO electrolyte tubes were immersed in the liquid metal. The dependence of current on immersion depth, applied potential, time, dissolved oxygen concentration, temperature, and the amplitude and frequency of vibration of the electrolyte was studied. The electrode reactions are reversible. At sufficiently high applied potentials, diffusion overpotential appears at the liquid metal electrode and, for small depths of immersion, limiting currents are eventually realized. They are directly proportional to the concentration of dissolved oxygen meaning that voltammetric measurements could be used to determine the dissolved oxygen content of liquid metals. This proportionality was verified from 0.002 to 0.15 a/o (atomic per cent) O in silver between 1000° and 1200°C and from 0.005 to 0.13 a/o O in copper between 1100° and 1300°C. Effective diffusion layer thicknesses are about 0.05 cm.

Electromotive force measurements on oxygen concentration cells with solid oxide electrolytes have been used for the *in situ* determination of dissolved oxygen in many liquid metals and alloys. For instance, results have been reported on the activity of oxygen in liquid silver (1-3) and copper (3-21). In several investigations, values for the solubility limit of oxygen in liquid copper were concurrently determined (6, 7, 10).

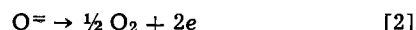
An earlier paper concerning the behavior of the liquid silver electrode during current flow (22) indicated the feasibility of analyzing liquid metals for dissolved oxygen using a voltammetric technique. This method depends upon the establishment of limiting currents at the metal-electrolyte interface during the electrochemical removal of oxygen from the liquid metal. The conditions necessary to observe limiting currents were defined in this investigation. The influence of the depth of immersion of the electrolyte tube is discussed in detail, and current-potential and current-time characteristics are shown. Results are given which relate the dissolved oxygen concentration to the limiting current density over a wide range of oxygen contents for both silver and copper.

The principle of the oxygen concentration cell when current is passed with the liquid metal electrode as the cathode is illustrated in Fig. 1 (O symbolizes dissolved oxygen in the figures). At the metal-electrolyte interface, dissolved oxygen (existing in solution as atoms or anions) is reduced according to



Hence, liquid metals can be electrolytically deoxidized, e.g., copper (23, 24). When the applied potential is high enough to lower the dissolved oxygen concentration at the interface below the bulk concentration, oxygen passes through a diffusion layer, which appears in the

liquid metal, in order to reach the interface. If the interfacial concentration becomes negligible with respect to the bulk concentration, limiting currents, controlled by diffusion and convection, will be observed. Forced convection in the metal results from vibrating the electrolyte, as indicated. As a consequence, the diffusion layer is set up more quickly and is more stable. Oxygen ions are transported through the solid electrolyte and are oxidized at the Pt, O_2 anode via the reaction



Experimental

The cell design used for the reported measurements is shown in Fig. 2. The electrolyte was an impervious tube of $\text{ZrO}_2 + 10$ m/o CaO , closed flat at one end. The inner surface of the closed end had been platinized by applying drops of a 5-10% chloroplatinic acid solution and decomposing the solution at 600°-700°C. The electrolyte tube was 24 in. long with a nominal ID of $\frac{3}{8}$ in. and OD of $\frac{1}{2}$ in.

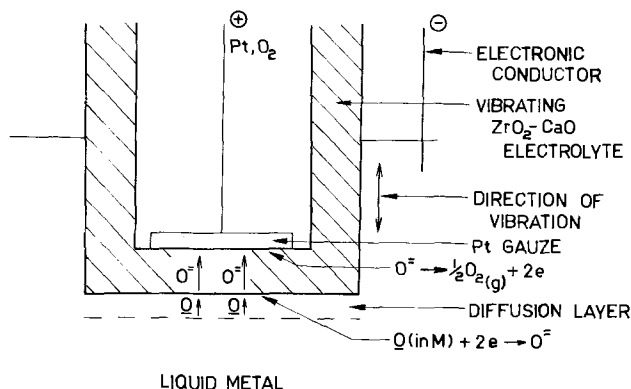


Fig. 1. Principle of the voltammetric determination of oxygen in liquid metals.

* Electrochemical Society Active Member.

Key words: solid electrolytes, zirconia, oxygen determination, voltammetry, limiting currents, diffusion overpotential, liquid metals, silver, copper.

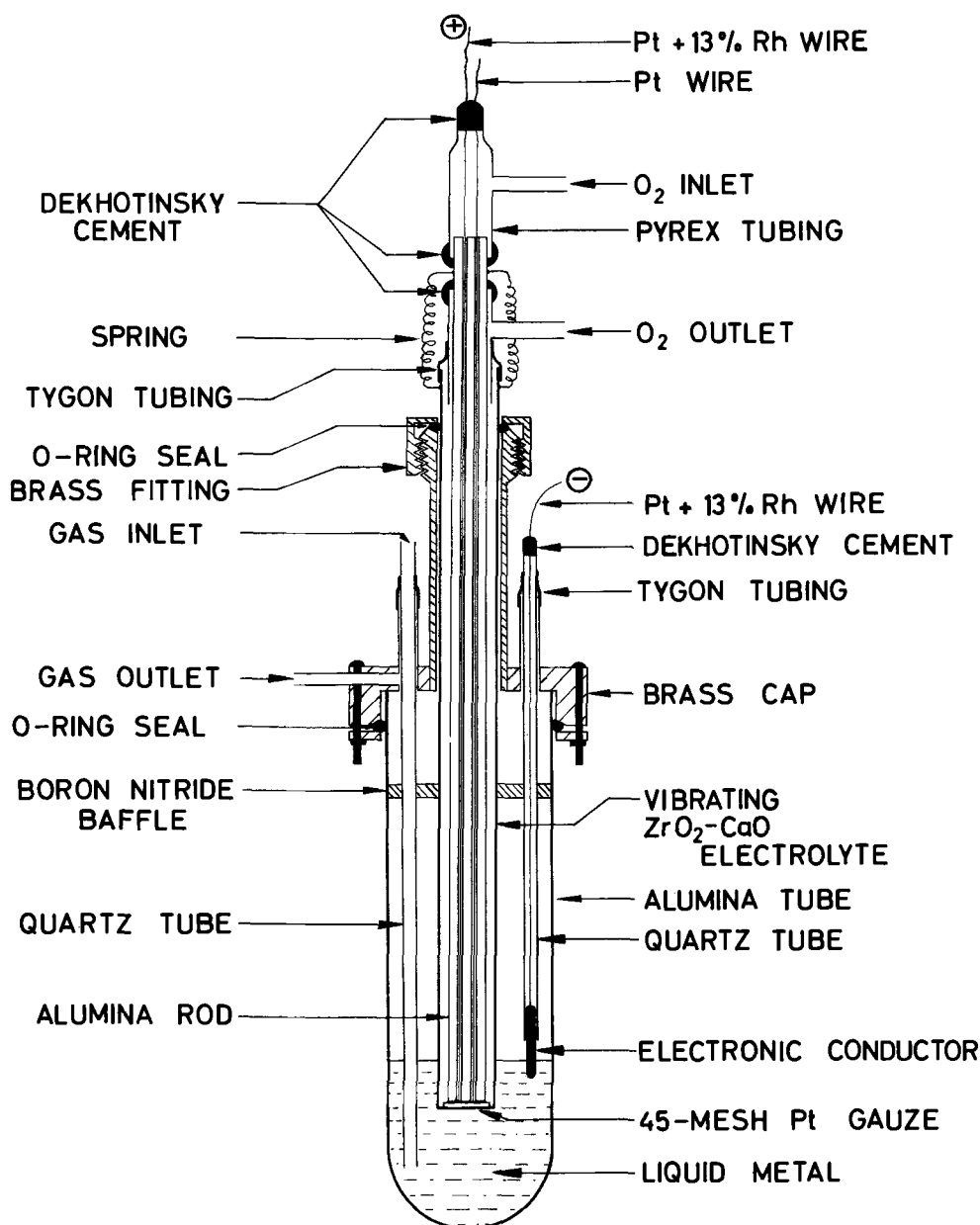


Fig. 2. Oxygen concentration cell.

The liquid metal was contained inside an alumina tube having a hemispherical closure which was 18 in. long with an ID of 1-1/16 in. and OD of 1-5/16 in. Enough 99.999+ % metal shot was initially added so that the liquid would have a height of 1 1/2 in.—175g of silver or 150g of copper.

To serve as a conducting lead for establishing electrical contact with the liquid metal, a 2 in. length of 0.057 in. Chromel A wire (80% Ni, 20% Cr) for the silver experiments and of 0.105 in. stainless steel wire (Type 314) for copper were used. The lead was spot-welded to a piece of 0.020 in. Pt + 13% Rh wire. Since the joint was in the hot zone, thermoelectric forces were virtually eliminated. The lead wire was held in a 4 mm OD quartz tube. (For copper, this tube was joined to a piece of 6 mm OD quartz tubing to accommodate the stainless steel.) The lead protruded 1 in. below the quartz tube and dipped about 1/4 in. into the metal. The space between it and the quartz tube was small enough to prevent attack of the Pt-Rh wire by metal vapor.

To control the concentration of dissolved oxygen, gas mixtures of known oxygen content (Ar-O₂ for silver and CO-CO₂ for copper) were bubbled through the liquid metal. They entered the cell via a quartz tube

with an ID of 2.5 mm and OD of 4 mm which was generally inserted about 1 1/4 in. into the metal. Both quartz tubes could be easily raised or lowered through the Tygon tubing seals.

The boron nitride radiation baffle, held 10 in. above the surface of the liquid metal by a piece of wire wound on the electrolyte tube, had been machined to fit tightly against the ceramic tubes to help achieve proper alignment. In order to prevent its reaction with quartz, the baffle was kept in the cold zone. Further alignment of the electrolyte tube was achieved because a 3 in. long brass tube with an ID of 1/2 in. was soldered to the brass cap. The brass fitting was adjusted so that the O-ring seal pressed very gently against the electrolyte which was coated with a thin layer of grease in this region. In this manner, a gas-tight seal could be maintained while the electrolyte tube was vibrated freely. A motor-driven steel rod was clamped to the tube immediately above the brass fitting (not shown).

A 1/4 in. alumina rod, which had two 1/16 in. holes and was 28 in. long, held a 3/8 in. diam circle of 45-mesh Pt gauze firmly against the inside of the electrolyte tube. Three springs located at 120° intervals around the cell ensured satisfactory electrical contact. Oxygen at a pressure of 1 atm was passed over the Pt gauze to

form the reference electrode. To facilitate the gas flow, slits had been cut into the bottom of the alumina rod. A Pt-Pt + 13% Rh thermocouple was welded to the Pt gauze. The Pt-Rh wire also served as the positive lead to the cell.

The cell was heated in a Pt resistance furnace with a 2 in. long constant temperature zone ($\pm 2^\circ\text{C}$). For electrical shielding, a grounded 0.025 in. thick Inconel tube lined the furnace walls. The rubber and cement connections were protected by a cooling coil soldered to the brass cap and a fan.

Before measurements were begun, the cell was heated to 1200°C to reduce contact resistance between the Pt gauze and the electrolyte. Suitable gas mixtures were bubbled, in turn, through the metal until the cell emf reached the theoretical value. Equilibrium was approached very slowly (several hours were often inadequate) for Ar-O₂ mixtures dilute in O₂ (<100 ppm) and CO-CO₂ mixtures dilute in CO (<1%), probably due to slow CO₂ decomposition in the latter case (8). It was usually achieved coulometrically for these mixtures. Prior to the voltammetric measurements, the gas flow was stopped. The experiments were not conducted above 1200°C for silver because of excessive evaporation, nor above 1300°C for copper because of excessive oxidation of the stainless steel lead wire. In the latter case, the oxide severely attacked the quartz sheath at 1300°C . Three independent runs for both silver and copper were made.

Results and Discussion

As inert conducting leads, Chromel A and Type 314 stainless steel functioned very well for silver and copper, respectively. They were not chemically attacked and the oxide films protecting them had a negligible resistance.

For liquid copper, 6 in. lengths of $\frac{1}{8}$ in. SiC rod, mechanically joined to either Chromel A or gold wire, were also tried. The rods had a density of 92% of the theoretical value. They were found to be quite satisfactory for emf measurements but unreliable for voltammetric measurements, probably due to the formation of a surface layer of SiO₂ which often caused a large increase in their resistance. A SiC lead could be useful for emf readings in liquid copper containing impurities such as sulfur and phosphorus which would restrict the use of stainless steel. In earlier work, a cermet of 72% Cr and 28% Al₂O₃ was successfully used (3, 8, 13, 14, 20, 21).

Initially, the resistance of the electrolyte varied somewhat with time due to a changing contact area with the Pt gauze electrode upon the evolution of oxygen during current flow. However, it soon became approximately constant ($\pm 5\%$). On an average, the a-c resistance of the cell (electrolyte and lead wires), measured at 3000 Hz, for an electrolyte immersion of $\frac{1}{8}$ in. into the liquid metal was 17.5, 8.2, 5.2, and 4.0 ohms at 1000° , 1100° , 1200° , and 1300°C , respectively.

Emf measurements.—The emf or reversible potential of the cell illustrated in Fig. 2 can be expressed as

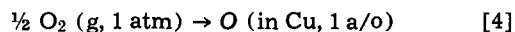
$$E_{\text{rev}} = -\frac{RT}{4F} \ln P_{\text{O}_2} \quad [3]$$

where P_{O_2} is the oxygen pressure imposed by the gas mixture in equilibrium with the liquid metal. When the electrolyte was submerged even slightly in the metal, the emf responded slowly to changes in the oxygen pressure above the metal relative to the virtually instantaneous response recorded for a Pt,gas electrode. Therefore, the emf is mainly dependent on the oxygen activity at the bottom of the electrolyte tube. Agreement between measured and theoretical values to within ± 1 mV for Ar-O₂ mixtures and ± 3 mV for CO-CO₂ mixtures was generally achieved. Thermoelectric forces were found to be no greater than 0.5 mV (the liquid metal electrode was positive).

After the gas flow was interrupted, emf's of 250 and 700 mV for silver and copper, respectively, remained essentially constant for 12 hr. These results indicated that the cells were gastight and verified the expected low electronic conductivity and porosity of the ZrO₂-CaO tubes.

Dissolved oxygen concentrations.—In the case of silver, the oxygen pressures calculated from Eq. [3] were converted into dissolved oxygen concentrations using available solubility data at an oxygen pressure of 1 atm and Sievert's law which has been verified for the Ag-O system (1, 25). At 1 atm, silver will dissolve 1.969, 1.793, and 1.649 a/o O at temperatures of 1000° , 1100° , and 1200°C , respectively (1, 25, 26).

For copper, the dissolved oxygen concentrations were determined from data recently reported by Fruehan and Richardson (14). The reaction



has partial free energies of solution of $-18,300$, $-18,130$, and $-18,020$ cal/g-atom at 1100° , 1200° , and 1300°C , respectively, whereby dissolved oxygen has the properties corresponding to infinite dilution. The former two values are in excellent agreement with the earlier results of Wilder (7) although the most recent data (21) indicate free energies about 130 cal/g-atom less negative. The equilibrium constant for reaction [4] is given by

$$K = \frac{\text{a/o O}}{P_{\text{O}_2}^{1/2}} \quad [5]$$

assuming Henry's law is obeyed—a reasonable assumption for the Cu-O system below 1 a/o O from 1100° to 1400°C (4-6, 7, 11, 12, 14, 17). At 1100° , 1200° , and 1300°C , $K \times 10^{-2} = 8.18$, 4.90, and 3.19 atm^{-1/2}, respectively. Using Eq. [5], the dissolved oxygen concentration can be readily calculated for any given oxygen pressure in equilibrium with liquid copper.

Cell reversibility.—The plot of cell potential vs. current in Fig. 3 for an electrolyte immersion depth of $\frac{1}{8}$ in. indicates that the oxygen concentration cell discharges reversibly. In agreement with earlier work on liquid silver (22), only resistance polarization is present since, within experimental error, the slopes of the lines approximate the corresponding a-c resistance of the cell. At lower oxygen concentrations, some diffusion overpotential caused by a buildup of dissolved oxygen at the metal-electrolyte interface was unavoidable, especially at high currents. The Pt, O₂ reference electrode was nonpolarizable, even at 200 mA and 1000°C .

Influence of the depth of immersion of the electrolyte tube.—During electrochemical removal of oxygen from

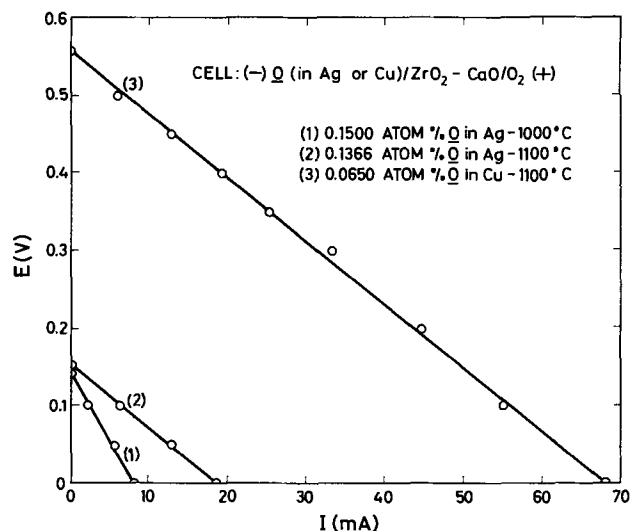


Fig. 3. Discharge curves. Cell potential is plotted against current.

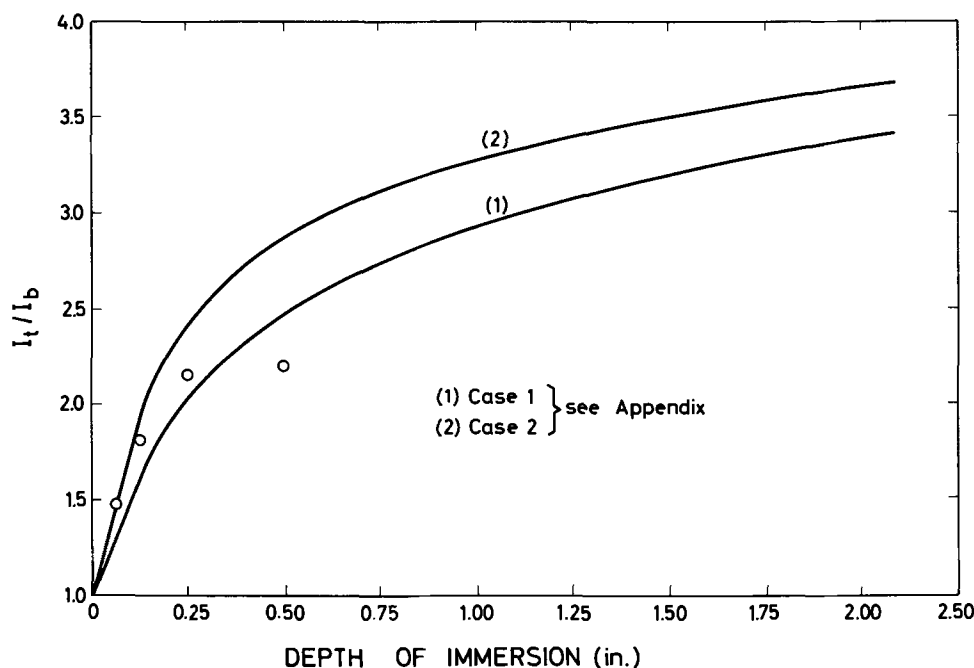


Fig. 4. Ratio of the total current to the current crossing the outside surface of the bottom of the electrolyte tube as a function of the depth of immersion of the electrolyte in the absence of diffusion overpotential. Both theoretical curves and experimental points are shown. The Pt gauze electrode has a diameter of $\frac{1}{4}$ in. for case 1 and $\frac{3}{8}$ in. for case 2.

the liquid metal, reaction [1] will occur over the entire metal-electrolyte interface, *i.e.*, some of the $O^=$ ions will be formed on the side of the electrolyte tube. Theoretical curves for the ratio of the total current, I_t , to the current carried across the bottom of the electrolyte tube, I_b , as a function of the depth of immersion are presented in Fig. 4. These curves were derived by dividing the tube into a number of parallel conductors; their derivation is given in the Appendix. It should be emphasized that the curves are applicable only when the current is controlled by the resistance of the electrolyte, *i.e.*, in the absence of diffusion overpotential.

Case 1 and case 2 refer to two different sizes of the circular Pt gauze electrode. Case 1 (diam = $\frac{1}{4}$ in.) would apply if only that portion of the Pt gauze directly under the alumina rod (Fig. 2) were making suitable contact with the electrolyte, whereas case 2 (diam = $\frac{3}{8}$ in.) would apply if the entire Pt gauze were making suitable contact. Although the currents are higher in case 2 (see Appendix), it results in a greater percentage of the current crossing the side of the electrolyte for a given depth of immersion. The experimental points, representing an average of several determinations of either the a-c resistance of the electrolyte or the d-c resistance at low currents and high oxygen concentrations at various depths of immersion, support the correctness of the model proposed in the Appendix and favor case 2 up to a depth of immersion of $\frac{1}{8}$ in. The agreement with case 2 is consistent with the observation made after the runs that both the Pt gauze electrode and Pt black deposit covered the entire inside of the bottom of the electrolyte tubes. At greater depths of immersion, the currents became more insensitive to changes in the depth than predicted from Fig. 4 indicating, undoubtedly, some interference among the competing currents in the various segments of the tube.

The effects presented in Fig. 4 would be less severe if the thickness of the bottom of the electrolyte tube were reduced. However, grinding the electrolyte with SiC powder led to a serious risk of cracking the ceramic tube. When diffusion overpotential appears, the influence of the depth of immersion becomes more pronounced since the longer resistance paths through the electrolyte for $O^=$ ions formed at the side of the tube (see Appendix) become less important. In the limit, when the oxygen concentration is very low along

the entire metal-electrolyte interface, the current will be proportional to the submerged outside area of the electrolyte tube (assuming a constant diffusion layer thickness). As the electrolyte tubes had an actual OD of 1.25 cm, the area of the metal-electrolyte interface was 1.23, 2.47, and 3.72 cm^2 for depths of immersion of 0, $\frac{1}{8}$, and $\frac{1}{4}$ in., respectively.

Establishment of limiting currents.—Most of the measurements were taken while the electrolyte tube was vibrated with an amplitude of $\frac{1}{16}$ in. and a frequency of 84 cycles/min. These conditions produced current fluctuations near the limiting currents of 2-3% and $<0.5\%$ of the readings for depths of immersion of $\frac{1}{8}$ and $\frac{1}{2}$ in., respectively. These percentages increased markedly at higher amplitudes and increased by a factor of about 1.5 at a frequency of 42 cycles/min.

Several important features of the preceding section are illustrated by the current-potential curves for 0.0622 a/o O in silver at 1000°C shown in Fig. 5. The potential was applied at a rate of 0.8 V/min to avoid lowering the bulk oxygen concentration significantly. A rate of 0.4 V/min was satisfactory if the initial reading was taken near the onset of appreciable diffusion overpotential.

At low currents, the d-c resistances, calculated from the slopes of the curves, were generally somewhat higher than the corresponding a-c resistance, *e.g.*, 17% higher for $\frac{1}{8}$ in. immersion in Fig. 5. The percentage increased when either the oxygen concentration or the a-c resistance was decreased. For instance, it was about 50% at 1000°C and 75% at 1200°C for 0.01 a/o O in silver. However, this disagreement was determined to be solely caused by diffusion overpotential at the liquid metal electrode and, consequently, reactions [1] and [2] proceed reversibly. Diffusion overpotential, η_d , in the absence of other types of overpotential, can be expressed as

$$\eta_d = E - E_{rev} - IR_{a-c} \quad [6]$$

where E is the applied potential, E_{rev} is the reversible potential ($I = 0$), and R_{a-c} is the a-c resistance of the cell. Close agreement was found between the diffusion overpotential, measured immediately after the current was interrupted, and the total overpotential, given by the right-hand side of Eq. [6]. Further evidence of diffusion overpotential was derived from the fact that, at low oxygen concentrations, the a-c resistance measured at 1000 Hz was often about 5% higher than that

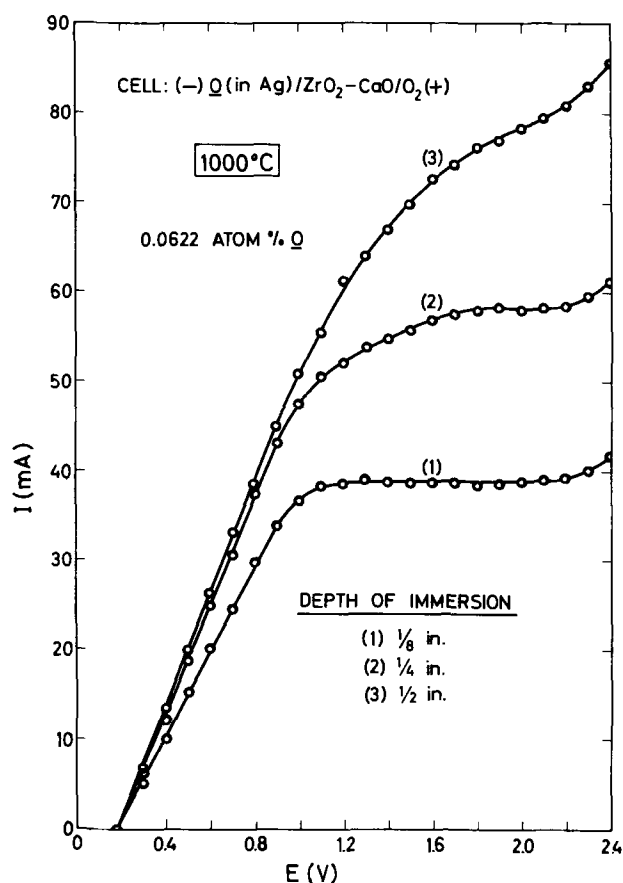


Fig. 5. Current vs. applied potential curves for 0.0622 a/o O in silver at 1000°C. The potential was applied at a rate of 0.8 V/min. Results are shown for three depths of immersion of the electrolyte tube. The amplitude of vibration of the electrolyte was 1/16 in. and the frequency of vibration was 84 cycles/min.

measured at 3000 Hz. It should be noted that the low-current points for 1/4 and 1/2 in. immersion are almost coincident as would be predicted from Fig. 4.

From the example in Fig. 5, it is evident that limiting currents were readily observed at a depth of immersion of 1/8 in. For this condition, the path lengths for the O⁼ ions formed at all points on the metal-electrolyte interface were similar (see Fig. 16b). At the higher applied potentials, there was a tendency for the current to drop because of a decrease in the bulk oxygen concentration. At 2.2V ($E - IR_{ac} > 1.5V$), reduction of the oxide electrolyte leading to n-type conductivity begins to interfere. For 1/4 in. immersion, the curve has an irregular shape since the current is a composite of contributions from competing sections of the electrolyte with varying path lengths. The O⁼ ions formed on the outside of the electrolyte tube near the surface of the metal must travel a relatively long distance to reach the Pt gauze electrode. Accordingly, higher applied potentials are required to achieve current control by diffusion overpotential, rather than the electrolyte resistance, in this region. Therefore, the limiting current is observed at higher applied potentials than that for 1/8 in. immersion. The ratio of the limiting currents (1.5) is in excellent agreement with the ratio of the areas of the metal-electrolyte interface, i.e., the limiting current densities are equal.

Unfortunately, limiting currents could not be measured at a depth of immersion of 1/2 in. Even in the flattest region of the curve, the current increases by about 2% per 0.1V increment. N-type conductivity near the bottom of the tube interfered before the oxygen concentration at the metal-electrolyte interface near the surface of the liquid metal could be significantly lowered. The limiting current would be 97 mA

if it continued to be proportional to the submerged outside area of the electrolyte.

Necessarily, from Fig. 5, the majority of the results were obtained at small depths of immersion. Accordingly, the depth of immersion had to be accurately controlled since the current is very sensitive to this variable (Fig. 4 and 5). Although limiting currents were observed to be independent of the cell resistance from 17.5 to 40 ohms at 1000°C, the attainment of a low cell resistance was very important for 1/4 in. immersion since limiting currents could then be established over a wider potential range. When the resistance was too high, the current-potential curves at 1/4 in. immersion took a similar shape to curve 3 in Fig. 5.

Possible interference from the gas phase due to either direct electrochemical reaction near the metal-electrolyte-gas boundary or chemical dissolution of oxygen from the gas phase into the diffusion layer must be considered, particularly at high oxygen pressures. However, limiting currents were not significantly affected by evacuating the system immediately prior to the voltammetric measurements. The large size of the electrolyte relative to the quantity of liquid metal rendered a noticeable drop in the bulk concentration of dissolved oxygen unavoidable. Nevertheless, by applying the potential at 0.8 V/min, it was calculated that this error caused the limiting currents to be low by no more than 1.5% at 1/8 in. immersion and 4% at 1/4 in. immersion.

Current-potential curves for two oxygen contents in liquid copper at 1200°C are plotted in Fig. 6. The depth of immersion of the electrolyte was 1/8 in. From the initial slopes of the curves, the d-c resistances are 15 and 50% higher than the a-c resistance (5.2 ohms) for the 0.0500 and 0.0146 a/o O compositions, respectively. Again, limiting currents are well-defined and n-type conductivity interferes at high applied potentials ($E - IR_{ac} > 1.4V$).

If the thickness of the diffusion layer (Fig. 1) is independent of the applied potential, then diffusion overpotential obeys the relationship

$$\eta_d = \frac{2.3RT}{nF} \log \frac{i_l}{i_l - i} \quad [7]$$

where n is the number of electrons involved in the electrode reaction, i is the current density, and i_l is the limiting current density. The plots of η_d vs. $\log [i_l/(i_l - i)]$ in Fig. 7 and 8 serve to verify the two-electron process at the cathode given by reaction [1]. Figure 7 is derived from curve 1 in Fig. 5 and Fig. 8 is derived from Fig. 6. Theoretical slopes are 0.126 and 0.146V at 1000° and 1200°C, respectively. The most accurate points were generally obtained in the range $0.1V < \eta_d < 0.2V$. Below 0.1V, small errors in i greatly affect η_d and, above 0.2V, small errors in i greatly affect $\log [i_l/(i_l - i)]$.

Linear plots only resulted from data obtained at 1/8 in. immersion of the electrolyte tube. For case 2 in Fig. 4 which represents resistance control of the current, $I_t/I_b \approx 1.93$ at 1/8 in. immersion. This factor becomes 2.01 for diffusion overpotential control (ratio of the appropriate areas). Consequently, the ratio is almost unaffected by the applied potential and theoretical behavior is observed. For greater depths of immersion, similar plots were displaced above the theoretical lines and were convex towards the abscissa.

Limiting currents could also be established by holding the applied potential constant as illustrated by the current-time curves for liquid silver in Fig. 9. Similar chronoamperometric results were obtained for copper. The applied potentials correspond to approximately the middle of the flat portions of the respective current-potential curves ($\eta_d = 0.4-0.6V$). At zero time ($\eta_d = 0$), the currents were equal to $(E - E_{rev})/R_{ac}$ in accordance with Eq. [6]. They were within 10% of the limiting values in 15 sec and were fully established in 1 to 1 1/2 min. The time required decreased when either the temperature or applied potential was increased or the depth of immersion of the electrolyte was de-

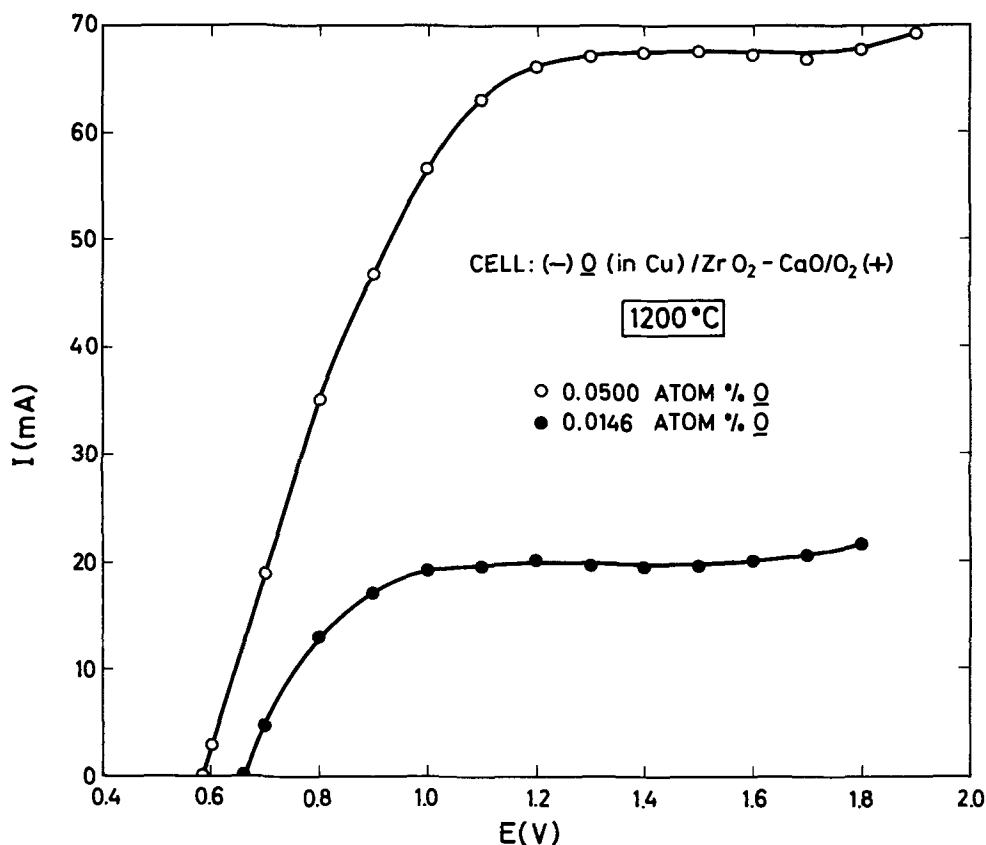


Fig. 6. Current vs. applied potential curves for two oxygen concentrations in liquid copper at 1200°C. The depth of immersion of the electrolyte tube was 1/8 in. The conditions were identical to those given for Fig. 5.

creased. After 1½ to 2 min, the currents dropped because of a decrease in the bulk oxygen concentration. This is more apparent for the lower curve in Fig. 9 since the limiting currents increase notably with temperature (next section). Even after 1 min, it can be calculated that the limiting currents can be up to 3% low on account of the decrease in the bulk oxygen concentration.

Effect of the dissolved oxygen concentration.—The relationship between the limiting current density and the dissolved oxygen concentration is presented for silver in Fig. 10 and 11 and for copper in Fig. 12. The log-log plot has been drawn for silver in Fig. 11 to enable the results for the entire oxygen concentration range which was studied to be seen more clearly. The depth of immersion of the electrolyte was either 1/8 or

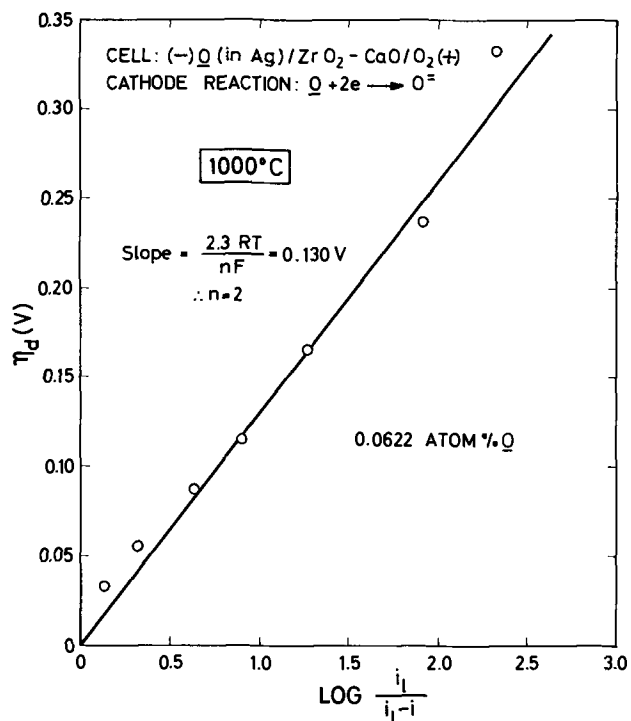


Fig. 7. Verification of the two-electron reaction at the liquid silver cathode. Derived from curve 1 in Fig. 5.

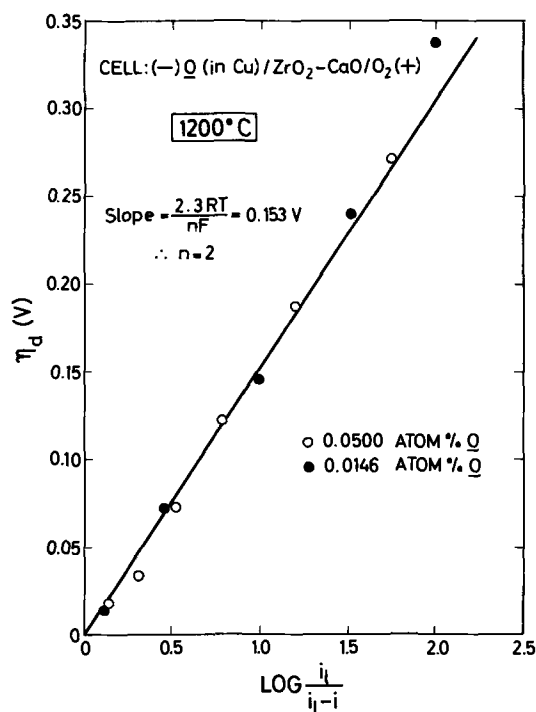


Fig. 8. Verification of the two-electron reaction at the liquid copper cathode. Derived from Fig. 6.

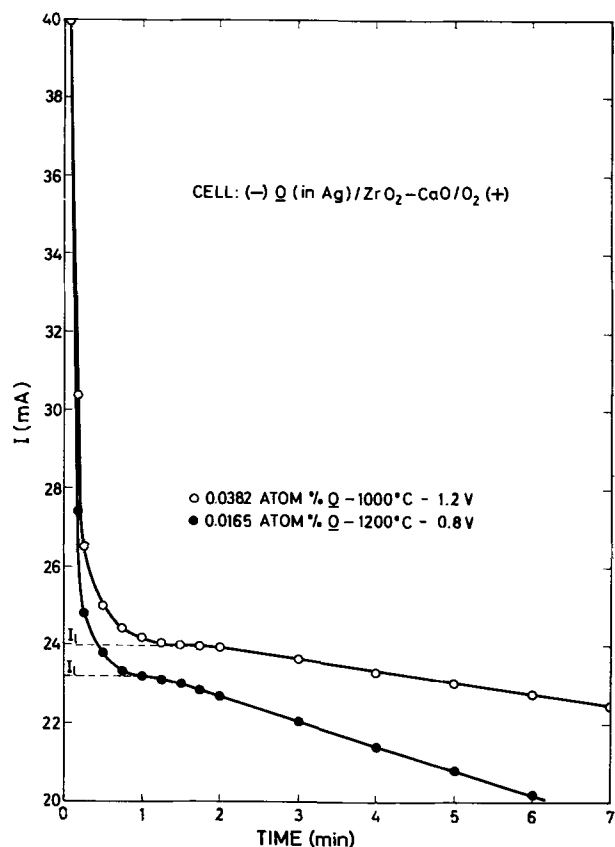


Fig. 9. Current-time curves for two oxygen concentrations in liquid silver. The depth of immersion of the electrolyte tube was $\frac{1}{8}$ in. The amplitude of vibration of the electrolyte was $\frac{1}{16}$ in. and the frequency of vibration was 84 cycles/min.

$\frac{1}{4}$ in. Current densities were calculated by dividing the currents by the geometric area of the metal-electrolyte interface, i.e., 2.47 or 3.72 cm^2 , respectively. However, these areas are somewhat uncertain because of the surface tension of the liquid metals. Since contact angles generally exceed 90° , the actual areas may be less than the calculated values which would make the current densities higher.

Generally, the data were reproducible to $\pm 3\%$ upon oxygen content or temperature cycling within a given run, but only to about $\pm 10\%$ from run to run. Points below 2 and above 50 mA/cm^2 were usually not as reproducible as those in the intermediate range.

Limiting currents are directly proportional to the dissolved oxygen concentration. They increase significantly with temperature and the lines in Fig. 10 and 12 pass through the origin. Calibration curves such as these could be used to analyze liquid metals for dissolved oxygen.

Using Fick's first law, the limiting current density can be written as

$$i_l = \frac{2FD_0c_0}{\delta} \quad [8]$$

where D_0 is the diffusion coefficient of oxygen in the liquid metal, c_0 is the bulk concentration of oxygen in the metal, and δ is the effective thickness of the diffusion layer. From the average of three recent independent investigations (27-29), $D_0 \times 10^4$ in silver is 0.99, 1.28, and 1.59 cm^2/sec at 1000°, 1100°, and 1200°C, respectively. The diffusion coefficient is independent of oxygen concentration (30). From the average of two recent independent studies (31,32), $D_0 \times 10^4$ in copper is 0.74, 0.98, and 1.27 cm^2/sec at 1100°, 1200°, and 1300°C, respectively. Converting concentrations to g-atoms/ cm^3 using the densities of liquid silver (33) and copper (34) enables effective diffusion layer thick-

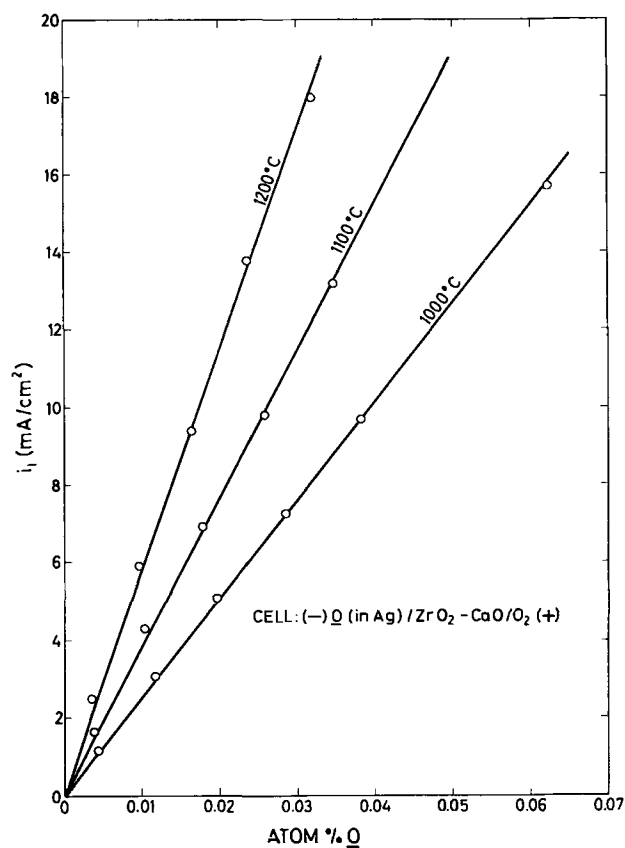


Fig. 10. Limiting current density vs. oxygen concentration at low oxygen concentrations in silver. The depth of immersion of the electrolyte tube was either $\frac{1}{8}$ or $\frac{1}{4}$ in. The amplitude of vibration of the electrolyte was $\frac{1}{16}$ in. and the frequency of vibration was 84 cycles/min.

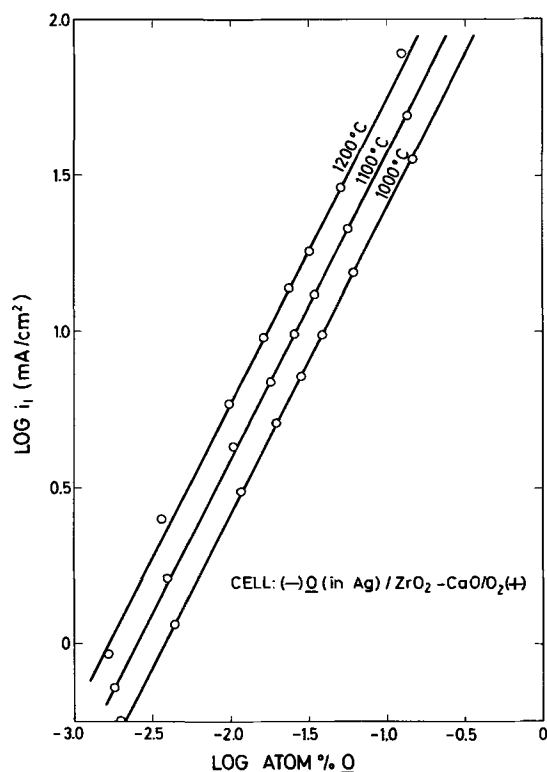


Fig. 11. Log limiting current density vs. log oxygen concentration for silver. The conditions were identical to those given for Fig. 10.

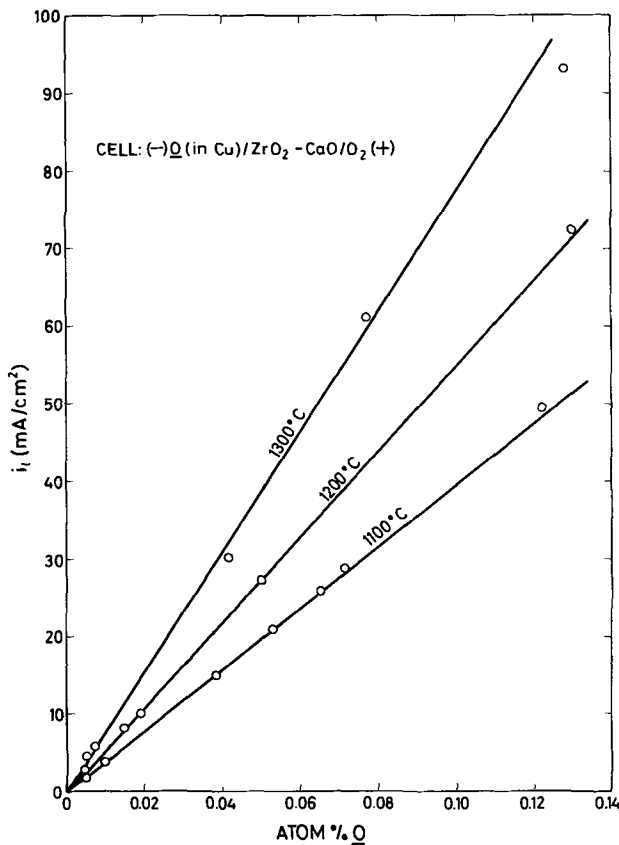


Fig. 12. Limiting current density vs. oxygen concentration for copper. The conditions were identical to those given for Fig. 10.

nesses to be found. For example, at 0.0385 a/o O in copper at 1100°C, since $i_l = 15.0 \times 10^{-3} \text{ A/cm}^2$, $F = 9.65 \times 10^4 \text{ coulomb/equiv}$, $D_0 = 0.74 \times 10^{-4} \text{ cm}^2/\text{sec}$, and $c_0 = 4.84 \times 10^{-5} \text{ g-atoms/cm}^3$, Eq. [8] gives $\delta = 0.046 \text{ cm}$. At 1100°C, a value of 0.054 cm was calculated for silver. At 1200°C, $\delta = 0.042$ and 0.045 cm for copper and silver, respectively. Consequently, the limiting currents increase with temperature due to both an increase in D_0 and a decrease in δ (Eq. [8]). The latter occurs because the viscosity of the liquid metal decreases as the temperature is increased.

The diffusion layer data are comparable for liquid silver and copper since their viscosities are similar (35). Nevertheless, the values are somewhat higher for silver, probably since D_0 is higher. Often, δ has been found to vary as D^x ($0 < x < 1$) in aqueous studies (36).

The effective thicknesses of the diffusion layer are relatively high implying that vibrating the electrolyte was not an efficient method of stirring the metal. However, this served to stabilize the diffusion layer (prevent it from spreading with time) and lower the time required to establish limiting currents. By continuing to bubble the gas mixtures through the metal during the measurements, i_l could be markedly increased and, accordingly, δ could be markedly decreased. However, limiting currents obtained in this manner were not very reproducible.

It should be noted that the results for δ are average values over the entire metal-electrolyte interface. They are not necessarily the same along the side as across the bottom of the electrolyte tube, nor are they probably even constant across the bottom of the tube. By sealing an electrolyte pellet into a quartz tube or pressing a pellet against a polished alumina tube, the diffusion conditions could be better-defined and uncertainties associated with measurements near the surface of the metal could be eliminated. Unfortunately, attempts to do this led to poorer reproducibility of

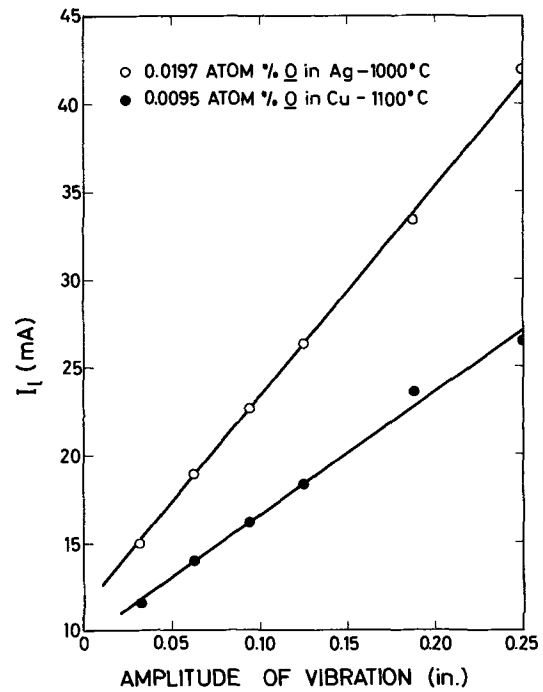


Fig. 13. Limiting current vs. amplitude of vibration of the electrolyte tube for silver and copper. The depth of immersion was $\frac{1}{4}$ in. and the frequency of vibration was 84 cycles/min.

the voltammetric measurements on account of leakage between the electrode compartments.

Effect of the amplitude and frequency of vibration of the electrolyte.—The effect of the amplitude of vibration of the electrolyte tube on the limiting current for both silver and copper is shown in Fig. 13. At lower temperatures, the dependence appeared somewhat more pronounced. The limiting current was approximately doubled by increasing the amplitude from $\frac{1}{16}$ to $\frac{1}{4}$ in. The currents at zero vibration were often higher than the extrapolated values, undoubtedly due to natural convection in the metal which arises from density gradients that are, in turn, caused by oxygen concentration and temperature gradients. The density increases as the oxygen concentration decreases.

Limiting current as a function of the frequency of vibration is plotted for both metals in Fig. 14. Again,

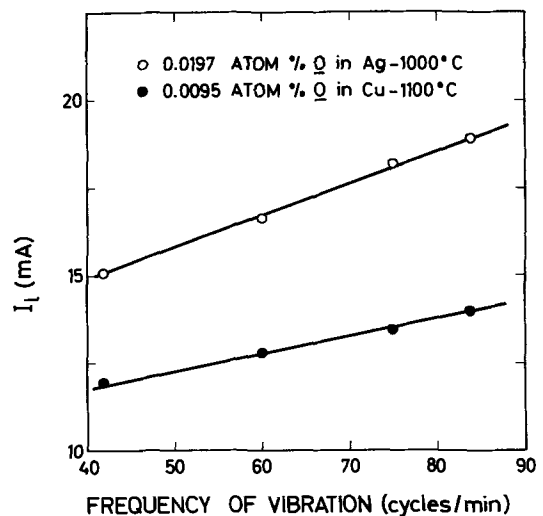


Fig. 14. Limiting current vs. frequency of vibration of the electrolyte tube for silver and copper. The depth of immersion was $\frac{1}{4}$ in. and the amplitude of vibration was $\frac{1}{16}$ in.

a linear dependence was observed which was stronger at lower temperatures.

Conclusions

By electrochemically removing dissolved oxygen from liquid metals in cells with impervious solid oxide electrolytes, limiting currents controlled by oxygen diffusion and convection in the liquid metal can be established. Either the applied potential can be increased at a rate of about 0.8 V/min or a suitable applied potential can be held constant for 1 to 1½ min. To achieve electrical contact, Chromel A wire for silver and Type 314 stainless steel wire for copper are very satisfactory. Using electrolyte tubes, the influence of the depth of immersion must be considered to interpret the results and small immersion depths are necessary to obtain limiting currents. Stability of the diffusion layer is ensured by providing forced convection in the metal, but natural convection may be sufficient.

Limiting currents are directly proportional to the dissolved oxygen concentration at low oxygen contents and increase substantially with temperature. Diffusion layer thicknesses decrease with temperature and are slightly greater for liquid silver than liquid copper. Voltammetric measurements could be used to analyze liquid metals and alloys for dissolved oxygen.

Acknowledgment

This research was supported by a grant from the Defence Research Board of Canada.

Manuscript submitted March 22, 1971; revised manuscript received ca. Sept. 20, 1971. This was, in part, Paper 329 presented at the Los Angeles Meeting of the Society, May 10-15, 1970.

Any discussion of this paper will appear in a Discussion Section to be published in the December 1972.

APPENDIX

Calculation of the Influence of the Depth of Immersion of a Solid Electrolyte Tube in a Liquid Metal

The following calculation is applicable to the influence of the depth of immersion on the current through the cell when the current is solely controlled by the resistance of the solid electrolyte, i.e., in the absence of diffusion overpotential. Regarding emf measurements, it could also be used to determine mixed potentials resulting from oxygen activity gradients along the liquid metal-electrolyte interface.

For an electrical conductor with potential-independent conductivity, the current, I , is given by

$$I = \frac{E\sigma A}{y} \quad [9]$$

where E is the applied potential (corrected for the cell emf in the case of an ionic conductor), σ is the specific conductivity, A is the area through which the current passes, and y is the path length for the current. In the case of an electrolyte tube immersed in a liquid metal depicted in Fig. 15, the path length for O^{2-} ions will be dependent upon the position on the liquid metal-electrolyte interface where they are either produced or consumed. Since the liquid metal conducts electroni-

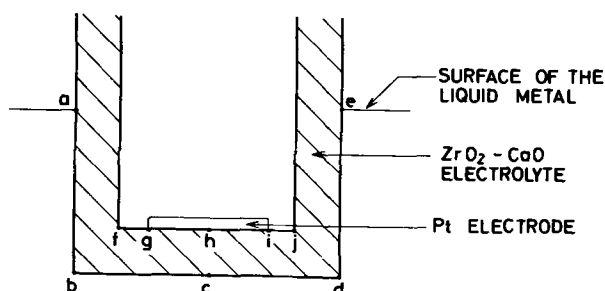


Fig. 15. Solid electrolyte tube immersed in a liquid metal

cally, the electrochemical reduction of oxygen dissolved in the metal will occur over the entire surface abcde. To be oxidized, the O^{2-} ions which are produced must migrate through the electrolyte to the Pt electrode. Oxygen ions formed at c must only travel a distance ch and those formed at b must travel a distance bg, while those formed at a must travel a distance afg.

Since E is constant over the surface abcde and σ is constant throughout the solid electrolyte (electronic conductivity is negligible), Eq. [9] predicts that

$$I \propto \frac{A}{y} \quad [10]$$

When y is not constant for a given area, then

$$A \left(\frac{1}{y} \right) = \frac{A}{y^*} = \lim_{n \rightarrow \infty} \left(\frac{\Delta_1 A}{y_1} + \frac{\Delta_2 A}{y_2} + \dots + \frac{\Delta_n A}{y_n} \right)$$

and, therefore

$$\frac{A}{y^*} = \int_{A_1}^{A_2} \left(\frac{1}{y} \right) dA \quad [11]$$

where A is the area on the outer surface of the electrolyte tube ($A_2 - A_1$), $(1/y)$ is the average value of $1/y$ for this area, and y^* is the effective path length which is the reciprocal of $(1/y)$. It is assumed that the current carried by each element $\Delta_i A/y_i$ is independent of the remaining elements since the elements unavoidably overlap, i.e., in Fig. 15, the area defined by abcde (the area of the liquid metal-electrolyte interface) is greater than the area defined by ghi (the area of the Pt-electrolyte interface).

When values of A/y^* for two or more areas are determined, then, if their currents are independent, the total current passing through them will simply be proportional to the sum of their A/y^* values. In effect, the electrolyte is divided into a number of parallel conductors. Calculations for the electrolyte tubes used in the present experiments for two different cases regarding the Pt electrode will now be given.

Cross sections containing the longitudinal axis of the electrolyte tube are drawn in Fig. 16. Each length on the outside surface defines an area—circular on the bottom and curved on the side. Each area involving a different type of calculation will be discussed in turn.

Case 1. The Pt electrode only partly covers the bottom surface of the inside of the electrolyte tube (Fig. 16a).—In Fig. 16a, the circular Pt gauze electrode has a diameter of ¼ in. This represents the smallest area of Pt-electrolyte contact possible in the present investigation since the Pt electrode was held firmly against the electrolyte with a ¼ in. alumina rod (Fig. 2).

Area fg. The path length for all the O^{2-} ions formed in this area is fi. Accordingly,

$$\frac{A}{y} = \frac{\pi(1/8)^2}{1/16} = 0.7854 \text{ in.} = 1.995 \text{ cm}$$

Area df. For a given element of this area at e, the path length y is $\sqrt{x^2 + (1/16)^2}$ where x is the distance fe and 1/16 in. is the thickness of the electrolyte tube. The area represented by fe is

$$A = \pi(x + 1/8)^2 - \pi(1/8)^2 \quad [12]$$

Therefore

$$dA = 2\pi(x + 1/8)dx \quad [13]$$

Substituting for y and dA in Eq. [11] and evaluating the integral gives

$$\frac{A}{y^*} = 2\pi \sqrt{x^2 + (1/16)^2} \Big|_{x_1}^{x_2} + \frac{\pi}{4} \ln \left(x + \sqrt{x^2 + (1/16)^2} \right) \Big|_{x_1}^{x_2} \quad [14]$$

Integration constants will be omitted since definite integrals are being considered. At f, $x = x_1 = 0$ and at d, $x = x_2 = 1/8$ in. Substituting into Eq. [14] yields the result that

$$\frac{A}{y^*} = 4.113 \text{ cm}$$

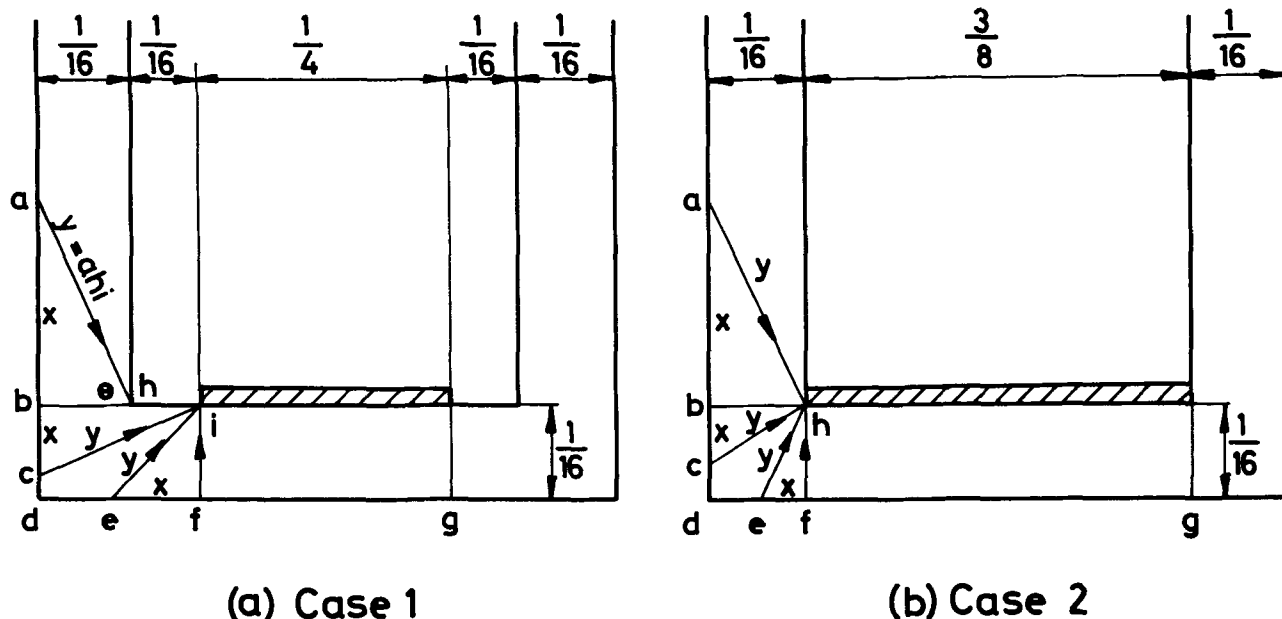


Fig. 16. Illustration of the method used to calculate the effect of the depth of immersion of a solid electrolyte tube on the current. Dimensions are in inches. The Pt electrode is hatched. Arrows are drawn on lines representing current paths through the solid electrolyte which was divided into sections fg, df, bd, and ab.

Area bd. The path length y for $O^=$ ions formed at any element c within this area is $\sqrt{x^2 + (1/16)^2}$ where x is the distance bc. The area defined by bc is simply given by

$$A = \frac{\pi}{2} x \quad [15]$$

since the electrolyte tube has an OD of $1/2$ in. Therefore

$$dA = \frac{\pi}{2} dx \quad [16]$$

Again, substituting for y and dA in Eq. [11] and evaluating gives

$$\frac{A}{y^*} = \frac{\pi}{2} \ln \left(x + \sqrt{x^2 + (1/16)^2} \right) \Big|_{x_1}^{x_2} \quad [17]$$

Here, $x = x_1 = 0$ at b and $x = x_2 = 1/16$ in. at d. Consequently

$$\frac{A}{y^*} = 1.920 \text{ cm}$$

Area ab. Oxygen ions formed at a must travel along ah to reach the Pt electrode. Accordingly, the path length y is $\sqrt{x^2 + (1/16)^2} + 1/16$ where x is the length ba. For the area defined by ba, Eq. [15] and [16] apply. Therefore, from Eq. [11]

$$\frac{A}{y^*} = \frac{\pi}{2} \int_{x_1}^{x_2} \frac{dx}{\sqrt{x^2 + (1/16)^2} + 1/16} \quad [18]$$

Evaluating this integral by rationalizing the denominator invalidates the situation where $x = 0$. For the general case, it can be determined by making the substitution $x = 1/16 \tan \theta$ where θ is the angle shown in Fig. 16a. Hence, $dx = 1/16 \sec^2 \theta d\theta$. The integral in Eq. [18] can now be written as

$$\int \frac{dx}{\sqrt{x^2 + (1/16)^2} + 1/16} = \int \frac{d\theta}{\cos \theta (1 + \cos \theta)} \quad [19]$$

Using the method of partial fractions and integrating yields

$$\int \frac{d\theta}{\cos \theta (1 + \cos \theta)} = \ln (\sec \theta + \tan \theta) - \frac{\sin \theta}{1 + \cos \theta} \quad [20]$$

Recalling that $\tan \theta = \frac{x}{1/16}$ results in an expression

for Eq. [18] of the form

$$\frac{A}{y^*} = \frac{\pi}{2} \ln \frac{\sqrt{x^2 + (1/16)^2} + x}{1/16} \Big|_{x_1}^{x_2} - \frac{\pi}{2} \frac{x}{\sqrt{x^2 + (1/16)^2} + 1/16} \Big|_{x_1}^{x_2} \quad [21]$$

At b, $x = x_1 = 0$ and at a, $x = x_2$. The value of x_2 will depend on the depth of immersion of the electrolyte tube. For example, if the depth of immersion is $1/2$ in., then $x_2 = 7/16$ in. and

$$\frac{A}{y^*} = 7.089 \text{ cm}$$

Case 2. The Pt electrode covers the entire bottom surface of the inside of the electrolyte tube (Fig. 16b).—This case would be experimentally realized in the present work if all of the Pt gauze electrode (diameter = $3/8$ in.) were in close contact with the electrolyte.

Area fg. The A/y value can be calculated as for case 1.

Area df. For $O^=$ ions formed at e, the path length y is $\sqrt{x^2 + (1/16)^2}$ where x is the distance fe. For the area defined by fe, $dA = 2\pi(x + 3/16) dx$. Substituting for y and dA into Eq. [11] produces a solution similar to Eq. [14]. Here, $x_1 = 0$ and $x_2 = 1/16$ in.

Area bd. Inserting $y = \sqrt{x^2 + (1/16)^2}$ and Eq. [16] into Eq. [11] gives a solution similar to Eq. [17]. Again, the limits of integration are 0 and $1/16$ in.

Area ab. Oxygen ions formed at a must travel a distance ah through the electrolyte (the Pt electrode is thin). The path length y is $\sqrt{x^2 + (1/16)^2}$ and Eq. [15] and [16] apply. The solution is identical to that for area bd. At b, $x = x_1 = 0$ and x_2 can have any desired value.

Some of the calculated values are recorded in Table I. It is apparent from these data and Eq. [17] and [21] that, if the $O^=$ ions migrating through the electrolyte do not interact, then as $x_2 \rightarrow \infty$ (area ab), $A/y^* \rightarrow \infty$ and the percentage of the current carried across the bottom of the electrolyte tube $\rightarrow 0$. Recalling Eq. [10], it is obvious that higher currents will be observed in case 2 than in case 1.

The total current for any depth of immersion, I_b , may now be easily compared to the current crossing the outside of the bottom of the electrolyte tube, I_o , i.e., the

Table I. A/y^* values (cm) for the solid electrolyte tube

Area	Case 1	Case 2
fg	1.995	4.489
df	4.113	3.051
bd	1.920	3.516
ab ($x_2 = 1/16$ in.)	1.864	3.516
ab ($x_2 = 3/16$ in.)	4.380	7.255
ab ($x_2 = 5/16$ in.)	5.955	9.226
ab ($x_2 = 7/16$ in.)	7.089	10.550

total current at zero depth of immersion. As an example, for case 1 and a depth of immersion of $\frac{1}{2}$ in. ($x_2 = 7/16$ in.), the ratio is

$$\frac{I_t}{I_b} = \frac{1.995 + 4.113 + 1.920 + 7.089}{1.995 + 4.113} = 2.475$$

Ratios calculated in this manner for nine depths of immersion were used to plot Fig. 4.

REFERENCES

- C. Diaz, C. R. Masson, and F. D. Richardson, *Trans. Inst. Mining Met., Sect. C*, **75**, 183 (1966).
- W. A. Fischer and W. Ackermann, *Arch. Eisenhüttenw.*, **37**, 697 (1966).
- C. M. Diaz and F. D. Richardson in "Electromotive Force Measurements in High-temperature Systems," p. 29, C. B. Alcock, Editor, Institution of Mining and Metallurgy, London (1968).
- W. Pluschkell and H.-J. Engell, *Z. Metallk.*, **56**, 450 (1965).
- W. A. Fischer and W. Ackermann, *Arch. Eisenhüttenw.*, **37**, 43 (1966).
- H. Rickert and H. Wagner, *Electrochim. Acta*, **11**, 83 (1966); H. Rickert, H. Wagner, and R. Steiner, *Chem.-Ing.-Tech.*, **38**, 618 (1966); H. Wagner and H. Sundermann, *Z. Anal. Chem.*, **222**, 217 (1966).
- T. C. Wilder, *Trans. Met. Soc. AIME*, **236**, 1035 (1966).
- C. Diaz and F. D. Richardson, *Trans. Inst. Mining Met., Sect. C*, **76**, 196 (1967).
- M. M. A. El-Naggar, G. B. Horsley, and N. A. D. Parlee, *Trans. Met. Soc. AIME*, **239**, 1994 (1967).
- J. Gerlach, J. Osterwald, and W. Stichel, *Z. Metallk.*, **59**, 576 (1968).
- Z. Kozuka, K. Suzuki, T. Oishi, and J. Moriyama, *Nippon Kinzoku Gakkaishi*, **32**, 1132 (1968).
- J. Osterwald, G. Reimann, and W. Stichel, *Z. Phys. Chem., N. F.*, **66**, 1 (1969).
- K. P. Abraham, *Trans. Indian Inst. Metals*, **22**, 5 (1969).
- R. J. Fruehan and F. D. Richardson, *Trans. Met. Soc. AIME*, **245**, 1721 (1969).
- C. R. Nanda and G. H. Geiger, *Met. Trans.*, **1**, 1235 (1970).
- W. A. Fischer and G. Pateisky, *Arch. Eisenhüttenw.*, **41**, 661 (1970).
- I. Tsukahara, *Nippon Kinzoku Gakkaishi*, **34**, 679 (1970).
- J. Dompas and J. Van Melle, *J. Inst. Metals*, **98**, 304 (1970).
- M. M. A. El-Naggar and N. A. D. Parlee, *Met. Trans.*, **1**, 2975 (1970).
- A. D. Kulkarni, R. E. Johnson, and G. W. Perbix, *J. Inst. Metals*, **99**, 15 (1971).
- K. T. Jacob and J. H. E. Jeffes, *Trans. Inst. Mining Met., Sect. C*, **80**, 32 (1971).
- T. H. Etsell and S. N. Flengas, *Met. Trans.*, **2**, 2829 (1971).
- B. Marincek, *Helv. Chim. Acta*, **50**, 988 (1967); B. Korousic and B. Marincek, *ibid.*, **51**, 907 (1968).
- B. Marincek, *Schweiz. Arch. Angew. Wiss. Tech.*, **33**, 143 (1967); B. Marincek and B. Korousic, *ibid.*, **34**, 209 (1968); B. Korousic and B. Marincek, *ibid.*, **34**, 264 (1968).
- N. A. D. Parlee and E. M. Sacris, *Trans. Met. Soc. AIME*, **233**, 1918 (1965).
- E. A. Mizikar, R. E. Grace, and N. A. D. Parlee, *Trans. Am. Soc. Metals*, **56**, 101 (1963).
- I. D. Shah and N. A. D. Parlee, *Trans. Met. Soc. AIME*, **239**, 763 (1967).
- C. R. Masson and S. G. Whiteway, *Can. Met. Quart.*, **6**, 199 (1967).
- N. Sano, S. Honma, and Y. Matsushita, *Trans. Iron Steel Inst. Japan*, **9**, 404 (1969); *Met. Trans.*, **1**, 301 (1970).
- N. A. D. Parlee and H. Seibel, *Trans. Met. Soc. AIME*, **233**, 1923 (1965).
- J. Osterwald and G. Schwarzlose, *Z. Phys. Chem., N. F.*, **62**, 119 (1968).
- H. Rickert and A. A. El Miligy, *Z. Metallk.*, **59**, 635 (1968).
- C. J. Smithells, "Metals Reference Book," Vol. III, 4th ed., p. 689, Butterworths, London (1967).
- J. A. Cahill and A. D. Kirshenbaum, *J. Phys. Chem.*, **66**, 1080 (1962).
- "Landolt-Börnstein Zahlenwerte und Functionen," Vol. II, Part 5, 6th ed., p. 124, Springer-Verlag, Berlin/Heidelberg (1969).
- V. G. Levich, "Physicochemical Hydrodynamics," Prentice-Hall, Inc., Englewood Cliffs, N. J. (1962).

Detection of Nonuniform Current Distribution on a Disk Electrode

William H. Smyrl*

Boeing Scientific Research Laboratories, Seattle, Washington 98124

and John Newman*

Inorganic Materials Research Division, Lawrence Radiation Laboratory, and
Department of Chemical Engineering, University of California, Berkeley, California 94720

ABSTRACT

The relative merits of different methods of detecting a nonuniform current distribution on a disk electrode are discussed. Some implications of such a distribution are presented. Experimental results are reported for collection efficiency measurements on the system of Albery and Ulstrup.

We consider here several aspects of the current and potential distribution on a rotating disk electrode, a problem for which a theoretical analysis has been presented earlier (1-4). Since this electrode is popularly regarded to have a uniform current distribution, it is appropriate to give examples illustrating under what

conditions a nonuniform distribution can be expected. We should also like to discuss possible methods of detecting that a nonuniform current distribution prevails. In this connection, new experimental data are given for one of these methods, that involving the rotating ring-disk electrode system as used by Albery and Ulstrup (5).

* Electrochemical Society Active Member.

Key words: ohmic potential drop, collection efficiency.

Current Distribution on a Disk Electrode

The current distribution on a rotating disk electrode is described in detail in Ref. (2). On the basis of mass-transfer considerations alone, Levich (6) has shown that the current distribution should be uniform, and the disk surface is said to be uniformly accessible from a mass-transfer standpoint. This conclusion is valid at the limiting current, where the concentration of the reactant is zero over the entire surface of the disk electrode. [See, however, the paper (7) on the effect of radial diffusion.]

At currents below the limiting current, the ohmic potential drop tends to produce a nonuniform current distribution. The extreme case is the primary current distribution (1)

$$\frac{i}{i_{\text{avg}}} = \frac{0.5}{(1 - r^2/r_0^2)^{1/2}} \quad [1]$$

which corresponds to the solution of Laplace's equation for the potential when the potential in the solution adjacent to the electrode is uniform. Here, the disk electrode is taken to be embedded in a large, insulating plane with the counterelectrode at infinity. The primary current distribution prevails when the surface overpotential for the electrode reaction is negligible and there are no mass-transfer limitations.

For intermediate cases, the current distribution can be described in terms of seven parameters (2), two of which we consider here

$$J = \frac{ZF r_0 i_0}{RT \kappa_x} \quad \text{and} \quad N = -\Gamma \left(\frac{4}{3} \right) \frac{ZF r_0 i_{\text{lim}}}{RT \kappa_x} \quad [2]$$

J can be regarded as a dimensionless exchange current density and N as a dimensionless limiting current density. Small values of J lead to a uniform current distribution; large values, to a nonuniform distribution. Even for a small value of J , the distribution can be nonuniform if the current is large. Here one can use as a parameter the average current density made dimensionless in the same manner as J in Eq. [2]. The value of N determines how large the dimensionless average current density can be without exceeding the limiting current. At the limiting current, the current distribution is uniform, but this mass-transfer effect loses force at currents only slightly below the limiting current.

The current density, whether it be the exchange current density, the limiting current density, or the average current density, is made dimensionless with the electrode radius r_0 , the solution conductivity κ_x , and other parameters over which there is little experimental control. Large disks and low conductivities promote a nonuniform current distribution, and *vice versa*. For laboratory work on polarography and electrode kinetics, small disks and small reactant concentrations with an excess of supporting electrolyte can be used to ensure a uniform current distribution. However, in engineering systems involving electroplating, corrosion, etc., a nonuniform current distribution must be expected. Ohmic effects can lead to the following undesirable results: (a) nonuniform deposition or dissolution, (b) errors in kinetic parameters calculated with neglect of current nonuniformities, (c) loss of control in analytical determinations [Harrar and Shain (8) give a lucid account of such an example in large cells], and (d) waste of current in cathodic protection in corroding systems.

Some numerical examples may be helpful. For $r_0 = 0.25$ cm, $\kappa_x = 0.1$ (ohm-cm)⁻¹, $i_0 = 1$ mA/cm², $Z = 1$, and $T = 298^\circ\text{K}$, the value of J is about 0.1. For small values of the average current density, this value of J implies a fairly uniform current distribution, but for an average current density of 0.1 A/cm², the current distribution will be nonuniform. However, for a value of $i_0 = 40$ A/cm², the value of J is about 4000, and the current distribution will be nonuniform at all current densities (except very close to the limiting

current). For this value of i_0 , it is unlikely that a large enough concentration of supporting electrolyte could be used to obtain a uniform current distribution.

As an example of the ohmic effect in corrosion studies, we might ask how large a disk electrode can be protected cathodically by a counterelectrode at infinity, without waste of current. We assume that the disk is rotated, the flow is laminar, and the limiting current for the oxygen reaction is uniform.

The desired current distribution for cathodic protection is determined by the limiting current distribution for oxygen reduction. This results in a potential variation in the solution adjacent to the protected surface. The potential difference $\Delta\Phi_0$ between the solution adjacent to the center of the disk and that adjacent to the outside edge of the disk, for a uniform current distribution, can be obtained from Ref. (2) as

$$\Delta\Phi_0 = 0.36338 r_0 i / \kappa_x \quad [3]$$

We want the electrode to have a potential between that necessary to prevent oxidation of the metal (say, -0.1V vs. NHE) and that at which hydrogen generation begins (say, -1.0V vs. NHE). This means that $\Delta\Phi_0$ should be no larger than 0.9V. For a limiting current density of 10 mA/cm² and a conductivity of 0.04 (ohm-cm)⁻¹, the largest disk which can be cathodically protected is $r_0 = 9.9$ cm.

The above equation can also be used for anodic protection of an electrode with active-passive kinetics. The potential of the electrode should be large enough to ensure that the surface is in the passive region and small enough to ensure that it is not in the transpassive region. Assume that this gives an allowed maximum of $\Delta\Phi_0$ of 0.5V and that the current density in the passive region is 10^{-5} A/cm². Then, the largest disk which can be protected anodically corresponds to $r_0 = 5500$ cm, again for a conductivity of 0.04 (ohm-cm)⁻¹. Equation [3] can also be used to guide the selection of conditions for constant-potential electrolysis.

Detection of the Current Distribution

Various methods are conceivable for detecting a nonuniform current distribution on a rotating disk electrode. Direct measurement of the deposit thickness has been used with success by Marathe and Newman (9). Irene Sun, at Berkeley, has sectioned a radioactive deposit on a disk electrode, and autoradiograms of radioactive deposits have been made by Jordan and Finston (10). Recently, Bruckenstein and Miller (11) have reported additional results of deposit thickness measurements.

Albery and Ulstrup (5) have measured collection efficiencies at the ring electrode of a ring-disk system with a view toward detecting a nonuniform current distribution on the disk electrode. If the current density is higher near the edge of the disk than at the center, then the collection efficiency at the ring should be higher than that calculated with the assumption of a uniform current density on the disk. A quantitative comparison of theory and experiment is made difficult by the fact that a current to the ring will accentuate the nonuniformity on the disk. Nevertheless, the results of Albery and Ulstrup show a lower measured collection efficiency. This conflict led us to repeat the experiments, as described in the next section. After completion of the present work, Bruckenstein and Miller (11) also reported results on this system, with conclusions which generally agree with those described below. Also, it is reported¹ that the results of Albery and Ulstrup have been recanted.

It would be more straightforward to use the ring-disk system as a sectioned electrode for the purpose of measuring the nonuniformity of current distribution. In this application, the ring and the disk would be held at the same potential so as to function as a single electrode to the parts of which the current

¹ Barry Miller, Private communication. See Ref. 8 of the paper by Bruckenstein and Miller (11).

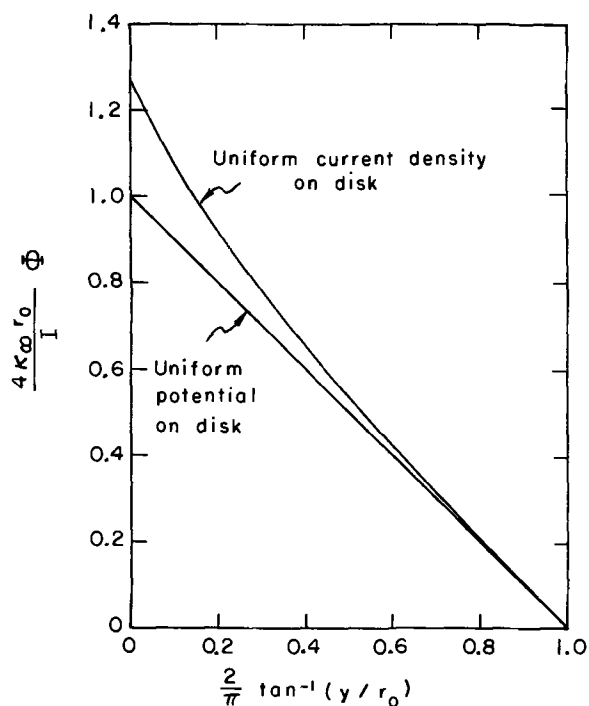


Fig. 1. Potential distribution along the axis of the disk

could be measured separately. Since this is a classical method of measuring current distributions, we have assessed in a separate paper (12) the error which might be introduced by the nonzero gap between the ring and the disk. Experimental measurements are also reported for this technique.

Angell, Dickinson, and Greef (13) have measured the potential distribution near a rotating disk electrode. In order for such measurements to detect a nonuniformity of current distribution on the disk, measurements would have to be made quite close to the electrode itself, as shown by the theoretical potential profiles along the disk axis (see Fig. 1). McIntyre and Peck (14) have developed an interrupter technique and applied it to the measurement of the ohmic potential drop at a rotating disk electrode. Although the ohmic potential drop to the center of the disk can vary by 27% depending on the uniformity of distribution of the same total current (2), an interrupter technique will ideally measure the ohmic potential drop corresponding to the primary current distribution, independent of the actual current distribution prevailing before interruption of the current (15).

Ring Collection Efficiencies for the Bromide-Bromine System

Albery and Ulstrup (5) have reported the results of experiments with a ring-disk assembly to test critically the predictions of current distribution on a disk electrode. The disk was operated at a given current as an anode, oxidizing bromide to bromine, which was then reduced back to bromide at the ring. The nonuniform current distribution on the disk should produce a concentration of bromine at the edge of the disk which is higher than that expected from the average current density.² This should result in a higher current on the ring (or a higher collection efficiency) than that predicted by Albery and Bruckenstein (16). In other words, bromine produced near the edge of the disk has less chance to diffuse away and therefore more chance to react at the ring. In contrast, Albery and Ulstrup report a lower current on the ring.

Three effects might complicate the interpretation of these results: (i) Operation of the ring cathodically enhances the nonuniformity of the current distribution

² Note however that the equation that they propose for predictions of this effect is incorrect (12).

on the disk and should lead to a still higher collection efficiency; (ii) the ohmic potential drop may have been large enough in some of the dilute solutions to obviate the limiting-current measurements on the ring, that is, the ring may not have been at limiting current at the potential of its operation; and (iii) kinetic complications on the disk might have resulted in the production of less bromine than was supposed.

For the rotating ring-disk system described below, calculations were made of the ohmic potential drop between the ring and the reference electrode, with the ring operating at limiting current. The results of Newman (2) and of Nanis (17) were used for the calculations. It was found that the ohmic effect was too small, and in the wrong direction, to be of importance for the concentrations and placement of reference electrode used in the measurements reported below.

Since the importance of the last possibility could not be determined from the data reported by Albery and Ulstrup, the measurements were repeated. The solutions were NaBr and HClO₄ in water. The ring, disk, and counterelectrodes were made of platinum. The dimensions of the ring-disk assembly (RD1) were $r_0 = 0.442$ cm, $r_1 = 0.504$ cm, and $r_2 = 0.621$ cm. The calculated collection efficiency was 0.340. The ring and disk were imbedded in epoxy, and the over-all radius was 1.27 cm. The reference electrode probe (Luggin capillary tip) was placed in the plane of the disk at $r = 2.27$ cm. A Regatron constant-current power supply maintained a constant disk current. A Wenking potentiostat and voltage-ramp generator were used to measure the limiting current curves on the ring. Currents were determined by measuring the potential drop across precision resistors. The vessel containing the solution and electrodes was open to ambient air and was at ambient temperature ($23 \pm 2^\circ\text{C}$). The ring-disk assembly was rotated at 1550 rpm.

Since this system has received recent attention (11), we shall describe our results briefly.

At high and moderate concentrations, the ring limiting current for bromine reduction was broad and well defined. At decreased concentrations, especially that of HClO₄, the region between attainment of limiting current and onset of reduction of oxide on the platinum was more narrow.

Results of collection efficiency measurements at moderate concentrations are given in Table I. The measured collection efficiency is greater than that calculated for all but three entries in the table. This indication of a nonuniform current distribution is in qualitative agreement with the predictions of Newman (2).

However, the more interesting systems are the dilute solutions in which Albery and Ulstrup found the anomalous collection efficiencies. To investigate the possibility that these results were caused by kinetic complications on the disk, disk polarization curves were

Table I. Collection efficiencies for NaBr-HClO₄ systems

Solution composition	Total disk current (mA)	$-I_r/I_d$
0.1M NaBr 0.1M HClO ₄	0.1	0.350
	1.0	0.345
	5.0	0.360
	10.0	0.350
0.01M NaBr 0.01M HClO ₄	0.01	0.350
	1.00	0.353
0.001M NaBr 0.1M HClO ₄	0.005	0.350
	0.010	0.350
	0.020	0.340
	0.030	0.340
	0.040	0.350
	0.050	0.350
	0.100	0.350
	0.050	0.354
0.001M NaBr 0.01M HClO ₄	0.010	0.340
	0.012	0.360
	0.050	0.360
	0.10	0.355
0.0001M NaBr 0.1M HClO ₄	0.02	0.350
	0.03	0.350

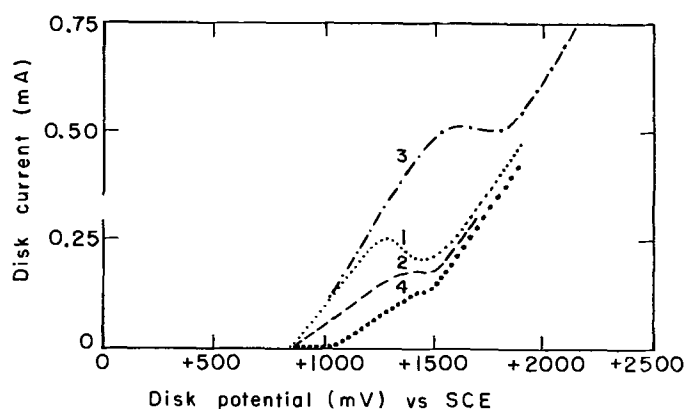


Fig. 2. Disk polarization curves in 0.001M NaBr-0.001M HClO₄: curve 1, freshly buffed; curve 2, run immediately after 1; curve 3, prereduced at -100 mV for 1 min; curve 4, preoxidized at +2500 mV for 1 min.

measured for different preparations of the surface. Typical results are shown in Fig. 2.

Curves 1-4 were obtained in a solution of 10⁻³M HClO₄, 10⁻³M NaBr, with RDI, and in the sequence numbered. Curve 1 was taken after the ring disk had been freshly buffed on a metallographer's wheel—our usual preparation. The run (and each subsequent run) was started at +500 mV (*vs.* SCE) and swept at 156 mV/min to more positive potentials, with simultaneous measurement of the disk current. Immediately after curve 1 was obtained, the potential was returned to +500 mV, another sweep was started, and curve 2 was obtained. The difference in the two was caused by the different state of the platinum surface in the two runs. This was confirmed by (i) prereducing the disk at -100 mV (*vs.* SCE) for 1.5 min before curve 3 was taken and then (ii) preoxidizing the disk at +2500 mV (*vs.* SCE) for 1 min before curve 4 was obtained. Finally, a curve was obtained after the disk had been prereduced at -100 mV (*vs.* SCE) for 5 min, and the results were identical to curve 3.

Similar investigations at concentrations of 10⁻²M HClO₄ and 10⁻³M NaBr revealed that the inhibition of Br₂ production on a preoxidized surface was much less important than for the above system. With a lower concentration of HClO₄ (10⁻⁴M, 10⁻³M NaBr), however, it was not possible to obtain a current due to Br⁻ oxidation of more than 0.12 mA (total disk current) no matter how much the disk had been prereduced. One may conclude that (i) bromine evolution on the disk is affected by the surface preparation, *i.e.*, inhibited by oxide on the platinum and (ii) a reproducible surface may be obtained by prereduction of the disk. Similar inhibition effects have been obtained recently for the Cl⁻-Cl₂ system (18).

The influence of the preparation of the disk surface on the collection efficiencies in dilute solutions is demonstrated by the results in Table II. For preoxidized platinum disks, these results are qualitatively in agreement with those of Alberty and Ulstrup. Presumably, the extra disk current on a preoxidized surface (above that required to produce the Br₂ detected on the ring) goes to produce oxygen which is not reduced on the ring in the potential region scanned. However, prereduced platinum shows a striking difference, *i.e.*, the collection efficiency is constant up to the disk limiting current. This indicates that all the disk current is going to produce Br₂, which is then detected on the ring. Bruckenstein and Miller (11) also obtained results on prereduced platinum but did not use the same system to obtain results on preoxidized surfaces. In general, their measured collection efficiencies are in agreement with ours but showed larger deviations from the calculated collection efficiencies

Table II. Surface treatment effects on collection efficiency in NaBr-HClO₄ systems

Solution composition	Total disk current (mA)	-I _r /I _d	Disk treatment
0.001M NaBr	0.01	0.330	Prereduced at -100 mV for 1 min
0.001M HClO ₄	0.02	0.330	Prereduced at -100 mV for 1 min
	0.03	0.330	Prereduced at -100 mV for 1 min
	0.05	0.340	Prereduced at -100 mV for 1 min
	0.10	0.340	Prereduced at -100 mV for 1 min
	0.25	0.350	Prereduced at -100 mV for 1 min
	0.30	0.340	Prereduced at -100 mV for 1 min
	0.40	0.330	Prereduced at -100 mV for 1 min
	0.25	0.120	Preoxidized at +2500 mV for 1 min
	0.40	0.075	Preoxidized at +2500 mV for 1 min
0.001M NaBr	0.01	0.340	Prereduced at -500 mV for 1 min
0.0001 HClO ₄	0.03	0.330	Prereduced at -500 mV for 1 min
	0.05	0.330	Prereduced at -500 mV for 1 min
	0.10	0.330	Prereduced at -500 mV for 1 min

than ours do. This may be due to a geometrical effect, but it seems premature to discuss such possibilities.

We have two general conclusions about this experimental work. First, the conditions of the platinum surface are important in the kinetics of formation of Br₂ from Br⁻ in dilute HClO₄ solutions. Preoxidized surfaces give collection efficiency results in agreement with those of Alberty and Ulstrup; prereduced surfaces give results in qualitative agreement with theoretical predictions. Second, these kinetic complications make the system a poor one for more extensive investigations of this type. Another, more reliable system should be used for more quantitative work on detecting nonuniform current distributions by collection efficiency measurements. On the other hand, it will be extremely difficult to obtain results by collection efficiency measurements which will be more than just qualitative tests of the theoretical predictions. The other methods, herein discussed, seem more suitable for quantitative work [see also Ref. (12)].

Conclusions

Nonuniform current distributions on a disk electrode may be detected in several ways. Of these, the method of measuring the deposit thickness on the disk and the technique of using the ring-disk system as a sectioned electrode are probably the most straightforward. The collection efficiency method, proposed by Alberty and Ulstrup (5) is *not* as simple to interpret, but it may be used to provide qualitative evidence for nonuniform current distributions. Experimental data have been reported here that support the predictions of theory (2) when the platinum surface is properly prepared.

Acknowledgment

This work was supported by the United States Atomic Energy Commission and by Boeing Scientific Research Laboratories.

We wish to acknowledge the help of Robert L. Lee of BSRL in making the experimental measurements.

Manuscript submitted Feb. 26, 1971; revised manuscript received *ca.* Sept. 29, 1971.

Any discussion of this paper will appear in a Discussion Section to be published in the December 1972 JOURNAL.

REFERENCES

- John Newman, *This Journal*, **113**, 501 (1966).
- John Newman, *ibid.*, **113**, 1235 (1966).
- John Newman, *ibid.*, **114**, 239 (1967).
- W. R. Parrish and John Newman, *ibid.*, **116**, 169 (1969).
- W. J. Alberty and J. Ulstrup, *Electrochim. Acta*, **13**, 281 (1968).
- V. Levich, *Acta Physicochim. U. R. S. S.*, **17**, 257-307 (1942).
- William H. Smyrl and John Newman, *This Journal*, **118**, 1079 (1971).
- J. E. Harrar and Irving Shain, *Anal. Chem.*, **38**, 1148 (1966).
- Vinay Marathe and John Newman, *This Journal*, **116**, 1704 (1969).

10. Joseph Jordan and H. L. Finston, "Identification of Active Electrode Sites by Radioactive Tracers," Brookhaven National Laboratory Report BNL-6110 (February 1962).
11. Stanley Bruckenstein and Barry Miller, *This Journal*, **117**, 1044 (1970).
12. William H. Smyrl and John Newman, *This Journal*, **119**, 212 (1972).
13. D. H. Angell, T. Dickinson, and R. Greef, *Electrochim. Acta*, **13**, 120 (1968).
14. J. D. E. McIntyre and W. F. Peck, Jr., *This Journal*, **117**, 747 (1970).
15. John Newman, *ibid.*, **117**, 507 (1970).
16. W. J. Albery and S. Bruckenstein, *Trans. Faraday Soc.*, **62**, 1920 (1966).
17. Leonard Nanis, Paper 150 presented at Electrochem Soc. Meeting, Dallas, May 7-12, 1967.
18. T. Dickinson, R. Greef, and Lord Wynne-Jones, *Electrochim. Acta*, **14**, 467 (1969).

Ring-Disk and Sectioned Disk Electrodes

William H. Smyrl*

Boeing Scientific Research Laboratories, Seattle, Washington 98124

and John Newman*

*Inorganic Materials Research Division, Lawrence Radiation Laboratory, and
Department of Chemical Engineering, University of California, Berkeley, California 94720*

ABSTRACT

Integrals relating surface concentration to surface flux for the diffusion layer on a rotating disk are used to evaluate collection efficiencies for a ring-disk system and to assess the error involved in using this system as a sectioned electrode to measure the current distribution. Experimental results are reported which confirm these predictions at the limiting current. Below the limiting current, a nonuniform current distribution is obtained.

The Diffusion Layer on a Rotating Disk

Equations relating to the diffusion layer on a rotating disk are used to rederive in a new way Albery and Bruckenstein's formula (1) for the collection efficiency of a rotating ring-disk system. The same method is then used to assess the accuracy of using a ring-disk electrode as a sectioned electrode for the direct measurement of the current distribution on a disk electrode.

Steady transfer of a solute species obeys the equation of convective diffusion

$$\underline{v} \cdot \nabla c_i = D_i \nabla^2 c_i \quad [1]$$

if, for one reason or another, electric migration of this species can be ignored. This condition applies to a neutral solute and to a minor ionic solute in a solution with an excess of inert, supporting electrolyte. The equation also applies to a solution of a single electrolyte where the migration terms can be eliminated by means of the electroneutrality condition (2-4). In this case, D_i is replaced by the diffusion coefficient of the electrolyte.

The appropriate form of this equation for the diffusion layer on a rotating disk is

$$ay\Omega(\Omega/\nu)^{1/2} \left(r \frac{\partial c_i}{\partial r} - y \frac{\partial c_i}{\partial y} \right) = D_i \frac{\partial^2 c_i}{\partial y^2} \quad [2]$$

The radial diffusion terms are neglected on the basis of the thinness of the diffusion layer, compared to the radius of the electrode. We treat the neglect of these terms in a separate paper (5). For large values of the Schmidt number $Sc = \nu/D_i$, as encountered in electrolytic solutions, the diffusion layer is also much thinner than the hydrodynamic boundary layer, and it is appropriate to approximate the normal and radial components v_y and v_r of the velocity by the first terms of their power-series expansions in the normal distance y from the disk. This introduces the rotation speed Ω , the kinematic viscosity ν , and the dimensionless constant a from the solution of the hydrodynamic problem (6-8),

where it is assumed that the mass-transfer process does not influence the fluid motion.

Equation [2] forms, in essence, the basis of the derivation of the limiting current at a disk electrode (3, 4). It is also the starting point for Newman's analysis of the current distribution on a disk electrode below the limiting current (9) and for Albery and Bruckenstein's analysis of the collection efficiency of a ring-disk system (1). It is convenient to introduce the dimensionless distance from the disk

$$\zeta = y(a\nu/3D_i)^{1/3} (\Omega/\nu)^{1/2} \quad [3]$$

so that Eq. [2] becomes

$$3\zeta \left(r \frac{\partial c_i}{\partial r} - \zeta \frac{\partial c_i}{\partial \zeta} \right) = \frac{\partial^2 c_i}{\partial \zeta^2} \quad [4]$$

The boundary conditions for Eq. [4] will normally include

$$c_i = c_\infty \text{ at } \zeta = \infty \text{ and } \partial c_i / \partial r = 0 \text{ at } r = 0 \quad [5]$$

as well as a specification of the concentration c_0 or the concentration derivative $\partial c_i / \partial \zeta$ or a combination of these on the surface of the disk at $\zeta = 0$. The problem can be solved formally to yield either the derivative at the surface in terms of the surface concentration (10)

$$\frac{\partial c_i}{\partial \zeta} \Big|_{\zeta=0} = \frac{-r}{\Gamma(4/3)} \int_0^r \frac{dc_0}{dr} \Big|_{r=r'} \frac{dr'}{(r^3 - r'^3)^{1/3}} \quad [6]$$

or vice versa (11)

$$c_0(r) - c_\infty = \frac{-1}{\Gamma(2/3)} \int_0^r \frac{\partial c_i}{\partial \zeta} \Big|_{\zeta=0} \frac{r' dr'}{(r^3 - r'^3)^{2/3}} \quad [7]$$

These equations are analogous to those integral equations commonly used to relate the surface concentration and the normal derivative of concentration for problems involving unsteady, linear diffusion in a stagnant medium. Equation [6] should be regarded as a Stieltjes integral.

Rosner (10, 12) has discussed the application of these equations to certain aspects of the ring-disk system

* Electrochemical Society Active Member.

Key words: current distribution, collection efficiency.

and to other geometries [see also Chambré (13) and Chambré and Acrivos (14)]. Analogous expressions have been derived for heat-transfer problem by Tribus and Klein (15). Appendix II treats other geometries at high Schmidt numbers.

At the limiting current, the concentration of the reactant is zero over the entire surface of the disk electrode. In Eq. [6], c_o is regarded in this case to change discontinuously from c_∞ to 0 at $r = 0$, and dc_o/dr is zero over the remainder of the electrode. This equation then yields

$$\left. \frac{\partial c_i}{\partial \xi} \right|_{\xi=0} = \frac{c_\infty}{\Gamma(4/3)} \quad [8]$$

the result of Levich (3).

Ring and Disk Electrodes

The integrals in Eq. [6] and [7] can be applied to evaluate the collection efficiency of a ring-disk system and to treat the limiting current on a sectioned disk electrode. We wish to treat three cases. It should be emphasized that the application of the mathematical expressions [6] and [7] represents a new treatment of these three cases and completely confirms the older work referenced. On the other hand, Eq. [6] and [7] and their extensions in Appendix II are more widely useful than just for the three cases described here, which illustrate their use for disk and sectioned-disk electrodes.

I. In most applications of rotating ring-disk electrodes, an unstable intermediate is generated on the disk and detected on the ring. The appropriate boundary conditions on the surface are

$$\left. \begin{array}{ll} 0 \leq r \leq r_o & (\text{on the disk}) & c_o = c_d \\ r_o < r < r_1 & (\text{on the insulating annulus}) & \partial c_i / \partial \xi = 0 \\ r_1 \leq r \leq r_2 & (\text{on the ring}) & c_o = 0 \end{array} \right\} \quad [9]$$

Here c_d is the concentration of this species on the disk, where it is produced. Normally the bulk value is $c_\infty = 0$. It should be pointed out that the condition of uniform concentration on the disk surface is, strictly speaking, an assumption, problems of current distribution on the disk having been ignored. Furthermore, Eq. [1] and [2] do not account for any homogeneous decomposition of the species produced on the disk.

II. When both the disk and the ring are at limiting current for the same reaction, the boundary conditions on the surface are

$$\left. \begin{array}{ll} 0 \leq r \leq r_o, & c_o = 0 \\ r_o < r < r_1, & \partial c_i / \partial \xi = 0 \\ r_1 \leq r \leq r_2, & c_o = 0 \end{array} \right\} \quad [10]$$

III. When no current is passed through the disk and the ring is at limiting current, the boundary conditions are

$$\left. \begin{array}{ll} 0 \leq r < r_1, & \partial c_i / \partial \xi = 0 \\ r_1 \leq r \leq r_2, & c_o = 0 \end{array} \right\} \quad [11]$$

This case, of course, also applies when there is no disk electrode. Obviously, $c_o = c_\infty$ for $0 \leq r < r_1$, as shown by Eq. [7].

These three cases will be discussed in detail, and the concentration and current distribution will be derived for each region on the rotating surface. These cases can be treated simultaneously with the appropriate values of c_∞ and c_d given in Table I.

On the disk, the surface flux is given by Eq. [6].

$$\left. \frac{\partial c_i}{\partial \xi} \right|_{\xi=0} = \frac{c_\infty - c_d}{\Gamma(4/3)} \quad (\text{disk}) \quad [12]$$

On the insulating annulus, the surface flux is zero. Hence, Eq. [7] can be used to determine the surface

Table I. Values of c_∞ and c_d for the various cases

Case	c_d	c_∞
I. Collection efficiencies	c_d	0
II. Sectioned disk	0	c_∞
III. Ring only	c_∞	c_∞

concentration, the surface flux on the disk being given by Eq. [12].

$$c_o = c_\infty - \frac{c_\infty - c_d}{\Gamma(2/3)\Gamma(4/3)} \int_0^{r_o} \frac{r' dr'}{(r^3 - r'^3)^{2/3}} \quad (\text{annulus}) \quad [13]$$

In Appendix I it is shown how to evaluate this integral. With that result, Eq. [13] can be expressed as

$$c_o = c_d + \frac{c_\infty - c_d}{\Gamma(2/3)\Gamma(4/3)} \left[\frac{\pi}{6\sqrt{3}} + \frac{1}{\sqrt{3}} \tan^{-1} \left(\frac{2\theta - 1}{\sqrt{3}} \right) + \frac{1}{6} \ln \frac{(1 + \theta)^3}{1 + \theta^3} \right] \quad [14]$$

where

$$\theta^3 = r^3/r_o^3 - 1 \quad [15]$$

On the ring electrode, the surface concentration is zero, and the surface flux can be obtained from Eq. [6], the surface concentration on the disk being given by c_d and the surface concentration on the annulus being given by Eq. [13] or [14].

$$\left. \frac{\partial c_i}{\partial \xi} \right|_{\xi=0} = \frac{-r}{\Gamma(4/3)} \left\{ \frac{c_d - c_\infty}{r} + \int_{r_o}^{r_1} \frac{dc_o}{dr} \bigg|_{r=r'} \frac{dr'}{(r^3 - r'^3)^{1/3}} - \frac{c_o(r_1)}{(r^3 - r_1^3)^{1/3}} \right\} \quad [16]$$

From Eq. [14]

$$\frac{dc_o}{dr} = \frac{c_\infty - c_d}{\Gamma(2/3)\Gamma(4/3)} \frac{r_o^2}{r(r^3 - r_o^3)^{2/3}} \quad (\text{annulus}) \quad [17]$$

and Eq. [16] becomes

$$\Gamma\left(\frac{4}{3}\right) \left. \frac{\partial c_i}{\partial \xi} \right|_{\xi=0} = c_\infty - c_d + \frac{rc_o(r_1)}{(r^3 - r_1^3)^{1/3}} - \frac{c_\infty - c_d}{\Gamma(2/3)\Gamma(4/3)} \int_{r_o}^{r_1} \frac{rr_o^2 dr'}{r'(r^3 - r_o^3)^{2/3} (r^3 - r'^3)^{1/3}} \quad [18]$$

Let us evaluate a quantity j_r , proportional to the total flow of the species to the ring

$$j_r = \int_{r_1}^{r_2} \left. \frac{\partial c_i}{\partial \xi} \right|_{\xi=0} r dr \quad [19]$$

Integration of Eq. [18] in this way over r gives

$$j_r = \frac{1}{2\Gamma(4/3)} \left\{ (c_\infty - c_d)(r_2^2 - r_1^2) + c_o(r_1)(r_2^3 - r_1^3)^{2/3} - \frac{(c_\infty - c_d)r_o^2}{\Gamma(2/3)\Gamma(4/3)} \int_{r_o}^{r_1} \frac{(r_2^3 - r'^3)^{2/3} - (r_1^3 - r'^3)^{2/3}}{(r'^3 - r_o^3)^{2/3}} \frac{dr'}{r'} \right\} \quad [20]$$

In Appendix I it is shown how to evaluate integrals of the type involved here. Similarly, let

$$j_d = \int_0^{r_o} \left. \frac{\partial c_i}{\partial \xi} \right|_{\xi=0} r dr = \frac{c_\infty - c_d}{2\Gamma(4/3)} r_o^2 \quad [21]$$

In order to avoid writing complicated expressions more than once, let us define N as the following function of the geometric ratios r_2/r_o and r_1/r_o

$$\begin{aligned}
N &= \frac{(r_2^3 - r_1^3)^{2/3}}{r_0^2 \Gamma(2/3) \Gamma(4/3)} \int_0^{r_0} \frac{r' dr'}{(r_1^3 - r'^3)^{2/3}} \\
&\quad - \frac{r_2^2 - r_1^2}{r_0^2} + \frac{1}{\Gamma(2/3) \Gamma(4/3)} \int_{r_0}^{r_1} \\
&\quad \frac{(r_2^3 - r'^3)^{2/3} - (r_1^3 - r'^3)^{2/3}}{(r'^3 - r_0^3)^{2/3}} \frac{dr'}{r'} \\
&= (A^3 - B^3)^{2/3} \left[\frac{\sqrt{3}}{4\pi} \ln \frac{1 + \theta^3}{(1 + \theta)^3} \right. \\
&\quad \left. - \frac{3}{2\pi} \tan^{-1} \left(\frac{2\theta - 1}{\sqrt{3}} \right) + \frac{3}{4} \right] \\
&\quad + \frac{\sqrt{3}}{4\pi} \ln \frac{1 + A^3 \psi^3}{(1 + A\psi)^3} + \frac{3}{2\pi} \tan^{-1} \left(\frac{2A\psi - 1}{\sqrt{3}} \right) + \frac{1}{4} \\
&\quad - A^2 \left[\frac{\sqrt{3}}{4\pi} \ln \frac{1 + \psi^3}{(1 + \psi)^3} \right. \\
&\quad \left. + \frac{3}{2\pi} \tan^{-1} \left(\frac{2\psi - 1}{\sqrt{3}} \right) + \frac{1}{4} \right] \quad [22]
\end{aligned}$$

where

$$\left. \begin{aligned}
A &= r_2/r_0, \quad B = r_1/r_0, \\
\theta &= (B^3 - 1)^{1/3}, \quad \psi = \frac{1}{A} \left(\frac{A^3 - B^3}{B^3 - 1} \right)^{1/3}
\end{aligned} \right\} \quad [23]$$

Then we can write

$$\begin{aligned}
j_r &= - \frac{c_a - c_d}{2\Gamma(4/3)} r_0^2 N + \frac{c_a (r_2^3 - r_1^3)^{2/3}}{2\Gamma(4/3)} = \\
&\quad - j_d N + \frac{c_a (r_2^3 - r_1^3)^{2/3}}{2\Gamma(4/3)} \quad [24]
\end{aligned}$$

If no other reactions occur, the ratio of the total ring current to the total disk current for the first case in Table I is found to be

$$-j_r/j_d = N \quad [25]$$

since in this case $c_a = 0$ and all the active intermediate which reacts on the ring is produced at the disk. Then, N is called the collection efficiency, and Eq. [22] agrees exactly with the expression derived by Albery and Bruckenstein (1) by another method. These authors have tabulated values of N for given values of r_1/r_0 and r_2/r_1 . The analytic form of the result makes it easy to evaluate N numerically for values of r_1/r_0 and r_2/r_1 outside those tabulated.

For case III, when there is no disk electrode, $c_d = c_a$, and the total flow to the ring reduces to

$$j_r = c_a \frac{(r_2^3 - r_1^3)^{2/3}}{2\Gamma(4/3)} \quad [26]$$

a result first obtained by Levich (16) and later by Ibl (17) and Rosner (10).

The geometric quantity N can also be measured with a ring-disk system where both electrodes are operated at the limiting current for the same reaction. Equations [21] and [24] then yield for the ratio of the total ring current to the total disk current, since $c_d = 0$ (case II in Table I)

$$\frac{j_r}{j_d} = \frac{(r_2^3 - r_1^3)^{2/3}}{r_0^2} - N \quad [27]$$

in agreement with the result of Bruckenstein (18).

The rotating ring-disk electrode system is usually used as a polarographic instrument; species which are generated at the disk are detected on the ring. The presence of unstable intermediates can be detected in this way, but it is difficult to treat quantitatively the

kinetics because of uncertainty in the relative importance of ohmic potential drop and concentration and surface overpotentials. On the ring, the influence of surface overpotential and ohmic potential drop is negligible when it is operated at the limiting current. The kinetics of generation of the active intermediate on the disk is less well known, however, because of the nonuniformity of the current distribution on the disk. The assumption of a uniform surface concentration on the disk surface is questionable for case I of Table I.

When the ring-disk system is used for plating-type applications, the same reaction would occur on both electrodes, and they would normally be operated at the same potential. If both are operated below the limiting current, the nonuniform current distribution on the disk again makes it difficult to analyze the electrochemical kinetics. However, it is just because of the nonuniform current distribution that a ring would be used with the disk. The ring-disk system might be used to determine the current distribution, or the ring might be included to make the current distribution more nearly uniform on the disk. Since the nonuniformities are greatest on the outer edge of a disk, the ring might be viewed as "soaking up" the nonuniformities. The justification for use of the ring for either purpose must come from an analysis of the current on a ring as compared to the current over an equivalent area of a disk electrode.

Since sectioned electrodes are commonly used to measure the current distribution on an electrode, frequently at the limiting current, it would be valuable to assess the error introduced by the nonzero thickness of the insulator. One standard of comparison would be the ring current divided by the current density on the disk and the area of the ring electrode. From Eq. [24], this ratio is given by

$$f_1 = \frac{(r_2^3 - r_1^3)^{2/3} - r_0^2 N}{r_2^2 - r_1^2} \quad [28]$$

and is tabulated in Table II. Departures of this ratio from unity show by how much the average current density on the ring exceeds the current density on the disk. Since limiting currents are being considered, this current density on the disk is the appropriate standard since it would prevail everywhere if the insulating annulus were of zero thickness.

As a second standard of comparison, we take the ring current divided by the current density on the disk and the area of both the ring electrode and the insulating annulus. This ratio is given by

$$f_2 = \frac{(r_2^3 - r_1^3)^{2/3} - r_0^2 N}{r_2^2 - r_0^2} \quad [29]$$

and is tabulated in Table III. Again, departures of this ratio from unity show by how much the average current density on the ring and annulus is less than the current density on the disk.

For thin insulators or wide rings, both of these ratios approach unity. For a ring electrode whose area

Table II. Total ring current divided by the current density on the disk and the area of the ring (from Eq. [28]) for the case where both the ring and the disk are at limiting current for the same reaction

r_2/r_0	1.1	1.2	1.5	2	3
$r_2^2 - r_0^2$					
$r_2^2 - r_1^2$					
0.05	1.0388	1.0390	1.0395	1.0401	1.0409
0.1	1.0720	1.0724	1.0735	1.0749	1.0767
0.2	1.1304	1.1313	1.1336	1.1366	1.1400
0.5	1.2713	1.2736	1.2795	1.2860	1.2928
1	1.4497	1.4540	1.4641	1.4746	1.4846
2	1.7112	1.7181	1.7337	1.7491	1.7628
5	2.2156	2.2269	2.2514	2.2744	2.2940
10	2.7431	2.7584	2.7910	2.8209	2.8459
20	3.4247	3.4446	3.4869	3.5252	3.5569

Table III. Total ring current divided by the current density on the disk and the area of both the ring and the annulus (from Eq. [29]) for the case where both the ring and the disk are at limiting current for the same reaction

r_2/r_o	1.1	1.2	1.5	2	3
$r_1^2 - r_o^2$					
$r_2^2 - r_1^2$					
0.05	0.9894	0.9895	0.9900	0.9906	0.9914
0.1	0.9746	0.9749	0.9759	0.9772	0.9788
0.2	0.9420	0.9427	0.9447	0.9471	0.9500
0.5	0.8475	0.8491	0.8530	0.8574	0.8619
1	0.7248	0.7270	0.7320	0.7373	0.7423
2	0.5704	0.5727	0.5779	0.5830	0.5876
5	0.3693	0.3712	0.3752	0.3791	0.3823
10	0.2494	0.2508	0.2537	0.2564	0.2587
20	0.1631	0.1640	0.1660	0.1679	0.1694

is ten times the area of the insulator, the error represented by the ratio f_2 can be expected to be less than 3% while that represented by f_1 can be greater than 7%. These ratios thus provide a basis for the design of ring-disk systems for current-distribution studies. Similar considerations apply to the design of sectioned electrodes for other geometries when mass-transfer limitations determine the current distribution (see Appendix II).

The ratio f_2 depends most strongly on the ratio of the area of the insulator to the area of the ring electrode. Consequently, we have used this for one of the geometric parameters in Tables II and III. With a strong dependence on this parameter, the choice of the other parameter becomes less important; we chose r_2/r_o , the ratio of the outer radius of the ring to the radius of the disk electrode. These geometric parameters replace the ratios r_1/r_o and r_2/r_1 .

Experimental Determination of Current Distributions

The experimental investigation of these predictions was divided into two parts. The first objective was to investigate whether or not Eq. [29] was obeyed at limiting current for the solutions used here. The second part was to investigate the departure from this equation below the limiting current, i.e., to determine whether or not a nonuniform current distribution could be observed.

The electrolytic solutions used were composed of KNO_3 , $\text{K}_4\text{Fe}(\text{CN})_6$, and $\text{K}_3\text{Fe}(\text{CN})_6$. The concentration of KNO_3 was always 1 molar, and the concentrations of the other two components were varied but their ratio was always 1. Fresh, filtered solutions were used for the determinations because it was found that the solutions decompose slowly upon exposure to light and air. The measurements were made at about 23°C.

The rotating ring-disks were constructed of platinum with epoxy insulation. The relevant dimensions of the assemblies were: ring-disk 1 (RD1), $r_o = 0.441$ cm, $r_1 = 0.502$ cm, $r_2 = 0.620$ cm, and over-all radius 1.27 cm; ring-disk 2 (RD2), $r_o = 0.322$ cm, $r_1 = 0.478$ cm, $r_2 = 0.633$ cm, and over-all radius 1.27 cm; ring-disk 3 (RD3), $r_o = 0.441$ cm, $r_1 = 0.498$ cm, $r_2 = 0.616$ cm, and over-all radius 1.27 cm. The ring-disks were polished before each run on a metallographic wheel with 0.05μ alumina.

The ring-disks were operated potentiostatically with a Wenking potentiostat. Both were operated anodically. One output from the potentiostat was taken to a parallel circuit in one leg of which was a precision resistor and the connection to the disk, and in the other leg was a variable resistor and the connection to the ring. For measurements at the limiting current, the potential drop across each resistor was measured, and the current was calculated from this and the measured resistance of each resistor. For measurements below the limiting current, the potential across the resistors was matched to within 0.05 mV. From this and the measured resistance, the current through each resistor was calculated. These potential drops were measured with a Honeywell potentiometric strip chart recorder.

Table IV. Sectioned-electrode measurements at limiting current. All solutions were 1M in KNO_3 . Solutions I, II, and III were 0.005, 0.01, and 0.05M respectively, in both $\text{K}_4\text{Fe}(\text{CN})_6$ and $\text{K}_3\text{Fe}(\text{CN})_6$

Ring-disk assembly	Solution	Rotation speed (rpm)	I_r/I_d	$I_r/r_o^2 / I_d/r_2^2 - r_o^2$	f_2 theory
RD1	I	1550	0.858 ± 0.1%	0.879	0.871
	II	1550	0.852 ± 0.9%	0.872	
	III	1550	0.852 ± 0.1%	0.872	
RD2	III	2500	0.847 ± 0.1%	0.867	0.798
	III	750	0.855 ± 0.1%	0.876	
	I	1550	2.300 ± 0.1%	0.801	
	II	1550	2.308 ± 0.2%	0.804	
	III	1550	2.312 ± 0.2%	0.805	
	III	2500	2.305 ± 0.1%	0.803	
RD3	III	750	2.295 ± 0.5%	0.800	0.879
	III	750	0.832 ± 0.02%	0.875	
	III	1550	0.833 ± 0.3%	0.876	
	III	2500	0.831 ± 0.03%	0.874	

The reference electrode was a strip of platinum partially immersed in a side arm compartment filled with the solution being investigated. The side compartment was connected through a Luggin capillary to the main solution. The capillary tip was positioned in the plane of the disk surface at 2.27 cm from the center of the ring-disk assembly.

The anodic limiting current was attained with overpotentials between +400 mV and +800 mV. In the limiting current region, both the ring current and disk current were constant with potential. In Table IV is listed the ratio of ring current to disk current, in the limiting current region, for each solution used and at several rotation speeds. The results are the average of several runs, and the per cent of average deviation is also given. Also given is this ratio multiplied by the ratio of disk area to the area of insulating annulus plus ring electrode. This may be compared to the value of f_2 , also listed, calculated from Eq. [29].

The experimental results agree with the predictions of Eq. [29] to better than 1%. Also, there is no dependence on concentration or rotation speed, which is also consistent with Eq. [29]. The deviation from f_2 (theory) is considered to be within experimental error. The largest error was probably the measurement of the electrode dimensions.

The second part of the investigation, i.e., sectioned electrode measurements below the limiting current, would be expected to reveal a higher value of f_2 (meas.) than predicted by Eq. [29]. This is the result obtained, as shown in Fig. 1 and 2. Δ is the deviation of the measured results from predictions of Eq. [29], plotted in Fig. 1 as a function of the fraction of limiting current on the disk plus ring. Δ is zero at limiting current, and increases with decreasing importance of the concentration overpotential and the increasing importance of ohmic potential drop as the current is decreased below the limiting current. The ferro-ferricyanide system was not under kinetic control in the concentration and potential ranges used here.

Curves A and B of Fig. 1 were obtained for RD2 and RD3 at the same rotation speed in solutions of the same composition. The difference between the two curves is due to the different gap widths of the two assemblies.

Since the outer radii of RD2 and RD3 are approximately equal, curves A and B were obtained with the same value of the dimensionless rotation speed, N , of Newman's theory (9) (not to be confused with the collection efficiency N). This parameter is defined as

$$N = -\Gamma(4/3) \frac{ZF r_2^{3/2} i_{lim}}{RT \kappa_x}$$

The values of N for curves A and B are 5.84 and 5.89, respectively. The parameter is a measure of the relative importance of the ohmic potential drop as com-

¹ The values of N were calculated from the limiting current density and the conductivity of 1M KNO_3 , i.e., $\kappa_x = 0.1$ ohm⁻¹ cm⁻¹.

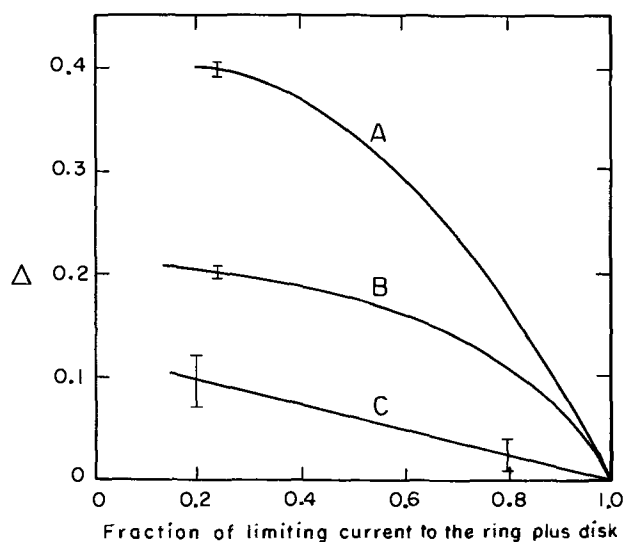


Fig. 1. Δ as a function of the fraction of limiting current. Curve A—RD3, 1550 rpm, 1M KNO_3 , 0.05M $\text{K}_3\text{Fe}(\text{CN})_6$, 0.05M $\text{K}_4\text{Fe}(\text{CN})_6$. Curve B—RD2, 1550 rpm, 1M KNO_3 , 0.05M $\text{K}_3\text{Fe}(\text{CN})_6$, 0.05M $\text{K}_4\text{Fe}(\text{CN})_6$. Curve C—RD3, 1550 rpm, 1M KNO_3 , 0.005M $\text{K}_3\text{Fe}(\text{CN})_6$, 0.005M $\text{K}_4\text{Fe}(\text{CN})_6$. I—indicates standard deviation.

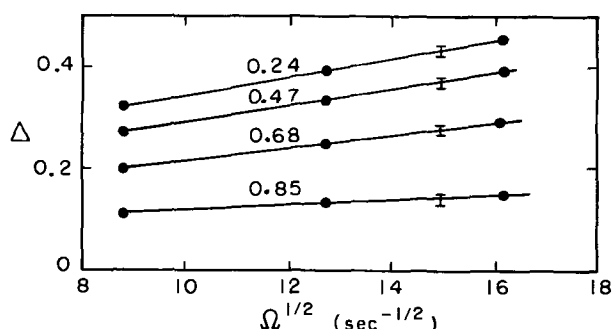


Fig. 2. Δ as a function of rotation speed. Numbers on the curves indicate the fraction of limiting current on ring plus disk. RD3—1M KNO_3 , 0.05M $\text{K}_3\text{Fe}(\text{CN})_6$, 0.05M $\text{K}_4\text{Fe}(\text{CN})_6$. I—indicates standard deviation.

pared to the concentration overpotential at a particular fraction of limiting current.

The effect of changing N was measured in two ways. First, the composition of the solution was changed from 0.05M in both ferrocyanide and ferricyanide to 0.005M in both ferrocyanide and ferricyanide. With this solution, the value of N is¹ 0.595 for RD3, and curve C of Fig. 1 was obtained. These results may be compared to curve A. Thus, by reducing the concentration of ferro-ferricyanide, one reduces the importance of the ohmic potential drop, at a particular fraction of limiting current, and the current becomes more uniform.

N was also changed by varying the rotation speed, with the results shown in Fig. 2. The increase of rotation speed increases N and thus the importance of the ohmic drop, producing a less uniform current distribution.

Conclusions

It has been possible to determine the error involved in using the ring-disk system as a sectioned electrode. The predictions for operation at limiting current were verified by experiment within 1%. When operated below the limiting current, a nonuniform current distribution is observed. The average current density on the ring is higher than the average current density on the disk—an observation which is consistent with Newman's theory (9).

Bruckenstein and Miller (21) recently reported measurements similar to those here but with a NaBr-HClO_4 system. Their measurements also revealed a nonuniform current distribution. They found that an increase in conductivity (thus reducing N) made the current distribution more uniform. They do not report values of the important parameters for their system, nor even the location of the reference electrode, so a more direct comparison with the present results is not possible. It is surprising, however, that the ratio of ring current density to disk current density, which they measure, is constant for various fractions of limiting current (which fractions they do not specify). This should be contrasted with the data reported here, in Fig. 1. The explanation for this behavior is not clear, but it may be related to the kinetic complications of the NaBr-HClO_4 system (22).

The diffusion coefficient for the ferrocyanide ion in the systems used here has been calculated from the measured anodic limiting currents, and the equation (3, 9)

$$i_{\text{lim}} = \frac{nFc_{\infty}}{\Gamma(4/3)} \left(\frac{a}{3}\right)^{1/3} \Omega^{1/2} D_i^{2/3} \nu^{-1/6}$$

In making the calculations, the viscosity of water and the density of 1M KNO_3 were used. The viscosity of 1M KNO_3 , 0.05M ferrocyanide, 0.05M ferricyanide was found to be the same as that for water (within 5%) at the same temperature. The results are:

- (i) 1M KNO_3 , 0.05M $\text{K}_3\text{Fe}(\text{CN})_6$, 0.05M $\text{K}_4\text{Fe}(\text{CN})_6$
rotation speeds of 750, 1550, and 2500 rpm
 $D_i = 0.567 \times 10^{-5} \text{ cm}^2/\text{sec}$ with a standard deviation of $0.0166 \times 10^{-5} \text{ cm}^2/\text{sec}$.
- (ii) 1M KNO_3 , 0.01M $\text{K}_3\text{Fe}(\text{CN})_6$, 0.01M $\text{K}_4\text{Fe}(\text{CN})_6$
rotation speed of 1550 rpm
 $D_i = 0.599 \times 10^{-5} \text{ cm}^2/\text{sec}$ with a standard deviation of $0.007 \times 10^{-5} \text{ cm}^2/\text{sec}$.
- (iii) 1M KNO_3 , 0.05M $\text{K}_3\text{Fe}(\text{CN})_6$, 0.005M $\text{K}_4\text{Fe}(\text{CN})_6$
rotation speed of 1550 rpm
 $D_i = 0.577 \times 10^{-5} \text{ cm}^2/\text{sec}$ with a standard deviation of $0.013 \times 10^{-5} \text{ cm}^2/\text{sec}$.

The value of $D_i = 0.606 \times 10^{-5} \text{ cm}^2/\text{sec}$ is predicted from the correlation of Gordon, Newman, and Tobias (23). This compares favorably with that reported here.

The theoretical results for sectioned electrodes can be extended to a variety of geometries involving forced, laminar convection, as shown in Appendix II.

Acknowledgment

This work was supported by the United States Atomic Energy Commission and by Boeing Scientific Research Laboratories.

We wish to acknowledge the help of Robert L. Lee of BSRL in making the experimental measurements.

Manuscript submitted March 8, 1971; revised manuscript received ca. Sept. 29, 1971.

Any discussion of this paper will appear in a Discussion Section to be published in the December 1972 JOURNAL.

APPENDIX I

First let us evaluate the integral

$$\int_0^x \frac{xdx}{(1-x^3)^{2/3}} = \int_0^1 \frac{xdx}{(1-x^3)^{2/3}} - \int_x^1 \frac{xdx}{(1-x^3)^{2/3}} \quad [30]$$

In the first integral, make the substitution $y = x^3$; in the second, make the substitution

$$\theta^3 = 1/x^3 - 1 \quad [31]$$

Then we have

$$\int_0^x \frac{x dx}{(1-x^3)^{2/3}} = \frac{1}{3} \int_0^1 \frac{dy}{y^{1/3}(1-y)^{2/3}} - \int_0^\theta \frac{d\theta}{1+\theta^3}$$

$$= \frac{1}{3} \Gamma\left(\frac{2}{3}\right) \Gamma\left(\frac{1}{3}\right) - \frac{1}{3} \int_0^\theta \frac{d\theta}{1+\theta^3}$$

$$- \frac{1}{3} \int_0^\theta \frac{2-\theta}{\theta^2-\theta+1} d\theta = \Gamma\left(\frac{2}{3}\right) \Gamma\left(\frac{4}{3}\right)$$

$$- \frac{1}{3} \ln(1+\theta) + \frac{1}{6} \ln(\theta^2-\theta+1)$$

$$- \frac{1}{\sqrt{3}} \tan^{-1} \frac{2\theta-1}{\sqrt{3}} \Big|_0^\theta = \Gamma\left(\frac{2}{3}\right) \Gamma\left(\frac{4}{3}\right)$$

$$+ \frac{1}{6} \ln \frac{1+\theta^3}{(1+\theta)^3} - \frac{1}{\sqrt{3}} \tan^{-1} \frac{2\theta-1}{\sqrt{3}} - \frac{\pi}{6\sqrt{3}} \quad [32]$$

Next we want to evaluate the integral

$$I = \int_1^x \frac{(A^3-x^3)^{2/3}}{(x^3-1)^{2/3}} \frac{dx}{x} \quad [33]$$

where $A \cong x > 1$. Let

$$\omega = x^3/(x^3-1) \quad [34]$$

Then

$$I = \frac{A^2}{3} \int_\omega^\infty \frac{(\beta\omega-1)^{2/3} d\omega}{\omega(\omega-1)} = \frac{A^2}{3} \left[\int_\omega^\infty \frac{d\omega}{\omega(\beta\omega-1)^{1/3}} \right. \\ \left. - (1-\beta) \int_\omega^\infty \frac{d\omega}{(\omega-1)(\beta\omega-1)^{1/3}} \right] \quad [35]$$

where

$$\beta = 1 - 1/A^3 \quad [36]$$

In the first integral, let $y^3 = \beta\omega - 1$; in the second integral, let $y^3 = (\beta\omega - 1)/(1 - \beta)$. Then we have

$$I = A^2 \int_\psi^\infty \frac{y dy}{1+y^3} - \int_{A\psi}^\infty \frac{y dy}{1+y^3} \quad [37]$$

where

$$\psi = (\beta\omega - 1)^{1/3} = \frac{1}{A} \left(\frac{A^3 - x^3}{x^3 - 1} \right)^{1/3} \quad [38]$$

The integrals here can now be evaluated in a manner used above for the first integral

$$I = (A^2 - 1) \int_0^\infty \frac{y dy}{1+y^3} + \int_0^{A\psi} \frac{y dy}{1+y^3}$$

$$- A^2 \int_0^\psi \frac{y dy}{1+y^3} = (A^2 - 1) \Gamma(4/3) \Gamma(2/3)$$

$$+ \frac{1}{6} \ln \frac{1+A^3\psi^3}{(1+A\psi)^3} + \frac{1}{\sqrt{3}} \tan^{-1} \left(\frac{2A\psi-1}{\sqrt{3}} \right) + \frac{\pi}{6\sqrt{3}}$$

$$- A^2 \left[\frac{1}{6} \ln \frac{1+\psi^3}{(1+\psi)^3} \right. \\ \left. + \frac{1}{\sqrt{3}} \tan^{-1} \left(\frac{2\psi-1}{\sqrt{3}} \right) + \frac{\pi}{6\sqrt{3}} \right] \quad [39]$$

Note that

$$\Gamma(2/3) \Gamma(4/3) = 2\pi/3\sqrt{3} \quad [40]$$

and that

$$\tan^{-1} \left(\frac{2\psi-1}{\sqrt{3}} \right) = \frac{\pi}{3} - \tan^{-1} \left(\frac{2/\psi-1}{\sqrt{3}} \right) \quad [41]$$

APPENDIX II

Diffusion Layers in Laminar Forced Convection at High Schmidt Numbers

Because the diffusion coefficient is so small in electrolytic solutions, the diffusion layer generally lies very close to the electrode surface and it is appropriate to approximate the velocity components by the first terms in their power-series expansions in the normal distance from the surface. The Lighthill transforma-

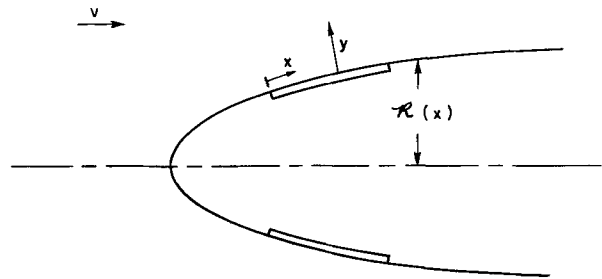


Fig. 3. An electrode on an axisymmetric body with axisymmetric flow.

tion (19, 20) is useful for treating such diffusion layers. The diffusion-layer form of Eq [1] then is

$$y\beta \frac{\partial c_i}{\partial x} - \frac{1}{2} y^2 \frac{(\mathcal{R}\beta)'}{\mathcal{R}} \frac{\partial c_i}{\partial y} = D_i \frac{\partial^2 c_i}{\partial y^2} \quad [42]$$

where the coordinate system is indicated in Fig. 3, $\beta(x)$ is the velocity derivative $\partial v_x/\partial y$ at $y = 0$, and for an axisymmetric body $\mathcal{R}(x)$ is the distance of the surface from the axis of symmetry. For two-dimensional diffusion layers, $\mathcal{R} = 1$. Outside the diffusion layer, at $y = \infty$, the concentration is $c_i = c_\infty$.

We solve the problem first for the boundary conditions on the surface

$$\left. \begin{aligned} c_i &= c_\infty \text{ at } y = 0, x < x_0 \\ c_i &= 0 \text{ at } y = 0, x \geq x_0 \end{aligned} \right\} \quad [43]$$

In terms of the similarity variable

$$\xi = y \sqrt{\mathcal{R}\beta} / \left[9D_i \int_{x_0}^x \mathcal{R} \sqrt{\mathcal{R}\beta} dx \right]^{1/3} \quad [44]$$

the solution is (for $x > x_0$)

$$\frac{c_i}{c_\infty} = \theta(\xi) = \frac{1}{\Gamma(4/3)} \int_0^\xi e^{-x^3} dx \quad [45]$$

which gives for the concentration derivative at the wall

$$\frac{\partial c_i}{\partial y} \Big|_{y=0} = \frac{c_\infty \sqrt{\mathcal{R}\beta}}{\Gamma(4/3)} / \left[9D_i \int_{x_0}^x \mathcal{R} \sqrt{\mathcal{R}\beta} dx \right]^{1/3} \quad [46]$$

The above solution can be used to treat the case of a varying surface concentration by superposition of results for appropriate changes in the surface concentration at many points x_0 along the surface

$$\frac{\partial c_i}{\partial y} \Big|_{y=0} = - \frac{\sqrt{\mathcal{R}\beta}}{\Gamma(4/3)} \int_0^x \frac{dc_0}{dx} \Big|_{x=x_0} \frac{dx_0}{\left[9D_i \int_{x_0}^x \mathcal{R} \sqrt{\mathcal{R}\beta} dx \right]^{1/3}} \quad [47]$$

By means of the coordinate transformation

$$r^3 = \int_0^x \mathcal{R} \sqrt{\mathcal{R}\beta} dx \text{ and } \zeta = y \sqrt{\mathcal{R}\beta} / \left[9D_i \int_0^x \mathcal{R} \sqrt{\mathcal{R}\beta} dx \right]^{1/3} \quad [48]$$

Eq. [47] becomes

$$\frac{\partial c_i}{\partial \zeta} \Big|_{\zeta=0} = \frac{-r}{\Gamma(4/3)} \int_0^r \frac{dc_0}{dr} \Big|_{r=r'} \frac{dr'}{(r^3 - r'^3)^{1/3}} \quad [49]$$

which is the same as Eq. [6]. The coordinate transformation [48] also reduces Eq. [42] to Eq. [4].

Equation [49] should have the same inverse [7] as Eq. [6]. We can derive this in a more straightforward manner than that used in Ref. (11) by following Tribus and Klein (15), p. 215. Write Eq. [49] as

$$\left. \frac{\partial c_i}{\partial \xi} \right|_{\substack{\xi=0 \\ r=r'}} = \frac{-r'}{\Gamma(4/3)} \int_0^r \frac{dc_o}{dr} \bigg|_{r=x} \frac{dx}{(r^3 - x^3)^{1/3}} \quad [50]$$

Multiply by $(r^3 - r'^3)^{-2/3} 3r'dr'$ and integrate from 0 to r .

$$3 \int_0^r \frac{\partial c_i}{\partial \xi} \bigg|_{\xi=0} \frac{r'dr'}{(r^3 - r'^3)^{2/3}} = - \int_0^r \frac{3r'^2}{\Gamma(4/3)} \int_0^r \frac{dc_o}{dr} \bigg|_{r=x} \frac{dx}{(r^3 - x^3)^{1/3}} \frac{dr'}{(r^3 - r'^3)^{2/3}} \quad [51]$$

Interchange the order of integration on the right.

$$3 \int_0^r \frac{\partial c_i}{\partial \xi} \bigg|_{\xi=0} \frac{r'dr'}{(r^3 - r'^3)^{2/3}} = \frac{-1}{\Gamma(4/3)} \int_0^r \frac{dc_o}{dr} \bigg|_{r=x} \int_x^r \frac{3r'^2 dr'}{(r^3 - x^3)^{1/3} (r^3 - r'^3)^{2/3}} dx \quad [52]$$

In the inner integral, let

$$y = (r'^3 - x^3)/(r^3 - x^3)$$

so that

$$\int_x^r \frac{3r'^2 dr'}{(r^3 - x^3)^{1/3} (r^3 - r'^3)^{2/3}} = \int_0^1 \frac{dy}{y^{1/3} (1-y)^{2/3}} = \Gamma\left(\frac{1}{3}\right) \Gamma\left(\frac{2}{3}\right) = \frac{2\pi}{\sqrt{3}} \quad [53]$$

Then we have

$$\int_0^r \frac{dc_o}{dr} \bigg|_{r=x} dx = c_o(r) - c_\infty = \frac{-1}{\Gamma(2/3)} \int_0^r \frac{\partial c_i}{\partial \xi} \bigg|_{\xi=0} \frac{r'dr'}{(r^3 - r'^3)^{2/3}} \quad [54]$$

in agreement with Eq. [7]. The inverse of Eq. [47] can thus be written, expressing the surface concentration as an integral over the flux

$$c_o(x) - c_\infty = - \frac{(D_i/3)^{1/3}}{\Gamma(2/3)} \int_0^x \frac{\partial c_i}{\partial y} \bigg|_{\substack{y=0 \\ z=x_0}} \frac{\mathcal{R}(x_0) dx_0}{\left[\int_{x_0}^x \mathcal{R} \sqrt{\mathcal{R}\beta} dx \right]^{2/3}} \quad [55]$$

With these results we can now work, for various geometries, the same problems as outlined in Table I. The collection efficiency problem may then not be realistic since we have no justification for assuming that the surface concentration is uniform on the first electrode (unless the first electrode is at limiting current for the reaction which produces the active intermediate). The third problem is trivial since we worked it out before the superposition (see Eq. [46]).

Let us have two electrodes given by

$$0 \leq r \leq r_o \text{ and } r_1 \leq r \leq r_2$$

with an insulator between ($r_o < r < r_1$). On the first electrode, $c_o = c_d$, and Eq. [12] gives the flux. On the insulator, $\partial c_i/\partial \xi = 0$ at $\xi = 0$, and the surface concentration is given by Eq. [13] or [14]. On the second electrode, $c_o = 0$, and the flux is given by Eq. [18].

Note that

$$j_r = \int_{r_1}^{r_2} \frac{\partial c_i}{\partial \xi} \bigg|_{\xi=0} r dr = \left(\frac{D_i}{3}\right)^{1/3} \int_{x_1}^{x_2} \frac{\partial c_i}{\partial y} \bigg|_{y=0} \mathcal{R} dx \quad [56]$$

and is proportional to the total flow to the second electrode. Similarly, j_d is proportional to the total flow to the first electrode, and Eq. [21] and [24] apply.

Furthermore, for sectioned electrodes at the limiting current, f_1 and f_2 have the meaning originally intended

(but not stated explicitly). f_1 is the current to the second electrode divided by the current which would flow to the area of the second electrode if the insulator were an electrode. f_2 is the current to the second electrode divided by the current which would flow to the combined area of the second electrode and the insulator if the insulator were an electrode.

Consider the special case of sectioned electrodes in the wall of a flow channel (or a tube or an annulus). $\beta = \beta_o$, a constant, and \mathcal{R} is a constant. Then, according to Eq. [48]

$$r^3 = x\mathcal{R}\sqrt{\mathcal{R}\beta_o} \quad [57]$$

Tables II and III still apply, but $A = r_2/r_o = (x_2/x_o)^{1/3}$ and $B = r_1/r_o = (x_1/x_o)^{1/3}$, and the parameters on those tables are

$$\frac{r_2}{r_o} = \left(\frac{x_2}{x_o}\right)^{1/3} \text{ and } \frac{r_1^2 - r_o^2}{r_2^2 - r_1^2} = \frac{x_1^{2/3} - x_o^{2/3}}{x_2^{2/3} - x_1^{2/3}} \quad [58]$$

NOMENCLATURE

a	$= 0.51023$
A	$= r_2/r_o$
B	$= r_1/r_o$
c_i	concentration of the species of interest (mole/cm ³)
c_o	surface concentration of the species of interest (mole/cm ³)
c_r	concentration of the species of interest outside the diffusion layer (mole/cm ³)
c_d	uniform concentration of the species of interest near the surface of the disk electrode (mole/cm ³)
D_i	diffusion coefficient of the species of interest (cm ² /sec)
f_1	see Eq. [28]
f_2	see Eq. [29]
i_{lim}	limiting current density on disk electrode (A/cm ²)
I	see Eq. [33]
j_d	proportional to the total mass-transfer rate to disk electrode (mole/cm)
j_r	proportional to total mass-transfer rate to ring electrode (mole/cm)
N	dimensionless limiting current density for disk electrode [see Ref. (9)]
N	collection efficiency for ring-disk system
r	radial distance from the axis of the disk
r_o	radius of disk electrode (cm)
r_1	inner radius of ring electrode (cm)
r_2	outer radius of ring electrode (cm)
\mathcal{R}	distance of axisymmetric surface from axis of symmetry (cm)
Sc	$= \nu/D_i$, the Schmidt number
ν	fluid velocity (cm/sec)
x	distance along electrode (cm)
y	normal distance from the electrode surface (cm)
β	velocity derivative at the wall (sec ⁻¹)
Γ	gamma function
ζ	dimensionless normal distance for the diffusion layer (see also Eq. [48])
θ	$= (r^3/r_o^3 - 1)^{1/3}$
θ	$= (B^3 - 1)^{1/3}$
κ_∞	solution conductivity outside the diffusion layer (mho/cm)
ν	kinematic viscosity (cm ² /sec)
ξ	see Eq. [44]
ψ	see Eq. [23]
Ω	rotation speed (radian/sec)

REFERENCES

- W. J. Albery and S. Bruckenstein, *Trans. Faraday Soc.*, **62**, 1920 (1966).
- W. Nernst, *Z. Physik. Chem.*, **2**, 613 (1888).
- V. Levich, *Acta Physicochim. U. R. S. S.*, **17**, 257 (1942).
- J. Newman, *Advan. Electrochem. Electrochem. Eng.*, **5**, 87 (1967).
- W. H. Smyrl and J. Newman, *This Journal*, **118**, 1079 (1971).
- Th. v. Kármán, *Z. Angew. Math. Mechan.*, **1**, 233 (1921).
- W. G. Cochran, *Proc. Cambridge Phil. Soc.*, **30**, 365 (1934).
- E. M. Sparrow and J. L. Gregg, *J. Heat Transfer*, **81C**, 249 (1959).
- J. Newman, *This Journal*, **113**, 1235 (1966).

10. D. E. Rosner, *ibid.*, **113**, 624 (1966).
11. J. Newman, *ibid.*, **114**, 239 (1967).
12. D. E. Rosner, *Symp. (International) Combust. 11th*, pp. 181-194 (1967).
13. P. L. Chambré, *Appl. Sci. Res.*, **6A**, 97 (1956).
14. P. L. Chambré and A. Acrivos, *J. Appl. Phys.*, **27**, 1322 (1956).
15. M. Tribus and J. Klein, *Heat Transfer Symp. Univ. Mich.* 1952, 211 (1953).
16. V. G. Levich, "Physicochemical Hydrodynamics," Sect. 18, Prentice-Hall, Inc., Englewood Cliffs, N. J. (1962).
17. N. Ibl, *This Journal*, **108**, 610 (1961).
- 18a. S. Bruckenstein, *Elektrokhimiya*, **2**, 1085 (1966).
- 18b. D. T. Napp, D. C. Johnson, and S. Bruckenstein, *Anal. Chem.*, **39**, 481 (1967).
19. M. J. Lighthill, *Proc. Roy. Soc., Ser. A*, **202**, 359 (1950).
20. J. Newman, *Ind. Eng. Chem.*, **60**, 12 (1968).
21. S. Bruckenstein and B. Miller, *This Journal*, **117**, 1044 (1970).
22. W. H. Smyrl and J. Newman, *This Journal*, **119**, 208 (1972).
23. S. L. Gordon, J. S. Newman, and C. W. Tobias, *Ber. Bunsen. Physik. Chemie*, **70**, 414 (1966).

Technical Note



Electrochemical and Chemical Corrosion of Tungsten Carbide (WC)

John D. Voorhies*¹

Chemical Engineering Department, Stanford University, Stanford, California 94305

Tungsten carbide (WC) has attracted interest in recent years because of its electrocatalytic properties in anodic reactions of H₂, CO, and other fuels (1-6). Bianchi *et al.* (7) have studied the general electrochemical properties of a low area WC surface and Mazza and Trasatti (8) have used WC as an "inert" electrode material for solution redox measurements.

In the work of Binder *et al.* (4, 5) and Pohl and Böhm (1-3), there is evidence for chemical and electrochemical reactivity of the WC surface in aqueous electrolytes. Binder cites anodic passivation of WC with evolution of CO₂ and speculates that the passivated surface consists of WO₃ which is reducible to a hydrogen tungsten bronze. Böhm (6) finds that preanodization is necessary to achieve moderate levels of hydrogen adsorption on WC. There is also a consensus that oxidation of the WC surface is necessary for electrocatalytic activity in the anodic oxidation of fuels.

The present work is a potentiostatic-coulometric study of the anodic corrosion of WC powder and the cathodic reduction of the surface anode product. Oxidation of WC by the one-electron oxidants, ceric sulfate, and ferricyanide is also described.

Experimental

The sample of WC powder (I) used almost exclusively in this work was gratefully received from Prof. Dr.-Ing. F. A. Pohl and Dr. H. Böhm of AEG-Telefunken, Forschungsinstitut Frankfurt, 6 Frankfurt (Main)-Niederrad, Goldsteinstrasse 235. The BET surface area of this material is 5 m²/g. X-ray diffraction shows a clean WC pattern with lattice constants for the simple hexagonal structure, $a = 2.9004\text{Å}$, $c = 2.8444\text{Å}$ and an average apparent particle size from x-ray line broadening of about 300Å. Deviation of the lattice constants from the accepted values, $a = 2.906\text{Å}$, $c = 2.837\text{Å}$ (9) may be interpreted as a slight deficiency of carbon, a condition which is claimed (5) to favor electrocatalytic activity of WC. Spectral analysis by uv emission indicates about 10 ppm Cu, 2 ppm Mg, and 20 ppm Si.

Sample II was obtained from Norton Company, Worcester, Mass., and also shows a clean diffraction pattern with exact WC stoichiometry. The surface area is 2 m²/g.

All electrochemical measurements were obtained with the Wenking 61-TR Standard Potentiostat used only in its simple static mode with manual adjustment of the controlled electrode potential in discrete potential steps. The working electrode compartment was a Pyrex glass tube 10 cm long with an I.D. of 11 mm and a fine fritted glass closure at one end, the bottom of the electrode compartment in its normal vertical orientation. In the first experiments, the working electrode was contained in this compartment, and the reference electrode was positioned in the electrolyte outside of the frit. As the frit resistance was 15 ohms saturated with 2N H₂SO₄ electrolyte, the "controlled potential" was actually the sum of a variable IR component and the electrode potential. Nevertheless, useful coulometric information was obtained in 200-300 mV intervals with this setup, and the first two entries in Table I are from measurements of this kind.

In order to obtain more meaningful current-electrode potential values, a glass sidearm was attached to the working electrode compartment and the reference electrode placed therein, thereby contacting the electrolyte within the working electrode compartment and eliminating the variable IR component.

Table I. Coulombic ratio—*anodic corrosion:*
cathodic reduction of corrosion product

Sample (AEG WC) (g)	Anodic corrosion ^(a) (coulombs)	Cathodic reduction ^(b) (coulombs)	Ratio (A:C)
0.49	15.2	0.806	18.8
0.224	7.61	0.377	20.2
0.125	5.32	0.246	21.6
0.50	32.9	1.65	19.9
0.50	17.6 ^(c)	0.437	40.2 ^(c)

^(a) Corrosion at one or more potentials in the range +0.45 to +0.75V vs. HE.

^(b) Net cathodic reduction of anodic corrosion product on surface of WC.

^(c) Experiment in 2M H₃PO₄, all others in 2N H₂SO₄.

* Electrochemical Society Active Member.

¹ 1970-71 Senior Educational Leave from American Cyanamid Company, Stamford, Connecticut 06904.

Key words: tungsten carbide (WC), corrosion, surface oxide.

The working electrode itself was a compacted slug of powdered material, WC or tungsten metal powder, contained in the annulus provided by a sleeve of polyethylene tubing (6 mm I.D.) extending 0.5-1 cm beyond the contact end of a spectrographic graphite rod which provided electronic contact to the potentiostat. The counterelectrode was a spectrographic graphite rod positioned in the simple beaker cell far from the working electrode to prevent contamination with gas from the counterelectrode.

The reference electrode was a small, stable Beckman fiber-junction saturated calomel electrode whose potential was checked frequently against several larger SCE's and measured against a platinized platinum wire hydrogen electrode [$p_{\text{H}_2} = 1 \text{ atm}$, $E(\text{SCE-HE}) = +249 \text{ mV}$] in the test electrolyte. All values of electrode potential are reported with respect to the hydrogen electrode in the test electrolyte (HE).

Two electrolytes were used, 2N H_2SO_4 and 2M H_3PO_4 , both prepared with doubly distilled water and Baker and Adamson reagent grade acid without further purification. The test electrolyte was not deaerated during or prior to an experiment, and therefore small residual oxygen currents were observed in cathodic measurements. These currents were accounted for in a small cathodic "blank" measured before the anodic corrosion-cathodic reduction measurements and subtracted from the coulombs for cathodic reduction.

Coulometric values for a specific faradaic process were obtained by integrating current-time curves at a given controlled potential or range of potentials. The coulombs required to charge the double layer on these high area powder electrodes were not subtracted from these values. An estimate of this capacitive charge in a potential step of 100 mV for an 0.50g sample of AEG WC (2.5 m^2 BET area) in 2N H_2SO_4 is 0.01-0.02 coulomb from the charging current in a step from +0.2 to +0.1V in the initial potentiostatic measurements before anodic corrosion. This charging error in the coulombic measurements cited in Table I is most significant for the cathodic reduction step. Although the error is partially compensated by the blank correction mentioned previously, it could make the smaller cathodic values in Table I 5-10% high.

Results

Potentiostatic-WC powder.—In the anodic corrosion of WC powder in dilute H_2SO_4 , the corrosion reaction forms a passive surface layer, and the current decreases irreversibly over periods up to 45 min as the active surface area is depleted. Even after excursions of several minutes into regions of cathodic reduction, a return to a given anodic corrosion potential produces no faradaic increase in anodic current over the prior level attained. This phenomenon was also cited by Binder *et al.* (4) using the triangular wave potential sweep method on resin-bonded WC powder electrodes.

Potentiostatic current-potential curves are shown in Fig. 1 for AEG WC (I) in 2N H_2SO_4 at room temperature, based on current observed after 2 and 5 min at each potential. Corrosion begins at relatively low anode potentials compared with titanium carbide in the same medium (10). At currents above 4 mA for a typical 0.50g test electrode, gas evolution is observed in the anode compartment. The gas contained CO_2 , identified by mass spectroscopy and acid titration after absorption in NaOH. Cathodic reduction of the surface oxide and the early part of the hydrogen evolution reaction are also shown in Fig. 1.

The two WC powder samples are surprisingly different in their anodic corrosion behavior. Sample II requires about 300 mV higher anode potential to produce corrosion current densities equivalent to I. Reduction of the surface oxide is similar qualitatively to sample I. Anode currents are so low in the normal corrosion range for I, however, that an accurate coulometric measure of reduction of anode product is impossible.

The extent of anodic corrosion before low currents of about 5% of the maximum faradaic current are

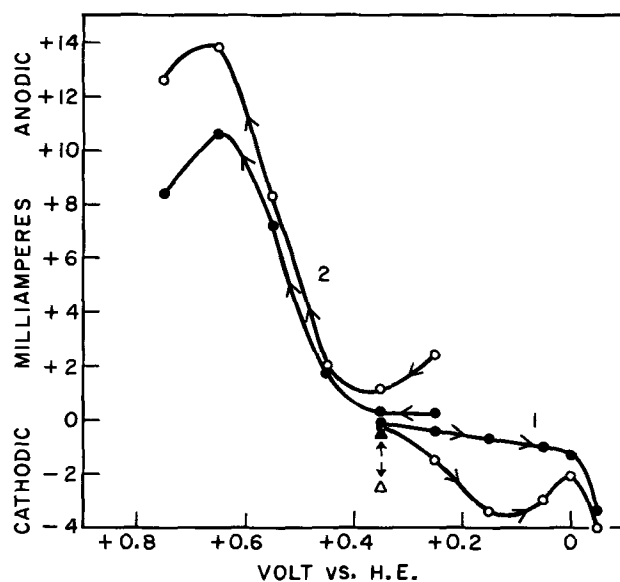


Fig. 1. Potentiostatic $I_{a,c}$ vs. E curves. 1, First measurements (cathodic direction); 2, second measurements (anodic direction); ○, 2 min points; ●, 5 min points; Δ, cathodic reduction of surface oxide—2 min; ▲, cathodic reduction of surface oxide—5 min; 0.50g AEG WC.

observed is in the order of 1-5 tungsten atom layers depending on the stoichiometry of the anode process, which could involve from 2-10 electrons per W atom. This assumes that all of the 5 m^2/g BET surface area is electroactive and that the average surface tungsten atom density is 1.3×10^{15} W atoms/ cm^2 .

Cathodic reduction of anode product.—The cathodic reduction of the surface corrosion product formed anodically occurs very rapidly in a narrow range of potential (+0.35 to +0.25V vs. HE, Fig. 1). The coulombic value associated with this process can be separated from the small background cathodic "blank" mentioned previously with reasonable accuracy. As the potential of reduction is about 350 mV anodic to the hydrogen evolution reaction, the electrode process must be the reduction of a tungsten species, possibly WO_3 .

The coulombic ratio of anodic corrosion to net cathodic reduction of the corrosion product is remarkably constant for several sample sizes, ranges of anode potential and extents of corrosion (Table I). The value of this ratio in 2N H_2SO_4 is about 20.

The experiment with 2M H_3PO_4 was prompted by expectation of a solubilizing or complexing effect of phosphate on the anodic tungsten oxide. The very large coulombic ratio of anodic corrosion to cathodic reduction indicates a surface reaction very different from that in sulfuric acid. The anode product does not, however, appear to be soluble in that the surface is still irreversibly passivated by the anode process.

Tungsten metal.—A comparison of the behavior of tungsten metal with WC under identical experimental conditions in 2N H_2SO_4 is also striking. Tungsten as a pure high area powder (2 m^2/g) or as a polycrystalline foil does not passivate under the current-potential-time conditions of the present study. Also, no easily reducible surface oxide is observed on W. Anode products are either soluble and thereby reducible over a broad and more cathodic range of potentials or insoluble and cathodically inert prior to hydrogen evolution.

Current-time curves.—The current-time curves at a fixed electrode potential were compared with the exponential curves predicted for a simple first order rate process at a two-dimensional surface layer in which the instantaneous current, i_t , is given by

$$i_t = k(N_s^0 - \int_0^t i_t dt) \quad [1]$$

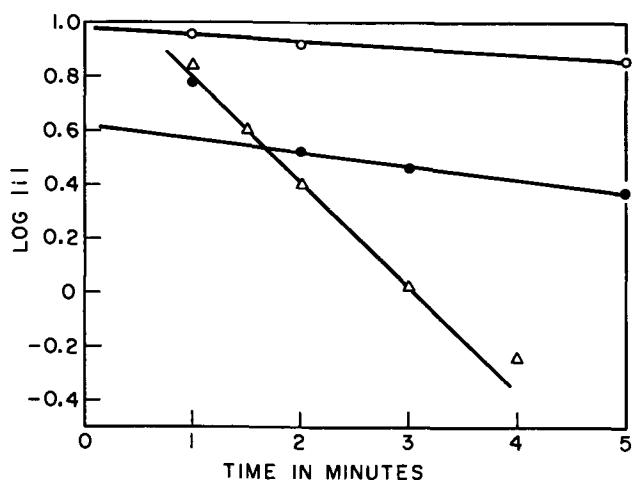


Fig. 2. Kinetic analysis of current-time data. ○, anodic corrosion at +0.55V (sample A); ●, anodic corrosion at +0.60V (sample B); △, cathodic reduction of oxide at +0.35V (sample A).

in which k is a first order rate constant which depends on potential and has the units sec^{-1} , and N_s^0 = initial surface sites for the electrode reaction expressed in coulombs. The anodic corrosion and cathodic reduction of WO_x should obey this relationship providing there are no slow diffusional processes in the liquid or solid phases at the electrode surface. For the case of anodic corrosion assuming $n = 10$ electrons per W atom, N_s^0 = (grams sample) \times (BET surface area, m^2/g) \times (20.8) coulombs.

A more convenient integrated form of Eq. [1] is

$$\log i_t = \frac{-kt}{2.303} + \log kN_s^0 \quad [2]$$

Figure 2 shows $\log i_t$ vs. t for several anodic and cathodic experiments. Experimental plots do not follow the expected rate law in the initial portion because of capacitive charging and in the final portion because of subsurface oxidation for the anodic process. Values of N_s^0 obtained from an extrapolation of the linear portion of the experimental curves are compared below with the calculated values for a complete BET monolayer corrosion.

WC Sample	N_s^0 (slope-intercept)	N_s^0 (calc.)
0.125g	2.08	13.0
0.500g	10.4	52.0

The low values of N_s^0 from this analysis of the i - t curves may mean that (i) the stoichiometry, $n = 10$ electrons, is too high, (ii) the measured BET area is not the effective corrosion area, or (iii) the total anodic coulombs passed in a given experiment represents several layers of subsurface oxidation on a fraction of the BET area rather than a real monolayer.

The i - t analysis of cathodic reduction of the anode product is also difficult because of small regions of linearity in $\log i_t$ vs. t . The best estimate of N_s^0 for one 0.50g sample of WC was 0.99 coulomb by the slope-intercept method compared with the measured 1.65 coulombs required to reduce the surface oxide.

The very high rate of reduction of oxide is indicated by a rate constant, k , of 0.03 sec^{-1} measured at +0.35V vs. HE compared with 0.0009 and 0.002 sec^{-1} at +0.55 and +0.60V respectively for anodic corrosion. The ratio of rate constants is even larger if N_s^0 is expressed as number of sites rather than as coulombs.

Hydrogen evolution reaction.—Binder *et al.* (4) and Böhm (6) have suggested that the electrocatalytic activity of WC for fuel cell anode reactions, *e.g.*, hy-

drogen ionization, is promoted by the formation of an oxygenated surface containing W, C, O, and H. A similar promotion effect might be observed in the hydrogen evolution reaction (h.e.r.) on "as is" WC and surface oxidized WC. The observed current-potential curves for the h.e.r. on these two surfaces (AEG WC) in 2N H_2SO_4 at room temperature were, however, identical.

Chemical oxidation.—A suspension of AEG WC in 0.2N ceric sulfate 2N in H_2SO_4 evolved gas rapidly at room temperature, and the fine particles were completely oxidized to a white material believed to be tungstic acid. An 0.099g sample completely decolorized 2.0 meq. of Ce^{+4} (40% bulk oxidation of WC assuming WO_3 , CO_2 , $n = 10$) and was about 50% oxidized in bulk by a further increment of Ce^{+4} , which was not fully decolorized. Apparently, the complete bulk oxidation of the sample was precluded by passivation of the large WC particles which settled under the layer of white tungstic acid precipitate.

In order to determine the CO_2 evolved quantitatively, the product gas was absorbed in 0.0924N NaOH and titrated with 0.0987N HCl. An excess of WC (0.101g = 5.1 meq. for bulk oxidation, $n = 10$) was reacted with 1.0 meq. of Ce^{+4} completely decolorizing the solution and evolving about 70% of the expected CO_2 . The low result was probably caused by inefficient collection of CO_2 .

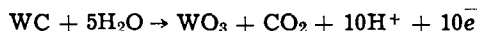
Ceric sulfate in 2N H_2SO_4 is strongly oxidizing (formal potential, $E^{01} = 1.459\text{V}$). Oxidation with ferricyanide in 2N H_2SO_4 , $E^{01} = +0.69\text{V}$, represents more closely the range of corrosion potentials in the electrochemical work. In 0.2N ferricyanide, 2N H_2SO_4 , AEG WC powder evolved gas very slowly and showed no evidence of bulk oxidation. In fact, the amount of CO_2 collected from 0.4-1.0g samples of WC in excess ferricyanide corresponded to surface monolayer or partial monolayer oxidation.

Discussion

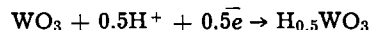
The primary result of this study is the ratio of about 20 between the coulombs required to oxidize a sample of WC anodically and the coulombs for reduction of the anode product. The constancy of this value in 2N H_2SO_4 under varying conditions of sample size, extent and potential of anode corrosion (Table I) suggests that there are single anodic and cathodic reactions rather than a multiplicity of poorly defined reactions. Moreover, for any anodic stoichiometry involving from 2 to 10 electrons per tungsten atom, the cathodic reduction requires only 0.1-0.5 electrons per tungsten atom oxidized. If a W(VI) oxide is the anode surface product, then the cathodic process is either a partial reduction of W(VI) to W(V) or the formation of $\text{H}_x\text{W(VI)}$ oxide in which $x = 0.1$ -0.5.

A possible scheme supported in part by the identification of CO_2 as an anode product, the chemical oxidation work described herein, and chemical and electrochemical reduction of bulk WO_3 to hydrogen tungsten bronzes (11-13) is

Anode



Cathode



Some evidence against the formation of "surface hydrogen tungsten bronzes" are the citations by Armstrong *et al.* (14) that "sodium tungsten bronzes are completely inactive for anodic hydrogen oxidation" and by Vondrak and Balej (15) that hydrogen on cation vacancies in the lattice of a sodium tungsten bronze is oxidized at -0.1V vs. RHE, while in the present study " H_xWO_3 " is formed at +0.35V.

The work of Böhm (6) on adsorption and anodic oxidation of hydrogen on WC is interesting and relevant in that the maximum value of hydrogen adsorption, 32.5 microcoulombs/ cm^2 , represents a coverage of only about 15% of the available surface tungsten atoms and in that an oxidative pretreatment of the

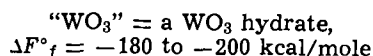
WC, namely several anodic square wave pulses to 1000 mV vs. hydrogen electrode, substantially increases hydrogen adsorption. Both facts can be explained by assuming that the hydrogen is "adsorbing" on a complete or partial surface oxide as H_xWO_3 , where x is small in the range 0.1-0.5.

The comparison of WC with W metal indicates a strong influence of carbon in the tungsten lattice on the electrochemistry of W. Although WC is an interstitial carbide, its crystal structure is simple hexagonal whereas W is body centered cubic. The shortest W-W distance is 2.86Å in WC and 2.74Å in W; the density of WC is 15.6 g/cc compared with 19.2 g/cc for W. It is difficult to imagine that this moderate expansion of the W lattice in WC is responsible for the differences in electrochemical behavior of W and WC. It is more likely that there is a chemical effect of carbon on the formation and reduction of the surface oxide.

The experiment on the hydrogen evolution reaction on "as is" WC and anodized WC is certainly not definitive in that "as is" WC may be covered with sorbed oxygen. It is noteworthy, however, that the h.e.r. occurs on WC with essentially no overvoltage whereas pure W powder requires an overvoltage of about 0.10V to achieve a given low current density for the h.e.r. in 2N H_2SO_4 .

The oxidation-reduction properties of WC in aqueous media are novel and interesting in several respects. It is surprising that the surface and bulk corrosion, both anodic and chemical, occur so easily at room temperature in aqueous solutions at "medium to high" anodic potentials. The almost complete bulk oxidation of WC by aqueous ceric sulfate is unexpected in view of the literature (9, 16) on the apparent kinetic

stability of WC to oxidation ($WC + O_2 \xrightarrow{>500^\circ C} \text{oxidation}$) and to the dissolving power of strong mineral acids. A thermodynamic estimate of standard free energy at room temperature of the reaction



is $\Delta F^\circ = -319$ kcal/mole, and it is apparent that one-electron oxidants with a potential as low as +0.1V vs.

the standard hydrogen electrode are possible oxidants for WC.

Acknowledgment

The author is sincerely grateful to Professor Michel Boudart for his invitation to study in the Chemical Engineering Department of Stanford University and for his encouragement and support of this work. Several of the physical measurements and many useful comments and suggestions were made by Mr. Ricardo Levy of the Chemical Engineering Department.

Manuscript submitted April 30, 1971; revised manuscript received Sept. 29, 1971.

Any discussion of this paper will appear in a Discussion Section to be published in the December 1972 JOURNAL.

REFERENCES

1. H. Böhm and F. Pohl, *Wiss. Ber. AEG—Telefunken*, **41**, 46 (1968).
2. F. Pohl and H. Böhm, in "Proc. III. Journées Internationales d'Etude des Piles a Combustible," p. 180, Brussels (1969).
3. H. Böhm and F. Pohl, *ibid.*, p. 183 (1969).
4. H. Binder, A. Köhling, W. Kuhn, W. Lindner, and G. Sanstede, *Energy Conversion*, **10**, 25 (1970).
5. H. Binder, A. Köhling, W. Kuhn, W. Lindner, and G. Sanstede, *Nature*, **224**, 1299 (1969).
6. H. Böhm, *Electrochim. Acta*, **15**, 1273 (1970).
7. G. Bianchi, F. Mazza, and S. Trasatti, *Z. Physik. Chem. (Leipzig)* **226**, 40 (1964).
8. F. Mazza and S. Trasatti, *This Journal*, **110**, 847 (1963).
9. G. D. Rieck, "Tungsten and Its Compounds," Pergamon Press, Oxford (1967).
10. R. Cowling and H. Hintermann, *This Journal*, **117**, 1447 (1970).
11. O. Glemser and C. Naumann, *Z. Anorg. Chem.*, **265**, 238 (1951).
12. J. Benson, H. Kohn, and M. Boudart, *J. Catalysis*, **5**, 307 (1966).
13. B. Hobbs and A. Tseung, *Nature*, **222**, 558 (1969).
14. R. Armstrong, A. Douglas, and D. Keene, *This Journal*, **118**, 568 (1971).
15. J. Vondrak and J. Balej, *Ext. Abstr.*, p. 361, 21st CITCE Meeting, Prague (1970).
16. E. Gulbransen and K. Andrew, *This Journal*, **107**, 619 (1960).



Oxide Charge Reduction by Chemical Gettering with Trichloroethylene During Thermal Oxidation of Silicon

Mao-Chieh Chen* and John W. Hile*

Electronics and Instrumentation Department, Research Laboratories,
General Motors Corporation, Warren, Michigan 48089

ABSTRACT

Silicon dioxide was thermally grown in an oxygen atmosphere containing a small percentage of trichloroethylene (C_2HCl_3) vapor. As a result of this process, it was possible to fabricate metal-oxide-semiconductor (MOS) diodes with greatly reduced oxide space charge. This reduction in oxide charge was accompanied by improved electrical stability under bias-temperature stress. It is believed that the pyrolysis product, chlorine, acts as a getter to continuously remove mobile impurity cations such as Na^+ during the oxidation process. Also described are various charge phenomena under bias-temperature stress conditions.

The performance of MOS devices depends critically on the stability of the insulating oxide between the silicon substrate and the metal counterelectrode. The most significant device instability generally arises from ionic contamination (such as sodium) which is unavoidably included in the oxide during thermal oxidation. These ions act as a positive space charge and are mobile under bias-temperature stresses (1-4). Thus the electrical characteristics of such devices are not predictable and are variant with time.

A number of researchers have developed techniques for eliminating or reducing the positive ion space charge in thermal oxide layers with varying degrees of success. These techniques include the use of phosphosilica layers (5-7) and the production of clean oxides by *in situ* gaseous etching with HCl and subsequent oxidation of the silicon by means of rf induction heating (8). More recently, Heiman and Robinson (9) and Kriegler *et al.* (10) have shown that clean oxides can be produced by the addition of HCl during thermal oxidation. In this paper the method disclosed is a similar technique, but it is much easier to implement since the gettering agent (C_2HCl_3) is noncorrosive and is very easy to handle safely. This process results in the reduction of oxide charges and in the stabilization of the ionic migration instability. Various charge phenomena under bias-temperature stress conditions are described.

Experimental Procedures

Silicon dioxide films were thermally grown in a dry oxygen atmosphere at $1050^\circ C$ with a small percentage of trichloroethylene (C_2HCl_3) vapor included.

The oxygen flow rate was 1.5 liters per minute. The trichloroethylene vapor was added by bubbling helium (at a slow rate of 0.05 liters per minute) through C_2HCl_3 maintained at room temperature. No

special mixing was employed. Epitaxial n/n^+ silicon wafers of 10 and 30 ohm-cm were used. The wafer orientation was (111). No special precautions were used with respect to furnace cleanliness. However, the wafers were degreased in trichloroethylene and acetone and rinsed in ultrasonically agitated, flowing, deionized water for 10 min before being loaded into the modified oxidation furnace. For comparison, wafers with conventionally grown, dry thermal oxide were also prepared.

Following oxidation, aluminum gate electrodes (26 mil diameter dots) were applied to the oxide films by means of vacuum evaporation and photomasking. Individual MOS devices were diced out, die bonded (at $400^\circ C$), and ultrasonically lead bonded to TO-5 headers.

Measurements of the MOS capacitance voltage characteristics were performed at 1 MHz and were automatically recorded on an X-Y plotter. The X-Y plotter scheme is a modification of that proposed by Zaininger (11).

Results

The flat-band voltages V_{FB} for a number of MOS devices are plotted in Fig. 1. It is clearly indicated that the effective oxide charge density is greatly reduced in samples exposed to C_2HCl_3 vapor during oxidation. It is also evident that the C_2HCl_3 treated samples have their flat-band voltages constrained to a much narrower range of values. In Fig. 2, the results of bias-temperature stress tests for oxide stability are shown. In these tests positive or negative bias voltages were applied for 30 min at the temperature indicated. The samples were then quenched to room temperature while still under bias. The improvement in stability afforded by the C_2HCl_3 process is obvious. It is, however, noted that at temperatures above $200^\circ C$, the flat-band voltage, V_{FB} , increases significantly upon prolonged stress.

* Electrochemical Society Active Member.

Key words: oxide charge, gettering, oxidation, clean oxide.

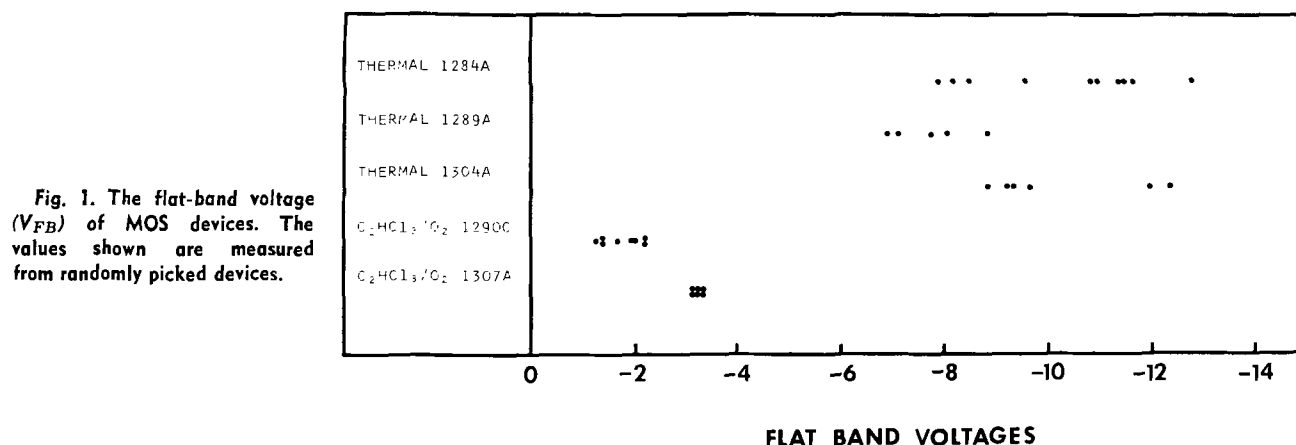


Fig. 1. The flat-band voltage (V_{FB}) of MOS devices. The values shown are measured from randomly picked devices.

It was observed that for C_2HCl_3 grown samples, both positive and negative B-T stress cause the flat-band voltage to shift slightly in the negative bias direction. A slight broadening of the C-V curve is also observed with this small increase in V_{FB} . With a positive bias of 20V applied to a 1500Å thick oxide, the flat-band voltage shift, ΔV_{FB} , was within half a volt after several days of stress at 150°C. At temperatures higher than 200°C, however, V_{FB} shows a large increase and slowly reaches a saturated value in approximately 10 hr. These saturated values are $V_{FB} = 1.6V$ at 200°C and $V_{FB} = 2.7V$ at 250°C. These high-temperature bias-stress shifts in the flat-band voltage cannot be recovered either by short circuiting the device at elevated temperature nor by reverse bias stresses. Since it has been shown that

ionic contamination within an SiO_2 layer can be rearranged in minutes at 150°C, the above high-temperature, slow bias-stress phenomenon cannot be attributed purely to ionic migration. The actual mechanism is not yet well understood.

Under negative bias-stress, the flat-band shift is in the negative bias direction even with bias voltages as low as -5V. The saturated values of ΔV_{FB} at 250°C (see Fig. 3) were observed to be proportional to the applied negative bias. This observation is similar to that reported by Deal *et al.* (12) and Miura *et al.* (13). The time to reach a saturated ΔV_{FB} condition is relatively long and requires several hours even at temperatures as high as 400°C. Only partial recovery of the shifted C-V curve can be obtained by a short circuit, high-temperature treatment. Slightly higher values of ΔV_{FB} were observed for higher stress temperatures. These observed phenomena suggest that it is intrinsically connected with the silicon dioxide/silicon interface, and that the dominant drift mechanism is carrier injection-trapping (8, 14, 15) although some ion migration appears to be active.

The exact mechanism by which the C_2HCl_3 vapor acts to reduce the oxide charge is not known. It is believed that the pyrolytic product, chlorine, acts as a gettering agent for sodium and other ionic contaminants during the oxidation process. Presumably the chlorine reacts with the metallic ions to form volatile chlorides which are removed as gases. It is also suggested that the carbon reacts with the oxygen to form carbon dioxide and escapes from the furnace as a gas.

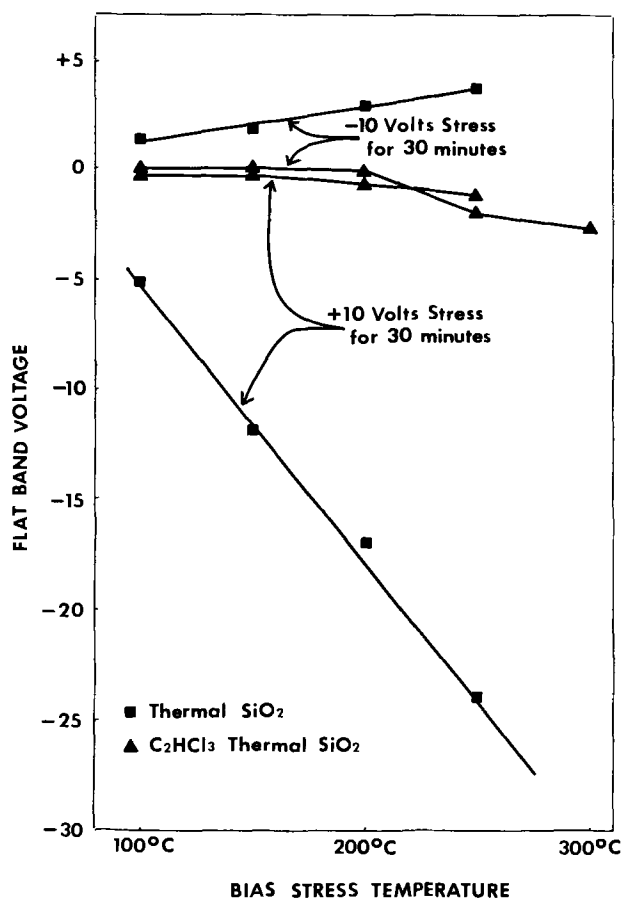


Fig. 2. The shift of flat-band voltage under bias-temperature stress at various temperatures. The stress was $\pm 10V$ bias for 30 min. The oxide thickness is about 1500Å.

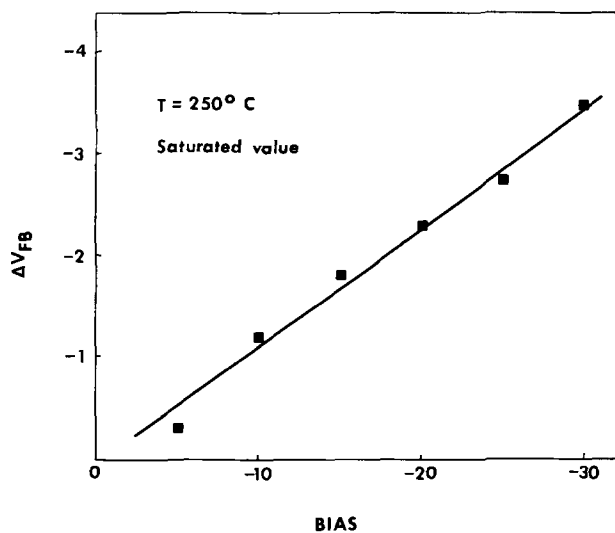


Fig. 3. Saturated values of flat-band voltage as a function of applied negative bias for MOS devices.

In addition to the possible gettering of alkali ions from the oxide, there also appears to be some kind of chemical reaction occurring which modifies the oxide structure. This is evidenced by the observed shifts in the C-V curve at bias-stress temperatures greater than or equal to 200°C. The fact that ΔV_{FB} is temperature dependent very likely reveals the creation of oxide charge (a slow state). Possibly this charge arises from the ionization of metallic chlorides which are formed and are not removed during the oxide growth process. These charged species may have very low mobilities and may be well trapped. It was found that high-temperature annealing of the sample in air without bias causes an increase in V_{FB} . The amount of increase is proportional to the annealing temperature and is in the order of 1V at 400°C. This would support our assumption.

In summary, it has been demonstrated that silicon dioxide grown in a C_2HCl_3/O_2 atmosphere has a much lower oxide charge. However, the exact mechanism controlling the high-temperature ($\geq 200^\circ C$) instability is not well understood and additional effort is required.

Acknowledgments

We would like to thank Mrs. C. M. Hoyland and Mr. A. Fritz who assisted in the fabrication of the devices.

Manuscript submitted June 22, 1971; revised manuscript received ca. Oct. 20, 1971.

Any discussion of this paper will appear in a Discussion Section to be published in the December 1972 JOURNAL.

REFERENCES

1. E. H. Snow, A. S. Grove, B. E. Deal, and C. T. Sah, *J. Appl. Phys.*, **36**, 1664 (1965).
2. E. Yon, W. H. Ko, and A. B. Kuper, *IEEE Trans. Electron Devices*, **ED-13**, 276 (1966).
3. J. Lindmayer, *Solid-State Electron.*, **9**, 225 (1966).
4. S. R. Hofstein, *IEEE Trans. Electron Devices*, **ED-13**, 222 (1966).
5. D. R. Keer, J. S. Logan, P. J. Burkhardt, and W. A. Pliskin, *IBM J. Res. and Develop.*, **8**, 376 (1964).
6. Y. Miura, S. Tanaka, Y. Matukura, and H. Osafune, *This Journal*, **113**, 399 (1966).
7. M. Yamin, *IEEE Trans. Electron Devices*, **ED-13**, 246 (1966).
8. S. R. Hofstein, *Solid-State Electron.*, **10**, 657 (1967).
9. R. H. Robinson and F. P. Heiman, *This Journal*, **118**, 141 (1971).
10. R. J. Kriegler, Y. C. Cheng, and D. R. Colton, Paper 79 presented at Electrochem. Soc. Meeting, Washington, D. C., May 9-13, 1971.
11. K. H. Zaininger, *RCA Rev.*, **27**, 341 (1966).
12. B. E. Deal, M. Sklar, A. S. Grove, and E. H. Snow, *This Journal*, **114**, 266 (1967).
13. Y. Miura and Y. Matukura, *Japan J. Appl. Phys.*, **5**, 180 (1966).
14. T. L. Chu, J. R. Szedon, and C. H. Lee, *Solid-State Electron.*, **10**, 897 (1967).
15. S. M. Hu, D. R. Kerr, and L. V. Gregor, *Appl. Phys. Letters*, **10**, 97 (1967).

Effects of Annealing on Luminescent Properties of (Zn,O)-Doped GaP[†]

H. D. Pruett and D. L. Hughes¹

Western Electric Engineering Research Center, Princeton, New Jersey 08540

and M. R. Notis*

Department of Metallurgy and Material Science, Lehigh University, Bethlehem, Pennsylvania 18015

ABSTRACT

Annealing studies were performed on (Zn,O)-doped GaP at 400°, 600°, and 900°C. The photoluminescent quantum efficiency and the visible/infrared emission ratio were both found to increase with decreasing annealing temperature. The increase in both quantities is primarily attributed to an increase in the concentration of nearest-neighbor (Zn,O)-pairs. Results are discussed and quantitatively compared to a recent theoretical model which predicts the equilibrium (Zn,O)-pair concentration as a function of temperature.

The purpose of this paper is to present preliminary results of annealing studies that were performed on samples of (Zn,O)-doped GaP. A particular objective of the present work was to evaluate the effects of low annealing temperatures ($\leq 600^\circ C$) in conjunction with long annealing times (many hours) to increase the equilibrium concentration of red-luminescence recombination centers. The present study differs from earlier work in that the investigation was made on bulk material, rather than on p-n junctions, and it included annealing temperatures lower than previously explored. Our investigation was limited to bulk material because evaluation of electroluminescent emission

from a p-n junction would have added another degree of complexity to the problem, as is discussed later.

Numerous fundamental studies have been made on red-luminescence emission of (Zn,O)-doped GaP (1, 2). Low-temperature investigations of Henry, Dean, and Cuthbert (3) and Morgan, Welber, and Bhargava (4) were responsible for clearly establishing the red-luminescence emission process. Basically, red emission is produced by either the decay of excitons bound to (Zn,O)-complexes or from recombination of electrons bound at (Zn,O)-complexes with holes trapped at distant zinc acceptors. At temperatures below approximately 60°K, pair luminescence dominates, but above 60°K, exciton luminescence dominates. However, the actual temperature at which exciton decay becomes predominant depends upon the zinc doping concentration and the excitation intensity (5). Infrared emission is produced by recombination of electrons at

[†] This paper is based upon a thesis submitted by D. L. Hughes to Lehigh University in partial fulfillment of the requirements for the M.S. degree.

* Electrochemical Society Active Member.

¹ Present address: Western Electric Company, Lee's Summit, Missouri 64063.

Key words: luminescence, semiconductors, gallium phosphide, annealing, dopants, photoluminescence.

unpaired-oxygen sites with either holes on distant zinc-acceptor sites (donor-acceptor pair recombination), or with free holes (bound-free recombination). Recent work has suggested that the latter is the dominant process at room temperature (6, 7).

Several previous investigations (8-13) have shown that the quantum efficiency, η_E , of GaP diodes can be improved by employing a suitable heat treatment. Part of the change in η_E can be attributed to an increase in the concentration of Zn-O pairs (8) and part can be attributed to a change in the electrical properties of the p-n junction. However, the change in the electrical properties may have an opposite effect to that of an increase in the Zn-O pair concentration. It is, therefore, difficult to quantitatively determine the increase in Zn-O pair concentration by studying electroluminescent emission from GaP diodes. For this reason, the present investigation was confined to an examination of photoluminescent emission from bulk GaP.

Experimental

The p-type GaP crystals used in this study were flux grown from a gallium phosphide saturated gallium solution by a slow cooling method. In addition to the GaP and Ga, the solution included 0.07 mole per cent (m/o) Zn and 0.04 m/o Ga_2O_3 . The small Ga samples produced by the growth process were first lapped into 15 mil thick platelets and then polished on one side. Next the samples were cut into a clover-leaf shape about 4 mm in diameter. Carrier concentrations and Hall mobility were determined using the van der Pauw technique (14).

In an attempt to inhibit out-diffusion of dopants, all of the samples (except for those in a control group) were coated with an rf-sputtered film of SiO_2 , approximately 3500 Å thick.

Samples were annealed in a quartz ampoule which, after being evacuated to 10^{-6} Torr, was filled with argon to atmospheric pressure. To establish an initial reference condition, all samples were first heated to 900°C for 10 min and then quenched by plunging the ampoule into a room-temperature water bath. After this initial heat treatment, but prior to further heat treatment, the samples were said to be in the "time-equal-zero" ($t = 0$) condition. The same quenching procedure was used after each annealing cycle to insure that the equilibrium defect concentration at a given annealing temperature would be fixed in the sample. If samples were cooled slowly, rather than quenched, further annealing would occur during the cool-down period and the defect concentration would generally not correspond to the equilibrium value for the annealing temperature that was used.

There are several approaches that can be used to obtain a time-temperature plot of the effects of annealing on a given parameter. One approach is to start with many groups of samples, one for each annealing time to be investigated. Each group is then annealed only once; the first group is annealed for a certain length of time and each successive group is annealed for a progressively longer time. Unless all of the samples have nearly identical properties, such an approach results in a considerable amount of scatter in the data. An alternative approach, and the one used in the present investigation, is to cycle the same group of samples in cumulative fashion assuming that N successive annealing cycles of duration Δt are equivalent to a single annealing cycle of duration N times Δt .

Two annealing temperatures, 400° and 600°C, were investigated in addition to the initial 900°C temperature. One group of SiO_2 coated samples was annealed at 400°C using 30 min time increments up to a cumulative value of 4 hr, after which the time increment was increased to 4 hr. A second group of coated samples was annealed at 600°C using 4 hr time increments. A third group of samples, not SiO_2 coated, was annealed at 400°C using 15 min increments for the first hour and one hour increments thereafter.

After every heat treatment, each sample's photoluminescent efficiency was measured and its 77°K emission spectra was recorded. Emission spectra measurements were performed at 77°K in order to completely resolve the red and infrared emission bands, the tails of which overlap each other at room temperature. Efficiency measurements were made only at room temperature because it was not possible to make absolute efficiency measurements at 77°K with the existing apparatus.

Results

Conventional x-ray methods were used to identify both the composition and orientation of grown crystals. Debye-Scherrer patterns and Laue photographs confirmed that the samples were gallium-phosphide single crystals with the polished face parallel to a (111) plane. Room temperature resistivity and Hall-effect measurements were made on five representative samples. The average resistivity and Hall coefficients obtained were 0.129 ohm-cm and 8.61 $\text{cm}^3/\text{coulombs}$, respectively, from which the corresponding average values of carrier concentration and Hall mobility were calculated to be $8.10 \times 10^{17} \text{ cm}^{-3}$ and 70 $\text{cm}^2/\text{V-sec}$.

In Fig. 1, the external photoluminescence quantum efficiency, η_p , is plotted as a function of annealing time for two temperatures, 400° and 600°C. The plotted data are for two specific samples, however, the shape of the curves obtained is typical for all samples. That is, there were variations in the initial values of η_p , but a plot of η_p vs. time annealed at a given temperature for all samples in a group showed a consistent trend in the data. The significant features of Fig. 1 are: first, the existence of a plateau in the values of η_p after long anneal times; second, a larger percentage increase in the plateau value of η_p for a 400°C anneal temperature than for a 600°C anneal temperature; and third, the observation that the plateau value of η_p for samples annealed at 600°C was reached in less than 4 hr, whereas approximately 16 hr were required to reach the corresponding plateau-value of η_p for samples annealed at 400°C. The short-term peak in η_p after approximately 1 hr of cumulative annealing at 400°C was observed for all samples that had been coated with an SiO_2 film, but was not observed for uncoated samples.

In Fig. 2 the integrated red to infrared emission ratio is shown as a function of annealing time for two representative samples annealed at 400° and 600°C. This ratio is seen to increase by a factor of 14 after 24 hr of cumulative annealing time at 400°C, whereas only a factor of four increase is observed for samples annealed at 600°C. Measurement of the red/infrared ratio for samples annealed at 600°C was discontinued after 12 hr of cumulative anneal time when it ap-

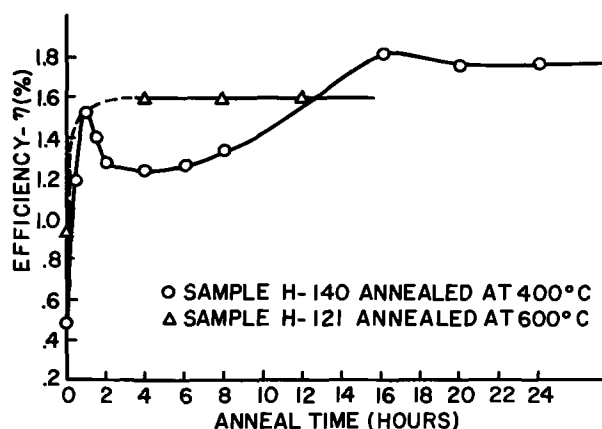


Fig. 1. Total radiative efficiency, using photoexcitation, is shown for two representative SiO_2 -coated GaP samples annealed at 400° and 600°C.

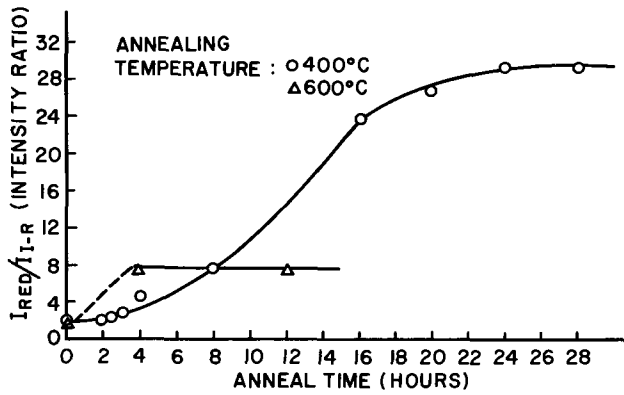


Fig. 2. The integrated red to infrared emission ratio at 77°K is shown for the two samples whose room temperature efficiency is shown in Fig. 1.

peared that this quantity had reached a maximum after less than 4 hr of annealing.

As indicated earlier, SiO₂ films were not deposited on one group of samples annealed at 400°C. The data obtained from measurements on these uncoated samples were not as consistent as the data from coated samples, but the following observations were made. The efficiency of uncoated samples steadily decreased for the first hour and then leveled off, or began to gradually increase with further heat treatment. For those samples whose efficiency did increase, approximately 16 hr of annealing at 400°C were required to reach the original $t = 0$ value (15). The appearance of the surfaces of uncoated samples indicated that some type of surface deposits were being produced. Etching the bulk samples produced only a slight improvement in the photoluminescent efficiency, whereas etching has been reported (13) to improve the efficiency of electroluminescent diodes by 20-30%. The increase in the integrated red-infrared emission ratio was also less for uncoated samples than for coated ones.

A brief experiment was performed to see if the difference between coated and uncoated samples could be explained by zinc out-diffusion from the uncoated samples. An uncoated sample was broken into two pieces, but only one was annealed in the usual manner. Both samples were then examined for zinc concentration by using d-c arc excitation to record optical emission of elemental zinc. Unfortunately, the results were inconclusive because the zinc concentrations were too near the detection limit of the equipment. However, no obvious loss of zinc was observed.

Discussion

The results shown in Fig. 1 and 2 are generally consistent with those obtained by Onton and Lorenz (8) in their annealing studies. It should be noted, however, that OL measured diode electroluminescence efficiency, η_E , rather than bulk photoluminescence efficiency, η_p . Thus, the "permanent" degradation in η_E which they observed after extended annealing at 600°-900°C may have been degradation of the p-n junction itself rather than being related to (Zn, O)-pairing. For example, extended annealing may have merely altered the impurity concentration at the p-n junction and thereby reduced the efficiency of injection of electrons into the (Zn, O)-doped p-side of the diode. By measuring η_p in bulk material, the present study concentrated on basic luminescent efficiency and avoided the complication of possible p-n junction degradation.

In agreement with the observations of Onton and Lorenz, the present results indicated that infrared emission could be shifted to red emission by annealing at temperatures of 400°-600°C. Conversely, red emission could be shifted into the infrared band by an-

nealing at a higher temperature. Onton and Lorenz suggested that such results could be explained in terms of the equilibrium number of Zn-O nearest-neighbor pairs formed at a given temperature. Assuming the total number of zinc and oxygen atoms in a sample to be constant, the number of oxygen atoms that can participate in infrared emission is reduced whenever zinc and oxygen atoms combine to form nearest-neighbor pairs. Thus an increase in red emission via exciton decay at Zn-O complexes is expected to be accompanied by a decrease in infrared emission whenever a sample is annealed at a temperature which favors formation of Zn-O pairs.

The above qualitative arguments were put in quantitative form by Onton and Lorenz and, more recently by Wiley (16). Both calculations are based upon the similarity between formation of Zn-O pairs in GaP and the formation of Coulomb-bonded donor-acceptor pairs in Ge and Si. Using the work of Lidiard (17) as a basis, Wiley has calculated a theoretical curve for the fraction, $F = [P]/[O]$, of oxygen atoms which are paired, where $[P]$ is the equilibrium (Zn, O)-pair concentration at a given temperature and $[O]$ is the total substitutional oxygen concentration, assumed to be temperature independent.

As will be shown, the red/infrared emission ratio obtained experimentally in the present investigation can be compared to Wiley's theoretical pairing fraction. However, it is first necessary to develop a model for minority carrier recombination in GaP using standard semiconductor statistics (18). Referring to Fig. 3, we see that there are three recombination paths labeled S, Q, and Y. The paths labeled S and Q correspond to minority-carrier capture by the (Zn,O) and O-centers, respectively, while the Y-path corresponds to nonradiative band-to-band recombination through some unknown center or centers. Path Y, the "shunt path," is used as a means of quantitatively accounting for all minority carriers which do not recombine through either (Zn, O) or O-centers.

After Dishman and DiDomencio (19), we define a branching ratio as the fraction of minority carriers that recombine through a given path. If R_s , R_q , and R_y denote the capture rates for the three recombination centers, the branching ratio for a given center is just the capture rate for that center divided by the sum of the three capture rates. Thus, the branching ratios s , q and y are

$$s = R_s / (R_s + R_q + R_y) \quad [1]$$

$$q = R_q / (R_s + R_q + R_y) \quad [2]$$

$$y = R_y / (R_s + R_q + R_y) \quad [3]$$

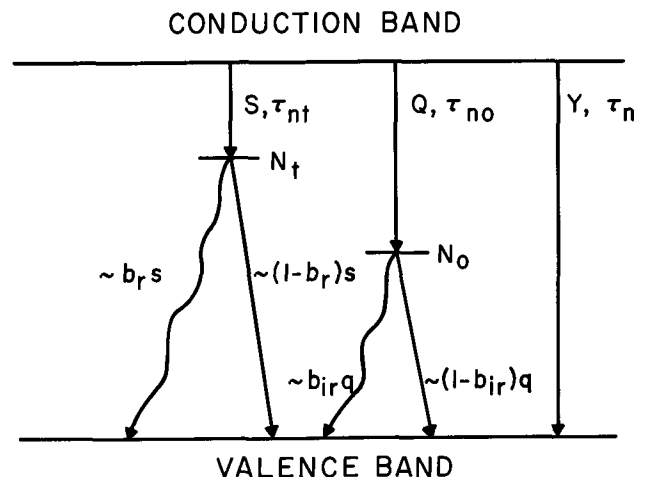


Fig. 3. The three minority-carrier capture paths, denoted S, Q, and Y, applicable to GaP at 77°K are shown along with other notation used in the text. Radiative transitions from the (Zn,O) and O-centers are indicated by wavy-line arrows.

At low excitation levels we can ignore the fraction of (Zn,O) or O-traps that are already electron-occupied (or exciton occupied) and take each capture rate to be simply the minority carrier concentration, n , divided by the appropriate capture lifetime. The capture rates are (19)

$$R_s = n/\tau_{nt} = n\nu\sigma_{nt} N_t \quad [4]$$

$$R_q = n/\tau_{no} = n\nu\sigma_{no} N_o \quad [5]$$

$$R_y = n/\tau_n \quad [6]$$

In the above equations, ν is the conduction-band-electron thermal velocity, τ is the capture lifetime, σ is the capture cross section, and N is the recombination-center concentration. Quantities subscripted with t refer to (Zn,O)-centers, while those subscripted with o refer to oxygen centers. Using the above expressions, and eliminating the common factor n , we obtain the following equations for the branching ratios

$$s = \frac{\nu\sigma_{nt} N_t}{\nu\sigma_{nt} N_t + \nu\sigma_{no} N_o + 1/\tau_n} \quad [7]$$

$$q = \frac{\nu\sigma_{no} N_o}{\nu\sigma_{nt} N_t + \nu\sigma_{no} N_o + 1/\tau_n} \quad [8]$$

$$y = \frac{1/\tau_n}{\nu\sigma_{nt} N_t + \nu\sigma_{no} N_o + 1/\tau_n} \quad [9]$$

It is convenient to define two more branching ratios, b_r and b_{ir} , in the following way (19). We are ultimately interested in radiative quantum efficiency, and, therefore, b_r or b_{ir} is defined as the fraction of the total recombination through (Zn,O) or O-centers, respectively, that is radiative. If, for example, $y = 0$ and $b_r = b_{ir} = 1$, the radiative quantum efficiency would be 100%.

We can now write down expressions for the red and infrared quantum efficiencies η_r and η_{ir} , respectively, for band-to-band excitation.

$$\eta_r = b_r s \quad [10]$$

$$\eta_{ir} = b_{ir} q \quad [11]$$

Denoting the integrated red/infrared emission ratio by α , we see that $\alpha = \eta_r/\eta_{ir}$ can be written as

$$\alpha = \frac{b_r s}{b_{ir} q} \quad [12]$$

$$= \frac{b_r \sigma_{nt} N_t}{b_{ir} \sigma_{no} N_o} \quad [13]$$

The above expression for α can be compared with the theoretical results of Wiley by making a few slight changes in his notation. Wiley calculated the fraction, F , of oxygen atoms that are paired into Zn-O complexes. Denoting the total substitutional oxygen concentration by N_{oo} , the fraction F can be written

$$F = N_t/N_{oo} \quad [14]$$

However, $N_o = N_{oo} - N_t$, and now α can be expressed in terms of F

$$\alpha = \frac{b_r \sigma_{nt}}{b_{ir} \sigma_{no}} \left(\frac{F}{1-F} \right) \quad [15]$$

The coefficient of $F/(1-F)$ in Eq. [15] can be considered a scale factor which will be denoted as K

$$K = \frac{b_r \sigma_{nt}}{b_{ir} \sigma_{no}} \quad [16]$$

Although not necessarily true, K will be assumed independent of heat treatment in the present discussion. Solving Eq. [15] for F we have

$$F = \frac{\alpha}{K + \alpha} \quad [17]$$

Thus, through Eq. [17], the present experimental values of α can be related to theoretical values of F in terms of the scale factor, K , given in Eq. [16].

To compare F and α , the scale factor K can either be calculated using Eq. [16], or empirically determined by curve fitting. Experimental work performed elsewhere (20) gave the following estimates for the branching ratios and capture cross sections: $b_r \approx 0.07$; $b_{ir} \approx 0.6-0.7$; $\sigma_{nt} \approx 10^{-16}$ cm²; and $\sigma_{no} \approx 1-2 \times 10^{-18}$ cm². More recent work (21) has indicated σ_{nt} is about a factor of twenty larger than the above value and that σ_{no} depends linearly on the hole concentration. For the present samples where $p \approx 8 \times 10^{17}$, the estimated value of σ_{no} is 4×10^{-16} cm². Using the more recent values of σ_{nt} and σ_{no} , the calculated value of the scale factor is $K \approx 5$.

When plots of K vs. temperature and α vs. temperature were made using the value $K = 5$, the two curves were found to have a similar shape but to differ in magnitude. In view of the uncertainties involved in the estimates given above, it was decided to use K as an empirically determined scale factor. This was accomplished by calculating the value of K required to make the curves coincide at 400°C. The empirical value ($K = 32$) was then used in conjunction with experimental values of α at 600° and 900°C to calculate, using Eq. [17], new values of F . The experimentally determined values of F are plotted in Fig. 4 along with the complete theoretically predicted curve of Wiley. As can be seen, the experimental agreement is quite good.

In the above mathematical development, the reason why (Zn-O)-pairing produces an increase in the red/infrared emission ratio can be easily seen. Less obvious is whether an increase in (Zn-O)-pairing can account for the observed increase in photoluminescent efficiency. To answer this question, η_p should be expressed in terms of F , σ , N , etc., and the resulting equation differentiated with respect to F . If $d\eta_p/dF > 0$, this indicates that (Zn-O)-pairing does improve the photoluminescent efficiency as well. The calculation is given here, but it is easy to show that $d\eta_p/dF$ is, in fact, always positive. This result is reasonable because, physically, radiative recombination is being shifted from the unpaired-oxygen center to the (Zn,O)-center which has a larger capture cross section and, hence, a faster minority-carrier capture rate.

Although (Zn,O)-pairing is seen to increase η_p , the amount of this increase could not be quantitatively determined. It was necessary to measure η_p at room temperature where the relationship between η_p and the various fundamental quantities becomes very complicated and involves additional parameters which depend on N_T (19). Thus, it is not practicable to calculate $d\eta_p/dF$ at room temperature. The observation that

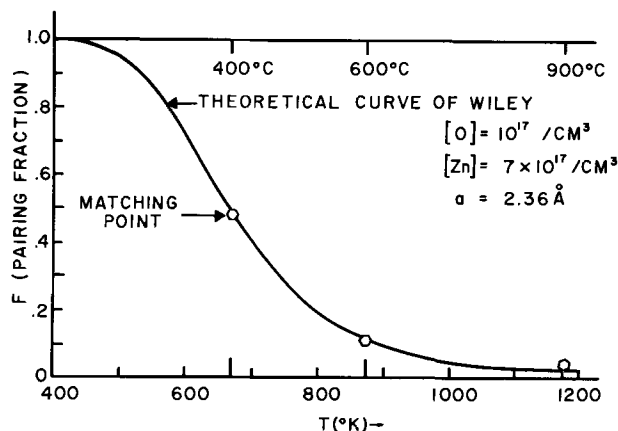


Fig. 4. A plot of the present experimental results is shown together with the theoretical pair-equilibrium curve of Wiley.

the plateau value of η_p was reached in about 16 hr of 400°C annealing, whereas α was still increasing at that time, indicates that η_p does not depend solely on F .

There are two other possibilities which can account for part of the increase in η_p with annealing. One possibility is that oxygen is liberated from compounds during annealing and, thereby, the total substitutional oxygen concentration in the lattice is increased. The basis for this suggestion is that Ga_2O_3 precipitates have been observed (22) in GaP crystals and there is the possibility that other compounds which dissociate at a lower temperature might also be present. A second explanation for part of the net increase in η_p is that annealing might produce a reduction in the amount of nonradiative recombination that occurs. If the recombination through shunt path Y were reduced, the photoluminescent efficiency would increase but the red/infrared ratio would not be affected, as shown by Eq. [13].

To investigate the reversibility of pairing, sample H-140 was heated to 900°C for 30 min and quenched after it had undergone an annealing cycle of 24 hr at 400°C. For comparison purposes, the original $t = 0$ values were $\eta_p = 0.47\%$, $\alpha = 2.2$, while the values after the final 30 min-900°C treatment were $\eta_p = 0.81\%$, $\alpha = 2.4$. The reset value of α is, within experimental error, equal to the original $t = 0$ value, thus demonstrating that emission can be shifted between the red and infrared emission bands by appropriate heat treatment and that no permanent degradation was observed in this sample. The reason why the efficiency, η_p , was not reset to its original $t = 0$ value is not clear but at least this result is not inconsistent with the two latter suggestions regarding the over-all increase in η_p with annealing. That is, annealing might have irreversibly increased the substitutional oxygen concentration and/or decreased the amount of nonradiative recombination.

Summary

In the present work we have investigated the effects of annealing on the photoluminescence efficiency of Zn-O doped GaP. Samples that were examined were solution-grown with doping concentrations similar to those used for the p-side of GaP light-emitting diodes. Photoluminescence emission spectra were obtained at 77°K in order to determine how the red and infrared emission bands are separately affected by heat treatment. Samples were cut in a small cloverleaf shape to insure that successive optical measurements would be made at the same position on the sample. A SiO_2 coating was applied to samples in an attempt to reduce factors which might adversely affect the reproducibility of the results.

The results obtained in the present investigation are in substantial agreement with those obtained by Onton and Lorenz (8). We did not observe any permanent degradation in the photoluminescence properties of bulk samples after prolonged heat treatment, and therefore we attribute the permanent degradation of diode efficiency observed by Onton and Lorenz to some adverse change in the electrical properties of their p-n junctions. The present results are consistent with the notion that low-temperature annealing promotes coulomb-bonding of Zn-O acceptor-donor pairs at nearest-neighbor lattice sites (16). Using a scale factor based upon a well-founded model (19), quantitative agreement between the present experimental results and the theoretically predicted (Zn,O)-pair equilibrium curve calculated by Wiley (16) has been obtained. It was shown that the increase in total radiative efficiency could be attributed in part to an increase in the number of (Zn, O)-pairs that results from low-temperature annealing. Other possible mechanisms that are proposed to explain part of the increase in η_p are: (i) an increase in the total amount of substitutional oxygen and (ii) a decrease in nonradiative transitions, particularly through the band-to-band

shunt path. The observation that the original efficiency could not be reset after a subsequent 900°C anneal-quench cycle is qualitatively explainable by either of the above arguments.

Conclusions

The results obtained in the present work indicated that annealing temperatures lower than 600°C are desirable in order to increase both the red-luminescence efficiency and the total luminescence efficiency of (Zn, O) doped GaP. Although the present work involved bulk material, similar results are expected for diodes fabricated with p-type material having similar doping concentrations. Inasmuch as luminescence recombination processes are the same for any band-to-band excitation method, the only reason for annealing diodes at temperatures higher than 400°C would be if the p-n junction were adversely affected by a long duration annealing at 400°C.

Although the present study was unable to completely evaluate the efficacy of the SiO_2 films used on the samples, the conclusions are that such films are generally beneficial. A further evaluation of the films should be made using GaP diodes similarly coated and subjected to the same type of heat treatment.

In view of the intentionally limited scope of the present investigation, further work of a similar nature is suggested in order to answer some of the unresolved questions. Additional information about radiative and nonradiative processes in GaP can be obtained by studying the luminescent time decay of the bound exciton emission, as shown recently by Jayson *et al.*²³ Measurements of photoluminescent efficiency and emission spectra, as performed in the present investigation, only determine steady-state luminescent properties, whereas decay measurements yield information about the kinetics of radiative and nonradiative recombination. Through an understanding of GaP recombination processes, obtained in such studies, it should be possible to improve the already-high electroluminescent efficiencies obtainable with GaP light-emitting diodes.

Acknowledgment

We are particularly indebted to J. D. Wiley for making the results of his pairing calculations available prior to publication. We would like to acknowledge many helpful discussions with L. Derick and F. A. Trumbore during the crystal growth portion of this work. Also, we would like to acknowledge the assistance of J. S. Jayson and W. A. Erdman in making their laboratory facilities available to us for electrical measurements and for sputtering the SiO_2 coatings.

Manuscript submitted June 22, 1971; revised manuscript received Sept. 29, 1971. This was Paper 210RNP presented at the Washington, D.C., Meeting of the Society, May 9-13, 1971.

Any discussion of this paper will appear in a Discussion Section to be published in the December 1972 JOURNAL.

REFERENCES

1. P. J. Dean, "Luminescence of Inorganic Solids," Paul Goldberg, Editor, p. 119, Academic Press, New York (1966).
2. M. Gershenson, "Semiconductors & Semimetals," R. K. Willardson, and A. C. Beer, Editors, Vol. 2, p. 289, Academic Press, New York (1966).
3. C. H. Henry, P. J. Dean, and J. D. Cuthbert, *Phys. Rev.*, **170**, 739 (1968).
4. T. N. Morgan, B. Welber, and R. N. Bhargava, *ibid.*, **166**, 751 (1968).
5. J. D. Cuthbert, C. H. Henry, and P. J. Dean, *ibid.*, **170**, 739 (1968).
6. R. N. Bhargava, *ibid.*, **B2**, 387 (1970).
7. J. M. Dishman, *ibid.*, **B3**, 2588 (1971).
8. A. Onton and M. R. Lorenz, *Appl. Phys. Letters*, **12**, 115 (1968).
9. R. A. Logan, H. G. White, and W. Wiegmann, *ibid.*, **13**, 139 (1969).
10. R. A. Logan, H. G. White, and F. A. Trumbore, *ibid.*, **10**, 206 (1967).

11. R. A. Logan, H. G. White, and F. A. Trumbore, *J. Appl. Phys.*, **38**, 2500 (1967).
12. M. Toyama, A. Kasami, M. Naito, and K. Maeda, *Trans. Met. Soc. AIME*, **245**, 551 (1969).
13. R. H. Saul, *J. Appl. Phys.*, **40**, 4977 (1969).
14. L. J. van der Pauw, *Philips Res. Rept.*, **13**, 1 (1958).
15. In a brief study involving five uncoated samples annealed for 5 hr at 600°C, J. M. Dishman, M. DiDomenico, Jr., and R. Caruso, *Phys. Rev. B*, **1**, 3381 (1970), also found that the quantum efficiency sometimes decreased upon annealing. Inasmuch as the efficiency of some samples increased, they were unable to make any definite conclusions regarding the effects of annealing on quantum efficiency.
16. J. D. Wiley, *J. Phys. Chem. Solids*, To be published.
17. A. B. Lidiard, *Phys. Rev.*, **94**, 29 (1954).
18. J. S. Blakemore, "Semiconductor Statistics," Pergamon Press, Inc. New York (1962).
19. J. M. Dishman and M. DiDomenico, Jr., *Phys. Rev.*, **B1**, 3381 (1970).
20. J. M. Dishman, Private communication.
21. J. S. Jayson, Private communication.
22. J. M. Dishman, M. DiDomenico, Jr., and R. Caruso, *Phys. Rev.* **B2**, 1988 (1970).
23. J. S. Jayson, R. N. Bhargava, and R. W. Dixon, *J. Appl. Phys.*, **41**, 4972 (1970).

Luminescence and Structural Properties of Thiogallate Phosphors Ce⁺³ and Eu⁺²-Activated Phosphors. Part I

T. E. Peters* and J. A. Baglio

The Bayside Research Center of GTE Laboratories, Incorporated, Bayside, New York 11360

ABSTRACT

Thiogallate compounds represented by the formula MGa_2S_4 [where $M = Ca^{+2}, Sr^{+2}, Ba^{+2}, Pb^{+2}, Eu^{+2}, (Na^{+1}La^{+3}),$ and $(Na^{+1}Ce^{+3})$] were prepared by solid-state reaction. Single crystals of the alkaline earth derivatives were also obtained by vapor transport of the corresponding polycrystalline material. X-ray diffraction analyses of the single crystals show that $BaGa_2S_4$ is cubic belonging to space group Th^0-Pa3 while $SrGa_2S_4$ and $CaGa_2S_4$ are isomorphous belonging to the orthorhombic space group $D_{2h}^{24}-Fddd$. X-ray powder diffraction results on the other derivatives indicate that they are all isostructural with the Sr analogue. The alkaline earth thiogallates are the basis of a new type of sulfide phosphor. Rare earth ions readily substitute for the alkaline earth in the host lattice resulting in phosphors that fluoresce strongly under ultraviolet and cathode rays. The luminescence properties of the host compounds and the Ce^{+3} and Eu^{+2} -activated phosphors are described.

In recent years much of the luminescence research has been concerned with the fluorescence of rare earth ions in oxygen dominated systems. The fluorescence of rare earth ions in sulfur dominated lattices has received considerably less attention. Contemporary research, for example, includes the work of Brown and Shand (1) and Suchow and Stemple (2) who reported on the emission of several of the trivalent rare earth ions in various semiconducting thiospinel host crystals. Anderson (3-4) investigated rare earth emission in zinc and cadmium sulfides and noted that the trivalent rare earth ion can associate with a variety of acceptor defects, and it thereby occupies a number of non-equivalent symmetry sites. This gives rise to complex emission and absorption spectra and consequent difficulty in theoretical interpretation. Additional complications arise as a result of broad band emissions originating from impurity levels within the bandgap of sulfide host. The only efficient sulfide phosphors based on rare earth activators were those described by Urbach (5), Ward (6) and their associates beginning in 1946-1947. These are the infrared stimulable alkaline earth sulfides doubly activated with Ce^{+3} , Eu^{+2} and Sm^{+3} . Keller and co-workers (7) later reported on the fluorescence of virtually all of the rare earth ions in SrS and recently Lehmann and Ryan (8) presented data on the cathodoluminescence of $CaS:Ce^{+3}$ and $CaS:Eu^{+2}$. Although the alkaline earth sulfides are efficient hosts for rare earth ions, phosphors of this type have not been widely used because of their susceptibility to hydrolysis. It was decided, therefore, to investigate binary compounds based on the alkaline earth sulfides since these materials should

readily accommodate substitutional rare earth ions and might also be more stable toward hydrolysis.

It has been shown (9) that the bandgap of a binary chalcogenide compound can be estimated from the arithmetic mean of the bandgaps of the unary components. The absorption spectra of SrS have been determined (10) and consequently the bandgap is known to be about 4.05 eV. Gallium sulfide (Ga_2S_3) was chosen as the second part of the binary system since it also possesses a relatively large bandgap (3.31 eV) (11). The absorption edge of the binary compound was calculated to be about 3.68 eV and it would therefore be transparent in the visible region of the spectrum. Evidence for the existence of such compounds was given by Bostsarron (12) who prepared $CaGa_2S_4$ and noted that it exhibited a complicated x-ray diffractogram.

Initially, the activators chosen for study included those in which $4f^{n-1}5d \rightarrow 4f^n$ transitions were known to play an important role in the emission process (i.e., Ce^{+3} , Eu^{+2} , Yb^{+2}). Of these only Ce^{+3} and Eu^{+2} were found to exhibit visible emission at 300°K. Subsequently, activators chosen from the remaining rare earth ions in which the fluorescence arises from transitions within the shielded 4f shell were also investigated. In this report the luminescence and structural properties of the host compounds and the Ce^{+3} and Eu^{+2} -activated phosphors are described. Applications of the Ce^{+3} and Eu^{+2} phosphors and the luminescent properties of the remaining rare earth ions will be the subject of subsequent articles.

Experimental

Materials preparation.—The starting materials employed in the preparation of the thiogallate compounds were high purity alkaline earth carbonates PbS, Ga_2O_3

* Electrochemical Society Active Member.
Key words: luminescence, phosphors, structural properties, Eu^{+2} activated, Ce^{+3} activated, thiogallate.

(99.99%) and the appropriate rare earth oxides (99.9%). All reagents except PbS were subsequently converted to their respective sulfides by reaction at 900°-1200°C in a stream of H₂S gas. Stoichiometric quantities of the various sulfides were then thoroughly mixed by grinding in a glass mortar and the resulting blend was subjected to a solid-state reaction at 900°-1000°C in H₂S. Under these conditions the reaction usually resulted in the formation of M²⁺Ga₂S₄ in about 2 hr. The compound was obtained in the form of a sintered cake which was then mortared and sieved prior to evaluation. The phosphors were formulated as: M_{1-x}Eu_xGa₂S₄ or M_{1-2x}Ce_xNa_xGa₂S₄ (M = Ca, Sr, Ba). Alternate compensation mechanisms for Ce³⁺ such as those expressed by the general formulas M²⁺_{1-3x}Ce_{2x}Ga₂S₄ and M²⁺_{1-x}Ce_xZn_xGa_{2-2x}S₄ were also investigated but sodium compensation proved to be the most effective in producing efficient phosphors. The monovalent sodium was usually introduced as NaCl but in some syntheses (*viz.* Na_{0.5}Ln_{0.5}Ga₂S₄) Na₂CO₃ was found to be more suitable. The Ce³⁺ and Eu²⁺ activators were generally introduced at a sufficiently high concentration level to assure accurate gravimetry and lower doping levels were achieved by dry dilution.

Alkaline earth thiogallate single crystals were grown from the corresponding polycrystalline compounds by iodine vapor transport. Quartz ampules 2.54 cm I.D. and 20. cm in length were filled with enough iodine so that the pressure was approximately 0.5 atm at the hot zone temperature of 960°C. The ampules were placed in a tube furnace with a 200°C temperature drop over the length of the tube. The reaction time was usually 5 days. The crystals thus obtained were usually in the 1 mm range or less. In one case, however, (SrGa₂S₄:Eu), it was possible to obtain a single crystal with dimensions 5 × 5 × 2 mm.

Measurement techniques.—X-ray powder diffraction techniques were employed in the identification of the various sulfide reagents and thiogallate compounds. Single crystal lattice parameters and space group determinations were obtained from Weissenberg photographs. In addition, emission spectroscopy and chemical analysis were employed to monitor the purity and stoichiometry of the starting materials, the sulfide reagents, and the finished phosphors. Emission and excitation spectra are given in terms of relative energy and relative energy efficiency *vs.* wavelength. Radiant efficiencies under cathode ray excitation were determined in a manner analogous to that described by Brill and Klasens (13). Photoluminescence was measured relative to suitable standard phosphors under excitation by a medium or low pressure mercury vapor lamp whose output was filtered by a Wratten No. 7-54 filter. The emission was detected by a Photovolt

Photometer equipped with a 1P21 phototube and a Wratten 106 filter.

Results and Discussion

Crystallography.—Optical and crystallographic examination of single crystals of BaGa₂S₄ show that it is cubic. The diffraction symmetry and systematic absences correspond to the tetrahedral space group Th⁶-Pa3 (14). Since the general position for this space group is twenty-four fold and because there are 12 formula-weight units per unit cell, the barium ions must be in two different sites; 8 Ba ions lie in the special position c with point symmetry 3, and 4 Ba ions lie in the special position a or b with point symmetry $\bar{3}$. Since it is assumed that activator ions substitute for Ba, these ions also lie in two different sites. The pertinent crystal data are compiled in Table I.

Microscopic examinations of the Sr and Ca analogues indicated that both these compounds are biaxial. Weissenberg patterns confirmed that they are isomorphous and belong to the orthorhombic crystal class. The diffraction symmetry and systematic absence are consistent with space group D_{2h}²⁴-Fddd. As shown, however, in Table I there are additional extinctions that are not accounted for by this space group. Attempts to reindex the patterns so as to be more consistent with other space groups were unsuccessful. An explanation for these anomalous extinctions is the possibility of twinning, although no evidence of this was detected by polarized microscopic studies. Even if Fddd is indeed the correct space group, the point symmetries for Ca and Sr atoms are not determinable from existing data because the general position is thirty-two fold and there are 32 formula-weight units per unit cell. The point symmetries of Ca and Sr would be low, however, since the highest possible site symmetry for this space group is 222 (positions 8a and b). Moreover, only half of the cations could occupy these positions; the remainder would be required to be in sites with either 2 or $\bar{1}$ point symmetry.

X-ray powder diffractograms on all the other related compounds show that they are isomorphous with SrGa₂S₄. The lattice parameters and other crystal data are listed in Table I. The observed interplanar spacings are compared in Table II with those obtained from the assumed crystal model.

In a recent article, Eholie and co-workers (15) reported the preparation and crystallographic properties of PbM₂X₄, EuM₂X₄, and SrM₂X₄ (M = Al, Ga and X = S, Se). The unit cell parameters for the supercell of EuGa₂S₄ (with their notation a and b interchanged) and density (32 formula units/unit cell) are in good agreement with our results as presented in Table I. (They did not report any lattice parameters for SrGa₂S₄.) Their single crystal studies on PbGa₂Se₄

Table I. Crystallographic data*

Compound	a	b	c	z	ρ_{obs}	ρ_{calc}	Sp.Gp.
BaGa ₂ S ₄	12.660 (4)	12.660 (4)	12.660 (4)	12	3.92	3.98	Th ⁶ -Pa3
SrGa ₂ S ₄	20.840 (4)	20.495 (4)	12.212 (4)	32	3.61	3.62	D _{2h} ²⁴ -Fddd
CaGa ₂ S ₄	20.087 (4)	20.087 (4)	12.112 (4)	32	3.38	3.34	D _{2h} ²⁴ -Fddd
EuGa ₂ S ₄	20.716 (5)	20.404 (5)	12.200 (5)	32	4.2	4.32	D _{2h} ²⁴ -Fddd
PbGa ₂ S ₄	20.706 (8)	20.380 (9)	12.156 (9)	32	4.6	4.92	D _{2h} ²⁴ -Fddd
Na _{0.5} La _{0.5} Ga ₂ S ₄	20.384 (9)	20.384 (9)	12.075 (9)	32	3.6	3.69	D _{2h} ²⁴ -Fddd
Na _{0.5} Ce _{0.5} Ga ₂ S ₄	20.230 (9)	20.230 (9)	12.130 (9)	32	3.5	3.74	D _{2h} ²⁴ -Fddd

Systematic absences for SrGa₂S₄ type structure

hkl: $h + k = 2n^{\dagger}$, $h + 1 = 2n^{\dagger}$, $k + 1 = 2n^{\dagger}$
 $k + 1 = 4n$ (when h is even)
 hko: $h, k = 4n$
 $(h + k = 4n)^{\dagger}$
 hol: $h, l = 4n$
 $(h + 1 = 4n)^{\dagger}$
 okl: $k + 1 = 4n^{\dagger}$
 hoo: $h = 4n^{\dagger}$
 Oko: $k = 4n^{\dagger}$
 OOl: $l = 4n^{\dagger}$

* Estimates of standard deviations are in parentheses.
 † Extinctions required by D_{2h}²⁴-Fddd.

Table II. Indexed x-ray powder diffraction data

BaGa ₂ S ₄				SrGa ₂ S ₄				CaGa ₂ S ₄				Na _{0.5} Ce _{0.5} Ga ₂ S ₄				
h	k	l	d _{calc} I/I ₀	h	k	l	d _{obs} d _{calc} I/I ₀	h	k	l	d _{obs} d _{calc} I/I ₀	h	k	l	d _{obs} d _{calc} I/I ₀	
0 0 2	6.33	5.25	1.923	2 3 4	1.923	1.929	0 4 0	5.03	5.02	100	1.933	1.933	3	0 2 2	5.20	5.20
0 0 2	5.66	5.21	1.863	4 2 6	1.863	1.864	2 2 2	4.60	4.60	3	1.906	1.907	9	0 4 0	5.05	5.06
0 2 2	4.48	4.22	1.848	7 2 2	1.848	1.848	1 1 3	3.88	3.88	3	1.875	1.875	1	0 0 0	5.05	5.06
1 1 3	4.21	3.91	1.835	4 4 4	1.835	1.837	3 3 3	3.74	3.75	3	1.873	1.873	1	2 2 2	4.62	4.63
1 1 3	3.814	3.817	1.835	8 8 0	1.835	1.835	9 3 3	3.607	3.608	25	1.843	1.843	3	1 1 1	3.89	3.89
0 2 3	3.507	3.511	1.821	5 1 1	1.821	1.821	2 10 2	3.549	3.551	3	1.842	1.842	3	1 5 1	3.77	3.77
1 2 3	3.381	3.384	1.821	8 8 0	1.821	1.821	4 4 0	3.407	3.407	2	1.841	1.841	3	4 2 2	3.62	3.63
0 0 4	3.166	3.165	1.821	4 4 0	1.821	1.821	7 1 5	3.407	3.407	2	1.841	1.841	3	0 6 6	3.571	3.575
0 4 1	3.071	3.071	1.821	3 3 3	1.821	1.821	3 1 3	3.407	3.407	2	1.841	1.841	3	4 4 2	3.417	3.418
2 2 3	2.986	2.984	1.821	3 3 3	1.821	1.821	4 2 6	3.407	3.407	2	1.841	1.841	3	1 3 3	3.417	3.418
1 1 4	2.832	2.831	1.821	3 3 3	1.821	1.821	4 2 6	3.407	3.407	2	1.841	1.841	3	3 1 3	3.417	3.418
0 2 4	2.758	2.763	1.821	6 6 2	1.821	1.821	4 2 6	3.407	3.407	2	1.841	1.841	3	3 5 1	3.333	3.335
1 2 3	2.685	2.689	1.821	2 6 6	1.821	1.821	3 8 4	3.308	3.313	3	1.796	1.798	2	5 3 1	3.333	3.335
2 2 4	2.583	2.584	1.821	2 6 6	1.821	1.821	8 1 1	2.927	2.930	8	1.796	1.798	2	0 3 4	3.032	3.034
1 3 4	2.479	2.483	1.821	6 6 2	1.821	1.821	11 1 1	2.803	2.812	17	1.782	1.784	2	0 6 2	2.945	2.947
1 1 5	2.432	2.436	1.821	2 10 6	1.821	1.821	7 3 5	2.803	2.812	17	1.782	1.784	2	2 6 2	2.829	2.829
3 3 3	2.348	2.351	1.821	6 10 2	1.821	1.821	7 3 5	2.763	2.766	4	1.740	1.743	2	7 1 1	2.789	2.784
0 2 5	2.310	2.311	1.821	3 1 7	1.821	1.821	4 10 2	2.594	2.593	1	1.740	1.743	2	1 7 1	2.789	2.784
1 2 5	2.232	2.238	1.821	12 2 2	1.821	1.821	11 3 1	2.575	2.577	1	1.740	1.743	2	3 5 3	2.630	2.633
0 4 4	2.200	2.203	1.821	5 10 4	1.821	1.821	6 2 6	2.575	2.577	1	1.740	1.743	2	7 7 5	2.630	2.633
2 2 5	2.110	2.110	1.821	4 12 0	1.821	1.821	5 7 5	2.511	2.511	43	1.681	1.681	2	0 4 4	2.594	2.601
0 0 6	2.081	2.081	1.821	7 7 5	1.821	1.821	7 5 5	2.511	2.511	43	1.681	1.681	2	4 0 4	2.594	2.601
0 6 1	2.051	2.054	1.821	8 8 0	1.821	1.821	0 12 0	2.511	2.511	43	1.681	1.681	2	4 0 4	2.594	2.601
3 3 5	1.929	1.930	1.821	8 8 0	1.821	1.821	12 0 0	2.511	2.511	43	1.681	1.681	2	4 0 4	2.594	2.601
1 3 6	1.865	1.867	1.821	4 8 0	1.821	1.821	12 0 0	2.511	2.511	43	1.681	1.681	2	4 0 4	2.594	2.601
2 3 6	1.807	1.809	1.821	4 8 0	1.821	1.821	12 0 0	2.511	2.511	43	1.681	1.681	2	4 0 4	2.594	2.601
1 2 7	1.723	1.723	1.821	4 8 0	1.821	1.821	12 0 0	2.511	2.511	43	1.681	1.681	2	4 0 4	2.594	2.601
3 3 6	1.675	1.677	1.821	4 8 0	1.821	1.821	12 0 0	2.511	2.511	43	1.681	1.681	2	4 0 4	2.594	2.601
4 4 5	1.645	1.648	1.821	4 8 0	1.821	1.821	12 0 0	2.511	2.511	43	1.681	1.681	2	4 0 4	2.594	2.601
3 5 5	1.603	1.608	1.821	4 8 0	1.821	1.821	12 0 0	2.511	2.511	43	1.681	1.681	2	4 0 4	2.594	2.601
0 0 8	1.584	1.583	1.821	4 8 0	1.821	1.821	12 0 0	2.511	2.511	43	1.681	1.681	2	4 0 4	2.594	2.601
3 5 6	1.510	1.513	1.821	4 8 0	1.821	1.821	12 0 0	2.511	2.511	43	1.681	1.681	2	4 0 4	2.594	2.601

plus others

Na _{0.5} La _{0.5} Ga ₂ S ₄											
h	k	l	d _{obs}	d _{calc}	I/I ₀	h	k	l	d _{obs}	d _{calc}	I/I ₀
0	0	0	5.24	1.774	1	1	1	1.774	1.772	2	3
0	0	0	5.10	1.744	1	1	6	1.744	1.745	3	3
0	0	2	5.10	1.725	1	1	10	1.725	1.727	10	8
0	2	0	4.67	1.720	1	1	8	1.720	1.721	8	8
1	1	1	3.91	1.704	1	1	3	1.704	1.705	2	2
1	1	5	3.801	1.702	1	1	11	1.702	1.702	2	2
4	4	2	3.678	1.698	1	1	3	1.698	1.699	3	3
4	4	4	3.633	1.688	1	1	6	1.688	1.689	3	3
3	1	3	3.446	1.688	1	1	10	1.688	1.689	3	3
3	3	1	3.376	1.688	1	1	2	1.688	1.688	4	2
3	3	5	3.048	1.653	1	1	6	1.653	1.654	4	4
0	0	4	2.968	1.640	1	1	4	1.640	1.640	10	10
0	0	6	2.878	1.638	1	1	11	1.638	1.638	10	10
0	0	2	2.855	1.635	1	1	12	1.635	1.635	12	12
2	5	1	2.824	1.628	1	1	4	1.628	1.628	1	1
2	5	5	2.852	1.624	1	1	10	1.624	1.624	1	1
7	7	3	2.652	1.615	1	1	3	1.615	1.615	3	3
0	0	4	2.615	1.616	1	1	5	1.616	1.615	3	3
0	0	8	2.586	1.579	1	1	8	1.579	1.580	3	3
2	2	4	2.551	1.561	1	1	5	1.561	1.561	8	8
2	2	4	2.535	1.550	1	1	6	1.550	1.550	2	2
4	4	4	2.334	1.486	1	1	4	1.486	1.447	4	4
4	4	4	2.307	1.447	1	1	4	1.447	1.447	4	4
8	8	2	2.307	1.441	1	1	3	1.441	1.441	3	3
4	4	0	2.288	1.440	1	1	4	1.440	1.440	5	5
4	4	0	2.216	1.428	1	1	3	1.428	1.428	3	3
1	1	9	2.084	1.419	1	1	14	1.419	1.418	2	2
5	5	5	2.084	1.406	1	1	4	1.406	1.406	2	2
0	0	2	1.991	1.387	1	1	8	1.387	1.387	2	2
9	9	1	1.972	1.372	1	1	12	1.372	1.372	3	3
2	2	6	1.956	1.366	1	1	7	1.366	1.366	5	5
0	0	8	1.951	1.352	1	1	10	1.352	1.352	3	3
8	8	2	1.951	1.352	1	1	23	1.352	1.352	2	2
4	4	2	1.859	1.330	1	1	10	1.330	1.330	3	3
4	4	8	1.829	1.317	1	1	4	1.317	1.317	4	4
8	8	0	1.813	1.313	1	1	10	1.313	1.313	4	4
4	4	0	1.813	1.313	1	1	10	1.313	1.313	4	4

plus others

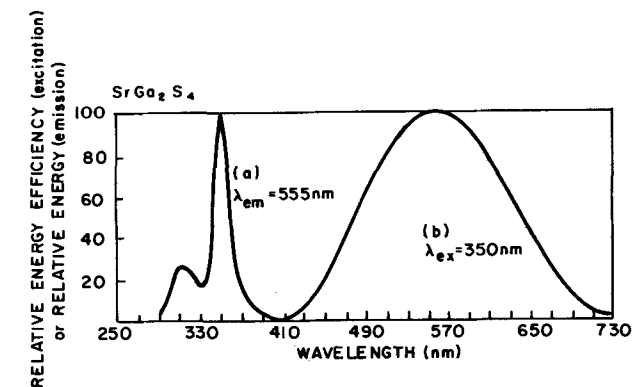


Fig. 1. Relative excitation spectra (a) and spectral energy distribution of fluorescence (b) for SrGa₂S₄.

showed that this compound is also orthorhombic $a = 21.28$, $b = 21.54$, and $c = 12.72\text{\AA}$, with 16 formula weight units/unit cell. These authors did not report a space group for this or any of the other compounds since, as in our case, there were more systematic absences observed than are strictly required by any orthorhombic space group. In order to explain the anomalous extinctions these authors also postulated the presence of twinning even though they were unable to interpret the diffraction data with this assumption. Attempts, moreover, to refine a proposed substructure with unit cell parameters $a/2$, $b/2$, and $c/2$ and space group Bmb were unsuccessful. The absences found for the "superstructure" are, at least, consistent with Fdd and until these anomalies can be resolved by more extensive structure analysis, it appears that in all cases Fdd would be the most consistent tentative space group for all these compounds.

Compound stability.—All of the MGa₂S₄ (M = Ca, Sr, Ba) phosphors appeared to have a satisfactory shelf life but efforts were made to ascertain their stability toward hydrolysis. This was accomplished by measuring the pH change of an aqueous dispersion of several representative samples of each of the alkaline earth phosphors. The results of these measurements indicate that the stability decreases in the order Ba > Sr > Ca.

Experiments employing SrGa₂S₄:Eu indicate that the phosphor undergoes limited hydrolysis after synthesis which imparts an alkaline pH to its aqueous dispersion. After repeated replacement of the dispersion medium the pH of the liquid returns to the neutral range and remains constant. The initial alkaline reaction is probably related to the hydrolysis of free SrS since phosphors prepared with a stoichiometric excess of Ga₂S₃ did not produce this phenomenon. However, chemical analyses indicated the presence of both gallium and strontium ions in the dispersion medium which suggests that the initial hydrolysis of SrS is followed by a much slower hydrolysis of the stoichiometric phosphor.

Luminescence.—The thiogallates exhibit many of the perversities observed in other sulfide phosphor systems with regard to nonreproducibility. This is particularly true with the unactivated thiogallates and is much less so for the activated products. Only the most consistently observed characteristics of the thiogallate phosphors are discussed in the following sections.

Unactivated phosphors.—Unactivated BaGa₂S₄ is inert at 300°K but calcium and strontium thiogallates exhibit a broad band luminescence. The intensity of the emission is stronger near the top surface of the reacted phosphor cake and diminishes near the core. Typical excitation and emission spectra, which are similar for both compounds, are presented in Fig. 1.

Initially it was assumed that the luminescent centers responsible for the host emission were cation vacancies introduced by the sulfurizing atmosphere em-

plus others

plus others

ployed in the synthesis. However, the same emission was observed when syntheses were conducted in N_2 or N_2-H_2 ambients and when a stoichiometric excess of either MS or Ga_2S_3 were provided in the formulation. In a subsequent investigation it was found that $MGa_2S_4:Pb^{2+}$ [$M = Ca, Sr; Pb \leq 0.5$ atomic per cent (a/o)] phosphors exhibited excitation and emission spectra similar to those of the unactivated products. However, none of the metallic ions with the ns^2 electronic configuration were detected by a spectrographic analysis of the sulfide starting materials or the unactivated thiogallate phosphors. Thus the luminescent center responsible for the emission of the unactivated thiogallates remains unassigned.

Ce^{+3} -activated phosphors.—The fluorescence in Ce^{+3} -activated phosphors arises from $^2D \rightarrow ^2F$ electronic transitions of the Ce^{+3} ion. Although visible emission has been reported (16) the fluorescence is usually characterized by broad bands appearing in the near ultraviolet region of the spectrum.

Emission and excitation spectra for the Ce^{+3} -activated thiogallates are presented in Fig. 2. The spectra are for samples containing 2 a/o Ce^{+3} . In the isomorphous calcium and strontium thiogallates significant levels of photoluminescence were observed for concentrations as small as 0.01 a/o and complete concentration quenching did not occur even when all of the alkaline earth cation was replaced, viz., $Na_{0.5}Ce_{0.5}Ga_2S_4$. Solid solutions of $BaGa_2S_4$ with $Na_{0.5}Ce_{0.5}Ga_2S_4$ are limited.

The emission spectra of all three phosphors are similar; two bands are observed and their separation corresponds to that usually found for the ground doublet $^2F_{7/2}, ^2F_{5/2}$. Furthermore the excitation spectra are identical for both emission bands. The excitation spectra for the isostructural calcium and strontium thiogallates are similar while that of the $BaGa_2S_4$:

Ce,Na differs slightly. Diffuse reflectance spectra of the unactivated thiogallate host compounds show no indication of a strong absorption corresponding to the principal excitation bands in the Ce^{+3} phosphors, while the Ce^{+3} activated compounds do absorb in this region. Consequently the principal excitation bands must be due to direct Ce^{+3} absorption. In the 310 nm region, however, both the unactivated and Ce^{+3} -activated compounds absorb strongly, and it is therefore quite likely that the shorter wavelength excitation bands are due to host absorption. The most apparent feature of these spectra is that the excitation and emission bands are located at longer wavelengths than are generally observed for Ce^{+3} in oxidic hosts, but a spectral shift of this type is expected as a consequence of the nephelauxetic effect (17).

The luminescence response of the $M^{+2}Ga_2S_4:Ce,Na$ phosphors is compared to that of blue-emitting standard phosphors in Table III. The radiant cathodoluminescence efficiency of the Ce^{+3} -activated calcium and strontium thiogallates are approximately equal to the $Ca_2Al_2SiO_7:Ce$ (P-16) phosphor while the barium thiogallate exhibits a slightly lower efficiency. The thiogallate phosphors also exhibit a strong response to the radiation from a medium pressure mercury vapor lamp but are less effectively excited by low pressure mercury vapor lamp radiation.

Eu^{+2} phosphors.—In Eu^{+2} -phosphors the fluorescence arises from transitions between the $4f^65d$ and $4f^7$ configurations. The fluorescence is characterized by broad bands whose peak wavelength is strongly influenced by the chemical nature and symmetry of the host crystal. Blasse *et al.* (18), for example, show that in a number of oxygen-dominated compounds the Eu^{+2} emission peaks in the wavelength interval 390–520 nm and in alkaline-earth sulfides the emission has been observed at longer wavelengths (viz., $CaS:Eu^{2+\lambda_{max}} = 650$ nm) (8).

The excitation and emission spectra for the Eu^{+2} -activated thiogallates are shown in Fig. 3. The spectral data are for phosphors activated with 2 a/o Eu^{+2} .

The excitation spectra consist of extremely broad bands which extend well into the visible region and overlap the emission bands to a considerable extent. The excitation bands in the visible are undoubtedly due to Eu^{+2} absorption since the unactivated host compounds do not absorb in this region. As a consequence of this strong visible absorption, the phosphors exhibit a light green to yellow body color.

Blasse *et al.* (18), using an approach similar to that employed by Wood and Kaiser (20) for Sm^{+2} , described an approximate energy level scheme for Eu^{+2} . As in the case of Ce^{+3} , the excitation spectrum was interpreted in terms of the crystal field splitting of the 5d levels. This approach was successful when applied to hosts where the Eu^{+2} ion is located in a lattice site of fairly high symmetry, but for lower symmetry sites such as in the present case the excitation spectrum is too complex for such an analysis.

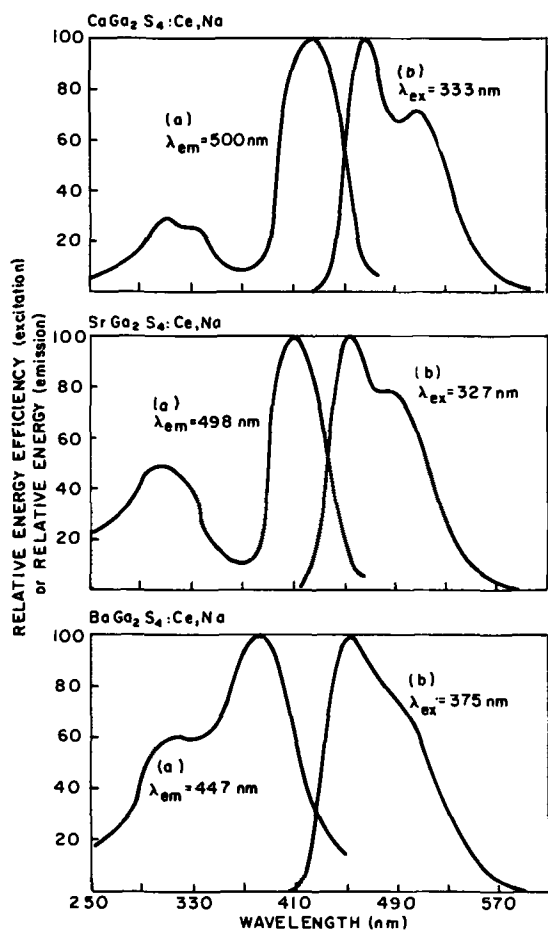


Fig. 2. Relative excitation spectra (a) and spectral distribution of fluorescence (b) for $M^{+2}Ga_2S_4:Ce,Na$ phosphors.

Table III. Performance data for $M^{+2}Ga_2S_4:Ce,Na$ and related phosphors

Phosphor*	Cathodoluminescence		Photoluminescence ^(e) relative luminance	
	$\lambda_{max},$ η_m	$\eta_{cr},$ ^(c) %	MPMV	LPMV
$CaGa_2S_4:Ce,Na$	468	4.5	69	10.5
$SrGa_2S_4:Ce,Na$	455	5.0	61.5	13.5
$BaGa_2S_4:Ce,Na$	455	2.9	105	9.2
$Ca_2Al_2SiO_7:Ce$	405	4.5 ^(d)	—	—
$MgWO_4$ ^(a)	490	—	—	100
$ZnS:Ag$ ^(b)	455	—	100	—

* Ce^{+3} conc—2 a/o.

^(a) $MgWO_4$ —NBS No. 1027.

^(b) $ZnS:Ag$ —NBS No. 1020.

^(c) η_{cr} —absolute radiative efficiency for 20 kV CR excitation.

^(d) Ref. (22)

^(e) MPMV, LPMV—medium pressure and low pressure mercury vapor lamp, respectively.

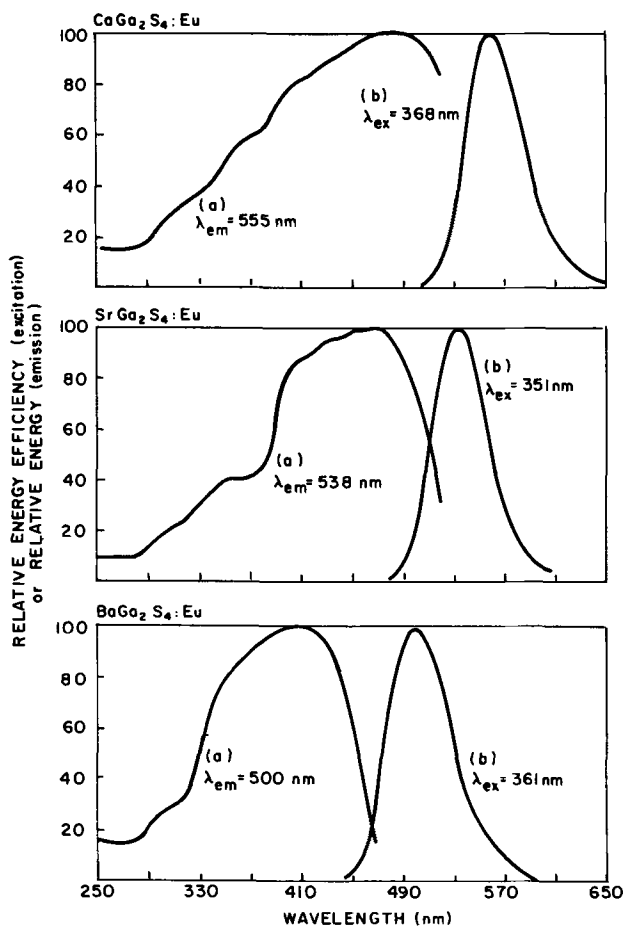


Fig. 3. Relative excitation spectra (a) and spectral energy distribution of fluorescence (b) for $M^{+2}Ga_2S_4:Eu$ phosphors.

As shown in Fig. 3, the emission bands are relatively narrow and depending on the choice of host cation they peak in the blue-green through yellow regions of the spectrum. The isostructural calcium and strontium thiogallates form a complete series of solid solutions whose spectral energy distribution vary uniformly from the green of $Sr_{1-x}Eu_xGa_2S_4$ ($\lambda = 535$ nm) to the yellow of $Ca_{1-x}Eu_xGa_2S_4$ ($\lambda = 555$ nm). Solid solutions in the barium-strontium system are limited.

Trichromatic coefficients derived from the cathodoluminescence spectra of the Eu^{+2} -activated $M^{+2}Ga_2S_4$ compounds and some of their binary solid solutions, together with those of several commercial phosphors, are given on the CIE diagram in Fig. 4. In the figure the lines connecting the coordinate points of the $M^{+2}Ga_2S_4:Eu$ phosphors indicate the range of chromaticity values that can be obtained from solid solutions of the type $Sr_{0.97-x}Eu_{0.03}M^{+2}_xGa_2S_4$ (where $M = Ca, Ba$ and $x = 0 \rightarrow 1.0$). The double lines on the $SrGa_2S_4:Eu$ - $BaGa_2S_4:Eu$ join indicate a region of mixed phase. Thus from $x = 0 \rightarrow 0.1$ the phosphors exhibit the $SrGa_2S_4$ crystal structure and from $x = 0.6-1.0$ they possess the $BaGa_2S_4$ structure.

One of the more interesting of these phosphors is $SrGa_2S_4:Eu$ whose chromaticity values indicate that it is more saturated in color than most of the commercially available phosphors. Employed in a color TV application as a substitute for the $(Zn,Cd)S:Ag$ green primary the $SrGa_2S_4:Eu$ phosphor would increase the gamut of obtainable colors approximately 10%. It is also interesting to note that small ($\sim 10\%$) substitutions of Ba for Sr actually improves the color slightly and at the same time improves the stability of the phosphor toward hydrolysis.

The Eu^{+2} -activated thiogallates exhibit an excellent cathodoluminescence response as demonstrated by the data presented in Table IV. The table also presents

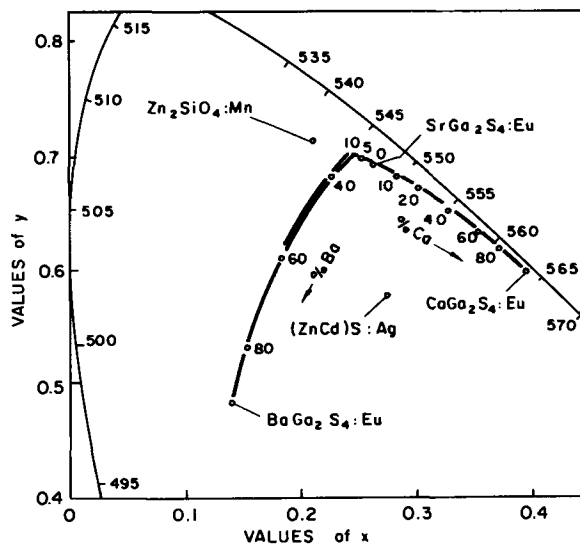


Fig. 4. Trichromatic coefficients of $M^{+2}Ga_2S_4:Eu$ and other green-emitting CRT phosphors.

analogous data for two commercial phosphors which have served as the green primary in color television picture tubes.

The radiant efficiency of the Eu^{+2} -activated thiogallates decreases in the order $Ca > Sr \gg Ba$. In general, the lumen equivalents follow this same progression and as a consequence the differences in the luminous efficiencies are larger.

A comparison of the cathodoluminescence data for the green-emitting phosphors is of particular interest because of the excellent color coordinates of the $SrGa_2S_4:Eu^{+2}$. The radiant efficiency of the $SrGa_2S_4:Eu^{+2}$ is observed to be only 38% that of the $(Zn,Cd)S:Ag$ but its lumen equivalent is approximately 30% higher. Thus it has a luminous efficiency which is 50% that of the green sulfide primary. Similarly, by virtues of its higher lumen equivalent and a slightly higher radiant efficiency the luminance of the $SrGa_2S_4:Eu$ exceeds that of $Zn_2SiO_4:Mn$ by about 19%.

At low current densities the emission intensity of a cathodoluminescent phosphor increases linearly with increasing beam current. At high current densities, however, ZnS type phosphors saturate or become non-linear in their response to current (21). The luminance of a $SrGa_2S_4:Eu$ phosphor relative to that of the green $(Zn,Cd)S:Ag$ primary is presented as a function of cathode current in Fig. 5. These measurements were obtained with a 25 kV electron beam scanned at the normal TV rate over a 4 in. \times 4 in. raster. The beam spot diameter was 0.010 in. and the dwell time was about 0.1 μ sec. The relative luminance is observed to increase linearly with current reaching a value of 85%.

Table IV. Luminescence data for $M^{+2}Ga_2S_4:Eu$ and related phosphors

Phosphor*	Coordinates		$\eta_{cr}^{(a)}$ %	Lumen equiv- alent	Relative luminance ^(c)		
	x	y			$L_{cr}^{(b)}$	MPMV LPMV	
$CaGa_2S_4:Eu$	0.39	0.59	7.8	594	46.3	134	91
$SrGa_2S_4:Eu$	0.26	0.69	7.6	560	42.6	80	72
$BaGa_2S_4:Eu$	0.14	0.48	4.5	325	14.6	37	18
$Zn_2SiO_4:Mn^{(d)}$	0.22	0.70	7.0	510	35.7	—	100
$(Zn,Cd)S:Ag$	0.25	0.56	20.0	428	85.6	100	—
$SrAl_2O_4:Eu$	0.28	0.55	1.5 ^(e)	—	—	129	154

* Eu^{+2} conc—2 a.o.
^(a) η_{cr} —absolute radiative efficiency for 20 kV CR excitation.
^(b) L_{cr} —luminous efficiency—lumens/elect. watt.
^(c) MPMV, LPMV—medium pressure and low pressure mercury vapor lamp, respectively.
^(d) NBS—1021.
^(e) Ref. (18).

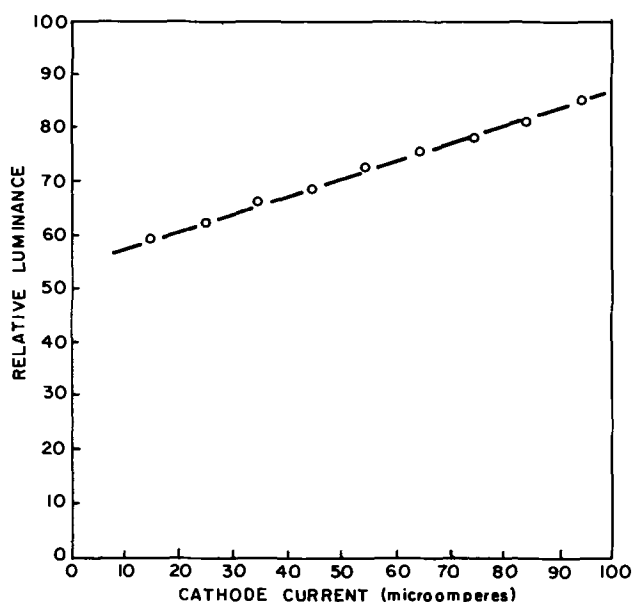


Fig. 5. Relative luminance of $\text{SrGa}_2\text{S}_4:\text{Eu}$ vs. cathode current

of the green $(\text{Zn,Cd})\text{S}:\text{Ag}$ at $95 \mu\text{A}$. Phosphors with a linear response are of interest for use in PDF (post deflection focusing) and Trinitron type CR tubes where they are subjected to higher current densities than those encountered in conventional TV picture tubes. Thus the $\text{SrGa}_2\text{S}_4:\text{Eu}$ phosphor might find application in one of these tube designs.

The response of the $\text{M}^{+2}\text{Ga}_2\text{S}_4:\text{Eu}$ phosphors to the radiation from low and medium pressure mercury vapor lamps is also given in Table IV. The Eu^{+2} -activated thiogallates are similar to the $\text{M}^{+2}\text{Ga}_2\text{S}_4:\text{Ce,Na}$ phosphors in that they have a somewhat higher response to the long uv radiation of the medium pressure mercury lamp. However, the Eu^{+2} -activated phosphors, in contrast to the $\text{M}^{+2}\text{Ga}_2\text{S}_4:\text{Ce,Na}$ materials, also respond rather well to short uv excitation.

Sulfide phosphors are generally avoided in fluorescent lighting applications because of their poor maintenance. The light output of a 40W lamp containing $(\text{Zn,Cd})\text{S}:\text{Ag}$, for example, drops to 73% of its initial value after 100 hr of operation. The $\text{SrGa}_2\text{S}_4:\text{Eu}$ phosphor, while it does not compare favorably to standard lamp phosphors for maintenance, is considerably better than the $(\text{Zn,Cd})\text{S}:\text{Ag}$ losing only 10% of its initial intensity in 100 hr.

Summary

The synthesis and crystallographic properties of thiogallate compounds of the general formula $\text{M}^{+2}\text{Ga}_2\text{S}_4$ [where $\text{M} = \text{Ca}^{+2}, \text{Sr}^{+2}, \text{Ba}^{+2}, \text{Pb}^{+2}, \text{Eu}^{+2}, (\text{Na}^{+1}\text{La}^{+3}),$ and $(\text{Na}^{+1}\text{Ce}^{+3})$] have been described. All of these compounds, except BaGa_2S_4 , are isomorphous and belong to the orthorhombic space group $D_{2h}^{24}-\text{Fddd}$. BaGa_2S_4 was found to be cubic and belongs to the space group $\text{Th}^6-\text{Pa}3$.

Unactivated BaGa_2S_4 does not fluoresce at 300°K but the calcium and strontium thiogallates exhibit a broad band emission peaking at 560 nm. Thus far the luminescent center responsible for this fluorescence has not been identified.

The Ce^{+3} -activated phosphors exhibit a strong blue fluorescence when excited by the radiation of a medium

pressure mercury vapor lamp or cathode rays. The Eu^{+2} -phosphors fluoresce in the blue-green through yellow region of the spectrum depending on the choice of host cation. The Eu^{+2} -activated phosphors are effectively excited by uv radiation from low and medium pressure mercury vapor lamps and by cathode ray.

The CIE coordinates of the $\text{SrGa}_2\text{S}_4:\text{Eu}$ phosphor ($x = 0.26, y = 0.69$) indicate that it is superior in color to most of the commercially available CRT phosphors. Optimum cathodoluminescence values are about 50% of the green $(\text{Zn,Cd})\text{S}:\text{Ag}$ primary employed in color CRT's. Relative luminances of 85% are achieved at higher current densities indicating the potential of this material in CRT systems requiring nonsaturable phosphors.

Acknowledgments

The authors wish to acknowledge the technical assistance of A. Alimonda and A. Calvano, who performed a large portion of the experimental work. Thanks are also due to V. D. Meyer for his determination of the absolute radiant efficiencies of the phosphors under cathode ray excitation.

Manuscript submitted Oct. 1, 1970; revised manuscript received ca. Oct. 11, 1971.

Any discussion of this paper will appear in a Discussion Section to be published in the December 1972 JOURNAL.

REFERENCES

1. M. R. Brown and W. A. Shand, *IEEE J. Quantum Electron.*, **4**, 712 (1968).
2. L. Suchow and N. R. Stemple, *This Journal*, **111**, 191 (1964).
3. W. W. Anderson, S. Razi, and D. J. Walsh, *J. Chem. Phys.*, **43**, 1153 (1965).
4. W. W. Anderson, *ibid.*, **44**, 3282 (1966).
5. F. Urbach, D. Pearlman, and H. Hemmendinger, *J. Opt. Soc. Am.*, **36**, 372 (1946).
6. E. Banks, V. Russo, and R. Ward, *J. Am. Chem. Soc.*, **72**, 3137 (1950); A. Dreeben and R. Ward, *ibid.*, **73**, 4679 (1951).
7. S. P. Keller, *J. Chem. Phys.*, **29**, 180 (1958); S. P. Keller and G. D. Pettit, *ibid.*, **30**, 434 (1959).
8. W. Lehmann and F. Ryan, *This Journal*, **118**, 477 (1971).
9. R. Nitsche and W. J. Merz, *Helv. Phys. Acta*, **35**, 274 (1962).
10. S. P. Keller, J. E. Mapes, and G. Cheroff, *Phys. Rev.*, **108**, 663 (1957).
11. M. Springford, *Proc. Phys. Soc.*, **82**, 1020 (1963).
12. A. M. Bostsarron, Doctoral Dissertation, University of Paris (1962).
13. A. Brill and H. A. Klasens, *Philips Res. Rept.*, **7**, 401 (1952).
14. International Tables for X-ray Crystallography, Vol. 1, The Kynock Press, Birmingham, England (1959).
15. R. Eholie *et al.*, *Bull. Soc. Chim. Fran.*, **3**, 747 (1971).
16. G. Blasse and A. Brill, *Appl. Phys. Letters*, **11**, 53 (1967).
17. C. K. Jørgensen, "Orbitals in Atoms and Molecules," Academic Press, New York (1962).
18. G. Blasse, W. L. Wanmaker, and J. W. ter Vrugt, *This Journal*, **115**, 673 (1968).
19. G. Blasse, W. L. Wanmaker, J. W. ter Vrugt, and A. Brill, *Philips Res. Rept.*, **23**, 189 (1968).
20. D. L. Wood and W. Kaiser, *Phys. Rev.*, **126**, 2079 (1962).
21. V. Meyer and F. Palilla, *This Journal*, **116**, 535 (1969).
22. A. Brill, G. Blasse, and J. A. de Poorter, *This Journal*, **117**, 346 (1970).

Measurement of Resistivity of Epitaxial Wafers Using a Voltage Relaxation Technique

Takashi Agatsuma*

Semiconductor & Integrated Circuits Division, Hitachi, Ltd., Kodaira, Tokyo, Japan

ABSTRACT

A voltage relaxation technique has been devised as a means of measuring the resistivity of epitaxial wafers. The principle, the method, and examples of the measurement are presented. In this approach, the steady-state value, V_s , of the voltage relaxation characteristic which is observed when a high-voltage ramp is applied in the reverse direction to a point contact diode, is related to the resistivity of the epitaxial wafer. V_s , measured on silicon slices, showed a power dependence of $k\rho^n$ where ρ is the resistivity of the silicon slice and k is a constant. This dependence was used to obtain calibration curves. It was also found, in the case of epitaxial wafers, that time spent in room air after epitaxial growth, and heat conduction from the back side of the wafers, had to be taken into consideration. V_s could not be measured for approximately 1 hr after epitaxial growth, but after 2 or 3 hr it was possible to take stable measurements; this can be explained in terms of slow surface states which grow with the silicon dioxide film on the surface of the wafers. When heat conduction from the back side of a wafer 200μ thick is considered, it was found that the pulse width of the measuring voltage ramp should be less than $100\mu\text{sec}$. If wafers were treated with hydrofluoric acid, then V_s could be measured immediately after such a treatment. However, when treatments were repeated on the same wafer and V_s was measured after every repetition, it was noted that V_s varied ± 4 to 5V . It is suggested that the variation of V_s would be reduced if the fast surface states at the interface of the SiO_2 film and the silicon bulk could be fully occupied.

The method for evaluating the resistivity of epitaxial wafers by utilizing the turnover breakdown of point contact diodes has been known as the point contact breakdown (PCB), or three-point probe breakdown, technique. This approach uses calibration curves obtained by measuring the turnover voltage as a function of the resistivity.

Three theories have been proposed in connection with the turnover phenomenon associated with point contact diodes. The first theory explains the turnover in terms of an avalanche effect, treating the point contact diode as a step PN junction (1). In the second theory, turnover is considered to be a thermal effect. It implies that turnover occurs when the temperature at the point contact has reached the intrinsic temperature of bulk silicon (2). The third theory states that the turnover phenomenon should not be considered to be a pure thermal effect, but that a field emission effect from surface states may be involved (3).

The PCB method has been explained in terms of the first or the second theory. However, this paper presents a method for measuring the resistivity of epitaxial wafers by the point contact breakdown technique based on the third theory. This method has been called the voltage relaxation technique (4).

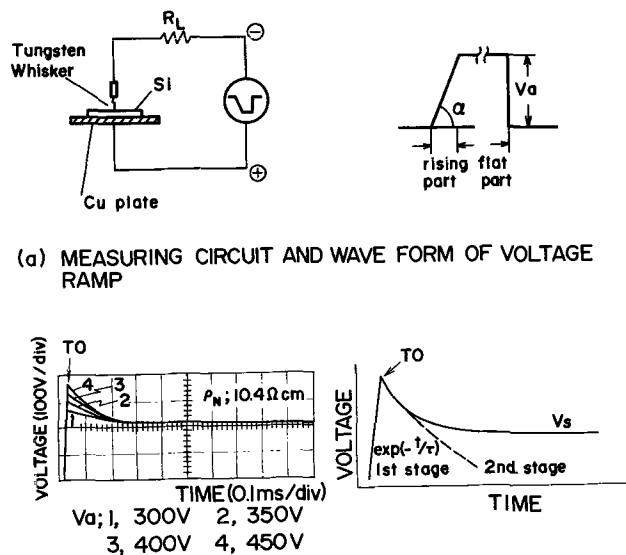
Principle of Measurement

Measurement of V_s .—The principle of measurement is based on the relaxation characteristics of the voltage past the turnover point when a silicon point contact diode is biased in the reverse direction. A schematic representation of the measuring circuit and a typical example of the voltage relaxation characteristic for an N-type Si slice are shown in Fig. 1 (a) and (b). The applied voltage consists of a ramp with a constant slope, $\sim 10^7$ V/sec, followed by a constant voltage region. The voltage ramp is applied in the reverse direction through the current limiting resistance, R_L .

As noted in Fig. 1 (b), the diode voltage rises steeply, corresponding to the rising slope of the applied voltage and then shows an exponential decay characterized by the time constant " τ ." This is the

first stage, Fig. 1 (b). Subsequently, the voltage approaches the steady-state value of V_s . This is the second stage. Initiation of turnover corresponds to the point where the voltage begins an exponential decay from its maximum value, T_0 .

As observed in Fig. 1 (b), the turnover voltage and the time constant in the first stage vary with the amplitude of the applied voltage V_a , but the voltage V_s in the second stage shows almost no variation with amplitude of the applied voltage. V_s , however, as shown in Fig. 2 (a) and (b), was found to show a power dependency on resistivity of the samples. The turnover voltage measured using the PCB method is shown as dotted lines in Fig. 2. The samples were mirror-polished silicon slices obtained from melt-



(b) RELAXATION CHARACTERISTICS OF VOLTAGE

Fig. 1. The Measuring circuit, waveform of the applied voltage, and relaxation characteristics of the voltage.

* Electrochemical Society Active Member.

Key words: silicon, point contact, turnover voltage, field emission.

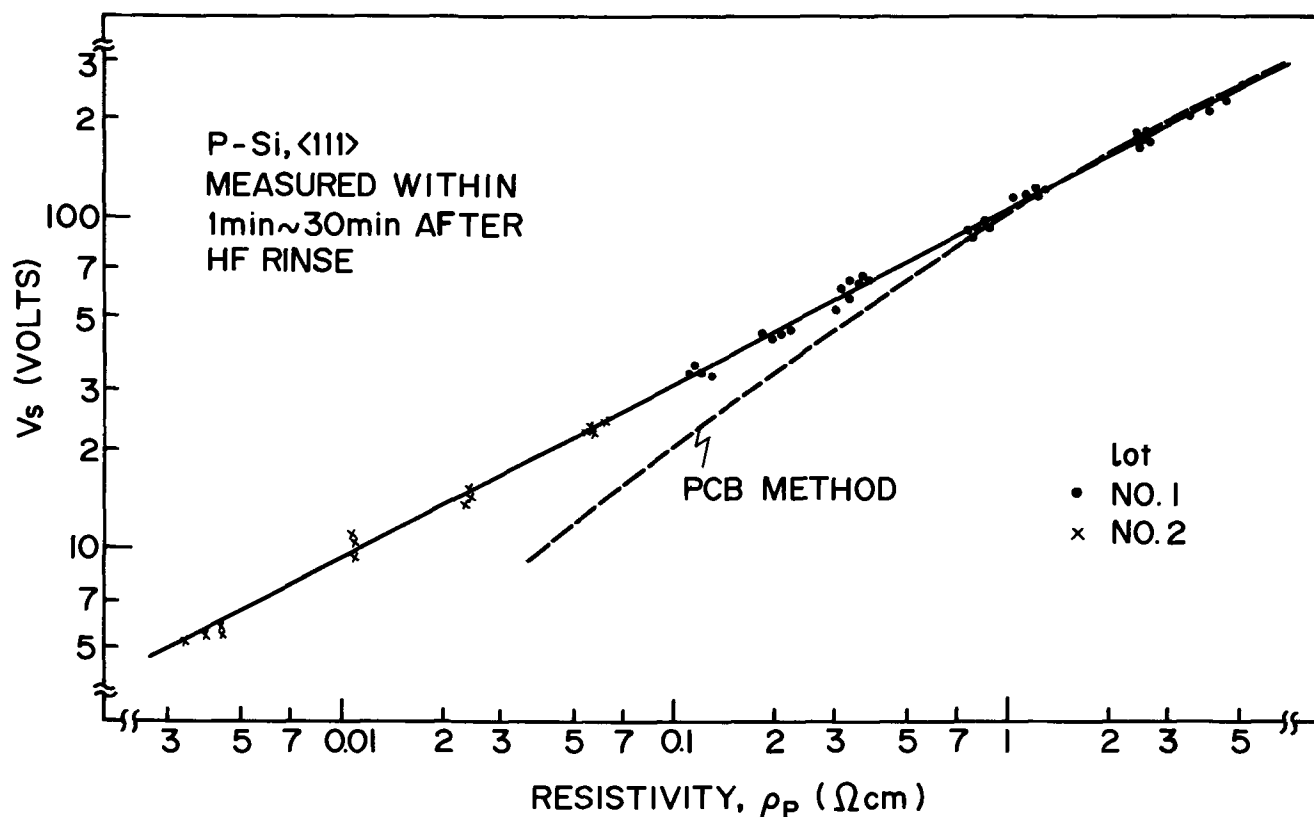
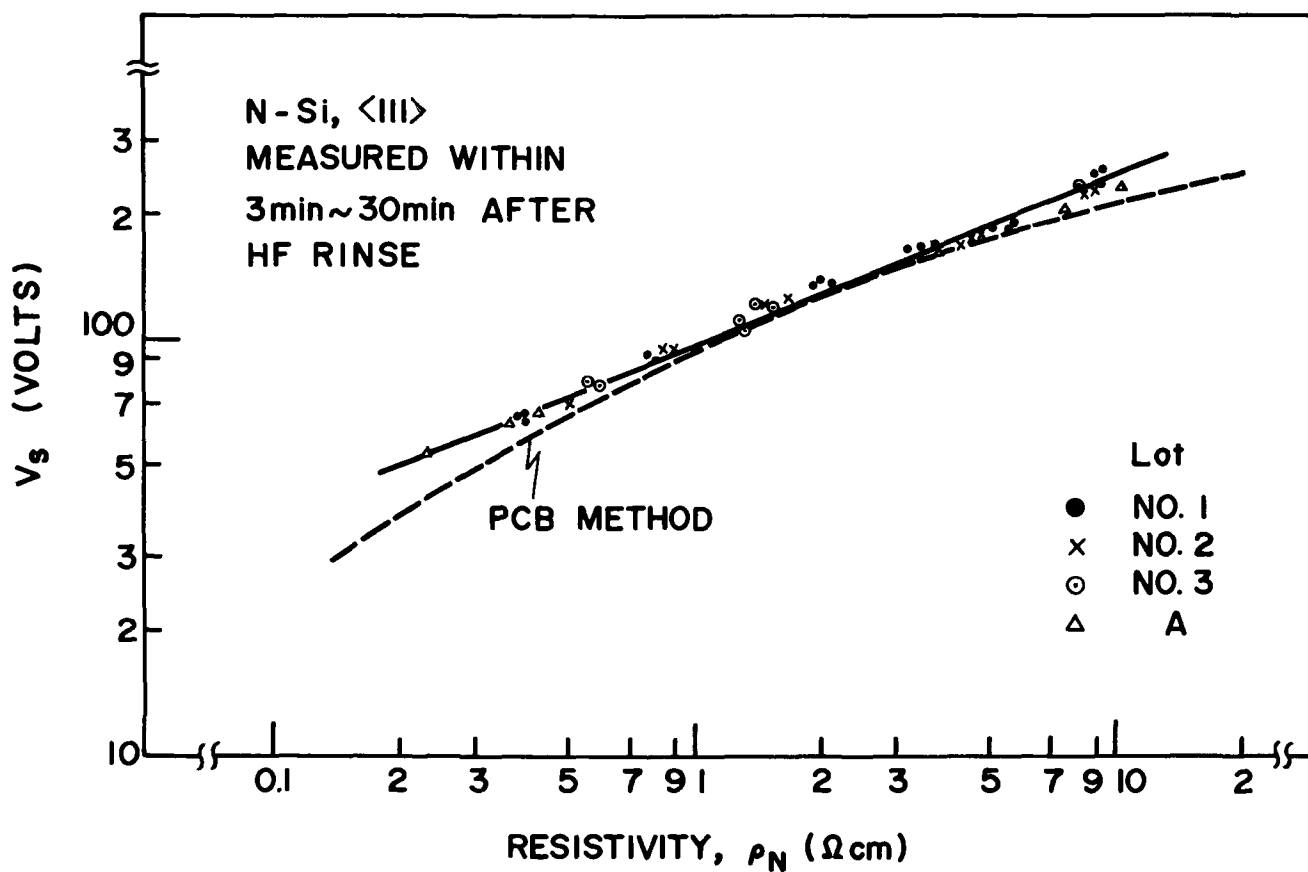


Fig. 2 (a) and (b). Calibration curves showing V_s as a function of resistivity for N- and P-type silicon

grown single crystals. Before measurement, specimens were dipped in hydrofluoric acid, followed by a deionized water rinse and a spin dry. A tungsten whisker with a $3 \sim 5\mu$ point diameter was used. The point loading was 4 grams.

The voltage relaxation technique uses the resistivity dependency of V_s to generate calibration curves in order to evaluate the resistivity of epitaxial wafers. Figure 3 is used to show how V_s is determined from the voltage-current and the voltage-time characteristics.

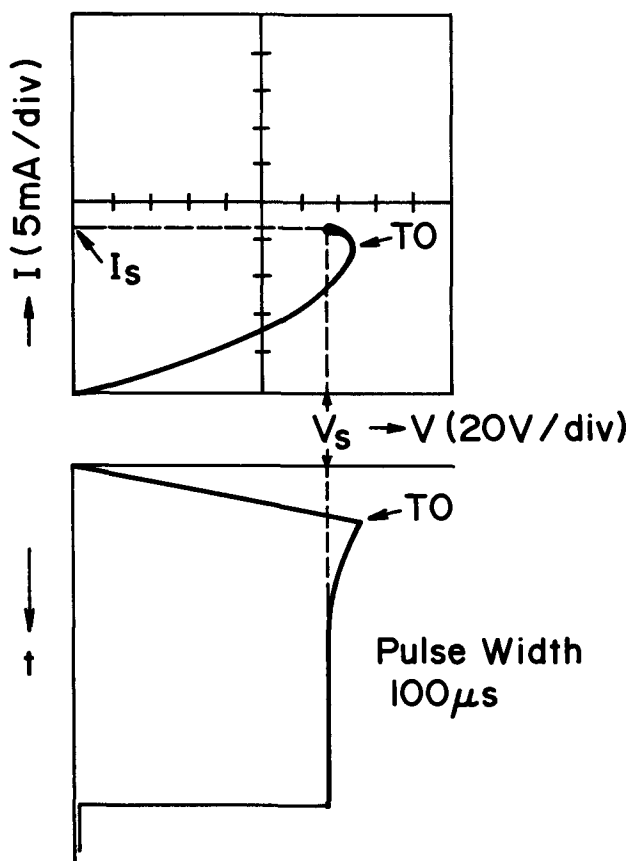


Fig. 3. Determination of V_s from I vs. V and V vs. t plots

It is seen that the dense spot in the V - I characteristic, after turnover, corresponds to the value of V_s .

Physical model of V_s .—The relaxation phenomenon shown in Fig. 1(b) can be understood as a process of charge transfer from a nonequilibrium to an equilibrium state (3). The process may be described in terms of the rate of change in the density of occupied slow surface donor states n_t . The rate, dn_t/dt is proportional to the product of n_t and the tunneling probability of electrons through the forbidden zone of Si, $\exp(-\alpha/F_s)$, where F_s is the electric field strength at the Si-SiO₂ interface and α is a constant depending on the properties of slow states.

The voltage drop V_s is considered to correspond to the condition $dn_t/dt = 0$, where the process of electron transfer comes to equilibrium such that the current due to emitted electrons from slow states balances the charging current from the metal (tungsten). Under this condition the interface electric field strength F_s reduces to a value (F_{ss}) just large enough to maintain the equilibrium state for the system.

An energy diagram showing nonequilibrium and equilibrium states for a tungsten point contact to N-Si is shown in Fig. 4.

The voltage drop V_s across the depletion layer in the equilibrium state is related to F_{ss} in terms of the depletion layer width *vs.* the resistivity of Si substrates. Therefore, V_s can be correlated with the resistivity of Si if an appropriate form of the junction is assumed at the point contact and F_{ss} is also assumed not to change with resistivity of the Si. However, the resistivity dependence of V_s will not be expressed explicitly, because the junction shape at the point contact is not established, and the dependence of the slow surface states on resistivity is not known. Hence the dependence of V_s on resistivity must be determined experimentally.

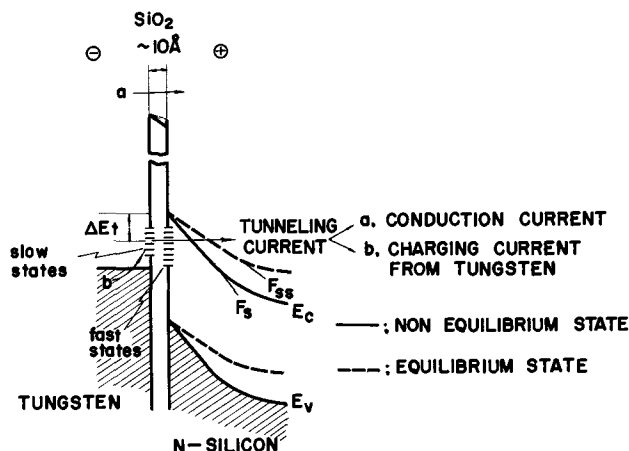


Fig. 4. Energy diagram for the system under the application of the voltage ramp.

Results and Discussion

The value of V_s was found to vary with many factors when using epitaxial wafers.

Variation of V_s with applied voltage.—The value of V_s was found to vary with temperature (3). Therefore, the measurement of V_s must be made by taking into consideration heat conduction from the wafer to the sample holder, since the wafer is of limited thickness and does not make a good thermal contact with the copper plate of the sample holder. The pulse width and the amplitude V_a of the applied voltage are subject to restrictions.

In order to eliminate the effect of heat conduction at the contact between the wafer surface and the copper plate, the pulse width of the applied voltage should be shorter than the time it takes the heat generated at the point contact to reach the back side of wafers; this is given by $t_r \approx 0.3 W^2/k$ (7), where W is the wafer thickness and k is the thermal diffusivity of silicon. If 200μ is substituted for W and $0.51 \text{ cm}^2/\text{sec}$ for k , $t_r \approx 0.24 \text{ msec}$. Figure 5 shows how the values of V_s vary with pulse width of the applied voltage for various wafers. V_s has a tendency to decrease with pulse width beyond $0.1 \sim 0.2 \text{ msec}$, which is of the same order of magnitude as the calculated value of t_r .

V_s for thick silicon slices ($5 \sim 6 \text{ mm}$) showed no variation with pulse width, so the decrease of V_s with

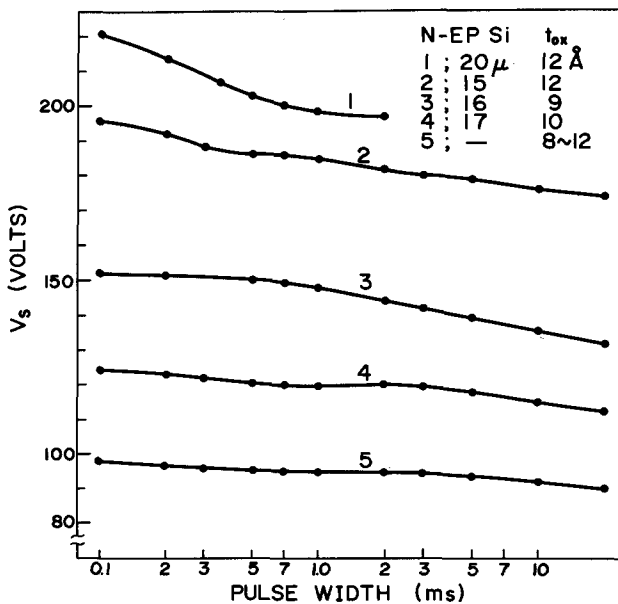


Fig. 5. Variation of V_s with pulse width of the applied voltage

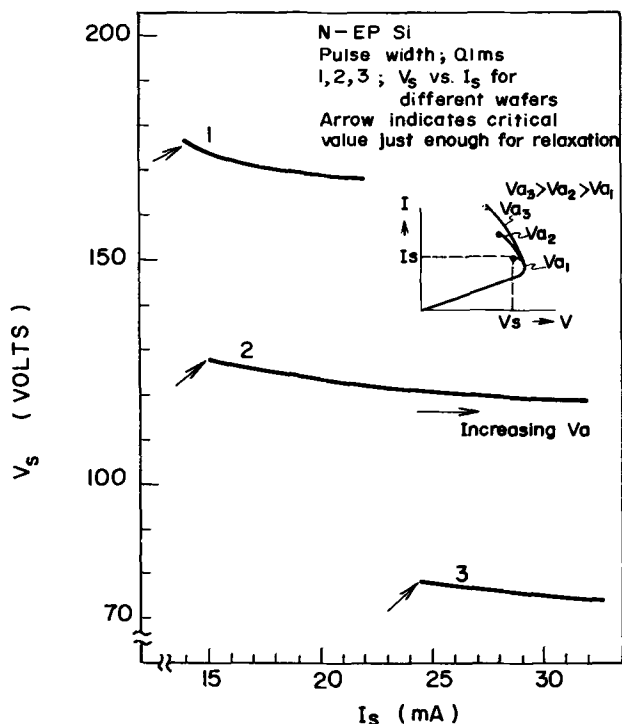


Fig. 6. Variation of V_s with I_s for a pulse width of 0.1 msec

pulse width for the thinner wafers may be explained in terms of the thermal effect mentioned above. Hence, for wafers of practical thickness, pulse width of the applied voltage should be kept below 0.1 ~ 0.2 msec.

When the amplitude of the applied voltage V_a is increased, V_s decreased slowly, but I_s , the current at V_s , increased noticeably. This is shown in Fig. 6 in terms of V_s vs. I_s curves, where pulse width was held to 0.1 msec. For thick silicon slices, V_s showed no variations with applied voltage. Therefore, the decrease of V_s with I_s is also considered to originate from a temperature rise at the point contact due to poor thermal conduction at the contact surface of the wafer and copper plate. Thus the amplitude of the applied voltage must be limited to a value just large enough for observing voltage relaxation.

Variation of V_s with time.—Figure 7 illustrates how V_s for N-type epitaxial wafers varies with time after a hydrofluoric acid etch. The width and amplitude of

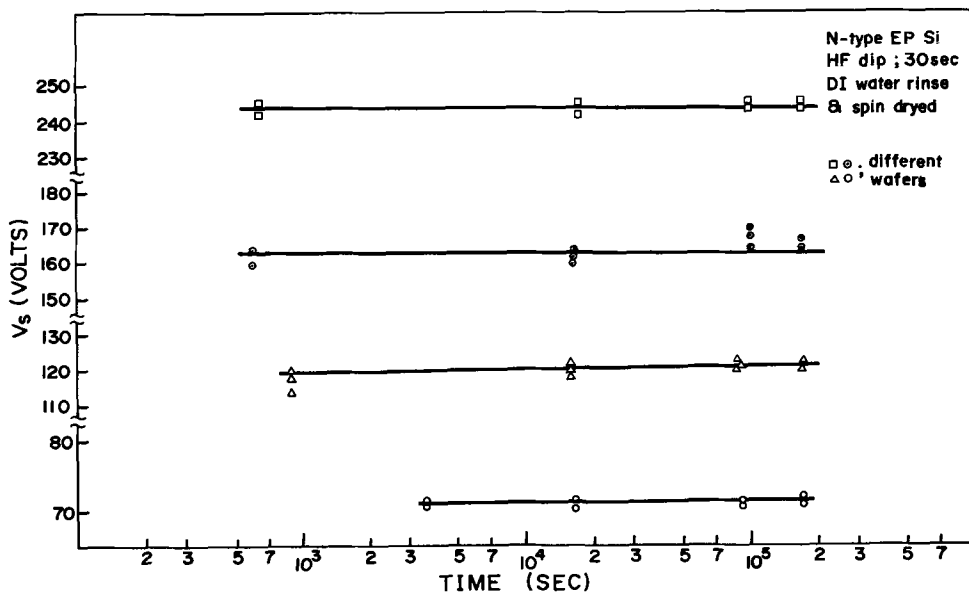
the applied voltage pulse were selected so as to give consistent results as discussed above. V_s showed a very slight increase with time, but for practical purposes, it may be considered as constant. The variation of V_s for N-type epitaxial wafers as a function of time after epitaxial growth is shown in Fig. 8. The sample was a lot consisting of six wafers made in the same epitaxial furnace. As shown in Fig. 8, different values of V_s were measured among the wafers as well as at various points on a given wafer within an hour or two after epitaxial growth. There were also points on wafers through which no current flowed. In this case, an oscillation appeared in the voltage-time characteristics. After 2-4 hr (or longer) V_s reached a uniform value without variation from wafer to wafer or from point to point on a given wafer.

The variations of V_s with time on wafers after hydrofluoric acid etching and after epitaxial growth are considered to be due to the different thicknesses of the insulating thin films on the surfaces of the wafers. These films probably increase in thickness with time after treatment. Thickness of the insulating thin film as a function of time after hydrofluoric acid treatment is shown in Fig. 9. These data were measured by ellipsometry (5). In this case, the extinction coefficient, $k = 0$, and the refractive index, $n = 1.45$ for SiO_2 were used for the insulating thin film. As can be seen in Fig. 9, an SiO_2 film of 8-12Å was formed immediately after the treatment; in a few days it became 17-19Å thick.

The variation of SiO_2 film thickness as a function of time in room air after epitaxial growth is shown in Fig. 10. Immediately after epitaxial growth, the surface is seen to be covered with an SiO_2 film of ~4Å. In a few hours the film gradually grew in thickness to ~14Å. However, it did not grow beyond ~14Å even after several weeks.

As shown in Fig. 8, within 1-2 hr after epitaxial growth V_s had different values from wafer to wafer, and from point to point on a given wafer. This period of 1 to 2 hr is considered to correspond to the time for which the thickness of the SiO_2 film is in the range of 4-8Å. After 3-4 hr, where V_s showed no variation from wafer to wafer, the SiO_2 film was observed to grow to 8-12Å (see Fig. 10). This may indicate that for the measurement of V_s on epitaxial wafers, an SiO_2 film of ~10Å in thickness is required on the surface. For wafers after a hydrofluoric acid treatment, an SiO_2 film of 8-12Å in thickness was formed on the surface immediately after treatment (Fig. 9). Thus, V_s can be measured immediately after a hydrofluoric acid treatment, Fig. 7.

Fig. 7. Variation of V_s with time after hydrofluoric acid treatments



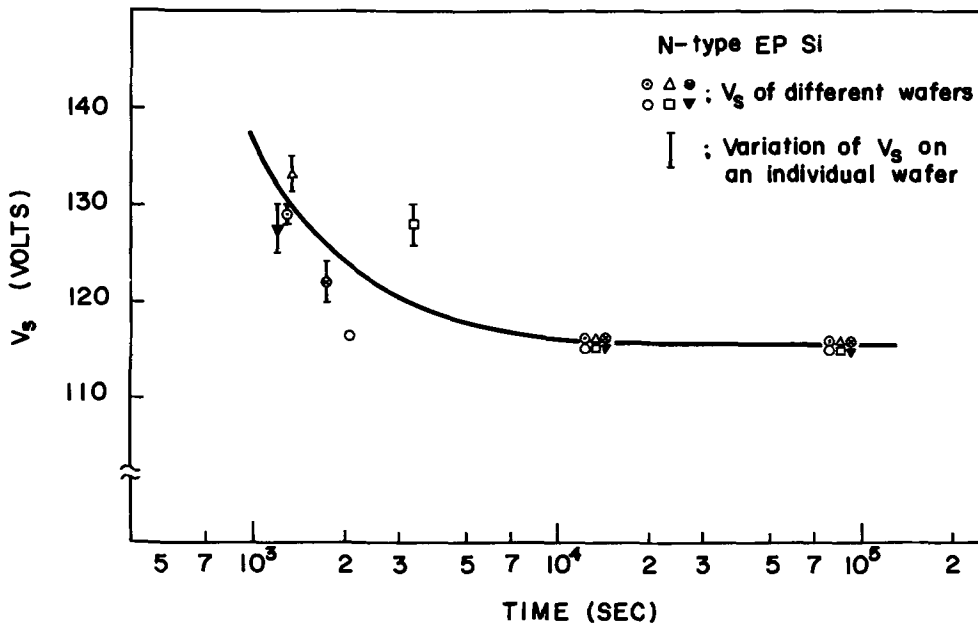


Fig. 8. Variation of V_s with time after epitaxial growth.

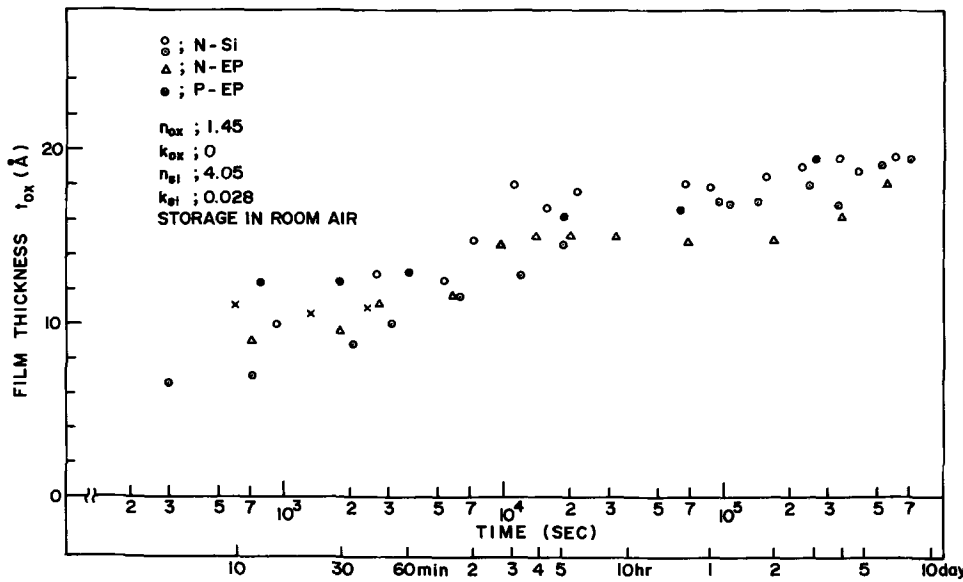


Fig. 9. Film thickness of SiO_2 as a function of time after hydrofluoric acid treatment.

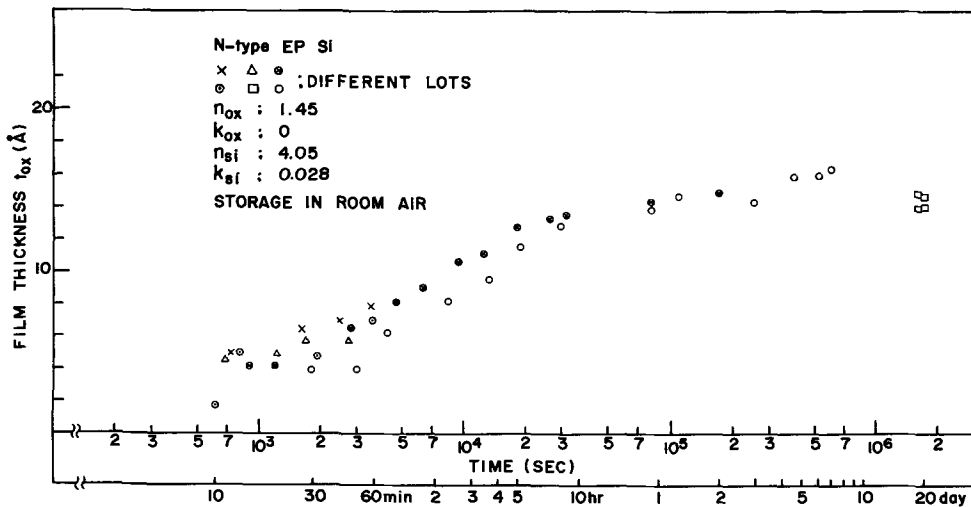


Fig. 10. Film thickness of SiO_2 as a function of time after epitaxial growth.

The requirement of an SiO_2 film $\sim 10\text{\AA}$ thick on the surface of Si for consistent results shows evidence that the slow surface states responsible for the voltage relaxation are formed after the SiO_2 film becomes $\sim 10\text{\AA}$ thick.

Waveform of voltage relaxation.—Figures 11(a) and (b) show the various types of voltage relaxation waveforms for N-EP Si wafers. Figure 11(a)-(1) gives the normal mode of voltage relaxation and Fig. 11(a)-(2) shows the case when secondary breakdown occurs (6).

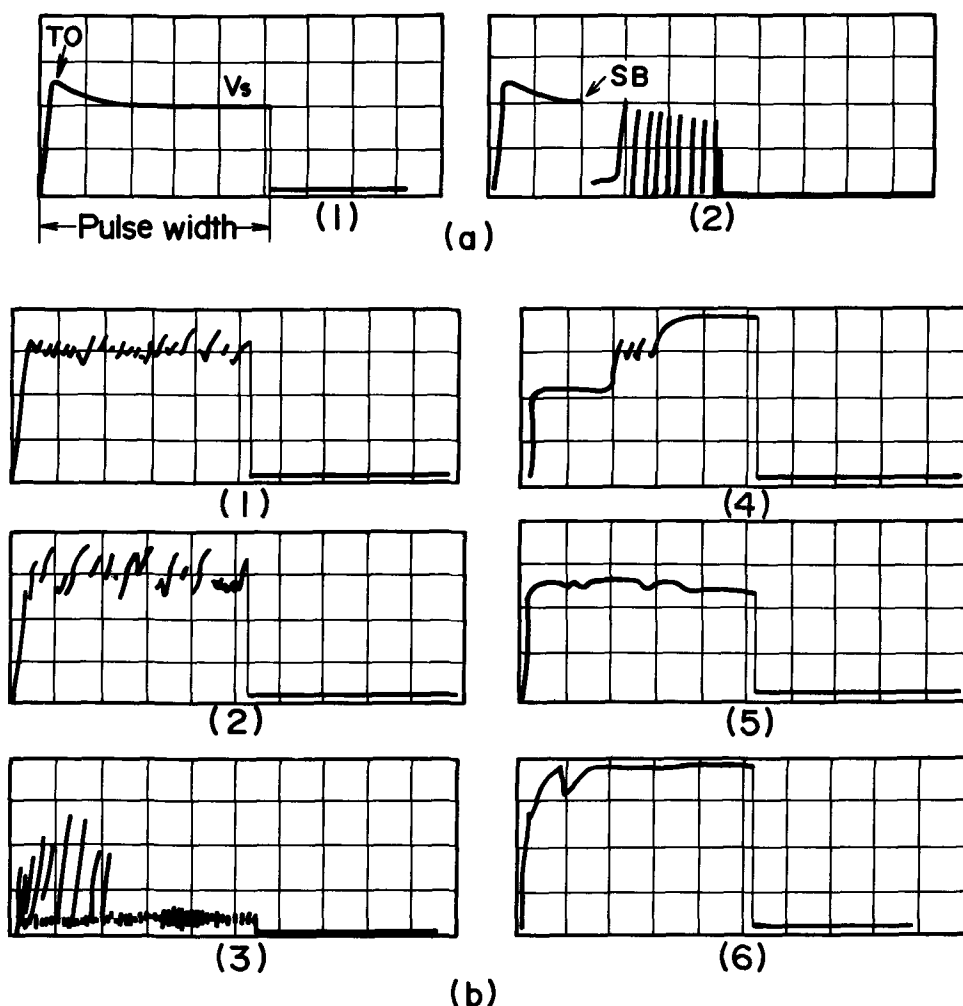


Fig. 11. Various modes of the relaxation voltage waveform.

ABSCISSA ; VOLTAGE (arbitrary unit)
ORDINATE ; TIME ($20\mu\text{s}/\text{div.}$)

(a) NORMAL MODE

(b) ABNORMAL MODE

This is observed in thinner, higher resistivity epitaxial layers. In this case, the initiating voltage of secondary breakdown is measured as V_s .

Figures 11(b)-(1) and (2) are used to show the condition for epitaxial wafers having an SiO_2 film $\sim 26\text{\AA}$ thick. No current was observed to flow and thus the measurement was not possible. Also, Figures 11(b)-(3), (4), (5), and (6) show abnormal modes observed during the first 10 min to 1 hr after epitaxial growth. As noted, V_s could not be defined.

Variations of V_s with successive hydrofluoric acid treatments.—The manner in which V_s for the same wafer of N-type EP Si varies as a function of the number of times it is subjected to hydrofluoric acid treatment is shown in Fig. 12. The treatments and the measurements were repeated every hour and repeated 9 times. Also shown in Fig. 12 are different V-I characteristics. For the "O" trace, $V_s \sim 90\text{V}$ and for the "X" trace, $V_s \sim 100\text{V}$.

When the voltage ramp was applied successively to the same point on a wafer, V_s was observed to increase at every repetition of the voltage pulse. The variation of V_s as a function of the number of times the ramp voltage was applied is shown in Fig. 13. (The sample used was the same as that of Fig. 12.) As shown in Fig. 13, when V_s was $\sim 90\text{V}$, the change of V_s was

small ($\sim 2\text{V}$). For a V_s of $\sim 100\text{V}$, the variation was as large as 6V .

The change of V_s when city water and deionized water were used alternately for rinsing after hydrofluoric acid treatment is shown in Fig. 14. (The same sample studied in Fig. 12 was used again.) V_s for the deionized water rinse was $\sim 100\text{V}$, but it became $\sim 90\text{V}$ when city water was used. The magnitude of this variation is consistent with that noted in Fig. 12. Thus, it is possible that the variations observed in Fig. 12 are due to fluctuations in the purity of water used for post rinsing after the hydrofluoric acid treatments.

As illustrated in Fig. 12 and 13, the variation of V_s with successive hydrofluoric acid treatments, as well as with every repetition of applied voltage, was accompanied by a different slope of the ohmic region in the V-I characteristics. Although the V-I characteristics in this region are not understood, it is assumed that fast states at the interface of the SiO_2 film and the silicon bulk are responsible for the current conduction of the region as shown in Fig. 4. Then, the rate equation for the number of electrons in fast states can be given in terms of the change in n_t (8), where n_t is the density of occupied fast states of the donor type capable of emitting electrons into the conduction band of Si.

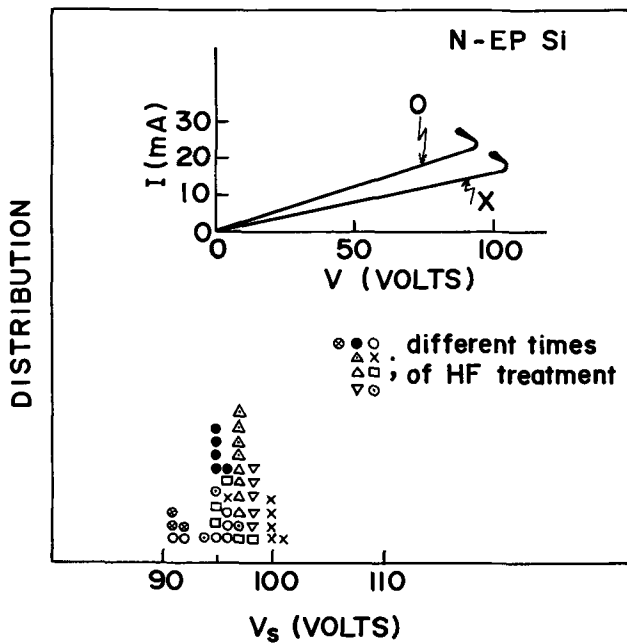


Fig. 12. The variation of V_s as a function of the number of times it is subjected to hydrofluoric acid treatments.

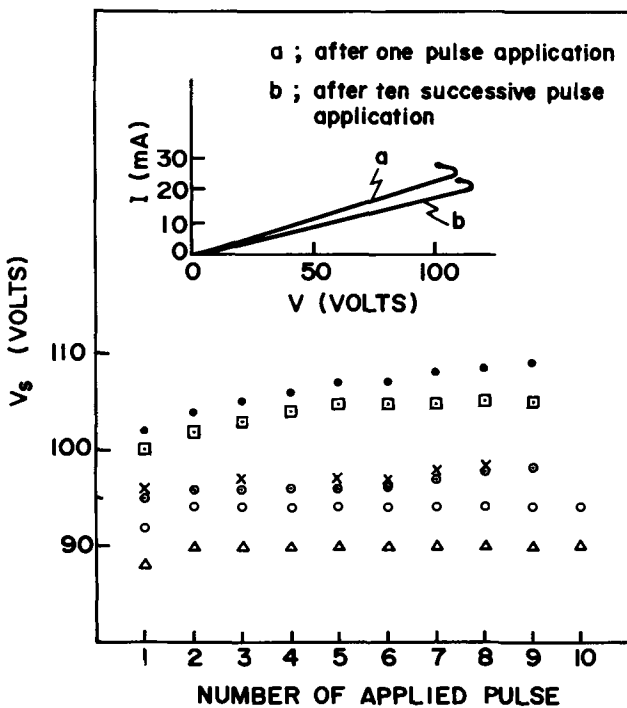


Fig. 13. The variation of V_s as a function of the number of times the ramp voltage is applied.

$$\frac{dn_t}{dt} = C_n (n_s p_t - n_t n_1) + J_t/q \quad [1]$$

with

$$n_1 = N_c \exp [-(E_c - E_t)/kT]$$

$$n_s = N_c \exp [-(E_c - E_{Fe})/kT]$$

$$p_t = N_t - n_t$$

where N_c is the effective density of states for the conduction band, N_t is the density of fast states, C_n is the capture coefficient of electrons, E_t is the energy level of fast states (assumed to have a single charged center) and E_{Fe} is the quasi-Fermi level of Si to which a

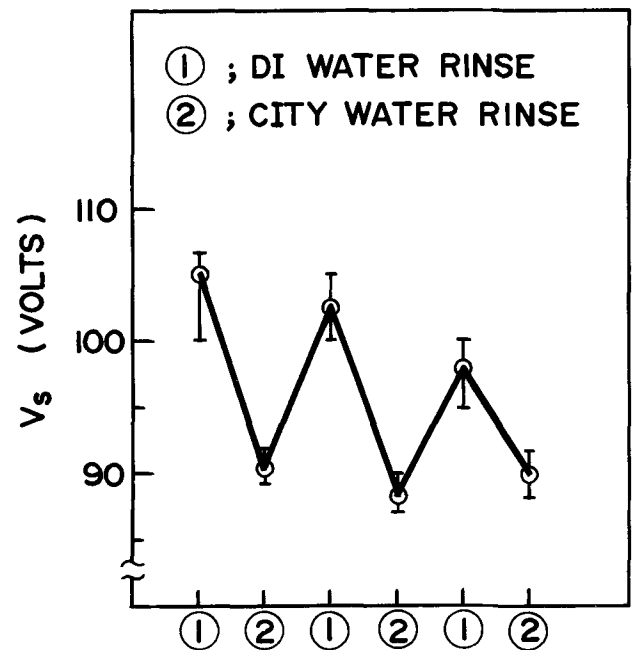


Fig. 14. The variation of V_s with rinsing water after hydrofluoric acid treatments.

negative bias is applied. J_t/q represents the charging current of electrons from tungsten.

In the present case where the rise time of the applied ramp is long enough compared to the time constant of fast states, the system can be regarded as being in a steady-state condition. Then, the current in the ohmic region is given by the first term of Eq. [1] as

$$J_s = qC_n N_c [p_t \exp \{-(qV + \phi_B)/kT\} - n_t \exp \{-(E_c - E_t)/kT\}] \quad [2]$$

where ϕ_B is the barrier height for a tungsten-silicon contact, and V is the reverse applied voltage. For large bias voltage the first term in Eq. [2] can be neglected, so J_s varies largely with the values of n_t and $E_c - E_t$. Substituting typical values for fast states under large bias voltage (8) ($C_n = 10^{-8}$ cm³/sec, $N_c = 2 \times 10^{20}$ cm³, $E_c - E_t = 0.15$ eV, $n_t = 10^{13}$ cm⁻², $kT = 0.025$ eV) in Eq. [2], J_s becomes 10^4 A/cm², which is found to correspond to the experiments, $\sim 10^4$ A/cm² for $I_s = 10$ mA and the radius at the point = 7.5μ .

Thus, for the sample that has $V_s \sim 90$ V and a steeper slope, the ohmic region is considered to have the higher density of occupied fast states, n_t . On the other hand, the sample that has a $V_s \sim 100$ V shows evidence of fast surface states that are partially occupied and that interact with the unoccupied fast states.

The V_s variations at every repetition of the applied voltage are assumed to result from a decrease in the density of fast states capable of emitting electrons, n_t , due to the trapping of electrons in the unoccupied fast states. If this is the case, it will be understood that for the sample of $V_s \sim 90$ V, which showed the lowest value of V_s variations in Fig. 13, the density of unoccupied fast states is considered to be minimum. The sample of $V_s \sim 100$ V which showed a large variation of V_s with repetitive pulse application has a large density of unoccupied fast states which act as a trapping center for electrons.

The variations of V_s with water after HF treatment may also be understood in terms of the density of occupied fast states which are able to emit an electron into the conduction band. The sample treated with city water has a higher density of occupied fast states. For the deionized water rinsed sample, the density of occupied fast states is considered to be lower, and is

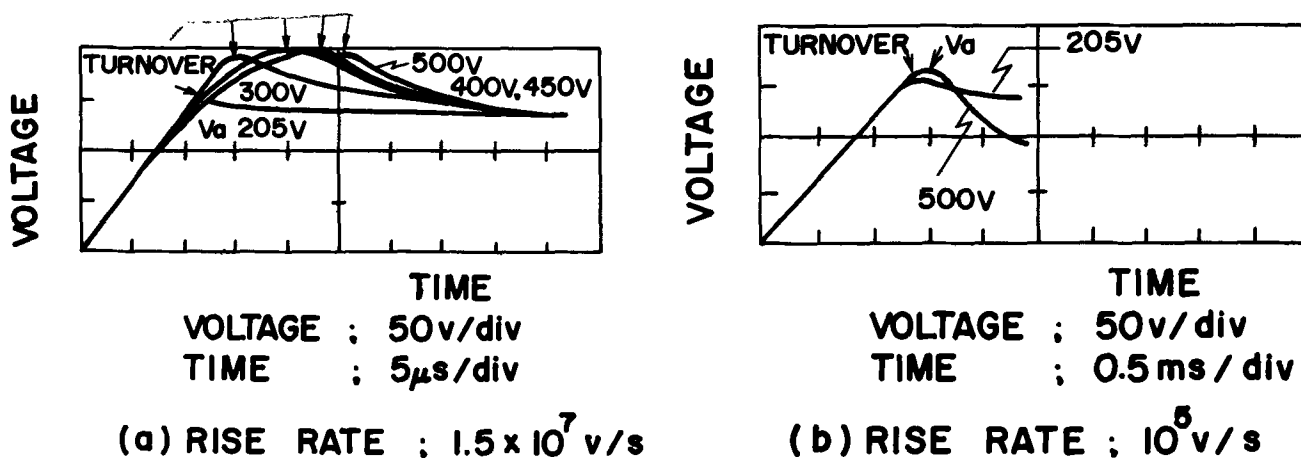


Fig. 15. Voltage relaxation curves for rising slopes of $\sim 10^7$ V/S and $\sim 10^5$ V/S

also subjected to variations with purity of the deionized water.

From the above experiments and discussions, it is evident that in order to measure V_s , the fast states must be fully occupied (metallic surface). Under this state, the effect of fast states on V_s will be eliminated.

Comparison with usual PCB method.—Figure 15 shows a comparison of the voltage relaxation curves for two cases where the rising slopes of the voltage ramp are 10^7 V/S and 10^5 V/S. A N-Si slice of 3.8 ohm-cm resistivity is used. The rising slope for the latter case corresponds closely to that of the PCB method which uses a 50 Hz half rectified voltage.

For Fig. 15-(a) many values of turnover are seen depending on the amplitude of the voltage ramp, but in each case the voltage relaxed towards its steady-state value, V_s . On the other hand, for Fig. 15-(b), it was not possible to define a steady-state value, V_s , since the turnovers were not characterized in terms of the relaxation process as described in Fig. 1(b). However, the turnovers occurred at nearly the same voltage, irrespective of the amplitude of the voltage ramp. This indicates that the turnover voltage can be correlated with the resistivity, as utilized in the PCB method. The turnover voltages as a function of Si resistivity however, as shown by the dotted lines in Fig. 2, were seen to depart from the V_s vs. resistivity curves for both the lower and higher resistivity ranges.

Summary and Conclusions

1. The steady-state value of V_s for voltage relaxation curves, which is observed when a high voltage ramp is applied in the reverse direction to a point contact Si diode, can be related to the resistivity of Si slices.

2. The voltage relaxation is due to the emission of current carriers from slow surface states at the interface of the tungsten point and the silicon dioxide film through the forbidden zone into the conduction band of Si; V_s corresponds to the voltage which gives a critical field strength at the interface of Si and SiO_2 film just large enough to hold a steady state of current flow for the system.

3. The voltage relaxation technique, which is based on V_s vs. the resistivity of Si slices, is applied to the

evaluation of the resistivity of NN^+ epitaxial wafers. In this case, the effects of heat conduction, slow surface states, and fast surface states on V_s must be taken into consideration.

4. The thermal consideration arising from the limited thickness of silicon wafers requires that the pulse width of the voltage ramp should be below ~ 100 μsec and the amplitude should be limited to a value just large enough for observing voltage relaxations.

5. For the measurement of V_s , an SiO_2 film ~ 10 Å in thickness is required for growth of the slow surface states necessary for voltage relaxation. Moreover, the fast states must be fully occupied. In this case, a higher slope of the ohmic region of V-I characteristic is obtained, and less variation with repetitive applications of the voltage ramp is seen.

Acknowledgment

The author wishes to express his sincere thanks to Drs. M. Tomono, S. Shibata, S. Tauchi, K. Miyake, and Mr. S. Nishida for their encouragement during this study. He is also indebted to Mr. S. Shimizu who performed the ellipsometry measurements.

Manuscript submitted Sept. 23, 1970; revised manuscript received ca. July 9, 1971. This was Paper 95 presented at the Los Angeles Meeting of the Society, May 10-15, 1970.

Any discussion of this paper will appear in a Discussion Section to be published in the December 1972 JOURNAL.

REFERENCES

1. E. E. Gardner and P. A. Schumann, *Solid State Electron.*, **8**, 165 (1965).
2. C. C. Allen, L. H. Clevenger, and D. C. Gupta, *This Journal*, **113**, 508 (1966).
3. P. A. Schumann, *This Journal*, **115**, 1197 (1968).
4. T. Agatsuma and K. Miyake, *ibid.*, **118**, 759 (1971).
5. T. Agatsuma, Paper 95 presented at Electrochem. Soc. Meeting, Los Angeles, May 10-15, 1970.
6. K. H. Zaininger and A. G. Revesz, *RCA Rev.*, March, **85** (1964).
7. T. Agatsuma, *Proc. IEEE*, **54**, 1206 (1966).
8. T. Agatsuma and K. Miyake, *This Journal*, **118**, 763 (1971).
9. D. J. Rose, *Phys. Rev.*, **105**, 413 (1957).
10. J. Shewchun, A. Waxman, and G. Warfield, *Solid State Electron.*, **10**, 1165 (1967).

Growth Mechanism for Germanium Deposition near a SiO₂-Ge Boundary

V. J. Silvestri,* R. Ghez, and T. O. Sedgwick*

IBM Thomas J. Watson Research Center, Yorktown Heights, New York 10598

ABSTRACT

Enhanced growth (ridge growth) of germanium on germanium near an oxide-germanium boundary has been studied in the Ge-H-Cl system as a function of temperature and oxide pad width. A model is presented assuming that surface diffusion of some germanium-containing species occurs along the SiO₂ pads, thereby feeding additional material to the germanium at the pad edge to form the ridge. It is shown that volume diffusion effects alone cannot explain the data. It appears that the reaction at the oxide-germanium boundary is much faster than surface diffusion and that adsorption of germanium-bearing species on the oxide mask constitutes a rate-limiting step.

A number of investigators (1-14) have studied the selective epitaxial deposition of silicon, germanium, and gallium arsenide through holes in thin SiO₂ masks. In some cases (6, 7, 8, 12) an enhanced growth or "ridge" on the otherwise planar Si epitaxy has been observed immediately adjacent to the edge of the SiO₂ mask. In attempting to prepare such structures for epitaxial depositions by either vapor phase or liquid etching, sometimes an enhanced etching or trough formation has been found in the semiconductor surface just at the edge of the mask (5, 7-9).

The ridge growth has not been studied in detail partly because of the prevalence of Si nucleation on the oxide. It has been reported, however, that the ridge growth could be reduced by using narrow oxide windows (7), or by lowering the temperature or reactant concentration (12). Alexander and Runyan (5) and Schnable *et al.* (7) showed that the reaction of Si and SiO₂ in the presence of H₂ (or H₂O) explains in part the trough formation above 1250°C. Oldham and Holmstrom (8) assumed that both ridge and trough formations are due to enhanced reactant concentrations and hence enhanced growth and etching rates at the edges of the holes. They develop a volume diffusion model and are able to explain qualitatively their observed trough formation. Shaw (10) speculates that in the liquid etching of GaAs there is a surface diffusion of etchant along the mask which leads to enhanced etching at the edge of the hole. Sirtl and Seiter (12) report that the use of silicon nitride masks eliminated both the trough and ridge formation in Si although very little experimental data was presented.

In the epitaxial deposition of Ge from GeCl₄ and H₂, we have found that ridge growths occur around the periphery of SiO₂ masking pads on the Ge surface. Trough formation has not been observed. In this system the Ge does not either nucleate on or react with the SiO₂ mask at the relatively low temperatures of 600°-875°C used. For these reasons and because the ridge growth was found to vary significantly over a wide range of growth conditions, this system was investigated in some detail both theoretically and experimentally.

A model has been developed assuming that surface diffusion of some Ge-containing species occurs along the SiO₂ pads, thereby feeding additional material to the Ge at the pad edge to form a ridge. The model is able to explain both the increase of ridge growth with temperature and the saturation of growth with increasing pad width. It is shown in the Appendix that a pure volume diffusion model cannot explain the experimental results.

Experimental

Oxide pad formation.—Preliminary observations of ridge growth on partially masked substrates indicated that the excess or ridge growth was sensitive to both temperature and oxide pad width. Therefore, ridge growth was investigated systematically as a function of these parameters. First, SiO₂ (2000Å) was deposited on <110> germanium substrates. Then oxide pads were formed on the substrate using conventional photoresist-etch techniques in the pattern shown in Fig. 1. These pads were rectangles in sets of three having a length to width ratio of 5:1. The oxide pad widths, equal to the interpad widths, varied from 40 to 588 μm. The oxide pads covered approximately 16% of the total germanium area. The germanium surrounding the oxide pads was then selectively etched to a depth of 1 μm using an H₂O₂-H₂O solution. During this etching an oxide overhang developed from the etch undercutting the oxide at the SiO₂ boundary. The amount of undercutting was the same as the etch depth of 1 μm thereby forming a 45° angle for the mesa side.

Germanium was deposited from a GeCl₄-H₂ mixture in a conventional vertical epitaxial reactor under the following conditions: substrate temperature range, 600°-875°C; Ge/H₂ = 3.6 × 10⁻⁴; linear gas stream velocity, 175 cm/min; growth times were constant at 11 min. Under these conditions the growth rate was constant at 0.099 μm/min (15), and ridge growth immediately adjacent to the oxide was noted for all samples.

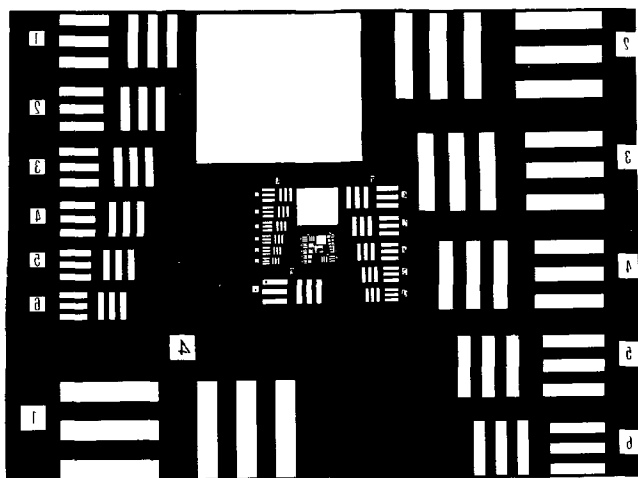


Fig. 1. Mask pattern

* Electrochemical Society Active Member.

Key words: ridge growth, selective epitaxial deposition.

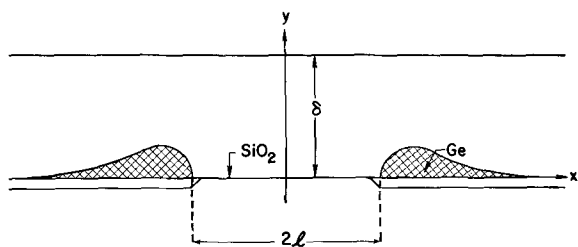


Fig. 2. Schematic of a representation of a section through a ridge showing coordinate system.

Ridge measurement.—Vertical profiles of the ridge were taken across the shorter dimension of the pads employing a stylus gauge. The top of the germanium epitaxy far from the oxide pads, extreme left or right (Fig. 2), was taken as the reference level. The excess growth area, A in square centimeters was calculated from the area under the Talysurf curve above the reference level which corresponded to the cross-hatched area in Fig. 2. Thus A is the growth above that which one would expect on a bare Ge wafer. The figure depicts a case where the epitaxial refill level corresponds exactly with the oxide level. Experimentally we could approach this exact refill case within 15% and in cases where there were deviations, corrections were made to simulate a perfect refill. In addition a small correction was made to the calculated excess area due to the nonplanarity of the germanium surface under the oxide overhang. This correction was no greater than 5% and usually was less than 1%. It was found that the excess growth between pads of a set was the same as that exterior to a set.

Results.—In Fig. 3 a scanning electron microscope photograph of a typical ridge surrounding an oxide pad is shown. Ridges were smooth, nonfaceted, and typically 1-2 μm high. A few ridges were 3 μm high. They could extend to a distance of 200 μm from the oxide. In Fig. 4 we plot the average excess growth area as a function of oxide pad width. The deposition temperatures for the samples range from 600°-875°C. The dashed curves through the experimental points are discussed later. We note that the experimental points for each excess growth curve seem to begin parabolically at the smaller pad widths but then saturate for larger pad widths. We also note that the maximum excess area increases with increasing temperature.

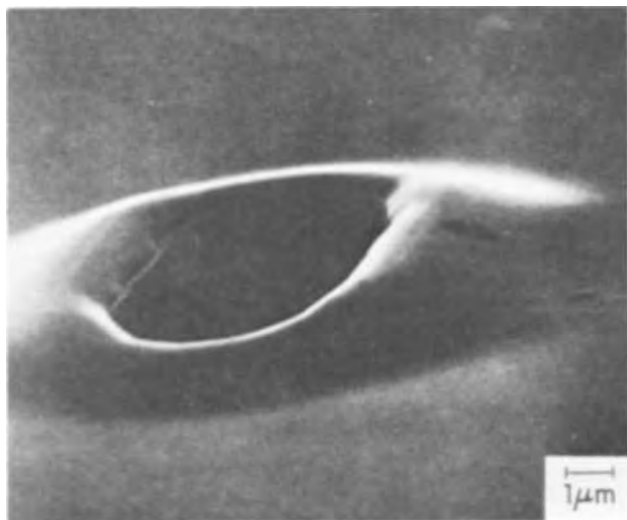


Fig. 3. Scanning electron microscope photograph of "ridge growth" surrounding an oxide pad.

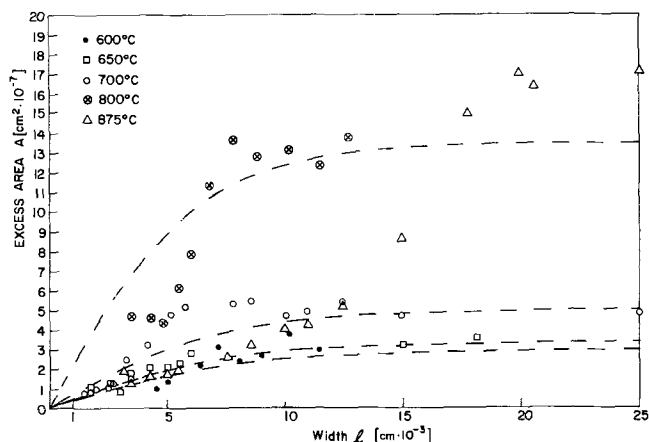


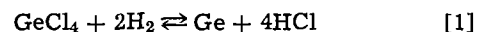
Fig. 4. Excess area of the ridge as a function of pad width. — — — Theoretical.

It was observed from ridge examination with the scanning electron microscope that the Ge-SiO₂ contact angle of the ridge varied markedly during growth as a function of time of growth. It was also noted that the overgrowth of Ge on the SiO₂ was a small fraction of the pad width.

Model

To our knowledge, the only quantitative analysis of excess growth during selective chemical vapor deposition is due to Oldham and Holmstrom (8). In a sense, their system is the "inverse" of ours since in their case the ratio of exposed Si area to that of the oxide mask is small. Their analysis is based on a calculation of an enhanced volume diffusion field. In the Appendix it is shown that this effect cannot explain our observations. However, the results of the preceding section suggest the following model: ridge growth is due to the surface diffusion on the oxide of some Ge-bearing species to the Ge-oxide boundary.

Referring to Fig. 2, a stagnant layer of thickness δ allows volume diffusion. The existence of a stagnant layer has been argued by several authors (16-19) as a convenient means of calculating mass transfer coefficients. The impinging molecules may then be incorporated directly at the Ge-vapor interface or be adsorbed on the oxide of width $2l$ where they will diffuse to the oxide-Ge boundary. In both cases, incorporation into the Ge lattice requires a chemical reaction. In the Ge-H-Cl system, the net reaction is



and it is assumed that GeCl₄ is the major chemically reactive species. A detailed thermodynamic analysis of this system, similar to that carried out by Lever (20) on the Si-H-Cl system, is contained in unpublished work by Silvestri. For low Cl to H ratios and for increasing temperatures, this analysis shows that most of the GeCl₄ will first be converted to GeHCl₃ and with further increase in temperature to GeCl₂. In lieu of any detailed kinetic information we simply point out that if this conversion is sufficiently rapid, then the major chemically reactive species diffusing through the stagnant layer could be GeHCl₃ or GeCl₂. Investigations by infrared spectroscopy (21-23) indicate that such might be the case, although operating conditions were different from ours. The over-all reaction [1] is assumed to hold also for the adsorbed GeCl₄ at the oxide-Ge boundary. Isothermal conditions are assumed since mainly processes at the interface are considered. Also it can be shown that essentially steady-state conditions prevail.

In order to set up the surface diffusion model, let $n(x)$ be the number of adsorbed molecules on the oxide per unit area. The coordinate x refers to the

direction parallel to the wafer in Fig. 2. It has been shown (24-26) that n must obey the mass-balance equation

$$D_s \frac{d^2 n}{dx^2} - \frac{n}{\tau} + \phi = 0, |x| < l \quad [2]$$

where D_s is the surface diffusion coefficient, τ the mean lifetime of an adsorbed molecule on the oxide, and ϕ is the flux of impinging molecules. Physically, the first term of [2] is the divergence of the surface flux which must accommodate the net flux from the vapor. This net flux may be viewed as a detailed balancing of two processes: a flux ϕ from the vapor to the oxide which may have to take an adsorption barrier into account and a reverse process $-n/\tau$ due to desorption. The surface flux at the oxide-Ge boundary is prescribed by a first-order chemical reaction

$$-D_s \frac{dn}{dx} = k_s n, x = l \quad [3]$$

where k_s is a reaction rate constant. We assume a first-order reaction since such is the case for growth on a bare Ge wafer (15). Defining a mean diffusion distance (24) $x_s = (D_s \tau)^{1/2}$, a symmetric solution of [2] and [3] is easily obtained

$$n(x) = \tau \phi \left[1 - \frac{\cosh x/x_s}{(D_s/k_s x_s) \sinh l/x_s + \cosh l/x_s} \right] \quad [4]$$

Physically, x_s is a capture distance; the density n varies largely within a distance x_s of the Ge-oxide boundary. The surface flux at the boundary is then

$$j_s = -D_s \frac{dn}{dx} \Big|_{x=l} = x_s \phi [D_s/k_s x_s + \coth l/x_s]^{-1} \quad [5]$$

and the average density is

$$\bar{n} = \frac{1}{l} \int_0^l n(x) dx = \tau \phi \left[1 - \frac{1}{(l/x_s) (D_s/k_s x_s + \coth l/x_s)} \right] \quad [6]$$

Turning now to the Ge ridge, the existence of such a smooth (*i.e.* nonfaceted) structure can be explained on the basis of Mullins' analysis (27, 28) of morphological changes due to capillarity. However, contrary to the case of grain boundary grooving, the Ge-oxide contact angle is not maintained, *i.e.*, local edge equilibrium is not satisfied. If it is assumed that each adsorbed molecule reacting at the Ge-oxide boundary according to [1] and [3] is then transported by surface diffusion over the ridge (formally, the surface flux is continuous at $x = l$), the excess area A , defined in the last section, is just

$$A = \Omega t j_s = \Omega t x_s \phi [D_s/k_s x_s + \coth l/x_s]^{-1} \quad [7]$$

where Ω is the atomic volume of Ge (2.21×10^{-23} cm³), t the time, and where [5] has been used. The argument leading to the first equality of [7] can be made rigorous by using Mullins' equation of motion of the ridge (27). It is seen that, as a function of pad width l , A is linear in l for $l \ll x_s$. The slope at the origin is

$$\frac{dA}{dl} \Big|_{l=0} = \Omega t \phi \quad [8]$$

and is independent of the surface processes. For $l \gg x_s$, A saturates reaching a maximum excess growth A_{\max}

$$A_{\max} = \Omega t x_s \phi / (1 + D_s/k_s x_s) \quad [9]$$

Discussion and Conclusions

To summarize, two extreme models are proposed. A surface diffusion model in which volume diffusion

through the stagnant layer is unperturbed by the oxide, and a volume diffusion model in which surface diffusion on the oxide is not operative. The calculated excess growth curves for large pad widths saturate for the first model ($l \gtrsim x_s$) and increase linearly for the second ($l \gtrsim \delta$). Since our observations (Fig. 4) show a plateau region for all temperatures, the surface diffusion mechanism is favored. However, this does not rule out some enhanced volume diffusion which is probably negligible at small pad widths, but which might dominate for larger ones. In fact, experimental observation on larger pads should show again a rise above the plateau level that has been observed. This might explain why Oldham and Holmstrom's calculations (8) fit their data. A more accurate description would have to couple the surface and volume diffusion processes.

At this point let us examine another mechanism leading to a saturation of growth curves. The reaction at the Ge-oxide boundary could become surface rate limited (29). Silvestri (15) has established under the same operating conditions that above 600°C the bare Ge wafer system is mass transport limited. However, just at the Ge-oxide boundary where the ridge is highest, the effective growth rate is about three times faster than on the remainder of the bare Ge surface. This enhanced growth rate must be due to an increase in the transport of reactants to (or reaction products from) the ridge. We can conceive that for sufficiently large enhanced transport rates due to large enough pads coupled with very fast surface diffusion or due to very high linear gas stream velocities as was observed by Reisman (29) in a different system, the growth rate will reach a maximum. This will occur when the partial pressures of the reactants at the surface become essentially equal to the input pressures or when the partial pressures of the products become either essentially uniform throughout the system or zero due to the fast effective removal of products from the ridge to the gas phase. Under these conditions the reaction is surface rate limited and further increase in transport rates, however accomplished, will not further increase the growth rate. How close are we to that condition in the present system? For a bare Ge wafer, Silvestri has shown (i) that the growth rate can be at least doubled by doubling the linear gas velocity [see Fig. 6, Ref. (15)] without showing any sign of saturation in growth rate which might occur if surface limited operation obtains (29), and alternatively (ii) at 800°C the growth rate would have to increase a factor of sixteen before the reaction becomes surface rate limited. In this latter case, we assume that an increase in the net transport of reactants to the ridge by the oxide pads is equivalent to the net increase in growth rate that occurs by increasing the Ge/H₂ ratio from 3.6×10^{-4} to $\sim 5.9 \times 10^{-3}$ as indicated by Fig. 2 and 3 of Ref. (15). Thus, we conclude that a surface rate limitation probably has not been reached in the neighborhood of the ridge, although any increase in transport rates unavoidably shifts the system closer to that condition.

The expression [7] for the excess area A , has been fitted to the experimental data of Fig. 4. To this effect, the observed plateau in A for large pad widths, l , was equated to A_{\max} . An initial slope was estimated so that the dashed (calculated) curves would go through most of the experimental points at the "knee." Such an estimate was not carried out for the 875°C data. A_{\max} and the slope are recorded as a function of temperature in Table I. In Fig. 5 and 6 of $\ln A_{\max}$ and $\ln dA/dl|_{l=0}$ vs. $1/T$, it is seen that the data points fall on straight lines. Since we have not measured a slope for 875°C, two least-squares lines have been calculated for A_{\max} corresponding to the case when one does or does not include the 875°C value of A_{\max} . These lines are almost coincident so that only the line correspond-

Table I.

	Temperature, °C				
	600	650	700	800	875
$dA/dl \times 10^6$ (cm)	3.3	4.8	8.8	16.7	—
$A_{\max} \times 10^7$ (cm ²)	2.9	3.3	5	13.5	16.5
$x_s \times 10^8$ (cm)					
(without 875°C point)	7.529	7.357	7.206	6.953	—
(with 875°C point)	7.7	7.36	7.07	6.6	6.312

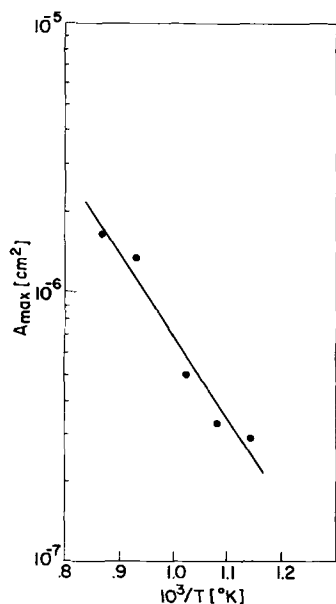
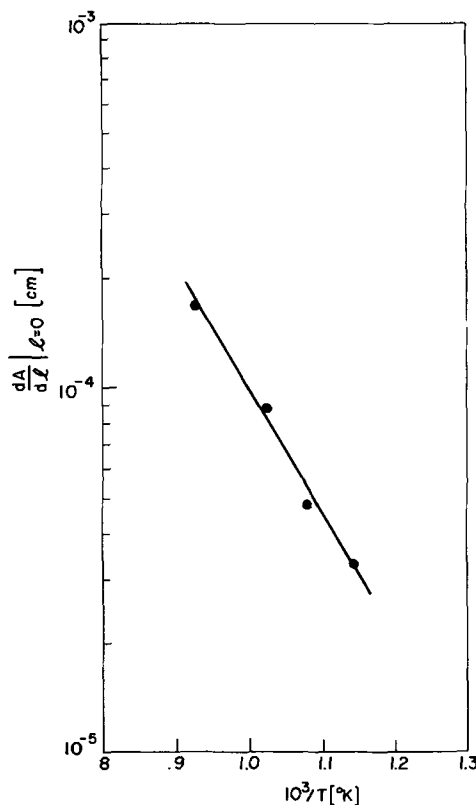
ing to the full data has been represented in Fig. 5. Preliminary numerical analysis has shown that an optimum fit requires that $D_s/k_s x_s \ll 1$ which means that the surface reaction is much faster than mass transport on the oxide. Equation [7] then reduces to

$$A = \Omega t \phi x_s \tanh l/x_s = A_{\max} \tanh l/x_s \quad [10]$$

Then, using Eq. [8], the mean diffusion distance can be expressed as

$$x_s = A_{\max} / \left. \frac{dA}{dl} \right|_{l=0} \quad [11]$$

As a function of temperature, values of x_s are calculated according to Eq. [11] by using the least-squares fit of A_{\max} and the slope. Corresponding to the two least-square lines of A_{\max} , two sets of values of x_s are calculated and are recorded in Table I. It is seen that x_s decreases slowly with temperature according to the relation $x_s = x_s^0 \exp E/kT$ which is consistent with the prediction of Burton, Cabrera, and Frank (24). The values of x_s just calculated and the measured values of A_{\max} allow the excess growth to be computed according to Eq. [10]. The computed curves are dashed in Fig. 4. Both sets of x_s are used and lead to curves differing at most by 5%. Although our surface diffusion model does predict a plateau, the calculated curves do not fit the initial portions of the experimental data, since these present an inflection point. In particular, the discrepancy between the data at 875°C and our model is so large that no curve representing these data has been shown. Although the reason for this lack of fit is not clear, we speculate that, in addition to reaction [1] there are other competing reactions as yet unaccounted for. For example, it might be postulated that HCl, liberated by the reaction, [1], on the Ge surface flows back over the oxide and is desorbed into the vapor. The inclusion of a second adsorbed species into the model could possibly explain the observed discrep-

Fig. 5. A_{\max} (cm²) as a function of $10^3/T$ (°K)Fig. 6. Initial slope $dA/dl|_{l=0}$ as a function of $10^3/T$ (°K)

ancy. In particular, such an improved model would have to explain the 875°C data where deviations to the present model are largest.

In spite of these limitations we have tried to obtain an understanding of the impingement flux ϕ . Figure 6 and Eq. [8] suggest that an Arrhenius form holds

$$\phi = \phi_0 e^{-Q/kT} \quad [12]$$

where k is Boltzmann's constant (8.62×10^{-5} eV/°K). Since $\Omega = 2.21 \times 10^{-23}$ cm³ and $t = 660$ sec, we calculate $\phi_0 = 1.69 \times 10^{19}$ cm⁻² sec⁻¹, $Q = 0.67$ eV. This suggests that an adsorption step (which might include a partial reaction with energy barrier Q) is rate limiting and that ϕ_0 is a frequency factor. The value of ϕ_0 may be compared with the molecular impingement flux Z given by kinetic theory (30)

$$Z = p(2\pi mkT)^{-1/2} \quad [13]$$

where p is the partial pressure and m is the mass of a molecule of GeCl₄. The GeCl₄ to H₂ concentration ratio is 3.6×10^{-4} the mass of a GeCl₄ molecule is 3.56×10^{-22} g. Z varies from 2.212×10^{19} cm⁻² sec⁻¹ at 600°C to 1.929×10^{19} cm⁻² sec⁻¹ at 875°C which is very close to the calculated value of ϕ_0 .

Finally an estimate of the surface diffusion coefficient (31) can be obtained with Eq. [6] and [10]. Since $A_{\max} \cong \Omega t \phi x_s$ and for large pad widths $\bar{n} \cong \tau \phi$

$$D_s = x_s^2/\tau = \left(\frac{A_{\max}}{\Omega t} \right)^2 \frac{1}{\bar{n} \phi} \quad [14]$$

For large l , when the effects of the oxide-Ge boundary can be neglected, \bar{n} could be estimated by an appropriate adsorption isotherm. This will not be pursued further since experimental data on D_s is unavailable.

In conclusion, we observe Ge ridges at the edges of SiO₂ masks. These growths increase with temperature and oxide pad width. A surface diffusion model is proposed which explains the saturation effect. It appears that the reaction at the oxide-Ge boundary is much faster than surface diffusion and that adsorption of Ge-

bearing species on the oxide mask constitutes a rate-limiting step. It is further shown that volume diffusion cannot explain the observations. However, certain details remain unexplained; in particular the inflection characteristic at higher temperatures indicates some competing process (or processes) not being considered. It should be noted that if the boundary condition [3] is altered to allow half- and second-order reactions, it can be shown that the curves obtained still exhibit the same behavior as [7]. Thus a more complete description will have to introduce more than one reaction and the diffusion paths of the products of the reactions.

APPENDIX

It remains to be investigated whether or not volume diffusion alone can explain the saturation effect. Let $N(x, y)$ be the density of Ge-bearing species (molecules/cubic centimeter) in the gas phase; x, y are the rectangular coordinates of Fig. 2. Under steady-state conditions, N must obey the time-independent diffusion equation (32)

$$\frac{\partial^2 N}{\partial x^2} + \frac{\partial^2 N}{\partial y^2} = 0 \quad [\text{A-1}]$$

Assume then that surface diffusion is not operative, i.e., n is a constant. Then Eq. [2] implies that the net flux above the oxide is zero

$$\left. \frac{\partial N}{\partial y} \right|_{y=0} = 0, \quad |x| < l \quad [\text{A-2}]$$

This boundary condition produces a bending of the flux lines toward the Ge, thereby enhancing the volume flux to the ridge. An explicit calculation is possible when the Ge-vapor reaction is much faster than mass transport. The density over the Ge is then constrained to its equilibrium value N_e

$$N(x, 0) = N_e, \quad |x| > l \quad [\text{A-3}]$$

Finally it is assumed that the density is maintained at a constant value N_0 (determined by the input) at the top of the stagnant layer

$$N(x, \delta) = N_0 \quad [\text{A-4}]$$

Since excess growth between pads is the same as that exterior to a set of pads, an infinite interpad distance can be assumed. The solution of [A-1] under the conditions [A-2-4] can be obtained by standard methods of conformal mapping (33). A mapping of the $z = x + iy$ plane into the (ω) plane can be found which conserves the boundary conditions and reduces the problem to a simple one-dimensional one. If I_m denotes the imaginary part and $\lambda = \pi l / 2\delta$, we get

$$N = N_e + (N_0 - N_e) I_m \omega / \pi$$

$$\omega + \lambda = \cosh^{-1} \left[\frac{\cosh \pi(|x| + iy) / \delta - \sinh 2\lambda}{\cosh \lambda} \right] \quad [\text{A-5}]$$

with the restriction $0 \leq I_m \omega \leq \pi$. Finally, the excess growth is given by

$$A / \Omega Dt = \int_l^\infty dx \left[\left. \frac{\partial N}{\partial y} \right|_{y=0} - \frac{N_0 - N_e}{\delta} \right]$$

$$= \frac{N_0 - N_e}{\pi} [2\lambda - \ln \cosh \lambda] \quad [\text{A-6}]$$

where in the integral, we have subtracted out the unperturbed flux, i.e., the flux derived from [A-5] for $l \rightarrow 0$. This function is plotted in Fig. 7. It depends solely on the characteristic ratio l/δ (experimentally always $\ll 1$) and does not saturate. The linear rise for $l > \delta$ is easily understood because the flux lines over the oxide are then essentially parallel to the x -axis.

Acknowledgments

The authors wish to thank S. A. Sharpe, S. A. Chan, and J. B. Bartivic for their technical assistance throughout the course of the work. Contributions by their colleagues, in particular, M. Berkenblit, M. E.

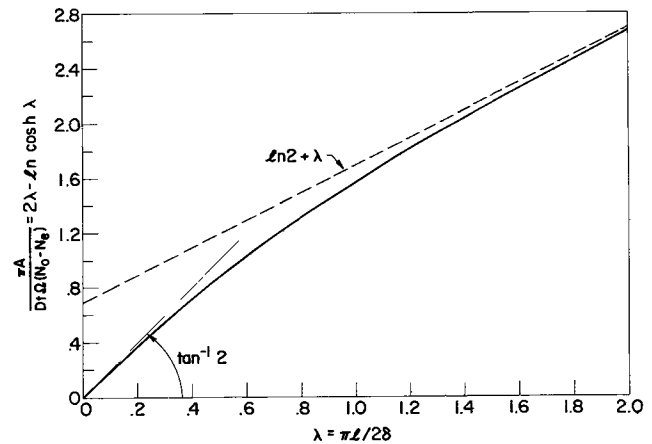


Fig. 7. Excess growth as a function of pad width for the volume diffusion model.

Cowher, J. M. Green, R. A. Laff, R. F. Lever, T. B. Light, and A. Reisman are gratefully acknowledged. O. C. Wells and C. G. Bremer furnished the scanning electron microscope photograph.

Manuscript submitted April 20, 1971; revised manuscript received ca. Oct. 8, 1971.

Any discussion of this paper will appear in a Discussion Section to be published in the December 1972 JOURNAL.

REFERENCES

1. B. D. Joyce and J. A. Baldrey, *Nature*, **195**, 485 (1962).
2. J. M. Hirshon, *This Journal*, **109**, 72C (Abstract No. 101) (1962).
3. A. F. McKelvey, Proc. 3rd Annual Microelectron Symposium, IEEE, St. Louis (1964).
4. D. M. Jackson, Jr., *Trans. Met. Soc., AIME*, **233**, 596 (1965).
5. E. G. Alexander and W. R. Runyan, *ibid.*, **236**, 284 (1966).
6. B. D. Joyce, N. P. Formigoni, C. C. Rose, and F. Schliesing, *Electrochem. Technol.*, **4**, 482 (1966).
7. G. L. Schnable, W. J. Hillegas, Jr., and C. G. Thornton, *ibid.*, **4**, 485 (1966).
8. W. G. Oldham and R. Holmstrom, *This Journal*, **114**, 381 (1967).
9. D. W. Shaw, *ibid.*, **113**, 904 (1966).
10. D. W. Shaw, *ibid.*, **113**, 958 (1966).
11. W. von Munch, H. Statz, and A. E. Blakeslee, *Solid State Electron.*, **9**, 826 (1966).
12. E. Sirtl and H. Seiter, "Semiconductor Silicon," p. 189, R. R. Haberecht and E. L. Kern, Editors, Electrochem Soc., New York (1969).
13. D. W. Shaw, *This Journal*, **115**, 777 (1968).
14. M. Berkenblit and A. Reisman, *Met. Trans., AIME*, **2**, (3), 803 (1971).
15. V. J. Silvestri, *This Journal*, **116**, 81 (1969).
16. J. J. Grossman, *ibid.*, **110**, 1065 (1963).
17. A. S. Grove, "Physics and Technology of Semiconductor Devices," John Wiley & Sons, Inc., New York (1967).
18. F. C. Eversteyn, P. J. W. Severin, C. H. J. v.d. Brekel, and H. L. Peek, *This Journal*, **117**, 925 (1970).
19. F. A. Kuznetsov and V. I. Belyi, *ibid.*, **117**, 785 (1970).
20. R. F. Lever, *IBM J. Res. & Dev.*, **8**, 460 (1964).
21. K. J. Miller and M. J. Grieco, *This Journal*, **111**, 1099 (1964).
22. K. E. Haq and W. Von Muench, *ibid.*, **113**, 260 (1966).
23. K. E. Haq, *ibid.*, **113**, 817 (1966).
24. W. K. Burton, N. Cabrera, and F. C. Frank, *Phil. Trans. Roy. Soc.*, **A243**, 299 (1951).
25. J. P. Hirth and G. M. Pound, *J. Chem. Phys.*, **26**, 1216 (1957).
26. R. Ghez, *Surf. Sci.*, **20**, 326 (1970).
27. W. W. Mullins, *J. Appl. Phys.*, **28**, 333 (1957).
28. W. W. Mullins, *ibid.*, **30**, 77 (1959).
29. A. Reisman and M. Berkenblit, *This Journal*, **113**, 146 (1966).

30. E. H. Kennard, "Kinetic Theory of Gases, McGraw-Hill Publishing Co., New York (1938).
 31. V. J. Silvestri and T. O. Sedgwick, *This Journal*, **117**, 198C (1970).
 32. W. Yost, "Diffusion in Solids, Liquids, Gases," Academic Press, New York (1952).
 33. Z. Nehari, "Conformal Mapping," McGraw-Hill Publishing Co., New York (1952).

High Apparent Mobility in Inhomogeneous Semiconductors

C. M. Wolfe,* G. E. Stillman,* and J. A. Rossi

Lincoln Laboratory, Massachusetts Institute of Technology, Lexington, Massachusetts 02173

ABSTRACT

In this paper we discuss in detail a simple model for an inhomogeneous semiconductor which leads to an anomalously high measured mobility. Quantitative results from this model are compared to experimental data from several different measurement configurations with intentionally introduced conducting inhomogeneities. These results cast doubt on the use of a high mobility as an indication of the quality of a semiconductor unless the homogeneity is unambiguously determined. These results may also qualitatively account for the behavior of samples with conducting inhomogeneities such as accumulation layers, metallic inclusions or precipitates, and doping variations due to polycrystalline growth or faceting effects.

The effects of various types of inhomogeneity on the mobility in semiconductors have been examined theoretically in some detail. Juretschke *et al.* (1) have treated the effects of nonconducting cavities in conducting materials. The properties of semiconductors with disordered regions produced by fast neutron irradiation have been discussed by Crawford and Cleland (2) and Gossick (3). A detailed treatment of the effects of random inhomogeneities has been given by Herring (4). Bate and Beer (5) and Bate *et al.* (6) have examined the influence of macroscopic conductivity gradients and discontinuities. Weisberg (7) has treated the scattering of current carriers by the space charge regions surrounding localized inhomogeneities. All of these treatments have shown that the mobility of inhomogeneous samples should be anomalously low either as a result of the averaging inherent in the Hall and resistivity measurements or as a result of carrier scattering.

Although anomalously low mobilities are commonly observed experimentally, anomalously high mobilities have also been observed in several semiconductors, including silicon where an accumulation layer was induced on a high-resistance n-type sample by an HF treatment (8) and GaAs which was grown under gallium-rich conditions (9). Mobilities which appear to be anomalously high have also been observed in other compound semiconductors which were grown under metal-rich conditions and which may have metallic inclusions or precipitates (10). By means of a simple model we have previously shown (11) that high apparent mobilities can be obtained in semiconductors with conducting inhomogeneities. Since this model may qualitatively account for the high measured mobilities in semiconductors with conducting inhomogeneities, we extend these results in the present paper and discuss in more detail the theoretical and experimental effects of conducting inhomogeneities on resistivity and Hall measurements in semiconductors.

Theoretical Model

The model which leads to an anomalously high measured mobility is shown in Fig. 1. This sample consists of a cylindrically symmetric van der Pauw configuration (12) of radius a , conductivity σ , and mobility μ , with a conducting inhomogeneity in the center of radius b , conductivity σ_0 , and mobility μ_0 . The ap-

parent resistivity of this sample is determined by measuring the voltage induced between contacts 3 and 4 with zero magnetic field while a current is flowing through contacts 1 and 2. The apparent Hall constant is obtained by measuring the voltage induced between contacts 2 and 4 by a magnetic field B while a current is flowing through contacts 1 and 3. (In this model we treat the conductivity and the mobility as fundamental parameters of the semiconductor, whereas we treat the apparent resistivity, the apparent Hall constant, and the apparent mobility as parameters of the measurement sample.) By assuming that the contacts have only one dimension along the sample thickness (t), general expressions are derived in the Appendix for the apparent resistivity (Eq. [A-5]) and the apparent Hall constant (Eq. [A-6]) of the measurement configuration. Although the numerical results to be presented later were calculated for various values of the conductivity ratio (σ_0/σ), for discussion purposes these expressions can be simplified by assuming that the conductivity of the inhomogeneity (σ_0) is much greater than the conductivity of the medium (σ). Thus, in the limit ($\sigma_0/\sigma \rightarrow \infty$) the apparent resistivity is given by

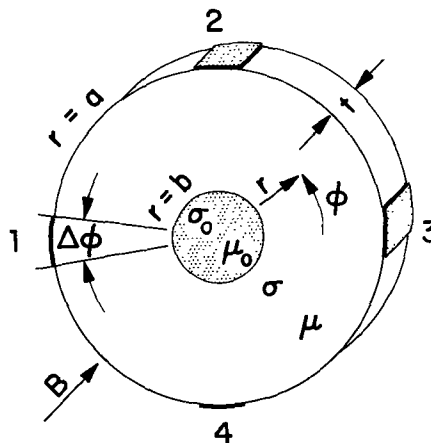


Fig. 1. Cylindrically symmetric van der Pauw configuration of radius $r = a$ with a conducting inhomogeneity of radius $r = b$ which leads to an anomalously high apparent mobility. The contacts are indicated by 1, 2, 3, and 4.

* Electrochemical Society Active Member.

Key words: high mobility, inhomogeneity, metallic inclusion, faceting effect.

$$\rho_{app}(\alpha) = \frac{1}{\sigma \ln 2} \sum_{n=1}^{\infty} \frac{(1 - \alpha^{2n})^3}{(1 + \alpha^{4n})(1 + \alpha^{2n})} \frac{(-1)^{n+1}}{n} \quad [1]$$

and the apparent Hall constant is given by

$$R_{app}(\alpha, \beta) = \frac{4}{\pi} \frac{\mu}{\sigma} \sum_{n=1}^{\infty} \frac{\left(\frac{1 - \alpha^{4n-2}}{1 + \alpha^{4n-2}}\right)^2 (1 + \beta^2) (-1)^{n+1}}{1 + \left(\frac{1 - \alpha^{4n-2}}{1 + \alpha^{4n-2}}\right)^2 \beta^2 (2n - 1)} \quad [2]$$

where α is the ratio of the radius of the inhomogeneity (b) to the radius of the sample (a) and β is the product of the real mobility of the semiconductor (μ) and the magnetic field (B).

From these equations we can examine qualitatively the effect of the inhomogeneity on the resistivity and Hall measurements. In the absence of an inhomogeneity ($\alpha = 0$) the series in Eq. [1] reduces to $\ln 2$, so $\rho_{app}(0) = 1/\sigma$. The series in Eq. [2] reduces to $\pi/4$ and $R_{app}(0, \beta) = \mu/\sigma$. The calculated mobility

$$\left[\mu_{app}(0, \beta) = \frac{R_{app}(0, \beta)}{\rho_{app}(0)} \right]$$

is then equal to the real mobility of the sample. (Actually, both the apparent Hall constant and the apparent mobility are independent of β in this case, since the effects of scattering mechanisms are not included in the model. The β arguments are maintained for notation consistency.)

In the low field limit ($\beta^2 \ll 1$), it can be seen that both the apparent resistivity and the apparent Hall constant decrease as the relative extent of the inhomogeneity is increased ($\alpha > 0$). However, the resistivity decreases faster than the Hall constant, thus resulting in a higher apparent mobility. Physically, this is a geometrical effect where the current lines in the Hall measurement configuration with an applied magnetic field tend to spread around the inhomogeneity more than the current lines in the resistivity measurement configuration. Thus, the Hall voltage is reduced less than the resistivity voltage by the inhomogeneity.

For a given size inhomogeneity as the magnetic field is increased the measured Hall constant increases and, since the resistivity is measured in zero magnetic field, the measured mobility increases. In the high field limit ($\beta^2 \gg 1$), the measured Hall constant is equal to μ/σ , which is the Hall constant of the homogeneous part of the sample. Physically, this effect is a result of the current lines being distorted out of the inhomogeneity by the magnetic field, until in the high field limit there is no current flow into the inhomogeneity. As has been pointed out by Herring (4) this is a consequence of the interactions of the boundary conditions between the inhomogeneity and the surrounding medium induced by the magnetic field.

Quantitative results for the dependence of the apparent resistivity, apparent Hall constant, and apparent mobility on the relative extent of the inhomogeneity (α), the normalized magnetic field (β), and the ratio of the conductivity of the inhomogeneity to the conductivity of the surrounding medium (σ_0/σ), have been calculated from the general expressions derived in the Appendix. Since the results are dominated by the discontinuity in conductivity σ_0/σ as opposed to the discontinuity in mobility (μ_0/μ), it was assumed that $\beta_0 = \beta$ in the calculations to avoid unnecessary complications. These results are plotted in Fig. 2, 3, and 4.

Figure 2 shows the dependence of the normalized resistivity $[\rho_{app}(\alpha, \sigma_0/\sigma)\sigma]$ on α and σ_0/σ . In addition to the decrease in $\rho_{app}(\alpha)$ with increasing α previously indicated, for small values of α the major decrease in $\rho_{app}(\alpha, \sigma_0/\sigma)$ occurs for σ_0/σ between 1 and about 10. Thus, relatively small values of σ_0/σ can significantly affect the resistivity measurement.

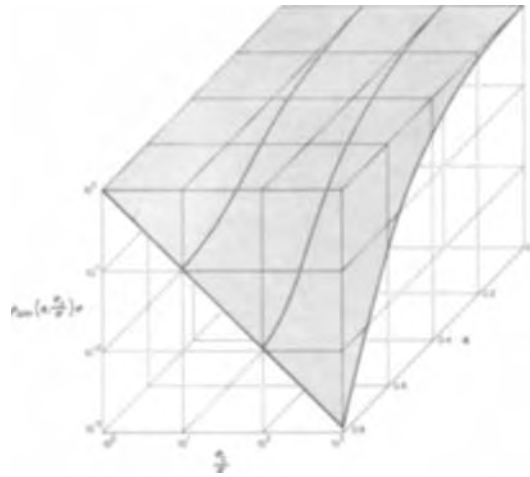


Fig. 2. Theoretical dependence of the normalized apparent resistivity $[\rho_{app}(\alpha, \sigma_0/\sigma)\sigma]$ on the relative extent of the inhomogeneity ($\alpha \equiv b/a$) and the ratio of the conductivity of the inhomogeneity (σ_0) to the conductivity of the medium (σ).

The dependence of the normalized Hall constant

$$\left[\frac{R_{app}\left(\alpha, \beta, \frac{\sigma_0}{\sigma}\right)\sigma}{\mu} \right]$$

on α , β , and σ_0/σ is shown in Fig. 3. Here we see the increase in $R_{app}(\alpha, \beta)$ with β previously indicated. However, these quantitative results for $R_{app}(\alpha, \beta, \sigma_0/\sigma)$ show that for values of β as low as about 10 the measured Hall constant approximates rather closely the Hall constant of a homogeneous sample for all values of α . Also, relatively small values of σ_0/σ have an appreciable effect on the Hall constant measurement (for values of α greater than about 0.2 which corresponds to 4% of the volume) as well as on the resistivity measurement.

Figure 4 shows the dependence of the normalized mobility

$$\left[\frac{\mu_{app}(\alpha, \beta, \sigma_0/\sigma)}{\mu} \right]$$

on α , β , and σ_0/σ . For low values of α and β we see the increase in apparent mobility with increasing α as previously indicated. However, for rather large values of α the apparent mobility begins to decrease. This is because in the low field region the relative shunting

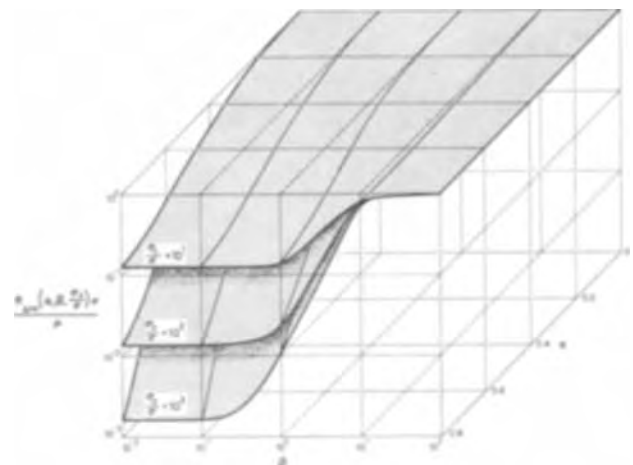


Fig. 3. Theoretical dependence of the normalized apparent Hall constant $[R_{app}(\alpha, \beta, \sigma_0/\sigma)\sigma/\mu]$ on the normalized magnetic field ($\beta \equiv \mu B$) and α for several values of σ_0/σ .

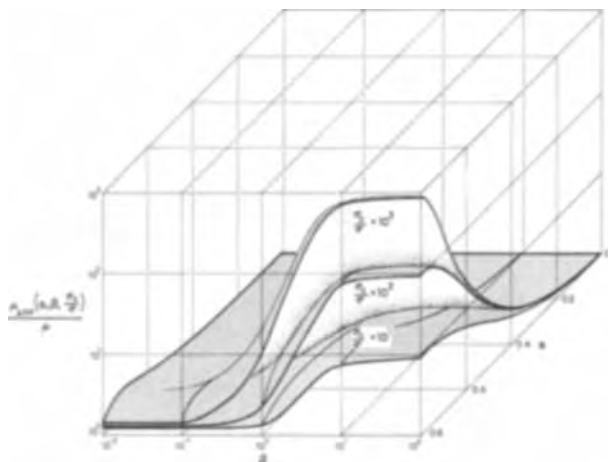


Fig. 4. Theoretical dependence of the normalized apparent mobility [$\mu_{APP}(\alpha, \beta, \sigma_0/\sigma)/\mu$] on β and α for several values of σ_0/σ .

effect of the inhomogeneity on the Hall voltage compared to the resistivity voltage begins to decrease for relatively large inhomogeneities. In the high field region, however, the apparent mobility continues to increase with α since almost all of the current is in the homogeneous part of the sample regardless of the size of the inhomogeneity. Here also for a given α we see rather sizable increases in apparent mobility with β and σ_0/σ , so that, depending on the various parameters, the apparent mobility can exceed the real mobility by as much as several orders of magnitude.

Experimental Verification

Since the theoretical model represents a rather idealized inhomogeneous measurement sample, a number of the more commonly used measurement configurations were investigated experimentally to test the generality of the model. For this purpose conducting inhomogeneities were intentionally introduced into thin epitaxial layers of GaAs which were grown on semi-insulating substrates. Conducting n^+ regions were obtained by alloying tin, and metallic inclusions were simulated by alloying gallium into the exposed surface of the epitaxial layers. This was expected to be a good representation of the theoretical model since the layers were thin compared to the extent of the inhomogeneity and also because the current flow tends to become two-dimensional with increasing magnetic field (4). In addition to a number of van der Pauw configurations, including cloverleaves, crosses, squares, and circles, the standard rectangular Hall configuration was also investigated. The real mobility (μ) was determined from resistivity and Hall measurements before the inhomogeneities were introduced, and the apparent mobility [$\mu_{APP}(\alpha, \beta)$] was determined by measurements after the inhomogeneities were introduced. In each configuration the apparent mobility after introducing inhomogeneities was greater than the real mobility.

Some of these results are shown in Fig. 5 where the ratio of the apparent mobility to the real mobility is plotted vs. the relative size of the inhomogeneity (α). Experimentally, the parameter α was estimated from the area of the inhomogeneity and the area of the portion of the sample which was measured. The different symbols indicate different measurement configurations. Experimental values of β were between 0.5 and 1.0 and the corresponding theoretical curves calculated for $\sigma_0 \gg \sigma$ are shown. Much of the scatter in the experimental data is caused by uncertainties in estimating area. Also we expect the effect to be quantitatively somewhat different in the various measurement configurations. However, it can be seen that in all configurations an anomalously high apparent mobility could be obtained by introducing a conducting in-

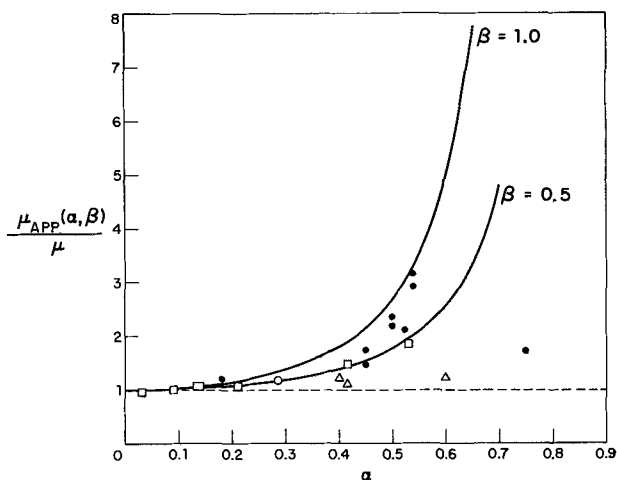


Fig. 5. Experimental dependence of $\mu_{APP}(\alpha, \beta)/\mu$ on α . The theoretical curves for $\sigma_0 \gg \sigma$ bracket the values of β for the experimental data. Different symbols indicate the different van der Pauw measurement configurations: \circ —cross, \triangle —cloverleaf, \square —square, and \bullet —circle. The rectangle indicates the standard Hall configuration.

homogeneity and that the experimental data are in reasonable agreement with the theoretical model.

In Fig. 6 we show the experimental dependence of the apparent mobility on the normalized magnetic field (β). The parameter β was varied either by changing the magnetic field or by changing the measurement temperature and thus the real mobility of the sample. As in the previous figure the different symbols represent the different measurement configurations and theoretical curves calculated for $\sigma_0 \gg \sigma$ bracket the estimated values of α for the experimental samples. As can be seen, the apparent mobility increases with β in reasonable agreement with the model.

Applicability

Since it has been shown that anomalously high apparent mobilities can be obtained as a result of conducting inhomogeneities in semiconductors, it is apparent that the homogeneity of the material must be determined before the mobility can be used as a figure of merit for the material. Although there are a number of techniques for detecting inhomogeneities (13), they may not produce definitive results for some types of

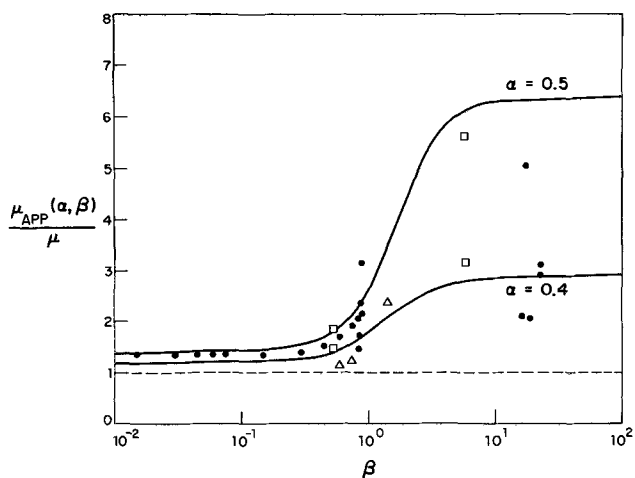


Fig. 6. Experimental dependence of $\mu_{APP}(\alpha, \beta)/\mu$ on β . The theoretical curves for $\sigma_0 \gg \sigma$ bracket the values of α for the experimental data. The symbols have the same meaning as in Fig. 5.

material inhomogeneity. Unintentionally introduced conducting inhomogeneities which are similar to the model constructed here are expected to have several characteristic features.

First, the observation of anomalously high mobilities is generally not expected to be very reproducible. The effect may be observed in samples prepared under conditions which result in accumulation layers on the surface of the measurement sample, or for compound semiconductors the effect may be most commonly observed in samples which are grown under metal-rich conditions and which may have metallic inclusions or precipitates. Doping variations in a sample may also lead to measurements of anomalously high apparent mobility. Since crystallites of different orientation can incorporate impurities at different rates during growth (14), the effect may be observed in polycrystalline samples. High apparent mobilities due to the so-called "facet effect" may also occur in Czochralski-grown crystals for measurement samples which are cut normal to the growth direction. [Expressions for the apparent resistivity and Hall constant of samples with conductivity gradients which approximate those observed in the "facet effect" (15) are derived in the Appendix.]

For pure samples the measured mobility in samples with conducting inhomogeneities may exceed the theoretical lattice scattering limited values. For example, in GaAs the polar optical phonon scattering limit (16) at 300°K is calculated to be 8000 ± 1000 cm²/V-sec using the most accurate experimental parameters. At 77°K a lattice limited mobility of about 240,000 cm²/V-sec has been calculated (17). However, by intentionally introducing conducting inhomogeneities in samples, we have increased the measured 300°K mobility from 7400 to 24,000 and the measured 77°K mobility from 150,000 to 740,000 cm²/V-sec.

Samples with conducting inhomogeneities may appear to be quite uncompensated. For measurements in low magnetic fields this is because the apparent carrier concentration is higher than the real concentration. However, this is also true for measurements in high magnetic fields, since, even though the apparent carrier concentration approaches the real concentration, the apparent mobility is higher.

One method of determining the presence of conducting inhomogeneities and thus estimating the homogeneity of a material is to examine the magnetic field dependence of the Hall constant. For a homogeneous sample the Hall constant should decrease with increasing magnetic field as expected by the magnetic field dependence of the Hall coefficient factor. This dependence can be estimated or calculated from the Hall coefficient factors for the relevant scattering mechanisms (18, 19). The effect of conducting inhomogeneities however, is to give an increase in Hall constant with magnetic field which may reduce or eliminate the expected variation. Thus, if the magnetic field dependence of the Hall constant is anomalous, then the presence of conducting inhomogeneities is indicated.

For the intentionally introduced inhomogeneities previously described, this effect is quite pronounced. This is shown in Fig. 7 where the magnetic field dependence of the normalized Hall constant is plotted for a GaAs sample before and after an inhomogeneity was introduced. The upper curve shows the variation expected due to the magnetic field dependence of the Hall coefficient factor (19) [$r(\beta) = neR(\beta)$] and the experimental data points for a homogeneous sample (open circles) are in reasonable agreement with the expected dependence. The lower theoretical curves and experimental data points (solid circles) indicate the dependence obtained after an inhomogeneity was introduced in the sample.

Conclusions

Since intentionally introduced conducting inhomogeneities result in anomalously high measured mobil-

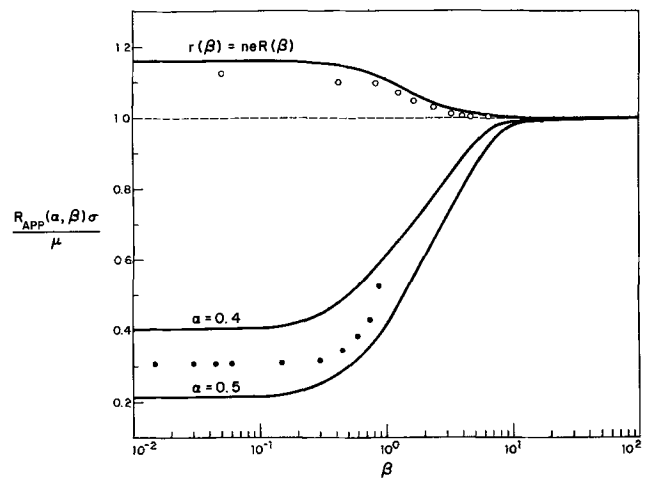


Fig. 7. Theoretical (curves) and experimental (circles) dependence of $R_{APP}(\alpha, \beta)\sigma/\mu$ on β for a homogeneous sample (upper) and a sample with an intentionally introduced inhomogeneity (lower) with α between 0.4 and 0.5.

ities, similar effects may be observable in samples with other conducting inhomogeneities such as accumulation layers, metallic inclusions and precipitates, and doping variations due to polycrystalline growth or faceting effects. This casts doubt on the use of mobility as a figure-of-merit for a material unless homogeneity can be established.

Acknowledgments

We would like to thank J. O. Dimmock, T. C. Harman, D. Hill, W. T. Lindley, D. L. Spears, A. J. Strauss, and F. V. Williams for useful discussions and L. Krohn and H. R. Favreau for technical assistance. This work was sponsored by the Department of the Air Force.

Manuscript submitted June 9, 1971; revised manuscript received Oct. 8, 1971. This was Paper 87 presented at the Washington, D. C., Meeting of the Society, May 9-13, 1971.

Any discussion of this paper will appear in a Discussion Section to be published in the December 1972 JOURNAL.

APPENDIX

Formulation of Model

Consider the cylindrically symmetric van der Pauw configuration with a radial change in conductivity (σ) shown in Fig. 1. The relationship between the current density, \vec{J} , and the potential, V , is given by $\vec{J} = \vec{\sigma} \text{grad } V$, where $\vec{\sigma}$ is the magnetoconductivity tensor. With the magnetic field B in the z direction

$$\vec{\sigma} = \begin{bmatrix} \frac{\sigma}{1 + \beta^2} & \beta \frac{\sigma}{1 + \beta^2} & 0 \\ -\beta \frac{\sigma}{1 + \beta^2} & \frac{\sigma}{1 + \beta^2} & 0 \\ 0 & 0 & \sigma \end{bmatrix}$$

where $\beta \equiv \mu B$. In the steady state $\text{div } \vec{J} = 0$ and the differential equation which determines the transport of charge is

$$\text{div } \vec{\sigma} \text{grad } V = 0 \quad [\text{A-1}]$$

We next consider a current I through any contact on the perimeter $r = a$. The current density at the contact is

$$J_r(a, \phi) = \frac{I}{ta\Delta\phi}$$

To simplify the problem we obtain one-dimensional contacts by letting $\Delta\phi$ approach zero.

$$\lim_{\Delta\phi \rightarrow 0} J_r(a, \phi) = \lim_{\Delta\phi \rightarrow 0} \frac{I}{ta\Delta\phi} = \frac{I}{ta} \delta(\phi - \phi_0)$$

where $\delta(\phi - \phi_0)$ is the Dirac delta function, and ϕ_0 is the angular position of the contact. In the resistivity calculation we pass a current through the contacts at $\phi = \pi/2$ and $\phi = 0$, which results in the boundary conditions

$$J_r(a, \phi) = \frac{I}{ta} \left[\delta\left(\phi - \frac{\pi}{2}\right) - \delta(\phi - 0) \right] \quad [\text{A-2}]$$

and determine the voltage induced between the contacts at $\phi = \pi$ and $\phi = 3\pi/2$ with zero magnetic field. In the Hall constant calculation we pass a current through the contacts at $\phi = \pi/2$ and $\phi = 3\pi/2$, which results in the boundary conditions

$$J_r(a, \phi) = \frac{I}{ta} \left[\delta\left(\phi - \frac{\pi}{2}\right) - \delta\left(\phi - \frac{3\pi}{2}\right) \right] \quad [\text{A-3}]$$

and determine the voltage induced between the contacts at $\phi = 0$ and $\phi = \pi$ by a magnetic field B .

Discontinuity in Conductivity

If we assume that the conductivity, σ , and the mobility, μ , are discontinuous at $r = b$, then Eq. [A-1] reduces to Laplace's equation which is separable. At the boundary between the two regions we require that the radial components of the current be equal, $J_r(b, \phi) = J_r^o(b, \phi)$, and that the tangential components of the field be equal, $E_\phi(b, \phi) = E_\phi^o(b, \phi)$. This gives us for the potential at any point (r, ϕ) in the outer region

$$V(r, \phi) = A_0 + \sum_{n=1}^{\infty} \{ [A_n r^n - b^{2n} r^{-n} (A_n \gamma + B_n \eta)] \cos n\phi + [B_n r^n - b^{2n} r^{-n} (B_n \gamma - A_n \eta)] \sin n\phi \} \quad [\text{A-4}]$$

where

$$\gamma \equiv \frac{(\omega_0^2 - \omega^2) + (\omega_0 \beta_0 - \omega \beta)^2}{(\omega_0 + \omega)^2 + (\omega_0 \beta_0 - \omega \beta)^2},$$

$$\eta \equiv \frac{2\omega(\omega_0 \beta_0 - \omega \beta)}{(\omega_0 + \omega)^2 + (\omega_0 \beta_0 - \omega \beta)^2},$$

$$\omega \equiv \frac{\sigma}{1 + \beta^2} \text{ and } \omega_0 \equiv \frac{\sigma_0}{1 + \beta_0^2}$$

(Note that $\frac{\sigma_0}{\sigma} \rightarrow \infty$ $\gamma = 1$, and $\frac{\sigma_0}{\sigma} \rightarrow \infty$ $\eta = 0$.)

A_n and B_n are then determined from the boundary conditions at $r = a$.

For the resistivity determination Eq. [A-4], boundary conditions [A-2], and van der Pauw's expression (12) for the resistivity in zero magnetic field, $\rho = (\pi/\ln 2)(Vt/I)$, yield an apparent resistivity given by

$$\rho_{\text{app}}\left(\alpha, \frac{\sigma_0}{\sigma}\right) = \frac{1}{\sigma \ln 2} \sum_{n=1}^{\infty} \left[\frac{2(1 - \gamma \alpha^{2n})}{(1 + \gamma \alpha^{2n})} - \frac{(1 - \gamma \alpha^{4n})}{(1 + \gamma \alpha^{4n})} \right] \frac{1}{n} (-1)^{n+1} \quad [\text{A-5}]$$

where $\alpha \equiv b/a$ and $\gamma = (\sigma_0^2 - \sigma^2)/(\sigma_0 + \sigma)^2$ for $\beta = 0$.

To obtain Eq. [1] $\lim_{\sigma_0/\sigma \rightarrow \infty} \rho_{\text{app}}(\alpha, \sigma_0/\sigma) \equiv \rho_{\text{app}}(\alpha)$.

For the Hall constant determination we use Eq. [A-4], boundary conditions [A-3], and the expression for the Hall constant, $R = Vt/IB$, to find an apparent Hall constant given by

$$R_{\text{app}}\left(\alpha, \beta, \frac{\sigma_0}{\sigma}\right) = \frac{\mu}{\omega} \frac{4}{\pi} \sum_{n=1}^{\infty} \frac{\left[(1 - \gamma \alpha^{4n-2})^2 + \eta^2 \alpha^{8n-4} + \frac{2}{\beta} \eta \alpha^{4n-2} \right]}{\left[(1 + \gamma \alpha^{4n-2})^2 + \beta^2 (1 - \gamma \alpha^{4n-2})^2 + (1 + \beta^2) \eta^2 \alpha^{8n-4} + 4\beta \eta \alpha^{4n-2} \right]} \times \frac{(-1)^{n+1}}{(2n-1)} \quad [\text{A-6}]$$

To obtain Eq. [2] $\lim_{\sigma_0/\sigma \rightarrow \infty} R_{\text{app}}(\alpha, \beta, \sigma_0/\sigma) \equiv R_{\text{app}}(\alpha, \beta)$. The apparent mobility is

$$\mu_{\text{app}}\left(\alpha, \beta, \frac{\sigma_0}{\sigma}\right) = \frac{R_{\text{app}}\left(\alpha, \beta, \frac{\sigma_0}{\sigma}\right)}{\rho_{\text{app}}\left(\alpha, \frac{\sigma_0}{\sigma}\right)}$$

which results in

$$\frac{\mu_{\text{app}}\left(\alpha, \beta, \frac{\sigma_0}{\sigma}\right)}{\mu} > 1$$

for $\alpha > 0$ and $\sigma_0/\sigma > 1$.

Gradient in Conductivity

If we assume that the conductivity has a radial dependence of the form $\sigma = \sigma_0(b/r)^{2\zeta}$ so that $(1/\sigma)(d\sigma/dr) = (-2\zeta/r)$, and the mobility is uniform, then Eq. [A-1] is again separable. The potential at any point (r, ϕ) in the outer region is

$$V(r, \phi) = A_0 + r^\zeta e^{\zeta\beta\phi} \sum_{n=1}^{\infty} r^{-\zeta(4n^2+1)^{1/2}}$$

$$[A_n \cos \zeta(4n^2 - \beta^2)^{1/2}\phi + B_n \sin \zeta(4n^2 - \beta^2)^{1/2}\phi] \quad [\text{A-7}]$$

for $2n > \beta$ and ζ positive. To determine A_n and B_n from the boundary conditions at $r = a$, it is necessary to construct a set of orthogonal solutions to Eq. [A-1]. Since this is quite cumbersome to do in general, we make the simplifying assumption that $\beta^2 \ll 1$ and then use the solutions [A-7] which are orthogonal on the interval 0 to 2π with respect to the weighting function $e^{-\zeta\beta\phi}$. To approximate the radial conductivity dependence observed experimentally for the "facet effect" in Czochralski-grown crystals, we use a value $\zeta = 1/2$ so that $\sigma = \sigma_0(b/r)$.

For the resistivity determination Eq. [A-7], boundary conditions [A-2], and van der Pauw's expression for the resistivity yield an apparent resistivity given by

$$\rho_{\text{app}} = \frac{1}{\sigma_0} \left(\frac{a}{b}\right) \frac{4}{\ln 2} \sum_{n=1}^{\infty} \frac{[(16n^2 + 1)^{1/2} - (4n^2 + 1)^{1/2}]}{[(16n^2 + 1)^{1/2} - 1][(4n^2 + 1)^{1/2} - 1]} (-1)^{n+1} \quad [\text{A-8}]$$

For the Hall constant determination we use Eq. [A-7], boundary conditions [A-3], and the expression for the Hall constant to find an apparent Hall constant given by

$$R_{\text{app}} = \frac{\mu}{\sigma_0} \left(\frac{a}{b}\right) \frac{16}{\pi} \sum_{n=1}^{\infty} \frac{(2n-1)}{\{[4(2n-1)^2 + 1]^{1/2} - 1\}^2} (-1)^{n+1} \quad [\text{A-9}]$$

For $\mu_{\text{app}} = \frac{R_{\text{app}}}{\rho_{\text{app}}}$, Eq. [A-8] and [A-9] give $\frac{\mu_{\text{app}}}{\mu} > 1$.

REFERENCES

- H. J. Juretschke, R. Landauer, and J. A. Swanson, *J. Appl. Phys.*, **27**, 838 (1956).
- J. H. Crawford, Jr., and J. W. Cleland, *ibid.*, **30**, 1204 (1959).
- B. R. Gossick, *ibid.*, **30**, 1214 (1959).
- C. Herring, *ibid.*, **31**, 1939 (1960).
- R. T. Bate and A. C. Beer, *ibid.*, **32**, 800 (1961).
- R. T. Bate, J. C. Bell, and A. C. Beer, *ibid.*, **32**, 806 (1961).
- L. R. Weisberg, *ibid.*, **33**, 1817 (1962).

8. D. Colman and D. L. Kendall, *ibid.*, **40**, 4662 (1969).
9. F. V. Williams and D. Hill, Private communication; L. F. Eastman, Private communication; S. Knight, Private communication.
10. G. A. Antcliffe and J. S. Wrobel, *Mater. Res. Bull.*, **5**, 747 (1970); T. C. Harman, Private communication.
11. C. M. Wolfe and G. E. Stillman, *Appl. Phys. Letters*, **18**, 205 (1971).
12. L. J. van der Pauw, *Philips Res. Rept.*, **13**, 1 (1958).
13. R. T. Bate, in "Semiconductors and Semimetals," Vol. 4, p. 459, "Physics of III-V Compounds," R. K. Willardson and A. C. Beer, Editors, Academic Press, New York (1968).
14. R. N. Hall, *J. Phys. Chem.*, **57**, 836 (1953).
15. J. B. Mullin and K. F. Hulme, *J. Phys. Chem. Solids*, **17**, 1 (1960); M. D. Banus and H. C. Gatos, *This Journal*, **109**, 829 (1962).
16. H. Ehrenreich, *J. Phys. Chem. Solids*, **8**, 130 (1959).
17. C. M. Wolfe, G. E. Stillman, and W. T. Lindley, *J. Appl. Phys.*, **41**, 3088 (1970); D. L. Rode, Private communication.
18. A. C. Beer, "Galvanomagnetic Effects in Semiconductors," p. 123, Academic Press, New York (1963).
19. S. S. Devlin, in "Physics and Chemistry of II-VI Compounds," p. 558, M. Aven and J. S. Prener, Editors, North-Holland Publishing Co., Amsterdam (1967).

Effects of Grown-In and Process-Induced Defects in Single Crystal Silicon

D. I. Pomerantz*

*P. R. Mallory & Co., Inc., Laboratory for Physical Science,
Northwest Industrial Park, Burlington, Massachusetts 01803*

ABSTRACT

Distributions of defects observed in single crystals of silicon grown from the melt are shown to be congruent with two well known growth inhomogeneities characterized either by a spiral ramp pattern or a faceted core pattern in the crystal. The consequences of these defects are traced through the oxidation of the substrate, as required for a subepitaxial diffusion, and (after removal of the oxide) the growth of an epitaxial layer. It will be shown that the defect distributions persist through these processes and, interacting with process induced defects, produce several characteristic distributions of stacking faults in the epitaxial layer.

The two most striking growth inhomogeneities of silicon single crystals grown from the melt are growth spirals and growth cores (1-5). Spiral growth (1-4) is produced when the axis of crystal rotating is not coincident with an axis of thermal symmetry so that the growing interface experiences temperature fluctuations with the period of the rotation. The result is a surface of constant (*e.g.*, maximum or minimum) growth rate which will normally have the shape of a spiral ramp distributed within the growing crystal with its axis parallel to the direction of growth.

Growth cores (4, 5) are characterized by a solid-liquid interface which is extremely flat and close to a (111) plane. This facet, which is usually in the center of the crystal is believed to be produced by rapid lateral growth.

The existence of both types of growth fluctuations described above is largely deduced from the presence of resistivity striations (1, 4) in the crystal which are caused by the variation of effective segregation coefficient with growth rate.

In the light of these results, it is reasonable to expect that the observed fluctuations in growth rate might also produce a defect structure resembling the structure of resistivity striations; and in fact defect structures which are similar to spiral growth patterns have been observed by several workers. In particular Schwuttke (6) and Kaiser and Keck (7) have shown the precipitation of oxygen in this pattern in crystals grown from quartz crucibles. In low dislocation, low oxygen crystals grown by the Dash technique Plaskett (8) and de Kock (9) have described a similar distribution of defects which are attributed to vacancy clusters. Both types of defect were found to be nucleation sites for the precipitation of copper, which by infrared microscopy enabled the distribution to be made visible.

* Electrochemical Society Active Member.

Key words: silicon, single crystals, defects, stacking faults, oxidation, epitaxy, sodium, copper.

It will be the purpose of this work to show that silicon crystals can contain defect distributions which are congruent to both spiral- and core-type growth inhomogeneities. We do not here attempt to identify the nature of these grown-in defects, but their effects will be traced through the processing of silicon slices as typically required for subepitaxial diffusion and the growth of an epitaxial layer. It will be seen that the over-all distribution of defects remains stable throughout these processes although the individual defects undergo characteristic changes. Specifically it will be shown that during thermal oxidation of a slice these grown-in defects can act as nucleation sites for the precipitation of fast diffusing impurities which form clusters characteristic of copper.

It will also be seen that these defect distributions, interacting with surface defects at the oxide-silicon interface, nucleate characteristic patterns of stacking faults in epitaxial layers.

Experimental Procedure

The single-crystal slices used in this study were obtained from several commercial sources and were grown either by the Czochralski method from quartz crucibles or by the Dash "pedestal" method (10-11). All crystals were grown on the <111> axis to a diameter of 1.25 in. and were doped with boron in the range 10^{15} - 10^{16} atoms/cm³. Dislocation density in the crucible-grown crystals was less than 1000/cm² and essentially zero in the Dash-grown crystals. Slices from these crystals were cut from 2-5° off the <111> axis along the <110> direction and were supplied with one side polished in such a way as to remove a minimum of two mils from the sawn surface. Final slice thickness was 7.5-9.5 mils. Various polishing methods were used, but to eliminate the possibility that any of the observed structures could be attributed to polishing variables; samples of as-received slices were further

polished to a depth of 1-2 mils using the nonpreferential etch described by Lawrence and Koehler (12). This etch was also used, where specified, to remove saw damage from the back of the slice.

Slices or portions of slices prepared as described above were oxidized under one of the following conditions: (i) wet oxygen, saturated with water vapor at 95°C, for a period of 1-2 hr at 1200°C, (ii) dry oxygen for periods ranging from 1-7 hr at 1200°C, (iii) steam at 1200°C for a period of 1-2 hr. All oxidations were carried out in an externally heated quartz tube with slices held by a quartz boat and the oxidation period was preceded and followed by a 5 min flush with dry oxygen.

In some cases where indicated below the quartz boat was deliberately contaminated with a drop of 0.1M sodium nitrate solution prior to insertion in the oxidation furnace. Oxidation tubes used for this purpose were not used for other types of oxidation.

Portions of slices which were oxidized as described above were etched in HF to remove the oxide and then used as substrates for epitaxial deposition of silicon layers by the hydrogen reduction of silicon tetrachloride. The growth conditions and substrate preparation are described in Ref. (13). In order to observe the effects of the oxidation, control slices which had not been oxidized were also subjected to the HF etch and processed in parallel with the oxidized slices through epitaxial deposition.

The defect structures in as-received, oxidized, and epitaxially deposited slices were revealed by means of the structural etch described by Sirtl and Adler (14) (Solution B). Epitaxial layers were etched 1-2 min to show stacking faults. Other samples were etched 2-5 min. To reveal the stacking fault distributions in the macrophotographs the samples were illuminated at glancing incidence in a direction normal to one of the stacking fault edges. In this way specular reflections are obtained from the etched stacking fault facets which produce the small bright spots in the photographs.

Results

The experimental procedure described above has been used to trace the evolution and effects of grown-in silicon crystal defects through the processes typically used to produce an epitaxial layer over a localized diffused layer as required for many electronic devices. These processes are the oxidation of a substrate as required for a subepitaxial diffusion followed by removal of the oxide and growth of the epitaxial layer.

Grown-in defects.—The defect distributions observed in this work will be seen below to be morphologically congruent to the growth inhomogeneities described in the introduction. In this work the defect pattern corresponding to spiral growth has been seen only in Dash-type crystals (10, 11). Such a "spiral-growth" type of defect distribution in a Dash crystal is seen in Fig. 1 which illustrates the structural etch pattern produced on the polished surface of a slice cut perpendicular to the growth direction. These "swirl patterns" are found on more careful examination to be spirals rather than concentric rings. They cannot be attributed to surface preparation since they penetrate the slice, as can be demonstrated by removing various thicknesses of the sample with a nonpreferential etch (12) followed by application of the structural etch (14). More complex swirl patterns are frequently observed, one of the more common being a double spiral as seen in Fig. 2. (This sample was oxidized to make the swirl pattern more visible, as explained below.)

Although the defect patterns seen in Fig. 1 and 2 appear similar to resistivity striations, the detailed structure is quite different as seen in Fig. 3. This shows the microstructure of the swirl pattern of Fig. 1 which is found to be composed of small, triangular, flat bot-

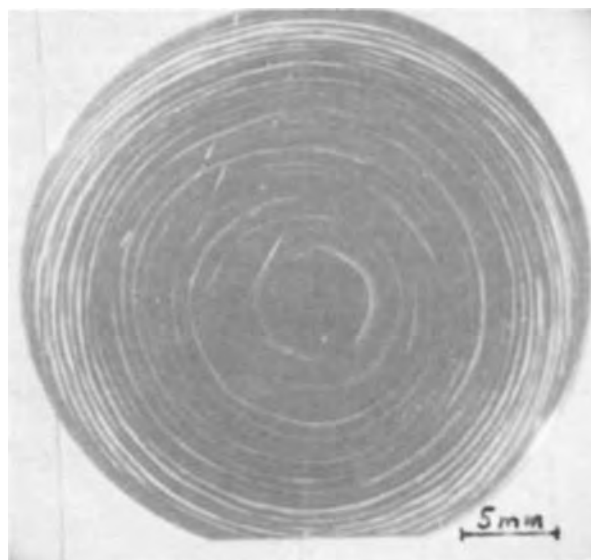


Fig. 1. Swirl pattern seen in low dislocation silicon crystal as grown

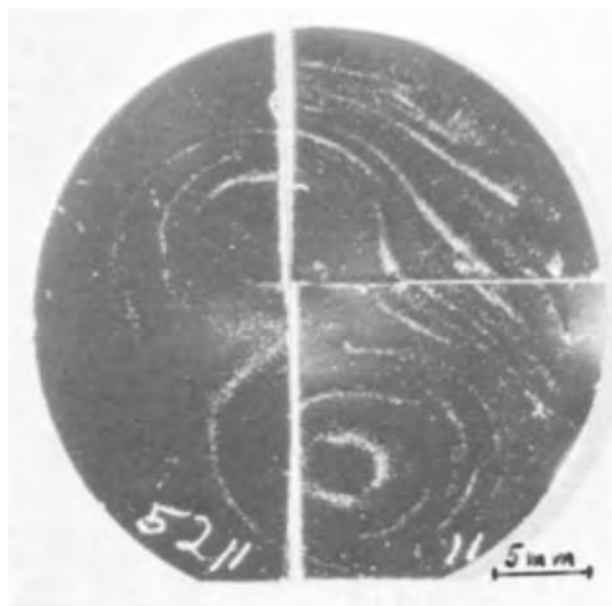


Fig. 2. Double swirl pattern in low dislocation silicon crystal after oxidation.

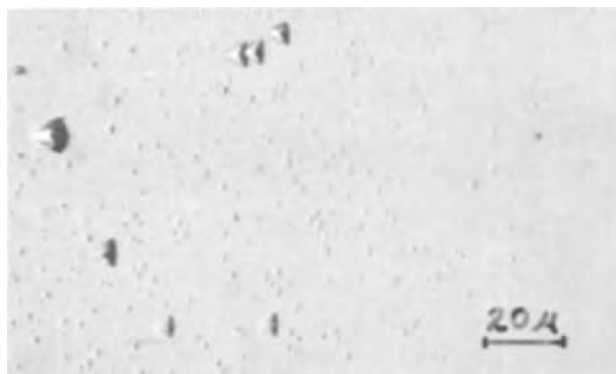


Fig. 3. Microstructure of the swirl pattern shown in Fig. 1 at the edge of a spiral band.

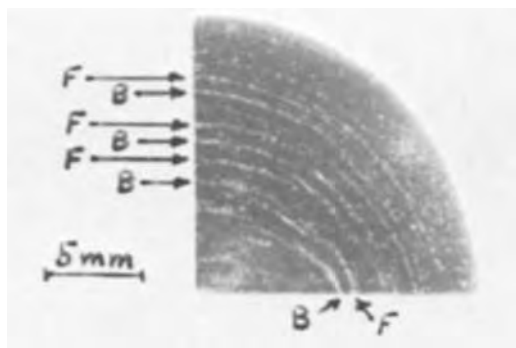


Fig. 4. A montage of the swirl pattern on the front (F) and back (B) surfaces of a slice illustrating the shape of the growth interface. Two mils removed from each side after oxidation by nonpreferential etch.

tomed pits mixed with a much lower density of larger pits having the same geometry. Both types of etch pit can vary considerably in density from crystal to crystal and at high densities the smaller pits merge to form an "orange peel" surface. Crystals from a number of commercial sources grown by the Dash method have been examined and all have shown this structure.

By comparing the spirals produced by etching the front and back surfaces of a slice it can be established that these patterns represent the intersection of the (111) faces of the slice with the spiral growth ramp surface described above. This is shown in Fig. 4 where photographs of the spiral pattern on the front and back surfaces are superimposed. From the spacing between the patterns on the front and back surface the contours of the growth interface can be determined. To enhance the visibility of the swirl pattern on this sample the slice was oxidized prior to structural etching as described below.

Corresponding to the observation of Wang (15) that growth cores are generally observed in crucible-grown crystals, this work has observed the corresponding core-type defect structure only in crystals of this type. The characteristic defect pattern in such a crystal is a core region consisting of a series of lamellar regions parallel to (111) planes with defect density alternating between high and low values in alternate lamellae.

When such a crystal is sliced more than a few degrees off the (111) plane these lamellar regions intersect the slice surface in a series of bands of alternating defect density. These bands are seen in Fig. 5 and the left-hand sample of Fig. 6. Both samples are oriented 4° from the (111) plane. The sample illustrated in Fig. 6 was etched nonpreferentially to a depth of 2 mils prior to the structural etch to eliminate the possibility that the observed structure was due to surface preparation of the slice. The apparent curvature of the core bands is due to slight curvature in the surface after the nonpreferential etch.

The straight core defect bands illustrated in Fig. 5 are characteristic of a flat polished surface. Although these are visible on the polished and etched surface of the as-grown slice, as in Fig. 6, this sample was oxidized prior to structural etching to improve contrast in the photograph.

A typical core-type defect pattern of a slice cut close to a (111) plane is shown in the left-hand sample of Fig. 7. The microstructure of as-grown core defects is similar to that found in growth spirals such as illustrated in Fig. 3.

Effects of oxidation.—Generally speaking all of the oxidation processes described above produce a coarsening of the defect structures observed in slices cut from the as-grown crystal; that is, the etched structures become larger and more distinct. However, the wet oxidation processes (steam or wet oxygen) gen-

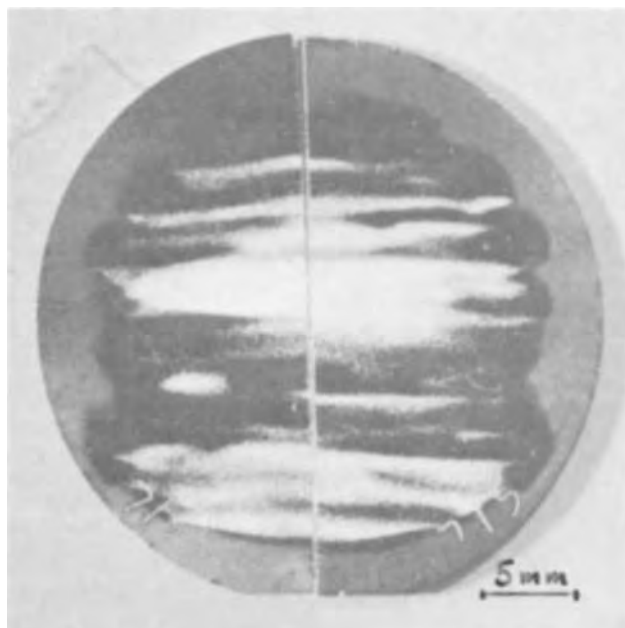


Fig. 5. The bands of structure in the center of this oxidized silicon slice are produced by a lamellar distribution of defects grown into the core of the crystal. The defects around the periphery occur at the oxide-silicon interface and are gettered by the core defects. Slice is from crucible-grown crystal cut 4° off (111) orientation with back surface etched nonpreferentially before oxidation.

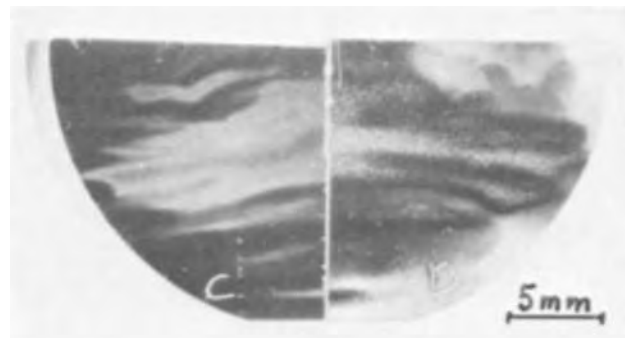


Fig. 6. Core band defects before oxidation (left) and after oxidation (right). Interfacial defects on the right-hand sample (bottom and upper right) are gettered from the surface in the clear areas around the oxidized core bands. Two mils removed from front and back of both samples by nonpreferential etch prior to treatment.

erally produce a much greater degree of coarsening than dry oxidation. This is true even when the oxides are grown to the same thickness.

The coarsening of the swirl microstructure after a 2 hr wet oxidation (procedure No. *i*) is illustrated in Fig. 8 and 9. Here it can readily be seen that the small pits present in as-grown crystals develop into large and distinct saucer pits after oxidation. This effect is not due to oxidation of the surface but penetrates through the slice as illustrated in Fig. 4 in which the sample after oxidation was etched nonpreferentially to a depth of 2 mils before structural etching.

When the as-grown crystal has a strongly developed swirl pattern, i.e., one where the pits are numerous and relatively well developed after structural etching, the microstructure produced after oxidation becomes more complex. In increasing order of complexity, the first stage results in increased size and definition of the saucer pits after structural etching. The second stage results in linear arrays of over-lapping saucer pits

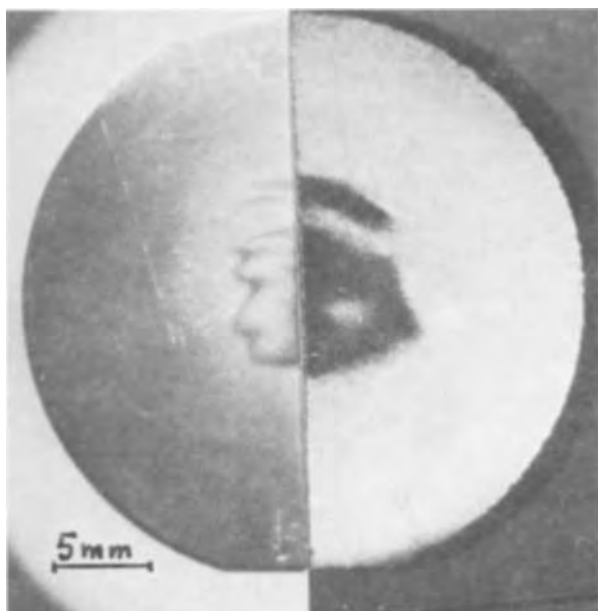


Fig. 7. Defect structure in a core cut close to a (111) plane; after oxidation (left) and core gettering effect on stacking faults in an epitaxial layer (right). Crucible-grown crystal with back surface etched nonpreferentially before oxidation.

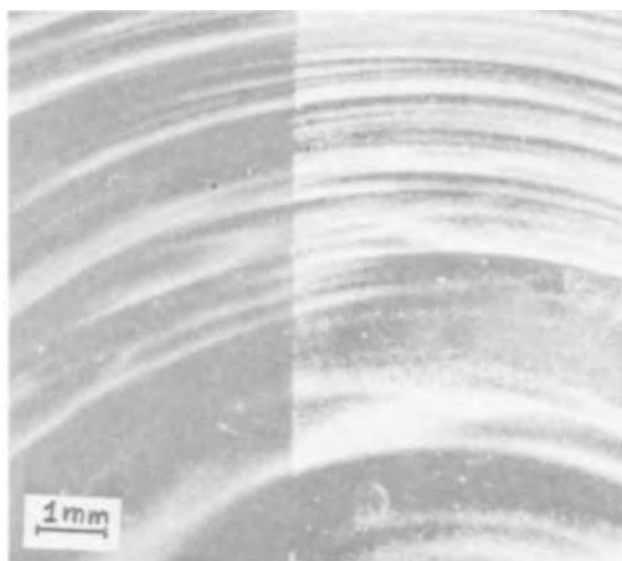


Fig. 8. Swirl structure after oxidation (right) is considerably coarser than before oxidation (left).

aligned in $\langle 112 \rangle$ directions. Finally, for very strongly developed swirl patterns in the as-received crystal, oxidation produces structures such as shown in Fig. 10. Here we see the $\langle 112 \rangle$ arrays of pits observed in the second stage producing deeply etched, structured grooves. At the same time a number of granular appearing linear structures aligned in the $\langle 110 \rangle$ direction appear. These $\langle 110 \rangle$ structures are much more superficial than those aligned in the $\langle 112 \rangle$ direction. The etch properties of these two types of arrays are evidently due to the fact that the $\langle 112 \rangle$ oriented structures are plate-like precipitates penetrating into the crystal whereas the $\langle 110 \rangle$ oriented figures are needle-like structures. The result is confirmed by sequential etching of the slice using alternating structural and nonstructural etchants.

The defects observed in crystal cores also exhibit a coarsening effect due to oxidation. The effect of oxida-

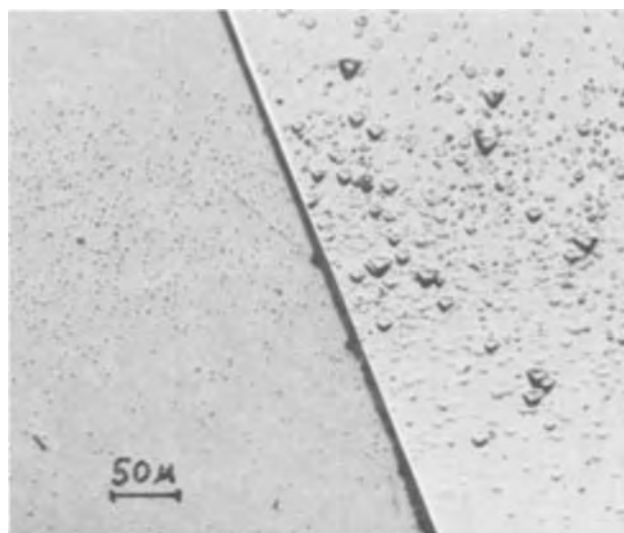


Fig. 9. Detail of Fig. 8 showing microstructure of swirl pattern before (left) and after oxidation (right).

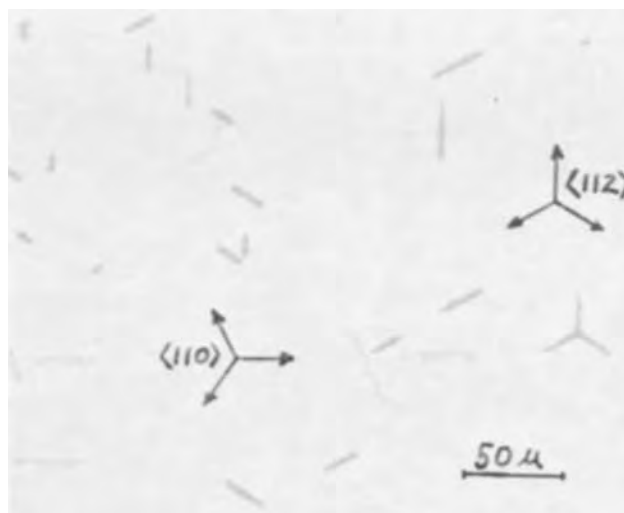


Fig. 10. Detail of a swirl pattern showing copper-like precipitates after oxidation.

tion on core defects is illustrated in Fig. 6. As with defects distributed in the form of growth spirals, this effect also penetrates the slice as seen in Fig. 11. In this figure the front and back surfaces of the sample are shown simultaneously, but offset so as to align corresponding band patterns. The core bands such as illustrated in Fig. 6 (left sample) produce a characteristic defect microstructure after oxidation. As illustrated in Fig. 12, short etching times produce an array of linear grooves oriented in the $\langle 110 \rangle$ directions. Further structural etching expands these grooves into trapezoids and finally into large triangular pits.

Considerable variation in the degree of coarsening of as-grown defect structure during oxidation is observed when different oxidation furnaces are used and when different oxidation boats are used. Variations are also observed due to differences in density of defect structure from crystal to crystal in the as-grown condition. A high degree of coarsening is frequently observed when the slices are oxidized in contact with specific "slab" type quartz boats while other boats of the same type produce lesser effects. These results are not altered by conventional techniques of cleaning or etching the quartz. Using a quartz slab which produces a high degree of coarsening, this effect can be

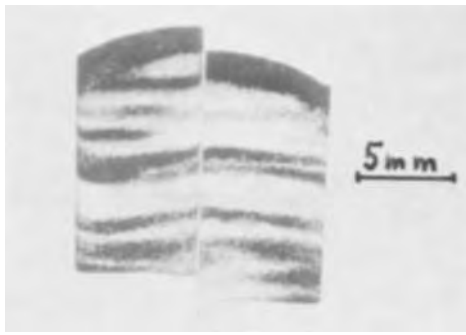


Fig. 11. The front (left) and back (right) surfaces of the same oxidized slice containing core band defects. The shift in core bands over the thickness of the slice is due to the slight misorientation of the slice surface from the (111) planes of the core lamellae. Two mils etch-polished from both sides after oxidation.

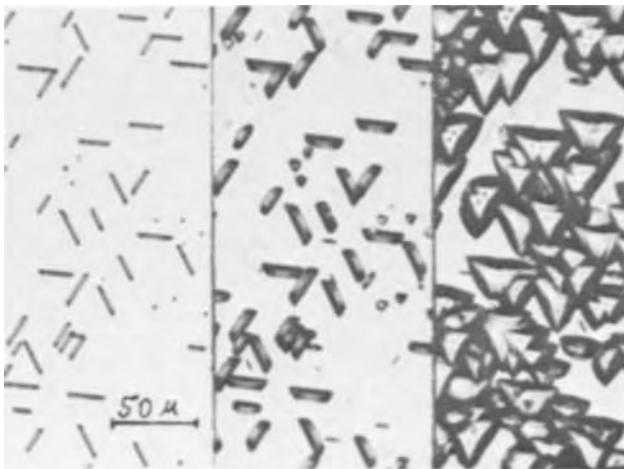


Fig. 12. The linear microstructures which develop in core bands after oxidation etch into triangles which penetrate the slice along (111) planes. Sirtl etched 1 min (left); 3 min (center); 8 min (right).

significantly reduced by inserting a dummy slice between the oxidized slice and the slab.

In contrast to the bulk defects described above, oxidation also introduces another type of defect which is largely confined to the region of the crystal near the oxide interface and will be referred to as an interfacial defect. The characteristic etch structure of these defects, like some of the bulk defects described above, is a shallow triangular "saucer" pit on (111) surfaces. The defects described in the previous work (13) were found to be of this type which was determined by the disappearance of these structures a few microns below the surface. [Analogous pits are not seen on (100) surfaces.] Unlike the bulk defects however, no evidence has been observed at or near the slice surface of any etch structures prior to oxidation which are precursors of interfacial defects.

It was speculated that the interfacial defect might be due to sodium, a prevalent contaminant and a rapid diffuser in the quartz tubes used for oxidation. To clarify this point some slices were oxidized by the methods described above except that the quartz boat or tube was contaminated with a drop of sodium nitrate solution. The result of such an experiment is shown in Fig. 13. To see the effect of the sodium more clearly the back surface of this slice was etched before oxidation to prevent gettering of the sodium (see below). The upper right-hand quarter which was oxidized in a sodium-contaminated tube clearly has a much higher density of defects than the upper left-hand quarter which was oxidized as control in an uncontaminated tube. As seen in Fig. 14 these sodium-

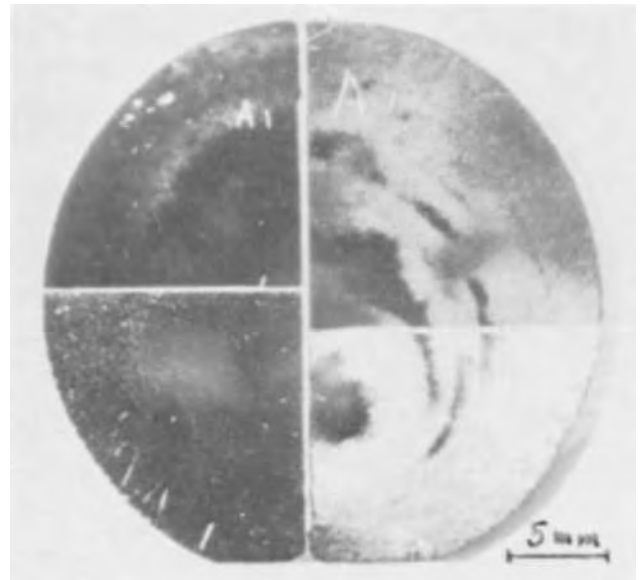


Fig. 13. The interfacial defects produced by sodium contamination during oxidation (upper right) nucleate stacking faults in a subsequent epitaxial layer (lower right). Both are gettered by underlying spiral defect pattern. The left half slice is a control sample similarly processed but oxidized in an uncontaminated furnace. Back surface nonpreferentially etched prior to oxidation.

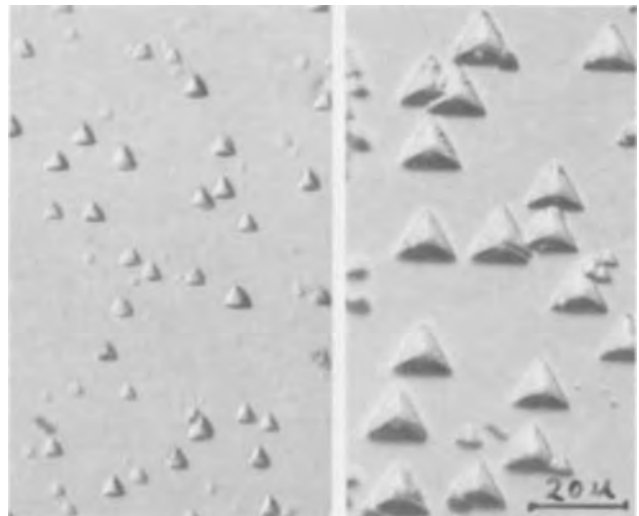


Fig. 14. The interfacial defects produced by sodium contamination during oxidation (left) and the stacking faults nucleated by such defects in an adjacent epitaxial layer (right). Detail from Fig. 13.

induced defects produce the characteristic saucer-shaped etch pit of an interfacial defect. The sodium-induced defects also occur quite close to the oxide interface; although for sufficiently contaminated samples they may penetrate to a depth of 5 to 10 μ . As will be seen they behave in other respects exactly like the saucer pits described above and in Ref. (13) which occur adventitiously during oxidation such as those seen in the upper left-hand sample of Fig. 13.

Like the interfacial saucer pits previously described, the sodium-induced defects produced during oxidation also have a strong orientation dependence. This is seen in Fig. 15 where a small, roughly hemispherical hole has been etched in the (111) surface prior to oxidation in a sodium-contaminated environment. Figure 15 is a scanning electron micrograph of such a

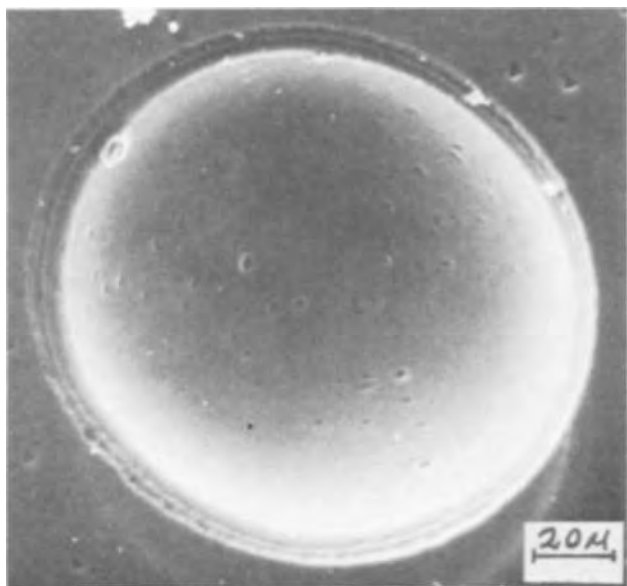


Fig. 15. Scanning electron micrograph of a hemispherical hole in a (111) silicon surface which has been oxidized in a sodium-contaminated environment. Sodium precipitates occur preferentially near the (111) surfaces of the hole.

hole after a structural etch. The sodium defects can be seen to cluster near the regions of the hole surface which are near the (111) orientation.

Gettering effect of bulk defects.—In this section it will be shown that the two types of defects described in the previous section, bulk and interfacial, interact in such a way during the oxidation process that the interfacial defects tend to disappear from regions of the interface which are closely approached by the bulk defect distribution. For reasons given below, this will be referred to as a gettering effect. The result is illustrated in Fig. 16 (upper segments). This slice was oxidized with the back surface etched nonpreferentially to remove saw damage. The left and right halves

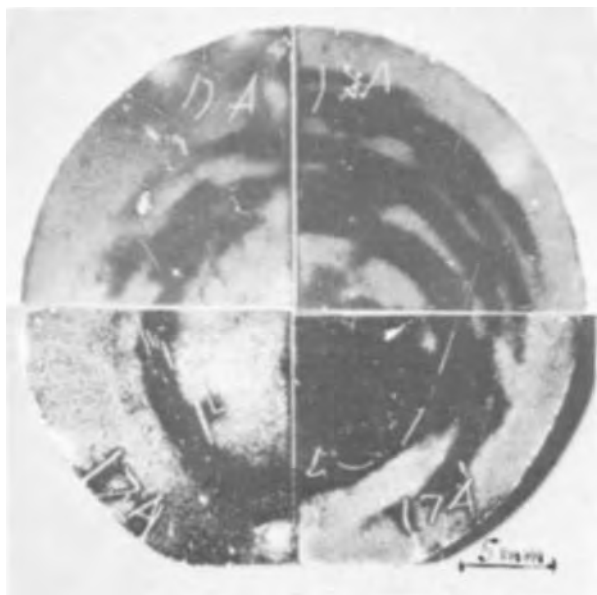


Fig. 16. The hazy rings in the upper segments are interfacial defects after oxidation which are gettered by the underlying swirl structure in the clear areas. The bottom segments show the stacking fault distribution produced by the interfacial defects in an epitaxial layer. Back surface nonpreferentially etched before oxidation.



Fig. 17. The interfacial defect structure of Fig. 16 (upper right segment) superimposed on the underlying swirl structure shown in Fig. 4.

were oxidized in two different furnaces but under the same conditions, namely 1200°C for 1 hr in dry oxygen. After removal of the oxide the upper two segments were structurally etched. The ring-like hazy regions, which in microstructure consist of densely packed saucer pits, are readily shown to be interfacial defects of the type described above, since they disappear if a few microns of the silicon surface are removed by a nonpreferential etch and the exposed surface is then re-etched structurally. The clear areas between these rings of structure have been gettered of interfacial defects by the underlying "spiral-growth" defect distribution. This is illustrated in Fig. 4 which depicts the upper right segment of Fig. 16 Sirtl-etched at a depth of 2 mils below the surface. The relationship between the bulk defect distribution of Fig. 4 and the surface defect distribution of Fig. 16 can be visualized by superimposing photographs of the two distributions as in Fig. 17. Here it can be seen that the swirl pattern is located close to the inner edge of the rings of interfacial defects. Interfacial defects produced by sodium contamination during oxidation are also gettered, as seen in Fig. 13, by grown-in bulk defects of the spiral distribution.

Gettering effects due to bulk defects are also observed in crystals having growth cores as seen in Fig. 5, 6, and 18. Figure 18 shows, in the top two quarters, the gettering of interfacial defects by subsurface core defects during oxidation. This slice was cut on the (111) plane and had a nonpreferentially etched back surface during oxidation. Figure 5 and the right-hand segment of Fig. 6 show the disappearance of interfacial defects during oxidation due to the gettering effect of core bands as observed when the slice is cut slightly off the (111) plane. In Fig. 5 the interfacial defect structure consists of a ring of saucer-shaped etch pits around the edge of the slice. This structure disappears due to gettering in the center of the slice inside a scalloped boundary which approximates the perimeter of the core band. A similar effect is seen in the right-hand segment of Fig. 6 where the interfacial defects appear in the lower and upper right areas.

Interfacial defects can be gettered by dislocations induced during oxidation as well as by defects grown into the crystal. One technique which was previously demonstrated to achieve this effect is to leave the back surface in a roughened condition during oxidation (13). The effect of this treatment can be seen by comparing the left-hand half slice shown in Fig. 19 with the slice shown in Fig. 5. The sample shown in Fig. 19 was oxidized with the back surface in a lapped condition while that shown in Fig. 5 was oxidized with the back surface etched nonpreferentially. The absence of interfacial defects around the perimeter of Fig. 19 is due to the gettering effect of the lapped back surface during oxidation. As can be seen in Fig. 19 this condition of the back surface during oxidation does not have any gettering effect on core-type defects. The

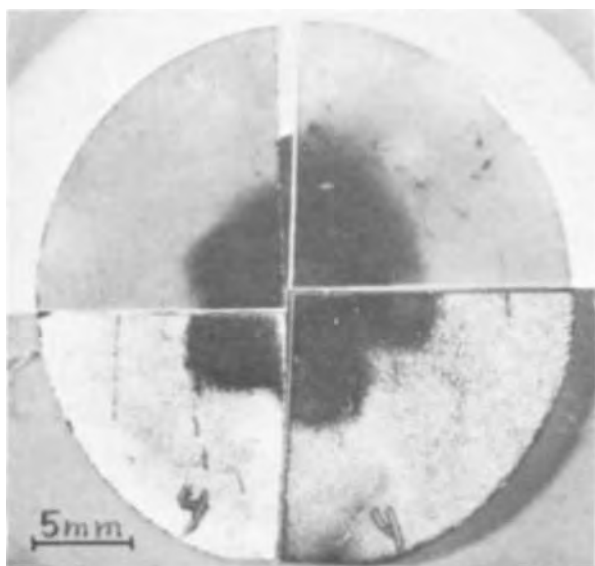


Fig. 18. Gettering of interfacial defects by a core after oxidation (upper segments) and the effect on stacking fault nucleation in a subsequent epitaxial layer (lower segments). Slice was cut on (111) plane and oxidized with a nonpreferentially etched back surface. Numerals on bottom segments scribed before oxidation.

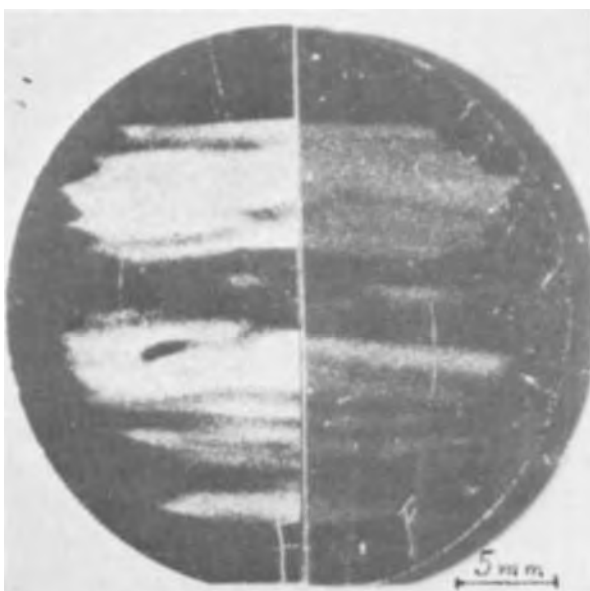


Fig. 19. The core defects (left) seen after oxidation nucleate bands of stacking faults (right) in a subsequent epitaxial layer. Back surface lapped before oxidation.

effect of process-induced dislocations is also illustrated in Fig. 20 and 21. In Fig. 20 the dislocations which propagate from the scribe mark during oxidation getter the interfacial defects around the rim of the slice. The same effect is seen in Fig. 21. This slice was oxidized with the central region in contact with a spacer on a quartz slab. The region with a high density of slip in the figure (bottom and left) overhung the spacer and slip is due to the thermal shock produced in this region when the slice was inserted into the oxidation furnace. The thermal shock of the central region was considerably less because it was in good thermal contact, through the silicon spacer, with the underlying quartz boat, a relatively large thermal mass. The hazy regions in this sample consist of interfacial precipitates and, especially at the boundary of the slipped region, one can clearly see the gettering

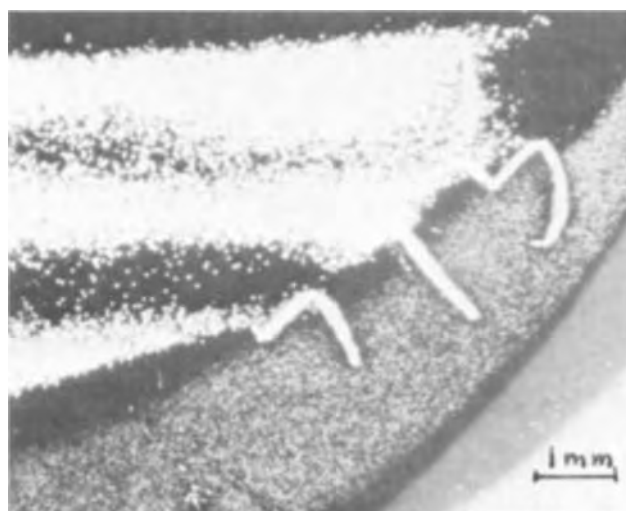


Fig. 20. A scribe mark produced before oxidation getters interfacial defects around the rim of this slice but not bulk defects occurring in the core region. Detail from Fig. 5.

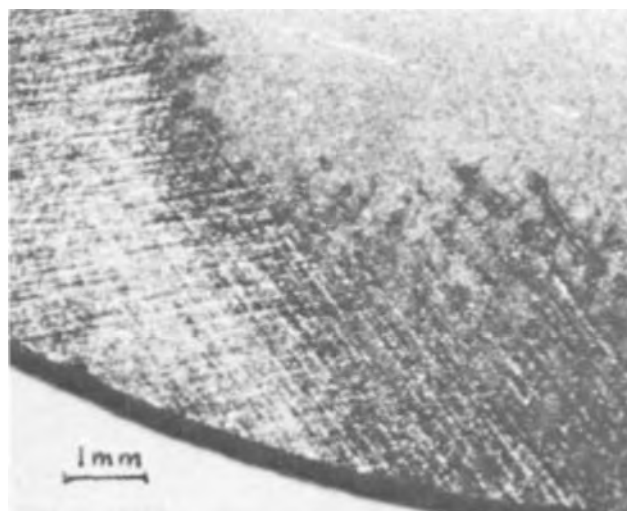


Fig. 21. The gettering of interfacial defects (upper right) by dislocation array (bottom and left) produced by thermal shock during oxidation.

effect of the dislocations introduced by thermal shock during oxidation. It can also be observed from Fig. 20 that the dislocations induced during oxidation do not produce any apparent gettering of the grown-in defects in the crystal core. In fact, it is observed that grown-in bulk defects in general are resistant to gettering by process-induced dislocations.

Nucleation of stacking faults.—Both interfacial defects, and bulk defects which intersect the oxidized surface, are found to nucleate stacking faults in epitaxial layers. Epitaxial growth conditions and the method of observing the stacking faults are given in the section on Experimental Procedure. Substrates from the same lots which had not been oxidized produced epitaxial layers with a uniformly low stacking fault density averaging less than $10/\text{cm}^2$.

The nucleating effects of interfacial defects are clearly seen in Fig. 16, 18, and the right-hand segments of Fig. 13. These slices were oxidized and after removal of the oxide the lower segments received an epitaxial deposit. In all three cases there is a clear-cut correlation between interfacial defects seen in the upper segments after oxidation and stacking faults nucleated in the epitaxial layer on the lower segments.

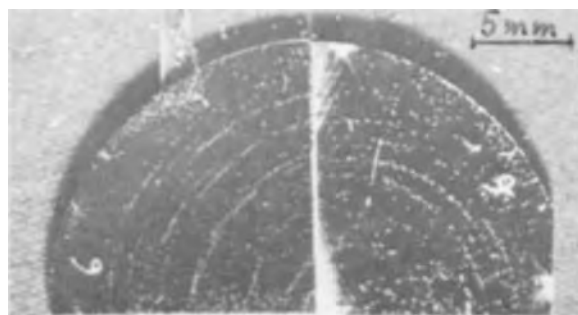


Fig. 22. The swirl pattern defects produced after oxidation (left) nucleate stacking faults (right) in a subsequent epitaxial layer. Back surface lapped before oxidation.

In the case of Fig. 13 the stacking fault density is extremely high due to deliberate sodium contamination. Figures 13, 16, and 18 also illustrate the effect of gettering on stacking fault nucleation. The underlying spiral defect pattern in Fig. 13 and 16 has gettering ring-like regions of the surface which are relatively free of interfacial defects and therefore have a much reduced stacking fault density. In Fig. 18 the same effect is seen in the core region. (Note also in Fig. 18 the gettering effect on stacking faults of the numerals, scribed before oxidation.)

To observe the nucleation of stacking faults by bulk defects it is generally necessary to suppress nucleation by interfacial defects. This can usually be done by oxidation of the slice with the back surface in a lapped or sawed condition. As mentioned above such a procedure has the effect of eliminating interfacial defects, but does not have any observable gettering effect on bulk defects. The result is illustrated in Fig. 22. Both segments of this slice were oxidized together for 2 hr in wet oxygen with back surfaces lapped. After oxide removal the right segment then received an epitaxial deposit subsequent to oxidation. The stacking fault distribution in this sample is seen to correlate closely with the distribution of defects in the core bands.

The linear type of defect found in core bands, as illustrated in Fig. 12, invariably produces a very high percentage of linear stacking faults in epitaxial overgrowths as opposed to the triangular stacking faults nucleated by saucer defects such as seen in Fig. 14. Such linear stacking faults are illustrated in Fig. 24. It can also be seen from this figure that the linear faults are equal in length or shorter than a side of a triangular fault. There are also many dislocation pairs separated by distances of this order. In many cases the stacking faults nucleated by linear-type core defects disappear entirely leaving only the dislocation pairs, as seen in Fig. 25.

As described above the incidence of interfacial defects on (100) surfaces after oxidation is much less common than on (111) surfaces. This was illustrated for sodium-induced defects in Fig. 15. The nucleation of stacking faults on oxidized (100) surfaces is similarly rare. Figure 26 illustrates the orientation de-

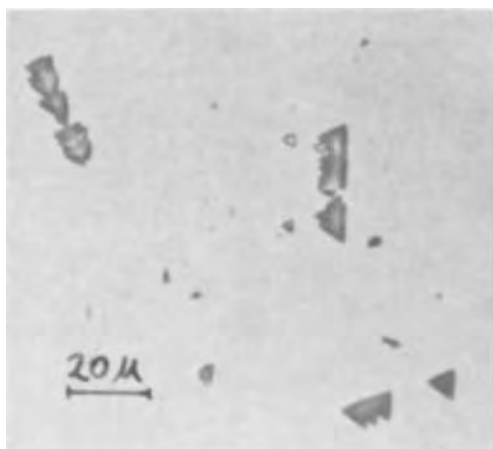


Fig. 23. These oriented lines of stacking faults are nucleated in epitaxial layers grown over substrates containing linear defects such as shown in Fig. 10.

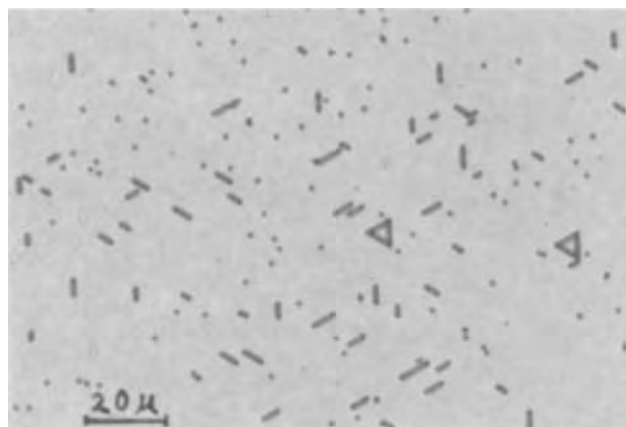


Fig. 24. Microstructure of the epitaxial layer from Fig. 19 (right) showing high density of linear stacking faults produced by core defects of the type shown in Fig. 12.

cleated by core defects unless those nucleated by interfacial defects are suppressed by gettering. An example is seen in Fig. 19 which shows a slice gettered during oxidation by means of a lapped back surface. As seen in the left-hand sample the gettering effect of the back surface does not prevent development of core defects during oxidation. (The same result as for swirl defects seen in Fig. 22.) The right-hand half of the sample shown in Fig. 19 received an epitaxial deposit subsequent to oxidation. The stacking fault distribution in this sample is seen to correlate closely with the distribution of defects in the core bands.

The linear type of defect found in core bands, as illustrated in Fig. 12, invariably produces a very high percentage of linear stacking faults in epitaxial overgrowths as opposed to the triangular stacking faults nucleated by saucer defects such as seen in Fig. 14. Such linear stacking faults are illustrated in Fig. 24. It can also be seen from this figure that the linear faults are equal in length or shorter than a side of a triangular fault. There are also many dislocation pairs separated by distances of this order. In many cases the stacking faults nucleated by linear-type core defects disappear entirely leaving only the dislocation pairs, as seen in Fig. 25.

As described above the incidence of interfacial defects on (100) surfaces after oxidation is much less common than on (111) surfaces. This was illustrated for sodium-induced defects in Fig. 15. The nucleation of stacking faults on oxidized (100) surfaces is similarly rare. Figure 26 illustrates the orientation de-

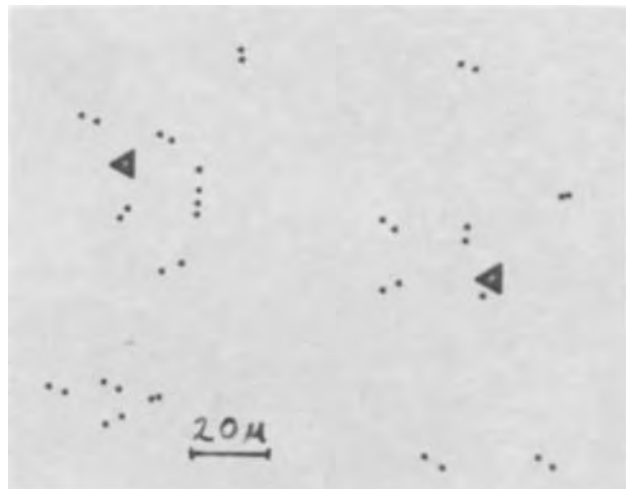


Fig. 25. Dislocation pairs seen in epitaxial layers grown over banded core defects appear to be annealed linear stacking faults.

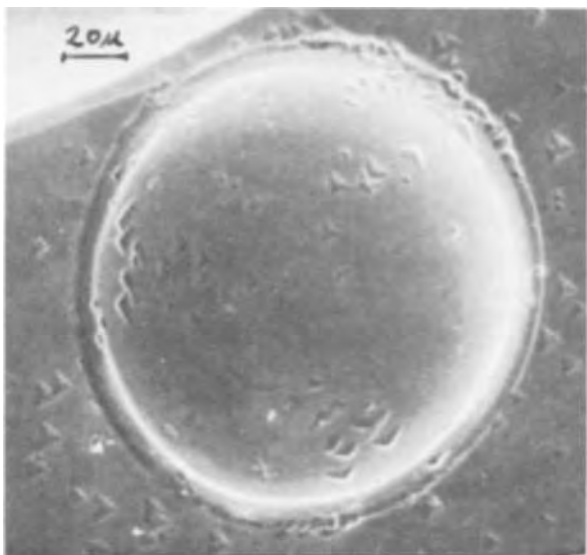


Fig. 26. Scanning electron micrograph of the stacking fault distribution in an epitaxial layer grown in a hemispherical hole on a (111) surface. The surface of the hole was previously oxidized in a sodium-contaminated environment as in Fig. 15.

pendence of stacking fault nucleation in a hemispherical hole previously oxidized in a sodium contaminated environment similarly to the sample shown in Fig. 15. Again, it can be seen that stacking faults nucleate preferentially close to the points of tangency of (111) planes with the hemispherical surface on which the epitaxial layer was deposited.

Interpretation of Results

The defect distributions described above which are observed in as-grown crystals have a striking similarity to the resistivity striations previously described (1-5). This suggests a common origin, namely, growth rate fluctuations. The spiral ramp type of growth inhomogeneity which is congruent with the "swirl"-type defect structures illustrated in Fig. 1 and 4 has been explained as due to a temperature fluctuation of one cycle per rotation of the crystal (1-3). This is produced when the temperature distribution around the circumference of the growth interface has one maximum and one minimum. The double spiral pattern seen in Fig. 2 where both spirals have the same rotational sense can be explained by a temperature distribution with two maxima separated by two minima around the circumference of the growth interface, thus producing two cycles of temperature fluctuation per crystal rotation.

Figures 5, 6, 11, and 19 show that the core defect distributions observed in this work are congruent with the faceted growth inhomogeneities previously reported (4,5); that is, the defects appear in a series of lamellae of alternating defect density which are parallel to (111) planes and located within the core region of the crystal. If the slice cut from the crystal is slightly misoriented from the $\langle 111 \rangle$ direction, this results in a series of bands of alternating defect density on the surface of the slice. The shift in the position of these bands from the front to the back surface of the slice as in Fig. 11 can, in fact, be used to estimate the misorientation of the slice surface which is equal (in radians) to the shift in position of the striations divided by the sample thickness. In the case of the sample of Fig. 11, the result is about 4° from the $\langle 111 \rangle$ direction toward the $\langle 110 \rangle$ direction.

The result of oxidation on the microstructure of grown-in defects implies that the coarsening of as-grown defect structure during oxidation is due to the decoration of the defects by impurities introduced in the oxidation process. The fact that the coarsening

effects penetrate the slice indicates that these impurities have high diffusion constants in silicon similar to copper, nickel, iron, manganese, or cobalt. The fact that many of these impurities also diffuse rapidly in quartz at the oxidation temperature probably explains the result obtained with quartz slabs as oxidation boats. It is probable that some degree of contamination also comes from diffusion of such impurities through the wall of the quartz furnace tube. In fact, it appears that the presence of contaminants from this class of impurities cannot be completely eliminated from conventional oxidation systems in spite of precautions taken to purify and clean the components of the system. If grown-in defects are present in the crystal, it is probable that these contaminants will precipitate on such defects.

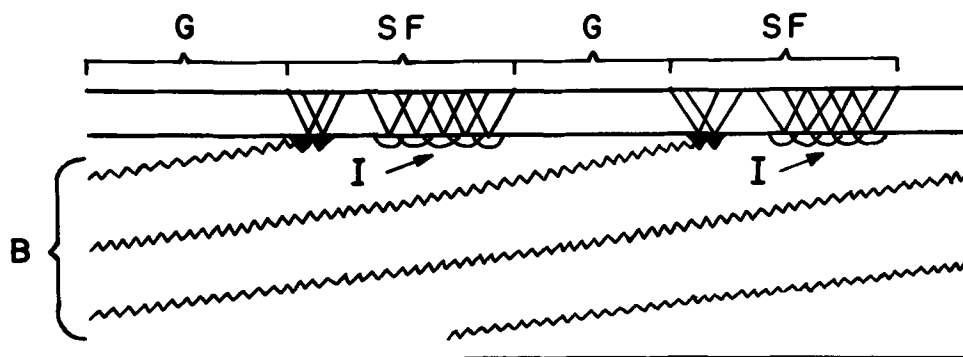
The bulk defects exhibited by oxidized swirl pattern (Fig. 10) have a form which is very close to the copper precipitates observed by Schwutke (6) in the form of needles oriented in the $\langle 100 \rangle$ direction and platelets which bisect the angles made by the needles when observed in the $\langle 111 \rangle$ direction.

The properties of linear defects produced in core bands (Fig. 12) could be explained if these defects existed in the form of triangular plates lying in (111) planes perpendicular to the growth direction. In a slice cut slightly off the (111) orientation only one edge of such a platelet could lie in the plane of the sample and would be the first to etch. On deeper etching the whole platelet would be delineated as in Fig. 12. This mode of etching suggests that these defects are very similar to the stacking faults reported by a number of workers (16-21) to be produced when surfaces damaged by abrasion or vacuum annealing are oxidized. The difference is that the faults observed in this work penetrate the crystal so that their appearance is not due to oxidation as such, but rather to the accompanying processes of annealing and/or the precipitation of fast diffusing impurities. A similar generation of bulk stacking faults is reported by de Kock (9). Thomas (17) and Lawrence (18) showed that linear defects of the type seen in core striations also nucleate the precipitation of copper.

The above results do not throw much light on the nature of the grown-in defects prior to oxidation. It is therefore not possible to decide whether these defects might be produced by oxygen as shown by Schwutke (16) or by vacancies as proposed by Dash (11), Plaskett (8), and de Kock (9). However, the resemblance to copper-like structures after oxidation suggests a third possibility, namely, that these bulk defects are initially due to copper, which combines a very low equilibrium segregation constant with a very low solid solubility. Because of its small segregation coefficient, fluctuations in growth rate will produce large changes in effective segregation coefficient and therefore large fluctuations in the amount of copper incorporated into the growing crystal. Because of its low and strongly temperature dependent solubility, the copper may be expected to precipitate out readily during cooling from the growth temperature. This idea is supported by the observation that bulk defects tend to be most prominent in crystals grown at high rates.

The interfacial defects described in this work which occur adventitiously during oxidation and those which are introduced deliberately during oxidation, by contamination with sodium, can be identified with the "saucer" defects described in Ref. (13) which produced the same etch structures. This is to say both nucleate stacking faults (see Fig. 13, 16, and 18) and are gettered both by dislocations (see Fig. 21) as well as by regions of surface damage (see Fig. 20 and 22). In addition to these previously described properties of interfacial defects this work has found that they are located within a few microns of the oxidized interface. Unlike the bulk defects described above, however, no evidence has been observed at or near the slice surface of any structures prior to oxidation which are precursors of interfacial defects. That is to say, the inter-

Fig. 27. Cross section through a slice explaining the relationship between bulk and interfacial defect structures seen in Fig. 17. The gettering effect, G, of the bulk defect distribution, B, is most pronounced where the bulk defect distribution approaches the surface of the slice. Both interfacial defects, I, and the bulk defect distribution, where it intersects the surface of the slice, nucleate stacking faults, SF.



facial defect is not due to the heterogeneous nucleation of impurities precipitating on a pre-existing site but rather the homogeneous nucleation of precipitates at the oxidized interface. Another property of interfacial defects which has been demonstrated here is that they are gettered by bulk defects of both the core and spiral patterns. Examples of core gettering are Fig. 5 and the upper segments of Fig. 18. Examples of spiral gettering are the upper segments of Fig. 16.

The variable density of interfacial defects can be explained by the variable gettering due to bulk defects such as those described above. This is understood with reference to Fig. 27 which diagrammatically shows a cross section of a slice such as the one shown in Fig. 4, 16, and 17. The spiral growth pattern is shown as concave toward the upper surface of the slice (as demonstrated in Fig. 4). The result is a periodic variation of spacing between this gettering sink and the surface, the separation being a maximum just at the outside edge of the swirl pattern and a minimum at the inside edge of the swirl pattern. This explains why the gettering effect of the spiral growth surface is greatest inside the swirl contour and least outside the swirl contour as seen in Fig. 17.

The difference between the left and right halves of the slice shown in Fig. 16 is believed to be due to the fact that the furnace used for oxidizing the left half was somewhat more contaminated so that more of the subsurface gettering structure was saturated with impurities during oxidation. In general, it has been found that in the absence of a gettering surface on the back of the slice during oxidation, considerable variations of this type exist. In fact, it is difficult with a tube-type oxidation furnace to maintain a (111) surface free of interfacial precipitates in the absence of some type of gettering sink.

The observations of the sodium-like species responsible for interfacial defects may be explained as follows. If the quantity of sodium contamination is small and the back surface of the slice is lapped or otherwise damaged prior to oxidation, the sodium will be quantitatively removed by this gettering sink. If the quantity of sodium present is large enough to saturate this gettering sink or to saturate the crystal in the absence of such a sink at the oxidation temperature, then, as the crystal is cooled down after oxidation, the sodium will be forced to precipitate either in the bulk or at the surface of the crystal. Since the diffusion constant of sodium is very high (22) it can freely move to either bulk or surface sites. Which site the sodium reaches will depend both on its proximity and affinity for the site. Where the bulk defect distribution approaches closely to the surface it getters sodium from the surface, indicating that it has a greater affinity for this species. Where the bulk defect distribution is further away from the surface, some sodium will precipitate at the oxide interface because of its closer proximity, in spite of the fact that this site has a smaller affinity for sodium.

As illustrated in Fig. 27 it has been shown that epitaxial stacking faults are nucleated both by interfacial defects and also by bulk defects where they intersect

the surface of an oxidized slice. In regions where bulk defects below the surface getter interfacial nuclei (e.g., Fig. 16 and 18) the stacking faults also disappear in the overlying epitaxial layer. The stacking faults produced by interfacial defects may also be eliminated if the back surface is left in a lapped or otherwise damaged condition during oxidation. This is probably due to the network of dislocations introduced by such a treatment and is similar to the gettering effect of dislocations seen in Fig. 21. Such a treatment does not however prevent the formation of stacking faults due to bulk defects (*viz.*, Fig. 19 and 22). These can only be eliminated either by preventing the formation of defects during crystal growth or by eliminating the impurities which precipitate on such defects in processing.

The linear stacking faults (Fig. 24) produced by core band defects seem to have a tendency to anneal out of the slice during epitaxial growth leaving as residue a shallow dislocation loop such as shown in Fig. 25.

The observation that stacking faults are relatively rare in epitaxial layers grown on previously oxidized (100) substrates compared with (111) substrates can be interpreted in the light of Fig. 15 and 26. It appears that this result is due to the strong tendency of interfacial precipitates to prefer (111) surfaces.

Conclusions

In summary, a relationship has been established between two types of defects in single-crystal silicon and two types of impurities which have properties similar to sodium and copper. The following properties of the defects have been demonstrated.

Properties of bulk defects:

1. They are present in the crystal, as grown, and distributed congruently with growth rate inhomogeneities either of the spiral or of the core (faceted) type.
2. They produce etch structures after oxidation which are similar to copper precipitates. The formation of these structures is not inhibited by known copper gettering centers such as dislocations or regions of surface damage.
3. Where close to the surface, they act as gettering sites during oxidation for the species responsible for interfacial defects and thus inhibit the nucleation of stacking faults by such defects in epitaxial layers.
4. Where they intersect an oxidized surface, they nucleate stacking faults in epitaxial layers. In particular linear defects nucleate linear stacking faults which tend to anneal out of the epitaxial layer.

Properties of interfacial defects:

1. They occur after oxidation at or near the oxide-silicon interface with a strong preference for (111) surfaces.
2. They are not correlated with observable surface structures prior to oxidation.
3. They are greatly enhanced by deliberate sodium contamination during oxidation.

4. They are gettered during oxidation by damaged regions of the crystal, by dislocations, and by bulk defects while lie close to the oxide interface.

5. They nucleate stacking faults in epitaxial layers.

Manuscript submitted June 12, 1970; revised manuscript received ca. Oct. 25, 1971. This was Paper 98 presented at the Los Angeles Meeting of the Society, May 10-15, 1970.

Any discussion of this paper will appear in a Discussion Section to be published in the December 1972 JOURNAL.

REFERENCES

1. J. R. Carruthers and K. E. Bensen, *Appl. Phys. Letters*, **3**, 100 (1963).
2. D. A. Petrov and A. A. Bukhanova, *Sov. Phys. Cryst.*, **7**, 349 (1962).
3. B. M. Turovskii and M. G. Mil'vidskii, *Sov. Phys.-Solid State*, **3**, 1834 (1962).
4. "Semiconductor Silicon," R. R. Haberecht and E. L. Kern, Editors, pp. 97, 146, 156, The Electrochemical Society Softbound Symposium Series (1969).
5. W. D. Edwards, *Can. J. Phys.*, **38**, 439 (1960).
6. G. H. Schwuttke, *This Journal*, **108**, 163 (1961).
7. W. Kaiser and P. H. Keck, *J. Appl. Phys.*, **28**, 882 (1957).
8. T. S. Plaskett, *Trans. Met. Soc. AIME*, **233**, 809 (1965).
9. A. J. R. de Kock, *Appl. Phys. Letters*, **16**, 100 (1970).
10. W. C. Dash, *J. Appl. Phys.*, **29**, 736 (1958).
11. W. C. Dash, *ibid.*, **30**, 459 (1959).
12. J. E. Lawrence and H. Koehler, *J. Sci. Instr.*, **42**, 270 (1965).
13. D. Pomerantz, *J. Appl. Phys.*, **35**, 695 (1964).
14. E. Sirtl and A. Adler, *Z. Metallk.*, **52**, 529 (1961).
15. Pei Wang, Private communication.
16. M. L. Joshi, *Acta Met.*, **14**, 1157 (1966).
17. D. J. D. Thomas, *Phys. Status Solidi*, **3**, 2261 (1963).
18. J. E. Lawrence, *Trans. Met. Soc. AIME*, **242**, 484 (1968).
19. A. W. Fisher and J. A. Amick, *This Journal*, **113**, 1055 (1966).
20. G. R. Booker and R. Stickler, *Phil. Mag.*, **11**, 1303 (1965).
21. H. J. Queisser and P. G. G. Van Loon, *J. Appl. Phys.*, **35**, 3066 (1964).
22. L. Svob, *Solid-State Electron.*, **10**, 991 (1967).

Oxygen Transport and Charge Storage in Calcium Orthovanadate

M. Sayer and H. Erdogan

Department of Physics, Queen's University, Kingston, Ontario, Canada

and C. D. Cox

Communications Research Centre, Shirley Bay, Ottawa, Ontario, Canada

ABSTRACT

Electrolytic effects, crystal coloration, and charge storage observed when an electric field is applied to single crystals of calcium orthovanadate at temperatures above 700°C are shown to be associated with oxygen migration and the creation of V⁴⁺ centers in the crystal. The oxygen transport number is shown to be constant at 0.9 over the temperature range 650°-900°C with an activation energy for predominantly ionic conduction of 1.05 ± 0.05 eV. The amount of recoverable charge stored in the crystal depends on the sample used and also on the charging current, but is about 15% for an average crystal with a charging current density of several milliamperes/square centimeter. The open-circuit voltage is of the order of several volts. Deterioration of the bulk material during electrolysis and barrier effects appear to be the major limitation on the use of the material as a charge storage medium.

Calcium orthovanadate has been grown as a single crystal and investigated for use as a laser host material (1, 2). Crystals grown from melts having stoichiometric proportions and in an atmosphere of excess oxygen are yellow in color, while growth in an atmosphere deficient in oxygen results in a strong black coloration. It has been found that a similar black coloration can be electrolytically induced into crystals of calcium orthovanadate by the application of an electric field at temperatures above about 700°C (3). On removal of the applied field, colored crystals are found to contain an excess charge which can be released by short-circuiting the crystal through an external circuit. This suggests applications such as current integrating devices.

Electrolytic coloration is well known in the alkali halides (4) and normally requires the migration of an ionic species (and/or its associated vacancy) with the injection and capture of electrons at an appropriate site in the crystal lattice. The main feature of the orthovanadate is the high current density achieved (10⁻³ A/cm² at tens of volts/centimeter) compared with the alkali halides where 10⁻⁸ A/cm² at hundreds of volts/centimeter is more usual. In the alkali halides,

the characteristic optical and electrical properties arise from electrons captured at halide ion vacancies to form F⁻centers. In calcium orthovanadate, Ca₃(VO₄)₂, the migrating ionic species is likely to be oxygen, while an optical absorption which causes a black coloration is known in other vanadium compounds to be due to V⁴⁺ ions (5). In this paper we report experiments which confirm these suggestions and describe an investigation of the charge storage process.

Experimental

Measurements of the oxygen transport number and of electrical conduction were undertaken in the apparatus shown in Fig. 1. The crystal was held between two ceramic tubes by spring pressure with a concentric pair of smaller diameter tubes allowing gases to be circulated near the crystal face. The central tubes also carried platinum wires which made contact to platinum electrodes evaporated on to the surface of the crystal. The crystal and electrode system were mounted within a small muffle furnace and a side window was used to view the crystal during the experiment. The furnace temperature was measured and controlled by means of an internal thermocouple and the gas flow rate and composition were regulated by an external gas mixing system. The crystals were Czochralski-grown and were prepared by cutting with a wire saw

Key words: solid-state electrolysis, ionic conductivity, charge storage, oxygen transport, calcium orthovanadate, and electrolytic coloration.

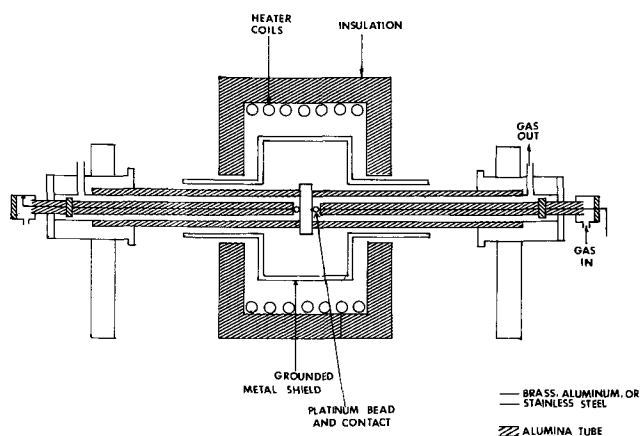


Fig. 1. High-temperature apparatus for conductivity and oxygen transport measurements.

and by subsequent mechanical polishing. A Keithley 610B electrometer having an input impedance of 10^{14} ohms was used to measure open-circuit voltages or emf's, while current was measured by a potentiometric recorder connected across a 100 ohm resistance placed in series with the crystal.

Results

Oxygen Transport

The theory and practice of transport number measurements have been discussed by Mitoff (6). If the partial pressure of a gaseous ion which is involved in transport within a membrane is p_1 and p_2 on either side of the membrane, respectively, an emf is developed across the membrane given by

$$E_{\text{theor}} = \frac{2.3 RT}{4F} \log \frac{p_1}{p_2} \quad [1]$$

where R is the gas constant, F is the Faraday constant, and T is the absolute temperature. However, if conduction within the membrane occurs also by the movement of other ions or by electrons, the observed emf, E_{exp} , is less than that calculated from Eq. [1] and the transport number t_i is defined by

$$t_i = \frac{E_{\text{exp}}}{E_{\text{theor}}} = \frac{\sigma_i}{\sigma_{\text{total}}} \quad [2]$$

The emf measured as a function of temperature between evaporated platinum contacts of an area much less than that exposed to the gas is shown in Fig. 2 for the case of pure oxygen ($p_1 = 1$ atm) maintained at one surface and air ($p_2 \sim 0.2$ atm) maintained at the other. Results for activated zirconia are also shown since it is known (7) that the transport number for this material is very close to unity and this fact was used as a form of calibration for the apparatus. The transport number calculated for calcium orthovanadate is shown as a function of temperature in Fig. 3. The transport number is constant at 0.9 over the temperature range from 650° to 900°C and the conduction process in as-grown crystals is therefore predominantly due to oxygen ion migration.

Measurements were also made of the conductivity of the crystals as a function of temperature, using either a constant current of less than 10^{-8} A/cm² or a small a-c voltage in an attempt to avoid polarization effects. In both cases the conductivity was found to be thermally activated with an activation energy of 1.05 ± 0.05 eV. The magnitude of the d-c conductivity for nearly stoichiometric crystals under these conditions was of the order of 10^{-8} (ohm-cm)⁻¹ at $T = 800^\circ\text{K}$. The conductivity was larger for crystals grown in an atmosphere deficient in oxygen, although such crystals

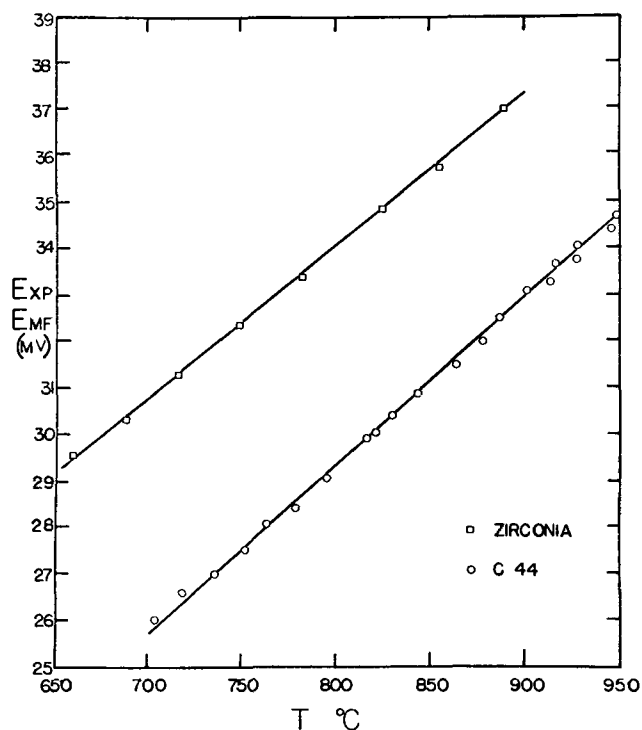


Fig. 2. EMF due to oxygen transport as a function of temperature. Air and oxygen on each side of the crystal, respectively. Measurements shown for a yellow crystal of calcium orthovanadate and for a slab of activated zirconia.

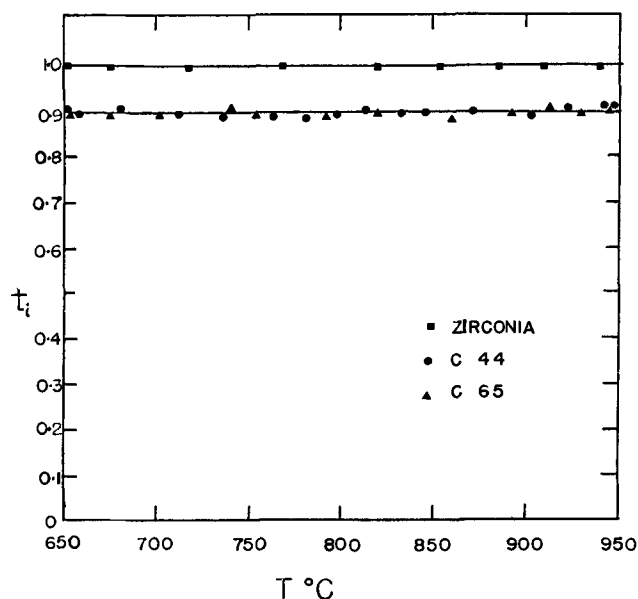


Fig. 3. Transport number of calcium orthovanadate as a function of temperature. Transport number for activated zirconia taken to be unity at 700°C.

were not colored as strongly as those colored electrically. The activation energy for conduction was similar for as-grown crystals of both yellow and black color.

Charge Storage

General.—Crystals were cut in the form of flat slabs 1-2 mm in thickness and 0.5 to 1.0 cm² in area. Platinum contacts were evaporated to completely cover the slab faces and the crystals were then mounted within the furnace. When the crystal was heated above 700°C and a voltage applied corresponding to a field of the order of 30-40 V/cm a black coloration was observed

to enter the crystal from the negative electrode and sweep across the crystal. The magnitude of the threshold voltage was not particularly reproducible suggesting that electrode conditions were of importance. On the assumption that the color was due to the injection and migration of electrons, an effective carrier mobility and concentration could be computed from the transit time for the color and from the calculated conductivity. This assumes a uniform field distribution within the crystal which is probably unwarranted and the calculation can only be regarded as providing an order of magnitude for the quantities. The values obtained for the effective mobility and carrier concentration at 730°C were $1 \times 10^{-4} \text{ cm}^2/\text{V-sec}$ and $3 \times 10^{19} \text{ cm}^{-3}$, respectively. Removal of the external field showed that the blackened crystal retained a potential difference between the electrodes of several volts with a polarity the same as that of the applied voltage. Short-circuiting the electrodes produced a current in the external circuit which decayed with time accompanied by the movement of the black color back toward the negative electrode.

Current and voltage as a function of time.—The crystal current and open-circuit voltage measured as a function of time are shown in Fig. 4. For voltages below 30 V/cm , no color could be observed to enter the crystal and the current decreased with time from an initial value indicating effects due to polarization. At higher voltages, carrier injection was observed and the current in the crystal increased monotonically. The open-circuit voltage measured on removal of the external voltage was found to increase with applied voltage, although no simple relationship could be deduced. The variation of open-circuit voltage with the charging time for fixed applied voltage was also complex as shown in Fig. 5. The longer charging times produced a smaller initial open-circuit voltage, but the time dependence was less pronounced. A similar effect has been observed in polyethylene (8).

Short-circuiting the electrodes caused a discharge current to flow in the external circuit. The discharge current time constant was longer than that for the charging process and integration of the charging and discharging current over time indicated that for an average crystal about 15% of the charge was recoverable. It may be noted that in a previous set of experiments (3) a larger recovery rate was obtained (up to 80%), particularly in crystals grown from a stoichiometric melt. These experiments were carried out with

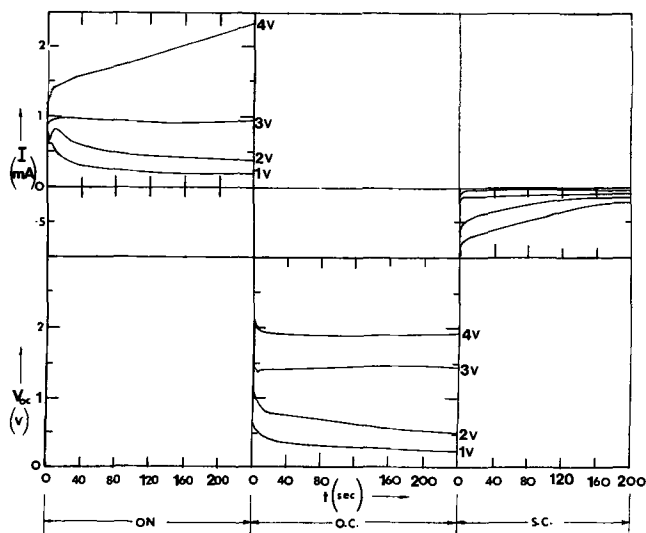


Fig. 4. Time dependence of current (upper) and open-circuit voltage (lower) for a cycle, i.e., applied voltage on, open circuit, short circuit. Voltages marked on diagram are those applied from the external voltage source. Crystal thickness 1.07 mm.

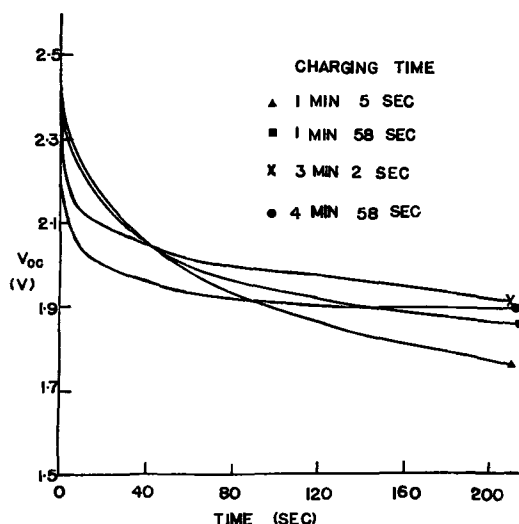


Fig. 5. Variation of open-circuit voltage with time for an applied voltage of 4V across a 1 mm thick crystal for successively increasing charging times. The crystal was discharged between each cycle.

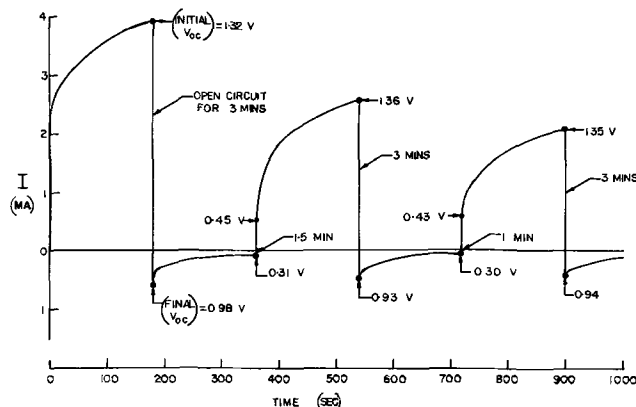


Fig. 6. Successive charging and discharging current cycles for a fixed applied voltage of 4V across 1 mm thick crystal.

charging currents about five or ten times smaller than those used in the present experiments and this could have had some bearing on the difference in results. The effect of repeated charging and discharging cycles is shown in Fig. 6. The current flowing for a given applied voltage becomes smaller on successive cycles, indicating a change in the bulk material or in the electrodes during the course of charge injection.

Potential distribution.—The internal potential distribution during coloration was estimated by wrapping a platinum wire around the center of a crystal of about 1 cm thickness and recording the potential of this electrode with respect to the left-hand electrode using a second Keithley 610B electrometer. As shown in Fig. 7, the electrode potential was roughly one half the applied voltage for the uncolored crystal but became smaller if the color entered from the left-hand side, or larger when the color entered from the right-hand side. The simplest interpretation of this behavior is that the conductivity of the blackened region of the crystal is higher than that of the uncolored material due to the presence of the injected charge.

Crystal decomposition.—On cooling crystals which had had currents of several mA/cm^2 passed for 10 min or so with the same polarity being maintained, the bulk material was found to become clouded and in some cases to be severely cracked. In addition the negative platinum electrode became blackened with

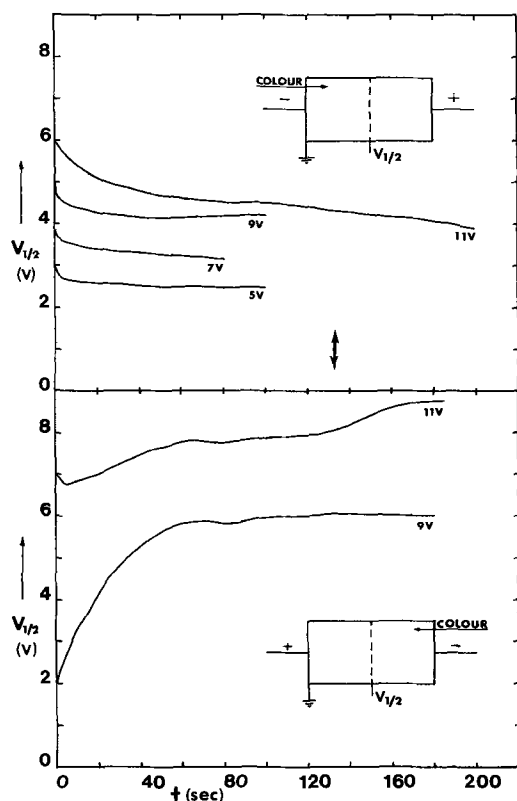


Fig. 7. Voltage measured between a central electrode and ground for various voltages applied across the full crystal; upper diagram, as the color is injected from the grounded electrode; lower diagram, as the color is injected from the ungrounded electrode. Arrows indicate approximate times when cloud is at mid-point and has completely traversed crystal.

some visible evidence of diffusion of the electrode material into the crystal. Although the color of the positive electrode was unchanged, microscopic examination showed large depressions had been formed under the electrode indicating that material had been lost from the crystal. These observations are consistent with electrolytic action within the material, with the movement of oxygen vacancies toward the negative electrode and the release of gaseous oxygen from the positive electrode.

Optical effects and electron paramagnetic resonance.—The optical absorption spectrum recorded by a Cary Model 15 spectrophotometer is shown in Fig. 8 for a yellow and blackened crystal, respectively. The black color is seen to arise from a broad absorption band extending the width of the visible spectrum (4). Direct evidence that the electron is associated with a vanadium site is shown by the electron paramagnetic resonance spectrum measured at 21 GHz at 70°K and shown in Fig. 9. A full analysis of this spectrum has not yet been carried out, but the two sets of eight lines could either arise from electrons trapped at two types of vanadium sites or from an electron trapped between a vanadium site and an associated defect such as an oxygen vacancy. Such V^{4+} sites have an electron spin $S = \frac{1}{2}$ and a nuclear spin $I = 7/2$ leading to a single resonance containing $(2I + 1) = 8$ lines. The concentration of paramagnetic spins in a colored crystal was found to be of the order of 10^{19} spins/cm³ which is in agreement with the carrier concentration estimated from the electrical data. As far as could be ascertained the resonance signals were similar for electrically colored crystals and for those grown in an oxygen-deficient atmosphere.

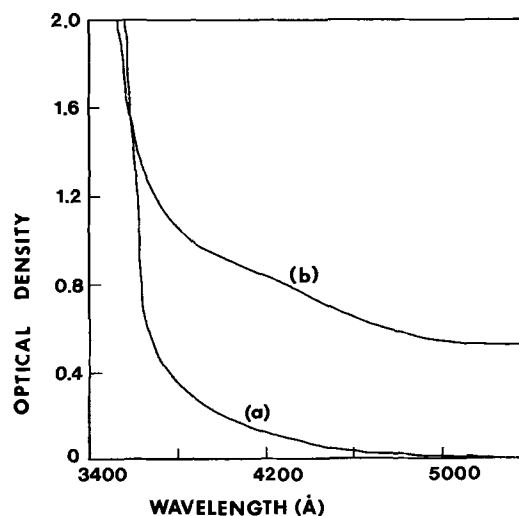


Fig. 8. Optical absorption spectra for calcium orthovanadate, (a) "Normal" yellow crystal, probably stoichiometric. (b) Blackened crystal.

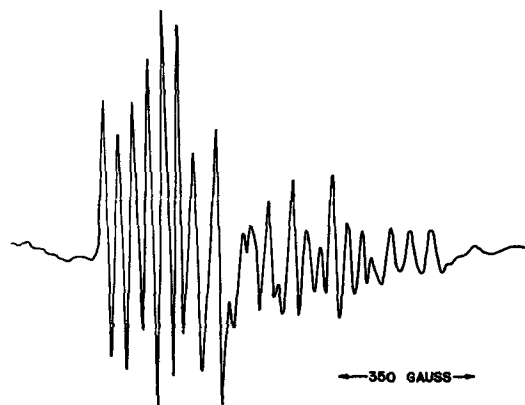


Fig. 9. Electron paramagnetic resonance spectrum of color centers in electrolytically colored calcium orthovanadate.

Discussion

The transport measurements indicate that conduction in stoichiometric calcium orthovanadate occurs predominantly by the movement of oxygen ions. The transport number of 0.9 implies that an emf may be developed in a cell based on calcium orthovanadate which is close to the thermodynamic maximum. The internal impedance of several such cells was in the range 10^5 - 10^6 ohms when operated in the temperature range near 1000°C.

The mechanisms of charge injection and crystal coloration in alkali halides and calcium orthovanadate are compared in Fig. 10. In the alkali halides, coloration involves the migration of halide ions toward the positive electrode, the movement of halide ion vacancies toward the negative electrode, and the injection of electrons from the negative electrode to form neutral F-centers at the halide ion vacancy sites. In the orthovanadate, where measurements show that oxygen migration is predominant, the corresponding process is that of oxygen migration to and release from the positive electrode, oxygen vacancy migration to the negative electrode, and electron injection and capture at oxygen vacancy sites. Local neutrality requires two electrons for each vacancy site and the optical and electron paramagnetic resonance results suggest that these electrons are located at vanadium sites adjacent to the vacancy. Electron migration by hopping between

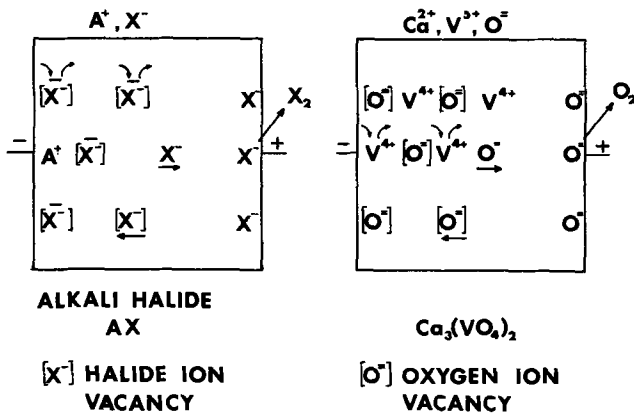


Fig. 10. Comparison of the mechanisms of electrolytic coloration in alkali halides and in calcium orthovanadate.

V^{4+} and V^{5+} sites is well known in vanadium compounds and the large number of available V^{5+} sites may account for the high current densities observed in the orthovanadate compared with alkali halides.

A full analysis of time-dependent space charge injection into insulators is normally difficult. In the present case, the evidence for local neutrality in the colored region, the comparable ionic and electronic contributions to the total conductivity, and the well-defined boundary of the charged region allow a quasi-static approach to be used to interpret the processes involved. This is illustrated in Fig. 11. The crystal is divided into colored and uncolored regions with a boundary at d , the conductivity in the colored region σ_1 being due to an ionic component σ_i and an electronic component σ_e , while that in the uncolored region σ_2 is totally ionic σ_i . The ratio of these conductivities is conveniently written as

$$\frac{\sigma_1}{\sigma_2} = 1 + \frac{\sigma_e}{\sigma_i} = 1 + m \quad [3]$$

Making an initial assumption of no space charge accumulation within the crystal, the partly colored crystal of area A can be regarded as two resistances in series

$$R_1 + R_2 = \frac{d}{\sigma_1 A} + \frac{(L-d)}{\sigma_2 A} \quad [4]$$

and the current and voltage distribution calculated as a function of the position of the boundary. Three quantities can be compared with experiment: the values of current when the boundary is at $d = 0$ and at $d = L$, and the voltage measured at an electrode situated at the mid-point of the crystal. The current should rise from an initial value $\sigma_2 AV/L$ to a value of $\sigma_1 AV/L$, an

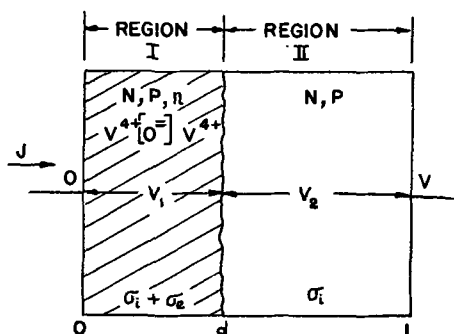


Fig. 11. Model for charging process. Region I is neutral but has conductivity $\sigma_1 + \sigma_e$, region II has purely ionic conductivity, σ_i .

increase of $(1 + m)$ due to the injection of electrons into the sample. It is easily shown that the voltage measured at an electrode placed at $L/2$ is given as a function of $y = d/L$ by the expression

$$V_{L/2} = \frac{V}{2[y + (1 - y)(1 + m)]} \quad [5]$$

This expression has a value of $V/2$ when the conductivity is uniform (with the boundary at $d = 0$ and $d = L$, respectively) and has a minimum value of $V/(2 + m)$ when the boundary is at $d = L/2$. A similar analysis can be made for the injection of electrons at $d = L$ with the voltage again being measured between electrodes at $d = 0$ and $d = L/2$. In this case the voltage at $L/2$ is expected to rise as the electron cloud penetrates the crystal.

Comparison of these results with the experimental data shown in Fig. 4 and 7 shows general agreement with this model. The approximate position of the boundary is shown by arrows on the diagram. The rise in current and fall in center electrode potential occur as predicted as the color enters the crystal and leads to a value of the parameter m between 2 and 3. However the rise in center electrode potential as the color crosses the mid-point does not occur and it is therefore necessary to consider other phenomena which may occur during coloration. These are illustrated in Fig. 12 and include the formation of a negative space charge region beneath the positive electrode due to the migration of negatively charged oxygen ions and the release of oxygen through the electrode.

The effect of a negative space charge layer may be evaluated by repeating the above analysis with the inclusion of a distribution of space charge within the crystal. For example, a distribution which can be justified on empirical grounds is a negative space charge density which increases linearly from the edge of the colored region toward the positive electrode. This corresponds to the accumulation of oxygen ions beneath this electrode. The effect of the distribution is included through Poisson's law and it is found that the center electrode potential falls continuously to zero when calculated as a function of increasing boundary parameter $y = d/L$. This polarization effect is not in accord with the experimental behavior shown in Fig. 7.

The experimental observation of a loss of material under the positive electrode is strong evidence that oxygen escapes through the electrode and that the total density of excess negative charge in the boundary

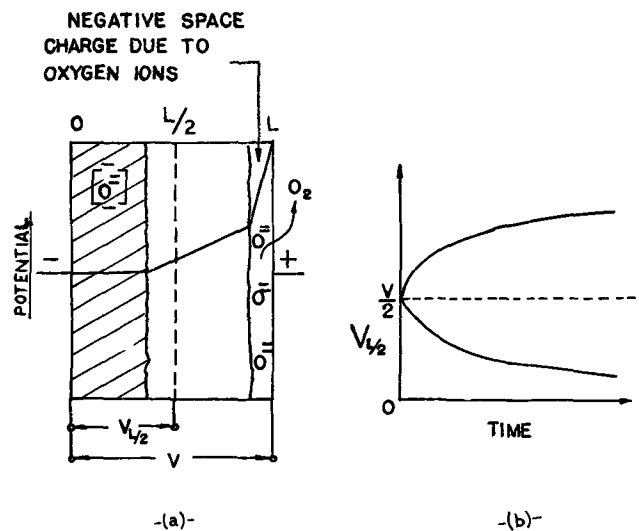


Fig. 12. Model including space charge at the positive electrode and oxygen loss from the crystal. The graph shows the expected change in the potential of the center electrode with the position of the boundary layer.

layer distribution is thereby reduced. Taking this effect into account is difficult to do in a quantitative fashion without further information regarding conditions at the boundary. However, qualitatively, oxygen loss would be expected to lead to a slower decrease in the center electrode potential as the color enters the crystal. This is shown in the graph in Fig. 12 and is in substantial agreement with the experimental behavior. Such a large effect due to electrode conditions would account for the difficulty of obtaining reproducible threshold and open-circuit voltages in repeated experiments on a single sample or between different samples.

The effect of electrolysis may be seen in the decreasing magnitude of the injected current on successive charging cycles shown in Fig. 6. If electrical neutrality is maintained in the colored region during the application of the external field, the injected charge must be located in the neighborhood of an oxygen vacancy. During electrolytic action and subsequent crystal decomposition, such vacancies will be progressively swept out of the crystal leading to a smaller charge injection during subsequent cycles.

Conclusions

Some application of calcium orthovanadate as a high temperature charge storage and oxygen transport medium appear to be possible. The principal limitation is contact and material deterioration due to electrolysis

within the bulk. An increase in lifetime and improved charge storage efficiency can be obtained by operating at low specimen currents.

Acknowledgments

The work was partly supported by the National Research Council of Canada. The assistance of Dr. H. J. Wintle is appreciated.

Manuscript submitted June 18, 1971; revised manuscript received Sept. 27, 1971.

Any discussion of this paper will appear in a Discussion Section to be published in the December 1972 JOURNAL.

REFERENCES

1. C. H. Brixner and P. A. Flournoy, *This Journal*, **112**, 303 (1965).
2. C. D. Cox and T. Surek, *J. Can. Ceram. Soc.*, **35**, 45 (1966).
3. C. D. Cox and P. C. Eastman, *ibid.*, **38**, 75 (1969).
4. J. H. Schulman and W. D. Compton, "Colour Centres in Solids," The MacMillan Co., New York (1962).
5. G. A. Anderson and W. D. Compton, *J. Chem. Phys.*, **52**, 6166 (1970).
6. S. P. Mitoff, *ibid.*, **36**, 1383 (1962).
7. H. Peters and H. H. Möbius, *Z. Physik. Chem.*, **209**, 298 (1958).
8. H. J. Wintle, *J. Appl. Phys.*, **41**, 4004 (1970).

A Radiochemical Technique for Determining Depth Distributions in Mo

M. R. Arora* and Roger Kelly*

Institute for Materials Research, McMaster University, Hamilton, Ontario, Canada

ABSTRACT

Molybdenum can be anodized at up to 235V in an electrolyte containing glacial acetic acid, $\text{Na}_2\text{B}_4\text{O}_7 \cdot 10 \text{H}_2\text{O}$, and water. The resulting oxide films, which must be stabilized by compressed-air drying, show brilliant interference colors, have a linear (or nearly linear) thickness-voltage relation, and can be formed with thicknesses of up to $380 \mu\text{g}/\text{cm}^2$ of oxide ($\sim 8400 \text{Å}$). When exposed to 1.0 g/liter aqueous KOH, the films dissolve ("strip") within 30 sec, whereas the underlying metal dissolves at a rate of only 20 Å/hr. The film thicknesses formed on Mo which has been subjected to Kr ion bombardment at doses of up to 4×10^{16} ions/ cm^2 are similar to those on unbombarded specimens. It follows from these results that the use of an anodizing-stripping sequence for determining depth distributions in Mo should be possible. Examples of depth distributions for 10-keV Kr implanted at doses from 4×10^{13} to 4×10^{16} ions/ cm^2 are given and are shown, by comparison both with theory and with previously obtained results for W, to be numerically plausible.

Although a great deal of effort has been devoted in recent years to studying the penetration of energetic charged particles into solids, most of the work has been restricted either to low-mass targets (Al, Si, Al_2O_3 , WO_3) or to high-mass targets (W, Au) (1-5). This leaves much to be done in the intermediate mass region, for example, work on maximum ranges (6) and on "supertails" (7). We propose to describe here an electrochemical technique suitable for depth-distribution measurements with Mo, mass 96; in addition, we demonstrate the plausibility of the technique by reporting preliminary depth-distribution measurements for Mo in the little-studied high-dose region.

The technique developed for studying the penetration of ions into Mo is similar in all respects to the anodizing-stripping methods previously developed by Davies and co-workers with Al (1), Si (2), W (3),

and Au (4). Thus, with all five materials under suitable anodizing conditions, an extremely uniform oxide layer can be formed, whose thickness is determined mainly by the applied formation voltage. Also with all five materials, solvents exist which will rapidly dissolve the anodic oxide layer but not attack the underlying metal.

We would point out that further possibilities for studying intermediate masses have recently presented themselves. Andersen and Sørensen (8) have demonstrated that well-defined halide films can be formed and stripped from Cu (mass 64) and Ag (mass 108). In addition, vibratory polishing (9) and sputtering (10) are nearly universally applicable. None of these alternatives is, however, as straightforward as might be desired.

Anodizing-Stripping Procedure for Mo

Specimen preparation.—Polycrystalline Mo foils, which were 0.1 mm thick and had purities of 99.8%,

* Electrochemical Society Active Member.

Key words: molybdenum, anodization, thin films, depth distributions.

were used as specimens throughout this work. They were degreased with petroleum ether and etched in dilute nitric acid; they were then anodized at 80-100V several times and the anodic oxide films thus formed were dissolved in dilute KOH solution (to be discussed later). This preanodizing treatment may be assumed by analogy with Al (1) to provide a reproducibly flat surface of constant area for thickness calibration and subsequent depth-distribution measurements.

Anodizing step.—There are at least two examples in the literature where Mo has been anodized under etching or polishing conditions (11, 12), although no examples at all are known to the authors where the anodizing of Mo led [as with the closely related W (3)] to a protective oxide film. For example, negative results were obtained by Wood and Pearson (13). While the initial results obtained here tended to confirm the difficulty of forming films, it was found, after a rather large number of unsuccessful experiments, that films could be readily grown using an electrolyte similar to that proposed by Keil and Salomon (14) for V: glacial acetic acid, 0.02M $\text{Na}_2\text{B}_4\text{O}_7 \cdot 10\text{H}_2\text{O}$, and either 1.0M or 2.0M water. Higher amounts of water (> 2.0M) resulted in excessively unstable films: specifically, with 5.0M water in the electrolyte, fresh films tended to become nonuniformly thinner in 25 sec when exposed to the surrounding air and could not be stabilized by compressed-air drying. Films formed in the electrolyte with 1.0M water were not affected by 45-sec exposure to air and were found to be particularly stable when dried with compressed air. They could then be preserved in air for more than a day and in a desiccator for more than two weeks. Films formed with 2.0M water showed an intermediate behavior, being closer, however, to those formed with 1.0M water. Water contents of less than 1.0M resulted in stable but nonuniform films, the nonuniformity being presumably due to the low conductivity of the electrolyte [cf. Ref. (15)]. These conclusions are all based on the observation of interference colors.

The experiments were carried out at $25^\circ \pm 1^\circ\text{C}$ and, on the basis of the above considerations, were confined mainly to the electrolyte with 1.0M water. A planar Pt foil, separated by about 1.0 cm from the Mo specimens, acted as cathode. A calomel reference electrode was occasionally inserted into the bath during anodizing to determine what portion of the applied voltage actually appeared across the oxide film on the Mo and what portion corresponded to the ohmic drop in the electrolyte. Except at the beginning of a run, the voltage across the film was similar (typically 97-98%) to the total applied voltage and corrections have therefore not been applied.

The anodizing was carried out at a constant current of 2.0 mA/cm² until the desired voltage had been reached and the current was then allowed to drop for a total anodizing time of 6 min. The current had by this time decreased to an almost limiting value of 0.1 to 0.3 mA/cm², most of which is believed to be electronic in nature (16).

Above 10 to 15V, the presence of the oxide films on Mo could be detected visually, and their uniformity verified, by means of the characteristic interference colors that occur. As described above, freshly prepared films were highly unstable, although they could be stabilized by exposing them for about 10 to 15 sec to a jet of compressed air immediately after withdrawal from the anodizing bath. The films were shown by reflection electron diffraction at 60 kV to be amorphous (Fig. 1a), although they were subject to crystallization at temperatures greater than about 400°C (Fig. 1b); they are similar in these respects to anodic WO_3 (17).

Apparently normal anodizing behavior was found up to a voltage of 235V, corresponding to an oxide film thickness of 380 $\mu\text{g}/\text{cm}^2$ of oxide ($\sim 8400\text{\AA}$). At that potential, film breakdown occurred as evidenced by

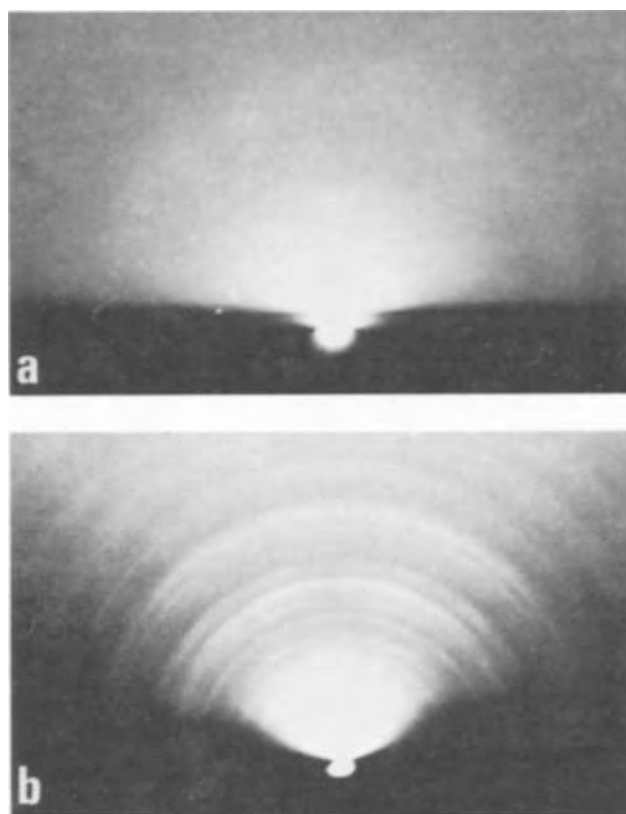


Fig. 1. Electron diffraction patterns taken by reflection in a Philips EM300 electron microscope operated at 60 kV. (a) Mo as anodized at 50V. (b) Mo which has been first anodized at 50V and then heated in air at 450°C for 5 min.

discoloration and a tendency for the voltage either to rise reluctantly or to fall.

Stripping step.—The only oxide solvent tried was, by analogy with WO_3 (3), 1.0 g/liter KOH. It was observed that the oxide interference colors disappeared within 30 sec. By using specimens first labeled with 35-keV Kr^{85} to a dose of 5×10^{15} ions/cm² and then anodized at 15, 30, or 60V, it was confirmed that film dissolution was complete within 30 sec and that the attack on the underlying metal occurred at about 20 $\text{\AA}/\text{hr}$.¹ Partial results are given in Table I.

The existence of a dissolution "end-point" at the oxide-metal interface is perhaps the most crucial consideration in setting up an anodizing-stripping procedure. It was therefore gratifying that the "end point" is so well-defined with Mo.

Thickness Calibration

Calibration for $\geq 10\text{V}$.—As a first step in establishing a thickness-voltage calibration for the anodizing-

¹ The ion bombardments used throughout this work were carried out with a high-current, 0-40 kV accelerator located in the Institute for Materials Research at McMaster University.

Table I. Stripping experiments*

Total time in KOH	Normalized residual target activity		
	15-V film	30-V film	60-V film
0	100	100	100
2 sec	72.8	74.0	82.0
5 sec	64.8	48.2	53.2
10 sec	64.1	39.8	33.7
30 sec	64.1	39.8	18.4
2 min	63.8	40.2	18.1
10 min	63.8	39.7	17.9
60 min	62.0	39.0	17.6

* The Mo specimens were labeled with 35-keV Kr^{85} , anodized at 15, 30, or 60V, and then exposed to 1.0 g/liter aqueous KOH for various times.

stripping procedure, the extent to which Mo went into solution during the anodizing step was estimated. Eight specimens were labeled with 10-keV Kr⁸⁵ to a dose of 5×10^{15} ions/cm² and were then counted three times: before anodizing, after anodizing at 3 to 50V, and after stripping. From 30 to 80% of the activity was found to be lost during anodizing, indicating that significant oxide-film dissolution was occurring. This means that Mo, as distinct from W (3), requires two types of thickness calibration, one for oxide-film thickness due to anodizing alone and the other for total metal removed in a full anodizing-stripping sequence.

In further experiments, it was shown that the oxide thickness and its uniformity, as inferred both from the interference colors and from the time to reach the limiting electronic current, did not depend significantly on whether the anode-cathode spacing was 0.5 or 1.0 cm provided the initial current density was at least 2.0 mA/cm² and the total anodizing time at least 6 min. Had the time been increased to 9 min, spacings of up to 2.0 cm could have been tolerated.

The main results, as determined by the conventional weight-loss procedure, are shown in Fig. 2 and can also be represented by the following expressions:

$$\begin{aligned} &\text{Thickness of oxide film for} \\ &\text{electrolyte with 1.0M water} \\ &= 1.4 + 1.58 \times V \quad \mu\text{g/cm}^2 \text{ of oxide} \\ &\text{Thickness of oxide film for} \\ &\text{electrolyte with 2.0M water} \\ &= 1.4 + 1.78 \times V \quad \mu\text{g/cm}^2 \text{ of oxide} \\ &\text{Total Mo removed for electro-} \\ &\text{lyte with 1.0M water; } \leq 10\text{V} \\ &= 1.5 + 1.60 \times V \quad \mu\text{g/cm}^2 \text{ of metal} \\ &\text{Total Mo removed for electro-} \\ &\text{lyte with 1.0M water; } \geq 10\text{V} \\ &= 7.3 + 1.02 \times V \quad \mu\text{g/cm}^2 \text{ of metal} \end{aligned}$$

Note how the curves for oxide thickness are given in units of micrograms/square centimeter of Mo [deduced by assuming the oxide to be MoO₃ (16)], whereas the corresponding analytical expressions are in terms of micrograms/square centimeter of total oxide (no

assumptions necessary as to its nature). Note also that the calibrations are not unique, but apply for an initial current density of 2.0 mA/cm², a total anodizing time of 6 min, and an anode-cathode separation of ≤ 1.0 cm.

Calibration at low voltages.—Since the precision of depth-distribution measurements depends mainly on the knowledge of small thicknesses ($< 10 \mu\text{g/cm}^2$), supplementary calibration experiments (*i.e.*, other than weight-loss measurements) were made in the low-voltage region.

Oxide films on Mo as prepared here were found to be sufficiently stable for the use of ellipsometry to measure their thickness. Six specimens, prepared with the electrolyte having 1.0M water, were therefore examined assuming the following refractive indices (18): $n_{\text{Mo}} = 3.14 - i 3.60$; $n_{\text{oxide}} = 1.55$. It was found that the thickness of a natural film was $31 \pm 2\text{\AA}$, of a 4-V film was $127 \pm 4\text{\AA}$, and of a 6-V film was $219 \pm 5\text{\AA}$. For an oxide density of 4.52 g/cm³ and an assumed composition MoO₃ (16), these thicknesses correspond to, respectively, 0.93, 3.84, and 6.61 $\mu\text{g/cm}^2$ of Mo.

Values for the total metal removed could be obtained using a technique based on comparing depth distributions. Twenty-four specimens were bombarded with 30-keV Kr⁸⁵ under identical conditions of dose (5×10^{15} ions/cm²). The specimens were then subdivided into eight groups and the Kr depth distributions were determined such that each group was anodized and stripped using only one voltage. By letting the total amounts of metal removed at the lower voltages (1, 2, 3, 6, and 8V) be unknowns, these amounts could be expressed relative to those at the higher voltages (10, 15, and 20V). A typical example, which serves to establish the 2-V amount as being 0.17 of the 10-V amount, is shown in Fig. 3.

Over-all low-voltage results are summarized in Fig. 4 and have been taken into account in the analytical expressions of the preceding section. The depth-distribution procedure, in particular, will be recognized as being related to that used by Whitton (9) for calibrating the vibratory polishing behavior of W and Ta₂O₅.

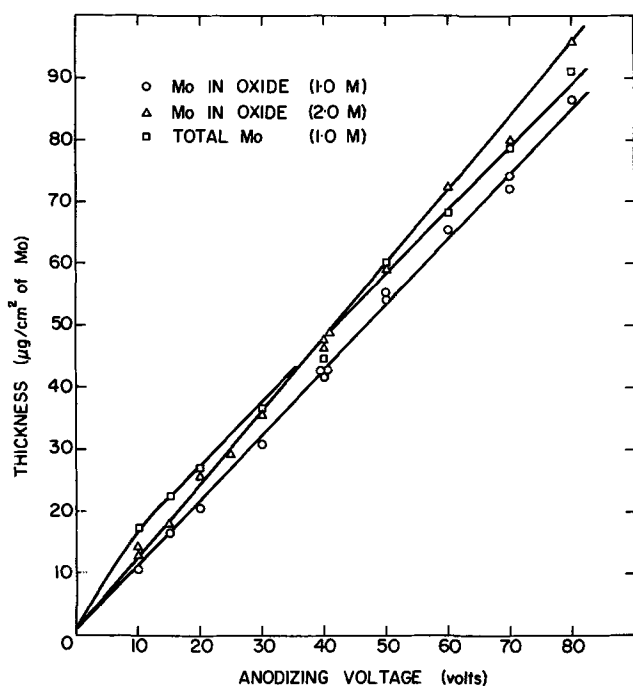


Fig. 2. Thickness-voltage calibration for anodization of Mo. \circ , Mo removed during stripping step alone when using electrolyte with 1.0M water; \triangle , like the preceding but electrolyte with 2.0M water; \square , total Mo removed in a full anodizing-stripping sequence when using electrolyte with 1.0M water.

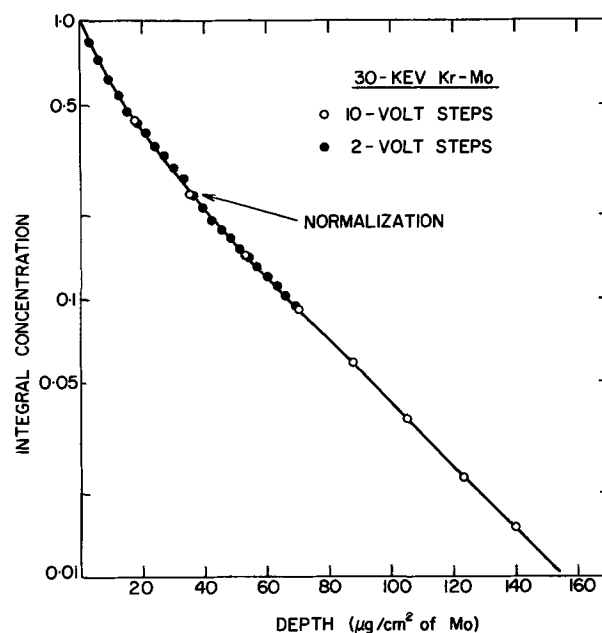


Fig. 3. Integral Kr depth distributions in Mo for 5×10^{15} ions/cm² of 30-keV Kr⁸⁵. \circ , curve determined by a sequence of 10V anodizings (1.0M water), each of which may be assumed to remove 17.5 $\mu\text{g/cm}^2$ of Mo; \bullet , curve determined by a sequence of 2V anodizings and normalized to the other curve at a residual target activity of 0.24. A 2V step may be inferred to remove 0.17 of a 10V step.

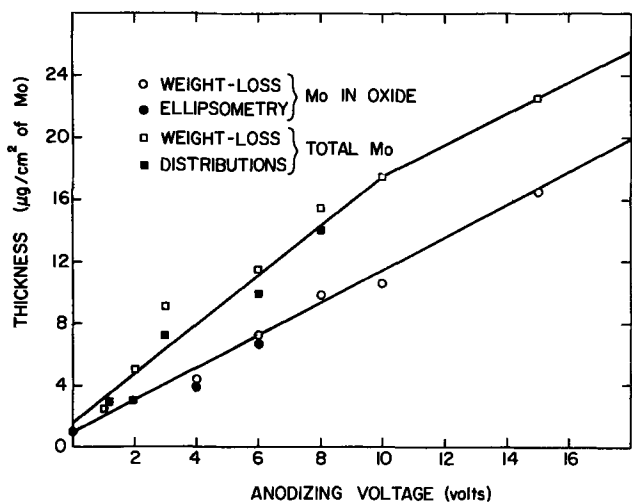


Fig. 4. Thickness calibration for Mo at low anodizing voltages. ○, Mo removed during stripping step alone (1.0M water) as determined by weight loss; ●, like the preceding but deduced by ellipsometry; □, total Mo removed in a full anodizing-stripping sequence (1.0M water) as determined by weight-loss; ■, like the preceding but deduced by comparing depth distributions as in Fig. 3.

Effect of radiation damage on thickness calibration.— Andersen and Sørensen (8) were concerned in their work on halide films on Cu with the effect of ion-bombardment damage on the thickness calibration. No effect was observed for doses of up to 10^{16} ions/cm². In the present work we have prepared a series of 12 specimens, bombarded them with 10-keV Kr to various doses, and then anodized them at 40V. The total amount of metal plus implanted Kr removed in a full anodizing-stripping sequence was then determined and from it the estimated weight of the Kr was subtracted. (The sticking probability of the incident ions was taken into account in making this correction.) The results are given in Table II and serve to confirm again the absence of a damage effect except perhaps at the highest dose (4×10^{17} ions/cm²).

Depth Distributions in Mo at High Doses

As a specific application of the anodizing-stripping procedure described here, we have undertaken experiments on Kr depth distributions in Mo in the little studied high-dose region. The results are still preliminary but one series in particular will be included here, since its plausibility serves as a good indication of the effectiveness of the anodizing-stripping procedure.

Figure 5 shows distribution curves of the residual target activity (i.e., integral concentration) for Kr⁸⁵ injected into Mo at a constant energy of 10 keV but at various doses. Each curve is based on at least 12 separate specimens with typically 8 to 15 points per specimen, and we note first of all that the reproducibility, as shown by the vertical bars, is rather good for this type of work [cf. Ref. (10)].

The theoretical curve was deduced from a knowledge of the Thomas-Fermi values of the mean projected range, $\langle x \rangle$, and mean projected straggling, $(\langle \Delta x^2 \rangle)^{1/2}$, as calculated by Schjøtt (19) assuming a

Table II. Effect of radiation damage

Kr dose (ions/cm ²)	Total metal removed in 40-V step (µg/cm ²)
Zero	47.9
5×10^{15}	47.0
4×10^{16}	48.4
4×10^{17}	42.4

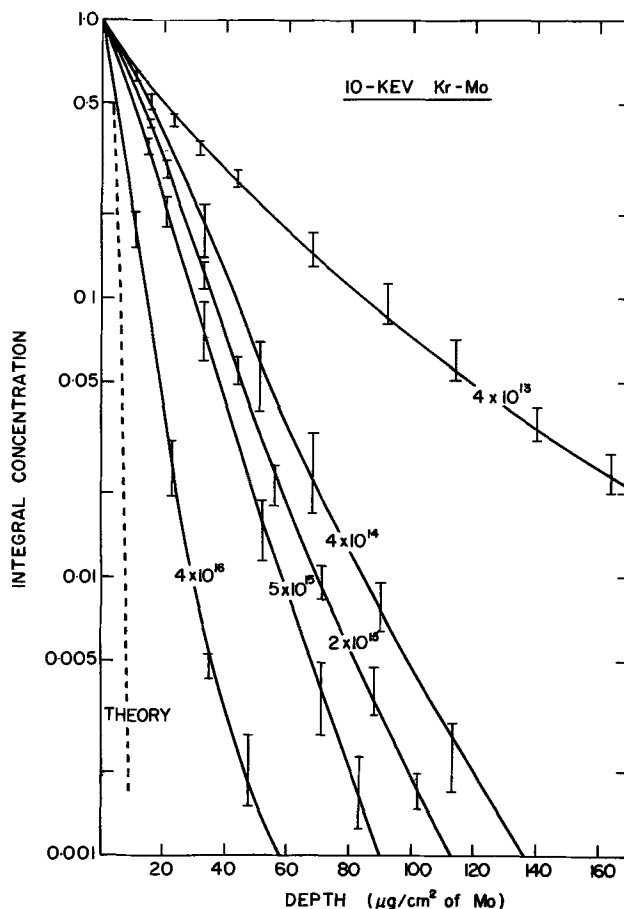


Fig. 5. Integral Kr depth distributions in Mo as a function of dose for a constant energy of 10 keV. Solid: experimental curves, each involving approximately 100 to 180 experimental points which have a scatter as shown by the vertical bars. Numbers such as 4×10^{13} refer to doses in ions/cm². Dashed: theoretical curve corresponding to $\langle x \rangle = 3.7 \mu\text{g/cm}^2$ and $(\langle \Delta x^2 \rangle)^{1/2} = 1.9 \mu\text{g/cm}^2$.

random (amorphous) solid

$$\left. \begin{aligned} \langle x \rangle &= 3.7 \mu\text{g/cm}^2 \\ (\langle \Delta x^2 \rangle)^{1/2} &= 1.9 \mu\text{g/cm}^2 \end{aligned} \right\} \text{for 10-keV Kr}^{85} \text{ in Mo}$$

These values were substituted into the leading term of an integral Edgeworth expansion (20)

$$\text{integral concentration} \approx (\frac{1}{2}) \operatorname{erfc} \left[\frac{x - \langle x \rangle}{2^{1/2} (\langle \Delta x^2 \rangle)^{1/2}} \right]$$

Table III enables a comparison to be made between the experimental median projected range, R_m , and the expected value $\langle x \rangle = 3.7 \mu\text{g/cm}^2$.

R_m is seen to be a factor of 5.4 larger than expected at the lowest dose used, 4×10^{13} ions/cm². We do not regard this as a sign of experimental error, but rather a normal result, due to there being mixed random and channeled stopping in nonamorphizable substances

Table III. Median ranges for 10-keV Kr in Mo

Kr dose (ions/cm ²)	Median range, R_m (µg/cm ² of Mo)	$R_m/\langle x \rangle^*$
4×10^{13}	20	5.4
4×10^{14}	15.5	4.2
2×10^{15}	12.5	3.4
5×10^{15}	10	2.7
4×10^{16}	4	1.1

* The expected value of $\langle x \rangle$ is $3.7 \mu\text{g/cm}^2$ of Mo (19).

such as Mo. Consider, for example, the behavior of low doses of Kr in W: for polycrystalline W, Davies *et al.* (21) found $R_m/\langle x \rangle$ to have an average value of 2.3, while for single-crystalline W with $\langle 111 \rangle$ or $\langle 100 \rangle$ orientations Kornelsen *et al.* (22) found values of 10 to 12. The Mo specimens were subsequently shown to have virtually only three orientations present, $\langle 100 \rangle$, $\langle 211 \rangle$, and $\langle 111 \rangle$, and it is thus not surprising that $R_m/\langle x \rangle$ was large.

R_m decreases with increasing dose, such that for a dose of 4×10^{16} ions/cm² it is comparable to the theoretical value. This is again an expected result, for in the context of mixed random and channeled stopping, one anticipates a progressive blocking of the channels both by incident ions and by lattice damage. The blocking is evidently complete in the near-surface region at a dose of 4×10^{16} ions/cm², although it is clearly incomplete at greater depths. The corresponding results for W include a bombardment to 5×10^{14} ions/cm² (22), where R_m was only slightly reduced from the value for 2×10^{13} ions/cm², and bombardments at 5×10^{15} ions/cm² (16), where $R_m/\langle x \rangle$ was 2.2 to 2.8. In addition, Eriksson (23) has showed that a dose of 3×10^{16} ions/cm² still yields a distribution of which the deeper portions are dominated by channeling effects. Reference to Table III or Fig. 5 reveals that these results are very similar to those obtained here for Mo.

One concludes that depth distributions can be obtained in Mo which are numerically plausible. Depending on the dose, R_m either deviates from theory in an expected way or else agrees with theory.

Other series of high-dose depth distributions are in the course of being obtained by the present authors for the metals Mo, Al, and W. One of the conclusions that is emerging is, however, already clear from the present work: Mo behaves, as far as stopping phenomena are concerned, more nearly like W than like Al. This means that Mo will be particularly effective for studying maximum ranges (6) and "supertails" (7).

Summary

A procedure is outlined whereby Mo can be anodized at voltages up to 235V. The resulting oxide films are highly unstable unless dried with a jet of compressed air immediately after withdrawal from the anodizing bath. The films are rapidly soluble in 1.0 g/liter aqueous KOH, whereas the underlying metal dissolves at a rate of only 20 A/hr.

Oxide thicknesses are determined both by the conventional techniques of weight-loss and ellipsometry, as well as by a procedure based on comparing depth distributions. For example, depth distributions for 30-keV Kr were obtained both from a sequence of 2-V anodizings and from a sequence of 10-V anodizings, and the value of the 2-V thickness increment was deduced as being 0.17 of the 10-V increment.

Sequences of anodizings and strippings enable depth distributions to be obtained only if the amount of metal removed in such a sequence is independent of ion-bombardment damage. This condition is shown to be met with Mo for Kr doses up to 4×10^{16} ions/cm².

Examples of depth distributions are given for various doses of 10-keV Kr in Mo. The median range exceeded the Thomas-Fermi value by a factor of 5.4 at a dose of 4×10^{13} ions/cm² but agreed at a dose of 4×10^{16} ions/cm². Since these results are numerically plausible, they indicate that an anodizing-stripping sequence is an effective depth probe with Mo.

Acknowledgments

The authors acknowledge with pleasure various discussions held with Dr. J. A. Davies (Chalk River) during the course of this work. Dr. D. C. Santry (Chalk River) read a preliminary version of this manuscript and made many constructive suggestions. In addition, Dr. J. Shewchun and Mr. E. C. Rowe (McMaster University) provided valuable assistance, as well as use of their equipment, in the ellipsometry measurements. This work was supported by a grant from the National Research Council, Ottawa, Ontario, Canada.

Manuscript submitted July 30, 1971; revised manuscript received Oct. 5, 1971.

Any discussion of this paper will appear in a Discussion Section to be published in the December 1972 issue of the JOURNAL.

REFERENCES

1. J. A. Davies, J. Friesen, and J. D. McIntyre, *Can. J. Chem.*, **38**, 1526 (1960).
2. J. A. Davies, G. C. Ball, F. Brown, and B. Domeij, *Can. J. Phys.*, **42**, 1070 (1964).
3. M. McCargo, J. A. Davies, and F. Brown, *ibid.*, **41**, 1231 (1963).
4. J. L. Whitton and J. A. Davies, *This Journal*, **111**, 1347 (1964).
5. B. Domeij, F. Brown, J. A. Davies, and M. McCargo, *Can. J. Phys.*, **42**, 1624 (1964).
6. L. Eriksson, J. A. Davies, and P. Jespersgaard, *Phys. Rev.*, **161**, 219 (1967).
7. J. A. Davies and P. Jespersgaard, *Can. J. Phys.*, **44**, 1631 (1966).
8. T. Andersen and G. Sørensen, *Rad. Effects*, **2**, 111 (1969).
9. J. L. Whitton, *J. Appl. Phys.*, **36**, 3917 (1965).
10. R. Kelly, *ibid.*, **39**, 5298 (1968).
11. V. A. Lavrenko and A. A. Pen'kov, *Russ. J. Phys. Chem. (English Transl.)*, **37**, 551 (1963).
12. I. A. Menzies, G. W. Marshall, and G. B. Griffin, *Corrosion Sci.*, **9**, 287 (1969).
13. G. C. Wood and C. Pearson, *ibid.*, **7**, 119 (1967).
14. R. G. Keil and R. E. Salomon, *This Journal*, **115**, 628 (1968).
15. A. Aladjem, *J. Mater. Sci.*, **3**, 328 (1968).
16. M. R. Arora, M.Sc. Thesis, McMaster University (1971).
17. N. Q. Lam and R. Kelly, Submitted to *Canadian Journal of Physics*.
18. E. C. Rowe, Private communication.
19. H. E. Schiøtt, Private communication. See also *Can. J. Phys.*, **46**, 449 (1968).
20. J. B. Sanders, *Can. J. Phys.*, **46**, 455 (1968).
21. J. A. Davies, B. Domeij, and J. Uhler, *Arkiv Fysik*, **24**, 377 (1963).
22. E. V. Kornelsen, F. Brown, J. A. Davies, B. Domeij, and G. R. Piercy, *Phys. Rev.*, **136**, A849 (1964).
23. L. Eriksson, *ibid.*, **161**, 235 (1967).



Fast Cathodoluminescent Calcium Sulfide Phosphors

W. Lehmann* and F. M. Ryan

Westinghouse Research Laboratories, Pittsburgh, Pennsylvania 15235

Calcium sulfide phosphors are attractive for use as luminescent materials in cathode ray tubes (1). Their decay of luminescence following excitation by a short electron beam pulse is primarily determined either by the electron transition within the used activator ion, or by carriers temporarily captured in various traps depending on which is slower. Since traps are always present in CaS phosphors, the phosphorescence decay (even of phosphors containing relatively fast activators) is slower than might be desired for some applications. As an example, the recombination time constant corresponding to the luminescent $5d \rightarrow 4f$ transition of Ce^{3+} in CaS is less than 10^{-7} sec while the observed decay time of the phosphorescence of normal CaS: Ce^{3+} phosphors is about 10^{-6} sec, somewhat dependent on the particular phosphor and the excitation conditions (1).

We have tried to reduce this afterglow by incorporating a suitable chemical "killer" element in the phosphor, without an excessive reduction in the emission intensity resulting. Killers of luminescence of ZnS-type phosphors are well known to be mainly Fe, Co, and Ni (2, 3), and of these, nickel comes closest to the ideal of affecting mainly the afterglow with a minimum reduction in efficiency (4), and is commercially used in the phosphors P-11, P-36, and P-37. Corresponding actions of various killers in CaS phosphors are less well known. We have observed that, in striking contrast to ZnS, nickel is almost ineffective in CaS¹ which tolerates appreciable amounts of it without much effect. This apparently was noted already by Avinor who proposed instead to reduce the afterglow of CaS phosphors by addition of cadmium (5). Our experience disagrees with this claim as we cannot see a clear action of Cd in CaS in this respect. However, we observe cobalt to perform well in CaS, about equal to the performance of nickel in ZnS.

The technically ideal killer would be one that removes all afterglow without reducing the efficiency of the phosphor. In practice this cannot be achieved as killer centers compete with radiative recombination centers for recombining carriers and thereby introduce energy losses. A more realistic goal is to seek for a killer which associates to some degree with deep traps and, in this way, reduces the long-time afterglow more than the short-time afterglow. One must then vary the killer concentration in order to reach an acceptable compromise between high efficiency and short decay. The following shows how this has been achieved in several CaS phosphors by adding cobalt in varying amounts.

Experimental

The general conditions of CaS phosphor preparations are described elsewhere (1, 7). Cobalt containing phosphors were made in the same way except for the addition of cobalt.

Emission spectra of CaS phosphors considered here are shown in Fig. 1. Neither excitation intensity nor

the addition of cobalt measurably altered these spectra. This contrasts with the behavior of nickel in ZnS which, besides its action as a killer, produces an intense optical absorption band in the blue which does change the emission spectrum, probably by selective reabsorption of the emission light. A corresponding strong absorption of cobalt in CaS is not observed.

Decay characteristics were measured under conditions approaching those encountered in flying-spot scanners. The phosphors were excited in a demountable system by an electron beam of 10 kV in pulses of 50 nanoseconds duration with a current density of between 10-100 mA/cm². The light emission was detected with a photomultiplier and displayed on an oscilloscope screen. The decay curves were photographed and evaluated afterwards. The RC-response time of the system was 27 nanoseconds, well below the decay rates of the phosphors. The efficiencies presented in this paper are time-average energy efficiencies determined under the same pulse excitation conditions as mentioned above by comparison of the phosphors to several standard phosphors whose efficiencies were known from other sources (8).

Decay times and efficiencies of various phosphors vary somewhat with variation of the excitation conditions which, in turn, may depend upon the desired application. Hence, we include data on several commercial fast phosphors excited under the same conditions as our CaS phosphors in order to provide a somewhat firmer base of evaluation.

Results

The decay of green emitting CaS: Ce^{3+} containing no cobalt consists of several subsequent t^{-n} branches probably due to thermal emptying of several groups of traps. Details vary somewhat from sample to sample, average times to decay to $1/e$ or to $1/10$ of the original

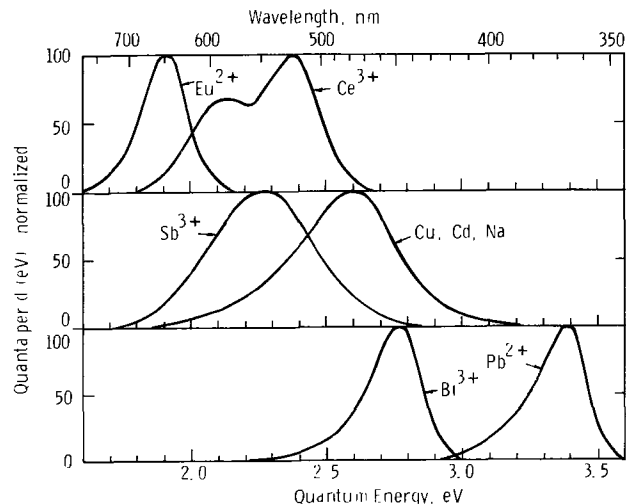


Fig. 1. Emission spectra of CaS phosphors

* Electrochemical Society Active Member.

Key words: phosphors, cathodoluminescence, decay, killer.

¹ There is even a CaS phosphor activated by Ni in combination with Cu or Ag (6).

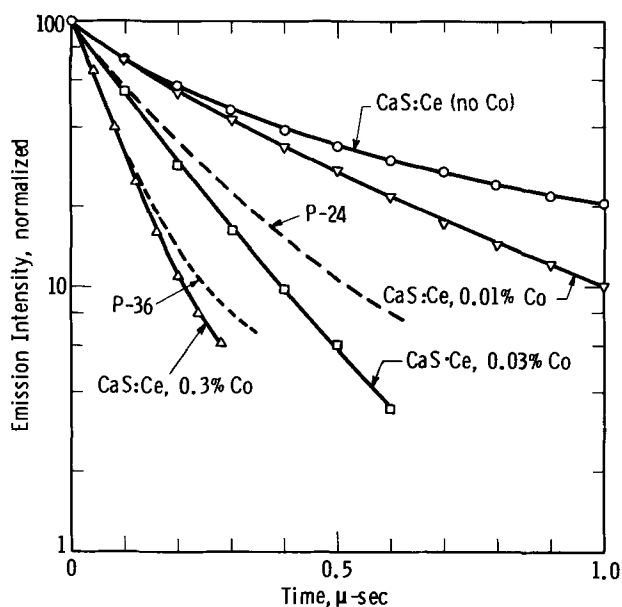


Fig. 2. Decay curves of $\text{CaS}:\text{Ce}^{3+}, \text{Co}$ compared to P-24 and P-36, all normalized to 100 at zero time.

intensity may be about 0.5 and 2 μsec respectively. A very weak tail of the afterglow may be observed even in the millisecond range.

Decay curves of several $\text{CaS}:\text{Ce}^{3+}$ phosphors containing different amounts of cobalt are shown in Fig. 2 and compared to those of commercially used P-24 (ZnO) and P-36 (ZnS-type, Ni). All of these phosphors are green emitters. The curves in Fig. 2. are normalized to 100 units at zero time. The time-average efficiencies of these phosphors under the used pulse excitation are listed in Table I. It may be noted that $\text{CaS}:\text{Ce}^{3+}$ containing properly adjusted amounts of cobalt easily matches P-24 and P-36 in speed of decay but is many times more efficient. Values of the efficiencies of $\text{CaS}:\text{Ce}^{3+}, \text{Co}$ and of the times required to decay to $1/e$ ($\tau_{1/e}$) and to $1/10$ ($\tau_{1/10}$) of the original as functions

Table I. Efficiencies and decay times

	Efficiency (%)	$\tau_{1/e}$ (μsec)	$\tau_{1/10}$ (μsec)
Green emitters:			
$\text{CaS}:\text{Ce}^{3+}$ (no Co)	20	0.5	~2
$\text{CaS}:\text{Ce}^{3+}, \text{Co}$ (0.03%)	4	0.16	0.4
$\text{CaS}:\text{Ce}^{3+}, \text{Co}$ (0.1%)	1.2	0.12	0.3
$\text{CaS}:\text{Ce}^{3+}, \text{Co}$ (0.3%)	0.24	0.08	0.2
$\text{CaS}:\text{Sb}^{3+}$ (no Co)	18	0.8	1.8
P-24 (ZnO)	0.8	0.2	0.5
P-36 (ZnS-type, Ni)	0.16	0.12	0.28
Red emitters:			
$\text{CaS}:\text{Eu}^{2+}$ (no Co)	12	0.6	~1.6
$\text{CaS}:\text{Eu}^{2+}, \text{Co}$ (0.03%)	3.2	0.25	0.6
$\text{CaS}:\text{Eu}^{2+}, \text{Co}$ (0.1%)	0.3	0.12	0.3
Blue emitters:			
$\text{CaS}:\text{Bi}^{3+}$ (no Co)	5	1.5	6-7
$\text{CaS}:\text{Bi}^{3+}, \text{Co}$ (0.05%)	0.4	0.3	0.8
$\text{CaS}:\text{Cd}, \text{Cu}$ (no Co)	12	5	10-15
$\text{CaS}:\text{Cd}, \text{Cu}, \text{Co}$ (0.1%)	0.5	1	4
P-11 (ZnS-type, Ni)	10	0.9	12
P-37 (ZnS-type, Ni)	0.4	0.15	0.36
Ultraviolet emitters:			
$\text{CaS}:\text{Pb}^{2+}$ (no Co)	16	0.6	3-4
$\text{CaS}:\text{Pb}^{2+}, \text{Co}$ (0.01%)	0.5	0.09	0.25
P-16 (silicate, Ce^{3+})	4	0.15	0.43

of the cobalt concentration are given in Fig. 3. Increasing amounts of cobalt reduce the decay until it finally approaches exponential shape with a time constant, $\tau_{1/e}$, of about 80 n-sec. This appears to be the final speed limit of this phosphor type. Excessively high cobalt concentrations only reduce the efficiencies without further reduction of the decay times.

This general behavior of $\text{CaS}:\text{Ce}^{3+}, \text{Co}$ is observed also in other CaS phosphors containing fast activators, all excited by electron beam pulses at room temperature² although minor details depend on the activator. Some performance data of CaS and, for comparison, of several commercial fast phosphors are given in Table I. In every case, cobalt reduces nonexponential decay of CaS until, with increasing amounts of cobalt,

² Striking differences are observed at low temperatures, however. For instance, $\text{CaS}:\text{Ce}^{3+}$ (no Co) is very efficiently excited to cathodoluminescence also at low temperatures and its decay becomes faster with decreasing temperature and is perfectly exponential ($\tau_{1/e} = 77$ n-sec) at about 10°K . In contrast, $\text{CaS}:\text{Eu}^{2+}$ (no Co) is extremely poorly excited at low temperatures and its decay becomes slower, not faster, with decreasing temperature down to about 10°K .

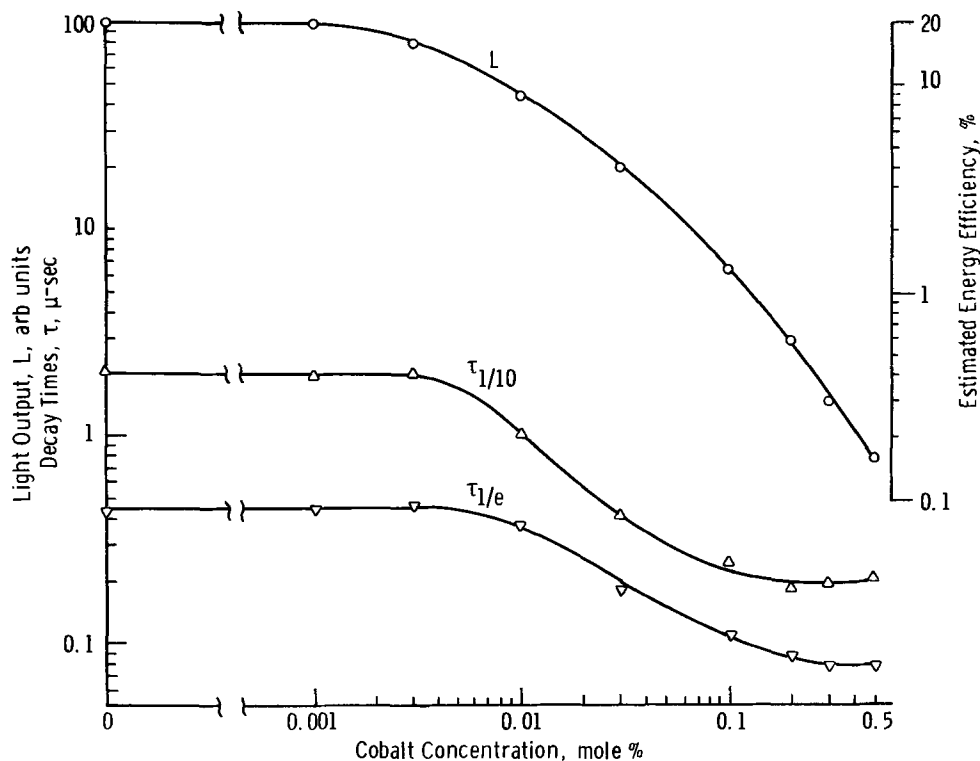


Fig. 3. Energy efficiencies and decay times of $\text{CaS}:\text{Ce}^{3+}, \text{Co}$.

it approaches exponential shape. The time constants, $\tau_{1/e}$, of decay at this ultimate limit are about 120 n-sec for Eu^{2+} and 80 n-sec for Pb^{2+} . The limits of the activators Bi^{3+} and Cu are still unknown. If the decay of a CaS-phosphor containing a particular activator is exponential already without cobalt, then addition of the latter only reduces the efficiency but not the decay times. An example of this case is CaS: Sb^{3+} whose exponential decay ($\tau_{1/e} = 0.8 \mu\text{sec}$) is not affected by the addition of cobalt.

Discussion

The observed action of cobalt on the luminescence decay of CaS-phosphors may be understood as follows.

The process of excitation and luminescence consists of a chain of events, the length of the afterglow is determined by the slowest link in the chain, and reduction of the afterglow by selective killing is possible only if the killer affects this slowest link. Well shielded 4f-states of trivalent rare earth ions are not affected by a killer in the surrounding lattice, for example, and since 4f \rightarrow 4f transitions generally are relatively slow, the afterglow of CaS-phosphors containing these ions is also slow and cannot be shortened by addition of cobalt or any other killer. The same holds true for the emission of Mn^{2+} and, more or less, for various other activators. Only activators with intrinsically fast electronic transitions permit a substantial reduction of the afterglow, and the ultimate speed limit attainable with increasing killer action is that of the intrinsic electron transition within the activator ion. Transitions between well-shielded states inside of an activator ion are first-order processes resulting in simple exponential decays but transitions involving states of the surrounding lattice normally are not. The chemical "killer" competes with the latter so that in the limit of high killer concentrations one approaches the simple exponential decay due to the first-order kinetics within the activator ion.

On the basis of this general picture one might describe the observed phenomena by a simplified model involving luminescence centers (activators), nonluminescent recombination centers (killers), traps, and various interactions between them. However, we believe any such model presently to be of little value since there are still too many unknowns, and we prefer not to go into details here.

A practical result of this investigation is the conclusion that some partly cobalt-killed CaS phosphors may advantageously replace conventional phosphors in applications where high speed of response is required. This includes mainly green CaS: Ce^{3+} and, perhaps, red CaS: Eu^{2+} . CaS phosphors containing the activators Pb^{2+} , Bi^{3+} , and Cu perform less well in this respect and are not likely to be competitive to conventional phosphors purely in terms of efficiency and speed.

Manuscript submitted Aug. 13, 1971; revised manuscript received Nov. 1, 1971. This was Paper 209RNP presented at the Washington, D.C., Meeting of the Society, May 9-13, 1971.

Any discussion of this paper will appear in a Discussion Section to be published in the December 1972 JOURNAL.

REFERENCES

1. W. Lehmann and F. M. Ryan, *This Journal*, **118**, 477 (1971).
2. F. A. Kröger, "Some Aspects of the Luminescence of Solids," p. 229, Elsevier Publishing Co. (1948).
3. H. W. Leverenz, "An Introduction to Luminescence of Solids," p. 309, 333, Wiley, Chapman & Hall, (1950).
4. L. A. Levy and D. W. West, Brit. Pat 424 195 (1935) and 440 818 (1936) and U.S. Pat. 2 075 399 (1937).
5. M. Avinor, U.S. Pat. 3 053 772 (1962).
6. M. Avinor, A. Carmi, and Z. Weinberger, *J. Chem. Phys.*, **35**, 1978 (1961).
7. W. Lehmann, *This Journal*, **117**, 1389 (1970).
8. W. Lehmann, *ibid.*, **118**, 1164 (1971).

A New Technique for Terminating Liquid Phase Epitaxial Growth

R. M. Potemski and J. M. Woodall*

IBM Thomas J. Watson Research Center, Yorktown Heights, New York 10598

A problem that is encountered with the liquid phase epitaxial growth method is that terminating growth by rapid cooling of the melt while it is still in contact with the substrate produces a gradient in composition along the growth direction (1) which is undesirable for certain device applications. Methods which have been employed to overcome this problem, such as withdrawal (2), tipping (3), and melt wiping (4) or a combination of these, suffer some disadvantages. For instance, gravitational methods such as tipping do not always remove the melt completely and droplets are left on the surface of the epitaxial layer. Wiping insures removal of the melt, but it is suitable only for carefully designed systems and can result in damage to the surface. Also, these methods expose the new surface to the atmosphere of the system at a high temperature with the possibility of contamination. This note describes a new method for terminating growth which can be easily applied to currently used growth systems. In this method the substrate is moved, along with a portion of the growth melt, from the growth melt into a quench melt which has a very low solubility for the solute species of the growth melt. When a small volume of this mixed melt, in contact with the wafer, is cooled to room temperature, an insigni-

ficant amount of growth occurs. Thus, the composition of the solid at the growing interface, as well as the surface morphology that existed just prior to termination of the layer growths, are essentially preserved.

Experimental Procedure

The system that was studied was the $\text{Ga}_{1-x}\text{Al}_x\text{As}$ LPE growth on (100) GaAs substrates. The apparatus shown assembled (top) and exploded (bottom) in Fig. 1 is a modification of that which has been previously described (5). Briefly, a substrate holder B can rotate with respect to melt chamber D, which can accommodate four separate melts. Spacer C fits between D and B to both hold the substrate in place and transfer a fixed volume of melt, depending on the spacer thickness, from one chamber into the other. Part A contains B, C, and D and fixes D in place during the rotation of B and C. The apparatus is such that the substrate can be rotated into a position between two melt chambers and be isolated from the melts.

Experiments were performed where all growth conditions were fixed except for the procedure for growth termination. In one case, the procedure of allowing the wafer to cool in the presence of a small volume of growth melt was followed. In the other, the wafer was brought into a quench melt prior to cooling. The growth melt consisted of 5g of Ga and 0.006g of Al, saturated with As from a bar of GaAs in

* Electrochemical Society Active Member.

Key words: crystal growth, liquid-phase epitaxy, heterostructures, compound semiconductors.

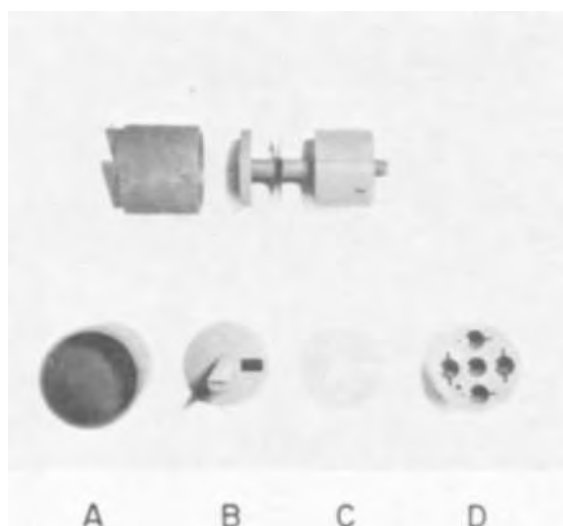


Fig. 1. Apparatus used for growth termination experiments. The diameter of part D is 2 in.

contact with the melt. The quench melt consisted of 2g of Ga, 0.200g of Al, and no GaAs. The growth schedule consisted of a 300°C vacuum bakeout, back filling and continuous flushing with palladium diffused H₂, and heating to 835°C. During this time the substrate was held between two chambers out of contact with any melt. After 55 min of soak time the substrate was moved into the growth melt and allowed to equilibrate for 10 min. Growth was then produced by lowering the temperature 0.1°C/min for 100 min. Next, the substrate was moved to a storage position between melts together with a small volume of growth melt carried along by the spacer. The run was then terminated by either (a) removal of the furnace, or (b) moving the substrate into the quench melt, holding for 30 sec while the carryover and quench melt mixed and then moving to a storage position followed by removal of the furnace. In both cases the substrate remained in the store position with a small amount of melt covering it until it was cooled to room temperature. Upon removal from the system the substrates were washed with hot water and detergent to remove any melt still present.

Results and Discussion

The wafers from the quench melt rapidly develop a blue film over the epitaxial layer surface when exposed to the air. The surface characteristics of such a layer are shown in Fig. 2a. This film (the dark regions of Fig. 2a), presumably Ga_{1-x}Al_xAs, with $x \sim 1$, readily oxidizes in moist air and is easily removed by washing in aqueous HCl (Fig. 2b). The surface structure of layer growth obtained by cooling in the presence of a small volume of growth melt is shown in Fig. 3. This surface does not exhibit oxidation because of its much lower aluminum content.

The wafers were cleaved parallel to the growth direction on (110) planes, etched in H₂O₂:HF:H₂O (1:1:10) to facilitate metallography and composition profiling. The composition profiles were measured with an electron beam microprobe. Figure 4 is a plot of the Al concentrations along the growth direction as a function of distance. Figure 4a shows the profile for growth terminated with a small volume of the growth melt. Figure 4b is the profile of the growth terminated with a quench melt and also etched in HCl. It is readily seen that both layers are initially uniform in composition. However, when growth is terminated by cooling in the presence of the growth melt, additional material is deposited in which the Al concentration decreases toward the surface. A comparison of the photomicrographs in Fig. 5 with the Al concentration

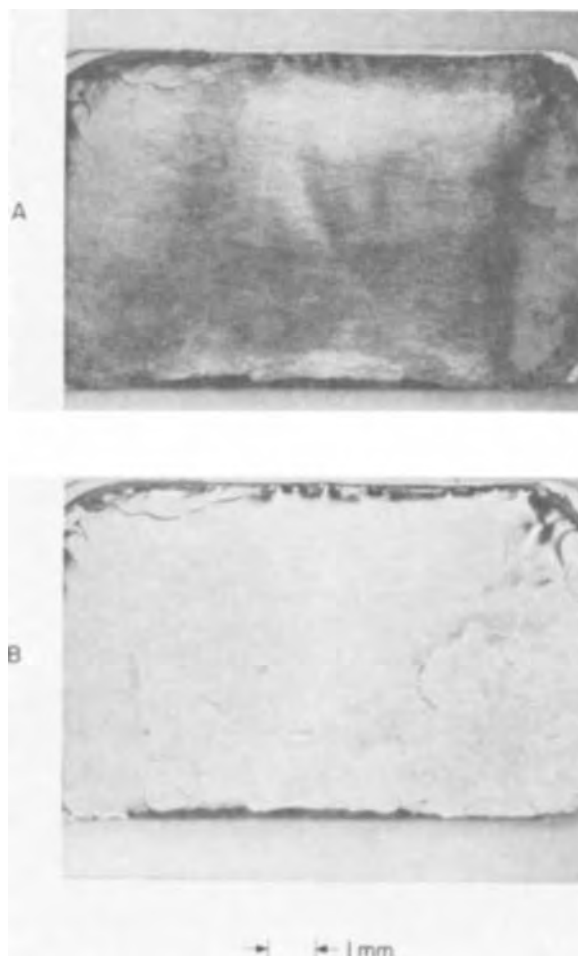


Fig. 2. Surface of a layer the growth of which was terminated by cooling in the presence of a mixed melt: (A) 1 hr exposure to air after growth, and (B) after washing in aqueous HCl.

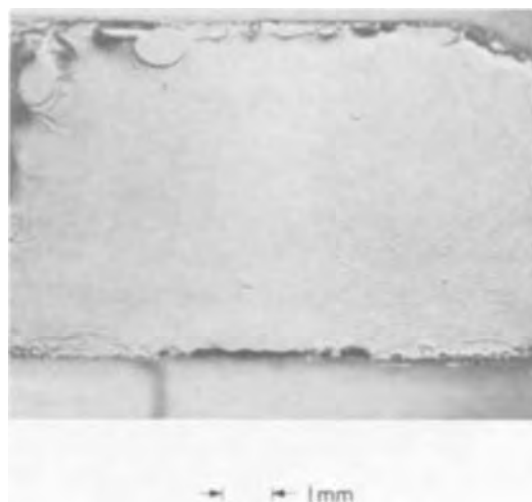


Fig. 3. Surface of a layer the growth of which was terminated by cooling in the presence of a growth melt.

profiles shown in Fig. 4 shows that terminating in contact with even a small volume of growth melt over the surface of a layer leaves behind an additional layer with a steep Al gradient along the growth direction. However, this additional layer growth is nearly eliminated using the growth-quenching technique and the small amount of growth that is present and nondetectable with an optical microscope is readily removed in HCl. Since cooling was done by rapidly

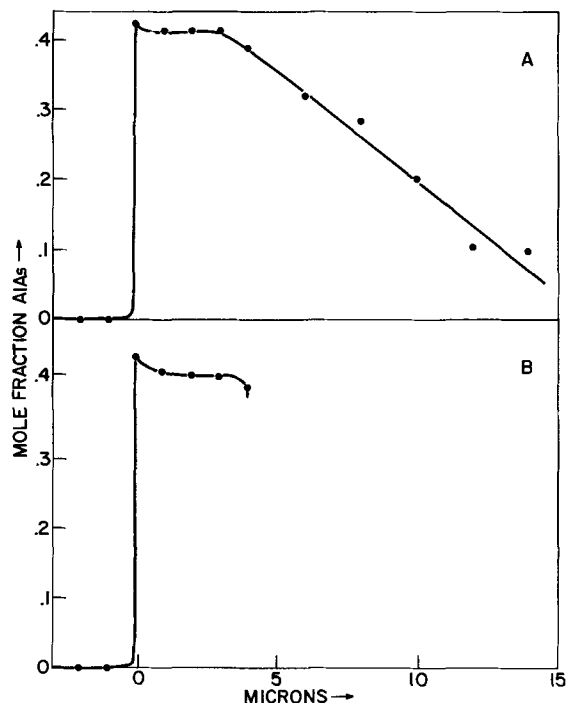


Fig. 4. Composition profile along the growth axis of (A) growth terminated by cooling in the presence of a growth melt and (B) growth terminated by cooling in the presence of a mixed melt.

removing the furnace from the melt and flushing with a large volume of H_2 gas, the amount of material that is deposited during cooling in the presence of a small volume of growth melt (Fig. 5a) represents the minimum amount of growth which will occur. Cooling more slowly produces termination layers even thicker than that shown in Fig. 5a. It is interesting to note that the surface morphology of the growth-melt cooled layer (Fig. 3) does not show constitutional supercooling effects such as deep valley cellular growth normally produced by large cooling rates.

An obvious application of the melt quench technique is the preparation of electroluminescent device structures of $Ga_{1-x}Al_xAs$ having sandwich layers which are optically transparent to light generated in an active region. The composition profile of a structure which should lead to devices with greatly improved external quantum efficiencies, provided the absorbing substrate can be etched away, is shown in Fig. 6. Even with the substrate intact, devices with this profile have had room temperature quantum efficiencies into air of 2% with the peak emission at 7900Å. This structure was grown from three different growth melts and terminated with a quench melt.

Acknowledgments

The authors wish to thank Mr. J. D. Kuptsis and Miss B. Chider for the microprobe analysis.

Manuscript submitted Aug. 20, 1971; revised manuscript received Oct. 27, 1971.

Any discussion of this paper will appear in a Discussion Section to be published in the December 1972 JOURNAL.

REFERENCES

1. J. M. Woodall, H. Rupprecht, and W. Reuter, *This Journal*, **116**, 899 (1969).

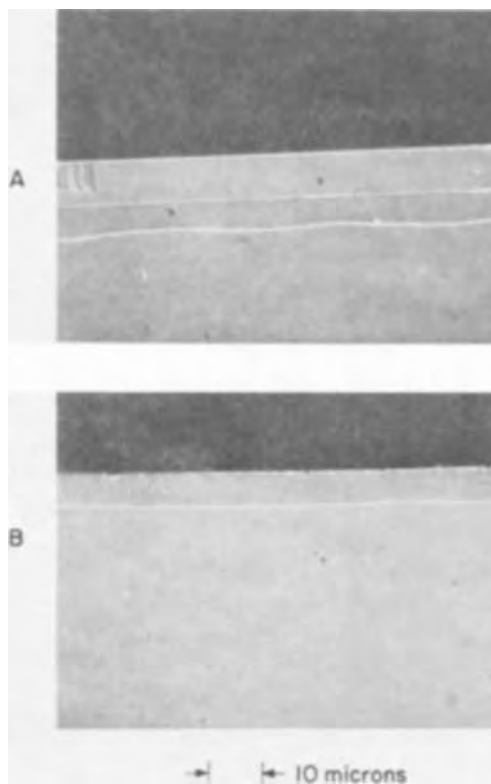


Fig. 5. Photomicrograph of (A) growth of Fig. 4a, and (B) growth of Fig. 4b.

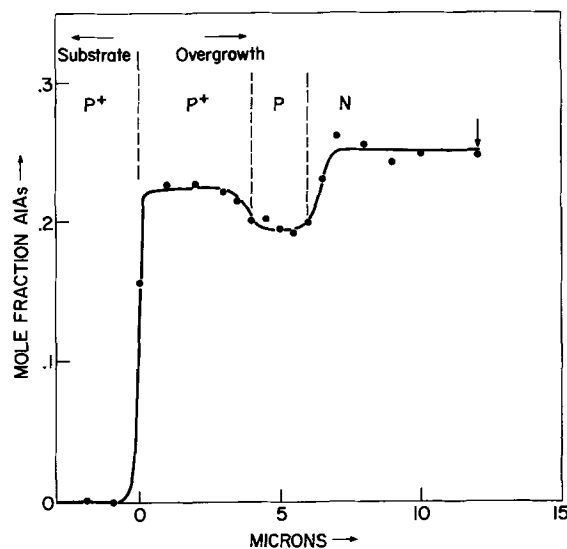


Fig. 6. Composition profile of three-layer electroluminescent diode structure. The arrow refers to the surface composition associated with melt quenching.

- H. Rupprecht, 1966 Proc. Int. Symp. on GaAs (London: The Institute of Physics and the Physical Society, 1967) p. 57.
- H. Nelson, *RCA Rev.*, **24**, 603 (1963).
- M. B. Panish, I. Hayashi, and S. Sumski, *Appl. Phys. Letters*, **16**, 326 (1970).
- J. M. Woodall, *This Journal*, **118**, 150 (1971).

Preparation and Semiconducting Properties of $\text{Cu}_2\text{In}_4\text{Te}_7$

A. Congiu, L. Garbato, P. Manca, and S. Serci

Istituto di Fisica dell'Università di Cagliari, Italy, Gruppo Nazionale di Struttura della Materia del C.N.R.

Following the current rules for normal valences and for valence electron concentrations used in the prediction of new semiconducting compounds (1) of tetrahedral structure, one can derive, for $A^I B^{III} C^{VI}$ group elements ($A^I = \text{Ag, Cu}$; $B^{III} = \text{Al, Ga, In}$; $C^{VI} = \text{S, Se, Te}$), the general composition formula $A^I_2 B^{III}_{2n} C^{VI}_{3n+1}$. This formula is equivalent to $(A^I_2 C^{VI}) (B^{III}_2 C^{VI}_3)_n$ in the $A^I_2 C^{VI} - B^{III}_2 C^{VI}_3$ pseudobinary system and predicts the possibility of preparing a number of isostructural semiconducting alloys with controlled cation vacancies.

The incorporation of cation vacancies makes it possible to satisfy the valence rules by nonintegral values of n , as well as by integral values of this coefficient. The formation of such an alloy system as n decreases can be regarded as a systematic filling, by atoms of the group A^I element, of the vacant lattice sites of the $B^{III}_2 \square C^{VI}_3$ defect structure in the range $0 \leq 1 - \frac{2n+2}{3n+1} < 0.33$, eventually reaching the normal tetrahedral phase $A^I B^{III} C^{VI}_2$ with $n = 1$.

Recent works (2-4) on the $A^I_2\text{Te}-\text{In}_2\text{Te}_3$ pseudobinary phase diagram, where the group A^I element is Ag or Cu, have shown the existence of the defect tetrahedral phases AgIn_3Te_5 , AgIn_5Te_8 , and $\text{AgIn}_9\text{Te}_{14}$, which are cases of the previous general composition formula with $n = 3, 5$, and 9 respectively.

AgIn_3Te_5 (2), AgIn_5Te_8 , and CuIn_5Te_8 (3) were shown to have the sphalerite (E_3) type structure, and $\text{AgIn}_9\text{Te}_{14}$ (4) seems to be of chalcopyrite (E_1) type.

The tetrahedral short-range order in these compounds is a consequence of the overlapping of sp^3 hybridized orbitals which can be assumed to be the predominant character of the bonding in these intermetallic alloys. All these phases are expected to be semiconductors but semiconducting properties have been investigated only for AgIn_3Te_5 (2) and $\text{AgIn}_9\text{Te}_{14}$ (4).

For the Cu-In-Te system the physical investigations are limited to normal tetrahedral phase CuInTe_2 (5, 6, 7). The pseudobinary $\text{Cu}_2\text{Te}-\text{In}_2\text{Te}_3$ diagram recently reported (3) contains a δ -phase region with sphalerite structure, stable at sufficiently high temperatures, which includes the $\text{Cu}_2\text{In}_4\text{Te}_7$ composition. In this note some results of our investigations concerning the synthesis and characterization of the defect phase $\text{Cu}_2\text{In}_4\text{Te}_7$ and its semiconducting properties are presented and briefly discussed.

Preparation and Metallurgical Properties

Polycrystalline ingots of nominal $\text{Cu}_2\text{In}_4\text{Te}_7$ composition were prepared by direct melting of the component elements (Johnson-Matthey quoted purity 99.999+%) sealed in evacuated silica tubes. To prevent surface oxidation, the tubes were first washed with $\text{HF} + \text{HNO}_3$ mixture, rinsed with deionized water, outgassed under dynamic vacuum (10^{-5} Torr) at 900°C over a period of 8 hr., and then cooled to room temperature under an argon atmosphere. Using a suitable temperature gradient along the furnace axis to pre-

Key words: compound semiconductors, ternary compounds, I-III-VI compounds, transport properties.

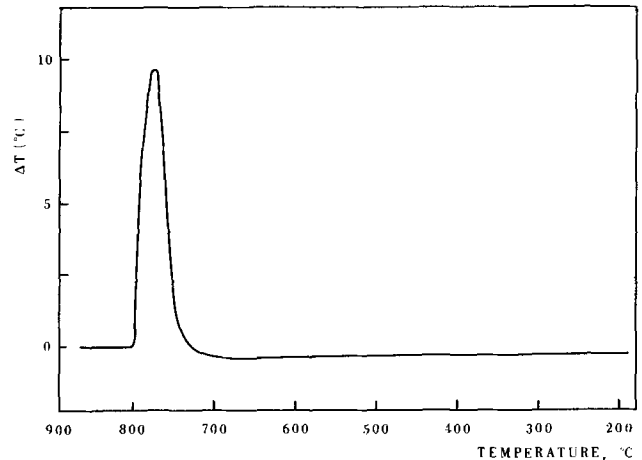


Fig. 1. Differential thermal analysis cooling curve

vent distillation of the volatile component, the samples were heated to 900°C with continuous 50 Hz vibration to assist mixing and left at this temperature for several hours. The ingots were obtained by slow cooling or by quenching in water from a temperature just below the melting point. Metallographic examination of mechanically and chemically polished surfaces showed the sample to be single-phase with a micro-hardness of (220 ± 20) kg/mm². The results of chemical analysis are consistent with the composition $\text{Cu}_2\text{In}_4\text{Te}_7$; the differences between the theoretical and the measured values for the components do not exceed 1%.

X-ray analysis on powders reveals the crystal structure to be of sphalerite type. At room temperature the lattice constant was found to be 6.16Å, the calculated density of 6.02 g/cm³ and the observed pycnometric density 5.93 g/cm³. By using the experimental data for the melting point and density, a Debye temperature of about 138°K has been evaluated according to the Lindeman melting formula (8).

The phase behavior has been investigated by DTA performed with a Netzsch differential thermal analyzer. Use of a sample heating rate of $2^\circ\text{C}/\text{min}$ and differential thermocouple sensitivity of 0.3°C permits the phase change temperature to be determined within $\pm 5^\circ\text{C}$.

The thermogram of Fig. 1 shows no solid-state phase change in the temperature range investigated and may be consistent with the small difference in liquidus and solidus temperatures indicated for this composition in Fig. 1 of Ref. (3). From a quantitative analysis of the DTA curves the heat of fusion was found to be approximately $\Delta Q_F = 168$ kcal/mole.

Some characteristic parameters of $\text{Cu}_2\text{In}_4\text{Te}_7$ are summarized in Table I.

Electrical and Thermoelectric Properties

All measurements were carried out on polycrystalline samples. Electrical conductivity measurements were made in the range $200^\circ - 570^\circ\text{K}$ by a conventional

Table I. Metallurgical properties of $\text{Cu}_2\text{In}_4\text{Te}_7$

Structure	Lattice parameter, Å	Density (exp), g/cm ³	Density (x-ray), g/cm ³	Micro-hardness, Kg/mm ²	Melting point, °C	Debye temperature, °K	Heat of fusion, kcal/mole
Sphalerite	6.16	5.93	6.0 ₂	220 ± 20	795 ± 5	138	168

Table II. Electrical and thermoelectric properties of $\text{Cu}_2\text{In}_4\text{Te}_7$ at 300°K

Energy gap, eV	Electrical conductivity (ohm-cm) ⁻¹	Hall mobility, cm ² /V-sec	Thermal conductivity, W/°C-cm	Thermoelectric power, $\mu\text{V}/^\circ\text{C}$	$\frac{m^*}{m_0}$	E_f , eV	Carrier concentration, cm ⁻³	Temperature dependence of Hall mobility	Thermoelectric figure of merit, °K ⁻¹
1.10	$3 \cdot 10^{-4}$	0.27	0.02	550-900	0.13	0.15	$7 \cdot 3 \cdot 10^{25}$	$T^{1.5}$	10^{-8}

d-c method with 4-probe contacts on samples with approximate dimensions $10 \times 4 \times 1$ mm. Both thermal conductivity and thermoelectric power were measured by the absolute method on cylindrical samples 2 cm long and 1 cm in diameter by using a slightly modified version of the apparatus reported by Klein and Caldwell (9). To minimize heat transfer by radiation, the sample was surrounded with a thermal shield. Steady-state heat flow conditions were reached at each temperature with a system isolated in vacuum. The tem-

peratures were measured by calibrated copper-constantan thermocouples soldered to the heater and sink. To insure low thermal resistance contacts, the heater, sink, and sample were lapped and then a thin layer of thermosetting silver (Johnson-Matthey) was introduced between the lapped surfaces.

The samples investigated, all of which were prepared by slow freezing, exhibit nondegenerate behavior in the electrical conductivity vs. temperature (200°-570°K) curves. The Hall effect (300°-400°K) and thermal emf

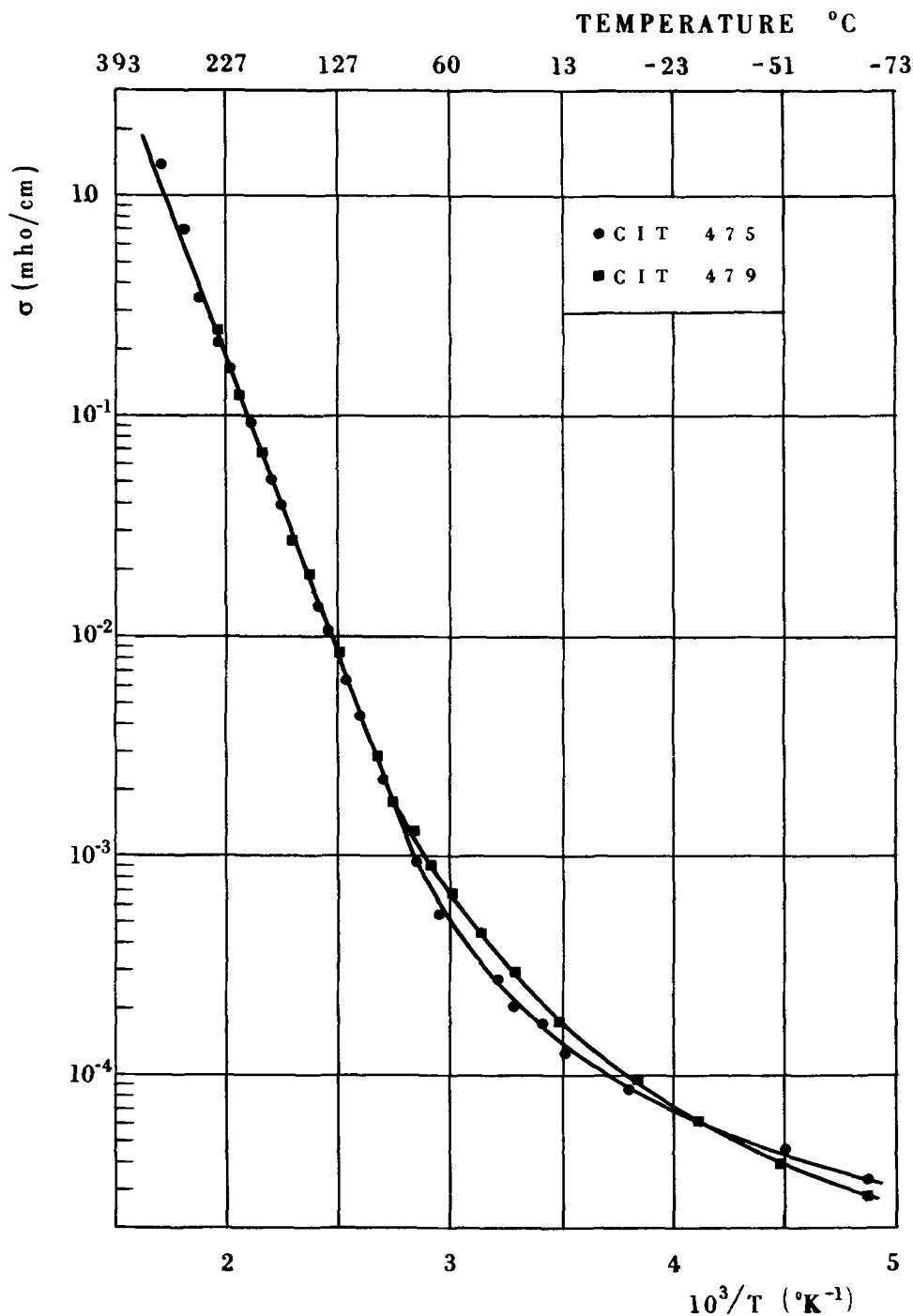


Fig. 2. Logarithm of electrical conductivity vs. reciprocal absolute temperature for two samples.

Table III. Some properties of CuInTe_2 and $\text{Cu}_2\text{In}_4\text{Te}_7$

Compound	Structure	Lattice parameter, Å	Melting point, °C	Micro-hardness, kg mm ⁻²	Energy gap, eV	Hole mobility, cm ² /V-sec
CuInTe_2	Chalcopyrite ^(a)	6.167-12.34 ^(a)	780 ^(b)	210 ± 20 ^(b)	1.05 ^(c)	100 ^(b)
$\text{Cu}_2\text{In}_4\text{Te}_7$	Sphalerite	6.16	795	220 ± 20	1.10	0.1-1

(a) Ref. (10).
 (b) Ref. (6).
 (c) Ref. (5).

(100°-300°K) measurements show that the predominant carriers are holes.

At room temperature the conductivity is about $3 \cdot 10^{-4}$ mho/cm and the hole concentration $p = 7 \cdot 10^{15}/\text{cm}^3$.

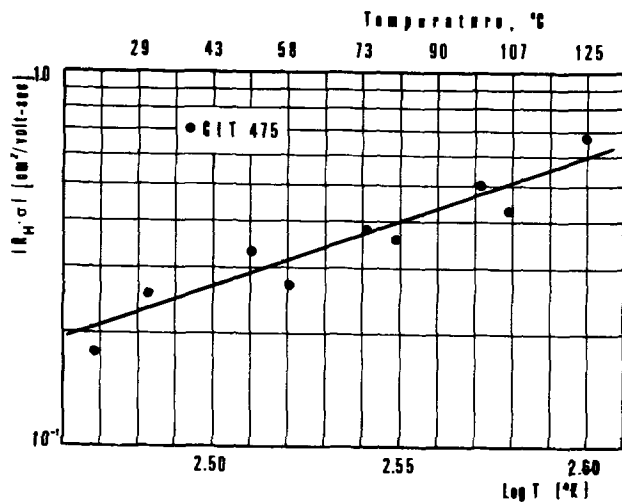


Fig. 3. Logarithm of Hall mobility plotted against logarithm of absolute temperature.

The typical curves of $\log \sigma$ vs. $10^3/T$ shown in Fig. 2 indicate that the intrinsic conductivity region begins at 390°K; above this temperature the slope of the line for the samples CIT 475 and 479 gives an energy gap of 1.10 eV.

The hole mobility calculated from the measured values of σ and R in the extrinsic range by using the single carrier approximation is between 0.3 and 1 cm²/V-sec. The mobility in this range is plotted against temperature on a logarithmic scale in Fig. 3. The value of the scattering parameter, of the order 3/2, calculated from the slope of this graph, indicates that ionized impurity scattering is dominant at these temperatures.

Figure 4 shows the temperature dependence of the thermal conductivity, for $\text{Cu}_2\text{In}_4\text{Te}_7$ ingots CIT 475, 479, 473. Its value varies between 0.017-0.023 W/°C-cm at room temperature.

The electronic contribution at this temperature, calculated according to the Wiedemann-Franz law, is negligible ($3 \cdot 10^{-9}$ W/°C-cm). The thermoelectric power at room temperature, for the same samples of Fig. 4, is of the order 550-900 $\mu\text{V}/^\circ\text{C}$. Its temperature variation is shown in Fig. 5.

From the measured values of thermoelectric power and Hall constant the effective mass of holes was found to be $m^*/m = 0.13$ by assuming ionized impurity scattering. The values of the figure of merit (Z), calcu-

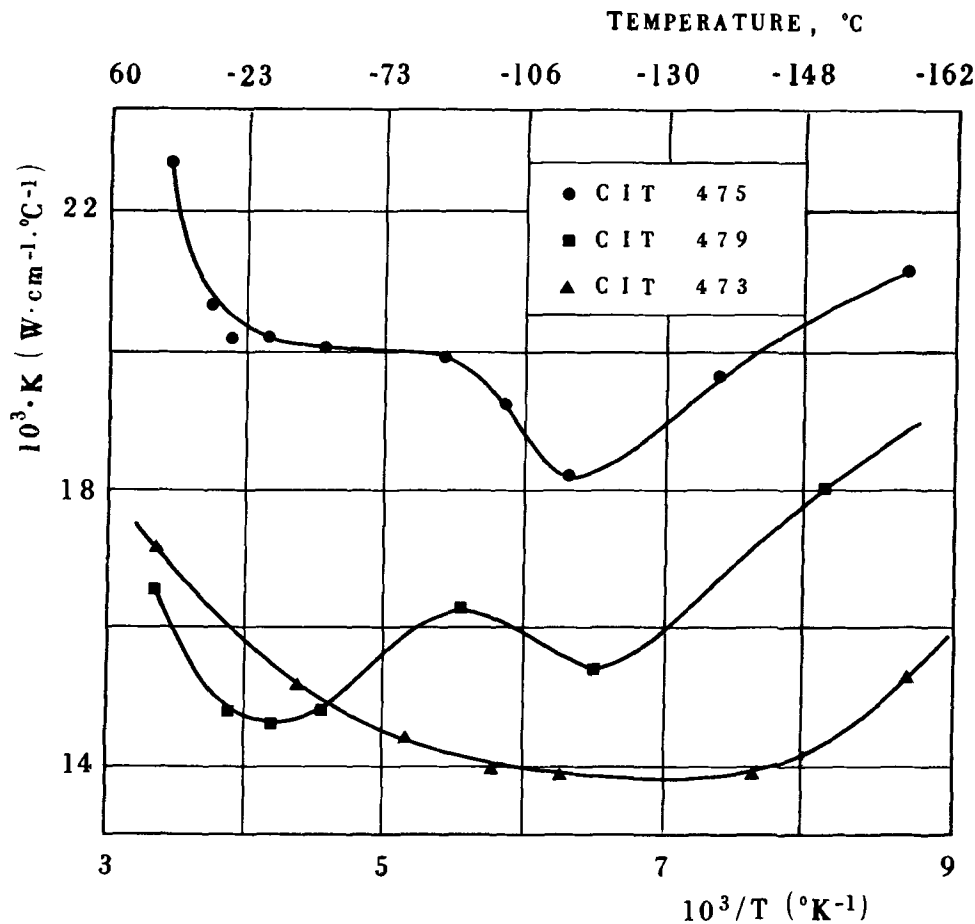


Fig. 4. Thermal conductivity vs. $1/T$ for three samples.

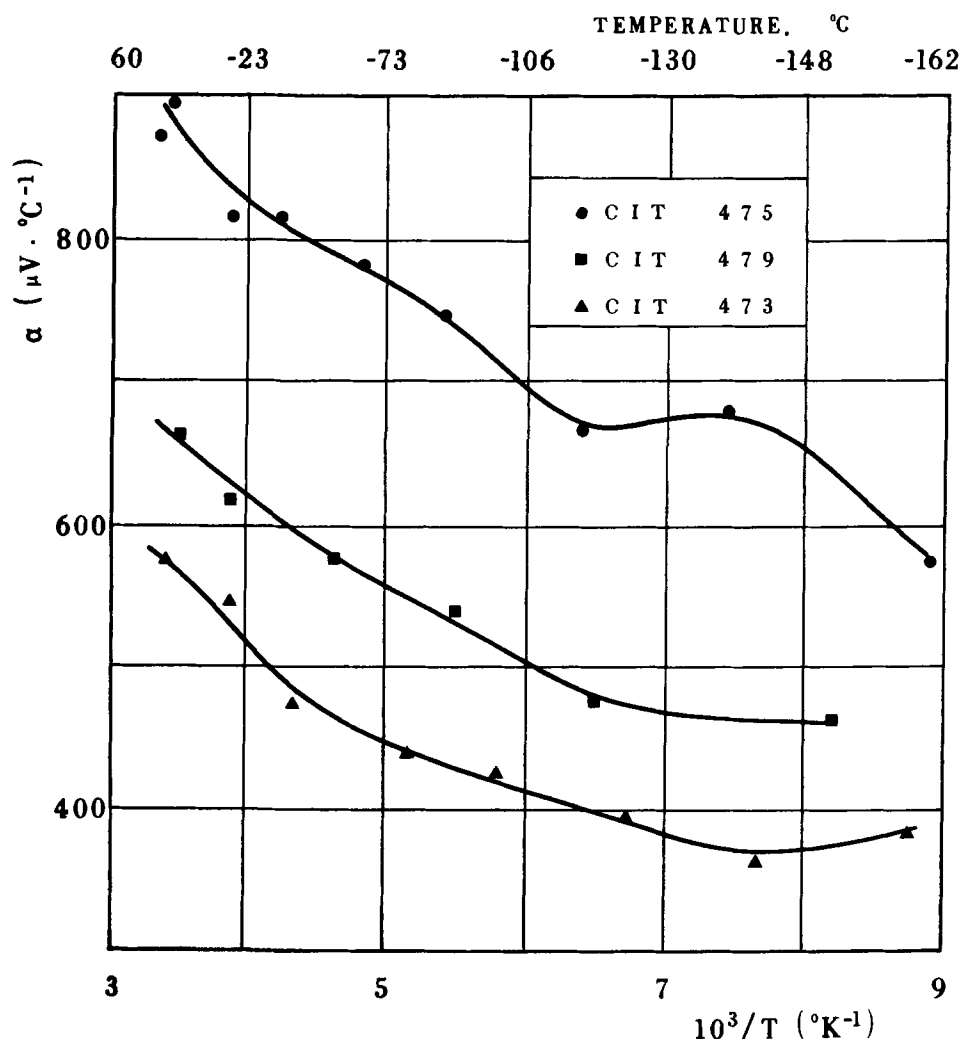


Fig. 5. Thermoelectric power vs. $1/T$ for three samples.

lated from the data for α , σ , and K is very small, reaching the value of $10^{-8} \text{ }^\circ\text{K}^{-1}$ at room temperature. Table II lists representative room temperature values of the fundamental electric and thermoelectric properties, based on the results of measurements on several samples.

Conclusion

According to the general composition formula $\text{A}^{1/2}\text{B}^{\text{III}}_{2n}\text{CVI}_{3n+1}$ derived for defect tetrahedral phases in $\text{A}^{\text{I}}\text{B}^{\text{III}}\text{CVI}$ system, a defect tetrahedral phase of $\text{Cu}_2\text{In}_4\text{Te}_7$ composition has been prepared and characterized by metallographic, x-ray structure, and differential thermal analysis, as a single phase of sphalerite-type structure.

$\text{Cu}_2\text{In}_4\text{Te}_7$ is a p-type semiconductor with an energy gap of 1.10 eV. Some of its properties are compared with those of CuInTe_2 in Table III.

Acknowledgment

This work was supported by C.N.R. under Contract No. 115-0717-0328.

Manuscript submitted Jan. 8, 1971; revised manuscript received Aug. 10, 1971.

Any discussion of this paper will appear in a Discussion Section to be published in the December 1972 JOURNAL.

REFERENCES

1. N. A. Goriunova, "The Chemistry of Diamond-like Semiconductors" Chapman and Hall (1965).
2. D. F. O'Kane and D. R. Mason, *This Journal*, **111**, 546 (1964).
3. L. S. Palatnik and E. I. Rogacheva, *Sov. Phys. Doklady*, **12**, 503 (1967).
4. P. W. Chiang, D. F. O'Kane, and D. R. Mason, *This Journal*, **114**, 759 (1967).
5. I. F. Austin, C. H. L. Goodman, and A. E. Pengelly, *ibid.*, **103**, 609 (1956).
6. V. P. Zhuze, V. M. Sergeeva, and E. L. Shtrum, *Sov. Phys. Tech. Phys.*, **3**, 1925 (1958).
7. S. M. Zalar, *This Journal*, **109**, 207 (1962); *J. Appl. Phys.*, **35**, 1988 (1964).
8. J. M. Ziman, "Electrons and Phonons" Oxford University Press (1960).
9. M. V. Klein and R. F. Caldwell, *Rev. Sci. Instr.*, **37**, 1291 (1966).
10. H. Hahn, G. Frank, W. Klingler, A. D. Meyer, and G. Storger, *Z. Anorg. Allgem. Chem.*, **271**, 153 (1953).



153

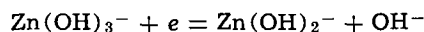
On the Deposition and Dissolution of Zinc in Alkaline Solutions

J. O'M. Bockris,* Z. Nagy,^{*1} and A. Damjanovic²

Electrochemistry Laboratory, University of Pennsylvania, Philadelphia, Pennsylvania 19104

ABSTRACT

The zinc/KOH-zincate electrode reaction was investigated under high purity conditions with galvanostatic and potentiostatic transient techniques in the 0.1-3.0M KOH and 0.0001-0.5M zincate concentration range. The exchange current density was found to be between 8 and 370 mA/cm², with 40 mV/decade anodic and 120 mV/decade cathodic nominal Tafel slopes; an overpotential range of ± 100 mV was covered. The cathodic reaction orders were 1 for zincate, and -1 for hydroxyl ions. A four-step mechanism, consistent with the kinetic data, is suggested. It consists of four consecutive dissociation reactions of the zincate complex, with two of them incorporating a single electron charge transfer. The rate-determining step is



The mechanism of the anodic and cathodic reactions is the same. The transients indicate only double layer charging and charge transfer processes. No surface diffusion effects or intermediate build-up was observed (no pseudocapacitance). A rationalization is given for the mechanism. The effect of zinc surface preparation is discussed.

The electrochemistry of metal deposition and dissolution, in the past, has been mostly an applied science, and only in recent years has some fundamental knowledge been accumulating in this field. These advances are summarized in a recent review (1). These reactions form a special section of electrochemistry because the electrode material itself is being formed or dissolved during the process. Therefore, in addition to the basic charge transfer step, and the preceding or following chemical steps and solution transfer processes, the crystal building or breaking of the solid and the surface transport of intermediate species must be considered. In certain cases one of these latter steps may be rate determining; e.g., the lattice building step was suggested as the rds in the electrodeposition of silver on carbon electrodes (2), and slow surface diffusion was found to be the rds for silver (3, 4) and copper (5) depositions at low overpotentials. Because of the direct involvement of the substrate in the reaction, any changes in its surface structure can have profound influence; the decrease of dislocation density can cause a shift from charge transfer control to surface diffusion control (6) and in the extreme case, on a dislocation free surface, the process may become controlled by two dimensional nucleation as was shown for silver (7, 8). These characteristics also introduce some experimental limitations, mainly the need for reproducible surface preparations, the necessity of short pulse measurements to avoid any changes in surface structure due to the measuring current, and special precautions to avoid spontaneous surface changes when in contact with the solution.

* Electrochemical Society Active Member.

¹ Present address: Diamond Shamrock Chemical Co., Painesville, Ohio 44077.

² Present address: Xerox Research Laboratories, Webster, New York 14580.

Key words: zinc/alkaline zincate electrode, reaction kinetics and mechanism, galvanostatic and potentiostatic transients, consecutive single electron transfers, predissociation, charge transfer rate-determining step.

Some fundamental work has been reported recently on the zinc/alkaline zincate system (9-13) but the experimental results and conclusions of the different investigators are contradictory. The lack of more extensive work and the poor agreement among the data are indicative of the complexity of the system; some of the difficulties arise from the possible surface changes by corrosion reaction and oxide formation. A better understanding of this system is desirable not only because of the fundamental interest in the metal deposition-dissolution reactions but also because of its technological importance. The silver-zinc battery is the only one among the presently commercially available electrochemical energy storers which approaches the power and energy density required for an electric car. However, a short cycle life limits its present use to air- and spacecraft applications (14-15). The zinc-air system seems one of the most promising future energy storers. The further improvement of this almost practical system is partly impaired by a lack of fundamental understanding of the electrode processes occurring, both at the angstrom and micron level. In this paper, the first of these levels is the subject.

Experimental

Galvanostatic and potentiostatic pulse techniques were used to examine both the transient and the steady-state current-potential behavior of the system.

Electrode preparation.—Polycrystalline zinc rods (99.999%), machined to 3 mm diameter, were used. The electrodes were first mechanically polished with silicon carbide papers (grits 180, 320, and 600), and then with alumina powders (1.0 and 0.3 μ). The surface was then anodically etched for 10 min in 2M KOH solution at a current density of 2.5 mA/cm² with a 100 Hz 3.25 mA/cm² (peak) a.c. superimposed. This treatment removed a layer more than twice as thick as the

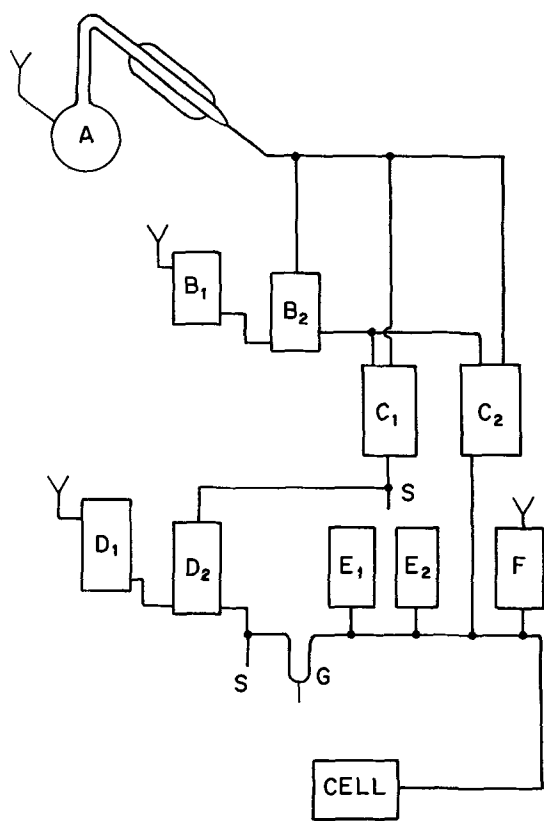


Fig. 1. Solution purification system. A: still. B₁, B₂: potassium amalgam preparation and decomposition cells. C₁, C₂: potassium hydroxide dilution vessels for test solution, and the 0.1M solution used in the reduction of the electrode. D₁, D₂: zinc amalgam preparation and decomposition cells. E₁, E₂: Test solution storage vessels. F: distilled water for washing cell. G: Mercury trap. S: sampling points.

last polishing powder and eliminated imbedded particles. After this treatment the rod was annealed in a purified nitrogen atmosphere at 200°C for 2 hr, followed by slow cooling. The electrode was then stored in a desiccator. A final treatment of the electrode was carried out in the test cell; it was an electrochemical reduction in 0.1M KOH solution at a current density of 50 mA/cm² for 8 min.

Solution preparation.—The solutions ranged from 0.1 to 3M KOH and from 0.0001 to 0.5M zincate. The equipment used for the solution preparation is shown schematically in Fig. 1. The procedure was as follows. Potassium amalgam was first made electrolytically from a solution of AR grade KOH dissolved in double-distilled water. The amalgam was then transferred under N₂ pressure into the decomposition vessel and electrolytically decomposed into triple-distilled water. The third distillation of the water was carried out under a nitrogen atmosphere directly into the decomposition vessel, just before preparation of the solution. This pure KOH solution was then transferred to another vessel (cf. D₂, Fig. 1) and left there for an extended time (10–20 hr) over zinc amalgam, prepared electrolytically from zinc sulfate solution, to remove any traces of dissolved mercury which may have been introduced during the preparation of pure KOH. Finally, the required amount of zinc was electrolyzed into the solution from the zinc amalgam. The counterelectrodes in these processes were platinum wires separated by glass frits from the main solutions. This type of purification has been shown to remove all metallic impurities below the 0.1 ppm level (16). The nonmetallic impurities were also removed since there always remained a mercury seal between the amalgam preparation and decomposition vessels and only the amalgam was transferred from one vessel to another.

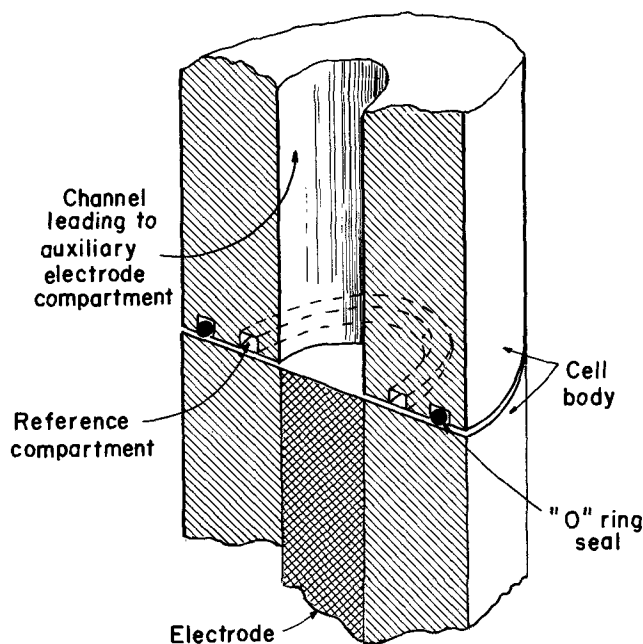


Fig. 2. Concept of cell design

During every stage of these operations, purified nitrogen was passed through the solutions. The gas was purified by passing it over 400°C copper turnings and then over 13X Molecular Sieve. The solutions were analyzed before being used by acidimetric and EDTA titrations (17). The solutions containing 0.6M KOH or less were supersaturated in zincate to avoid diffusional limitations in the measurements. The stability of the supersaturated solutions has been shown before (27).

Cell.—The measuring cell was designed to give low IR drop between the reference and the working electrode and at the same time provide a uniform current distribution and small interelectrode stray capacitances. These features were necessary to provide a short rise time for the potentiostatic transients (18). This was achieved by a cell construction which completely eliminates the "classical Luggin-capillary." The basic concept of the cell is illustrated in Fig. 2. The working electrode is pressfitted into a Teflon holder comprising the bottom of the cell. The top portion (made of KEL-F) contains the reference electrode compartment and the auxiliary electrode chamber. The latter is connected to the working electrode by a channel exactly matching the size and position of the working electrode to assure uniform current distribution. This channel is surrounded by a concentric groove which serves as the reference compartment. The cell bottom and top are held apart by a suitable spacer providing a gap between them. This circular gap serves as a connector between the working and reference electrodes and provides (i) a very low IR drop between the point of potential measurement and the surface of the working electrode, (ii) a low internal resistance, and (iii) a minimal interference with the current distribution. The gap thicknesses used in the present experiments were 0.0025 and 0.0125 cm. The counterelectrode was a platinum wire spiral; the reference was a zinc wire immersed in the test solution. The potential of the zinc reference was often checked against an outside Hg/HgO electrode with KOH concentration the same as that of the test solution. Purified nitrogen was bubbled continuously through the cell. A detailed description of the cell is given elsewhere (18).

Electronics.—**Galvanostat.**—The galvanostat was basically a transistor amplifier in the emitter-follower configuration (Fig. 3). A fixed reference voltage is supplied by the Zener diode, which results in a fixed

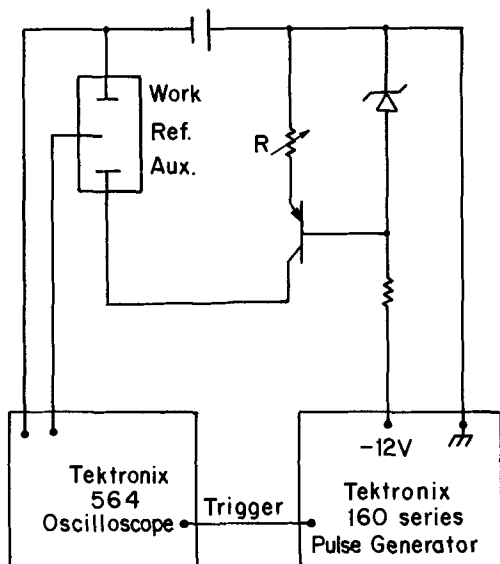


Fig. 3. Schematic of the galvanostatic equipment

voltage drop over the variable resistor, R . The current is set by the reference voltage and the value of R , and will remain constant independently of the resistance of the cell and the supply voltage. A similar type galvanostat, using a common power source for the Zener and the cell circuits, was previously described (19). When a separate pulse generator is used for the Zener it is possible to control precisely the pulse length. This is necessary in order to reduce the total charge passed during the experiments and hence to avoid excessive changes of the electrode surface.² In Fig. 3 the cathodic galvanostat is shown: the anodic one was similar, *mutatis mutandis*, using an n-p-n transistor. Two different circuits are needed to provide low noise sources. The potential-time transients were recorded with a Tektronix 564 storage scope connected to the cell through a voltage-follower buffer stage (20) to avoid loading the cell.

Potentiostat.—The potentiostat was a wide-band, differential input unit built of operational amplifiers. It was equipped with variable phase compensator and IR compensation features to allow fast and close control of the potential. It is described in detail elsewhere (20).

Experimental procedures.—The pulses applied were usually of 5 msec duration or shorter. Longer pulses were made only occasionally. All measurements were made at room temperature.

Galvanostatic experiment.—A galvanostatic experiment proceeded as follows. The cell was flushed and filled with 0.1M KOH solution and the working electrode was reduced. The cell then was flushed and filled with the test solution and the measurements were made. During the course of a run an arbitrarily selected current point was often repeated to check reproducibility. Usually a range of ± 100 mV overpotential was covered. Current densities up to 4 A/cm² were used. Some examples of the galvanostatic transients are shown in Fig. 4. In spite of the special cell used there still remained a measurable IR drop; a correction for this was applied in the determination of the overpotential. Examples of Tafel and linear plots constructed from the steady-state portion of the transients are shown in Fig. 5 and 6.

Potentiostatic run.—A potentiostatic run was completed in the following way. The electrode was reduced galvanostatically as described above. After the cell was filled with test solution, a galvanostatic pulse was applied to determine the IR drop between the reference and the working electrodes, and the IR

² A set-up like this could also be used to supply a galvanostatic pulse train or repetitive pulses.

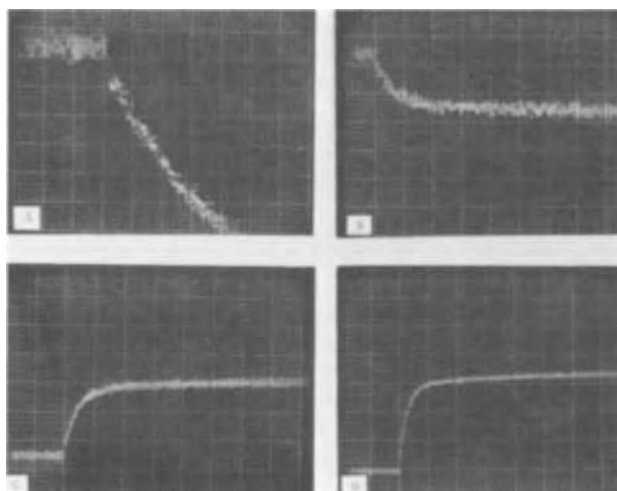


Fig. 4. Examples of the galvanostatic transients. Solution: 3.0M KOH, 0.018M Zn(OH)₄²⁻; $i_0 = 65$ mA/cm². A: 50 mA/cm², cathodic; 1 mV/cm, 2 μ sec/cm; $C_{dl} = 50$ μ F/cm². B: 16.5 mA/cm², cathodic; 2 mV/cm; 20 μ sec/cm; calculated rise time: 40 μ sec. C: 58 mA/cm², anodic; 5 mV/cm, 20 μ sec/cm. D: 193 mA/cm², anodic; 10 mV/cm, 20 μ sec/cm.

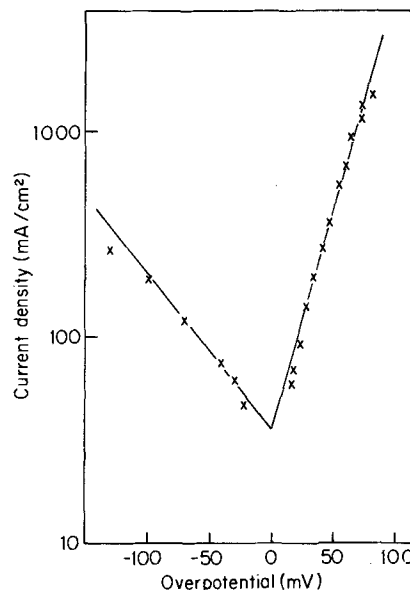


Fig. 5. Example of Tafel plot (electrolyte: 1.8M KOH, 0.018M zincate).

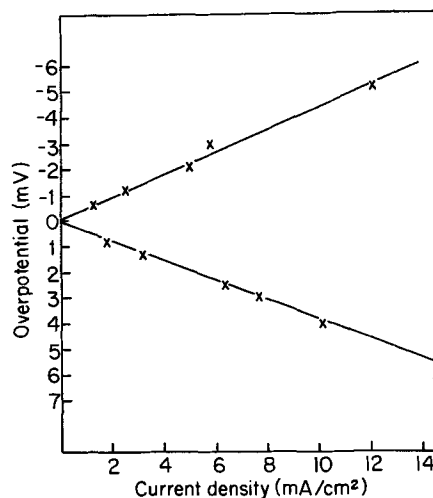


Fig. 6. Example of linear i - η plot (electrolyte: as in Fig. 15). Exchange current density determined from the anodic slope, 34 mA/cm²; from cathodic slope, 30 mA/cm².

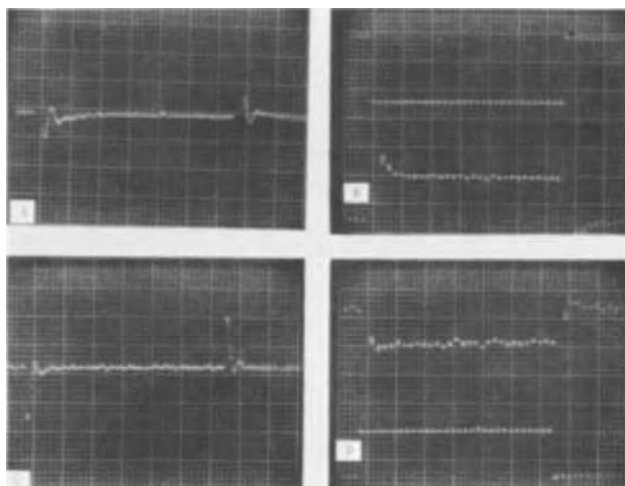


Fig. 7. Examples of potentiostatic oscillograms. Electrolyte: 1M KOH, 0.02M $Zn(OH)_4^{2-}$. A and B cathodic, C and D anodic. A: Error signal; 10 mV/cm, 20 μ sec/cm. B: Top. Potential signal to potentiostat 20 mV/cm, 20 μ sec/cm. Bottom. Current, 5 mA/cm, 20 μ sec/cm. C: Error signal, 5 mV/cm, 20 μ sec/cm. D: Bottom. Potential signal to potentiostat, 5 mV/cm, 20 μ sec/cm. Top. Current, 2 mA/cm, 20 μ sec/cm.

compensation of the potentiostat was adjusted accordingly. The electrode was potentiostated at its rest potential and then a few short pulses of the desired potential were applied in order to allow optimum adjustment of the potentiostat. The error-signal of the potentiostat (the difference between the desired and actual electrode potentials) was displayed on the scope, and the phase compensation of the potentiostat was adjusted to eliminate or minimize ringing and achieve the shortest possible settling time. The measuring pulse was then applied and the current-time transient recorded. The error-signal was checked before each pulse, but the phase compensation needed only occasional readjustments. Examples of oscillograms are shown in Fig. 7.

Although the cell was designed to provide minimal IR drop, and so to avoid the necessity of IR compensation in the potentiostat, the error was still significant at the high exchange current densities, even with the smallest (0.0025 cm) gap distance. (E.g., at 3M KOH concentration the solution resistance was 7×10^{-3} ohm cm^2 while the reaction resistance could be as low as 35×10^{-3} ohm cm^2 , a 20% error). Therefore, a wider gap (0.0125 cm) and IR compensation was used in many of the experiments resulting in settling times of 10-30 μ sec. The selection of gap thickness and the choice of operation with or without IR compensation are discussed in detail elsewhere (18, 20).

Determination of reaction orders (galvanostatic method).—Because the exchange current density vs. concentration plots (see Fig. 8 and 9) had a considerable spread of points, additional experiments of other types were carried out to confirm the reaction orders by the measurement of $[\partial \log i_0 / \partial \log C_1]_{C_2, E}$. Since the spread of the i_0 was attributed to the day-to-day variations of the surface of the working electrodes, in these additional experiments the electrolyte concentration was changed during the test itself with a single electrode. In this type of experiment, the electrolyte concentration was varied and at each concentration a quick galvanostatic cathodic run was made to establish Tafel lines. The electrode was reduced before each run.

Determination of reaction orders (potentiostatic method).—An even faster way (therefore, affording less chance for surface change) was to measure the change of current at a constant potential (NHE) as a function of solution concentrations. This required tak-

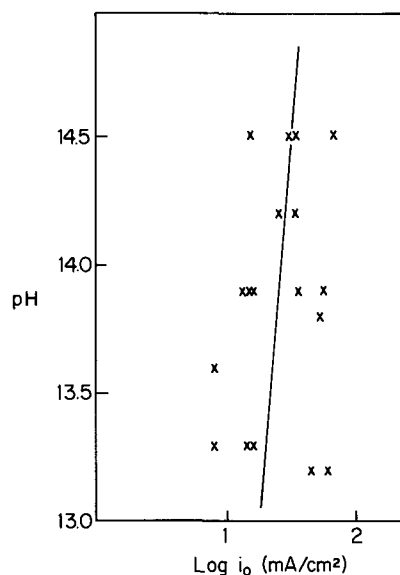


Fig. 8. The pH dependence of exchange current density (zincate concentration: 0.019M).

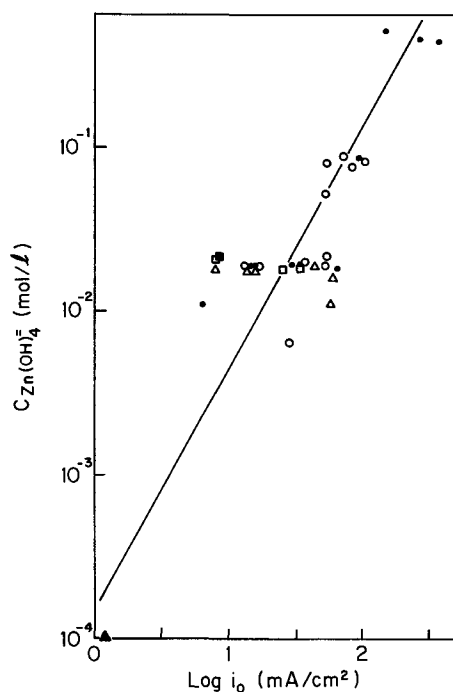


Fig. 9. The dependence of exchange current density on zincate concentration. Symbols: \bullet , 3.0; \square , 1.8; \circ , 1.0; \blacksquare , 0.6; \triangle , 0.3; \blacktriangle , 0.1M KOH.

ing only one point at each concentration. It was carried out for varying zincate at constant pH and for varying pH at constant zincate concentration.

Corrosion rate measurements.—The corrosion rate of zinc in various test solutions was measured by immersing zinc wire in nitrogen stirred solutions for 74 hr; the increase of zincate concentration of the solution was determined by titration (17). The measurements were carried out at room temperature, in duplicates.

Results

Rest potentials.—The rest potential of zinc in different alkaline zincate solutions is compared to the calculated equilibrium potentials in Table I. The equilibrium values were obtained using the equation (21)

$$E = 0.441 - 0.1182 \text{ pH} + 0.0295 \log a_{Zn(OH)_4^{2-}}$$

and the potential of the Hg/HgO reference electrode was taken as (22)

Table I. Measured and calculated electrode potentials

Solution composition		Activity coefficient		Potential (NHE)	
KOH (mol/l)	K ₂ Zn(OH) ₄ (mol/l)	KOH	K ₂ Zn(OH) ₄	Calculated (V)	Measured (V)
0.3	0.011	0.74	0.44	-1.205	-1.187
1.0	0.087	0.78	0.30	-1.248	-1.230
1.0	0.022	0.76	0.31	-1.264	-1.249
1.0	0.0065	0.75	0.32	-1.278	-1.257
3.0	0.435	1.39	0.21	-1.318	-1.291
3.0	0.085	1.12	0.22	-1.327	-1.300

$$E = 0.926 - 0.059 \text{ pH}$$

There are no activity data available for alkaline zincate solutions, and the following approximations were made to obtain the activity coefficients. For potassium hydroxide the tables of Harned and Owen (23) were used, taking the values at the appropriate ionic strengths of the test solutions, with the assumption that addition of zincate has no specific effect. Activity coefficients of a number of 1-2 electrolytes are tabulated by Robinson and Stokes (24) and the values of all the salts reported seem to be in fair agreement with each other. Therefore, as a first approximation, the coefficients reported for K₂CrO₄ were used for the zincate, taken at the appropriate ionic strengths.

Transition times.—Since the potential of zinc is negative to the reversible hydrogen potential a possibility of hydrogen evolution interference with the test measurements exists. To investigate this effect transition times of the zincate deposition reaction were measured galvanostatically in the milliamperes to the ampere per square centimeter current density range, at different zincate concentrations. The calculated and measured transition times agreed within the limit of experimental error [a *D* value of 0.7×10^{-5} cm²/sec was used (25) in the Sand's equation].

Corrosion rates.—The corrosion rate of zinc in 1.8M KOH solution was found to be equivalent to a current of 45 μA/cm². Addition of 0.03 and 0.1M zincate to the above solution decreased the corrosion rate below 1 μA/cm² (the sensitivity of the measurement).

Galvanostatic steady-state data.—Tafel slopes.—The steady-state activation overpotentials, taken from the flat portion of the galvanostatic transients, were plotted in the usual manner (Fig. 5) and the Tafel slopes were determined. The cathodic slopes were 113 ± 30 mV/decade, and the anodic ones 49 ± 13 mV/decade. The slopes were found to be independent of solution composition.

Exchange current densities.—These were determined by extrapolation of cathodic and anodic Tafel lines (Fig. 5), and also from the polarization resistance values measured at low overpotentials (Fig. 6). The agreement among these four *i*₀ values was better than ±10% in most cases, in a few instances deviations up to ±30% were observed. For each test, an average value was calculated and these are plotted as a function of solution composition in Fig. 8 and 9. The value of the exchange current density was found to be practically independent of pH, the statistical best line through the points of Fig. 8 gives

$$\left[\frac{\partial \log i_0}{\partial \text{pH}} \right]_{C_{\text{Zn}(\text{OH})_4} =} = 0.14$$

The dependence of the exchange current density on zincate concentration is shown in Fig. 9. The best fitting line has a slope of

$$\left[\frac{\partial \log i_0}{\partial \log C_{\text{Zn}(\text{OH})_4} =} \right] = 0.67$$

The *i*₀ values measured at all pH's fell on the same line, confirming the virtual pH independence of the exchange current density.

Potentiostatic steady-state data.—Only a limited number of potentiostatic experiments were carried out. The resulting Tafel slopes and exchange current densities were within ±10% of those measured galvanostatically on the same electrode.

Determination of reaction orders.—In the determination of reaction orders, the activity of water was considered constant. Calculations using the Gibbs-Duhem equation have shown that, within the limits of solution concentrations used in these experiments, the maximum change in the activity of water is 12%.

Concentration dependence.—From the concentration dependence of exchange current density, the reaction orders can be obtained by taking into account the concentration dependence of the equilibrium potential (38). By this method reaction orders of 0.94 (cathodic) and 0.06 (anodic) were found for zincate, and -0.92 (cathodic) and 2.59 (anodic) with respect to the hydroxyl ions.

Direct determination of reaction orders.—Two methods were used. The results of the galvanostatic method [cf. section on Determination of reaction orders (galvanostatic method)] for zincate are shown in Fig. 10. The current density values taken at a constant potential were then plotted in Fig. 11 against zincate concentration. The resulting cathodic reaction order was

$$\left[\frac{\partial \log i}{\partial \log C_{\text{Zn}(\text{OH})_4} =} \right]_{\text{pH}, E} = 0.85$$

With the potentiostatic technique [cf. section on Determination of reaction orders (potentiostatic method)] the cathodic reaction order was found to be 0.75 and 1.05 with respect of zincate ions in two separate experiments (Fig. 11).

Three measurements were made with the potentiostatic technique [cf. section on Determination of reaction orders (potentiostatic method)] to determine the reaction order with respect of hydroxyl ions, and the value of the cathodic

$$\left[\frac{\partial \log i}{\partial \text{pH}} \right]_{E, C_{\text{Zn}(\text{OH})_4} =}$$

was found to be -0.75, -1.04, and -1.06 (Fig. 12).

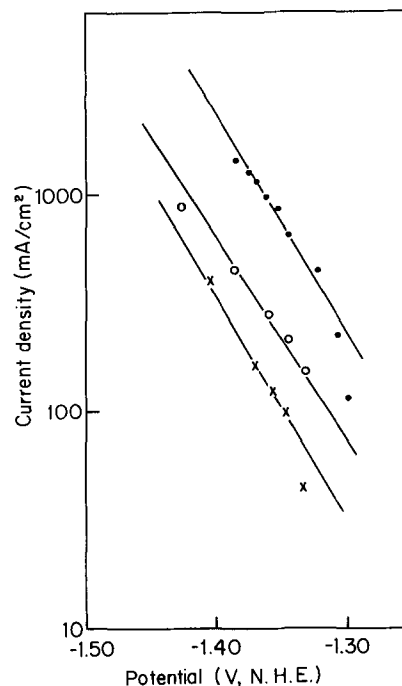


Fig. 10. Tafel lines obtained at different zincate concentrations with the same electrode. 3M KOH solutions. Symbols: ●, 0.50; ○, 0.082; x, 0.051M zincate.

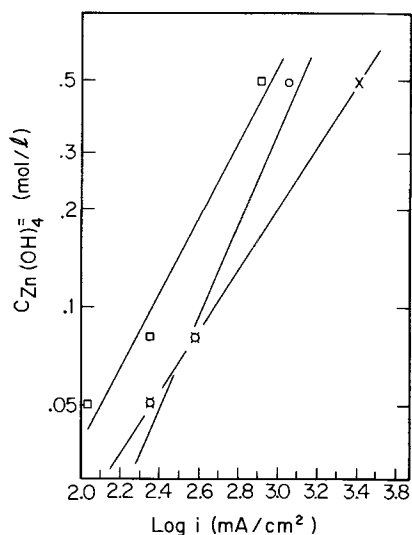


Fig. 11. Determination of cathodic reaction orders in zincate. 3M KOH. \square , Galvanostatic data, taken at -1.350V from Fig. 10. \circ , \times , Potentiostatic data taken at a fixed potential of -1.363V (NHE).

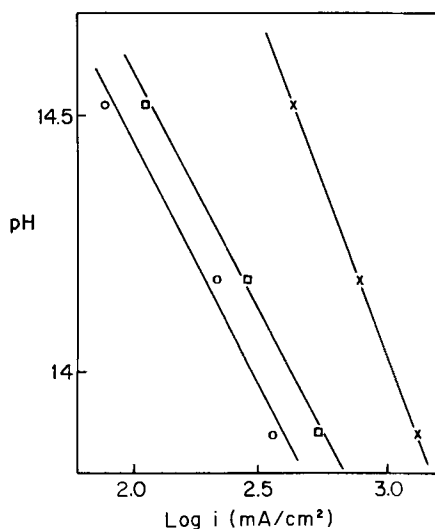


Fig. 12. Determination of cathodic reaction order in hydroxyl ions from potentiostatic (-1.358V , NHE) measurements. Zincate concentration: 0.08M . Results of three separate experiments.

Galvanostatic transient data.—Double layer capacitance.—Double layer capacitance values were obtained from the slope of the tangent drawn to the beginning of the galvanostatic transients. In summary, C was between 40 and $85 \mu\text{F}/\text{cm}^2$ in most cases and did not show any dependence on solution composition.

Rise time of galvanostatic transients.—Rise times were measured in the linear current-potential region. Assuming that the only processes taking place are the charging of the double layer, and a charge transfer reaction, a τ value can be calculated as

$$\tau = \frac{RT}{nFi_0} \cdot C_{dl}$$

and the full rise time is expected to be about 4τ . The calculated and measured rise times agreed within 20%.

Potentiostatic transient data.—After the settling time of the system (10 – $30 \mu\text{sec}$) only steady-state currents were observed, and no transient results were obtained.

Effect of cathodic reduction of the electrode.—The final reduction of the electrode in the test cell (cf. section on Electrode preparation) was found to be a critical step in the surface preparation. Some preliminary

Table II. Effect of reduction time on i_0 and C_{dl}

Total time of reduction (min)	i_0 (mA/cm^2)	C_{dl} ($\mu\text{F}/\text{cm}^2$)
0	8	60
0.05	14	60
5	30	85
8	30	85

data, taken with electrodes subject to a shorter or no reduction treatment, gave irreproducible results which are summarized in the following. The apparent exchange current density was not reproducible, it was strongly dependent on the duration of the reduction, increasing with increasing length of reduction and leveling off after about 5 min, with further reduction having no effect on i_0 . The observed changes were of an order of magnitude; an example is given in Table II. The Tafel slopes were independent of the reduction treatment. The C_{dl} values were irreproducible, sometimes very high (several hundred $\mu\text{F}/\text{cm}^2$) capacitances were observed with unreduced electrodes, but usually the capacitance was normal and increased slightly with reduction (Table II). The transition behavior to hydrogen evolution was also variable: with fully reduced surfaces a long, flat plateau was observed for zincate reduction (cf. section on Transition times) with subsequent quick potential rise to hydrogen evolution (Fig. 13A); with nonreduced surfaces no flat potential plateau for zinc deposition was observed but a continuous slow rise of potential to that of hydrogen evolution (Fig. 13B,C); occasionally irreproducible shoulders appeared (Fig. 13D). After a full reduction (8 min) the electrode remains in the "reproducible" state in the solution for about $\frac{1}{2}$ –1 hr, then it slowly reverts to its original behavior; with repeated reduction the "reproducible" state can again be obtained.

Discussion

Rest potentials and the effect of hydrogen evolution.—The rest potential of zinc in these solutions is a mixed potential set up by the zinc dissolution-hydrogen evolution corrosion couple. Since the corrosion current is small (cf. section on Corrosion rates) and the exchange current density of the zinc dissolution is high (Fig. 8, 9), this rest potential will differ only slightly (less than 1 mV) from the equilibrium zinc potential (37). The rest potentials, therefore, can be directly compared to the calculated thermodynamic equilibrium potentials (Table I). The observed values are 21 ± 6 mV less negative than the calculated poten-

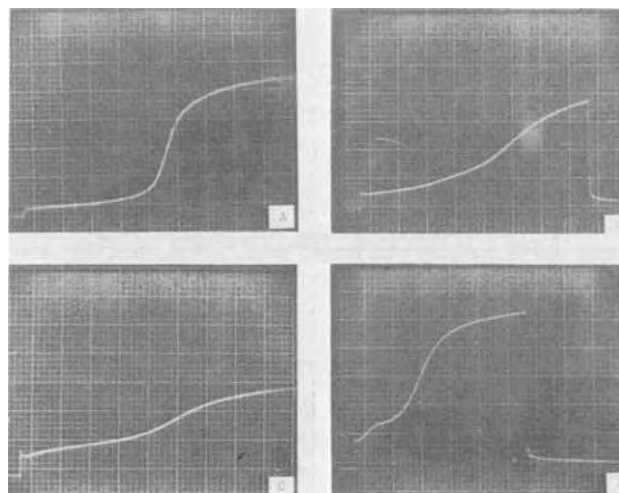
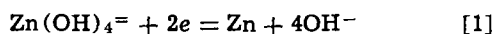


Fig. 13. Examples of zinc-hydrogen transitions. Current density: $50 \text{ mA}/\text{cm}^2$. Scale: $100 \text{ mV}/\text{cm}$ and $100 \text{ msec}/\text{cm}$ (A,B,C), and $200 \text{ msec}/\text{cm}$ (D). A: Fully reduced electrode. B,C,D: Not fully reduced electrodes. Solution: 1M KOH , $0.07\text{M Zn(OH)}_4^{2-}$. Calculated transition time: 440 msec .

tials, a fair agreement considering the approximate nature of the activity coefficients (cf. section on Rest potentials). From the measured corrosion rates, and the known 120 mV/decade Tafel slope of h.e.r. on zinc (26), it can be concluded that the contribution of the h.e.r. to the cathodic current will be negligible (less than 3%) within the limits of the experimental conditions. The negligible hydrogen effect is also corroborated by the good agreement of the measured and calculated transition times for the zincate reduction reaction. The hydrogen contribution can also be calculated from h.e.r. kinetic data reported for zinc in KOH solutions (26). The exchange current density is in the range of 10^{-10} - 10^{-12} A/cm², with a 120 mV Tafel slope. According to these data the h.e.r. current would not exceed 10 μ A/cm² in the whole potential range investigated in the present work; this is in good order of magnitude agreement with the conclusions reached above.

Surface state of the test electrodes.—It was found that a strong cathodic reduction (cf. section on Electrode preparation), carried out shortly before the measurements, was necessary to obtain reasonable reproducibility for the data (less than one order of magnitude spread in the i_0 values). It is suggested that the unreproducible behavior of the electrodes not subjected to this treatment (cf. section on Effect of cathodic reduction of the electrode) was due to residual oxide (or hydroxide) film on the zinc surface. The electrodes were in contact with air prior to assembly of the cell and therefore were covered by an oxide film; the chemical dissolution of this film by the solution is assumed to be incomplete. Such surface films have been proposed specifically for zinc by previous workers (27-28), and it has been shown in general (29-31), that a monomolecular layer of film can exist below the appropriate thermodynamic reversible potentials if the surface free energy of the electrode-electrolyte interface is reduced by the film formation. The transient behavior of the electrodes with the occasional potential arrests corroborates this suggestion. All the data used in the following mechanism determination were taken on "fully reduced" electrodes.

Selection of the reaction mechanism.—The predominant solution species has been identified as the tetrahedral $Zn(OH)_4^{2-}$ ion by potentiometric and solubility studies (32-34), IR and Raman spectra (35), and NMR (36); and the over-all electrode reaction has been shown (27) to be



Therefore, the simplest possible reaction mechanism must consist of at least four steps, the consecutive dissociation of the complex ion, with two steps including a charge transfer each. Different combinations of these four steps give rise to a number of possible paths. Furthermore, the charge transfer need not occur directly to or from a zinc complex, it could involve a charge transfer between the electrode and some other solution species (H_3O^+ , OH^- , H_2O), and the intermediate reacting further with a zinc complex. In principle, a very large number of possible reaction paths could be suggested. In reality, the comparison of measured kinetic parameters with those predicted by the different mechanisms will considerably reduce the possibilities. The experimental facts which can be used in this selection process are summarized in Table III.

The first conclusion suggested by the experimental results is that the mechanism of the anodic and the cathodic reactions is the same (cf. the agreement between anodic and cathodic exchange current densities, and the fact that $\alpha_a + \alpha_c \approx 2$). In the following discussion the mechanism in the cathodic direction will be examined in detail with the full analysis applicable, *mutatis mutandis*, to the anodic reaction.

Rate-determining step.—Considering the theory of multistep electrode reactions (37-38) the Butler-

Table III. Summary of steady-state results

Measured parameter	Value
Cathodic transfer coefficient (α_c)	0.56 ± 0.15
Anodic transfer coefficient (α_a)	1.3 ± 0.35
$\left[\frac{\partial \log i_0}{\partial \log C_{Zn(OH)_4^{2-}}} \right]_{pH}$	0.67
$\left[\frac{\partial \log i_0}{\partial pH} \right]_{C_{Zn(OH)_4^{2-}}}$	0.14
Cathodic reaction order for zincate	0.72-1.05
Cathodic reaction order for hydroxyl	(-0.75)-(-1.06)
Anodic reaction order for zincate	0.06
Anodic reaction order for hydroxyl	2.59

Volmer equation can be written as

$$i = i_0 \left[\exp \left(\frac{\alpha_a F \eta}{RT} \right) - \exp \left(- \frac{\alpha_c F \eta}{RT} \right) \right]$$

where

$$\alpha_c = \frac{\gamma_c}{\nu} + r\beta$$

$$\alpha_a = \frac{n - \gamma_c}{\nu} - r\beta$$

giving

$$\alpha_c + \alpha_a = \frac{n}{\nu}$$

where γ_c is the number of electrons transferred before the rds in the cathodic direction; ν is the stoichiometric number; n is the total number of electrons transferred in the over-all reaction; β is the symmetry factor; and r is the number of electrons transferred in a single occurrence of the rds.

Since

$$n = 2, \text{ and } \alpha_c + \alpha_a \approx 2 \\ \nu = 1$$

Therefore

$$\alpha_c = \gamma_c + 0.5r$$

$$\alpha_a = 2 - \gamma_c - 0.5r$$

The calculated possible values of transfer coefficients are given in Table IV. Comparison with experimental values reveals that only a type B mechanism could explain the data.

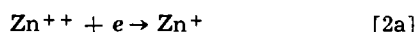
Nature of the rate-determining charge transfer.—Selection among the different charge transfer reaction possibilities can be made on the basis of their predicted reaction orders with respect to zincate and hydroxyl ions. All but the zinc complex would predict a zeroth order in zincate for the cathodic reaction, furthermore, reactions with H_2O would give a cathodic zeroth order for hydroxyl, and if OH^- were in the rds one would predict an anodic first order with respect to hydroxyl. These predictions are in contradiction with the experimental facts (Table III) eliminating all but

Table IV. Calculated values of transfer coefficients

	A	B	C	D	E	F
Number of electrons transferred in the rds (r)	2	1	1	0	0	0
Number of electrons transferred before the rds in the cathodic direction (γ_c)	0	0	1	0	1	2
Cathodic transfer coefficient (α_c)	1	0.5	1.5	0	1	2
Anodic transfer coefficients (α_a)	1	1.5	0.5	2	1	0

A represents a two electron transfer rate-determining step (rds).
 B represents two consecutive electron transfer steps, with the first one in the cathodic direction being the rds.
 C represents two consecutive electron transfer steps, with the second one in the cathodic direction being the rds.
 D represents a chemical step rate control, rds occurs before charge transfer in the cathodic direction.
 E represents a chemical rds between two single electron transfer steps.
 F represents chemical rate control, the rds occurs after two cathodic charge transfer steps.

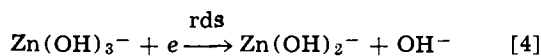
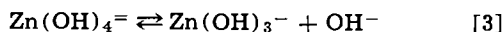
a zinc-containing species as reactant in the charge transfer step, which can then be written as



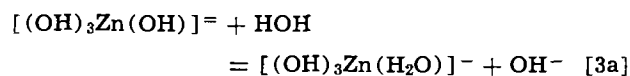
or



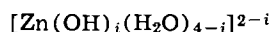
This leaves five different possibilities, as reaction [2b] can be written with "i" ranging from 1 to 4. A selection is, however, possible comparing the predicted reaction orders in hydroxyl ion of the five reactions with the experimental values (Table III). Agreement is obtained with [2b] if $i = 3$, therefore, the first two steps of the reaction are



Estimation of the rate of the chemical predissociation step—According to the above mechanism the chemical dissociation step (Eq. [3]) should be faster than the charge transfer step (Eq. [4]). An estimate of the rate of the dissociation can be obtained as follows. There are a number of reasons to suggest that the dissociation step is really a proton transfer reaction

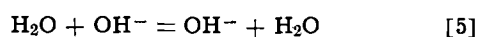


that is the complex species in solution are



rather than $[\text{Zn}(\text{OH})_i]^{2-i}$. (i) It is known (39) that ($pK_n - pK_{n-1}$) values remain constant with changing n (cf. Table V) unless there is a change in the symmetry of the complex. (ii) There is evidence for a tightly held inner coordination sphere for Zn^{++} by NMR technique (40) of about 4. (iii) The existence of tetrahedral $\text{Zn}(\text{H}_2\text{O})_4^{++}$ ion was shown in nearly neutral aqueous solutions by a temperature-pH transient technique (41).

The proton transfer between OH^- ion and water molecules has been shown (42-44) to proceed by proton tunneling and the rate-determining step was found to be the orientation of the water molecule in the field of the ion to a position required for tunneling. It is suggested that reaction [3a] also proceeds by this path. The pseudo first order rate constant of the reaction



was reported (45) to be $2.1 \times 10^{11} \text{ sec}^{-1}$. For reaction [3] this should be diminished by a Boltzmann factor arising from the fact that the free energy of the reaction [3] is 4.7 kcal (cf. Table V). The rate of the reaction [3] can then be calculated to be between 5×10^5 and $5 \times 10^8 \text{ mol/liter sec}$, for the present zincate concentration range. This estimate gives a minimum value for the rates, the real rates are expected to be higher for the following reason. In reaction [5] the proton transfer occurs from a water molecule which is part of the water structure and its rotation is therefore hindered. In the vicinity of large ions, the first layer of water has been shown (46) to consist of free monomers which will rotate more freely than the water of reaction [5]. This minimum rate of reaction [3] can now be compared to rates of reaction [4] which were calculated from the maximum currents applied in the given zincate range as 10^4 to $4 \times 10^5 \text{ mole/liter sec}$.³

Table V. Formation constants of zincates

[Gubeli and Ste-Marie (34)]	
pK_4	= -17.7
pK_3	= -14.3
pK_2	= -11.2
pK_1	= -6.3
$C_{\text{Zn}(\text{OH})_i}^{2-i}$	
$K_1 = \frac{C_{\text{Zn}(\text{OH})_3^-} C_{\text{OH}^-}}{C_{\text{Zn}^{++}} C_{\text{OH}^-}^2}$	

Double layer effects on the rds.—The double layer structure on solid electrodes is much less known than that of mercury, and the literature data are often contradictory and nonreproducible. Such is also the case for zinc. The value of the potential of zero charge (pzc) is not known in alkaline zincate solutions. For sulfate solutions a good agreement exists among different authors and techniques (47) giving a pzc value of $-0.64 \pm 0.04 \text{ V}$. There is some evidence from capacitance minimum determinations that in chloride solutions the pzc is about 0.25V more negative, but there is no firm confirmation of this value (48-51). The potential range of the present investigation therefore, was taken to be 0.5 to 0.9V negative to the pzc of zinc in the following evaluation of double layer effects.

(i) At such negative potentials, and in the concentration range covered, the double layer corrections for the Tafel slope, and for reaction order determination, can be considered negligible. These corrections depend on the parameters $(\partial\phi_2/\partial\eta)$ and $(\partial\phi_2/\partial E_{\text{rev}})$ (52) which are not known for zinc but in analogy with Hg data (53) can be assumed to be less than 0.1.

(ii) Complications from specific adsorption of anions can also be disregarded since at such highly negatively charged electrode the adsorption of anions was found to be negligible (54-56).

(iii) The species reacting in the rds are negatively charged and therefore will have a negative surface excess under the prevailing conditions. Numerical values for the zinc/KOH system, again, are not known. By analogy to mercury (57) the concentration at the Helmholtz plane is expected to be 10 to 100 times lower than the bulk concentration, a decrease not large enough to be an objection against the proposed mechanism.

(iv) For the discharge of anions at a potential negative to the pzc a further effect should also be considered. It has been suggested (58-59) that under these conditions a limiting current may arise due to the influence of the diffuse double layer (especially at low concentrations and far from the pzc where ϕ_2 is larger). An approximate equation for this limiting current was given (58)

$$i_1 = \frac{FDC\kappa}{2} \exp \frac{F\phi_2}{RT}$$

where κ is the Debye-Hueckel reciprocal length. Limiting currents calculated with this equation for the present reaction [using ϕ_2 values from 30 to 100 mV (52)] gave at least two orders of magnitude larger current densities than the currents used in this study, showing that this effect is also negligible.

Nature of the nonrate-determining charge transfer.—The considerations of the section on the Nature of the rate-determining charge transfer refer only to the rds and give no clues as far as the other charge transfer step is concerned. A selection can, however, be made based on thermodynamic and kinetic considerations of the oxygen and hydrogen evolution reactions since the steps suggested for the charge transfer are part of these reactions. The potential range investigated extended from about -1.3 to -1.6V of the standard oxygen potential in the test solutions, thereby excluding the possibility of any charge transfer step which would be part of the oxygen evolution reaction. The hydrogen evolution reaction has been investigated in KOH solution on zinc electrodes by Iofa and co-workers (26). The exchange current density was measured to be in the order of 10^{-10} - 10^{-12} A/cm^2 and the charge transfer step was found to be the rate-determining step. Since the exchange current densities observed for the zincate electrode reaction are about ten orders of magnitude larger, the charge transfer to form H_{ads} cannot be part of the mechanism. It can be concluded there-

³ In these calculations a 5Å double layer thickness was assumed.

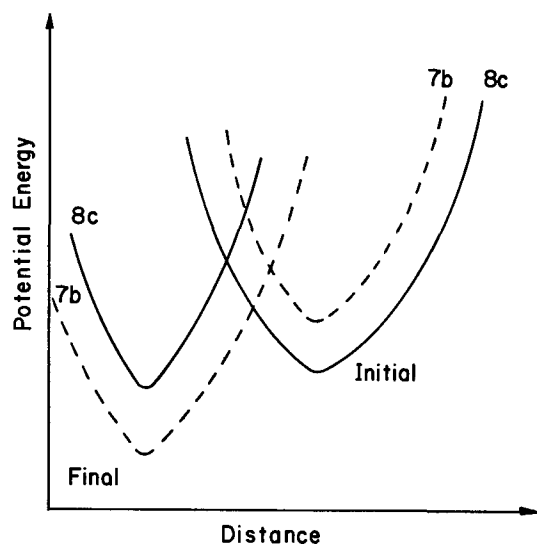
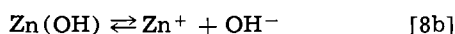
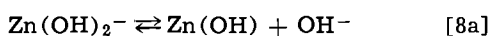
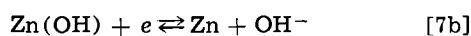
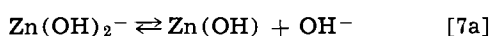
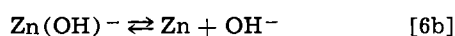
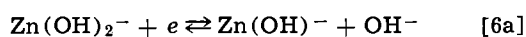


Fig. 14. Potential energy-distance curves for reactions [7b] and [8c].

fore, that the nonrate-determining charge transfer also occurs with a zinc complex reactant.

Steps occurring after the rds.—There remain but three possibilities to write up the steps following the rds



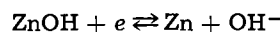
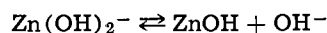
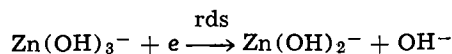
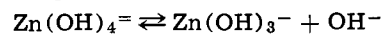
None of the measured kinetic parameters gives help in selecting between these three possibilities and there is little known about the chemistry or stereochemistry of Zn^+ complexes. The single charged Zn^+ ion is very unstable in aqueous solutions, its half-life was measured in the order of $100 \mu\text{sec}$ (60). Some speculative considerations can be made to suggest the most probable path. Changes in the activation energy of the charge transfer can be estimated using the Bockris-Matthews theory of charge transfer (61-62). Reaction [6a] produces a negatively charged species which will not be adsorbed on the electrode at the prevailing high negative potentials (cf. section on Double layer effects on the rds) and therefore is energetically unfavorable compared to [7] and [8] where adsorption stabilizes the charge transfer product. Furthermore, [6a] suggests that an uncharged zinc atom, coordinated by an OH^- ion, exists at the Helmholtz plane and in reaction [6b] this uncharged Zn atom transfers from the Helmholtz plane to the surface of the electrode, a rather unlikely mechanism.

For the selection between paths [7] and [8] a relative potential energy-distance diagram is used (61-62), (Fig. 14).⁴ The parameters needed for the calculation of these curves are not all known, but since it is the difference between the activation energies, rather than their absolute values that is needed, only the relative positions of the curves have to be established. The curves for reaction [7b] were, therefore, drawn arbitrarily. The final state of reaction [8c] will differ from that of [7b] only by the heat of hydration of hydroxyl ions which is -110 kcal/mol (63). The initial curves will differ by the difference of heat of hydrations of Zn^+ and ZnOH . The former is estimated to be between -65 and -70 kcal/mole based on its diameter

⁴ The implicit assumption is, of course, adiabaticity.

(46), while the latter (being a neutral molecule) will be negligible in comparison. These effects are shown in Fig. 14. There is one further term to be taken into account for the initial curve, and this is the Zn-OH bond energy. This value is not known but it certainly will be less than 175 kcal/mol which would be needed to overcome the above two effects. The activation energy change is therefore in favor of reaction [7].

Suggested mechanism.—From the above considerations, the following reaction path is the most probable



The mechanism is written in the cathodic direction, the anodic reaction proceeds through the exact reverse of the above path. This mechanism is in agreement with all the experimental facts given in Table III.

In this analysis, all data taken with supersaturated solution were included. Exclusion of these points does not alter the conclusions. This indicates that supersaturation of the solution with respect to zincate, has no effect on the mechanism.

Mechanism at low overpotentials.—Surface diffusion, rather than charge transfer, has been suggested for several metal deposition reaction (3-5) as the rate-determining step in the low overpotential region. In the present case this possibility was eliminated by the fact that the exchange current densities obtained from the extrapolation of the Tafel lines and from the slope of linear $i - \eta$ plots at low overpotentials are in complete agreement. This was further substantiated by the fact that the rise times of the galvanostatic transients can be explained by considering only the double layer charging and charge transfer processes.

Concentration of the intermediate species containing Zn^+ .—The fact that no pseudocapacitance was observed indicates that the change of concentration of Zn^+ -containing species in the Helmholtz plane is very small and so is its equilibrium concentration [cf. Ref. (6)]. This is also corroborated by the rise time of the potentiostatic transients which was found to be less than the $10\text{-}30 \mu\text{sec}$ settling time of the potentiostat. With considerable intermediate concentrations a larger rise time would be expected even if the fastest step (which determines the rise time of the potentiostatic transients) in the mechanism has a rate constant 100 times that of the rds (64-65). This low concentration is in agreement with the known reactivity of single charged zinc (60).

Comparison of the results to data of other workers.—A series of papers was published by Hampson and co-workers (10-12) on the electrochemical behavior of solid zinc in alkaline electrolytes. Both the anodic and the cathodic processes were investigated in a wide range of overpotentials and solution compositions. Armstrong and Bulman (13) investigated the anodic dissolution of solid zinc in 1 and 2M sodium hydroxide solutions using a rotating disk electrode. A very brief report is given on zinc dissolution in KOH by Kabanov (9). The experimental data of these workers is summarized in Table VI and compared to the results of this work. A good agreement is found with the results of Armstrong and Bulman and with those of Kabanov; also with some of Hampson's data. There are, however, three areas of disagreement with the data of Hampson and co-workers; (i) the dependence of exchange current density on zincate concentration; (ii) the value of Tafel slopes; and (iii) the value of the double layer capacitance. These are discussed in detail in the following paragraphs.

The dependence of the exchange current density on the concentration of zincate, and the transfer co-

Table VI. Comparison of experimental data

Parameter	Hampson and co-workers (10-12)	Armstrong and Bulman (13)	Kabanov (9)	Present work
i_0 (mA/cm ²)	40-250	—	—	8-370
$\left[\frac{\partial \log i_0}{\partial \text{pH}} \right]_{C_{Zn(OH)_2}^-}$	0.2	—	—	0.14
$\left[\frac{\partial \log i_{an}}{\partial \text{pH}} \right]_{\beta}$	—	ca 3.5	3	2.6
$\left[\frac{\partial \log i_0}{\partial \log C_{Zn(OH)_2}^-} \right]_{\mu\text{H}}$	0	—	—	0.67
C_d ($\mu\text{F/cm}^2$)	30-600	—	—	40-120
Anodic Tafel slope (mV/decade)	65 \pm 10 (at low η)* 320 (at high η)*	42 \pm 5	30	49 \pm 13
Cathodic Tafel slope (mV/decade)	55 \pm 8 (at low η)* 280 \pm 40 (at high η)*	—	—	113 \pm 30

* Calculated from the reported transfer coefficients.

efficients at low overvoltages were determined by galvanostatic double pulse technique in the linear $i - \eta$ range (11). The tacit assumption was made (66) that the solution resistance between the Luggin capillary and the surface of the electrode is small compared to the reaction resistance. [This assumption was also extended to some of their high overvoltage measurements (67), although later the authors themselves (12) realized the ohmic errors thus introduced at the high overpotentials.] The validity of this assumption can be examined by calculating the reaction resistance and the solution resistance for a number of their reported experiments. For the calculation of the solution resistance it will be assumed that the distance between the Luggin and the electrode surface was 0.3 mm (a rather close placing). The values of reaction resistance were calculated from their reported exchange current densities. The resulting values are shown in Table VII. Clearly, although the absolute value of the solution resistance is very small because of the high conductivity of the solution, it is not negligible compared to the reaction resistance due to the large exchange current density of the reaction. It therefore seems probable that the ohmic overpotential was a considerable part of the total overpotential for these workers. The following observations are consistent with this suggestion:

(i) The claimed independence of i_0 from the zincate concentration is understandable since the addition of zincate causes little change in the conductivity.

(ii) The reported slight pH effect on i_0 could also be, at least partially, due to the decrease of solution conductivity as NaOH was replaced by NaClO₄ ($\kappa_{\text{NaOH}} \approx 2.3\kappa_{\text{NaClO}_4}$) (68)

(iii) The reported $\left(\frac{\partial \log i_0}{\partial 1/T} \right) = 0.65$ in 7M KOH solutions, compares with $\frac{\partial \log \kappa}{\partial 1/T} = 0.72$ (69).

The above suggestion is thus consistent with their observations.

The Tafel slopes reported in a recent paper (12) for the high polarization range are surprisingly high, about 300 mV/decade for both the anodic and the cathodic processes. These measurements were done in 7M KOH solutions and Tafel behavior was reported over the 80-300 mV range. Both the solution concentration and the

Table VII. Comparison of Farr and Hampson's solution and reaction resistances

Solution	i_0 (mA/cm ²)	κ (68) (ohm ⁻¹ cm ⁻¹)	R_p (ohm cm ²)	R_s (ohm cm ²)
7M KOH	238	0.54	0.054	0.056
5M LiOH	185	0.33	0.070	0.091
7M NaOH	140	0.30	0.092	0.100

overpotentials are outside the range of the present work, therefore direct comparison is not possible. In fact, however, a linear $\eta - \log i$ relationship with a slope of about 40 mV (in agreement with the present work) exist below 80 mV polarization on the anodic curves of these workers.

The capacitance values (10) were bridge measurements taken on electrodes "equilibrated" with the solution for many hours; a strong time dependence of the values was reported. A time-dependent electrochemical behavior and some high values of capacitances for nonreduced electrodes were also found in this study (section on Effect of cathodic reduction of the electrode). It seems, therefore, that the capacitances measured with our freshly reduced zinc electrodes cannot be compared directly with those taken under quite different surface conditions.

Acknowledgments

Useful discussions with Dr. M.A. Genshaw and Dr. D. Drazic are gratefully acknowledged. Our thanks are also due to Dr. B. D. Cahan for his advice in the design of the apparatus. Financial assistance for this work was provided by the National Science Foundation under grants NSF-GK-1724, and -16550; and the A.R.P.A. Program in Materials Science (University of Pennsylvania).

Manuscript submitted June 8, 1971; revised manuscript received Oct. 28, 1971. Part of this work was presented as Paper 14 at the Detroit Meeting of the Society, Oct. 5-9, 1969.

Any discussion of this paper will appear in a Discussion Section to be published in the December 1972 JOURNAL.

REFERENCES

- J. O'M. Bockris and A. R. Despic, in "Physical Chemistry," Vol. 9B, chap. 7, H. Eyring, D. Henderson, and W. Jost, Editors, Academic Press, New York (1970).
- D. J. Astley,* J. A. Harrison, and H. R. Thirsk, *Trans. Faraday Soc.*, **64**, 192 (1968).
- W. Mehl and J. O'M. Bockris, *J. Chem. Phys.*, **27**, 818 (1957).
- W. Mehl and J. O'M. Bockris, *Can. J. Chem.*, **37**, 190 (1959).
- E. Mattson and J. O'M. Bockris, *Trans. Faraday Soc.*, **55**, 1586 (1959).
- J. O'M. Bockris and M. Enyo, *ibid.*, **58**, 1187 (1962).
- E. Budevski, *Electrochim. Metal.*, **2**, 1 (1966).
- E. Budevski, W. Bostanov, T. Vitanov, Z. Stojnov, A. Kotzeva, and R. Kaishev, *Electrochim. Acta*, **11**, 1697 (1966).
- B. N. Kabanov, *Izv. Akad. Nauk SSSR*, 980 (1962).
- J. P. G. Farr and N. A. Hampson, *Trans. Faraday Soc.*, **62**, 3493 (1966).
- J. P. G. Farr and N. A. Hampson, *J. Electroanal. Chem.*, **13**, 433 (1967).
- N. A. Hampson, G. A. Herdman, and R. Taylor, *ibid.*, **25**, 9 (1970).
- R. D. Armstrong and G. M. Bulman, *ibid.*, **25**, 121 (1970).
- S. U. Falk and A. J. Salkind, "Alkaline Storage Batteries," John Wiley & Sons, Inc., New York (1969).
- A. Fleischer and J. J. Lander, Editors, "Zinc-Silver Oxide Batteries," John Wiley & Sons, Inc., New York (1971).
- B. P. Kiselev and V. L. Balashov, *Elektrokhimiya*, **5**, 631 (1969).
- F. J. Welcher, "The Analytical Uses of EDTA," p. 149, D. Van Nostrand Co., Inc., Princeton, N. J. (1958).
- B. D. Cahan, Z. Nagy, and M. A. Genshaw, *This Journal*, **119**, 64 (1972).
- J. O'M. Bockris, H. Wroblowa, E. Gileadi, and B. J. Piersma, *Trans. Faraday Soc.*, **61**, 2531 (1965).
- Z. Nagy, Thesis, Univ. of Pennsylvania (1972).
- M. Pourbaix, "Atlas of Electrochemical Equilibria in Aqueous Solutions," p. 406, Pergamon Press, Oxford (1966).
- M. Pourbaix, *ibid.*, p. 421.
- H. S. Harned and B. B. Owen, "The Physical Chemistry of Electrolytic Solutions," 3rd ed., p. 498, Reinhold Publishing Corp., New York (1958).

24. R. A. Robinson and R. H. Stokes, "Electrolyte Solutions," 2nd ed., p. 501, Butterworths, London (1959).
25. J. McBreen, Study to Investigate and Improve the Zinc Electrode for Spacecraft Electrochemical Cells, Yardney Electric Corp., Contract NAS 5-10231 (June 1967).
26. Z. A. Iofa, L. V. Komlev, and V. S. Bagotskii, *Zh. Fiz. Khim.*, **35**, 1571 (1961).
27. T. P. Dirkse, *This Journal*, **102**, 497 (1955).
28. H. Bode and A. Oliapuram, *Electrochim. Acta*, **13**, 71 (1968).
29. D. A. Vermilyea, "Advances in Electrochemistry and Electrochemical Engineering," Vol. 3, chap. 4, P. Delahay and C. W. Tobias, Editors, Interscience Publishers Inc., New York (1963).
30. R. D. Armstrong, M. Fleischmann, and J. W. Oldfield, *J. Electroanal. Chem.*, **14**, 235 (1967).
31. D. J. Astley, J. A. Harrison, and H. R. Thirsk, *ibid.*, **19**, 325 (1968).
32. T. P. Dirkse, *This Journal*, **101**, 328 (1954).
33. T. P. Dirkse, C. Postmus, Jr., and R. Vandenbosch, *J. Am. Chem. Soc.*, **76**, 6022 (1954).
34. A. O. Gubeli and J. Ste-Marie, *Can. J. Chem.*, **45**, 827 (1967).
35. J. S. Fordyce and R. L. Baum, *J. Chem. Phys.*, **43**, 843 (1965).
36. G. H. Newman and G. E. Blomgren, *ibid.*, **43**, 2744 (1965).
37. J. O'M. Bockris, "Modern Aspects of Electrochemistry," No. 1, chap. 4, J. O'M. Bockris and B. E. Conway, Editors, Butterworths, London (1954).
38. J. O'M. Bockris and A. K. N. Reddy, "Modern Electrochemistry," chap. 9, Plenum Press, New York (1970).
39. D. D. Perrin, "Organic Complexing Reagents," p. 34, Interscience Publishers Inc., New York (1964).
40. T. J. Swift and W. G. Sayre, *J. Chem. Phys.*, **44**, 3567 (1966).
41. T. J. Swift, *Inorg. Chem.*, **3**, 526 (1964).
42. B. E. Conway, J. O'M. Bockris, and H. Linton, *J. Chem. Phys.*, **24**, 834 (1956).
43. B. E. Conway, "Modern Aspects of Electrochemistry," No. 3, chap. 2, J. O'M. Bockris and B. E. Conway, Editors, Butterworths, Washington (1964).
44. B. E. Conway and M. Salomon in "Chemical Physics of Ionic Solutions," B. E. Conway and R. G. Barradas, Editors, John Wiley & Sons, Inc., New York (1966).
45. S. Meiboom, *J. Chem. Phys.*, **34**, 375 (1961).
46. J. O'M. Bockris and P. P. S. Saluja, To be published.
47. R. S. Perkins and T. N. Anderson, "Modern Aspects of Electrochemistry," No. 5, chap. 3, J. O'M. Bockris and B. E. Conway, Editors, Plenum Press, New York (1969).
48. D. S. Brown, J. P. G. Farr, N. A. Hampson, D. Larkin, and C. Lewis, *J. Electroanal. Chem.*, **17**, 421 (1968).
49. P. Caswell, N. A. Hampson, and D. Larkin, *ibid.*, **20**, 335 (1969).
50. C. S. Cha and Z. A. Iofa, *Dokl. Akad. Nauk SSSR*, **131**, 137 (1960).
51. J. W. Diggle and B. Lovrecek, *J. Electroanal. Chem.*, **24**, 119 (1970).
52. P. Delahay, "Double Layer and Electrode Kinetics," pp. 201, 204, Interscience Publishers Inc., New York (1965).
53. R. Parsons, "Advances in Electrochemistry and Electrochemical Engineering," Vol. 1, chap. 1, P. Delahay and C. W. Tobias, Editors, Interscience Publishers Inc., New York (1961).
54. H. Wroblowa, Z. Kovac, and J. O'M. Bockris, *Trans. Faraday Soc.*, **61**, 1523 (1965).
55. Y. C. Chiu and M. A. Genshaw, *J. Phys. Chem.*, **73**, 3571 (1969).
56. W. Paik, M. A. Genshaw, and J. O'M. Bockris, *ibid.*, **74**, 4266 (1970).
57. Ref. 52, p. 46.
58. V. G. Levich, *Dokl. Akad. Nauk SSSR*, **67**, 309 (1949).
59. V. G. Levich, *ibid.*, **124**, 869 (1959).
60. D. Meyerstein and W. A. Mulac, *J. Phys. Chem.*, **72**, 784 (1968).
61. J. O'M. Bockris and D. B. Matthews, *Proc. Roy. Soc., London*, **A292**, 479 (1966).
62. D. B. Matthews and J. O'M. Bockris, "Modern Aspects of Electrochemistry," No. 6, chap. 4, J. O'M. Bockris and B. E. Conway, Editors, Plenum Press, New York (1971).
63. H. F. Halliwell and S. C. Nyburg, *Trans. Faraday Soc.*, **59**, 1126 (1963).
64. A. Damjanovic and J. O'M. Bockris, *This Journal*, **110**, 1035 (1963).
65. J. A. Harrison, S. K. Rangarajan, and H. R. Thirsk, *ibid.*, **113**, 1120 (1966).
66. J. P. G. Farr, N. A. Hampson, and M. E. Williamson, *J. Electroanal. Chem.*, **13**, 462 (1967).
67. N. A. Hampson, P. E. Shaw, and R. Taylor, *Brit. Corrosion J.*, **4**, 207 (1969).
68. International Critical Tables, McGraw-Hill Publishing Co., New York (1929).
69. W. H. Dyson, L. A. Schreier, W. P. Sholette, and A. J. Salkind, *This Journal*, **115**, 566 (1968).

Performance of Aluminum-Manganese Dioxide Dry Cells

David Belitskus

Aluminum Company of America, Alcoa Technical Center, Pittsburgh, Pennsylvania 15230

ABSTRACT

Aluminum-manganese dioxide dry cells were constructed and discharged to determine voltages, capacities, corrosion rates, pH changes, and internal resistances. Aluminum cells showed promise for moderate to heavy-duty discharge but had lower capacities than commercial general purpose zinc cells on more intermittent discharge. Anode corrosion during discharge and on open circuit following partial discharge raised cell pH and decreased capacity. The internal resistances of the aluminum cells decreased during initial discharge, indicating dissolution or alteration of the original anode film. Substitution of electrolytic for natural manganese dioxide increased cell capacity, as did certain acid additions to the electrolyte. Use of a high potential anode alloy or addition of lithium chloride to the electrolyte increased cell voltages during initial discharge but did not increase capacity. Amine additions to the electrolyte reduced corrosion but did not increase capacity.

Aluminum is a theoretically attractive anode material for primary cells, from the standpoints of electrochemical equivalence (2.98 A-hr/g, vs. 0.82 for Zn) and reversible electrode potential (E_0 acid = $-1.66V$,

Key words: discharge, capacity, voltage, resistance, pH.

vs. -0.76 for Zn). However, rapid formation of an oxide film on aluminum in air or water prevents the reversible electrode potential from being reached (1). With electrolytes in which the oxide layer is soluble, potentials are higher but corrosion becomes a problem.

Table I. Dry cell electrolytes for use with aluminum anodes (14)

	A	B	C	D
AlCl ₃ ·6H ₂ O (aluminum chloride hexahydrate)	8.1%	13.6%	—	6.9%
CrCl ₃ ·6H ₂ O (chromic chloride hexahydrate)	3.4%	5.7%	6.1%	3.5%
NH ₄ Cl (ammonium chloride)	—	—	6.1%	6.9%
(NH ₄) ₂ CrO ₄ (ammonium chromate)	4.5%	9.1%	4.5%	—
HCl (hydrochloric acid)	2.9%	—	—	—
KHC ₈ H ₄ O ₄ (potassium acid phthalate)	4.8%	—	—	—
MnO ₂ (manganese dioxide)	63.6%	62.6%	69.4%	68.9%
C (Shawinigan black)	12.7%	9.0%	13.9%	13.8%
H ₂ O (water [cc/100g dry mix])	43	30	43	42

Factors associated with use of aluminum, magnesium (whose chemistry also is largely dominated by its oxide film), and zinc primary cell anodes have been reviewed by Glicksman (2).

Although the subject of numerous patents (3-13), primary cells containing aluminum anodes are not in commercial production. The present work was undertaken to further characterize and improve the aluminum cells described by Stokes (14).

Cell Construction

Size D cells were constructed from the duplex alloy aluminum cans (0.010 in. thick 99% Al, 99.8% pure-1% Zn inner layer, 0.004 in. thick 3003 alloy outer layer) previously found to reduce pitting perforation (6, 14). Separators made from 0.16 mm thick, medium weight chromatography paper were employed along with paper washers and paraffin-impregnated carbon rods identical to those in zinc dry cells. Cells were constructed using the electrolyte formulations listed by Stokes (14) and repeated here as Table I. Water contents were adjusted to give consistencies comparable to those of commercial zinc cells. The black mix, including natural (African) MnO₂ ore, 50% compressed Shawinigan black, and the electrolyte, was compacted at 200 psi in cans lined with dry paper, with the electrolyte exuding from the mix to wet the paper. Cells were sealed with either pitch of the type used in zinc cells or with a 1:1 mixture (by weight) of beeswax and rosin.

Capacity

Testing was concentrated on "B" formulation aluminum cells, found to have the greatest capacity, and "C" formulation cells, reported to have a long shelf life (8). Six different brands of general purpose zinc cells purchased through normal sources and aluminum cells aged for one week or more after assembly were discharged in 4- and 2.25-ohm continuous and intermittent tests. The intermittent testing employed automated apparatus.

Each curve in Fig. 1 represents an average from 2-6 zinc or "B" formulation aluminum cells in 4-ohm tests. Capacities of aluminum cells increased as testing became more intermittent, from continuous discharge, to the heavy industrial flashlight test (4 min discharge per 15 min period, 8 hr per day), to the light industrial flashlight test (4 min discharge per hour, 8 hr per day), but dropped off on the general purpose test (5 min discharge per day).¹ Increase in performance with intermittent testing was much greater for zinc cells. Some 2.25-ohm tests, continuous and general purpose,² were also performed with the following results: continuous discharge, 255 min for Al cell and 200 min for Zn cell; general purpose test, 225 min for Al cell and 490 min for Zn cell. Some of the discharge times to cut-off in Table II of the original report on these cells (14) are believed to be high because of contact resistances that devel-

¹ The heavy industrial flashlight test (4-ohm) and light industrial flashlight test (4-ohm) are standard tests (National Bureau of Standards Annual Qualifications Tests) for D-size cells. The general purpose test (4-ohm) has been discontinued for D-size cells.

² The general purpose test (2.25-ohm) is a standard test for D-size cells.

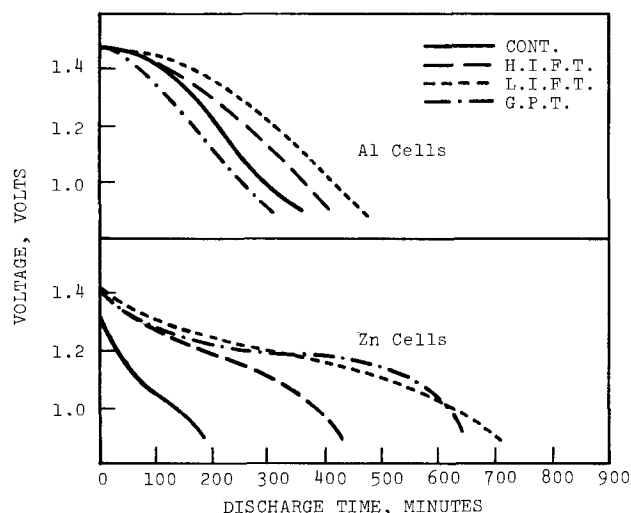


Fig. 1. Discharge curves for "B" formulation aluminum dry cells and commercial general purpose zinc dry cells: 4-ohm discharges. [Cont. = Continuous Discharge; H.I.F.T. = Heavy Industrial Flashlight Test; L.I.F.T. = Light Industrial Flashlight Test; G.P.T. = General Purpose Test.]

oped in the automatic intermittent discharging apparatus.

The ratios of "B" formulation aluminum cell capacity to zinc cell capacity (in terms of minutes of service to cut-off voltage for each of the various tests performed, i.e., 0.90V for the 4-ohm tests, 0.65V for the 2.25-ohm tests) are plotted against minutes of discharge per day in Fig. 2. For comparison of cells under continuous discharge, minutes-per-day was arbitrarily taken as the average of aluminum and zinc cell service to the cut-off voltage. On this basis, formulation "B" aluminum cells outperform general purpose zinc cells in discharges where the cell is under load for more than about 2 hr per day. From the discharge curves from both the 4- and 2.25-ohm tests, energy (watt-hours) extracted from the cells (to the cut-off voltage) was also determined and the ratios are included in Fig. 2. Because of initially higher voltages under load (about 0.07V higher under either 4- or 2.25-ohm load), the aluminum cells performed even better on this basis, yielding greater watt-hour capacities than zinc cells when discharged for more than about 1.25 hr per day. Considering that the commercial zinc cells undoubtedly contained some electrolytic ore, which increased capacity, these aluminum cells show promise for moderate to heavy-duty discharges.

Aluminum cells with the "C" formulation had lower capacities, yielding 270 min of service to 0.90V

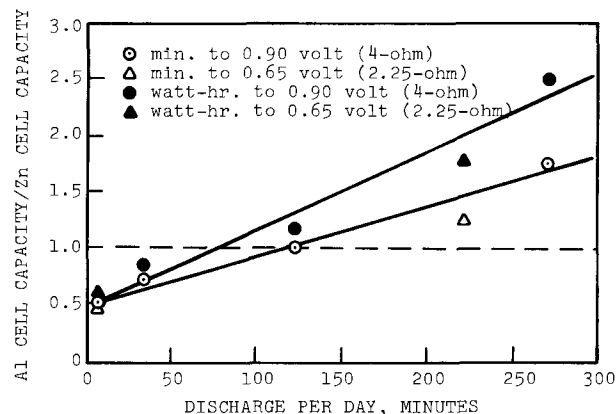


Fig. 2. Comparison of capacities of "B" formulation aluminum dry cells and commercial general purpose zinc cells. [Time for continuous discharge is average for Al and Zn cell to cut-off voltage; intermediate times are for standard discharge tests.]

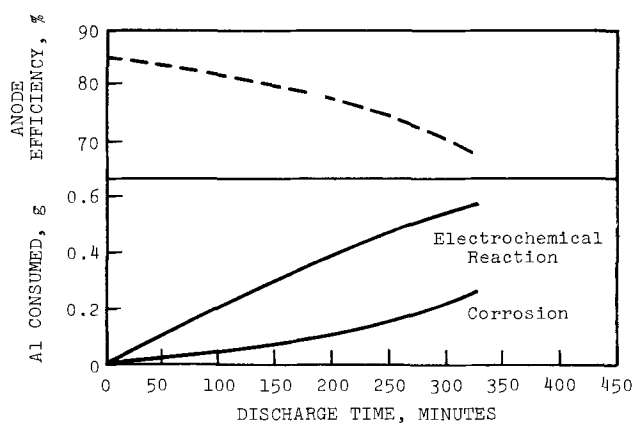


Fig. 3. Anode consumption and efficiency of a "B" formulation aluminum dry cell during a 4-ohm continuous discharge.

when discharged continuously under 4-ohm load and 350 min on the heavy industrial flashlight test (4-ohm), for example. Cells having the "A" and "D" formulations had intermediate capacities.

Corrosion

Corrosion of aluminum, with the evolution of hydrogen, was significant under all discharge conditions as in Fig. 3 for 4-ohm continuous discharge of a "B" formulation cell. Over-all anode ampere-hour efficiency to a 0.90V cut-off was 71%, calculated from the discharge curve in Fig. 1 and simultaneous gas evolution data (not shown). Total gas evolution was 300 ml (NTP). During intermittent discharge gassing continued during periods on open circuit, but at a reduced rate. The ammonium chromate in the black mix inhibits corrosion of unused cells but apparently is of less value after a cell has been partially discharged. The corrosion on open circuit decreased anode efficiencies as discharge became more intermittent. During the heavy industrial flashlight test (4-ohm), gas evolution to a 0.90V cut-off increased to 550 ml, corresponding to an anode efficiency of 65%; during the light industrial flashlight test (4-ohm), gas evolution and anode efficiency were 800 ml and 57%, respectively. During the general purpose test (4-ohm), gassing was not recorded during an entire discharge, but efficiency extrapolated from gas evolution during one week was 33%. Cells which had undergone the general purpose test for one week continued to evolve gas for at least two weeks after discharging. The low capacity of aluminum cells on the general purpose test was probably due to this extensive corrosion.

Gas evolution invariably caused seal rupture and leakage of cells during continuous discharge, and usually during the heavy industrial flashlight test. Paraffin-impregnated carbon rods sufficiently porous to permit escape of gas can undoubtedly be developed. A few cells vented through dimethyl silicone membranes did not leak during continuous discharge.

Acidity of Electrolyte

Numerous studies on zinc dry cells have indicated that during intermittent discharge the MnO₂ is reduced according to the reaction



so that cell voltage is a function of pH [-0.059 V/pH at 25°C theoretically, although this value is seldom observed (15)]. Hydrogen ions are replenished by hydrolysis of zinc ions added in the original formulation and generated during the cell reaction. During continuous discharge hydrolysis and diffusion are apparently not rapid enough to maintain acidity, and cell capacity is low.

The change in acidity of the cathode-electrolyte mix of aluminum cells with extent and type of dis-

charge was measured and compared with zinc cells. To prevent any effect from differences in cathode-electrolyte mix, comparisons were made between aluminum and zinc anode cells having the identical mix. This consisted of: 15% NH₄Cl, 5% ZnCl₂, 1% (NH₄)₂CrO₄, 70% natural MnO₂, 9% Shawinigan black, and ~25 ml H₂O/100g black mix.

The mix is similar to that used in zinc cells, except for the (NH₄)₂CrO₄ added to reduce aluminum corrosion. These zinc cells had lower capacities than the commercially available cells but showed the same large increase in capacity during the heavy industrial flashlight test (relative to continuous discharge) as commercial cells.

The change in pH during discharge was measured by a glass electrode pressed into finely ground black mix removed from cells subjected to continuous discharge (4-ohm), the heavy industrial flashlight test (4-ohm), and the light industrial flashlight test (4-ohm) for various predetermined times.

The initial cell pH of 5.2 for zinc cells in Fig. 4 increased during continuous discharge and cell capacity was correspondingly low. During the heavy industrial flashlight test, pH leveled off near 6 and cell capacity was correspondingly much greater. A small additional increase in capacity (and a marginally flatter pH curve) was obtained during the light industrial flashlight test.

As with the aluminum cells described previously, the capacities in Fig. 5 for cells with aluminum anodes increased slightly as discharge became more intermittent. The pH increased most rapidly during continuous discharge and less rapidly as discharge became more intermittent, but did not level off even during the light industrial flashlight test. The pH increased in the same way during discharge of cells having the formulations in Table I, even though initial pH was lower. For example, pH of a "C" formulation aluminum cell was 3.5 before discharge and 7.8 after a 4-ohm continuous discharge to 0.90V.

Thus, capacity of an aluminum anode cell, like capacity of a zinc cell, is related to changes in pH of the cathode-electrolyte mix during discharge. The present formulations for aluminum cells probably do not maintain a low pH during either continuous or intermittent discharge because of the extensive corrosion that consumes hydrogen ions both during discharge and, to a lesser extent, on open circuit, as represented below

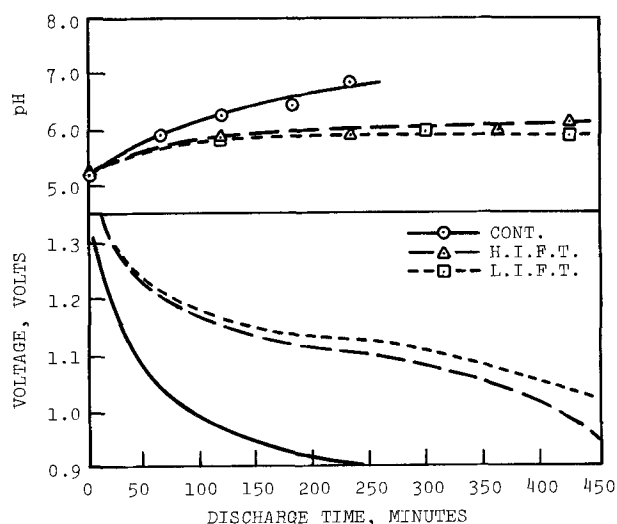
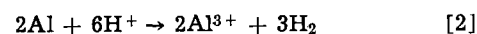


Fig. 4. Discharge curves and pH changes of the electrolyte of specially constructed zinc dry cells: 4-ohm discharges. [Cont. = Continuous Discharge; H.I.F.T. = Heavy Industrial Flashlight Test; L.I.F.T. = Light Industrial Flashlight Test.]

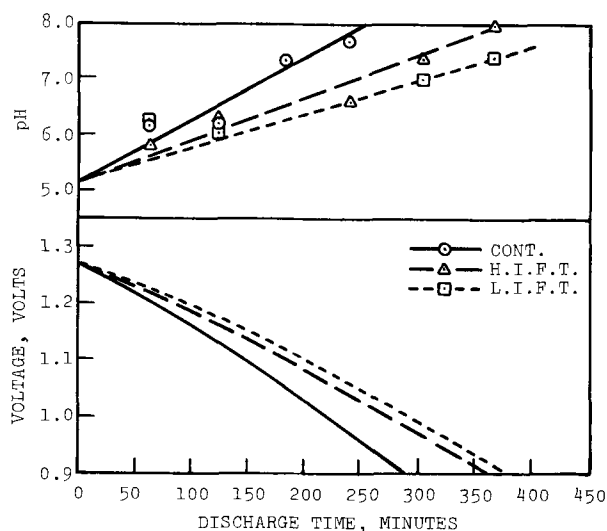


Fig. 5. Discharge curves and pH changes of the electrolyte of aluminum dry cells (having the same electrolyte as zinc cells shown in Fig. 4): 4-ohm discharges. [Cont. = Continuous Discharge; H.I.F.T. = Heavy Industrial Flashlight Test; L.I.F.T. = Light Industrial Flashlight Test.]

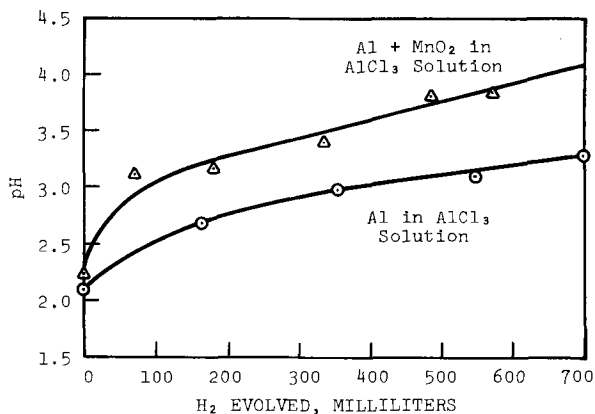


Fig. 6. Change in pH of an electrolyte caused by aluminum corrosion and by reduction of manganese dioxide: 6g $\text{AlCl}_3 \cdot 6\text{H}_2\text{O}$ /20 ml H_2O + 2g Al powder, with or without 3g MnO_2 .

Although hydrogen ions can be regenerated by hydrolysis of the aluminum ions formed, they are consumed more rapidly and pH increases. This was demonstrated by hydrogen evolution and pH changes in Fig. 6 for mixtures prepared by adding 2g of atomized aluminum powder ($0.85 \text{ m}^2/\text{g}$ surface area) to a solution of 6g $\text{AlCl}_3 \cdot 6\text{H}_2\text{O}$ dissolved in 20 ml of water and the same mixture with 3g of natural manganese dioxide added. The latter test simulates hydrogen ion consumption by cell discharge (Reaction [1]) and the accompanying aluminum corrosion (Reaction [2]). These tests were, of course, only qualitative since the electrolyte composition and aluminum surface area differed from those in an actual cell.

Internal Resistance

Another possible cause of relatively low capacity of the present aluminum cells was high internal resistance from an anode film or reaction products such as $\text{Al}(\text{OH})_3$. Comparative internal resistances of zinc and formulation "B" and "C" aluminum cells were measured with an oscilloscope, milliammeter, and a mercury switch by interrupting the current momentarily during discharge across a 3-ohm resistance.

As for magnesium dry cells (16) the instantaneous voltage changed more for aluminum cells than for commercial zinc cells. An oscillographic trace for the "B" formulation aluminum cell one minute after the start of discharge is shown in Fig. 7(a). While the

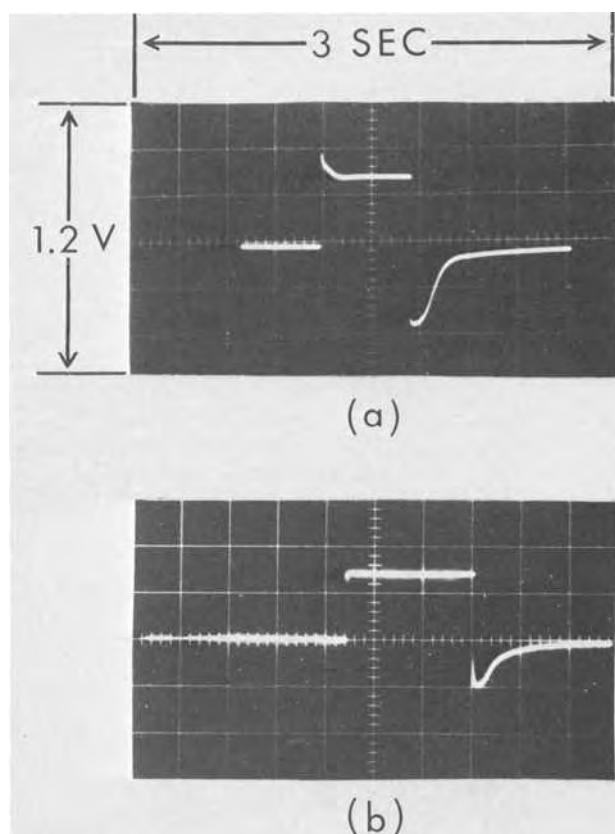


Fig. 7. Voltage of an Al dry cell (formulation "B") for a 3-ohm discharge, with (from left to right) the circuit closed, opened, and reclosed: (a) 1 min after start of discharge; (b) 2 hr after start of discharge.

circuit was closed, the aluminum anode was either film free or the film was readily penetrated by electrolyte species, probably chloride ions. When the circuit was opened, the anode was in an active condition, but passivated in about 0.1 sec to attain a steady voltage. Reclosing the circuit decreased the voltage below the steady closed-circuit voltage until the oxide film could be fully penetrated, which required over 0.5 sec. The difference between the instantaneous and steady closed-circuit voltage early in the discharge was about 0.34V for "B" formulation cells and 0.52V for "C" formulation cells. Zinc anode chemistry is not dominated by the presence of a surface oxide film, and the voltage changed only 0.05V instantaneously in opening or closing the circuit.

As discharge proceeded, two changes in aluminum cell ("B" formulation) behavior took place in Fig. 7(b). The voltage instantaneously attained a constant value on opening the circuit, and the difference between the instantaneous and steady closed-circuit voltage decreased. Both of these changes indicate a trend toward decreased film formation, possibly because the chromate inhibitor was losing effectiveness. This correlates with the increase in corrosion rate during discharge (cf. Fig. 3).

The internal cell resistances obtained by dividing the instantaneous change in voltage produced by opening the circuit³ by the current at each of several stages of discharge are plotted against discharge time in Fig. 8. The zinc cell resistance was essentially constant during discharge, while resistances of both types of aluminum cells were about constant for 30 min, decreased sharply, then gradually increased. The large increase

³ The rapidity of this measurement should minimize any polarization effects. During the subsequent period on open circuit (~ 0.5 -1 sec), the voltage of the zinc cell gradually increased, indicating polarization. This effect increased with extent of discharge. There was no change in the open-circuit voltage of the aluminum cells in the same time span except for the passivation phenomenon mentioned above.

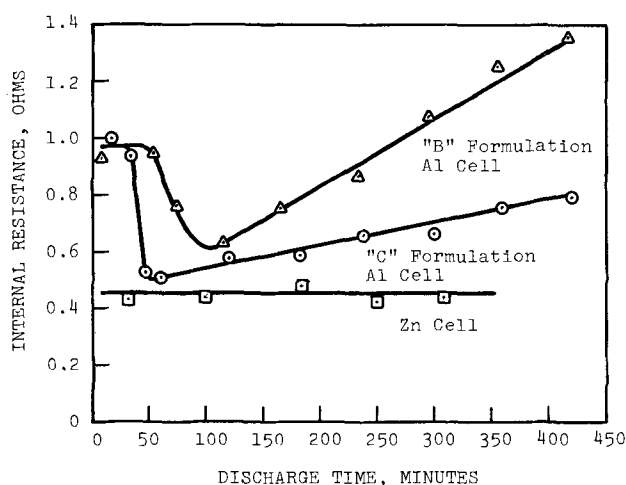


Fig. 8. Internal resistances of two aluminum dry cells and a commercial general purpose zinc dry cell: 3-ohm discharges. [Continuous discharge, except for momentary interruptions.]

in internal resistance of the "B" formulation aluminum cell correlates with the voltage drop in the discharge curve for this cell. During continuous discharge, the voltage for a "B" formulation cell decreases slowly initially but then drops rapidly [cf. Fig. 1(a)], whereas the voltages of a zinc cell [cf. Fig. 1(b)] and "C" formulation aluminum cell drop rapidly at first, then more slowly. The large increase in resistance of the "B" formulation cell could be the result of a build-up of amorphous $\text{Al}(\text{OH})_3$ ⁴ produced from the large amount of $\text{AlCl}_3 \cdot 6\text{H}_2\text{O}$ in the cell formulation and the added aluminum ions formed by the discharge and corrosion reactions. The "C" formulation cell does not include $\text{AlCl}_3 \cdot 6\text{H}_2\text{O}$ in the electrolyte formulation so might be expected to show less of a resistance increase, as is the case.

The high internal resistance of the undischarged aluminum cells appears to be an anode phenomenon. A cell with "B" formulation electrolyte but a zinc anode had an initial resistance similar to that of a commercial zinc cell and an increase in resistance with discharge time. Also, the minima in resistance of the aluminum cells in Fig. 8 correspond closely to a noticeable decrease in the difference in instantaneous closed-circuit voltage and the steady closed-circuit voltage, as shown in Fig. 7. The aluminum anode of an undischarged cell is probably covered with a resistant oxide or chromate film which decreases working cell voltage during the early part of the discharge. During continued discharge, this film is dissolved or modified and cell resistance decreases. The straight line portions of both aluminum cell curves in Fig. 8 extrapolate to about 0.4 ohm. The difference between actual initial resistance and this value, about 0.5 ohm, could be attributed to the initial resistance of the anode film. While reducing cell capacity by increasing internal resistance, this film undoubtedly improves the storage capabilities of new or slightly discharged cells.

Aluminum Cell Modifications

Use of electrolytic manganese dioxide.—Substitution of electrolytic (Mitsui) manganese dioxide for natural ore improved aluminum cell capacity significantly: a "B" formulation aluminum cell containing electrolytic manganese dioxide had a capacity of 580 min (to 0.90V) on the heavy industrial flashlight test (4-ohm), 35% greater than a cell with natural ore. Initial voltage under load was 1.50V, 0.03V higher than a cell with natural ore.

Anode alloy change.—While the potentials of binary aluminum-zinc alloys are higher than aluminum, they

are lower than zinc. A ternary galvanic anode alloy, CB75⁵ (Al-7.2% Zn-0.12% Sn), with a potential of -0.85V (vs. H_2 electrode) in 0.5M $\text{AlCl}_3 + 0.2\text{M}$ $(\text{NH}_4)_2\text{CrO}_4$, compared with -0.66V for Al-1% Zn, and -0.77V for zinc, was tried as a dry cell anode in "B" formulation cells. The initial cell voltage was 1.65V on the heavy industrial flashlight test (4-ohm) but capacity was not improved over a cell with Al-1% Zn. A black coating which may have increased cell resistance formed on the anode.

Electrolyte changes.—"B" formulation cells containing 1 ml of various corrosion inhibiting amines and amino alcohols (triethanolamine, triethylenetetramine, n-isopropylethylenediamine, or 2-(isoamylamino)-ethanol) were tested under the heavy industrial flashlight test (4-ohm). Although gassing in some cases was only 70% that of cells without the additions, capacity was not correspondingly increased. A film which decreased corrosion but increased cell resistance may have formed.

Two acids which are solids at room temperature, citric and oxalic, were mixed into the black mix of "C" formulation aluminum cells (1.5 g/cell) in an attempt to maintain a low pH during discharge without overly lowering initial pH (which would increase corrosion on shelf stand). It was hoped that solid acid would slowly dissolve during discharge. While the cells had higher capacities than cells without the additions (50% greater for the cell with oxalic acid) on the heavy industrial flashlight test (4-ohm), an initial gas-producing reaction of the acids with manganese dioxide made sealing of the cells difficult. A buffer system, included in "A" formulation cells, did not produce a high capacity.

Substitution of lithium chloride for chromic chloride in "B" formulation aluminum cells, to reduce internal resistance, increased closed circuit (4-ohm resistance) voltage 0.10V, but reduced capacity during the heavy industrial flashlight test. The lithium chloride perforated the aluminum anode cans during discharge, reducing capacity.

Discussion

Capacities of some D-size aluminum dry cells containing natural manganese dioxide exceeded those of commercial general purpose zinc cells on heavy-duty discharge, and capacity was increased substantially by use of electrolytic manganese dioxide. Because of higher initial potentials under load, the aluminum cells performed even more favorably on a watt-hour basis.

On continuous 4-ohm discharge, an aluminum anode yielded 71% of its theoretical ampere-hour capacity, or 2.1 A-hr/g, comparable to the theoretical capacity of a magnesium anode, and about 2.5 times the theoretical capacity of a zinc anode. Even under the most unfavorable discharge condition (general purpose test), an aluminum anode yielded 1.0 A-hr/g.

The ammonium chromate added to aluminum cell electrolytes to reduce corrosion of undischarged cells loses effectiveness during discharge until the anode of a partially discharged cell corrodes even on open circuit. In addition to decreasing anode efficiency and producing hydrogen, the corrosive reaction raises cell pH, decreasing manganese dioxide capacity. Although a certain amount of corrosion may be inevitable while the cell is under load and the anode surface is relatively film free, an alloy-electrolyte-inhibitor combination which would effectively inhibit corrosion of a partially discharged cell on open circuit, should increase capacity on intermittent discharge as with zinc cells. An alternate, although less satisfactory, method of increasing capacity on intermittent discharge may be adding materials which can help maintain a low pH. Additions of this type present a trade-off by re-

⁴ X-ray diffraction examination of the black mix, material in the separator, and material adhering to the anode surface revealed no crystalline alumina.

⁵ Patented, Aluminum Company of America.

ducing the amount of manganese dioxide which can be included in the cell.

After remaining fairly constant for a short time, the internal resistance of an aluminum dry cell decreases during discharge because of dissolution or modification of the anode film, then increases. A cell formulation high in aluminum chloride produces the largest increase, possibly due to $\text{Al}(\text{OH})_3$ formation. However, since a cell with this formulation has a high capacity, other factors such as pH control must be more important.

Acknowledgment

The author is grateful for the technical assistance of Mr. W. W. Hill.

Manuscript submitted Aug. 20, 1971; revised manuscript received Oct. 25, 1971.

Any discussion of this paper will appear in a Discussion Section to be published in the December 1972 JOURNAL.

REFERENCES

1. R. B. Mears and C. D. Brown, *Corrosion*, **1**, 113 (1945).
2. R. Glicksman, *This Journal*, **106**, 457 (1959).
3. D. E. Sargent, U.S. Pat. 2,554,447 (1951).
4. S. Ruben, U.S. Pat. 2,638,489 (1953).
5. S. Ruben, U.S. Pat. 2,783,292 (1957).
6. J. J. Stokes, Jr., U.S. Pat. 2,796,456 (1957).
7. J. J. Stokes, Jr., U.S. Pat. 2,828,591 (1958).
8. J. J. Stokes, Jr., U.S. Pat. 3,307,976 (1967).
9. G. S. Lozier et al., U.S. Pat. 2,874,079 (1956).
10. M. J. Pryor et al., U.S. Pat. 3,240,629 (1966).
11. M. J. Pryor et al., U.S. Pat. 3,368,958 (1968).
12. Jean Foucry, U.S. Pat. 3,415,688 (1968).
13. M. P. Korver and N. C. Cahoon, Can. Pat. 683,182 (1964).
14. J. J. Stokes, Jr., *Electrochem. Technol.*, **6**, 36 (1968).
15. P. Benson, W. B. Price, and F. L. Tye, *ibid.*, **5**, 571 (1967).
16. R. Glicksman and C. K. Morehouse, *This Journal*, **102**, 273 (1955).

Hydrogen Ion (Proton) Conduction in Thoria-Base Solid Electrolytes

David A. Shores* and Robert A. Rapp*

Department of Metallurgical Engineering, The Ohio State University, Columbus, Ohio 43210

ABSTRACT

The total conductivities of a series of ThO_2 -base electrolytes have been determined over a wide range of oxygen activity in atmospheres of $\text{H}_2/\text{H}_2\text{O}/\text{Ar}$ mixtures. At 1200° and 1400°C and low oxygen activities, a significant conductivity contribution corresponding to hydrogen ion (proton) conduction was found for electrolytes with high dopant contents. The experiments are interpreted in terms of a defect model involving two dopants.

When high temperature equilibration with a gas phase containing H_2 - H_2O , CO - CO_2 , etc. is used to establish the oxygen activity of a compound, it is important to know the extent to which the second components of the gas mixtures are soluble and mobile in the compound, particularly in experiments concerned with the nature, concentrations, and mobilities of charged point defects. Stotz and Wagner (1) have analyzed several defect reactions whereby hydrogen or water vapor may dissolve into oxides as protons or hydride ions at high temperatures. If a substantial solubility for these dopant ions exists, the defect-dependent properties of the oxide will be altered.

Hydrogen dissolved in crystalline oxide can be treated as a dopant whose concentration is established by equilibration with an atmosphere containing hydrogen. In the following discussion, the dissolved hydrogen is considered to be fully ionized either as H^+ or H^- , and thus the concentration of dissolved neutral hydrogen atoms is assumed to be negligibly small. To maintain electrical neutrality in the presence of dissolved hydrogen ions, compensating changes in the concentration of the predominant defects in the host crystal will occur according to the arguments of Koch and Wagner (2) and Kröger and Vink (3). In the present work, with the dissolution of hydrogen into doped oxide electrolytes, the base oxide, ThO_2 , is actually doped with two components, i.e., hydrogen ions and aliovalent metal ions. In the absence of hydrogen and over a range of relatively low oxygen activities, the predominant ionic defect is the oxygen vacancy

whose concentration is essentially established by the metal dopant content, eg., Y_2O_3 , La_2O_3 , or Sm_2O_3 in ThO_2 (4-6). Within this P_{O_2} -range, and with the presence of hydrogen, electrical compensation of dissolved hydrogen ions is assumed to occur by changes in the concentration of oxygen vacancies. At oxygen activities above and below the P_{O_2} -range of predominant ionic conduction, the effect of dissolved hydrogen on the positive hole and excess electron concentrations might become observable.

Wagner (7, 8) and Kröger (9, 10) have shown that each dopant affects the solubility of the other dopant. The interaction is such that the solubility of each is increased if the dissolved ions have relative charges of opposite sign and is decreased in the case of relative charges of the same sign. The interaction between dopants arises from the electrical neutrality condition, which in the present study is

$$n + 2[\text{O}_i'] + [\text{F}_{\text{Th}}'] = p + 2[\text{V}_{\text{O}}'] + [\text{H}'] \quad [1]$$

where according to the defect notation of Kröger and Vink (3), n and p are the concentrations of electrons and positive holes respectively, V_{O}' is an oxygen vacancy, O_i' is an interstitial oxygen ion, H^- is a dissolved hydrogen ion (proton), F_{Th}' denotes La_{Th}' , Sm_{Th}' or Y_{Th}' , etc., and the brackets denote concentrations. There are numerous examples of controlled doping with two or more components in both elemental semiconductors and in simple ionic compounds (9) in which the description by an algebraic summation was adequate. On the other hand, in a discussion of the effects of multicomponent doping in calcia-stabilized zirconia, Kröger (10) found it useful to postulate the

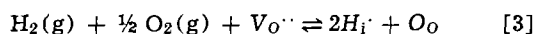
* Electrochemical Society Active Member.

Key words: ionic conductivity, proton conduction, ThO_2 -base electrolytes.

existence of uncharged associates, $(Ca_{Zr}V_O)^x$, which in effect, reduced the concentration of dopant calcium ions $[Ca_{Zr}]$ that entered the electrical neutrality condition. In the present study, it is assumed that interactions between defects, such as the formation of associates, do not occur.

Stotz and Wagner (1) have proposed some defect reactions whereby hydrogen can dissolve into an oxide which contains oxygen vacancies as the predominant defect. Two possibilities involve either interstitial protons (H_i^+) or hydride ions (H^-) located on oxygen lattice sites (H_O^-). Both defects have a net electrical charge of +1 relative to the host crystal.

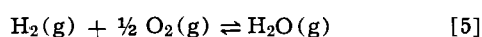
For the case of interstitial protons, an oxide crystal containing anion vacancies as the predominant ionic defect could equilibrate with an atmosphere containing $H_2(g)$ and $O_2(g)$ by



where O_O denotes an oxygen ion on a normal lattice site. From the law of mass action corresponding to the assumption of a dilute solution of defects

$$K_3 = \frac{[H_i^+]^2}{[V_{O^{\cdot\cdot}}] P_{H_2} P_{O_2}^{1/2}} \quad [4]$$

Further, for equilibrium in the gas phase



so that

$$[H_i^+] = K_3^{1/2} K_5^{-1/2} [V_{O^{\cdot\cdot}}]^{1/2} P_{H_2O}^{1/2} \quad [6]$$

The partial electrical conductivity of a charged species is given by

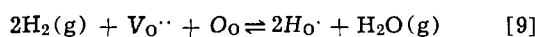
$$\sigma_i = c_i q_i u_i \quad [7]$$

where σ_i is the partial conductivity ($\text{ohm}^{-1}\text{-cm}^{-1}$), c_i is the carrier concentration (number/cm³), q_i is the charge on the species (coulombs), and u_i is the electrochemical mobility ($\frac{\text{cm/sec}}{\text{V/cm}}$). Thus it follows from

Eq. [6] and [7] that at constant temperature

$$\sigma_{H_i^+} \propto [V_{O^{\cdot\cdot}}]^{1/2} P_{H_2O}^{1/2} \quad [8]$$

Alternatively, if negatively charged hydride ions are situated on oxygen lattice sites, then



From the law of mass action

$$K_9 = \frac{[H_O^-]^2 P_{H_2O}}{P_{H_2}^2 [V_{O^{\cdot\cdot}}]} \quad [10]$$

From Eq. [5] and [10]

$$[H_O^-] = K_9^{1/2} K_5^{-1} [V_{O^{\cdot\cdot}}]^{1/2} P_{H_2O}^{1/2} P_{O_2}^{-1/2} \quad [11]$$

From Eq. [7] and [11]

$$\sigma_{H_O^-} \propto [V_{O^{\cdot\cdot}}]^{1/2} P_{H_2O}^{1/2} P_{O_2}^{-1/2} \quad [12]$$

A comparison of Eq. [6] with [11] and [8] with [12] shows that the solubility and partial conductivity of interstitial protons are independent of P_{O_2} , whereas the solubility and partial conductivity of hydride ions are proportional to $P_{O_2}^{-1/2}$. Measurements of the partial hydrogen ion conductivity as a function of P_{O_2} at constant P_{H_2O} may be used to distinguish between the two defect models. Equations [6] and [11] show explicitly that the solubility of hydrogen depends on the concentration of the other dopant, viz., with $2[V_{O^{\cdot\cdot}}] \approx [F_{Th}']$ (when $[H^+]$ is small)

$$[H^+] \propto [F_{Th}']^{1/2} \quad [13]$$

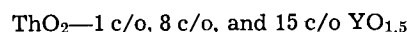
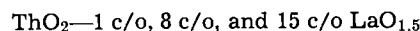
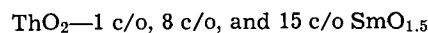
If an oxide solid electrolyte dissolves a significant concentration of hydrogen ions, then the use of H_2 - H_2O mixtures as an oxygen electrode in a galvanic cell could lead to mixed electrode reactions and hence to an ambiguous cell voltage with an unreliable determi-

nation of oxygen activities. Further, the doping effect of hydrogen ions could conceivably affect the partial electronic conductivities (to be discussed) and thereby change the range of oxygen activities over which the electrolyte exhibits predominant ionic conduction ($t_{ion} \cong 0.99$). For other applications (11) a significant solubility and partial conductivity of hydrogen ions in a solid electrolyte might affect the experiment or process in other ways.

Only one measurement of the solubility of hydrogen or water vapor in solid oxide electrolytes has been reported. Wagner (12) found that the solubility of water vapor in ZrO_2 containing 8 or 17 weight per cent (w/o) Y_2O_3 at relatively low temperature (near 900°-1000°C) was rather low, about 13-30 parts per million. However, the activities of hydrogen and oxygen in the gas phase were not fixed and known, but rather were established through the dissociation of water molecules. In another paper, Primas *et al.* (6) reported electrical conductivities in thoria-base solid solutions which appear to have a significant hydrogen ion component under certain conditions. The present study was an extension of that aspect of Primas' work, and its purpose was to test the proposals of Stotz and Wagner (1) which concerned the dissolution of hydrogen or water vapor in solid oxides containing oxygen vacancies as the predominant ionic defect.

Experimental Procedure

Electrical (a-c) conductivity measurements were made on thoria-base solid solutions at 800°, 1000°, 1200°, and 1400°C with equilibration in H_2 - H_2O -Ar or H_2O - O_2 -Ar atmospheres. Specimens in the shape of "pills" (5/16 in. diameter by 1/16 in. thick) were prepared from high-purity oxide powders (99.9% purity) obtained from the Rare Earth Division of American Potash and Chemical Corporation. The following compositions in cation per cent (c/o) were prepared:



The components were blended for one or more days, calcined overnight, ground, screened, blended again, and cold pressed into pills. The pills were pre-fired overnight at 1100°C and then sintered at 1950°C or higher for 3-4 hr in air to obtain dense samples.

Several pills of differing compositions were platinized on their faces and were assembled and held in an alumina cell holder with spring pressure. The pills were separated from each other by 5-mil thick platinum sheets which also served as electrodes. The alumina cell holder was placed in an impervious alumina combustion tube in a noninductively wound furnace which was controlled to $\pm \frac{1}{2}^\circ\text{C}$ while conductance measurements were being made. The design of the cell holder, as well as general procedures and precautions for conductivity measurements, have been described in detail elsewhere (13). Previous measurements (6) had established that the conductances were independent of frequency over a broad range; a Wayne-Kerr conductivity bridge with 1592 Hz was used in the present study. As is usual with sintered specimens, duplicate runs on different pills of the same composition yielded conductivities which differed slightly in absolute magnitude; however, such specimens exhibited the same conductivity increments with respect to changes in P_{H_2} . Since, for the most part, only changes in conductivity were important in the present study, the agreement between duplicate runs was quite satisfactory.

Electrical conductivities were determined in separate runs at both low and relatively high oxygen activities. For low oxygen activities, H_2 - H_2O -Ar atmospheres were prepared by passing accurately metered flows of argon and hydrogen through a water saturator which was maintained at carefully controlled tem-

peratures. A P_{H_2}/P_{H_2O} ratio of 0.40 was chosen and held constant throughout this experiment, and hence an unvarying oxygen activity was established over the samples by the equilibrium between H_2 and H_2O at each temperature, i.e., at 800°C , $P_{O_2} = 10^{-17.55}$ atm; at 1000°C , $P_{O_2} = 10^{-13.74}$ atm; at 1200°C , $P_{O_2} = 10^{-10.95}$ atm; at 1400°C , $P_{O_2} = 10^{-8.84}$ atm. The oxygen partial pressure can be expressed in terms of the experimental variables as

$$P_{O_2} = \left(\frac{P_{H_2O}}{P_T - P_{H_2O}} \right)^2 \left(\frac{N_{Ar} + N_{H_2}}{N_{H_2}} \right)^2 \exp \left(\frac{2\Delta G^\circ_{H_2O}}{RT} \right) \quad [14]$$

where P_{H_2O} is the vapor pressure of water at the temperature of the water saturation unit, P_T is the total pressure, N_{Ar} and N_{H_2} are the flow rates of argon and hydrogen, $\Delta G^\circ_{H_2O}$ is the standard free energy of formation of H_2O at the furnace temperature T . The partial pressure of hydrogen (and necessarily that of water) was varied by the simultaneous adjustment of the flow rates of hydrogen and argon and the temperature of the water saturation unit.

In another experiment, conductances were measured as a function of P_{O_2} in H_2 - H_2O -Ar atmospheres at constant P_{H_2O} . A few conductance measurements were made in CO - CO_2 atmospheres having the same low oxygen pressure at a given temperature as the H_2 - H_2O -Ar mixtures, but these values appeared to be inconsistently low (perhaps because of electrode polarization by adsorbed CO_2) and were not used in subsequent calculations.

Atmospheres with high oxygen activity were achieved by passing mixtures of oxygen and argon through the water saturation unit held at various temperatures. With this procedure, the oxygen partial pressure was maintained at approximately 0.263 atm at all furnace temperatures. The resulting hydrogen partial pressures are listed in Table I.

Results and Discussion

The conductivity measurements at low P_{O_2} , where ionic conduction predominates, and at high P_{O_2} , where mixed ionic and positive hole conduction occurs, will be discussed separately. The results for the fixed relatively low P_{O_2} , where P_{H_2}/P_{H_2O} was held constant, are presented in Fig. 1-3 as plots of log total conductivity as a function of $\log P_{H_2}$ (or equivalently $\log P_{H_2O}$) at constant P_{O_2} . Those lines with slopes significantly greater than zero indicate a contribution of mobile hydrogen ions to the total conductivity; one possible exception is the data for 1 c/o dopant samples at 800°C , which will be discussed subsequently. Thus, significant hydrogen ion conduction occurs at high temperatures (1200° and 1400°C) and in samples with high metal ion dopant contents (8 and 15 c/o). No appreciable difference in behavior was noted between equivalent compositions with differing metal ion dopants.

In Fig. 4 is shown a plot of log hydrogen ion conductivity vs. $\log P_{H_2}$ (or $\log P_{H_2O}$) for samples with high dopant contents and at high temperatures. This hydrogen ion component was computed as the total conductivity minus the oxygen vacancy partial conductivity which is essentially independent of P_{H_2} for a small solubility of hydrogen. The oxygen vacancy

partial conductivity was obtained as the intercept at $P_{H_2} = 0$ of a plot of the total conductivity vs. $P_{H_2}^{1/2}$. A slope of $1/2$ on a plot of $\log \sigma_H$ vs. $\log P_{H_2O}$ is predicted for both the interstitial hydrogen ion model (Eq. [8]) and the hydride ion model (Eq. [12]). With consideration of the inherent uncertainty for a small difference between two large quantities, the agreement of the experimental curves with the predicted slope is satisfactory.

The effect of the concentration of metal ion dopant on the partial conductivity of hydrogen ions is shown in Fig. 5. The rather considerable scatter of the data in this plot is not unusual when comparing the behavior of different sintered pills. However, from Fig. 5, the

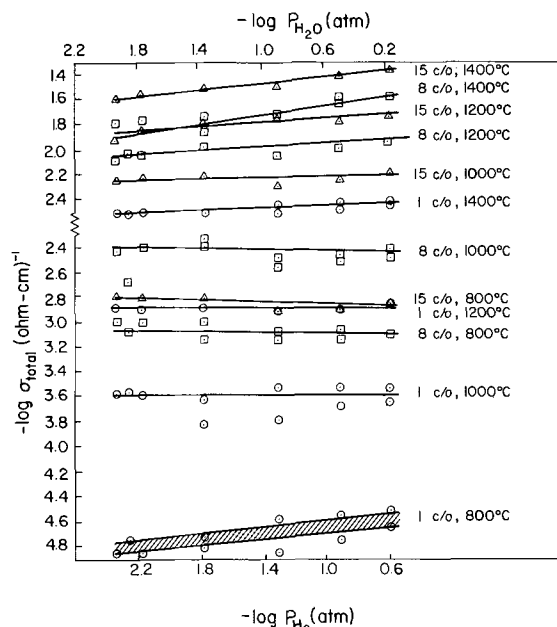


Fig. 1. Total conductivity of thoria-yttria solid solutions at fixed oxygen activities as a function of partial pressure of hydrogen.

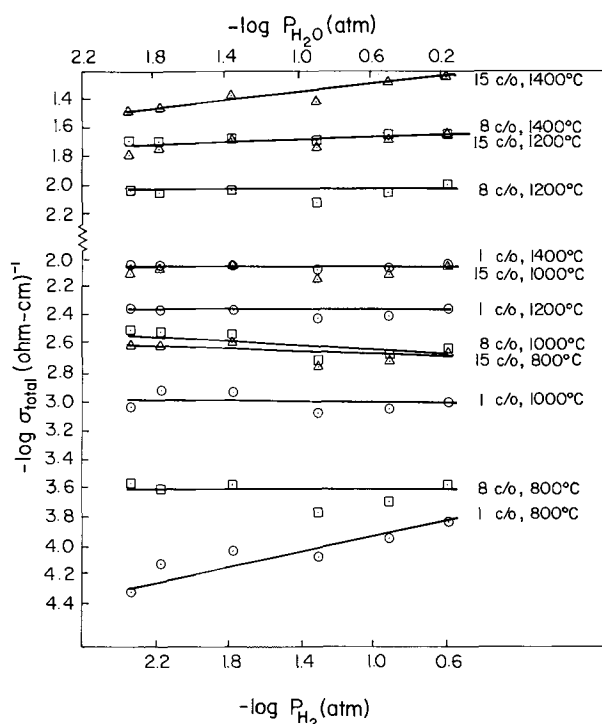


Fig. 2. Total conductivity of thoria-samarium solid solutions at fixed oxygen activities as a function of partial pressure of hydrogen.

Table I. Calculated partial pressures of hydrogen in H_2O - O_2 -Ar Atmospheres

$\log P_{H_2O}$ (atm)	$\log P_{H_2}$ (atm)			
	800	1000	1200	
		Furnace temperature, $^\circ\text{C}$		
		1000	1200	1400
-1.38	-10.26	-8.35	-6.96	-5.90
-0.91	-9.80	-7.89	-6.50	-5.44
-0.51	-9.40	-7.49	-6.10	-5.04
-0.20	-9.13	-7.22	-5.83	-4.77

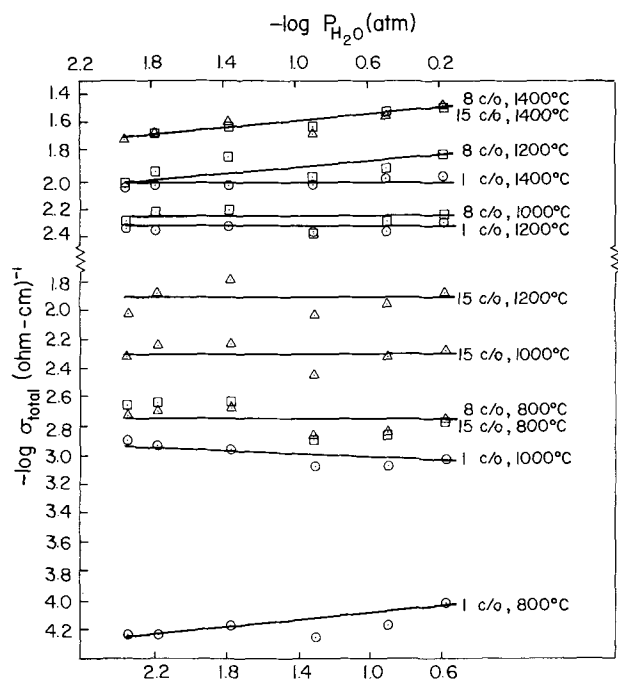


Fig. 3. Total conductivity of thoria-lanthana solid solutions at fixed oxygen activities as a function of partial pressure of hydrogen.

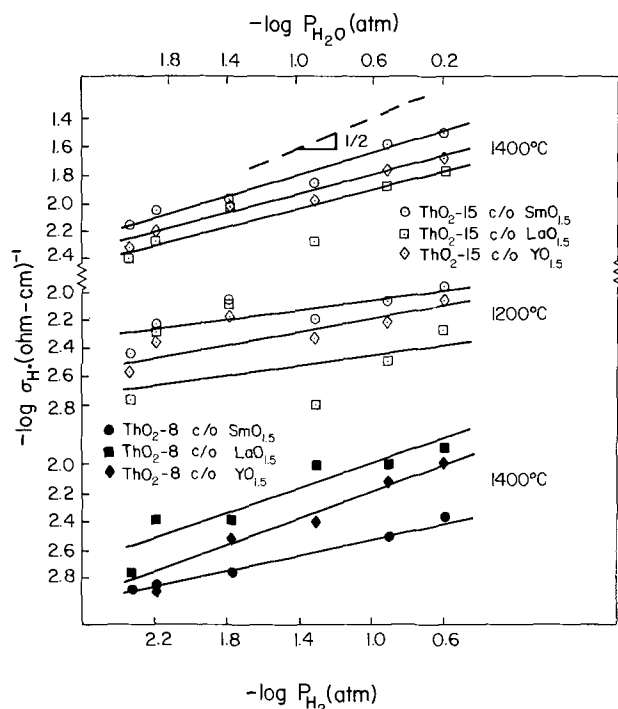


Fig. 4. Hydrogen ion conductivity of thoria-base solid solutions at 1400°C ($P_{O_2} = 10^{-8.8}$ atm) and at 1200°C ($P_{O_2} = 10^{-10.9}$) as a function of partial pressure of hydrogen. A slope of $\frac{1}{2}$ is predicted by the interstitial proton model.

hydrogen ion partial conductivity increases with increasing dopant content in qualitative agreement with Eq. [8] or [12]. Recent conductivity measurements on pure ThO₂ in H₂-H₂O mixtures at 1000° and 1200°C by Bransky and Tallan (14) show no indication of a proton conductivity contribution.

In Fig. 6 are shown the results of a separate set of conductivity measurements in which P_{H_2O} was held constant while P_{O_2} was varied. These conductivities

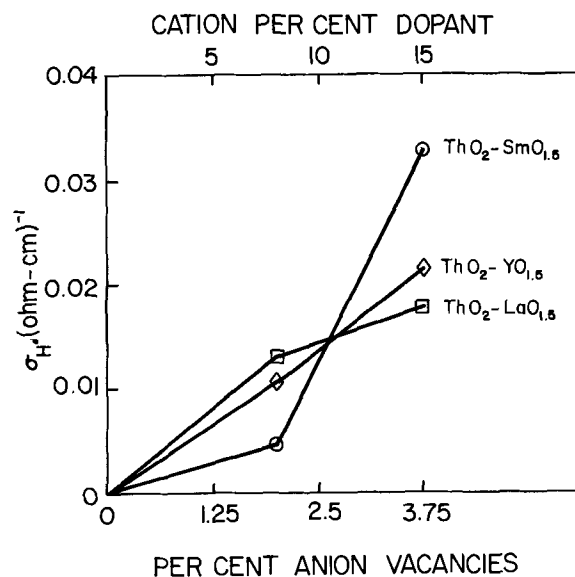


Fig. 5. Hydrogen ion conductivity of thoria-base solid solutions at 1400°C and at a hydrogen activity of $10^{-0.59}$ atm as a function of dopant content.

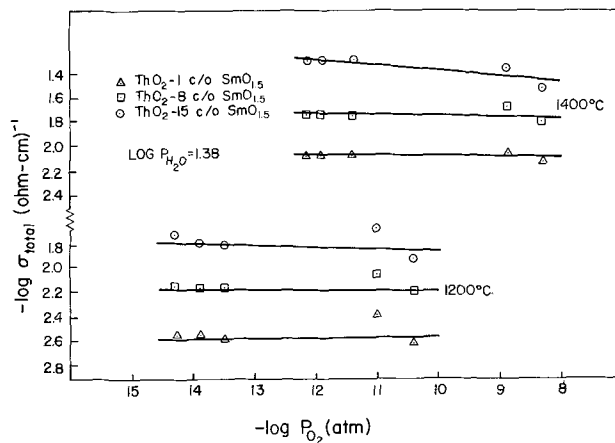


Fig. 6. Total conductivity of thoria-base solid solutions at a constant water vapor pressure of $10^{-1.38}$ atm as a function of oxygen activity. A slope of $-\frac{1}{2}$ is predicted by the hydride ion model; a slope of zero is predicted by the interstitial proton model.

were found to be independent of P_{O_2} which is consistent only with the interstitial hydrogen ion model; a $P_{O_2}^{-1/2}$ dependence is predicted from the hydride ion model. Thus, it is concluded that the interstitial hydrogen ion model is appropriate for the dissolution of hydrogen into thoria-base electrolytes in the P_{O_2} -range of predominant ionic conduction. According to the model, electrical compensation of the dopant protons is accomplished by an equivalent (small) reduction in the concentration of oxygen vacancies.

The increasing total conductivity with increasing P_{H_2} for samples containing 1 c/o dopant at 800°C (Fig. 1-3) probably does not represent hydrogen ion conduction. This conclusion is based on the observations that (i) the conductivities of samples containing 8 and 15 c/o dopant at 800°C indicated no partial hydrogen ion conductivity (see Eq. [6]), and (ii) the conductivities of 1 c/o doped samples at higher temperatures, where a greater solubility and hence a larger partial hydrogen ion conductivity would be expected, indicated no hydrogen ion conduction. The results of Primas *et al.* (6) for some dilute ThO₂-Sm₂O₃ electrolytes at 800°C showed similar behavior. In their work, the conductivities in H₂-H₂O-O₂ atmospheres were significantly higher than the value extrapolated from data obtained in higher oxygen activity atmospheres containing no hydrogen.

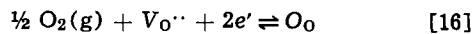
The apparently anomalous behavior for the 1 c/o dopant specimens at 800°C at a fixed low oxygen activity may represent a significant contribution from excess electron conduction. Lasker and Rapp (4) have shown for doped oxide electrolytes that in the absence of proton doping, $\sigma_{\theta} \propto [F_{Th}']^{-1/2}$ is expected. Thus, it is unlikely that a σ_{θ} conductivity contribution could be detected in the 8 and 15 c/o specimens, particularly in view of the higher σ_{ion} . A tentative explanation of the anomalous behavior is proposed as follows.

The reduced electrical neutrality condition for the 1 c/o dopant specimens at 800°C and low P_{O_2} would be

$$n + [F_{Th}'] = 2[V_{O''}] + [H_i'] \quad [15]$$

With consideration of the expected relative mobilities of the species and the observed conductivity behavior, one could conclude that the terms $[F_{Th}']$ and $[V_{O''}]$ greatly exceed $[H_i']$ which, in turn, greatly exceeds n .

For equilibrium of the specimen with the gas phase



and at constant P_{O_2} , as in Fig. 1-3

$$[V_{O''}] n^2 = K_{16}' \quad [17]$$

From Eq. [15]

$$[V_{O''}] = \frac{1}{2} (n + [F_{Th}'] - [H_i']) \quad [18]$$

Solving Eq. [17] for $[V_{O''}]$ with substitution into Eq. [18]

$$n^3 + [F_{Th}'] n^2 - [H_i'] n^2 = \text{constant} \quad [19]$$

Upon differentiation, the fractional change in n with increasing $[H_i']$ is given by

$$\frac{1}{n} \frac{dn}{d[H_i']} = \frac{1}{2} \frac{1}{[F_{M}'] - [H_i']} \quad [20]$$

Integration between a hydrogen-free state with excess electron concentration n^* to a hydrogen-containing state with excess electron concentration n_H yields

$$n_H = n^* \left(\frac{[F_{M}']}{[F_{M}'] - [H_i']} \right)^{+1/2} \quad [21]$$

considering that $n^* \propto [F_{M}']^{-1/2}$ gives

$$n_H \propto ([F_{M}'] - [H_i'])^{-1/2} \quad [22]$$

Thus, an excess electron conductivity contribution might become observable in a hydrogen-containing atmosphere when $[H_i']$ approaches $[F_{M}']$ (at low $[F_{M}']$), and at a low temperature where σ_{ion} is sufficiently low to allow the detection of σ_{θ} by a measurement of σ_{total} .

The above development has described the effect on an electronic concentration n_H caused by compensation of a dopant H_i' by the change in the concentration of an ionic defect $V_{O''}$. This interpretation may describe the conductivity behavior of the 1 c/o dopant specimens at 800°C in Fig. 1-3, as well as the behavior of the 0.5, 1, and 3 c/o $SmO_{1.5}$ specimens at 800°C from the work of Primas *et al.* (6). Unexplained, and apparently inconsistent, is the fact that the "pure" ThO_2 , 0.1 c/o $SmO_{1.5}$, and the dilute $LaO_{1.5}$ -doped specimens of Primas *et al.* (6) did not exhibit analogous behavior.

The results of conductivity measurements as a function of P_{H_2} at a constant, relatively high P_{O_2} (0.263 atm) are shown in Fig. 7-9. The calculated hydrogen activities for these conditions are presented in Table I. The total conductivity of such compositions at this P_{O_2} in H_2O -free atmospheres is composed of ionic and positive hole contributions of comparable magnitudes (4, 6). From Eq. [8] and [12], conduction by both protons and hydride ions should be proportional to $P_{H_2O}^{1/2}$. However, conduction by hydride ions is otherwise excluded because of its $P_{O_2}^{-1/2}$ dependence in Eq. [12]. On the other hand, because the same range of P_{H_2O} was used in the high P_{O_2} measurements as in the

low P_{O_2} measurements, proton conduction according to Eq. [8] would be expected at high P_{O_2} in a magnitude equal to that found at low P_{O_2} and plotted in Fig. 4.

Except for 1 c/o doped samples at low temperatures, the total conductivities at high P_{O_2} were independent of P_{H_2O} or P_{H_2} and therefore proton conduction was not detected. However, this result is not unexpected because the magnitudes of σ_{proton} of Fig. 4 are sufficiently lower than the corresponding total conductivities of Fig. 7-9.

Interestingly, the dissolution of protons from H_2O at high P_{O_2} caused no detectable change in σ_{θ} , except possibly for the 1 c/o dopant specimens at 800°C. Considerations of intrinsic electronic equilibrium in the crystal with

$$n \cdot p = K_1 \quad [23]$$

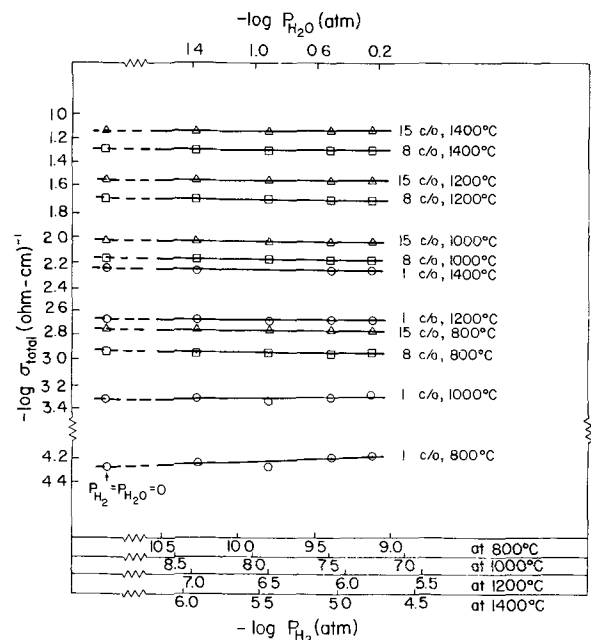


Fig. 7. Total conductivity of thoria-yttria electrolytes at a constant oxygen activity of 0.263 atm as a function of partial pressure of hydrogen and water vapor.

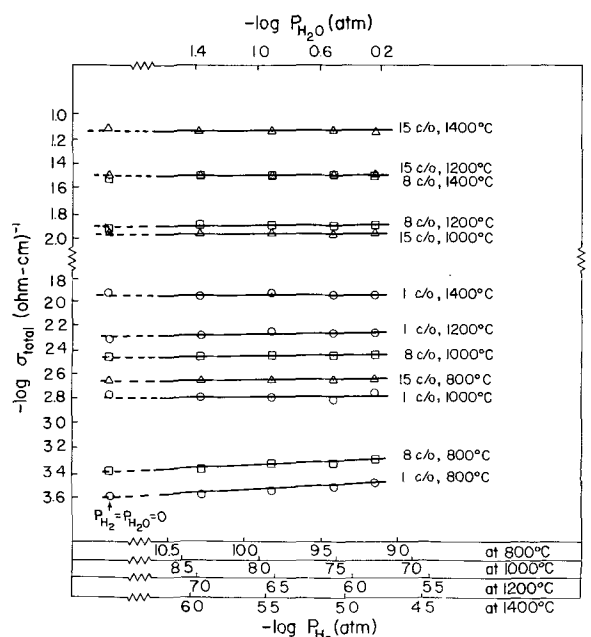


Fig. 8. Total conductivity of thoria-samarium electrolytes at a constant oxygen activity of 0.263 atm as a function of partial pressure of hydrogen and water vapor.

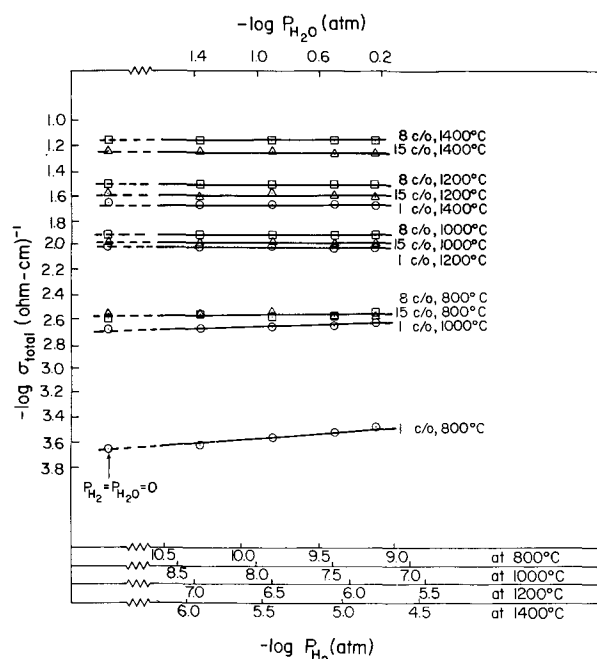


Fig. 9. Total conductivity of thoria-lanthana electrolytes at a constant oxygen activity of 0.263 atm as a function of partial pressure of hydrogen and water vapor.

and use of Eq. [21] with $p_{\alpha}[F_{Th}']^{1/2}$ gives

$$p_H \propto ([F_{M'}] - [H_i'])^{1/2} \quad [24]$$

where p_H is the concentration of positive holes in the H_2O (or H_2) containing environment. The observed low slopes of the lines for 1 c/o dopant specimens are of the opposite sign compared to the expected effect of dissolved protons on positive hole conduction. Further interpretation of these results is not obvious.

Summary and Conclusions

A-C conductivities of nine thoria-base solid electrolytes have been measured at high temperatures as a function of the partial pressure of hydrogen at fixed oxygen partial pressures. The present study encompassed oxygen activities in both the ionic (low P_{O_2}) and the mixed (high P_{O_2}) conduction ranges. The re-

sults have shown that appreciable hydrogen ion conduction by protons occurs at 1200° and 1400°C at low P_{O_2} in samples with high aliovalent metal dopant contents. At high P_{O_2} (low P_{H_2}) significant hydrogen ion conduction was not detected and the dissolved protons did not affect the positive hole conductivity contribution. The results were consistent with the interstitial proton model of Stotz and Wagner (1). Seemingly anomalous behavior for 1 c/o dopant specimens at low P_{O_2} at 800°C was interpreted as excess electronic conduction.

Acknowledgment

This research was supported under Contract No. AT(11-1)-1440 by the U. S. Atomic Energy Commission.

Manuscript submitted Sept. 13, 1971; revised manuscript received ca. Nov. 19, 1971.

Any discussion of this paper will appear in a Discussion Section to be published in the December 1972 JOURNAL.

REFERENCES

1. S. Stotz and C. Wagner, *Ber. Bunsenges. Phys. Chem.*, **70**, 781 (1966).
2. E. Koch and C. Wagner, *Z. Phys. Chem.*, **B38**, 295 (1938).
3. F. A. Kröger and H. J. Vink, "Solid State Physics," Vol. 3, p. 307, Academic Press, New York (1956).
4. M. F. Lasker and R. A. Rapp, *Z. Phys. Chem. N.F.*, **49**, 198 (1966).
5. R. A. Rapp, "Thermodynamics of Nuclear Materials," p. 559, IAEA, Vienna (1968).
6. D. H. Primas, D. A. Shores, and R. A. Rapp, Paper in preparation.
7. C. Wagner and K. E. Zimens, *Acta Chem. Scand.*, **1**, 539 (1947).
8. C. Wagner, *J. Chem. Phys.*, **18**, 62 (1950); C. Wagner, *J. Phys. Chem.*, **57**, 738 (1953).
9. F. A. Kröger, "The Chemistry of Imperfect Crystals," p. 716, North-Holland Publishing Co., Amsterdam (1964); F. A. Kröger and H. J. Vink, *J. Phys. Chem. Solids*, **5**, 208 (1958).
10. F. A. Kröger, *J. Am. Ceram. Soc.*, **49**, 215 (1966).
11. H. S. Spacil and C. S. Tedmon, *This Journal*, **116**, 1618; *ibid.*, 1627 (1969); *Chem. and Eng. News*, Nov. 4, 48 (1968).
12. C. Wagner, *Ber. Bunsenges. Phys. Chem.*, **72**, 778 (1968).
13. R. A. Rapp and D. A. Shores, "Techniques of Metals Research, IV," R. A. Rapp, Editor, Part 2, p. 123, Interscience Publishers, New York (1970).
14. I. Bransky and N. M. Tallan, *J. Am. Ceram. Soc.*, **53**, 625 (1970).

Sputtered Fe_2O_3 Films for Use in "See Through" Masks

F. G. Peters, W. Robert Sinclair,* and M. V. Sullivan

Bell Telephone Laboratories, Incorporated, Murray Hill, New Jersey 07974

ABSTRACT

A sputtering technique has been devised for preparing Fe_2O_3 films with rates of solubility in 6M HCl and with transmission spectra appropriate for use as "see-through" photomasks (i.e., photomasks sufficiently transparent at 589 nm for viewing purposes and opaque in the spectral region 360-400 nm). This method involves rf or d-c sputtering of Fe electrodes in CO-CO₂ mixtures or rf sputtering of Fe_2O_3 electrodes in CO-CO₂ mixtures. To achieve films with acceptable transmission spectra the CO content must not exceed 82% with the metal electrode and must not exceed 87% with the oxide electrode. The fastest deposition rate obtained was 120 Å/min for 350W input rf power using an Fe electrode and an 80% CO/20% CO₂ ambient. Measurements of scratch resistance, defect density, and film morphology are presented.

The requirements for a "see through" mask for use in integrated circuit technology have been stated recently (1). These are primarily: (a) sufficient absorption (<ca. 1% transmission) of light in the spectral

region near 360-400 nm, (b) sufficient transmission (ca. 30%) at the sodium D line for viewing purposes, (c) a rate of solubility in selected solvents (in our case 6M HCl) appropriate to photoresist technology, and (d) a hard, abrasion resistant film. MacChesney et al. (2) have shown that Fe_2O_3 films prepared by

* Electrochemical Society Active Member.

Key words: semitransparent photomasks, thin films, sputtering.

chemical vapor decomposition (CVD) of $\text{Fe}(\text{CO})_5$ on a glass surface in the presence of oxygen can have these properties if prepared in the proper temperature range (ca. $100^\circ\text{--}160^\circ\text{C}$). Reid and Cukor (3) have also described a process for preparing iron oxide films for "see through" masks by decomposition of iron organics (4) at about 500°C .

Attempts to prepare iron oxide films by reactive d-c sputtering of Fe in O_2 (1) have led at best to highly strained films which dissolve with removal of curled chunks of film and are, therefore, useless for preparing precision masks. In this paper we explore the possibilities of preparing Fe_2O_3 films suitable for mask use by sputtering. Initially, our interest was solely in the rf sputtering of Fe_2O_3 . However, this interest was broadened to reactive rf sputtering of Fe and reactive d-c sputtering when the essentials of the solution were perceived.

There are three main reasons why a sputtering process for preparing Fe_2O_3 films suitable for masks could be of interest. First, toxicity problems for personnel are not usually encountered in sputtering as they can be in the CVD method. Second, the process of sputtering onto large numbers of substrates has already been automated (5) so that for large scale production of masks commercially available equipment can be used. Third, if at some later date masks of dimensions greater than the present 2×2 in. size are desired, scaling up the procedure to larger areas may be more straightforward than for MacChesney's CVD process (2) or Reid and Cukor's spun film process (3).

Apparatus and Experimental Procedure

The rf sputtering apparatus used in these studies is shown schematically in Fig. 1. The sputtering electrodes consisted of 6 in. disks of hot pressed Fe_2O_3 and cold-rolled steel. Some work was done with Fe_3O_4 electrodes also but these results will not be included as no significantly different results were obtained. These targets were placed on the bottom electrode assembly and sputtering was upwards to minimize pinholes caused by dust. The iron oxide films were deposited onto cleaned 2×2 in. soda-lime glass substrates. Because the strain in the films was found to

be a function of the efficiency of the water cooling of the electrodes a special electrode was fabricated of copper for holding substrates. Etching studies indicate that films deposited onto substrates attached to the more efficiently cooled copper holder were usually less strained than those prepared using the usual stainless steel assembly. Films were deposited onto substrates that were either electrically floating or attached to a grounded electrode. However, when sputtering in CO-CO_2 mixtures, the preferred ambient, the electrical condition (i.e., floating or grounded) was not important and the water cooling not as critical.

The Pyrex chamber was evacuated by a turbomolecular pump to 1×10^{-5} Torr prior to establishing the sputtering gas pressure range of 20 to 40 mTorr through needle and throttle valve adjustments. Various compositions (0 to 100%) of Ar-CO_2 , CO-CO_2 , and Ar-O_2 were used directly from commercial grade tanks (Matheson Company Inc.) without further purification. Some compositions were obtained from cylinders containing known gas mixtures. In other cases the preparation of known mixtures was achieved in the deposition chamber by admitting the gases successively and measuring the pressure after the addition of each gas. When sputtering in an atmosphere containing CO, a heated nichrome screen was situated over the exit port of the vacuum chamber to decompose any iron carbonyl being pumped from the system. However, no evidence of any decomposition to Fe_2O_3 was found on this screen. As another safety precaution, the mechanical pump was exhausted through a line to a fume hood. A focus coil located around the electrodes and outside the chamber was used to obtain a concentrated plasma between the sputtering target and the substrate. A presputtering period of 30 min was employed with the substrates shielded from the depositing material. In some experiments the substrates were also sputter etched just before film deposition. This was done by interchanging the cathode and anode leads. After sputter etching the leads were switched back and film deposition started without breaking vacuum.

Typical sputtering conditions involved the use of a net power of 270W at a gas pressure of 28 mTorr with a target-to-substrate distance of 1.5 in. The operating frequency was 13.56 MHz. The deposition rate varied considerably as shown in Fig. 2 and was dependent on the gas composition, sputtering target, and power. Sputtering of the cold-rolled steel in 50% CO-50\% CO_2 at 270W resulted in iron oxide being deposited at a rate of 52 Å/min. The deposition rate of iron oxide was increased to 110 Å/min by sputtering the same steel electrode in 80% CO-20\% CO_2 at 350W.

After the successful rf sputtering in CO-CO_2 mixtures, the d-c reactive sputtering technique was employed using the cold-rolled steel electrode in 80% CO-20\% CO_2 . The apparatus was the same as that used in the rf studies except that a d-c power supply was substituted for the rf supply. The d-c sputtering was conducted at a 3.5 kV cathode potential, a current of 62 mA, and a gas pressure of 60 mTorr. Under these conditions the deposition rate of iron oxide was 55 Å/min onto electrically floating substrates.

Experiments and Discussion

Ar-O₂ and Ar-CO₂ ambients.—Presumably the main reason that sputtered Fe_2O_3 films prepared by reactive sputtering in O_2 dissolve more slowly in dilute HCl, our selected etchant, than the low-temperature CVD films is that they are produced at a higher surface temperature and, therefore, have larger crystallites. Since the reactively sputtered films studied previously were in some cases prepared on water-cooled substrate holders whose temperatures did not exceed 25°C and since the CVD films were deposited at $100^\circ\text{--}160^\circ\text{C}$, this may seem inaccurate. However, it has long been recognized that the temperature on a thermally insulating substrate where a film is being formed can differ con-

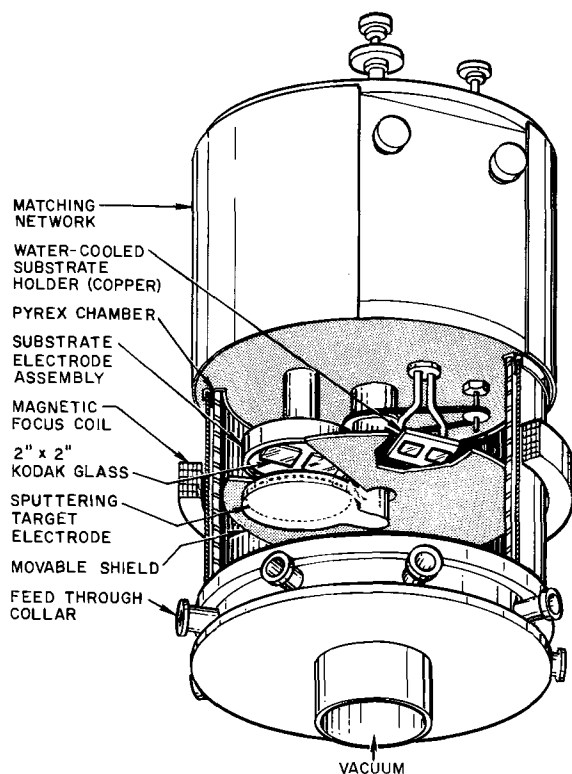


Fig. 1. RF sputtering apparatus

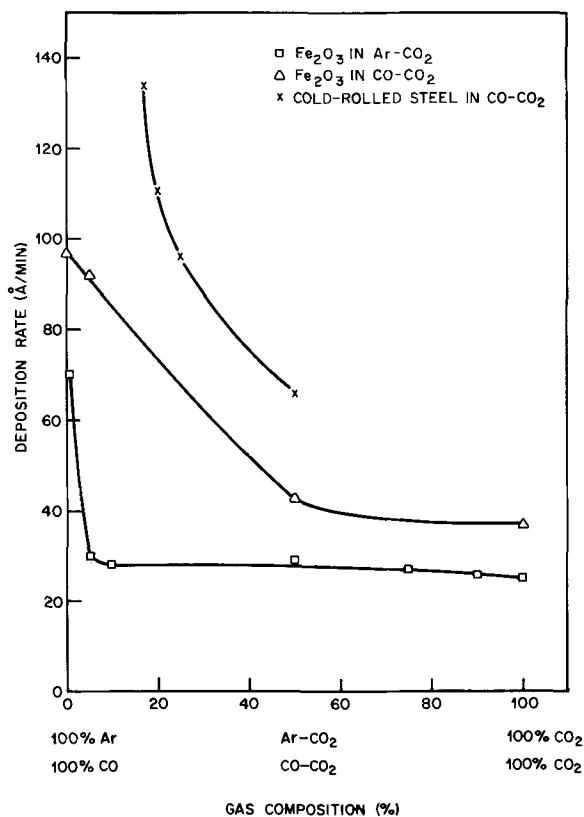


Fig. 2. Decomposition rates of Fe_2O_3 as a function of gas composition and electrode material. \square , Fe_2O_3 electrode sputtered in Ar- CO_2 at 270W net input. \triangle , Fe_2O_3 electrode sputtered in CO- CO_2 ambients at 270W net input. \times , Cold-rolled steel sputtered in CO- CO_2 ambients at 350W net input.

siderably from the temperature as measured by a nearby thermocouple. For instance, Pliskin and Lehman (6) using refractive index and etch rates as analytical tools found that reactively sputtered SiO_2 prepared at 25°C resembled SiO_2 grown thermally at 950°C more closely than SiO_2 films prepared by CVD at 675°C.

The three main causes of this local heating during film formation by sputtering are chemical heats of reaction (e.g., $2\text{Fe} + 3/2\text{O}_2 \rightarrow \text{Fe}_2\text{O}_3$), electron and ion bombardment of the substrate surface during deposition, and bombardment by energetic neutrals. In our first study (1), the heat of reaction where the film was grown was unknown because for reactive sputtering of iron we did not know what molecular species were hitting the substrate. In rf sputtering of Fe_2O_3 we likewise do not know what the sputtered species are and oxidation of Fe neutrals at the substrate could still be the dominant reaction, but presumably there is a greater possibility of depositing an already oxidized iron atom. Reduction of heating effects from ion and electron bombardment can be accomplished by electrically isolating or biasing the substrate holder. The effects of bombardment of the substrate by energetic neutrals can be lessened by working at higher pressures and keeping the input rf power reasonably low. Thus, our initial approach in this study was aimed at lowering the deposition temperature by sputtering from an oxide cathode using rf excitation, by electrically isolating the substrate, and by working at somewhat higher pressures than usual.

The first gas discharge system studied for sputtering was Ar- O_2 . The film which was sputtered in pure argon dissolved in 6M HCl in a few seconds at 25°C. However, the spectrum was unsatisfactory being too strongly absorbent at 590 nm as indicated in Fig. 3a. Visually the film was black. If O_2 was added to the sputtering gas in concentrations ranging from about

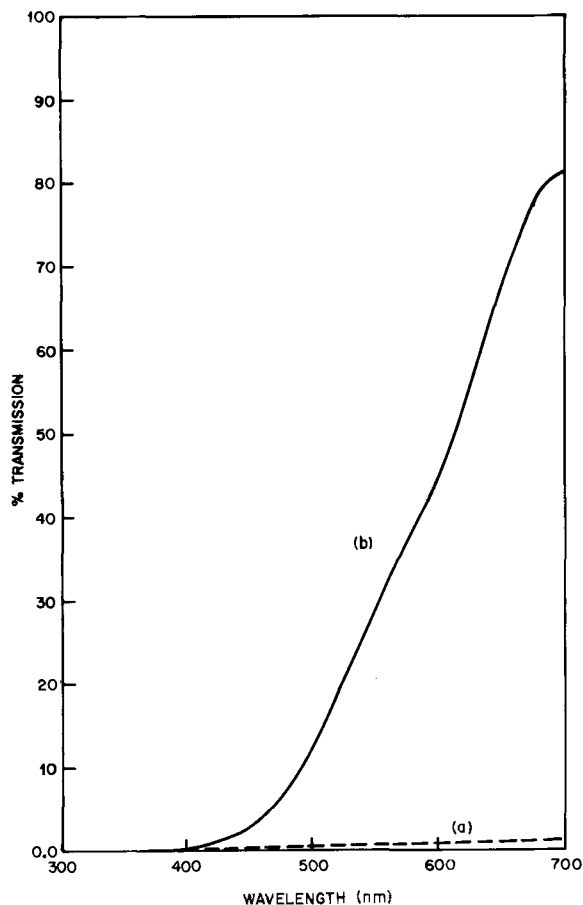


Fig. 3. Transmission spectra of films sputtered from Fe_2O_3 electrode; (a) Film sputtered in 100% Ar (black color) (2500Å). (b) Film sputtered in 100% O_2 (orange or rust color) (2100Å).

1 to 100% O_2 , absorption spectra similar to that shown in Fig. 3b were obtained. These films were orange or rust colored. Unfortunately, although the spectra for films obtained using these Ar- O_2 mixtures were acceptable the solubility of these films in 6M HCl was much too slow to be useful (> 1 hr at 25°C). It is evident, we believe, that neither reactive sputtering in O_2 -Ar mixtures, nor rf sputtering of Fe_2O_3 electrodes in O_2 -Ar mixtures, will lead to films having the desired rate of solubility in 6M HCl along with an acceptable spectrum.

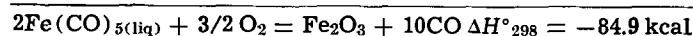
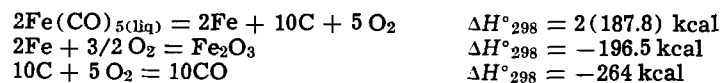
In an effort to come up with some solution to this problem we decided to substitute CO_2 for O_2 in the discharge gas. The reasons for this approach were more speculative than solid. One hope was that the effects of bombardment by ions and neutrals might be lessened by having a heavier gas molecule, but there was no firm basis for this hope. Another possibility was that ferric carbonate might be formed which presumably would be quite acid soluble. The existence of ferric carbonate has not been shown, however (7), nor have we found a spectrum attributed to it in the chemical literature. Despite the flimsy basis of these speculations we found on sputtering in 100% CO_2 that a film with an acceptable spectrum very similar to that of Fig. 3b was obtained. [In this paper we discuss the transmission spectra as being either of type a or type b of Fig. 3. This oversimplifies, of course, because there are thickness effects on the transmission curves and there are intermediate situations in going between the two types. The thickness effects (i.e., deviations from Beer's law behavior) are comparatively small and the change from one type of spectrum to the other occurs over a very small change in gas composition and is not of interest to us. Another important optical property of the films that will not be discussed is the

reflectivity. Kerwin (8) has found the reflectivity of Fe_2O_3 films to be low.]

The film also dissolved in 6M HCl at room temperature in about 2 min analogous to the rate of solubility obtained using Fe_2O_3 films formed at 110°C by the CVD method. Films sputtered in Ar- CO_2 mixtures in the range of 4-100% CO_2 have absorption spectra similar to Fig. 3b. The solubility of the rust-colored films becomes progressively slower as the CO_2 percentage decreases. With CO_2 contents lower than 4%, black films are obtained.

CO- CO_2 mixtures.—Having obtained films with both transmission spectra and solubility in 6M HCl appropriate for making "see through" photomasks by sputtering in Ar- CO_2 ambients, plasmas of CO- CO_2 compositions were tested. All gas compositions in this system yielded films easily soluble in 6M HCl and acceptable spectra were obtained with a CO_2 composition above 18% using an Fe electrode or with a CO_2 composition above 13% using an Fe_2O_3 electrode. D-C reactive sputtering of Fe in CO- CO_2 mixtures also can give acceptable films.

At this time it is perhaps appropriate to inquire as to the reason for our choice of a CO- CO_2 ambient and to propose some explanation for the successful use of this mixture, unusual in sputtering. We first discuss the CVD method, the reaction of $\text{Fe}(\text{CO})_5$ and O_2 to form Fe_2O_3 . Following MacChesney *et al.* (2) we say that the solubility is inversely related to the crystallite size which is presumably directly related to the temperature where the reaction occurs. We have previously commented that the heat of reaction is of importance here. The thermodynamics is suggestive (9).



It is seen that the standard heat of formation of a mole of Fe_2O_3 at 25°C is more than a factor of 2 smaller starting with $\text{Fe}(\text{CO})_5$ rather than Fe which may be the reactant in our sputtering experiments thus far. However, this alone is not sufficient to explain the easy formation of acid-soluble Fe_2O_3 at a low temperature. In addition to the lower heat of reaction we must assume a very low activation energy as was pointed out by MacChesney *et al.* (2). The known ease with which $\text{Fe}(\text{CO})_5$ decomposes to give an active iron is probably the significant feature here (10). It is, therefore, this combination of having a reaction which cuts down the heat of reaction where the film is formed and use of a molecule with a low activation energy for decomposition which is probably at the root of the explanation for the success of the pentacarbonyl method. This almost unique property of the iron carbonyls makes it doubtful that a better system can be found with commonly available iron compounds to make Fe_2O_3 films of high rate of acid solubility at a low temperature.

Returning now to sputtering in CO_2 , a possibility for explaining the easy solubility in acids (and, therefore, lower formation temperature) of the Fe_2O_3 films obtained is suggested by a reaction which is known to occur in CO_2 discharges (11).



The reactive sputtering of metal carbides has been studied previously (12). The discharge gas in such a system rapidly becomes a mixture of CO and CO_2 . It was noted at the time that Cr_2O_3 was formed at a much faster rate (from 5 to 15 times faster) from the carbide than Al_2O_3 from Al_4C_3 and SiO_2 from SiC (sputtering of iron carbide was not studied). No explanation of this fact was offered at the time but later the possibility that $\text{Cr}(\text{CO})_6$ was being formed and evaporat-

ing from the cathode was pointed out (13). Because of the chemical similarities between $\text{Cr}(\text{CO})_6$ and $\text{Fe}(\text{CO})_5$ it is natural to consider the possibility that we are forming $\text{Fe}(\text{CO})_5$ ¹ at the cathode during the discharge and this is evaporating from the cathode. If, indeed, this is occurring one should be able to increase the rate of film formation by using CO- CO_2 mixtures rather than pure CO_2 without adversely affecting the acid solubility of the films.

Thus far we have not considered deposition rates in any detail. In Fig. 2 deposition rates are presented graphically as a function of gas composition and target material. It is seen that the highest deposition rates are obtained with the Fe electrode and the highest CO/ CO_2 ratios. Rates above 100 A/min can be obtained using 350W input power to give films with good spectra as in Fig. 3b and good solubility (complete solution in less than 2 min in 6M HCl at 25°C with no evidence of strain). It is noted that the sputtering rate in CO_2 -Ar mixtures is relatively low unless one is sputtering in pure or almost pure Ar. The same type of results are obtained in Ar- O_2 mixtures. The deleterious effects of oxygen in plasmas on the deposition rate of oxides is known (15). It is seen that the deposition rate in the CO- CO_2 ambients is different in behavior increasing strongly throughout as one increases the CO/ CO_2 ratio. This is consistent with our suggestion that an iron carbonyl is evaporating. However, we hasten to add that the evidence is by no means conclusive. Also to be considered is the fact that the concentration of oxygen species (e.g., O, O^+ , etc.) is kept at a very low level by the presence of scavenging CO molecules.

Physical properties of films.—Approximate measurements have been made on the scratch resistance of these films and of the CVD films. The measurement technique involves weighting a diamond stylus until the film is scratched on dragging the stylus over the film surface. The test is similar to that of Benjamin and Weaver (16). The results are shown in Table I. The films sputtered in CO- CO_2 mixtures are identical to those of the CVD method. The films formed in pure CO_2 are considerably more scratch resistant. All of the oxide films are more scratch resistant than a chromium film.

Some pictures of film texture have been obtained using the scanning electron microscope (SEM). Figure 4a shows a film obtained by rf sputtering from an Fe_2O_3 target in pure CO_2 . The large particles are about 1500Å in diameter. That some control of the concentration of these large particles is possible is indicated by the significantly smaller number of large particles obtained by sputtering from an Fe target in 80% CO-20% CO_2 as shown in Fig. 4b. The desired result, total elimination of these large particles, is obtained by sputter etching about 600Å of glass substrate in 80% CO-20% CO_2 before depositing Fe_2O_3 using the

¹ We recognize that the system is much more complex than sketched here [cf. Ref (14)] but the picture presented here suffices for our purpose.

Table I. Results of approximate measurements of scratch resistance of some films

Sample description	Force in grams needed to scratch film
Fe_2O_3 , CVD deposited	350-400
Fe_2O_3 , sputtered in 80% CO-20% CO_2	350-400
Fe_2O_3 , sputtered in 100% CO_2	750-800
Cr, evaporated	<250

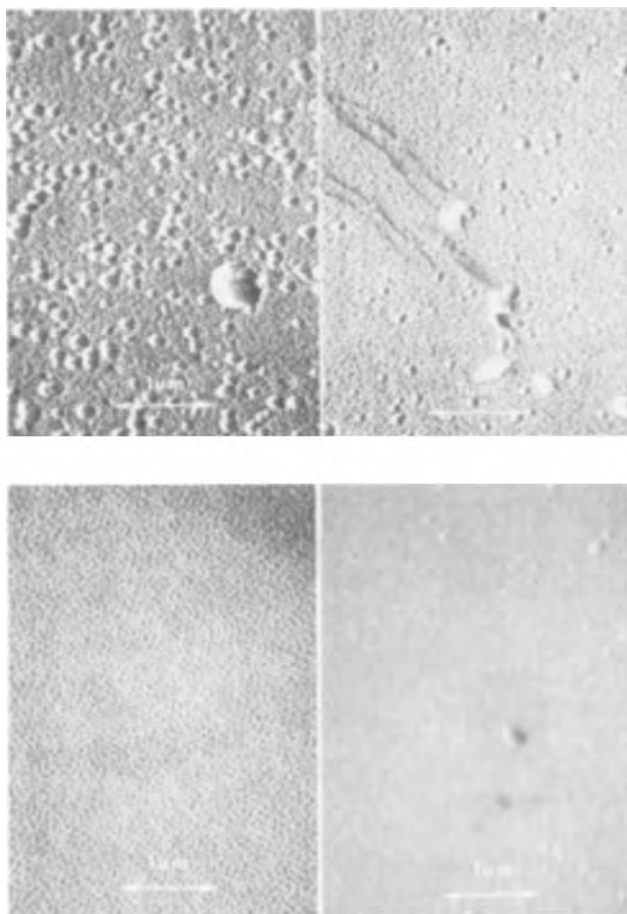


Fig. 4. Scanning electron microscope pictures of Fe_2O_3 film textures. (a, upper left), Sputtered Fe_2O_3 film from Fe_2O_3 electrode and a 100% CO_2 atmosphere. (b, upper right), Sputtered Fe_2O_3 film from an Fe electrode and a 80% CO -20% CO_2 atmosphere. (c, lower left), Sputtered Fe_2O_3 film formed in same way as (b) film but with the substrate sputter etched before deposition. (d, lower right), Fe_2O_3 film prepared by CVD.

same ambient. Evidently surface structure and/or surface impurities cause these large particles but no detailed investigations have been made. The particle size of the sputtered film (Fig. 4c) is about 500Å which is comparable with the low-temperature CVD films (Fig. 4d). This particle size is much smaller than can be taken advantage of in present photoresist technology. It is possible that the process by which the film is generated is not the limiting determinant of the film particle size but rather the chemistry and topography of the substrate is limiting.

The defect density and defect size for Fe_2O_3 films prepared in various ways were estimated after studying the SEM photographs and are shown in Table II. They are essentially equal in the various films considering the poor statistics one gets with such small numbers. This suggests that the defects may be in the glass substrate and that the number of actual film defects may be considerably fewer in number. Partial support

Table II. Results of defect density measurements made on Fe_2O_3 films using scanning electron microscope

Film	Total area scanned by SEM, mm^2	Total No. defects found	Defect diameter, μm
Fe_2O_3 by CVD	3.0	6	1
RF sput. Fe_2O_3 (80% CO -20% CO_2)	0.6	3	0.5
RF sput. Fe_2O_3 with pre dep. sputter etch (600Å glass removed, 80% CO -20% CO_2)	0.6	2	0.5

for this hypothesis was found in an optical examination of the films at 500X by transmitted light. Pinhole densities were $\sim 1/\text{cm}^2$ whereas the SEM examination had indicated defects $\sim 1/\text{mm}^2$. It should also be pointed out that defects smaller than 1 μm will probably be insignificant for most present day device fabrication.

Conclusions

RF sputtering of Fe_2O_3 electrodes and rf or d-c sputtering of Fe electrodes in CO - CO_2 plasmas can give Fe_2O_3 films with a sufficiently high dissolution rate in 6M HCl and transmission spectra appropriate for use in making "see-through" photomasks if the CO_2 content is above 13% with the Fe_2O_3 electrode and above 18% with the Fe electrode. Somewhat similar results are obtained with Ar - CO_2 plasmas but deposition rates are smaller. RF sputtering of Fe_2O_3 in Ar - O_2 mixtures yields films which have either a poor rate of solution or an unacceptable transmission spectrum. The scratch resistance of the films sputtered in CO - CO_2 are essentially equivalent to Fe_2O_3 films prepared by CVD and both are superior to evaporated Cr films. The defect density for both the sputtered films and for the CVD films is low. Film particle size in the sputtered films is affected by plasma composition and surface conditions on the substrate. Best results were found using a gas composition of 80% CO -20% CO_2 and sputter etching the substrate before deposition. In this case particle size was about 500Å.

Acknowledgments

We are pleased to acknowledge the assistance we have received from colleagues in various portions of this work. G. W. Kammlott performed the SEM measurements. Spectra were obtained by Mrs. G. A. Pasteur. Miss B. E. Prescott also helped in interpretation of some spectra. E. E. Francois made the scratch tests.

Manuscript submitted June 14, 1971; revised manuscript received Oct. 29, 1971.

Any discussion of this paper will appear in a Discussion Section to be published in the December 1972 JOURNAL.

REFERENCES

- W. R. Sinclair, M. V. Sullivan, and R. A. Fastnacht, *This Journal*, **118**, 341 (1971).
- J. B. MacChesney, P. B. O'Connor, and M. V. Sullivan, *ibid.*, **118**, 776 (1971).
- F. J. Reid and P. Cukor, Extended Abstract No. 127, Electrochemical Society Meeting, Los Angeles, May 10-15, 1970.
- W. B. Shelby and P. Cukor, *Anal. Chim. Acta*, **49**, 275 (1970).
- R. W. Berry, P. M. Hall, and M. T. Harris, "Thin Film Technology," p. 638, D. Van Nostrand Co. Inc., New York (1968).
- W. A. Pliskin and H. S. Lehman, *This Journal*, **112**, 1013 (1965).
- J. W. Mellor, "A Comprehensive Treatise on Inorganic and Theoretical Chemistry," XIV, p. 370, Longmans and Co., London (1935).
- R. E. Kerwin, *Bell System Tech. J.*, **49**, 2179 (1970).
- R. C. Weast, Editor, "Handbook of Chemistry and Physics," p. D-56 et seq., The Chemical Rubber Co., Cleveland (1969).
- H. E. Carlton and J. H. Oxley, *Am. Inst. Chem. Engrs. J.*, **11**, 79 (1965).
- M. J. Barton and A. Von Engel, *Phys. Letters*, **32A/3**, 173 (1970).
- W. R. Sinclair and D. W. Stillinger, Abstract No. 15-E-66, *Bull. Am. Ceram. Soc.*, **45**, 405 (1966).
- F. Vratny, Personal communication.
- G. Distefano, *J. Res. Nat. Bur. Std.*, **74A**, 233 (1970).
- R. E. Jones, H. F. Winters, and L. I. Maissel, *J. Vacuum Sci. Technol.*, **5**, 84 (1968).
- P. Benjamin and C. Weaver, *Proc. Roy. Soc. London*, **A254**, 163 (1950).

Jet Polishing of Semiconductors

I. Automatic Jet Thinning of GaP for Transmission Electron Microscopy

B. D. Chase, D. B. Holt, and B. A. Unvala

Metallurgy Department, Imperial College of Science and Technology, London S.W.7, England

ABSTRACT

A method has been developed for thinning localized regions in GaP for examination by means of transmission electron microscopy. A jet of chlorine in methanol was used to chemically polish slices from the P(111) face. To thin specimens from the Ga(111) face the same reagent and apparatus were used, but a voltage was applied so that the specimen was anodic with respect to an electrode inserted in the jet. In this case the surface was free from etch pits, but yellowish surface films were formed which could be removed by a short chemical polish. GaP is optically transparent, but if it is illuminated only with wavelengths for which it has a sufficiently large absorption coefficient, it can be arranged that significant transmission of light begins only when the material is thin enough for electron transmission. This light can be detected by a photomultiplier and the resultant signal used to automatically terminate the thinning. The principles of this method are discussed, and the equipment required for its utilization is described. Large transparent areas were produced in material of various dopings and defect contents with a 100% success rate.

Chemical etching and polishing reagents have been developed to produce required types of attack on a great variety of crystallographic faces of many semiconducting compounds in numerous conditions of doping (1-3). It was reported in an earlier paper that several of the reagents described in the literature could be used to thin samples of a number of the more important III-V and II-VI compounds for transmission electron microscopy (4). The area to be examined in an electron microscope must be uniformly thin. In general it must be less than 1 μm thick and in the case of the more electron-opaque materials, only a few thousand angstroms thick. The thin area should preferably be produced by localized attack, so that the remainder of the specimen, shaped to fit the electron microscope holder, is left in the form of a relatively thick and sturdy rim of a disk. This type of localized attack can be achieved by several techniques falling into two classes. Either the specimen disk is immersed in a bath of the reagent but has the edges masked in some way or a jet of the reagent is used to bring about contact only with the chosen central area of one face (4). The latter techniques are referred to as jet polishing or thinning and have been long and widely used, generally with an electropolishing action. Chemical polishing has important advantages however. Chemical polishes have been developed for many important compounds (1-3) for which electropolishing reagents are not known. Moreover, the turbulent conditions involved in jet polishing in our experience tend to produce a smoother surface than is otherwise obtained with the same chemical reagent. Thus the published reagents generally work well in jets without modification. Chemical polishing rates are often less dependent on the doping of the semiconductor than are electropolishing rates. That is because the current flowing for a given applied voltage varies directly with the conductivity which varies rapidly in magnitude and in charge carrier sign at the doping levels used in semiconductor technology. Uniform electropolishing of nonuniformly doped microcircuit slices is therefore not possible.

Later development (5) showed that in the thinning of GaAs, which is an opaque material, a microscope and photomultiplier could be used to detect the moment at which a selected level of light transmission occurred. The photomultiplier signal was then used to trigger a solenoid which removed the specimen from

the chemical polishing jet to a nearby washing jet. With this equipment large (80 μm diam) areas could be produced in areas on GaAs laser diodes, preselected by optical microscopy (6), with a 100% success rate (5). The use of a microscope and photomultiplier to produce a signal which turned off a jet electropolishing current when the specimen was thin enough was first introduced for Ge, another opaque material, by Riesz and Bjorling (7).

In the present paper a development of this technique is described that is applicable to an optically transparent material such as GaP. The most suitable reagent was found to be chlorine in methanol (8), and this was used for both chemical and electrochemical polishing. The electrochemical polishing of the Ga(111) face of GaP was found to produce a yellowish surface film. Transmission electron microscope studies established that this surface film was actually a region of tunnel etching, and this work is described in part II of this paper (9).

Recently equipment was developed for scanning the point of impingement of a jet of a chemical polishing reagent over the face of a rapidly spinning slice of germanium. It was found that this technique produced smooth, flat surfaces (10). Further work has shown that an improved version of this equipment will not only polish slices of Si, GaAs, and GaP as well as Ge, but it can be used to shape silicon slices that have been masked. This work is reported in the third paper in this series (11).

Experimental Methods

The Thinning Apparatus

The thinning apparatus, shown in Fig. 1, was similar to that described previously (5), but was modified as follows. To prevent the escape of gases to the atmosphere the reagent and washing jets were enclosed in a PVC box. This made it unnecessary to operate the apparatus in a fume cupboard. The specimens, mounted as discussed below, were fitted into a PTFE disk, which acted as the lid of the box. Once a solenoid had been actuated the lid rotated, so moving the specimen from a position above the polishing jet to one above the washing jet. A weight connected to the lid by a nylon cord provided the rotational force. Optical filters were added to the light detection system so that the thinning of a transparent material like GaP could be controlled. This will be discussed below. Arrangements were also

Key words: polishing, thinning, semiconductors, electron microscopy.

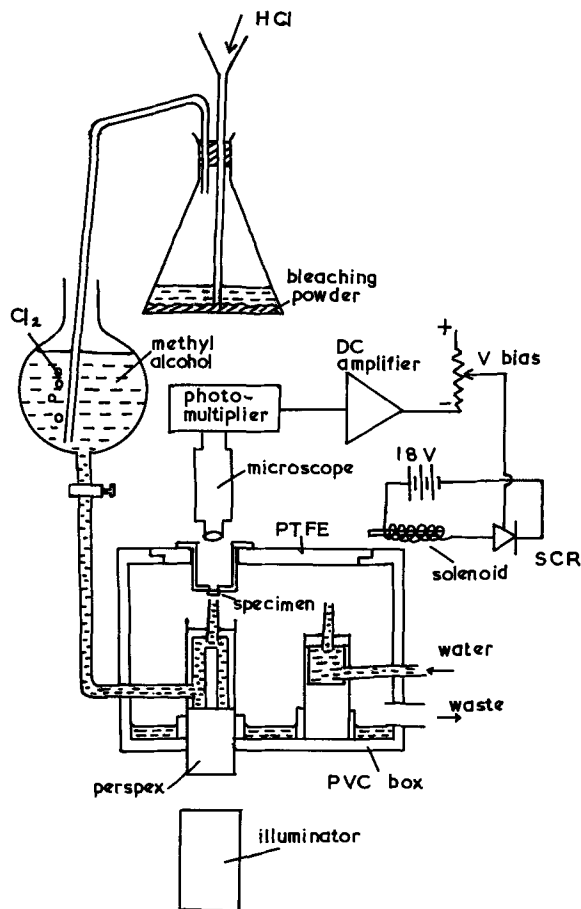


Fig. 1. Jet thinning apparatus. The polishing jet (chlorine in methanol) and the washing jet of water were enclosed in a PVC box with a rotating lid of PTFE which carried the specimen. For electropolishing, a short tungsten wire cathode (not shown) was introduced into the polishing jet.

made so that either chemical or electrochemical thinning could be employed.

The jet nozzles were drawn from glass tubing. A perspex (or lucite, i.e. PMMA) light guide was built into the polishing jet to make it possible to illuminate the specimen through the jet. This guide was sealed into the PVC box with an O-ring. A microscope was used to position the specimen over the center of the polishing jet nozzle, and to observe light transmitted through the specimen during thinning. A photomultiplier (E.M.I. Type 9664B) with an S10 photocathode could be substituted for the eyepiece. The output from the photomultiplier was fed into a stabilized d-c amplifier and on reaching a selected level triggered an SCR, which activated the solenoid. As a result, when the intensity of the light reaching the photomultiplier through the specimen had increased by a predetermined amount, the specimen was automatically repositioned over the washing jet and thinning ceased.

The photomultiplier was sensitive to wavelengths of light which were transmitted by GaP with little absorption. To obtain adequate variation of photomultiplier signal with specimen thickness, it was necessary to selectively remove these wavelengths by the use of filters. It was found that Kodak Wratten filter No. 47B used together with a Chance Pilkington OB 10 metal oxide filter to remove infrared gave satisfactory results. The principles of the control process will be discussed below. The two filters were positioned inside the photomultiplier case rather than at the source of illumination to reduce the influence of extraneous light. As a result it was found possible to operate the system under conditions of normal room lighting.

The Thinning Process

This work was undertaken with a view to analyzing defects in electroluminescent GaP diodes in relation to their performance as light sources. Results obtained in this way will be reported elsewhere (12, 13). Initially interest was centered on material grown by vapor phase epitaxy on GaAs substrates. Thinning was done from the GaAs surface which presented the P(111) or B face. This ensured that the final thin area contained material distant from the GaP/GaAs interface. Since it is relatively simple to obtain a good polish on the P(111) face of GaP, smooth well-shaped dimples with large thin areas were formed.

The chemical polishes generally used for GaAs had much lower polishing rates when applied to GaP. Three of the more rapidly acting reagents were considered. Boiling aqua regia although commonly used as a polish for GaP was not suitable for jet thinning. Br in methanol, although suitable as a polish, was unusable because of the effect of the Br in absorbing light passing through the jet. With the filters in place no light could be detected by the photomultiplier even without a specimen in position. The third alternative, Cl in methanol (8), was found to be satisfactory. This was produced in the equipment illustrated in Fig. 1, by feeding concentrated HCl into a conical flask containing bleaching powder. The chlorine gas that was evolved was bubbled through a flask containing methanol, which could then be fed directly to the jet.

Later in the work it became necessary to examine GaP grown by liquid phase epitaxy on the P(111) faces of GaP substrates. In order to thin the material from the substrate side it was necessary to find means to polish the Ga(111) or A faces of these specimens. Cl in methanol would not form satisfactory dimples by chemical polishing. Preferential edge attack left a raised pitted portion in the center of the specimen. An electrochemical technique for dimpling of Ga(111) faces was developed using the same apparatus and reagent. The specimen was connected to the positive terminal of a battery. The negative electrode consisted of a short length of tungsten wire inserted into the jet nozzle from below. With an applied potential difference of 120V the current flow was about 20 mA and a smooth-sided dimple could be produced on Ga(111) faces.

The surfaces of electrochemically jet-polished dimples in Ga(111) faces were covered by an orange film which could be removed by chemical action when the current was switched off for a few seconds. Unfortunately this surface film had a very high optical absorption coefficient in the relevant range of wavelengths, so that the automatic detection system was triggered only when a hole appeared in the thin area. This was unsatisfactory and better results could be obtained in two alternative ways. The first successful method developed was to use visual control. By repeatedly turning off the current to disperse the surface film the true appearance of the thin area could be observed. The specimen thickness was correct when light which appeared nearly white to the eye was transmitted. The second successful method was to use electrochemical polishing to produce an initial dimple on the Ga(111) face of the specimen. The specimen was then reversed in the mount and finally thinned chemically from the P(111) face. In this way the automatic mechanism could be used in the final stage of the process. This also had the advantage of removing any possible surface damage and meant that no special surface polishing was required prior to thinning. Some specimens were examined in the transmission electron microscope with the orange surface film remaining in order to try to establish its nature. The results are reported in a later paper (9). In the majority of specimens it was removed by a short chemical polish. It was found that the films could be removed from the

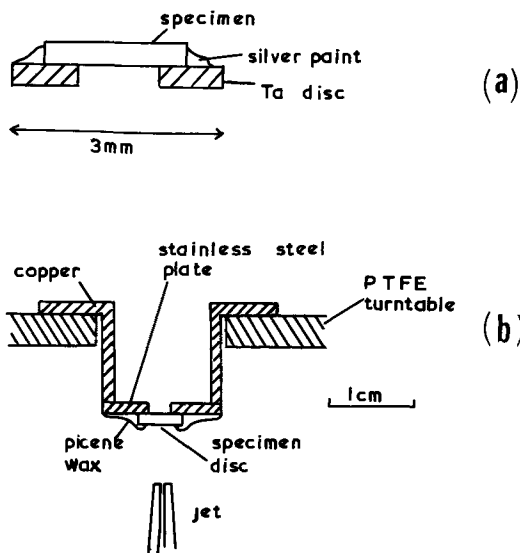


Fig. 2. Techniques for mounting specimens for thinning: (a) Small, fragile specimens were first mounted over holes in Ta disks, 2.3 mm diam. Larger samples were ultrasonically cut to form 2.3 mm diam disks of GaP. (b) The specimens were then affixed to a metal holder and mounted in the rotating lid of the apparatus shown in Fig. 1.

Ga(111) faces in this way without causing any detectable etching of the surfaces.

Mounting Specimens for Thinning

The vapor-grown GaP was received in the form of very thin layers. To facilitate handling, small pieces were cleaved off and mounted, using silver paint over small holes drilled in 2.3 mm diam Ta disks as illustrated in Fig. 2(a). The liquid phase epitaxy and pulled samples were large and disks of 2.3 mm diam were cut ultrasonically from this material.

The specimen holder for the jet thinner is illustrated in Fig. 2(b). The specimens were positioned beneath a 1.5 mm hole in a stainless steel plate. Silver paint was used to ensure electrical contact for the electrochemical process. When this had dried, the metal plate and the edges of the specimen were coated with a layer of picene wax so that just the area to be thinned was exposed. After thinning, the picene wax was dissolved in trichlorethylene and the silver paint was peeled off with tweezers. The specimens were then washed in hot trichlorethylene followed by rinsing in ethyl alcohol and deionized water.

Automatic Control of Thinning

When opaque semiconductors such as Ge, Si, or GaAs are thinned for electron microscopy they become transparent to visible light, appearing orange to the eye when a suitable thickness is reached. When an automatic thinning system is used it is this light which is detected by the photomultiplier (5, 7). GaP, however, is transparent to certain regions of the spectrum to which both the photomultiplier and the human eye are sensitive. The absorption edges of intrinsic GaAs (14) and GaP (15) are shown in Fig. 3, together with the spectral response curve of the S10 type photocathode used in the photomultiplier. It is apparent that the photomultiplier is completely insensitive to wavelengths of light transmitted by a thick specimen of GaAs. However, a specimen of thickness near 5000Å (0.5 μm) will transmit sufficient light to be detected.

For an order of magnitude calculation of the conditions required to automatically detect the desired thickness in the case of GaP, suppose that the photomultiplier triggers the solenoid when 1% of the intensity of the light incident on the specimen in the relevant wavelength range is transmitted. Assuming reflection to be negligible the transmitted intensity is given

by

$$I = I_0 \exp(-\alpha t)$$

where I_0 is the intensity of the incident light, α is the linear absorption coefficient, and t is the specimen thickness. On the assumption therefore that $I/I_0 = 0.01$ for the SCR to be triggered

$$\alpha t = 4.6$$

And for

$$t = 0.5 \mu\text{m}$$

$$\alpha = 9.2 \times 10^6 \text{ m}^{-1}$$

Thus a wavelength of light with a linear absorption coefficient near 10^7 per meter will be transmitted through a specimen, thin enough to be electron transparent, with sufficient intensity to trigger the detection system. In practice a range of wavelengths and absorption coefficients are involved, but the simple calculation serves to illustrate the principle.

The same principles apply in the case of GaAs. Extrapolation of the absorption data for n-type with a

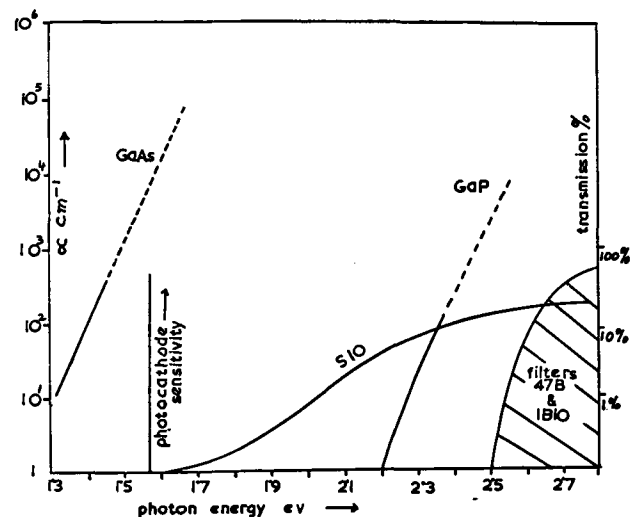


Fig. 3. Comparison of the linear absorption coefficients for light of GaAs and GaP with the spectral sensitivity range of the photomultiplier photocathode and the wavelength range passed by the two filters.

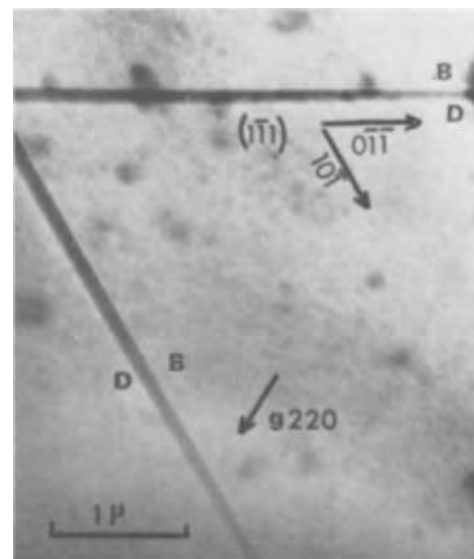


Fig. 4. Transmission electron micrograph of a tetrahedral stacking fault in Te-doped GaP grown from the vapor phase on a GaAs substrate. B and D indicate the bright and dark bounding fringes of the stacking faults. It can be deduced that the faults are intrinsic (12).

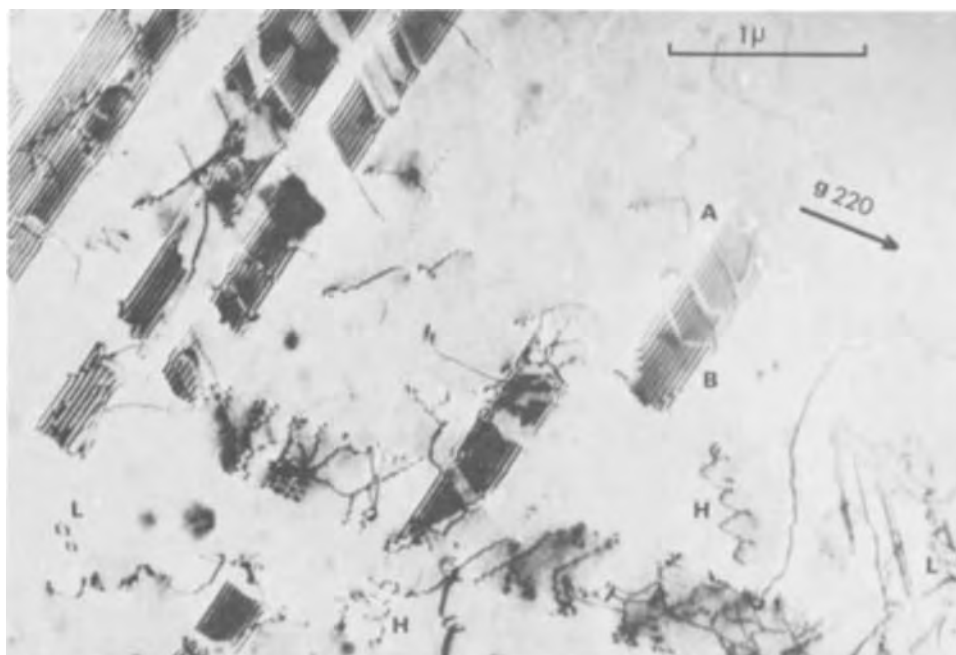


Fig. 5. Dark field micrographs showing defects in Te-doped vapor phase grown GaP. Helices are marked H and loops are marked L. At A-B there is a set of overlapping stacking faults.

free carrier concentration of $2 \times 10^{18} \text{ cm}^{-3}$ indicates (14) that a wavelength of about $0.75 \mu\text{m}$ (with a photon energy of $h\nu \approx 1.8 \text{ eV}$ in Fig. 3) corresponds to a value of α of 10^7 per meter. This corresponds to light of a reddish orange color which is just detectable by both the photomultiplier and the human eye.

The absorption edge of GaP lies at a much lower wavelength than that of GaAs. Even a thick specimen will transmit visible (yellow-orange) light with very little absorption. For automatic thinning it was necessary to use optical filters to cut out the portion of the transmitted spectrum to which the photomultiplier was sensitive. Ideally an interference filter would provide a suitable narrow band width for which α has a value near 10^7 m^{-1} . A satisfactory and cheaper alternative was found using a Kodak Wratten filter No. 47B in conjunction with a Chance Pilkington OB 10 filter to remove the infrared component. The combined region of transmission is illustrated by the shaded area in Fig. 3.

Results

In those cases in which it was possible to thin from the P(111) faces of the specimens the automatic system for terminating thinning could be used. It was found that the technique worked less well than in the case of GaAs which could be reduced to a reproducible thickness with a 100% success rate (5). Drift in the electronics made it impossible to obtain reproducible thicknesses by adjusting the brightness of the light source and the voltage applied to the photomultiplier. It was found best to set the system to cut off at too great a specimen thickness and to give a final manually controlled thinning. Thinning was then terminated when the transmitted light appeared white. Specimens of different dopings have slightly different absorption edges. Therefore it was necessary to obtain settings for each batch of material by trial and error. Nevertheless the technique was a great convenience since visual control was not required except during the brief and crucial final stage of thinning.

Large ($40\text{--}50 \mu\text{m}$ diam) electron transparent areas were produced in thinning from both the Ga(111) side and from the P(111) side. It was found that GaP was transparent to the beam in a conventional 100 kV transmission electron microscope up to a thickness greater than $0.8 \mu\text{m}$ (8000 \AA). This is the thickness of

the specimen shown in Fig. 4 as determined from the projected widths of the tetrahedral stacking fault.

The present thinning technique was used successfully on heavily doped material as shown in Fig. 4 and on material containing a profusion of stacking faults as shown in Fig. 5.

Acknowledgments

Thanks are due to Professor J. G. Ball for the provision of research facilities and to the Services Electronics Research Laboratory for the supply of material. This work was supported by a CVD contract and is published by permission of the Ministry of Defence.

Manuscript submitted May 11, 1971; revised manuscript received ca. Nov. 15, 1971.

Any discussion of this paper will appear in a Discussion Section to be published in the December 1972 JOURNAL.

REFERENCES

1. J. W. Faust, in "Semiconducting Compounds," Vol. I, "The Preparation of III-V Compounds," pp. 445-468, R. K. Willardson and H. L. Goering, Editors, Reinhold, New York (1962).
2. M. Aven and J. S. Prener, "The Physics and Chemistry of II-VI Compounds," pp. 141, 155, 773, North-Holland, Amsterdam (1967).
3. S. Amelinckx, "Methods for Observing Dislocations," Solid State Physics Suppl. 6, pp. 40-49, Academic Press, New York (1964).
4. D. B. Holt, R. Porter, and B. A. Unvala, *J. Sci. Instrum.*, **43**, 371 (1966).
5. M. J. Hill, D. B. Holt, and B. A. Unvala, *ibid.*, **1**, 301 (1968).
6. M. J. Hill and D. B. Holt, *J. Mater. Sci.*, **3**, 244 (1968).
7. R. P. Riesz and C. G. Bjorling, *Rev. Sci. Instrum.*, **32**, 889 (1961).
8. C. S. Fuller and H. W. Allison, *This Journal*, **109**, 880 (1962).
9. B. D. Chase and D. B. Holt, *ibid.*, **119**, 314 (1972).
10. B. A. Unvala, Aung San, and D. B. Holt, *J. Sci. Instrum.*, **2**, 119 (1969).
11. B. A. Unvala, Aung San, and D. B. Holt, *This Journal*, **119**, 318 (1972).
12. B. D. Chase and D. B. Holt, *J. Mater. Sci.*, To be published.
13. D. B. Holt and B. D. Chase, To be published.
14. D. E. Hill, *Phys. Rev.*, **133**, A.866 (1964).
15. M. R. Lorenz, G. D. Pettit, and R. C. Taylor, *ibid.*, **171**, 876 (1968).

Jet Polishing of Semiconductors

II. Electrochemically Formed Tunnels in GaP

B. D. Chase and D. B. Holt

Metallurgy Department, Imperial College of Science and Technology, London S.W.7, England

ABSTRACT

Transmission electron microscopy showed that high density networks of tunnels about 300Å in diameter were formed in {111} foils of GaP thinned by jet electropolishing using a chlorine in methanol solution. These tunnels ran in <111> directions, in the polar sense from the gallium to the phosphorus atom along a chemical bond. They were unrelated to any of the pre-existing defects in the material that could be seen by transmission electron microscopy.

Deep, narrow, optically resolvable tunnels produced in crystalline materials by dissolution processes have long been known to mineralogists as "anomalous solution phenomena" (1). Later such a process described as tunnel etching producing "negative whiskers" was studied in LiF (2). A similar phenomenon of tunnel corrosion has recently been observed on a transmission electron microscope scale in Cu₃Au alloys (3).

We observed that narrow crystallographic channels were produced in GaP in the course of electrochemical thinning of this material for transmission electron microscopy (4). The results of a microscopic study of these etch tunnels are presented in this paper.

Experimental Methods

The method of thinning the specimens was described in the previous paper (4). It involved directing a jet of chlorine in methanol on the GaP specimens. This worked well when the P(111) face was to be attacked. When the Ga(111) side had to be attacked however, it was found necessary to employ electropolishing. The specimen was made. The anode and a potential difference of 120V was applied between it and a tungsten electrode inside the jet nozzle. A current of about 20 mA then flowed, and rapid localized attack on the GaP occurred. An orange surface film was formed during electrochemical thinning from the Ga(111) face. This surface film could be removed by a final 15 sec chemical attack in the chlorine in methanol jet with no voltage applied. The evidence to be discussed below showed a dense network of tunnels to be present in the orange films. The scattering of light from these networks of tunnels caused the translucence of the films and the diffuse nature of light reflected from them when observed in the optical microscope.

Results

In GaP specimens which were prepared by electrochemical polishing alone, dense networks of linear features were visible in transmission electron microscopy. Examination using the stereo pair technique, in which two micrographs like those in Fig. 1 were taken with a difference in specimen tilt of about 10°, showed that the features formed a three-dimensional array with each one penetrating the foil from top to bottom.

Selected area diffraction patterns from regions of high tunnel concentrations showed no additional diffraction spots or rings. This ruled out the possibility of the presence of a second phase or of extensive precipitation.

All the specimens examined were close to a {111} orientation and the tunnels projected onto the three <211> directions in this plane. Examination of the (111) stereogram shows that this condition is met if the tunnels lie either in the <111> or in the <110> direction. To decide between these two possible direc-

tions a series of micrographs was taken at widely differing angles of tilt, using a high tilt goniometer stage in the electron microscope. The angles between the projected tunnel directions were measured on each micrograph, and the beam directions were determined by analysis of the diffraction pattern relative to a foil normal of [111]. The results established that the tunnels lay along the [111], [111], and [111] directions at 70.5° to the [111] foil normal (7).

At extinction contours the absence of material in the tunnels gave rise to characteristic contrast. In Fig. 2 it can be seen that the contours are displaced where they are crossed by a tunnel. Also given in Fig. 2 is a cross-sectional diagram showing the relation of the tunnel at A to the top and bottom surfaces of the foil. By counting extinction contours on the micrograph it was established that the bottom of the etch pit was the equivalent of 1.5 extinction distances ξg from the unetched base of the foil. In each such case the projected length of the tunnel was in proportion to the depth of material below the pit.

The displacement of the extinction contours where they crossed the tunnels was measured as about two-thirds of the contour separation ξg for a tunnel diameter of 0.4 μ m on the micrograph. Thus the effective thickness of the tunnel as seen by the electron beam can be written

$$t = \frac{0.4}{\sin \theta} = \frac{2}{3} \xi g \quad [1]$$

where θ is the angle between the tunnel and the normal to the foil. Moreover, a tunnel of measured length 3 μ m on the micrograph penetrated a thickness of material

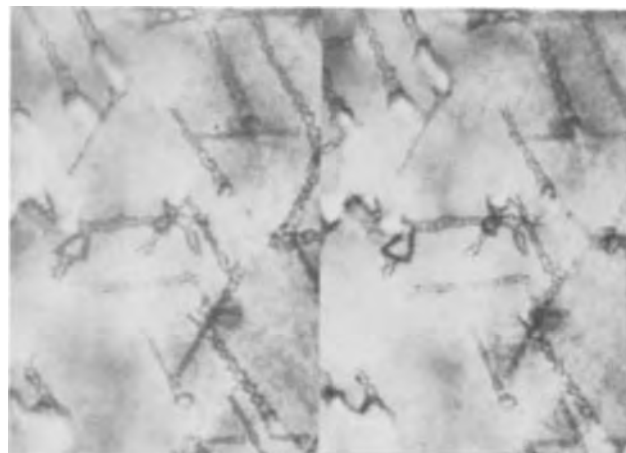


Fig. 1. Stereo pair of transmission electron micrographs of an area of an electrochemically polished GaP specimen showing crystallographic etch tunnels. The micrographs were taken at specimen tilts differing by about 10°.

Key words: localized attack, polarity, tunnels, GaP.

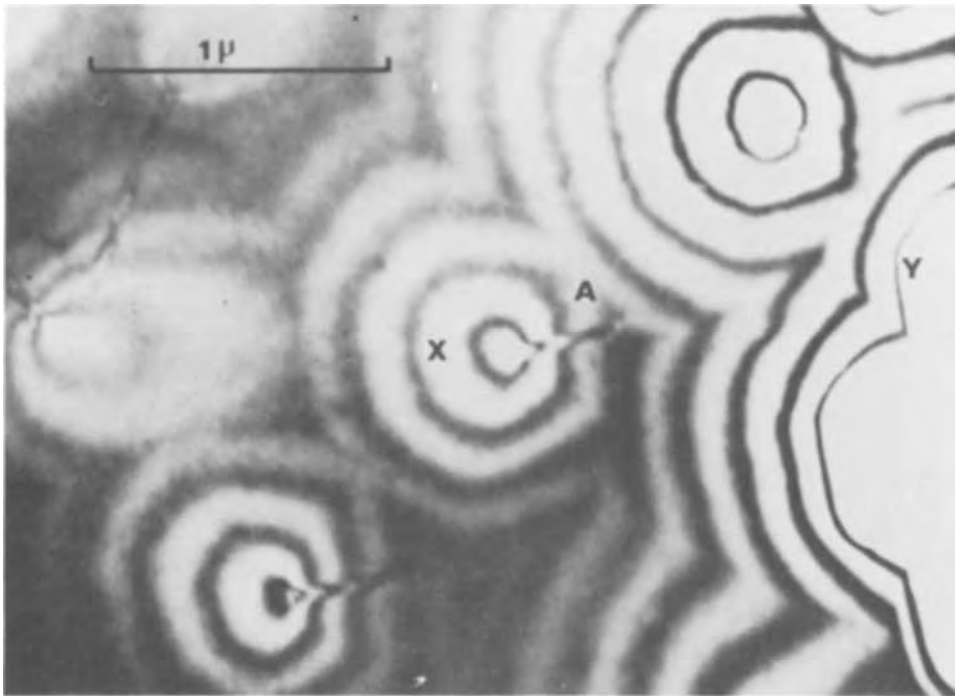


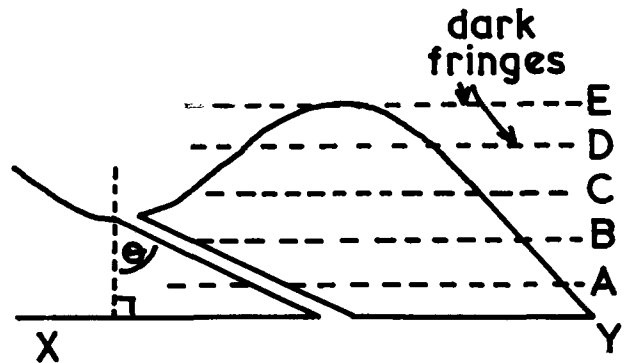
Fig. 2. Contrast effect obtained when an etch tunnel crosses an extinction contour: (left) micrograph showing displacements of the contours and (below) cross-sectional diagram of the tunnel orientation through the foil.

equal to $1.5 \xi g$. Therefore

$$\tan \theta = \frac{3}{1.5 \xi g} \quad [2]$$

Combining Eq. [1] and [2] to eliminate ξg gives a value for θ of 72.5° which is close to the value of 70.5° of the angle between $\langle 111 \rangle$ directions. This therefore supports the finding that the tunnels lay in the $\langle 111 \rangle$ directions. The mechanism of extinction is that of the scattering of the electrons by the specimen material. The observed displacements of the extinction contours therefore also support the supposition that the linear features were empty tunnels.

The opposite contrast effects shown by the linear features in Fig. 3(a) and (b) can also be understood on the basis that they are tunnels. Both these micrographs were taken in a two-beam condition with a



single extinction contour operating over the whole area of the micrograph. Extinction contours arise because as the thickness of the material changes, the extinction



Fig. 3. Opposite contrast conditions exhibited by tunnels: (a) dark contrast (left) and (b) bright contrast (right).



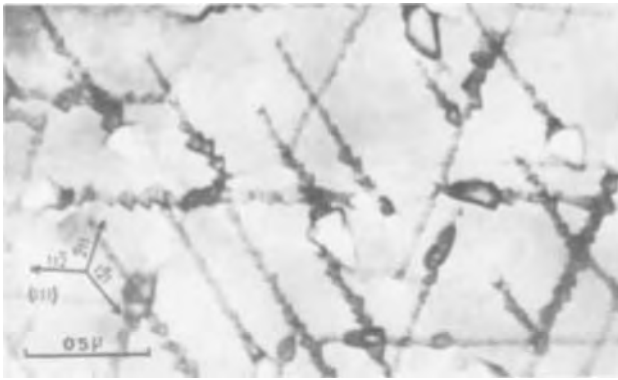


Fig. 4. Etch tunnels of crystallographic internal form, produced by low voltage polishing (less than 120V). At the points marked A tunnels terminate inside the material but are continued by much narrower channels.

conditions change cyclically, so that the effective transmission of electrons changes. This gives rise to a variation of intensity in the form of successive bright and dark fringes. The reduction in the thickness of the material traversed by the beam, due to the presence of etch tunnels, can change the extinction conditions so as to increase, or reduce, the brightness depending on the point in the cyclic variation of the extinction representing the situation in the specimen in the absence of any tunnel. In the case shown in Fig. 3(a) the reduction in thickness due to the tunnels shifts the extinction to a more absorbing condition and the tunnels appear in dark contrast. In case 3(b) the tunnels alter the extinction conditions so that a greater beam intensity is transmitted and they appear bright.

Thus the linear features were tunnels about 300Å in diameter.

Tunnels were observed apparently in various stages of formation. In some cases the main tunnel was found to penetrate only part of the foil while the continuation of the line of the tunnel was marked by a narrow trace. Examples of this type can be seen in Fig. 4 at the points marked A.

Tunnels of crystallographic shape like those in Fig. 4 were only observed in specimens electrochemically polished at low voltages of less than 120V. Specimens that were thinned at high applied voltages (near 240V) contained tunnels with rounder shapes like those in

Fig. 3(b). It appears, therefore, that only at lower voltages were the conditions such that some degree of crystallographic etching within the tunnels themselves could occur.

In some specimens it was found that the tunnels lay mainly in one preferred $\langle 111 \rangle$ direction as in Fig. 3(b). In some cases this was limited to one portion of a thin foil while other regions contained tunnels equally distributed among the three available directions.

These electrochemical etch tunnels were first discovered due to the fact that it was found necessary to use electrochemical polishing to thin $\{111\}$ GaP specimens from the Ga(111) face. Most observations were made on tunnels produced by electrochemical attack on this side of the specimens. This resulted, as reported above, in the formation of tunnels lying only along the three $\langle 111 \rangle$ directions at 70.5° to the specimen surface. In cases of electrochemical action on the $P(\bar{1}\bar{1}\bar{1})$ surface tunnels were also formed. However, in this case most of them ran in the $\langle 111 \rangle$ direction normal to the surface as shown in Fig. 5. This evidence indicates that the tunnels were etched in specific polar directions.

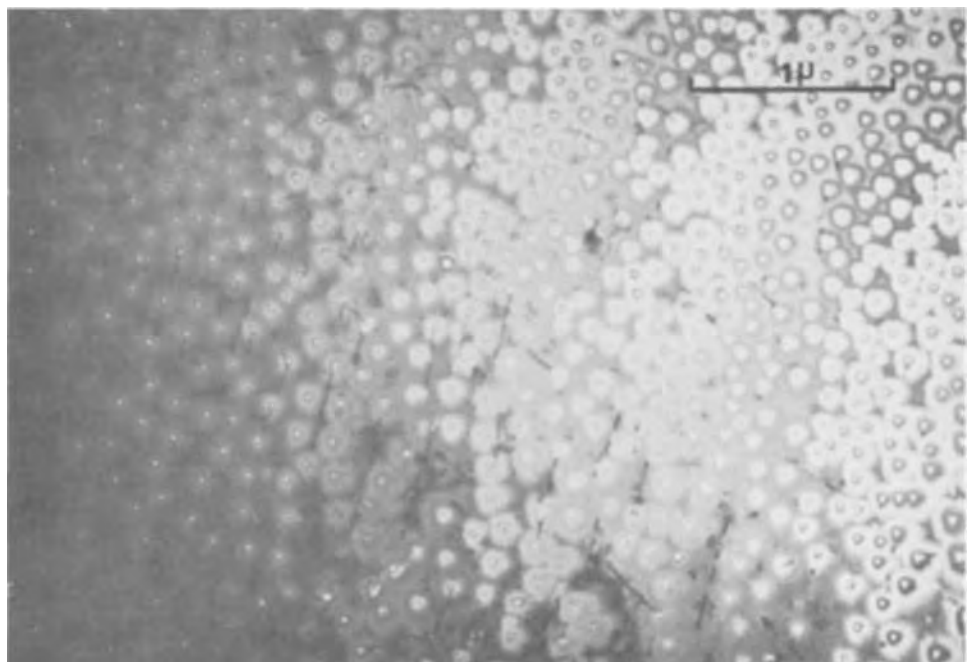
Discussion

Figure 6 indicates that these observations are consistent with the tunnels preferentially propagating in the Ga-to-P directions along the bonds as indicated by the arrows. The other tunnels occurring in films thinned from the $P(\bar{1}\bar{1}\bar{1})$ side may be spurious. The mounting of some of the specimens was not leakproof and the reagent was observed to creep around and attack the Ga(111) faces of these specimens. The tunnels inclined at 70° to the normal in the specimens thinned from the $P(\bar{1}\bar{1}\bar{1})$ side may have resulted from this unintended Ga(111) attack.

The presence of etch tunnels on a transmission electron microscope scale has not previously been reported in GaP or any other semiconducting material. This also appears to be the first report of an example of electrochemical tunnel etching. Tunnels have, however, been observed in certain other materials under particular conditions.

Westwood and Rubin (2) investigated the growth and dissolution of LiF crystals in aqueous solutions containing long-chain fatty acids. Both "positive and negative whiskers," that is, both growth whiskers and dissolution tunnels of similar form, could be formed

Fig. 5. GaP specimen electrochemically attacked from the $P(\bar{1}\bar{1}\bar{1})$ surface. About half of the etch tunnels lie along the $\langle 111 \rangle$ direction normal to the specimen surface. No tunnels were formed in this direction when the specimens were attacked from the Ga(111) side as in all the previous figures.



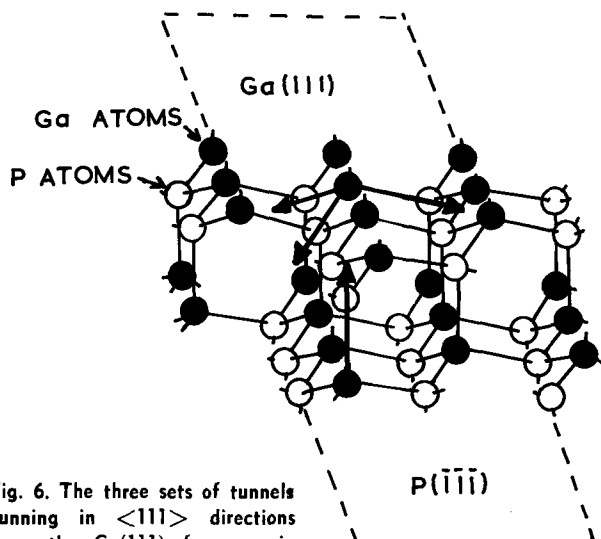


Fig. 6. The three sets of tunnels running in $\langle 111 \rangle$ directions from the Ga(111) face, as in Fig. 1, 3(a) and 4, are consistent with preferential propagation in the polar Ga-to-P directions along the bonds as indicated by the three arrows. The tunnels running vertically through the foils from the P(111) faces as in Fig. 5 are also consistent with preferential propagation in the Ga-to-P polar direction as indicated by the single vertical arrow.

using supersaturated and undersaturated solutions, respectively, containing identical concentrations of stearic acid. It was thus possible to equate the formation of tunnels with a reversal of crystal growth. It was suggested that the fatty acids acted as step poisons and were less concentrated at the base of the tunnels than at the surface. The maximum depth of the tunnels in LiF was 200 μm and their diameter was between 1 and 2 μm . Thus they were orders of magnitude larger than those reported above.

Swann (3) observed corrosion tunneling in the dissolution of Cu_3Au in ferric chloride solution. Electron microscope studies showed that a passive layer of gold was formed on the tunnel walls. A theory was developed to explain the longitudinal rather than lateral growth of the tunnels. According to this, passivation of the tunnel walls would occur at a critical radius found by equating the number of gold atoms in the tunnel with the number of copper surface sites on the tunnel walls. This radius was found to be two-thirds of the maximum radius of the hemispherical pit at the base of the tunnel. Thus the tunnel walls become passivated before the base and the tunnels grow longitudinally.

The formation of tunnels in GaP, however, appears to be purely an electrochemical phenomenon and there is no evidence that passivation is involved. No electron diffraction effects attributable to surface layers of a different structure or composition than the bulk material were ever seen.

Electrochemically formed tunnels similar to those reported here have been observed by transmission electron microscopy in GaAs and Si.¹ Theunissen *et al.* (5) in a study of the electropolishing of Si in hydrofluoric acid reported that a thin dark brown layer formed on n^+ material. Sirtl etching of cross sections of these specimens "revealed a high density of etch channels (about 10^8 cm^{-1}) extending a few microns (0.5 μm)" into the specimen. It seems probable that the dark brown layers observed by Theunissen *et al.*, like those

reported above, contained a high density of tunnels on an electron microscopic scale and the Sirtl etch enlarged some or all of the deeper ones to produce the optically visible etch channels. Subsequently Theunissen (6) reported scanning electron microscope (SEM) observations of channels in these electropolished slices. The intermediate resolution of the SEM means that those channels were probably on a rather larger scale than those reported here.

No relation was found between the formation of tunnels and any defects originally present in the materials examined in this paper. It is certain that the tunnels in GaP do not follow lines of dislocations as they formed in material in which the dislocation density was too small by several orders of magnitude to account for all the tunnels. The observed density of tunnels varied from about 10^6 to 10^8 cm^{-2} , and this density was found to increase with the electropolishing voltage used. The density of dislocations in this material was 10^4 to 10^5 cm^{-2} . Furthermore, dislocations in GaP tend to lie along $\langle 110 \rangle$ directions (7, 8), whereas the tunnels were invariably formed along $\langle 111 \rangle$ directions. It therefore seems certain that the tunnels are formed by localized electrochemical reaction occurring at the semiconductor-electrolyte interface. It is possible, however, that the tunnels initiate at some form of minor surface defect.

An hypothesis that appears to be consistent with our observations is that localized electrochemical attack is the result of avalanche breakdown of the surface depletion layer of the semiconductor due to the large applied field in this layer. Avalanche breakdown produces a localized microplasma. This contains a high density of the electron holes that are required for electrochemical attack. A similar idea was put forward by Theunissen (6). However, he appeared to suggest that the phenomenon was unique to n^+n epitaxial slices of Si and reported that in some cases the channel networks could be related to dislocation networks. The present work, however, as just discussed, shows that in GaP the tunnels are not related to dislocations.

Acknowledgments

This work was supported by a C.V.D. contract and is published by permission of the Ministry of Defence. Thanks are due to the Services Electronics Research Laboratory for the supply of material and to Professor J. G. Ball for the provision of research facilities.

Manuscript submitted May 11, 1971; revised manuscript received ca. Nov. 15, 1971.

Any discussion of this paper will appear in a Discussion Section to be published in the December 1972 JOURNAL.

REFERENCES

1. A. P. Honess, "Etch Figures on Crystals," p. 43, John Wiley & Sons, Inc., New York (1927).
2. A. R. C. Westwood and H. Rubin, *J. Appl. Phys.*, **33**, 2001 (1962).
3. P. R. Swann, *Corrosion*, **25**, 147 (1970).
4. B. D. Chase, D. B. Holt, and B. A. Unvala, *This Journal*, **119**, 310 (1972).
5. M. J. J. Theunissen, J. A. Appels, and W. H. C. G. Verkuylen, *ibid.*, **117**, 959 (1970).
6. M. J. J. Theunissen, Paper presented at the Institute of Physics and Physical Society Conference on Solid State Devices at Exeter, England, Sept. 15-18, 1970.
7. B. D. Chase, Ph.D. Thesis, University of London (1970).
8. B. D. Chase and D. B. Holt, *J. Mater. Sci.*, To be published.

¹ M. J. Hill, Private communication.

Jet Polishing of Semiconductors

III. Polishing and Shaping of Si, Ge, GaAs, and GaP Slices

B. A. Unvala, D. B. Holt, and Aung San

Metallurgy Department, Imperial College of Science and Technology, London S.W.7, England

ABSTRACT

Clean, flat, strain-free surfaces of Si, Ge, GaAs, and of the P($\bar{1}\bar{1}\bar{1}$) faces of GaP were prepared by scanning jets of chemical polishing reagents across one side of the rotating slices. The Ga(111) faces of GaP were electrochemically polished in the same apparatus. It was found possible to reduce the central areas of large diameter Si slices to thicknesses of tens of microns while retaining thick, mechanically strong rims with this technique by masking the edges of the slices. Whole slices of Si were also reduced to uniform thicknesses of under 20 μm by this technique.

Chemical polishing reagents are available for the more important semiconductors. [Tabulations of these reagents were listed in the first paper in this series (1).] By using jets of these reagents improved polishing action in our experience is generally obtained. Techniques for thinning small areas for transmission electron microscopy in several semiconducting materials by chemical jet polishing were successfully developed (1-3). It was also shown that by rotating germanium slices under a chemically polishing jet which scanned over one side it was possible to produce clean, flat, and strain-free surfaces for use as epitaxial substrates (4). This method has been improved and applied to the polishing of silicon, germanium, GaAs, and GaP slices in this present work.

For the production of certain semiconductor devices and for optical transmission studies, it is desirable to produce large areas that are uniformly thin but have thick, mechanically strong rims. A method for doing this has been developed for silicon and is reported here.

Some evidence is also reported which indicates that the very thin slices required for certain types of integrated circuits can be produced by the technique described here.

Equipment

The apparatus used to scan the jet across an arc under which the rapidly rotating slices passed is shown in Fig. 1(a). The slices were given a planetary motion, that is a rotating platform was used which carried the slice mounts, each rotating about an axis parallel to and moving round the axis of rotation of the platform as indicated in Fig. 1(b). This prevented the formation of raised central spikes that were occasionally produced when slices were rotated on a stationary axis beneath a scanning jet (4). Electrical contacts for electropolishing were made to the stainless steel jet nozzle and to the rotating platform.

The planetary gear ratio was approximately four to one. The central spindle was rotated at speeds of about 300 rpm and the reciprocator carrying the jet nozzle was driven at about 950 cycles per minute in all the experiments.

Before chemical polishing the slices were mounted on the spinner disks and mechanically polished in a special jig as described previously (4).

Slices were successfully polished using standard reagents. For polishing silicon a mixture of HF:HNO₃:HAc in the volume ratio 5:15:3 at room temperature was used. With a flow rate of about 4 cm³ sec⁻¹ for all the polishing experiments, the rate of removal of Si was about 0.5 μm sec⁻¹ for both n- and p-type materials. Ge was polished using CP-4 at 47°C. The rate of removal was again about 0.5 μm sec⁻¹. Heavily Cr-doped GaAs was polished using 2% of Br in methanol

at room temperature. The rate of attack was about 8 μm min⁻¹.

A solution of H₂O:NaOCl:HCl in the volume ratio 16:2:2 was employed to polish the P($\bar{1}\bar{1}\bar{1}$) sides of GaP{111} slices. The slices were attached to the stainless steel platform with silver paint. The Ga(111) sides of the slices were polished with the same reagent but a current of 35 mA was passed between the slice and the nozzle. (The Ga(111) and P($\bar{1}\bar{1}\bar{1}$) sides of the slices were identified by etching in hot aqua regia. The Ga faces were etched and the P faces were polished.)

Results and Discussion

Polishing

The polished Si slices were flat as was shown by the straightness of optical interference fringes. That they were microscopically smooth was demonstrated by the absence of any detail due to asperities on dark field optical microscope observations of these surfaces. The use of planetary motion eliminated the central spikes which sometimes resulted when slices were rotated about a stationary central axis during jet polishing (4).

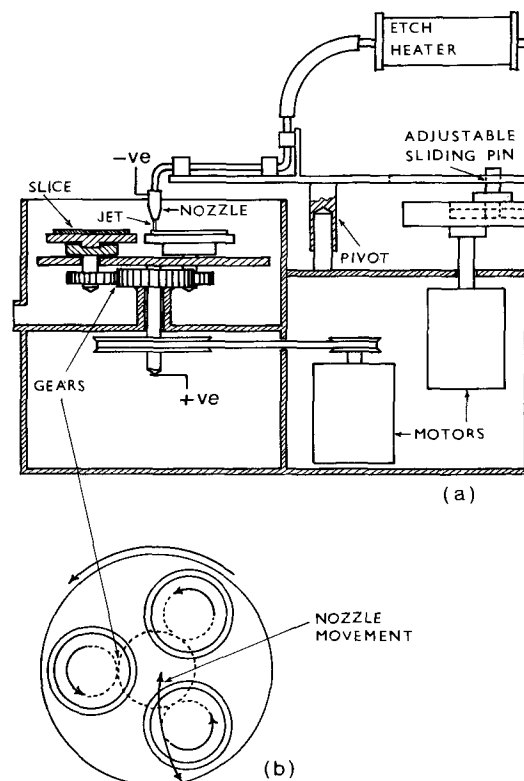


Fig. 1. Modified apparatus for the jet polishing of rotating slices

Key words: polishing, shaping, semiconductor slices.

Germanium slices were polished to a similar standard.

The polish achieved on the GaAs slices, despite their being heavily Cr-doped, was of the same quality as that on Si and Ge. That is, chemical polishing produced surfaces that were optically smooth and flat on both Ga(111) and As(111) faces. Attempts were also made to electropolish GaAs. $H_2O:HCl:NaOCl$ (about 10% available chlorine) in the volume ratio 170:10:20 was used. At 200-240V applied, 30 to 40 mA flowed and the rate of attack was about $150 \mu\text{m}/\text{min}$. The surfaces so produced were, however, found to be tunnel-etched similarly to GaP as described previously (5).

The P(111) faces of GaP slices were also chemically polished, flat, and smooth to optical standards. Smooth, flat Ga(111) surfaces could, however, only be produced electrochemically as described above. These faces had a thin yellow surface film. All semiconductor slices polished by this method were rounded at the edges.

Shaping and Thinning Silicon

For a certain device application large thin areas of silicon were required with a thick strong rim. The ability of this method to produce silicon slices with this shape was tested. Regions about 2 mm wide around the edge of Si slices 2.54 cm in diameter and $125 \mu\text{m}$ thick were masked with a gold-chromium alloy. The slices were then hollowed by chemical polishing as described above. A central area about 1.9 cm in diameter was found to be uniformly thick. Figure 2 is a Tallysurf trace showing the shape of the rim produced by polishing a masked slice. No undercutting or formation of stress-concentrating sharp corners occurred. Thicknesses of the central area less than $20 \mu\text{m}$ could be achieved. The thicknesses were determined by an infrared interference method (6).

There is also currently a growing interest in uniformly thin slices of Si for the production of integrated

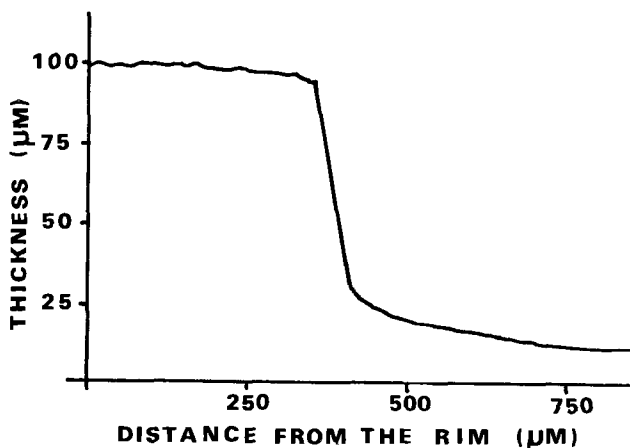


Fig. 2. Tallysurf trace of the rim of a hollowed Si slice

circuits involving only p-n junctions oriented normal to the slice. Recently it has been pointed out that electropolishing can be used to preferentially attack a substrate leaving only the thin, differently doped epitaxial layer in the cases both of Si (7) and of GaAs (8). Mash *et al.* (9) have reported a mechanical polishing technique for thinning Si slices to $10 \mu\text{m}$. This process must however introduce some degree of mechanical damage.

Using the method described above Si slices were successfully reduced to less than $20 \mu\text{m}$ in thickness at which value they were beginning to be optically transparent. Without special apparatus to prepare slices with faces that were initially accurately parallel and to monitor thickness continuously during final thinning it was not practical to reduce thicknesses much below about $20 \mu\text{m}$. However there is no reason in principle why the technique should not be used for this purpose. The present technique can be used for uniformly doped slices and not only for removing substrates from differently doped layers. Moreover, due to the insensitivity of chemical polishing rates to semiconductor levels of doping, this technique, using chemical polishing reagents, should be capable of thinning slices containing n- and p-type areas.

Acknowledgments

One of us (AS) would like to thank the S.R.C. for financial support. It is a pleasure to thank C. Marsh for the construction of the polishing device, P. Steigman of Marconi Ltd., Witham, Essex, for supplying the masked silicon slices and determining their final thicknesses, Dr. M. J. Hill for determining the polishing conditions for GaP, and Prof. J. G. Ball for the provision of research facilities.

Manuscript submitted May 11, 1971; revised manuscript received *ca.* Nov. 15, 1971.

Any discussion of this paper will appear in a Discussion Section to be published in the December 1972 JOURNAL.

REFERENCES

1. B. D. Chase, D. B. Holt, and B. A. Unvala, *This Journal*, **119**, 310 (1972).
2. D. B. Holt, R. Porter, and B. A. Unvala, *J. Sci. Instrum.*, **43**, 371 (1966).
3. M. J. Hill, D. B. Holt, and B. A. Unvala, *ibid.*, **1**, 301 (1968).
4. B. A. Unvala, Aung San, and D. B. Holt, *ibid.*, **2**, 119 (1969).
5. B. D. Chase and D. B. Holt, *This Journal*, **119**, 314 (1972).
6. M. P. Albert and J. F. Combs, *ibid.*, **109**, 708 (1962).
7. M. J. Theunissen, J. A. Appels, and W. H. C. G. Verkuylen, *ibid.*, **117**, 959 (1970).
8. C. J. Nuese and J. J. Gannon, *ibid.*, **117**, 1094 (1970).
9. D. H. Mash, G. D. Henshall, and B. A. Eales, *J. Phys. D.*, **3**, 1199 (1970).

Analysis of a Chlorate Cell System with Separate Reactor

T. R. Beck*

Boeing Scientific Research Laboratories, Seattle, Washington 98124
and Department of Chemical Engineering, University of Washington, Seattle, Washington 98105

and R. Brännland

Mo och Domsjö Aktiebolag Husums Sulfatfabrik, Sweden

ABSTRACT

Equations previously formulated for a model electrolyzer-reactor system for production of sodium chlorate are tested with experimental pilot-plant data. The reactor volume and circulation rate between the electrolyzer and reactor were systematically varied in the pilot-plant tests. Mass-transfer coefficients for hypochlorite discharge and the Foerster rate constant for formation of chlorate in solution determined from these data were compared to laboratory data from the literature. Literature rate constants were put in the model equations and calculated efficiencies were found to vary with reactor volume and circulation rate in a similar way as pilot-plant efficiency data.

An equation relating current efficiency to the significant parameters of a model electrolyzer-reactor system for producing chlorate was presented in a prior paper (1). The model was based on the Foerster mechanism (2) of homogeneous formation of chlorate from hypochlorite in solution and of mass-transport-limited anodic discharge of hypochlorite. Only beaker-scale laboratory data from the literature were available to the author at the time of development of the model so it did not receive a critical test.

Pilot-plant studies were made with a separate electrolyzer-reactor system providing data with which to test the applicability of the model. The pilot plant was installed at the Domsjo chlorine plant in Sweden where studies were made on the effect of circulation rate and reactor volume on current efficiency. Fortuitous circumstances brought the two authors together for collaboration on this paper.

Pilot Plant Description

The arrangement of the pilot plant is illustrated in Fig. 1. The pilot plant consisted of a rectifier, an electrolytic cell with a plastic cover, two reaction tanks, a circulation pump of rubber lined iron, a tube cooler

* Electrochemical Society Active Member.

Key words: current efficiency, recirculation, electrolyzer, pilot plant, hypochlorite.

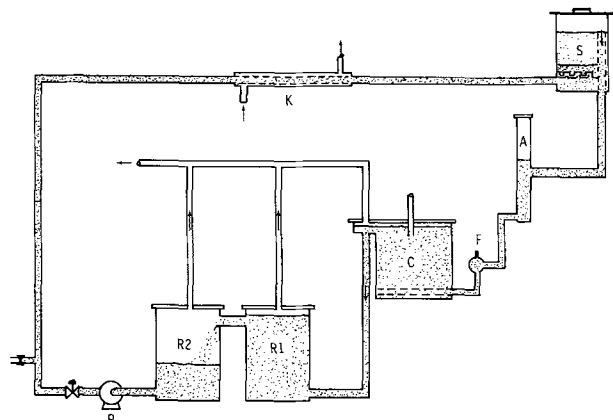


Fig. 1. Arrangement of pilot plant for electrolytic chlorate production. A—Deaerator, C—electrolytic cell, F—distribution tube, K—titanium cooler, P—circulation pump, R—reactor tanks, S—salt dissolver.

of titanium, and a salt dissolver. The tubing, reactors, and dissolver were made of polyvinyl chloride plastic (PVC).

Rectifier.—An air-cooled rectifier made by ASEA, Type RPI G, equipped with germanium cells was used. The rated output was 2400A at 2.5-8.0V d.c.

Cell.—The electrolytic cell was made of mild steel and had the internal dimensions; length 63 cm, height 67 cm, and width 47 cm. The anodes consisted of impregnated graphite plates with length 62.5 cm, width 15.0 cm, and thickness 5.0 cm. Twenty plates of this size were arranged in four rows with five in each row. An anode immersion depth of 48 cm gave a total anode area of 4.0×10^4 cm² and an area directly facing the cathodes of 3.05×10^4 cm². From the main busbar four copper bars conducted the current to the electrodes as shown in Fig. 2. The cathodes consisted of 1.0 cm thick mild steel plates welded between the anodes, forming five compartments in the cell. The distance between two plates was 7.0 cm, and the distance between anode

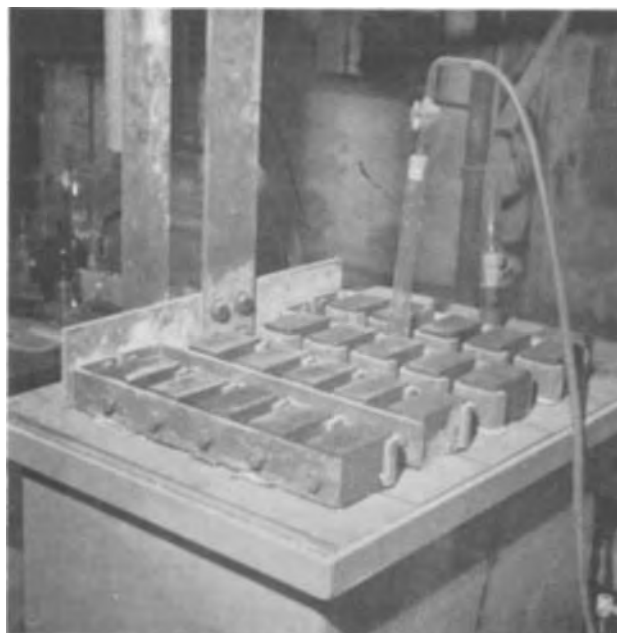


Fig. 2. Top view of electrolytic cell

and cathode thus 1.0 cm. The cathode busbar was bolted to the bottom of the cell.

In order to keep the graphite anodes in place there was a set of plastic spacers in the bottom and on the top of the cathode plates. The electrolyte was introduced through five perforated pipes, one in each compartment with eight 0.4 cm holes evenly distributed along each. These tubes were introduced through the end at the bottom of the cell.

The electrolyte left the cell through an overflow placed in the upper part of the cell at the same side as the inlet tubes. In the end box the gas was separated from the solution and was removed through a plastic pipe with a fan.

In the middle of the cell cover, which was divided in five parts, a plastic tube was arranged and submerged into the electrolyte. From this tube gas samples were taken for analysis. The cover was sealed with asphalt.

Reactors.—From the cell the solution flowed by gravity to the bottom of reactor No. 1 through a 3.0 cm plastic hose, and then from the upper part of this reactor to the upper part of reactor No. 2. From the covers of the reactors any chlorine-containing vapors were removed with plastic hoses which were connected to the gas pipe from the cell. The two reactors had the same volume, about 450 liters, but reactor No. 2 was only partly filled during the main part of the experiments. In the cover of reactor No. 1 two quartz heaters were arranged for heating the solution. They were not in use during normal operation, since the cell then developed enough heat for keeping the temperature at the desired level.

Pump.—The solution flowed from the bottom of reactor No. 2 through the pump to the titanium cooler. The cast-iron, rubber-lined pump was of centrifugal type with a Teflon-stuffed packing gland. The circulation rate was controlled with a valve placed on the pressure side of the pump. The pump was operated with a 3 HP motor at 1450 rpm.

Cooler.—From the pump the solution flowed through a 2.5 cm plastic tube to the titanium cooler which consisted of an outer steel tube (4.5 cm diameter and 520 cm length) and an inner 2.5 cm titanium tube. Between the inner and outer tube the water was fed concurrently to the electrolyte in the inner tube.

Salt dissolver.—The electrolyte flowed from the cooler through a 2.5 cm pipe to the salt dissolver. This consisted of a plastic vessel with 50 cm diameter and 100 cm length. At the inlet were two 2.5 cm tubes placed 6.0 cm above the bottom. Just above the inlet tubes there was a bubble cap plate with seven caps. Salt was dissolved as the electrolyte passed through the caps. The solution left the vessel through an overflow about 60 cm above the bottom. The required amount of salt was added hourly. In the outlet the solution passed a perforated plastic disk, and thereby solid particles were separated.

Deaeration tube and distribution tube.—The electrolyte flowed by gravity from the saturator through a 5.0 cm tube to a deaerator in which the air was removed which had been taken up by the solution in the dissolver. With respect to the gas analyses air was not desired in the cell. The deaerating tube had a diameter of 16 cm and a length of 160 cm.

The solution then passed through a distribution tube, which distributed the solution to five channels connected to the five compartments of the cell. Above the outlet channels pitot tubes were placed, indicating the flow to each compartment. Both the deaeration and the distribution tube were made of PVC.

Experimental

The pertinent experimental conditions used are summarized in Table I. A constant current of 2250A was used in all tests reported here. The total immersed

Table I. Experimental conditions

Current	2250A	
Cell voltage	3.0-3.4V	
Anode area	$4.0 \times 10^4 \text{ cm}^2$	
Volume of electrolyte in cell	$9.0 \times 10^4 \text{ cm}^3$	
Volume of electrolyte in reactors and circulation loop exclusive of cell	$80 \times 10^4 \text{ cm}^3$ in circulation rate experiments (where $q = 170\text{-}1010 \text{ cm}^3/\text{sec}$)	
Circulation rate	$830 \text{ cm}^3/\text{sec}$ in reactor volume experiments (where $V_r = 30 \times 10^4$ to $100 \times 10^4 \text{ cm}^3$)	
Temperature	$40 \pm 2^\circ\text{C}$	
Electrolyte composition:	Set I	Set II
NaCl	200 g/liter	100 g/liter
NaClO ₂	0-400 g/liter	600 g/liter
Na ₂ Cr ₂ O ₇	2 g/liter	2 g/liter
pH in reactor	6.7-6.9	6.75

anode area is listed and was used in the calculations. The total immersed area is accessible to diffusion and discharge of hypochlorite. The total current density would not be uniform, however, and this could cause some departure from the model equations.

The volume of electrolyte in the cell was calculated by deducting the volume of the anodes, cathodes, and spacers from the internal cell volume. The volume of electrolyte in the reactors was controlled by measuring the height of the liquid. The value of V_r is the volume of liquid in the reactors and recirculation loop exclusive of the cell. The circulation rate was controlled by measurement of pressure drop in a calibrated section of pipe in the rising part of the circulation loop.

The electrolyte composition was maintained by salt additions to the dissolver. The concentration of NaClO₂ was allowed to build up during the experiments to the levels indicated in Table I. The pH was maintained in the reactor at 6.75 by addition of dilute HCl under the liquid surface in the second reactor at hourly intervals. Chemical analyses were made at intervals during the runs for total hypochlorite, chlorate, chloride, and chromate. Orsat analyses of the cell gas for oxygen and CO₂ were made for the determination of current efficiency.

Experimental results for the reactor volume experiments are given in Table II and results for the circulation-rate experiments are given in Table III.

Current efficiency of hypochlorite discharge was calculated from the gas analysis by

$$\epsilon_2 = \frac{2(\% \text{O}_2 + \% \text{CO}_2)}{100 - (\% \text{O}_2 + \% \text{CO}_2)} \quad [1]$$

Equation [1] is based on the assumptions that all of the O₂ and CO₂ are produced from discharge of hypochlorite and that hydrogen is produced at 100% current efficiency at the cathode.

The mass-transfer coefficient for hypochlorite discharge was calculated (1) from

$$K_L = \frac{I \epsilon_2}{ACF} \quad [2]$$

The gas evolution rate was calculated from (1)

$$v = \frac{IRT \epsilon_2}{4APF} \quad [3]$$

The rate constant for auto-oxidation of hypochlorite in solution by the Foerster mechanism to form chlorate was calculated (1) for perfect mixing in the reactor by material balance from

$$kf_r = \frac{q(C_e - C_r)}{V_r C_e^3} \quad [4]$$

and for plug flow in the reactor from

$$kf_r = \frac{q}{2V_r} \left(\frac{1}{C_r^2} - \frac{1}{C_e^2} \right)^2 \quad [5]$$

¹ Obtained by integration of $dC/d\tau = -kf_r C^3$ in reactor with residence time $\Delta\tau = V_r/q$.

Table II. Data for reactor volume experiments with circulation rate of 830 cm³/sec

	Experimental data					Derived values				
	V_r (liters)	C_e (m mol/ liter)	C_r (m mol/ liter)	% O ₂	% CO ₂	ϵ_2	$K_L \times 10^4$ (cm/sec)	$v \times 10^4$ (cm/sec)	$kf_r \times 10^{-3}$ [(mole/cm ³) ⁻² sec ⁻¹]	
									Perfect mixing	Plug flow
Set I	300	115.3	112.3	5.15	0.30	0.115	5.8	4.3	5.85	5.5
	400	113.3	110.2	4.75	0	0.100	5.2	3.7	4.8	4.5
	550	110.8	105.3	4.1	0	0.0855	4.5	3.2	7.1	6.4
	600	109.8	102.8	3.9	0	0.081	4.3	3.0	9.0	8.3
	700	106.5	96.2	3.65	0	0.076	4.1	2.8	13.7	11.9
	800	104.0	93.2	3.57	0	0.074	4.1	2.8	13.8	11.8
	1000	94.2	87.0	3.45	0	0.0715	4.4	2.7	9.05	8.0
									9.05 Avg.	8.05 Avg.
Set II	275	126	86	3.4	0	0.0705	3.3	2.6	189	109
	400	116	89	3.1	0	0.064	3.2	2.4	80	54
	600	104	79	2.6	0	0.0535	3.0	2.0	70	47
	800	99	65	2.7	0	0.0555*	3.3	2.1	126	70
									116 Avg.	70 Avg.

* Value of ϵ_2 based on chlorate analyses was 0.13 to 0.17 for this condition.

Table III. Data for circulation rate experiments with reactor volume of 800 liters

	Experimental data					Derived values				
	q (cm ³ /sec)	C_e (m mol/ liter)	C_r (m mol/ liter)	% O ₂	% CO ₂	ϵ_2	$K_L \times 10^4$ (cm/sec)	$v \times 10^4$ (cm/sec)	$kf_r \times 10^{-3}$ [(mole/cm ³) ⁻² sec ⁻¹]	
									Perfect mixing	Plug flow
Set I	169	—	—	7.4	0	0.160	—	6.0	—	—
	250	—	—	5.5	0	0.117	—	4.4	—	—
	338	—	—	4.6	0	0.096	—	3.6	—	—
	500	—	—	4.0	0	0.083	—	3.1	—	—
	675	—	—	3.55	0	0.073	—	2.7	—	—
	840	104	93	3.50	0	0.072	4.0	2.7	14.3	12.6
	1010	106	94	3.45	0	0.071	3.9	2.7	18.2	15.1
									16.2 Avg.	13.8 Avg.
Set II	332	104	63	3.6	0.2	0.079	4.4	3.0	68	33
	520	99	66	3.2	0.2	0.070	4.1	2.6	75	42
	830	99	65	2.8	0.2	0.062	3.6	2.3	128	70
									90 Avg.	48 Avg.

Discussion

Mass-transfer coefficient.—A plot of the mass-transfer coefficient for hypochlorite discharge vs. anodic gas evolution rate from Tables II and III is shown in Fig. 3. On the basis of theory (1), a line for the one-half-power law expressed by

$$K_L = 2.4 \times 10^{-2} v^{1/2} \quad [6]$$

was drawn through the data. The value of the coefficient on the right hand side is smaller than that calculated from laboratory data on hypochlorite discharge

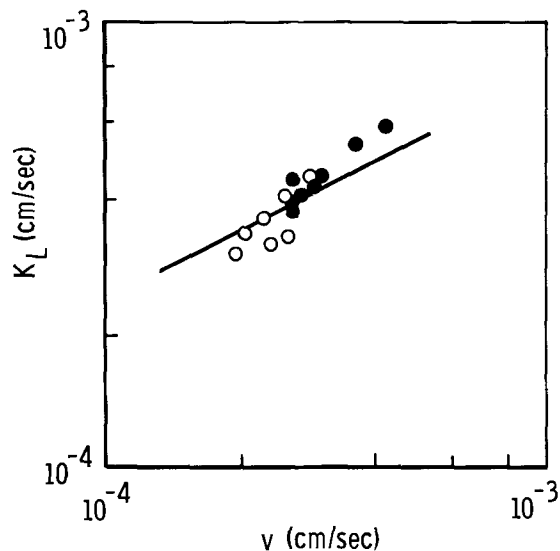


Fig. 3. Relation of mass transfer coefficient for hypochlorite discharge to anodic gas evolution rate.

(1) as indicated in Fig. 4, in which the ratio of coefficients for hypochlorite discharge (B) to the coefficient in the one-half-power law for the Ibl-Venczel data (3) for Fe³⁺ reduction in 1M H₂SO₄ ($B_0 = 2.2 \times 10^{-2}$) is shown. The expected effect of temperature on diffusivity (4) and thus B/B_0 (3) is indicated by the function $a(T/\mu)$, which was adjusted to pass through the Foerster data. Viscosity data for NaCl and NaClO₃

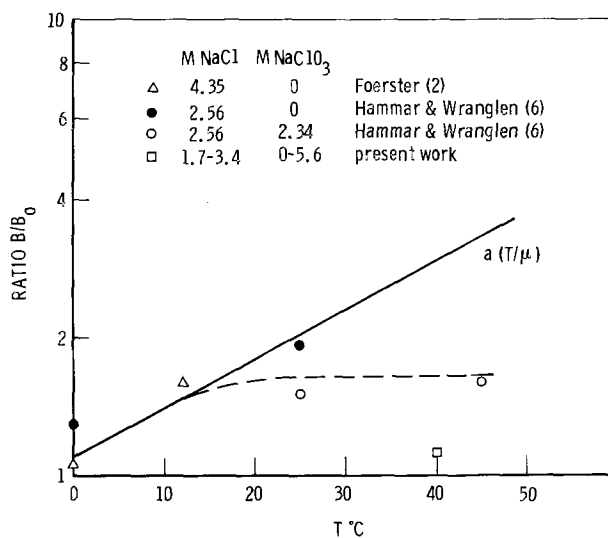


Fig. 4. Extrapolation of B/B_0 to higher temperature

solutions were from International Critical Tables (5). The Foerster data (2) and the Hammar and Wranglen data (6) for NaCl solutions were reasonably close to the line in Fig. 4. The Hammar and Wranglen data and the present pilot plant data for solutions containing NaClO₃ were below the line.

There are at least two important factors affecting the prediction of mass transfer coefficients for hypochlorite discharge from the Ibl-Venczel data (3) for cathodic reduction at a hydrogen evolving electrode. First, Janssen and Hoogland (7) observed that mass transfer coefficients for oxidation of Ce³⁺ at an oxygen evolving electrode was about a factor of two larger than for reduction of Ce⁴⁺ at a hydrogen evolving electrode at the same volumetric gas rate per unit area at 25°C. The value of the correlation line at 25°C in Fig. 4 is consistent with this observation. Second, Landolt and Ibl (8) found with 4M NaCl solutions containing hypochlorite in forced convection experiments, for which the hydrodynamics were well characterized, that the anodic chlorate formation rate was smaller than predicted by a purely diffusional process. This may account in part for the negative deviations from the correlation line in Fig. 4 for the more concentrated solutions. Janssen and Hoogland further found that their mass transfer rates were a function of electrode height. This perhaps is related to effects of convection currents established by the gas bubbles.

The dashed line in Fig. 4 through the Hammar and Wranglen data give

$$K_L = 3.7 \times 10^{-2} v^{1/2} \quad [7]$$

at 40°C which is used in predicting pilot-plant performance.

Rate constant for chemical chlorate formation.—Values of k_f , determined in the experiments (Tables II and III) and from the literature are compared in Table IV. Values from the pilot plant varied by more than an order of magnitude between Set I and Set II and fell on either side of the value calculated from literature data. Values of k_f were calculated for the limiting conditions of perfect mixing and plug flow in the reactors as it was expected that the actual condition would be between these two limits. The value calculated for perfect mixing is larger because this is a less efficient condition and a higher rate constant is required to achieve the same amount of reaction. The high values of the rate constant for Set II are discussed in the next section.

In obtaining a calculated value of k_f from literature data the Knibbs and Palfreeman (9) value of the Foerster rate constant, k , was used. Their value was determined at 40°C in a concentrated NaCl solution.

Table IV. Comparison of values of k_f calculated from pilot plant data and from literature data

	$k_f \times 10^{-3}$ (mole/cm ³) ⁻² sec ⁻¹	
	Perfect mixing	Plug flow
Pilot plant values (from Tables II and III)		
Set I		
Reactor volume experiments	9.0	8.0
Circulation rate experiments	16.2	13.8
Set II		
Reactor volume experiments	116	70
Circulation rate experiments	90	48
Calculation from literature data		
k Knibbs and Palfreeman (9) (concentrated NaCl solution at 40°C) 9.6 (mole/liter) ⁻² min ⁻¹ = 1.60×10^5 (mole/cm ³) ⁻² sec ⁻¹		
C_{H^+} (for pH = 6.75 in reactor) = 1.8×10^{-7} mole/liter		
$K_i^{40^\circ}$ (calculated from $K_i^{25^\circ} = 3.2 \times 10^{-8}$ (10) and $\frac{dT}{d \ln K} = \frac{\Delta H^\circ}{RT^2}$ where $\Delta H^\circ = +3.95$ kcal (10)) = 4.5×10^{-8} mole/liter		
$f_r = \left(\frac{1}{1 + K_i/C_{H^+}} \right)^2 \left(1 - \frac{1}{1 + K_i/C_{H^+}} \right)$ (1)		
= 0.128		
$k_{f_r} = (1.60 \times 10^5) (0.128) =$		

20.5

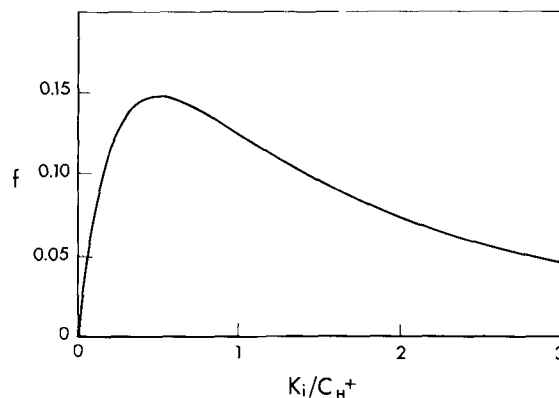


Fig. 5. Plot of $f = \left(\frac{1}{1 + K_i/C_{H^+}} \right)^2 \left(1 - \frac{1}{1 + K_i/C_{H^+}} \right)$

The dimensionless concentration factor, f_r , was calculated from an expression previously derived (1). A plot of f_r vs. K_i/C_{H^+} shown in Fig. 5 indicates that conditions in the electrolyzer were nearly optimum for maximum conversion rate.

Correlation of efficiency data.—Pilot-plant current efficiency data are now compared to predictions of the model equations for efficiency of a separate electrolyzer-reactor system (1) using values of K_L and k_f based on laboratory data from literature cited above. The parameters used in the model equations are given in Table V. No data were available on the pH in the electrolyzer but it was assumed to be less acidic than in the reactor. Therefore $k_{f_e} = k_{f_r}$ (curve A) and $k_{f_e} = 0$ (curve B) were considered as limiting conditions based on Fig. 5.

The parameters of Table V substituted in the model equation [Eq. [11-14], ref. (1)] give (Curve A)

$$V_r = \frac{[3.40\epsilon_2^{3/2} - 10.2\epsilon_2^{5/2} - 9.0\epsilon_2^3] \times 10^4}{[0.141\epsilon_2^2 + 0.163\epsilon_2^{3/2} + \epsilon_2 - 0.0542\epsilon_2^{1/2}]^3} \quad [8a]$$

(Curve B)

$$V_r = \frac{[3.40\epsilon_2^{3/2} - 10.2\epsilon_2^{5/2}] \times 10^4}{[0.163\epsilon_2^{3/2} + \epsilon_2 - 0.0542\epsilon_2^{1/2}]^3} \quad [8b]$$

for the reactor volume experiments, and

(Curve A)

$$q = \frac{[119\epsilon_2^2 + 135\epsilon_2^{3/2} - 45\epsilon_2^{1/2}]}{[0.0427\epsilon_2^{3/2} - 0.128\epsilon_2^{5/2} - 0.113\epsilon_2^3]^{1/3} - \epsilon_2} \quad [9a]$$

(Curve B)

$$q = \frac{[135\epsilon_2^{3/2} - 45\epsilon_2^{1/2}]}{[0.0427\epsilon_2^{3/2} - 0.128\epsilon_2^{5/2}]^{1/3} - \epsilon_2} \quad [9b]$$

for the circulation rate experiments. Equations [8] and [9] are plotted in Fig. 6 and 7 in terms of ϵ_1 (where $\epsilon_1 = 1 - \epsilon_2$) and compared to Set I and Set II data.

Several important observations can be made in Fig. 6 and 7:

(i) Current efficiencies based on gas analyses and on the model equations followed the same trends in respect to reactor volume and to circulation rate.

(ii) Set I data are closer to the model equations than Set II data.

Table V. Values of parameters used in model equations

I	= 2250A
A	= 4.0×10^4 cm ²
V_e	= 9.0×10^4 cm ³
V_r	= 80×10^4 cm ³ in circulation rate experiments
q	= 830 cm ³ /sec in reactor volume experiments
K_L	= $3.7 \times 10^{-2} v^{1/2}$ cm/sec
k_{f_r}	= 20×10^3 (mole/cm ³) ⁻² sec ⁻¹
k_{f_e}	= 20×10^3 (mole/cm ³) ⁻² sec ⁻¹ (Curve A)
k_{f_e}	= 0 (Curve B)

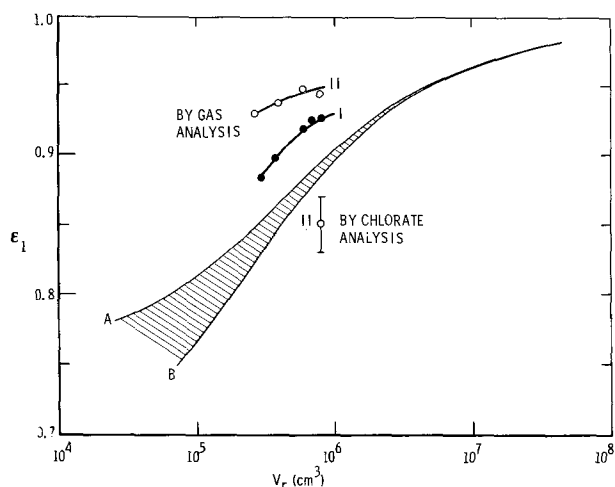


Fig. 6. Comparison of model equation to Set I and Set II data for reactor volume experiments.

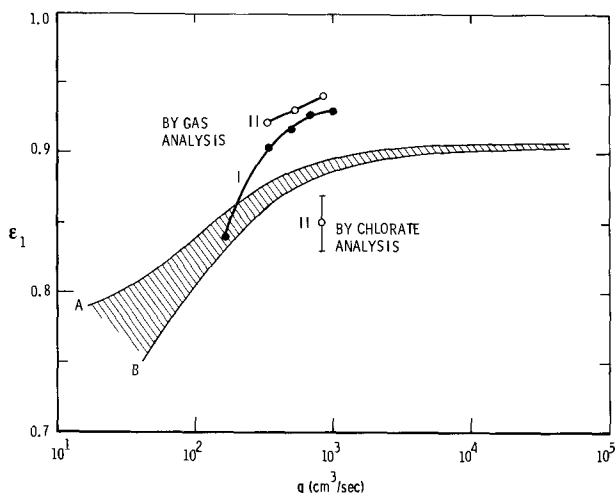


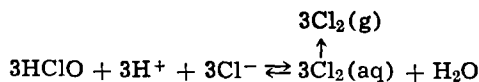
Fig. 7. Comparison of model equation to Set I and Set II data for circulation rate experiments.

(iii) The experimental current efficiency had a stronger dependence on circulation rate than that of the model equations.

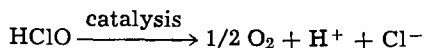
(iv) Set II current efficiencies based on gas analyses were above, and current efficiencies based on chlorate analyses were below, the values for the model equations.

It would appear that there were some systematic errors in the experimental data. Possible systematic errors of differences in the experimental data are:

(i) Loss of chlorine from cell and reactors by



(ii) Decomposition of hypochlorite by



(iii) Cathodic reduction of hypochlorite.

(iv) Effect of high salt and chlorate concentrations on k_f and K_L .

(v) Flow conditions not exactly defined.

(vi) Nonuniform anode current density.

(vii) Catalysis of Foerster reaction.

The difference between current efficiency determined by gas analyses and by chlorate analyses indicates a loss of hypochlorite as by items (i), (ii), or (iii), although cathodic reduction would not be expected to be

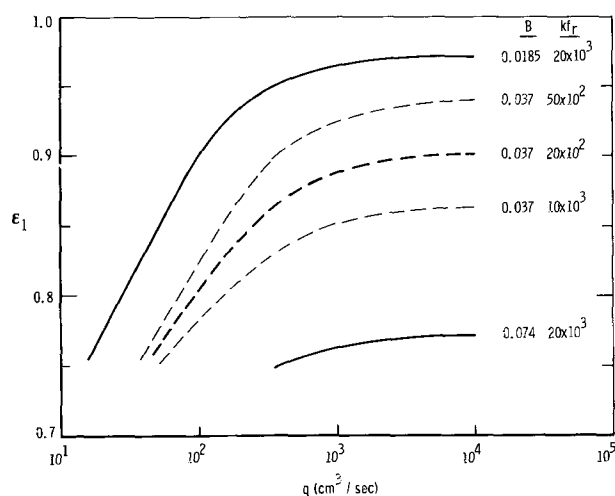


Fig. 8. Relative effect of mass transport and kinetic parameters on predicted current efficiency.

significant with sufficient chromate present. The difference between Set II and Set I current efficiencies indicates an abrupt change such as through solution contamination affecting catalysis in items (ii) and (vii). The steep dependence of current efficiency on circulation rate and the apparent increase in k_f with q noted in Table II suggest a loss of chlorine due to agitation. On balance it appears that chlorine losses and catalytic decomposition may both have occurred in the pilot plant. It also appears that the model equations predicted current efficiency more accurately than the calculation from gas analyses.

The relative effect of values of the two rate parameters, B and k_f on current efficiency (Curve B) is indicated in Fig. 8. It is seen that current efficiency is more sensitive to B than to k_f . This is because an increase in the value of B increases hypochlorite discharge and increases gas evolution giving a greater effect on K_L and current inefficiency, ϵ_2 , whereas an increase in k_f causes a decrease in concentration of hypochlorite diminishing the increase in rate of formation of chlorate. Thus it appears to be more important to get accurate mass-transport data than reaction kinetics data for this system.

Perhaps the greatest utility of the model equations is that they permit extrapolation of the system performance from experimental data. Thus Fig. 6 indicates that current efficiency could be further increased by increasing reactor volume, whereas Fig. 7 indicates that efficiency is near the plateau for circulation rate. Furthermore the model equations would allow interpolations of the data for combinations of reactor volume and circulation rate different than used in the experiments. The interpolations and extrapolations could be used in determining the economic optimum combination of pump and reactor.

Conclusions

Calculations performed on pilot plant data for a separate electrolyzer-reactor system for production of sodium chlorate showed:

1. Mass-transfer coefficients for anodic hypochlorite discharge and the Foerster rate constant for formation of chlorate were consistent in respect to order of magnitude with laboratory data in the literature.

2. Previously derived equations expressing current efficiency as a function of system parameters using mass transfer coefficients and Foerster rate constant from laboratory data in the literature gave trends of current efficiency vs. reactor volume and circulation rate consistent with pilot plant data.

Manuscript received April 30, 1969; revised manuscript received Nov. 11, 1971. This was Paper 253 presented at the Boston Meeting of the Society, May 5-9, 1968.

Any discussion of this paper will appear in a Discussion Section to be published in the December 1972 JOURNAL.

NOMENCLATURE

a	constant
A	anode area, cm^2
B	constant in $K_L = Bv^{1/2}$, $(\text{cm}/\text{sec})^{1/2}$
C	concentration of total hypochlorite, mole/cm^3
f	$\left(\frac{1}{1 + K_i/C_{H^+}}\right)^2 \left(1 - \frac{1}{1 + K_i/C_{H^+}}\right)$, dimensionless
F	Faraday, 96,500 coulombs/equiv
ΔH°	standard enthalpy of reaction, cal/mole
I	current, A
k	Foerster rate constant, $(\text{mole}/\text{cm}^3)^{-2} \text{sec}^{-1}$
K_i	ionization constant for HClO , $(\text{mole}/\text{cm}^3)$
K_L	mass transfer coefficient for hypochlorite discharge, cm/sec
P	pressure, atm
q	circulation rate, cm^3/sec
R	gas constant, $\text{cm}^3 \text{atm}/\text{deg mole}$
T	absolute temperature, $^\circ\text{K}$
v	anodic gas evolution rate, $\text{cm}^3/\text{cm}^2 \text{sec}$
V	volume, cm^3
ϵ	current efficiency, dimensionless
μ	viscosity
τ	time, sec

Subscripts

1	refers to current efficiency for Cl^- discharge or for chlorate formation
2	refers to current efficiency for hypochlorite discharge or oxygen formation
e	electrolyzer
r	reactor

REFERENCES

1. T. R. Beck, *This Journal*, **116**, 1038 (1969).
2. F. Foerster, *Trans. Am. Electrochem. Soc.*, **46**, 23 (1924).
3. N. Ibl and J. Venczel, Presented at 11th and 12th CITCE meetings 1959 and 1961 and Paper 94 presented at Electrochem. Soc. Meeting, Cleveland, Ohio, May 1-6, 1966.
4. C. R. Wilke and P. Chang, *AIChE J.*, **1**, 264 (1955).
5. "International Critical Tables", V, McGraw-Hill Book Company, New York (1929).
6. L. Hammar and Wranglen, *Electrochim. Acta*, **9**, 1 (1964).
7. L. J. Janssen and J. G. Hoogland, *ibid.*, **15**, 1013 (1970).
8. D. Landolt and N. Ibl, *ibid.*, **15**, 1165 (1970).
9. N. V. S. Knibbs and H. Palfreeman, *Trans. Faraday Soc.*, **16**, 402 (1921); *ibid.*, 415 (1921).
10. W. Latimer, "Oxidation Potentials," 2nd ed., Prentice-Hall, Englewood Cliffs, N. J. (1952).

The Differential Capacitance of Polycrystalline Gold in Aqueous Solutions

J. P. Carr and N. A. Hampson

Chemistry Department, Loughborough University of Technology, Loughborough, Leicestershire, England

ABSTRACT

The impedance of polycrystalline gold in aqueous NaOH and H_2SO_4 solutions has been studied as a function of bias potential. The pzc is estimated to be $0.33 \pm 0.02\text{V}$ in H_2SO_4 solutions. Evidence is found for the adsorption of oxygen species. Addition of n-butylamine to the electrolyte solutions inhibits adsorption of oxygen species from NaOH solutions. In H_2SO_4 solutions n-butylamine is apparently absorbed as the quaternary ammonium ion and is adsorbed only at negative rational potentials.

The gold/aqueous solution interphase has been studied by a number of workers (1-14, 16, 17) however there is considerable disagreement regarding the position of the potential of zero charge, E_z . Reported values of E_z range from -0.47 to 0.5V .¹ Table I summarizes the previous work and the wide range of E_z values indicates that the double layer structure on gold electrodes in aqueous solutions may be complicated by oxide films and adsorption of solution species.

Studies concerning oxide formation and the anodic dissolution of gold in aqueous solutions have been reported (18-34) however most of the work has been performed under acid conditions. In alkaline and neutral solutions there is a limited amount of data (26, 27, 31). Thermodynamically Au_2O_3 can exist on gold electrodes under alkaline conditions (35) and the possibility of adsorption of hydroxyl species from the solution giving rise to adsorbed OH and O species at the electrode has been discussed by a number of workers (30, 32-34), however the absence of hydrogen adsorption was shown by Bauman and Shain (28).

In this paper we present the results of a study of the differential capacitance of polycrystalline gold in aqueous NaOH solutions from which inferences con-

cerning oxide formation or adsorption at the electrode within the polarizable region could be made. The results obtained under alkaline conditions are compared with complementary results in acid solutions.

Experimental

The experimental procedure has been described previously (36, 37). The test electrode ($3.48 \times 10^{-2} \text{cm}^2$ superficial surface area) was prepared from 99.999% pure gold wire supplied by Johnson Matthey and Company and sheathed in polythene (38). The adhesion of the polythene to gold was found to be excellent (liquid-tight junctions were invariably obtained) and was found to be the most satisfactory way of mounting the gold micro electrodes. The counterelectrode was of platinum gauze of high surface area² and contained in a compartment separated from the test electrode compartment by a glass frit. Electrolyte solutions were prepared from AR quality reagents and twice distilled water from deionized stock and subjected to continuous purification over cleaned activated charcoal (the electrolyte from the counterelectrode compartment being passed through the charcoal and the purified solution passing into the test electrode com-

Key words: gold, differential capacitance, adsorption, n-butylamine.

¹ All potentials are reported with respect to the normal hydrogen electrode.

² The use of platinum counterelectrodes was shown to be satisfactory since the magnitude and the time stability of the impedance measurements was the same irrespective of whether a platinum or "glassy carbon" counterelectrode was used.

Table I

Solution	Method	p.z.c. (volts)	Refer- ence
1N HCl	Calculation from work functions	-0.45	(15)
0.1N KCl } 0.1N HCl } 2N H ₂ SO ₄	Open circuit scrape	-0.06	(8)
	Calculation from work functions	0.23	(5)
0.001N HClO ₄	Capacitance of single crystals	(110) plane 0.24 (100) plane 0.19	(4)
0.001 mol l ⁻¹ HClO ₄ and 0.001 mol l ⁻¹ HClO ₄ + 1 mol l ⁻¹ NaClO ₄	Organic adsorption	0.3	(6)
0.001 mol l ⁻¹ HClO ₄	Capacitance	0.17	(11)
0.1 mol l ⁻¹ HClO ₄	Friction method	0.1	(11)
0.01 mol l ⁻¹ HClO ₄	Friction method	0.15	(11)
1N KNO ₃	Deformation of wires	0.43	(1)
0.02-0.0025 mol l ⁻¹ NaF	Capacitance of single crystals	(110) plane 0.2 (100) plane 0.4 (111) plane 0.5	(13)
0.1N NaF	Open circuit scrape	0.15	(8)
0.1 mol l ⁻¹ KCl (pH = 7)	Open circuit scrape	-0.09	(7)
1N KCl	Friction and hardness measurements	0.15	(2)
0.001N KCl, 0.0005N La(NO ₃) ₃	Crossed polarized metal threads	0.05	(3)
0.1N KBr } 0.1N NaBr }	Open circuit scrape	-0.24	(8)
0.1N KI } 0.1N NaI }	Open circuit scrape	-0.47	(8)
0.001 mol l ⁻¹ NaClO ₄	Capacitance	(pH3) 0.15 (pH4) 0.18	(11)
NaClO ₄ (various conc)	Organic adsorption	0.37	(11)
0.02N Na ₂ SO ₄	Capacitance	0.23	(5)
0.1N Na ₂ SO ₄ } 0.1N Na ₂ SO ₄ }	Open circuit scrape	0.13	(8)
0.01, 0.005 and 0.0025 mol l ⁻¹ Na ₂ SO ₄	Capacitance of single crystals	(110) plane 0.1 (100) plane 0.02 (111) plane 0.45	(12)
0.0167 mol l ⁻¹ K ₂ SO ₄	Capacitance	0.1	(9)
0.1N NaOH	Open circuit scrape	-0.08	(8)

partment). When adding the n-butylamine the purification procedure was stopped and the solution left to equilibrate for 12 hr before taking any readings. At all times the test solutions were kept under an atmosphere of N₂.

The electrode impedance was matched as a series combination of resistance and capacitance using a modified Schering bridge. Before each experimental run the test electrode was mechanically polished on roughened glass using bidistilled water as a lubricant, immersed in nitric acid (50%) for 3 sec followed by

a bidistilled water wash and placed in the test solution. The electrode was held on open circuit until stable impedance readings were obtained.

Results

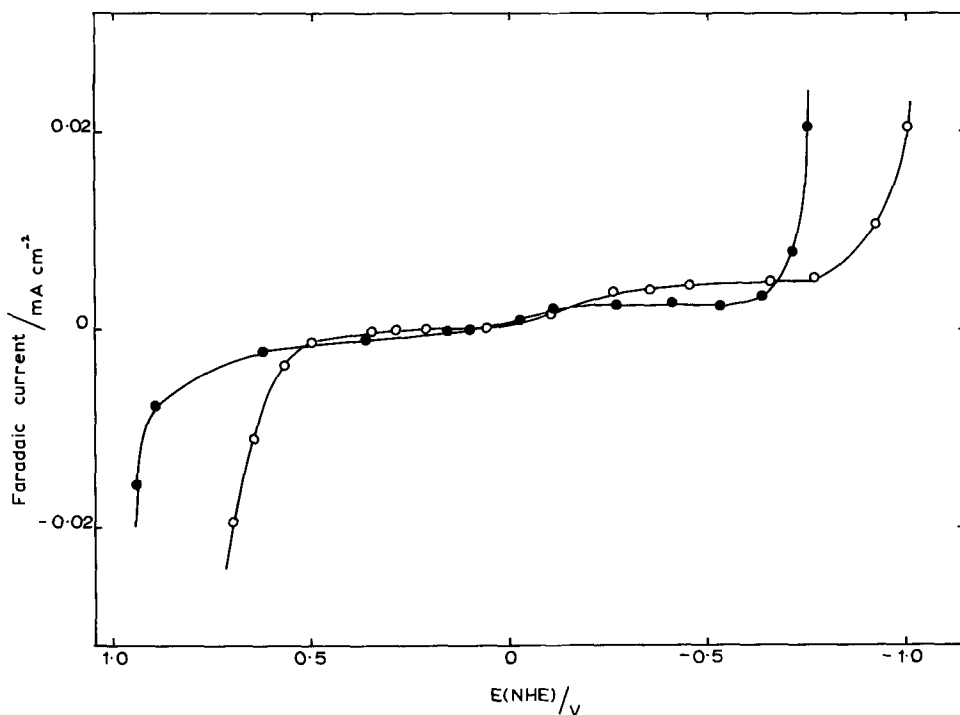
Figure 1 shows typical faradaic current vs. bias potential curves for the electrolytes investigated. The gold electrode is nowhere ideally polarizable however there exists an experimental region in which faradaic current is negligible. The extent of this region is ~0.9- -0.7V for H₂SO₄ and ~0.6- -0.8V for NaOH solutions. The negative extreme of this region is determined by H₂ evolution and the rise at the positive limit can possibly be related to the compression of the solvent monolayer at the electrode by the electric field across the electrical double layer; however, the situation is complicated by OH⁻ adsorption from solution.

The electrode/electrolyte contact times required for electrode stability were ~30 min for both electrolytes, thereafter the electrodes remained reasonably stable for ~24 hr. Electrodes forced to potentials outside the extremes of the polarizable region showed only slight hysteresis in both electrolytes being more predominant at the negative extremity. Stable impedance measurements were rapidly established after small potential changes of the test electrode within the polarizable region, however longer times were required when large capacitance changes occurred for small potential changes.

Figure 2 shows a series of differential capacitance vs. bias potential curves for polycrystalline gold in aqueous NaOH electrolytes. The direction of the potential sweep had no significant effect on the shape and magnitude of the capacitance curves. Impedance readings were reproducible to ± 3% about a mean. The capacitance curves showed a capacitance peak at ~0.4V and a capacitance minimum at -0.26V. Also in Fig. 2 is shown a typical electrode resistance, R_E,³ vs. bias potential curve which shows a rapid rise at the positive extremity of the polarizable region, a peak at ~ -0.25V complementary to the capacitance peak observed and a decrease in resistance at the negative extremity. Figure 3 shows a typical frequency dispersion of the capacitance curves in aqueous NaOH solution. With decreasing frequency the peak observed in

³ It was not possible in the present experiments to correct R_E for electrolyte resistance. Thus values of R_E are only of qualitative significance.

Fig. 1. Typical faradaic current vs. bias potential curves for polycrystalline gold at 23°C. (○) 0.194 mol l⁻¹ NaOH; (●) 0.06 mol l⁻¹ H₂SO₄.



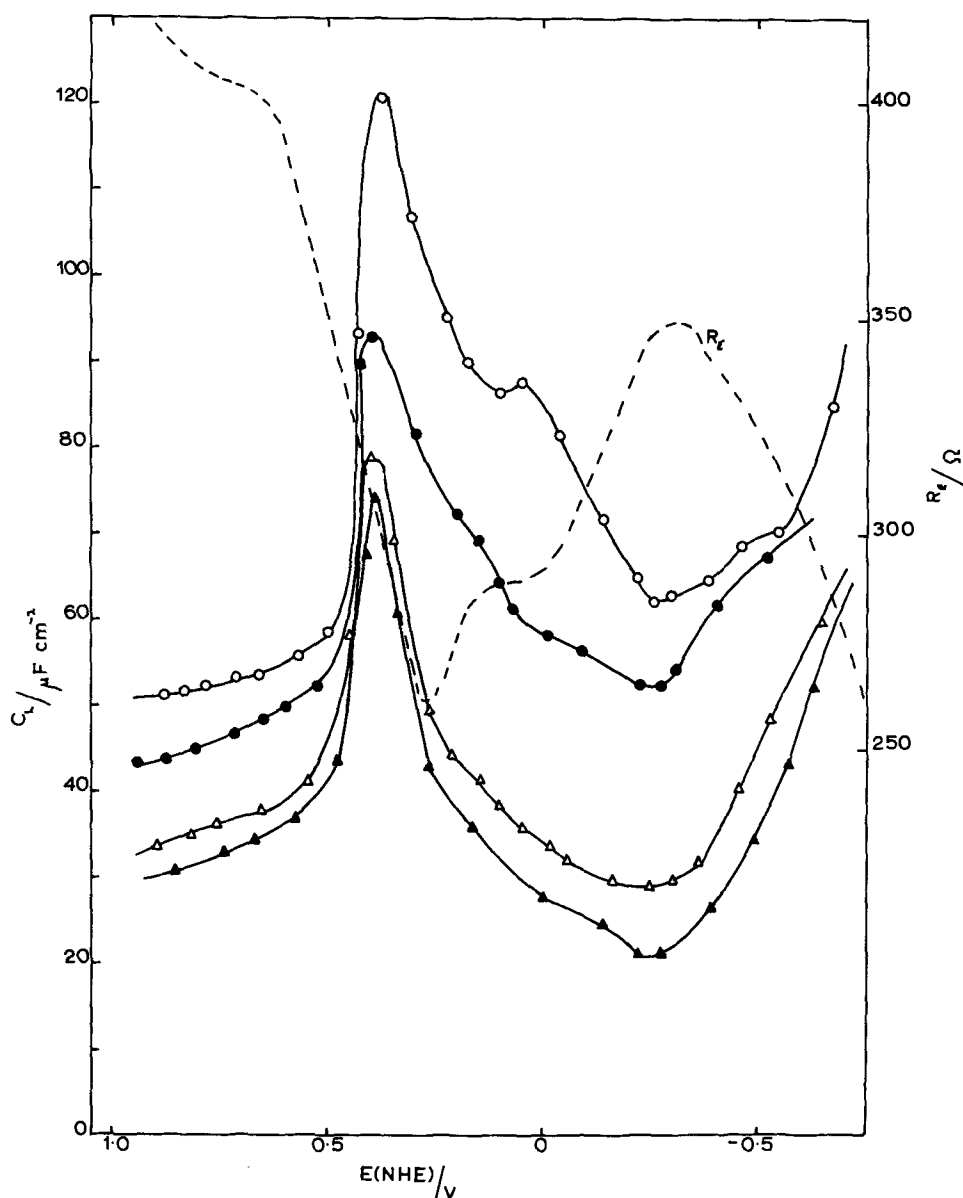


Fig. 2. Differential capacitance curves for polycrystalline gold in aqueous NaOH solutions at 23°C, 1000 Hz; (○) 0.81 mol l⁻¹; (●) 0.194 mol l⁻¹; (△) 0.0635 mol l⁻¹; (▲) 0.0091 mol l⁻¹. Broken line shows electrode resistance, R_E , vs. bias potential at 23°C, 1000 Hz, electrode area 3.48×10^{-2} cm²; 0.81 mol l⁻¹ NaOH.

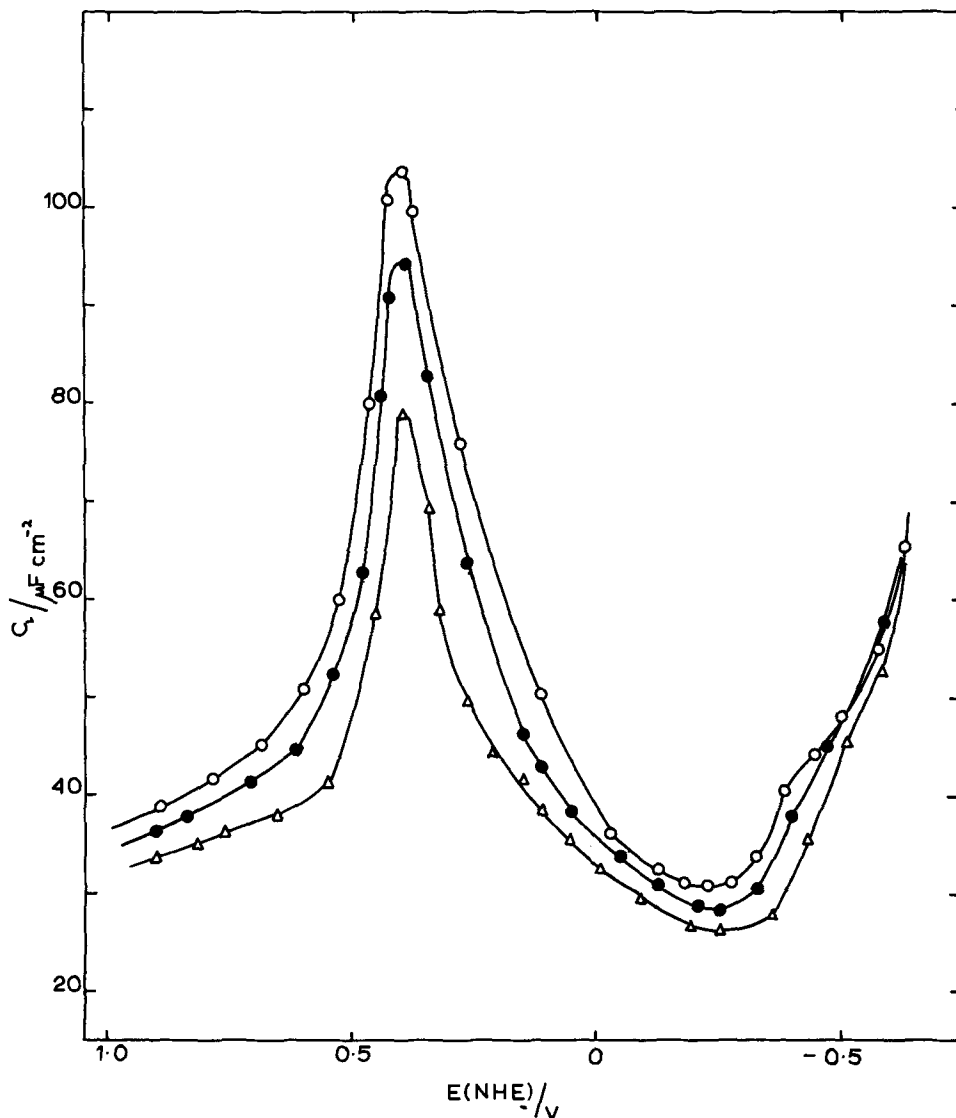
the capacitance curves at ~ 0.4 V increases in magnitude, however for all frequencies a capacitance minimum was observed at -0.26 V at which potential the frequency dispersion tended to be minimal.

Figure 4 shows the influence on the differential capacitance curves of small additions of n-butylamine. The magnitude of the resulting capacitance was reduced by these additions at all potentials within the polarizable region, however at the extremities of the experimental polarizable region the values obtained resembled those in organic free NaOH solutions. The capacitance curves obtained when the potential was varied cathodically showed a capacitance peak at ~ 0.4 V and a capacitance minimum as in organic free NaOH solution, however the capacitance minimum observed was much broader than that observed in organic free NaOH solutions. Anodic potential sweeps gave capacitance curves showing a broad capacitance minimum and an absence of a peak at ~ 0.4 V. For concentrations of n-butylamine greater than 0.03 mol l⁻¹ little further effect on the capacitance curves was observed. The starting potential of both anodic and cathodic potential sweeps were varied and in the case of cathodic sweeps seemed to have little effect on the shape and magnitude of the curves, however for the anodic sweeps with starting potentials > 0.3 V the capacitance peak could be observed whereas for starting potentials < 0.0 V no peak appeared.

Figure 5 shows a series of differential capacitance vs. bias potential curves for polycrystalline gold in aqueous H₂SO₄ solution. The direction of potential sweeping had little effect on the shape and magnitude of the capacitance curves except that the small peak observed at $\sim +0.15$ V in the more concentrated solutions was more pronounced for cathodic sweeps. The capacitance curves were reproducible to $\pm 5\%$ about a mean. All the curves showed a characteristic capacitance peak at ~ 0.8 – 0.85 V and a minimum at 0.33 V. Also on Fig. 5 is shown the electrode resistance, R_E , as a function of bias potential characterized by a rapid rise at both extremities of the polarizable region and a resistance peak at ~ 0.3 V complementary to the capacitance minimum.

Figure 6 shows the influence of additions of low concentrations of n-butylamine on the differential capacitance curves in H₂SO₄ solutions. At the more negative potentials the curves show a progressive lowering of the capacitance values in the concentration range up to 0.03 mol l⁻¹ n-butylamine thereafter further additions having no significant effect on the capacitance curves. At more positive potentials a capacitance peak was observed at a potential corresponding to that of the capacitance peak observed in organic free H₂SO₄ solutions. The direction of the potential sweep and the initial potential had no effect on the curves.

Fig. 3. Typical frequency dispersion of the differential capacitance curves for polycrystalline gold in aqueous NaOH solution (0.0635 mol l⁻¹, 23°C, (○) 120 Hz; (●) 500 Hz; (△) 1000 Hz.



Discussion

The time stability of the electrode impedance, in all the electrolytes investigated indicates that no irreversible chemical or structural changes occur at the electrode surface for potentials within the experimental polarizable region. The magnitude of the differential capacitance is similar to that observed for lead electrodes (39) which have a low roughness factor. This, taken with the small degree of frequency dispersion, indicates that the gold electrode has a relatively smooth surface.

The capacitance minimum in dilute NaOH solutions at -0.26V is well removed from the value of E_z , 0.23V , which has been estimated from work function data. It is suggested that for the potentials studied ($\sim +0.6$ – -0.6V) adsorption of OH^- from solution occurs. This is evidenced by a slight shift in the capacitance minimum (Fig. 2) observed with increasing concentration of NaOH and also by the rise in R_E values at potentials of ~ 0.2 – -0.2V . At the negative extremity the adsorbed species is expelled from the electrode, as would be expected at high negative rational potentials, and results in a decrease in R_E and rise in capacitance values. The fall in R_E and the capacitance peak at $\sim 0.4\text{V}$ could indicate a possible valency change of the adsorbed species at this potential.

In H_2SO_4 solutions the capacitance minimum at 0.33V is in agreement with previous work in which pzc values of Au were reported (Table I), and it appears that the gold electrode interphase is relatively uncomplicated by adsorbed species.

The capacitance peaks, $\sim 0.4\text{V}$ and $\sim 0.8\text{V}$ in Fig. 2 and 5 respectively are associated with adsorption of hydroxyl species from the solutions giving rise to adsorbed OH and O species (30, 32–34) prior to formation of an insoluble gold compound.⁴ The increased frequency dispersion of the capacitance at potentials in the region of the capacitance peak (Fig. 3) indicates that the adsorbed compounds are able to undergo redox reactions at the electrode which can follow changes in the electrode potential.

The adsorption of *n*-butylamine from NaOH solutions shows differing behavior depending on the direction of the potential sweeps. For cathodic sweeps the capacitance peak, associated with hydroxyl adsorption, is unaltered in potential by adsorption of *n*-butylamine; however for anodic sweeps such a peak is absent indicating inhibition of hydroxyl adsorption by an adsorbed organic layer. By starting potential sweeps at more positive potentials the gold electrode is initially covered with a layer of an insoluble gold compound and on moving to more negative potentials this layer is reduced. Starting the sweep from potentials negative with respect to the polarizable region excludes O and OH adsorption leaving the gold electrode free for adsorption of *n*-butylamine and on proceeding to more positive potentials the adsorbed organic layer prevents any adsorption of oxygen species at potentials where the adsorption pseudocapacitance peak is observed for organic free NaOH solutions.

⁴The exact constitution of the insoluble gold film could not be determined by these experiments.

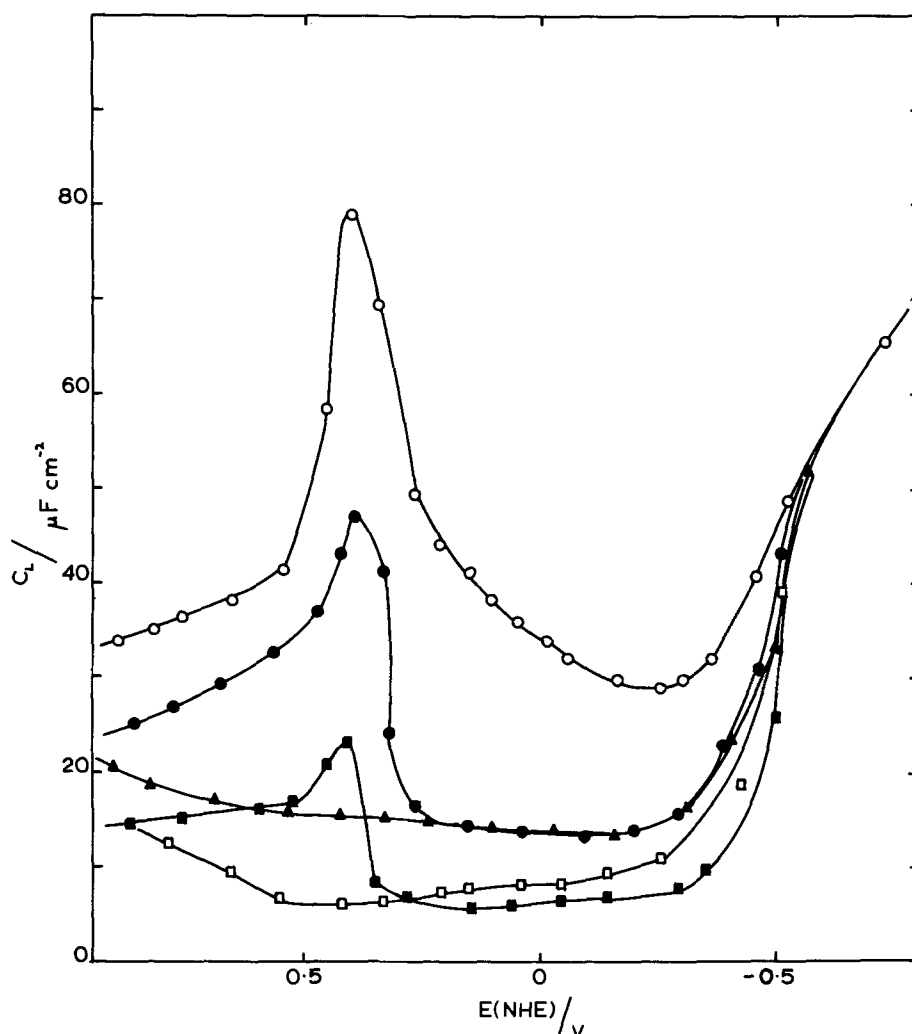


Fig. 4. Effect of addition of n-butylamine on the differential capacitance of polycrystalline gold in aqueous NaOH solution ($0.0635 \text{ mol l}^{-1}$) at 23°C , 1000 Hz. (○) no n-butylamine; (●) 0.003 mol l^{-1} n-butylamine, cathodic potential sweep; (△) 0.003 mol l^{-1} n-butylamine, anodic potential sweep; (■) 0.03 mol l^{-1} n-butylamine, cathodic potential sweep; (□) 0.03 mol l^{-1} n-butylamine, anodic potential sweep.

It is expected that organic molecules which have a lower polarizability than water would be adsorbed at low rational and desorbed at high rational potentials. This type of agreement has been very useful in estimating potential regions where adsorption of an organic substrate is to be expected and the fall of the differential capacitance values in the presence of amine, observed in the present case (Fig. 4 and 6) is fairly typical of the adsorption of aliphatic compounds on Hg from aqueous solution. In the case of NaOH solutions adsorption of n-butylamine causes the largest capacitance reduction (compared with organic free solutions) at potentials neighboring -0.26V indicating that at this potential the gold interphase, although complicated by adsorption, has zero net charge. For acid solutions it is suggested that n-butylamine forms the quaternary ammonium ions which would be expected to be adsorbed at negative rational potentials and desorbed at positive rational potentials. In the present capacitance curves (Fig. 6), it appears that little adsorption occurs at potentials positive of 0.33V but at potentials negative of this value the capacitance magnitude is significantly reduced indicating adsorption and suggests that the pzc of Au is at $0.33 \pm 0.02\text{V}$ in H_2SO_4 solutions.

Conclusions

(i) The pzc of polycrystalline gold in H_2SO_4 solutions is estimated at $0.33 \pm 0.02\text{V}$.

(ii) There is evidence for adsorption of oxygen species at gold electrodes and in the case of NaOH solutions adsorption seems to occur throughout the polarizable region.

(iii) In acid solutions n-butylamine is adsorbed as the quaternary ammonium ion, adsorption only occurring at potentials negative of the pzc. At positive

rational potentials n-butylamine does not appear to be adsorbed to any great extent.

Manuscript submitted July 26, 1971; revised manuscript received ca. Nov. 15, 1971.

Any discussion of this paper will appear in a Discussion Section to be published in the December 1972 JOURNAL.

REFERENCES

1. A. Pfützenreuter and G. Masing, *Z. Metallk.*, **42**, 361 (1951).
2. E. K. Venstren, V. I. Likhtman, and P. A. Rehbinder, *Dokl. Akad. Nauk. SSSR*, **107**, 106 (1956).
3. T. N. Voropaeva, B. V. Deryagin, and B. N. Kabanov, *Kolloidn. Zh.*, **24**, 396 (1962); *Izv. Akad. Nauk. S.S.S.R. Otd. Khim. Nauk.*, 257 (1963).
4. G. M. Schmid and N. Hackerman, *This Journal*, **109**, 243 (1962); **110**, 440 (1963).
5. B. S. Krasikov, *Zh. Prikl. Khim.*, **37**, 2420 (1964); "The Potentials of Zero Charge of Metals and Alloys," LDNTP, Leningrad 1963.
6. M. Green and H. Dahms, *This Journal*, **110**, 466 (1963).
7. T. N. Andersen, R. S. Perkins, and H. Eyring, *J. Am. Chem. Soc.*, **86**, 4496 (1964).
8. D. D. Bode, Jr., T. N. Andersen, and H. Eyring, *J. Phys. Chem.*, **71**, 792 (1967).
9. M. Petit and J. Clavilier, *Compt. Rend., Ser. C*, **265**, 145 (1967).
10. J. Clavilier, A. Hamelin, and G. Valette, *ibid.*, **265**, 221 (1967).
11. J. O'M. Bockris, S. D. Argade, and E. Gileadi, *Electrochim. Acta*, **14**, 1259 (1969).
12. A. Hamelin, M. Sotro, and G. Valette, *Compt. Rend., Ser. C*, **268**, 213 (1969).
13. A. Hamelin and J. Lecoqeur, *Coll. Czech. Chem. Commun.*, **36**, 714 (1971).
14. J. Clavilier and N. Van Houg, *Compt. Rend., Ser. C*, **270**, 982 (1970).

Fig. 5. Differential capacitance curves for polycrystalline gold in aqueous H_2SO_4 solutions at 23°C, 1000 Hz. (○) 0.45 mol l^{-1} , cathodic potential sweep; (●) 0.45 mol l^{-1} , anodic potential sweep; (□) 0.06 mol l^{-1} , anodic potential sweep; (△) 0.0087 mol l^{-1} , anodic potential sweep. Broken line shows electrode resistance, R_E , vs. bias potential at 23°C, 1000 Hz, electrode area $3.48 \times 10^{-2} \text{ cm}^2$, 0.45 mol $l^{-1} H_2SO_4$.

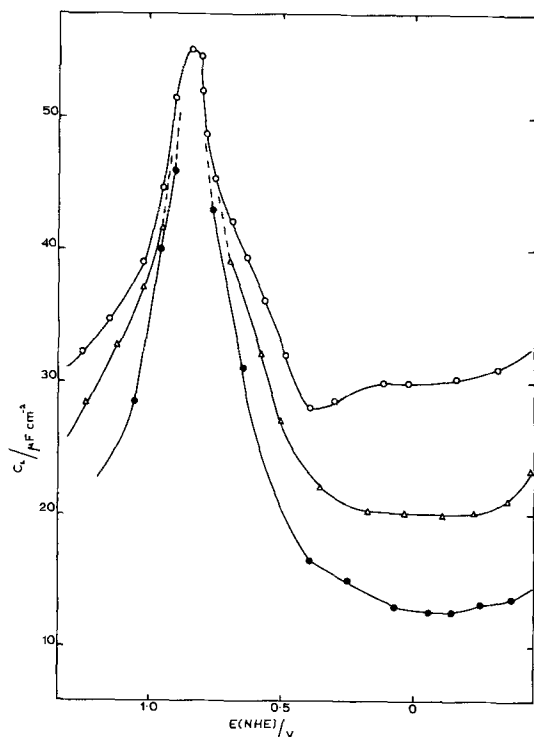
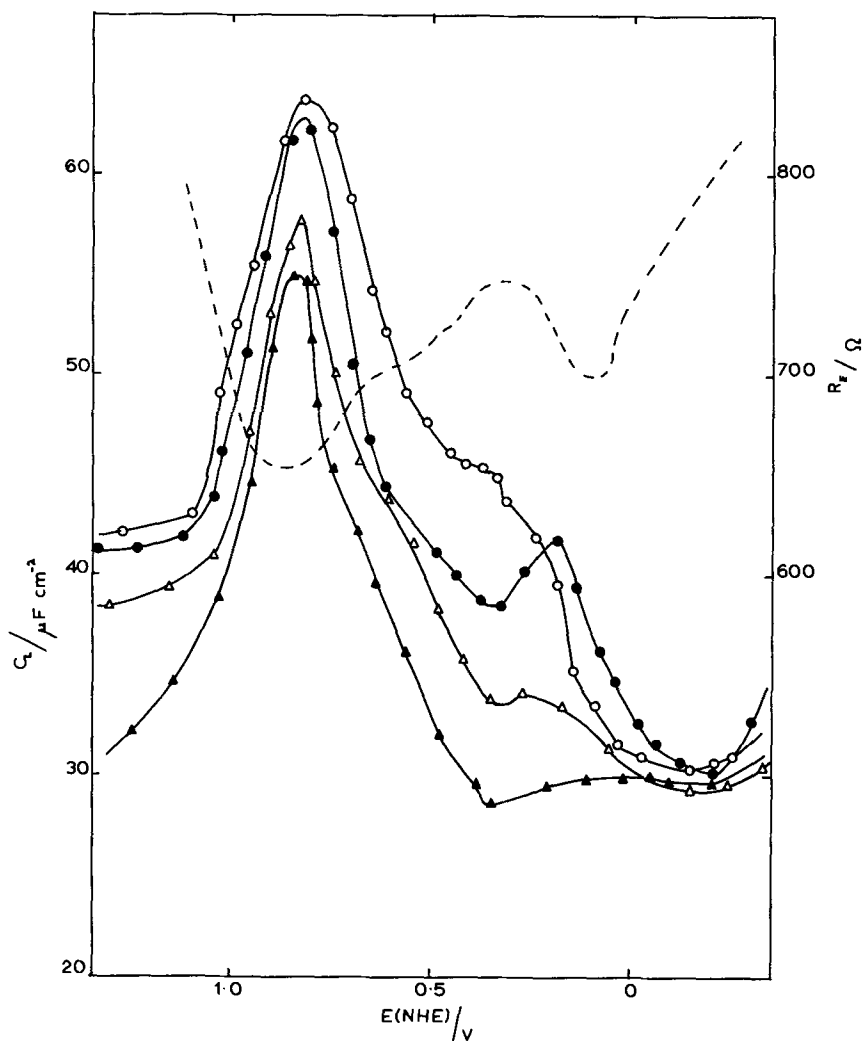


Fig. 6. Effect of addition of *n*-butylamine on the differential capacitance of polycrystalline gold in aqueous H_2SO_4 solution (0.0087 mol l^{-1}) at 23°C, 1000 Hz, anodic potential sweep. (○) no *n*-butylamine; (△) 0.003 mol l^{-1} *n*-butylamine; (●) 0.03 mol l^{-1} *n*-butylamine.

15. V. S. Fomenko, "The Emission Properties of the Chemical Elements and their Compounds," Naukova Dumka (1964).
16. V. Jendrasic, *J. Electroanal. Chem.*, **32**, 157 (1969).
17. T. R. Beck, Paper presented at the 19th Meeting of CITCE, Detroit, September, 1968.
18. F. H. Jeffery, *Trans. Faraday Soc.*, **11**, 172 (1915).
19. F. Jirsa and O. Buryanek, *Z. Elektrochem.*, **29**, 126 (1923).
20. F. Jirsa and H. Jelinek, *ibid.*, **30**, 286, 534 (1924).
21. R. H. Gerke and M. D. Rourke, *J. Am. Chem. Soc.*, **49**, 1855 (1927).
22. T. F. Buehrer and W. E. Roseveare, *ibid.*, **49**, 1989 (1927).
23. W. J. Shutt and A. Walton, *Trans. Faraday Soc.*, **30**, 914 (1934).
24. G. Armstrong, F. R. Himsworth, and J. A. V. Butler, *Proc. Roy. Soc.*, **143A**, 89 (1934).
25. G. Deborin and B. V. Ershler, *Acta Physicochem. URSS*, **13**, 347 (1940).
26. A. Hickling, *Trans. Faraday Soc.*, **42**, 518 (1946).
27. S. E. S. El Wakkad and A. M. Shams El Din, *J. Chem. Soc.*, **9**, 3098 (1954).
28. F. Bauman and I. Shain, *Anal. Chem.*, **29**, 303 (1957).
29. S. Barnatt, *This Journal*, **106**, 722 (1959).
30. H. A. Laitinen and M. S. Chao, *ibid.*, **108**, 726 (1961).
31. S. B. Brummer and A. C. Makrides, *ibid.*, **111**, 1122 (1964).
32. G. M. Schmid and R. W. O'Brien, *ibid.*, **111**, 832 (1964).
33. F. F. Faizullin and N. P. Nikandrov, *Elektrokhimiya*, **3**, 988 (1967).
34. J. N. Gaur and G. M. Schmid, *J. Electroanal. Chem.*, **24**, 279 (1970).
35. M. Pourbaix, "Atlas d'équilibres Electrochimique," p. 399, Paris (1963).

36. J. P. G. Farr and N. A. Hampson, *Trans. Faraday Soc.*, **62**, 3494 (1966).
37. D. Armstrong, N. A. Hampson, and R. J. Latham, *J. Electroanal. Chem.*, **23**, 361 (1969).
38. J. T. Clarke, G. S. Dale, R. J. Latham, and J. R. Morley, *Lab. Pract.*, **18**, 950 (1969).
39. J. P. Carr, N. A. Hampson, S. N. Holley, and R. Taylor, *In press*.

A Study of the Adsorption and Desorption of Iodine and Iodide at Platinum Electrodes in 1.0M Sulfuric Acid

Dennis C. Johnson*

Department of Chemistry, Iowa State University, Ames, Iowa 50010

ABSTRACT

Various reactions involving adsorption and desorption of I_2 and I^- at platinum electrodes in 1.0M H_2SO_4 were studied using a rotating, ring-disk electrode. Reversibly adsorbed I_2 was found to be desorbed in the potential region of the limiting current for the oxidation of I^- to I_2 . Iodine was found to coexist with I^- in an irreversible state of adsorption. The irreversibly adsorbed I_2 is electrochemically reduced to I^- at $E < 0.1V$ vs. SCE. The presence of irreversibly adsorbed I_2 was determined to result in a positive shift of the potential for desorption of I_2 from the reversible state of adsorption. Also found was evidence that I_2 will slowly pass from the reversible to the irreversible state of adsorption at an electrode surface covered with irreversibly adsorbed I^- .

The adsorption and desorption of I_2 and I^- at platinum electrodes in acidic media have been studied using radiochemical (1-10) and electrochemical (8, 11-17) methods. Iodide ions are rapidly adsorbed on a platinum surface which previously has been electrochemically reduced. The adsorption process is irreversible and the adsorbed I^- is not removed if the electrode is taken from the solution and the surface rinsed with an I^- -free solution of electrolyte (17). Nor is the adsorbed I^- oxidized if the potential of the electrode is adjusted to a value at which I^- from the bulk solution is oxidized to I_2 at the electrode surface (17). This absence of any apparent electroactivity for adsorbed I^- led some investigators to conclude that I^- is not adsorbed at platinum surfaces (15). The maximum coverage of a platinum electrode by irreversibly adsorbed I^- was reported as 1.5×10^{-9} g ion/cm² (5) on the basis of radiochemical data and 1.6×10^{-9} g ion/cm² (17) on the basis of electrochemical data. Irreversibly adsorbed I^- is removed from the electrode surface when the potential of the electrode is adjusted to a value at which I^- is oxidized to IO_3^- (5, 10, 17), e.g., $E > 1.1V$ vs. SCE for 1.0M H_2SO_4 . Oxidation of the platinum surface occurs simultaneously. There is no adsorption of I^- at a platinum surface covered with platinum oxide (7, 9, 10, 17).

Studies using electrochemical techniques (8, 13-17) resulted in conclusions that I_2 is adsorbed at platinum surfaces. Hubbard, Osteryoung, and Anson (17), using thin-layer cells and radiochemical tracers, differentiated between reversible and irreversible adsorption of I_2 . They determined that I_2 is adsorbed by an irreversible process at a platinum surface bearing no adsorbed I^- . They reported a surface coverage by irreversibly adsorbed I_2 equal to 1.6×10^{-9} mol/cm² at an electrode in $1.00 \times 10^{-3}M$ I_2 . These authors showed that I_2 is adsorbed by a reversible process at a platinum surface covered with I^- or I_2 adsorbed in irreversible states. They reported that the coverage by reversibly adsorbed I_2 is 0.9×10^{-9} mol/cm² at such an electrode in $1.14 \times 10^{-3}M$ I_2 (17). Iodine adsorbed in both reversible and irreversible states is reportedly removed electrochemically from the electrode surface during anodization, being oxidized to IO_3^- (17).

The purpose of this research was the correlation of the various adsorption and desorption processes for I^- and I_2 with the observed current-potential behavior of platinum electrodes in 1.0M H_2SO_4 containing NaI. This study was made using a rotating ring-disk electrode (RRDE) for which both the ring and the disk electrodes were platinum. Use of a RRDE for investigating mechanisms of electrode reactions has been described (18-23). Johnson and Bruckenstein (24) reported use of a RRDE for study of the adsorption and desorption of Br^- at a platinum electrode in 1.0M H_2SO_4 . Bromide is adsorbed by an irreversible process and is oxidized to $HOBr$ at $E > 1.25V$ vs. SCE. Bromine is not adsorbed in observable quantities in this media.

Experimental

Instrumentation.—The RRDE used in this study was constructed by Pine Instrument Company of Grove City, Pennsylvania. The electrode dimensions are given in Table I of Ref. (23) where the electrode is designated as B. For this electrode $\alpha = 0.089$, $\beta^{2/3} = 0.151$, and $N = 0.090$. The geometric area of the disk electrode equals 0.470 cm². The bipotentiostat used is described in Ref. (22). Signal voltages were obtained from the circuit described in Ref. (25). Current-potential ($I-E$) curves were recorded on an Electronic Associates Inc., Model 1131, XYY' Recorder. The electrolysis cell is described in Ref. (24). Experimental work was performed at $25^\circ \pm 2^\circ C$. Integration of $I-E$ data was performed on the original $I-E$ recordings using a Keuffel and Esser Compensating Polar Planimeter.

Chemicals.—1.0M H_2SO_4 and solutions of NaI were prepared using Mallinckrodt Analytical Reagents. All water was triply distilled with a deionization following the first distillation and the second distillation being from alkaline permanganate. Due to the heat resulting from addition of concentrated H_2SO_4 to water, the 1.0M H_2SO_4 was cooled to room temperature before stock solution of NaI was added. At room temperature, oxidation of I^- to I_2 by O_2 in 1.0M H_2SO_4 was found to be negligible. Solutions were deaerated prior to the electrochemical experiments using Air Products Pre-purified N_2 (99.9995%) saturated with H_2O . During experimentation, an N_2 atmosphere was maintained over the solution.

* Electrochemical Society Active Member.

Key words: rotating ring-disk electrode, iodide adsorption, iodine adsorption, platinum electrode.

Notation.—Notation used is that described in Ref. (24). All potentials were measured and are reported in V vs. SCE.

Current-potential curves.—The surface of the RRDE was polished with 0.3μ Buehler alumina on Buehler microcloth using water as lubricant and then thoroughly rinsed with triply distilled water. Following insertion of the electrode into a solution, E_d was scanned approximately 100 times between the limits $E_d^a = 1.6V$ and $E_d^c = -0.2V$. Except as stated otherwise, electrical treatment prior to recording I - E data consisted of scanning E_d between the limits specified by that experiment until the I - E curves produced on subsequent scans were reproducible. The I - E curves for the second and third scans were invariably identical. All scans of E_d had a triangular wave form.

To determine I - E behavior of soluble and electroactive species produced by reactions at the surface of the disk electrode, I_r was recorded vs. E_d , during the triangular potential scan, for fixed values of E_r . Values of E_r were varied by 50 mV increments between the potential limits set by solvent decomposition. The shapes of I_r - E_d curves is determined by: (i) convective-diffusional transport of electroactive species present in the bulk of the solution to the ring electrode, (ii) collection of a fraction of any electroactive species produced at the disk electrode, and (iii) decrease of the flux of an electroactive species at the surface of the ring electrode due to reactions at the disk surface (22).

Variations of the I_d - E_d and I_r - E_d curves obtained for particular values of E_r , while scanning E_d , which resulted from changes in the bulk concentration of I^- , scan rate of E_d , or rotation velocity of the electrode were diagnostically used to differentiate processes limited by the surface area of the disk electrode from those limited by the rate of convective-diffusional mass transport. Electrical currents from electrochemical processes limited by the rate of mass transport show linear dependences on bulk concentration and the square root of rotation velocity and no dependence on the rate of potential scan after correcting for charging current. Electrical currents from electrochemical processes limited by the surface area of the electrode are proportional to the scan rate of applied potential. Because the scan of E_d was a linear function of time, the I_r - E_d curves were also I_r - t curves. The quantity of an electroactive species involved in a reaction controlled by the surface area of the disk electrode was estimated from the difference in the time integrals of the I_r - E_d curves obtained at rates of E_d scan equal to 6.0 V/min and 0.0 V/min over the potential region where the reaction occurred. The I_r - E_d curve for an effective scan rate of 0.0 V/min was determined as the best smooth curve fitting steady-state values of I_r measured at fixed values of E_d . At a scan rate of 6.0 V/min and the rotation speed used (2500 RPM), the average time required for transit of electroactive species from the disk electrode to the ring electrode was negligible (80 msec). Evidence is presented that this procedure may be in error for surface processes occurring in the vicinity of the $E_{1/2}$ of the I - E curve for the species involved in the surface process.

Results and Discussion

I_d - E_d curves for NaI.—A I_d - E_d curve obtained for 1.0M H_2SO_4 containing $3.0 \times 10^{-4}M$ NaI is shown in Fig. 1. The solid and dashed lines correspond to the anodic and cathodic portions, respectively, of the triangular scan of E_d at 6.0 V/min. The dotted line between 0.4 and 0.7V corresponds to the curve obtained under steady-state conditions, i.e., an effective scan rate of 0.0 V/min. This was included to assist in distinguishing surface-controlled processes from those limited by the rate of convective-diffusional mass transport.

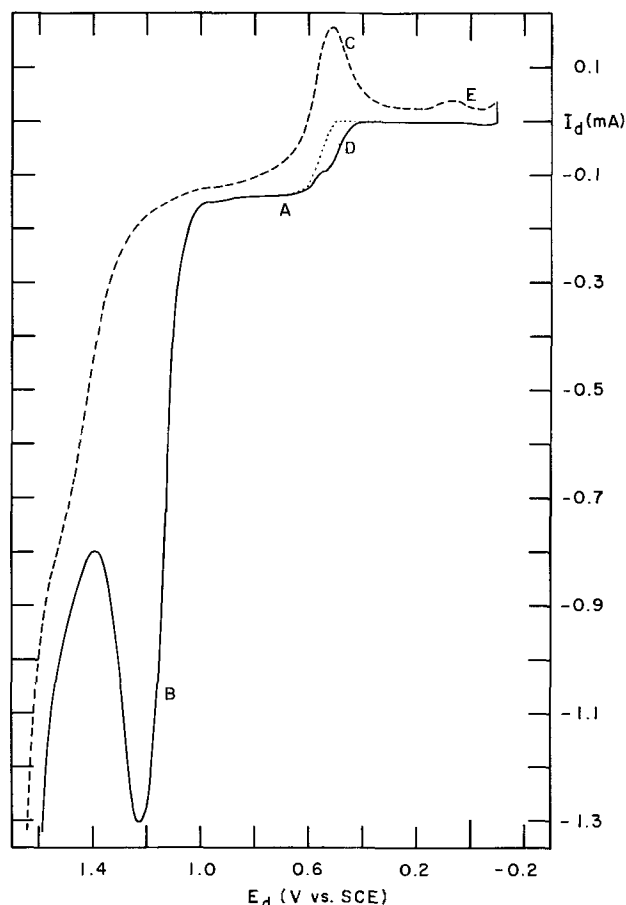


Fig. 1. I_d - E_d curve for $3.0 \times 10^{-4}M$ NaI in 1.0M H_2SO_4 ; 1600 rev/min, 6.0 V/min. $E_d^a = 1.6V$, $E_d^c = -0.2V$, — is anodic scan, - - - is cathodic scan, is steady-state curve.

Wave A in Fig. 1, with a limiting-current plateau between 0.6 and 1.0V, results from the oxidation of I^- to I_2 . The anodic peak, B, obtained for $E_d > 1.0V$ results from oxidation of I^- to IO_3^- at the electrode surface (17). The production of IO_3^- does not result in a limiting-current plateau and is apparently inhibited by the formation of platinum oxide on the electrode surface. The cathodic peak at 0.6V, C, observed during the cathodic E_d scan is the result of reduction of the platinum oxide formed during the anodic potential scan for $E_d > 1.1V$.

The prewave to wave A, designated D in Fig. 1, results from the oxidation of I^- at the electrode surface and adsorption of the I_2 produced. This process occurs at potentials less than those predicted by the Nernst equation when calculated for a soluble product because of the stabilization of I_2 by adsorption. The height of the prewave was found to be a linear function of the scan rate of E_d as is expected for a surface-controlled process such as adsorption.

Oxygen is evolved at the disk electrode for $E_d > 1.4V$ and H_2 is evolved for $E_d < -0.2V$.

I_r - E_d curves for NaI.— I_r - E_d curves were obtained at various values of E_r under the conditions of Fig. 1. Figure 2 contains curves for selected values of E_r . The I_d - E_d curves recorded simultaneously were identical to that of Fig. 1. Wave P in Fig. 2 obtained at $E_r = 0.0$ and 0.2V results from the reduction of soluble I_2 produced at the disk electrode by oxidation of I^- , wave A of Fig. 1, which is transported to the ring electrode by convective-diffusional processes. The ratio of ring-to-disk currents at $E_d = 0.7V$ is -0.094 which compares favorably with the value of $-N$ for this electrode. From I_r - E_r curves obtained in 1.0M H_2SO_4 containing $NaIO_3$ and O_2 it was determined that IO_3^-

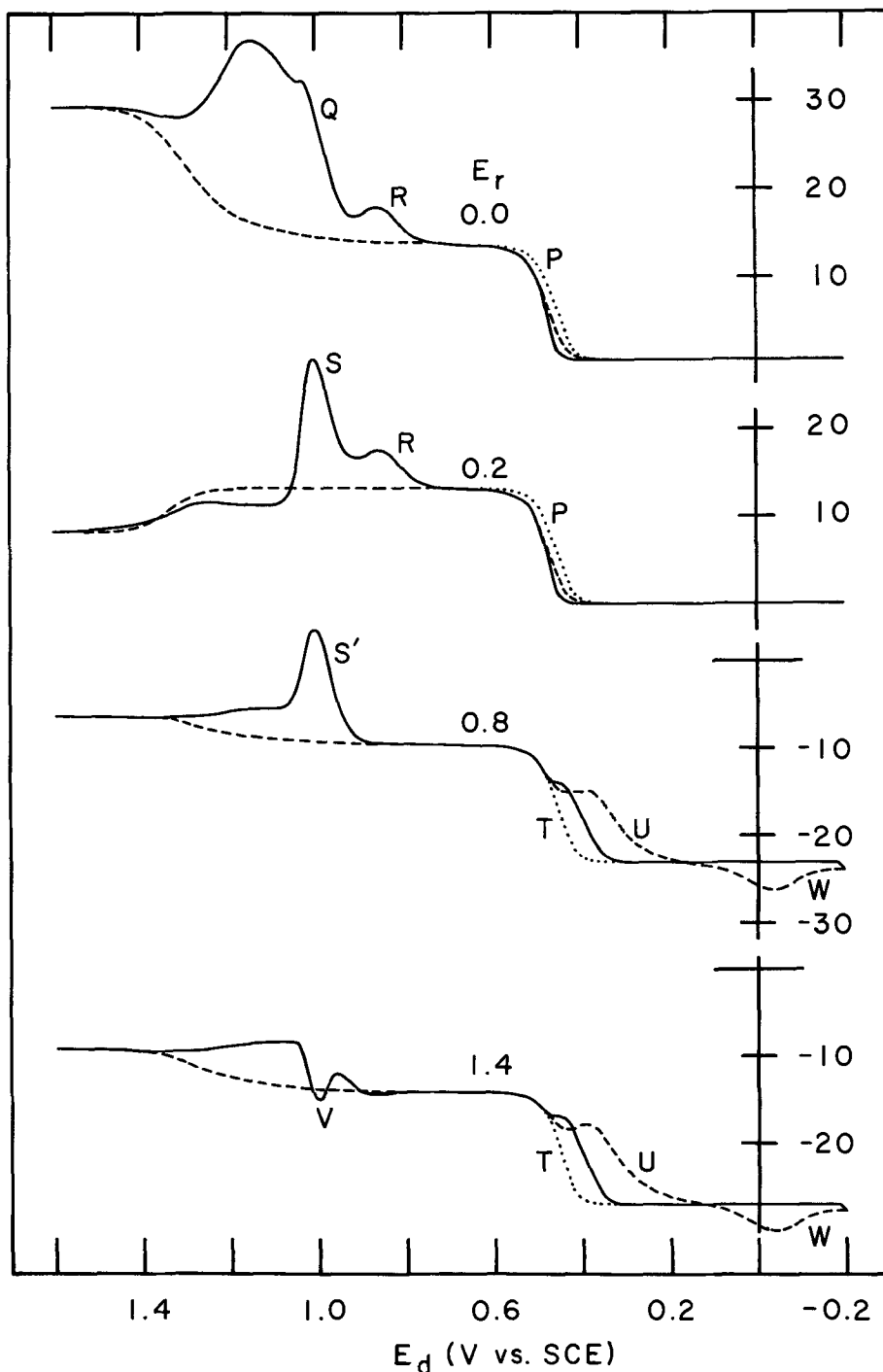


Fig. 2. I_r - E_d curves for $3.0 \times 10^{-4}M$ NaI in $1.0M$ H_2SO_4 ; 1600 rev/min, 6.0 V/min, $E_d^a = 1.6V$, $E_d^c = -0.2V$ ——— is anodic scan, - - - - is cathodic scan, ······ is steady-state curve.

and O_2 are reduced at a platinum-ring electrode at $E_r < 0.1V$. Iodate ions produced at the disk electrode during the anodic E_d scan in the region of wave B are reduced at the ring electrode when $E_r = 0.0V$ with the resultant appearance of wave Q.

No I_2 reaches the ring electrode when E_d is in the region of wave D during the anodic potential scan. This is consistent with the interpretation of wave D wherein I^- is oxidized to I_2 which is adsorbed at the surface of the disk electrode.

Peak R observed during the anodic scan of E_d results from a species which was found to have the electrochemical properties of I_2 . Because of the absence of a significant peak on the I_d - E_d curve of Fig. 1 in this region of the I_d - E_d curve, it is my conclusion that this I_2 is produced at the disk electrode by a desorption process.

Iodate and O_2 are not reduced at the ring electrode in $1.0M$ H_2SO_4 for $E_r \approx 0.2V$. The I_r - E_d curve shown

for $E_r = 0.2V$ is identical to those obtained for $0.2V < E_r \leq 0.4V$. Again, a peak is observed for the reduction of the I_2 desorbed at the disk surface during the anodic scan at $E_d = 0.8V$. Peak S observed at $E_d = 1.0V$ cannot be the result of reduction of IO_3^- or I_2 at the ring electrode. The height of peak S was found to be nearly independent of the scan rate of E_d contrary to the behavior expected for a surface-controlled process. The peak height is a linear function of C_T^{-b} and $\omega^{1/2}$. Apparently, the species whose reduction produces peak S is an intermediate in the production of IO_3^- at the disk electrode, possibly $I(+1)$.

For $E_r = 0.8V$, I^- is oxidized quantitatively to I_2 at the ring electrode. The I_r - E_d curve shown for $E_r = 0.8V$ is identical to those obtained for $0.6V \leq E_r \leq 0.9V$. The ratio of I_r measured at $E_d = 0.2V$ to I_d measured at $E_d = 0.6V$ is 0.164 in fair agreement with the value of $\beta^{2/3}$ for this electrode. A cathodic ring current, peak S', was obtained at $E_d = 1.05V$ for the spe-

cies concluded to be an intermediate in the production of IO_3^- at the disk electrode. This is evidence sufficient to prove that species is not I_2 .

The difference between the I_r - E_d curve for $E_r = 0.8\text{V}$ obtained during the anodic scan of E_d at 6.0 V/min and the steady-state curve in the region designated T is the result of consumption of I^- at the disk electrode. Wave D is obtained simultaneously on the I_d - E_d curve. This result is consistent with the conclusion that I^- is oxidized to I_2 , in the region of wave D, which is subsequently adsorbed at the disk surface.

The interpretation of the portion of the I_d - E_d curve of Fig. 1 obtained during the cathodic scan of E_d is complicated by the large cathodic current resulting from reduction of platinum oxide. On the basis of radiochemical studies it has been concluded that I^- is not adsorbed at a platinum surface covered with oxide (7, 9, 10). The reduction of platinum oxide in this study during the cathodic scan of E_d for $E_d < 0.5\text{V}$ results in electrochemical preparation of the disk surface for I^- adsorption. The adsorption of I^- at the disk electrode results in the shielding of the flux of I^- at the ring electrode and wave U results on the I_r - E_d curve obtained at $E_r = 0.80\text{V}$. Inspection of the I_r - E_d curve for $E_r = 0.2\text{V}$ reveals that no I_2 is collected at the ring in this region of the I - E curve.

Some IO_3^- is produced at the ring electrode by oxidation of I^- for $E_r = 1.4\text{V}$. As a result the anodic currents observed when $E_d < 0.5\text{V}$ for $E_r = 1.4\text{V}$ are greater than for $E_r = 0.8\text{V}$. The intermediate from the production of IO_3^- at the disk electrode, detected at the ring electrode during the anodic scan of E_d , is oxidized at the ring electrode for $E_r = 1.4\text{V}$, peak V. The oxidation product presumably is IO_3^- .

Intermediate from the production of IO_3^- .—Figure 3 is of the approximate I_r - E_r curve constructed for the electroactive species which was detected at the ring electrode during the anodic scan of E_d at $E_d = 1.05\text{V}$ and concluded to be an intermediate in the electrochemical production of IO_3^- . The curve is of the difference between I_r measured at $E_d = 1.05\text{V}$ and that measured at $E_d = 0.8\text{V}$ plotted vs. E_r . The curve reflects the fact that the intermediate species can be oxidized and reduced at the ring electrode. The anodic process at the ring electrode for $E_r > 1.1\text{V}$ is quite irreversible which may be the result of platinum oxide present on the ring surface.

In an earlier study of the adsorption of Br^- at a platinum electrode (24), it was determined that the adsorbed Br^- is oxidized and desorbed as HOBr during the anodic potential scan. It might appear consistent in this study that adsorbed I^- is the precursor of the species concluded to be the intermediate. This is not the case, however. As stated earlier, the height of peak S is a linear function of $\omega^{1/2}$ and C_1^{-b} and independent of the scan rate of E_d . These evidences are not characteristic of a desorption process. Further sup-

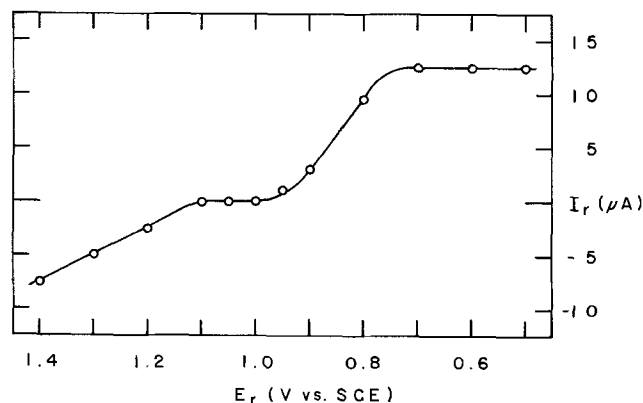


Fig. 3. I_r - E_d curve for intermediate detected at onset of oxidation of I^- to IO_3^- ; $3.0 \times 10^{-4}\text{M NaI}$, $1.0\text{M H}_2\text{SO}_4$, 1600 rev/min , 6.0 V/min .

port for the conclusion that the species which produces peak S does not originate as irreversibly adsorbed I^- is given below. Essentially it is that no adsorbed I^- was determined to be desorbed from an electrode during the anodic scan of E_d until $E_d > 1.1\text{V}$. The species in question is produced at the disk electrode during the anodic scan of E_d in the region of the I_d - E_d curve corresponding to onset of the oxidation of I^- to IO_3^- . No experimental evidence was obtained which is inconsistent with the conclusion that the species is an intermediate in the electrochemical oxidation of I^- to IO_3^- at the disk electrode.

No intermediate was detected during a cathodic scan of E_d originating at $E_d > 1.2\text{V}$. Figure 1 reflects the inhibition of the production of IO_3^- at the disk electrode due to the formation of platinum oxide. As reported in a later section, formation of platinum oxide was found to occur with the concurrent loss of irreversibly adsorbed I^- . This change in the surface composition of the disk electrode probably results in a change of the mechanism for IO_3^- production to one in which this intermediate is not involved.

Attempts to prepare solutions of HIO and obtain its I - E characteristics failed. HIO rapidly decomposes to IO_3^- and I_2 in acidic media.

Irreversible adsorption of I_2 .—Hubbard, Osteryoung, and Anson (17) determined that both I^- and I_2 are adsorbed at a reduced platinum surface in solutions of I^- or I_2 , respectively. The adsorption processes are irreversible and both species are removed from the electrode by oxidation to IO_3^- at $E > 1.1\text{V}$. These authors found that $1.6 \times 10^{-9}\text{ mol/cm}^2$ of I_2 is adsorbed in an irreversible state at a platinum electrode in $1.00 \times 10^{-3}\text{M I}_2$.

The reduction of platinum oxide at the disk surface in $1.0\text{M H}_2\text{SO}_4$ occurs on the cathodic scan of E_d at a value where both I_2 and I^- are present at the electrode surface (see Fig. 1 and 2). These two species are probably simultaneously adsorbed at the disk surface and may coexist in their respective irreversible states of adsorption. The I_d - E_d curve of Fig. 1 obtained at 6.0 V/min has a cathodic peak, E, on the cathodic half of the potential scan at $E_d = 0.0\text{V}$. The I_r - E_d curve of Fig. 2 obtained for $E_r = 0.8\text{V}$ has an anodic peak, W, which was obtained simultaneously with the appearance of peak E. The species produced at the disk electrode was found to have the electrochemical properties of I^- . It is my conclusion that peak E results from the electrochemical reduction of I_2 present at the disk surface in an irreversible state of adsorption. Further experimental evidence supporting this conclusion is that if, during the cathodic scan of E_d , the value of E_d is stepped rather than scanned over the region from 0.6 to 0.3V , peaks E and W are not obtained. In this experiment the I_2 produced at the disk surface of the rotating electrode when $E_d > 0.6\text{V}$ is transported away from the electrode surface before the platinum oxide is electrochemically removed from the disk electrode and only I^- is adsorbed. The ratio of the height of peak W to peak E, correcting for charging current at the disk electrode, equals -0.09 approximately the value of $-N$ for this electrode.

Isotherm for irreversible adsorption of I^- .—The adsorption isotherm for I^- at the platinum disk electrode in $1.0\text{M H}_2\text{SO}_4$ was determined using the RRDE according to a procedure described by Bruckenstein and Napp (26). Advantage was taken of the fact that I^- cannot remain adsorbed at the disk electrode when $E_d = 1.6\text{V}$ (17) and that adsorption proceeds after E_d is stepped to a value at which the surface oxide is reduced. The surface coverage by irreversibly adsorbed I^- was calculated as a function of C_1^{-b} from I_r - t curves obtained for $E_r = 0.8\text{V}$ when E_d was stepped from 1.6 to 0.2V and to -0.1V . It was concluded earlier that no I_2 is adsorbed by an irreversible process under these conditions. The adsorption isotherms calculated

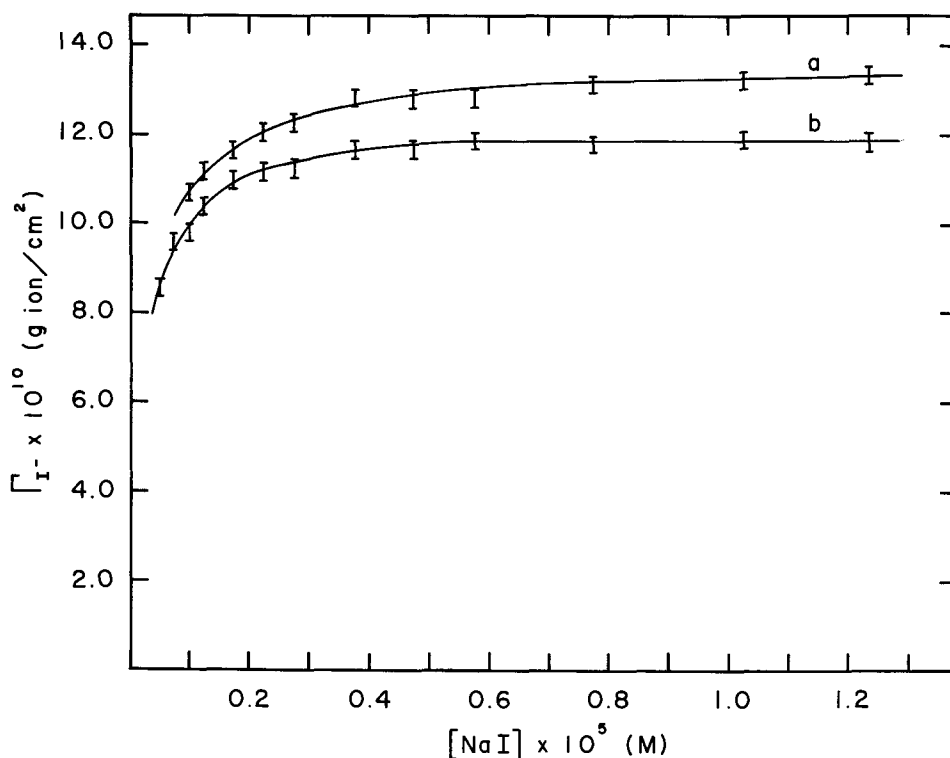


Fig. 4. Isotherm for I^- adsorbed in irreversible state at platinum disk electrode; 1.0M H_2SO_4 ; a, results for E_d step to 0.2V vs. SCE, b, results for E_d step to $-0.1V$ vs. SCE.

are given in Fig. 4. The maximum surface coverage observed at 0.2V is 1.3×10^{-9} g ion/cm² and at $-0.1V$ is 1.2×10^{-9} g ion/cm². These values are in fair agreement with those obtained by electrochemical (17) and radiochemical (10) techniques in view of the possible differences in surface roughness of the electrodes used in the various studies.

The value of E_d for which desorption of I^- commences on an anodic potential scan was determined by measuring the quantity of I^- adsorbed following a step of E_d from various anodic values to 0.2V. From this study it was found that no I^- is desorbed for $E \leq 1.1V$ and that the desorption is complete for $E \geq 1.4V$.

Reversible adsorption of I_2 .—Figure 5 is of I_d - E_d and I_r - E_d curves obtained for 1.0M H_2SO_4 containing NaI. For these curves $E_d^a = 1.0V$ and $E_d^c = -0.2V$. Within these scan limits the disk surface is not oxidized and I^- adsorbed in an irreversible state is not oxidized or desorbed. As a result there is no irreversibly adsorbed I_2 at the electrode surface as evidenced by the absence of peaks E and W. Production and adsorption of I_2 at the disk electrode by oxidation of I^- results in wave D on the I_d - E_d curve obtained during the anodic scan of E_d . This adsorption occurs at an electrode surface covered by irreversibly adsorbed I^- and is a reversible process (17). For $E_d < 0.4V$ on the cathodic scan, the reversible adsorbed I_2 is reduced to I^- resulting in peak F on the I_d - E_d curve. The I^- produced is soluble and the resulting increase in the flux of I^- at the ring electrode in excess of the steady-state value results in peak Y for $E_r = 0.8V$. The surface coverage of the disk electrode by reversibly adsorbed I_2 was calculated from the difference between the time integrals of the I_r - E_d curves, for $E_r = 0.8V$, obtained on the cathodic scan of E_d at scan rates equal to 6.0 V/min. and 0.0 V/min. The isotherms are shown in Fig. 6. Curves a and b correspond to those obtained by integration from 0.60 to 0.35V and to 0.15V, respectively. The isotherms in Fig. 6 do not show a limiting surface coverage as C_{1-b} is increased. Hubbard, Osteryoung, and Anson found that 9×10^{-10} mol/cm² of I_2 is adsorbed in the reversible state at a platinum electrode in $1.14 \times 10^{-3}M$ I_2 .

Peak R is observed on the I_r - E_d curve of Fig. 5 for $E_r = 0.2V$. The presence of this peak is concluded to result from the reduction at the ring electrode of I_2 produced at the disk surface by desorption of I_2 from

the reversible state of adsorption. Following reversal of the E_d scan at 1.0V, I_2 is reabsorbed at the disk surface, when $E_d < 0.9V$, resulting in peak X on the I_r - E_d curve in Fig. 5. Cycling E_d between the limits $E_d^a =$

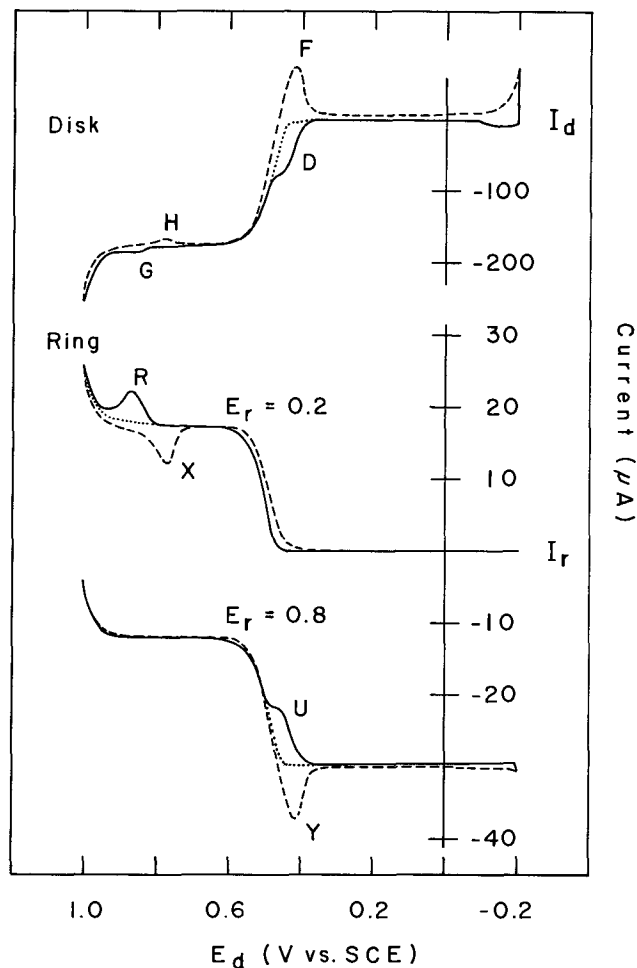


Fig. 5. I_d - E_d and I_r - E_d curves for $3.0 \times 10^{-4}M$ NaI in 1.0M H_2SO_4 ; 2500 rev/min, 6.0 V/min, — is anodic scan, --- is cathodic scan, is steady-state curve.

Fig. 6. Isotherm for I_2 adsorption in reversible state at platinum disk electrode; 1.0M H_2SO_4 ; a, results for integration from $E_d = 0.60-0.15V$; b, results for integration from $E_d = 0.60-0.35V$.

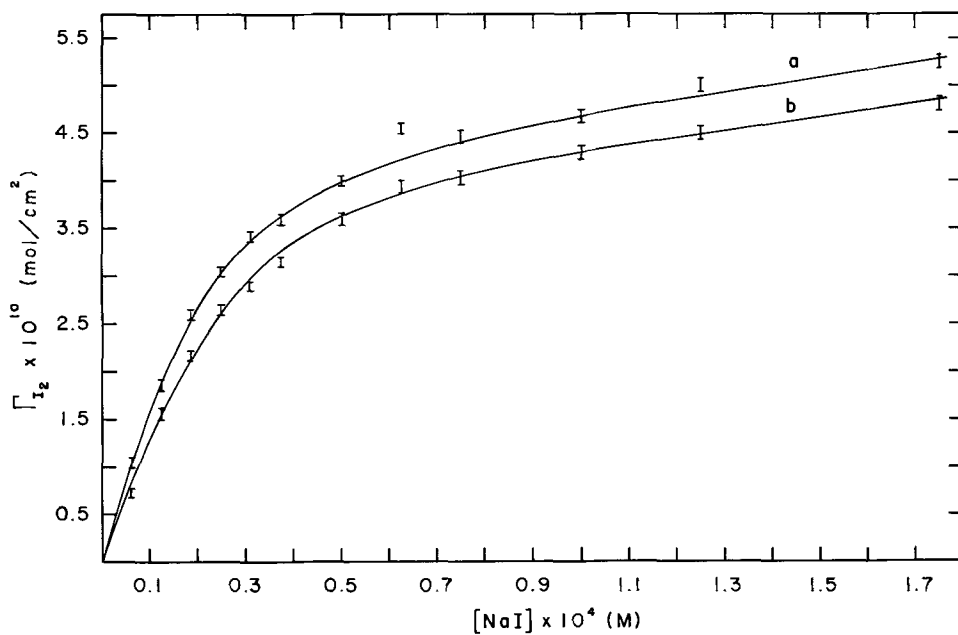
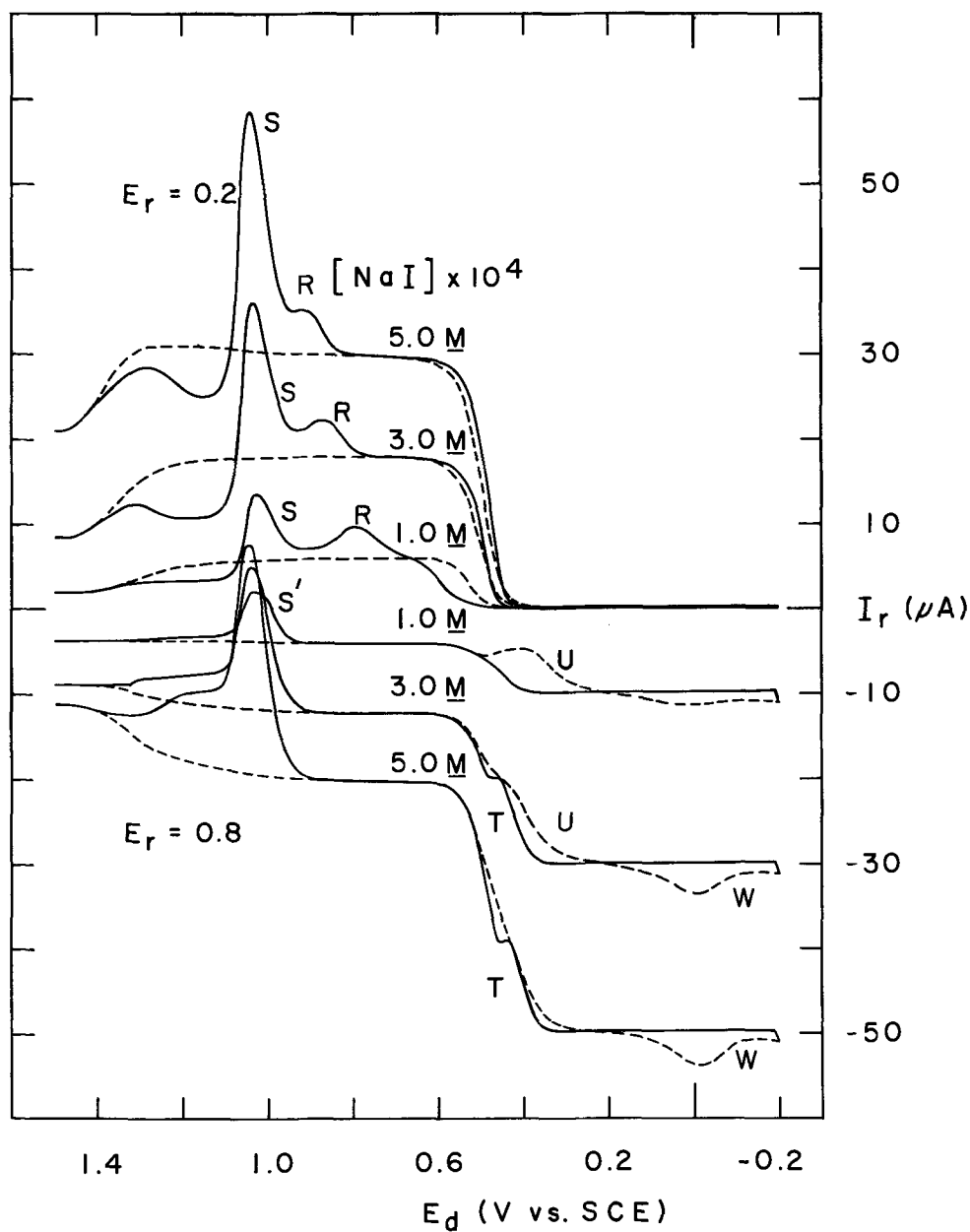


Fig. 7. I_r-E_d curves for NaI in 1.0M H_2SO_4 ; 2500 rev/min, 6.0 V/min, — is anodic scan, - - - is cathodic scan.



1.0V and $E_d^c \approx 0.6V$ produced I_r-E_d curves reflecting repeated adsorption and desorption of I_2 at the disk surface.

Very small peak currents G and H can be observed on the I_r-E_d curve of Fig. 5. The magnitude of these peaks is much less than would be obtained if the phenomena at the disk surface resulting in peaks R and X were only Faradaic in nature. Apparently, desorption of I_2 from the disk surface is accompanied by the loss of a very small quantity of I^- which is subsequently oxidized. During the cathodic E_d scan, I_2 is re-adsorbed and a small quantity of I^- is reincorporated into the adsorption layer.

I_r-E_d curves for $E_r = 0.2$ and $0.8V$ were obtained for various values of C_{I^-} and are shown in Fig. 7. Peak R observed for $E_r = 0.2V$ is shifted to more positive values of E_d as C_{I^-} increases. This is expected since the surface process at the disk electrode is reversible and increasing C_{I^-} results in increasing surface concentrations of I_2 at the disk electrode in the potential region $0.6V < E_d < 1.0V$. The position of peak R does not shift when C_{I^-} is constant and ω is varied. This is expected since increasing ω , while increasing the flux of I^- to the disk electrode, does not result in a change of surface concentration of I_2 .

Wave U, obtained during the cathodic E_d scan for $E_r = 0.8V$, becomes less evident as C_{I^-} is increased. This results since the time required to obtain the equilibrium surface coverage by adsorbed species decreases as bulk concentration of adsorbing species is increased.

Effect of irreversibly adsorbed I_2 on the desorption of reversibly adsorbed I_2 .—The presence of I_2 adsorbed in an irreversible state at the disk surface prevents the desorption of I_2 during an anodic scan at $E_d = 0.8V$ and, therefore, the appearance of peak R on the I_r-E_d curve. This is demonstrated by the I_r-E_d curves in

Fig. 8. The program for the scan of E_d for obtaining the curves in Fig. 8 is given in Fig. 9. The recording of the I_r-E_d curves was begun at point a of the E_d program. Peaks R and X were obtained only during the scans following the cathodic scan for which $E_d^c = -0.20V$. It should be noted that electrochemical reduction of irreversibly adsorbed I_2 occurs at $E_d < 0.1V$.

In a separate experiment, I_r-E_d curves were obtained at $E_r = -0.2V$ using $E_d^a = 1.60V$ and a value of E_d^c varied by 50 mV increments from -0.20 to $0.20V$. As E_d^c increased such that successively greater amounts of irreversibly adsorbed I_2 remained at the disk surface, peak R was observed to be shifted to more positive potentials and to finally converge with peak S. As a result, the height of peak S increased. Repeating the experiment using $E_r = 0.8V$ yielded I_r-E_d curves on which the height of peak S' did not vary. Apparently, the reversibly adsorbed I_2 , even though desorbed in a region of the I_d-E_d curve corresponding to the onset of IO_3^- production, is not oxidized to IO_3^- . Nor is it oxidized to the oxidation state of the intermediate species detected on the anodic scan of E_d during the onset of IO_3^- production.

The dotted line in Fig. 8 represents the I_r-E_d curve obtained under steady-state conditions. The quantities of material produced or consumed by the various surface-controlled processes at the disk electrode were estimated from the area between the steady-state curve and those curves obtained at an E_d scan of 6.0 V/min. The results are tabulated in Table I for waves T, U, W, and Y.

The calculated quantity of I_2 adsorbed into a reversible state (from curve 2 of Fig. 8) during the anodic half of a scan of E_d for which $E_d^c = 0.15V$ is 4.0×10^{-10} mol/cm². However, the calculated amount of I_2 desorbed at the disk surface on the subsequent

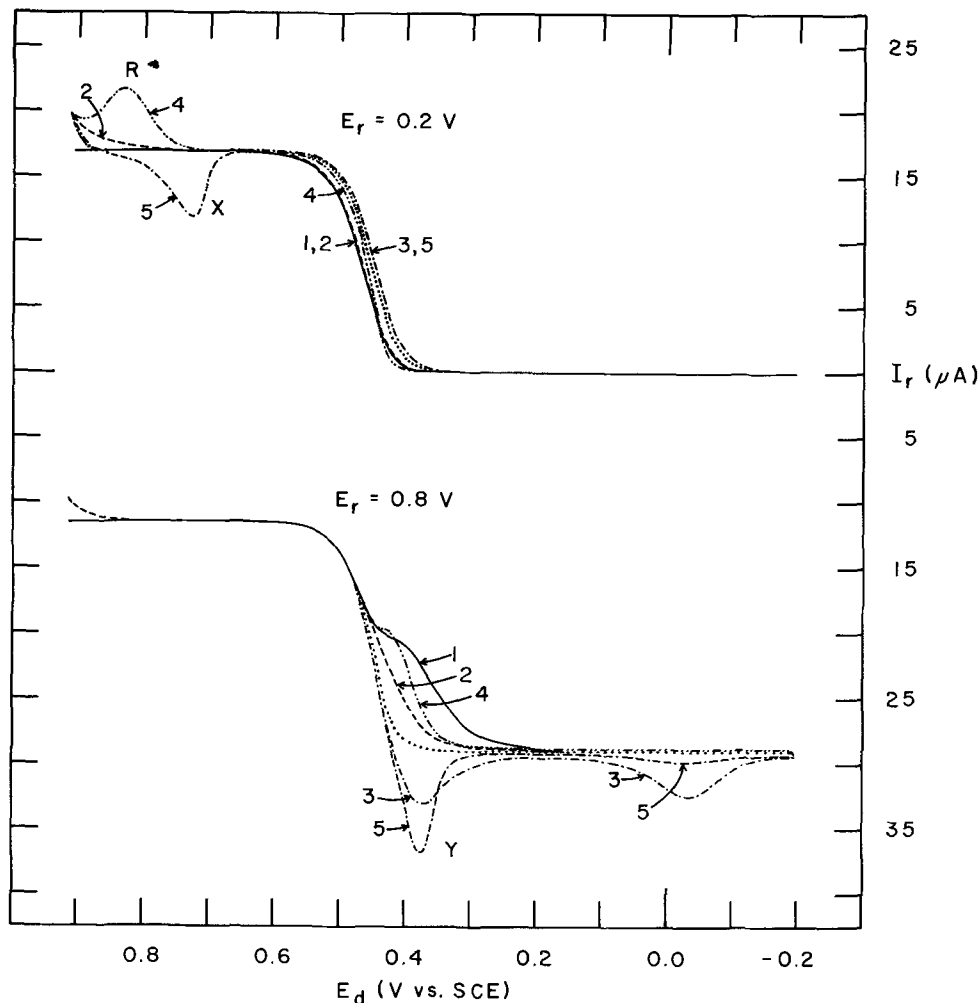
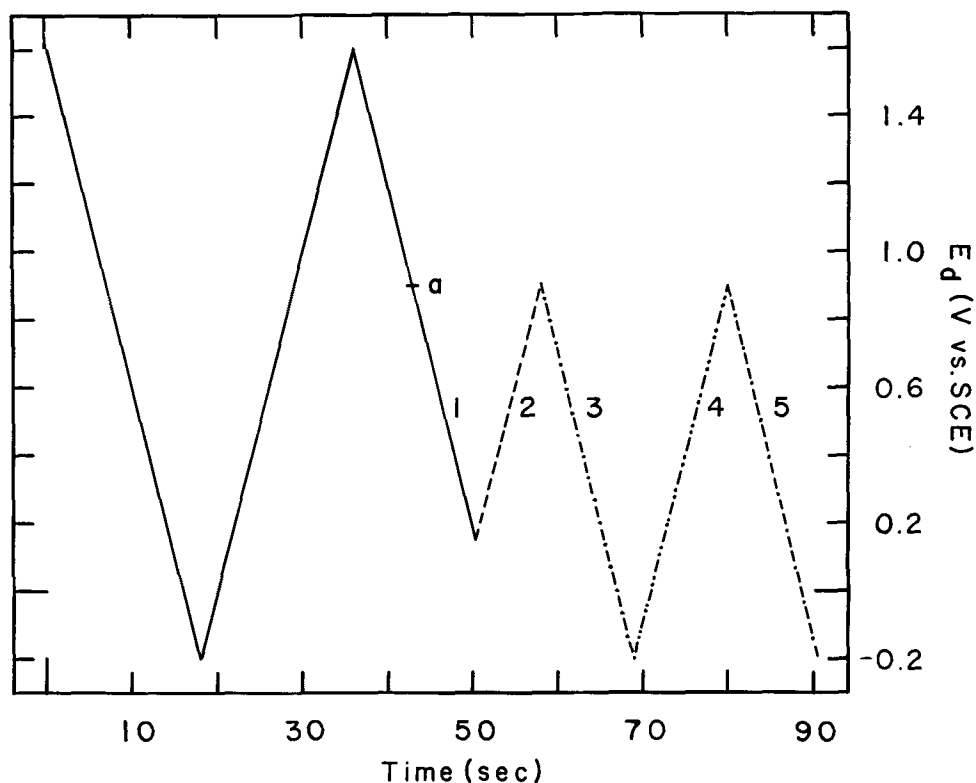


Fig. 8. I_r-E_d curves for $3.0 \times 10^{-4}M$ NaI in $1.0M$ H_2SO_4 ; 2500 rev/min, 6.0 V/min, program for scan of E_d given in Fig. 9.

Fig. 9. Program for scan of E_d used in Fig. 8; 6.0 V/min, recording of I_r-E_d curves started at a.



cathodic scan (from curve 3 of Fig. 8) is 6.0×10^{-10} mol/cm². I_r-E_d curves obtained during repeated cyclic E_d scans between the limits $E_d^c = 0.15$ V and $E_d^a = 0.90$ V were identical to those in Fig. 8. Since more I_2 cannot be desorbed than is previously adsorbed, it is apparent the use of the steady-state curve as a reference for the calculation of values in Table I is not correct. This would be the case if the $E_{1/2}$ for the oxidation of I^- to I_2 on the steady-state curve differs from the $E_{1/2}$ on curves obtained during cathodic and/or anodic scans of E_d at 6.0 V/min.

The surface coverage by reversibly adsorbed I_2 at a disk surface bearing only I^- in an irreversible state of adsorption (from curve 5 of Fig. 8) was found to be approximately the same as that adsorbed at a surface bearing both I^- and I_2 in irreversible states of adsorption (from curve 3 of Fig. 8). This is in agreement with the findings of Hubbard, Osteryoung, and Anson (17).

An accurate calculation of the quantity of I_2 adsorbed in a reversible state at a surface covered with I^- is based on the areas under peak R and X. On that basis 5.5×10^{-10} mol/cm² of I_2 is adsorbed at an electrode in 3.0×10^{-4} M NaI. This result is consistent with results given in Fig. 6.

The quantity of species adsorbed at the disk electrode in the region of wave T (curve 1 in Fig. 8) was calculated as 2.1×10^{-9} g eq/cm². The isotherm for adsorption of I^- in an irreversible state (Fig. 4) shows a maximum surface coverage of 1.3×10^{-9} g ion/cm². It does not seem possible that this large difference can be accounted on the basis of the possible incorrect use of the steady-state curve. Hubbard, Osteryoung, and

Anson (17) found that 3.2×10^{-9} g eq/cm² of I_2 may be adsorbed in an irreversible state at a platinum electrode. The value calculated here is intermediate the values for surface coverage by I^- and by I_2 .

As stated earlier, the height of peak W is equal to $-N$ times the height of peak E after correcting for charging current. On the basis of this evidence, it is my conclusion that the quantity of I^- removed from the disk surface during reduction of the irreversibly adsorbed I_2 is equal to the quantity of I^- produced at the disk surface by the reduction. It is clear that the inclusion of I_2 as an irreversibly adsorbed species does not prevent the value of surface coverage by irreversibly adsorbed I^- from being equal to the maximum value, 1.3×10^{-9} g ion/cm².

Rate of exchange between reversible and irreversible states of I_2 adsorption.—The knowledge that I_2 and I^- can be adsorbed simultaneously at the electrode surface and that the quantity of I^- adsorbed is equal to that adsorbed if no I_2 were present leads immediately to a question. Will I_2 which is adsorbed in a reversible state at a platinum surface covered with irreversibly adsorbed I^- enter a state of irreversible adsorption? To obtain an experimental answer, I_r-E_d curves were obtained as follows: E_d was adjusted to 1.6V, then stepped to -0.20 V, and then to 0.70V. E_d was maintained at 0.70V for time, t , from 0 to 360 sec. After the desired time period, the I_r-E_d curve was recorded while scanning E_d from 0.7 to -0.20 V at 6.0 V/min. The I_r-E_d curves are shown in Fig. 10 for $t = 5, 60,$ and 360 sec. It is clear that I_2 is slowly adsorbed into the irreversible state at a surface covered with ir-

Table I. Quantities of material involved in surface reactions at the disk electrode
Data calculated from I_r-E_d curves shown in Fig. 8

E_d scan	No.	E_r	Wave	Surface-controlled reaction at disk	Quantity
— — — — —	1	0.8	U	Irreversible adsorption of I^- and I_2	2.1×10^{-9} g eq/cm ²
— — — — —	2	0.8	T	Reversible adsorption of I_2	4.0×10^{-10} mol/cm ²
— • — • —	3	0.8	Y	Desorption and reduction of reversibly adsorbed I_2	6.0×10^{-10} mol/cm ²
— • — • —	3	0.8	W	Reduction of irreversibly adsorbed I_2	4.0×10^{-10} mol/cm ²
— • — • —	4	0.8	T	Reversible adsorption of I_2	6.5×10^{-10} mol/cm ²
— • — • —	4	0.2	R	Desorption of I_2 from reversible state	5.5×10^{-10} mol/cm ²
— • — • —	5	0.2	X	Adsorption of I_2 into reversible state	5.5×10^{-10} mol/cm ²
— • — • —	5	0.8	Y	Desorption and reduction of reversibly adsorbed I_2	6.5×10^{-10} mol/cm ²

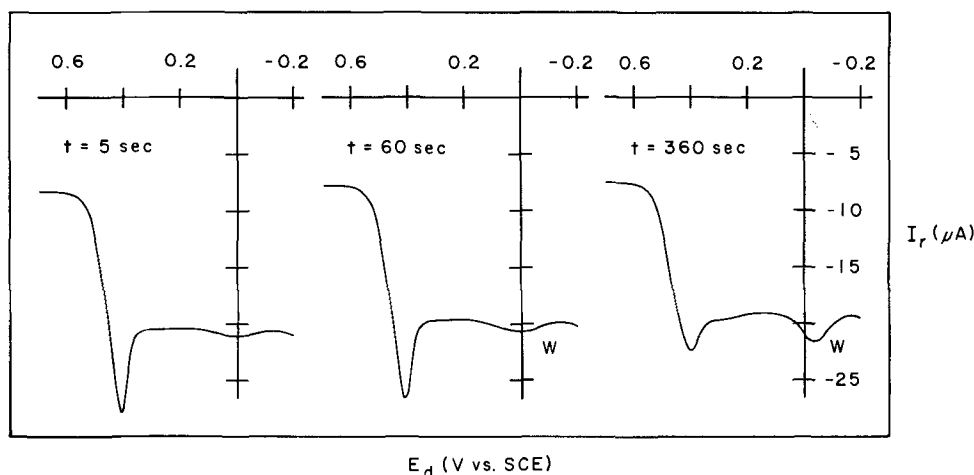


Fig. 10. I_r - E_d curves illustrating exchange of I_2 between reversible and irreversible states of adsorption; $2.0 \times 10^{-4}M$ NaI , $1.0M$ H_2SO_4 , 2500 rev/min, 6.0 V/min.

reversibly adsorbed I^- as evidenced by the increase in the size of wave W for longer t values.

In a similar experiment, E_d was stepped from 1.6 to $-0.20V$ and then to $0.90V$ at which it was maintained for values of t ranging from 0 to 360 sec. The I_r - E_d curves were then recorded while scanning E_d from 0.90 to $-0.20V$ at 6.0 V/min. It is shown above that in this experiment no I_2 was present at the disk surface in a reversible state of adsorption even though a potential of $0.90V$ is in the limiting-current region of the wave for oxidation of I^- to I_2 . The size of wave W was no larger after $t = 360$ sec than when $t = 0$ sec. Thus, the mechanism whereby I_2 is slowly adsorbed into an irreversible state at a surface covered with irreversibly adsorbed I^- requires preliminary adsorption to the reversible state.

Summary

New conclusions about the processes of adsorption and desorption of I^- and I_2 at platinum electrodes in $1.0M$ H_2SO_4 have resulted from this study. Iodine was determined to rapidly and simultaneously adsorb with I^- by an irreversible process following electrochemical reduction of an anodized platinum electrode. The irreversible adsorption of I_2 does not result in a decrease of the surface coverage by I^- from that determined in the absence of I_2 . Iodine was found to adsorb equally to a surface covered with irreversibly adsorbed I^- or a mixture of I^- and I_2 . This is in agreement with the findings of Hubbard, Osteryoung, and Anson (17) who determined that I_2 adsorbs by a reversible process to the same extent at a surface covered by irreversibly adsorbed I^- or irreversibly adsorbed I_2 . Iodine is desorbed from the reversible state of adsorption by a potential-dependent mechanism at a surface covered with irreversibly adsorbed I^- at $E = 0.8V$. The presence of I_2 in an irreversible state causes the desorption to shift to more positive values. Irreversibly adsorbed I_2 is electrochemically reduced and the I^- produced is desorbed at $E < 0.1V$. It was also found that I_2 undergoes slow adsorption to the irreversible state at an electrode surface covered by irreversibly adsorbed I^- and this proceeds by a mechanism involving preliminary adsorption of I_2 to the reversible state.

Acknowledgment

Equipment used in this study was purchased with funds supplied by the General Electric Corporation and administered by the Department of Chemistry at

Iowa State University. The author acknowledges the graduate students in his research group for their helpful discussions of this work.

Manuscript submitted June 4, 1971; revised manuscript received ca. Sept. 28, 1971.

Any discussion of this paper will appear in a Discussion Section to be published in the December 1972 JOURNAL.

REFERENCES

1. K. Schwabe, K. Wagner, and Ch. Weischmantel, *Z. Phys. Chem.*, **206**, 309 (1957).
2. N. A. Balashova, *ibid.*, **207**, 340 (1957).
3. N. A. Balashova, *Zh. Fiz. Khim.*, **32**, 2264 (1958).
4. W. Lorenz and H. Mühlberg, *Z. Phys. Chem.*, **17**, 129 (1958).
5. V. E. Kazarinov and N. A. Balashova, *Dokl. Akad. Nauk SSSR*, **134**, 864 (1960).
6. N. A. Balashova, *Wiss. Z. Tech. Univ. Dresden*, **12**, 1177 (1963).
7. K. Schwabe and W. Schwenk, *Electrochim. Acta*, **9**, 975 (1964).
8. R. A. Osteryoung and F. C. Anson, *Anal. Chem.*, **36**, 975 (1964).
9. N. A. Balashova and V. E. Kazarinov, *Elektrokhimiya*, **1**, 512 (1965).
10. V. E. Kazarinov, *ibid.*, **2**, 1389 (1966).
11. W. Lorenz and H. Mühlberg, *Z. Electrochem.*, **59**, 736 (1955).
12. M. W. Breiter, *Electrochim. Acta*, **8**, 925 (1963).
13. R. A. Osteryoung, *Anal. Chem.*, **35**, 1100 (1963).
14. H. B. Herman, S. V. Tatwawadi, and A. J. Bard, *Anal. Chem.*, **35**, 2211 (1963).
15. R. A. Osteryoung, G. Lauer, and F. C. Anson, *This Journal*, **110**, 926 (1963).
16. E. C. Toren, Jr. and C. P. Driscoll, *Anal. Chem.*, **38**, 872 (1966).
17. A. T. Hubbard, R. A. Osteryoung, and F. C. Anson, *ibid.*, **38**, 692 (1966).
18. V. G. Levich, "Physicochemical Hydrodynamics," pp. 60-72, Prentice-Hall, New York (1962).
19. A. N. Frumkin and L. N. Nekrosov, *Dokl. Akad. Nauk SSSR*, **142**, 820 (1962).
20. L. M. Nekrosov and N. P. Berezina, *ibid.*, 855 (1962).
21. W. J. Albery and S. Bruckenstein, *Trans. Faraday Soc.*, **62**, 1920 (1966).
22. D. T. Napp, D. C. Johnson, and S. Bruckenstein, *Anal. Chem.*, **39**, 481 (1967).
23. D. C. Johnson, D. T. Napp, and S. Bruckenstein, *ibid.*, **40**, 482 (1968).
24. D. C. Johnson and S. Bruckenstein, *This Journal*, **117**, 460 (1970).
25. D. C. Johnson, *Talanta*, **16**, 1481 (1969).
26. S. Bruckenstein and D. T. Napp, *J. Am. Chem. Soc.*, **90**, 6303 (1968).

Current Distribution Along an Electrode of High Resistance During Unsteady-State Diffusion

Richard C. Alkire*¹ and Aladar Tvarusko*

Engineering Research Center, Western Electric Company, Princeton, New Jersey 08540

ABSTRACT

Current-time behavior is predicted following a step-change in applied potential for electrolysis at a straight wire electrode of high resistance in unstirred solution. Transport equations are integrated by finite difference techniques on a digital computer. Six classes of electrode behavior are described in accord with the relative importance of diffusion, charge-transfer, and ohmic resistance effects. A high electrode resistance leads to nonuniform current distribution along the wire whereas diffusion resistance in the electrolyte causes appreciable transient current decay.

The surface on which an electrochemical reaction takes place may not be equipotential if the resistance of the electrode phase is large. Accordingly, the electrochemical reaction may proceed at different rates along the electrode surface. The variation of the reaction rate along the electrode depends upon the kinetic, geometric, and transport characteristics of the specific electrochemical system involved. The over-all behavior of such a distributed reaction system can be quite complicated since it is the result of several competing factors such as ohmic resistance of the wire and solution, mass transport by diffusion and migration in the electrolytic solution, hydrodynamic motion of the solution, charge-transfer overpotential, and geometry of the electrolysis cell.

In the past, several studies have been conducted on straight wire electrodes of small diameter immersed in electrolytic solution and surrounded by cylindrical counterelectrodes. These analyses have shown how the current and potential distributions along a wire electrode depend upon ohmic electrolyte resistance and upon the rate of sluggish electrode reaction (1-8). Calculations were carried out by treating the electrode as a one-dimensional region along which electrochemical reaction takes place.

To date, no theoretical analyses are known to be reported which take into consideration mass transfer effects during electrolysis at electrodes of high resistance. Such mass transfer effects may be complicated when there is convective motion of solution as, for example, encountered in axial flow during the electroplating of moving wires, transverse forced flow through a wire grid or porous electrode, and natural convection at stationary electrodes.

In the present study, an analysis of potentiostatic electrolysis is conducted on a wire electrode immersed simply in stationary electrolyte and surrounded by a cylindrical counterelectrode. If the applied potential is sufficiently cathodic, the concentration of reacting species at the electrode surface would be quickly reduced to nearly zero along the entire electrode surface. In such cases the current density distribution would be uniform, the total current would decrease according to unsteady-state radial diffusion (9), and electrode operation would be under pure mass transfer control. On the other hand, if the mass transport process proceeds with ease, the concentration of reacting species at the electrode surface may not be appreciably reduced below the value in the bulk electrolyte so that diffusion-controlled transient behavior would not be anticipated. Instead, a steady-state condition would be obtained immediately following the double-layer charging process. If the resistance of the wire electrode is sufficiently high, then ohmic losses in the metal phase may

consume much of the applied potential so that the current distribution along the electrode would not be uniform. At intermediate conditions, ohmic resistance of the wire electrode may lead to a nonuniform current distribution while, at the same time, the concentration of reacting species at the electrode surface is reduced to a value between the bulk value and zero. The transient current response may then be expected to deviate significantly from that predicted on the basis of simple radial diffusion at the limiting current. Establishment of a constant applied potential does not fix the surface concentration on the wire surface since there is more than one series resistance in the distributed reaction circuit. In the present study, conditions are ascertained under which mass-transfer transient behavior and/or a nonuniform current distribution may be anticipated. The theoretical model predicts the current and potential distributions along the electrode as a function of time during electrolysis. The investigation of this simple case can illuminate how the reaction distribution depends upon mass transport, ohmic, and charge-transfer effects, and can serve as a basis for extension of model studies to more complex conditions such as continuous electrodeposition on moving wire.

Model Formulation

The model for the resistive wire electrode is based on consideration of a single straight metal wire which extends the entire length of an electrolysis cell as shown in Fig. 1. The cylindrical counterelectrode surrounds the wire and the primary current distribution is supposed to be uniform. Electrical contact is made at one end of the wire. The other end of the wire is insulated and no current passes through it; alternatively a plane of symmetry may exist. There is no motion of fluid relative to the solid surface. The potential of the wire electrode is maintained at a desired value with respect to a reference electrode placed in the solution near the wire at the end of the cell closest to the electrical contact point.

The theoretical model presented below may be employed for predicting either anodic or cathodic behavior. For convenience of presentation, however, only cathodic electrodeposition of metal onto a wire electrode is chosen for discussion.

Prior to the application of potential, the electrode is supposed to be at its rest potential so that no current passes and the metal-ion concentration is uniform throughout the electrolyte. Following the sudden application of cathodic potential, current flows through the electrode at a rate which is limited "initially" by charge-transfer overpotential and/or ohmic resistance.²

² In a metallic conductor, electrons attain their steady-state velocity within approximately 10^{-14} sec. The establishment of an electrical double layer at the metal-solution interface is typically completed within approximately 10^{-4} sec, depending upon the resistance of the metal, the capacity of the double layer, and the charging current. The theoretical model presented here does not apply to behavior during these processes.

* Electrochemical Society Active Member.

¹ Permanent address: Department of Chemical Engineering, University of Illinois, Urbana, Illinois 61801.

Key words: current distribution, electrodeposition on wire, non-equipotential surface, potentiostatic transients.

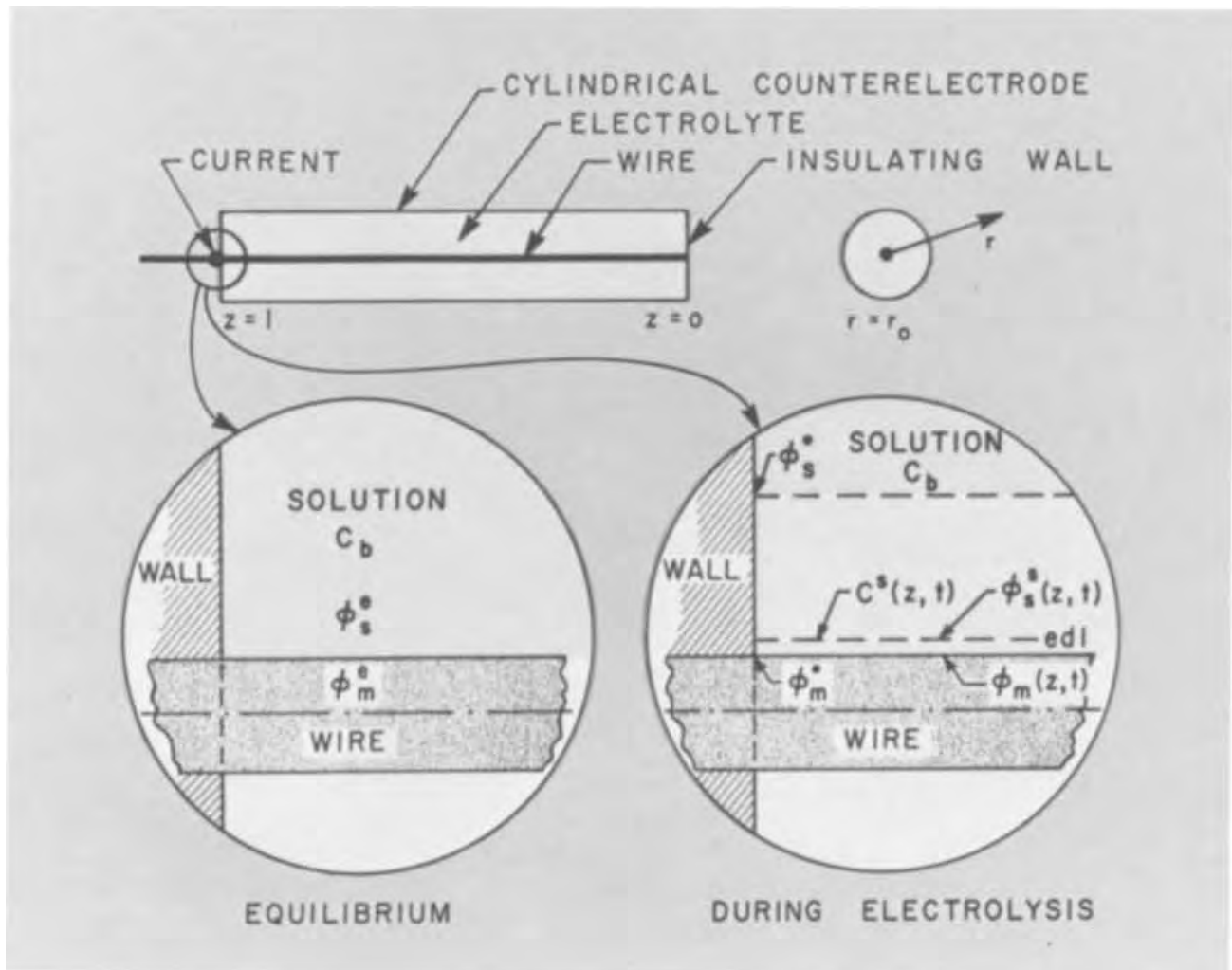


Fig. 1. Electrolysis cell and schematic diagram of the model for stationary wire electrode

If the transference number of the reacting ion is less than one, a concentration gradient is caused to form in the solution. The concentration of reacting species at the surface of the cathode thus decreases below the bulk value to an extent which depends upon the applied potential and upon the competing series resistance: ohmic and charge-transfer.

The current in the metal is carried by the electrons and in the solution by the ions. The local concentrations and potentials may be obtained by solving the transport equations in each phase. If these concentration and potential distributions are known throughout both phases, the local reaction rate may be calculated, in principle, by a relation which suitably describes the kinetics of the electrode process. Thus the local current distribution may be determined along the wire.

Because rigorous calculations are cumbersome, several simplifying assumptions have been introduced. Although these assumptions restrict somewhat the range of validity of the model, they do not obviate the essential features of behavior which are of interest.

(i) The wire is a straight circular cylinder, and the counterelectrode configuration is such that the primary current distribution along the wire is uniform. The wire diameter is not appreciably altered by conduct of electrolysis.

(ii) The rate of establishment of the electrical double layer is rapid with respect to any transient electrode behavior under consideration.

(iii) The wire diameter is small with respect to distances over which significant potential variation takes place in the metal phase so that the one-dimensional

macroscopic method is applicable for calculation of the potential field in the metal electrode.

(iv) There is negligible ohmic resistance in the contact wires external to the electrolysis cell.

(v) Only one electrochemical reaction takes place and the overpotential of the reaction sequence is adequately characterized by a Volmer-type expression (Eq. [3]).

(vi) The metal ions are present in small concentration in an electrolytic solution containing a large excess of nonreactive charged species. Thus motion of the metal ions is not appreciably affected by the presence of the potential field in the electrolyte.

(vii) The resistance of the electrolytic solution is negligible with respect to other resistances in the cell and thus does not tend to alter the current distribution along the wire.

(viii) There is no hydrodynamic motion in the electrolyte.

(ix) The ratio of wire length/diameter is sufficiently large that, in the electrolyte, axial diffusion along the wire is everywhere negligible in comparison with radial diffusion away from the wire.

(x) The system is isothermal.

(xi) Nonelectrochemical reactions do not occur.

The spatial coordinate along the wire, z , extends from the insulated end ($z = 0$) to the current feeder side ($z = l$). The radial coordinate, r , has the value r_0 at the wire surface. The electronic current and potential along the wire are related by Ohm's law.

$$i(z,t) = -\sigma \frac{d\phi_m(z,t)}{dz} \quad [1]$$

The electronic current in the wire, $i(z,t)$, varies with position owing to the electrochemical reaction taking place at the wire surface

$$\frac{di(z,t)}{dz} = -\frac{2}{r_o} j(z,t) \quad [2]$$

The local reaction rate along the wire, $j(z,t)$, is related to the local metal ion concentration at the surface, $c^s(z,t)$ and to the potentials in both phases by the kinetic expression associated with the metal deposition process. The Volmer equation (10) has found particularly widespread use and will be used in this study. For application to electrodeposition systems, this equation is written

$$j(z,t) = i_o \left\{ \exp \left[\frac{\alpha n F}{R T} \eta(z,t) \right] - \frac{c^s(z,t)}{c_b} \exp \left[\frac{(\alpha - 1) n F}{R T} \eta(z,t) \right] \right\} \quad [3]$$

The exchange current density, i_o , has the value which corresponds to the reactant concentration in the bulk of the electrolyte, c_b . The quantity $\eta(z,t)$ is defined as the potential difference between metal and solution, outside the diffusion layer, during passage of current minus the potential difference existing under equilibrium conditions. This quantity thus includes both charge-transfer overpotential and concentration overpotential. It is convenient to introduce two additional potentials, ϕ_m^\bullet and ϕ_s^\bullet , which are defined as the potentials during electrolysis at the current feeder side of the electrolysis cell in the metal and in the bulk solution, respectively. Thus

$$\eta(z,t) = [\phi_m(z,t) - \phi_s^\bullet] - [\phi_m^e - \phi_s^e] \quad [4]$$

By denoting the potential in the electrolyte "at the surface of the wire" as $\phi_s^s(z,t)$, the right-hand side of Eq. [4] may be rearranged to

$$\begin{aligned} & [(\phi_m^\bullet - \phi_s^\bullet) - (\phi_m^e - \phi_s^e)] = [\phi_m^\bullet - \phi_m(z,t)] \\ & + [\phi_s^s(z,t) - \phi_s^\bullet] + \{[\phi_m(z,t) - \phi_s^s(z,t)] \\ & - [\phi_m^e - \phi_s^e]\} \quad [5] \end{aligned}$$

If a reference electrode is placed outside the diffusion layer at the current-feeder side of the electrolysis cell, then the quantity on the left side of Eq. [5] is the applied or control potential. Equation [5] indicates that the applied potential is consumed within the cell by (i) ohmic losses in the metal electrode, $[\phi_m^\bullet - \phi_m(z,t)]$, (ii) concentration overpotential in the electrolyte, $[\phi_s^s(z,t) - \phi_s^\bullet]$, and (iii) charge-transfer overpotential at the electrode surface, $\{[\phi_m(z,t) - \phi_s^s(z,t)] - [\phi_m^e - \phi_s^e]\}$. The concentration overpotential is related to the concentration difference across the diffusion layer in accord with the formula

$$\phi_s^s(z,t) - \phi_s^\bullet = \frac{R T}{n F} \ln \frac{c^s(z,t)}{c_b} \quad [6]$$

The relative magnitude of the three overpotentials vary in distance along the electrode and in time during electrolysis, but their sum remains constant. The sum of potential losses (ii) and (iii) constitute the quantity $\eta(z,t)$, as already indicated by Eq. [4].

Combination of Eq. [1] to [5] gives

$$\begin{aligned} \frac{d^2 \phi_m}{dz^2} = \frac{2i_o}{r_o \sigma} \left[\exp \left\{ \frac{\alpha n F}{R T} [(\phi_m - \phi_m^\bullet) \right. \right. \\ \left. \left. + (\phi_m^\bullet - \phi_s^\bullet) - (\phi_m^e - \phi_s^e)] \right\} \right. \\ \left. - \left(\frac{c^s}{c_b} \right) \exp \left\{ - \frac{(1 - \alpha) n F}{R T} [(\phi_m - \phi_m^\bullet) \right. \right. \right. \\ \left. \left. + (\phi_m^\bullet - \phi_s^\bullet) \right. \right. \\ \left. \left. - (\phi_m^e - \phi_s^e)] \right\} \right] \quad [7] \end{aligned}$$

where, for compactness, the functional dependence upon the z -coordinate and upon time has been deleted from the variable notation. Equation [7] is to be integrated subject to two boundary conditions:

1. Current does not pass through the insulated end of the wire

$$\frac{d\phi_m}{dz} = 0 \quad \text{at } z = 0 \quad [8]$$

2. During electrolysis the potential at the current-feeder end of the wire is constant

$$\phi_m - \phi_m^\bullet = 0 \quad \text{at } z = l \quad [9]$$

Equation [7] has two unknown variables: the potential in the metal, $\phi_m(z,t)$, and the concentration of reacting metal ion along the surface of the electrode, $c^s(z,t)$. In order to determine the distribution of surface concentration along the nonequipotential surface of the wire, diffusion in the solution must be taken into consideration. Thus, in accord with the conditions listed above, the radial diffusion equation is applied locally along the wire with neglect of axial terms

$$\left[\frac{\partial c(r,t)}{\partial t} \right]_z = D \left[\frac{\partial^2 c(r,t)}{\partial r^2} + \frac{1}{r} \frac{\partial c(r,t)}{\partial r} \right]_z \quad [10]$$

At the onset of electrolysis, the concentration of reactant species in the electrolyte is everywhere uniform

$$c(r,t) = c_b \quad (t = 0, \text{ all } r > r_o) \quad [11]$$

During electrolysis, the concentration far from the electrode remains constant

$$c(r,t) = c_b \quad (r = \infty, \text{ all } t) \quad [12]$$

At the surface of the wire, the local current density is related to the local concentration gradient in the solution

$$\left[D \frac{\partial c(r,t)}{\partial r} \right]_z = -\frac{j(z,t)}{n F} \quad (r = r_o, \text{ all } t) \quad [13]$$

Equation [13] states Fick's first law which is valid in the absence of migration effects. The time dependence of the local current density, $j(z,t)$, indicates that Eq. [13] does not correspond to a constant current boundary condition. Since neither the concentration c^s nor the current j are constant in time or in distance, both need to be calculated during the transient period; the calculation is performed such that Eq. [13] is obeyed.

In accord with the assumptions of the model, the potential and current distributions during transient operation may be determined from the solution of the coupled equations, [7] and [10], subject to the boundary conditions [8], [9], [11], [12], and [13]. Before proceeding with the analysis of these equations, it is worthwhile to reformulate the variables into dimensionless form. For this purpose the following relations seem convenient

$$\begin{aligned} Z = \frac{z}{l} \quad R = \frac{r}{r_o} \\ \tau = \frac{D t}{r_o^2} \quad C(R, \tau) = \frac{c(r,t)}{c_b} \end{aligned}$$

$$\Phi_m(Z, \tau) = \frac{n\mathbf{F}}{\mathcal{R}T} [\phi_m(z, t) - \phi_m^\bullet]$$

$$\Phi_a = \frac{n\mathbf{F}}{\mathcal{R}T} [(\phi_m^\bullet - \phi_s^\bullet) - (\phi_m^e - \phi_s^e)]$$

When the above variables are introduced into Eq. [7]-[13], the following dimensionless groupings of the system parameters arise

$$\xi = \frac{2n\mathbf{F}l^2i_0}{\sigma r_0 \mathcal{R}T} \quad \chi = \frac{\sigma r_0^2 \mathcal{R}T}{2n^2 l^2 \mathbf{F}^2 c_b D}$$

$$\beta(\tau) = \frac{n\mathbf{F}l i^\bullet(t)}{\sigma \mathcal{R}T} \quad J(Z, \tau) = \frac{2lj(z, t)}{r_0 i^\bullet(t)}$$

$$\theta(Z, \tau) = \beta J \chi \quad [14]$$

The parameter ξ is seen to be proportional to the ratio of exchange current density to metal conductivity and thereby is a measure of charge-transfer *vs.* ohmic effects. In a similar manner, the parameter χ is a measure of the relative importance of ohmic *vs.* diffusion resistances.

Equations [7]-[13] which describe the model used in this study may now be written in dimensionless form

$$\frac{d^2\Phi_m}{dZ^2} = \xi \{ \exp[\alpha(\Phi_m + \Phi_a)] - C^s \exp[(\alpha - 1)(\Phi_m + \Phi_a)] \} \quad [15]$$

$$\frac{d\Phi_m}{dZ} = 0 \quad (Z = 0, \text{all } \tau) \quad [16]$$

$$\Phi_m = 0 \quad (Z = 1, \text{all } \tau) \quad [17]$$

$$\frac{\partial C}{\partial \tau} = \frac{\partial^2 C}{\partial R^2} + \frac{1}{R} \frac{\partial C}{\partial R} \quad [18]$$

$$C = 1 \quad (\tau = 0, R > 1) \quad [19]$$

$$C = 1 \quad (R = \infty, \text{all } \tau) \quad [20]$$

$$\frac{\partial C}{\partial R} = -\theta \quad (R = 1, \tau > 0) \quad [21]$$

Once the potential and concentration distributions along the wire surface are known, the current distribution may be calculated by

$$J(Z, \tau) = \frac{\xi}{\beta} \{ \exp[\alpha(\Phi_m + \Phi_a)] - C^s \exp[(\alpha - 1)(\Phi_m + \Phi_a)] \} \quad [22]$$

It is interesting to observe that the current distribution in porous electrodes obeys Eq. [15] in the absence of concentration gradients in the pores (11, 12). The above model also characterizes certain transient processes which may occur during electrocrystallization (13).

Method of Solution

The solution of the set of equations and boundary conditions which describe the wire electrode model, Eq. [15]-[21], was carried out by a computer-implemented numerical procedure. In principle the transient calculation was accomplished by uncoupling Eq. [15] and [18] and solving each equation alternately in a stepwise manner with use of finite difference representations to the differential equations at each time step. First, Eq. [15] was solved with the surface concentration set equal to the bulk value ($C^s = 1$), and the current distribution was determined with Eq. [22]. These results correspond to the potential and current distributions prevailing before depletion of metal ions commences. Calculations were then carried out at specified time intervals during the ensuing mass-transfer transient

period. Equation [18] was applied at each spatial incremental element along the wire, with the surface flux (θ) set equal to the local current density in accord with its definition, Eq. [14]. The initial time increment was chosen so that the surface concentration at the current-feeder end of the wire decreased by 3%; the numerical results were not appreciably improved with use of smaller time increments. After a specified incremental period of radial diffusion under a given current distribution, the concentration distribution was re-evaluated. With the values thus determined for the surface concentration distribution along the wire, Eq. [15] was again solved for a new current distribution and the sequence repeated for as many time intervals as required.

The central problem of these calculations is the solution of two second-order differential equations. Equation [15] was first linearized about an approximate solution and then put into finite difference form. The tridiagonal matrix was solved in accord with the method of Newman (14). The solution of the nonlinear problem was obtained by iteration with successive correction of the approximate solution. The transient diffusion equation, Eq. [18] was placed into finite difference representation in accord with the Crank-Nicolson symmetric form, and the tridiagonal matrix was inverted at each time step with use of an algorithm attributed to Thomas (15). Quarter-point representation of the finite difference equations was employed for the boundary conditions at the wire surface in accord with the discussion of Beck and Dhanak (16).

Results presented in this work were determined with use of 100 Z -increments in the axial direction and 40 R -increments in the radial direction ($\Delta R = 0.05$). For the range of parameters under study, this choice gave numerical results which were not appreciably improved by use of smaller mesh sizes. Between successive time steps, the time increment was increased by a factor of 1.1 in order to conserve computer time. A typical single time-step calculation involving 100 Z -increments with 40 R -increments at each Z -increment was found to take approximately 0.8 sec on an IBM 360 computer when the program is compiled in FORTRAN G.

Results and Discussion

The simple theoretical model developed above was used to predict several essential features of wire electrode behavior. The dimensionless quantities used in presentation permit evaluation of a wide variety of actual systems. All calculations were carried out for cathodic deposition (negative applied potentials) with use of the values $n = 2.0$ and $\alpha = 0.5$.

First consider the state which exists in the absence of significant concentration overpotential. As shown in Fig. 2, the current density distribution depends upon the value of the parameter ξ . For highly resistive wires, or reversible reactions (large values of ξ), electrochemical reaction takes place mainly near the current feeder end of the wire. For sluggish reactions on good conductors, charge-transfer overpotential near the current feeder end of the wire forces the electronic current to pass further along the wire so that for a given current density the reaction is more uniformly distributed at the expense of higher overpotential. Figure 3 illustrates how the total current passing to the wire electrode increases with applied potential. For small values of ξ , the total current β increases in direct proportion to an increase in ξ ; that is, since the current distribution is uniform for small ξ , the total current is proportional to the exchange current density, as may be seen in Eq. [3] and [22]. For large values of ξ , Fig. 3 indicates that the total current increases with approximately the square root of ξ for a given potential. For large ξ , the potential in the electrode varies with position, Eq. [1], so that the exponential terms in Eq. [22] become dependent upon the value of ξ .

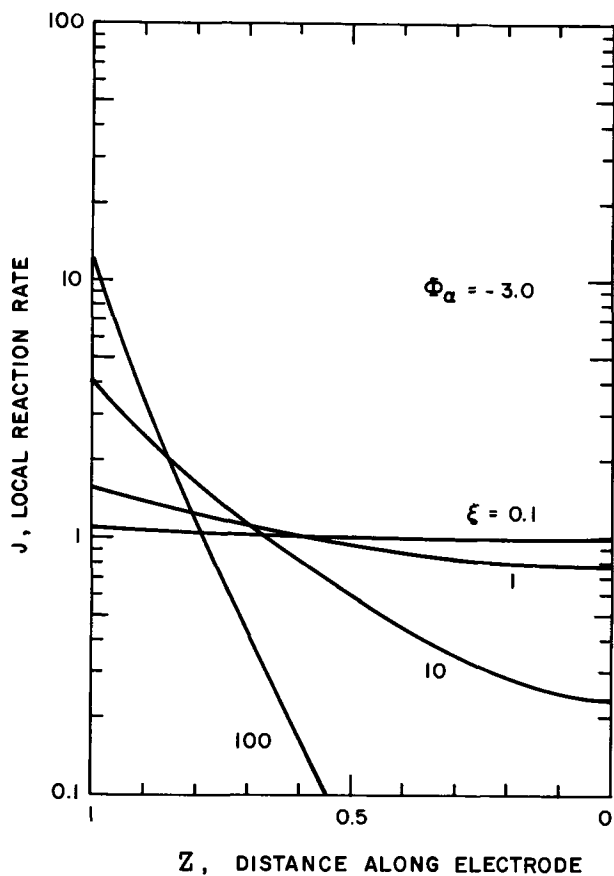


Fig. 2. Current density distribution along a wire electrode of high resistance in the absence of mass transport effects.

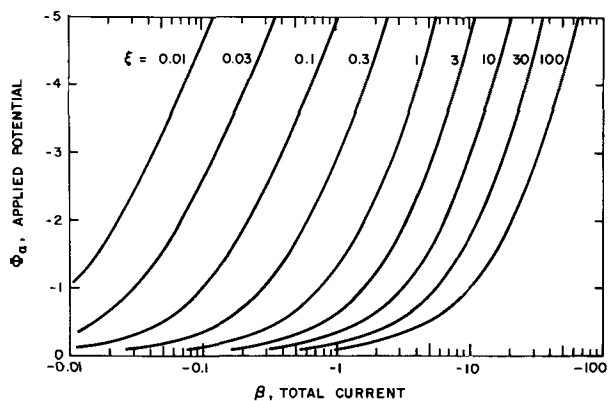


Fig. 3. Current-potential curves in the absence of concentration overpotential for high resistance wire electrodes at several values of the parameter ξ .

Let us now consider the effect of diffusional resistance on electrode behavior. The applied cathodic potential will be partitioned into ohmic, charge-transfer, and concentration overpotentials (Eq. [5]) according to the system parameters ξ and χ . The surface concentration at any point along the electrode may have a value between that in the bulk electrolyte and the minimum value

$$C_{\min}^s = \exp(\Phi_a) \quad [23]$$

given by the Nernst equation. If the ohmic resistance of the electrode is important, the reaction distribution will be nonuniform; if the mass transport resistance is important, diffusion-controlled transient behavior will be observed. "Initially," the concentration overpotential will be zero since the concentration distribution is uniform at the onset of electrolysis. The applied potential is thus initially partitioned between charge-transfer overpotential and ohmic losses in the wire accord-

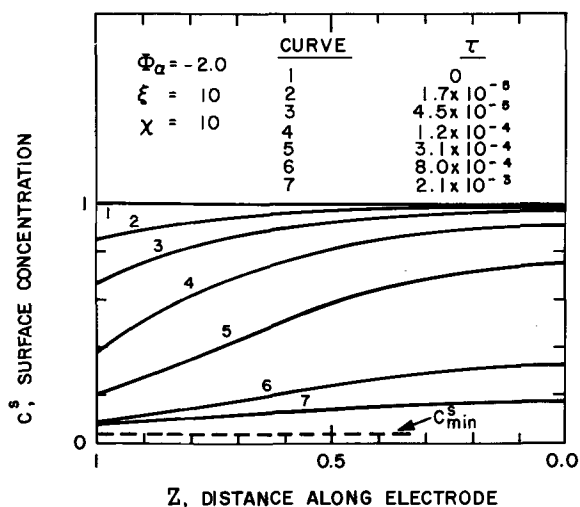


Fig. 4. Concentration variation at the surface of wire electrode of high resistance during unsteady-state potentiostatic electrodeposition at various dimensionless times.

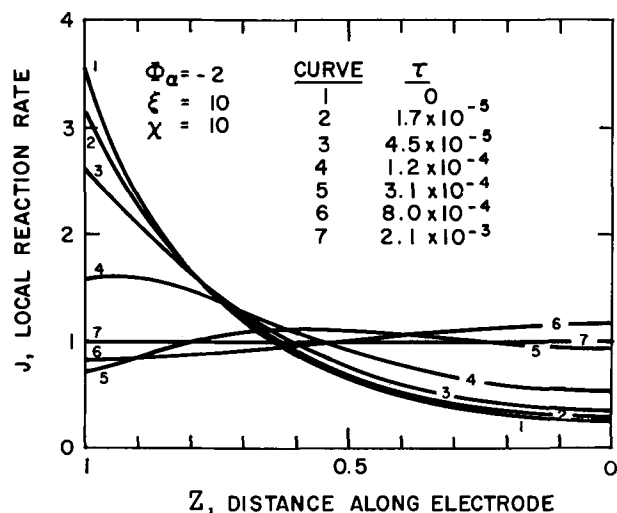


Fig. 5. Current density distribution on a wire cathode of high resistance during unsteady-state potentiostatic electrodeposition.

ing to the parameter ξ . With subsequent passage of current, concentration overpotential will eventually become significant if the parameter χ has a large value. As shown in Fig. 4, the concentration of metal ions at the cathode surface decreases during electrolysis at a rate which is in accord with the prevailing current density distribution. Eventually, for large χ , concentration overpotential can become the predominant resistance to current flow in the cell.³ The current density distributions which correspond to the results depicted in Fig. 4 are nonuniform (large ξ) and, indeed, the concentration decreases most rapidly near the current-feeder, where the local reaction rate is highest. As electrolysis proceeds, the region depleted in reacting species propagates along the wire. The minimum possible surface concentration, attained when ohmic and charge-transfer resistances are essentially negligible, has the value given by Eq. [23]. This lower limiting value is shown as the dashed line for the applied potential employed in Fig. 4.

Naturally, the variation of concentration during electrolysis has a dramatic effect on the current density distribution along the wire. Figure 5 shows the current distributions on the wire during electrolysis under the same conditions as in Fig. 4. Initially, the local reaction rate varies along the length of wire in a nearly exponential fashion as was already indicated

³Because the diffusion field is unbounded, the transient process does not attain a steady state and the diffusion layer grows indefinitely.

in Fig. 2. As concentration overpotential sets in near the current feeder end of the wire, however, reaction takes place further along the wire. At sufficiently long times, the mass transfer restriction near the current feeder becomes so severe that the most favorable reaction zone shifts away from the end of the wire. This most favorable reaction zone is sufficiently far from the current feeder end of the wire that concentration overpotential does not dominate, but yet not so far down the wire that ohmic losses in the electrode consume the applied potential. In this intermediate zone, the parameter ξ will influence the value of the maximum in the local current density. As electrolysis proceeds further, the most favorable reaction zone propagates down the wire owing to further depletion of metal ions near the current feeder side of the zone. Eventually, the most favorable zone reaches the far end of the wire, in which case the current distribution becomes nearly uniform along the entire electrode.

During the transient behavior depicted in Fig. 4 and 5, the individual overpotentials (ohmic, charge-transfer, and concentration) all vary with position and time in such a way that the applied potential remains constant throughout electrolysis.

The preceding discussion of events occurring locally along the wire surface during electrolysis has emphasized the interplay between diffusion, ohmic and charge-transfer overpotentials. Now, consider how such local behavior influences the total current flowing to the electrode, an easily accessible experimental quantity. For a given applied potential, two independent parameters, ξ and χ , are necessary to characterize the relative importance of the three effects. As shown in Table I, six possible combinations for the order of relative importance of diffusional, ohmic, and charge-transfer resistances can be ascertained according to the values of ξ and χ . It has already been mentioned that, generally speaking, a large value of ξ corresponds to a nonuniform current distribution owing to large ohmic resistance losses. In addition, a large value of χ corresponds to the predominance of diffusional resistance in comparison to ohmic resistance. Therefore, a large value of the product $\xi\chi$ indicates that concentration overpotential will eventually surpass the charge-transfer overpotential.

At the onset of electrolysis the total current, β , is determined by the applied potential, Φ_a , and by the parameter ξ . The subsequent timewise variations of β depend upon whether or not concentration gradients form near the electrode, i.e., upon the value of χ . In Fig. 6, ξ has a low value which corresponds to nearly uniform current distribution at the onset of electrolysis as already indicated in Fig. 2. For small values of χ , concentration overpotential does not set in since the over-all process is primarily limited by charge-transfer overpotential. For increased values of χ , however, transient behavior becomes more pronounced since the diffusional process becomes rate limiting. In Fig. 7, ξ has a large value which corresponds to a nonuniform current distribution at the onset of electrolysis. Once again it may be seen that transient behavior sets in to an extent which depends upon the value of the parameter χ .

Table I. Interpretation of the parameters ξ and χ

Case	ξ	χ	$\xi\chi$	Order of importance of competing effects
1	small	large	large	C > S > O
2	large	large	large	C > O > S
3	small	small	small	S > O > C
4	small	large	small	S > C > O
5	large	small	small	O > S > C
6	large	small	large	O > C > S

C—concentration overpotential.
S—surface overpotential.
O—ohmic loss in wire electrode.

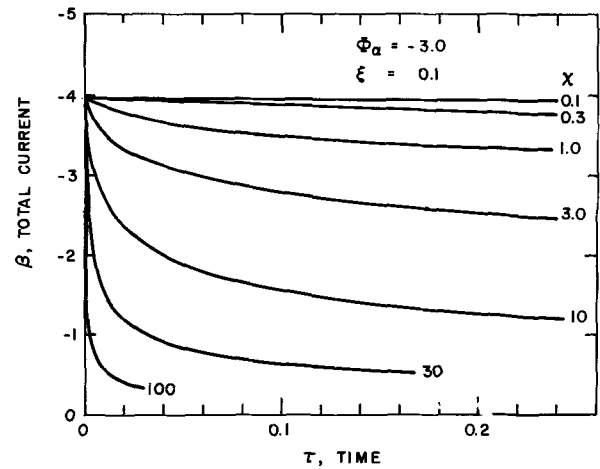


Fig. 6. Importance of mass transfer resistance (χ) at low ξ value on variation of total current during unsteady-state potentiostatic deposition at a wire electrode of high resistance.

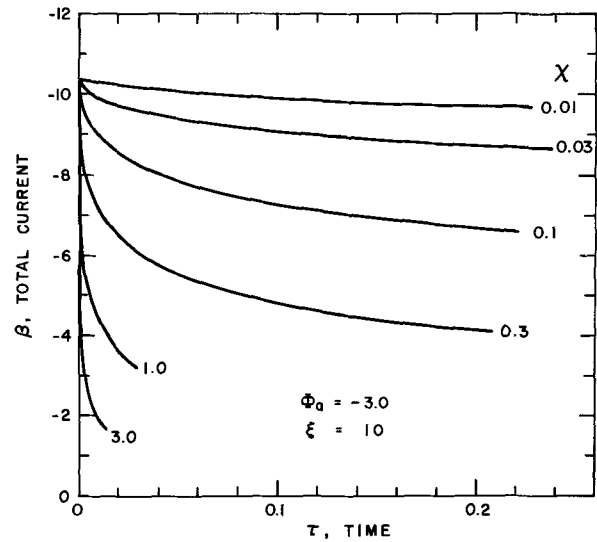


Fig. 7. Importance of mass transfer resistance (χ) at high ξ value on variation of total current during unsteady-state potentiostatic deposition at a wire electrode of high resistance.

It is illustrative to compare the above predictions with the "ideal" situation of pure radial diffusion under which both the current distribution is uniform and the concentration overpotential predominates at all times. Such a situation corresponds to one-dimensional unsteady-state radial diffusion from a circular cylinder with (constant) surface concentration equal to the value $c^{s_{min}}$. The analytical solution (9) is

$$\frac{j r_o}{n F D (c^{s_{min}} - c_b)} = f \left(\frac{D t}{r_o^2} \right) \quad [24]$$

The quantity on the left is a dimensionless ratio of the mass flux to the mass transfer driving force, that is, a Nusselt number for pure mass transport in an electrochemical system. In dimensionless form, Eq. [24] is

$$\frac{\beta \chi}{e \Phi_a - 1} = f(\tau) \quad [25]$$

where

$$f(\tau) = (\pi \tau)^{-1/2} + \frac{1}{2} - \frac{1}{4} \left(\frac{\tau}{\pi} \right)^{1/2} + \frac{1}{8} \dots \quad [26]$$

for short times and

$$f(\tau) = \frac{1}{\ln(4\tau) - 2\gamma} - \frac{\gamma}{[\ln(4\tau) - 2\gamma]^2} \quad [27]$$

for long times. The quantity γ is Euler's constant

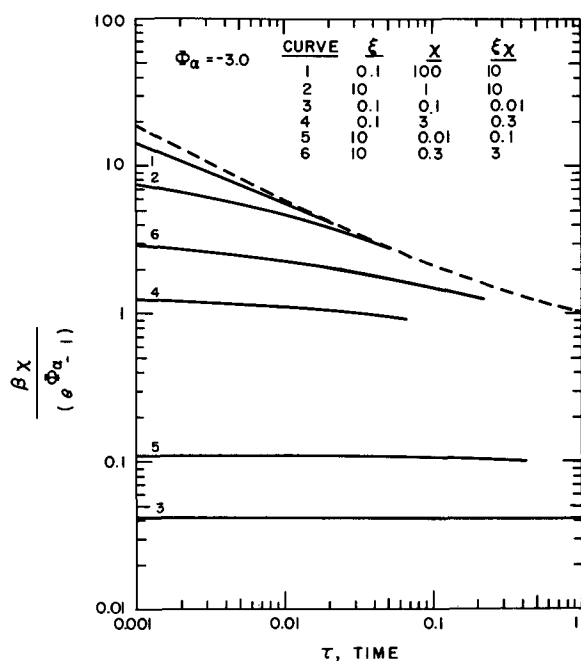


Fig. 8. Comparison of transient current response of resistive wire electrodes with idealized situation of pure diffusion control.

(0.57722). Notice from Eq. [26] that at time zero the current density would be infinitely large since competing resistances were not accounted for. The transient current response which corresponds to this limiting situation is shown by the dashed line in Fig. 8.

The limiting case of Eq. [25]-[27] may be compared with predictions based on the foregoing theoretical model. Deviations from the dashed line in Fig. 8 will always be observed for sufficiently small times, when ohmic or charge-transfer resistance prevail. The predicted results, of course, are invalid for extremely small times since the model does not include effects associated with the double layer charging process. Sample calculations for each of the six cases of behavior (Table I) are reported in Fig. 8 for an applied potential of $\Phi_a = -3.0$. Curve 1 corresponds very nearly to the limiting situation of Eq. [25] except that an infinitely large current is not passed at short times; the current density distribution is uniform at all times owing to the small value of ξ . For curve 2, the initial current distribution is nonuniform and, as previously illustrated in Fig. 4 and 5, concentration overpotential propagates down the wire; eventually diffusion resistances predominate along the entire length, and the current distribution is forced to become uniform. In curve 3, charge-transfer overpotential predominates at all times so that the current distribution is uniform and no transient diffusion behavior is observed. In curve 4, although charge-transfer predominates, a weak transient response is predicted since diffusional restrictions are not completely negligible owing to the large value of χ . In curves 5 and 6, ohmic effects predominate at all times so that the current distribution is highly non-uniform; in the former case, appreciable concentration gradients are not formed in the solution ($\chi = 0.01$) whereas, in the latter case, concentration overpotential develops to a moderate extent ($\chi = 0.3$). The various example curves shown in Fig. 8 will depend upon the value chosen for the applied potential. In general, more cathodic applied potentials will shift all curves upward and to the left, will tend to enhance the formation of concentration gradients, and will result in more non-uniform current distributions along the wire.

Conclusions

The behavior of resistive wire electrodes as illustrated by the preceding calculated results is consistent in pattern with what should be expected on the basis of

qualitative reasoning. The predicted behavior is subject to the limitations imposed by the assumptions which define the model.

By assumption (ix), axial diffusion along the wire is considered negligible in comparison with radial diffusion away from the wire. The appropriateness of this assumption may be tested by examination of the computed results. For the most nonuniform concentration distribution reported above, the axial diffusion flux attains only 1% of the value of the radial diffusion flux if the wire length/diameter ratio has the value 80. A smaller length/diameter ratio would also satisfy the assumption at smaller values of ξ and χ .

The conductivity of electrolytic solutions is less than the conductivity of common metallic electrode materials. Thus assumption (vii), that the ohmic resistance of the solution is negligible with respect to other resistances, may be expected to be good when the total current density in the wire is large with respect to the reaction rate at the wire surface. The ohmic overpotential in the solution phase will be less than 5% of the applied potential when the inequality

$$11 \frac{\sigma r_o^2}{kl^2} \frac{J\beta}{\Phi_a} \leq 1$$

is satisfied, where k is the conductivity of the electrolytic solution.

In the absence of concentration polarization, the uniformity of the current density distribution at a given applied potential depends solely upon the parameter ξ . Consequently, experimental methods which require uniform current density distribution for proper methodology or analysis of results should be designed such that ξ has a small value. Alternatively, the foregoing model may be employed to analyze the experimental data.

The effect of transport restrictions on electrode behavior is determined in accord with the value of χ . A value greater than unity indicates that transient response will be observed whether the current distribution is uniform or not. In the case of a nonuniform distribution, the most favorable region for reaction propagates along the wire as transport restrictions develop at the current feeder end of the electrode. For large values of χ , the current distribution will eventually be forced to become uniform regardless of the value of ξ .

Manuscript submitted July 30, 1971; revised manuscript received ca. Oct. 28, 1971. This was Paper 110 presented at the Cleveland, Ohio, Meeting of the Society, Oct. 3-7, 1971.

Any discussion of this paper will appear in a Discussion Section to be published in the December 1972 JOURNAL.

LIST OF SYMBOLS

English Characters

- c Concentration of reacting species, g mol/cm³
- c_b Concentration of reacting species in bulk electrolyte, g mol/cm³
- C c/c_b , concentration of reacting species, dimensionless
- D Diffusion coefficient, cm²/sec
- F Faraday's constant, 96,500 coulombs/g-equiv
- i Current density in the wire, A/cm²
- i_0 Current density in the wire at the current-feeder side, A/cm²
- i_o Apparent exchange current density of the electrode reaction, evaluated at the bulk concentration, A/cm²
- j Local reaction rate (current density) along wire surface, A/cm²
- J $2lj/i_0 r_o$, local reaction rate along wire, dimensionless
- l Length of wire, cm
- n Number of electrons taking part in electrode reaction, g-equiv/g mol
- r Spatial variable in radial direction, cm
- r_o Radius of wire electrode, cm

R	r/r_o , spatial variable in radial direction, dimensionless
\mathcal{R}	Gas constant, 8.31 joules/g mol °K
t	Time, sec
T	Temperature, °K
z	Spatial variable along wire, cm
Z	z/l , spatial variable along wire, dimensionless

Greek Characters

α	Transfer coefficient in reaction rate expression, Eq. [3]
β	$n\mathcal{F}li/\sigma\mathcal{R}T$, current density in the wire at the current-feeder side, dimensionless
κ	Electrolytic conductivity of solution, $\text{ohm}^{-1}\text{cm}^{-1}$
η	Electrode overpotential as defined by Eq. [4], V
θ	$j\tau_o/n\mathcal{F}c_bD$, local reaction rate along wire, dimensionless
ξ	$2n\mathcal{F}i_o l^2/\sigma\tau_o\mathcal{R}T$, kinetic parameter, dimensionless
σ	Electrical conductivity of wire electrode, $\text{ohm}^{-1}\text{cm}^{-1}$
τ	Dt/r_o^2 , time, dimensionless
ϕ	Potential, V
Φ	Potential, dimensionless
Φ_a	Potential applied by potentiostatic power supply, dimensionless
χ	$\frac{\sigma\tau_o^2\mathcal{R}T}{2n^2l^2\mathcal{F}^2c_bD}$, mass transfer resistance parameter, dimensionless

Subscripts

b	Denotes value in bulk of electrolytic solution
s	Pertains to electrolytic solution phase
m	Pertains to metallic electrode phase

Superscripts

e	Pertains to equilibrium conditions
s	Pertains to values prevailing at the electrode sur-

- face outside the double layer region but at the inner edge of the diffusion layer
- Pertains to reference position at $Z = 1$

REFERENCES

1. A. Weisselberg, *Trans. Electrochem. Soc.*, **90**, 235 (1946).
2. S. Ishizaka, H. Matsuda, and Y. Wada, *J. Electrochem. Soc. Japan*, **22**, 420 (1954).
3. C. Tobias and R. Wijnsman, *This Journal*, **100**, 459 (1953).
4. W. Harvey, *ibid.*, **109**, 638 (1962).
5. B. Conway, E. Gileadi, and H. Oswin, *Can. J. Chem.*, **41**, 2447 (1963).
6. S. Rangarajan, M. Dignam, and B. Conway, *ibid.*, **45**, 422 (1967).
7. J. Wojtowicz, L. Laliberte, and B. Conway, *Electrochim. Acta*, **13**, 361 (1968).
8. V. Fomichev, *Sov. Electrochem.*, **4**, 708 (1968).
9. H. Carslaw and J. Jaeger, "Conduction of Heat in Solids," 2nd ed., p. 334, Oxford University Press (1959).
10. T. Erdey-Gruz and M. Volmer, *Z. Physik. Chem.*, **150A**, 203 (1930).
11. F. Posey, *This Journal*, **111**, 1173 (1964).
12. R. de Levie, Electrochemical Response of Porous and Rough Electrodes, in "Advances in Electrochemistry and Electrochemical Engineering," Vol. 6, P. Delahay and C. Tobias, Editors, Interscience, New York (1967).
13. M. Fleishmann, S. Rangarajan, and H. Thirsk, *Trans. Faraday Soc.*, **63**, 533, 1240 (1967).
14. J. Newman, *I. & E. C. Fund.*, **7**, 514 (1968).
15. D. von Rosenberg, "Methods for the Numerical Solution of Partial Differential Equations," American Elsevier, New York (1969).
16. J. Beck and A. Dhanak, ASME Publ. 65-HT 14 (1965).

Technical Note



Transient Pressure Considerations in Charge Control of Sealed Batteries

Sidney Gross*

The Boeing Company, Seattle, Washington 98124

When sealed batteries with imperfect charge efficiency approach full charge, gas often evolves and increases pressure. In addition to the problems caused by increased heat and pressure, gassing causes mechanical forces within pores that contribute to structural breakdown; mechanical breakage causes loss in capacity and promotes shorting, and thus should be minimized (1). In this Technical Note it is shown that cell structural damage, when it occurs, can be greatest at the start of gassing due to transient pressure effects. An analysis is developed to compare the relative severity of this effect by the use of cell transient pressure data.

Analysis

The physical model postulated consists of a small pore of gas volume V_1 within a plate connected by a flow restriction to the larger gas volume V outside the plate. The pressures inside and outside the pore are P_1

and P , respectively. Gas of mass W leaving the pore either recombines on another electrode or causes a pressure increase in the sealed cell. The gas recombination rate may be approximated by

$$\frac{dW'}{dt} = KP \quad [1]$$

where W' is the unit mass of recombining gas, t is the unit time, and K is the gas recombination coefficient, determined experimentally.

The gas flow associated with cell pressurization is derived by differentiating the gas equation

$$W'' = C_1 \frac{PV}{T} \quad [2]$$

where W'' is the unit mass of pressurizing gas, T is temperature absolute, and C_1 is a gas constant. Hence

$$\frac{dW''}{dt} = \frac{C_1 V}{T} \left(\frac{dP}{dt} \right) \quad [3]$$

* Electrochemical Society Active Member.

Key words: charge control, batteries, electrode gassing, gassing, pressure transients, sealed batteries.

Thus, the total gas flow from the pore is

$$\frac{dW}{dt} = \frac{dW'}{dt} + \frac{dW''}{dt} \quad [4]$$

$$\frac{dW}{dt} = KP + \frac{C_1 V}{T} \frac{dP}{dt} \quad [5]$$

The gas flow results from a pressure difference between P_1 and P . If this pressure difference is small relative to P , then the gas flow rate may be defined by the conventional orifice flow equation [Ref. (2), Eq. VIII.71, or Ref. (3), Eq. D] as follows

$$\frac{dW}{dt} = C_2 \left[\frac{P(P_1 - P)}{T} \right]^{1/2} \quad [6]$$

where C_2 is a constant related to geometry and gas composition.

Equation [6] and the subsequent Eq. [7], [8], and [9] describe incompressible flow conditions in which density change is negligibly small. Nevertheless, these incompressible relationships may be used for many compressible flow conditions with acceptable error. For example, when $P_1 - P$ is less than 10% of P , the error does not exceed 2%; when it is less than 25% of P , the error does not exceed 15% (4). A more precise form of Eq. [6], not used in this analysis, is

$$\frac{dW}{dt} = C_2 Y \left[\frac{P(P_1 - P)}{T} \right]^{1/2} \quad [6a]$$

which includes the expansion factor Y , derived and tabulated in Ref. (4). Combining Eq. [5] and [6]

$$P_1 - P = \frac{T}{C_2^2 P} \left[KP + \frac{C_1 V}{T} \frac{dP}{dt} \right]^2 \quad [7]$$

The pressure difference $P_1 - P$ is directly related to stresses on the plate structure due to gassing.

When the pressure is stabilized, Eq. [7] reduces to

$$P_1 - P = \frac{K^2 P T}{C_2^2} \quad [8]$$

When the gas recombination is small relative to the rate of gas generation, Eq. [7] reduces to

$$P_1 - P = \frac{1}{T} \left[\frac{C_1 V}{C_2} \right]^2 \left[\frac{\left(\frac{dP}{dt} \right)^2}{P} \right] \quad [9]$$

where the first bracketed term shows the influence of the configuration and the second bracketed term shows the influence of the cell charge control method.

A useful application of these results is in the evaluation of charge control designs for sealed cells, especially those types for which overcharge is known to cause structural damage to positive plates. The forces in plates resulting from gassing are proportional to the pressure change parameter $(dP/dt)^2/P$ of Eq. [9], which can be calculated from the transient pressure curve during charging.

The significance of this can be illustrated using two typical pressure rise curves (Fig. 1) for charging with relatively slow gas recombination rate. Both cases start and end with equal pressures and rise with equal slopes; they differ only in the initial transient at the start of gassing. Calculation of the pressure change parameter (Fig. 2) shows that it is highest toward the start of gassing. Since this is directly related to stresses on the plate structure due to gassing, the highest stresses in plates can occur long before maximum pressure is reached, and occurs at the start of gassing if the initial pressure rise is linear. Charging that results in a transition pressure rise phase (curve A) develops smaller stresses than when the initial pressure change is abrupt (curve B).

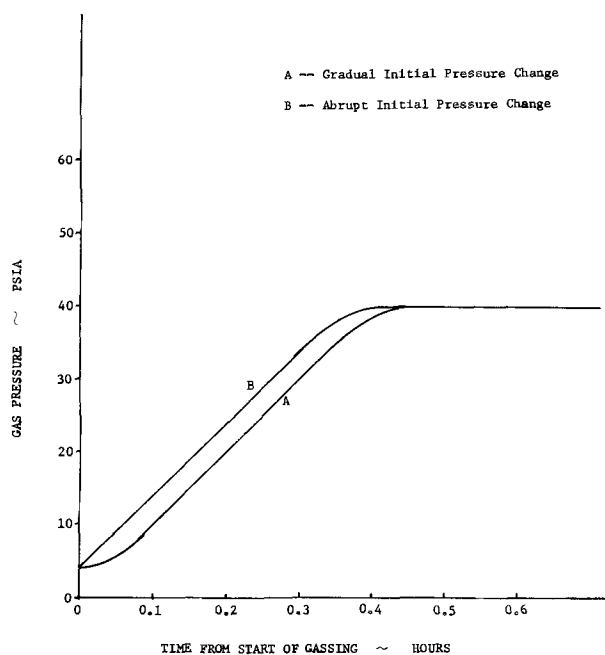


Fig. 1. Typical pressure rise in sealed cells

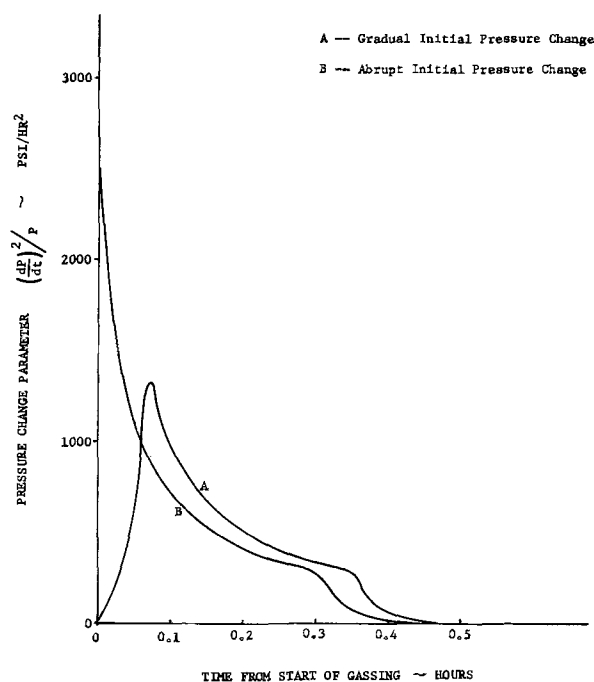


Fig. 2. Pressure change parameter for typical pressure rise

Discussion

The greatest stresses in plates due to gassing in sealed cells can often occur before maximum pressure is obtained. Thus, current tapering should start early enough to influence the initial gassing behavior, when stresses can be highest. Reliance entirely on methods that provide a charge termination signal is not sufficient, for this gives no consideration to transient pressure effects.

An order-of-magnitude estimate can be made of structural stress caused by gas evolution. Assume a cell pressure of one atmosphere, with an instantaneous pressure difference across a pore of 0.1 atm, and assume the pressure difference is developed across a particle 0.1 mil \times 0.1 mil \times 0.6 mil which is cantilevered from one end. With uniform loading across one face, the moment is 2.64×10^{-11} inch-lb, and the stress on the attached end is 160 psi. If the particle dimensions are

reduced by a factor of 100, the stress increases to 16,000 psi. Thus, gas evolution can develop substantial stresses on some particles, especially those that are small and poorly attached. As a point of comparison, lead and carbon have yield strengths of approximately 1200 and 900 psi, respectively, which could be much less at particle attachment points.

Experimental evidence for structural change caused by gas evolution has been obtained for the PbO_2 electrode (5, 6). These studies showed that gas generation within the structure formed channels through which gas escaped to the surface of the plate. Apparently the gas evolution dislodged many of the more loosely attached PbO_2 particles and carried them to the surface. Gas evolution is a common problem also with dry cells, resulting in movement of the electrolyte paste and bobbin (7). Even the sintered nickel positive electrode, though relatively strong, can also be damaged by gas evolution, especially plates weakened by cycling and corrosion; a common commercial manufacturing test to screen for weak plate structures is to overcharge for several days and observe structural damage caused by gassing.

Designing cells for maximum gas recombination rate can sometimes be questioned, based on this analysis; gas recombination electrodes can maintain low cell pressure during overcharge and give the illusion of safely controlling charge. Also, this causes pressure to be very low at the commencement of gassing, which is seen to be detrimental (Eq. [7]). Even for applica-

tions where continuous overcharge must be endured, low cell pressures could be harmful for a given gassing rate. Inert gas in sealed cells could be beneficial by providing at least a known minimum pressure, though there are disadvantages in other respects, such as decreased gas diffusion rates.

Manuscript submitted May 27, 1971; revised manuscript received ca. Nov. 12, 1971.

Any discussion of this paper will appear in a Discussion Section to be published in the December 1972 JOURNAL.

REFERENCES

1. S. Gross, *J. Energy Conversion*, **11**, 39 (1971).
2. B. F. Dodge, "Chemical Engineering Thermodynamics," p. 334, McGraw-Hill Book Co., New York (1944).
3. S. A. Moss, "Measurement of Flow of Air and Gas with Nozzles," *Trans. ASME, Appl. Mech.*, **50**, (1928).
4. R. C. Binder, "Fluid Mechanics," 2nd ed., pp. 219 and 235, Prentice-Hall, Inc., New York (1949).
5. A. C. Simon and S. M. Caulder, *This Journal*, **118**, 659 (1971).
6. C. F. Yarnell, M. C. Week, R. V. Biagetti, and G. W. Kammlott, Paper 18, presented at Electrochem. Soc. Meeting, Cleveland, Ohio, Oct. 3-7, 1971.
7. F. Aufenast and J. Muller, Gas Formation in Dry Cells in "Power Sources 1962," D. H. Collins, Editor, pp. 335-355, Pergamon Press, Oxford (1963).

Brief Communication



A Method for the Stripping of Anodic Titanium Oxide Films from Metal by Using A-C Current

Masaki Yamazaki and Hiroshi Nozaki

Institute of Industrial Science, University of Tokyo, Roppongi, Minato-ku, Tokyo, Japan

Stripping of anodic oxide films from metals is of importance in connection with investigation on a structure of the oxide films, which would be provided for x-ray analysis or for electron diffraction analysis. Isolation of the films has been usually carried out by dipping the oxide films in a suitable solution which selectively attacks the film/metal interface without dissolution of the oxide films (1). However, it often happens that the films are not stripped completely from a metal substrate by employing this method.

Recently, it has been found that the pretreatment of titanium by using a-c current in a H_2SO_4 solution is effective in producing good insulating oxide films (2), and in fact the a-c pretreatment has been used in the formation of electrolytic titanium oxide films (3, 4). It is also found that this a-c procedure has an effect on stripping of the titanium oxide films from the titanium substrate. Thus, in this work we report the stripping of the anodic oxide films, using the a-c procedure.

Titanium electrodes, 50 mm \times 20 mm \times 1 mm, were prepared from ST-40 titanium (H_2 , < 0.02%; O_2 , < 0.20%; N_2 , < 0.05%; Fe, < 0.20%). The electrodes have very thin films of unknown composition, and it is necessary to remove these films from the electrodes to do analyses. In order to make the surface clean, the

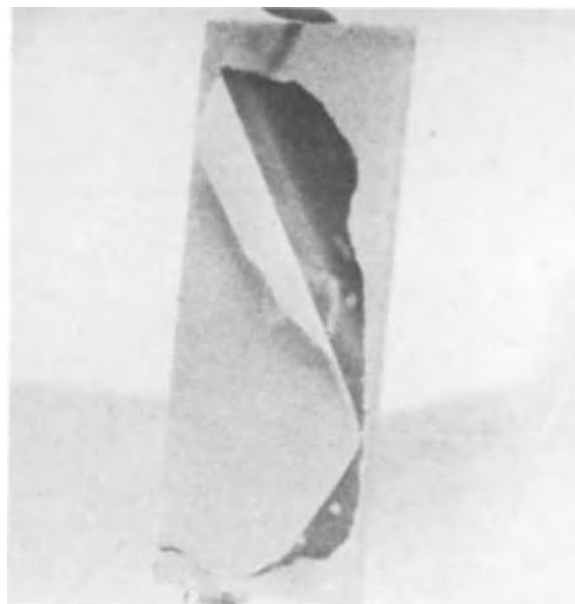


Fig. 1. Photograph of the stripping of an anodic film from titanium by using a-c current in H_2SO_4 solution.

Key words: stripping, titanium oxide, oxide films, a-c current.

electrodes were first treated in a 16 weight per cent (w/o) H_2SO_4 aqueous solution at 25°C , using a-c current (50 Hz) at $50 \sim 70 \text{ mA/cm}^2$ for 2 hr. After the pretreatment, the electrodes were anodized in a 8 w/o H_3PO_4 aqueous solution at 25°C with a current density of 3 mA/cm^2 . The oxide films of controlled thickness from 500 to 3500\AA were formed in this anodization.

The electrodes with the oxide films obtained were then electrolyzed by using a-c current in the same H_2SO_4 solution with the same current density mentioned above. After $10 \sim 20$ min, the oxide films were beautifully stripped from the titanium substrate. A photograph of the stripping of a film (ca. 3500\AA) is shown in Fig. 1.

Of course, the above method is applicable to the stripping of other titanium oxide films which are produced by other anodizations. It is considered that the stripping effect is based on a process in which the metal surface is dissolved without dissolution of the oxide films by applying a-c current in the H_2SO_4

solution. However, a detailed mechanism of the process is not clear at present.

Acknowledgments

The authors are indebted to M. Nakagawa for his help and assistance during the experiments.

Manuscript received Oct. 25, 1971.

Any discussion of this paper will appear in a Discussion Section to be published in the December 1972 JOURNAL.

REFERENCES

1. M. J. Pryor and D. S. Keir, *This Journal*, **102**, 370 (1955).
2. M. Yamazaki, M. Nakagawa, and H. Nozaki, *Bull. Chem. Soc. Japan*, **44**, 3200 (1971).
3. M. Yamazaki and H. Nozaki, *This Journal*, **118**, 400 (1971).
4. M. Yamazaki and H. Nozaki, *Japan. J. Appl. Phys.*, **10**, 1529 (1971).



Etch Channel Formation during Anodic Dissolution of N-Type Silicon in Aqueous Hydrofluoric Acid

M. J. J. Theunissen*¹

Philips Research Laboratories, N.V. Philips' Gloeilampenfabrieken, Eindhoven, The Netherlands

ABSTRACT

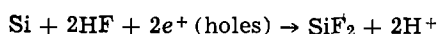
Anodic dissolution of n^+ -, n -, and n^- -type silicon in 5% aqueous hydrofluoric acid at moderate current densities results in the formation of etch channels which propagate in crystal-oriented directions in the monocrystal. Density and depth of the channels are a function of the applied voltage, the donor concentration, and the exposure time of the electrolyte under anodic bias conditions. It is assumed that the channel formation originates at spots with a lower breakdown voltage of the depletion layer which exists on the surface of the crystal under reverse bias conditions. Channel formation in epitaxial n layers can occur during preferential electrochemical etching of the n^+ substrate of n^+n^- structures. This is the case when the n^+ to n^- interface profile is not abrupt and when defects in the epitaxial layer are present. Some methods of restricting the influence of channels occurring during device processing are mentioned.

Several phenomena have been reported occurring during the anodic dissolution of n -type silicon in fluoride-containing solutions. In general terms the experimental conditions determine whether dissolution is complete, partial, or absent. One set of conditions of practical importance is that which leads to the complete dissolution of n^+ material but not n^- . In this case it is possible, for example, to remove by electrochemical etching the n^+ substrate from an n^+n^- structure while the very thin epilayer remains unattacked. This etching process was originally presented by van Dijk and de Jonge (1) and was more recently described (2-4).

Partial dissolution of n -type silicon was observed, and it was reported that preferential electrochemical etching of n^+n^- structures can lead to the formation of etch channels in the remaining thin n -type layer (2). Etch channel formation was also observed in homogeneously doped n -type silicon (2). During etching channels form and extend in crystallographical directions, leading to a complex network of caverns beneath the silicon surface.

In anodization experiments with n -type germanium and silicon, Uhler (5) observed etch pits growing in crystallographically well-defined directions into the monocrystal.

Turner *et al.* (6) observed thick film formation on n -type silicon anodized in HF solutions. To explain the presence of the elemental silicon found in this film they suggested that after a primary dissolution reaction



the SiF_2 rapidly disproportionates into Si and SiF_4 according to



A brown layer was also observed on the etched side of the n^- layer after the selective removal of the n^+ substrate (1, 2).

In a recent paper by Meek (7) connection was made between the current density and the appearance of the silicon surface. For highly doped silicon three types of etching behavior were distinguished. Below a critical current density, J_{crit} (which depends on resistivity and orientation), a brown layer was found to be formed on the etched surface. In an intermediate range of current densities (from J_{crit} to J_{max}), dissolution occurred without film formation, but the surface was rough and pitted. Beyond J_{max} bright electropolishing occurred. For low doped n -type silicon Meek observed etch pit formation at all current densities, even at current densities below the saturation current.

In this paper a systematic experimental study of the occurrence of channels in silicon as a function of donor concentration and silicon voltage or current density is reported. The formation of channels during etching and the dependence of their density, length, and propagation direction upon conditions used are demonstrated. It is further shown that the published reports of brown layers, etch pits, and channels in n -type silicon refer essentially to the same phenomenon of partial dissolution and that these apparently different features are all attributable to various degrees of attack of the monocrystal.

Experimental

n -type, Czochralski-grown, antimony-doped silicon was used. After the sawing and lapping procedures, the slices were etched for 3 min in 1 vol HF (48%), 2 vol HAc (98%), and 3 vol HNO_3 (fuming). The etch rate of this mixture is about 15 $\mu\text{m}/\text{min}$. The surface orientations used were (111), (110), and (100).

* Electrochemical Society Active Member.

¹ Present address: Laboratoire d'Electronique et de Physique Appliquée, 94-Limeil-Brévannes, France.

Key words: anodic dissolution, etch channels, silicon, brown layers, crystal-oriented attack, monocrystal.

The donor concentration, deduced from resistivities, ranged from $4 \cdot 10^{18}$ to $5 \cdot 10^{14}$ cm^{-3} . The three concentration ranges n^+ ($N_D > 2 \cdot 10^{18}$), n ($2 \cdot 10^{18} > N_D > 2 \cdot 10^{16}$), and n^- ($N_D < 2 \cdot 10^{16}$) differ from each other in electrochemical etch behavior at 10V as mentioned in (2).

The epitaxial slices used were n^+n^- structures with a highly doped substrate ($N_D > 2 \cdot 10^{18}$ cm^{-3}) and epitaxial layers phosphorus-doped to about $5 \cdot 10^{15}$ cm^{-3} . The epitaxial growth was by either a SiCl_4 process at 1220°C as described in (2) or a SiH_4 process. The latter was carried out at 1050°C in a water-cooled horizontal reactor (8), using a SiH_4 and H_2 gas mixture. The growth rate was about 0.25 $\mu\text{m}/\text{min}$.

The procedure for the electrochemical etching of the slices has been described (2). Most of the experiments were carried out at a potential difference of 10V between anode and cathode in a 5% aqueous HF solution. If necessary, ohmic contact between the platinum contact strip and silicon was made by an additional n^+ diffusion.

Measurements of the current density J against the silicon potential V were carried out using an arrangement as sketched in Fig. 1(a) and 1(b). The potential difference between anode and cathode was increased manually. The potential of the silicon working electrode was measured against a calomel reference electrode (saturated KCl). As can be seen in Fig. 1(b) the silicon slice is contacted at the rear by an outer and an inner contact. The outer contact was used for the application of the potential difference between the silicon and a platinum mesh electrode. The inner contact was used to measure the silicon electrode potential against the calomel electrode for very low current densities at the silicon-metal contact.

Etch channels, formed during the electrochemical dissolution process were studied with a microscope at surfaces or cross sections of the slices. The cross sections were mostly $\{111\}$ planes obtained by cleavage. A 3-5 sec treatment in Sirtl etchant (9) was used to reveal the channels.

Laue diffraction patterns were used to determine the degree of crystallinity of brown, channel-rich layers and infrared absorption measurements for determining the composition.

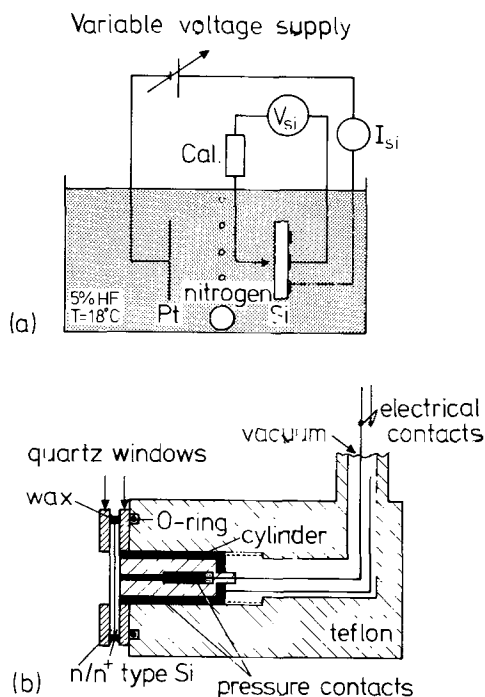
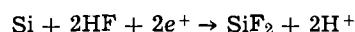


Fig. 1. (a) Current vs. voltage measurement apparatus and (b) detail of the silicon anode and its electrical contacts.

Experimental Results and Discussion

Anodic Dissolution of N-Type Silicon

The charge distribution at an n-type silicon anode in an aqueous HF solution is shown in Fig. 2(a). Because of the positive bias of the silicon, a positively charged depletion layer forms at its surface. A thin layer containing a high concentration of negatively charged ions is formed in the electrolyte. As shown by Myamlin and Pleskov (10), the potential drop in the electrolyte and the Helmholtz layer in sufficiently concentrated solutions (relative to the free charge concentration in the semiconductor) can be neglected. The voltage drop in the system is almost completely supported by the depletion layer in the semiconductor. The depletion thickness and the corresponding electric field are functions of the donor concentration of the n-type silicon. Anodic dissolution is governed by the supply of holes at the surface of the semiconductor (6). Taking the dissolution as divalent (6), then the following reaction may be assumed to occur



Without an additional generation or injection mechanism there will be essentially very few holes at the surface of the n-type material. Hole concentration at the silicon surface can be increased in several ways (6), one of which is the application of a sufficiently high reverse bias voltage. Excess holes are generated by impact ionization or Zener breakdown at the depletion layer and silicon can dissolve. The evidence of a breakdown mechanism has been demonstrated by Uhlir (5). The selective electrochemical etching of n^+n^- slices can be explained on the basis of the difference in breakdown voltage between n^+ and n^- silicon.

In order to predict whether or not breakdown occurs, the maximum electric field of the depletion layer, E_{max} , will be calculated and compared with the critical field, E_{crit} . The situation as sketched in Fig. 2(a) can be treated as a metal-n silicon or an abrupt p^+n junction under reverse bias. The following simplifying assumptions must be made: (i) The semiconductor-electrolyte interface is planar and infinitely extended (width \gg depl. depth). (ii) The semiconductor is homogeneously doped and no defects are present which lower the breakdown voltage. (iii) The electrolyte n-type Si system has a charge distribution

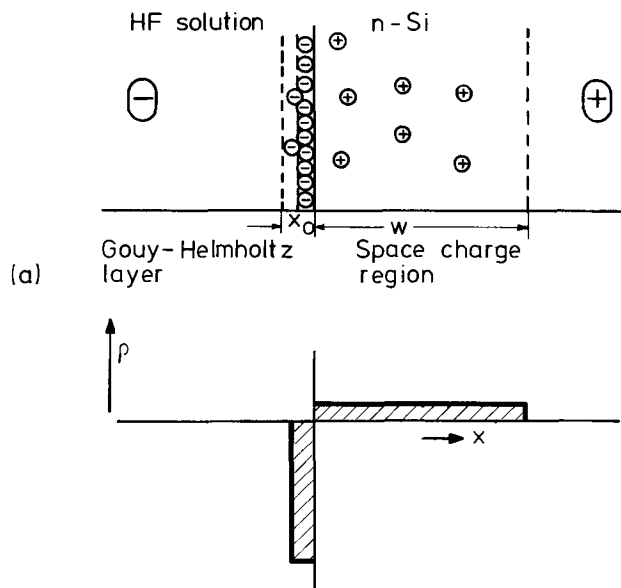


Fig. 2. (a) The HF electrolyte-n-type Si interface under anodic bias conditions and (b) schematic representation of the charge distribution.

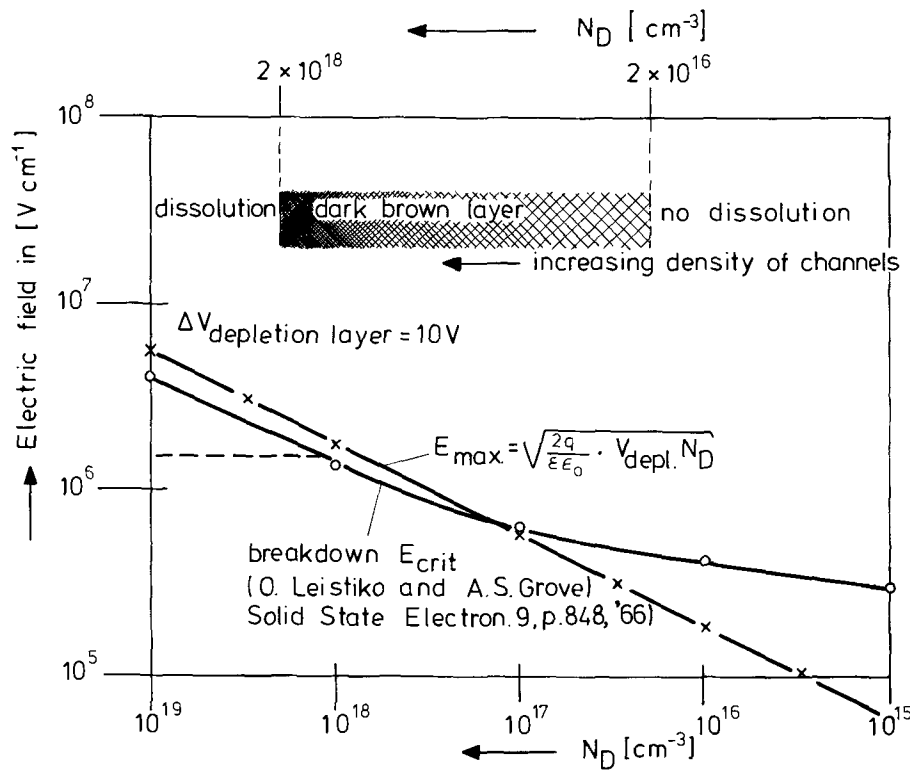


Fig. 3. The calculated maximum electric field, E_{max} , and the value of the breakdown field, E_{crit} , as a function of the donor concentration N_D . The upper part of the graph schematically indicates the three ranges of different etch character found in practice after 30 min etching.

as sketched in Fig. 2(b); the maximum field, E_{max} , exists at the silicon-electrolyte interface.

The value of E_{crit} as a function of the donor concentration is given in (11). Figure 3 gives the values of E_{crit} and E_{max} for a 10V drop across the depletion layer. In the upper part of the same graph, an indication is given of what has happened in practice during 30 min etching of dislocation-free material. It can be seen that the E_{max} value exceeds the value of E_{crit} at donor concentrations above 2×10^{17} donors/cm³ and dissolution due to breakdown of the depletion layer may be expected. Above 10^{18} donor/cm³ tunneling is the most probable breakdown mechanism. The field at which tunneling may occur is indicated by the broken line. In the donor concentration range below 2×10^{17} cm⁻³, E_{max} is lower than E_{crit} . It is expected that no holes are generated by impact ionization and no dissolution should occur.

The influence on the etching behavior of the donor concentration and defects.—In practice the situation is much more complicated as some of the approximations made are not valid. In fact three ranges of different etch character were found after a 30 min etch of dislocation-free, homogeneously doped n-type ma-

terial (2). Anodic dissolution occurred (at 10V) when the donor concentration was higher than about 2×10^{18} cm⁻³. For impurity concentrations between 2×10^{18} and 2×10^{16} cm⁻³ a brownish-black, pitted surface was formed. Sections of the slices showed higher density of channels at the higher donor concentrations. In the range below about 2×10^{16} cm⁻³ no measurable dissolution occurred and no channels were detected.

Figure 4 shows the current density vs. time plot for dislocation-free, float zone silicon of various donor concentrations at a potential difference of 10V between anode and cathode. Pre-etched samples were used. The increase of the current density for the samples of $(1.3-3.7) \times 10^{16}$ and $(2.5-13) \times 10^{15}$ cm⁻³ coincides with the formation of etch channels which were found in these samples. The observed higher current density may be explained as an increase in real etching surface, which means that the real current density does not necessarily change. The other samples exhibited no channels; uniform etching was observed with the highly doped sample ($N_D = 4 \times 10^{18}$ cm⁻³); the low-doped samples did not show a visible attack. However when silicon material with dislocations,

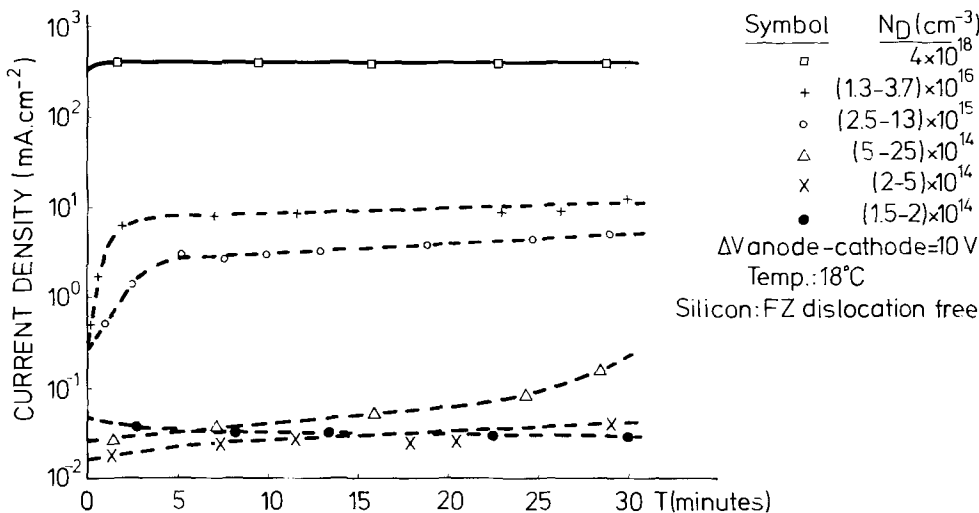


Fig. 4. Current density vs. time for silicon of various donor concentrations for an etching time of 30 min at 10V.

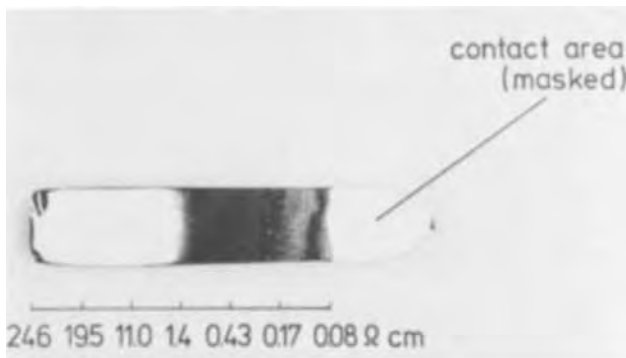


Fig. 5. Longitudinal section of a silicon bar (float zone, dislocation free) with varying resistivity. The surface of the section has been subjected to the electrochemical etching process for 60 min.

scratches or other kinds of mechanical damage was used, etch pits surrounded by a pattern of fine lines were found in low-doped samples. Cross sections of these slices revealed networks of etch channels around these pits. Bellin and Zwicker (12) did anodization experiments on n^- silicon in hydrofluoric acid and copper sulfate. They found a remarkable agreement between the channel and dislocation networks which are often observed around defects.

Figure 5 shows the etched side of a longitudinal section of a float zone, dislocation-free silicon bar of varying resistivity. This bar had been subjected to the electrochemical etching process with an anode-cathode voltage of 10V. The dark area of the n^- zone and the bright unattacked n^- zone are clearly visible; the transition between the two zones shifts to higher resistivity material when the etching time increases.

Figure 6, shows J - V curves for some silicon samples of various donor concentrations. The dislocation density of these samples was low. The potential difference between anode and cathode was increased stepwise. Current and voltage were measured within 30 sec after the application of the potential. The total measuring time was less than 30 min. Because the high resistivity samples exhibited J - V curves that were very sensitive to surface damage such as

scratches, lapping, polishing processes, or surface contamination, pre-etched samples were used. As can be seen the low-doped samples exhibited breakdown-like characteristics. The breakdown voltage seems to be inversely proportional to the donor concentration, but it is still much lower than that expected theoretically. The explanation may be that during the measurement of the J - V curves channels are etched which influence the shape of these curves. Meek (7), for example, observed etch pits even at current densities below the saturation current. The influence of the channel formation on the J - V measurement can easily be demonstrated by repeating a J - V curve of the same slice. This is shown in Fig. 7. J - V curves for the n^+ (and p)-type silicon appeared to be much more reproducible (7).

Channel Etching in n -Type and n^+ -Type Silicon

At silicon electrode voltages of 10V etch channels were always formed in moderately doped n -type silicon ($2 \times 10^{18} > N_D > 2 \times 10^{16} \text{ cm}^{-3}$), but the attack did not seem to be related to crystal defects. The density of the channels increased with the donor concentration. With N_D about 10^{18} cm^{-3} cross sections showed a brownish layer in which the channel density was so high that the individual channels were hardly visible. Figure 8(a) and 8(b) show cross sections of two n -type samples with donor concentrations $N_D = 2 \times 10^{18} \text{ cm}^{-3}$ and $N_D = 2 \times 10^{16} \text{ cm}^{-3}$. As can be seen the channel density in the highly doped sample is much higher than in the lower doped sample. Moreover the highly doped sample shows a straight line between the brown, channel-rich structure and unattacked silicon substrate whereas the low-doped sample shows fluctuations of the channel depth along the section. The fluctuations could be attributed to fluctuations of the donor concentration (resistivity striations) along the section. For the low-doped samples the local etch rate seems to be a function of the local donor concentration. This is not the case with the highly doped samples although striations were found to be present.

For n^+ silicon ($N_D > 2 \cdot 10^{18} \text{ cm}^{-3}$) it was found that etching at 10V resulted in a bright electropolished surface. The corresponding current density was about $130 \text{ mA} \cdot \text{cm}^{-2}$, but this value could be considerably

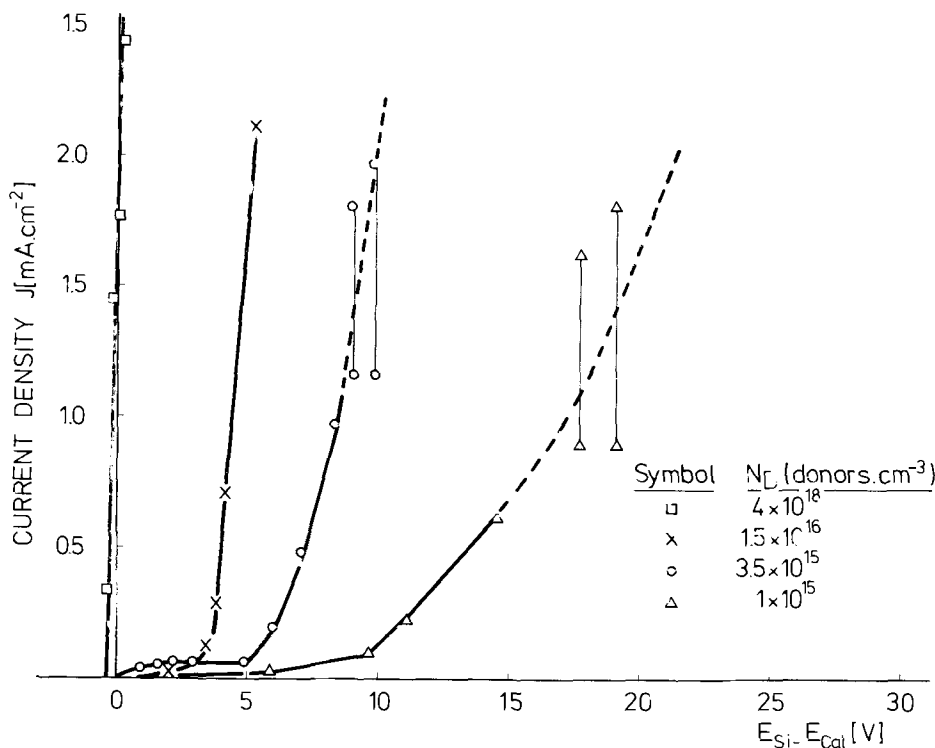


Fig. 6. Current density vs. electrode potential for various donor concentrations.

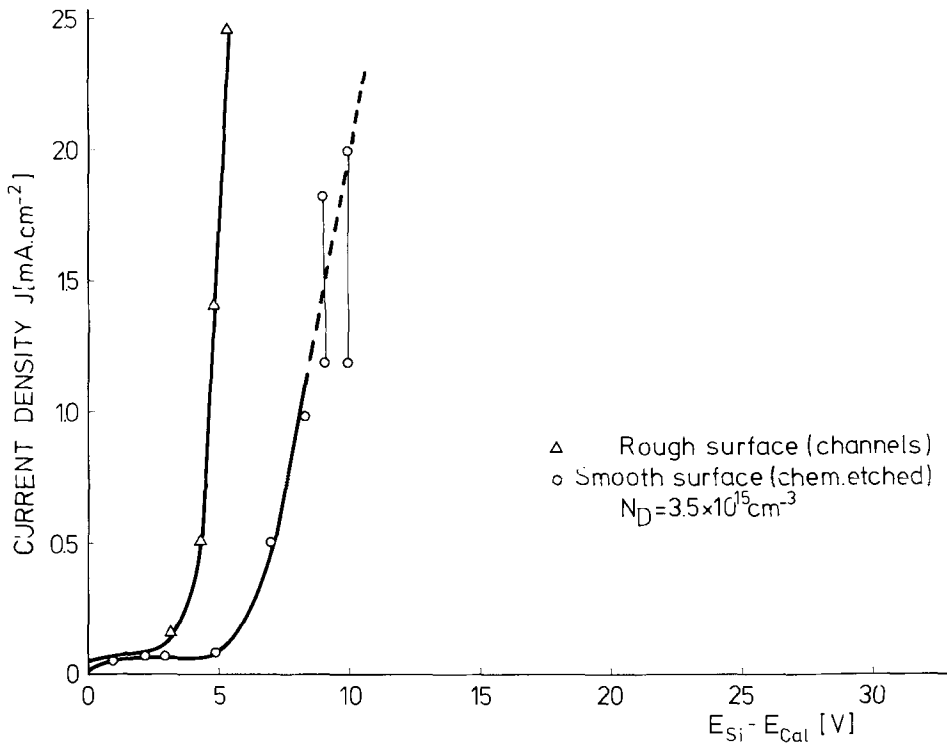


Fig. 7. Current density vs. electrode potential for a smooth and a rough surface.

increased by stirring, which implies that the etch rate is controlled by diffusion. This is in agreement with Turner's observation (6). At lower voltages (or current densities), depending on the donor concentration, the formation of a brownish layer was observed. In order to determine the crystallinity of the brown layers, n⁺- and n-type silicon samples were totally converted to channel-rich structures. X-ray diffraction patterns [Fig. 9(a) and 9(b)] showed that except for minor differences, the monocrystalline character was unchanged. Infrared transmission spectra confirmed that the brown layer samples were almost pure silicon. These observations are consistent with the idea that the brown layers consist of a framework of the monocrystal, which is left after the channel etching.

As reported by Meek (7) the brownish layer formation on n⁺ samples is typical for current densities below J_{crit} . J_{crit} is the current density at which the brown layer starts to be detached. Above J_{crit} it is not likely that the etch rate is determined by the availability of holes, but rather by the supply of F⁻ ions to the etching surface. At current densities lower than J_{crit} it is difficult to say which step determines the etch rate. Meek's measurements (13) suggest that a trap to band transition mechanism supplies holes to the etching interface. The dissolution process itself seems to be divalent (7).

As indicated by the short time needed to reveal the channels in Sirtl etchant, inside these channels there is probably some fast etching material. Amorphous

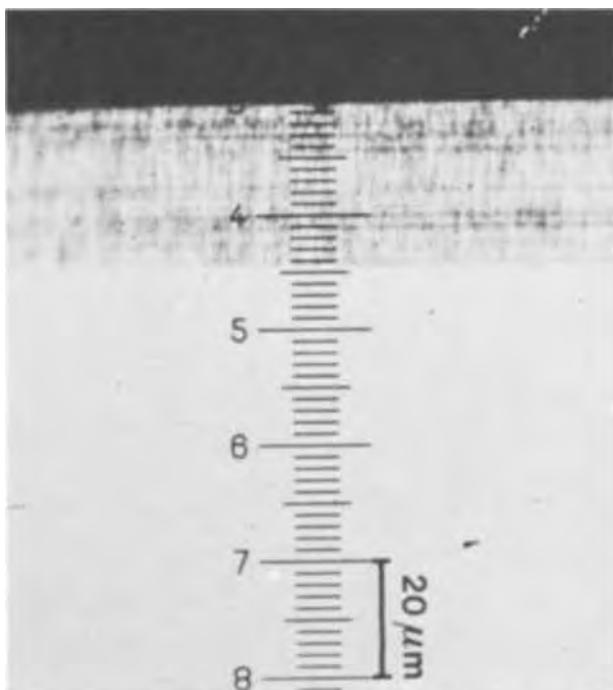


Fig. 8(a). Section of a (100) sample of n⁺-type Si ($N_D = 2 \times 10^{18} \text{ cm}^{-3}$) after 30 min etching at $J = 20 \text{ mA cm}^{-2}$.

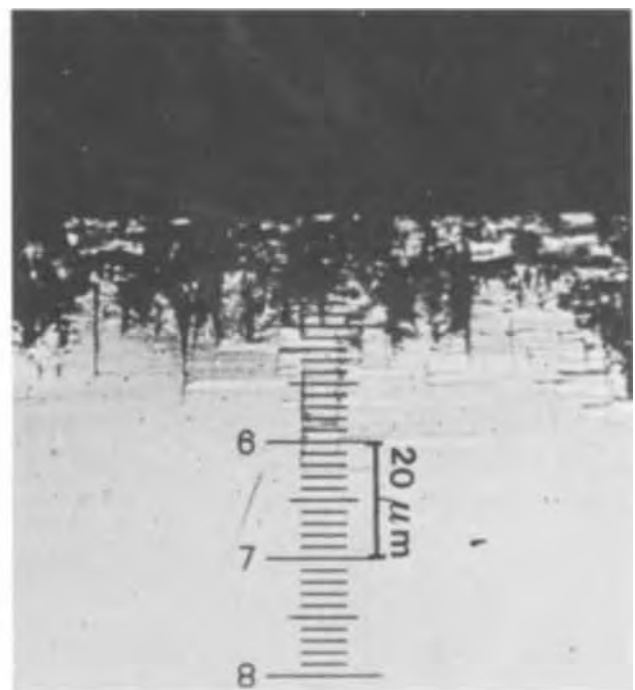


Fig. 8(b) Section of a (100) sample of n-type Si ($N_D = 2 \times 10^{16} \text{ cm}^{-3}$) after 30 min etching at $J = 15 \text{ mA cm}^{-2}$.

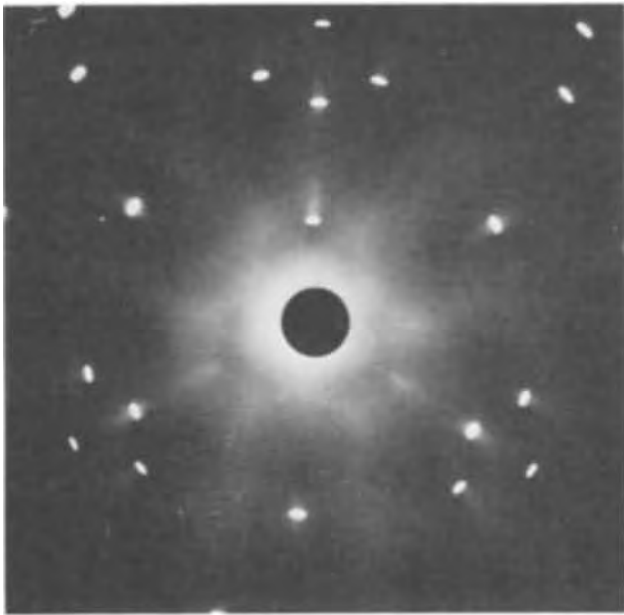


Fig. 9(a). X-ray diffraction pattern of a (111) surface-oriented slice.

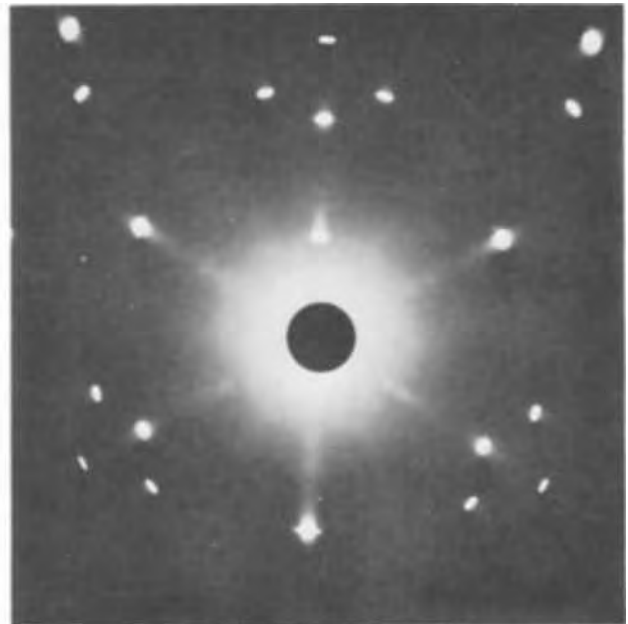
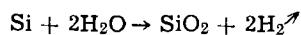
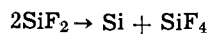
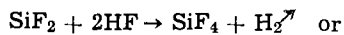


Fig. 9(b). X-ray pattern of the same slice electrochemically converted into "brown layer" structures.

silicon or silicon hydride compounds have been reported elsewhere (14). The presence of the amorphous silicon had been explained by Turner (6) by the disproportionation of SiF_2 . The presence of SiH_4 -like compounds may be due to hydrogen passivation of the surface. At current densities lower than J_{crit} hydrogen evolution was observed. As described by Memming and Schwandt (15), hydrogen may be evolved with the reactions



However, more information will be needed to support

this hypothesis, because most of the relevant interface processes are still unknown.

The Direction of the Channels in the Monocrystal

Figure 10 shows the surface and (111) cleaved sections of (111), (100), and (110) oriented silicon slices. The channels or the points of intersection of the channels with the surface or cleavage planes were made visible after 3 sec Sirtl etching. Slices with a (111) surface orientation were found to give channels lying in {111} planes and in the [110] directions. The fact that the channels grow out in well-defined directions can point to either a bulk property of the silicon lattice (open directions where impurities prefer to collect) or to a surface mechanism (influence of the

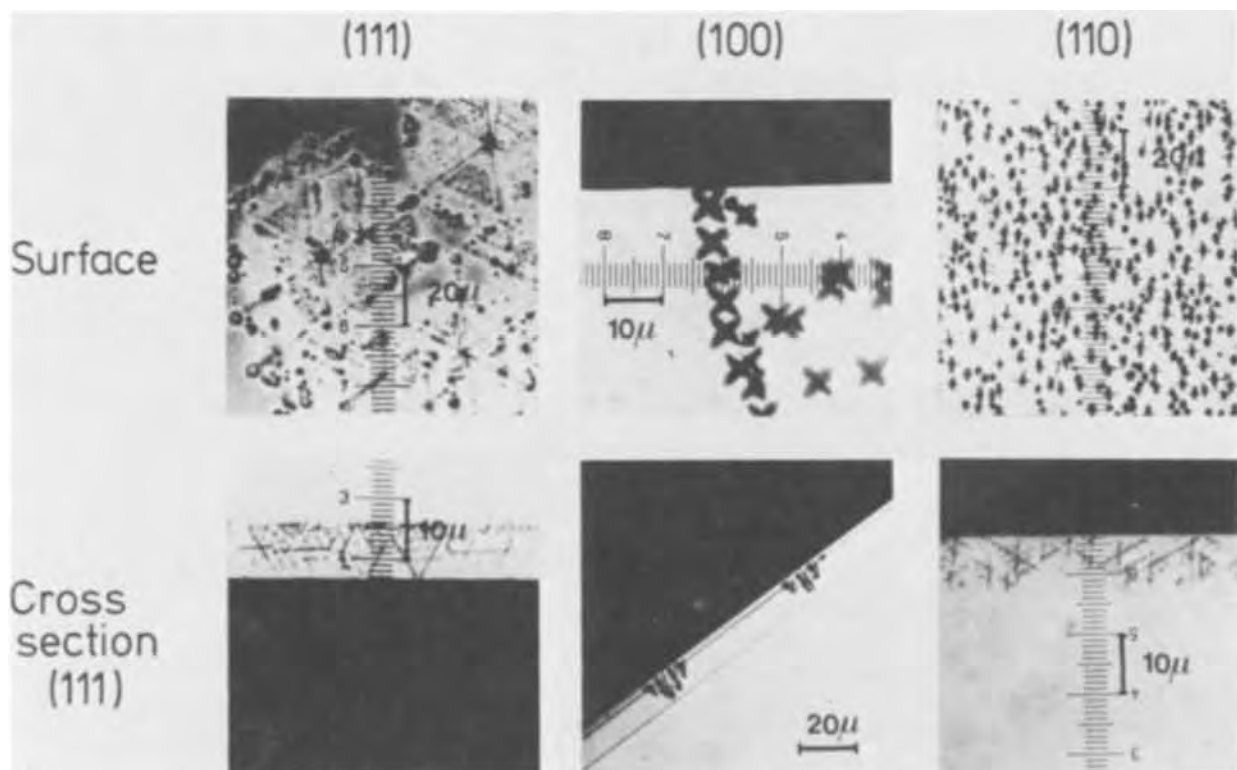


Fig. 10. Surface and (111) cleavage sections of slices of the (111), (100), and (110) orientations

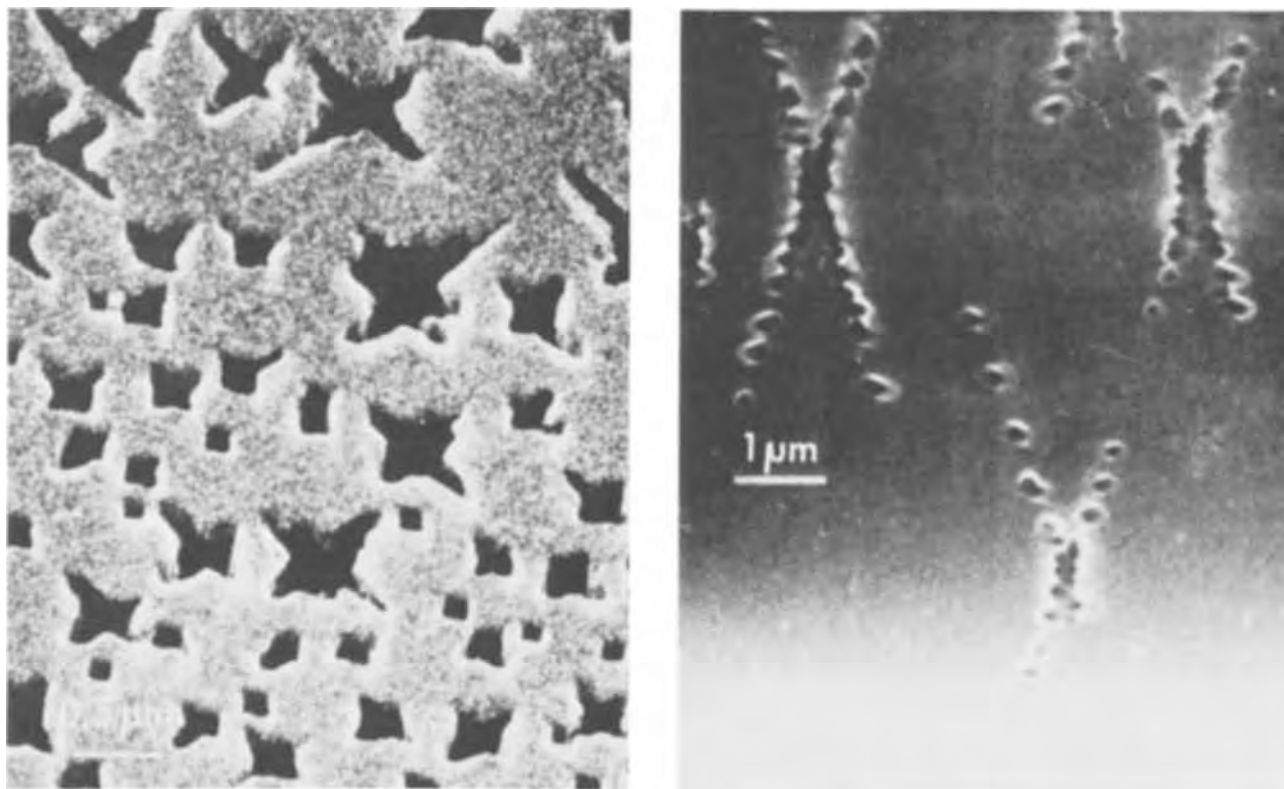


Fig. 11. SEM photograph of the etched side of a (100) epitaxial layer after removing the n^+ substrate and after 5 sec Sirtl etching: (left) the surface and (right) a section of the layer.

adsorbed or chemisorbed ions at the surface). As mentioned before, it is reported elsewhere (14) that brown layers contain, in addition to silicon, SiH_4 -like compounds. Hydrogen passivation of the interior surfaces other than in the channel propagation directions might explain the anisotropic etching behavior.

Etching of Epitaxially Grown Structures

Preferential etching of $n^+ n^-$ structures was carried out at 10V (2). The thin n^- layer was always covered by a brown layer. In practice the $n^+ n^-$ interface profile is not abrupt; its slope depends on the time and temperature of growth, autodoping, and subsequent heat treatment. In fact it is a $n^+ n^-$

structure, in which the thickness of the intermediate n layer depends on the processing. During the electrochemical treatment the n -type layer is converted into a brown, channel-rich layer. Moreover it was observed that the high resistivity epitaxial n^- layer, which is not expected to etch, sometimes contains channels (Fig. 11). From the n layer a minor part of the channels grows out into the n^- layer. Because the channel formation is a time-dependent process, the channel depth across the n^- layer (2) will follow a distribution schematically indicated in the figure (Fig. 12). In this figure diffused areas in the epitaxial layer are indicated. The areas which are farthest from the contact are attacked because the electrolyte can communicate

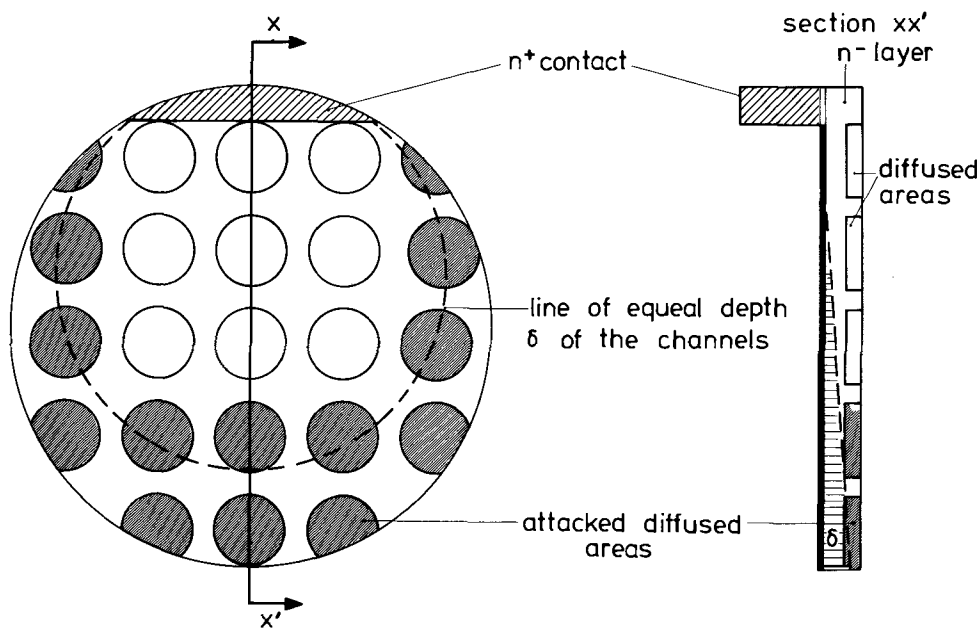


Fig. 12. Schematic representation of the attack of diffused areas through channels.

δ = depth of channel region

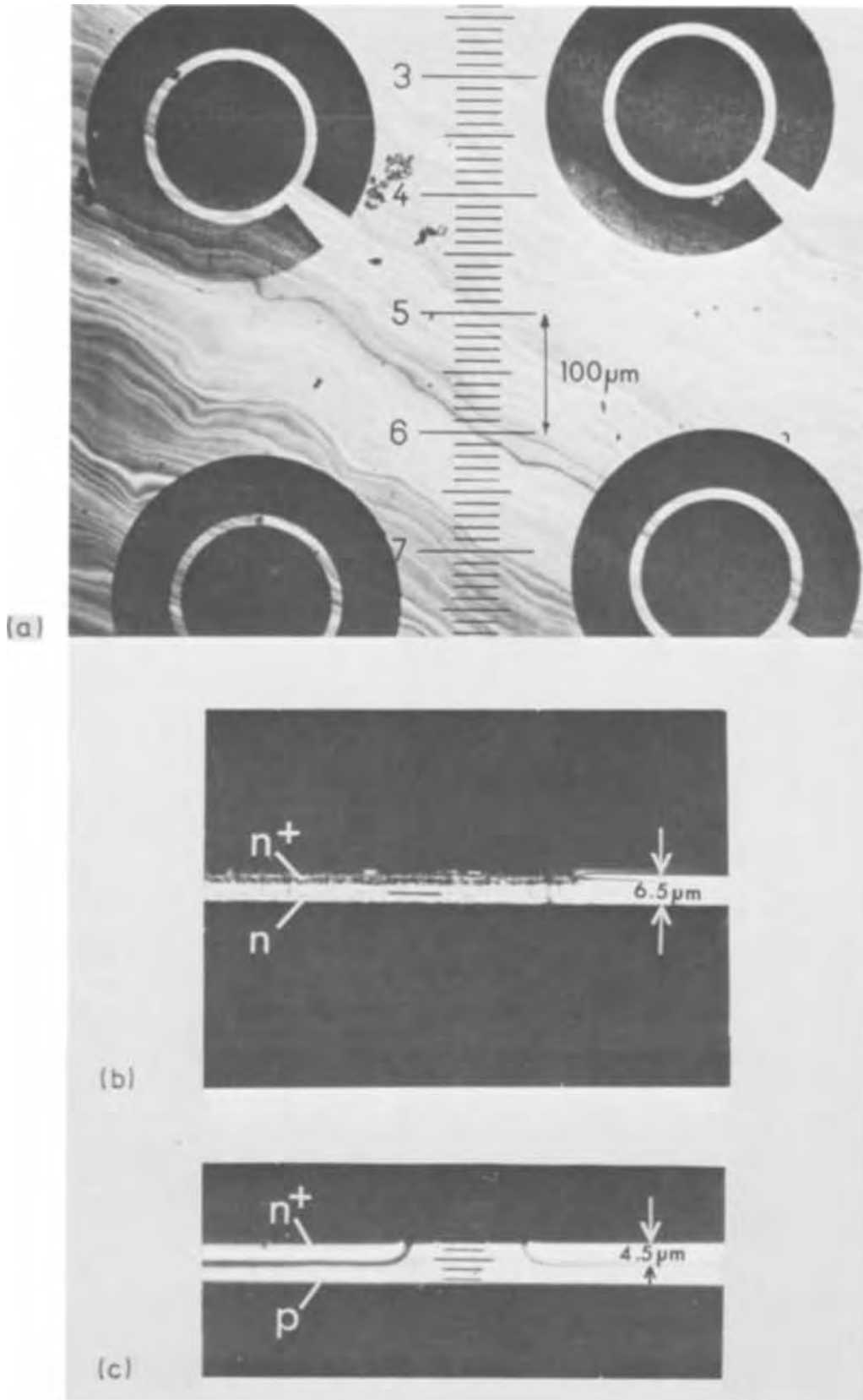


Fig. 13. Photograph of the attack of n^+ diffused areas: (a) the etched side of the n^- layer, (b) detail of a cross section, which shows that the n^+ areas are attacked through the thin intermediate n^- layer, and (c) cross section of a thin p-type layer, in which n^+ areas have been made by diffusion. The n^+ areas and the p-type layer are not attacked.

here with the highly doped regions. This distribution of the attacked diffused areas was often observed. Moreover n^+ diffused areas were found to be readily attacked with respect to p^+ diffused areas, as demonstrated in Fig. 13(a) and 13(b). This is probably due to the increased hole generation at defects (dislocations, precipitates) at the n^+ diffused regions. Meek (4) points to the field-aided diffusion of minority carriers (holes) toward the etching interface. This may also be the case with n^+ diffusions in p layers, but no influence on the etching behavior would be expected

because holes are already the majority carriers. That n^+ diffusions in p-type layers are not attacked is demonstrated in Fig. 13(c).

One means of preventing attack of the diffused areas is to take a relatively thick intermediate n^- layer between the n^+ diffusion area and the n^+ substrate. A second method employs an additional p-type layer which can be made between the n^+ substrate and an n-type epitaxial layer. P-type silicon exhibits no etch channels. Some other methods are suggested in Ref. (4).

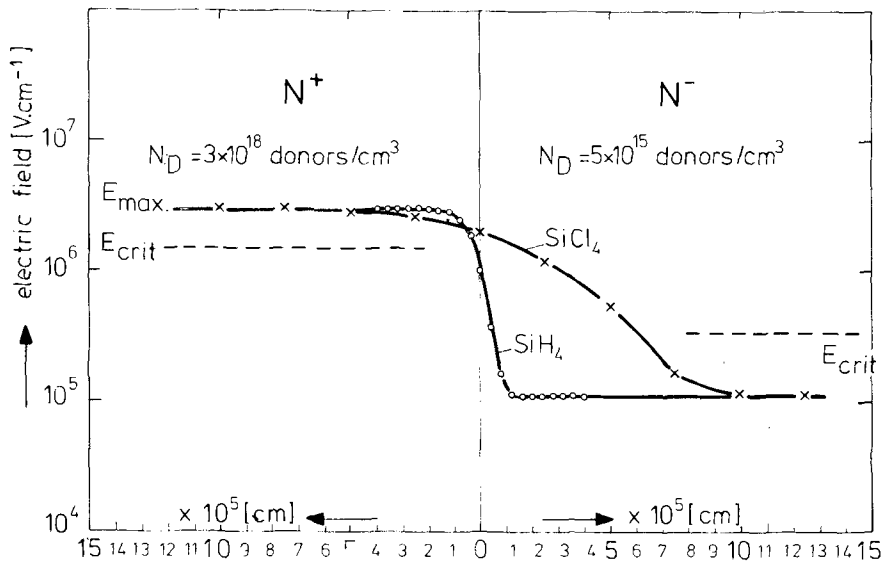


Fig. 14. The calculated electric field, E_{\max} , near the epitaxial interface during etching, assuming $V_{\text{depletion layer}} = 10\text{V}$; the distribution of donor atoms is given by $N(x) = N_0/2 \operatorname{erfc}\left(\frac{x}{2\sqrt{DT}}\right)$. Heat-treatment during epitaxy gives $\sqrt{DT} = 4 \cdot 10^{-6}$ cm for SiH_4 and $25 \cdot 10^{-6}$ cm for SiCl_4 . The breakdown field, E_{crit} , has been indicated by the broken line.

In order to reduce the thickness of the outdiffused layer between the n^+ substrate and the n^- epilayer, epitaxial structures were made at relatively low temperatures (1050°C) using SiH_4 epitaxy. The donor concentration of the n^- layer did not exceed $5 \times 10^{15} \text{ cm}^{-3}$. It was found that when such structures were etched preferentially at 10V , no channels were detected in the n^- layer. This contrasts with a silane-grown n^+n^- slice that has been subjected to an additional high-temperature treatment and with an n^+n^- slice made by SiCl_4 epitaxy at 1220°C . Typical etch times were about half an hour in both cases. The difference in etching behavior might be explained by the difference in outdiffusion profile of the donor concentration. Assuming that the interface profile of n^+ to n^- is determined only by outdiffusion and not by autodoping (16) during epitaxy, we can calculate E_{\max} from the Poisson equation, using $V_{\text{depl.}} = 10\text{V}$, and $N(x)$ should be given by

$$N(x) = \frac{N_0}{2} \operatorname{erfc}\left(\frac{x}{2\sqrt{DT}}\right)$$

$N(x)$ is the donor concentration at a distance x from the interface, N_0 the concentration of the n^+ silicon, D the diffusion coefficient, and T the diffusion time. Figure 14 shows the variation of the E_{\max} value across the interface for epitaxial slices made by the SiH_4 and SiCl_4 process. The value of E_{crit} has been indicated for the n^+ and n^- silicon. The intermediate layer, which is converted into a brown, channel-rich zone, is much thinner in the SiH_4 slices. Moreover, E_{\max} drops sharply for SiH_4 , whereas the corresponding change in E_{crit} is more gradual.

N^- type layers made by SiH_4 and SiCl_4 epitaxy having equal resistivities and thicknesses were compared by four-point-probe resistivity measurements after etching of the n^+ substrate. It was found that SiH_4 -made layers systematically showed higher resistivities. Apparently for the SiCl_4 -made layers the tail of the outdiffusion profile and the monocrystalline framework of the brown layer contribute to the conductance. This means that in the case of SiH_4 the potential drop alongside the slice is greater. Areas farthest from the contact place have such a low electrode voltage that the channel etching process probably does not occur.

Conclusion

During the anodic dissolution process of n^- , n^- , or n^+n^- type silicon, etched channels can be formed, which grow out in crystallographically well-defined directions in the monocrystal. The origin of these etch channels is ascribed to the local breakdown of a barrier at the surface of the silicon. This provides holes

which are necessary for the etching process. For high resistivity silicon a depletion layer model can be used. The maximum electric field E_{\max} at an electrolyte-silicon interface is a function of the voltage across the layer and the donor concentration. Breakdown will occur when $E_{\max} > E_{\text{crit}}$. In practice local breakdown will occur, dependent on crystal defects, impurities, fluctuations of the donor concentration, etc. Highly doped silicon exhibits a high channel density only at low values of the silicon electrode potential.

J - V curves for low-doped silicon are dependent on the growing process of the channels. This means the shape of the curves is time dependent.

The occurrence of etch channels in the n^- layer during preferential electrochemical etching of n^+n^- can be easily explained with the results of the homogeneously doped samples. The anode voltage, the donor concentration of the n^+ - and n^- -type silicon, the steepness of the n^+n^- interface profile, the presence of defects in the n^- layer (often introduced by diffusions), and the total exposure time of the n^- layer to the electrolyte must be taken into account. Using standard etching conditions (10V) it was found that etch-through effects between the diffused areas and the n^+ substrate can be eliminated in the following ways: (i) Take a relatively thick intermediate n^- -type layer between the n^+ substrate and the diffused areas. (ii) Use an additional p layer between the n^+ substrate and the n^- layer. (iii) Reduce the total amount of heat-treatment which precedes the electrochemical process. Good results were obtained with SiH_4 epitaxy carried out at 1050°C and $N_D = 5 \times 10^{15} \text{ cm}^{-3}$ for the n^- layer. Typical etch times were half an hour.

Acknowledgments

The author wishes to thank Mrs. E. Olijdam, who carried out much of the experimental work, W. J. Schouten for the scanning electron microscopy, C. Langereis for the x-ray diffraction techniques, and C. Albrecht for mathematical assistance.

Comments by T. L. Tansley, E. Kooi, J. de Jonge, and G. Schwandt were very helpful.

Manuscript submitted May 19, 1971; revised manuscript received Oct. 13, 1971.

Any discussion of this paper will appear in a Discussion Section to be published in the December 1972 JOURNAL.

REFERENCES

- H. J. A. van Dijk and J. de Jonge, *This Journal*, **117**, 553 (1970).
- M. J. J. Theunissen, J. A. Appels, and W. H. C. G. Verkuijlen, *ibid.*, **117**, 959 (1970).

3. M. J. J. Theunissen, Paper presented at the Fourth Annual Conference on Solid State Devices, Exeter, N. H., Sept. 14-18, 1970.
4. R. L. Meek, *This Journal*, **118**, 1240 (1971).
5. A. Uhlir, Jr., *Bell System Tech. J.*, **35**, 333 (1956).
6. D. R. Turner, in "The Electrochemistry of Semiconductors," p. 179, P. J. Holmes, Editor, Academic Press, London (1962).
7. R. L. Meek, *This Journal*, **118**, 437 (1971).
8. F. C. Eversteijn, P. J. W. Severin, C. H. J. v.d. Brekel, and H. L. Peek, *ibid.*, **117**, 925 (1970).
9. E. Sirtl and A. Adler, *Z. Metallk.*, **52**, 529 (1961).
10. V. A. Myamlin and Y. V. Pleskov, "Electrochemistry of Semiconductors," p. 30, Plenum Press, New York (1967).
11. A. S. Grove, "Physics and Technology of Semiconductor Devices," p. 193, John Wiley and Sons, Inc. (1967).
12. P. H. Bellin and W. K. Zwicker, *J. Appl. Phys.*, **42**, 1216 (1971).
13. R. L. Meek, *Surface Sci.*, **25**, 526 (1971).
14. K. H. Beckmann, *Surface Sci.*, **3**, 314 (1965).
15. R. Memming and G. Schwandt, *ibid.*, **4**, 109 (1966).
16. K. Suzuki and M. Endo, Paper 96 presented at Electrochem. Soc. Meeting, Los Angeles, May 10-15, 1970.

The Chromium-Glass Interface

R. G. Frieser

IBM Components Division, East Fishkill Facility, Hopewell Junction, New York 12533

ABSTRACT

Using a combination of etch and contact angle techniques, three regions were identified in the thin chromium films deposited on glass substrates. It appears that the thin native oxide surfaces do not usually etch homogeneously. The glass/chromium interface, approximately 50-100Å thick, is formed by modifying the original glass due to the penetration of the chromium during the oxidation process. The interface seems to become a chrome-glass with the chromium concentration decreasing as a function of the depth of penetration.

The prevalence of the use of thin chromium films on oxides and glass substrates in the present technology makes the study of the chromium-glass interface particularly relevant.

Chromium was chosen for many applications because of its good adhesion to glass, its hardness, and the relative inertness which is protected by a supposedly uniform layer of oxide. Attempts to peel chromium films ~1000Å or less from glass substrates invariably resulted in a layer of glass coming off with the chromium. This indicates that rupture occurs below the "interface," since apparently the cohesive forces in the glass adjacent to the interface are smaller than the adhesive forces of the chromium to the glass. Furthermore, the original glass surface may have become modified during the chromium deposition process, in which case one would expect an interfacial region rather than a sharp interface. The properties in this interfacial region would change gradually from the properties of pure chromium to that of the glass.

By etching off successive layers of the chromium films below the "interface" and measuring the contact angles that drops of water form with the respective surfaces, it appears that an interfacial region was located.

Experimental Procedure

Contact angles were measured using a Ramé-Hart Contact Angle Goniometer. Uniform water drops were dispensed from a precision liquid dispenser with 0.1% accuracy of the dispensed volume through a 0.1 ml range. The actual volume of the drops used was 2×10^{-4} ml. Only water distilled in a quartz still from a potassium permanganate solution was used. Photographs of three drops on each respective surface were taken and the contact angles were determined using a geometric technique. Thus, the contact angles could be measured to $\pm 1^\circ$. An acidic ceric sulfate solution (20g $\text{Ce}(\text{SO}_4)_2$, 164 ml HNO_3 conc, 6 ml H_2SO_4 conc, and 330 ml D.I. water) was used to etch the chromium films.

Surface Cleaning

Meaningful contact angle measurements can only be made on homogeneous surfaces. However, highly

nonuniform etch rates on large area chromium films were noted in spite of the fact that the optical density of these films was uniform prior to etching. Similar results were obtained with conventional standard alkaline etchants. Ordinarily this effect may escape attention, because the chromium is completely removed between patterns etched into the chromium films. It was further noted that this phenomenon is highly surface sensitive. Various schemes of cleaning the chromium surface followed by an annealing procedure at different temperatures in a nitrogen furnace resulted in even more irregular etch rates across the treated films. The etch rates were particularly irregular when organic solvents such as acetone, trichloroethylene, methanol, or freon were part of the cleaning cycle. This was true even when either was preceded or followed by an oxidant.

However, it was possible to obtain sufficiently homogeneous surfaces by the following technique: One-half hour boiling of the chromium-coated substrate in an ammonia-hydrogen peroxide solution (80 ml 30% hydrogen peroxide, 35 ml 58% ammonium hydroxide, and 885 ml water) at 80°C, rinsing in deionized water at R.T., boiling for 15 min in deionized water, rinsing again in deionized water (R.T.), and inserting into the etching solution while still covered with a uniform film of water.

Presumably, this procedure not only cleaned the surface but hydrated the thin native oxide on top of the chromium film.

Further verification for the inhomogeneity of the surface was obtained from ellipsometric studies of the surfaces of thin chromium films on glass substrates prior to cleaning.

Because neither the type of oxide, much less the optical constants, were known, the delta and psi values which are complex functions of the refractive index, the wavelength, and the angle of incident light could only be compared (1). Employing an immersion technique, data on the chromium-glass interface were obtained in the same study. The following conclusions support the observations noted during the etching experiments: (i) The free chromium surface is very nonuniform; data were highly ambiguous. (ii) The chromium/glass interface data were extremely uniform.

Table I. Freshly cleaned vs. aged chromium surface

Position of contact angle on surface	Top	Center	Bottom
Freshly cleaned	16°	24°	21°
24 hr aging in air	45°	46°	43°
Optical densities	2.89	2.81	2.80
Recleaned	18°	18°	21°
24 hr aging in air	52°	42°	40°
Optical densities	2.86	2.81	2.78

Table II. Chromium-glass interface

Position of contact angle on the surface	Chromium glass		Bare glass	
	Original chromium	Etched 14'30"	Original glass	Etched 14'30"
Fresh				
Top	17	90	6	13
Center	19	91	7	17
Bottom	20	83	5	9
Aged for 24 hr				
Top	38	86	12	14
Center	37	81	6	14
Bottom	41	88	9	19

(iii) No obvious correlation was observed between the optical density of the films and delta values.

Contact Angle Study

After obtaining homogeneous surfaces by the above technique, contact angles were measured before etching the chromium films, on freshly etched, as well as aged chromium and glass surfaces.

Table I is a summary of representative data of contact angles of water on cleaned and air-aged chromium surfaces. Three drops on each sample were measured. Top, center and bottom refers to the location of the drop on the surface to be measured.

These data indicate that the increase in the contact angle on aging were repeatable and probably a function of the degree of hydration of the surface. The

Table III. Contact angles of water

Position of contact angle on surface	Etched in Ce (SO ₄) ₂ H ⁺				
	Original chromium	3'20"	3'45"	3'55"	4'00"
Top	45°	17°	20°	57°	85°
Center	56°	23°	24°	49°	89°
Bottom	50°	25°	26°	62°	89°
Optical density	1.45	0.40	0.22	0.13	0.07

constancy of the optical densities shows that the observed surface changes should be attributed to a reversible transformation of the surface and that no loss of chromium metal seems to be involved. The effect of overetching on the chromium and bare glass side is shown in Table II. The samples were exposed to the etchant approximately twice as long as required to completely remove the chromium film.

Only the original chromium surface exhibits an increase in the contact angle. However, a dramatic increase in the contact angle after etching on the chromium side is observed—indicating that the glass adjacent to the chromium has different etch characteristics. Replica electron micrographs showed that the high contact angle was not due to surface roughness. Figure 1 shows that, on the scale 24,800X, the surface with the lower contact angle (16°) appears rougher than the high angle surface (85°). It appears that the noted roughness is much too small to have an effect on the contact angle.

The same observation can be made in Fig. 2 (176X). Again, little, if any, surface roughness can be noted which could account for the difference in contact angles. Table III shows the variation of the contact angles on one and the same plate as a function of depth from the surface after repeated etchings. The optical density shows the thinning of the chromium film. At an optical density of 0.40, a very thin

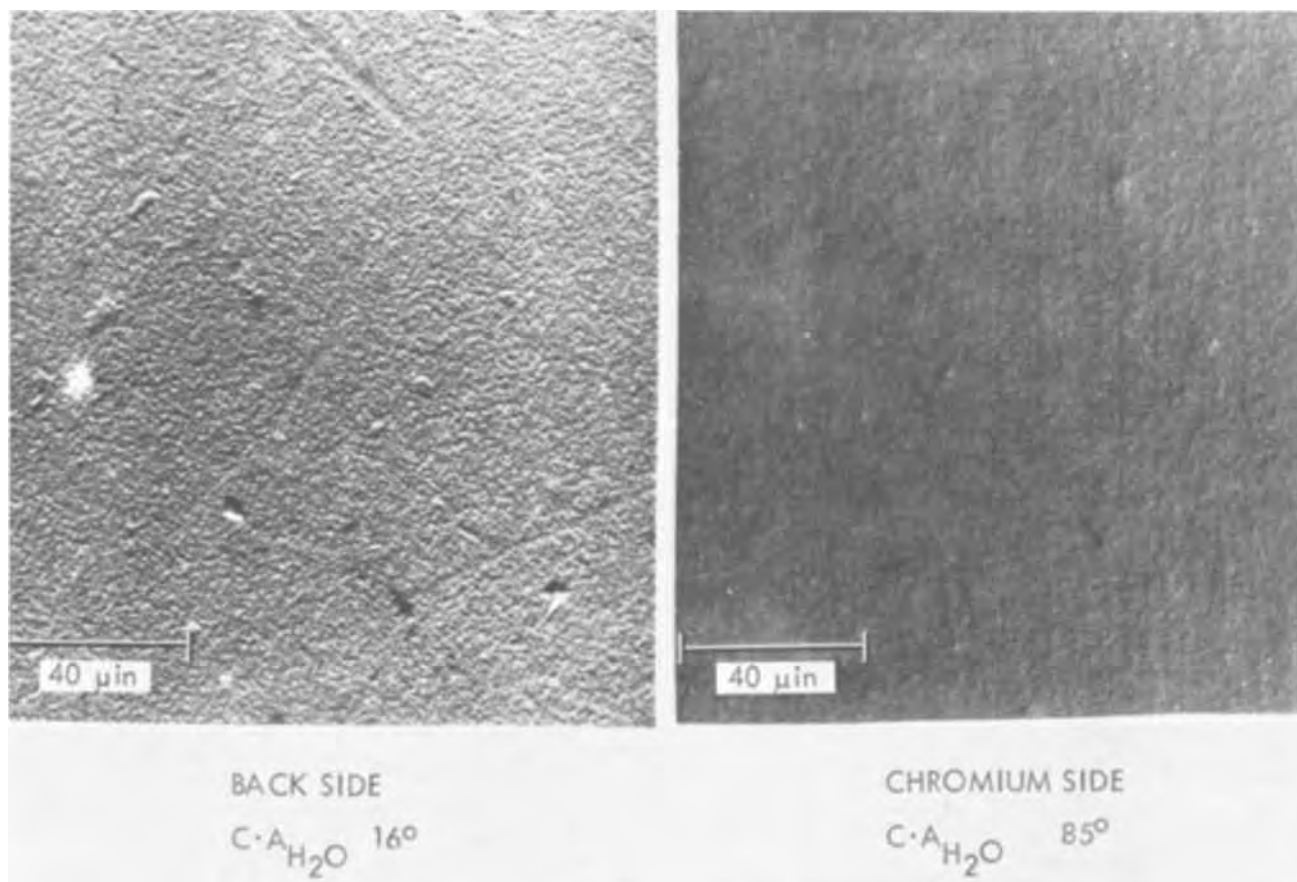


Fig. 1. Replica electron micrograph, 24,800X. (Both etched in ceric sulfate solution for 3'15")

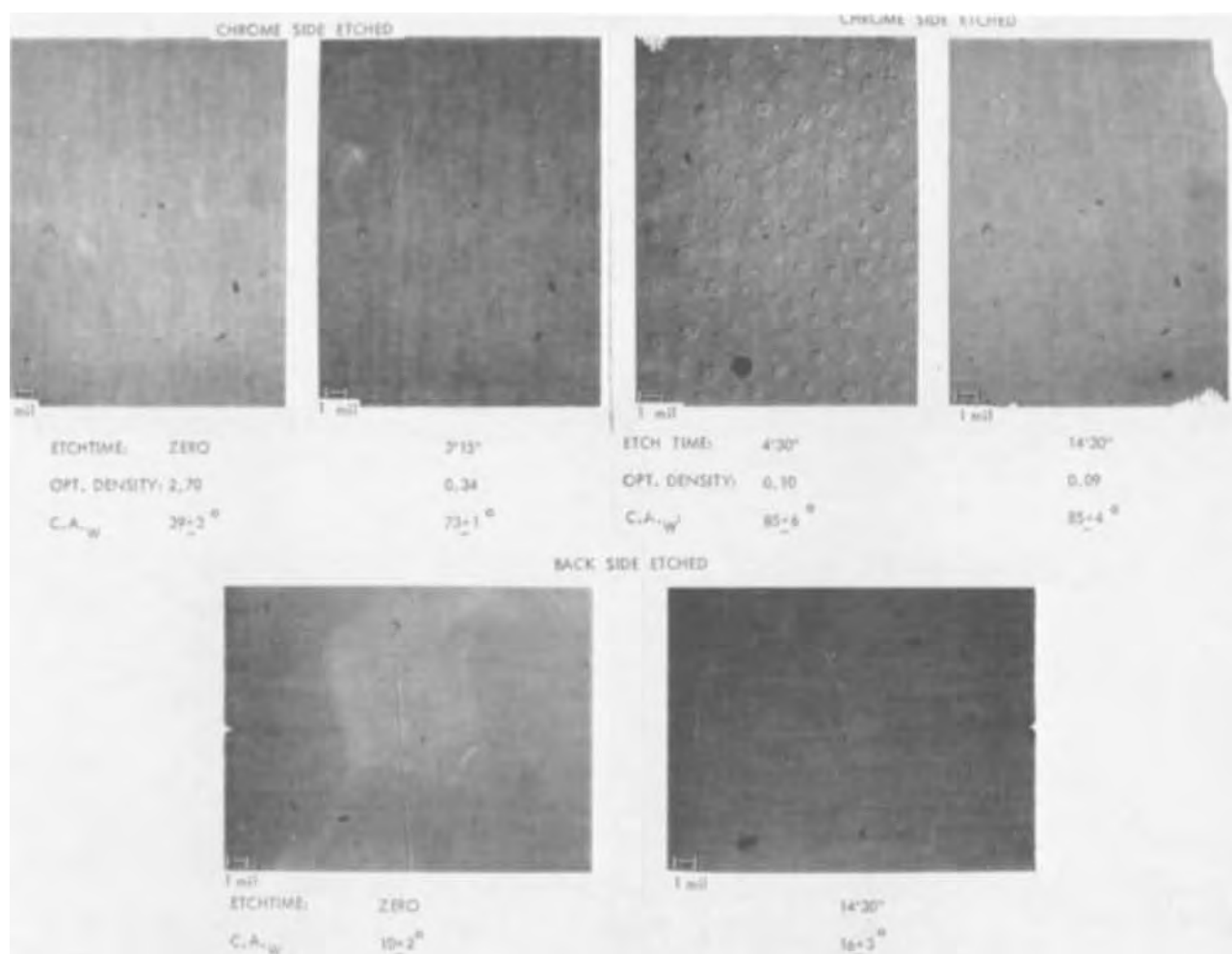


Fig. 2. Chrome and back-side etched

film of chromium was present—indeed a faint gray haze was still visible with the unaided eye. The contact angle is low (as might be expected) on a freshly hydrated chromium surface. At optical densities between 0.22 and 0.13, no chromium was visible to the unaided eye and the contact angles increased to what was previously observed on an overetched plate.

Figure 2 is a summary of the above experiment: A chromium-coated substrate was cut into six pieces. Each piece was etched in ceric sulfate etchant at room temperature as indicated below the respective pictures. After all the samples had been prepared, water contact angles were measured. Results were essentially similar to those observed in the previous experiment. The first etched sample (3'15") still had some chromium on the surface, but showed a higher contact angle than the respective sample in the previous experiment because of aging.

An electron microprobe analysis showed that the chrome side etched for 4'30" and 14'30" showed the presence of Cr on both sides. The significance of this test is qualitative, although the electron microprobe showed the presence of 0.07 and 0.02 weight per cent (w/o) Cr of the volume as compared to the standard. The Cr was in the glass below the original surface and none could be detected on the back-side, etched nor unetched. The electron beam was 10 Kv with a 25 diameter spot and an approximate penetration of 9000Å. In a subsequent experiment, 0.02% Cr was noted on a substrate which was etched for 7 min (optical density was 0.02) until all chromium has disappeared, but not in a second substrate. The inference from these experiments is that chromium, on sputtered as well as evaporated glass substrates, can be found in layers below the original surface—though

in some instances, it is readily leached-out by the etchant.

Discussion

The deposition of a chromium film on top of a glass substrate appears to modify the glass immediately beneath the chromium films. This interfacial region seems to be rather shallow, probably in the order of 50-100Å. These figures are based on etch-rate studies of the chromium-glass system. It appears that chromium penetrates the glass surface and is oxidized in the process since on etching much of it is readily leached-out. In some experiments performed under the same conditions, some chromium was detected after etching below the original glass surface indicating the presence of chromium ions loosely held by the glass. Further evidence for the penetration of chromium comes from carbon replicas on angle lapped surfaces. In Fig. 3, a region of cracks appears at the interface. Such cracks are attributed to the penetration of metal atoms and/or have been reported previously in the literature (2).

This study indicates then that three distinct regions can be identified in thin chromium films on glass on the basis of contact angle studies. This is further supported in etch studies by this laboratory and elsewhere (3). Figure 4 shows that the optical density is a linear function of the thickness of the films in Å. Thus optical density was used to determine film thickness in the etch studies. Figure 5 is an anticipated generalized etching curve. Regardless of the etchant employed or the type of chromium film, the character and the slopes of the "bulk" portion of the films of the curves obtained are similar, thus indicating three distinct regions or phases but not the slope which must be found experimentally.

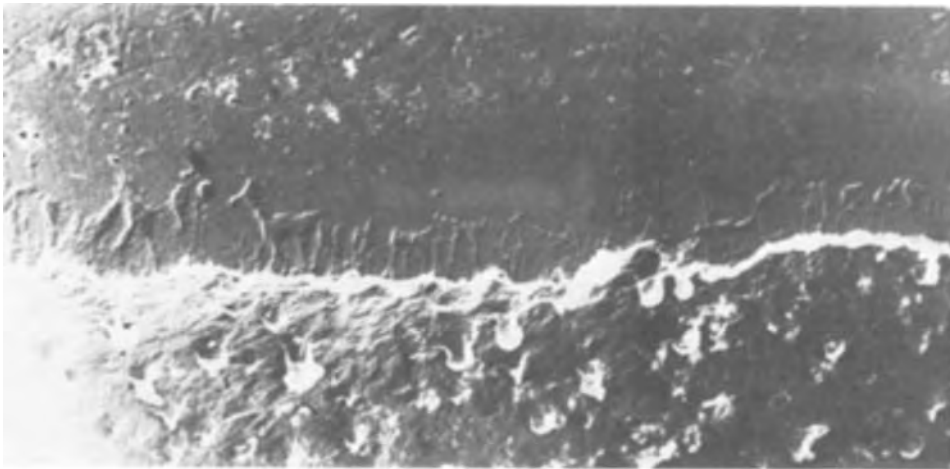


Fig. 3. Polished section of Cr/glass interface (unetched showing fissures), 13,400X.

These three regions are as follows:

(i) The surface of the chromium film which may be, but more likely is not homogeneous, due to organic or other contamination. This effect is aggravated on heating in air or nitrogen because it can modify the oxide, and in turn the etch rate. This could account for the observation that the slope of the section A of the curve in Fig. 5 varies more widely than the slopes of the "bulk" portions of this curve.

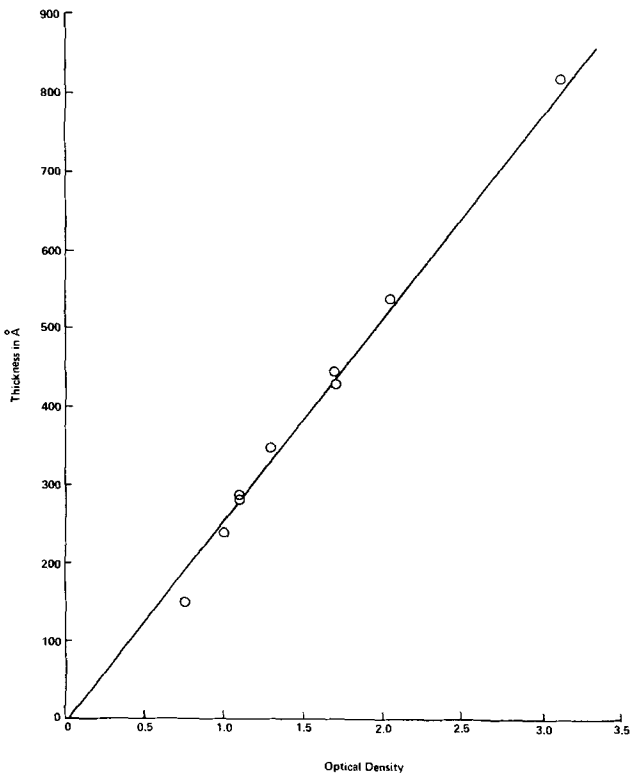


Fig. 4. Optical density vs. thickness of thin chromium films on glass substrates.

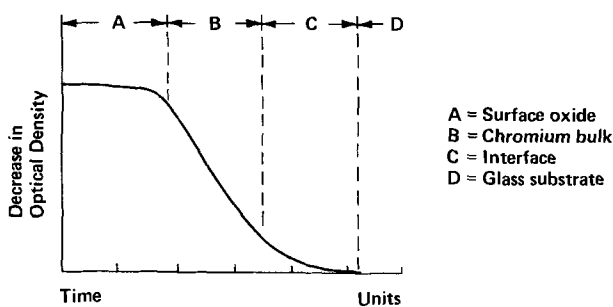


Fig. 5. Anticipated generalized etch curve

(ii) The bulk of the chromium film (section B in Fig. 5) has a relatively constant etch rate of $\sim 100 \text{ \AA}/\text{min}$ for acidic ceric sulfate etchant regardless of the manner in which the chromium film was deposited. Figure 6 represents experimental etch curves of chromium film deposited by three different techniques.

(iii) The interface proper which constitutes the modified original glass surface has again a much lower etch rate than the chrome but presumably faster than the glass itself. This is assumed because the etch rate of glass is $\sim 1 \text{ \AA}/\text{min}$, but the permanent steps can be etched into the glass when etching off the chromium on a partially coated glass substrate. It is impossible to avoid such steps even if etching is stopped as soon as the chromium film has disappeared by visual inspection.

Thus, this interfacial layer is formed by chromium ions penetrating into the original glass surface forming presumably a chromium-glass, with the chromium concentration decreasing as a function of depth into the glass.

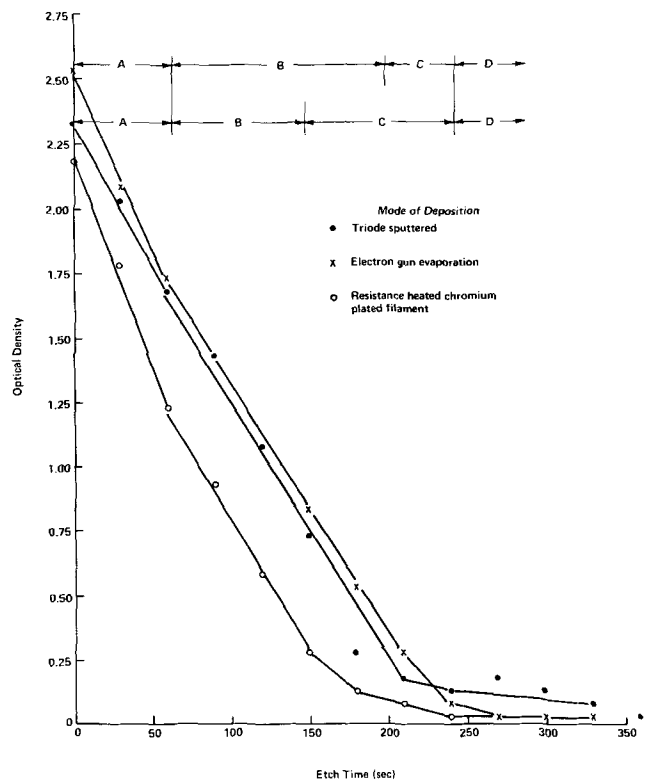


Fig. 6. Optical density vs. etch time of chromium films deposited on glass by three different techniques.

Acknowledgment

The author gratefully acknowledges the cooperation of many of his colleagues especially, T. Reith for peel test studies, D. P. Cameron for replica electron micrographs, Dr. B. H. Vromen and E. F. Gorey for ellipsometric studies, V. C. Marcotte for his electron microprobe analysis of the films, J. W. O'Brien for assisting with the contact angle and optical density measurements, and Dr. R. C. Buchanan for permission to use Fig. 3.

Manuscript submitted September 8, 1971; revised manuscript received ca. Nov. 8, 1971. This was Paper 72

presented at the Washington, D. C., Meeting of the Society, May 9-13, 1971.

Any discussion of this paper will appear in a Discussion Section to be published in the December 1972 JOURNAL.

REFERENCES

1. R. J. Archer, *J. Opt. Soc. Am.*, **52**, 970 (1962).
2. F. M. Ernsberger, *Proc. Roy. Soc. Ser. A*, **257**, 213 (1960).
3. A. Janus, Paper 109 presented at Electrochem. Soc. Meeting, Washington, D. C., May 9-13, 1971.

Selective Deposition of Silver on Silicon by Reaction with Silver Fluoride Vapor

R. J. H. Voorhoeve and J. W. Merewether

Bell Telephone Laboratories, Incorporated, Murray Hill, New Jersey 07974

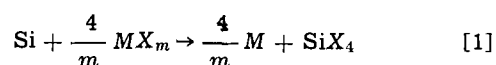
ABSTRACT

Reaction of silver fluoride vapor with a silicon surface has been shown to produce a smooth silver film at temperatures from 80° to nearly 600°C. The silicon surface is etched in the beginning of the deposition process, and silicon is continuously removed from the silicon-silver interface, leading to improved adherence of the film. Films of up to 1 μm have been obtained. On surfaces which are partly covered by an oxide pattern, selective deposition on bare silicon occurs in the range of 80°-600°C. This method is, in principle, applicable to the deposition of a wide variety of metals on elemental and compound semiconductors.

For the manufacture of electronic devices, *e.g.*, of silicon integrated circuits, depositions of metals and semiconductors onto selected areas of the substrate have been of interest to reduce the number of diffusion, photolithography, and masking steps. In particular for microminiaturization, where definition of fine lines is essential, selective depositions appear to be attractive, especially in combination with electron beam delineation techniques.

The deposition of semiconductors on selected areas has been successfully accomplished by those deposition processes which are surface-reaction limited. Disproportionation of GeI₂ at 350°C has been used for selective germanium deposition onto Ge and GaAs (1). Selective epitaxy using silane and germane has been done under high-temperature conditions (> 1175°C for Si, > 800°C for Ge), where the mobility of the Si and Ge atoms over the oxide parts of the substrate, in conjunction with a low sticking coefficient on the oxide, produce preferential growth on the bare semiconductor (2-4).

Selective depositions of metals are possible also and seem widely applicable in the deposition of metal films on silicon, germanium, and compound semiconductors such as GaAs or ZnS. For convenience, the discussion will be limited to silicon. A necessary condition is that the reaction



will go to completion. M is here a metal of valency *m*, X is a halogen. A further condition is that diffusion of the metal or of silicon in the deposited layer must be sufficiently fast to allow a film of practical thickness to form. The metal halide must have enough stability and volatility to yield a reasonable evaporation

rate. The halide produced in the plating reaction should be volatile at the temperatures and pressures employed. The process may be carried out in a flow system for metal halides with high volatility, such as WF₆ and PtF₆, or in a vacuum evaporator for many metal halides with low vapor pressure.

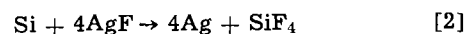
Selective depositions are possible if reaction [1] is sufficiently faster than the reaction of metal halide with the silicon dioxide or silicon nitride mask. Reaction with the mask seems likely only for metal fluorides.

The expected advantages of this metallization process over physical vapor plating (5) are the selectivity of the deposition and the inherent etching of the semiconductor surface, leading to well-adherent films. Possible disadvantages include the limited film thickness and the possibility of halogen incorporation in the films.

Examples of metals which have been deposited through their halides are tungsten and copper (6-10).

Some metals which judged on the basis of thermodynamic data could be deposited this way are, in addition to copper and tungsten, silver, tin, lead, vanadium, tantalum, chromium, molybdenum, iron, cobalt, nickel, and platinum. These metals have one or more halides of sufficient volatility, and for which reaction [1] is favorable ($\Delta F^\circ \ll 0$). Available diffusion data for these systems are not sufficient to predict the thickness limits for such films, since diffusion in these thin films, with halogen present, is generally appreciably faster than volume diffusion.

In the present paper, the deposition of silver on silicon through the reaction



is described.

With an oxide layer the following reaction is possible

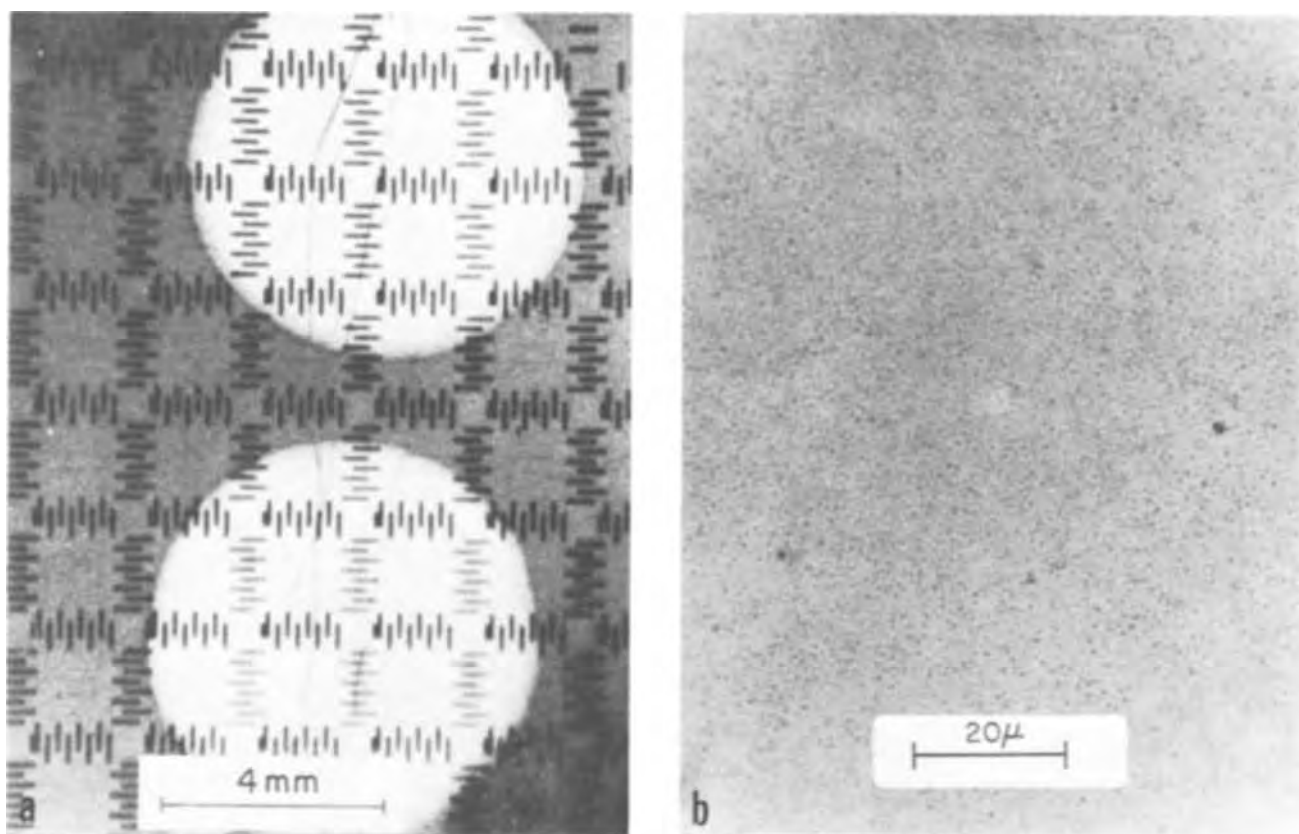
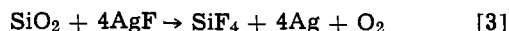


Fig. 1. Silver (2000Å thick) deposited at 100°C; (a) on a rectangular oxide island pattern; oxide is black, silicon gray, and silver white (b) on "plain" silicon.



but this is much less favorable thermodynamically than reaction [2].

Experimental

The depositions were carried out in an ion-pumped 12 in. Viton-sealed bell jar evaporator with a base pressure of 6×10^{-8} Torr. During depositions the pressure was about 10^{-6} Torr.

A (111) silicon wafer, 0.010 in. thick, is mounted against a molybdenum heater plate, which is heated by electron bombardment or by passage of a current. The silicon temperature is measured with a thermocouple spot-welded to the molybdenum plate or, at high temperature, by pyrometry. Temperatures indicated in the following are therefore only approximate.

Three types of silicon slices were used: (i) unoxidized ("plain"), (ii) with a pattern of rectangular oxide islands of 1600Å thickness, and (iii) with a PICTUREPHONE® pattern of bare silicon windows in an oxide mask. Before use, each slice was degreased, washed with HF, and rinsed with deionized water. Slices with oxide patterns were washed with a 1:3 HF solution to thin the oxide to 1000Å. Before depositions were made, the silicon wafers were cleaned by heating in $<10^{-6}$ Torr for a few minutes, to 1100°C for "plain" wafers, or to 750°C for wafers with an oxide pattern.

Silver fluoride was evaporated from a graphite crucible mounted in a strip-heater. The powder (Ventron, Alfa Inorganics) was thoroughly outgassed by melting in the graphite crucible at 10^{-6} Torr.

A shutter with a 0.125 in. hole was placed between the source and the silicon wafer. This allowed several consecutive depositions to be made on a single wafer.

After deposition of the metal layer, the wafers were immediately rinsed in deionized water to remove any unreacted silver fluoride from the surface. This is necessary because unreacted fluoride causes rapid de-

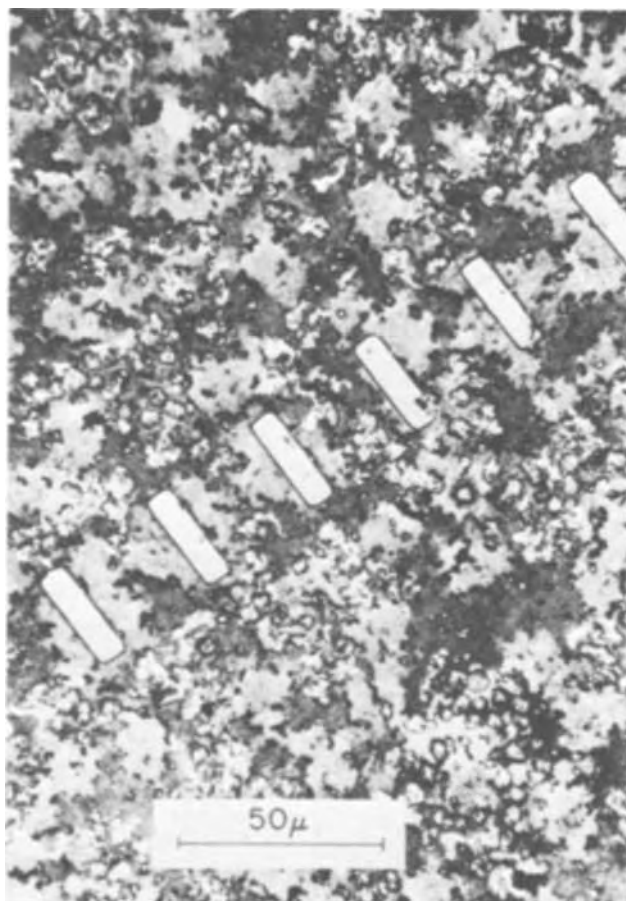


Fig 2. Silver deposited at 60°C. The irregularly shaped smooth and bright areas are silver, the grainy deposit is AgF, the rectangles are oxide islands.

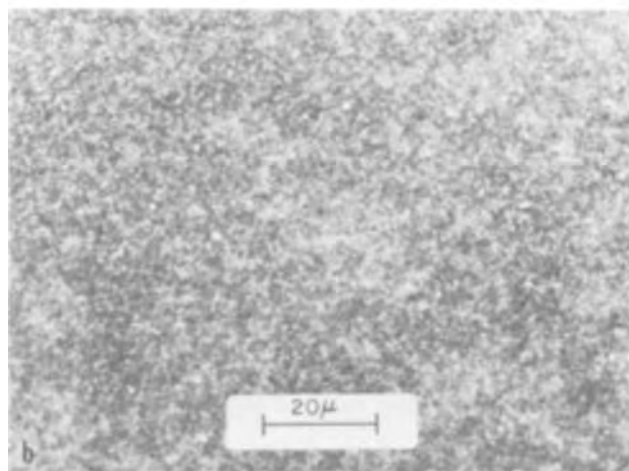
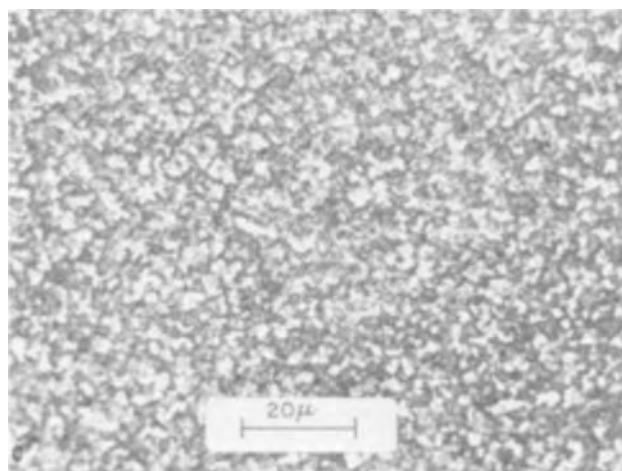
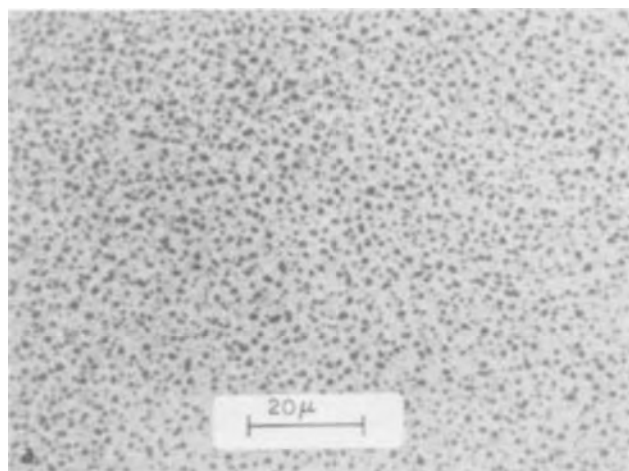


Fig. 3. Silver deposited at 600°C; (a) approximately 200Å, (b) 1200Å, (c) 1μ.

terioration of the silver and silicon oxide surfaces in air.

Results

General characteristics of the deposition process.—Deposits of silver on silicon could be readily distinguished because of the higher reflectivity of silver, compared to silicon and silicon dioxide (Fig. 1a). The optimal deposition temperature and the structure of the silver deposit were studied on "plain" silicon substrates (p-type, 4-15 ohm-cm), at AgF impingement rates of about $2 \times 10^{16} \text{ cm}^{-2} \text{ sec}^{-1}$, equivalent to 50Å of silver per second if the reaction is complete. The substrate temperature was varied from 900°C to room temperature.

A smooth silver deposit was obtained with the substrate between 80° and 600°C. A typical example of a deposit in that range is shown in Fig. 1b. The structure of the deposit was determined by x-ray to be polycrystalline, but with the Ag (111) preferentially parallel to the substrate, Si (111).

The thickness of these films is limited by the temperature-dependent rate of diffusion of silver and/or silicon. At 400°C, a film of 1 μm could be obtained in 2-5 min, at lower temperatures (100°-200°C) the limit was about 1000-2000Å. Even at 80°C films of about 1000Å were obtained in a few minutes. This indicates rather fast diffusion, which may be enhanced by the presence of the halide (11).

The silver films showed better adherence to the substrate than evaporated films and were not removed with the "scotch tape method." This is probably due to etching of the interface during the deposition process.

Two phenomena interfere with the formation of smooth films. At room temperature, reaction of AgF with silicon is very slow. At 40°-60°C, only a patchy silver deposit is formed, with codeposition of AgF

(Fig. 2). Grain growth becomes evident at 600°C, especially in thicker films (Fig. 3). At 700°C, the mobility of the silver under deposition conditions becomes excessive, leading to agglomeration and formation of large crystals, up to 5 μm in size (Fig. 4). Some of these form on top of the oxide, where nucleation is presumably facilitated by etching, which becomes especially prominent beyond 700°C.

The structure of the interface between silver and silicon was observed by etching off silver with HNO₃/HCl and removing any oxide pattern with HF. Difficulty was experienced in dissolving silver deposits in HNO₃ alone. This may be due to the presence of silicon in solid solution or at the grain boundaries (12). The silicon surface remaining presented a hazy appearance at spots where silver had been deposited. The haze is due to the presence of a roughness with a "grain" of 0.3 μm or less resulting from the reaction with AgF (Fig. 5). A few larger pits were observed. Etching of the interface is most noticeable at the borderline of the oxide pattern. The resulting depression lining the islands is less pronounced at higher temperatures (compare Fig. 5a and 5b.). It may be due to stress-enhanced etching.

Selectivity on SiO₂/Si patterns.—Between 80°-600°C silver deposition occurs exclusively on the bare silicon. The selectivity indicated in Fig. 1a is further illustrated by scanning electron micrographs of the small rectangular features in the rectangular pattern (Fig. 6). The secondary electron pattern shows the definition of the features to be quite good (Fig. 6a). The scanning electron microscope was also used to scan the surface specifically for silver, using an x-ray detector and a multi-channel analyzer tuned to the Ag L_α + L_β x-ray fluorescence. It was shown that very little, if any, silver is deposited on the oxide (Fig. 6b). The difference in appearance of silicon

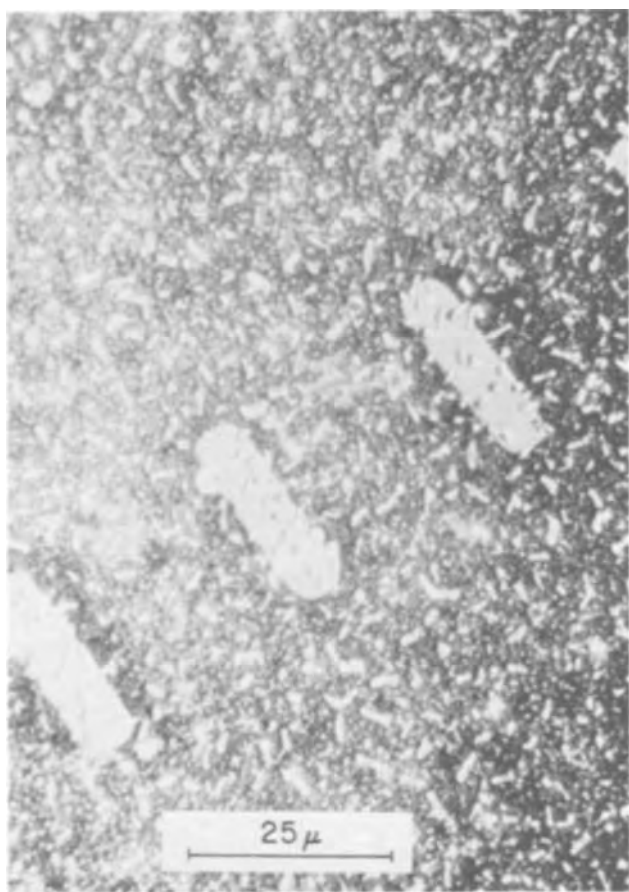
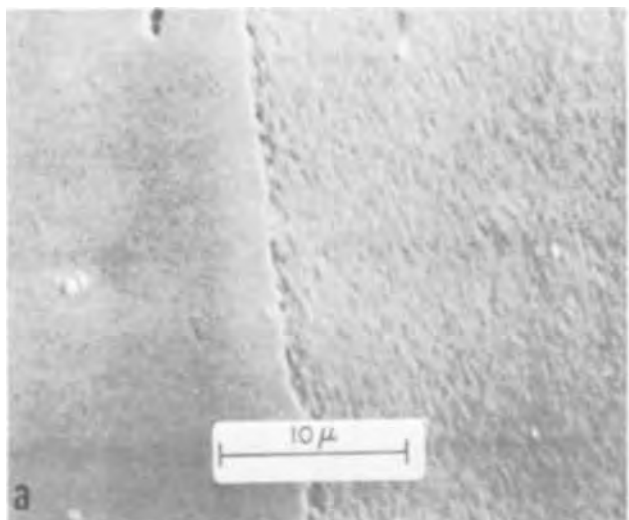


Fig. 4. Silver deposited at 700°C. Except for the light rectangular oxide islands, the whole surface is covered by silver. Bright Ag crystals cover part of the oxide.

underlying oxide islands and silicon on which silver had been deposited (Fig. 5) also shows the good selectivity of the method.

The rectangular pattern consists of oxide islands on a silicon substrate. Selective deposition was also tested for an array of circular windows in an oxide mask on silicon (PICTUREPHONE® array). The objective was to deposit silver in the windows only. Figure 7 shows that selective deposition is possible for such configurations, even at 100°C. Some spurious growth of silver adjacent to the windows does occur,



however. No effort has been made to find the optimal conditions for this deposition.

A feature of some of the deposits is the collection of a somewhat heavier silver deposit on the silicon near the edges of the oxide. This may give rise to the formation of rings, rather than solid dots, in the PICTUREPHONE® pattern. This may be due to AgF molecules landing on the oxide surface and migrating to the edge of the oxide film. Similar effects have been shown for the Ge deposition from GeI₂ (Ref. 1).

Discussion and Conclusions

In this largely exploratory study, it has been shown that the deposition of silver on silicon through the reaction of AgF with the silicon surface is a feasible process. The reaction is sufficiently fast to allow depositions of films at substrate temperatures of 80°C and higher. In the range from 80°C to nearly 600°C, the films are smooth, with small grains (<0.3 μm). Thicknesses from 1000Å to 1 μm are obtained in a few minutes. Thicker films could be built up, e.g., by electroplating, electroless plating, or both.

The films adhere well to the silicon surface. The silicon-silver interface is etched by the deposition process, and this may contribute to the good adherence and the preferred orientation of silver crystallites.

Selective deposition of silver has been obtained through windows on an oxide-masked silicon substrate, and also on a silicon surface partly covered with oxide islands. The oxide surface remains free of silver between 80° and 600°C, and pattern details are well preserved. Deposited films can probably be heated to 700°C long enough to allow deposition of Si₃N₄ protective coatings or to anneal out ion implantation damage in silicon [see e.g., Ref. (13)].

Two subjects not covered in the present study are the possible incorporation of fluorine in the metal film, and the specific resistivity of the films in comparison with bulk silver.

The method may be applicable for the deposition of several other metals mentioned in the introductory remarks of this paper allowing selective depositions at conveniently low temperatures.

Acknowledgments

We would like to thank K. E. Benson for supplying silicon slices, and R. E. Caffrey and A. C. Dumbri for the oxide-patterned silicon wafers. We also thank H. J. Leamy and S. D. Ferris for the scanning electron microscope results, and Mrs. Mildred H. Read for determining the preferred orientation of the deposits.

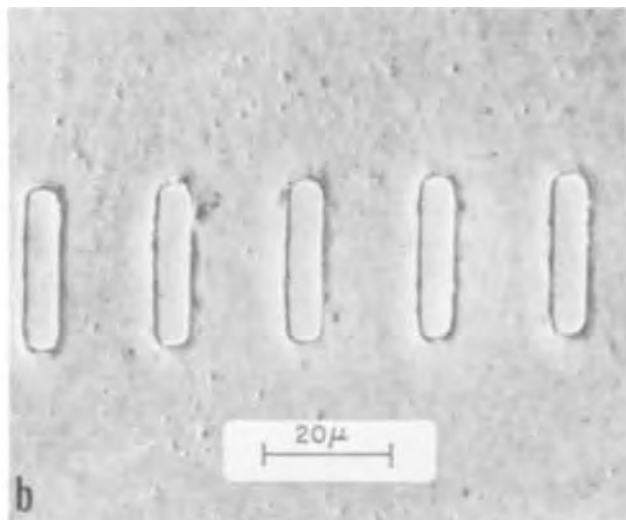


Fig. 5. Silicon/silver interface, revealed by etching off silver and oxide; (a) deposit made at 750°C, oxide island was at left, silver deposit at right; (b) deposit made at 200°C, rectangles were oxide islands, their position is marked by an etch groove around them.

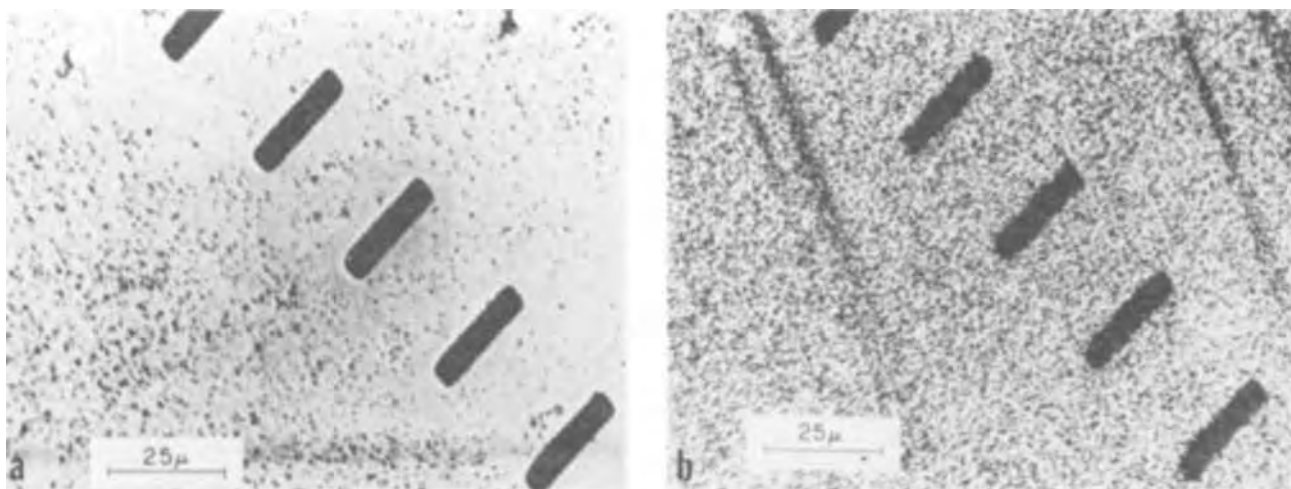


Fig. 6. Scanning electron micrographs of silver on the rectangular pattern, about 300\AA thick, deposited at 100°C ; (a) secondary electron emission; (b) Ag $L\alpha$ and $L\beta$ x-ray fluorescence; the rectangles are oxide islands.

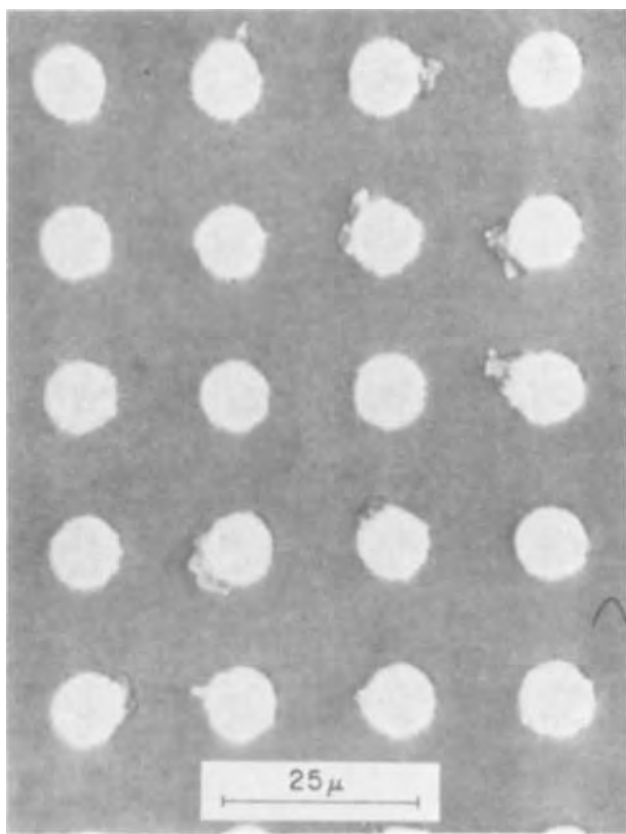


Fig. 7. Silver (2000\AA thick) deposited at 100°C through windows in an oxide mask (PICTUREPHONE® pattern).

We thank R. S. Wagner, G. E. Smith, and P. A. Turner for their helpful comments on the manuscript.

Manuscript submitted July 26, 1971; revised manuscript received ca. Oct. 12, 1971.

Any discussion of this paper will appear in a Discussion Section to be published in the December 1972 JOURNAL.

REFERENCES

1. M. Berkenblit and A. Reisman, *Met. Trans.*, **2**, 803 (1971).
2. D. J. Dumin, *J. Cryst. Growth*, **8**, 33 (1971), see also references given in this paper.
3. P. Rai-Choudhury and D. K. Schroder, *This Journal*, **118**, 107 (1971).
4. W. E. Engeler, M. Blumenfeld, and E. A. Taft, *Appl. Phys. Letters*, **16**, 202 (1970).
5. C. F. Powell, J. H. Oxley, and J. M. Blocher, Jr., Editors, "Vapor Deposition," John Wiley & Sons, New York (1966).
6. R. J. H. Voorhoeve, Thesis Techn. Univ. Delft, 115 (1964).
7. R. J. H. Voorhoeve, "Organohalosilanes, Precursors to Silicones," p. 255, Elsevier Publishing Co., Amsterdam (1967).
8. F. A. Veer, B. H. Kolster, and W. G. Burgers, *Trans. Met. Soc. AIME*, **242**, 669 (1968).
9. C. R. Crowell, J. C. Sarace, and S. M. Sze, *ibid.*, **233**, 478 (1965).
10. J. M. Shaw and J. A. Amick, *RCA Rev.*, **31**, 306-316 (1970).
11. F. Delamare and G. E. Rhead, *Compt. Rend. Acad. Sci. Paris*, **270**, C, 249 (1970).
12. H. M. Schadel, G. Derge, and C. E. Birchenall, *Trans. Met. Soc. AIME*, **188**, 1282 (1950).
13. M. T. Duffy and W. Kern, *RCA Rev.*, **31**, 742 (1970).

The Use of Laser-Induced Photoluminescence to Evaluate GaAsP Wafers for Red-Light Emitting Diodes

J. F. Black*

Bayside Research Center, GTE Laboratories Incorporated, Bayside, New York 11360

and T. Sentementes* and G. Duggan*

GTE Sylvania Incorporated, Danvers, Massachusetts 01923

ABSTRACT

A method based on photoluminescence measurements is described to determine the suitability of GaAsP wafers for red-light emitting devices. Using a focused laser beam as an excitation source, testing was carried out in the open at room temperature, assuring simplicity and speed of wafer evaluation. It is shown that one can readily determine whether a wafer is uniform in composition and/or uniform in external quantum efficiency and determine what the spectral characteristics of diodes fabricated from a given wafer will be. It is also shown that one can study the effects of wafer processing on the radiative recombination of electron-hole pairs, which will allow one to rapidly develop optimum device fabrication procedures.

This paper describes one phase of a continuing study of optical methods for nondestructive evaluation and characterization of semiconductors (1). Nondestructive testing of semiconductor wafers for light-emitting diodes (LEDs) allows one to reject unsatisfactory material before a valuable effort is wasted in fabricating it into diodes. It also provides a check on device fabrication procedures, *i.e.*, if a material checks out as high quality before processing and then yields LEDs of low performance, it is evidence of faulty fabrication procedures. Such a test, besides being non-destructive in nature, should be sensitive, accurate, simply and rapidly executed, capable of high spatial resolution and, of particular importance for LEDs, possess high spectral resolution. In addition, the test should be a direct reflection of the performance of an LED made from the material under examination, and it should be capable of examining, as nearly as possible, the same region (both in area and in depth) that is to be effective in producing light in the finished device.

The end result of electro-excitation, *i.e.*, as in a forward biased p-n junction, and photo-excitation is the same, namely, radiative recombination of electron-hole pairs to produce electroluminescence (EL) and photoluminescence (PL), respectively. Thus a PL test should provide a direct means for evaluation of many of the materials parameters of importance for LEDs.

The use of a laser as an excitation source offers significant advantages in screening out scattered exciting radiation during PL measurements and in achieving sufficiently intense levels of excitation via focusing optics to produce strong PL spectra (2). Recent work has shown that measurements of photoluminescence, especially when generated by lasers can be extremely useful for fundamental studies of semiconductor properties (3). Less attention has been paid to laser-induced photoluminescence for materials evaluation purposes. This paper describes a method, based on photoluminescence (PL) measurements and using a laser as an excitation source, which meets all of the requirements noted above. The method is applied to determine the suitability of GaAsP wafers for red-light-emitting devices. The measurement is carried out with the wafer in the open and at room temperature, assuring simplicity and speed of evaluation.

Apparatus and Experimental Techniques

The PL apparatus consists of the following arrangement: a 6328Å He-Ne laser, designed and built at the

* Electrochemical Society Active Member.

Key words: photoluminescence, electroluminescence, semiconductors, light-emitting diodes, gallium arsenide-phosphide.

Bayside Research Center, operating in a single (TEM₀₀) mode with a nominal power output of 15 milliwatts; a 50Å bandwidth filter peaked at 6328Å with peak transmission of 47%, and with long wavelength and short wavelength rejection of $> 10^4$ at $\pm 150\text{Å}$ of peak transmission (to remove extraneous He-Ne emissions). This arrangement is followed by a selection of neutral density filters capable of reducing the beam power incident on the sample by a factor of 10^3 ; a beam power meter for monitoring the laser power incident on the sample; an objective lens system for focusing the laser beam down to a fine spot; an x-y-z micrometer stage which carries the sample mounting assembly for holding and positioning the GaAsP wafer; a highly absorbing beam trap for the reflected laser beam, and a high-pass filter to absorb scattered laser radiation. A schematic of the apparatus is shown in Fig. 1.

The PL signal was collected and focused onto the entrance slit of a Perkin-Elmer 112C Recording Spectrometer by the standard front-end optical system supplied with this instrument. The half angle of the cone of acceptance, dictated by the size and tilt of the plane mirror and its distance from the GaAsP wafer, was 6°.

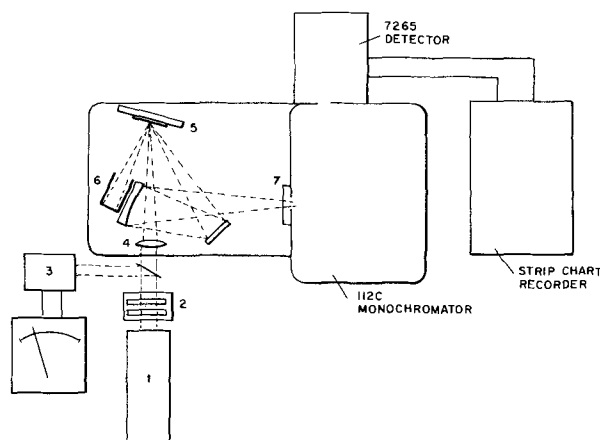


Fig. 1. Schematic of the apparatus used for photoluminescence measurements of $\text{GaP}_x\text{As}_{1-x}$ ($x \leq 0.4$) epitaxial wafers: 1, 6328Å He-Ne laser; 2, filter rack for 50Å bandwidth filter and for neutral-density filters; 3, beam power meter; 4, objective lens system for focusing the laser beam; 5, x-y-z sample mount; 6, trap for reflected laser beam; 7, filter for absorbing scattered laser radiation.

Laser radiation scattered from the sample was absorbed by a CS2-58 or, in a few instances, by a CS2-64 Corning glass filter placed over the entrance slit of the monochromator. Photoluminescence spectra were measured using a DF-2 prism in the monochromator generally working at a slit opening yielding a bandwidth of 40Å, and using an RCA 7265 photomultiplier (PM) tube as a detector. Provision was made for cooling the PM tube to improve signal-to-noise ratio. All photoluminescence measurements were conducted with the GaAsP wafer at room temperature, in the open. The diffraction-limited spot size calculated from the optical parameters of the system was 5.6×10^{-3} cm. Experiments using thin metal masks with various hole sizes showed that the actual diameter of the focused laser spot was not more than 10^{-2} cm. Laser-stimulated PL was restricted to GaAsP wafers with compositions ≤ 40 mole per cent (m/o) GaP (emission energy ≤ 1.91 eV), largely because of limitations imposed by the photon energy (1.96 eV) of the He-Ne laser radiation, but also because of limitations imposed by the absorption edge of the CS2-58 and CS2-64 filters.

Because the two parameters of most importance in LEDs, the radiative quantum efficiency and the ratio of near-band-edge to impurity emission, are sensitive to the concentration of electron-hole pairs produced per unit time (4), it was important that our PL test apparatus be capable of exciting electron-hole pairs in GaAsP wafers comparable in density to those generated in the average LED. Typically, LEDs operate at a current density from 1 A/cm² to 50 A/cm² (d.c.). All of the electron-hole pairs in an LED are injected into a layer about one micrometer thick near the p-n junction. Corresponding electron-hole pair production is 6.3×10^{22} /cm³ sec and 3.1×10^{24} /cm³ sec. A well-focused laser beam of moderate power can excite an electron-hole pair population equal to or greater than that typical of LEDs operated at room temperature, as shown in the following calculation.

The laser output of 15 mW was focused to a circular spot of minimum area 2.47×10^{-5} cm², maximum area 7.85×10^{-5} cm². Taking into account losses due to the narrow-pass laser filter ($T = 47\%$) and reflection from the sample ($R = 35\%$), the laser power available for creating electron-hole pairs in the sample provided a minimum of 50 W/cm² and a maximum of 235 W/cm². One watt of 6328Å radiation is equivalent to 3.3×10^{18} photons/sec. If it is assumed that every photon absorbed creates one electron-hole pair, then the electron-hole pair flux produced by the He-Ne laser was not less than 1.65×10^{20} /cm²/sec nor more than 7.75×10^{20} /cm²/sec. The absorption coefficient (α) for 6328Å radiation in the GaAsP epitaxial layers used for this investigation ranged from about 2000 cm⁻¹ to 10,000 cm⁻¹, depending on exact composition (5). Thus we calculate that 9/10 or $[1 - (1/e^2)]$ of the optical power absorbed in generating PL was absorbed in a layer from 2.0 to 10.0 micrometers thick at the surface of the wafer. The corresponding lower and upper limit for electron-hole pairs excited is accordingly 1.65×10^{23} /cm³ sec and 3.9×10^{24} /cm³ sec, respectively. Thus ample laser power density is available to effect good correlation between PL and EL. Photoluminescence signals were produced which were strong enough to allow detection of shifts of peak wavelength of 5Å, corresponding to differences in GaAsP composition—in the composition range of interest—of about 0.1 m/o (6).

The angle of incidence of the focused laser beam on the GaAsP wafer was made as near normal as possible (never greater than 10° from the normal), commensurate with keeping scattered laser light to a minimum, to insure an essentially symmetrical (nearly circular) focused laser spot. At the same time the take-off angle between the optical axis of the cone of acceptance and the surface of the sample was kept as near normal as

possible to take advantage of the fact that for a given solid angle there is more PL power at near normal incidence in this type of PL source. A take-off angle of 30° was found to be optimum for all samples measured. GaAsP wafers or wafer sections with area ranging from 1 to 2 cm² were mounted on thin metal plates with a low-melting-point wax. Photographs of each sample were taken and either imperfections on the surface of the wafer or the corners of the metal plate or wafer were used as fiducial marks. The mounted sample was placed on the x-y-z stage and the fiducial marks were referenced to an x-y position coordinate. The sample was then divided into a reference grid array of 2 × 2 mm squares and PL measurements were made in the center of each square. Anywhere from 20 to 100 measurements were made on a sample.

The GaAsP LEDs, which were fabricated from epitaxial wafers by zinc diffusion, generally contained an emitting region 0.38 mm in diameter, but diodes with an emitting region as small as 0.1 mm in diameter were also made. The p-n junctions in all of these diodes ranged from 3 to 5 micrometers below the surface. Thus the region in which most of the PL test signals were generated included the region in which the EL was subsequently generated.

A random sample of several dozen diodes was taken from the four or five hundred diodes that were usually produced from each wafer section. This was considered adequate to expect reasonably good correlation between photoluminescence and electroluminescence.

Experimental Results and Discussion

Since the total PL power emitted from the GaAsP samples under the action of the focused laser beam is of some importance, several experiments were devoted to obtaining this information. In a well-polished or highly reflecting semiconductor wafer, internally generated emission (for either PL or EL) exits from the surface with a Lambertian-like distribution (7). Therefore it is important to define the take-off angle of the PL as well as the angle of the cone of acceptance of the front end of the spectrometer to arrive at an accurate determination of the "total" PL power output. With a take-off angle 30° from the normal and a cone of acceptance of 12°, the fraction of the PL power entering the spectrometer is calculated to be slightly less than 1%.

A convenient optical power reference for calculating PL output in our system is the laser beam itself. The slit opening of the monochromator was set to produce a spectral bandwidth of about 40Å over the spectral range of interest. This was more than adequate to allow all of the 6328Å laser output to pass through the monochromator to the detector, but it only allowed 20% of the PL output to pass through. An appropriate multiplication factor was applied to arrive at a correct total PL output. The focused laser beam was reflected onto the entrance slit of the monochromator from a front surface aluminized mirror substituted in place of the GaAsP sample. By comparison of PL output with laser output, it was determined that the "total" PL power emitted from a good GaAsP wafer was 1.5×10^{-6} watts.

Figure 2a shows a 5 × 6 PL scan of a GaAsP epitaxial layer with variations in peak emission wavelength that indicate compositional homogeneity within 0.3 m/o. It was noted that there is a slight but definite trend to longer PL wavelength (lower phosphorus content) toward the upper-right-hand corner of the scanned area. In Fig. 2b is shown a nearly complete 6 × 8 scan of another epitaxial layer. The variation of the PL emission peaks in this sample suggest random compositional inhomogeneity of 1.0 m/o.

There was no significant heating of the GaAsP area illuminated. This was established by measurements of PL spectra at successively lower laser power using neutral density filters to attenuate the laser beam. The PL wavelength showed no shift (within 5Å) to shorter

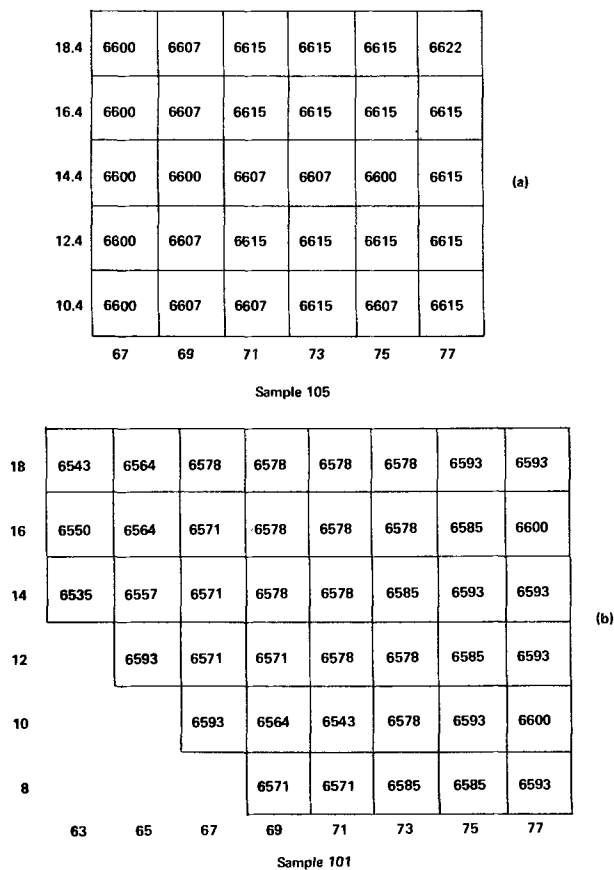


Fig. 2. (a) Map of photoluminescence measurements which show the variation of peak wavelength in reasonably homogeneous epitaxial wafer of GaAsP. The numbers outside of the 5 × 6 array represent position coordinates in units of millimeters. The number within each box is the peak wavelength of photoluminescence (expressed in Å) measured for an illuminated area between 0.01 cm and 0.005 cm in diameter, located in the center of the box. (b) Map of photoluminescence measurements which suggest compositional inhomogeneity of 1 m/o in a GaAsP epitaxy. The regions in the lower left hand corner were not measured because they were close to the edge of the wafer.

wavelength such as would have occurred had there been even moderate heating at the maximum laser power. (A rise of 1°C would cause an increase of 2.4Å in peak emission wavelength.)

The average peak emission wavelength observed for PL of a given wafer usually agreed within 10Å with the average peak emission wavelength for diodes made from that wafer. Table I compares PL and EL for four different samples of GaAsP. Care was taken in our diode measurements to keep the current low enough (generally less than 10 A/cm²) to preclude wavelength shifts due to self-heating of the diode. Photoluminescence and electroluminescence measurements involving near-bandgap emissions from a III-V semiconductor wafer do not usually show peak wavelengths that agree as closely as those shown in Table I. There are several reasons for this; first, the energy of a conventional excitation source for PL is usually high compared to the energy gap of the semiconductor

Table I. Comparison of PL measurements with LED measurements

Sample number	Photoluminescence peak wavelength (Å)		Diode luminescence peak wavelength (Å)	
	Average	Range	Average	Range
101	6576	6535-6600	6578	6571-6586
105	6609	6600-6622	6597	6585-6607
112	6580	6557-6585	6581	6578-6593
114	6572	6557-6593	6573	6564-6578

and, typically, generates electron-hole pairs within a region only a few tenths of a micrometer below the surface. The region where most of the recombination occurs may be much deeper than this, but it is not likely to be more than a few micrometers from the surface in the GaAsP which was the subject of this investigation. Diode emissions, on the other hand, are generated many micrometers below the surface and self-absorption causes strong attenuation of the high energy portion of the electroluminescence resulting in a shift of the peak wavelength to lower energy. The good agreement between EL and PL peaks shown in Table I may be explained in part by the close correspondence of p-n junction depth and the thickness of the layer sampled by the He-Ne laser.

Second, and more important, EL in III-V diodes is usually dominated by recombination on the p-side of the junction through acceptor centers that lie several hundredths of an electron volt above the edge of the valence band (8). One must account for the apparent absence of a strong shift in peak emission to longer wavelength between original (n-type) and p-diffused wafers that would be consistent with the generally observed situation. The results in Table I are most simply explained if the emission in these diodes is dominated by recombination on the n-side of the junction, through donor impurities, which in direct band gap III-V's lie only a few thousandths of an electron volt from the edge of the conduction band.

In two instances the emission wavelength (both PL and EL) was at variance with that expected from the composition of the GaAsP epitaxial layer stated by the supplier. An emission wavelength of energy lower than that expected from the stated composition can be explained in terms of impurity recombinations or near-band-edge recombinations. However, in the two cases cited here the emission wavelength was at higher energy than could be ascribed to the wafer composition, a practical impossibility. In each case, precision lattice parameter measurements confirmed the composition, within 0.2 m/o, deduced from PL and EL (LED) measurements. Table II compares the stated composition of five epitaxial wafers with composition deduced by means of PL or EL measurements and by x-ray techniques.

Photoluminescence measurements were also used to investigate changes in the quantum efficiency of the epitaxial material after chemical processing of the surface. Table III shows the results of measurements of PL in a GaAsP layer as received, and after treatment with Br₂-CH₃OH solution to remove about

Table II. Comparison of GaAsP wafer composition determined by different measurement techniques

Sample number	Stated	m/o GaP PL or EL	X-ray
108	38.2	38.5	—
104	39.0	40.7	40.5
120	36.0	38.5	38.7
126	40.4	40.3	—
130	38.8	38.6	—

Table III. Comparison of PL measurements on a GaAsP wafer as-received and after chemical treatment of the surface (Sample 101)

Position coordinates	As-Received		After surface treatment	
	Peak wavelength (Å)	Peak intensity	Peak wavelength (Å)	Peak intensity
10-71	6578	148	6571	294
10-67	6557	98	6550	214
14-73	6585	200	6578	330
14-69	6578	130	6571	280
14-65	6557	97	6557	225
18-75	6593	170	6585	385
18-71	6578	155	6578	308
18-67	6578	122	6571	245
18-63	6543	120	6543	185

5 μm from the surface. Note that the peak wavelength at each point is practically identical, but the peak intensity, which is a measure of the quantum efficiency, has increased markedly at each point sampled. The precision with which a particular point on a sample could be located on successive measurements was 0.1 mm, or about 0.004 in., equal to the maximum diameter of the focused laser beam.

Since the area that is sampled in each PL measurement is no more than 10^{-2} cm in diameter, a highly detailed map of the photoluminescence response of a wafer can be constructed. If we could generate PL maps or images with high spatial resolution in a reasonably short space of time, similar to the way in which infrared maps or images are produced by scanned laser techniques (1), we would have a valuable new technique for evaluating LED wafers.

Conclusions

This investigation has provided strong evidence that PL testing can be employed as a process control and process development tool as well as a tool for rapid, accurate evaluation of the results of semiconductor materials synthesis and purification procedures. The effects of wafer processing on quantum efficiency (including steps such as SiO_2 masking) that are involved in fabricating a wafer into LEDs can be studied. Peak emission wavelength and variations thereof can be determined with an accuracy of 10Å, relative quantum efficiency and variation within a given wafer can be determined within 10%.

PL measurements have been used to establish the beneficial effects of chemical treatments on GaAsP wafers prior to the formation of diffused light-emitting junctions. Photoluminescence testing of wafers has also been used to check the phosphorus content stated by the supplier and to check for the presence of undesired impurity radiations. In addition, this nondestructive test technique has been employed to determine whether point-to-point variations in wafer composition exist that would cause serious variations in LED emission wavelength. Finally, it is clear that the extension of these PL techniques to the evaluation of other higher energy-gap semiconductors is largely a matter of substituting another laser, for example an argon-ion laser ($\Delta E = 2.41\text{--}3.35$ eV), for the He-Ne laser.

Acknowledgments

The authors would like to acknowledge Mr. F. Scutto for his assistance in measurements of photoluminescence and electroluminescence and Mr. R. Copolla for his assistance in fabricating light-emitting diodes.

Manuscript submitted April 12, 1971; revised manuscript received Oct. 27, 1971. This was Paper 72 presented at the Los Angeles Meeting of the Society, May 10-15, 1970.

Any discussion of this paper will appear in a Discussion Section to be published in the December 1972 JOURNAL.

REFERENCES

1. J. F. Black, E. Lanning, and S. Perkowitz, *Infrared Phys.*, **10**, 125 (1970); D. C. Gupta, *Solid-State Electron.*, **13**, 543 (1970); S. Perkowitz, *J. Appl. Phys.*, **40**, 3751 (1969); R. R. Alfano and D. H. Baird, *ibid.*, **39**, 2931 (1968); E. D. Jungbluth, *Met. Trans.*, **1**, 575 (1970); J. F. Black, B. Sherman, and V. Fowler, "Semiconductor Silicon," R. R. Haberecht and E. L. Kerr, Editors, p. 693, The Electrochemical Society Softbound Symposium Series, New York (1969); B. Sherman and J. F. Black, *Appl. Opt.*, **10**, 125 (1970); E. D. Jungbluth, *Appl. Phys. Letters*, **17**, 473 (1970); D. C. Gupta, E. D. Jungbluth, B. Sherman, and J. F. Black, *Solid State Technol.*, March 1971.
2. P. J. Dean, *Trans. Met. Soc. AIME*, **242**, 384 (1968).
3. C. J. Hwang, *J. Appl. Phys.*, **39**, 5347 (1968); E. W. Williams and D. M. Blacknall, *Trans. Met. Soc. AIME*, **239**, 387 (1967); K. Era and D. W. Langer, *J. Lum.*, **1**, 2, 514 (1970); H. J. Queisser and M. B. Panish, *J. Phys. Chem. Solids*, **28**, 1177 (1967).
4. S. Mayburg and J. F. Black, *J. Appl. Phys.*, **34**, 1521 (1963); S. M. Ku and J. F. Black, *Solid-State Electron.*, **6**, 505 (1963); See also the excellent survey on "Radiative Recombination in the III-V Compounds" by M. Gershenzon, Chap. 13 Semiconductors & Semimetals, Vol. II, "Physics of III-V Compounds," Willardson and Beer, Editors, Academic Press, New York (1966).
5. G. D. Clark, Jr. and N. Holonyak, Jr., *Phys. Rev.*, **156**, 913 (1967).
6. A. H. Herzog, W. O. Groves, and M. G. Craford, *J. Appl. Phys.*, **40**, 1830 (1969).
7. H. F. Lockwood, *ibid.*, **34**, 2110 (1963).
8. C. J. Nuese, J. J. Tietjen, J. J. Gannon, and H. F. Gussenberger, *This Journal*, **116**, 248 (1969).

Control of the Deposition of Silicon Nitride Layers by 2537Å Radiation

C. H. J. v. d. Brekel and P. J. Severin

Philips Research Laboratories, N. V. Philips' Gloeilampenfabrieken, Eindhoven, Netherlands

ABSTRACT

Thin Si_3N_4 films were deposited on polished Si crystals at low temperatures using the Hg-photosensitized reaction of N_2H_4 and SiH_4 . The deposition rate increases linearly with the light intensity. The experiments showed that destructive interference between multiply reflected beams has a pronounced effect in limiting film thickness to a well-defined value with a high degree of uniformity over the slice.

The formation of silicon nitride films by a number of methods has been reported including the reaction of ammonia and silane under an rf discharge (1), the pyrolytic reaction of the silane-ammonia system (2, 3), the silane-hydrazine system (3) or the silicon tetra-

chloride-ammonia system (4), and reactive sputtering of silicon in nitrogen (5, 6). These are chemically activated processes which are effected at a relatively high temperature. The Hg-photosensitized decomposition of hydrazine and of silane has been described by Mitchell and Zemansky (7). Collet (8) has used the Hg-photosensitized decomposition of hydrazine and silane for

chloride-ammonia system (4), and reactive sputtering of silicon in nitrogen (5, 6). These are chemically activated processes which are effected at a relatively high temperature. The Hg-photosensitized decomposition of hydrazine and of silane has been described by Mitchell and Zemansky (7). Collet (8) has used the Hg-photosensitized decomposition of hydrazine and silane for

Key words: Si_3N_4 -deposition, destructive interference, stepwise growth, Hg-photosensitized, uniform thickness layers.

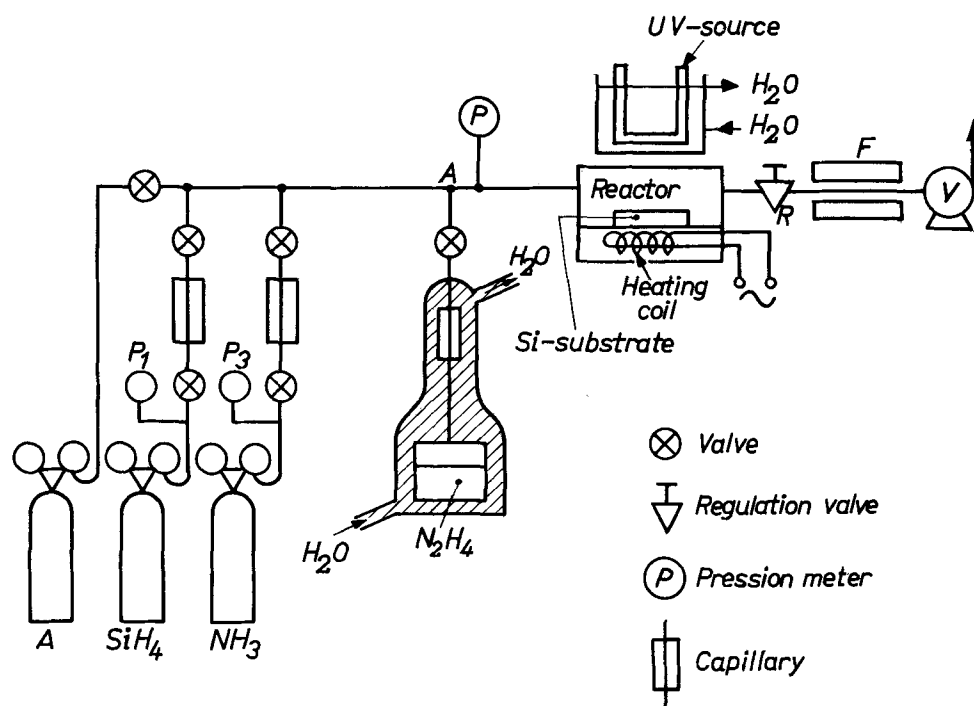


Fig. 1. Apparatus for depositing Si_3N_4 .

the deposition of silicon nitride films at low temperatures. This technique works with a closed system, which results in a varying deposition rate, due to a gradual consumption of the reactants from the gaseous phase and an increase in total gas pressure. In order to maintain a reasonable growth rate the system has to be refilled after a certain exposure time with a fresh $\text{N}_2\text{H}_4/\text{SiH}_4$ mixture. To eliminate this effect we used a fast-flow system with a constant input of the reactive species. At a constant intensity of uv radiation, the growth rate of silicon nitride was expected to have a constant value. A second advantage is the additional possibility of using ammonia instead of hydrazine as the nitrogen delivering compound, because in a fast-flow system ammonia is photochemically converted into hydrazine (9). In practice it is much easier to remove traces of water from gaseous ammonia than from liquid hydrazine.

Apparatus

The apparatus is shown schematically in Fig. 1. It consists of a gas supply, the reactor and a vacuum system. The pump (V) maintains a constant pressure P in the system. The silane, ammonia, and hydrazine vapor are forced into the system through capillaries by the difference in pressure ($P_1 - P$), ($P_3 - P$), and ($P_2 - P$), respectively.

The vapor pressure P_2 of hydrazine is fixed by the temperature of the thermostated water bath which surrounds the bottle containing the liquid hydrazine. By adjusting the needle valve (R) a constant total pressure range within the reactor can be reached. Variation of P_1 with respect to P_2 or P_3 permits variable ratios of silane to hydrazine or ammonia flow.

The quartz reactor is 10 cm long, 3.5 cm wide, and 4 mm high. A heating coil under the bottom of the reactor keeps the sample at a constant deposition temperature (maximum, 500°C). A low-pressure mercury discharge tube (40W) acts as the radiation source situated just above the reactor. To avoid Doppler-broadening of the resonance line, the tube is cooled in a quartz tank with running water.

A drop of mercury at the inlet of the reactor dopes the gas mixture with mercury vapor.

The exhaust gases are decomposed into hydrogen, nitrogen, and solid products in the furnace (F) at 900°C and the gases are pumped off.

By repeated pumping and filling of the system with argon, the apparatus can be emptied of the highly reactive silane before the reactor is opened.

Experimental

Water-free hydrazine, distilled from sodium hydroxide (10), and silane (Matheson) were used to deposit silicon nitride layers on 10 ohm-cm n-type polished silicon substrates of about 3 cm diameter.

In the experiments the hydrazine or ammonia flow was set to at least $2/3$ times that of the silane being the stoichiometric ratio to prevent the deposition of a white-yellow film of polymerized silicon hydrides by the decomposition of silane (11, 12). In general this ratio was set to unity.

At constant total pressure P , flow rates, and temperature, the influence of the intensity of the uv radiation on the growth rate was investigated. The light intensity was varied by changing the distance between the substrate and uv source. The thickness of the deposited layers were estimated from their interference colors (6). Figure 2 shows that the growth rate G increases with decreasing distance x as x^{-2} .

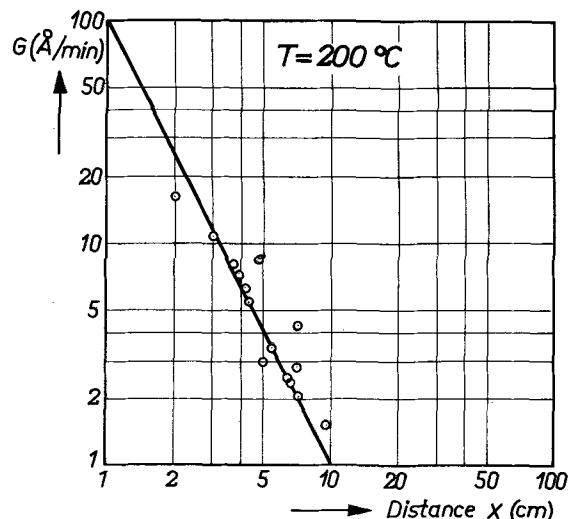


Fig. 2 Growth rate G of Si_3N_4 vs. distance x between the sample and light source.

Considering the mercury tube as a point source, Fig. 2 indicates a direct proportionality of the growth rate to the uv intensity.

The growth rate of the Si_3N_4 film was roughly constant. A closer examination, however, revealed that the precise growth rate depends on the layer thickness. In fact, at some thickness the growth rate turns out to be greatly reduced. This phenomenon will be explained in detail in the next section by taking into account the interference between multiply reflected beams close to the nitride-gas interface. The same effect in photoresist films has been described recently by Middelhoeck (14) and Fried *et al.* (15).

Theory

Figure 3 shows schematically the experimental situation. A silicon wafer is covered by a silicon nitride layer. Only the mercury line $\lambda = 2537\text{\AA}$ is used for the experiments as has been substantiated by filtering the different wavelengths. It has been experimentally verified that the layers discussed in this paper actually have within 2% the value for the index of refraction for 5860\AA as published by Reizmann and van Gelder (6). Therefore we assume the index of refraction for Si_3N_4 at 2537\AA to be also as measured by those workers, *viz.*, 2.18. The index of refraction for Si at 2537\AA has been found (17) to be 1.65. As Fig. 2 suggests the radiation may be considered as normally incident. Absorption in the Si_3N_4 layer is neglected and light reflects at the Si surface with a phase change π . The light intensity at the silicon nitride-vacuum interface if the relevant values of the refractive indices are substituted in (A1) can, as shown in Appendix A, be represented by

$$R = \frac{I_R}{I_0} = \frac{0.05 + 0.20 \sin^2 \phi/2}{0.90 + 0.20 \sin^2 \phi/2} \quad [1]$$

where I_R and I_0 are the intensities of incident and reflected beams, and

$$\phi = 2hn\pi/\lambda \quad [1a]$$

where h = layer thickness and n = refractive index of Si_3N_4 , which is assumed to be independent of both growth rate and layer thickness.

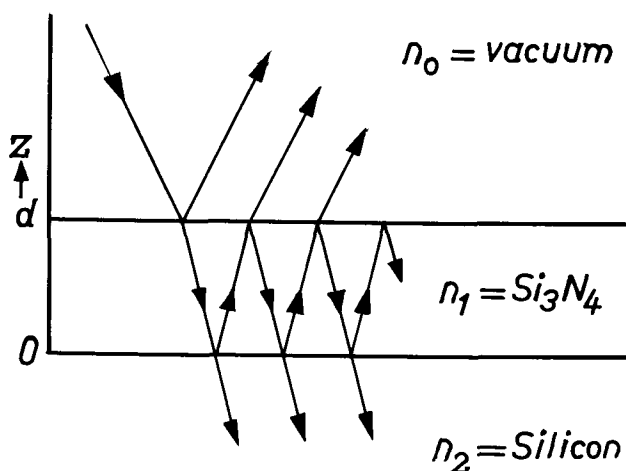


Fig. 3. Schematic representation of the optical system. For clarity the incoming beam is shown at an angle of incidence θ .

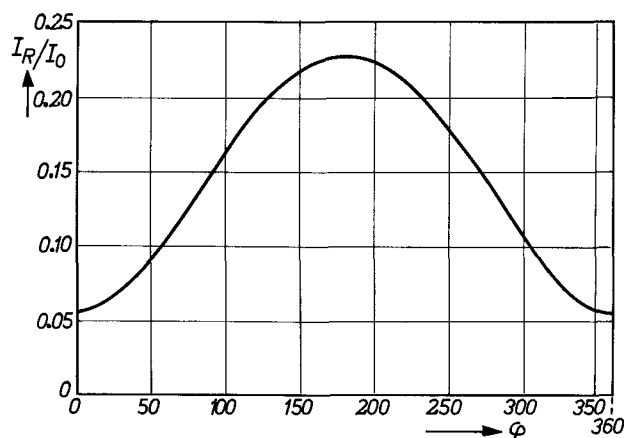


Fig. 4. Relative surface light intensity vs. layer thickness

The deposition rate G is found to be directly proportional to the intensity I_0 of the radiation (Fig. 2)

$$G = C \cdot I_0 \quad [2]$$

The intensity at the surface I_R depends on the thickness, and shows maxima and minima, and it has experimentally been observed that G also depends on the thickness. Therefore we assume that in fact $G \sim I_R$. Figure 4 shows the intensity I_R at the interface as a function of the reduced layer thickness, in fact a plot of Eq. [1]. From the definition of the growth rate

$$G(h) = \frac{d}{dt} h(t) \quad [3]$$

The time t required to grow in thickness from 0 to $h(t)$ is found to be equal to

$$t = \int_0^{h(t)} \frac{dh}{G(h)}$$

or with Eq. [1], [1a], and [2]

$$A I_0 t = \int_0^{\phi(t)} \frac{0.90 + 0.20 \sin^2 \phi/2}{0.05 + 0.20 \sin^2 \phi/2} d\phi \quad [4]$$

This integral is evaluated in Appendix B.

The constant $A = 2n\pi C/\lambda$, which is a function of the quantum efficiency of the process, the pressure in the reactor and partial pressures of the reactive species, can be calculated by substituting the experimental values of t at which the growth retardation occurs. When A is known, the thickness *vs.* time curve can be plotted from Eq. [4].

Figure 5 shows the result of a calculation for one experiment. As shown, a good agreement between theory and experiment is obtained. The critical thickness is defined as the value at which a minimum in growth rate occurs.

Discussion

The deposition of Si_3N_4 was carried out in a temperature range of 100° - 400°C , therefore thermal degradation of the compounds was negligible.

As neither gaseous hydrazine nor silane shows absorption of 2537\AA radiation, the process must be initiated by excited mercury. Thus the reaction is Hg-photosensitized. It was noticed that across the wafer the growth rate decreased strongly in the downstream direction, owing to depletion of the reactants in the gaseous phase. Thus a nonuniform Si_3N_4 film resulted, even up to a decline of 500\AA over 2 cm. The film, however, was always uniform across the slice at about the critical values of the Si_3N_4 thickness. This phenomenon can be explained by the model. When the film at the gas inlet edge of the wafer ($x = 0$) approaches a critical thickness, the growth rate is retarded drastically since $G \sim I_0$ and I_R decreases as $\phi \rightarrow 2\pi$. At other points

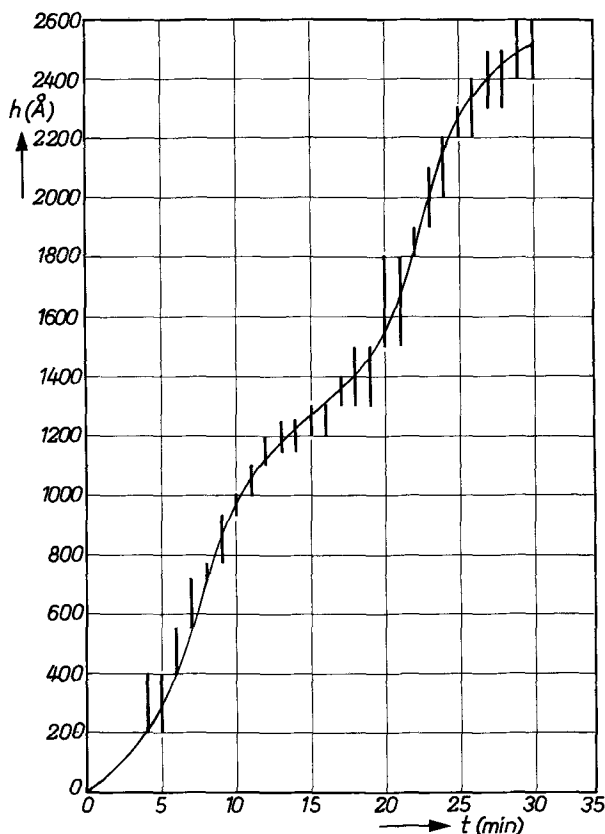


Fig. 5. Thickness increase vs. exposure time curve according to the model. Vertical lines represent the experimental precision. The film was deposited at 200°C, at a reactor pressure of 1.5 Torr and $P_{N_2H_4}/P_{SiH_4} = 1$. The light source was at 20 mm distance.

($x > 0$) the growth rate has a higher value, because $h_x < h_{crit}$ or $\phi < 2\pi$. The thickness increase in t seconds at $x > 0$ will be larger than at $x = 0$. The film consequently changes from wedge-shaped into a layer of uniform thickness. By stopping the process at the appropriate moment, we were able to deposit Si₃N₄ films in integer times 1268Å thick with a thickness variation of less than 20Å over 3 cm (see Appendix A).

The experiment confirms that the intensity at the interface is the major factor which controls the decomposition of the compounds, and that accordingly the contribution of both in the gas phase excited mercury atoms, and obliquely incident light can be neglected. Both these factors would make the growth rate thickness independent. As a consequence it may be concluded that the mercury atoms adsorbed on to the surface catalyze the decomposition only if these are activated *in situ* by the radiation. In other words the sensitized decomposition shows itself as a heterogeneous process. A relatively high surface concentration of hydrazine and mercury due to specific adsorption may be present on the sample surface, increasing the chance for a collision between an excited mercury atom and a hydrazine molecule.

The above theory and experiments apply more generally to any chemical surface reaction which is rate controlled by any photosensitive process step and which produces or destroys a layer transparent to the radiation.

Acknowledgment

One of the authors (C.B.) wishes to thank Dr. J. de Jonge for stimulating discussions.

Manuscript submitted Sept. 1, 1971; revised manuscript received ca. Nov. 4, 1971.

Any discussion of this paper will appear in a Discussion Section to be published in the December 1972 JOURNAL.

APPENDIX A

Application of Multiple Reflection (18-20)

It can be shown that the rays directly reflected at the (0,1) interface (Fig. 3) interfere with the rays transmitted through layer (1) and reflected at the (1,2) interface producing effective reflection coefficient R . In the case of normal incidence and refractive indices with no imaginary part, the pertinent equation becomes (20)

$$R = 1 - \frac{(1 - r_{01}^2)(1 - r_{12}^2)}{(1 - r_{01}r_{12})^2 + 4r_{01}r_{12} \sin(-\phi/2)} \quad [A-1]$$

where $R = I_R/I_0$: ratio of the reflected and incident light.

The amplitude reflection coefficients r_{01} and r_{12} are given by Fresnel's equations

$$r_{01} = \left| \frac{n_0 - n_1}{n_0 + n_1} \right| ; r_{12} = \left| \frac{n_1 - n_2}{n_1 + n_2} \right| \quad [A-2]$$

At the (0,1) interface a phase shift equal to π occurs. Maxima and minima occur at certain optical path differences yielding

$$\text{for } \phi = l \cdot 2\pi \quad \text{minima with } R = \frac{(r_{01} - r_{12})^2}{(1 - r_{01}r_{12})^2} \quad [A-3a]$$

and

$$\text{for } \phi = (l + \frac{1}{2})2\pi \quad \text{maxima with } R = \frac{(r_{01} + r_{12})^2}{(1 + r_{01}r_{12})^2} \quad [A-3b]$$

with l being an integer.

Insertion of the numerical values mentioned in the text leads to Eq. [1]. Eq. [A-3a] and [A-3b] give

$$I_{min} = 0.05 I_0 \text{ for } h = 1268\text{Å}, \dots \quad [A-4a]$$

$$I_{max} = 0.23 I_0 \text{ for } h = 634\text{Å}, \dots \quad [A-4b]$$

APPENDIX B

The integral in Eq. [4]

$$A I_0 t = \int_0^{\phi(t)} \frac{0.90 + 0.20 \sin^2 \phi/2}{0.05 + 0.20 \sin^2 \phi/2} d\phi \quad [B-1]$$

can be evaluated to be equal to

$$A I_0 t = B \cdot \phi(t) + D \arctan (E \tan \phi/2) \quad [B-2]$$

B and C being constants

The shape of the t vs. ϕ curve is controlled by the value of the parameter E . It can be seen that for $E = 1$ a straight line and for $E \neq 1$ a set of S-shaped curves is found (Fig. 6). The role of the parameter E can be demonstrated when the integrand in Eq. [B-1] is rewritten also in terms of E by differentiating [B-2]

$$\frac{1}{G} = \frac{1}{2} \frac{ED}{E^2 \sin^2 \phi/2 \cos^2 \phi/2} \quad [B-3]$$

The curves start at $\phi = 0$ with a slope equal to $\frac{1}{2}E$. All curves cross at $\phi = l \cdot \pi$. For values of E exceeding

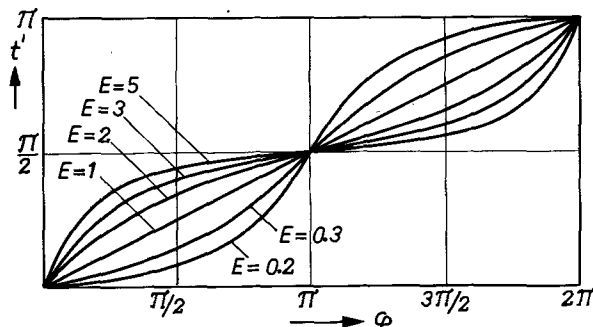


Fig. 6. Plot of the reduced time $t' = \frac{A I_0}{D} t$ vs. ϕ curves according to Eq. [B-2] for a number of E values. For clarity the term $B \cdot \phi(t)$ is omitted.

unity this point of inflection corresponds to a maximum in growth rate. The maximum value increases with E . For values of E smaller than unity this point corresponds to a minimum growth rate. For any particular combination of optical parameters of a layered system E should be calculated.

REFERENCES

1. H. F. Sterling and R. C. G. Swann, *Solid-State Electron.*, **8**, 653 (1965).
2. V. Y. Doo, R. D. Nichols, and G. A. Silvey, *This Journal*, **113**, 1279 (1966).
3. S. Yoshioka and S. Takayanagi, *ibid.*, **114**, 962 (1967).
4. H. F. Grieco, F. L. Worthing, and B. Schwartz, Paper 148 presented at Electrochem. Soc. Meeting, Philadelphia, Oct. 9-14, 1966.
5. S. M. Hu, *This Journal*, **113**, 693 (1966).
6. T. Reizmann and W. van Gelder, *Solid-State Electron.*, **10**, 625 (1967).
7. A. Mitchell and M. Zemansky, "Resonance Radiation and Excited Atoms," University Press, Cambridge (1961).
8. M. J. Collet, *This Journal*, **116**, 110 (1969).
9. C. C. McDonald and M. E. Gunning, *J. Chem. Phys.*, **23**, 532 (1955).
10. G. Brauer, "Handbuch der Präparativen Anorganischen Chemie," 1st ed., p. 360, Enke Verlag, Stuttgart (1954).
11. H. Niki and G. J. Mains, *J. Phys. Chem.*, **68**, 304 (1964).
12. H. J. Emelús and J. Stewart, *Trans. Faraday Soc.*, **32**, 1577 (1936).
13. J. C. Elgin and H. S. Taylor, *J. Am. Soc.*, **51**, 2059 (1929).
14. S. Middelhoek, *IBM J. Res. Develop.*, **14**, 117 (1970).
15. L. J. Fried, R. Flachbart, D. F. Itlen, J. W. Ranisesky, F. W. Anderson, and K. V. Patel, *This Journal*, **117**, 1079 (1970).
16. J. Franz and W. Langheinreich, *Solid-State Electron.*, **11**, 59 (1968).
17. H. R. Philipp and E. A. Taft, *Phys. Rev.*, **120**, 37 (1960).
18. M. Born and E. Wolf, "Principles of Optics," Sec. 16, Pergamon Press, Oxford (1965).
19. J. A. Stratton, "Electromagnetic Theory," Chap. 9, McGraw Hill Book Co., New York (1941).
20. O. Heavens, "The Optical Properties of Thin Solid Films," Chap. 4, Butterworths, London (1955).

Electron Trapping in Single Crystal Cuprous Oxide

Jerome D. Schick*¹ and Dan Trivich*

Department of Chemistry, Wayne State University, Detroit, Michigan 48202

ABSTRACT

Samples of Cu_2O after illumination at low temperatures possess a higher electrical conductance than the same samples without preillumination. The excess conductance is removed by heating above 100°C . The possibility that this "photomemory" effect is due to electron trapping was investigated by methods analogous to thermally stimulated conductivity. When the preilluminated samples are heated at a constant rate with time, $\beta = dT/dt = \text{constant}$, the plots of excess conductance vs. temperature are characterized by two maxima lying at about 25° and 100°C . Under different heating rates, the temperatures of the maxima, T_m , are shifted according to the function $\ln(T_m^2/\beta) = E_t/kT_m + \text{constant}$. The values of E_t obtained are interpreted as indicating traps lying 1.03 and 1.34 eV below the conduction band, with a precision of $\pm 15\%$.

The semiconducting properties of cuprous oxide have been of interest for many years and recently developed methods (1,2) for reliable preparation of single-crystal Cu_2O have allowed new measurements of properties which had previously been performed only on polycrystalline material. The considerable variation found in the previous data could be due to impure materials, variations in sample preparation, and the effects of grain size and grain boundaries in the polycrystalline cuprous oxide samples. New data have been obtained in our laboratory using these single crystals.

Electrical conductivity measurements have been performed (3) on single-crystal samples of cuprous oxide which had been quenched from high temperatures and controlled oxygen pressures. Optical transmission measurements (4) have been carried out on similarly prepared samples. In particular we have observed that the electrical conductivity of quenched samples decreases irreversibly when the sample is heated to somewhat above room temperature. This phenomenon, which is called "aging," may be similar to the aging in cuprous oxide rectifiers (5) and in polycrystalline cuprous oxide (6). The aging effect may be simulated by first preilluminating the aged sample and

then measuring the conductivity in the dark. The increase in conductivity due to preillumination has been called a "photomemory effect" and has been studied by several investigators (7), especially by Kužel (8). In order to gain information which might explain these results, in particular the photomemory effect, we have been led to a consideration of electron trapping as a possible explanation for the variations in the conductivity results and a possible correlation between the conductivity and optical data.

Methods for studying electron trapping in solids include the method of thermally stimulated conductivity. In this method, the sample is illuminated at low temperatures and then, in the dark, the temperature is increased, e.g., at a constant rate with time, while the conductivity is measured. The difference between the conductivity of a preilluminated sample as a function of temperature and the normal dark conductivity as a function of temperature is called the thermally stimulated conductivity (TSC). In an attempt to better understand the electron trapping phenomenon as it pertains to cuprous oxide, a study of single-crystal cuprous oxide was undertaken using methods related to thermally stimulated conductivity.

Much of the work done on investigating trapping levels by thermally stimulated current measurements has been done on CdS (9) and other similar materials (10). There are a number of studies in the literature that compare various methods of analyzing TSC data

* Electrochemical Society Active Member.

¹ Present address: IBM Corporation, East Fishkill Facility, Hopewell Junction, New York 12533.

Key words: cuprous oxide, electron trapping, photomemory, thermally stimulated conductivity.

(9). In general, the temperature of the TSC maximum gives information regarding the magnitude of the trap depth (E_t), the area under the TSC curve gives information about the density of traps, and in some cases, the detailed shape of the TSC curve may give information about the capture cross section of the trap (11). The methods used for analyzing TSC data are generally applicable to all the materials studied, since they are primarily n-type materials with similar properties. In these cases, the thermally stimulated conductivity, σ^* , is due to a transient increase in the number of free electrons during trap emptying. For cuprous oxide, the interpretation of the data may be complicated by interdependent electronic processes. In fact, we have shown that σ^* for Cu_2O increases significantly before trapped electrons are released, making the application of TSC-like measurements to cuprous oxide considerably different from that for n-type materials in general. Thus we have chosen to call the difference between the preilluminated conductivity and the dark conductivity, that is σ^* for cuprous oxide, the excess conductivity (EC).

A center may be considered a trapping center or a recombination center (12) depending on the relative magnitudes of (a) the probability of thermal freeing of the carrier from the center and (b) the probability of recombination of the carrier at the center occurring with a free carrier of opposite sign. Imperfection levels lying E_t below the conduction band will behave as trapping centers if

$$n_t p v S_p \ll n_t S_n v N_c \exp(-E_t/kT) \quad [1]$$

where n_t is the density of centers occupied by electrons, p is the density of free holes, and S_n and S_p are the capture cross sections for a free electron (and hole) by a center occupied by a hole (electron), N_c is the effective density of states in the conduction band, and v is the thermal velocity of an electron.

Figure 1 shows a model for a material with N_A acceptors, N'_A of which are ionized, N_t trapping states, and N_{dt} deep trapping states. The trapping level lies E_t below the conduction band and is occupied by n_t trapped electrons. The electronic transitions for thermal freeing and retrapping are labeled with their respective probabilities, γ and α .

Let us consider the situation where $n_t = 0$, and let us also neglect the deep trapping level. With these restrictions we may plot $\ln \sigma$ against $1/T$ and the slope of this plot may be used to calculate the energy for ionization of an acceptor. This information is obtained from what may be called dark conductivity curves, that is, no illumination reaches the sample insuring that the conductivity is due to the thermal interaction of the valence electrons with the acceptor level.

Now suppose that, due to preillumination, $n_t \neq 0$, that is, there are n_t trapped electrons at E_t below the conduction band. Suppose also that the preilluminated conductivity, $\sigma'(T)$, is greater than $\sigma(T)$, at some temperature far below trap emptying temperatures.

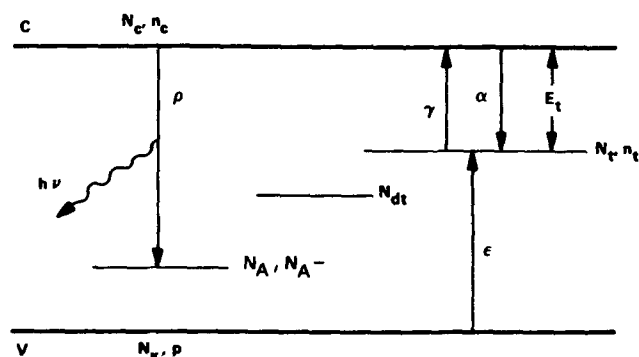


Fig. 1. Energy level diagram for a p-type material with trapping levels.

This greater conductivity could be attributed to an increase in the hole concentration as a result of removing electrons from the valence band/acceptor level equilibrium. These effects are complicated and interdependent; however, under no circumstances should $\sigma'(T) < \sigma(T)$.

Let us consider the variation of σ^* with increasing temperature. In the low-temperature region, the p-type conductivity, $\sigma'(T)$ is larger than the dark conductivity, $\sigma(T)$, due to the previous removal of n_t electrons from the valence band/acceptor equilibrium system. This leads to an increase in σ^* with increasing temperature. As the temperature approaches the region where n_t is affected, electrons are liberated from the traps by being excited to the conduction band from which, by recombination, they re-enter the valence band/acceptor equilibrium system leading to a reduction in $\sigma^*(T)$. Since the free carrier lifetime should be relatively constant over the small temperature range of trap emptying, a maximum in the number of excess free electrons, available for recombination, should occur where the rate of trap emptying is a maximum. These effects will eventually die out as $n_t \rightarrow 0$ and $\sigma^*(T) \rightarrow 0$. This will produce a maximum in the σ^* vs. T curve and the maximum will occur in the temperature region where the rate of change of n_t becomes significant.

In thermally stimulated conductivity of n-type materials, the TSC curves are explained in terms of an increased conductivity as a result of an increase in the number of electrons in the conduction band. In this case, the rate of change in the concentration of free carriers is

$$dn_c/dt = -(n_c/\tau) - (dn_t/dt) \quad [2]$$

where τ is the recombination lifetime for the excess free electrons. Beginning with this expression and using definitions for γ and α , one may arrive at expressions which relate the trap depth E_t to the temperature T_m at which the maximum excess conductivity occurs. For the case of a constant heating rate, $\beta = dT/dt = \text{constant}$, with no retrapping, Bube (13) obtained the relation

$$\ln(T_m^2/\beta) = (E_t/kT_m) - \ln(N_c S_n v k/E_t) \quad [3]$$

We found that a similar analysis could be applied to cuprous oxide to interpret the maxima in the EC curves, and that an expression similar to Eq. [3] could be applied. In the application of the heating-rate method to cuprous oxide, T_m was determined for several values of the heating rate, β , and the first term of Eq. [3], $\ln(T_m^2/\beta)$, was plotted against $1/T_m$ resulting in a straight line whose slope taken as E_t/k gave a value for the trap depth E_t . The justification for this treatment is given in the discussion.

Experimental

The single-crystal cuprous oxide samples were prepared using the method developed in this laboratory by Toth, Kilkson, and Trivich (1) and modified by Kellogg (14). In this method, high-purity copper sheets were oxidized at 1000°C to polycrystalline cuprous oxide and subsequently annealed at higher temperatures to form large area single crystals in the plate. The single-crystal samples cut from this plate were polished to a thickness of 0.02 cm and then equilibrated. Equilibration was accomplished at 1020° or 750°C in an atmosphere of known and controlled oxygen partial pressure. The purpose of the equilibration procedure was to fix the departure from stoichiometry. The concentration of defect species, e.g., copper atom vacancies, presumably varies according to the oxygen pressure used in the equilibration. Oxygen partial pressures used were in the range of 112 to 8.9×10^{-2} Torr for 1020°C and 1.48 to 7.5×10^{-4} Torr for 750°C , thus covering a wide region of conditions in which Cu_2O is stable.

The single-crystal samples were quenched to liquid nitrogen temperatures from equilibration temperatures. This technique was presumed to "freeze-in" the departure from stoichiometry determined during equilibration. After gold ohmic contacts were evaporated on the sample, it was placed in the measuring system. This system allowed measurements of conductivity, photoconductivity, minority carrier lifetime, and excess conductivity. Measurements could be performed under illuminated conditions or total darkness and at a pressure less than 5×10^{-7} Torr.

The samples were mounted on a holder in the system which allowed cooling to liquid nitrogen temperatures and heating to 300°C . A control thermocouple was connected from the sample holder to a modified Fisher DTA programmer/controller. Two additional Chromel/Alumel thermocouples were attached to the sample holder and connected to a recorder for time/temperature curves and a plotter for current/temperature plots. The sample current was plotted on the vertical axis of the plotter.

Illumination of the sample was performed by using either a tungsten filament source, a pulsed light source, or a monochromatic source. Each of these could be positioned adjacent to the quartz window of the vacuum system.

After the sample was placed in the system it was initially heated to above 100°C after which it was cooled to -160°C in the dark. The temperature was then linearly increased and sample current plotted as a function of temperature on the X-Y plotter. This gave the dark conductivity curve. The sample was again cooled to -160°C and illuminated, e.g., for precisely 4 min with white light. Then in total darkness, it was again heated at a linear rate producing the preilluminated curve. The difference in conductivity between the two curves is called the excess conductivity curve.

Results

Figure 2 gives a typical recorder plot of conductance curves for cuprous oxide, showing the dark conductance, σ , the conductance after preillumination, σ' , and the difference or excess conductance, σ^* . In this plot, the difference is doubled in conductance to accentuate the shape of the EC curve. Since only relative values of the conductivity are required, the directly recorded values of the conductance in ohm^{-1} are given

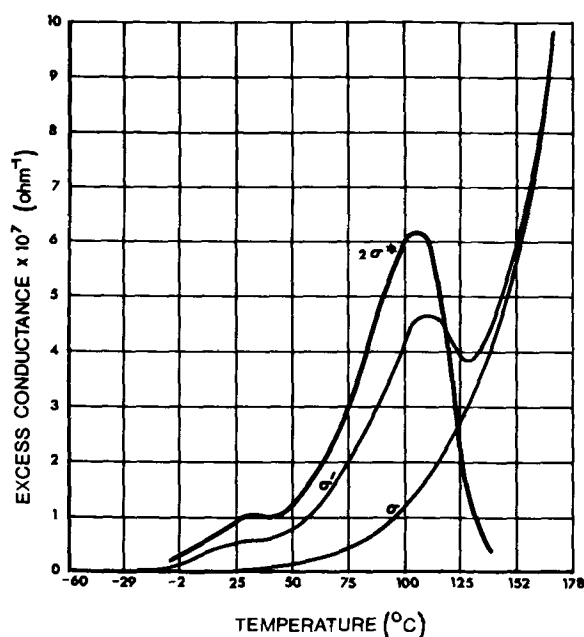


Fig. 2. Typical excess conductance curve, showing the dark conductance, σ , the conductance after preillumination, σ' , and the difference, σ^* , the last on a doubled scale.

in the plots, but in the discussion the term, conductivity, is used.

The dark conductivity curves were very nearly identical for all the samples run which had been equilibrated at oxygen pressures of 14.2 to 7.4×10^{-4} Torr and quenched from 1020° and 750°C . These curves were used to obtain plots of $\log \sigma$ vs. $1/T$ which were straight lines whose slopes of $-E/2.303 kT$ gave $E = 0.4$ eV in all cases. The dark curve was repeated through as many as thirty cooling-heating cycles for a given sample.

The curves for conductance after preillumination all showed two maxima producing two peaks in the EC curves near 298° and 373°K . As indicated by Eq. [3], a change in the heating rate, β , causes a shift in the temperature at which the EC peak occurs. This then provided a method of determining the trap depth, E_t . In this work, heating rates of 0.09 to $0.4^\circ\text{C}/\text{sec}$ were used to produce the shifts in the EC maximum temperatures as shown in Fig. 3. From these curves, the maxima were determined, T_{m1} , for 298°K peak and T_{m2} for the 373°K peak, and plots were made of $\log (T_{m2}^2/\beta)$ vs. $1/T_{m1}$. Figure 4 shows these two plots which can be used to determine the electron trap depths associated with the two peaks in the EC curves. Thus an average value of 1.03 eV for the trap depth was obtained from the 298°K peak and 1.34 eV for the trap depth associated with the 373°K peak. Values for the trap depths from the EC curves of all the samples varied by as much as 15%, but this was judged to be the limit of the precision of reading and treating the data, rather than being due to significant variations among the samples.

In order to determine the minimum photon energy for trap filling, an experiment using monochromatic light was performed. Monochromatic light of controlled intensity was directed on the sample at low temperatures for 1 hr, and then the curves for the conductance of the sample after preillumination and for the dark conductance were run in the normal manner. The heights of the EC curves at the maxima were then plotted against the photon energies of monochromatic light. Figure 5 shows the results of these measurements. For measurement of the higher temperature peak, the preillumination was done at room tempera-

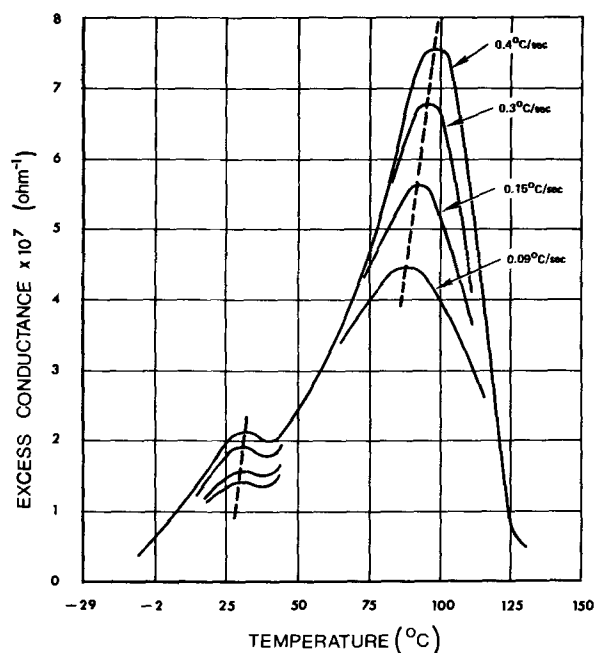


Fig. 3. Excess conductance curves at various heating rates. For clarity only the portions in the vicinity of the maxima are shown for the curves below the topmost; all curves tend to merge at the lowest and highest temperatures.

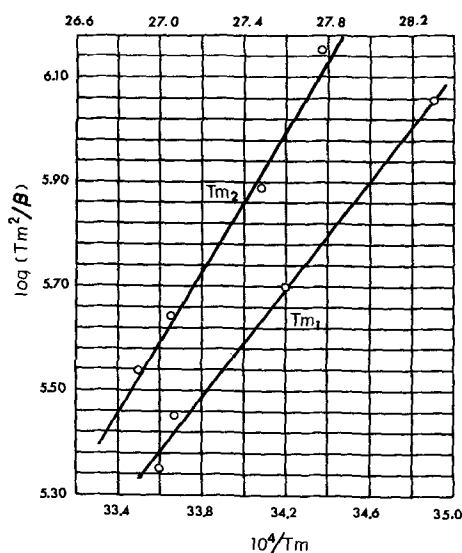


Fig. 4. Plots of $\log (T_m^2/\beta)$ vs. $1/T_m$ whose slopes give the trap depth. The lower horizontal scale applies to the lower curve and the upper scale to the upper curve.

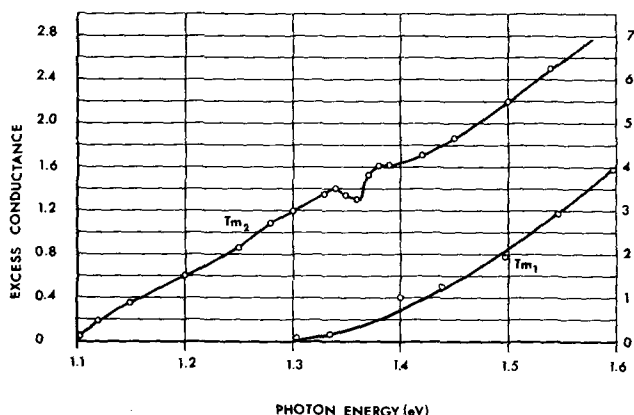


Fig. 5. Effect of wavelength of monochromatic light used in preillumination on the magnitude of the excess conductance. The left scale applies to the left curve and is in units of 10^{-8} ohm^{-1} . The right scale for the right curve is in units of 10^{-9} ohm^{-1} .

ture since this resulted in elimination of the lower temperature peak. In fact, separation of the two peaks was frequently used, e.g., by warming a preilluminated sample to room temperature, cooling the sample again, and then making a normal programmed run with only the higher temperature peak present.

No significance is attached to the detailed shape of the curves in Fig. 5 except to the tendency to approach a threshold. The threshold energy for filling of the 1.03 eV trapping level was found to be about 1.3 eV and the threshold energy for filling of the 1.34 eV trapping level was about 1.1 eV. A discussion of the consequences of these results appears later.

The proposed energy level diagram for cuprous oxide as determined from this work is shown in Fig. 6. Level 1 is the 0.4 eV acceptor level, and levels 2 and 3 are the two electron trapping levels whose depths and threshold energies were determined independently in this work.

Discussion

To explain these results one must make some assumptions concerning a model for cuprous oxide. A widely accepted model is that by Wagner (15), which describes cuprous oxide as a defect compound in which an excess of oxygen gives rise to copper atom vacancies. These vacancies act as acceptors thus explaining the observed p-type character. Since this model, while moderately successful in explaining high-temperature

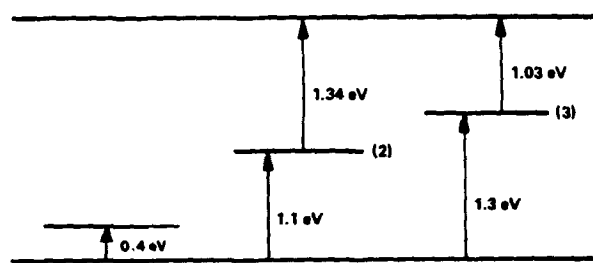


Fig. 6. Proposed energy level diagram for Cu_2O . The lowest level is an acceptor level; the higher levels are trap levels. The values associated with the trap levels are approximate, with an estimated precision of $\pm 15\%$.

properties, is inadequate for low temperatures, more elaborate models have been proposed, largely based on Bloem's (16) work and more recently treated by the Strasbourg group (7, 17). The principal species postulated are copper atom vacancies, oxygen vacancies, which can be singly and doubly ionized, and also complexes among these various species. While these postulates are plausible, very little concrete evidence is yet available to assign the various species to the energy levels that are invoked to explain the experimental results.

The dark conductivity and the conductivity after preillumination at temperatures below the maximum can be described by the functions $\sigma = K \exp(-E/kT)$ and $\sigma' = K' \exp(-E'/kT)$, respectively, in which $E \approx E' \approx 0.4 \text{ eV}$ within the precision of measurements, and $K' > K$. In this region, which has been called the "photomemory" region, the problem is to explain the increase in the pre-exponential factor, K , due to preillumination. Kužel (8) has proposed that K is dependent on the concentration of isolated copper atom vacancies which act as acceptors. Heating in the dark removes some of these by forming associates, e.g., copper atom divacancies, and preillumination causes a dissociation of these complexes, enlarging the concentration of single atom vacancies. While Kužel's model is a possible one, our results are better explained by a model which is based on a changed concentration of un-ionized acceptors due to preillumination. A similar model is apparently preferred by the Strasbourg group.

Let K be proportional to the concentration of un-ionized acceptors, $K = BN_{A_0}$. It is possible that even at absolute zero some of the acceptors are ionized, thus implying a partially compensated model, so that $N_{A_0} = N_A - (N_{A-})$ at $T = 0^\circ\text{K}$. Here N_A is the total concentration of acceptors and N_{A-} is the concentration of ionized acceptors at 0°K .

As the temperature is increased, electrons are excited from the valence band to the acceptor levels, giving rise to more ionized acceptors and p-type conductivity, so that $N_{A_0} = N_A - [(N_{A-}) + p]$, where p is the hole concentration. We assume $p \ll [N_A - (N_{A-})]$.

The effect of preillumination is to remove some electrons from the ionized acceptors and place them in higher, trapping states. The details of this process need not be specified since the equilibrium between the valence band and the acceptor states allows the removal to occur from both of these. The net effect is to increase the concentration of un-ionized acceptors so that after illumination $N_{A_0} = N_A - [(N_{A-}) - n_t]$ where n_t is the concentration of trapped electrons. Thus K is increased to K' giving rise to a greater conductivity due to preillumination.

The above discussion applies to the temperature region below the maximum in the EC curve. The effect of further increase in temperature is to excite electrons out of the traps to the conduction band from which they re-enter the valence band/acceptor equilibrium system by way of recombination centers. The net effect

is to regenerate the ionized acceptors which had been bared by preillumination. This tendency toward a decrease superimposed on a rising EC curve then gives rise to a maximum in the curve. The temperature at which this occurs, T_m , can be used to locate the depth of the trap level by methods analogous to those used for the TSC case.

Neglecting the contribution to the conductivity by the electrons in the conduction band, the excess conductivity $\sigma^* = (K' - K) \exp(-E_A/kT) \propto (p' - p)$ and $(K' - K) = Bn_t$. We modify Bube's treatment of the heating rate method for locating trap depth by postulating that the rate of trap emptying determines the rate of regenerating ionized acceptors, i.e., the lifetime of the excess electrons in the conduction band is very small.

Thus at the maximum, $d\sigma^*/dT = 0$ and also $d\Delta p/dT = 0$ if one neglects the temperature variation of the hole mobility, μ_p . At a constant heating rate, $\beta = dT/dt = \text{constant}$, we have $d\Delta p/dT = \beta^{-1}d\Delta p/dt$. Now setting $d(\ln \Delta p)/dt = 0$, and noting that $\sigma^* = q\mu_p\Delta p$, we obtain

$$\frac{d}{dt} [\ln(B/q\mu_p) + \ln n_t - E_A/kT] = 0 \quad \text{at } T = T_m \quad [4]$$

so that

$$\frac{\beta E_A}{kT_m^2} = -\frac{1}{n_t} \frac{dn_t}{dt} \quad [5]$$

The factor on the right of Eq. [5] represents the probability of escape from traps and this is given by Bube (18) as

$$-n_t^{-1}(dn_t/dt) = P = N_c v S_t \exp(-E_t/kT) \quad [6]$$

where S_t is the capture cross-section of the traps. Then for $T = T_m$, we obtain

$$\beta E_A/kT_m^2 = -n_t^{-1}(dn_t/dt) = P = N_c v S_t \exp(-E_t/kT_m) \quad [7]$$

so that

$$\ln(T_m^2/\beta) = (E_t/kT_m) - \ln(N_c v S_t/k/E_A) \quad [8]$$

Equation [8] is analogous to Eq. [3] previously derived for the treatment of the TSC curves. Thus by the present model, plots of $\ln(T_m^2/\beta)$ vs. $1/T_m$ can be used to evaluate the trap depth by setting the slope equal to E_t/k , as was done in the Results section.

The model proposed is also in accord with the results of Zouaghi *et al.* (17) who showed by Hall measurements that the effect of the preillumination is primarily to increase the density of holes. Further support may be found in the work of Fortin *et al.* (20) who related the photomemory effect to high-temperature photoconductivity for which the time constants vary from minutes to fractions of a second over temperature ranges from room temperature to 250°C.

While the above is apparently the most economical model that could be used to explain the present data, it is possible to make a more detailed model by making further postulates which are quite plausible. In the model thus far we have not identified the source of the ionization of the originally ionized acceptors of concentration, N_{A-} . It is conceivable that both donors and acceptors exist in cuprous oxide with a predominance of acceptors. The neutral donors would lose electrons to the acceptors (not necessarily rapidly), thus leading to partial compensation. As shown by Brattain (19)

for partially compensated cuprous oxide, the hole concentration would be given by

$$p = \frac{N_A - (N_{D+} + p)}{N_{D+} + p} N_v \exp(-E_A/kT) \quad [9]$$

where N_{D+} is the concentration of ionized donors.² For the condition $p \ll N_{D+} < N_A$

$$p = \frac{(N_A - N_{D+})}{N_{D+}} N_v \exp(-E_A/kT) \quad [10]$$

which is identical to our previous treatment with $N_{D+} = N_{A-}$ and $B/q\mu_p = N_v/N_{D+}$. Further the effect of preillumination may be to move the electrons from the ionized acceptors to the ionized (empty) donor states so that

$$N_{A0} = N_A - N_{D+} \quad \text{and} \quad N_{D+} = N_D - n_t$$

A further elaboration of the model could proceed by attempting an identification of the species responsible for the various levels. Following Bloem, one could assign the two trap levels to oxygen vacancies which can be singly and doubly ionized. The acceptor levels could be assigned to copper atom vacancies or some complex arising from them. Still further levels are presumably necessary to explain other results. However the identification of the species responsible for these levels must await more definitive experiments.

Manuscript submitted May 20, 1971; revised manuscript received Nov. 3, 1971.

Any discussion of this paper will appear in a Discussion Section to be published in the December 1972 JOURNAL.

REFERENCES

1. R. S. Toth, R. Kilkson, and D. Trivich, *J. Appl. Phys.*, **31**, 1117 (1960).
2. Y. Ebisuzaki, *ibid.*, **32**, 2027 (1961).
3. M. R. Wright, J. D. Schick, and D. Trivich, "Proceedings from Colloque sur les Propriétés Physique de la Cuprite, a Symposium held at Strasbourg, France, March 1968," p. 76.
4. L. M. Kellogg and D. Trivich, *ibid.*, p. 36.
5. A. L. Williams and L. E. Thompson, *J. Inst. Elec. Engrs. (London)*, **88**, 353 (1941).
6. S. J. Angello, *Phys. Rev.*, **62**, 371 (1942).
7. J. P. Zielinger, M. Tapiero, Mme. C. Roubaud, and M. Zouaghi, *Solid State Commun.*, **8**, 1299 (1970).
8. R. Kuzel, *Czech. J. Phys.*, **B11**, 133 (1961); R. Kuzel, Paper B in "Proceedings of Second Cuprite Colloquium, University of Alberta, Edmonton, Canada, August 1968."
9. H. J. Dittfield and J. Voigt, *Phys. Status Solidi*, **3**, 1941 (1963); K. H. Nicholas and J. Woods, *Brit. J. Appl. Phys.*, **15**, 783 (1964).
10. G. F. J. Garlick and A. F. Gibson, *Proc. Phys. Soc. (London)*, **A60**, 574 (1948).
11. G. A. Dussel and R. H. Bube, *Phys. Rev.*, **155**, 764 (1967).
12. R. H. Bube, "Photoconductivity of Solids," John Wiley & Sons, Inc., New York (1960).
13. Ref. 12, p. 295.
14. L. M. Kellogg, Ph.D. Thesis, Wayne State University, Detroit, 1967.
15. C. Wagner and H. Hammen, *Z. Physik. Chem. (Leipzig)*, **B40**, 197 (1938).
16. J. Bloem, *Philips Res. Rept.*, **13**, 167 (1958).
17. M. Zouaghi, M. Tapiero, J. P. Zielinger, and R. Burgraf, *Solid State Commun.*, **8**, 1823 (1970).
18. Ref. 12, p. 278.
19. W. H. Brattain, *Rev. Mod. Phys.*, **23**, 203 (1951).
20. E. Fortin, M. Zouaghi, and J. P. Zielinger, *Phys. Letters*, **24A**, 180 (1967).

² If the acceptors are not compensated, the dark conductivity activation energy is $E_A/2$, giving $E_A = 0.8$ eV.

Vapor-Phase Epitaxial Growth and Some Properties of ZnSe, ZnS, and CdS

W. M. Yim and E. J. Stofko

RCA Laboratories, Princeton, New Jersey 08540

ABSTRACT

Single-crystal layers of ZnSe, ZnS, and CdS have been grown epitaxially on GaAs, GaP, and sapphire substrates in an open-tube system by reaction of the metal vapors with the nonmetal hydride gases. Various factors are discussed which were found to affect the epitaxial growth. These include the role of vapor compositions and growth temperatures in controlling stoichiometry and polymorphism, and the choice of substrate materials with particular emphasis on the effects of lattice and thermal expansion match between the substrate and the epitaxial layer. High crystalline quality of the epitaxially grown layers was evidenced by the Kikuchi lines present in their electron diffraction patterns. As-grown layers of ZnSe and ZnS, both undoped and doped, were high resistivity, while CdS was readily grown n-type. These epitaxial layers showed at room temperature a bright, visible cathodoluminescence, and for each compound different emission colors were observed with specimens grown at different temperatures.

Although published literature abounds with reports describing crystal growth of II-VI compounds, relatively little information is available on vapor-phase epitaxial growth of these compounds. The lack of information is particularly true for epitaxial growth using gaseous starting sources of the component elements, since in nearly all of previous work (1-3) the starting materials used were presynthesized bulk compounds.

In this paper, we report the heteroepitaxial growth of single-crystal ZnSe, ZnS, and CdS layers on GaAs, GaP, and sapphire substrates in an open-tube system by reaction of the metal vapors with the nonmetal hydride gases. The results presented include growth morphology, crystalline perfection, and some of the electrical and luminescent properties of these epitaxially grown layers.

Experimental

The epitaxial growth of ZnSe, ZnS, and CdS on various substrates was investigated with the apparatus (4) shown schematically in Fig. 1.¹ In this apparatus the Group II element (Zn or Cd) was transported as the vapor by passing H₂ over the molten metal located in the source zone at a temperature T₁. The Group VI element (Se or S) was introduced as gaseous hydride (H₂Se or H₂S) diluted in H₂. The Groups II and VI gases were brought together in the reaction zone at a temperature T₃, and growth of the II-VI compound occurred on a substrate in the deposition zone maintained at a temperature T₅.

The substrate material most extensively used was GaAs of (100) and (111)² orientations, but we also used (100)- and (111)²-oriented GaP and (0001)-oriented sapphire, while the use of other substrate materials such as Si and Ge was limited to only a few experiments. The GaAs and GaP substrates were first mechanically polished to a mirror-smooth finish, followed by chemical polish in a dilute bromine-methanol solution with or without H₃PO₄. The sapphire substrates (which were furnished with a smooth surface finish by the supplier³) were annealed *in situ*, prior

Key words: II-IV compounds, heteroepitaxy, vapor-phase growth, electrical properties, cathodoluminescence.

¹ Shown also in Fig. 1 are the provisions for growth of III-V compounds and for introduction of doping impurities, but these were not used in the present study, except in several experiments to dope ZnSe and ZnS with Al, which was added as volatile chlorides through the side arm into the reaction zone by passing an H₂-HCl mixture over molten aluminum at T₄ = 1000°C.

² All were specifically of the type (111A) with the gallium face up.

³ Insaco, Inc., Quakertown, Pennsylvania.

to epitaxial growth, in flowing H₂ for about 15 min at 1300°C. This simple treatment was found satisfactory for single-crystal epitaxy. Although we have explored other methods of sapphire surface preparation, which included chemical etch in hot H₃PO₄ followed by Caro's acid etch, as well as gas-phase etch in flowing HCl-H₂ at temperatures from between 1000° and 1250°C, the substrates thus treated did not provide single-crystal epitaxy within the experimental conditions investigated.

Virtually all of the present II-VI compound epitaxial layers were deposited directly onto the substrates prepared as above. However, as is discussed later, for ZnS we also used GaAs substrates coated with thin layers of single-crystal GaP.

A comprehensive series of experiments with various reactant gas compositions, flow rates, and zone temperatures led to the selection of the optimum growth conditions, the discussion of which follows.

Results and Discussion

Effect of Growth Conditions

Of various growth parameters investigated, the reactant gas compositions and particularly the substrate temperatures had the most significant effects upon stoichiometry, growth rate, and crystallinity. In addition, the choice of substrate materials had an important bearing on the crystallinity of the deposited layer, as is discussed in a later section.

Reactant gas compositions.—The effect of reactant gas compositions on epitaxial synthesis was investigated primarily with the growth of ZnSe on GaAs substrates near 700°C; the most significant data are given in Table I.

The gaseous flow rates (200 cm³/min H₂ over molten Zn and 15 cm³/min H₂Se) listed first in Table I were

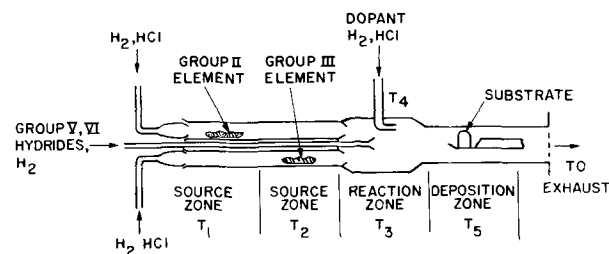


Fig. 1. Vapor-phase epitaxial growth apparatus, [Ref. (4)]

Table I. Effect of reactant gas compositions on epitaxial growth of ZnSe

Parameters	Substrate		Flow (cm ³ /min) over Zn (530°C), H ₂	Flow (cm ³ /min) to reaction zone (925°-1000°C) H ₂ Se H ₂		Subst. temp (°C)	Growth rate (μ/hr)	Deposit composition	Crystallinity
	Mater.	(hkl)							
1. Effect of H ₂ Se concentration	GaAs	(100)	200	15	700	700	2	Major Ga ₂ Se ₃ -ZnSe alloy	Poly
	GaAs	(100)	200	10	700	675	1	Minor ZnSe(Zb,W)*	Poly
	Sapph.	(0001)	200	10	700	675	1	Major ZnSe(Zb)	Poly
2. Effect of Zn vapor concentration	GaAs	(100)	200	5	700	700	5	Minor Ga ₂ Se ₃ alloy	Single-poly**
	GaAs	(100)	200	3	700	700	5	ZnSe(Zb,W)	Single
	GaAs	(100)	40	3	700	700	1	ZnSe(Zb)	Single-poly
	GaAs	(100)	200	3	700	700	5	ZnSe(Zb)	Single

* (Zb,W): Nearly all zincblende form with small amount of wurtzite form.
 ** Single-poly: Nearly all single with very small portions polycrystalline.

Table II. Effect of substrate temperatures on epitaxial growth of ZnSe, ZnS, and CdS

Epitaxial layer	Substrate		Subst. temp (°C)	Growth rate (μ/hr)	Epi-layer crystallinity			Cathodoluminescence
	Mater.	(hkl)			Cryst.	Struct.	(hkl)	
ZnSe ^a	GaAs	(100)	650	2	Single	Zb ^f	(100)	Red
	GaAs	(100)	700	5	Single	Zb	(100)	Red
	GaAs	(100)	750	6	Single-poly ^g	Zb-W ^g	(100)	Orange
	GaAs	(100)	800	9	Single-poly	Zb-W	(100)	Orange
	GaAs	(100)	830	13	Single	Zb	(100)	Yellow
	GaAs	(100)	850	18	Single	Zb	(100)	Yellow
	GaAs	(100)	890	36	Single	Zb	(100)	Yellow
	GaAs	(111)	890	29	Single	Zb	(111)	Yellow
	Sapph.	(0001)	850	15	Single	Zb	(111)	Yellow
	ZnS ^b	Sapph.	(0001)	650	9	Poly	W	(0001) ^h
Sapph.		(0001)	750	15	Poly	W	(0001) ^h	Blue
Sapph.		(0001)	810	12	Poly	W	(0001) ^h	Blue
Sapph.		(0001)	890	7	Poly	W	(0001) ^h	Blue
GaAs ^d		(111)	825	15	Single	Zb	(111)	Blue
GaAs		(100)	775	13	Single	Zb	(100)	Blue
GaP		(100)	825	18	Single	Zb	(100)	Blue
Sapph.		(0001)	690	33	Single	W	(0001)	Green
CdS ^c	GaAs	(111)	690	50	Single	W	(0001)	Green
	GaAs	(111)	750	10	Single	W	(0001)	Red
	Sapph.	(0001)	810	~0	—	—	—	—
	Sapph.	(0001)	890	0	—	—	—	—

^a H₂ flow over Zn (530°C) = 200 cm³/min. H₂Se and H₂ flow to reactive zone (925°C) = 3 and 700 cm³/min, respectively.

^b H₂ flow over Zn (530°C) = 200 cm³/min. H₂S and H₂ flow to reactive zone (925°C) = 3 and 700 cm³/min, respectively.

^c H₂ flow over Cd (580°C) = 200 cm³/min. H₂S and H₂ flow to reactive zone (1000°C) = 5 and 700 cm³/min, respectively.

^d Substrate coated with (111) GaP after grading the composition from GaAs to GaP.

^e Nearly all single with very small portions poly.

^f Zincblende form.

^g Major = zincblende, minor = wurtzite.

^h (0001) preferred orientation.

calculated to give an approximately equal number of moles (10⁻⁵ moles/min) of Zn and Se for deposition of stoichiometric ZnSe. This, however, resulted in polycrystalline, multiphased material. The major phase consisted of a Ga₂Se₃-ZnSe alloy⁴ and the minor phase was ZnSe of zincblende form mixed with a small amount of wurtzite form. The Ga₂Se₃-ZnSe alloy apparently resulted from the reaction between excess H₂Se and the GaAs substrate, since no Ga₂Se₃ alloy formed when sapphire substrates were used. By reducing the H₂Se flow to 10 cm³/min, the Ga₂Se₃ alloy formation was substantially suppressed, and by further reducing the H₂Se flow to 3 cm³/min the single-crystal epitaxy of ZnSe was achieved. On the other hand, the Zn vapor concentration had relatively little effect on formation of ZnSe within the Zn concentration range investigated of 10⁻⁶-10⁻⁵ moles/min, as shown in Table I.

For ZnS and CdS deposition, we used approximately the same gas flow rates as that found to be optimum for the growth of ZnSe.

Substrate temperatures.—The growth rate of ZnSe epitaxial layers was found to increase with increasing substrate temperature, as shown in Table II. At deposition temperatures below 700°C, the growth rates were small (1-5 μ/hr). Faster growth occurred in the temperature range of 700°-800°C, but with mixtures of zincblende (cubic) and wurtzite (hexagonal) polymorphs. The wurtzite polymorph generally disap-

peared at temperatures higher than 830°C, leading to return of the single-phase cubic form with a growth rate as high as 36 μ/hr at 890°C.

For ZnS the growth rate increased also with increasing temperature to more than 15 μ/hr at 830°C, but it decreased with further increase in temperature. The zincblende-wurtzite polymorphism was also observed for ZnS, but we defer general discussion of the observed phenomenon to a later section.

In contrast to relatively high temperatures found for optimum growth of ZnSe and ZnS, 890°C and 830°C, respectively, the optimum growth temperature for CdS was found to be near 700°C with a growth rate of 50 μ/hr. Above 700°C the growth rate decreased, and no CdS deposit formed beyond 800°C.

The observed dependence on substrate temperature of the growth rate could not be predicted on the basis of equilibrium thermodynamics. The free energy changes (ΔF_T) in chemical reactions postulated for the vapor deposition of ZnSe, ZnS, and CdS (see Appendix) are all negative in the range of substrate temperatures investigated, as shown in Fig. 2. Further, the ΔF_T values become more negative with decreasing temperature. Therefore, the deposition rate would probably increase monotonically with substrate temperature, contrary to the present experimental data, if equilibrium thermodynamics is the only factor that affects the vapor deposition process. The assumption, however, is not valid as amply demonstrated in recent studies, which showed that considerable deviations from thermochemical equilibrium exist (5) in an open-tube growth system such as the present one, and

⁴ Our unpublished results indicated that Ga₂Se₃, with a defect zincblende structure having a lattice constant of 5.42Å, forms continuous solid-solution alloys with ZnSe.

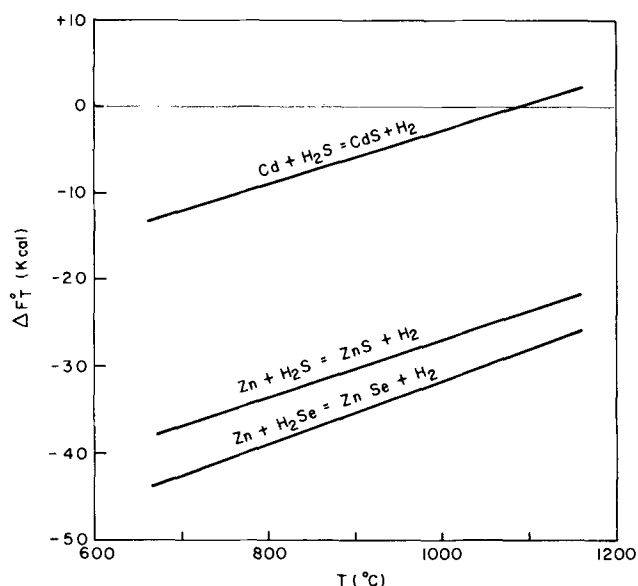


Fig. 2. Free energy of reaction (ΔF°_T) for vapor deposition of ZnSe, ZnS, and CdS.

that kinetic factors significantly influence the deposition process (6).

While simple arguments based on equilibrium are inadequate to describe the present vapor growth process, it is, nonetheless, noteworthy that the experimental optimum growth temperatures are lower for materials of smaller calculated ΔF°_T values than for materials of larger ΔF°_T . Namely, the optimum growth temperature listed in Table III for CdS of 700°C is lower than that for ZnS of 830°C which is yet lower than that for ZnSe of 890°C, and this is to be correlated with the trend shown in Fig. 2 of $|\Delta F^{\circ}_T|_{\text{CdS}} < |\Delta F^{\circ}_T|_{\text{ZnS}} < |\Delta F^{\circ}_T|_{\text{ZnSe}}$ below about 1100°C. The above observation is not limited to the case of II-VI compound vapor deposition. Previously, in an open-tube vapor growth of III-V compounds, we also observed (7) the similar relationship between experimental optimum growth temperature (T_{opt}) and ΔF°_T ; for example, $(T_{\text{opt}} = 700^{\circ}\text{C})_{\text{InP}} < (T_{\text{opt}} = 750^{\circ}\text{C})_{\text{GaAs}} < (T_{\text{opt}} = 800^{\circ}\text{C})_{\text{GaP}}$ and $|\Delta F^{\circ}_T|_{\text{InP}} < |\Delta F^{\circ}_T|_{\text{GaAs}} < |\Delta F^{\circ}_T|_{\text{GaP}}$. It is certain that any attempt to explain the above relationship must include considerations not only of equilibrium thermochemistry but also of kinetics, for which experimental data are lacking at the present time.

Structure and Crystallinity

ZnSe epitaxial layers.—Typical microstructure of a single-crystalline cubic ZnSe layer grown epitaxially on a (100)-GaAs substrate is shown in Fig. 3a. The layer was grown at 890°C and, as shown, it is well oriented. The reflection electron diffraction pattern in Fig. 3b confirms the (100) epitaxy. In addition to the well-defined diffraction spots, Kikuchi lines are present, which indicate high crystalline perfection. Simi-

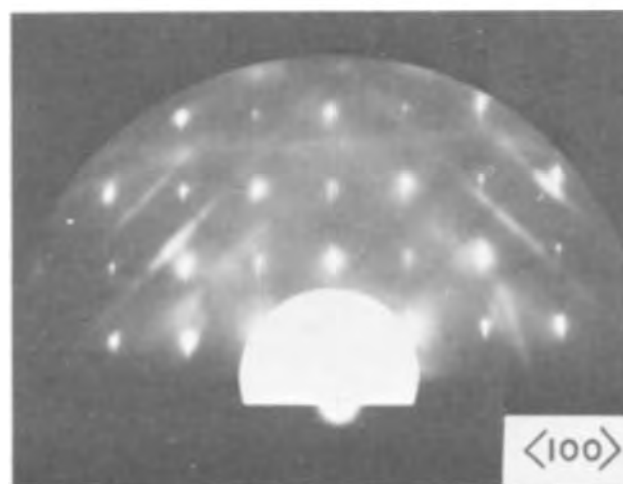
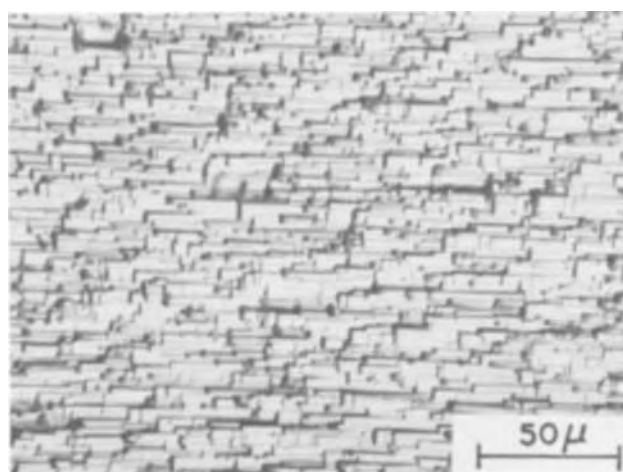


Fig. 3. (a, top) Photomicrograph, and (b, bottom) reflection electron diffraction pattern, of (100) ZnSe grown epitaxially on (100) GaAs.

larly, epitaxial layers on (111)-GaAs substrates (not shown) revealed well-oriented triangular growth patterns, characteristic of the (111) epitaxy. The cubic (111) ZnSe was also found to grow on (0001)-sapphire substrates; a microstructure of the (111)-oriented ZnSe single-crystal layer is shown in Fig. 4a.

The excellent epitaxy of ZnSe on GaAs can be understood in the light of complete solid-solution alloying (4), and good match both in the lattice constant and in the thermal expansion coefficient, between ZnSe and GaAs; and this makes possible a smooth transition between the substrate and the grown layer with minimal strains involved. As shown in Table IV, the difference in their lattice constants at room temperature is only 0.3%, and it increases slightly to about 0.6% at 800°C. Even with this good lattice match, rapid cooling sometimes caused the epitaxial layers to crack. However, cracking was com-

Table III. Optimum growth conditions for ZnSe, ZnS, and CdS

Epitaxial material	Cryst. struct.*	(hkl)	Substrate Material (hkl)		Flow (cm ³ /min) over		Flow (cm ³ /min) to reaction zone (925°-1000°C)			Substrate temp (°C)	Max. growth rate (μ/hr)
					Zn (530°C) H ₂	Cd (580°C) H ₂	H ₂ Se	H ₂ S	H ₂		
ZnSe	Zb	(100)	GaAs	(100)	200	—	3	—	700	890	36
			GaAs	(111)							
			Sapphire	(0001)							
ZnS	Zb	(100)	GaAs†	(111)	200	—	—	3	700	825	15
			GaAs	(100)							
			GaP	(100)							
CdS	W	(0001)	GaAs	(111)	—	200	—	15	700	690	50
			Sapphire	(0001)							

* Zb: zincblende; W: wurtzite.

† Substrate was graded in composition from GaAs to GaP prior to ZnS deposition.

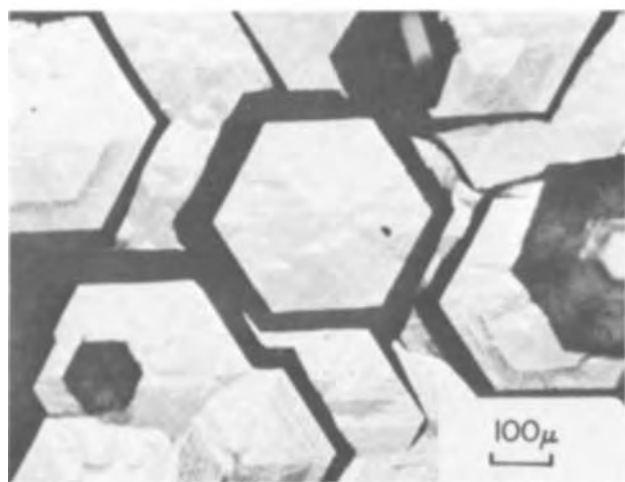


Fig. 4. (a, top) Photomicrograph of (111) ZnSe, and (b, bottom) photomicrograph of (0001) CdS, grown on (0001) sapphire. These layers were determined to be single crystalline by x-ray Laue back reflection.

pletely eliminated by slowly cooling the specimens from the growth temperature.

ZnS epitaxial layers.—The room-temperature lattice constant of GaP matches that of cubic ZnS to within 0.7%, and their thermal expansion coefficients are not appreciably different from each other (see, Table IV). Furthermore, GaP and ZnS form complete solid solutions (4), and therefore GaP appears to be a good substrate material for epitaxial growth of ZnS. The thermal expansion match is one of the most important factors to be considered in selecting suitable substrate materials. Silicon, in spite of its good lattice match to within 0.4% of ZnS at room temperature, is not a good substrate material, since ZnS layers grown on Si substrates were frequently found to crack. This is probably due to a relatively large difference in the thermal expansion between ZnS and Si. Since high-quality GaP single crystals of large dimensions were not readily available when the present study was undertaken, we initially used GaAs substrates after slowly varying the composition through graded regions of Ga(As, P) alloys from GaAs to GaP, using a vapor-phase growth technique previously developed by Tietjen and Amick (8). Subsequently, however, we used (100)-GaP as well as (100)-GaAs substrates for direct deposition of (100)-oriented cubic ZnS.

Typical microstructure of a cubic (111)-ZnS layer epitaxially grown on (111) GaP on a (111)-oriented GaAs substrate is shown in Fig. 5a, and the reflection electron diffraction pattern of Fig. 5b confirms the epitaxy. The pyramid-shaped growth patterns were formed during the epitaxial growth of GaP, with the

Table IV. Lattice constants and thermal expansion coefficients

Material	Struct.	Lattice constant (room temp)		Avg linear thermal exp. coeff. (RT up to about 800°C)	
		(Å)	Ref.*	(10 ⁻⁶ /°C)	Ref.*
ZnSe	Zb	5.6687	i, ii	9.44	vii
	W	<i>a</i> = 4.003		—	—
		<i>c</i> = 6.540	i		
ZnS	Zb	5.4093	i, ii	6.5-8.5	viii
	W	<i>a</i> = 3.820		<i>c</i> 5.9-6.5	
		<i>c</i> = 6.260	i		<i>c</i> 4.4-4.6
CdS	Zb	5.820	i	~6	iii
	Zb	5.8378	iii		
	W	<i>a</i> = 4.1368		<i>c</i> 5.0	
<i>c</i> = 6.7163		i, ii		<i>c</i> 2.5	ix
GaAs	Zb	5.6533	ii	6.72	x
GaP	Zb	5.4506	ii	5.78	x
Ge	Zb	5.6576	iv	6.2	iv
Si	Zb	5.4309	v	~4	v
α-Al ₂ O ₃	Trig.	<i>a</i> = 4.758		<i>c</i> 9.2	vi
		<i>c</i> = 12.991	vi	<i>c</i> 9.8	
	Cubic	3.839	iii	—	—

- * Ref. i. W. L. Roth, in "Physics and Chemistry of II-VI Compounds," pp. 127-128, M. Aven and J. S. Prener, Editors, North-Holland Publishing Co., Amsterdam (1967).
 ii. This work.
 iii. Calculated.
 iv. J. A. Amick, *RCA Rev.*, 24, 556 (1963).
 v. H. P. Wolf, "Silicon Semiconductor Data," p. 100, Pergamon Press, London (1966).
 vi. W. J. Campbell and C. Grain, U.S. Bur. of Mines Rept. Invest. 5757 (1961).
 vii. H. P. Singh and B. Dayal, *Phys. Status Solidi*, 23, K93 (1967).
 viii. R. R. Reeber and D. McLachlin, Jr., Tech. Report ARL-68-0183, Aerospace Research Laboratories, Wright-Patterson Air Force Base, October (1968).
 ix. R. R. Reeber and B. A. Kulp, *Trans. AIME*, 233, 698 (1965).
 x. E. D. Pierron, D. J. Parker, and J. B. McNeely, *J. Appl. Phys.*, 38, 4669 (1967); and M. S. Abrahams, J. J. Tietjen, and R. J. Paff, Unpublished results.

result that they also appeared in the ZnS epitaxial layer. By contrast, the single-crystal ZnS layers deposited directly on (100)-GaP or on (100)-GaAs substrates showed less well-defined microstructure, e.g., Fig. 6a; but, as shown in Fig. 6b, the Laue picture proved the deposited layers to be single-crystal cubic ZnS of the (100) orientation.

CdS epitaxial layers.—Epitaxial layers of (0001) CdS grown on (111)-GaAs substrates show a distinct growth feature consisting of many flat-topped and some pointed hexagonal pyramids. The surface microstructure of one such layer is shown in Fig. 7a and the epitaxial relation was determined to be (0001) CdS // (111) GaAs from the reflection electron diffraction pattern shown in Fig. 7b. The hexagonal patterns are apparently a common growth morphology for the (0001)-oriented CdS epitaxial layer, found not only in the layers grown on (111) GaAs and (0001) sapphire (Fig. 4b), but also in the films deposited on many other substrate materials such as ZnS, Ge, SrF₂, mica, CaF₂, and CdS itself (9). These morphological patterns are believed to indicate the characteristic growth mechanism (surface nucleation) of the epitaxial CdS layers (9).

There is a relatively large difference (3.2%) in the room temperature lattice constant between CdS and GaAs, although the difference in their thermal expansion coefficients is small. Since the present CdS layers were directly deposited on GaAs substrates, a considerable strain would be present in the CdS layers, particularly if the grown layers were thin. The strain arising from the lattice mismatch would, however, diminish with increasing distance away from the CdS-GaAs interface. In fact, for specimens with CdS layers thicker than about 50μ, Kikuchi lines were sometimes observed in the electron diffraction patterns.

Polymorphism.—It is well known (2) that many II-VI compounds exhibit zincblende-wurtzite polymorphism, as well as polytypism in the wurtzite form. The zincblende form is closely related to the wurtzite form by a simple lattice stacking difference, and the free energy difference between the two phases is prob-

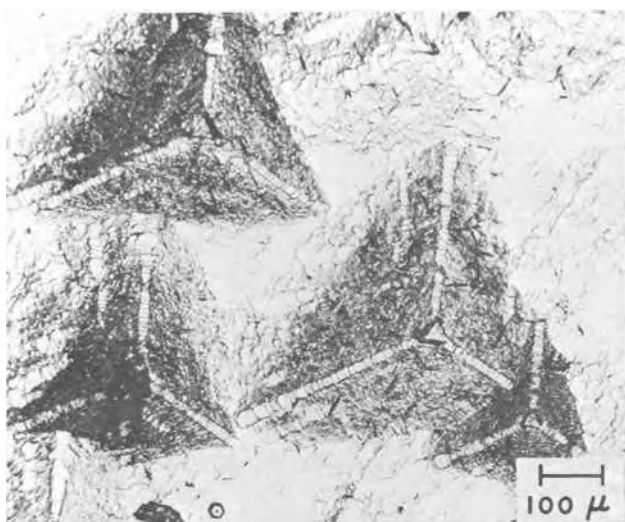


Fig. 5. (a, top) Photomicrograph, and (b, bottom) reflection electron diffraction pattern, of (111) ZnS grown epitaxially on (111) GaP on (111) GaAs.

ably small since they frequently coexist in one sample, as mentioned in a previous section. Although the zincblende phase is generally thought to occur at low temperatures and the wurtzite phase at high temperatures, previous results on this are widely conflicting. For instance, in the case of ZnSe, the wurtzite polymorph was reported (10) to appear in vacuum-sputtered films at substrate temperatures above 210°C. On the other hand, we did not observe (11) the hexagonal phase either in flash-evaporated ZnSe films deposited at temperatures up to 600°C, or in closed-tube chemically transported ZnSe grown at temperatures up to 950°C. A much higher temperature, $> 1000^{\circ}\text{C}$, was reported (12) for the occurrence of the wurtzite phase in vapor-transported ZnSe using Ar as a carrier gas.

In the present study with an open-tube chemical vapor deposition process, the temperature range where the wurtzite form of ZnSe appeared most frequently was between 700° and 830°C, as shown in Table II. The ZnSe layers grown outside of this temperature range were entirely in the cubic form, except when the vapor deposition was carried out in large excess H_2Se (see, Table I); and under this condition the hexagonal polymorph appeared, mixed with the cubic form in varying proportions, at all deposition temperatures investigated.

For bulk ZnS, it is also generally accepted that wurtzite is the stable form at high temperature, and that the hexagonal to cubic transition takes place at a temperature between 1020° and 1150°C (2, 13). In the present vapor-deposited ZnS, the wurtzite modification was obtained at growth temperatures as low as 650°C, and this was the only form that grew on (0001)-sapphire substrates throughout the entire range of

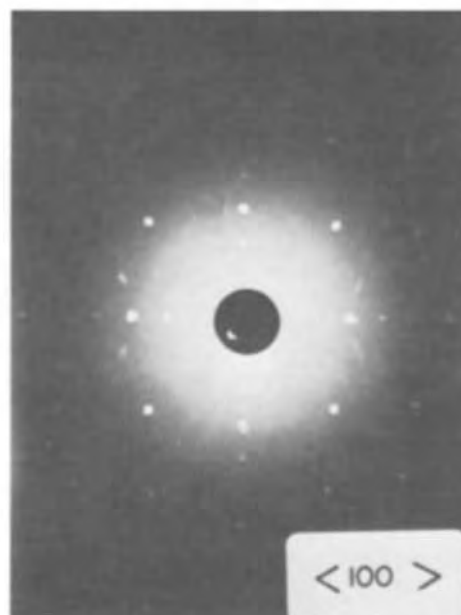
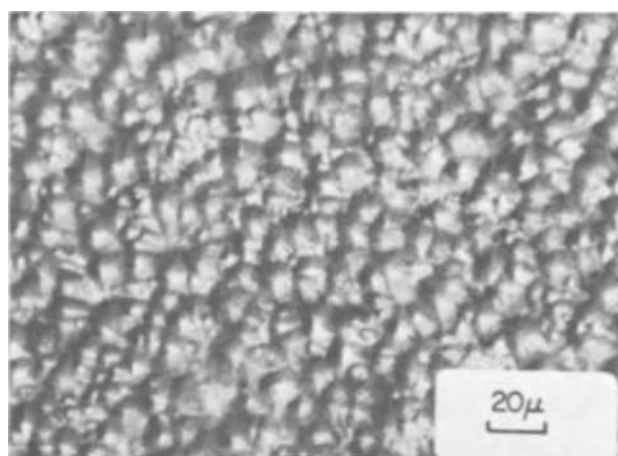


Fig. 6. (a, top) Photomicrograph, and (b, bottom) Laue back reflection pattern, of (100) ZnS grown directly on (100) GaAs.

deposition temperatures investigated up to 900°C. The crystal structure of substrate materials had a very significant effect on the type of polymorph to be obtained, since the ZnS epitaxial layers deposited near 800°C on GaAs and GaP consisted entirely of the cubic form, as opposed to the hexagonal form that grew on sapphire under otherwise identical growth conditions (see, Table II).

In contrast to the epitaxially grown ZnSe and ZnS, no polymorphism was observed in the present CdS epitaxial layers, which were all in the wurtzite form. This is in agreement with general observations that the zincblende form of CdS occurs only rarely in nature or in synthesized bulk material.

It is clear from the above discussion that the occurrence of polymorphism is a sensitive function of such variables as preparative techniques, growth temperatures, substrate materials, and reactant gas compositions. In addition to the aforementioned variables, previous investigations (2, 13) on the polymorphism in II-VI compounds, particularly in ZnS, list such factors as impurity effects, cooling rates, pressure, and mechanical strain that significantly affect the structure, and thus emphasize even more the complexity of the problem involved. The frequently quoted hexagonal to cubic transition temperature for ZnS, 1020°-1150°C, is for the bulk crystal probably under equilibrium conditions. Accordingly, it is not too surprising that the data are at variance in the present case, where the epitaxial layers were grown under

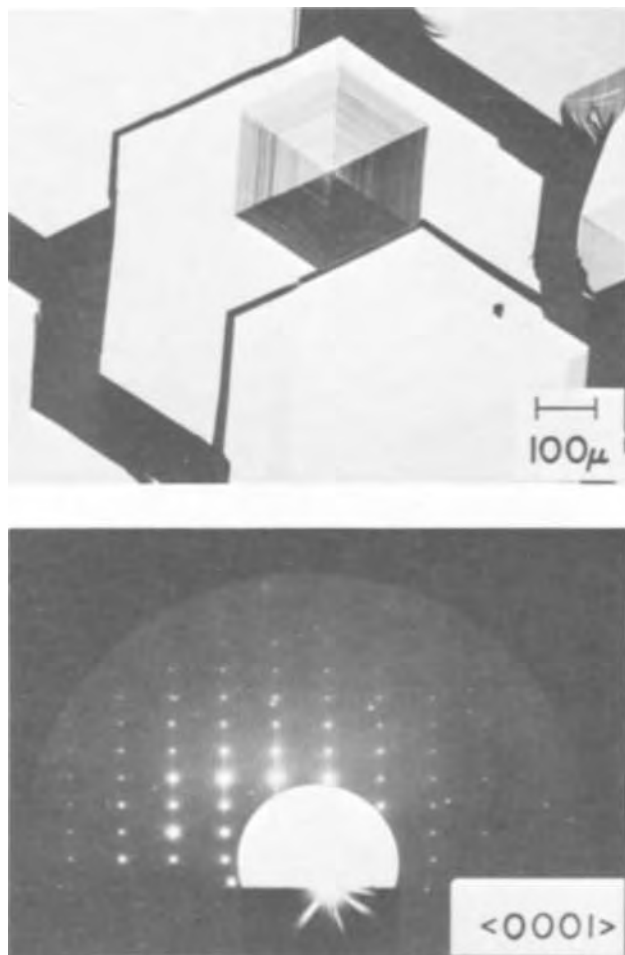


Fig. 7. (a, top) Photomicrograph, and (b, bottom) reflection electron diffraction pattern, of (0001) CdS grown on (111) GaAs.

conditions deviating appreciably from equilibrium and where the structure of the grown layers was dictated largely by that of the substrate.

Electrical Properties

Epitaxial layers of ZnSe grown without intentional doping were high resistivity, $> 10^8$ ohm-cm. N-type specimens were obtained by doping during growth with 300-3000 ppm Al, but the resistivity still remained high, $\sim 10^5$ ohm-cm. The difficulty of obtaining low-resistivity wide-bandgap II-VI compounds is well known, and it is attributed to the process whereby added doping impurities are compensated by native lattice defects (14). The most effective method to induce a high n-type conductivity in ZnSe involves annealing the specimen submerged in molten Zn containing the desired donor impurities such as Al (15). The zinc liquid suppresses the formation of Zn vacancies and, at the same time, helps the electrically active donor element to be incorporated into the lattice. The liquid anneal also helps to extract any acceptor impurities that may be present in the specimen.

Our preliminary experiments showed that high-resistivity melt-grown ZnSe can indeed be converted to n-type (e. g., to a resistivity of 5×10^{-2} ohm-cm, with corresponding carrier concentration of $4 \times 10^{17}/\text{cm}^3$ and Hall mobility of $313 \text{ cm}^2/\text{V}\cdot\text{sec}$) after about 70-hr annealing in $\text{Zn}_{0.97}\text{Al}_{0.03}$ liquid at 1000°C . Although successful for bulk crystals, this annealing condition was found unsuitable for epitaxially grown ZnSe layers on GaAs substrates, since both the ZnSe and the GaAs dissolved completely in the zinc liquid after annealing treatment. In fact, even for the bulk crystals, it was subsequently determined that the zinc

melt dissolved more than 20% of ZnSe upon annealing as above. Shorter periods of anneal, however, were ineffective in rendering ZnSe high conductivity.

Since the liquid annealing procedure thus involved drastic conditions, annealing of Al-doped ZnSe epitaxial layers was carried out in approximately 1-atm Zn vapor in the temperature range 800°C - 1000°C for periods of 1-100 hr; however, all specimens remained high resistivity. The vapor anneal was motivated by previous reports (15) that a highly conducting ZnSe:Al (obtained by zinc-liquid anneal similar to that described above) can be rendered insulating by a brief annealing in vacuum at 850°C , but that it can be completely restored to the original conductivity by reannealing in about 0.5-atm Zn vapor at the same temperature. However, our experience with melt-grown bulk ZnSe showed that the zinc-vapor anneal can effect only a partial restoration of the original conductivity (e. g., to a resistivity of 7×10^{-1} ohm-cm from the original value of 5×10^{-2} ohm-cm), and this indicated that the vapor anneal is not as effective as the liquid anneal. With ZnSe:Al epitaxial layers on GaAs substrates, a further complication is that GaAs dissociates during high-temperature anneal to dope ZnSe:Al with As (acceptor), thus resulting in compensation and high resistivity, as observed in the above vapor anneal of the ZnSe:Al epitaxial layers.

The ZnS layers grown without intentional doping, much like ZnSe, were high resistivity, and neither Al-doping nor postgrowth anneal in Zn-Al liquid or in Zn vapor rendered them low-resistivity n-type. It is worth mentioning in this connection that melt-grown bulk crystals of ZnS, when annealed for a long time (~ 10 days) in $\text{Zn}_{0.97}\text{Al}_{0.03}$ liquid at 1000°C , became multiphased showing a dark metallic color, and x-ray powder patterns revealed the presence of a cubic material of the form ZnAl_2S_4 in the annealed specimens. The present data indicate that it is difficult to obtain high-conductivity ZnSe and ZnS epitaxial layers by vapor-phase synthesis, and this is true even by using postgrowth annealing techniques.

In comparison, the majority of the epitaxially grown CdS was conducting n-type with resistivities in the 10^{-2} ohm-cm range. A relatively high resistivity of 10^2 ohm-cm (n-type) was obtained for the layers grown at higher substrate temperatures than the optimum shown in Table III, or by intentionally doping them with acceptor impurities such as As and Li.

Observations on Cathodoluminescence

We have described earlier the occurrence of polymorphism in ZnSe. Associated with the dependence of polymorph type on deposition temperature, a variation was observed in the color of cathodoluminescence in ZnSe specimens grown at different temperatures. The colors observed at room temperature were bright yellow, orange, and red for the specimens grown in the temperature ranges 890°C - 830°C , 800°C - 700°C , and 700°C - 600°C , respectively. Although quantitative information is lacking at present, this could be due to small variations with temperature in the stoichiometry, or impurity concentration, of the epitaxially deposited ZnSe. The ZnSe samples prepared at 890°C were of sufficient purity to permit an observation of near-bandgap cathodoluminescence, 2.76 eV, at 77°K (16).

The epitaxially grown ZnS showed a bright blue cathodoluminescence at room temperature, and this might have emanated from the self-activated emission process (2) involving Zn vacancies and some unknown ionized donors.

As for the epitaxial layers of CdS, a green cathodoluminescence was observed at room temperature for the majority of conducting n-type specimens. A red cathodoluminescence was also observed, but with specimens showing relatively high resistivities ($\sim 10^2$ ohm-cm) due probably to the compensation by acceptor impurities. Similar observations of luminescence

Table V. Thermodynamic data

Species	H [°] ₂₉₈ (kcal/ mole)	S [°] ₂₉₈ (eu)	Cp (cal/°K/mole)	H [°] _T (cal)	S [°] _T (eu)	Ref.*
Zn(g)	31.18	38.45	4.97	4.97T + 29,700	4.97lnT + 10.2	i, ii
Cd(g)	26.75	40.07	4.97	4.97T + 25,300	4.97lnT + 11.8	i, ii
H ₂ Se(g)	9.174	54.9	7.59 + 3.5 × 10 ⁻³ T - 0.31 × 10 ⁵ T ⁻²	7.59T + 6,700	7.59lnT + 11.7	iii, ii
Se ₂ (g)	34.12	60.23	8.73 + 0.32 × 10 ⁻³ T - 0.34 × 10 ⁵ T ⁻²	8.73T + 31,400	8.73lnT + 10.4	i, ii
H ₂ S(g)	-4.9	49.15	7.81 + 2.9 × 10 ⁻³ T - 0.46 × 10 ⁵ T ⁻²	7.81T - 7,500	7.81lnT + 4.9	iv, ii
S ₂ (g)	30.84	54.51	8.72 + 0.16 × 10 ⁻³ T - 0.9 × 10 ⁵ T ⁻²	8.72T + 27,900	8.72lnT + 4.9	i, ii
H ₂ (g)	0	31.22	6.52 + 0.78 × 10 ⁻³ T + 0.12 × 10 ⁵ T ⁻²	6.52T - 1,600	6.52lnT - 5.3	v
ZnSe(s)	-44.2	15.4	11.99 + 1.38 × 10 ⁻³ T	11.99T + 0.69 × 10 ⁻³ T ² - 47,800	11.99lnT + 1.38 × 10 ⁻³ T - 53.2	vi
ZnS(s)	-48.5	13.8	12.16 + 1.24 × 10 ⁻³ T - 1.36 × 10 ⁵ T ⁻²	12.16T + 0.62 × 10 ⁻³ T ² - 52,600	12.16lnT + 1.24 × 10 ⁻³ T - 55.8	vii, ii
CdS(s)	-34.5	17	12.9 + 0.9 × 10 ⁻³ T	12.9T + 0.45 × 10 ⁻³ T ² - 30,600	12.9lnT + 0.9 × 10 ⁻³ T - 56.6	vii, ii

- * Ref. i. D. R. Stull and G. C. Sinke, "Thermodynamic Properties of the Elements," American Chemical Society (1956).
 ii. K. K. Kelley, "Contribution to the Data on Theoretical Metallurgy XIII," Bull. 584, U.S. Bur. Mines (1960).
 iii. J. R. Rawling and J. M. Toguri, *Can. J. Chem.*, **44**, 451 (1966).
 iv. O. Kubaschewski, E. L. L. Evans, and C. B. Alcock, "Metallurgical Thermochemistry," 4th ed. Pergamon Press Ltd., New York (1967).
 v. C. E. Wicks and F. E. Block, "Thermodynamic Properties of 85 Elements—Their Oxides, Halides, Carbides, and Nitrides," Bull. 605, U.S. Bur. Mines (1963).
 vi. T. O. Sedgwick and B. J. Agule, *This Journal*, **113**, 54 (1966).
 vii. F. D. Rossini, D. D. Wagman, W. H. Evans, S. Levine, and I. Jaffe, "Selected Values of Chemical Thermodynamic Properties," Circular 500, Nat. Bur. Standards (1952).

Table VI. Free energy of reactions

Reaction	ΔF [°] _T (cal)	ΔF [°] _{1000°K} (kcal)	ΔF [°] _{1800°K} (kcal)
[1] Zn(g) + H ₂ Se(g) = ZnSe(s) + H ₂ (g)	86.4T - 5.95TlnT - 0.69 × 10 ⁻³ T ² - 85,800	-41.1	-30.3
[1]' Zn(g) + ½Se ₂ (g) = ZnSe(s)	71.3T - 2.65TlnT - 0.69 × 10 ⁻³ T ² - 93,200	-40.9	-26.3
[2] Zn(g) + H ₂ S(g) = ZnS(s) + H ₂ (g)	82.1T - 5.9TlnT - 0.62 × 10 ⁻³ T ² - 76,400	-35.6	-25.8
[2]' Zn(g) + ½S ₂ (g) = ZnS(s)	71.3T - 2.83TlnT - 0.62 × 10 ⁻³ T ² - 96,300	-45.1	-31
[3] Cd(g) + H ₂ S(g) = CdS(s) + H ₂ (g)	85.2T - 6.64TlnT - 0.45 × 10 ⁻³ T ² - 50,000	-11.1	-1.6
[3]' Cd(g) + ½S ₂ (g) = CdS(s)	74.5T - 3.57TlnT - 0.45 × 10 ⁻³ T ² - 69,900	-20.5	-7.2

in CdS of different electrical resistivities have been reported previously by Aven and Garwacki (3), but detailed studies of the exact nature of the luminescent centers have not been made.

Conclusions

Single-crystal layers of ZnSe, ZnS, and CdS have been epitaxially grown on GaAs, GaP, and sapphire substrates in a flow system by reaction of the metal vapors with the nonmetal hydride gases. The growth morphology, crystalline perfection, and some of the electrical and luminescent properties of these epitaxially grown materials have been studied. Although the present paper is concerned with the above three compounds, the results obtained suggest that other II-VI compounds may also be grown with equal success using the present vapor-phase epitaxial growth technique. HgTe is one such compound recently reported (17) to have been grown by a growth technique similar to that used in the present study.

Acknowledgments

The authors are grateful to D. Richman and J. J. Tietjen for valuable discussions, and to W. C. Roth and R. T. Smith for electron diffraction and x-ray work. The research herein reported was made possible by the support of the Advanced Research Projects Agency under Order No. 1034, through the United States Army Electronics Command, Fort Monmouth, New Jersey, under Contract No. DAAB07-68-C-0129 and DAAB07-69-C-0145.

Manuscript submitted March 11, 1971; revised manuscript received Oct. 27, 1971.

Any discussion of this paper will appear in a Discussion Section to be published in the December 1972 JOURNAL.

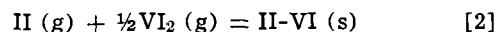
APPENDIX

In the absence of direct determination such as by mass spectrometry (5) of the chemical species present in the vapor phase we cannot unambiguously identify the chemical reactions responsible for the present II-VI compound vapor deposition. However, the most

reasonable chemical reactions, consistent with the initial reactant gases used and the final solid products formed, are of the type either



or



where II = Zn or Cd and VI = Se or S. The free energies of the appropriate reactions are calculated from the known sources (Table V) and are tabulated in Table VI. It should be noted that the calculated values of the free energy change (Table VI) are all negative in the temperature range of interest, and that the values are roughly similar whether they are calculated for reaction [1] or [2].

REFERENCES

- For ZnSe, see, A. Baczewski, *This Journal*, **112**, 577 (1965); J. T. Calow, S. J. T. Owen, and P. W. Webb, *Phys. Status Solidi*, **28**, 295 (1968); and H. J. Hovel and A. G. Milnes, *This Journal*, **116**, 843 (1969).
- For ZnS, see, articles in "Physics and Chemistry of II-VI Compounds," p. 720, M. Aven and J. S. Prener, Editors, North-Holland Publishing Co., Amsterdam (1967); P. Jones, C. N. W. Litting, D. E. Mason, and V. A. Williams, *Brit. J. Appl. Phys. (J. Phys. D) Ser. 2*, **1**, 283 (1968); and R. J. Caveney, *J. Crystal Growth*, **2**, 85 (1968).
- For CdS, see, M. Aven and W. Garwacki, *This Journal*, **110**, 401 (1963); H. V. Dijk and J. Gooissen, in "Crystal Growth," p. 531, H. S. Peiser, Editor, Pergamon Press Inc., New York (1967); M. Weinstein and G. A. Wolff, *ibid.*, p. 537; and B. J. Curtis and H. Brunner, *J. Crystal Growth*, **6**, 269 (1970).
- W. M. Yim, J. P. Dismukes, and H. Kressel, *RCA Rev.*, **31**, 662 (1970).
- V. S. Ban, *This Journal*, **118**, 1473 (1971).
- D. W. Shaw, *ibid.*, **115**, 405 (1968).
- W. M. Yim, Unpublished data.
- J. J. Tietjen and J. A. Amick, *This Journal*, **113**, 724 (1966).
- W. H. Strehlow, *J. Appl. Phys.*, **41**, 1810 (1970).
- I. Dima, *Soviet Phys.-Crystal. (English transl.)*, **9**, 338 (1964).
- W. M. Yim, *J. Appl. Phys.*, **40**, 2617 (1969).
- A. S. Pashinkin, G. N. Tischenko, I. V. Korneeva, and B. N. Ryzhenko, *Soviet Phys.-Crystal. (En-*

- lish transl.), 5, 243 (1960); Y. S. Park and F. L. Chan, *J. Appl. Phys.*, **36**, 800 (1965); and A. G. Fitzgerald, M. Mannami, E. H. Pogson, and A. D. Yoffe, *Phil. Mag.*, **14**, 197 (1966).
13. P. Goldberg, in "Luminescence of Inorganic Solids," p. 385, P. Goldberg, Editor, Academic Press, New York (1966).
14. G. Mandel, *Phys. Rev.*, **134**, A1073 (1964).
15. M. Aven and H. H. Woodbury, *Appl. Phys. Letters*, **1**, 53 (1962); M. Aven and B. Segall, *Phys. Rev.*, **130**, 81 (1963); and M. Aven and R. E. Halsted, *ibid.*, **137**, A228 (1965).
16. F. H. Nicoll and H. Kressel, Private communication.
17. G. A. Antcliffe and H. Kraus, *J. Phys. Chem. Solids*, **30**, 243 (1969).

The Effect of HCl and Cl₂ on the Thermal Oxidation of Silicon

R. J. Kriegler, Y. C. Cheng, and D. R. Colton*

Bell-Northern Research, Ottawa, Ontario, Canada

ABSTRACT

The addition of a few mole per cent of HCl or Cl₂ to the oxidizing atmosphere has been found to significantly improve the electrical stability of dry-grown SiO₂ films. The results reported here were obtained with 30 min oxidation at 1150°C. The process not only decreases the mobile ion contamination originating from the furnace tube, but to a large extent also passivates the films against ionic instabilities caused by contaminated metallization. The use of HCl or Cl₂ apparently also reduces the number of surface states at the Si-SiO₂ interface. No significant change between standard and HCl or Cl₂ oxides was observed in oxide charge, dielectric strength, dielectric constant and index of refraction, but the oxidation rate of Si is considerably increased in the presence of HCl or Cl₂. The mixture of HCl and dry O₂ was also found to be very effective for the "cleaning" of quartz furnace tubes.

A major cause of electrical instabilities in MOS devices is the migration of positive ions [see, e.g., Ref. (1)], particularly of sodium in the oxide, although not all of the sodium incorporated into the oxide is electrically active. Most of the effort to produce highly stable MOS structures using SiO₂ has been concentrated on avoiding sodium contamination as much as possible during the various stages of processing, rather than on the immobilization of easily ionizable or ionic species already incorporated into the structures. The only exception was perhaps the use of a phosphosilicate glass layer on top of the oxide, but the instability introduced by the polarizability of the phosphorus glass itself (2) has prevented this technique from being universally accepted. The purpose of this paper is to report preliminary experimental results on the apparent immobilization of ionic contaminants in SiO₂ films by the use of HCl or Cl₂ during dry oxidation.

The development of this process was instigated by our accidental observation that SiO₂ films grown in a furnace tube containing NaCl were found to contain a much smaller concentration of mobile ions than those grown in the presence of Na₂CO₃. These results lead to the speculation that, in the presence of chlorine, at least some of the sodium being incorporated into the oxide may have entered in an electrically inactive form, such that it remained immobile even under the influence of high electric fields at elevated temperatures. Based upon this premise, we investigated the electrical stability of SiO₂ samples grown in the presence of HCl or Cl₂ and found (3) that these "HCl oxides" and "Cl₂ oxides" were indeed more stable than their counterparts grown in pure oxygen ("standard oxides"). We have since extended our work particularly for the HCl oxides to assess their immobilizing effects on contaminations introduced from various sources during processing, and have also observed various other properties of these oxides.

Experimental Details

To evaluate the "resistance" of HCl oxides to different sources of contamination, first a systematic study

was undertaken in which the amount of contamination originating from our various laboratory processing steps was determined. In agreement with previous investigators (4) we found that by far the most significant contribution to the mobile ion content in the final MOS structures came from contaminated metallization. The only other detectable amount of contamination was introduced from the high temperature furnace tube during oxidation and *in situ* annealing. The elimination of the cleaning of the silicon slices before oxidation did not result in a measurable increase in the mobile ion contamination of our oxides. To separate the above two contributions of contamination, various methods were developed in which the amount of contamination could at least partially be controlled. As the experimental results to be given below will demonstrate, the contamination originating from the furnace tube could be completely eliminated by the prolonged exposure of the tube to a mixture of HCl and dry O₂. The mobile ion contamination originating from the metallization could be reduced at most to the 10⁹ ions/cm² level, and even then, only by a special process, not applicable for routine evaporation. Our routine processes produced ion concentrations in the range of 10¹⁰ to 10¹² ions/cm² for both aluminum and gold metallization. Aluminum was evaporated both by an electron beam and from a resistance-heated tungsten basket, the latter method resulting in considerably higher values of contamination. To avoid any considerable degree of radiation damage, gold was always evaporated from a resistance-heated molybdenum boat and in this case the level of contamination was controlled by the length of the vacuum prefire of the molybdenum. Our study confirmed that oxidized slices could be stored in room air under cover for at least several days without picking up any measurable amount of contamination from the surroundings. It was also found that, at least for lower levels of contamination, samples processed in an identical way and metallized simultaneously, exhibited approximately the same level of mobile ion concentrations; this observation allowed the comparison of slices processed in various ways, i.e., grown with various HCl or Cl₂ concentrations. Based upon the previous results and somewhat

* Electrochemical Society Active Member.

Key words: SiO₂, MOS structure, electrical stability.

arbitrarily chosen parameters the following procedure was adopted for sample preparation:

(i) N-type 10 ohm-cm (100) Si slices were used, as received from Monsanto without any cleaning process before oxidation.

(ii) Slices were oxidized for 30 min at 1150°C in various mixtures of HCl or Cl₂ and dry O₂. The flow rate of O₂ was always maintained at 800 cc/min.

(iii) *In situ* annealing in a He ambient was carried out at 1050°C for a period of 15-30 min. The oxidation and annealing steps were carried out in a double walled quartz tube in which the space between the tubes was also flushed with the oxidizing or annealing gas. No liner of any kind was used.

(iv) Oxidized slices were kept in the laboratory under cover until metallization.

(v) Front oxide surfaces were metallized first; all oxides grown for a given experiment were metallized simultaneously.

(vi) Back oxides were removed with HF, the bare Si surface was metallized with Al, and finished samples were sintered at 470°C for 10 min in N₂.

Electrical testing of the samples mainly consisted of the determination of their C-V characteristics measured at 1 mHz. The oxide charge, Q_{ox} , was directly calculated from the initial room temperature flat-band voltage taking account of the metal-semiconductor work function difference (5). The number of fast interface states, N_{ss} , obtained according to the Gray and Brown technique (6), was calculated from the shift of the flat-band voltage between room and liquid nitrogen temperatures, taking into account the change of silicon depletion layer capacitance and the change of the metal-semiconductor work function difference between the two temperatures. The mobile ion concentration was directly calculated from the shift of the flat-band voltage after a 5 min positive bias-temperature stress at 250°C with a field of 10⁶ V/cm, provided that the flat-band shift after negative bias-temperature stressing was negligible, which was found to be the case for most samples tested. Only in special instances, when the ultraclean metallization technique was used, was the ion concentration determined from current-voltage measurements using a constant rate voltage ramp (7, 8). Such a voltage ramp was also used to determine the approximate breakdown field in the oxide. The thickness of the samples and their index of refraction at a wavelength of 5461Å was determined by ellipsometry with an average accuracy of ±5Å and 0.005, respectively. The dielectric constant was determined at room temperature at 10 kHz on samples having aluminum electrodes of 0.02 cm² area. The amount of HCl added to the oxygen flow was measured by dissolving the HCl in water and titrating it with NaOH, while Cl₂ was allowed to react with a solution of KI and the precipitated iodine was titrated with Na₂S₂O₃. The maximum concentration of Cl₂ used in these experiments corresponded to a Cl₂/O₂ mole ratio of 0.035,

and was limited by the tendency of chlorine to cause peeling of the oxide, presumably due to the etching of the silicon substrate by chlorine penetrating through the pinholes in the oxide. No similar effect was observed with HCl at least up to a 0.2 HCl/O₂ mole ratio, which was the highest employed. For the sake of brevity, HCl/O₂ and Cl₂/O₂ mole ratios will subsequently be referred to as percentage HCl and Cl₂ content, respectively.

Results and Discussion

Basic observations.—The results presented here are representative of a large number of experiments and were chosen to demonstrate some important characteristics of the HCl and Cl₂ oxides. Table I shows the effect of HCl on the electrical stability of SiO₂ samples grown in a furnace tube which became contaminated from a methanol rinse, and for comparison, includes data on samples grown in a steam-cleaned furnace tube. Two sets of samples were prepared and metallized in separate evaporations. The cleanliness of the metallization was different in the two instances; significantly however, the difference between the mobile ion concentrations of the standard oxides grown in the steam-cleaned tube and in the ethanol-rinsed tube is about the same for the two evaporations, and therefore this difference, approximately $1.5 \times 10^{10}/\text{cm}^2$, can be attributed to contamination introduced from the furnace tube. Oxides grown with increasing HCl concentrations show decreasing mobile ion content, which at 6% HCl content reduces to the 10⁹/cm² region, well below the figure that would be expected to result from contamination introduced by either of the metallizations. In addition, standard oxides grown in the contaminated tube after the preparation of the HCl oxides, *i.e.*, after the tube had been exposed to an HCl-O₂ flow for some time, are considerably cleaner than the first ones grown in the same tube, and have mobile ion concentrations just slightly below those samples grown in the steam-cleaned tube. These results suggest that: (i) the presence of HCl during the oxidation can render electrically inactive ionic impurities resulting from both a contaminated furnace tube and contaminated metallization, and (ii) the oxidation furnace tube itself can be cleaned with a prolonged exposure to an HCl-O₂ atmosphere at a high temperature. The following experiments were designed to confirm these two observations separately.

Furnace tube cleaning.—Table II shows two examples of the cleaning effect of HCl on the furnace tube. In one case a methanol-contaminated furnace tube is cleaned by steam and a subsequent HCl process. The cleanliness of the tube was measured by the mobile ion contamination detected in standard oxides, which were grown before and after each cleaning step and metallized together with our ultraclean evaporation process. Dry oxides grown after contamination contained an average of $1.9 \times 10^{10}/\text{cm}^2$ mobile ions (which figure here is attributable to the oxidation furnace tube only). After 6 hr of steam cleaning (1800 cc/min H₂ burned in approximately stoichiometric O₂)

Table I. The effect of HCl on the electrical stability of SiO₂ grown in a contaminated furnace tube

Sample description	HCl/O ₂ mole ratio (%)	Thickness (Å)	Metallization I		Metallization II	
			ΔV_{FB} (V)	N_{ion} (10 ¹⁰ /cm ²)	ΔV_{FB} (V)	N_{ion} (10 ¹⁰ /cm ²)
Standard oxide grown in steam-cleaned furnace tube	0	1100	0.35	6.6	0.16	3.6
Standard oxide grown in tube contaminated with ethanol rinse	0	1100	0.43	8.1	0.23	5.2
HCl oxides grown in contaminated tube	2 4 6	1210	0.42	7.2	0.15	2.8
		1340	0.40	6.2	0.12	2.0
		1380	0.05	0.8	0.0	<0.3
Standard oxide grown after HCl oxides in contaminated tube	0	1100	0.34	6.4	0.14	3.1

All oxidations were carried out for a period of 30 min at ~1150°C. ΔV_{FB} was negligible on all samples and N_{ion} was calculated from ΔV_{FB} . Q_{ox} for all samples was in the region of 10¹⁰ charges/cm², apparently unaffected by the HCl concentration.

Table II. The cleaning effect of HCl on the oxidation furnace tube

Time of oxide growth (all standard oxides)		N_{ion} (from I-V measurements) ($10^{10}/cm^2$)
	A) Steam and HCl cleaning of methanol contaminated furnace tube	
Immediately after contami- nation	Dry oxides (avg.)	1.9
After 6 hr of steam	Dry oxides (avg.)	1.75
	Wet oxides (avg.)	1.31
After 6 hr with 10% HCl/O ₂	Dry oxides (avg.)	0.1
	Wet oxides (avg.)	0.1
After additional 2 hr of steam	Dry oxides (avg.)	0.3
	Wet oxides (avg.)	0.1
	B) Pure O ₂ and HCl cleaning of tube contaminated with 0.01N NaOH solution. (All tests done on dry oxides)	
One hr after contamination without any previous gas-flow		170
After 6 hr of gas-flow	O ₂ cleaning	5.0
After 24 hr of gas-flow		4.8
After 2 hr of HCl-O ₂ flow		1.0
After 6 hr of HCl-O ₂ flow	5% HCl cleaning	0.47
After 12 hr of HCl-O ₂ flow		0.15
After 6 additional hr of 25% HCl cleaning		0.25

at 1150°C the mobile ion contamination measured in 1700Å thick dry and wet oxides only reduced to 1.75 and 1.3×10^{10} ions/cm², respectively. On the other hand, a subsequent 6 hr period of cleaning with an HCl-O₂ mixture of 10% HCl content at 1150°C reduced the mobile ion contamination in both dry and wet oxides to the low 10^9 ions/cm² region, which is just on the limit of detectability even with the I-V measurements. A further 2 hr period of steam cleaning did not introduce any statistically significant change in the cleanliness of the oxide. The second example compares the effect of pure O₂ cleaning with HCl cleaning of a tube that was contaminated with 0.01N NaOH solution. 1100Å thick oxides grown 1 hr after the NaOH rinse exhibited levels of contamination in the 1.3×10^{12} ions/cm² range. As a result of O₂ flushing (800 cc/min) at the normal oxidation temperature, in a matter of 6 hr the contamination was reduced to 5×10^{10} ions/cm², without any appreciable further reduction in the subsequent 18 hr. By contrast, HCl cleaning of an initially identically contaminated tube, employing as low as 5% HCl content, eliminated even the last trace of contamination in a matter of half a day. Beyond this no further improvement could be obtained, and the

small variation observed may be attributed to fluctuations in the cleanliness of the metallization.

Passivating effect.—Samples prepared to establish the behavior of HCl oxides after metallization from contaminated sources were always grown in an HCl cleaned furnace tube, so that the metallization gave the only detectable contribution to the contamination. Table III compares the flat-band shift on standard and HCl oxides measured after a negative and positive bias-temperature stress, respectively, for two aluminum and one gold metallization process. Taking the appropriate thickness into account, N_{ion} was calculated from ΔV_{FB}^+ , except where ΔV_{FB}^+ became so low as to be comparable with the generally small ΔV_{FB}^- shift, in which case the $\Delta V_{FB}^+ - \Delta V_{FB}^-$ difference was used for the calculation. The possible percentage error in the ion concentration, of course, increased with diminishing N_{ion} value. The results indicate that oxides grown with higher concentration of HCl have decreasing concentrations of mobile ions for all three levels of metallization contamination resulting from the three different metallizations. Comparison of samples metallized with aluminum shows that a higher amount of initial contamination requires higher HCl concentrations to reach comparable electrical stability, while the comparison between the resistance-heated aluminum and the resistance-heated gold evaporations suggests that the immobilization of contaminating ions may be easier for gold-metallized than for aluminum-metallized MOS samples. This latter observation was also borne out by experiments in which the mobile ion contamination was measured in oxides grown with identical HCl concentrations and metallized with gold and aluminum electrodes that introduced approximately the same level of contamination in standard oxides. It is interesting to observe that even though the use of a small amount of HCl results in an increased electrical instability, a certain HCl concentration, somewhere between 6-8% HCl content for these experiments, brings about a sudden large reduction in the mobile ion concentration for the two more heavily contaminated metallizations. This threshold-like effect has been frequently observed but the HCl concentration at which it occurs has varied somewhat and its origin is not yet understood.

Other properties.—Various other HCl oxide properties of interest are summarized in Table IV, where

Table III. The effect of contaminated metallization on the electrical stability of HCl oxides

HCl/O ₂ mole ratio %	Metallization									Thickness* (Å)
	E-Gun aluminum			Resistance-heated aluminum			Resistance-heated gold			
	ΔV_{FB} (V)	ΔV_{FB}^+ (V)	N_{ion} ($10^{10}/cm^2$)	ΔV_{FB} (V)	ΔV_{FB}^+ (V)	N_{ion} ($10^{10}/cm^2$)	ΔV_{FB} (V)	ΔV_{FB}^+ (V)	N_{ion} ($10^{10}/cm^2$)	
0	0.02	-0.40	7.6	0.01	-4.26	81	-0.29	-10.5	198	1100
4	0.04	-0.34	5.3	0.00	-4.14	64	-0.17	-8.9	138	1340
6	0.00	-0.10	1.5	0.02	-3.34	50	-0.01	-7.8	118	1380
8	0.04	-0.01	0.7	0.00	-0.26	3.8	0.05	-0.66	10.4	1420
10	0.01	0.01	<0.1	0.00	-0.21	3.0	0.11	-0.25	5.1	1470

* All oxides were grown for a period of 30 min at approximately 1150°C.

Table IV. Comparison of various properties of standard and HCl oxides

	Au metallization HCl/O ₂ mole ratio (%)					Al metallization HCl/O ₂ mole ratio (%)				
	0	4	6	8	10	0	4	6	8	10
	V_{FB}^* at room temperature (V)	-0.55	-0.57	-0.51	-0.58	-0.61	0.12	0.13	0.12	0.02
Q_{ox}/e ($10^{10}/cm^2$)	10.4	8.8	7.7	8.5	8.6	1.5	1.5	0.8	0.6	0.9
N_{ss}^{**} ($10^{10}/cm^2$)	2.7	2.2	2.1	2.0	2.1	7.0	7.2	7.1	7.2	7.2
$E_{breakdown}$ (10^6 V/cm)						1.5	1.5	0.8	0.6	0.9
ϵ (10 kHz at 25°C)						1.460	1.462	3.76 ± 0.04	1.480	1.495
n ($\lambda = 5461\text{Å}$)										

* Corrected for metal-semiconductor work-function difference.

** Estimated on the basis of the Gray and Brown technique.

again samples having both gold and aluminum electrodes are listed. As is well known, because of the sintering of slices as a last step in their preparation, samples metallized with aluminum show properties attributable to hydrogen annealing (9). It is seen that for neither metal is there any systematic change in the room temperature flat-band voltage between the standard and HCl oxides, and consequently no fixed charge appears to be introduced into the oxide by the HCl process. V_{FB} was not converted to oxide charge figures for the case of aluminum metallization, because even for the standard oxide, a small negative rather than positive charge would have resulted; this apparently unusual behavior however, is most likely due to an error in the metal semiconductor work function difference assumed for the samples. The number of fast interface states are seen to be generally lower for HCl oxides than for standard oxides, and of course, samples metallized with aluminum all exhibit lower values than the corresponding gold-metallized samples. The breakdown field, which was determined from the point where the first rapid increase in current across the samples occurred, and therefore would probably be best described as a self-healing breakdown (10), shows little systematic change between standard and HCl oxides, although a small improvement with increasing HCl concentrations is suggested from the data. While the dielectric constant shows no variation with HCl concentration within experimental error, the index of refraction displays a slight increase with increasing HCl concentration. It is not certain whether the apparent increase in the index of refraction for HCl oxides is a real one, or whether it is caused by a small absorption in the oxides, the net effect of which on the ellipsometric data is the same as if the index of refraction had changed in the absence of absorption.

Effect on Si oxidation rate.—As the data from Tables I and III imply, the oxidation rate of silicon is increased in the presence of HCl. This is shown in somewhat more detail on a log-log scale in Fig. 1, where the ratio of the cycle lengths of the ordinate and abscissa scales are 2:1. In the thickness range indicated, oxidation in pure oxygen results in an approximately parabolic time dependence; the solid lines for other oxides were obtained by fitting the experimental points with lines parallel to that for the standard oxide. Apart

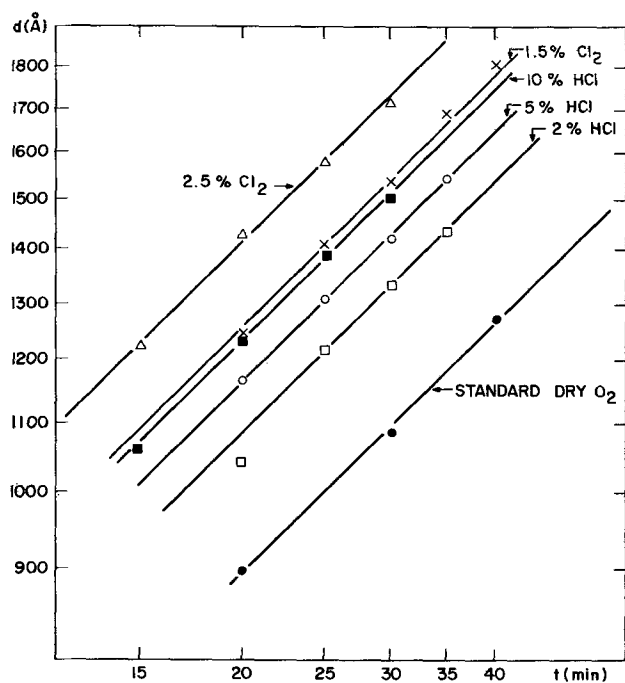


Fig. 1. Oxidation rate of (100) Si at 1150°C in the presence of HCl and Cl₂.

from one experimental point, the rather good fit suggests that at least for the limited range of thickness covered here, the effect of HCl can be described as an increase in the parabolic coefficient (11), which depends linearly on the effective diffusion rate of the oxidizing species in the bulk of the silicon dioxide. Based upon the extrapolation of data obtained for the oxidation rate of silicon in the mixture of O₂ and H₂O (12), it is easy to conclude that the formation of water vapor in the HCl-O₂ mixture is insufficient to account for the observed degree of enhancement of the parabolic rate constant. At equilibrium, the reaction, $2\text{HCl} + \frac{1}{2}\text{O}_2 \rightleftharpoons \text{H}_2\text{O} + \text{Cl}_2$, for a 1:10 mixture of HCl and O₂ results in a H₂O/O₂ ratio of 0.0142 at 1150°C, which amount of water would cause less than half of the observed effect. On the other hand, the fact that a 1.5% dry Cl₂ content results in a growth rate somewhat higher than a 10% HCl content could indicate that chlorine may be mainly responsible for the higher oxidation rate.

Cl₂ oxides.—As previously mentioned, we have found that the use of Cl₂ during oxidation also has beneficial effects on the electrical properties of the oxides. A comparison between the properties of the HCl and Cl₂ oxides is given in Table V. Since it was obvious even from the preliminary experiments that the passivation effect of HCl is not due to Cl₂ "molecules" alone, the samples listed in the table were prepared with HCl and Cl₂ concentrations such that the effect of the same total number of chlorine "atoms" could be compared. All the samples were oxidized for 30 min at 1150°C and metallized with aluminum. The data indeed show that the two forms of chlorine, HCl and Cl₂, are about equally effective in the reduction of the mobile ion concentration in the oxides. The surface state density at the silicon-oxide interface is approximately the same for Cl₂ as for HCl oxides. This effect however, may be due to minute amounts of water vapor present in our Cl₂ source.

Related experiments.—It is noteworthy that other effects of HCl, of somewhat similar nature to those described here, were reported recently. MacKenna *et al.* (13), observed that the introduction of mobile ion impurities into thermally grown silicon dioxide during a subsequent pyrolytic deposition of silicon nitride was much reduced when SiCl₄ was used instead of SiH₄. Robinson and Heiman (14), found an increased minority carrier lifetime in silicon under an oxide layer when the oxide was grown with an HCl concentration as low as 0.5 to 1%, presumably due to a gettering effect of heavy metal ions. This latter paper, published during the course of our work, and referring to a private communication by A. Mayer, has also alluded to the gettering effect of HCl for sodium when an HCl solution was used as a source for steam oxidation, but no experimental facts in this regard were given.

Conclusions

The results presented here have all been derived from experiments carried out with dry oxygen at 1150°C using (100) Si, and all samples were oxidized for a period of 30 min. Within these limitations it has been demonstrated that the addition of HCl or Cl₂ to

Table V. Comparison of some properties of HCl and Cl₂ oxides

Sample description	Thickness (Å)	V_{FB} (V)	ΔV_{FB} (V)	ΔV_{FB}^+ (V)	N_{ion} (10 ¹⁰ /cm ²)	N_{ss} (10 ¹⁰ /cm ²)
Standard	1050	-0.18	0.00	-2.12	42.0	1.6
1.5% Cl ₂	1560	-0.24	-0.07	-0.90	12.7	1.1
3.0% HCl	1340	-0.22	0.00	-0.65	9.6	0.95
2.5% Cl ₂	1670	-0.16	0.00	-0.08	1.0	0.40
5.0% HCl	1480	-0.23	0.00	-0.07	1.0	0.73

Slices were oxidized for approximately 30 min at 1150°C and metallized with Al.

O₂ during the thermal growth of SiO₂ has beneficial effects on the oxide properties: the main effect is the increased electrical stability, observable in oxides grown in a contaminated furnace tube as well as in oxides metallized by a contaminated metallization; in addition, at least the use of HCl, also reduces the surface state density at the silicon-oxide interface. It has been established furthermore that a mixture of HCl and O₂ can "clean" a quartz furnace tube so effectively that, even in the absence of chlorine in any form, no contamination can be detected to enter into the silicon dioxide during its thermal growth or high temperature anneal.

All the results, and in particular, the fact that contamination introduced into MOS structures after oxidation is rendered, at least partially electrically inactive, strongly suggest that chlorine becomes incorporated into the oxide during growth. However, neither the nature of this chlorine species, nor the mechanism leading to the increased electrical stability has been established so far. Further work now in progress is directed towards the understanding of the mechanisms involved, along with the extension of the present experimental data to include a wider range of time and temperature.

Acknowledgments

The authors are indebted to Miss Grace Massolin for performing a large part of the experimental work and to Mr. Tibor Devenyi for carrying out the current-voltage measurements. This work was in part supported by the Defence Research Board of Canada through its Directorate of Industrial Research.

Manuscript submitted Aug. 25, 1971; revised manuscript received ca. Nov. 12, 1971. This was Paper 79 presented at the Washington, D. C., Meeting of the Society, May 9-13, 1971.

Any discussion of this paper will appear in a Discussion Section to be published in the December 1972 JOURNAL.

REFERENCES

1. S. R. Hofstein, *IEEE Trans. Electron Devices*, **ED-14**, 749 (1967).
2. E. H. Snow and B. E. Deal, *This Journal*, **113**, 263 (1966).
3. R. J. Krieger, Paper presented at the Local Meeting of the Ontario-Quebec Section of the Electrochemical Society, Ottawa, Canada, Nov. 1970.
4. S. R. Hofstein, *Solid-State Electron.*, **10**, 657 (1967).
5. B. E. Deal, E. H. Snow, and C. A. Mead, *J. Phys. Chem. Solids*, **27**, 1873 (1966).
6. D. M. Brown and P. V. Gray, *This Journal*, **115**, 760 (1968).
7. D. R. Kerr, Paper 14 presented at Electrochem. Soc., Meeting, Cleveland, Ohio, May 1-5, 1966.
8. M. Kuhn and D. J. Silversmith, *This Journal*, **118**, 966 (1971).
9. P. L. Castro and B. E. Deal, *ibid.*, **118**, 280 (1971).
10. C. M. Osburn, Paper 95 presented at Electrochemical Soc. Meeting, Washington, D. C., May 9-13, 1971.
11. B. E. Deal and A. S. Grove, *J. Appl. Phys.*, **36**, 3770 (1965).
12. A. M. Smith, "Integrated Silicon Device Technology," Vol. 7 pp. 62-63, Research Triangle Institute AD 618 704.
13. E. MacKenna, V. Rodriguez, and P. Kodama, Paper 146 presented at Electrochem. Soc. Meeting, Atlantic City, Oct. 4-8, 1970.
14. P. M. Robinson and F. P. Heiman, *This Journal*, **118**, 141 (1971).

Chemical Etch Rate Studies on Sputtered Chromium Films

Alan R. Janus*

Roanoke College, Salem, Virginia 24153

ABSTRACT

An etch rate measurement technique is proposed for the study of compositional variants through the thickness of sputtered chromium thin films. Verification of the technique is given by a correlation of chemical etch rate measurements with variations in deposition conditions. These included deposition rate, substrate potential, reactive sputtering in oxygen, and postdeposition air bake.

While the practice of sputtering chromium has been generally adopted by the major razor blade manufacturers throughout the world as a means of prolonging razor blade life, very little effort has been given to understanding the mechanism by which this improvement is operative or to the optimization of deposition parameters with regard to a maximum improvement. Both areas have suffered for lack of a convenient analytical technique pertinent to compositional variants through the thickness of a thin film; that is, the oxide layer formation necessary for corrosion passivation. Until recently, resistivity measurements have offered the only means of determining the effect on thin films of variations in deposition and postdeposition conditions (1). These, however, relate to gross effects.

Within the past year, ion probe measurements (2) have yielded infinitely more detailed information on compositional variants in thin films. Since this method requires the use of expensive equipment and detailed interpretive effort, it is not yet in wide use.

The subject of this effort was, therefore, to develop a simple technique to detect compositional variants in thin films and to monitor these variations relative to deposition and postdeposition procedures related to the sputtering technique.

Initial verification of a chemical etch rate technique involved the use of a chromium film deposited in an rf tubular cathode sputtering system. Subsequent experiments were directed to a variation in chromium deposition conditions in a d-c triode system. In particular, the latter effort was directed to the effect of deposition rate in inert atmospheres on oxidative compositional variants through the thickness of the thin film. The etch rate relationship was observed at different substrate bias potentials. Etch characteristics were also measured on films intentionally subjected to oxidizing conditions. These included a postdeposition air bake as well as reactive sputtering in a range of partial pressures of oxygen.

Experimental

The etch rate measurement technique has previously been utilized in the study of thermally grown silicon dioxide films (3) as well as reactively sputtered silicon

* Electrochemical Society Active Member.

¹ Present address: Electronic Materials Division, Bell & Howell Company, 360 Sierra Madre Villa, Pasadena, California 91109.

Key words: sputtering, chromium thin films, etch rate measurement, multiple beam interferometry.

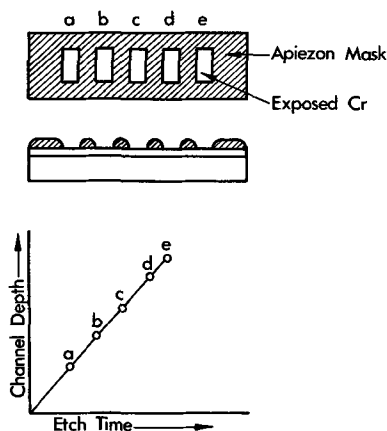


Fig. 1. Chemical etch technique used

nitride films (4). The method is described in Fig. 1. Apiezon Q wax is dissolved in trichloroethylene to form a viscous solution. This solution is used to define the mask pattern on the film as illustrated.

The masked slide is immersed in an appropriate etchant for a timed period. On withdrawal from the etch solution, the slide is dipped into deionized water to stop the etching action. It is then blown dry and one of the exposed areas masked over with the masking solution. This operation is repeated until all exposed portions of the film have been utilized in a progressive fashion. The slide is then immersed in the trichloroethylene solvent to remove the masking material. The operation results in a series of progressively deepening channels in the film, extending to the film-substrate interface. The etched film is next coated with evaporated aluminum for thickness measurement by multiple beam interferometry. The depth of the individual channels is measured and plotted *vs.* corresponding etch time. The slope of the curve is the etch rate.

In this particular study a Varian A Scope was utilized as a means of thickness measurement. The etchant, at a temperature of $28^\circ \pm 2^\circ\text{C}$ was a variant of a commercially available chromium etch: $\text{Ce}(\text{SO}_4)_2 \cdot 2(\text{NH}_4)_2\text{SO}_4 \cdot 2\text{H}_2\text{O}$, 2g; HNO_3 (conc), 10 ml; and H_2O , 50 ml. The triode investigation utilized a more dilute solution containing twice the amount of water.

Sputtering systems were the MRC 30-in. Tubular Cathode Unit and the Bendix AST-100 Triode apparatus. In both cases MARZ grade chromium targets were used. Similarly, both systems were evacuated by 6-in. oil diffusion pumps to less than 5×10^{-6} Torr prior to deposition. In the former case a Freon refrigerated chevron baffle was employed; in the latter system, a combination of ambient and an uncooled liquid nitrogen chevron baffle were utilized.

With regard to the metallic depositions, AIRCO welding grade argon was employed. In the reactive sputtering experiments, partial pressures of oxygen and argon were read by an ion gauge located in base plate throat calibrated to chamber pressure. Gauge pressures rather than nitrogen equivalent calibrations were employed. Utilization of the ion gauge in this manner was accomplished by interposition of a variable restricted orifice at the base plate. This method was found to be an effective means of controlling relative reactive gas compositions in the micron range. Pirani gauge and flowmeter techniques were found to be inadequate for this purpose.

Bias variation in the triode system was accomplished by grounding and floating the substrate holder. It has been observed that a minimum of a 50V differential exists in the triode configuration for an applied anode voltage of 75V. In the presence of a 5.0A magnet current, a 3.0A plasma current is obtained between filament and anode. The self-bias condition

satisfies levels of voltage both above ($\sim 60\text{V}$) and below ($\sim 10\text{V}$) the sputtering threshold of chromium.

Substrate holder geometry was such in the tubular rf unit that neither target presputtering nor substrate glow discharge cleaning could be accomplished prior to deposition. The target-to-substrate distance was 7-in. The pressure of argon in the sputtering chamber was 2.6×10^{-3} Torr.

In the triode system, at a total gas pressure of 1.5×10^{-3} Torr, a rotating substrate holder allowed for a 10-min glow discharge cleaning of the substrates as well as a 10-min target preconditioning period prior to the actual deposition. The target-substrate distance was 2 in.

Substrates in all cases were 1×3 in. Bioloid brand microscope slides (Will Corporation) used as supplied without further cleaning other than a compressed air blowoff.

Postdeposition baking conditions for the tubular films were 179°C for 3 hr. The triode films were baked at $350^\circ \pm 25^\circ\text{C}$ for 30 min.

Results

Ideally it is expected that an invariant slope in the etch rate plot would be obtained for a unicompositional film on the basis of Fig. 1. Further, one would expect that on the cessation of etching activity, a plateau would be established in the curve. In Fig. 2, relating to the rf deposition, this plateau is seen to occur at 1340\AA and yields a deposition rate of $89\text{ \AA}/\text{min}$. However, the data through the thickness of the film do not hold for a single composition, but indicate three distinct regions. These regions are designated as surface layer (A), inner layer (B), and interfacial layer (C).

The surface layer, 100-200 \AA in thickness represents 8-15% of the film thickness. This value is slightly greater than the 80-100 \AA value reported in the literature for the ambient oxide. The increase could be a consequence of exposure of the film to atmosphere while still hot. The etch rate of this layer is a minimum $3.3\text{ \AA}/\text{min}$.

The inner layer, probably chromium, etches at a slower rate of $1.4\text{ \AA}/\text{sec}$, and at 520-620 \AA , represents 39-46% of the total film thickness.

The layer at the film-substrate interface is of the same thickness as the inner layer, but according to an etch rate of $3.4\text{ \AA}/\text{sec}$, could represent a composition similar to that of the ambient oxide.

Postdeposition baking under the conditions listed does not alter this compositional variation.

Deposition rate variation with target voltage is plotted in Fig. 3 for the triode system. Under otherwise constant conditions, the target current was found to vary between 0.68 and $0.46\text{ mA}/\text{cm}^2$. It can be seen that little difference exists between the floating and grounded substrate condition at a given voltage.

Figures 4 and 5 detail etch rate measurements on films prepared at varying deposition rates on both floating and grounded substrate holders. The expected

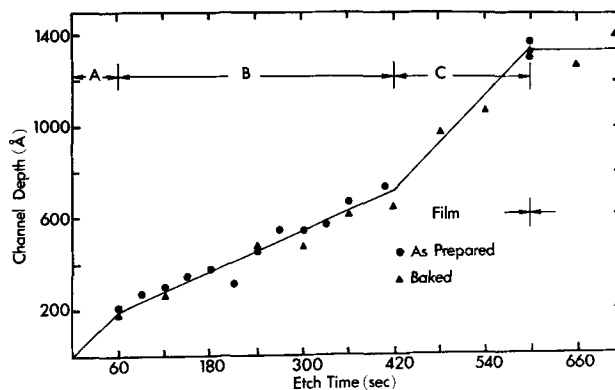


Fig. 2. Etch rate characteristic of rf sputtered chromium

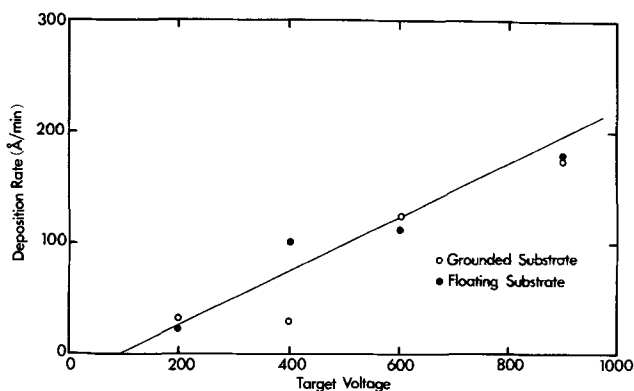


Fig. 3. Deposition rate as function of target voltage

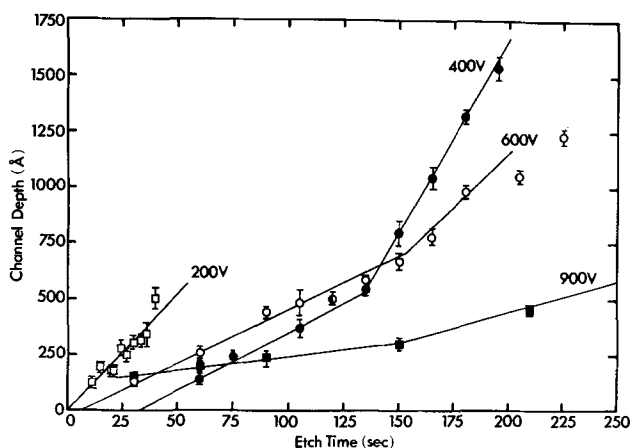


Fig. 4. Etch rate of chromium deposited on floating substrate related to variation in target voltage.

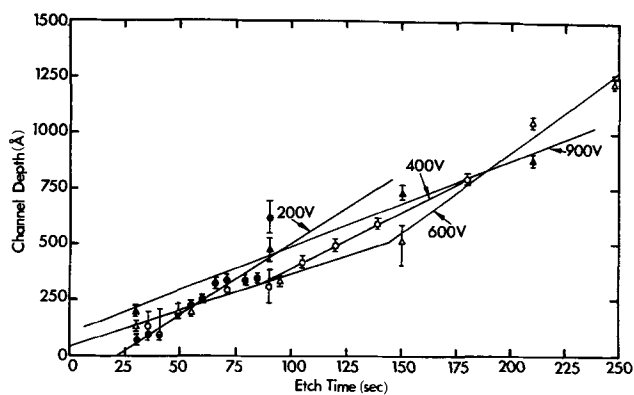


Fig. 5. Etch rate of chromium deposited on grounded substrates related to variation in target voltage.

increase in film purity with increase in deposition rate is observed in both cases (5-7). However, a comparison of Fig. 4 and 5 shows that the grounded substrate favors a generally lower etch rate and a more homogeneous film than does the floating substrate under the same deposition conditions. Here, homogeneity is defined as a relatively lower degree of etch rate variation through the thickness of the film. Independent of deposition rate, films prepared on grounded substrate undergo a lower degree of oxidation during deposition. The data are in general agreement with previous resistivity data and detail more precisely the distribution of oxide layers in the film for various deposition conditions. In addition, it is seen that less variation in etch rate with regard to deposition rate is observed in the grounded condition over the range of deposition rates. That is, ion bombardment during deposition can be a stronger influence in determining film purity than deposition rate under certain conditions. This factor

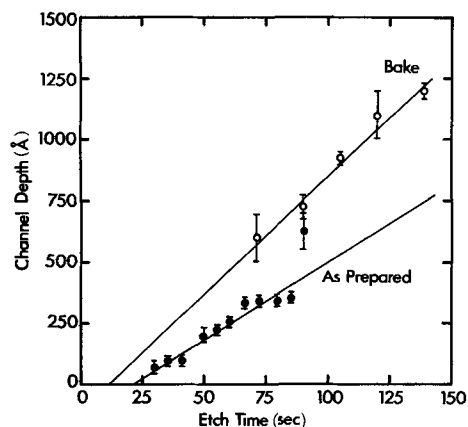


Fig. 6. Effect of postdeposition bake on etch rate of films prepared at 200V, ground potential.

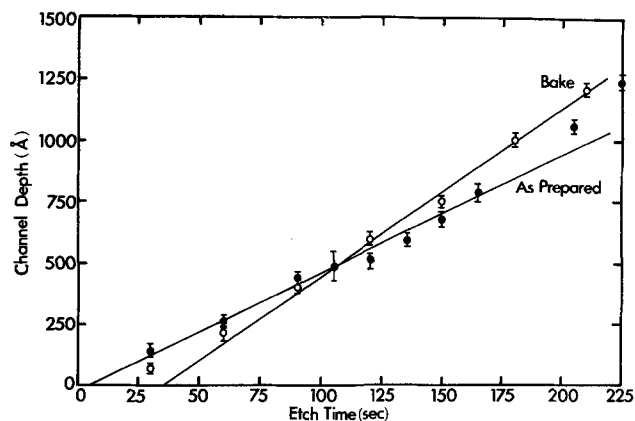


Fig. 7. Effect of postdeposition bake on etch rate of films prepared at 600V, floating potential.

is stronger at lower deposition rates. At higher deposition rates, the effect is minimized.

The assumption that oxidation will cause an increase in etch rate is verified by the results of a postdeposition air bake. Figures 6 and 7 are typical of films prepared below 900V and compare the etch rate characteristic of baked and nonbaked films prepared under identical conditions. For the 900V films, however, an apparent reversal of this trend is observed in Fig. 8 and 9 in that the baked films etch at a lower rate for both the floating and grounded cases. An explanation of this anomaly cannot be given. It is apparent that other factors become operative at the higher deposition rates. However, Fig. 10 reveals that the homogenizing effect of the higher substrate bias observed previously is still evident.

Figures 11 and 12 compare etch rate data on films sputtered in the presence of varying partial pressures of oxygen. The increase in etch rate with increase in the amount of oxygen in the sputtering gas pro-

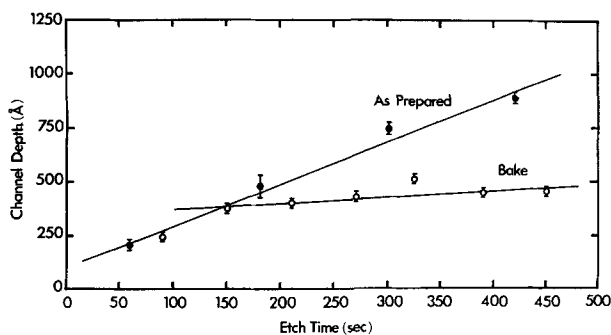


Fig. 8. Effect of postdeposition bake on etch rate of films prepared at 900V, ground potential.

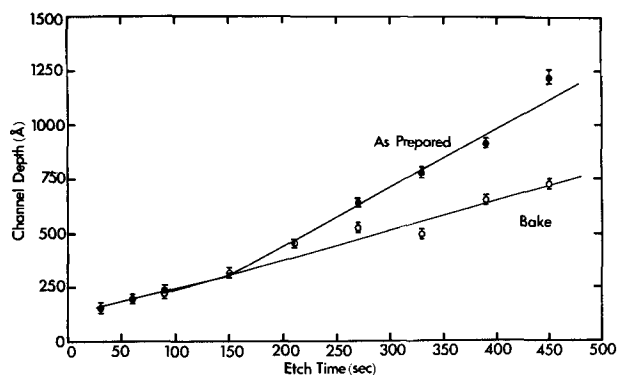


Fig. 9. Effect of postdeposition bake on etch rate of films prepared at 900V, floating potential.

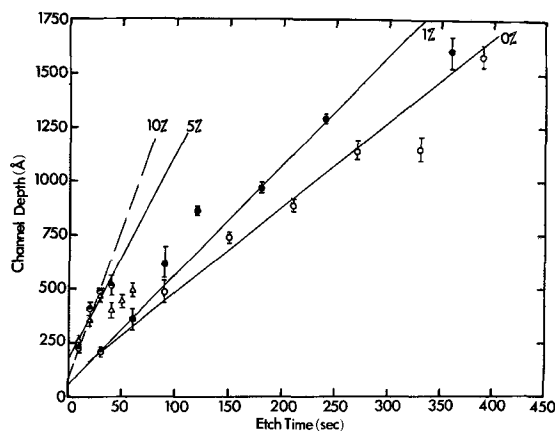


Fig. 12. Effect of reactive sputtering in oxygen (gauge per cent) at 900V on etch rate at ground substrate potential.

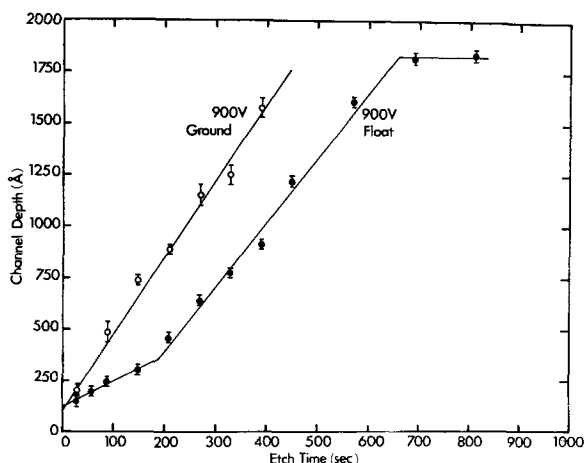


Fig. 10. Comparison of substrate potential variation at constant sputtering voltage.

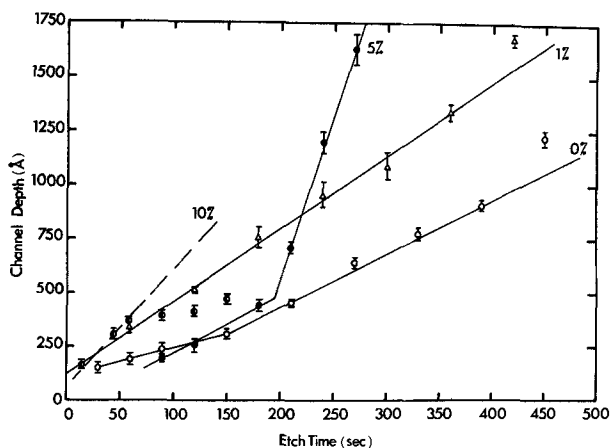


Fig. 11. Effect of reactive sputtering in oxygen (gauge per cent) at 900V on etch rate at floating substrate potential.

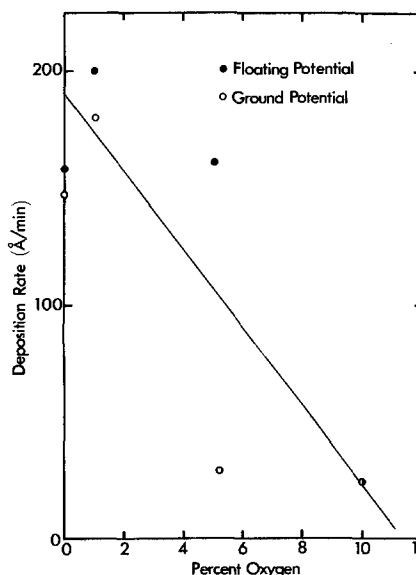


Fig. 13. Effect of oxygen on deposition rate at 900V

due to differences in deposition rate as indicated in Fig. 13.

Summary

It is shown that the proposed etch rate measurement technique is sensitive to compositional variants in thin films produced by variations in deposition conditions.

The method indicates that deposition rate has a strong influence on film composition and homogeneity. Further, the method reveals that a d-c substrate bias in excess of sputtering threshold is a profoundly influential variable even on nonconducting substrates. It enhances film reproducibility and homogeneity under a variety of deposition conditions. In inert atmospheres, film purity is increased, while compound formation is furthered in the presence of reactive gases.

The effect of postdeposition baking of sputtered films depends in large measure on deposition conditions.

Acknowledgment

I would like to express my thanks to J. W. Downing and Susan M. Janus for experimental work and to Dr. C. G. Dodd for his encouragement and support. This work was supported by the American Safety Razor Division of the Philip Morris Corporation.

Manuscript submitted Aug. 18, 1971; revised manuscript received Oct. 19, 1971. This was Paper 109 presented at the Washington, D. C., Meeting of the Society, May 9-13, 1971.

vides independent confirmation of the hypothesis that the etching mechanism proceeds by an attack of the oxide. Again, the grounded substrate provides a more homogeneous film. The fact that these films etch at a higher rate under otherwise identical conditions can be explained if one postulates the existence of O_2^+ species in the plasma. Enhanced bombardment of the growing film with this specie as favored by a grounded substrate condition would be expected to increase the oxygen content of the film. Direct evidence of this reaction lies in the fact that while both the grounded 5 and 10 gauge per cent oxygen films were transparent, only the 10% floating film was not opaque. Measurements have confirmed that differences observed between the floating and grounded situations were not

Any discussion of this paper will appear in a Discussion Section to be published in the December 1972 JOURNAL.

REFERENCES

1. D. Hoffman and J. Riseman, "Vacuum Symposium Transactions," p. 218, Pergamon Press, Philadelphia (1959).
2. A. Socha, "Transaction Symposium of Surface Sciences," New York (1970) (To be published).
3. R. Dreiner, Paper 15, Electrochemical Society Meeting, Cleveland, May 1-6, 1966.
4. A. Janus and G. Shirn, *J. Vacuum Sci. Technol.*, **4** 37 (1967).
5. K. Scow and R. Thun, "Vacuum Symposium Transactions," p. 151, Pergamon Press, Los Angeles (1962).
6. H. Schwarz, *J. Appl. Phys.*, **34** 2053 (1963).
7. P. Gould, *Brit. J. Appl. Phys.*, **16** 1481 (1965).

Technical Note



Cyclic Oxidation of Hastelloy X

S. K. Rhee and A. R. Spencer

Research Laboratories, Bendix Corporation, Southfield, Michigan 48076

This investigation has been conducted as a part of a program to evaluate and select high-temperature alloys which are particularly suitable for fabricating transpiration-cooled (porous) materials used in turbine blades and similar engine components.

The kinetics of cyclic oxidation of Hastelloy X in the form of sheet and wire were studied over the temperature range 760°-1200°C. The chemical composition of the alloy is listed in Table I, as provided by the manufacturer. Sheet specimens were cut to nominal dimensions of $6 \times 0.5 \times 0.060$ in. Wire specimens were 0.005 ± 0.0005 in. in diameter. Surface contamination of specimens was removed by sonic-cleaning in hot trichloroethylene followed by acetone rinsing. After cleaning the specimens were annealed for 8 hr at 1150°C in dry hydrogen (dew point below -62°C). Wires were loosely wound around prefired mullite tubes for support during the annealing cycle. The specimens appeared clean and bright after the anneal. The sheet specimens were then polished with successively finer grades of abrasives, and were finished with 320 grit silicon carbide. A bright, smooth surface of approximately 10 μ in. RMS roughness was produced. Final sonic cleaning was accomplished in hot trichloroethylene with an acetone rinse.

Sheet specimens were contained in zircon ceramic thimbles with four-point minimum contact at the corners of the specimen. Wire specimens consisted of loose bundles about 6 in. long and $1\frac{1}{2}$ in. in diameter containing approximately 100 ft of 0.005 in. diameter wire which weighed about 3g. Each wire bundle was placed in a separate zircon thimble. All thimbles were fired at 1600°C and baked out at 760°C to constant weight before using. Separate specimens (a total of 9 for each temperature) were subjected to cyclic oxidation in air for times of 4, 16, 64, 100, 200, 300, 400, 500, and 600 hr at each given temperature. After each exposure cycle, a tray containing all specimens was removed from the furnace and air-cooled. One specimen was removed for evaluation and the rest returned to the furnace. Temperatures are generally $\pm 5^\circ$.

Key words: oxidation, oxidation of superalloy, cyclic oxidation, cyclic oxidation of superalloy, oxidation of Hastelloy X.

Calibrated Chromel-Alumel thermocouples of heavy wire were placed at several locations on each tray and temperatures recorded continuously. At higher temperatures, thermocouples were replaced frequently. Specimen weight and oxidation weight gain were determined to ± 0.1 mg with an analytical balance after each oxidation cycle. At high temperatures where the amount of oxide spall was large, the ceramic thimble and the specimen were weighed together before and after oxidation, and this method was found to be more reproducible than direct weighing. Further details of the experimental procedure together with the resulting data, which is analyzed herein, have been reported elsewhere (1, 2).

The weight-gain vs. oxidation, time curves for the sheet specimens and for the wire specimens are shown in Fig. 1 and 2, respectively; in the case of wire specimens, the mean surface area was used for calculating the specific weight gain, based on the initial and final diameters of the metal. In all cases, initially the weight increases parabolically in a manner similar to that often found for continuous oxidation (3, 4). At higher temperatures and longer times sheet specimen behavior was observed to be erratic. In these cases, the differing spall behavior of the individual specimens explains the observed results because fresh surfaces oxidize rapidly. Also, a few points seem to show a large experimental error at lower temperatures, partly because weight gain was small.

The oxidation rate constants calculated for the sheet specimens are given in Table II, and for the wire specimens in Table III. The rate constants are plotted as an inverse function of temperature in Fig. 3. The rate constants obtained from continuous oxidation of Hastelloy X wire (5) and sheet (6) are also included in Fig. 3 for comparison. A least-squares fit to the Arrhenius plots yields an activation energy of 49.9 ± 2.6 kcal/mole for the sheet specimens and 51.6 ± 1.5 kcal/mole for the wire specimens, respectively. Taking into account the estimated experimental errors ($\pm 5\%$), the activation energies become 49.9 ± 5.1 kcal/mole, and 51.6 ± 4.1 kcal/mole, respectively. The activation energies are practically equal for both types of speci-

Table I. Chemical composition of Hastelloy X, weight per cent

	Ni	Cr	Fe	Mo	Co	Si	Mn	W	C	P	S
Sheet	Bal.	22.47	18.35	9.12	0.93	0.84	0.57	0.57	0.015	0.018	0.007
Wire	Bal.	21.57	18.07	9.08	1.45	0.57	0.58	0.52	0.09	0.016	0.004

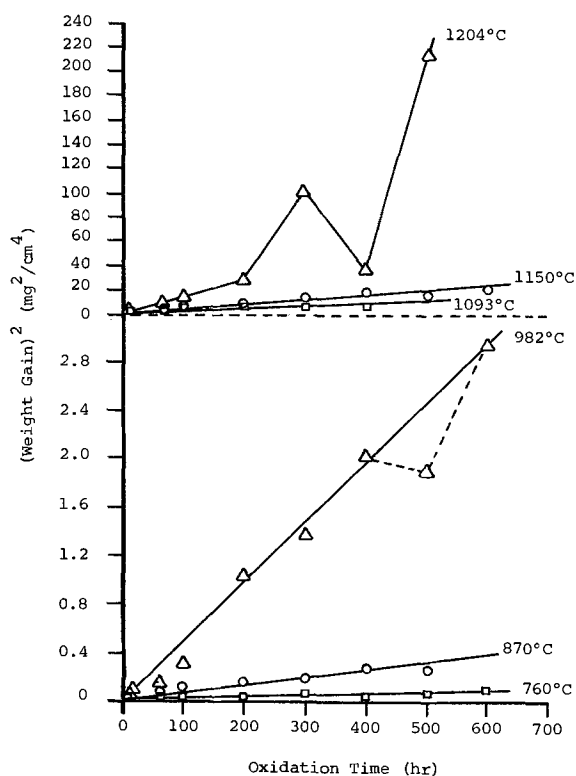


Fig. 1. Cyclic oxidation of Hastelloy X sheet

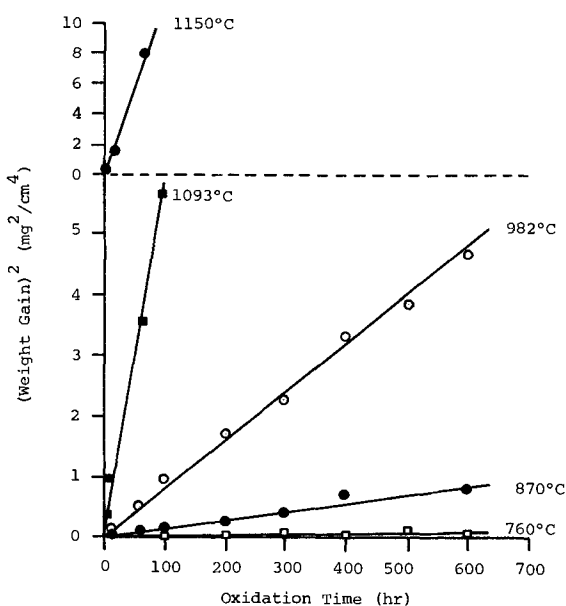


Fig. 2. Cyclic oxidation of Hastelloy X wire

mens, indicating that the same activation process is rate-controlling for the cyclic oxidation. The parabolic rate constants for the sheet specimens used in the present work are substantially smaller than the constants found for the wire and sheet specimens in continuous, or cyclic oxidation (Fig. 3). This difference in rate constants is probably due to various factors such as surface preparation, composition, and history

Table II. Parabolic rate constants for sheet specimens

T (°C)	k [g ² /cm ⁴ /sec]	Time (hr)
760	2.22 × 10 ⁻¹⁵	>600
870	1.80 × 10 ⁻¹⁴	500
982	1.38 × 10 ⁻¹³	>600
1093	6.68 × 10 ⁻¹³	400
1150	1.11 × 10 ⁻¹²	>600
1204	3.67 × 10 ⁻¹²	300

Table III. Parabolic rate constants for wire specimens

T (°C)	k [g ² /cm ⁴ /sec]	Time (hr)
760	3.61 × 10 ⁻¹⁴	>600
870	3.56 × 10 ⁻¹³	>600
982	2.02 × 10 ⁻¹²	>600
1093	1.55 × 10 ⁻¹¹	100
1150	3.57 × 10 ⁻¹¹	64

of heat-treatment. For example, according to Caplan *et al.* (7) the oxidation rate of the Fe-26% Cr-0.5% Si alloy was found to increase in the following order of surface treatment, electropolished plus etched, abraded plus etched, machined, abraded, and electropolished. They found that the weight gain after 210 min at 1100°C was 0.4 mg/cm² on the electropolished and etched surface, compared with 1.05 mg/cm² on the electropolished surface. It was suggested that the effects were due to the differences in defect concentrations in the oxide films produced by the various pretreatments. Similarly, in the case of Ni-Cr alloys, the oxidation rate was increased when the surface was grit-blasted, compared with the grit-blasted and annealed surface, and the effects of surface preparation also depended on the composition of the alloys (8). Wlodek (6) found that the rate constants varied with a small variation in the composition of Hastelloy X. According to Wood and Wright (9), the oxidation rate of Ni-Co alloys was very sensitive to the previous history of the specimen; coherent or noncoherent oxides were observed depending on the previous history.

Metallographic and x-ray analyses were performed on the oxide scales formed on the sheet specimens (10). Metallographic examinations revealed that dark spots started to form along surface scratches after 4 hr at 982°C, and almost the entire surface was covered with the dark phase and with some lighter phase after 100 hr at 982°C. The 600 hr 1093°C specimen had an adherent scale, which was light green near the substrate, while it gradually darkened near the surface, indicating either a change in the oxide Cr₂O₃ or the presence of a finely dispersed, dark second phase. The x-ray diffraction and fluorescence studies showed that the major phases of the scale were Cr₂O₃ and (Fe, Ni) (Cr, Mn)₂O₄ up to 1093°C, and mostly Cr₂O₃ at 1204°C.

In the case of continuous oxidation of Hastelloy X wires, the activation energy is reported to be 63.1 ± 2.3 kcal/mole, and this value was attributed to chromium ion diffusion in Cr₂O₃ (5). In the case of continuous oxidation of Hastelloy sheets, the activation energy is reported to be 60 kcal/mole for the early stage and 57 kcal/mole for the late stage (6). The low values

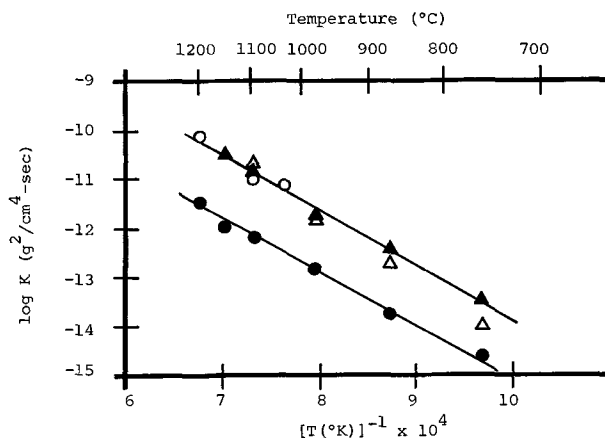


Fig. 3. Temperature dependence of parabolic rate constants for cyclic oxidation of Hastelloy X: Q = 51.6 ± 4.1 kcal/mole for wire specimens (▲) and Q = 49.9 ± 5.1 kcal/mole for sheet specimens (●). Δ represents K values obtained from continuous oxidation of Hastelloy X wire (Ref. 5) and O from continuous oxidation of Hastelloy X sheet (Ref. 6).

determined in the present work indicate that a different mechanism is rate-controlling for the cyclic oxidation. According to Gulbransen and Andrew (11) a Ni-Cr alloy containing approximately 20% Cr exhibits two rate constants during continuous oxidation. They proposed that the early stage was due to the initial oxide NiO and the late stage due to Cr₂O₃. The activation energy for the early stage was 49,739 cal/mole, which is very near the values found in the present work. Also, an activation energy of 53.6 ± 3.8 kcal/mole was found for cyclic oxidation of TD-Ni (12). According to Iitaka *et al.* (13) the Fe-18% Cr-9% Ni alloy was found to form a very thin layer of NiO between the outer oxide layer [(Fe, Cr)₂O₃ plus spinell] and the alloy substrate during high-temperature oxidation. Thus, it appears that the NiO formation might be rate-controlling for the cyclic oxidation of Hastelloy X. However, this conclusion is rather tentative.

In summary, the cyclic oxidation of Hastelloy X can be described by the parabolic rate law, and the activation energy is 49.9 ± 5.1 kcal/mole for the sheet specimens and 51.6 ± 4.1 kcal/mole for the wire specimens. These values are approximately 10 kcal/mole lower than the activation energy found for continuous oxidation.

Acknowledgment

The authors wish to thank the Research Laboratories of The Bendix Corporation for permission and assistance in publishing this paper.

Manuscript submitted Aug. 27, 1971; revised manuscript received ca. Nov. 10, 1971.

Any discussion of this paper will appear in a Discussion Section to be published in the December 1972 JOURNAL.

REFERENCES

1. F. W. Cole, J. B. Padden, and A. R. Spencer: Oxidation Resistant Materials for Transpiration-Cooled Gas Turbine Blades (I. Sheet Specimen Screening Tests), NASA CR-930, February 1968.
2. F. W. Cole, J. B. Padden, and A. R. Spencer: Oxidation Resistant Materials for Transpiration-Cooled Gas Turbine Blades (II. Wire Specimen Tests), NASA CR-1184, September 1968.
3. C. Wagner, in "Atom Movements," ASM, 153 (1951).
4. P. Kofstad, "High Temperature Oxidation of Metals," pp. 12, 18, John Wiley & Sons, Inc., New York (1966).
5. S. K. Rhee and A. R. Spencer, *Met. Trans.*, **1**, 2021 (1970).
6. S. T. Wlodek, *Trans. Met. Soc. AIME*, **230**, 177 (1964).
7. D. Caplan, A. Harvey, and M. Cohen, *This Journal*, **108**, 132 (1961).
8. C. S. Giggins and F. S. Pettit, *Trans. Met. Soc. AIME*, **245**, 2509 (1969).
9. G. C. Wood and I. G. Wright, *Corrosion Sci.*, **5**, 841 (1965).
10. S. J. Grisaffe and C. E. Lowell, Examination of Oxide Scales on Heat Resisting Alloys, NASA TN D-5019, February 1969.
11. E. A. Gulbransen and K. F. Andrew, *This Journal*, **106**, 941 (1959).
12. S. K. Rhee and A. R. Spencer, *Met. Trans.*, **2**, 2285 (1971).
13. I. Iitaka, T. Nakayama, and K. Sekiguchi, *J. Sci. Res. Inst. (Tokyo)*, **45**, 57 (1951).



Electromotive Force Measurements on High-Temperature Sulfide Formation Cells

W. T. Thompson*¹ and S. N. Flengas*

Department of Metallurgy and Materials Science, University of Toronto, Toronto 5, Ontario, Canada

ABSTRACT

Using formation cells with a sulfur vapor electrode, relative partial molar thermochemical properties are reported for the sulfide-rich region of the molten lead sulfide-lead chloride and silver sulfide-silver chloride systems. Negative deviations from Raoultian ideality observed in the former system and positive deviations in the latter are tentatively related to available molar conductance data.

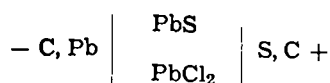
Most base metal reduction practices involve some stage in which solid or liquid sulfides are reacted with oxygen. As a result metal production is attended by the evolution of large volumes of sulfur dioxide. Sulfur dioxide emission could be eliminated if it were possible to reduce the metal directly from the sulfide by a method which yields only the more easily handled elemental sulfur as a by-product.

It is known that base metal sulfides are soluble in chloride melts particularly those containing a cation common to the sulfide (1-4). Further, it has been found that such melts when dilute in sulfide (containing less than 0.1 mole fraction sulfide) are electrolytes (5,6). As a result of such findings, one method of reducing base metal sulfide that has been proposed is fused salt electrolysis (7-9). In this process, the products of electrolysis are metal and sulfur gas.

In previous publications, the reversibility of a sulfur vapor electrode was demonstrated (10), and free energies of formation of silver and lead sulfide were determined (11). This paper reports measurements, using this electrode, of partial molar properties in the lead sulfide-lead chloride and silver sulfide-silver chloride systems. This study was intended to supplement other investigations of the physical chemistry of sulfide-chloride melts carried out in this laboratory (1-6) and in particular establish any relationships which may exist between melt structure, as inferred from the thermodynamics, and the electrical conductance behavior.

Experimental

Details of the cell



are shown in Fig. 1. The electrode compartments, as in previous work, were separated with an asbestos diaphragm. This feature, which restricts sulfur diffusion to the lead electrode, is most important if a reproducible stable emf is to be observed. The upper portion

of the apparatus, showing the arrangement of the molten sulfur bath used to establish a sulfur pressure in an argon flow over the positive electrode, is identical to that shown in a previous publication (10). The molten lead used for one of the electrodes was cominco five nine grade etched with dilute nitric acid prior to melting. The lead sulfide was prepared by reacting stoichiometric quantities of the high purity lead with doubly distilled sulfur in vacuum sealed quartz cells as described previously (5, 11). The lead chloride was vacuum oven dried Fisher reagent grade. The graphite electrodes were spectroscopic grade. Since considerable glass blowing was involved in setting up each cell, the entire apparatus was evacuated for an hour or more while those portions of the apparatus enclosed by the furnace assembly were warmed to about 150°C. The salts were then fused and dried argon was slowly passed through the lead electrode compartment; at the same time, the sulfur argon mixture was admitted to the other compartment and circulated over the graphite rod thereby creating a sulfur electrode. When measurements on an electrolyte of one composition were complete, the cell was discarded and a new one constructed. Temperature measurements of the sulfur bath

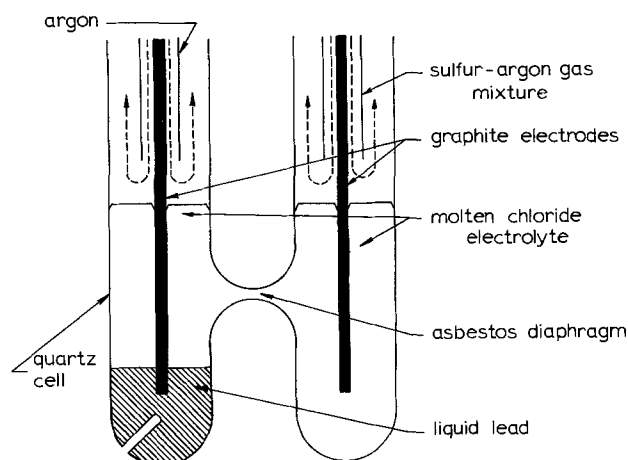


Fig. 1. Lead sulfide formation cell

* Electrochemical Society Active Member.
¹ Present address: Department of Metallurgical Engineering, McGill University, Montreal 110, Quebec, Canada.
 Key words: molten solutions, fused salts, chloride, sulfide, sulfur electrode, formation cell, thermodynamics, electrochemistry.

Table I. EMF measurements of the lead sulfide formation cell

X_{PbS}	$T_{\text{sulfur}} \text{ } ^\circ\text{C}$	$T_{\text{electrolyte}} \text{ } ^\circ\text{C}$	$\bar{E} \text{ (mV)}$	$E \text{ (mV)}$
0.013	217	508	521	592.6
0.013	217	511	519	590.6
0.013	226	525	525	592.3
0.013	244	534	528	587.6
0.013	216	567	511	585.1
0.013	221	602	508	581.5
0.013	221	602	508	581.5
0.019	185	513	493	582.6
0.019	191	561	487	577.4
0.019	194	525	497	579.9
0.019	180	547	485	581.9
0.019	181	610	468	570.9
0.019	182	576	476	574.3
0.034	190	516	474	566.6
0.034	195	500	484	568.6
0.034	198	563	470	555.7
0.034	198	535	484	567.3
0.034	194	504	484	567.3
0.034	197	599	462	551.5
0.034	197	649	449	543.4
0.055	199	494	472	552.5
0.055	201	541	465	545.1
0.055	203	561	462	543.9
0.055	207	579	456	536.3
0.055	207	602	447	529.7
0.055	204	620	442	528.5
0.100	180	478	433	523.1
0.100	195	567	419	506.8
0.100	192	533	424	510.7
0.100	190	517	427	513.7
0.100	187	481	435	521.3
0.100	200	629	400	490.2
0.100	198	576	418	504.6
0.100	196	593	414	503.6

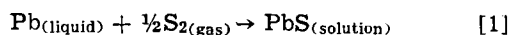
and molten electrolyte were made with Chromel-Alumel thermocouples. The output of the thermocouples and the cell voltage were determined with a Leeds and Northrup K-3 potentiometer.

Results

The emf measurements, \bar{E} , are reported in Table I to the nearest mV. The potentials were measured on both increasing and decreasing temperature cycles and found to be reproducible over periods of up to three days. During this period, the sulfur electrode was operated at relatively low S_2 partial pressure, in the range 10^{-2} to 10^{-3} atm. The electrolyte compositions were calculated from the initial weighings.

To facilitate thermodynamic calculations on the electrolyte, the measured potentials were adjusted to the condition corresponding to S_2 gas at one atmosphere pressure.

Since the cell reaction may be written



for which the Nernst expression is

$$\bar{E} - \frac{RT}{4F} \ln (P_{S_2}) = E^\circ - \frac{RT}{2F} \ln a_{\text{PbS}} \quad [2]$$

The adjusted potentials, E , are therefore given by

$$E = \bar{E} - \frac{RT}{4F} \ln (P_{S_2}) \quad [3]$$

In these equations, R is the gas constant, T is the electrolyte temperature, and F is the Faraday. P_{S_2} is the actual partial pressure of S_2 in the sulfur-argon mixture when the cell emf was determined. Since sulfur vapor in the temperature range of this investigation exists in a complex molecular state, this partial pressure is not directly available from the experimental measurements. The partial S_2 pressure may however be calculated from a knowledge of the liquid sulfur temperature and the electrolyte temperature since the equilibrium constants for sulfur vapor association



are known (12); these data covering the range $3 \leq \nu \leq 8$ include all the important sulfur gas molecules. The details of this rather involved calculation have been described elsewhere (10, 11). The S_2 pressures have been estimated to be accurate to about $\pm 5\%$ (11).

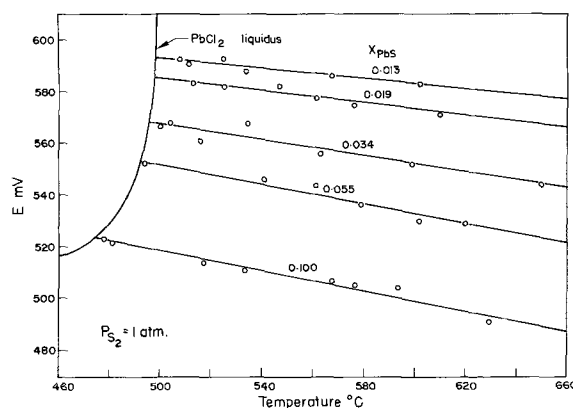


Fig. 2. EMF vs. temperature for lead sulfide formation cell

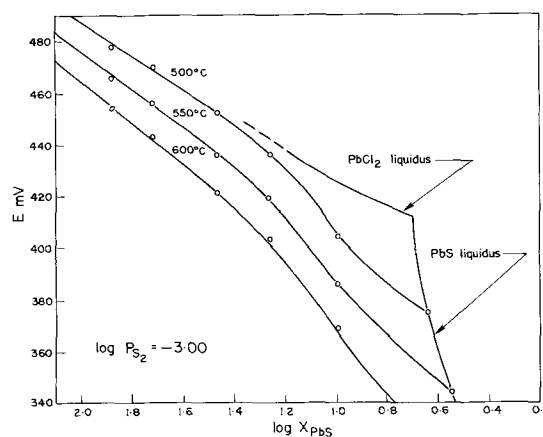


Fig. 3. Nernst plot for lead sulfide formation cell

The adjusted emf measurements are plotted against temperature for various sulfide concentrations in Fig. 2. The lead chloride liquidus that limits the lower temperature is taken from the work of Bell and Flengas (2). The upper experimental temperature limit was determined by the volatility of lead chloride. Electrolytes more concentrated than 0.1 mole fraction lead sulfide were not studied since the more concentrated melts are not truly electrolytes but conduct current to some extent electronically (6). This mode of conduction makes it difficult to interpret the cell voltages in a thermochemical manner. The equations of the least squares lines through the data points are given in Table II together with standard deviations. A Nernst plot is shown in Fig. 3. This was constructed by interpolation from Fig. 2 using the equations for the straight lines. A sulfur pressure adjustment to 10^{-3} atm S_2 was made in order to separate the isotherms. The limiting slopes of the plots correspond to 2 electrons per sulfur atom.

Measurements made with the sulfur vapor electrode on multicomponent sulfide saturated melts (11) gave the equation (mV - °K)

$$E^\circ = 867.4 - 0.4884T \quad [5]$$

for a cell reaction corresponding to the formation of pure solid lead sulfide from pure liquid lead and S_2 gas at one atmosphere pressure over the temperature range 876°-1075°K. The standard deviation for this equation

Table II. Temperature-emf relationships in lead sulfide formation cells

X_{PbS}	Equation (mV - °K)	Std. dev. (mV)
0.013	$E = 685.4 - 0.1193 T$	1.3
0.019	$E = 686.0 - 0.1302 T$	1.4
0.034	$E = 689.0 - 0.1576 T$	3.0
0.055	$E = 678.1 - 0.1670 T$	4.8
0.100	$E = 667.2 - 0.1927 T$	2.0

Table III. Partial molar properties* of PbS in PbS-PbCl₂ melts

X_{PbS}	$(\Delta\bar{H}_m)^S$ cal/g mole	$(\Delta\bar{S}_m)^S$ gibbs/g mole	a
0.013	8394	17.02	0.024
0.019	8366	16.52	0.030
0.034	8228	15.26	0.053
0.055	8770	14.32	0.088
0.100	9233	13.64	0.214

* At 600°C relative to pure solid lead sulfide.

was 4.5 mV. Equation [5] together with those in Table II, allow calculation of the partial molar enthalpy and entropy of mixing as well as the activity of the sulfides.

The partial molar enthalpy and entropy of mixing, taking pure solid sulfide as the standard state, $(\Delta\bar{H}_m)^S$ and $(\Delta\bar{S}_m)^S$ respectively, were calculated for each melt composition by applying the equations

$$(\Delta\bar{H}_m)^S = -2F \frac{d((E - E^\circ)/T)}{d(1/T)} \quad [6]$$

$$(\Delta\bar{S}_m)^S = 2F \frac{d(E - E^\circ)}{dT} \quad [7]$$

The activity of lead sulfide relative to pure solid at 600°C was calculated using the equation

$$a^S = \exp \left[\frac{(\Delta\bar{H}_m)^S}{RT} - \frac{(\Delta\bar{S}_m)^S}{R} \right] \quad [8]$$

All the calculated properties are listed in Table III.

For the purpose of making inferences about melt structure, it is usual to refer partial molar properties to the liquid state. Unfortunately, there is insufficient accurate thermal data on the heat of fusion and liquid heat capacity to make this change of state calculation reliable for lead sulfide particularly since its melting point is about 600°C higher than the temperature range examined experimentally for this system.

A least squares fit of the data in Table III resulted in the equations

$$(\Delta\bar{H}_m)_{\text{PbS}}^S = 13.761 - 5.654X_{\text{PbCl}_2}^2 \quad [9]$$

$$(\Delta\bar{S}_m)_{\text{PbS}}^S = 12.354 - 3.952X_{\text{PbCl}_2}^2 - R \ln X_{\text{PbS}} \quad [10]$$

The standard deviations for these fits were 174 cal/g mole and 0.184 gibbs/g mole respectively. The constants 13.761 and 12.354 appear in these expressions because the standard state for lead sulfide is pure solid. The constants are in fact related to the enthalpy and entropy of fusion at 600°C, but are about 35% higher than one might expect based upon a reported value for the enthalpy of fusion of 8700 ± 800 cal/g mole at the melting point of 1113°C (3, 13). Physical significance however, can only be attached to these constants if the other terms in Eq. [9] and [10] are absolutely correct. It is probably better to view the equations as empirical expressions, valid for the range $0 \leq X_{\text{PbS}} \leq 0.1$, that have a form consistent with thermodynamic requirements. In this connection, the first power term in X_{PbCl_2} does not appear in the equations in order that Raoult's law will apply as a limiting condition to the lead chloride solvent.

The partial molar properties of lead chloride were calculated at 600°C by an analytical integration of the Gibbs-Duhem equation. The expressions taking pure liquid as the standard state are

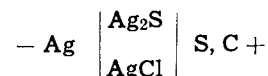
$$(\Delta\bar{H}_m)_{\text{PbCl}_2}^L = -5.654X_{\text{PbS}}^2 \quad [11]$$

$$(\Delta\bar{S}_m)_{\text{PbCl}_2}^L = -3.952X_{\text{PbS}}^2 - R \ln X_{\text{PbCl}_2} \quad [12]$$

The partial molar properties are depicted in Fig. 4 along with the data points listed in Table III.

Calculations for the Silver Chloride-Silver Sulfide System

In a previous paper (10), emf measurements of the cell



were reported for sulfide concentrations less than 0.12 mole fraction. Subsequent work by a modified technique (11) yielded the standard cell potential for the formation of silver sulfide. As for the lead sulfide-lead chloride system, these data make it possible to determine partial molar property data for the sulfide-rich melts. For comparison purposes, the results of these calculations are presented in this section. A plot of measured emf data appears in Fig. 5. This plot differs slightly from the one reported originally (10) in that the

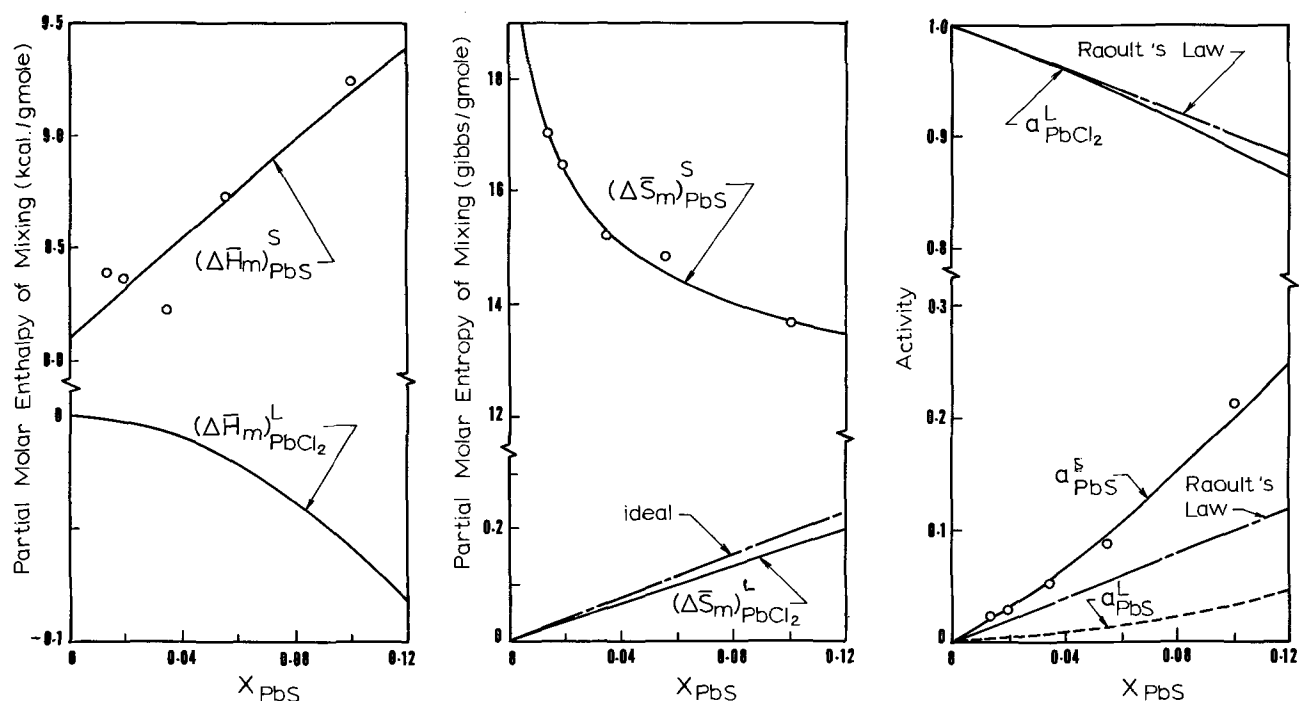


Fig. 4. Partial molar properties for sulfide-rich melts of lead sulfide and lead chloride

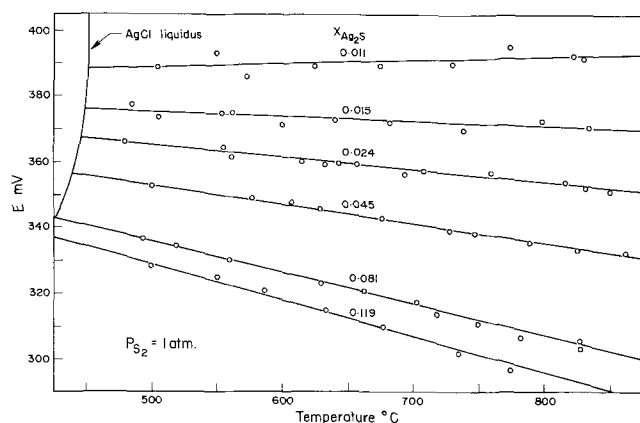


Fig. 5. EMF vs. temperature for silver sulfide formation cell

+Ag/C-thermoelectric voltage (11) was added to the measured cell potentials. In computing the magnitude of the thermoelectric voltage, the cold junction temperature was taken to be equal to that for the liquid sulfur since the silver connections from the potentiometer were located directly below the sulfur bulb. This voltage correction amounts to about 5 mV and consequently has a significant effect on the calculation of thermodynamic properties of the electrolyte. The equations of the least square lines through the data points in Fig. 5 are given in Table IV together with standard deviations.

For the cell which realized the formation of solid silver sulfide from pure solid silver and S₂ gas at one atmosphere pressure (11), the equation (mV - °K) was

$$E^{\circ} = 455.3 - 0.1919T \quad [13]$$

over the temperature range 773°-1071°K. The standard deviation was 3.2 mV. Partial molar property data for silver sulfide relative to solid sulfide were calculated using Eq. [6] and [7]. In the case of silver sulfide however, it is possible to refer the properties to the pure liquid sulfide since enthalpy of fusion and heat capacity data for solid and liquid sulfide are available from calorimetric work by the present authors (14). Defining the difference in heat capacity between solid and liquid silver sulfide as

$$(C_p)^L - (C_p)^S = \Delta\alpha \quad [14]$$

the partial molar enthalpy and entropy of mixing referred to pure liquid silver sulfide, $(\Delta\bar{H}_m)^L$ and $(\Delta\bar{S}_m)^S$ respectively, were calculated at 600°C for each melt composition studied by applying the equations

$$(\Delta\bar{H}_m)^L = (\Delta\bar{H}_m)^S - \Delta\alpha (T - T_f) - \Delta H_f \quad [15]$$

$$(\Delta\bar{S}_m)^L = (\Delta\bar{S}_m)^S - (\Delta H_f/T_f) - \Delta\alpha \ln (T/T_f) \quad [16]$$

In these equations ΔH_f is the enthalpy of fusion of silver sulfide, 1880 cal/g mole (14) at the fusion temperature, T_f , of 830°C (1). The calculated properties are listed in Table V.

In order to determine partial molar properties for silver chloride at 600°C, $(\Delta\bar{H}_m)^L$ and $(\Delta\bar{S}_m)^L$ were first fit by the method of least squares to equations in mole fraction. The following expressions were obtained

$$(\Delta\bar{H}_m)^L_{Ag_2S} = -14.123X_{AgCl}^2 + 16.201X_{AgCl}^3 \quad [17]$$

$$(\Delta\bar{S}_m)^L_{Ag_2S} = -14.798X_{AgCl}^2 + 13.785X_{AgCl}^3 - R \ln X_{Ag_2S} \quad [18]$$

The standard deviations for these equations are 164 cal/g mole and 0.255 cal/g mole respectively. By integrating the Gibbs-Duhem equation, expressions for the partial molar enthalpy and entropy of mixing for silver chloride with the pure liquid as standard state were obtained.

Table IV. Temperature-emf relationships in silver sulfide formation cells

X_{Ag_2S}	Equation (mV - °K)	Std. dev. (mV)
0.011	$E = 382.0 + 0.00896 T$	3.7
0.015	$E = 388.3 - 0.01694 T$	1.6
0.024	$E = 395.4 - 0.03921 T$	1.1
0.045	$E = 401.9 - 0.06243 T$	0.8
0.081	$E = 415.5 - 0.1019 T$	1.1
0.119	$E = 421.5 - 0.1185 T$	1.3

Table V. Partial molar properties* of Ag₂S in Ag₂S-AgCl melts

X_{Ag_2S}	$(\Delta\bar{H}_m)^L$ cal/g mole	$(\Delta\bar{S}_m)^L$ gibbs/g mole	α
0.011	2072	8.14	0.055
0.015	1782	6.95	0.085
0.024	1454	5.92	0.118
0.045	1155	4.85	0.169
0.081	527	3.03	0.295
0.119	251	2.26	0.370

* At 600°C relative to pure liquid silver sulfide.

$$(\Delta\bar{H}_m)^L_{AgCl} = -6.023 + 28.247X_{AgCl} - 38.425X_{AgCl}^2 + 16.201X_{AgCl}^3 \quad [19]$$

$$(\Delta\bar{S}_m)^L_{AgCl} = -7.905 + 29.596X_{AgCl} - 35.476X_{AgCl}^2 + 13.785X_{AgCl}^3 - R \ln X_{AgCl} \quad [20]$$

Equations [17]-[20] apply when $0 \leq X_{Ag_2S} \leq 0.12$.

The partial molar properties given by these equations together with the calculated activities are depicted in Fig. 6. Included in this presentation are the data points listed in Table V.

Discussion

A rough approximation of the lead sulfide activity isotherm relative to pure liquid is shown in Fig. 4. A temperature independent enthalpy of fusion of 8700 cal/g mole (13) was assumed for this calculation in the absence of more complete data referred to previously. Moderately negative departure from Raoultian ideality is indicated therefore for both lead sulfide and lead chloride, a situation generally taken to be indicative of a tendency toward weak compound formation in the melt. This inference is supported by the negative partial molar enthalpy of mixing of lead chloride and is consistent with an identified solid compound occurring at lower temperatures in this system (15). Furthermore, the partial molar entropy of mixing of lead chloride exhibits a negative departure from ideal behavior.

The thermodynamic properties in Fig. 6 indicate a general tendency toward immiscibility for silver sulfide-silver chloride melts, at least for those dilute in sulfide. This is evidenced by the positively deviating activity isotherms and positive enthalpy of mixing. It appears in Fig. 6 that the partial molar enthalpy of mixing of silver sulfide may change sign. This was found to be the case in calorimetric data reported previously (14). These results, represented in Fig. 6, indicate that cross-over takes place at 0.23 mole fraction silver sulfide compared to an estimated 0.13 resulting from the emf measurements. This change in sign of the enthalpy of mixing may be indicative of unusual structural changes occurring in melts of this system and may be consistent with the partial molar entropy of mixing of silver chloride being unexpectedly greater than the ideal value.

Figure 7 shows some of the liquidus data reported by Bell and Flengas (1). Since solid solubility is negligible, limiting liquidus slopes were obtained by application of the equation

$$\Delta T = \frac{\nu XRT_f^2}{\Delta H_f} \quad [21]$$

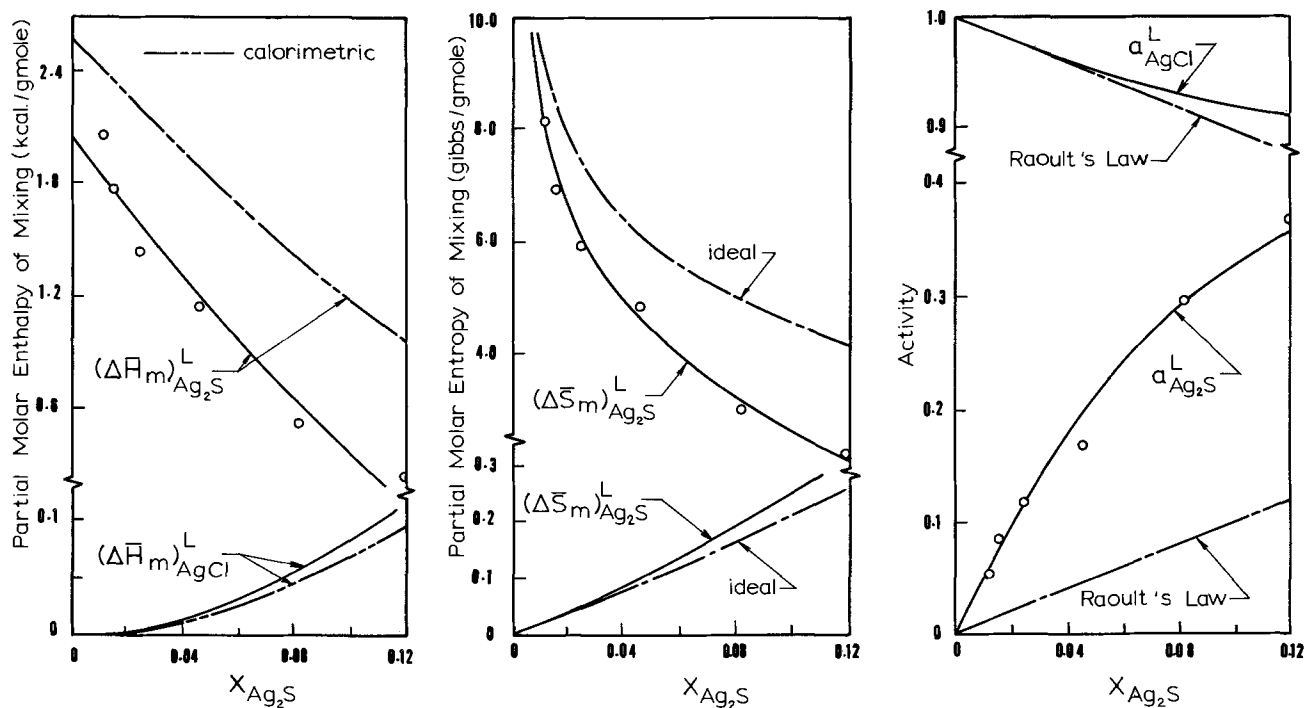


Fig. 6. Partial molar properties for sulfide-rich melts of silver sulfide and silver chloride.

In this equation ΔT is the freezing point depression, X is the mole fraction of solute, and ν is the number of moles of foreign particles contributed to the solution per mole of solute; other symbols are as previously defined. The sparse amount of data suggests that silver chloride contributes two moles of foreign particles per mole to silver sulfide-rich melts but that silver sulfide contributes only one to silver chloride-rich melts. A possible explanation requires that silver sulfide exist as a molecule-like entity in the melt in which silver atoms are linked to a sulfur. Similar references to apparently molecule-like entities have appeared for other high temperature solutions, notably molten metal-oxygen systems (16). At the present time, there is in-

sufficient cryoscopic and heat of fusion data to show that lead chloride dissolves to yield three foreign particles in lead sulfide. On the lead chloride-rich side of the system there appears to be significant solid solubility.

Molecule-like sulfide entities offer a convenient qualitative way of accounting for the observed conductance behavior. Measurements of Bell and Flengas (5, 6) have shown that for both melt systems molar conductance is ionic on the chloride side, decreases in magnitude as the sulfide is dissolved and then rapidly increases while changing in character to electronic. In the silver sulfide-silver chloride system, the increase occurs at about 0.15 mole fraction sulfide while in the lead sulfide-lead chloride systems it occurs near 0.25. Electronic conduction requires the existence of a continuous sulfide network in the melt similar to what must exist in the pure molten sulfide. Random mixing considerations indicate that when about one fifth or greater mole fraction sulfide exists in the melt, the probability of adjacent sulfide entities forming continuous chains is unity. At significantly lower sulfide concentrations, it is improbable that such continuous chains exist when random mixing is assumed. The implication is that in chloride-rich melts molar conductance is totally ionic but decreases as the population of noncharge-carrying sulfide particles increase. In sulfide-rich melts molar conductance is large and virtually totally electronic as the sulfide network develops with increasing sulfide concentration to more closely resemble that for the pure molten sulfide.

The difference in the extent of the ionic range of conductance is consistent with the thermodynamic properties. In the silver sulfide-silver chloride system, the tendency exhibited toward immiscibility suggests that the proposed sulfide particles prefer being adjacent to others, in this way making it possible to establish continuity at concentrations lower than expected on a random mixing basis. The opposite situation is indicated for the negatively deviating lead sulfide-lead chloride system. Accordingly, electronic conduction is exhibited at lower sulfide concentrations in the silver system compared to the lead system.

The proposal of metal sulfide existing in these melts predominantly as molecule-like entities is not inconsistent with it being possible to set up a reversible

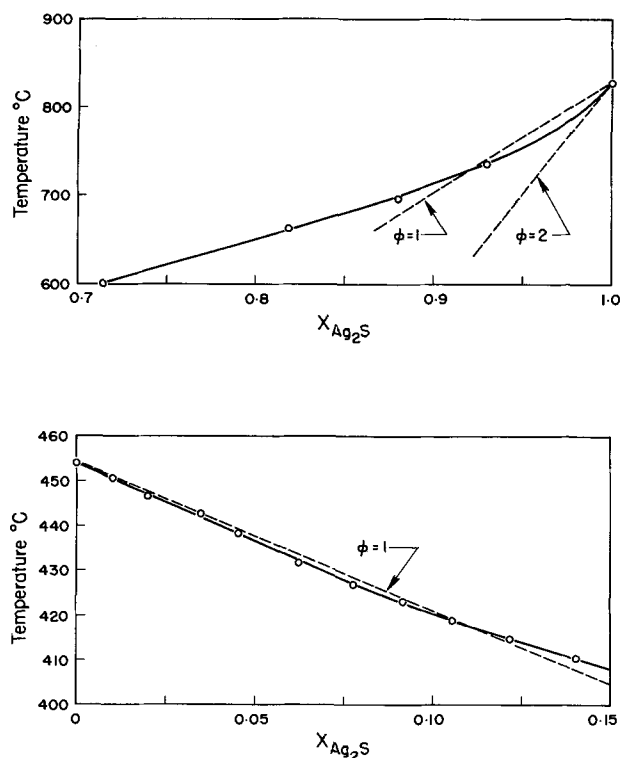
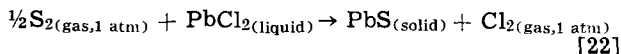


Fig. 7. The silver sulfide and silver chloride liquid

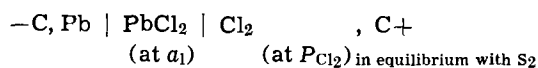
electrochemical cell with a sulfur electrode. Even in the complete absence of sulfide ions, the sulfur electrode could reach the expected sulfide-sulfur potential via the chloride ion. For example, although the standard free energy change, ΔG° , for the reaction



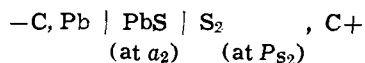
is about +35 kcal/g mole PbS, a very small chlorine partial pressure, P_{Cl_2} , exists which is closely approximated by

$$P_{\text{Cl}_2} = P_{\text{S}_2}^{1/2} \cdot \frac{a_1}{a_2} \cdot \exp \frac{-\Delta G^\circ}{RT} \quad [23]$$

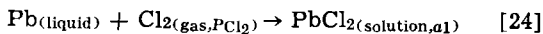
In this equation, P_{S_2} is the partial S_2 pressure fixed experimentally, and a_1 and a_2 are the activities of lead chloride and lead sulfide respectively in a melt of given composition. Since the chlorine pressure is quite small, the melt composition changes insignificantly with time. It follows, however, since there is some chlorine at the positive electrode, the formation cell may be schematically represented by



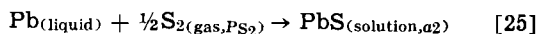
instead of



since the free energy changes for the primary reactions, respectively,



and



are equal. The potential at the positive electrode may therefore be due to $\text{S}^=/\text{S}_2$ or Cl^-/Cl_2 or both with no mixed potential resulting. These arguments may be readily extended to include the trace concentrations of S_2Cl_2 , known to exist at the temperatures and gas pressures under consideration. In this connection, it is noteworthy that chlorine, sulfur, and sulfane reactions have been reported at liquid sulfur electrodes by Delarue (17) and Bodewig and Plambeck (18) as a result of polarographic studies.

The foregoing concept of sulfide-chloride melts would affect the igneous electrolysis of base metal sulfide. During the passage of current, electrochemically oxidized chloride ion would have to react chemically to reestablish as equilibrium for reaction [22] as it applies to sulfide dissolved in the anolyte. This might result in a rate-limiting condition related to sulfide-chlorine diffusion and reaction if it were desired to generate predominantly sulfur at the anode during electrolysis.

Conclusions

Electromotive force measurements on sulfide formation cells in the vicinity of 600°C employing a sulfur vapor electrode were reported. These showed that melts containing up to 0.1 mole fraction lead sulfide in molten lead chloride exhibit negative deviation from Raoultian ideality. Similar measurements indicated positive deviations for the sulfide-rich region of silver sulfide-silver chloride melts. These data in conjunction with published molar conductance data suggest that the sulfide may dissolve to yield little or no free sulfide ion. Instead, molecule-like sulfide entities were postulated to exist. The consequences of this proposal were briefly explored.

Acknowledgments

The authors wish to thank the National Research Council of Canada for financial support.

They thank Mr. R. H. Chappell for his assistance in constructing the glass cells.

Manuscript submitted July 1, 1971; revised manuscript received ca. Nov. 15, 1971.

Any discussion of this paper will appear in a Discussion Section to be published in the December 1972 JOURNAL.

REFERENCES

1. M. C. Bell and S. N. Flengas, *This Journal*, **111**, 569 (1964).
2. M. C. Bell and S. N. Flengas, *ibid.*, **113**, 27 (1966).
3. A. D. Pelton and S. N. Flengas, *Can. J. Chem.*, **48**, 2016 (1970).
4. A. K. Garbee, Ph.D. Thesis, University of Toronto, Toronto, Ontario, 1969.
5. M. C. Bell and S. N. Flengas, *This Journal*, **111**, 574 (1964).
6. M. C. Bell and S. N. Flengas, *ibid.*, **113**, 31 (1966).
7. T. Yanagase, Y. Suginoara, and I. Kyono, *Denki Kagaku*, **36**, 129 (1968).
8. H. Winterhager and R. Kammel, *Z. Erzberbau Metallhüttenw.*, **9**, 97 (1956).
9. H. Sawanoto and T. Saito, *J. Min. Inst. Jap.*, **68**, 555 (1952).
10. W. T. Thompson and S. N. Flengas, *Can. J. Chem.*, **46**, 1611 (1968).
11. W. T. Thompson and S. N. Flengas, *This Journal*, **118**, 419 (1971).
12. D. Detry, J. Drowart, P. Goldfinger, H. Keller, and H. Rickert, *Z. Phys. Chem.*, **55**, 314 (1967).
13. O. Kubaschewski, E. W. Evans, and C. B. Alcock, "Metallurgical Thermochemistry," 4th ed., Pergamon Press, New York (1967).
14. W. T. Thompson and S. N. Flengas, *Can. J. Chem.*, **49**, 1550 (1971).
15. Swanson and Fuyat, N.B.S. Circular 539, Vol. 2, 45 (1953).
16. G. R. Belton and E. S. Tankins, *Trans. AIME*, **233**, 1892 (1965).
17. G. Delarue, *Bull. Soc. Chim. France*, 906, 1654 (1960).
18. F. G. Bodewig and J. A. Plambeck, *This Journal*, **116**, 607 (1969).

A Theory for the Propagation of Stress Corrosion Cracks in Metals

David A. Vermilyea*

Corporate Research and Development, General Electric Company, Schenectady, New York 12301

ABSTRACT

A quantitative theory for the rate of propagation of stress corrosion cracks in metals is presented and discussed. The theory is based on the film rupture mechanism and is valid when phenomena at the crack tip control the propagation rate. The important parameters in the theory are the strain required to rupture the passive film, the amount of corrosion before repassivation, and the creep rate of material at the crack tip. Plausibility of the theory is demonstrated for stainless steel and for a magnesium alloy.

The objective of this paper is to present and discuss a model which makes it possible to predict the rates of propagation of stress corrosion cracks in metals in terms of experimentally accessible characteristics of the system. The theory is based upon the film rupture mechanism (1, 2) and is applicable to situations in which phenomena at the crack tip control the propagation rate. The theory accepts the generally held view that during stress corrosion cracking metal strain and corrosion are mutually stimulative. Strain accelerates corrosion by periodically causing film rupture, while, as suggested by Hart (3), corrosion accelerates strain by removing the most severely strain hardened material in the immediate vicinity of the crack tip. From the point of view of the theory, adequate information is not presently available about all of the system characteristics, especially about the details of stress and strain at the crack tip, in order to permit accurate rate predictions. Nevertheless the theory provides a conceptual framework which is amenable to further development and identifies the relevant material characteristics so that their influence on the process can be discussed from at least a semiquantitative point of view.

Theory

Model.—The model is outlined in Table I.

The metal is assumed to be homogeneous, isotropic, and uniform, and the detailed atom motions involved in creep strain, including dislocation motion, are ignored. The rate of crack propagation, \dot{l} , according to this model is

$$\dot{l} = \frac{L}{t_c} \quad [1]$$

Corrosion is assumed to proceed at a negligible rate when the metal is passive.

Figure 1 portrays schematically the strain rate and strain during crack propagation. Following film rupture an abrupt increase in strain rate occurs because the restraining influence of the surface film is removed. During corrosion prior to repassivation a further strain rate increase occurs as the most highly strained material near the crack tip is removed. After repassivation the strain rate decreases because of the presence of the surface film and because of strain hardening.

* Electrochemical Society Active Member.
Key words: film rupture, creep.

Table I. Model of stress corrosion cracking mechanism

Event	Time
1. Passive film ruptures	$t = t_0$
2. Metal corrodes to a depth L	$t = t_l$
3. Repassivation occurs	$t = t_L$
4. Creep strain continues	
5. Passive film ruptures at a critical strain ϵ_c	$t = t_c$

In order to predict crack propagation rates it is necessary to determine the values of L , ϵ_c , t_L , and t_c . Values for L , ϵ_c , and t_L can be obtained from transient experiments in which specimens covered with films formed in a solution chosen to simulate the crack-tip solution are strained while maintained at the crack-tip potential. If the specimen is strained slowly ϵ_c can be determined from the specimen strain at which a marked current change occurs. Values for L and t_L can be obtained from the current transient following a sudden extension of the specimen.

The film rupture time, given by $t_c - t_L$, is found from the creep strain *vs.* time behavior of the metal and the value of the critical strain. The creep behavior must be known for the material present a distance L ahead of the crack tip, that is, for the material at the

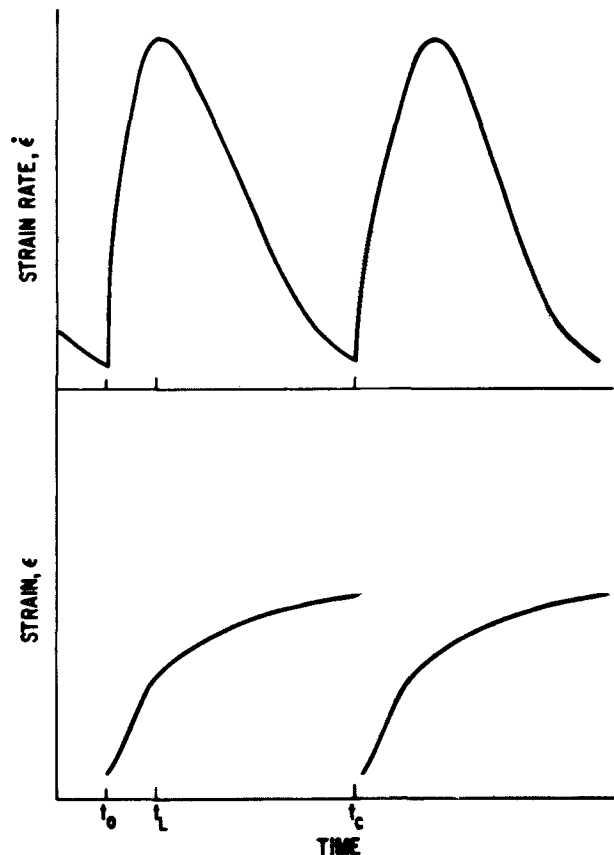


Fig. 1. Variations of crack tip strain and strain rate during stress corrosion cracking. Film rupture occurs at $t = 0$; corrosion occurs to t_L ; repassivation occurs at t_L ; creep continues to t_c at which film rupture occurs again and the cycle repeats.

position of the crack tip after film rupture and re-passivation.

The most difficult quantity to determine is undoubtedly the film rupture time, because creep behavior, especially in response to sudden large stress transients at low temperatures, is poorly understood. In addition, the distribution of stress and strain near the crack tip in an elastic-plastic medium is not amenable to exact treatment, so that approximations must be made in determining crack tip conditions. The characteristics of stress corrosion cracks suggest that the plastic strain near crack tips is less than 0.2, for no gross deformation is visible from the microstructure, but more than 0.05, for the cracks are generally sharp and represent large stress concentrators. A reasonable assumption might be that the plastic strain near the crack tip is 15%. Transient creep measurements using material cold-worked 15% should then provide data from which the film rupture time can be estimated.

Applications of the Theory

The literature does not presently supply enough data for any system to make an adequate test of the theory. The only useful data are for the creep strain *vs.* time behavior of stainless steel in boiling magnesium chloride, and for a magnesium alloy at ambient temperature. Although the available data were not originally obtained with the objective of duplicating crack-tip conditions, they do at least give an order-of-magnitude idea about the rates involved. Values of *L*, ϵ_c , and t_L are also not available. The best that can be done is to demonstrate plausibility by assuming reasonable values for ϵ_c ; assuming that t_L is small compared to t_c ; and using the available creep data and stress corrosion crack propagation rates to calculate values for *L*.

The fracture strain, ϵ_c , for aluminum oxide has been reported by Cochrane and Block (4) to be $3 \cdot 10^{-4}$; by Bradhurst and Leach (5) to be $3 \cdot 10^{-3}$; by Brummer and Cocks (6) to be 10^{-3} to $5 \cdot 10^{-3}$; and by Grosskreutz (7) to be $1.5 \cdot 10^{-3}$ to $3 \cdot 10^{-3}$. These average to about $2 \cdot 10^{-3}$, and accordingly a value of $2 \cdot 10^{-3}$ for ϵ_c will be used, the assumption being made that the fracture strain would be about the same for most oxides, at least as to order of magnitude.

Brauns and Ternes (8) reported that the creep strain rate, $\dot{\epsilon}$, for an AISI 304 stainless steel at the temperature of boiling $MgCl_2$ obeyed the relationship

$$\dot{\epsilon} = kt^{-m} \quad [2]$$

in which $m \approx 1.1$ to 1.3 and *k* is a constant. From their data for 20 kg/mm² (28,300 psi) $k = 1.45 \cdot 10^{-3}$. From Eq. [2] by integration, taking $m = 1.2$

$$\dot{\epsilon} = \text{const} - 5kt^{-0.2} \quad [3]$$

Assuming re-passivation to be complete at 1 sec, Eq. [3] gives 5 sec for the strain to reach $2 \cdot 10^{-3}$. According to Brauns and Ternes the time to crack a 0.35 cm test specimen at 20 kg/mm² and at a potential of -80 mV is 2 hr, so that the crack propagation rate is about $5 \cdot 10^{-5}$ cm/sec. From Eq. [1] $L \approx 3 \cdot 10^{-4}$ cm. At $E = -110$ mV the failure time increased to about 200 hr, and the corresponding value of *L* would be $3 \cdot 10^{-6}$ cm. Brauns and Ternes also give values for the creep strain rate at 10 kg/mm² and 30 kg/mm², and also for the cracking time at those stresses. At 30 kg/mm² the creep strain rate is about a factor of 2 greater than at 20 kg/mm², and the failure time at -80 mV is about half that at 20 kg/mm². At 10 kg/mm² the creep rate is lower by a factor of 3 and the failure time longer by a factor of 5. All these data are consistent with a constant value of *L* at a given corrosion potential, and the values deduced for *L* seem reasonable.

Logan (9) gave data for the creep strain rate of magnesium alloy AZ31. An analysis similar to that above gives a value of *L* of 10^{-2} cm, which at first glance seems rather large. On the other hand the specimens cracked in only a few minutes, and the cracks appeared

from the $10 \times$ photographs to be rather wide. The value of *L* of 10^{-2} cm is at least conceivable. It is also possible that the value assumed for ϵ_c is too high, or that the re-passivation times are very short so that creep strain below one second is important.

Discussion

The parameters of the model.—The critical strain, ϵ_c , will depend on the nature of the film which forms and on its homogeneity, and hence in turn primarily on the alloy but also possibly on the solution composition. Film rupture probably nucleates at flaws, and hence the nature and distribution of precipitate particles in the metal will be important. If the reaction product exhibits considerable plasticity, stress corrosion cracking may be impossible.

The value of *L* will be influenced by the metal, the solution (a possible role for inhibitors), and especially the potential. If the potential is low enough (cathodic protection) the value of *L* will be too small for crack propagation. A minimum value for *L* can be computed as follows. It is necessary for corrosion to result in a change $\Delta\epsilon$ in the crack tip strain of at least ϵ_c . $\Delta\epsilon$ is given by

$$\Delta\epsilon = \epsilon_0 - \epsilon_{(\rho+L)} \quad [4]$$

where ϵ_0 is the crack tip strain and $\epsilon_{(\rho+L)}$ is the strain at the crack tip after corrosion to the depth *L*. Tetelman and McEvily (10) state that the plastic strain varies approximately as x^{-1} , so that

$$\epsilon_x = \frac{\rho\epsilon_0}{x} \quad [5]$$

in which ϵ_x is the strain at distance *x* and ρ is the radius of curvature at the crack tip. Using Eq. [5] to find $\epsilon_{(\rho+L)}$ gives

$$\Delta\epsilon = \epsilon_0 \left(1 - \frac{\rho}{\rho + L} \right) \quad [6]$$

Setting $\Delta\epsilon \geq \epsilon_c$ and solving for *L* gives

$$L \geq \frac{\epsilon_c}{\epsilon_0} (\rho + L) \quad [7]$$

and a minimum value for *L* is given by

$$L_{\min} = \frac{\rho\epsilon_c}{\epsilon_0 - \epsilon_c} \quad [8]$$

Taking $\epsilon_c = 10^{-3}$, $\epsilon_0 = 10^{-1}$, $\rho = 10^{-4}$ gives $L_{\min} = 10^{-6}$ cm, while if $\epsilon_c = 10^{-3}$, $\epsilon_0 = 10^{-2}$, $\rho = 10^{-3}$ the value of L_{\min} is about 10^{-4} cm. Note that *L* may be associated with the striations often observed on stress corrosion fracture surfaces, and that the value obtained for *L* can be confirmed from a measurement of the spacing of such striations. A casual perusal of the literature shows striation spacings of about 0.03 to 1 μm .

The re-passivation time, t_L , will be influenced by the metal, the potential, and especially by the solution composition. Aggressive species like chlorides may cause a large increase of t_L .

Following film rupture the creep rate which determines the time to cause cracking, t_c , is influenced by the stress, the metal composition, and by *L*. The effect of stress is particularly important and is discussed below. Metal composition determines the detailed transient creep response to a stress change. An example of an important metal composition effect is represented by the possibility of strain aging. Strain aging should play a very important role in stress corrosion cracking for two reasons. In a strain aging alloy a large value of $\Delta\sigma$ may be required to start plastic deformation, and the ensuing transient creep may be sharply curtailed so that stress corrosion cracking might not occur. The role of *L* in determining the creep rate arises from the fact that a large *L* results in larger increments of

stress and strain following crack advance, so that a large L should result in faster creep.

Roles of temperature and stress.—The temperature will influence the creep rate and the corrosion process. An increase in temperature would always be expected to increase the creep rate, and usually would increase the value of L . In special cases an increase in temperature may decrease L and decrease the rate of stress corrosion cracking. For instance, a higher temperature may increase the rate of repassivation more than it increases the rate of corrosion prior to repassivation.

The stress dependence of the creep rate can be expressed by the equation

$$\dot{\epsilon} = \text{const} \cdot \sigma^a \quad [9]$$

where a is a constant (the strain rate exponent) which, for low homologous temperatures, has values of about 5-10. A smaller dependence of the creep rate on applied stress may be expected in stress corrosion cracking, however, since an increase in applied stress will produce a proportionately smaller increase in the stress at the crack tip where plastic strain has occurred. A high-power dependence of crack propagation rate on stress can be expected when stress corrosion cracking occurs with crack tip stresses which are just above the yield stress, i.e., at low applied stresses, and when the strain rate exponent is high. On the other hand there may be a value of strain rate exponent above which stress corrosion cracking does not occur at all. If the strain rate exponent is very large then the film rupture induced application of a stress increment to material just ahead of the crack tip will result in a very large creep rate. In consequence nearly all the deformation following film rupture may ensue before repassivation occurs, with the result that the total remaining creep strain is insufficient to rupture the film again. In short, not only the magnitude of the strain transient but also its detailed time-dependence determine whether the crack can progress. It should especially be noted that if the total strain transient following repassivation is less than ϵ_c stress corrosion cracking by this mechanism is impossible.

The influence of cold work, strain hardening, and grain boundaries.—Cold work should have an influence on the rate of stress corrosion cracking through its influence on the creep rate and because some grains will be left in residual tension. Small amounts of cold work may increase the dislocation density and creep rate, while large amounts of cold work may produce dislocation structures in which few free dislocations are available and in which transient creep may be very small.

The strain hardening exponent will be important in determining the distribution of stress and strain near the crack tip. If the material strain hardens relatively little, there will be a gradient of strain but little gradient of stress near the crack tip. When corrosion allows the tip to advance the same stress will therefore act on a material which is plastically strained a smaller

amount and creep will occur. For materials which strain harden markedly there will be gradients of both stress and strain near the crack tip, so that after crack advance not only will the material at the new crack tip be plastically strained less than it was before crack advance but also the stress acting on that material will be greater than before the advance of the crack. Accurate predictions require more detailed knowledge of these gradients, but it may be that materials which strain harden markedly are more susceptible to stress corrosion cracking because crack advance results in faster creep than in those materials which do not strain harden much.

Grain boundaries could influence stress corrosion in several ways. First, strain is likely to be greater near the grain boundary, which may also be the site of numerous dislocation pile-ups. Second, the composition at the grain boundary may differ from the bulk composition. Third, the grain boundary may contain precipitate particles which change ϵ_c . There are therefore several reasons to expect that stress corrosion cracking should be predominantly intergranular. On the other hand, for several reasons slip at low stresses may often be easier within the bulk of the grains than near the grain boundaries. Then providing L is large enough to give an adequate crack advance per film rupture event so that the new creep rate can be large the material may be susceptible to transgranular cracking.

Acknowledgment

Conversations with L. F. Coffin, Jr., M. E. Indig, E. W. Hart, D. Lee, H. W. Schadler, H. D. Solomon, and C. S. Tedmon, Jr. contributed in an important way to the development of the ideas incorporated into this paper.

Manuscript submitted Aug. 6, 1971; revised manuscript received Nov. 1, 1971.

Any discussion of this paper will appear in a Discussion Section to be published in the December 1972 JOURNAL.

REFERENCES

1. F. A. Champion, "Symposium on Internal Stresses in Metals and Alloys," p. 468, Inst. of Metals, London (1948).
2. H. Logan, *J. Res. Nat. Bur. Std.*, **48**, 99 (1952).
3. E. W. Hart, Proc. 14th Sagamore Army Materials Research Conference, p. 210, Syracuse U. Press (1966).
4. N. J. Cochrane and R. J. Block, *This Journal*, **117**, 225 (1970).
5. D. H. Bradhurst and J. S. L. Leach, *ibid.*, **113**, 1245 (1966).
6. S. B. Brummer and F. H. Cocks, Gordon Research Conference (Corrosion), 1970.
7. J. C. Grosskreutz, *This Journal*, **116**, 1232 (1969).
8. E. Brauns and H. Ternes, *Werkstoffe Korrosion*, **19**, 1 (1968).
9. H. Logan, "The Stress Corrosion of Metals," p. 234, John Wiley & Sons, New York (1966).
10. A. S. Tetelman and A. J. McEvily, Jr., "Fracture of Structural Materials," John Wiley & Sons, New York (1967).

Silicon Nitride Coatings on Copper

Sylvain C. Audisio and Henry Leidheiser, Jr.*

Center for Surface and Coatings Research, Lehigh University, Bethlehem, Pennsylvania 18015

ABSTRACT

Silicon nitride was deposited on copper substrates at room temperature by a reactive sputtering technique. The coatings, in the thickness range 500-1500Å, were amorphous, transparent, and had glass-like smoothness. They were tightly adherent to the substrate. Infrared analysis indicated the coatings were pure silicon nitride when precautions were taken to eliminate oxygen and water from the system. The coatings exhibited dielectric constants of 8-11 with a dissipation factor less than 10^{-2} at 1000 cycles/sec. The ductility approached 1% as measured on a copper substrate. The coatings reduced the charge passing across the metal/electrolyte interface when the coated samples were anodically treated in sodium hydroxide, sulfuric acid, and phosphoric acid. The coatings provided good resistance to attack of the copper surface in ammonium hydroxide and sodium hypochlorite; provided moderate protection in concentrated acids, mediocre protection in sodium thiosulfate and sodium sulfide solutions, and very little protection in concentrated nitric acid.

Silicon nitride has been known for a long time for its chemical inertness, high temperature strength, high electrical resistivity, good thermal shock resistance, and extreme hardness. It has very attractive chemical and physical properties which have encouraged its use as a coating material for microelectronic devices. Several methods (1-14) of preparing silicon nitride have been reported in the literature. The three major methods for depositing silicon nitride on high melting substrates are: (i) chemical vapor deposition, (ii) reactive sputtering, and (iii) rf glow discharge. The chemical vapor deposition (1-7) of silicon nitride is carried out by reacting a silicon compound such as SiH_4 , SiBr_4 or SiCl_4 with nitrogen or ammonia at temperatures above 800°C . Reactive sputtering (8-11) is a technique which involves the sputtering of silicon in a nitrogen plasma. In the rf glow discharge method, the silicon nitride is deposited by reacting ammonia and SiH_4 in a radio frequency glow discharge (12-13). Several other techniques have also been used to form silicon nitride coatings, but these methods have shortcomings which do not make them suitable candidates for use with copper substrates (14).

The first method (CVD) is not attractive for use with copper alloys because the high temperature required leads to changes in the metallurgical structure and consequent changes in physical properties. Both reactive sputtering and rf glow discharge could be used to deposit silicon nitride films on copper, but reactive sputtering was chosen over radiofrequency glow discharge because of its simplicity, the ease in changing experimental variables, and because preliminary experiments indicated high quality coatings were obtained. The three important steps which govern the formation of silicon nitride coatings by reactive sputtering are: (i) sputtering of silicon atoms from the cathode, (ii) activation of the sputtered silicon atoms and interaction with nitrogen species, and (iii) condensation of the silicon-nitrogen compound on the anode and on the substrate (copper).

In order to attain a high rate of deposition of silicon nitride, it is important to maximize the number of silicon atoms permanently sputtered from the cathode. The number of atoms permanently sputtered from the surface is the difference between those sputtered and those which recondense on the silicon as a consequence of collision with gaseous species. Thus the gas pressure must be sufficiently high to maintain the discharge and yet low enough to reduce sufficiently the number of collisions in the gas phase. The voltage between the cathode and anode must be high enough to maintain the glow discharge yet low enough to avoid

sparking. The cathode-anode distance must be optimized to maximize the rate of deposition of silicon nitride and yet avoid sparking.

Experimental Procedure

The apparatus used in this study is shown schematically in Fig. 1. After achieving a vacuum of 10^{-6} Torr, ultrapure nitrogen is flowed through the system at a pressure of 0.2-0.3 Torr. The nitrogen gas was supplied through a trap cooled by liquid nitrogen. A d-c glow discharge is maintained between a water-cooled silicon cathode and a copper anode arranged at 90° to the cathode by application of a potential of 1500-2000V. The current passed between the anode and the cathode is of the order of 3 mA/cm^2 under the conditions used. The copper substrate, on which the silicon nitride coatings is desired, is placed in the gas stream, in a parallel position with the silicon cathode.

Both electrodes were protected on their periphery by quartz sleeves. If this precaution was not observed, sparking occurred at the edges with rapid deterioration of the electrodes and consequent inability to maintain a good discharge without sparking. In order to obtain high quality coatings it was essential to avoid sparking

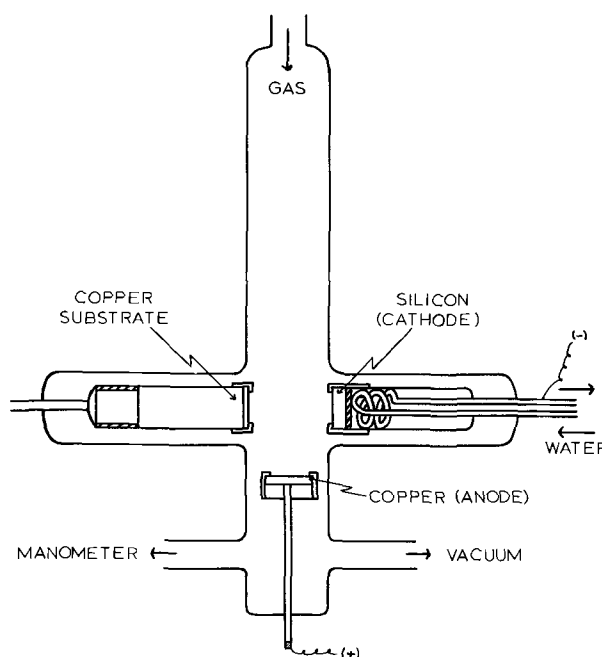


Fig. 1. Schematic diagram of the apparatus used for the deposition of silicon nitride coatings by reactive sputtering.

* Electrochemical Society Active Member.

Key words: corrosion, protection, refractories, sputtering, coating.

when the voltage was first applied by gradually increasing the potential until the glow discharge was observed. The cathode-substrate spacing finally adopted was 2.5 cm.

The copper substrate in the form of a square sheet, $1.5 \times 1.5 \times 0.1$ cm, was surfaced before each deposition either by electrolytic polishing in phosphoric acid or by metallographic polishing and washing in deionized water. No difference was observed between these two types of surfacing procedures.

All samples on which property measurements were made were prepared under the following experimental conditions: nitrogen gas pressure 0.2-0.3 Torr; cathode-substrate spacing, 2.5 cm; potential between cathode and anode 1500-2000V; current density, 3 mA/cm².

Experimental Results

Rate of coating growth.—The thickness of the coating was determined with an ellipsometer. A computer program was developed to calculate film thickness from readings obtained from the ellipsometer.

Typical growth rates were of the order of 15Å per min. Figure 2 shows the rate of film growth. The film growth rate increases with increase in anode-cathode potential, with increase in current density, and with decrease in anode-substrate spacing.

Composition of the coating.—Analysis of the coating was performed by infrared absorption. Highly polished silicon or germanium substrates, which are transparent to infrared radiation in the area of interest, were substituted for copper. During the early stages of the program, oxygen contamination was recognized by the fact that absorption bands characteristic of silicon dioxide were observed along with those of silicon nitride. The preparation method was then modified as follows to minimize oxygen and water contamination in the system: use of ultrapure nitrogen; pumping the system down to 10^{-6} Torr before admission of nitrogen; flushing the system with nitrogen before starting the experiment; and maintaining the system under vacuum when not in use.

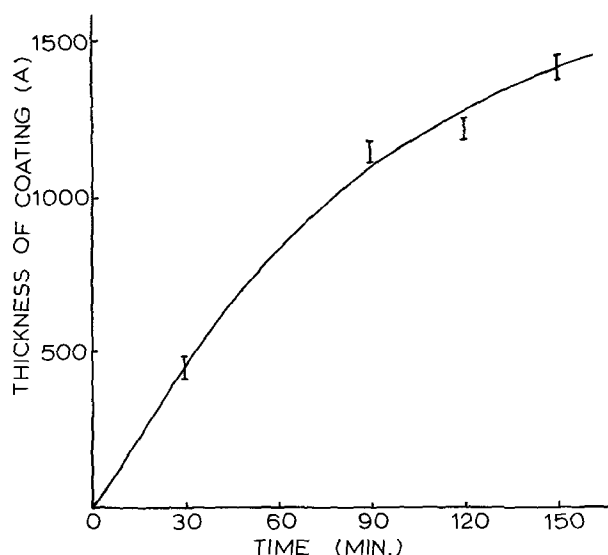


Fig. 2. Rate of growth of silicon nitride coatings under the slow-growth conditions used.

A typical infrared absorption spectrum of the silicon nitride coating is given in Fig. 3. The broad absorption band centered at 900 cm^{-1} is characteristic of silicon nitride (3, 4). The absorption band centered at 2200 cm^{-1} has been attributed to a silicon nitride triple bond and may indicate a lack of stoichiometry in the coating.

Adherence and color of the coating.—The coatings were smooth and very tightly adherent to the substrate as judged by the fact that hard rubbing with non-abrasive papers or cloths had no effect on the coating. The sample could be severely bent without macroscopic separation of the coating from the substrate. The films were smooth and mirrored the smoothness of the substrate. They imparted slight color presumably as a

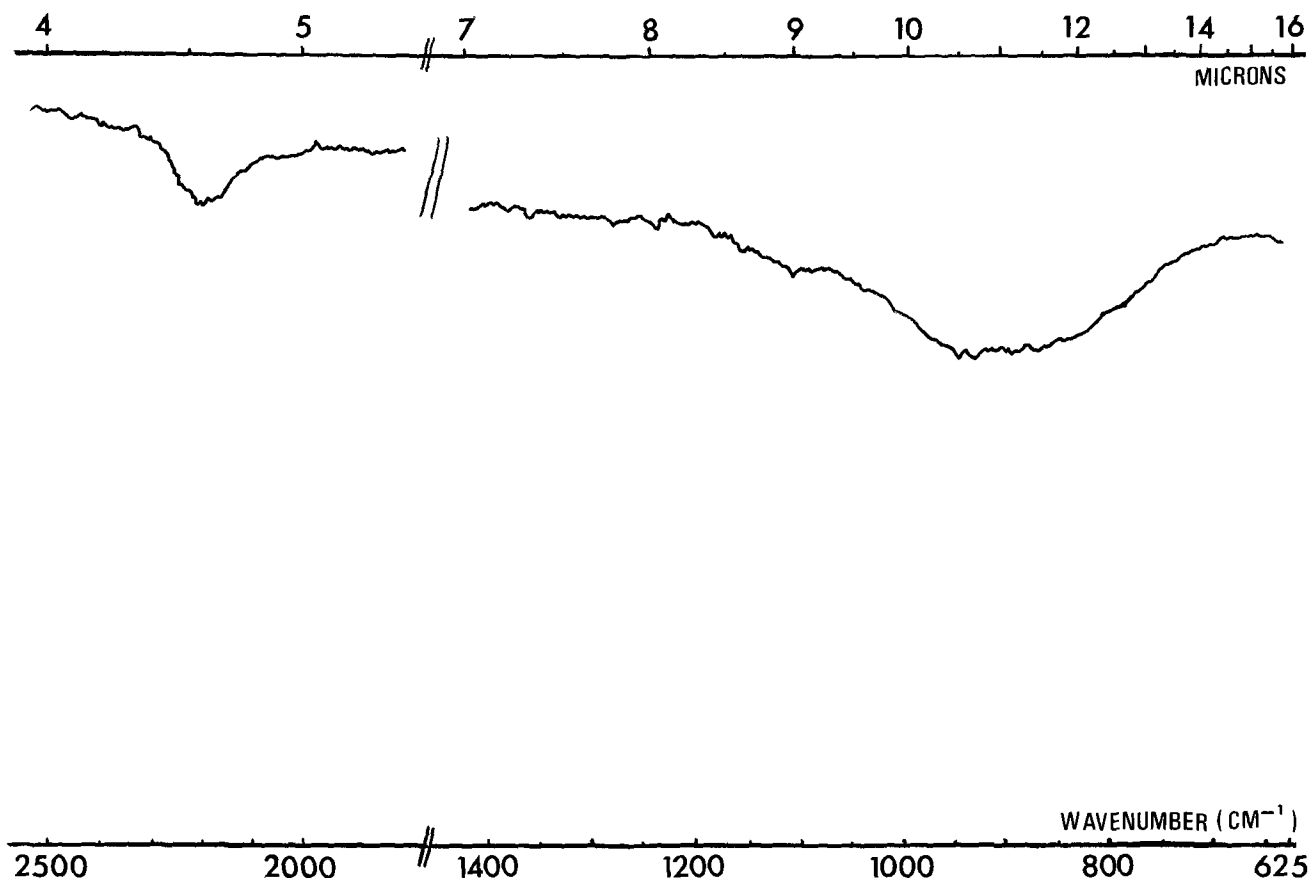


Fig. 3. Infrared absorption spectrum of silicon nitride coating formed on a germanium substrate

consequence of interference between light reflected from the silicon nitride-air interface and the copper-silicon nitride interface. Films, 200-400Å in thickness, were reddish to brown in color, and films, 1000-1500Å in thickness, were yellow to gold in color. The coating appeared transparent and structureless under the microscope and the grain boundaries of the substrate were readily visible.

Dielectric constant.—The dielectric constant of films ranging in thickness from 500-1500Å was determined at 1000 cycles/sec. There was no unique value of the dielectric constant for the amorphous silicon nitride films. It varied with the conditions under which the films were formed, and ranged from 8 to 11. It is likely that the dielectric constant is intimately associated with the structure and stoichiometry of the coating. The possible cause for the high dielectric constant of the coating is the increase in molecular and dipole polarizabilities of the amorphous structure or the presence of shallow impurity levels in the films causing higher electronic polarization. The dissipation factor at 1000 cycles/sec was less than 10^{-2} .

Behavior of coatings upon polarization.—In order to obtain information about charge motion across the copper-environment interface, potentiostatic polarization curves were determined in several electrolytes. Typical polarization curves are given in Fig. 4-6. All potentials are given with respect to a mercurous sulfate reference electrode.

Anodic polarization of the silicon nitride-coated copper in sulfuric acid (1M), phosphoric acid (1M), and sodium hydroxide electrolytes (1M) yielded polarization curves in which the current passed at equivalent anodic potentials was appreciably less than that of uncoated copper.

Prepolarization of samples in phosphoric acid caused a significant reduction in current at equivalent anodic potentials upon anodic treatment in sulfuric acid solution. Sealing of pores in the coating is the likely explanation. The localized nature of the attack of the copper upon anodic treatment as observed by the naked eye and under the microscope suggests that defects in the coating are largely responsible for charge movement through the coating.

Corrosion resistance.—The coated samples were exposed at room temperatures to a number of aqueous corrosive environments. In each case a 0.5 cm² section

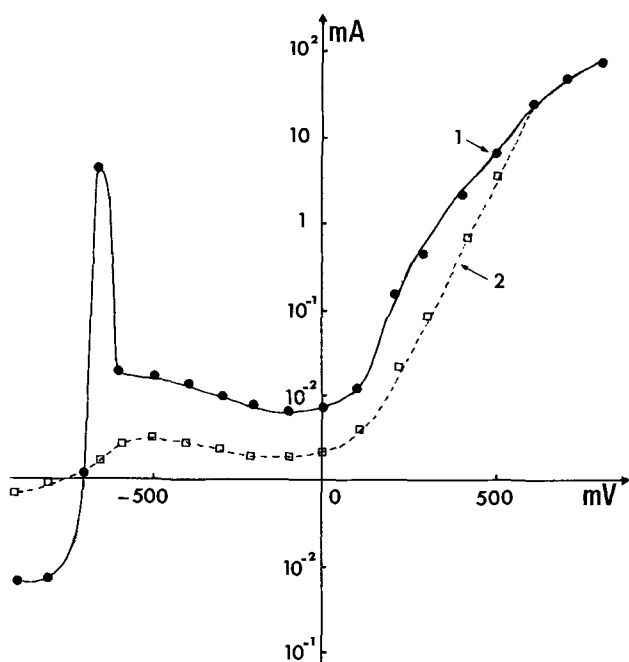


Fig. 4. Polarization curves of copper (curve 1) and silicon nitride-coated copper (curve 2) in 1N sodium hydroxide.

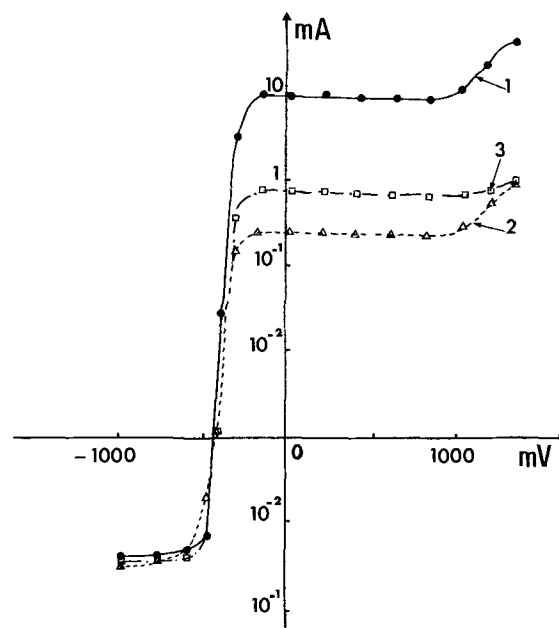


Fig. 5. Polarization curves of pure copper (curve 1) and silicon nitride-coated copper (curve 2) in 2N phosphoric acid. Curve 3 is a second polarization curve on the same silicon nitride-coated sample. Note that current plateau is at the same position as the highest current used in determining curve 2.

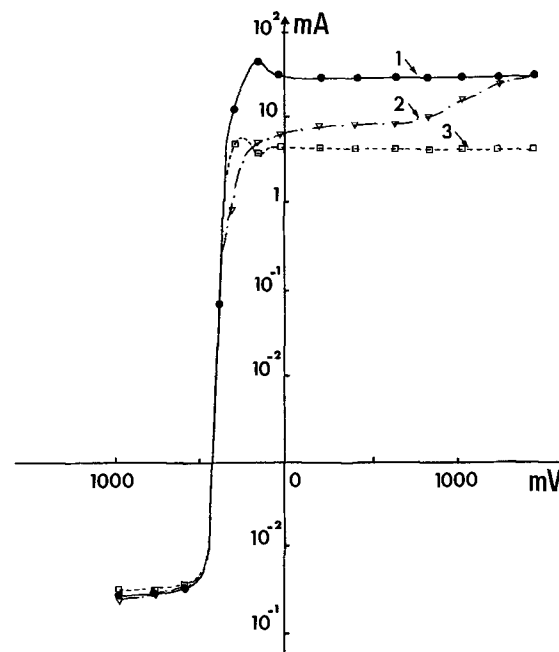


Fig. 6. Polarization curves of pure copper (curve 1) and silicon nitride coated copper in 2N sulfuric acid (curve 2). Curve 3 is a polarization curve after the silicon nitride-coated sample was polarized anodically in 2N phosphoric acid. The lower current observed with the "phosphated" copper suggests that pores in the coating were sealed.

in the center of the coated sample was isolated by masking off the remainder of the surface with a proprietary resistant lacquer. Control samples of electrolytically polished copper were attacked immediately or within a short time in the same environments. The results of these experiments are summarized in Table I.

The coated samples afforded a good resistance to corrosion in sodium hypochlorite and ammonium hydroxide solutions; moderate resistance in phosphoric and sulfuric acids; short-term protection in sodium



Fig. 7. Photomicrograph of silicon nitride-coated copper strained 1% in tension. Cracks are readily identified by interference fringes adjoining crack.

thiosulfate and sodium sulfide solutions; and little or no protection in nitric acid.

Complete protection was afforded to coated surfaces adjoining uncoated surfaces during electrolytic polishing in phosphoric acid solutions.

Mechanical properties of the coating.—Qualitative tests involving severe bending of the silicon nitride-coated samples indicated that the coating had ductility and that sharp bends did not cause the deposit to flake from the surface. Quantitative experiments were then performed by straining coated copper samples on an Instron Universal Testing Machine at a cross head speed of 0.02 in./min. Conventional tensile test specimens were coated with silicon nitride.

In order to determine the mechanical behavior of the coating, axial tensile loads were applied in successive elongation steps of 0.3%, 0.5%, 0.7%, and 1%. After each degree of elongation, the sample was examined microscopically for indication of fracture in the coating. No cracks were detected on samples strained 0.3%, 0.5%, and 0.7%. At 1% elongation, however, short cracks largely at right angles to the loading axis were detected as shown in Fig. 7. The cracks were readily identifiable by the interference fringes which occurred in areas adjoining the cracks. Presumably the coating broke from the substrate in these highly localized sites and the silicon nitride film formed an angle with the surface.

Summary and Conclusions

Amorphous films of silicon nitride have been deposited on copper substrates at room temperature by reactive sputtering. Because of the greater reactivity of silicon towards oxygen, the partial pressure of oxygen in nitrogen must be carefully controlled. No problems have been encountered with adherence of the

Table I. Behavior of 1000 Å-thick silicon nitride coatings on electrolytically polished copper substrates upon exposure to corrosive environments

Phosphoric acid, conc	First attack on the coating noted after 24 hr
Sulfuric acid, conc	First attack on the coating noted after 24 hr
Nitric acid, conc	First deterioration of the coating noted in 5 min
Nitric acid, 10%	Samples resisted attack for 3 hr
Ammonium hydroxide, conc	No observable deterioration of the coating within 24 hr
Sodium hypochlorite, conc	No observable deterioration of the coating within 24 hr
Sodium thiosulfate, 1M	First attack visible after 2 hr
Sodium sulfide, 0.1M	First attack visible after 2 hr with buckling of coating and darkening of the copper

coating to the copper or with macroscopic defects in the coating. The coatings were crack free and gross-defect free.

It does appear, however, that 1000-1500Å thick coatings were porous to electrolytes as judged from the fact that coatings passed appreciable current when subjected to an applied potential in media such as sulfuric acid, phosphoric acid, and sodium hydroxide. Nevertheless, the silicon nitride coating did reduce greatly the rate of anodic copper dissolution and did afford short-term protection in aggressive environments.

Improvements remain to be made in the direction of a decrease in the porosity through modification in the rate or method of formation, or through a post-treatment such as heat treatment.

The coatings tolerated strains less than 1% without apparent fracture.

Acknowledgment

The authors acknowledge with appreciation support of this work by the International Copper Research Association. The advice of Frederick M. Fowkes is gratefully acknowledged.

Manuscript received Oct. 14, 1971. This was Paper 63 presented at the Cleveland, Ohio, Meeting of the Society, Oct. 3-7, 1971.

Any discussion of this paper will appear in a Discussion Section to be published in the December 1972 JOURNAL.

REFERENCES

1. K. E. Bean, P. S. Gleim, R. L. Yeakley, and W. R. Runyan, *This Journal*, **114**, 733 (1967).
2. V. Y. Doo, D. R. Nichols, and G. A. Silvey, *ibid.*, **113**, 1279 (1966).
3. S. M. Hu, *ibid.*, **113**, 693 (1966).
4. T. L. Chu, C. H. Lee, and G. A. Gruber, *ibid.*, **114**, 717 (1967).
5. M. J. Grieco, F. L. Worthing, and B. Schwartz, *ibid.*, **115**, 525 (1968).
6. T. Sugano, K. Hirai, K. Kuroiwa, and K. Hoh, *Jap. J. Appl. Phys.*, **7**, 122 (1968).
7. J. A. Aboaf, *This Journal*, **116**, 1736 (1969).
8. C. Constantin, *L'onde Electrique*, **48**, 327 (1968).
9. R. C. G. Swann, R. R. Mehta, and T. P. Cauge, *This Journal*, **114**, 713 (1967).
10. Y. Kuwano, *Jap. J. Appl. Phys.*, **7**, 88 (1968).
11. Y. Kuwano, *ibid.*, **8**, 876 (1969).
12. S. M. Hu and L. V. Gregor, *This Journal*, **114**, 826 (1967).
13. H. F. Sterling and R. C. G. Swann, *Solid-State Electron.*, **8**, 653 (1965).
14. M. G. Collet, *This Journal*, **116**, 110 (1969).

Characterization of Platinum Electrodes in H₂-Saturated Sulfuric Acid Solution

I. Transient Conditions

Murray Rosen,* Sigmund Schuldiner,* and David R. Flinn*¹

Electrochemistry Branch, Naval Research Laboratory, Washington, D. C. 20390

ABSTRACT

A single cycle of anodic-cathodic constant current pulses (1-3 A/cm²) were applied to a normal hydrogen Pt electrode. Following anodic charging to between 0.4 and 1.75V, the total faradaic and nonfaradaic cathodic charge to the H₂ evolution plateau was equal to the net anodic charge. The distribution of total faradaic charge into hydrogen and oxygen processes in each half-cycle, as based on a geometric separation of charging regions, showed that anodic charging gave a much better resolution of each of these processes. The irreversible reduction of Pt-O occurred in two separate regions of unequal charge content. The two regions represent a complex reduction of Pt-O where the O is held with different bonding energies rather than a sequence of two one electron steps. The amount of H deposited up to the negative limiting potential plateau where H₂ evolution occurred is numerically equal to the amount of H that is associated with Pt at the normal H⁺/H₂ equilibrium.

There is a great deal of confusion and conflict in the literature concerning the transient amounts of anodically oxidized H and generated Pt-O and the subsequent reduction of the Pt-O and regeneration of H. Table I in the Discussion Section will review some of this literature. Differences appear to be the result of solution purity, voltage ramp and galvanostatic pulse rates, potential or current control in between transients, and pretreatment. Pursuit of the last point has resulted in data in which the state of the Pt system between cyclic pretreatment (n cycles) and the electrochemical measurement perturbation (n + 1 cycles) hardly differed, but the question as to the effect of n cycles on the electrode character was unanswered.

In the present work, a high-purity, normal hydrogen electrode (NHE) with no immediate pretreatment was subjected to a single cycle of constant high current density pulses in the order anodic, cathodic. When the potential at which the anodic pulse was switched to a cathodic pulse, E_{sw} , ranged from 0.4 to 1.75V, the total faradaic and nonfaradaic anodic charge was equal to the cathodic charge. However, the distribution of the total faradaic charge into hydrogen and oxygen processes in each half-cycle, as based on the geometric regions of the charging curves, had to be resolved.

Experimental

The high-purity, gas-tight electrochemical system and experimental conditions were the same as previously used (1-3). Two working Pt bead electrodes were used. Their true areas (2) were 0.37 and 0.42 cm². The temperature was 25° ± 1°C, and all measurements were made in 1M H₂SO₄ stirred with H₂ and measured vs. the NHE.

The circuit used is shown in Fig. 1. The Pt working electrode was polarized by an anodic, constant current pulse (1-3 A/cm²) to various potentials between equilibrium and 1.8V. This anodic current pulse was triggered (START) by depressing the RESET button on the Hewlett-Packard 5214L Electronic Preset Counter. At the end of the preset count, which corresponded to selected potentials along the anodic charging curve, the Preset Counter (STOP) triggered the cathode pulse generator on. The latter in turn produced a TURN-OFF pulse which shut-off the anodic pulse generator. The pulse generators were EH Models 132A that were adapted here to accept turn-off pulses. Tek-

tronix 454 and 547 oscilloscopes, the latter using a Type W plug-in, were used to display the anodic and cathodic charging curves, respectively. In order to locate the start of cathodic polarization in a photograph of the oscilloscope display, a second sequence of current pulses was applied but this time only the cathodic polarization was recorded at a 1 μsec/cm sweep rate. By extrapolating to zero time, the initial point of the cathodic charging curve and any potential at any time on the full charging curve could be determined.

In some cases, a third pulse was applied, that is, an anodic pulse was applied at some point during the cathodic polarization. For this phase of the work, the first anodic polarization was recorded on the Tektronix 454 oscilloscope. The cathodic and second anodic polarizations were recorded on a Tektronix 565 Dual-Beam (Type 3A6 plug-ins). The second anodic current pulse was provided by a third EH Pulse Generator triggered by the 565 oscilloscope's DEL'D TRIG. OUT, which was positioned along the horizontal time axis of the cathodic charging curve to correspond to the desired switching point. As before, when the second anodic pulse generator was triggered, it simultaneously provided a turn-off trigger pulse to the cathodic pulse generator. In summary, by using this arrangement, an anodic followed by cathodic followed by anodic sequence of high, constant current pulses, with switching times of about 500 nsec, were applied. By merely depressing the RESET button of the Preset Counter a sequence of events occurred that resulted in photographed oscilloscope traces of the resultant polarizations.

Except where otherwise indicated, anodic and cathodic measurements of q in μC/cm² were corrected for

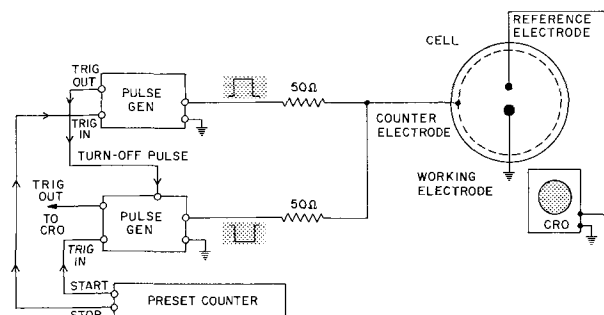


Fig. 1. Circuit for applying a constant, anodic current pulse that is terminated by a constant, cathodic current pulse at switching times less than 1 μsec. See text for explanation.

* Electrochemical Society Active Member.
¹ National Academy of Sciences-National Research Council Postdoctoral Research Associate at NRL.
Key words: platinum, hydrogen, oxygen, adsorption, transient polarization, fast switching.

the double layer contribution following previously established procedures (1). The vertical and horizontal deflections of the scopes were periodically checked. Numerous checks of the current density and of the true areas of the bead were also made. The current from the pulse generators was determined either by measurement with a Tektronix P6042 Current Probe, positioned in the current path where the Pt working electrode was grounded or by differential measurement of the voltage drop across the individual series resistors using Type W or Type 1A5 plug-ins. Throughout the course of this work it was found that the cyclic pulsing had little effect on the true area. Variations in area measurements were random and dependent on electronic effects, that is, calibrations, etc., and how the oscilloscope traces were read. When care was taken, the true area as determined from the three pulse generators would agree with an average deviation of about $\pm 0.007 \text{ cm}^2$ ($\pm 2\%$). An average deviation of $\pm 0.010 \text{ cm}^2$ ($\pm 2.5\%$) was observed for the deviation of six average areas of which each one was determined as the average one measured from three pulse generators.

Results

Anodic-cathodic polarization.—The anodic polarization response below 1.76V for Pt bead electrodes to a high current density galvanostatic pulse results in potential-time regions representing two faradaic processes. From 0.0 to about 0.88V, hydrogen atoms which were associated with the electrode at equilibrium (NHE) are oxidized ($276 \mu\text{C}/\text{cm}^2$). Following the oxidation, a monolayer of Pt-O ($420 \mu\text{C}/\text{cm}^2$) is formed from the oxidation of water. Consequently, the reactions that occur and the resultant potential-time responses of the cathodic pulse depend on the selection of E_{sw} .

Potential vs. time curves for cathodic polarization following current reversal at various E_{sw} are shown in Fig. 2. From the several breaks that can be observed in the charging curves only two major potential-time regions were used for quantitative study. The first one, given the symbol "□," begins at the anodic to cathodic switching potential, E_{sw} , and includes all the charge found in the rising portion of the curve. The second region, given the symbol "○," begins at the end of region □ where there is a large slope change and extends all the way to the beginning of the long plateau. Since the faradaic reactions of the first anodic pulse are H oxidation followed by Pt-O formation, it is logical to expect only two faradaic reactions during the cathodic pulse, namely, Pt-O reduction followed by H formation. Consequently, the data for regions □ and ○ should primarily represent these two processes. The ratio of the total charge (faradaic and nonfaradaic),

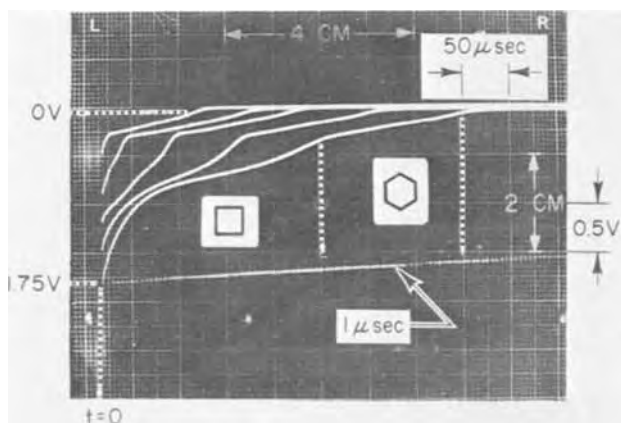


Fig. 2. Potential vs. time response for cathodic pulses terminating anodic pulses at E_{sw} (top to bottom) 0.38, 0.78, 1.1, 1.4, and 1.75V. (□), First reduction region; (○), second reduction region. Arrow ($1 \mu\text{sec}$) refers to the cathodic charging curve polarization at the rate of $1 \mu\text{sec}/\text{div}$.

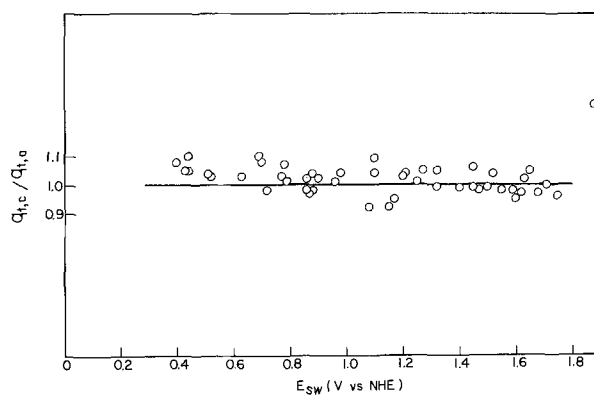


Fig. 3. The ratio as a function of E_{sw} for the total coulombs of faradaic and nonfaradaic processes of the cathodic branch divided by the total coulombs of faradaic and nonfaradaic processes of the anodic branch.

$q_{t,c}/q_{t,a}$, is plotted vs. E_{sw} in Fig. 3, where $q_{t,c}$ is the total cathodic charge and $q_{t,a}$ is the total anodic charge.

Hydrogen oxidation/formation.—The amount of hydrogen atoms, q_H , oxidized up to E_{sw} is shown in Fig. 4 as open circles. Beyond 0.9V the amount of q_H determined below this potential should be constant since all the H is oxidized below this potential. The mean for this q_H is $276 \pm 14 \mu\text{C}/\text{cm}^2$ where the second term is the standard deviation. The charge consumed in the ○ region primarily represents the formation and accumulating of atomic H. The amount of q found in region ○ vs. E_{sw} is plotted in Fig. 4 as ⊙. The mean for $q_{\odot} > 0.88\text{V}$ is $258 \pm 21 \mu\text{C}/\text{cm}^2$. The potential for the start of region ○ vs. E_{sw} is shown in the upper portion of Fig. 4. The potential for the end of the region, or the beginning of the long plateau, is about 50 to 100 mV negative.

Oxygen formation/reduction.—The amount of Pt-O formed, as determined from an anodic pulse, up to E_{sw} is shown in Fig. 5 as open circles. Symbol ■ is for the data when $0.4 \leq E_{sw} \leq 0.88\text{V}$ where no Pt-O was formed and □ is for $E_{sw} > 0.88\text{V}$ where Pt-O was formed. Although there is some scatter, the data points, □ and ○, could be separated over the potential range 0.9 to 1.7V by individual computer-fitted straight lines. The dashed line ($q_{\square} = 416 E_{sw} - 345$) is for the rapid transient formation of O, and the solid line ($q_{\square} = 316 E_{sw} - 262$) is for the total faradaic charge in region □ (both corrected for double-layer charging).

Discussion

Cathodic/anodic ratio of total charge.—Table I compiles data comparing the q_c/q_a ratios for oxygen spe-

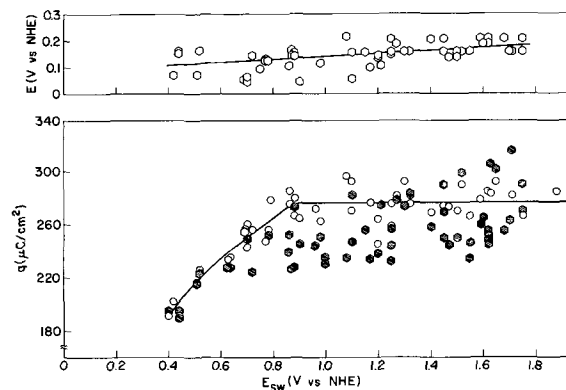


Fig. 4. Upper curve, relation between potential for the start of region ○ vs. E_{sw} . Lower curve, relation between amount of H oxidized by an anodic pulse up to E_{sw} (o) and the amount of charge consumed in region ○ (⊙) vs. E_{sw} .

Table I. Comparison with literature results

Ref.	Sulfuric acid+ electrolyte concentration	Intensity of applied perturbation	Voltage limits (V)	Condition prior to perturbation	q_c/q_a for oxygen species
(4)	1M, N ₂ -Sat.	10 ⁻⁴ A/cm ²	-0.16, 1.54	a, b, c*	<0.15
(5)	0.5M, N ₂ -Sat. degassed electrode	3.6 × 10 ⁻³ A/cm ²	0.2, 1.2	open-circuit, c	0.2
(6)	0.5M, N ₂ -Sat. degassed electrode	0.2 V/sec 1 V/sec	0.2, 1.4	open-circuit, c d*	>0.5 ≈1
(7)	0.5M, N ₂ -Sat.	0.2-40 V/sec	50 mV, 1.5	d*	<1
(8)	"Dilute", N ₂ -Sat.	3.2 × 10 ⁻⁵ A/cm ²	>0, 1.2	a, b, c*	0.8
(9)	4M, N ₂ -Sat.	1 A/cm ²	0, 1.6	a, b, c*	>1
(10)	0.8M HClO ₄ CO ₂ -Sat.	1 V/sec	0.6, 1.4	a, b, d	≈1 (within ±1%)
(11)	0.5M, He-Sat.	6.8 × 10 ⁻⁵ A/cm ²	0.5, 1.4	3 hr steady-state, c	0.5
		30 mV/sec	0.2, 1.5	10-20 cycles	~1
				30 min open-circuit, c	0.5
				120th cycle	0.75
This work	1M, H ₂ -Sat.	>1 A/cm ²	0.0, 1.75	NHE, c	1

* Except where otherwise noted.

a. Some form of pre-anodization and/or cathodization is mentioned.

b. Whether equilibrium or steady-state is prior condition before measurement cycle is applied is not specifically stated.

c. First cycle.

c.* First cycle is assumed.

d. Some nth cycle is assumed.

cies. Our ratio $q_{t,c}/q_{t,a}$ being one over the E_{sw} range 0.4 to 1.75V shows that when a single cycle of high intensity galvanostatic pulses is applied to a NHE, all the oxygen formed is reduced and that all the hydrogen oxidized is reformed at the negative plateau (Fig. 2), no matter how the faradaic charge is divided between hydrogen and oxygen.

Pearson and Butler in 1938 (8) applied high current density pulses to electrodes that had been previously cathodized in N₂-saturated solutions. From the shape of their anodic charging curves and the -0.6V limiting potential of the cathodic charging curves, it is apparent that their electrodes were not free of impurities. They

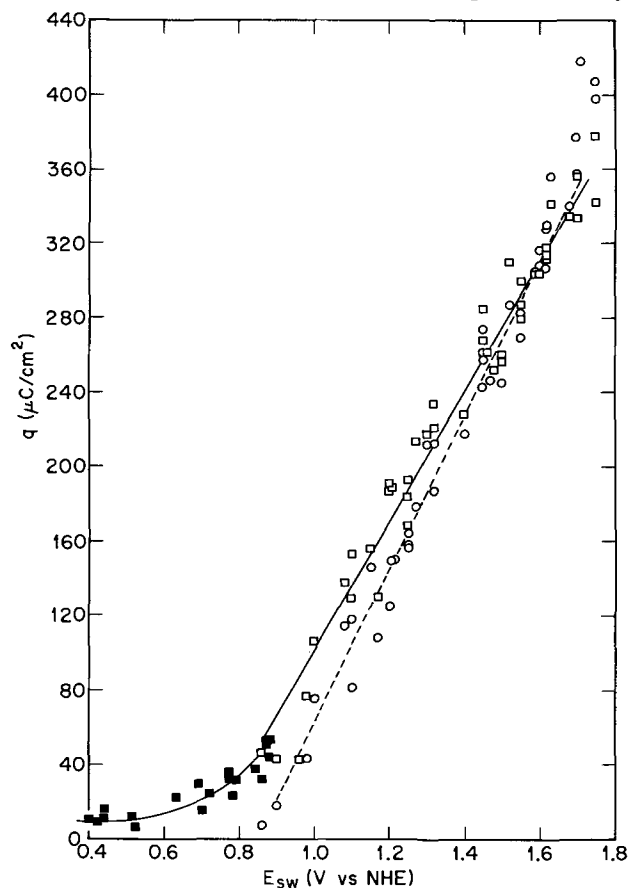


Fig. 5. Relation between faradaic charge in region \square vs. E_{sw} $\leq 0.88V$ (\blacksquare) and for $E_{sw} \geq 0.88V$ (\square). The straight lines between 0.9 and 1.7V are computed least square fits; (solid) $q_{\square} = 316 E_{sw} - 262$, (dashed) $q_{\circ} = 416 E_{sw} - 345$. Amount of O formed by anodic charging to E_{sw} (\circ).

did not determine the amount of H oxidized in the 0.4-0.8V region.

Will and Knorr (9) found equal amounts of charge for the anodic and cathodic hydrogen regions. However, their determination gave 640 $\mu C/cm^2$ for each q_H and q_O . They did not state if the determination was for the first or nth cycle.

The charge ratios shown in Table I for just the oxygen reactions demonstrate the confusion encountered in the literature concerning this measurement. The major problems are solution purity and the fact that the measurement cycle was not the first cycle applied at an initial, well-defined condition. Indiscriminate "activation" leads to undefined conditions. A clean system does not require immediate pre-anodization. Paper II (12) of this series shows in detail how stable O and anion species, which may be generated during pretreatment, do affect the character of Pt.

The cathodic potential plateau at the end of region \circ (Fig. 2) being negative to zero V indicates that the H atoms formed during the rapid transients are not associated with Pt as would an equivalent amount of H at the NHE (1). Counting the charge back to this plateau rather than to 0.0V is logical because the plateau in effect represents a limiting condition for the transient perturbation. Making the comparison of total charge by including nonfaradaic coulombs precludes any possible error due to area determination or double-layer correction. Even though the cathodic plateau may go to -0.1V, the additional double layer charge from 0 to -0.1V would be less than 2 $\mu C/cm^2$, which is well below our experimental error.

Faradaic charge distribution.—Although the faradaic charge can be adequately separated into hydrogen and oxygen regions, there is a significant amount of overlap. The q_H anodic average (Fig. 4) of 276 $\mu C/cm^2$ is greater than the q_{\circ} cathodic average of 258 $\mu C/cm^2$.

Figure 5 shows that there is excess faradaic charge (q_{\square}) for $E_{sw} \leq 0.88V$ and that more charge is consumed in region \square than is necessary to reduce Pt-O formed in the preceding anodic pulse. Because the anodic-cathodic charging curves are unsymmetrical, a geometric method for separating reaction regions may show significant differences in the amount of charge. To determine in a charging curve where one process ends and the next one begins, an electrochemical end point is assumed by drawing straight lines through the charging curves near the transition region. If the geometric and electrochemical end points do not coincide, then overlapping occurs.

Previous measurements (2) of anodic charging curves have shown that below E_{sw} of 0.88V (the geometric separation point between the hydrogen and oxygen regions) no oxygen intermediates are formed.

Table II. Ratio of hydrogen formed by cathodic pulse to hydrogen oxidized by second anodic pulse

Potential E_{sw}	Cathodic $\mu\text{C}/\text{cm}^2$, region \square	Cathodic $\mu\text{C}/\text{cm}^2$, total
	Anodic $\mu\text{C}/\text{cm}^2$ q_{\square}/q_H	Anodic $\mu\text{C}/\text{cm}^2$ $(q_{\square} + q_{\blacksquare, \blacktriangle})/q_H$
0.44	0.90	0.97
0.84	0.87	1.04
1.20	0.83	0.92
1.25	0.91	0.99
	0.91	0.96
1.45	0.91	0.93
	0.95	1.05
1.48	0.96	0.98
1.50	0.93	0.98
1.55	0.96	0.96
	0.89	0.94
1.60	0.95	0.95
1.70	0.99	0.99
1.75	1.03	1.03
Average	0.93 ± 0.04	0.98 ± 0.03
Std. Dev.	0.05	0.04

This means that an accurate separation of the hydrogen and oxygen regions is possible in the anodic charging curve. Hence, the excess charge shown in the cathodic charging curve results of Fig. 5 may be due to significant H⁺ reduction in the \square region. Since the possibility of H⁺ reduction at potentials around 0.4V is open to question other reasons for the excess charge may be possible. However, a reasonable alternate explanation has not been found and we assume that this excess charge is due to H⁺ reduction.

The experiments in which 1½ cycles were applied, i.e., anodic, cathodic, and anodic, showed that in order to account for all the faradaic charge (see Table II, column 2) used for H oxidation in the second anodic pulse, q_{\blacksquare} or q_{\blacktriangle} ($q_{\blacksquare, \blacktriangle} = q_{\square} - q_{\circ}$) had to be added to q_{\circ} , i.e., $q_{\circ} + q_{\blacksquare, \blacktriangle}$. This sum is plotted in Fig. 6 as filled-in circles. The continuous line is the same as in Fig. 4.

Table II compares both the ratio of the H formed in the \circ region, q_{\circ} , and total H formed ($q_{\circ} + q_{\blacksquare, \blacktriangle}$) to the q_H measured by the second anodic pulse. Included are cases in which the cathodic pulse was terminated before the end of region \circ to avoid the plateau. Since for the $E_{sw} = 0.44\text{V}$, not all of the H is oxidized by the first anodic pulse, the H not oxidized was subtracted from the q_H of the second anodic pulse. This correction was the difference between 276 $\mu\text{C}/\text{cm}^2$ and the amount oxidized by the first pulse, e.g.,

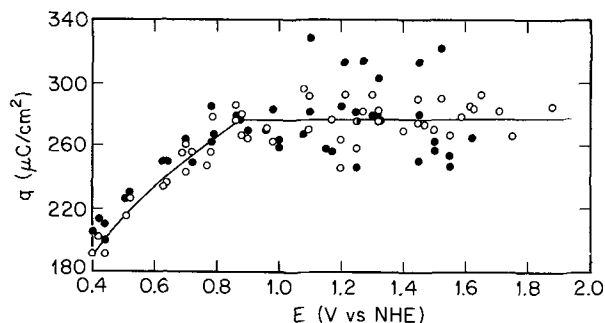


Fig. 6. Relation between amount of H oxidized by an anodic pulse up to E_{sw} (\circ) and the sum (\bullet) vs. E_{sw} for the amount of faradaic charge in region \circ plus the faradaic charge in region \square less any charge for oxygen reduction (q_{\circ}).

at $E_{sw} = 0.44\text{V}$

$$\frac{(q_{\circ} + q_{\blacksquare, \blacktriangle})}{[q_H - (276 - q_{H'})]} = \frac{(195 + 15)}{[300 - (276 - 191)]} = 0.97$$

where, $q_{H'}$ and q_H is the number of $\mu\text{C}/\text{cm}^2$ of H oxidized in the first and second anodic pulses, respectively.

Further evidence that part of the charge in region \square was the result of a faradaic process when Pt-O was not formed was shown by the capacitance, as measured by the slope of the charging curve prior to the beginning of region \circ . Slope determinations for the portion of the cathodic charging curves just before the beginning of region \circ for E_{sw} equal to 0.44 and 0.77V gave capacitances of 57 and 70 $\mu\text{F}/\text{cm}^2$, respectively. The double layer capacitance at the beginning of region \circ in these solutions is about 30 $\mu\text{F}/\text{cm}^2$ (13, 14).

This overlapping of the two reduction processes complicates a determination of Pt-O reduction in the second part of region \square . Nevertheless, qualitative inspection of the charging curves (Fig. 2) shows that in the higher potential portion of region \square more charge is consumed than in the lower potential portion. For example, at E_{sw} of 1.75V, this ratio is nearly 2:1. Consequently, it is concluded that the two breaks do not simply mean consecutive one electron steps, but actually involve a complex reduction of Pt-O where the O is held with different bonding energies so that the potential vs. time relation does not follow the simple linear relation found during formation.

Previous work (2) has shown that the anodic oxygen region was not dependent on the initial presence of H on the electrode. It is therefore evident from the present work that anodic charging curves give a better separation of the H and O regions than are possible by the cathodic charging curves.

Manuscript submitted Dec. 11, 1970; revised manuscript received ca. Nov. 9, 1971. This was Paper 180 presented at the Washington, D. C., Meeting of the Society, May 9-13, 1971.

Any discussion of this paper will appear in a Discussion Section to be published in the December 1972 JOURNAL.

REFERENCES

1. M. Rosen and S. Schuldiner, *This Journal*, **117**, 35 (1970).
2. S. Schuldiner and R. M. Roe, *ibid.*, **110**, 332 (1963).
3. S. Schuldiner, T. B. Warner, and B. J. Piersma, *ibid.*, **114**, 343 (1967).
4. Fred C. Anson and James J. Lingane, *J. Am. Chem. Soc.*, **79**, 4901 (1957).
5. V. I. Luk'yanycheva and V. S. Bagotskii, *Dokl. Akad. Nauk SSSR*, **155**, 160 (1964).
6. V. I. Luk'yanycheva, V. I. Tikhomirova, and V. S. Bagotskii, *Elektrokhimiya*, **1**, 262 (1965).
7. K. Ohashi, K. Sasaki, and S. Nagaura, *Bull. Chem. Soc. Japan*, **39**, 2066 (1966).
8. J. D. Pearson and J. A. V. Butler, *Trans. Faraday Soc.*, **34**, 1163 (1938).
9. F. G. Will and C. A. Knorr, *Z. Elektrochem.*, **64**, 258 (1960).
10. S. W. Feldberg, C. G. Enke, and C. E. Bricker, *This Journal*, **110**, 826 (1963).
11. M. W. Breiter, *Electrochim. Acta*, **11**, 905 (1966).
12. S. Schuldiner, M. Rosen, and D. R. Flinn, *Electrochim. Acta*, Submitted for publication.
13. M. Rosen, D. R. Flinn, and S. Schuldiner, *This Journal*, **116**, 1112 (1969).
14. D. R. Flinn, M. Rosen, and S. Schuldiner, *Coll. Czech. Chem. Commun.*, **36**, 454 (1971).

On the Potentiostatic Oxidation of Iron in Neutral Sulfate Solution

I. "Oxide-Free" Specimens

D. Barry Gibbs¹ and Morris Cohen*

Division of Chemistry, National Research Council of Canada, Ottawa, Ontario, Canada

ABSTRACT

The anodic oxidation of electropolished iron in deaerated sodium sulfate solution (pH 8.4) has been studied by a potential-step method over the range -500 to +1550 mV vs. SHE. The iron surfaces were prepared by cathodic reduction in a borate buffer solution immediately prior to oxidation. The anodic behavior of an "oxide-free" surface so obtained was found to be markedly different from that of a surface which had not been completely reduced.

Neutral sulfate solutions are relatively corrosive media for iron (1-3). However, studies of anodic passivation of iron in this system have been reported, notably by Freiman and Kolotyrlin (4-7), much of whose work has been concerned with two active-passive transitions, and the dependence of the transition potentials on pH and sulfate ion concentration.

Most work to date has been carried out using iron specimens initially carrying at least an air-formed film. In contrast, the data presented below describe the anodic behavior of iron which has been cathodically reduced in a deaerated borate buffer solution immediately before oxidation in the sulfate solution, with no intervening exposure to air. The results, which are rather different from those of Freiman and Kolotyrlin, for example, indicate that even a thin air-formed film exerts a major influence on the passivation characteristics of iron.

The present paper is intended mainly to describe the electrochemical behavior of the initially "oxide-free" iron in deaerated Na₂SO₄ solution. The effects of the air-formed film will be explored more fully in a subsequent report.

Experimental

Apparatus.—The cell was similar to that described previously (8) except that the counterelectrode consisted of two pieces of fine mesh platinum gauze surrounding the working electrode. The cell was fitted with Teflon stopcocks for solution transfer. A saturated calomel reference electrode was used; however all potentials are quoted with respect to the standard hydrogen electrode. All runs were carried out at a temperature of 25° ± 0.2°C.

A Wenking Model 61 RS fast-rise potentiostat was used for anodic oxidation, the variation of current with time being followed by a Texas Instruments Servo/Riter II chart recorder (1 or 10 mV full scale). For galvanostatic reduction, a constant-current source constructed from operational amplifiers was employed, with an E-H Research Laboratories electrometer coupled to a Leeds and Northrup Speedomax G recorder being used to monitor the potential of the working electrode.

Solutions.—Solutions were prepared from AR grade reagents and doubly distilled water. The borate buffer solution (pH 8.4) used for cathodic reduction was an equivolume mixture of a solution of 28.6 g/liter sodium tetraborate decahydrate and a solution of 18.5 g/liter boric acid. The pH of the 0.15N sodium sulfate solution was adjusted to 8.4 by addition of 1N sodium hydroxide. This pH was chosen for oxidation since no change of bulk pH from this value was observed during a

run (solutions of lower initial pH rapidly approached a pH of approximately 8.4 upon application of current).

Argon was used for deaerating solutions and for providing an inert atmosphere for experiments. Commercial high-purity argon was further purified by passage through a column packed with finely dispersed copper on Kieselguhr heated to 200°C (9). The solutions were deaerated in storage vessels by bubbling argon through them for 48 hr. They could then be transferred to the cell under an argon atmosphere.

Iron electrodes.—Ferrovac E sheets 0.015 in. (0.038 cm) in thickness and 1, 2, 5, or 10 cm² in area (depending on the magnitude of the current) were suspended in solution by means of narrow handles. Surface preparation steps were carried out in the following sequence: (i) degreasing in benzene in Soxhlet extractor for several hours; (ii) chemical polishing for 4 min in oxalic acid-hydrogen peroxide bath; (iii) electropolishing for 1 min in acetic acid-perchloric acid bath (10); (iv) annealing in hydrogen in a system capable of ultra-high vacuum (2.5 hr at 700°C, hydrogen pressure 1-2 Torr); (v) re-electropolishing for 1 min just before installation in the cell. If a specimen was to be reused for a later experiment, it was again electropolished as in step (v).

For oxidation experiments, three types of surface were used, classified according to the initial degree of oxidation. These are designated C (complete preliminary cathodic reduction), B (incomplete preliminary reduction), and A (specimen carrying air-formed film). These will now be described more fully:

C specimens were subjected to thorough cathodic reduction in the borate solution immediately before oxidation. All reductions were carried out at a current density of 10 μA/cm² while passing argon over the solution (the solution was not stirred). These electrodes were distinguished by the magnitude and rate of attainment of the initial rest potential upon immersion in the sulfate solution. This potential was approximately -565 ± 5 mV vs. SHE and was reached very rapidly, i.e., within 1-2 sec. If left on open circuit it would remain constant at this value for extended periods of time.

B specimens could be prepared either by interrupting the current before cathodic reduction was complete, or by carrying out the reduction in a borate solution which had not been sufficiently deoxygenated. In contrast to those of type C, these assumed an unsteady initial potential in sulfate of -400 to -500 mV, which decreased very slowly toward the C value. The surfaces of the B electrodes always contained a small amount of electrochemically reducible oxide which was, however, much less than the air-formed film.

An A specimen was prepared by first cathodically reducing as for type C. It was next removed from the

* Electrochemical Society Active Member.

¹ Former NRC Post-doctorate Fellow. Present address: Noranda Research Centre, Pointe Claire, Quebec, Canada.

Key words: iron passivity, anodic oxidation, oxide films.

cell, washed with freshly redistilled water, and quickly dried by blotting lightly with Fisher lens paper. It was reinstalled in the cell just before introduction of the sulfate solution for anodic oxidation, the total time of exposure to air being exactly 15 min.

Procedure.—After obtaining the desired starting surface (see preceding section) the cell was rinsed carefully with the sulfate solution to remove all traces of borate. An argon atmosphere was maintained (except in the case of A electrodes) to prevent air oxidation of the specimens.

Upon immersion in sulfate, the initial open circuit potential was noted; the potentiostat was then immediately switched on. Each run was carried out at a single potential, this being applied in one step from the rest potential. During oxidation, argon was bubbled through the solution at a constant rate.

Following oxidation for the desired period, the working electrode was again cathodically reduced in the borate solution.

Results

The behavior of C electrodes will be described first. It is convenient to divide the potential range covered (-500 to $+1550$ mV) into three regions, based on the nature of the current-time curves. These are (a) the low potential region, -500 to -385 mV; (b) the major active region, -385 to $+1450$ mV; and (c) the region of vigorous oxygen evolution, $> +1550$ mV. Representative current-time curves are given in Fig. 1.

Because the cell currents did not, in general, readily attain steady values (especially at the low potentials), a "steady-state" polarization curve was not plotted. However, polarization curves could be made for fixed periods of oxidation. An over-all picture of C electrode behavior can be had from such a curve for an oxidation time of 15 minutes, shown in Fig. 2.

Region (a).—Upon application of low potentials, the current density rapidly decreased from the initial high-current peak to relatively small values, of the order of $100 \mu\text{A}/\text{cm}^2$. The data in Fig. 2 suggest that there is an active region centered at ca. -450 mV, the currents, however, being fairly small. An active-passive transition is found at ca. -400 mV.

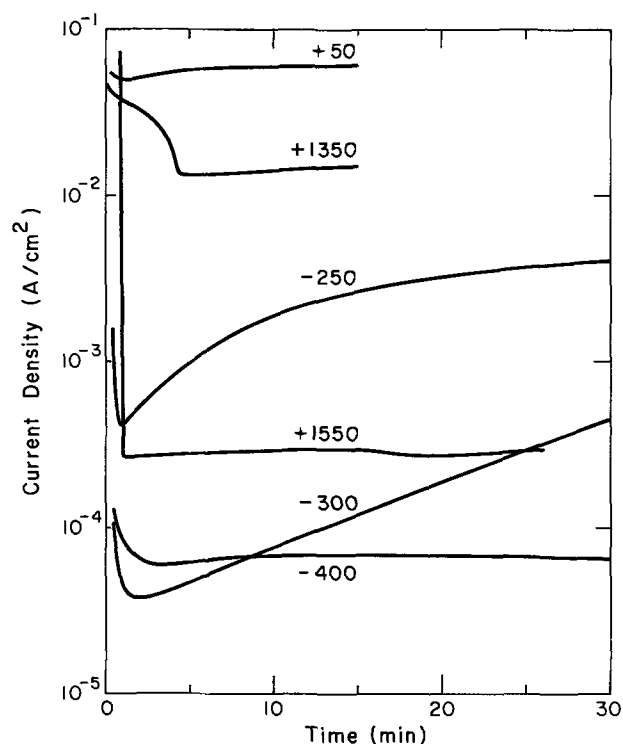


Fig. 1. Representative curves of current vs. time for potentiostatic oxidation of C electrodes. The numbers on the curves give the potential of oxidation in millivolts vs. SHE.

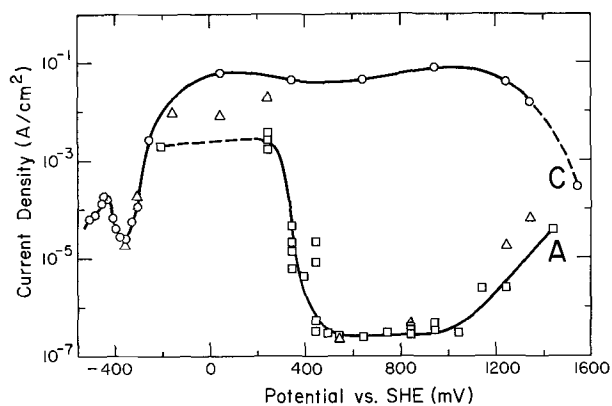


Fig. 2. Polarization curves for C and A electrodes, plotted for an oxidation time of 15 min. The points Δ are for B electrodes. Region (a) -500 to -385 mV; (b) -385 to -1450 ; (c) vigorous O_2 evolution $> +1550$ mV.

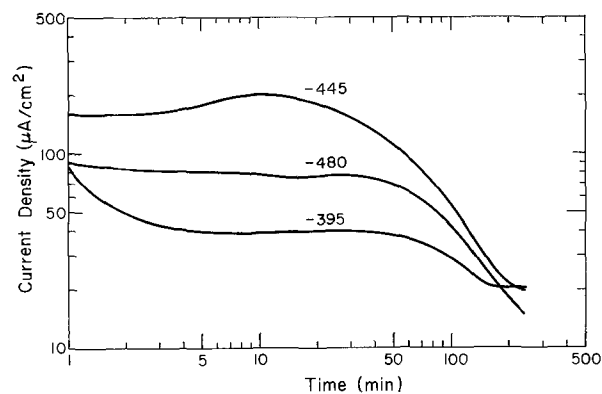


Fig. 3. Current-time curves for long-time potentiostatic oxidation of C electrodes at certain low potentials. The numbers on the curves give the potentials in millivolts vs. SHE.

Examination of the current-time curves in Fig. 3 shows that these conclusions are not valid for long periods of polarization. In this figure, the behavior at three different potentials for oxidation times of four hours are plotted. It is seen that much lower currents may eventually be reached, so that a polarization curve plotted for a prolonged period of oxidation would display no active peak around -450 mV, and no active-passive transition.

For short oxidation times (up to 30 min) at these potentials, apparent surface attack was comparatively slight; only a small number of tiny pits (diameter < 0.001 mm) could be seen at low magnifications. In contrast, after several hours of oxidation the nature of the attack changed and the specimen became coated with a spongy, poorly adherent green film which could not be completely removed by cathodic reduction. The underlying surface exhibited fairly severe general etching, the degree of attack increasing with potential. Identification of the film was not attempted because of its susceptibility to air oxidation. This film was probably a ferrous hydroxy sulfate. Exposure of the specimen to air produced a very rapid color change from green to orange.

The cathodic reduction curves (potential vs. time) obtained after oxidation resembled in shape those of Nagayama and Cohen (11) for iron oxidized in a borate solution. However, they tended to be diffuse and poorly defined. Film thicknesses estimated from the curves were small, amounting to only a few tens of angstroms.

Transition from Region (a) to Region (b).—These two regions have been defined arbitrarily in terms of the current-time behavior. At potentials less than about -385 mV, the current always decreases monotonically following the initial transient peak. (A very broad,

superficial second peak was sometimes observed; see Fig. 3). At potentials greater than this value, on the other hand, the current reaches a minimum after a period of 1 to 5 min, and then begins to increase. By carrying out a number of runs at potentials in the range -400 to -350 mV, the potential at which the current just failed to decrease at long times could be determined fairly accurately as -385 ± 5 mV.

It is to be noted that the current minimum around -360 mV (Fig. 2) falls within the active range (b) according to this criterion. This serves to emphasize how much the shape of the polarization curve is dependent on time. At a potential of -360 mV, for example, the current density reaches a minimum of about $20 \mu\text{A}/\text{cm}^2$ after a few minutes. Four hours later, however, it has increased to a value of a few milliamperes per square centimeter.

The change in the nature of the transition region with time is depicted in Fig. 4.

Region (b).—In this potential range, the current passes through a minimum after a few minutes and then increases, eventually levelling off at a much greater value which is dependent on potential. With increasing potential, the minimum current becomes greater, and the long-time steady-state current is reached sooner (Fig. 1).

At potentials greater than about 0 mV, the minimum is barely discernible, and the very high currents cause rapid dissolution of the specimen and formation of a thick green precipitate. The current densities given are only estimates based on unit roughness factor; they are doubtless too high because of the severe attack and roughening of the metal surface.

Such behavior is observed up to about $+1250$ mV. From $+1250$ to $+1450$ mV, very high currents are still observed, but the shapes of the current-time curves are different (see Fig. 1).

During oxidation at the lower potentials in this region (up to ca. 0 mV), the specimen became covered with a loose green film. After cathodic reduction, nu-

merous very tiny pits (0.001 to 0.005 mm in diameter) could be seen distributed more or less uniformly over the metal surface. With increasing potential, the number of pits became greater, attack evidently proceeding by an increase in the density of pits rather than by the growth of a few pits.

At higher potentials, the pits became numerous enough to coalesce into patches, giving the appearance of uneven general attack. The patches appeared to be free of a colored overlying film, in contrast to the remainder of the surface, which became covered with a gold-colored film. Examination by reflection high-energy electron diffraction of a specimen oxidized at $+650$ mV showed this film to consist of $\gamma\text{-FeOOH}$ and Fe_3O_4 . A satisfactory diffraction pattern could not be obtained from the "bare metal" patches.

In all cases, cathodic reduction curves obtained after oxidation consisted of two well-defined waves as for Fe oxidized in borate solution (11), the lengths of the waves depending on potential and time of oxidation. Film thicknesses estimated from these curves were relatively large; for example, for 15 min oxidation at $+650$ mV, the amount of charge associated with the first wave corresponded to a Fe(III) oxide film thickness of a few hundred angstroms. Some of this Fe(III) oxide was probably deposited from Fe(II) in solution by anodic deposition (8).

Region (c).—At a potential of $+1550$ mV, bubbles of oxygen were rapidly evolved from the electrode surface. After about one minute of polarization, the concentration of oxygen in solution reached a value sufficiently large to cause a rapid drop in current density (Fig. 1) to a few hundred microamperes per square centimeter. The presence of oxygen was emphasized by formation of a yellow precipitate in the solution, in contrast to the green precipitate observed at lower potentials.

B and A electrodes.—At potentials from -350 to -150 mV, B specimens showed qualitatively the same behavior as those of type C. In general, the initial current peak was smaller for the former type (presumably because of the film already present), and the current density increased less rapidly following the minimum. Specimens of type A could not be examined at potentials less than about -200 mV, the initial open circuit potential of an A electrode in the sulfate solution.

Around -100 mV, very marked differences became evident, not only in the magnitudes of the currents (Fig. 2), but also in the type of surface attack. The B and A specimens showed intensely localized attack, with formation of only a few large pits (up to 0.5 mm in diameter), in contrast to the much more general attack observed for C electrodes.

Both B and A electrodes exhibited a most important change for potentials in the range $+550$ to $+1100$ mV, where such attack ceases due to passivation. The active-passive transition occurs over the range $+350$ to $+550$ mV. Upon application of a potential in this passive region, the current density rapidly falls to a fraction of a microampere per square centimeter, and metal dissolution virtually stops. Even at very high potentials, the presence of an initial film greatly reduces the rate of metal attack.

Discussion

The anodic behavior of iron in a deaerated neutral sulfate solution has been shown to be strongly dependent on the initial degree of oxidation of the surface. In particular, the passive region at high potentials, extensively studied by Freiman and Kolotyarkin (4-7), is seen to be entirely absent for electrodes which have been completely cathodically reduced before oxidation. This passive region evidently exists only if an air-formed film is initially present on the surface. The present results for B electrodes indicate that even a very thin initial film, such as might result when preliminary cathodic reduction is carried out with insufficient care, is able to give rise to such a region of passivity.

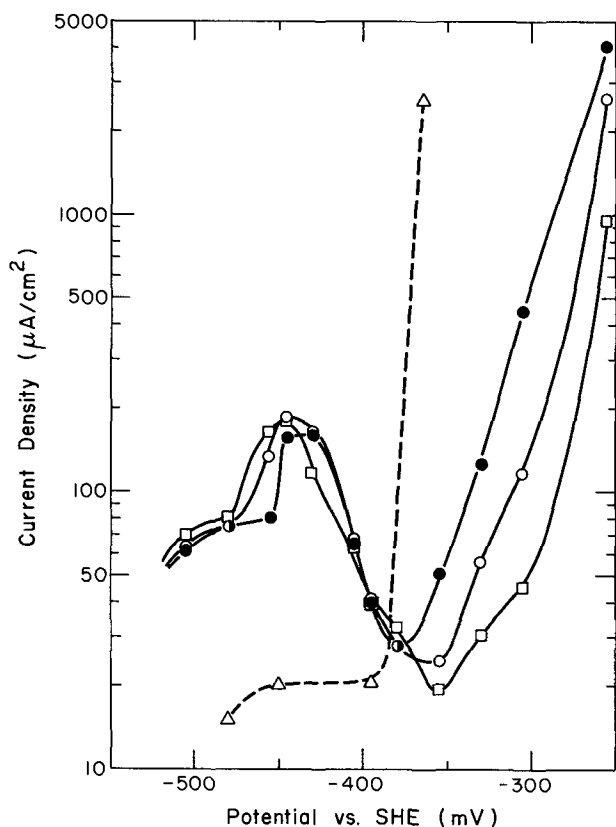


Fig. 4 Polarization curves for C electrodes at low potentials, plotted for oxidation times of \square -5 min, \circ -15 min, and \bullet 30 min. The points indicated by Δ are for an oxidation time of 240 min.

On C electrodes, the anodic film formed at all potentials more positive than -385 mV is nonprotective and gradually suffers general breakdown, the rate of breakdown increasing as the potential becomes more "noble." Attack probably begins at a few discrete points but soon becomes widespread. The film is not able to repair itself and the electrode remains active. Thus the cell current, which is the resultant of components due to film formation (including any deposition of oxide from iron in solution) and metal dissolution, reaches a minimum a few minutes after the potential is applied, and then begins to increase. The sulfate ion may prevent the formation and/or repair of a protective layer by adsorption (12) at the metal surface with displacement of water molecules, by altering the interfacial potential distribution so as to favor metal dissolution, by its incorporation into the film lattice (13), or by some other mechanism.

In Region (a), it is possible that the sulfate ion plays a smaller role, so that the anodic film resembles more closely that formed at corresponding potentials in borate solution; the potentials associated with the critical passivating current and active-passive transition are similar (11).

It is concluded that C electrodes do not become satisfactorily passive at any potential. While low currents do result after long polarization times at low potentials, this is only after considerable attack of the metal surface has taken place, with formation of a thick, spongy precipitated film. The data in Fig. 4 illustrate the danger of drawing conclusions from short-term polarization measurements: thus, the active region around -450 mV "disappears" at very long times, while the apparent region of passivity around -360 mV soon gives way to rapid corrosion.

An obvious question is that of how much oxide must be present initially in order to cause a departure from C behavior at high potentials. Experiments with B electrodes, which may be thought of as intermediate between C and A, ought to allow examination of this question. Unfortunately, B electrodes do not lend themselves readily to experiment because of the non-

reproducible nature of the rest potential on immersion in the sulfate solution. This potential is believed to be a sensitive measure of the amount of oxide initially present; it is, however, difficult to prepare a specimen whose immersion potential has a specified value.

The initial film on A specimens can be prepared more reproducibly, and the behavior of these electrodes, particularly in the passive region at high potentials, will be the subject of a future communication.

Manuscript submitted Aug. 16, 1971; revised manuscript received Dec. 2, 1971.

Any discussion of this paper will appear in a Discussion Section to be published in the December 1972 JOURNAL.

REFERENCES

1. P. Hancock and J. E. O. Mayne, *J. Appl. Chem.*, **9**, 345 (1959); K. F. Lorking and J. E. O. Mayne, *ibid.*, **10**, 262 (1960).
2. W. T. Denholm, *J. Australian Inst. Metals*, **7**, 141 (1962).
3. D. Gilroy and J. E. O. Mayne, *Brit. Corr. J.*, **1**, 102, 107, 161 (1965-1966).
4. L. I. Freiman and Ya. M. Kolotyrykin, *Zashchita Metallov*, **1**, 77, 161 (1965).
5. L. I. Freiman and Ya. M. Kolotyrykin, *ibid.*, **1**, 725 (1965).
6. L. I. Freiman and Ya. M. Kolotyrykin, *Dokl. Akad. Nauk SSSR*, **171**, 1138 (1966).
7. L. I. Freiman and Ya. M. Kolotyrykin, *Zashchita Metallov*, **5**, 139 (1969).
8. V. Markovac and M. Cohen, *This Journal*, **114**, 674 (1967).
9. F. R. Meyer and G. Ronge, *Angew. Chem.*, **52**, 637 (1939).
10. P. B. Sewell, C. D. Stockbridge, and M. Cohen, *Can. J. Chem.*, **37**, 1813 (1959).
11. M. Nagayama and M. Cohen, *This Journal*, **109**, 781 (1962).
12. N. Hackerman and S. J. Stephens, *J. Phys. Chem.*, **58**, 904 (1954).
13. J. L. Leibenguth and M. Cohen. Submitted to *This Journal*.

Anodic Film Studies on Steel in Nitrate-Based Electrolytes for Electrochemical Machining

Kao-Wen Mao,* Mitchell A. LaBoda,* and James P. Hoare*

Electrochemistry Department, Research Laboratories, General Motors Corporation, Warren, Michigan 48090

ABSTRACT

Steady-state polarization measurements along with constant-current film stripping determinations were carried out on steel wires in solutions of NaNO_3 , NaClO_4 , and mixtures of NaNO_3 and NaClO_4 from which it was found that ClO_4^- ion can efficiently remove the film formed by nitrate by a potential-dependent mechanism. In a closed system employing an ECM test rig, mass balance studies showed that the film formed by NO_3^- ion is electronically conducting since most of the current is consumed in O_2 evolution instead of metal removal. With additions of ClO_4^- ion to the nitrate, the current efficiency for metal removal is increased to 100%. The character of the surface finish in the mixed electrolytes is highly dependent on the flow rate of the solution which was confirmed by the machining of fully hardened type 5160H steel bushings in a through-hole ECM machine. To account for these results, an ion exchange model for metal removal in the transpassive region is suggested.

Since Keeleric (1) announced the commercial development of an electrolytic grinding machine and Anocut Engineering Company (2) published the details

* Electrochemical Society Active Member.
Key words: electrochemical machining, anodic films, steel anodes, metal removal, surface finish.

of a pure electrochemical machining (ECM) device, considerable effort has been expended in developing and refining the ECM process (3, 4) to the growing commercially important machining method of today. One of the important steps in achieving such progress was the

realization that an understanding of the electrochemical processes underlying the ECM operation is essential to further progress. From research on ECM electrolytes carried out by LaBoda and co-workers, the use of solutions of NaClO_3 as a superior ECM electrolyte was published (5).

It was soon realized (6-9) that the nature of the anodic films formed on the workpiece metal by contact with the given electrolyte profoundly affected the quality of the finished product. Because there is a limit to the number of single-salt electrolytes available for use in an ECM operation, interest was generated in the possible modification of the electrolyte properties by investigating the ECM behavior of mixed electrolytes.

If the film formed is too highly protective such as that formed in chromate-based electrolytes, little or no ECM takes place (9). If, however, a poorly protective film is formed such as that produced in chloride-based electrolytes, stray cutting impairs the integrity of the workpiece. By mixing electrolytes, it may be possible to form protective films on the metal surface with the most desirable properties of high metal removal rate with good control of geometry and dimensions. Nitrate-based electrolytes form protective films on iron and steel, and the ClO_4^- ion is known (9a) to be a good dissolver of films formed on iron. It is thought that electrolytes composed of mixtures of NO_3^- and ClO_4^- ions may possess the properties of a good ECM electrolyte.

It is the purpose of this report to describe the results of an investigation of the anodic corrosion of mild steel in mixtures of solutions of NaNO_3 and NaClO_4 as a function of the composition of the electrolyte and the potential. These results were compared with the actual machining of steel bushings in a through-hole, sizing-and-finishing, ECM test rig as a function of solution flow rate and applied voltage as well as electrolyte composition.

Experimental

Polarization Studies

Steady-state, anodic potentiostatic polarization curves were obtained on mild steel wire electrodes which had been abraded with fine emery cloth, degreased in benzene, washed in acetone, rinsed in distilled water, and embedded in polyethylene so that a measurable length of wire was exposed. Three such electrodes to be used as checks were sealed in one compartment of a dual Teflon cell (10), and a probe-type, saturated calomel electrode (SCE) was placed in the other compartment connected by a glass frit. To minimize the effects of mass transfer, the solutions were stirred with purified O_2 at a rate of about 200 to 300 cm^3/min . Stock solutions, 3M in NaNO_3 and 3M in NaClO_4 , were made from reagent grade chemicals in triply distilled water so that all mixtures contained a total anion concentration of 3M.

When the output of the Wenking 61R potentiostat had come to a steady value, as noted on a strip recorder driven by a Keithley Model 600A electrometer, the potentiostat was removed from the circuit by a mechanical switch and a constant current cathodic stripping pulse was applied to the steel wire anode by means of a mercury-wetted relay (11). The resulting transient was displayed on a Tektronix 541 oscilloscope and recorded photographically. From a determination of the transition times (12) associated with the arrests on the transients and from the known value of the constant current applied, it was possible to determine the amount of charge, Q , associated with the film adsorbed on the steel wire surface at the potential held by the potentiostat (7). In this way, the amount of charge associated with the film could be determined for each point on the anodic polarization curve. The temperature at which these experiments were carried out was $24^\circ \pm 1^\circ\text{C}$.

Current Efficiency Studies

The ends of mild steel tubes were machined at constant current in the fixed-cathode, ECM test rig in the closed system described in detail elsewhere (8, 13) to carry out mass-balance and current efficiency determinations. The gases evolved in the process were passed through a series of traps designed to give quantitative analyses for H_2 and O_2 liberated (13). The chemical analyses of the electrolytes and the sludges were carried out in the Chemistry Department of Research Laboratories, General Motors Corporation. Calculations of current efficiencies for iron removal were based on the two-electron dissolution of iron to ferrous ion, and the Type 1020 steel was assumed to be 100% iron. When NO_3^- ion is present in the electrolyte, the NO_3^- ion is reduced at the cathode to form NH_3 , NO_2^- ion, and NH_2OH (13) instead of the evolution of H_2 . In this case, the NH_3 was absorbed in a trap containing 20% H_2SO_4 solution.

Through-Hole ECM Studies

To assess the metal removal rate and the quality of the surface finish as a function of electrolyte composition and flow rate, mild steel (Type 1020) and fully hardened steel (Type 5160H) bushings were machined in a through-hole ECM test rig described before (5). In this device, the anodic bushing is clamped in place so that the Elkonite (Cu-W) rod cathode extended about halfway into the bushing. After the electrolyte flow rate had been set at the desired value, either 1.5 or 4.5 gpm (electrolyte was pumped from the bottom of the fixture through the gap between the anode and cathode and out of the top of the cell), and the desired applied cell voltage had been set, the inside wall of the bushing was machined for 30 sec. The amount of metal removed was determined from the increase in the ID of the bushing with a bore gauge. In this way, only the desired metal removal in the high current density region is determined, and unwanted stray metal removal in the low current density region is eliminated from the measurements. The quality of the surface finish as well as the profile of the bore was obtained by means of a Proficorder.

Results

Polarization Studies

Steady-state polarization curves obtained on mild steel anodes in mixtures of NaNO_3 and NaClO_4 for the following compositions expressed in terms of per cent NO_3^- ion 100, 90, 84, 67, 50, 33, 10, and 0 are presented in Fig. 1, and the amount of charge, Q , in millicuries/apparent square inch associated with film stripped from the electrode for each point on the polarization curves is plotted in Fig. 2. A roughness factor of 10 was used in the calculation of apparent area, using the geometric dimensions of the wire anode.

As ClO_4^- ion is added to pure NO_3^- ion solutions, the current in the passive region becomes smaller, and the film thickens with ClO_4^- ion concentrations up to about 16%. Also, the transition from the passive to the transpassive regions becomes sharper. When the NO_3^- ion concentration falls below 84% NO_3^- ion, the transpassive region appears at less noble values with increasing ClO_4^- ion concentrations until a minimum potential is reached at 67% ClO_4^- ion. Afterwards, the transpassive region appears at more noble potentials again with further increases of ClO_4^- ion. It was found (Fig. 2) that for all solutions below 90% NO_3^- ion, a potential is reached where all trace of the surface film disappears. This potential is a function of the composition of the electrolyte and is in direct correlation with the potential at which the transpassive region begins as shown in Fig. 3. Here, the potential at which the transpassive region begins (circles) and the potential at which a surface film can no longer be detected (triangles) are plotted as a function of per cent ClO_4^- ion.

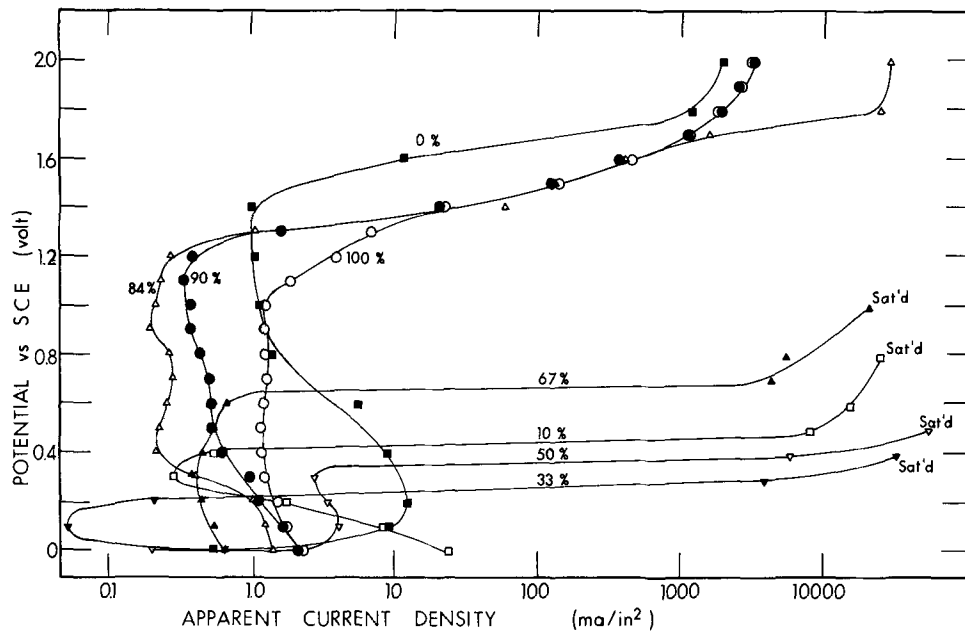


Fig. 1. Steady-state potentiostatic polarization curves obtained on mild steel wire anodes in 3M solutions of mixtures of NaNO₃ and NaClO₄. The per cent NaNO₃ is indicated on the respective curve. The point at which the potentiostat loses control (potential cannot be raised further, current determined by resistance of the cell) is noted by "Sat'd."

The upturning of the curves in Fig. 1 toward a limiting current at the highest current densities investigated is due to mass transfer effects since these points are stirring-dependent. For those curves where the transpassive region lies below 1000 mV such high currents are drawn that the current becomes limited by the resistance of the cell, and the potentiostat loses control. This situation is indicated on Fig. 1 by the notation "Sat'd" (saturated). This saturation current had a value of about 30 A/in.².

Consider, for example, the 67% NO₃⁻ ion curve in Fig. 1. When the potential was raised from 600 to 700 mV, the current shifted four orders of magnitude to the saturation value in about 100 to 200 sec, which indicated that once a threshold potential was reached it required a certain amount of time to remove the film. If, now, the potential was lowered below 400 mV, the potentiostat would regain control and the polarization curve could be retraced down to 0V.

Current Efficiency Studies

The results of the machining of mild steel tube ends in electrolytes composed of mixtures of NO₃⁻ and ClO₄⁻ ions expressed in terms of the current efficiency for metal removal as a function of electrolyte composition and applied current density are given in Table I. The appearance of the machined tube ends is shown in Fig. 4.

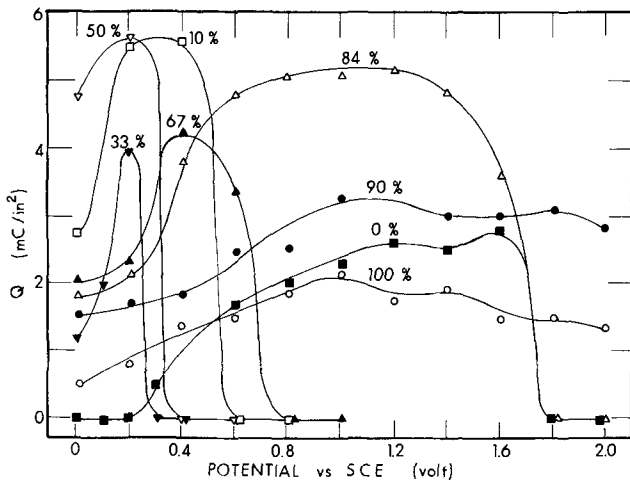


Fig. 2. The amount of charge, Q, per apparent square inch associated with the surface film present at each point of the polarization curve in Fig. 1.

The fact that the current efficiency for O₂ evolution is so large in pure NaNO₃ solutions gives evidence that the protective film formed on steel is electronically conducting. The actual metal removal is very low, thus accounting for the observation that in the ECM process using NaNO₃ electrolytes, metal removal is slower than that in NaCl or NaClO₃ solutions. In pure NaClO₄ solutions some current is used in the evolution of O₂, but in the mixtures of NaNO₃ and NaClO₄ all the anodic current is used in the metal removal process.

The formation of NH₃ at the cathode in the NaNO₃ electrolyte changes the pH of the electrolyte from the initial value of 6 to a final steady value of 11. In pure NaClO₄ solutions the final steady pH value of the ECM electrolyte is about 9, which agrees well with the pH value of a saturated solution of Fe(OH)₂. It may be noted that the color of the sludge in NaClO₄ elec-

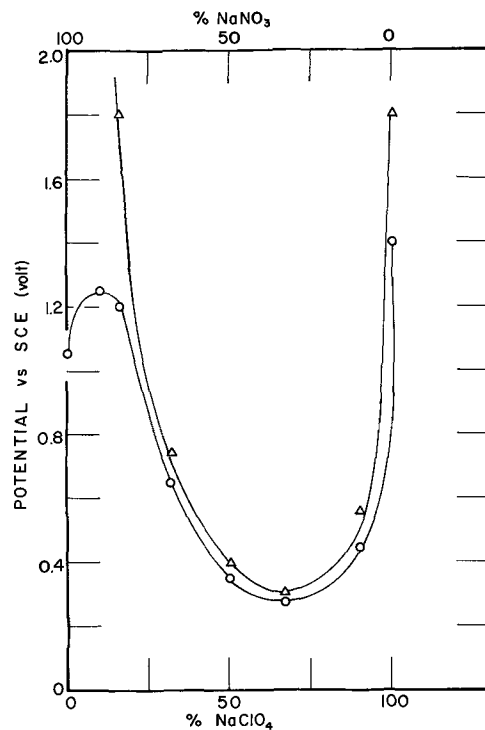


Fig. 3. A plot of the potential above which a surface film cannot be detected (triangles) as well as the potential where the transpassive region of Fig. 1 begins (circles) as a function of the composition of the electrolyte.

Table I. Current efficiency for metal removal in ECM of Type 1020 steel

Composition of electrolyte	Apparent current density (A/in. ²)	Current eff. for O ₂ evol. (%)	Current eff. for Fe removal (%)	Iron removal (Mole)	Final pH
3M NaClO ₄	300	6	90	0.0327	9
2.5M NaClO ₄ + 0.5M NaNO ₃	240	—	97	—	11
2M NaClO ₄ + 1M NaNO ₃	240	0	100	—	11
1.5M NaClO ₄ + 1.5M NaNO ₃	300	0	112*	—	11
1M NaClO ₄ + 2M NaNO ₃	300	0	112*	0.0406	11
0.5M NaClO ₄ + 2.5M NaNO ₃	300	0	106*	—	11
0.3M NaClO ₄ + 2.7M NaNO ₃	300	—	82	—	11
4.5M NaNO ₃	300	56	33	0.0120	11
2M NaNO ₃	300	85	12	0.00418	11
4.5M NaClO ₃	300	25	79	0.0285	6
2.0M NaClO ₃	300	38	63	0.0230	6

* During metal corrosion, severe grain boundary attack may account for apparent efficiencies greater than 100%.

trolyte, as well as in the NO₃⁻-ClO₄⁻ mixtures, is greenish black.

An interesting point in Fig. 4 is the brightening of the lip of the tube machined in the mixed electrolyte.

Through-Hole ECM Studies

After machining in the through-hole ECM device, the steel bushings were cut open. The hardened steel (Type 5160H) bushings are pictured in Fig. 5 and Proficorder tracings are displayed in Fig. 6. Since the cathode extended only about halfway into the bushing, only about one-half of the bushing is machined. The area machined is referred to as the high current density (hcd) region; beyond this area is the low current density (lcd) region.

In pure NaNO₃, the steel surface is relatively poor and covered with a black film. In pure NaClO₄, the surface in the hcd region is smooth and somewhat bright, and its quality is improved at higher potentials and lower flow rates. This observation is different from that obtained in NaClO₃ where the surface brightness is virtually independent of the flow rate. Another difference between the NaClO₄ and NaClO₃ solutions is found in the lcd region. Whereas pitting is found in the lcd region in NaClO₄, no attack in the lcd region is observed in NaClO₃.

The results obtained in the mixed electrolytes is very dependent on the flow rate. At high flow rates, no brightening is obtained [Fig. 5(G)]; but as the flow rate is lowered, the amount of brightening is increased [Fig. 5(H)]. In general, the best results are obtained at high applied voltage and low flow rate. There is a difference in the kind of brightening one obtains in mixed electrolytes [Fig. 5(F)] as compared with that obtained in NaClO₃ [Fig. 5(C)]. The surface machined in NaClO₃ seems to be more mirror bright. The metal removal rate in the mixed electrolytes is higher than that in other electrolytes for the same operating conditions (Tables I, II), and the black film characteristic of iron in nitrate electrolytes is found in the lcd region even though the surface in the hcd region is bright.

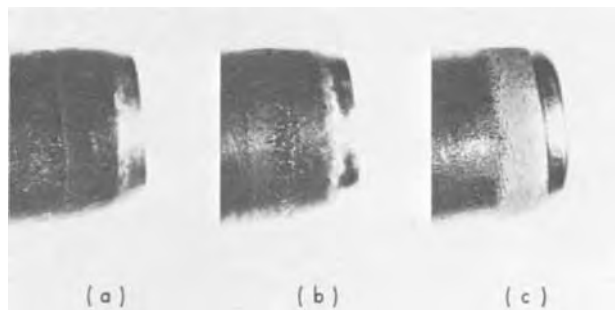


Fig. 4. Photomicrographs of mild steel tube ends which had been machined in 50% NaNO₃ (a), 66.7% NaNO₃ (b), and 100% NaClO₃ (4.5M) (c) at 300 A/in.². Note reflectance and evenness of cut on lip of tube ends.

A summary of the through-hole cuts of the steel bushings is given in Table II. The results of both the polarization studies and the ECM studies indicate that similar behavior is obtained on both mild and fully hardened steel.

Discussion

The NaNO₃ Electrolyte

The steady-state polarization curve for mild steel in pure NaNO₃ electrolyte (open circles in Fig. 1) exhibits more of a limiting current region than a passive region, although relatively thick films are present on the surface as noted by the data (open circles in Fig. 2). Such behavior could be explained if the film were electronically conducting. In this case, the double layer would extend from the solution side of the film into the solution so that one would expect that anodic current would be consumed by the discharge of a chemical

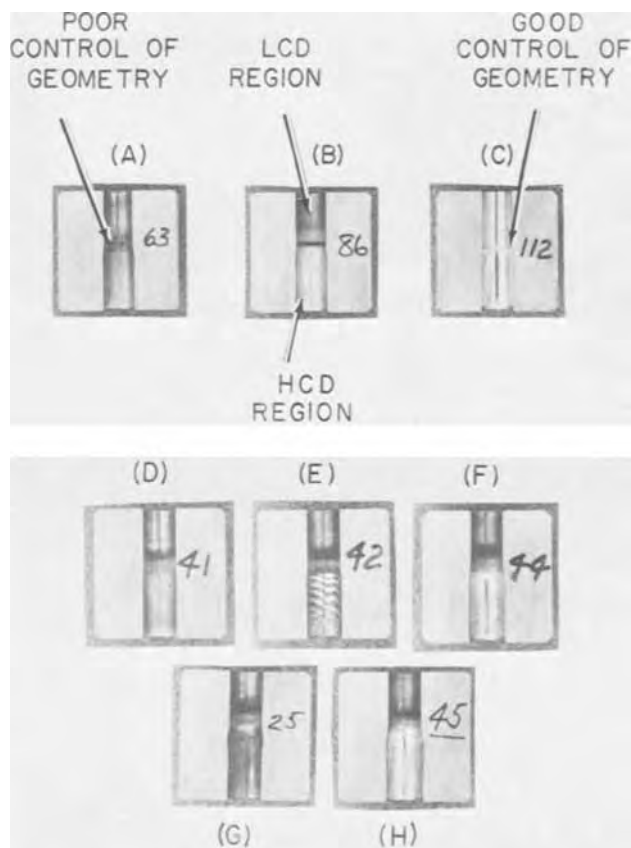


Fig. 5. Photographs of fully hardened steel bushings cut open to show quality of the metal removal operation for samples machined for 30 sec in NaNO₃ (A), NaClO₄ (B), NaClO₃ (C), 1M NaClO₄ + 2M NaNO₃ (D)-(G); applied cell voltage is 20V (A)-(C), 10V (D), 15V (E), 25V (F), 30V (G), (H); solution flow rate is 1.5 gpm (A)-(F) and (H), 4.5 gpm (G).

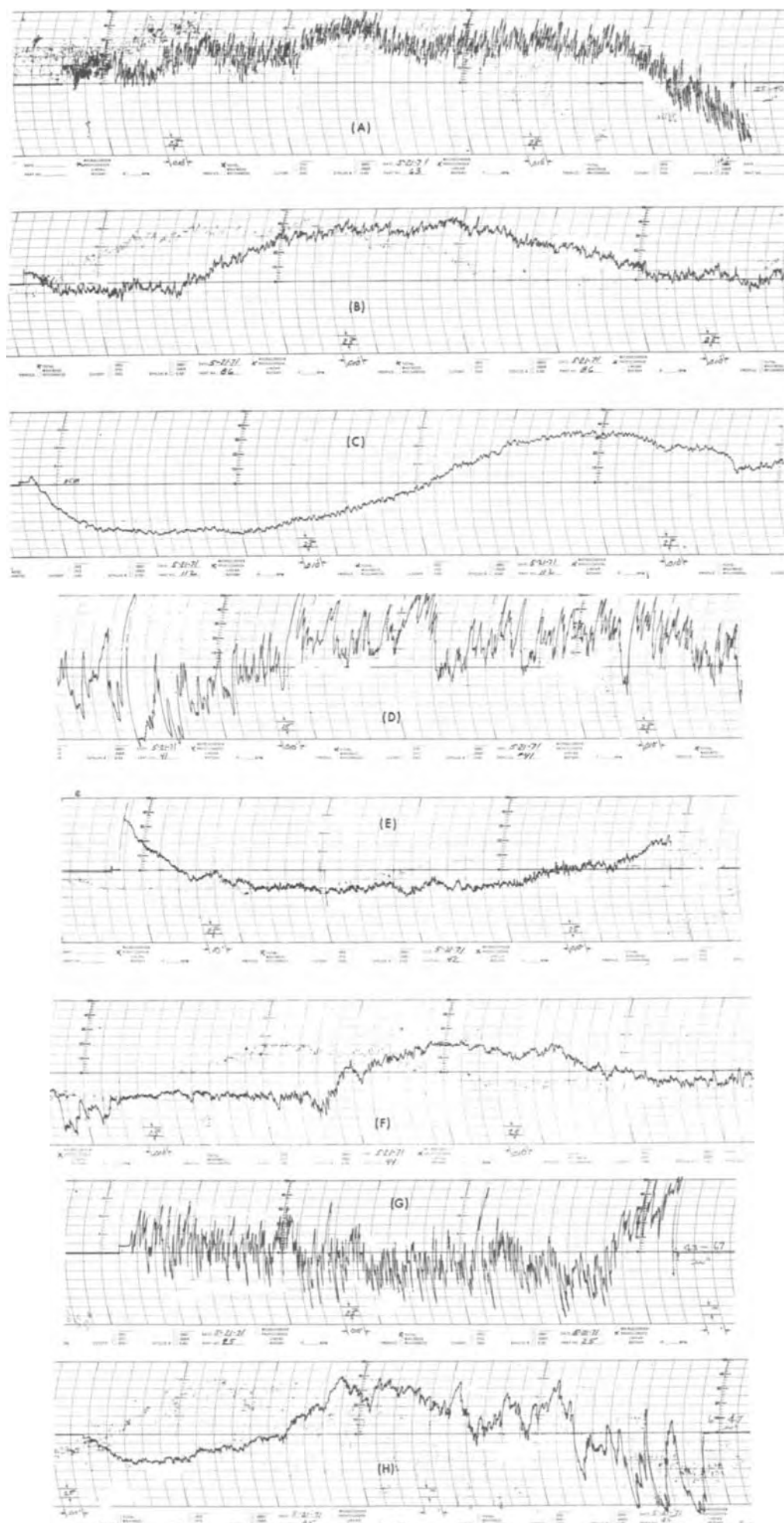


Fig. 6. Proficorder traces of the machined surface for each sample shown in Fig. 5. As one progresses up the bore as shown in Fig. 5, the trace is read from right to left, each unit being 0.01 in. On the y-axis, the scale is given in μin . The RMS value of surface roughness reported in Table II is estimated from the trace by taking 1/3 of the peak-to-peak value.

Table II. Machining data for the ECM of steel bushings

Sample number	Composition of electrolyte	Applied voltage (V)	Flow rate (gpm)	Metal removal rate (in./side)	Surface roughness μ in. RMS	Figure number
Type 5160H fully hardened steel						
63	3M NaNO ₃ *	20	1.5	0.0122	25-40	5(A), 6(A)
64	3M NaNO ₃ *	25	1.5	0.0140	—	—
86	3M NaClO ₄	20	1.5	0.0108	10-13	5(B), 6(B)
87	3M NaClO ₄	20	1.5	0.0180	—	—
112	3M NaClO ₃	30	1.5	0.0104	5-8	5(C), 6(C)
114	3M NaClO ₃	30	1.5	0.0155	—	—
41	1M NaClO ₄ + 2M NaNO ₃	10	1.5	0.0053	53-62	5(D), 6(D)
42	1M NaClO ₄ + 2M NaNO ₃	15	1.5	0.0088	7-13	5(E), 6(E)
43	1M NaClO ₄ + 2M NaNO ₃	20	1.5	0.0130	—	—
44	1M NaClO ₄ + 2M NaNO ₃	25	1.5	0.1065	5-12	5(F), 6(F)
45	1M NaClO ₄ + 2M NaNO ₃	30	1.5	0.0208	6-47	5(H), 6(H)
25	1M NaClO ₄ + 2M NaNO ₃	30	4.5	0.0060	43-67	5(G), 6(G)
Type 1020 mild steel						
58	3M NaNO ₃ *	20	1.5	0.0135	—	—
82	3M NaClO ₄	20	1.5	0.0095	—	—
108	3M NaClO ₃	20	1.5	0.0075	—	—
37	1M NaClO ₄ + 2M NaNO ₃	15	1.5	0.0104	—	—
38	1M NaClO ₄ + 2M NaNO ₃	20	1.5	0.0145	—	—
39	1M NaClO ₄ + 2M NaNO ₃	25	1.5	0.0180	—	—
40	1M NaClO ₄ + 2M NaNO ₃	30	1.5	0.0240	—	—
15	1M NaClO ₄ + 2M NaNO ₃	30	4.5	0.0080	—	—

* It is to be noted that the metal removal rate in pure NaNO₃ electrolyte is much higher in Table II than that observed previously (13) or in the current efficiency studies (Table I) of this work. It is possible that interfering amounts of NaClO₄ or NaClO₃ were occluded in the pumping system of the through-hole machine from previous runs and were later leached out into NaNO₃ electrolyte producing the anomalously high metal removal rate.

entity present in solution rather than by the dissolution of the metal lattice of the anode.

This conclusion is supported by the current efficiency studies (Table I), where it is seen that nearly all the current (85%) is consumed in the evolution of oxygen with only about 12% used in metal dissolution. Additional evidence in favor of the conducting film concept is the fact that a black smut or film is always obtained on steel surfaces machined in NaNO₃ solutions. Such a black film is evidence for the formation of Fe₃O₄. It has been found (14) that ferrous hydroxide can be oxidized chemically by the nitrate ion, but in all cases Fe₃O₄ was the resultant product. The presence of the electronically conducting protective film on steel in NaNO₃ solutions accounts for the slower metal removal obtained for the machining of steel in this electrolyte as compared with NaCl or NaClO₃ solutions under similar conditions.

Even at the high potentials in the transpassive region (see Fig. 1 and 2), the film on steel in NaNO₃ solution is not greatly reduced in thickness. As noted by Hoar (15, 16), a thin compact film is required to give an electropolishing of the surface so that one does not expect a brightening of the steel surface machined in NaNO₃ solutions due to the presence of the thick conducting film of Fe₃O₄. The surface of the bushings machined in NaNO₃ [Fig. 5(A) and 6(A); Table II] is relatively poor.

The NaClO₄ Electrolyte

In pure NaClO₄ solutions, the polarization curve for steel (filled squares in Fig. 1) has a sharp transition from the passive to the transpassive state. This property of the system, it has been suggested (6-10), is responsible for the good control of geometry and dimensions obtained in the machining of steel in such an electrolyte because the hcd region of the machined piece is associated with the transpassive region of the polarization curve and the lcd region with the passive region. It has been observed from rotating disk studies (17) that the critical current at the point where the transition from the active to the passive region takes place is a function of the stirring rate of the solution. As the stirring rate increases, the critical point is shifted to more noble potentials. Such behavior is characteristic of a salt film, the thickness of which may be reduced by increased agitation. With increasing

potential, a point is reached where a more compact film is formed by precipitation of a salt from the salt film onto the metal surface followed by conversion of the salt to the more protecting oxide-type film. The relatively slow buildup of the protective film (Fig. 2) accompanied by the gradual onset of passivity (Fig. 1) is in agreement with this interpretation. Finally a potential is reached above which the film becomes unstable and can no longer be detected on the anode surface.

This behavior is different from that reported (7, 9) for steel in NaClO₃ solutions where a compact oxide film is formed quickly and independently of the rate of solution stirring (18). In the transpassive region some oxide film may still be detected which is believed (8) to be responsible for the brightening and good surface finishes obtained on steel with NaClO₃ electrolytes. Since the film formed in NaClO₄ is not so compact, it is expected that the quality of the surface finish obtained on steel in NaClO₄ will not be as good as that in NaClO₃. In Fig. 5 and 6 it is seen that the surfaces of the bushings machined in NaClO₄ [Fig. 5(B)] are not as bright as those machined in NaClO₃ [Fig. 5(C)] in the hcd region for a given set of conditions and there is an area of pitting in the lcd region. For high potentials and low flow rates the surface finish of the bushings machined in NaClO₄ approaches that in NaClO₃ [Fig. 6(B) and 6(C)].

Mixed NaNO₃/NaClO₄ Electrolytes

Consider now the data for mixed electrolytes. As NaClO₄ concentration is increased in the series of mixed electrolytes, the film formed on the steel surface becomes less and less electronically conducting as noted by the decreasing value of the current in the passive region for 90% and 84% NO₃⁻ ion solution in Fig. 1 and by the increase in the current efficiency for metal removal in Table I. For concentrations of NO₃⁻ less than 85%, a potential may be reached where the presence of the adsorbed film can no longer be detected (Fig. 2), and the potential is shifted to less noble values as the ClO₄⁻ ion concentration is increased until a minimum value is reached at about 33% NO₃⁻ ion. As a consequence, the transpassive region appears at less noble values in correspondence with the disappearance of the surface film as noted in Fig. 3. With further increases in the ClO₄⁻ ion concentration, the

potential above which surface films are not observed is shifted once more to more noble values. Current efficiencies for metal removal equal 100% (see Table I) for these solutions which is to be expected if adsorbed films are absent.

These data suggest that the metal removal rate for steel in $\text{NaNO}_3/\text{NaClO}_4$ mixtures with NO_3^- ion concentrations between 70 and 10% should be higher than in any other electrolyte studied so far for a given set of conditions. Since the transpassive region for these mixtures lies at such low potentials, good dimensional control of the machining of steel in such mixtures is not expected. These predictions were confirmed by the machining of the bushings. As observed in Fig. 5, more metal was removed (Table II), but the region of wild cutting (metal removal in the lcd region) was greater in the mixtures [Fig. 5(E) and (F)] than in NaClO_3 [Fig. 5(C)].

When the bushings were machined in the mixed electrolytes at high flow rates (4.5 gpm), the machined surfaces were dark [Fig. 5(G)] and relatively rough [Fig. 6(G)], but when the flow rate was lowered to 1.5 gpm, the surface became smoother [Fig. 6(H)]. At this low flow rate, the surface became brighter as the applied voltage was raised from 5 to 30V until, at this highest voltage, the surface was highly reflecting.

Brightening of the surface, then, can take place by at least two different mechanisms. In one case where a thin uniform porous oxide film is formed on the steel surface in an electrolyte such as NaClO_3 (8), electropolishing occurs virtually independently of the flow rate (19) and takes place by the mechanism suggested by Hoar (15, 16, 20).

In the absence of adsorbed oxide films, metal may be dissolved rapidly, forming a thick salt layer next to the metal surface. When the concentration of salt becomes high enough, a salt film may be precipitated onto the surface; and if the potential is high enough, the salt film may be converted to a thin oxide film. Under these conditions electropolishing can take place. If, however, the flow rate is high, the salt concentration in the salt layer cannot reach a value high enough to precipitate a salt film on the metal surface; and if the applied potential is too low, the thin oxide film necessary for electropolishing cannot be formed. Thus, polishing of the machined surface in the presence of salt films is highly dependent on the applied potential and the solution flow rate as observed in the machining of steel bushings in the $\text{NaNO}_3/\text{NaClO}_4$ mixed electrolytes [Fig. 5(D)-5(H)]. Because the films formed from salt layers are not as compact or protecting as those formed by a passivating electrolyte such as NaClO_3 , pitting of the surface in the lcd region usually occurs and the dimensional control is not as good in the mixed electrolytes as in NaClO_3 solutions. An advantage, however, of the mixed NO_3^- -based electrolytes is the ability to ECM steel at high metal removal rates with little or no evolution of H_2 .

Anion Effects and the Ion-Exchange Model of Anodic Films on Iron

From these studies it becomes a matter of concern how these adsorbed anodic films become unstable and dissolve in the transpassive region. It appears that this phenomenon may be associated with the type of anion present in solution (20). For a small anion such as Cl^- ion, it may be possible for this ion to penetrate the pores of the film (21), causing a breakdown of the film particularly since the Cl^- ion easily forms soluble complexes with iron (22).

It has been pointed out (9a, 23, 24) that the ClO_4^- ion is as good as Cl^- ion, or better in some cases, as an aggressive agent for the breakdown of iron oxide films. Because the ClO_4^- ion is much larger than the Cl^- ion, it is difficult to see how such an anion can penetrate the oxide film lattice or be such an efficient agent for film dissolution.

A possible mechanism called the mechanical mechanism has been suggested by Hoar (21) to account for

the ClO_4^- activity. According to this scheme, the anions are adsorbed on the surface of the oxide film; and with increasing potential, more and more anions become adsorbed. The repulsive forces between the adsorbed anions can reach a point where the film may be ruptured at weak spots caused by dislocations, inclusions, etc. On the new surface caused by this rupture, more anions can be adsorbed causing a further rupture of the film and exposure of the underlying metal to attack. It may be possible that the exceptional ability of the ClO_4^- ion to dissolve iron oxide films in the transpassive region may be attributed to the symmetrical, nonpolarizable nature of the ion (25, 26). Such behavior may lead to weak chemical bonding.

The only really protective film is one that is electronically conducting (24); but for anodic brightening, the adsorbed film must be a good ionic conductor. Hoar (24) reasoned that the passive films on metal anodes cannot merely be composed of the metal oxides. He speaks of a "contaminated" film in which anions and water molecules are occluded in the oxide layer. In this way the ionic conductivity of the film is increased to the extent that metal ions may pass easily through the film producing a brightening of the surface. It has been suggested (27) that the protective film formed on steel in these neutral-salt electrolytes may have properties similar to an ion exchange membrane.

With these ideas in mind and from analyses of the data obtained on steel anodes in $\text{NaNO}_3/\text{NaClO}_4$ mixed electrolytes, we conclude that the structure of these anodic films most likely takes the form of a matrix-type honeycomb in which water molecules and anions reside in the interstices. It is proposed that the material of the matrix network is composed of iron and oxygen atoms with the stoichiometry, but not necessarily the properties, of bulk iron oxide.

When Cl^- ions are present, soluble complexes are made with the iron ions so that the matrix of iron oxide units cannot be formed. This accounts for the fact that protective films are not formed on steel in NaCl electrolytes (7, 9).

In NaNO_3 solutions, black films of Fe_3O_4 are formed on the steel surface. Such a film is likely to be a ferrous ferrite, $\text{Fe}(\text{FeO}_2)_2$ which is a good electronic conductor (28). The matrix of the protective film is composed then of ferrous ferrite units, and the electronically conducting network is truly protective so that the current is consumed by the discharge of a chemical species in solution on the surface of the adsorbed film as observed experimentally (discharge of H_2O to O_2 evolution, Table I).

A compact film of $\gamma\text{-Fe}_2\text{O}_3$ is formed on the steel surface in solutions of chromates (29, 30), carbonates (31), phosphates (32), and chlorates (18). On the steel surface in these electrolytes, the matrix network is made up of the poorly conducting Fe_2O_3 units by the strong oxidizing power of these anions. Any current that flows in the passive region is accounted for by whatever ferrous ions can migrate through the interstices of the Fe_2O_3 network.

Once the oxide matrix is formed on the passivated steel surface by well-known methods (33, 34) of film nucleation and growth, anions may be adsorbed not only on the external but also the internal surfaces of the network by exchanging with adsorbed water. The presence of these adsorbed anions can increase the ionic conductivity of the adsorbed film (24). Although the concentration of adsorbed anions increases with potential (36), it is suggested that at high enough potentials these adsorbed anions can exchange with the oxygen ions of the iron oxide matrix. Eventually, a point is reached where so many oxide sites are replaced with anions from solution that the matrix breaks down and dissolves. It may be expected that the concentration of replaced oxide sites would be greatest at the solution side of the adsorbed film (36). This viewpoint would account for the thinning of the passivating film

observed (7) in the transpassive region for steel in chromate, nitrate, and chlorate electrolytes.

This ion-replacement model can also explain the effect of concentration of the electrolyte on the metal removal rate. Not only was it observed in this work but also in previous studies (9, 13, 37) that the metal removal rate, as well as the current efficiency, increased with increasing concentration of NaNO_3 or NaClO_3 electrolytes. With increasing concentration, more anions can be adsorbed on the surface of the film for a given potential causing the film to be thinned quicker, besides increasing its ionic conductivity. This effect, in turn, produces a lowering of the transition region of the polarization curve (37) and an increase in the rate of metal removal as well as current efficiency at the given potential.

The more difficult it is for a given anion to replace an oxide ion in the matrix of the passive film, the higher will be the potential at which the transpassive region will appear. Since the transpassive region lies at higher potentials on steel in $\text{Na}_2\text{Cr}_2\text{O}_7$ than in NaClO_3 solutions (7), it is concluded that chromate ions exchange with more difficulty than chlorate ions. It may be possible that the presence of dislocations or inclusions may make one part of the matrix more susceptible to anion exchange and an uneven removal of the film could take place.

In the case of solutions of NaClO_4 , a compact film of Fe_2O_3 units is not built up on the steel surface at low anodic potentials since the ClO_4^- is a weak oxidizing agent (26). As a result, a salt film is formed, [see e.g. (35)], and at a high enough potential, the layer of ferrous perchlorate precipitated out on the steel surface is oxidized to a passivating oxide film similar to that formed on steel in NaClO_3 solutions. With further increases in potential, the adsorbed ClO_4^- ions can exchange with the oxide ions of the Fe_2O_3 matrix causing the oxide film to disintegrate. It appears that the film is completely removed when the ClO_4^- ion is the chemical species which is exchanged. Possibly because of the highly symmetrical structure of the ClO_4^- ion, the oxide matrix with substituted ClO_4^- units is more soluble than that with ClO_3^- units.

In electrolytes where both NO_3^- and ClO_4^- ions are present at a steel anode at low potentials, the NO_3^- ions can form a passivating ferrous ferrite film on the steel surface. The symmetrical ClO_4^- ions can adsorb more easily on the conducting Fe_3O_4 surface than on the poorly conducting Fe_2O_3 surface; but since ClO_4^- is in competition with NO_3^- for adsorption sites, a threshold concentration must be reached before the effect of ClO_4^- ion addition can be observed. With increasing addition of ClO_4^- ion to a NaNO_3 solution above about 15% ClO_4^- ion, the adsorbed ClO_4^- ions can exchange with the ferrous ferrite units of the oxide matrix at increasingly less noble potentials with the consequent dissolution of the protective film and lowering of the potential of the transpassive region to less noble values.

Further increases in ClO_4^- ion beyond the maximum lowering of the transpassive region at about 70% ClO_4^- ion impairs the electronic conductivity by contaminating the ferrous ferrite film with ClO_4^- salt films or Fe_2O_3 units and hence impairs the ability of ClO_4^- ion to adsorb on the surface of the passive film. Consequently, the transpassive region appears at more noble potentials again at very high concentrations of ClO_4^- ion. With complete destruction of the protecting films on steel in mixtures of NO_3^- and ClO_4^- ions, the very high metal removal rates observed in this work may be accounted for.

The breakup of the protective film on the steel surface in the mixed electrolyte with increasing potential can be observed in the series of photographs, Fig. 5(D)-5(F). At low applied voltage, the surface is covered with the black ferrous ferrite film in Fig. 5(D), the surface is very rough [Fig. 6(D)], and a

small amount of metal is removed (see Table II). The breakup of the film is seen in Fig. 5(E) by noting the patterns of light and dark bands. Corresponding undulations of the Proficorder trace can be detected in Fig. 6(E). At high enough potentials, in Fig. 5(F), the film is removed; and at the low flow rate and high metal removal rate, a salt film produces a brightening of the surface.

Because brightening of the steel surface is caused by the salt film as described in the previous section, the process is very dependent on the electrolyte flow pattern as observed in Fig. 6(H) as well as on the flow rate [see Fig. 6(G) and 6(H)]. At the entrance to the bushing [extreme right-hand side of Fig. 6(H)], the turbulence of the solution is great and the structure of the salt film is highly disorganized. This situation produces a high degree of surface roughness (47 $\mu\text{in.}$, Table II). As the electrolyte progresses upward along the channel [from right to left in Fig. 6(H)], the flow pattern becomes more regular and the structure of the salt film becomes more uniform with a resulting decrease in surface roughness (6 $\mu\text{in.}$, Table II) and an increase in the reflectance of the surface.

Acknowledgments

The authors are indebted to R. B. Loranger, H. E. Vergosen, and Dr. J. L. Johnson of the Chemistry Department, General Motors Corporation, who carried out the chemical analyses; to T. L. Davis of the Processing Department, GMR, for his assistance in sample preparation; and to C. Eib of the Processing Department, GMR, for the Proficorder trace measurements.

Manuscript submitted Sept. 1, 1971; revised manuscript received Nov. 30, 1971. This was Paper 72 presented at the Cleveland Meeting of the Society, Oct. 3-7, 1971.

Any discussion of this paper will appear in a Discussion Section to be published in the December 1972 JOURNAL.

REFERENCES

1. G. Keeleric, *Steel*, **130**, 84 (1952); L. H. Metzger and G. Keeleric, *Am. Machinist*, **96**, 154 (1952).
2. Anon., *Am. Machinist*, **103**, 99 (1959).
3. A. E. DeBarr and D. A. Oliver, "Electrochemical Machining," Elsevier, New York (1968).
4. J. P. Hoare and M. A. LaBoda, "Electrochemical Machining," in "Applied and Industrial Electrochemistry," E. Yeager and A. Salkind, Editors, To be published by Wiley, New York.
5. M. A. LaBoda and M. L. McMillan, *Electrochem. Technol.*, **5**, 340 (1967).
6. J. P. Hoare, M. A. LaBoda, M. L. McMillan, and A. J. Wallace, *This Journal*, **116**, 199 (1969).
7. J. P. Hoare, *ibid.*, **117**, 142 (1970); *Nature*, **219**, 1034 (1968).
8. J. P. Hoare, K.-W. Mao, and A. J. Wallace, *Corrosion*, **27**, 211 (1971); *Corrosion Sci.*, In press.
9. M. A. LaBoda, J. P. Hoare, and S. E. Beacom, *Coll. Czech. Chem. Commun.*, **36**, 380 (1970).
- 9a. T. P. Hoar, *Trans. Faraday Soc.*, **45**, 683 (1949).
10. J. P. Hoare, *This Journal*, **109**, 858 (1962).
11. J. P. Hoare, *Electrochim. Acta*, **9**, 599 (1964).
12. R. Thacker and J. P. Hoare, *J. Electroanal. Chem.*, **30**, 1 (1971).
13. K.-W. Mao, *This Journal*, **118**, 1870, 1876 (1971).
14. S. H. Carsley, *J. Phys. Chem.*, **34**, 178 (1930).
15. T. P. Hoar and J. A. S. Mowat, *Nature*, **165**, 64 (1950); *Electrodepositors Tech. Soc.*, **26**, 7 (1950).
16. T. P. Hoar and T. W. Farthing, *Nature*, **169**, 324 (1952).
17. D. T. Chin, Private communication.
18. M. L. McMillan and M. A. LaBoda, *Electrochem. Technol.*, **5**, 346 (1967).
19. M. A. LaBoda, To be published.
20. T. P. Hoar, in "Modern Aspects of Electrochemistry," Vol. II, p. 262, J. O'M Bockris, Editor, Academic Press, New York (1959).
21. T. P. Hoar, *Corrosion Sci.*, **7**, 341 (1967).
22. N. V. Sidgwick, "The Chemical Elements and Their Compounds," p. 1356, Oxford Univ. Press, London (1950).

23. T. P. Hoar, *Trans. Faraday Soc.*, **33**, 1152 (1937).
24. T. P. Hoar, D. C. Mears, and G. P. Rothwell, *Corrosion Sci.*, **5**, 279 (1965).
25. N. V. Sidgwick, *op. cit.*, p. 1231.
26. T. Moeller, "Inorganic Chemistry," p. 443, Wiley, New York (1952).
27. A. H. Gropp, Private communication.
28. N. V. Sidgwick, *op. cit.*, p. 1353.
29. T. P. Hoar and U. R. Evans, *J. Chem. Soc.*, **134**, 2476 (1932).
30. M. Cohen and A. F. Beck, *Z. Elektrochem.*, **62**, 696 (1958).
31. M. J. Pryor and M. Cohen, *This Journal*, **100**, 203 (1953).
32. H. H. Uhlig, D. N. Triadis, and M. Stern, *ibid.*, **102**, 59 (1955).
33. L. Young, "Anodic Oxide Films," Academic Press, New York (1961).
34. D. A. Vermilyea, in "Advances in Electrochemistry and Electrochemical Engineering," Vol. III, p. 211, P. Delahay, Editor, Interscience (1963).
35. D. R. Turner, *This Journal*, **98**, 434 (1951).
36. J. J. Randall, W. J. Bernard, and R. R. Wilkinson, *Electrochim. Acta*, **10**, 183 (1965).
37. M. A. LaBoda and J. P. Hoare, in "Fundamentals of Electrochemical Machining," C. L. Faust, Editor, p. 227, The Electrochemical Society Soft-bound Symposium Series, Princeton, N. J. (1971).

Preparation and Properties of Pyrolysis of Vanadium Oxide Films

L. A. Ryabova, I. A. Serbinov, and A. S. Darevsky

Institute of Radio Engineering & Electronics, Academy of Science, Prospect Marx, 18, Moscow K-9, U.S.S.R.

ABSTRACT

Vanadium oxide films (V_2O_3 , VO_2 , V_2O_5) were obtained by the pyrolysis of vanadium acetylacetonate $(C_5H_7O_2)_4V$ in controlled atmosphere. The influence of deposition parameters on the film composition is studied. It was revealed that the composition of the gas carrier is the main factor determining the film composition. Electron diffraction and electron microscopy analysis of films are carried out. Temperature dependence of resistance was studied. VO_2 films deposited on glazed ceramic and sapphire change resistance by factor 10^3 at about $340^\circ K$. V_2O_5 films had an activated conductivity.

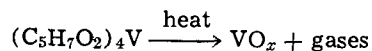
Currently, thin films and single crystals of vanadium oxides attracted attention of investigators due to the phase transitions in VO_2 and V_2O_3 . Thin films and crystals were grown by the decomposition of $VOCl_3$ in controlled atmosphere (1, 2) and by the reactive sputtering using post deposition treatment (3).

This report concerns the preparation of thin films of V_2O_3 , VO_2 , V_2O_5 (thickness 600-10,000Å) by the pyrolysis method and investigation of their properties.

Pyrolysis makes it possible to prepare any of these oxides by the thermal decomposition of vanadium acetylacetonate in the corresponding atmosphere. This method was chosen because of: (i) the simplicity of the equipment, (ii) the few parameters to be controlled in the process, and (iii) the high reproducibility of film properties.

Experimental

Acetylacetonates of 4-valent vanadium $(C_5H_7O_2)_4V$ were used as the initial substance. Films were deposited on the substrates of various materials by the thermal decomposition of vanadium acetylacetonate in vacuum and in the flow of the gas carrier by the reaction



The composition of vanadium oxide films changed in dependence on the composition of the reaction medium.

The technique of the film preparation is the same as described in Ref. (4). In the process of film preparation in vacuum, in the absence of foreign gases, films consisting of a mixture of stoichiometric and intermediate oxides are formed. The temperature dependence of the resistivity did not have the sharp transition as did single crystals of stoichiometric VO_2 and V_2O_3 . VO_2 films with the resistivity change by a factor of 10^2 at 60° were obtained by introducing oxygen (oxygen pressure 10^{-2} - 10^{-1} Torr) during the

pyrolysis process in vacuum. Probably there was a small amount ($\sim 1\%$) of intermediate oxide. The composition and properties of these films were poorly reproduced. Increasing the oxygen amount (oxygen pressure, 10 Torr) leads to the formation of dense, uniform in thickness films of V_2O_5 .

Successful deposition of V_2O_3 , VO_2 , and V_2O_5 films was finally effected by using a carrier gas flow of nitrogen or appropriate mixtures of nitrogen and oxygen.

Experimental equipment for film preparation in the gas flow is analogous to that described in Ref. (5). It consists of a 2-zone resistance oven where the reaction quartz tube is placed (diameter 50 mm, length 1000 mm). A quartz boat with vanadium acetylacetonate is placed at a distance of 200 mm from the substrates, which are placed on the quartz holder.

Glass, glazed ceramic, KCl, sapphire, muscovite mica, and single crystal quartz were used as substrates. The structure and phase control were carried out by means of electron diffraction and electron microscopy. Data on the phase analysis are given in Table I.

Experiments showed that the film composition and their properties mostly depend on the composition of the gas carrier.

V_2O_3 films are formed when the reaction is carried out in the flow of pure nitrogen. Films are smooth, dense; the grain size is about 1000Å. Polycrystalline films are formed on glazed ceramic (Fig. 1a). In the reflection diffraction pattern of this film there are three extra lines: $d = 3.07\text{Å}$, $d = 2.82\text{Å}$, $d = 1.37\text{Å}$ (Table Ia). Probably these lines are of intermediate oxide. Single crystal films are formed on mica; the "c" axis is perpendicular to substrate plane (Fig. 1b). This figure shows that separate crystallites have a characteristic for hexagonal phase of V_2O_3 angle relations between planes. On the temperature dependence of the resistance of these films deposited on glazed ceramic and mica, there is no sharp transi-

Key words: pyrolysis, vanadium oxide, films, resistivity, deposition.

Table I. Data on electronographic analysis

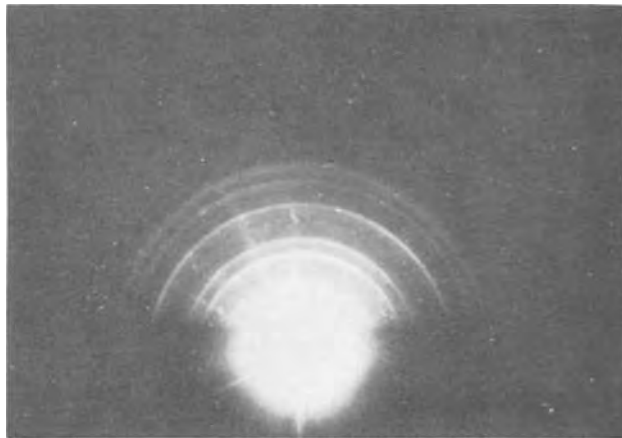
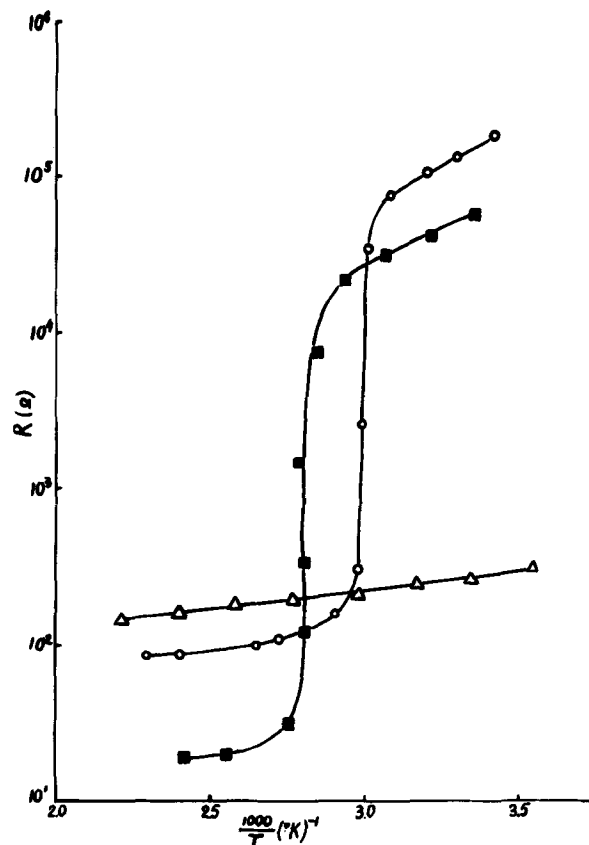
Table Ia For V ₂ O ₃ films				Table Ib For V ₂ O ₅ films			
Thin films		Polycryst. (6)		Thin films		Polycryst. (6)	
d, Å	Relative Intens.*	d, Å	Relative Intens.*	d, Å	Relative Intens.*	d, Å	Relative Intens.*
3.60	40	3.65	60	3.41	100	3.39	83
3.07	10			2.87	10	2.87	53
2.82	10			2.58	70	2.61	13
2.47	100	2.47	60	1.96	40	1.99	7
2.19	70	2.18	20	1.83	60	1.86	7
2.08	10	2.03	2	1.76	10	1.77	10
1.80	10	1.83	25	1.54	60	1.56	7
1.70	70	1.69	100				
1.47	80	1.47	25				
1.37	70						
1.34	50	1.33	10				
1.20	50	1.218	2				
1.10	30	1.093	6				

* Estimated.

tion at 150°K characteristic for V₂O₃ single crystals. Probably it is an evidence of the existence of the impurities of intermediate oxides (composition between V₂O₃ and VO₂).

It may be possible to prepare a pure V₂O₃ phase, either by choosing corresponding composition of gas carrier or by using as the initial substance acetylacetonate of 3-valent vanadium.

The temperature dependence of the resistance of films prepared in the flow N₂/O₂ = 10/1 is shown in Fig. 2. This figure shows that films on glazed ceramic and sapphire have a characteristic for VO₂ phase transition, the resistance changes with a factor 10³. Resistance of the films obtained on mica slightly depends on the temperature (Fig. 2).

Fig. 1 (a). Reflection electron diffraction from V₂O₃ film deposited onto ceramics.Fig. 1 (b). Platinum-carbon replica of the surface of V₂O₃ deposited onto mica. Particles of V₂O₃ are partially extracted. Shade angle is 10°.Fig. 2. Resistance vs. $1000/T(^{\circ}\text{K})^{-1}$ for VO₂ films deposited on glazed ceramics (○), sapphire (■), and mica (△).

In the process of film formation in the mixture of nitrogen and oxygen (N₂/O₂ = 1/1) polycrystalline textured films of V₂O₅ are formed (Table Ib). Resistance of these films in the temperature range from the room temperature to 200°C has an activated character with activation energy 0.1-0.2 eV. These films are needle-like with the "c" axis parallel to the substrate plane (Fig. 3a, b). Polycrystalline films of V₂O₅ are formed on the glazed ceramic. The grain size is about 2000Å (Fig. 3c). Highly oriented films with platelet crystallites of V₂O₅ are formed on mica (Fig. 3d, e). Data on electron diffraction analysis of polycrystalline V₂O₅ films are given in Table Ib. Optimum conditions of preparation of vanadium oxide films (dense, transparent, uniform in thickness) in the flow of gas are given in Table II.

Conclusions

Thin films of vanadium oxides (V₂O₃, VO₂, V₂O₅) are obtained by the pyrolysis method. The technique of film preparation is very simple. The composition of the gas carrier is the main factor determining the film composition.

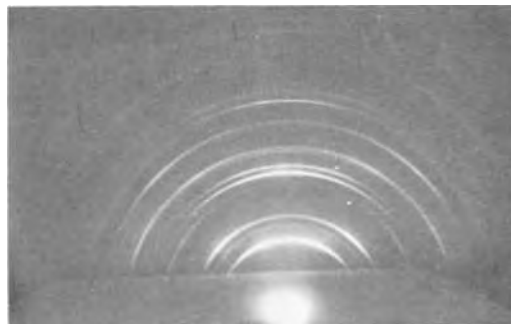
Fig. 3 (a). Reflection electron diffraction of V₂O₅ film deposited onto quartz.

Table II. Optimum conditions of the preparation of vanadium oxide films

Film composition	Composition of gas carrier		Substrate temperature, °C
	N ₂ flow rate ml/min	O ₂ flow rate ml/min	
V ₂ O ₅	500	—	420
VO ₂	500	50	400
V ₂ O ₃	500	500	340

Polycrystalline textured films are formed on unoriented substrates. Highly oriented and single crystal films are formed on oriented substrates.

The temperature dependence of the resistance of VO₂ films on glazed ceramic and sapphire have a transition by a factor 10³. Phase transition in V₂O₃ films was not observed, probably because of nonstoichiometric composition of oxide.

Acknowledgments

The authors wish to acknowledge helpful discussions with Y. S. Savitskaya and to thank V. U. Antokhina for carrying out the synthesis of the initial substance.

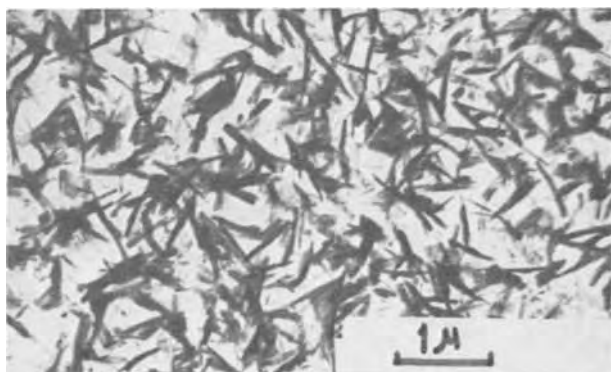


Fig. 3 (b). Transmission electron micrograph of V₂O₅ film surface on quartz. Magnification X20,000.

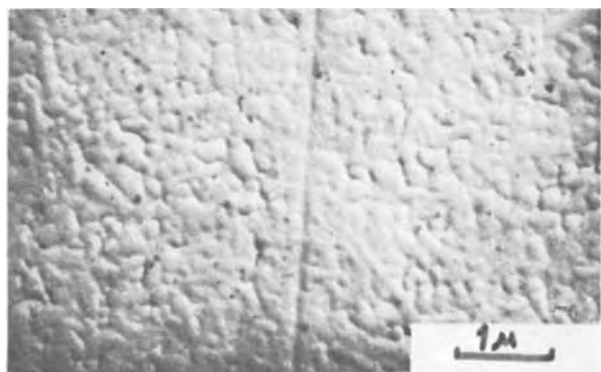


Fig. 3 (c). Carbon-platinum replica of V₂O₅ film surface on glazed ceramics, shade angle 10°.

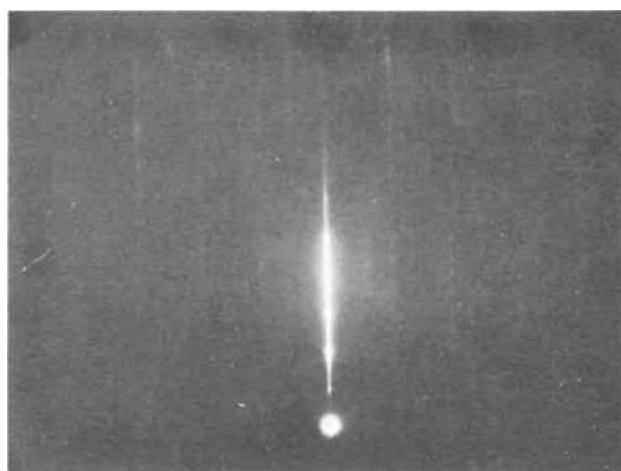


Fig. 3 (d). Reflection electron diffraction of V₂O₅ film on mica



Fig. 3 (e). Carbon-platinum replica of V₂O₅ film surface on mica, shade angle 10°.

Manuscript submitted May 11, 1971; revised manuscript received ca. Dec. 13, 1971.

Any discussion of this paper will appear in a Discussion Section to be published in the December 1972 JOURNAL.

REFERENCES

1. J. Fan and W. Paul, "Preparation and properties of thin films of vanadium oxides," Report on Cannes Conference on Thin films, April 1970.
2. G. A. Rozgonyi and W. J. Polito, *This Journal*, **115**, 56 (1968).
3. H. Takei, *Japan. J. Appl. Phys.*, **7**, 8, 827 (1968).
4. L. A. Ryabova and Ya. S. Savitskaya, *Thin Solid Films*, **2**, 141 (1968).
5. M. Prutton, "Thin Ferromagnetic Films," London (1964).
6. L. I. Mirkin, "Handbook of X-ray structural analysis of polycrystals," Moscow (1961).

Sputtered Manganese Dioxide as Counterelectrodes in Thin Film Capacitors

R. W. Landorf¹ and S. J. Licht

Bell Telephone Laboratories, Incorporated, Murray Hill, New Jersey 07974

ABSTRACT

Manganese dioxide films were sputtered with resistivities as low as 0.3 ohm-cm. Ta-Ta₂O₅-MnO₂-Metal (TMM) capacitors were fabricated and found to have dissipation factors of 0.008 at 1 kHz and 0.011 at 100 kHz. Leakage currents for the TMM capacitors were 10⁻⁹A when measured at 75V (33% of the anodizing voltage). By chemically removing the sputtered MnO₂ from the capacitors and then replacing the counterelectrodes the effect of sputtering on the dielectric could be observed. It was found that rf + 2 kV d-c sputtering conditions increased the dielectric dissipation factor by $\leq 20\%$ while the 3 kV d-c + rf conditions caused a 50% increase in the dielectric dissipation factor. The sputtered MnO₂ films were found to be γ -MnO₂ and showed a conduction activation energy of 0.10 eV (± 0.01) for 3 kV d-c + rf and 2 kV d-c + rf indicating that similar material has been deposited under both sputtering conditions.

The use of manganese dioxide in thin film capacitors has been studied by McLean and Rosztochy (1) and various techniques have been used to deposit the manganese dioxide films. These methods include pyrolytic spraying (1), electroless deposition (2), reactive evaporation (3), and reactive sputtering (4, 5). The results of these studies, in general, were: (i) MnO₂ is beneficial to thin film capacitor reliability and initial yield, (ii) the dissipation factor of the capacitors were an order of magnitude higher at 1 kHz than the equivalent Ta-Ta₂O₅-Metal (TM) capacitor, (iii) the dissipation factor became much higher at higher frequencies, and (iv) the resistivity of the MnO₂ was always > 5 ohm-cm, if, in fact, MnO₂ was deposited.

The bulk of the work on Ta-Ta₂O₅-MnO_x-Metal (TMM) capacitors has involved only pyrolytically deposited MnO_x films of high resistivity ($\sim 10^3$ ohm-cm) and the purpose of this study was to investigate the properties of TMM capacitors with sputtered MnO₂ films. The effects of various sputtering conditions on dissipation losses in the dielectric, the effect of MnO₂ on the dissipation factor, and the effect of counterelectrode area were studied. In addition to capacitance measurements, capacitor yields, and leakage current measurements were made for comparison with TM capacitors.

Experimental

The manganese dioxide films were sputtered in a conventional, diffusion pumped vacuum system as shown in Fig. 1. The sputtering cathode was in two equal area sections so the rf supply could be operated in the push-pull mode. The rf supply was operated at 7.5 MHz for the present experiments with a constant 100W power input. The cathode-substrate separation was 6.3 cm. The cathode was 8 in. in diameter and made of electrodeposited Mn metal (99.5% Mn). Three 7050 glass slides were mounted on the substrate table for each run.

The substrates were 1 in. \times 3 in. glass slides with the tantalum and the Ta₂O₅ dielectric predeposited on the slides. Details on the fabrication of the tantalum thin film capacitors are given elsewhere (6) and are only briefly mentioned here. Before sputtering the MnO₂ films, the tantalum was anodized to 170V, heat stabilized at 350°C for 1 hr, back-etched for 5 sec at 90V, and reanodized to 230V. Anodization was

Table I. Conditions investigated

Independent variables				Dependent variables		
D-C + rf	Pressure (μ)	D-C current drawn (mA)	Grid used	Substrate temp.	Deposition rate (A/min)	ρ range (ohm-cm)
3 kV + rf	20	40-45	NO	207°C	17	0.2-5.0
2 kV + rf	20	0	NO	170°C	15	0.5-1.6
1.5 kV + rf	20	0	NO	150°C	23	0.4-0.6
3 kV + rf	20	45	+50V	140°C	4.3	> 5
3 kV + rf	20	33	+5V	170°C	8.8	4.3-9.1
3 kV + rf	20	35	-25V	230°C	8.2	1.5-4.0
3 kV + rf	20	45	-100V	200°C	16	0.4-2.4

carried out in 0.01% citric acid at 25°C with a constant current density of 0.5 mA/cm².

The deposition temperature was measured by a Pt-Pt 10% Rh thermocouple clamped to a glass substrate. Temperatures read in this manner were compared with temperature measurements made with a thin film Pt-Pt 10% Rh thermocouple. The thin film thermocouple measurements were found to read $\sim 30^\circ\text{C}$ higher than the temperature measurements with the conventional thermocouple. The deposition temperatures reported in Table I were made with the conventional thermocouple.

Before each sputtering run the vacuum chamber was pumped to 1×10^{-6} Torr and given a mild (hot

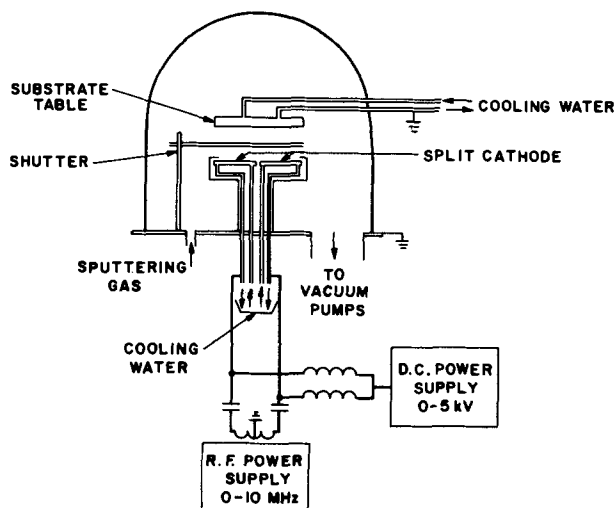


Fig. 1. Diagram of the sputtering system used in this experiment

¹ Present address, Bell Telephone Laboratories, Holmdel, New Jersey 07733.

Key words: thin films, sputtering, capacitor technology, manganese dioxide.

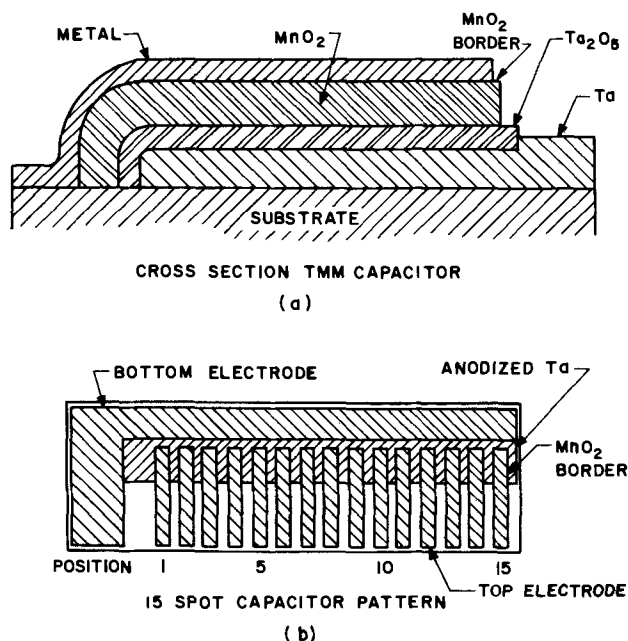


Fig. 2. (a). Shows the cross section of capacitor. (b). Shows the 15 spot capacitor pattern.

water) bake. A 15 min presputter in oxygen was completed before opening the shutter for deposition on the substrate. Manganese dioxide was then sputtered over the entire slide and nichrome-gold counterelectrodes were applied. The capacitor pattern, shown in Fig. 2b, was generated in two ways. First, evaporation of the counterelectrode through a mask was followed by photoetching and removal of the unwanted MnO_2 . This technique left a 0.025 cm border of MnO_2 around the nichrome-gold counterelectrode. Second, the counterelectrode was evaporated over the entire slide and then the capacitor was defined by photoetching techniques that required the removal of nichrome-gold and MnO_2 from the unwanted areas. This method left no border around the nichrome-gold counterelectrode. Some undercutting of the counterelectrode took place with this method, but this effect was minimized by reducing the time in the etching solution.

The cross-sectional thicknesses of the capacitor, (TMM) as shown in Fig. 2a, were: Ta = 3500Å, Ta_2O_5 = 3600Å, MnO_2 can be chosen, nichrome-gold counterelectrode = 5000Å. The TM capacitors were made with the same thicknesses but without MnO_2 ; the TM capacitors were used as monitors throughout the experiments.

The experimental conditions for the deposition of MnO_2 films are given in Table I. The experiments which used a biasing grid had that grid placed 2.5 cm from the substrate table. Special emphasis was placed on the work at 2 kV + rf because there was some indication that these conditions were the best conditions of those studied here.

The TMM capacitors were measured for leakage current at 75V; capacitance and dissipation factor were measured from 400 Hz to 100 kHz on many capacitors. Dissipation factors and capacitance were routinely measured at 1 kHz on an automatic capacitance bridge assembly (General Radio Model 1680). The MnO_2 films were checked for carrier type, resistivity, and x-ray diffraction techniques were used to check the phase or phases of MnO_2 present (7).

To investigate the effect of sputtering on the Ta_2O_5 , a number of TMM capacitors were etched in a KI- I_2 solution to remove the nichrome-gold counterelectrode. The MnO_2 could then be removed with a solution of 10 cc HNO_3 , 5 cc superoxol, 85 cc water. These solutions did not attack the Ta_2O_5 . The ni-

chrome-gold counterelectrode was then evaporated on the Ta_2O_5 . These capacitors are designated as TMM-M capacitors.

As a check on the effect of the etching solutions on the dissipation factor and leakage current, control TM capacitors were made after exposure to the etching solutions. No change in either leakage current or dissipation factor was found.

Results

MnO₂ films.—The MnO_2 films were sputtered on clean glass substrates for x-ray diffraction analysis. The deposits were mainly amorphous with diffuse rings indicating the presence of pyrolusite and/or γ - MnO_2 . Films were sputtered in pure oxygen with rf and 2 or 3 kV d-c power (Table I).

The density of the sputtered MnO_2 was found to be 3.0 g/cc, as determined by weight difference, area, and thickness measurements. The theoretical density is 5.0 g/cm³ (8) and 4.7 g/cm³ has been obtained experimentally by Klose (9) on pyrolyzed samples of MnO_2 . The resistivity of MnO_2 is as low as 0.0028 ohm-cm for bulk pyrolyzed samples (9). The MnO_2 films sputtered in the present experiments had apparent (measured) resistivities as low as 0.3 ohm-cm. Using the equation of Wiley and Knight (10) to correct for the porosity of the MnO_2 films, the sputtered MnO_2 films have resistivities as low as 0.2 ohm-cm. Valletta and Pluskin (5) obtained MnO_2 films of 5 ohm-cm using d-c sputtering.

The activation energy for conduction was measured for various samples with resistivities from 1 to 5 ohm-cm. Typical data are shown in Fig. 3. The change in activation energy at approximately 60°C was not found when the samples were remeasured. This nonreversible behavior of the activation energy indicates that there may be a small change in stoichiometry. The initial measured activation energy between -55°C and 60°C was found to be 0.10 eV (± 0.01) for all samples and the initial activation energy measured from 65° to 125°C was 0.21 eV (± 0.03). This higher activation energy was not observed when the samples were remeasured and an activation energy of 0.10 eV was found over the temperature range of from, -55° to 125°C. The measured activation energy and the initial anomaly temperature were similar to those values found by Bhide and Damle (11) on both natural ores and chemically pure β - MnO_2 pellets. Wiley and Knight (10) observed a change in activation energy at 115°-140°C while

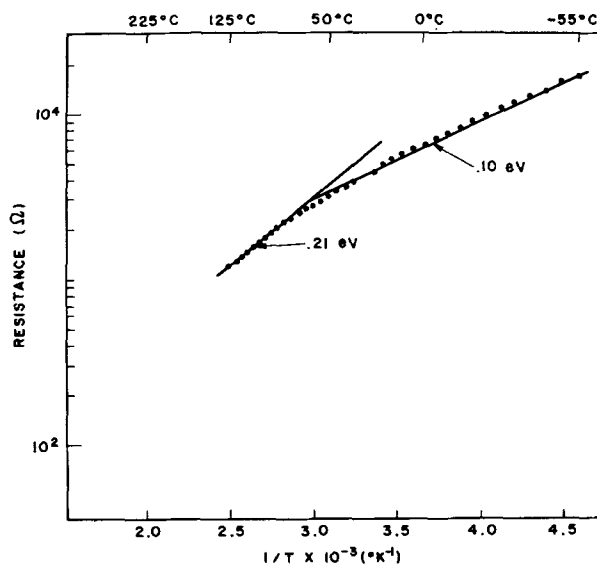


Fig. 3. Typical plot of resistivity vs. $1/T$ for activation energy determination.

other workers (12, 13) found no change in activation energy.

The MnO_2 films used in the TMM capacitors were always n-type and had apparent resistivities of less than 1 ohm-cm. The MnO_2 sputtered in these experiments is thought to be nonstoichiometric but not differing by more than 5% from an O/Mn ratio of 2, on the basis of the resistivity vs. O/Mn data of Wiley and Knight (10).

Capacitors.—Using the model of McLean (14), the measured dissipation factor was taken as

$$\tan \delta = \tan \delta' + \omega R_s C$$

where $\tan \delta'$ represents the dissipation in the dielectric and R_s represents dissipation losses due to the resistance of the electrodes, MnO_2 , and geometry. From the data in Fig. 4, it can be seen that the series resistance, R_s , is most important at high frequencies and can be neglected at 1 kHz. The TMM-M curve of Fig. 4 represents the same capacitors as in the TMM curve, however, the counterelectrode and the MnO_2 have been removed from the dielectric. After replacing the counterelectrode, the TMM-M curve was taken. At 1 kHz it can be seen that the $\tan \delta'$ for the TMM-M has been reduced, but remains higher than the $\tan \delta'$ value for the monitor capacitors. This indicates some change in the dielectric due to the sputtering process. Whether this increase in $\tan \delta'$ is due to substrate heating or bombardment by energetic particles cannot be determined at this time. The series resistance for the TMM capacitors is ~ 17 ohms; R_s for the TMM-M is ~ 4 ohms and R_s for the monitor (TM) is ~ 3 ohms. The TMM capacitors have higher capacitance values because they have an area of 0.192 cm^2 as compared with an area of 0.132 cm^2 for the TMM-M and TM capacitors. This difference is due to the 0.025 cm border on the TMM capacitors. The capacitance density for all the capacitors is $0.052 \mu\text{F}/\text{cm}^2$ at 1 kHz.

The data in Fig. 5 show the effect of d-c sputtering voltage on the dissipation in the dielectric; at 1 kHz the $\tan \delta'$ value is lowered by a factor of 3 when sputtering is done at 2 kV d.c. Removal of the border of the 3 kV sputtered TMM capacitors shows a drop in the series resistance from ~ 16 to ~ 3 ohms. The $\tan \delta$ curve of the TMM capacitors without the border is very close to the curve for the TMM capacitors with the MnO_2 removed. This drop in R_s is due to the removal of the high series resistance capacitor elements located at the edges of the MnO_2 border. Calculations show that these outer elements have a series resistance of approximately 10^5 ohms and could

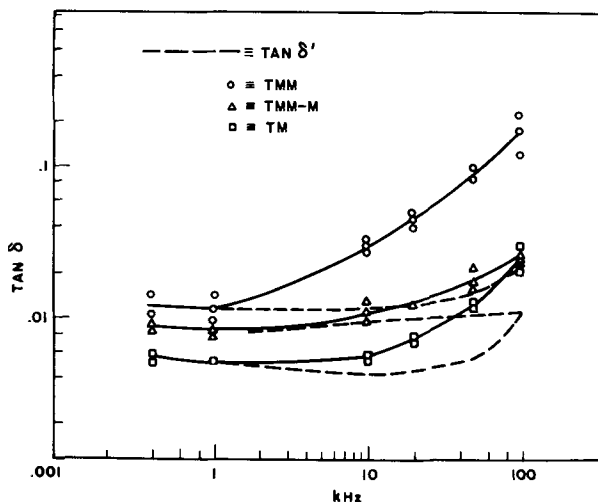


Fig. 4. Separation of the series resistance, R_s , from $\tan \delta$ for TMM, TMM-M, and TM capacitors.

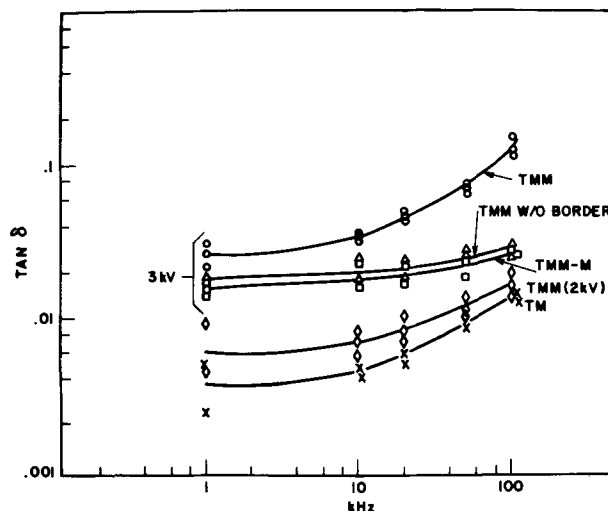


Fig. 5. Log dissipation factor vs. log frequency for capacitors sputtered at 3 kV + rf and 2 kV + rf. Also the effect of the MnO_2 border on dissipation factor is shown.

add several ohms to the measured series resistance of the TMM capacitors. The TM monitor capacitors and the TMM capacitors (without the MnO_2) border have similar series resistances because the MnO_2 layer between the dielectric and the metal counterelectrode only contributes about 10^{-4} ohms to R_s . The curves for the 2 kV sputtered depositions show similar results. In the case of the 2 kV depositions there is still some change in the $\tan \delta'$ at 1 kHz, however, it is much less than the results at 3 kV when compared with the TM capacitors.

The effect of thickness of the MnO_2 on the dissipation factor was found to be negligible for MnO_2 films from 750 to 1800 \AA thick. Dissipation factors (1 kHz) and leakage currents were measured on 150 TMM capacitors with $1120 \pm 80 \text{ \AA}$ of sputtered MnO_2 . These capacitors were fabricated without the 0.025 cm border. The dissipation factor was uniform from slide to slide to 12% and the MnO_2 thickness as measured by a Taly-Step was uniform to 7%. Variations in $\tan \delta$ must be due to localized temperature gradients and/or plasma variations.

Leakage current measurements were made on these capacitors at 75V. It was found that higher leakage currents were observed in the capacitors that had high dissipation factors. The initial yield of the TMM capacitors was 96%, while the monitors had an initial yield of 100%. The initial yield is determined by the number of shorts at 60V. Leakage current measurements at 75V on the TMM capacitors showed that 91% had acceptable leakage currents; there were no additional shorts at 75V. An acceptable leakage current was taken as 1 A/F or $7 \times 10^{-9} \text{ A}$ for these TMM capacitors. The test condition for the monitors (TM capacitors) was 50V with a leakage current of 2 A/F to be acceptable. Under this condition, no monitors had acceptable leakage currents.

The dissipation factors for the TMM capacitors with 1120 \AA of MnO_2 sputtered at 2 kV d.c. were measured as a function of frequency and can be compared with the TM capacitors from the same batch. The dissipation is slightly higher than the values for the TM capacitors, but a significant decrease in $\tan \delta$ is obtained over 3 kV d-c sputtered TMM capacitors.

Conclusions

It has been demonstrated that low resistivity MnO_2 can be sputtered with deposition rates of 15 $\text{ \AA}/\text{min}$ and with resistivities as low as 0.3 ohm-cm; 1 ohm-cm material can be sputtered routinely and reproducibly.

It has also been shown that TMM capacitors can be fabricated with sputtered MnO_2 films that have repro-

ducible dissipation factors of 0.008 at 1 kHz and 0.011 at 100 kHz. This is a large improvement over the dissipation factors for TMM capacitors produced with chemically deposited MnO₂ (0.015 at 1 kHz and 0.06 at 100 kHz). Leakage currents for the TMM capacitors with sputtered MnO₂ were on the average 1×10^{-9} A with 7×10^{-9} A being acceptable. Deposition of MnO₂ by 3 kV d-c + rf sputtering was found to increase the dissipation factor of the dielectric (at 1 kHz) by 50% when compared with TM monitors. This increase in the dielectric dissipation factor was reduced to $\leq 20\%$ when 2 kV d.c. + rf was used.

Acknowledgments

The authors would like to thank R. S. Wagner, H. J. Levinstein, and N. Schwartz for many helpful discussions and M. H. Read for the x-ray diffraction measurements.

Manuscript submitted July 23, 1971; revised manuscript received ca. Nov. 4, 1971.

Any discussion of this paper will appear in a Discussion Section to be published in the December 1972 JOURNAL.

REFERENCES

1. D. A. McLean and F. E. Rosztochy, *Electrochem. Technol.*, **4**, 523 (1966).
2. W. Mindt, *This Journal*, **118**, 93 (1971).
3. L. Slack, Unpublished results.
4. J. H. Cash, Jr. and R. Scott Clark, *This Journal*, **113**, 58C (1966).
5. R. M. Valletta and W. A. Pliskin, *ibid.*, **114**, 944 (1966).
6. R. W. Berry, P. M. Hall, and M. T. Harris, "Thin Film Technology," p. 380, D. Van Nostrand Co., Inc., Princeton, N. J.
7. G. Gattow and O. Glemser, *Z. Anorg. Allgem. Chem.*, **309**, 121 (1961).
8. Handbook of Chemistry and Physics, 47th ed., The Chemical Rubber Co. (1966).
9. P. H. Klose, *This Journal*, **117**, 854 (1970).
10. J. S. Wiley and H. T. Knight, *ibid.*, **111**, 656 (1964).
11. V. G. Bhide and R. V. Damle, *Physica*, **26**, 33 (1960).
12. J. Brenet, *Compt. Rend.*, **248**, 776 (1959).
13. J. N. Das, *Z. Physik*, **151**, 345 (1958).
14. D. A. McLean, *This Journal*, **108**, 48 (1961).

Solution Chemistry and Colloid Formation in the Tin Chloride Sensitizing Process

R. L. Cohen and K. W. West

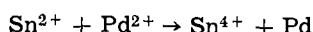
Bell Telephone Laboratories, Incorporated, Murray Hill, New Jersey 07974

ABSTRACT

For many years, stannous chloride solutions have been used to prepare surfaces so that they would catalyze deposition from electroless plating solutions. This paper discusses the colloid and solution chemistry of such baths, including the colloid formation, size mediation, and aging processes. The colloid is shown to be nucleated by stannic ions, and mediated by stannous ions. The investigation was carried out primarily using Mössbauer spectroscopy to characterize the materials involved.

For many years, dilute solutions of stannous chloride in HCl have been used to prepare surfaces for electroless plating. Typically, the technique used has been to dip the object to be plated in the tin solution, wash it, and then dip it into another solution containing, e.g., Pd ions. This treatment can be used to prepare a wide range of materials for electroless plating by copper, nickel, gold, or other metals. A recent useful review (1) of this topic lists patents going back to 1933, and a wide range of variations on the basic approach.

Generally in the literature, the tin bath treatment is called "sensitization" and the Pd (or similar) second treatment is called "activation." The technique is believed to work (1) via the deposition of Sn²⁺ ions from the tin bath, and subsequent reduction of Pd ions by the tin



The Pd deposited in this way serves to nucleate the deposition from the electroless plating bath.

Despite the extensive practical application of the process and its variants, relatively little fundamental research into the chemical processes and surface physics at work has been reported. The importance of such research has increased recently with the demonstration that the sensitizer is photosensitive (2) and that the sensitizer could be applied to specific areas of the substrate (3); either of these approaches allows generation of controlled patterns. The application of these

processes for manufacture of printed cables and wiring boards has considerably increased the possible use of the traditional technique.

Recently, a number of studies have been reported dealing with the nucleation and growth of the plated metal layer (4-6), and the morphology of the sensitizing layer. However, we have been able to find no published work studying in detail the chemical composition of the film deposited by the tin chloride bath, or on the chemistry of the bath itself. Sard (4) showed that the electron diffraction pattern of the tin coating on the sensitized substrate was identifiable as belonging to SnO₂, but was careful to point out that the material might have undergone some change in handling. Recent unpublished work (7) found an electron diffraction pattern which could be attributed to a mixture of SnO and SnO₂, but also pointed out that the high vacuum environment, heating from the electron beam, and oxidation during handling might have affected the results. Thus, further research on the chemical composition of the sensitizing layer seemed indicated. At the time we began this work (8), we could find no published research discussing the formation of the sensitized layer from the tin chloride solution, though the chemistry of such solutions has been extensively studied.

On the other hand, the morphology of the sensitized surface has been studied (4, 5) by electron microscopy, and the studies have shown that the layer produced by the tin chloride bath consists of (typically) 100Å

clumps of 25Å particles, covering ~25% of the surface area. The amount of tin deposited typically ranges from about 1-10 $\mu\text{g}/\text{cm}^2$, measured by x-ray fluorescence analysis (7, 8).

There are basically two pieces of evidence showing that the sensitizing material deposited on the substrate is present as a colloid in the bath. The first is Sard's observation (4) that the sensitized surface contains small discrete particles. The second is the fact, discussed elsewhere (9) that the Mössbauer spectrum of the layer deposited by the tin bath is distinctive and unusual, but identical with the spectrum of colloidal particles centrifuged from the solution. These facts suggest that a study of the sensitization process should begin with a study of chemical processes in the bath itself. There will be no further discussion here of the chemical makeup of the deposited layer itself.

We present here the results of recent studies of the "front end" of the sensitization process—the tin solution chemistry and the formation of the colloid. Data are presented to establish

- (i) that the colloid is based on Sn^{4+} , but contains roughly half as much Sn^{2+} ,
- (ii) the mechanism of colloid formation and size mediation,
- (iii) the details of the solution aging.

The discussion proceeds in four parts: We first show briefly the applications of Mössbauer spectroscopy to the study of tin chemistry. Second, the experimental techniques are described. Third, we discuss the colloid formation in terms of the well-known tin solution chemistry. The model developed in this way is then confirmed with some further experiments.

Mössbauer Spectroscopy

Mössbauer spectroscopy (MS), known more formally as recoil-free nuclear gamma ray resonance spectroscopy (10), has in recent years been increasingly used for studying the chemistry and bonding of various elements, and has more recently been used for analytical determinations as well. The elements that have been the most used in chemical research have been iron and tin. A review of the use of MS in chemistry generally has been given by Herber (11); a brief discussion of the MS of tin compounds has been given by Donaldson (12), and an exhaustive survey of Sn organic compounds has been done by Zuckerman (13). The MS technique is one in which the changes in energy levels of nuclei (in this case, Sn^{119} nuclei are the resonant species) due to electronic perturbations are studied. The effects important in the work here are the presence of the 5s electrons (in stannous ions) which tend to increase the nuclear transition energy over that observed in the Sn^{4+} ions, and quadrupole interaction, which splits the absorption line into a doublet. Generally, the stannous ions have larger quadrupole splittings than the stannic, and in most of the spectra shown here the splitting of the divalent tin absorption lines is large enough to be resolved.

Experiments are performed by varying the source gamma-ray energy by small amounts (using the Doppler effect), and measuring the transmission of the sample as a function of gamma-ray energy. A "dip" in the spectrum then corresponds to resonance absorption by Sn^{119} nuclei in the absorber. The energy of the resonance absorption, and the quadrupole splitting of the Sn^{2+} peaks, are characteristics of particular ionic surroundings and can be used to identify compounds in favorable cases. Examples of spectra of some well-characterized tin compounds are shown in Fig. 1. Since the experiments were done with a source containing Sn^{4+} nuclei of stannic ions in the absorbing materials resonantly absorb near the source emission energy, i.e., near zero (Doppler shift) velocity. The isomer shift between Sn^{2+} and Sn^{4+} corresponds to about 3-4 mm/sec, so that the (quadrupole split) divalent lines are centered about this region.

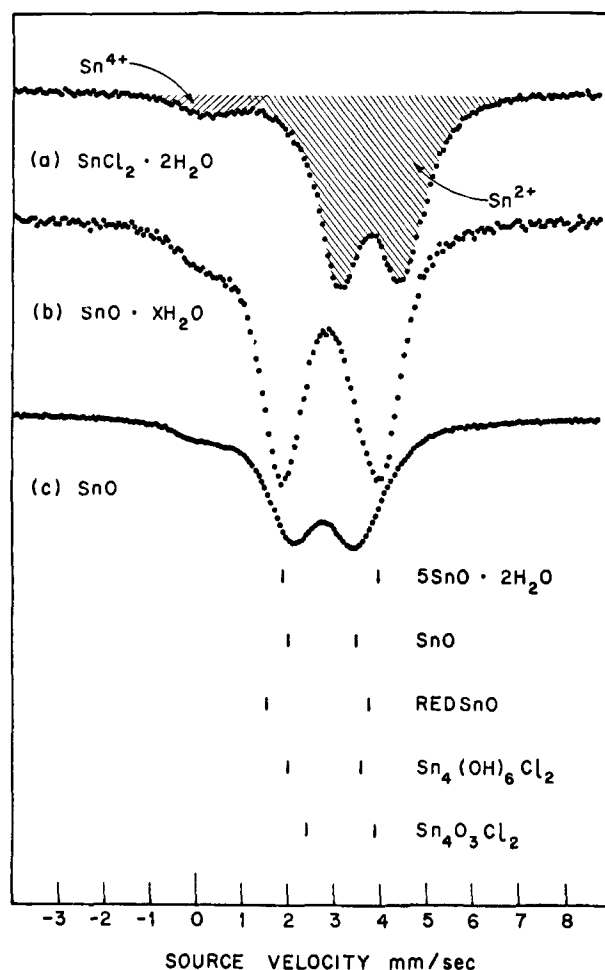


Fig 1. Observed spectra of 3 stannous compounds. The $\text{SnCl}_2 \cdot 2\text{H}_2\text{O}$ was Baker, reagent grade; the other two were made in our laboratory by standard preparative techniques. Note the existence of a line due to Sn^{4+} in all samples. Line positions reported in Ref. (14) for various well-characterized tin compounds are shown below the spectra.

Experimental

The Mössbauer spectroscopy experiments were done with standard techniques: Transmission geometry was used, with a source of $\sim 2\text{mCi}$ $\text{Sn}^{119\text{m}}$ in the form of BaSnO_3 . Both the source and absorber were maintained at $\sim 80^\circ\text{K}$ during the measurements to increase the resonance strength. The gamma rays were detected with a sodium iodide scintillation crystal and photomultiplier. A "critical absorber" of 45μ Pd was used to separate the Sn x-rays from the desired 23.8 keV gamma rays. Standard nuclear electronics were used for counting. The data were taken with a constant-acceleration drive (15) and multichannel analyzer used in the multiscaling mode. Up-down multiscaling was used to fold the two halves of the spectrum in the analyzer, and the spectra shown were traced directly from X-Y plots produced by the analyzer. The absorber was in the Dewar vacuum, and was inserted with the Dewar precooled. Thus, the absorber was frozen (in a nitrogen gas atmosphere) to very low temperatures before being subjected to vacuum; this should have greatly reduced alteration due to dehydration. "Frozen solution" (16) samples were prepared by mixing the tin solution with 50% of its own volume of methanol, placing in a 5 mm deep polyethylene dish, covering, and quick-freezing in liquid nitrogen. Additional experiments with different amounts of methanol and with glycerol showed that a glass was being formed by this process.

Unless otherwise stated, the solutions studied here were made by dissolving reagent grade $\text{SnCl}_2 \cdot 2\text{H}_2\text{O}$

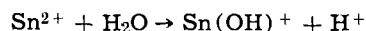
in water, and promptly adding reagent grade (37%) HCl. The concentrations used were 20g $\text{SnCl}_2 \cdot 2\text{H}_2\text{O}/1$ (0.089M) and 10 ml HCl/1 (0.1M). Solutions were mixed at room temperature and kept under nitrogen gas to inhibit oxidation.

Tin Chloride Solution Chemistry

The colloid and solution chemistry of the tin chlorides has been extensively studied, and we can use the existing information, in combination with our Mössbauer spectroscopy measurements, to analyze the solutions and precipitates made in this process.

We will begin with some of the basic reactions and equilibria which are important for the system:

1. The solution of divalent tin in water results in hydrolysis



Divalent tin ions can hydrolyze more than one molecule of water; in fact the dominant complexed species is the polynuclear $\text{Sn}_3(\text{OH})_4^{2+}$ ion (17). Figure 2 shows the relative concentration of the various complexes as a function of pH. The results shown in Fig. 2 are for a perchloric acid medium, which was used to eliminate the effects of chloride complex formation. It can be seen that in the concentration range used in our solutions, the hydroxy complexes form a relatively small fraction of the total divalent tin.

2. Sn^{2+} ions also complex with Cl^- ions in solution; an indication of the relative population of these complexes (18) (under slightly different conditions from those existing in our solutions) is shown in Fig. 3. Other results published in Ref. (19) show that the complex formation is not very different for the tin and chloride ion concentrations used by us, except that the SnCl_4^{2-} complex is probably not present.

The data in Fig. 2 and 3 show that as HCl is added, the fraction of chloride-complexed Sn^{2+} is increased, while the hydroxy complex is decreased. Reducing the H^+ concentration, though, (e.g., by neutralizing with NH_4OH) increases the fraction of the $\text{Sn}_3(\text{OH})_4^{2+}$ complex, culminating in the precipitation of some form of stannous hydroxide (or hydrous stannous oxide) typically around pH 1-3, depending on conditions.

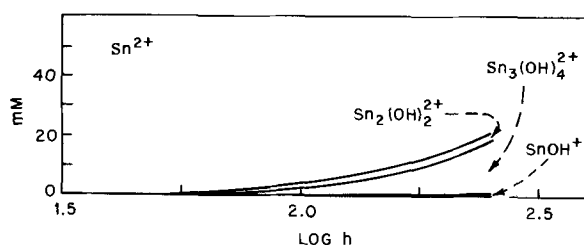


Fig. 2. Distribution of hydrolyzed complexes in solution [from Ref. (17)].

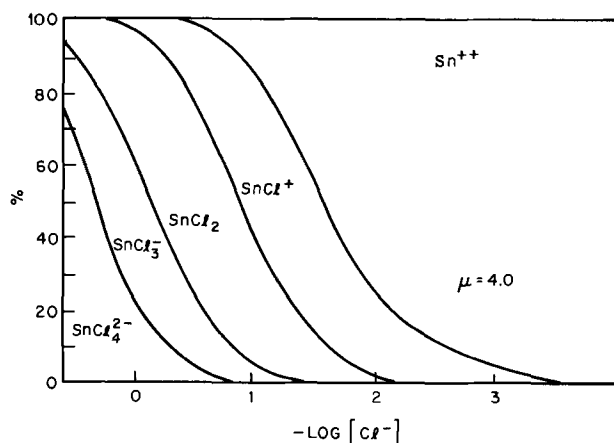


Fig. 3. Chloride complex formation by stannous ions [from Ref. (20), ion strength 4.0].

3. Though the solution preparation procedures used do not intentionally generate Sn^{4+} ions, our results show that stannic ions are present in large quantity, and seem to be important for the working of the process. There are two obvious ways for stannic ions to get into the solution initially: as an impurity in the starting $\text{SnCl}_2 \cdot 2\text{H}_2\text{O}$, and by oxidation of the stannous ions by oxygen dissolved in the bath water. The $\text{SnCl}_2 \cdot 2\text{H}_2\text{O}$ spectrum shown in Fig. 1 shows that even in the fresh reagent grade material used there, ~5% (21) of the tin ions are tetravalent, and will appear in the bath in that form. The solubility of oxygen in water is enough so that dissolved oxygen can convert an additional ~1% of the stannous ions to stannic form. This reaction proceeds rapidly, especially in the presence of light. Once the bath is made up, of course, the continued oxidation from atmospheric oxygen will contribute to the aging process.

4. No spectra attributable to dissolved mixed valence ($\text{Sn}^{2+}\text{-Sn}^{4+}$) complexes were observed in this work.

The solution chemistry of the stannic ion is dominated by the complete hydrolysis in aqueous solutions, with almost 4H^+ ions being produced per Sn^{4+} ion (22). It seems to be unclear, however, despite extensive research, whether essentially all the tin ions have been complexed as $\text{Sn}(\text{OH})_4$, or whether a distribution of species with different degrees of hydrolysis (as in the Sn^{2+} case) exists. The hydrolysis can be inhibited (23) by the presence of more than 0.5M Cl^- ions; presumably the SnCl_6^{2-} complex becomes the dominant species in that case.

Thus, combining this information, we would expect our freshly made tin sensitizing solutions to consist of about 95% Sn^{2+} ions, mostly complexed with Cl^- ions, and 5% Sn^{4+} ions, which we will for simplicity assume to be complexed as $\text{Sn}(\text{OH})_4$. However, this situation is not stable, because of the tendency of the hydrolyzed stannic ions to polymerize and precipitate as $\text{Sn}(\text{OH})_4 \cdot n\text{H}_2\text{O}$. This reaction has been studied in solutions of pure SnCl_4 (23) and as a function of added bases and acids (24). Depending on the concentration of various ionic species, the colloid formation and subsequent precipitation can take from a few minutes to months (23, 24).

Our results, which show (Fig. 4a) that divalent tin is present in the colloidal precipitate in a pH and chloride ion concentration range where it should be dissolved, suggest that the colloid formed by the stannic ions also bonds stannous ions. The great relative abundance of the stannous ions (~20X Sn^{4+} concentration at the beginning of colloid formation, and increasing as the stannic ions get removed from solution by the polymerization) should encourage this process.

The sensitizing bath, then, appears to work in this way: the tin chloride solution forms a colloidal suspension which is based on the polymerization of hydrolyzed Sn^{4+} ions. Because of the large relative abundance of Sn^{2+} ions, they are bound in the colloid as it forms, roughly in the ratio of one Sn^{2+} per 2Sn^{4+} ions. (Estimated from the areas in the respective spectral regions.) When the substrate is dipped into the bath, the colloidal particles adhere to (or are adsorbed on) it, and these contain the divalent tin which later deposits the Pd from the Pd bath.

The description contains two new features, as pointed out by D'Amico *et al.* (8): First, the view that the material deposited on the substrate is present as a colloid in the bath, and second, the idea that the colloid itself is based on Sn^{4+} . Though colloidal systems involving more than one cation species have been extensively studied (25), we believe this to be the first case in which different valence states of the same element play distinct roles.

It is interesting to see how this approach can explain some of the aspects of the bath formation process. For example, sensitizing baths are often made (as we

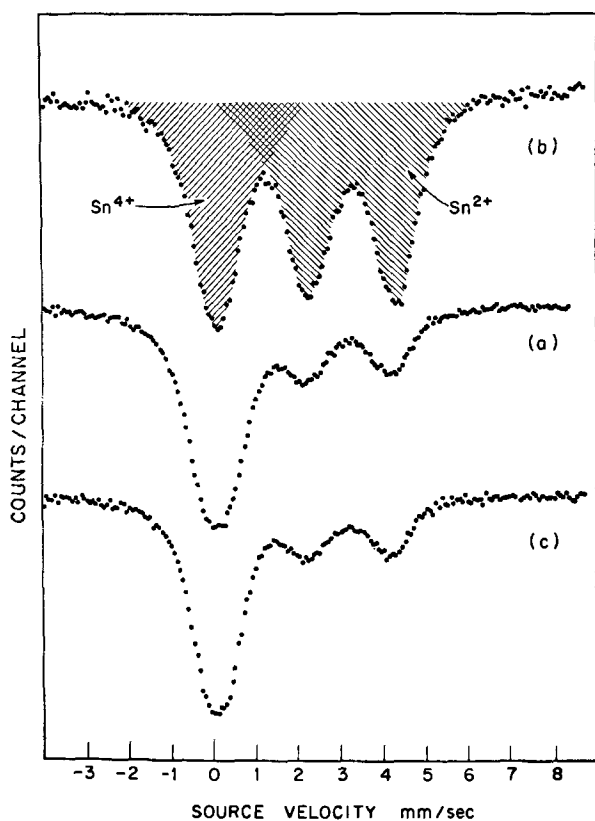


Fig. 4. Spectra of precipitates from various tin chloride baths: (a) colloid centrifuged from solution "A" as discussed in text; (b) heavy precipitate following solution of 2g $\text{SnCl}_2 \cdot 2\text{H}_2\text{O}$ in 100 ml water (no acid); (c) colloid centrifuged from solution "C." Note that the solids formed in the acidified solutions have far less divalent tin than the material shown in (b).

describe above) by first putting the tin chloride in the water, and then adding the acid. When this procedure is followed, a heavy precipitate forms immediately, while the tin chloride is dissolving. (If left for a few minutes, the precipitate coagulates and settles.) Prompt addition of the acid "dissolves" the precipitate, leaving a slightly opalescent solution (which we call "A"). If the tin chloride is dissolved in the acid first, and then the water added, a relatively clear solution is obtained (which we call "B"). If the acid is added to the water first and then the tin chloride is added, the solution formed (C) is slightly less milky than A.

With the interpretation we have given above, plus the discussion in the references, it would appear that "A," the technique of redissolving the precipitate, is a controlled way of generating the colloid. As a step in understanding the formation process, we have studied the Mössbauer spectrum of the heavy precipitate formed in the first stage of "A," before the acid is added to redissolve it. The results are shown in Fig. 4b. Comparison with Fig. 4a shows that the divalent line positions are the same as those in the colloid, but that relatively more of the tin is divalent.

Our MS experiments have indicated that essentially all the tetravalent tin in the fresh "A" solutions is tied up in the colloid (26). Figure 5 shows (for an aged solution) that the tetravalent tin is in the colloid and the dissolved ions are essentially all divalent. Thus, the solution is mostly depleted of its Sn^{4+} , and the ratio of dissolved $\text{Sn}^{4+}/\text{Sn}^{2+}$ must have decreased as the colloid grew. This would make the colloidal particles richer and richer in Sn^{2+} as they increased in size. Adding the acid, then, dissolves the Sn^{2+} -rich outer layers.

This picture is supported by an experiment in which we added perchloric acid (instead of HCl) to increase the H^+ concentration without increasing the Cl^- con-

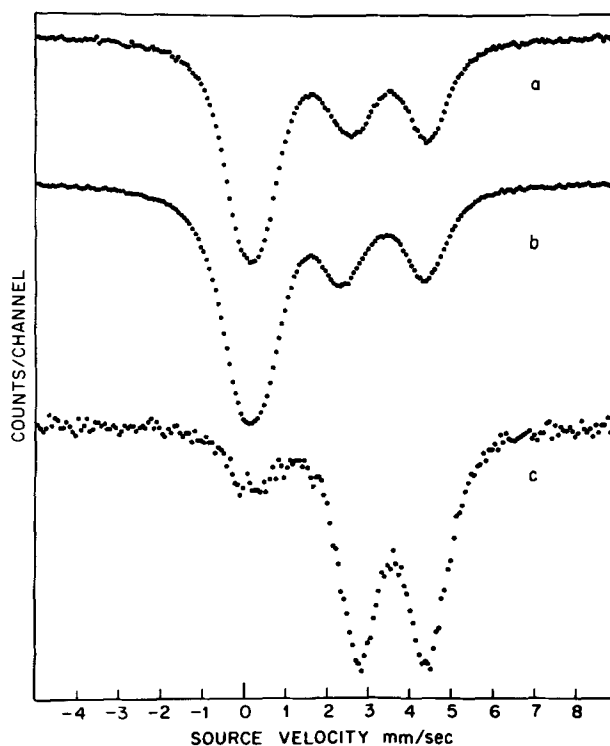


Fig. 5. Mössbauer spectrum of a frozen tin chloride bath is shown in (a). Centrifugation (100,000G for 16 hr) removes most of the colloid, the spectrum of which is shown in (b). The spectrum of the (frozen) supernatant solution is shown in (c). Note that essentially all the ions in solution are divalent. The bath was aged three days exposed to air before the separation and measurements.

centration. Increase in H^+ concentration is effective in dissolving precipitates of divalent tin, which are strongly pH controlled, but ineffective (23) in dissolving the hydrolyzed Sn^{4+} precipitate, which is Cl^- sensitive. Since the perchloric acid was effective in dissolving the heavy precipitate (leaving again a slightly opalescent solution), it would appear that the divalent tin is the dominant species in coagulating the mixed $2^+ - 4^+$ colloid initially formed on dissolving the tin chloride in water. When the $\text{SnCl}_2 \cdot 2\text{H}_2\text{O}$ is dissolved in water, the colloid forms, coagulates, and settles, and the visible reactions cease. This can be explained by the fact that as the hydrolyzed stannous ions precipitate out, the solution is further hydrolyzed to maintain an appropriate fraction of OH-complexed ions in solution. Thus the H^+ ion concentration increases from $\sim 0.02\text{M}$ (due to hydrolysis of the stannic ions) initially until the bath is acid enough to keep the remaining Sn^{2+} ions in solution. At this point the precipitation of Sn^{2+} to resume, while addition of acid tends to redissolve the divalent-rich precipitate. We have determined that the precipitate formed by the addition of alkali in fact has a still higher ratio (Fig. 6) of $\text{Sn}^{2+}/\text{Sn}^{4+}$ than that shown in Fig. 4, as would be expected.

The clear solution B, made by dissolving the tin chloride in acid first, appears to contain much smaller colloidal particles. The solution used by Sard (4) was made up in this way, and showed a deposit of particles mostly smaller than 30Å diameter, too small to have been separated by our centrifuging conditions (27). Thus the transparency of those solutions means that the colloid is only partly formed (i.e., Sn^{4+} still in solution) and/or is much finer than the colloid in A. Solution C (tin chloride into acidified water) has also had the colloid forming slowly (relatively to the heavy and rapid precipitation of the first step of A). The colloid formed in C appears (see Fig. 4c) identical to that formed from the A solution. The greater transparency

of C, however, suggests that the particle size range is somewhat smaller.

This analysis of the situation, in which the coagulation and precipitation are limited by the cumulative hydrolysis of the Sn^{2+} ions, helps to explain why such a wide range of tin concentrations [solutions containing from 0.16g to 200g $\text{SnCl}_2 \cdot 2\text{H}_2\text{O}$ /liter H_2O have been mentioned by Ref. (1)] has proved useful in making sensitizing baths. The HCl concentration is also not very critical, because of the relatively wide range of Cl^- concentrations over which the colloid forms, the slow solution of the colloid even in solutions containing large concentration of Cl^- , and possibly, shielding of the Sn^{4+} cores by the divalent-rich outer layer.

We now turn to the evidence that the colloid is not simply a mixture of two compounds, one stannous and the other stannic.

One of the strong indications is that the line positions of the divalent ions do not correspond to those reported for known divalent compounds in the oxychloride or hydroxide family. The picture we have presented, of tetravalent tin hydroxide particles picking up divalent tin ions from solution, makes possible an additional test. If $\text{SnCl}_2 \cdot 2\text{H}_2\text{O}$ is dissolved in water, a heavy precipitate is formed, as stated previously, and then visible reactions stop, leaving a slightly milky solution above the precipitate. According to our model and measurements, that precipitate should contain most of the stannic ions. If alkali (NaOH or NH_4OH solution) is added to the liquid, additional precipitate is formed, leaving again a slightly milky solution. This new precipitate can be removed, and the process repeated. Mössbauer spectra of the resultant solid products at various stages of this reaction are shown in Fig. 6. The spectrum of 6c can be readily identified as belonging to the hydrous oxide $5\text{SnO} \cdot 2\text{H}_2\text{O}$, and appears after the Sn^{4+} ions have been precipitated. The line positions of the Sn^{2+} ions precipitated with the Sn^{4+} ions are significantly different, and we have only found spectra with these line positions in mixed valence materials. It is important to note that except for the number of Sn^{4+} ions present, the concentrations of the various ionic species do not change greatly during the successive stages depicted in 6A, 6B, 6C. Even the pH remains roughly constant

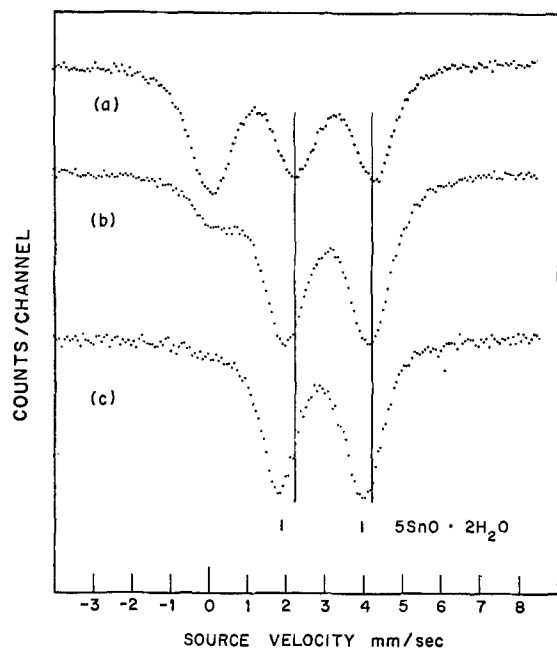


Fig. 6. (a). ppt from solution of 2g $\text{SnCl}_2 \cdot 2\text{H}_2\text{O}$ in 100 ml H_2O . (b). additional ppt obtained by adding 8 ml 1M NaOH to milky solution remaining after A ppt; (c). ppt obtained between addition of 10 ml and 16 ml NaOH. Line positions [from Ref. (14)] for $5\text{SnO} \cdot 2\text{H}_2\text{O}$ are shown.

(~ 1.5) as the additional precipitate is formed. Thus, the distinctive line positions shown by the Sn^{2+} ions in the colloid appear only when Sn^{4+} ions are present in the precipitate as well.

The failure of the divalent ions alone to form a colloid in the tin chloride solution would also be expected from the complex-formation studies discussed earlier which indicate solubility of the divalent species in this range of ionic concentration. We have directly confirmed this by making up a solution of the same ion concentrations specified above, but essentially free of Sn^{4+} ions (28). Such a solution remains absolutely clear for days when stored under nitrogen gas to prevent oxidation of the Sn^{2+} . However, if this solution is then oxygenated, (by bubbling O_2 through it for 5 min) a visible opalescence appears in a day or so. This suggests again that stannic ions are necessary for colloid formation. A similar result is reported by D'Amico *et al.* (8), who also show that, in the absence of colloid formation, sensitization may occur via the precipitation of hydrous SnO during the water rinse step.

This analysis envisages the tin chloride sensitizing bath as a suspension of colloidal particles, based on Sn^{4+} , with Sn^{2+} -rich outer layers, in a bath of bare and complexed Sn^{2+} ions. With this picture in mind, it is easy to see what the "aging" process during normal use of the bath does. Exposure to atmospheric oxygen produces Sn^{4+} ions in the solution; but these are precipitated on the existing colloid particles, and also nucleate new colloidal particles. Spectra in Fig. 7 show the oxidation of an A solution with time.

The discussion above suggests that the best way to maintain the desired colloid during operation is to prevent the production of Sn^{4+} ions; a gas shield over the

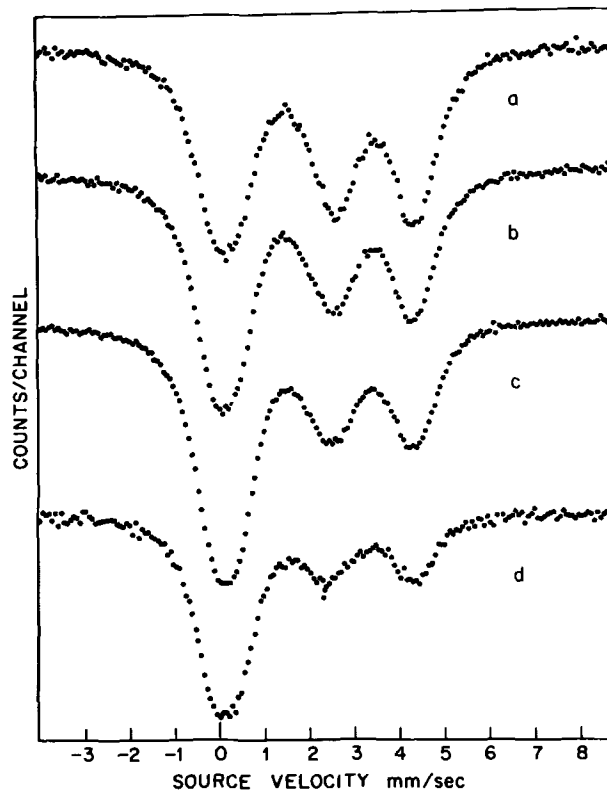


Fig. 7. Spectra of frozen solutions after exposure to air for (a) 1 day, (b) 2 days, (c) 4 days, (d) 6 days in loosely covered beaker. Note that initially, the spectrum of the divalent tin is that shown by Sn^{2+} ions in solution (compare Fig. 5c). As the stannic fraction (line near zero velocity) increases with air oxidation, it forms more colloid, and the divalent tin spectrum gradually changes to that of stannous ions in the colloid (compare Fig. 4a). This shows explicitly that the stannous ions, which are initially dissolved, are incorporated into the tetravalent-based colloid as it forms.

bath to exclude atmospheric oxygen (nitrogen would be satisfactory, but CO₂ or argon would be easier to maintain) should be effective for this. It would probably be much more difficult to remove or reduce Sn⁴⁺ ions which have gotten into the bath by oxidation.

Although it might appear that this would lead to eventual depletion of the sensitizing colloid in the bath, a simple estimate shows that with the known coating density of 5-10 μg Sn/cm², bulk depletion (due to mechanical carry-out on the substrate) will severely reduce the bath volume before the colloid is exhausted.

One additional aspect of the process should be discussed here. Some of the substrate pretreatments involve an etch using NaOH just before immersion into the tin bath. Any carry over of OH⁻ from this bath will tend to precipitate additional Sn²⁺ on the colloid (see Fig. 6 and discussion); this could lead to changes in colloid size and copper deposition.

Conclusions

This research on the tin chloride sensitization process by Mössbauer spectroscopy has been successful in investigating the chemistry and chemical intermediates appearing at various stages. We have developed a detailed picture of the colloid formation mechanisms and size mediation reaction. This information has been used to discuss some of the possible difficulties which might arise in production applications.

Acknowledgments

We are greatly indebted to J. F. D'Amico and other members of the Western Electric (ERC) Chemical Process Technology Department for frequent discussions during the course of this work, and for making reports available to us before publication. Work on the colloids was greatly aided by the availability of the Biophysics Research Department's ultracentrifuge, and advice from T. Yamane. R. Sard provided helpful discussions on the structure of sensitized surfaces.

Manuscript submitted June 22, 1971; revised manuscript received ca. Nov. 19, 1971.

Any discussion of this paper will appear in a Discussion Section to be published in the December 1972 JOURNAL.

REFERENCES

- W. Goldie, "Metallic Coating of Plastics," Vol. I., p. 39ff Electrochemical Publications Limited, Middlesex (1968).
- D. J. Sharp, Abs. 262, p. 651, Electrochem. Soc. Extended Abstracts, Spring Meeting, New York, May 4-9, 1969; D. J. Sharp, J. Henrickson, J. D'Amico, and J. Kenney, Paper 136 presented at Electrochem. Soc. Meeting, Detroit, Oct. 5-9, 1969; D. J. Sharp, J. F. Henrickson, J. F. D'Amico, and J. T. Kenney, 23rd Annual Conference, Photographic Science and Engineering, New York, May 1970; D. J. Sharp, Proceedings of the Third Plating in the Electronics Industry Symposium, American Electroplaters Society, Palo Alto, California, Feb. 1971, p. 103.
- D. R. Turner, Paper 137 presented at Electrochem. Soc. Meeting, Detroit, Oct. 5-9, 1969.
- R. Sard, *This Journal*, **117**, 864 (1970).
- J. P. Marton and M. Schlesinger, *ibid.*, **115**, 16 (1968).
- A. S. Frieze, R. Sard, and R. Weil, *ibid.*, **115**, 586 (1968).
- P. Sewall, "Characterization of a Photosensitive Tin (II) Compound" Masters Degree thesis, Lehigh University (1969).
- The conclusions reached here closely parallel those reported by J. F. D'Amico and M. A. De Angelo (Private Communication, unpublished report) and J. F. D'Amico, M. A. De Angelo, J. F. Henrickson, J. T. Kenney, and D. J. Sharp, *This Journal*, **118**, 1695 (1971).
- R. L. Cohen, J. F. D'Amico, and K. W. West, *This Journal*, **118**, 2042 (1971).
- R. L. Mössbauer, *Z. Physik*, **151**, 124 (1958). For a general survey, see G. K. Wertheim, "Mössbauer Effect: Principles and Applications," Academic Press Inc., New York (1964). A brief elementary discussion is given by R. L. Cohen, Physics Teacher, p. 308, Oct. 1965.
- R. H. Herber in "Progress in Inorganic Chemistry," F. A. Cotton, Editor, Vol. 8, p. 1, John Wiley & Sons, New York (1967).
- J. D. Donaldson in "Progress in Inorganic Chemistry," F. A. Cotton, Editor, Vol. 8, p. 287, John Wiley & Sons, New York (1967).
- J. J. Zuckerman, in "Advances in Organometallic Chemistry," Vol. 9, p. 21, Academic Press Inc., New York (1970).
- C. G. Davies and J. D. Donaldson, *J. Chem. Soc. (A)*, 948 (1968).
- R. L. Cohen, *Rev. Sci. Instr.*, **37**, 260 (1966) and **37**, 957 (1966).
- See, e.g., R. L. Cohen and K. W. West, *Chem. Phys. Letters*, In press.
- R. S. Tobias, *Acta Chem. Scand.*, **12**, 198 (1958).
- C. E. Vanderzee and D. E. Rhodes, *J. Am. Chem. Soc.*, **74**, 3552 (1952).
- R. S. Tobias and Z. Z. Hugus, Jr., *J. Phys. Chem.*, **65**, 2165 (1961). These authors also show that mixed chlorohydroxy complexes do not appear in solution concentrations used here.
- G. P. Haight, Jr., J. Zoltewicz, and W. Evans, *Acta Chem. Scand.*, **16**, 311 (1962).
- We assume throughout that the "f value" (recoil-free fraction, related to the strength of the Mössbauer effect) is the same for both the di- and tetravalent tin ions. For the mixed-valence materials we have measured, we have verified this to ~ ±20% by converting all the ions to Sn⁴⁺. Any change in f is not very significant for the interpretation of the data, which is based primarily on the relative proportion of divalent tin under various conditions, rather than the absolute 2+/4+ ratio.
- G. E. Collins and J. K. Wood, *J. Chem. Soc.*, **121**, 441 (1922).
- J. S. Johnson and K. A. Kraus, *J. Am. Chem. Soc.*, **63**, 440 (1959).
- J. Guéron, *Compt. Rend.*, **197**, 247 (1933); N. K. Kulrestha, A. K. Dey, and S. Ghosh, *Kolloid-Z.*, **132**, 143 (1953) and **141**, 106 (1955).
- E. Matijević and J. E. Janauer, *J. Coll. Int. Sci.*, **21**, 197 (1966) and references therein.
- This view is based on a number of experiments with different tin solutions, centrifuging conditions, and measurements on both precipitates and supernatant liquids. Though it is impossible to remove completely the Sn⁴⁺ based colloid from solution by centrifuging, all our experiments suggest that few, if any, of the stannic ions are in solution.
- If we assume that the density of the colloid particles is 2 g/cm³, centrifuging for 2 hr at 100,000G separates particles down to 60Å diameter.
- J. D. Donaldson, W. Moser, and W. B. Simpson, *J. Chem. Soc.*, 1727 (1963).

The Field-Dependence of the Dielectric Constant during the Anodic Oxidation of Tantalum, Niobium, and Tungsten

J. L. Ord,* M. A. Hopper,* and W. P. Wang**

Department of Physics, University of Waterloo, Waterloo, Ontario, Canada

ABSTRACT

In situ ellipsometric measurements on the galvanostatic oxidation of tantalum, niobium, and tungsten show that both the refractive index and the thickness of the oxide change suddenly on changing the current applied to the film. For all three metals the thickness was found to increase linearly with the electric field, whereas both the refractive index and low frequency (1000 Hz) dielectric constant were found to decrease linearly with increasing field. The magnitudes of the changes in dielectric constant and refractive index that were detected experimentally, when compared with theoretical predictions using standard dielectric theory and the observed change in thickness, indicate that these changes are due to the variation in the density of the film with the applied field. The inclusion of the linear dependence of the dielectric constant on field into an effective field model of the ionic conduction process is shown to be a possible explanation of the curvature in the plot of $\ln(i)$ vs. E for the anodic oxidation process.

It has been known for quite some time that the dielectric constants of valve metal oxides vary with the electric field in the film. Guenterschultze and Betz (1) reported results on a wide variety of valve metals in 1931, and results reported recently (2, 3) show a continuing interest in this phenomenon.

The measurements of refractive index variations with field were carried out in our laboratory in the spring of 1966 to determine whether our recently completed ellipsometer (4) had sufficient sensitivity to detect small variations in the refractive index of a growing film. Also in the spring of 1966, Young and Zobel (5) reported results of experiments which found a curvature in the plot of $\ln(i)$ vs. E for the anodic oxidation of niobium, and they confirmed the earlier measurements (6) of this curvature on tantalum. In that paper and in the oral discussion of it at The Electrochemical Society meeting, several possible reasons for this effect were suggested.

The experiments we report in this paper were designed to determine whether the curvature could be explained using a model in which the local electric field controls the ionic conduction process. The logarithm of the current density can be linearly dependent on the local electric field and yet show a quadratic dependence on the external field if the dielectric constant varies with the field. We present results of measurements on the field-dependence of the dielectric constants of the anodic oxides of tantalum, niobium, and tungsten and test the local field model by comparing its predictions with the data of Young and Zobel for tantalum and niobium.

Experimental

The ellipsometer used to obtain the data reported in this paper was the second of two following ellipsometers built in this laboratory and has been described in detail elsewhere (7). This instrument differs little from the first instrument on which the initial measurements were made. Both instruments have 0.01° resolution, and the *in situ* nulling time on thin anodic oxides is typically less than 1 sec. The nulling times for the measurements reported here are somewhat longer than this because they were carried out at film thicknesses for which it is possible to distinguish between small variations in film thickness and

index. Under these experimental conditions the analyzer null readings are generally in excess of 70° and the intensity of light detected by the photomultiplier is not very sensitive to angular displacement from the null position, particularly in the case of the polarizer. The increased sensitivity to thickness and index variations at large A values more than compensates for any increases in nulling times and standard deviation of the data. The light source used with the ellipsometer is a low-power helium-neon gas laser, and all refractive indexes calculated in this paper are pertinent to its wavelength 6328Å.

The initial measurements were all made using a cell with windows mounted for an angle of incidence of 75°, but the more recent results reported in this paper were all obtained at an angle of incidence of 60° using a cell made from a hollow equilateral prism. The cell has standard-taper joints for mounting the electrode holder, platinum counterelectrode, mercury-mercurous sulfate reference electrode (fitted with a 0.1N K₂SO₄ salt bridge), and gas dispersion tube. The electrolyte, 0.2N H₂SO₄, is saturated with argon, and argon is bubbled through the solution during the experiments. All experiments were performed at room temperature (23°C).

Cylindrical samples were prepared from single crystals of tantalum, niobium, and tungsten. When a sample is mounted between Teflon washers in the electrode holder, a vertical surface of approximately 1.2 cm² area is exposed to the solution. Optical measurements are made on a flat on one side of the cylinder. The surfaces are prepared initially by chemically polishing niobium and tantalum and by electropolishing tungsten. In all the experiments reported here, the surface treatment just prior to an experiment consisted of dissolution of the oxide film left by a previous experiment in a solution consisting of hydrofluoric acid saturated with ammonium fluoride for tantalum and niobium and in dilute sodium hydroxide for tungsten. In the case of tantalum, the process progressively etches the sample with each successive run and care must be taken to orient the optical flat parallel to a crystallographic plane that does not tend to roughen when the sample is etched. This was necessary to ensure reproducibility in the optical data which tend to be affected by surface roughness.

The electronic circuitry used with the cell consists of a set of five operational amplifiers, three of which are used to apply constant currents, constant poten-

* Electrochemical Society Active Member.

** Electrochemical Society Student Associate.

Key words: anodic oxidation, valve metals, ellipsometry, dielectric constant.

tials, or linear potential sweeps to the cell. Of the remaining two, one is used to follow the potential and the other is used as a transresistor to monitor the current. In these experiments the galvanostat is the most critical circuit component. Measurements are made as the galvanostat is switched through a sequence of preset d-c currents, all with a superposed a-c current whose amplitude and phase are required to be independent of the d-c current. The output of the potential follower is connected to a lock-in amplifier whose internal reference potential is used to drive the a-c section of the galvanostat. Tests of the galvanostat with passive circuit components show that the a-c current is independent of the d-c current to better than the 0.1% required for these measurements. The 0.1% accuracy is imposed by the fact that when the lock-in amplifier is set 90° out of phase with the current, the a-c potential measured is inversely proportional to the equivalent series capacitance of the cell rather than the capacitance of the oxide layer. The extent to which changes in the equivalent series capacitance are due to changes in the capacitance of the oxide layer rather than its resistance depend on the frequency of the a-c current and the magnitude of the d-c currents. At a frequency of 1000 Hz, changes in the layer resistance for the range of currents used in our experiments produce changes in the equivalent series capacitance of less than 0.1%. The changes we measure in the equivalent series capacitance are typically a few per cent, and hence are mainly due to variations in the capacitance of the oxide film.

The experimental data were recorded on a digital printer, except for the output of the lock-in amplifier which was recorded on an X-Y plotter with calibrated offset. The laboratory HP2114B computer was used for the analysis of the optical data using a program written in BASIC, but it was not used for data acquisition in these experiments.

Results

The first series of experiments were carried out using samples of tantalum, the metal whose oxide turns out to be the least sensitive to field variations of the three metals studied. The ellipsometric data obtained during the anodic oxidation of tantalum at 100 $\mu\text{A}/\text{cm}^2$ are plotted in Fig. 1. In the upper portion of the figure, the polarizer null readings, P , are plotted *vs.* the analyzer null readings, A . The data points start at A and trace out the clockwise loop A - B - C - H - I - J - K , point K overlapping the initial point, A . The complete set of data points would appear as a continuous curve if plotted on the scale of Fig. 1. The points in the figure are a set of points selected from the data at approximately 5° increments. The curve passing through the points is a theoretical curve for the growth of a film of index 2.2 on a substrate of index 3.02-2.57i. In the lower part of the figure the thickness of the film determined from the theoretical curve in the upper portion of the figure is plotted *vs.* potential. The slope of this plot, 5.85×10^6 V/cm, gives the field in the film at a current density of 100 $\mu\text{A}/\text{cm}^2$. Its intercept gives an initial thickness of 30Å of oxide at the beginning of the experiment. When the optical data return to their starting point, the thickness of the oxide on the electrode is 1720Å.

The design of an experiment to test for a field-dependent refractive index makes use of the fact that as the layer is grown at a constant rate, the optical data points trace out the loop at a very non-uniform rate. The rate at which the segment between C and H is traced out is more than 14 times the rate at which the segment J - K is traced out. The nonuniformity can be seen in Fig. 1 by comparing the thickness intervals between the lettered points with the

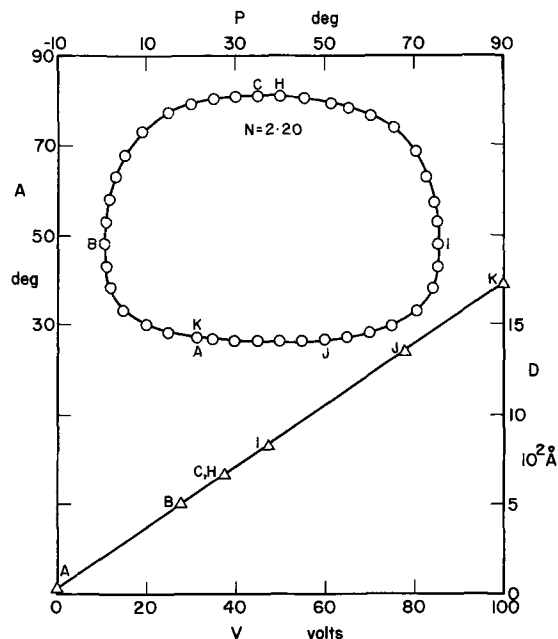


Fig. 1. Anodic oxidation of tantalum at 100 $\mu\text{A}/\text{cm}^2$ in 0.2N H_2SO_4 . The optical data in the upper part of the figure start from point A and trace out the loop A - B - C - H - I - J - K as the oxide film grows. The curve fitted to the optical data is for the growth of a film of index 2.20 on a substrate of index 3.02-2.57i. The film thickness determined from this fitted curve plotted *vs.* potential in the lower part of the figure.

lengths of the corresponding arcs on the P - A plot in the upper part of the figure. In the region between C and H the optical data are most sensitive to slight changes in film thickness. In addition, changes in thickness give rise to changes in P with virtually no changes in A , whereas changes in index at constant thickness give changes in both P and A . Hence, if the current density is switched to another value as the layer is grown through this region, it is possible both to detect and to distinguish between small changes in film thickness and in film index.

The results of an experiment in which the current density is switched from 20 $\mu\text{A}/\text{cm}^2$ to 1 $\mu\text{A}/\text{cm}^2$, then back to 20 $\mu\text{A}/\text{cm}^2$ are plotted in Fig. 2. The optical data are depicted on a P - A plot in the upper section of the figure, and the plot of the potential *vs.* time is given in the lower section. For segments CD and GH the current density is 20 $\mu\text{A}/\text{cm}^2$ and all the optical data points are plotted; for the segment EF the current density is 1 $\mu\text{A}/\text{cm}^2$ and points are plotted at 0.1° intervals in P . In this figure the analyzer scale is expanded tenfold over the polarizer scale to show the fine structure in the data. With this expansion, the most significant feature of the optical data is the shift to higher A values as the current is lowered, and the shift back when the current is raised again. A theoretical curve for the growth of a layer of index 2.2045 is fitted to the data at 20 $\mu\text{A}/\text{cm}^2$, and a curve for a layer of index 2.2059 is fitted to the 1 $\mu\text{A}/\text{cm}^2$ data. The number of figures to which these indexes are quoted is sufficient to allow us to estimate that the difference in the indexes, 1.4×10^{-3} , is accurate to within about 10% although the absolute values of the indexes themselves are not significant to 4 decimal places. An important feature to note is the sign of the index change: as the field and current density increase, the refractive index decreases.

An explicit equation can be written to express the dependence of the refractive index on the steady-state field. If a range of current densities is used in the experiment, a linear dependence of the refractive index on the steady-state field is found in contrast

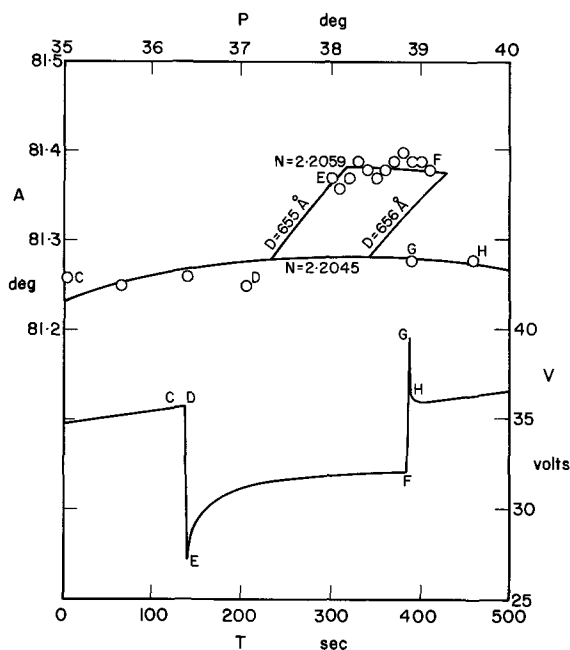


Fig. 2. Transients observed on switching the current density from 20 to 1 to 20 $\mu\text{A}/\text{cm}^2$ in the region between C and H in Fig. 1. Theoretical curves for layer growth at indexes of 2.2045 and 2.2059 and index change at thicknesses of 655 and 656 Å are fitted to the optical data in the upper part of the figure. Potential is plotted vs. time in the lower part of the figure.

to the quadratic field dependence common in nonlinear optics. If an equation of the form

$$n = n_0 (1 - \alpha E) \quad [1]$$

is used to fit the data of Fig. 2, α must have a value of 0.117 Å/V. Another significant feature of the dependence of the index on the field is a lack of overshoot in the optical data during the overshoot in potential. The lack of overshoot in the optical data is an important result which turns out to hold true for all the metal oxides we have studied.

It may be possible to interpret the data plotted in Fig. 2 as resulting from some process other than a change in the layer index, perhaps from a process taking place at the oxide-electrolyte interface. That this is not the case can be demonstrated by measurements at other layer thicknesses. The simplest experiment which demonstrates that the entire layer is involved in the optical changes consists of comparing the results produced by changes in current density at points A and K in Fig. 1. The optical conditions are the same at these two points, but the layer thicknesses differ by a factor of over 50. No optical changes can be detected when the current is switched at point A, whereas significant changes are produced at point K. We do not present the results of this experiment here because in the region of points A and K the optical results do not enable changes in index to be differentiated clearly from changes in layer thickness. We choose instead to present the results of an experiment in which film growth is continued beyond the potential range plotted in Fig. 1 to return the optical conditions to what they were at points C through H in Fig. 1 and 2. Although this experiment is designed mainly to determine whether or not the thickness remains constant as the index changes, its results exhibit the larger optical shift on the second cycle of film growth expected for a process involving the whole film.

Although we plotted curves of constant thickness and variable index in Fig. 2 for thicknesses of 655 and 656 Å, we have as yet said nothing about variations in film thickness as the applied current density

is changed. Because of problems arising from the limited following speed of the ellipsometer, it is difficult to determine whether or not a film thickness change accompanies the index changes by direct inspection of Fig. 2. The data points plotted in Fig. 2 are not simultaneous values of the polarizer and analyzer null positions, because the polarizer and analyzer are nulled sequentially, polarizer before analyzer. At high A values the time required to null the polarizer is considerably longer than that required to null the analyzer, thus complicating corrections to the data to allow for the limited following speed of the instrument. If we do attempt to make following speed corrections to the data of Fig. 2, the strongest conclusion we can reach concerning thickness changes is that the thickness changes by about the same percentage as the change in index, the direction of the change being such as to keep the optical thickness constant. Thickness changes can be detected far more readily if the experiment is performed on the second optical cycle of layer growth rather than the first.

The optical results obtained on performing current-switching experiments on a tantalum sample during the first (points A1 through E1) and second (points A2 through E2) optical cycles are plotted in Fig. 3. The current density is 20 $\mu\text{A}/\text{cm}^2$ for the segments A1-B1 and A2-B2; changing the current to 1 $\mu\text{A}/\text{cm}^2$ shifts the optical null readings to points C1 and C2 on the first and second cycles, respectively. The applied current density is then returned to 20 $\mu\text{A}/\text{cm}^2$ before significant film growth occurs, and the optical data trace out the segments D1-E1 and D2-E2. The continuous lines plotted in Fig. 3 are theoretical curves for both the growth films of constant refractive index, and the variation in index of films of constant thickness on a tantalum substrate of index 3.02-2.57i. Ideally, the second cycle data should retrace the first cycle data rather than fall on a curve of slightly different index. The offset between the two cycles gives an indication of the absolute accuracy of our index measurements. The index variation curves in the figure indicate that the P-A behavior in this region changes on the second cycle of film growth.

For the first cycle data of Fig. 3 the difference in refractive index between the data obtained at 20 and 1 $\mu\text{A}/\text{cm}^2$, 1.5×10^{-3} , is in good agreement with the data reported in Fig. 2. For the second cycle experiment the change in index, 2.2×10^{-3} , and in field are larger

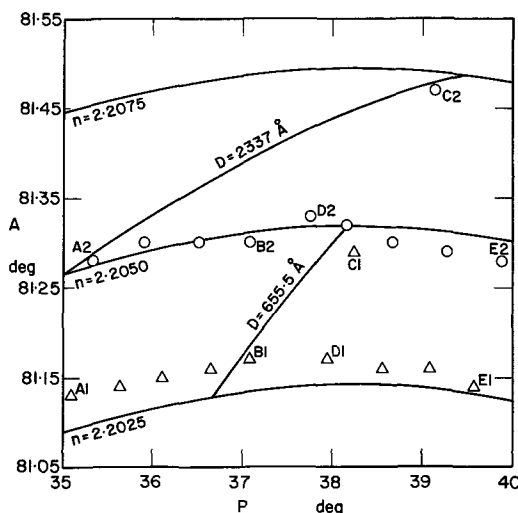


Fig. 3. Transients observed on switching the current density from 20 to 1 to 20 $\mu\text{A}/\text{cm}^2$ on the first cycle (A1-B1-C1-D1-E1) and second cycle (A2-B2-C2-D2-E2) of layer growth through the region plotted in Fig. 2. Theoretical layer growth curves for indexes of 2.2025, 2.2050, and 2.2075, and index variation curves at layer thicknesses of 655.5 and 2337 Å are superimposed on the experimental data.

than in the first cycle, indicating that electronic leakage accounts for a significant fraction of the $1 \mu\text{A}/\text{cm}^2$ current at this thickness, 2350\AA , and potential, 130V . For the first cycle experiment we estimate that the fractional decrease in thickness is almost exactly equal to the fractional increase in refractive index on switching the current from 20 to $1 \mu\text{A}/\text{cm}^2$. For the data obtained in the second cycle experiment the thickness of the film, of index 2.2050 , prior to switching the current was calculated, by extrapolating along A2-B2, and checked, by extrapolating back along D2-E2, to be 2339.32\AA . The point C2, obtained at $1 \mu\text{A}/\text{cm}^2$, falls on a theoretical curve of index 2.2072 , and the film thickness at this point is 2337.18\AA . This experiment confirms that the fractional change in film thickness, 9.14×10^{-4} , and refractive index, 10^{-3} , are approximately equal in magnitude and opposite in sign. The fractional changes in thickness and refractive index may be related by the expression

$$\Delta d/d = -C \Delta n/n \quad [2]$$

We have determined the coefficient C in Eq. [2] using data from several experiments on tantalum, and estimate that the average value we obtain, 0.872 , is accurate to within 15% . All these optical experiments display two important features. First, the optical changes are due to changes in the whole film rather than in a surface layer or in the double layer in the electrolyte, and second, the thickness of the film increased linearly on application of the electric field in contrast with the prediction that the layer will undergo a compression proportional to the square of the field (8, 9).

Measurements of changes in the low-frequency dielectric constant can be made by following changes in the capacitance when the applied current density is switched to different values. It is not possible to distinguish between thickness variations and dielectric constant changes as was possible with the optical measurements, but the thickness variation can be taken as known from the optical measurements. In any event, the thickness variations detected optically for films on tantalum are small and comparable to the error estimated for the determination of the capacitance from a measurement of the a-c potential 90° out of phase with the applied a-c current. Unless simultaneous optical data are required, capacitance measurements can be made at any convenient thickness. In Fig. 4 we plot the results of an experiment in which the d-c current is switched from $200 \mu\text{A}/\text{cm}^2$ to $1 \mu\text{A}/\text{cm}^2$ and then back to $200 \mu\text{A}/\text{cm}^2$ while the a-c current is held constant at $2.5 \mu\text{A}/\text{cm}^2$. Both the d-c potential and the a-c potential 90° out of phase with the current are plotted in the figure. The a-c potential follows the d-c potential to some extent, both showing

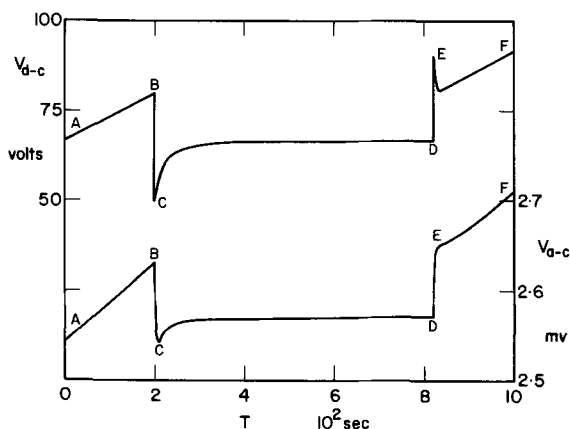


Fig. 4. Transients observed on switching the d-c current density from 200 to 1 to $200 \mu\text{A}/\text{cm}^2$ while superimposed 1000 Hz a-c current is held constant at $2.5 \mu\text{A}/\text{cm}^2$. The d-c potential is plotted in the upper part of the figure, and the a-c potential 90° out of phase with the current is plotted in the lower part.

overshoot, but the a-c potential shows less overshoot than the d-c potential even after taking into consideration the effect of the 0.3 sec time constant of the lock-in amplifier used in the experiment. An equation similar to Eq. [1] can be written to describe the dependence of the low-frequency dielectric constant, K , on the field.

$$K = K_0 (1 - \gamma E) \quad [3]$$

We have verified that the dielectric constant varies linearly with E , the electric field, and the constant, γ , in Eq. [3] has a value of $2.42 \text{ \AA}/\text{V}$ for the data of Fig. 4. Assuming a roughness factor of unity, we calculate the dielectric constant of the tantalum oxide layer as 24 at an applied current density of $200 \mu\text{A}/\text{cm}^2$ in fair agreement with the previously published value of 27.6 (10). It should be noticed that the percentage change in the a-c potential on switching the current, 2.5% , exceeds by more than an order of magnitude both the anticipated $1/C$ error and the percentage change in film thickness. These quantities are thus small compared with changes in the dielectric constant. Considerable difficulty was encountered in attaining reproducibility in the current dependence measurements of the dielectric constant of tantalum oxide. We attribute this difficulty to factors in sample preparation over which we had inadequate control. As a result we estimate a possible error of about a factor of two in the value of γ quoted above. No difficulties were encountered in attaining reproducibility in these measurements with the other two metals.

Similar sets of measurements to those described above were carried out on niobium and tungsten, and we describe these results more briefly. Figure 5 shows the data obtained during the anodic oxidation of niobium at a current density of $100 \mu\text{A}/\text{cm}^2$. The optical P - A data are shown in the upper part of the figure fitted to the growth of a film of index 2.30 . The film thickness as determined from the fitted theoretical curve is plotted against potential in the lower section of the figure. Corresponding points on the two curves are designated A through N. Points K through N lie on the second cycle of the P - A curve, and the region between C and H is chosen for the current switching experiments plotted in Fig. 6 and 7. The same scales are used in Fig. 5 as in Fig. 1 to facilitate direct com-

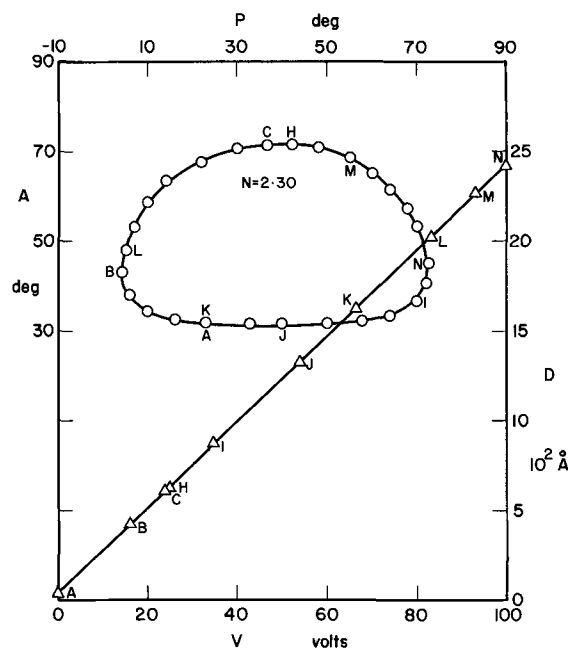


Fig. 5. Anodic oxidation of niobium at $100 \mu\text{A}/\text{cm}^2$ in $0.2N \text{ H}_2\text{SO}_4$. The curve fitted to the optical data in the upper part of the figure is for the growth of a layer of index 2.30 on a substrate of index 3.03 - 3.61 . The film thickness determined from this fitted curve is plotted vs. potential in the lower part of the figure.

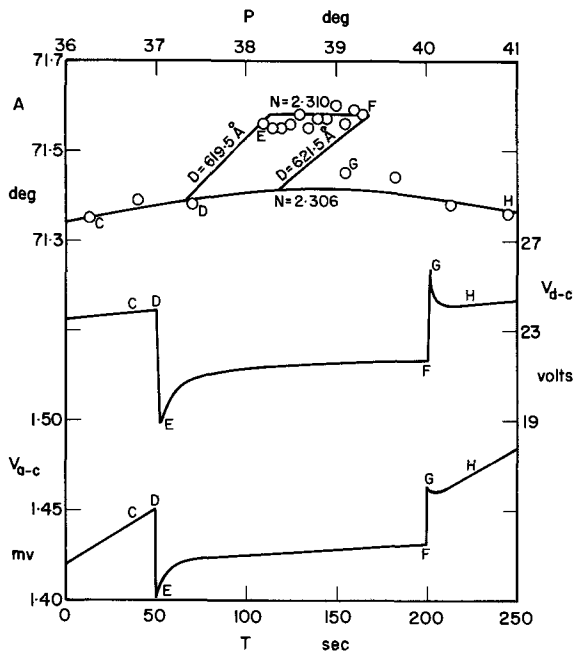


Fig. 6. Transients observed in the region between C and H in Fig. 5 when the d-c current density is switched from 30 to 3 to 30 $\mu\text{A}/\text{cm}^2$ with a superimposed 1000 Hz a-c current density of 5 $\mu\text{A}/\text{cm}^2$. The optical data, along with theoretical layer growth curves for indexes of 2.306 and 2.310 and index variation curves at thicknesses of 619.5 and 621.5 Å, are plotted in the upper third of the figure, and the d-c potential and a-c potential 90° out of phase with the current are plotted vs. time in the lower part.

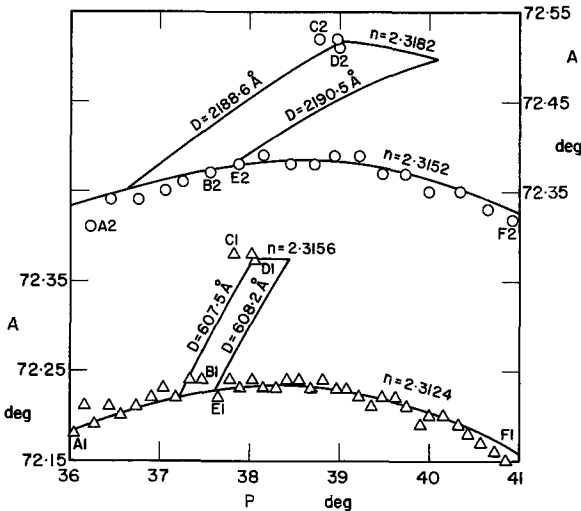


Fig. 7. Transients observed on switching the current density from 30 to 3 to 30 $\mu\text{A}/\text{cm}^2$ on the first cycle (A1-B1-C1-D1-E1-F1) and second cycle (A2-B2-C2-D2-E2-F2) of layer growth through the region plotted in Fig. 6. Offset analyzer scales are used to avoid overlap of the two sets of data. Theoretical layer growth curves for indexes of 2.3124 and 2.3156 and index variation curves at thicknesses of 607.5 and 608.2 Å are fitted to the first cycle data, and layer growth curves for indexes of 2.3152 and 2.3182 and index variation curves at thicknesses of 2188.6 and 2190.5 Å are fitted to the second cycle data.

parison. The electric field in the oxide, 4.16×10^6 V/cm, is considerably lower than that for tantalum, and the refractive index is a little higher. Generally larger refractive indexes result in the optical data falling on larger loops in the P-A plane, but the refractive index of the niobium substrate, 3.03-3.6i, differs sufficiently from that of tantalum to cause the data to fall on a smaller loop. This behavior is important in the current-switching experiments performed in the region between C and H, because the nulling time of

the instrument increases markedly at large A values. The initial film thickness is calculated to be 30 Å, the same value as for tantalum. The optical loop closes at a thickness of 1620 Å at a potential of 67V.

The results of a current-switching experiment during the first optical cycle, in which the d-c current is switched from 30 $\mu\text{A}/\text{cm}^2$ (segment CD) to 3 $\mu\text{A}/\text{cm}^2$ (segment EF) and then returned to 30 $\mu\text{A}/\text{cm}^2$ (segment GH) while the a-c current is held constant at 5 $\mu\text{A}/\text{cm}^2$ and 1000 Hz, are plotted in Fig. 6. As was found for the tantalum system, the d-c and a-c potentials show overshoot, but no overshoot could be detected in the optical results. In addition, both the dielectric constant and the refractive index are linearly dependent on the electric field, decreasing with increasing field. The values of the coefficients α and γ of Eq. [1] and [3] were determined to be 0.457 and 8.61 Å/V, respectively, for the niobium system. The value of the dielectric constant at 30 $\mu\text{A}/\text{cm}^2$, assuming a roughness factor of unity, was found to be 38.5 in fairly good agreement with previous measurements (10). The change in thickness on switching the current can also be estimated from these results. On switching to the lower current the decrease in thickness observed has approximately the magnitude required to maintain constancy of the optical thickness.

Figure 7 presents the results of an experiment similar to that performed on tantalum, and summarized by Fig. 3, to determine the change in thickness that occurs upon changing the current density. In Fig. 7 the optical data for both the first and second optical cycles are presented. The experiment involves growing the oxide at 30 $\mu\text{A}/\text{cm}^2$ (segments A1-B1 and A2-B2), switching the current to 3 $\mu\text{A}/\text{cm}^2$ (segments C1-D1 and C2-D2), and returning to 30 $\mu\text{A}/\text{cm}^2$ (segments E1-F1 and E2-F2) before much layer growth can occur. This experiment confirms that the thickness of the layer decreases as the refractive index increases and that the fractional change in index is related to the fractional change in thickness by a relation of the form of Eq. [2], the coefficient C having a value of 0.78 with an estimated error of 20%.

Figure 8 shows the data obtained during the anodic oxidation of tungsten at an applied current of 200 $\mu\text{A}/\text{cm}^2$. The optical data obtained in the experiment are

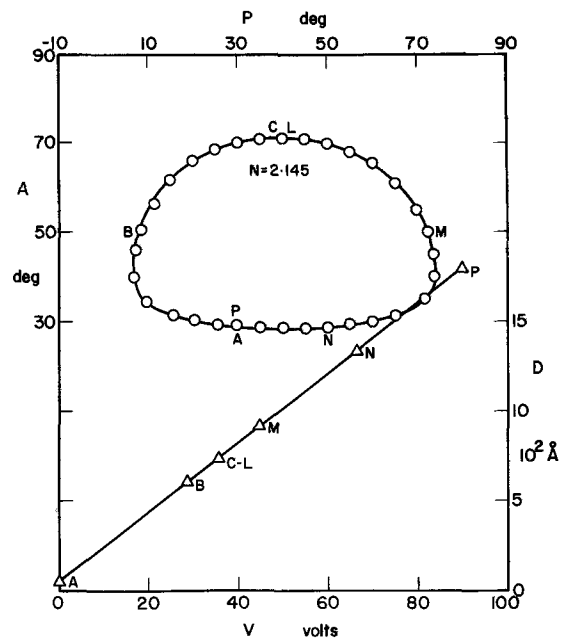


Fig. 8. Anodic oxidation of tungsten at 200 $\mu\text{A}/\text{cm}^2$ in 0.2N H_2SO_4 . The curve fitted to the optical data in the upper part of the figure is for the growth of a layer of index 2.145 on a substrate of index 4.30-3.10i. The film thickness determined from this fitted curve is plotted vs. potential in the lower part of the figure.

shown in the upper portion of the figure fitted to the growth of a layer of refractive index 2.145 on a substrate of refractive index 4.3-3.1i. The film thickness, determined from the theoretical fit to the data, is plotted against potential in the lower section of the figure. From this plot the field in the film is determined to be 5.2×10^6 V/cm at an applied current of $200 \mu\text{A}/\text{cm}^2$. Corresponding points on the two curves are designated A through P. At point P, corresponding to approximately 90V, film growth ceases presumably due to breakdown. In addition to this effect, the tungsten system exhibits other effects which complicate the interpretation of optical and electrical data.

In the initial stages of galvanostatic oxidation, before the potential increases linearly with time, the metal exhibits an active state. Typical valve metal behavior commences at 0.25V with 50Å of oxide covering the surface of the electrode. Optical results show that tungsten oxide also tends to dissolve in the electrolyte under anodic currents less than $20 \mu\text{A}/\text{cm}^2$, although the electric field in the layer does not drop appreciably under these conditions.

We have performed current-switching experiments on this system to determine whether or not it shows the same behavior found for both tantalum and niobium. Figure 9 presents the results obtained for a current-switching experiment performed in the region between points C and L in Fig. 8. The optical data obtained are recorded in a P-A plot in the upper part of Fig. 9. During this experiment the current is switched from $100 \mu\text{A}/\text{cm}^2$ (segment CD) to $10 \mu\text{A}/\text{cm}^2$ (segment EF) to $30 \mu\text{A}/\text{cm}^2$ (segment GH) to $3 \mu\text{A}/\text{cm}^2$ (segment IJ) and returned to $100 \mu\text{A}/\text{cm}^2$ (segment KL). In the center and lower sections of the figure, the d-c potential and the a-c potential which is 90° out of phase with an a-c current density of $4.9 \mu\text{A}/\text{cm}^2$ at 1000 Hz are recorded. From this experiment we conclude that both the refractive index and the dielectric constant have a field dependence similar to that found for the oxides of tantalum and niobium. The values of α and γ in Eq. [1] and [3] are determined to

be 0.61 and 8.4 Å/V, respectively, for the tungsten system. The dielectric constant at $100 \mu\text{A}/\text{cm}^2$ was determined, using a roughness factor of unity, to be 31.5. Measurements of thickness change accompanying changes in index are difficult to determine exactly as data on the second optical cycle cannot be obtained, but the thickness does increase as the index decreases. We estimate the coefficient C in Eq. [3] to have a value of 1.2 to within an error of 30% for this system.

Discussion

Theoretical descriptions of the ionic conduction process occurring during the anodic oxidation of valve metals have generally invoked a classical field-assisted transport model. This treatment leads to the well-known form

$$i = i_0 \exp - (U/kT) \exp (qaE/kT) \quad [4]$$

for the relation between the ionic current density, i , and the electric field strength, E .

In 1960, Young (6) reported experimental results on the oxidation of tantalum, which showed that the relation between $\ln(i)$ and E was not linear and that a better fit to the data could be obtained by replacing the term qaE in Eq. [4] by $q(\alpha - \beta E)E$. This result was confirmed by the results of Young and Zobel (5) who in addition showed the necessity for including the non-linear term in the fit of data obtained on niobium oxidation.

Our measurements were undertaken to determine whether a local field model could account for the curvature in the plot of $\ln(i)$ against E . The possibility that the local electric field rather than the external field controls the ionic conduction process in some solids has been suggested by Maurer (11), Young (6, 12), and Dignam (13, 14). In this model qaE , of Eq. [4], is replaced by $qa'E_e$, where E_e , the effective field is related to the applied field by the expression

$$E_e = E (K + 2)/3 \quad [5]$$

Experimentally we find that the dielectric constant varies with the field in the manner described by Eq. [3], and substituting this dependence into Eq. [5] gives

$$E_e = E (K_0 + 2)/3 - E^2 K_0 \gamma /3 \quad [6]$$

This relation has the same form as the expression used by Young and Zobel and their data could be accounted for by a local field model if

$$K_0 \gamma / (K_0 + 2) = \beta / \alpha \quad [7]$$

For tantalum our results give 2.23 Å/V for the left side of Eq. [7], whereas Young's results give 4.8 Å/V for the right-hand side. For niobium our results give 8.2 Å/V compared with Young and Zobel's value of 7.78 Å/V. The effective field model thus gives both the correct sign and order of magnitude of β/α for tantalum and niobium. Little work has been published on tungsten, and it is not known if the $\ln(i)$ vs. E plot is non-linear. Our results indicate that there should be curvature in the tungsten system, the left-hand side of Eq. [7] having a value of 7.9 Å/V. The close agreement between the values for niobium indicates that an effective field model merits serious consideration in this case. In the case of tantalum, it is more difficult to reach a firm conclusion; although our result is too low by a factor of slightly more than two to account for all the $\ln(i)$ vs. E curvature, the problems we encountered with reproducibility in the data for the dependence of K on the field in this system forced us to estimate a possible error of a factor of two in our quoted γ value. Dell'Oca and Young (15) have recently shown that incorporation of electrolyte into the oxide film causes an increase in the curvature in the plot of $\ln(i)$ vs. E for tantalum. They suggest that some of the curvature for tantalum, even when grown in 0.2N H_2SO_4 , might be due to electrolyte incorporation. We have, however,

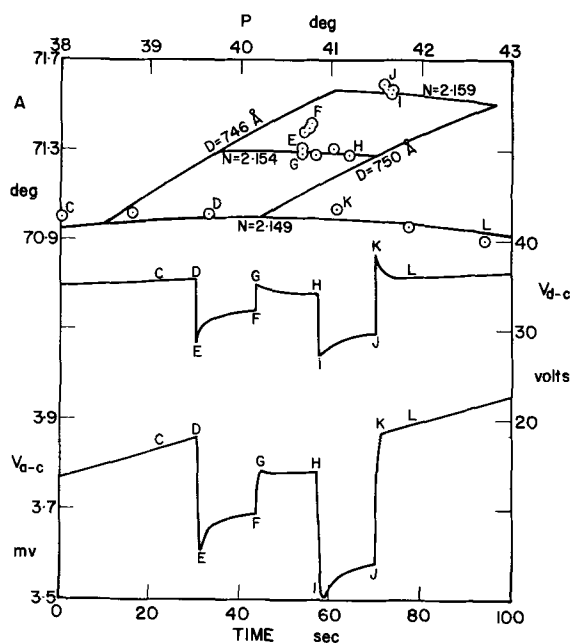


Fig. 9. Transients observed in the region between C and L in Fig. 8 when the d-c current density is switched from 100 (CD) to 10 (EF) to 30 (GH) to 3 (IJ) to $100 \mu\text{A}/\text{cm}^2$ (KL) with a superimposed 1000 Hz a-c current density of $4.9 \mu\text{A}/\text{cm}^2$. The optical data, along with theoretical layer growth curves for indexes of 2.149, 2.154, and 2.159, and index variation curves at thicknesses of 746 and 750Å are plotted in the upper third of the figure, and the d-c potential and a-c potential 90° out of phase with the a-c current are plotted vs. time in the lower part.

found no optical evidence for any nonuniformity in the oxide film grown in tantalum in 0.2N H₂SO₄. Variations in the dielectric constant certainly appear to contribute to the $\ln(i)$ vs. E curvature for tantalum, but whether or not they are a major contributing factor, as seems to be the case for niobium, will have to be decided by further measurements.

Our ellipsometric measurements on the variation of refractive index with change in applied current, and thus in field, resulted in the detection of the important result that a change of thickness accompanies a refractive index change. We find, for all three systems studied, that the thickness change depends linearly on the field change, the thickness increasing with increasing field. All other investigations on anodic oxides have assumed that an electrostrictive effect was exhibited by these systems. Why the thickness changes should be linearly dependent on field is difficult to explain, but a knowledge of the magnitude and direction of the effect allows us to account for changes in the dielectric properties that occur on changing the field.

The change in thickness accompanying the change of field, in a current switching experiment, occurs without any charge being passed through the system; the total mass of the layer thus remains constant. Assuming that the only dimension which changes is the thickness, the fractional change in density, ρ , of the layer is related to the fractional change in thickness by the relation

$$\Delta\rho/\rho = -\Delta d/d \quad [8]$$

For solids of the type under consideration, the Lorentz-Lorenz relation between the refractive index and density

$$(n^2 - 1)/(n^2 + 2) = A\rho \quad [9]$$

where A is a constant, depending on the nature of the material and the wavelength of the light, should apply. Appropriate manipulation of Eq. [9] and substitution into Eq. [8] gives

$$\Delta d/d = -6(n^2 + 1 - 2/n^2)^{-1} \Delta n/n \quad [10]$$

Comparing this equation with our empirical relation in Eq. [2], we see that the two would be identical if

$$C = 6/(n^2 + 1 - 2/n^2) \quad [11]$$

From our optical results we can calculate the values for the right-hand side of Eq [11], and the values are 1.1, 1.0, and 1.16 for tantalum, niobium, and tungsten, respectively. Our measurements of C for the three systems are 0.872, 0.78, and 1.2, respectively, in quite reasonable agreement with the theoretically predicted values. This agreement indicates that the only contribution to the change in refractive index with field is a change in the bulk density. Our results for the change of refractive index with field are larger, by almost two orders of magnitude, than those reported by Frova and Migliorato (3) who used a field-modulated reflectance technique. They assumed that the film thickness did not change on applying a field to the electrode and that all the shift in the reflectance spectrum was due to the change in the refractive index of the film. The reflectance technique is actually sensitive to changes in optical thickness, the product nd , and as we have found that an increase in the refractive index is accompanied by a decrease in field, their results are expected to be far smaller than those we have observed.

The low-frequency dielectric constant changes may be predicted by a method similar to that described above for refractive index changes. The dielectric constant of the oxide should depend on the density through the Clausius-Mossotti relation

$$(K - 1)/(K + 2) = B\rho \quad [12]$$

where B is a constant. From Eq. [12] the change in K due to a change in density would be

$$\Delta K = (K + 2)(K - 1) \Delta\rho/3\rho \quad [13]$$

Equation [13] when combined with Eq. [8], [2], [3], and [1] yields the equality

$$\gamma/\alpha = C(K^2 + K - 2)/3K \quad [14]$$

which will be true provided all the change in the dielectric constant is due to a change in the bulk density of the oxide. Our experimental values of the ratio γ/α are 20.5, 14.1, and 13.8 for tantalum, niobium, and tungsten, respectively. The values of the right-hand side of Eq. [14] for the three metals are 9.13, 13.6, and 12.5. The agreement is excellent for niobium and tungsten, but not for tantalum, perhaps due to the poor accuracy to which we determined γ for the tantalum system.

One other result obtained in this investigation, one which should be of use in the development of a more detailed and satisfactory model for the high-field ionic conduction process in anodic oxides, is the observation of overshoot in measurements of the dielectric constant at low frequencies but not at optical frequencies. The existing theories of the ionic conduction process do not give an adequate prediction of the behavior of the anodic oxide under the transient conditions that occur when the applied current, or field, is suddenly changed. The existence of overshoot in the low-frequency measurements would seem to suggest that the processes which dominate at this frequency and not at optical frequencies are intimately connected with the ionic conduction process.

Conclusion

The linear increase of thickness with increase in field we observe in ellipsometric measurements on the anodic oxides of tantalum, niobium, and tungsten results in the variation of the dielectric constant, at both high and low frequencies, with steady-state field. The variation in the dielectric constant with field, in combination with an effective field model for the ionic conduction process, can explain the existence of non-linearity in the $\ln(i)$ vs. E plot observed by many other investigators for tantalum and niobium oxidation.

Acknowledgment

The authors would like to acknowledge the assistance given by Dr. J. D. Leslie in the preliminary measurements of the field-dependence of the low-frequency dielectric constant. This work was supported in part by the National Research Council of Canada under Grant No. A-1151.

Manuscript submitted Sept. 16, 1971; revised manuscript received Dec. 3, 1971.

Any discussion of this paper will appear in a Discussion Section to be published in the December 1972 JOURNAL.

REFERENCES

1. A. Guenterschultze and H. Betz, *Z. Phys.*, **71**, 106 (1931).
2. B. J. Holden and F. G. Ullman, *This Journal*, **116**, 280 (1969).
3. A. Frova and P. Migliorato, *Appl. Phys. Letters*, **13**, 328 (1968).
4. J. L. Ord and B. L. Wills, *Appl. Opt.*, **6**, 1673 (1967).
5. L. Young and F. G. R. Zobel, *This Journal*, **113**, 277 (1966).
6. L. Young, *Proc. Roy. Soc. (London)*, *Ser. A*, **258**, 496 (1960).
7. J. L. Ord, *Surface Sci.*, **16**, 155 (1969).
8. L. Young, *This Journal*, **110**, 589 (1963).
9. M. J. Dignam and D. B. Gibbs, *J. Phys. Chem. Solids*, **30**, 375 (1969).
10. L. Young, "Anodic Oxide Films," Academic Press, London and New York (1961).
11. R. J. Maurer, *J. Chem. Phys.*, **9**, 579 (1941).
12. L. Young, *Trans. Faraday Soc.*, **50**, 159 (1954).
13. M. J. Dignam, *This Journal*, **112**, 722 (1965).
14. M. J. Dignam and P. J. Ryan, *Can. J. Chem.*, **46**, 535 (1968).
15. C. J. Dell'Oca and L. Young, *This Journal*, **117**, 1548 (1970).

Electrolytic Determination of Porosity in Gold Electroplates

II. Controlled-Potential Techniques

Ronald J. Morrissey*

Research Division, AMP Incorporated, Harrisburg, Pennsylvania 17105

ABSTRACT

Anodic polarization curves of gold and gold-plated copper specimens have been obtained at a sweep rate of 10 mV/min in 0.1M NH₄Cl electrolyte. The curves obtained are found to be linear over ranges of potential approaching 50 mV displacement from the free corrosion potential. From the data obtained, values of the free corrosion potential, the polarization admittance, and the leakage current are extracted and compared for each specimen. Agreement between the corrosion potential and polarization admittance values is excellent. It is shown that the polarization admittances of gold-plated copper specimens in 0.1M NH₄Cl vary with the apparent exposed area fraction of copper according to expressions derived by Stern. Agreement between the corrosion potential and leakage current values is fair, becoming poorer as the polarizing potential is displaced farther from the free corrosion potential. It is shown that at a given value of the polarizing potential, leakage currents passed by gold-plated copper specimens in 0.1M NH₄Cl vary directly with the apparent exposed copper area. Anodic current densities and minimum limits of detectability for the various techniques are discussed.

In a previous paper (1) it was shown that the corrosion potentials of gold-plated copper specimens in 0.1M NH₄Cl electrolyte are related to the exposed basis metal area fractions of the specimens by means of an expression originally derived by Stern (2), and that this relationship affords a convenient and sensitive means of electroplate porosity determination. The object of the present paper is to examine two additional electrolytic techniques: linear polarization measurements and leakage current measurements, which have proven useful in electroplate porosity determinations, and to present comparisons of data obtained from corrosion potential, linear polarization, and leakage current measurements performed sequentially on the same specimens.

Linear Polarization Methods

Linear polarization methods were first applied to the determination of electroplate porosity by Clarke and Britton (3). Beginning with studies of tin-nickel platings on steel, these authors and subsequent co-workers have investigated the effects of various preplating treatments of the substrate on the porosity of electrodeposits subsequently applied (4), and have extended the use of the porosity test to a number of plating-substrate systems, including gold on copper (5, 6).

Clarke and Britton found that, in electrolytes chosen so as to corrode only those areas of substrate exposed at pores in a noncorroding metal electroplate and to do so without formation of insoluble corrosion products, the anodic polarization curves of potential vs. current density for electroplated specimens were linear over ranges of potential approaching 100 mV displacement from the free corrosion potential; and that the slopes of the linear plots thus obtained appeared to be directly related to the resistivity of the electrolyte and inversely related to the average porosities of the test specimens. Analyzing these data, they suggested that under these conditions, current was passed by the exposed basis metal only and was effectively controlled by the resistance of the electrolyte in the pore channels. Assuming that the change in polarization of the basis metal was negligibly small, the slope of the polarization curve for a given specimen would then be a measure of the sum of the parallel resistances

of the electrolyte-filled pore channels, and the greater the value of $\Delta V/\Delta I$, the smaller would be the apparent porosity.

In this work, we consider an alternative hypothesis, namely, that the initial linear slopes of the anodic polarization curves of basis metal specimens coated with porous noble metal electrodeposits may be governed, in certain electrolytes, by the area relationships of the exposed anodic and cathodic constituents according to expressions derived by Stern (2). We do this for two reasons: first, because our own previous work has shown (1) that the Stern expressions adequately describe the corrosion potentials of gold-plated copper specimens in 0.1M NH₄Cl solution. It is also felt that an approach based on the use of the Stern expressions, if applicable, represents a more general case than that treated by Clarke and Britton; and particularly avoids the perhaps questionable requirement that the polarization of the exposed basis metal remain substantially invariant as the over-all mixed potential of the plated specimen is varied over several tens of millivolts.

For the corrosion current of a binary galvanic couple controlled by activation polarization, Stern writes

$$\log I_{\text{corr}} = \frac{E_a}{\beta_a + \beta_c} + \frac{\beta_c}{\beta_a + \beta_c} \log A_c i_{oc} + \frac{\beta_a}{\beta_a + \beta_c} \log A_a i_{oa} \quad [1]$$

where E_a is the free corrosion potential of pure anodic material, measured with respect to the equilibrium potential of pure cathodic material in the same electrolyte, which is taken as zero. β_a and β_c are the anodic and cathodic Tafel constants, and i_{oa} and i_{oc} are the respective exchange current densities for the anodic and cathodic processes. A_a and A_c are the area fractions of anodic and cathodic materials in the actual couple (such that $A_a + A_c = 1$).

Following the analysis presented previously (1), we note that for a given base metal-noble metal couple in a given corrodant bath the electrochemical parameters E_a , β_a , β_c , i_{oa} , and i_{oc} , as well as the equilibrium potential of the pure cathodic material, are constants. Further, for the case of base metal specimens coated with noble metal electroplates of moderate to low porosity, $A_c \gg A_a$. In this case, A_c approaches unity, and the term in $(\log A_c i_{oc})$ may be considered a constant. It is thus possible to rearrange expression [1], combining

* Electrochemical Society Active Member.

Key words: electroplates, porosity, porosity testing, gold, copper, galvanic cells, corrosion potential, polarization admittance, linear polarization, leakage current.

and substituting terms to yield an expression of the form

$$I_{\text{corr}} = C_1 A_a \frac{\beta_a}{\beta_a + \beta_c} \quad [2]$$

Thus, for a base metal specimen of specified total area, coated with a noble metal electroplate of moderate to low porosity, the corrosion current is found to vary as a power of the area fraction of basis metal exposed to the electrolyte.

It is now of interest to compare expression [2] with the linear polarization expression of Stern and Geary (7)

$$\frac{\Delta I}{\Delta V} = \frac{(2.3) I_{\text{corr}} (\beta_a + \beta_c)}{\beta_a \beta_c} \quad [3]$$

that relates the corrosion current of a freely corroding specimen to the slope of that linear portion of the cathodic or anodic polarization curve which is found to occur at potentials close to the free corrosion potential. The range of potential over which such linear kinetics are observed is usually small. Stern (8) estimated the expected range to be only of the order of ± 10 mV from the free corrosion potential. Cases of linear polarization behavior extending over potential ranges of several times this figure are, however, well documented in practice. These and the occurrence of asymmetric behavior (in which the potential range of linear kinetic behavior is greater in one direction from the free corrosion potential than in the other) have been discussed by Barnartt (9).

Combining expressions [2] and [3] and simplifying, we obtain

$$\frac{\Delta I}{\Delta V} = C_1 C_2 A_a \frac{\beta_a}{\beta_a + \beta_c} \quad [4]$$

where the constant C_1 results from grouping the various constant terms in expression [1], and the constant C_2 is equal to $(2.3) (\beta_a + \beta_c) / \beta_a \beta_c$. According to this expression, and subject to experimental conditions as specified above, a plot of the logarithm of the linear polarization slope for a plated specimen *vs.* the logarithm of the area fraction of basis metal exposed to the electrolyte should yield a linear trace, the slope of which is in turn given by $\beta_a / (\beta_a + \beta_c)$.

Leakage Current Methods

Leakage current measurements were first applied to the determination of porosity in electrodeposits of nickel and cobalt on steel by Shome and Evans (10). Their procedure was to measure the cell current passed when the specimens were connected, in an electrolyte of 3% NaCl + 0.1% Rochelle salt, to a large copper gauze which served as an auxiliary cathode. No reference electrode was used. They reasoned that if the copper gauze were made sufficiently large, the cell current would be limited only by the rate of anodic dissolution and would thus be directly proportional to the exposed area of bare steel. This technique was subsequently extended by Ehrhardt (11) with the addition of an external power supply with which the potential between the specimen and the auxiliary cathode could be controlled. Again, no reference electrode was employed. Using an applied potential of 0.75V, Ehrhardt measured porosity values for gold-plated copper specimens in 5% H₂SO₄ electrolyte. Kamm, Willey, and co-workers (12) have employed a variation of the leakage current technique to determine the continuity of the iron-tin alloy layer in electrolytic tinplates on steel.

In their critique of leakage current methods, Clarke and Leeds (5) pointed out that the potential of the auxiliary cathode as employed in such measurements is itself a corrosion potential, subject to change from polarization by current flow or from other experimental variables. They suggested that such measurements might be improved by polarizing the specimen

with respect to a reference electrode rather than with respect to the auxiliary cathode. Barnartt (13) has shown that, if the partial cathodic current can be neglected, the cell current under such conditions is approximated by

$$I = A_{\text{anodic}} i_{\text{oa}} \exp [2.3(E - E_{r,a})/\beta_a] \quad [5]$$

where E is the polarizing potential and $E_{r,a}$ is the reversible potential for the anodic process, both measured with respect to a suitable reference electrode; and A_{anodic} is the exposed basis metal area. Thus, under conditions of simple anodic dissolution of the exposed basis metal to form soluble corrosion products, and provided that the effects of concentration and resistance polarization can be kept small (*i.e.*, by restricting the investigation to fairly thin electroplates and by restricting anodic current densities to the smallest practicable values), anodic polarization of a series of plated specimens to the same potential *vs.* a suitable reference electrode should yield cell currents that in each case are proportional to the area of basis metal exposed to the test electrolyte.

Experimental

The general approach taken in this work has been to examine the anodic polarization curves of gold and gold-plated copper specimens, obtained potentiodynamically at low sweep rates (10 mV/min) in 0.1M NH₄Cl test electrolyte. The curves obtained were found to be linear over ranges of potential approaching 50 mV displacement from the free corrosion potential. The slopes of these linear plots were taken to be equal to the polarization admittance $\Delta I/\Delta V$ (14) of the various specimens. Comparisons were then drawn between the observed values of the free corrosion potential, the polarization admittance, and the leakage current (determined at several potentials with respect to a saturated calomel reference electrode) for each specimen.

A Pyrex resin kettle of 500 ml capacity served as the reaction vessel. This was equipped with a Plexiglas cap through which the electrodes could be immersed into the bath. Experiments were performed at room temperature, approximately 23°C. Solutions were made up using Analytical Reagent grade chemicals in boiled, demineralized water, the specific resistance of which was typically in the range of 200,000 ohms. The specific resistance of the 0.1M NH₄Cl solution as made up was 83 ohms.

The reference electrode employed was a Beckman No. 39170 saturated calomel electrode having a fiber junction. For convenience, this was located in the electrolyte at a distance of 3.5 cm from the test specimen, which was itself suspended in the bath by means of a 99.99% gold wire.¹ It had been shown in previous work (1, 3) that the position of the reference electrode is of negligible influence in determining the corrosion potentials of specimens coated with porous electrodeposits. Prior to each experiment, the potential of the saturated calomel electrode was checked *vs.* that of a Beckman No. 41236 silver-silver chloride electrode that was reserved as a standard. A pair of 99.99% platinum spirals, each of 9.1 cm² immersed area, served as counterelectrodes. These were located at a distance of 7 cm from each other in the bath, with the test specimen suspended midway between them.

The test specimens were small OFHC copper electrical terminals, each of 2.5 cm² gross geometric surface area. These were barrel plated in small lots with Temperex HD gold² to thicknesses of 50, 100, and 400 μ m. (1.27, 2.54, and 10.16 μ). Additionally, data were obtained using two circular gold coupons, each of 10.8 cm² geometric surface area, which had been stamped from sheet stock of 99.9% purity.³ Cleaning and preparation of the various specimens prior to each experiment was accomplished as previously outlined (1).

¹ Obtained from the Sigmund Cohn Corporation, Mount Vernon, New York.

² Sel-Rex Corporation, Nutley, New Jersey.

³ Handy and Harman, Incorporated, New York, New York.

The electrical apparatus consisted of a Wenking Model 68TS1 potentiostat, equipped with a Wenking Model MP165 motor potentiometer. Recording of the polarization curves was accomplished using a Hewlett-Packard Model 7005B X-Y recorder. Potential of the specimen with respect to the reference electrode was read using a Keithley Model 610B electrometer voltmeter, the output of which was relayed to the X-axis of the recorder. Current was read by monitoring the potential drop across a one megohm precision resistor which was inserted between the potentiostat and the twin counterelectrodes. The use of this rather large resistance served to restrict the magnitude of the cell currents obtained, as well as providing a convenient means of current measurement. The potential drop across this resistance was read using a Keithley Model 610A electrometer voltmeter, the amplified output of which was relayed to the Y-axis of the recorder.

The experimental procedure was as follows: after cleaning and preparation, the test specimen was suspended in the bath by means of a 99.99% gold wire and was allowed to attain a steady corrosion potential with respect to the reference electrode. In all cases, an equilibration time of at least 1 hr was allowed for this purpose. In this work, corrosion potential measurements have been employed as the "referee" technique, and the apparent basis metal (copper) area fractions of the test specimens have been determined from the corrosion potentials by reference to the calibration curve previously obtained (1). This is shown in Fig. 1.

When a steady corrosion potential had been attained, the potentiostat was switched into the circuit and the anodic polarization curve of the specimen was obtained at a potential sweep rate of 10 mV/min. Some representative curves obtained in this manner are shown in Fig. 2. In general, the curves obtained for the gold-plated copper specimens were found to be linear over a potential range approaching 50 mV displacement from the free corrosion potential. For the gold specimens, the linear range approached 150 mV.

A comparison of free corrosion potential and polarization admittance values for a series of gold and gold-plated copper specimens is shown in Fig. 3. The agreement in the results obtained using these two methods is felt to be excellent. Polarization admittances shown in Fig. 3 have been calculated on a gross area current

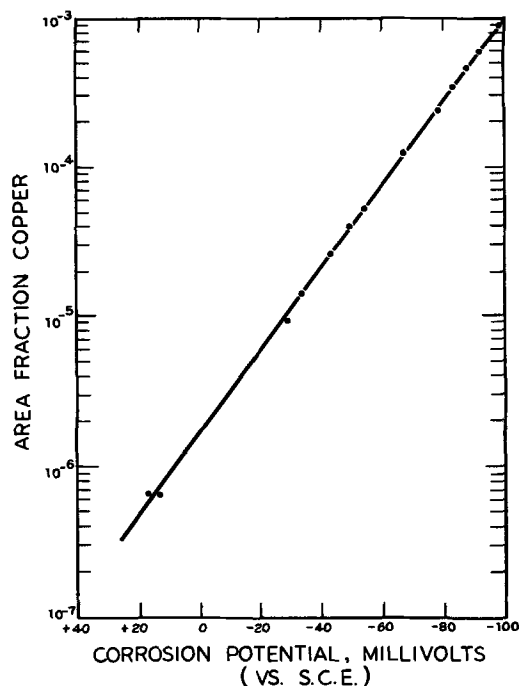


Fig. 1. Variation of corrosion potential with immersed copper area fraction.

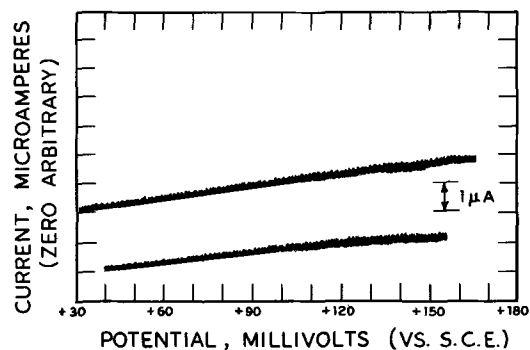


Fig. 2. Anodic polarization curves of gold-plated copper specimens in 0.1M NH_4Cl . (Deposit thickness 50 μin .)

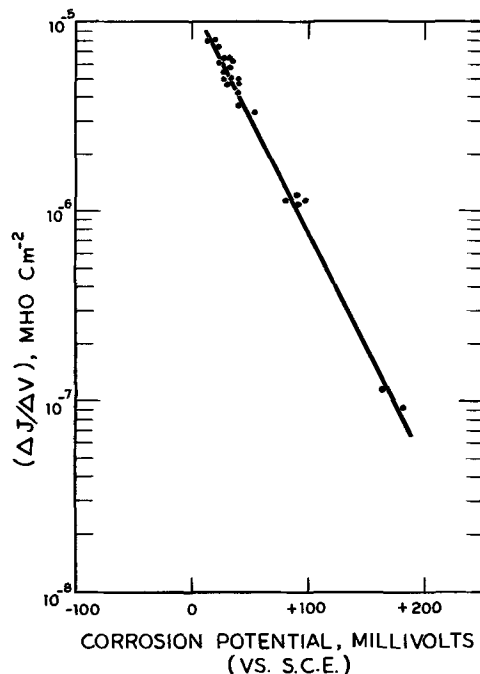


Fig. 3. Comparison of corrosion potential and polarization admittance values.

density basis to compensate for the difference in geometric surface area between the gold ($A = 10.8 \text{ cm}^2$) and gold-plated copper ($A = 2.5 \text{ cm}^2$) specimens. The slight differences noted in corrosion potential and polarization admittance values for the two gold specimens (shown at the lower right of Fig. 3) are felt to be attributable to slight differences in their respective impurity concentrations. In both gold specimens, the major impurity was copper.

Converting the corrosion potential values for the gold-plated copper specimens to corresponding values of the apparent area fraction of exposed copper by reference to Fig. 1, it is possible to replot the polarization admittance data for these specimens in the form $[\log(\Delta I/\Delta V) \text{ vs. } \log A_a]$. Such a plot is shown in Fig. 4. Data for specimens plated with 400 μin . deposits are omitted from this figure because their apparent exposed basis metal area fractions are considerably smaller than the lower limit of calibration shown in Fig. 1. The slope of Fig. 4 is 0.384, which is in excellent agreement with the value of 0.352 calculated for $(\beta_a/\beta_c + \beta_c)$ from the observed values for β_c of gold (0.0935V) and β_a of copper (0.0507V) in this electrolyte (1). This evidence is taken to indicate that, under experimental conditions as described herein, the polarization admittances of gold-plated copper specimens in 0.1M NH_4Cl electrolyte are adequately described by an expression of the form of Eq. [4].

Leakage current values were obtained in this work by reading directly from the polarization curves. A

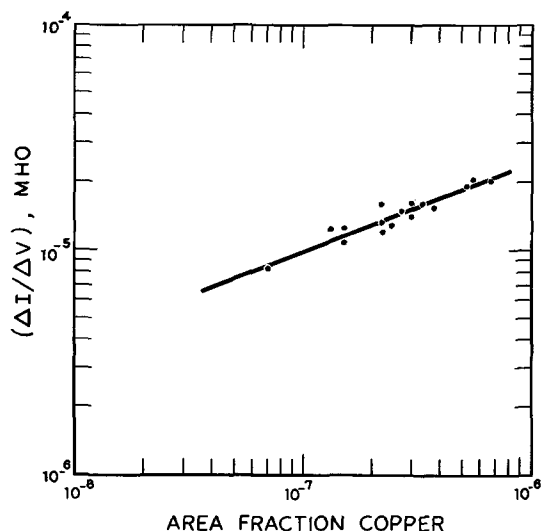


Fig. 4. Variation of polarization admittance with exposed copper area fraction.

plot of leakage currents obtained at potentials of +0.050 and +0.100V (*vs.* SCE) *vs.* the apparent areas of exposed copper for the plated specimens is shown in Fig. 5. Values of the apparent exposed area of copper for these specimens were obtained, as previously, from their corrosion potentials by reference to Fig. 1; multiplying the indicated values of the apparent area fraction by the gross geometric surface area (2.5 cm²) of the plated specimens.

The plots shown in Fig. 5 are of unit slope, indicating that in the range considered the leakage currents obtained are directly proportional to the area of copper exposed to the electrolyte. The scatter of the experimental data, however, is observed to increase as the polarizing potential is displaced farther from the free corrosion potential; indicating that, as might be expected, the effects of various experimental artifacts become increasingly significant as the anodic current density is increased. In general, the agreement between corrosion potential and leakage current results in this work was fair.

Discussion

The employment in this work of a potential-scan technique for the determination of polarization admittance and leakage current values departs somewhat from the potential-step procedures ordinarily used. It was felt that for purposes of obtaining comparative data the scanning technique offered potentially greater reproducibility in handling numbers of specimens. The sweep rate of 10 mV/min was chosen to be sufficiently slow as to avoid double layer charging effects near the

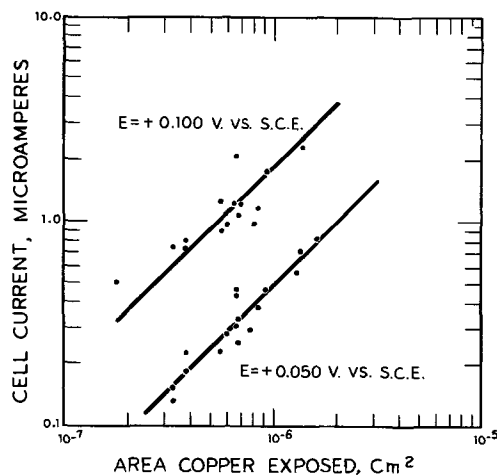


Fig. 5. Variation of leakage current with exposed copper area

free corrosion potential, and sufficiently rapid as to avoid excessive erosion of the pore channels in obtaining the remainder of the polarization curve.

We have not attempted to evaluate the effects of electrolyte pH, oxygenation, or cupric ion accumulation on the results of the various determinations. Previous work had shown (1) that these factors influence the corrosion potentials of gold-plated copper specimens in 0.1M NH₄Cl, and presumably they would affect polarization admittance determinations as well, both by affecting the corrosion rates of the specimens and because the initial potential in such determinations is the corrosion potential. The experimental scatter observed in leakage current determinations in this work would appear to indicate that various experimental artifacts can and do exert a significant influence on such measurements, particularly at large current densities.

As was mentioned earlier, the agreement obtained between corrosion potential and polarization admittance determinations in this work was considered excellent. The evidence of Fig. 3 would indicate that either of these techniques, given a suitable means of calibration, could be extended to the lower limiting case of pure gold. This, of course, is subject in both techniques to the limitations imposed by the inability of the electrolyte to penetrate very fine or very deep pores (1, 4, 15). In the upper limit, it was shown (1) that the corrosion potentials of gold-plated copper specimens in 0.1M NH₄Cl approach a plateau at values of A_a larger than about 1%, and that the method would thus fail as a porosity test in this range. It might be expected that the upper limit of applicability for polarization admittance measurements as a porosity test would be somewhat higher than this, but we have not attempted to establish such an upper limit.

The agreement obtained between corrosion potential and leakage current results was fair, becoming poorer as the polarizing potential was progressively displaced from the free corrosion potential. The major advantage of the leakage current technique is in speed of measurement, as it is not necessary when using this technique to determine the corrosion potentials of the various specimens before energizing them. This ability, however, is achieved at the cost of high anodic current densities when the specimens are energized. It can be shown from Fig. 5 that under the conditions of these experiments, polarization of gold-plated copper specimens to a potential of +0.100V *vs.* SCE produces an anodic current density of approximately 2 A/cm² of exposed copper. By contrast, the free corrosion current densities of the plated specimens employed in this work can be calculated from polarization admittance values to be of the order of 100-500 mA/cm² of exposed copper, increasing with decreasing values of A_a . A plot of free corrosion current densities for gold-plated copper specimens in 0.1M NH₄Cl solution, calculated on the basis of Fig. 4 using expression [3], is shown in Fig. 6. This illustrates a major point of difference between the corrosion potential and polarization admittance techniques, in both of which the free corrosion current density varies with A_a as shown in Fig. 6; and leakage current measurements, in which, at a given polarizing potential, anodic current density is invariant with A_a . A further difference, as was mentioned previously, is that the lower limit of detectability in porosity determinations by corrosion potential or polarization admittance measurements appears to be determined primarily by the ability of the electrolyte to penetrate very fine or very deep pores, whereas in leakage current measurements, the lower limit is also determined by the magnitude of the polarizing potential. Polarization of gold-plated copper specimens to +0.050V *vs.* SCE under the conditions of these experiments yields an anodic current density of 500 mA/cm² of exposed copper. At this polarizing potential, anodic currents would be passed

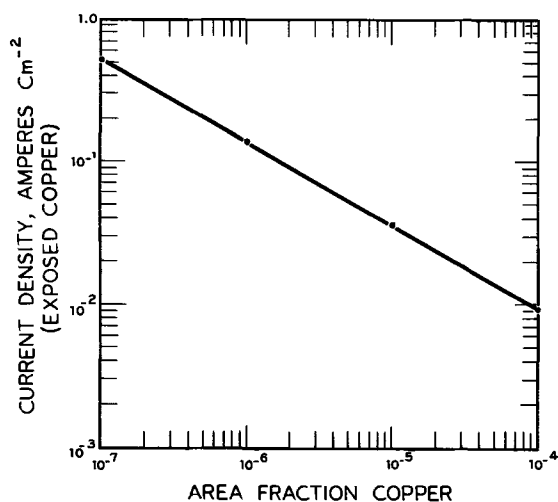


Fig. 6. Variation of free corrosion current density with exposed copper area fraction.

only by specimens having free corrosion potentials more negative than this value, thus introducing a minimum limit of detectability in A_a of approximately 10^{-7} .

In view of this work and of that previously reported (1) it now appears that, within limits at least, the results of electrolytic porosity determinations on base metal specimens coated with noble metal electroplates are expressible in terms of the electrochemical theory of galvanic couples; and that, in the case of corrosion potential measurements, it is possible to prepare calibration curves such that values of the exposed basis metal area fraction in electroplated specimens can be estimated to a reasonable approximation. Cross-calibrations of polarization admittance and of leakage current measurements with respect to corrosion potential measurements are also obtainable and are illustrated in this work. This is in contrast, particularly, to chemical porosity test methods, correlations between which are usually possible only on an empirical basis.

Acknowledgment

The author would like to thank Dr. Sidney Barnartt for helpful discussions concerning this work.

Manuscript submitted Sept. 13, 1971, revised manuscript received Nov. 29, 1971.

Any discussion of this paper will appear in a Discussion Section to be published in the December 1972 JOURNAL.

LIST OF SYMBOLS

I_{corr}	Corrosion current of a galvanic couple at the free corrosion potential (A)
E_a	Corrosion potential of pure anodic material as measured with respect to the equilibrium potential of pure cathode material in the same electrolyte (V)
$E_{r,a}$	Reversible potential of the anodic dissolution process measured with respect to a suitable reference electrode (V)
β_c	Cathodic Tafel slope (V)
β_a	Anodic Tafel slope (V)
i_{oc}	Cathodic exchange current density (A/cm ²)
i_{oa}	Anodic exchange current density (A/cm ²)
A_c	Cathodic area fraction (dimensionless)
A_a	Anode area fraction (dimensionless)
$(\Delta I/\Delta V)$	Polarization admittance, measured as the slope of that linear portion of a polarization curve which is observed at potentials near the free corrosion potential (mho)
$(\Delta J/\Delta V)$	Polarization admittance per unit gross surface area of the specimens (mho/cm ²)

REFERENCES

1. R. J. Morrissey, *This Journal*, **117**, 742 (1970).
2. M. Stern, *Corrosion*, **14**, 329t (1958).
3. M. Clarke and S. C. Britton, *Trans. Inst. Metal Finishing*, **36**, 58 (1958).
4. M. Clarke and S. C. Britton, *ibid.*, **37**, 110 (1960).
5. M. Clarke and J. M. Leeds, *ibid.*, **43**, 50 (1965).
6. M. Clarke and A. M. Chakrabarty, *ibid.*, **48**, 99 (1970).
7. M. Stern and A. L. Geary, *This Journal*, **104**, 56 (1957).
8. M. Stern, *Corrosion*, **14**, 440t (1958).
9. S. Barnartt, *Corrosion Sci.*, **9**, 145 (1969).
10. S. C. Shome and U. R. Evans, *J. Electrodepositors Tech. Soc.*, **27**, 45 (1951).
11. R. A. Ehrhardt, *Tech. Proc. Am. Electroplaters' Soc.*, **47**, 78 (1960).
12. G. G. Kamm, A. R. Willey, R. E. Beese, and J. L. Krickl, *Corrosion*, **17**, 84t (1961).
13. S. Barnartt, Private communication.
14. R. Annand, *Corrosion*, **22**, 215 (1966).
15. F. Ogburn, D. W. Ernst, and W. H. Roberts, *Plating*, **46**, 1952 (1959).

Organosilicon Films Formed by an RF Plasma Polymerization Process

M. J. Vasile and G. Smolinsky

Bell Telephone Laboratories, Incorporated, Murray Hill, New Jersey 07974

ABSTRACT

The purpose of this research was to develop a plasma polymerization process for producing polymeric films and to achieve an understanding of the chemistry involved. A technique for the production of polymer coatings from a capacitively coupled RF plasma is presented. The resulting films contain trapped free radical sites which can react with oxygen and nitric oxide. The rate of polymer formation is a complicated function of power input, total system pressure, and partial pressure of monomer. The rates of reaction differ for different monomers under identical reaction conditions. The stoichiometry and infrared spectra of the polymers indicate that considerable fragmentation and bond reorganization of the monomeric starting material occurs during the polymerization process. A mechanism is proposed to account for conversion of monomer to polymer by formation and fragmentation of ionic species in the discharge. Neutralization of the ionic fragments at the walls yields radicals which can react with adsorbed species and be cross-linked to form polymer.

There is a growing interest in coating solid surfaces with thin polymeric films by reactions resulting from electron bombardment, ultraviolet radiation, or electrical discharges in an atmosphere containing a low molecular weight organic compound. Since 1967 three reviews (1-3) have been written on this subject. It is well known that polymer can be produced on the walls and electrodes of a discharge apparatus containing a reactive gas or a mixture of inert and reactive gases. The electrical discharge may be supported by static, radio frequency, or microwave fields, or some combination of these. A polymeric film that is clear, smooth, and pin-hole free can be produced by the proper choice of discharge conditions. These films adhere well to most substrates and can be made from approximately 200Å to several microns thick. Polymers that are synthesized in electrical discharges are usually highly cross-linked, *i.e.*, they possess two or three dimensional bonding, rather than linear structures. As a result of cross-linking, the polymer films have good thermal stability and are inert to mild acids, alkalis, and most organic solvents. In this paper we describe our apparatus and experimental procedure for discharge polymerization and some of the properties of polymers formed from vinyltrimethylsilane, $\text{CH}_2=\text{CHSi}(\text{CH}_3)_3$ and hexamethyldisiloxane, $(\text{CH}_3)_3\text{SiOSi}(\text{CH}_3)_3$ (abbreviated VTMS and HMDS, respectively).

Experimental

A schematic representation of the discharge chamber is shown in Fig. 1. The lower electrode, E, is connected to the output of a 13.56 MHz generator through an impedance matching network. This electrode is supported 10 cm above the base plate by insulating legs, and it has provisions for water to be circulated to it from a constant temperature bath. The upper electrode, G, is supported from the top plate and is held at ground potential. The top plate contains the monomer and gas inlet tube and is supported by a glass cylinder 20 cm in diameter and 21 cm in height. The electrodes are 15 cm in diameter, and the interelectrode separation is 4 cm. All feed throughs and vacuum seals utilize Viton gaskets or Swagelok fittings.

Substrates upon which polymer is to be deposited are placed on the electrode E. The chamber is then evacuated by a 6-in. diffusion pump to a pressure of 2×10^{-6} Torr or less. The gate valve is then closed, and a throttle valve leading to a mechanical pump is

opened. Argon is admitted to the chamber to the desired pressure through a variable leak valve which leads into the gas inlet tube. Gas pressure in the discharge chamber is measured to the nearest 0.01 Torr on a calibrated capacitance manometer. Monomer vapors are then introduced into the argon stream from heated reservoirs through variable leak valves. In this way, the partial pressure of each component in the discharge tube is known. The entire gas inlet is kept about 20°C warmer than the monomer reservoirs to prevent condensation. Gas flow is maintained throughout the duration of the discharge by pumping through the throttle valve.

The discharges were operated at a variety of pressures and power levels in order to investigate the effects of different reaction conditions on the produc-

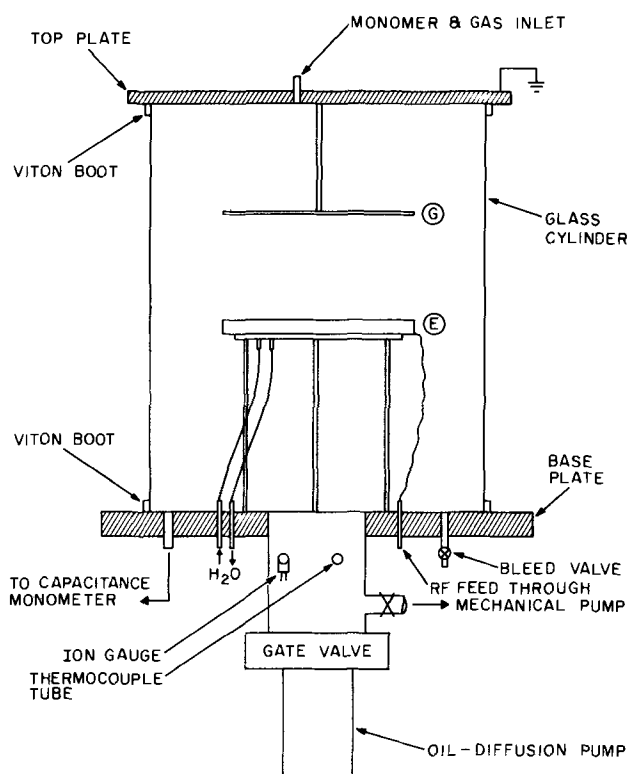


Fig. 1. Schematic representation of glow discharge reaction chamber

Key words: organosilicon films, RF plasma, polymerization.

tion of polymer films. Rate measurements were made by weighing the amount of polymer deposited on 5×5 cm aluminum foil substrates for a given discharge duration, power level, gas composition, and total pressure. Unless otherwise stated, polymer samples for chemical analysis, IR and ESR spectra, and differential scanning calorimetry were prepared using the same set of conditions, *viz.*, 0.4 Torr total pressure, 0.3 Torr monomer pressure, 200W input power, and 25°C electrode temperature. Infrared spectra were obtained using the attenuated total reflectance technique from polymer deposited on highly reflecting aluminum strips. Samples used for ESR measurements and elemental analysis were scraped from glass slides which had been coated with polymer.

Upon termination of the discharge the chamber was again evacuated using the diffusion pump. The discharge chamber could be back-filled with any desired gas at this point. Polymer samples that were to be heat-treated in air, vacuum, or oxygen were transferred to another apparatus that was built especially for that purpose.

Results and Discussion

Under all conditions used in this study to form polymer, a glow was visible around both electrodes, and a striated glow was observed in the interelectrode region. Polymer formation occurred in all regions of the discharge tube and under some conditions, macroscopic polymer particles were observed to form in the gas phase. The thickest deposits were on the electrodes and the walls of the chamber; deposition occurred to a lesser extent on the base plate and the top plate. In our discussion of film growth rate, we do not mean to imply a true reaction rate measurement, since all our data were obtained just on the surface of the active electrode, E, and the rate of film growth differs in different regions of the reaction chamber. However, polymer deposition on the substrate should be a function of the kinetic rate of polymerization as well as such factors as gas diffusion, mixing, and substrate temperature.

The rate of deposition of VTMS and HMDS polymers was linear with time for any particular choice of discharge conditions for reaction times up to 60 min. No tests were carried out for durations longer than 60 min. This linear growth rate is an expected result since the gas flow through the discharge tube was sufficient to maintain a constant monomer partial pressure. Furthermore, the degree of ionization in the discharge is undoubtedly low, which further insures against depletion of the monomer.

Additional information on the kinetics of the depositing polymer is obtained from the data in Fig. 2 which shows the rate of polymerization of a three-component system of VTMS, HMDS, and argon as a function of the monomer composition. The argon partial pressure was maintained at 0.1 Torr, and the total partial pressure of monomers was 0.3 Torr. The data points shown in Fig. 2 are the averages of several determinations at each composition. The scatter obtained for each of the points is principally due to the experimental difficulties encountered in maintaining the feed and power input constant. Figure 3 is a plot of the ratio of the carbon:silicon content of the films shown in Fig. 2. It is evident from Fig. 2 that HMDS films grow at approximately one-half the rate of VTMS films, while the rate of polymerization of mixtures of the two monomers is merely the sum of the individual rates. In addition the elemental composition of polymer prepared from mixtures of HMDS and VTMS (Fig. 3) is also the sum of the composition of the polymers prepared from each component. The data presented in Fig. 2 and 3 suggest that both HMDS and VTMS react independently of each other.

The rate of deposition of VTMS polymer was studied as a function of power input, total pressure, and par-

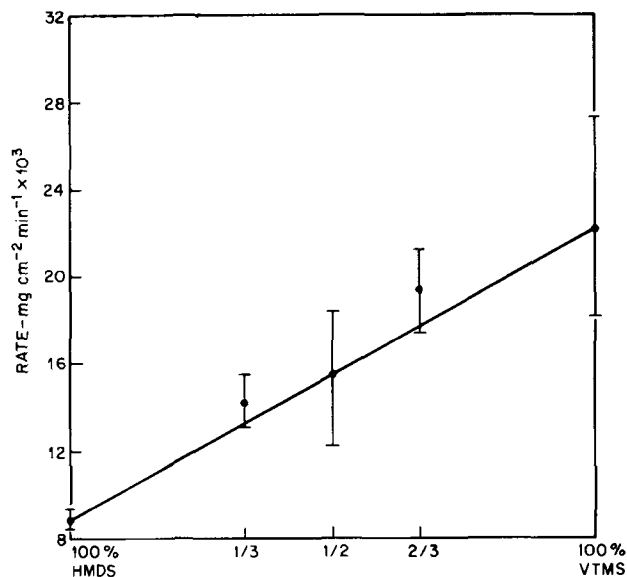


Fig. 2. Rate of polymer deposition as a function of monomer composition (VTMS and HMDS). Total partial pressure of monomers was 0.3 Torr, argon 0.1 Torr. Power 200W.

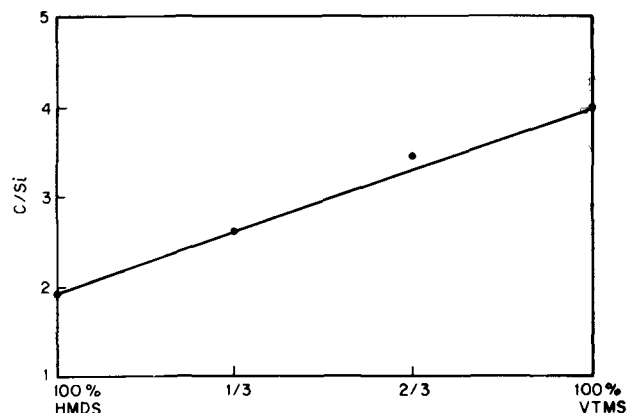


Fig. 3. Carbon to silicon ratio of polymers prepared from HMDS and VTMS.

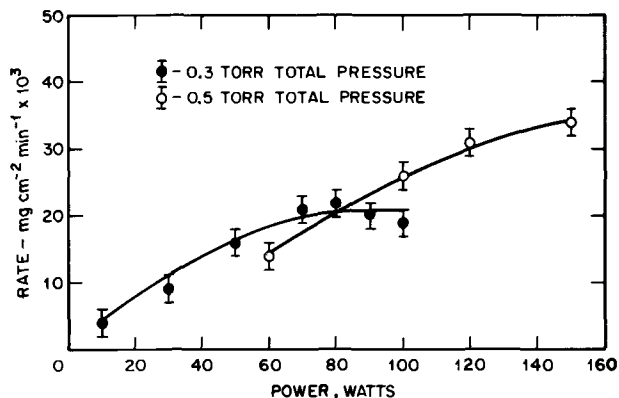


Fig. 4. Rate of VTMS polymer deposition as a function of power at constant pressure. (Equal partial pressure of argon and VTMS.)

tial pressure of the monomer. Figure 4 shows the rate as a function of power for constant total pressures of 0.3 and 0.5 Torr with equal partial pressures of argon and VTMS. In both cases, the rate increased to a plateau as the input power increased. This behavior is probably due to an increase in the electron temperature and number density with a higher power level, which in turn would enhance the rate of production of ions and radicals and hence increase the rate of polymerization. Figure 5 shows the rates obtained for VTMS polymer deposition as a function of partial pressure in

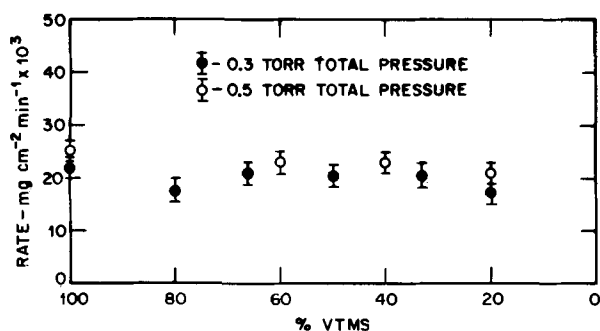


Fig. 5. Rate of polymer deposition as a function of monomer concentration in argon at constant total pressure and power (80W).

argon for constant total pressures of 0.3 and 0.5 Torr, with a constant power input of 80W. There was no significant difference in deposition rate between 100% and 20% VTMS at either total pressure. (Note that Fig. 4 shows that the rate curves obtained at 0.3 and 0.5 Torr intersect at 80W.) In addition, the data presented in Fig. 5 show that the rate of polymer deposition is controlled not simply by the concentration of monomer but perhaps by the rate at which monomer can be converted to a reactive species, since film growth remains essentially constant even though the concentration of monomer is reduced by a factor of five. Figure 6 shows the rate of polymer deposition obtained in pure VTMS at 80W as a function of pressure. At 0.1 Torr VTMS with no argon present, the rate of film growth is about 4×10^{-3} mg cm⁻² min⁻¹, whereas at 0.1 Torr partial pressure VTMS in the argon mixtures, the rate is about five times as fast (Fig. 5). It is probable that the presence of argon helps to sustain the discharge and thus prevents the decrease in rate as the monomer pressure is decreased. The sharp drop in deposition rate between 0.5 and 0.6 Torr (Fig. 6) may be a result of having increased the frequency of inelastic collisions to the point where the electrons do not reach a temperature high enough to maintain the plasma at previous levels. It must be emphasized at this point that a precise and definitive explanation of these rate data requires diagnostics of the electron temperature and concentration while the polymerization is taking place, and such diagnostics are not conveniently performed.

Several different experiments lead to the conclusion that glow discharge polymers possess potentially reactive radical sites. Some of these sites are obviously very reactive toward oxygen since samples of VTMS polymer for which the discharge vessel was back-filled with air were found to contain 11.6 and 14.3% oxygen, while back-filling with nitric oxide reduced the oxygen content in the polymer to less than half this amount (see Tables I and II). In addition, the infrared

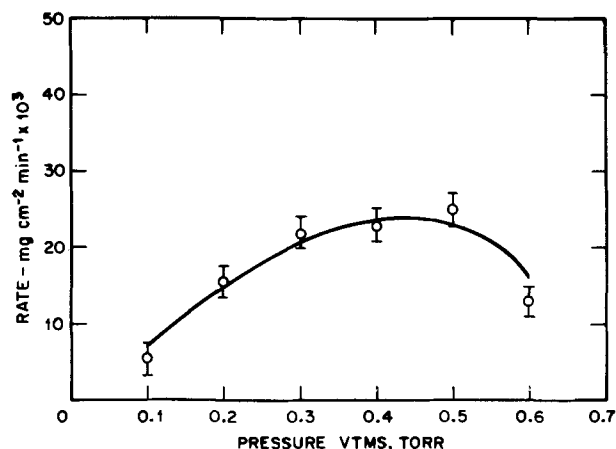


Fig. 6. Rate of polymer deposition as a function of monomer pressure at constant power (80W).

Table I. Elemental composition of polymers prepared from VTMS and HMDS

Starting materials	Power input, W	Element and weight per cent in polymer				Atom ratio in polymer, C/Si
		C	H	Si	O*	
VTMS	200	41.1	8.9	35.7	14.3	2.7
VTMS + Ar, 3:1	200	49.6	9.6	29.2	11.6	4
VTMS† + Ar, 4:3	150	51.1	9.8	36.0	2.0	3.3
VTMS† + Ar, 3:1	200	51.3	10.1	34.1	4.5	3.5
HMDS	200	33.5	8.7	44.5	13.3	1.8
HMDS + Ar, 3:1	200	36.5	8.8	44.1	10.6	1.9

* Weight per cent of C, H, and Si were determined directly. Weight per cent O is the difference between the total found for C, H, and Si and 100%.

† Polymer treated with NO before exposure to air.

Table II. Elemental composition of monomers

	Element and weight per cent				Atom ratio		
	C	H	Si	O	C/Si	C/H	C/O
VTMS	60.0	12.0	28.0	—	5	0.416	—
HMDS	44.4	11.1	34.6	9.8	3	0.333	6

spectrum of a VTMS film initially exposed to air exhibited weak broad absorption at 3380 cm⁻¹ (O-H) and 1720 cm⁻¹ (C=O), and strong absorption at 1050 cm⁻¹ (Si-O) along with the expected absorption at 2960 and 2910 cm⁻¹ (CH₂ and CH₃, respectively), 2120 cm⁻¹ (Si-H), and 1245 cm⁻¹ (Si-CH₃). Heating the above films at 150°C for 3 hr in oxygen increased the intensities of the O-H, C=O, and Si-O bands, while the C-H and Si-H absorption essentially vanished. On the other hand, VTMS films that were initially exposed to a 3 Torr atmosphere of nitric oxide for 16 hr before exposure to air showed absorption bands at 2950 and 2900 cm⁻¹ (CH₂ and CH₃), 2110 cm⁻¹ (Si-H), and 1243 cm⁻¹ (Si-CH₃), with virtually no absorption for O-H, C=O, and Si-O bonds. The incorporation of oxygen by glow discharge polymers on exposure to air has also been observed by Westwood (4); the amount depended on the nature of the polymer and the conditions under which it was formed.

Radical sites which were less reactive toward oxygen were detected by electron spin resonance measurements. VTMS polymer showed a broad line absorption from 6 to 13 gauss wide at $g = 2$. Heat treatment (150°C) of the polymer in air or in vacuum resulted in almost total loss of this signal. It is interesting to note that complete quenching of the free radicals and relief of conformational strain in the polymer required heating to about 150°C. Trapped free radicals in discharge produced polymers have also been observed by Schurov *et al.* (5).

Differential scanning calorimetry of VTMS and HMDS polymer indicates that the former material has a much greater concentration of potentially reactive sites than the latter, even after both polymers have been exposed to air. For example, samples of VTMS polymer produced strongly exothermic thermograms over the entire temperature range 35°-460°C, while HMDS polymer samples gave thermograms which were only slightly exothermic from 35° to 180°C and then endothermic to 460°C. After heating freshly prepared VTMS polymer at 150°C for 20 hr in vacuum, a thermogram very similar to that of HMDS was obtained. We interpret the strong exothermic behavior as due to chemical reaction, perhaps with atmospheric oxygen and/or as radical recombination.

The results of combustion analyses of VTMS and HMDS polymers are given in Tables I and II. The weight per cent of carbon, hydrogen, and silicon were determined directly; the difference between the total for these elements and 100% was assumed to be the oxygen content. The carbon to silicon atom ratio of each sample is also reported in the tables. These re-

sults demonstrate quite clearly that the elemental compositions of the polymers of HMDS and VTMS differ significantly from the compositions of the monomers. In the case of the VTMS polymer, the C/Si ratio varies from 2.7 to 4 and apparently depends on the power input and the partial pressure of argon. The VTMS monomer has a C/Si ratio of 5, so that at least one carbon atom per monomer unit must be lost when forming polymer. Similarly, HMDS polymer has a C/Si ratio of about 2, while the monomer has a C/Si ratio of 3. Tkachuk *et al.* (6) have found C/Si ratios of 1.85 and 1.59 for polymer prepared from HMDS by the action of gas discharges, as well as a dependence of this ratio on the presence of argon. Further evidence of major structural reorganization occurring in the transition from monomer to polymer is found in the infrared spectra. VTMS polymer contains Si-H bonds and lacks double bonds. HMDS polymer also contains Si-H bonds. In both cases, the monomers have no Si-H bonds.

Many workers have proposed a variety of mechanisms for the formation of glow discharge polymers. Three of these are discussed briefly to give some idea of the diversity of thinking in this area. Yasuda and Lamaze (7) studied the polymerization of styrene in an electrodeless, inductively coupled glow discharge system. They concluded that in their system polymerization is initiated (whether by a radical or ion is not mentioned) and propagates in the vapor phase until the growing polymer is too large to remain as a vapor and deposits on the wall. Westwood (8) studied the polymerization of ten conventional vinyl polymers, including styrene, in a capacitively coupled discharge. He concluded that positive ions and ionic fragments attracted to the electrode surface and walls initiate polymerization of adsorbed neutral monomer molecules. The proportion of ionic fragments to intact monomer incorporated in the polymer depended on the conditions of the reaction. Denaro *et al.* studied the polymerization of styrene (9a), styrene derivatives (9b), allyl alcohol (9c), and crotyl alcohol (9c) in a capacitively coupled discharge. These workers concluded that the reaction of radicals produced in the vapor phase was of little importance, and that the mechanism of polymerization involved competitive reactions of radicals formed on the electrodes by electron bombardment.

All the above workers have used compounds which readily polymerize by cationic and/or radical mechanisms. We have studied compounds, VTMS and HMDS, which are not suitable for polymerization by ordinary means. Experimental observations in this study which may be relevant to postulating a mechanism follow: the stoichiometry of the polymer indicates a lower carbon content and the infrared spectra show bond reorganization, both of which must occur in the transition from monomer to polymer. Potentially reactive radical sites are trapped in the polymer. Polymerization was observed in the gas phase when the input power and total pressure were high. Fragmentation of VTMS under electron impact was studied in a mass spectrometer as a function of electron energy. The parent molecular ion was found to be very unstable even at electron energies as low as 10 eV. The major ionic fragments at high or low energies had values of M/e of 85 and 59. Figure 7 shows the relative intensities of the various fragment ions for electron energies from 10 to 40 eV. The mass 85 fragment ion corresponds to a loss of the methyl radical from the parent ion, and the mass 59 fragment ion results from a loss of acetylene from the mass 85 fragment ion.

A likely mechanism of polymer formation at the walls of an RF discharge for a compound such as VTMS can now be postulated. The process is initiated in the gas phase by electron impact and formation of a radical ion. Since electrons with energies in excess of 20 eV are rare in the plasma, the major fragments

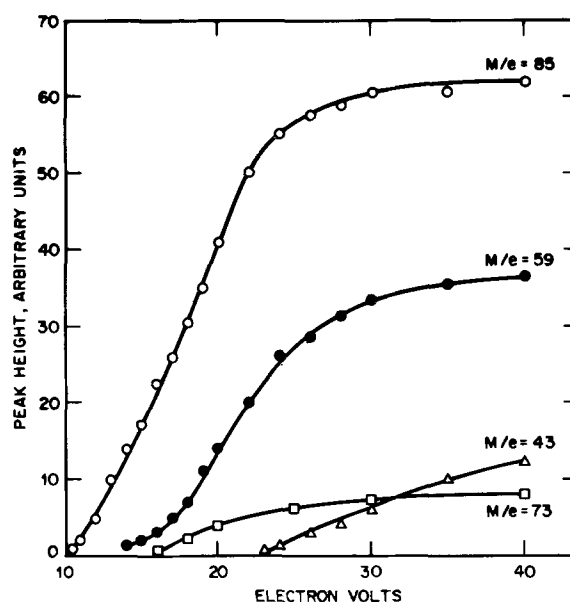


Fig. 7. Ionic fragments from VTMS on electron impact

expected due to a single electron impact on the VTMS molecule are ions of mass 85, $(C_4H_9Si)^+$, and mass 59, $(C_2H_7Si)^+$, acetylene, and methyl radicals. Ionic fragments formed near the sheath boundary are accelerated to the walls of the vessel by the plasma-to-wall potential difference. On reaching the walls, the ions recombine with electrons forming radicals. These radicals can then react with adsorbed monomer or other radical sites and become incorporated into the polymeric structure. Ionic fragments formed in the plasma at relatively long distances from the sheath boundary may react with a neutral or radical species to form higher molecular weight positive ions. If the rate of growth of this ionic chain is slow enough to allow migration to a wall, electron-ion recombination will produce a short chain radical which can then become incorporated into the polymer. If, on the other hand, the growth of the ionic chain is fast, it can continue to grow in size until it becomes large enough (i.e., macroscopic) to act as a virtual wall. Radical site production in existing polymer on the walls should be a continuous process resulting from photon and ion impact. (Electrons from the plasma are retarded as they approach the walls and thus lose energy.)

Polymer production on the electrode surfaces should proceed by essentially the same mechanism, with the exception that a strong alternating electric field is present in the dark space between the plasma and the electrode surface. Electron energies are likely to be much higher in this region, resulting in increased monomer fragmentation. Charged particles of either polarity will be accelerated to the electrode on each half cycle, so the effects of high-energy electron impact must also be considered as a source of cross-linking.

This postulated mechanism is consistent with many of the observed experimental results; however, it must be emphasized that it is only one of a number of possibilities. Experiments involving the diagnostics of chemically reactive plasmas are now in progress in this laboratory and should provide more definitive data on the mechanism of polymer formation.

Manuscript submitted June 22, 1971; revised manuscript received Nov. 16, 1971.

Any discussion of this paper will appear in a Discussion Section to be published in the December 1972 JOURNAL.

REFERENCES

1. P. White, *Insulation*, **13**, 52 (1967).
2. V. M. Kolotyarkin, A. B. Gil'man, and A. K. Tsapuk, *Russ. Chem. Rev. (English Transl.)*, **36**, 579 (1967).

3. A. M. Mearns, *Thin Solid Films*, **3**, 201 (1969).
4. A. R. Westwood, *European Polymer J.*, **7**, 377 (1971).
5. A. N. Schurov, L. S. Tuzov., A. B. Gil'man, V. M. Kolotyrlin, and N. N. Tunitskii, *Polymer Sci. (USSR) (English Transl.)*, **11**, 660 (1969).
6. R. V. Tkackuk, V. V. Bushin, V. M. Kolotyrlin, and N. P. Smetankina, *ibid.*, **9**, 2281 (1967).
7. H. Yasuda and C. E. Lamaze, *J. Appl. Polymer Sci.*, **15**, 2277 (1971).
8. A. R. Westwood, *European Polymer J.*, **7**, 363 (1971).
9. (a) A. R. Denaro, P. A. Owens, and A. Crawshaw, *European Polymer J.*, **4**, 93 (1968); (b) *ibid.*, **5**, 471 (1969); (c) *ibid.*, **6**, 487 (1970).

Calibration of Electrochemical Oxygen Meters in Sodium Using Uranium

Hugh S. Isaacs*

Brookhaven National Laboratory, Upton, New York 11973

ABSTRACT

Methods using uranium to remove or getter oxygen quantitatively from sodium have been used to calibrate the potential of the meter as a function of the oxygen concentration in sodium. The oxygen meters were constructed with sodium-sodium oxide reference electrodes and ThO₂-Y₂O₃ electrolytes. The calibration methods depended on the deviation of these meters from ideal behavior. The methods involved the summation of the weight gains of uranium, i.e., the weights of oxygen removed from the sodium, the derivative of the weight gains for a given potential change as a function of the number of repetitive oxygen removal steps, and the time dependence of the potential during the removal of oxygen from sodium by uranium. The behavior of a meter depended on the purity of the ThO₂-Y₂O₃ electrolyte used. High-purity electrolytes gave the theoretical dependence of potential on concentration but impure tubes showed marked deviations from theoretical behavior at low concentrations at temperatures of 500°C.

The necessity for measuring oxygen concentration in sodium used as a coolant in fast breeder nuclear reactors is related to the corrosion and mass transfer of metals in these systems. The corrosion of many metals (1) and iron-base alloys, including stainless steels (1,2), have been found to increase with higher oxygen concentrations in sodium. Increased corrosion rates would lead to increased transfer of radioactive materials from the reactor core to the rest of the primary system, and, to minimize these effects, the concentration of oxygen should be kept as low as possible and monitored to detect any concentration changes.

Electrochemical cells using solid oxide electrolytes (3) offer a possible method for continuously monitoring oxygen concentrations in the sodium. However, the potentials developed by these cells or meters have not been reproducible (3,4) and in some cases their response to changes in oxygen concentration have not been the same for one or more meters in the same system.

In order to study the variables which could influence the reproducibility of these meters, a rapid method for calibrating meters was required. For this study the use of small sodium containers was more desirable than the large sodium loops most frequently used for investigations of the behavior of sodium. The advantages of small containers are that impurities in the sodium, including oxygen, could be controlled more readily and rapidly than in a large nonisothermal system.

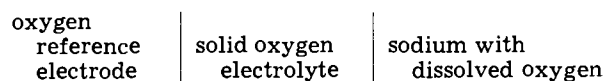
During a study of methods for removing oxygen from sodium it was found that uranium reacted rapidly with oxygen dissolved in sodium and formed uranium oxide. This oxide adhered to the uranium when the temperature was 500°C and above giving weight gains of the uranium equal to the amount of oxygen removed. The rate of reaction was also found to be proportional to the oxygen concentration and the rate was con-

trolled by diffusion in the sodium or the mass transfer coefficient for oxygen in sodium (5). Uranium, therefore, appeared to be ideal for removing oxygen from sodium and also offered several alternative techniques for determining the relationship between the potential of the meter and the oxygen concentration in sodium. It is the purpose of this paper to describe these techniques and discuss some of the results obtained.

Theory

Electrochemistry

An electrochemical oxygen meter for monitoring oxygen in sodium is basically an electrochemical cell which may be represented by



where the sodium with dissolved oxygen forms the second electrode and the potential of the cell (E) is given by the Nernst equation

$$E = E_0 + \alpha \ln \frac{C_s}{C} \quad [1]$$

where $\alpha = RT/nF$, E_0 is the potential of the meter when the concentration of oxygen in the sodium, C , is at saturation, C_s , and R , T , and F are, respectively, the gas constant, the absolute temperature, and the Faraday. The solubility of sodium oxide in sodium is low (~1200 ppm) and the solution may therefore be considered as dilute. Hence Henry's law is applicable and the concentration of oxygen in solution is proportional to its activity (6). The value of E_0 depends on the reference electrode used and is determined by the free energy of formation of sodium oxide from the reaction of sodium with the reference electrode; when a sodium-sodium oxide reference is used its value is theoretically zero.

* Electrochemical Society Active Member.

Key words: sodium, electrochemical oxygen meter, thoria-electrolyte, uranium.

Calibration Methods Using Uranium

In this section the equations that may be used for the calibration of oxygen meters using uranium are derived and their application is discussed in the following section.

Summation method.—Consider an initial potential of the oxygen meter as E_1 , then this potential corresponds to an oxygen concentration C_1 and the potential increases as oxygen is removed from the sodium by reaction with uranium. When the uranium is removed from the sodium the potential will have increased to a value E_2 corresponding to a lower oxygen concentration C_2 . From the weight gain of the uranium, ΔW_1 , the relationship between the concentrations is

$$C_1 = C_2 + \frac{\Delta W_1}{W_{Na}} \quad [2]$$

where W_{Na} is the weight of sodium. As the measurements are related to weight changes rather than concentration changes, the weights of oxygen are considered. It is a simple matter to convert weights to concentrations when the calibration curve is obtained. If the weight of oxygen in the sodium, W , corresponds to an oxygen concentration, C , then multiplying both sides of Eq. [2] by W_{Na} gives

$$W_1 = W_2 + \Delta W \quad [3]$$

If oxygen was removed from the sodium in Z steps then

$$W_1 = W_{Z+1} + \sum_{n=1}^Z \Delta W_n \quad [4]$$

where W_{Z+1} is the weight of oxygen remaining in the sodium after Z getting steps and $\Delta W_{n=Z}$ is the weight of oxygen removed by uranium for the Z th step. The corresponding weight of oxygen in the sodium before the n th getting step is

$$W_n = W_{Z+1} + \sum_{n=n}^Z \Delta W_n \quad [5]$$

In the above equation the value of W_{Z+1} is unknown, but if $W_{Z+1} \ll W_n$ this quantity may be neglected and Eq. [5] becomes

$$W_n = \sum_{n=n}^Z \Delta W_n \quad [6]$$

The potential of the meter prior to each getting is given by E_n and a plot of E_n vs. W_n would give the calibration curve for the meter where $W_n \gg W_{Z+1}$.

This method has the advantage that the period of getting or the resulting potential changes need not be controlled as is required in some of the methods described below. However, to overcome the restriction that the weight of oxygen remaining in the sodium must be negligible compared with the total weight of oxygen at a given potential necessitates the use of a method requiring a specific experimental procedure for each getting.

Method using constant potential steps.—In this method a series of getting steps are performed and n refers to a particular step as in the summation method. The weight gain for a given step is again ΔW_n . However, in this method the potential step (ΔE) for all steps must be the same (i.e., $\Delta E_1 = \Delta E_n$).

The potential change for the first step is given by

$$\Delta E = \alpha \ln \frac{W_1}{W_2} \quad [7]$$

and is derived from Eq. [1]. After $n - 1$ steps the potential change is

$$(n - 1) \Delta E = \ln \frac{W_1}{W_n} \quad [8]$$

Equation [7] with Eq. [3] can be rearranged to give

$$\Delta W_1 = W_1 \left(1 - \exp \left\{ -\frac{\Delta E}{\alpha} \right\} \right) \quad [9]$$

and, in general

$$\Delta W_n = W_n \left(1 - \exp \left\{ -\frac{\Delta E}{\alpha} \right\} \right) \quad [10]$$

Equations [9] and [10] indicate that the weight gain (or change in concentration) is proportional to the initial weight (or concentration) of oxygen for that getting step on the assumption that the value of α remains constant.

Substituting Eq. [9] and [10] in [8] for the $(n - 1)$ step gives

$$(n - 1) \Delta E = \alpha \ln \frac{\Delta W_1}{\Delta W_n} \quad [11]$$

which on differentiating gives

$$\frac{d \ln \Delta W_n}{dn} = -\frac{\Delta E}{\alpha} \quad [12]$$

Equation [11] shows that a plot of the logarithm of the weight gain as a function of the number of gettings (n) has a slope as given by Eq. [12] equal to the (constant) potential change ΔE for each getting divided by the value of α . The slope of this curve can be measured and as ΔE is known, the value of α can be calculated.

If the value of α is constant this plot is linear, but if α changes as the oxygen concentration is reduced this is reflected in a change in slope of this plot.

Variation of potential with time during uranium getting.—The rate of change in oxygen concentration is related to the rate at which uranium removes oxygen from sodium. When uranium is inserted into sodium the rate of change in concentration (dc/dt) is proportional to the oxygen concentration in the sodium (5), i.e.

$$-\frac{dc}{dt} = Ck \quad \text{or} \quad -\frac{d \ln C}{dt} = k \quad [13]$$

where k is the rate constant which is equal to the mass transfer coefficient (5). The rate of potential change is also related to the rate of change in oxygen concentration as can be seen on differentiating Eq. (1)

$$\frac{dE}{dt} = \alpha \frac{d \ln C}{dt} \quad [14]$$

Substituting Eq. [13] in Eq. [14] gives

$$\frac{dE}{dt} = \alpha k \quad [15]$$

If the value of α remains constant and the mass transfer coefficient is kept constant (by controlling the geometry of the system and the sodium velocity during uranium getting) then the product of α and k is a constant and from Eq. [15] the potential increases linearly with time. If α decreases, the rate of change in potential also decreases.

Experimental

The oxygen meters used in this work were of similar construction to those with a copper-copper oxide reference electrode (3) except the reference electrode was replaced by sodium and sodium oxide. The thoriatytria electrolyte tubes all containing 15% yttria by weight were about 6-8 in. long and $\frac{1}{4}$ - $\frac{1}{2}$ in. in diameter. The tubes were leak tested and showed a leak rate of less than 10^{-10} cm³/sec. The slip-cast tubes were obtained from Zirconium Corporation of American and the isostatically pressed tubes were obtained from General Electric Corporation. The insidious impurity in the slip-cast tubes was SiO₂ at concentrations of 100-300

Table I. Impurities in ThO₂-15 w/o Y₂O₃ tubes

Element	Slip-cast	Isostatically pressed
Si	300	<10
Fe	300	<10
Mo	10	<10
Mg	300	<1
Ni	50	<1
Mn	10	<1
Pb	5	<1
Co	5	<1
Cu	50	<1

ppm that formed a second grain boundary phase by reacting with Y₂O₃ (7). The isostatically pressed tubes had an impurity level of less than 35 ppm. Representative compositions of the two types of tubes determined spectrographically are shown in Table I. The high-purity tubes were white in color and remained white after firing in air at 700°C. The impure tubes were brown after air firing. This difference suggests that impurities in the oxide play a part in developing the brown coloration when exposed to high-oxygen activities rather than being caused by some property of the oxide solution itself (8).

Impurities present in "as-received" sodium gave reactions which tended to buffer the oxygen concentration in sodium and could act as a source or sink for oxygen (9). Distilled sodium was consequently used in these experiments. Containers of zirconium oxidized in oxygen for 3 hr at 700°C, or of stainless steel showed no difference in results. The sodium weighed 310 ± 20g and was stirred with a hermetically sealed stirrer. Stringent precautions were taken to prevent contamination of the sodium or the added sodium oxide (5) with air or water vapor. A helium cover gas at pressure above atmospheric, containing less than 10 ppm oxygen and water vapor protected the sodium from contamination by gaseous impurities.

Uranium strips were usually 5 x 1 x 0.1 cm in size. The strips were electropolished in equal volumes of ethanol and phosphoric acid at 6-12V, washed in water, and weighed to ±0.03 mg before use. After exposure to sodium the sodium adhering to the uranium was dissolved in methanol and the uranium was then washed in water and air dried prior to reweighing (5).

Results and Discussion

When oxygen is removed from the sodium the oxygen concentration decreases and the potential of the meter according to Eq. [1] increases. Figure 1 shows an example of the variation of potential with time when uranium was used to remove oxygen in a series of gettering steps. The meter was constructed with the high-purity isostatically pressed oxide tube. When uranium was inserted in the sodium the potential increased linearly with time in agreement with Eq.

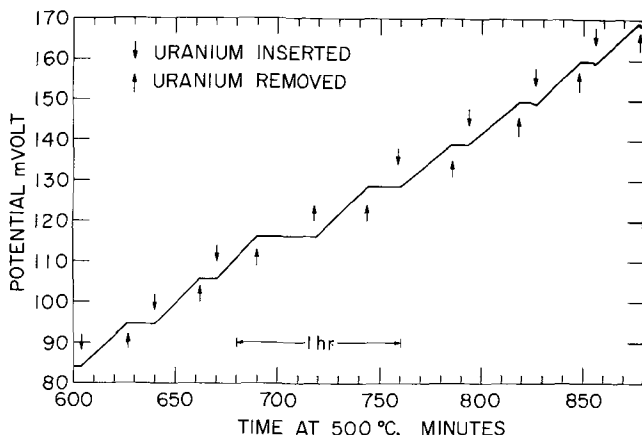


Fig. 1. Variations of potential with time during oxygen gettering with uranium for a meter with a high-purity electrolyte.

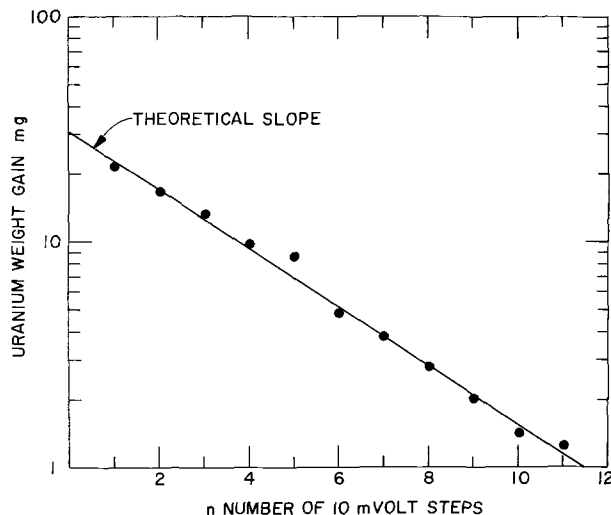


Fig. 2. Variation of uranium weight gain as a function of the number of repetitive gettering steps for a high-purity electrolyte.

[15]. Upon removing the uranium the potential no longer increased and gave the series of steps shown in Fig. 1. The weight gains of uranium tubes after each gettering shown in Fig. 1 and those obtained at higher potentials are plotted in Fig. 2 as a function of the gettering step. These results can be used to determine the calibration curve for the meter, *i.e.*, the relation between the potential and the logarithm of the oxygen concentration. The slope of this curve α can be determined from Fig. 2 as indicated by Eq. [12]. This equation can be expressed to base 10 as

$$\frac{d \log \Delta W}{dn} = \frac{\Delta E}{2F} \left/ \frac{2.3 RT}{2F} \right. \quad [16]$$

The theoretical slope is equal to 1/7.7 mV⁻¹ at 500°C for 10 mV potential changes. The observed slope in Fig. 2 is in good agreement with the theoretical slope indicating that the value of α was in accord with the Nernst equation. An extrapolation of these results can also be used to determine the calibration curve shown in Fig. 3. The value of α determined from this curve was 79 mV/decade change in oxygen concentration which deviates by less than 3% from the theoretical value.

Three meters constructed with isostatically pressed tubes were calibrated after holding at 500°C for one

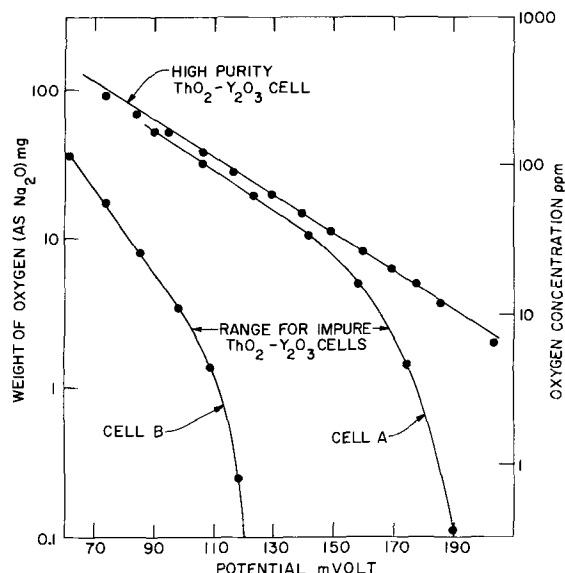


Fig. 3. Calibration curves for cells constructed with high purity and impure ThO₂-Y₂O₃ electrolytes.

day. The potential difference between the calibration curves at a given oxygen concentration varied by close to 20 mV. The curves were parallel being within 5% of the theoretical slope down to oxygen concentrations of 1 ppm. The potential of the meters, however, decreased with time but their response to changes in oxygen concentration remained the same for a period of 40 days. The decrease in potential was found to be approximately 2 mV/day when only a small excess of solid Na_2O was present in the reference electrode. Additions of Na_2O to the reference electrode after the drift had occurred increased the potential of a cell and suggested that the drift and the potential differences after one day were probably a result of the reaction between the oxide and the electrolyte at the higher oxygen activity in the reference electrode. Reactions have been observed to take place at higher temperatures and at a rate which increased oxygen concentrations in the sodium (10).

The calibration curves of 15 oxygen meters constructed with slip-cast $\text{ThO}_2\text{-Y}_2\text{O}_3$ tubes that were less pure than the isostatically pressed tubes, were highly variable. The results for two of the meters which represented the range of behavior of the slip-cast tubes tested at 500°C are shown in Fig. 4. This figure shows the variation of the logarithm of the weight gains for a series of gettering steps. The measurements have been normalized to effectively 10 mV steps for direct comparison between the results. Curves A and B were obtained with 17 ± 2 (for meter A) and 10 ± 2 mV steps (for meter B), respectively. Results with a high-purity isostatically pressed tube gettered to give 20 mV steps are also shown for comparison. The results using the slip-cast tubes show pronounced curvature, while those for the isostatically pressed tube are linear, and theoretical. Curve A shows that the value of α is close to but slightly greater than theoretical at weight gains above 3.5 mg. However, at lower weight gains a marked decrease was observed. This deviation is indicative of a decreased value of α with decreasing oxygen concentration. The results for meter B with the high slope indicates that the value of α was low throughout the range of oxygen concentration investigated. The value of α determined from the slope for the higher weight gains is 33 mV which is 43% of the theoretical value. This value also shows a decrease with decreased weight gains or lower oxygen concentrations.

Extrapolation of both curves A and B to weight gains below 0.1 mg indicates that very small quantities

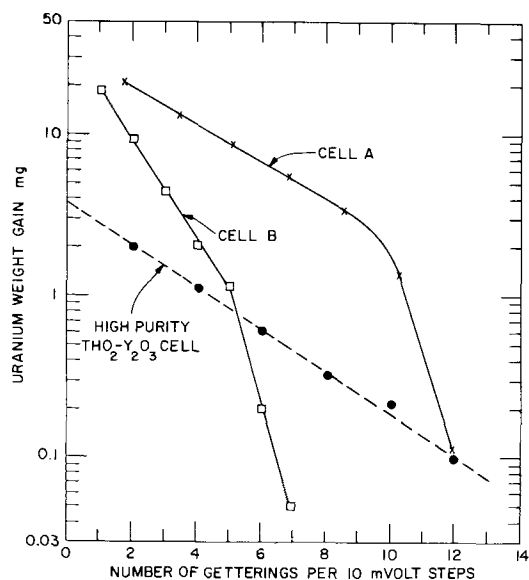


Fig. 4. Variation of uranium weight gain as a function of repetitive gettering steps for high-purity and impure $\text{ThO}_2\text{-Y}_2\text{O}_3$ electrolytes.

of oxygen would be removed from the sodium if the number of gettering steps were increased, or the weight of oxygen remaining in the sodium was extremely small. The amounts of oxygen in the sodium after the last getterings were therefore negligible and the calibration curves for these meters were constructed using the summation method (Eq. [6]). The calibration curves obtained by summation of the weight gains and plotting the related concentrations against the potential are also shown in Fig. 3. Above 30 ppm curve A shows a theoretical slope. At oxygen concentrations below 30 ppm for meter A and for the entire range of oxygen concentration investigated with meter B, the calibration curves show less than the theoretical value of α . This behavior was indicated by the results shown in Fig. 4.

Indications of this decrease in α could also be deduced from the behavior of the rate of potential change during removal of oxygen by uranium. During gettering the rate was observed to fall continuously at the higher potentials for all slip-cast tubes tested. For example in the case of cell A the rate decreased when the potential was above 140 mV and continued to decrease at still higher potentials. It may be seen from Eq. [15] that the rate of potential change is proportional to the value of α and the observed decreased rate therefore suggested a decrease in the value of α .

Measurements of the oxygen ionic transference number have been made on thoria-ytria electrolyte of similar composition to those of the slip-cast tubes (11). These results showed that the observed decrease in α from the theoretical value could not be attributed to deviations of the transference number from unity at the oxygen activities in sodium. The observed decrease in α is probably a result of interactions of sodium with impurities present in the slip-cast tubes which also act to influence the characteristics of the electrochemical system.

Conclusion

Uranium offers a rapid and sensitive method for calibrating oxygen meters in sodium at temperatures of 500°C . The high-purity isostatically pressed $\text{ThO}_2\text{-Y}_2\text{O}_3$ electrolyte tubes are far superior to less pure slip-cast tubes. The former show theoretical slopes down to oxygen concentrations of 1 ppm while the slip-cast tubes are highly variable in behavior and deviate from the theoretically expected variation of potential with oxygen concentration.

Acknowledgments

The author wishes to thank Dr. D. H. Gurinsky and Dr. L. Newman for their helpful discussions during the course of this work and Mr. W. W. Becker and G. C. Spira for their assistance in conducting the experiments. This work was performed under the auspices of the United States Atomic Energy Commission.

Manuscript submitted Aug. 27, 1971; revised manuscript received Nov. 11, 1971.

Any discussion of this paper will appear in a Discussion Section to be published in the December 1972 JOURNAL.

REFERENCES

1. J. H. Stang, E. M. Simons, J. A. DeMastry, and J. M. Genco, Battelle Memorial Inst., DMIC Report, 1966.
2. J. R. Weeks, C. J. Klamut, and D. H. Gurinsky, Alkali Metal Coolants, IAEA, Vienna, 1967, p. 3.
3. M. Kolodney, B. Minushkin, and H. Steinmetz, *Electrochem. Technol.*, **3**, 244 (1966).
4. J. E. Meyers and R. A. Hunter, Proc. Int. Conf. on Sodium Technology, Nov. 7-9, 1968, Argonne Natl. Lab., ANL 7520, Pt. 1, p. 233.
5. H. S. Isaacs, *J. Nucl. Mater.*, **36**, 322 (1970).
6. O. Kubaschewski, E. L. Evans, and C. B. Alcock, "Metallurgical Thermodynamics," p. 60, Pergamon Press (1967).
7. L. Bates, Private communication, 1968.
8. J. E. Bauerle, *J. Chem. Phys.*, **45**, 4162 (1966).

9. H. S. Isaacs, B. Minushkin, and F. J. Salzano, Proc. Int. Conf. on Sodium Technology, Nov. 7-9, 1968, Argonne Natl. Lab., ANL 7520, Pt. 1, p. 460.
10. W. A. Ross, Westinghouse Atomic Development Co.,

- Report HEDL-TME-71-29, Vol. 3, p. 5., Oct-Dec 1970.
11. F. J. Salzano, H. S. Isaacs, and B. Minushkin, *This Journal*, **118**, 412 (1971).

Technical Notes



D-Size Lithium Cupric Sulfide Cells

J. P. Gabano, V. Déchenaux, G. Gerbier, and J. Jammet

Societe des Accumulateurs Fixes et de Traction, Département la Pile Leclanché, Poitiers, France

Research at SAFT on high-energy primary batteries with a lithium anode and a nonaqueous electrolyte has resulted in the design of a lithium cupric sulfide cell using an electrolyte made of a LiClO_4 solution in a combined solvent comprising 10% tetrahydrofuran (THF) (1) and 30% 1,2 dimethoxyethan (1,2-DME) (2). Prismatic cells of 30 A-hr capable of reaching and even exceeding 300 W-hr/kg and 400 W-hr/dm³ have been developed in the past (3, 4) for the determination of the reliability of the system. The results indicated that this couple can be stored more than one year under normal conditions and six months at 45°C without appreciable loss of energy. On the basis of these studies D-size lithium cupric sulfide cells have been designed.

The purpose of this paper is to present the data obtained on D-size cells after optimization and to discuss their characteristics and performance in comparison with carbon-zinc and alkaline manganese dioxide cells of the same size.

Cell Design

Completely sealed D-size cells were made using cans of nickel-plated steel. The cylindrical cell has the distinguished feature of a coiled element for improving cell performance under heavy discharge rates.

The cupric sulfide used for the cathode was prepared by the thermal combination of sulfur and copper. Very pure sulfur free cupric sulfide was synthesized by this method. For the making of the cathode, cupric sulfide powder was mixed with a Teflon binder and cold-pressed onto a very thin nickel-plated steel strip of a suitable length. Then the cathode was cured at 280°C for 2 hr. This process gave a flexible electrode which could be rolled very easily. The cathode was entirely sealed in a nonwoven polypropylene bag which acted as a separator.

The lithium anode was made of a pure lithium strip with a terminal made of a tab of stainless steel soldered to one end of the strip.

The solvents used were the purest commercially available and were dried by standing one week over molecular sieves. The LiClO_4 solute was of the highest

purity available (GF Smith Chemical Co.); it was dried at 150°C for 48 hr before use.

Cells were filled with a molar solution of LiClO_4 in the combined solvent (THF + 1,2-DME) before sealing. Their capacity varied according to the length and the thickness of the cathode, that is to say between 11 and 14 A-hr for the cells we studied. Anode capacity was about 30% higher than cathode capacity. Moreover the amount of electrolyte was approximately 17 cm³ per cell. The open-circuit voltage (O.C.V.) of these cells was about 2.15V and their ohmic resistance 0.3 ohm, the total weight of a single cell was about 95g, its volume 55 cm³.

Cell Optimization

In order to achieve cell optimization, D-size cells with cathodes of different length and thickness were tested under continuous discharge through a 5 ohm load at ordinary temperature.

Table I gives the theoretical capacity of these cells according to the thickness and length of the cathode. The height was kept to a constant value of 47 mm.

Figure 1 shows the variations of the cell energy as a function of the length of the cathode, for these conditions of discharge. It can be seen that the cell energy is markedly affected by decreasing the length of the cathode below 250 mm, but remains approximately constant beyond this value.

In our further determinations, all the cells were designed with a 250 mm cathode length. This electrode gives a theoretical capacity of 13 A-hr.

Cell Discharge Characteristics

Different test loads were used in this evaluation under various conditions of continuous and intermit-

Table I. Effect of length and thickness of the cathode on theoretical cell capacity

Length of the cathode (mm)	Thickness of the cathode (mm)	Theoretical cell capacity (A-hr)
120	2.80	14.2
250	1.50	13.0
360	1.15	11.5

Key words: nonaqueous cell, organic solvents, tetrahydrofuran, 1,2 dimethoxyethan, lithium, copper sulfide.

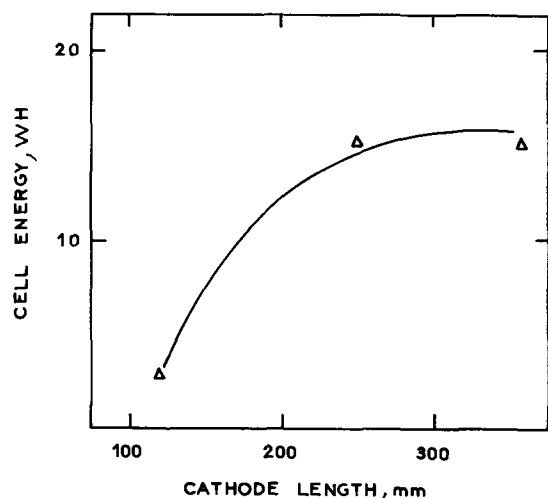


Fig. 1. Effect of cathode length on cell energy under 5 ohm continuous discharge load.

tent discharges. Regular carbon-zinc and alkaline manganese dioxide cells of the same size were discharged in the same time; however, in order to account for the difference of voltage of each system, suitable loads were selected to give the same average current drain in order to have a better comparison. All the discharges were performed to a cutoff voltage equal to 50% of the starting voltage.

Continuous Discharges

Figure 2 shows discharge characteristics of a 13 A-hr Li/CuS D-cell. It can be seen that the discharge curve has two steps corresponding to the two levels of reduction of cupric sulfide (3). However, the voltage steps become more and more diffuse when the discharge rate is increased.

Figure 3 shows the relationship between cell energy and current drain for the three systems. These results were deduced from the discharge curves of each system obtained under suitable loads. In both cases the Li/CuS cell gave better performance than the two other couples studied. Nevertheless at current drain more than 500 mA, the energy of Li/CuS cell was only slightly greater than that of the alkaline manganese dioxide system.

Intermittent Discharges

The accepted method of assessing the performance of primary D-size cells in intermittent discharge accord-

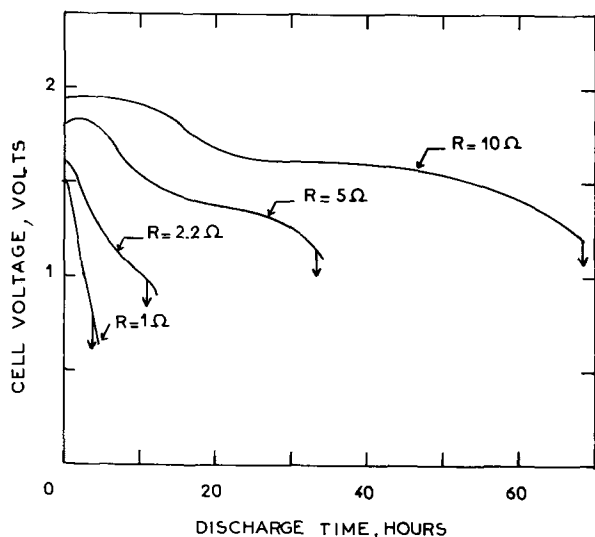


Fig. 2. Discharge characteristics of a 13 A-hr D-size Li/CuS cell as a function of various loads.

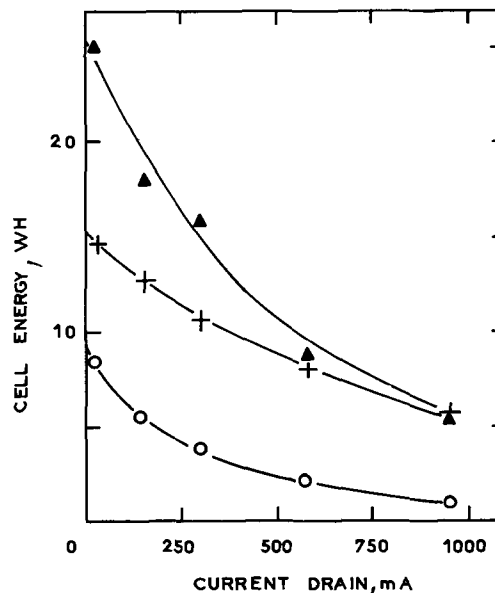


Fig. 3. Relative energy of D-size cells under continuous loads: \blacktriangle , Li/CuS cell; +, regular alkaline manganese dioxide; \circ , regular carbon-zinc cell.

ing to the various consumer applications were applied here, as is shown in the following tables.

Table II shows the results obtained for a radio intermittent duty. It can be seen from this table that the Li/CuS cell delivered a significant amount of energy in comparison with the carbon-zinc and alkaline manganese dioxide cells and had a longer discharge duration.

Table III gives the results obtained on the cassette players/recorders intermittent duty. The discharge duration for the Li/CuS cell was approximately three times more than for the carbon-zinc cell; moreover the total cell energy was four times higher. The difference in performance with the alkaline manganese dioxide cell was, however, less pronounced.

Table IV pertains to a lighting intermittent duty. This table shows the superiority of the Li/CuS cell to the two other systems. Nevertheless, the energy difference between the carbon-zinc, alkaline manganese dioxide, and Li/CuS cell is less pronounced than in the case of radio and cassette players intermittent duty. The reason is that the carbon-zinc cell does not lose much energy on intermittent heavy drains due to its capability of recovery. The difference of performance with the alkaline manganese dioxide cell is still small, especially for discharge durations which are quite similar.

Finally, the technical performances of a battery system in a given application should be estimated from

Table II. Transistor radio intermittent duty, 30 mA, 4 hr per 24 hr day

Couple	Cell capacity (A-hr)	Cell average voltage (V)	Cell energy (W-hr)	Time of service (hr)
Carbon-zinc	6.8	1.25	8.5	225
Alkaline MnO ₂ /Zn	11.8	1.24	14.6	395
Li/CuS	13.0	1.8	23.4	435

Table III. Cassette players/recorders intermittent duty, 150 mA, 4 hr per 24 hr day

Couple	Cell capacity (A-hr)	Cell average voltage (V)	Cell energy (W-hr)	Time of service (hr)
Carbon-zinc	4.8	1.20	5.8	32
Alkaline MnO ₂ /Zn	11.2	1.15	12.9	75
Li/CuS	12.6	1.58	20.0	84

Table IV. Flashlight intermittent duty,
210 mA, 3 times for 30 min per 24 hr day

Couple	Cell capacity (A-hr)	Cell average voltage (V)	Cell energy (W-hr)	Time of service (hr)
Carbon-zinc	6.1	1.20	7.3	29
Alkaline				
MnO ₂ /Zn	12.0	1.07	12.8	57
Li/CuS	12.2	1.52	18.5	58

the volume, since available volume is usually the most critical parameter to the designer of equipment. In both applications that we have mentioned, ranging in power load from radios at the low end to flashlights at the high end, we can use a stack of three Li/CuS cells instead of four conventional primary cells for reaching approximately the same voltage. This important fact can be deduced from the values of the single-cell average voltage in Tables II, III, and IV.

Conclusions

This small test program has shown that the D-size Li/CuS cell is capable of giving useful energy within the range of rates and types of discharge applied.

A comparison with carbon zinc and alkaline manganese dioxide D-size cells has shown the superiority of the Li/CuS cell over the common primary systems in the case of consumer applications.

The best performance obtained at low drain was 25 W-hr. This corresponds to a specific volumetric energy of 470 W-hr/dm³. This value is considerably greater than can be obtained with the HgO/Zn system, which has the best volumetric energy density (350 W-hr/dm³) in aqueous electrolytes for the D-size cell.

Manuscript submitted June 9, 1971; revised manuscript received Nov. 11, 1971. This was Paper 40 presented at the Cleveland Meeting of the Society, Oct. 3-8, 1971.

Any discussion of this paper will appear in a Discussion Section to be published in the December 1972 JOURNAL.

REFERENCES

1. J. P. Gabano, U. S. Pat. 3, 542, 601.
2. J. P. Gabano *et al.*, U. S. Pat. 3, 511, 716.
3. J. P. Gabano, G. Gerbier, and J. F. Laurent, "Proc. 22th Ann. Power Sources Conf.," p. 84, Atlantic City, N.J. (1969).
4. V. Dechenaux, G. Gerbier, and J. F. Laurent, "Final Report, Contract SEFT No. 507/197/50" (1969).

Photoelectrochemical Image Conversion

M. M. Nicholson*

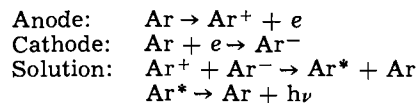
Atomics International, A Division of North American Rockwell Corporation, Canoga Park, California 91304

Imaging devices that convert infrared to visible light generally involve all solid-state systems and may require high voltages to achieve the desired image intensity. This note describes an electrochemical scheme for infrared-to-visible conversion in a single cell operated by a low-voltage power supply. Efficiencies and other performance characteristics have not yet been determined, but available information on the essential processes involved supports the feasibility of the concept.

The schematic design of the electrochemical image conversion device is shown in Fig. 1, where the cell is envisioned as a thin-layer structure. The essential elements are (a) a semiconductor control electrode, which is responsive to infrared light, (b) a solution containing a supporting electrolyte and a regenerative faradaic system capable of producing electrochemiluminescence, and (c) a perforated or transparent counterelectrode through which the resultant image

may be viewed. For discussion, it may be assumed that the semiconductor is germanium or silicon and that the solution consists of an electroactive aromatic hydrocarbon such as rubrene, dissolved in benzonitrile, with tetrabutylammonium perchlorate as the supporting electrolyte (1). The counterelectrode may be a platinum screen. The device is not limited to this type of system, although present information suggests that these materials would be appropriate for an experimental study.

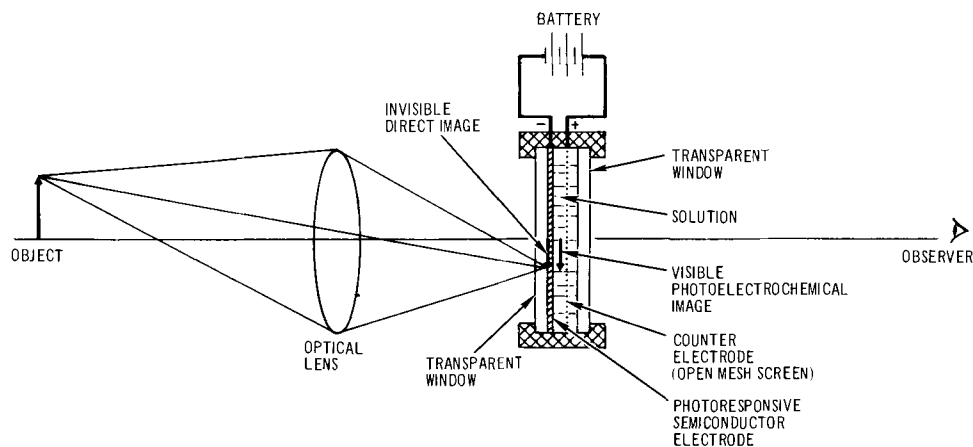
It is known that many aromatic hydrocarbon systems emit light when electrolyzed at ~3V between two inert metal electrodes (2, 3). The luminescence is due primarily to the annihilation reaction between the electrolytically formed hydrocarbon cations and anions, which occurs in the solution phase when these species are brought together by diffusion. The over-all process may be represented as follows:



* Electrochemical Society Active Member.

Key words: Images, semiconductors, electrochemiluminescence, hydrocarbons.

Fig. 1. Photoelectrochemical image converter.



The last two equations are consistent with an excited singlet state for the light-emitting species; detailed mechanisms are discussed elsewhere (3). For the present application it is essential to note that the net result of these reactions is the conversion of electrical energy to light, with regeneration of the hydrocarbon.

It is expected that similar reactions will occur at semiconductor electrodes. Further, if a semiconductor is chosen so that one of the faradaic processes is limited by the minority carrier concentration, the electrode will be photosensitive (4). For example, if the control electrode in Fig. 1 is p-type and the reduction of Ar requires conduction electrons, very little current will flow through the cell in the absence of light. When an infrared (or visible) image is focused on the outer surface of this electrode, a large increase in conduction electrons will occur in the areas of high light intensity. The faradaic current will then follow a corresponding pattern at the semiconductor/solution interface, and shortly thereafter, a luminescent image will appear in the solution layer, due to the anion-cation reaction. Thus, by coupling a semiconductor electrode with an electrochemiluminescent system, one may convert an infrared image to a visible image and measure a total current for the process. The sharpness of the visible image will depend on the distances traveled by carrier species in the semiconductor and solution

layers. The absolute image intensity cannot be predicted at present, but luminescence from diffusion-controlled currents in $10^{-3}M$ hydrocarbon solutions is readily visible (2). Other practical details include the stability of the hydrocarbon ions and the influences of impurities.

Of interest for sensor applications is the possibility of light amplification in the cell, due to absorption of luminescence light by the semiconductor. This would, in turn, produce additional current and generate more light. Although such feedback may diminish the sharpness of a visual display, it would be advantageous in a light detection system.

Manuscript received Oct. 18, 1971.

Any discussion of this paper will appear in a Discussion Section to be published in the December 1972 JOURNAL.

REFERENCES

1. R. E. Visco and E. A. Chandross, *Electrochim. Acta*, **13**, 1187 (1968).
2. D. M. Hercules, *Science*, **145**, 808 (1964).
3. A. Zweig in "Advances in Photochemistry," Vol. 6, W. A. Noyes, Jr., G. S. Hammond, and J. N. Pitts, Jr., Editors, Interscience, New York (1968).
4. H. Gerischer in "Advances in Electrochemistry and Electrochemical Engineering," Vol. 1, Chap. 4, P. Delahay and C. W. Tobias, Editors, Interscience, New York (1961).

Brief Communication



The Influence of Chloride Ion on the Pitting of Aluminum

F. D. Bogar*¹ and R. T. Foley**

Chemistry Department, The American University, Washington, D. C. 20016

Engell and Stolica (1), and later Hoar and Jacob (2), devised a technique to measure the kinetics of breakdown of passivity of iron and stainless steel by halide ions. In this technique the metal electrode is held potentiostatically in the passive range in sulfuric acid solution, a specific concentration of chloride is injected, and the induction time, τ , for a sharp rise in current is recorded. The rise in current is correlated with the breakdown of passivity and the initiation of pitting. This technique is of particular interest because the dependence of the induction time, τ , on the chloride concentration has been related to the stoichiometry of the initial metal dissolution reaction. The investigators cited above used different arguments but reached the same conclusion with respect to the significance of the chloride dependence. Further, the temperature dependence of τ can be related to the apparent energy of activation for the process, whatever the mechanism of the process might involve. In the present investigation the kinetics of pitting of aluminum and an aluminum alloy have been measured by this technique from the standpoint of achieving a better understanding of the mechanism by which chloride ion participates in the pitting process.

Experimental

The experiment was conducted in a modified H-cell in which the working compartment was separated from the counterelectrode compartment by a fine-porosity glass frit. The working compartment had a volume of 250 ml allowing the placement of a Luggin capillary and a gas dispersion tube in addition to the working electrode. An electrode holder similar to that described by Myers *et al.* (3) which exposed an electrode area of 0.637 cm^2 was used. The counterelectrode was a platinum electrode of 57 cm^2 . Oxygen was removed from the solution by dispersing high purity N_2 through the electrolyte for 30 min prior to electrolysis and for an additional 30 min while the current of the polarized electrode came to a steady-state value, and for the duration of the experiment. The bubbling nitrogen excluded air and provided stirring to the system. Stirring was also provided in the cell with a magnetic stirrer. When nitrogen was bubbled through the system, the corrosion potential became more active, the major change occurring in the first 30 min. Polarization of the electrodes after 1 hr of deaeration with nitrogen produces current-potential curves with little or no difference from curves obtained from electrodes which were deaerated for 24 hr. The cell was thermostated at a preset temperature $\pm 0.1^\circ\text{C}$ in the range of $15^\circ\text{--}40^\circ\text{C}$.

The potential of the working electrode was regulated either with an Anotrol Model 4100 Research Potential

* Electrochemical Society Student Associate Member.

** Electrochemical Society Active Member.

¹ Present address: Physical Metallurgy Division (Code 6324), U.S. Naval Research Laboratory, Washington, D. C. 20390.

Key words: corrosion, aluminum alloy 1199, aluminum alloy 2024, kinetics, activation energy.

Controller or a Wenking Model 61 RS Potentiostat. In either case, the potential of the working electrode was measured with a Keithley Model 621 Electrometer in preference to that provided by the potentiostat circuit. The current from the output terminal of the potentiostat was recorded by a Sargent Model SRL Recorder which has a 1 sec full-scale response time.

Two aluminum alloys, Type 1199-H14 and 2024-T6, were used as electrodes. Aluminum alloy 2024 was of the nominal commercial composition. Aluminum alloy 1199-H14 was 99.99% Al and contained Si, 0.001%, Fe, 0.001%, Mg, 0.001%, and Cu, Mn, Cr, Ni, Zn, and Ti less than 0.001%. These alloys were cleaned by conventional procedures and following cleaning, were kept for 24 hr in a dessicator.

In a typical experiment, after the assembled cell had reached a preset temperature, the potential of the aluminum electrode was set at the mid-point of the passive region, usually at +0.18V with respect to the Hg|Hg₂SO₄ electrode. The current was allowed to reach a steady-state value and then a known volume of sodium chloride solution was injected rapidly into the cell with an all glass syringe. The mixing time for the electrolyte was estimated to be 4-5 sec as judged by the time required for uniform color to be achieved when KMnO₄ solutions of concentrations equal to those of the chloride solutions were injected. The time required for the current to rise was measured as τ , the induction time. Figure 1, the current plot for a 2024 alloy electrode potentiostated in H₂SO₄ at pH 3.5 represents a typical measurement.

Results and Discussion

The dependence of the induction time on chloride concentration was measured at 25°C for alloy 1199 at pH 0.0 and for alloy 2024 at pH's 0.0 and 3.5. The data for the series of experiments with alloy 2024 are plotted in Fig. 2. The plots for the other series of experiments are quite similar. The temperature depen-

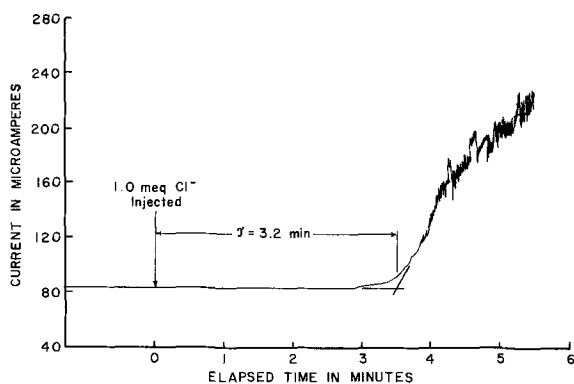


Fig. 1. Current-time plot for a 2024 aluminum alloy electrode potentiostated at 0.18V (Hg|Hg₂SO₄) in H₂SO₄ at pH 3.5 and at 25°C.

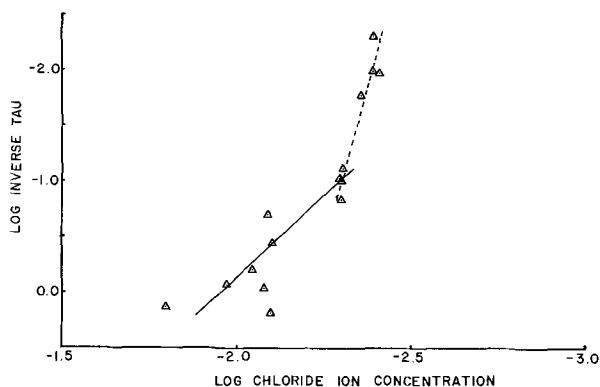


Fig. 2. Dependence of induction time on chloride ion concentration. Alloy 2024 in H₂SO₄ at pH 0.0 and at 25°C.

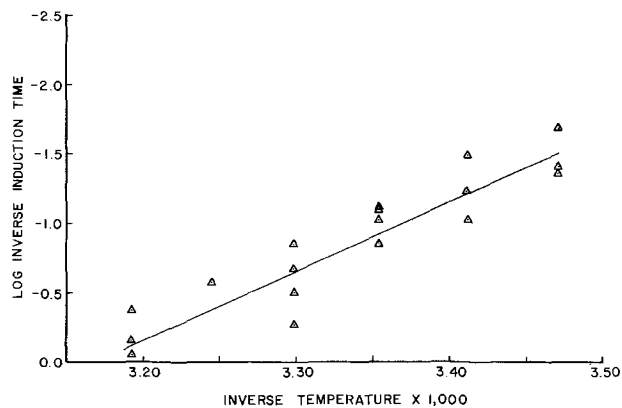


Fig. 3. Arrhenius-type plot for temperature dependence of induction time. Alloy 1199, H₂SO₄ at pH 0.0.

dence of the induction time was investigated over the temperature range of 15°-40°C for alloy 1199 at pH's 0.0, 3.5, and 6.08 and for alloy 2024 at pH 0.0. In these experiments chloride concentrations of 2.58×10^{-3} , 5.00×10^{-3} , and 7.75×10^{-3} molar were used. The plot for alloy 1199 in pH 0.0 H₂SO₄ in Fig. 3 is typical although at pH 6.08 (phosphate buffer) the scatter of the experimental points was greater.

Following the arguments of Engell and Stolica (1) and Hoar and Jacob (2) the reciprocal of τ is taken as a measure of the rate of the "breakdown" process. Then the slope of the line, which is plotted in Fig. 2, equals " n ," wherein " n " is interpreted as the order of the reaction. From the data, the stoichiometry of the reaction of aluminum with chloride ion is not independent of the concentration of the chloride ion. Two values of n can be calculated from these data. The first corresponds to low chloride ion concentrations and is designated in Table I as n' . This stoichiometric factor was evaluated by the use of a computer which was programmed to evaluate the least squares slope of the data plot. Starting from the highest chloride ion concentration, a data point at a time was dropped and the least squares slope of the data was recalculated. The program continued in this manner comparing the least squares slope until agreement was achieved to one significant figure after the decimal point. The computer was programmed to print out the equation of the least squares line and to plot the data and the resultant line. The dotted line in Fig. 2 was obtained from the computer. The solid line which corresponds to high chloride ion concentrations was calculated manually as the least squares fit to the data excluded by the computer. This second value is designated in Table I as n . Also, following the Arrhenius treatment for the temperature dependence of the kinetic data, an apparent energy of activation for the process was calculated from the least squares slope of all the data; Fig. 3 is also a plot obtained from the computer. The stoichiometric factors and the energy of activation are summarized in Table I.

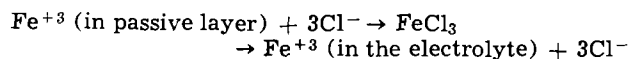
With the exception of the reaction at pH 6.08 the energy of activation is high, approximately 20.0 kcal/mole. Hoar and Jacobs (2) reported a value of 60 kcal/mole for the reaction associated with the breakdown of passivity of stainless steel by chloride ions. In both cases, the energy of activation is considerably higher than one associated with an adsorption process. A diffusion process such as diffusion through Al₂O₃ via lat-

Table I. Summary of kinetic data

Aluminum alloy	0.00	pH 3.50	6.08
1199	$n = 4.0$ $n' = 11.1$ $E = 22.9$ kcal	$E = 20.7$ kcal	$E = 12.0$ kcal
2024	$n = 3.0$ $n' = 8.8$ $E = 20.1$ kcal	$n = 4.8$	—

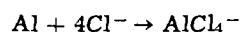
tice defects would have an activation energy in the same range but the diffusion rate itself would be much too low to account for the induction times observed (4).

The value of "n" from the $\log \tau$ - $\log c_{Cl^-}$ plot is interpreted as the number of chloride ions participating in the pitting process per metal atom. Engell and Stolica (1) found that their kinetics followed the third power of chloride ion concentration and postulate a sequence of the form



Hoar and Jacob (2) found "n" values in the range 2.5-4.5 for 18-8 stainless steel and concluded that pitting was initiated by 3-4 halide ions adsorbed around a lattice cation.

The present results indicate that n appears to be 3.0-4.8 for higher chloride ion concentrations. This is interpreted to mean that the primary reaction involves a reaction such as



Such a complex would be transitory, would separate from the metal-oxide interface, and would essentially perform a catalytic function as previously suggested (2). For lower chloride ion concentrations, n' appears to be close to multiples of 4 (8 and 12).

These three investigations have established that the primary role of the anion in the initiation of pitting in chloride solutions in moderately concentrated solutions is chemical rather than physical in nature.

Acknowledgment

This research was supported by the Advanced Research Projects Agency of the Department of Defense and was monitored by the U. S. Naval Research Laboratory under Contract No. N 0014-68-A-0245-0001. The interest and discussion of Dr. B. F. Brown of the Naval Research Laboratory has been appreciated. The aluminum alloy 1199 was supplied by Mr. William Ailor of the Reynolds Metals Company, in Richmond, Virginia.

Manuscript submitted July 13, 1971; revised manuscript received ca. Dec. 16, 1971.

Any discussion of this paper will appear in a Discussion Section to be published in the December 1972 JOURNAL.

REFERENCES

1. H. Engell and N. Stolica, *Z. Physik Chem. N. F.*, **20**, 113 (1959).
2. T. P. Hoar and W. R. Jacob, *Nature*, **216**, 1299 (1967).
3. J. Myers, E. Gruenler, and L. Smulczynski, *Corrosion*, **24**, 352 (1968).
4. A. E. Paladino and W. D. Kingery, *J. Chem. Phys.*, **37**, 457 (1962).



The Effect of Stress on the Low-Temperature Oxidation of Niobium

I. Stresses Involved in the Oxidation Process

L. J. Weirick*¹ and W. L. Larsen

Ames Laboratory, USAEC and Department of Metallurgy, Iowa State University, Ames, Iowa 50010

ABSTRACT

Oxidation, cooling, dissolution, and annealing flexure measurements were performed on thin coupons of niobium presaturated with oxygen. Oxidation was done near 425°C in dry oxygen, dissolution in hydrofluoric acid, cooling and annealing in vacuum. From curvature measurements during each process, bending stresses were determined and correlated with oxidation rate and surface morphology. A thin-film model was applied to the bending due to niobium pentoxide formation. The resulting calculated compressive stress of about 123,000 psi agreed well with the known compressive strength of Nb₂O₅. Application of the thin-film model to an "effective" film of niobium suboxide gave compressive stresses of 125, 150, and 177 thousand psi for Nb₆O, Nb₅O, and Nb₄O, respectively, the reported formulas for NbO_x. Suboxide formation was found to cause bending during early stages of the oxidation process. An oxygen solution model did not adequately explain bending during early oxidation times for oxygen-presaturated niobium specimens. The resulting tensile stress on the substrate surface caused by oxidation was found to be significant, possibly approaching the yield stress.

The kinetics of the oxidation of niobium in the vicinity of 425°C are sufficiently well known (1, 2) that it is possible to calculate with fair precision the lifetime of a part made from niobium sheet. In the case of tubing, however, premature failure has been observed in as little as one-tenth the expected time as a result of the formation of "wedges" of Nb₂O₅ growing normal to the oxidizing surface (3, 4).

Preliminary work at this laboratory (5) established that bent specimens of sheet niobium oxidized at 425°C exhibited wedges on the concave surface. These wedges increased in number with decreasing initial radius of curvature and increasing prior cold work and were apparently unaffected by surface preparation. During oxidation, bent specimens were observed to approach straightness.

During oxidation, when one solid phase is forming upon another under isothermal conditions, elastic strains may arise as a result of any of several possible mechanisms. These sources of strain may be classified generally as those associated with (i) the establishment of defect or oxygen gradients, (ii) epitaxial effects, and (iii) volume changes during the reaction.

The relationship between defect gradients and stress gradients has been treated theoretically by Richmond *et al.* (6) and experimentally by Pawel *et al.* (7). Pawel *et al.* applied a flexure technique to the oxidation of niobium near 425°C and obtained data which indicated a compressive stress of about 35,000 psi existed in the surface layer of niobium metal due to oxygen solution.

Epitaxial strains have not been observed upon oxidation of niobium (7). It was originally postulated by Pilling and Bedworth (8) that the majority of oxide films should form in a state of compression since the volume of the oxide is usually greater than the metal oxidized. For the case where anion diffusion predominates and the oxide grows isotropically and adherently to the metal, or anisotropically and adherently but is not allowed to expand easily, stresses sufficient to deform and/or fracture the oxide may eventually exist. For the case where cation diffusion predominates, the oxide is formed at the oxide/oxygen phase boundary. Therefore, no restraints should act upon the newly formed oxide and it remains adherent and stress-free even for very large oxide/metal volume ratios.

Dankov and Chureav (9) derived an experimental equation for the compressive stress in a thin film of oxide as a function of bending stress as measured by flexure techniques. Pawel and Campbell (10) applied this technique to the oxidation of niobium near 425°C and obtained preliminary data which indicates that the thin-film stress would be quite high, perhaps approaching 100,000 psi.

Based upon these observations, the authors of this paper hypothesized that lateral stresses induced in the metal surface by the growth of Nb₂O₅ into a constricted volume produce a tensile strain in the underlying metal which, when exceeding the ultimate strain of the (oxygen-saturated) metal surface, produce a mechanical crack in the embrittled metal. Subsequent oxidation of the interior of the crack produces additional tensile stress and oxygen-solution embrittlement at the crack tip, resulting in a self-propagating crack. A program of research was initiated in order to test

* Electrochemical Society Active Member.

¹ Present address: Metallurgy Division, Sandia Laboratories, Livermore, California 94550.

Key words: suboxide, cracks, Nb₂O₅.

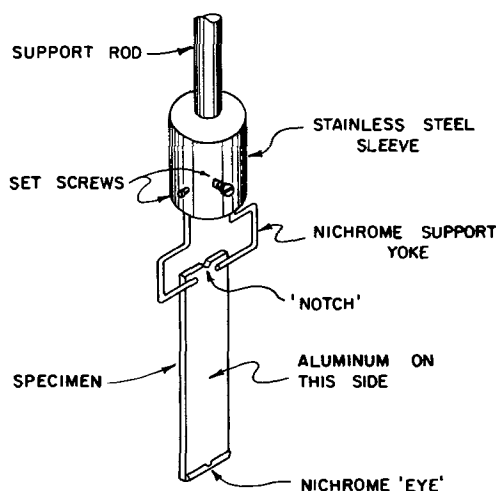


Fig. 1. Schematic drawing of flexure measurement specimen

this hypothesis and to gain further understanding of this gas-phase stress-corrosion cracking in niobium.

The present work was designed to measure that stress created in a niobium metal substrate by the formation of a thin film of oxide. By using only metal which had been previously saturated with oxygen, it was expected that the effects of concentration gradients could be eliminated and that the resultant stress would be entirely due to "Pilling-Bedworth effects." Moreover, it was felt that the results would more nearly approximate those conditions of service wherein oxygen concentrations are sufficiently low that near-saturation could occur before the formation of significant amounts of surface scale. Such conditions might be found in nuclear reactors.

Experimental Procedure

Niobium specimens² were cut from a 0.010 in. sheet as rectangular coupons 1 × 4.5 cm and polished on both sides with 600 grit silicon carbide paper. The polished coupons were suspended in a thermogravimetric system and oxidized to a predetermined weight gain to form a thin, adherent Nb₂O₅ layer. They were then vacuum annealed at temperatures from 500° to 1200°C for times up to 14 or 3 days respectively. This procedure gave specimens saturated with oxygen at various temperatures. The oxygen was retained upon cooling and thus the specimens had oxygen contents above the saturation value at 425°C (11, 12). These oxygen-supersaturated coupons were again polished on both sides with 600 grit silicon carbide paper and subsequently one side only was further polished with 15, 1, and 0.3μ levigated alumina. A 0.5 × 1 cm piece was cut from the end of each specimen to be vacuum-fusion analyzed for oxygen, nitrogen, and hydrogen. The coupons were first cleaned in a solution containing 50 parts lactic acid, 30 parts nitric acid, 2 parts hydrofluoric acid, and 18 parts water and then were dried with alcohol.

A support yoke of Nichrome wire was welded on the polished side of the coupon (Fig. 1). On this side at the other end, a piece of Nichrome wire was welded across the tip and a hole drilled at the middle to form a small "eye." The specimen was again cleaned in acid and alcohol and placed in a vacuum evaporator with the Nichrome wire side up. Aluminum was plated onto this side to a thickness of about 6μ. A subsequent vacuum annealing at 600°C for 24 hr formed a diffusion bond making the aluminum an excellent protective film. Specimens prepared in this manner were subsequently subjected to flexure measurements during four

consecutive processes: oxidation, cooling, dissolution, and annealing.

Oxidation.—For oxidation flexure measurements, the specimen was suspended by the Nichrome yoke in a furnace (Fig. 2). A quartz fiber, 235 mm long, was hung onto the specimen with its free end threaded through the "eye." Deflection measurements could be made by sighting through a quartz window in that part of the furnace tube extending below the furnace using a traveling microscope which was converted to an x-y cathetometer. A total deflection of about 4 cm could be measured with the accuracy of individual readings being ±0.05 mm.

The system was evacuated to a pressure less than 3×10^{-6} Torr and the temperature slowly raised to within five degrees of the desired reaction temperature. A "zero" reading was taken and dry, preheated oxygen allowed to leak into the system, raising the specimen temperature five degrees. The specimen bent as it was oxidized on the unprotected side, the aluminum being on the concave side. The quartz fiber maintained a position corresponding to the chord of the arc of the deflecting specimen and thus the end of the fiber deflected proportionately with the curvature of the specimen. A correction for elastic bending of the cantilever fiber was determined experimentally.

Following the method of Pawel *et al.* (7), these fiber deflections were converted to radii of curvature, ρ , and thus maximum bending stress, S_m , through the use of the simple flexure formula (for bending in two dimensions occurring without distortion)

$$S_m = \frac{E_m h}{2\rho} \left(\frac{1}{1 - \nu} \right) \quad [1]$$

Thus the oxidation bending stress, $S_m(\text{Ox})$, could be plotted *vs.* oxidation time.

The bending of the specimen during oxidation flexure measurements was found to be the result of a combination of growth of a very thin layer of niobium suboxide, NbO₂, just under the surface of the niobium and of a niobium pentoxide film upon the metal surface. If the flexure were due to the growth of Nb₂O₅ alone, the thin-film compressive stress within the Nb₂O₅ could be calculated using the following equation (10)

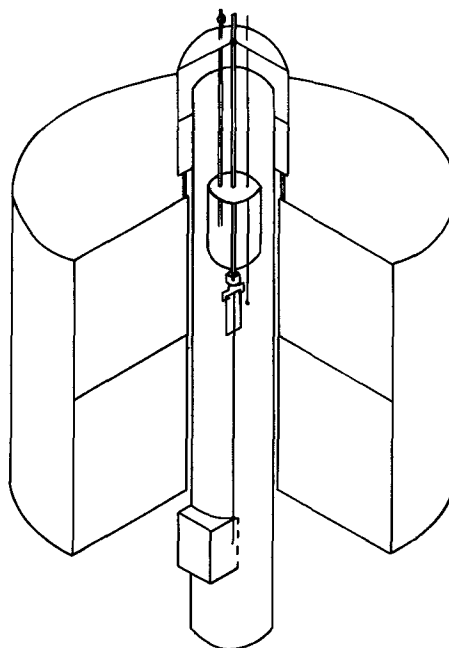


Fig. 2. Schematic drawing of flexure measurement apparatus

² Supplied by Fansteel Metallurgical Corporation with given nominal analysis of about 99.7-8% Nb with Ta, Fe, Mo, Ti, and Zr being major metallic impurities; interstitial content determined from vacuum fusion analysis was about 650 ppm O₂, 300 ppm N₂, and 5 ppm H₂.

$$S_{1(Ox)} = \frac{1}{3} S_{m(Ox)1} \frac{h}{t_1} \quad [2]$$

Similarly, if the flexure were due to the growth of NbO_x alone

$$S_{2(Ox)} = \frac{1}{3} S_{m(Ox)2} \frac{h}{t_2} \quad [3]$$

Since weight gain measurements could not be made concurrently with flexure measurements, values of t were obtained from geometrically similar samples whose oxidation curves were previously established as being very reproducible.

Thickness was computed from weight gain measurements assuming the following:

1. Since the initial oxygen content of the specimens was higher than the oxygen solubility limit in niobium at 425°C, there should be no oxygen going into solution.

2. Since the oxide thickness on the top surface is the desired quantity, the weight of oxide on the sample edges (6.25% of the total area) must be deducted from the total.

3. The density is about 5.17 g/cc (19). Thus for Nb_2O_5

$$t_1 (\text{mil}) = W_o \times 0.0593 \quad [4]$$

where W_o is the weight gain, in milligrams, for the 1×4 cm sample.

4. For NbO_x , the reported formulas are Nb_6O , Nb_5O , and Nb_4O which give oxygen contents of 2.79, 3.33, and 4.13 w/o (weight per cent), respectively.

5. For NbO_x , by analogy to the data of Magneli *et al.* (20) on Ti, V, Zr, and Hf and by using data from Brauer *et al.* (21) on a tetragonal niobium suboxide (about Nb_6O), densities derived from a plot of density vs. oxygen/niobium ratio for Nb_6O , Nb_5O , and Nb_4O are 8.33, 8.28, and 8.20 g/cc, respectively. Thus, for Nb_5O

$$t_2 (\text{mil}) = W_o \times 0.3346 \quad [5]$$

Using the densities for Nb_6O and Nb_4O gives variations of calculated film thickness of plus 18% and minus 18%, respectively, from the value for Nb_5O .

Cooling.—Following the oxidation, the system was evacuated and the furnace power shut off. Deflection readings were taken intermittently during cooling. Thus cooling bending stress, $S_{m(Cl)}$, could be plotted vs. temperature.

The bending of the specimen during cooling resulted from the relative difference in the thermal expansion coefficients of Nb and Nb_2O_5 . Using Timoshenko's (22) equation for the cooling of a bimetallic strip and applying boundary conditions for the present Nb- Nb_2O_5 composite, the following equation was derived and subsequently verified by Bradhurst and Heuer (23)

$$1/\rho = 3n(\alpha_m - \alpha_o)\Delta T \frac{2t_1}{h^2} \quad [6]$$

Using the radius of curvature calculated from this equation, the maximum bending stress in the metal surface caused by cooling, $S_{m(Exp)}$, was calculated using Eq. [1] and compared with the cooling bending stress determined directly from deflection measurements during cooling, $S_{m(Cl)}$.

The stress in the thin film of Nb_2O_5 caused by differential thermal contraction during cooling, $S_{1(Cl)}$, is given by the application of the thin-film stress equation (10)

$$S_{1(Cl)} = \frac{1}{3} S_{m(Cl)} \frac{h}{t_1} \quad [7]$$

Oxidation and cooling flexure measurements gave bending in the same (positive) direction. After cooling a photograph was taken of the specimen profile. Measurements made on an enlargement established that the radius of the curved specimen varied less than 1% from that of an arc of a circle, thus validating the as-

sumption used in converting deflection measurements to radii of curvature. The curvature measured photographically also agreed within 3% of that calculated from oxidation and cooling fiber deflection measurements.

To separate the contributions to specimen bending from Nb_2O_5 and NbO_x growth, dissolution and annealing flexure measurements were performed.

Dissolution.—Deflections were measured during the removal of the Nb_2O_5 film by a method analogous to that described for oxidation except for the substitution of a molybdenum wire for the quartz fiber. Oxides were stripped with a 25% HF-water solution. The protective layer of aluminum is dissolved quickly with no resultant effect on sample curvature. Nb_2O_5 is dissolved easily but there is little effect of HF on Nb or NbO_2 (24).

As oxide was removed, the specimen approached straightness. The resulting loss of curvature was converted to a bending stress, $S_{m(Ds)}$, which was negative in sign, using Eq. [1].

The stress in the thin film of Nb_2O_5 removed by dissolution, is given by an application of the thin-film stress equation, Eq. [2], which relates metal surface stress to corresponding oxide film stress

$$S_{1(Ds)} = \frac{1}{3} S_{m(Ds)} \frac{h}{t_1} \quad [8]$$

Annealing.—If the curvature resulting from the oxidation process was due to the niobium pentoxide film growth alone, the removal of this film should cause the specimen to return to straightness. Since after the dissolution process the specimens still retained some curvature, a second process was apparently contributing stress during the oxidation process. This additional process is thought to be the formation of the niobium suboxide, NbO_x , near the surface of the niobium substrate. Vacuum annealing was performed in an attempt to remove this stress by removing the concentration gradient associated with the suboxide, thereby returning the specimens to straightness.

The specimen was replaced in the controlled atmosphere furnace system which was evacuated to a pressure of 2×10^{-6} Torr. The temperature was slowly raised to 300°C to outgas. When the pressure was again acceptably low, the temperature was quickly raised to 550°C and a "zero" cathetometer reading taken. Annealing for 3 days at 550°C was usually sufficient to return the specimen to straightness. Intermittent readings were taken with the cathetometer for the duration of the annealing process. The resulting loss of curvature was converted to a bending stress, $S_{m(An)}$, which was also negative in sign, by using Eq. [1].

The magnitude of the stress in the thin layer of niobium near the substrate surface due to the "removal" or redistribution of the niobium suboxide, NbO_x , is

$$S_{2(An)} = \frac{1}{3} S_{m(An)} \frac{h}{t_2} \quad [9]$$

Since the cooling stress can be accounted for entirely by the differential thermal expansion of the metal and Nb_2O_5 alone, and since dissolution appears not to affect the suboxide, it is assumed that NbO_x affects bending only during the oxidation and annealing processes. Thus, we equate the magnitudes of the NbO_x film stresses created during oxidation and removed during annealing

$$S_{2(An)} = S_{2(Ox)} \quad [10]$$

or, equating the corresponding bending stresses induced in the metal

$$\frac{1}{3} S_{m(An)} \frac{h}{t_2} = \frac{1}{3} S_{m(Ox)2} \frac{h}{t_2} \quad [11]$$

giving

$$S_{m(An)} = S_{m(Ox)2} \quad [12]$$

Table I. Summary of data for flexure measurement specimens (69-86) (6-8 μ annealed aluminum coating)

Specimen No.	$S_{m(Ox)}$ $\times 10^3$ psi	$S_{m(Cl)}$ $\times 10^3$ psi	Total positive stress $\times 10^3$ psi	$S_{m(Ds)}$ $\times 10^3$ psi	$S_{m(An)}$ $\times 10^3$ psi	Total negative stress $\times 10^3$ psi	% Diff., $S_{pos}-S_{neg}$	$S_{1(Ox)}$ $\times 10^8$ psi
69	22.50	6.03	28.53	20.97	8.15	29.12	2.0	107.69
70	15.60	3.55	19.15	13.07	6.48	19.55	2.0	113.09
71	15.27	3.68	18.95	12.58	6.29	18.87	0.4	117.19
72	19.07	4.90	23.97	16.87	7.50	24.37	1.6	108.41
73	18.50	5.10	23.60	19.69	4.11	23.80	0.8	125.86
77	17.82	3.79	21.61	14.60	7.18	21.78	0.8	122.92
79	18.23	3.63	21.86	14.84	6.61	21.45	1.9	147.06
81	17.65	4.05	21.70	14.74	6.95	21.69	—	126.36
83	18.55	4.39	22.94	15.55	7.19	22.74	0.9	115.97
85	16.57	4.06	20.63	16.24	4.52	20.76	0.6	133.34
86	20.53	4.79	25.32	20.16	5.16	26.32	—	137.99
							Avg.	123.26

where $S_{m(Ox)2}$ is the oxidation bending stress due to NbO_x .

Combination of results.—The dissolution and annealing flexure measurements gave the total unbending which should then equal the total bending in the positive direction during the oxidation and cooling processes. This equality can be expressed through the summation of induced bending stresses in the metal since, by Eq. [1], these stresses are a direct function of measured curvatures

$$S_{m(Ox)} + S_{m(Cl)} = S_{m(Ds)} + S_{m(An)} \quad [13]$$

or

$$S_{m(Ox)} - S_{m(An)} = S_{m(Ds)} - S_{m(Cl)} \quad [14]$$

The deflection of the sample, and thus the stress induced in the metal, during oxidation is a result of stresses in both a suboxide layer and an Nb_2O_5 film. The stress in the Nb_2O_5 film can be separately determined as follows.

First it is noted that the stress in the Nb_2O_5 film, $S_{1(Ox)}$, is given by Eq. [2] as a function of the stress in the metal surface, S_m , which in turn is calculated from specimen curvature using Eq. [1]. The metal surface stress arising from Nb_2O_5 alone is the total induced surface stress caused by oxidation, $S_{m(Ox)}$, minus the stress induced by suboxide—the stress which is later removed by annealing. Thus, we can write

$$S_{m(Ox)1} = S_{m(Ox)} - S_{m(An)} \quad [15]$$

Substituting this value of $S_{m(Ox)1}$ into Eq. [2] yields

$$S_{1(Ox)} = \frac{1}{3} [S_{m(Ox)} - S_{m(An)}] \frac{h}{t_1} \quad [16]$$

This equation is valid if an oxide film at a given stress level will yield the same deflection when acting in conjunction with a suboxide as it will acting alone. This is the case in these experiments.

The stress in the Nb_2O_5 layer can also be computed another way. The deflection induced in the metal by differential contraction during cooling has been calculated using Eq. [6] assuming that Nb_2O_5 is the only

oxide layer present. The calculated result is virtually identical to the deflection observed at the end of cooling (Fig. 7). Further, in the process of dissolution only Nb_2O_5 is attacked. Therefore, the deflections involved in cooling and dissolution can be attributed entirely to Nb_2O_5 . Consequently, at the end of the oxidation process the portion of the deflection caused by stress in the Nb_2O_5 layer is equal to the difference between the total deflection removed by dissolution of the Nb_2O_5 layer and that deflection added during cooling by differential contraction of the Nb_2O_5 layer. Relating these deflections to stresses at the metal surface using Eq. [1] we have

$$S_{m(Ox)1} = S_{m(Ds)} - S_{m(Cl)} \quad [17]$$

Substituting as before into Eq. [2], we have

$$S_{1(Ox)} = \frac{1}{3} [S_{m(Ds)} - S_{m(Cl)}] \frac{h}{t_1} \quad [18]$$

Since bending deflections very nearly equal unbending deflections, the positive and negative metal stresses, S_m , also agree closely, as shown in Table I. In effect, this verifies Eq. [13] and [14]. Equations [16] and [18] thus yield equivalent values of the Nb_2O_5 stress, $S_{1(Ox)}$, since these equations differ only in that the terms in brackets are the two sides of Eq. [14]. This agreement with experiment further validates the assumptions underlying Eq. [16] that the stress in the Nb_2O_5 layer, computed from a deflection measurement, is essentially independent of the presence of a suboxide layer.

Results and Interpretation

Oxidation.—Table II lists the initial specimen conditions along with the accompanying oxidation parameters for a sampling of specimens upon which the four described flexure measurement techniques were performed. Figure 3 illustrates typical deflection-time curves for niobium specimens presaturated with oxygen and oxidized near 425°C in preheated, dry oxygen at 1 atm. The scale on the right side of this figure indicates the magnitude of oxidation bending stresses, $S_{m(Ox)}$, calculated from the deflections using Eq. [1].

Table II. Conditions for flexure measurement specimens (69-86) (6-8 μ annealed aluminum coating)

Specimen No.	Thickness, mil	Anneal temp., °C	Oxygen content, ppm	Oxdn. temp., °C	Oxdn. time, min.	Oxygen added, mg.	Calc. cool. bend. stress, $S_{m(Ox)}$ $\times 10^3$ psi
69	10.00	500	1292	425 ^(a)	240	7.3	5.97
70	9.75	500	1415	430	120	4.3	3.63
71	9.75	500	1432	420	240	4.1	3.47
72	9.75	500	1483	430	150	5.7	4.84
73	9.75	500	1521	425	180	6.1	5.16
77	9.50	800	2825	420	240	4.5	3.95
79	9.00	800	2931	430	150	3.9	3.63
81	9.50	1000	3566	425	180	4.4	3.87
83	9.50	1000	3436	430 ^(b)	150	5.1	4.52
85	9.50	1200	4008	425	180	4.7	4.11
86	9.50	1200	3985	430	150	5.8	4.76

(a) Start temperature was high.

(b) Start temperature was low.

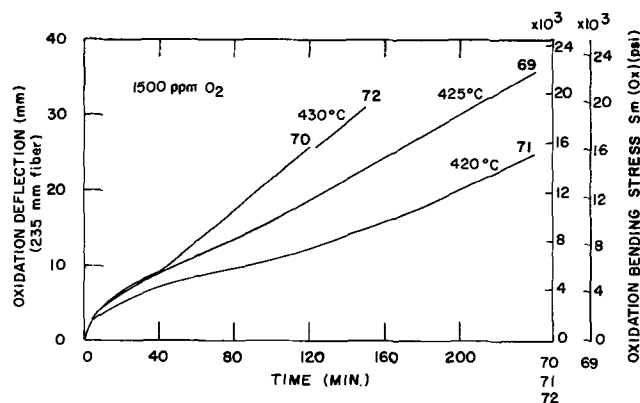


Fig. 3. Oxidation deflection and bending stress curves for specimens 69, 70, 71, and 72.

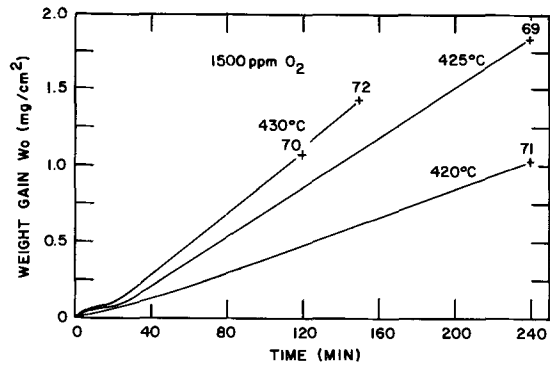


Fig. 4. Weight gain due to oxygen vs. time for specimens 69, 70, 71, and 72.

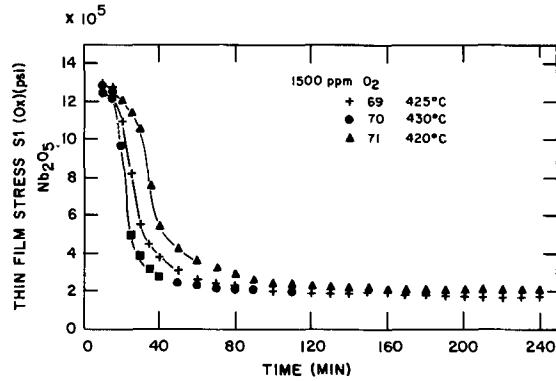


Fig. 5. Thin-film stress curves, $S_{1(Ox)}$, for niobium pentoxide on specimens 69, 70, and 71.

Figure 4 illustrates typical weight gain curves for oxygen-presaturated specimens geometrically similar to the corresponding flexure specimens. The end point of each curve is the actual measured weight gain for the complementary flexure specimen. As previously described, these curves are used to calculate the corresponding Nb_2O_5 or NbO_x film thickness for the oxidation process.

Taking data from curves such as shown in Fig. 3 and 4 and applying Eq. 2, gave plots of $S_{1(Ox)}$ (for Nb_2O_5 film only), an example of which is shown in Fig. 5. At early oxidation times when no Nb_2O_5 is observed to form, the calculated film thicknesses for the small weight gains were very small although the bending stresses were appreciable so that very high $S_{1(Ox)}$ values are obtained, around 1,000,000 psi. The $S_{1(Ox)}$ stresses drop and level off at times corresponding with the times for observed Nb_2O_5 formation and film growth.

Since published solubility limits (11, 12) may be in error, the possibility that high stresses observed at short oxidation times were due to increased oxygen solution was considered. However, calculations led to surface stresses of 90,000 psi, using Pawel's (7) equations, and surface oxygen concentrations of 8000 ppm, using Richmond's (6) equations. Both results are considered unreasonable.

Another characteristic of the early oxidation of niobium near 425°C is the formation of a niobium suboxide, designated NbO_x (1). Specimens oxidized from 10 to 20 min near 425°C were examined by x-ray diffraction. A similar occurrence to that found by previous authors (1, 25) was observed in that small peaks appear adjacent to the niobium x-ray diffraction peaks. Upon further oxidation, these extra peaks disappeared, apparently due to an overgrowth of Nb_2O_5 .

Plots of $S_{2(Ox)}$ (for Nb_5O film only) are shown in Fig. 6. These stresses varied as expected for a thin film, the influence of which was important early in the oxidation and became masked when Nb_2O_5 formation was predominant. These $S_{2(Ox)}$ stresses would be 18%

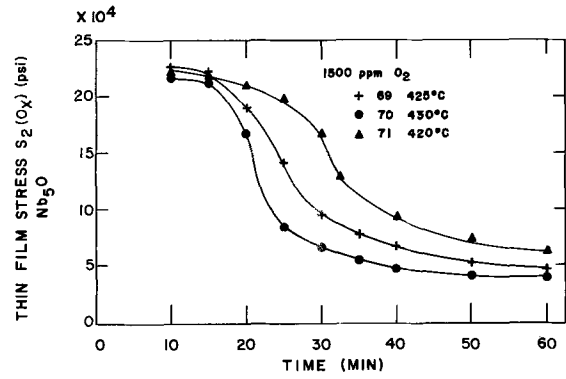


Fig. 6. Thin-film stress curves, $S_{2(Ox)}$, for niobium suboxide (Nb_5O) on specimens 69, 70, and 71.

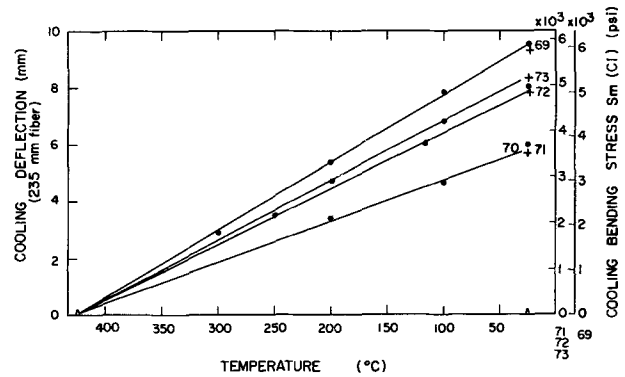


Fig. 7. Cooling deflection and bending stress curves for specimens 69, 70, 71, and 72 compared to final calculated cooling bending stress (+).

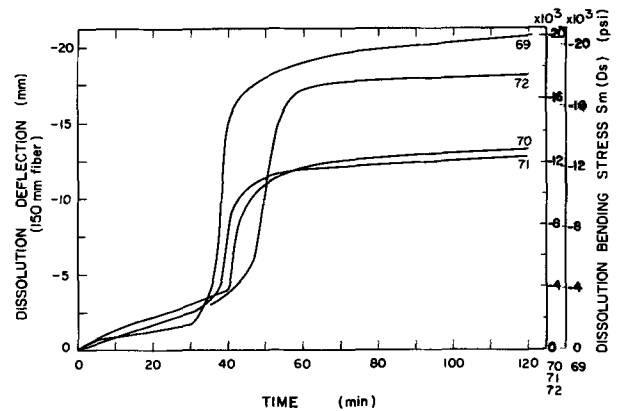


Fig. 8. Dissolution deflection and bending stress curves for specimens 69, 70, 71, and 72.

higher if the film analysis were made with values for Nb_4O and 18% lower for Nb_6O . Therefore, using an "effective" thin-film model³ for NbO_x , the induced tensile stress in the substrate surface, S_m , would be at least 125, 150, or 177 thousand psi for Nb_6O , Nb_5O , or Nb_4O , respectively.

Cooling.—Typical curves of deflection and cooling bending stress, $S_{m(Cl)}$, are shown in Fig. 7 along with the theoretically calculated end point (+) for the cooling process using Eq. [6]. Thus, taking Nb and Nb_2O_5 as the controlling components and setting $n = 1/2$ gave results in good theoretical agreement with experimental observations of bending magnitude.

Dissolution.—Examples of deflection and dissolution bending stress, $S_{m(Ds)}$, curves are shown in Fig. 8. The dissolution process proceeded slowly for a time as the acid attacked the oxide/metal interface as well as the

³ This assumes the oxide is a discrete layer of uniform thickness and composition.

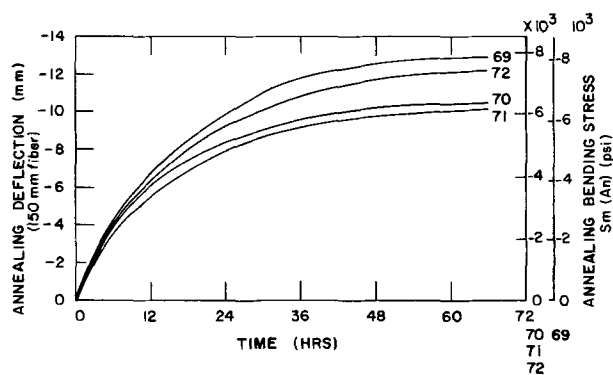


Fig. 9. Annealing deflection and bending stress curves for specimens 69, 70, 71, and 72.

oxide/solution surface. When enough oxide was dissolved at the oxide/metal interface to prevent adequate mechanical bonding of the oxide, the scale flaked off the metal substrate causing the specimen to straighten rapidly.

Annealing.—Typical deflection and annealing bending stress, $S_{m(An)}$, curves are shown in Fig. 9. The annealing procedure did remove the "additional" contribution to the cause of specimen bending, that attributed to NbO_x formation, so the specimens did return to straightness.

Although it is believed that this stress removal is associated with a diffusional process whereby oxygen concentration gradients are diminished, no precise statement of the mechanism is possible since the exact nature of the state of aggregation of oxygen at low concentrations is presently unknown. Gibala and Wert (26), using internal friction measurements, have identified oxygen clusters in niobium containing up to 2500 ppm oxygen. Van Landuyt (27) has found ordering reactions in oxygen-supersaturated niobium using electron microscopy and diffraction. Hurlen *et al.* (1) using x-ray diffraction have identified the suboxide " NbO_x " (probable formula Nb_6O) during oxidation at 425°C. Thus the actual stress reduction may involve a change in clusters or ordering or possibly the redistribution of a phase. The role of stress in promoting phase stability or in providing the driving force for change is not known. However, it was found that the " NbO_x " x-ray diffraction peak diminishes in intensity as annealing time increases. The peak does not vanish, presumably because of the presence of excess or supersaturated oxygen which results from the quenching of samples from temperatures where oxygen solubility is higher than at the test temperature.

Combination of results.—Table I summarizes the maximum bending stresses for these four processes and includes the total bending (positive) and unbending (negative) stresses with their per cent differences. This per cent difference shows that the experimental data differ by a maximum of only 2% from the theoretical Eq. [13]. Therefore, Eq. [14] holds true also to within 2%.

The last column in Table I lists the compressive stress in the thin film of Nb_2O_5 , $S_{1(Ox)}$, calculated using Eq. [18]. The value for $S_{1(Ox)}$ is approximately 123,000 psi. This value compared well with the value of 117,000 psi measured by Douglass (28) as the compressive strength of Nb_2O_5 at room temperature. This agreement suggested that in this "break away" oxidation range, the individual Nb_2O_5 nuclei grow until they impinge upon one another laterally. The compressive stress increases to the ultimate compressive strength whereupon the oxide fractures or "breaks away." Since this is happening randomly over the specimen surface, the over-all compressive stress in the oxide layer approximates that of the ultimate compressive strength.

A few samples were prepared similarly to the flexure specimens but without the Nichrome wires attached. They were suspended in the thermogravimetric system and oxidized near 425°C in air for extended lengths of time. Two of these samples are shown in Fig. 10. The fact that a sample oxidized for 30 hr forms a cylinder adds support to the argument that the bending follows an arc of a circle. This resulting shape was somewhat different, but experimentally more desirable, than the spirals obtained by Pawel (10). Also, upon mounting, sectioning, and polishing these specimens, oxide wedges growing into the convex side of the niobium substrate were observed. Therefore, originally flat flexure specimens can eventually deform and form oxide wedges.

Conclusions

1. When oxygen-saturated niobium is oxidized in dry oxygen near 425°C, the oxides consist of a surface layer of Nb_2O_5 and, below it, a suboxide layer. Agreement with experiment is found when this layer is assumed to be Nb_5O .
2. The stress in the layer of Nb_2O_5 approaches a limiting value of approximately 123,000 psi, in fair agreement with the reported ultimate compressive strength.
3. Niobium pentoxide is probably nonprotective after approximately 30 min of oxidation near 425°C because its lateral growth results in compressive fracture.
4. The compressive stress in the oxide induces a tensile stress in the underlying metal which varies with time. Stresses of approximately 20,000 psi were observed after 240 min of oxidation at 425°C.

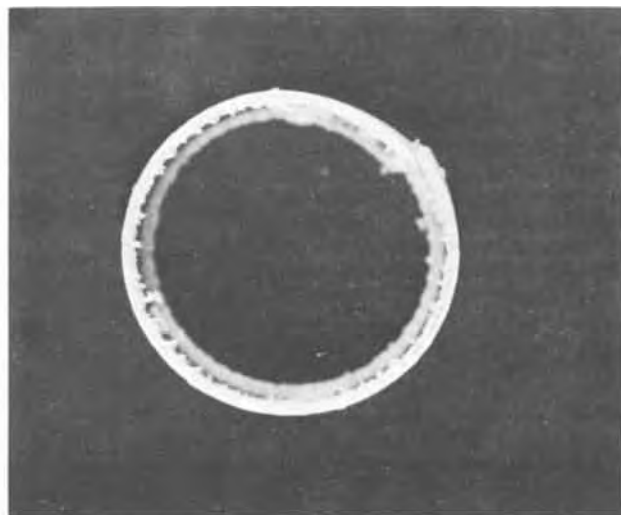
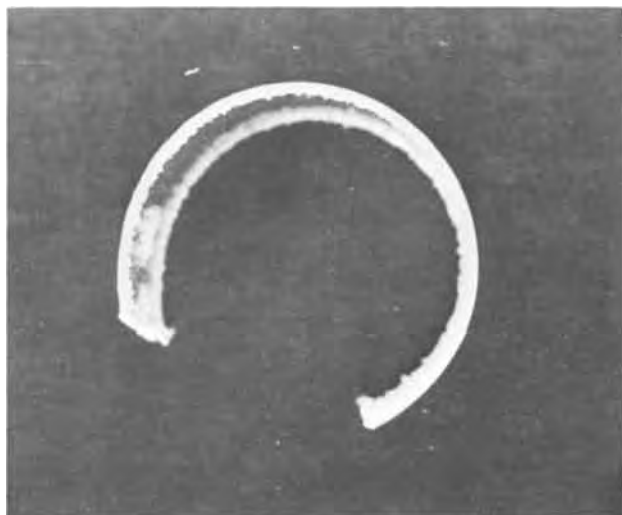


Fig. 10. 10-mil niobium specimen oxidized on one side at 425°C in air for 24 hr (left) and 30 hr (right), respectively

Manuscript submitted April 23, 1971; revised manuscript received Dec. 13, 1971. This was Paper 109 presented at the Atlantic City Meeting of the Society, Oct. 4-8, 1970.

Any discussion of the paper will appear in a Discussion Section to be published in the December 1972 JOURNAL.

LIST OF SYMBOLS

S_m	Bending stress existing at the surface of the niobium metal, calculated from deflection measurements.
S_1	Compressive stress existing in the thin film of Nb_2O_5 , calculated from deflection and weight gain measurements.
S_2	Compressive stress existing in the thin film of suboxide, NbO_x , calculated from deflection and weight gain measurements.
Ox	Subscript referring to oxidation process.
Cl	Subscript referring to cooling process.
Ds	Subscript referring to dissolution process.
An	Subscript referring to annealing process.
Exp	Subscript referring to bending stresses calculated from thermal expansion data.
h	Niobium metal thickness, 0.010 in.
E_m	Young's modulus for niobium at 425°C, 14.5×10^6 psi (13).
E_o	Young's modulus for niobium pentoxide at 425°C, 7×10^6 psi (14, 15).
ρ	Radius of curvature calculated from deflection measurements, in.
ν	Poisson's ratio for niobium, 0.38 (16).
t_1	Thickness of Nb_2O_5 , mils = $0.0593 W_o$.
t_2	Thickness of NbO_x , mils = $0.3346 W_o$.
W_o	Weight gain due to oxidation, mg.
n	Ratio of elastic moduli of oxide and metal, E_o/E_m ($\cong 1/2$ for Nb_2O_5/Nb).
α_n	Thermal expansion coefficient of Nb, $7.5 \times 10^{-6}/^\circ C$ (17).
α_o	Thermal expansion coefficient of Nb_2O_5 , $-1.0 \times 10^{-6}/^\circ C$ (18).
ΔT	Difference between oxidation and room temperature, °C.

REFERENCES

- H. Hurlen, H. Kjøllesdal, J. Markali, and N. Norman, Central Institute for Industrial Research, Blindern-Oslo, Norway Technical Note No. 1 (1959).
- J. Cathcart, J. Campbell, and G. Smith, *This Journal*, **105**, 442 (1958).
- T. Kolski, *Am. Soc. Metals Trans. Quart.*, **55**, 119 (1962).
- J. H. Doyle, Unpublished M.S. thesis. Ames, Iowa, Library, Iowa State University of Science and Technology (1964).
- D. B. Fox, Private communication.
- O. Richmond, W. Leslie, and H. Wriedt, *Am. Soc. Metals Trans.*, **57**, 294 (1964).
- R. Pawel, J. Cathcart, and J. Campbell, *This Journal*, **110**, 551 (1963).
- N. Pilling and R. Bedworth, *J. Inst. Metals*, **29**, 529 (1923).
- P. Dankov and P. Churaev, Technical Translation TT-245, National Research Council of Canada, Ottawa, Canada (1951).
- R. Pawel and J. Campbell, *Acta Met.* **14**, 1827 (1966).
- E. Gebhardt and R. Rothenbacher, *Z. Metallk.* **54**, 623 (1963).
- A. Taylor and N. J. Doyle, *J. Less-Common Metals*, **13**, 313 (1967).
- C. A. Hampel, Editor, "Rare Metals Handbook," 2nd ed., Reinhold Publishing Co., New York (1961).
- E. Durbin, H. Wagner, and C. Harmon, U.S. Atomic Energy Commission Report BMI-792, Battelle Memorial Institute, Columbus, Ohio (1952).
- W. Manning, Private communication. Ames Laboratory, Iowa State University, Ames, Iowa (1964).
- W. Koster, *Appl. Sci. Res. Sect. A*, **4**, 324 (1954).
- T. Lyman, "Metals Handbook," Vol. I, American Society for Metals, Metals Park, Ohio (1961).
- E. A. Durbin and C. G. Harman, U.S. Atomic Energy Commission Report BMI-791, Battelle Memorial Institute, Columbus, Ohio (1952).
- F. Holtzberg, A. Reisman, M. Berry, and M. Berkenblit, *J. Am. Chem. Soc.*, **79**, 2039 (1957).
- A. Magneli, S. Andersson, L. Kohlborg, S. Asbrink, S. Westman, B. Holmberg, and C. Nordmark, Institute of Inorganic and Physical Chemistry, Stockholm, Sweden, Technical Report No. 1 (1959).
- G. Brauer, H. Muller, and G. Kuhner, *J. Less-Common Metals*, **4**, 533 (1962).
- S. Timoshenko, *Opt. Soc. Am.* **11**, 233 (1925).
- D. H. Bradhurst and P. M. Heuer, *J. Nuclear Mater.*, **37**, 35 (1970).
- C. D. Hodgman, Editor, "Handbook of Chemistry and Physics," 34th ed., Chemical Rubber Publishing Co., Cleveland, Ohio (1952).
- M. A. Goldschmidt, Air Force Materials Laboratory Report AFML-TR-65-332, University of Dayton, Dayton, Ohio (1965).
- R. Gibala and C. A. Wert, *Acta Met.*, **14**, 1095 (1966).
- J. Van Landuyt, European Atomic Energy Community Report EURAEC-1184, Centre d'Etude de L'Énergie Nucleaire, Mol, Belgium (1965).
- D. Douglass, *J. Less-Common Metals*, **5**, 151 (1963).
- R. E. Pawel, *This Journal*, **116**, 1144 (1969).

The Effect of Stress on the Low-Temperature Oxidation of Niobium

II. Oxide Wedge Formation

L. J. Weirick*¹ and W. L. Larsen

Ames Laboratory, USAEC and Department of Metallurgy, Iowa State University, Ames, Iowa 50010

ABSTRACT

It was found that the formation of suboxide needles or plates, NbO_2 , during the oxidation of niobium in the temperature range of 425°-440°C was a function of initial specimen oxygen concentration, oxidation temperature, and applied tensile stress. It was further found that when the oxygen concentration at the substrate surface had reached an equilibrium level and the suboxide plates had formed, only a small tensile stress (less than 10,000 psi on low oxygen content niobium) was needed to form microcracks in a surface of the metal associated with these suboxide needles. Upon further oxidation these microcracks formed niobium pentoxide wedges penetrating the metal causing premature failure of niobium metal sheet.

Premature failure has been observed in oxidizing niobium tubing in as little as one-tenth the expected lifetime (1, 2) as a result of the formation of "oxide wedges" growing normal to the oxidizing surface (3, 4).

Preliminary work at this laboratory (5) established that bent specimens of sheet niobium oxidized at 425° in air exhibited wedges on the concave surface whose number increased with decreasing initial radius of curvature and increasing prior cold work. These bent specimens were observed to approach straightness during the oxidation.

Based upon these observations, it was hypothesized (6) that lateral stresses induced in the metal surface by the growth of Nb_2O_5 into a constricted volume produce a tensile strain in the underlying metal which, when exceeding the ultimate strain of the (oxygen-saturated) metal surface, produce a mechanical crack in the embrittled metal. It was further hypothesized that subsequent oxidation of the interior of the crack produces additional tensile stress and oxygen-solution embrittlement at the crack tip resulting in a self-propagating crack. A program of research was initiated in order to test this hypothesis and to gain further understanding of this gas-phase stress-corrosion cracking in niobium.

Part I of this study (6) established that stresses in the Nb_2O_5 film formed at 425°C increase initially with time but after approximately 30 min, level off at approximately 123,000 psi, the apparent ultimate compressive stress of Nb_2O_5 . In addition, suboxides, probably Nb_3O , were found to form near the surface of oxygen-saturated niobium, adding to the strain of the underlying metal. With the growth of the oxide film, the stress on the underlying metal increased.

Part I of this study was limited to elastic deformations (6). Quantitative stress measurements could not be made readily at stress levels high enough to cause substrate cracking or plastic deformation. It was the purpose of Part II of the research to measure the additional tensile stress needed to be applied to the surface of a metal substrate to produce cracking and resultant oxide wedges. Using a sample loaded in tension, it was possible to measure the mechanical stress equivalent to the stress which exists at the surface of a freely flexing oxidizing sheet or freely opening tube oxidizing until wedges form. Thus, useful information could be obtained for this gas-phase stress-corrosion cracking problem in niobium.

Experimental Procedure

Niobium sheet² of 0.020 in. thickness was cut into strips and machined to form sheet tensile specimens with a 4 cm gauge length and a 1 cm width. The surfaces were mechanically polished through 600 grit silicon carbide paper and cleaned in alcohol. The specimens were suspended in a thermogravimetric system and oxidized in air to form thin adherent layers of Nb_2O_5 of predetermined thickness. Upon subsequently vacuum homogenization annealing at various temperatures, a range of oxygen contents was obtained. Vacuum fusion analysis, checked by microhardness measurements (7, 8), gave the nominal oxygen contents obtained. Microhardness measurements across the samples indicated that the oxygen concentrations were uniform. The specimens were given a final polish with 600 grit silicon carbide paper.

In order to obtain background data on the tensile properties of niobium as a function of initial oxygen content, stress-strain measurements were made at room temperature and at 425°C in helium.

The effect of stress upon oxidation might be approached by at least four methods of testing. Stress could be constant (stress-rupture) or variable (tensile test); the oxidation state could be constant (previously oxidized) or variable (oxidizing while stressing). Since oxidation itself induces stresses in the metal, actual service conditions consist of a variable stress imposed upon continuously oxidizing metal. The combination of steady stress imposed on oxidizing metal was selected as the combination most nearly approximating service conditions and at the same time being a simple enough stress state to readily permit some form of analysis of results.

Because of the linearity of the oxidation rate in the temperature range of interest, the thickness of an oxidizing specimen diminishes linearly with time. Therefore, in order to maintain a constant applied tensile stress upon an oxidizing specimen, it was necessary to decrease the applied load proportionately with time.

The specimen was mounted in a conventional creep machine using water as the load since the quantity could be conveniently and continuously varied with time. Stress was measured by a load cell and automatically recorded. The specimen was attached by wedge grips between support rods inside a glass sleeve containing alumina chips. Air which had been previously dried using sulfuric acid was preheated by the alumina chips and then passed across the specimen.

* Electrochemical Society Active Member.
¹ Present address: Metallurgy Division, Sandia Laboratories, Livermore, California 94550.
Key words: oxide, Nb_2O_5 , suboxide, flexure, films.

² Supplied by Fansteel Metallurgical Corporation with given nominal analysis of about 99.7-8% Nb with Ta, Fe, Mo, Ti, and Zr being the metallic impurities; interstitial contents determined from vacuum fusion analysis were about 300 ppm O_2 , 40 ppm N_2 , and 5 ppm H₂.

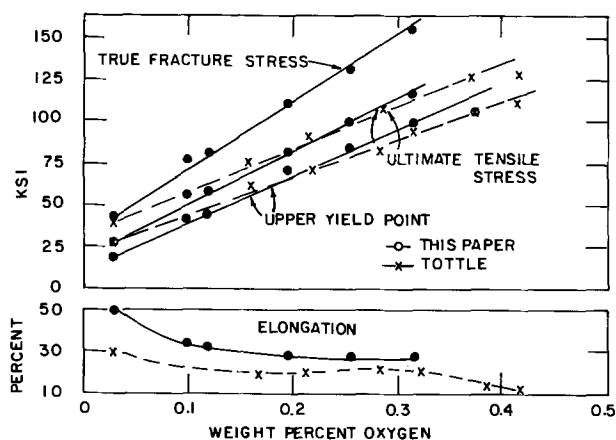


Fig. 1. Upper yield point, ultimate tensile stress, true fracture stress, and elongation vs. weight per cent oxygen at 25°C.

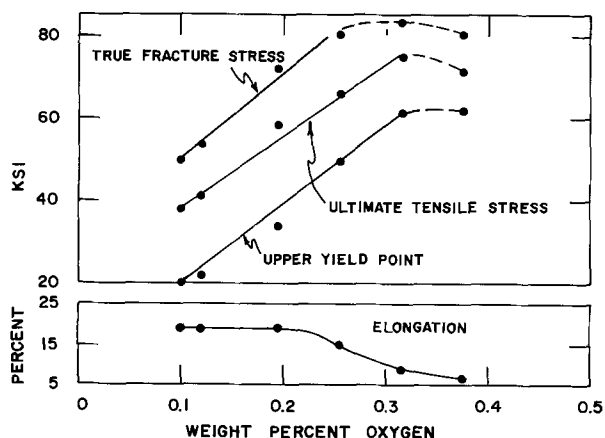


Fig. 2. Upper yield point, ultimate tensile stress, true fracture stress, and elongation vs. weight per cent oxygen at 425°C in helium.

Results

Load-elongation curves as a function of oxygen content were obtained at 25° and 425°C. Figures 1 and 2 show plots of upper yield point, ultimate tensile stress, true fracture stress, and elongation as a function of oxygen content at 25° and 425°C. The data shown in Fig. 1 show very good agreement with the data of Tottle (7). At 425°C, the true fracture stress increases linearly with oxygen content to about 0.25 weight per cent (w/o) oxygen, leveling off thereafter at approximately 80,000 psi. How oxygen is distributed in niobium at this temperature and whether saturation actually exists at oxygen contents below 0.25 w/o are questions which have never been fully answered, but it appears that if an oxygen-embrittled zone occurs at 425°C the total stress required for fracture cannot greatly exceed 80,000 psi.

In order to test the mechanics of the constant-applied-tensile-stress apparatus, a niobium specimen with an initial oxygen content of about 1000 ppm (which happened to be made from a piece of cold worked niobium sheet) was oxidized at 435°C in air while maintaining an approximate constant tensile stress of 15,000 psi. The intention was to oxidize the specimen for one week but it failed on the fifth day. Upon sectioning and mounting the specimen, numerous oxide wedges were observed. To check the validity of this result, two specimens (which were prepared as discussed from annealed sheet) were oxidized in air for 48 hr at 440° and 435°C, respectively, under a constant tensile stress of approximately 15,000 psi. Figure 3 shows an example of oxide wedges formed in the specimen oxidized at 435°C. The specimens were carefully polished and the niobium-oxide interface was ob-



Fig. 3. Oxide wedges formed in niobium tensile specimens oxidized at 435°C in air while a constant tensile stress of approximately 15,000 psi was applied; 100X.

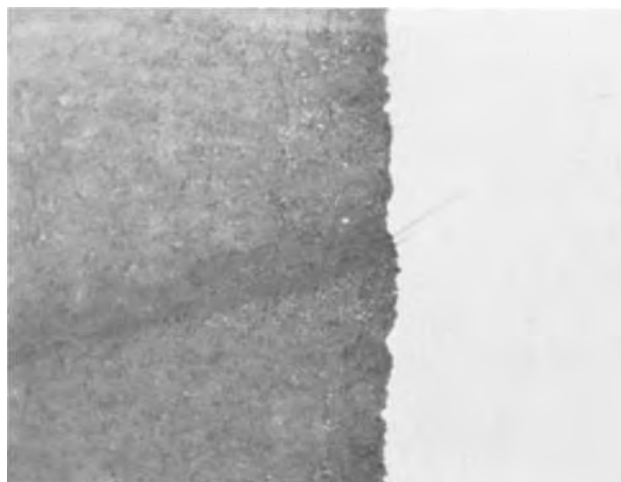


Fig. 4. Suboxide needles formed in niobium tensile specimens oxidized at 435°C in air while a constant tensile stress of approximately 15,000 psi was applied; 1400X.

served on a metallograph at 1400X. Suboxide needles as shown in Fig. 4 were observed penetrating into the metal.

Figures 5 and 6 show the microstructures of the metal-oxide interface of niobium specimens oxidized in air at 425°C for 48 hr and at 500°C for 24 hr, respectively, with no applied stress. Note the layering of the grayish niobium pentoxide upon the clear, light niobium. Also in Fig. 6 needles are observed which were not observed to occur at 430°C. These needles have been previously observed (1,4) at oxidation temperatures from about 475° to 650°C. They were designated as a suboxide of niobium, NbO_z (1).

As shown in Fig. 4, the suboxide needles formed in the oxidized tensile specimen look very much like the needles of NbO_z as shown in Fig. 6 for the specimen oxidized at 500°C. A trail of pores and slight discoloration of the overlying niobium pentoxide were observed in both specimens. The presence of pores indicates that the needles were present during the entire oxidation process (9). The micrographic evidence strongly suggested the similarity of the suboxide needles in the two specimens.

Further observation of the suboxide needles in the specimens oxidized while being subjected to a tensile stress showed that a number of these needles had microcracks associated with them, as shown in the example in Fig. 7. Some cracks were within the needles,



Fig. 5. Microstructure of niobium-oxide interface of niobium specimen oxidized at 430°C for 48 hr; 1400X.

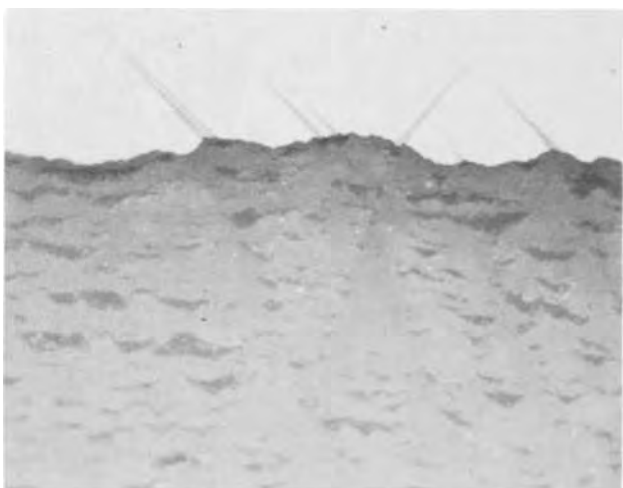


Fig. 6. Microstructure of niobium-oxide interface of niobium specimen oxidized at 500°C for 24 hr. Note the addition of NbO_2 needles; 1400X.

some extended from the base of the needles, some were at the needle tip, and some occurred between a few needles. It was thus suspected that the oxide wedge formation was initiated by the microcracks associated with the niobium suboxide needles. Further evidence



Fig. 7. Two examples showing cracks associated with niobium suboxide needles; 1400X

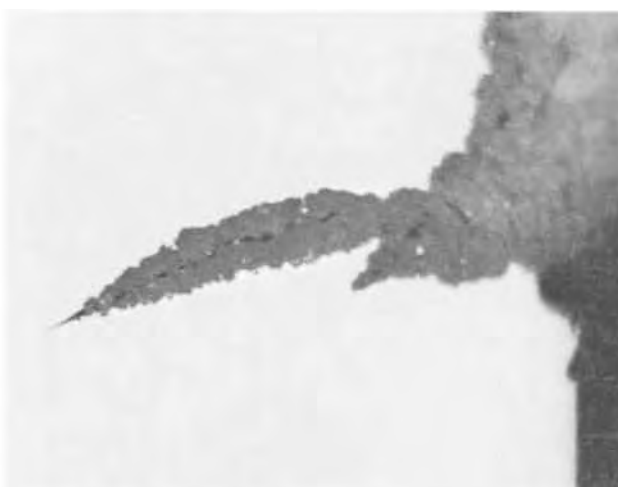


Fig. 8a. Oxide wedge in niobium tensile specimen; 1400X

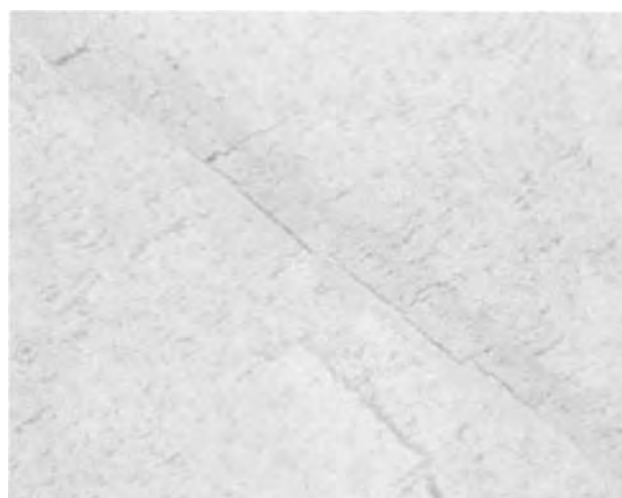


Fig. 8b. Holes in niobium pentoxide associated with oxide wedge shown above; 1400X.

of this was shown by Fig. 8a and 8b. Figure 8a is a photomicrograph of a niobium pentoxide wedge in niobium at a magnification of 1400X. A point to observe is the initial direction of the oxide wedge formation before propagating more perpendicularly into the niobium. This direction was similar to that for most niobium suboxide needles indicating that the oxide wedge



Table I. Results for constant stress tensile specimens (30B-71B)

Specimen No.	Oxygen content, ppm	Oxdn. temp., °C	Oxdn. time, hr	Stress, start, × 10 ³ psi	Stress, finish, × 10 ³ psi	Suboxide needles	Oxide wedges
30B	1000	440	36	15	17	Yes	Yes
31B	1000	435	48	15	16	Yes	Yes
39B	1950	420	48	20	20	No	No
51B	2550	420	72	30	28	No	No
54B	3150	420	20	50	50	No	No
55B	3150	435	36	40	45	Few	Few
64B	1300	420	72	20	18	No	No
66B	1300	435	48	25	25	Yes	Yes
67B	1300	435	48	20	21	Yes	Yes
68B	1300	435	48	15	15	Yes	Yes
70B	1300	435	48	10	10	Few	Few
71B	1300	435	46	20	22	Yes	Yes

Table II. Results for constant stress tensile specimens (72B-82B)

Specimen No.	Oxygen content, ppm	Oxdn. temp., °C	Oxdn. time, hr	Stress, start, × 10 ³ psi	Stress, finish, × 10 ³ psi	Suboxide needles	Oxide wedges
72B	1950	435	46	30	30	Yes	Yes
73B	1950	435	46	20	20	Yes	Yes
74B	1950	435	48	15	15	Few	Few
75B	1950	430	40	30	30	Few	Few
76B	3150	435	48	15	14	No	No
77B	3150	435	48	20	18	No	No
78B	3150	435	48	20	19	No	No
79B	3150	435	48	30	28	No	No
80B	2550	435	48	30	30	No	No
81B	2550	435	20	40	41	Yes	Yes
82B	2550	435	36	35	35	Few	Few

may have started from a microcrack inside of a suboxide needle. Figure 8b shows an area in the niobium pentoxide layers directly adjacent to the oxide wedge shown in Fig. 8a. The trail of pores and slight oxide discoloration observed is similar to that associated with niobium suboxide needles as shown in Fig. 4. Thus there was evidence of a direct relationship between niobium suboxide needles, microcracks associated with them and niobium pentoxide wedges.

To obtain a more complete understanding of the suboxide needle and subsequent oxide wedge formation phenomena, niobium tensile specimens with different initial oxygen contents were oxidized at temperatures near 425°C while maintaining various applied constant tensile stresses. Tables I and II summarize the results for these tensile specimens. The oxidizing temperature at which most data were taken was 435°C and these data are best shown in Fig. 9. The results showed a correspondence of suboxide needle formation and oxide wedge formation with the frequency of oxide wedges increasing with the frequency of suboxide needles. Also, the frequency of suboxide needles increased and length decreased with increasing applied tensile stress for specimens with the same initial oxygen content oxidized at the same temperature for the same time (as shown in Fig. 10a and 10b).

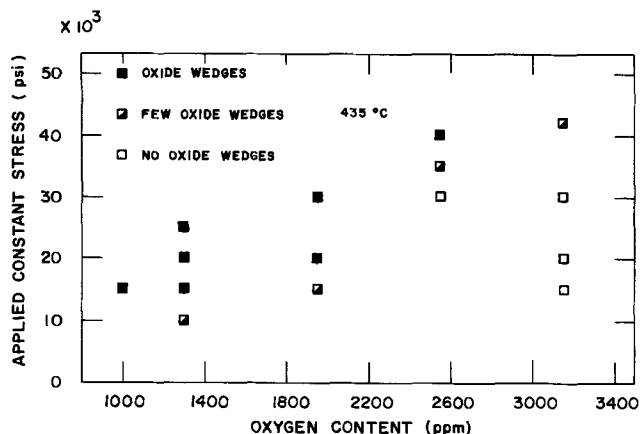


Fig. 9. Plot of applied tensile stress vs. initial oxygen content for niobium tensile specimens oxidized at 435°C in air indicating the formation of oxide wedges.

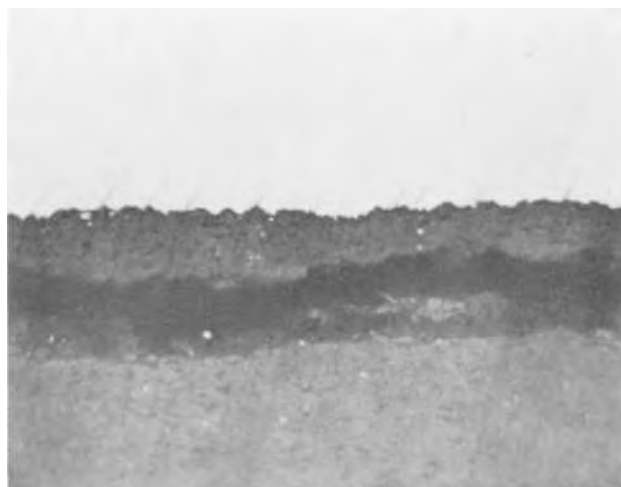


Fig. 10a. Suboxide needles formed in a niobium tensile specimen oxidized at 435°C in air while a constant tensile stress of 25,000 psi was applied; 1400X.

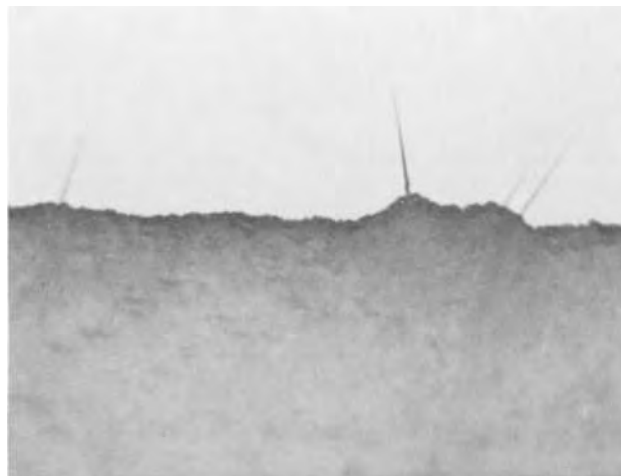


Fig. 10b. Suboxide needles formed in a niobium tensile specimen oxidized at 435°C in air while a constant tensile stress of 10,000 psi was applied; 1400X.

An important result was that there existed a critical minimum applied tensile stress required for the formation of suboxide needles and subsequent oxide wedges. This critical stress was a function of both temperature and oxygen content. At 435°C in air the critical stress was approximately 16,000 psi less than the upper yield point over the range of oxygen contents studied whereas at 430°C the critical stress was only about 5000 psi less than the upper yield point.

An additional observation was that the first tensile specimen oxidized, which was made from a cold-worked niobium sheet, showed many more oxide wedges than specimens made from the annealed sheet which were oxidized at the same temperature and had about the same initial oxygen content. This result agreed with the observation of Doyle (4) that cold working a specimen reduces the temperature required for suboxide needle formation.

Interpretation and Discussion

A detailed study of the formation of these niobium suboxide needles in niobium has not been made. Van Landuyt and Wayman (10) did perform a detailed study of the suboxide needle formation in tantalum. As outlined in their paper, the formation of tantalum suboxide, TaO_y , needles was shown to proceed in a martensitic manner. A subsequent overgrowth of another suboxide, TaO_z , then made the needles more readily visible by optical microscopy. They noted that the two-dimensional needles were actually sections of three-dimensional plates. These authors further indicated that the actual details of formation of the TaO_y plates are still largely conjectural, but certain pieces of evidence obtained shed additional light on the situation. First, the TaO_y plates did not form until a certain incubation period had passed. Second, their work established that the TaO_y plates form only near the surface. They postulated that since it appeared that during the incubation period the oxygen concentration in a surface layer is increasing, the oxygen-saturated Ta transforms to the orthorhombic suboxide plates, TaO_y , upon reaching some critical oxygen content.

Since the oxidation characteristics of niobium and tantalum are very similar, the assumption that the niobium suboxide needles are also forming in a martensitic manner would not seem unreasonable. Supporting this assumption was the observation that an incubation time was also needed in niobium to allow the surface oxygen concentration to increase. Tetragonal suboxides of niobium, NbO_x and NbO_z , corresponding to the tetragonal suboxides of tantalum, TaO_x and TaO_z , were observed, adding support to this view. Also, the information reported (11) on the indices of the plane on which these NbO_z plates lie agreed with the $\{100\}$ indices observed (10) for the habit plane of TaO_z , the overgrowth phase.

However, the actual martensite phase underneath this overgrowth of TaO_z was the orthorhombic, TaO_y , with $\{320\}$ habit planes. One correspondence which has not been observed is the existence of an orthorhombic niobium suboxide, NbO_y , similar to the orthorhombic tantalum suboxide, TaO_y . Since the existence of these orthorhombic suboxides is very critical to the argument favoring the mechanism of martensitic formation, a doubt exists as to the applicability of the mechanism of martensitic formation in the niobium system.

As indicated by Van Landuyt and Wayman (10), the problem is not easily analyzed because of the closeness of the $\{100\}$ and $\{320\}$ planes in a body-centered cubic system to one another and to the theoretical plane of maximum shear stress. Also, the overgrowth of one oxide upon another adds confusion. Therefore, because of the ambiguities of the proposed mechanism with observations, exactly which mechanism is involved in the niobium suboxide needle formation cannot be determined without further study.

The change in frequency and length of suboxide needles as a function of applied tensile stress cannot be explained unambiguously. However, a simple nucleation and growth model may be applicable. A higher applied tensile stress may increase the number of nucleation sites (possibly dislocation lines) (12) and hence the number of needles. The nucleation of a larger number of suboxide needles may cause a reduction in the stress gradient in their immediate vicinity, thus causing a reduction in the driving force for growth and a consequent reduction in length.

Regardless of the nucleation and growth or the formation mechanism of these suboxide plates, the important finding of this study was that under the proper conditions of oxygen concentration gradient, temperature, and stress these plates do form. Once they are formed, in areas where the local frequency is high, only a very small applied tensile stress (less than 10,000 psi) is needed to produce a microcrack. Once this microcrack is formed, it further oxidizes to form an oxide wedge. If the conditions of oxygen concentration gradient, temperature, and stress are not right to form suboxide plates, no microcracks or oxide wedges are observed. It appears that suboxide plates and subsequently microcracks, must occur before the oxide wedges, which are the ultimate destructive agent, can occur.

Summary

It has been shown (6) that the resulting tensile stress on a niobium metal substrate due to the formation of Nb_2O_5 may approach the yield point of the oxygen-hardened niobium surface.

No matter what the actual tensile stress is, this stress would be approximately the same for the cases of oxidizing niobium tubes, coupon specimens, flexure specimens, or sheet tensile specimens. It is the addition of an applied tensile stress either by bending (as in the case of tubes or flexure specimens) or by pulling (as in the case of tensile specimens) on the oxygen-saturated metal surface which causes the formation of suboxide needles, subsequent cracking of the metal in some localized areas where there is a high frequency of needles and a final formation of an oxide wedge.

Manuscript submitted April 23, 1971; revised manuscript received Dec. 13, 1971. This was Paper 109 presented at the Atlantic City Meeting of the Society, Oct. 4-8, 1970.

Any discussion of this paper will appear in a Discussion Section to be published in the December 1972 JOURNAL.

REFERENCES

1. T. Hurlen, H. Kjøllesdal, J. Markali, and N. Norman, Central Institute for Industrial Research, Blindern-Oslo, Norway, Technical Note No. 1 (1959).
2. R. Pawel and J. Campbell, *Acta Met.*, **14**, 1827 (1966).
3. T. Kolski, *Trans. Am. Soc. Metals*, **55**, 119 (1962).
4. J. H. Doyle, Unpublished M.S. thesis, Ames, Iowa, Library, Iowa State University of Science and Technology (1964).
5. D. B. Fox, Private communication.
6. L. J. Weirick and W. L. Larsen, *This Journal*, **119**, 465 (1972).
7. G. R. Tottle, *Inst. Metals*, **85**, 375 (1957).
8. J. R. DiStefano, U.S. Atomic Energy Commission Report ORNL-3551, Oak Ridge National Laboratory, Oak Ridge, Tennessee (1964).
9. J. Stringer, *J. Less-Common Metals*, **11**, 111 (1966).
10. J. Van Landuyt and C. Wayman, *Acta Met.*, **16**, 803 (1968).
11. N. Norman, *J. Less-Common Metals*, **4**, 52 (1962).
12. J. Van Landuyt, European Atomic Energy Community Report EURAEC-1184, Centre d'Etude de l'Energie Nucleaire, Mol, Belgium (1965).

Solid-State Ionics—Solids with High Ionic Conductivity in the Systems Silver Iodide-Silver Oxyacid Salts

Takehiko Takahashi,* Shoichiro Ikeda, and Osamu Yamamoto

Department of Applied Chemistry, Faculty of Engineering, Nagoya University, Nagoya, Japan

ABSTRACT

Two kinds of high ionic conductivity solids, $\text{Ag}_7\text{I}_4\text{PO}_4$ and $\text{Ag}_{19}\text{I}_{15}\text{P}_2\text{O}_7$, have been found in the systems $\text{AgI-Ag}_3\text{PO}_4$, and $\text{AgI-Ag}_4\text{P}_2\text{O}_7$ at ambient temperature. $\text{Ag}_7\text{I}_4\text{PO}_4$ has a silver ion conductivity of $0.019 (\text{ohm}\cdot\text{cm})^{-1}$ at 25°C and an activation energy for conduction of 3.8 kcal/mole between 20° and 79°C . $\text{Ag}_{19}\text{I}_{15}\text{P}_2\text{O}_7$ has a silver ion conductivity of $0.09 (\text{ohm}\cdot\text{cm})^{-1}$ at 25°C and an activation energy for conduction of 3.3 kcal/mole between 20° and 147°C . The $\text{Ag}/\text{electrolyte}/\text{I}_2$ solid-state cells using these electrolytes showed open circuit voltages of 684 mV for $\text{Ag}_7\text{I}_4\text{PO}_4$, and 689 mV for $\text{Ag}_{19}\text{I}_{15}\text{P}_2\text{O}_7$, which agree well with the value of 687 mV calculated from ΔG° of the cell reaction. Transport number measurements using Tubandt's method showed that the transport numbers of silver ions in both new compounds are 1.00 within the experimental error. The phase diagrams of the systems $\text{AgI-Ag}_3\text{PO}_4$, and $\text{AgI-Ag}_4\text{P}_2\text{O}_7$ have been determined.

Recently, a new solid electrolyte group of the type MAg_4I_5 , where M is K, Rb, or NH_4 , was reported by Bradley and Greene (1), and independently by Owens and Argue (2), to have a high ionic conductivity of $0.27 (\text{ohm}\cdot\text{cm})^{-1}$ at 25°C . Many solid electrolyte batteries and electrochemical devices with MAg_4I_5 , particularly with RbAg_4I_5 , have been investigated by many authors (3-6), because of its being relatively stable to light, moisture, and handling within this group.

It was found, however, by Topol and Owens (7), and Takahashi *et al.* (8) that RbAg_4I_5 reacted rapidly with iodine to decompose to RbI_3 and AgI when it was maintained in an iodine atmosphere. In a $\text{Ag}/\text{RbAg}_4\text{I}_5/\text{I}_2$ cell, therefore, the internal resistance increases so fast that the cell fails its performance. Further, the decomposition of MAg_4I_5 to AgI and M_2AgI_3 was found to be promoted by moisture, when it was in contact with silver plate.

In this study, therefore, a number of investigations on some double salts with silver iodide, such as the systems silver iodide-silver oxyacid salts, have been carried out in order to find new high ionic conductivity solids which are not decomposed by iodine and moisture. Ag_3PO_4 , $\text{Ag}_4\text{P}_2\text{O}_7$, $(\text{AgPO}_3)_n$, Ag_3AsO_3 , Ag_3AsO_4 , and AgIO_3 have been examined as silver oxyacid salts.

Two new high ionic conductivity solid electrolytes have been found in the systems silver iodide-silver phosphate, and silver iodide-silver pyrophosphate. The properties of both new compounds have been investigated, and the phase diagrams of these systems have been determined.

Experimental

Preparation of samples.—The following grades of starting materials were used: special grade: AgNO_3 , KI , $\text{Na}_2\text{HPO}_4\cdot 12\text{H}_2\text{O}$, $\text{Na}_4\text{P}_2\text{O}_7\cdot 10\text{H}_2\text{O}$, and KIO_3 ; extra pure reagent: $(\text{NaPO}_3)_n$, and sodium arsenite; guaranteed reagent: $\text{Na}_2\text{HAsO}_4\cdot 7\text{H}_2\text{O}$. All of the silver compounds were prepared by precipitation from aqueous solutions of silver nitrate with the other starting materials under safe-lights. The precipitates were washed seven or eight times with distilled water, and dried under nitrogen flow at 100° - 120°C . The x-ray diffraction patterns of them were confirmed to agree with those listed in the A.S.T.M. cards.

Weighing of silver iodide and the other material was followed by mixing and grinding, and the mixture was

sealed in a Pyrex tube under vacuum and heated for about 18 hr in the temperature range between 200° - 400°C , according to its composition. The resulting material was ground and pressed by a hand press under 4 tons/cm² to form a pellet which was 13 mm in diameter and about 2 mm thick.

X-ray diffraction.—Geigerflex D-3F (Rigaku Denki Company, Ltd.) was used for x-ray diffraction analysis. A copper anode tube was operated at 15 mA and 35 kV. The shape of each specimen was a pellet as described above. A sample holder made in our laboratory was used to determine the change in structure at high temperatures.

Differential thermal analysis (D.T.A.).—A sample of 0.8g was sealed in a Vycor tube under vacuum, and α -alumina powder sealed in the same size of Vycor tube was used for the standard material. The heating rate was $3.5^\circ\text{C}/\text{min}$, controlled by a PID controller (YEW, Model EGC 5-10) and a programmer (YEW, Model PGE-12).

Conductivity measurement.—In order to reduce the contact resistance in the measurements of the conductivity change with temperature, a mixture of powdered silver and the sample was used for electrode. Namely, a mixture of 0.9g of the sample and 0.3g of 200 mesh silver powder was applied to the electrode material. The sample of 1.2g was stacked between the electrodes and pressed into a pellet of 13 mm in diameter. The electrical conductivity was measured with a 1 kHz impedance bridge (YEW, Model BV-Z-13A).

Transport number measurement.—The transport number of silver ion in both of the new high conductivity compounds was measured by Tubandt's method (9). In order to reduce an anodic polarization, an amalgamated silver plate was used for an anode material, and the change of the mass of the anode and sample-1, which directly contacted the anode, was not measured (see Fig. 1). Four specimens, 13 mm in diameter and about 1.2 mm thick, were weighed separately and stacked into a measuring cell as shown in Fig. 1. A solution of 20 w/o (weight per cent) silver nitrate was used for an electrolyte for the silver coulometer. A stabilized direct current was passed through the cells for about 4 hr at the current densities of 1.2 and 1.5 mA/cm² for $\text{Ag}_7\text{I}_4\text{PO}_4$ and $\text{Ag}_{19}\text{I}_{15}\text{P}_2\text{O}_7$, respectively.

Results and Discussion

$\text{AgI-Ag}_3\text{PO}_4$ system.—A plot of the electrical conductivity of the system $\text{AgI-Ag}_3\text{PO}_4$ at room tempera-

* Electrochemical Society Active Member.

Key words: silver iodide, ionic conductivity, solid-state battery.

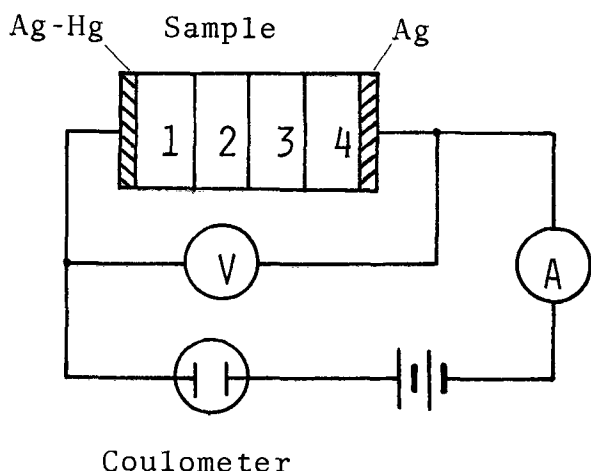


Fig. 1. Schematic diagram of the circuit of transport number measurement.

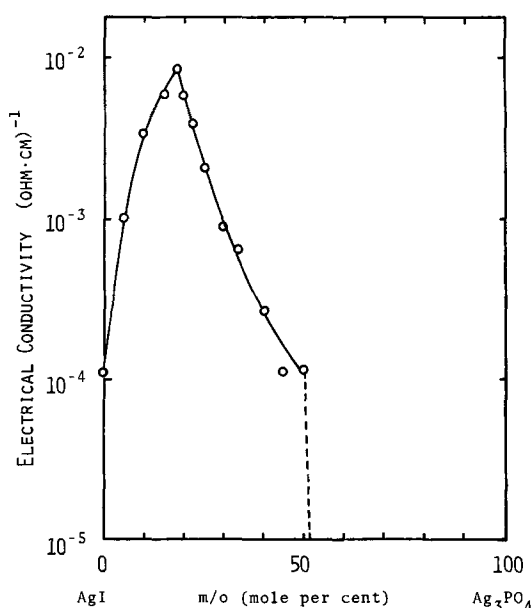


Fig. 2. Electrical conductivities in the system AgI-Ag₃PO₄ vs. the composition of Ag₃PO₄ at room temperature.

ture against the Ag₃PO₄ content is shown in Fig. 2, where silver plates were used for electrodes. All the samples were prepared by heating at 400°C and cooling naturally to room temperature, where the cooling rate was about 1.5°C/min. The conductivity curve suggests that two intermediate compounds may be present in this system, because the conductivity of the system showed a maximum at the composition of 20 m/o (mole per cent) and suddenly falls above 50 m/o of Ag₃PO₄.

Results of the x-ray diffraction carried out at room temperature on the samples using nickel filtered Cu-K α radiation are listed in Table I. In the range of 0-20 m/o of Ag₃PO₄, diffraction peaks of γ phase silver iodide and Phase I appeared. Lines due to Ag₃PO₄ were observed in samples containing 60 m/o or more Ag₃PO₄, the intensity of those lines increased gradually with increasing content of Ag₃PO₄. The pattern of 20 m/o of Ag₃PO₄, Phase I, is simple to predict a new compound, which may be written as Ag₇I₄PO₄, and that of 50 m/o, Phase II, is also due to a single phase and is sufficiently different from those of α -, β -, and γ -AgI, Ag₃PO₄, and Ag₇I₄PO₄ to predict another new compound, which may be written as Ag₄IPO₄.

The electrical conductivity of Ag₇I₄PO₄ plotted as a function of the reciprocal of the absolute temperature is shown in Fig. 3. In the range of room temperature

Table I. Results of x-ray investigations on the system AgI-Ag₃PO₄ at room temperature

m/o Ag ₃ PO ₄	Phase observed	Symmetry	Structure type	Lattice parameter (Å)	Reference
0	γ -AgI	Cubic	Zinc blende	6.495	(10)
5, 10, 15	γ -AgI + Phase I				
20	Phase I	Cubic		10.6	
25, 33, 40	Phase I + Phase II				
50	Phase II	Complex pattern			
60, 67, 80, 90	Phase II + Ag ₃ PO ₄				
100	Ag ₃ PO ₄	Cubic		6.013	(11)

to 79°C, the conductivity increases linearly, and the activation energy for conduction is obtained from this slope to be 3.8 kcal/mole. At 25°C, the conductivity is $(1.9 \pm 0.1) \times 10^{-2}$ (ohm \cdot cm)⁻¹. Above 79°C, however, the electrical conductivity decreases with increasing temperature, but it abruptly increases about 6-7 times at about 147°C, corresponding to the transition of silver iodide from β to α phase. This discontinuity was thought to be caused by the transition of the resulting silver iodide. The conductivity decreases again with temperature above this transition.

Figure 4 shows the x-ray diffraction patterns of Ag₇I₄PO₄ measured at various temperatures to compare with the conductivity measurements. The starting material was prepared by heating at 400°C and cooling naturally to room temperature. Each measurement was taken after the sample was kept at the desired temperature for about 20 min. At 80°C, a few small peaks different from those obtained at room temperature are seen, and at 120°C the pattern is quite different from that of Ag₇I₄PO₄. Above 150°C, the peaks of β -AgI were changed to those of α -AgI, suggesting that Ag₇I₄PO₄ was decomposed to AgI and a compound of another composition at 80°C. Both the samples which were quenched from 400°C and cooled gradually from 400°C to room temperature, the cooling rate of which was about 3-5°C/hr, showed the same x-ray diffraction patterns as those of Fig. 4.

As the x-ray diffraction pattern measured at room temperature of the sample annealed at 150°C was found to be nearly equal to that measured at 120°C, the x-ray diffraction patterns of the specimens of the other compositions annealed at 160°C for 1 or 2 hr in air were also measured at room temperature. The results of these measurements are summarized in Table II. Though in the composition range of 50 to 100 m/o of Ag₃PO₄ the patterns were quite equal to those of unannealed samples of the corresponding compositions, it was found that the x-ray diffraction patterns of the samples containing between 0-50 m/o of Ag₃PO₄ were fairly different from those measured on the unannealed samples. Namely, between 0-33 m/o of Ag₃PO₄, the peaks of Ag₇I₄PO₄ (Phase I) vanished, and the peaks

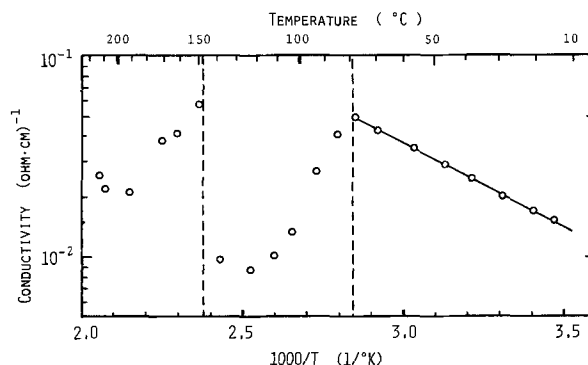


Fig. 3. Electrical conductivity of Ag₇I₄PO₄ vs. the reciprocal of the absolute temperature.

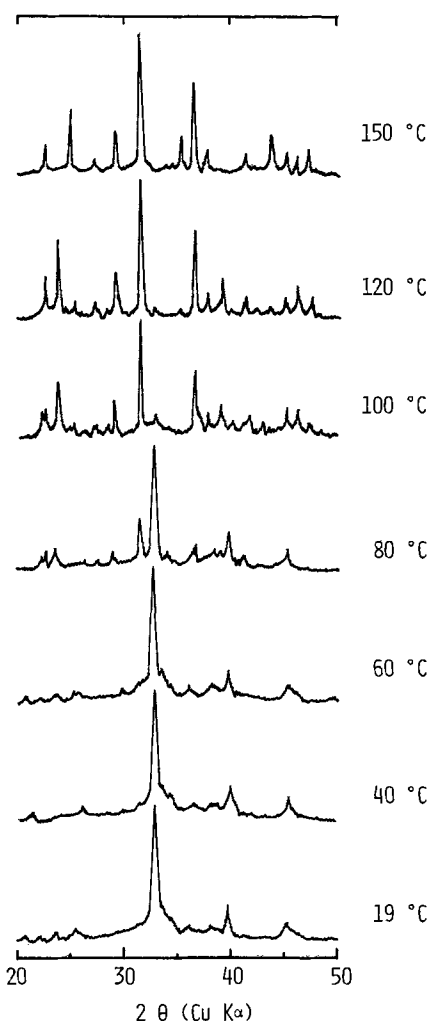


Fig. 4. X-ray diffraction patterns of $\text{Ag}_7\text{I}_4\text{PO}_4$ measured at various temperatures.

of β -AgI and 33 m/o of Ag_3PO_4 (Phase III, which may be written as $\text{Ag}_5\text{I}_2\text{PO}_4$) appeared. And between 33-50 m/o of Ag_3PO_4 , the mixed patterns of Phase II and Phase III were observed.

From these results described above, it has been thought that $\text{Ag}_7\text{I}_4\text{PO}_4$ would be completely decomposed according to the reaction



by annealing above 79°C , and the rate of the recombination reaction of the resulting materials would be fairly slow at room temperature. A mass change of the sample before and after the annealing procedure was not observed, so it was found that $\text{Ag}_7\text{I}_4\text{PO}_4$ was merely decomposed to AgI and $\text{Ag}_5\text{I}_2\text{PO}_4$, and no change of the number of oxygen atoms bonded to

Table II. Results of x-ray investigations on the system AgI- Ag_3PO_4 annealed at 160°C

m/o Ag_3PO_4	Phase observed	Symmetry	Structure type	Lattice parameter (Å)	Reference
0	β -AgI	Hexagonal	Wurtzite	a = 4.592 c = 7.510	(12)
15, 20, 27.5	β -AgI + Phase III				
33.3	Phase III	Complex pattern			
40	Phase III + Phase II				
50	Phase II	Complex pattern			
60, 67, 80	Phase II + Ag_3PO_4				
100	Ag_3PO_4	Cubic		6.013	

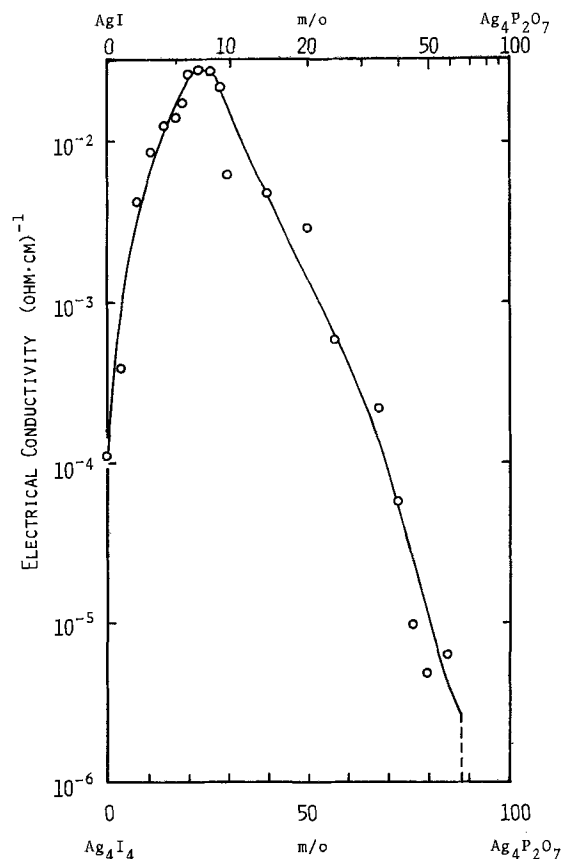


Fig. 5. Electrical conductivities in the system AgI- $\text{Ag}_4\text{P}_2\text{O}_7$ vs. the content of $\text{Ag}_4\text{P}_2\text{O}_7$ at room temperature.

phosphorous atoms occurred by annealing. The sample prepared at 400°C , however, was extremely stable at room temperature, as the electrical conductivity and the x-ray diffraction pattern of it have been confirmed to be maintained constantly for at least 3 yr.

The crystal structure of $\text{Ag}_7\text{I}_4\text{PO}_4$ is estimated to be a cubic structure having a lattice constant of 10.6Å from the x-ray analysis.

AgI- $\text{Ag}_4\text{P}_2\text{O}_7$ system.—Figure 5 shows the result of the electrical conductivity of the system AgI- $\text{Ag}_4\text{P}_2\text{O}_7$ at room temperature, plotted against the composition of $\text{Ag}_4\text{P}_2\text{O}_7$, where silver plates were used for electrodes. The samples containing between 0-25 m/o of $\text{Ag}_4\text{P}_2\text{O}_7$ were prepared at 200°C , and the samples containing between 30-50 m/o and between 60-90 m/o were prepared at 300° and at 400°C , respectively, where the cooling rate was about $1.5^\circ\text{C}/\text{min}$ for all samples. Considering the phase diagram and the experimental results, $\text{Ag}_{19}\text{I}_{13}\text{P}_2\text{O}_7$ was mainly prepared by heating at 250°C for about 20 hr and cooling naturally to room temperature (the cooling rate was about $1.5^\circ\text{C}/\text{min}$). The conductivity curve suggests that a new compound having a high conductivity may be present in this system.

Results of the x-ray diffraction carried out at room temperature are listed in Table III. Peaks of γ -phase silver iodide were observed in samples containing less than 5 m/o of $\text{Ag}_4\text{P}_2\text{O}_7$, and new lines were observed in the samples containing about 7 and 33 m/o of $\text{Ag}_4\text{P}_2\text{O}_7$. In the sample containing more than 67 m/o, peaks of $\text{Ag}_4\text{P}_2\text{O}_7$ appeared. It could be concluded, therefore, that three new intermediate compounds are present at room temperature in this system.

From the results described above, it has been found that the new high conductivity solid containing about 7 m/o of $\text{Ag}_4\text{P}_2\text{O}_7$ is not a solid solution of AgI and $\text{Ag}_4\text{P}_2\text{O}_7$, but a new compound, so several experiments have been done in order to decide the composition of this compound. Figure 6 shows the logarithm of the conductivities of the samples of the composition rang-

Table III. Results of x-ray investigations on the system $\text{AgI-Ag}_4\text{P}_2\text{O}_7$ at room temperature

m/o $\text{Ag}_4\text{P}_2\text{O}_7$	Phase observed	Symmetry	Structure type	Lattice parameter (Å)	Reference
0	γ -AgI	Cubic	Zinc blende	6.495	
3, 5	γ -AgI + Phase IV				
6, 7	Phase IV	Cubic		11.2	
10, 20, 30	Phase IV + Phase V				
33, 35	Phase V	Complex pattern			
40, 50, 60	Phase V + Phase VI				
66.7	Phase VI	Complex pattern			
70, 80, 90	Phase VI + $\text{Ag}_4\text{P}_2\text{O}_7$				
100	$\text{Ag}_4\text{P}_2\text{O}_7$				(13)

ing from 6 to 8 m/o of $\text{Ag}_4\text{P}_2\text{O}_7$ plotted against the reciprocal of the absolute temperature. The conductivity curves of 6.00 and 6.25 m/o have an abrupt change near 147°C, corresponding to the transition of silver iodide from β to α phase. In the sample containing 8.00 m/o it was found that the conductivity was decreased above 147°C. On the other hand, the conductivity curves of the sample containing 7.00 m/o showed the Arrhenius type curve in the range of the temperature investigated.

The results of D.T.A. of this system show endothermic peaks at 147°C on heating in the composition range of 0-17 m/o of $\text{Ag}_4\text{P}_2\text{O}_7$.

The x-ray diffraction patterns of the samples containing 6 and 7 m/o of $\text{Ag}_4\text{P}_2\text{O}_7$ showed a cubic structure with a lattice constant of 11.2Å, and it was assumed from the analysis of the lattice constant, specific gravity, and the ionic radii that the new compound may be written as $\text{Ag}_{19}\text{I}_{15}\text{P}_2\text{O}_7$.

Other systems.—The same procedure described in the previous section has been carried out on the systems, $\text{AgI-(AgPO}_3)_n$, $\text{AgI-Ag}_3\text{AsO}_3$, $\text{AgI-Ag}_3\text{AsO}_4$, and AgI-AgIO_3 , and also on the systems, $\text{AgBr-Ag}_3\text{PO}_4$, and $\text{AgCl-Ag}_3\text{PO}_4$.

It was indicated by the results of the electrical conductivity measurements that no high conductivity compounds were present in these systems at room temperature. The electrical conductivities of these systems measured at room temperature were lower than that of pure silver iodide (γ phase) (14). In the $\text{AgI-Ag}_3\text{PO}_4$ system, exchange of silver iodide with silver bromide or silver chloride did not improve the electrical conductivity.

Properties of $\text{Ag}_7\text{I}_4\text{PO}_4$ and $\text{Ag}_{19}\text{I}_{15}\text{P}_2\text{O}_7$.—The compound $\text{Ag}_7\text{I}_4\text{PO}_4$ is an orange colored solid, and the compound $\text{Ag}_{19}\text{I}_{15}\text{P}_2\text{O}_7$ is a yellow solid at room temperature. The former was darkened by exposure to visible light in a powder state, but the latter has little

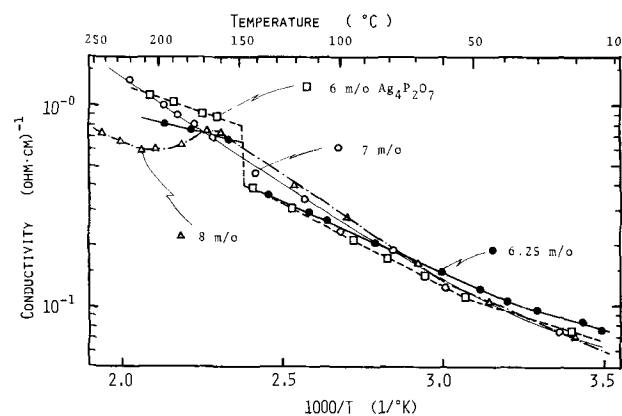


Fig. 6. Temperature dependence of electrical conductivities in the system $\text{AgI-Ag}_4\text{P}_2\text{O}_7$.

Table IV. Activation energies for conduction in high ionic conductors having average structures

Substance	Conductivity at 25°C ($\text{ohm} \cdot \text{cm}$) ⁻²	Activation energy (kcal/mole)	Reference
Ag_3SI	1×10^{-2}	4.0	(15)
$\text{Ag}_2\text{Hg}_{0.25}\text{S}_{0.5}\text{I}_{1.5}$	1.5×10^{-1}	3.2	(16)
$\text{Ag}_4\text{HgSe}_2\text{I}_2$	1.2×10^{-2}	3.5	(17)
RbAg_4I_5	2.7×10^{-1}	1.7	(18)
QAg_6I_7			(19)
Q = Tetramethyl ammonium	4×10^{-2}	4.0	
Diethylidimethyl ammonium	6×10^{-2}	3.6	
$\text{Ag}_7\text{I}_4\text{PO}_4$	1.9×10^{-2}	3.8	
$\text{Ag}_{19}\text{I}_{15}\text{P}_2\text{O}_7$	9.0×10^{-2}	3.3	

Table V. Transport numbers in $\text{Ag}_7\text{I}_4\text{PO}_4$ and $\text{Ag}_{19}\text{I}_{15}\text{P}_2\text{O}_7$

	Change in mass (mg)	
	$\text{Ag}_7\text{I}_4\text{PO}_4$	$\text{Ag}_{19}\text{I}_{15}\text{P}_2\text{O}_7$
Ag-Hg anode	—	—
Sample 1	—	—
Sample 2	-0.03	-0.05
Sample 3	-0.10	-0.02
Sample 4		
Ag cathode	+19.89	+31.91
Ag deposited in coulometer	19.84	31.91
Transport number of Ag^+	0.998 ± 0.005	0.999 ± 0.005

sensitivity to light. The electrical conductivities of both compounds are 0.019 ± 0.001 and 0.090 ± 0.002 ($\text{ohm} \cdot \text{cm}$)⁻¹ at 25°C, respectively. The activation energies for conduction of both compounds are 3.8 and 3.3 kcal/mole, respectively. These values are so low for ionic compounds that they are thought to have the average structures. The compounds which are known to have the average structures are listed in Table IV.

In the experiments to find the transport numbers of these compounds, it was found that the total current passed through both cells (see Fig. 1) corresponded to the quantities of silver deposited at the cathodes, as shown in Table V, and the transport numbers of silver ion are unity within the experimental error. Figure 7 shows the results of the changes of the internal resistances of the following cells in process of time: Graphite/ $\text{Ag}_7\text{I}_4\text{PO}_4$ + I_2 /Graphite, Graphite/ $\text{Ag}_{19}\text{I}_{15}\text{P}_2\text{O}_7$ + I_2 /Graphite, and Graphite/ RbAg_4I_5 + I_2 /Graphite. A mixture of 1.3g of each sample and 0.3g

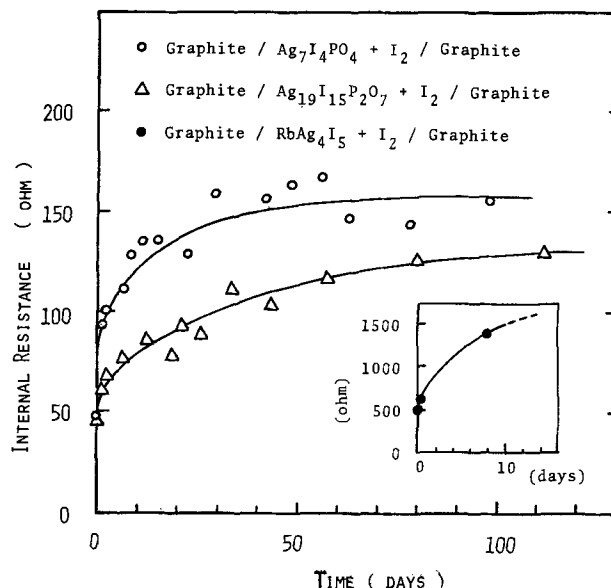
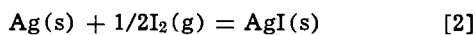


Fig. 7. The changes of the internal resistances of the cells: Graphite/ $\text{Ag}_7\text{I}_4\text{PO}_4$ + I_2 /Graphite, Graphite/ $\text{Ag}_{19}\text{I}_{15}\text{P}_2\text{O}_7$ + I_2 /Graphite, and Graphite/ RbAg_4I_5 + I_2 /Graphite.

of iodine was used, and platinum plates were used for the current collectors. In the former two cells, the resistances increased gradually with time for about a month, and then were maintained at constant values. The resistance of the last cell, however, increased about 100 times greater than those of the former two cells. This result indicates that two new compounds found in this study provide a good performance in silver-iodine solid-state batteries. The cells, $\text{Ag}/\text{Ag}_7\text{I}_4\text{PO}_4/\text{I}_2 + \text{C}$, and $\text{Ag}/\text{Ag}_{19}\text{I}_{15}\text{P}_2\text{O}_7/\text{I}_2 + \text{C}$, showed open circuit voltages of 684 and 689 mV at 25°C, respectively. These values agree fairly well with the value, 687 mV, calculated from the change of free energy of formation of silver iodide at 25°C according to Eq. [2]



that is, the ionic transport numbers of these compounds are unity. And these results are in good agreement with the transport numbers measured by Tubandt's method.

As no other cations are present except silver ions in both compounds, the conduction in $\text{Ag}_7\text{I}_4\text{PO}_4$ and $\text{Ag}_{19}\text{I}_{15}\text{P}_2\text{O}_7$ is mainly due to the migrations of Ag^+ ions, because anions such as I^- , PO_4^{3-} , and $\text{P}_2\text{O}_7^{4-}$ ions have large ionic radii and usually do not migrate in solids at ambient temperature.

Phase diagrams of the systems $\text{AgI}-\text{Ag}_3\text{PO}_4$, and $\text{AgI}-\text{Ag}_4\text{P}_2\text{O}_7$.—Figures 8 and 9 show the phase diagrams of the systems $\text{AgI}-\text{Ag}_3\text{PO}_4$, and $\text{AgI}-\text{Ag}_4\text{P}_2\text{O}_7$, respectively, determined from the results of the measurements of electrical conductivities, x-ray diffractions, and differential thermal analysis.

In the former system, there are two intermediate compounds at room temperature at the compositions of 20 and 50 m/o of Ag_3PO_4 . The high conductivity compound, $\text{Ag}_7\text{I}_4\text{PO}_4$, decomposes to AgI and a compound with 33.3 m/o of Ag_3PO_4 above 79°C. The compounds, $\text{Ag}_5\text{I}_2\text{PO}_4$ and Ag_4IPO_4 melt incongruently at 236° and 320°C, respectively. The eutectic composition is estimated to be 16 m/o of Ag_3PO_4 , at 225°C. The liquidus line of the samples containing more than 67 m/o of Ag_3PO_4 was obtained by extrapolation. A

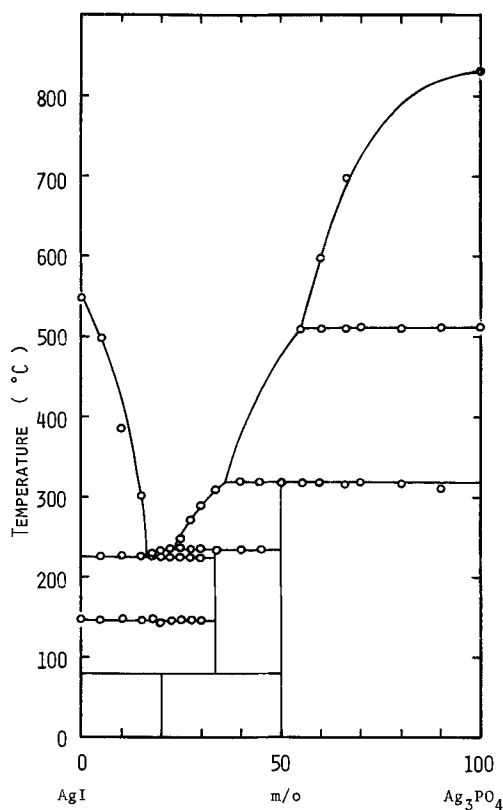


Fig. 8. Phase diagram of the system $\text{AgI}-\text{Ag}_3\text{PO}_4$

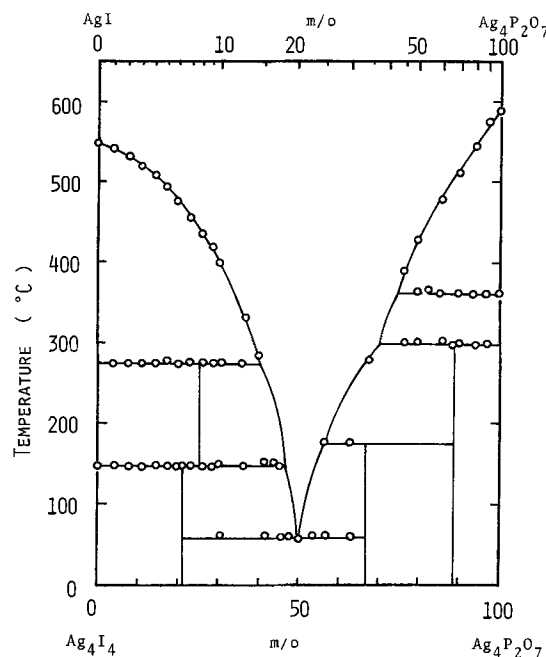


Fig. 9. Phase diagram of the system $\text{AgI}-\text{Ag}_4\text{P}_2\text{O}_7$

thermal arrest (a peak in the D.T.A. trace) at 512°C was observed for all compositions containing between 60-100 m/o of Ag_3PO_4 .

In the latter system, there are three intermediate compounds at room temperature at the compositions of 6.25, 33.3, and 66.7 m/o of $\text{Ag}_4\text{P}_2\text{O}_7$. The high conductivity compound, $\text{Ag}_{19}\text{I}_{15}\text{P}_2\text{O}_7$, decomposes to AgI and $\text{Ag}_{16}\text{I}_{12}\text{P}_2\text{O}_7$, which is the compound at the composition of 7.69 m/o of $\text{Ag}_4\text{P}_2\text{O}_7$, above 147°C. $\text{Ag}_{16}\text{I}_{12}\text{P}_2\text{O}_7$ has an incongruent melting point at 274°C. $\text{Ag}_6\text{I}_2\text{P}_2\text{O}_7$ and $\text{Ag}_9\text{IP}_4\text{O}_{14}$ melt incongruently at 178° and 295°C, respectively.

When the mixture containing 6.25 m/o of $\text{Ag}_4\text{P}_2\text{O}_7$ was heated above 274°C and cooled to room temperature naturally, the x-ray diffraction peaks were mainly those of γ -phase silver iodide and those of $\text{Ag}_{19}\text{I}_{15}\text{P}_2\text{O}_7$ were absent. This result indicates that the peritectic reaction at 274°C produces the glassy product containing near the composition of 20 m/o $\text{Ag}_4\text{P}_2\text{O}_7$ and AgI , and these products may be hard to recombine to form $\text{Ag}_{16}\text{I}_{12}\text{P}_2\text{O}_7$. The electrical conductivity of the product was nearly equal to that of γ - AgI , but when the sample was annealed between 147° and 274°C, the new high conductivity compound was formed again. In the former system, however, when the mixture containing 20 m/o of Ag_3PO_4 was melted above 225°C and cooled to room temperature, the electrical conductivity was so high as to indicate the formation of $\text{Ag}_7\text{I}_4\text{PO}_4$, and the annealing procedure between 79° and 225°C gave the opposite result.

Conclusion

Though compounds in the MAG_4I_5 group have specific conductivities as high as $0.27 (\text{ohm} \cdot \text{cm})^{-1}$ at 25°C, they seem to be somewhat unstable to moisture, handling, and especially to an iodine atmosphere. So the search for high ionic conductivity solid electrolytes has been carried on the new systems, silver iodide-silver oxyacid salts.

$\text{Ag}_7\text{I}_4\text{PO}_4$ and $\text{Ag}_{19}\text{I}_{15}\text{P}_2\text{O}_7$ have pure silver ion conductivities as high as 0.019 and 0.090 $(\text{ohm} \cdot \text{cm})^{-1}$ at 25°C, and activation energies for conduction of 3.8 and 3.3 kcal/mole, respectively. Both compounds are more stable than RbAg_4I_5 in an iodine atmosphere. The transport numbers of silver ions in both compounds are 1.00 within the experimental error. The silver-iodine solid state batteries using these new compounds for the electrolyte materials showed open circuit voltages as high as 684 and 689 mV at 25°C, respectively, which are in good agreement with the value, 687

mV, calculated from ΔG° , the free energy of formation of silver iodide(s) from silver(s) and iodine(g) at 25°C.

$\text{Ag}_7\text{I}_4\text{PO}_4$ is stable up to 79°C, and though $\text{Ag}_{19}\text{I}_{15}\text{P}_2\text{O}_7$ decomposes to AgI and $\text{Ag}_{16}\text{I}_{12}\text{P}_2\text{O}_7$ above 147°C, $\text{Ag}_{16}\text{I}_{12}\text{P}_2\text{O}_7$ has a high ionic conductivity up to 274°C in the solid state, and it is a promising material for use as a solid electrolyte for electrochemical devices.

Manuscript submitted July 13, 1971; revised manuscript received Nov. 26, 1971.

Any discussion of this paper will appear in a Discussion Section to be published in the December 1972 JOURNAL.

REFERENCES

1. J. N. Bradley and P. D. Greene, *Trans. Faraday Soc.*, **62**, 2069 (1966), **63**, 424 (1967).
2. B. B. Owens and G. R. Argue, *Science*, **157**, 308 (1967).
3. T. Takahashi, O. Yamamoto, and E. Nomura, *Denki Kagaku*, **38**, 360 (1970).
4. T. Takahashi and O. Yamamoto, *This Journal*, **117**, 1 (1970).
5. M. de Rossi, G. Pistoia, and B. Scrosati, *ibid.*, **116**, 1642 (1969).

6. G. R. Argue, I. J. Groce, and B. B. Owens, The Sixth International Power Source Symposium, Brighton, Sussex, Sept. 23-25, 1968.
7. L. E. Topol and B. B. Owens, *J. Phys. Chem.*, **72**, 2106 (1968).
8. T. Takahashi, O. Yamamoto, and S. Ikeda, *Denki Kagaku*, **37**, 843 (1969).
9. C. Tubandt, *Handbuch Exp. Phys.*, **12**, 383 (1932).
10. NBS Circular 539, "Standard X-ray Diffraction Powder Patterns," H. E. Swanson *et al.*, Editors, Vol. 9, p. 49, Nat. Bur. Std., Washington, D.C., (1960).
11. *Ibid.*, Vol. 5, p. 62, (1955).
12. *Ibid.*, Vol. 8, p. 51, (1959).
13. ASTM cards File No. 11-637.
14. T. Takahashi, K. Kuwabara, and O. Yamamoto, *This Journal*, **116**, 357 (1967).
15. T. Takahashi and O. Yamamoto, *Denki Kagaku*, **32**, 610 (1964).
16. T. Takahashi and O. Yamamoto, *ibid.*, **35**, 651 (1967).
17. T. Takahashi, K. Kuwabara, and O. Yamamoto, *ibid.*, **35**, 264 (1967).
18. B. B. Owens and G. R. Argue, *This Journal*, **117**, 899 (1970).
19. B. B. Owens, *ibid.*, **117**, 1536 (1970).

A Very Precise Sectioning Method for Measuring Concentration Profiles in Anodic Tantalum Oxide

J. P. S. Pringle*

Chalk River Nuclear Laboratories, Atomic Energy of Canada Limited, Chalk River, Ontario, Canada

ABSTRACT

Concentration profiles can be measured by removing thin uniform layers from the surface of a solid and determining the amount of the species left after the removal of each layer. The precision of such measurements depends on four factors: the thinness of the layers removed, the accuracy with which their thickness can be measured, the uniformity of the layers, and the accuracy with which the amount of the species present may be determined. The present paper describes a sectioning technique for anodic tantalum oxide, based on slow dissolution of the oxide in HF almost saturated with NH_4F . Layers as thin as 5Å have been repeatedly and reproducibly removed, and the standard error in the total thickness removed is effectively about 3Å for the purpose of profile measurements. Furthermore, the layers are removed with extreme uniformity. In effect, therefore, anodic oxide films on tantalum can be sectioned almost atom layer by atom layer.

The migration of atoms across oxide films is of great importance for the theory of metal oxidation, and of great practical significance in device technology. Study of these migrations requires that the concentration profile of the atomic species be measured before and after the migration event, and methods are therefore needed for measuring its concentration as a function of distance beneath the oxide surface. The obvious way of doing this is to section the oxide; that is, to remove thin uniform layers in succession and determine the amount of the species present in the oxide after the removal of each layer. Such a method is reported here for films of tantalum oxide formed by anodization. Since many of the species were incorporated by ion implantation, it was necessary to study the effect of ion implantation on the sectioning technique, and this is done in a separate paper (1). Other papers describe the application of the technique to the measurement of implantation profiles (2), transport numbers of metal and oxygen (3), and oxygen migration (4).

Comparison of the concentration profiles before and after the migration event yields two kinds of measurement. The relative mobility of the migrating spe-

cies can be determined by measuring the change in its mean position within the oxide; that is, relative to one of the oxide surfaces. In another paper of this series (3), it is shown that it is possible to define a position in the oxide that corresponds to zero migration, and hence to calculate the absolute mobility. Second, by measuring the change, or more specifically the broadening of the concentration profile, it is possible to obtain information on the nature of the migration process itself. Experimentally, the difference between the two kinds of measurement is that the second requires a technique roughly ten times as precise as the first, and no such technique has hitherto been available. The present paper repairs this omission.

In developing a sectioning technique to this degree of precision, several factors assume an importance they do not otherwise have, and it was therefore necessary to consider them in some detail. The precision of a sectioning technique is limited by the following considerations.

(A) The number of experimental measurements must be sufficient to characterize the concentration profile. This means that the thickness of each layer must be considerably less than the width of the profile investigated. A method for removing layers as thin as

* Electrochemical Society Active Member.

Key words: tantalum, anodic oxidation, oxide dissolution, sectioning method, concentration profiles.

5Å is described under Sectioning Anodic Tantalum Oxide.

(B) The accuracy with which the mean thickness of each layer can be measured. The section on Measuring the Average Thickness of Each Layer Removed describes a spectrophotometric method for measuring anodic oxide thickness, from which the thickness of the removed layers can be obtained by difference; the standard error in these measurements is generally less than 3Å.

(C) The uniformity of the layers removed. Concentration profiles obtained by removing layers of irregular thickness are broader than the true profiles. The reanodization method described in the section on Uniformity of the Oxide Layers Removed shows that the effect of the irregularities is negligible for all but the very narrowest profiles.

(D) The accuracy with which the amount of the atomic species present in each layer can be measured. Most of the species used here were radioactive, and so their concentrations could be estimated by standard nuclear techniques; the special technique used to estimate ^{18}O is described in (4).

Once the data has been obtained, it must be analyzed to obtain the parameters of the concentration profile. Mathematical procedures for doing this, involving a computer, are described elsewhere (2-4).

Sectioning Anodic Tantalum Oxide

Preparation of Tantalum Specimens

Tantalum sheets, 99.9% pure, were obtained from Fansteel Metallurgical Corporation, and cut to shape as required. The usual specimen size was rectangular, $3.5 \times 1.0 \text{ cm}^2$, cut from 0.037 cm (0.015 in.) sheet, with a 0.05 cm (0.020 in.) diameter tantalum wire spot welded on one corner to provide electrical contact. The coupons were then treated much as described by Randall, Bernard, and Wilkinson (5): 10 min each in hot Alconox and trichlorethylene to remove grease, followed by 30 min in concentrated HNO_3 to remove any copper left by the welding process. A chemical or electrochemical polish was next; either 10 sec in the usual 5:2:2 mixture of concentrated sulfuric, nitric, and hydrofluoric acids, or 10-20 min at 100 mA/cm² in a 9:1 mixture of concentrated sulfuric and hydrofluoric acids (6). Finally, the specimens were dipped for 2 min in the $\text{HF-NH}_4\text{F}$ reagent described below to remove any film left by the polishing process. It has recently been demonstrated that this procedure is excellent for removing fluoride contaminants (7).

Anodic Oxidation

The tantalum coupons were anodized at constant current using an apparatus designed and built by Walker (8). This consisted of a Northeast Scientific Model RI-234 constant current supply, governed by an electronic control unit similar to that described by Young (6), which shut off the current automatically when the required voltage was reached. The anodizing cell was normally a stainless steel beaker, which also served as cathode, and the electrolyte was 0.1M H_2SO_4 , as used by Young (9) in making the thickness calibration described later. Anodizing voltages were measured with respect to a Beckman General Purpose glass reference electrode, since absolute accuracy was not required, and the temperature of the electrolyte was maintained within 0.2° of 25°C by immersing the beaker in a water bath.

Procedure for Removing Oxide Layers

The anodic tantalum oxide was stripped in concentrated HF almost saturated with NH_4F . By varying the proportion of NH_4F , stripping rates ranging from 25 to 150 Å/min were obtained. One such solution, prepared from 200 mliters 48% HF and 80g NH_4F , stripped the oxide at the rate of 60 Å/min; by adding another 20 mliters 48% HF, the rate was increased to 140

Å/min. The uniformity of the stripping, as determined from the interference color of the remaining oxide, was excellent throughout the range quoted, but for rates faster than 150 Å/min it deteriorated. There was no evidence for any variation in the stripping rate as a function of remaining oxide thickness; the oxide dissolved as though it was completely homogeneous.

Since the time in the stripping solution was being used only as a control on the thickness removed and not as a measure of it, the stripping rate did not have to be known very accurately. No detailed study of the dependence on temperature, acidity, fluoride concentration, and oxide preparation was therefore undertaken. Qualitatively, however, it was observed that the rate increased with increasing HF concentration and with increasing temperature, and that the uniformity improved with increasing fluoride concentration. Freshly prepared solutions dissolved the oxide somewhat more rapidly; after about a week, the rate fell to an almost constant value. Similarly, freshly prepared oxides dissolved faster than aged samples, in agreement with previous observations by Vermilyea (10).

The stripping procedure was as follows. After measuring the thickness of the oxide film by the method described in the next section, the coupon was dipped into the $\text{HF-NH}_4\text{F}$ reagent, with agitation, for the time necessary to remove the desired thickness of oxide. The coupon was then transferred rapidly to distilled water, which quenched the dissolution. After 10 sec in the first water wash and 20 sec in a second, the specimen was transferred to acetone for 15 sec, after which it was dried in a blast of cold air. Remasurement of the oxide film thickness gave, by difference, the amount dissolved by the stripping agent.

Masking of Selected Areas

For certain experiments, it was necessary to mask portions of the specimen and then either thicken (anodize) or thin (strip) the oxide film on the remainder. The masking material had, therefore, to meet several requirements. It had to have a high resistivity to prevent current flow on anodizing, and it had to be inert to the hydrofluoric acid in the stripping reagent. It had to be readily removable, but preferably insoluble in the acetone used for washing. Furthermore, it had to make a good seal with itself so that different areas could be masked in succession. Above all, it had to cover the surface without leaving pinholes.

After various trials, it was found that the vacuum grease Apiezon N was ideal for the purpose. Tests showed that this grease could be used up to at least 200V on anodizing, and for any amount of stripping. Boundaries between masked and unmasked areas were extremely sharp, as demonstrated by the interference colors, and the colors of the masked areas remained in their original state, thus demonstrating the absence of pinholes. Furthermore, Apiezon N made an excellent seal to itself, was apparently insoluble in acetone, yet readily soluble in trichlorethylene.

By masking different areas in succession, therefore, it was possible to form the anodic film to different thicknesses on different parts of the same specimen, and either anodizing or stripping could be used to achieve this. The former was used in the uniformity of stripping tests described in the section on Uniformity of Oxide Layers Removed, while the latter was used for the consistency tests in the section on Measuring the Average Thickness of Each Layer Removed and for the study on oxygen migration described elsewhere (4).

Measuring the Average Thickness of Each Layer Removed

Spectrophotometric Method of Measuring Oxide Thickness

The mean thickness of the layers removed was obtained as the difference between the mean thickness of the oxide film before and after stripping. The prob-

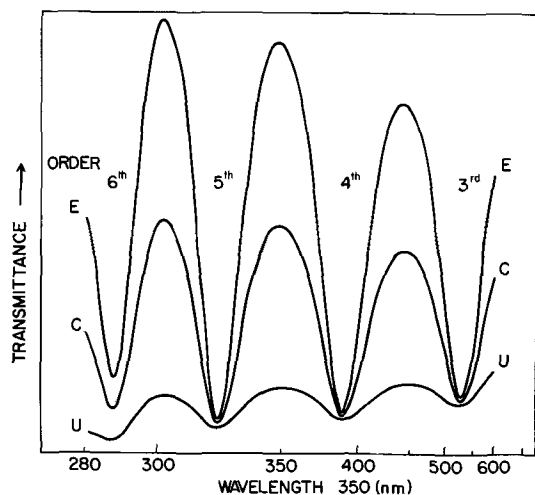


Fig. 1. Interference spectra from three tantalum specimens anodized simultaneously to show the effect of surface roughness. Anodizing conditions: 1 mA/cm² at 25°C to 172V in 0.1M H₂SO₄. Oxide thickness 2630 ± 2Å. U, unpolished; C, chemically polished; E, electrochemically polished.

lem, therefore, was one of measuring the mean oxide thickness with sufficient accuracy, and to do this, a spectrophotometric technique developed by Young (9) was employed. The specular reflectance of an anodized tantalum specimen exhibits minima at certain wavelengths (Fig. 1) due to interference between the light reflected at the oxide surface and that reflected at the oxide/metal interface. By measuring the wavelength, λ , of these minima at known orders, n , of interference, the mean thickness, h , of the oxide films could be calculated.

The conditions for interference is

$$h = \frac{(n - \frac{1}{2}) \cdot \lambda}{2\eta \cdot \cos \phi} - X \quad [1]$$

where η is the refractive index of the oxide, ϕ the angle of refraction, and X accounts for the phase change on reflection at the oxide/metal interface. Both η and X vary significantly with the wavelength of the measuring light, and the variations are not independently known. Young (9) was, however, able to form oxides of known thickness by means of a rather complex procedure involving Faraday's law, capacity, and refractive index, and he then used these oxides to establish the variation of η and X . His interference spectra were measured at an 11° angle of incidence, so that $\cos \phi$ was effectively unity; a polished but unanodized tantalum specimen was placed at the equivalent position in the reference beam of the Cary Model 14 spectrophotometer. Exactly the same procedure was followed here using a Beckman DK2 spectrophotometer, with a light beam of area 0.8 × 0.2 cm² incident on the sample.

As can be seen from Fig. 1, the interference minima are quite broad, and so there is a difficulty in determining the exact minimum wavelength. Excellent results, however, were obtained by means of the following procedure. With the DK2 set at the 0-10% transmittance scale to magnify changes in reflectance, the wavelengths about the minimum were manually scanned. Provided the scanning was done slowly enough, the recorder pen would give a distinct upward kick after passing through the minimum, and the wavelength at which this occurred was recorded. By scanning through the minimum in both directions, two such wavelengths were obtained, and their average was taken as the wavelength of the interference minimum. Justification for this procedure is provided by the symmetry of the interference spectra and by the extreme reproducibility, usually better than 0.2 nm, of the "kick" wavelengths.

Interference minima can be satisfactorily measured from about 280 to about 600 nm. Below 280 nm, the interference is masked by the intrinsic absorption of the oxide, while above 600 nm the intensity of the maxima are reduced so much that the minima become too broad to measure. As Young has pointed out, best results are obtained in the region from 300 to 400 nm, where the minima are most intense. The requirement for at least one minimum between 280 and 600 nm limits the method at small oxide thicknesses; the first-order minimum covers the range from 160Å at 280 nm to 520Å at 600 nm, while the second-order begins at 660Å with a minimum at 280 nm. Thicknesses between 520-660Å cannot therefore be measured, but above 660Å coverage is continuous. Wherever possible, therefore, experiments were performed using thicknesses greater than 660Å.

Surface Roughness and the Nature of the Thickness Measured

The thickness of a uniform film formed on a perfectly smooth flat surface is unambiguously defined, as illustrated in Fig. 2a. Real surfaces, however, are more or less rough, as illustrated schematically in Fig. 2b and 2c, and this complicates the definition. Evans (11) has suggested two measures for the film thickness on rough surfaces. The mean general intercept, MGI, is the average thickness of the film measured perpendicular to the general plane of the surface, and is equal to the film weight divided by the film density and apparent area of the metal surface. The second measure, the mean local intercept, MLI, is the average film thickness measured normal to the local metal surface; it can be calculated in the same way as the MGI, but using the real area in place of the apparent area. The real area equals the apparent area times the roughness factor, which is always greater than unity; the MGI is therefore always larger than the MLI. However, when the roughness pitch is smaller than the MGI, the definition of the MLI is no longer valid, as can be seen from Fig. 2c.

The surface roughness in a metal/anodic oxide system is very considerably influenced by the nature of the anodic oxidation. In a later section of this paper it is shown that the oxide thickness measured perpen-

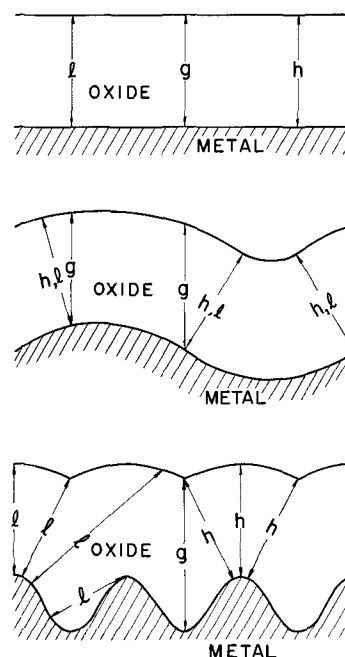


Fig. 2. Effect of surface roughness on the definition of film thickness. (a, Top) perfectly smooth flat oxide; (b, center) surface roughness of large pitch; (c, bottom) surface roughness of small pitch; g thickness averaged for mean general intercept (MGI); l thickness averaged for mean local intercept (MLI); h thickness controlling the kinetics of anodization.

dicular to the local metal surface must be exceedingly uniform at all points on the specimen, and that this must be true throughout the anodization process. It follows immediately that the amount of metal consumed in forming oxide is greater at a convexity in the metal surface than at a concavity, and that the rate of consumption is proportional to the local convexity of the curvature. The formation of an anodic oxide therefore leads to a smoothing of the metal surface, the sharpest asperities being smoothed first. Lewis and Plumb have demonstrated this smoothing experimentally during the anodic oxidation of aluminum (12).

Because of the smoothing, Fig. 2c is not a reasonable picture for an anodic oxide, and so the definition of the MLI is valid. Young (9) has measured the roughness factor for chemically polished tantalum specimens that had been subsequently anodized and found that it was within 3% of unity; the MGI and the MLI are therefore almost identical.

The over-all surface roughness is therefore small, but it might still be sufficient to affect the interference minimum, and hence the measured film thickness. To test this, the following experiment was performed. Three tantalum foils, one electrochemically polished, one chemically polished, and one not polished at all were connected together by their lead wires and anodized simultaneously to 172V at approximately 1 mA/cm². The resulting interference spectra are shown in Fig. 1; the residual roughness obviously does have an effect on the over-all shape of the spectra. Nevertheless, the average of the kick wavelengths was the same for all three specimens, as is demonstrated later.

A simple argument suffices to explain the results of Fig. 1. Parallel light incident at a certain angle on a rough surface is reflected in various directions, depending on the local orientation of the surface at reflection. In the apparatus used here, the phototube subtended an angle of about 2° at the sample, which meant that only those portions of the surface oriented within a certain 1° range would reflect light into it. To a first approximation, the rougher the surface, the smaller the area covered by the favorable orientations, and hence the smaller the intensity of the reflected light recorded by the phototube. On a film-covered surface, therefore, the roughness will have the effect of reducing the intensity of the interference spectrum by approximately the same factor at all wavelengths. When plotted on a scale linear in transmittance, as in Fig. 1, the maxima are depressed much more than the minima, since they are reduced by a greater absolute amount. Increasing roughness therefore tends to compress the interference spectra, as is observed, and this in turn leads to an increased difference between the two kick wavelengths, which was also observed.

The surface roughness of the specimens, then, affects the precision with which the oxide thickness can be measured, since this depends on the difference between the two kick wavelengths, but it does not affect the measurement itself. It but remains to show what kind of thickness is being measured. Obviously, the light beam is sampling those portions of the surface that are favorably oriented, and on which it measures the thickness normal to the local metal surface. The result, an average of all the sampling points, is therefore an excellent approximation to the mean local intercept. Fortunately, this is just the thickness measure that is required, for the kinetics of the anodization are determined by the thickness normal to the local metal surface.

Sources of Error in the Thickness Measurements

Calibration errors.—As recreated here from the data in Young's paper (9), the thickness calibration was found to have certain inconsistencies; thus for oxide thicknesses near 1300Å, the third-order minimum at about 295 nm would regularly give thicknesses some 10Å greater than the second-order at about 430 nm.

These inconsistencies may well be artifacts due to the different apparatus used, but they were unacceptable for the experiments to be performed here. The calibration was therefore revised as follows.

By means of the successive masking and stripping procedure previously described, an electropolished tantalum coupon was prepared with twelve different oxide thicknesses across its surface. The thicknesses ranged from about 2320 to about 1450Å, and all interference minima between 280 and 600 nm were measured at each thickness. The foil was then dipped in the HF-NH₄F reagent to remove approximately 650Å of oxide, so that the oxide thicknesses remaining now ranged from about 1670 to about 800Å. Again all interference minima were measured at each thickness. The cycle was repeated twice more, removing about 300 and 340Å in succession, so that the final thicknesses ranged from about 1030 to about 160Å.

This experiment tested Eq. [1] by providing: (A) Measurements of λ for different known n at the same h . (B) Measurements of λ at known n for constant differences in h .

Statement B rests on the assumption that the stripping proceeds uniformly all over the specimen surface; this is confirmed experimentally in the next section.

The object of the revision was to adjust the parameters η and X in [1], both of which vary with λ , in such a way as to obtain a consistent relationship between λ , n , and h . To do this, the individual oxide thicknesses were first calculated from Young's original calibration using the interference minimum closest to 350 nm. The next step was to calculate the difference in thickness between adjacent oxide areas after each stripping operation, and on the same area after successive strippings, in a manner similar to that shown in Table I. By a series of successive adjustments to the calibration, these differences were equalized as much as possible, thus meeting criterion B above. This largely set the calibration for the favored 300-400 nm region. Adjustments under criterion A were used to refine the calibration and to extend it to other wavelengths. Opportunity was taken to adjust the base of the calibration so that the oxide thicknesses for first-, second-, third-, and fourth-order interference at 350 nm were 270, 1007, 1744, and 2481Å, respectively; these figures are Young's recommended thicknesses (13) corrected for the 1 mA/cm² anodizing current used here (14). A final, minor, adjustment to the calibration ensured that η and X would vary smoothly with λ .

Information needed to recreate the revised calibration is given in Table II, and a test of the new calibration is presented in Table I. The test specimen was prepared and measured in the same way as that used to revise the calibration, but the oxide thicknesses were so chosen that, except for the extreme values in second order, the interference minima could always be measured in the favored 300-400 nm region, and in a single order after each stripping operation.

Table I. Thickness measurements on an oxide film with seven different thicknesses. The film was stripped three times. Thickness differences are in parentheses. Figures are in angstroms using the calibration given in Table II

Area No.	Original, measured in 5th order	After one stripping, measured in 4th order	After two strippings, measured in 3rd order	After three strippings, measured in 2nd order
1	3227 (618)	2609 (631)	1978 (748)	1230 (174)
2	3058 (76)	2441 (74)	1806 (72)	1056 (75)
3	2982 (44)	2367 (46)	1734 (49)	981 (47)
4	2938 (46)	2321 (49)	1685 (42)	934 (43)
5	2892 (97)	2272 (94)	1643 (96)	891 (96)
6	2795 (127)	2178 (123)	1547 (120)	795 (125)
7	2668 (613)	2055 (628)	1427 (757)	670

Table II. Revised third-order film thickness, $h = (3 \cdot 1/2) \cdot \lambda / (2\eta \cdot \cos \phi) - X$, and thickness increment between orders, $\lambda / \eta \cdot \cos \phi$, as a function of interference wavelength. Anodizing conditions. 25°C, 1 mA/cm², 0.1M H₂SO₄.

Wavelength for interference (nm)	Third-order thickness (Å)	Thickness increments between orders (Å)
280	1160	500
290	1268	544
300	1360	581
320	1526	648
340	1674	708
350 (base)	1744	737
360	1812	765
380	1945	819
400	2074	871
420	2199	921
440	2321	971
460	2441	1020
480	2559	1069
500	2675	1118
520	2789	1166
540	2901	1214
560	3012	1262
580	3122	1310
600	3231	1358

Random errors in the measurement of λ .—As the oxide thickness increases, the interference minima become narrower, and so the error in the measurement of λ decreases. At the same time, $dh/d\lambda$ increases so that, as Young (13) has noted, the sensitivity of h to errors in λ remains practically constant. This has been confirmed here, using the difference between the kick wavelengths as a measure of the sharpness of the interference minima. On chemically polished specimens for wavelengths near 350 nm, these differences were about 20, 6.0, 3.5, 2.6, and 2.2 nm for the 1st to 5th orders, respectively, with a range of about 10% on either side of the values quoted; when multiplied by $dh/d\lambda$, the equivalent oxide thicknesses were 24, 24, 24, 25, and 28Å respectively. The standard error in h due to random errors in λ can therefore be represented satisfactorily by a single value, obviously much less than 25Å.

A reasonable estimate of the standard error for chemically polished samples can be obtained from the differences listed in Table I. Analysis shows that the root mean square deviation for all the differences is 2.6Å, from which it may be inferred that the standard error in each thickness measurement is $2.6/\sqrt{2}$ Å or 1.8Å. Reproducibility checks on the amount of oxide removed by the stripping agent in a given time improve this figure; thus in one series of forty-seven measurements, using the same stripping solution on several samples over a period of a few weeks, the mean thickness removed in 7½ sec was 5.3 ± 2.1 Å, so that the standard error in each thickness measurement was $2.1/\sqrt{2}$ or 1.5Å. In early experiments (2), therefore, the standard error was taken as 1.8Å, but this was subsequently replaced by the formula

$$\frac{2}{3} \times \left(\frac{\lambda' - \lambda''}{10} \right) \times \frac{dh}{d\lambda} \text{ Å}$$

where λ' and λ'' are the two kick wavelengths measured in nanometers, and $dh/d\lambda$ is the rate, in angstroms per nanometer, at which the oxide thickness h changes with change in the interference wavelength. Using the error formula given above, the thicknesses on the electrochemically, chemically, and nonpolished specimens of Fig. 1 were found to be 2829.3 ± 1.7 , 2828.0 ± 2.4 , and 2836.6 ± 4.8 Å for the fourth order at about 390 nm, and 2833.7 ± 1.6 , 2830.0 , ± 2.0 , and 2828.5 ± 4.1 Å for the fifth order at about 320 nm; obviously, therefore, the precision decreases with increasing surface roughness. The errors quoted are standard errors, which must be doubled to obtain the 95% confidence limits; it is then apparent that the individual measurements do not differ significantly among themselves.

Absolute accuracy.—The absolute accuracy of the revised calibration depends on the accuracy with which

Young's standard thicknesses are known, and these in turn depend on the refractive index of the oxide. The absolute value of the latter is not known to better than 1% (13), and so this limits the accuracy to an absolute standard error of about 0.5%. Errors of this kind and of this magnitude were not important for the experiments described in subsequent papers; the transport numbers, for example, were calculated as a ratio of thicknesses (3).

Refractive index variations.—Fluctuations in refractive index, both from sample to sample, and within the different parts of the same sample, could have an important bearing on the accuracy of the measurements. A fractional change of 0.001 from the value used in the calibration, from Eq. [1], gives rise to a fractional error of like amount in the measured oxide thickness.

Masing, Orme, and Young (14) have shown that the refractive index of the oxide varies somewhat with the temperature and current density during its formation, and that it is determined largely by conditions in the final stages of anodization. In the course of their work, they measured the refractive index several times under nominally identical conditions; analysis of these results indicates that the scatter of the individual measurements about the mean corresponds to a fractional standard deviation of 0.00144. How much of this scatter was due to real fluctuations in the refractive index is uncertain, since Masing *et al.* do not quote the precision of their measurements; the figure quoted here, therefore, is a maximum value. Errors of this kind are important for measurements involving successive anodizations of the same foil, as in the transport number measurements (3).

The term refractive index has thus far referred to the average refractive index for the whole oxide. Using ³⁵S labeled 0.1M H₂SO₄ as the electrolyte, Randall, Bernard, and Wilkinson (5) were able to show that ³⁵S was incorporated into the outer half of the oxide film at uniform concentration; assuming that the sulfur was incorporated as sulfate, their figures show that the ratio of sulfate to oxide was about 1:100 by weight or 1:600 by frequency. On stripping, therefore, the proportion of the two layers changes, and so, if the refractive indices are different, the average also changes. In the specimen of Table I, the sulfur would be uniformly distributed down to about 1600Å; no discontinuities about 1600Å are apparent in the table. Nor were any differences apparent in the stripping rates for the two layers. Films formed in dilute sulfuric acid thus appear to be effectively homogeneous, despite the variation in their composition: the optical homogeneity of such films has been confirmed ellipsometrically by Dell'Oca and Young (15).

Accuracy of the Oxide Thickness Measurements When Used for the Determination of Concentration Profiles

Random errors in the thickness measurements are important for the best squares fit computer programs described in subsequent papers (2-4). They arise from two sources; the error in measuring the wavelength of minimum interference, and the possibility of fluctuations in the average refractive index of the oxide. The total random standard error in each individual thickness measurement is given by combining these two errors in quadrature; the error is thus

$$\left[\left(\frac{2}{3} \times \frac{(\lambda' - \lambda'')}{10} \times \frac{dh}{d\lambda} \right)^2 + (0.00144 \times h)^2 \right]^{1/2} \text{ angstroms}$$

where the second term represents the maximum possible error due to refractive index fluctuations.

Systematic errors in the thickness measurements can arise from four sources.

Error in refractive index. As already stated, the absolute value of the refractive index is not known to better than 1%.

Surface roughness. As previously discussed, the thicknesses of importance in the anodic Ta₂O₅/Ta system all correspond to the MLI. From the results presented in the next section, it would appear that the oxide is sectioned parallel to the underlying metal surface and so the thickness of films which have been stripped after anodizing can also be described by the MLI.

A further problem arises from the way in which the foreign atoms have been incorporated in the oxide film. If the atoms have been implanted at normal incidence using the mass separator as in (2) and (3), their concentration profiles should properly be measured perpendicular to the general plane of the metal surface; that is, using MGI measurements. The use of MLI measurements leads to the range parameters being underestimated by the roughness factor; the underestimate could, therefore, be as large as 3% (9). The problem does not arise with atoms incorporated from the electrolyte (4), for then the MLI measurements are appropriate.

Calibration errors. In view of the excellent results obtained in Table I, the systematic calibration errors in Table II must be small compared to the random errors, at least over the favored 300-400 nm region.

Spectrophotometric errors. Since the calibration of Table II is relative rather than absolute, the only errors that could be important were changes in the characteristics of Beckmann DK2. Small changes were occasionally observed after the instrument had been serviced, but these were readily compensated with the aid of standard oxide specimens.

To sum up, the absolute standard error in the oxide thickness measured by the spectrophotometric method is about 0.5% due to the uncertainty in the refractive index, while the relative error is the greater of 2Å, due to the random errors in the measurement, or 0.15%, due to fluctuations in the average refractive index.

Uniformity of the Oxide Layers Removed

Anodic oxide films on tantalum must, for the kinetic reasons given below, be extremely uniform in thickness. Any nonuniformity in the stripping, therefore, gives rise to irregularities in the thickness of the oxide film remaining on the metal surface. Such irregularities can be qualitatively characterized by a wavelength, describing their extent on the surface, and by an amplitude, which takes account of the magnitude of their deviation from the mean thickness. The spectrophotometric method of measuring thickness is rather insensitive to such irregularities because, as discussed previously, it takes an average over an area of 0.8×10^{-2} cm².

Uniformity of interference colors on stripping.—Thickness irregularities with a wavelength greater than a millimeter or so are apparent to the eye as a different interference color. Except as noted below, the interference colors observed on thinning the films by dissolution were just as uniform as those obtained on thickening by anodizing. This was confirmed by measurement of the oxide thickness at fourteen different points across a tantalum foil. As anodized, the thickness ranged from 3592.4 to 3587.6Å (380.8-380.4 nm in fifth order) with a mean of 3590Å. The foil was then placed in the stripping solution, with agitation, for ten successive 4-min periods, and was washed and dried in the usual fashion between each strip. Remasurement showed that the remaining oxide thickness ranged from 1913.7 to 1907.4Å (375.2-374.3 nm in third order) with a mean of 1911Å, so that the amount removed was $1679 \pm 2\text{Å}$ (standard error).

The interference colors would not remain uniform on stripping if:

(a) The specimens were held stationary in the stripping bath. Under these circumstances, the specimens would sometimes develop spots of different color.

(b) The same specimen was used repeatedly, as in the range measurements reported in (2). After anodizing and stripping the same foil half a dozen times, small irregularities became noticeable on stripping; these were probably due to the cumulative effects of field crystallization (16).

(c) The specimens were anodized past the breakdown voltage, at which point the character of the oxide film changes (6).

(d) The specimens were subjected to ion implantation at large fluence, as discussed in (1).

(e) The specimens were contaminated with carbonaceous polymers during ion implantation (1).

Flaws in the oxide film.—Flaws of short wavelength and large amplitude arise in the vicinity of impurities in the tantalum surface; for example, carbide particles. Vermilyea (17) has shown that these flaws are thin spots in the oxide film, and that they dissolve unusually rapidly in HF; the effect is, therefore, to punch holes through the film at these points. The area covered by these holes is, however, a very small fraction of the area sampled by the spectrophotometer, and so they are of little importance for the sectioning procedure. Another type of flaw studied by Vermilyea (16) arises from field crystallization, in which the amorphous oxide at certain places on the oxide surface is replaced by a more crystalline oxide. The latter is insoluble in HF (10) and so any radioactive species incorporated in it is retained on stripping; this has the effect of raising the background count when measuring the distribution of radioactive species in the oxide (2). Again, however, the area covered by these flaws is usually negligible, except when the same coupon is used repeatedly (2).

Effect of nonuniformity in the stripping on the measurement of profile widths.—The irregularities described so far are extreme examples arising from unusual local conditions at the tantalum surface. Of greater interest, especially for the experiments on transport number (3) and oxygen migration (4), are the small amplitude irregularities that could exist on the rest of the oxide surface, for these would affect the observed widths of the concentration profiles. Thus, if the concentration profile was normally distributed with a correct standard deviation, σ_c , the observed standard deviation, σ_o , would be given by

$$\sigma_o = (\sigma_c^2 + \sigma_h^2)^{1/2} \quad [2]$$

where σ_h is the root mean square deviation associated with the fluctuations in oxide thickness. If σ_h was a sizable fraction of σ_c , σ_o would differ significantly from σ_c ; the magnitude of σ_h was therefore important. To measure σ_h , the following procedure was used.

Theory of the reanodization method for measuring the uniformity of the anodic film after stripping.—For the purpose of discussion, the equation governing anodic oxidation can be written in the simple form

$$i = D \cdot \exp(BV/h) \quad [3]$$

where i is the current density and V is the potential across the oxide film of thickness h , defined as in Fig. 2b; D and B are constants. Suppose that at a certain point in the oxide the thickness is less than h ; then, from Eq. [3], the current density at that point is greater than i . If the current density is greater than normal, the oxide thickens more rapidly, and so the thickness irregularity tends to disappear as anodizing is continued. Anodic films must, therefore, be extremely uniform in thickness, a conclusion used earlier in this paper. It has also been used to advantage by Davies and co-workers in the sectioning of Al (18) and W (19).

In reanodizing a stripped oxide film at constant current, therefore, the current initially flows through the thinnest parts of the film; that is, Vermilyea's flaws. Since these cover a very small portion of the surface area, the effective current density is very high, and the applied voltage has to increase very rapidly in order to maintain the total current at its constant value. As the deeper irregularities fill up, current starts to flow through the less deep as well, so that the average current density decreases; the rate at which the applied voltage must be increased therefore decreases as well. Eventually, when all the irregularities have been filled in, the anodization proceeds in the normal fashion, with the current uniformly distributed over the whole surface and a relatively small rate of voltage increase. By monitoring the voltage as a function of time therefore, information can be obtained on the irregularities left by the stripping, and hence on the uniformity of the stripping process itself.

In practice, for reasons that become apparent later, reanodization experiments were performed on oxide films of the type illustrated in Fig. 3a. A small area A_1 of a tantalum coupon was covered with an oxide of mean (MLI) thickness h_1 , and the remainder of the surface, area A_2 , was covered with a larger thickness h_2 . Reanodization of such a system at constant current I is governed by the following set of equations.

Anodization kinetics

$$i_1 = D \cdot \exp(BV/h_1); \quad i_2 = D \cdot \exp(BV/h_2) \quad [4a]$$

Current density

$$I = A_1 \cdot i_1 + A_2 \cdot i_2 \quad [4b]$$

Faraday's law

$$It = (A_1 \cdot \Delta h_1 + A_2 \cdot \Delta h_2) \cdot \rho \cdot F/Q \quad [4c]$$

Here i_1 and i_2 are current densities in the areas A_1 and A_2 , Δh_1 and Δh_2 the resulting increases in oxide thickness after an anodizing time t , ρ the density of the oxide, F the Faraday, and Q the equivalent weight of Ta_2O_5 .

Initially, since $h_1 < h_2$, $i_1 \gg i_2$ and so the current effectively flows through the area A_1 only. Under these conditions i_1 is constant and equal to I/A_1 ; by [4a] and [4c] V and h_1 increase linearly with time at a rate proportional to I/A_1 . As h_1 approaches the thickness h_2 , however, i_2 becomes significant and hence by [4b], i_1 must decrease; h_1 and V continue to increase but at a slower rate than before, while h_2 starts to increase. At the limit, h_1 catches up to h_2 so that $i_1 = i_2 = I/(A_1 + A_2)$; V , h_1 , and h_2 again increase linearly, but at a rate proportional to $I/(A_1 + A_2)$. The variations of V , h_1 , and h_2 with time

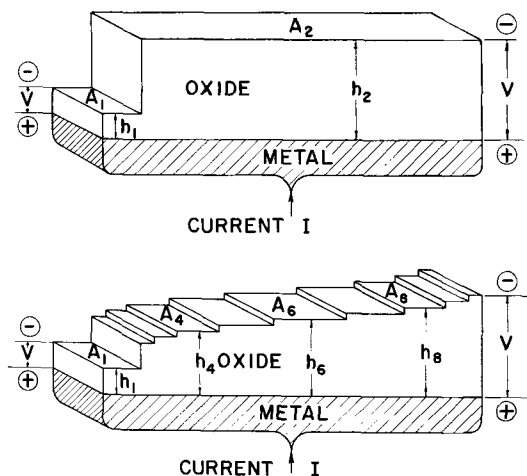


Fig. 3. Types of oxide film used in the reanodization experiments to measure the uniformity of stripping. (Type a, top) oxide of uniform thickness, (type b, bottom) simulation as per Fig. 5, to an oxide with random thickness fluctuations.

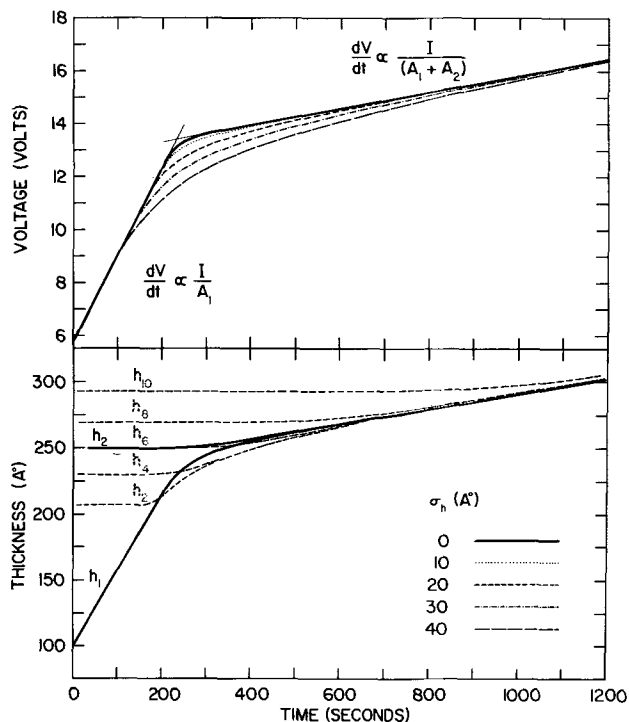


Fig. 4. Computed voltage-time and thickness-time plots for oxide films of the types depicted in Fig. 3. The heavy solid lines refer to the oxide of uniform thickness, type a of Fig. 3, and the lighter broken lines to the oxide with the random thickness fluctuations, type b of Fig. 3. Input data: $h_1 = 100\text{Å}$, $h_2(h_8) = 250\text{Å}$, initial current density $i_1 = 0.1 \text{ mA/cm}^2$, final current density $i_2 = 0.01 \text{ mA/cm}^2$, area $A_2 = 9 \times \text{area } A_1$.

are illustrated by the solid lines in Fig. 4, from which it may be seen that the voltage time plot consists of two straight lines connected by a curved knee.

To compute the exact shape of the knee it is necessary to solve Eq. [4a-c] with h_1 nearly equal to h_2 . This was done by means of a Runge-Kutta procedure (20), in which the variables i_1 , i_2 , h_1 , h_2 , and V were replaced by their time differentials. By integrating over successive short periods of time, values for the several variables could be computed at a series of different times. The integrations were performed on a CDC G-20 computer, with the simple form of the anodizing Eq. [3] replaced by the more precise quadratic form given by Young (12).

To find out how random fluctuations in the oxide thickness would affect the shape of the voltage-time curve, the following computations were performed. The oxide thickness on A_2 was assumed to be normally distributed about its mean h_2 with a standard deviation, σ_h , as illustrated in the top part of Fig. 5. Random fluctuations like this are equivalent to the smooth error function complement shown in the center of the figure, but the effect of this on the voltage-time plot cannot be computed by the Runge-Kutta procedure. Instead, it must be replaced by the equivalent histogram shown in the bottom of Fig. 5, and this gives an oxide film of the type shown in Fig. 3b. Time differentials for the current density and thickness of each element were derived as before, and the Runge-Kutta procedure applied. The resulting voltage-time and thickness-time plots are given in Fig. 4 for various values of σ_h .

Elimination of voltage transients from the experimental reanodization.—When an oxide film of area A and uniform thickness h is reanodized at constant current I , the current density changes almost instantly from zero to I/A . Changes in current density are associated with voltage transients (21), whose magnitude and sign are roughly proportional to the rate of change in the current density, di/dt . As the current

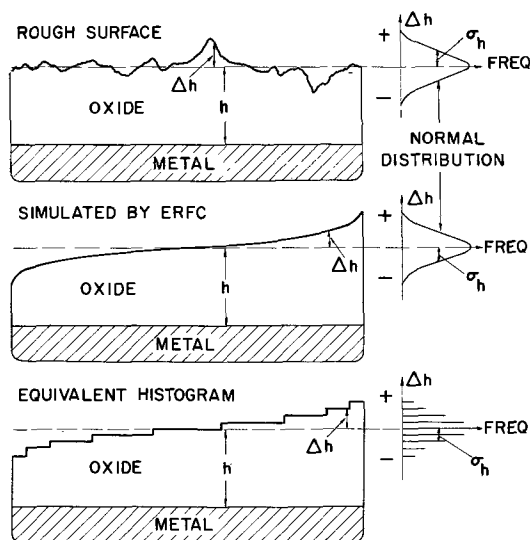


Fig. 5. Simulation of an oxide with random thickness fluctuations for the purpose of computing voltage-time plots by the Runge-Kutta procedure.

density changes from zero to I/A , di/dt is very large; within the same period, therefore the voltage V overshoots the steady-state value predicted from Eq. [3] and the values of $i(=I/A)$ and h . Adequate mathematical description of these transients is lacking, and so a satisfactory analysis of the voltage-time plots depends on their elimination.

Obviously, di/dt must be reduced as much as possible, and it was for this reason that oxide films of the type shown in Fig. 3 were used. When such an oxide is reanodized, the current density changes only as h_1 catches up to h_2 , and this takes a relatively long time. The voltage transients therefore are relatively small, and only occur about the knee position. Furthermore, the current density, i_1 , over the smaller area A_1 is decreasing and would normally give rise to a negative transient, or reduction in the recorded voltage; the current, i_2 , over the larger area, A_2 , is increasing, and so would normally give rise to a positive transient. Since the applied voltage must be the same all over the coupon surface, the outcome of the competition between the two effects is difficult to predict; experiments such as those illustrated in Fig. 6 show that there is in fact a net positive transient.

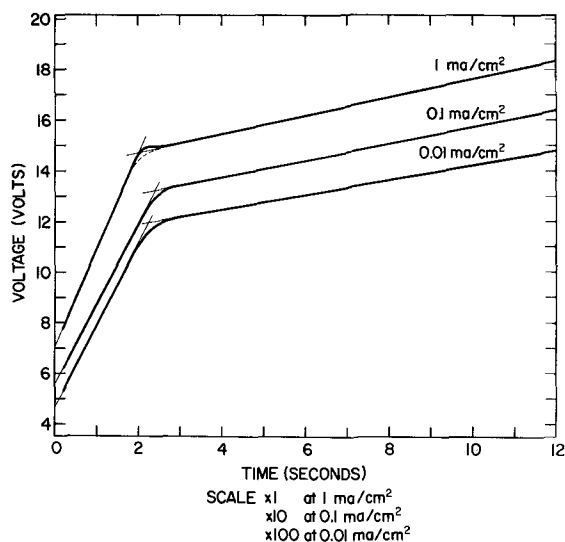


Fig. 6. Elimination of voltage transients, using oxide films of the type shown in Fig. 3a. Initial anodizations to 5.5V at 1 mA/cm², and 16V at 10 mA/cm²; reanodizations at current densities indicated. Conditions: 25°C, 0.1M H₂SO₄.

The general features of these transients are quite well known (21, 22) and so it was a relatively simple matter to minimize their effect still further. By using the lowest possible current density, 0.01 mA/cm², the time scale for the reanodization was much extended, and di/dt correspondingly reduced; this by itself effectively eliminated the transients, as shown in Fig. 6. To minimize annealing (22), initial anodizations were performed at 10 mA/cm², and the reanodizations were performed as soon as possible thereafter. The low current density on reanodization made it desirable to use thin oxides, so that the experiment would not be unduly prolonged; this was fortunate, because the sensitivity of the voltage-time relation to thickness irregularities is greatest when the irregularities are a large fraction of the mean thickness. The application of rather extreme currents, 10 and 0.01 mA/cm², to relatively thin films, 250Å, presents no problems in the analysis, for, as Young himself has shown (13), the quadratic equation gives a perfectly adequate description of the kinetics under these conditions.

Experimental reanodizations.—All anodizations and reanodizations were performed in 0.1M H₂SO₄ at 25°C, using the constant current circuit (8).

Electropolished tantalum coupons were anodized in such a way that one tenth of their total area was covered with thin oxide. The thickness h_1 was usually about 90Å, equivalent to 5.3V at 0.1 mA/cm², while h_2 was normally fixed at 200-250Å, equivalent to 11-14V at 0.01 mA/cm². The voltage was recorded using a Non-Linear Systems V91P digital voltmeter, equipped with a Hewlett-Packard Model 155 data printer. The rate of printout was a little less than 5/sec, the exact rate for each anodization being calculated by dividing the anodizing time into the total number of prints recorded. Four significant figures were obtained for each voltage printed; least squares fit analyses on the straight line portion of the voltage plots showed that the deviations were consistent with the rounding errors expected. That is, the error in 10-20V region was of the order of 0.005V.

The results illustrated in Fig. 6 were obtained to make sure that voltage transients had been eliminated by the procedure used. Suitable oxide films were prepared by anodizing the whole of an electrochemically polished tantalum coupon to 5.5V at 1 mA/cm², masking one tenth of the area with Apiezon N, and then anodizing the rest to 16V at 10 mA/cm². A voltage transient is clearly visible in the sample reanodized at 1 mA/cm², but not in those reanodized at 0.1 mA/cm² or 0.01 mA/cm². By reanodizing at 0.01 mA/cm², therefore, voltage transients were effectively absent from the system.

Analysis of the voltage-time data required a knowledge of A_1 , A_2 , h_1 , and h_2 , all of which could be calculated from the straight line sections of the $V-t$ plot. From the slopes, dV/dt , of these sections, the current densities I/A_1 and $I/(A_1 + A_2)$ could be computed, using Eq. [4a-c]: since the total current, I , was known, A_1 and A_2 could be calculated. With the current densities known, the relation between oxide thickness and applied voltage (the angstrom/volt values) could be calculated from Eq. [4a-c], as could the rates, dh/dt , at which the oxide thickened. The thickness, h_1 , was then calculated by multiplying the voltage at zero time, extrapolated from the initial straight line portion of the plot, by the appropriate angstrom/volt value. To obtain h_2 , the two equations for dh/dt were solved simultaneously.

Given these values of A_1 , A_2 , h_1 , and h_2 a voltage-time plot could be computed, as in Fig. 4, to reproduce the straight line portions of the experimental curve exactly. To reproduce the shape around the knee, σ_h had to be adjusted to the best value, and this was done by means of a least squares procedure. A suitable value of σ_h was used to compute voltages, $V_{calc}(J)$, for a series $J = 1, 2, \dots, N$ of time t (J) about the knee. The quantity

$$\sum_{j=1}^N [(V_{\text{obs}}(j) - V_{\text{calc}}(j))/0.005]^2$$

was then computed, where $V_{\text{obs}}(j)$ were the observed voltages at the corresponding times, and 0.005V the standard error in each voltage measured. The best value for σ_h was then obtained by varying σ_h in units of 1Å until this sum was minimized. As a test, the 0.1 and 0.01 mA/cm² reanodizations in Fig. 6 were analyzed, and σ_h found to be 0 and 6Å, respectively. The expected value of σ_h was of course 0Å, since these specimens had been anodized but not stripped. In view of the insensitivity of the knee shape to very small values of σ_h , as demonstrated in Fig. 4, the agreement can be considered acceptable.

The uniformity of the stripping was tested as follows. Two tantalum coupons were anodized at 10 mA/cm², one to 61.45V (934Å) and the other to 121.4V (1857Å). Nine-tenths of each coupon was then masked with Apiezon N, and approximately 200Å stripped off the remainder, leaving thicknesses of 721 and 1633Å, respectively. The Apiezon was then removed, and both foils stripped in the NH₄F-HF reagent until the mean oxide thickness, h_2 , on the larger area was 337 and 296Å, respectively. Accordingly, 597 and 1561Å of oxide had been stripped away, leaving a thickness, h_1 , of 124 and 72Å, respectively, on the smaller area. Reanodization of these two specimens at 0.01 mA/cm² gave the voltage-time plots shown in Fig. 7, which are almost identical to the plots in Fig. 6. The great bulk of the oxide is therefore almost as uniform after stripping as it was after anodizing.

The voltage-time plots in Fig. 7 do differ from those in Fig. 6, however, in that the sections on either side of the knee are not quite straight. Above the knee, the slope decreases very slightly with time, but the resulting curvature is so small that it is not apparent in Fig. 7. Below the knee, however, the curvature is much more pronounced and is continuous. This indicates that a small fraction of the oxide film has been stripped to thicknesses between h_1 and h_2 , which is precisely what would be expected from the behavior of Vermilyea's flaws (17) discussed previously. The curvature does, however, affect the calculations for h_1 , h_2 , A_1 , and A_2 , since these assume that the voltage-time plot is linear on either side of the knee. Tangents to either end of the curved portion have been drawn in Fig. 7 and give some idea of the uncertainty; obviously, σ_h depends on which is chosen. Using the tangents nearer the knee, represented by the solid lines in Fig. 7, σ_h

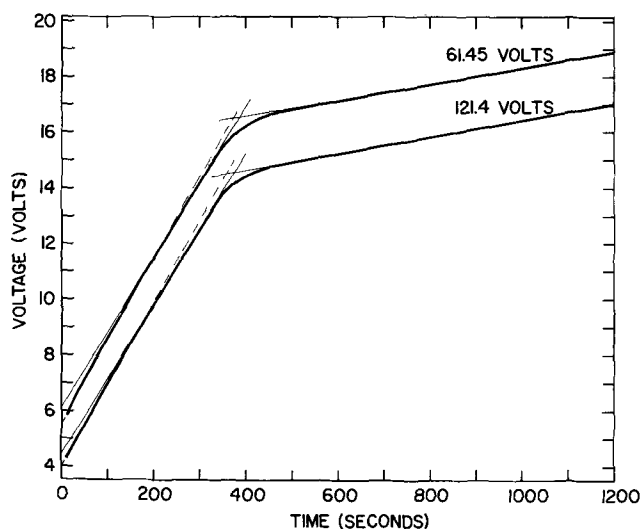


Fig. 7. Reanodization of stripped oxide films. Initial anodization at 10 mA/cm² to voltages indicated, followed by stripping in HF-NH₄F reagent; reanodizations at 0.01 mA/cm². Conditions: 25°C, 0.1M H₂SO₄.

was found to be 9Å for the sample anodized originally to 61.45V, and 8Å for that anodized to 121.4V.

The thickness irregularities left after stripping are therefore not normally distributed, as the difference between Fig. 4 and Fig. 7 makes clear, but they must be small. The question then arises as to whether they would be significant for the measurement of concentration profiles. Assuming that $\sigma_h = 10\text{Å}$, and that the correct standard deviation of a normally distributed profile, σ_c , is 30Å, it follows from Eq. [2] that the observed deviation would be $(30^2 + 10^2)^{1/2}$ or 32Å. Since the error in the measurement is itself of the order of 2Å (2, 3), the difference between correct and observed is definitely not significant. Observed deviations less than 30Å were obtained for low energy implantations (2), but the amount of stripping required to obtain these was so small that σ_h would probably be less than 10Å. The conclusion is, therefore, that irregularities in the stripping have no effect on the measurements of concentration profile.

Possible explanation for the uniformity of the stripping.—As is well known, most etchants act on surfaces in an irregular manner, dissolving more material from one area than another. This is particularly true of crystalline solids, where the rate of attack may vary with the crystal plane exposed (23); it can also vary substantially near imperfections such as dislocations or grain boundaries. At first sight, therefore, the extreme uniformity of the present sectioning technique seems surprising, but anodic tantalum oxide is unusual in that it is apparently both amorphous (10) and highly homogeneous. The anisotropy arising from crystal orientation is thereby eliminated, as are effects due to lattice imperfections; the small nonuniformity that remains has been attributed to impurities in the tantalum surface. The influence of the radiation damage accompanying ion implantation is discussed in another paper (1).

Nevertheless, it might seem reasonable to consider the dissolution of an amorphous solid statistically. If an average of n atomic layers be removed, the fluctuation from place to place on the surface should be proportional to a standard deviation of \sqrt{n} layers. The deviations actually observed are, however, much less than this, and so some leveling process must be at work. Presumably this is related to the local curvature of the oxide surface in the same way as the smoothing action of anodic oxidation is related to the local curvature of the metal surface; that is, areas with convex curvature dissolve faster than those with concave curvature.

Conclusions

The precision of the sectioning technique is limited by the following factors.

(a) Oxide layers as thin as 5Å have been reproducibly removed. Since the minimum FWHM of the concentration profiles reported in subsequent papers (2-4) is about 10Å, the layers removed can always be made thinner than the width of the profile being investigated.

(b) The mean thickness of the oxide remaining after the removal of each layer can be measured with a relative standard error of about 2Å or 0.15% of the thickness, whichever is greater; the absolute error is about 0.5%, due to the uncertainty in the absolute value of the refractive index. The relative standard error in the mean thickness removed, which is the difference between two oxide thickness measurements, is therefore $2\sqrt{2}\text{Å}$ or about 3Å.

(c) The uniformity of the layers removed is effectively perfect as far as the measurement of concentration profiles is concerned.

At a density of 8.03 g/cm³ (24), a molecule of Ta₂O₅ occupies a cube of side 4.5Å, so that "one atom layer" would correspond to a thickness about half this. In the present experiments, therefore, anodic tantalum oxide has been sectioned two atom layers at a time; by

reducing the stripping time still further, it would be possible to section atom layer by atom layer.

Acknowledgments

It is a pleasure to acknowledge the assistance of D. Phillips, who performed many of the experimental measurements. A stimulating conversation with J. A. Davies answered the problem of measuring the uniformity of stripping, and Mrs. F. E. Lane kindly supplied the Runge-Kutta programs for the G-20 computer. B. Cox, T. A. Eastwood, and D. Marsden read the manuscript and made valuable suggestions for improvement.

Manuscript submitted July 30, 1971; revised manuscript received Dec. 2, 1971.

Any discussion of this paper will appear in a Discussion Section to be published in the December 1972 JOURNAL.

REFERENCES

1. J. P. S. Pringle, *This Journal*, To be submitted.
2. J. P. S. Pringle, *ibid.*, To be submitted.
3. J. P. S. Pringle, *ibid.*, To be submitted.
4. J. P. S. Pringle, *ibid.*, To be submitted.
5. J. J. Randall, Jr., W. J. Bernard, and R. R. Wilkinson, *Electrochim. Acta*, **10**, 183 (1965).
6. L. Young, "Anodic Oxide Films," Academic Press, London and New York (1961).
7. B. Maurel, D. Dieumegard, and G. Amsel, Paper 88, Extended Abstracts, Cleveland Meeting of the Society, Oct. 3-8, 1971.
8. D. Walker, Atomic Energy of Canada Ltd. Report AECL-2502, Chalk River, 1965.
9. L. Young, *Proc. Roy. Soc., Ser. A.*, **244**, 41 (1958).
10. D. A. Vermilyea, *This Journal*, **104**, 485 (1957).
11. U. R. Evans, "The Corrosion and Oxidation of Metals," Arnold, London (1960).
12. J. E. Lewis and R. C. Plumb, *Intern. J. Appl. Radiation Isotopes*, **1**, 33 (1956).
13. L. Young, *Proc. Roy. Soc., Ser. A.*, **258**, 496 (1960).
14. L. Masing, J. E. Orme, and L. Young, *This Journal*, **108**, 428 (1961).
15. C. J. Dell'Oca and L. Young, *ibid.*, **117**, 1545 (1970).
16. D. A. Vermilyea, *ibid.*, **102**, 207 (1955).
17. D. A. Vermilyea, *ibid.*, **110**, 250 (1963).
18. J. A. Davies, J. Friesen, and J. D. McIntyre, *Can. J. Chem.*, **38**, 1526 (1960).
19. M. McCargo, J. A. Davies, and F. Brown, *ibid.*, **41**, 1231 (1963).
20. E. A. Okazaki and J. K. Fowler, Atomic Energy of Canada Ltd. Report AECL-1744, Chalk River, 1963.
21. J. F. Dewald, *J. Phys. Chem. Solids*, **2**, 55 (1957).
22. D. A. Vermilyea, *This Journal*, **104**, 427 (1957).
23. J. W. Faust, Jr., in "Compound Semiconductors," Vol. I. p. 445, Reinhold Publishing Corp., New York (1962).
24. A. J. Schrijner and A. Middelhoek, *This Journal*, **111**, 1167 (1964).

Internal Stresses in Multilayered Structures

P. B. Ghate and Lou H. Hall*

Semiconductor Research and Development Laboratory, Texas Instruments Incorporated, Dallas, Texas 75222

ABSTRACT

Internal stresses in vacuum-deposited aluminum films are measured by x-ray diffraction techniques and by the Newton's rings method. The effects of annealing on the internal stresses are also determined. Aluminum films deposited at room temperature (25°C) are found to have an average stress of $(0 \pm 0.5) \times 10^9$ dynes/cm² prior to heat-treatment. Aluminum films deposited at 200°C are in tension with a stress of 2.6×10^9 dynes/cm². Films annealed at 450°C exhibit tensile stress at the same value as the films deposited at 200°C. This stress value is equivalent to a ΔT of 125°C if the stress is due to thermal considerations only. The Newton's rings method is extended to measure the changes in stresses after the processing steps required in a multilayered structure of Al/silane SiO₂/Al. The composite films are found to be in tension and the silane SiO₂ is found to have a high tensile intrinsic stress.

The desire for increased packing density in integrated circuits has resulted in the advent of medium scale and large scale integration. This technology requires a highly reliable interconnection system. Depending on the complexity of the circuits, a two or three level interconnection system is required. Some of the slice processing difficulties encountered in the development of multilevel interconnections are a consequence of the internal stresses in the multilayered composite. The use of alternate layers of aluminum/silicon dioxide/aluminum films is one of the methods used for achieving multilevel interconnections. The present investigation was undertaken to understand the nature of internal stresses in aluminum, silane silicon dioxide films, and a multilayered composite of Al/SiO₂/Al two-level structures.

The existence of internal stresses in evaporated films deposited on a substrate is well known (1, 2). Stresses in films may be calculated from a determination of either the curvature of the substrate or of the lattice distortion in the substrate or in the film. Several authors have studied stresses in thin films of aluminum

(3, 4). Others (5-7) have also reported on stresses in films. In particular, Sunami *et al.* (8) and Lathlaen and Diehl (9) have reported studies on the stress in CVD silane silicon dioxide films.

The present investigation uses x-ray diffraction techniques and the Newton's rings method to determine stress in individual films and in multilayered composite films. The Newton's rings method is particularly applicable to following the changes in stress in slice form that is a consequence of sequential integrated circuit processing.

Experimental Procedures

Internal stresses in vacuum-deposited aluminum films on oxidized silicon substrates have been determined by x-ray diffraction techniques and by the Newton's rings method. Two types of aluminum films, one deposited on cold substrates Al-I, and another film deposited on hot substrates (200°C) Al-II, have been used in these experiments. The x-ray diffraction technique is employed to determine the deviations in the interplanar spacings from the known values of the strain-free material. Subsequently, stress is calculated from the lattice strain and the appropriate modulus of elasticity. In the Newton's rings method, the curva-

* Electrochemical Society Active Member.

Key words: multilevel technology, internal stress, interconnections, thin films.

ture of the substrate on the film side is measured and the stress in the metal film is calculated from the curvature, thickness, and the appropriate modulus of elasticity of the substrate. The values of the stresses determined from the two methods have been compared. Stress changes in aluminum films due to a 450°C anneal in N₂ for 30 min have also been determined. The Newton's rings method has been extended to determine the stresses in the various layers of the multilayered composite Al/silane SiO₂/Al. The Newton's rings patterns were obtained at the following stages of fabrication: (a) Al, (b) Al/silane SiO₂, (c) Al/silane SiO₂/Al, and (d) after 450°C anneal in N₂ for 30 min. The effects of processing parameters on the internal stresses are also examined.

X-ray diffraction technique for stress measurement.

—Stresses in films can be determined by measuring the changes in lattice parameters. According to Bragg's law

$$2d_{hkl} \sin \theta_{hkl} = \lambda \quad [1]$$

where d_{hkl} = interplanar spacing for the set of (hkl) planes, θ_{hkl} = Bragg angle for the hkl reflection, and λ = wavelength of X-radiation (CuK α).

If the Al film is free of stress, then the interplanar spacing for the set of (hkl) planes corresponds to the known interplanar spacing in strain-free crystallites (reference: ASTM Data). Let d_{hkl}^0 denote the interplanar spacing in strain-free crystallites. If the Al film were under tension, then the interplanar spacing d_{hkl}^τ (superscript τ denotes tension) parallel to the substrate would be smaller than d_{hkl}^0 . Thus

$$d_{hkl}^\tau < d_{hkl}^0 \quad \text{and hence} \quad \theta_{hkl}^\tau > \theta_{hkl}^0 \quad [2]$$

Similar arguments can be extended to Al films under compression

$$d_{hkl}^c > d_{hkl}^0 \quad \text{and hence} \quad \theta_{hkl}^c < \theta_{hkl}^0 \quad [3]$$

If the deviation in the interplanar spacing d is assumed to be due to the mean isotropic strain of crystal in the film plane, then the average stress in the film is given by

$$\sigma_f = \frac{E_f}{2\nu_f} \cdot \epsilon \quad [4]$$

where ϵ = strain = $(d_0 - d)/d_0$, $d_0 = 2.3380 \text{ \AA}$ (ASTM value of d_{111}^0 for aluminum), E_f = Young's modulus of aluminum = 7×10^{11} dynes/cm², and ν_f = Poisson's ratio for aluminum = 0.33.

Newton's rings method for stress measurements.—

The average film stress can be calculated from the relationship between the stress and strain of circular substrate. It is assumed that the film strains the substrate which bends until equilibrium is reached. The adhesion of the film to the substrate is assumed to be adequately strong to suppress slippage. Since the average stress in the film is calculated from the strains in the substrate, the elastic constants and thickness of the substrate are taken into account. The following equation allows calculation of the average film stress (2)

$$\sigma_f = \frac{E_s}{6(1-\nu_s)} \frac{d_s^2}{t_f} \cdot \frac{1}{R_s} \quad [5]$$

where σ_f = average stress in the film, t_f = film thickness, E_s = Young's modulus of the substrate, ν_s = Poisson's ratio of the substrate, d_s = thickness of the substrate, and R_s = radius of curvature of the substrate.

The radius of curvature of the substrate can be determined by using the Newton's rings interference technique. The film side of the substrate is placed against an optically flat surface. The radius of curvature R_s of the substrate is determined from the radii of the Newton's rings and wavelength of light (10)

$$R_s = \frac{r_{m+p}^2 - r_m^2}{P\lambda} \quad [6]$$

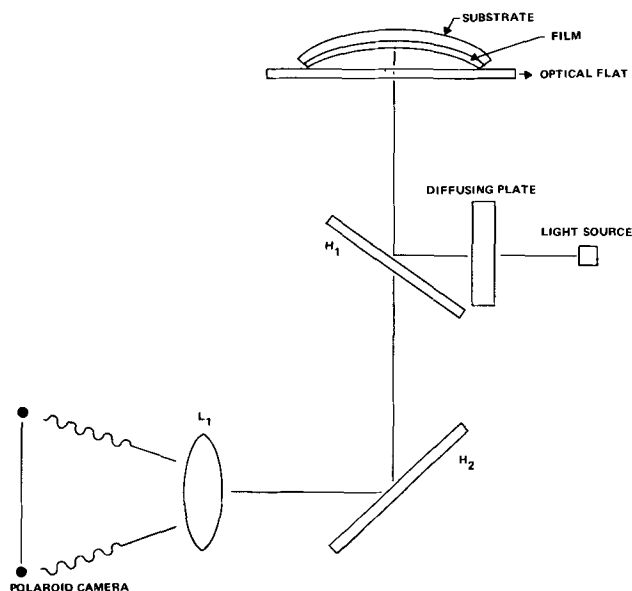


Fig. 1. Schematic of experimental setup (not to scale). L₁ lens, H₁ and H₂ are partially silvered optical flats, light source is a neon laser ($\lambda = 6328 \text{ \AA}$).

where r_m = radius of the m 'th dark ring, r_{m+p} = radius of the $(m+p)$ 'th dark ring, λ = wavelength of the light, and R_s = radius of curvature of the substrate.

A schematic of the experimental setup used in our experiments is shown in Fig. 1. A He-Ne laser is used to provide the monochromatic light of wavelength $\lambda = 6328 \text{ \AA}$. The Newton's rings are photographed with a polaroid camera.

It was essential to screen the starting oxidized silicon slices for this experiment. A number of slices, whose thicknesses were close to $300 \pm 10 \text{ \mu m}$, were examined to check if the slices produced acceptable Newton's rings pattern. Only those slices which produced almost circular fringe patterns were considered acceptable and were used in further experiments. In order to examine the behavior of aluminum films on plane silicon slices, i.e., on slices not oxidized, a number of bare silicon slices were also chosen for further study.

The following arbitrary guidelines were used in processing the data:

1. If the center of the ring was lying closer to the edge rather than the center of the slice, then the data were discarded.
2. If the rings were circular or close to being elliptic, then the Newton's rings data were considered acceptable.
3. The average radius of curvature of the substrate (R_s) was determined from the radii of the 4th and 8th rings along the major and minor axes of the elliptic fringe pattern. The following expression was used

$$\frac{1}{R_s} = 2\lambda \left[\frac{1}{(r_8^2 - r_4^2)_x} + \frac{1}{(r_8^2 - r_4^2)_y} \right] \quad [7]$$

where λ = wavelength of the light = 6328 \AA , and x and y denote the directions along the major and minor axes.

Results and Discussion

The aluminum films, Al-I and Al-II, thicknesses were close to 8000 \AA . The metalized slice was mounted on the goniometer of a Norelco Diffractometer unit, and the x-ray diffraction pattern corresponding to the (111) reflection was scanned using the CuK α radiation ($\lambda = 1.5405 \text{ \AA}$). The (111) reflection from the silicon substrate served as an internal standard. The Bragg angle θ_{111} for Al was obtained from the position of the (111) diffraction peak. The diffraction traces of Al-I

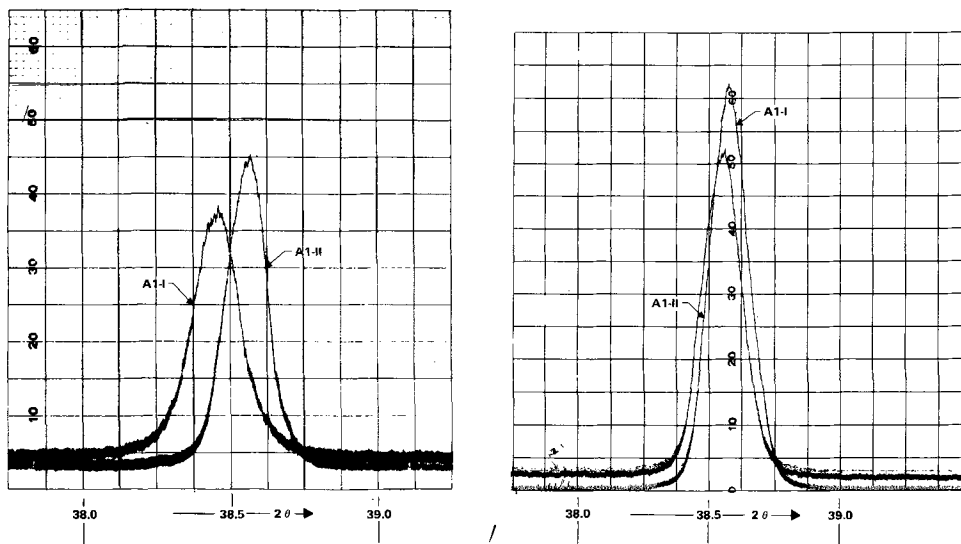


Fig. 2. X-ray diffraction traces of Al-I and Al-II films using $\text{CuK}\alpha$ radiation. Intensity scales have been appropriately chosen to permit an easy comparison of the peak positions. a (Left), unannealed films; b (right) annealed at 450°C for 30 min in N_2 .

and Al-II are shown in Fig. 2. The scan speed was $(1/8)$ degree/minute and the chart speed was 0.5 in./min. The intensities of these peaks were so chosen that the positions of the peaks could be easily compared. The metalized slices were annealed in N_2 ambient for 30 min at 450°C . The positions of the (111) diffraction peaks of the annealed Al-I and the Al-II films were determined. The diffraction traces corresponding to the annealed films are also shown in Fig. 2. Similar diffraction traces were examined for other samples. The peak position for Al-I films before anneal was always reproducible with $\pm 0.02^\circ$. The peak position of Al-II films varied by $\pm 0.06^\circ$. For a given sample, the peak position was reproducible within $\pm 0.01^\circ$. After a 450°C anneal, the peak position of the (111) reflection for Al-I always shifted toward higher angles. The Bragg angles for Al-I and Al-II were almost equal. For some films, the Bragg angle θ_{111} for Al-I was greater than that for Al-II. In the last column of Table I, the average values of the stresses are summarized. These results suggest that the internal stresses in Al-I and Al-II films are almost equal after a 450°C anneal.

The average stresses in Al-I films are found to be $(0 \pm 0.5) \times 10^9$ dynes/cm² prior to any heat-treatment. Since these films are deposited at room temperature and the stress measurements are made at room temperature, the internal stresses in Al-I films can be considered as intrinsic. It appears that the intrinsic stresses in room temperature deposited Al films are small and are close to zero within the accuracy of our measurements. The stresses in Al-II films deposited at 200°C , are tensile and the average stress = 2.6×10^9 dynes/cm².

The thermal stress component can be calculated from the known values of the coefficients of thermal expansion and moduli of elasticity for the substrate and the film (1, 2). The film is considered to be bonded perfectly to the substrate and assumed to be in zero stress at the deposition temperature. The constraints imposed by the bonding of the film to the substrate give the following strain value at the measurement temperature if the substrate temperature is constant during film deposition

Table I. Stresses in Al-I and Al-II films before and after a 450°C anneal as determined by x-ray diffraction using $\text{CuK}\alpha$ radiation

Sample	Status of film	Average stress, $\bar{\sigma}$ (dynes/cm ²)
Al-I	Before anneal	$\pm 0.5 \times 10^9$
Al-II	Before anneal	2.6×10^9
Al-I	After anneal	2.6×10^9
Al-II	After anneal	2.6×10^9

$$\epsilon = (\alpha_f - \alpha_s) (T_2 - T_1) \quad [8]$$

$$= \Delta\alpha \cdot \Delta T$$

where ϵ = strain in film, α_f = coefficient of thermal expansion of film ($= 23 \times 10^{-6}/^\circ\text{C}$ for aluminum), α_s = coefficient of thermal expansion of substrate ($= 3 \times 10^{-6}/^\circ\text{C}$ for silicon), T_2 = film deposition temperature, and T_1 = temperature at which stress is measured.

The stresses are obtained by multiplying the strain value with the appropriate elastic modulus. The sign agrees with the usual convention: it is positive for tension, and negative for compression.

If it is assumed that the stress in Al-II films can be accounted for by thermal stress alone, then ΔT can be estimated from Eq. [4] and [8]. After substitution of the appropriate values, in Eq. [8] one finds that

$$\Delta T = \frac{2\rho_f}{E_f} \cdot \frac{\sigma_f}{\Delta\alpha} \quad [9]$$

$$\Delta T \approx 125^\circ\text{C}$$

Since $T_1 = 25^\circ\text{C}$ (room temperature at which stress is measured), the apparent $T_2 \approx 150^\circ\text{C}$. Even though this aluminum film was deposited at 200°C , the analysis of data suggests that the film has retained a thermal stress corresponding to a deposition temperature of 150°C . It appears that, as the substrates are cooled from the deposition temperature of 200°C down to room temperature, the film remains stress-free down to 150°C , and after that the thermal stress is locked in. This is ascribed to the fact that the recrystallization temperature is in the range of 150°C , and in addition the free surface of the film permits stress relief by mass migration above 150°C (4).

Figure 3 shows a Newton's rings pattern corresponding to the same slice (e.g., Al-I film on oxidized silicon substrate) before and after a 30-min anneal at 450°C in N_2 ambient. The magnification of the photograph is determined from the known value of the diameter of the slice (diameter of slice = 1.5 in.). The radii of the Newton's rings as determined from the photograph are used to calculate the radius of curvature of the substrate.

The data in Table II indicate that the radius of curvature of Al-I slice decreases after a 450°C anneal. This is interpreted as clear evidence of an increase in the tensile stress in Al-I films due to 450°C annealing. The numerical values of $\Delta\sigma$ (change in stress) as determined from the Newton's rings experiments are smaller than the ones determined from the x-ray diffraction techniques. This is possibly due to the errors in the curvature determination. In the case of slices metalized at 200°C (Al-II slices), a 450°C anneal did not appreciably change the curvature and hence it is

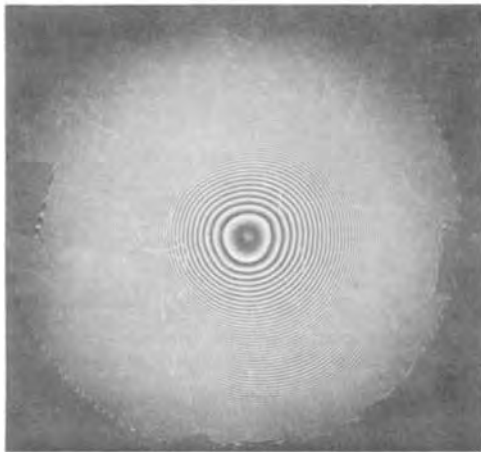
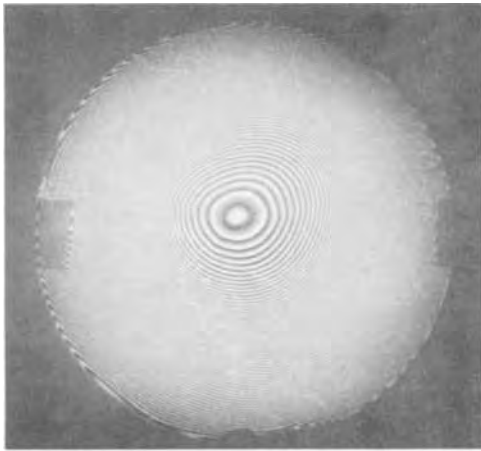


Fig. 3 Newton's rings for aluminum film Al-I on oxidized silicon substrates. a (Upper) before 450°C anneal for 30 min in N₂; b (lower), after 450°C anneal for 30 min in N₂.

considered that the stress levels in Al-II films are almost equal before and after annealing.

The absolute values of the stresses in aluminum films may be calculated from the radii of curvature listed in Table II. However, such a determination is possible only if the curvatures of the slices prior to metal depositions are known. Because the final curvature is dependent on parameters such as initial slice curvature, and bulk modulus of the substrate, the errors are propagated and stress values are good up to $\pm 10\%$. The radius of curvature of the slices used in this experiment ranged from 900 to 1200 cm. When these de-

Table II. Internal stress changes in aluminum films due to 450°C anneal

Metal film	Slice No.	Radius of curvature (cm) Before	After	$\Delta\sigma$ (10^9 dynes/cm ²)
Al-I RT 20 A/sec	G-1-1	823	622	1.6
	G-1-3	622	526	1.2
	O-3	698	578	1.2
	O-4	998	559	3.1
	N-2	912	589	2.4
Al-II 200°C 20 A/sec	N-4	1382	823	2.0
	G-2-1	551	555	-0.1
	G-2-3	547	541	+0.1
	O-11	801	698	+0.7
	O-14	493	497	-0.1
	N-10	896	885	+0.9
	N-15	875	678	+1.4

$$\Delta\sigma = \frac{E_s}{6(1-\nu_s)} \cdot \frac{d_s^2}{t_t} \left[\left(\frac{1}{R_s} \right)_{After} - \left(\frac{1}{R_s} \right)_{Before} \right]$$

$$\frac{E_s}{6(1-\nu_s)} = 2.305 \times 10^{12} \text{ dynes/cm}^2 \text{ for oxidized substrates}$$

where d_s = thickness of the substrate = 300 μm , t_t = thickness of aluminum film = 0.80 μm , G and O = oxidized silicon substrate, and N = unoxidized silicon substrate.

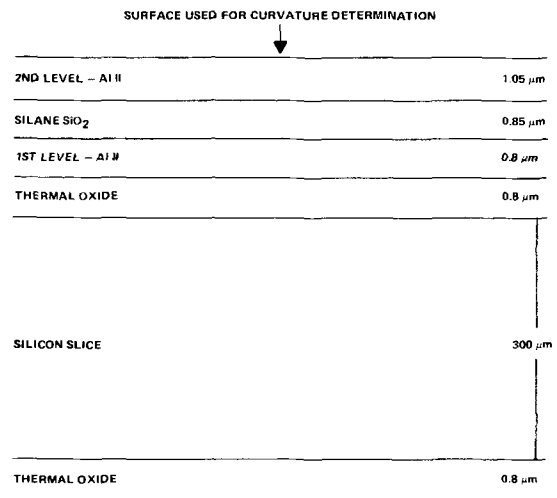


Fig. 4. Schematic of two-layered structure: Al/SiO₂/Al

tails are considered, the internal stresses in Al-I and Al-II films are found to be (0 to 2.5) and (1 to 3.4) $\times 10^9$ dynes/cm², respectively. The stress levels determined from Newton's rings method are in fair agreement with those determined from the x-ray diffraction methods.

Stresses in multilayered structure.—Example Al/SiO₂/Al: the Newton's rings method is used to monitor the changes in slice curvature after the successive processing steps needed in the fabrication of two-level test structures. A schematic of the different layers in the test structure is shown in Fig. 4. The data on the curvature of the various slices are presented in Table III. In the same table, the values of the product of stress and thickness of the layer are also presented.

The stresses in multilayered films are discussed on a model based on the following assumptions:

1. Each layer adheres perfectly to the one next to it.
2. Each layer has a uniform thickness.
3. The material is elastic.
4. The material is isotropic.
5. Only thermal stresses need to be considered (for metal films intrinsic stresses are small).
6. Each layer is in a state of plane stress and the stress in each layer is assumed to be uniform throughout.

Consider the fabrication of Al-II/SiO₂/Al-II on oxidized silicon substrates. The aluminum film deposited at 200°C remains stress-free above 150°C and the thermal stress is locked in after the film cools below 150°C. Thus, the internal stress in Al-II is (intrinsic stresses

Table III. Radii of curvature and product (σt) after successive stages in fabricating two-level test structures

Metal film	Slice No.	Radius of curvature, R	Al, $t = 0.80 \mu$	Al/SiO ₂ , $t = 1.65 \mu\text{m}$	Al/SiO ₂ /Al, $t = 2.70 \mu\text{m}$	After bake, $t = 2.70 \mu\text{m}$
Al-I RT 20 A/sec	O-6	R	601	388	339	327
		σt	56.6	87.5	100.0	103.8
		σt	916	481	530	379
Al-II 200°C 20 A/sec	O-7	R	39.0	74.1	67.3	94.0
		σt	1176	514	545	467
		σt	30.9	70.6	66.5	777
Al-II 200°C 20 A/sec	O-8	R	528	362	303	321
		σt	65.4	98.0	113.9	107.3
		σt	492	354	297	307
Al-II 200°C 20 A/sec	O-10	R	66.7	92.6	110.5	106.9
		σt	531	356	321	318
		σt	67.3	100.2	111.0	112.0

$$R_s = \text{radius of curvature in cm}$$

$$\sigma t t = \text{stress} \times \text{thickness in } 10^9 \text{ dynes/cm}$$

$$\sigma t t = \frac{E_s d_s^2}{6(1-\nu_s) R_s}$$

are approximated to zero and only the thermal stresses are considered)

$$\sigma_{Al} = E'_{Al} (\alpha_{Al} - \alpha_{Si}) \cdot \Delta T$$

$$E' = E/1 - \nu$$

We find

$$\sigma_{Al} = 2.6 \times 10^9 \text{ dynes/cm}^2$$

and

$$\sigma_{Al} t_{Al} = 20.8 \times 10^4 \text{ dynes/cm}$$

This tensile stress in the film bends the slice, and as a result the radius of curvature decreases. For slice 0-8 (see Table III), the radius of curvature has decreased to 528 cm from its initial value (approximately 1000 cm).

The substrates are heated to 350°C prior to silane SiO₂ deposition. When the substrates have equilibrated to 350°C, the metal film relaxes to a state of zero stress. As the substrate is cooled from 350°C to room temperature, the top layer of SiO₂ may cool to 150°C without any built-in thermal stress (due to the yielding of the aluminum film above 150°C). Below 150°C the composite layers assume a size equilibrium with the substrate and the deformation in SiO₂ is determined by the silicon substrate. The thermal stress in SiO₂ can be calculated as follows

$$(\sigma_{\text{thermal}})_{SiO_2} = E'_{SiO_2} (\alpha_{SiO_2} - \alpha_{Si}) \Delta T$$

$$= -0.26 \times 10^9 \text{ dynes/cm}^2$$

and

$$(\sigma_{\text{thermal}})_{SiO_2} \cdot t_{SiO_2} = -2.2 \times 10^4 \text{ dynes/cm}$$

In the framework of the model, which assumes no interaction of the two films to relieve stress, σ_{rf} is additive.

$$(\sigma t)_{Al/SiO_2} = \sigma_{Al} t_{Al} + \sigma_{SiO_2} t_{SiO_2}$$

The product σt of the composite Al/SiO₂ should decrease after the SiO₂ deposition by -2.2×10^4 dynes/cm if the internal stresses are composed of thermal stresses alone. However, Table III shows

$$\sigma_{SiO_2} t_{SiO_2} \approx 30 \times 10^4 \text{ dynes/cm}$$

and suggests large tensile stresses are present

$$\sigma = \sigma_{\text{thermal}} + \sigma_{\text{intrinsic}}$$

$$\sigma_{\text{intrinsic}} \times t_{SiO_2} \approx 32.2 \times 10^4 \text{ dynes/cm}$$

$$\sigma_{\text{intrinsic}} \approx 4 \times 10^9 \text{ dynes/cm}^2 \text{ (tensile)}$$

Thus, the intrinsic stresses in silane SiO₂ films are tensile. In another series of experiments (11), the internal stresses in silane SiO₂ films on silicon substrates were studied by use of Newton's rings method and a 5000Å SiO₂ film was found to be in tension with $\sigma \approx 1.5 \times 10^9$ dynes/cm². It was also found that on phosphorous doping of SiO₂ the films were still in tension while on boron doping the films were in compression. Aboaf (12) has observed the intrinsic stresses to be tensile for chemically vapor-deposited SiO₂ films; these SiO₂ films were prepared by the reaction of tetraethylorthosilicate whereas the films used in our experiments have been deposited by the oxidation of silane. Sunami *et al.* (8) and Lathlaen *et al.* (9) report results on stress in silane SiO₂ in agreement with ours.

The stresses after the second layer of Al-II and 450°C anneal are given in Table III. This level of metal is also in tension. The changes in σt after 450°C bake are the results of annealing of intrinsic stresses in three-layered structures and are difficult to interpret. Silane oxide films can undergo stress relief on annealing while aluminum films can undergo a stress increase. The interaction of the two make analysis of the stress difficult.

From the view point of slice processing in multilevel technology we have noted the following:

1. Aluminum films deposited on silicon substrates at temperatures of 150°C or above have the same thermal stress value ($\sim 2.6 \times 10^9$ dynes/cm²).

2. Cracks can develop in thick undoped silane oxides ($> 1 \mu\text{m}$) because of the high intrinsic tensile stress. Doping the oxide reduces the stress in the oxide film.

3. Increasing the oxide thickness to cover the first-level metal increases the slice curvature; moreover, an increase in second-metal thickness is needed to avoid open metal at second level and this further increases the tensile stress.

4. Slice bending results in poor photoresist definition with the increased probability of stress enhanced etching.

5. Internal stresses in multilayered structures can manifest themselves in terms of oxide cracking, stress enhanced etching at steps, and open metalization.

6. Thicknesses of individual layers and the deposition parameters used in multilevel interconnections need to be optimized in order to minimize the over-all stresses.

Conclusions

X-ray diffraction techniques and the Newton's rings method have been used to examine the internal stresses in aluminum films vacuum deposited on oxidized silicon substrates at room temperature (25°C) and at 200°C. The results indicate that the room temperature aluminum film is in a state of approximately zero stress, and the 200°C aluminum film is in tension with a stress of 2.6×10^9 dynes/cm². Both of the films have a tensile stress of 2.6×10^9 dynes/cm² after 450°C anneal. The films have a thermal stress equivalent to a temperature difference of 125°C.

The Newton's rings method has been extended to understand the internal stresses in various layers of the multilayered structure Al/SiO₂/Al. The silane SiO₂ film is in high intrinsic tensile stress and the over-all composite is also in high tensile stress.

The results presented here are in agreement with previously reported data (3, 4, 8). The severe slice bending which results from the internal stresses of the composite multilayered structure and the hillocks formed during annealing of the aluminum (4) or during the silane oxide deposition make slice processing more difficult.

Acknowledgments

It is a pleasure to acknowledge the technical assistance of Joe Bob Leake, Naomi White, and Imogene Killen. We also wish to thank John Pankratz for helpful discussion on internal stresses in multilayered structures. This work was supported by Air Force Systems Command, Rome Air Development Center, Griffiss Air Force Base, New York.

Manuscript submitted Sept. 7, 1971; revised manuscript received Dec. 10, 1971.

Any discussion of this paper will appear in a Discussion Section to be published in the December 1972 JOURNAL.

REFERENCES

1. K. L. Chopra, "Thin Film Phenomena," McGraw-Hill Book Co., New York (1969).
2. R. W. Hoffman, "Physics of Thin Films," Vol. 2, pp. 211-273, G. Haas and R. F. Thun, Editors, Academic Press, New York (1966).
3. P. L. Castro and J. F. Campbell, "Ohmic Contacts to Semiconductors," p. 332, B. Schwartz, Editor, Electrochemical Society, New York (1969).
4. F. d'Heurle, L. Berenbaum, and R. Rosenberg, *Trans. Met. Soc. AIME*, **242**, 502 (1968).
5. C. M. Drum and M. J. Rand, *J. Appl. Phys.*, **39**, 4458 (1968).
6. J. D. Finegan and R. W. Hoffman, *ibid.*, **30**, 597 (1959).
7. R. Glang, R. A. Holmwood, and R. L. Rosenfeld, *Rev. Sci. Instr.*, **36**, 7 (1965).
8. H. Sunami, Y. Itoh, and K. Sato, *J. Appl. Phys.*, **41**, 5115 (1970).
9. R. Lathlaen and D. A. Diehl, *This Journal*, **116**, 620 (1969).
10. F. A. Jenkins and H. F. White, "Fundamentals of Optics," p. 261, McGraw-Hill Book Co., New York (1950).
11. L. H. Hall, Unpublished results.
12. J. A. Aboaf, *This Journal*, **116**, 1732 (1969).

Si Contamination in Open Flow Quartz Systems for the Growth of GaAs and GaP

M. E. Weiner*

Bell Telephone Laboratories, Incorporated, Murray Hill, New Jersey 07974

ABSTRACT

Silicon contamination of III-V compounds is a potentially serious problem because of silicon's amphoteric behavior and its high affinity for oxygen. A potential source of silicon is fused quartz, which is widely used in systems for the growth of GaAs and GaP. Most open growth systems use flowing hydrogen because it is easily purified and it can remove solid gallium sesquioxide from the system. In this paper, calculations are presented for the rates of contamination of liquid gallium with silicon and of flowing H₂-HCl mixtures with volatile silicon compounds. Ideal gas behavior and local thermodynamic equilibrium are assumed. It is shown that the contact of Ga or HCl with quartz at normal growth temperatures can lead to significant silicon contamination in very dry systems. In addition, it is found that at 800°C, the pressure of water cannot be controlled below 10⁻⁸ atm for H₂ in contact with SiO₂ and 5 × 10⁻⁷ atm for HCl in contact with SiO₂, regardless of the initial purity of the H₂. These pressures rise appreciably with increasing temperature. In addition, models are presented for the formation of high concentrations of Si at the substrate-epitaxial interface and for the formation of SiO₂ precipitates in vapor growth systems. The former has previously been associated with the formation of "I" or insulating layers. The calculations show that HCl synthesis-type systems should give rise to much less silicon contamination than transport-type systems, and vapor growth systems using H₂O as a transporting agent give rise to nearly negligible Si contamination below 1000°C. Other possible ways to minimize silicon contamination are also discussed.

Fused quartz is a widely used material for the construction of high-temperature apparatus used for melt, solution, and vapor growth of GaAs and GaP. Although SiO₂ has a high free energy of formation (1), it cannot be considered completely inert when in contact with such reactive materials as Ga, H₂, HCl, C, and BN. Contamination of GaAs with Si during melt growth in quartz crucibles or boats has been treated fairly extensively both thermodynamically (2) and experimentally (3-6). Some evidence of Si contamination in open flow solution and vapor growth of GaAs and GaP has also been reported (6-11). Very little work on the rates of Si contamination in the latter system has been carried out. It is the purpose of this paper to examine the rates of Si contamination in open flow quartz systems in some detail under a variety of conditions and to determine how such contamination can be avoided or minimized.

General Assumptions

The following calculations of Si contamination in open flow quartz systems are for systems in which hydrogen, at atmospheric pressure, is flowing through the system at a flow rate F . The objective is to calculate the rate of contamination of Ga (of mass M_{Ga}) by Si, i.e., to calculate dx_{Si}/dt where x_{Si} is the atom fraction of Si in the liquid gallium.¹ In order that the results be related to the more or less typical conditions prevalent in open tube experiments, values were chosen for F and M_{Ga} . Specifically, $M_{\text{Ga}} = 20\text{g}$ and $F = 100\text{ cm}^3/\text{min}$ at the growth temperature (note that $F = F_{298} \cdot T(^{\circ}\text{K})/298$). It will become evident that dx_{Si}/dt is proportional to F/M_{Ga} ; hence, to consider flow rates or masses of Ga other than 100 cm³/min and 20g, respectively, one need only expand or contract the time scale proportionately in the results of the Si contamination rate calculations. In these calculations, the following assumptions were made:

1. The flowing gas stream is in thermodynamic equilibrium with its immediate surroundings (i.e., no forward or back diffusion of gaseous species).

* Electrochemical Society Active Member.
Key words: silicon contamination, GaAs, GaP, compound semiconductors.

¹ The activity of liquid Ga is unity. (At the temperatures of interest, the activity of liquid gallium is not far from unity even if saturated with a III-V compound.)

2. Si is always distributed homogeneously in liquid Ga.
3. The solubility of SiO₂ in liquid Ga is neglected.
4. The pressures of elemental silicon, SiO₂, SiCl, SiCl₂, and SiCl₃ are neglected. The only volatile silicon compounds considered are SiO, SiH₃Cl, SiH₂Cl₂, SiHCl₃, and SiCl₄.
5. Any oxygen in the gas stream reacts with H₂ to form H₂O.
6. All gases obey the ideal gas law.

Specific Cases

A. Contamination of liquid Ga in an inert crucible or boat in flowing H₂.—A schematic diagram of the system under consideration is shown in Fig. 1. This situation could exist in the solution growth of GaAs and GaP.

The only volatile silicon compound to be considered in this case is SiO.

Let

- $P_{\text{SiO input}}$ = pressure of SiO upstream from the liquid Ga
 $P_{\text{SiO eq}}$ = pressure of SiO in equilibrium with the liquid Ga
 $P_{\text{H}_2\text{O}}^0$ = initial pressure of water in the system (including any water from reaction between H₂ and O₂)

In general, "input" implies values upstream from the liquid Ga and "eq" implies values at the liquid Ga. Thus, since SiO resulting from the reaction of H₂ with SiO₂ is the only source for Si contamination

$$\frac{dx_{\text{Si}}}{dt} = \frac{F}{N_{\text{Ga}}RT} (P_{\text{SiO input}} - P_{\text{SiO eq}}) \quad [1]^2$$

The following reactions are of interest in case A:

² This equation is a differential form of the ideal gas law under the assumption that $V = 0$. (V is the effective reaction volume). If ΔN moles are transferred from the gas phase to the liquid phase

$$\begin{aligned} V\Delta p &= RT\Delta N \\ \text{By differentiating, setting } V &= 0, \text{ setting } \frac{dV}{dt} = F \text{ and } \frac{d\Delta N}{dt} = \\ \frac{dN}{dt} &= N_{\text{Ga}} \frac{dx}{dt}, \text{ Eq. [1] is obtained.} \end{aligned}$$

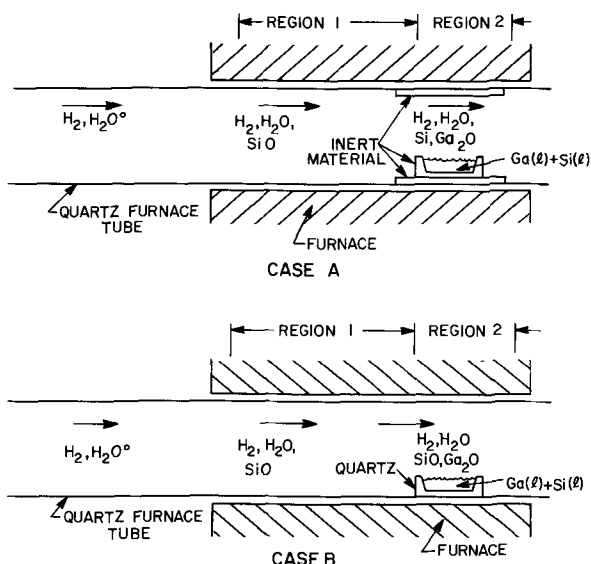
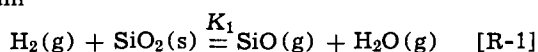
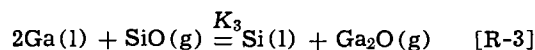
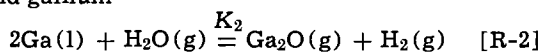


Fig. 1. Diagram of the growth systems considered in cases A and B, silicon contamination of liquid Ga. Region 1, "input" values; Region 2, "equilibrium" values.

Upstream



At liquid gallium



Values for $P_{\text{SiO input}}$ and $P_{\text{SiO eq}}$ may be calculated from the equilibrium products of reactions [R-1], [R-2], and [R-3] and substituted into Eq. [1]. These calculations are given in Appendix I. The result is

$$\frac{dx_{\text{Si}}}{dt} = \frac{FP_{\text{H}_2\text{O}^0}}{2RTN_{\text{Ga}}} \left[\sqrt{1 + \frac{4K_1}{(P_{\text{H}_2\text{O}^0})^2}} \frac{(K_3 + K_3K_2 - K_2x_{\text{Si}})}{K_3 + K_3K_2 - K_2x_{\text{Si}}} - 1 \right] \quad [2]$$

The activity coefficient for silicon dissolved in liquid gallium is included in K_3 . An exact solution of Eq. [2] is given in Appendix I. In order to calculate K_1 , K_2 , and K_3 , free energies of formation of $\text{SiO}_2(\text{s})$, $\text{SiO}(\text{g})$, and $\text{Si}(\text{l})$ were obtained from the JANAF tables (1); the free energy of formation of $\text{Ga}_2\text{O}(\text{g})$ was obtained from data compiled by Bass and Oliver (12), and the activity coefficient for $\text{Si}(\text{l})$ was obtained from the Ga-Si phase diagram (13). From these data, it is easily seen that the term K_2x_{Si} in Eq. [2] is negligible if $x_{\text{Si}} < 10^{-4}$. This is equivalent to the assumption that $P_{\text{SiO input}} \gg P_{\text{SiO eq}}$ and all SiO input is incorporated into the liquid gallium as dissolved silicon. Then Eq. [1] takes the form

$$\frac{dx_{\text{Si}}}{dt} = C(T) \quad \text{or} \quad x_{\text{Si}} - x_{\text{Si}}^0 = C(T)t \quad [3]$$

where $C(T)$ is a constant which is only a function of temperature and x_{Si}^0 is the initial concentration of Si in the Ga. Some values of $C(T)$ are given in Table I. It is easily seen that the approximation $x_{\text{Si}} < 10^{-4}$ is valid up to 10^3 or more hours.

Equation [2] also allows the calculation of a steady-state value of x_{Si} . This value occurs when $dx_{\text{Si}}/dt = 0$. Some values of x_{Si} (steady state) are also given in Table I.

B. Contamination of liquid Ga in a quartz crucible in flowing H_2 .—There are now two sources of Si contamination of the liquid Ga. These are H_2 reduction of the quartz (as in case A) and Ga reduction of quartz (see Fig. 1, case B). The generation of Si from the Ga

Table I. Calculated rates (C) and steady-state [x_{Si} (steady state)] values of Si contamination of Ga in an open flow quartz system with the Ga in an inert crucible or boat (case A) Assumed: local thermodynamic equilibrium, $P_{\text{H}_2} = 1 \text{ atm}$, $F = 100 \text{ cm}^3/\text{min}$, $M_{\text{Ga}} = 20\text{g}$

T ($^{\circ}\text{C}$)	$P_{\text{H}_2\text{O}^0}$ (atm)	C (atom fraction/hr)	x_{Si} (steady state)
800	10^{-8}	8.9×10^{-10}	7.6×10^{-3}
800	10^{-7}	1.2×10^{-10}	1.4×10^{-1}
800	10^{-6}	1.2×10^{-11}	1.4×10^{-6}
900	10^{-8}	2.0×10^{-8}	1.4×10^{-2}
900	10^{-7}	1.3×10^{-8}	5.9×10^{-3}
900	10^{-6}	2.1×10^{-9}	1.5×10^{-4}
1000	10^{-8}	1.8×10^{-7}	1.2×10^{-2}
1000	10^{-7}	1.7×10^{-7}	1.1×10^{-2}
1000	10^{-6}	1.0×10^{-7}	4.2×10^{-3}

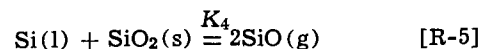
reduction of quartz results from the reaction



Thus, for each mole of Si generated from this reaction, two moles of Ga_2O are generated. Therefore

$$\frac{dx_{\text{Si}}}{dt} = \frac{F}{RTN_{\text{Ga}}} [P_{\text{SiO input}} - P_{\text{SiO eq}} + \frac{1}{2}P_{\text{Ga}_2\text{O gen}(\text{Ga} + \text{SiO}_2)}] \quad [4]$$

As a result of the addition of the term $P_{\text{Ga}_2\text{O gen}(\text{Ga} + \text{SiO}_2)}$, it is helpful to use the equilibrium product of the reaction



Note that $K_4 = K_1K_2/K_3$. Following case A and from Appendix I

$$\frac{dx_{\text{Si}}}{dt} = \frac{F}{2RTN_{\text{Ga}}} \left[\frac{K_3K_4^{1/2} + K_3K_2K_4^{1/2}}{K_2x_{\text{Si}}^{1/2}} - K_4^{1/2}x_{\text{Si}}^{1/2} - P_{\text{H}_2\text{O}^0} \right] \quad [5]$$

The equilibrium constant K_4 includes a value for the activity coefficient for silicon. The data required to calculate K_4 were obtained from Ref. (1) and (13). Equation [5] can be solved in closed form. However, a numerical integration by Simpson's rule is straightforward, comparable in accuracy, and much simpler. This procedure was carried out on a computer using 100 equally spaced intervals for each integration. Some results are shown in Fig. 3-5.

The steady-state values of Si activity are calculated (as in case A) by setting $dx_{\text{Si}}/dt = 0$. Some results of

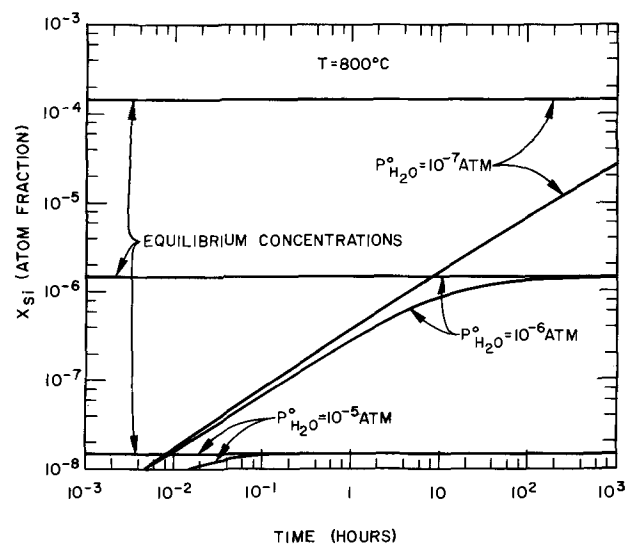


Fig. 2. Calculated rate of Si contamination of liquid Ga in an open flow quartz system with the Ga in a quartz crucible or boat ($T = 800^{\circ}\text{C}$). Assumed: local thermodynamic equilibrium, $P_{\text{H}_2} = 1 \text{ atm}$, $F = 100 \text{ cm}^3/\text{min}$, $M_{\text{Ga}} = 20\text{g}$.

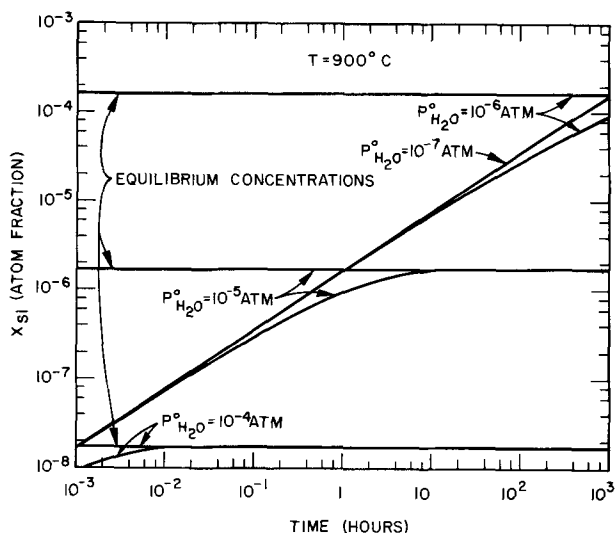


Fig. 3. Calculated rate of Si contamination of liquid Ga in an open flow quartz system with the Ga in a quartz crucible or boat ($T = 900^\circ\text{C}$). Assumed: local thermodynamic equilibrium, $P_{\text{H}_2} = 1 \text{ atm}$, $F = 100 \text{ cm}^3/\text{min}$, $M_{\text{Ga}} = 20\text{g}$.

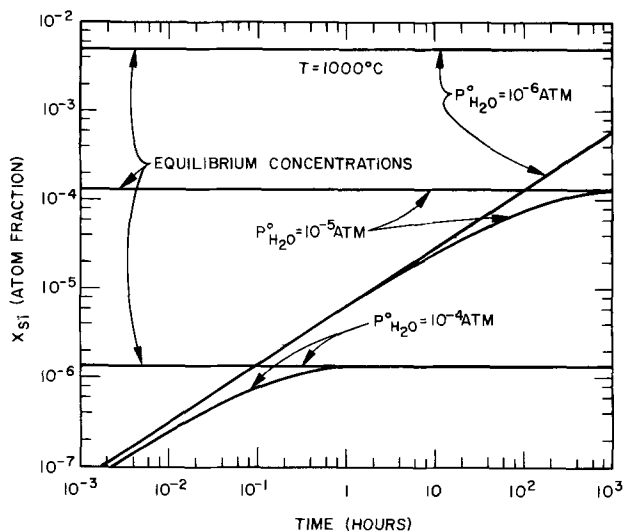


Fig. 4. Calculated rate of Si contamination of liquid Ga in an open flow quartz system with the Ga in a quartz crucible or boat ($T = 1000^\circ\text{C}$). Assumed: local thermodynamic equilibrium, $P_{\text{H}_2} = 1 \text{ atm}$, $F = 100 \text{ cm}^3/\text{min}$, $M_{\text{Ga}} = 20\text{g}$.

this calculation are also shown in Fig. 2-4. Note that steady-state values of Si contamination can be approached in the range of times of interest in liquid phase growth. Note also that these steady-state values are close to those given in Table I for case A. This is because the influence of the term $P_{\text{Ga}_2\text{O gen}}(\text{Ga} + \text{SiO}_2)$ on Eq. [4] becomes minimal near steady state, and Eq. [4] becomes similar to Eq. [1].

C. Si contamination in an open flow quartz system in the presence of flowing H_2 and HCl .—This case is applicable to vapor growth systems. A diagram of the systems to be discussed below is given in Fig. 5. Therefore, it is of interest to calculate the quantity of volatile Si compounds in the gas stream before considering effects due to liquid gallium.

There are five volatile Si compounds to be considered. These are SiO , SiH_3Cl , SiH_2Cl_2 , SiHCl_3 , and SiCl_4 . Unfortunately, none of the chloride species can be completely neglected over a wide range of temperatures and values of P_{HCl}^0 . As above, "input" refers to values upstream of any liquid Ga and superscript "O" refers to initial values. Then

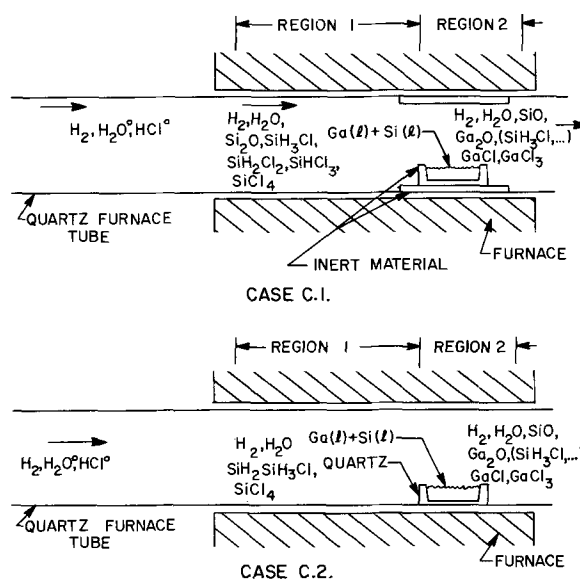
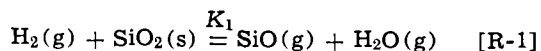
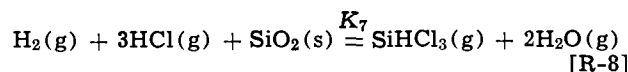
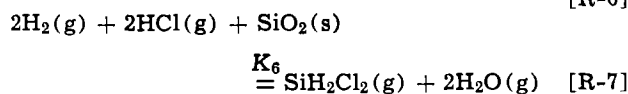
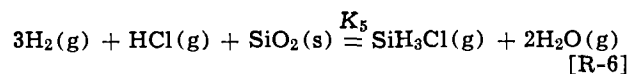


Fig. 5. Diagram of the growth systems considered in case C, silicon contamination of liquid Ga and of a gas stream containing H_2 and HCl . Region 1, "input" values; Region 2, "equilibrium" values.



In principle, the equilibrium products of these reactions allow the calculation of the total pressure of volatile silicon compounds. In practice, the calculation is greatly simplified by assuming $P_{\text{HCl}}^0 = P_{\text{HCl input}}$. Actually, under normal conditions of interest, the maximum fraction of HCl lost to other compounds is about 3×10^{-3} so that this assumption is reasonable. The detailed calculation of the total pressure of volatile Si compounds is carried out in Appendix II. The equilibrium constants K_5 , K_6 , K_7 , and K_8 were calculated from free energies of formation in the JANAF tables (1). Some results of this calculation are shown in Fig. 6.

C-1. Ga in inert crucible or boat.—In order to see how liquid Ga affects the system described in case C, it is necessary to calculate the rate of Si contamination of the liquid Ga. This will enable us to determine what happens to the gas stream after it passes over the Ga into the region of vapor growth. A diagram for case C-1 is shown in Fig. 5. Calculations for case C-1 require free energy data on the formation of GaCl and GaCl_3 . These were calculated from thermodynamic data tabulated by Fergusson and Gabor (14), and Stull and Sinke (15). These calculations are similar to those for case A with the result

$$\frac{dx_{\text{Si}}}{dt} = C'(T) \quad \text{or} \quad x_{\text{Si}} = x_{\text{Si}}^0 = C'(T)t \quad [6]$$

Details of this calculation are given in Appendix III. Some values for $C'(T)$ are given in Table II. It is seen that the approximate form given by Eq. [6] is valid for times up to 10^2 hr . Since HCl would not normally be run continuously through a hot system, as might H_2 , steady-state values of Si contamination would be far removed from the region of interest. A calculation of steady-state values could be carried out as in cases A and B. However, some of the approximations made

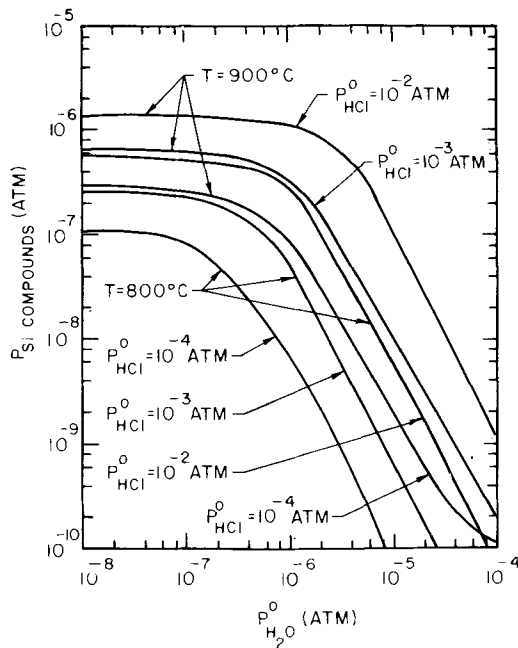


Fig. 6. Calculated total pressure of gaseous Si compounds ($P_{SiO} + P_{SiH_3Cl} + P_{SiH_2Cl_2} + P_{SiHCl_3} + P_{SiCl_4}$) in equilibrium with quartz as functions of initial pressures of H_2O and HCl . $P_{H_2} = 1$ atm.

will break down and the calculation would become very tedious. The significance of Eq. [6] is that in its range of validity, all of the Si in the gas stream is removed by the liquid Ga.

C-2. Ga in quartz crucible or boat.—Following case B (see Fig. 5)

$$\frac{dx_{Si}}{dt} = \frac{F}{RTN_{Ga}} [(P_{SiO} \text{ input} + P_{silanes} \text{ input} + P_{SiCl_4} \text{ input}) - (P_{SiO} \text{ eq} + P_{silanes} \text{ eq} + P_{SiCl_4} \text{ eq}) + \frac{1}{2}P_{Ga_2O} \text{ gen}(Ga + SiO_2)] \quad [7]$$

From Appendix III, it is shown that Eq. [7] becomes

$$\frac{dx_{Si}}{dt} = \frac{F}{2RTN_{Ga}} \left[\frac{K_3K_4^{1/2} \left(1 + \frac{1}{K_2} \right)}{x_{Si}^{1/2}} - K_4^{1/2}x_{Si}^{1/2} - P_{H_2O}^0 - 2x_{Si} \left(\frac{P_{GaCl} \text{ eq}}{K_9} + \frac{P_{GaCl} \text{ eq}^2}{K_{10}} + \frac{P_{GaCl} \text{ eq}^3}{K_{11}} + \frac{P_{GaCl} \text{ eq}^4}{K_{12}} \right) \right] \quad [8]$$

It is interesting to note that Eq. [8] is identical to Eq. [5] with the exception of the term linear in x_{Si} . Furthermore, this term is rather small except at fairly high values of x_{Si} . In general, the terms in $x_{Si}^{1/2}$ and x_{Si}

Table II. Calculated rates (C') of Si contamination of Ga in an open flow quartz system with the Ga in an inert crucible or boat (case C-1)

Assumed: local thermodynamic equilibrium, $P_{H_2} = 1$ atm, $P_{HCl}^0 = 10^{-3}$ atm, $F = 100$ cm³/min, $M_{Ga} = 20g$

T (°C)	$P_{H_2O}^0$	C' (atom fraction/hr)
800	10^{-8}	5.9×10^{-8}
800	10^{-7}	5.3×10^{-8}
800	10^{-6}	1.2×10^{-8}
800	10^{-5}	1.5×10^{-10}
900	10^{-8}	1.4×10^{-7}
900	10^{-7}	1.3×10^{-7}
900	10^{-6}	7.8×10^{-8}
900	10^{-5}	2.5×10^{-8}

are less significant than the other terms. Thus, the curves of Fig. 2-4 are, for the most part, applicable to case C-2. For this reason, no further numerical calculations were made. From a comparison of Fig. 2-4 with Table II, it is clear that the Ga reduction of quartz still provides most of the Si contamination of the liquid Ga. However, the fact that equilibrium values of x_{Si} are still approached slowly indicates that a significant fraction of the Si compounds in the gas stream is absorbed by the liquid Ga. It is easily seen that the equilibrium pressures of gaseous Si compounds above the liquid Ga are several orders of magnitude below the "input" pressures when x_{Si} is on the order of 10^{-5} . For smaller values of x_{Si} , an even greater fraction of the gaseous Si compounds is absorbed.

Discussion

Case A.—This case is mainly of interest in open tube solution growth. From Table I, it is clear that Si contamination under the conditions of case A is of significance only at higher temperatures in very dry systems and for times on the order of days, weeks, or months, depending on the contamination level which is of concern. From Table I it is seen that the addition of water to the hydrogen stream can greatly decrease Si contamination. In very dry systems, the rate of contamination depends only slightly on $P_{H_2O}^0$. However, as $P_{H_2O}^0$ is increased, the rate of contamination drops rapidly. The reason for this is that in very dry systems, a significant fraction of the total water content is generated by the H_2 reduction of SiO_2 . Thus, the effect of input H_2O is less significant than in "wetter" systems. In general, the use of an inert crucible in solution growth of GaAs and GaP should prevent serious Si contamination if small amounts of H_2O (or O_2) are added to the system, if turbulence in the flow stream is avoided (to avoid equilibration of the liquid Ga with a quartz furnace tube), and if the liquid Ga is changed after being at temperature for times on the order of 1-1000 hr, depending on specific experimental conditions and allowable contamination levels.

Case B.—This case, again, is mainly of interest in open tube solution growth. It is readily seen from Fig. 2-4 that Si contamination can arise very rapidly under the conditions of case B (i.e., the liquid Ga is in a quartz crucible or boat). For example, after one hour at temperature, 1-10 ppm (atomic) of Si can contaminate the Ga, depending on specific experimental conditions. The main reason for such rapid contamination is removal of Ga_2O from the surface of the liquid Ga both by physical flow and by reaction with H_2 . The addition of H_2O significantly affects steady-state values of x_{Si} (see Fig. 2-4), but has no effect on initial rates of contamination (see Fig. 2-4, and Eq. [5]). Replacing H_2 with an inert gas should lead to a significant decrease in the amount of Si contamination at any level of x_{Si} . This calculation can be performed by letting $K_2 \rightarrow \infty$ in Eq. [5]. Clearly, contact of liquid Ga with quartz is to be avoided in a system where the surface of the Ga is exposed to a flowing gas. If it is desired to use quartz as a crucible or boat, one might minimize Si contamination by growing under conditions such that a GaAs or GaP compound skin forms on the surface or by covering the surface with an inert liquid in a fashion similar to the liquid encapsulation process (12), as is done in melt growth of GaAs and GaP compounds. If the surface of the Ga is protected, the removal of Ga_2O from the surface of the Ga is minimized and the rate of Si contamination can be decreased.

There is some experimental evidence available on silicon contamination under case B conditions. Wolfstirn and Dawson (16) have measured the contamination of liquid Ga with Si from irradiated SiO_2 . After 15g of liquid Ga were in a furnace at 800°C for 2½ hr under 50 cm³/min of flowing H_2 they found 3.8×10^{-7} atm fraction of Si. They measured the input pressure

of H_2O at less than 10^{-6} atm. From Fig. 3 (note that the effective time is 6 hr due to the different mass of Ga and flow rate of hydrogen), a calculated view of about 8×10^{-7} atm fraction is obtained. In view of the assumptions in these calculations and the accuracy of thermochemical data, the agreement between these two numbers is quite good.

Hicks and Greene (17) have also studied silicon contamination under case B conditions and found that the amount of contamination was somewhat less than their calculation of the steady-state value. Their information on growth conditions is not complete. However, from the case B calculations, it seems clear that they were far from steady-state conditions. Their amounts of contamination (estimated from electrical properties of solution-grown GaAs) is still less than that calculated for case B. However, the agreement between their measurements and case B calculations is much better than with their equilibrium theory.

Case C.—This case is of particular interest in vapor phase growth of GaAs and GaP. First, it is of interest to consider the pressure of volatile Si compounds resulting from the combined reactions of HCl and H_2 . These are shown in Fig. 6. It can be seen that in very dry systems, it is possible to obtain ratios of Si compounds to P_{HCl}^0 of above 10^{-3} . This is undoubtedly a much higher ratio than used with dopant gases. Under almost all conditions, chloride compounds of Si provide nearly all of the pressure of gaseous Si compounds. From reactions [R-6] through [R-9], it is seen that two moles of water are generated for each mole of a silicon chloride. Thus, from Fig. 6, it can be readily seen that extreme efforts to reduce oxygen and water pressures below roughly 10^{-6} atm have very little effect on the total H_2O pressure in the system. Clearly the contact of HCl with quartz at elevated temperatures should be avoided if either Si contamination or oxygen contamination is believed to be a problem. One possible problem could be the formation of very fine precipitates of SiO_2 which must come out of the gas stream in a decreasing temperature. Such precipitates might not affect electrical properties at low fields and could be too fine to see by optical microscopy. Thus, their presence might be difficult to determine. DiLorenzo *et al.* have found Si in GaAs grown by the $AsCl_3$ transport method by use of a Direct Image Mass Analyzer (18). Unfortunately, this technique does not allow quantitative measurements of impurity concentrations. However, since the $AsCl_3$ growth technique leads to very high mobilities and low values of N_D-N_A , it is possible that part of this Si is in the form of SiO_2 precipitates. Luther has analyzed wall deposits of GaP grown in a PCl_3 transport system at $900^\circ C$ for Si by a chemical transport method (6). He found about 30 ppm atomic of Si (19) presumably from the fused quartz furnace tube. Since typical N_D-N_A values were well below this value, it seems likely that part of this Si was in the form of SiO_2 .

From the analysis of cases C-1 and C-2, it is seen that liquid Ga is capable of removing considerable amounts of Si from the gas stream. Furthermore, GaCl is significantly more stable than HCl so that very little HCl remains in the gas stream past the liquid Ga. Thus, further attack on the quartz prior to deposition of the GaAs or GaP should be considerably reduced. Hence, synthesis systems should have a considerable effect on reduction of Si contamination.³ In addition, the use of an inert crucible or boat to hold the liquid Ga results in one to two orders of magnitude less Si in the gas stream than the use of a quartz crucible or boat (compare Fig. 2-4 with Table II).

³ The use of the word "synthesis" in this context means that Ga and arsenic are fed into the system separately, and are not mixed until they reach the growth region. In the case considered, Ga would be transported as GaCl from the reaction of HCl and Ga, and As would be transported in the vapor as an elemental molecule (either As_2 or As_4). In contrast in a transport system, GaAs is either placed or formed upstream of the growth region, then decomposed by reaction with HCl, and reformed in the growth region.

In transport systems, the situation is considerably different. [The standard (As,P) Cl_3 -Ga- H_2 system is really a transport system since the Ga is covered by a skin of GaAs or GaP.] First, the Ga is no longer available to remove Si from the gas stream. Second, the free energy of formation of GaAs or GaP is sufficient to prevent nearly complete conversion of HCl to GaCl, and a significant fraction of the input HCl remains in the gas stream (20-21). Thus, reactions with SiO_2 can continue to occur after the formation of GaCl. The boat or crucible material in these systems should have little effect on Si contamination.

One problem which is believed to be associated with Si contamination is the formation of "I" or insulating layers at the beginning of growth of GaAs (18). Concentrations of Si estimated at above 1 a/o (atom per cent) have been observed at the interface between the substrate and the epitaxial layer (18). Casey has suggested (22) that this layer results from the formation of a very thin layer of liquid Ga when the substrate is placed in the reactor and arsenic evaporates from it. This layer of Ga then "soaks up" silicon. It is easily seen that SiH_3Cl is the dominant equilibrium species of all of the gaseous Si compounds in case C. Thus, if we consider the equilibrium product of reaction [R-10]

$$\frac{P_{GaCl}x_{Si}}{P_{SiH_3Cl}} = K_9$$

at $800^\circ C$ and let $P_{GaCl} = 10^{-3}$ atm and $P_{SiH_3Cl} = 10^{-7}$ atm, we find

$$x_{Si} = \frac{1.2 \times 10^{-7}}{10^{-3}} = 1.2 \times 10^{-4} \text{ (atom fraction)}$$

Thus, this source of the Si observed in Ref. (18) seems reasonable. It should be noted that the rate of Si contamination is inversely proportional to the mass of liquid Ga. In this case when the amount of Ga is very small, equilibrium values of x_{Si} could be reached rapidly. Once no liquid Ga is available (when arsenic is fed into the system, the Ga is converted to GaAs), the activity of Ga drops sharply and the amount of Si contamination drops, even though the gas stream composition should stay constant. The formation of liquid Ga could be avoided either by keeping the substrate below the congruent evaporation temperature until the Group V element is fed into the system (22) or by maintaining a Group V element pressure at all times in excess of that pressure at the Ga-GaAs or Ga-GaP liquidus line. Iwasaki and Sugibuchi have recently reported the elimination of high resistance layers in GaAs by initiating growth under high arsenic pressures (23). If the "I" layer problem is truly caused by Si, then the addition of H_2O or the use of a synthesis system should also help to alleviate the problem.

It is of interest to compare water vapor transport growth of GaAs and GaP with HCl transport or synthesis from the point of view of Si contamination. For this purpose, a temperature of $1000^\circ C$ and $P_{H_2O}^0 = 10^{-3}$ atm are assumed. These conditions are typical of water vapor transport system (24). At this water pressure, we can assume that $P_{H_2O \text{ input}} = P_{H_2O}^0$. Furthermore, from thermodynamic data, it is seen that the pressure of water changes only slightly after transport and before deposition. Then, from reaction [R-1]

$$P_{SiO \text{ input}} = \frac{K_1}{P_{H_2O}^0} = 7.8 \times 10^{-10} \text{ atm}$$

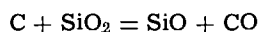
Thus, the total pressure of volatile Si compounds in the gas stream is about 10^3 times less than that in a dry HCl system (see Fig. 5). In addition, the equilibrium concentration of Si in liquid Ga under the above conditions is, from Eq. [4]

$$x_{Si} \approx \frac{K_3 + K_3K_2}{K_2} \frac{K_1}{(P_{H_2O}^0)^2} \approx 10^{-8}$$

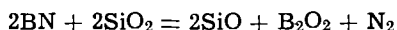
This value is about 10^4 times less than in a dry HCl system. Thus, if "I" layer formation is truly caused by Si contamination of a very thin Ga layer on the GaAs or GaP substrate, the problem of "I" layer formation in water vapor systems should be nearly non-existent.

Some mention has been made above of the differences between transport systems and synthesis systems. One further difference is of interest. In a transport system, it is always necessary to have the GaAs or GaP to be transported at a higher temperature than the substrate. This is because the equilibrium Ga/Cl or Ga/O ratios increase with temperature and deposition takes place only when these ratios exceed the values in equilibrium with the substrate. The free energy of formation of the GaAs or GaP is a significant factor in determining these ratios. Thus, in a synthesis system, these ratios will always be higher than in a transport system at the same temperature. Therefore, the liquid and the walls of the reactor in a synthesis system can be cooler than the substrate. Then, Si contamination will decrease and SiO_2 is less likely to precipitate out of the gas stream if the temperature of the gas stream is rising at the substrate.

Other sources of Si contamination which could be analyzed in a fashion similar to the above cases are Ga in a carbon boat or crucible in contact with quartz and Ga in a BN boat or crucible in contact with quartz. In these cases, the reactions



and



could be significant. The second of these might be complicated the possible formation of Si_3N_4 and B_2O_3 .

The problem of what materials can be considered inert when in contact with liquid Ga and quartz was not discussed above. It is believed that Al_2O_3 (possibly in the form of single-crystal sapphire) comes closest to being satisfactory. It has the advantages that it is highly stable, it is available in fairly high purity form, it can be shaped to some extent, and Al is iso-electronic with Ga and should not be electrically active in GaAs or GaP. Another possible inert system is a complete graphite system with no contact between graphite and quartz at elevated temperatures. Other possibilities might include coating of boats, crucibles, and/or reactors with materials such as AlN or alkaline earth fluorides.

Conclusions

It has been shown that serious Si contamination of liquid Ga in a quartz crucible or boat can occur in an open flow system under conditions used in the growth of GaAs or GaP from a Ga solution. In addition, serious Si contamination of the gas stream in HCl vapor systems can occur under typical vapor growth conditions. Furthermore, in either case, Si contamination is related to the formation of gaseous oxides, and efforts to obtain very dry systems may have little effect on oxygen contamination. It has been shown that H_2O vapor systems should not suffer from Si contamination nearly as much as HCl systems. Of course, the problem of oxygen contamination may be very severe in H_2O vapor systems. It has also been shown how large amounts of Si can pile up at the substrate-epitaxial interface in HCl systems. Such a Si rich layer is not expected in H_2O systems.

Some experimental evidence for the contamination of Ga, GaAs, and GaP with Si has been presented. Clearly more work needs to be done. Perhaps the best techniques for quantitative chemical analysis for Si in Ga, GaAs, and GaP are radio tracer methods (25) and Luther's chemical transport method (6). The former allow the best chance of an unambiguous determination of the source of Si contamination. Dean *et al.* (26) have observed evidence of optical phonons bound to

neutral donors in Raman scattering experiments on GaP. This technique is expected to allow a measurement of the total number of Si donors in GaP in the range $8 \times 10^{16} \text{ cm}^{-3}$ to $2 \times 10^{18} \text{ cm}^{-3}$ (27) and could help to distinguish between total chemical Si and electrically active Si.

In summary, significant silicon contamination of GaP and GaAs from fused quartz is expected to occur rapidly under some conditions, leading to potentially serious problems. Experimental work is clearly required to determine the accuracy of the calculations described in this paper. However, the trends implied by the calculations should be valid and of use in designing open flow quartz systems and in choosing gas stream compositions.

Acknowledgments

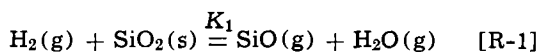
I would like to acknowledge many enlightening hours of discussion of the problem of silicon contamination with C. D. Thurmond. My level of understanding of thermochemical problems has been greatly enhanced as a result. I would also like to thank J. V. DiLorenzo, L. R. Dawson, L. C. Luther, and B. Schwartz for informing me of many of the details of epitaxial growth systems. H. C. Casey, Jr. suggested a possible mechanism for "I" layer formation, which was discussed in this paper. I wish to acknowledge discussions of the thermodynamics of silicon contamination with A. S. Jordan, who also offered help on the use of thermodynamic data. This manuscript was critically reviewed by A. S. Jordan, B. Schwartz, and F. A. Trumbore.

Manuscript submitted July 23, 1971; revised manuscript received Dec. 4, 1971.

Any discussion of this paper will appear in a Discussion Section to be published in the December 1972 JOURNAL.

APPENDIX I

Case A.—Calculation of $P_{\text{SiO input}}$



Thus

$$P_{\text{H}_2\text{O input}} = P_{\text{H}_2\text{O}^0} + P_{\text{SiO input}}$$

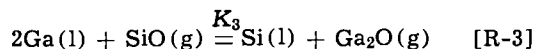
Therefore

$$P_{\text{SiO input}} (P_{\text{H}_2\text{O}^0} + P_{\text{SiO input}}) = K_1$$

and

$$P_{\text{SiO input}} = \frac{P_{\text{H}_2\text{O}^0}}{2} \left[\sqrt{1 + \frac{4K_1}{(P_{\text{H}_2\text{O}^0})^2}} - 1 \right] \quad [\text{A-1}]$$

Derivation of Eq. [2]: The following reactions occur at the crucible or boat containing the liquid Ga



From conservation of oxygen (see Fig. 1)

$$P_{\text{H}_2\text{O eq}} + P_{\text{Ga}_2\text{O eq}} + P_{\text{SiO eq}} = P_{\text{H}_2\text{O input}} + P_{\text{SiO input}} \quad [\text{A-2}]$$

Then, the equilibrium products of reactions [R-2] and [R-3] and Eq. [1], [A-1], and [A-2] may be solved simultaneously, yielding

$$\frac{dx_{\text{Si}}}{dt} = \frac{FP_{\text{H}_2\text{O}^0}}{2RTN_{\text{Ga}}} \left[\sqrt{1 + \frac{4K_1}{(P_{\text{H}_2\text{O}^0})^2}} - 1 \right] \frac{(K_3 + K_3K_2 - K_2x_{\text{Si}})}{K_3 + K_3K_2 + K_2x_{\text{Si}}} - 1 \quad [2]$$

Solution of Eq. [2]: Since there are no explicit functions of time on the right side of Eq. [2], the solution consists simply of an integration.

Let

$$A_I = \frac{FP_{H_2O}^0}{2RTN_{Ga}}$$

$$B_I = \sqrt{1 + \frac{4K_1}{(P_{H_2O}^0)^2}}$$

$$C_I = K_3(1 + K_2)$$

$$D_I = K_2$$

$$x = x_{Si}$$

Thus, Eq. [2] becomes

$$\frac{dx}{dt} = A_I \left[B_I \frac{(C_I - D_I x)}{C_I + D_I x} - 1 \right] \quad [A-3]$$

Then

$$\text{Let } B_I C_I - C_I = E$$

$$B_I D_I + D_I = F$$

The solution to [A-3] is

$$\int_{x_0}^x \frac{C_I + D_I x}{E - Fx} dx = A_I t \quad [A-4]$$

From integral tables

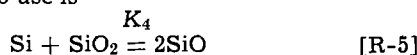
$$\frac{D_I}{F} (x - x_0) + \left(\frac{C_I}{F} + \frac{D_I E}{F^2} \right) \ln \left[\frac{\frac{E}{F} - x}{\frac{E}{F} - x_0} \right] = -A_I t \quad [A-5]$$

Note that x_0 refers to x_{Si} at $t = 0$. Thus, this solution is valid not only for calculating the rate of silicon contamination when starting with pure Ga, but may also be used to calculate the rate of change of Si when the Ga is purposely doped with Si.

Case B.—Following case A, the term $P_{Ga_2O \text{ gen}(Ga + SiO_2)}$ is added to the right side of Eq. [A-2] so that

$$P_{H_2O \text{ eq}} + P_{Ga_2O \text{ eq}} + P_{SiO \text{ eq}} = P_{H_2O \text{ input}} + P_{SiO \text{ input}} + P_{Ga_2O \text{ gen}(Ga + SiO_2)} \quad [A-6]$$

A further equilibrium product is helpful because of the addition of the term $P_{Ga_2O \text{ gen}(Ga + SiO_2)}$. A convenient reaction to use is



Note that $K_4 = K_1 K_2 / K_3$. Following case A again

$$\frac{dx_{Si}}{dt} = \frac{F}{2RTN_{Ga}} \left[\frac{K_3 K_4^{1/2} + K_3 K_2 K_4^{1/2}}{K_2 x_{Si}^{1/2}} - K_4^{1/2} x_{Si}^{1/2} - P_{H_2O}^0 \right] \quad [5]$$

APPENDIX II

Case C.—Calculation of total pressure of volatile Si compounds.—It may be seen from reactions [R-1] and [R-6]–[R-9] that

$$P_{HCl \text{ input}} = P_{HCl}^0 - P_{SiH_3Cl \text{ input}} - 2P_{SiH_2Cl_2 \text{ input}} - 3P_{SiHCl_3 \text{ input}} - 4P_{SiCl_4 \text{ input}} \quad [A-7]$$

and

$$P_{H_2O \text{ input}} = P_{H_2O}^0 + P_{SiO \text{ input}} + 2(P_{SiH_3Cl \text{ input}} + P_{SiH_2Cl_2 \text{ input}} + P_{SiHCl_3 \text{ input}} + P_{SiCl_4 \text{ input}}) \quad [A-8]$$

By substituting the equilibrium products of reactions [R-1] and [R-6] through [R-9] into Eq. [A-7] and [A-8]

$$P_{HCl \text{ input}} = P_{HCl}^0 - \frac{K_5 P_{HCl \text{ input}}}{P_{H_2O \text{ input}}^2} - \frac{2K_6 P_{HCl \text{ input}}^2}{P_{H_2O \text{ input}}^2} - \frac{3K_7 P_{HCl \text{ input}}^3}{P_{H_2O \text{ input}}^2} - \frac{4K_8 P_{HCl \text{ input}}^4}{P_{H_2O \text{ input}}^2} \quad [A-9]$$

and

$$P_{H_2O \text{ input}} = P_{H_2O}^0 + \frac{K_1}{P_{H_2O \text{ input}}} + \frac{2K_5 P_{HCl \text{ input}}}{P_{H_2O \text{ input}}^2} + \frac{2K_6 P_{HCl \text{ input}}^2}{P_{H_2O \text{ input}}^2} + \frac{2K_7 P_{HCl \text{ input}}^3}{P_{H_2O \text{ input}}^2} + \frac{2K_8 P_{HCl \text{ input}}^4}{P_{H_2O \text{ input}}^2} \quad [A-10]$$

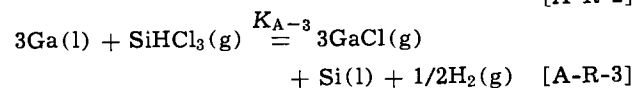
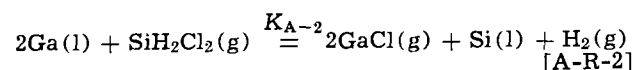
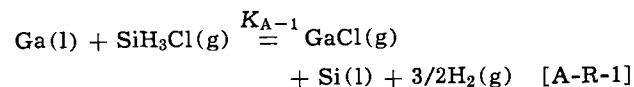
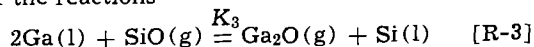
In principle, Eq. [A-9] and [A-10] allow the calculation of $P_{H_2O \text{ input}}$ and $P_{HCl \text{ input}}$. These in turn can easily be used to find the pressures of all of the gaseous Si compounds. However, an exact calculation along these lines would be very tedious and of dubious value. Great simplification will arise by assuming that $P_{HCl \text{ input}} = P_{HCl}^0$. This is equivalent to assuming that only a negligibly small fraction of the HCl fed into the system is converted to Si compounds. Actually, it will be shown that the maximum fraction of HCl lost to Si compounds under the conditions assumed is only about 3×10^{-3} under the conditions of interest. Thus, the assumption that $P_{HCl \text{ input}} = P_{HCl}^0$ seems valid. Once this assumption is made, Eq. [A-10] may be converted to a cubic equation in $P_{H_2O \text{ input}}$, which is easily solved numerically. Then, the equilibrium constants K_1 , K_5 , K_6 , K_7 , and K_8 allow the calculation of the total pressure of all volatile Si compounds. (Note that each compound has only one Si atom per molecule.) Some results of this calculation are shown in Fig. 6.

APPENDIX III

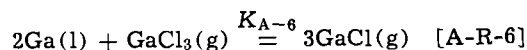
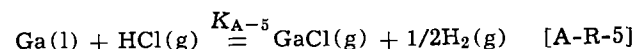
Calculations for case C-1.—Let $P_{SiH_3Cl} + P_{SiH_2Cl_2} + SiHCl_3 = P_{silanes}$. Then, following case A

$$\frac{dx_{Si}}{dt} = \frac{F}{RTN_{Ga}} [(P_{SiO \text{ input}} + P_{silanes \text{ input}} + P_{SiCl_4 \text{ input}}) - (P_{SiO \text{ eq}} + P_{silanes \text{ eq}} + P_{SiCl_4 \text{ eq}})] \quad [A-11]$$

The input terms were calculated in Appendix II. In order to calculate the "eq" terms (see Fig. 2), we must consider the reactions



and



From reactions [R-3] and [A-R-1] through [A-R-4]

$$(P_{SiO \text{ eq}} + P_{silanes \text{ eq}} + P_{SiCl_4 \text{ eq}}) = x_{Si} \left(\frac{P_{Ga_2O \text{ eq}}}{K_3} + \frac{P_{GaCl \text{ eq}}}{K_{A-1}} + \frac{P_{GaCl \text{ eq}}^2}{K_{A-2}} + \frac{P_{GaCl \text{ eq}}^3}{K_{A-3}} + \frac{P_{GaCl \text{ eq}}^4}{K_{A-4}} \right) \quad [A-12]$$

Thus, it is necessary to calculate $P_{Ga_2O \text{ eq}}$ and $P_{GaCl \text{ eq}}$. Equation [A-2] is valid for this case. Thus

$$P_{\text{Ga}_2\text{O eq}} + P_{\text{H}_2\text{O eq}} + P_{\text{SiO eq}} = P_{\text{H}_2\text{O input}} + P_{\text{SiO input}} \quad [\text{A-2}]$$

Then, using the equilibrium products of reactions [R-2] and [R-3]

$$P_{\text{Ga}_2\text{O eq}} \left(1 + \frac{1}{K_2} + \frac{x_{\text{Si}}}{K_3} \right) = P_{\text{H}_2\text{O input}} + P_{\text{SiO input}}$$

The values of $P_{\text{H}_2\text{O input}}$ and $P_{\text{SiO input}}$ may be calculated from information in Appendix I. Therefore

$$P_{\text{Ga}_2\text{O eq}} = \frac{P_{\text{H}_2\text{O input}} + P_{\text{SiO input}}}{1 + \frac{1}{K_2} + \frac{x_{\text{Si}}}{K_3}} \quad [\text{A-13}]$$

Since chlorine must be conserved

$$P_{\text{GaCl eq}} + P_{\text{HCl eq}} + \frac{1}{3} P_{\text{GaCl}_3 \text{ eq}} = P_{\text{HCl input}} + P_{\text{SiH}_3\text{Cl input}} - P_{\text{SiH}_3\text{Cl eq}} + \dots \quad [\text{A-14}]$$

Then, by substituting the equilibrium products of reactions [A-R-1] through [A-R-6] into Eq. [A-14]

$$P_{\text{GaCl eq}} \left(1 + \frac{1}{K_{A-5}} \right) + \frac{1}{3} \frac{P_{\text{GaCl eq}}^3}{K_{A-6}} = P_{\text{HCl input}} + P_{\text{SiH}_3\text{Cl input}} + 2P_{\text{SiH}_2\text{Cl}_2 \text{ input}} + 3P_{\text{SiHCl}_3 \text{ input}} + 4P_{\text{SiCl}_4 \text{ input}} - x_{\text{Si}} \left(\frac{P_{\text{GaCl eq}}}{K_{A-1}} + \frac{2P_{\text{GaCl eq}}^2}{K_{A-2}} + \frac{3P_{\text{GaCl eq}}^3}{K_{A-3}} + \frac{4P_{\text{GaCl eq}}^4}{K_{A-4}} \right) \quad [\text{A-15}]$$

The calculation of the input terms was described in Appendix II. Thus, Eq. [A-15] becomes a fourth order equation allowing, in principle, the calculation of $P_{\text{GaCl eq}}$ as a function of x_{Si} . Then, Eq. [A-11], [A-12], [A-13], and [A-15] may, in principle, be used to obtain a differential equation of the form

$$\frac{dx_{\text{Si}}}{dt} = f(x_{\text{Si}}) \quad [\text{A-16}]$$

Equation [A-16] can then be integrated numerically to obtain an equation of the form

$$x_{\text{Si}} = f(x_{\text{Si}}^0, t) \quad [\text{A-17}]$$

Thus, the formalism has been presented for an exact solution of case C-1. However, the conversion of Eq. [A-11] to [A-16] is very tedious. In practice, examination of thermodynamic data allows some reasonable approximations. The input data may be approximated in the manner previously described and shown in Fig. 6. Then, from calculations of various equilibrium constants, the following approximations were considered reasonable

$$P_{\text{GaCl eq}} \approx P_{\text{HCl input}} \approx P_{\text{HCl}}^0 \quad [\text{A-18}]$$

$$\frac{P_{\text{GaCl eq}}^2}{K_{10}} + \frac{P_{\text{GaCl eq}}^3}{K_{11}} + \frac{P_{\text{GaCl eq}}^4}{K_{12}} \approx 0 \quad [\text{A-19}]$$

$$x_{\text{Si}} \ll K_3 \left(1 + \frac{1}{K_2} \right) \quad [\text{A-20}]$$

Equation [A-18] means that very little HCl is lost by reaction with quartz, that virtually all HCl is converted to GaCl, and that GaCl₃ may be neglected. Equation [A-19] states that the equilibrium pressures of SiH₂Cl₂, SiHCl₃, and SiCl₄ in contact with liquid Ga are negligible. This is due to the fact that P_{HCl} is greatly reduced, favoring decomposition of these chlorides. Equation [A-20] means that $P_{\text{SiO}} \ll P_{\text{H}_2\text{O eq}} + P_{\text{Ga}_2\text{O eq}}$. This is because low values of x_{Si} favor the decomposition of SiO. Then, by using these approximations, Eq. [A-11] becomes

$$\frac{dx_{\text{Si}}}{dt} = \frac{F}{RTN_{\text{Ga}}} \left[(P_{\text{SiO input}} + P_{\text{silanes input}} + P_{\text{SiCl}_4 \text{ input}}) - x_{\text{Si}} \left[\frac{P_{\text{H}_2\text{O input}} + P_{\text{SiO input}}}{K_3 + \frac{K_3}{K_2}} + \frac{P_{\text{HCl}}^0}{K_9} \right] \right] \quad [\text{A-21}]$$

It may be shown that the term $x_{\text{Si}}(\dots)$ in Eq. [A-21] is negligible if $x_{\text{Si}} < 10^{-3}$. Equation [A-21] then takes the form

$$\frac{dx_{\text{Si}}}{dt} = C'(T) \quad \text{or} \quad x_{\text{Si}} - x_{\text{Si}}^0 = C'(T)t \quad [6]$$

Calculations for case C-2.—Equations [A-6], [A-12], and [A-15] are still valid for this case. Therefore, following cases A, B, and C-1

$$\frac{dx_{\text{Si}}}{dt} = \frac{F}{RTN_{\text{Ga}}} \left[\left(\frac{P_{\text{SiO input}}}{2} - \frac{P_{\text{H}_2\text{O input}}}{2} + P_{\text{silanes input}} + P_{\text{SiCl}_4 \text{ input}} \right) - x_{\text{Si}} \left(\frac{K_4}{2[x_{\text{Si}}^{1/2}]} + \frac{P_{\text{GaCl eq}}}{K_9} + \frac{P_{\text{GaCl eq}}^2}{K_{10}} + \frac{P_{\text{GaCl eq}}^3}{K_{11}} + \frac{P_{\text{GaCl eq}}^4}{K_{12}} \right) + \frac{1}{2} \frac{K_3 K_4^{1/2}}{x_{\text{Si}}^{1/2}} \left(1 + \frac{1}{K_2} \right) \right] \quad [\text{A-22}]$$

Then, using Eq. [A-8], the input terms add up to $-P_{\text{H}_2\text{O}}^0/2$. Thus, Eq. [A-22] becomes

$$\frac{dx_{\text{Si}}}{dt} = \frac{F}{2RTN_{\text{Ga}}} \left[\frac{K_3 K_4^{1/2} \left(1 + \frac{1}{K_2} \right)}{x_{\text{Si}}^{1/2}} - K_4^{1/2} x_{\text{Si}}^{1/2} - P_{\text{H}_2\text{O}}^0 - 2x_{\text{Si}} \left(\frac{P_{\text{GaCl eq}}}{K_9} + \frac{P_{\text{GaCl eq}}^2}{K_{10}} + \frac{P_{\text{GaCl eq}}^3}{K_{11}} + \frac{P_{\text{GaCl eq}}^4}{K_{12}} \right) \right] \quad [8]$$

REFERENCES

1. JANAF Thermochemical Tables, Published by U.S. Department of Commerce (1965).
2. C. N. Cochran and L. M. Foster, *This Journal*, **109**, 149 (1962).
3. J. M. Woodall, *Trans. Met. Soc. AIME*, **239**, 378 (1967).
4. J. F. Woods and N. G. Ainslie, *J. Appl. Phys.*, **34**, 1469 (1963).
5. M. E. Weiner and D. T. Lassota, Unpublished.
6. L. C. Luther and H. W. Verleur, *This Journal*, **118**, 1221 (1971).
7. C. J. Frosch, C. D. Thurmond, H. G. White, and J. A. May, *Trans. Met. Soc. AIME*, **239**, 365 (1967).
8. P. J. Dean, C. J. Frosch, and C. H. Henry, *J. Appl. Phys.*, **39**, 5631 (1968).
9. C. M. Ringle, *This Journal*, **118**, 609 (1971).
10. G. E. Moore and L. R. Dawson, Unpublished.
11. J. V. DiLorenzo, G. E. Moore, and A. E. Machala, Talk given at Electrochemical Society Meeting, Los Angeles, May 10-15, 1970.
12. S. J. Bass and P. E. Oliver, "Gallium Arsenide, Proceedings of the International Symposium," Inst. of Phys. and the Phys. Soc., p. 41 (1966).
13. M. Hansen and K. Anderko, "Constitution of Binary Alloys," McGraw-Hill Publishing Co., New York (1958).
14. R. R. Fergusson and T. Gabor, *This Journal*, **111**, 585 (1964).
15. Stull and Sinke, "Thermodynamic Properties of the Elements," Am. Chem. Soc. Advances in Chem. Series (1956).
16. K. B. Wolfstirn and L. R. Dawson, Private communication.

17. H. G. B. Hicks and P. D. Green, "Proceedings of 3rd International Symposium on Gallium Arsenide," Inst. of Phys. and Phys. Soc., p. 92 (1970).
18. J. V. DiLorenzo, R. B. Marcus, and R. Lewis, *J. Appl. Phys.*, **42**, 729 (1971).
19. L. C. Luther, Private communication.
20. D. T. J. Hurle and J. B. Mullin, "Crystal Growth," H. Steffen Peiser, Editor, pp. 241-248, Pergamon Press (1967).
21. L. C. Luther and D. D. Roccasecca, *This Journal*, **115**, 850 (1968).
22. H. C. Casey, Jr., Private communication.
23. H. Iwasaki and K. Sugibuchi, *Appl. Phys. Letters*, **18**, 420 (1971).
24. B. Schwartz, Private communication.
25. K. B. Wolfstirn, *J. Phys. Chem. Solids*, **31**, 601 (1970).
26. P. J. Dean, D. D. Manchon, and J. J. Hopfield, *Phys. Rev. Letters*, **52**, 1027 (1970).
27. D. D. Manchon, Private communication.

Thermodynamic Analysis of the III-V Alloy Semiconductor Phase Diagrams

II. The GaSb-GaAs System

L. M. Foster* and J. F. Woods

IBM Thomas J. Watson Research Center, Yorktown Heights, New York 10598

ABSTRACT

A thermodynamic analysis was made of the GaSb-GaAs pseudobinary phase diagram. The solid solutions in this system exhibit strong positive deviations from ideality, as evidenced by the large excess free energy of mixing, $B^s x_1 x_2$. An excellent fit of the experimental liquidus and solidus points was obtained with $B^s/RT = 2.00$ and $B^l/RT = -0.100$. These values designate the liquid as nearly ideal and the solid as bordering on phase separation. The latter is consistent with the observation that composition homogeneity is extremely difficult to achieve in this system. The large deviation from ideality in the solid is attributed to lattice strain resulting from the large lattice mismatch between the two components.

Alloys between the Group III-Group V semiconductor compounds offer some attractive features for the design of electronic and optical devices because of the possibility of obtaining a desired forbidden energy gap by selection of the alloy system and adjustment of the composition within the system (1-3). This presupposes that there is complete miscibility throughout the solid and that no metallurgical or chemical inhomogeneities are introduced by alloying that would adversely effect device performance.

In an earlier paper (4) we presented thermodynamic arguments which suggested that under some circumstances complete homogeneity and a smooth blending of crystal properties might in fact be lacking in some of the alloys as a consequence of the large excess free energy of mixing involved in their formation. The three systems that were investigated in that study were the pseudobinary alloys, InSb-GaSb, InAs-GaAs, and InP-GaP. They constitute a homologous series where only the Group V atom changes. In each system the departure from Raoult's law of mixing is positive; that is, the excess free energy of mixing is positive, increasing from the antimonides to the arsenides to the phosphides. This is also the order of increasing lattice parameter mismatch between the two components of the alloys.

A group of alloys such as III-(As, Sb), III-(As, P), and III-(Sb, P) would constitute another homologous series, in this case with a fixed Group III atom and different pairs of Group V atoms. Unfortunately, data for both the liquidus and solidus boundaries are not yet available for all of these alloys and, in fact, there is evidence that the III-(Sb, P) systems do not form

miscible solid solutions across the entire phase diagrams (5).

Recently our attention was called to unpublished data (6) for the liquidus of one of these systems (GaSb-GaAs) which, together with solidus data from the literature, permits calculation of the excess thermodynamic quantities and a comparison with the findings and conclusions of the earlier series.

Calculation procedure.—Details of the thermodynamic analysis were given in the earlier paper (4) and will not be repeated here. Briefly, the excess free energy of mixing for the liquid and solid solutions is given by $B^l x_1 x_2$ and $B^s x_1 x_2$, respectively, where x_1 and x_2 are mole fractions of components 1 and 2. The total free energy of mixing for the liquid then becomes

$$\Delta F^{M(l)} = RT(x_1 \ln x_1 + x_2 \ln x_2) + B^l x_1 x_2 \quad [1]$$

and for the solid

$$\Delta F^{M(s)} = RT(x_1 \ln x_1 + x_2 \ln x_2) + x_1 L_1 (T/T_1 - 1) + x_2 L_2 (T/T_2 - 1) + B^s x_1 x_2 \quad [2]$$

where T_1 and T_2 are the melting points and L_1 and L_2 are the latent heats of fusion for the two pure components. The parameters B are related to the activity coefficients through the relations (4)

$$\begin{aligned} \ln \gamma_1 &= (B/RT)x_2^2 \\ \ln \gamma_2 &= (B/RT)x_1^2 \end{aligned} \quad [3]$$

Reference (4) derives expressions for B^l and B^s at temperature T in terms of the liquidus and solidus compositions, x^l and x^s , taken from an experimentally determined binary phase diagram, as follows

* Electrochemical Society Active Member.
Key words: phase diagrams, compound semiconductors, solution theory.

$$B^l = \frac{RT \{ (1 - x^s)^2 \ln [(1 - x^l)/(1 - x^s)] - (x^s)^2 \ln (x^l/x^s) \}}{(x^s)^2 (1 - x^l)^2 - (x^l)^2 (1 - x^s)^2} - \frac{(1 - x^s)^2 L_1 (T - T_1)/T_1 - (x^s)^2 L_2 (T - T_2)/T_2}{(x^s)^2 (1 - x^l)^2 - (x^l)^2 (1 - x^s)^2} \quad [4]$$

$$B^s = \frac{RT \{ (1 - x^l)^2 \ln [(1 - x^s)/(1 - x^l)] - (x^l)^2 \ln (x^s/x^l) \}}{(x^l)^2 (1 - x^s)^2 - (x^s)^2 (1 - x^l)^2} + \frac{(1 - x^l)^2 L_1 (T - T_1)/T_1 - (x^l)^2 L_2 (T - T_2)/T_2}{(x^l)^2 (1 - x^s)^2 - (x^s)^2 (1 - x^l)^2} \quad [5]$$

Results

Kulwicki (6) obtained points on the liquidus boundary by differential thermal analysis of samples that had been equilibrated for 72 days at 695°C (Table I). These data are shown as open circles in Fig. 1. Points on the solidus boundary (filled circles) were obtained by Woolley and Smith (7) by an x-ray method, assuming that Vegard's rule applies. Equilibrium could not be achieved for compositions of lower GaAs content than those shown.¹ The dashed curves in Fig. 1 are the ideal liquidus and solidus boundaries calculated from Eq. 13 and 14 of Ref. (4), with $T_1 = 712^\circ\text{C}$ (10), $T_2 = 1240^\circ\text{C}$ (11), $L_1 = 15.56$ kcal/mole (10), and $L_2 = 25.18$ kcal/mole (11). The solid curves of Fig. 1 are calculated boundaries that meet certain criteria for acceptable data, as set forth in Ref. (4) and discussed in the next section.

Discussion

The GaSb-GaAs phase diagram appears to indicate strong positive deviations from ideality in the solid solution. As pointed out in Ref. (4), however, the degree to which the solid and liquid contribute separately to the gross features of the diagram cannot be guessed by cursory examination. This information can only come from actual calculation of pairs of B^s and B^l at selected temperatures, and the assignment of excess free energies therefrom. Figure 2 shows the excess free energy, Bx_1x_2 , for each phase, with the B parameters calculated from Eq. [5] and [6]. It is seen that the pronounced lowering of the solidus boundary is indeed attributable to the large positive $B^s x_1 x_2$. The liquid is almost ideal, and the very small negative excess free energy could be disregarded in an approximate calculation. It is interesting, however, that the arsenide system that was studied previously [InAs-GaAs (4)] also showed small negative deviations in the liquid. This could result from a small positive excess entropy of mixing, which implies a degree of ordering in one of the pure components which is lost in mixing. This property has been suggested for arsenic melts where there is some evidence of polymeric As molecules (12).

Figure 3 gives the plot of B/RT vs. x for GaSb-GaAs, and similar plots for the three systems from Ref. (4) for comparison. (The relationship between B/RT and the activity coefficients is shown by Eq. [3].) It was suggested in Ref. (4) that linearity of this plot might

¹ Straumanis and Kim (8) showed that Vegard's law was obeyed up to 34 m/o (mole per cent) GaAs, but could not obtain equilibrated samples after annealing up to 20 days beyond 60% GaAs. Muller and Richards (9) found that Vegard's law was obeyed in one determination at 50 m/o GaAs.

Table I. Differential thermal analysis of samples

Mole fraction GaAs	Liquidus temp. °C
0.20	990
0.30	1043
0.40	1085
0.50	1123
0.60	1154
0.72	1180
0.80	1200

be taken as a criterion of acceptable experimental data. Its B/RT plot for the available data is exactly linear for both the liquid and solid. Moreover, the plots are flat with $B^l/RT = -0.100$ and $B^s/RT = 2.00$, thus strengthening our earlier contention (4) that this family of binary alloys appears to be characterized by $B/RT \approx \text{constant}$.

The significance of B/RT is illustrated in Fig. 4 (the figures are exaggerated to illustrate the effects). With

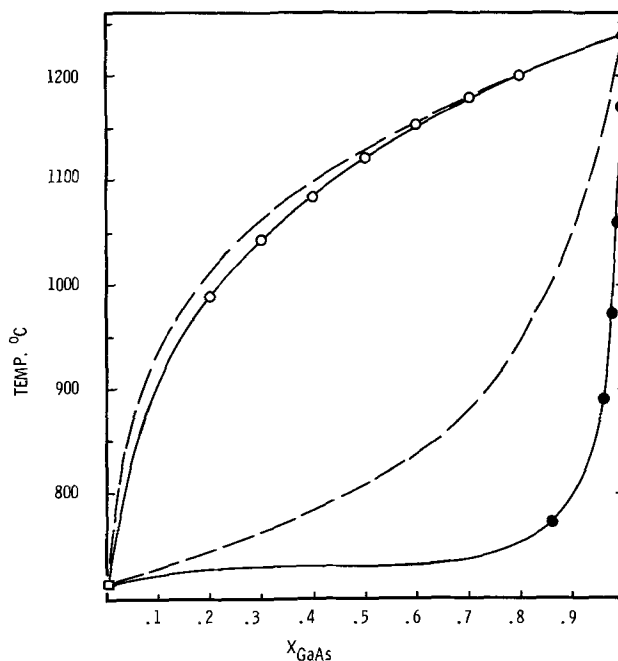


Fig. 1. GaSb-GaAs system. ○, Ref. (6); ●, Ref. (7); □, Ref. (10); △, Ref. (11).

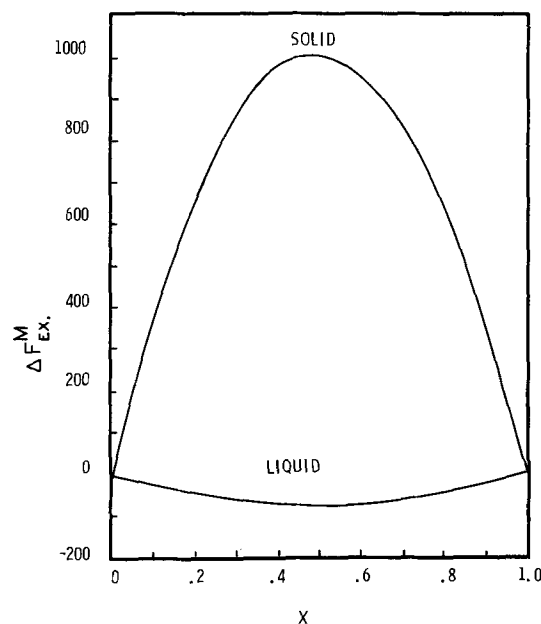


Fig. 2. Excess free energy of mixing in the GaSb-GaAs system

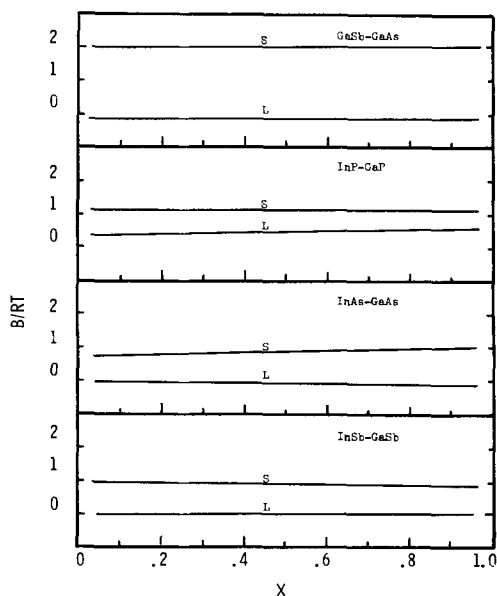


Fig. 3. B/RT vs. composition for III-V alloy systems

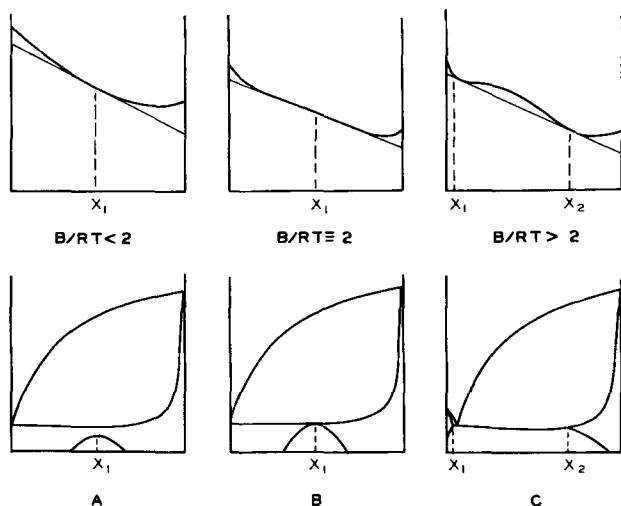


Fig. 4. Free energy of mixing of the solid and corresponding phase diagrams for cases where $B^s/RT \approx 2$.

$B^s/RT \leq 2$, the plot of $\Delta F^{M(s)}$ vs. x is concave upward throughout its entire course and at any value of x there is a unique tangent whose slope is the change in chemical potential of component 2. A miscibility gap should appear at a critical temperature, $T_c = B^s/RT$, which will be entirely within the solid phase. This is illustrated in Fig. 4A. $B^s/RT = 2$ is the upper limit of this quantity for which there is still a unique tangent to the free energy curve at any value of x and the maximum of the miscibility gap is coincident with the solidus at $x = 0.5$, as in Fig. 4B. For $B^s/RT > 2$, two inflection points appear in the $\Delta F^{M(s)}$ curve as the contribution of $B^s x_1 x_2$ in Eq. [2] becomes large in the vicinity of $x = 0.5$. There are two points of tangency where the slope is the same, corresponding to the same chemical potential at two compositions, and the solid, at equilibrium, separates into two phases, as in Fig. 4C.

The GaSb-GaAs system, with $B^s/RT = 2$, is of the type shown in Fig. 4B. The situation is very sensitive when B^s/RT is near 2, however, and values of this quantity just slightly greater or lesser would give calculated solidus and liquidus curves that would be acceptable fits to the data points, but which would predict phase separation in the solid at all temperatures on one hand, and complete miscibility just beneath the solidus on the other. (This assumes that B^s determined at a particular composition on the solidus

boundary remains constant down into the solid.) For example, with $B^s/RT = 2.01$, $\Delta F^{M(s)}$ already shows two tangents corresponding to a miscibility gap of 0.12 in mole fraction (from $x = 0.44$ to $x = 0.56$) in place of the continuous solidus line; whereas, with $B^s/RT = 1.99$ the peak of the miscibility gap is at 728°C , about 6° below the solidus at $x = 0.5$. It would be extremely difficult to establish experimentally whether the solidus of the GaSb-GaAs system does indeed follow the calculated curve, shown in Fig. 1, from the melting point of GaSb to the left-most data point because of the very narrow temperature range where homogenization of samples could be accomplished in this critical region. Both Kulwicki (6) and Woolley and Smith (7) noted their inability to equilibrate solid samples in this part of the diagram.

It is particularly significant that a constant B/RT fits the available data for both phases of the GaSb-GaAs system, for this is the fourth III-V alloy system that exhibits such behavior (Fig. 3). The implications of a constant B/RT were discussed in detail in Ref. (4). Briefly, if B is not dependent on composition, $B \propto T$ and the entire excess free energy of mixing, $B^s x_1 x_2$, appears as the entropy term, $T\Delta S$, in $\Delta F^{M_{ex}} = \Delta H^{M_{ex}} - T\Delta S^{M_{ex}}$, leaving no excess enthalpy of mixing. This outcome is not permitted by either the regular (13) or the quasichemical (14) treatments of solutions. The implication of this finding in terms of the properties of the III-V alloys is not clear at this time [see Ref. (4)].

The severe departure from ideality in the solid of the GaSb-GaAs system is consistent with the large lattice mismatch between the pure components, according to the pattern established in Ref. (4). The mismatch in the GaSb-GaAs system of 7.52% (0.442Å) is greatest of the four systems studied thus far and, as a rule of thumb, might be considered as the maximum mismatch that can be tolerated in this class of alloys for complete miscibility near the freezing point. According to this rule, of the eighteen possible pseudobinary alloys between the nine III-V compounds of Al, Ga, and In with P, As, and Sb, three (InSb-InP, GaSb-GaP, and AlSb-AlP) should not form miscible solid solutions, and one (AlSb-AlAs) would be doubtful. Many others would be expected to undergo spinodal decomposition when held for extended periods somewhat below their freezing points.

The fact that nonideality of the solids and the lattice mismatch vary in a parallel manner in the III-V alloys studied thus far, and the fact that the liquids depart only slightly from ideality, suggest that lattice strain is the principal contributor to the excess free energy in these systems.

Acknowledgment

The authors wish to thank Dr. B. M. Kulwicki of the Texas Instruments Inc., Attleboro, Massachusetts, for calling our attention to his work on the GaSb-GaAs system and for making his unpublished data available to us.

Manuscript submitted Sept. 16, 1971; revised manuscript received ca. Dec. 5, 1971.

Any discussion of this paper will appear in a Discussion Section to be published in the December 1972 JOURNAL.

REFERENCES

- O. G. Folberth, *Z. Naturforsch.*, **10a**, 502 (1955).
- H. Weiss, *ibid.*, **11a**, 430 (1956).
- C. Hilsum, "Proceedings 7th International Conference on Physics of Semiconductors," Paris, 1964, p. 1127.
- L. M. Foster and J. F. Woods, *This Journal*, **118**, 1175 (1971).
- E. K. Muller and J. L. Richards, *J. App. Phys.*, **35**, 1233 (1964).
- M. Miksovsky and B. M. Kulwicki, RNP presented at Electrochem. Soc. Meeting, San Francisco, May

- 9-13, 1965; *This Journal*, **112**, 149C (1965). The data are not supplied in this reference but were transmitted privately by Dr. Kulwicki.
7. "Compound Semiconductors," p. 12, R. K. Willardson and H. L. Goering, Editors, Reinhold Publishing Corp., New York (1962).
8. M. E. Straumanis and C. D. Kim, *This Journal*, **112**, 112 (1965).
9. E. K. Muller and J. L. Richards, *J. App. Phys.*, **35**, 1233 (1964).
10. B. D. Lichter and P. Sommelet, *Trans. AIME*, **245**, 99 (1969).
11. B. D. Lichter and P. Sommelet, *ibid.*, **245**, 1021 (1969).
12. J. R. Arthur, *J. Phys. Chem. Solids*, **28**, 2257 (1967).
13. J. H. Hildebrand and R. L. Scott, "Solubility of Non-electrolytes," Reinhold Publishing Corp., New York (1950).
14. E. A. Guggenheim, *Proc. Roy. Soc. (London)*, **A148**, 304 (1935).

Contact Resistance and Contact Resistivity

H. H. Berger

IBM Laboratory, 703 Boeblingen/Württ, West Germany

ABSTRACT

This paper mainly offers guidance to the technologist who has to characterize metal-semiconductor contacts for process development and production control. To abolish confusion clear definitions are proposed for the terms contact resistance and contact resistivity. Based on these definitions, methods of determining contact resistivity are discussed, revealing the common source of error of the methods and making comparisons. New methods like the TLM method are described and included in the comparison. Results of contact resistivity measurements on Al-Si contacts over a wide range of silicon surface doping are presented.

One of the obvious measures that have been taken to obtain higher densities in monolithic circuits has been to decrease the area provided for the metal-semiconductor interconnection contacts on the circuit chips. This has put a severe burden on the technologist, who has to develop proper production processes for small area contacts of low resistance and high reliability.

For this development work and for the process control, he needs clearly defined terms to describe the practically important contact qualities, as well as proper methods to measure them.

Such terms widely used are contact resistance and contact resistivity. However, there has been a lack of common understanding of their meaning. Moreover, although a number of methods to determine contact resistivity have been offered, a clear conception of their validity and accuracy has not always been worked out.

Accordingly the purpose of this paper is to offer suitable definitions for both contact resistance and contact resistivity and then to discuss several measurement methods for contact resistivity mainly to reveal their common source of measurement error. The comparison points out that there are three new methods which offer considerable less error than conventional procedures and simultaneously are well adapted to present fabrication processes. Finally, results of such contact resistivity measurements on aluminum-silicon contacts are reported, which enlarge the relatively rare data presently available.

Definition of Contact Resistance

Experience shows that the access to a semiconductor region via a metal contact usually exhibits higher resistance than expected from an ideal contact. The additional resistance may be imagined as being a series resistor in the lead to the ideal contact. It shall be referred to as "contact resistance."

The theoretical treatment of semiconductor devices has been facilitated by this mental image. Namely, it allows the consideration of the device behavior first under the simplifying condition of ideal contacts and later adding the experimentally or theoretically derived contact resistances that provide the corrections

Key words: ohmic contacts, contact resistance, contact resistivity, contact resistivity measurement, contact characterization.

for the actual contacts. Furthermore, it has provided a simple basis for comparing different contact-making processes.

The still rather vague notion of contact resistance as a series resistance describing the deviation of an actual contact from its ideal condition would be strengthened by a precise definition. But this requires first a clear conception of the ideal contact.

Practical contacts are nonideal for two basic reasons:

1. In a thin surface layer of the semiconductor beneath the contact metal the charge carrier density differs from that of the semiconductor bulk (accumulation or depletion layer) due to differences in work function of metal and semiconductor or due to surface states of the semiconductor.

2. Layers of foreign matter sometimes impede a rigorous contact of metal and semiconductor.

In contrast, an ideal contact does not exhibit any interface layers. Hence, its potential may be identified with the potential ϕ' in the contact plane of the semiconductor after extending the latter by its mirror image on that contact plane (Fig. 1).

To compare now the access via the actual contact with that via its ideal counterpart, a common reference plane P_r within the semiconductor must be identified. This plane must coincide with a plane of constant potential and must carry the total contact current. The

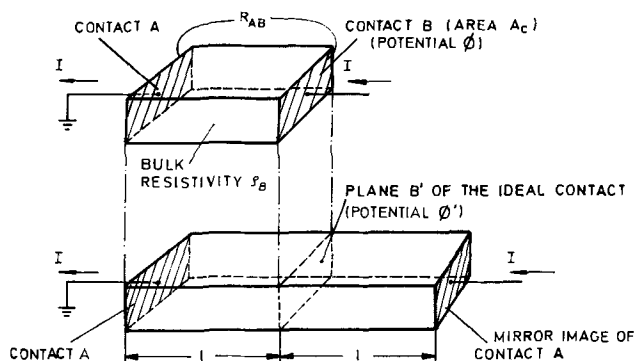


Fig. 1. Derivation of the potential ϕ' of the ideal contact (B') pertaining to the real contact (B) by mirror-imaging.

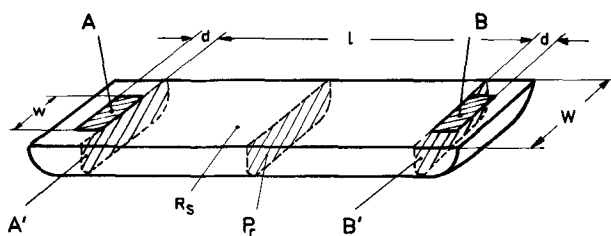


Fig. 2. Planar resistor with real contacts A and B and the most practicable locations A' and B' for the corresponding ideal contacts.

resistance between P_r and the actual contact is R_a , that between P_r and the ideal contact R_i . The contact resistance is then defined by the difference of these two resistances

$$R_c = R_a - R_i \quad [1]$$

Of course, for this comparison of R_a with R_i , the reference plane P_r must (practically) remain a plane of constant potential when the actual contact is replaced by its ideal counterpart. Hence, the mental image underlying the contact resistance concept fails where such a reference plane cannot be found. In such cases the contacts must be considered an integral part of the whole semiconductor device.

With the sample shown in Fig. 1, however, any plane parallel to the contacts may be taken for P_r provided that the contacts are uniform. Although no assumptions have been made in the definition of contact resistance regarding the position of the ideal contact, for the sample in Fig. 1, it is most convenient to let ideal and actual contact coincide. Taking, e.g., the grounded contact A as the reference plane P_r , the contact resistance of contact B may be written according to Eq. [1] as the difference of the potential ϕ of the actual contact and the potential ϕ' of its ideal counterpart, divided by the current I

$$R_c = \frac{\phi - \phi'}{I} \quad [2]$$

With other structures it might prove advantageous to choose a plane for the ideal contact that does not coincide with that of the actual contact. This is the case with the contact on a diffused resistor¹ shown in Fig. 2. By using the planes A' and B' for the ideal contacts, one facilitates the calculation of R_i in Eq. [1]. Thus, with the reference plane P_r in the center of the resistor² one obtains for equal contacts

$$R_c = \frac{1}{2} \left(R_{AB} - R_s \cdot \frac{l}{W} \right) \quad [3]$$

where R_s is the sheet resistance of the resistor layer. Solved for R_{AB}

$$R_{AB} = R_s \cdot \frac{l}{W} + 2R_c \quad [4]$$

it corresponds to the widely used formulation in terms of an "end correction" (equivalent number of squares k of the resistor layer)

$$R_{AB} = R_s \left(\frac{l}{W} + 2k \right) \quad [5]$$

Equation [4] leads to a practicable way of measuring the so defined contact resistance of a planar resistor. Such a resistor having three equal contacts A, B, C arranged in different distances l_1 and l_2 (Fig. 3) exhibits different resistances between A and B (R_1) and B and C (R_2). The contact resistance R_c can be eliminated by applying Eq. [4] to R_1 and R_2 , which results in

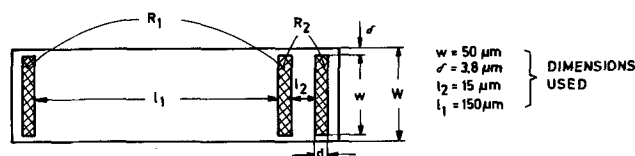


Fig. 3. Planar resistor having three contacts for contact resistance determination.

$$R_c = \frac{R_2 \cdot l_1 - R_1 \cdot l_2}{2(l_1 - l_2)} \quad [6]$$

It might appear peculiar that in this paper contact resistance has been defined in such a way as to allow a free choice of the position of the ideal contact, thus permitting the arbitrary introduction of semiconductor bulk portions into the contact resistance. Clearly, this would be a disadvantage if there were reasons to assume that coinciding ideal and actual contact planes would generally lead to a contact resistance being free of any semiconductor bulk influence and thus describing solely the metal-semiconductor interface. However, the replacement of the actual by the ideal contact alters the boundary conditions for the electric field in the semiconductor and hence changes the current distribution in the vicinity of the contact, unless it is fixed by the geometry of the sample as in Fig. 1. Obviously, a change of current distribution will introduce different bulk influence into R_a and R_i (Eq. [1]) and thus introduce bulk resistance into the contact resistance.³ Generally attempts to split the total contact resistance into interface and bulk contribution in the form of concentrated series resistors must be rather fruitless according to the foregoing discussion. Actually, it suffices to make this separation only for infinitesimal sections of the contact. This leads to the term "contact resistivity" solely describing the metal-semiconductor interface independent of contact geometry.⁴

Contact Resistivity

Contact resistivity ρ_c can be derived formally from the contact resistance definition. Consider a tube of current streamlines in the semiconductor device carrying a portion ΔI of the total current. In the plane of the contact the tube has a cross section of ΔA_c . The tube with its portion ΔA_c of the contact may now be considered as a device with a contact, for which a contact resistance R_c can be defined according to Eq. [1]. For this purpose, the plane of the ideal contact coincides with that of the actual one. Furthermore, it is assumed that the current flow within the interface portion of the tube is directed vertically to the contact plane. Then contact resistivity is defined as

$$\rho_c [\text{ohm cm}^2] = \lim_{\Delta A_c \rightarrow 0} (R_c \cdot \Delta A_c) \quad [7]$$

thus taking an infinitesimal tube of streamlines.

³ Hence, since the author believes that the expression contact resistance is worth being preserved, he had either to detach it from the described mental image underlying its usage or to refrain from the widespread association of contact resistance exclusively with the metal-semiconductor interface. The latter alternative was chosen in this paper from the outset. This choice is mainly based on the consideration that there is a sufficient reservoir of other expressions clearly referring solely to the resistance of the metal-semiconductor interface, like "transitional resistance", "interface resistance," or the geometry independent term "contact resistivity." The other choice has been tried by Ting and Chen (2). They have associated "contact resistance" solely with the metal-semiconductor interface and have used the expression "correction term" for the resistance defined by Eq. [3] ("contact resistance" in the present paper). The contact resistance contribution $R_{c,eff}$ to the correction term (in Ting and Chen's terminology) has been rated according to the power dissipation N in the interface layer: $R_{c,eff} = N \cdot I^{-2}$ (I = total current). Unfortunately, Ting and Chen have not subsequently applied this interesting concept to the semiconductor bulk resistance contributions, as these have not been rated via power dissipation. Instead, resistance calculations assuming ideal boundary conditions have been used. The error of such an approximation is probably not easy to assess. Also since $R_{c,eff}$ is difficult to determine, the practical value of Ting and Chen's concept appears questionable.

⁴ For metal-metal contacts treated by Holm (3) contact resistivity to a large extent is comprised of an average constriction resistance, which means that a strict separation between bulk and interface is not made there because of the somewhat different nature of metal-metal contacts.

¹ Very likely the contact on a diffused resistor is typical also for many contacts on other planar devices (1).

² Obviously, the resistor has to be sufficiently long to fulfill the condition that the coincidence of P_r and a constant potential plane be maintained when either one of the contacts is replaced by its ideal counterpart.

With Eq. [2] it can be written as

$$\rho_c = \lim_{\Delta A_c \rightarrow 0} \left[(\phi - \phi') \frac{\Delta A_c}{\Delta I} \right] \quad [8]$$

$$= \frac{1}{j_c} \lim_{\Delta A_c \rightarrow 0} (\phi - \phi') \quad [9]$$

where j_c stands for current density at the contact.

For a homogeneous contact having uniform current density as in Fig. 1, Eq. [7] simplifies to

$$\rho_c = R_c \cdot A_c \quad (j_c = \text{const.}) \quad [10]$$

This equation has been used to determine ρ_c via contact resistance and contact area A_c . However, it must be kept in mind, that it is valid only for contacts having uniform current distribution dictated by the sample geometry.

The assumption of vertical current flow in the interface layer is, of course, fulfilled with the sample in Fig. 1. It is also practically fulfilled even with adverse sample geometries, if the resistivity of the interface layer is much larger than that of the undisturbed semiconductor bulk. Most practical contacts indeed exhibit very thin depletion layers of very high resistivities.⁵ For these, without noticeable error, the thin depletion layer may even be considered as lying outside of the semiconductor like a possible layer of foreign matter. The potential difference $\phi - \phi'$ in Eq. [9] then becomes the total voltage drop v_c across these outside layers

$$\rho_c \approx \frac{v_c}{j_c} \quad [11]$$

This is the form⁶ most readily used in practical applications of ρ_c . Of course, a definite value ρ_c can only be given for contacts which are sufficiently ohmic within the range of current density under study.

Determination of Contact Resistivity

In determining contact resistivity the essential problem is to separate the metal-semiconductor interface resistance from the semiconductor bulk resistance. There are methods devised for d-c measurement and others for a-c measurement. The latter rely on the relatively large capacitance of the interface, which practically shorts its resistance at sufficiently high frequencies. Thus the interface resistance appears as the difference of a low and a high frequency resistance measured on suitable samples. Besides detrimental parasitic influences, the difficulty lies in taking small differences of large quantities.

D-C methods suffer from the latter difficulty as well; however, they are much more accurate than a-c measurements at very high frequency. In the following only d-c methods are considered.

The first three methods to be discussed (twin contact, differential, and interface probing methods) rely on samples that provide uniform current distribution so that Eq. [10] may be used. The remaining two (TLM and interface probing methods), however, utilize samples of nonuniform current distribution and thus are based on different relations for contact resistivity.⁷ It is shown that in spite of these differences, the main error of all d-c methods can be commonly described by the basic equation

$$\left| \frac{\Delta \rho_c}{\rho_c} \right| \lesssim \frac{\rho_B}{\rho_c} \cdot |\Delta l|_{\text{eff}} \quad [12]$$

⁵ The measurements on typical Al-Si that are presented in the section on Measurements on Al-Si Contacts indicate average resistivities of the depletion layers that are 100 to 1000 times larger than that of the semiconductor bulk.

⁶ Also compare the definition of "specific contact resistance" by Chang *et al.* (4).

⁷ There is another method proposed by Cox and Strack (5) that utilizes samples of nonuniform current distribution. This, however, tacitly assumes Eq. [10] to be valid in spite of a nonuniform current distribution. It appears very difficult to obtain an estimate of the error that is introduced by the contradicting assumption. Therefore, it has been excluded from the following discussion.

which considerably facilitates their comparison. In this equation, $|\Delta l|_{\text{eff}}$ is the effective error of one or more crucial length measurements which are required to separate the metal-semiconductor interface from the semiconductor bulk resistance. The accompanying electrical measurements are usually much more accurate with readily available equipment, so that they have a minor influence. The ratio of semiconductor bulk resistivity ρ_B to contact resistivity ρ_c is fixed by the nature of the contact under investigation. Thus, the relative error of the ρ_c determination for a given contact depends only on the absolute error of the crucial length measurements. According to the measurement results to be described in the section on Measurements on Al-Si Contacts, for aluminum-silicon contacts a $\rho_B/\rho_c = 0.1/\mu\text{m}$ might be used for a rough orientation. With this figure, an effective length measurement error $|\Delta l|_{\text{eff}} = 5 \mu\text{m}$ would cause a relative ρ_c error as large as 50%! Or, to obtain less than 10% error, $|\Delta l|_{\text{eff}} < 1 \mu\text{m}$ would be required.

*Twin contact method.*⁸—This measurement follows Eq. [1] and [10]. A homogeneous semiconductor body as in Fig. 1 carrying two equal contacts on opposite faces (area A_c) provides uniform current distribution so that Eq. [10] is valid. With the coinciding actual and ideal contact planes one obtains from Eq. [1]

$$R_c = \frac{1}{2} \left(R_{AB} - \rho_B \cdot \frac{l}{A_c} \right) \quad [13]$$

(compare with Fig. 1) or with Eq. [10]

$$\rho_c = \frac{1}{2} (R_{AB} \cdot A_c - \rho_B \cdot l) \quad [14]$$

The contact resistivity determined according to this equation is very sensitive to measurement errors, since usually a small difference of large terms appears. As shown in the Appendix, length measurement errors $|\Delta l|_{\text{eff}}$ have the largest influence, in agreement with Eq. [12].

When the Van der Pauw method (7) is used for ρ_B measurement, $|\Delta l|_{\text{eff}}$ in Eq. [12] becomes identical with the error $|\Delta l|$ of the probe thickness measurement. Practicable samples have a thickness of about 300 μm . $|\Delta l|$ within 5 to 10 μm can then be expected.⁹ According to the foregoing discussion this is too large for an accurate ρ_c determination on typical Al-Si contacts.

Differential method.—Compared with the twin contact method this new approach improves the accuracy by more than an order of magnitude. Figure 4 shows the sample structure and the measurement principle. A direct comparison is made of contact B under investigation with the contacts A and C, having negligible interface resistance due to a highly doped layer beneath the contact metal. The areas of all three contacts are equal.

This structure reflects the definition of R_c , where a real contact (B) is compared with an ideal contact (A or C) under otherwise equal conditions. Hence, the potential difference $\phi - \phi'$ (compare with Eq. [2]) can

⁸ Compare, e.g., Sullivan and Eigler (6).

⁹ Four-point probe measurements (8) yield about the same $|\Delta l|_{\text{eff}}$.

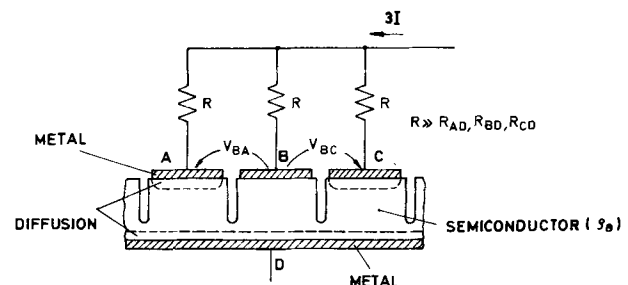


Fig. 4. Differential method for determining contact resistivity ρ_c

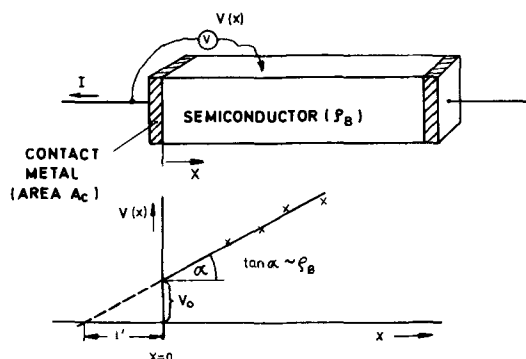


Fig. 5. Extrapolation method for determining contact resistivity ρ_c .

be directly measured as V_{BA} or V_{BC} . Usually a gradient of the sample thickness will disturb the result but can be eliminated by taking the average of V_{BA} and V_{BC} . Moreover, an error is introduced by the finite thickness x_j of the highly doped layers beneath A and C, which reduces the vertical resistance of the bulk by R_d . Hence one obtains

$$R_c = \frac{V_{BA} + V_{BC}}{2I} - R_d \quad [15]$$

For diffused layers beneath A and C, R_d can be approximated by

$$R_d \approx \rho_B \cdot \frac{x_j}{A_c} \quad [16]$$

where x_j is the junction depth obtained by the same diffusion in test wafers of equal bulk doping but opposite conduction type. Considering that Eq. [10] is valid for the sample structure, one arrives at

$$\rho_c = A_c \left(\frac{V_{BA} + V_{BC}}{2I} \right) - \rho_B \cdot x_j \quad [17]$$

Considerations similar to those explained in the Appendix for the twin contact method lead again to Eq. [12]. Of $|\Delta l|_{\text{eff}}$ the major portion here is the error in determining the thickness x_j of the highly doped layers beneath contacts A and C. Thus one obtains

$$\left| \frac{\Delta \rho_c}{\rho_c} \right| \approx \frac{\rho_B}{\rho_c} |\Delta x_j| \quad [18]$$

$|\Delta x_j|$ can be kept very small, usually about $0.2 \mu\text{m}$, showing the main advantage of this differential method.

Extrapolation method.¹⁰—Figure 5 explains this method. The voltage distribution $V(x)$ is measured along the homogeneous semiconductor bulk of constant cross section using a fine probe needle. The results then allow an extrapolation to the metal-semiconductor interface ($x = 0$) thus obtaining a voltage drop V_0 . This can be attributed to the contact resistance, since an ideal contact would show the voltage $V' = 0$ at this point. Hence, according to Eq. [2] the contact resistance becomes

$$R_c = \frac{\phi - \phi'}{I} = \frac{V_0}{I} \quad [19]$$

and with Eq. [10] one obtains

$$\rho_c = A_c \frac{V_0}{I} \quad [20]$$

The source of measurement error becomes obvious, when V_0 is replaced by the extrapolated length l' and by the bulk resistivity ρ_B (compare with Fig. 5)

¹⁰ In its essential part the extrapolation method has been described already by Joffe (9). It has been refined by Mengall and Seiler (10). Hooper *et al.* (11) have made the first larger series of measurements on contacts to silicon using this method.

$$V_0 = I \cdot \rho_B \cdot \frac{l'}{A_c} \quad [21]$$

which leads to (compare with Eq. [20])

$$\rho_c = \rho_B \cdot l' \quad [22]$$

or

$$\frac{\Delta \rho_c}{\rho_c} = \frac{\rho_B}{\rho_c} \Delta l' \quad [23]$$

This equation complies again with Eq. [12] as do the other methods. The error $\Delta l'$ is actually the uncertainty in determining the distance between contact interface and the probe needle tip. Most likely it lies in the order of $5 \mu\text{m}$, which makes this extrapolation method only somewhat superior to the twin contact method in accuracy.

TLM method (1, 12-15).—Berger (1, 12) as well as Murrmann and Widman (13-15) have shown that contacts to planar devices like the diffused resistor in Fig. 3 can be described by their geometry, the semiconductor sheet resistance R_s beneath the contact, and the contact resistivity ρ_c , when a transmission line model (TLM) is used.

In the TLM the following important parameters have been used

characteristic contact resistance

$$Z = \frac{1}{w} \sqrt{R_s \cdot \rho_c} \quad [24]$$

attenuation constant

$$\alpha = \sqrt{\frac{R_s}{\rho_c}} \quad [25]$$

where w = contact width (compare with Fig. 2).

For sufficiently wide contacts ($w \rightarrow W$) the contact resistance according to Eq. [3] becomes (2)

$$R_c = Z \coth \alpha d \quad [26]$$

where d is the contact length (compare with Fig. 2). Thus an "electrically long" contact ($\alpha d \gtrsim 2$) exhibits a contact resistance

$$R_c \approx Z \quad (\alpha d \gtrsim 2) \quad [27]$$

Hence, from a R_c measurement¹¹ on an electrically long contact one can determine the contact resistivity using Eq. [24]¹²

$$\rho_c = \frac{w^2 \cdot R_c^2}{R_s} \quad (\alpha d \gtrsim 2) \quad [28]$$

As is derived in the Appendix for the sample structure of Fig. 3, the relative error becomes

$$\frac{\Delta \rho_c}{\rho_c} \approx \alpha \Delta d \quad [29]$$

Once more, the main error is due to a length determination. To allow for easy comparison with an equation of type [12], a homogeneously doped layer having a resistivity ρ_B may be assumed instead of the diffused resistor layer. If the thickness of the resistor layer is properly chosen, a measurement error as small as

$$\frac{\Delta \rho_c}{\rho_c} \approx \frac{\rho_B}{\rho_c} \cdot 1.4 \cdot \Delta d \quad [30]$$

can be achieved (see Appendix).

Using a light microscope for measuring d , $|\Delta d|$ of less than $0.3 \mu\text{m}$ may be assumed yielding a comparative $|\Delta l|_{\text{eff}}$ (Eq. [12]) of about $0.4 \mu\text{m}$.

¹¹ Compare with Eq. [6].

¹² The method is not entirely restricted to electrically long contacts; using the diagram of Fig. 10 in Appendix 3, shorter contacts can be utilized as well.

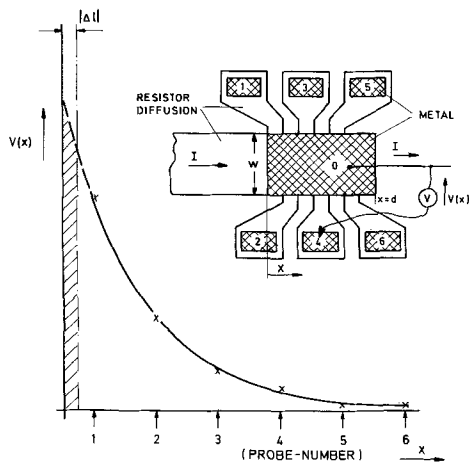


Fig. 6. Sample for the interface probing method of determining contact resistivity ρ_c after Ting and Chen (2), and typical voltage profile $V(x)$. Effect of length measurement error $|\Delta l|$ on $\int V(x) dx$ is indicated.

Interface probing method.—Ting and Chen (2) have determined contact resistivities of contacts on diffused layers by probing the voltage drop across the metal-semiconductor interface. The sample structure is shown in Fig. 6.

As the TLM indicates (1, 12-15), the current density in such a contact subsides along the x-direction and accordingly so does the voltage across the metal-semiconductor interface (compare with Eq. [11]). Assuming that the vertical voltage drop in the semiconductor layer is negligible compared with the interface voltage,¹³ the interface voltage profile can be probed by measuring the voltage difference between the resistor contact 0 and the contacts 1 through 6 (Fig. 6). The TLM predicts a nearly exponential voltage drop along x as the measurements by Ting and Chen have confirmed.

From this plot $V(x)$ as in Fig. 6, ρ_c can be calculated according to the following considerations

$$j(x) = \frac{V(x)}{\rho_c} \quad (\text{compare with Eq. [11]}) \quad [31]$$

$$I = W \int_0^d j(x) dx = \frac{W}{\rho_c} \int_0^d V(x) dx \quad [32]$$

$$\rho_c = \frac{W}{I} \int_0^d V(x) dx \quad [33]$$

The possible error in determining ρ_c will not be due to variations of the mutual distances of the probe fingers as these are fixed on a single mask. However, the distance of at least one probing point from the leading contact edge has to be measured, since here the alignment of two separate masks and etching tolerances are involved. The error of this length measurement Δl can be identified with the uncertainty of the position of the y-axis relative to the probing points (Fig. 6). The effect on ρ_c is then according to Eq. [33]

$$\Delta \rho_c \approx \frac{W}{I} \cdot V(0) \cdot \Delta l \quad [34]$$

For $V(0)$, the TLM yields approximately

$$V(0) \approx \rho_c \cdot \alpha \cdot \frac{I}{W} \quad [35]$$

The insertion of $V(0)$ into Eq. [34] yields the relative error

¹³ This is also one of the basic assumptions for the TLM and is correct in most of the practical cases of at least aluminum-silicon contacts (1).

	TWIN CONTACT	EXTRAPOLATION	DIFFERENTIAL	T L M	INTERFACE PROBING
LINEARITY CHECK	NO	YES	YES	YES	YES
ERROR $ \Delta l _{\text{eff}}$ [μm]	5	5	0.2	0.4	0.6
HOMOGENEITY CHECK	NO	NO	NO	YES	YES
$\frac{A_c \text{ SAMPLE}}{A_c \text{ DEVICE}}$	$\approx 10^4$	$\approx 10^4$	$\approx 10^4$	≈ 1	≈ 1

Fig. 7. Comparison of methods for determining contact resistivity ρ_c .

$$\frac{\Delta \rho_c}{\rho_c} \approx \alpha \cdot \Delta l \quad [36]$$

This compares with Eq. [29] derived for the TLM method. Hence, Eq. [30] is valid also for the interface probing method, if Δd is replaced by Δl .

The determination of the distance between a probing point and the leading contact edge causing the error Δl , requires two separate measurements, namely the probing finger to contact edge distance and the finger width. The finger width has to be divided by 2, assuming that the actual probing point lies on the center line of the finger.¹⁴ Thus in the worst case the total length measurement error is 1.5 times that of the TLM method. This results in a comparative value $|\Delta l|_{\text{eff}} \approx 0.6 \mu\text{m}$. Although less accurate under regular conditions, the extrapolation method appears superior to the TLM method in cases where the sheet resistance R_s of the semiconductor layer is altered beneath the contact by the contact making process. In this case it becomes intricate to determine the right value of R_s needed in the TLM method according to Eq. [28] [compare with Chang (16)], whereas the interface probing method does not require a R_s measurement at all.

Concluding comparison.—In the foregoing analysis of various d-c methods for contact resistivity determination the emphasis has been on measurement accuracy. It has been shown that Eq. [12] is indeed valid for all these methods, so that their error may be compared on the basis of the error $|\Delta l|_{\text{eff}}$ of the crucial length measurements.

However, besides accuracy a few other criteria should be considered as listed in Fig. 7. One wants to know whether the contact is indeed ohmic, which requires a linearity check. Checks for homogeneity are also important to confirm that the contact resistivity determined is meaningful and, of course, a good method uses sample dimensions that are representative for the actual device contacts. Figure 7 gives a clear cut between positive and negative answers to these criteria.¹⁵ There only remain the TLM and the interface probing methods with all positive answers. From the other methods, the differential method is still attractive as it offers high accuracy and as it can be easily applied to lightly doped semiconductor samples.

Measurements on Al-Si Contacts

The differential and the TLM methods have been used to determine the dependence of ρ_c on semiconductor doping level for Al-Si contacts. All contacts were on <100> oriented silicon and had been sintered at

¹⁴ For completeness it ought to be mentioned that this would be exactly true only in case of a uniform potential distribution along the finger width. The deviation of the actual probing point, from the center line, however, should be equal for all fingers (except near the contact end) due to the nearly exponential voltage drop. A corresponding correction of the position of the y-axis is principally possible from model measurements, if necessary at all.

¹⁵ For the measurement error criterion a $|\Delta l|_{\text{eff}}$ of $1 \mu\text{m}$ was chosen as a border between "positive" and "negative" answer, corresponding to a ρ_c error of 10% if a ratio $\rho_B/\rho_c = 0.1 \mu\text{m}$ is assumed.

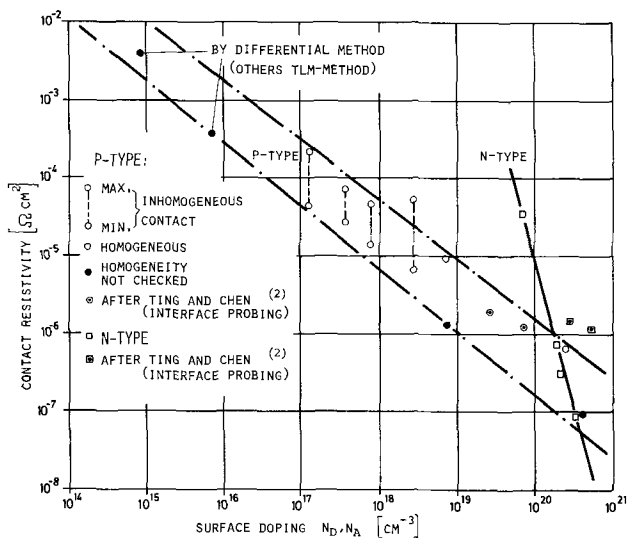


Fig. 8. Contact resistivity vs. surface doping of $\langle 100 \rangle$ oriented silicon for Al contacts, measured with differential or TLM method. Results by Ting and Chen (2) included for comparison (interface probing method).

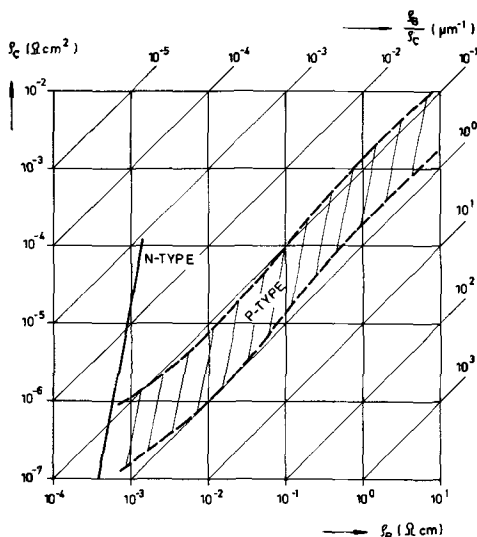


Fig. 9. Contact resistivity ρ_c vs. bulk resistivity ρ_B according to Fig. 8 for determination of measurement accuracy.

$\approx 400^\circ\text{C}$ for 20 min. The differential method has been most convenient for the high-ohmic p-type samples. In all other cases the TLM method has been applied using the sample structure of Fig. 3.

Figure 8 shows a plot of the results vs. surface doping of the silicon. Good ohmic contacts on n-type material could be achieved only above $\approx 5 \cdot 10^{19}/\text{cm}^3$. Below this doping level the contacts become at least partly Schottky diodes,¹⁶ and a meaningful contact resistivity cannot be specified.

On p-type silicon the very wide doping range of 10^{15} . . . $10^{21}/\text{cm}^3$ could be covered. Some of the samples, however, were inhomogeneous, with different contact resistivities at the contact edges and the center. By using different contact lengths and a supplement to the TLM method as described in Appendix 3, an upper and a lower limit for ρ_c have been determined in these cases.

The results by Ting and Chen (2) who used the interface probing method show some disagreement with the author's measurements on the highly doped n-type samples (compare with Fig. 9). However, the difference might be due to the difficulties of determining surface

¹⁶ The measurements on different contact lengths indicated that Schottky diodes with a very strong edge leakage have been obtained.

concentration especially in the high doping range. The author has used differential sheet resistance measurement on these n-type samples. For the p-type sample a gaussian profile has been assumed, allowing the use of Irvin's curves (17).

The measurements have demonstrated the applicability of the differential and the TLM methods. But they have pointed also to the general difficulty that inhomogeneities in the contact can appear and thus proper checks are necessary. The conditions which give rise to such inhomogeneities and their control deserves investigation, as fluctuating contact resistivities lead to uncontrolled current densities and thus are a potential reliability risk.

To get an impression on the possible effect of the length measurement on the contact resistivity errors according to Eq. [12], a diagram ρ_c vs. ρ_B (Fig. 9) has been derived from Fig. 8, using Irvin's curves (17) of resistivity vs. doping. In such a log/log-plot curves of constant ρ_B/ρ_c become straight lines, e.g., for p-type silicon the error becomes almost independent of doping level; according to the range of uncertainty shown, it lies between 4 and 40%, assuming a $|\Delta l|_{\text{eff}}$ of $0.4 \mu\text{m}$. For n-type silicon the error is a very strong function of bulk resistivity.

Summary

The definitions of the terms contact resistance and contact resistivity offered in this paper prevent confusion especially when dealing with contacts of nonuniform current distribution. Concurrently, the definitions are well adapted to measurement requirements.

In the discussion of different d-c methods for contact resistance determination, crucial length measurements have been revealed as a common main source of error. Considering all pertinent requirements, the TLM method, the interface probing method, and the differential method are the most promising.

Measurement results on Al-Si contacts using the differential and the TLM methods have enlarged the rare data on contact resistivities. From these results a diagram for predicting the error of contact resistance determination has been derived.

This paper can render some guidance to the technologist, how to characterize contacts during process development work and in production control. Moreover, the newer methods offered and the better appreciation of measurement accuracy might help the theorist as well in relating theoretical results with experimental data.

Acknowledgment

The author is indebted to Professors Dr. H. Beneking and Dr. D. Mlynski of the Technische Hochschule Aachen for helpful discussions. Thanks are due also to colleagues of the German IBM Laboratory for preparing measurement samples. This paper is part of a doctoral thesis approved by the Electrotechnical Faculty of the Technische Hochschule Aachen, Germany.

Manuscript submitted July 8, 1971; revised manuscript received Nov. 15, 1971. This was Paper 167 presented at the Cleveland Meeting of the Society, Oct. 3-8, 1971.

Any discussion of this paper will appear in a Discussion Section to be published in the December 1972 JOURNAL.

APPENDIX

1. Measurement Error of the Twin Contact Method

According to Eq. [14]

$$\rho_c = \frac{1}{2} (R_{AB} \cdot A_c - \rho_B \cdot l) \quad [\text{A-1}]$$

ρ_B is determined in a preceding measurement on the semiconductor body. No matter whether a four-point probe (8) or the Van der Pauw method (7) is used

here, ρ_B can be traced back to

$$\rho_B = R_x \cdot l^* \quad [\text{A-2}]$$

which says that both a resistance and a length measurement¹⁷ are necessary, each with its inherent error.

Using [A-1] and [A-2] and applying the total differential, one obtains for the error of ρ_c as a function of the contributing errors

$$\begin{aligned} |\Delta\rho_c| \leq & \frac{R_x \cdot l \cdot l^*}{2} \left[\frac{R_{AB} \cdot A_c}{R_x \cdot l \cdot l^*} \left(\left| \frac{\Delta R_{AB}}{R_{AB}} \right| \right. \right. \\ & \left. \left. + \left| \frac{\Delta A_c}{A_c} \right| \right) + \left| \frac{\Delta l^*}{l^*} \right| + \left| \frac{\Delta l}{l} \right| + \left| \frac{\Delta R_x}{R_x} \right| \right] \quad [\text{A-3}] \end{aligned}$$

Dividing by ρ_c , resubstituting $R_x \cdot l^*$ by ρ_B and replacing $R_{AB} \cdot A_c / \rho_B \cdot l$ by $1 + (2\rho_c / \rho_B \cdot l)$ according to Eq. [A-1], one obtains the relative error

$$\begin{aligned} \frac{\Delta\rho_c}{\rho_c} \leq & \frac{\rho_B \cdot l}{2\rho_c} \left[\left(1 + \frac{2\rho_c}{\rho_B \cdot l} \right) \left(\left| \frac{\Delta R_{AB}}{R_{AB}} \right| \right. \right. \\ & \left. \left. + \left| \frac{\Delta A_c}{A_c} \right| + \left| \frac{\Delta l^*}{l^*} \right| + \left| \frac{\Delta l}{l} \right| + \left| \frac{\Delta R_x}{R_x} \right| \right) \right] \quad [\text{A-4}] \end{aligned}$$

The ρ_c determination is critical, since both terms on the right-hand side of Eq. [A-1] are usually large as compared to ρ_c . Hence in these critical cases the term $2\rho_c / \rho_B \cdot l$, in Eq. [A-4] may be neglected, which yields

$$\begin{aligned} \left| \frac{\Delta\rho_c}{\rho_c} \right| \leq & \frac{\rho_B \cdot l}{2\rho_c} \left(\left| \frac{\Delta R_{AB}}{R_{AB}} \right| + \left| \frac{\Delta A_c}{A_c} \right| \right. \\ & \left. + \left| \frac{\Delta l^*}{l^*} \right| + \left| \frac{\Delta l}{l} \right| + \left| \frac{\Delta R_x}{R_x} \right| \right) \quad [\text{A-5}] \end{aligned}$$

Using accurate equipment, the errors of resistor measurement can be kept much smaller than usual length measurement errors. Thus by neglecting the resistor errors, Eq. [A-5] can be written as

$$\left| \frac{\Delta\rho_c}{\rho_c} \right| \leq \frac{\rho_B}{\rho_c} \cdot |\Delta l|_{\text{eff}} \quad [\text{A-6}]$$

where

$$|\Delta l|_{\text{eff}} = \frac{l}{2} \cdot \left(\left| \frac{\Delta A_c}{A_c} \right| + \left| \frac{\Delta l^*}{l^*} \right| + \left| \frac{\Delta l}{l} \right| \right) \quad [\text{A-7}]$$

Assuming a sufficiently large contact area A_c , the error $\left| \frac{\Delta A_c}{A_c} \right|$ can also be neglected, so that for the Van der Pauw method with $l^* = l$, one simply obtains

$$|\Delta l|_{\text{eff}} = |\Delta l| \quad [\text{A-8}]$$

2. Measurement Error of the TLM Method

Starting with Eq. [28]

$$\rho_c = \frac{w^2 \cdot R_c^2}{R_s}$$

one obtains

$$\ln \rho_c = 2 \ln w - \ln R_s + 2 \ln R_c \quad [\text{A-9}]$$

or

$$\frac{d\rho_c}{\rho_c} = 2 \frac{dw}{w} - \frac{dR_s}{R_s} + 2 \frac{dR_c}{R_c} \quad [\text{A-10}]$$

Doubtlessly, the main error will be due to the error in determining R_c , because of the small differences of large numbers to be taken in Eq. [6], so that

$$\frac{\Delta\rho_c}{\rho_c} = 2 \frac{\Delta R_c}{R_c} \quad [\text{A-11}]$$

It is convenient to introduce a term $y = l_1/l_2$ in Eq. [6]

$$R_c = \frac{R_2 \cdot y - R_1}{2(y - 1)} \quad [\text{A-12}]$$

¹⁷ Van der Pauw method: $l^* = l =$ thickness of the sample. Four-point probe: $l^* = s =$ distance between probe tips if $l \gg s$.

The total differential then becomes

$$\begin{aligned} dR_c = & \frac{\partial R_c}{\partial y} \cdot \frac{\partial y}{\partial l_1} \cdot dl_1 + \frac{\partial R_c}{\partial y} \cdot \frac{\partial y}{\partial l_2} \cdot dl_2 \\ & + \frac{\partial R_c}{\partial R_2} \cdot dR_2 + \frac{\partial R_c}{\partial R_1} \cdot dR_1 \quad [\text{A-13}] \end{aligned}$$

From these error constituents the part due to length measurement errors will be considered first

$$\Delta R_c(\Delta l) \approx \frac{\partial R_c}{\partial y} \left(\frac{\partial y}{\partial l_1} \Delta l_1 + \frac{\partial y}{\partial l_2} \Delta l_2 \right) \quad [\text{A-14}]$$

Looking at Fig. 3 one conceives that Δl_1 or Δl_2 are related to the variations Δd of contact hole lengths, as the center distances of the contact holes are fixed by the photomask. Within the small area of a diffused resistor the over- or underetching of contact holes is tracking, so that one can assume

$$\Delta l_1 = \Delta l_2 = -\Delta d \quad [\text{A-15}]$$

thus getting from Eq. [A-14]

$$\Delta R_c(\Delta l) \approx -\frac{\partial R_c}{\partial y} \cdot \Delta d \left(\frac{\partial y}{\partial l_1} + \frac{\partial y}{\partial l_2} \right) \quad [\text{A-16}]$$

Carrying out the differentiations, one obtains

$$\frac{\Delta R_c(\Delta l)}{R_c} \approx \frac{1}{R_c} \cdot \frac{R_1 - R_2}{(y - 1)} \cdot \frac{\Delta d}{l_2} \quad [\text{A-17}]$$

Assuming a sufficiently long contact, so that $R_c \approx Z$ (Eq. [26] and [27] and considering Eq. [5] one can write

$$\frac{\Delta R_c(\Delta l)}{R_c} \approx \frac{R_s}{2W \cdot Z} \cdot \Delta d \quad [\text{A-18}]$$

With $w \approx W$ from Eq. [24] and [25] one recognizes this as

$$\frac{\Delta R_c(\Delta l)}{R_c} \approx \frac{\alpha}{2} \cdot \Delta d \quad [\text{A-19}]$$

The second error contribution by resistor measurement errors (Eq. [13]) can be written as

$$\Delta R_c(\Delta R) \approx \frac{\partial R_c}{\partial R_2} \cdot \frac{\Delta R_2}{R_2} \cdot R_2 + \frac{\partial R_c}{\partial R_1} \cdot \frac{\Delta R_1}{R_1} \cdot R_1 \quad [\text{A-20}]$$

A constant relative error of resistor measurement shall be assumed for simplicity

$$\left| \frac{\Delta R_2}{R_2} \right| = \left| \frac{\Delta R_1}{R_1} \right| = M \quad [\text{A-21}]$$

so that Eq. [A-20] leads to

$$\frac{\Delta R_c(\Delta R)}{R_c} \leq \frac{M}{R_c} \left(\left| \frac{\partial R_c}{\partial R_2} \right| \cdot R_2 + \left| \frac{\partial R_c}{\partial R_1} \right| \cdot R_1 \right) \quad [\text{A-22}]$$

Carrying out the differentiations on Eq. [A-12] one arrives at

$$\left| \frac{\Delta R_c(\Delta R)}{R_c} \right| \leq M \cdot \frac{R_2 \cdot y + R_1}{R_2 \cdot y - R_1} \quad [\text{A-23}]$$

After some conversions using Eq. [3] for R_1 and R_2 and taking $R_c \approx Z$, $w \approx W$ with Eq. [24] and [25], [A-23] becomes

$$\left| \frac{\Delta R_c(\Delta R)}{R_c} \right| \leq M \cdot \frac{\alpha l_2 y + y + 1}{y - 1} \quad [\text{A-24}]$$

This error is minimized by choosing $y \gg 1$

$$\left| \frac{\Delta R_c(\Delta R)}{R_c} \right| \leq M (\alpha l_2 + 1) \quad (y \gg 1) \quad [\text{A-25}]$$

Now this result can be compared with the error contribution $\left| \frac{\Delta R_c(\Delta l)}{R_c} \right|$ after Eq. [A-19]. One may assume that usually $\alpha l_2 > 1$. Thus it is sufficient to compare

$M \cdot \alpha \cdot l_2$ with $\frac{1}{2}\alpha|\Delta d|$. In the sample structure according to Fig. 3, $l_2 = 15 \mu\text{m}$ has been used, but it is possible to reduce it to $\approx 7 \mu\text{m}$. With precision equipment $M \leq 3 \cdot 10^{-3}$ can be achieved. Using a light microscope for measuring d , $|\Delta d| \leq 3 \cdot 10^{-1} \mu\text{m}$ would be possible, so that $Ml_2 \ll \left| \frac{\Delta d}{2} \right|$ is true. This might change, if, e.g., an electron scanning microscope is used for the measurement of d . So far, however, the prevailing error of ρ_c is according to Eq. [A-19] and [A-11]

$$\frac{\Delta \rho_c}{\rho_c} \approx \alpha \Delta d \quad [\text{A-26}]$$

α can be related to a quotient ρ_B/ρ_c as it appears in Eq. [12] by taking a homogeneously doped resistor. According to an extended TLM (-ETLM) (1) the corresponding α becomes

$$\alpha^* = \frac{1}{\sqrt{\eta + 0.2}} \cdot \frac{1}{h} \quad [\text{A-27}]$$

where $\eta = \frac{\rho_c}{\rho_B \cdot h}$ and $h =$ semiconductor layer thickness.

For reasons of accuracy one requires a minimum η of 2, which also allows the term 0.2 in Eq. [A-27] to be neglected.¹⁸ Multiplying with η/η one then obtains

$$\alpha^* = \frac{\rho_B}{\rho_c} \sqrt{\eta} \quad [\text{A-28}]$$

Adjusting the structure for the minimum η of 2, one then obtains with Eq. [A-26]

$$\frac{\Delta \rho_c}{\rho_c} \approx \frac{\rho_B}{\rho_c} \cdot 1.4 \cdot \Delta d \quad [\text{A-29}]$$

3. Supplement to the TLM Method

Contacts having $ad \lesssim 2$ can be treated as follows: combining Eq. [24], [25], and [26] one obtains

$$\frac{R_s \cdot d}{R_c \cdot w} = ad \cdot \tanh ad \quad [\text{A-30}]$$

from which via the diagram, Fig. 10, α can be determined when R_s , d , R_c , and w are known. Equation [25] then yields

$$\rho_c = \frac{R_s}{\alpha^2} \quad [\text{A-31}]$$

There are two more possibilities of determining α required in Eq. [A-31]. A measurement according to Fig. 11 leads to a "contact end resistance" value $R_e = v_2/i_1$, which according to the TLM becomes

$$R_e = \frac{Z}{\sinh ad} \quad [\text{A-32}]$$

Thus from the quotient (compare Eq. [26])

$$\frac{R_c}{R_e} = \cosh ad \quad [\text{A-33}]$$

α can be determined.

If the contact again is electrically long ($ad \gtrsim 2$), Eq. [A-32] can be approximated by

$$R_e \approx \frac{Z}{2} \cdot e^{-ad} \quad [\text{A-34}]$$

Taking two contacts with a length difference $\Delta d =$

¹⁸ However, this term may not be neglected in the result ρ_c which has to be corrected by $\approx -\frac{0.2}{\eta}$ (1).

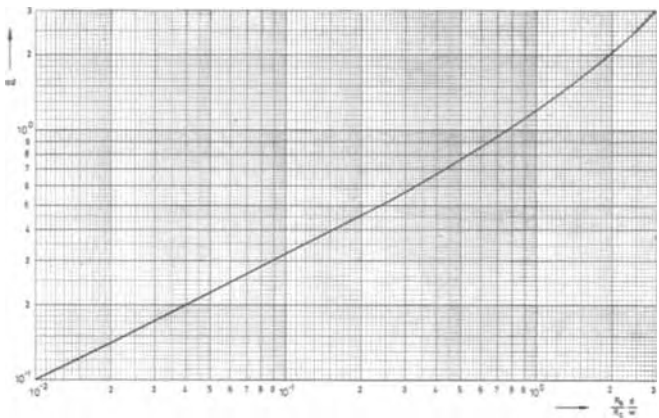


Fig. 10. Diagram for determination of attenuation constant α via contact resistance R_c .

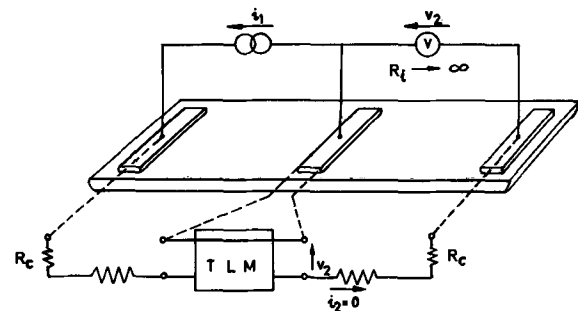


Fig. 11. Measurement of contact end resistance R_e

($d_1 - d_2$) one obtains

$$\frac{R_{e2}}{R_{e1}} \approx e^{\alpha \Delta d} \quad [\text{A-35}]$$

yielding α . This procedure offers an advantageous means of process control as the difference Δd is fixed by the photomask and is influenced only very little by the contact opening process. Thus the critical length measurement can be saved. The ρ_c results, however, are influenced much more by small contact homogeneities than when using the more averaging R_c according to Eq. [28].

REFERENCES

- H. H. Berger, *Solid-State Electron.*, **15**, 145 (1972).
- C. Y. Ting and C. Y. Chen, *Solid-State Electron.*, **14**, 433 (1971).
- R. Holm, "Electric Contacts," Springer-Verlag, Berlin, Heidelberg, New York (1967).
- C. Y. Chang et al., *Solid-State Electron.*, **14**, 541 (1971).
- R. H. Cox and H. Strack, *ibid.*, **10**, 1213 (1967).
- M. V. Sullivan and J. H. Eigler, *This Journal*, **103**, 218 (1956).
- J. Van der Pauw, *Philips Res. Rept.*, **13**, 1 (1958).
- L. B. Valdes, *Proc. IRE*, **42**, 420 (1954).
- A. V. Joffe, *J. Phys. USSR*, **10**, 49 (1946).
- O. J. Mengali and M. R. Seiler, *Advan. Energy Conversion*, **2**, 59 (1962).
- R. C. Hooper et al., *Solid-State Electron.*, **8**, 831 (1965).
- H. H. Berger, Dig. Techn. Papers ISSCC 1969, pp. 160-161.
- H. Murrmann and D. Widman, *ibid.*, pp. 162-163.
- H. Murrmann and D. Widman, *Solid-State Electron.*, **12**, 879 (1969).
- H. Murrmann and D. Widman, *IEEE*, **ED-16**, 1022 (1969).
- I. F. Chang, *This Journal*, **117**, 368 (1970).
- J. C. Irvin, *Bell System Tech. J.*, **41**, 387 (1962).

The Nature of Semiconductivity in Polycrystalline Tin Oxide

Colin A. Vincent

Department of Chemistry, University of St. Andrews, St. Andrews, Fife, Scotland

ABSTRACT

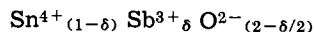
The differences in nonstoichiometric and controlled valence n-type semiconductors based on tin oxide are considered. The thermodynamic stability of tin and antimony oxides are calculated, and an assessment is made of the likely stabilities of the various forms of semiconductor.

Conducting tin oxides have been known for many years; thus Foex (1) reviewing work done up to 1943 cites investigations reported as early as 1910. However, although a number of authors have recently described methods for producing n-type semiconducting tin oxides, they have not always made clear what chemical species were responsible for producing the conductivity. Thus, for instance, Miloslavskii (2) employed pyrolytic decomposition of mixtures of SnII and SnIV chlorides at 500°-600°C to produce a semiconducting film on glass, whereas Bartholomew and Garfinkel (3) used SnCl₂ and Arai and co-workers (4) used SnCl₄. More commonly a mixture of SnIV and SbIII or FI compounds are used. It was therefore thought useful prior to attempting to prepare tin oxide semiconductors from solution to investigate the types of semiconductor which might be produced by different dopants as well as their probable stability.

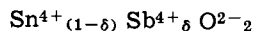
Nonstoichiometric and Controlled Valence Semiconductors

Verwey (5) has described the basic difference between nonstoichiometric and controlled valence semiconductors. In the former, for every ion of deviating valency inserted into the lattice a defect such as a lattice vacancy must also be introduced; in the latter, extra ions are added so that there is no incorporation of lattice defects.

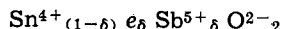
Consider a fraction δ of the SnIV sites in a SnO₂ crystal to be substituted by SbIII, by formally taking $\delta/2$ moles of Sb₂O₃ and $(1 - \delta)$ moles of SnO₂ to give



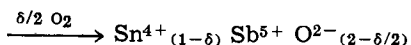
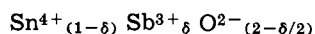
Such a system, which has correctly balanced charges of $(4 - \delta)^+$ and $(4 - \delta)^-$, if based on a cassiterite lattice has $\delta/2$ moles of vacancies on oxide sites. These may be filled if the material is heated in an oxygen-containing atmosphere, provided that there are electrons available within it to reduce the oxygen. Here we have $\text{Sn}^{4+}_{(1-\delta)} \text{Sb}^{3+}_{\delta} \text{O}^{2-}_{(2-\delta/2)}$ reacting with $\delta/4$ O₂ to give



i.e.



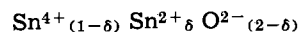
where there are δ moles of electrons donated to the conduction band of the lattice. This material has no defects and is a controlled valence semiconductor. For the successful formation of such a substance it is essential that complete air oxidation of antimony to Sb₂O₅ does not occur



This system is an insulator.

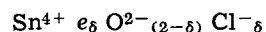
Key words: tin oxide, semiconductivity, thermodynamic stability.

In contrast with the SnIV/SbIII system it is impossible to produce a controlled valence SnIV/SnII semiconductor. On combining δ moles of SnO with $(1 - \delta)$ moles of SnO₂ the nonstoichiometric oxide



is formed. This is likely to be a semiconductor since the 2 moles of electrons formally assigned to the Sn²⁺ ions will be free to move to other Sn⁴⁺ sites. However, to form a controlled valence semiconductor an additional $\delta/2$ moles of oxygen would be required to be incorporated with an associated transfer of 2δ moles of electrons from the SnII. Thus pure insulating SnO₂ would be formed. The stability of the nonstoichiometric tin oxide under different conditions of temperature and oxygen partial pressure will depend basically on the relative stabilities of SnO and SnO₂. A similar argument may be advanced for a system containing Sn, such as $\text{Sn}^{4+}_{(1-\delta)} \text{Sn}_{\delta} \text{O}^{2-}_{(2-2\delta)}$.

A controlled valence semiconductor may however be formed by substituting δ moles of oxide ions by chloride ions in the lattice to give



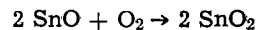
Since chlorine has one less 2p orbital to fill than oxygen, for every chloride substitution a tin atom must retain an extra 5s electron which enters the conduction band of the lattice.

Thermodynamic Stability of the Oxides

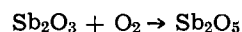
The stabilities of the oxides of tin and antimony over the range of temperatures 300°-1500°K were calculated using the equation

$$\Delta G^{\circ} = \Delta H^{\circ} + aT \ln T + bT^2 + cT^{-1} + IT$$

and values for the parameters from the U. S. Bureau of Mines Bulletin 542 (1954). Ellingham diagrams for the formation of SnO and SnO₂ and for Sb₂O₃ and Sb₂O₅ are shown in Fig. 1 and 2, respectively. From the functions illustrated the free energy changes for the reactions



and



were determined and are given in Fig. 3 together with the corresponding equilibrium constant functions in Fig. 4. It is apparent that in the presence of oxygen SnO₂ is considerably more stable than SnO over the whole temperature range investigated. On the other hand the difference in stabilities between Sb₂O₃ and Sb₂O₅ is not so great and above 1240°K the former is the more stable. In interpreting this result it is important to note that it holds for pure Sb₂O₃ with respect to Sb₂O₅ and that it is not possible to conclude that SbIII is never stable in oxygen below this temperature.

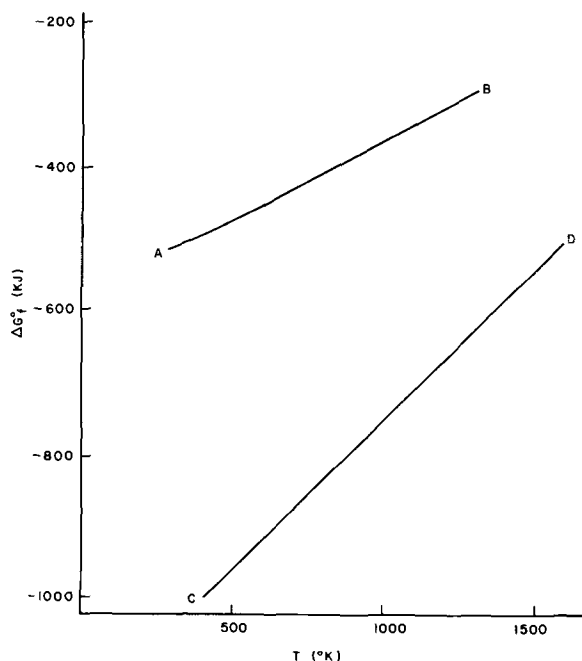


Fig. 1. AB: free energy of formation of 2SnO , CD: free energy of formation of 2SnO_2 .

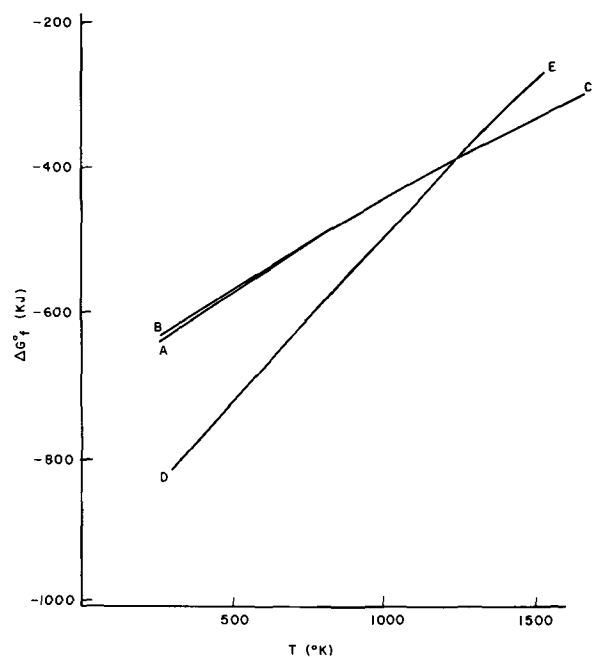
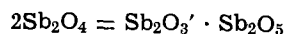


Fig. 2. AC: free energy of formation of Sb_2O_3 (cubic in solid state), BC: free energy of formation of Sb_2O_3 (orthorhombic in solid state), DE: free energy of formation of Sb_2O_5 .

A number of other antimony oxides are known, such as α - and β - Sb_2O_4 and Sb_6O_{13} , which contain antimony in III and V oxidation states. X-ray crystallographic studies (6) of the two Sb_2O_4 oxides have shown them to consist of units of SbV octahedrally surrounded by oxygen and SbIII having a "one-sided" fourfold coordination. The latter environment is very different from that of Sb in either orthorhombic (low temperature) or cubic Sb_2O_3 .

Sb_2O_4 consists of an equal number of SbIII and SbV units and we take



where $\text{Sb}_2\text{O}_3'$ represents the trivalent antimony oxide in Sb_2O_4 . Assuming that the pentavalent oxide in this compound is very similar to Sb_2O_5 , the free energy of

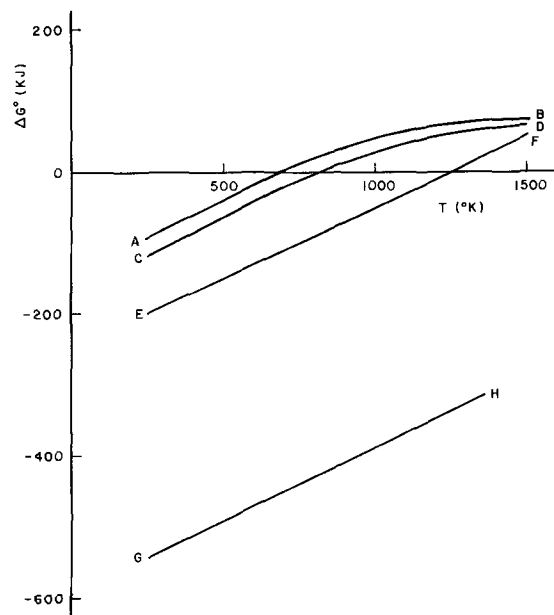


Fig. 3. AB: free energy of oxidation of $\text{Sb}_2\text{O}_3''$ to Sb_2O_5 , CD: free energy of oxidation of $\text{Sb}_2\text{O}_3'$ to Sb_2O_5 , EF: free energy of oxidation of Sb_2O_3 to Sb_2O_5 , GH: free energy of 2SnO to 2SnO_2 .

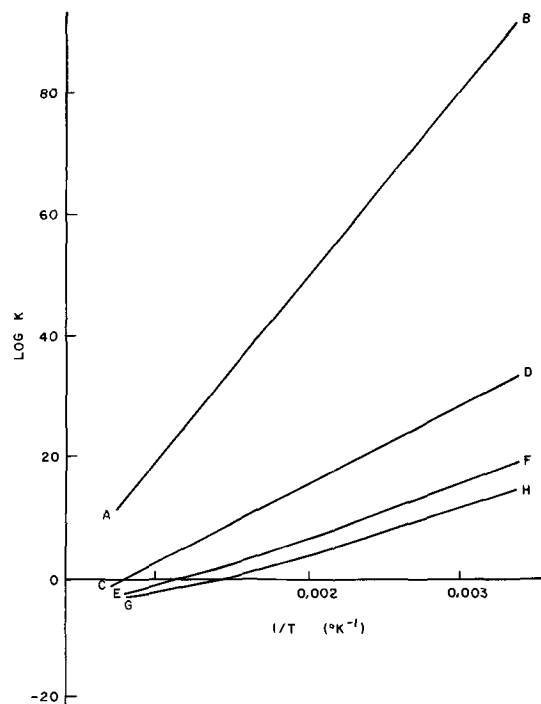


Fig. 4. AB: $2\text{SnO} + \text{O}_2 \rightarrow 2\text{SnO}_2$, CD: $\text{Sb}_2\text{O}_3 + \text{O}_2 \rightarrow 2\text{Sb}_2\text{O}_5$, EF: $\text{Sb}_2\text{O}_3' + \text{O}_2 \rightarrow \text{Sb}_2\text{O}_5$, GH: $\text{Sb}_2\text{O}_3'' + \text{O}_2 \rightarrow \text{Sb}_2\text{O}_5$.

formation of a mole of Sb_2O_3 in the Sb_2O_4 system was estimated as

$$(\Delta G^\circ_f)_{\text{Sb}_2\text{O}_3'} = 2(\Delta G^\circ_f)_{\text{Sb}_2\text{O}_4} - (\Delta G^\circ_f)_{\text{Sb}_2\text{O}_5}$$

This function is shown as curve CD in Fig. 5. It is seen that the stability of $\text{Sb}_2\text{O}_3'$ is so much enhanced that Sb_2O_4 is stable to oxidation at much lower temperatures than Sb_2O_3 . Another well-characterized oxide, Sb_6O_{13} may be treated in a similar way as $\text{Sb}_2\text{O}_3'' \cdot 2\text{Sb}_2\text{O}_5$. ΔG°_f for 1 mole of Sb_2O_3 in Sb_6O_{13} was estimated as

$$(\Delta G^\circ_f)_{\text{Sb}_2\text{O}_3''} = (\Delta G^\circ_f)_{\text{Sb}_6\text{O}_{13}} - 2(\Delta G^\circ_f)_{\text{Sb}_2\text{O}_5}$$

and is shown in Fig. 5 as curve EF. The SbIII is seen to be further stabilized to oxidation.

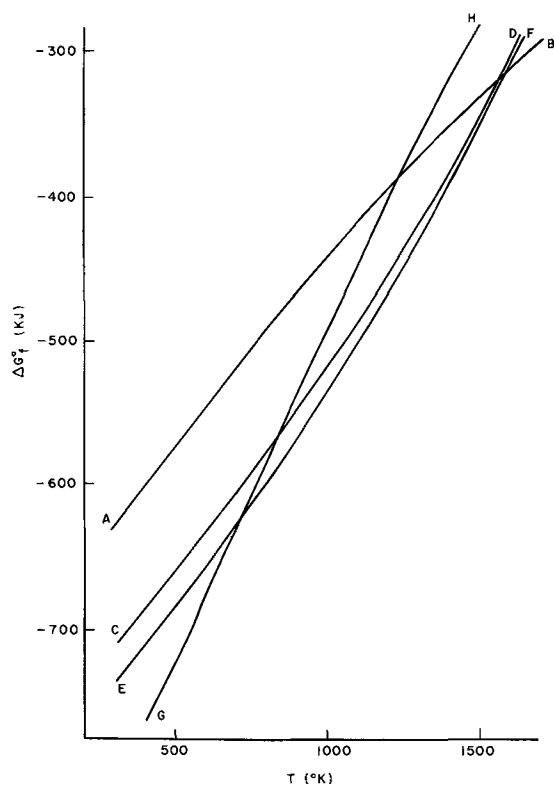


Fig. 5. AB: free energy of formation of Sb_2O_3 , CD: free energy of formation of $\text{Sb}_2\text{O}_3'$, EF: free energy of formation of $\text{Sb}_2\text{O}_3''$, GH: free energy of formation of Sb_2O_5 .

Tin does not possess a similar stable group of mixed oxides. Some evidence for the existence of Sn_3O_4 has been suggested as a result of thermochemical investigations of SnO (7) and a quantity of a compound with formula Sn_5O_6 has been reported, produced by heating SnO *in vacuo* or under argon above 750°K (8). However the experiments of Niwa, Yamai, and Wada (9) suggest that such materials are composed of a mixture of SnO_2 and Sn .

So far we have considered the stability of the lower oxidation states of tin and antimony to oxidation. One must also take into account disproportionation reactions of the type



and



There have been a number of reports on the stability of stannous oxide with respect to disproportionation. Platteeuw and Meyer (10) heated SnO *in vacuo* above 300°C and completely decomposed it into Sn and SnO_2 . Niwa *et al.* (9) in their x-ray study found that at 550°C the decomposition was rapid and complete, but that below 500°C the kinetics were slow. On the other hand they noted that heating a mixture of Sn and SnO_2 at 400°C did not result in the production of any SnO . In Fig. 6 the standard free energy changes of the SnO and Sb_2O_3 disproportionation reactions are plotted as a function of temperature, and it is seen that solid SnO is thermodynamically unstable over the entire temperature range considered. In contrast, Sb_2O_3 is completely stable to disproportionation.

Conclusions

A number of conclusions may be drawn from the above calculations. First, since SnO is very susceptible to air oxidation nonstoichiometric semiconductors of the type $\text{Sn}^{4+}_{(1-\delta)}\text{Sn}^{2+}_{\delta}\text{O}^{2-}_{(2-\delta)}$ are not likely to be stable in air. Further, at high temperatures in the absence of oxygen SnO disproportionates to Sn and SnO_2 . Therefore although it may be difficult but possible to make reproducible SnII/SnIV semiconductors, it is

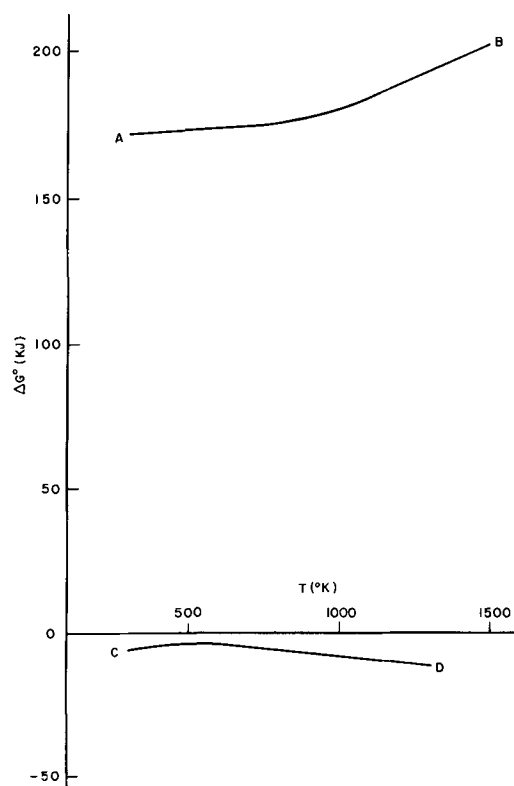
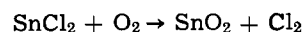


Fig. 6. AB: free energy change for $5/4\text{Sb}_2\text{O}_3 \rightarrow \text{Sb} + 3/4\text{Sb}_2\text{O}_5$, CD: free energy change for $2\text{SnO} \rightarrow \text{Sn} + \text{SnO}_2$.

very unlikely that they will be stable in air. Several types of dopant may exist in a lattice. Nevertheless it is concluded that conducting tin oxide films formed by pyrolysis of tin (II or IV) chlorides probably owe their conductivity almost entirely to the inclusion of chloride ions in the lattice. Although the free energy change for the reaction



has been calculated (3) to be -1368 kJ at 700°K , it is

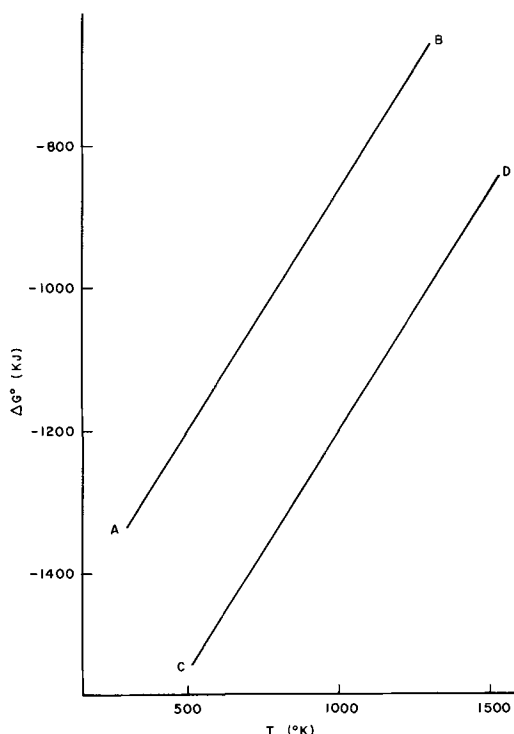
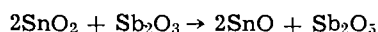


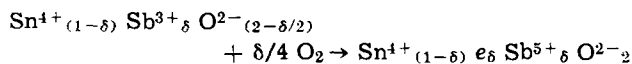
Fig. 7. AB: free energy of $2\text{SnO} + \text{Sb}_2\text{O}_5$, CD: free energy of $2\text{SnO}_2 + \text{Sb}_2\text{O}_3$.

not necessary that the replacement of chloride ions by oxygen be fast. Indeed Miloslavskii noted an irreversible decrease in conductance after long baking at temperatures above 350°C, which may be due to such a slow replacement (2).

A result of the relative instability of SnO with respect to SnO₂ is that the reaction



is not feasible, as is seen in Fig. 7, there being a free energy increase of 335 kJ associated with the process. The equivalent redox reactions with Sb₂O₄ or Sb₆O₁₃ are even less likely. This reaction must not however be confused with



the process which gives rise to the controlled valence semiconductor.

The relative stability of trivalent antimony oxide species would suggest the possibility of forming the controlled valence semiconductor rather than the complete oxidation of the antimony to Sb₂O₅.

Manuscript submitted June 20, 1971; revised manuscript received Sept. 16, 1971.

Any discussion of this paper will appear in a Discussion Section to be published in the December 1972 JOURNAL.

REFERENCES

1. M. Foex, *Bull. Soc. Chim. France*, **11**, 6 (1944).
2. V. K. Miloslavskii, *Opt. Spectr. (USSR) (English Transl.)*, **7**, 154 (1959).
3. R. F. Bartholomew and H. M. Garfinkel, *This Journal*, **116**, 1205 (1969).
4. T. Arai, K. Ishiguro, T. Sasaki, and I. Imai, *J. Phys. Soc. Japan*, **13**, 296 (1958).
5. E. J. W. Verwey, "Semiconducting Materials," H. K. Henisch, Editor, Butterworth, London (1951).
6. A. C. Skapski and D. Rogers, *Chem. Comm.*, 611 (1965).
7. H. Spandau and E. J. Kohlmeyer, *Z. Anorg. Allgem. Chem.*, **254**, 65 (1947).
8. C. Decroly and M. Ghodsi, *Compt. Rend.*, **261**, 2659 (1965).
9. K. Niwa, I. Yamai, and T. Wada, *Bull. Chem. Soc. Japan*, **31**, 725 (1958).
10. J. C. Platteeuw and G. Meyer, *Trans. Faraday Soc.*, **52**, 1066 (1956).

Preparation and Properties of Semiconducting Polycrystalline Tin Oxide

Colin A. Vincent and Derek G. C. Weston

Department of Chemistry, University of St. Andrews, St. Andrews, Fife, Scotland

ABSTRACT

A method is described for preparing semiconducting tin oxide by precipitation from solution. Materials subjected to heat treatment at a number of temperatures have been characterized by x-ray, spectroscopic, and conductance measurements.

There has recently been considerable interest in the electrochemical behavior of semiconducting tin oxides (1-3, etc.). Up until now the work has been mainly concerned with the use of thin films of this material deposited on a glass or quartz substrate. In this form electrodes have been prepared which can be used to observe electroactive species near the electrode-solution interface by internal reflectance spectroscopy in the visible region of the spectrum (2-5). Such electrodes are usually prepared by hydrolyzing a volatile tin compound, together with a suitable dopant, on a glass substrate at high temperature. A detailed method for preparing thick crystalline films in anhydrous conditions has been reported by Bartholomew and Garfinkel (6). The use of semiconductors in the form of thin films, however, has disadvantages for many applications. Further, the method of preparation makes it necessary to treat the samples at a minimum of 400°C, thus excluding investigations of the very interesting low-temperature types of semiconductor. Finally to produce exactly reproducible samples by the pyrolytic method requires considerable experimental technique. This paper describes a method of producing the semiconductors by precipitation from solution.

Verwey (7) has defined controlled valence oxidic semiconductors as oxides to whose lattices have been added a number of ions of deviating valency without the simultaneous incorporation of lattice defects, i.e. appropriate counterions must be included. The ions

of deviating valency are substituted for the main lattice ions and thus must be of similar size and charge. Controlled valence n-type semiconductors may be prepared by substituting ions such as SbIII for the SnIV of the cassiterite lattice, or FI, or even CII for the OII. [The conductance of SnO₂ thin films prepared by the pyrolysis of pure SnCl₄ is probably due entirely to residual chloride in the lattice (9, 13).] In this work we have investigated the preparation and properties of "bulk" SbIII-doped (controlled valence) and SnII-doped (nonstoichiometric) SnO₂ semiconductors.

Preparation

Antimony-doped semiconductors were prepared by the coprecipitation with ammonium hydroxide of antimony and tin hydroxides from appropriate mixtures of antimony and tin chloride solutions in HCl, followed by a washing procedure and heat treatment. SnII/SnIV semiconductors were made in a similar manner, taking particular care to exclude air from the system at all times.

Stock solutions of SbCl₃, SnCl₂, and SnCl₄ were prepared in HCl using "Analar" grade reagents. Volumes of these were taken to give 0.1 mole of tin oxide with a composition range of dopant of 0.1-5.0 m/o (mole per cent) for SbIII-doped samples and 1.0-5.0 m/o for SnII-doped samples. On mixing the SnCl₄ and dopant solutions a yellow-orange color of a solution interaction species (9, 10) was always observed. Oxygen-free nitrogen was passed through the solution to provide stirring and to prevent air oxidation of the SnII in the case of the SnIV-SnII

system. The solution was maintained at 100°C on a steam bath and 3.5% ammonia solution was added dropwise until a pH of 3.2 had been achieved. The resulting mixed hydroxide precipitate was washed alternately with NH_4NO_3 solution (to prevent peptization) and with water until the washings showed no trace of chloride ion. The precipitate was then peptized to release any further occluded chloride and reprecipitated with NH_4NO_3 solution. Finally the precipitate was washed with water and filtered.

Since the presence of chloride ion was likely to seriously affect the semiconducting properties of the material, it was necessary to minimize contamination of the final product by this species. Kirkov (11, 12) favors the fast precipitation of $\text{Sn}(\text{OH})_4$ in the cold in order to lessen the danger of occluding chloride in the precipitate. A precipitate formed in this way is, however, almost colloidal in nature, and the large surface area causes a high chloride adsorption. Since the precipitate does not settle well, it is difficult to remove the chloride-rich mother liquor right after the precipitation. With our technique, a precipitate was formed which settled well and allowed this liquor and subsequent washings to be readily decanted. The bulk of the chloride was thus removed before the precipitate was peptized and subjected to final washing. A test for chloride ion was made by refluxing approximately 1g of powdered sample of precipitate which had been dried at 45°C, in 50 ml of concentrated NaOH until it dissolved. The tin was precipitated from this solution as metastannic acid, using HNO_3 , and filtered off. The resulting filtrate was tested for chloride by adding acidified 0.1M AgNO_3 ; no turbidity was found. Since it was considered very unlikely that a large proportion of any chloride ion present in the original sample would coprecipitate with the metastannic acid, it was concluded that any contamination by chloride was too low to be significant.

The yellow gel-like precipitates were dried for 48 hr at 45°C, in air for the SbIII-doped samples and under a nitrogen flow for the SnII-doped samples, to give large (0.5 cm) pieces of a transparent amber material. Samples of this material were broken up and subjected to heat treatment at temperatures from 100° to 1200°C.

Results and Discussion

Stability

It was found that all the SbIII-doped materials were completely stable and had reproducible properties throughout the composition and heat-treatment ranges investigated. On the other hand it was very difficult to prepare reproducible SnII-doped materials because (a) under the low oxygen partial pressures necessary to prevent oxidation there was oxygen loss from the sample and the production of variable non-stoichiometric semiconductors and (b) the semiconductors once prepared, especially those dried at low temperatures, varied in weight and resistivity on standing exposed to the air.

These results agree with the predictions made in the preceding study where the stability of possible semiconducting materials was considered (13).

Thermogravimetric analysis.—Samples of the clear amber material which had been held at 45°C for 48 hr were subjected to thermogravimetric analysis in a Stanton Massflow Thermobalance. In Fig. 1 the lower curve corresponds to a TGA performed at a heating rate of approximately 2°C/min up to 200°C and 4°C/min above 200°C. The points on the upper curve represent "equilibrated" weight losses occurring when samples were heated to the appropriate temperature and maintained there for periods ranging from 1 to 10 hr.

The total weight loss observed in the equilibration experiments was approximately 19%; this took place

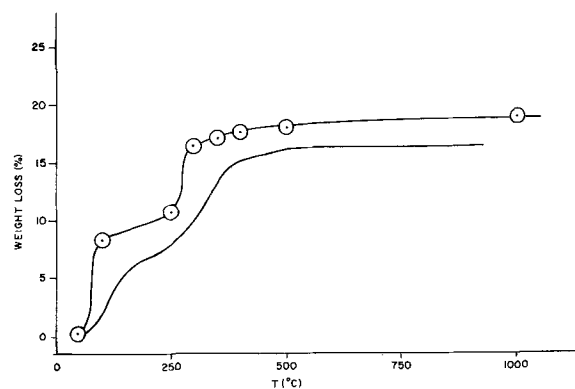


Fig. 1. Upper curve: equilibrated weight loss; lower curve: TGA scan.

in two stages, an initial loss of 8% by 100°C and a second 11% step, most of which was over by 300°C. The height of the first step varied slightly from sample to sample.

The first step corresponds to the loss of ≤ 1 mole of water per mole of SnO_2 , together with small quantities of impurity such as NH_4NO_3 retained from the washing stages. Differences in the height of this step may be explained as due to a variable quantity of water being retained in the samples dried at 45°C. The 11% loss observed in both TGA and equilibration experiments agrees well with the loss of 1 mole of water per mole of SnO_2 , i.e. with the conversion



reported by Giesekke, Gutowsky, Kirkov, and Laitinen (11). (In an NMR investigation these authors showed that this compound could not be written simply as $\text{SnO}_2 \cdot \text{H}_2\text{O}$.)

In detail however, the present TGA behavior is completely different from that reported by the above authors, who found a series of four distinct dehydration steps over the temperature range 100°-700°C, corresponding to the scheme



The absence of these additional compounds in our work is further confirmed by the x-ray results reported below.

X-ray diffraction.—X-ray diffraction measurements were carried out on powdered samples of semiconductors which had been prepared at different temperatures, using an x-ray spectrometer and Philips PW 1049 diffraction goniometer. The quantity of Sb present was too small to affect the diffraction pattern.

In all cases a cassiterite pattern was produced: this was well developed for the samples treated at the higher temperatures, but even for the 45°C samples strong broad lines were present corresponding to d-spacings of 0.335, 0.264, 0.176, and 0.149 nm. This would imply that even the glassy, highly hydrated low-temperature form contained considerable regions of SnO_2 structure. The diffraction pattern of a 500°C sample is shown in Fig. 2 as a plot of diffracted intensity against 2θ for copper K_α radiation. Peaks corresponding to d-spacings of 0.335, 0.264, 0.237, 0.176, 0.167, 0.159, 0.149, and 0.141 nm may be clearly seen,

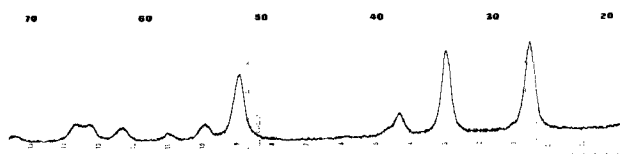


Fig. 2. Diffracted intensity of 500°C sample vs. 2θ for CuK_α radiation.

and the results are similar to those obtained for 500°C material by Niwa, Yamai, and Wada (14). Such behavior, however, contrasts markedly with the electron diffraction results of Giesekke *et al.* (11), which seem to indicate the existence of different crystalline substances formed by heating to different temperatures. For instance the d-spacings reported for their 520°C sample were 0.239, 0.199, 0.189, 0.172, 0.166, 0.156 and 0.141, 0.129 nm *etc.*, the majority of which are not to be found in cassiterite. There is even less correspondence for lower temperature samples.

The very presence of x-ray diffraction lines indicated that the semiconductors were microcrystalline in nature rather than glasses. The mean size of the microcrystals was investigated by considering the diffraction broadening of the peaks corresponding to the 110 and 101 planes. The peaks were approximately Gaussian, with half-widths in the range 0.25°–3.25°. Measurements were first made on the peaks at 19° 9' and 22° 20' of an aluminum dust standard. It was assumed that the latter had such large crystals that diffraction broadening would be absent, and thus a measure of instrumental broadening was obtained. Jones' conversion curves (15, 16) were then used to determine the pure diffraction broadening of the SnO₂ peaks. The mean dimension of the microcrystals, *D*, was calculated using Scherrer's formula

$$D = \frac{0.9 \lambda}{\beta_{1/2} \cos \theta}$$

where $\beta_{1/2}$ is the corrected width of the diffraction peak at half height, λ is the wavelength of the x-ray, and θ is the diffraction angle. Since the uncertainty in determining the diffraction broadening increases with increasing crystal size, *D* values for the high temperature samples are not very accurate. Results of the measurements (made on 1 m/o Sb semiconductors) are given in Table I.

Spectroscopy

A spectroscopic examination was carried out on equilibrated samples of 1 m/o antimony-doped tin oxides.

Visible region.—The color of the material heated to various temperatures is given in Table II.

Reflectance spectra using a freshly prepared MgO standard were obtained using a Unicam SP 300 spectrometer and are shown in Fig. 3. From these it is seen that the high-temperature specimens have a considerable absorption of energy at the red end of the spectrum, extending into the infrared. The origin of such absorption is considered below. Low-temperature samples have little absorption at long wavelengths, but

Table I. Results of measurements made on Sb semiconductors

Preparation temperature	Plane	Measured width	Corrected width	<i>D</i> (nm)
45°C	110	3.2° ± 0.1°	3.2°	2.5 ± 0.3
	101	3.0° ± 0.1°	3.0°	
300°C	110	1.75° ± 0.05°	1.71°	5.4 ± 0.4
	101	1.45° ± 0.05°	1.41°	
500°C	110	0.98° ± 0.02°	0.94°	9.1 ± 0.5
	101	0.92° ± 0.02°	0.87°	
700°C	110	0.65° ± 0.02°	0.59°	15.0 ± 2.0
	101	0.58° ± 0.02°	0.51°	
1000°C	110	0.37° ± 0.01°	0.24°	59.0 ± 10.0
	101	0.35° ± 0.01°	0.22°	

Table II. Color of material heated to various temperatures

Equilibration temperature	Color of sample
45°C	Amber, transparent
100°C	Amber, transparent
300°C	Yellow-green, transparent
500°C	Very dark green/black, very thin sections, transparent
600°C	Very dark blue, opaque
800°C	Light blue, opaque
1000°C	Very light blue, opaque

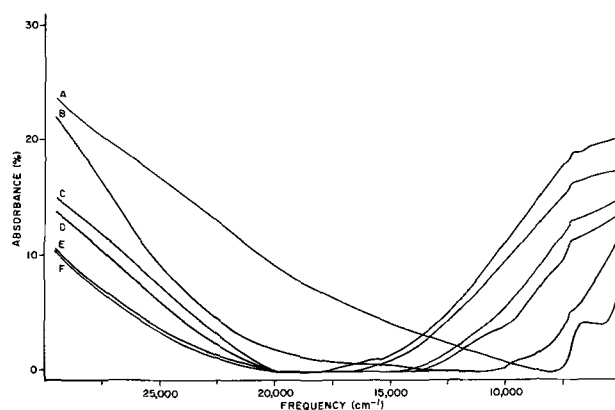


Fig. 3. Reflectance spectra. Heat treatment: A = 45°C, B = 300°C, C = 500°C, D = 700°C, E = 1000°C, F = 1200°C.

strong absorption in the violet. In pure SnO₂, optical excitation of electrons to the conduction band occurs at wave numbers greater than 30,000 cm⁻¹ (17, 18), *i.e.* there is a large forbidden gap. Arai (17) has shown that the absorption edge may move to shorter wavelengths in conducting oxides if the bottom of the conduction band is occupied, so that transitions must take place from the valence band to higher levels than the ground level of the latter. In the presence of antimony, one must also consider transitions from antimony to tin levels.

In solution a SnIV/SbIII species was formed which gave rise to "interaction absorption" in the blue similar to that investigated by Whitney and Davidson in SnIV/SnII and in SbV/SbIII systems. Recently the origins of such interaction absorption have been examined by Robin and Day (19). As might be expected the highly hydrated sample (45°C) had an absorption similar to that of the SnIV/SbIII solution.

Infrared.—Spectra of 1% KBr disk samples of material dried below 300°C contained a large absorption band corresponding to water and to NH₄⁺ and NO₃⁻ from the washing electrolyte which had not been completely removed. These bands were absent from samples dried at over 500°C, but these samples showed instead a broad transmission loss from 1000 cm⁻¹ to 4000 cm⁻¹ with a maximum loss near 2000 cm⁻¹. The intensity of this band increased with the temperature at which the sample had been treated.

This large drop in transmission is similar to that observed by Miloslavskii (8) in pyrolytically decomposed SnCl₂/SnCl₄ mixtures where a wide band in the 700–5000 cm⁻¹ region centered at 1200 cm⁻¹ was noted. This band was attributed to electronic transitions from the ground state of impurity centers to an excited state, such as transitions to the conduction band. Arai, Imai, and co-workers (20) also investigated pyrolytic antimony-free semiconductors. Free electrons are able to absorb energy from electromagnetic radiation only when they can interact with a crystal lattice, so that the transfer satisfies conservation both of energy and momentum. Since the absorption is a function of electron-lattice interaction frequency, it is closely connected with the conductance of the crystal. Free electron absorption or plasma oscillation increases monotonically with frequency (for a constant number of carriers and specific conductance). Although Arai *et al.* claim to have found such behavior, close examination of their results would seem to show a minimum in the transmission at about 1300 cm⁻¹. Miloslavskii (18) also went on to investigate antimony-doped films and reported a further marked decrease in the transmission above 10,000 cm⁻¹. Here the transmission did fall monotonically, *i.e.*, it was apparently due to free electron absorption.

The present results are not consistent with plasma oscillation. Rather it is suggested that the band arises

from promotion of electrons from antimony ground-state levels high in the SnO_2 forbidden band to the conduction band. The presence of the band in samples heated to 500°C and above parallels the greatly increased conductance of these samples.

Far infrared.—An absorption band in the $30\text{--}45\mu$ region was observed for all samples, including those dried at low temperatures. This absorption corresponds to the tin-oxygen lattice vibrations reported at 33 and 39μ for SnO_2 by Ishiguro *et al.* (21). These authors point out that there is no further optical absorption at shorter wavelengths than 33μ due to lattice vibration.

We however have noticed an additional broad band in the $14\text{--}25\mu$ region. This band is also present in natural cassiterite and in commercial SnO_2 (Fisons Ltd., reagent grade). Since this absorption was not affected by the heat-treatment of the sample nor by the presence or absence of antimony, it is not connected with the band observed by Miloslavskii (8) centered at 16.4μ and shown to be due to excitation of impurity centers. Sn-O vibrations are known in this region, for instance in tin alkoxides (22) and have been reported (23) in the region from 15.4 to 23.5μ for Sn-O-Sn vibrations in polymeric species formed from alkyl tin halides. Further, Dupuis (24) has reported tin oxide absorption bands at 16.1 , 21.0 , and 29.4μ .

Conductance.—D-C conductances were found of samples which had been powdered in an agate ball mill and enclosed under pressure between steel electrodes in an insulating former for the purpose of the measurement. The apparatus for this measurement will be described elsewhere (25). Resistivities of specimens of 1 m/o antimony-doped SnO_2 prepared at different temperatures and measured at room temperatures are shown in Fig. 4.

Verwey (7) has pointed out that there is a special problem in the study of the conductance of polycrystalline semiconductors, namely the existence of grain boundaries within each particle of the material, which greatly affects the impedance behavior. In the simplest cases there are layers of increased resistance due to air gaps between the grains; while in more complex situations, the chemical constitution of the surface layers may differ from the bulk of the microcrystal. Thus the d-c conductance (although completely reproducible) has only relative significance and is likely to be much lower than the "true" conductance of the material, which may only be determined at very high frequencies.

The nature of the conductance in completely dehydrated tin oxide has been investigated by a number of workers, and it is generally accepted that the position of the antimony level with respect to the conduction band is such that there is no restriction to transfer of

electrons to the latter. The electrical resistance within the microcrystal is thus due entirely to electron scattering. This theory is confirmed by the findings that the temperature coefficient of conductance is relatively low and, as with metals, the conductance falls as the temperature rises. Arai (17) noted that for antimony-doped SnO_2 the conductance fell when the doping rose above 1% due to increased scattering by the impurity centers.

From Fig. 4 it is seen that the conductance of samples having different heat treatments falls into two distinct regions. Samples equilibrated below 250°C had high specific resistances, of the order of 1-10 ohm-m, while those treated above 500°C were below 0.02 ohm-m. The sudden drop in resistance corresponds to the elimination of the majority of the water from the material, *i.e.*, to the conversion of SnO_3H_2 to SnO_2 . This finding is understandable since water is not a bridging ligand and when present in large quantities tends to form an insulating system.

The slow rise in conductance in samples treated from 500° to 1200°C may be attributed to the increase in the size of the microcrystals (discussed above in the section on X-ray diffraction) and to the consequent reduction of grain boundary impedance.

Acknowledgment

We wish to thank the Department of Geology, University of St. Andrews for carrying out the x-ray diffraction measurements.

Manuscript submitted June 20, 1971; revised manuscript received Sept. 16, 1971.

Any discussion of this paper will appear in a Discussion Section to be published in the December 1972 JOURNAL.

REFERENCES

- H. A. Laitinen, C. A. Vincent, and T. M. Bednarski, *This Journal*, **115**, 1024 (1968).
- T. Kuwana, R. K. Dovington, and D. W. Leedy, *Anal. Chem.*, **36**, 2023 (1964).
- J. W. Strojek and T. Kuwana, *J. Electroanal. Chem.*, **16**, 471 (1968).
- T. Osa and T. Kuwana, *ibid.*, **22**, 209 (1969).
- N. Winograd and T. Kuwana, *ibid.*, **23**, 333 (1969).
- R. F. Bartholomew and H. N. Garfinkel, *This Journal*, **116**, 1205 (1969).
- E. J. W. Verwey, "Semiconducting Materials," H. K. Henisch, Editor, Butterworth, London (1951).
- V. K. Miloslavskii, *Opt. Spectr. (USSR) (English Transl.)*, **7**, 154 (1959).
- J. E. Whitney and N. Davidson, *J. Am. Chem. Soc.*, **69**, 2076 (1947).
- J. E. Whitney and N. Davidson, *ibid.*, **71**, 3809 (1949).
- E. W. Giesekke, H. S. Gutowsky, P. Kirkov, and H. A. Laitinen, *Inorg. Chem.*, **6**, 1294 (1967).
- P. Kirkov, Private communication.
- C. A. Vincent, *This Journal*, **119**, 515 (1972).
- K. Niwa, I. Yamai, and T. Wada, *Bull. Chem. Soc. Japan*, **31**, 725 (1958).
- F. W. Jones, *Proc. Roy. Soc. London, A*, **16**, 166 (1938).
- L. Alexander, *J. Appl. Phys.*, **21**, 137 (1950).
- T. Arai, *J. Phys. Soc. Japan*, **15**, 916 (1960).
- V. K. Miloslavskii and S. P. Lyashenko, *Opt. Spectr. (USSR) (English Transl.)*, **8**, 455 (1960).
- M. B. Robin and P. Day, *Advan. Inorg. Chem. Radiochem.*, **10**, 247 (1967).
- T. Arai, K. Ishiguro, T. Sasaki, and I. Imai, *J. Phys. Soc. Japan*, **13**, 296 (1958).
- K. Ishiguro, T. Sasaki, T. Arai, and I. Imai, *J. Phys. Soc. Japan*, **13**, 755 (1958).
- F. K. Butcher, W. Gerrard, E. F. Mooney, R. G. Rees, and H. A. Willis, *Spectrochim. Acta*, **20**, 51 (1964).
- H. Kriegsman and S. Panly, *Z. Anorg. Allgem. Chem.*, **330**, 275 (1964).
- T. Dupuis, *Mikrochim. Acta*, 963 (1962).
- J. Rennie and C. A. Vincent, Unpublished work.

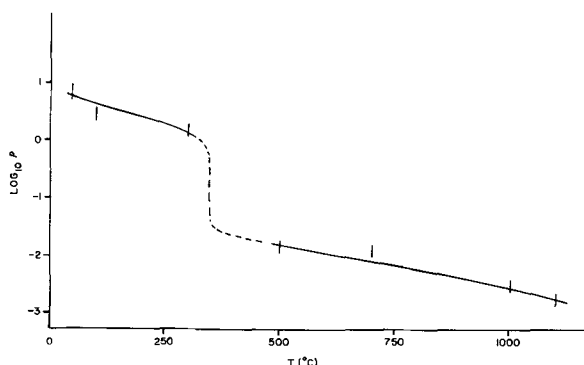


Fig. 4. Graph of $\log_{10} \rho$ measured at room temperature, against temperature of heat treatment.

Pseudo-Brewster Angle Concentration Determination: Apparatus, Reproducibility, and Accuracy

W. A. Keenan,* C. J. Liu, and C. P. Schneider

IBM Components Division, East Fishkill Facility, Hopewell Junction, New York 12533

ABSTRACT

The angle of incidence at which the parallel component of polarized infrared reflected light attains a minimum (the pseudo-Brewster angle, or PBA) is used to determine semiconductor carrier concentrations. A PBA apparatus using a 3.391 He-Ne laser as a polarized light source is described. Experimental results for n- and p-type silicon are compared with plasma resonance and sheet resistance measurements to determine best fit of theoretical calibration curves. Results of reproducibility and correlation studies are also presented.

Optical techniques, such as infrared interference and plasma resonance for example, are very attractive for characterizing processed semiconductor material because they are in general nondestructive and contactless (1). The Brewster angle, the angle of incidence at which the parallel component of reflectivity goes to zero, has long been used to determine the index of refraction of nonabsorbing material. Semiconductors and other absorbing materials exhibit a nonzero minimum at a "pseudo-Brewster" angle which depends on the wavelength of the incident light and the optical constants of the material. Since the semiconductor optical constants are strongly dependent on the free carrier density (2), the pseudo-Brewster angle is an indication of this density.

Theory

The variation of polarized monochromatic infrared reflectivity with angle of incidence can be used to determine the carrier concentration of a semiconductor. The reflection coefficients for the parallel and perpendicular components of polarized reflectivity for an infinitely thick homogeneous material are approximately (3)

$$R_p(\theta) = \frac{(n^2 + k^2) \cos^2 \theta - 2n \cos \theta + 1}{(n^2 + k^2) \cos^2 \theta + 2n \cos \theta + 1} \quad [1]$$

and

$$R_s(\theta) = \frac{(n^2 + k^2) - 2n \cos \theta + \cos^2 \theta}{(n^2 + k^2) + 2n \cos \theta + \cos^2 \theta} \quad [2]$$

respectively, where θ = angle of incidence, n = index of refraction, and k = extinction coefficient. These approximations are accurate for $n^2 + k^2 > 1$, which is always the case for semiconductors in the infrared region of the spectrum. $R_s(\theta)$, the component of polarized reflectivity with electric vector perpendicular to the plane of incidence, increases monotonically as the angle of incidence increases from 0° to 90° . $R_p(\theta)$, the component of polarized reflectivity with electric vector parallel to the plane of incidence, exhibits a minimum at an angle θ_B

$$\theta_B = \cos^{-1} \frac{1}{(n^2 + k^2)^{1/2}} \quad [3]$$

For a nonabsorbing material where $k = 0$, substitution of Eq. [3] into [1] will yield $R_p(\theta_B) = 0$. The Brewster angle for a nonabsorbing material is defined as the angle at which the parallel component of polarized reflectivity goes to zero.

For a noninsulating or semiconducting material which has a nonzero extinction coefficient k , the minimum in the parallel component of reflectivity is not zero, but

$$R_p(\theta_B) = \frac{(n^2 + k^2)^{1/2} - n}{(n^2 + k^2)^{1/2} + n} \quad [3a]$$

$$= \frac{1 - n \cos \theta_B}{1 + n \cos \theta_B}$$

The angle at which this parallel component of reflectivity attains its nonzero minimum is defined as the pseudo-Brewster angle (PBA). Figure 1 shows curves of calculated $R_p(\theta)$ and $R_s(\theta)$ for n-type silicon with an impurity concentration of $N = 1 \times 10^{19} \text{ cm}^{-3}$, a d-c resistivity of $\rho_0 = 6.9 \times 10^{-3} \text{ ohm-cm}$ for a wavelength of $\lambda = 3.391$ using the free carrier infrared optical constant model of Schumann and Phillips (4), an assumed effective mass ratio $a = m^*/m = 0.26$, and an assumed relative lattice dielectric constant (no free carrier contribution) $K_L = \epsilon_L/\epsilon_0 = 11.7$. $R_p(\theta)$ appears to go to zero on the linear reflectivity scale used, but the insert showing the logarithm of $R_p(\theta)$ around θ_B shows that this minimum is indeed not equal to zero.

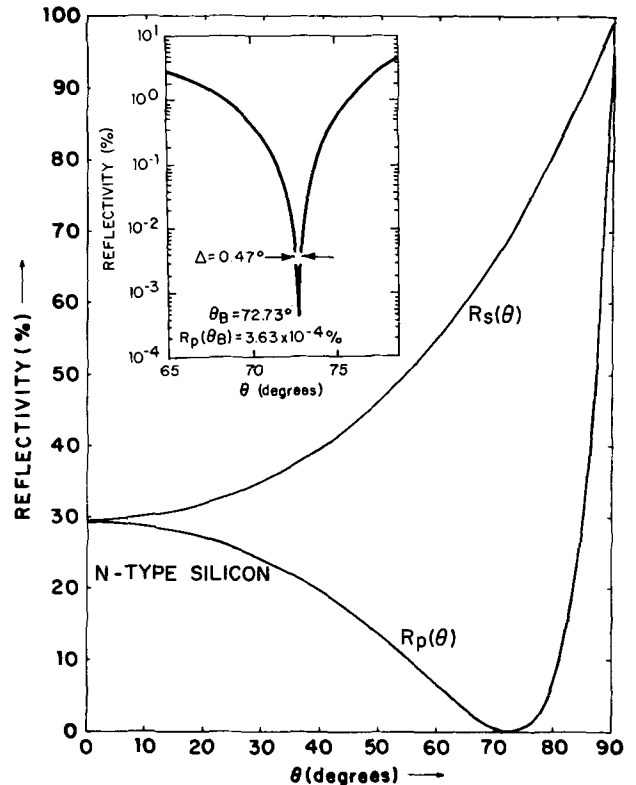


Fig. 1. Theoretically calculated $R_p(\theta)$ and $R_s(\theta)$ for n-type silicon with $N = 1 \times 10^{19} \text{ cm}^{-3}$ at $\lambda = 3.391 \text{ } \mu\text{m}$. Insert shows $\log R_p(\theta)$ around θ_B .

* Electrochemical Society Active Member.
Key words: semiconductor carrier concentration, polarized infrared light, silicon, Brewster angle, plasma resonance.

The PBA depends on n and k , the optical constants of the material. In the infrared region of the spectrum the optical constants of a semiconductor are strongly dependent on the free carrier density of the material. The above infrared optical constant theory relates n and k to the impurity concentration N and to the d-c resistivity ρ_0 of the material (4). These formulas can be schematically represented

$$\left. \begin{aligned} n &= F_1 \left(\frac{N}{a}, \rho_0, K_L, \lambda \right) \\ \text{and} \\ k &= F_2 \left(\frac{N}{a}, \rho_0, K_L, \lambda \right) \end{aligned} \right\} \quad [4]$$

where N = impurity concentration, ρ_0 = d-c resistivity, $K_L = \epsilon_L/\epsilon_0$ = relative lattice dielectric constant, $a = m^*/m$ = effective mass ratio of majority carrier, and λ = wavelength of radiation. The optical constants are thus dependent on the ratio of the impurity density divided by the effective mass ratio.

Calibration curves relating θ_B , the PBA, to N , the impurity concentration, have been calculated using the above formulas. Clearly N and ρ_0 are not independent, and for this work their relationship was assumed to be given by Irvin's (5) curves. Figure 2 shows a family of calibration curves for n-type silicon for several wavelengths with assumed values of $K_L = 11.7$ and $a = 0.26$. The strong dependence of these calibration curves on wavelength reflects the strong dependence of the optical constants n and k on wavelength. As concentration decreases, all the calibration curves approach 73.00° , the PBA for intrinsic silicon for the assumed value of $K_L = 11.7$. For values of PBA less than the intrinsic PBA, N is not a single-valued function of θ_B . For short wavelengths, the concentration range over which N is a single-valued function of θ_B is small, but θ_B is very sensitive to N for this range of concentration. As wavelength increases, the sensitivity of θ_B to N decreases but the single-valued range of N increases. This problem of N being a double-valued function of θ_B for θ_B less than the intrinsic PBA can be overcome by using two wavelengths, by observing the sharpness of the minimum around θ_B , or by monitoring $R_p(\theta_B)$ or $R_s(\theta_B)$ (6). Note that the lower limit concentration that can be detected by PBA depends only on the wavelength employed; the longer the wavelength, the lower the detectable limit of concentration. The wavelength employed in this investigation of the PBA concentration determination technique was $3.391 \mu\text{m}$, the output of a He-Ne laser with special resonator windows. This proved to be a most convenient source of monochromatic polarized infrared light.

The PBA calibration curves for $\lambda = 3.391 \mu\text{m}$ are shown in Fig. 3A and 3B for silicon. Figure 3A is for

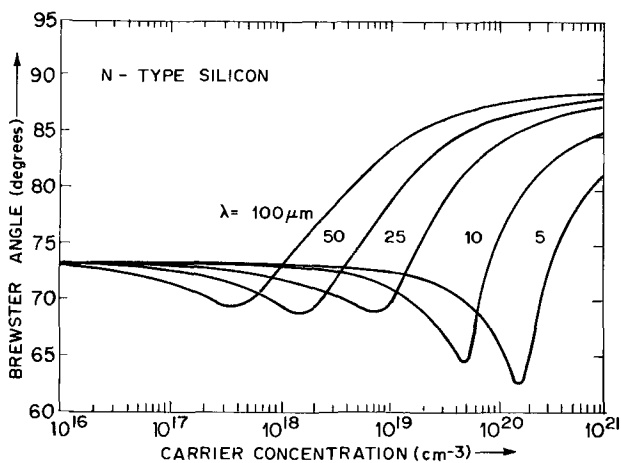


Fig. 2. Family of pseudo-Brewster angle calibration curves for n-type silicon, calculated assuming $K_L = 11.7$ and $m^*/m = 0.26$.

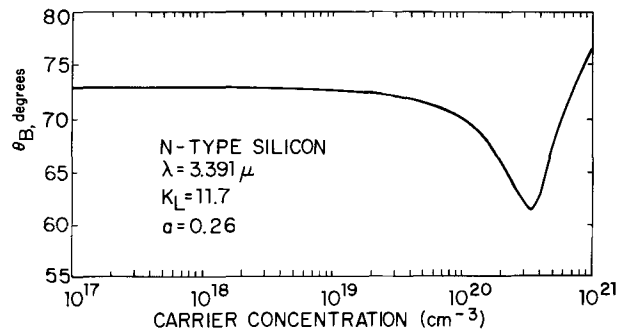


Fig. 3A. PBA calibration curves for $\lambda = 3.391 \mu\text{m}$ for n-type silicon.

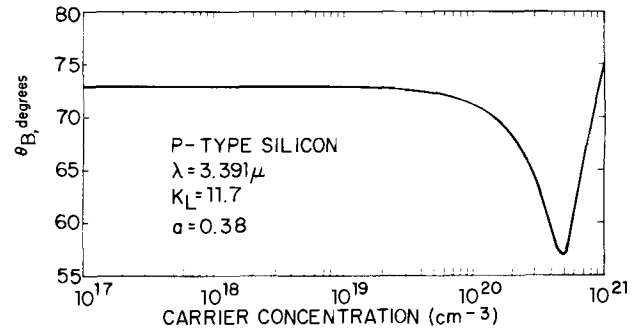


Fig. 3B. PBA calibration curves for $\lambda = 3.391 \mu\text{m}$ for p-type silicon.

n-type silicon and an assumed value of $K_L = 11.7$ and $a = 0.26$. Figure 3B is for p-type silicon with an assumed value of $K_L = 11.7$ and $a = 0.37$. Figures 4A and B emphasize the dependence of these calibration curves on the assumed values of a and K_L . Figure 4A shows θ_B vs. N for n-type silicon for $K_L = 11.7$ and several assumed values of a . Since it is the ratio N/a that appears in the optical constant formulas, an increase in a is equivalent to a decrease in N and has the effect of shifting the calibration curves to higher concentration. Thus a shift in N or a horizontal shift in the calibration curve is obtained by increasing a . A shift in θ_B or a vertical shift in the calibration curve is obtained by changing K_L , the relative lattice dielectric constant. This is demonstrated in Fig. 4B, which shows a family of θ_B vs. N calibration curves for p-type silicon for $a = 0.38$ and several assumed values of K_L . Clearly a change in K_L will change θ_B , since as N approaches zero, k approaches zero, and

$$n = (K_L)^{1/2} \quad [5]$$

Thus, Eq. [3] above reduces to

$$\begin{aligned} \theta_B &= \cos^{-1} \frac{1}{n} \\ &= \cos^{-1} \frac{1}{(K_L)^{1/2}} \end{aligned} \quad [6]$$

where the value of the pseudo-Brewster angle for intrinsic material depends only on the relative lattice dielectric constant.

Apparatus

The apparatus for determining carrier concentration by the pseudo-Brewster angle technique consists essentially of a source of polarized infrared light, a detector, and a means of varying the angles of incidence and reflectance so that they are kept equal. The experimental setup is shown schematically in Fig. 5. The light must be polarized with the electric vector parallel to the plane of incidence, that is the plane perpendicular to the sample surface which contains the incident (and hence also reflected) beam. The beam is

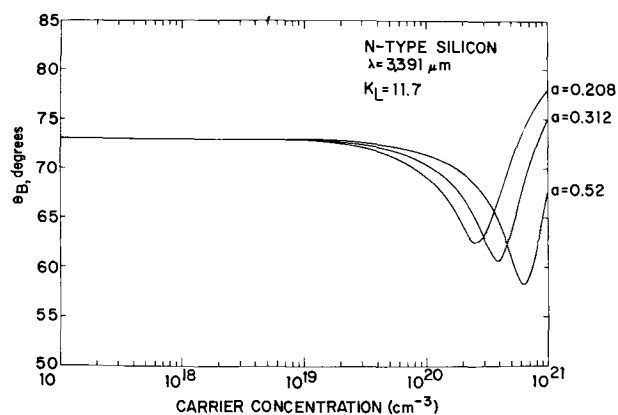


Fig. 4A. N-type silicon PBA calibration curves for $\lambda = 3.391 \mu\text{m}$, $K_L = 11.7$ and several assumed values of $a = m^*/m$.

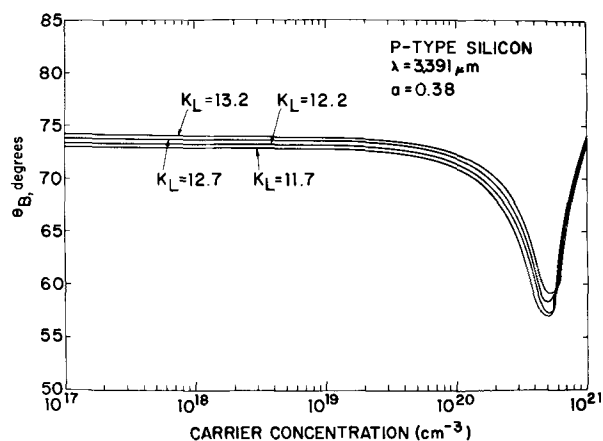


Fig. 4B. P-type silicon PBA calibration curves for $\lambda = 3.391 \mu\text{m}$, $a = m^*/m = 0.38$ and several assumed values of K_L .

incident on the sample surface at θ_i and reflected at θ_r to the detector which monitors the reflected light intensity as the angle of incidence and reflectance are simultaneously scanned. Figure 6 is a close-up of the laser, diffractometer, and detector system. Figure 7 shows the complete apparatus used in this work, with the X-Y recorder on top of the detector amplifier in the foreground, and the laser, diffractometer, and detector on a vibration-free table in the background.

A Spectra-Physics Model 122 He-Ne laser, adjusted to resonate at $\lambda = 3.391 \mu\text{m}$, was used as the polarized infrared light source. As it normally stands, this laser has its output linearly polarized with electric vector vertical to a tolerance of $\pm 5^\circ$. At the laser exit port the beam diameter (to points where the intensity falls off

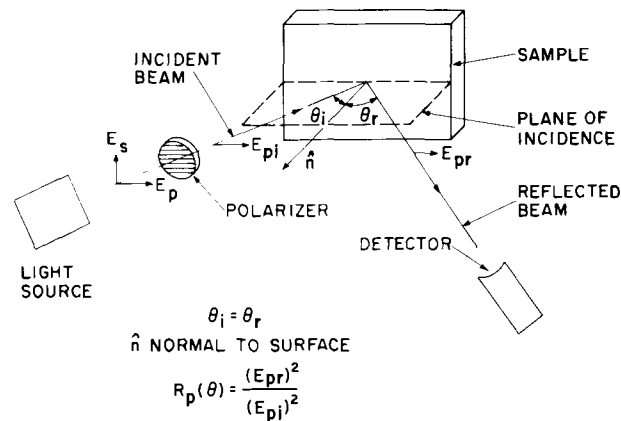


Fig. 5. Schematic of pseudo-Brewster angle apparatus

to e^{-2}) is 0.4 mm. The full angle beam divergence is 1.6 milliradians. The laser was mounted on a specially designed stand with adjustments to align the optical axis of the laser with the rotational axis of the stand. This stand allowed rotation of the laser, and hence the polarization of the beam 90° , which is essential if $R_s(\theta)$, the perpendicular component of reflectivity, is to be measured as well as $R_p(\theta)$. Adjustable stops on the rotation frame allow accurate trimming of the limits of rotation, and thus the polarization.

The silicon wafer mounted on the light chopper is used as a polarization filter, transmitting the light with electric vector polarized predominantly parallel to the test wafer plane of incidence. This half wafer is oriented in a plane perpendicular to the plane of incidence of the sample, and at an angle with respect to the light beam equal to its PBA. Since the PBA is the angle of incidence at which the minimum amount of parallel polarized light is reflected, it is the angle at which the maximum is transmitted for this polarization. The perpendicular polarized reflectivity is much greater at PBA, and hence its transmission is much smaller.

The Siemens diffractometer (Fig. 6) scans the angle of incidence by rotating the sample through an angle β while rotating the detector through an angle 2β , thus maintaining the angle of incidence equal to the angle of reflectance. A change in the angle of incidence as small as 0.005° can be detected with this instrument. The diffractometer is attached to the base plate of the laser-rotator stand to prevent disturbing the alignment. Much faster angular scan speeds were possible by using, instead of the diffractometer's internal drive, a variable speed motor coupled to the drive shaft of the diffractometer via a rubber hose; the hose minimized the coupling of motor vibrations into the dif-

Fig. 6. PBA apparatus



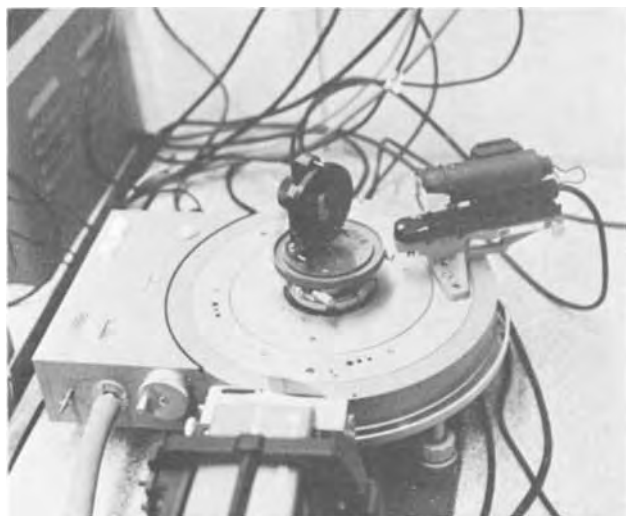


Fig. 7. Close-up of laser, diffractometer, and detector system

fractometer. Angular scan speeds of 5 to 20 degrees per minute were achieved.

An Eppley Lab Golay infrared detector was used to measure the reflected light intensity as the angle of incidence was scanned. The chopper of this detector was placed as close as possible to the output port of the laser to minimize the amount of stray chopped light reaching the detector. A silicon wafer taped to the aperture of the detector head (Fig. 6) was used to prevent visible light from reaching the detector. The Y-axis of a Hewlett-Packard Moseley Model 7000 AM X-Y recorder was used to display the output of the Golay detector, with the X-axis representing time. A capacitive discharge system in the diffractometer was used to superimpose a marker pip on the trace for every 0.5° change in the angle of incidence.

Experimental Results

Pseudo-Brewster angle measurements were made on silicon wafers doped with arsenic, boron, and phosphorus. The impurity concentrations of these bulk and diffused wafers were also measured by four-point probe and plasma resonance.

A typical detector response of reflectivity vs. angle of incidence is shown in Fig. 8 for a p-type silicon bulk wafer with impurity concentration $N = 2.75 \times 10^{20} \text{ cm}^{-3}$ and d-c resistivity $\rho_0 = 4.52 \times 10^{-4} \text{ ohm-cm}$ (plasma resonance results). The lower curve of Fig. 8 is the original scan, whereas the upper curve is that

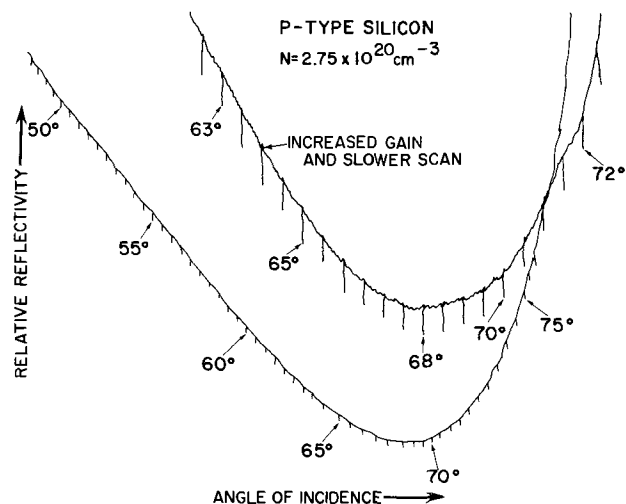


Fig. 8. Typical detector response for PBA measurement on p-type silicon bulk wafer with $N = 2.75 \times 10^{20} \text{ cm}^{-3}$ at $\lambda = 3.391 \mu\text{m}$.

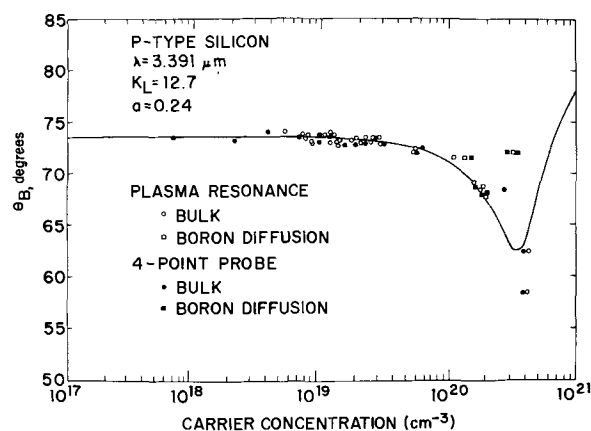


Fig. 9. Experimental results for p-type silicon samples and best fit theoretical calibration curve.

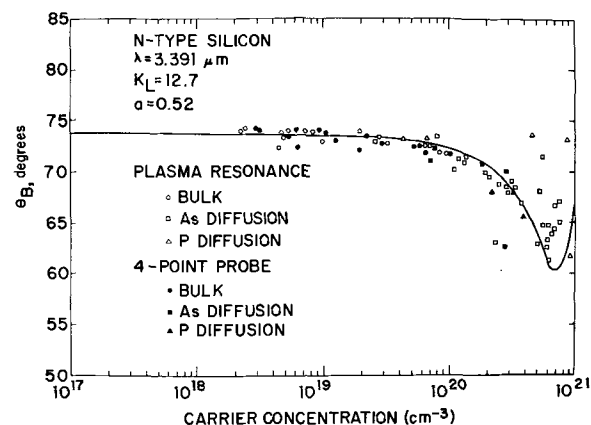


Fig. 10. Experimental results for n-type silicon wafers and best fit theoretical calibration curve.

which was recorded at increased detector gain and slower angular scan speed. Every half degree of angle of incidence is indicated by the marker pip superimposed on the trace.

The experimental results for n- and p-type silicon are shown in Fig. 9 and 10, where the experimentally determined PBA is plotted against the impurity concentration determined by either plasma resonance or four-point probe. The data points on these figures indicate the reference method of concentration determination, whether the sample is a bulk or diffused wafer (Fig. 9); and for n-type material they also indicate the dopant used, arsenic or phosphorus (Fig. 10). The data represented in these figures were used to determine the best values of the relative lattice dielectric constant K_L and the effective mass ratio a for use in calculating the theoretical calibration curves. The lower concentration data were first used to determine K_L , and then a was determined to obtain the best fit of the higher concentration data. The best fit theoretical PBA calibration curve for n-type silicon uses $K_L = 12.7$ and $a = 0.52$ (Fig. 9). The best fit theoretical PBA calibration curve for p-type silicon uses $K_L = 12.7$ and $a = 0.24$ (Fig. 10). It must be emphasized that a constant value of a was used to fit the data for each conductivity type. But since effective mass is known to vary with concentration at high impurity levels, a varying a should perhaps have been employed.

A correlation analysis was made of the measured PBA and that predicted by the theoretical calibration curves shown in Fig. 9 and 10. The correlation coefficient for all 87 n-type data points was 0.832. The correlation coefficient for all 66 p-type data points was 0.779. The confidence level, or T-value, for both are very good, as shown in Table I.

Table I. Correlation analysis

Samples	Number	Correlation coefficient	T-value
All n-type	87	0.832	13.82
N-type $\Delta\theta_B < 3^\circ$	73	0.960	28.76
All p-type	66	0.779	9.94
P-type $\Delta\theta_B < 4.5^\circ$	60	0.971	30.97

However, there are good reasons for disregarding some of the data points shown in Fig. 9 and 10:

Plasma resonance is known to be inaccurate on very thin diffusions (7) due to penetration of the light into the diffused layer and reflection from regions with concentration lower than the surface.

The resistivity determined by the four-point probe technique depends on accurate determination of the junction depth (7), which is extremely difficult for thin diffusions.

On wafers where both measurements were made, the plasma resonance and four-point probe concentration results differed by an average of about 30%, and in some cases by more than 100%.

Irvin's curves (5), which were used to determine the impurity concentration from the four-point probe sheet resistivity, are inaccurate at the high concentrations.

If the high concentration samples, where the measured PBA differs with the theoretical PBA by more than several degrees, are excluded from the linear regression analysis, much higher correlation coefficients are obtained. For the 73 n-type samples with $\Delta\theta_B < 3^\circ$ the correlation coefficient is 0.96 with a confidence level, or T-value, of 28.76. For the 60 p-type samples with $\Delta\theta_B < 4.5^\circ$, the correlation coefficient is 0.97 and the T-value is 30.97. These results indicate that the theoretical model of the PBA determination of concentration is accurate. The results are surprisingly good when it is considered that the model assumes an infinitely thick (no reflection from the back surface) and homogeneous sample (no variation of the optical constants with depth).

Table II. Reproducibility study

Sample	N-type	P-type	P-type
Mean θ_B	$N = 3.16 \times 10^{16} \text{ cm}^{-3}$ 73.97°	$1.01 \times 10^{20} \text{ cm}^{-3}$ 71.76°	$2.75 \times 10^{20} \text{ cm}^{-3}$ 69.47°
Range	1.0°	1.4°	1.0°
Standard deviation	0.253°	0.344°	0.348°

A reproducibility study, the results of which are shown in Table II, was made using three different wafers. Forty different PBA determinations were made for each wafer on different days. The standard deviation for all three wafers was less than 0.35° (or 0.6%) with a range of less than 1.5° (or 2%), indicating that the PBA technique is highly reproducible.

Conclusions

While the theoretical calibration curves with adjusted values of relative lattice dielectric constant and effective mass ratio agree very well with the experimental results, this agreement could perhaps be improved by introducing a variable effective mass ratio at high values of concentration.

The accuracy with which the PBA technique can determine carrier concentration for a particular semiconductor depends both on the sharpness of the reflectivity minimum (that is, the ease of determining the PBA) and also on the sensitivity of PBA to N on the calibration curve. For a given wavelength, the sharpness of the reflectivity minimum increases as concentration decreases, but the minimum is easily read at high concentration, as shown in Fig. 9.

Since the calibration curve of PBA vs. concentration is nonlinear and double-valued, the sensitivity of PBA to changes in N depends both on the range of concentration being investigated and the wavelength employed, as shown in Fig. 2. Once a concentration range is specified (by a particular diffusion process, for example), a wavelength can be chosen to yield the required sensitivity and accuracy. This feature of the pseudo-Brewster angle technique makes it an ideal process monitor.

Manuscript submitted July 1, 1971; revised manuscript received Dec. 10, 1971.

Any discussion of this paper will appear in a Discussion Section to be published in the December 1972 JOURNAL.

REFERENCES

1. P. A. Schumann, Jr., "Semiconductor Silicon," R. R. Habrecht and E. L. Kern, Editors, p. 662, The Electrochemical Society Softbound Symposium Series, New York (1969).
2. P. A. Schumann, Jr., W. A. Keenan, A. H. Tong, H. H. Gegenwarth, and C. P. Schneider, *This Journal*, **118**, 145 (1971).
3. O. S. Heavens, "Optical Properties of Thin Films," p. 54, Dover Publications, New York (1965).
4. P. A. Schumann, Jr., and R. P. Phillips, *Solid-State Electron.*, **10**, 943 (1967).
5. J. C. Irvin, *Bell System Tech. J.*, **41**, 387 (1962).
6. W. A. Keenan and P. A. Schumann, Jr., *This Journal*, **118**, 2010 (1971).
7. J. C. Irvin, Proceedings of the Symposium on Silicon Device Processing, NBS Special Publication 337, 99-110 (1970).

Phase Transformations in Eutectic Gold-Silicon Alloys on Single-Crystal Silicon

E. Philofsky,* K. V. Ravi, J. Brooks, and E. Hall

Motorola Semiconductor, Phoenix, Arizona 85008

ABSTRACT

Phase transformations in eutectic gold-silicon alloy thin films on single-crystal silicon substrates have been studied as a function of the rate of cooling from the melt by utilizing metallography, resistivity measurements, and x-ray and electron diffraction. Cooling at rates $<10^3$ °C/sec results in the eutectic structure, which becomes finer with increased rate of cooling. The silicon is found to nucleate and grow epitaxially from the substrate silicon with different shapes and orientations depending on the orientation of the substrate. At cooling rates $>10^3$ °C/sec the eutectic transformation is suppressed, and metastable structures are obtained. Isothermal annealing studies show that the reversion of the metastable structures on heating occurs via a series of both diffusionless and diffusion-controlled transformations.

Gold-silicon alloys are commonly used in semiconductor devices for bonding silicon dice to packages. The alloy is either a eutectic preform which is sandwiched between the bare silicon and the package, or is developed by depositing gold on the silicon and alloying above the eutectic temperature (370°C). During the bonding process the alloy can be slowly furnace cooled or rapidly quenched on a cold plate or in water. Despite the extensive use of this eutectic solder, little work has been published on phase transformations in this alloy. Heath (1) has determined the eutectic composition to be 18.6 a/o (atomic per cent) silicon by metallography. The eutectic structure is composed of pure gold and silicon as there is negligible mutual solubility of the components (2). Several investigators (3-7) have reported obtaining metastable cubic phases and amorphous structures in gold-silicon alloys cooled at rates greater than 10^6 °C/sec. However, no work has been reported on the phase transformations encountered in eutectic gold-silicon alloys cooled from the melt at commercially obtainable cooling rates. The present study is intended to fill this void.

Experimental Procedure

To prepare the gold-silicon alloys, 1-5 μm layers of 99.99% gold were evaporated onto 150 μm thick single-crystal silicon wafers of (100) or (111) orientation. The wafers were etched in HF solution prior to evaporation to remove any oxide which may have formed on the surface. The gold-deposited wafers were alloyed on a graphite strip heater at 400°C as monitored by a Chromel-Alumel thermocouple. The liquid alloys on both (100) and (111) silicon substrates were cooled at various rates up to 5°C/sec by reducing the power to the strip heater. Faster cooling rates were obtained by quenching with compressed N₂ gas or in water. These cooling rates were estimated by assuming Newton's law of cooling (8).

The alloy structures obtained on the two substrate orientations at various cooling rates were examined directly using optical metallography, resistivity measurements, and x-ray diffraction. The resistivity was measured using a four-point probe. Phase identifications were confirmed using a Norelco x-ray diffractometer with CuK α radiation. The orientation of the silicon in the alloy specimens was determined by Laue x-ray diffraction techniques.

For cooling rates higher than 10^3 °C/sec, metastable structures were obtained. To study the reversion of these structures to equilibrium gold and silicon phases,

beams 3×0.3 cm were cut from the silicon wafers and mounted on a hot plate for aging studies conducted at fixed temperatures between 25° and 200°C. A Chromel-Alumel thermocouple pressure-mounted to the specimen monitored the temperature, which was stable to $\pm 2^\circ\text{C}$. Resistivity changes during aging were continuously monitored with a four-point probe accurate to $\pm 1.5\%$. X-ray diffractometer studies were also conducted on several samples at different intervals of aging.

Experimental Results and Discussion

Eutectic structures (cooling rate $<10^3$ °C/sec).—Typical microstructures obtained at various cooling rates up to 150°C/sec on (111) and (100) silicon substrates are illustrated in Fig. 1 and 2, respectively. The

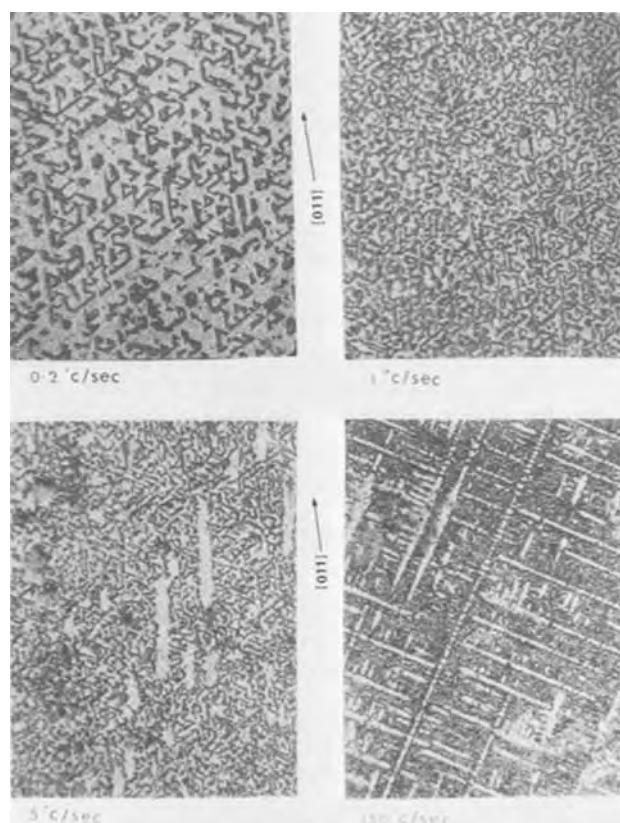


Fig. 1. Optical micrographs of gold-silicon eutectic alloy formed on (111) silicon at various cooling rates. The dark areas are silicon and the light areas are gold. Magnification X390.

* Electrochemical Society Active Member.
Key words: metastable phase, epitaxial growth, quenching, cooling curve.

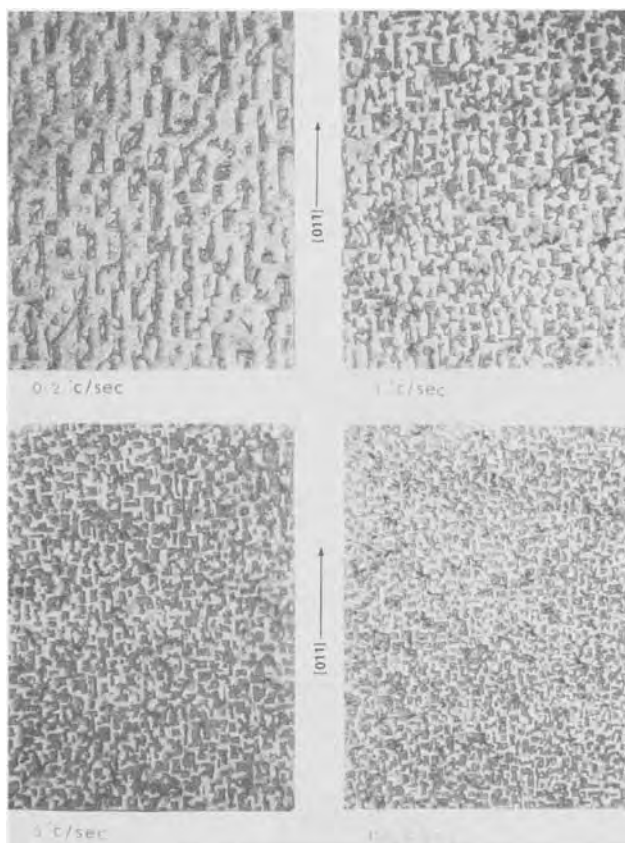


Fig. 2. Optical micrographs of gold-silicon eutectic alloy formed on (100) silicon at various cooling rates. The dark areas are silicon and the light areas are gold. Magnification X390.

structures consist of geometrically shaped pillars of silicon growing from the substrate in a matrix of gold. The pillar size and the interpillar spacing decrease as the cooling rate increases. This effect has been observed previously for a variety of eutectic morphologies (9). The shape of the silicon pillars is determined by the substrate orientation. Pillars on (111) substrates have triangular and plate-like cross sections with perimeters strongly oriented in $\langle 110 \rangle$, while the morphology of pillars on (100) substrates consists of squares and rectangles with perimeters also oriented in $\langle 110 \rangle$. Laue patterns show that these eutectic silicon pillars grow epitaxially from the substrate, while the gold is randomly oriented.

It can be observed by comparing microstructures for identical cooling rates in Fig. 1 and 2 that nucleation of the eutectic occurred much more rapidly on (100) silicon. Comparable interpillar spacings are obtained by cooling at $150^\circ\text{C}/\text{sec}$ on (100) and $5^\circ\text{C}/\text{sec}$ on (111). Because of the slow nucleation of the epitaxial eutectic, at cooling rates faster than $5^\circ\text{C}/\text{sec}$ on (111) substrates sufficient undercooling can be achieved for pure gold dendrites to nucleate independently of the substrate and grow within the melt. The remaining silicon-rich liquid in these specimens still grows epitaxially with the very fine pillar size and interpillar spacing characteristic of the greater undercooling. Cooling rates faster than $150^\circ\text{C}/\text{sec}$ were necessary for nucleation of gold dendrites on (100) substrates.

From these experimental observations, a model can be postulated for the solidification of the eutectic. The eutectic nucleates at the silicon substrate and grows toward the surface (in the direction of heat flow) with silicon as the primary phase. The silicon grows epitaxially with (111) sidewalls and the symmetry being governed by the substrate orientation (Fig. 3). Since the (111) sidewalls are not orthogonal to (100) or (111) substrates, the sidewalls grow at obtuse or acute angles depending on the local availability of silicon.

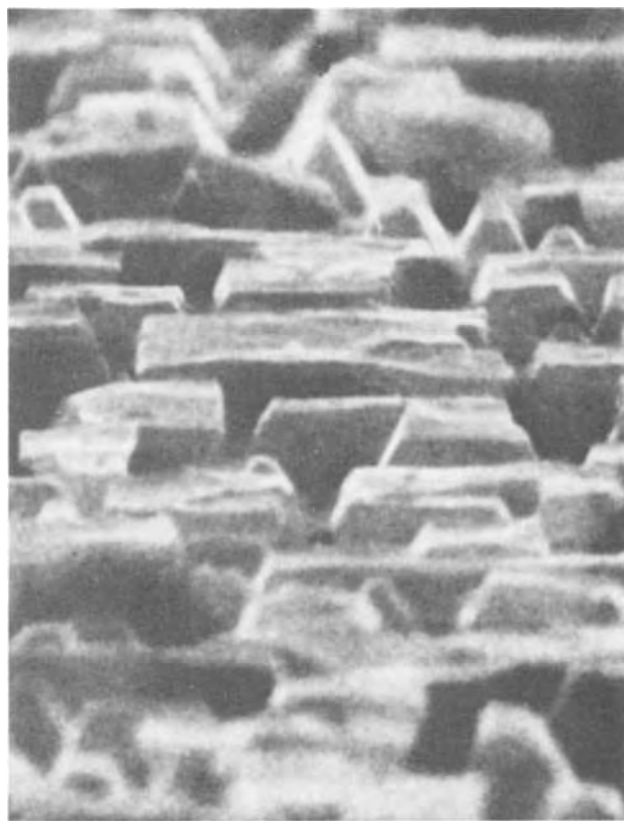


Fig. 3. Scanning electron micrograph of eutectic silicon pillars on (100) silicon. Cooling rate was $5^\circ\text{C}/\text{sec}$. The gold was removed by etching in an organic cyanide solution. Tilt- 75° , magnification X7800.

The pure gold liquid between these silicon pillars solidifies with many nuclei in a polycrystalline array. Since the nucleation and growth of epitaxial silicon is more rapid on (100) substrates, for a given cooling rate coarser structures result on (100) than on (111) substrates.

The epitaxial growth of the gold-silicon eutectic occurs only for thin films on a silicon substrate. Bulk gold-silicon eutectic nucleated from the melt in a graphite crucible is illustrated in Fig. 4. The silicon grows as a discontinuous precipitate yielding a structure similar to that observed for Al-Si eutectic (9).

Metastable structures (cooling rate $>10^3$ °C/sec).— For cooling rates faster than $\sim 1000^\circ\text{C}/\text{sec}$, the macroscopic appearance of the eutectic was silver instead of the gold color obtained at slower rates. Microscopically, the structure appears under polarized light to be composed of many small grains of a single phase with no evidence of gold or silicon. The resistivity of the silver phase is ~ 100 $\mu\text{ohm-cm}$, two orders of magnitude higher than that for normal gold-silicon.

The x-ray peaks obtained from a diffractometer trace of this phase are listed in Table I. Luo, Klement, and Anantharaman (5) had previously studied Au-Si alloys quenched at extremely fast rates. They reported a distribution of two phases, both fcc, depending on the initial atomic per cent silicon in the alloy. Predecki, Giessen, and Grant (6) found a rapidly quenched eutectic alloy to have a bcc γ -brass structure. Columns 3-6 of Table I indicate which of the observed peaks can be assigned to silicon, gold, or the reported metastable phases. It is seen that the peaks of the γ -fcc metastable phase most closely match those found in our work. However, several other lines cannot be indexed.

To study the quenched films further, electron microscopy and diffraction were utilized. The electron diffraction patterns showed that the structure was much



Fig. 4. Optical micrograph of bulk gold-silicon eutectic alloy. Magnification X800.

more complicated than previously believed. It was impossible to index these patterns on the basis of any of the reported cubic structures (5, 6). All indications are that the structure has a lower symmetry. Aging the quenched films indicated that the reverse transformation to equilibrium gold-silicon proceeds through the formation of a faulted structure. The faulted phase is also found if the water quench is inefficient, indicating the possibility that a finite amount of the faulted phase is present in the quenched films. This fact may account for the strong intensities seen at d spacings slightly shifted from that of pure gold (10). Anantharaman (3) also reports the presence of stacking faults, as evi-

denced by x-ray line broadening effects, in rapidly cooled eutectic alloys of Ag-Si, Ag-Ge, Au-Si, and Au-Ge.

Aging of metastable structures.—The reversion of the metastable phase to equilibrium gold-silicon aged in both air and N₂ atmospheres was monitored by following resistance changes during isothermal annealing. X-ray diffractometer traces were also taken on several samples at various intervals of aging. There appeared to be good correlation between the fraction of metastable phase transformed as given by the fractional change in resistivity, $(\rho_i - \rho)/(\rho_i - \rho_f)$, and that obtained from measurements of x-ray peak intensity changes between the metastable and equilibrium gold peaks. Figure 5 shows the S-shaped transformation curves obtained by resistivity measurements at three temperatures.

The kinetics of the reversion to equilibrium structure over the temperature range of 25°-200°C are given in Fig. 6. The abscissa, τ , is the time for one-half the entire resistivity change to occur. It is seen that the transformation rate is affected by the annealing atmosphere, with less time required for transformation in air than in N₂ at temperatures below 150°C. The activation energy of the line drawn through the data for annealing in N₂ is 34 kcal/mole. Macroscopically, the surface of the specimens annealed in air turned a gold color immediately on annealing, before x-ray or re-

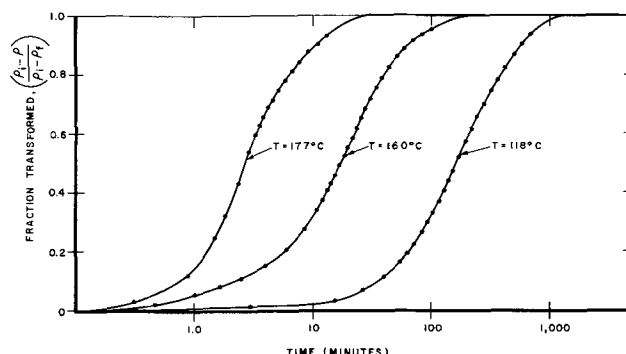


Fig. 5. Fraction of metastable gold-silicon transformed to eutectic gold-silicon vs. time for annealing in air at three temperatures.

Table I. d-Spacings obtained from quenched gold-silicon

d-Spacing (Å)	Intensity	Si and Au	β -FCC (5) (a = 7.844Å)	γ -FCC (5) (a = 19.5Å)	γ -Brass-bcc (6) (a = 9.6Å)
11.2	M			111	
6.2	W			~220	
5.84	W			311	
4.56	VVW		111		
4.03	M		200	422	
3.93	VW			333-511	211
3.72	M			400	
3.46	VVW			~531	220
3.34	W				
3.21*	VS	Si (111)			
3.13	VVS				
3.03	W			533	310
2.95	W			622	
2.90*	S				
2.78	M		220		222
2.63	W			642	
2.54	W			731-553	321
2.45	M			800	
2.40	W				400
2.36	M	Au (111)	311	820, 644	
2.32*	VS				
2.26	M		222	751-555	411
2.24	M			662	
2.18	W			840	
2.13	VS			842	420
2.07	S			664	
2.04	VW	Au (200)		931	332
2.02*	M				
1.96	W		400		422

* Not identified.

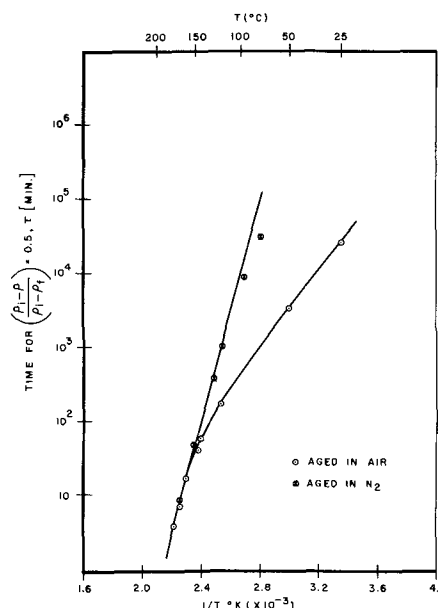


Fig. 6. Time for half completion of transformation from metastable to eutectic gold-silicon vs. reciprocal of absolute temperature over the range 25°-200°C for specimens aged in air and N₂.

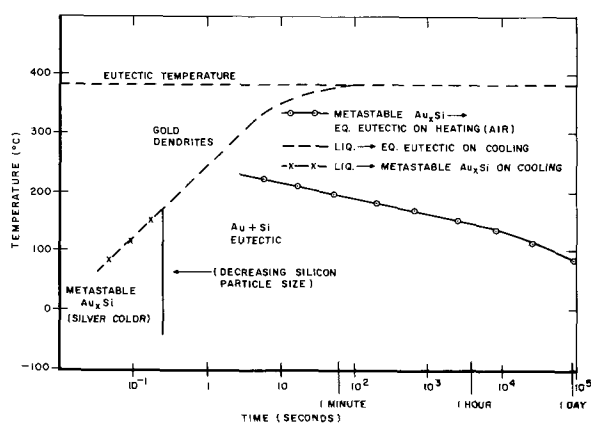


Fig. 7. Isothermal transformation diagram for gold-silicon eutectic alloy.

sistivity data showed any transformation had occurred. Analysis of the film in a Cameca ion microanalyzer showed the gold color to be caused by a surface layer $<1000\text{\AA}$ thick and composed of gold, silicon, oxygen, and nitrogen. Films annealed in N_2 remained silver-colored until the transformation was near completion. The rate data indicate this surface phenomenon in air significantly influences the transformation below 150°C .

From preliminary results obtained by transmission electron microscopy it appears that the transformation is complex, involving intermediate diffusionless steps as well as nucleation and growth. Thus, it is not surprising that the kinetics do not follow a simple Arrhenius relationship with a single activation energy. A more detailed investigation of the steps in this transformation is underway and will be discussed in a later paper.

Summary

From the observations presented in this paper it is seen that gold-silicon eutectic alloys can have a wide

variety of structures depending on thermal treatment. This range of structures can perhaps best be summarized by borrowing a tool from the ferrous metallurgist viz., the isothermal transformation diagram (11). Figure 7 is an attempt at such a diagram for gold-silicon eutectic alloys. The various types of broken lines represent completed transformation (see legend in Fig. 7). The position of the various transformation curves depends on experimental conditions. For instance, the curves for freezing are shifted upward if (100) silicon is used as a substrate instead of (111). Likewise, the metastable heating transformation curve is shifted to the right below 150°C if annealing is done in N_2 instead of air. Nevertheless, the form of the diagram, regardless of substrate or atmosphere, should appear similar to that in Fig. 7.

Manuscript submitted Jan. 8, 1971; revised manuscript received Oct. 22, 1971. This was Paper 190 presented at the Atlantic City Meeting of the Society, Oct. 4-8, 1970.

Any discussion of this paper will appear in a Discussion Section to be published in the December 1972 JOURNAL.

REFERENCES

1. E. G. Heath, *J. Electron Control*, **11**, 13 (1961).
2. E. R. Jette and E. B. Gebert, *J. Chem. Phys.*, **1**, 753 (1933).
3. T. R. Anantharaman, *Current Sci. (India)*, **27**, 238, 287 (1959).
4. W. Klement, Jr., R. H. Willens, and P. Duwez, *Nature*, **187**, 869 (1960).
5. H. L. Luo, W. Klement, Jr., and T. R. Anantharaman, *Trans. Indian Inst. Metals*, **20**, 214 (1965).
6. P. Predecki, B. Giessen, and N. Grant, *Trans. AIME*, **233**, 1438 (1965).
7. J. Dixmier and A. Guinier, *Rev. Met.*, **64**, 53 (1967).
8. P. Predecki, A. Mullendore, and N. Grant, *Trans. AIME*, **233**, 1581 (1965).
9. G. A. Chadwick, *Prog. Mater. Sci.*, **12**, 97 (1963).
10. M. S. Patterson, *J. Appl. Phys.*, **23**, 805 (1952).
11. E. S. Davenport, "Metals Handbook," p. 607 American Society for Metals (1948).

Kinetics of Thermal Growth of Ultra-Thin Layers of SiO_2 on Silicon

I. Experiment

Y. J. van der Meulen*

IBM Thomas J. Watson Research Center, Yorktown Heights, New York 10598

ABSTRACT

The rate of formation of very thin SiO_2 films thermally grown on [111] and [100] oriented silicon wafers was studied using ellipsometry to measure oxide thickness. Film thicknesses from $10\text{-}300\text{\AA}$ were obtained by varying oxidation time, oxidation temperature ($700^\circ\text{-}1000^\circ\text{C}$), and oxygen concentration in $\text{O}_2\text{-N}_2$ mixtures at 1 atm total pressure. The applicability of ellipsometry for such a study is discussed. Reproducibility of oxide films grown to thicknesses of $20\text{-}30\text{\AA}$ was approx. $\pm 1.0\text{\AA}$. Under otherwise equal conditions the oxide thickness grown differs for [100] and [111] oriented wafers. The pressure and temperature dependence of the linear rate constant, k_{lin} , show that the SiO_2 growth reaction is more complicated than was suggested earlier. In particular, a different pressure dependence for the two substrate orientations used indicates that several oxygen species participate in the rate determining steps.

Over the last decade, the increasing importance of silicon dioxide films in semiconductor technology has been evidenced by the large number of studies dealing

with its thermal formation on silicon, many of which are listed in Ref. (1-3). In classifying the results, a distinction can be made between the so-called "wet" oxidation in which water vapor is the principal oxidant, and "dry" oxidation where the principal oxidizing species generally is oxygen. As the oxide film grows

* Electrochemical Society Active Member.
Key words: ellipsometry, oxygen, (linear) rate constant, pressure dependence.

thicker, both the wet and the dry process eventually follow a parabolic rate law (thickness \propto time^{1/2}) of the type originally observed by Tammann (4) and theoretically treated by Wagner (5). This time dependence is a consequence of the fact that the transport of material through the thickening scale has become the slowest or rate-limiting step in the overall process. For smaller thicknesses, the oxide formation is not yet diffusion-controlled and slower surface (interface) reactions are rate-determining, resulting for SiO₂ in a linear relation between thickness and time. At intermediate thicknesses where neither the parabolic nor the linear step alone is rate-limiting, a mixed linear-parabolic equation combining them does describe the growth of SiO₂ as a function of time quite adequately over a range of conditions (1, 2).

Unfortunately, few published results are available describing the growth of SiO₂ in the thickness range between 0 and 300Å. In this interval, past work has been concerned mainly with the very slow oxidation of silicon near room temperature for thicknesses up to 25Å (6, 17); one of the few exceptions is a study by Goodman and Breece (7) of the oxide growth at 600°C for thicknesses up to ~30Å for the "dry" and ~60Å for the "wet" process. However, as the trend towards the use of thinner oxide layers continues, it is essential to further study their formation. The present article describes the thermal growth of SiO₂ films (10-300Å) on [100] and [111] oriented silicon wafers in O₂-N₂ mixtures of various oxygen concentration (1-100%) over a range of temperatures (700°-1000°C).

Experimental Procedures

In this investigation, chem-mechanically polished silicon wafers ([100] and [111] oriented, 1¼ in. diam, p-type, 2 ohm-cm) were used. They were cleaned by a standard process;¹ subjected to a clean-up oxidation in O₂ at 1050°C to form ~2000Å of SiO₂; recleaned;¹ blown dry in filtered, purified N₂ while being transferred to a quartz rack; and within 150 sec after leaving the water placed in the oxidation furnace tube which was filled with high purity N₂.

It has been reported that cleaned silicon surfaces can be temporarily protected by quenching freshly etched wafers in a saturated solution of iodine in methanol (8). The iodine can be removed by heating in N₂ (500°-550°C, atmospheric pressure) to leave a bare Si surface. We found that the index of refraction of the surface n_{Si} was not changed by such a treatment and that, on the average, oxide thicknesses were equal to those obtained without quenching in I₂. However, the scatter in the data was somewhat higher, and the method was therefore abandoned.

Oxidations were carried out in a double-walled, high purity, fused silica tube. Purified N₂ was passed through the outer jacket (2 liters/min). The water content of the effluent from the inner tube was less than 0.1 ppm. In each run, four wafers, vertically arranged on a quartz carrier, were warmed up in N₂ (15 min); oxidized at the desired oxygen partial pressure (\bar{p}_{O_2}) in an O₂-N₂ mixture (1 atm) for the desired length of time (t_{ox}); flushed with N₂ (15 min) and finally cooled down in N₂. This procedure gave a reasonable degree of accuracy in defining smaller values of t_{ox} (the minimum value of which was 15 min), in spite of mixing between the N₂ and the O₂-N₂ mixture. Control runs were made in pure N₂.

The oxide thickness was measured by ellipsometry. Alignment of the ellipsometer was done according to standard procedure (10). The ellipticity of the polarizer was shown to be negligible (9). The adjustments necessary for the optimal alignment of the mounted sample were done as follows: The polarizer (P) and analyzer (A) were roughly adjusted to yield the mini-

mum photo-detector response (i.e., extinction); the analyzer was then rotated by 90° and the sample was adjusted until the response of the detector was at a maximum; with the sample in this position the measurements were made. This procedure gave the same results as alignment of the sample with P and the quarter-waveplate (Q) put at zero but it is much faster. All data points were measured in 2 zones with Q = 45.00°, at a wavelength $\lambda = 5461\text{Å}$ and with an angle of incidence $\phi = 70.00^\circ$. Two measurements were usually made on each oxidized wafer. The data were numerically evaluated using an IBM 360/91 computer and McCrackin's program which allows one to make a number of different calculations (10).

Ellipsometric Evaluation

Proper interpretation of the ellipsometric results in terms of the complex refractive indices of the substrate ($n_s^* = n_s [1 - i \cdot \kappa_s]$) and the film ($n_F^* = n_F [1 - i \cdot \kappa_F]$), and of the film thickness (d_F), requires that a few limitations of this technique be kept in mind. A single ellipsometric measurement yields a set of two parameters (Δ, ψ), that characterize the change in polarization of the light upon reflection by the surface

$$\frac{R_p}{R_s} = \tan \psi e^{i\Delta} \quad [1]$$

where R_p and R_s are the complex reflection coefficients for light polarized parallel and normal to the plane of incidence of the light beam. For transparent films, Δ and ψ are cyclic functions of the oxide thickness. From these parameters no more than two of the five unknown material parameters, defined above, can be deduced.

In order to simplify the analysis, the SiO₂ films are assumed to be completely transparent, i.e., $\kappa_{SiO_2} = 0$. In addition, ellipsometry cannot be used to determine the imaginary part of the substrate index (κ_{Si}) unless the silicon has an atomically clean surface. This is because both a change in κ_{Si} and the presence of a very thin oxide film cause a shift in Δ only, which can be made to coincide to within a fraction of the experimental error (Fig. 1). Thus a value of $\kappa_{Si} = 0.00685$, obtained from optical transmission experiments (11), was used in this study. A small change in the real part of the substrate index (n_{Si}) on the other hand results almost exclusively in a shift in ψ (Fig. 2). All of this serves to reduce the number of unknown material parameters to three ($n_{Si}, n_{SiO_2}, d_{SiO_2}$).

Consider now the relation between these parameters and the ellipsometric data (Δ, ψ). It can be understood

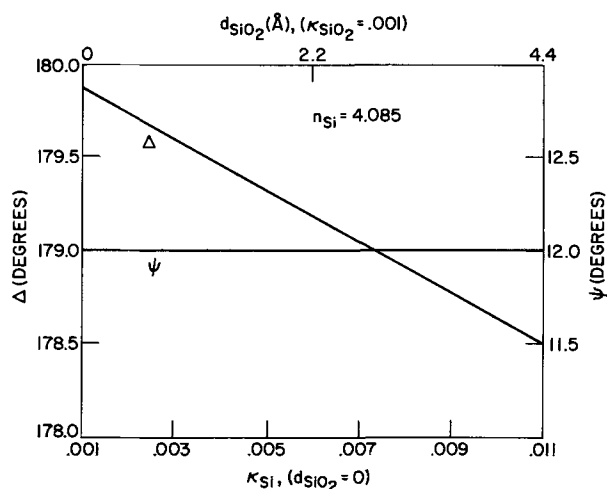


Fig. 1. The effect on (Δ, ψ) of a change in the imaginary part of the refractive index (κ_{Si}) at a constant value of the real part ($n_{Si} = 4.085$) for an unoxidized substrate. Also shown is the equivalency of such a variation of κ_{Si} and the presence of a thin SiO₂ film for a fixed value of κ_{Si} .

¹ Cleaning sequence: deionized H₂O; NH₄OH:H₂O₂:H₂O = 1:1:5, 65°C, ultrasonically agitated; d.i. H₂O; HCl:H₂O₂:H₂O = 1:1:5, 65°C, u.a.; d.i. H₂O; HF:H₂O = 1:1; d.i. H₂O.

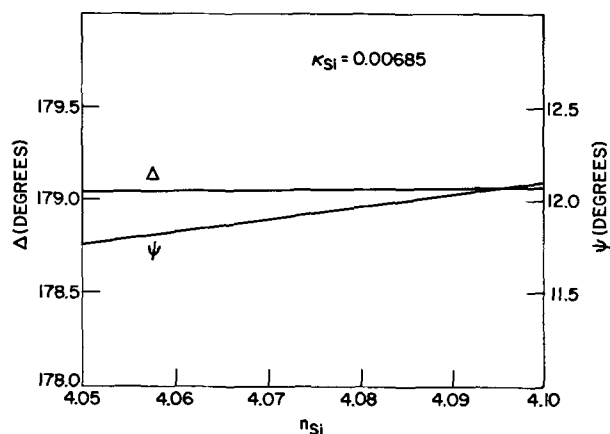


Fig. 2. The effect on (Δ, ψ) of a change in the real part of the refractive index (n_{Si}) at a constant value of the imaginary part ($\kappa_{Si} = 0.00685$). Unoxidized surface.

that as d_{SiO_2} becomes smaller, the influence of n_{Si}^* becomes dominant. Thus, for a fixed value of n_{Si}^* and small d_{SiO_2} it is not possible to determine n_{SiO_2} accurately. At the same time, some uncertainty is introduced into the determination of d_{SiO_2} . As shown in Table I(a) for $d_{SiO_2} \approx 30\text{\AA}$, very small changes in Δ and ψ suffice to change n_{SiO_2} considerably. Taking into account the experimental errors in Δ and ψ (± 0.015), the estimated accuracy in n_{SiO_2} in this thickness range is approx. $\pm 20\%$. At greater oxide thickness ($d_{SiO_2} \approx 500\text{\AA}$) the influence of a change of 1% in n_{SiO_2} already exceeds the experimental uncertainty [Table I(b)]. Determination of n_{Si} , however, is best done on surfaces covered with as thin a film as possible: Even with a small variation possible in n_{SiO_2} , the effect of a shift in n_{Si} at $d_{SiO_2} \approx 30\text{\AA}$ quickly exceeds the experimental error in ψ , whereas at $d_{SiO_2} \approx 500\text{\AA}$ the same uncertainty in n_{SiO_2} effectively prevents determination of n_{Si} (Table II).

The best procedure is thus to first compute n_{Si} from (Δ, ψ) measured on very thin films ($d_{SiO_2} < 20\text{\AA}$) using a reasonable value of n_{SiO_2} (e.g., 1.50), followed by a more precise determination of n_{SiO_2} from sets of data (Δ, ψ) taken on thicker films ($d_{SiO_2} > 200\text{\AA}$). This calculation can be reiterated until consistent values of both n_{Si} and n_{SiO_2} are obtained. Once these values are known, one can make an accurate calculation of d_{SiO_2} for all films regardless of thickness. The tacit assumption here is that the optical constants do not depend on d_{SiO_2} . This is the case if all data in the range of observation can be evaluated using the same values of n_{Si} and n_{SiO_2} , and it was indeed found that throughout our experiments consistent results could be obtained using $n_{Si} = 4.085 \pm 0.003$ and $n_{SiO_2} = 1.47 \pm 0.01$. Finally, it

Table I. Effect of variations in n_{SiO_2} on the ellipsometric parameters (Δ, ψ) ; $n_{Si}^* = 4.085 [1 - i \times 0.00685]$

(a) $\Delta = 169.855, \psi = 12.121$ (corresponding to $d_{SiO_2} = 30\text{\AA}$ at $n_{SiO_2} = 1.47$)			
n_{SiO_2}	d_{SiO_2}	$\delta\Delta$	$\delta\psi$
1.40	32.5	0.002	0.004
1.42	31.7	0.002	0.003
1.44	30.9	0.001	0.002
1.46	30.3	0.000	0.001
1.48	29.7	-0.000	-0.001
1.50	29.2	-0.001	-0.002
(b) $\Delta = 91.657, \psi = 26.336$ (corresponding to $d_{SiO_2} = 500\text{\AA}$ at $n_{SiO_2} = 1.47$)			
n_{SiO_2}	d_{SiO_2}	$\delta\Delta$	$\delta\psi$
1.40	547.8	1.756	0.467
1.42	532.6	1.203	0.336
1.44	518.7	0.695	0.203
1.46	506.0	0.224	0.068
1.48	494.3	-0.215	-0.068
1.50	483.6	-0.628	-0.206

Table II. Effect of variations in n_{Si} on the ellipsometric parameters (Δ, ψ) ; $n_{SiO_2} = 1.46 - 1.48$

(a) $\Delta = 169.855, \psi = 12.121$ (corresponding to $d_{SiO_2} = 30\text{\AA}$ at $n_{Si} = 4.085 [1 - i \times 0.00685]$)				
n_{Si}	n_{SiO_2}	d_{SiO_2}	$\delta\Delta$	$\delta\psi$
4.055	1.46	30.3	-0.118	-0.201
4.065	1.46	30.3	-0.078	-0.134
4.075	1.46	30.3	-0.038	-0.066
4.085	1.47	30.0	0.000	0.000
4.095	1.48	29.7	0.038	0.067
4.105	1.48	29.7	0.075	0.133
4.115	1.48	29.7	0.112	0.200
(b) $\Delta = 91.657, \psi = 26.336$ (corresponding to $d_{SiO_2} = 500\text{\AA}$ at $n_{Si} = 4.085 [1 - i \times 0.00685]$ and $n_{SiO_2} = 1.47$)				
n_{Si}	n_{SiO_2}	d_{SiO_2}	$\delta\Delta$	$\delta\psi$
4.055	1.46	508.5	0.000	0.000
4.065	1.46	505.6	0.000	0.000
4.075	1.47	502.8	0.000	0.000
4.085	1.47	500.0	0.000	0.000
4.095	1.47	497.3	0.000	0.000
4.105	1.48	494.5	0.000	0.000
4.115	1.48	491.8	0.000	0.000

has been shown that, for a silicon wafer covered with SiO_2 , the reflectance (R), as calculated from Δ and ψ , is constant within experimental error up to $d_{SiO_2} \approx 150\text{\AA}$ (12). This was conveniently used to check on the constancy of n_{Si} after various cleaning and oxidizing treatments.

Results and Discussion

For a given set of conditions (silicon orientation, temperature, oxygen partial pressure) an oxide thickness vs. oxidation time plot was always characterized by a fast initial rise followed by a (almost) linear region. The rapid initial growth process is known to have a $d_{SiO_2} \propto \log t_{ox}$ dependence at room temperature (6) and ceases to be important with increasing thickness (7). At lower temperatures ($T \leq 800^\circ\text{C}$) and oxygen partial pressures ($\bar{p}_{O_2} \leq 0.1$ atm) the data fit quite closely to the linear relationship

$$d_{SiO_2} = k_{lin} t_{ox} + d_0 \quad [2]$$

where k_{lin} is a linear rate constant and d_0 is a correction due to the fact that the linear region does not extrapolate back to the origin, but is preceded by the logarithmic growth. Thus we can also write

$$\frac{\partial d_{SiO_2}}{\partial t_{ox}} = k_{lin} = f(\bar{p}_{O_2}, T, \text{orientation}) \quad [3]$$

At higher temperatures and pressures, the oxide thickness did not increase exactly linearly with time, and allowance had to be made for the onset of a diffusion-controlled oxidation mechanism by using a mixed linear-parabolic equation

$$\frac{d_{SiO_2}^2 - d_0^2}{k_{par}} + \frac{d_{SiO_2} - d_0}{k_{lin}} = t_{ox} \quad [4]$$

where k_{par} is the parabolic rate constant, connected with the transport of oxidant through the oxide film.

Typical results, illustrating the large effects of silicon orientation and oxygen concentration are presented in Fig. 3 for $T_{ox} = 850^\circ\text{C}$. Most of the data points represent the average value of two measurements on each of four wafers. Standard deviations are indicated for the top three curves and are smaller than 1.0Å for the lowest curve. The small standard deviations in the latter case for oxide thickness of approx. 20-35Å makes these films very suitable for use in MNOS type structures based on direct tunneling phenomena (18). The solid lines were obtained by curve fitting using Eq. [4]. Values for the parabolic rate constant were obtained from the data of Deal and Grove (1) who, with others (13), also established the proportionality of k_{par} with partial oxygen pressures albeit at higher temperatures ($> 950^\circ\text{C}$) than some of the temperatures used in the

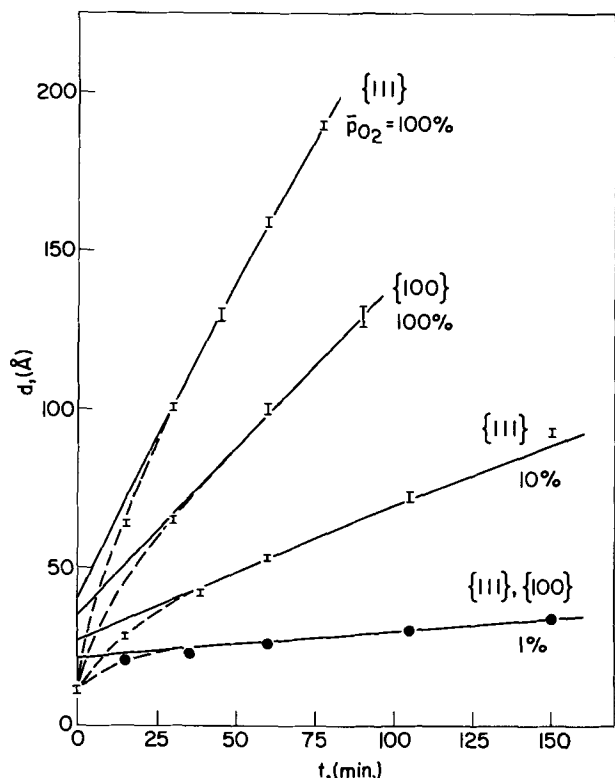


Fig. 3. Plot of oxide thickness vs. oxidation time at 850°C. Orientation and \bar{p}_{O_2} have been indicated. Error bars are shown in the upper curves. Standard deviations for the lowest curve were approx. 1.0Å.

present study. At $\bar{p}_{O_2} = 1$ atm, the difference in k_{lin} between the [111] and [100] surfaces amounts to a factor two; at $\bar{p}_{O_2} = 0.01$ atm no difference could be measured between the two orientations.

Curves similar to those in Fig. 3 were measured at five different temperatures (700°, 800°, 850°, 900°, 1000°C) for [111] oriented wafers and at two temperatures (850°, 1000°C) for [100] oriented wafers. Values of the linear rate constant (k_{lin}) were obtained and are shown in Fig. 4, along with two lines having slopes of

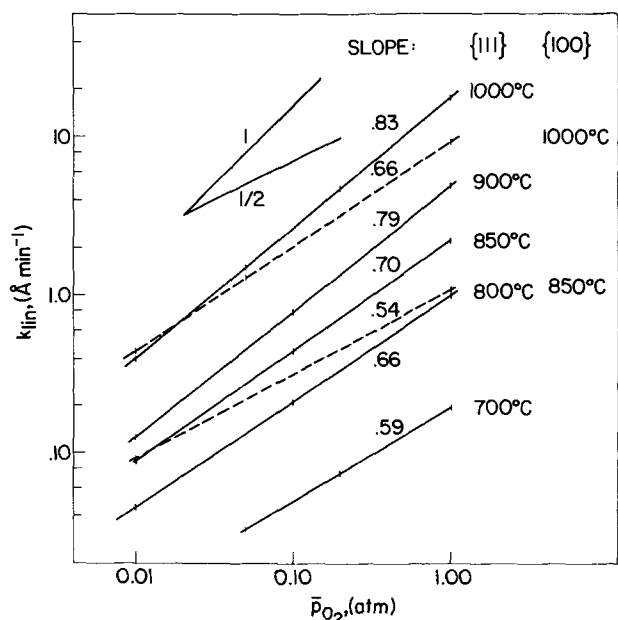


Fig. 4. Plot of $\log k_{lin}$ vs. $\log \bar{p}_{O_2}$. Drawn lines: [111] wafers; dashed lines: [100] wafers. Oxygen partial pressures where measurements were taken are indicated. Shown in the upper left-hand corner are two lines with slopes 0.5 and 1.0, respectively.

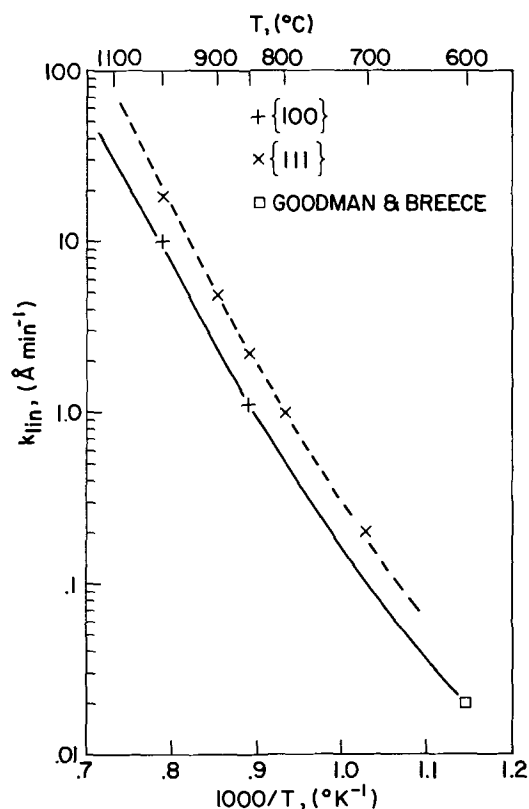


Fig. 5. Arrhenius plot of k_{lin} at $\bar{p}_{O_2} = 100\%$ (1.0 atm)

$\frac{1}{2}$ and 1. With the possible exceptions of the [100] data at 850°C (slope : 0.54) and the [111] data at 700°C (slope : 0.59) none of the curves measured exhibit a simple pressure dependence, i.e., $k_{lin} \propto \bar{p}_{O_2}^y$, where y equals either $\frac{1}{2}$ or 1. Small values ($k_{lin} < 0.1 \text{ Å min}^{-1}$) are harder to determine accurately and accordingly the scatter in the data was somewhat larger in that range. However, it is evident from the curves in Fig. 4 obtained for the [111] oriented wafers that the slopes increase as the temperature rises from 700° to 1000°C. Although our data collected on [100] oriented wafers are more limited, they indicate a similar trend. All values obtained for k_{lin} at $\bar{p}_{O_2} = 1.0$ atm have been plotted in Fig. 5 as a function of temperature. Also shown is a point taken from recently published work (7) on the oxidation of [100] oriented wafers at 600°C. From this graph, it is clearly apparent that the data for one orientation cannot be fitted using a single activation energy (ΔE) in an Arrhenius expression

$$k_{lin} = k_{lin}^{\circ} \exp \left(\frac{-\Delta E}{kT} \right) \quad [5]$$

Instead a considerably more complicated mechanism must be operative. These findings will be treated in detail in Part II of this investigation.

Consideration of both earlier published data and the present experimental results makes it possible to lay down a few ground rules that any description of the silicon oxidation mechanism should conform to. The oxide growth takes place at the silicon-silicon dioxide interface (14). Earlier work showed the oxidation in the parabolic region to be independent of wafer orientation, as indeed it must be when the process is diffusion-controlled. It was also found (1, 13) that the parabolic rate constant increases linearly with the oxidant partial pressure from 950° to 1200°C. This adherence to Henry's law thermodynamically means that molecular oxygen, perhaps as a molecule ion (14-16), must be the principal diffusing species. In this work, we measured different values of the linear rate constant at $\bar{p}_{O_2} = 1.0$ atm for wafers having a different orienta-

tion. Previously, this had only been reported for "wet" oxidation (2). This orientation dependence could simply be the result of the different atomic structure of the surface and need not imply a basically different reaction mechanism. It was also found, however, that at a given temperature the pressure dependence of k_{lin} depends on the orientation of the substrate. Thus the apparent order of the reaction is different for different orientations which means that more than one oxygen species must be involved in the rate-limiting step. In other words, the two orientations studied have different rate-limiting steps. Taken together with the fact that even for a single orientation the slope of k_{lin} vs. \bar{p}_{O_2} changes with temperature, it means that the rate-limiting step is more complicated than was thought before and may well be comprised of various competing reactions involving different oxygen species at the Si-SiO₂ interface. The mathematical description to be presented in Part II will attempt to take these complexities into account.

The values calculated for k_{lin} from the experimental data at $\bar{p}_{O_2} = 1$ atm presented here—although roughly comparable—are not in complete numerical agreement with earlier values (3). This can be ascribed to the fact that the mixed linear-parabolic mechanism in prior work normally was diffusion dominated, the surface reaction giving rise to a linear correction only, whereas in the present study surface reactions are dominant. There seems to be one fundamental aspect where at first sight the discrepancy is of a more fundamental character: Deal and Grove (1) reported that k_{lin} too varies linearly with the oxygen pressure. Further examination of their data shows, however, that the observations—probably made on [111] oriented wafers—in dry oxygen were made at a single temperature (1200°C) and over a rather limited range of partial pressures ($\bar{p}_{O_2} = 190$ -760 mm Hg). Thus no real discrepancy with the data presented here need exist, because the relation between k_{lin} and \bar{p}_{O_2} becomes more linear with rising temperature (Fig. 4).

Summary

The thermal dry oxidation of silicon under ultraclean conditions has been studied in the region where the kinetics are predominantly linear with time and controlled by a reaction at the SiO₂ outer surface, where the incorporation of oxygen into the SiO₂ takes place, or at the SiO₂-Si interface, where the oxide growth occurs. The following findings seem to be most significant:

(i) For a given temperature and oxygen partial pressure the linear oxidation rate is different for [111] and [100] oriented wafers.

(ii) For a given temperature and orientation the pressure dependence of the linear rate constant is complicated and seems to preclude a simple reaction mechanism.

(iii) For a given temperature the oxygen pressure dependence of the linear rate constant is different for [111] and [100] oriented wafers.

(iv) For a given wafer orientation the oxygen pressure dependence of the linear rate constant varies with temperature.

The data do not seem to contradict earlier work but they definitely require a more complex reaction scheme than has been proposed for this process in the past. Possible solutions to this problem will be discussed in Part II of this investigation.

Acknowledgments

The author gratefully acknowledges his discussions with Drs. J. M. Eldridge and W. A. Pliskin and the experimental assistance of Mr. H. P. Crowder.

Manuscript submitted Sept. 8, 1971; revised manuscript received Dec. 10, 1971. This was Paper 80 presented at the Washington, D. C., Meeting of the Society, May 9-13, 1971.

Any discussion of this paper will appear in a Discussion Section to be published in the December 1972 JOURNAL.

REFERENCES

1. B. E. Deal and A. S. Grove, *J. Appl. Phys.*, **36**, 3770 (1965).
2. W. A. Pliskin, *IBM J. Res. Develop.*, **10**, 198 (1966).
3. A. G. Revesz and R. J. Evans, *J. Phys. Chem. Solids*, **30**, 551 (1969).
4. G. Tammann, *Z. Anorg. Allgem. Chem.*, **111**, 78 (1920).
5. C. Wagner, *Z. Phys. Chem.*, **B21**, 25 (1932); **B32**, 447 (1936).
6. R. J. Archer, *This Journal*, **104**, 619 (1957).
7. A. M. Goodman and J. M. Breece, *ibid.*, **117**, 982 (1970).
8. R. Lieberman and D. L. Klein, *ibid.*, **113**, 956 (1966).
9. W. R. Hunter, D. H. Eaton, and C. T. Sah, *Surface Sci.*, **20**, 355 (1970).
10. F. L. McCrackin, NBS Technical Note 479 (April 1969) U. S. Government Printing Office, Washington, D. C.
11. W. C. Dash and R. Newman, *Phys. Rev.*, **99**, 1151 (1955).
12. K. Vedam, W. Knausenberger, and F. Lukes, *J. Opt. Soc. Am.*, **59**, 64 (1969).
13. P. J. Burkhardt and L. V. Gregor, *Trans. Met. Soc. AIME*, **236**, 299 (1966).
14. P. J. Jorgensen, *J. Chem. Phys.*, **37**, 874 (1962).
15. D. O. Raleigh, *This Journal*, **113**, 782 (1966).
16. P. J. Jorgensen, *ibid.*, **114**, 820 (1967).
17. J. T. Law, *J. Phys. Chem. Solids*, **4**, 91 (1958).
18. A. M. Goodman, E. C. Ross, and M. T. Duffy, *RCA Rev.*, **31**, 342 (1970).

A Survey of the Cr-Rich Area of the Cr-Si-C Phase Diagram

P. W. Pellegrini, B. C. Giessen, and J. M. Feldman

Department of Electrical Engineering and Department of Chemistry,
Northeastern University, Boston, Massachusetts 02115

ABSTRACT

An investigation of the ternary phase diagram Cr-Si-C has been completed in the region Cr-Cr₃C₂-Cr₅Si₃. Phase boundaries have been established to an accuracy of ± 2 a/o (atomic per cent). The extent of a ternary single-phase region of approximate stoichiometry Cr₅Si₃C_x is established. Lattice parameter measurements of this phase show that all or nearly all C enters the D8₈-Mn₅Si₃ structure at interstitial sites, rather than substitutionally as previously reported. Finally, the possibility of SiC crystal growth from solutions of transition metal silicides is discussed.

Chromium has been considered as a solvent for the solution growth of single crystal silicon carbide, based essentially on initial phase diagram work by Griffiths and Mlavski (1) and Griffiths (2) that indicated a two-phase equilibrium Cr-SiC. Griffiths (3) subsequently corrected the earlier diagram and reported that binary Cr₃C₂ is in equilibrium with a ternary Cr-Si-C phase; this rules out a Cr-SiC pseudobinary system at least at low temperatures. A tentative Cr-Si-C ternary diagram was later given by Wolff and Das (4) which is based on the constitution of several alloys with compositions in the partial system Cr₃C₂-SiC-Cr₅Si₃-Si, supplemented by tentative tie-lines in the Cr-rich portion. They report the existence of the equilibria Cr₂₃C₆-Cr₃Si, Cr₇C₃-Cr₃Si, Cr₃C₂-Cr₃Si, Cr₃C₂-T (T = ternary phase), Cr₅Si₃-T, Cr₃Si₂-T, Cr₃C₂-SiC, T-SiC, CrSi-SiC, and CrSi₂-SiC.

We report here a reasonably detailed survey of the Cr-rich region of the Cr-Si-C isotherm at 1400°C which is shown in Fig. 1. The constitution of alloys in the Cr-Cr₃C₂-T-Cr₅Si₃ partial diagram was studied; thus, the present work is complementary to that reported in Ref. (4).

Techniques

Samples of ~ 5 g weight were prepared by arc-melting in a Ti-gettered argon atmosphere from 99.999% Cr, 99.99% Si and C with < 5 ppm ash. Cr-Si and Cr-C master alloys were used to make the ternary alloys. In the preparation of the alloys in the partial system Cr₅Si₃-T-SiC-Si, SiC (99+%) was also used as a starting material. Weight losses on melting depended on the Cr content, and amounted to ~ 1 w/o (weight per cent) at 70 a/o Cr and 2 w/o at 90 a/o Cr. Considering the high vapor pressure of Cr, these losses could be taken as Cr losses; after correcting for them, the nominal compositions of the alloys were used, with a remaining uncertainty of ± 1 a/o. No oxidation was noted. The dash-dotted line in Fig. 1 indicates the approximate limit of the compositions of alloys that could be prepared by arc-melting as described; in alloys with compositions beyond this limit large evaporation losses occurred.

The alloys were examined in the as-cast state and after annealing for 6 to 7 hr at 1400°C in He at 1 atm (< 5 ppm impurities). This period of time was found to be sufficient to produce equilibrium, as shown by the removal of nonequilibrium structures such as those due to incomplete peritectic reactions. Metallographic samples were electrolytically etched in dilute HCl; x-ray patterns of ground samples were taken on a GEXRD6 diffractometer with filtered Cr K α -radiation. All phases were identified by matching of the diffraction patterns with the data in the JCPDS Powder Diffraction File; phase proportions were estimated from microscopic examination of the polished, annealed sam-

Key words: ternary phase diagram, C-Cr-Si system, SiC, solution growth, x-ray diffraction.

ples and by comparing x-ray intensities using our own diffraction pattern matching program. Lattice parameters for T are shown in Fig. 2; they were calculated from high-angle reflections with $2\theta > 140^\circ$ and have error limits of < 1 to 2×10^{-3} Å, as indicated in Fig. 2.

Results and Discussion

The Cr-Si-C system.—On the basis of these alloys, the nature of the phase equilibria in the investigated portion of the 1400°C isotherm (Fig. 1) has been established unambiguously. A more accurate location of the boundaries between the two- and three-phase fields beyond the present accuracy of $\sim \pm 2$ a/o (for boundaries given in solid lines) would have required a much larger number of alloys and was not attempted. The extent of ternary homogeneity ranges of the binary Cr-C phases was not studied but they are probably small, judging from the absence of lattice parameter changes. Cr₃Si has a limited solubility for carbon of 4 ± 1.5 a/o; Cr₅Si₃ has no noticeable solubility for carbon (this may be due to the formation of the ternary phase T with the formula Cr₅Si₃C_x which lowers the solubility of carbon in Cr₅Si₃).

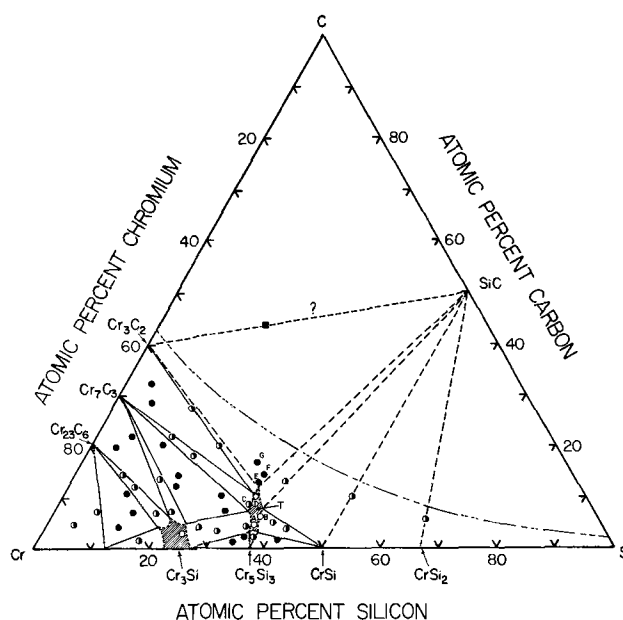


Fig. 1. Isothermal section of the ternary system Cr-Si-C at 1400°C. Binary Cr-C, Si-C, and Cr-Si phases and their compositions are taken from Ref. (5-7) respectively. ○: single phase; ◐: two-phase; ●: three phase. Dash-dotted curve indicates limit of compositions of alloys accessible by arc-melting as described in text. Alloy marked ■ was prepared by sintering a mechanical mixture of the elements, and consisted of Cr₃C₂, SiC, and T.

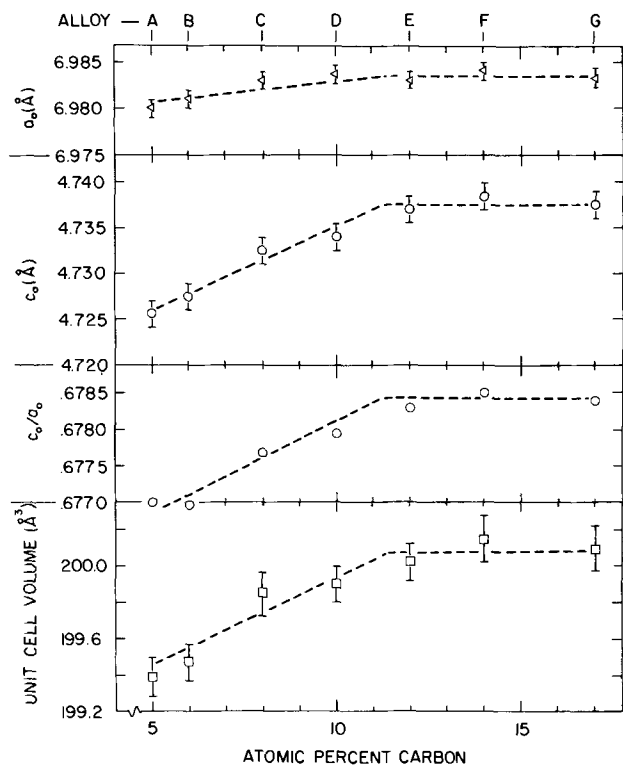


Fig. 2. Lattice parameters, axial ratios, and unit cell volumes of the ternary Cr-Si-C phase T ($\text{Cr}_5\text{Si}_3\text{C}_x$) in alloys A-G on or near the section $\text{Cr}_5\text{Si}_3\text{-C}$ (see Fig. 1). Small departures of alloy compositions from section $\text{Cr}_5\text{Si}_3\text{-C}$ have negligible effect on unit cell parameters due to the similar sizes of Cr and Si in $\text{Cr}_5\text{Si}_3\text{C}_x$.

The phase diagram shows clearly that combinations of silicides and carbides of Cr, such as $\text{Cr}_7\text{C}_3 + \text{Cr}_3\text{Si}$ or $\text{Cr}_3\text{C}_2 + \text{T}$ have lower free energies than the combination $\text{Cr} + \text{SiC}$. The zigzagging of the tie-lines between the silicides and carbides up to Cr_3C_2 and T, and the absence of a Cr-SiC equilibrium is possibly related qualitatively to the average valence electron concentration per atom (8) (VEC) of the silicides and carbides which changes monotonically with the C and Si contents, as shown by the following argument. It is often observed in ternary systems that two VEC-determined binary phases (such as σ -phase-related transition metal phases and noble metal Hume-Rothery phases) with a common constituent are connected by a pseudobinary solid solution range of constant VEC (8). In addition, Pfeifer *et al.* (9) noted that in the absence of a complete solid solution, tie-lines will tend to connect two phases with similar VEC's rather than two phases with a large VEC difference. As the phase diagram shows, the Cr-rich phases in the Cr-Si-C system may follow this rule.

The main changes in the present phase diagram over the tentative diagram of Ref. (4) are: (i) no tie-line exists between Cr_3C_2 and Cr_3Si ; instead there is a tie-line between Cr_7C_3 and T (see Fig. 1); (ii) the region $\text{Cr}_3\text{Si-T-CrSi}$ has been worked out; a nonexistent phase Cr_3Si_2 has been removed and replaced by Cr_5Si_3 ; (iii) missing tie-lines such as those between Cr_3Si and T or CrSi and T were established and a number of phase boundaries were refined.

The ternary phase.—Some interesting results concern the ternary phase, T. Its stoichiometry range was found to conform to the ideal formula $\text{Cr}_5\text{Si}_3\text{C}_x$, (approximate homogeneity range $\text{Cr}_{5\pm 0.2}\text{Si}_{3\pm 0.1}\text{C}_x$) with $0.25 < x < 1.05$. Its lattice parameters and atomic volumes (Fig. 2) show a pronounced increase with increasing x . This indicates that additional carbon does not substitute for Cr or Si, as implied by the formula $\text{Cr}_{5-x}\text{Si}_{3-y}\text{C}_{x+y}$ [Ref. (10)] but that it occupies unfilled sites of the $\text{D}_{8h}\text{-Mn}_5\text{Si}_3$ type structure of $\text{Cr}_5\text{Si}_3\text{C}_x$. The Mn_5Si_3 struc-

ture type provides vacant hole sites formed by the metal octahedra which are uniquely favorable for the accommodation of interstitial atoms (11). A neutron diffraction study (12) of the related Nowotny phase $\text{Mo}_{4.8}\text{Si}_3\text{C}_{0.6}$, confirmed that carbon occupies the octahedral hole positions. (In $\text{Mo}_{4.8}\text{Si}_3\text{C}_{0.6}$, the ratio Mo:Si = 1.60 causes 10% vacancies in the fourfold Mo positions, with the sixfold Mo positions being completely occupied; however, in $\text{Cr}_5\text{Si}_3\text{C}_x$ there are probably no such metal vacancies).

The present investigation provides strong support for the model (11, 12) for the C positions. Since there is one hole site per formula unit, the maximum solubility of carbon due to this position would be 11.1 a/o C ($x = 1$). This agrees well with the experimental value of 11.5 ± 1 a/o C ($x = 1.05 \pm 0.1$) from metallographic observation and the discontinuities of the lattice parameters and atomic volume (Fig. 2). As in other alloy phases stabilized by interstitial atoms, additional bonding is probably provided in $\text{Cr}_5\text{Si}_3\text{C}_x$ by interaction of the s,p-states of carbon with the d-states of the transition metal (13), stabilizing the ternary phase.

Growth of SiC.—Concerning the possibility of growing SiC from Cr solutions, it can be seen in Fig. 1 that SiC is not in equilibrium with Cr at 1400°C , nor is there likely to be an equilibrium between SiC and melt at elevated temperatures in the partial system Cr- Cr_7C_3 - Cr_3Si . To grow SiC from Cr-SiC melts, compositions in the partial system Cr_3C_2 -T-SiC would be necessary. These would require high temperatures ($1900^\circ\text{-}2000^\circ\text{C}$) with attendant, relatively high partial pressures of Cr ($\sim 1\text{-}10$ Torr). This makes Cr an unattractive base for equilibrium solution growth of SiC even if one were willing to operate in the requisite temperature and composition range.

Concerning other potential transition metal solvents for SiC, the following statements are possible. In accordance with the general VEC principle stated above (9), ternary Si-C-transition metal phase diagrams with transition metals between Group IVB (Ti) and Group VIII (Ni), will either have similar stable tie-lines between metal carbides and silicides as in Cr-Si-C (if the third element is an early transition metal such as Ti, V, Cr), or there will be tie-lines between the metal silicides and C (if the third element is a later transition metal such as Co and Ni). Unalloyed transition metals are, therefore, not prospective solvents for SiC; SiC growth is possible, perhaps, if one used as a solvent a relatively low melting binary or ternary intermetallic phase which is in equilibrium with SiC at all temperatures.

Acknowledgment

We would like to thank Mr. Steven Goldberg for his able assistance in developing a diffraction pattern matching program. This work was supported by N.S.F. under Grant GK-2572; one of us (B.C.G.) acknowledges support by ARO(D) under Contract 31-124-G1127.

Manuscript submitted May 3, 1971; revised manuscript received ca. Nov. 2, 1971.

Any discussion of this paper will appear in a Discussion Section to be published in the December 1972 JOURNAL.

REFERENCES

- L. B. Griffiths and I. A. Mlavski, *This Journal*, **111**, 806 (1964).
- L. B. Griffiths, *J. Phys. Chem. Solids*, **27**, 261 (1966).
- L. B. Griffiths, *ibid.*, **27**, 1368 (1966).
- G. A. Wolff and B. N. Das, "The Investigation of SiC by a Traveling Solvent Method," Final Report, AF19(628)-4384, p. 8 (1967).
- M. Hansen and K. Anderko, "Constitution of Binary Alloys," 2nd edition, p. 351, McGraw-Hill Book Co., New York (1958).
- R. P. Elliot, "Constitution of Binary Alloys," First Supplement, p. 227, McGraw-Hill Book Co., New York (1965).

7. F. A. Shunk, "Constitution of Binary Alloys," Second Supplement, p. 279, McGraw-Hill Book Co., New York (1969).
8. T. B. Massalski, in "Physical Metallurgy," 2nd edition, R. W. Cahn, Editor, pp. 167 and 196, North Holland/American Elsevier, New York (1970).
9. H. U. Pfeifer, S. Bhan, and K. Schubert, *J. Less Common Metals*, **14**, 291 (1968).
10. E. Parthe, H. Schachner, and H. Nowotny, *Monatsh. Chem.*, **86**, 182 (1955).
11. B. Aronsson, *Acta Chem. Scand.*, **14**, 1414 (1960).
12. E. Parthe, W. Jeitschko, and V. Sadagopan, *Acta Cryst.*, **19**, 1031 (1965).
13. H. H. Stadelmaier, in "Developments in the Structural Chemistry of Alloy Phases," B. C. Giessen, Editor, p. 141, Plenum Press, New York, (1969).

Technical Notes



Spectrophotometric Determination of Photoresist Photosensitivity

I. A Theoretical Discussion of Those Photoresist Reactions Which Entail the Depletion of a Photoactive Species¹

D. F. Ilten*

IBM Components Division, East Fishkill Facility, Hopewell Junction, New York 12533

Many of the commonly used photoresist systems consist of two components: a polymer and a photoactive species dissolved in an organic solvent system (1, 2). During exposure, light is absorbed by the photoactive species which undergoes a chemical change promoting either a solubilization or a desolubilization reaction in the polymer. To be capable of reacting the photoactive species must, of course, according to the Grothus-Draper law (3), have an absorption band in the region of emission of the radiation source used for the exposure. As the photoactive species is depleted, its absorbance decreases also. Assuming no product arises which absorbs at the same wavelength as the photoactive species, the change in absorbance of the latter as a function of exposure can be directly determined spectrophotometrically. These facts suggest a method of monitoring the photoresist photoreaction by measuring the rate of change of the photoactive species' concentration as a function of exposure time. The theory of this method will be developed in the following sections.²

Discussion of Photoresist Reaction Kinetics

Assuming monochromatic radiation in all cases, the analysis is based on the following mechanism (4-8): the photoactive species, A, upon absorbing a quantum of radiation gives the excited species, A*. This may either relax to the ground state with the emission of radiation or form one or more product species, B



It is assumed that the rate of disappearance of A is directly proportional to the rate of the absorption of light, where the proportionality constant is the primary quantum yield, $\phi = \phi(\lambda)$. Then the rate equation for the net reaction

* Electrochemical Society Active Member.

¹ This article is Part I of a series, the second part of which is found on p. 539.

Key words: photoresist, kinetics, photochemistry, microelectronics, S₁S reaction.

² The method would not be applicable to photoresist systems which employ an energy transfer dye which is not depleted during exposure or in cases where only a very small change in the concentration of the photoactive species is observed, e.g., Kodak Photoresist (KPR).

$$A \rightarrow B$$

may be written as

$$\frac{d(nl)}{dt} = -\phi I_a \quad [2]$$

where n = the number of moles of A/cm³; I_a = the number of moles of quanta (Einstein) of monochromatic light absorbed per cm²/sec; l = the optical path length, i.e., the photoresist film thickness in cm, ϕ = the primary quantum yield = $\frac{\text{No. of molecules which react}}{\text{No. of photons absorbed}}$.

It is further assumed that the Lambert-Beer law holds for the photoactive species in the model chosen

$$I = I_0 e^{-\epsilon'cl} \quad [3]$$

where I_0 = the incident light intensity; I = the transmitted light intensity; ϵ' = 2.303 ϵ ; ϵ = the molar absorptivity in liters/mole/cm; c = the molar concentration of unreacted molecules in moles/liter. Further, x = the absorbance at the measured wavelength = $\log I_0/I = \epsilon cl$, again assuming Beer's law to hold, also $x' = 2.303x$.

The absorbed light intensity is given by

$$I_a = I_0 (1 - e^{-x'}) \quad [4]$$

Upon substitution of Eq. [4] into Eq. [2], and using the definition of x one obtains

$$\frac{dx}{dt} = -10^3 \epsilon \phi I_0 (1 - e^{-x'}) = -a \phi (1 - e^{-x'}) \quad [5]$$

where $a = 10^3 \epsilon I_0$ and $a' = 2.303a$

This yields

$$\int_{x_0}^{x'} \frac{dx'}{1 - e^{-x'}} = -a' \phi \int_0^t dt \quad [6]$$

Upon integration, the expression

$$\ln \left| \frac{e^{x_0} - 1}{e^{x'} - 1} \right| = a' \phi t \quad [7]$$

is obtained.

Finally, after cancelling the factors 2.303, the primary quantum yield can be expressed as

$$\phi = \frac{1}{at} \log \left| \frac{e^{x'_0} - 1}{e^{x'} - 1} \right| \quad [8]$$

Letting $x' = x'_{0/2}$ and expanding the exponentials as a truncated power series, one obtains

$$\phi = \frac{1}{at_{1/2}} \log \left| \frac{e^{x'_{0/2}} - 1}{e^{x'_{0/2}} - 1} \right| \quad [9]$$

$$\phi \sim \frac{1}{at_{1/2}} \log 2 = \frac{0.301}{at_{1/2}} \quad [10]$$

Equation [10] is a reasonable approximation of Eq. [9] for values of $x' < 1$. The half-time, $t_{1/2}$, is the exposure time necessary to reduce x' to one half its initial value. More generally, ϕ may also be expressed in terms of $t_{1/n}$, where n is any arbitrary value, as

$$\phi \sim \frac{1}{at_{1/n}} \log |n| \quad [10a]$$

Determination of x' as a function of time.—The values of the absorbance, x' , may also be obtained as a function of time from Eq. [7].

Setting $b = e^{x'_0} - 1$, Eq. [7] becomes

$$\frac{b}{e^{x'} - 1} = e^{a\phi t} = e^{t/\tau} \text{ where } \tau = \frac{1}{a'\phi} \quad [11]$$

$$e^{x'} = 1 + be^{-a'\phi t} = 1 + be^{-t/\tau} \quad [12]$$

$$x'(t) = \ln(1 + be^{-a'\phi t}) = \ln(1 + be^{-t/\tau}) \quad [13]$$

$x'(t)$ is plotted in Fig. 1 as a function of time for various values of $a'\phi$. For small values of the variable, $a'\phi t$, Eq. [13] becomes

$$x' \sim be^{-a'\phi t} \quad [14]$$

or

$$x \sim \frac{b}{2.303} e^{-a'\phi t} \quad [14b]$$

Taking logarithms of Eq. [14b] gives

$$\log x = \log \left| \frac{b}{2.303} \right| - a\phi t \quad [15]$$

For reasonably low concentrations, the disappearance of x should approximate an exponential decay and a plot of $\log x$ vs. time should give a straight line. Values of $t_{1/2}$ taken from such plots of experimental data can be used to calculate the primary quantum yield, ϕ . Expression [15] also predicts a series of parallel lines for differing values of initial absorbance, x' , resulting from either variations of film thickness or of the concentrations of the photoactive species.

Exposure.—Exposure is defined as the integral of the absorbed radiation over time

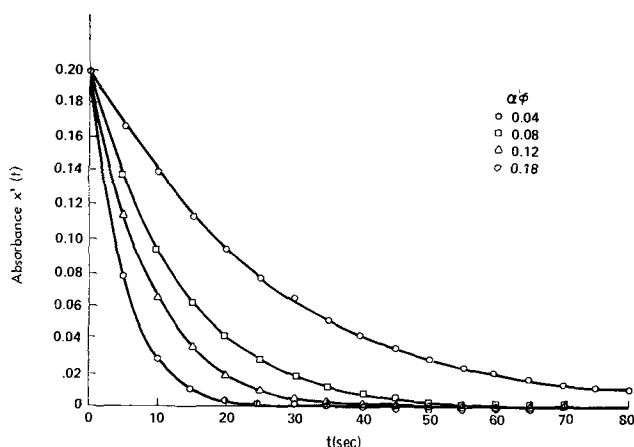


Fig. 1. Depletion of the photoactive species with constant exposure intensity.

$$E = \int_0^t I_a dt \quad [16]$$

Utilizing Eq. [4], expression [16] becomes

$$E = \int_0^t I_0(1 - e^{-x'}) dt$$

$$E = I_0 \int_0^t [1 - \exp\{-\ln(1 + be^{-a'\phi t})\}] dt$$

$$= I_0 \int_0^t \left(1 - \frac{1}{1 + be^{-a'\phi t}} \right) dt \quad [17]$$

Upon integration this yields

$$E = -I_0 \left[\frac{1}{a'\phi} \ln(1 + be^{-a'\phi t}) \right]_0^t$$

$$= \frac{I_0}{a'\phi} [\ln(1 + b) - \ln(1 + be^{-a'\phi t})] \quad [18]$$

$$= \frac{1}{a'\phi} |x'_0 - x'| \quad [19]$$

Expression [19] reduces to

$$E(t) = \frac{l}{10^3\phi} (c_0 - c(t)) \quad [20]$$

Values for the extreme cases of zero and infinite exposure time are

$$E(0) = 0 \text{ and } E(\infty) = \frac{lc_0}{10^3\phi}$$

Calculated values for $E(t)$ as a function of time for various values of the product, $a\phi \propto I_0\phi$, are presented in Fig. 2.

Reciprocity.—Considering Eq. [18] and expanding the logarithmic terms, assuming the variables to be $\ll 1$, one obtains

$$E(t) = \frac{I_0 b}{a\phi} (1 - e^{-a'\phi t}) = I_0 b \tau (1 - e^{-t/\tau}) \quad [21]$$

Expanding the exponential this becomes

$$E(t) \sim I_0 b t \text{ or } E \propto I_0 t$$

for low photoactivator concentrations and light intensities and for short exposure times. Thus, under these conditions reciprocity between exposure intensity and time appears to hold.

Conclusions

Starting from a simple kinetic model, the rate equations for the depletion of the photoactive species during the course of photochemical reactions under conditions of continuous monochromatic irradiation have been derived. An expression has been obtained for ϕ ,

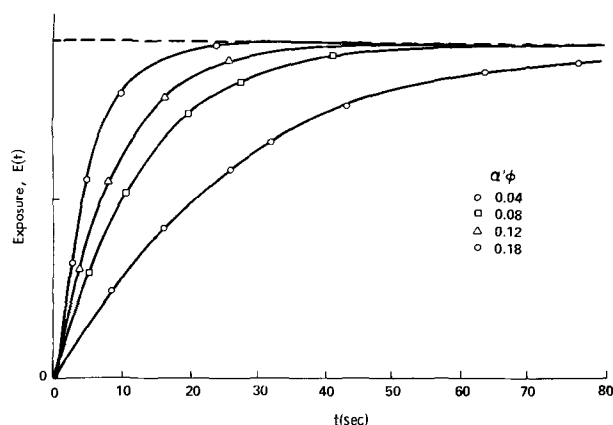


Fig. 2. Normalized exposure curves.

the primary quantum yield of the disappearance of the photoactivator, as a function of experimentally determined halftimes. For reasonably low absorbances (concentrations), *i.e.*, $x < 1$, this becomes

$$\phi \sim \frac{0.301}{at_{1/2}}, \text{ where } a = 10^3 \epsilon I_0 \quad [23]$$

This expression also shows the inverse proportionality between $t_{1/2}$ and exposure intensity

$$t_{1/2} \sim \frac{0.301}{10^3 \epsilon \phi I_0} \quad [24]$$

Expressions are given for $x(t)$, the absorbance (which is proportional to the photoactivator concentration), and for $E(t)$, the exposure, as functions of exposure time. Again, for values of $x < 1$ and $a\phi\epsilon < 1$, the exposure relation reduces to

$$E \propto I_0 t$$

indicating that reciprocity can be expected for this rather limited condition.

Manuscript received June 28, 1971; revised manuscript received *ca.* Nov. 10, 1971.

Any discussion of this paper will appear in a Discussion Section to be published in the December 1972 JOURNAL.

REFERENCES

1. D. L. Klein and J. W. Raniseski, "Photomasks and Photolithography," American Institute of Chemical Engineers, Proceedings of Atlanta Materials Conference (1970).
2. R. W. Berry, P. M. Hall, and M. T. Harris, "Thin Film Technology," p. 448, Van Nostrand, Princeton, New Jersey (1968).
3. J. Kosar, "Light Sensitive Systems," pp. 3, 199, John Wiley & Sons, Inc., New York (1965).
4. H. J. A. Dartnall, C. F. Goodeve, and R. J. Lythgoe, *Proc. Roy. Soc. (London)*, **164A**, 216 (1938).
5. H. J. A. Dartnall, C. F. Goodeve, and R. J. Lythgoe, *Proc. Roy. Soc. (London)*, **156A**, 158 (1938).
6. C. F. Goodeve and L. J. Wood, *Proc. Roy. Soc. (London)*, **166A**, 342 (1938).
7. R. Moraw and J. Munder, "Kolloquium über Wiss. Photographie," Sect. IV/II Zürich (1961).
8. J. G. Calvert and J. N. Pitts, "Photochemistry," pp. 518ff., John Wiley & Sons, Inc., New York (1966).

Spectrophotometric Determination of Photoresist Photosensitivity

II. Comparison of the Theoretical Model with Experimental Studies on AZ-1350¹

D. F. Ilten* and R. J. Sutton

IBM Components Division, East Fishkill Facility, Hopewell Junction, New York 12533

Having completed a general theoretical analysis of the exposure kinetics of an idealized photoresist (1), the next step is a comparison of the results predicted with those obtained experimentally for an actual photoresist system. For this purpose the positive photoresist AZ-1350² was chosen. The principal reaction involved is thought to be the photochemical S_{is} reaction (2-5) as illustrated in Fig. 1. The diazooxide group of the photoactive species evolves nitrogen when irradiated and forms a carbene intermediate. This leads to ring contraction accompanied by the formation of a ketene. Upon hydrolysis the corresponding carboxylic acid results. It is basically the kinetics of the initial step of this reaction which will concern us here. In none of the studies was the photoresist developed, nor was the actual product of the photoreaction isolated.

Experimental

A spectrophotometric method as described in Part I was used for following the first step of the AZ-1350

* Electrochemical Society Active Member.

¹ This article is Part II of a series, the first part of which is found on p. 537.

Key words: photoresist, kinetics, photochemistry, microelectronics, S_{is} reaction.

² Shipley Company, Newton, Massachusetts.

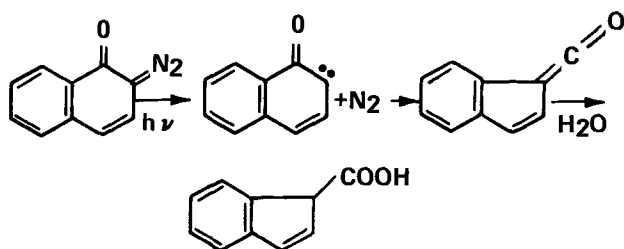


Fig. 1. The S_{is} reaction

exposure reaction. Both absolute and difference spectra of spin-cast films of the photoresist were taken. Typical sets of these types of spectra can be seen in Fig. 2 and 3. The difference method was found to be more satisfactory because the spectrum of the photoactive species itself and changes therein can be measured directly. The absorption of the polymer and of any reaction products is compensated for by using them as the reference in a dual beam spectrophotometer.³ Samples were prepared as follows: two quartz wafers, 32 mm in diameter and 3.2 mm thick, were cleaned using acetone, water, and ultrasonic treatment. They were spin-

³ Cary model 14.

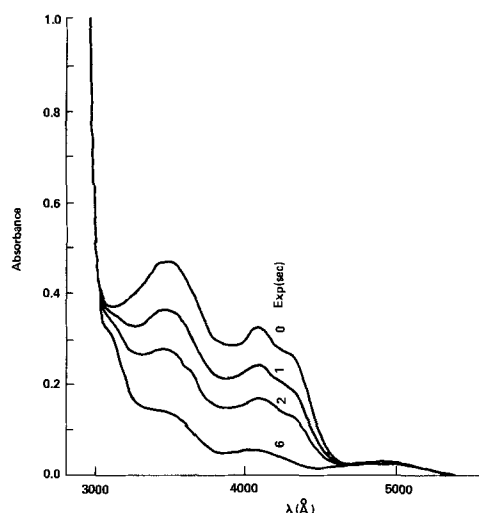


Fig. 2. Absolute spectrum. Decrease in absorbance as a function of exposure time in seconds.

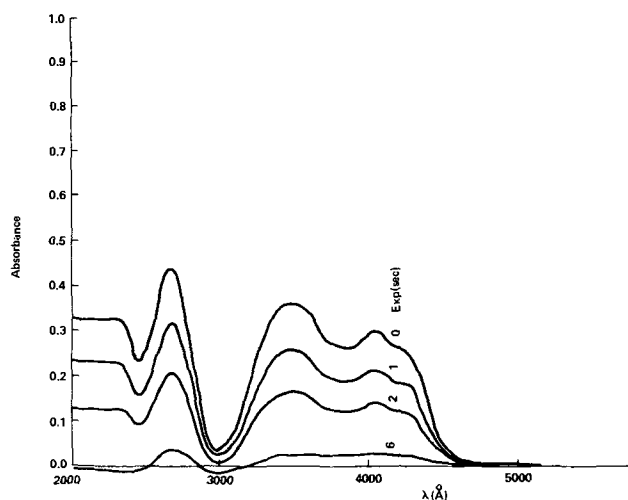


Fig. 3. Difference spectrum, AZ-1350 vs. exposed photoresist film, both on quartz substrates. Decrease in absorbance as a function of exposure time in seconds.

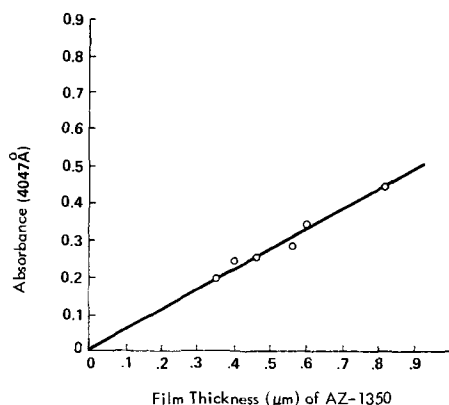


Fig. 4. Photoactivator absorbance at 4047 Å of AZ-1350 films as a function of film thickness.

coated with AZ-1350 to give film thicknesses of $\sim 5000 \text{ \AA}$ and an initial absorbance of 0.30 after a prebake of 80°C for 30 min. One film was exposed for one-half hour using an HBO-200 hp Hg lamp.⁴ Complete reaction of the photoactivator was assumed and the film was used in the reference beam of the spectrometer. The second, unexposed, film was placed in the sample beam and the spectrum was taken over the 2000-6000 Å wavelength region. The wafer was exposed very briefly using a black absorbent background to prevent exposure from reflected light and the spectrum was taken once again. The process was repeated until no further change in the spectrum was observed and a family of spectra as shown in Fig. 3 had been obtained. The intensity of the exposing radiation was measured using a thermopile⁵ (6). The applicability of the Lambert-Beer law was tested by casting films at a variety of spinning speeds to give a range of film thicknesses. These were measured by the Talystep (7), a stylus instrument for thickness determination. The absorbance of these samples at 4047 Å was determined and the results were plotted as a function of the film thickness (Fig. 4). The linear relationship obtained indicates that the Lambert-Beer law holds, at least over the range of values investigated, and that concentrations can be determined spectrophotometrically by linear interpolation.

Results

Semilogarithmic plots of the absorbance, x , at 4047 Å as a function of the exposure time, t , were made as shown in Fig. 5. A straight line resulted, in agreement with Eq. [15] of Part I (1). The exposure halftimes

⁴ Osram.

⁵ Eppley Laboratory, Inc., Newport, Rhode Island.

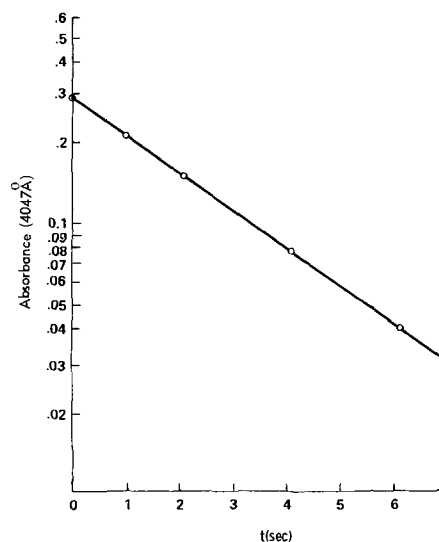


Fig. 5. Absorbance at 4047 Å of an AZ-1350 film vs. exposure time ($t_{1/2} = 2.1$ sec).

for the depletion of the photoactivator were determined from these linear plots both for full spectrum exposure and for exposure using the 3650, 4047, and 4358 Å Hg lines, isolated using band pass filters⁶ having a bandwidth of 100 Å and a maximum transmission of $\sim 30\%$. By employing Eq. [9] of the kinetics section Part I (1), values of ϕ , the primary quantum yield, were obtained. The data are given in Table I. The $t_{1/2}$ values were also determined as a function of the intensity of the exposing light by using neutral density filters⁷ in combination with the band pass filters. The results are presented in Table II.

Studies were conducted on films varying in thickness from 4400-10,000 Å, as determined by Talystep thickness measurements. A family of straight lines was obtained, demonstrating the applicability of Eq. [15], Part I (1), over this thickness range. Also, the effects of the reflectivity of the substrate on the exposure halftimes were studied. Quartz wafers were exposed using an aluminum reflective backing and a black paper, essentially nonreflective backing. This experiment was carried out, both for full spectrum exposure and for monochromatic exposure, employing each of the three principal Hg lines in the near uv-blue region. These results are given in Table III. In all cases a reduction of exposure time of approximately one-third was found for the reflective as opposed to the nonreflective backing.

Plots of the reciprocal of the intensity as a function of $t_{1/2}$ were made also for full spectrum exposure and for monochromatic exposure using each of the 3650, 4047, and 4358 Å Hg lines. Figures 6 and 7 illustrate that reasonable approximations to straight lines pass-

⁶ Filter Types G-572, Oriol Optics Corporation, Stamford, Connecticut.

⁷ Oriol, Type G-63.

Table I. Primary quantum yield of AZ-1350

λ (Å) (a)	mW/cm ²	I_0 Einstein/sec cm ² $\times 10^{18}$ (b)	$\epsilon \times 10^{-4}$			ϕ (λ)
			$\frac{1}{M}$ cm ²	$t_{1/2}$ (sec)	(c)	
3650	1.875	1.07	1.16	34	0.15	
4047	1.585	0.53	0.97	32	0.20	
4358	2.918	0.57	0.68	32	0.14	

(a) Oriol GS-572 filters, Oriol Optics Corporation, Stamford, Connecticut.

(b) Measured using Eppley thermopile, Eppley Laboratories, Newport, Rhode Island.

(c) Based on an estimated concentration of the photoactive species in the polymer of one molar.

The values obtained are in all cases averages of three measurements.

Table II. Primary quantum yield of AZ-1350 as a function of intensity

% T of Neutral density filter ^(a)	$t_{1/2}$ (sec)	$a \times 10$	ϕ (λ)	Average ϕ
Bandpass filter 3650 \pm 100Å ^(b)				
100	34	0.666	0.15	0.15 \pm 0.02
41.7	73	0.278	0.16	
33.5	98	0.223	0.15	
12.1	310	0.081	0.13	
Bandpass filter 4047 \pm 100Å				
100	32	0.518	0.20	0.23 \pm 0.04
42.6	53	0.221	0.28	
32.4	84	0.168	0.23	
11.8	277	0.061	0.19	
Bandpass filter 4358 \pm 100Å				
100	32	0.727	0.14	0.16 \pm 0.02
42.2	63	0.307	0.17	
31.2	84	0.227	0.17	
11.5	272	0.083	0.15	
No bandpass filter				
		I_0 (erg/cm ² /sec) $\times 10^{-5}$		
100	2.1	9		0.2 ^(c)
50	4.2	4.5		0.2
32	6.9	3		0.2
10	19.8	1		0.2

(a) Oriel G-63.

(b) Oriel G-572 filters. The transmission was measured using a Cary Model 14 Spectrophotometer.

(c) An estimated value based on an average ϵ of 1×10^4 and an $I_0 = 5 \times 10^5$ ergs/cm²/sec.

The values obtained are in all cases averages of three measurements.

Table III. Effects of reflective backing on exposure halftimes

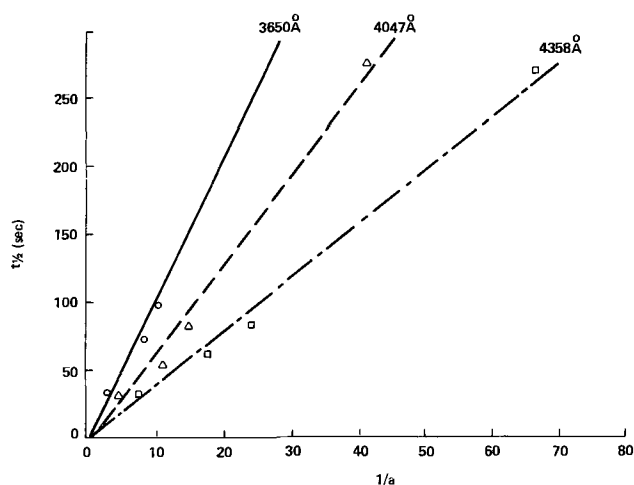
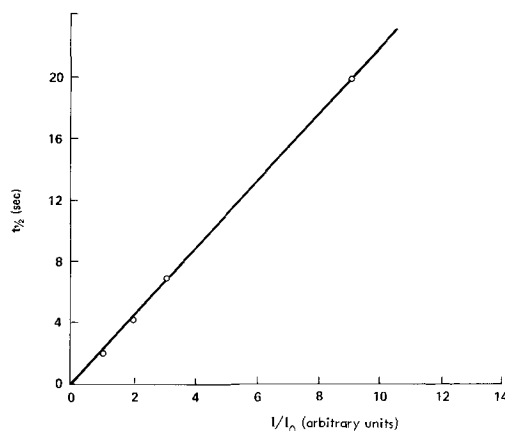
λ (Å) \pm 100	Backing	$t_{1/2}$ (sec)
3650	Al	21.2
	B	33.0
4047	Al	22.0
	B	29.5
4358	Al	15.5
	B	25.0
None	Al	2.0
	B	2.8

Al = Aluminum backing for quartz disks during exposure.
B = Black paper backing.

ing through the origin are obtained. This behavior is predicted by Eq. [24] of Part I (1) for moderately low concentrations of the photoactive species, i.e., corresponding to absorbance values less than one. It might be noted that the exposure values measured were in reasonable agreement with data obtained by Htoo (8). Also, the quantum yield values of 0.2 for the diazoxide reaction agreed approximately with those obtained by Fedorov and others by measuring N₂ evolution (9, 10). These results were also confirmed by infrared spectroscopic studies carried out in this laboratory.

Conclusions

The primary quantum yield for the depletion of the AZ-1350 photoactivator has been determined to be 0.15, 0.20, and 0.14, respectively, for the 3650, 4047, and 4358Å Hg lines. The use of an aluminum reflective backing for the quartz wafers during irradiation resulted in a reduction of $t_{1/2}$ values by \sim 30%. This demonstrates the important role played by reflected light in photoresist exposure. A straight line was obtained when $t_{1/2}$ values were plotted against the reciprocal of intensity. Thus, $t_{1/2}I_0 = \text{const.}$ when the entire spectrum of the lamp is used for exposure. That is, knowing the exposure intensity and the constant for the sample it is possible to calculate the expected $t_{1/2}$ value. Likewise, similar linear relationships exist for the exposure carried out using the three main Hg lines in the near uv-blue region. In conclusion, a measurement of $t_{1/2}$ values for a known light intensity appears to be a useful means of characterizing photoresists. By this procedure, various photoresist samples can be compared and their

Fig. 6. Exposure half-time values for AZ-1350 as a function of reciprocal absorbance $\frac{1}{a} = \frac{1}{10^3 \epsilon(\lambda) I_0}$.Fig. 7. Exposure half-time for AZ-1350 as a function of reciprocal intensity (full spectrum exposure $I_0 \sim 5 \times 10^5$ ergs/cm²/sec = 1).

proper exposure times determined independently of development conditions.

Acknowledgment

We wish to express our appreciation to Dr. J. W. Raniseski for his continued interest in this work and for his critical reading of the manuscript.

Manuscript received June 28, 1971; revised manuscript received ca. Nov. 10, 1971.

Any discussion of this paper will appear in a Discussion Section to be published in the December 1972 JOURNAL.

REFERENCES

1. D. F. Ilten, *This Journal*, **119**, 537 (1972).
2. O. Süss, *Liebigs Ann. Chem.*, **556**, 65 (1944).
3. O. Süss, *Liebigs Ann. Chem.*, **556**, 85 (1944).
4. A. Schönberg, "Preparative Organic Photochemistry," pp. 304ff, Springer-Verlag, Inc., New York (1968).
5. H. A. Levine, Photochemistry of Positive Resist Systems, *Polymer Reprints*, **10**, 377 (1969), ACS 157th National Meeting, Minneapolis, Minnesota.
6. J. G. Calvert and J. M. Pitts, "Photochemistry," pp. 765ff, John Wiley & Sons, Inc., New York (1966).
7. W. Pliskin and S. Zanin, "Handbook of Thin Film Technology," L. I. Maissel and R. Glang, Editors, pp.11-29, McGraw-Hill Book Co. (1970).
8. M. S. Htoo, *Phot. Sci. and Eng.*, **12**, 169 (1968).
9. Y. Fedorov, A. V. Ryabov, and R. D. Maltseva, *Tr. Khim. Khim. Tekhol.*, **1**, 64 (1968); C. A. **70**, 105737 (1969).
10. I. L. Volodarskii, B. I. Belov, and V. V. Kozlov, *Zh. Obshch. Khim.*, **35**, 2071 (1965).

On the Incorporation of Oxygen in GaP Liquid Phase Epitaxy Layers

R. H. Saul and W. H. Hackett, Jr.

Bell Telephone Laboratories, Incorporated, Murray Hill, New Jersey 07974

Previous optical absorption studies suggest the presence of significant background concentrations of oxygen in GaP (1). According to Miyauchi *et al.* (2), residual oxygen could be comparable to the total oxygen concentration¹ in O-doped crystals. In other experiments (4), the oxygen concentration could not be correlated with the Ga₂O₃ addition to the growth solution, and changes in oxygen concentration were reported to occur during low-temperature annealing. More recently, electrically inactive oxygen, in the form of β-Ga₂O₃ precipitates, have been observed in O-doped SG (solution grown) and LPE (liquid phase epitaxy) crystals (5). The possibility of such large variations in the oxygen concentration and concomitant variation in the number of Zn-O (red) radiative centers (6) have important consequences on the reproducibility of luminescent properties. In this work, we have studied the importance of the above factors in determining the oxygen concentration in GaP LPE layers. We have also examined several aspects of dynamic oxygen incorporation which clarify earlier results on O-doping (7-9) and have determined the maximum oxygen concentration which can be incorporated via LPE growth at ~1025°C.

Experimental

Both Zn- and Zn,O-doped layers were grown on Te-doped ($N_D - N_A \approx 8 \times 10^{17}$) SG or LEC (liquid encapsulation Czochralski) substrates using a fused quartz sealed-tube LPE system which has been described elsewhere (9). Except where indicated, layers were grown in evacuated ampoules which were cooled from 1025° to 600°C at a rate of 10°/min. For several cases, encapsulated mesa diodes were fabricated (8) and the electroluminescent quantum efficiency η of representative diodes was measured at 300°K in a calibrated integrating sphere. The electroluminescent time-decay τ_D was also measured at 300°K using pulsed current excitation and an appropriate detection system (10). Near-junction oxygen concentrations were computed (9) from high resolution doping profiles (11) of the Zn- and Zn,O-doped LPE layers. Table I summarizes some of the experimental results.

Results and Discussion

Residual Oxygen

We have previously shown (8) that at a relatively high Zn concentration of $\sim 1.3 \times 10^{18}$ atoms/cm⁻³ [0.15 mole per cent (m/o) in the LPE solution], η increases monotonically with Ga₂O₃ addition, demonstrating that substantial and controlled additions of oxygen can be incorporated by LPE, contrasting with the results recently reported for SG crystals (1, 2, 4).

The most efficient GaP red-emitting diodes have been fabricated, using additions of 0.03 m/o Zn and 0.35 m/o Ga₂O₃ to the LPE solution (8) (entry A in Table I). The addition of Ga₂O₃ results in compensation of Zn acceptors equivalent to an increase in donor concentration of 2.7×10^{17} atoms/cm³, which has been interpreted to be entirely due to the deep O donor (9). To substantiate this interpretation, an O-doped LPE layer was grown using the same Ga₂O₃ addition. The

shallow donor concentration in this layer is $N_D - N_A \approx 4 \times 10^{16}$ which is comparable to our undoped layers. Consequently, negligible additions of shallow donor impurities accompany the Ga₂O₃ additions and the tacit assumption (9) of equivalent background levels for the Zn- and Zn,O-doped layers is reasonable. [At lower epitaxy temperatures, it has been observed that significant S incorporation can accompany additions of Ga₂O₃ (12).] The oxygen concentration for our red-emitting LPE diodes (8) is thus about a factor of ~10 higher than the background concentration of uncompensated shallow donor impurities in these LPE layers. As discussed below, this oxygen concentration is also a factor of ~10 higher than the residual oxygen concentration.

The ratio of oxygen donor concentrations in Zn and Zn,O-doped LPE layers in the present work is estimated from the measured time decay τ_D and efficiency η of the red emission and from the net acceptor concentration, using a recent analysis (13) relating τ_D to the ratio τ_n/τ_{nt} (shunt path capture lifetime/Zn-O complex capture lifetime). For both layers we used the same 0.03 m/o Zn addition, and for the Zn,O-doped layer, a 0.35 m/o Ga₂O₃ addition. If we refer to Fig. 1 of Ref. (13), assume 80% Zn ionization (7), and use the measured values of $N_A - N_D = 5.3 \times 10^{17}$ cm⁻³ and $\tau_D = 175$ nsec for the Zn-doped junction and $N_A - N_D = 4.0 \times 10^{17}$ cm⁻³ and $\tau_D = 310$ nsec for the Zn,O-doped junction we conclude τ_n/τ_{nt} increases from ~0.3 to 3.0 with the O-doping. Correspondingly, the measured (peak) electroluminescent efficiency increased from 1.5% (no Ga₂O₃ added) to 5.5% with the O-doping. Using Fig. 3 of Ref. (13) and the above values of τ_n/τ_{nt} , theoretical quantum efficiencies of ~2% and 10% are obtained for the Zn-doped and Zn,O-doped layers, respectively, in reasonable agreement with the measured values if we allow for ~60-80% light extraction and ~60-70% electron injection efficiencies. Thus assuming τ_n is constant, O-doping increases the concentration of Zn-O radiative centers by a factor of ~10. (If τ_n decreases due to impurities introduced by the Ga₂O₃, this factor will be larger.) To calculate relative O concentrations, we expect from pairing theory (14) for Zn $\sim 5 \times 10^{17}$ atoms/cm³ and O $\leq 5 \times 10^{17}$ atoms/cm³ that the (equilibrium) Zn-O complex concentration is approximately proportional to the oxygen

Table I. Near-junction oxygen concentration for LPE layers grown from an initial temperature of 1025°C

Entry	Zn (m/o)	Ga ₂ O ₃ (m/o)	Comments	Near-junction O donor concentration (atoms/cm ³)
A	0.03	0.35	—	$2.7 \pm 0.4 \times 10^{17}$
B	0.03	0.35	Capsule backfilled	2.6×10^{17}
C	0.03	0.6	—	2.6×10^{17}
D	0.03	0.02	Capsule backfilled	2.7×10^{17}
E	0.03	0.005	Capsule backfilled	0.3×10^{17}
F	0.03	0.35	Cooling rate of 1°/min	1.4×10^{17}
G	0.03	0.6	Cooling rate of 1°/min	3.1×10^{17}

All layers were grown in evacuated ampoules using a cooling rate of 10°/min, except as indicated. Ga₂O₃ levels refer to additions to the ampoule rather than the actual growth solution concentrations. The computed O donor concentration refers to levels above the background O concentration (see text). The uncertainty in O concentration for entry A reflects the range of values obtained for 26 LPE layers. Entry A corresponds to the doping levels used to achieve 7% diode efficiencies (10).

Key words: gallium phosphide, oxygen incorporation, luminescence, liquid phase epitaxy.

¹ Hereafter, oxygen concentration is used to denote only electrically (or optically) active forms, excluding the electrically inactive oxygen which has been suggested to exist (3).

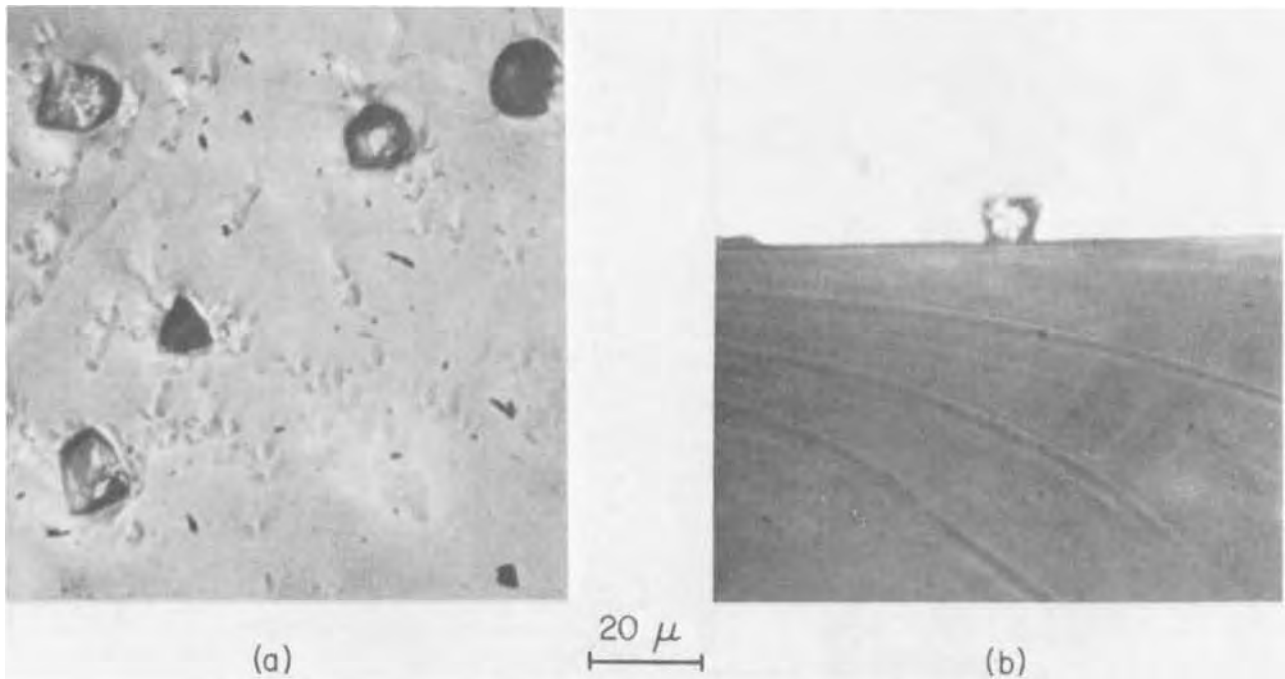


Fig. 1. (a) Granular precipitates penetrating the P{111} surface of a Zn,O-doped LPE layer, as viewed with combined incident and transmitted illumination. (b) Granular precipitate remaining after GaP matrix was removed by etching the P{111} surface, as viewed normal to the P{111} face with transmitted illumination.

concentration. Hence the oxygen concentration in the Zn,O-doped layers is expected to be at least an order of magnitude greater than for the Zn-doped layers, and the background oxygen concentration is thus $< 3 \times 10^{16}$ atoms/cm³. This background level should not be sufficient to hamper controlled incorporation of oxygen in LPE layers, but it may be detrimental in green-emitting GaP where oxygen must be excluded from the crystal.

This background oxygen level may arise from the GaP starting material,² air entrapped in the Ga, or by the reaction of Ga with SiO₂ (15). We note that the substitutional oxygen concentration in SG crystals, as previously determined (7) by the degree of compensation in Zn,O-doped crystals, is only $\sim 7 \times 10^{16}$ cm⁻³ (a factor of 4 lower than for our LPE layers). Also, at the higher temperatures and slower cooling rates that are generally employed in solution growth we may expect increased oxygen incorporation from the SiO₂ growth vessel. Thus for SG crystals, unintentionally incorporated oxygen may be a substantial fraction of the total oxygen concentration as was claimed by Miyauchi (2). Variations in this background oxygen level may account for the lack of correlation between photoluminescence efficiency and O-doping reported by Dishman *et al.* (4).

Thermal Conversion of Oxygen by Annealing

Using He-3 activation, Kim (3) has determined the total oxygen concentration in SG O-doped GaP to be $\sim 2 \times 10^{19}$ cm⁻³ which is a factor of ~ 100 greater than the oxygen donor concentration determined in this work. These observations suggest that a considerable amount of oxygen can be present in electrically inactive forms, *e.g.*, interstitials, Ga₂O₃ or neutral O-complexes. In view of Kim's work, it is worthwhile to consider if thermal conversion of electrically inactive to electrically active (substitutional) O can be accomplished by low temperature annealing. On the basis of photoluminescent and absorption measurements of Zn,O-doped SG crystals, Dishman *et al.* (4) have sug-

gested that low-temperature annealing increases the substitutional oxygen concentration. The Zn,O-doped LPE layers described in the present work were annealed for ~ 22 hr at temperatures in the range of 500°-600°C, a procedure which has been shown to increase η by a factor of $\sim 3-4$ (8). However, for Zn,O-doped layers the oxygen donor concentration before annealing was found to be the same as after annealing, demonstrating that thermal conversion of oxygen by low-temperature annealing is not significant for these LPE layers. This result is substantiated by reverse-bias junction capacitance measurements which indicate no change in doping levels following annealing.

Dynamic Oxygen Incorporation and Ga₂O₃ Precipitation

For several O-doped layers, optical transmission microscopy has revealed precipitates which were thought to be similar to the β -Ga₂O₃ needles previously observed by Kowalchik *et al.* (5) in O-doped GaP, SG and LPE crystals. However, careful sectioning of an O-doped layer by selective etching of the GaP matrix with hot aqua regia indicates that for these layers the precipitates are granular rather than acicular in shape and are mostly confined to the top surface of the layer. (See Fig. 1.) X-ray analysis confirmed that these precipitates are β -Ga₂O₃. The oxygen donor concentration was determined for a number of Zn,O-doped layers and found to be independent of the precipitate density. Since the precipitates are not in the vicinity of the p-n junction and contribute negligible absorption losses, they are not expected to deleteriously affect η . Indeed, re-examining our earlier (8) LPE diodes, we have found that η is independent of the presence of precipitates.

It has been previously suggested (5) that oxygen depletion of an LPE solution can occur due to the high partial pressure (~ 10 Torr) of Ga₂O over Ga saturated with oxygen at typical LPE temperatures (16). This depletion will always tend to occur in open-tube systems and can also occur in sealed-tube systems if thermal gradients exist. Measurements of the dynamic temperature profile within our growth ampoules indicate that, although the temperature along the length of the boat (containing the substrate and LPE solution) remains constant to within $\pm 3^\circ$, the sealing plug can be

² The total oxygen concentration in our GaP source material is estimated to be 1.5×10^{17} atoms/cm³, based on mass spectroscopy and He-3 activation analysis of similar material. (S. F. Nygren, Private communication.)

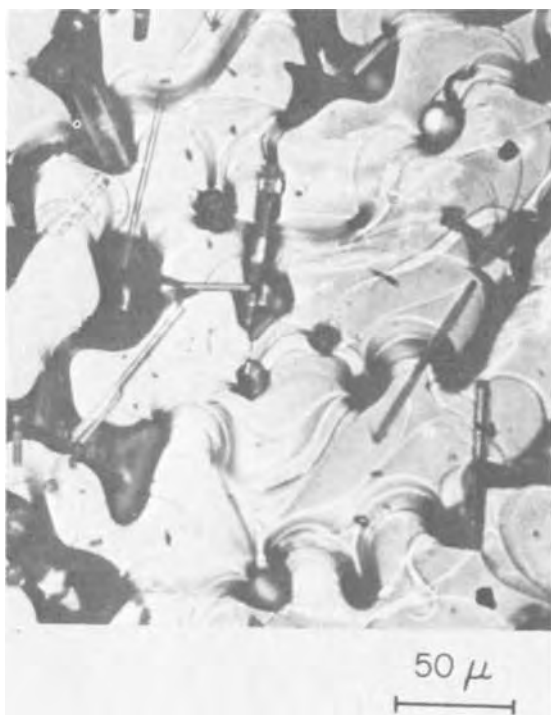


Fig. 2. Acicular precipitates on the surface of a Zn,O-doped LPE layer grown from an O saturated solution, as viewed by Nomarski interference microscopy. (See text.)

as much as 15° cooler. This temperature differential is apparently sufficient to efficiently transport oxygen (via Ga₂O pumping) since we find that reducing the mean free path, by backfilling with an inert ambient, results in a large excess of undissolved Ga₂O₃ remaining in contact with the Ga during growth. (Excess Ga₂O₃ was not observed with evacuated capsules.) In this case the LPE layers are laden with needlelike precipitates which penetrate the entire LPE layer, as observed by Kowalchik *et al.* (5). (See Fig. 2.)³ The near junction oxygen concentration for such a layer (entry B in Table I) was found to be the same as for the LPE layers described above.

The fact that the O concentration is essentially a constant implies that either (a) the GaP layer is saturated with oxygen if the Ga₂O₃ precipitates within the GaP matrix during cooling of the LPE layer or (b) the LPE solution is nearly saturated with oxygen if the Ga₂O₃ coprecipitates with the GaP. The large size of the precipitates and lack of a common growth habit suggest that solid-solution precipitation is not occurring. Moreover, the disappearance of the precipitates when the Ga₂O₃ addition is lowered below the solubility limit of O in Ga (5), supports the contention that coprecipitation is occurring. Substantially larger Ga₂O₃ additions are thus not expected to appreciably increase the incorporated oxygen concentration, in agreement with our observation of no detectable increase in oxygen level for a 70% increase in Ga₂O₃ addition (entry C in Table I). Thus the maximum oxygen concentration which can be incorporated at 1025°C is $\sim 3 \times 10^{17}$ atoms/cm³. This limiting value corresponds to growth from an O-saturated growth solution.⁴ The effect of growth temperature on oxygen incorporation is reported elsewhere (12).

³ For layers grown in evacuated capsules, the precipitates are confined to the surface of the LPE layer and appear to be granular; hence, the supersaturation sufficient to result in gross precipitation apparently occurs only at the lowest temperatures encountered during growth ($\sim 800^\circ\text{C}$). Extrapolating the data of Ref. (7), we estimate the solubility of oxygen in Ga to decrease by a factor of ~ 30 during cooling from 1000° to 800°C.

⁴ We note that if the (growing) GaP solid is in equilibrium with the O-saturated liquid, i.e., the chemical potential of oxygen is the same in these phases, the incorporated oxygen concentration corresponds to the maximum solid solubility.

The solubility limit of Ga₂O₃ in Ga at 1025°C has been determined to be ~ 0.01 m/o (7). When the Ga solution is saturated with GaP, the liquid concentration where Ga-GaP-Ga₂O₃ are in equilibrium shifts to ~ 0.008 m/o Ga₂O₃ (5). Since the maximum incorporated O level is thought to correspond to an O-saturated LPE solution, it follows that when Ga₂O transport is suppressed, this maximum value should be achieved with Ga₂O₃ additions of ~ 0.01 m/o, while for lower Ga₂O₃ additions, the oxygen concentration will be reduced. These expectations are borne out by entries D and E in Table I. O-depletion of the growth solution thus accounts for the large disparity between the low Ga₂O₃ solubility and the large Ga₂O₃ additions previously used to achieve comparable O concentrations in 7% diodes (8, 9). In this vein, it is worth noting our previous work (9) which suggested that decreasing the LPE cooling rate from 10°/min to 1°/min decreases the incorporated O level by a factor of ~ 2 (cf., entries A and F). The reduced O level with slower cooling was probably the result of O-depletion of the Ga and serves to emphasize the dynamic nature of O incorporation. We now find that by increasing the Ga₂O₃ concentration, the limiting O concentration of $\sim 3 \times 10^{17}$ atoms/cm³ can be attained at the slower cooling rate (see entry G). Identical results are obtained by backfilling the growth ampoules with an inert ambient.

Summary and Conclusions

The residual O concentration in GaP LPE layers grown at $\sim 1000^\circ\text{C}$ in a quartz system has been estimated to be $\sim 3 \times 10^{16}$ atoms/cm³. This value is about a factor of 10 lower than the intentionally added O in Zn,O-doped layers and thus it should not affect the reproducibility of the red luminescence. The high radiative efficiency [$\eta(\text{red}) = 1\%$ for SG substrates] which can result from the residual O, may prove detrimental in green-emitting GaP.

We have found no evidence of changes in near-junction doping levels resulting from annealing in the range of 500°-600°C. The increased efficiency brought about by annealing is thus not the result of changes in electrically active O concentration.

The maximum oxygen concentration which can be incorporated by LPE at 1025°C is $\sim 3 \times 10^{17}$ atoms/cm³; this value corresponds to an O-saturated LPE solution. For this case, β -Ga₂O₃ coprecipitates with GaP during cooling but has no effect on the electrically active O concentration. An oxygen concentration of $\sim 3 \times 10^{17}$ atoms/cm³ can be incorporated for Ga₂O₃ additions as low as ~ 0.02 m/o by minimizing Ga₂O transport. When Ga₂O transport occurs, very large Ga₂O₃ additions may be required to maintain saturation of the LPE solution, and the incorporated oxygen concentration will tend to decrease with slower cooling rates.

Acknowledgments

We are indebted to Mrs. J. Armstrong and T. E. McGahan for their skilled technical assistance and to Mrs. M. H. Read for performing the x-ray analysis.

Manuscript submitted Aug. 25, 1971; revised manuscript received ca. Nov. 5, 1971.

Any discussion of this paper will appear in a Discussion Section to be published in the December 1972 JOURNAL.

REFERENCES

1. J. D. Cuthbert, C. H. Henry, and P. J. Dean, *Phys. Rev.*, **170**, 739 (1968).
2. T. Miyauchi, H. Sonomura, and N. Yamamoto, *Jap. J. Appl. Phys.*, **8**, 886 (1969).
3. C. K. Kim, *Radiochem. and Radioannal. Letters*, **2**, 53 (1969).
4. J. M. Dishman, M. DiDomenico, Jr., and R. Caruso, *Phys. Rev. B2*, 1988 (1970).
5. M. Kowalchik, A. S. Jordan, and M. H. Read, *This Journal*, **117**, 407C (1970).
6. T. N. Morgan, B. Welber, and R. N. Bhargava, *Phys. Rev.*, **166**, 751 (1968); C. H. Henry, P. J. Dean, and J. D. Cuthbert, *ibid.*, 754 (1968).

7. L. M. Foster and J. Scardefield, *This Journal*, **116**, 494 (1969).
8. R. H. Saul, J. Armstrong, and W. H. Hackett, Jr., *Appl. Phys. Letters*, **15**, 229 (1969).
9. R. H. Saul and W. H. Hackett, Jr., *This Journal*, **117**, 921 (1970).
10. W. H. Hackett, Jr. and R. N. Bhargava, *J. Appl. Phys.*, **41**, 3306 (1970).
11. T. E. McGahan and W. H. Hackett, Jr., *Rev. Sci. Instr.*, **41**, 1182 (1970).
12. R. H. Saul, Paper presented at Technical Conference on Recent Advances in Electronic, Optical, and Magnetic Materials (AIME), San Francisco, August 29-September 1, 1971; also *J. Electronic Materials*, **1**, 16 (1972).
13. J. S. Jayson, R. N. Bhargava, and R. W. Dixon, *J. Appl. Phys.*, **41**, 4972 (1970).
14. J. D. Wiley, *J. Phys. Chem. Solids*, To be published.
15. C. N. Cochran and L. M. Foster, *This Journal*, **109**, 149 (1962).
16. C. J. Frosch and C. D. Thurmond, *J. Phys. Chem.*, **66**, 877 (1962).

Low-Temperature Electrostatic Silicon-to-Silicon Seals Using Sputtered Borosilicate Glass

A. D. Brooks* and R. P. Donovan*

Research Triangle Institute, Research Triangle Park, North Carolina 27709

and C. A. Hardesty

National Aeronautics and Space Administration, Langley Research Center, Hampton, Virginia 23365

The Mallory electrostatic sealing process (1, 2) is a method of anodically bonding two dissimilar materials together to form a strong, hermetic seal which involves little alteration in the shape, size, and dimensions of the members making up the joint. Previous applications have involved the sealing of a metal or semiconductor to an insulator, such as glass or ceramic. In this brief note we describe a method for sealing two silicon surfaces together by depositing a thin, borosilicate glass layer on one of the polished silicon members to be sealed. Our method for depositing the borosilicate glass layer is sputtering. Most likely the method is equally applicable with other deposition methods capable of similar control of film composition and thickness.

Experimental Technique

The surfaces of the silicon members to be sealed are polished by either mechanical, electrochemical, or high-quality chemical methods. These surfaces are cleaned and stripped of any residual oxide by immersion in concentrated hydrofluoric acid. The surfaces are then coated with sputtered borosilicate glass. We used an MRC-340 sputtering unit fitted with a 5 in. Corning 7740 ("Pyrex") borosilicate glass target. R-F sputtering was carried out in a 1% oxygen in argon atmosphere. Power levels varied between 150 and 800W. The critical property for satisfactory sealing is a minimum glass thickness of approximately 4 μm . Below this thickness the areas of satisfactory seal between the two silicon members are patchy and discontinuous. Substrate temperature during deposition was not controlled directly; the copper block upon which the silicon samples rested was either held at a temperature of about 50°C by water cooling or allowed to reach a temperature as high as 380°C when no water cooling was used. The sealing behavior of the sputtered film appeared insensitive to the deposition temperature over this span. No means of insuring good thermal contact between the silicon and the copper block was employed so that the temperature of the silicon samples themselves was most likely higher than that of the measured temperature of the copper block.

After sputtering the borosilicate glass layer, each coated silicon substrate was annealed, most often in steam, at a temperature between 500°-900°C. This steam annealing greatly improved yield during the

subsequent sealing operation. The annealing temperature and ambient are not critical, but inclusion of some high-temperature heat cycle is required for satisfactory seals. Oxygen and nitrogen ambients during annealing were also used. Slightly higher yield during sealing seemed to be associated with the steam anneal.

To carry out the silicon-to-silicon electrostatic seal, a second polished silicon chip is placed on top of the first silicon member which is already coated with borosilicate glass. This second silicon member is polished by the same technique used to prepare the first surface. The two members are aligned in the desired orientation and held in position by a weight which is electrically conductive so as to serve as a top electrode as well as a pressure load. The combination is then heated on a graphite strip to a temperature of 450°-550°C. After the sandwich is stabilized at temperature, a slowly increasing d-c voltage is applied across the silicon-borosilicate glass-silicon sandwich, the uncoated silicon member being positively biased with respect to the glass-coated member. The primary control during sealing is total current flow which was limited to about 0.5 mA for these samples (corresponding to a current density of approximately 1 mA/cm²). The voltage is advanced in steps as the current decreases with time. A maximum voltage of 50V is adequate for a satisfactory seal. After reaching the maximum voltage, the sandwich is left at temperature and voltage for 5 min. The substrate heater is then shut off so that the temperature of the sandwich can decrease to near room temperature before the voltage is turned off. This completes the sealing operation.

To evaluate the hermeticity of such a seal a number of silicon-to-silicon seals were prepared in which one silicon member of the silicon-borosilicate glass-silicon sandwich had a deep cavity etched part way through it. The second silicon member was then thinned to a total thickness of 0.025-0.1 mm (1-4 mils) and the sealing operation was carried out inside a vacuum chamber at a pressure of approximately 10⁻⁵ Torr. Upon completing the seal and removing the unit from within the chamber, atmospheric loading on the top, thin member of the sandwich produces a visible depression in the top member above the cavity in the bottom member, as illustrated in Fig. 1.

The top member of this particular unit is a piezoresistive silicon diaphragm with twelve junction isolated resistors ion implanted into its top surface. These resistors are positioned so that some are in tension and

* Electrochemical Society Active Member.

Key words: sealing, electrostatic sealing, hermetic, housing, packaging, silicon-to-silicon seals.

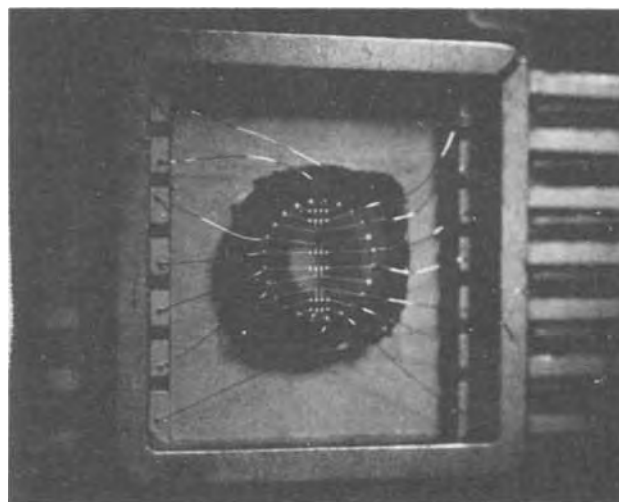
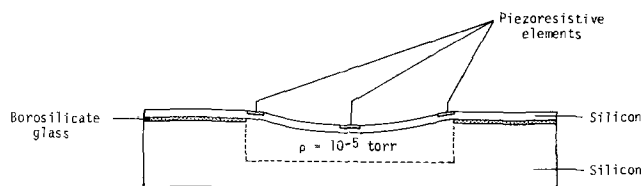


Fig. 1. Electrostatically sealed piezoresistive pressure transducer. (a, left) Sketch, (b, right) Photograph

others in compression because of the atmospheric pressure. When these resistors are externally connected in a Wheatstone bridge configuration, the output voltage of the bridge is a measure of the atmospheric pressure. The cavity diameter across which the thin silicon diaphragm is suspended is 2 mm in this illustration; the sealing area is a 1 mm ring surrounding the cavity. Reducing the ambient pressure surrounding the structure of Fig. 1b causes the dimple to disappear because the diaphragm is thereby unloaded.

Bottom views of similarly sealed units are shown in Fig. 2. The unit on the left is a silicon diaphragm electrostatically sealed to a borosilicate glass cavity. The cavity dimensions and position are clearly visible in this unit; the silicon unit on the right is identically shaped and has been sealed using the borosilicate glass methods described in this paper. These units are only one example of the application of this technique; both larger and smaller areas have been sealed. No effect associated with area has been identified. Current density during sealing has been held to $\lesssim 1 \text{ mA/cm}^2$, but this current density is not optimum or anything more than an arbitrarily selected, convenient value.

An evacuated cavity such as that illustrated in Fig. 1 has been measured as essentially leak-free by helium leak-testing. Even after 63 thermal cycles between $+100^\circ$ and -40°C , the unit showed no loss of dimple or measurable leak rate by helium leak-testing. To carry out the helium leak test, the unit was stored in a helium atmosphere for approximately 3 weeks at a pressure of $2 \times 10^5 \text{ N/m}^2$ (2 atmospheres) of helium.



Fig. 2. Bottom view of electrostatically sealed piezoresistive pressure transducers. (a) Borosilicate glass cavity, (b) Silicon cavity.

The unit was then placed in the helium detection chamber in order to measure trace quantities of escaping helium. No traces of helium could be detected.

No other evaluation of the quality of this seal (such as tensile or shear tests) has been made; the thermal shock limits have not been determined. The value of the process is its compatibility with sealing to silicon device structures which have already been metallized with aluminum. Previous methods for housing silicon elements in silicon packages have involved higher temperature processes and have therefore required that metallization follow the sealing (3). Elimination of this restriction allows greater freedom in both device and package design.

Conclusion

A technique has been described for hermetically sealing silicon members to each other at a temperature $\lesssim 500^\circ\text{C}$. The method involves no measurable deformation of the surfaces being sealed and hence is compatible with package designs of tight tolerance. The advantages of the all-silicon package are especially important for compensating the effect of temperature upon piezoresistive and piezjunction sensors. Since a low-pressure reference can be sealed between two members, the technique is compatible with the construction of absolute pressure transducers.

Acknowledgments

The sputtering apparatus employed in this work was made available to us by the Electrical Engineering Department at North Carolina State University, Raleigh, North Carolina, through the courtesy of Dr. M. A. Littlejohn. It is a pleasure to acknowledge helpful suggestions for this work from Drs. G. Wallis and D. Pomerantz of P. R. Mallory Company, Burlington, Massachusetts, and Drs. L. Maissel and W. Pliskin of IBM Corporation, East Fishkill, New York.

This work was sponsored by NASA, LRC, Hampton, Virginia 23365, under Contract NAS1-9005.

Manuscript submitted July 20, 1971; revised manuscript received Nov. 22, 1971.

Any discussion of this paper will appear in a Discussion Section to be published in the December 1972 JOURNAL.

REFERENCES

1. D. I. Pomerantz, U.S. Pat. 3,397,278, August 13, 1968.
2. G. Wallis and D. I. Pomerantz, *J. Appl. Phys.*, **40**, 3946 (1969).
3. G. Wallis, Paper 239 RNP presented at Electrochem. Soc. Meeting, Atlantic City, Oct. 4-8, 1970.

Preferential Electrochemical Etching of P⁺ Silicon in an Aqueous HF-H₂SO₄ Electrolyte

C. P. Wen and K. P. Weller

RCA Laboratories, Princeton, New Jersey 08540

Electrochemical polishing and preferential etching techniques and their application to thin-film silicon device technology have been described by many workers (1-3). A major difficulty encountered has been the continued formation of thick brown films on the semiconductor surface during etching under low-current-density conditions (1). At the high bias voltages commonly employed to achieve sufficiently high current densities and insure the elimination of brown-film formation, preferential removal of a p⁺ layer from a higher resistivity n layer leaves a rough surface (3) which is undesirable for device fabrication. The addition of sulfuric acid to the standard HF-H₂O solution employed by most previous workers permits a reduction of the bias to less than 0.5V yet maintains a high current density. As a result the effectiveness of the self-limiting preferential etching is increased because the higher current density eliminates the build-up of thick brown films on the p⁺ silicon surface and leaves a smooth surface on the unetched higher resistivity silicon layer.

Preferential removal of p⁺ silicon by the electrochemical etching process has been carried out on heavily doped substrates with epitaxially grown 5- μ m-thick n-type layers ($n \cong 2 \times 10^{16}/\text{cm}^3$). The sample, with a 0.5V bias applied, is etched in a freshly mixed electrolytic solution (500 ml H₂O, 100 ml 50% HF, 100 ml 98% H₂SO₄) using a platinum cathode. Constant agitation during the etching process is required. Over 200 mA/cm² current density has been obtained at the 0.5V bias. Abrupt termination of the etching takes place as soon as the p-type substrate layer is completely removed and the total current then drops to less than 5% of its original value. Accompanied with the drastic drop in current is the formation of a very thin dark brown film on the exposed n-layer. This film is removed by etching the sample in a 97% HNO₃-3% HF mixture for a few seconds thereby yielding a smooth n-type silicon surface. The low bias voltage employed in this etching process reduces the possibility of hole injection from the p⁺ layer into the n-layer and results in a more abrupt termination of the etching process; the increase in current density obtained by the addition of the H₂SO₄ probably provides a smoother post-etched surface condition for the n-type layer. This process has been carried out successfully under normal room illumination conditions, eliminating the complete darkness requirement mentioned by previous workers (3).

A comparison has been made of the characteristics of these three component electrolyte with the traditional aqueous HF solutions. The effect of electrolyte composition on the current density (the current density is directly proportional to etch rate) is shown in Fig. 1 for HF-H₂SO₄-H₂O, and HF-HClO₄-H₂O solutions. With an initial electrolyte composition of 100 ml 50% HF in 500 ml distilled water, the current density is slightly over 20 mA/cm² at 0.5V bias. Commercially available concentrated acids are added to the initial solution. To allow thorough mixing the current density measurements are taken 30 sec after the addition of acid. As shown in Fig. 1 the addition of sulfuric acid to the initial HF-H₂O solution is found to increase the current density and, therefore, enhance the etch rate considerably. A current density of 218 mA/cm² at 0.5V bias has been obtained with 100 ml of H₂SO₄ added to

the initial aqueous HF electrolyte. Most important of all, the current density rises well above the critical value of ~ 70 mA/cm². Above this critical value brown film build-up on the p⁺ silicon surface does not occur (1). The change in current density caused by the addition of HF or HClO₄ is found to be less striking and the formation of brown film on the sample surface is observed at 0.5V bias. The brown film is removed with a quick etch in 97:3 HNO₃ (70%), HF (50%) after each data point is taken. The rise in current density in the freshly mixed HF-H₂SO₄ electrolyte is found to be caused at least partially by the 40° temperature rise in the solution when concentrated H₂SO₄ is diluted. No such change in temperature is observed when HF or HClO₄ is mixed with water.

The effect of temperature on the current density at 0.5V is shown in Fig. 2 for both the HF-H₂SO₄ - H₂O and HF-H₂O electrolyte of composition designated. The current density at 0.5V bias is monitored as the solutions cool by natural convection. No brown film formation has been observed on the p⁺ substrate surface in the HF-H₂SO₄ - H₂O electrolyte, within the experimental temperature range (25°-66°C) while increas-

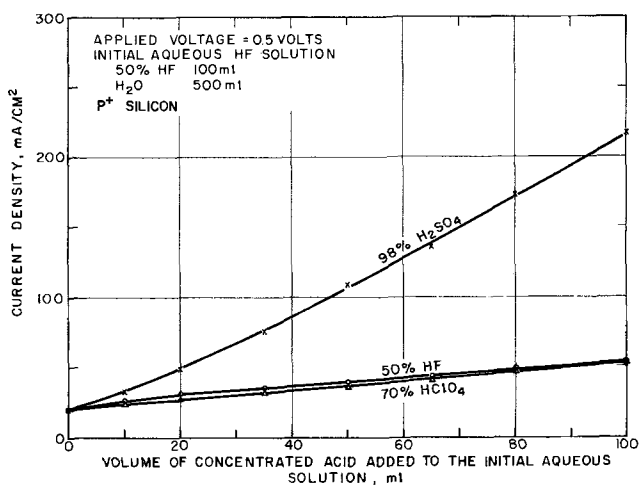


Figure 1

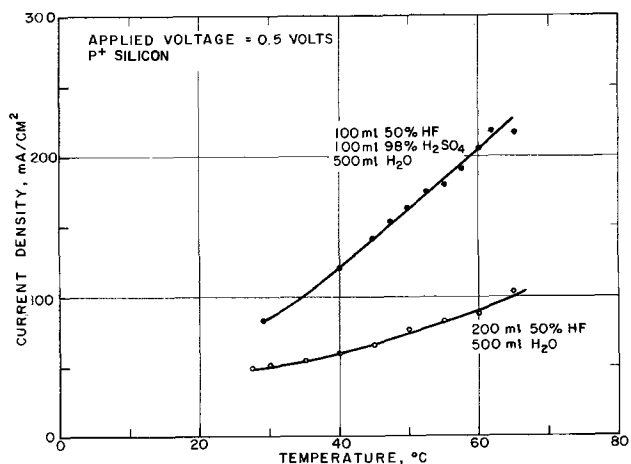


Figure 2

Key words: preferential etching, electrolytic etching, etching silicon.

ingly rapid formation of brown film on the surface of the same sample is observed with increasing temperature when the HF-H₂O solution is employed. The incorporation of H₂SO₄ into the electrolyte appears to increase the etch rate without undesirable side effects.

In summary, an HF-H₂SO₄ - H₂O electrolyte is found to be suitable for electrochemical preferential removal of p⁺ silicon from epitaxially grown n-type layers. The introduction of H₂SO₄ to the electrolyte tends to increase the etch rate and reduce the bias requirement to less than 0.5V. This self-limiting preferential-etching process leaves a smooth surface on the unetched higher resistivity n-type layer.

Acknowledgment

The authors wish to thank H. Davis, J. Jaklik, and A. Young for their assistance in sample preparations and

Y. S. Chiang for helpful suggestions and advice during the preparation of the Si epitaxial layers.

Manuscript submitted July 27, 1971; revised manuscript received Dec. 13, 1971.

Any discussion of this paper will appear in a Discussion Section to be published in the December 1972 JOURNAL.

REFERENCES

1. D. R. Turner, *This Journal*, **105**, 402 (1958).
2. H. J. A. van Dijk and J. deJonge, *ibid.*, **117**, 553 (1970).
3. M. J. J. Theunissen, J. A. Appels, and W. C. G. Verkuylen, *ibid.*, **117**, 959 (1970).

Brief Communication



A Note on Manganese-Activated Magnesium Arsenate

E. Kostiner* and P. W. Bless

Baker Laboratory of Chemistry, Cornell University, Ithaca, New York 14850

Magnesium arsenate has been reported (1) as a red-emitting phosphor activated by quadrivalent manganese having the composition 6MgO · As₂O₅. Its emission spectrum has been investigated (1, 2) and compared with manganese-activated magnesium fluorogermanate (3, 4). As part of a program investigating the structural parameters of manganese(IV)-activated phosphor systems (5-7), we have prepared single crystals of magnesium arsenate by standard flux growth techniques. This note reports the crystal growth and powder x-ray crystallographic data for this compound.

Experimental

The phosphor was prepared by standard ceramic technique. Magnesium oxide (Mallinckrodt Analytical Reagent) and arsenic pentoxide (Fisher Certified Reagent) in a 6:1 mole ratio with 1 mole per cent (m/o) manganese carbonate (Fisher Certified Reagent) added as an activator were mixed and ground under acetone. After removal of the acetone at 110°C, the mixture was fired in a platinum crucible at 1000°C in air for 1 hr, reground and fired for 16 hr at 1200°C.

A suitable high-temperature flux for the crystal growth of the arsenate was found to be a eutectic in the PbO-As₂O₅ system occurring at approximately 83 m/o PbO-17 m/o As₂O₅ (8). Then 33.67g of this eutectic mixture (0.150 "mole") and 7.08g of the composition 6MgO · As₂O₅ (0.015 mole) were mixed and packed into a 25 cm³ platinum crucible. The tightly covered crucible was placed in a silicon carbide resistance-heated furnace, held at 1225°C for 4 hr, cooled at a rate of 8°C/hr to 600°C, and then removed from the furnace. To protect the platinum crucible, dry oxygen was passed through the furnace. The arsenate crystals were removed from the flux by leaching with hot, very dilute hydrochloric acid and by ultrasonic cleaning in water.

* Electrochemical Society Active Member.

Key words: crystal growth, magnesium arsenate, Mn⁴⁺-activated phosphors.

Results

The grown crystals were irregularly shaped with maximum dimension of about 2 mm. Occasionally, hexagonal plates up to 0.5 mm thick and 2 mm cross section were found. The experimental density (buoyant force) was 3.96(1) g/cm³.

Single-crystal precession and Weissenberg photographs indicated rhombohedral symmetry; the space group was identified as R_{3m}. The composition of magnesium arsenate was determined to be approximately

Table I. Magnesium arsenate; a₀ = 6.034 (2)Å, c₀ = 27.67 (2)Å

d	l	hkl	Sin ² θ (× 10 ⁴)	
			Obs.	Calc.
5.151	80	101	223.6	224.9
4.624	11	006	277.5	279.0
4.211	5	104	334.6	341.1
3.803	100	015	410.2	410.8
3.072	24	009	628.6	627.7
3.023	32	110	649.1	651.3
2.882	24	018	714.1	713.1
2.605	23	021	874.4	876.3
2.573	18	202	896.3	899.5
2.526	70	116	929.9	930.4
2.443	62	024	993.8	992.5
2.365	19	205	1060.5	1062.2
2.309	3	00, 12	1112.7	1115.9
2.267	6	01, 11	1154.7	1154.8
2.084	49	208	1365.9	1364.3
1.9717	10	211	1526.1	1527.4
1.8997	5	214	1644.0	1643.9
1.8610	10	125	1713.1	1713.5
1.8110	8	20, 11	1808.9	1806.2
1.7388	4	300	1962.4	1976.7
1.7131	6	128	2021.7	2015.8
1.6284	10	306	2237.4	2233.0
1.6065	18	21, 10	2298.9	2294.8
1.5700	76	11, 15	2407.0	2395.0
1.5523	6	12, 11	2462.1	2457.4
1.5069	46	220	2612.7	2605.5
1.4401	20	312	2860.8	2853.6
1.4024	5	315	3016.7	3016.1
1.3798	4	20, 17	3116.1	3108.0
1.3553	3	229	3229.8	3233.2

$\text{Mg}_{8.5}\text{As}_3\text{O}_{16}$ ($5.67 \text{ MgO} \cdot \text{As}_2\text{O}_5$) by analytical results (Mg: calc 30.06, obs 29.6; As: calc 32.70, obs 32.7) and by a complete three-dimensional structural analysis (9). It has the same structure as the compound " $\text{Co}_8\text{As}_3\text{O}_{16}$ " reported recently by Calvo (10), which is based on a twelve-layer cubic close-packed array of oxygen atoms. A detailed discussion of the structure will be presented with the completed structural analysis.

The indexed powder pattern of ground single crystals (x-ray diffractometer, Cu $K\alpha$ radiation) is given in Table I. The refined unit cell dimensions are $a_o = 6.034$ (2) Å, $c_o = 27.67$ (2) Å (hexagonal setting); $a_R = 9.859$ (6) Å, $\alpha = 35.64$ (3)° (rhombohedral setting).

In summary, single crystals of the phosphor manganese-activated magnesium arsenate have been prepared and the indexed powder pattern has been reported. The complete three-dimensional structural analysis will be published shortly.

Acknowledgment

This work was supported in part by the Advanced Research Projects Agency through the Materials Sci-

ence Center, Cornell University, Ithaca, New York 14850.

Manuscript received Nov. 24, 1971.

Any discussion of this paper will appear in a Discussion Section to be published in the December 1972 JOURNAL.

REFERENCES

1. M. Travnicek, F. A. Kröger, T. P. J. Botden, and P. Zalm, *Physica*, **18**, 33 (1952).
2. H. A. Klasens, *Philips Res. Repts.*, **9**, 337 (1954).
3. A. H. McKeag, *Acta Phys. Hung.*, **14**, 301 (1962).
4. S. Ibuki, K. Awazu, and T. Hata, *Proc. Internat. Conf. Luminescence*, Budapest, Hungary, 1465 (1966).
5. E. Kostiner and P. W. Bless, *This Journal*, **118**, 351 (1971).
6. R. B. Von Dreele, P. W. Bless, E. Kostiner, and R. E. Hughes, *J. Solid State Chem.*, **2**, 612 (1970).
7. P. W. Bless, R. B. Von Dreele, E. Kostiner, and R. E. Hughes, *J. Solid State Chem.*, **4**, 262 (1972).
8. E. M. Levin, C. R. Robbins, and H. F. McMurdie, "Phase Diagrams for Ceramists," American Ceramic Society, Columbus, Ohio (1964).
9. P. W. Bless and E. Kostiner, *J. Solid State Chem.*, **5** (1972).
10. N. Krishnamachari and C. Calvo, *Can. J. Chem.*, **48**, 3124 (1970).



Molecular Understanding of Electrochemical Processes by Ice Research¹

A. von Hippel

Laboratory for Insulation Research, Massachusetts Institute of Technology, Cambridge, Massachusetts 02139



Your kind invitation to give the opening lecture at this annual meeting of the Electrochemical Society greatly honored and slightly worried me. When one is exposed like a political candidate (Fig. 1), the audience expects last words of wisdom, and then the let-down comes in one way (Fig. 2) or another (Fig. 3). Fortunately, as scientists and engineers we are supposed to be experts in something, have doubts about certain developments, and ideas about others. To look

¹This is the Electrochemical Society Lecture delivered at the Cleveland, Ohio Meeting of the Society, October 4, 1971.



Fig. 1. "Pyramids rise and fall. But what our next speaker has to say will always be remembered as . . ."

at the field of electrochemistry with such doubts and ideas, however controversial they may be, I believe is the task you have set me.

From turbulence to deep-freeze.—Electrochemistry was born during the French Revolution, the unexpected offspring of the frog leg experiment on this balcony in Bologna during a thunderstorm by the physician Dr. Galvani (Fig. 4). How could its youth be anything else but stormy. Not only the political but the scientific world was in violent upheaval. Cavendish had just demolished the nearly religious Aristotelian conviction held for more than 2000 years that water is one of the "four elements," by generating it from a mixture of air and "inflammable" air (alias hydrogen) with an electric spark. Actually, since nitrogen was

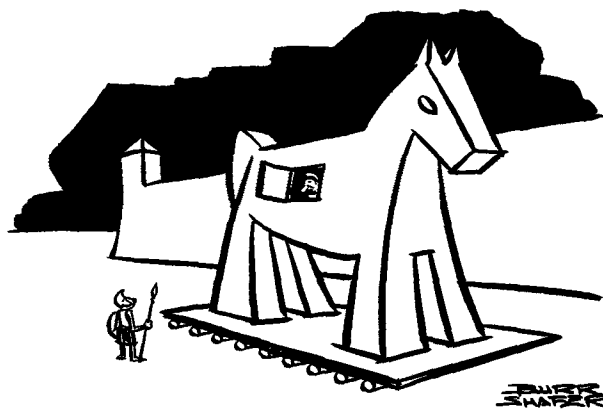


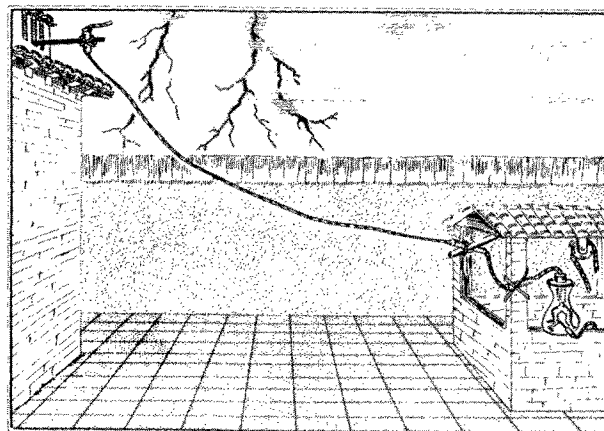
Fig. 2. "I said it's stuffy in here"



Fig. 3. "It's still in the experimental stage"



Fig. 4. Galvani and the balcony scene during the frog leg experiment (Sept. 1786)



present, the end product proved to be nitrous acid generated by an electric spark, the first certified case of automotive air pollution. This still confused Winston Churchill about one hundred years later, when he wrote from prep-school in amazement: "is it not wonderful to think that water is made of two gases, namely, hydrogen and nitroden." But in the meantime, Dr. Volta with his cell (Fig. 5) had opened the way to quantitative electric experimentation with low d-c voltages, and Dr. Galvani's "Animal Electricity" had fallen into disgrace. The president of the Royal Society, in presenting the Copley medal to Volta (1794), rubbed it in: "The experiments of Professor Galvani, until commented upon by Professor Volta, had too much astonished, and perhaps, in some degree perplexed many of the learned in various parts of Europe. To Professor Volta was reserved the merit of bringing his countryman's experiments to the test of sound reasoning and accurate investigation; he has explained them to Dr. Galvani himself and to the whole of Europe. . ."

Electrochemistry, thanks to the electric cell, became proprietor of the whole field of electrolytic conduction with its science and technology of ionic systems. Its findings were of decisive help for the formulation of the periodic system. The currents of its batteries led to the discovery of electromagnetism by Oersted (1820) and, in turn, to Faraday's reverse experiment of electromagnetic induction (1831). Thus electromagnetism and electrical engineering, concerned mainly with fields, insulators, and metallic conductors, became its progenies. Electrochemistry, centered on liquid systems and ionic conductors, cast them off and chose physical chemistry, the treatment of thermodynamic and statistical equilibria, as its guide for theoretical insight.

I still had the privilege to see several of its pioneers in action. From childhood I remember Professor Nernst setting out on his impossible 120-mile trip from Göttingen to Berlin by automobile in 1905, horn-blowing and the faculty cheering and waving handkerchiefs (Fig. 6). In the dark of night, there was the auto again, broken down and pulled by two oxen, but with an undaunted Professor Nernst. He took a train to

a city near Berlin, bought a new car and held his entry triumphantly at the appointed hour. Professor Tammann, his successor in Göttingen, cheered me up



Fig. 5. Alessandro Volta



Fig. 6. Professor Nernst and family setting out for Berlin.

no end when I was sitting as a young student in his lecture and thermodynamics seemed beyond my grasp: "Hü," he exclaimed, "there is 'that man' in Berlin who says he invented a Third Law of Thermodynamics; we need not to learn it." But "that man" took those laws seriously. Retiring in old age to his farms, he proclaimed: "Cattle raising is thermodynamically wrong because it heats the universe; I am growing carps"—and so he did.

As the memory drum whirls on, the sky of electrochemistry, studded with stars of the first magnitude, clouds over and a snowstorm of mathematical equations approaches, covering the landscape with semi-empirical assumptions and frozen activity coefficients. Volta's field of electrolytes seems paralyzed and Galvani is now in the ascendancy with "animal electricity" an exciting center-piece of molecular biology. What has gone wrong?

Water and ice.—Water is the basic fluid of electrochemistry and "the staff of life" for biology, but what do we really know about it? "Nearly everything that thermodynamics can measure and statistics interpret," the physical chemist is bound to answer (1). "Nearly nothing," the molecular scientist will retort "because those tools lead only to surmises." Both are right from their points of view. Physical chemistry finds itself today in the same dilemma that afflicted electrical engineering two to three decades ago. Circuit and field theory, akin to thermodynamics and statistics, could describe materials and their properties in reference to vacuum, but only the advent of "molecular science and molecular engineering" allowed us to understand them and to tailor them to order (2).

This understanding is still essentially restricted to gasses and solids. We cannot really visualize the molecular structure of water nor, in molecular detail, the happenings in aqueous solutions and on their surfaces and interfaces, because these liquids are in chameleon-like structure transitions. H_2O in the gaseous state behaves like a harmless dipole molecule with typical infrared modes of vibration and rotation and with Rydberg series of electronic excitation in the far ultraviolet

(Fig. 7). In the condensed states, however, it tends to be tetrahedrally interconnected by hydrogen bonds (Fig. 8). These weak bonds of ca. 5 kcal/mole break about every 10^{-12} sec in thermal fluctuations at room temperature, hence the need for statistical surmises about the actual happenings behind this fluctuating structure screen. To perceive events in clear detail, we must nail the H_2O molecules into place. We have done so by shifting the emphasis from water to ice and operating with single crystals.

Several times before, our laboratory has used that roundabout approach with success in various fields to clear up tantalizing questions about the behavior of materials. Many years ago, for example, the electrical engineer tried to understand and control electric breakdown by statistical studies on materials like air, oil, paper, and glass. By choosing instead, single crystals of the alkali halides as test objects with their well-known lattice structure and wide range of ionic substitution, we could discern in detail the development of electric breakdown as a sequence of electrochemical events (Fig. 9): injection of electrons from the cathode, of copper ions from the anode, and their recombination as copper colloid; discharge of alkali ions at the cathode and dendrite growth of an alkali metal Christmas tree; electron avalanche formation leading to the drilling of a plasma path from anode toward cathode in preferential lattice direction; finally melting of the crystal when this thunderbolt hits the dendrite tree (3). From these experiments a way of understanding could be found to solids, liquids, and gases of technical importance (4). Thus, hopefully, we may learn to understand aqueous systems better by research on ice single crystals. In the time remaining, allow me to present some of the results obtained thus far.

The phase diagram of ice and its molecular interpretation.—The complexity and beauty of ice research becomes apparent when one looks at the phase diagram (Fig. 10) known, thanks to the pioneering effort of Tammann (5) and Bridgman (6) and recently completed research, especially the excellent work of Kamb (7), Whalley (8), and co-workers. Thermodynamically

Fig. 7. The H_2O molecule and its spectrum.

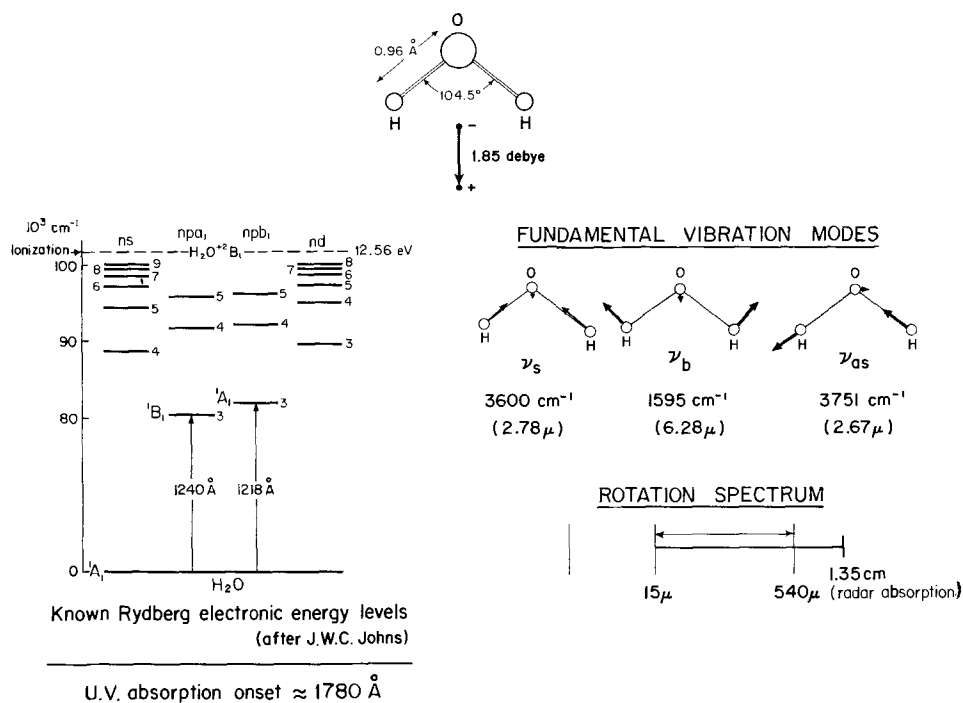
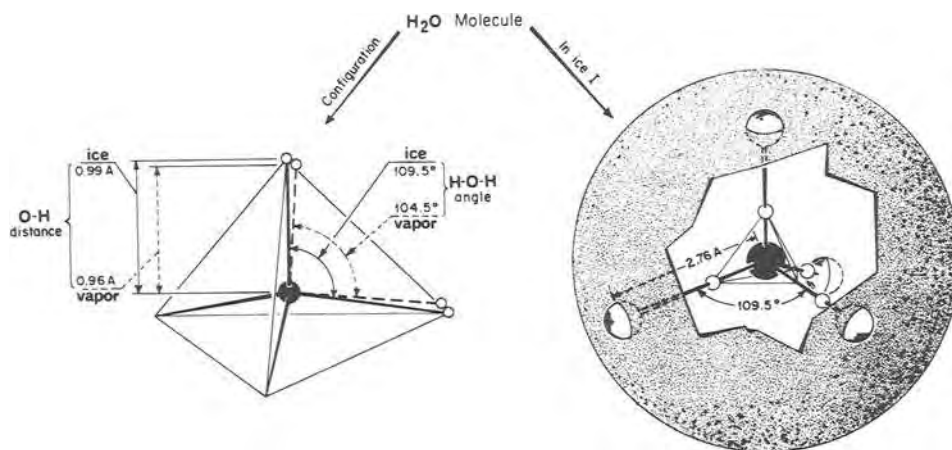


Fig. 8. The H_2O molecule in vapor and Ice I.



speaking, it is one of the most complex diagrams yet found for a simple compound. Diffraction analysis certifies that one deals with tetrahedrally bonded H_2O molecules throughout. An inquiry, how the individual water molecules must shift to produce these structures, leads to some intrinsic insight about the interaction between such molecules as function of temperature and approach distance. Let me illustrate the type of information obtainable from such a study (9).

Ice in nature crystallizes in the hexagonal wurtzite structure, puckered hexagonal chair-rings forming planes stacked in ABABAB etc., sequence normal to the c axis (Fig. 11). Open hexagonal channels traverse the crystal in the axis direction and lower the density of ice by *ca.* 10% compared to that of water. Since the channels offer freely available space, they are bound to play a vital role under pressure and in accommodating addition agents.

In the Ice I \rightarrow Ice II transition, the H_2O molecules remain in their puckered planes but, squeezed into the channels, tend to form diagonal bonds across them; one half of all the hexagon columns are destroyed in the bargain. The surviving ones are alternately pushed up and down; the old c axis survives as a threefold axis (Fig. 12). The Ice I \rightarrow Ice III transition, in contrast,

proceeds by hydrogen bond formation to second-nearest neighbors across the hexagon chair-rings in the puckered planes as well as across the hexagon boating normal to these planes. All hexagon rings are destroyed and pentagon rings are formed instead. While in Ice II, all the H_2O molecules of the Ice I structure can be accommodated, in Ice III every fourth water molecule is squeezed out. These rejects may form the elusive Ice IV phase.

Focusing on oxygen positions and bond directions, one can develop systematically the structures from Ice I to Ice IX, but this is only one half of the story. The other half comes into view when one inquires about proton locations. A tetrahedral array of N water molecules has $2N$ O-O links, hence one proton per link, while two equivalent proton positions are offered in an ideal tetrahedral structure of six equal bond angles $\text{H-O-H} \approx 109.5^\circ$. Ice I approaches this ideal situation; in consequence, the protons distribute themselves more or less at random over the competing sites as Pauling first concluded from zero-point entropy measurements (10). In the higher ice structures, however, large deviations from the tetrahedral bond angle may occur and proton ordering, preferentially seeking the smaller

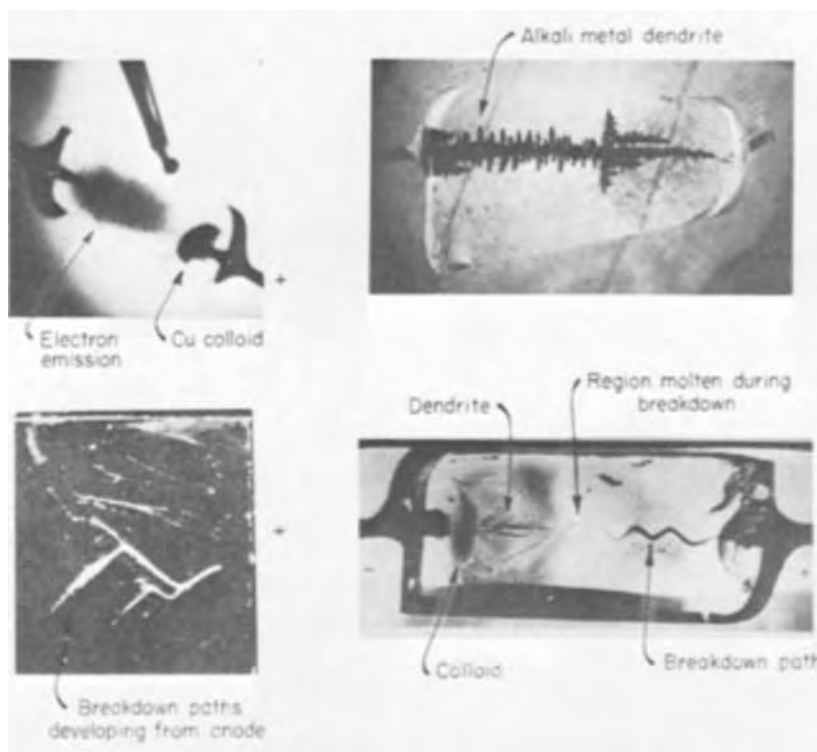


Fig. 9. Events before and during breakdown (NaCl crystal, Cu electrodes).

angles, can lower the lattice energy. Figures 13a, b show two typical situations of antiferroelectric ordering, first recognized by Whalley and co-workers (8): in the Ice I → Ice II transition, immediate proton ordering occurs and the permittivity drops to its near infrared value; the Ice I → Ice III transition offers less

incentive for ordering, hence the protons stay randomized until temperature decrease allows successive ordering accompanied by lattice distortion to the Ice IX phase.

Much more can be learned from the phase diagram about molecular phenomena (9), but let us hurry on to our central theme, the elucidation of electrochemical processes by ice research.

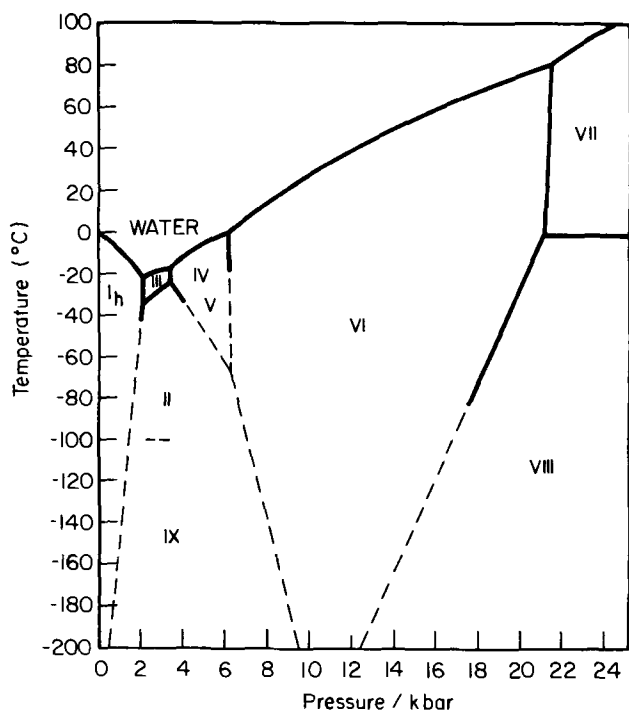


Fig. 10. Phase diagram of ice

Polarization and conduction in ice—Seen from the standpoint of ideal crystal structure, the application of an electric field to ice should result in a slight charge displacement akin to its infrared dielectric constant $k_i' \approx 3$. Instead, a big relaxation spectrum appears as in water, but is displaced by about a factor 10^7 toward lower frequencies (Fig. 14). The original explanation that ice behaves water-like but that the viscosity resisting the orientation of the H_2O molecules has increased by a factor 10^7 , is obviously nonsense; the crystal lattice stays intact. Bjerrum (11) came nearer to the truth by postulating two thermal excitation processes: molecule rotation requiring the breaking of three hydrogen bonds and placing two protons on one O-O link ("D" defect), none on another ("L" defect); and proton transfer to a neighboring H_2O molecule, creating an H_3O^+ and OH^- ion. He also saw that the movement of these two types of defects by proton exchange caused proton ordering, producing polarization and antipolarization, respectively, in the affected ice lattice.

Operating with these two defect pairs, their dissociation products, proton tunneling, and extensive sets of balancing equations, subsequent investigators arrived at an impressive theory of "ice as a protonic semiconductor," the next of kin to electronic semiconductors (12).

Not convinced of the validity of these ideas, we decided to remeasure the relaxation spectrum of "pure"

Fig. 11. Structure of Ice I_h single crystal.

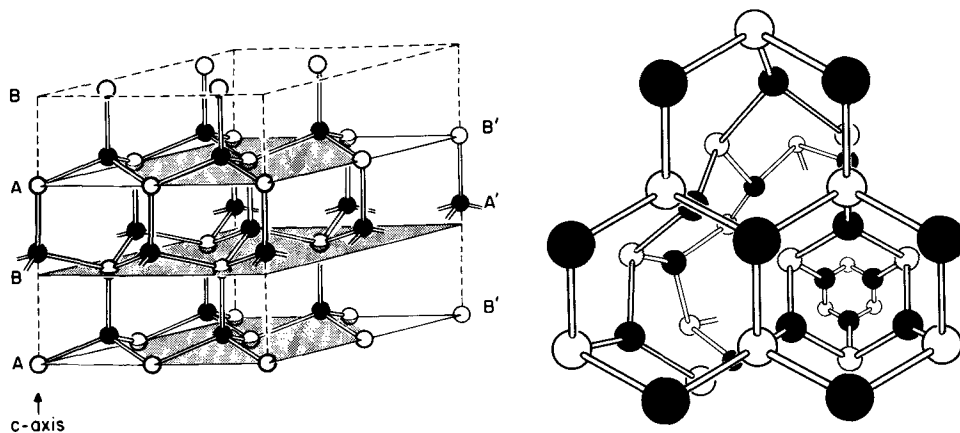
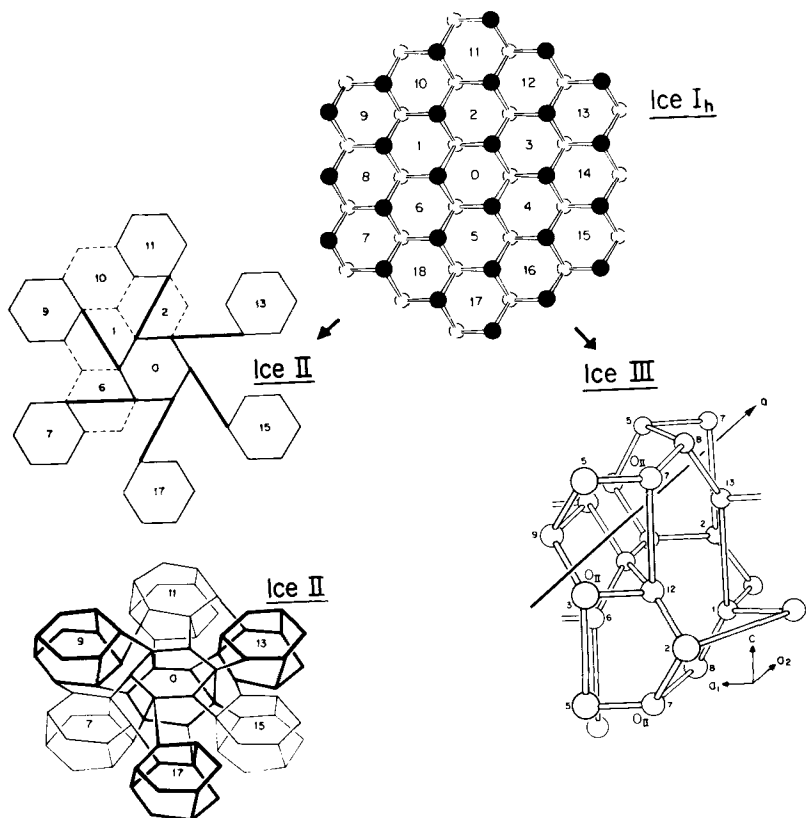


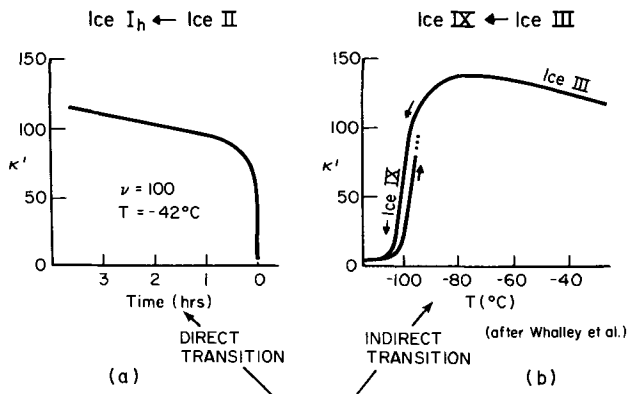
Fig. 12. Bond changes in Ice I → Ice II and Ice I → Ice III transition.



Ice I_h single crystals with improved resolving power over a wide range of frequencies (8×10^{-3} to 10^5 Hz) and temperatures (-5°C to -80°C). And indeed, we

found seven well resolved relaxation spectra (Fig. 15). Spectrum 3 is the standard volume polarization spectrum of ice previously seen; the activation energy of its time constant ($\mathcal{E}_c = 13.8$ kcal/mole) corresponds to the breaking of three hydrogen bonds as required for Bjerrum's L-, D-defect pair formation by molecule rotation. Expanding Bjerrum's concepts, we believe at present that the following molecular picture may adequately describe this polarization mechanism.

Creation of an L-, D-defect pair requires the thermal activation energy and proper infrared vibration to transfer a proton to an empty corner (unshared electron pair) of its H₂O tetrahedron (Fig. 16). The pair drifts apart a field-directed diffusion distance by subsequent proton exchanges until the defects are annihilated by counterdefects. These proton exchanges cause proton ordering in the ice lattice, i.e., the ice matrix acts like an electric memory system in which each vanishing L-, D-defect pair inscribes a polarization dipole (Fig. 17). Each molecule of the volume will have a chance to re-enact this pair creation after a statistical waiting time τ , the relaxation time of the process. Thus τ is connected to the number N of dipole



Figs. 13a,b. Antiferroelectric proton ordering in ice as observed by dielectric-constant measurements.

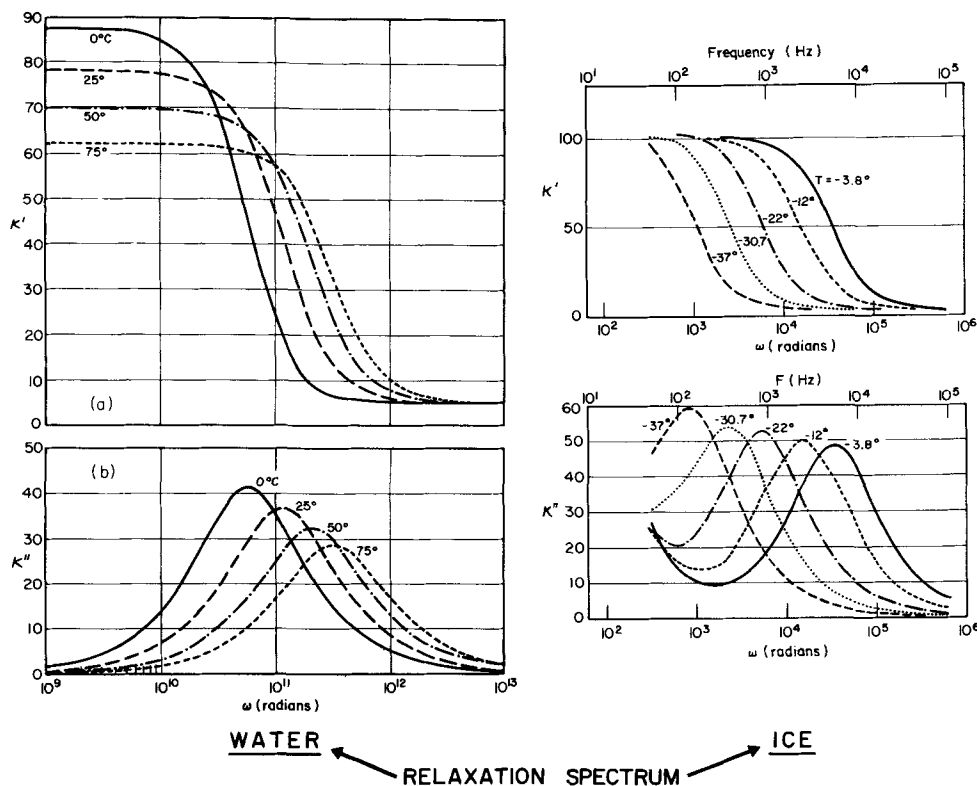


Fig. 14. Relaxation spectrum of water vs. ice.

WATER ← RELAXATION SPECTRUM → ICE

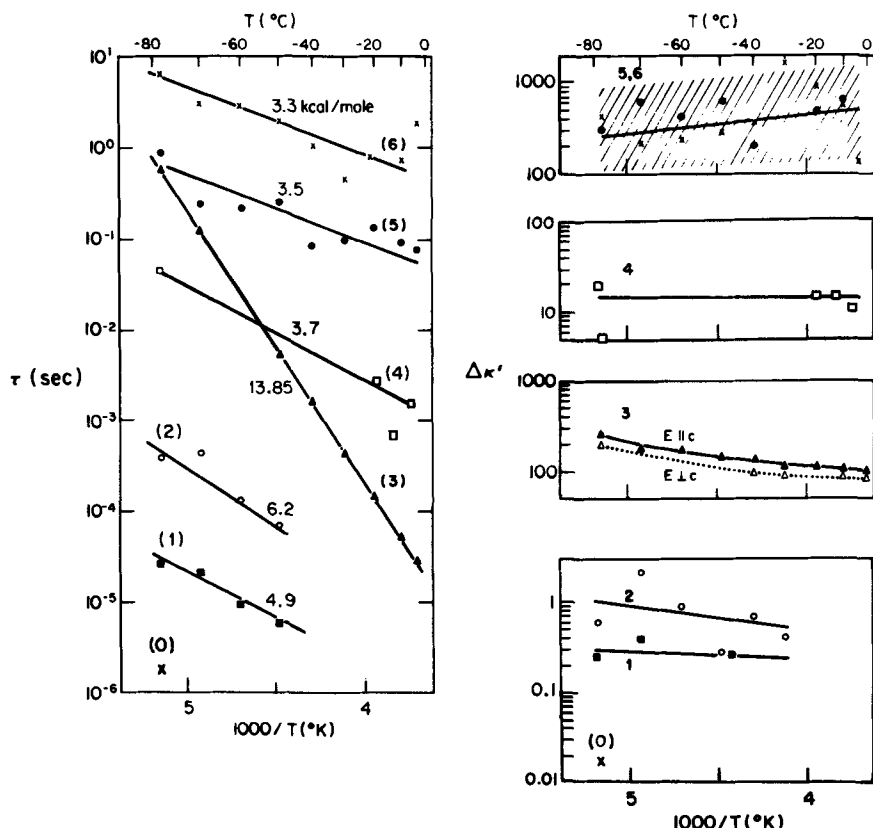


Fig. 15. Seven polarization spectra in "pure" ice I_h single crystals.

molecules per unit volume, not, as in previous models, to the orientation of dipole moments μ .

If one applies the same reasoning to the formation of an ionic defect pair and the migration of H_3O^+ and OH^- by intermolecular proton transfer toward cathode and anode, the memory system of the ice matrix puts a stop to this process: an antipolarization arises which pumps just as much charge uphill as the ions take downhill, thus uncoupling the ions from the driving

field (cf. Fig. 17). This strange situation became experimentally confirmed when we measured the trans-conduction of ice. Here the literature conveyed complete confusion by ascribing to the conductivity of pure ice thermal activation energies \mathcal{E}_σ ranging from 0 to ca. 33 kcal/mole. All our measurements of polarization and conduction were made on single crystals, carefully shielded from surface effects by guarded three-terminal electrodes. Suddenly a sample cracked in its holder exposing a fresh unguarded surface (Fig.

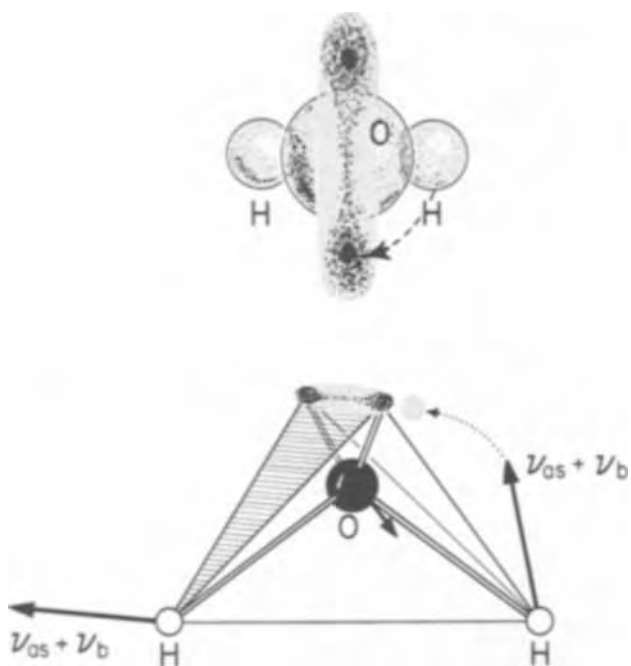
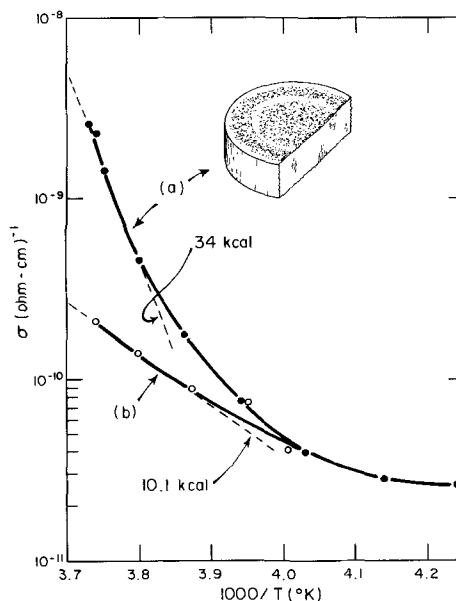


Fig. 16. L-, D-defect pair formation by intramolecular proton transfer.

18); the conductivity jumped up by an order of magnitude and \mathcal{E}_o rose from about 10 to ca. 34 kcal/mole. Obviously, these were not simple "activation energies."

Closer inspection showed that between ca. 0°C and -30°C the main current in ice actually flows over its



3-Terminal ice single crystal sample
 a) cracked
 b) fully guarded

Fig. 18. Surface vs. volume conductivity of Ice I_h

surface, where the lattice is destroyed and its anti-polarization memory inactivated. Multicrystallinity has

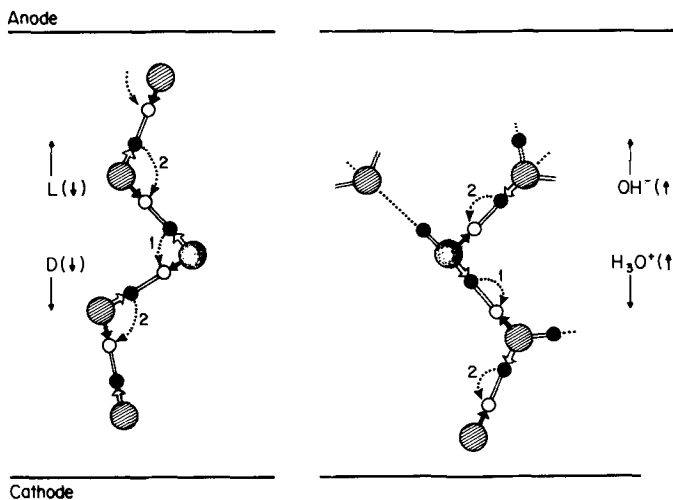
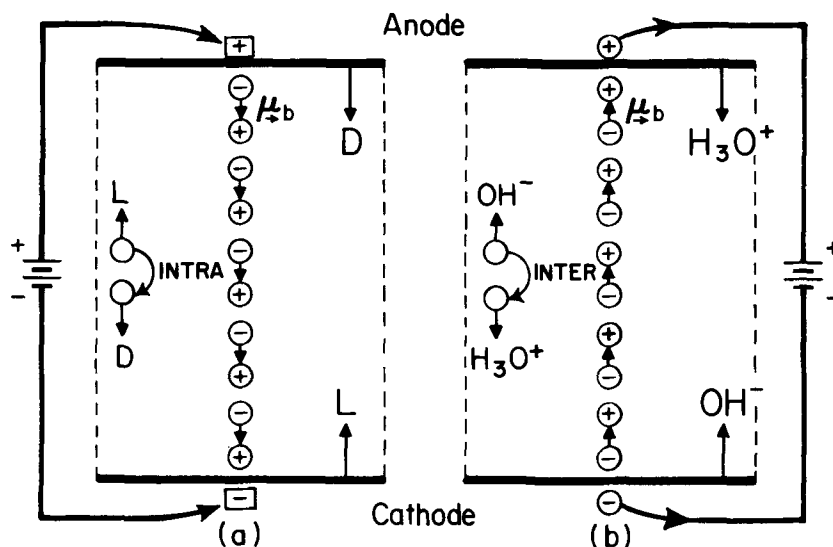


Fig. 17. Polarization by L and D defects and antipolarization by ionic defects in Ice I_h single crystals.



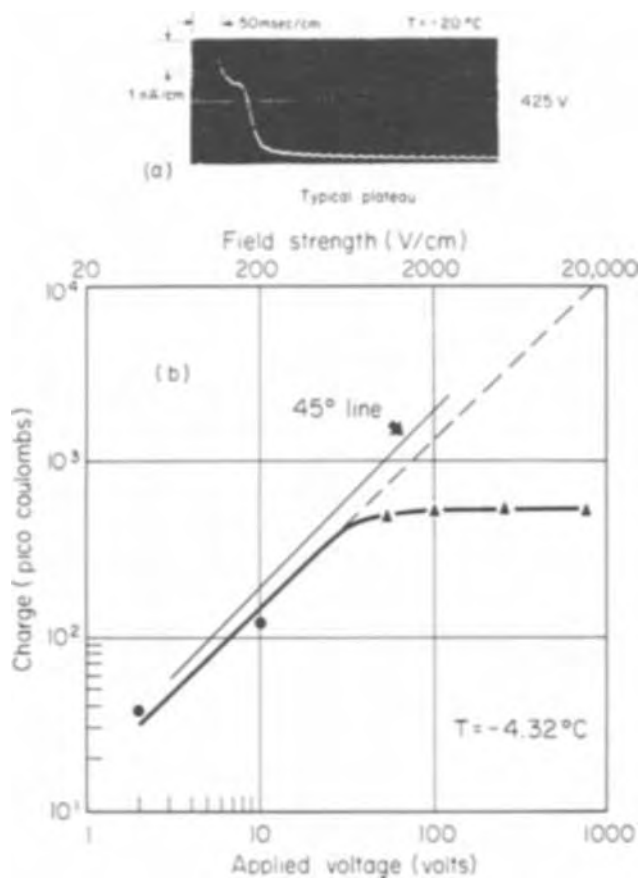


Fig. 19. Extrinsic charge-carrier removal from Ice I_h crystal by high fields.

corresponding effects by creating inner surfaces and additional polarization spectra. A small amount of extrinsic carriers is normally held loosely in an ice crystal (e.g., ca. 3×10^{11} carriers/cm³ in the case shown); it appears as a hump in the current-time characteristic and can be pulled out with near zero activation energy (Fig. 19). The effects of prehistory are pronounced. In short, surface conduction and space-charge effects have falsified the measurements of most previous observers, and a new picture begins to emerge about protons and their actions (13). Extensive new measurements on the interpretation of spectra 1 \rightarrow 6, the correlation of electrical and mechanical data, and the effects of HF doping have just been completed

(14), and we begin to talk with increasing confidence about "Molecular Phenomena in H₂O Systems."

Ice is not, as people previously believed, a chemically inert environment. Polishing it with alcohol, as recommended in bars around the world, creates dielectric absorption bands. Introducing fluorine softens ice crystals excessively, tempting one to offer toothpaste manufacturers a new advertising slogan: "When you sit on a glacier and brush with Crest, an ice-fall will propel you to your eternal rest."

Everywhere we find ourselves today confronted with the ecological dilemma of fitting man's activities, based on incomplete understanding, into nature's ways without ruinous results. One answer is to forego new knowledge and to plod along old pathways; the other, to seek more complete understanding and to apply it with more compassionate insight. I believe we have no choice but to go forward trusting Michelangelo's vision: "God gave a divine spark to Man" (Fig. 20).

Acknowledgment

Figures 1-3 reprinted by permission of the publisher, The Vanguard Press, from "Through History with J. Wesley Smith" by Burr Shafer. Copyright, 1950, by The Vanguard Press, Inc.

The pictures of Drs. Galvani and Volta (Fig. 4 and 5) and the quotation from the Copley medal presentation, may be found in the delightful booklet by Dr. Bern Dibner, "Galvani-Volta," Burndy Library, Norwalk, Conn. (1952).

The photograph of Professor Nernst and family in his automobile (Fig. 6) was obtained through courtesy of Mrs. von Zanthier-Nernst and of Professor W. Jost, Director of the Institut für Physikalische Chemie, Göttingen. The oxen story belongs to the "Apocrypha of local lore."

This research was sponsored by the Office of Naval Research under Contracts N00014-67A-0204-0003 (Medicine and Dentistry Branch) and N00014-67-A-0204-0053 (Chemistry Program and Atmospheric Sciences Program).

REFERENCES

1. Cf. the summarizing account of D. Eisenberg and W. Kauzmann, "The Structure and Properties of Water," Oxford University Press, New York (1969).
2. Cf. A. von Hippel, "Dielectrics and Waves," John Wiley & Sons, Inc., New York (1954); "Molecular Science and Molecular Engineering," M.I.T. Press (1959).
3. Cf. A. von Hippel, *Ergeb. Exakt. Naturw.* 14, 79-129 (1935); *J. Appl. Phys.*, 8, 815-832 (1937).



Fig. 20. Michelangelo's vision of God awakening man (Sistine Chapel)

4. Cf. A. von Hippel, "The Molecular Designing of Materials and Devices," Chap. 20, M.I.T. Press (1965).
5. Cf. G. Tammann, "States of Aggregation," D. Van Nostrand Co., New York (1925).
6. Cf. P. W. Bridgman, "The Physics of High Pressure," G. Bell & Sons, London (1949).
7. Cf. B. Kamb, "Ice Polymorphism and the Structure of Water," in "Structural Chemistry and Molecular Biology," A. Rich and N. Davidson, Editors, pp. 507-542, Freeman & Company, San Francisco (1968); and B. Kamb, *Trans. Am. Crystallogr. Assoc.*, **5**, 61 (1969).
8. Cf. E. Whalley, "Structure Problems of Ice," in "Physics of Ice," N. Riehl, B. Bullemer, and H. Engelhardt, Editors, pp. 19-43, Plenum Press, New York (1969).
9. A. von Hippel and E. F. Farrell, "Molecular Phenomena in H₂O Systems, I. A Molecular Interpretation of the Phase Diagram of Ice," Tech. Rept. 9 (New Series), Lab. Ins. Res. M.I.T., April 1971.
10. L. Pauling, *J. Am. Chem. Soc.*, **57**, 2680 (1935).
11. N. Bjerrum, *Kgl. Danske Videnskab. Selskab., Mat.-Fys. Medd.*, **27**, 32, 41 (1951).
12. H. Gränicher, *Physik Kondensierten Materie*, **1**, 1 (1963); C. Jaccard, *ibid.*, **3**, 99 (1964).
13. A. von Hippel, D. B. Knoll, and W. B. Westphal, "Transfer of Protons Through 'Pure' Ice I_h Single Crystals. I. Polarization Spectra of Ice I_h," *J. Chem. Phys.*, **54**, 134-144 (1971); A. von Hippel, "Transfer of Protons Through 'Pure' Ice I_h Single Crystals. II. Molecular Models for Polarization and Conduction," *ibid.*, **54**, 145-149 (1971); M. A. Maidique, A. von Hippel, and W. B. Westphal, "Transfer of Protons Through 'Pure' Ice I_h Single Crystals. III. Extrinsic versus Intrinsic Polarization Surface versus Volume Conduction," *ibid.*, **54**, 150-160 (1971).
14. A. von Hippel, R. Mykolajewycz, A. H. Runck, and W. B. Westphal, "Molecular Phenomena in H₂O Systems," II. The Dielectric and Mechanical Response of Ice I_h Single Crystals and Its Interpretation, Tech. Rept. 10 (New Series), Lab. Ins. Res., M.I.T., October 1971.

Reports on Electrochemical Society Summer Fellowship Awards

During the summer of 1971, the following graduate students received \$1000 each, representing the three Summer Fellowship Awards of The Electrochemical Society:

Miss Jean Horkans, Case Western Reserve University, Cleveland, Ohio, was awarded the Edward Weston Fellowship.

Mr. Robert R. Fike, University of Massachusetts, Amherst, Mass., was designated as the recipient of the Colin Garfield Fink Fellowship.

Mr. James Webb, University of Michigan, Ann Arbor, Mich., received the James W. Richards Fellowship.

The Summer Fellowship Awards are made "without regard to sex, citizenship, race, or financial need, to a fellow or teaching assistant pursuing work between the degree of B.S. and Ph.D. on a subject in a field of interest to The Electrochemical Society." It is intended to cover a period during which the recipient has no financial support for the continuance of his work.

The Edward Weston Summer Fellowship Report

A summary of Miss Horkans' report is given below.

The Electroreflectance Study of Gold

The use of optical reflection techniques in conjunction with electrochemical methods has made available a powerful additional tool for *in situ* studies of the electrode-electrolyte interface. For example, optical techniques have been used to measure the extent of adsorption of a species (1-4), to study passivation of surfaces (5), to indicate the extent of surface roughening caused by an electrochemical process (5), to follow short-lived intermediate species in solution (6, 7) to investigate the band structure and surface states of semiconductors (8-10), and to study the nature of the forces involved in adsorption (11).

In addition, the optical data obtained for gold have stimulated a discussion (12) on the mechanism of electrochromism and the importance of considering the unique electronic properties of the surface in developing a detailed understanding of the electrode-electrolyte interface. Our laboratory is currently involved in an effort to elucidate further the nature of the gold-electrolyte interface and to determine the roles played by the free electrons (those in the 6s conduction band) and by the 5d electrons at the surface. It is felt that the 5d-surface electrons and their interactions with species in the double layer are important in determining the electrochromism of gold, and that this phenomenon cannot be explained as due to modulation of the free electrons alone.

Figure 1 shows the change in relative reflectivity at

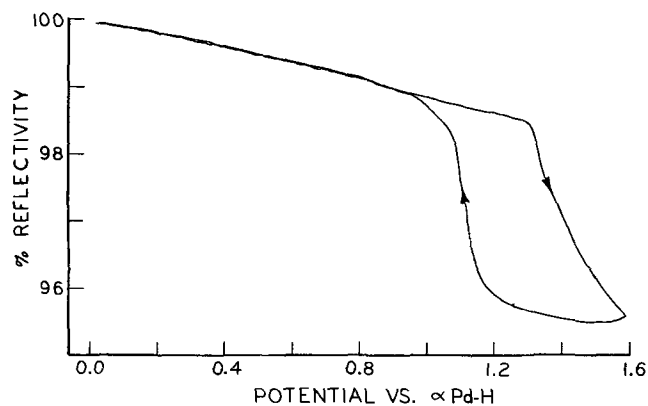


Fig. 1. The voltage dependence of the reflectivity of an evaporated gold electrode in 1N HClO₄ at 500 nm. The sweep rate is 0.1 V/sec.

500 nm of a gold electrode in 1N HClO₄ as a triangular potential sweep is applied. The formation of a layer of oxygen on gold at ~1.3V and its reduction at ~1.2V on the reverse sweep are clearly visible; but the nature of the smaller, but real changes in reflectivity occurring outside of this region is less clear. Such changes are much more obvious when a derivative reflectance technique is used, and various applications of modulated electroreflectance have been successful in studying surface films (13, 14). A variable angle specular reflection instrument with the capability of doing derivative measurements has been built in this laboratory.

The variable angle reflectance spectrometer consists of an optical cell mounted on the axis of a θ - 2θ goniometer. The tungsten filament light source is mounted



Galvanic Cells in Molten Sodium Bisulfate

M. C. B. Hotz*

Hydrologic Sciences Division, Inland Waters Branch, Department of the Environment, Ottawa, Ontario, Canada

and R. C. Kerby, and T. R. Ingraham

*Extraction Metallurgy Research Section, Mines Branch,
 Department of Energy, Mines, and Resources, Ottawa, Ontario, Canada*

ABSTRACT

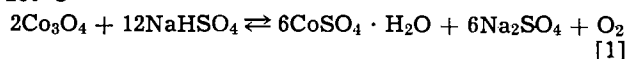
Study of the cells Pt, H₂|NaHSO₄|H₂, Pt and Pt, H₂|NaHSO₄||Ag₂SO₄, NaHSO₄|Ag shows that the hydrogen electrode behaves reversibly in molten sodium bisulfate. Emf's of the cell Pt, H₂|CoSO₄(m₂), NaHSO₄|CoSO₄(m₁), NaHSO₄|Co in the range 200°-270°C have been used to calculate thermodynamic data for the reaction



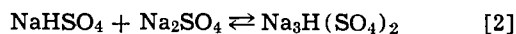
A plot of emf against log m₁/m₂ is linear, but the slope is steeper than predicted.

In previous papers (1,2), we have shown that molten sodium bisulfate and sodium pyrosulfate are the sulfating agents in the sulfate-catalyzed roasting of sulfide ores containing cobalt and nickel. More recently, we have published data on the stability and the thermodynamics of decomposition of these compounds, and a partial phase diagram for the sodium pyrosulfate-water system, in which sodium bisulfate appears as a constituent (3, 4).

The sodium bisulfate roasting cycle includes two reactions that occur simultaneously at temperatures between the melting point of NaHSO₄ (187°C) and 250°C



and



so that it is difficult to obtain thermodynamic and kinetic data for the commercially significant reaction [1]. A possible approach seemed to be through the development of satisfactory nickel and cobalt electrodes in molten sodium bisulfate, and this paper describes attempts to examine the behavior of a cobalt electrode in this environment with respect to a hydrogen electrode.

The literature contains very few papers on the electrochemistry of solutions in molten bisulfates. Tajima, Soda, Mori, and Baba (5) showed that hydrogen and oxygen were obtained in a molar ratio of 2:1 when KHSO₄ was electrolyzed with platinum electrodes, and Shams El Din (6) studied overpotentials in the same system. Le Ber (7) briefly considered the H₂|H⁺ system, but had some difficulty in achieving reversibility. Arvia and his co-workers appear to be the first to have considered the hydrogen electrode as the basis of an electrochemical series in a bisulfate melt (8-10). They found the electrode reaction to be reversible and determined its potential against a silver|silver sulfate refer-

ence electrode. Their attempt to establish an electrochemical series was based on corrosion potentials of a number of metals.

The only other studies of equilibrium systems involving bisulfates are those of Seward and Miller (11) on the Hg|Hg²⁺ and Ag|Ag⁺ electrodes in NaHSO₄ and Le Ber (7) on the Ag|Ag⁺ electrode in KHSO₄|NaHSO₄ eutectic.

The decomposition of molten bisulfate to pyrosulfate poses a major problem in maintaining the purity levels of the bisulfate melts, and those used in many of the investigations quoted were likely contaminated by pyrosulfates, as well as water and sulfuric acid.

Our study of the stability of sodium bisulfate at temperatures between 100° and 400°C showed that sodium bisulfate starts to lose water at temperatures just below the melting point (187°C) to form sodium pyrosulfate. In order to effectively prevent pyrosulfate formation in our sodium bisulfate melts, we used a closed system in the present investigation.

Experimental

Preparation of materials.—Sodium bisulfate was prepared by adding stoichiometric amounts of water to sodium pyrosulfate that had been made by direct reaction between sodium sulfate and sulfur trioxide (4).

Cobalt sulfate was made by heating Fisher Certified CoSO₄ · 7H₂O at 400°C for 8 hr, crushing the product, and reheating for a further 8 hr (1).

Johnson, Matthey and Mallory cobalt wire and platinum foil were washed with acetone and distilled water, and oven-dried before use.

Linde hydrogen was purified by passage through a Deoxo tube, and then over copper mesh at 500°C.

Fisher Certified sodium sulfate was oven-dried at 200°C before use.

The double salt Na₂Co(SO₄)₂ was prepared by precipitation of its tetrahydrate from a mixed solution of the two sulfates, followed by dehydration at 400°C for 8 hr.

* Electrochemical Society Active Member.

Key words: galvanic, galvanic cells, molten, sodium bisulfate.

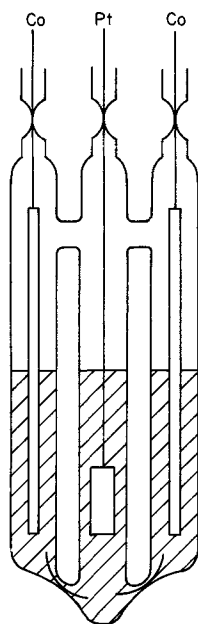


Fig. 1. Cell vessel

Apparatus and procedure: Emf's were measured with a L&N Type K2 potentiometer, using a Pye nanoammeter as a null detector. Readings were steady within 1 mV over periods of several hours.

The cell vessels were made of Pyrex glass; junctions between the half-cell containers were made with asbestos fibers (12). In such dilute solutions the activities would not differ significantly on either side of the junction, and transport should be almost exclusively by the predominating sodium and bisulfate ions. A diagram of the cell is shown in Fig. 1. The outer compartments contained cobalt electrodes and solutions of cobalt sulfate in molten sodium bisulfate. The electrodes were 1.3 mm diameter lengths of cobalt wire welded to 0.4 mm diameter support wires. A piece of bright platinum foil 1 cm² in cross-section was welded to 0.4 mm platinum wire to form the reference electrode in the center compartment. This arrangement permitted two series of measurements to be made simultaneously. The cells were sealed to prevent decomposition of sodium bisulfate, and their construction ensured that all three compartments were at the same pressure during the measurement.

The vessels used for the study of hydrogen electrodes were similar in that junctions were made through asbestos fibers, but some cells were designed to permit bubbling of hydrogen, while others had half cells in which the platinum electrodes were isolated completely from gaseous hydrogen. Various combinations of these half cells were used to check for zero emf between isolated and bubbling electrodes. Reversible behavior of the hydrogen electrodes was also established with respect to a silver|silver sulfate electrode.

The cells were packed in alumina powder in a Pyrex tube that fitted closely into a cylindrical brass block furnace heated by four GE 150W Type 186 H cartridge heaters. The block was insulated by layers of glass wool, firebrick, and transite. Temperatures were controlled by a Honeywell Pulse-Pyrovan unit, and cell temperatures were measured on the K2 potentiometer with a platinum-10% rhodium platinum thermocouple in conjunction with a Kaye Ice-point Reference Standard. Temperature control was within $\pm 0.2^\circ\text{C}$.

Apparatus used for the associated differential thermal analysis and x-ray powder diffraction analysis were described in an earlier paper (2).

Results and Discussion

Differential thermal analyses on mixtures of cobalt powder and sodium bisulfate were done at a programmed temperature increase of $2^\circ\text{C}/\text{min}$ between

Table I.
Pt, H₂ | NaHSO₄ || NaHSO₄ | H₂, Pt

Cells	Emf, V	Flow rate, cc/min	Temperature, °C
Pt:Pt, H ₂ (gas)	0.0003	5.0	233
Pt:Pt	0.0006	—	233

Ag Ag ₂ SO ₄ (m) NaHSO ₄ Pt, H ₂			
Concentration (m)	Emf, V	Temperature, °C	
0.184	-0.183	214.0	
0.184	-0.182	215.0	
0.184	-0.194	240.0	
0.184	-0.200	240.3	
0.184	-0.211	270.0	

room temperature and 500°C . The sodium bisulfate fusion endotherm at 187°C was followed immediately by a large exothermic peak. X-ray powder diffraction analysis identified the products of this reaction as cobalt sulfate and sodium sulfate when the reaction was allowed to proceed at temperatures below 250°C , and the double salt Na₂Co(SO₄)₂ when the reaction proceeded above this temperature. Other endothermic peaks appearing at 455° and 470°C were identified as phase transitions of the system CoSO₄-Na₂SO₄ (13). Hydrogen was also produced by the above reaction. The suggested stoichiometry is



This is apparently the reaction for the galvanic cell Pt, H₂|NaHSO₄, CoSO₄(m₂)||NaHSO₄, CoSO₄(m₁)|Co. Measurement of the emf's of such a cell in which $m_1 = m_2$ should provide thermodynamic data for reaction [3], if the cobalt and hydrogen electrodes operate reversibly in a bisulfate melt.

In order to demonstrate that a reversible hydrogen electrode is formed in molten sodium bisulfate, the cells Pt, H₂|NaHSO₄||NaHSO₄|H₂, Pt and Pt, H₂|NaHSO₄||NaHSO₄, Ag₂SO₄|Ag were examined, and the results are shown in Table I.

The potential of the platinum|hydrogen electrode is shown to be independent of the gaseous hydrogen partial pressure, implying that the melt is saturated with respect to hydrogen and that the activity of the hydrogen in the melt is constant. Arvia (9) has demonstrated that a reversible hydrogen electrode is formed in potassium bisulfate melts, and that once the platinum electrode was saturated with hydrogen from the cathodic reaction, bubbling hydrogen over its surface did not change the emf. In the present case, it would appear that the platinum surface has become saturated with hydrogen without the necessity of a prior electrolysis to saturate the surface; alternatively, mere adjustment of the potentiometer balance may have sufficed to saturate the surface.

The emf of the cell, H₂, Pt|NaHSO₄||NaHSO₄, Ag₂SO₄|Ag varies linearly with temperature and is reversible (Table I). The hydrogen electrode has also been found to be reversible with respect to a silver|silver sulfate electrode in the systems KHSO₄ (9), KHSO₄|NaHSO₄ eutectic (7), and NH₄HSO₄ (11). Because the potential of the hydrogen electrode does not vary with the partial pressure of hydrogen gas, melt decomposition to pyrosulfate can be prevented by using platinum immersed in the melt in a sealed system as a reversible hydrogen electrode. This also prevents contamination with atmospheric moisture; sealed vessels were therefore used in the experiments involving the cobalt electrode.

The range of molalities in which a cobalt electrode will function reversibly is restricted by the corrosion of the metal by sodium bisulfate, and by the solubility of cobalt sulfate in the melt. In experiments using the cell Pt, H₂|CoSO₄(m₂), NaHSO₄||CoSO₄(m₁), NaHSO₄|Co, for the determination of the thermodynamic data

Table II.

Emf of the cell H₂ | CoSO₄ (0.0350m), NaHSO₄ || CoSO₄ (0.0350m), NaHSO₄ | Co
and thermodynamic data for the reaction
 $\frac{1}{2}\text{Co} + \text{NaHSO}_4 = \frac{1}{2}\text{Na}_2\text{SO}_4 + \frac{1}{2}\text{CoSO}_4 + \frac{1}{2}\text{H}_2$

Temperature, °K	Emf, V	-ΔG, cal	Equilibrium constant	-ΔH, kcal
475.2	-0.3314	7644	3270.0	34.0
496.4	-0.2761	6369	636.0	34.4
501.2	-0.2707	6245	528.0	34.5
518.9	-0.2305	5316	173.0	34.6
542.0	-0.1671	3853	35.8	34.4
543.0	-0.1645	3794	33.7	34.4

Table III.

Emf of the cell H₂ | CoSO₄(m₂), NaHSO₄ || CoSO₄(m₁), NaHSO₄ | Co
at 511.2°K. m₁ = 0.0350m

m ₂ , mole kg ⁻¹	Emf, V
0.0177	-0.2668
0.0350	-0.2425
0.0530	-0.2301
0.0750	-0.2152

for reaction [3], the molalities m_1 and m_2 were set at 0.0350m. Effective inhibition of corrosion by the solute at this concentration was indicated by the absence of observable attack on the cobalt electrode during the course of an experiment. Emf's were measured at temperatures between 200° and 270°C, and were found to vary linearly with temperature. The measured emf's were constant within 1 mV for several hours. This excludes the possibility of mixed potentials due to continuing corrosion of the cobalt electrode, which would change the cobalt ion activity in the melt and alter the emf.

The measured emf's and the calculated free energies, enthalpies, and equilibrium constants for reaction [3] are shown in Table II. The entropy change for the corrosion of cobalt by molten sodium bisulfate is $\Delta S = 56.4 \pm 1.4$ eu. Using standard entropy values for aqueous solutions for a comparison

$$\Delta S = \frac{1}{2}S^\circ_{\text{H}_2(\text{g})} + \frac{1}{2}S^\circ_{\text{Na}_2\text{SO}_4(\text{aq})} + \frac{1}{2}S^\circ_{\text{CoSO}_4(\text{aq})} - \frac{1}{2}S^\circ_{\text{Co}(\text{s})} - S^\circ_{\text{NaHSO}_4(\text{l})} \quad [4]$$

provides an entropy change of $\Delta S^\circ = 51.9$ eu at 500°K. Application of the van't Hoff isochore to the equilibrium constant data leads to an enthalpy at 500°K of $\Delta H = -34.5$ kcal · mole⁻¹, in good agreement with values calculated from the Gibbs-Helmholtz equation, providing further justification for the validity of the data.

Addition of an equivalent molar amount of sodium sulfate to the cobalt electrode vessel did not change

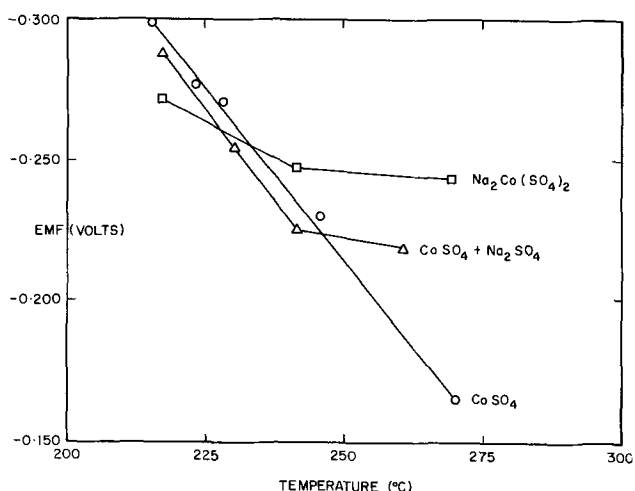


Fig. 2. Effect of addition of Na₂SO₄ and Na₂Co(SO₄)₂ on the emf of Pt, H₂ | CoSO₄(m₂), NaHSO₄ || CoSO₄(m₁), NaHSO₄ | Co.

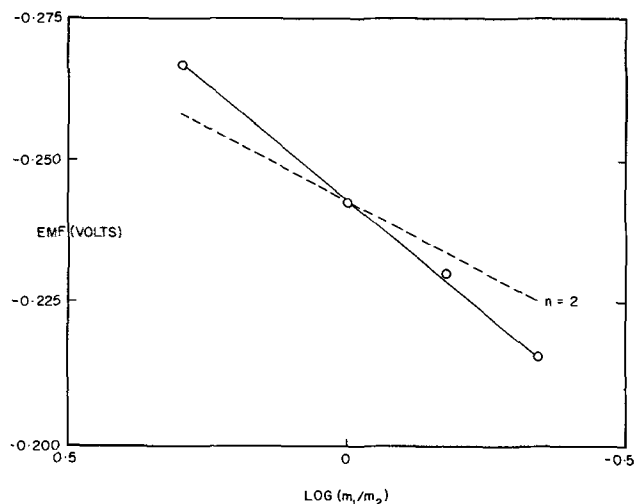


Fig. 3. Theoretical (---) and observed (—) Nernst plots for Pt, H₂ | CoSO₄(m₂), NaHSO₄ || CoSO₄(m₁), NaHSO₄ | Co.

the slope of the emf-temperature relationship below 240°C, but the measured emf's were about 10 mV lower. Above 250°C, however, there is a marked change in slope, the new slope approximating that found when cobalt sulfate and sodium sulfate are replaced by an equal amount of the double salt Na₂Co(SO₄)₂. These effects are shown in Fig. 2. Seward and Miller (11) observed that the addition of sulfate ion to their cell lowered the emf, implying an increase in the activity of the silver ion. In spite of viscosity studies that indicated structural changes in the melt, they were unable to explain the increase in silver ion activity. The same effect occurs in the present work with the cobalt electrode, an increase in cobalt ion activity occurring on addition of sodium sulfate. Sodium bisulfate forms highly structured melts (14), with extensive hydrogen bonding (15), and it seems likely that the added sulfate ions would be incorporated into this structure. This would reduce association of the divalent sulfate ion with the cobalt ion, thereby increasing its activity. At higher temperatures, where the hydrogen bonding breaks down, this trend should be reversed, as is evidenced by the behavior of the cells on sulfate addition at temperatures above 250°C.

A series of experiments were done with the cell Pt, H₂ | CoSO₄(m₂), NaHSO₄ || CoSO₄(m₁), NaHSO₄ | Co in which the molality m_1 was maintained at 0.0350m, and m_2 varied between 0.0177 and 0.0750m. Emf's measured at 238°C are shown in Table III; the cells usually reached equilibrium within 6-7 hr. A plot of emf against the logarithm of the ratio of the molalities is linear but the slope is about 55% steeper than that predicted by the Nernst equation (Fig. 3).

Although the Nernst slope indicates that the behavior of the cobalt ion in a bisulfate melt is complex, this effect may be qualitatively explained by reasoning similar to that used for the addition of sodium sulfate, that is, the incorporation of sulfate ion into the melt structure effectively increases the cobalt activity.

Acknowledgment

The authors are grateful to M. R. Hughson for the x-ray power diffraction analyses.

Manuscript submitted Aug. 25, 1969; revised manuscript received July 21, 1971. This was Paper 284 presented at the Boston Meeting of the Society, May 5-9, 1968.

Any discussion of this paper will appear in a Discussion Section to be published in the December 1972 JOURNAL.

REFERENCES

1. M. C. B. Hotz and T. R. Ingraham, *Can. Met. Quart.*, **4**, 295 (1965).

2. M. C. B. Hotz and T. R. Ingraham, *ibid.*, **5**, 237 (1966).
3. T. R. Ingraham and M. C. B. Hotz, *ibid.*, **7**, 139 (1968).
4. M. C. B. Hotz and T. R. Ingraham, *ibid.*, **7**, 147 (1968).
5. S. Tajima, M. Soda, T. Mori, and N. Baba, *Electrochim. Acta*, **4**, 205 (1959).
6. A. M. Shams El Din, *ibid.*, **7**, 613 (1962).
7. F. Le Ber, Commissariat à l'Énergie Atomique. Rapport CEA-R-2567 (1964).
8. H. A. Videla and A. J. Arvia, *Electrochim. Acta*, **10**, 21 (1965).
9. A. J. Arvia, A. J. Callandra, and H. A. Videla, *ibid.*, **10**, 33 (1965).
10. A. J. Arvia and H. A. Videla, *ibid.*, **11**, 537 (1966).
11. R. P. Seward and J. P. Miller, *J. Phys. Chem.*, **69**, 3156 (1965).
12. S. N. Flengas and T. R. Ingraham, *Can. J. Chem.*, **35**, 1139 (1957).
13. K. A. Bolshakov and P. I. Federov, *Zh. Obshch. Khim.*, **26**, 348 (1956).
14. S. E. Rogers and A. R. Ubbelohde, *Trans. Faraday Soc.*, **46**, 1051 (1950).
15. M. C. B. Hotz and N. J. Ramey, Extended Abstracts Electrochem. Soc. (Industrial Electrolytic Div.), **5**, 501 (1969).

Electrode Processes in Sodium Polysulfide Melts

K. D. South, J. L. Sudworth, and J. G. Gibson

British Railways Research Department, Derby, England

ABSTRACT

Results are reported of three-electrode measurements in sodium polysulfide melts. The composition range covered was Na_2S_3 - Na_2S_5 and the temperature range 300° - 400°C . The electrode material used was vitreous carbon. Voltammetric, chronopotentiometric, and current interruption techniques were used to investigate cathodic and anodic processes. Evidence is produced that sulfide films are formed at the cathode and that these result in limiting currents. The lowest value of limiting current density was $28 \text{ mA} \cdot \text{cm}^{-2}$ obtained for Na_2S_3 at 350°C . At the anode the current appears to be limited by accumulation of liquid sulfur. The value of the limiting current density in Na_2S_5 was $100 \text{ mA} \cdot \text{cm}^{-2}$ at 350°C . A reaction scheme which best fits our results is suggested.

Interest in the electrochemistry of sodium polysulfides has recently been stimulated by the development of the sodium/sulfur battery (1-3), in which the overall process at the cathode is the reduction of sulfur to sulfide ions. In order to gain a further understanding of the electrode processes we decided to study the behavior of a nonporous carbon electrode in three different polysulfide melts. Vitreous carbon was deemed a suitable material for this purpose.

Following a suggestion (4) that lithium polysulfides might exhibit electronic conductivity, we decided to investigate the electronic conductivity of sodium polysulfides. Although this work is not yet complete, preliminary results indicate that the electronic contribution to the conduction in these melts is very small, and in the interpretation of our results we have assumed electronic conductivity in these melts to be negligible.

The phase diagram for the system $\text{Na}_2\text{S}/\text{S}$ has been constructed by Pearson and Robinson (5) and revised by others (6, 7). At 350°C , if precipitation of solids is to be avoided, the sodium content of the melt must not exceed 40 atomic per cent (a/o) (Na_2S_3). Experience in our laboratory indicates that polarization of the sulfur electrode is most severe in the one-phase region (Na_2S_5 - Na_2S_3). We therefore decided to study three different compositions corresponding to melts in this region, viz., $\text{Na}_2\text{S}_{5.5}$ (two-phase, Na_2S_5 + sulfur), Na_2S_4 , and Na_2S_3 . Results in $\text{Na}_2\text{S}_{5.5}$ refer to the sulfide-rich phase (Na_2S_5).

Very little work has been reported on the electrochemistry of the alkali metal polysulfides, but recently, mass transfer effects in molten $\text{Na}_2\text{S}/\text{S}$ mixtures were investigated by Selis (8). He used voltammetric sweeps to distinguish between the electrode behavior in the two liquids present in the two-phase region. Results in the sulfide-rich phase indicated that the current maxi-

mum was associated with an irreversible oxidation process. At cathodic potentials a current maximum followed by a current surge was observed. In a recent paper by Bodewig and Plambeck (9) concerning the S^{2-}/S^0 electrode in molten LiCl-KCl , a voltammetric curve was shown for the reduction of S^0 to S^{2-} at a graphite electrode. Only one current surge was evident.

In this work we have used voltammetric sweeps, current interruption experiments, and chronopotentiometry in an attempt to determine the electrode reactions.

Experimental

Apparatus.—Voltammetry experiments were performed with a Wenking 61 RH Potentiostat coupled to a Wenking SMP 61 sweep unit (max rate $50 \text{ mV} \cdot \text{sec}^{-1}$). A few faster cyclic voltammetric sweeps were performed with the potentiostat coupled to a Hewlett-Packard 3310A function generator. Voltammetric curves were recorded on a Bryans 26000 Series XY plotter. Chronopotentiometric experiments were carried out with the aid of a 5A max constant current unit in conjunction with a mercury-wetted relay switch. Both pieces of equipment were built in the laboratory. Chronopotentiograms were recorded on the Bryans XY plotter set in the Y/t mode. Electrode potentials were measured with a Vibron electrometer backed-off with a Pye portable potentiometer. A Techne fluidized sand bath was used to maintain the temperature at 300° - 400°C . A molten salt bath would have allowed better temperature control, but was not used for safety reasons. Temperature control was by "Cal" proportional controller unit, which maintained the temperature to $\pm 3^\circ\text{C}$.

The experimental cell is shown diagrammatically in Fig. 1. The side arm containing a porous sinter was incorporated to enable melt to be filtered *in situ* into the electrochemical compartment. Ground-glass joints were greased with Apiezon T compound.

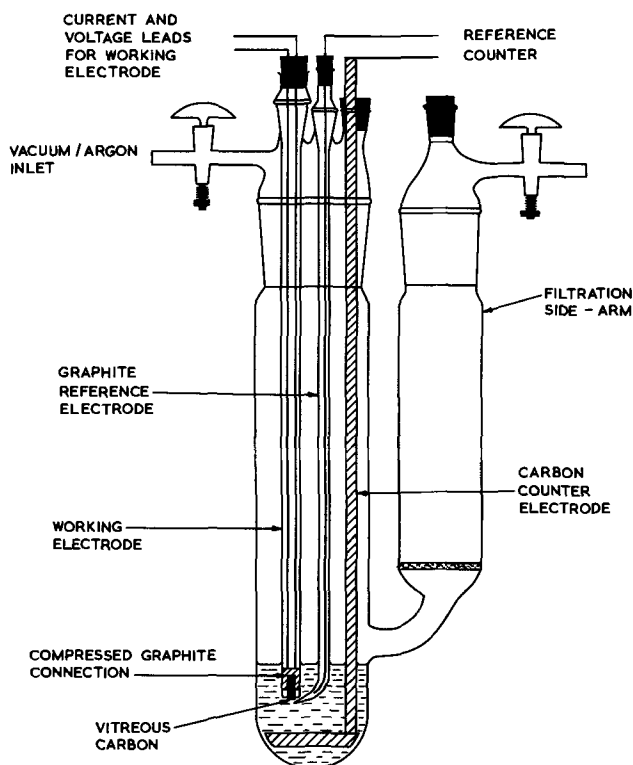


Fig. 1. Electrochemical cell assembly

Electrodes.—A conventional three-electrode assembly was used. The working electrode material, vitreous carbon, was supplied in the form of 0.32 cm diameter rod. A short length was sealed into a Pyrex tube and faced off to expose a disk of area 0.08 cm². The electrode was polished to 0.25 μ surface finish. The sealing of vitreous carbon rod into Pyrex was carried out by the Allen Clarke Research Centre, Towcester, following several unsuccessful attempts in our laboratory to obtain a leakproof seal. The counterelectrode consisted of a large carbon disk attached to a threaded carbon rod; both pieces were spectrographic grade porous carbon. Electrode potentials were measured using a carbon/sodium polysulfide reference electrode. This electrode, which consisted of a strip of flexible graphite sheet ("Grafoil," Union Carbide Corporation) immersed in a melt of the same composition as the bulk melt, was contained in a Luggin capillary. The potential of this carbon/polysulfide reference electrode which has been shown to be reversible (10), was consequently dependent upon the composition of the melt under investigation. All electrode potentials have therefore been corrected to the carbon/Na₂S₅/S electrode, using the potential/composition relationship for the cell Na/ β alumina/Na₂S_x/carbon (where $x = 3-5$), determined independently by Gupta and Tischer (7) and Davies (10).

Melt.—Sodium polysulfide (Na₂S₃) was prepared electrochemically in a specially designed sodium/sulfur cell. Special care was taken in handling the sodium trisulfide which was removed from the preparation cell in the molten state using a large argon-purged pipette. This was allowed to cool, transferred to a glove box and removed from the pipette by breaking the glass. A dry argon atmosphere was maintained at all times in the glove box, where the trisulfide was stored until required. Higher polysulfides were obtained from the trisulfide by mutually melting with the appropriate amount of sulfur.

Procedure.—The introduction of electrolyte into the filtration side arm of the cell was done in the glove box. The electrolyte was filtered into the cell through a porosity 4 sinter under an argon atmosphere.

On completion of the filtration, rest potentials of both counter and working electrodes were measured. The cell impedance was also determined using an a-c bridge (automatic Wayne Kerr B641). These measurements were repeated at intervals of 1-2 days as a check on the condition of the cell and electrodes. Experiments were continued on any one melt for a maximum of 10 days.

Voltammetric curves were obtained at different sweep rates at both positive and negative potentials. In each case the start of the sweep corresponded to the initial rest potential of the electrode which was 2-3 mV, wrt the graphite reference electrode described previously. After each run the electrode was allowed to attain its rest potential before proceeding with further measurements.

The interruption experiments were performed by holding the electrode at a given potential with the potentiostat for 1 min, opening the circuit with a high speed switch and simultaneously recording the subsequent behavior of the electrode potential with time on an oscilloscope (Hewlett Packard 141) or an XY recorder. The rise times of the switch and the oscilloscope were less than 1 μ sec.

The procedure for chronopotentiometric measurements was straightforward using the equipment already described. The same cell and electrode geometry were employed.

Results

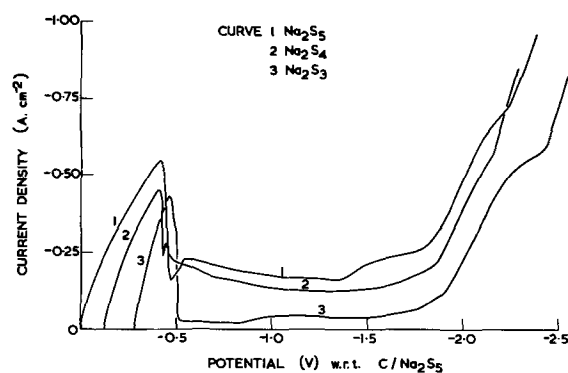
Voltammetry.—Cathodic voltammetric curves at 350°C are shown in Fig. 2. Salient features are a current maximum followed by a sharp drop in the current, a region of limiting current and a final current surge at about -1.7 to -1.8V. The height of the current peak was proportional to the square root of the sweep rate, in accordance with the equation for peak voltammetry (11).

$$i_p = Kn^{3/2} D^{1/2} C v^{1/2} \quad [1]$$

where i_p = peak current density; K = Randles-Sevcik constant, n = number of electrons transferred, D = diffusion coefficient, C = bulk concentration of reducible species, and v = potential sweep rate.

Values of the slope of the plot i_p vs. $v^{1/2}$ which was a good straight line, were 1.9 - 2.1 A \cdot V^{-1/2} \cdot cm⁻² \cdot sec^{1/2} and showed no significant variation with melt composition. Peak potentials were displaced in the cathodic direction with increasing sweep rates suggesting uncompensated IR effects due to the large currents obtained. In successive runs at lower sweep rates, a second, more complex peak appeared on the curves (Fig. 3). The height of this peak was virtually constant below sweep rates of 16 mV \cdot sec⁻¹.

Values of the limiting current were determined in each melt at sweep rates at which they became constant (less than 10 mV \cdot s⁻¹). Actual values at 350°C were 28 mA \cdot cm⁻² in Na₂S₃; 45 mA \cdot cm⁻² in Na₂S₄; and 100 mA \cdot cm⁻² in Na₂S₅. The temperature dependence of limiting current density in Na₂S₃ is shown in Fig. 4.

Fig. 2. Cathodic voltammetric curves for different melt compositions at 350°C. Sweep rate v , 50 mV \cdot sec⁻¹.

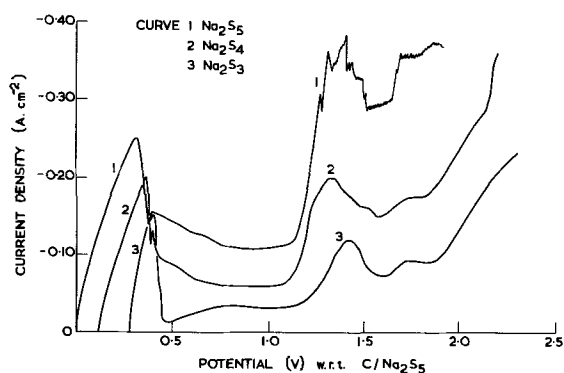


Fig. 3. Cathodic voltammograms for different melt compositions at 350°C showing the second current maxima. Sweep rate ν , 8.33 mV \cdot sec $^{-1}$.

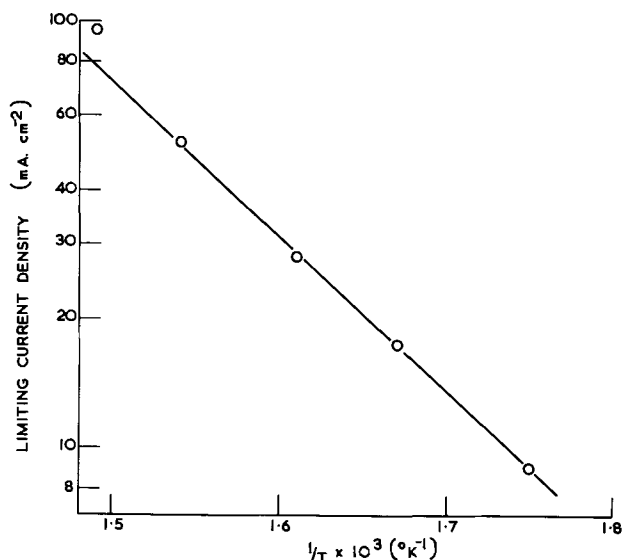


Fig. 4. Temperature dependence of the limiting current density for the composition Na₂S₃.

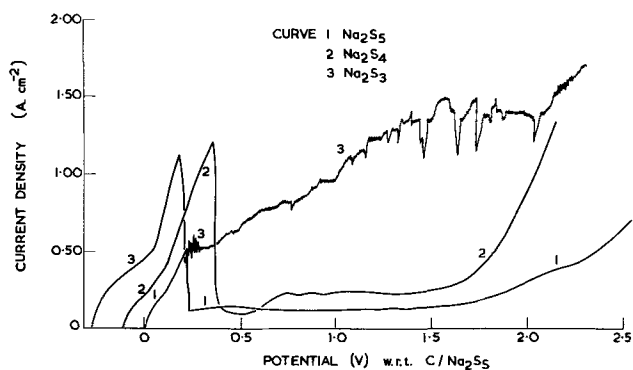


Fig. 5. Anodic voltammograms for different melt compositions at 350°C. Sweep rate ν , 50 mV \cdot sec $^{-1}$.

Results of anodic voltammograms are shown in Fig. 5. These curves were less reproducible than the corresponding cathodic ones. This was particularly so in the case of the Na₂S₃ melt composition. In this melt the curve rarely showed a current maximum. The current continued to increase up to a value corresponding to the maximum capability of the potentiostat. When a current peak was obtained in this melt as in Fig. 5, it was followed by a region of oscillating current. In the other two melt compositions the current maximum was followed by a limiting current region. The value of the limiting current in Na₂S₅ was about 100 mA \cdot cm $^{-2}$. Again the height of the current density peak was proportional to the square root of the sweep rate. In Na₂S₄ the value of the slope,

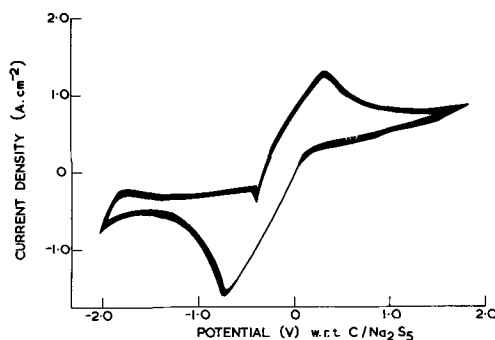


Fig. 6. Cyclic voltammogram for the composition Na₂S₄ at 350°C. Sweep rate ν , 0.4 V \cdot sec $^{-1}$.

5.5 A \cdot V $^{-1/2}$ \cdot cm $^{-2}$ \cdot sec $^{1/2}$, was more than twice the value obtained from the cathodic results. However, in Na₂S₅ the value of slope of 0.8 A \cdot V $^{-1/2}$ \cdot cm $^{-2}$ \cdot sec $^{1/2}$ was less than half the corresponding cathodic value.

An example of a cyclic voltammogram is shown in Fig. 6. Noteworthy features are the peak separation of a 1.04V, and the greater height of the cathodic current maximum. The peak separation is very much greater than the value expected at 350°C for a reversible couple (11).

In the single sweeps the anodic current maximum was higher than the cathodic one in this composition, yet this situation is reversed in the cyclic sweep.

Interruption experiments.—These experiments were conducted in two different melts and the results for Na₂S₃ are given in Table I. Results for Na₂S₅ showed a similar trend although values of R were generally lower. Anodic experiments were not conducted above 120 mV in Na₂S₃ as the current exceeded the maximum control capability of the potentiostat. An initial sharp drop, ΔE , in the potential was noted. This was ascribed to IR drop and found to occur in less than 1 μ sec. From the knowledge of I , the current flowing prior to switch off, a value for the electrode resistance, R , was obtained. Both sets of results showed an increase in the electrode resistance up to approximately -1.1V, thereafter the resistance showed a decreasing trend. Another significant feature was the sharp increase in the resistance at cathodic potentials which approximately correspond to the initial current density maxima on the voltammograms. Two stable potentials were evident on the cathodic decay curves, one at -340 mV and the other at about -1.9V.

Chronopotentiometry.—All measurements were made with a vitreous carbon disk electrode of geometric area 0.08 cm 2 . Figure 7 shows a chronopotentiogram for Na₂S₃ together with the potential decay curve

Table I. Results of interruption experiments in Na₂S₃ at 350°C
Geometric electrode area = 0.08 cm 2

Potentiostated potential (mV) wrt C/Na ₂ S ₃	Current, I (mA)	E (mV)	Resistance R (ohm)	Potential following interruption (mV) wrt C/Na ₂ S ₃
120	60	130	2.2	-10
20	30	70	2.3	-50
-80	5.8	12	2.1	-95
-180	3.0	16	2.0	-190
-330	1.9	4	2.1	-326
-380	3.8	8	2.1	-372
-430	2.5	86	34	-340
-480	2.4	140	58	-340
-680	2.4	230	96	-340
-880	2.4	430	180	Arrest at -450 -340
-1080	2.4	640	266	Arrest at -450 -340
-1280	5.6	940	168	Arrest at -450 -340
-1480	8.8	1140	130	-346
-1680	6.2	200	32	Arrest at -1480 & -450
-1880	3.3	40	12	-1840
-2280	8.8	350	40	-1930
-2680	220	770	3.5	-1910

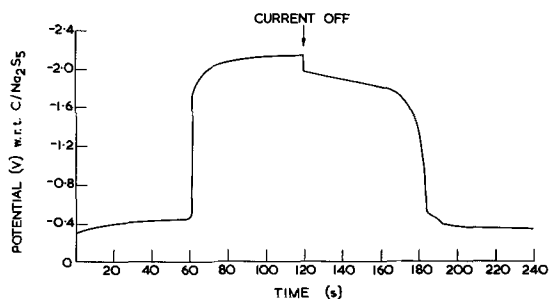


Fig. 7. Chronopotentiogram for the composition Na_2S_3 at 350°C , showing the potential decay pattern after switching off the current. Current density, $80 \text{ mA} \cdot \text{cm}^{-2}$.

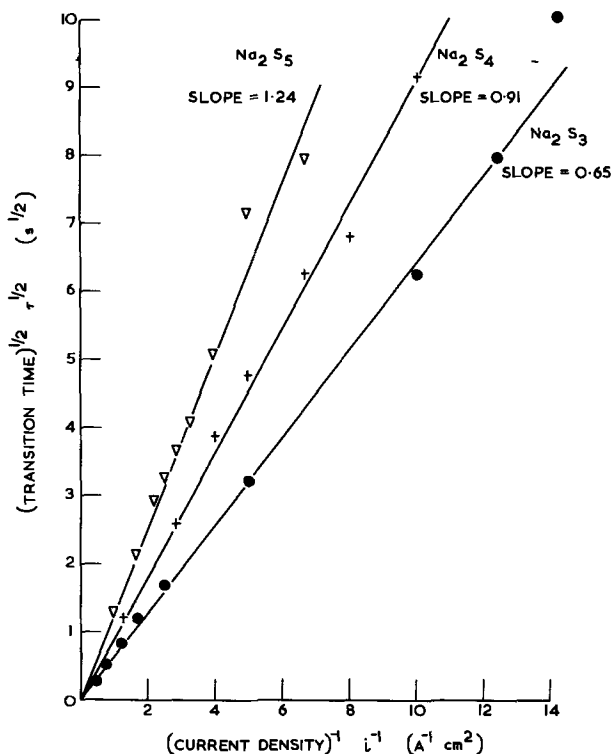


Fig. 8. Chronopotentiometric results. Dependence of $\tau^{1/2}$ on i^{-1} for different melt compositions at 350°C .

following the opening of the circuit. The chronopotentiograms obtained in Na_2S_4 and Na_2S_5 were similar.

For cathodically impressed currents the observed transition time, τ , is proportional to the reciprocal of the current density. Results are shown in Fig. 8 and suggest that the process is controlled by diffusion in accordance with the Sand equation

$$i\tau^{1/2} = \frac{1}{2}\pi^{1/2}nFCD^{1/2} \quad [2]$$

where symbols have their usual significance and i is the current density.

Anodic chronopotentiograms were only recorded for Na_2S_5 . The traces were again characterized by very sharp end points. The observed transition times, however, were not in accordance with the Sand equation since the plot of $\tau^{1/2}$ vs. i^{-1} was nonlinear.

Discussion

The linear dependence of both i_p and $\tau^{1/2}$ on $v^{1/2}$ and i^{-1} respectively suggests that the electroactive species are transported predominantly by a diffusion process. Simultaneous solution of the voltammetric and chronopotentiometric equations gave a value of K , the Randles-Sevcik constant, which was dependent on melt composition, viz., 1.95×10^{-5} in Na_2S_3 , 1.3×10^{-5} in Na_2S_4 , and 1.0×10^{-5} in Na_2S_5 . The theoretical value of the constant at 350°C for a reversible process

is 1.88×10^{-5} (13). Experimental values are therefore in fair agreement with the theoretical value particularly in the Na_2S_3 melt where the agreement is within 5%. This suggests that under these experimental conditions effects other than those due to diffusion can be neglected. This is somewhat surprising in view of the fact that no supporting electrolyte was used.

From the shape of the cathodic voltammetric curves it is evident that several processes are occurring at the electrode. Unfortunately, lack of experimental data on the species present in sodium polysulfide melts makes interpretation of our results rather difficult. Recently, however, some data (10) on the activity of sulfur in the melts have become available. Values obtained were 0.9 in Na_2S_5 , 0.2 in Na_2S_4 , and 0.04 in Na_2S_3 . In the light of these results we are inclined to ascribe the first current maximum in all melts to the reduction of a polysulfide ion rather than elemental sulfur. This step appears to be diffusion-controlled as indicated by the linear dependence of i_p on $v^{1/2}$. The chronopotentiometric results also confirm diffusion-control, and further imply that the diffusing species is not the same in all melts. Analysis of the current maxima over a range of sweep rates yields horizontal straight line plots of $i_E/v^{1/2}$ vs. $v^{1/2}$, (where i_E is the current density at a potential, E , less cathodic than E_p) suggesting a fast, reversible electron-transfer process. Further analysis of the current maxima indicates the occurrence of a following chemical reaction, thus the plot of $i_p/v^{1/2}$ vs. $v^{1/2}$ which should be a horizontal straight line for an uncomplicated electron-transfer step shows a positive deviation from linearity at low sweep rates in accordance with the diagnostic criteria for a chemical reaction following the initial electrochemical step (12). This is found in Na_2S_5 and Na_2S_4 melts but not in Na_2S_3 as seen in Fig. 9. We therefore conclude that this chemical step involves elemental sulfur.

The sharp drop in the current following the initial maximum could be associated with the formation of a film of Na_2S_2 . The fact that this sharp drop is observed even at very low sweep rates ($0.6 \text{ mV} \cdot \text{min}^{-1}$) tends to support the formation of a film. The sharpness of the transitions in the chronopotentiograms are also indicative of film formation. The reduction of a higher polysulfide ion could give rise to S_2^{2-} ions which would precipitate in accordance with the phase diagram. Other S_2^{2-} ions could diffuse away into the bulk melt and recombine with sulfur to form the original polysulfide ion. This step would constitute the chemical step observed in Na_2S_5 and Na_2S_4 melts. The fact that the following chemical reaction is faster in Na_2S_5 (see Fig. 9) which is the melt having the highest sulfur activity lends support to the above explanation.

In Na_2S_5 and Na_2S_4 there is evidence of a small current peak immediately following the initial peak (Fig. 2 and 3). This could be associated with the re-

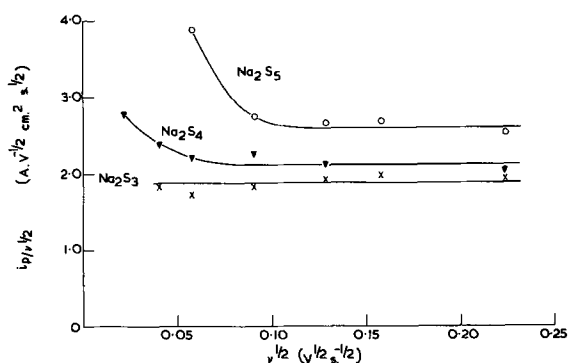


Fig. 9. Dependence of the voltammetric function $i_p/v^{1/2}$ on $v^{1/2}$ for cathodic sweeps in different melt compositions at 350°C showing the effect of a following chemical reaction at lower sweep rates [Ref. (12)].

duction of either elemental sulfur or a different polysulfide ion.

In the region of limiting current, the resistance ascribed to the film of Na_2S_2 continues to increase to a maximum at about -1.1V . In Na_2S_3 , where the activity of sulfur is very low, we might expect a more stable film since the rate of reaction of the film with sulfur to form higher polysulfides will be much slower. This is in fact the case, as indicated by the high values of electrode resistance obtained in this melt.

The second current maximum, which is observed at about -1.3V , we believe to be associated with the reduction of the Na_2S_2 film to Na_2S . At this potential, however, the value of the electrode resistance began to decrease (Table I). This may be interpreted as the faster rate of dissolution of Na_2S than Na_2S_2 in the bulk melt. Alternatively, the film of Na_2S may assume some degree of electronic conductivity although there does not appear to be any independent evidence for this.

We believe the final current surge to be associated with the production of metallic sodium. This is contrary to the suggestion put forward by Selis that this surge is due to the formation of sulfide ions. Our opinion is substantiated by the agreement between the corresponding potential, about -1.8V , and the free energy of formation of sodium polysulfides (7). Maintaining the electrode at potentials more cathodic than -1.9V resulted in a potential of about -1.9V persisting for several minutes after the current had been switched off. The existence of metallic sodium at the electrode in such a reactive medium could be explained by a thin sodium ion conducting film of Na_2S protecting the metal from the melt.

The shape of the anodic current maximum suggests the occurrence of two different electrochemical steps. The first process could be the oxidation of a lower polysulfide ion to form a higher species. As the potential is increased the higher polysulfide is then itself oxidized, and the current increases until the point is reached when the electrode becomes covered by a film of liquid sulfur. The current therefore drops sharply and is subsequently limited by this film. This situation would be accentuated in melts containing sulfur at a higher activity, which was found to be the case. Conversely, the electrochemically produced sulfur could react quite rapidly with Na_2S_3 and this would explain the rarity of a limiting current in this melt.

The final current surge at around 1.8V on the voltammetric curves is difficult to explain. One explanation could be interference by the products of a cath-

odic process at the counterelectrode, although the high current reached renders this view somewhat doubtful.

Conclusions

At the carbon cathode the first step in the reduction of sodium polysulfide appears to be the reversible formation of a lower polysulfide species. In Na_2S_4 and Na_2S_5 melts this is followed by a chemical reaction involving sulfur. Available evidence suggests that the current becomes limited by the formation of sodium sulfide films at the electrode. At higher potentials, -1.7 to -1.8V , metallic sodium is formed.

At the anode the current is limited by the formation of a film of liquid sulfur and this limitation is greatest in the Na_2S_5 melt.

Acknowledgments

The authors express thanks to the British Railways Board for permission to publish this paper and acknowledge the helpful discussions with Dr. B. Cleaver of Southampton University.

Manuscript submitted Oct. 7, 1971; revised manuscript received ca. Dec. 21, 1971.

Any discussion of this paper will appear in a Discussion Section to be published in the December 1972 JOURNAL.

REFERENCES

1. J. K. Kummer and N. A. Weber, Society of Automotive Engineers, Automotive Engineering Congress, Detroit, Mich., January (1967).
2. L. J. Miles and I. Wynn Jones, "Proceedings of the 6th International Power Sources Symposium Brighton 1970."
3. J. L. Sudworth and M. D. Hames, "Proceedings of the 6th Power Sources Symposium, Brighton, 1970."
4. E. J. Cairns, Private communication (1970).
5. T. G. Pearson and P. L. Robinson, *J. Chem. Soc.*, **132**, 1473 (1930).
6. M. D. Hames, Thesis, University of Southampton (1970).
7. N. K. Gupta and R. P. Tischer, Abs. 344, p. 769, Electrochem. Soc. Extended Abstracts, Spring Meeting, Los Angeles, May 10-15, 1970.
8. S. M. Selis, *Electrochim. Acta*, **15**, 1285 (1970).
9. F. G. Bodewig and J. A. Plambeck, *This Journal*, **116**, 607 (1969).
10. A. Davies, Private communication.
11. R. N. Adams, "Electrochemistry at Solid Electrodes," Chap. 5, Marcel Dekker, Inc., New York (1969).
12. R. S. Nicholson and I. Shain, *Anal. Chem.*, **36**, 706 (1964).
13. P. Delahay, "New Instrumental Methods in Electrochemistry," p. 119, Interscience, New York (1954).

The Electrochemical Activity of Dispersed Platinum

K. F. Blurton,* P. Greenberg, H. G. Oswin,* and D. R. Rutt

Energetics Science Inc., New York, New York 10470

ABSTRACT

A highly dispersed platinum catalyst (platinum crystallite size less than 15Å) on a conductive carbon support was prepared. These doped carbons were made into Teflon-bonded fuel cell electrodes and the platinum surface area and the dispersed platinum specific activity (i.e., the activity per unit area of platinum) for oxygen electroreduction in acid electrolyte was determined. The specific activity of the dispersed platinum was found to be approximately twenty times less than that of crystalline platinum black. The lower activity of this catalyst compared with that of platinum black may be due either to the difference in the platinum crystallite sizes, or to the influence of the support on the platinum activity, or to a combination of both these factors.

To build low cost acid electrolyte fuel cells with platinum as the cathode catalyst, it is desirable to utilize Pt with the maximum activity and one method of achieving this is to use Pt with the maximum surface area. High degrees of dispersion of Pt (defined as the ratio of surface metal atoms to total number of atoms) have been prepared by supporting the platinum on a porous, conducting substrate. However a basic question which must be answered before using these supported Pt catalysts is whether the support and/or Pt crystallite size affects the platinum specific activity (i.e., the activity per unit area of Pt).

Many dispersed metal catalysts supported on non-metallic substrates have been prepared (1, 2) and in some cases the ultimate goal of an atomic dispersion of the metal has been claimed (3, 4). These dispersed metal catalysts have been used in many studies with gas reactants. The reactions have been divided into two classes: structure insensitive or facile reactions and structure sensitive or demanding reactions. Examples of the former are the dehydrogenation of cyclohexane (5), the hydrogenation of ethylene (6), and the hydrogenation of cyclopropane (7). Examples of demanding (1) reactions are propane cracking (8), the hydrogenation of benzene (9), ethane hydrogenolysis (10), and the isomerization of neopentane (11).

To relate the specific activity of metals and supported metals to the metal crystallite size, the catalyst activity free of mass transfer limitations and the catalyst area must be measured. Zeliger (12) showed that the specific activity of Pt supported on asbestos for the electroreduction of oxygen was constant for Pt crystallites in the range of 50-100Å. Bett *et al.* (13) extended this observation and showed that the specific activity of unsupported Pt for the same reaction was independent of the Pt crystallite size in the range of 100-400Å. Thus it would appear that this reaction was facile. However these observations may not be applicable to smaller Pt crystallites since the influence of the crystallite size on the specific activity of a metal is expected (1) to be much more significant for crystallites smaller than 40Å.

In the present paper we describe the preparation of a highly dispersed platinum catalyst (platinum crystallite size less than 15Å) on a conductive carbon support and the specific activity of this dispersed Pt for oxygen electroreduction. Polarization curves for oxygen reduction on Teflon-bonded diffusion electrodes prepared from these catalysts were determined in oxygen-saturated 20% H₂SO₄ solution at 70°C and the Pt area of the catalyst was measured by the electrochemical oxidation of adsorbed hydrogen and of adsorbed carbon monoxide. We have shown that the specific activity of this highly dispersed Pt for the

electroreduction of oxygen is approximately twenty times less than that of crystalline Pt black.

High dispersions of Pt on nonconducting supports have been prepared either by localizing metal ions at specific sites by ion exchange prior to reduction with hydrogen (4, 14) or by using a low Pt concentration [less than 1 weight per cent (w/o)] (3, 6). The limitation of the latter method is that, at these low Pt concentrations, the minimum Pt crystallite size which can be detected by x-ray diffraction is approximately 50Å (15). Thus we prepared the highly dispersed platinum catalysts on a conducting substrate by localizing the platinum ions through exchange with ions in a commercial ion exchange resin and subsequently reducing the metal ions by resin pyrolysis in an inert atmosphere. Thus the initial stage fixes the platinum ions at specific sites while in the second stage a conducting substrate is produced and the metal ions are reduced. We have termed this material a Pt-doped carbon in order to differentiate it from the material prepared by the reduction of chloroplatinic acid adsorbed on a preformed carbon.

Experimental

Preparation of the highly dispersed platinum.—The procedure used to prepare the highly dispersed platinum was similar to that used by Pohl (16) and by Pohl and Rosen (17) in the preparation of metal-doped, semiconductor, polymer carbons.

Cation exchange resins were received in the free acid form and they were converted into the calcium form with calcium hydroxide solution. The platinum solution consisted of 3 g/liter of diamminoplatinum (II) dinitrite dissolved in a calcium hydroxide solution of pH 9. Fifty milliliters of the calcium form of the resin [measured in Ca(OH)₂ solution] was stirred in 500 ml of the hot platinum solution for 3 hr. The resin was doped with platinum ions in this way to ensure uniform distribution of the ions throughout the resin. The resin was decanted from the platinum solution, washed with water, dried at 110°C for 24 hr and then at 200°C for 24 hr. It was then pyrolyzed in an inert atmosphere at a temperature in the range 700°-900°C for 24 hr. The pyrolyzed material was washed thoroughly with dilute nitric acid and then water to remove the calcium salt and finally dried at 110°C in a vacuum oven.

Highly dispersed platinum was formed in the platinum-doped carbon only with weak acid cationic resins which were neutralized with calcium hydroxide solution (18). The two commercial weak acid cation exchange resins used in this work were: Amberlite IRC 50 (Rohm & Haas Company) which is based on methacrylic acid and has a particle size of 16-50 mesh and Amberlite CG50 (Rohm & Haas Company) which has a similar structure but a particle size of 200-400 mesh.

The noncombustible gases are listed in Table I and the pyrolysis time was 24 hr for all samples.

* Electrochemical Society Active Member.

Key words: catalytic activity, dispersed platinum, oxygen cathodes, fuel cells.

Table I. The preparation conditions of Pt-doped carbons containing highly dispersed Pt^a

Sample No.	Pyrolysis temperature	Furnace atmosphere	Weight ^b % Pt
1	700	N ₂	6.1
2 ^c	700	N ₂	6.1
3	700	N ₂	6.2
4	700	N ₂	7.3
5	700	N ₂	7.8
6	700	N ₂	12.2
7	700	10% CO, 90% N ₂	8.1
8	700	50% CO, 50% N ₂	9.7
9	700	10% C ₂ H ₄ , 90% N ₂	8.0
10	800	N ₂	8.4

^a These samples contained no detectable Pt crystallites.

^b The ratio of the weight of Pt to the total weight of Pt and carbon.

^c Sample 2 was prepared from Amberlite CG50 resin, the remainder were prepared from Amberlite IRC50 resin.

Characterization of the highly dispersed platinum.—The particle sizes of the Pt-doped carbons were in the range 0.4–12 μ and it was possible to prepare Teflon-bonded diffusion electrodes from all these catalysts. Clearly it was essential to prepare reproducible electrodes and this was achieved by using the same procedure as that of Vogel and Lundquist (19). As a check on the electrode preparation technique, electrodes were also prepared from commercial Pt black (Engelhard Industries) and 5% Pt supported on graphite. The latter catalyst was prepared by the reduction of chloroplatinic acid adsorbed on graphite.

The polarization curves for oxygen reduction were determined galvanostatically in oxygen saturated 20% H₂SO₄ solution at 70°C using the floating electrode technique (20). The cell was a 500 ml round-bottom flask, and its temperature was maintained by placing in a heating mantle. The electrodes were inserted through ground glass joints in the flask. The working electrode was supported in a gold foil spring, and it was floated on the surface of the electrolyte. Current collection from the gold foil to the external circuit was made via a platinum wire. The counterelectrode was a platinum gauze on which platinum was electrodeposited. The reference electrode was a reversible hydrogen electrode which was placed in a Luggin capillary and immersed in the test electrolyte. The IR drop between the floating electrode and the tip of the Luggin capillary was determined using an interrupter technique. All potentials given in this paper refer to the reversible hydrogen electrode in the same electrolyte and are corrected for IR drop.

The available Pt area of the electrodes was measured by determining the charge due to the oxidation of adsorbed H₂ and of adsorbed CO in N₂ purged 1M H₂SO₄ solution at 30°C using the periodic triangular voltage sweep technique. These sweeps were made using an Electroscan 30 (Beckman Instrument Company).

The platinum concentrations in the doped carbons were determined by measuring the weight loss after heating in a muffle furnace at 900°C. These concentrations were checked in selected doped carbons by dissolving the platinum in aqua regia and measuring the absorbance of the stannous chloride complex (21). The size of the platinum crystallites in the Pt-doped carbons was determined from the broadening of the x-ray diffraction line from the (111) plane using a Norelco diffractometer.

Results

Preparation of highly dispersed platinum catalysts.—The minimum Pt crystallite size which can be detected depends on the Pt concentration (15). Preliminary experiments showed that 15Å or bigger Pt crystallites were detected by x-ray diffraction providing the Pt concentration was greater than 5 w/o. Thus the samples with greater than 5 w/o Pt in which Pt could not be detected by x-ray diffraction contained highly dispersed platinum. It is not known whether the Pt was monatomically dispersed or whether it existed as

small crystallites but the average crystallite size was less than 15Å.

Table I lists the preparation conditions of platinum-doped carbons containing highly dispersed Pt (samples 1–10). All these samples had greater than 5 w/o Pt and Pt crystallites could not be detected by x-ray diffraction. The concentration of the highly dispersed Pt in the doped carbon could not be increased above 12.2 w/o (18) (Table I.)

In the preparation of the highly dispersed platinum it was important to ensure that all the platinum ions were ion exchanged and that no platinum salt was precipitated in the resin pores. This was achieved by doping the resin in a hot platinum solution. When the resin doping solution was at room temperature, platinum crystallites were detected in the doped carbons after pyrolysis and it was presumed that these crystallites were formed by platinum salt precipitated in the resin pores. Highly dispersed Pt was formed when either of the resins was used as the starting material and when any of the gases was used as the furnace atmosphere.

To compare the electrochemical activity of crystalline and subcrystalline platinum, three platinum-doped carbons were prepared containing platinum crystallites. These platinum crystallites were formed in the doped carbons either by precipitating platinum salt in the resin pores and pyrolyzing at 700°C (samples 12 and 13), or by doping the resin in a hot platinum solution and pyrolyzing at 900°C (Table II).

The specific resistance of several Pt-doped carbons was measured (18). The values of the materials prepared by resin pyrolysis at 700°C were approximately 0.01 ohm-cm and this is in agreement with the values determined by Pohl (16). This resistance was sufficiently low for there to be no ohmic drop in the electrode at the low experimental current densities.

Platinum surface areas.—The platinum surface areas of the doped carbons were measured by determining the charge associated with the electrochemical oxidation of adsorbed hydrogen and of adsorbed carbon monoxide. This was carried out by measuring the current/potential curve during the application of a periodic triangular potential sweep to the electrode in nitrogen-purged 1M H₂SO₄ solution at 30°C at a sweep rate of 10 mV/sec. This sweep rate was chosen since faster rates gave ill-defined oxidation peaks in the current/potential curves.

In agreement with the work of Giner *et al.* (22) we found that it was not possible to obtain reproducible values for the charge associated with the oxidation of adsorbed hydrogen (Q_H) with a floating electrode due to hydrogen evolution at potentials cathodic to approximately 0.3V. Also it was not possible to determine the charge due to the reduction of chemisorbed oxygen (Q_{PtO}) by galvanostatic stripping since there was no arrest in the potential/time curve due to chemisorbed oxygen reduction. Thus Q_H was determined on a submerged electrode.

Figures 1, 2, and 3 show the current/potential curves determined on the application of a potential sweep in the range 0.05–1.45V to electrodes prepared from sample 5, Pt black and Pt supported on graphite, respectively. Similar current/potential curves to Fig. 1 were observed with all the electrodes prepared from the Pt-

Table II. Preparation of platinum-doped carbons containing Pt crystallites

Ion exchange resin: Amberlite IRC50; pyrolysis atmosphere: N₂

Sample No.	Pyrolysis temperature (°C)	Weight % Pt	Pt crystallite diameter (Å) (from x-ray diffraction data)
11	900	9.4	55
12	700 ^a	11.0	40
13	700 ^a	6.7	25

^a The Pt crystallites were formed by precipitating the Pt salt in the resin pores prior to pyrolysis.

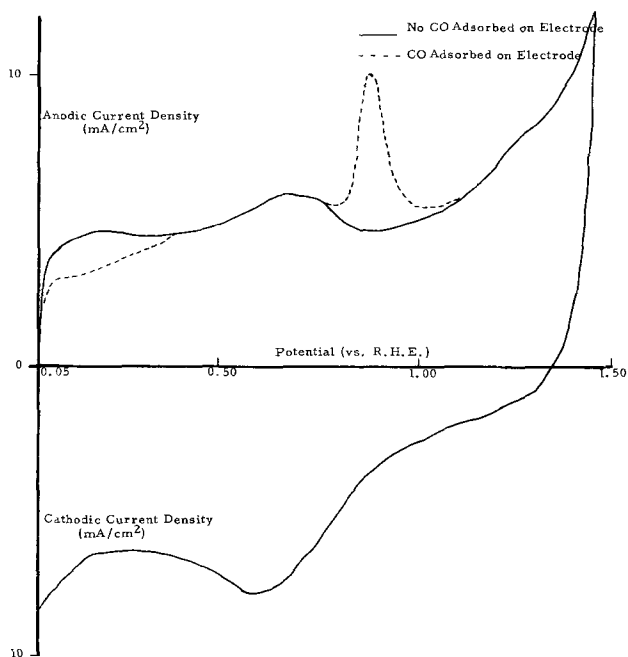


Fig. 1. Potential sweeps on electrodes prepared from sample 5. Pt loading 0.6 mg/cm^2 , $1\text{M H}_2\text{SO}_4$ solution at 30°C .

doped carbons containing dispersed Pt (samples 1-10) and with those containing crystalline Pt (samples 11-13).

The current/potential curves obtained with Pt black (Fig. 2) and Pt/graphite (Fig. 3) electrodes are the same as those obtained with Pt foil electrodes (23). The unusual characteristics of the current/potential curves with Pt-doped carbon (Fig. 1) were: (i) it had a large capacity current in the potential range of 0.05-0.40V which interfered with the measurement of Q_H on Pt, (ii) it had no peak due to the reduction of chemisorbed oxygen, and (iii) it had an anodic peak at 0.71V and a cathodic peak at 0.68V.

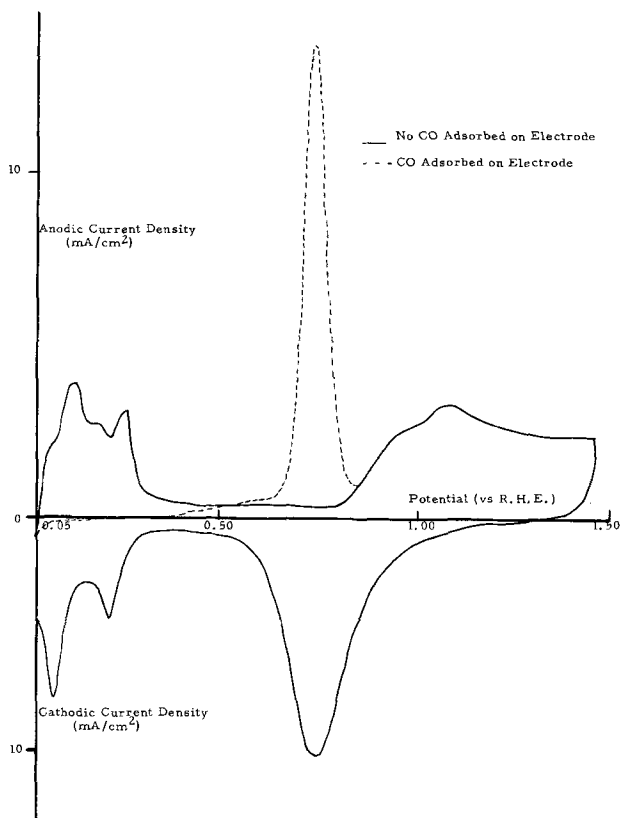


Fig. 2. Potential sweeps on Pt black electrodes. Pt loading 9.2 mg/cm^2 , $1\text{M H}_2\text{SO}_4$ solution at 30°C .

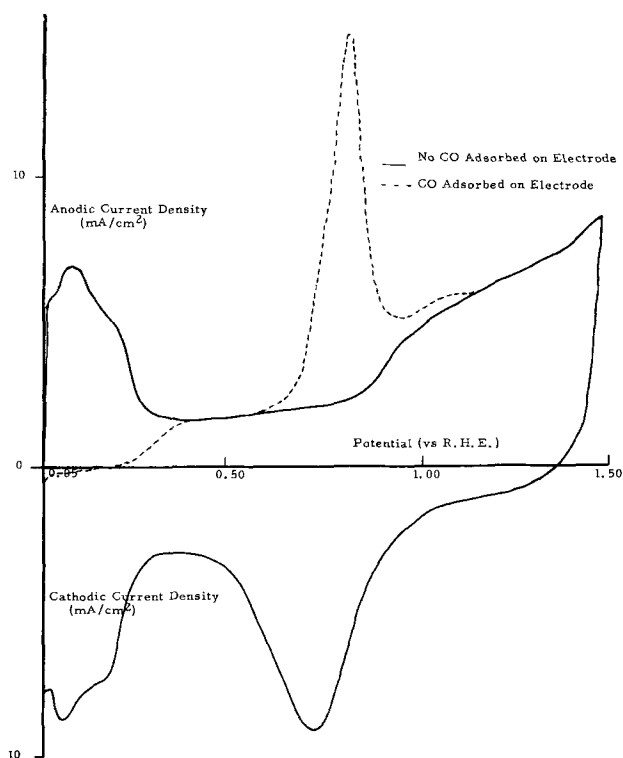


Fig. 3. Potential sweeps on 5% Pt/graphite electrode. Pt loading 0.7 mg/cm^2 , $1\text{M H}_2\text{SO}_4$ solution at 30°C .

Since Q_H could not be determined on the Pt-doped carbon electrodes from the potential sweeps in nitrogen-purged electrolyte, it was determined by comparing the potential sweeps with and without carbon monoxide adsorbed on the electrode surface. The same measurements were also made with the Pt black and the Pt/graphite electrodes.

Figures 1, 2, and 3 show the current/potential curves determined by the application of a potential sweep with (dashed line) and without (solid line) carbon monoxide adsorbed on electrodes prepared from sample 5 (Fig. 1), Pt black (Fig. 2), and Pt supported on graphite (Fig. 3), respectively, in N_2 -purged $1\text{M H}_2\text{SO}_4$ at 30°C . These measurements were made by first performing the potential sweep on the electrode in nitrogen-purged electrolyte (solid lines, Fig. 1-3). The electrolyte was then purged with CO for 1 min while the electrode was on open circuit (approximately 0.20V) and then with N_2 for 5 min to remove dissolved CO. The cyclic voltammetric sweep on the electrode was then repeated in the N_2 -purged electrolyte (dashed) lines (Fig. 1-3). The difference in the shape of the two curves in the potential region 0.05-0.45V is due to the adsorption of CO on the electrode and in the potential region 0.60-0.80V it is due to the oxidation of CO. Preliminary experiments indicated that a 5 min N_2 purge was sufficient to remove all the dissolved CO from the electrolyte with minimal desorption of carbon monoxide from the electrode surface.

Figure 4 shows the potential sweeps in nitrogen-purged electrolyte on an electrode prepared from a carbon. This carbon was prepared by the pyrolysis at 700°C of the calcium form of Amberlite IRC50 ion exchange resin but similar current/potential curves were also observed with graphite electrodes. There is no peak due to the oxidation of adsorbed hydrogen or of adsorbed carbon monoxide on carbon (Fig. 4) and hence the values of Q_H and Q_{CO} calculated from Fig. 1 and 3 are due solely to reactions occurring on Pt. Also Fig. 4 indicates that the anodic and cathodic peaks at 0.71 and 0.68V, respectively, Fig. 1, are due to the oxidation and reduction of surface groups on the carbon.

Pt-doped carbons prepared by resin pyrolysis at 500° and 600°C also contained highly dispersed Pt (18).

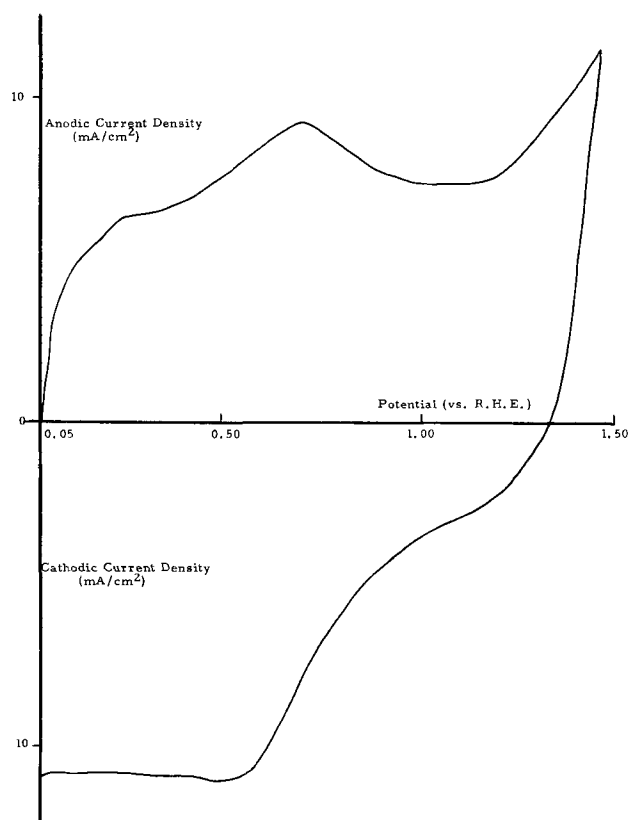


Fig. 4. Potential sweep on carbon electrode 1M H_2SO_4 solution at 30°C.

However no well-defined peaks in the current/potential curves were obtained with these materials and no further studies were made with them since it was not possible to measure their Pt areas.

For the Pt-doped carbons (samples 1-13), the ratio of Q_{CO} to Q_H was in the range 1.5-2.0 to 1. The slightly low value of Q_{CO} is probably caused by CO desorption during the N_2 purge. The values of Q_H and Q_{CO} of selected Pt-doped carbons were measured in 20% H_2SO_4 solution at 70°C as well as in 1M H_2SO_4 solution at 30°C and the same values were obtained in each of two electrolytes. With Pt black and Pt supported on graphite, the ratio of $Q_H:Q_{PtO}:Q_{CO}$ was 1:2:2 within $\pm 10\%$. Thus the oxidation of CO was a 2 electron process on dispersed and on crystalline Pt.

The values of the Pt areas (expressed as m^2/g) of the Pt-doped carbons (samples 1-13), Pt black, and Pt supported on graphite are given in Table III. They were calculated from the experimental values of Q_H and the Pt loading on the electrode by assuming that the average density of Pt atoms is 1.12×10^{15} atoms/ cm^2 (3). The values of the Pt area reported in Table III are average values obtained with 3 electrodes and the Pt area of these electrodes agreed within $\pm 10\%$. The area of the Pt black (Table III) agreed with other data with Engelhard Pt black (19).

The Pt areas calculated from the CO oxidation data are not included in Table III. However these values were the same as those calculated from Q_H since the ratio of $Q_H:Q_{CO}$ was 1:2.

The calculated areas of a monatomic Pt dispersion and of a 14Å Pt crystallite are (3) 276 m^2/g and 167 m^2/g , respectively. The experimental values of the areas of highly dispersed platinum (samples 1-10) are less than the calculated values for a 14Å crystal indicating that a significant fraction of the platinum is buried inside the carbon during the resin pyrolysis and is therefore not wetted by the electrolyte.

Thus the x-ray diffraction measurements (Table I) show that there are no platinum crystallites in samples 1 through 10 greater than 14Å and the surface area data (Table III) indicates the Pt available for

Table III. Values of the available Pt surface areas of the activity of Pt of Pt-doped carbons, Pt black, and Pt supported on graphite

Sample No.	Pt surface area (m^2/g of Pt) (from H_2 oxidation data)	Activity of Pt	
		mA at 0.9V/mg of Pt ^a	mA at 0.9V/mC H_2 oxidation ^{b,c}
1	132	1.5	0.007
2	54	0.7	0.007
3	108	0.9	0.007
4	58	0.6	0.005
5	102	1.6	0.008
6	143	1.0	0.004
7	84	0.3	0.002
8	22	0.1	0.002
9	69	0.3	0.002
10	84	0.4	0.003
11	39	1.3	0.030
12	49	3.0	0.041
13	84	9.1	0.063
Pt black	24	2.5	0.071
5% Pt/graphite	50	6.3	0.101

^a The current was calculated by extrapolating the Tafel plot to 0.9V.

^b This is the specific activity (i.e., the activity per unit area) of the Pt.

^c The average value of the specific activity of highly dispersed Pt catalysts (samples 1-10) was 0.004.

the electrochemical reaction. The "burying" of Pt makes it impossible to calculate the actual degree of dispersion of Pt.

The relatively low platinum area of sample 8 (Table III) indicates that a particularly large fraction of platinum was buried during resin pyrolysis in the N_2/CO (50% CO) furnace atmosphere. This is substantiated by the fact that calcium was detected in this sample by x-ray diffraction and it was not possible to wash it out. Hence it appears that the furnace atmosphere does influence the pyrolysis reaction but it does not measurably affect the size of the platinum crystallites (18).

Activity of highly dispersed platinum.—Figure 5 shows the steady-state polarization curves for oxygen

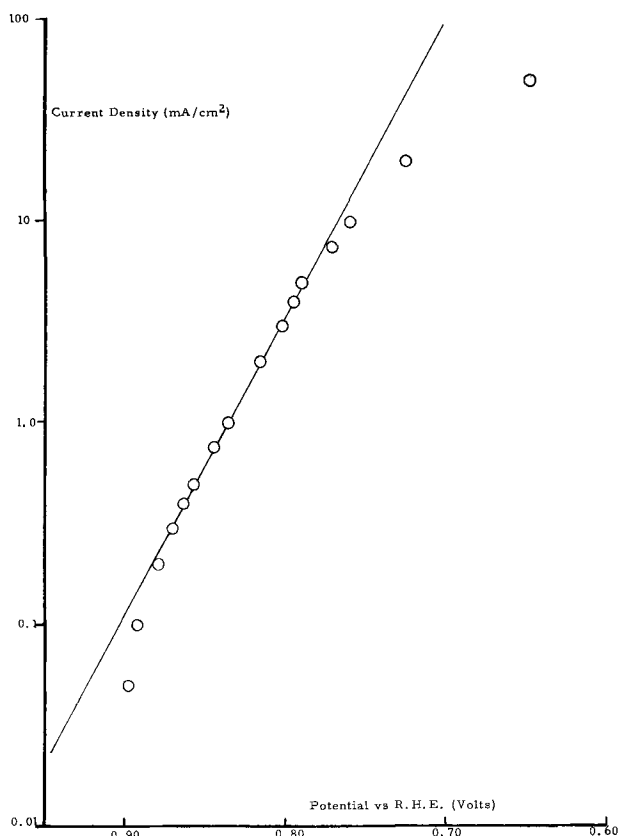


Fig. 5. Cathode performance on oxygen. Sample 4, Pt loading 0.2 mg/cm^2 , 20% H_2SO_4 at 70°C.

reduction in oxygen-saturated 20% H₂SO₄ solution at 70°C on an electrode prepared from sample 4. The data obtained with the other electrodes followed the same general pattern and the slopes of the semi-logarithmic plots were equal to 70 ± 5 mV. These plots were linear over $1\frac{1}{2}$ decades of current for electrodes prepared from the platinum-doped carbons (samples 1-13) and from Pt supported on graphite and over 3 decades of current for those prepared from Pt black. Since these plots are linear over a large current density range, it is possible to obtain the activation polarization for oxygen reduction on the electrodes.

In the potential range of the oxygen reduction measurements (i.e., 0.9-0.6V), there was no significant current (approximately $1 \mu\text{A}/\text{cm}^2$) due to oxygen reduction on carbon and on the Au electrode holder and there was no current due to carbon corrosion in N₂-saturated 20% H₂SO₄ solution at 70°C. Thus the experimental polarization curves represent oxygen reduction on Pt.

The activity of Pt in Table III is expressed in two ways: (i) the ratio of the current at 0.9V to the weight of Pt on the electrode (mA at 0.9 V/mg of Pt) and (ii) the ratio of the current at 0.9V to mC for H₂ oxidation. The value of the current at 0.9V was obtained by extrapolating the semilogarithmic plot to 0.9V and hence these values of the Pt activity are free of mass transfer effects.

The first method of expressing the Pt activity (mA at 0.9 V/mg of Pt) is of practical importance since it allows the calculation of the activation polarization per unit weight of Pt. The second method (mA at 0.9 V/mC for H₂ oxidation) is used in the theoretical discussion since it is a measure of the specific activity (i.e., the activity per unit Pt area) of Pt for oxygen reduction.

The average value of the specific activity of the highly dispersed Pt was 0.004 and it was apparently independent of its preparation conditions (furnace atmosphere and ion exchange resin particle size). The values of the specific activity of Pt black and of Pt supported on graphite were in excellent agreement with the value calculated from other Pt black data (19).

It can be seen from Table III that the specific activity of highly dispersed Pt is significantly lower than that of Pt-doped carbons containing crystallites, Pt black, and Pt supported on graphite. This low value was not due to an experimental artifact. Thus the high activity of Pt-doped carbons containing crystallites demonstrated that the low activity of dispersed Pt was not due to catalyst inhibition during resin pyrolysis, large carbon corrosion currents in oxygen-saturated electrolyte, and high ohmic losses between the catalyst and current collector; and the high activity of samples 11-13, Pt black and Pt supported on graphite demonstrated that it was not caused by inadequate electrode structures.

Discussion

The x-ray diffraction data indicate that a highly dispersed Pt catalyst was prepared. It was not possible from the Pt surface area data to determine whether a monatomic dispersion of Pt was prepared but the average Pt crystallite size in the samples was less than 15Å.

It was shown (24), from measurements of the rate of hydrogen chemisorption on platinized carbon from the gas phase, that hydrogen was initially adsorbed on the metal and it then migrated over the carbon surface. This process was termed hydrogen spillover (1), and it has resulted (1, 4, 24, 25) in anomalously high Pt areas for platinum supported on carbon, zeolites, and tungsten oxide.

Carbon monoxide spillover onto a support has not been reported in the literature. Thus hydrogen spillover onto the support did not occur in the present work since the ratio of $Q_{\text{H}}:Q_{\text{CO}}$ was 1:2. Hence the Pt areas (Table III) are not anomalously high and the specific activities of Pt (Table III) are correct values.

Table IV. Elemental analysis of Pt-doped carbons

Sample No.	Atomic per cent			
	C	H	O	Pt
4	77.4	13.9	8.4	0.4
6	65.0	22.1	12.0	0.9
7	73.0	20.5	5.8	0.5
9	77.3	15.5	6.7	0.5

The specific activity of the highly dispersed Pt for O₂ electroreduction in acid electrolyte was considerably lower than that of crystalline Pt (Table III). The specific activity of Pt foil has not been measured. However the current/potential curve in the Tafel region is the same in concentrated phosphoric and sulfuric acid solutions (19) and thus using data in H₃PO₄ (26) solution and assuming 0.21 mC/cm² for H₂ oxidation, the specific activity of Pt foil at 76°C is 0.02. This value is significantly lower than those of Pt black and Pt supported on graphite but greater than that of dispersed Pt.

The lower activity of the dispersed Pt catalysts may be due either to the difference in the Pt crystallite sizes, or to the influence of the support on the Pt activity, or to a combination of both these factors. It is not possible from the present data to determine which has the major influence.

The influence of Pt crystallite size on the activity of Pt arises since the coordination number of the surface atoms depends on the crystallite size. For example, Poltorak and Boronin (27) have shown that in a 14Å crystal only 33% of the surface atoms have the coordination number of atoms in an infinite, ideal face, whereas in a 50Å crystal 85% of the surface atoms have the coordination number of atoms in an infinite face. It is clear that the Pt crystallite size distribution may also affect the Pt activity.

Evidence for an interaction between Pt and the support was obtained by Nicolau, Thom, and Pobitschka (28) and by Hillenbrand and Lacksonen (29, 30). Nicolau, Thom, and Pobitschka (28) found that the sample prepared by the reduction of chloroplatinic acid adsorbed on charcoal exhibited strong paramagnetic resonance absorption but that the paramagnetic resonance absorption was weaker when Pt was mixed with the charcoal. Hillenbrand and Lacksonen (29, 30) found that adsorption of Pt on carbon altered the number of unpaired electrons in the carbon and this modification depended on the pretreatment of the carbon. There are no measurements of the interaction between the metal and the support as a function of metal crystallite size but it is expected that this interaction will be greater for the smaller metal crystallites.

The catalysts prepared by the pyrolysis of an ion exchange resin at 700°C do not consist solely of Pt and carbon, and selected doped-carbons were analyzed¹ to determine the fraction of hydrogen and oxygen atoms in each support. These results are reported in Table IV.

It can be seen from Table IV that the supports contained significant fractions of hydrogen and oxygen. Comparison of the analysis results (Table IV) with the Pt specific activity data (Table III) indicates that small changes in the composition of the support does not change the activity of Pt for oxygen reduction, but this does not prove that the support is not influencing the activity of platinum. Further work aimed at larger variations in support composition is required to extend the present study.

This work demonstrates that the activity for oxygen reduction of highly dispersed Pt on a support prepared by the pyrolysis of an ion exchange resin is less than that of crystalline Pt. This may not hold true for all dispersed Pt catalysts but it may only be applicable to the Pt dispersion prepared by this particular method.

¹ Analyses were made by Schwarzkopf Microanalytical Laboratories, New York, New York.

In addition the low activity of dispersed Pt catalyst may be applicable only to the electroreduction of oxygen and the relative activity of highly dispersed and crystalline platinum will probably depend on the nature of the reactant and even of the electrolyte. For example, Poltorak and Boronin (31) using highly dispersed Pt on silica gel found that many hydrogenation, dehydrogenation, and hydrogenolysis reactions were independent of the platinum crystallite sizes. However when the same catalysts were used for reactions involving oxygen species (e.g., hydrogen peroxide decomposition, methanol and ethanol oxidation, and acetaldehyde oxidation) their activity was at least one order of magnitude lower than that of Pt black. It was claimed (31) that in the latter reactions the platinum was completely covered with oxygen and consequently it lost its metallic character.

The highly dispersed Pt catalyst prepared by the pyrolysis of an ion exchange resin in which Pt ions were adsorbed is not suitable as cathode catalysts in acid fuel cells since the increase in Pt area is more than outweighed by the decrease in Pt specific activity.

Manuscript submitted Aug. 13, 1971; revised manuscript received ca. Jan. 7, 1972.

Any discussion of this paper will appear in a Discussion Section to be published in the December 1972 JOURNAL.

REFERENCES

1. M. Boudart, in "Advances in Catalysis," Vol. 20, p. 153, D. D. Eley, H. Pines, and P. B. Weisz, Editors, Academic Press (1969).
2. E. I. Gil'debrand, *Intern. Chem. Eng.*, **6**, 449 (1966).
3. L. Spenadel and M. Boudart, *J. Phys. Chem.*, **64**, 204 (1960).
4. J. A. Rabo, V. Schomaker, and P. E. Pickert, "Proc. 3rd Intern. Congr. Catalysis, Amsterdam, 1964," Vol. 2, p. 1277, North-Holland Pub., Amsterdam (1965).
5. J. A. Cusumano, G. W. Dembinski, and J. H. Sinfelt, *J. Catalysis*, **5**, 471 (1966).
6. T. A. Dorling, M. J. Eastlake, and R. L. Moss, *ibid.*, **14**, 23 (1969).
7. G. K. Boreskov and V. S. Chesalova, *Zh. Fiz. Khim.*, **30**, 2560 (1956).
8. D. W. McKee, *J. Phys. Chem.*, **67**, 841 (1963).
9. T. A. Dorling and R. L. Moss, *J. Catalysis*, **5**, 111 (1966).
10. D. J. C. Yates and J. H. Sinfelt, *ibid.*, **8**, 348 (1967).
11. M. Boudart, A. W. Aldag, L. D. Ptak, and J. E. Benson, *ibid.*, **11**, 35 (1968).
12. H. I. Zeliger, *This Journal*, **114**, 144 (1967).
13. J. A. S. Bett, E. Washington, and K. Routsis, Paper 285 presented at the Electrochem. Soc. Meeting, Los Angeles, May 10-15, 1970.
14. H. A. Benesi, R. M. Curtis, and H. P. Studer, *J. Catalysis*, **10**, 328 (1968).
15. R. A. Van Nordstrand, A. J. Lincoln, and A. Carnevale, *Anal. Chem.*, **36**, 819 (1964).
16. H. A. Pohl, "Proc. 4th Carbon Conference," p. 241, Pergamon Press (1960).
17. H. A. Pohl and S. L. Rosen, "Proc. 5th Carbon Conference," p. 113, Pergamon Press (1962).
18. K. F. Blurton, *Carbon*, Accepted for publication.
19. W. M. Vogel and J. T. Lundquist, *This Journal*, **117**, 1512 (1970).
20. J. Giner and S. Smith, *Electrochem. Technol.*, **5**, 61 (1967).
21. W. M. MacNevin and W. B. Crummett, *Anal. Chem.*, **25**, 1628 (1953).
22. J. Giner, J. M. Parry, S. Smith, and M. Turchan, *This Journal*, **116**, 1692 (1969).
23. S. Gilman, "Electroanalytical Chemistry," Vol. 2, p. 112, A. J. Bard, Editor, Marcel Dekker, New York (1967).
24. A. J. Robell, E. V. Ballou, and M. Boudart, *J. Phys. Chem.*, **68**, 2748 (1964).
25. J. E. Benson, H. W. Kohn, and M. Boudart, *J. Catalysis*, **5**, 307 (1966).
26. A. J. Appleby, *This Journal*, **117**, 328 (1970).
27. O. M. Poltorak and V. S. Boronin, *Intern. Chem. Eng.*, **7**, 452 (1967).
28. C. S. Nicolau, H. G. Thom, and E. Pobitschka, *Trans. Faraday Soc.*, **55**, 1430 (1959).
29. L. J. Hillenbrand and J. W. Lacksonen, *This Journal*, **112**, 245 (1965).
30. L. J. Hillenbrand and J. W. Lacksonen, *ibid.*, **112**, 249 (1965).
31. O. M. Poltorak and V. S. Boronin, *Zh. Fiz. Khim.*, **40**, 2671 (1966).

Hermetic Compression Seals for Alkaline Batteries

E. J. McHenry* and P. Hubbauer

Bell Telephone Laboratories, Incorporated, Murray Hill, New Jersey 07974

ABSTRACT

An accelerated thermal cycle test is described which has been used to evaluate the long-term reliability of seals for nickel-cadmium batteries in Bell System use. Results of this test correlate well with life test results on long-term overcharge. Two new types of seal have been developed for use in nickel-cadmium or other alkaline batteries. The first is a simple modification of the seal developed by A. W. Ziegler for submarine cable use. It entails substitution of an injection molded nylon bushing for the machined Kel-F bushing used by Ziegler, thus eliminating a costly machining operation and greatly simplifying fabrication of the seal. The second is a design employing the same principles as the Ziegler seal but is simpler and can be made in smaller sizes than the Ziegler seal. Both designs have been subjected to accelerated thermal cycle tests and found to be superior to the seals used on commercial alkaline cells.

The maintenance-free rechargeable nickel-cadmium cell depends on a proper balance among oxygen pressure, state-of-charge of the electrodes, electrolyte content, and positive-to-negative capacity in order to function dependably. This balance can be maintained only as long as there is no material transport across the walls of the container. A leakage rate of as little as

10 std cm³ of oxygen per month (4×10^{-6} std cm³/sec) would result in an increase of 480 mA-hr in negative state-of-charge in one year. This represents approximately one third of the excess negative capacity in a typical D (4 A-hr) cell and would result in cell failure within three years.

Leakage is a problem which seriously limits the life of nickel-cadmium batteries in Bell System service. These batteries contain conventional commercial cells

* Electrochemical Society Active Member.
Key words: injection molding, terminal seals.

in which economic and size limitations usually dictate the use of a seal based on a compressed plastic gasket. Aerospace cells, having no such economic limitations, have traditionally used ceramic-to-metal and glass-to-metal seals in an attempt to achieve long life. However, NASA data (1) indicate that despite their high cost, leakage occurred in 33% of the cells tested containing ceramic-to-metal seals and 53% of the cells tested containing glass-to-metal seals. In addition to the fact that glass and ceramic seals are expensive, inherently fragile, and subject to chemical degradation, previous work in the laboratory (see section on Ziegler seal) has shown better results with properly designed compression seals. Therefore, this work was directed toward improvement of the compression seal.

Experimental

Theory and accelerated testing.—The basic principle of the compression seal is shown in Fig. 1. In its simplest form the seal is composed of a plastic gasket, 1, compressed between the negative terminal, 2, and the positive terminal, 3, sealing leakage paths, A. Provided there is continuous contact between the metal and gasket surfaces and sufficient pressure is maintained on the gasket, this seal will effectively prevent leakage. When metal-to-plastic contact is not continuous or contact pressure is not maintained above a critical point, failure occurs. Failure of compression seals may be the result of any one or combination of the following:

1. Improper construction (misaligned gasket, feathered edges, burrs, etc.).
2. Poor design.
3. Chemical or thermal degradation of the gasket.
4. Thermal or mechanical fatigue of the gasket.

Chemical or thermal degradation of the gasket is normally not encountered at room temperature or below but may be serious at higher temperatures. Diffusion of gas or liquid through the gasket occurs at an appreciable rate only at high temperature or pressure. Seal failures are normally due to poor design, improper construction, or gasket fatigue, all of which result in insufficient contact pressure between the gasket and metal surfaces.

Fatigue results from pressure fluctuations inside the cell or from stress variations caused by thermal cycle of components with large differences in thermal expansion coefficients. The internal gas pressure of a sealed Ni-Cd cell varies with the state of charge and rate of overcharging. This differential may be as great as 5 atm between the end of charge and the end of discharge. In conventional cells the area of the cover acted on by the internal pressure is considerably

greater than the bearing (contact) surface between the cover and the gasket. Thus the resulting stress in the gasket is of the order of 10 times the internal gas pressure. Normal operation also entails thermal cycle (daily temperature variation superimposed on a seasonal temperature cycle) which causes expansion and contraction of the seal components. Gasket materials generally have thermal expansion coefficients ten times that of metal container materials so that expansion of the gasket is restricted by the container. Heating and cooling cause a fluctuating stress on the gasket which eventually results in fatigue failure. Thus rapid, broad range thermal cycling would be expected to greatly accelerate seal failures which would result from any of the causes listed above. This test would rapidly provide comparative data on seal quality which might otherwise take months or years to accumulate.

The temperature profile that was used in our experiments is shown in Fig. 2. It consisted of cycling between -40°F and $+160^{\circ}\text{F}$, one full cycle every 2 hr. The lag time required for the chamber to come to the set temperature was approximately 20 min on both rise and fall. Thermal cycling was continuous seven days a week with no rest period until failure of the seal. Failure was determined by applying wet multi-range pH paper to the seal and observing color change after 5 min. If the paper indicated a pH of 9 or greater, the seal was considered failed. Leak checks were made every day during the first week of testing and every week thereafter.

Experimental evidence of the correlation between thermal cycle and overcharge tests is shown in Fig. 3. The upper graph is a conglomerate of leakage data on 60 commercial D cells of four manufacturers which were tested at 20°F , 32°F , and room temperature at 200 mA constant overcharge (2). The lower graph shows results of thermal cycle tests on 20 additional D cells taken from the same lots. As can be seen, there is one-to-one correspondence in relative seal quality exhibited in the two types of tests. Thus, the thermal

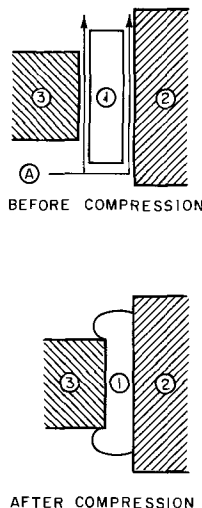


Fig. 1. Compression seal principles

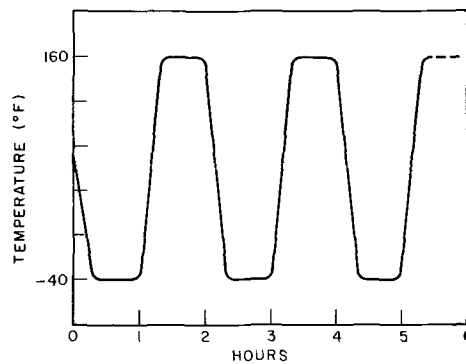


Fig. 2. Thermal cycle test temperature profile

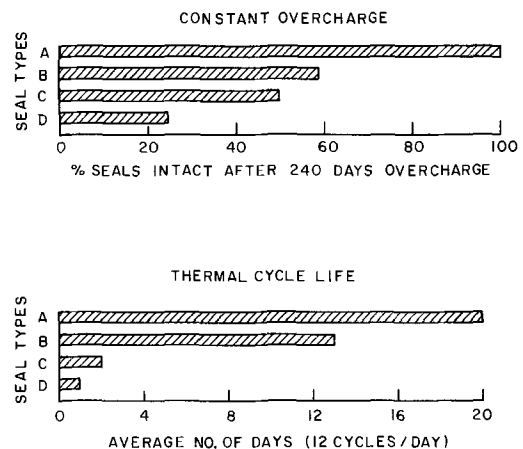


Fig. 3. Commercial battery seal performance

Table I. Leakage tests, TELSTAR® battery seals

Type of seal	No. of seals	% Failed after 4 yr Overcharge at C/100	% Failed after 5 yr Additional O.C. stand
Glass-to-metal	50	100	100
Ceramic-to-metal	400	50	100
Ziegler	50	0	0

cycle test is established as a valid accelerated test of relative quality of compression seals.

Ziegler seal.—Among the seals developed for use with nickel-cadmium batteries for TELSTAR® (3) was a plastic compression seal designed by Ziegler (4) originally for use in submarine cable repeaters. Although the reliability of the seal design was not established in time for the TELSTAR® flights, long-term experiments carried out subsequently showed them to be superior to glass and ceramic seals as seen in Table I. More important, they show it to be capable of eliminating the leakage problem in long-term service.

A diagram of the Ziegler seal used in these experiments is shown in Fig. 4. The threaded metal barrel is first brazed into the lid of a cell. The Kel-F bushing is then screwed into the barrel and the central lead wire inserted through the bushing. Radial compression is then applied to reduce the barrel diameter from 0.250 to 0.234 in.

In order to insure continuous uniform compression of the threaded Kel-F bushing, a 0.156-32 Whitworth thread is used. The important feature of this thread is the rounded roots and crests. Normal threads with sharp roots and crests are very difficult to match by a machining operation so that a helical leakage path along the sharp root is a primary failure mode. High precision is required in machining the threads to prevent burrs which would mar the Kel-F during assembly. This construction is referred to as the standard Ziegler seal.

Injection molded Ziegler seal.—Although the Ziegler seal is very effective, the precision machining required is time-consuming and expensive. Of the possible fabrication techniques available, injection molding appeared most suitable for our design objectives of simplicity and economy. This technique is rapid, economical, and faithfully reproduces the surface characteristics of the threaded barrel. It has the added advantage of eliminating the assembly operation since the bushing is formed *in situ*.

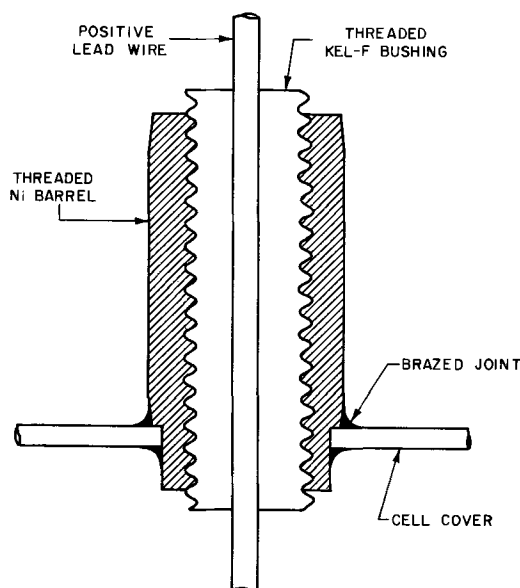


Fig. 4. Construction of Ziegler seal

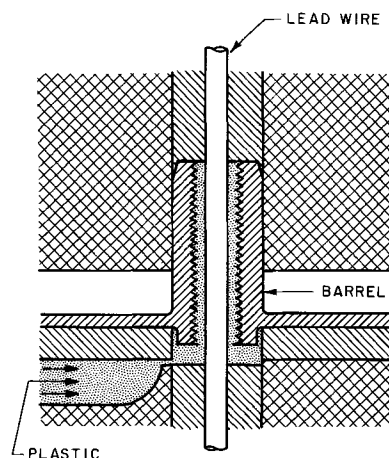


Fig. 5. Injection mold for Ziegler seal

Starting with the basic Ziegler design, a modified seal was fabricated by injection molding a nylon 6-6 bushing into a nickel barrel. The barrel was identical to the standard Ziegler barrel (shown in Fig. 4) with the exception of the thread which was cut with a standard 8-32 tap. Threaded barrels were brazed into covers made to fit a standard D cell can. The cover and lead wire were placed in a mold (Fig. 5) and plastic material was injected into the cavity to form a bushing. Molding conditions are shown in Table II. A cylindrical electrode core taken from a standard commercial D cell was then placed in a can and the cover with the injection molded seal was welded onto the can. The barrel was then crimped in the same manner as the standard Ziegler seal. At this point the cells were pressurized with 60 psig of helium and placed on a mass spectrometer leak detection device. This instrument is capable of detecting a leak rate of 2×10^{-10} std cm³/sec or 0.0063 std cm³/yr. No leakage was detected on any of the cells. Approximately 18 ml of electrolyte was then added to the cell through a fill tube on the bottom of the can. The cells were placed on thermal cycle at 50 mA overcharge. Results of these tests are presented in Table III.

As can be seen, these seals are equally as effective as the standard Ziegler seal. A major difference between the two types of seal is the quality of workmanship required in their fabrication. To illustrate this

Table II. Operating conditions for injection molding Ziegler seals using a one-half ounce-12 ton Unex jet molding machine

	Nylon 6-6	Nylon 6-10	Nylon 12
Die temperature, °F	170	170	170
Cylinder temperature, °F	600	500	510
Injection time, sec	12	12	12
Clamp closing time, sec	30	30	30
Over-all time, sec	60	60	60
Injection pressure, psi	6000	5000	6000
Feed, in.	1¼	1¼	1¼

Nylon was dried for 16 hr at 72°C prior to molding.

Table III. Thermal cycle performance of Ziegler seals

No. of seals	Plastic material	Assembly method	No. of thermal cycles	No. of seals failed
5	Nylon 12	Injection mold	1236	0
5	Nylon 6-6	Injection mold	1236	0
5*	Nylon 6-6	Injection mold	1236	0
4	Nylon 6-10	Injection mold	1101	0
5**	Nylon 6-6	Injection mold	3410	0
5	Kel-F	Standard	1101	0

* Heat and oxidation stabilized.

** 304L stainless steel barrel was used in place of nickel.

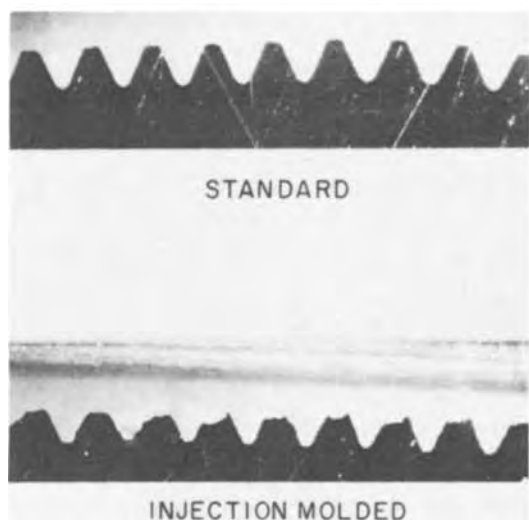


Fig. 6. Thread design for Ziegler seals

point, seals were constructed using a worn 8-32 tap to produce deliberately poor thread quality. Figure 6 shows a comparison between the threads of the standard and these injection molded seals. Both of the seals shown have withstood over 1000 thermal cycles without any indication of leakage.

Multiple crimp seal.—The proportionally large increase in over-all cell height accompanying the use of the Ziegler seal on small cylindrical cells is a major disadvantage. For this reason another design (5) operating on principles similar to that of the Ziegler seal was developed in which the seal is inverted and extends into the central void of the cylindrically wound core of the cell as shown in Fig. 7.

It consists of a metal tube containing a coaxial plastic tube and a central metal lead wire. The lead wire is normally nickel and serves as the positive terminal of the cell. The outer metal tubing is brazed into the cell cover, and the plastic tubing and wire are inserted into it. Multiple crimps compress the plastic tubing between the outer metal tubing and the central lead wire, thus effecting a seal. A 0.125 in. OD by 0.062 in. ID nickel tubing was employed in all of these seals with a 0.060 in. OD by 0.031 in. ID plastic tubing. The central wire was drawn to approximately 0.001 in. less than the plastic tubing ID. In all cases the crimping operation reduced the outside metal tubing diameter

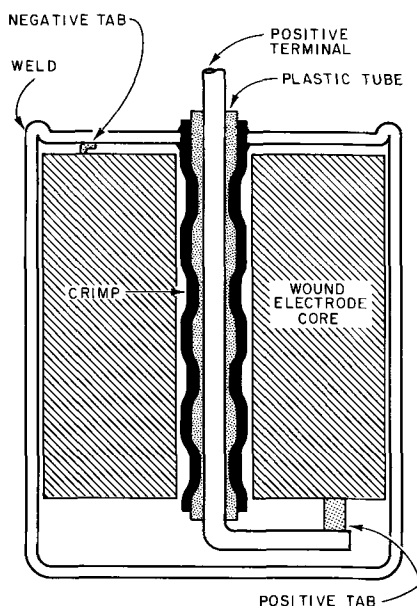


Fig. 7. Diagram of crimp seal

by approximately 0.017 in. Each crimp was 1/8 in. long, and the space between crimps was 1/8 in. Two groups of seals were made 2 in. long with seven crimps, and two groups were made with two crimps and a length of 3/8 in.

Injection molding was also applied to the crimp seal in order to simplify construction and avoid assembly errors. A larger tubing measuring 0.187 in. OD by 0.125 in. ID by 1 in. long was used with a 0.060 in. diameter nickel lead wire. Plastic material was injected into the annulus between the wire and the metal tubing. The tubing was crimped in four equally spaced sections of 1/8 in. length. Crimping reduced the tubing OD from 0.187 to 0.176 in. on the crimped portion.

Since this type of seal extends into the cell it is not possible to crimp after the welding operation. Therefore, adequate heat sinking is required to prevent the seal from being heated above 200°F during welding. Helium leak check and electrolyte addition were performed in the same manner described for the Ziegler seals. Thermal cycle performance of the new seals is presented in Table IV.

Discussion

Values of gas diffusion rates through plastic bodies comparable in size to the Ziegler seal have been calculated. These values are presented in Table V for 1/4 in. diameter by 1/2 in. long bodies of nylon 6 and Kel-F and are based on diffusion rates reported in the literature (6) and a 1 atm pressure differential at room temperature. Leakage of helium through the standard and injection molded Ziegler seals as well as the crimp seal has been measured as less than 6.3×10^{-3} std cm³/year (2×10^{-10} std cm³/sec). This value is of the same order as the calculated gas diffusion rates shown in Table V. Thus gas diffusion is not considered to be a life-limiting factor. Accelerated thermal cycle tests indicate that fatigue failure may also be eliminated as a failure mode in a five to ten year life. All available evidence suggests that leakage is no longer a problem in any application where the Ziegler or crimp seals can be employed.

A major advantage of the new seals over the standard Ziegler or ceramic seals is the simplicity and expected economy in their fabrication techniques. Costly precision machining has been eliminated and replaced by punching, drawing, stamping, and welding operations. It is expected that relatively unskilled workers can assemble these seals quickly with very low in-

Table IV. Thermal cycle performance of multiple crimp seals with nylon 6-6 bushings

No. of seals	Seal OD, in.	No. of crimps	No. of thermal cycles	No. of seals failed
3	0.125	7	2070	0
5	0.125	7	1596	0
2	0.125	2	996	0
7	0.125	2	588	0
5*	0.187	4	744	0

* Injection molded.

Table V. Diffusion rates of gases through 1/4 in. diameter 1/2 in. long plastic bodies

Component	Nylon		KEL-F	
	g/yr	std cm ³ /yr	g/yr	std cm ³ /yr
N ₂	4×10^{-7}	3×10^{-4}	2×10^{-7}	2×10^{-4}
O ₂	2×10^{-6}	1×10^{-3}	2×10^{-6}	1×10^{-3}
CO ₂	2×10^{-7}	1×10^{-4}	5×10^{-7}	3×10^{-4}
H ₂	2×10^{-7}	2×10^{-3}	5×10^{-9}	5×10^{-5}
H ₂ O	2×10^{-4}	0.2	4×10^{-7}	4×10^{-4}

Calculations based on 1 atm pressure differential at room temperature.

cidence of rejects. The new seals have the added advantage of flexibility in design change. That is, the seal dimensions need not be changed at all unless a gross change is made in the cell design. Thus exactly the same seal design can be used in the size range from "sub C" to D cell without any change in any dimension of the seal. It is conceivable that in small quantities of special cells it may be cheaper to use the Ziegler or crimp seal rather than the ordinary commercial seal.

All of the seals studied in this work employed a nylon insulating bushing. Ease of fabrication, prior experience with nylon in Ni-Cd cells, and physical and chemical properties were the main reasons for this choice. Other materials such as polypropylene, FEP Teflon, Kel-F, and Kynar appear to be suitable for use in these types of seals. Some of these materials were used in preliminary experiments, and results indicate that with proper control, they will be equally suitable in these designs. Further work is planned to investigate other plastic materials and to develop a seal which will withstand sterilization at 135°C for 72 hr.

Conclusions

The injection molded Ziegler seal and the multiple crimp seal perform far better on accelerated thermal

cycle testing than do ordinary commercial seals and are expected to perform satisfactorily for five to ten years of normal operation. These seals are simple in construction and can be produced at a cost considerably below that for ceramic seals, which they will outperform under most conditions.

Manuscript submitted Oct. 14, 1971; revised manuscript received Jan. 10, 1972. This was Paper 72 presented at the Atlantic City Meeting of the Society, Oct. 4-8, 1970.

Any discussion of this paper will appear in a Discussion Section to be published in the December 1972 JOURNAL.

REFERENCES

1. "Evaluation Program for Secondary Spacecraft Cells—Fifth Annual Report of Cycle Life Test," QEL Report QE/C 69-244, April 7, 1969.
2. M. L. Cassotta, Unpublished work.
3. D. C. Bomberger and L. F. Moose, *Bell System Tech. J.*, **42**, 1687 (1963).
4. A. W. Ziegler, U.S. Pat. 3, 109, 055.
5. E. J. McHenry, U.S. Pat. 3, 510, 353.
6. J. Brandrup and E. H. Immergut, "Polymer Handbook," Interscience Publishers, Inc., New York (1967).

A New Water-Activated Lead-Acid Battery Concept

R. F. Amlie,* E. Y. Weissman,* C. K. Morehouse,* and N. M. Qureshi

Globe-Union, Inc., Milwaukee, Wisconsin 53201

ABSTRACT

A discussion is presented of a reserve lead-acid battery concept based on water-soluble sulfuric acid gels. The gels consist primarily of 100% sulfuric acid plus small amounts of boric and phosphoric acids. These gels exhibit excellent mechanical and thermal stability characteristics when prepared with a relatively large molar excess of boric acid with respect to phosphoric acid. The rate of water activation of a battery containing this gel is controllable, and no solid residues are left after the activation has been completed. Performance, life, and electrolyte composition aspects are covered in this discussion, with a view to defining the advantages and limitations of the system and its future possibilities.

The development of a satisfactory water-activated dry-charged lead-acid battery is of particular interest since it would fill a definite need that exists in military and possibly also commercial applications for a reserve system. A water-activated battery would have several advantages over the widely accepted acid-activated battery in that no separate acid volume is required and shipment, storage, and activation are inherently less costly, safer, and simpler. A satisfactory water-activated concept requires the internal storage of concentrated sulfuric acid (or its precursor) in a mechanically and thermally stable form which will produce sufficient sulfuric acid electrolyte in a safe yet sufficiently rapid manner upon addition of water. Other characteristics for a practical concept require that the acid concentrate occupy essentially a minimal volume, since internal free space is greatly limited in conventional batteries, and that it produce no degradation of cell components. Further, performance should be comparable to that of a conventional battery of the same external dimensions.

Various concepts for water-activated lead-acid batteries are described primarily in the patent literature

and have appeared at an increasing rate in recent years following a feasibility study reported in 1965 (1). Briefly, these concepts could be described as involving the immobilization of concentrated sulfuric acid by mechanical encasement of the liquid (2-4), physical sorption (5-9), chemical reaction (10), and gelation (11-17), although this classification may not always be completely rigorous.

Stable Boron Phosphate Gels

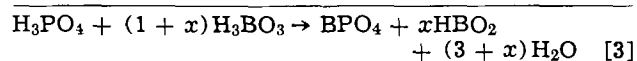
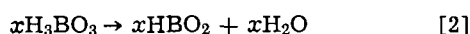
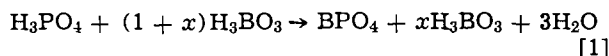
This paper presents a water-activated lead-acid battery concept based on the use of stable "boron phosphate" gels of concentrated sulfuric acid. Gelation of concentrated sulfuric acid and oleum by the addition of essentially equimolecular amounts of boric and phosphoric acids was described by Leicester in 1948 (18). Leicester suggested that gelation is due to the formation of a boron phosphate, (BPO₄), structure which may be isomorphous with a silicic acid gel of sulfuric acid in which the silicon atoms are alternately replaced by boron and phosphorous atoms. He describes general properties of these gels including the observation that, "Equimolecular proportions of the two acids (H₃BO₃ and H₃PO₄) gave the best gels, but the quantities could be varied within wide limits (±30%) with-

* Electrochemical Society Active Member.

Key words: gelled sulfuric acid, boron phosphate gels, water-activated battery, lead-acid battery, dry-charged battery.

out seriously affecting gel formation for the 1/100 (mole ratio $\text{BPO}_4/\text{H}_2\text{SO}_4$) and more concentrated gels." Other properties listed included: (a) increased firmness with concentration, (b) faint to strong opalescence, (c) slight syneresis (separation of liquid phase due to gel contraction) with little indication of thixotropic properties, (d) readily broken down and dissolved by the addition of water, (e) good thermal stability at 100°C , and (f) good room temperature stability for several months. Leicester also shows that gelation time decreased rapidly with increasing water content and moderately with increased BPO_4 content.

We found these gels to be easily prepared starting with boric acid crystals, 85% orthophosphoric acid, concentrated sulfuric and oleum solutions. Since the composition of the sulfuric acid component (or $\text{H}_2\text{O}/\text{SO}_3$ ratio) of the mixture greatly influences gel stability, we assumed the gelation reactions shown below in order to define a calculated $\text{H}_2\text{O}-\text{SO}_3$ composition



In addition to the water introduced in the gelation process, the 85% phosphoric acid and the concentrated sulfuric acid ingredients also introduce water into the system. This water is effectively removed by the addition of oleum (free SO_3) and the resulting H_2SO_4 and H_2O , or SO_3 contents were calculated according to the above assumptions. Laborious material balance equations involving different ingredient concentrations and gel compositions were avoided by use of a FORTRAN program in our computer facility.

In actual practice, it was found that gel preparation can be readily monitored by measuring the electrolyte solution conductivity which is very sensitive to concentration in the range of interest. Specific conductance values of liquid gelling mixtures with an acid mole ratio of $2\text{H}_3\text{PO}_4/5\text{H}_3\text{BO}_3/100\text{H}_2\text{SO}_4$ are plotted in Fig. 1 as a function of the weight per cent (w/o) H_2SO_4 . The weight per cent H_2SO_4 calculated for each solution is based on the total SO_3 content, and H_2O which was both added and assumed to be derived from gelation and dehydration. Gel compositions with this 2/5/100 mole ratio exhibit excellent stabilities in the calculated H_2SO_4 concentration range from about 99 to 101%, above which SO_3 fuming becomes progressively evident. The specific conductance curve of a pure sulfuric acid solution with a minimum at 99.7 w/o H_2SO_4 (19) is also included in Fig. 1. It is evident that the minimum, as calculated for the gelling solution, exceeds that of pure H_2SO_4 by approximately 1 w/o. This would indicate that the assumed gelation reaction [3] does not provide a complete description of this complex system which may involve interaction of acid species. A systematic study of the boron phosphate-sulfuric acid system is required to clarify these results.

Gels prepared in our laboratory using Leicester's formulations did not exhibit satisfactory thermal and storage stabilities toward syneresis as deemed necessary for a water-activated battery application. The hygroscopic gels were stored in tightly capped glass bottles at temperatures up to 100°C . In agreement with Leicester, it was found that gel stability was improved by decreasing the water content and increasing the BPO_4 content, but neither the equimolar gels nor gels containing up to 30% excess of boric or phosphoric acid were sufficiently stable.

Gel stabilities were found to be greatly improved when a relatively large molar excess of boric acid relative to phosphoric acid is used (16). Table I summarizes the optimum ranges of acid mole ratios necessary to produce battery-stable gels. An approximate stability-composition domain for gels containing a 99-

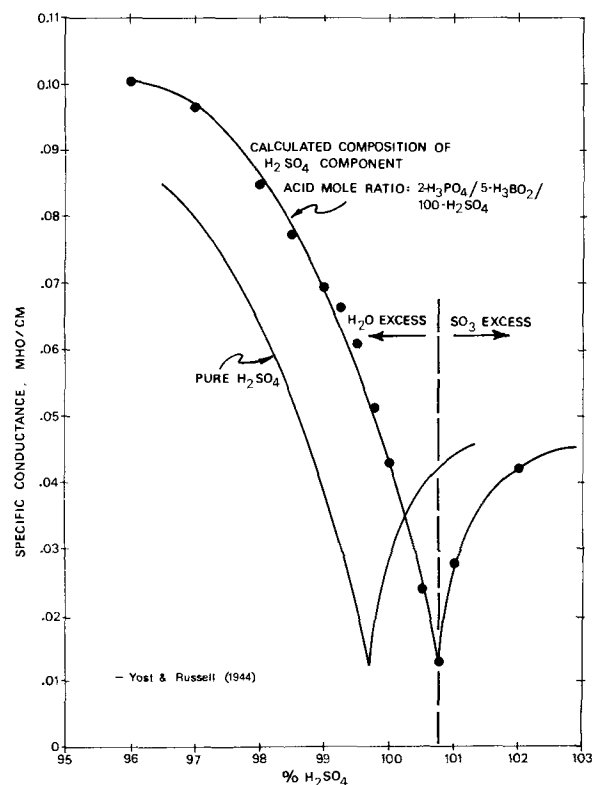


Fig. 1. Specific conductance vs. per cent H_2SO_4 at 30°C

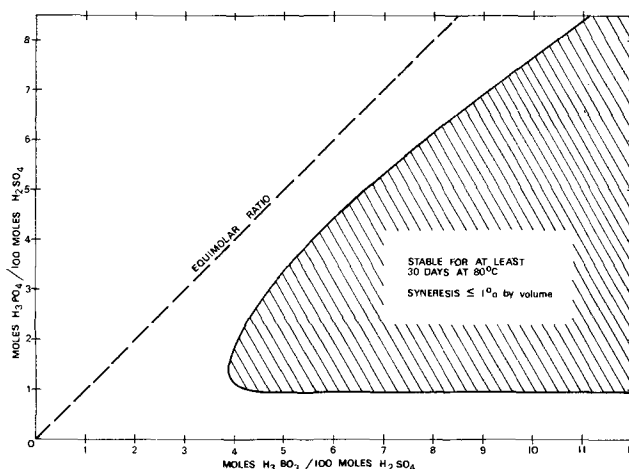


Fig. 2. Approximate stability composition domain for $\text{H}_3\text{PO}_4/\text{H}_3\text{BO}_3/\text{H}_2\text{SO}_4$ gels containing 99-100% calculated H_2SO_4 .

100% calculated (aqueous) H_2SO_4 component, wherein syneresis was less than 1% by volume after 30 days' storage at 80°C , is shown in Fig. 2. Acid composition of the gels is given in moles of phosphoric and boric acid per 100 moles of calculated (100%) sulfuric acid. Stabilities of these gels were generally best in the lower portion of the composition domain where the H_3PO_4 content exceeded 1 mole per 100 moles H_2SO_4 and the maximum $\text{H}_3\text{BO}_3/\text{H}_3\text{PO}_4$ mole ratios were attained. The more stable gels exhibited no evidence of syneresis or breakdown after 100 days' storage at 100°C

Table I. Optimum acid ingredient mole ratios for stable $\text{BPO}_4-\text{H}_2\text{SO}_4$ gels

$\text{H}_3\text{BO}_3/\text{H}_3\text{PO}_4 > 1.3$ and, preferably > 1.5
$3.5 \leq \text{H}_3\text{BO}_3/100 \text{ moles } \text{H}_2\text{SO}_4 \leq 12$
$1 \leq \text{H}_3\text{PO}_4/100 \text{ moles } \text{H}_2\text{SO}_4 \leq 5$



Fig. 3. Photograph of a water-clear gel

at which time the tests were discontinued. Attempts to liquify the most stable gels at even higher temperatures produced instead a surface decomposition with gradual reduction of the gel body size.

Gel appearance varied from strongly opalescent to water-clear and was found to be dependent on the H_3PO_4/H_3BO_3 ratio, the water content, and the setting temperature. Water-clear gels generally exhibited the greatest stability and were obtained only with an excess of boric acid and minimal (or no) calculated water content. A photograph of a water-clear gel sample is shown in Fig. 3.

A particular advantage with this gel is that it can be combined rapidly with water without the hazard encountered with concentrated sulfuric acid liquid.

Having established that gels could be prepared with excellent mechanical, thermal, and storage stabilities, effort in this development was devoted to determining the effect of gel-prepared electrolytes on battery performance.

Water-Activated Battery Performance

Electrochemical phenomena arising from the use of solutions prepared from gelled acids rather than pure sulfuric acid are primarily due to the presence of orthophosphoric acid. Furthermore, our measurements and observations support Leicester's view that the addition of water (at least 10-15% by volume of gel) readily hydrolyzes the gels to the constituent acids yielding a clear solution (18).

The addition of phosphoric acid to the lead-acid battery has been rather extensively tried (20) and will not be reviewed here. Definitive conclusions have often been dependent on the materials, design, and test mode or service employed. While the earliest patents claimed such general improvements as "the elimination of harmful sulfation" (21), it is now generally accepted that phosphoric acid additions are of particular benefit in improving the cycle life of nonantimonial grid batteries (22, 23). More fundamental investigations of the reactions of phosphoric acid with the lead dioxide electrode have also been reported (23-27) and we have carried out measurements on the electroanalytical determination of Pb(IV) phosphate species in solution (28). Nevertheless, a more comprehensive understanding of the incorporation of phosphoric acid in the positive plate and the changes it produces is definitely needed.

Activation of Prototype Batteries

Initial 20-min activation performances of prototype water-activated batteries are superior to comparable commercial acid-activated batteries owing to the heat of dilution of the concentrated sulfuric acid gel. This advantage is illustrated in Fig. 4 wherein discharges are plotted for 12V-60 A-hr batteries activated and discharged according to the standard SAE $\sim 0^\circ C$ ($30^\circ F$)-150A discharge test specification. These batteries were assembled with production dry-charged 60

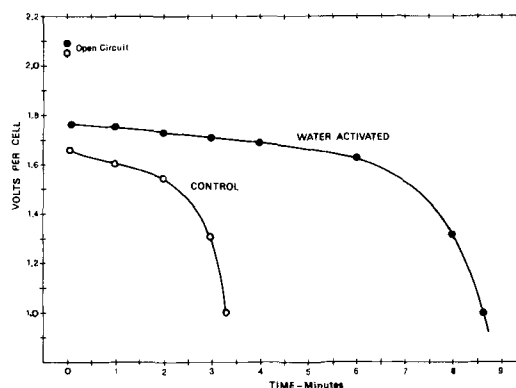


Fig. 4. Performance of 12V-60 A-hr water-activated batteries on the SAE 20-min activation test at $-1^\circ C$ ($30^\circ F$), 150A.

A-hr elements in polypropylene containers (and covers). The water-activated batteries contained 210 cc (388g) of gel mounted above each cell element (16). Prior to activation, the batteries and the (1,270 sp. gr.) sulfuric acid solution had been cooled to $\sim 0^\circ C$ ($30^\circ F$) and the water to $+1^\circ C$. These water-activated batteries were designed to dissolve the gel body in about 20 min after the addition of water and the dissolution occurred with no emission of liquid from the filling ports. The 150A discharge was started 20 min after filling, at which time the average temperatures of the commercial acid-activated and water-activated batteries were 3.5° and $69.5^\circ C$, respectively.

Short and Long Term Results

Only a brief summary of available storage, cycle-life, overcharge, and field service results for one gelled electrolyte composition will be given at this time. A more detailed presentation of design and performance characteristics will be given elsewhere (29).

Standard production dry-charged 12V-60 A-hr batteries with 6% antimonial-lead grid alloy have frequently been used to compare the performance of solutions prepared from gelled acids with the standard sulfuric acid solutions. No effort was made to optimize or alter the batteries for this application. To make this extensive comparison, gel with an acid mole ratio of $2H_3PO_4/5H_3BO_3/100H_2SO_4$ was selected based on initial laboratory test results. The acid concentrations of a solution prepared from this gel are typically 9, 14, and 455g per liter of phosphoric, boric, and sulfuric acid, respectively. The solution prepared by the addition of 480g of a 2/5/100 gel containing 0.5 w/o "excess" water to 802g of water has a specific gravity of 1.282 at $21^\circ C$. The control batteries were filled with 1,270 sp. gr. sulfuric acid (460 g/liter).

The most significant available results can be summarized as follows:

1. The 60 A-hr sealed, dry-charged, SLI-type batteries with gel mounted above the plate elements continue to show satisfactory storage after more than six months in a $60^\circ C$ -100% relative humidity environment.
2. Gel prepared electrolyte capacities on the 20-hr (3A) discharge at $27^\circ C$ ($80^\circ F$) have shown an average reduction of 6% relative to their respective controls.
3. At low temperatures (0 to $-29^\circ C$) and high discharge rates (150 and 300A), the 2/5/100 gel prepared electrolyte solution has exhibited increased 5 sec voltages¹ of 3 to 6% and reduced discharge times ranging from 5 to 33% relative to the control.
4. When cycled according to the SAE cycle-life specification (30), the 60 A-hr SLI batteries with the 2/5/100 composition electrolyte have averaged only 2/3 of the control cycles. On the other hand, Edison Cycle Life Test (see Appendix) results average about 10% higher for the experimental batteries. Field test results are still inconclusive but seem to suggest a detrimental effect on life in hot climate use.

¹ Voltage measured after 5 sec of discharge at the given rate.

5. Overcharge life test comparisons for 60 A-hr batteries on the standard SAE overcharge test (30) routine have shown the same performance for the 2/5/100 acid solution and the sulfuric acid control.

6. There appears to be a structure-dependent scale effect when evaluating experimental and control batteries so much so that certain types of low-capacity batteries (not of the SLI variety) have not exhibited the above-mentioned performance differences. This aspect will be discussed at a later date.

7. Gel prepared electrolyte solutions used in batteries fabricated with nonantimonial lead alloy grids are expected to improve positive paste adherence. Fortunately, a practical phosphoric acid concentration for typical nonantimonial systems (e.g., lead-acid batteries having lead-calcium grids), namely 10 g/liter of solution, corresponds to what results from the utilization of the gelled acids described in this paper.

Conclusions

The technical feasibility of a water-activated, dry-charged lead-acid battery based on stable boron phosphate-concentrated sulfuric acid gels has been demonstrated. Properly formulated gels have been developed which exhibit superior mechanical, thermal, and shelf stabilities when stored out of contact with moisture. The low-temperature activation performance of prototype SLI batteries is excellent due to the H_2SO_4 heat of dilution released. Laboratory cycle life, and field testing of SLI prototype batteries indicate that the gelled acid may reduce the performance of standard batteries in certain SLI applications, although optimization of the system to compensate for the modified electrolyte effects is possible.

Finally, while this discussion addresses itself to the SLI type of battery, it should be obvious that the water-activation principle described here is adaptable to any battery system utilizing a sulfuric acid electrolyte.

Manuscript submitted Nov. 1, 1972; revised manuscript received Dec. 20, 1971. This was presented at the Cleveland Meeting of the Society, Oct. 3-8, 1971.

Any discussion of this paper will appear in a Discussion Section to be published in the December 1972 JOURNAL.

APPENDIX

Edison Cycle Life Test for Lead-Acid SLI Batteries

Temperature:	38°-43°C in air environment	
Cycle time:	10 min; 1000 cycles/week	
Charge	— 6 min, 27 sec at 5-6A	} 10 min
Discharge	— 10 sec at 150A	
Rest	— 3 min, 23 sec	
Capacity test:	150A to 7.2V (1.2 V/cell)	

Specified minimums:

Capacity	— > 0.5 min to 7.2V
Life	— 10 weeks (10,000 cycles) for 60 A-hr battery

REFERENCES

- G. L. Simmons, R. W. Adler, W. E. Elliott, and W. L. Towle, "Immobilized Electrolyte Feasibility Study," U.S. Army Tank Automotive Center, Contract DA-11-022-AMC-2236(T), Dec. 21, 1965, AD 678594.
- T. Yeoman, U.S. Pat. 2,773,927 (1956).
- A. Sam, U.S. Pat. 3,304,202 (1963).
- J. T. Redmon, U.S. Pat. 3,525,639 (1970).
- G. W. Vinal, "Storage Batteries," John Wiley & Sons, Inc., New York (1955).
- R. G. Robinson, Brit. Pat. 785,848 (1957).
- K. Parker and J. L. Brosilow, U.S. Pat. 3,408,233 (1968).
- J. P. Badger and H. A. Bernholtz, U.S. Pat. 3,540,939 (1970).
- H. A. Bernholtz and J. P. Badger, U.S. Pat. 3,591,422 (1971).
- L. E. Solomon, U.S. Pat. 3,067,275 (1962).
- H. H. Roth, U.S. Pat. 2,596,046 (1952).
- J. T. Rivers, U.S. Pat. 2,684,950 (1954).
- D. L. Douglas, R. E. Biddick, and J. B. Ockerman, "Power Sources 2" (1968), p. 93, D. H. Collins, Editor, Pergamon Press, Inc., New York.
- D. L. Douglas and H. J. Banas, U.S. Pat. 3,556,850 (1971) and 3,556,851 (1971).
- M. H. Little, U.S. Pat. 3,530,002 (1970).
- R. F. Amlie, U.S. Pat. 3,556,860 (1971).
- H. Lauck, U.S. Pat. 3,586,539 (1971).
- J. Leicester, *J. Soc. Chem. Ind. (London)*, **67** 433 (1948).
- D. M. Yost and H. Russell, Jr., "Systematic Inorganic Chemistry of the Fifth and Sixth Group Non-Metallic Elements," p. 340, Prentice-Hall Inc., Englewood Cliffs, N. J. (1944).
- C. Drotschmann, "Bleiakkumulatoren," p. 160, Verlag Chemie, GmbH, Weinheim (1951).
- M. Kugel, U.S. Pat. 1,748,485 (1930).
- S. Tudor, A. Weisstuch, and S. H. Davang, *Electrochem. Technol.*, **3**, 90 (1965); **4**, 406 (1966); **5**, 21 (1967).
- K. Eberts, "Power Sources 2" (1968), p. 61, D. H. Collins, Editor, Pergamon Press Inc., New York.
- E. Voss, "Proceedings of the 2nd International Symposium on Batteries," Bournemouth (1960), Paper No. 16.
- H. Bode and E. Voss, *Electrochim. Acta*, **6**, 11 (1962).
- P. Ness, *ibid.*, **12**, 161 (1967).
- F. Huber and M. S. A. El-Meligy, *Z. Anorg. Allgem. Chem.*, **367**, 154 (1969).
- R. F. Amlie and T. A. Berger, To be published in *Journal Electroanalytical Chemistry, Interfacial Electrochemistry*.
- R. F. Amlie, E. Y. Weissman, and N. M. Qureshi, "Proceedings of the Twenty-Fifth Power Sources Symposium, Atlantic City, May 23-25, 1972," To be published.
- "The Storage Battery Manufacturing Industry—1970 Yearbook," Battery Council International, Burlingame, California.

Effect of Chloride Ion on Iron Corrosion in NaOH Solution

Clarence M. Shepherd* and Sigmund Schuldiner*

Naval Research Laboratory, Electrochemistry Branch, Washington, D. C. 20390

ABSTRACT

Potentiostatic polarization curves for the system Fe-NaOH, in which the level of reactable impurities had been reduced to 10^{-6} ppm, showed that Fe did not corrode and that the Fe behavior was similar to Pt. Introduction of chloride ion changed the potentiostatic polarization behavior and at Cl^- concentrations $\geq 2 \mu\text{g}/\text{cc}$ Fe corrosion occurred. Chloride ion also caused the development of a pronounced active dissolution region in the anodic polarization curves. At $0.2 \mu\text{g}/\text{cc}$ of chloride ion, the changes in the polarization curve were small. At $2 \mu\text{g}/\text{cc}$ of chloride ion a typical pattern had developed which showed a definite corrosion region, followed by "passivity" as the potential was increased. At $2000 \mu\text{g}/\text{cc}$ of chloride ion corrosion was marked, even in the "passive" region.

The present work extends our previous (1) study of the effects of chloride ion on the potentiostatic behavior of iron in oxygen-free ($<10^{-6}$ ppm) NaOH solution. Mayne, Mentor, and Pryor (2) showed that in oxygen-free solution chloride ion concentrations from 3.5 to $35 \mu\text{g}/\text{cc}$ will cause iron to corrode, however no corrosion occurred when oxygen was present. The chloride ion concentration in our high-purity 0.2M NaOH was approximately $0.01 \mu\text{g}/\text{cc}$ so that we were able, under O_2 -free conditions, to determine the effects of chloride ion at considerably lower levels than previously had been investigated.

Experimental

The electrode was a high purity Fe wire immersed in 0.2M NaOH under an atmosphere of helium at 25°C . The closed system and measuring equipment have been previously described (1, 3, 4). The 20 mm diameter Fe wire was fabricated from 3 pass electron beam zone refined iron which was reported by the supplier to contain less than 4 ppm metallic impurities. The NaOH electrolyte was prepared by dissolving high purity sodium from a glass capsule inside the closed cell (1). Final purification was by electrolysis to remove traces of heavy metals and organic material. A point on the curves shown was determined by potentiostating the Fe electrode until a constant current was reached. The potential was then increased and another steady-state current was obtained. The process was repeated until the potential was well up into the O_2 generating region after which the potential was decreased stepwise until well into the H_2 generating region. The potential was then increased stepwise back to its original value, thus completing a cycle. Repeated cycling gave essentially the same results.

Results and Discussion

The results for the highly purified system, Fe/0.2M NaOH containing about $0.01 \mu\text{g}/\text{cc}$ Cl^- (from NaCl) as an impurity, are shown in Fig. 1 where the constant value of the apparent current density is plotted against the potential measured against the normal hydrogen electrode (NHE). This curve is used as a standard for comparison with the results that were obtained when small known amounts of Cl^- were added to the pure system. No visual corrosion or changes in the Fe were observed under low power microscopy nor was Fe found in the analyzed solution.

When Cl^- is added to the system the potentiostatic polarization curve of Fig. 1 is affected. The results are shown in Fig. 2-5 for concentrations of Cl^- from $0.2 \mu\text{g}/\text{cc}$ to $2000 \mu\text{g}/\text{cc}$. The concentration of O_2 in these systems was less than 10^{-6} ppm (4).

When the chloride ion concentration reached $2 \mu\text{g}/\text{cc}$ (Fig. 3-5), one observes a large increase in the anodic

current density, particularly in the region of the loop where the potential is being increased from point C through K to L. This increase in current is accompanied by corrosion. This confirms the Mayne, Mentor, and Pryor (2) finding of iron corrosion in O_2 -free solution containing 3.5 to $35 \mu\text{g}/\text{cc}$ of Cl^- . Under conditions in which no chloride has been added to the electrolyte the iron remains bright and shiny over repeated cyclings. After 2 cycles in the solution containing $2000 \mu\text{g}/\text{cc}$ of chloride ion, the iron electrode was pitted appreciably. Considerable amounts of dark brown corrosion products were observed, particularly in the

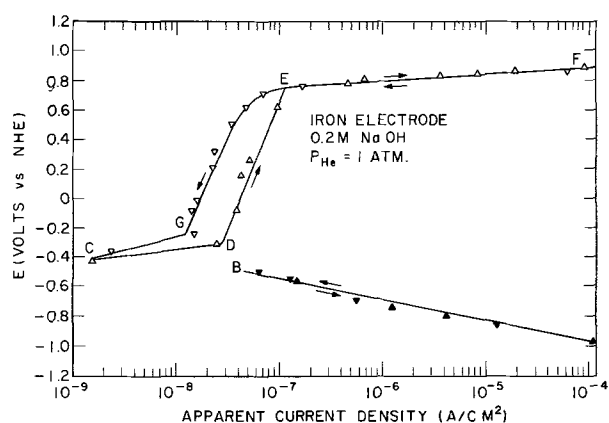


Fig. 1. Fe potentiostatic polarization curves in 0.2M NaOH at 25°C . Δ anodic current, increasing potential; ∇ anodic current, decreasing potential; \blacktriangle cathodic current, increasing potential; \blacktriangledown cathodic current, decreasing potential.

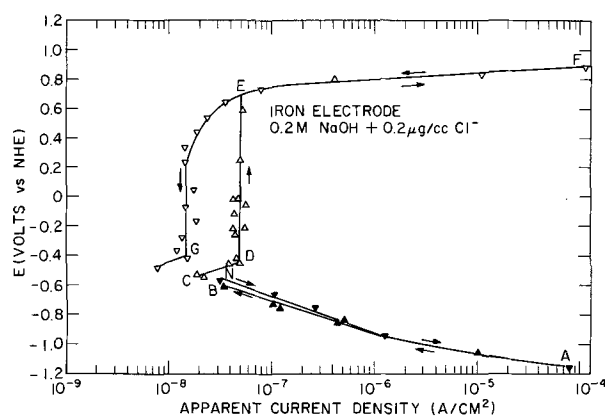


Fig. 2. Effect of addition of $0.2 \mu\text{g}/\text{cc}$ of Cl^- ion on Fe potentiostatic polarization curves in 0.2M NaOH at 25°C and $P_{\text{He}} = 1$ atm. See Fig. 1 for symbols.

* Electrochemical Society Active Member.

Key words: corrosion, iron, chloride ion, passivity, polarization, potentiostatic, high purity.

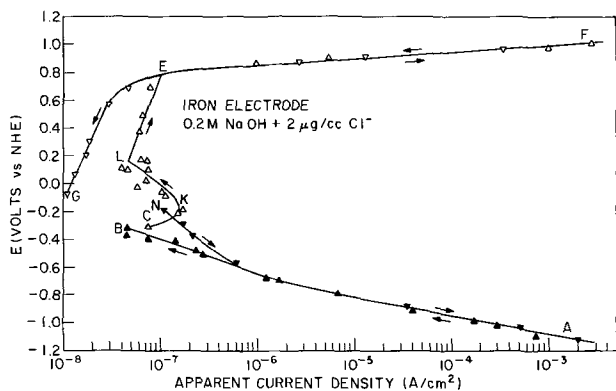


Fig. 3. Effect of addition of 2 $\mu\text{g/cc}$ of Cl^- ion on Fe potentiostatic polarization curves in 0.2M NaOH at 25°C and $P_{\text{He}} = 1$ atm. See Fig. 1 for symbols.

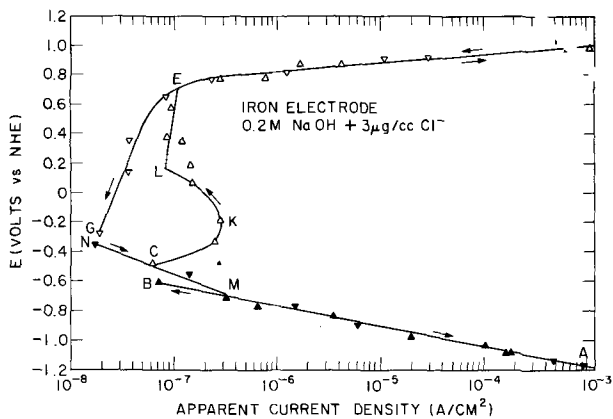


Fig. 4. Effect of addition of 3 $\mu\text{g/cc}$ of Cl^- ion on Fe potentiostatic polarization curves in 0.2M NaOH at 25°C and $P_{\text{He}} = 1$ atm. See Fig. 1 for symbols.

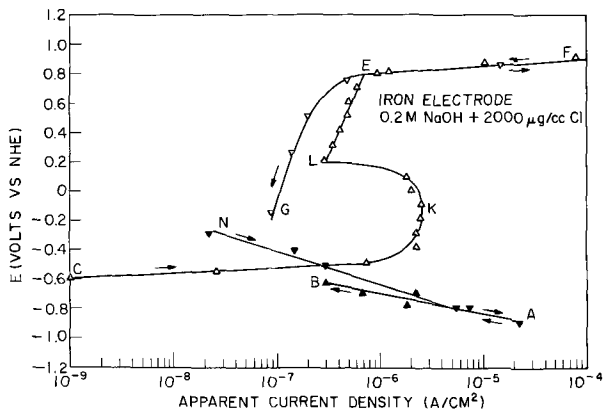


Fig. 5. Effect of addition of 2000 $\mu\text{g/cc}$ of Cl^- ion on Fe potentiostatic polarization curves in 0.2M NaOH at 25°C and $P_{\text{He}} = 1$ atm. See Fig. 1 for symbols.

pits. These pits were not randomly distributed but tended to occur in clusters.

In Fig. 3-5 the Fe electrode is exhibiting normal passive behavior. At a potential in the neighborhood of C, a reaction is initiated involving the oxidation of iron. The current reaches a maximum at the point K, declines, and enters the passive region along line L-E. As the amount of chloride ion increases, the nature of the passive region changes as is evident by the higher current densities. The current density at 2000 $\mu\text{g/cc}$ of chloride ion is several times that at low concentrations of chloride. If the reactions that take place in the system shown in Fig. 1 take place at the same rate in the systems shown in Fig. 3-5, their current density in the passive region is being masked by a reaction or

reactions, whose current density is several hundred per cent higher. If this latter reaction or reactions involve the oxidation of iron, then an appreciable amount of corrosion is being experienced in the so-called "passive" region. Around point K in Fig. 5 the current densities are 100 times higher than found in Fig. 1. As the potential moves upward from E toward F (the transpassive region), the current density involved in the production of O_2 becomes so high that it completely masks out the effect of the impurities. Consequently, this portion of the potentiostatic polarization curve was not affected by change in chloride content.

As the potential was decreased the current went from anodic to cathodic at about -0.22V in the presence of 2000 $\mu\text{g/cc}$ of Cl^- . When the potential was increased the current went from cathodic to anodic at about -0.61V . The difference between these two potentials, ΔE , is 0.39V. This difference in changeover potentials is characteristic of impure systems and decreases monotonically as the amount of impurity decreases, as can be seen in Fig. 6 where ΔE is plotted as a function of the chloride content of the electrolyte. As the chloride content is increased, the value of ΔE appears to be leveling off in the neighborhood of a value of 0.4V. As the chloride value is decreased ΔE approaches zero in value (1). Similar results have been observed qualitatively with other impurities.

In Fig. 3-5 it can be seen in each case that the potential at point K remains fairly constant at -0.2V , whereas the potential at point C decreases appreciably with increase in chloride content.

The maximum current, i_M , is a good measure of the extent of corrosion in the system. In Fig. 7, the current density at the potential of -0.2V has been plotted as a function of the chloride content. This is the potential that gives the maximum current density at point K in those cases where the chloride content is sufficiently high to show a corrosion loop. The relationship is

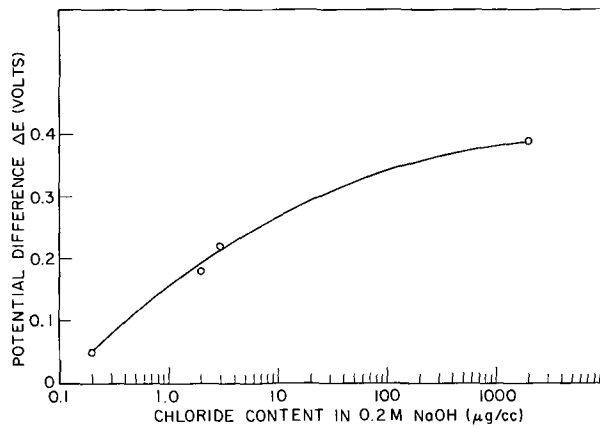


Fig. 6. The effect of Cl^- ion content on ΔE , the potential at which the current changes from anodic to cathodic minus the potential at which the current changes from cathodic to anodic.

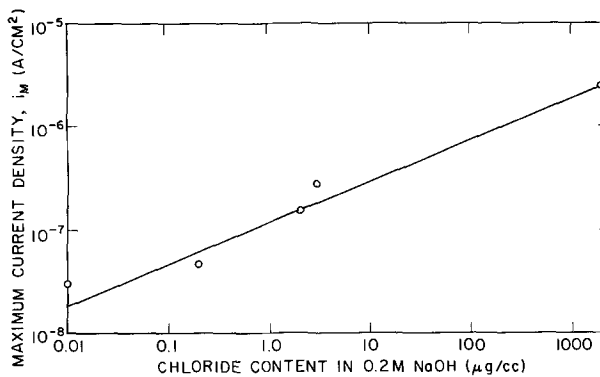


Fig. 7. The effect of Cl^- ion on the maximum corrosion current (current density measured at -0.2V).

logarithmic and can be expressed as the equation

$$i_M = 1.2 \times 10^{-7} C^{0.4}$$

where C is the concentration of chloride ion in $\mu\text{g}/\text{cc}$ and i_M is the current density at -0.2V vs. the normal hydrogen electrode (NHE) and is measured on the increasing potential curve. In the standard system, where impurity effects have been minimized, there is no visible corrosion and the potential-current relationships, as shown in Fig. 1, are essentially straight lines, it seems quite likely that the low chloride content of approximately $0.01 \mu\text{g}/\text{cc}$ neither causes Fe corrosion nor typical passive behavior. At a level of $0.2 \mu\text{g}/\text{cc}$ of chloride ion in the electrolyte (Fig. 2), definite changes have occurred in the potentiostatic polarization curve, and at $2 \mu\text{g}/\text{cc}$ of Cl^- (Fig. 3), there is the first evidence of an active dissolution region. This indicates that a concentration of 10^{-1} to $1 \mu\text{g}/\text{cc}$ of chloride ion must be present to initiate corrosion or the steps that lead to corrosion.

The variation in results obtained using two successive cycles in a given purified electrolyte is not large, in most cases, and is much less than the variation in results obtained between separately prepared and purified electrolytes unless the chloride content is high. At $2000 \mu\text{g}/\text{cc}$ of chloride ion the iron is corroding and pitting rapidly, thus causing a rapid increase in the surface area which resulted in an increase of 50% in the current density in going from one cycle to the next. The data in Fig. 1-5, as well as each of the points plotted in Fig. 6 and 7 were obtained from separate solutions. The variation between results would probably have been much less for low chloride contents if the data had been taken on a single solution for each of the successively added increments of chloride ion.

It has been observed that a silver or a silver-silver oxide anode would under certain conditions remove Cl^- from a 15% KOH solution as AgCl on the electrode. The optimum conditions were not determined nor is it known to how low a level the Cl^- can be reduced. It does suggest the possibility that the Cl^- content of existing purified electrolytes could be lowered even more in this manner. The silver introduced into the system could be removed by electrodeposition.

This technique might also be useful commercially in keeping the Cl^- content low enough to inhibit appreciably metallic corrosion in a system.

Techniques of this sort might lead the way to the possibility of efficiently removing unreactable impurities. For a given electrolyte containing a given unreactable ionic impurity, a suitable electrode material, temperature, potential, etc., might be found which would make it possible for this ion to react with the electrode and form an insoluble film which then could be removed from the system by removing the electrode.

Highly porous metallic electrodes can be prepared (5) which have surface areas so large that the formation of even a fraction of a monomolecular layer would remove relatively large amounts of a given ionic impurity. This would thus open up the possibility of removing nearly all of the impurities in an electrolyte down to levels that in many cases might approach the approximately 10^{-6} ppm that is now being obtained with reactable impurities. Under these conditions it would be possible to prepare a wide range of reagents whose impurity levels would be several orders of magnitude less than can be achieved with current techniques.

Acknowledgment

This research was supported by the Advanced Research Projects Agency of the Department of Defense, ARPA Order No. 878, under Problem No. M04-08.

Manuscript submitted July 23, 1971; revised manuscript received ca. Dec. 7, 1971.

Any discussion of this paper will appear in a Discussion Section to be published in the December 1972 JOURNAL.

REFERENCES

1. C. M. Shepherd and S. Schuldiner, *This Journal*, **115**, 1124 (1968).
2. J. E. O. Mayne, J. W. Mentor, and M. J. Pryor, *J. Chem. Soc.*, **1950**, 3229.
3. S. Schuldiner and R. M. Roe, *This Journal*, **110**, 332 (1963).
4. S. Schuldiner, T. B. Warner, and B. J. Piersma, *ibid.*, **114**, 343 (1967).
5. C. M. Shepherd and H. C. Langelan, *ibid.*, **109**, 657 (1962).

Anodic Oxidation of Ethylenediaminetetraacetic Acid on Pt in Acid Sulfate Solutions

J. W. Johnson,* H. W. Jiang, S. B. Hanna, and W. J. James*

Departments of Chemical Engineering and Chemistry and the Graduate Center for Materials Research, University of Missouri-Rolla, Rolla, Missouri 65401

ABSTRACT

The anodic oxidation of EDTA was studied in acid sulfate solutions on platinumized-Pt at 25°C . Polarization relationships were obtained for the EDTA concentration range 3.42×10^{-5} to $3.42 \times 10^{-3}\text{M}$ and pH range 0.35 to 3.80. Numerous reaction products were identified that indicated a sequential removal of acetate groups from the EDTA, each by an initial decarboxylation followed by a reverse Schiff-type reaction, that produced formaldehyde and the corresponding amine. A reaction sequence which correlated the experimental data involved Frumkin-type adsorption of the EDTA species through an un-ionized acetate group followed by a rate-determining electrochemical decarboxylation.

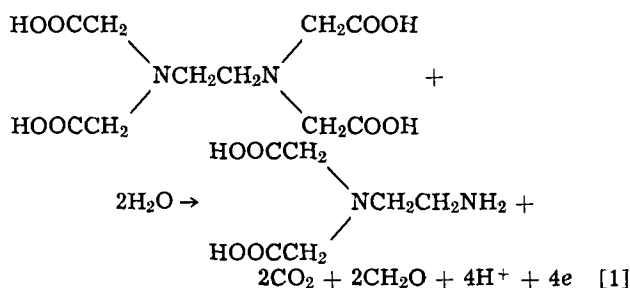
Ethylenediaminetetraacetic acid, commonly abbreviated "EDTA," forms very stable, water-soluble complexes with many metal ions. Because of this, studies

involving EDTA have dealt mainly with complex formation and associated analytical and industrial applications. A few reports have been concerned with electrochemical aspects. One, a polarographic investigation of the products of the anodic oxidation of EDTA on Pt in alkaline solutions, was made by Kopek'a (1).

* Electrochemical Society Active Member.

Key words: ethylenediaminetetraacetic acid, anodic oxidation, decarboxylation.

The over-all anodic reaction proposed was



In another, Rêishakhrit *et al.* (2) studied the oxidation of EDTA on a Pt rotating-disk anode and found increases in the limiting currents with pH. Shifts in the polarization curves with pH were attributed to shifts in the dissociation equilibrium. With carbon paste indicator electrodes, Kitagawa and Tsushima (3) reported a single anodic wave for EDTA in acidic media with $E_{p/2} = 0.93\text{V}$ (vs. SCE).

The presence of EDTA during electrochemical processes (e.g., corrosion, metal dissolution, metal deposition, etc.) is not uncommon. Thus, it is of interest to know if EDTA itself is reactive. The purpose of this investigation was to determine if it could be oxidized on platinized platinum, and if so, to obtain information about the electrochemical reaction kinetics. The investigation included polarization measurements in acid sulfate solutions of various pH, the determination of reaction products and coulombic efficiency for CO_2 production, and the effect of temperature on the reaction rate.

Experimental

The electrolyses were carried out in the usual H-cell (400 ml capacity). All solutions employed analytical grade chemicals and conductivity water. Prepurified nitrogen was bubbled through the electrolyte to provide an inert atmosphere and for stirring. A constant flow rate (50 cm^3/min STP) was maintained through the anode compartment. The electrodes consisted of 52-mesh Pt gauze folded on Pt wire frames for support. They were platinized using a platinum chloride solution to which a trace of lead acetate had been added. The anode had a geometric surface area of 11.5 cm^2 . It was activated in $1.0\text{N H}_2\text{SO}_4$ before each experiment as described previously (4).

The electrolytes for the studies were $\text{H}_2\text{SO}_4 + \text{Na}_2\text{SO}_4$ solutions (pH 0.35-4.0) in which the sulfate concentration was kept constant at unit normality. The EDTA concentration was varied from 3.42×10^{-5} to $3.42 \times 10^{-3}\text{M}$. The polarization measurements were made potentiostatically. A $\text{Hg}/\text{Hg}_2\text{SO}_4$ (1N H_2SO_4) reference electrode was used in conjunction with a salt bridge of the same electrolyte as in the cell. The potentials are reported vs. the standard hydrogen electrode (SHE) at 25°C . Reaction products were determined by standard qualitative analyses and paper electrophoresis. All studies were carried out at 25°C except as noted.

Results

Polarization measurements.—The rest potentials, Tafel slopes, and limiting currents from the polarization studies are summarized in Table I. The rest potentials and limiting currents were affected by the N_2 bubbling rate (the rest potentials decreased and limiting currents increased with increasing bubbling rate). There was no effect on currents in the linear Tafel region. All reported data were taken with the constant N_2 bubbling rate mentioned above. Steady currents at a given potential were obtained within about 25 min and remained quite stable for hours. Individual points were reproducible within $\pm 10\%$.

Semilogarithmic plots of the polarization curves are shown in Fig. 1. There are linear sections in the potential regions slightly above the rest potentials, with

Table I. Rest potentials, Tafel slopes, and limiting currents for the anodic oxidation of EDTA in acid sulfate solutions on Pt at 25°C

EDTA, $\text{M} \times 10^4$	Electrolyte concentration			Rest potential V (SHE)	Tafel slope, V	Limiting current, $\text{A}/\text{cm}^2 \times 10^5$
	$\text{H}_2\text{SO}_4, \text{N}$	$\text{Na}_2\text{SO}_4, \text{N}$	pH			
3.42	1.00	—	0.35	0.803	0.125	1.9
1.027	1.00	—	0.35	0.842	0.130	1.1
0.342	1.00	—	0.35	0.889	0.120	0.65
3.42	0.100	0.900	1.78	0.660	0.130	8.7
1.027	0.100	0.900	1.78	0.698	0.130	2.0
13.7	0.010	0.990	2.74	0.650	0.115	13
3.42	0.010	0.990	2.78	0.679	0.110	3.7
1.027	0.010	0.990	2.80	0.700	0.110	1.9
0.342	0.010	0.990	2.72	0.730	0.120	0.96
34.2	0.001	0.999	2.93	0.623	0.120	30
13.7	0.001	0.999	3.10	0.652	0.105	20
3.42	0.001	0.999	3.59	0.648	0.110	3.4
1.027	0.001	0.999	3.72	0.645	0.110	1.7
0.342	0.001	0.999	3.80	0.665	0.120	0.65

slopes varying from 105 to 130 mV. The limiting current region was reached at potentials of about 0.95V (SHE). No pronounced passivation regions were found.

Two basic solutions, 3.42×10^{-2} and $1.028 \times 10^{-1}\text{M}$ EDTA in 1N NaOH, were also investigated. The polarization curves are shown in Fig. 2. Very small limiting currents were reached at potentials immediately above the rest potentials. Visible oxygen evolution occurred at potentials above 0.78V.

Reaction products.—Qualitative analyses showed the anodic oxidation products of EDTA to be quite numerous. A positive test for CO_2 was obtained by passing the N_2 purge through a saturated $\text{Ba}(\text{OH})_2$ solu-

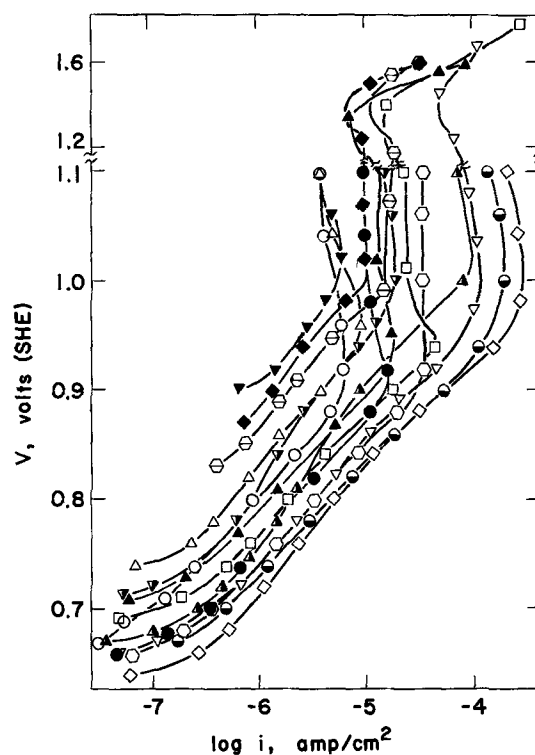


Fig. 1. Polarization curves for EDTA oxidation on Pt in acidic sulfate solutions at 25°C . \ominus , $3.42 \times 10^{-4}\text{M}$ EDTA in 1N H_2SO_4 ; \blacklozenge , $1.027 \times 10^{-4}\text{M}$ EDTA in 1N H_2SO_4 ; \blacktriangledown , $3.42 \times 10^{-5}\text{M}$ EDTA in 1N H_2SO_4 ; \blacktriangle , $3.42 \times 10^{-4}\text{M}$ EDTA in 0.1N $\text{H}_2\text{SO}_4 + 0.9\text{N Na}_2\text{SO}_4$; \blacktriangledown , $1.027 \times 10^{-4}\text{M}$ EDTA in 0.1N $\text{H}_2\text{SO}_4 + 0.9\text{N Na}_2\text{SO}_4$; ∇ , $1.37 \times 10^{-3}\text{M}$ EDTA in 0.01N $\text{H}_2\text{SO}_4 + 0.99\text{N Na}_2\text{SO}_4$; \square , $3.42 \times 10^{-4}\text{M}$ EDTA in 0.01N $\text{H}_2\text{SO}_4 + 0.99\text{N Na}_2\text{SO}_4$; \blacktriangle , $1.027 \times 10^{-4}\text{M}$ EDTA in 0.01N $\text{H}_2\text{SO}_4 + 0.99\text{N Na}_2\text{SO}_4$; \triangle , $3.42 \times 10^{-5}\text{M}$ EDTA in 0.01N $\text{H}_2\text{SO}_4 + 0.99\text{N Na}_2\text{SO}_4$; \diamond , $3.42 \times 10^{-3}\text{M}$ EDTA in 0.001N $\text{H}_2\text{SO}_4 + 0.999\text{N Na}_2\text{SO}_4$; \bullet , $1.37 \times 10^{-3}\text{M}$ EDTA in 0.001N $\text{H}_2\text{SO}_4 + 0.999\text{N Na}_2\text{SO}_4$; \circ , $3.42 \times 10^{-4}\text{M}$ EDTA in 0.001N $\text{H}_2\text{SO}_4 + 0.999\text{N Na}_2\text{SO}_4$; \bullet , $1.027 \times 10^{-4}\text{M}$ EDTA in 0.001N $\text{H}_2\text{SO}_4 + 0.999\text{N Na}_2\text{SO}_4$; \circ , $3.42 \times 10^{-5}\text{M}$ EDTA in 0.001N $\text{H}_2\text{SO}_4 + 0.999\text{N Na}_2\text{SO}_4$.

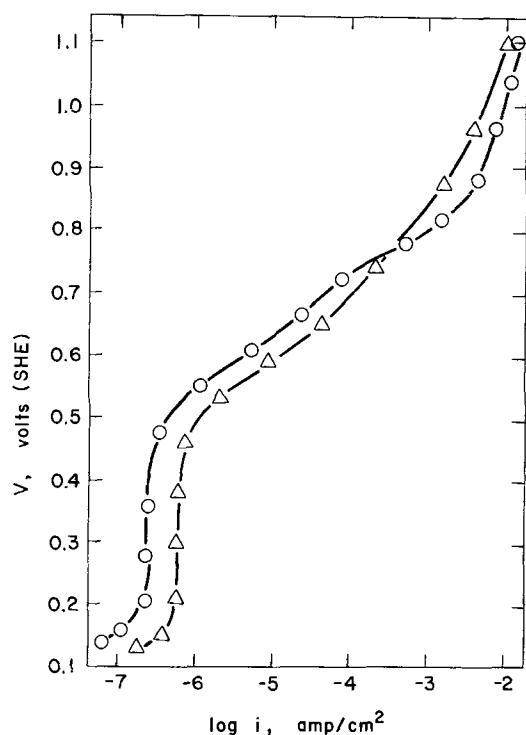


Fig. 2. Polarization curves for EDTA oxidation on Pt in basic solutions at 25°C. ○, 3.42×10^{-2} M EDTA in 1N NaOH; △, 1.027×10^{-1} M EDTA in 1N NaOH.

tion where a white precipitate (BaCO_3) was formed (5). Formaldehyde was detected by determining the melting point of a yellow precipitate formed on addition of a saturated solution of 2,4-dinitrophenylhydrazine (6). Other products in the electrolyte were identified by paper electrophoresis (7), the results of which are shown schematically in Fig. 3. Quantitative measurements of CO_2 production were made galvanostatically for 3.42×10^{-3} M EDTA in 10^{-3} N $\text{H}_2\text{SO}_4 + 0.999$ N Na_2SO_4 at potentials in the linear Tafel region. The average efficiency based on Eq. [1] was $124 \pm 6\%$.

Temperature dependence.—Arrhenius plots of current vs. temperature for 3.42×10^{-3} M EDTA in 10^{-3} N $\text{H}_2\text{SO}_4 + 0.999$ N Na_2SO_4 are shown in Fig. 4 for poten-

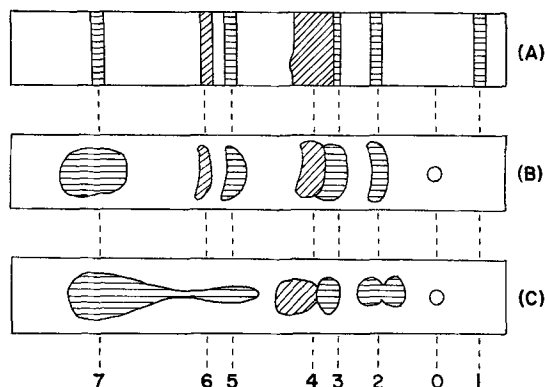


Fig. 3. Products of EDTA oxidation on Pt in acidic sulfate solutions at 25°C. (A) Standard tape. (B) 3.42×10^{-4} M EDTA in 1N H_2SO_4 , polarized at 1.2×10^{-4} A for 83 hr. (C) 3.42×10^{-4} M EDTA in 0.01N H_2SO_4 , polarized at 1.1×10^{-3} A for 75 hr. Electrophoretic separation in 1M acetic acid at 5 mA for 45 min, color developed with ninhydrin: horizontal hatch, purple bands; diagonal hatch, yellow bands. Bands: 1. IMDA and ED3A (iminodiacetic acid and ethylenedinitrioltriacetic acid), 2. S-EDDA and U-EDDA (N,N'-ethylenediglycine and N,N'-ethylenediglycine), 3. GL (glycine), 4. S-KP (2-oxo-1-piperazineacetic acid), 5. EDMA (N-(2-aminoethyl)glycine), 6. 2-KP (2-oxopiperazine), 7. EDA (ethylenediamine).

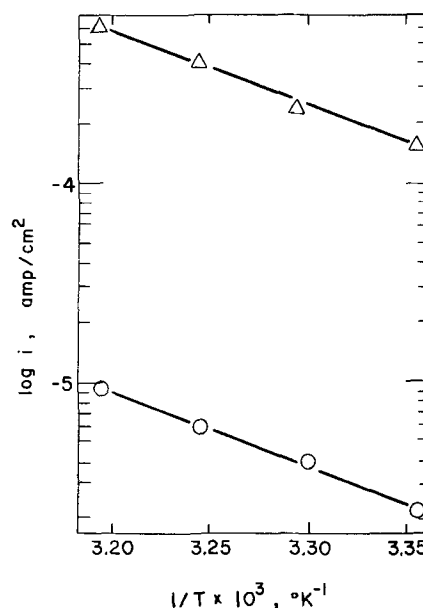
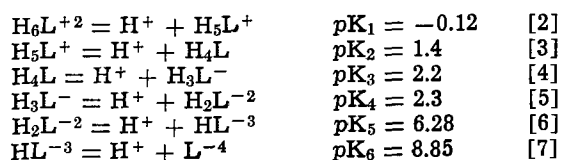


Fig. 4. Effect of temperature on current for oxidation of 3.42×10^{-3} M EDTA in 0.001N $\text{H}_2\text{SO}_4 + 0.999$ N Na_2SO_4 on Pt. ○, 0.76V; △, 0.86V.

tials of 0.76 and 0.86V (SHE). The slopes of the two straight lines yielded activation energies of 18.4 and 17.0 kcal, respectively. These further give an effect of potential on the activation energy, $\partial E_a/\partial V$, of ca. -14 kcal/V which is consistent with the Tafel slopes.

Discussion

Limiting currents.—An initial consideration of the limiting (potential-independent) currents, i_L , from the polarization curves indicated them to be of the same order of magnitude as diffusion currents. However, the expected first-order dependence between current and concentration (8) was not found when the total EDTA concentration was used. This, together with the absence of reaction prior to oxygen evolution in basic solutions, suggested that some EDTA species may be preferentially participating. It is well known that EDTA engages in various equilibria with hydrogen ions with reported species covering the complete spectrum from H_6L^{+2} to L^{-4} .¹ Constants for these equilibria have been reported and are given in Eq. [2]-[7].



There is a considerable variation in the values of these constants reported by various investigators. All the values in Eq. [2]-[7] were from a single source, those reported by Anderegg (9). The concentrations of the EDTA species in all the electrolytes were calculated and are shown in Table II. The hydrogen ion activities used in the calculations were evaluated directly from the measured pH. For all other species, the activities and concentrations were assumed equal.

A comparison of the limiting currents with concentrations of the individual species (Tables I and II) shows that no single species can account for the reaction over the entire region studied. Various combinations of species were tried and the one most successful in correlating the data was the summation of the concentrations of the species H_5L^+ , H_4L , H_3L^- , H_2L^{-2} , and HL^{-3} . A log-log plot of i_L vs. C_{Σ}^2 is shown in Fig. 5 with a straight line of unit slope drawn through the

¹ With this symbolic representation, H_6L = un-ionized EDTA.
² Sum of the concentrations of species H_5L^+ through HL^{-3} .

Table II. Concentrations of EDTA species in acid sulfate solutions at 25°C

pH	a_{H^+}	$[H_4L]_0, M$	$[H_5L^{+2}], M$	$[H_6L^+], M$	$[H_7L], M$	$[H_8L^-], M$	$[H_9L^{-2}], M$	$[HL^{-3}], M$	$[L^{-4}], M$
0.35	0.447	3.422×10^{-4}	8.112×10^{-4}	2.394×10^{-4}	2.134×10^{-5}	3.014×10^{-7}	3.382×10^{-9}	3.973×10^{-15}	1.256×10^{-28}
0.35	0.447	1.027×10^{-4}	2.434×10^{-5}	7.182×10^{-5}	6.401×10^{-5}	9.042×10^{-8}	1.018×10^{-9}	1.192×10^{-15}	3.769×10^{-24}
0.35	0.447	3.422×10^{-5}	8.112×10^{-6}	2.394×10^{-5}	2.134×10^{-6}	3.014×10^{-8}	3.382×10^{-10}	3.973×10^{-16}	1.256×10^{-24}
1.78	1.660×10^{-2}	3.422×10^{-4}	9.367×10^{-7}	7.440×10^{-5}	1.785×10^{-4}	6.786×10^{-5}	2.049×10^{-5}	6.480×10^{-10}	5.516×10^{-17}
1.78	1.660×10^{-2}	1.027×10^{-4}	2.810×10^{-7}	2.232×10^{-5}	5.354×10^{-5}	2.036×10^{-5}	6.148×10^{-6}	1.944×10^{-10}	1.655×10^{-17}
2.74	1.820×10^{-3}	1.369×10^{-3}	6.140×10^{-9}	4.448×10^{-6}	9.732×10^{-4}	3.374×10^{-4}	9.293×10^{-4}	2.680×10^{-7}	2.080×10^{-13}
2.78	1.660×10^{-3}	3.422×10^{-4}	1.100×10^{-9}	8.736×10^{-7}	2.096×10^{-5}	7.967×10^{-5}	2.406×10^{-4}	7.608×10^{-8}	6.476×10^{-14}
2.80	1.585×10^{-3}	1.027×10^{-4}	2.789×10^{-10}	2.320×10^{-7}	5.828×10^{-6}	2.320×10^{-5}	7.337×10^{-5}	2.429×10^{-8}	2.165×10^{-11}
2.72	1.906×10^{-3}	3.422×10^{-5}	1.811×10^{-10}	1.253×10^{-7}	2.618×10^{-6}	8.668×10^{-6}	2.280×10^{-5}	6.280×10^{-9}	4.655×10^{-15}
2.93	1.175×10^{-3}	3.422×10^{-3}	3.070×10^{-9}	3.444×10^{-6}	1.167×10^{-4}	6.268×10^{-4}	2.674×10^{-3}	1.194×10^{-6}	1.436×10^{-12}
3.10	7.943×10^{-4}	1.369×10^{-3}	2.784×10^{-10}	4.620×10^{-7}	2.315×10^{-5}	1.839×10^{-4}	1.160×10^{-3}	7.667×10^{-7}	1.363×10^{-12}
3.59	2.570×10^{-4}	3.422×10^{-4}	8.528×10^{-13}	4.373×10^{-9}	6.774×10^{-7}	1.663×10^{-5}	3.242×10^{-4}	6.619×10^{-7}	3.638×10^{-12}
3.72	1.906×10^{-4}	1.027×10^{-4}	7.826×10^{-14}	5.414×10^{-10}	1.131×10^{-7}	3.746×10^{-6}	9.852×10^{-5}	2.714×10^{-7}	2.012×10^{-12}
3.80	1.585×10^{-4}	3.422×10^{-5}	1.256×10^{-14}	1.045×10^{-10}	2.624×10^{-8}	1.045×10^{-6}	3.304×10^{-5}	1.094×10^{-7}	9.750×10^{-38}

points. Although there is a great deal of scatter, the trend is correct and covers the entire concentration range. A least squares analysis of the data gives a slope of 0.8 ± 0.1 .

Product analyses.—The product analyses suggest that the oxidation of EDTA proceeds along at least two

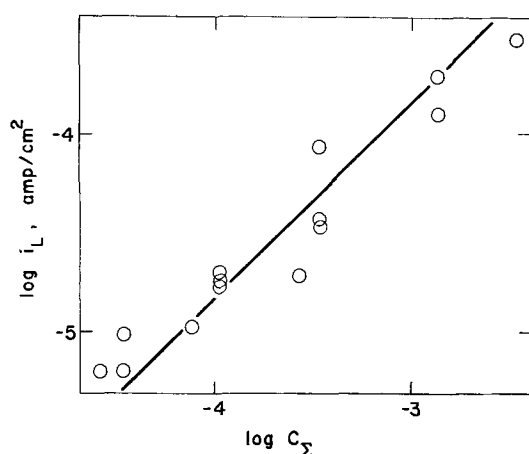


Fig. 5. Limiting currents for EDTA oxidation on Pt in acidic sulfate solutions at 25°C.

paths. Such a reaction scheme is shown in Fig. 6 for which all the species were identified with the exception of ED3A, 3-KP, U-KP, and S-KP. The paper-electrophoresis method used was not sensitive to the latter three, and according to Doran (7), the cyclization of ED3A to 3-KP is so extensive in acid solutions that ED3A cannot be detected. Separate studies have indicated that equilibria are reached in the other cyclization reactions ($U-KP \rightleftharpoons U-EDDA$, $S-KP \rightleftharpoons S-EDDA$, and $2-KP \rightleftharpoons EDMA$) in which appreciable quantities of both species exist (10). From the product distribution, it appears that each decarboxylation step is a separate electrochemical reaction that gives a desorbed product capable of further similar reactions as long as acetate groups are available. This indicates adsorption through the carboxylate group with a Hofer-Moest-type reaction (11) occurring which involves the loss of two electrons, decarboxylation, and a reaction with water (not necessarily in that order) to form an alcohol. The two most common sequences offered to explain such reactions involve free-radical and/or carbonium ion intermediates. In both sequences, the first electron transfer is thought to form a free radical which leads to decarboxylation, i.e.

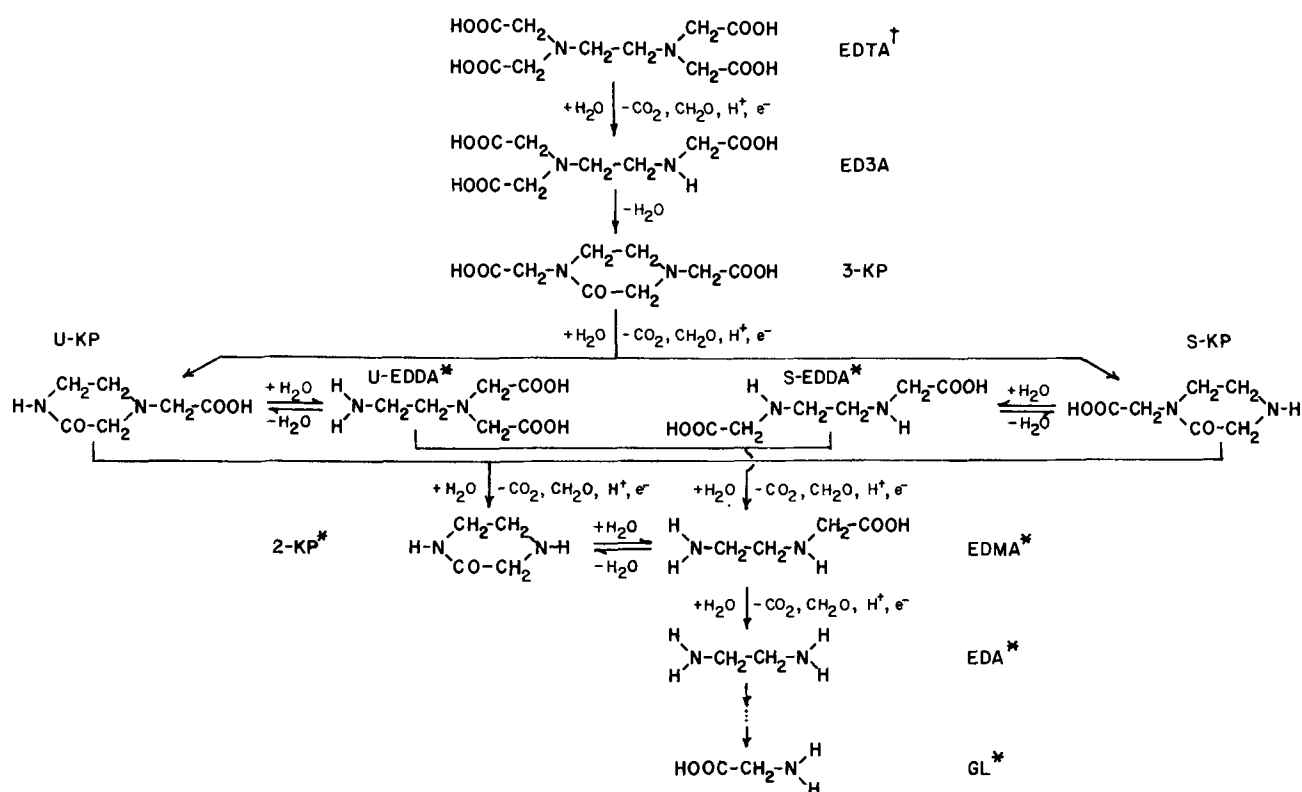
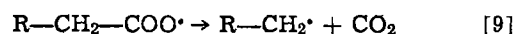
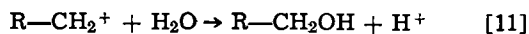
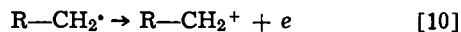
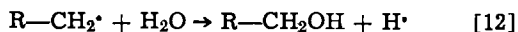


Fig. 6. Suggested reaction scheme for EDTA oxidation on Pt in acidic sulfate solutions at 25°C. †, Representative of any of the reactive species; *, species identified by paper electrophoresis, bands shown in Fig. 3.

At this point the sequences diverge with $R-CH_2\cdot$ either forming a carbonium ion by the second electron transfer or reacting to form another intermediate that may or may not involve an electron transfer. These can be represented by



and

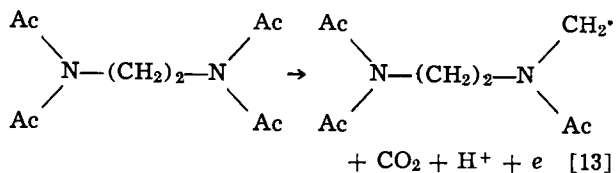


In either case with EDTA, the group $-N-CH_2OH$ is formed which is unstable and produces formaldehyde

through a reverse Schiff-type reaction, leaving $-NH$ (12). A feature that might allow one to distinguish between these two possibilities is the opportunity for different coulombic efficiencies for CO_2 production. In the first case (Eq. [10] and [11]), the carbonium ion is believed to be formed by electron transfer to the anode (13) which gives 1 mole of CO_2 per 2F of charge as shown in Eq. [1]. (Also implied here is the continued adsorption of the reacting species until after formation of the carbonium ion.) In the second case, it is possible that the radical $R-CH_2\cdot$ may have been desorbed during decarboxylation and that Eq. [12] represents a homogeneous reaction. (This is consistent with adsorption through the carboxylate group as mentioned above.) The $H\cdot$ produced in this manner could be oxidized at the anode which would again give $1CO_2/2F$, but there is also opportunity for it to participate in some homogeneous reaction which would lead to $1CO_2/F$. If this latter reaction should occur, CO_2 efficiencies (based on Eq. [1]) greater than 100% would be observed. As seen above, efficiencies greater than 100% were found experimentally, thus favoring the sequence of Eq. [8], [9], and [12].

If adsorption had occurred through bonding with the nitrogen (as opposed to adsorption through the carboxylate), one would expect both the acetate groups to be removed before desorption with only U-EDDA and EDA as products as well as a $1CO_2/2F$ coulombic efficiency.

Rest potentials.—According to the reaction scheme shown in Fig. 6 and discussed in the above section, the initial electrochemical reaction is between EDTA and the precursor to ED3A and involves only one electron. (The proceeding reactions will become significant only when sufficient current has passed so that appreciable quantities of the subsequent reactants are produced.) Thus, the measured rest potentials may reflect the reaction



Although the CO_2 and ED3A precursor ($R\cdot$) concentrations are not known and their standard free energies of formation are not available to allow a comparison of the rest and calculated potentials, the Nernst equation will allow a test of the effect of EDTA concentration and pH on the potential. At 25°C, the relation for Eq. [13] is

$$E = E_{13} - 0.0591 \log(a_{EDTA}) / (a_{R\cdot})(a_{CO_2})(a_{H^+}) \quad [14]$$

Assuming $a_{R\cdot}$ and a_{CO_2} constant and $a_{EDTA} = C_{\Sigma}$ gives

$$E = E_{13} - 0.0591 \log(C_{\Sigma}/a_{H^+}) \quad [15]$$

(C_{Σ} is the concentration of the species as mentioned previously.) A plot of E_{rest} vs. $\log(C_{\Sigma}/a_{H^+})$ is shown in Fig. 7. The relationship is linear and has a slope

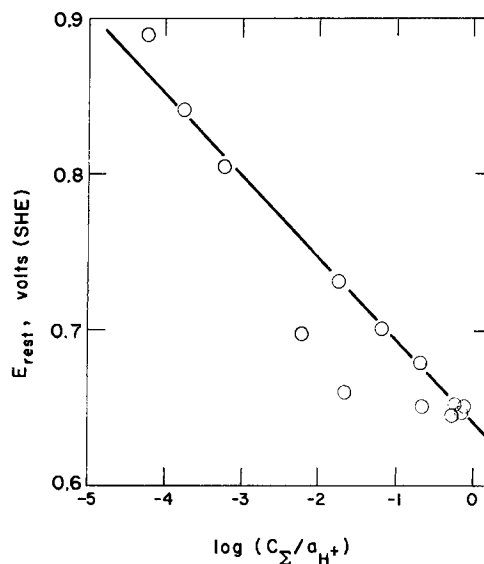


Fig. 7. Rest potentials for EDTA on Pt in acidic sulfate solutions at 25°C.

of 55 mV, in good agreement with that predicted by Eq. [15].

Polarization curves.—The oxidation of EDTA is seen to occur at potentials somewhat more positive than those for other organic compounds where CO_2 is produced (exclusive of Kolbe-type syntheses). For example in 1N H_2SO_4 , ethylene (4) oxidizes in the potential region from ca. 0.35 to 0.75V; formic acid (14), 0.15 to 0.45V; oxalic acid (15), 0.5 to 0.8V; and maleic acid (16), 0.35 to 0.60V. Acetic acid has been reported not to be reactive (17). In the majority of these cases, adsorption of the organic species was thought to involve the formation of bonds between C and Pt atoms, and passivation was observed between the upper potential limit for the organic oxidation and that for the commencement of oxygen evolution. The passivation ordinarily occurred in the region where EDTA has been found to be oxidized. This absence of passivation with EDTA indicates a different type of adsorption bonding that can presumably take place on an oxide-covered surface. Considering the apparent step-wise decarboxylation, the adsorption reaction thus appears to involve the carboxylate group and the electrode surface.

The Tafel slopes of ca. 120 mV or $2(2.3RT/F)$, are ones frequently encountered in electrochemical kinetic studies and normally associated with first-electron-transfer rate determining steps. The concentration and pH effects were unusual in that they were both fractional and approximately equal. The EDTA concentration effect (reaction order) was fairly well defined as 0.36 from the experiments in 1N H_2SO_4 where the pH was constant. It should be noted from Table I for 1N H_2SO_4 that the fraction of EDTA forming any of the individual species is independent of the initial EDTA concentration. Thus, the same reaction order (~ 0.36) would be found for any individual or combination of EDTA species. By a trial and error procedure, it was found that a pH effect also of 0.36 in conjunction with the concentration of EDTA species, C_{Σ} , best correlated the data. A log-log plot of i vs. $(C_{\Sigma}/a_{H^+})^{0.36}$ is shown in Fig. 8 for the entire EDTA concentration and pH region of the study. The line of unit slope drawn through the points show the data to be reasonably well correlated. This gives an empirical expression for the current as

$$i = nFk(C_{\Sigma}/a_{H^+})^{0.36} \exp(\alpha FV/RT) \quad [16]$$

Reaction mechanism.—From the preceding, several qualitative conclusions can be drawn about the reaction mechanism:

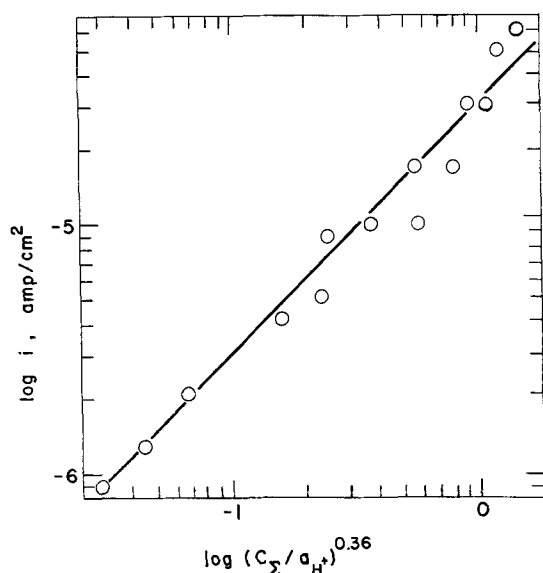


Fig. 8. Effect of concentration and pH on current for EDTA oxidation on Pt in acidic sulfate solutions at 25°C.

1. The rds (rate determining step) involves EDTA species or species derived therefrom since the concentration effect is positive.

2. The fractional concentration effect indicates that the EDTA species are adsorbed and that significant, although not complete, coverages are involved.

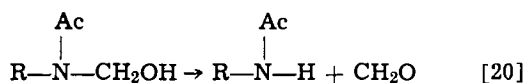
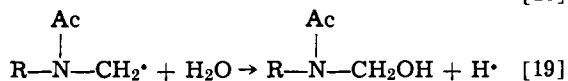
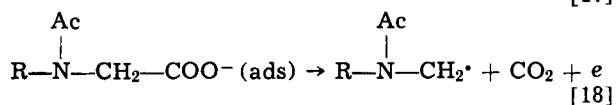
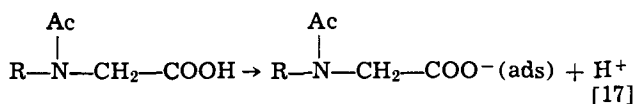
3. The positive pH effect indicates OH^- as a reactant or H^+ as a product during or prior to the rds. Since the OH^- concentration is very small, the latter case would be the most probable and would necessarily occur in an equilibrium step prior to the rds.

4. From the product analyses, there appears to be separate step-wise over-all reactions involving the acetate groups on EDTA, each of which yields CO_2 and CH_2O . From the rest potential and CO_2 efficiency studies, it further appears that only one electron is transferred to the faradaic circuit during the reaction that directly involves CO_2 production from the acetate group of the EDTA species.

5. From the concentration correlations for both the current and rest potentials, the pH effect, and the absence of reaction in basic solutions where L^{-4} is the predominant species, it appears that an un-ionized carboxyl group may be initially involved in the reaction sequence.

6. The occurrence of the reaction in a potential region where the anodic oxidation of ethylene, acetylene, etc. is passivated indicates that water discharge is not involved.

With these considerations, the initial electrochemical sequence ($\text{EDTA} \rightarrow \text{ED3A}$, Fig. 6) can be represented as follows³



The atomic hydrogen produced by reaction [19] can be oxidized at the anode and contribute to the faradaic

³ Species shown in these reactions are nonadsorbed unless otherwise indicated.

process or be removed by some nonelectrochemical reaction causing the CO_2 efficiency (based on Eq. [1]) to be increased. The ED3A thus produced can participate further in the sequence as shown in Fig. 6.

The type of adsorption (e.g., Langmuir, Temkin, etc.) as well as the nature and position of the rds in a reaction sequence can affect the associated kinetic parameters. For Langmuir-type adsorption, a first electron transfer rds is normally associated with the Tafel slope of 120 mV. For this case (reaction [18]), an EDTA concentration effect either close to zero or unity should be observed for conditions where this type adsorption is applicable, i.e., either high or low coverages. This does not appear to be the case.

The Temkin isotherm is often assumed for intermediate coverages when lateral interactions between adsorbed species are appreciable. For EDTA with the same rds (reaction [18]), Temkin-type adsorption gives a Tafel slope of 120 mV and concentration dependences $(a_{\text{EDTA}}/a_{\text{H}^+})^{0.5}$. These concentration effects are reasonably close to the observed values although 0.5 gives a poorer correlation than the value of 0.36 illustrated in Fig. 8. The use of the Frumkin isotherm allows a better correlation, primarily due to the added adjustable parameter associated with the variation of free energy of adsorption with coverage (18). This isotherm takes into account long-range interactions between adsorbed species which may be especially applicable due to the geometry of the EDTA molecule. Its application to the present case is as follows:

$$\begin{aligned} \tau_{17} = & k_{17} a_{\text{EDTA}} \theta_v \exp(-\beta\theta/RT) \\ & - k_{-17} \theta_R \cdot a_{\text{H}^+} \exp[(f-\beta)\theta/RT] \end{aligned} \quad [21]^4$$

Assuming quasi-equilibrium and the effect of coverage to be predominately controlled by the exponential terms gives

$$f\theta/RT = \ln(K_{17} a_{\text{EDTA}}/a_{\text{H}^+}) \quad [22]$$

From the rate determining step, reaction [18]

$$i = nFk_{18} \theta_R \cdot \exp(\alpha FV/RT) \exp(\beta\theta/RT) \quad [23]^4$$

Again assuming the exponential term to dominate the effect of coverage and substituting Eq. [22] into Eq. [23]

$$i = nFk' (a_{\text{EDTA}}/a_{\text{H}^+})^{\beta/f} \exp(\alpha FV/RT) \quad [24]$$

The term β/f can be made equal to 0.36 by assigning the appropriate value to the adjustable parameter f , thus making Eq. [24] correspond to the empirical rate expression, Eq. [16]. For the present case, f would equal 1.4 (assuming $\beta = 0.5$).

Acknowledgments

This paper is based on a thesis submitted by one of us (H.W.J.) for the M.S. degree in Chemical Engineering at the University of Missouri-Rolla. It is Contribution No. 131 from the Graduate Center for Materials Research, UMR.

Manuscript submitted July 6, 1971; revised manuscript received Dec. 18, 1971.

Any discussion of this paper will appear in a Discussion Section to be published in the December 1972 JOURNAL.

⁴ The symbols θ_v and θ_R refer to the fractions of the reaction surface that are available for reaction and covered by R, respectively.

REFERENCES

1. L. Kopeck'a, *Chem. Listy*, **50**, 1085 (1956).
2. L. S. Reishakhrit, V. N. Martynova, and Z. I. Tikhonova, *Ser. Fiz. Khim.*, **1**, 146 (1965).
3. T. Kitagawa and S. Tsushima, *Bull. Chem. Soc. Japan*, **39**, 636 (1966).
4. H. Wroblowa, B. J. Piersma, and J. O'M. Bockris, *J. Electroanal. Chem.*, **6**, 401 (1963).
5. R. K. McAlpine and B. A. Soule, "Qualitative Chemical Analysis," p. 448, D. Van Nostrand Co., New York (1933).

6. N. D. Cheronis and J. B. Entrikin, "Identification of Organic Compounds," p. 137, John Wiley & Sons Inc., New York (1967).
7. M. A. Doran, *Anal. Chem.*, **33**, 1752 (1961).
8. E. C. Potter, "Electrochemistry," p. 144, MacMillan Co., New York (1961).
9. G. Anderegg, *Helv. Chim. Acta*, **50**, 2333 (1967).
10. S. B. Hanna, Private communication.
11. B. J. Piersma and E. Gileadi, "Modern Aspects of Electrochemistry," Vol. 4, p. 52, J. O'M. Bockris, Editor, Plenum Press, New York (1966).
12. R. Q. Brewster, "Organic Chemistry," p. 271, Prentice-Hall, Inc., New York (1948).
13. A. K. Vijh and B. E. Conway, *Chem. Rev.*, 623 (1967).
14. S. B. Brummer and A. C. Makrides, *J. Phys. Chem.*, **68**, 1448 (1964); C. W. Fleischmann, G. K. Johnson, and A. T. Kuhn, *This Journal*, **111**, 602 (1964); M. H. Gottlieb, *This Journal*, **111**, 465 (1964).
15. J. W. Johnson, H. Wroblowa, and J. O'M. Bockris, *Electrochim. Acta*, **9**, 639 (1964).
16. J. W. Johnson and L. D. Gilmartin, *J. Electroanal. Chem.*, **15**, 231 (1967).
17. B. J. Piersma and E. Gileadi, "Modern Aspects of Electrochemistry," Vol. 4, p. 118, J. O'M. Bockris, Editor, Plenum Press, New York (1966).
18. E. Gileadi, "Electrosorption," p. 12, Plenum Press, New York (1967).

The Anodic Oxidation of Hydrogen on Platinized Tungsten Oxides

I. Composition of Tungsten Blue in Platinized WO₃ Hydrogen Electrocatalyst

B. S. Hobbs¹ and A. C. C. Tseung

Department of Chemistry, The City University, St. John Street, London EC1V 4PB, England

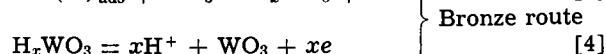
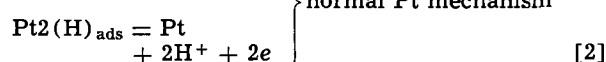
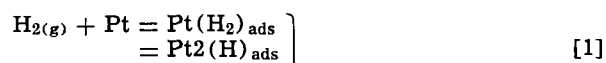
ABSTRACT

A synergistic effect is apparent when Pt/WO₃ catalysts are used in hydrogen electrodes. The exact mechanism of this effect depends on the composition and mode of formation of a reduced intermediate tungsten oxide. Chemical analysis and x-ray studies confirmed that this intermediate oxide consists of blue tungsten bronzes. The influence of Pt loading, platinizing technique, temperature, and pH on the bronze composition was investigated. The maximum reduction (H_{0.44}WO₃) was obtained using WO₃ impregnated with 0.8 weight per cent (w/o) Pt in acidic solution between 25° and 100°C.

When platinum is admixed with WO₃, it undergoes an apparent enhancement in its ability to catalyze the anodic oxidation of hydrogen in acid solution (1-3). WO₃ alone has no activity towards H₂-oxidation. Past workers have been unable to make definite conclusions on the origin of this effect owing to difficulties encountered in eliminating electrode structural effects from their results. Thus, the higher activity observed with WO₃ electrodes compared to other platinized substrates [e.g., graphite or TaC (2, 3)] could have arisen from differences in Pt morphology or physical electrode parameters such as wetting, permeability, etc. However, an alternative explanation has been proposed in which WO₃, in physical contact with Pt, participates in the electrode reaction via formation of hydrogen tungsten bronzes (2).

Hydrogen tungsten bronzes belong to a general class of nonstoichiometric mixed oxides (4) of general formula A_xM_yO_z; where M is a transition metal, M_yO_z its highest binary oxide, A is some other metal or hydrogen, and x is a variable, usually 0 < x < 1. Formation of blue hydrogen tungsten bronzes generally occurs whenever WO₃ is exposed to reducing conditions, e.g., gaseous atomic hydrogen (5-10), treatment of aqueous suspensions of WO₃ with reducing agents (11-14) (*viz.* Zn/HCl, SnCl₂, etc.), but of special interest to this study is their appearance in mixtures of platinized WO₃ when exposed to H₂, particularly in the presence of water vapor (15, 16). According to Benson *et al.*, gaseous H₂ dissociatively chemisorbs on the Pt then

migrates across the metal/oxide interface to form bronzes. The migration is considerably aided by the presence of an adsorbed water layer when an exchange mechanism operates and the WO₃ particles are rapidly reduced in depth. Bronze oxides are characteristically chemically inert, metallic conductors of electricity and the H-compounds are typical group members, except that they are sensitive towards oxidizing conditions which reconvert them to the parent oxide (13), e.g., air, hydrogen peroxide, oxidizing ions such as Fe³⁺ and Ce⁴⁺, and presumably anodic potentials. Thus a reaction scheme can be formulated for the H₂-electrode to include the WO₃ support, namely



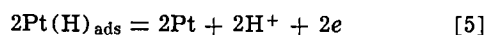
By means of the bronze route the reaction zone can be extended and the Pt appears to increase its activity. No such possibility exists for graphite or TaC which can be termed "passive" catalyst supports, WO₃ being an "active" support.

Both moist Pt/WO₃ powders, and suspensions in acidic solutions, rapidly turn blue when exposed to H₂, indicating partial reduction of the oxide. However, this "tungsten blue" may consist of either, or both, of two classes of compound, namely the lower tungsten oxides (17, 18) (WO_x, where 2 < x < 3) or hydrogen

¹ Present address: Electrical Research Association, Cleeve Road, Leatherhead, Surrey, England.

Key words: hydrogen, oxidation, platinized tungsten oxides, tungsten bronzes, tungsten blue, chemical analysis, x-ray studies, H₂ uptake, crystal structure.

bronzes. Although direct reduction of WO_3 to lower oxides by H_2 at room temperature does not occur (19), they could form by local cell action between the hydrogenated Pt surface and WO_3



Although the reduction of WO_3 to W_2O_5 (or $\text{WO}_{2.5}$) is not thermodynamically favored at normal H_2 anode potentials [$E^\circ \text{WO}_3/\text{W}_2\text{O}_5 = -0.03\text{V}$ (20)], reduction might occur through the formation of nonstoichiometric WO_3 [$\text{WO}_{3.00-2.95}$ (18)], the stable intermediate phase $\text{W}_{20}\text{O}_{58}$ (17, 18) or solid solutions of lower oxide phases, for which no thermodynamic data could be found. Bronze formation is also possible by local cell action and again no thermodynamic data is available for such reactions



In any system whereby local cells are the sole means of WO_3 reduction, e.g., via the lower oxides of tungsten, no net contribution to the steady state anodic current is possible since all the anodic current will be cancelled by the cathodic reducing current (reactions [6] and [7] above). The oxide will equilibrate at any given working potential and the local cells will merely provide a mechanism for electron conduction between the Pt particles and current collector.

Benson *et al.* (15, 16) have studied tungsten blue formation in a vacuum system and shown it to consist exclusively of bronzes formed by chemical reduction (reaction [3]). However, in view of the importance of the nature and mode of formation of the reduction product to the electrochemical oxidation of H_2 , it is necessary to confirm this finding under conditions closer to those in a fuel electrode, *viz.* Pt/ WO_3 slurries in 5N H_2SO_4 between ambient temperature and 80°C and 1 atm of bubbling H_2 .

Experimental

Using x-ray diffraction and analytical techniques, the tungsten blue composition was determined as a function of: (i) platinizing method, *viz.* mechanical mixing and impregnation—this has been shown to exert considerable influence on both the rate of tungsten blue formation (15) and the electrochemical performance (2); (ii) Pt content; (iii) pH of slurry; and (iv) temperature.

Due to the extreme sensitivity of tungsten blue to air, all preparations and analyses were carried out in completely O_2 -free conditions.

Materials.—(i) Impregnation of WO_3 —to ensure a high, uniform and intimate dispersion of Pt on the oxide, a freeze drying technique was employed for the impregnation (21, 22): A slurry of WO_3 powder, suspended in chloroplatinic acid solution, was quickly frozen by pouring into liquid nitrogen. The water was then removed by vacuum sublimation and the Pt-salt reduced to metal in a warm H_2 stream (50°C) below its melting point (60°C). Complete decomposition was checked by weighing before and after reduction.

The Pt content was analyzed by extracting the WO_3 with warm NaOH solution and weighing the washed and dried Pt residue. This residue was also used for surface area determination by "BET nitrogen adsorption." Blank Pt black samples were measured for surface area before and after NaOH treatment to ensure that the area remained unaltered during the extraction procedure. Specific surface areas of extracted Pt residues were all around 35 m^2/g .

(ii) WO_3 and chloroplatinic acid—Hopkin and Williams laboratory reagent grade chemicals were used without further purification. The measured specific surface area of WO_3 was 8 m^2/g .

(iii) Pt-black used in mechanical mixtures—Johnson Matthey Company fuel cell grade, specific surface area 30 m^2/g .

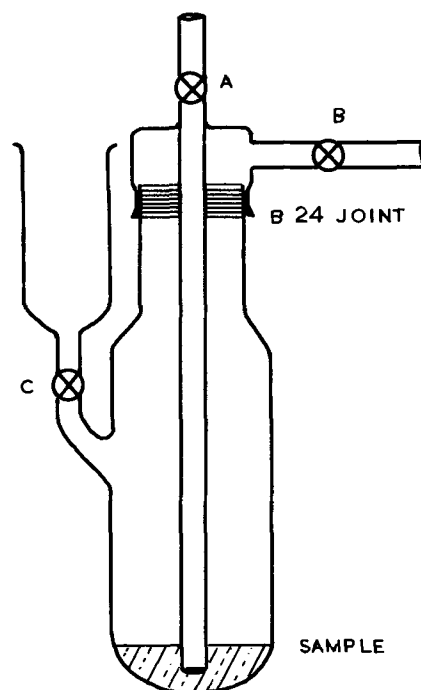


Fig. 1. Apparatus for tungsten blue analysis

(iv) 5N sulfuric acid was prepared from ANALAR grade concentrated acid and distilled/deionized water.
(v) White spot H_2 , purified with a palladium diffuser, was used throughout.

H_2 -uptake experiments.—Before carrying out the tungsten blue preparations, the time required to reach equilibrium was determined using a conventional volumetric apparatus at 1 atm pressure and ambient temperature. With impregnated powders the H_2 -uptake volume reached a limiting value after about 1 hr corresponding to a tungsten blue composition of $\text{H}_{0.44}\text{WO}_3$ or $\text{WO}_{2.78}$. The time taken to reach this value is almost certainly controlled by H_2 mass transfer through the slurry. In practical fuel electrodes the conditions are designed to achieve high transfer rates and the oxide composition will change much more rapidly.

In all experiments involving tungsten blue preparation a standard H_2 -contact time of 2 hr was used.

Analysis of tungsten blue.—Tungsten blue was prepared and analyzed in the apparatus shown in Fig. 1 as follows: Tap A was connected to N_2 (O_2 -free) and H_2 supplies. After N_2 purging, H_2 was bubbled from A through a weighed platinized WO_3 sample suspended in 5N H_2SO_4 . The H_2 was turned off after 2 hr and a measured volume of standard potassium dichromate solution admitted through tap C. The vessel contents were heated to ca. 60°C, when the blue color changed to yellow indicating complete oxidation. The cooled vessel contents were transferred to a beaker and the excess dichromate back-titrated with standardized ferrous ammonium sulfate solution. The end point was determined potentiometrically using a platinized wire indicator electrode with a glass standard electrode. In all cases a small correction was made to the titre to allow for reaction with H_2 adsorbed on the Pt surface.

Preparation of tungsten blue for x-ray diffraction.—The apparatus, shown schematically in Fig. 2, is a modified version of that described by Glemser and Naumann (13). Taps A_1 , A_2 , and A_3 were connected to N_2 (O_2 -free) and H_2 supplies. The flask contained distilled water, freed of O_2 by boiling during the passage of N_2 from A_2 and out the pressure release valve. After purging with N_2 and sealing the capillary, H_2 was bubbled through the sample suspended in H_2SO_4 , from A_2 and out B_2 , for 2 hr. The tungsten blue formed

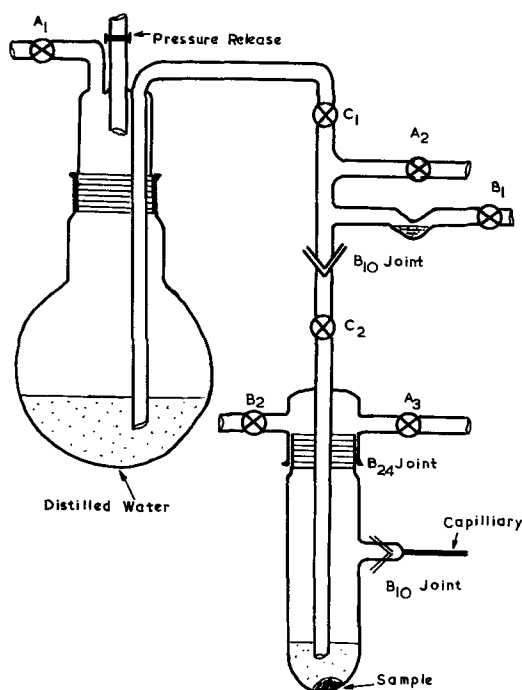


Fig. 2. Preparation of tungsten blue for x-ray examination

was washed by decantation—pressurized H_2 from A_3 forced the supernatant liquor from the settled suspension through C_2 and out B_1 . Water from the flask was forced onto the sample by pressurizing at A_1 . This procedure was repeated until the washings were neutral (pH 7.0). After the final wash all taps were closed and the apparatus below the B_{10} joint (between C_1 and C_2) detached and fused into a high vacuum line ($< 10^{-5}$ Torr) at the B_2 outlet. The product was dried by evacuation through B_2 , then after closing B_2 and detaching from the vacuum line, a sample of powder was sealed into the capillary by lying the vessel on its side, gently vibrating the powder, then when sufficiently full, applying a spot flame to remove and seal the capillary without releasing the vacuum.

X-ray powder photographs were taken of the samples using an 11.4 cm Phillips camera, copper $K\alpha$ radiation and exposure times of 8 hr. Lattice d-spacings were calculated from the patterns to within $\pm 0.005\text{\AA}$ from the Bragg equation.

In order to simplify the glassblowing of the apparatus, Pyrex capillaries were used instead of the usual Lindemann glass. Diffraction photographs of WO_3 using both materials showed no differences.

Results and Discussion

Analytical results.—The analytical results are summarized in Table I. The reproducibilities of the quoted values agreed closely with the estimated limits of experimental error which were as follows: tungsten oxi-

Table I. Analytical data for platinized WO_3

Powder	Platinum (wt %)	Temperature ($^{\circ}C$)	pH	W oxidation state	Equivalent bronze	Equivalent lower oxide
Pt/ WO_3 mech. mixt.	2	25	-0.3	5.86	$H_{0.14}WO_3$	$WO_{2.03}$
Pt/ WO_3 mech. mixt.	2	25	-0.3	5.86	$H_{0.14}WO_3$	$WO_{2.03}$
Pt/ WO_3 mech. mixt.	2	25	7.0	5.99	$H_{0.01}WO_3$	$WO_{2.005}$
Pt/ WO_3 mech. mixt.	2	25	2.0	5.86	$H_{0.14}WO_3$	$WO_{2.03}$
Pt/ WO_3 mech. mixt.	2	25	0.5	5.86	$H_{0.14}WO_3$	$WO_{2.03}$
Pt/ WO_3 mech. mixt.	10	25	-0.3	5.73	$H_{0.27}WO_3$	$WO_{2.87}$
Pt/ WO_3 mech. mixt.	10	25	-0.3	5.77	$H_{0.29}WO_3$	$WO_{2.89}$
Pt/ WO_3 impreg.	0.8	25	-0.3	5.56	$H_{0.44}WO_3$	$WO_{2.78}$
Pt/ WO_3 impreg.	0.8	25	-0.3	5.56	$H_{0.44}WO_3$	$WO_{2.78}$
Pt/ WO_3 impreg.	0.8	25	-0.3	5.58	$H_{0.42}WO_3$	$WO_{2.79}$
Pt/ WO_3 impreg.	0.8	72	-0.3	5.62	$H_{0.88}WO_3$	$WO_{2.81}$
Pt/ WO_3 impreg.	0.8	100	-0.3	5.62	$H_{0.86}WO_3$	$WO_{2.81}$
Pt/ WO_3 impreg.	10	25	-0.3	5.68	$H_{0.86}WO_3$	$WO_{2.84}$
Pt/ WO_3 impreg.	0.1	25	-0.3	5.88	$H_{0.13}WO_3$	$WO_{2.94}$

datation state $\pm 0.2\%$, tungsten oxide composition $\pm 0.2\%$, and bronze composition $\pm 7\%$.

The most notable result in Table I is the considerably higher extent of reduction achieved by impregnation methods over straight mechanical mixtures. This result parallels previous findings (2, 15), and is certainly due to the higher dispersion of the Pt and intimacy of contact with the oxide.

The analytical result for a 0.8 w/o Pt impregnated powder in 5N H_2SO_4 agreed with the H_2 -uptake value of $H_{0.44}WO_3$ or $WO_{2.78}$.

The Pt content of impregnated powders had little effect on the oxide composition above 0.8 w/o, but when reduced to 0.1 w/o a drastic fall in the degree of reduction occurred. This effect is explained in Part II dealing with the electrochemistry of the Pt/ WO_3 system. The small decrease in the reduction of the 10 w/o powder could have arisen from greater uncertainties in the correction applied for H adsorbed on the Pt.

With mechanical mixtures, reduction was significantly increased by changing the Pt content from 2 to 10 w/o. Even at 10 w/o Pt however, the reduction was still only about half that achieved with 0.8 w/o impregnated powders.

As long as the solution remained acidic the extent of reduction remained independent of pH. In neutral solutions however, blue formation was severely restricted.

Increasing the temperature to $100^{\circ}C$ resulted in a slight decrease in reduction of an impregnated powder.

X-ray diffraction results.—Measured d-spacings (within $\pm 0.005\text{\AA}$) and relative line intensities are recorded in Table II for diffraction patterns obtained from a 2 w/o Pt/ WO_3 mechanical mixture and 0.8 w/o Pt impregnation. Both patterns exhibited line broadening at high diffraction angles due to small particle size (23), but the lines were sharp enough for accurate measurements of angles corresponding to d-spacings above 1.2\AA .

Comparison of the d-spacings with the A.S.T.M. index values for the possible species showed no evidence for the presence of lower tungsten oxides and interpretation could be made entirely in terms of the bronze phases, $H_{0.1}WO_3$, $H_{0.33}WO_3$, and $H_{0.5}WO_3$ (13). The Pt concentration was below the detection limits for any diffraction lines to be discernible.

The mechanically mixed powder had a complex pattern which proved difficult to index. Most lines were attributable to $H_{0.1}WO_3$ and $H_{0.33}WO_3$, or solid solutions of these phases—as evidenced by lines having intermediate values between those quoted for the separate phases. This conclusion was supported by the empirical formula $H_{0.14}WO_3$ obtained by analysis. Some

Table II. Experimental x-ray data for tungsten blues

2% Pt mechanical mixture		0.8% Pt impregnation		
d (Å)	Intensity	d (Å)	Intensity	h k l
3.840	f	3.745	vs	001
3.713	vs	2.651	s	110
3.645	vs	2.168	m	111
3.087	f	1.883	m	002
2.650	vs	1.866	f	200
2.591	m	1.681	s	210
2.157	s	1.678	vf	102
1.993	f	1.533	m	112, 211
1.933	f	1.329	f	022, 220
1.884	f	1.252	m	122, 221
1.836	f			
1.809	f	1.19		
1.709	vf	1.18		
1.682	m	1.134		
1.664	m	1.129		
1.644	m	1.09		
1.533	m	1.045		
1.515	m	1.039		
1.486	f	1.005		
1.330	vvf			
1.253	vs			

Intensity key: vs = very strong, s = strong, m = medium, f = faint, vf = very faint.

lines remained which were best interpreted as being due to unreacted WO_3 , possibly in solid solution with the bronzes.

The impregnated powder had a far simpler pattern and evidently consisted of a solid solution of $\text{H}_{0.33}\text{WO}_3$ and $\text{H}_{0.5}\text{WO}_3$ (cf. data in Tables II and III). Using a Bunn Chart (24), the "blue" was shown to possess a tetragonal unit cell and assigned the hkl values given in Table II. The unit cell parameters a_0 and c_0 were calculated from the relationship (24)

$$d_{\text{tetragonal}} = \frac{1}{\sqrt{\frac{h^2 + k^2}{a_0^2} + \frac{l^2}{c_0^2}}}$$

using d -spacings of the 110 and 002 planes respectively. The choice of these planes gave maximum accuracy and ease of calculation. Closer spacings and secondary reflections at higher diffraction angles (e.g., 220, 003, etc.) had diffuse lines due to particle size effects, and the sharp 001 lines had a high inherent error due to the finite specimen thickness (25).

The a_0 and c_0 values are compared with those quoted for $\text{H}_{0.5}\text{WO}_3$ and $\text{H}_{0.33}\text{WO}_3$ (13) in Table IV. Differences in a_0 were too small to draw any conclusions as to the composition of the solid solution, but the c_0 -axis for the tungsten blue had an intermediate value between $\text{H}_{0.5}\text{WO}_3$ and $\text{H}_{0.33}\text{WO}_3$. Assuming that as H_2 progressively enters the tetragonal $\text{H}_{0.33}\text{WO}_3$ lattice, the c_0 -axis linearly decreases until the system becomes cubic at $\text{H}_{0.5}\text{WO}_3$, then an empirical formula can be calculated for the "blue" of $\text{H}_{0.42 \pm 0.06}\text{WO}_3$. This is in good agreement with the analytical result of $\text{H}_{0.44 \pm 0.03}\text{WO}_3$.

Final confirmation of the composition of the impregnated powder was obtained by reducing some plain WO_3 with zinc and hydrochloric acid to the same reduction state—previously determined by analysis of various Zn/WO_3 mixtures. This method which is definitely known to form bronzes (13, 26), produced an identical diffraction pattern.

Table III. A.S.T.M. d -spacings for hydrogen bronzes (13)

$\text{H}_{0.1}\text{WO}_3$		$\text{H}_{0.33}\text{WO}_3$		$\text{H}_{0.5}\text{WO}_3$	
d (Å)	Intensity	d (Å)	Intensity	d (Å)	Intensity
4.00	10	3.79	80	3.68	50
3.84	60	2.69	80	2.63	50
3.64	100	2.19	10	2.16	10
3.11	10	1.91	20	1.87	30
2.67	60	1.87	10	1.68	100
2.61	20	1.69	100	1.53	80
2.16	10	1.68	20	1.33	30
2.00	10	1.55	100	1.25	80
1.92	10	1.34	10	1.19	30
1.84	40	1.26	100	1.13	30
1.82	40	1.20	10	1.09	10
1.71	10	1.185	10	1.05	50
1.66	20	1.14	10	1.01	80
1.64	20	1.13	10		
1.58	5	1.09	10		
1.54	5	1.05	10		
1.51	20	1.04	10		
1.485	20	1.01	50		
		1.01	50		

Table IV. Unit cell dimensions for impregnated WO_3 powders and hydrogen bronzes prepared by other authors (13)

	Experimental values	$\text{H}_{0.33}\text{WO}_3$ (13)	$\text{H}_{0.5}\text{WO}_3$ (13)
a_0 (Å)	3.750 ± 0.006 ($\sqrt{2d_{110}}$)	3.751 ± 0.006	3.755 ± 0.006
c_0 (Å)	3.77 ± 0.01 ($\sqrt{2d_{002}}$)	3.796 ± 0.006	3.755 ± 0.006

Conclusions

Hydrogen tungsten bronzes (H_xWO_3) are formed in platinumized WO_3 under the prevailing conditions in a fuel cell hydrogen electrode. The highest degree of reduction $\text{H}_{0.44}\text{WO}_3$, was obtained at 25°C using an impregnation technique for platinizing with 0.8 w/o Pt. Mechanical mixtures do not produce very intimate mixing, resulting in slower, incomplete reduction which can be improved by increasing the Pt loading. So long as the electrolyte is acidic, pH has no effect on the reduction.

Although bronzes are the major product when platinumized WO_3 is reduced in acid slurries by H_2 , it is not apparent whether they form by chemical reduction or by local cell action. Whether or not the bronzes contribute to the net anodic current of a H_2 -anode will depend on which of these mechanisms predominates, as well as the relative rates of bronze formation and anodic oxidation. Part II describes work aimed at answering these questions.

Acknowledgment

This work was supported by the Ministry of Defence.

Manuscript submitted Nov. 1, 1971; revised manuscript received Dec. 21, 1971.

Any discussion of this paper will appear in a Discussion Section to be published in the December 1972 JOURNAL.

REFERENCES

- L. W. Niedrach and I. B. Weinstock, *Electrochem. Technol.*, **3**, 270 (1965).
- B. S. Hobbs and A. C. C. Tseung, *Nature*, **222**, 556 (1969).
- A. C. C. Tseung and B. S. Hobbs, *Platinum Metals Rev.*, **13**, 14 (1970).
- P. G. Dickens and M. S. Whittingham, *Quart. Rev. (London)*, **30** (1968).
- T. H. Johnson, *J. Franklin Inst.*, **207**, 629 (1929).
- D. Brennan and P. C. Fletcher, *Nature*, **183**, 249 (1959).
- J. R. Arthur, **164**, 537 (1949).
- J. C. Robb and H. W. Melville, *Discussions Faraday Soc.*, **2**, 132 (1947).
- J. C. Robb and H. W. Melville, *Proc. Roy. Soc. (London)*, **A196**, 445 (1949).
- O. Glemser, U. Hauschild, and G. Lutz, *Z. Anorg. Allgem. Chem.*, **269**, 93 (1952).
- O. Glemser and H. Sauer, *Z. Anorg. Chem.*, **252**, 144 (1943).
- O. Glemser, J. Weidelt, and F. Freund, *Z. Anorg. Allgem. Chem.*, **332**, 299 (1964).
- O. Glemser and C. Naumann, *Z. Anorg. Chem.*, **265**, 288 (1951).
- O. Glemser and G. Lutz, *ibid.*, **264**, 17 (1951).
- J. E. Benson, H. W. Kohn, and M. Boudart, *J. Catalysis*, **5**, 307 (1966).
- M. Boudart, M. A. Vannice, and J. E. Benson, *Z. Physik. Chem. Neue Folge*, **64**, 171 (1969).
- A. E. Vol, in "Handbook of Binary Metallic Systems," Israel Program Sci. Trans., N. V. Ageev, Editor, 727 (1966).
- K. C. Li and C. Y. Wang, "Tungsten," Reinhold Press (1955).
- A. J. Hegedus, T. Millner, J. Neugebauer, and K. Sasvari, *Z. Anorg. Allgem. Chem.*, **281**, 64 (1955).
- W. M. Latimer, "Oxidation Potentials", p. 254, Prentice Hall Inc., Englewood Cliffs, N. J. (1952).
- A. C. C. Tseung and H. L. Bevan, *J. Mater. Sci.*, **5**, 604 (1970).
- L. Wong, M. Phil Thesis, The City University, London (1969).
- C. W. Bunn, "Chemical Crystallography," p. 107, Oxford Press (1961).
- C. W. Bunn, *ibid.*, p. 144.
- C. W. Bunn, *ibid.*, p. 127.
- P. G. Dickens and R. J. Hurditch, *Nature*, **215**, 1266 (1967).

The Effect of Viscous Shear on a Meniscus in an Electrochemical System

P. C. Wayner, Jr.

Fluid, Chemical, and Thermal Processes Division, Rensselaer Polytechnic Institute, Troy, New York 12181

ABSTRACT

Fluid flow in the evaporating meniscus of an electrode-gas-electrolyte reacting system has been studied to examine the effect of viscous shear on the meniscus profile. The evaporating meniscus profile, the pressure derivative profile, and the curvature profile for various assumed evaporation profiles were calculated for 1N H₂SO₄. Due to the thinness of the meniscus profile in the interline region, large pressure gradients were needed to balance the viscous shear stress. The resulting evaporating meniscus profile was significantly different from the static profile. Depending on the evaporation rate the interline radius of curvature could be micron size for a large meniscus. Heat and mass transfer rates would also be significantly effected by these changes during an electrochemical reaction. Therefore, the effect of viscous shear should not be neglected in analyzing electrochemical processes in a "finite contact angle" meniscus.

The triple interline region of a meniscus formed on an immersed solid surface has been the subject of considerable research. In part, this derives from interest in the potentially high heat and mass transfer rates associated with a large surface area covered by a thin liquid film in the form of a myriad of menisci (porous fuel cell electrodes are of particular interest herein). The study of electrochemical processes on wetted metallic surfaces partially immersed in an electrolyte could be classified according to whether or not a thin film extends above the intrinsic meniscus. The obvious and significant characteristic of a meniscus without a thin film ["finite contact angle meniscus" (1)] is that the diffusion path length across the liquid film approaches zero at the interline. This study is particularly concerned with the outstanding work of Bockris and Cahan (1) which discusses the effect of a finite contact angle meniscus on kinetics in porous electrode systems. Conversely, various other authors (2-4) considered models and systems that included a thin film above the intrinsic meniscus. Due to the large number of experimental variables, the complete set of conditions that insure the presence of a particular type of meniscus is still questionable.

The following three of many conclusions concerning electrochemical kinetics in a meniscus presented by Bockris and Cahan (1) are of particular interest herein: (i) "most of the current is produced in the first 1% of the meniscus;" (ii) "the extreme concentration of current density into this small area can produce local heating and create a dynamic situation in the physical location of the meniscus;" and (iii) "the local geometry of the meniscus, particularly in the three-phase region, dominates the behavior of porous electrodes." They also state that some of the heat is readily removed by evaporation. In their analysis of this extremely complex system, the geometry of the meniscus is represented by the equation for a cylindrical surface, thereby neglecting the effect of viscous flow of the evaporating liquid on the meniscus profile. The major effect of this shear stress would be in the thinnest and most important region of the meniscus. Recently, a procedure to evaluate the effect of viscous flow on the profile has been developed (5). Although it is not the present objective to completely reanalyze the very complex transport processes occurring in an active electrochemical meniscus, the results presented below demonstrate that it is very instructive to examine the effect of viscous flow in a few selected and related cases.

* Key words: meniscus profile, capillarity, porous gas electrode, planar electrode.

Synopsis of Reference (1)

In Ref. (1) a 1N, H₂SO₄ meniscus was formed between two parallel optical glass flats. One glass surface of the resulting slot was coated with Pt to serve as an electrode. Optical measurements of the resulting meniscus were made through the other glass surface. Using reflectometric techniques, the slope was determined as a function of distance from the interline at intervals of approximately 12.7 μ . Interferometrically, fringes of the same kind reoccurred at film thickness differences of 2945 \AA . Simultaneously, the steady-state total current-potential behavior of the system was also measured for both H₂ and O₂ dissolution in the electrolyte. Within the accuracy of the experiments, the results indicated that the most stable meniscus configuration was one with a finite contact angle between 1° and 3°, and that it could be represented by the surface of a cylinder with a diameter equal to the slot width. On the basis of the experimental measurements, a detailed second-order nonlinear nonhomogeneous differential equation describing the reaction zone was derived and solved numerically. The microscopic description of the reaction zone was a strong function of the meniscus profile. The calculated relationship between the total current and potential which depended on many variables agreed well with the experimental results.

Qualitative Description of an Evaporating Meniscus

Consideration is given herein to an evaporating meniscus formed on a vertical flat plate immersed in a pool of liquid. The pressure gradient for fluid flow from the pool to the zone of evaporation results from a change in the meniscus profile (curvature). Relative to the isothermal case, the interline of the evaporating meniscus has migrated down the plate so that the profile can accommodate the increased pressure gradient needed to balance the viscous stresses of fluid flow. Assuming that the contact angle remains constant, the average curvature of the evaporating meniscus is larger than that of the isothermal meniscus and varies with heat flux. The present analysis only evaluates the effect of capillary pressure given by σ/R and does not include the additional effects of a disjoining pressure, surface tension variation, and surface viscosity. Insufficient data are presently available to include these additional factors. Therefore, bulk fluid properties and Newtonian flow are assumed applicable in the interline region. The effect of surface tension variation on thin supermeniscus electrolyte films of a uniform thickness has been analyzed by Lightfoot and Ludviksson (6). Comparable effects would be present in that portion of a finite contact angle meniscus where

the pressure gradient becomes relatively small. The principal conclusions of the present study are primarily concerned with that portion of the meniscus where the pressure gradient is relatively large and the effect of surface tension variation relatively small. A significant amount of research has been done using a fluid flow model in which the average velocity was assumed to be zero (7, 8).

Quantitative Description of the Evaporating Meniscus

Basic relations.—The following treatment parallels that developed in Ref. (5) except for the use of a different boundary condition at the meniscus base. The four fluid mechanical conditions at the boundaries of the liquid are (i) the base pressure of the meniscus is given by

$$P_f = P_a - \frac{\sigma_{fv}}{R} \tag{1}$$

with $R = R_b$, the radius of curvature at the base of the meniscus; (ii) the fluid velocity goes to zero at the wall; (iii) the force balance per unit length at the interline is given by the well-known Young-Dupré equation

$$\sigma_{sv} = \sigma_{sl} + \sigma_{fv} \cos \theta_c \tag{2}$$

and (iv) the following normal stress for a constant $R = R_i$ surface represents the local stress on the liquid at the interface

$$\tau_{RR} = -P_f = -P_a + \frac{\sigma_{fv}}{R} \tag{3}$$

Some of the nomenclature for the present analysis is presented in Fig. 1 with a cross-sectional drawing of the meniscus. The local curvature, $1/R_i$, of the meniscus at location "i" is

$$K_i = \left(\frac{d\theta}{dS} \right)_i = \left[\frac{\frac{d^2t}{dy^2}}{1 + \left(\frac{dt}{dy} \right)^2} \right]^{3/2}_i \tag{4}$$

At equilibrium $p_g = -\rho g(Y - y)$, $K_i = \rho g(Y - y)_i / \sigma_{fv}$, and $(\partial p_g / \partial r)_i = \rho g \cos \theta_i$. With evaporation, $p_g < -\rho g(Y - y)$ as a result of the additional pressure gradient required to balance liquid acceleration and viscous shear stresses. Since the pressure in the liquid at the liquid-vapor interface is a function of the curvature, $p_{g|i} = -K_i \sigma_{fv} < -\rho g(Y - y)_i$ when there is evaporation. Using Eq. [4] with the modified pressure $P = p_g + \rho g(Y - y)$

$$\left(\frac{\partial P}{\partial r} \right)_i = - \frac{\partial}{\partial r} \left[\frac{\sigma_{fv} \frac{d^2t}{dy^2}}{\left[1 + \left(\frac{dt}{dy} \right)^2 \right]^{3/2}} - \rho g(Y - y) \right]_i \tag{5}$$

The results of Sparrow and Starr (9) for fluid flow in a wedge are now used to approximate the dependence of the local average velocity, \bar{u}_i , on the local pressure gradient and film geometry. Using a linearized momentum equation, they obtained Eq. [6] for the velocity in a converging plane-walled passage with the half-taper angle, θ_i . Since this result is symmetrical with respect to the mid-plane where the shear stress vanishes, Eq. [6] applies locally in the present system for small angles and thin films.

$$u(r_i, \zeta) = \frac{\bar{u}_i [\cos \lambda_i - \cos \lambda_i \zeta]}{\left[\cos \lambda_i - \frac{1}{\lambda_i} \sin \lambda_i \right]} \tag{6}$$

in which $\zeta = \phi / \theta_i$, and

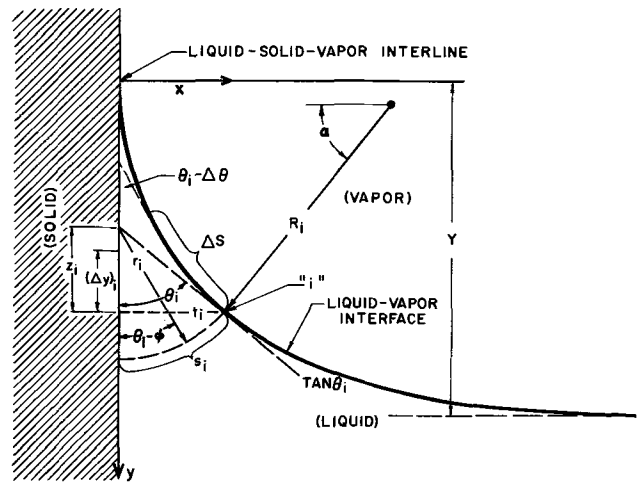


Fig. 1. Nomenclature for the analysis of an evaporating meniscus

$$\lambda_i = \left(4 + \frac{\epsilon Re_i}{2\theta_i} \right)^{1/2} \theta_i \tag{7}$$

where

$$Re_i = \left(\frac{\bar{u} 2\theta r}{\nu} \right)_i$$

In this approach the normal acceleration to the interface is assumed to have negligible effect. Their results can also be used to obtain Eq. [8] which relates the velocity to the pressure gradient.

$$u(r, \zeta) = \frac{\bar{u} \lambda^2 \cos \lambda}{4\theta^2 \left(\cos \lambda - \frac{1}{\lambda} \sin \lambda \right)} - \frac{r^2}{4\rho\nu} \frac{\partial P}{\partial r} \tag{8}$$

These last two equations can be combined to give

$$\bar{u}_i = \frac{z_i^2 \left(\frac{\partial P}{\partial r} \right)_i \left(\cos \lambda_i - \frac{1}{\lambda_i} \sin \lambda_i \right)}{\rho\nu \cos^2 \theta_i \left[\left(\frac{\epsilon Re_i}{2\theta} \right)_i \cos \lambda_i + 4 \right]} \tag{9}$$

Taking the normal force due to curvature to be the predominant interfacial effect the radial pressure gradient, $\frac{\partial P}{\partial r} \Big|_i$ is given by Eq. [5].

Numerical.—Using a finite difference technique, the above equations are sufficient to calculate the meniscus profile for a given heat flux at the vapor-liquid interface which can be assumed equal to a given per cent of the total thermal energy generated. The rest of the heat is conducted away through the solid. Assuming that all the fluid entering the initial interval, $(\Delta y)_i$, is evaporated, the average velocity of the fluid entering the initial wedge is

$$\bar{u}_1 = \left(\frac{q\Delta y}{\rho\lambda S} \right)_i \tag{10}$$

The initial arc length, s_1 , is

$$s_1 = \frac{\theta_1 (\Delta y)_1 (\tan \theta_c + \tan \theta_1)}{2 \sin \theta_1} \tag{11}$$

The wedge angle, θ_i , which is the inverse tangent of the slope at i is obtained from the slope and curvature at i-1 using the Euler finite difference approximation of curvature, K_i . This requires that the initial values of curvature, K_0 , and contact angle, θ_c , be assumed. The change in meniscus thickness, $(\delta t)_i$, is the product of the step size and the average slope between i and i-1. Knowing the average velocity and the geometry of the wedge at i, the derivative of the pressure and curvature are obtained from Eq. [9] and [5]. The volumetric flow entering each wedge is equal to the total fluid

evaporated in the meniscus above that level. Using Euler's method the above process can now be continued until either the heat flux becomes negligible or the wedge angle equals ninety degrees. In the present case, the effect of evaporation on the meniscus profile is significant only at small angles. However, continuing the analysis until $\theta = 90^\circ$, allows the use of the boundary condition at the base of the meniscus ($K = 1/R_b$, $\theta = 90^\circ$) to select the initial curvature.

Evaporation in H₂SO₄ Meniscus

The above analysis is now applied to three arbitrarily selected evaporation rates, water vapor equivalent of 8, 24, and 72 W/cm², which are assumed to occur over the top 250Å of a 1N, H₂SO₄ meniscus. Although these flux profiles are not intended as a definitive description of the evaporation zone described in Ref. (1), which is beyond the scope of this work, the results based on their use significantly improve the understanding of the transport process occurring in a reacting system. Alternatively, considering the large IR drop and polarizations calculated for the finite contact angle meniscus in Ref. (1), these evaporation rates are possible in the interline region. Since we are only investigating the general effect of viscous flow, the size of the evaporation region is purposely limited. As a result of the thinness of the interline region, the effect of the same evaporation occurring further down the meniscus would be substantially less. In this model, the generated vapor could easily diffuse away under a vapor pressure gradient and condense on a surface at a lower temperature. Even with an enlarged zone of evaporation, the total power dissipation would remain small in the finite contact angle model because the upper limit on the zone is very small. In this analysis, Δy was equal to 250Å for the initial five intervals, 625Å for the next ten intervals, 1.25×10^{-4} cm for the next 380 steps, and 6×10^{-3} cm for the remaining distance. The radius of curvature at the base of the meniscus is assumed to be 0.5 mm (one half the slot width), and the fluid properties are assumed constant and evaluated at 25°C.

Results

The calculated meniscus thickness at 250Å below the interline and the meniscus heights for the assumed heat fluxes and contact angles are presented in Table I. Comparing the isothermal and evaporating cases, these results demonstrate that the meniscus interline migrates a small, though measurable distance as a result of viscous shear. There is a possible +6% error in the calculated meniscus height due to the use of only the boundary condition for curvature at the base of the meniscus instead of both the meniscus thickness and curvature. Since the approximate size and sign of the error is the same in all cases, the error in the migration distance is less than 6%. Auxiliary work (not presented herein), in which a fixed height at $\theta = 90^\circ$ was used as a boundary condition, demonstrated that the meniscus profile in the interline region is not significantly different from the results presented herein. However, the profile at the base of the meniscus

Table I. Meniscus thickness at 250Å below the interline and over-all meniscus height

Conditions	Meniscus thickness, Å, at $y = 250\text{Å}$	Meniscus height, cm
$\theta_c = 0^\circ$ isothermal	Less than mono layer	0.0558
$\theta_c = 2^\circ$ isothermal	8.75	0.0546
$\theta_c = 0^\circ$ $q = 8 \text{ W/cm}^2$	11.4	0.0532
$\theta_c = 0^\circ$ $q = 24 \text{ W/cm}^2$	15.1	0.0521
$\theta_c = 0^\circ$ $q = 72 \text{ W/cm}^2$	19.8	0.0507
$\theta_c = 2^\circ$ $q = 72 \text{ W/cm}^2$	20.2	0.0508
$\theta_c = 2^\circ$ cylindrical surface	8.73	0.0483

is significantly different. The average radius of curvature for the fixed height boundary value analysis is approximately 5% less. Previous work (5) demonstrated that the error due to step size is small. It is interesting to note that for the cases studied the evaporating meniscus height is not strongly affected by the initial contact angle and that the height for the larger contact angle is slightly larger. This results from the slightly larger pressure gradient (curvature change) in the initial portion of the meniscus with a zero contact angle where the film is thinner.

Comparing the film thicknesses for the various cases at a point 250Å below the interline demonstrates the following: (i) the film thickness of an evaporating meniscus is substantially larger than the film thickness of an isothermal meniscus with the same contact angle; (ii) the film thickness of an evaporating meniscus with a 0° contact angle is larger than the film thickness of an isothermal meniscus with a contact angle of 2° (however, the 0° contact angle meniscus must start smaller in the interline region); (iii) the film thickness for the present isothermal model and the cylindrical surface model are approximately the same; and (iv) an increase in the heat flux and/or the contact angle results in a larger film thickness. These substantial changes in the film thickness due to viscous shear would have a correspondingly large effect on the transport processes occurring in this region of potentially high current densities.

The liquid-vapor interfacial height and the logarithm of the reciprocal of the distance from the interline are plotted vs. the logarithm of the meniscus thickness in Fig. 2. The curves for the reciprocal distance from the interline start at $y = 125\text{Å}$. These curves show the substantial effect of evaporation on the meniscus profile. At a given distance from the interline (for $y > 175\text{Å}$) the evaporating meniscus with a zero contact angle for the heat fluxes analyzed is always thicker than the isothermal meniscus with a contact angle equal to 2° . Previous analysis (1) indicated that 90% of the current is produced in the region $y < 10^{-4}$ - 10^{-5} cm, with the largest current density in the immediate vicinity of the interline. These results were partly based on diffused interferences fringes that reoccurred every 2.9×10^{-5} cm. The interaction of these results indicates that it is theoretically possible to define an evaporating meniscus with a contact angle equal to 0° that is indistinguishable from an isothermal meniscus with a 3° contact angle

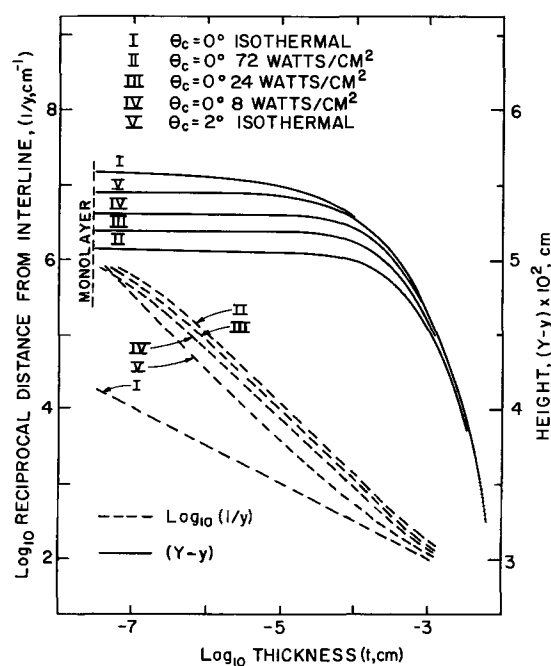


Fig. 2. Calculated meniscus profiles

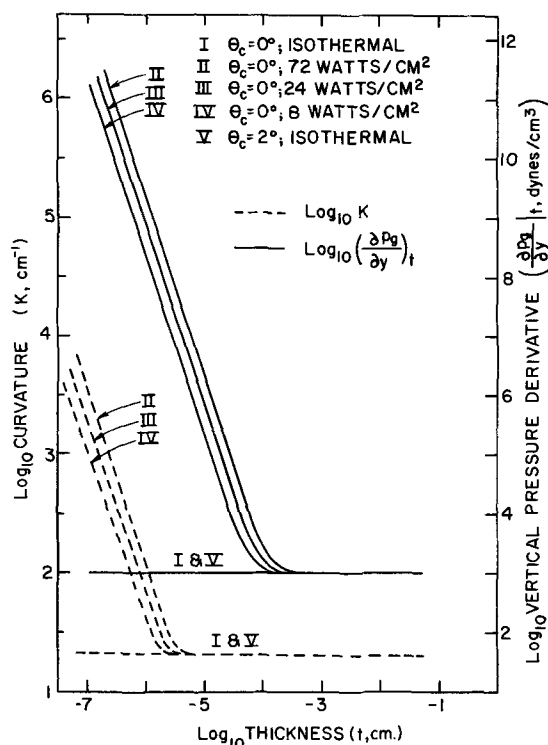


Fig. 3. Calculated vertical pressure derivative and curvature vs. the calculated meniscus thickness.

within the accuracy of the described experimental data and theoretical analysis. Considering this conclusion and the current understanding of transport processes in the critical interline region, considerable additional study of this area is needed to properly model the electrochemical reaction zone.

The logarithm of the meniscus curvature and the vertical pressure derivative are plotted vs. the logarithm of the film thickness for the upper portion of the meniscus in Fig. 3. These results demonstrate that there are orders-of-magnitude increases in the pressure gradient to balance the effect of viscous flow. The horizontal solid line near the bottom of the figure is the weight density of the fluid. The effect of viscous shear becomes negligible before the wedge angle is equal to 10° . The absolute value of the approximate wall shear stress can be calculated using

$$|\tau_s| = \left(\frac{\partial p_g}{\partial y} \Big|_{x=t} - \rho g \right) t \quad [12]$$

In this analysis the integrated product of the local wall shear stress and the area would be equal to the decrease in weight of the meniscus. These results also indicate that there are orders-of-magnitude increases in the radius of curvature near the interline. The average radius of curvature in the first interval for run No. 4 in Fig. 3 is 2.5μ vs. 479μ for the isothermal meniscus. Therefore, the meniscus profile in the interline region more closely resembles the meniscus found in a pore than that found on an immersed flat plate.

Discussion

Curve IV presented in Fig. 2 and 3 represents a system with an evaporative heat flux of 8 W/cm^2 which is assumed to occur over only the top 250\AA of the meniscus. This is 30% of the average thermal energy generated in the top 250\AA of the meniscus presented in Fig. 24e of Ref. (1), and a small per cent of the total heat generated. A substantial flow profile change occurs when the evaporating fluid flow results from a curvature change, which gives a plausible mechanism for the flow. This particular evaporating meniscus profile starts with a zero contact angle but resembles an isothermal meniscus with a 4° contact

angle for a large portion of the main reaction region. Curve III (72 W/cm^2 over 250\AA , 0° contact angle) corresponds closely to an isothermal curve with a 6° contact angle in a large portion of the main reaction region. If a reliable method of predicting the relative percentage of the thermal energy removed by evaporation were available, the method described herein could be used to improve the results of Bockris and Cahan. At present, these results give a good estimate of the effect of contact angle on the current vs. overpotential curve if the apparent contact angle is used. For example, in Fig. 17 of Ref. (1), the per cent decrease in the current at an overpotential of one volt for a change in the apparent contact angle from 1° to 4° is 26%. Additional results are presented in Ref. (10). The same change would occur if the profile change was due to fluid flow instead of the contact angle. This supports the model of an evaporative heat sink by giving a plausible mechanism for fluid flow. The large predicted increase in evaporative heat flux required to go from an apparent contact angle of 4° to 6° indicates that sufficient fluid flow is available for even the highest thermal fluxes. A similar effect could be expected to occur in porous electrodes.

In the complete system, conduction in the electrode would also remove some of the thermal energy. Therefore, it is instructive to make an order-of-magnitude calculation of the unit thermal conductance in a porous solid (k_{eff}/L) and compare it to a "mass conductance" in the pores. The unit thermal solid conductance ($L = 1\mu$) is $1400 \text{ cal/sec-cm}^2\text{-K}^\circ$ in nickel, 100 in carbon, 31 in quartz, and 5.6 in Teflon. The conduction path in Ref. (1) was quartz with a thin surface film of sputtered Pt. The unit thermal conductance in a porous media is much lower than this and is a strong function of the manufacturing process. For example, the conductance in strongly consolidated sintered metals is an order-of-magnitude less than the solid conductance and could be a factor of 100 less in poorly sintered specimens. For unconsolidated packed material, the ratio of the two conductances could be 1000. Therefore, thermal conductance in a porous electrode is a strong function of the material, the manufacturing process, and the meniscus location (relative to the junction between two particles).

Assuming that molecular diffusion through a stagnant gas occurs in a uniform pore, the conductance of the vapor space for water can be estimated to be (in equivalent thermal units) $7 \text{ cal/cm}^2\text{-sec-K}^\circ$ at 25°C . This is obtained using Eq. [13] with $T = 298^\circ\text{K}$, $L = 1\mu$, $p = 1 \text{ atm}$, $D_{\text{H}_2\text{O-H}_2} = 0.825 \text{ cm}^2/\text{sec}$, and a water vapor pressure difference corresponding to a temperature difference of 1°C

$$N_A = \frac{p D_{AB}}{RTL} \ln \left(1 + \frac{\Delta p_B}{p_B} \right) \quad [13]$$

This is larger at higher temperatures since the rate of change of vapor pressure with temperature and the diffusivity increase with temperature. Like the thermal conductance, the effective mass conductance in a porous material is a function of its manufacturing process. These calculations indicate that the evaporative heat flux in porous electrodes made from carbon and Teflon is relatively large. Alternately, the solid heat conduction process is much more effective than evaporation in well-sintered metal electrodes. However, in both cases, the evaporation-condensation mechanism could cause meniscus migration but at different velocities. In addition, if vaporization occurred at a surface with a large radius of curvature and condensation occurred in a crevice with a small radius of curvature, vapor transport would be enhanced. Theoretically, once the ideal electrochemical meniscus is completely described, the porous electrode design can be optimized.

The above analysis is based on the premise that a fully developed wedge flow model can be used in the meniscus. A partial feeling for the correct velocity

distribution can be obtained from a boundary layer calculation of the distance required for the boundary layer thickness for flow over a flat plate to be equal to 1×10^{-3} cm. This is the approximate thickness of the meniscus in the region where viscous effects become negligible. A simple form of the boundary layer equation is

$$x = \frac{t^2 u_s}{30\nu} \quad [14]$$

Using the interfacial velocity at $t = 1 \times 10^{-3}$ cm for u_s , the calculated distance is negligible compared to the distance from the bottom of the plate to this point. In fact the velocity is so low and thickness so small, that the use of the simple form of the boundary layer equation is not justified. However, the large difference between these two distances definitely indicates that the accelerating velocity profile is well developed in and above this region. In addition, since the angle θ_i is still small in this region, θ -direction flow has a small effect on the meniscus profile. These two results demonstrate that the wedge flow model is a good approximation to the flow field in the upper portion of the meniscus. Since viscous effects become negligible below this region, the continued use of the model does not effect the validity of the rest of the profile.

The thermocapillary shear stress at the liquid-vapor interface is assumed to be negligible in the present analysis. This assumption is based on the results of Ref. (5) which demonstrated that the thermocapillary effect in the upper portion of the meniscus was small compared to the curvature effect. Thermocapillary flow would have an effect on the profile in the lower and less important portion of the meniscus. Further, inclusion of this effect requires *a priori* knowledge of the temperature gradient. Since this gradient is unknown, its inclusion would require an additional set of iterations which is beyond the scope of the present study.

Conclusions

Fluid flow in the evaporating meniscus of an electrode-gas-electrolyte reacting system was modeled and analyzed. The meniscus profile, the curvature profile, and pressure derivative profile were calculated for 1N H_2SO_4 using various assumed evaporation profiles. The results demonstrate that: (I) A sufficiently large capillary force was available to supply the required fluid flow for a large evaporative heat sink. (II) Due to the thinness of the meniscus profile in the interline region large pressure gradients were needed to balance the viscous shear stress. (III) The change in curvature due to viscous flow had a significant effect on the meniscus profile in the critical interline region. (IV) Depending on the evaporation rate, the interline radius of curvature could be micron size for a large meniscus. (V) This change in meniscus profile would have an equally significant effect on the transport and kinetic processes occurring. (VI) The effect of viscous shear on the meniscus profile should not be neglected in analyzing electrochemical processes in a finite contact angle meniscus. (VII) Currently used optical techniques are not sufficiently accurate to measure the meniscus profile in the critical region.

SYMBOLS

D	molecular diffusivity, cm^2/sec
g	gravitational acceleration, cm/sec^2
k	thermal conductivity, $cal/cm\text{-}^\circ K$
K	curvature, cm^{-1}

L	conductance path length, cm
N	mass flux, moles/ $cm^2\text{-}sec$
P	modified pressure, $p_g - \rho g(Y - y)$, dynes/ cm^2
p	pressure, dynes/ cm^2 ; partial pressure
q	heat flux, W/cm^2
Re	Reynolds number, $(2u\theta r/\nu)$
R	radius of curvature, cm; gas constant, $cm^3\text{-}atm/\text{moles}\text{-}K^\circ$
r	radial direction (see Fig. 1), cm
s	arc length (see Fig. 1), cm
S	arc length (see Fig. 1), cm
t	meniscus thickness, cm
u	velocity, cm/sec
V	specific volume of vapor, cm^3/g
x	x coordinate
Y	interline distance from meniscus base, cm
y	y coordinate distance from interline, cm
z	distance (see Fig. 1), cm
Δ	difference
ϵ	velocity weighting factor [Ref. (6)]
θ	angle (see Fig. 1), radians
λ	function of Re and θ , see Eq. [7]
ν	kinematic viscosity, cm^2/sec
ζ	$= (\phi/\theta_i)$
ρ	density, g/cm^3
σ	surface tension, dynes/cm
ϕ	coordinate angle (see Fig. 2), radians

Subscripts

A	component A
B	component B
a	atmospheric
c	contact
eff	effective
f	liquid surface
g	gauge
i	location "i" (see Fig. 1)
R	R coordinate surface or direction
r	r coordinate surface or direction
s	solid surface
t	liquid vapor interface
v	vapor
1	initial interval

Acknowledgment

This research was supported by the Department of the Army Contract No. DAA B07-69-c 0063 entitled "Electrochemical Power Sources."

The computational assistance of M. Potash is gratefully acknowledged.

Manuscript submitted Jan. 27, 1971; revised manuscript received ca. Sept. 4, 1971.

Any discussion of this paper will appear in a Discussion Section to be published in the December 1972 JOURNAL.

REFERENCES

1. J. O'M. Bockris and B. D. Cahan, *J. Chem. Phys.*, **50**, 1307 (1969).
2. F. G. Will, *This Journal*, **110**, 145, 152 (1963).
3. R. P. Iczkowski, *ibid.*, **111**, 1078 (1964).
4. D. N. Bennion and C. W. Tobias, *ibid.*, **113**, 589 (1966).
5. P. C. Wayner, Jr. and M. Potash, Jr., Preprint No. 30b, 63rd Annual Meeting A.I.Ch.E., Chicago (1970); To be published.
6. E. N. Lightfoot and V. Ludviksson, *This Journal*, **113**, 1325 (1966).
7. Yu. A. Chizmadzke and V. S. Markin, *Electrokhimiya*, **2**, 1360 (1966).
8. Yu. G. Chirkov, V. S. Markin, and V. S. Chesnokov, *ibid.*, **6**, 889 (1970).
9. E. M. Sparrow and J. B. Starr, *J. App. Mech.*, **32E**, 684 (1965).
10. B. D. Cahan, Ph.D. Thesis, University of Pennsylvania, Philadelphia (1968).

Low Current Density Microcell Diffusion Layer Thickness at Shallow Vertical Electrodes

R. N. O'Brien

Chemistry Department, University of Victoria, Victoria, British Columbia, Canada

Use of microcell interferometry techniques which have been well reported (1-4) permit detailed analysis of the limiting effect of natural convection at vertical electrodes. A number of authors (5-9) have evolved equations to describe natural or free convection at vertical electrodes. Only that evolved by Wilke, Eisenberg, and Tobias (10) has been tested for microcells and found satisfactory (11, 12). Since the testing of this expression by conventional means, interferometric data has become available and is presented here. Microcells are for the purposes of this work defined as those with electrolyte volumes of 0.5 ml or less. Those used also had electrode area to electrolyte volume ratios of about 10^4 in contrast with conventional cells which have ratios usually in the range of 10^{-2} cm^{-1} .

The cell used was very similar to that reported in Ref. (1). The electrodes were 0.31 cm apart and were 0.191 cm thick, of high purity microcrystalline copper carefully prepared and polished to give a vertical edge to avoid shadowing. The experiments were done at room temperature (22°C).

The limitation of the extent of the diffusion layer by natural convection is shown in Fig. 1. Fig. 1(a) shows the concentration gradients for horizontal electrodes with the cathode over the anode (C/A) previously published in Ref. (3), and Fig. 1(b) shows them for shallow vertical (S/V) electrodes in the cell $\text{Cu}/\text{CuSO}_4/\text{Cu}$ at the natural pH of 4.3 of 0.05M CuSO_4 at a nominal $1 \text{ mA}/\text{cm}^2$ C. D. ($0.902 \text{ mA}/\text{cm}^2$). For short periods of electrolysis, irregularities of the surface of horizontal electrodes, small departures from the truly horizontal position, and inequalities of electrode areas in activity have usually not produced detectable convection.

The differences between the convecting system and the nonconvecting system are that the diffusion layer constantly expands for the horizontal C/A system and is limited after about 15 sec by convection in the S/V arrangement of electrodes to about 0.025 cm. The differences under these conditions are more easily seen in Fig. 2(a) and (b) where the concentration at a given distance out from the electrode is plotted at various times. An idea of the uncertainty of the measurements is given by the scatter of points shown in Fig. 2(b) at times less than 10 sec.

Contrasting Fig. 2(b) with 2(a) convection appears to have begun at the anode first and is detectable as an undulation in the curve at 10-15 sec after electrolysis was begun. The first irregularity in the cathode side occurred farther out from the electrode at just over 20 sec and was more severe, the slope of the concentration contour actually reversing. Close to the electrode, the anode exhibited 3 anomalous changes in concentration contour until settling down at about 45

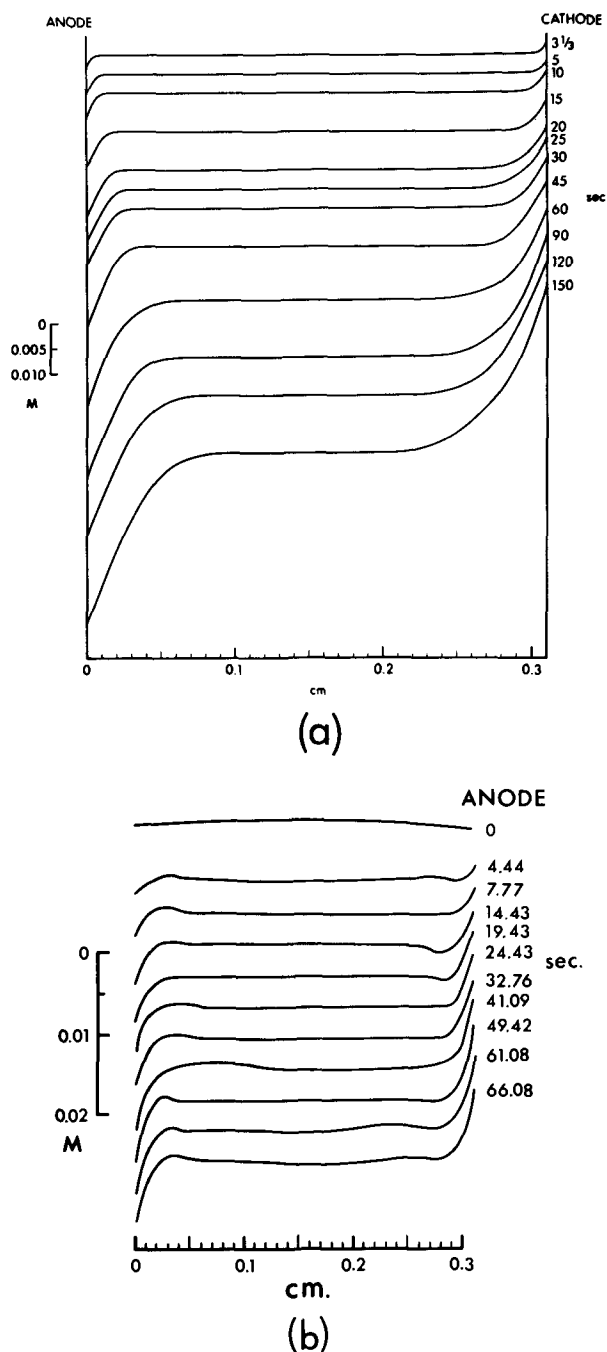


Fig. 1. Reproductions of interferograms: (a) no convection, cathode over anode and (b) shallow vertical electrodes, natural convection occurring, limiting the diffusion layer to about 0.03 cm.

* Electrochemical Society Active Member.
Key words: diffusion layer thickness, natural convection, interferometry.

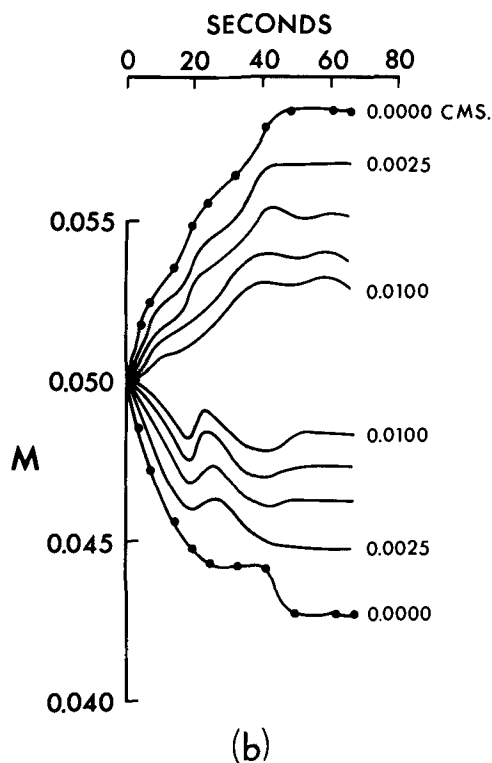
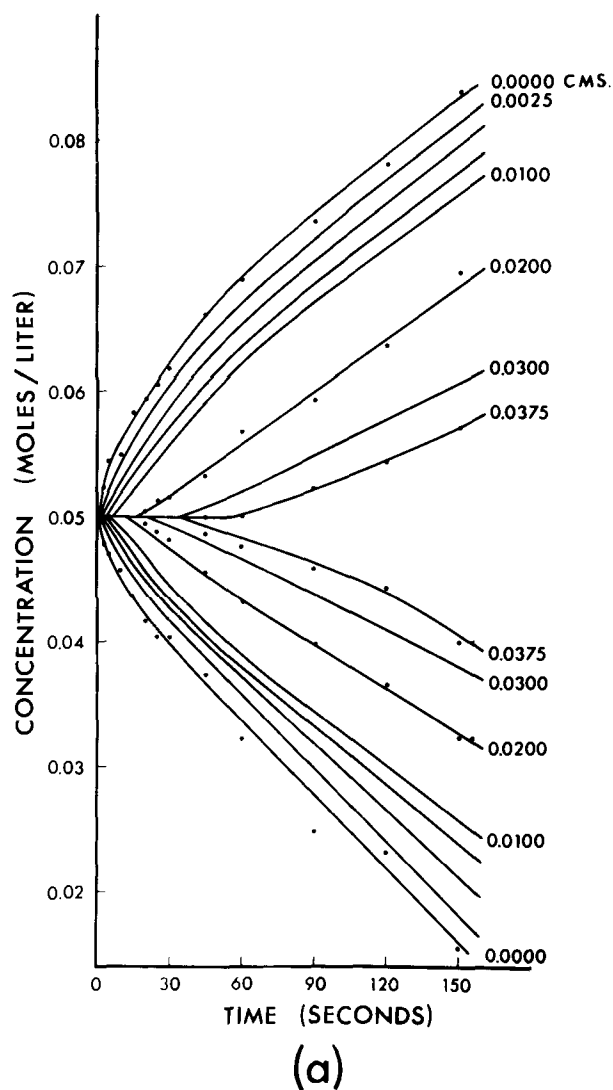


Fig. 2. Concentration changes at various times of electrolysis at various distances from the electrodes: (a) no convection and (b) natural convection limiting the diffusion layer.

sec to a constant concentration value and a pseudo-steady state. At 0.01 cm out from the anode small changes in concentration were still occurring at 60 sec. At the cathode, stability at the electrode and at 0.01 cm from it occurred at the same time, about 50 sec, and only two major perturbations to the smooth curve occurred. Two convective vortices were set up by 50 sec with overflow and underflow between them as described previously (4).

The characteristics shown in this experiment are generally true, that is, although the number of changes of slope to the pseudo-steady state is not constant, the anode region has the most, and they begin and end there first. The initial 10 sec has a smooth concentration change form similar to that of a convectionless system and like it, gives a linear plot of ΔC vs. \sqrt{t} , but the plot does not go through the origin. Higher current densities produce noticeable convection a little sooner and have less extensive diffusion layers as shown in a recent paper by Tvarusko and Watkins (13). Ibl and Bohm (12) have found a similar instability in a redox system when similar heights and separations of electrodes were used. Optical errors calculated according to Ibl (14) are negligibly small, of the order of 1% for these concentrations and current densities.

Manuscript submitted Sept. 27, 1971; revised manuscript received ca. Jan. 18, 1972.

Any discussion of this paper will appear in a Discussion Section to be published in the December 1972 JOURNAL.

REFERENCES

1. R. N. O'Brien, *Rev. Sci. Instr.*, **35**, 803 (1964).
2. R. N. O'Brien, *This Journal*, **111**, 1300 (1964).
3. R. N. O'Brien, *ibid.*, **113**, 389 (1966).
4. R. N. O'Brien, *Nature*, **201**, 74 (1964).
5. B. Levich, *Acta Physicochim. U.R.S.S.*, **19**, 117 (1944).
6. C. Wagner, *J. (and Trans.) Electrochem. Soc.*, **95**, 161 (1949).
7. G. H. Keulegan, *J. Res. Nat. Bur. Std.*, **47**, 156 (1951).
8. J. N. Agar, *Discussions Faraday Soc.*, **26**, 1937).
9. J. R. Selman and John Newman, *This Journal*, **118**, 1070 (1971).
10. C. R. Wilke, M. Eisenberg, and C. W. Tobias, *ibid.*, **100**, 513 (1953).
11. R. N. O'Brien and L. M. Mikhherjee, *ibid.*, **111**, 1358 (1964).
12. Ursula Bohm and N. Ibl, *Electrochim. Acta.*, **13**, 891 (1968).
13. A. Tvarusko and L. S. Watkins, *ibid.*, **14**, 1969).
14. N. Ibl, *Proceedings of the 7th Meeting C.I.T.C.E.*, Lindau, Butterworths, London (1955).



Dielectric Breakdown in Silicon Dioxide Films on Silicon

I. Measurement and Interpretation

C. M. Osburn* and D. W. Ormond

IBM Thomas J. Watson Research Center, Yorktown Heights, New York 10598

ABSTRACT

Depending on how one measures the dielectric breakdown strength of thermally grown SiO_2 films in the thickness range useful for MOSFET applications, different results may be obtained. These results are shown not to be an intrinsic property of the SiO_2 but rather are artifacts dependent on metallurgical contact thickness, oxide thickness, capacitor area, applied bias voltage, instrument impedance, and time constant. These parameters lead to phenomena commonly referred to as self-healing (or nonshorting) breakdowns which represent a voltage collapse followed by thermal processes that vaporize the shorting electrode metal allowing the capacitor to break down repeatedly at higher fields. Statistical distributions of breakdown fields for the initial breakdown event point to a continuum of oxide defects having different breakdown fields in contrast to prior work showing specific defect types. Measurements of the final shorting voltage (after self-healing breakdown events no longer occurred) are useful in determining the maximum dielectric strength of a defect-free film. A ramp-rate dependence of the breakdown field is observed for slow ramps, and a time instability is seen in the high-field conduction which leads to breakdown.

The dielectric strength of SiO_2 films on silicon is important to the performance of MOSFET devices. Both the initial yield and the reliability of these devices during operation can be related, at least in part, to the breakdown characteristics of the SiO_2 gate dielectric.

Dielectric breakdown in materials has been of interest for many years, particularly as related to high-voltage insulators and capacitors. More recently, growing interest in the large-scale integration of transistors and other thin-film components has shifted attention to breakdown in very thin films, and, consequently, breakdown strengths have been measured for films of many different materials. Unfortunately, only a limited amount of work has been done to relate materials and processing parameters to the breakdown characteristics in SiO_2 , in order to both improve the oxide integrity as well as to determine the major breakdown mechanisms.

Several ways of describing the dielectric strength of thin insulating films have been developed and refined in recent years (1). The following three methods have received special attention: (i) measuring one capacitor sample having thin metal electrodes in order to allow self-healing breakdowns (2) to take place by vaporizing the metalization over the failed or weak spot in the dielectric, thereby eliminating the weak spots; (ii) constructing a statistical distribution of breakdown values by using a large number of test specimens (3-4); and (iii) determining the current-voltage characteristics of a capacitor, just prior to the breakdown event (5). Each method has certain advantages and disadvantages, and the choice is important. For in-

stance, the first method permits the taking of a large amount of data from a single capacitor structure, but its usefulness is usually restricted to studying the so-called primary, or high-field, breakdown strength; as such, it tells little about the low-field breakdown strength which is important for device applications, and it does not reveal the effect of materials and processing parameters on the number of oxide defects. The statistical approach (ii) gives perhaps the best indication of when an actual MOSFET device might fail during loading, but it does not shed as much light as the former technique on the nature of the breakdown mechanism. While current-voltage measurements (iii) provide additional information on the breakdown mechanism, their usefulness is restricted mainly to observing primary-type breakdowns; furthermore, the measurements can be very tedious and difficult to interpret when other time-dependent components (e.g., from ionic displacements) appear in the total current.

When measuring breakdown in MOS capacitors, the statistical approach is often employed because it is probably most directly related to device reliability. It has the additional advantage of being the most sensitive measure of the effect of materials and processing parameter changes. However, it will be shown that the procedure used in measuring statistical distributions does affect the results obtained and that care must be taken in interpreting data. In this paper, the results of an attempt by the authors to interrelate various materials and measuring parameters to the dielectric breakdown characteristics of thermally grown SiO_2 films are reported. The interactions of such variables as oxide thickness, metal electrode area and thickness (here, aluminum), time response, and impedance of the electrical measuring circuit, as well as testing ramp rate

* Electrochemical Society Active Member.

Key words: dielectric breakdown, silicon dioxide films, metal-oxide-semiconductor (MOS), self-healing breakdown, conduction.

591

and polarity, are discussed. In addition, certain implications of the current-voltage characteristics are considered since they suggest a likely breakdown mechanism.

Experimental Procedure

Metal-oxide-semiconductor capacitors were fabricated on 2 ohm-cm, p- and n-type $\langle 100 \rangle$ -oriented silicon wafers. The wafers were ultrasonically cleaned using $\text{NH}_4\text{OH}-\text{H}_2\text{O}_2$, $\text{HCl}-\text{H}_2\text{O}_2$, and HF solutions, while the quartz glassware was etched with HNO_3-HF ; oxides from 200 to 2000Å thick were then grown in dry oxygen at 1000°C . By using all reasonable precautions to insure pure SiO_2 films, mobile Na^+ ion concentrations on the order of $5 \times 10^{10}/\text{cm}^2$ were obtained as determined by the flatband voltage shift technique (6). One hundred aluminum electrode dots were electron-gun evaporated through metal masks onto each wafer in a clean evaporation system, and the wafers were then given a 5-min anneal at 500°C in dry nitrogen.

Measurements were made with the circuit shown in Fig. 1, wherein a ramp voltage (i.e., increasing linearly with time) was applied to the MOS sample. Breakdown was accompanied by a rapid voltage drop across the MOS capacitor which was sensed by a special triggering circuit that would record the breakdown voltage on a voltmeter. Often, particularly if the aluminum electrode was thin, the MOS capacitor would not short out but would recover and continue increasing in voltage as the ramp voltage increased until another breakdown event occurred. This process of recovering is the well-known phenomenon of self-healing whereby the capacitor discharges through the breakdown path and vaporizes the metalization over the path leaving a nonshorted capacitor containing a small, burned-out area. Up to several hundred of these self-healing events could take place before the sample would short permanently. The voltage at which this shorting, or final, destructive breakdown, took place was recorded on a second, peak-reading voltmeter. Thus only the initial, self-healing breakdown voltage and the final, destructive breakdown voltage were recorded and the intermediate breakdown events were ignored. When the aluminum was thick and self-healing did not occur, both breakdown values were the same. After all the capacitor specimens on a wafer were tested, histograms giving the percentage of capacitors that broke down vs. the voltage of breakdown for the initial and the final breakdown were constructed. From a practical point of view, only the initial breakdown distribution was important; from the point of view of understanding breakdown processes in defect-free SiO_2 , the final one was important. This measuring procedure combined methods (i) and (ii) described earlier in that (a) statistical distributions were constructed in order to study low-field breakdown events, and (b) self-healing events were allowed in order to measure the intrinsic breakdown strength of SiO_2 . Intermediate-field breakdown events gave no additional information since the use of statistical distributions made it possible to determine the probability of breakdown at any given field.

The voltage ramp was obtained by charging a fixed capacitor by means of a constant current generator,

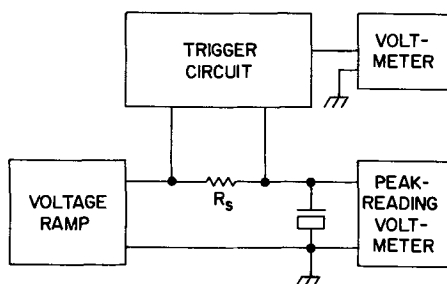


Fig. 1. Diagram of the breakdown measuring circuit

and its speed was varied by adjusting the current. The value of the series resistor (R_s) ranged from 10 ohms to 100 kilohms. The triggering circuit was basically the nanoampere sensing arrangement described elsewhere (7) with the input impedance reduced in order to speed the response time to under $1 \mu\text{sec}$. The circuit would trip a relay when a 1-volt, $1-\mu\text{sec}$ pulse appeared across R_s . With a large series resistor, the time constant for recharging the MOS after a self-healing event was larger than $1 \mu\text{sec}$ so that the circuit would detect all of the self-healing events in which the capacitor voltage dropped by one volt or more; later considerations show that the chances of self-healing occurring with less than a one-volt drop are quite remote.

Results and Discussion

Measurement of statistical distributions.—When the series resistor was 100 ohms or less, the initial and final breakdown distributions were identical, and visual inspection at 100 magnifications showed that no self-healing breakdowns had occurred. For larger R_s values (>10 kilohms) self-healing breakdowns occurred which were later observed as small black specks on the aluminum electrodes under this magnification. Accordingly a 100-kilohms series resistor was used subsequently to permit self-healing so that the maximum breakdown strength of each sample could be evaluated. Figure 2 compares the initial and final breakdown distributions for a typical wafer with the metal biased negatively. It was found that the initial breakdown values were continuously distributed over the entire field range from 0 to 10 MV/cm and did not show distinct peaks in general. More careful preparation of the SiO_2 films did, however, reduce the frequency of breakdowns occurring below 2 MV/cm. The final (i.e., destructive) distribution, on the other hand, consisted of distinct peaks similar to those observed earlier by Fritzsche (3) as well as by Chou and Eldridge (4). The measuring circuit of Chou and Eldridge was identical to the one used here for measuring the final breakdown voltage except that their series resistor was even larger (250 kilohms); furthermore, visual inspection did show that their samples experienced self-healing which was undetected by their slower responding (~ 0.1 sec) testing circuitry; hence, their data are probably more representative of the final breakdown phenomena. The presence of a low-field peak in the final breakdown distribution can be explained simply by the lack of sufficient energy stored in the MOS capacitor to promote self-healing at low fields. At low fields, breakdowns are shorting giving rise to a low-field peak while at intermediate fields breakdowns are self-healing. This behavior is explained more fully later. The occurrence of this peak in the final break-

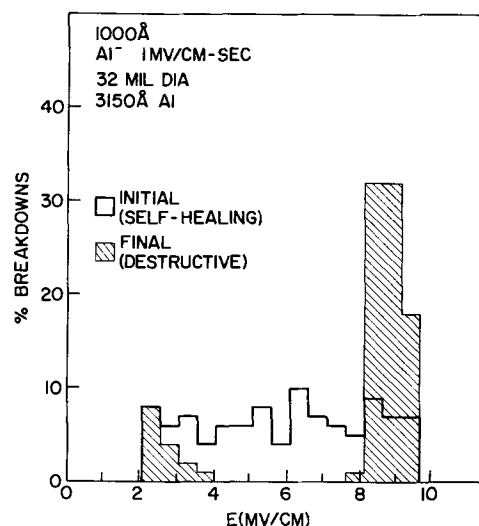


Fig. 2. Initial and final breakdown distributions

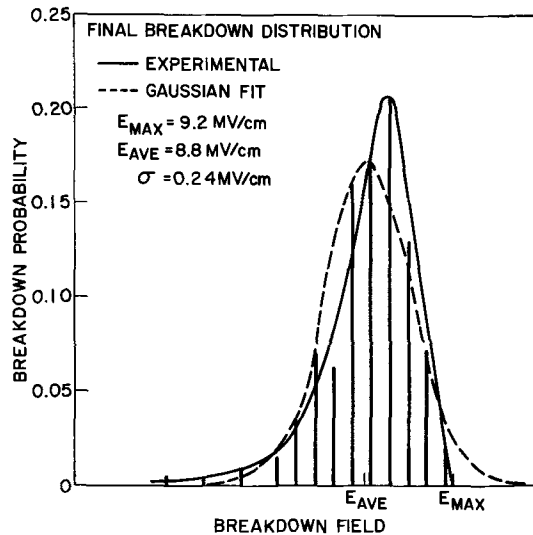


Fig. 3. Shape of typical final breakdown distribution

down distribution does not reflect any property of the SiO₂ film but is rather a consequence of measuring conditions. The wide distribution of breakdown fields across a wafer, as determined from the initial self-healing breakdown events, indicates either a distribution of weak spot sizes or several breakdown mechanisms. Both initial and final distributions were dependent on the electrode area since the frequency of low-field breakdown events increased with increasing electrode area.

A more expanded plot of a typical final breakdown distribution, as used to determine the maximum dielectric strength (see Fig. 3), shows that the high-field curve is not Gaussian but rather is skewed at low fields and has a sharp cutoff at the upper end (E_{max}). Furthermore, the peak of the experimental distribution occurs at a field that is greater than the average field. The variance of the distribution in most cases is two to five times larger than would be expected from thickness fluctuations over the wafer and must be explained in terms of other mechanisms, possibly large numbers of very small defects. The shape of the final distribution is largely independent of measuring temperature. The variance of the distribution remains about 4% of the average field down to 400Å thick films. Distributions for thinner oxides have larger standard deviations which can be attributed to the lack of self-healing.

A correlation has been observed between the initial and the final breakdown strength of a particular capacitor. Those which had a low initial, self-healing breakdown also had low final breakdown voltages; conversely high final breakdown usually followed high initial breakdown voltages. It has not been possible to determine whether the process of self-healing weakens the remainder of the film or whether both breakdowns are associated with a generally defective film. Destructive breakdown usually involves a series of propagating breakdowns in a cluster until the breakdown area is so large that insufficient energy is stored to sustain further clearing of shorted regions.

Polarity.—When the aluminum is biased negatively in p-type MOS capacitors, the silicon surface is in accumulation and the entire applied voltage appears across the oxide. When the aluminum is positive, however, the surface can be either depleted or inverted, depending on the field applied and the minority carrier generation rate. In the equilibrium case, the maximum voltage across the silicon is equal to the maximum amount of band bending allowed or about 1 volt; this is a small correction factor for samples that break down at roughly 50V or more. On the other hand, when the carrier generation rate is slow compared to the measuring ramp, deep depletion can occur, and

most of the applied field can be in the silicon. Avalanche in the silicon could possibly trigger the breakdown in this case. Because of this potential difficulty, most of the measurements in this study were made with the aluminum negative; a comparison was made with the aluminum positive, however. Under room lighting and with a ramp rate of 1 MV/cm-sec, the distribution for the aluminum positive was spread out over a very large range. The maximum breakdown voltage ranged up to 150V for 1000Å films and went over 80V for 200Å films (15 and 40 MV/cm, respectively, if the entire voltage were across the oxide). This compares with maximum breakdown strengths of 92 and 25.8V for 1000 and 200Å films (9.2 and 12.9 MV/cm, respectively) with the aluminum negative. As expected, the Al(+) distribution results were very light sensitive since light increases the carrier generation rate and gives faster equilibration; strong illumination reduced the maximum breakdown voltage in a 200Å film from over 80 to 19.4V and from 150 to 89V in a 1000Å film. Comparisons of breakdown distributions measured under strong illumination with both polarities gave identical results for the most part. The maximum dielectric strength for Si(+) is about 0.4 MV/cm less than for Si(−) however. Occasionally a capacitor withstood an abnormally high voltage with depletion bias even under illumination. Subsequent examination showed that these capacitors exhibited a high leakage current through the oxide. The authors attributed the high breakdown voltage in this case to the high oxide leakage prohibiting the formation of an inversion layer in the silicon and not to superior breakdown strength. Thus care must be taken to insure that equilibrium occurs if meaningful breakdown measurements are to be made with the silicon depleted. Many measurements were made on n-type Si wafers with the aluminum biased positively. The behavior observed was the same as that with Al(−) on p-type wafers. Apparently the measuring polarity is not an important factor in itself but rather the condition of the silicon surface (i.e., accumulated or depleted).

The tendency for self-healing was found to be very polarity dependent; *viz.*, self-healing breakdowns would occur for both polarities but were much less frequent when the aluminum was biased positively. For a sample to self-heal with positive aluminum, thinner aluminum, larger capacitor area, or thicker oxide was required than for Al(−). Klein (2) found that for p-type samples of 0.3 and 9 ohm-cm the resistance of the discharge path was an order of magnitude greater for Al(+) than for Al(−) so that the initial current surge through the discharge path was an order of magnitude greater for negative aluminum. It could be argued that the high-current, Al(−) breakdown could vaporize the discharge path more effectively (and, hence, self-heal) while the low-current, Al(+) breakdown could not. In an actual device, only the first breakdown event is important, of course, and is not affected by self-healing and hence is not affected by polarity.

Ramp rate.—If the breakdown mechanism in SiO₂ is thermal in nature, one would expect to find a ramp-rate dependence of the maximum breakdown strength. In this study, the ramp rate was varied from 0.05 to 10⁵ MV/cm-sec with only subtle changes in breakdown strength. For Al(−) the high-field, or primary, breakdown peak was observed to shift to higher field values by about 7% when the ramp rate was increased from 0.05 to 2 MV/cm-sec, as shown in Fig. 4. No statistically significant changes in the lower field breakdowns could be discerned. Breakdown measurements on a single sample using the self-healing technique (2) showed that the breakdown strength was constant for ramp rate over 2 MV/cm-sec (see Fig. 5). These results extend the work of Fritzsche (3) who found no pulse duration effect from 8 to 400 μsec. With the silicon depleted in room light, the faster ramp in-

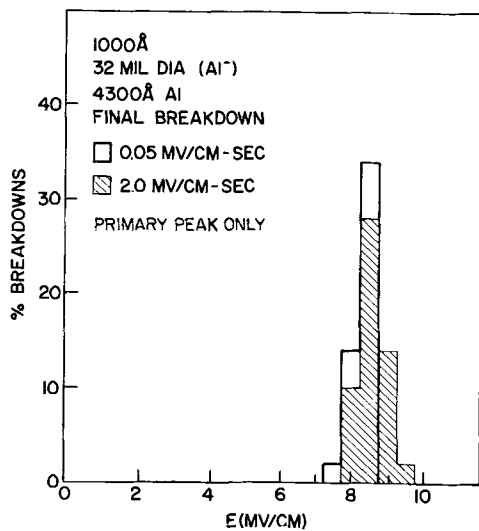


Fig. 4. Ramp-rate dependence of breakdown distributions

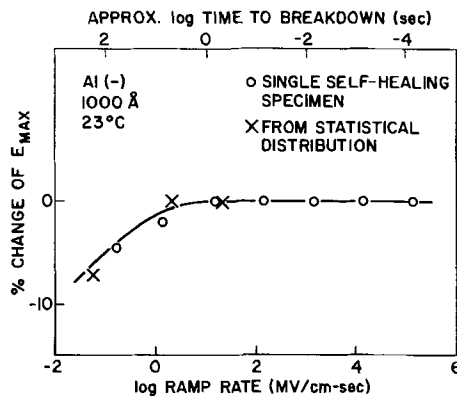


Fig. 5. Ramp-rate dependence of maximum dielectric strength

creased the low-field breakdowns but had no real discernable effect at high fields. It should be noted that even in room light, many samples withstood voltages that would create fields in the oxide greater than 10 MV/cm for over 5 min (this anomalously high voltage is divided between the oxide and the silicon and results from a low minority carrier generation rate as compared to the rate of loss of carriers through oxide conduction). Previous studies of low-frequency C-V characteristics (8, 9) also found very slow carrier generation rates.

Effect of material parameters on breakdown distributions.—Oxide thickness.—One significant finding here where the breakdown distributions were determined for various oxide thicknesses is that fewer self-healing breakdowns occur in thinner SiO₂ samples. Thus, for thin films (e.g., 200 Å), the initial and the final breakdown distributions are almost identical while they are quite different for much thicker SiO₂ layers. One qualitative explanation for this behavior is apparent; namely, the energy (W) stored in a capacitor of area F and oxide thickness d is

$$W \propto F \cdot d \cdot E^2 \quad [1]$$

where E is the electric field strength applied across the oxide. For a given field and area, thinner oxide samples store proportionately less energy that can be subsequently released for volatilizing a portion of the metal, thereby resulting in a self-healing event. The implications of this observation are important when it is realized that several breakdown studies in the past have measured the final breakdown only. The final breakdown voltage in a thick film is usually much higher than the initial breakdown because the MOS capacitor can self-heal; in contrast, the final break-

down in a thinner film is identical to the initial breakdown. Hence, a determination of only the final breakdown distributions can make the apparent intrinsic breakdown strength and the apparent high-field breakdown frequency decrease with decreasing SiO₂ thickness; these observations are artifacts of the measurement and do not represent the properties of the film itself.

Aluminum thickness.—The electrode area dependence of the fraction of capacitors having final breakdown strengths within the range of the high-field, or primary, breakdown peak (i.e., the high-field peak of the final breakdown distribution in Fig. 2) has been used to characterize a defect density of the oxide film. For example, Chou and Eldridge reported defect densities for several oxide thicknesses wherein the mobile Na⁺ concentration was $\sim 2 \times 10^{11}/\text{cm}^2$ and the immobile sodium was not determined. Since self-healing breakdowns were present but undetected in their samples, it was necessary to determine the extent of any interaction between their measurements and results. Accordingly, the aluminum thickness was varied, and, as expected, those samples having thicker aluminum contacts showed fewer self-healing breakdowns and therefore more low-field, final shorting breakdowns; however, some self-healing events were observed with over 10,000 Å of aluminum thicknesses. The electrode area dependence of the fraction of high-field breakdowns is shown in Fig. 6 for several thicknesses of aluminum; the oxide defect density, ρ , can be determined from this figure using the relation

$$-\ln P = \rho F \quad [2]$$

where F is the electrode area and P is the probability of a primary breakdown. Since ρ , as computed from final breakdown distributions, is a function of aluminum thickness (see Fig. 7), it is not a true measure of a density of defects in the oxide but is apparently a more complicated indicator of the defect density coupled with the aluminum thickness. The occurrence of undetected self-healing events can greatly distort results obtained for defect densities. The initial breakdown distribution, on the other hand, was independent of aluminum thickness to first order at least; although the wafer dependence precluded an exact comparison of wafers having different thicknesses of metal, no statistically significant difference was ever observed.

Capacitor area and defect density.—In examining the initial and final breakdown distributions, one observes a more or less definite threshold field (V_t) below which no self-healing breakdowns occur. In practice, it was found that most samples with initial breakdown above this threshold do self-heal but no samples self-heal below the threshold. This threshold voltage varied with the capacitor area, F , as

$$K = \frac{kF}{2d} (V_t^2 - V_r^2) \quad [3]$$

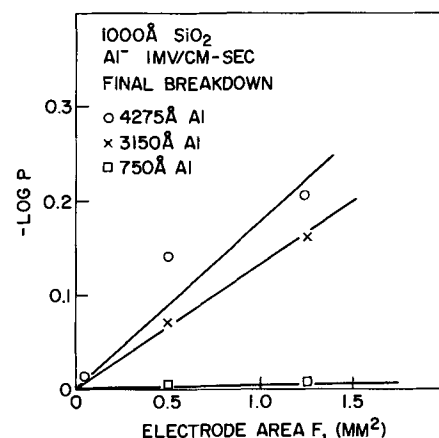


Fig. 6. Electrode area dependence of breakdown

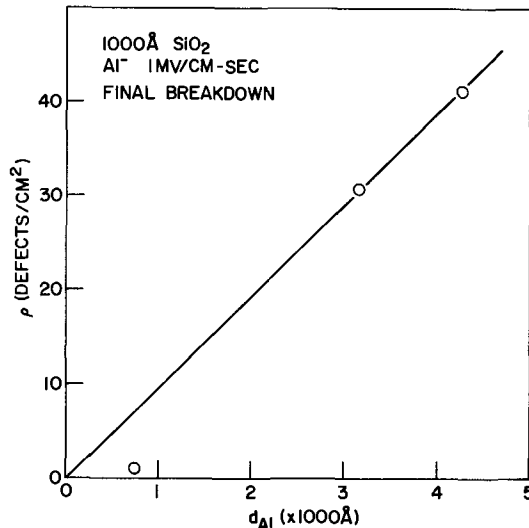


Fig. 7. Aluminum thickness dependence of breakdown

where V_r is associated with the minimum voltage remaining across the capacitor during a self-healing breakdown event; d is the thickness of the oxide having dielectric constant k ; and K represents the minimum energy required to vaporize the discharge path for self-healing and is dependent on aluminum thickness. A value of V_r about 23V gave the best fit to the experimental data for the present films. By comparison, Klein (2) found that the theoretical lower limit of V_r should be 12.2V for SiO₂ films; this value is considered to be the minimum voltage needed to support a gas discharge and is composed of the aluminum work function plus the silicon ionization potential. High-speed oscilloscope traces showing the voltage across the capacitor during a self-healing breakdown event with the wafers used in this study further verified the minimum value of V_r as 22-24V; Klein found an experimental value of 16V for V_r by using oscilloscope traces.

Since the fraction of the final, secondary breakdown events varies with aluminum thickness and since the self-healing threshold voltage of the secondary breakdown varies with capacitor area, it becomes necessary to re-examine the defect density, ρ , as used first by Fritzsche and then by Chou and Eldridge. The past work has made the assumption of a single type of defect responsible for the secondary breakdown peak; this study finds the absence of a well-defined secondary peak for the initial breakdown distribution. Instead the breakdowns are distributed over a wide range of fields. The probability, $p_F(E)$, that a capacitor of area F will break down between E and $E + dE$ can be determined from the initial breakdown histograms. Typical distributions of the breakdown probability for three different capacitor diameters are given in Fig. 8. In the most general case, three regions can be discerned: (i) high fields ($0.8 E_{max}$ to E_{max}) where $p_F(E)$ does not depend on the area F and can be associated with the intrinsic breakdown of the film, (ii) low fields (0 to $0.8 E_{max}$) where $p_F(E)$ can be expressed as $F \times \rho(E)$, and $\rho(E)$ can be considered as the density of defects having breakdown E , and (iii) moderately high fields ($0.6 E_{max}$ to E_{max}) where $p_F(E)$ increases with increasing area but not linearly and appears to be a transition between the intrinsic breakdown region and the defect-related breakdown region. It should be noted that the range of each region varied from one sample to another. The use of the defect densities as a function of field was a very sensitive indicator of the variability in breakdown properties of different wafers. Some wafers did show a distinct peak in the defect density at lower fields indicating a high incidence of a single type of defect in those particular wafers. Most wafers, however, showed a continuum of defect sizes or properties. As expected the

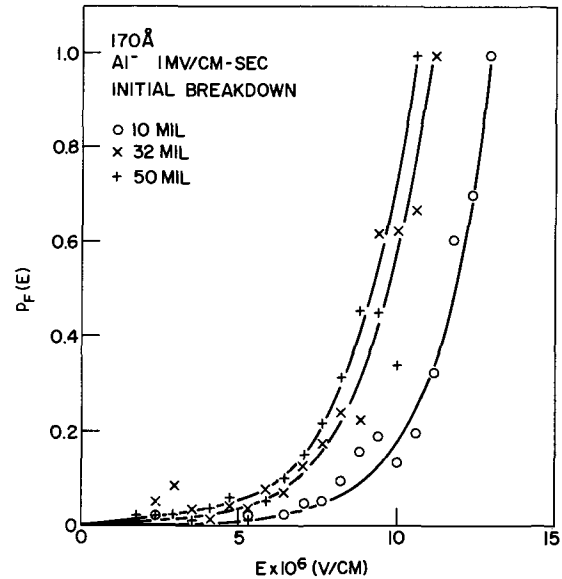


Fig. 8. Breakdown probability as a function of field

probability of a defect being present increases as the defect size decreases. No significant variations in the defect densities have been observed as a function of oxide thickness beyond normal wafer to wafer differences.

The mathematical treatment of a distributed defect density is only slightly more complicated than for the discrete defect case. In the defect-related breakdown region, if we let $P(E)$ be the probability that a capacitor of area F has a defect with breakdown less than or equal to E , then

$$P(E) = \int_0^E F \rho(\xi) [1 - P(\xi)] d\xi \quad [4]$$

Solving gives

$$P(E) = 1 - \exp \left\{ - \int_0^E F \rho(\xi) d\xi \right\} \quad [5]$$

If $P'(E)$ is the probability that the capacitor has breakdown greater than E , then

$$P'(E) = \exp \left\{ - \int_0^E F \rho(\xi) d\xi \right\} \quad [6]$$

or

$$-\ln P'(E) = F \int_0^E \rho(\xi) d\xi \quad [7]$$

which is the same as Eq. [2] with an integral replaced for a discrete density. It should be noted that the data of Fig. 8 fit Eq. [7] at all oxide thicknesses for $E = 0.8 E_{max}$ with

$$\int_0^{0.8 E_{max}} \rho(\xi) d\xi \simeq 120/\text{cm}^2 \quad [8]$$

Measurement of current-voltage characteristics.— Figure 9 gives the steady-state I-V curves for a 1300Å oxide film at room temperature. The data were taken after the field had been applied for a few hours to drive the mobile ions to one electrode or the other. The data are quite similar to those of Lenzlinger and Snow (10) showing Fowler-Nordheim tunneling. In the present case Al(+) gives higher current at a given field than Al(−) which is opposite of their result indicating different barrier heights. There is one major difference in the results: at the high fields, particularly with Al(−), the current increases with time (½ to 10 min) from its instantaneous value to a stable, equilibrium value. This change is repeatable: if the voltage is reduced, the current decreases with time to its original value at the voltage. When the voltage is increased again, both the instantaneous current and

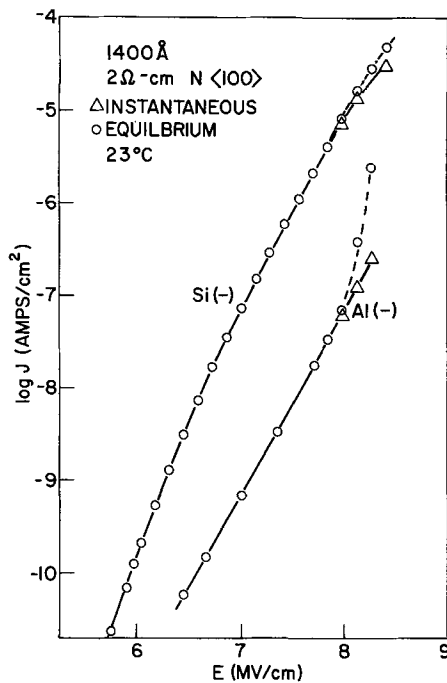


Fig. 9. Current-voltage characteristics of SiO_2

the equilibrium current are the same as they were initially. The range over which this instability could be observed was only about 4% of the entire voltage range; at any higher field the current would run away at too fast a rate to stop. Conduction measurements made on capacitor structures with a guard ring ensured that surface conduction does not affect these results. Although this instability is suggestive of joule heating in the sample, the power levels are too low to cause heating (see Appendix). Furthermore, the onset of the instability occurs at the same field for both polarities although the power levels are two to three orders of magnitude different. This field-dependent mechanism is thus more likely associated with an electronic process having a long time constant.

These steady-state I-V characteristics also shed light on the effect of breakdown measurement on the results obtained. If the breakdown voltage is defined to be the voltage at which a prescribed current flows (for example $1 \mu\text{A}$), then the breakdown for Al(-) will always be 1 to 1.5 MV/cm higher than for Al(+). If the runaway point is defined as being the breakdown point, this polarity difference will be smaller since the instability occurs at the same field for both polarities.

Summary

The dielectric breakdown properties of thermally grown SiO_2 films show a wide variability. Depending on the measuring conditions, this variability may or may not be observed. Statistical breakdown distributions as determined from the initial breakdown event can be considerably different from distributions of final destructive breakdown when self-healing or non-shortening breakdowns occur. Initial breakdown distributions reveal a continuum of defects having different breakdown fields rather than distinct defect types while final distributions show a low-field peak which is an artifact of the measurement.

The initial breakdown distributions were largely independent of materials and measuring parameters. Metalization thickness, oxide thickness, capacitor area, and measuring circuit impedance did not affect the initial, self-healing results. Final distributions, on the other hand, were very strongly influenced by these parameters.

The differences in the two distributions are best explained in terms of the self-healing breakdown proc-

ess. Only when self-healing takes place is the final distribution different from the initial. The final distribution depends on the number of self-healing breakdown events while the initial distribution is not influenced by these events. For a nonshorting breakdown to occur, sufficient energy must be stored on a capacitor to vaporize the metalization over a breakdown path. The metal thickness, oxide thickness, capacitor area, and circuit impedance are merely the parameters that affect the stored energy or the energy required for self-healing and would be expected to influence the final breakdown. It should be emphasized that the phenomena of self-healing breakdowns is not related to any fundamental property of the SiO_2 film but rather is related to the measuring parameters.

Due to the interaction of the materials and measuring parameters with the final breakdown, it is concluded that the initial distribution gives the better measure of the breakdown characteristics of the SiO_2 film itself. Furthermore, since actual devices use thicker metalization which is covered with glass, self-healing does not occur readily, and the initial breakdown is destructive and is therefore the important one. Final breakdown distributions are useful, however, for determining the maximum dielectric strength of the film and the mechanism of breakdown.

Measurements of the ramp-rate dependence of the breakdown distribution, coupled with steady-state I-V characteristics, indicate that for the aluminum-biased negatively the breakdown occurs via an electronic instability.

APPENDIX

The equation governing heating in a film per unit area on silicon with no radial heat loss is

$$J \cdot V - k \frac{dT}{dx} = dC \frac{dT}{dt}$$

where T = temperature of the film, J = current density flowing through film, V = voltage across film, k = coefficient of thermal conductivity (11) $\approx 3 \times 10^{-3} \text{ cal cm}^{-1} \text{ sec}^{-1} \text{ }^\circ\text{K}^{-1}$, C = heat capacity (11) $\approx 0.4 \text{ cal/cm}^2$, d = thickness of film, x = vertical dimension, and t = time.

The highest observed current density from Fig. 9 was 10^{-5} A/cm^2 at about 100V, thus the first term giving the heat input is about $2.5 \times 10^{-4} \text{ cal/cm}^2\text{-sec}$. Assuming even a minimal 1°C temperature difference across the 1000Å film gives a thermal conductance loss (second term) of $3 \times 10^2 \text{ cal/cm}^2\text{-sec}$ or six orders larger than the heat generated. Thermal runaway seems highly unlikely under these conditions. In 5000Å films of evaporated silicon oxide Klein and Burstein (12) observe thermal runaway when the $J \cdot V$ term is about $1 \text{ cal/cm}^2\text{-sec}$ or four orders higher than ever attained with SiO_2 ; in addition their thermal conductance loss should be at least one order of magnitude less than for the 1000Å films here.

Acknowledgments

The authors would like to thank Dr. J. Eldridge and Dr. N. Chou for many interesting and stimulating discussions during the course of this work and for critically reviewing the results. Dr. D. Young was consulted several times and his comments are gratefully acknowledged. They would also like to thank R. Hammer for the test probe used in breakdown measurements.

Manuscript submitted Sept. 1, 1971; revised manuscript received Dec. 10, 1971.

Any discussion of this paper will appear in a Discussion Section to be published in the December 1972 JOURNAL.

REFERENCES

1. N. Klein, *Advan. Electron. Electron Phys.*, **26**, 309 (1969).
2. N. Klein, *IEEE Trans. Electron Devices*, **ED-13**, 788 (1966).

3. C. Fritzsche, *Z. Angew. Phys.*, **24**, 43 (1967).
4. N. Chou and J. Eldridge, *This Journal*, **117**, 1287 (1970).
5. N. Klein and H. Grafni, *IEEE Trans. Electron Devices*, **ED-13**, 281 (1966).
6. E. H. Snow, A. S. Grove, B. E. Deal, and C. T. Sah, *J. Appl. Phys.*, **36**, 1664 (1965).
7. General Electric Transistor Manual, p. 325, 7th Edition (1964).
8. T. Hickmott, Private communication.
9. M. Kuhn and E. H. Nicollian, *This Journal*, **118**, 370 (1971).
10. M. Lenzlinger and E. Snow, *J. Appl. Phys.*, **40**, 278 (1969).
11. D. W. Kingery, "Introduction to Ceramics," p. 446, 490, John Wiley & Sons, Inc., New York (1960).
12. N. Klein and E. Burstein, *J. Appl. Phys.*, **40**, 2728 (1969).

Dielectric Breakdown in Silicon Dioxide Films on Silicon

II. Influence of Processing and Materials

C. M. Osburn* and D. W. Ormond

IBM Thomas J. Watson Research Center, Yorktown Heights, New York 10598

ABSTRACT

The breakdown characteristics of thermally grown SiO₂ films on Si are shown to depend on oxide thickness, substrate doping concentration, sample preparation, presence of passivating layers, and testing temperatures. The maximum breakdown strength varies as [thickness]^{-0.21} below 800Å, is essentially constant from 1000 to 2000Å, and increases slightly (8%) with increasing testing temperature in the range -196° to +300°C. The breakdown strength is only moderately affected by the dopant-type level in the starting silicon wafer: 10²⁰ phosphorus atoms/cm³ in the silicon reduced the breakdown strength in 200Å thick oxides by only 20%. The initial condition of the silicon wafer, cleaning procedure, oxidation temperature, passivation layer, and postmetalization anneal are important parameters in the control of defect-related, low-field breakdowns, while the oxidation ambient, substrate doping, oxide thickness, metalization, and measuring temperature have little or no influence on this process.

The fabrication of MOSFET devices requires the growth of SiO₂ films that will withstand moderate electric fields. Defects in the oxide that lead to dielectric breakdown reduce both the yield and the reliability of devices. For this reason, it is important to study processing and other material parameters that could lead to breakdown.

Low-field breakdown in SiO₂ films has previously been attributed to flaws or defects in the oxide or silicon by several investigators (1-5). Considerable work has been done to establish the conditions which reduce defect concentrations and thereby maximize the dielectric strength. The effects of oxide thickness (2, 3, 5-11), substrate doping (3, 4, 6), reactivity of the metal electrode (2), postmetalization annealing (2), passivating layers (2), and temperature (3, 9) have been examined, but, unfortunately, the results have not always been in agreement. For instance, it has been reported that SiO₂ breakdown strengths increase (2), decrease (3, 5-9), or are constant (10) as the oxide thickness is increased. One common problem of many past studies is that breakdown measuring conditions have not been well defined; as a consequence, defect-related breakdowns have obfuscated the results of investigations made to determine the thickness and temperature dependence of the maximum breakdown strength, and the occurrence of undetected self-healing events has distorted statistical breakdown characteristics. Consequently, earlier papers report breakdown strengths in the range 5-7 MV/cm, while later ones give values of 8-10 MV/cm. This study represents an attempt to systematically determine the effect of different processing and material variables on breakdown strengths through more carefully controlled, well-defined measurements.

* Electrochemical Society Active Member.

Key words: dielectric breakdown, silicon dioxide films, silicon processing; MOS, silicon dioxide defects.

Experimental Procedure

Metal-oxide-semiconductor capacitors were fabricated on silicon wafers using procedures previously described (1). Both p-type and n-type substrates, having from 10¹⁴ to 10²⁰ dopant atoms/cm³ of phosphorus or boron, were used in growing SiO₂ films from 50 to 2000Å thick. Oxide thicknesses were measured ellipsometrically. Dry oxygen as well as oxygen saturated with water at 95°C were used as ambients, and oxidations were carried out from 900° to 1200°C. The standard processing involved dry oxidation at 1000°C of 2 ohm-cm material. Phosphosilicate glass layers were grown on some samples by depositing P₂O₅ onto SiO₂ at 800°C in an ambient of 91% N₂, 9% O₂, and a small amount (0.02-0.3%) of POCl₃ followed by a drive-in at 975°C. One hundred metal electrode dots were electron-gun evaporated onto each wafer through masks in a clean evaporation system, and the wafers were given a 5-min postmetalization anneal at 500°C in dry nitrogen. Aluminum, magnesium, chromium, molybdenum, gold, and platinum electrodes were added, but aluminum ones were used for most of this work. A standard metal thickness of 3000Å was used to permit self-healing breakdown events to occur (1). Statistical breakdown distributions were measured, and care was taken to measure the voltage of the first, self-healing breakdown as well as the voltage of the final destruction (1). For device applications, only the voltage of the first breakdown event is of interest since it would render a device useless; furthermore, initial breakdown distributions are used to determine the defect density as a function of breakdown field as discussed in Part I (1). The final breakdown field is important only in studying the maximum dielectric strength of a defect-free film. The measuring polarity was selected to accumulate the silicon surface thereby minimizing the voltage drop in the wafer.

Results and Discussion

Oxide thickness.—When the distribution of final breakdown voltages is measured (self-healing events ignored), the fraction of high-field breakdown events increases with increasing oxide thickness as shown in Fig. 1 [the field value of $0.8 E_{max}$ is used as the dividing line between low-field, defect-related breakdowns and high-field, intrinsic breakdown as discussed in the previous paper (1)]. This thickness behavior, first reported by Chou and Eldridge (2), occurs because low-field breakdown events are more likely to recover through self-healing if the oxide is thick (1). Thus for thick oxides, the breakdown events are self-healing until the intrinsic dielectric strength is attained; for thin oxides, all breakdown events are destructive. It therefore must be emphasized that the behavior in Fig. 1 is the result of a peculiarity in the measurement and cannot be related to any fundamental property of the oxide.

On the other hand, distributions of the initial breakdown voltages show a markedly different oxide thickness dependence. From the results in Fig. 2 for three different capacitor areas, it is evident that the fraction of high-field breakdowns is independent of oxide thickness, within experimental error. Even though each point represents an average of several wafers (or 400 to 1000 capacitors tested), the data show a large amount of scatter because the breakdown characteristics have a strong wafer dependency. The capacitor area dependence of the breakdown probability is consistent with films having 120 defects/cm². It is clear that the occurrence of high-field breakdowns does not fall off markedly, even for oxides as thin as 200Å. Films thinner than 100Å do show increased low-field failures, suggesting that nonuniformities in the Si/SiO₂ or SiO₂/Al interface regions have dimensions that are

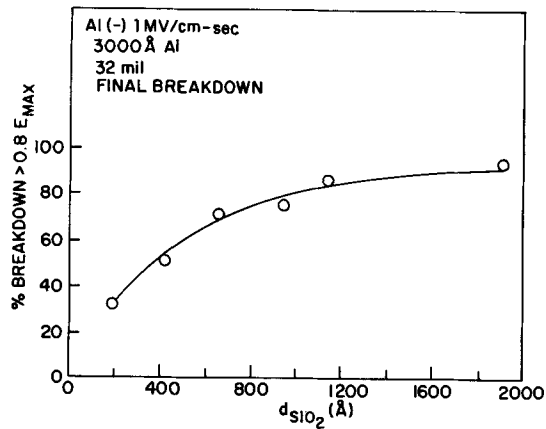


Fig. 1. Oxide thickness dependence of final breakdown distribution.

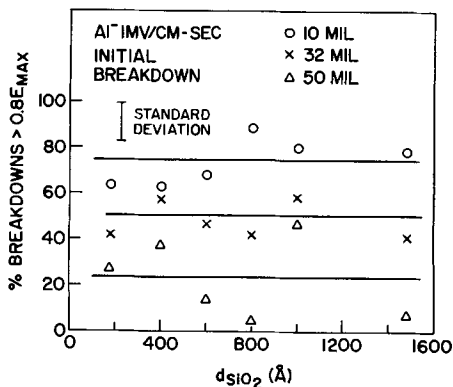


Fig. 2. Oxide thickness dependence of initial breakdown distribution for capacitors that have electrode diameters of 10, 32, and 50 mils.

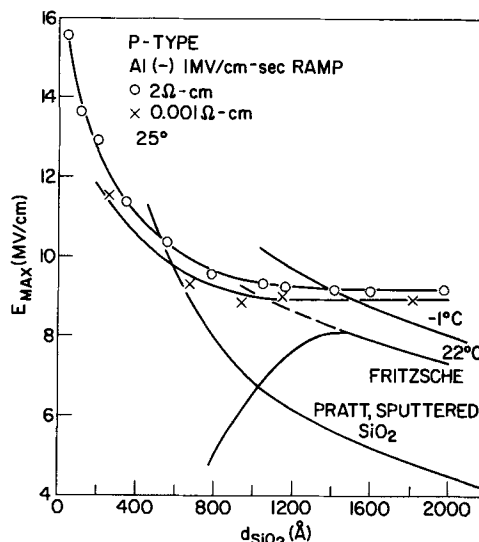


Fig. 3. Oxide thickness dependence of maximum breakdown strength.

at least a sensible fraction of $\sim 100\text{Å}$. On occasion, exceptionally defect-free (≈ 20 defects/cm²) oxides were grown which did seem to show a few more defects in 200-500Å films as compared to 1000Å thick ones. The authors observed that the initial breakdown voltage distribution provides a more sensitive measure of wafer-to-wafer defect variations than does the final breakdown one. When self-healing can occur, the final breakdown distribution reflects the maximum breakdown strength of a uniform film rather than the breakdown strength of a defective area. Initial breakdown voltages give results that can be interpreted in terms of a property of the film (such as a defect density from the data in Fig. 2) while the final breakdown voltage cannot be easily related to the quality of the film.

The oxide thickness dependence of the maximum breakdown strength shows still another type of behavior (Fig. 3). The maximum dielectric strength actually increases with decreasing thickness as observed by some previous investigations (3, 5-9, 11) and as predicted by both thermal (12-13) and electronic (13-15) breakdown models. Due to the limited range of data available, it is not possible to precisely determine the relationship between E_{max} and d . With 2 ohm-cm Si and $d \gtrsim 1000\text{Å}$, the breakdown strength is constant; however, with film less than 800Å the maximum breakdown strength varies as $d^{-0.21}$. The oxide thickness dependence is smaller for more heavily doped silicon wafers and is discussed later. This is smaller than the usual $d^{-0.50}$ dependence associated with the simplest models for electronic or avalanche breakdown but it does approximate the $d^{-0.25}$ behavior predicted by Forlani and Minnaja (15). Furthermore, O'Dwyer's (13, 16) consideration of space charge buildup due to avalanching as well as collision ionization gives breakdown strengths which do not vary with thickness as strongly as $d^{-0.50}$.

Data of Fritzsche (3) and Pratt (11) are also included in Fig. 3 for reference. Both show increasing breakdown strength with decreasing oxide thickness with the exception of Fritzsche's curve at 22°C where defects have possibly masked the intrinsic breakdown strength. Samples used in this study did not exhibit as pronounced a temperature dependence as reported by Fritzsche. In Pratt's sputtered SiO₂, $E_{max} \propto d^{-0.66}$ for films up to 10,000Å thick in contrast to the constant breakdown strength observed here above 1000Å. This thickness independence of the dielectric strength for thicker films is even more surprising in view of theoretical (13) and experimental (14, 15) evidence showing a varying dielectric strength for bulk dielectric

layers of other materials. This finding suggests that the breakdown process in thin-film structures is initiated in a small region of fixed thickness, possibly near the injecting electrode.

The data in Fig. 3 also fit reasonably well to a $E_{max}^{1/2} \propto \log(1/d)$ plot, which would indicate that the breakdown is thermal in nature. However, this alternate failure mechanism seems remote because of the low power input levels supported by the capacitor just prior to breakdown and because of the observed temperature dependence of breakdown. The high-field instability in the current-voltage characteristics prior to breakdown (1) is more likely associated with collision ionization and Fowler-Nordheim emission (16).

Substrate doping.—In the MOSFET configuration, the gate electrode extends over the diffused source and drain regions. Limited data in the literature (3, 6) (see Fig. 4) indicate that the SiO₂ breakdown strength decreases markedly as the substrate doping increases from 10¹⁴ to 10¹⁹/cm. Extrapolation of this data, to ~10²⁰ dopant atoms/cm³ typically used in the source and drain regions of an FET device, reveals a maximum breakdown strength in the range 3-5 MV/cm, about twice that encountered in proper device operation.

The maximum breakdown fields, obtained using 100 capacitors for each condition, are shown in Fig. 4 and 5 as a function of dopant concentration for several SiO₂ thicknesses. Clearly substrate doping has a rather small influence on dielectric strength since only a 10-20% decrease in the usual strength was observed for the extreme case of 200Å films with 10²⁰ impurity atoms/cm³. The effect was even less pronounced for thicker SiO₂ films, as summarized in Fig. 3 and 6, where the thickness dependence of the maximum breakdown field for 2 and 0.001 ohm-cm wafers with boron and phosphorus doping, respectively, are plotted. It should be noted that the behavior is roughly the same for all cases: i.e., increasing breakdown strength with increasing thickness. The effect of thick-

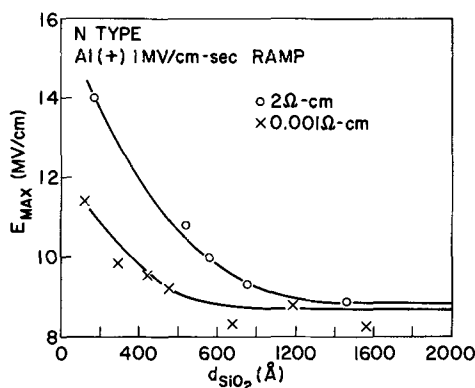


Fig. 6. Oxide thickness dependence of maximum breakdown strength with phosphorus-doped wafers.

ness is somewhat more pronounced for the more lightly doped substrate. For thicker films (over 800Å), high substrate doping reduces the breakdown strength by a few per cent at most. The effect of doping becomes as large as 20% when the SiO₂ thickness is reduced to 200Å. This change must be considered minor, however, in light of the more pronounced SiO₂ thickness dependence which improves oxide breakdown over both heavily and lightly doped wafers. Curiously, high phosphorus concentrations have more influence than boron does. The reverse situation might have been expected since phosphorus segregates to the silicon during the SiO₂ growth while boron moves into the oxide (17-19).

Substrate doping had no significant effect on the statistical distribution of initial breakdown events when evaluated in terms of two statistical parameters: namely, the fractions of very low-field (<0.2E_{max}) and of very high-field (>0.8E_{max}) initial breakdown strengths. (Neither of these parameters correlated with the doping level in the silicon.) Statistical comparison did show, however, that certain wafers exhibited substantially poorer breakdown characteristics than usual. Quite possibly, surface defects associated with a given lot of wafers can be more important than dopant concentration. Although the heavily doped wafers (0.001 ohm-cm) contained spiral rings of differing color (presumably nonuniformities introduced during growth), they exhibited typical breakdown properties. For some unknown reason, the n-type samples used here were consistently poorer than the p-type ones for all doping levels. Typically there were ~300 defects/cm² in n-type samples but only ~150/cm² in p-type specimens, as estimated from the relationship

$$-\ln P = \rho A \quad [1]$$

where ρ is the defect density, A is the area of a capacitor dot, and P is the fraction of very high-field (>0.8E_{max}) breakdown events (1). The difference might be attributed to intrinsically higher defect densities for SiO₂ film grown on n-type silicon wafers or, more likely, to the use of different oxidation furnaces for n- and p-type materials.

Steady-state current-voltage measurements were taken on MOS structures fabricated from 2 ohm-cm p-type as well as on 2 and 0.001 ohm-cm n-type Si wafers. When the capacitors were biased sufficiently long for the low-field transient to decay, the resulting I-V characteristics were essentially identical. The slight differences were well within the normal wafer-to-wafer variation and are most likely explained by minor variations in SiO₂ thicknesses across the wafers. Since conduction is limited by the barrier height of the injecting electrode (20), these measurements further support the observation (21) that the barrier height does not vary with silicon doping.

It is evident that any breakdown mechanism must explain: (i) the effect of substrate doping increases

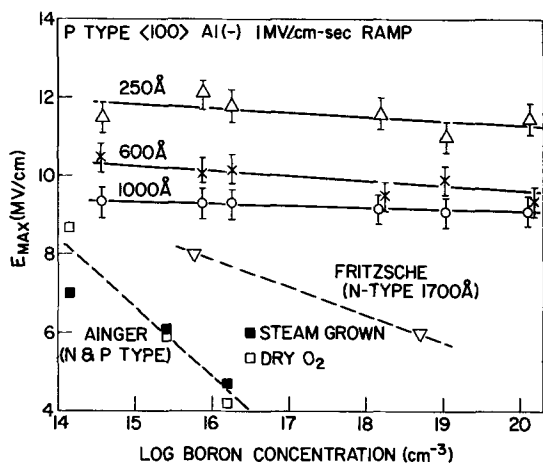


Fig. 4. Maximum breakdown strength vs. boron concentration

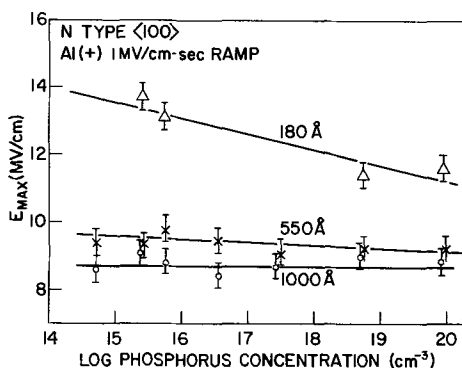


Fig. 5. Maximum breakdown strength vs. phosphorus concentration

with decreasing oxide thickness and (ii) phosphorus doping has more influence with Al(+) than boron does with Al(-). The reported segregation coefficient (17-19) for phosphorus is 10 compared to 0.1-0.3 for boron. Thus the difference between dopant concentrations in the oxide and the silicon is greater for phosphorus, but the absolute dopant concentration in the oxide is greater over the boron-doped substrates. If a certain fraction of the dopant ions in the oxide were charged (i.e., P⁺ and B⁻), the excess positive charge in the phosphorus-doped sample would enhance the electric field for the injected electrons while the negatively charged boron atoms would reduce the field. This mechanism would explain the first observation; unfortunately capacitance-voltage curves do not show any fixed charge in the oxide. In addition a charged-impurity model leading to a field enhancement would predict lower dielectric strengths for thicker films since the magnitude of the enhancement is related to the total charge in the film.

Wafer processing.—In order to determine some possible origins of defects in thermally grown SiO₂ films, specimens were prepared under various conditions including different SiO₂ growth temperatures in both O₂ and steam; the possible effects of different metal electrodes and the postmetalization anneal were also studied.

Clearly, one obvious source of oxide defects stems from surface faults (e.g., scratches, pits, bumps) in the starting silicon wafer. Chou and Eldridge (2) found that an HCl vapor polish of the silicon followed by *in-situ* oxidation using rf heating resulted in far fewer defect-related breakdowns, but apparently this reduction of defects was related more to the oxidation step than to the surface etching. A strong wafer dependency of breakdown was already noted for Fig. 2 where the data are quite scattered even though the points actually represent averages over many wafers each having 100 capacitor dots. Caines and Duffy (22) have correlated the position of breakdown in pyrolytically grown Al₂O₃ with defects or contamination of the starting silicon wafer.

In order to better understand the role of the substrate in breakdown, wafers from three suppliers were cleaned, oxidized, and metalized in the same run. Large area electrodes (50 mil diameter) were used to raise the frequency of defect-related breakdowns. The resultant defect densities (computed using Eq. [1]) were 29, 16, and 27 defects/cm² ± 5/cm² for the three wafer sources; it thus appears that defects related to the silicon polishing can vary slightly from one lot of wafers to another. However, the defect densities that can be attributed to silicon defects here (~25/cm²) are only a fraction of the defects computed from the data of Fig. 2 (i.e., 120/cm²) and from the experiments with high dopant concentrations (150-300/cm²). Thus, much of the wafer dependency of the defect density apparently arises from processing variations such as: solvent residues left on wafers during cleaning, incomplete drying, or dirty or partially devitrified furnace tubes. For instance, wafers given a cleaning sequence of trichloroethylene, isopropyl alcohol, and HF solution had 160 defects/cm² while control wafers had only 50/cm² after cleaning with NH₄OH-H₂O₂, HCl-H₂O₂, and HF. It has been also observed on many wafers that low breakdown capacitors are spacially clustered indicating the presence of either a larger defective area or a line defect. A large defect area (> 200 mil diameter) would more likely be due to processing than to wafer defects, although line defects could be due to scratches or crystallographic steps. Scratches introduced during handling have been observed to cause clustering of low-breakdown capacitors; otherwise, microscopic examination at 500 magnifications has generally failed to detect this defective area.

Laverty and Ryan (5) have previously reported an effect of the oxidation temperature on breakdown distributions. Unfortunately, their distributions were not

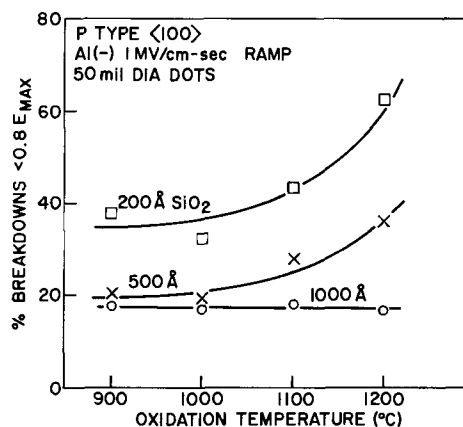


Fig. 7. Effect of oxidation temperature on breakdown distributions.

very similar in shape to those encountered in other studies (1-3); they represent very substandard oxide films. This effect, as found on oxide films typical of this study, is shown in Fig. 7 where the oxidation temperature has very little effect on films over 1000 Å thick; for thinner films higher oxidation temperatures promote defects. The effect of oxide thickness becomes more important as oxidation temperature is increased. When grown at 900° or 1000°C, the 200 Å films in this particular lot had about 15% more low-field breakdowns than 1000 Å films; when grown at 1200°C, they had 45% more low-field breakdowns.

Since oxidation temperature influences breakdown, one might expect to find a correlation of breakdown characteristics with oxidation ambient. Strangely enough it does not matter whether oxidation is done in dry O₂ or in oxygen saturated with water at 95°C. No difference in defect densities could be seen in oxides from 200 to 1000 Å thick grown under either condition at 1000° or 1200°C. These findings are in agreement with the more recent results of Fritzsche (3), but disagree with those of Ainger (6) and Deal (23), who reported much lower dielectric strengths for their samples. High-temperature annealing in nitrogen (15 min at 1000°C), following oxidation, increased defect densities by 50% in 1000 Å films and by 400% in 200 Å ones. Cleaning of the oxidation tube at 1150°C with a 6% HCl/O₂ mixture (24-25) followed by oxidation at 1150°C resulted in a 60% decrease in defect density. Other work (26) has shown that oxidation in 1% HCl/O₂ at 1000°C is likewise effective in reducing the number of defects causing dielectric breakdown. These results suggest that the improved breakdown characteristics seen with HCl vapor-polished wafers (2) may be due to the presence of HCl in the system rather than due to a better surface polish.

Several oxide films were deliberately contaminated with NaCl, during or after growth, to gain an understanding of the role contaminant ions play in defect formation and growth. Films having 10¹⁴ Na⁺/cm², evaporated onto the SiO₂ prior to electroding, showed normal breakdown behavior when the aluminum electrodes were biased negatively; for Al(+) however the peak of the breakdown distribution was shifted to a lower field as seen earlier by Raider (27). Other films were grown to half their final thickness, were contaminated with 10¹⁴/cm² sodium ions, and were then grown to the desired final thickness. These films showed 5 × 10¹² mobile charges/cm². It was not determined if the remaining sodium evaporated during the final growth period or if it was left immobile in the film. Breakdown measurements with Al(-) showed no degradation while Al(+) slightly lowered the field at which the peak in the distribution occurred; nevertheless, the fraction of lower field or defect-related breakdowns did not increase due to the presence of the sodium.

The oxidation temperature and the nitrogen annealing dependence of the defect density support a model where a metal excess in the oxide favors increased numbers of defects. As the oxidation temperature increases or after a high-temperature N₂ anneal, the oxygen content of the oxide would be expected to be reduced; both conditions give high defect densities particularly for thin films. The rate of oxide growth is irrelevant as seen with the steam oxidation. Although crystallization was suspected, the data do not support this mechanism since both steam and NaCl should enhance recrystallization.

The choice of metallization material did not influence breakdown to any significant extent either. When biased negatively, magnesium, chromium, aluminum, molybdenum, gold, and platinum all gave similar breakdown distributions with a maximum breakdown strength of over 8 MV/cm. However, conduction measurements (28) show many orders of magnitude difference in current levels at a fixed field for injection from magnesium and for gold verifying the Fowler-Nordheim, barrier-height-limited conduction mechanism.

The postmetallization annealing treatment (5 min at 500°C in N₂) resulted in a slight improvement of oxide integrity by reducing the defect density from 32 defects/cm² to 11/cm² on 1000Å test films. This reduction of defects is believed to be due to the elimination of interface states, which if present, could create internal fields which would then enhance the applied field. Thus it appears feasible that at least some of the oxide defects are electrically charged clusters rather than structural or geometrical defects. Chou and Eldridge (2) report that a short anneal improves the shape of the final breakdown distribution and that a more protracted anneal at 500°C would induce structural defects which are responsible for shorts. Figure 8 extends the temperature range of that work down to 200°C. No measurable effect is observed after 800 hr at 200°C while at 300°C annealing doubles the defect density in only a few hundred hours. Even at 250°C only a minor change is observed after 900 hr. The degradation after prolonged annealing at 500°C in the work of Chou and Eldridge was related to the reactivity of the metal used for electrodes. Likewise with this lower temperature testing the onset of defect formation at 300°C correlates well with the onset of injection of aluminum into SiO₂ (29). Samples made with Pt electrodes do not show the pronounced deterioration at 300°C. The degradation in breakdown characteristics is dependent on oxide thickness as well as temperature; 200Å thick oxides show a high defect density after a few hundred hours at 250°C.

Oxide passivation.—Earlier work (2) has shown that a thin phosphosilicate glass layer was effective in reducing the low-field or so-called secondary breakdown events and hence in reducing the measured defect den-

Table I. Effect of phosphosilicate glass layers on defects causing dielectric breakdown in SiO₂ films

PSG thickness (Å)	P ₂ O ₅ concentration (%)	Defect density* (cm ⁻²)
0 (starting oxide)	0	15
0 (30 min 975°C, N ₂)	0	37
60	2.1	19
60	3.7	17
60	4.0	12
60	5.4	6
15	3	22
35	3	18
60	3	17

* ±30% as measured on 500Å SiO₂ films.

sity. Furthermore the PSG increased the resistance of undoped and Na⁺-doped wafers to extended annealing in N₂ at 500°C. The improved properties are explained by a continuous film of PSG over the underlying SiO₂ thereby filling pinholes or cracks in the film. The thickness and concentration of the passivating PSG required to eliminate defects has not been fully explored however. In this investigation PSG layers were deposited on both good (<30 defects/cm²) and poorer (>100 defects/cm²) films of SiO₂. The standard films were fabricated with an organic cleaning step, and oxidation was followed by a 1 hr anneal in N₂ at 1000°C; both conditions were previously shown to increase the number of defects in the film.

The results obtained with the good oxide are summarized in Table I. One immediately sees that the 30 min nitrogen drive-in at 975°C more than doubles the defect density; hence, it is not surprising that in many cases (when PSG thickness and concentration are low) the defect density is higher in glassed films than it is in the starting films. Nevertheless, the defect density does decrease with both increasing PSG thickness and P₂O₅ concentration in the glass. At least 60Å of 4% P₂O₅ glass is needed to obtain films that are substantially better than the starting films. Defect densities less than 5/cm² were never observed even with 200Å of 9% P₂O₅ glass layers. Apparently these defects (5-10/cm²) were due to defects in the wafer and could not be eliminated with PSG. We have already shown that wafers obtained from different sources result in defect densities that vary by over 10 defects/cm². It should also be emphasized that the improvement in breakdown characteristics seen with thicker PSG is very substantial particularly in eliminating low-field (<0.2E_{max}) breakdown events. A PSG layer, 10% of the total oxide thickness, can give an 80% improvement in the breakdown strength of a capacitor. Apparently very deep pinholes or cracks in the SiO₂ layer are filled with the PSG. Since 60Å of PSG is needed to realize better films, it appears that the pinholes are of the order of 100Å in diameter.

With the poorer films (≈100 defects/cm²), the PSG addition markedly reduced the defect density. The defect density dropped to 60/cm² with 60Å of 2% P₂O₅ and to 40/cm² with 60Å of 5% P₂O₅ glass. Although this improvement is substantial, it is not as large fractionally as the improvement seen with good starting films. It is apparent that the effectiveness of PSG in improving breakdown characteristics is closely linked to the condition of the starting oxide films.

Temperature.—The temperature dependence of the breakdown strength is expected to be very helpful in analyzing the nature of the intrinsic breakdown mechanism. Fritzsche (3) reported that the intrinsic maximum dielectric strength decreases with increasing temperature from 0° to 80°C in much the same way as amorphous quartz. Chou and Eldridge (2) found very little change in breakdown characteristics in the 25°-150°C range. Korzo (9) on the other hand reports an increasing breakdown strength up to about 25°C followed by a slight drop at 50°C; his measurements were on oxides grown by pyrolytic decomposition of

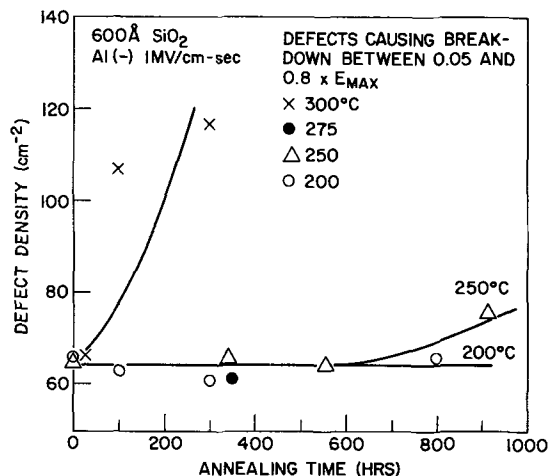


Fig. 8. Effect of extended annealing on defect densities

ethylates and had unusually low over-all breakdown strengths leading one to suspect defect-related breakdown.

To evaluate the effect of measuring temperature, a matrix of samples with 200, 400, 600, 800, 1000, and 1500Å SiO₂ layers were tested at -30°, +25°, 70°, 130°, and 200°C; in addition, several wafers were also measured at -196° and +300°C. Figure 9 gives some typical results showing a very slight increase ($\approx 8\%$) in maximum dielectric strength on going from liquid nitrogen to 300°C. Breakdown distributions were also only slightly affected by temperature. The defect density could not be correlated with measuring temperature other than by noting that the fraction of very low-field ($\leq 0.2E_{\text{max}}$) events increased by a few per cent on going from -30° to 185°C. These results further support the conclusion that most defects are present in the MOS structures after fabrication, and, except for the lowest field breakdown, are largely unaffected by measuring temperature.

The temperature dependence of breakdown supports an electronic rather than thermal mechanism for breakdown. With thermal breakdown, models indicate that $E_{\text{max}}^{1/2}$ should decrease linearly with increasing temperature (13), a trend that is contrary to the present data. Although it will not be dealt with in detail here, it should be remarked that the analysis of the temperature dependence of electronic breakdown is by no means complete. This dependence enters into electronic models via the temperature dependence of various ionizing processes that can take place in the oxide layer and is presumed to have a small effect on E_{max} . Thus the behavior observed in Fig. 9 is consistent with most electronic breakdown models and inconsistent with the temperature dependence expected for thermal breakdown. A ramp-rate dependence of the breakdown distribution similar to that reported earlier (1) was observed over the entire temperature range giving further support to the electronic breakdown model. The observation of the ramp-rate dependence at liquid nitrogen temperatures suggests that a space charge redistribution in the oxide occurs and is due to electronic rather than ionic charges.

Summary

Many processing and material variables are important to the breakdown characteristics of thermally grown SiO₂ films. The condition of the starting silicon wafer, the wafer cleaning sequence, the oxidation temperature, the passivation layer, and the postmetalization anneal are important parameters in the control of defects that have low breakdown strengths. No single factor was ever responsible for all of the defect-related breakdowns although poor wafer cleaning would substantially decrease yield. A number of the defects can be associated with the wafer as determined by comparison of wafers from different sources; others can probably be associated with electrically charged clusters that are neutralized during the post-metalization anneal, and the rest can be attributed to defects introduced during growth. A 1200°C oxida-

tion substantially increases the defect density in 200Å films.

Surprisingly enough, oxidation ambient (wet or dry O₂), substrate doping, oxide thickness, metalization, and temperature had little or no influence on defect-related breakdowns. High temperatures seemed to favor more low-field breakdowns although the increase was only a few per cent for a 200°C increase. Even though the maximum breakdown strength increased with decreasing oxide thickness, the number of defect-related breakdowns remained constant down to 200Å. Below that thickness the percentage of low-field failures increased. A very strong wafer dependence was observed, however, and several lots of wafers showed poorer than average characteristics for thin samples. High oxidation temperatures did aggravate the influence of the thickness dependence on breakdown distributions.

Oxide thickness, temperature, and substrate doping influenced the maximum breakdown strength. Films grown on 2 ohm-cm p-type wafers from 60-800Å followed the relationship $E_{\text{max}} \propto d^{-0.21}$; above 1000Å the dielectric strength was 9.2 MV/cm. More heavily doped wafers resulted in a less pronounced thickness dependence. The breakdown strength increased very slightly (8% over a 500°C range) with increasing temperature. This behavior points to an electronic breakdown mechanism; the observation of a high-field instability in the current voltage characteristics (1) provides experimental evidence of a space charge redistribution possibly due to internal collision ionization (13, 16). Substrate doping had only a minor (20%) effect on dielectric strength and was most noticeable for thinner films although phosphorus doping of the silicon wafers had a greater influence than boron doping.

Acknowledgments

The authors wish to thank Dr. N Chou and Dr. J. Eldridge for support and discussions during this work and for reviewing the results. The experimental work was aided by R. Hammer.

Manuscript submitted Sept. 1, 1971; revised manuscript received Dec. 10, 1971.

Any discussion of this paper will appear in a Discussion Section to be published in the December 1972 JOURNAL.

REFERENCES

1. C. M. Osburn and D. W. Ormond, Part I, *This Journal*, **119**, 591 (1972).
2. N. Chou and J. Eldridge, *ibid.*, **117**, 1287 (1970).
3. C. Fritzsche, *Z. Angew. Phys.*, **24**, 43 (1967).
4. N. Klein, *IEEE Trans. Electron Devices*, **ED-13**, 788 (1966).
5. S. J. Laverty and W. O. Ryan, *Intern. J. Electron.*, **26**, 471 (1969).
6. F. W. Ainger, *J. Mater. Sci.*, **1**, 1 (1966).
7. V. F. Korzo, *Soviet Phys.-Solid State*, **8**, 494 (1966).
8. V. F. Korzo, *ibid.*, **8**, 2003 (1967).
9. V. F. Korzo, *ibid.*, **10**, 1256 (1968).
10. F. L. Worthing, *This Journal*, **115**, 88 (1968).
11. I. H. Pratt, *Solid State Technol.*, Dec. (1969).
12. N. Klein, *Advan. Electron. Electron Phys.*, **26**, 309 (1969).
13. J. J. O'Dwyer, *This Journal*, **116**, 239 (1969).
14. J. J. O'Dwyer, *J. Phys. Chem. Solids*, **28**, 1137 (1967).
15. F. Forlani and N. Minnaja, *Phys. Status Solidi*, **4**, 311 (1964).
16. J. J. O'Dwyer, *J. Appl. Phys.*, **40**, 3887 (1969).
17. A. S. Grove, O. Leisteko, Jr., and C. T. Sah, *ibid.*, **35**, 2695 (1964).
18. B. E. Deal, A. S. Grove, E. H. Snow, and C. T. Sah, *This Journal*, **112**, 308 (1965).
19. J. S. T. Huang and L. C. Welliver, *ibid.*, **117**, 1577 (1970).
20. M. Lenzlinger and E. Snow, *J. Appl. Phys.*, **40**, 278 (1969).
21. R. Williams, *Phys. Rev.*, **140A**, 569 (1965).
22. J. E. Carnes and M. T. Duffy, *J. Appl. Phys.*, To be published.
23. B. E. Deal, *This Journal*, **110**, 527 (1963).

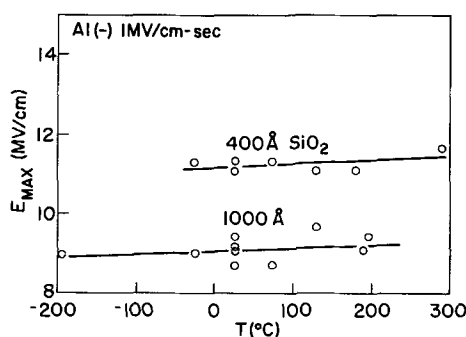


Fig. 9. Effect of measuring temperature on maximum breakdown strength.

24. P. H. Robinson and F. P. Herman, *ibid.*, **118**, 141 (1971).
 25. R. J. Kriegler, Y. C. Cheng, and D. R. Colton, *ibid.*, **118**, 73C (1971).
 26. E. Terner, IBM internal communication.
 27. S. Raider, To be published.
 28. C. M. Osburn and E. Weitzman, To be published.
 29. N. J. Chou, *This Journal*, **117**, 260C (1970).

Electrical Conduction and Dielectric Breakdown in Silicon Dioxide Films on Silicon

C. M. Osburn* and E. J. Weitzman

IBM Thomas J. Watson Research Center, Yorktown Heights, New York 10598

ABSTRACT

Conduction through SiO₂ films, thermally grown on Si substrates, was found to take place via a Fowler-Nordheim (F-N) tunneling mechanism, after an initial transient current associated with trapping of charge, mobile ions, and space charge redistribution has died away. The temperature dependence of the steady-state F-N current decreases with increasing applied field and was found to be smaller in magnitude than previously reported. Typical post-metalization annealing treatments (e.g., 5 min at 500°C in dry N₂) lowers the conductivity of the MOS capacitor structures by two to three orders of magnitude, an effect that can be attributed to the elimination of either traps or fixed charge distributed throughout the oxide. For applied fields larger than 8 MV/cm, a current instability arises which can lead to dielectric breakdown. For a wide range of different electrode materials, the onset of this instability appears to correlate well with the temperature and oxide thickness dependences of breakdown, as observed earlier (10). These findings are discussed in terms of a model which suggests that carriers can be generated and redistributed by collision ionization processes within the oxide.

Electrical conduction in SiO₂ films grown on Si substrates has been studied by several investigators (1-9) largely because of the importance of this insulator in silicon transistor technology. In particular, it is well known that metal-oxide-semiconductor FET's are operated with extremely large electric fields (e.g., 1 to 2 mV/cm) so that during testing dielectric breakdown can substantially lower the performance of these devices. As part of a continuing effort to investigate the electrical integrity of thermally grown SiO₂ films (10), prebreakdown current-voltage characteristics become important for gaining insight into the major breakdown mechanisms and for relating various materials and processing parameters to the resultant intrinsic dielectric strength.

Since several authors (11-13) have recently reviewed the various conduction mechanisms taking place in thin insulating films, this topic will not be detailed here other than to remind the reader that it is essential to distinguish between bulk-limited and electrode-limited conduction processes. In general, electronic conduction, space-charge-limited conduction, nonblocked ionic conduction, and impurity conduction are bulk limited while Fowler-Nordheim (F-N) tunneling and Schottky emission are electrode limited. Since SiO₂ is such an effective insulator, measurements of conduction in Metal/SiO₂/Si capacitors are highly sensitive to preparation and purity; consequently, results vary widely from one investigator to another. Earlier studies (3-5) indicated that the process was ionic in nature due to the presence of mobile impurities. Refinements in processing of MOS capacitors reduced the impurity content (notably Na⁺ ions) to the point where electronic conduction could be observed, wherein the currents were believed to be space-charge-limited modified by traps (6) or space-charge-limited with tunneling at the electrodes (7). Later, multiple conduction states were observed in both

thermally grown (8) and pyrolytically deposited SiO₂ films (9), and the switching from one state to another was linked to the presence of certain impurities in the oxide. Finally, conduction through high-purity SiO₂ has been demonstrated to occur via a Fowler-Nordheim tunneling mechanism (1-2).

This paper deals with conduction through high-purity SiO₂ in MOS capacitors and its relationship to dielectric breakdown. The parameters describing F-N conduction are evaluated from experimental data, particularly the temperature and voltage dependence of the current. Finally an instability in the conduction is compared to the oxide thickness and temperature dependence of breakdown.

Experimental Procedure

Silicon wafers, 2 ohm-cm p-type as well as 2 and 0.001 ohm-cm n-type, were cleaned in solutions of NH₄OH-H₂O₂, HCl-H₂O₂, and HF and then oxidized in dry O₂ at 1000°C to form oxides from 200 to 1500 Å thick. An array of 100 metal electrodes, 32 mils in diameter, were electron-gun evaporated through metal masks. Aluminum, chromium, magnesium, molybdenum, gold, and platinum were deposited for this purpose since they cover a wide range of electrode work functions. The MOS samples were subsequently annealed for 5 min at 500°C in dry N₂ in order to remove radiation damage from the evaporation step (14). Capacitance-voltage tests made on electrothermally stressed capacitors indicated typical mobile ion concentrations of less than 5 × 10¹⁰ cm⁻².

Current-voltage characteristics were measured with a Keithley 416 picoammeter. For measurements from room temperature to 325°C, the samples were placed on a small hot stage inside a shielded box with a dry N₂ ambient. Measurements were also made in liquid nitrogen. Care was taken to ensure that external leakage was negligible. Special measuring procedures were required to obtain repeatable results because the I-V characteristics were not at first reproducible (see Fig. 1). Note that the applied field must be cycled between

* Electrochemical Society Active Member.

Key words: dielectric breakdown, electrical conduction, silicon dioxide films, MOS, Fowler-Nordheim tunneling, electron injection, transient conduction, collision ionization.

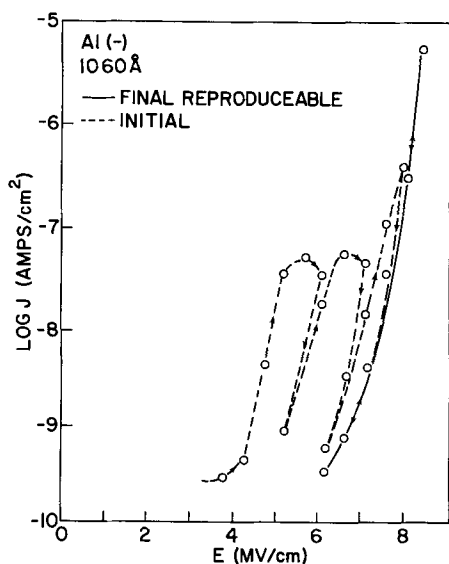


Fig. 1. Current-voltage characteristics of typical MOS capacitor showing cycling needed to achieve reproducibility.

low and high values several times before the I-V curves for increasing and decreasing fields coincide. This same degree of reproducibility could be attained by stressing the capacitor at moderately high fields ($E \approx 7$ MV/cm) for several hours while the current decreased with time to a steady-state value. Although this behavior was similar to ionic polarization effects frequently seen in other glasses, its appearance at temperatures as low as that of liquid nitrogen pointed to an electronic rather than ionic polarization in this case. No appreciable flatband voltage shift ($< 5 \times 10^{10}$ charges/cm²) was seen as a result of cycling or pre-stressing.

Using thin metalization ($< 3000\text{\AA}$) so that weak spots or flaws in the oxide would be eliminated by self-healing breakdown processes (15), it was possible to obtain on a wafer, I-V characteristics for several capacitors that were within a few per cent of one another. This high degree of reproducibility, coupled with earlier observations that the current scaled with the capacitor area (1), indicated that the measured current was distributed over the entire electrode area and not localized.

Results and Discussion

Transient conduction.—The temperature and the field dependencies of the initial current transient were studied in order to determine the origin of the decay seen here. Previous workers have reported similar transients and have attributed them to ion motion (2, 5, 17) notably sodium or protons, charge trapped or released by irradiation (18) or charge storage (4). Not surprisingly, the transient decay rate increased at higher applied voltages. The decay was not accompanied by a current transient in the opposite direction when the voltage was reduced to zero as is often seen (19) when polarization occurs. The charge levels involved in the decay, as determined by integration of current-time plots (16), were typically 10^{11} – 10^{14} /cm² and were found to increase with increasing voltage as might be expected with trapped charge and in contrast to mobile charge. It thus appears that the transient is due to trapped charges being released at high fields. The trap depth determines the field required for release. It should be noted that a current decay is observed at a high field after steady-state conduction was attained at a lower field, giving further evidence that the transient species is released by the high field. The almost linear increase in the transient charge concentration, with applied field in one sample from 3 to 7 mV/cm, indicates that the trap density must be uniformly distributed over this energy range in that

sample. The transient behavior is observed for both polarities of applied field with roughly the same amount of charge involved. Nevertheless, capacitance-voltage measurements have not been able to detect an appreciable flatband voltage shift ($> 0.1V$) after the decay has occurred. Thus if traps are involved in the process, they must be located near the metal SiO₂ interface as concluded earlier (4). Calculations show that for these traps to account for 10^{14} transient charges/cm², they must be located within 0.2Å of the metal-oxide interface for less than 0.1V flatband voltage shift in a 1000Å thick film. In addition, 10^{14} charges/cm² in the oxide would create fields up to 50 MV/cm. It appears more reasonable to postulate a lower number of traps (i.e., 10^{11} – 10^{12} /cm²); the field created by these trapped charges could then enhance the injected current. The transient would thus be due to two components: (i) mobile charge released from traps and (ii) injected electron current due to an internal space charge region.

The shape of the current decay curve shows a large variability although it is similar to an exponential curve. A single time constant τ in $I \propto I_0 e^{-t/\tau}$ does not satisfactorily describe the data at room temperature. Instead two different time constants must be considered. Likewise the data could be represented by $I \propto \beta_1 t^{-1/2} + \beta_2 t^{-1/2}$ as might be expected with ionic motion of different species (3, 17). The time constant for the fast decay in one sample was about 15 sec at room temperature, about twice that at -200°C and half that at 75°C , making an exponentially activated process unlikely since it would have such a low activation energy (~ 0.01 eV). These time constants are not within the range observed for sodium or proton release from traps as reported by Hofstein (17) and probably represent electronic traps. The slow decay ($\tau \approx 150$ sec at 23°C) is within the range described for ionic motion although its smaller contribution to the total current prohibited accurate temperature measurements. Likewise the complexity of this current decay made it impractical to get estimates of the distribution of trap energies. Occasionally with the metal biased positively, the current would increase with time for the first 50 sec and then decay. At this time the origin of this behavior is not known although the characteristics are similar to those involving space-charge-limited (SCL) transients (5, 17, 20) with a very long transit time. The lack of a steady-state current after the peak (rounded cusp for SCL transient) indicates trapping is important.

Conduction mechanism.—The conduction process is not affected by the oxide thickness in the 200–1500Å range since the applied fields required to produce given current densities are independent of thickness, in accord with the earlier results reported by Lenzlinger and Snow (1) (see Fig. 2). Furthermore, to within experimental error, the currents are independent of substrate type and dopant concentration for injection from either electrode. Figure 3 shows typical I-V characteristics for various electrode metals; the curve for injection from the bulk silicon is independent of the counterelectrode material. The spread in behavior is indeed very large. For the most part, the logarithm of the current density (J) is roughly proportional to the applied field (E), although at higher fields a deviation from this behavior is observed with Mg electrodes. In addition, for high-field injection from Al, Mo, Pt, and Si (at least), another type of instability occurs in which the current increases with time until a stable value is reached within a few minutes. Figure 4 illustrates this effect in more detail for a 1400Å-thick oxide grown on a 2 ohm-cm n-type wafer; since the same type of behavior was seen with p- and n-type substrates, it can be concluded that this particular instability is not due to minority carrier generation effects taking place in the Si depletion region. This high-field instability occurs at roughly the same field (8 MV/cm) independent of electrode

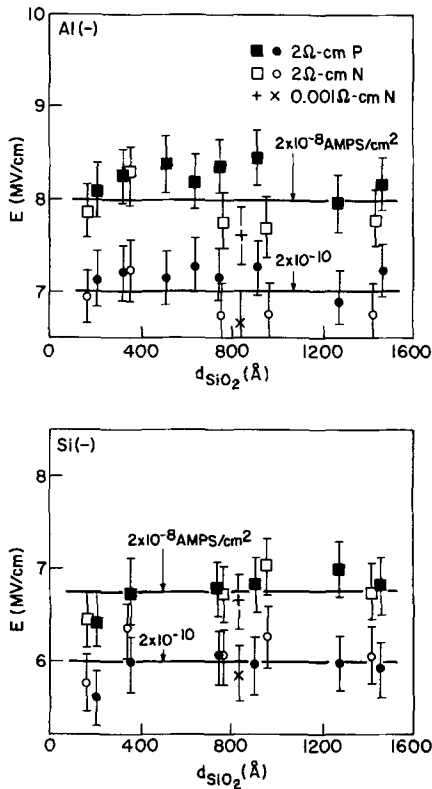


Fig. 2. Oxide thickness dependence of conduction in SiO₂ showing applied field required to produce fixed current. (a, top) Electron injection from aluminum electrode; (b, bottom) electron injection from silicon.

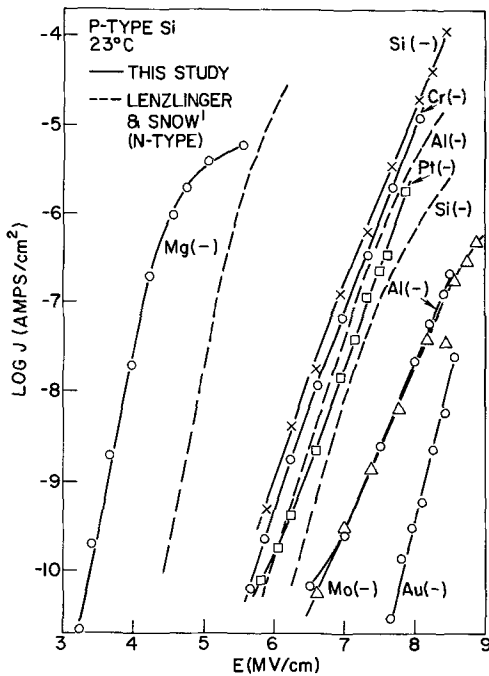


Fig. 3. Current-voltage characteristics resulting from electron injection into the SiO₂ from various metals.

material although the current levels may be considerably different when it is observed.

Both the Fowler-Nordheim and the Schottky conduction mechanisms are highly sensitive to the barrier height at the injecting electrode, and hence to the metal as observed in Fig. 3. The distinction between Fowler-Nordheim and Schottky emission are best seen with the energy level diagram of Fig. 5a. The energy difference between the metal Fermi level and the oxide conduction band presents a barrier (ϕ) for the electrons in the electrode to enter the oxide which is tri-

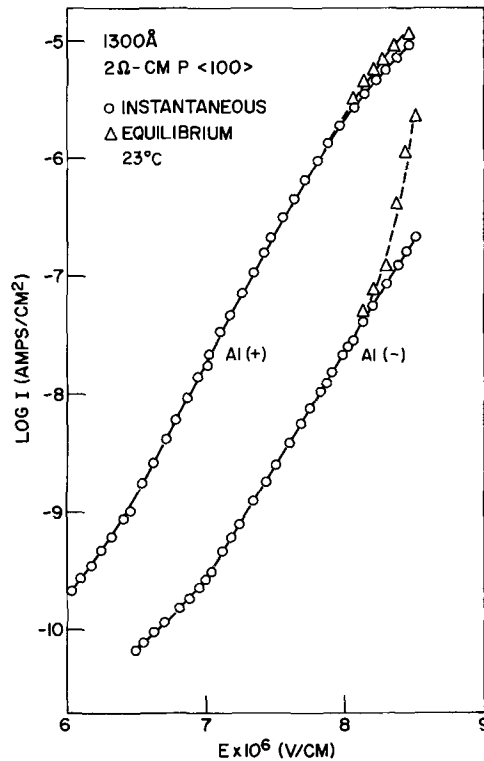


Fig. 4. Instability in I-V characteristics

angular-shaped when an electric field is applied. Electrons can tunnel through the barrier from the metal Fermi level (Fowler-Nordheim) or can be emitted over the barrier by thermal emission (Schottky). The intermediate conduction mechanism is thermally assisted electrode tunneling whereby thermally excited electrons tunnel through the upper portion of the energy barrier. The actual barrier is not a sharp tri-

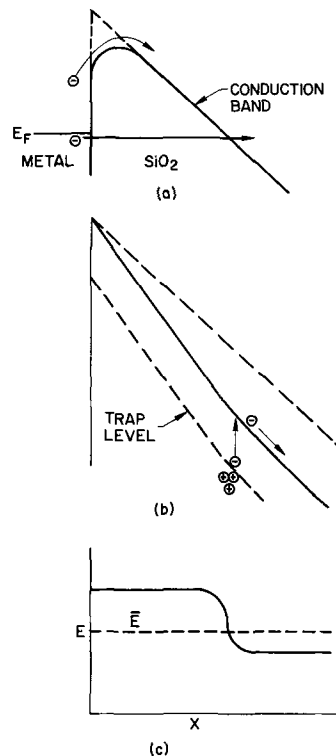


Fig. 5. Energy and field distribution near metal-silicon dioxide interface. (a) Under applied field showing image force lowering; (b) after collision ionization leaves relatively immobile positive charge (image force lowering neglected); (c) field distribution showing high-field region near interface and low-field region in bulk.

angle but is curved and has a height less than ϕ because of image-force lowering. The image-force lowering term arises from the potential redistribution in the oxide as a result of image charge induced in the metal from charge in the oxide.

The Fowler-Nordheim tunneling current J_{FN} into a solid with a barrier height of ϕ with image-force lowering is given by (1)

$$J_{FN} = (q^3 E^2 m / 8\pi h \phi m^*) [1/t^2(y)] [\pi C k T / \sin(\pi C k T)] \quad [1]$$

$$X \exp\{-[4(2m^*)^{1/2} \phi^{3/2} / 3 h q E] v(y)\}$$

where m^* is the electron effective mass in the SiO_2 , E is the applied field, q , m , h , k are the electronic charge, electron mass, Planck's constant, and Boltzmann's constant, respectively, and

$$C = 2(2m^* \phi)^{1/2} t(y) / h q E \quad [2]$$

$$y = 1/\phi (q^3 E / 4\pi \epsilon_r \epsilon_0)^{1/2} \quad [3]$$

with ϵ_r being the relative dielectric constant of SiO_2 and ϵ_0 the permittivity of free space. The correction for image-force lowering appears in the elliptic integrals $t(y)$ and $v(y)$ and are tabulated elsewhere (21).

The Schottky current J_S is given by (13, 20)

$$J_S = (4\pi m q k^2 / h^3) T^2 \times \exp\{-[\phi - \sqrt{E} (q^3 / 4\pi \epsilon_r \epsilon_0)^{1/2}] / kT\} \quad [4]$$

This Schottky conduction mechanism can be rejected for several reasons: (i) It predicts an exponentially activated temperature dependence which is not observed in Fig. 6 and 7. (ii) The slope $d \log J_S / d\sqrt{E}$, at room temperature gives a dielectric constant of only 0.35, well below even the optical value of 2.2. (iii) Temperature-field plots (13) giving regions for Fowler-Nordheim tunneling, thermally assisted tunneling, and Schottky emission show that Fowler-Nordheim conduction is expected for the conditions in this work with the possible exception of the highest temperature ($\sim 300^\circ\text{C}$) at lower fields where conduction does appear to vary exponentially with reciprocal temperature. The intermediate mechanism of thermally

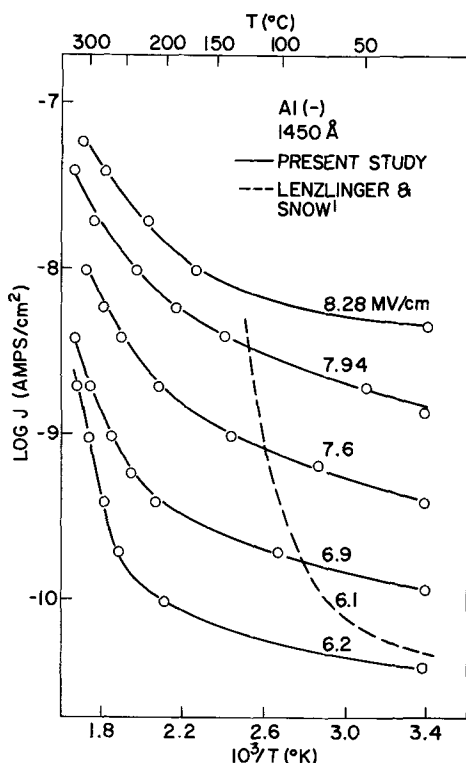


Fig. 6. Temperature dependence of conduction for electron injection from aluminum.

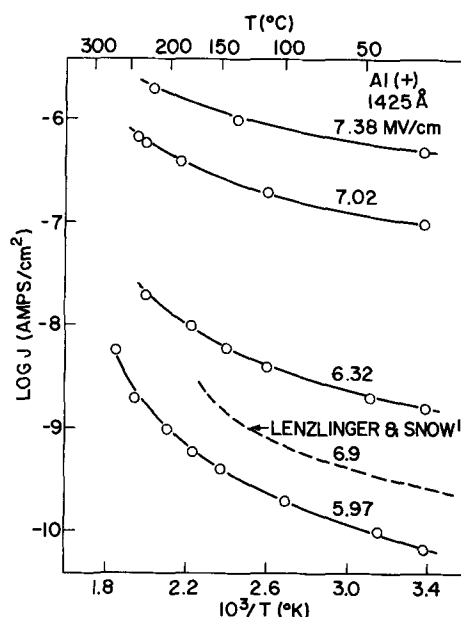


Fig. 7. Temperature dependence of conduction for electron injection from silicon.

assisted tunneling can also be ruled out since that current should vary roughly exponentially with $1/T$.

For a given field, the currents observed in this study were one-to-three orders of magnitude greater than those reported by Lenzlinger and Snow, with the exception of aluminum injection where it was two orders less (see Fig. 3). It should be noted that a layer of phosphosilicate glass (100Å, 5% P_2O_5) under the aluminum contact did not change the normally observed current. Within the limits of experimental error, the present data would fit Eq. [1]; furthermore, Lenzlinger and Snow's observation of the absolute magnitude of the current being one order of magnitude low can be explained by only a few per cent error in barrier height, effective mass, or even oxide thickness which seems very reasonable in view of their discrepancies in effective mass.

Due to the dominant exponential term in Eq. [1], it was not possible to independently determine the barrier height and the effective mass from the data but only their product. Lenzlinger and Snow used additional barrier height measurements to determine the effective mass; they found a best fit for a mass ratio of about 0.43, but this ratio varied by over 10% depending on the metal electrode, and it was not sufficient to explain their observed temperature dependence.

Table I gives the slope of the J/E^2 vs. $1/E$ plot for injection from various metals in column 2; column 3 gives the barrier height if one assumes $m^*/m = 0.5$ with the standard deviation for the least squares fit

Table I. Conduction and breakdown strengths for injection from various metals

Metal	$\phi^{3/2} \cdot \sqrt{\frac{m^*}{m}} \cdot v(y)$	Barrier height, eV		Breakdown strength E_{max} (mV/cm)
		This study†	Literature	
Mg	1.7	1.9 [0.3]	2.4 (1)	8.3
Si (bulk)	3.6	3.1 [0.1]	2.25-2.5 (2) 3.25 (1) 3.15 (18, 22), 3.29 (23)	8.9
Cr	3.6	3.1 [0.3]	3.2 (22)	8.0
Pt	3.7	3.2 [1.1]	—	8.8
Mo	4.0	3.4 [0.2]	—	9.2
Al (23°C)	4.2	3.5 [0.3]	3.2 (1, 21)	9.2
(100°C)	3.6	3.1 [0.5]	—	—
(200°C)	3.4	3.0 [0.3]	—	—
Au	7.8	5.2 [0.6]	4.2 (1) 4.0-4.1 (21)	8.0

† Assuming $m^*/m = 0.5$.

given in brackets [the correction for image-force lowering, from $v(y)$, is about 7% using the optical dielectric constant of 2.2]. The barrier heights are within 10% of those reported (1, 18, 22-24) elsewhere for Si, Cr, Mg, and Al; the agreement for the Au barrier heights is not as good where the experimental error is large. Despite the high work function of Pt, the Pt-SiO₂ barrier was only 3.2 eV high, as determined by I-V measurements. Quite possibly this unexpectedly low value as well as differences in conduction levels between this work and that of Lenzlinger and Snow can be explained in terms of impurities at the M/SiO₂ interface altering work functions. As shown by the measured barrier heights in Table I, there is a reasonable spread in the values from one study to another.

The most obvious temperature-dependent term in the Fowler-Nordheim conduction equation is $(\pi CkT)/\sin(\pi CkT)$. By adjusting the effective electron mass, Lenzlinger and Snow could fit their data to that functional form for one given field strength but then show that such a mass adjustment is unwarranted. They subsequently calculated the temperature dependence of the barrier height that would give such results. An examination of the temperature dependence of the conduction in Fig. 6 and 7 for several different field strengths show: (i) the temperature dependence is smaller for higher fields; (ii) the Si(-) polarity condition gives a more pronounced variation with temperature than the Al(-) one; and (iii) at lower fields, the current at higher temperatures begins to increase very rapidly. On the basis of these observations, it seems that more than one term in Eq. [1] is temperature dependent. Although the $\pi CkT/\sin(\pi CkT)$ term does give a more pronounced temperature dependence at low fields since $C \propto 1/E$, it does not quantitatively describe the variation of temperature dependence with field. In the exponential term, m^* , ϕ , and the dielectric constant in $v(y)$ could vary with temperature; a variation in barrier height seems most likely to explain the second observation. Table I also gives the least squares slope of the conduction for a few temperatures and shows that the exponential term in Eq. [1] decreases with increasing temperature. The rapid increase in current at high temperature and low field can be accounted for by either the $\pi CkT/\sin(\pi CkT)$ term which becomes infinite at $CkT \rightarrow 1$ or by a change of conduction mechanism to one that is activated such as Schottky emission or even bulk conduction; Faradaic currents are probably too small to make any contribution at these temperatures (25). Higher temperature measurements will be necessary to resolve this conduction mechanism. Although the temperature and field dependence of the current are more complex than originally reported (1), the magnitude of the variation is smaller particularly with Al(-). This may be attributed in part to a transient species that required special precautions to insure steady-state results as discussed earlier. Often a very large temperature dependence of conduction was observed on initial thermal cycling. These data were not repeatable however, and the final reproducible data showed much less variation with temperature.

Annealing of the SiO₂ films after metalization had a very important effect as shown in Fig. 8 by markedly reducing the current resulting from a given applied field for electron injection from both the Al and the Si contacts. Additional heat treatment (5 min or more at 500°C) did not further shift the 10 min, 500°C curves by more than a few per cent. Analysis of the data reveals that the Fowler-Nordheim slopes of the unannealed specimens give barrier heights for both electrodes that are 1.5 eV lower than those of annealed specimens. It seems unlikely that this is a true barrier height lowering due to impurities or surface states at the injecting interface since the apparent barrier lowering is the same for the Si/SiO₂ interface as for the Al/SiO₂ one. Instead two alternate models are proposed. First there is a trap level 1.5 eV below the con-

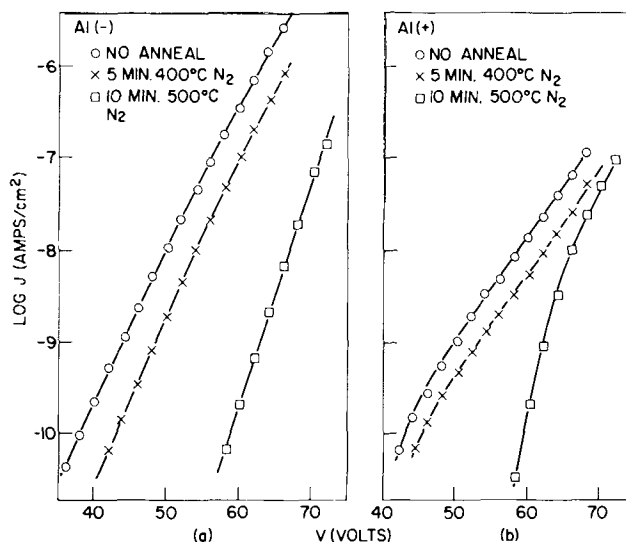


Fig. 8. Effect of postmetalization annealing on the I-V characteristics of an Al-SiO₂-Si capacitor. (a) Electron injection from aluminum electrode; (b) electron injection from silicon.

duction band in SiO₂ that can be annealed out; electrons are injected into this level with the unannealed samples and have sufficient mobility to travel along this trap level through the sample. It should be noted that trap levels (18) 2.0 eV below the conduction band have been reported and that irradiation has changed barrier heights at Si-SiO₂ and Cr-SiO₂ interfaces (23). In the second model, unannealed charge trapped in the bulk varies the potential distribution within the oxide resulting in a nonlinear potential *vs.* distance profile thereby altering the shape of the tunneling barrier. If the trapped charge is somewhat uniformly distributed throughout the oxide, the tunneling barriers at both interfaces will be equally reduced. Flatband voltage shifts during the anneal show relatively small changes in charge ($\sim 10^{12}/\text{cm}^2$) compared to the amount of charge necessary to Schottky lower the barrier by 1.5 eV ($\approx 2 \times 10^{13}/\text{cm}^2$); nevertheless, localized charges are not detected by the flatband voltage measurement. Without additional measurements it is not possible to determine which model is more correct. Since samples metalized from a tungsten filament instead of with an electron gun did not show as large an effect of annealing, the traps or oxide charge are presumed to be induced during metalization rather than present in as-grown oxide films.

Dielectric breakdown.—The high-field current instability is of particular interest in the study of dielectric breakdown. Figure 9 shows a typical current *vs.* time plot in this region of instability. The time constant associated with this current buildup appears to decrease slightly as the applied voltage increases. This instability is observed over only a small upper field region with a width of about 5% of the applied field making it somewhat difficult to observe experimentally. As Fig. 4 shows, there is a voltage at which the steady-state I-V curve becomes vertical and results in breakdown. The instability in Fig. 9 also occurs at a comparable rate when the sample is immersed in liquid nitrogen making a thermal breakdown mechanism unlikely. Likewise, any redistribution of space charge by motion of ionic carriers seems unreasonable particularly since the low-field I-V characteristics are reproducible after the conduction has been unstable. When the field is reduced after a period of time in the unstable region, the current relaxes to its original low value at that field; the time constants for this relaxation are about the same at -196° and 23°C . Capacitance-voltage flatband measurements made immediately after the instability had occurred showed at least 0.2V shift for the M(-) instability and $\approx 1\text{V}$ for the M(+) one. This C-V shift apparently indicates posi-

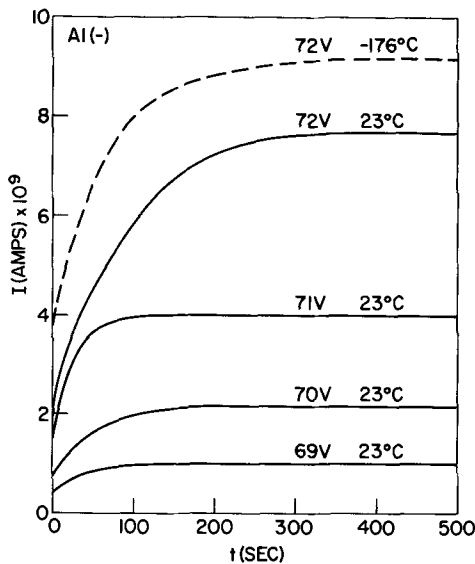


Fig. 9. Time dependence of current instability for various applied voltages.

tive charge in the oxide near the injecting electrode as a result of the high-field instability.

This onset of this instability correlates very well with the maximum breakdown strength [measured with a voltage ramp (10)] in both thickness and temperature dependence. Figure 10 shows the onset current increasing markedly with decreasing oxide thickness for films less than 800Å thick and remaining constant for thicker films. Data showing the increasing dielectric strength with decreasing thickness below 800Å are included for reference (10). The current region over which stable Fowler-Nordheim tunneling occurs is merely extended for thin oxides. The temperature dependence of the maximum breakdown strength (10) is plotted in Fig. 11 along with that of the onset of the instability. The scale is greatly expanded, and both the breakdown field and the instability field increase by a few per cent with increasing temperature. The observation that the instability occurs at a fixed field regardless of the barrier height of the injecting electrode is further substantiated by breakdown measurements included in Table I showing the maximum breakdown strength is constant to within 10% for the different metals tested.

The relative temperature and barrier height independence of the current instability are evidence that the instability is field-controlled. In this regard, it is possible to associate the instability with the onset of nondestructive avalanching in the oxide in a region, probably close to the injecting electrode. After injected electrons drift under the influence of the applied field,

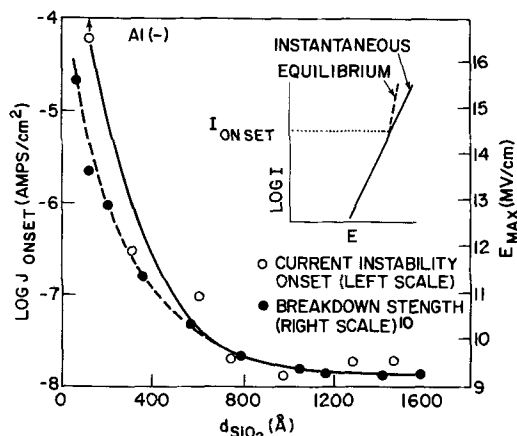


Fig. 10. Oxide thickness dependence of current instability and breakdown strength.

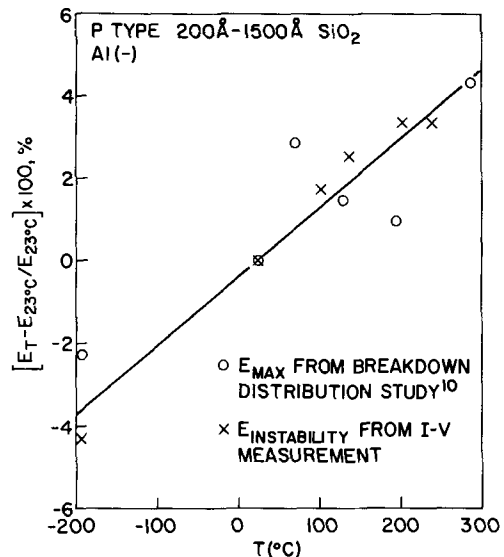


Fig. 11. Temperature dependence of current instability and breakdown strength.

additional carriers are created by collision ionization forming a space charge region which can modify the shape of the previously triangular tunneling barrier. The process is diagrammed in Fig. 5b and c, wherein, under the application of a field \vec{E} , injected electrons with mean free path λ gain energy $\vec{E}\lambda$; above a critical field this energy becomes enough to excite carriers from an energy level within the bandgap upon collision. The excited electrons are rapidly swept to the collecting electrode leaving positive charge a distance of λ from the injecting electrode. This charge modifies the potential and field distribution as seen in Fig. 5b and c with the effect of increasing the field in a narrow region around the injecting constant and reducing the field in the rest of the bulk. The reduced field prevents further collision ionization in the bulk that could lead to complete breakdown. Ionization at the interface continues until all the available traps are excited or until recombination and ionization rates equalize resulting in a steady-state condition after a few minutes (see Fig. 9). The current enhancement is due to the reduction in the size of the tunneling barrier (Fig. 5b); calculations with a 4 eV high barrier demonstrate over a 30% reduction in barrier area with 10^{13} charges/cm² (0.01 of a monolayer) located 100Å from the interface. With a 34Å mean free path (26) and an 8 MV/cm nominal field, the injected carriers should be able to excite traps 2.7 eV below the conduction band. Certainly a sophisticated treatment of the process would consider the energy distribution of traps and the variance of the mean free path. It is surprising, however, that an electronic process should have such a long time constant (*viz.*, 100-500 sec).

Recently, O'Dwyer (27-28) has made theoretical calculations of high-field conduction for a dielectric material in which collision ionization processes are taken into account. His I-V curves for both Fowler-Nordheim and Schottky cathode emission show a negative resistance instability which he associates with breakdown observed here can be associated with breakdown. The dielectric thickness coefficient (γ) of breakdown as computed in $E_{\max} \propto d^{-\gamma}$ using his model is generally less than one half which is usually associated with electronic breakdown and one quarter which has been predicted under certain conditions (29). Samples similar to those used there (10) showed $E_{\max} \propto d^{-0.21}$. This work then provides qualitative experimental support for O'Dwyer's model. More precise quantitative comparisons will need to be based on physically determined properties such as ionization coefficients and

carrier mobilities; these data, unfortunately, are not yet available.

Summary

The initial conduction in thermal SiO₂ films is seen to decrease with time. The decay can be characterized by at least two different exponential time constants. The fast decay is nearly temperature dependent while the magnitude and temperature dependence of the slow component agrees with data (17) on release of mobile ions from traps. Due to the lack of an appreciable flatband voltage change during decay, only a small component of the transient current can be attributed to mobile ion motion or polarization. A steady-state conduction is observed after several hours under high-field (7 MV/cm) stressing. The data equally well fit $\log J$ vs. $E^{1/2}$ and $\log J/E^2$ vs. $1/E$ plots indicative of Schottky and Fowler-Nordheim emission processes, respectively. The former mechanism seems unlikely because it predicts a dielectric constant value for SiO₂ which is much less than the experimentally observed one and the temperature dependence of J is not exponentially activated, as expected. The data fit the Fowler-Nordheim conduction equation, although both the effective mass and the barrier height could not be independently computed because the results were not sufficiently accurate. However, assuming a reasonable effective mass, the calculated barrier heights give good agreement (to within 10-20%) to previously measured values.

The temperature dependence of the conduction is more complex than previously reported (1) since it was found to decrease with increasing applied field, vary with electrode material, and become exponentially activated at low fields. The results cannot be explained in terms of the usual temperature dependence of Fowler-Nordheim conduction; rather, one is forced to consider a temperature-dependent barrier height or effective mass. It is not known whether the activated region represents Schottky or bulk conduction.

The postmetalization anneal reduced the current level by up to three orders of magnitude for both polarities. The mechanism proposed involves charged defects or traps in the unannealed oxide film. It was not possible to determine if tunneling and conduction were via these trap levels rather than the oxide conduction band or if the charged defects modified the internal potential distribution so as to reduce the size of the tunneling barrier.

A high-field current instability was observed that could lead to dielectric breakdown; the onset field of this instability was about 8 MV/cm and was independent of the electrode material. Likewise maximum breakdown strengths were not significantly influenced by the choice of the electrode metal. The onset of the instability increases with decreasing oxide thickness and increasing temperature in much the same way as dielectric strength. The observation of this instability at low temperatures points to an electronic mechanism. The results qualitatively fit O'Dwyer's (27-28)

model where the instability is due to collision ionization. Further calculations with this model must await additional data on ionization and drift kinetics in SiO₂.

Acknowledgments

The authors would like to express their gratitude to Dr. J. Eldridge and Dr. N. Chou for stimulating discussions and reviewing this work and to Dr. S. Raider and Dr. T. Hickmott for helpful discussions and exchange of ideas. They are also indebted to D. Ormond for the preparation of samples.

Manuscript submitted Sept. 1, 1971; revised manuscript received Dec. 10, 1971.

Any discussion of this paper will appear in a Discussion Section to be published in the December 1972 JOURNAL.

REFERENCES

1. M. Lenzlinger and E. H. Snow, *J. Appl. Phys.*, **40**, 278 (1969).
2. E. H. Snow, *Solid State Commun.*, **5**, 813 (1967).
3. E. H. Snow, A. S. Grove, B. E. Deal, and C. T. Sah, *J. Appl. Phys.*, **36**, 1664 (1965).
4. M. Yamin, *IEEE Trans. Electron Devices*, **ED-12**, 88 (1965).
5. S. R. Hofstein, *Appl. Phys. Letters*, **10**, 291 (1967).
6. R. W. Brander, D. R. Lamb, and P. C. Rundle, *Brit. J. Appl. Phys.*, **18**, 23 (1967).
7. A. G. Revesz, *Phys. Status Solidi*, **24**, 115 (1967).
8. D. R. Lamb and P. C. Rundle, *Brit. J. Appl. Phys.*, **18**, 29 (1967).
9. V. F. Korzo, *Fiz. Tverd. Tela.*, **11**, 1758 (1969).
10. C. M. Osburn and D. W. Ormond, To be published.
11. D. R. Lamb, "Electrical Conduction Mechanisms in Thin Insulating Films," Methuen and Co., London (1967).
12. A. K. Jonscher, *Thin Solid Films*, **1**, 213 (1967).
13. R. M. Hill, *ibid.*, **1**, 39 (1967).
14. P. Balk, *This Journal*, **112**, 185C (1965).
15. N. Klein, *IEEE Trans. Electron Devices*, **ED-13**, 788 (1966).
16. W. A. Pliskin, D. R. Kerr, and J. A. Ferri, "Physics of Thin Films," Vol. 4, pp. 257-324, Academic Press, Inc., New York (1967).
17. S. R. Hofstein, *IEEE Trans. Electron Devices*, **ED-14**, 749 (1967).
18. R. Williams, *Phys. Rev.*, **140**, A569 (1965).
19. R. H. Waiden and R. J. Strain, 8th Annual Proc. Reliability Physics, Las Vegas, Nevada, April 7-10, pp. 23-28 (1970).
20. M. A. Lampert and P. Mark, "Current Injection in Solids," pp. 113-139, 187, Academic Press, New York (1970).
21. R. E. Burgess, H. Kroemer, and J. M. Houston, *Phys. Rev.*, **90**, 515 (1953).
22. B. E. Deal, E. H. Snow, and C. A. Mead, *J. Phys. Chem. Solids*, **27**, 1873 (1966).
23. J. L. Peel, R. A. Kjar, and R. C. Eden, *Appl. Phys. Letters*, **17**, 3 (1970).
24. A. M. Goodman, *Phys. Rev.*, **152**, 785 (1966).
25. N. J. Chou, *This Journal*, **118**, 601 (1971).
26. C. N. Berglund and R. J. Powell, *Appl. Phys.*, **42**, 573 (1971).
27. J. J. O'Dwyer, *J. Appl. Phys.*, **40**, 3887 (1969).
28. J. J. O'Dwyer, *ibid.*, **39**, 4356 (1968).
29. F. Forlani and N. Minnaja, *Phys. Status Solidi*, **4**, 311 (1964).

Preparation of (Y,Yb,Er)F₃ Phosphors for Green-Light Emission

Sidney G. Parker* and Rowland E. Johnson

Texas Instruments Incorporated, Dallas, Texas 75222

ABSTRACT

A coprecipitation method has been used to prepare (Y,Yb,Er)F₃ phosphor powders for conversion of infrared to visible light. The coprecipitated material was treated in a stream of HF at 800°-900°C to dehydrate the powder and convert oxyfluorides to the fluorides. An interesting example of crystal growth occurred which gave a stable phosphor of the desired particle size. The phosphor converted up to 3% of the infrared radiation of GaAs:Si diodes to green light at 5400Å.

(Y,Yb,Er)F₃ has been used for conversion of infrared light of 9300-9600Å to green light having a wavelength of 5400Å (1). The phosphor has previously been prepared by melting the fluorides of Y, Yb, and Er together or by heating the fluorides together in a flux such as BeF₂, then leaching out the flux (1,2). The material obtained by melting the fluorides was uniform in composition, but the particles were too large for an application which required a particle size ≤ 20 μ m. When ground to the desired particle size, the crystals were apparently damaged, seriously reducing the phosphor conversion efficiency by 50% or more. Flux-grown material also required grinding and, in addition, was nonuniform and contained a high concentration of flux even after extensive leaching. A further disadvantage is the highly toxic nature of BeF₂. In both methods, the starting material must be the anhydrous, high-purity rare-earth fluorides.

We describe a method of coprecipitation of the rare earth fluorides, washing and filtering the precipitate, and treatment with HF at 900°C to prepare the phosphors. The phosphors are uniform, of the proper particle size and show a high conversion efficiency. The starting materials are rare earth oxides which are readily available in high purity at relatively modest price levels.

Experimental

Oxides of Y, Yb, and Er of 99.999%, 99.999% and 99.9999% purity (with respect to other rare earths) were used. Approximately 10g of the oxides in the desired mole ratio were dissolved in 25 ml of hot concentrated HCl. The clear solution was diluted with 50 ml H₂O and cooled to room temperature. To this solution in a polyethylene beaker we slowly added, while stirring vigorously, a mixture of 10 ml concentrated HF and 10 ml concentrated HNO₃. The gelatinous precipitate which formed was digested at $\sim 70^\circ\text{C}$ with constant stirring for 20-24 hr during which the precipitate became more crystalline. The supernatant liquid was decanted and the precipitate washed with 10% HF-10% HNO₃ until the wash was free of chlorides. The digestion and washing with 10% HF-HNO₃ was repeated several times. The precipitate was then rinsed with methanol, filtered, and air-dried at 110°C; it was a free-flowing powder which was probably a mixed rare earth fluoride and oxyfluoride with an unknown amount of water of hydration.

The material was heated slowly to 800°C over a period of 2 hr in a stream of He or N₂. Anhydrous HF was then mixed into the gas stream and the material was heated at 900°C for 4-8 hr. The reaction chamber was a vitreous carbon tube or an iridium tube with carbon liner; the phosphor was held in a platinum or vitreous carbon boat. The final product

from this dehydration-crystal growth treatment was very stable in air and could be used as a phosphor without further processing. It is routinely stored in a desiccator or drying oven and has shown no degradation of phosphor efficiency in more than a year.

Optimum processing conditions were selected by comparing conversion efficiencies of the phosphors. We define efficiency as the ratio of green-light output to infrared power emitted by a GaAs diode; an efficiency of 3.0% was achieved with our best phosphors.

Results and Discussion

Composition and Purity

An optimum phosphor composition was Y_{0.80}Yb_{0.19}Er_{0.01}F₃ as determined by varying the Y/Yb and Yb/Er ratios independently. The source of the starting materials greatly influenced the efficiency of the resulting phosphor. For example, Y and Yb, reported to be 99.999% purity, from two different sources gave phosphors of 1.5 and 2.5% efficiency. Analysis of the rare-earth elements and their compounds is very difficult; although emission spectroscopy is frequently used, the complex spectra make detection of many impurities impossible. Table I shows emission spectrographic analysis of typical phosphors; in this series, only Batch 36 had a high efficiency, and it also had the highest purity.

Table II shows the results obtained by mass spectrographic analysis on phosphor material as coprecipitated and after the dehydration-crystal growth steps and indicates the large number of impurities present. The concentration of all impurities except carbon and gold was decreased by the dehydration-crystal growth in HF. The amount of oxygen in the material was rather high even after dehydration and suggests that the final product may still contain oxyfluoride. Carbon could come from the organic compounds used for extraction and purification of the rare-earth oxides or from the carbon tube and boat used during dehydration. The effects of various impurities on phosphor performance were not studied. Electron microprobe analysis showed the particles to be homogeneous within the accuracy of the instrument which was $\pm 2\%$.

Coprecipitation Conditions

It was necessary to exercise control over the coprecipitation conditions to give a material easy to handle,

Table I. Emission spectrographic analyses of Y_{0.80}Yb_{0.19}Er_{0.01}F₃ phosphors

Batch No.	Impurities in ppm by weight				
	Mg	Mn	Cu	Si	B
36	0.1-1	ND	0.1-1	1-10	ND
62	0.1-1	ND	0.1-1	1-10	1-10
64	0.5-5	0.1-1	0.1-1	1-10	ND

* Electrochemical Society Active Member.
Key words: phosphors, infrared conversion, rare-earth compounds, coprecipitation, crystal growth.

Table II. Mass spectrographic analyses of $Y_{0.80}Yb_{0.19}Er_{0.01}F_3$ phosphors (ppm atomic)

Impurity	Coprecipitated material	Dehydrated-sintered material
C	1200	2200
O	20,000	8000
Na	560	115
Mg	28	10
Al	430	11.3
P	10	2.8
Cr	10	1.6
Ni	6.5	—
Cu	580	13
Zn	177	4.4
Te	50	19
Ba	1.1	0.28
Au	4.3	6.1
Hg	0.89	—
Pb	4.1	3.3
Si	1800	—

as established in past work (3), as well as a material which has a high conversion efficiency. Standard procedures described for gelatinous precipitates include low temperature (25°C) precipitation, dilute solutions, and slow addition of the precipitant with stirring. Phosphors prepared from concentrated solutions or at elevated temperatures gave approximately 1/20 the conversion efficiency of the best phosphors. The poor phosphors were presumably due to occlusion of impurities or water during precipitation which could not be removed in subsequent handling.

Homogeneous precipitation (4) to produce the mixed fluoride would presumably be of value here. A method has been reported by Vecht (5) which produces fluoride ion by acid hydrolysis of fluoroborate ion, $(BF_4)^-$, but we have not tested his method on this system.

Digestion and Washing

The digestion and washing conditions had a great effect on the phosphors. The best phosphors were formed by digestion for 24 hr at about 70°C with a 10% HF-10% HNO_3 solution followed by washing and additional digestion with dilute HF- HNO_3 solution. Digestion is a well-known method of obtaining particle growth and exclusion of impurities (3). Digestion of our gelatinous precipitate made it denser until it was transformed into a fine powder.

Analysis of phosphor efficiency indicated that it was necessary to use an acidic wash solution and to repeat the wash and digestion step a number of times. Digestion and washing in water alone gave phosphors with 0.1% efficiency compared with 3.0% for the best. This "water only" material could be improved to 2.5% by acid digestion and wash. Material which was digested once for only 24 hr or which was washed in water after acid digestion gave low-efficiency phosphors. Repeated digestions and washings seemed necessary to obtain breakdown of the gelatinous precipitate and to give a crystalline material containing much less water of hydration. Debye-Scherrer x-ray diffraction patterns of the material after the digestion washing in dilute acid solutions showed that the material was crystalline although the lines were rather diffuse and weak in intensity.

Dehydration—Crystal Growth

The dehydration period and temperature were also important factors in producing a good phosphor. The highest efficiency phosphors were obtained by starting a flow of N_2 or He, increasing the temperature over a period of 2 hr to 800°C and then maintaining at that temperature for 1 hr. TGA and gas chromatography showed H_2O was evolved, starting at about 500°C. After complete dehydration, anhydrous HF was added to the gas stream, the temperature raised to 900°C, and the system maintained for 4 hr. Heating at temperatures greater than 900°C gave inferior phosphors as did heating at 800°C for up to 12 hr in anhydrous HF. Bringing the temperature directly to 900°C also gave

a degraded phosphor. Heating at 900°C for periods longer than 4 hr did not improve the phosphor.

Phosphors with almost identical conversion efficiencies were formed when the dehydration-crystal growth steps were carried out in either a vitreous carbon boat or a Pt boat in a vitreous carbon tube. Mass spectrographic analysis of phosphors treated in Pt boats showed 0.2-2 ppm(wt) Pt in the final product. Using an iridium tube resulted in doping the phosphor to 500 ppm with Ir which reduced the conversion efficiency to 1/10 of its normal value. However, reaction of HF with Ir could be prevented by placing a carbon foil inside the Ir tube. There was little or no reaction of carbon foil or vitreous carbon if exposed to anhydrous HF. The phosphor was packed roughly into the boat; presumably these processes would occur more efficiently if the powder were spread in a thin layer or if gas flow could be directed through a bed of the powder.

As indicated in Table III, x-ray diffraction patterns on the freshly coprecipitated material which had been air dried at 110°C were diffuse, but after heating in HF the lines were sharp. This suggested that crystal growth occurred as well as dehydration. The diffraction pattern for the final product corresponded to that for the material produced by melting the anhydrous fluorides together in a dry HF ambient. Scanning electron micrographs of the phosphor at various stages confirmed that crystal growth occurred during heating in HF at 800°C and higher. Little if any crystal growth occurred by heating in the absence of HF. Figure 1(a) shows a scanning electron micrograph of the material after heating for 1 hr at 800°C in He; the appearance is identical to the unheated powder. Figure 1(b) shows the same powder after He treatment followed by treatment in HF at 800°C for 1 hr. It can be seen by comparison that the particles have increased in size by sintering together during the HF treatment. Continued heating in HF at 800°-900°C for 4 hr or more gave well-shaped crystals $\leq 20 \mu m$ in diameter, as shown by microscopic examination. Previous treatment also affected crystal growth. Thus, a fluoride precipitate which had been washed with H_2O , rather than the HF- HNO_3 mixture, showed very little crystal growth under the standard treatment and showed poor conversion efficiency as a phosphor.

Figure 2 shows photomicrographs of samples in index matching oil in transmitted light and crossed polarized light of material treated in HF at 900°C for 4 hr. It can be seen from the shape of the well-faceted

Table III. Comparison of d-spacings for $Y_{0.80}Yb_{0.19}Er_{0.01}F_3$ phosphors for different stages of hydration

Line No.	Co-ppt phosphor		Dehydrated phosphor		Melted phosphor	
	"d", Å	l/l ₀	"d", Å	l/l ₀	"d", Å	l/l ₀
1	3.70	Very diffuse	3.65	15	3.67	15
2	3.44	Sharp	3.56	50	3.57	50
3	3.24	Very diffuse	3.38	25	3.39	25
4	2.84	Diffuse	3.16	100	3.17	100
5	2.52	Very diffuse	2.85	30	2.86	30
6	2.31	Very diffuse	2.47	15	2.49	15
7	2.06	Very diffuse	2.39	2	2.40	2
8	1.95	Very diffuse	2.18	10	2.31	2
9	1.89	Very diffuse	2.04	20	2.19	10
10	1.85	Diffuse	1.98	30	2.05	20
11	1.72	Very diffuse	1.92	90	1.93	30
12	1.66	Very diffuse	1.90	25	1.92	90
13	1.56	Very diffuse	1.84	90	1.90	25
14			1.83	15	1.85	90
15			1.77	30	1.83	15
16			1.74	30	1.77	30
17			1.70	20	1.74	30
18			1.66	20	1.71	20
19			1.58	10	1.66	20
20			1.54	10	1.58	10
21			1.53	10	1.54	10
22			1.48	10	1.48	10
23			1.46	10	1.46	10
24			1.43	10	1.43	10
25			1.41	10	1.41	10
26			1.35	5		
27			1.33	5		
28			1.28	2		
29			1.27	5		

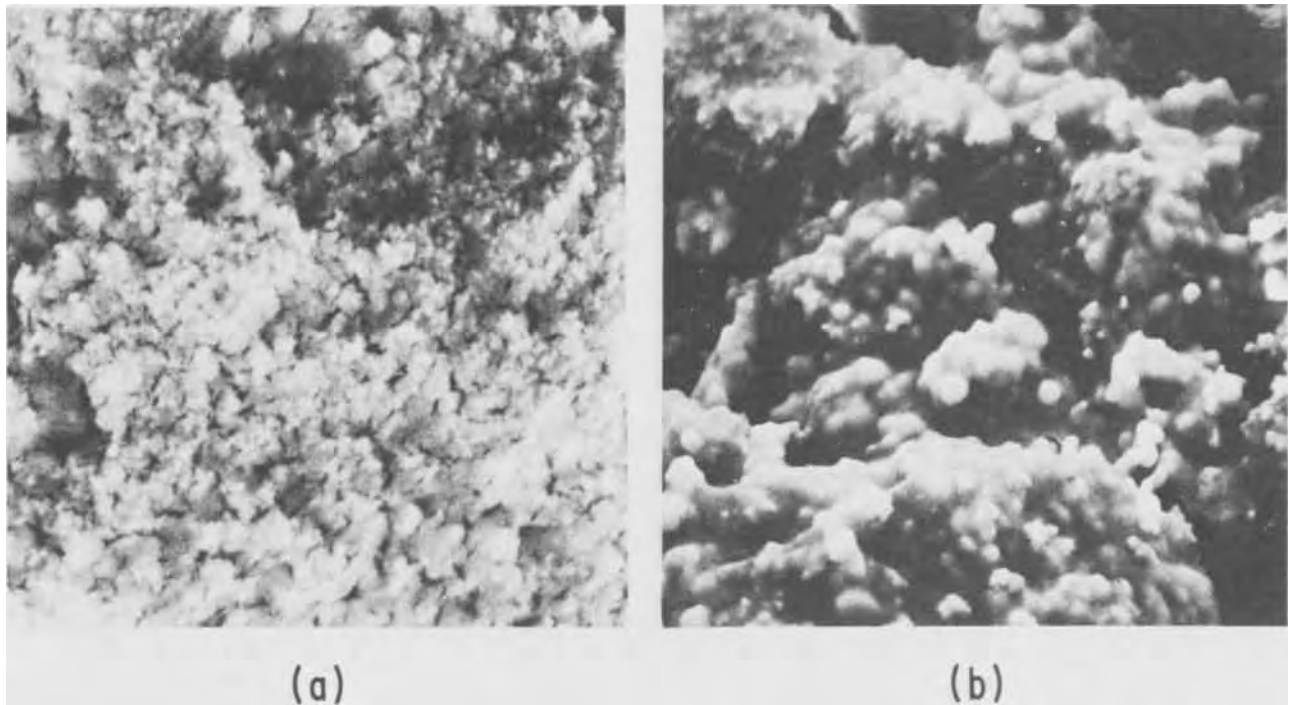


Fig. 1. Scanning electron micrographs (3000X) of (a) phosphor heated in He at 800°C for 1 hr (unheated phosphor showed identical appearance) and (b) phosphor from (a) heated in HF at 800°C for 1 hr.

particles that crystal growth has occurred. There is some strain in the crystals as evidenced by the shading. It is also apparent that during sintering or crystal growth, occlusions were formed in the crystals, most likely due to the pores or holes between the small particles during agglomeration (6). Heating in HF at 800°C did not give the pores; however, the particles

treated at 800°C were less efficient light converters than those treated at 900°C. It was possible that the pores acted as scattering centers and increased the conversion efficiency. Prolonged sintering in anhydrous HF at 900°C did not reduce the number or size of the pores. We conclude that dehydration, in the absence of HF, is necessary before the fluoridation step. This latter

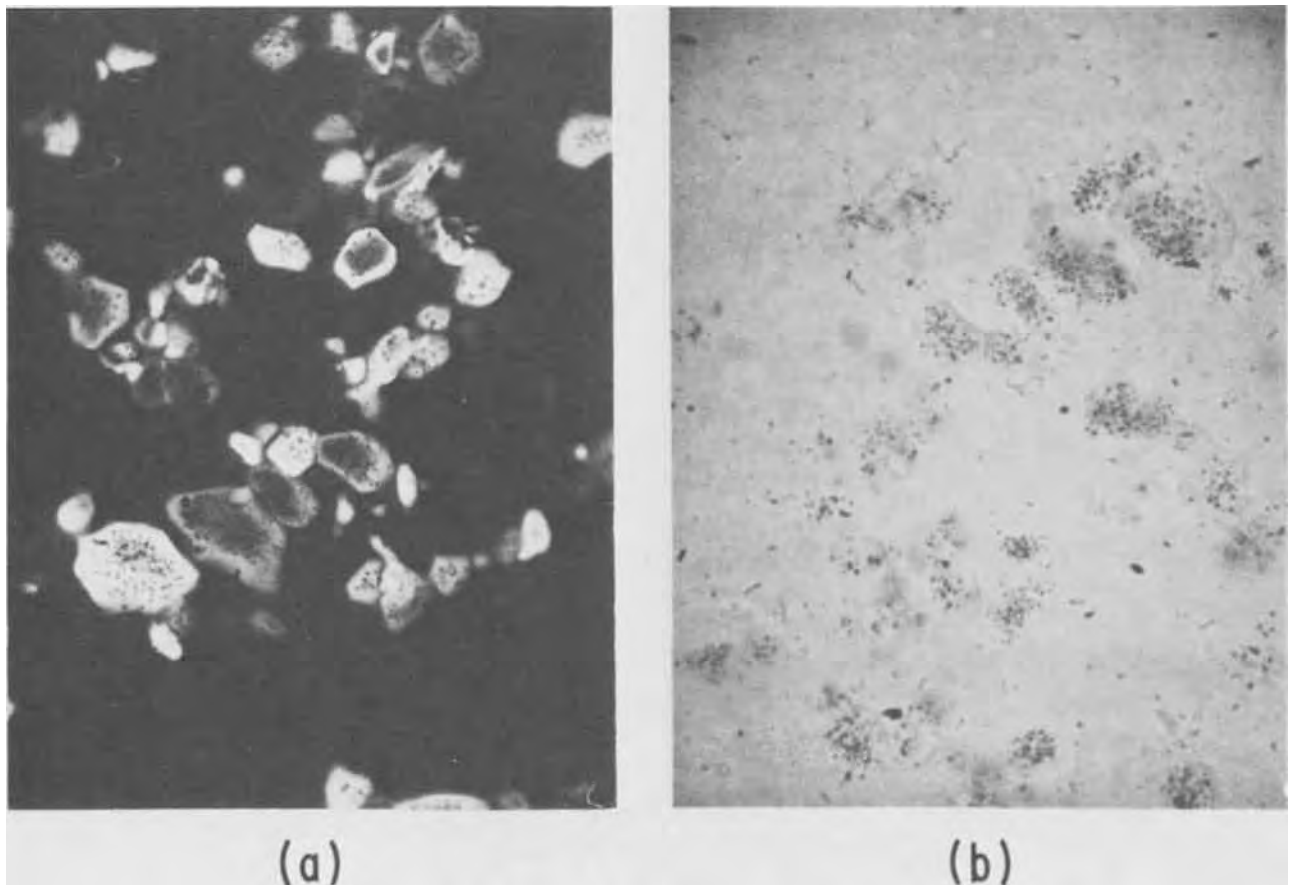


Fig. 2. Phosphor particles in index matching oil: (a) cross-polarized light and (b) transmitted light. Magnification 360X

process converts any oxyfluoride to fluoride and induces the desired crystal growth at about 900°C. Moisture in the HF stream could degrade the phosphor by forming an excessive amount of oxyfluoride or by attacking the carbon tube or boat and dispersing carbon particles throughout the system.

Testing and Application of the Phosphor

The method for evaluating the phosphors gave a rapid relative comparison but was not optimized for maximum output. For testing, the phosphor powder was mixed with silicone oil to form a viscous slurry with about 75% phosphor by weight. The slurry was applied to a 0.072-in. diameter domed GaAs:Si diode which gave infrared of 9300-9600 Å. Slurry was applied until maximum green light output was obtained. The GaAs diode was operated at 2A at a power level of 3.36W. The diode was well heat-sinked and operated for only short periods. The green-light intensity was determined with a silicon solar cell, filtered to remove the infrared. The solar cell voltage was measured across a fixed resistor and had been calibrated to give output power. The maximum conversion of diode infrared output to green light output was 3.0% which represented a brightness of ~8000 ft-L. No effort was made to obtain the maximum in light output by use of reflective surfaces, index-matching media, or a particular particle size, although some preliminary experiments indicated that the green-light output could be doubled by use of reflective coatings. The test method was reproducible to 1% and accurate to probably $\pm 10\%$; it enabled phosphors to be checked for conversion efficiency in only a few minutes. The phosphor-oil slurry was readily removed so the same diode was used for all tests.

Evaluation devices were made from diode chips, 0.024 in. square. An epoxy was applied; then the phosphor powder was allowed to settle through the epoxy. After curing, the epoxy-phosphor layer was ~200 μm thick and roughly 50% phosphor. Characteristics of some devices are given in Table IV. Since the phosphor emission depends on a 2-(or more) photon absorption, there is a nonlinear relation of infrared emission to green-light emission. Again, no effort was made to optimize the brightness of these devices. These green-light emitters showed little or no degradation in light output after 6 months under constant load at 50 mA but did show 10% degradation at 100 mA load. This

Table IV. Green light output at various current levels for $\text{Y}_{0.80}\text{Yb}_{0.19}\text{Er}_{0.01}\text{F}_3$ on GaAs:Si diodes

Diode No.	IR power (mW)		Brightness, ft-L			
	50 mA	100 mA	25 mA	50 mA*	100 mA**	125 mA
49	2.42	4.93	17	77	250	325
23	2.76	5.77	27	130	430	560
25	2.90	6.19	49	210	640	850

* Brightness 99% after 6 months at 50 mA.

** Brightness 90% after 6 months at 100 mA.

was caused by degradation of the diode rather than the phosphor. There appeared to be no reaction of the phosphor with the epoxy. Phosphors tested periodically over the span of one year showed no decrease in conversion activity. This suggests that the lifetime of a green-light emitter would be determined by the lifetime of the GaAs diode.

Acknowledgments

We wish to acknowledge the help of Mr. Jack E. Pinnell in the preparation of the phosphors. Dr. Kent Watts provided valuable aid in measuring the efficiencies of the phosphor, and Mr. Kent Carson obtained the scanning electron micrographs.

Manuscript received Oct. 12, 1971. This was Paper 55 presented at the Washington, D. C., Meeting of the Society, May 9-13, 1971.

Any discussion of this paper will appear in a Discussion Section to be published in the December 1972 JOURNAL.

REFERENCES

1. L. G. Van Uitert, L. Pictroski, and W. H. Grodkiewicz, *Mater. Res. Bull.*, **4**, 777 (1969).
2. R. A. Hewes and J. F. Sarver, *Phys. Rev.*, **182**, 427 (1969).
3. I. M. Kolthoff and E. B. Sandell, "Textbook of Quantitative Inorganic Analysis," pp. 103-117, Macmillan, New York (1937).
4. C. N. Reilly, Editor, "Advances in Analytical Chemistry and Instrumentation," Vol. 4, p. 1, Interscience, New York (1965).
5. A. Vecht and A. Hickey, Paper 54 presented at Electrochem. Soc. Meeting, Washington, D.C., May 9-13, 1971.
6. W. D. Kingery, "Introduction to Ceramics," p. 369, John Wiley and Sons, New York (1963).

Thermodynamic Calculations for $\text{GaAs}_{1-x}\text{P}_x$ Vapor Growth

M. Bleicher

Technische Universität, Institut für Technische Elektronik, 8 München 2, Germany

ABSTRACT

The combined transport of GaAs and GaP to form $\text{GaAs}_{1-x}\text{P}_x$ mixed crystals in an open-flow system by AsCl_3 and PCl_3 with two separate Ga sources has been calculated, based on simple thermochemical considerations. A new approach has been taken to determine theoretically the solid composition of the $\text{GaAs}_{1-x}\text{P}_x$ mixed crystal. The influence of the seed temperature on the solid composition has been studied as well as the influence of the total concentration of the incoming gases.

Production of $\text{GaAs}_{1-x}\text{P}_x$ mixed crystals has become very important in recent years. Two ranges of composition are especially favored: first the composition of x

Key words: vapor phase deposition, thermodynamics, $\text{GaAs}_{1-x}\text{P}_x$, computer calculations.

about 0.4 for applications in the visible, and second very low-phosphorus contents to produce GaAs heterojunction lasers (1). One of the reasons for the great interest in the $\text{GaAs}_{1-x}\text{P}_x$ mixed crystals is their relatively easy and cheap production by means of epitaxial

growth from the vapor phase. A well-known system is the Ga-As-P-Cl-H open tube flow system, which uses Ga, AsCl₃, and PCl₃ as starting materials and hydrogen as a carrier gas.

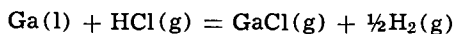
Since the early investigations (2, 3) much work has been done on the arsenic half of this system, for example by Boucher and Hollan (4), Shaw (5), and Kirwan (6). On the phosphorus half Luther and Roccasecca (7), Seki *et al.* (8, 9), and Kirwan (6) have made a new approach experimentally as well as theoretically since the early work of Oldham (10). For the whole complex system however only experimental studies of the preparation and investigation of the crystals are known.

This paper carries out thermodynamic calculations for the complex system and highlights the influence of the substrate temperature on the composition of the epitaxial deposit.

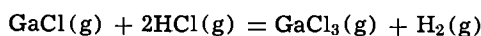
Computer Calculations

Chemical and thermodynamical background.—Calculations are made for a system containing two separate gallium sources, which are fed by PCl₃ and AsCl₃, respectively. The incoming pressures p_{PCl_3} and p_{AsCl_3} are varied from 10⁻⁴ up to 0.1 atm.

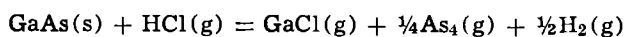
Within the reacting tube nine different vapor species are taken into account, which are assumed to govern seven dominant chemical reactions, taking place at the usual operation temperature range between 700° and 1000°C. These reactions are listed below together with their equilibrium constants.¹



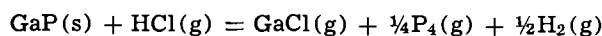
$$K_1 = \frac{p_{\text{GaCl}} p_{\text{H}_2}^{1/2}}{p_{\text{HCl}}} \quad [1]$$



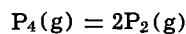
$$K_2 = \frac{p_{\text{GaCl}_3} p_{\text{H}_2}}{p_{\text{GaCl}} p_{\text{HCl}}^2} \quad [2]$$



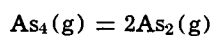
$$K_3 = \frac{p_{\text{GaCl}} p_{\text{As}_4}^{1/4} p_{\text{H}_2}^{1/2}}{p_{\text{HCl}}} \quad [3]$$



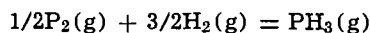
$$K_4 = \frac{p_{\text{GaCl}} p_{\text{P}_4}^{1/4} p_{\text{H}_2}^{1/2}}{p_{\text{HCl}}} \quad [4]$$



$$K_5 = \frac{p_{\text{P}_2}^2}{p_{\text{P}_4}} \quad [5]$$



$$K_6 = \frac{p_{\text{As}_2}^2}{p_{\text{As}_4}} \quad [6]$$



$$K_7 = \frac{p_{\text{PH}_3}}{p_{\text{P}_2}^{1/2} p_{\text{H}_2}^{3/2}} \quad [7]$$

Recently it has been shown by Ban (17) that the assumption for the reactions is justified especially for the deposition process (Eq. [3] and [4]). All of the itemized vapor species, except PH₃, are commonly expected to occur in systems like the one described. But, concerning PH₃, Ban (17) stated its existence in a relative high concentration experimentally.

Combinations between phosphorus and arsenic like AsP, As₂P₂, As₃P, or AsP₃ are not taken into considera-

¹ Some further possible vapor species were estimated and found to lie several magnitudes below that of the interesting ones. Over the whole range of considered temperatures and input concentrations $p_{\text{AsCl}_3} < 10^{-7}$ atm, $p_{\text{PCl}_3} < 10^{-8}$, $p_{\text{AsH}_3} < 10^{-10}$ atm, and $p_{\text{Cl}_2} < 10^{-13}$ atm; hence these species are ignored in the analysis.

Table I. Equilibrium constants, atm units

$\log_{10} K_1 = 3.67 - 0.87 \times 10^3/T - 0.16 \ln T$
$\log_{10} K_2 = -13.95 + 9.58 \times 10^3/T + 0.92 \ln T$
$\log_{10} K_3 = 8.04 - 6.99 \times 10^3/T - 0.35 \times 10^{-3}T - 0.22 \ln T$
$\log_{10} K_4 = 6.08 - 7.255 \times 10^3/T - 0.03 \ln T$
$\log_{10} K_5 = 11.5 - 1.21 \times 10^4/T - 0.5 \ln T$
$\log_{10} K_6 = 11.5 - 1.59 \times 10^4/T - 0.43 \ln T$
$\log_{10} K_7 = -4.04 + 3.58 \times 10^3/T - 0.207 \ln T$

tion because of the lack of thermodynamical data. As soon as this information becomes available, there will be no difficulty in introducing them in the given set of reactions. The values for the reaction equilibria constants, which are related to the standard free energy change of the concerned reaction in the form $-\Delta G_i = RT \ln K_i$, are taken from a list given by Kirwan (6) for the first five equations, while the sixth is taken from Hurle and Mullin (13) and the seventh is calculated from data of the JANAF Tables (14). These values which are listed in Table I originate from a careful literature survey and have been found to be the least contradictory ones.

Arsenic-saturated source reaction equilibria.—For source temperatures of the Ga boat of about 925°C it is assumed that after some time of saturation with arsenic a thin layer of GaAs will cover the liquid gallium. Therefore the reaction equations [2], [3], and [6] must be applied. Because the pressures of six different vapor species are involved at this place, three more equations are required. The latter are denoted as equations of conservation. In general, for such problems one gets for n different vapor species always $n-3$ equations from the chemical reactions and three equations of conservation, from which one describes the conservation of the total pressure of the system. For an open-flow system this is expressed as

$$\Sigma p_i = 1 \text{ atm} \quad [8]$$

The remaining two equations are given in the case regarded here by conservation of chlorine

$$p_{\text{GaCl}} + 3p_{\text{GaCl}_3} + p_{\text{HCl}} = 3p_{\text{AsCl}_3} \quad [9]$$

and conservation of arsenic

$$4p_{\text{As}_4} + 2p_{\text{As}_2} = p_{\text{AsCl}_3} \quad [10]$$

where p_{AsCl_3} denotes the partial pressure of the incoming AsCl₃.

It must be stated at this point that due to the criterion of constant pressure a volume change is induced in the system while the reactions are taking place, because mole numbers are changing. For this reason the equations of conservation Eq. [9] and [10] should be expressed in terms of moles instead of partial pressures. Since the relative volume change for the whole system has been estimated to be smaller than 3%, this error will be ignored in the calculations. Equation [10] is only true for the source region, where no deposition can occur. The etch rate ER of the gallium source in grams per minute is expressed by

$$\text{ER} = \frac{(p_{\text{GaCl}} + p_{\text{GaCl}_3}) g_{\text{Ga}}}{RT_0} \cdot V_0 \quad [11]$$

where g_{Ga} is the atomic weight of Ga, T_0 the temperature at which the reaction products are entering the tube, and V_0 is the total flow rate (cubic centimeters per minute).

Phosphorus-saturated source reaction equilibria.—The same procedure described above is now applied to this source, also containing gallium. In this case, however, Luther (7) and Seki (8) have pointed out that no skin of GaP forms. For this reason Eq. [1], [2], [5], [7], [8] and in addition

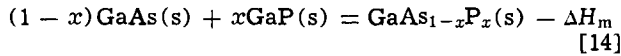
$$p_{\text{GaCl}} + 3p_{\text{GaCl}_3} + p_{\text{HCl}} = 3p_{\text{PCl}_3} \quad [12]$$

and

$$4p_{\text{P}_4} + 2p_{\text{P}_2} + p_{\text{PH}_3} = p_{\text{PCl}_3} \quad [13]$$

have to be taken into account.

Deposition reaction equilibria.—In the deposition zone of the reaction tube the incoming vapor mixture is allowed to form an equilibrium phase between all its species and solid GaAs and GaP, respectively, for all temperatures considered. This assumption is only true for low flow rates as well as for a long deposition region. Here Eq. [2] to [7] must be applied and, in addition, the heat of mixing which occurs at the reaction



The heat of mixing is given by

$$\Delta H_m = \Omega x(1 - x) \quad [15]$$

Huber (15) has calculated Ω to be 1 kcal/mole, i.e., the maximum heat of mixing at $x = 0.5$ is 0.25 kcal/mole. The resulting modification in the equilibrium constants is negligible and therefore ignored in the following. Equation [8] and the conservation of chlorine is still valid

$$p_{\text{GaCl}} + 3p_{\text{GaCl}_3} + p_{\text{HCl}} = 3p_{\text{AsCl}_3} + 3p_{\text{PCl}_3} \quad [16]$$

The third equation of conservation states that the sum of arsenic and phosphorus atoms precipitating out of the vapor phase must be equal to that of the gallium atoms

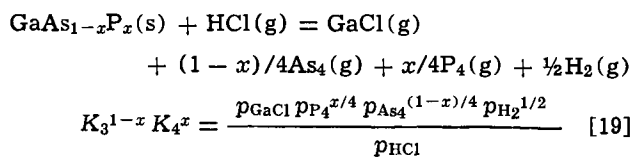
$$4p_{\text{As}_4} + 2p_{\text{As}_2} + p_{\text{PH}_3} + 4p_{\text{P}_4} + 2p_{\text{P}_2} - 4p_{\text{As}_4} - 2p_{\text{As}_2} - p_{\text{PH}_3} - 4p_{\text{P}_4} - 2p_{\text{P}_2} = p_{\text{GaCl}} + p_{\text{GaCl}_3} - p_{\text{GaCl}} - p_{\text{GaCl}_3} \quad [17]$$

where the p_{oi} 's indicate the partial pressures coming from the source into the deposition zone of the reactor.

This new equilibrium yields the amount of GaAs and GaP depositing at the seed dependent only on the input partial pressures of AsCl₃ and PCl₃, the source and the substrate temperature. The concentration x of GaP in the solid is given by the rates of precipitation similar to Eq. [17]

$$x = \frac{p_{\text{PH}_3} + 4p_{\text{P}_4} + 2p_{\text{P}_2} - p_{\text{PH}_3} - 4p_{\text{P}_4} - 2p_{\text{P}_2}}{p_{\text{GaCl}} + p_{\text{GaCl}_3} - p_{\text{GaCl}} - p_{\text{GaCl}_3}} \quad [18]$$

On the other hand it is possible to express x in terms of vapor pressures and equilibrium constants by combining Eq. [3] and [4] in the form



where x becomes

$$x = \frac{\ln \left[\left(\frac{p_{\text{HCl}}}{p_{\text{GaCl}} p_{\text{H}_2}^{1/2}} \right)^4 \frac{K_3^4}{p_{\text{As}_4}} \right]}{\ln \left[\left(\frac{K_3}{K_4} \right)^4 \frac{p_{\text{P}_4}}{p_{\text{As}_4}} \right]} \quad [20]$$

Equation [20] serves to predict in what direction x will change as soon as equilibrium is no longer maintained.

Results

The model proposed here is based only on simple chemothermodynamical relations. No account is taken of the kinetic mechanisms which might control the growth of an epitaxial layer in reality. Also no regard has been paid to the fact that in practice total homogeneity is not achievable.

Figure 1 shows the equilibrium partial pressures of the different vapor species over the arsenic- and phosphorus-saturated gallium source at 1200°K over various input pressures of AsCl₃ and PCl₃, respectively. It must be noted that in contrast to the negligible arsine pressure (8, 9), phosphine by Eq. [7] has a remarkably high vapor pressure. This plot is for a single source

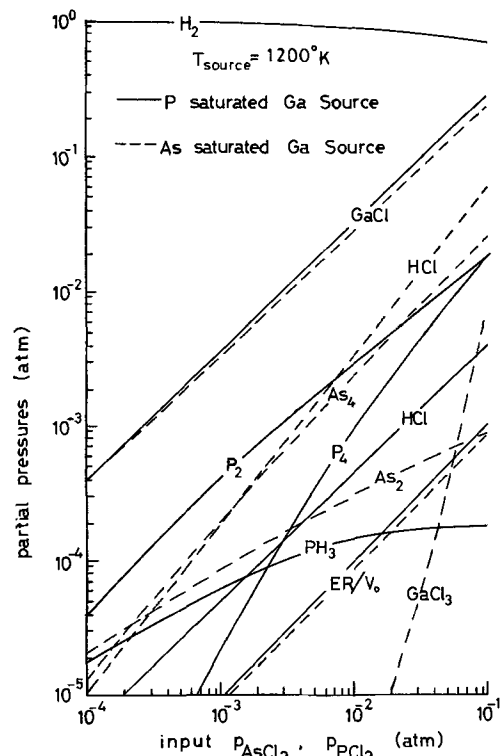


Fig. 1. Partial pressures and etch rates over a arsenic and phosphorus saturated Ga source, respectively, vs. the AsCl₃ and PCl₃ input partial pressures, respectively, for a constant 1200°K source temperature.

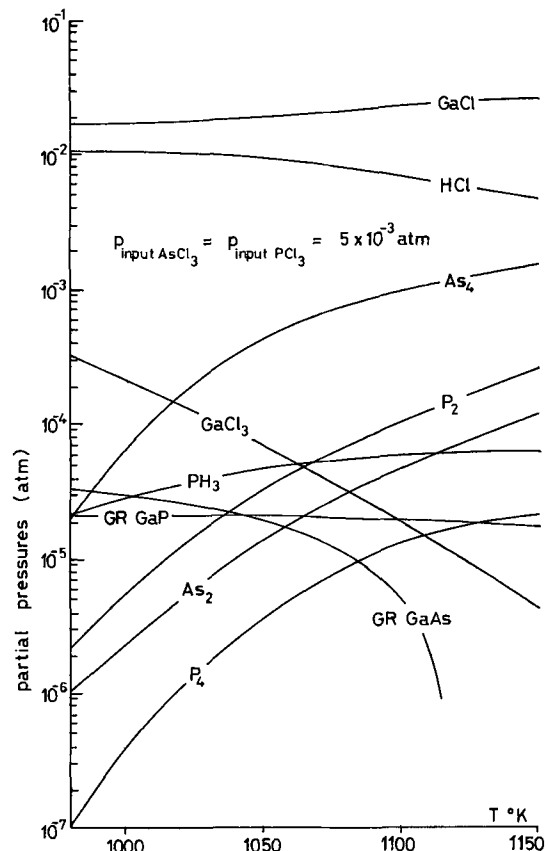


Fig. 2. Partial pressures and growth rates over a GaAs_{1-x}P_x deposit vs. the deposit temperature.

temperature but above 920°C there is little influence on growth. For the Group V elements only the ratio of dimers to tetramers is varying, while their total concentration remains constant. The dominant Group III

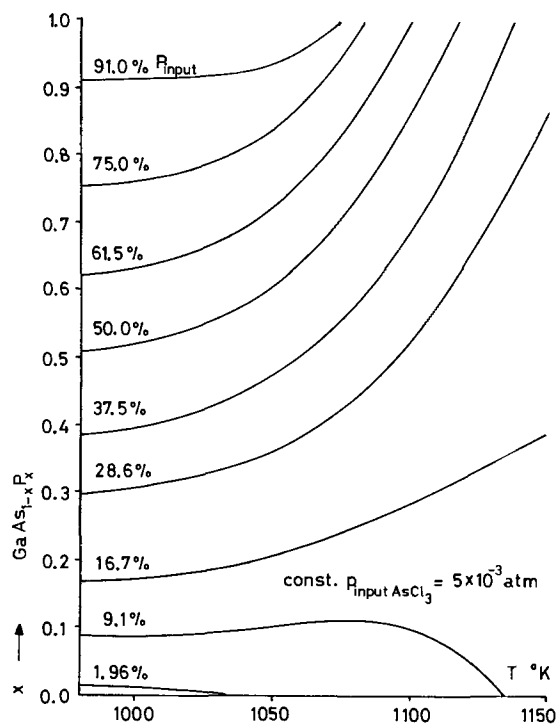


Fig. 3. $\text{GaAs}_{1-x}\text{P}_x$ deposit composition vs. the deposit temperature for several phosphorus percentages of the PCl_3 and AsCl_3 input gases.

element pressure, p_{GaCl} , is about constant too, because the HCl pressure lies more than one magnitude lower.

In Fig. 2 the equilibrium pressures in the deposition zone are plotted vs. the seed temperature for equal incoming pressures of AsCl_3 and PCl_3 . Two things are most interesting. First again the high phosphine pressure, which dominates until about 1060°K , second the behavior of the growth rates (denoted as GR GaAs and GR GaP and weighted with their molecular weight) while the growth rate of GaP stays nearly constant, the GaAs growth rate reveals a steep slope at higher temperatures. This behavior may be explained by the temperature dependence of Eq. [3]. In any case this phenomenon causes mostly the strong variation of the GaP solid concentration vs. deposition temperature shown in Fig. 3. According to this figure it should be possible to grow pure GaP crystals within a vapor containing arsenic at elevated temperatures. Further-

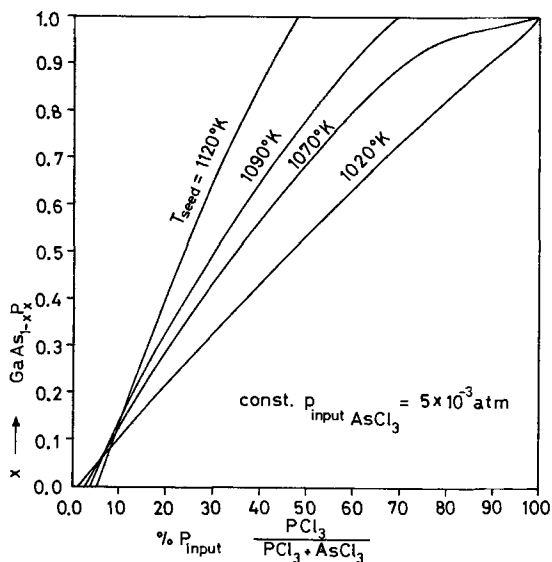


Fig. 4. $\text{GaAs}_{1-x}\text{P}_x$ deposit composition vs. the phosphorus percentage of the PCl_3 and AsCl_3 input gases.

more in this region a GaAs seed will be etched away. Figure 4 illustrates the solid composition x vs. the percentage of PCl_3 to AsCl_3 in the input gas. Once more the strong influence of the seed temperature can be seen. This is not in agreement with Finch and Mehal (11) who observed a straight relationship for temperatures between 775° and 820°C , but they used only one source, which is not comparable with the calculations done here. Stewart (16) with the AsH_3 , PH_3 , HCl/Ga system at $\sim 780^\circ\text{C}$ obtains a GaP solid concentration of 0.4 employing a P to As input vapor percentage of 28.6%, a point that fits exactly the calculations here. He also observed a composition variation by varying the HCl flow. This may be explained by Eq. [20], if the equilibrium over the source is not reached completely, i.e., the ratio p_{HCl} to p_{GaCl} changes. Finally it can be seen from Fig. 3 and 4 that for very low-phosphorus input concentrations no GaP is forming, in fact in this range all the available phosphorus is used in forming phosphine.

The great influence of the substrate temperature on the composition of the deposit diminishes with the higher concentrations of the input gases, indicated in Fig. 5. Here the solid composition approaches exactly the same value given by the ratio of the input gas concentration.

Conclusions

Applying the AsCl_3 , PCl_3 , Ga, H_2 system for growth of $\text{GaAs}_{1-x}\text{P}_x$ mixed crystals the seed temperature influences strongly the solid composition of the crystal. This dependence becomes smaller with increasing input concentrations of the trichlorides. Within the reactor a relatively high, at any case, a nonnegligible vapor pressure of phosphine exists. Above about 920°C , variation of the source temperature has little influence on the growth conditions.

Acknowledgment

The author would like to thank Professor W. G. Oldham for his encouragement, his valuable criticism of the manuscript, and his helpful discussions.

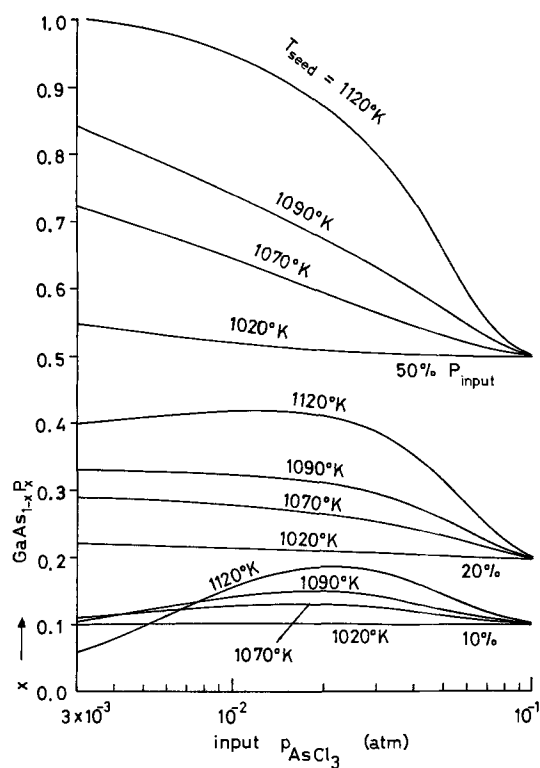


Fig. 5. $\text{GaAs}_{1-x}\text{P}_x$ deposit composition vs. the AsCl_3 input pressure for several phosphorus percentages and several deposit temperatures.

Manuscript submitted Aug. 20, 1971; revised manuscript received ca. Dec. 6, 1971.

Any discussion of this paper will appear in a Discussion Section to be published in the December 1972 JOURNAL.

REFERENCES

1. M. G. Craford, W. O. Grovesand, and M. J. Fox, *This Journal*, **118**, 355 (1971).
2. R. R. Fergusson and T. Gabor, *ibid.*, **111**, 585 (1964).
3. D. Effer, *ibid.*, **112**, 1020 (1965).
4. A. Boucher and L. Hollan, *ibid.*, **117**, 932 (1970).
5. D. W. Shaw, *ibid.*, **117**, 683 (1970).
6. D. J. Kirwan, *ibid.*, **117**, 1572 (1970).
7. L. C. Luther and D. D. Roccasecca, *ibid.*, **115**, 850 (1968).
8. H. Seki, H. Eguchi, and T. Gejo, *Jap. J. Appl. Phys.*, **10**, 39 (1971).
9. H. Seki and H. Araki, *ibid.*, **6**, 1414 (1967).
10. W. G. Oldham, *J. Appl. Phys.*, **36**, 2887 (1965).
11. W. F. Finch and E. W. Mehal, *This Journal*, **111**, 814 (1964).
12. R. W. Haisty, L. G. Baily, and R. C. Sangster, First Interim Report for Development of GaAsP Graded-Band-Gap-Base Transistor Structures, Texas Instruments Report No. 08-64-154 (1964).
13. D. T. J. Hurle and J. B. Mullin, Proc. Internat. Conf. on Crystal Growth, Boston, p. 241 (1966).
14. JANAF, "Interim Thermochemical Tables," Vol. 5, Thermal Laboratories, Dow Chemical Co.
15. D. Huber, Proc. Internat. Conf. on Heterojunctions, Budapest, I, p. 195 (1971).
16. C. E. E. Stewart, *J. Crystal Growth*, **8**, 269 (1971).
17. V. S. Ban, *This Journal*, **118**, 1473 (1971).

A Cross-Hatch Pattern in GaAs_{1-x}P_x Epitaxially Grown on GaAs Substrate

Seigo Kishinô, Masahiko Ogirima, and Kazuhiro Kurata*

Central Research Laboratory, Hitachi Ltd., Kokubunji, Tokyo, Japan

ABSTRACT

A cross-hatch pattern which appears on the surface of GaAs_{1-x}P_x epitaxially grown on the GaAs substrate was studied by x-ray diffraction techniques. The origin of this structure was determined by x-ray diffraction topography to be a misfit dislocation array aligned along lines perpendicular to each other in the layer of graded composition. The composition profile normal to the wafer was also determined by electron microprobe analyses. Furthermore, the growth mechanism of the aligned dislocations was proposed from the fact that aligned dislocations enable a considerable reduction in the curvature of the wafer which is due to the lattice mismatch between the GaAs_{1-x}P_x epitaxial layer and the GaAs substrate. The GaAs_{1-x}P_x wafer having the cross-hatch pattern was determined to be high in quality from the half width of the rocking curve.

GaAs_{1-x}P_x ($x \lesssim 0.4$) is one of the most promising materials currently being utilized for visible injection electroluminescence. The efficiency of emission which is in the red at room temperature is high because the bandgap is direct, and the material can be made high conductivity n- or p-type. At present, GaAs_{1-x}P_x has a technological advantage over Ga_{1-x}Al_xAs and GaP for display application because relatively large areas of GaAs_{1-x}P_x wafer suitable for use in electroluminescent devices can be readily obtained by the vapor phase growth technique. An understanding of the role of the crystal defects in the growth mechanism is important in order to control and improve the efficiency.

The crystal defects such as dislocations and stacking faults which may be important in determining the properties of vapor phase epitaxially grown GaAs_{1-x}P_x wafers have been described by a number of investigators (1-5).

This paper deals with the relationship between the cross-hatch pattern (6) and the dislocations and specifically with the origin of the dislocations and their effects on the perfection of epitaxially grown GaAs_{1-x}P_x wafer.

Experimental

The GaAs_{1-x}P_x crystals doped with Te were epitaxially grown on GaAs substrate in an open-tube system using Ga, PCl₃, As, and H₂ (7). Hydrogen, purified by Pd diffusion, was metered into the system through two

flowmeters. One of them was connected to PCl₃ bubblers while the other controlled further dilution of the displaced PCl₃ vapors. The diluted vapors then passed over Ga feed material. The alloy composition was controlled by the temperature of arsenic source. Mechanically and chemically polished surfaces of (100) oriented seeds were used.

Typical operating conditions were: gallium temperature, 900°C; seed temperature, 810°C; PCl₃ bubbler (0°C) flow rate, 40 cc/min; dilution hydrogen flow rate, 160 cc/min; temperature gradient at the substrate, 10°C/cm; arsenic source temperature, 430°C.

To minimize strains and crystal imperfections due to lattice mismatch between GaAs_{1-x}P_x and GaAs, a layer of continuously graded composition was grown before growing a thick layer of uniform composition. The layer of graded composition was grown by controlling the temperature of arsenic source in the range of 430°-530°C. The thickness of the epitaxially grown layer was usually 100 μm and the growth rate was usually 25 μm/hr. As mentioned later, the optimum thickness of the graded composition was 20-40 μm. So the temperature of arsenic source was varied from 530° to 430°C continuously for 1 hr in the initial period of epitaxial process. When the thickness of the graded composition layer was out of the range of the optimum thickness described above, the cross-hatch pattern was hardly observed.

Dislocations were observed by the Lang method, in which AgK_{α1} radiation from microfocus x-ray equipment was used, with the use of two kinds of specimens. (i) One specimen was the epitaxially grown GaAs_{1-x}P_x

* Electrochemical Society Active Member.
Key words: GaAs_{1-x}P_x, x-ray diffraction, x-ray topography, dislocation, epitaxial layer.

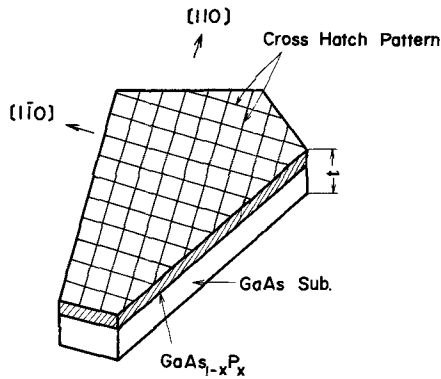


Fig. 1. The shape of specimen 1 from which x-ray topographs were taken.

wafer 50-100 μm thick including the GaAs substrate, which was reduced to 100 μm thickness by mechanical polishing with 2000 mesh carborundum and chemical etching with an etch solution of $3\text{H}_2\text{SO}_4:1\text{H}_2\text{O}:1\text{H}_2\text{O}_2$. The schematic diagram of the specimen is shown in Fig. 1. (ii) The wafer composed of the epitaxially grown $\text{GaAs}_{1-x}\text{P}_x$ layer and the GaAs substrate was angle lapped at 5° in order to reveal dislocations in the substrate, the graded composition layer, and the constant composition layer. This specimen was also etched with a similar lapping described above after mechanical lapping. The schematic diagram of the specimen is shown in Fig. 2(a) and (b).

The composition profiles of the phosphorus content in the $\text{GaAs}_{1-x}\text{P}_x$ layer normal to the GaAs substrate were examined by electron microprobe analyses. A particular precaution was taken to detect the variation of the phosphorus content in the graded composition layer. At the same time variation of the arsenic content was observed throughout the depth of the wafer for supporting the results.

The difference in lattice parameter between the $\text{GaAs}_{1-x}\text{P}_x$ epitaxial layer and the GaAs substrate causes a pronounced curvature in the structure. This curvature was measured by an x-ray diffraction technique (8). Prior to measurement, the thickness of the GaAs substrate was kept constant because the curvature of the wafer depends on the thickness of the substrate. In this case (400) $\text{CuK}\alpha_1$ diffraction in the Bragg case was used. The x-ray beam was incident not at the $\text{GaAs}_{1-x}\text{P}_x$ epitaxial layer but at the GaAs substrate because the measured results were governed by the compositional variation when the epitaxially grown $\text{GaAs}_{1-x}\text{P}_x$ surface was used for measurement.

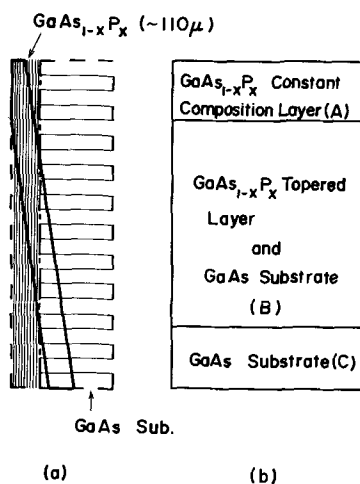


Fig. 2. The angle lapped specimen which is composed of the $\text{GaAs}_{1-x}\text{P}_x$ constant composition layer, the graded composition layer, and the GaAs substrate, respectively. (a) and (b) show the section and the plane figures, respectively.

The perfection of the epitaxially grown $\text{GaAs}_{1-x}\text{P}_x$ wafer was also examined by an x-ray diffraction technique (9) in which two different wavelengths of x-ray beams (10) were used for diffraction. X-ray radiation of two wavelengths, $\text{CuK}\alpha_1$ and $\text{CuK}\beta_1$, were used. With the use of this method the phosphorus content, assuming that Vegard's law of solid solutions holds for this GaAs-GaP system (11), was also examined. The perfection of the $\text{GaAs}_{1-x}\text{P}_x$ wafer was examined from the half width of the rocking curve which was the diffracted intensity *vs.* a small fraction of the incident angle $\Delta\theta$ around the Bragg angle.

The efficiency of junction luminescence was measured by silicon photocells at 10 A/cm² of diode current.

Results and Discussion

X-ray topographs were taken from the specimen whose surface revealed the cross-hatch pattern as shown in Fig. 3, and they are shown in Fig. 4(a), (b), (c), (d), and (e). The shape of the specimen in this



Fig. 3. The optical photograph of the surface which reveals the cross-hatch pattern.

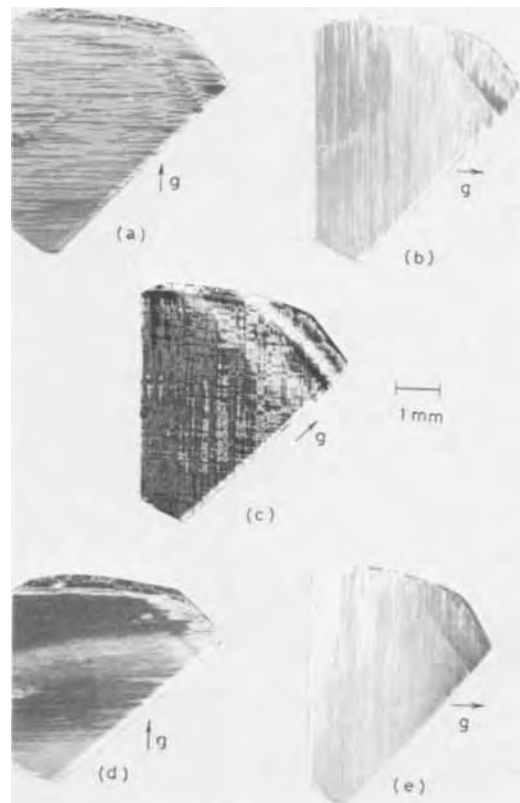


Fig. 4. X-ray topographs of the specimen 1. (a), (b), (c), (d), and (e) show topographs from (220), (220), (040), (111), and ($1\bar{1}\bar{1}$) diffractions, respectively.

case is shown in Fig. 1. The type of the dislocation observed here is similar to one observed by Ewing (2), that is, dislocation networks are aligned along [011] and [01 $\bar{1}$] directions with $\frac{1}{2}a[01\bar{1}]$ and $\frac{1}{2}a[011]$ Burger's vectors, respectively. X-ray topographs using the diffraction vectors [111] and $[\bar{1}\bar{1}\bar{1}]$ are also reproduced in Fig. 4(d) and (e) for determining the Burger's vector more accurately. The diffraction planes used here are shown in the pole figure, Fig. 5. From these x-ray topographs and the pole figure, Burger's vector of two kinds of the dislocations aligned along lines perpendicular to each other were determined exactly to be $\frac{1}{2}a [01\bar{1}]$ and $\frac{1}{2}a [011]$. The image contrast criterion (12), for [011] and [01 $\bar{1}$] dislocations only, is violated in some local areas. Therefore, where contrast violations exist, dislocations may have screw component or interact each other. Detailed examinations were not established at this stage.

X-ray topographs of a similar specimen are also reproduced in Fig. 6(a) and (b), in which the shape of the specimen is shown in Fig. 2(a) and (b). From these x-ray topographs it is obvious that dislocation densities in both the GaAs substrate and the constant composition layer, are rather low, while the aligned dislocations gather in the graded composition layer of the specimen. This may be the result of the large lattice mismatch between the GaAs substrate and the GaAs_{1-x}P_x layer.

An x-ray topograph was also taken from the specimen whose surface does not reveal the cross-hatch pattern as shown in Fig. 7. The shape of the specimen is similar to that shown in Fig. 1. In this case there is the irregular form in the image of dislocations because

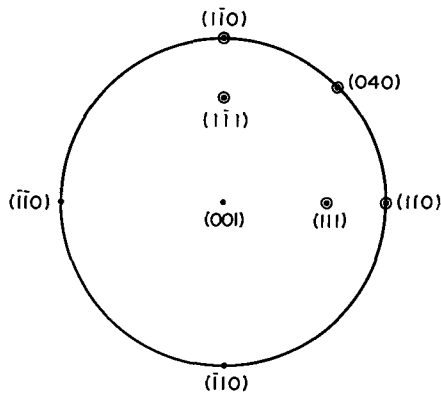


Fig. 5. The pole figure of specimen 1 from which x-ray topographs were taken.

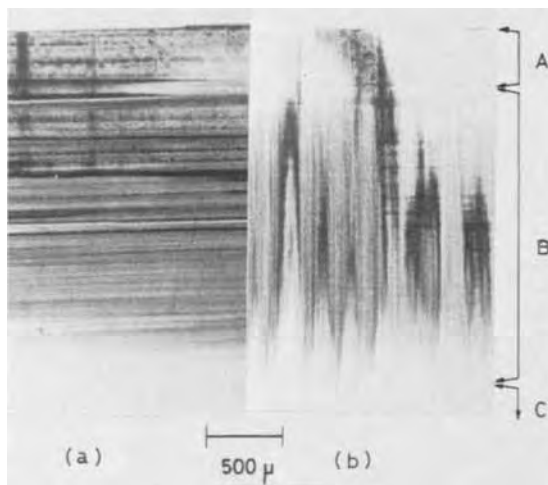


Fig. 6. X-ray topographs of specimen 2 in which signs A, B, and C correspond to those in Fig. 2(b). (a) and (b) are topographs from (220) and $(\bar{2}\bar{2}\bar{0})$ diffractions, respectively.



Fig. 7. X-ray topograph obtained by (220) diffraction from the GaAs_{1-x}P_x wafer whose surface does not reveal the cross-hatch pattern.

dislocations could not align along the line. The lattice strain might be too large to be compensated by making the misfit-dislocations array in the graded composition layer because of the sudden change of the phosphorus content as discussed later.

Variation of the phosphorus contents in the growth layer were measured by electron microprobe analyses as shown in Fig. 8(a) and (b). Figures 8(a) and (b) are obtained from the specimens which reveal, respectively, the cross-hatch pattern clearly and obscurely on the surface of the epitaxial GaAs_{1-x}P_x wafer. It is fairly obvious that the aligned dislocations were introduced in the graded composition layer when the epitaxial GaAs_{1-x}P_x wafer has the graded composition layer of 40 μm width as shown in Fig. 8(a).

If the lattice mismatch between the GaAs_{1-x}P_x epitaxial layer and the GaAs substrate causes the curvature and no dislocations are introduced to compensate the elastic strain, the curvature ρ can be obtained from the following equation (13-15)

$$\rho = \frac{6 \left[t_0 \sum_{j=1}^N t_j \left(\frac{d_0 - d_j}{d_0} \right) + \sum_{i=1}^N \sum_{j>i}^N t_i t_j \left(\frac{d_i - d_j}{d_0} \right) \right]}{\left[\sum_{j=0}^N t_j \right]^3} \quad [1]$$

where t_0 , $t_{i(j)}$, $d_{i(j)}$, and d_0 are the thickness of the substrate, the thickness of the $i(j)$ th epitaxial layer, the lattice parameter of the $i(j)$ th epitaxial layer, and the lattice parameter of the substrate, respectively. Figure 9 shows schematically the representative epitaxial layer which is composed of eight different layers. The result calculated by Eq. [1] is shown in Fig. 10 with a solid line. In this case the thickness of the substrate is 400 μm and the epitaxial layer is composed of eight layers each of 5 μm thickness but each layer has different phosphorus contents. The curvature of the wafers measured by an x-ray diffraction technique (8) are also shown in Fig. 10 in order to make correlation to the visibility of the cross-hatch pattern. Signs O, Δ, and X show the wafers which reveal the cross-hatch pattern clearly, rather clearly, and obscurely, respectively. It is evident that the curvature of the wafer in which the cross-hatch pattern is visible clearly is always smaller than that of the wafer in which the cross-

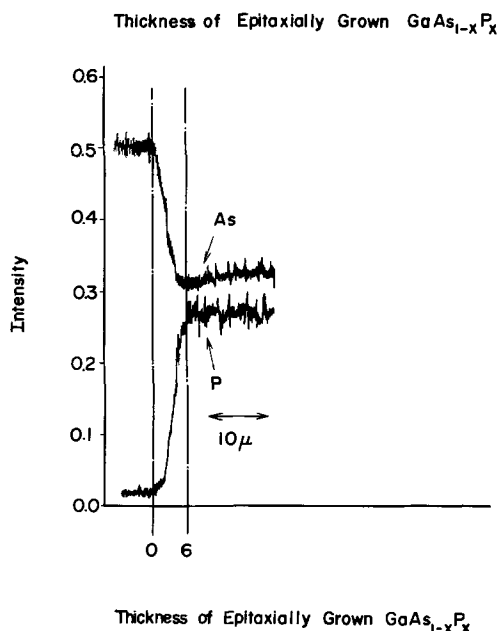
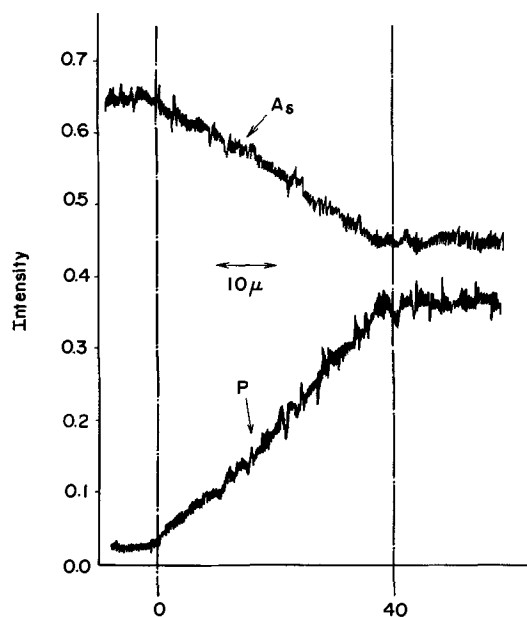


Fig. 8. Variation of the phosphorus content by electron microprobe analyses in the graded composition layer. (a, above) and (b, below) show the result from the $\text{GaAs}_{1-x}\text{P}_x$ wafer which reveals and does not reveal the cross-hatch pattern on the surface, respectively.

hatch pattern is obscure. In this experiment a convex configuration as viewed from the GaAs side was observed. It is also to be noted that the sign of the curvature is always reverse of those observed by Saul (16). From the result that a concave configuration was observed as viewed from the GaAs side, Saul determined that the thermal mismatch was larger than the lattice mismatch between the GaP epitaxial layer and the

Table I. Mole fraction of GaP (x)

Specimen No.	From the lattice parameter	From the energy gap
1	0.417	0.42
2	0.404	—
3	0.421	0.42
4	0.382	0.38
5	0.372	0.37
6	0.389	—
7	0.380	0.38
8	0.476	—
9	0.427	0.40

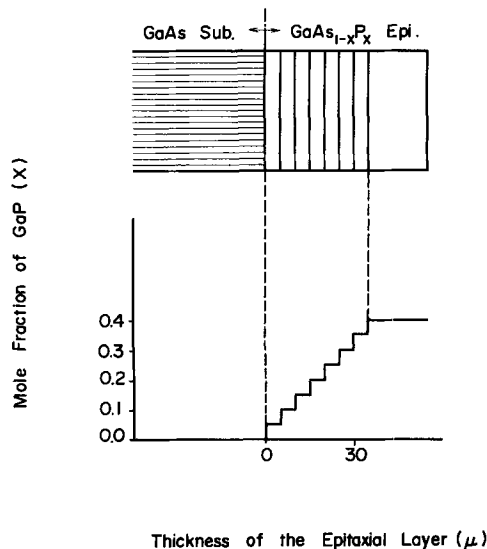


Fig. 9. The model from which the curvature of the $\text{GaAs}_{1-x}\text{P}_x$ wafer was calculated. It is postulated that the misfit dislocations are not introduced.

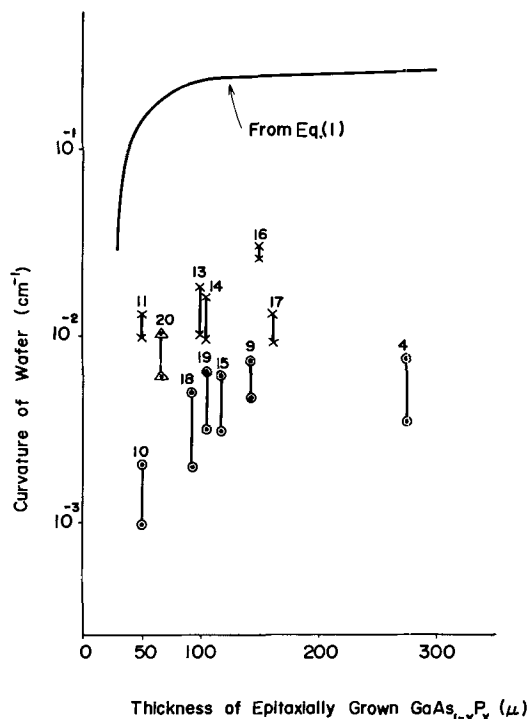


Fig. 10. Relation between the visibility of the cross-hatch pattern and the curvature. Signs \circ , Δ , and \times show the $\text{GaAs}_{1-x}\text{P}_x$ wafer which reveal the cross-hatch pattern clearly, rather clearly, and obscurely, respectively. Solid line shows the result obtained from Eq. [1].

GaAs substrate. However, the present observed sign of the curvature supports that the stress due to lattice mismatch considerably exceeds the stress due to differential thermal contraction in the $\text{GaAs}_{1-x}\text{P}_x$ -GaAs system, as Abrahams *et al.* have already reported (5).

Contrary to the result by Saul, it is reasonable to assume from our results that the wafer bends progressively during growth, if the lattice mismatch is not perfectly compensated by misfit dislocations. From the experimental results described above, a model of the formation mechanism of the misfit dislocation array in this case is proposed as shown in Fig. 11 and 12, where (a) and (b) show the plane and the section views of the wafer, respectively. Figures 11 and 12 show the model of the wafer in which the cross-hatch pattern is visible and obscure, respectively.

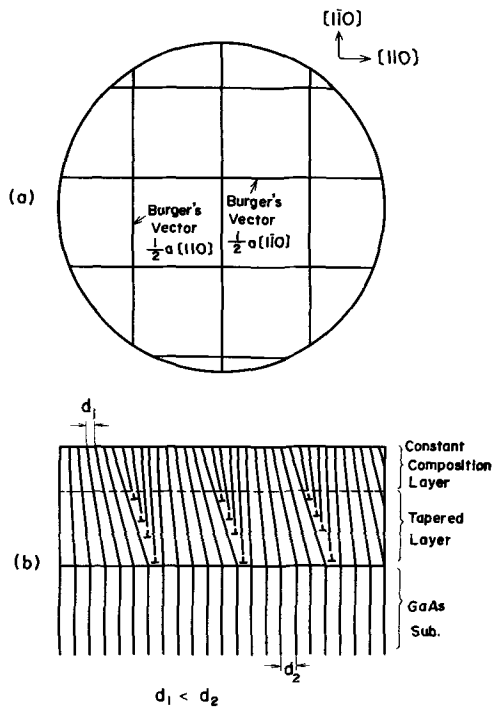


Fig. 11. The model of crystal growth in which dislocations are lined up in the graded composition layer. (a) and (b) show the plane and the section figures, respectively.

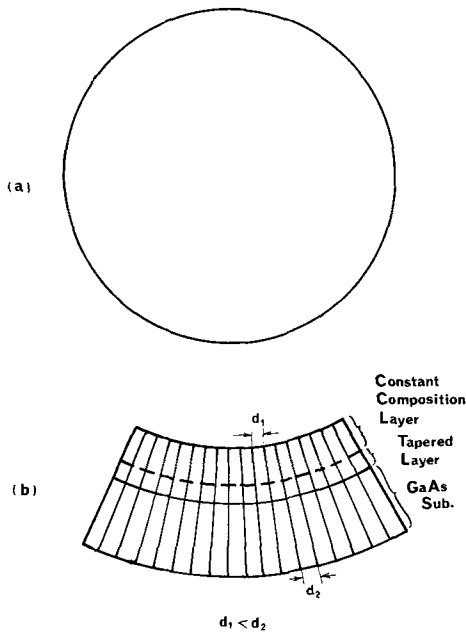


Fig. 12. The model of the crystal exhibiting curvature due to lattice mismatch between the $\text{GaAs}_{1-x}\text{P}_x$ layer and the GaAs substrate. (a) and (b) show the plane and the section figures, respectively.

When the cross-hatch pattern is visible, the aligned dislocations observed by x-ray topography may be composed of many dislocations which line up as if the small grain boundary is constructed. If the dislocations are arranged as shown in Fig. 11, the lattice mismatch at the graded composition layer can be compensated easily by the dislocations induced. The cross-hatch pattern visible on the surface, however, does not show the aligned dislocations themselves, because the aligned dislocations are existing in the graded composition layer and they are materially reduced in number on the surface as shown in Fig. 6. The cross-hatch pattern may be formed on the surface because growth rate variation of the epi-

taxial layer are initiated by: (i) the impurity concentration difference at the dislocation lines in the graded composition layer, and (ii) the screw components of some parts of the aligned dislocations which are visible in the x-ray topographs shown in Fig. 4.

If this model is used, it is easy to explain that the curvature of the wafer is small when the cross-hatch pattern is clearly visible. When the gradient of the phosphorus content is very sharp as shown in Fig. 8(b), the formation of the lattice strain during growth may be too large to be released by introducing the aligned dislocation array. In such a case dislocations may have a random distribution and consequently the cross-hatch pattern cannot be visible.

The phosphorus contents at the surfaces of the epitaxially grown $\text{GaAs}_{1-x}\text{P}_x$ wafers are shown in Table I with the results obtained from the energy gap data. The phosphorus contents were obtained from the lattice parameters which were measured from the differences of the two peak profiles obtained from (511) $\text{CuK}\alpha_1$ and (400) $\text{CuK}\beta_1$ diffractions (10, 17). The representative peak profiles are shown in Fig. 13 and 14 in which the upper and the lower profiles show (400) $\text{CuK}\beta_1$, and (511) $\text{CuK}\alpha_1$ diffractions, respectively. Figures 13 and 14 show the peak profiles obtained from the specimens where the cross-hatch pattern is clearly visible and obscure, respectively. This peak profile is a kind of the rocking curve, although the incident beam is not perfectly monochromatic. The

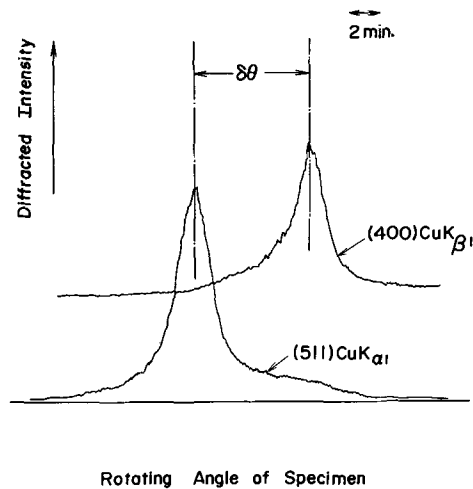


Fig. 13. Rocking curves of the $\text{GaAs}_{1-x}\text{P}_x$ wafer whose surface reveals the cross-hatch pattern clearly. In this figure $\delta\theta$ shows the lattice parameter, and the half width shows the perfection of the crystal.

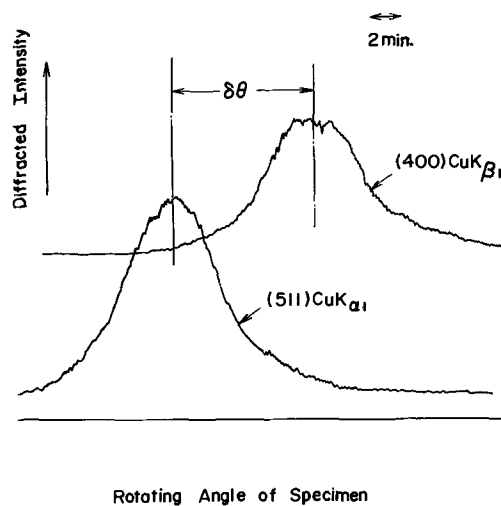


Fig. 14. Rocking curves of the $\text{GaAs}_{1-x}\text{P}_x$ wafer whose surface does not reveal the cross-hatch pattern.

perfection of the crystal, however, can be similarly estimated from the half width of the peak profile shown in Fig. 13 and 14. The half width of the peak profile of the epitaxially grown $\text{GaAs}_{1-x}\text{P}_x$ wafer, with a clearly revealed cross-hatch pattern, is comparable to that of the GaAs substrate in which dislocation density is lower than 10^4 cm^{-2} . The half width of the peak profile is broader, as shown in Fig. 14, when the wafer does not reveal the cross-hatch pattern. This high quality of the epitaxially grown $\text{GaAs}_{1-x}\text{P}_x$ wafer could be also expected from the model shown in Fig. 11 because the aligned dislocations need not be introduced at the surface.

When light emitting diodes are fabricated from the wafer which reveals the cross-hatch pattern clearly, the electroluminescent efficiency is higher by about 50% than that of the wafer with no cross-hatch pattern.

Conclusions

1. A cross-hatch pattern on the surface of $\text{GaAs}_{1-x}\text{P}_x$ layer appears when the graded composition layer of $20 \sim 40 \mu\text{m}$ width is formed in the initial period of epitaxial process.

2. The origin of the cross-hatch pattern was determined by x-ray topography to be a misfit dislocation array aligned along lines perpendicular to each other in the graded composition layer.

3. The curvature of the $\text{GaAs}_{1-x}\text{P}_x$ wafer is small or large depending on whether the cross-hatch pattern is clear or obscure on the surface.

4. When the cross-hatch pattern is visible on the surface, the $\text{GaAs}_{1-x}\text{P}_x$ wafer is high in quality on the surface because the half width of the rocking curve is as narrow as that of the GaAs substrate.

5. These results support the proposed model with regard to the growth mechanism of the aligned dislocation array.

Acknowledgment

The authors wish to express their appreciation to Dr. H. Kusumoto for his encouragement, to Mr. Y. Taguchi for making electron microprobe analyses, and also to Messrs. Y. Ono, K. Homma, and Y. Kekoin for their helpful support. The authors gratefully acknowledge the assistance of Mr. S. Aoki in carrying out part of the experimental portion of this study.

Manuscript submitted Aug. 13, 1971; revised manuscript received Nov. 22, 1971.

Any discussion of this paper will appear in a Discussion Section to be published in the December 1972 JOURNAL.

REFERENCES

1. C. M. Wolfe, C. J. Nuese, and N. Holonyak, Jr., *J. Appl. Phys.*, **36**, 3790 (1965).
2. R. E. Ewing and D. K. Smith, *ibid.*, **39**, 5943 (1968).
3. G. B. Stringfellow and P. E. Greene, *ibid.*, **40**, 502 (1969).
4. M. S. Abrahams, L. R. Weisberg, C. J. Buiocchi, and J. Blanc, *J. Mater. Sci.*, **4**, 223 (1969).
5. M. S. Abrahams, L. R. Weisberg, and J. J. Tietjen, *J. Appl. Phys.*, **40**, 3754 (1969).
6. R. A. Burmeister, Jr., G. P. Pighini, and P. E. Greene, *Trans. TMS-AIME*, **245**, 587 (1969).
7. M. Ogirima and K. Kurata, *Japan J. Appl. Phys.*, **10**, 1474 (1971).
8. T. Tokuyama, Y. Fujii, Y. Sugita, and S. Kishino, *ibid.*, **6**, 1252 (1967).
9. J. K. Howard and R. D. Dobrott, *This Journal*, **113**, 567 (1966).
10. S. Kishino, *Japan J. Appl. Phys.*, **10**, 1113 (1971).
11. M. Rubenstein, *This Journal*, **112**, 426 (1965).
12. A. R. Lang, *J. Appl. Phys.*, **30**, 1748 (1959).
13. S. Timoshenko, *J. Opt. Soc. Am.*, **11**, 23 (1925).
14. R. H. Saul, *J. Appl. Phys.*, **40**, 3273 (1969).
15. T. Mitsuishi, S. Kishino, and A. Noda, *Japan J. Appl. Phys.*, **10**, 1734 (1971).
16. R. H. Saul, *This Journal*, **115**, 1184 (1968).
17. S. Kishino, To be published.

The Equilibrium Pressure of N_2 over GaN

C. D. Thurmond* and R. A. Logan

Bell Telephone Laboratories, Incorporated, Murray Hill, New Jersey 07974

ABSTRACT

The equilibrium pressures of N_2 over GaN and Ga are not known. Values of the heat and entropy of formation of GaN are proposed that give equilibrium N_2 pressures as a function of temperature. Experiments reported in the literature lead to consistent upper and lower bounds to the calculated curve but do not define its position very well. We report the results of three different types of experiments, using NH_3 in H_2 , which tighten the bounds to the equilibrium curve: the NH_3 pressures at which GaN could be seen to form from Ga were upper limits; the pressure of NH_3 in the exiting gas stream after reaction with Ga gives a qualified upper limit; and of greatest importance, we believe, are the measurements of the NH_3 pressures generated when H_2 is passed over GaN. These latter pressures are lower limits to the equilibrium curve and are believed to lie close to it. The experimental results are in agreement with the calculated equilibrium pressures of N_2 over GaN and Ga obtained using the heat of formation of GaN based on the measurements of Hahn and Juza, and Mah and the assumption that the entropy and heat capacity of GaN are the same as those of ZnO.

The temperature and nitrogen pressure ranges over which GaN is stable are not known. It is believed that very high pressures of nitrogen are required to form GaN from Ga(l) at temperatures above 1000°C (1). At lower temperatures a skin forms on the Ga(l), presumably GaN, impeding further reaction (1). NH_3 at a pressure 1 atm reacts with Ga(l) above 1050°C

(2), any reaction below this temperature also is impeded by a thin GaN film.

It has been suggested (3) that the decomposition of GaN(s) may lead to polymeric nitride molecules, $(\text{GaN})_x$. Transport experiments offered some support for the existence of such species (4) but no evidence of polymeric nitride molecules was obtained from mass-spectrometer studies (5, 6).

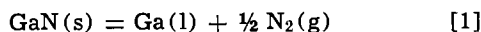
It is the purpose of this paper to calculate the equilibrium pressure of N_2 over GaN and Ga as a function

* Electrochemical Society Active Member.
Key words: gallium nitride, equilibrium, decomposition pressure, heat of formation, entropy.

of temperature from a heat of formation in the literature and an estimated entropy and heat capacity of GaN. It will then be shown that this curve is consistent with previously reported experimental results which, however, do not define the position of the curve very well, and is in good agreement with our experimental results which do define the position much more sharply.

Equilibrium Pressure Curve

The equilibrium between GaN, liquid Ga, and N₂ is described by the following reaction



The equilibrium N₂ pressure is related to the standard free energy change of reaction [1] by the expression

$$\frac{1}{2} RT \ln P_{\text{N}_2} = -\Delta G^\circ_1 \quad [2]$$

It has been assumed that GaN has a narrow non-stoichiometry range and that the solubility of GaN in Ga is negligible. The standard free energy change, in turn, is related to the free energy of formation of GaN, and the heat and entropy of formation by

$$-\Delta G^\circ_1 = \Delta G^\circ_{\text{GaN}} = (\Delta H^\circ_{\text{GaN}} - T\Delta S^\circ_{\text{GaN}}) \quad [3]$$

The heat of formation of GaN at 298°K given in the NBS tables (7), is -26.4 kcal. It is based on the heat of combustion of GaN measured by Hahn and Juza (2) and the heat of combustion of Ga measured by Mah (8). The entropy of formation of GaN has not been measured, but following a suggestion by Sime and Margrave (4), we have estimated the entropy of GaN by assuming it is the same as that of ZnO which is the same crystal structure (wurtzite), is isoelectronic, and is of nearly the same molecular weight. The entropy of ZnO at 298°C is 10.43 eu (9). In addition, we have assumed that the heat capacity of GaN is the same as that of ZnO (10). With the available thermodynamic information on liquid Ga (11) and on N₂ (12), the heat and entropy of formation of GaN can be obtained, from which the equilibrium N₂ pressure can be calculated.

The equilibrium N₂ pressure, estimated as described above, has been plotted in Fig. 1. At temperatures higher than 800°C, the calculated N₂ pressure is greater than 1 atm; at 1200°C, the pressure is 1000 atm, reaching 100,000 atm at about 1700°C.

Comparison with Available Experimental Data

The calculated N₂ pressures can be compared to related observations reported by a number of workers.

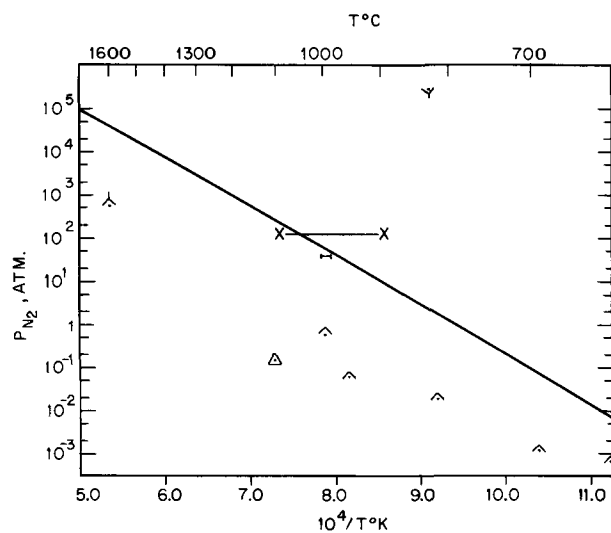
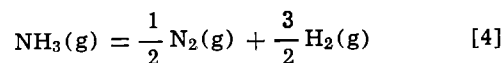


Fig. 1. Pressure of N₂ over GaN(s)-Ga(l), ($\log P_{\text{N}_2}$ vs. $10^4/T$). The solid line is calculated. Lower limits to the equilibrium curve: \blacktriangle MacChesney and co-workers (13), \triangle Juza and Hahn (2), \blacktriangle Lorenz and Binkowski (14). Upper limits to the equilibrium curve: ∇ Maruska and Tietjen (16), \times Logan and co-workers (17), \blacktriangle Lorimor and co-workers (18).

The most direct information comes from a measurement by MacChesney and co-workers (13) who found that at 1600°C, under a pressure of about 700 atm of N₂, GaN decomposed. This observation gives a lower limit to the equilibrium curve and, as plotted in Fig. 1, is consistent with the calculated curve. Lorenz and Binkowski (14) studied the rate of decomposition of GaN over the temperature range from 600° to 1000°C. They noted the highest N₂ pressures reached at the time the rate measurements were discontinued. These pressures also represent lower limits to the equilibrium curve and are plotted in Fig. 1. The five points are consistent with the estimated curve. Juza and Hahn (15) provide one point obtained by the same method.

The three sets of measurements just cited represent all of the information found in the literature that could be used to give lower limits to the equilibrium curve. There are three reports, however, on the reaction of NH₃ with Ga that can also be used to give upper limits to the equilibrium curve.

The first of these is by Maruska and Tietjen (16) who prepared GaN by passing GaCl and NH₃ in H₂ over a sapphire substrate at 825°C and at atmospheric pressure. The fact that GaN was formed in the presence of 0.14 atm of NH₃ and 0.86 atm of H₂ permits an upper limit to the equilibrium N₂ pressure over GaN and liquid Ga to be calculated. It is equal to the N₂ pressure corresponding to equilibrium with the NH₃ and H₂ pressures used in growing the GaN layers. This equilibrium is described by the equation



which leads to the following expression relating the partial pressures to the equilibrium constant, K_4

$$P_{\text{N}_2}^{1/2} = K_4 \frac{P_{\text{NH}_3}}{P_{\text{H}_2}^{3/2}} \quad [5]$$

The value of K_4 obtained from the JANAF Tables (12) is about 3×10^3 at 825°C, leading to a value for the N₂ pressure of 3×10^5 atm. This point is plotted in Fig. 1 and lies far above the calculated equilibrium curve. It is, of course, consistent with this curve but does not help appreciably to define it.

Recently, two additional observations related to the reaction of NH₃ with Ga provide upper limits to the equilibrium N₂ pressure curve. Logan and co-workers (17) have added N to GaP by passing NH₃ in H₂ over liquid Ga containing dissolved phosphorus from which GaP was grown by cooling. It was found that the N concentration in GaP was proportional to the NH₃ pressure and there was an NH₃ pressure above which good crystal growth of GaP was not possible. Lorimor and co-workers (18), in applying Logan's technique to the addition of N to GaP, observed that the concentration of N saturated. That is, crystal growth could be obtained with some difficulty at higher NH₃ pressures but no further increase in N concentration was found. They observed altered crystal growth and reported that GaN was formed.

The NH₃ pressures in H₂, at which GaN was formed from Ga in the studies of N doping of GaP, were in the range of 10⁻³ atm at temperatures of approximately 1000°C. Equivalent N₂ pressure can be calculated from the conditions used and have been plotted in Fig. 1. It is seen that Logan's point straddles the calculated curve, while Lorimor's point lies slightly below the curve. The temperature range of each of these points corresponds to the range over which GaP epitaxial layers were grown.

It is concluded that the equilibrium N₂ pressure curve lies on or below the curve plotted in Fig. 1 but not lower than 1 to 2 decades below it.

We have attempted to obtain improved upper limits to the equilibrium N₂ pressures by finding the mini-

mum NH_3 pressures at which GaN can be formed from Ga. Additional information has been obtained from the NH_3 pressure leaving the tube after reaction with Ga. The discovery that high pressures of NH_3 , relatively speaking, are generated by the reaction of H_2 with GaN, has led to greatly improved lower limits to the equilibrium curve.

Experimental

Most of the GaN used in these studies was grown by reacting a partial pressure of NH_3 in H_2 with Ga at 1150°C in a furnace system that was previously used (17) to grow epitaxial layers of N-doped GaP. The furnace was modified so that an easily replaceable quartz liner was used inside the main quartz furnace tube. The NH_3 pressure ranged from 10^{-3} to 5×10^{-2} atm in H_2 , with gas flow rates of 70 to 280 cc/min and a tube ID of 2.1 cm. The GaN formed was in the form of small, black, irregularly shaped crystals with dimensions ranging from 75 to 500 μm . The other GaN studied was composed of smaller crystals, gray in color, grown by Zetterstrom (19) by reacting Ga with 1 atm of NH_3 at 1100°C in a similar furnace. To separate out the very small crystals formed in this growth, the batch was repeatedly rinsed with agitation and the larger crystals retained. They ranged in size from 20 to 100 μm . In all cases, the GaN was separated from the Ga growth melt by digestion in aqua regia.

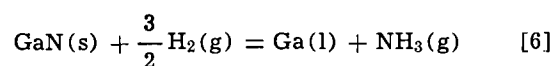
P_{NH_3} was determined by causing the NH_3 - H_2 furnace exhaust gas to bubble through a 4 cm high column of HCl solution of known column and normality, and containing methyl red indicator. The normality of the HCl solution was adjusted to give a convenient titration time of 5 to 10 min so that the uncertainty (a few seconds) in the determination of the time of the indicator color change was negligible. The contribution of the indicator to the normality of the solution became significant ($\sim 10\%$) only at the lowest normality used ($2 \times 10^{-5}N$). Since the furnace gas flowed at constant rate rather than at constant pressure, the gas flow rate was unaffected by the small change in gas pressure due to the titration. The NH_3 dissolution into the HCl solution was complete as evidenced by doubling the column height of the HCl solution by the addition of H_2O , without changing the titration time for a given gas mixture. P_{NH_3} is determined from the gas flow rate and the titration time of the solution of known volume and normality.

The system was routinely monitored for evidence of dissociation of NH_3 in the furnace. A clear indication of dissociation was the variation of P_{NH_3} with furnace temperature. Dissociation could be made negligible by use of new quartz furnace liner which was cleaned in deionized H_2O and alcohol prior to use. No bake-out was necessary. The main quartz furnace tube caused NH_3 dissociation after continual use for one to three months. The dissociation correlated with devitrification of the tube and was rectified by replacement with a new quartz tube. It was observed that the low oxygen (and water vapor) level in the furnace ambient was essential to achieve negligible NH_3 dissociation. The pyrolytic graphite crucibles used both in the formation and dissociation studies of GaN did not cause NH_3 decomposition and the crucible weight loss during an experiment was less than 1 mg.

The NH_3 pressure from the reaction of H_2 with GaN was determined by inserting 1-13g of GaN crystals, contained in a pyrolytic graphite crucible, into the furnace, at uniform temperature and with a pure H_2 ambient. The NH_3 pressure in the exit gas was monitored continuously and increased to a constant value in about 60 min. This is about the time required to achieve a constant value of the NH_3 pressure when H_2 and NH_3 are mixed and passed through the empty tube. Typically, about 25 w/o (weight per cent) of the GaN dissociated, leaving Ga, in heating times which ranged from 16 hr at 925°C to 4 hr at 1175°C .

Results and Discussion

In the work reported here, the reaction of NH_3 with Ga has been used to give upper limits to the N_2 equilibrium pressure over GaN and Ga. The reaction H_2 with GaN has been used to give lower limits to the N_2 equilibrium pressure. Both of these reactions can be described by the following equation



The equilibrium constant relates the equilibrium pressures of NH_3 and H_2 in the equation

$$\frac{P_{\text{NH}_3}}{P_{\text{H}_2}^{3/2}} = K_6 \quad [7]$$

It has again been assumed that the nonstoichiometry range of GaN is small and that the solubility of GaN in Ga is negligible. The pressure ratio $P_{\text{NH}_3}/P_{\text{H}_2}^{3/2}$ is also given in Eq. [5] from which the following equations can be written

$$\frac{P_{\text{NH}_3}}{P_{\text{H}_2}^{3/2}} = K_6 = \frac{P_{\text{N}_2}^{1/2}}{K_4} \quad [8]$$

Since K_4 can be obtained from the JANAF Tables (12), the values of $P_{\text{NH}_3}/P_{\text{H}_2}^{3/2}$ can be calculated for the equilibrium N_2 pressures given in Fig. 1. They are plotted in Fig. 2 as $\log P_{\text{NH}_3}$ vs. $10^4/T$ and give the solid line. This is the reverse of the calculations made in the section on Comparison with Available Experimental Data to obtain upper limits to the equilibrium N_2 line from NH_3 and H_2 pressures at which GaN formed.

The minimum NH_3 pressures in H_2 at which GaN was seen to form when passed over liquid Ga, have been plotted in Fig. 2 and are upper limits to the equilibrium NH_3 pressure. Measurements made independently by Ilegems (20) are included.

An independent upper limit to the equilibrium curve is obtained from the pressure of NH_3 leaving the reaction tube. This pressure is always less than that entering. Measurements of the NH_3 pressure after NH_3 in H_2 was passed through clean empty tubes showed that negligible decomposition occurred. However, it cannot be ruled out that some decomposition of NH_3 to H_2 and N_2 occurred during the reaction with liquid

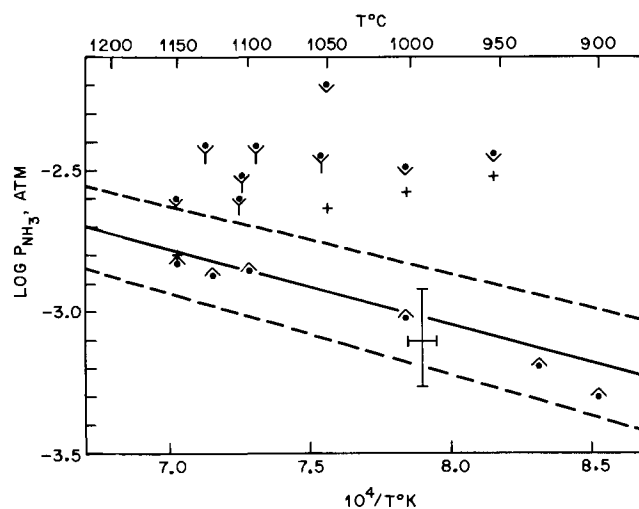


Fig. 2. Pressure of NH_3 in H_2 over GaN(s)-Ga(l), ($\log P_{\text{NH}_3}$ vs. $10^4/T$). The solid line is equivalent to the calculated line of Fig. 1. The dashed lines represent a ± 1 kcal uncertainty in the free energy of formation of GaN. ∇ Minimum NH_3 pressures at which GaN was seen to form from Ga. $+$ NH_3 pressures in exiting gas stream. ∇ Independent measurements by M. Ilegems of minimum input NH_3 pressures at which GaN was seen to form from Ga. \triangle NH_3 pressures from the reaction of H_2 with GaN. --- Lorimer and co-workers (18).

Ga. At lower NH₃ pressures where GaN is not formed, the NH₃ pressure decreased about 10% in passing through the reaction zone. We have taken this to be an estimate of the extent of dissociation of NH₃ in these experiments. The lowest observed exit pressures at several temperatures where GaN was formed are plotted in Fig. 2. These points may be too low by as much as 10%.

All of the upper limit points plotted in Fig. 2 are consistent with the calculated equilibrium line except for one point at the highest temperature which, however, agrees within the 10% estimated uncertainty.

We have found that impressively high pressures of NH₃ are generated when H₂ is passed over GaN. The measured pressures set lower limits to the equilibrium curve. The points plotted in Fig. 2 are the highest pressures measured at each temperature and are steady-state values achieved after about 1 hr of heating. They all are consistent with the estimated line and fall well within the band resulting from the 1 kcal uncertainty in the heat of formation of GaN.

The dependence of the NH₃ pressure on flow rate and sample area suggested that equilibrium was near. The observed NH₃ pressure increased ~20% as the flow rate decreased from 280 to 70 cc/min and a similar small increase was observed when the GaN area increased by a factor of 5. The GaN area was varied by changing the weight of crystals of a given mesh size. The points plotted in Fig. 2 are the highest NH₃ pressures measured at each temperature, obtained with the largest GaN area and smallest flow rate used at each temperature. It is possible, however, that equilibrium pressures were not attained because appreciable catalytic decomposition of NH₃ may have taken place in the hot tube down stream from the GaN. This possibility restrains us from accepting these as equilibrium measurements. They are, however, completely acceptable lower limits to the equilibrium curve.

On the basis of the lower and upper limiting points that we have obtained, we conclude that the equilibrium pressure of NH₃, given by the calculated line of Fig. 2, is consistent with all of the experimental information available as is true also for the pressure of N₂ given by the line of Fig. 1. The data of Lorimor *et al.* (18), plotted in Fig. 1 in terms of N₂ pressure, is plotted in Fig. 2 in terms of NH₃ pressure and provides an upper limit, with the indicated uncertainty in the NH₃ pressure. The data of Fig. 2 are summarized in Table I.

These results, then, are consistent with a heat of formation of GaN of -26.4 ± 1.0 kcal (2, 7, 8) and an entropy and heat capacity the same as those of ZnO

Table I. Pressure of NH₃ in H₂ over GaN(s)-Ga(l) vs. T°C (data of Fig. 2)

Experimental conditions	T°C	P _{NH₃} (10 ⁻³ atm)
(✓) Minimum input NH ₃ pressure at which GaN was seen to form from Ga	1150	2.5
	1050	7.0
	1000	3.2
	950	3.5
(+) NH ₃ pressures in exiting gas stream	1150	1.58
	1050	2.30
	1000	2.60
	950	3.00
(⊙) Independent measurements of M. Ilegems of minimum input NH ₃ pressures at which GaN was seen to form from Ga	1130	3.85
	1105	3.04
	1100	2.51
	1095	3.81
	1055	3.49
(←) Lorimor and co-workers (18)	1000-985	1.48
(∧) NH ₃ pressures from the reaction of H ₂ with GaN	1149	1.48
	1125	1.34
	1100	1.39
	1002	0.905
	929	0.645
	899	0.501

Table II. Heat and free energy of formation of GaN(s)

T, °K	-ΔH ^o , kcal	ΔG ^o , kcal
298	26.40 ± 1.0	-33.04 ± 1.0
900	26.94	-4.06
1000	26.74	-1.54
1100	26.52	+0.97
1200	26.29	+3.46
1300	26.04	+5.93
1400	25.78	+8.39
1500	25.52	+10.81
1600	25.24	+13.21

(9, 10). The heats of formation and free energies of formation used to calculate the curve of Fig. 1 are given in Table II.

Two criteria have been used to determine limits to equilibrium conditions: GaN must decompose or it must form. The fact that GaN may appear not to decompose under certain conditions does not give useful information since the rate of decomposition may be too slow to be observed. Similarly, Ga may appear not to react with N₂ or NH₃ and H₂ when, in fact, the reaction may be impeded by a thin surface nitride film. Conclusions can be drawn when changes occur; they cannot be drawn when changes do not occur.

We have taken advantage of two slow kinetic processes in order to closely approximate the equilibrium properties of GaN: the slow rate of decomposition of GaN to form Ga and N₂, and the slow rate of decomposition of NH₃ to N₂ and H₂. The iron-nitrogen system has been studied under somewhat related circumstances and equilibrium nitrogen pressures up to hundreds of thousands of atmospheres have been deduced from the much lower NH₃ pressures in H₂ used to control the nitrogen chemical potential (21).

Summary

The equilibrium pressure of N₂ over GaN and liquid Ga has been calculated from available thermodynamic functions with the assumption that the entropy and heat capacity of GaN are the same as those of ZnO. The calculated equilibrium pressure curve was found to be consistent with a number of reported experiments although the spread between upper and lower bounds was rather broad. NH₃ pressures in H₂, which were found to be the maximum pressures at which GaP, doped with N, could be grown (17, 18), gave equivalent nitrogen pressures in agreement with those calculated.

Three different experimental methods are reported here which were used to narrow the gap between upper and lower limits to the equilibrium pressure curve. In one method the minimum NH₃ pressure at which GaN could be seen to form on the surface of Ga was measured. Another consisted of measuring the NH₃ partial pressure in H₂ after passing over liquid Ga. Of importance is the last method, which appears to give results near equilibrium, where measurement was made of the NH₃ pressure generated by the reaction of H₂ with GaN. All measurements were consistent with the calculated equilibrium curve.

Acknowledgments

We are indebted to H. G. White for his assistance in performing these experiments. We thank M. Ilegems for helpful comments and for the experimental data used in Fig. 2 and R. B. Zetterstrom for providing the GaN crystals grown by reacting Ga with 1 atm of NH₃.

Manuscript submitted Sept. 22, 1971; revised manuscript received Dec. 27, 1971.

Any discussion of this paper will appear in a Discussion Section to be published in the December 1972 JOURNAL.

REFERENCES

1. A. Rabenau, "Compound Semiconductors," Vol. 1, p. 174, R. K. Willardson and H. L. Goering, Edi-

- tors, Reinhold Publishing Corp., New York (1962).
2. H. Hahn and R. Juza, *Z. Anorg. u. allgem. Chem.*, **244**, 111 (1940).
 3. J. L. Margrave and P. Sthapitanonda, *J. Phys. Chem.*, **59**, 1231 (1955).
 4. R. J. Sime and J. L. Margrave, *ibid.*, **60**, 810 (1970).
 5. Z. A. Munir and A. W. Searcy, *J. Chem. Phys.*, **42**, 4223 (1965).
 6. R. C. Schoonmaker, A. Buhl, and J. Lemley, *J. Phys. Chem.*, **69**, 3455 (1965).
 7. D. D. Wagman, W. H. Evans, V. B. Parker, I. Halow, S. M. Bailey, and R. H. Schumm, *Nat. Bur. Std., Tech. Note* 270-3 (1968).
 8. A. D. Mah, *Nat. Bur. Mines, Rept.* 5965 (1962).
 9. K. K. Kelley, *Bur. Mines, Bull.* 477 (1950).
 10. K. K. Kelley, *Bur. Mines, Bull.* 548 (1960).
 11. D. R. Stull and G. C. Sinke, "Thermodynamic Properties of the Elements," *Am. Chem. Soc.* (1956).
 12. D. R. Stull, Project Director, "JANAF Thermochemical Tables," (1967).
 13. J. B. MacChesney, P. M. Bridenbaugh, and P. B. O'Conner, *Mater. Res. Bull.*, **5**, 783 (1970).
 14. M. R. Lorenz and B. B. Binkowski, *This Journal*, **109**, 24 (1962).
 15. R. Juza and H. Hahn, *Z. Anorg. u. allgem. Chem.*, **244**, 133 (1940).
 16. H. P. Maruska and J. J. Tietjen, *Appl. Phys. Letters*, **15**, 327 (1969).
 17. R. A. Logan, H. G. White, and W. Wiegmann, *Solid State Electron.*, **14**, 55 (1971).
 18. O. G. Lorimer and L. R. Dawson, *This Journal*, **118**, 292C (1971).
 19. R. B. Zetterstrom, *J. Mater. Sci.*, **5**, 1102 (1970).
 20. M. Ilegems, Private communication.
 21. L. S. Darken and R. W. Gurry, "Physical Chemistry of Metals," p. 378, McGraw Hill Publishing Co., New York (1953).

Kinetics of Manganeseo-Wustite Scale Formation on Iron-Manganese Alloys

P. Mayer* and W. W. Smeltzer**

Department of Metallurgy and Materials Science, McMaster University, Hamilton, Ontario, Canada

ABSTRACT

The oxidation kinetics of Fe-Mn alloys containing up to 59 w/o (weight per cent) Mn exposed to carbon dioxide-carbon monoxide atmospheres at 1000°C have been determined by a thermogravimetric technique. The experimental conditions were chosen in order that the reaction would lead to formation of a single-phase manganeseo-wustite [(Fe Mn)O] scale. The rate of parabolic oxidation decreased and the manganese content in wustite increased with increasing manganese content in the alloy. A diffusion model, which is based on equations derived by Wagner for metal diffusion through the scale under chemical activity gradients, leads to a description of the scaling kinetics, and to evaluations for the self-diffusion coefficients of iron and manganese and the nonstoichiometry as a function of the manganese content in wustite.

A major objective of this investigation was to contribute to the understanding of the oxidation mechanism of binary alloys when a single-phase superficial oxide scale is formed as the major reaction product with only a relatively small degree of oxide precipitation in an internal oxidation zone. In recent papers, Wagner (1), and Coates and Dalvi (2) have advanced methods for calculating the distribution of cations in a metal-conducting scale growing by parabolic kinetics. The Fe-Mn-O system could meet these requirements since Foster and Welch (3) have demonstrated that wustite and manganous oxide form a continuous solid solution.

In the present work, the oxidation kinetics, morphological development, and composition of the wustite scale on Fe-Mn alloys exposed to CO₂-CO atmospheres at 1000°C were investigated under conditions to insure formation of (FeMn)O scale by parabolic kinetics. These results are used in combination with diffusional and thermodynamic properties of this ternary system and the above-mentioned theoretical considerations to gain an insight into the mechanism of scale growth and the metal transport properties of the oxide solid solution.

Experimental

The alloys were prepared from electrolytic iron, 99.96 w/o (weight per cent) pure, and manganese, 99.99 w/o

pure. Approximately 300g of material were placed in the melting chamber of a nonconsumable arc furnace with a tungsten electrode operating under argon. In order to prevent any long range segregation, each charge was melted, inverted, and then remelted until a total of four melting operations had been completed. It was then sealed in a quartz tube filled with argon and annealed for five days at 1000°C. The compositions of the alloys are given in Table I.

Alloy buttons were hot-rolled at 800°C to a thickness of 4 mm. The surface of each sheet was cleaned by pickling in dilute hydrochloric acid and by abrasion using 600 grit silicon carbide paper. The sheets were then cold-rolled to a thickness of approximately 2.5 mm. Test specimens, 10 × 10 × 2 mm, were prepared from these sheets by mounting plates in Bakelite and metallographically polishing all surfaces to 1μ diamond abrasive using kerosene as lubricant. After removal from the Bakelite mountings, specimens were washed with petroleum ether and stored in dried acetone.

Table I. Chemical analyses of Fe-Mn alloys based on manganese determinations

Alloy number in text	Nominal composition of alloys, w/o Mn	w/o Mn in alloys
1	0	0.0
2	1	0.93
3	12	12.33
4	27	27.35
5	32	31.83
6	59	58.94

* Electrochemical Society Student Associate.

** Electrochemical Society Active Member.

Key words: Fe-Mn alloys, parabolic oxidation, manganeseo-wustite scale.

An Ainsworth, Type RV, continuous recording microbalance was used to determine the weight change of a specimen exposed to a reaction atmosphere. The thermogravimetric assembly has been described previously (4); the temperature of the reaction zone in the furnace was controlled to $\pm 2^\circ\text{C}$. A specimen was lowered into the reaction atmosphere which was maintained at a flow rate of 0.6 cm/sec to prevent thermal segregation of the gases. Carbon dioxide, 99.95 v/o (volume per cent) pure, was dried by passage through columns containing magnesium perchlorate, reduced copper oxide, and activated alumina. Carbon monoxide, minimum purity of 99.6 v/o, was purified by passage through columns containing magnesium perchlorate and ascarite.

Oxidized specimens were mounted in epoxy, cold, self-setting resin, the final polishing being done with 1μ diamond abrasive and kerosene as lubricant. Chemical analyses were carried out by means of a Cameca electron-probe microanalyzer operating at 15 keV and a specimen current 50-80 nanoA. This instrument was calibrated as described previously (5). Standards for checking the calibration curves for the alloys were alloys of several known compositions. The calibration procedure for the wustite phase could be verified only for pure wustite. The Debye-Scherrer method of x-ray analysis using Co $K\alpha$ radiation was used to determine oxide crystallographic structures.

Results

The dependences of the oxidation kinetics on the compositions of the exposed alloys and on the CO_2/CO ratios in the reaction atmospheres are illustrated by the parabolic plots [(oxygen weight gain/unit area) 2 vs. (time)] in Fig. 1 and 2. These curves, which were reproducible within $\pm 15\%$, are of the same shape as those obtained for pure iron due to a relatively smaller reaction rate before onset of parabolic kinetics (6, 7). The plots in Fig. 3 illustrate that the values of the

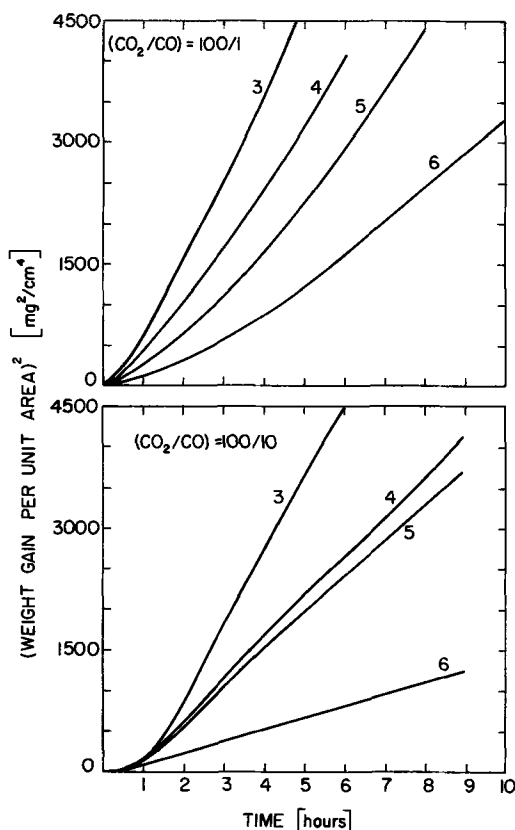


Fig. 1. Parabolic plots for the oxidation kinetics of Fe-Mn alloys in 100/1 and 100/10 CO_2 -CO atmospheres at 1000°C . The numbers on curves correspond to the alloy composition designations in Table I.

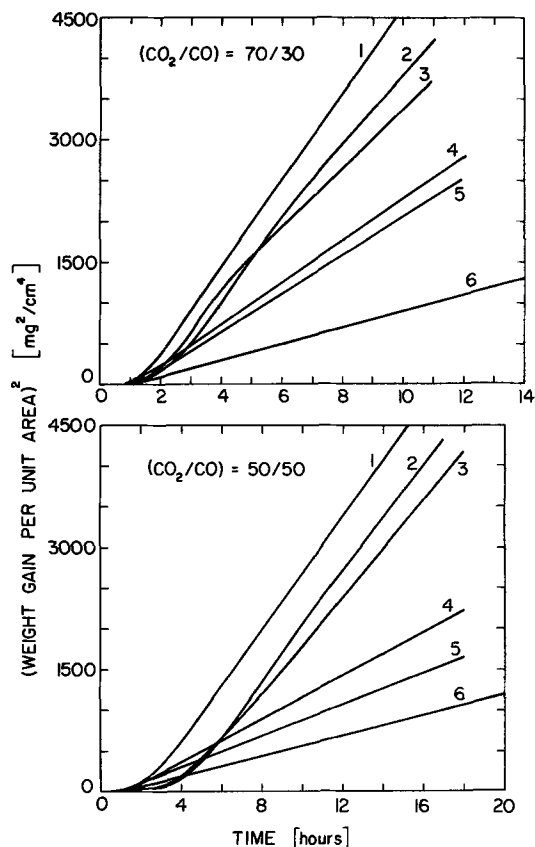


Fig. 2. Parabolic plots for the oxidation kinetics of Fe-Mn alloys in 70/30 and 50/50 CO_2 -CO atmospheres at 1000°C . The numbers on curves correspond to the alloy composition designations in Table I.

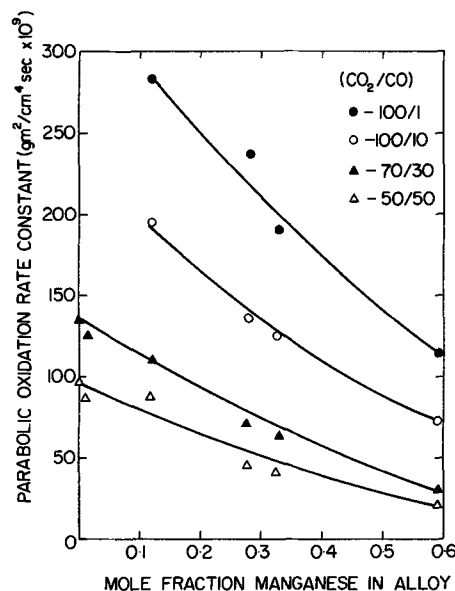


Fig. 3. Parabolic oxidation constants for Fe-Mn alloys as a function of manganese content.

parabolic oxidation constants decrease with increasing alloy manganese contents and carbon monoxide partial pressures.

Powder x-ray analyses of the scales demonstrated that they were composed of $(\text{FeMn})\text{O}$ with exception of those formed on pure iron and the alloy containing 10 w/o Mn exposed to pure carbon dioxide and a 100/10 CO_2 -CO atmosphere. In these cases, the presence of magnetite was identified. The mean lattice parameter of the single-phase scales, Fig. 4, exhibited a variation linearly related to the MnO content of the oxide solid solution.

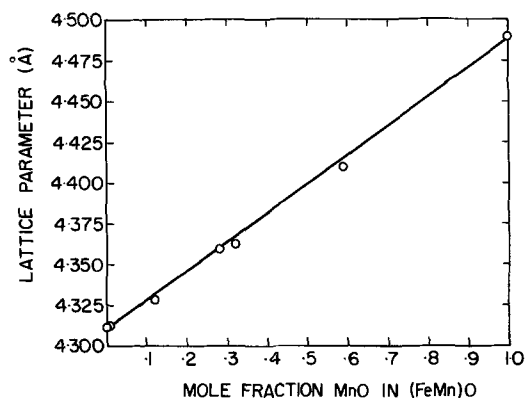


Fig. 4. Mean lattice parameter of the (FeMn)O solid solution scales.

A scale was essentially compact and uniformly thick during its growth. There was a small degree of internal oxidation but the penetration depth of its zone was negligible compared to the thickness of the scale. These features are illustrated by the micrographs in Fig. 5 and 6. Internal oxidation for the Fe-1% Mn alloy was so small that its penetration distance could not be determined at the comparatively high magnification of 1000X. In the alloy of highest manganese content, 59 w/o Mn, the penetration depth of oxide never exceeded 10% of the scale thickness. The only oxide identified in both the scales and internal zones was (FeMn)O.

Manganese concentration profiles in the scales and alloy substrates of specimens exposed to the various atmospheres for different intervals in the regions of parabolic oxidation were determined by the electron microprobe technique. The profiles shown in Fig. 7 and 8 for the alloy specimens containing 1 and 59 w/o Mn illustrate typical distributions for the alloying element between the metal and scale. The manganese concentrations were determined to within $\pm 0.5\%$ of

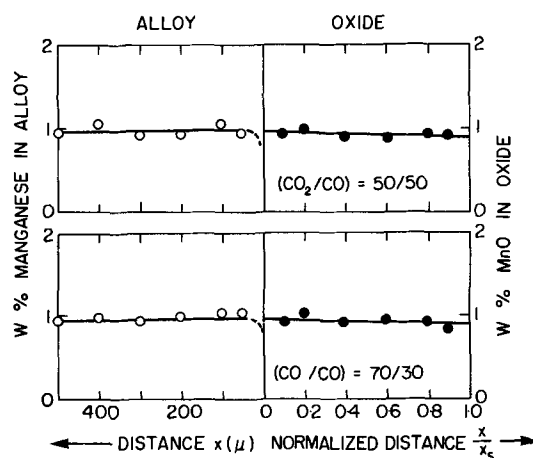


Fig. 7. Manganese concentration profiles in the metal and (FeMn)O scale of an Fe-1 w/o Mn alloy oxidized at 1000°C. The scale thickness has been standardized to $y = x/x_s$.

the determined values. Manganese depletion from an alloy was small, the depletion distance never extending inward more than 50μ from the alloy interface. The change of manganese concentration across a scale was small but the decrease in its concentration toward the outer surface gave rise to a linear manganese gradient. These gradients in the scales formed on the different alloys under various atmospheric conditions are recorded in Table II. Values are also tabulated for the MnO concentration at the outer scale surfaces as determined by extrapolation of the linear profiles.

Discussion

Oxidation of the alloys gave rise predominately to a scale consisting of a solid solution of the divalent oxides. An oxidation curve exhibited a region of slow reaction before onset of parabolic kinetics due to interfacial control at the scale/gas boundary. Oxidation in all atmospheres, nevertheless, proceeded at significant

Fig. 5. The metallographic cross-sections and the interfaces between the scales formed on Fe-1 w/o Mn and Fe-12 w/o Mn alloys exposed to a 70/30 CO₂-CO atmosphere at 1000°C (X130).

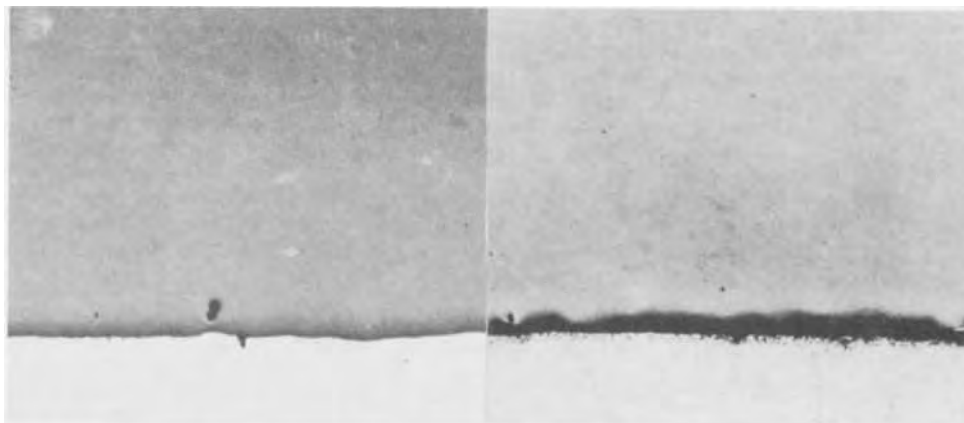
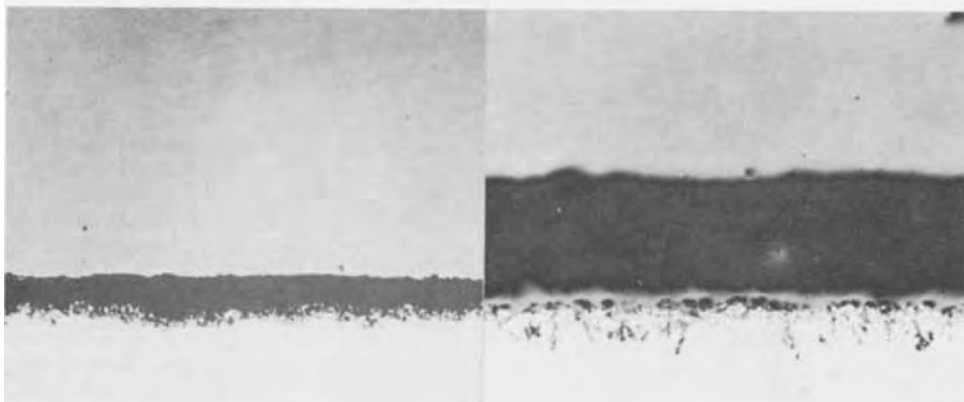


Fig. 6. The metallographic cross sections and the interfaces between the scales formed on Fe-32 w/o Mn and Fe-59 w/o Mn alloys exposed to a 70/30 CO₂-CO atmosphere at 1000°C (X130).



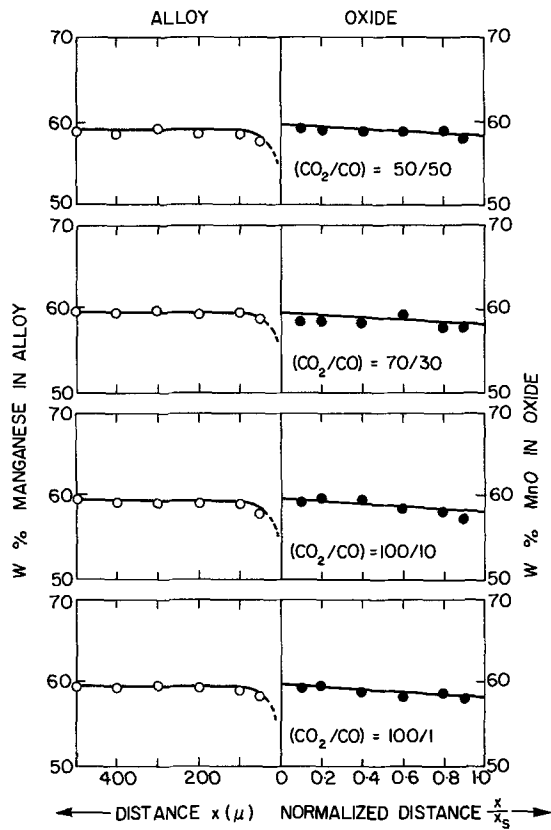


Fig. 8. Manganese concentration profiles in the metal and (FeMn)O scale of an Fe-59 w/o Mn alloy oxidized at 1000°C. The scale thickness has been standardized to $y = x/x_s$.

rates because of rapid metal diffusion within the oxide layer of large nonstoichiometry. The metal ratio in the scale was only slightly different from that in the alloy inasmuch as manganese, the less noble metal, entered the scale preferentially. Further, the ratio of manganese to iron in the scale decreased with distance from the alloy interface due to manganese exhibiting a smaller mobility than iron in the oxide solid solution. The metal gradients, nevertheless, attained a steady-state value during the stages of parabolic oxidation kinetics (Fig. 7 and 8).

The occurrence of parabolic kinetics governing growth of a relatively uniform scale with steady-state gradients in the oxide solid solution and the absence of an appreciable degree of internal oxidation meet the requirements of the theoretical analysis carried out by Wagner (1) for the distribution of cations in a metal conducting scale. Accordingly, the equations that he has deduced may be utilized with the present experimental results to calculate the metal diffusion coefficients in (FeMn)O and the dependence of its nonstoichiometry on the MnO content. His formalism is used and the reader is referred to the original paper for mathematical details.

The equations for the flux of metal cations through the scale are

$$j_{Fe}(eq) = -D_{Fe} \frac{1 - \xi}{V} \frac{\partial \ln a_{Fe}}{\partial x} \quad [1]$$

$$j_{Mn}(eq) = -D_{Mn} \frac{\xi}{V} \frac{\partial \ln a_{Mn}}{\partial x} \quad [2]$$

when correlation effects are disregarded. In these equations, D is a metal self-diffusion coefficient, ξ/V is the local concentration of manganese in equivalents per unit volume, and a is a local activity. Since the parabolic scaling rate is supposed to be controlled by diffusion, the above relationships yield Equation 11 from Ref. (1) for the parabolic oxidation rate constant

$$D_{Fe} (1 - \xi) \left(-\frac{\partial \ln a_{FeO}}{\partial \xi} \frac{d\xi}{dy} + \frac{z_{Fe}}{z_o} \frac{d \ln a_o}{dy} \right) + D_{Mn} \xi \left(-\frac{\partial \ln a_{MnO}}{\partial \xi} \frac{d\xi}{dy} + \frac{z_{Mn}}{z_o} \frac{d \ln a_o}{dy} \right) = k \quad [3]$$

where ξ is the mole fraction of MnO in the oxide and $y = x/x_s$ is the normalized scale thickness.

The Gibbs-Duhem equation for the oxide solid solution may be expressed as

$$(1 - \xi) d \ln a_{FeO} + \xi d \ln a_{MnO} = 0 \quad [4]$$

Since the (FeMn)O solid solution may be considered as nearly ideal (3)

$$\frac{d \ln a_{MnO}}{d \ln \xi} = 1 \quad [5]$$

Utilizing the equalities of the absolute valences, $z_{Fe} = z_{Mn} = z_o = 2$, we can express Eq. [3] upon substitution of [4] and [5] as

$$(1 - p) \frac{d\xi}{dy} + \frac{d \ln a_o}{dy} [(1 - \xi) + p\xi] = k^* \quad [6]$$

where

$$k^* = k/D_{Fe} \text{ and } p = D_{Mn}/D_{Fe} \quad [7]$$

The metal profiles in the oxide scales which were stationary and very flat under conditions for parabolic oxidation could be approximated to a linear gradient

$$\xi = a + by \quad [8]$$

where, $a = \xi'$ is the mole fraction of MnO in the scale at its inner interface and b is the gradient across the oxide. On substitution of Eq. [7] and [8] into [6]

$$\frac{d \ln a_o}{dy} = \frac{k^* + (p - 1)b}{1 + (p - 1)\xi} \quad [9]$$

The second equation that may be utilized in this calculation from Wagner's analysis is the algebraic expression 39 in Ref. (1) for material balance at the outer interface for manganese

$$- \left[D_{Mn} \xi \left(\frac{d \ln a_{MnO}}{d\xi} \cdot \frac{d\xi}{dy} - \frac{d \ln a_o}{dy} \right) \right]_{y=1} = \xi'' k \quad [10]$$

On applying the same simplifications as in the previous case, the resulting expression is

Table II. The values for the linear gradient, b , and the concentration at the outer oxide interface, ξ'' , of MnO in scales on alloys exposed to CO₂-CO atmospheres. The values of b and ξ'' from Eq. [8] are expressed as MnO mole fractions

Oxidation atmospheres, v/o [CO ₂ /CO]	Alloy composition, w/o Mn									
	0.93		12.33		27.35		31.83		59.04	
	$b \times 10^4$	ξ''	$b \times 10^4$	ξ''	$b \times 10^4$	ξ''	$b \times 10^4$	ξ''	$b \times 10^4$	ξ''
50/50	-0.9	0.0092	-12.3	0.121	-27.0	0.271	-31.4	0.314	-59.2	0.584
70/30	-0.9	0.0091	-12.2	0.122	-27.8	0.270	-31.8	0.313	-53.3	0.584
100/10	—	—	-12.2	0.120	-27.8	0.269	-31.2	0.315	-59.1	0.586
100/1	—	—	-12.3	0.121	-27.7	0.271	-31.6	0.315	-59.0	0.584

$$k^* = p \frac{d \ln a_o}{dy} - \frac{pb}{\xi''} \quad [11]$$

Substitution of Eq [9] into [11] yields

$$k^* = \frac{pb}{(p-1)(1-\xi'')\xi''} \quad [12]$$

These equations allow one to express the cation self-diffusivities in the following forms

$$D_{Fe} = \frac{k \xi'' (p-1)(1-\xi'')}{pb} \quad [13]$$

$$D_{Mn} = \frac{k \xi'' (p-1)(1-\xi'')}{b} \quad [14]$$

where the parabolic rate constant k is related to the experimental rate constant k_p by the relation

$$k \left(\frac{\text{cm}^2}{\text{sec}} \right) = \frac{k_p}{2} \left(\frac{V}{16} \right)^2 \quad [15]$$

In order to carry out calculations for metal self-diffusion coefficients and oxide nonstoichiometry, certain assumptions and approximations must be made to evaluate the constant p . The manganese concentration in the scale at its outer surface for an alloy of given composition was not measurably dependent on the oxygen potential of the atmosphere over the CO₂/CO ratios examined (Table II). This result and in view of previous findings that the (FeMn)O solid solution is nearly ideal allows one to invoke the assumption by Wagner that the enrichment of a metal toward the outer surface in a scale (in this case iron) results from its larger mobility. Since there is general agreement that the transport of iron and manganese in FeO and MnO takes place by a vacancy mechanism (8, 10), we may approximate the self-diffusion coefficients to

$$D_{Mn} = D^{\circ}_{Mn} \frac{x_{\square}}{(x^{\circ}_{\square})_{MnO}}; \quad D_{Fe} = D^{\circ}_{Fe} \frac{x_{\square}}{(x^{\circ}_{\square})_{FeO}} \quad [16]$$

Here D° and x°_{\square} refer to the self-diffusivities and vacancy concentrations for the pure oxides, and x_{\square} refers to the vacancy concentration in (FeMn)O. The ratio for the diffusivities in the oxide solid solution

$$\frac{D_{Mn}}{D_{Fe}} = \frac{D^{\circ}_{Mn}}{(x^{\circ}_{\square})_{MnO}} \bigg/ \frac{D^{\circ}_{Fe}}{(x^{\circ}_{\square})_{FeO}} \quad [17]$$

therefore essentially corresponds to the ratio of the jump frequencies for manganese and iron into an adjacent cation vacancy. Hence, the factor for manganese depletion across the scale may be regarded as corresponding to the mobility ratio of manganese to iron. That is

$$p = \frac{D_{Mn}}{D_{Fe}} = \frac{\xi''}{\xi'} \quad [18]$$

where from Eq. [8], $\xi''/\xi' = 1 + (b/a)$. A value of $p = 0.99 \pm 0.004$ is obtained using the results given in Table II.

The metal self-diffusivities are therefore related as follows

$$D_{Fe} = 1.01 D_{Mn} \quad [19]$$

The self-diffusion coefficient of iron may now be determined by substituting the value for p and the experimental values for the oxidation parameters in Eq. [12]. These results are presented in Fig. 9. Addition of MnO to FeO decreased the diffusion rate of both cations. The values for the self-diffusion coefficient of iron in wustite for oxygen potentials corresponding to 50/50

and 70/30 CO₂-CO atmospheres may be evaluated from published results (8, 9). It is seen that the plots determined for this diffusivity in (FeMn)O under these conditions extrapolate to these limiting values.

Wustite and manganous oxide exhibit metal deficiencies associated with occurrence of cation vacancies (8, 10). The former oxide shows by far the largest range of nonstoichiometry at 1000°C and the magnitude of the self-diffusion coefficient for iron is directly proportional to nonstoichiometry (8, 9). We therefore express the dependence of the diffusivity on nonstoichiometry for the ternary oxide solid solution as

$$D_{Fe} = D^{\circ}_{Fe} \frac{x_{\square}}{(x^{\circ}_{\square})_{FeO}} = D^{\circ}_{Fe} \frac{(X-1)X^{\circ}}{(X^{\circ}-1)X} \quad [20]$$

and where X° and X are the ratios of the atomic fractions of oxygen to metal in pure wustite and the ternary oxide. Consequently, we may utilize diffusion evaluations from this investigation to determine the variation of (FeMn)O nonstoichiometry with increasing manganese content.

The results of these calculations using Eq. [20] are shown in Fig. 10. A comparison is also given between the calculated values and those determined by Voetzel

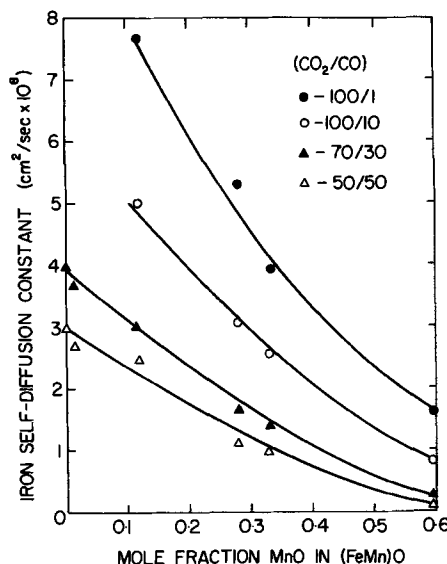


Fig. 9. Self-diffusion coefficient of iron in the (FeMn)O solid solution at 1000°C.

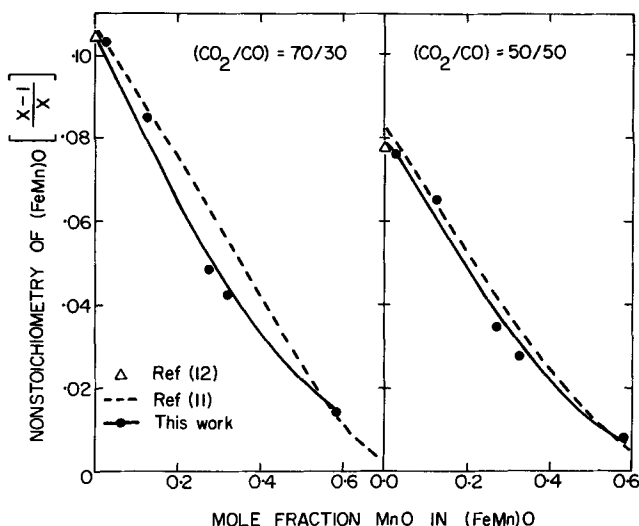


Fig. 10. Nonstoichiometry of the (FeMn)O solid solution at 1000°C. The dashed curve represents values obtained at 1100°C by Voetzel and Manenc (11) on equilibration of (FeMn)O in atmospheres undergoing the water-gas reaction. The values for pure FeO are those determined at 1000°C by Swaroop and Wagner (12).

and Manenc (11) and Swaroop and Wagner (12). The determinations from the first investigation are those obtained at 1100°C, but the investigators report that the nonstoichiometry was practically identical within the experimental precision at 1100° and 1000°C in atmospheres of constant CO₂/CO ratio (11). A very small variation in nonstoichiometry of pure wustite only occurs over the temperature range 1000°-1100°C, the nonstoichiometry at 1000°C being 2-3% smaller than that at 1100°C for atmospheres of constant CO₂/CO ratio. Within these limitations, it can be seen from Fig. 10 that there is good agreement between values obtained in this investigation and those in the literature. This consideration offers additional substantiation to the diffusion model and analysis adopted to describe the parabolic oxidation kinetics of the Fe-Mn alloys in CO₂-CO atmospheres.

Summary

The parabolic kinetics were determined for the formation of the manganese-wustite scale on Fe-Mn alloys exposed to CO₂-CO atmospheres at 1000°C. The morphological development and manganese gradients in the scale and metal demonstrated that the reaction proceeded under steady-state conditions. A model based on a diffusion analysis was shown to account for this kinetic behavior. It was possible by this analysis to evaluate the self-diffusion coefficients for iron and manganese and the nonstoichiometry of wustite as a function of manganese content. All of these parameters were found to decrease with increasing amounts of manganese dissolved in the (FeMn)O solid solution.

Acknowledgments

This research was carried out under the auspices of the National Research Council of Canada. The paper is based on the thesis submitted by P. Mayer to McMaster University in partial fulfillment of the requirements for the M. Eng. degree.

Manuscript submitted Sept. 16, 1971; revised manuscript received Jan. 12, 1972.

Any discussion of this paper will appear in a Discussion Section to be published in the December 1972 JOURNAL.

REFERENCES

1. C. Wagner, *Corrosion Sci.*, **9**, 91 (1969).
2. D. E. Coates and A. D. Dalvi, *J. Oxidation Metals*, **2**, 331 (1970).
3. P. K. Foster and A. J. E. Welch, *Trans. Faraday Soc.*, **52**, 1626 (1956).
4. R. Logani and W. W. Smeltzer, *J. Oxidation Metals*, **1**, 3 (1969).
5. A. D. Dalvi and W. W. Smeltzer, *This Journal*, **117**, 1431 (1970).
6. W. W. Smeltzer, *Acta Met.*, **8**, 377 (1960).
7. F. S. Pettit and J. B. Wagner, Jr., *ibid.*, **12**, 35 (1964).
8. L. Himmel, R. F. Mehl, and C. E. Birchenell, *Trans. AIME*, **197**, 827 (1953).
9. P. Hembree and J. B. Wagner, Jr., *ibid.*, **245**, 1547 (1969).
10. I. Bransky and N. M. Tallan, *This Journal*, **118**, 788 (1971).
11. J. Voeltzel and J. Manenc, *Mem. Sc. Rev. Metallurg.*, **64**, 8 (1967).
12. B. Swaroop and J. B. Wagner, Jr., *Trans. AIME*, **239**, 1215 (1967).

Electrical and Structural Properties of Metal Sulfides in Chloride Melts

The Systems Cu₂S-CuCl and FeS-FeCl₂

A. K. Garbee¹ and S. N. Flengas*

Department of Metallurgy and Materials Science, University of Toronto, Toronto, Ontario, Canada

ABSTRACT

The phase diagrams of the systems Cu₂S-CuCl and FeS-FeCl₂ and the densities of the liquid solutions have been measured over the permissible concentration and temperature ranges. Specific conductivities of the liquid mixtures have also been determined. The results indicate that the Cu₂S-CuCl solutions, for concentrations up to about 30 m/o (mole per cent) Cu₂S and temperatures below 1000°C, are essentially ionic conductors. Electronic conductance becomes evident for the more concentrated solutions. In the FeS-FeCl₂ solutions, ionic conductivity appears to be restricted to concentrations below 10 m/o FeS.

The thermodynamic calculations from the Cu₂S-CuCl phase diagram and the structural interpretation of the density measurements indicate that (Cu₂S)₂ dimers are present in dilute solutions. Further association occurs at higher concentrations and the formation of a continuous sulfide network appears to be related to the onset of electronic conduction. The solubility of copper metal in cuprous chloride is very low, and the conductivity of cuprous chloride, and of cuprous chloride-rich melts with cuprous sulfide, appears unaffected by the presence of copper metal. The addition of excess copper metal to molten cuprous sulfide, however, greatly increases its electrical conductivity.

Because the electrical conductivities of cuprous and ferrous sulfides are predominantly electronic in nature electrodeposition from the molten sulfides is not feasible. Electrolysis of solutions of Cu₂S in CuCl in the composition and temperature ranges of ionic behavior yielded copper metal at the cathode with high current efficiencies. Copper metal was also recovered selectively from solutions of a synthetic Cu-Fe-S matte dissolved in molten CuCl. It is also shown that FeS may be extracted from a synthetic FeS-Cu₂S matte by solvent extraction using molten CuCl at the appropriate temperatures. The extraction is attributed to an exchange reaction which converts the FeS component into the soluble ionic form of FeCl₂.

Previous work in this laboratory (1-4) and elsewhere (5-9) has indicated that the molten solutions

* Electrochemical Society Active Member.

¹ Present address: Armco Steel Corporation, Middletown, Ohio 45042.

Key words: electrical conductivities, metal sulfides, metal chlorides, electrical properties of mattes, densities of metal sulfides.

of metal sulfides in their corresponding metal chlorides exhibit interesting thermodynamic and electrical properties. Within specific temperature and composition ranges such solutions, rather dilute in metal sulfide, behave like ionic conductors. As the sulfide con-

tent and the temperature are increased electronic conductivity sets in, and the concentrated solutions behave more like the electronically conducting "pure" molten metal sulfide. It is evident that in the range of ionic behavior the recovery of metals from their sulfide ores by fused salt electrolysis should be feasible. In addition to this practical aspect, the factors determining the ionic to electronic transitions as well as the thermodynamic and structural properties of such high-temperature liquid semiconductors are of theoretical interest.

The sulfide solutions investigated previously in this laboratory include $\text{Ag}_2\text{S}-\text{AgCl}$ (1-2) and the $\text{PbS}-\text{PbCl}_2$ (3-4) binary systems. The present paper describes work on the thermodynamic and structural properties of the molten salt solutions of Cu_2S and of FeS in CuCl and FeCl_2 , respectively. The investigation includes the determination of the liquidus curves of the binary systems $\text{Cu}_2\text{S}-\text{CuCl}$ and $\text{FeS}-\text{FeCl}_2$, and measurements of densities and electrical conductivities in these systems. Finally, copper metal has been recovered by electrolysis of the $\text{Cu}_2\text{S}-\text{CuCl}$ solutions and from a synthetic matte containing $\text{Cu}-\text{Fe}-\text{S}$ dissolved in molten CuCl .

Experimental

Preparation of materials.—Anhydrous CuCl was prepared from an aqueous solution of cupric chloride by reduction with sulfurous acid. The precipitated CuCl was washed with anhydrous alcohol and was dehydrated by treatment under vacuum for several hours, followed by melting and sublimation in a stream of dry hydrogen chloride gas. Chemical analysis of the product indicated a purity of better than 99.7% by weight.

Anhydrous FeCl_2 was prepared from reagent-grade hydrated FeCl_2 dried in a vacuum oven at 110°C for several days. This partly dehydrated solid was finely ground in a dry box filled with purified argon and then was treated with dry hydrogen chloride gas at about 500°C . The chemical analysis of this product corresponded to a 99.7% FeCl_2 content.

Pure Cu_2S was prepared by direct reaction between stoichiometric amounts of hydrogen-reduced copper metal powder and sulfur which had been previously purified by sublimation. The reactants were charged to quartz ampoules which were then flame-sealed under vacuum. The reaction was completed by heating at about 600°C for at least three days.

The chemical analysis of the reaction product indicated a Cu_2S compound in the composition range $\text{Cu}_{1.97}\text{S}$ to $\text{Cu}_{2.00}\text{S}$. The x-ray analysis was in excellent agreement with the established diffraction patterns for Cu_2S .

Stoichiometric FeS was also prepared by reacting equivalent quantities of hydrogen-reduced iron metal powder (99.999% by weight) with sublimed sulfur in double-wall glass ampoules which were sealed under vacuum. This type of reaction cell was found necessary as, during heating, volume changes within the reacting mixtures tended to crack the inner compartment. The reaction between iron and sulfur was highly exothermic and could be initiated simply by touching the walls of the reaction site with a gas flame. When this initial violent reaction had subsided, the reaction cell was transferred to a furnace and heated to 600°C for a period of six days. The chemical analysis of the reaction product indicated an FeS composition between $\text{FeS}_{1.00}$ and $\text{FeS}_{1.01}$. X-ray analysis was in excellent agreement with the established diffraction patterns for FeS .

All other chemicals used in the course of this investigation (NaCl , KCl , and BaCl_2) were of reagent grade and were dried in a vacuum oven at 110°C prior to use.

Materials handling and transfer were always conducted in a dry box filled with purified argon gas, fitted with an air-lock.

Thermal stability of systems investigated.—Because of the pronounced dependence of the electrical properties of Cu_2S and FeS on stoichiometry the thermal stability of Cu_2S , FeS , and of their solutions with CuCl and FeCl_2 , respectively, was investigated. This information was a prerequisite for designing appropriate freezing-point depression apparatus, the density measuring apparatus, and the cells for measuring the electrical conductivities. The arbitrary temperature of 750°C was selected for comparison, simply on the basis of its being about half-way between the melting points of Cu_2S and CuCl . For this measurement, about 4g of material was added to a thin-walled quartz basket which was suspended from a quartz spring thermobalance in a closed all-silica-glass system. After the entire system had been evacuated argon gas was introduced and a movable furnace kept at 750°C was raised until the part of the quartz tubing containing the basket was in the hot zone of the furnace. The observed loss of weight was then recorded as a function of time over a period of 18 hr.

Weight losses in pure Cu_2S and FeS were not detected. However, a solution containing 11 m/o (mole per cent) Cu_2S lost about 8% by weight due to vaporization of CuCl . With pure CuCl and FeCl_2 the weight losses due to vaporization were alarmingly high. Both samples lost about 20% by weight after 18 hr of exposure. A sample of Cu_2S of 4.642g was also studied thermogravimetrically at a temperature of 1150°C . The complete heating and holding at 1150°C for 1 hr resulted in a loss of weight of 17 mg due to sulfur evolution which is equivalent to 0.36% of the original weight. When cooled to room temperature the solidified melt had acquired star-shaped copper metal crystallites which were visible around the circumference.

Hence, at the higher temperatures in an open experimental apparatus some unavoidable desulfurization should be expected to occur. For this reason it was decided to conduct the experiments in closed systems, where possible, or otherwise to measure a given property over the shortest possible period of time which would be compatible with the establishment of equilibrium and the reproducibility of the measurement.

Experimental.—Liquidus temperatures in the $\text{Cu}_2\text{S}-\text{CuCl}$ system were determined using a previously described technique (1, 3) and existing apparatus. Cooling rates were varied between 0.57° and $1.5^\circ\text{C}/\text{min}$. For these measurements the heart-shaped quartz cells fitted with a thermocouple well and containing about 15g of salt mixture were sealed under vacuum. Temperatures below 800°C were recorded using a 1 mV full-scale recorder and 24-gauge Chromel-Alumel thermocouples. For higher temperatures the thermocouples were platinum-13% platinum-rhodium. The sensitivity of the recorder was about 0.25°C , but the accuracy of the melting points should be taken as to the nearest degree. For chloride-rich compositions supercooling was not noticeable. However, supercooling did occur in the sulfide-rich melts and was minimized by vibrating the cells.

For the $\text{FeS}-\text{FeCl}_2$ mixtures, the steepness of the liquidus curve and the limited solubilities did not permit accurate cryoscopic measurements by this method. Only the melting point of pure FeCl_2 and the eutectic temperature could be detected. Hence, a decantation technique was employed. The measurements involved the equilibration at a given temperature of the sulfide-chloride mixtures placed in decantation quartz cells fitted with two side arms as described elsewhere (10).

At the beginning of a run, the cell with the salt mixture was sealed under vacuum and placed inside a graphite cylinder also containing the thermocouple wells and radiation baffles. The assembled system could be lowered into the hot zone of a cylindrical tilting furnace. The temperature along the 4-in. long graphite block was maintained constant to within $+3^\circ\text{C}$. When heated to the desired temperature the liquid phase

saturated with FeS was decanted into the second side arm of the cell by tilting the entire furnace. Prior to decantation the solutions were allowed to remain for several hours at temperature to ensure equilibration. After cooling, the cell was opened and the decanted phase was analyzed by extracting the water-soluble FeCl₂ with distilled water. The accuracy of the method was established from separate blank experiments during which both fused samples and mechanically mixed FeS and FeCl₂ were used. The former method yielded consistently slightly lower FeS contents by less than 0.5%. Thus, even for the smallest sulfide composition studied, 2.34% by weight FeS, the absolute error was only 0.012%. The only significant uncertainty in this type of measurement originated from the difficulty in maintaining a temperature control over the 4-in. long decantation cell of better than ±3°C.

The densities of the molten solutions in the Cu₂S-CuCl and FeS-FeCl₂ systems were determined by measuring the apparent loss of weight of a density sinker dipping into a melt at given compositions and temperatures. The density sinker was made by encapsulating a tungsten rod in quartz glass. For the oxygen-free melts quartz was found to be an excellent container material. All measurements were conducted in an atmosphere of purified argon using the quartz spring thermobalance apparatus and the cathetometer described previously (1, 3).

For the present measurements the quartz spring under a load of 5g had a total extension of 65 cm, allowing the detection of weight changes of the order of ±0.2 mg. The results were corrected for the slight increase in weight due to condensation of the salt on the quartz fiber supporting the density sinker.

The densities for pure Cu₂S could not be measured by this method because of the high viscosity and high surface tension of the melts.

Electrical conductivities in the systems Cu₂S-CuCl and FeS-FeCl₂ were measured as functions of melt composition and temperature, using the U-tube quartz capillary cells of 2 mm diameter described previously (2, 4). All measurements were taken under an atmosphere of oxygen-free argon gas. Cell constants varied between 500 and 900 cm⁻¹. Calibrations were made using a 1.0 demal KCl solution (11). The electrical conductivities were measured using an a-c conductivity bridge equipped with a Wagner ground and an oscilloscope detector. The bridge was operated at a frequency of 3000 Hz and resistances could be measured to within ±0.02 ohms. All values were corrected for lead

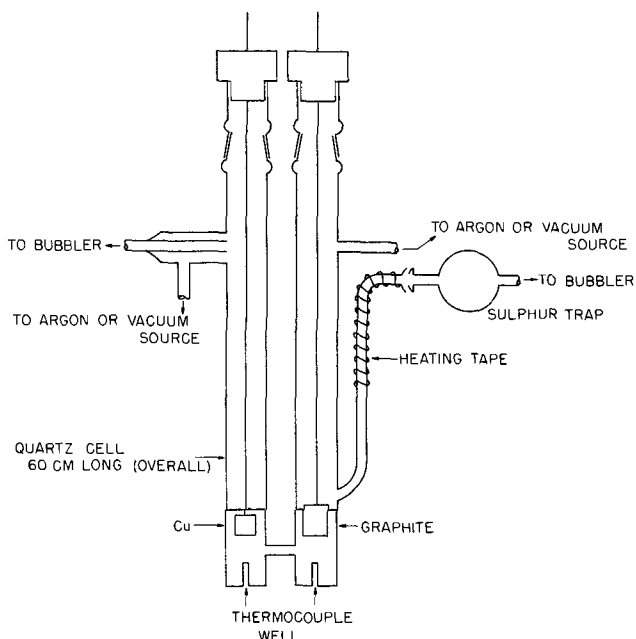


Fig. 1. Electrolysis cell

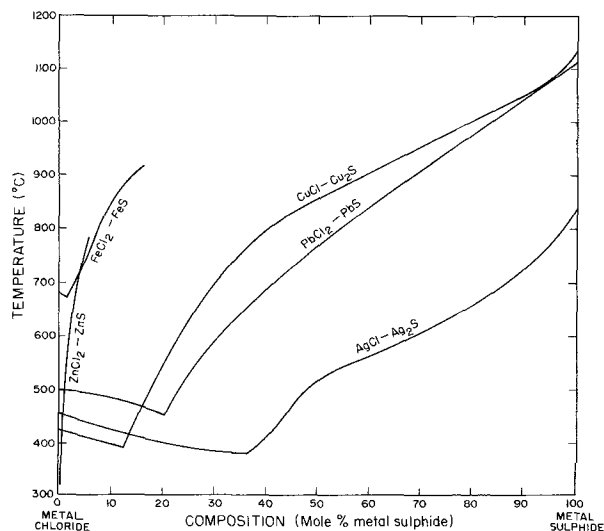


Fig. 2. Comparison between the phase diagrams of the systems: Cu₂S-CuCl, FeS-FeCl₂, PbS-PbCl₂, Ag₂S-AgCl, and ZnS-ZnCl₂.

and electrode resistances. For the lower temperatures the temperature control throughout the length of the cell was better than ±1.5°C, but between 1100° and 1200°C, it was only ±3°C.

Finally, the electrolysis experiments were conducted in the quartz cells shown in Fig. 1. Electrode materials were copper for the cathode and graphite for the anode. These cells were also operated under an atmosphere of purified argon.

Experimental Results

Phase diagram determination.—The liquidus curves for the system Cu₂S-CuCl and part of that for the system FeS-FeCl₂ are given in Fig. 2, where they are compared with those for similar systems.

The Cu₂S-CuCl system is of the simple eutectic type. The characteristic points are the melting points of CuCl and Cu₂S given as 422.9° ± 1.0°C and 1127.7° ± 2.0°C, respectively, and the eutectic temperature at 389.5° ± 1.5°C. The eutectic occurs at 12.1 m/o Cu₂S. The detailed data of the measured liquidus and eutectic temperatures are given in Table I.

Table I. Phase diagram measurements

Composition X _{Cu₂S}	Liquidus temperature (°C)	Eutectic temperature (°C)
Cu ₂ S-CuCl system		
1.0 (Pure Cu ₂ S)	1128 (m.p.)	—
0.950	1083	—
0.900	1047	—
0.850	1027	—
0.800	994.2	—
0.734	963.3	388.0
0.635	942.2	386.3
0.499	880.8	389.5
0.417	846.9	391.0
0.346	793.2	389.6
0.254	—	390.6
0.231	—	391.8
0.183	—	390.0
0.145	—	389.0
0.109	392.8	389.2
0.075	401.0	389.5
0.041	410.2	389.5
0 (Pure CuCl)	422.9 (m.p.)	—
	Temperature (°C)	Solubility X _{FeS}
FeS-FeCl ₂ system		
	697	0.032
	730	0.057
	735	0.058
	800	0.072
	857	0.108
	868	0.100
	890	0.120
	898	0.138

The present data should be compared with previous measurements by Urazov and Schleide (12) and by Truthe (13). The agreement is generally poor on the Cu_2S side of the eutectic where there is a 36°C spread in the reported values for the melting point of "pure" Cu_2S . In the composition range between 70-90 m/o Cu_2S , Truthe's (13) measurements differ by about 60°C from the present results. Urazov and Schleide (12) did not report any measurements beyond 48 m/o Cu_2S .

X-ray studies on material cooled from the eutectic, on both the sulfide and the chloride-rich sides, did not show any peak shift or line broadening. Therefore, solid solubility in this system is slight, if it occurs at all.

The cooling curves for pure CuCl and for compositions rich in CuCl indicate an exothermic reaction at 406°C which should be associated with the phase transformation of CuCl (14) from α -wüstite to the β -zinc blende type structure.

Cooling curves for the system FeS-FeCl_2 for compositions up to 40 m/o FeS showed only one inflection at a eutectic temperature of 674°C . In nine determinations FeCl_2 was found to melt at $679.4^\circ \pm 0.7^\circ\text{C}$. The solubility of FeS in FeCl_2 is limited and was measured by the decantation technique. The results are given in Fig. 2 and in Table I.

In Fig. 2, the liquidus curves of the systems FeS-FeCl_2 and $\text{Cu}_2\text{S-CuCl}$ are compared with those for Pb-PbCl_2 (3), $\text{Ag}_2\text{S-AgCl}$ (1), and ZnS-ZnCl_2 (15).

It may be seen that at corresponding temperatures the solubility of the sulfides in the chloride melt decreases in the order: $\text{Ag}_2\text{S-PbS-Cu}_2\text{S-FeS-ZnS}$, which is in the same order as the cation-ionic radius, or in the approximate order of the melting points of the pure metal sulfides. Work in this laboratory (10) on the reciprocal systems, PbS-NaCl , PbS-KCl , PbS-RbCl , and PbS-CsCl has indicated solubilities of the order of only 2 to 5 m/o sulfide which increased from the NaCl-PbS to the CsCl-PbS systems. Thus, the solubility trends in common cation and in reciprocal systems are entirely different.

Cryoscopic calculations.—In order to clarify the transformation for CuCl , and also for the purpose of obtaining information regarding the nature and the activities of the ionic species present in these solutions and of their degree of dissociation, freezing point depression measurements were also made on the systems CuCl-NaCl , CuCl-KCl , and CuCl-BaCl_2 .

From the results for the Cu_2S -rich liquidus curve, the activities of Cu_2S have been calculated using the simplified form of the van't Hoff equation

$$\ln a_{\text{solvent}} = \frac{-\Delta H_F}{R} \left[\frac{1}{T_L} - \frac{1}{T_F} \right] \quad [1]$$

where, T_L and T_F are, respectively, the liquidus and the fusion temperature of pure Cu_2S , and ΔH_F is the heat of fusion of Cu_2S given (16) as 2600 ± 500 cal. The results of the calculations are presented in Table II and indicate positive deviations from ideality.

Activity calculations were also made for CuCl for compositions along the CuCl liquidus. For this calculation the new heat of fusion for CuCl , determined calorimetrically in this laboratory (16), was used. The calorimetric measurements have shown that the solid transformation for CuCl at 406°C is accompanied by a heat effect of 1550 ± 50 cal/mole. Fusion occurs at 422.9°C and has a heat effect of only 1800 ± 50 cal/mole. It should be noted that the solid transformation is not mentioned in compilations of thermodynamic data and the heat of fusion is reported as having such widely different values as 2430 cal/mole (17) and 3879 cal/mole (18).

For the calculation of the activities of CuCl at temperatures below the transformation temperature, the

Table II. Activity calculations

System	X_{CuCl}	T_L (Liquidus temp. $^\circ\text{C}$)	a_{CuCl}	γ_{CuCl}
$\text{CuCl} + \text{BaCl}_2$	1.000	422.9	—	—
	0.990	417.0	0.989	0.999
	0.987	414.9	0.985	0.998
	0.981	411.6	0.979	0.998
	0.976	408.0	0.972	0.996
$\text{CuCl} + \text{KCl}$	0.992	418.1	0.990	0.999
	0.988	415.9	0.987	0.999
	0.978	410.2	0.976	0.997
	0.969	405.2	0.965	0.995
	0.966	403.4	0.959	0.992
	0.956	398.7	0.941	0.984
	0.952	396.6	0.935	0.982
$\text{CuCl} + \text{NaCl}$	0.931	386.2	0.808	0.965
	0.992	418.9	0.992	1.000
	0.983	414.5	0.984	1.001
	0.974	410.3	0.976	1.001
	0.965	405.5	0.966	1.001
	0.958	403.5	0.959	1.000
	0.953	401.5	0.952	0.999
$\text{CuCl} + \text{Cu}_2\text{S}$	0.934	394.5	0.928	0.988
	0.890	379.6	0.875	0.984
	0.995	421.1	0.996	1.001
	0.988	419.0	0.992	1.005
	0.978	416.6	0.988	1.010
	0.974	414.6	0.984	1.010
	0.965	412.2	0.980	1.015
	0.958	409.5	0.975	1.017
	0.951	407.5	0.971	1.020
	0.936	403.5	0.959	1.024
$\text{Cu}_2\text{S-CuCl}$	0.923	400.2	0.947	1.027
	0.917	399.0	0.943	1.028
	0.907	396.5	0.934	1.030
	0.898	394.4	0.927	1.032
	0.891	392.8	0.921	1.034
	$X_{\text{Cu}_2\text{S}}$		$a_{\text{Cu}_2\text{S}}$	$\gamma_{\text{Cu}_2\text{S}}$
	1.000	1128	—	—
	0.9765	1101	0.9865	1.0102
	0.9612	1092	0.9757	1.0151
	0.9500	1083	0.9685	1.0205
0.9000	1047	0.9443	1.0492	
$\text{Cu}_2\text{S-BaCl}_2$	0.9748	1108	0.9867	1.0511
	0.9432	1118	—	—

van't Hoff equation was used in the form

$$\ln \frac{a_{T_L}}{a_{T_T}} = - \frac{(\Delta H_F + \Delta H_T)}{R} \left[\frac{1}{T_L} - \frac{1}{T_T} \right] \quad [2]$$

where, a_{T_L} and a_{T_T} , are the activities at the liquidus and the transformation temperatures, respectively. ΔH_F is the heat of fusion of (β)- CuCl , and ΔH_T is the heat for the $\alpha \rightarrow \beta$ transformation.

All activity calculations are referred to pure super-cooled CuCl as the state of reference. Table II also includes the activities of CuCl in the binary systems CuCl-BaCl_2 , CuCl-KCl , and CuCl-NaCl , calculated from the cryoscopic results. It is readily seen that in these systems the deviations from ideality are slightly negative, while in the $\text{Cu}_2\text{S-CuCl}$ system the deviations are positive. The positive deviations from ideality in the $\text{CuCl-Cu}_2\text{S}$ system may be considered as evidence that Cu_2S is present in the liquid solutions as associated species.

Solute association may be evaluated quantitatively by applying the limiting law to the van't Hoff relationship. For the very dilute solutions, Eq. [1] may be written as

$$\Delta T = -n \frac{RT_F^2}{\Delta H_F} \cdot \frac{M_{\text{CuCl}}}{1000} \cdot m \quad [3]$$

where, ΔT , is the measured freezing point depression, m is the molality of Cu_2S , and n has the significance of the number of foreign particles produced from one molecule of solute.

Using Eq. [3], n has been calculated from the experimental ΔT values, and the calculations are summarized in Table III.

For a molten salt system with a common ion, $n = 1$ if the solute salt is totally dissociated. Inspection of the data in Table III shows that n is essentially unity for the systems NaCl-CuCl , KCl-CuCl , and CuCl-BaCl_2 . For the system $\text{CuCl-Cu}_2\text{S}$, n is about 0.6, indicating that Cu_2S exists as an associated species.

If it is assumed that Cu_2S in solution is present as

Table III. Cryoscopic calculations of the number of foreign particles in CuCl solutions

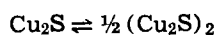
Solute	m^* solute, molality	n
Cu ₂ S	0.04964	0.6850
	0.12569	0.5851
	0.22564	0.5274
	0.26857	0.5838
	0.36853	0.5484
KCl	0.44405	0.5700
	0.51487	0.5650
	0.08444	1.0742
	0.12455	1.0616
	0.22395	1.0712
NaCl	0.08156	0.9265
	0.17625	0.9003
	0.26527	0.8972
BaCl ₂	0.10326	1.0975
	0.13906	1.1003
	0.19569	1.1004
	0.25092	1.1292

* For dilute solutions

$$X_{\text{solute}} = \frac{M_{\text{CuCl}}}{1000} \cdot m$$

where, M_{CuCl} is the molecular weight and X is the mole fraction.

the dimer $(\text{Cu}_2\text{S})_2$, the following association reaction should be expected to have occurred



The equilibrium constant for this reaction may be written as

$$K = \frac{\frac{\alpha}{2} X}{(1-n)X} \quad [4]$$

where, α represents the fraction of Cu_2S which forms the associated species and X is the solute mole fraction.

From a mass balance calculation it is readily shown that

$$n = 1 - \frac{\alpha}{2} \quad [5]$$

From Eq. [4] and [5]

$$K = \frac{(1-n)X}{(2n-1)} \quad [6]$$

Using the n values determined by cryoscopy for the dilute solutions containing up to 5 m/o Cu_2S , K is found to be practically constant for all compositions and to have the average value of $K = 1.3$.

From the α values obtained from Eq. [5] it is seen that about 80% of Cu_2S is present in the dilute solutions in the form of $(\text{Cu}_2\text{S})_2$ dimers.

The behavior of Cu_2S in the Cu_2S - CuCl system bears close resemblance with that of PbS in the PbS - PbCl_2 system previously investigated (3), which also showed positive deviations from ideality. However, in the Ag_2S - AgCl (1) system the dilute solutions of Ag_2S were shown to obey Temkin's rule, thus indicating that Ag_2S could be present either as a dissociated compound or as a monomer (Ag_2S).

Similar calculations have not been performed on the FeS - FeCl_2 system owing to the limited solubilities observed and also because of the lack of reliable data for the heat of fusion. It is evident, however, from the low solubilities that this system should also be characterized by large positive deviations from ideality.

Density measurements.—Densities were measured as functions of composition from pure CuCl to solutions containing 69.4 m/o Cu_2S . Because of the volatilization of CuCl at high temperatures, most of the measurements with melts rich in CuCl were conducted at temperatures below 750°C.

Similar measurements for the FeS - FeCl_2 system could only be obtained over the narrow composition range permitted by the phase diagram. Reproducibility for all these measurements was better than $\pm 0.3\%$. The density data for each composition were fitted by

Table IV. Density measurements ($d = a + bt$) (°C) $\text{g} \cdot \text{cm}^{-3}$

X_{CuCl}	a	$b \times 10^4$	Stand. dev.	Temp range (°C)
System Cu_2S - CuCl				
1.000	4.0829	-7.9298	0.007	465-838
0.964	4.2173	-8.4622	0.005	411-662
0.952	4.2535	-8.6774	0.003	492-639
0.943	4.2478	-8.3090	0.002	452-749
0.934	4.2888	-8.2019	0.002	464-794
0.903	4.3635	-8.4947	0.003	426-697
0.864	4.4708	-7.3269	0.005	539-699
0.825	4.4236	-8.1457	0.004	509-787
0.790	4.6189	-8.2951	0.003	613-795
0.746	4.5462	-6.0143	0.003	672-899
0.668	4.5840	-4.7936	0.003	842-1018
0.633	4.7182	-5.5801	0.001	902-1000
0.551	4.7514	-5.0319	0.002	902-1054
0.450	4.7159	-3.4010	0.002	908-1074
0.306	4.9236	-3.5308	0.001	1043-1150
System FeS - FeCl_2				
1.000	2.7237	-5.5488	0.003	685-884
0.946	2.7378	-5.5913	0.002	727-884
0.916	2.7430	-5.5758	0.001	830-851

the least squares method to linear equations of the type

$$d = a + bt$$

where a and b are constants, and t is the temperature in °C. The equations for the two systems, Cu_2S - CuCl and FeS - FeCl_2 are given in Table IV, together with the corresponding standard deviations.

Densities for pure CuCl have also been measured by Klemm (19) and are in agreement with the present results to within $\pm 0.5\%$.

From the results shown in Table IV molar volume isotherms for the Cu_2S - CuCl system were calculated at the selected temperatures of 500°, 750°, and 1000°C, and are shown in Fig. 3.

The dominant feature of the molar volume isotherms is a pronounced minimum occurring at about 30 m/o Cu_2S at 1000°C. The minimum is shifted to lower Cu_2S contents as the temperature is decreased.

The isotherm at 1000°C indicates negative deviations from apparent additivity. The approximate partial molar volumes that may be obtained from the isotherm at 1000°C by the method of tangents indicate two distinct trends. Below about 30 m/o sulfide, CuCl in solution should have about the same packing as in pure CuCl . Molten CuCl in this sense appears to be an associated liquid and to have a loosely packed structure. Cu_2S enters these solutions at a substantially decreased partial molar volume of about 25.9 cm^3/mole . For compositions containing more than 30 m/o Cu_2S the trend is reversed and CuCl appears to enter an essentially unaltered Cu_2S structure at the smaller

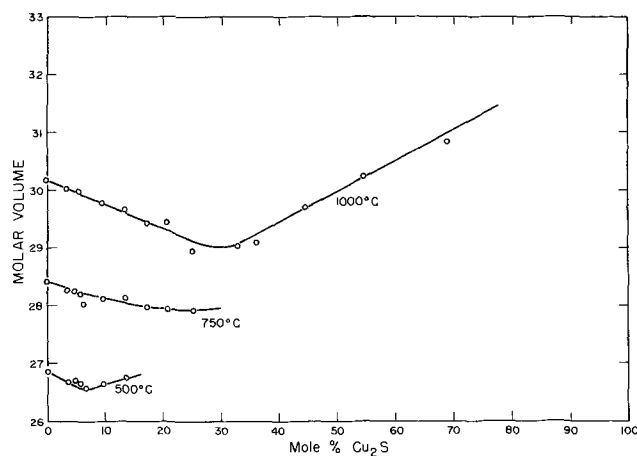


Fig. 3. Molar volume isotherms in the Cu_2S - CuCl system

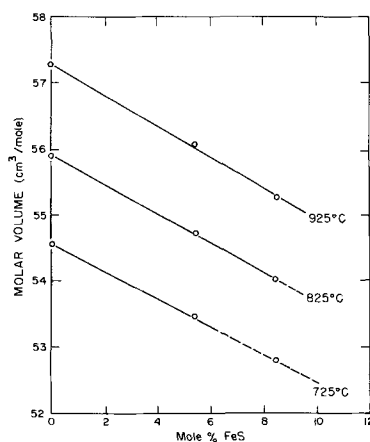


Fig. 4. Molar volume isotherms in the FeS-FeCl₂ system

partial molar volume of about 27.2 cm³/mole. The partial molar volume of Cu₂S in this range appears to be approximately the same as for pure Cu₂S.

These effects may be understood if it is considered that in concentrated solutions Cu₂S exists as a heavily associated structure of rather poor packing where CuCl can be easily accommodated. The decrease of the partial molar volume of Cu₂S for compositions below 30 m/o Cu₂S is indicative of the more efficient accommodation of the sulfide within the open CuCl structure because of dissociation of the polymeric Cu₂S to simpler species. This interpretation is in agreement with the cryoscopic calculations which indicated the presence of Cu₂S dimers in dilute solutions.

The shift with decreasing temperature of the minimum in the volume isotherms toward lower sulfide concentrations indicates the possible increase in the covalency of the melts at the lower temperatures.

The transition toward increased association at about 30 m/o Cu₂S at 1000°C roughly corresponds to the composition at which, as it will be shown shortly, significant electronic conduction appears to be setting in.

For the few compositions studied, molar volume isotherms have been calculated for the FeS-FeCl₂ system and are given in Fig. 4. It is seen that the molar volume decreases linearly with increasing FeS content. The initial decrease of the molar volume on addi-

Table V. Specific conductivity in the Cu₂S-CuCl system

Composition X _{Cu₂S}	Specific conductivity (mhos/cm)					
	500°C	600°C	700°C	800°C	900°C	1000°C
CuCl	3.55	3.78	3.89	3.96	3.99	3.96
0.035	3.39	3.59	3.73	3.81	3.80	—
0.077	3.00	3.50	3.67	(3.82)	—	—
0.093	3.30	3.45	3.48	—	—	—
0.125	3.28	3.46	3.65	—	—	—
0.162	3.25	3.45	3.67	3.87	—	—
0.192	—	3.43	3.72	4.00	4.18	—
0.260	—	—	3.75	4.04	4.33	4.46
0.267	—	—	—	4.04	4.41	4.52
0.304	—	—	—	4.15	4.40	4.72
0.360	—	—	—	4.21	4.88	5.48
0.506	—	—	—	—	5.17	6.06
0.652	—	—	—	—	(7.47)	10.45
0.752	—	—	—	—	—	12.20
0.853	—	—	—	—	—	(12.9)

Parentheses indicate extrapolated values.

tion of FeS appears to follow the same trend as with the copper system.

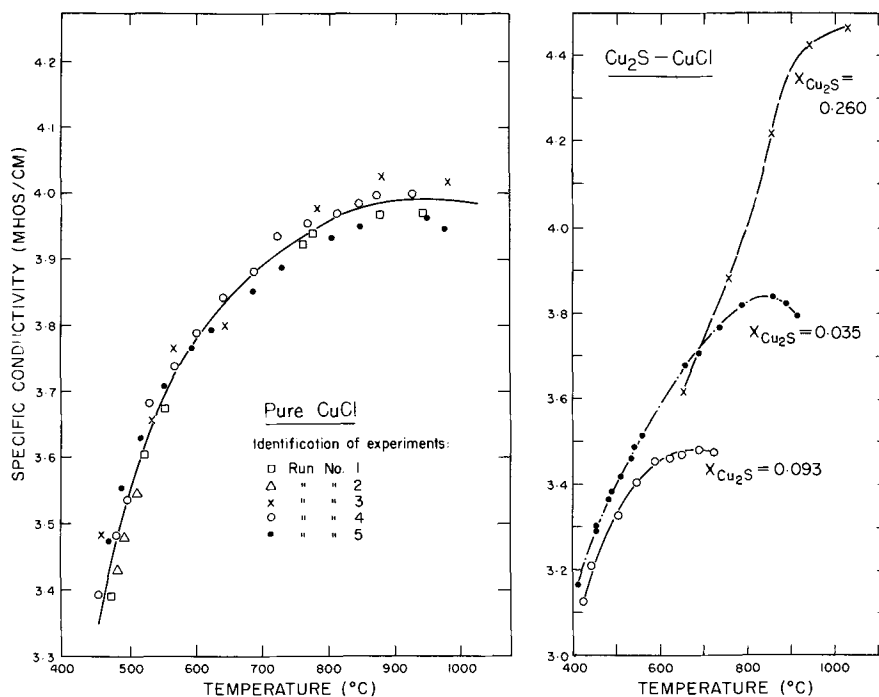
Electrical conductivity measurements.—Cu₂S-CuCl system.—Specific conductivities for pure molten CuCl were determined at temperatures between 450° and 970°C, and are given in Fig. 5 and in Table V.

The system has also been investigated by Grantham and Yosim (20) in the temperature range 475°-1157°C, and by Sakai (21) in temperature of 475°C to about 600°C. The present results are in excellent agreement with the former. It is of interest to note the nonlinear increase of the electrical conductivity of CuCl with temperature. At about 900°C the conductivity curve reaches a maximum and then the conductivity acquires a negative temperature coefficient. This abnormal behavior has also been detected by Grantham and Yosim (20) and has been explained as indicating increased covalency in CuCl at the high temperatures. Nevertheless, the magnitude of the conductance is typical of that encountered with ionic melts. Additional evidence for the ionic behavior of molten CuCl is provided from electrolysis experiments which have been reported to proceed with 100% current efficiency (8).

The specific conductivity of pure molten Cu₂S has also been measured in the temperature range 1130°-1195°C and is represented by the equation

$$K \text{ mho} \cdot \text{cm}^{-1} = 19.5010 + 0.1235 (t - 1000^\circ) \text{ in } ^\circ\text{C} \quad [7]$$

Fig. 5. Specific conductivities of pure molten CuCl and Cu₂S-CuCl melts containing 3.5, 9.3, and 26.0 m/o Cu₂S, respectively.



The standard deviation is 0.365 mho/cm. Molten Cu_2S may be described as a liquid semiconductor having conductivities which increase from 35 mho/cm at 1130°C to 44 mho/cm at 1195°C. At temperatures higher than 1200°C significant desulfurization of the molten sulfide was evident and measurements were not taken.

The specific conductivities of nonstoichiometric molten Cu_2S containing excess copper were also measured at 1150°C and the results are given in Fig. 6. For these measurements the nonstoichiometric Cu_2S was prepared by melting together in the conductivity cell known amounts of copper metal powder with stoichiometric sulfide. Clearly, the presence of excess copper causes a significant increase in the conductivity of molten Cu_2S .

The present results on "stoichiometric" Cu_2S are about 35% lower and less temperature dependent than the values reported by Yang, Pound, and Derge (8), although the Cu_2S used by the latter contained between 0.44 and 1.64% excess copper and should be expected to yield higher conductivities. Knacke and Strese (22) have also reported values for the conductivities of Cu_2S which change from 25 mho/cm at 1130°C to 97 mho/cm at 1480°C and are much lower than the present results.

The specific conductivities of the Cu_2S - CuCl solutions were also measured as functions of melt composition and temperature and the results are summarized in Table V. The specific conductance curves for melts containing 3.5, 9.3, and 26 m/o Cu_2S are also given in Fig. 5.

The conductivities for the latter were not linear functions of temperature and could not be represented by linear equations. The transition from a positive to a negative temperature coefficient which was observed with pure CuCl also characterized the Cu_2S - CuCl melts containing up to about 27 m/o Cu_2S .

The specific conductivity isotherms in the low-temperature range up to 700°C for solutions containing up to 25 m/o Cu_2S are given in Fig. 7. It is evident that the specific conductivity of the solutions decreases initially on addition of sulfide. For the isotherm at 700°C, the conductivities reach a minimum at about 10 m/o Cu_2S and then increase up to the liquidus composition. These solutions should be considered as ionic as their conductivities are still lower than the conductivities of pure CuCl at the same temperatures.

The initial decrease of the conductivity on addition of sulfide should be attributed to the lower mobility of the divalent sulfide anion and to its anchoring effect on the surrounding cations. The thermodynamic cal-

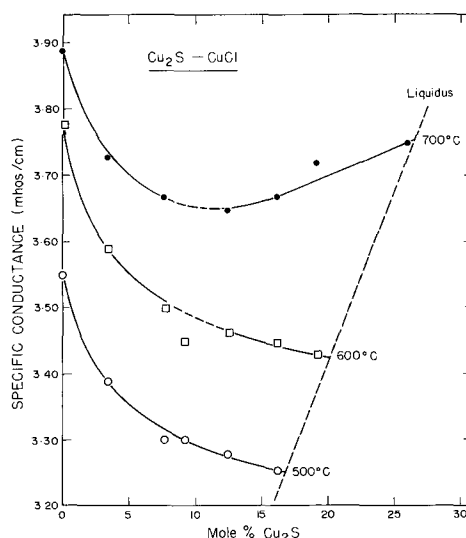


Fig. 7. Specific conductivity isotherms of dilute solutions of Cu_2S in CuCl .

culations have indicated the presence of associated $(\text{Cu}_2\text{S})_2$ dimers and such nonionic groups are not expected to contribute to the ionic conductivity. The conductance minima shift toward higher sulfide concentrations at lower temperatures.

The specific conductivity data at 1000°C given in Table V have been converted to molar conductivities and are presented in Fig. 8. A significant increase in the specific conductance is observed at higher temperatures when the sulfide content exceeds about 30 m/o. Thus, the molar conductivity of a solution containing 30 m/o Cu_2S is about 30% higher than that of pure CuCl . As the associated Cu_2S in solution is not expected to contribute to the conductance, as shown by the initial decrease in conductance on the addition of Cu_2S , it follows that the increase in conductance must be attributed to electronic contributions.

When the present results are compared with the measurements by Yang, Pound, and Derge (8), there is disagreement with regard to the sulfide content at which electronic conductivity sets in. At 1200°C

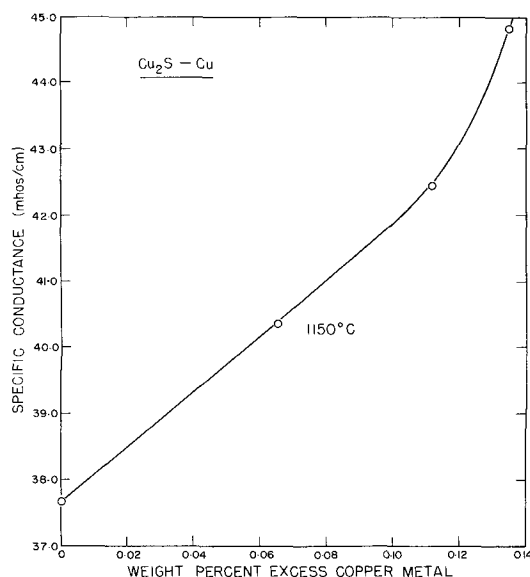


Fig. 6. Conductivities of nonstoichiometric Cu-rich cuprous sulfide at 1150°C.

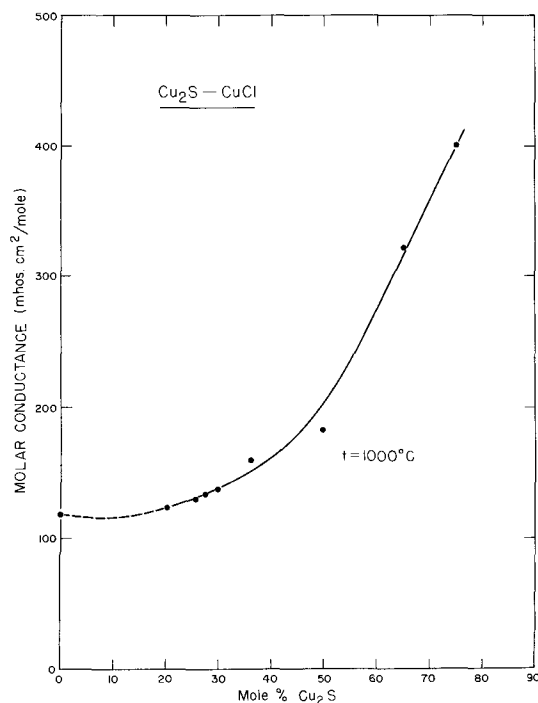


Fig. 8. Molar conductivity isotherm at 1000°C of the Cu_2S - CuCl system.

the specific conductivities measured by these authors remained almost constant at 5 mho/cm, from pure CuCl to about 50 m/o Cu₂S, and then increased to about 77 mho/cm for "pure" molten Cu₂S. Hence, melts containing up to 50 m/o Cu₂S were considered to be ionic conductors. In the present study even at 1000°C electronic conductivity sets in at about 30 m/o Cu₂S, and at 1200°C it should be expected that the onset of electronic conduction would occur at even lower Cu₂S contents.

Considering the effect of dissolved copper on the specific conductivities of the Cu₂S-CuCl melts, measurements were also obtained with conductivity cells fitted with copper electrodes immersed in melts containing pure CuCl and a Cu₂S-CuCl solution (15 m/o Cu₂S), respectively, at a temperature of 700°C. Both these solutions had previously been equilibrated with Cu metal. The resistance of these cells was monitored as a function of time. After 72 hr of operation the resistance change was only 0.5%, indicating that for all practical purposes the presence of dissolved copper in these melts, if any, does not introduce electronic contributions.

FeS-FeCl₂ system.—The specific conductivity for pure FeCl₂ was also measured as a function of temperature and may be expressed by the equation

$$K_{\text{FeCl}_2} (\text{mho} \cdot \text{cm}^{-1}) = 0.00149 + 1.889 \times 10^{-3} t \quad (\text{in } ^\circ\text{C}) \quad [8]$$

with a standard deviation of 0.004. Other data for this system are not available in the literature.

As was the case with the density measurements with the FeS-FeCl₂ melts the specific conductivity measurements presented in Fig. 9 are restricted to a narrow range of compositions. The dotted lines represent extrapolated values obtained from measurements at higher temperature where the system is miscible. It is evident that in this system a conductivity minimum does not occur.

From the conductivity isotherm at 925°C it is seen that the FeS-FeCl₂ solutions probably remain essentially ionic up to a composition of 10 m/o FeS, and that the more rapid increase in conductance at higher concentrations could indicate possible electronic contributions.

Accuracy of results.—With regard to the accuracy and reproducibility of the results, the reproducibility of the specific conductivities for CuCl between runs was of the order of ± 0.03 mho/cm, or within $\pm 0.9\%$. For FeCl₂ the reproducibility was of the order of ± 0.01 mho/cm, or better than $\pm 0.8\%$. The electrical con-

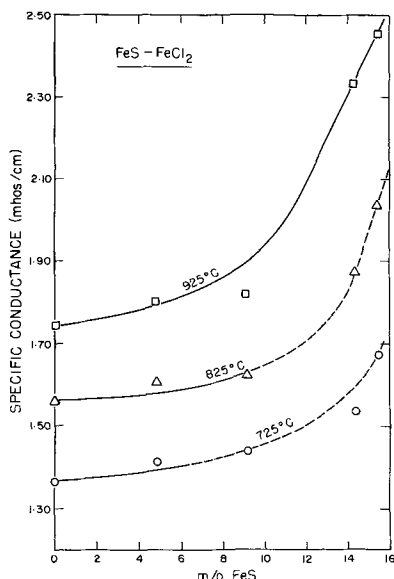


Fig. 9. Specific conductivity isotherms in the FeS-FeCl₂ system

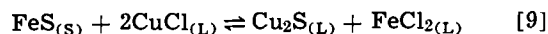
ductivity of cuprous sulfide could be reproduced within ± 0.15 mho/cm, or better than $\pm 0.4\%$. Reproducibilities of the conductivities of the solutions were of comparable magnitude. However, taking into account the additional factors of calibrating procedure and temperature uncertainty, the accuracy of the conductivity measurements reported herein is given with 1% confidence.

Electrolysis experiments.—For the binary mixtures Cu₂S-CuCl the electrolyte contained 10 to 20 m/o Cu₂S and the temperature was varied between 450° and 600°C. Electrolysis of Cu₂S dissolved in molten CuCl, and of a synthetic Cu₂S + FeS matte dissolved in molten CuCl, produced copper metal at the cathode and sulfur gas at the anode. The choice of electrolyte composition was made so as to obtain the highest sulfide content in the ionic composition range indicated by the conductivity results. Also, it was desirable that the solutions should remain liquid at low enough temperatures. The boiling point of sulfur (444.6°C) was used as the lower temperature limit for the experiments, and therefore, the anodic reaction product was always a vapor which could be swept out of the anode compartment by the argon carrier gas.

The current efficiencies were obtained by weighing the cathodic deposits and were found to vary. Low values for the current efficiencies for small amounts of deposits could be attributed to the fragile structure of the dendritic deposits and to the resulting breakage of the dendrites while the cathodes were being removed from the melts. Continuous electrolysis produced large well-shaped copper crystals. The structure of the deposits was not uniform throughout deposition. At the initial stage of electrolysis the deposits were generally coarse and multipyramidal but further deposition led to the formation of rather large dendritic crystals having fine needle-like projections. In all 25 electrodeposition runs the measured deposition potentials were of the order of 0.3-0.5V, which values are lower than 0.63V representing the theoretical (17) decomposition potential of Cu₂S in an ideal solution.

Current efficiencies of about 80% were obtained in the low-temperature range 450°-500°C with low apparent current densities up to 15 mA/cm², and with Cu₂S concentrations not exceeding 30 m/o. An electrolyte containing 6.6 m/o Cu₂S, at a cathodic current density of 0.3 mA/cm², yielded a current efficiency of 97.3%. Apparent current densities of the order 20-40 mA/cm² usually yielded poorly defined deposits and low current efficiencies of about 50%. At 650°C, a solution containing 46.4 m/o Cu₂S yielded a small amount of spongy deposit mixed with electrolyte with practically zero current efficiency, because of the electronic conductance at such high Cu₂S concentrations.

With the ternary solutions, FeS-Cu₂S-CuCl, which are the equivalent of dissolving the synthetic matte in a CuCl solvent, electrolysis produced copper metal at the cathode and chlorine-contaminated sulfur gas at the anode. Deposition of iron metal appeared to be totally absent. This behavior should be understood in terms of the exchange reaction



which is thermodynamically favored and has a standard free energy of -9800 kcal/mole at 1100°C. The implications are that in the molten salt mixture of the synthetic matte Cu₂S-FeS dissolved in excess CuCl, the stable components are FeCl₂ and Cu₂S. Considering 1 g-mole of solution having the initial composition: X₁ g-moles CuCl, X₂ g-moles Cu₂S, and X₃ g-moles FeS, where X₃ \leq X₁ and X₂, the final composition after the exchange reaction has taken place is readily calculated as

$$X_{\text{CuCl}} = \frac{2X_1 - X_3}{2X_1 + 2X_2 + 3X_3}, \quad X_{\text{Cu}_2\text{S}} = \frac{2X_2 + 2X_3}{2X_1 + 2X_2 + 3X_3}$$

$$X_{\text{FeCl}_2} = \frac{2X_3}{2X_1 + 2X_2}, \quad \text{and } X_{\text{FeS}} = 0 \quad [10]$$

Table VI. Effect of exchange reaction on composition: FeS-CuCl-Cu₂S solutions

Composition (mole fraction)								Calculated decomposition potentials (V)							
Initial mixture				Calculated after exchange reaction				500°C				1000°C			
CuCl	Cu ₂ S	FeS	FeCl ₂	CuCl	Cu ₂ S	FeS	FeCl ₂	CuCl	Cu ₂ S	FeCl ₂	FeS	CuCl	Cu ₂ S	FeCl ₂	FeS
0.500	0.375	0.125	—	0.375	0.500	—	0.125	1.004	0.583	1.349	—	0.831	0.518	1.178	—
0.750	0.125	0.125	—	0.625	0.250	—	0.125	0.969	0.606	1.349	—	0.774	0.556	1.178	—
0.500	0.250	0.250	—	0.250	0.500	—	0.250	1.030	0.583	1.326	—	0.875	0.518	1.140	—

These solutions must contain an excess of CuCl for the purpose of insuring complete solubility of the sulfides, and ionic type conductivities.

The approximate decomposition potentials may be calculated using Raoultian activities as

$$E_{\text{dec.}} = E^{\circ}_{\text{AX}} - \frac{RT}{ZF} \ln X_{\text{AX}} \quad [11]$$

where, E°_{AX} is the standard potential for pure liquid AX at a temperature T , and X_{AX} represents the final concentrations of a given species AX, which is calculated taking into account the exchange reaction. The standard potentials may be calculated from available free energy data for pure CuCl (23), Cu₂S (17), and FeCl₂ (17), respectively.

The effect of the exchange reaction on the decomposition potentials of the species in solution is demonstrated by the sample calculation in Table VI. It is evident from Table VI that the Cu-S pair has the lowest decomposition potential of about 0.5-0.6V, which is in agreement with the observed decomposition voltages in all experiments. The decomposition voltage of FeCl₂, which is formed as the result of the exchange reaction, is greater than 1.0V and hence it should not interfere with the deposition of copper. Thus, the selective separation of copper from iron by electrolysis of a Cu-Fe-S matte dissolved in a cuprous chloride solvent is feasible.

The above conclusion appears to be more valuable than the conclusion that copper metal can be electrodeposited from the solution of Cu₂S-CuCl. In traditional copper extraction from sulfide ores a substantially pure Cu₂S product is only obtained after treatment of the reverberatory matte. If the matte consists essentially of Cu₂S and FeS, direct recovery of copper by molten salt electrolysis might be suggested. However, the exchange reaction (9), while it does make possible the selective electrodeposition of copper, is also consuming copper-containing solvent (CuCl).

Molten salt solvent extraction.—From previous work in this laboratory (10) on alkali halide-metal sulfide systems and from the present results it has been established that limited solubility is common in reciprocal chloride-sulfide mixtures. However, utilizing the exchange reaction [9], FeS may be separated from the Cu₂S present in a synthetic FeS-Cu₂S matte by a solvent extraction process involving the use of molten CuCl.

Exchange reaction [9] predicts that the nominal ternary system Cu₂S-FeS-CuCl in the presence of excess CuCl, is best represented by the system Cu₂S-CuCl-FeCl₂. In the latter the solubility of iron which is now present as the ionic component FeCl₂ is expected to be quite high even at relatively low temperatures.

To substantiate the above possibility, quartz cells of the same type as the FeS-FeCl₂ decantation studies were used to sample the liquid phase representing the saturated solutions of Cu₂S and FeS in molten CuCl. Chemical analysis for iron and copper of the samples obtained by decantation at various temperatures indicated that the ratio of iron to copper in the molten CuCl phase was greater than in the remaining solid mixture, except at the highest temperatures studied. The iron to copper ratios are summarized in Table VII. The decreasing ratio with increasing temperature is likely due to increased solubility of Cu₂S at

the higher temperatures. Therefore, it is concluded that molten salt solvent extraction can separate iron from copper at appropriate temperatures. As shown, the iron-rich melt thus produced may be electrolyzed directly to yield electrolytic copper. Also, if desired, FeCl₂ may be separated from the sparingly soluble Cu₂S by aqueous leaching, as indicated in the experimental section.

It may be concluded that the combination of molten salt solvent extraction with electrolysis could provide the basis for a new process leading to the recovery of copper and possibly of iron from copper-iron mattes.

Discussion

When the electrical properties of the Cu₂S-CuCl and the FeS-FeCl₂ melts are compared with the previously investigated systems Ag₂S-AgCl (1, 2) and PbS-PbCl₂ (3, 4), there are several common characteristics which become evident. In dilute solutions of sulfide and at low temperatures the electrical conductivities in these four systems appear to be ionic. As the sulfide content and the temperature are increased electronic conductivity sets in and the solutions behave like liquid semi-conductors.

In the Ag₂S-AgCl (2) system, 1% electronic conduction appears at about 15 m/o Ag₂S at 750°C, and at about 25 m/o Ag₂S at 530°C. In the PbS-PbCl₂ system (4) electronic conduction starts at about 35 m/o PbS. In this respect the Cu₂S-CuCl system behaves more like the lead than the silver systems. In addition, both pure molten PbS and pure molten Cu₂S exhibit positive temperature coefficients for conduction. The conductance of Ag₂S is relatively insensitive to temperature changes. Also, the specific conductance appears to increase for both PbS and Cu₂S on melting. There is a corresponding decrease for Ag₂S.

The more "ionic" character of the Cu₂S-CuCl solutions may be related to the weaker electronic character of the "pure" molten Cu₂S. A comparison of the specific conductivities of a number of "pure" metal sulfide is given in Table VIII. It is readily seen that on the basis of the electronic conductivities, Cu₂S is a more "ionic" sulfide than either PbS, Ag₂S, or FeS.

The electrical properties of the metal sulfide-metal chloride solutions, namely, the magnitude of electronic conductivity at some common concentration of sulfide, and the sulfide composition at which electronic contributions set in, indicate similar trends. Thus, the order of increasing electronic conductance in the sulfide-chloride melts follows the sequence Cu₂S, PbS, Ag₂S, and FeS, and the order of sulfide content in the MS-MCl binary systems at which electronic conductivity sets in appears to increase in the opposite direction.

Table VII. Solvent extraction of iron by molten CuCl from a synthetic FeS-Cu₂S matte

Temperature of decantation (°C)	Original solid mixture			Decanted liquid		
	% Fe	% Cu	% Fe	% Fe	% Cu	% Fe
			% Cu			% Cu
660	8.83	56.95	0.155	10.2	43.2	0.236
765	7.99	58.06	0.138	8.82	48.9	0.180
870	3.79	61.55	0.0616	2.72	59.4	0.046
929	5.78	59.87	0.0965	4.15	56.4	0.074

Table VIII. Electrical conductance of molten sulfides near their melting points

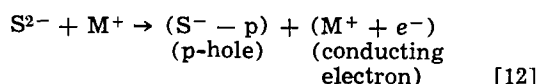
Compound	Temperature (°C)	Specific conductance (mho/cm)	Temperature coefficient of conductance (mho/cm · °C)	Reference
Cu ₂ S	1130	36	+ 0.12	Present study
PbS	1120	116	+ 0.30	Bell and Flengas (4)
Ag ₂ S	840	202.5	Nil	Bell and Flengas (2)
FeS	1200	400	- 0.5	Argyriades et al. (24)
CoS	1182	1410	- 10.0	Velikanov (25)
NiS	797	4055	- 11.0	Velikanov (25)
Sb ₂ S ₃	550	0.17	+ 0.00275	Velikanov (25)
TlS	375	0.10	+ 0.0133	Stoneburner (26)
Tl ₂ S ₃	216	0.017	+ 0.0026	Stoneburner (26)
GeS	664	1.33	+ 0.0209	Handfield et al. (27)
SnS	895	24	+ 0.0065	Boutin and Bourgon (28)

For the dilute solutions of the metal sulfides in their chlorides the thermodynamic calculations and the interpretation of the molar volumes for these systems are in substantial agreement in indicating the dissociation of the sulfides into monomeric- or dimeric-type species. These solutions appear to be ionic conductors.

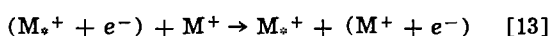
The electronic conductivity in the sulfide-rich melts appears to be related to the association of the sulfide species and to the creation of a continuous sulfide network acting as a suitable path for electron transfer. This was particularly evident in the Ag₂S-AgCl and Cu₂S-CuCl melts where the abnormally high partial molar volumes of the metal sulfides for the sulfide-rich compositions indicated the presence of the associated sulfide network of rather poor packing capacity. The breakdown of the electronic conductivity on the addition of the metal chloride is at least partially due to the dissociation of the structure into monomeric or dimeric species and to their subsequent isolation by the chloride solvent. The electronic conductivity in molten metal sulfides may be understood in terms of a modified "band model."

In a perfect covalently bonded material the electrons are generally restricted in their directional bonds and cannot contribute to the conductance. The appearance of electronic conductivity requires the promotion of electrons from their valence band to a conducting energy level. At high temperatures such transitions are probable and in addition impurity-type mechanisms may arise as the result of the thermal decomposition of the sulfides which is expected to create some nonstoichiometry. Also, in polar crystals the electrons of the negative ions may be excited to a conduction band of positive ions creating positive holes which offer a convenient path for p-type semiconductivity. Electrons excited to a conduction band may contribute to the electronic conductivity by moving from one positive ion to the next.

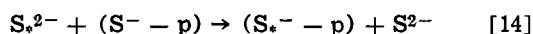
Thus, the conductivity mechanism for monovalent molten sulfides may be described by exchange reactions of the type



followed by



for n-type conductivity and by



for p-type conductivity. In addition, electron trapping should not be excluded and the melts could become predominantly p- or n-type semiconductors.

The excitation of electrons from the valence band of S²⁻ species to the conductance band of the M⁺ species requires a certain energy E_g , and in an electronically conducting liquid the concept of the band model must be modified to account for the lack of long-range order. However, the degree of directional long-range order which appears to exist in these polymeric sulfides should be helpful for the purpose of understand-

ing the conductivity path for electron transfer. In addition, collisions between polymeric chains and chain rearrangements should present instantaneous energetically favorable conditions for electron transfer from chain to chain. Apparently, the presence of the ionic component MCl in a binary system MCl-MS has the effect of decreasing the size of the polymeric M-S chains through the normal route of dissociation and the over-all energy gap for the transfer process increases with increasing MCl content until the solutions become ionic.

The measured activation energies (4) in the PbS-PbCl₂ system support this interpretation. The activation energy for electronic conduction which is about 8 kcal in "pure" molten PbS increases to 18, 22, 25, and 38 kcal/mole as the concentration of PbS in the binary PbS-PbCl₂ systems decreases to 80, -6, 45, and 40 m/o, respectively. The number of thermally activated carriers for electronic conductivity, if nonstoichiometry effects are ignored, should also be a function of temperature and increase as the temperature increases.

The addition of excess dissolved metal increases the total electronic conductivity because the added M atoms act as electron donors according to reaction [4]



However, it should also be expected that such electrons are donated at a conduction band level and accordingly the activation energy for conduction should not be affected to any large extent. The behavior of the previously investigated Pb-PbS-PbCl₂ (4) ternary system supports this interpretation. For solubilities of Pb in PbS ($X = 0.45$) - PbCl₂ melts varying between 0.01 and 1.13 m/o Pb the activation energy for conduction remains constant at about 25 kcal/mole. This activation energy is about the same for the binary PbS-PbCl₂ melt containing 45 m/o PbS which do not contain any dissolved "excess" lead.

It appears, however, that the ionization reaction [16] does not proceed to completion and that only a fraction of the "excess" metal atoms present are capable of providing conducting electrons. For example, a Cu₂S-Cu melt containing 0.012 w/o (weight per cent) dissolved copper has a conductivity which is only 4 mhos/cm higher than that of pure molten Cu₂S. Similarly, in the case of the PbS-PbCl₂-Pb system (4) it has been calculated that if all the added metal atoms were ionized giving free electrons in the conduction band, then a concentration of 0.014 m/o excess Pb should have increased the melt conductivity by about 1000 times.

Thus, it is evident that excess metal solubility should be accounted for by both "ionized" and "nonionized" species, the latter being the most numerous. The excess metal solubility in the corresponding pure metal sulfides at comparable temperatures appears to decrease in the order Cu₂S-PbS-Ag₂S. However, the magnitude of the electronic conductivity in these liquids does not appear to be directly related to the metal solubility.

Acknowledgments

The financial support of the National Research Council of Canada is gratefully acknowledged. The authors wish to thank Dr. W. T. Thompson for helpful discussions.

Manuscript submitted April 30, 1971; revised manuscript received Dec. 1, 1971.

Any discussion of this paper will appear in a Discussion Section to be published in the December 1972 JOURNAL.

REFERENCES

1. M. C. Bell and S. N. Flengas, *This Journal*, **111**, 569 (1964).
2. M. C. Bell and S. N. Flengas, *ibid.*, **111**, 575 (1964).
3. M. C. Bell and S. N. Flengas, *ibid.*, **113**, 27 (1966).
4. M. C. Bell and S. N. Flengas, *ibid.*, **113**, 31 (1966).

5. I. Gul'din, A. Buzhinskaya, V. Borseg'yan, and V. Ruppul, *Zh. Prikl. Khim.*, **33**, 378 (1960), *English translation, Soviet Electrochemistry*, **3**, 100 (1961), Consultants Bureau, New York.
6. H. Sawamoto and T. Saito, *Nippon Kogyo Kaishi*, **68**, 555 (1952).
7. V. Winterhager and R. Kammel, *Z. Erzbergbau Metallhuttew.*, **9**, (3), 97 (1956).
8. L. Yang, G. Pound, and G. Derge, *Trans. AIME*, **206**, 783 (1956).
9. T. Hoar and R. Ward, *Trans. Inst. Min. & Met.*, **67**, 393 (1958).
10. A. D. Pelton and S. N. Flengas, *Can. J. Chem.*, **48**, 2016 (1970).
11. M. C. Bell, Ph.D. Thesis, p. 37, 1964. Dept. Metallurgy and Materials Science, University of Toronto, Toronto, Ontario, Canada.
12. G. Urazov and L. Tschleide, *Akad. Nauk SSSR Izvestia*, Phys. Chem. Section, Analysis, **13**, 263 (1941).
13. W. Truthe, *Z. Anorg. Chem.*, **76**, 161 (1912).
14. M. Lorenz and J. Prener, *Acta. Cryst.*, **9**, 538 (1956).
15. G. Gashurov and A. Levine, *J. Chem. Eng. Data*, **5**, 517 (1960).
16. W. T. Thompson and S. N. Flengas, *Can. J. Chem.*, **49**, 1550 (1971).
17. O. Kubaschewski, L. E. Evans, and C. B. Alcock, "Metallurgical Thermochemistry," pp. 366-389, Pergamon Press, Toronto (1967).
18. J. Lumsden, "Thermodynamics of Molten Salt Mixtures," p. 313, Academic Press, New York (1966).
19. W. Klemm, *Zh. Anorg. Chem.*, **152**, 235 (1926).
20. L. Grantham and S. Yosim, *J. Chem. Phys.*, **45**, 1192 (1966).
21. K. Sakai, *J. Chem. Soc. Japan*, **75**, 182 (1954).
22. O. Knacke and G. Strese, *Z. Erzbergbau Metallhuttew.*, **10**, 207 (1957).
23. H. Kellogg, *Trans. AIME*, **188**, 862 (1950).
24. D. Argvriades, G. Derge, and G. Pound, *Trans. AIME*, **215**, 909 (1959).
25. A. A. Velikanov, Proc. of the All-Union Conf. on Phys. Chem. of Molten Salts and Slags, 1960. U.S. AEC Translation No. 5948, 1963.
26. D. Stoneburner, *Trans. AIME*, **233**, 153 (1965).
27. G. Hanfield, M. D'Amboise, and M. Bourgon, *Can. J. Chem.*, **44**, 853 (1966).
28. D. Boutin and M. Bourgon, *Can. J. Chem.*, **39**, 915 (1961).

On the Transition from Internal to External Oxidation in Ternary Alloys

Howard W. Pickering*

Edgar C. Bain Laboratory, United States Steel Corporation, Research Center, Monroeville, Pennsylvania 15146

ABSTRACT

Addition of certain metals to binary A-B alloys can markedly improve oxidation resistance through formation of a dense layer of BO_x on the surface, e.g., the addition of Cr to Fe-Al alloys with the formation of a dense layer of Al_2O_3 . The reason for the improved oxidation resistance is the subject of this paper. Experiments are described for the model alloy system, Ag-Zn-Al. A Ag-3 atomic per cent (a/o) Al alloy exhibits internal oxidation without formation of an Al_2O_3 layer on the surface. Upon addition of 21 or 25 a/o Zn, internal oxidation is completely suppressed and a dense, highly protective Al_2O_3 layer is formed. These data support the mechanism originally advanced by Wagner whereby Zn functions as a secondary getter for oxygen atoms. Other aspects of the results pertaining to the occurrence of exclusive internal oxidation in the alloys of low solute content and to the complex transient behavior exhibited by alloys of intermediate solute content are also discussed.

Oxidation resistant alloys for industrial use at elevated temperatures are usually ternary or multicomponent alloys rather than binary alloys. The low oxidation rate of Fe-Cr-Al alloys, for example, is well known (1-6). The good performance of these alloys results from the formation of a dense Al_2O_3 layer over the surface. The presence of Cr in the alloy in relatively large amounts is essential for the formation of this layer at feasible Al contents. Yet, Cr does not appear to enter the Al_2O_3 layer to an appreciable extent. Addition of other elements to Fe-Al alloys (in place of Cr) are in certain instances even more beneficial for the formation of an Al_2O_3 layer (7).

Wagner (8) has tentatively outlined the basic principles underlying the oxidation resistance of such alloys. In essence he suggested that one or more of the components functions as a getter for oxygen along with the component of highest affinity for oxygen. The action of the secondary getters supposedly decreases the diffusion of oxygen inward when the dissolved primary getter is depleted in the surface layers. In discussing the Cu-Zn-Al system Wagner points out that the oxygen concentration in the alloy next to the ZnO layer, determined by equilibrium between ZnO

and Zn in the alloy, may be as small as 10^{-6} of that determined by the coexistence of Cu and Cu_2O , as in the case of a copper alloy containing 1 or 2 a/o Al but no Zn. Hence virtually no oxygen diffusion into the alloy is to be expected when Zn is present in rather large amounts. As a result Al atoms may diffuse to the depleted surface region without being intercepted by oxygen atoms. They may then react with oxygen and also with the Cu_2O and ZnO which are formed at the beginning of oxidation (along with nuclei of Al_2O_3) to form more Al_2O_3 by a displacement reaction.

Wagner (8) specifically explained in this manner the excellent oxidation resistance of the Fe-Cr-Al alloys as well as that of the Cu-Zn-Al alloys as reported by Dunn (9) already four decades ago. The possibility of forming a dense Al_2O_3 layer by addition to the alloy of other metals has considerable technological importance since the ternary alloys with low Al content not only give excellent oxidation resistance but at the same time exhibit good mechanical behavior—quite the contrary of their counterpart binary alloys which have poor mechanical properties as a result of the high Al contents required for the formation of a protective Al_2O_3 layer.

Pfeiffer's (5) x-ray and electron diffraction data of the oxide scales which form on Fe-20% Cr-5% Al at 1073°-1473°K in air may be an indication that the

* Electrochemical Society Active Member.

Key words: alloys, elevated temperature properties, mechanism, oxidation, silver.

Table I. Composition of alloys—mean and standard deviation
Number of samples analyzed for each determination are given in parenthesis

Alloy	a/o Zn	a/o Al	Alloy	a/o Zn	a/o Al
Ag3Al	0	3.0 ± 0.1 (7)	Ag5Zn3Al	5.2 ± 0.4 (2)	3.1 ± 0.1 (4)
Ag6Al	0	6.1 ± 0.2 (9)	Ag10Zn3Al	10.0 ± 0.1 (4)	3.2 ± 0.2 (4)
Ag10Al	0	9.5 ± 0.4 (3)	Ag12Zn3Al	12.2 ± 0.8 (7)	3.1 ± 0.1 (3)
Ag14Al	0	14.0 ± 0.3 (3)	Ag21Zn3Al	20.6 ± 0.5 (2)	3.0 ± 0.1 (3)
Ag5Zn	4.7 ± 0.2 (2)	0	Ag24Zn3Al	24.1 ± 0.2 (3)	2.6 ± 0.3 (3)
Ag9Zn	9.3 ± 0.1 (3)	0	Ag5Zn6Al	5.1 ± 0.2 (3)	5.9 ± 0.2 (2)
Ag15Zn	14.8 ± 0.1 (2)	0	Ag10Zn6Al	9.5 ± 0.4 (4)	6.0
Ag21Zn	20.9 ± 0.8 (5)	0	Ag15Zn6Al	14.8 ± 1.1 (4)	6.0 ± 0.2 (2)
			Ag20Zn6Al	20.2 ± 0.6 (4)	6.1 ± 0.3 (2)

Wagner mechanism operates in this system. At early stages of oxidation, corresponding to the formation of $\sim 3 \times 10^{-6}$ cm-thick scales, Al_2O_3 , FeAl_2O_4 , and Cr_2O_3 were identified, whereas at longer times ($\sim \mu\text{m}$ -thick scales) only Al_2O_3 could be found.

It is the purpose of the present work to obtain a more definite validation of Wagner's tentative proposal by systematically investigating the oxidation behavior of a series of binary and ternary alloys. For ease of interpretation and experimentation Ag was chosen as the principal component since it does not form a stable oxide above 460°K at one atmosphere of oxygen, and Zn and Al were chosen as the secondary getter and the protective scale former, respectively, in accord with their relative tendencies to form stable oxides. The system Ag-Zn-Al is thus a model system in which the complexities of multiphase and multilayer surface oxides are not encountered.

As a result of prior investigations on Ag-In (10,11) and other alloys (12-17), in the present study one may expect that Ag-Al and Ag-Zn alloys with low Al and Zn contents would show internal oxidation, whereas

those of higher (> 15 a/o) Al and Zn contents would show external oxidation. The ternary Ag alloys of low Al and Zn contents also may show internal oxidation whereas if the Wagner hypothesis holds, ternary alloys of low Al but high Zn content should exhibit external oxidation and a low rate of oxidation through formation of an Al_2O_3 surface layer.

Experimental Procedure

Alloy samples were exposed to 1 atm of oxygen at 823°K (550°C) and in a few cases at 923°K (650°C). Except where specifically stated, data are for 823°K. The alloys, Table I, were prepared from 99.9999% Ag, 99.9999% Al, and 99.999% Zn by zone leveling in a high-purity graphite boat under an atmosphere of Pd-purified hydrogen; the Ag and Zn metals were deoxidized prior to alloying by melting under the same atmosphere. This melting procedure was found to be the best of several tried; appreciable Zn loss was encountered in the melting of the high Zn alloys but since the loss per zone leveling pass was fairly reproducible, sufficiently close estimates of the required Zn content in the initial charge could be made. The zone-leveling homogenization was determined to be satisfactory by chemical analysis. Subsequent electron microprobe examination of the specimens detected no microsegregation in the alloys. The alloys are all well within the composition range of the terminal fcc phase of the binary Ag alloys so that metallic-metallic phase transformations are not likely during oxidation. A section of each ingot was cleaned of oxide by grinding and was cold-rolled to 0.05 cm. Specimens 1.3 cm on edge were cut from the strip and a small hole drilled at one corner for suspension. The specimens were then cleaned in chloroform, rinsed in alcohol, and dried prior to a recrystallization anneal at 873°K in an evacuated silica capsule for 7.2 ksec (20 hr). Grain size of several of the alloys was measured and found to be in the range of 0.05 to 0.2 mm. Immediately prior to a run the specimen was electrolytically etched in 1N HNO_3 at 0.06 A cm^{-2} for 30 sec, as suggested by Rapp (11). This procedure gave sufficiently reproduc-

ible results in the oxidation runs. A 3-winding, vertical-(silica) tube furnace (18, 19) with a 4-cm uniform-temperature zone of $\pm 0.2^\circ\text{K}$ was used for the oxidation experiments.

Before a run a specimen was weighed by a balance precise to 0.05 mg and then suspended in the cold zone above the furnace by a silica hook and stainless steel chain. With the reaction zone at 823°K (or 923°K) and a steady upward oxygen flow of approximately 2 $\text{cm}^3 \text{sec}^{-1}$ the specimen was lowered into the reaction zone, held there for a prescribed time, and then raised to the cold zone. After cooling the specimen was removed and weighed. Weight gain data as a function of oxidation time were obtained by oxidizing several specimens of a given alloy for different times in this manner. Each specimen was then examined by cross-section metallography and other methods. In a few experiments continuous weighings were made using another furnace of similar design and a thermobalance; this produced complete weight gain-time data with one specimen. Results were essentially the same with both weighing methods; unless otherwise stated, data in this paper were obtained by the discontinuous weighing method. Cross-section metallographic examination and electron microprobe analysis after completion of a run helped ascertain the structure and composition of the oxidation zone.

Results

The data are presented and analyzed in separate sections, first those pertaining directly to the Wagner hypothesis and subsequently two other sections, one on the Ag alloys of low solute content which undergo exclusive internal oxidation and the other on the alloys of intermediate solute content which eventually exhibit a low oxidation rate after an initial period of high oxygen uptake.

Transition in ternary alloys (Wagner hypothesis).—Weight-gain, m , and thickness, ξ , of the zone of internal oxidation, for reaction of Ag-Al and Ag-Zn specimens with oxygen at 1 atm and 823°K (550°C), are shown in Fig. 1-3. Ag3Al (Ag-3 a/o Al) was found to oxidize at a very high rate, and according to the parabolic law for the duration of the test of 61.2 ksec (17 hr) except for a relatively short initial period. This, along with other information to be presented, established that the Ag3Al alloy undergoes essentially exclusive internal oxidation, and, hence, is suitable for investigating the role of Zn additions. In contrast the rate of oxidation of Ag10Al and Ag14Al is very low (Fig. 1) as a result of the formation of a dense, protective Al_2O_3 layer. The addition of Zn by itself to Ag is not as effective as Al additions in reducing the oxidation rate (Fig. 3), e.g., the Ag21Zn alloy oxidizes at a rate nearly matching that of Ag3Al.

The weight-gain at 823°K for ternary Ag-Zn-Al alloys containing 3 a/o Al and various amounts of Zn are shown in Fig. 4. Additions of 21 or 25 a/o Zn to the Ag3Al alloy are sufficient to reduce the rate of oxidation to a very low value, similar to that of the Ag14Al alloy. Actually the rate attained after an initial period is even lower than that indicated by the total weight gain of 150 μg since extrapolation of the data to zero time gives a nonzero intercept (100 to 150 μg), i.e., there is an initial, though brief, higher rate

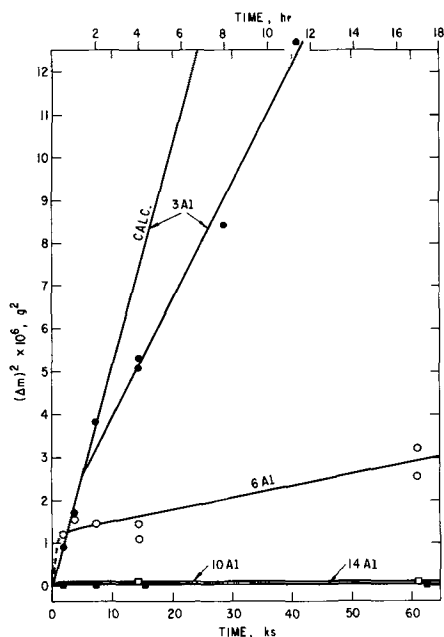


Fig. 1. Weight gain-time data for Ag3Al(●), Ag6Al(○), Ag10Al(□), and Ag14Al(■) specimens at 823°K. Calculated weight gain for exclusive internal oxidation (Eq. [7]) are given for comparison.

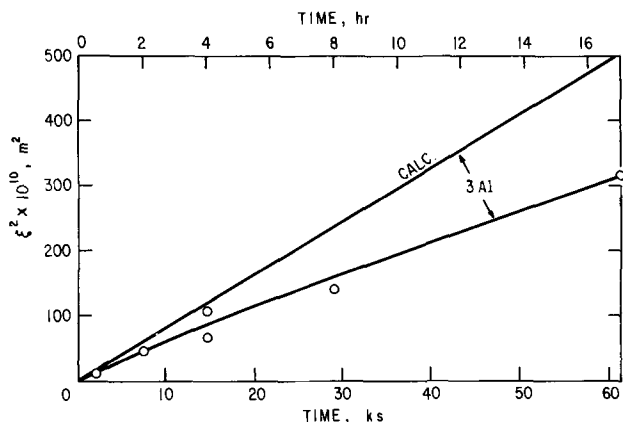


Fig. 2. Measured thickness-time data of the zone of internal oxidation on Ag3Al(●) specimens. Each point represents the mean value of 16 or more measurements on each specimen; the largest standard deviation was only $2.2 \times 10^{-5} m$ for the mean value at 61.2 ksec. Calculated thicknesses (Eq. [5]) of the internal oxidation zones are given for comparison.

of oxidation. Similarly there was found an initial higher rate of oxidation for the binary Ag10Al and Ag14Al alloys. The exceedingly low rate of oxidation attained in the second period is essentially the same for the alloys, Ag10Al, Ag14Al, Ag21Zn3Al, and Ag25Zn3Al, in agreement with the formation of a dense, protective Al₂O₃ layer on each of the alloys.

Similar oxidation results were obtained for the ternary alloys containing 6 a/o Al and varying amounts of Zn. These data, though, are less instructive since according to Fig. 1, the Ag6Al alloy already exhibits partial formation of a protective Al₂O₃ layer.

Cross-section metallographic observations of the specimens are in agreement with the above interpretation of the kinetic data. Oxidized Ag3Al specimens show a zone of internal oxidation (Fig. 5).

In contrast the Ag10Al, Ag14Al, Ag21Zn3Al, and Ag25Zn3Al specimens form only a thin oxidized region along the surface (Fig. 6 and 7). The detailed morphology of this region is the same for all four alloys, and is more complicated than the formation merely of a dense Al₂O₃ layer at the surface. Proceeding outward

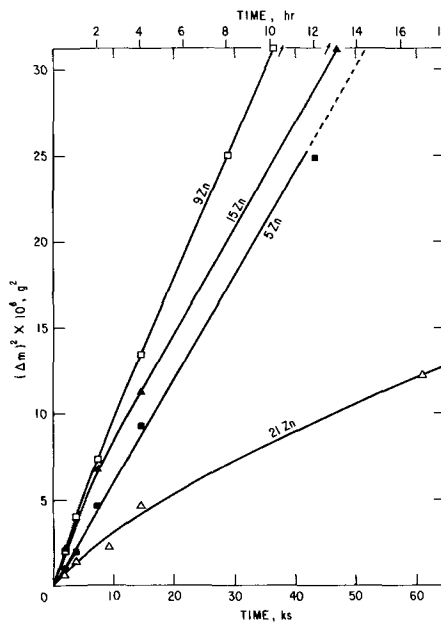


Fig. 3. Weight gain-time data for Ag5Zn(■), Ag9Zn(□), Ag15Zn(▲), and Ag21Zn(△) specimens.

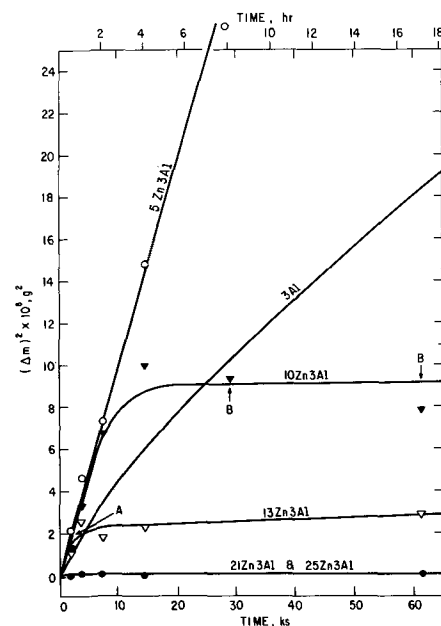


Fig. 4. Weight gain-time data for Ag5Zn3Al(○), Ag10Zn3Al(▼), Ag13Zn3Al(▽), Ag21Zn3Al(●), and Ag25Zn3Al(●) specimens, and for Ag3Al from Fig. 1.



Fig. 5. Cross-section micrograph showing a zone of internal oxidation (Z.I.O.) in a Ag3Al sample which was oxidized for 29 ksec at 823°K. Etched.

from the alloy there is often a discontinuous porous layer, then a dense layer, and finally patches of a white, metallic-appearing material. A porous region appears as a cavity or gap unless precautions are taken to avoid pullout during metallographic preparation as in the middle micrograph of Fig. 6.

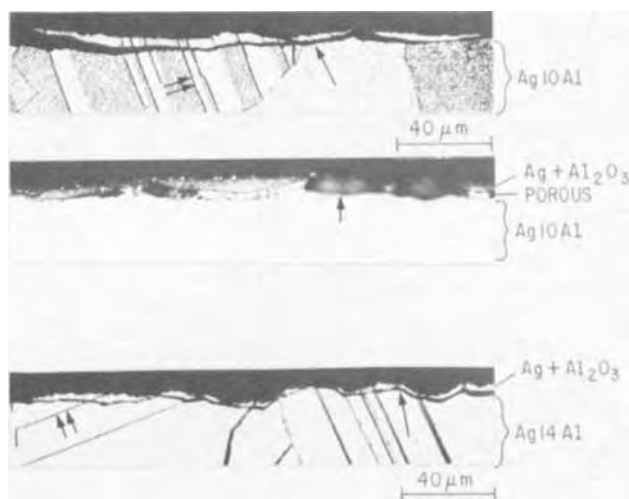


Fig. 6. Cross-section micrographs of oxidized Ag10Al and Ag14Al samples. The top and bottom micrographs are etched. \uparrow indicates gap. $\uparrow\uparrow$ indicates twin boundary.

The patches of white material were identified as Ag by electron microprobe examination. Silver was seen on the surfaces of many specimens, and particularly those containing higher amounts of solute as in Fig. 7. Wriedt and Darken (20) also observed Ag patches on the surface of internally oxidized Ag-Al alloys, and found that the amount increased with time of oxidation. They identified them by x-ray diffraction. Two sets of Ag lines were observed: one from the Ag patches on the surface and the other from an expanded and distorted Ag matrix within the internal oxidation zone.

The dense layer contains the alloy microstructure (Fig. 6 and 7), *i.e.*, grain and twin boundaries, characteristic of a zone of internal oxidation. Yet, for the ternary alloys in particular, these layers reflect light rather poorly, much as oxide layers do. Furthermore, in the case of the ternary alloys the dense layer is decidedly enriched in Zn and approximately unchanged in Al relative to the bulk alloy according to electron microprobe examination; this indicates a high volume per cent of oxide, mainly ZnO, in the layer. The Ag content in the layer on the other hand is lower than in the alloy, in agreement with the presence of Ag on the surface.

Electron microprobe examination was not made for Ag10Al and Ag14Al alloys. Presumably the dense layer has a higher ratio of Ag/Al₂O₃ than in the ternary alloys, since the (alloy) microstructure was more readily revealed by etching and the amount of Ag on the surface was less.

The occurrence of some, albeit very little, "internal" oxidation during exposure of the oxidation-resistant

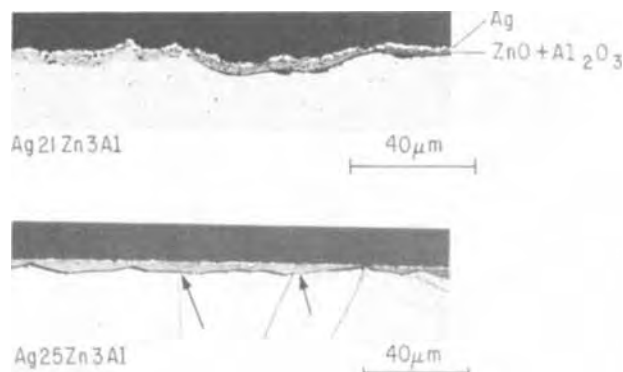
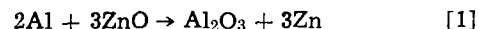


Fig. 7. Cross-section micrographs of oxidized Ag21Zn3Al and Ag25Zn3Al specimens. The bottom micrograph is etched. \uparrow points to twin boundaries in the oxidized region.

binary and ternary alloys to oxygen agrees with the brief, higher oxidation rate prior to the establishment of the exceedingly low oxidation rate shown for these alloys in Fig. 1 and 4. The dense Al₂O₃ layer which ultimately forms and reduces the oxidation rate to virtually nil is probably very thin and is not resolved by optical microscopy.

Discussion.—These data show that the addition of Zn to a Ag alloy containing a relatively small amount of Al results in the formation of a dense, protective Al₂O₃ layer. The beneficial effect of Zn in the formation of this layer is illustrated in Fig. 8. These data support the Wagner hypothesis (8, 21, 22) for the transition from internal to external oxidation in ternary alloys and, along with other data to be described, give some clue as to further details. On the basis of the data the transition is visualized as follows: When the surface of a Ag21Zn3Al alloy is initially bare, ZnO and Al₂O₃ are nucleated at the beginning of oxidation. The relatively large amount of Zn provides for the formation of sufficient oxide in the surface region to effectively block the diffusion of oxygen. Much of the initial silver in this region is "extruded" (20) or migrates to the surface; the latter may occur if the activity of Ag in the zone of internal oxidation is greater than unity as a result of strain. The presence of a ZnO layer ensures that the activity of oxygen in the alloy is very low, since it is determined by the coexistence of ZnO and Zn. As a result, the diffusion of oxygen into the alloy is negligible. In view of the depletion of Al in the alloy next to the surface, Al atoms migrate towards the surface without being converted to Al₂O₃ on their way. Hence, the supply of Al atoms diffusing toward the surface is sufficient for preferential reaction of the oxygen with Al. In addition, the initially formed nuclei of ZnO may be converted at least in part to Al₂O₃ by the displacement reaction



Once a dense Al₂O₃ layer is formed between the outer Zn-rich oxide layer and the bulk alloy the oxidation rate falls to the very low value determined by transport through Al₂O₃.

Hagel (23) offers an alternative explanation of the role that a third component plays in the formation of a protective layer; it is based on the degree of protection afforded by an α -Al₂O₃ vs. a γ -Al₂O₃ layer. He suggests that transformation from γ -Al₂O₃ to a more protective α -Al₂O₃ layer is enhanced by the presence of certain alloying elements. This mechanism, however,

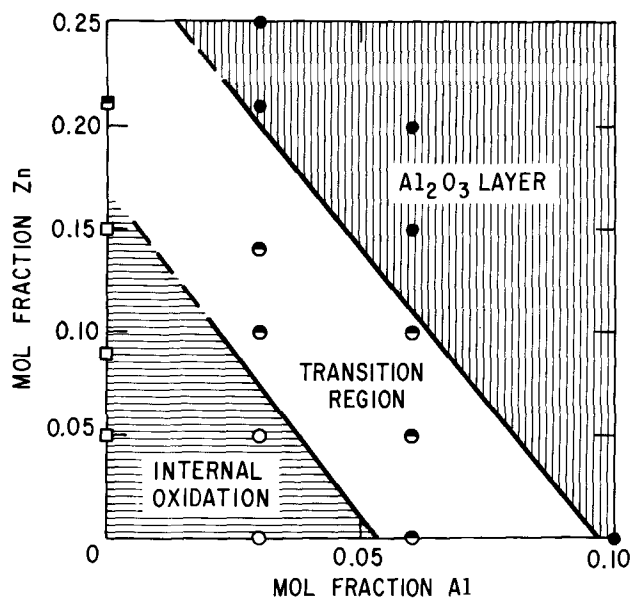


Fig. 8. Chart illustrating the beneficial effect of Zn in Ag-Zn-Al alloys for promoting the formation of a protective Al₂O₃ layer.

cannot be responsible for the transition to low oxygen uptake upon the addition of Zn to Ag-Al alloys since Ag₃Al without Zn additions does not form any Al₂O₃ layer.

Hence it seems reasonable to proceed on the basis that some, and perhaps many, of the multicomponent industrial alloys rely for their superior oxidation resistance on the "gettering action" of certain components which themselves may not be a constituent of the final protective oxide layer. It follows that the basic principles advanced by Wagner (8) may be used in the development of new alloys. Certain complications, however, must be avoided. Wood (24) points out that, depending on the kinetics of growth of the solvent metal oxide and on the alloy interdiffusion coefficient, the solvent metal oxide may engulf (overgrow) the nuclei of the solute metal oxide in accord with the earlier theoretical consideration of Wagner (21) and thereby preclude the formation of a protective solute metal oxide layer. He shows for Fe-Cr-Al alloys of relatively low chromium and aluminum contents that it is possible for the iron oxides to overgrow and undercut the Cr₂O₃ and spinel nuclei. This seemingly is not a problem with the higher alloyed Fe-Cr-Al alloys where a protective layer is well known to form at low total oxygen uptake (1-6), nor with certain other oxidation-resistant, Fe-base alloys, according to recent data of Boggs (7).

Exclusive internal oxidation.—For diffusion control and fixed boundary conditions the depth, ξ , of the zone of internal oxidation is given as a parabolic function of the time, t ,

$$\xi = 2 \gamma (D_0 t)^{1/2} \quad [2]$$

where D_0 is the diffusivity of oxygen in the two phase (solvent metal + solute oxide) zone of internal oxidation, and γ is a dimensionless parameter. Darken (25),

Wagner (26), Rhines *et al.* (27), and Meijering and Druyvesteyn (28) have solved the relevant diffusion equation. For the special case that movement of the front is completely determined by diffusion of oxygen in the metal one has the conditions (26)

$$\gamma \ll 1 \quad [3]$$

and

$$\gamma D_0/D_M \gg 1 \quad [4]$$

in which case Eq. [2] becomes

$$\xi \cong \left[\frac{2N_{O(s)} D_0 t}{\nu N_M^{(o)}} \right]^{1/2} \quad [5]$$

where $N_{O(s)}$ is the solubility of oxygen in the external interface of the solvent metal, ν is the atomic ratio of oxygen to metal in the internal oxide and $N_M^{(o)}$ is the mol fraction of the metal M in the bulk alloy. The solubility product of the internal oxide is here assumed to be negligibly small. The conditions of Eq. [3] and [4] were found to be satisfied for the alloys in the present investigation which contain low amounts of Al and Zn. For example, after internal oxidation of Ag₃Al for 14.4 ksec (4 hr) the measured ξ is 8.7×10^{-3} cm (Fig. 2), and $\gamma = 0.03$ which satisfies conditions in Eq. [3] and also Eq. [4] since D_0/D_M is very large.

Modification of Eq. [5] gives a relation for the weight gain, Δm , of the specimen

$$\frac{\Delta m}{A} \cong \xi \frac{N_M^{(o)}}{V_m} \cdot \nu W_O \quad [6]$$

where V_m is the molar volume of the alloy and W_O is the atomic weight of oxygen. Substituting Eq. [5] into Eq. [6] one has

$$\frac{\Delta m}{A} \cong \frac{W_O}{V_m} [2\nu N_M^{(o)} N_{O(s)} D_0 t]^{1/2} \quad [7]$$

Values for $N_{O(s)}$ and D_0 in Eq. [5-7] were assumed to be the solubility and diffusivity, respectively, of pure Ag as reported by Eichenauer and Müller (29), ν was assumed to be 1.5 and 1.0 corresponding to the

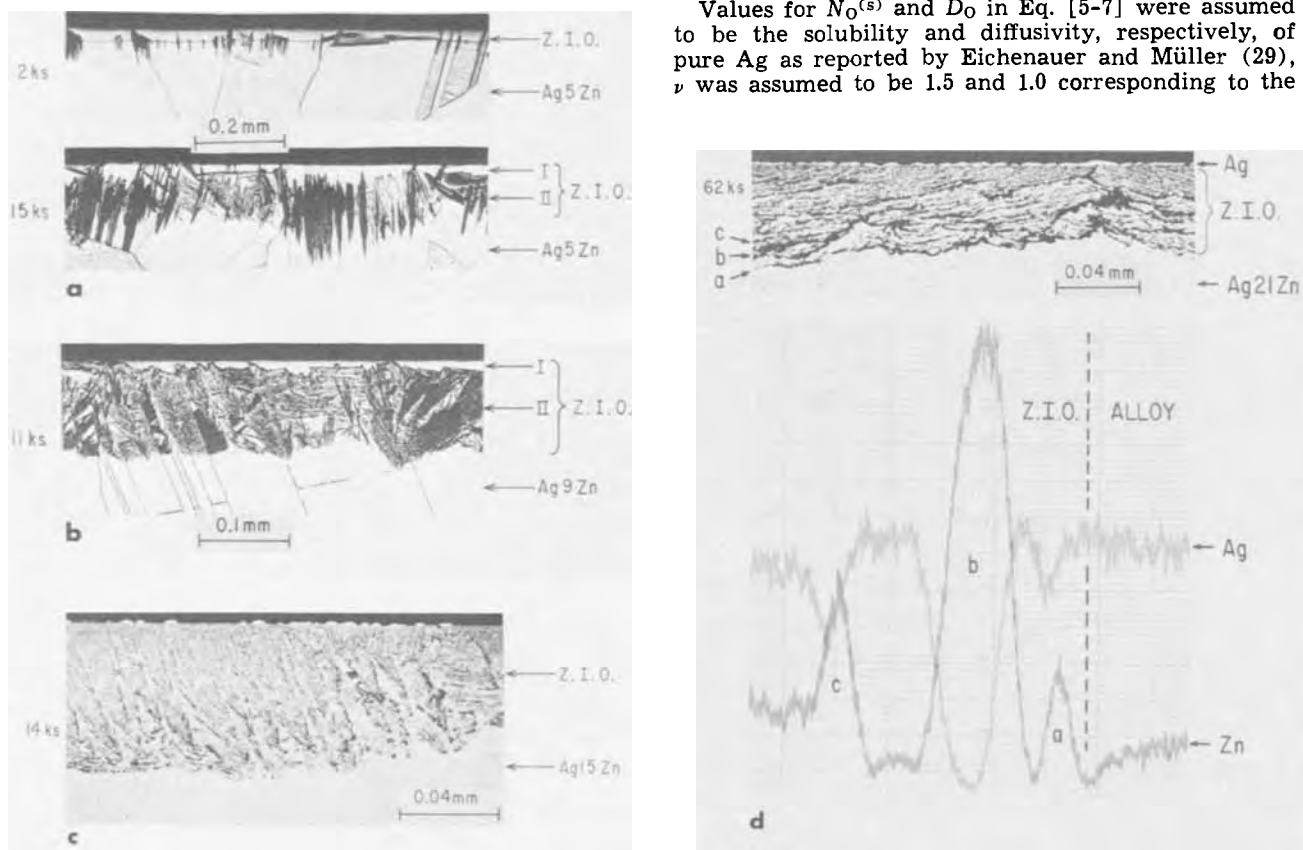


Fig. 9. Cross-section micrograph showing morphologically different zones of internal oxidation in Ag-Zn specimens, and an electron microprobe analysis which shows that the black "lines" within the zone of internal oxidation (Z.I.O.) of the Ag₂₁Zn specimen are Zn-rich. Ag trace lags the Zn trace by 1.2 μ m; probe traverse was from right to left. Specimens in (a) and (b) were etched.

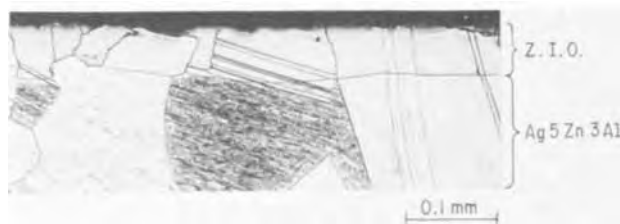


Fig. 10. Cross-section micrograph of a Ag5Zn3Al sample after 7.2 ksec at 823°K showing a zone of internal oxidation. Etched.

formation of stoichiometric Al_2O_3 and ZnO , respectively, $V_M = 10 \text{ cm}^3 \text{ mol}^{-1}$ and $A = 3.5 \text{ cm}^2$. Data in Fig. 1-4 indicate that the alloys Ag3Al, Ag5Zn, Ag9Zn, and Ag5Zn3Al undergo exclusive internal oxidation. On the other hand definite departures occur for all other alloys, e.g., the weight gain for Ag15Zn (Fig. 3) is lower than that for Ag9Zn and significantly lower than the calculated value from Eq. [7]. Still, Ag15Zn and some of the other alloys of intermediate solute content undergo appreciable internal oxidation and are discussed later in the section on transition alloys.

Cross-section metallographic examination shows a zone of internal oxidation for the Ag3Al (Fig. 5), Ag5Zn, Ag9Zn (Fig. 9a and 9b), and Ag5Zn3Al alloys (Fig. 10). Internal oxidation of the Ag-Zn alloys is complex. Examination of oxidized Ag5Zn specimens after polishing and etching reveals what appears as a "normal" zone of internal oxidation next to the surface and a second morphology (of internal oxidation) next to it which is comprised of acicular segments aligned mostly perpendicular to the surface (Fig. 9a). The acicular segments begin to develop after about 2 ksec oxidation as seen in the top micrograph, and to line up along twin boundaries or other planes which presumably are unresolved (micro) twin boundaries. At higher magnification the acicular segments are seen to be comprised of fine, parallel-arranged rows of material; this material may be porous as indicated by the fact that pull-out occurs during metallographic polishing. After etching, this structure is readily revealed as gaps or cavities in the scanning electron microscope (Fig. 11). The change from the normal to the acicular morphology occurs in the absence of a noticeable change in the kinetics of oxidation (Fig. 3).

Two morphologies of internal oxidation are also observed for Ag9Zn (Fig. 9b). The second morphology for Ag9Zn forms at an earlier stage and appears less acicular and less aligned perpendicular to the surface. In the higher Zn, binary alloys, on the other hand, only the second morphology, in further modified form, is observed. In the most Zn-rich alloy (Ag21Zn) the rows of material lie mainly parallel to the surface. It is shown in the next section that the formation of layers parallel to the surface is characteristic of alloys of intermediate solute content, i.e., those which often exhibit a two-stage kinetic behavior, and a total oxygen uptake between that for exclusive internal oxidation and that for formation of a dense, protective oxide layer at the surface.

Electron microprobe examination of the cross-sectioned Ag3Al and Ag5Zn specimens showed that the contents of the component metals within the zones of internal oxidation were essentially the same as in the original (unoxidized) alloys. Individual internal oxide precipitates are not resolved since the area analyzed by the beam is large relative to the precipitate size. The absence of solute enrichment within the zone of internal oxidation is additional justification for the assumption that for these alloys the kinetics of the internal oxidation process are controlled by the diffusion of oxygen within the zone of internal oxidation and, hence, of the applicability of Eq. [5].

Discussion.—The internal oxidation of Ag3Al appears to be uncomplicated in comparison to that of Ag5Zn and other alloys of higher solute content. The somewhat lower-than-calculated values of ξ and Δm for Ag3Al may be the result of a slightly reduced oxygen flux as a result of incipient "blocking" by the Al_2O_3 precipitates, or the solubility of oxygen may be lower as a result of strain (30).

For the other alloys, in which the thickness of the zone of internal oxidation was irregular the "average" observed ξ for each alloy is in accord with Eq. [5] and values of $N_0^{(s)}D_0$ in the literature. However, the maximum ξ observed at only a few locations yields a significantly larger $N_0^{(s)}D_0$ product, e.g., $N_0^{(s)}D_0(\text{max})$ for Ag5Zn equals $9 \times 10^{-10} \text{ cm}^2 \text{ sec}^{-1}$ vs. $1.85 \times 10^{-10} \text{ cm}^2 \text{ sec}^{-1}$ for pure Ag (29). This may be explained by significant interface diffusion or gas phase transport through pores of the acicular structure.

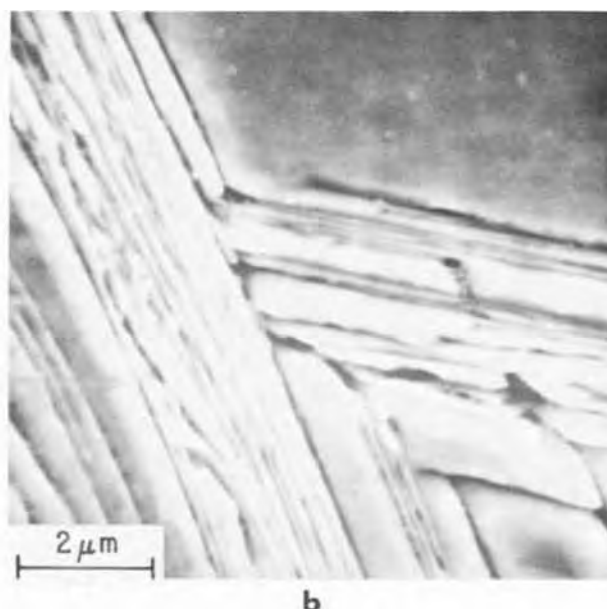
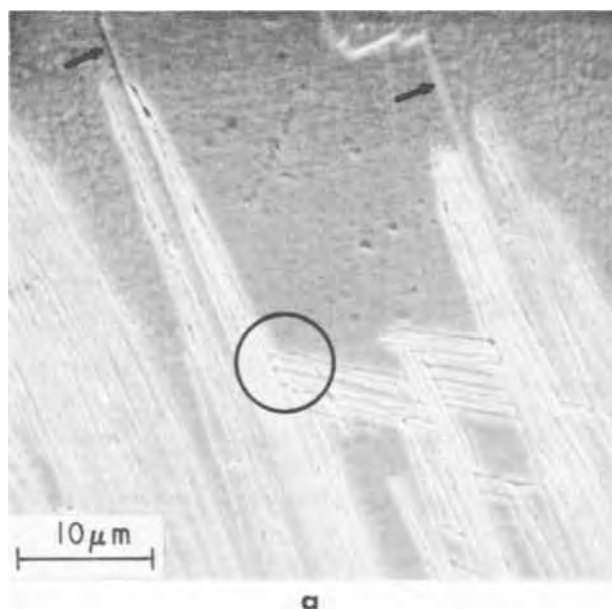


Fig. 11. Cross-section, scanning electron micrographs of an oxidized Ag5Zn specimen showing the acicular structure as gaps or cavities after pullout during mechanical polishing and subsequent etching. Micrograph in (b) is enlargement of circled region in (a). \uparrow indicates twin boundary.

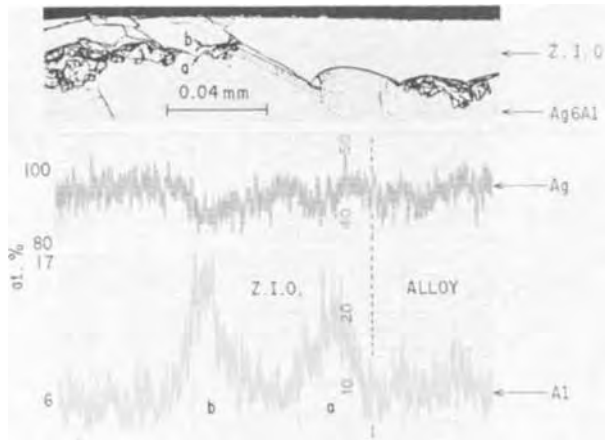


Fig. 12. Cross-section micrograph of an etched Ag6Al sample after 62 ksec of oxidation at 823°K, and an electron microprobe analysis which shows that the black "lines" in the region of the boundary between the alloy and the zone of internal oxidation (Z.I.O.) are Al-rich. Ag trace lags Al trace by 1.2 μm ; probe traverse was from right to left.

Transition region in binary and ternary alloys.—Data in Fig. 1-4 show that an induction period of large oxygen uptake precedes a falloff in the oxidation rate for the alloys of intermediate solute content, i.e., Ag6Al, Ag21Zn, Ag10Zn3Al¹, and Ag13Zn3Al. In a sense, the oxidation resistant alloys, Ag10Al, Ag14Al, Ag21Zn3Al, and Ag25Zn3Al also belong in this group since they, too, exhibited an, albeit very short, induction period.

Cross-section optical metallographic examination of oxidized specimens of the Ag6Al, Ag21Zn, Ag10Zn3Al, and Ag13Zn3Al alloys always shows a zone of internal oxidation containing what appears as black, ragged lines usually aligned roughly parallel to the surface (Fig. 9d and 12). These "lines," sometimes referred to in the literature as films, have been observed in Cu-Si (12), Ag alloys (31, 32, 11), Fe-Al (33), Ni-Al (34), and other alloys. Meijering (32) found that their frequency and thickness increased with solute content and that alloys which contain them oxidize at a lower rate. Elongated shapes and alignment of internal oxide precipitates including needles, plates, and dendrites have also been observed by electron microscopy for

¹ Continuous weighing measurements give a weight-time curve similar to that shown and indicate that the unusually large scatter of points from the discontinuous weighing measurements for Ag10Zn3Al is not significant.

various systems by Kahlweit and co-workers (35, 36) and others (33).

The material appearing as black lines in Fig. 9d and 12 is shown to be porous by the fact that pullout readily occurs during metallographic preparation. After appreciable pullout, gaps or cavities remain which are revealed by scanning electron microscopy (Fig. 13). Microhardness measurements show that these regions are softer than the neighboring two-phase material (Ag + oxide), in agreement with their porous structure.

Electron microprobe analysis shows that the layers even after appreciable pullout are rich in the solute metal, undoubtedly in the form of oxide (Fig. 9d and 12). The traces give average values, i.e., the magnitudes of the local departures from the alloy composition are probably greater than indicated in the microprobe traces. The layers within the zone of internal oxidation for Ag10Zn3Al consist of oxides of both Al and Zn, according to electron microprobe analyses.

The top micrograph of Fig. 14 is of the Ag10Zn3Al alloy after 1.8 ksec (30 min) of oxidation and corresponds to the initial period of the high rate of oxidation (point A in Fig. 4). At these early stages of oxidation porous oxide layers are, for the most part, absent within the zone of internal oxidation. They are first observed along grain boundaries between the surface and the internal oxidation front and then along the front itself. The middle and bottom micrographs of Fig. 14 are of other specimens of the same alloy, but correspond to the later, very low rate of oxidation (point B in Fig. 4). In the bottom micrograph the specimen was etched to reveal the twin and grain boundaries. At these longer oxidation times the layers are common features within and at the front of the zone of internal oxidation, as they are after comparable oxidation times for Ag21Zn and Ag6Al (Fig. 9 and 12).

The thickness of the zone of internal oxidation varies appreciably for these alloys, in contrast to the alloys of lower solute content which do not form protective oxide layers. Some regions, usually amounting to less than 5% of the surface, are observed in cross-section to be free from internal oxidation. Presumably in these regions a protective oxide layer forms immediately upon contact of the specimen with the oxidizing environment. Such behavior has previously been observed by Rapp (11) and others.

A slight drop of the Zn content in the unoxidized portion of the Ag21Zn specimen at the internal oxidation front in Fig. 9d indicates enrichment of Zn in the zone of internal oxidation. Diffusion of solute metal and, in addition, of oxygen along grain boundaries in the alloy ahead of the internal oxidation front were

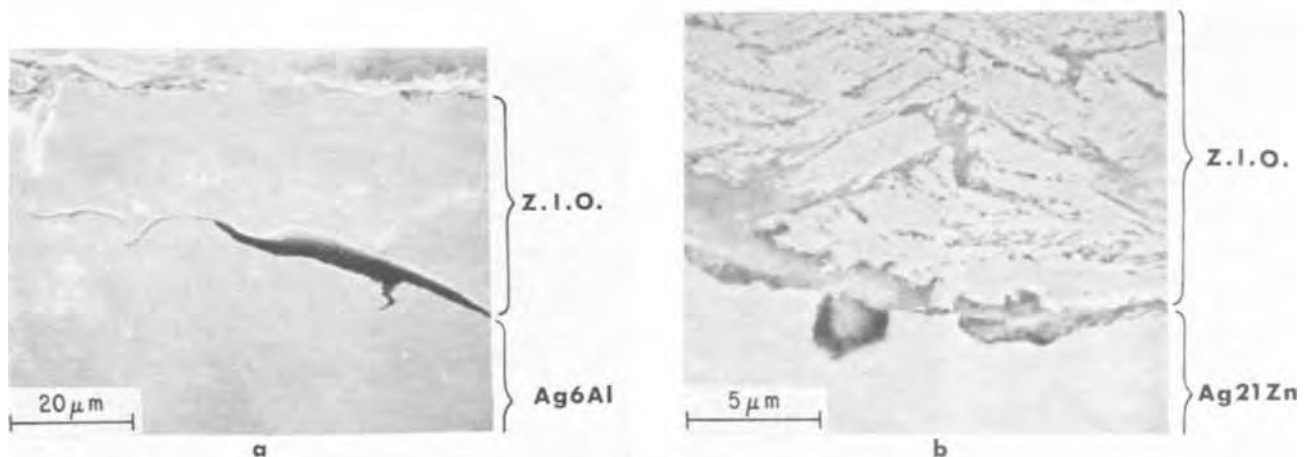


Fig. 13. Cross-section, scanning electron micrographs showing a gap(s) along the boundary between the alloy and the zone of internal oxidation (a) for an oxidized (923°K) Ag6Al specimen, mechanically polished and etched, and (b) for an oxidized Ag21Zn specimen, mechanically polished. Different phases are not distinguishable.

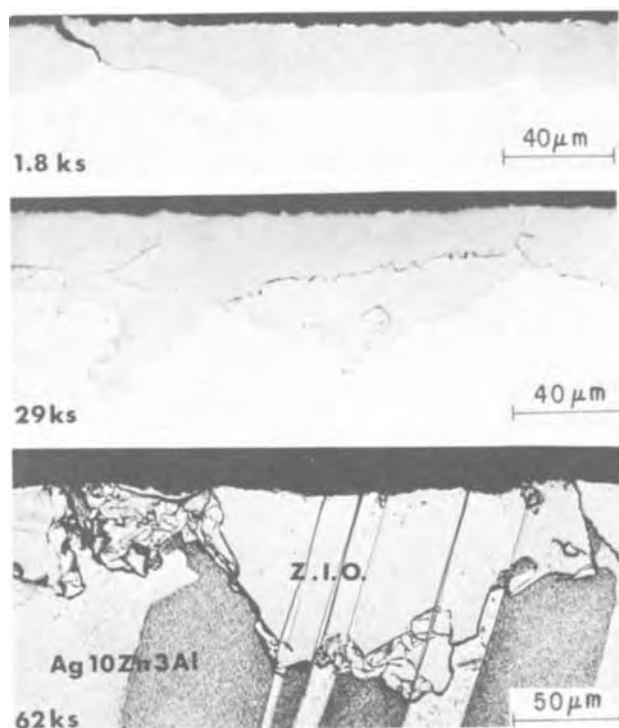


Fig. 14. Cross-section micrographs of oxidized Ag10Zn3Al specimens illustrating black "lines," identified as Al- and Zn-rich regions, within the zone of internal oxidation. The bottom micrograph is etched.

indicated also for Ag6Al and the ternary alloys which oxidize according to the kinetics of the transition region. Subsequent deformation of these specimens revealed that grain boundaries within the nominally unoxidized portion of the specimens had become embrittled.

Discussion.—Transition from internal to external oxidation does not take place at a definite concentration in these alloys but rather over a fairly wide composition range (Fig. 8). This occurs for specimens of identical thermal and mechanical history and surface preparation. Rapp has already showed that the boundary of the transition region depends to some extent on the prior surface preparation.

The data in the present paper show further that for alloys in the transition region the attainment of a low rate of oxidation is preceded by an induction period during which the oxidation rate is much higher and a zone of internal oxidation forms. The occurrence of an induction period is not surprising in view of early considerations by Wagner (21, 22). Chattopadhyay and Wood (37) have recently emphasized the occurrence of transient behavior during initial external scale formation accompanied by internal oxidation.

The main question for binary and ternary alloys in the transition region (and seemingly general to all of the alloys which attain a low oxidation rate) is where and how a dense oxide layer of the solute metal is formed once internal oxidation has transpired. Time invariant diffusion behavior is usually assumed in analyses of oxidation processes, except initially when diffusion control would require an infinite rate. Applying the concept generally means that for a given set of experimental conditions (p_{O_2} , solute content, etc.) a single oxidation process, e.g., internal oxidation, occurs for the duration of the experiment and a single rate constant is obtained. When exceptions to such behavior are observed during internal oxidation they can sometimes be traced to the initial period (prior to the establishment of diffusion control) when starting conditions allow oxidation to occur heterogeneously over the surface. One specific explanation of the transient

behavior is that patches of dense oxide which form initially spread sideways and eventually impinge to give a dense oxide layer at the external surface (38). Then one has the end of inward transport of oxygen, i.e., the extremely low oxidation rate which is observed after an initial period of a high rate of oxygen uptake. For this mechanism to operate it is necessary that Al can diffuse to the surface after internal oxidation begins. This would appear to be possible along segments of unoxidized alloy which extend to the surface. A surface scale is sometimes observed on the Ag6Al specimens; portions of one are barely visible in Fig. 12.

Another factor which may account for a change in the diffusion kinetics at some stage of the oxidation process is void formation during the internal oxidation process; voids may block the diffusion of an important species and thereby be a precursor to the formation of a dense Al_2O_3 layer along the boundary between the zone of internal oxidation and the alloy.

There is some reason to suspect that voids do form at temperature as part of the internal oxidation process. The easy pullout of material within the zone of internal oxidation indicates porosity which is developed either as a result of internal oxidation or of cooling after the oxidation run. Features usually associated with nonuniform contraction during cooling, however, such as matching surfaces, are not very evident.

Conclusions

Weight gain data and cross-sectional metallographic examination show that whereas a Ag3Al alloy exhibits internal oxidation without formation of a dense Al_2O_3 layer, upon addition of 21 or 25 a/o Zn internal oxidation is completely suppressed and a dense highly protective Al_2O_3 layer is formed. These data support the hypothesis advanced by Wagner (8) that Zn may be considered as a secondary getter for oxygen atoms so that virtually no oxygen atoms diffuse into the alloy and, therefore, aluminum atoms can diffuse to the surface without being intercepted by oxygen atoms. Newly arriving Al atoms may then form additional Al_2O_3 by a displacement reaction with initially formed nuclei of ZnO. Other metals such as chromium and silicon in base metal alloys containing aluminum as the least noble constituent, e.g., Fe-Cr-Al, may be expected to behave similarly in the formation of a highly protective layer of Al_2O_3 .

For Ag5Zn and Ag9Zn the internal oxidation process changes at a certain depth to one which is strongly influenced by the microstructure. The front of internal oxidation is irregular. At points of greater penetration the $N_{O^{(s)}}D_{O_2}$ product is significantly larger than that for pure Ag.

For the "transition" alloys the formation of a protective Al_2O_3 layer is preceded by an induction period during which internal oxidation occurs. Rows of aluminum oxide and/or zinc oxide form in alignment roughly parallel to the surface within the zone of internal oxidation. It is not clear though if these layer-like regions are instrumental in the eventual attainment of a lower rate of oxidation or are simply a consequence of a reduced inward flux of oxygen caused by the eventual formation of a continuous, dense Al_2O_3 layer at the surface.

Acknowledgments

It is a pleasure to acknowledge the considerable contribution of C. Wagner of the Max Planck Institut für Physikalische Chemie who outlined the experiments in this paper and made many helpful comments throughout the course of this investigation. Valuable discussions with several colleagues are also gratefully acknowledged, especially those with L. S. Darken and W. E. Boggs. Considerable assistance was provided on the oxidation experiments by H. A. Hughes, in the metallographic examinations by R. M. Lytle, P. J. Byrne, C. E. Brickner, and W. Gundaker, and on alloy preparation by B. B. Rice. The author is also grateful

to B. F. Oliver of the University of Tennessee for advice on preparation of the various alloys.

Manuscript submitted June 25, 1971; revised manuscript received ca. Oct. 5, 1971. This was Paper 116 presented at the Atlantic City Meeting of the Society, Oct. 4-8, 1970.

Any discussion of this paper will appear in a Discussion Section to be published in the December 1972 JOURNAL.

REFERENCES

1. A. Portevin, E. Pretet, and H. Jolivet, *Rev. Met.*, **31**, 101, 186, 219 (1934).
2. E. Scheil and E. H. Schulz, *Arch. Eisenhuettenw.*, **6**, 155 (1932/33).
3. E. Scheil and K. Kiwit, *ibid.*, **9**, 405 (1935/36).
4. E. A. Gulbransen and K. F. Andrew, *This Journal*, **106**, 294 (1959).
5. I. Pfeiffer, *Z. Metallk.*, **53**, 309 (1962).
6. G. C. Wood and M. G. Hobby, *Proc. Intern. Congr. Met. Corr.*, 3rd Moscow, Vol. 3, 102 (1966).
7. W. E. Boggs, Applied Research Laboratory, U.S. Steel Corp., Monroeville, Pa., Private communication (1970).
8. C. Wagner, *Corrosion Sci.*, **5**, 751 (1965).
9. J. S. Dunn, *J. Inst. Metals*, **46**, 25 (1931).
10. I. Dietrich and L. Koch, *Z. Metallk.*, **50**, 31 (1959).
11. R. A. Rapp, *Acta Met.*, **9**, 730 (1961).
12. K. W. Fröhlich, *Z. Metallk.*, **28**, 368 (1936).
13. J. P. Dennison and A. Preece, *J. Inst. Metals*, **81**, 229 (1952/53).
14. L. E. Price and G. J. Thomas, *ibid.*, **63**, 21 (1938).
15. F. N. Rhines and B. J. Nelson, *Trans. Am. Inst. Min. Met. Eng.*, **156**, 171 (1944).
16. F. Maak, *Z. Metallk.*, **52**, 538, 545 (1961).
17. W. E. Boggs, *This Journal*, **118**, 906 (1971).
18. L. S. Darken, *Trans. AIME*, **180**, 430 (1949).
19. R. P. Smith, *Acta Met.*, **1**, 578 (1953).
20. D. R. Wriedt and L. S. Darken, summarized in part by L. S. Darken, *Trans. Am. Soc. Metals*, **54**, 600 (1961).
21. C. Wagner, *This Journal*, **103**, 627 (1956).
22. C. Wagner, *ibid.*, **99**, 369 (1952).
23. W. C. Hagel, *Corrosion*, **21**, 316 (1965).
24. G. C. Wood, *Oxid. Metals*, **2**, 11 (1970).
25. L. S. Darken, *Trans. AIME*, **150**, 157 (1942).
26. C. Wagner, *Z. Elektrochem.*, **63**, 772 (1959).
27. F. N. Rhines, W. A. Johnson, and W. A. Anderson, *Trans. AIME*, **147**, 205 (1942).
28. J. L. Meijering and M. J. Druyvesteyn, *Philips Res. Rept.*, **2**, 81, 260 (1947).
29. W. Eichenauer and G. Müller, *Z. Metallk.*, **53**, 321, 700 (1962).
30. J. C. M. Li, R. A. Oriani, and L. S. Darken, *Z. Physikalische Chemie Neue Folge*, **49**, 271 (1966).
31. F. N. Rhines and A. H. Grobe, *Trans. AIME*, **147**, 318 (1942).
32. J. L. Meijering, *Pgh. Internat. Conf. on Surface Reactions*, (1948), p. 101.
33. R. P. Smith, formerly with E. C. Bain Laboratory for Fundamental Research, U.S. Steel Corp., Monroeville, Pa., Private communication (1958).
34. F. S. Pettit, *Trans. AIME*, **239**, 1296 (1967).
35. G. Böhm and M. Kahlweit, *Acta Met.*, **12**, 641 (1964).
36. P. Bolsaitis and M. Kahlweit, *ibid.*, **15**, 765 (1967).
37. B. Chattopadhyay and G. C. Wood, *Oxid. Metals*, **2**, 373 (1970).
38. C. Wagner, Private communication (1970).

Technical Notes



Electrical Switching in Anodic Oxide Films on Zircaloy-2

N. Ramasubramanian

Chalk River Nuclear Laboratories, Atomic Energy of Canada Limited, Chalk River, Ontario, Canada

The advantage of using the Widmanstätten morphology for locating weak spots in anodic oxide films on Zircaloy-2 was reported by us (1). It was shown that the initial electrical breakdowns were centered on the α -platelet boundaries where the intermetallic precipitates and second phase impurities have segregated during cooling the alloy in vacuum from the β phase. These breakdowns were always preceded by switchings to a high conductivity state; the occurrence of one or the other was governed by the load resistance in the circuit. The results obtained on such switching phenomena are presented here.

Experimental

The details regarding material, heat treatment, surface preparation, anodization, and current-voltage measurements have been described elsewhere (1). Zircaloy-2/anodic oxide/metal sandwiches were prepared by evaporation of gold or silver contacts through masks to a thickness of 1000-1500Å (monitored by a quartz crystal). Silver counterelectrodes were also formed utilizing the Eccobond Solder 56C supplied by Emerson and Cuming Inc. and G. C. Electronics' silver paint. The Eccobond contact was cured at 70°C for 2

hr, and the paint was air-dried. The voltage sources were an Electro Pulse Inc. Model 2140A pulse generator, d.c. from dry cells and a.c. from a Variac. The series resistance was 10 kohm during switch ON operation (high to low impedance state) and varied from 3 to 1 ohm during the low to high impedance, switch OFF operation. Impedance measurements were made using a GR-1680A automatic capacitance bridge.

Results

The electrical switching characteristics of the anodic oxide films on Zircaloy-2 could be classified into three types: (a) the most commonly observed one, associated with the delayed type of breakdown, (b) a nondestructive bistable switching, and (c) transitory switching observed in thin films, 250 to 750Å thick. Out of a total of thirty tested (as-received material), each carrying four or more diodes, all the specimens exhibited the type (a) and about 15% of the diodes the type (b) switching behavior. All the thin films tested showed the transitory switchings.

Bistable switching, type (a).—The current-voltage characteristics of the diode were traced first at 80° and 190°K; only the leakage currents were measured for potentials of both polarities up to ~60% of the anodizing voltage. Time of holding at various applied volt-

Electrochemical Society Active Member.

Key words: Zircaloy-2, anodic oxide, electrical switching, transition metal alloying additions.

ages was varied from a few seconds to ~ 5 min, with no detectable change in conductivity. Similarly at room temperature a positive bias on the alloy in the same range of voltages did not produce any change in conductivity. However, when a negative potential was applied at room temperature, current bursts were observed at ~ 15 V and holding the alloy at the voltage for a few minutes brought about a switch to the ON state. In this initial ON condition the $i \times V$ relation was ohmic, and the temperature coefficient of resistance was positive.

Considering the case of a 50V film as a typical example, -16.5 V on the alloy for $\frac{1}{2}$ min duration at room temperature turned the diode ON; in the ON state the resistances were 63 and 54 ohm at 300° and 80° K, respectively. A current of 100 mA (60 Hz from a Variac) turned the diode OFF. In the case of diodes carrying evaporated electrodes this initial switch OFF operation resulted in the "single-hole" type of breakdowns (1). When Eccobond solder or silver paint formed the counterelectrode, it was noticed that after the initial switching OFF operation the diode could be turned ON by a positive or a negative bias on the alloy.

A number of ON \rightleftharpoons OFF operations were carried out and the behavior was quite varied: switch ON voltages were in the range of 5 to 27V; OFF currents varied from 75 to 150 mA and the $i \times V$ relation was either ohmic or nonohmic with a positive or negative temperature coefficient of resistance, respectively.

Bistable switching, type (b).—A few of the diodes exhibited the type (b) switching which occurred in the temperature range of 80° to 300° K when the applied bias exceeded ± 6 V. As the d-c voltage across the oxide film was gradually increased, a sharp increase followed by a rapid decrease in current was observed at ~ 6 V. More such current transients were observed when the applied voltage was increased to ~ 10 V. Then at some stage, when lowering the applied bias, the current suddenly increased by more than two orders of magnitude at around 4V i.e., a switch to the low impedance ON state. The current-voltage curves showed the following characteristics in the ON state: an initial ohmic portion, a zero temperature coefficient of resistance, a zero differential resistance region, and multiple conduction levels. Any systematic variation of the minimum voltage required for the onset of current bursts with the oxide thickness was not found.

A typical example of the conductivity changes is illustrated in Fig. 1 and 2 for a 2100Å film carrying an evaporated gold contact and tested at liquid nitrogen temperature. In the low impedance ON state a slight instability in current was observed and the $i \times V$ curves were nearly symmetrical for positive and negative bias on the alloy, curves c and d. On warming the sample to room temperature no changes in the $i \times V$ relation were noticed, and the same curves c, d were traced. From the ohmic portion of the curves a resistance of 18.5 kohm can be calculated.

Then the impedance of the diode was measured at 1 kHz, and it was found that this act had effected an ON to OFF switching. The curves shown in Fig. 2 were traced subsequently. At ~ 3 V current transients were noticed and the diode switched ON at 3.2V, (curve a_2 in the figure). Curves a_3 and a_4 were traced in the ON state; a_4 was found to be symmetrical with a_3 until the current through the diode exceeded $90 \mu\text{A}$, the maximum passed immediately after OFF \rightarrow ON switching (curve a_3). When the current through the diode was increased beyond this maximum value, a zero differential resistance portion a_5 was traced, with the increases in applied voltage going almost entirely across the series resistor. Finally the curves a_6 and a_7 were traced. A similar type of behavior was observed when the alloy was biased negative following another impedance measurement, curves b_1 to b_7 in the figure. Switching times for OFF \rightarrow ON transitions (curves a_2

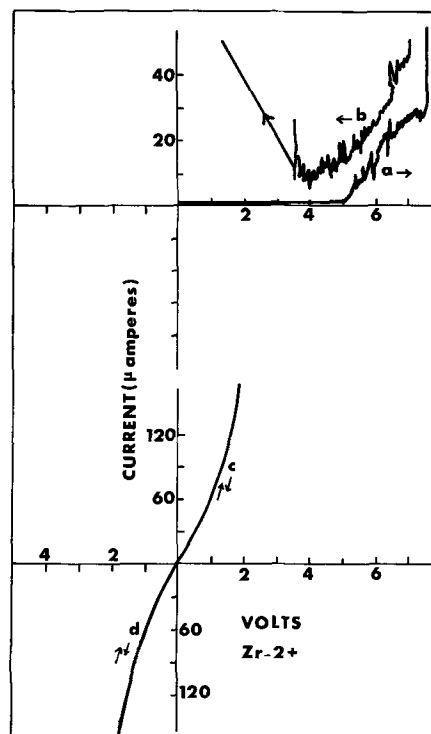


Fig. 1. Tracing of x-y recorder plots of the establishment of conductivity and switching in Zircaloy-2/2100Å anodic oxide film/gold (0.27 cm^2) at 80°K .

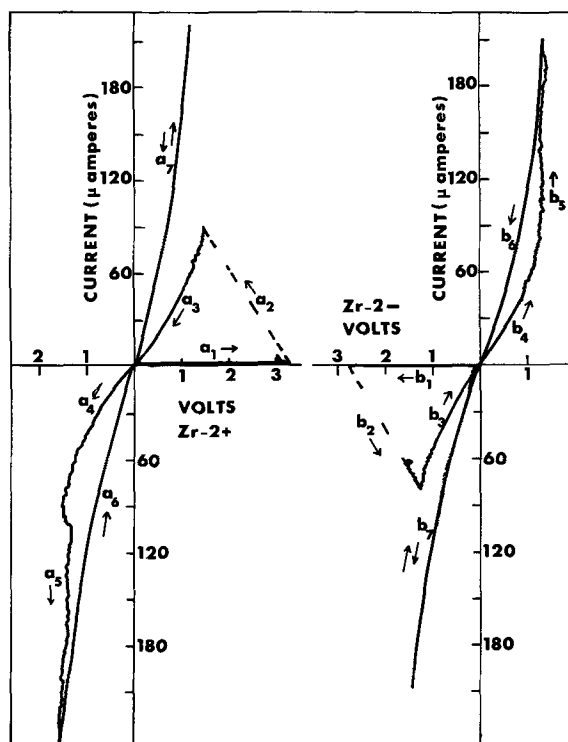


Fig. 2. Switching, zero differential resistance regions and multiple conduction levels; tracing of x-y recorder plots obtained during the tests at 80°K on the diode referred to in Fig. 1.

and b_2 in the figure) were less than 10^{-8} sec, and attempts to trace these current-time curves were unsuccessful.

A number of ON \rightleftharpoons OFF operations similar to that in Fig. 2 were carried out and the $i \times V$ tracings recorded for various maximum currents through the diode in the low impedance state. Switch ON voltages were all around ± 2.5 V. The zero differential resistance region on both the positive and negative sides was seen to cover a current range from ~ 30 to >240

μA . The curves were similar in shape and symmetrical about the origin; the resistances of the ohmic portions varied from 30 to 10 kohm and the switch off currents varied from 500 to 750 μA . No surface changes were noticed on the evaporated counterelectrodes.

Transitory switchings in thin films.—A set of $i \times V$ curves, selected from those obtained at room temperature on a 25V ($\sim 700\text{\AA}$) film, is shown in Fig. 3. At 8.7V negative bias on the alloy the current through the diode increased abruptly, a_1 in the figure followed by a zero differential resistance portion a_2 . Instability in the current flow was noticed when the diode tended to switch OFF and then ON as shown by the loop a_3 , a_4 and a_5 in the $i \times V$ characteristics. When the current through the diode was decreased, slight instability was still noticed and the portion a_7 was traced which passed through the origin. In tracing a_7 the current was gradually reduced to zero, over a period of 15 sec.

Immediately after tracing a_7 the diode was found in the high-impedance state. Then a number of $i \times V$ tracings were made; in each instance the diode was highly resistive to start, was turned to the ON state at about $\pm 1.4\text{V}$ and the $i \times V$ curve in the ON state passed through the origin. In the ON state, during the transitory switching, the $i \times V$ curves were almost linear and the resistance varied in the range of 5 to 8 kohm. Then the diode settled to bistable switching, and the ON state was characterized by an ohmic $i \times V$ relation and zero temperature coefficient of resistance.

Some of the diodes were tested at 80° and 190°K before the room temperature experiments. For voltages up to $\sim 50\%$ of the anodizing voltage, at lower temperatures only the leakage current flow was noticed. At room temperature transitory switching occurred, the easy direction for the first one to be initiated being Zircaloy-2 negative. The number of transitory operations prior to the onset of bistable mode varied among the various specimens and also on a single specimen carrying a number of diodes.

Vacuum-cooled material.—The oxide thickness varied from 1200 to 2500 \AA and a total of 50 diodes carrying evaporated gold electrodes were tested. All these were characterized by the type (a) bistable switching. The switch ON voltage did not vary with the oxide thickness and was $18 \pm 2\text{V}$. The initial switch OFF operation led to a few isolated single-hole breakdowns centered on the boundaries between the α platelets (1). Subsequent to this initial switch OFF operation, a second set of breakdowns were produced in some of the diodes by having a low series resistance in the circuit and by applying a negative potential of $20 \pm 2\text{V}$ on the alloy. These breakdowns

were more in number than the initial ones and their density averaged to $\sim 10^2/\text{cm}^2$. The diodes were highly conducting following this step; Park and Basavaiah have reported a similar type of behavior in oxide films on evaporated zirconium (2). The scanning electron micrographs of a second set of breakdowns are shown in Fig. 4. Almost all such breakdown spots were also found to be located on the α -platelet boundaries.

Discussion

When Zircaloy-2 is cooled in vacuum from the β phase, second phase intermetallic (Zr-Fe-Cr and Zr-Fe-Ni) particles are precipitated along the α -platelet boundaries. Second phase impurity particles (Zr and C, P, or Si present in ppm quantities) are probably the nucleation sites for the growth of the α -platelets (3). The initial and the subsequent breakdowns, in oxide films on the vacuum-cooled material, were all located on the α -platelet boundaries; the delayed type of bistable switching in these films is in the majority observed in oxide films grown on the alloy in the as-received condition. Therefore, it is reasonable to conclude that the second phase particles in the as-received alloy are the sites of such switching and the associated breakdowns.

Park and Basavaiah identified the conducting filament with the rim around the breakdown spots (2). In our experiments, however, the switch ON operation did not result in a breakdown when the series resist-

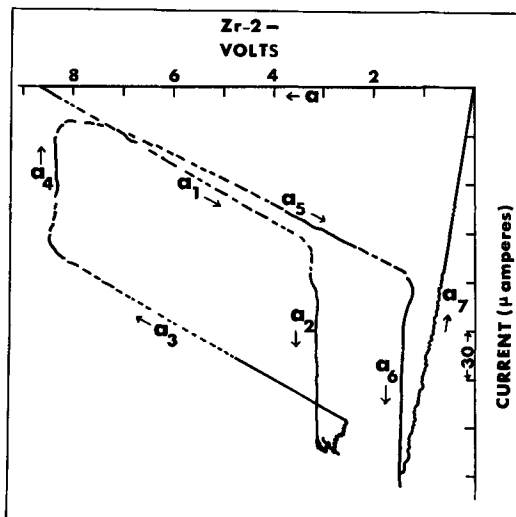


Fig. 3. Zircaloy-2/25 V anodic oxide film/silver (Eccobond, 0.12 cm^2) tested at atmospheric conditions; x-y recorder plots of the transitory switchings.

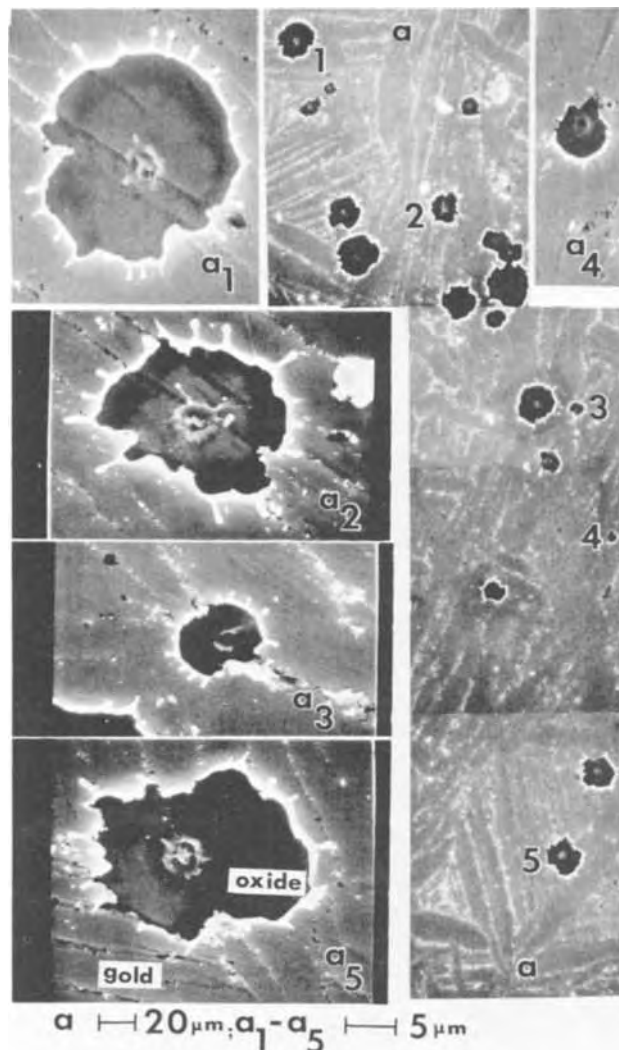


Fig. 4. Scanning electron micrographs of the second set of breakdowns in anodic oxide (2100 \AA thick) grown on the vacuum-cooled Zircaloy-2.

ance in the circuit was sufficiently high; also, the initial switch OFF operation resulted most often in single breakdown spots and the diode subsequently was highly resistive. Therefore, Park and Basavaiah's observation might represent an intermediate state and the current carrying filament present prior to breakdown is likely to be very different from that produced after the breakdown. The breakdown spots generally were 3 to 4 μm in diameter (cf. Fig. 4); however, the original current carrying filament is likely to have been much smaller in dimensions. Moreover, the oxide grown on the second phase particles has been shown to be highly heterogeneous and porous (1). Therefore, calculation of the resistivity of the filament based on the diameter of the breakdown spot and the anodic oxide (zirconia matrix) thickness would be meaningless. Though a positive temperature coefficient of resistance was found in the ON state, the nature of the filament material thus remains unknown.

At this stage, any attempt to interpret the mechanism of the initial switching would be highly speculative because the composition of the second phase particles, their behavior during wet anodization, the type of oxide grown on them, etc., remain unknown. In this connection, a study of the oxide growth on the inter-

metallics of zirconium and iron, chromium or nickel and their electrical properties might be helpful.

Conclusions

In anodic oxide films on Zircaloy-2, the second phase particles are the sites where a majority of the bistable switchings and the associated breakdowns occur.

Acknowledgments

The author remains indebted to Dr. B. Cox for several profitable discussions. He is most grateful to Mr. T. Trottier who assisted in carrying out the experiments.

Manuscript submitted Feb. 22, 1971; revised manuscript received ca. Jan. 12, 1972. This was Paper 152 presented at the Atlantic City Meeting of the Society, Oct. 4-8, 1970.

Any discussion of this paper will appear in a Discussion Section to be published in the December 1972 JOURNAL.

REFERENCES

1. N. Ramasubramanian and T. Trottier, *This Journal*, **118**, 1797 (1971).
2. K. C. Park and S. Basavaiah, *J. Non-Crystalline Solids*, **2**, 284 (1970).
3. R. A. Holt, *J. Nucl. Mater.*, **35**, 322 (1970).

The Composition of $\text{Ga}_{1-x}\text{Al}_x\text{As}$ Grown from Ga-Rich Solutions as a Function of Growth Temperature and Solution Composition

W. G. Rado, W. J. Johnson, and R. L. Crawley

Scientific Research Staff, Ford Motor Company, Dearborn, Michigan 48121

It has been shown that efficient visible light emitting diodes can be fabricated from liquid phase epitaxially (LPE) grown layers of $\text{Ga}_{1-x}\text{Al}_x\text{As}$ (1). The maximum direct energy gap obtainable is 1.9 eV corresponding to a composition of $x = 0.37$ (2). The work of Panish and Sumski (3) and Ilegems and Pearson (4) on the Ga-Al-As ternary system indicates that $\text{Ga}_{1-x}\text{Al}_x\text{As}$ in the range of $0 < x < 0.37$ can be grown by LPE at or below 1000°C from solutions containing less than about 0.007 atom fraction Al. This communication presents experimental data for $\text{Ga}_{1-x}\text{Al}_x\text{As}$ grown in the temperature range of $800^\circ\text{--}950^\circ\text{C}$ from Ga-Al-As solutions containing 0.002-0.014 atom fraction Al.

The $\text{Ga}_{1-x}\text{Al}_x\text{As}$ was grown by LPE on (111)-Ga and As faces of single crystal GaAs substrates that were doped with Te or Se in the range of 0.5 to 2.5×10^{18} electron/cm³. The growth apparatus was similar to that of Hayashi *et al.* (5) in that the solution was pushed over the substrate. Our apparatus also employed a special provision to shear the solution during its push in order to expose a fresh, unoxidized surface. The solution typically contained 4g of six nines pure Ga and the appropriate amounts of six nines pure Al and polycrystalline undoped GaAs. For each run, the saturation temperature, T_s , the temperature at which the Ga-Al solution is just saturated with the specific amount of GaAs used, was determined by using the ternary phase diagram of Ilegems and Pearson (4).

The substrates were lapped with 1 μm alumina, etched in 10 HNO₃:1 HF:5 H₂O for 10 sec, rinsed and dried before being loaded into the boat. The GaAs source material was heavily etched, rinsed, dried, and then wetted with Ga before placement in the solution.

Key words: LPE, LED, phase diagram, direct energy gap semiconductors, electron microprobe.

During loading, the solution was heated to 50°C to insure that the Al was dissolved properly. After positioning in the furnace, the system was flushed overnight with H₂ purified by Pd. The system was then heated to an equilibration temperature, T_e , either equal to T_s or exceeding T_s by about 40°C . After at least one hour at T_e , cooling at 40°C per hour was initiated. The solution was pushed over the substrate at $3^\circ\text{--}5^\circ\text{C}$ below T_s and allowed to cool to room temperature. Typical grown layers were 30 to 200 μm thick.

The x-ray emission produced from the layers by the electron beam of an ARL model EMX electron microprobe was analyzed to yield the alloy composition. Measurements were made as a function of position along the growth direction in 2-20 μm steps. The composition at the onset of growth was then obtained by interpolation to zero thickness. The error was estimated at $\pm 2\%$. The variation of the initial solid composition with atom fraction Al in the solution, $X_{\text{Al}}(1)$, and saturation temperature, T_s , is shown in Fig. 1.

Within the experimental uncertainties, the measured concentration of AlAs in the solid did not depend on substrate orientation, the physical properties of the substrate (doping level, dopant, etchpits density, etc.) or on the equilibration temperature, T_e . Examination of the metallurgical interface between the substrates and the grown layers indicated that no etchback of more than a few micrometers took place. Post-growth inspection of the solution revealed no undissolved GaAs source material. From these observations we concluded that a condition close to equilibrium existed in the solution before the initiation of growth.

In Fig. 2, our experimental values are compared to the calculations of Ilegems and Pearson (4). Our data are in moderately good agreement with the calculated

ance in the circuit was sufficiently high; also, the initial switch OFF operation resulted most often in single breakdown spots and the diode subsequently was highly resistive. Therefore, Park and Basavaiah's observation might represent an intermediate state and the current carrying filament present prior to breakdown is likely to be very different from that produced after the breakdown. The breakdown spots generally were 3 to 4 μm in diameter (cf. Fig. 4); however, the original current carrying filament is likely to have been much smaller in dimensions. Moreover, the oxide grown on the second phase particles has been shown to be highly heterogeneous and porous (1). Therefore, calculation of the resistivity of the filament based on the diameter of the breakdown spot and the anodic oxide (zirconia matrix) thickness would be meaningless. Though a positive temperature coefficient of resistance was found in the ON state, the nature of the filament material thus remains unknown.

At this stage, any attempt to interpret the mechanism of the initial switching would be highly speculative because the composition of the second phase particles, their behavior during wet anodization, the type of oxide grown on them, etc., remain unknown. In this connection, a study of the oxide growth on the inter-

metallics of zirconium and iron, chromium or nickel and their electrical properties might be helpful.

Conclusions

In anodic oxide films on Zircaloy-2, the second phase particles are the sites where a majority of the bistable switchings and the associated breakdowns occur.

Acknowledgments

The author remains indebted to Dr. B. Cox for several profitable discussions. He is most grateful to Mr. T. Trottier who assisted in carrying out the experiments.

Manuscript submitted Feb. 22, 1971; revised manuscript received ca. Jan. 12, 1972. This was Paper 152 presented at the Atlantic City Meeting of the Society, Oct. 4-8, 1970.

Any discussion of this paper will appear in a Discussion Section to be published in the December 1972 JOURNAL.

REFERENCES

1. N. Ramasubramanian and T. Trottier, *This Journal*, **118**, 1797 (1971).
2. K. C. Park and S. Basavaiah, *J. Non-Crystalline Solids*, **2**, 284 (1970).
3. R. A. Holt, *J. Nucl. Mater.*, **35**, 322 (1970).

The Composition of $\text{Ga}_{1-x}\text{Al}_x\text{As}$ Grown from Ga-Rich Solutions as a Function of Growth Temperature and Solution Composition

W. G. Rado, W. J. Johnson, and R. L. Crawley

Scientific Research Staff, Ford Motor Company, Dearborn, Michigan 48121

It has been shown that efficient visible light emitting diodes can be fabricated from liquid phase epitaxially (LPE) grown layers of $\text{Ga}_{1-x}\text{Al}_x\text{As}$ (1). The maximum direct energy gap obtainable is 1.9 eV corresponding to a composition of $x = 0.37$ (2). The work of Panish and Sumski (3) and Ilegems and Pearson (4) on the Ga-Al-As ternary system indicates that $\text{Ga}_{1-x}\text{Al}_x\text{As}$ in the range of $0 < x < 0.37$ can be grown by LPE at or below 1000°C from solutions containing less than about 0.007 atom fraction Al. This communication presents experimental data for $\text{Ga}_{1-x}\text{Al}_x\text{As}$ grown in the temperature range of $800^\circ\text{--}950^\circ\text{C}$ from Ga-Al-As solutions containing 0.002-0.014 atom fraction Al.

The $\text{Ga}_{1-x}\text{Al}_x\text{As}$ was grown by LPE on (111)-Ga and As faces of single crystal GaAs substrates that were doped with Te or Se in the range of 0.5 to 2.5×10^{18} electron/cm³. The growth apparatus was similar to that of Hayashi *et al.* (5) in that the solution was pushed over the substrate. Our apparatus also employed a special provision to shear the solution during its push in order to expose a fresh, unoxidized surface. The solution typically contained 4g of six nines pure Ga and the appropriate amounts of six nines pure Al and polycrystalline undoped GaAs. For each run, the saturation temperature, T_s , the temperature at which the Ga-Al solution is just saturated with the specific amount of GaAs used, was determined by using the ternary phase diagram of Ilegems and Pearson (4).

The substrates were lapped with 1 μm alumina, etched in 10 HNO₃:1 HF:5 H₂O for 10 sec, rinsed and dried before being loaded into the boat. The GaAs source material was heavily etched, rinsed, dried, and then wetted with Ga before placement in the solution.

Key words: LPE, LED, phase diagram, direct energy gap semiconductors, electron microprobe.

During loading, the solution was heated to 50°C to insure that the Al was dissolved properly. After positioning in the furnace, the system was flushed overnight with H₂ purified by Pd. The system was then heated to an equilibration temperature, T_e , either equal to T_s or exceeding T_s by about 40°C . After at least one hour at T_e , cooling at 40°C per hour was initiated. The solution was pushed over the substrate at $3^\circ\text{--}5^\circ\text{C}$ below T_s and allowed to cool to room temperature. Typical grown layers were 30 to 200 μm thick.

The x-ray emission produced from the layers by the electron beam of an ARL model EMX electron microprobe was analyzed to yield the alloy composition. Measurements were made as a function of position along the growth direction in 2-20 μm steps. The composition at the onset of growth was then obtained by interpolation to zero thickness. The error was estimated at $\pm 2\%$. The variation of the initial solid composition with atom fraction Al in the solution, $X_{\text{Al}}(1)$, and saturation temperature, T_s , is shown in Fig. 1.

Within the experimental uncertainties, the measured concentration of AlAs in the solid did not depend on substrate orientation, the physical properties of the substrate (doping level, dopant, etchpits density, etc.) or on the equilibration temperature, T_e . Examination of the metallurgical interface between the substrates and the grown layers indicated that no etchback of more than a few micrometers took place. Post-growth inspection of the solution revealed no undissolved GaAs source material. From these observations we concluded that a condition close to equilibrium existed in the solution before the initiation of growth.

In Fig. 2, our experimental values are compared to the calculations of Ilegems and Pearson (4). Our data are in moderately good agreement with the calculated

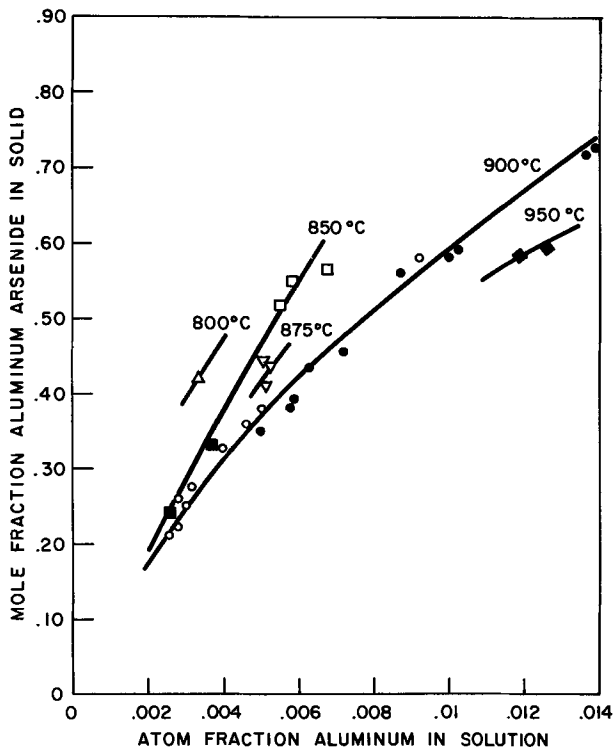


Fig. 1. Initial AlAs concentration in solid $\text{Ga}_{1-x}\text{Al}_x\text{As}$ vs. Al atom fraction in Ga-Al-As solution for specific values of T_s . For $T_s = T_e$, Δ 800°-805°C, \square 850°-855°C, ∇ 875°C, \circ 895°-905°C. For $T_s = T_e - 40^\circ\text{C}$, \blacksquare 850°-855°C, \bullet 895°-905°C, \blacklozenge 945°-950°C.

isotherms, but deviations as high as 30% are found for Al solution compositions in the 0.003-0.006 atom fraction range. A much better agreement is found between our data and the experimental values of Alferov *et al.* (6).

In conclusion, experimental data are presented establishing the relationship between the AlAs concentration in solid $\text{Ga}_{1-x}\text{Al}_x\text{As}$ and the Al concentration in the solution for crystal growth by LPE in the 800°-950°C range. These data should prove useful in the growth of direct energy gap $\text{Ga}_{1-x}\text{Al}_x\text{As}$ for use in efficient light emitting diodes.

Manuscript submitted Nov. 11, 1971; revised manuscript received ca. Jan. 28, 1972.

Any discussion of this paper will appear in a Discussion Section to be published in the December 1972 JOURNAL.

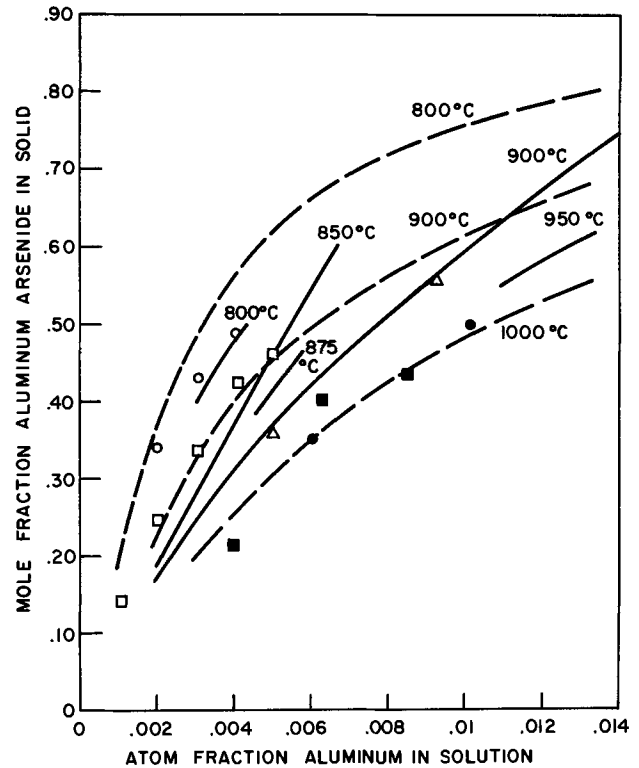


Fig. 2. Experimental isotherms from Fig. 1 (solid lines) and those calculated by Ilegems and Pearson (4) (dashed lines). For comparison purposes, the following data points are also included: \bullet 1000°C Ref. (3), \blacksquare 1000°C Ref. (4), \circ 802°C, \square 852°C and Δ 900°C Ref. (6).

REFERENCES

1. H. C. Casey, Jr. and F. A. Trumbore, *Mater. Sci. Eng.*, **6**, 69 (1970).
2. H. C. Casey, Jr. and M. B. Panish, *J. Appl. Phys.*, **40**, 4910 (1969).
3. M. B. Panish and S. Sumski, *J. Phys. Chem. Solids*, **30**, 129 (1969).
4. M. Ilegems and G. L. Pearson, "1968 Symposium on GaAs," pp. 3-10, Institute of Physics and The Physical Society, London (1969).
5. I. Hayashi, M. B. Panish, P. W. Foy, and S. Sumski, *Appl. Phys. Letters*, **17**, 109 (1970).
6. Zh. I. Alferov, V. M. Andreyev, S. G. Konnikov, V. G. Nikitin, and D. N. Tretyakov, *Proc. Internat. Conf. on Heterojunctions I*, p. 93, Academy of Sciences, Budapest, 1971.

Erratum

Regarding the paper "Electroplating of Osmium" by A. J. Appleby which appeared on p. 1610 in the December 1970 JOURNAL, Vol. 117, No. 12, it has recently been brought to the author's attention that a practical aqueous bath for obtaining bright osmium electrodeposits was described by L. Greenspan [*Engelhard Ind. Tech. Bull.* **10**, 48 (1969)] as the above paper was in final preparation. As stated by Mr. Greenspan: "This bath contains osmium in alkaline solution as an anionic complex formed by reacting osmium tetroxide

with sulfamic acid. Using this bath at a temperature of 65°-75°C, and with current densities of 2-10 A/ft², deposits at a rate of about 100 $\mu\text{in.}/\text{hr}$ are obtained with current efficiencies of the order of 40-80%. Deposits of about 50 $\mu\text{in.}$ are from lustrous to bright; those of 100 $\mu\text{in.}$ and above are dull but smooth. This bath appears more suited for practical electrodeposition of osmium than the cyanide bath and is commercially available." The author is indebted to Mr. Greenspan for bringing this omission to his attention.



Removal of Surface Antimony from Antimony Lead Alloys by Sulfuric Acid-Hydrogen Peroxide Pickling

T. R. Crompton and G. Uitenbroek*

Oldham & Son Limited, Denton, Manchester, England

ABSTRACT

It has been shown that treatment of cast antimonial lead alloys with mixtures of hydrogen peroxide and sulfuric acid at 20°C dissolves surface antimony at an appreciably greater rate than occurs with sulfuric acid alone, even at elevated temperatures. Optimum hydrogen peroxide-sulfuric acid reagent compositions have been established for the maximum solution of antimony from the alloy. A correlation exists between the quantity of antimony removed by this treatment and the quantity of antimony that is subsequently released from the alloy into sulfuric acid electrolyte when it is set up as an anode against pure lead cathodes. Batteries made using positive grids which have been pickled in hydrogen peroxide-sulfuric acid mixtures, then brightened by dipping in a 10% aqueous solution of diethylene triamine have been shown to have a greater life on charge/discharge cycles than batteries made using standard unpickled grids.

Antimony is added as an alloying constituent to impart increased hardness to lead used in the manufacture of grids for lead-acid batteries. Alloy grids are much less liable to distortion during battery manufacturing operations. However, positive battery plates used in lead-acid battery manufacture, made from such castings, will, during plate formation, release a large proportion of their surface antimony, which will migrate towards the negative plate, thereby contaminating the formation electrolyte, the negative active material, and the positive active material. Similarly, in battery operation, antimony contamination of plates will occur. Both forms of antimony contamination have adverse effects on battery performance such as increases in positive plate corrosion (i.e., shorter life) and in self-discharge rates; also it prevents the positive plate from reaching its true potential. For these reasons research has been undertaken to study removal of antimony from such grids.

Burbank and Simon (1) have shown the manner in which the anodic corrosion of lead and its hypoeutectic antimony alloys takes place in sulfuric acid and how such corrosion is related to the microstructure of these alloys. Pure lead and alloys containing up to 0.5% antimony corrode intergranularly (i.e., grain boundary attack). At higher concentrations a combination of intergranular and interdendritic penetration occurs, but up to 6% antimony the attack remains preferentially intergranular. At higher antimony concentration (6-12%) the corrosion is more evenly distributed between intergranular attack and attack along the interdendritic network of segregated antimony. Burbank and Simon also revealed by x-ray diffraction that the surface of castings containing 6% or more antimony is richer in antimony than within the bulk of the castings, i.e., an antimony-rich surface layer is present.

A search brought to light one patent, by Bosch (2), which involves a pickling treatment for removing con-

centrations of antimony on the surface of cast lead-antimony alloys used in lead acid battery manufacture. This process involves dipping the as-cast metal in sulfuric acid of 1.75 sp gr. This treatment it is claimed will remove antimony from a surface layer of at least 10^{-6} mm thickness of alloy.

The work described below for removing surface antimony from antimonial lead differs from that described by Bosch in that it incorporates a sulfuric acid-hydrogen peroxide reagent which has been shown to be much more effective than sulfuric acid alone in removing surface antimony from antimonial lead.

Experimental

Pickling in sulfuric acid.—Experiments were first carried out to establish the extent to which pickling in aqueous sulfuric acid dissolved antimony from 7% antimonial lead. One kilogram of metal was immersed in 2 liters of sulfuric acid of known specific gravity and maintained at a constant temperature. In the work described in this paper the lead was in the form of cast grids of the type used in the manufacture of lead acid batteries. After various time intervals portions of the acid were removed and dissolved antimony determined by a procedure which is sensitive enough to detect down to 0.2 mg antimony in a liter of test solution.

Pickling in sulfuric acid-hydrogen peroxide mixture.—A range of solutions were prepared such that the final mixtures had a known specific gravity with respect to sulfuric acid (between 1.03 and 1.60 sp gr at 20°C) and contained a known concentration of hydrogen peroxide (between 2 volume and 5 volume concentration).¹ In all cases the solutions were prepared immediately prior to use. The pickling experiments were then carried out as discussed above.

Determination of antimony in sulfuric acid-hydrogen peroxide mixtures.—**Reagents.**—Standard antimony so-

* Electrochemical Society Active Member.

Key words: battery, lead-acid, alloys, antimony, battery grids, pickling.

¹ One volume concentration H_2O_2 is that concentration (0.3g H_2O_2 /liter) which upon decomposition produces 1 ml oxygen at STP per milliliter of the peroxide solution.

lution, prepared from potassium antimonyl tartrate "ANALAR" to contain 0.1 mg antimony per milliliter.

Ascorbic acid/potassium iodide reagent was prepared by dissolving 70g potassium iodide "ANALAR" and 5g ascorbic acid in deionized water and making up to 500 ml. This solution must be prepared freshly as required.

Sulfuric acid was 1.2 sp gr, aqueous.

Potassium permanganate (1*N*) aqueous, was prepared from "ANALAR" solid.

Calibration curve.—Into seven 100 ml volumetric flasks, pipette 0.0, 0.1, 0.2, 0.3, 0.5, 0.7, and 1.0 ml of standard antimony solution (e.g., 0.0 to 0.1 mg Sb) then add 10 ml of 1.2 gravity sulfuric acid. Add 25 ml potassium iodide/ascorbic acid reagent to each flask then make up to 100 ml with 1.2 sp gr sulfuric acid.

Fill two 10 mm glass spectrophotometer cells, respectively with the solution which is free from antimony (control) and the solution containing 0.1 ml standard antimony solution.

Place the two cells in spectrophotometer and measure the optical density at 425 m μ of the sample solution relative to the control (antimony free) solution in the reference beam. Repeat with each of the standard antimony solutions.

Plot a curve of milligrams antimony in the original 100 ml test solution vs. the corresponding optical densities obtained.

Analysis of pickling solutions.—Transfer a suitable volume (maximum 10 ml) of pickling solution into a 100 ml volumetric flask. If the specific gravity of the sulfuric acid in the pickling solution is less than 1.2 then add a calculated volume of 1.6 sp gr sulfuric acid to adjust the gravity in the final mixture to 1.2. If the specific gravity of the pickling solution exceeds 1.2 then add a calculated volume of deionized water sufficient to adjust the gravity of the final mixture to 1.2. Add sufficient 1.2 sp gr sulfuric acid to make the volume up to 10 ml. To a second control 100 ml volumetric flask add 10 ml 1.2 sp gr sulfuric acid. To both solutions add dropwise from a burette, potassium permanganate solution until a faint pink color is produced which persists for 5 min, indicating complete neutralization of hydrogen peroxide. Add 25 ml potassium iodide/ascorbic acid reagent and make up to 100 ml with 1.2 sp gr sulfuric acid. Refer the optical density to the calibration curve to obtain the weight of antimony present in the original 100 ml of diluted pickling solution.

If it is found that the concentration of antimony in the original pickling solutions is too high, then this solution should be diluted by a known amount with sulfuric acid of the same specific gravity and the above analysis repeated.

Measurement of the release of antimony from alloys under electrochemical conditions.—Pickled and unpickled castings (150g) in 4.5, 7, and 10% antimonial lead were set up as anodes, against pure lead cathodes in cells containing a liter of 1.25 sp gr sulfuric acid. A 2A current was passed through the castings and the antimony content of the electrolyte determined at intervals.

Construction of test batteries.—The test batteries used in the study were Miners Caplamps batteries constructed with two cells, each containing a tubular positive plate and two negative plates and a standard separator system.

A low antimonial alloy (4.5% antimony) was used throughout; only the positive grids were pickled.

Pickling was conducted for 8 hr at 15°–20°C in a solution consisting of 4 volume strength hydrogen peroxide in 1.200 sp gr sulfuric acid. The solution was contained in a glass or polyethylene tank and the lead grids were suspended, without touching in this solution at a ratio of 1 kg of lead to 2 liters of solution.

In some experiments the grids were then rinsed in cold running water to remove acid and were then allowed to dry. Such grids had on the surface a very

thin whitish layer, presumably of lead sulfate. In other experiments, pickled grids were immediately dipped in a 10% aqueous solution of diethylene triamine for a few minutes until lead sulfate had been completely removed and the metal was bright. The plates were then quickly rinsed in water and left to air dry.

Batches of batteries containing unpickled, pickled and water washed, and pickled and amine washed positive grids were then assembled by standard manufacturing methods.

The batteries were then continuously cycled according to the following schedule: charge: constant voltage charge at 4.90 to 2.45V per cell (about 15 hr); discharge: for 9 hr through a 1A calibrated bulb recording the time taken to reach 1.85V per cell. Cycling tests were discontinued when the discharge time dropped below 7 hr, i.e., end of battery life.

Results

Sulfuric acid pickling.—Antimony extraction was extremely low at acid gravities of 1.2 and 1.4 even at operating temperatures up to 80°C. At 1.6 gravity and 80°C, 72 mg of antimony was dissolved from the alloy in 300 hr from 1 kilo of alloy, i.e., only 0.1% of the antimony content of the original alloy (7%) was dissolved into the pickling solution. At 80°C in 1.4 gravity acid, a small amount of white precipitate was noted in the acid, presumably lead sulfate. At 80°C in 1.6 gravity acid, a small amount of a brown orange precipitate was noted in suspension in the solution and as a coating on the metal. This solid contained about 4% antimony and, presumably by its color, contained antimony sulfide. The solution itself had a deep brown discoloration. In the same experiment, a bubbler containing 10% aqueous silver nitrate solution was connected to the sealed vessel in which the pickling was carried out and it was observed that during the experiment, a black precipitate formed in the silver nitrate solution. This was presumably, silver stibnide and/or silver sulfide produced by reaction of silver ions with stibine and/or hydrogen sulfide produced during pickling. These observations fit in with the reactions known to occur between antimony and hot sulfuric acid solutions of specific gravity greater than 1.55. Decomposition products of this type were not observed in pickling experiments conducted in acid gravities below 1.4

Sulfuric acid-hydrogen peroxide pickling.—Figure 1 compares the rate of extraction of antimony from 7% antimonial lead by strong sulfuric acid at 80°C and by various acid-hydrogen peroxide mixtures at normal ambient temperatures. The dramatic increase in antimony extraction resulting upon incorporation of hydrogen peroxide is immediately evident.

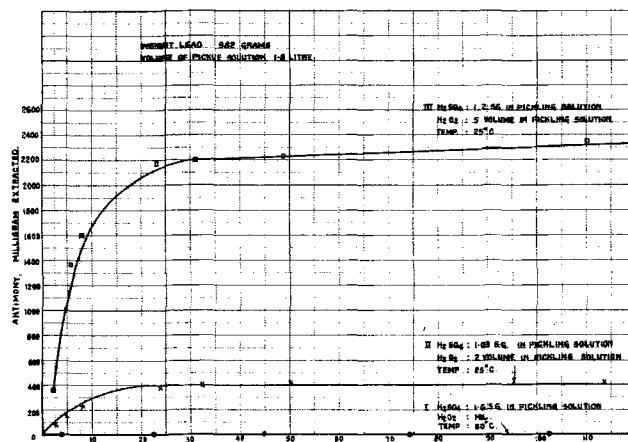


Fig. 1. Comparison of pickling rates of 7% antimonial lead in sulfuric acid and hydrogen peroxide/sulfuric acid.

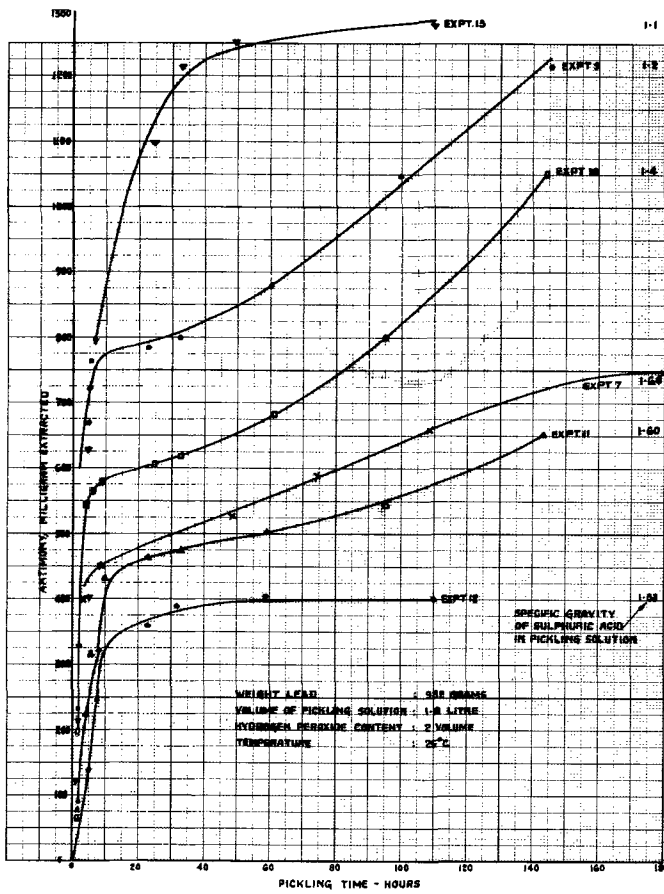


Fig. 2. Influence of sulfuric acid concentration on pickling rate of 7% antimonial lead.

Increase in the concentrations of acid and peroxide leads to higher antimony extractions (compare curves II and III, Fig. 1).

Effect of sulfuric acid concentration.—The curves in Fig. 2 plot the course of antimony extraction occurring from 7% antimonial lead during pickling times of up to 180 hr at 25°C in a reagent consisting of hydrogen peroxide (2 volume) and sulfuric acid (between 1.03 and 1.60 sp gr). Experimental replication is satisfactory (compare curves 7 and 11). At acid gravities of under 1.1, antimony extraction ceased after 40-50 hr, reaching 70-80% of this value in 10 hr. At acid gravities higher than 1.1 antimony extraction from the grid still continued after 180 hr with no evidence of leveling out. The highest antimony extraction recorded was obtained with 1.1 to 1.2 gravity acid. Also, at acid gravities in this range, antimony extraction following a 5 hr pickling was about half that obtained during a 140 hr pickle. After pickling, the metal became eventually gray or white colored and, at certain acid concentrations a turbidity or precipitate, presumably of lead sulfate, formed in the solution. At acid concentrations of 1.2-1.3 sp gr and pickling times up to 30 hr no insoluble matter was evident in the solution.

Effect of hydrogen peroxide concentration.—The results in Fig. 2 show that extension of the pickling time above 10-20 hr is not a very efficient method of increasing the antimony extraction rate in the case of a reagent consisting of 2 volume hydrogen peroxide and sulfuric acid in the 1.1-1.2 sp gr range. Next, a comparison was made between antimony extraction obtained for 7% antimonial lead using 2 volume and 5 volume hydrogen peroxide, both with 1.2 gravity acid at 25°C. After 10 hr the antimony extraction increased almost *pro rata* with increase of hydrogen peroxide concentration, and, in fact, the solution containing 5 volume hydrogen peroxide removed as much antimony in 5-10 hr as did the weaker reagent in 140 hr. The

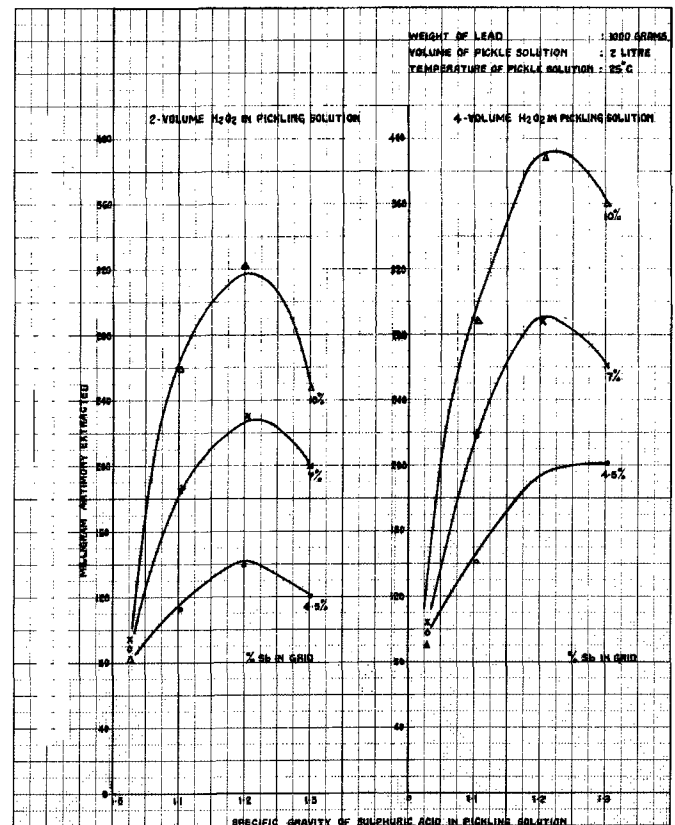


Fig. 3. Influence of acid gravity and hydrogen peroxide concentration on antimony extraction in 8 hr pickle of 4.5, 7, and 10% antimonial lead.

quantities of antimony dissolved from approximately 1 kilo of lead in a 140 hr pickle using the two and five volume hydrogen peroxide were respectively 1.3g and 2.4g. Thus, increasing the concentration of peroxide in the reagent is a more effective method of increasing antimony extraction than extension of pickling time.

Figure 3 shows the effect of sulfuric acid and hydrogen peroxide concentration on antimony extraction during an 8 hr pickle at 25°C for freshly cast lead alloys containing 4.5, 7.0, and 10% antimony. For each alloy, antimony extraction was highest at an acid gravity of 1.2 and at the higher peroxide concentration. A repeat experiment on these alloys three weeks after casting gave an identical set of curves. A plot of weight of antimony extracted during an 8 hr pickle against the antimony content of the alloy showed a linear relationship for each of the eight reagent systems quoted in Fig. 3.

Tables I and II show the effect of reagent composition and pickling time on the percentage of the original

Table I. Percentage dissolution of antimony from 7% antimonial lead (thin section 1/16 in.)

Sulfuric acid gravity	Per cent of original antimony content of alloy extracted into pickling solution		
	10 hr	Pickling time 20 hr	Extended*
1.6 (nil hydrogen peroxide) at 80°C	<0.001	0.001	0.1 (300.I)
1.03 (2 vol. H ₂ O ₂) at 25°C	0.45	0.5	0.6 (40.M)
1.1 (2 vol. H ₂ O ₂) at 25°C	1.2	1.5	1.9 (70.M)
1.2 (2 vol. H ₂ O ₂) at 25°C	1.0	1.1	1.7 (140.I)
1.2 (5 vol. H ₂ O ₂) at 25°C	2.6	3.0	3.3 (70.M)
1.4 (2 vol. H ₂ O ₂) at 25°C	0.8	0.9	1.4 (145.I)
1.6 (2 vol. H ₂ O ₂) at 25°C	0.6	0.65	1.0 (160-180.I)

* Numerals in brackets indicate prolonged pickling time in hours. I indicates that antimony concentration of solution is still increasing at end of test period. M indicates that it had reached a maximum at end of test period.

Table II. Percentage dissolution of antimony from various antimonial lead (thicker section 1/8-1/4 in.)

Sulfuric acid gravity	% hr	Per cent of original content of alloy extracted into pickling solution				
		4.5% antimonial lead pickling time		Extended*	7% antimonial lead pickling time	10% antimonial lead pickling time
		10 hr	20 hr		% hr	% hr
1.03 (2 vol. H ₂ O ₂) at 25°C	0.2	0.3	0.4	0.5 (50)	0.1	0.1
1.03 (4 vol. H ₂ O ₂) at 25°C	0.2	—	—	—	0.15	0.1
1.1 (2 vol. H ₂ O ₂) at 25°C	0.25	0.5	0.6	0.7 (50)	0.3	0.25
1.1 (4 vol. H ₂ O ₂) at 25°C	0.3	—	—	—	0.3	0.3
1.2 (2 vol. H ₂ O ₂) at 25°C	0.3	0.9	0.9	—	0.3	0.3
1.2 (4 vol. H ₂ O ₂) at 25°C	0.4	0.75	—	—	0.4	0.4
1.3 (2 vol. H ₂ O ₂) at 25°C	0.3	—	—	—	0.3	0.25
1.3 (4 vol. H ₂ O ₂) at 25°C	0.4	—	—	—	0.4	0.4

* Numerals in brackets indicate pickling time in hours, antimony extraction had reached a maximum within these times.

antimony content of the alloy which is removed by pickling. Comparison of these results show that with similar reagents the percentage of the original antimony content of the alloy which is extracted from thinner section moldings is higher than with thicker section moldings, due, presumably to the higher area to volume ratio of the former with its consequent increased surface area per unit weight of lead available for antimony dissolution. The inefficiency of pickling with strong sulfuric acid without peroxide at 80°C is clearly evident in Table I, which shows that only 0.001% of the original antimony content of the alloy has been extracted. Contrasted with this and confirming the earlier experiments, 3% antimony extraction occurs when pickling is carried out at 25°C in 1.2 gravity acid containing 5 volume peroxide. Clearly, this antimony removal must occur principally at the metal surface (or in the region near to the surface). If, with an as-cast alloy there is no enrichment of antimony at the surface above the normal level this result implies that, on the average, the pickling reagent penetrates only to a depth of between 0.001 and 3% of the average thickness of the metal. If, on the other hand, as had been postulated, antimonial lead castings have a very thin surface layer of appreciably higher antimony content than the bulk of the alloy, then the average depth of reagent penetration into the grid to produce the observed antimony extractions would be less than those quoted above.

Hydrogen peroxide decomposition.—It was observed that gas bubbles were continuously formed on the surface of grids during pickling at 25°C. The gas is produced by a gradual decomposition of hydrogen peroxide to oxygen and water and is presumably catalytically induced by lead or by impurities therein. Peroxide decomposition was monitored during pickling by analyzing timed samples by titration with standard potassium permanganate.

Figure 4, shows, for 7% antimonial grids during a 40 hr pickle, the influence of acid gravity on antimony extraction and the parallel decomposition of hydrogen peroxide. It is seen that hydrogen peroxide decomposi-

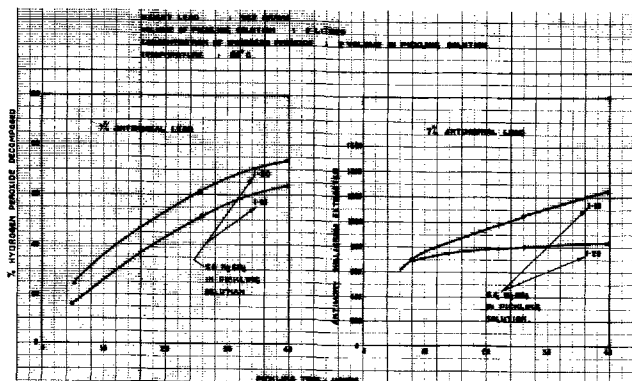


Fig. 4. Relation between pickling time, antimony extraction, and hydrogen peroxide decomposition.

tion is highest under those conditions under which antimony extractions are highest.

Effect of pickling on subsequent release of antimony from alloys under electrochemical conditions.—Obviously, the more efficient the removal of antimony by pickling then the lower will be the equilibrium antimony content of the electrolyte in an electrolysis experiment, compared to the equilibrium antimony content obtained by electrolysis of unpickled control alloys. This procedure therefore offers a method of ascertaining the influence of chemical pickling in acid hydrogen peroxide on the subsequent rate of removal of antimony from the alloy under conditions where a current flows.

Figure 5 plots the relationship between the antimony content of the original alloy and the weight of antimony removed from 150g of three lead alloys during a 25 hr electrolysis. It is seen that less antimony is removed by electrolysis of alloys which have been previously pickled compared to the unpickled controls. The effect of chemical pickling upon subsequent antimony removal occurring upon electrolysis, is greatest

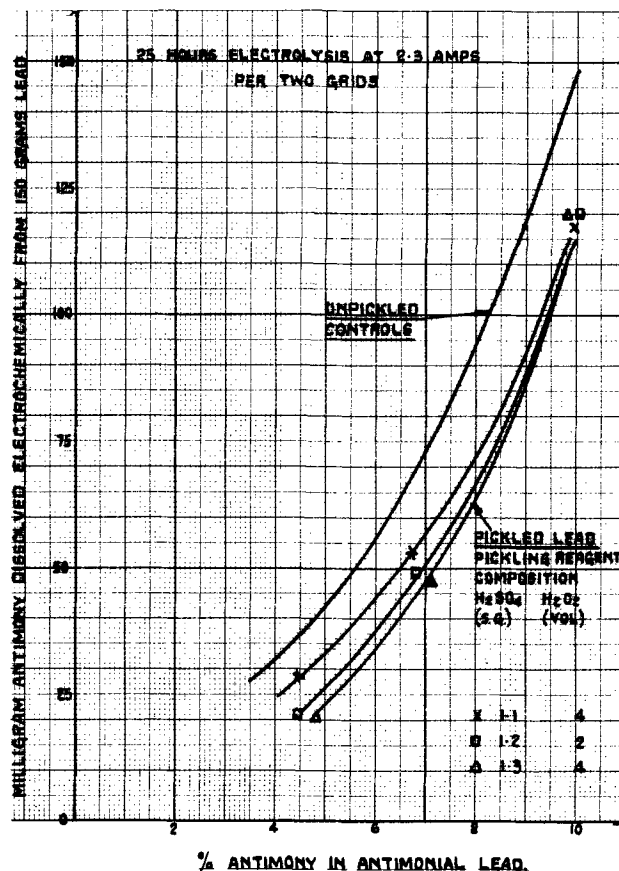


Fig. 5. Electrochemical removal of antimony from pickled and unpickled lead as a function of original antimony content of alloy.

in the case of the 4.5% antimonial alloy in which antimony removal upon electrolysis is about half the value obtained for the unpickled control. Smaller effects of pickling on antimony removal during electrolysis were noted in the case of the two higher antimonial alloys.

It was attempted to ascertain whether a relationship existed between antimony removal from the grid during chemical pickling and the amount of antimony which is subsequently removed from the grid upon electrolysis.

If, during electrolysis of an unpickled metal casting, the concentration of antimony that builds up in the electrolyte in time T is denoted by X mg Sb/g alloy and if, during the same time interval, the concentration of antimony that builds up in the electrolyte in contact with pickled alloy at the same initial antimony content is denoted by Y mg Sb/g alloy, then $(X - Y)$ is a measure of the efficiency of the chemical pickling process in removing surface antimony from the alloys. If the weight of antimony removed from the alloy during pickling is denoted by Z mg/g alloy, then it follows that for an alloy of a particular composition, an increase in the value of Z should be accompanied by a decrease in the value of Y , i.e., an increase in the value of $(X - Y)$ for each of the three alloys examined. That this is so is confirmed by examination of Table III.

It follows from the previous discussion that $(X - Y) 100/X$ represents the percentage reduction in extractable antimony that occurs as a result of chemical pickling of alloys compared to unpickled controls in the same antimonial alloy. This quantity is a direct measure of the reduced amount of electroextraction of antimony from alloys that occurs under standard electrochemical conditions as a result of various chemical pickling treatments of the alloys. It is interesting to examine, therefore, the influence of increasing the antimony removal from alloys, i.e., increasing Z during pickling (by using different pickling reagents) on $(X - Y) 100/X$. This is shown in Fig. 6 which plots Z against $(X - Y) 100/X$. It is seen that three groups of results are obtained corresponding to the 4.5, 7, and 10% antimonial alloys. At each alloy composition, as expected, an increase in antimony removal (Z) during pickling is accompanied by an increase in the percentage reduction of electroextractable antimony $(X - Y) 100/X$. The latter is greater in the case of the 4.5% antimonial alloy (viz. 40-50%) and least in the case of the 10% alloy (viz. about 20%).

Mining caplamp battery cycling tests.—The results in Table IV give distinct evidence that batteries made up with 4.5% antimonial lead positive grids which have been pickled and amine washed have a longer cycle life than batteries made using either unpickled grids of the same antimony content or grids which have been pickled but not amine washed.

Table III. Influence of pickling the alloy on subsequent solution of antimony by electrolysis

Alloy composition w/w % Sb	Pickling reagent composition		Z	Y* (25 hr electrolysis)	(X - Y)* (25 hr electrolysis)
	H ₂ SO ₄ sp gr	H ₂ O ₂ vol.			
4.5	1.03	2	13	32	4
	1.1	4	22	28	8
	1.2	2	21.5	21	15
	1.3	4	31	22	14
7.0	1.03	2	14	66	6
	1.1	4	34	66	17
	1.2	2	35	52	20
	1.3	4	40	52	20
10.0	1.03	2	13	138	10
	1.1	4	44	120	28
	1.2	2	50	120	28
	1.3	4	55.5	120	28

* For explanation of terms see text.

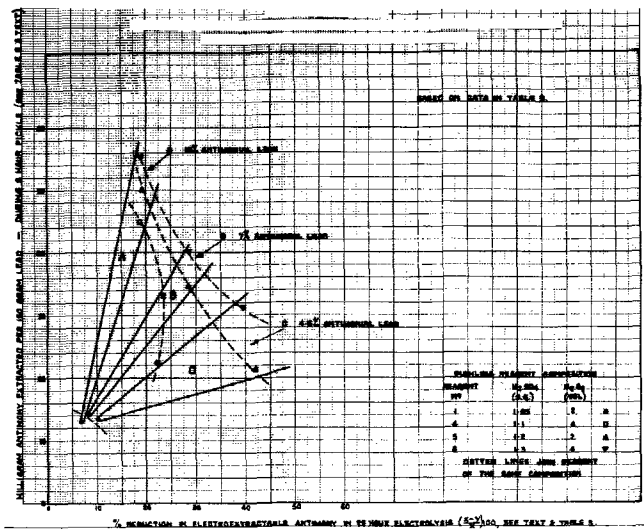


Fig. 6. Effect of efficiency of antimony removal during pickling on per cent reduction in electroextractable antimony from lead.

Discussion

Pickling of antimonial lead at ambient temperature in mixtures of hydrogen peroxide and sulfuric acid is a considerably more efficient method of stripping off the surface rich antimony layer that has been postulated to exist on these alloys than is achieved by pickling in sulfuric acid alone, even at elevated temperatures. For alloys in the composition range studied up to 10% antimony, antimony extraction is highest at a sulfuric acid concentration in the pickling solution corresponding to 1.20 ± 0.10 sp gr.

This applies at all hydrogen peroxide concentrations between the extremes of the range studied (2-5 volume strength). At any particular hydrogen peroxide concentration in the reagent, the extraction of antimony during a standard pickling time decreases as the sulfuric acid concentration is decreased below or is increased above the acid gravity of 1.20 ± 0.10 . At a particular acid concentration and pickling time, antimony extraction increases with increase in hydrogen peroxide concentration. Increase of the concentration of hydrogen peroxide in the pickling solution is usually a more efficient method of antimony removal than extension of the pickling time.

Depending on various factors viz. reagent composition, pickling time, surface area/volume ratio of lead, antimony content of alloy, between 0.1 and 3.3% of the original total antimony content of the alloy is extracted during pickling processes (Tables I and II). Also, as indicated in Table III, the greater the amount of antimony that is removed from the surface of the lead by pickling prior to electrolysis then the smaller the amount of surface antimony that is left on the grid. This indicates that both pickling and electrolysis

Table IV. Effect of grid pickling on cyclic life tests of mining caplamp cells

Battery No.	Positive spine pickling	No. pickle	Grid pickled then water washed	Grid pickled then amine washed	Cycles to end of life (when discharge time to 3.70V decreases to less than 7 hr)
1		360	80		500
2		480	360		540
3		340	340		440
4		360	360		420
5		300	400		440
6		340	500		540
7		400	400		440
8			360		420
9			380		540
10			400		500
11			340		560
12			420		440
13			240		480
14			400		520
Average		368	377		484

remove antimony from the surface, only, of the lead. Obviously, the higher the extraction of surface antimony during pickling the less are adverse effects to be expected by antimony in subsequent battery operation. Data in Fig. 5 and 6 indicate that positive 4.5% antimonial lead grids that have been pickled for 8 hr in a 1.2-1.3 gravity sulfuric acid/2-4 volume hydrogen peroxide pickling solution would be expected under electrochemical conditions to release only approximately 50% of the amount of antimony obtained from an unpickled 4.5% antimonial alloy. The corresponding figure for pickled 10% antimonial alloy is 80% of the amount of extracted antimony that would be obtained for the unpickled alloy. Thus the beneficial effects of pickling on subsequent battery performance would be expected to be greater in the case of lower antimonial alloys.

The data in Table IV indicate that an 8 hr pickling of 4.5% antimonial positive grids in a reagent comprising sulfuric acid (1.20 sp gr) and hydrogen peroxide (4 volume) followed by amine treatment to remove surface deposits leads to an approximately 30% increase in cyclic life of the particular type of battery studied. Examination of the data in Table II shows that extension of the pickling time with this reagent to times greater than 8 hr would have removed considerably more antimony (perhaps 2-3 times as much) than was in fact removed during 8 hr. Possibly, positive grids which had been given an extended pickling time would lead to further improvements in

cyclic life to that obtained in the experiments described above. Additionally, it is possible that negative grid pickling would have further beneficial effects.

It is clear that, to obtain maximum benefits from grid pickling, a careful study should first be conducted of the effect of pickling reagent composition, pickling time and other factors on antimony removal occurring during pickling for the types of plates it is intended to use in each particular type of battery.

Acknowledgments

Acknowledgments are made to Mr. D. Andrew and Mr. D. Butterworth who assisted in the experimental work and to the Directors of Oldham & Son Limited for their permission to publish the work.

The work described in this paper is the subject of the following British patent application: No. 18551/70 filed April 17, 1970 entitled "Improvements in Methods of Treating Grids for Electric Storage Battery plates."

Manuscript submitted Aug. 9, 1971; revised manuscript received ca. Feb. 2, 1972.

Any discussion of this paper will appear in a Discussion Section to be published in the December 1972 JOURNAL.

REFERENCES

1. J. B. Burbank and A. C. Simon, *This Journal*, **100**, 11 (1953).
2. Robert Bosch, G.m.B.H. Germany, Brit. Pat. 837,-969 (1960).

Lead-Fluoroboric Acid Battery

G. D. McDonald,* E. Y. Weissman,* and T. S. Roemer

Globe-Union, Inc., Milwaukee, Wisconsin 53201

ABSTRACT

A reserve battery is described that can operate over a wide temperature range, including temperatures as low as -60°C at coulombic efficiencies of 16% or better. The battery is based on the system: lead/fluoroboric acid/lead dioxide and utilizes a bonded lead dioxide cathode. The system is discussed based on data such as: capacities, current-voltage relationships, and coulombic efficiencies, as a function of temperature; self-discharge characteristics; specific energy; and cost considerations.

The lead/fluoroboric acid/lead dioxide battery has typically been used for applications requiring an inexpensive reserve-type power supply capable of high discharge rates over a wide temperature range. An example of such an application is the proximity fuze battery (1, 2). The characteristics of a typical Pb/HBF₄/PbO₂ battery are summarized in Table I, where the listed specifications have been all exceeded to a significant degree (e.g., 50 sec of 0.040A discharge, above 18V at $+60^{\circ}\text{C}$; 90 sec of 30 mA discharge, above 15V, at -40°C).

* Electrochemical Society Active Member.

Key words: fluoroboric acid battery, lead dioxide electrode, bonded lead dioxide electrode, lead-fluoroboric acid battery.

Table I. Characteristics of a fluoroboric acid proximity fuze battery

Number of cells:	14
Minimum voltage:	15V
Current:	0.030A
Discharge duration:	20 sec
Temperature range:	-40° to $+60^{\circ}\text{C}$
Activation time:	<0.4 sec
Battery volume:	2.5 cc
Battery weight:	approx. 4g
Special features:	a) shelf life of up to 20 yr b) low cost of raw materials (lead at 45¢/kg; fluoroboric acid at 55¢/kg)

Fluoroboric acid is particularly well suited for such types of reserve batteries because of its wide liquidus range, good conductivity, and ready availability (used in the electroplating industry). Table II summarizes its properties as well as the over-all electrochemical reaction in which it participates. The boric acid is present in order to suppress hydrolysis in which the fluorine atoms attached to the boron are stepwise replaced by hydroxyl groups, with the other hydrolysis product being hydrofluoric acid.

An important feature of this electrochemical system is the solubility of lead fluoroborate, the reaction product formed at each electrode (approximately 380g per liter). Because of this property, dense, nonporous,

Table II. The fluoroboric acid electrolyte

Over-all reaction	$\text{Pb} + \text{PbO}_2 + 4\text{HBF}_4 \rightarrow 2\text{Pb}(\text{BF}_4)_2 + 2\text{H}_2\text{O}$ / $E = 1.86$ at 25°C /
Electrolyte characteristics	Available as 48% aq. solution (with $\sim 2.5\%$ H ₃ BO ₃)
Freezing point:	-78°C
Decomposition point:	$+130^{\circ}\text{C}$
Conductivity	
at room temp.:	0.61 ohm ⁻¹ cm ⁻¹
at -60°C :	0.06 ohm ⁻¹ cm ⁻¹

and structurally stable electrodes can effectively be used with a resultant savings in required battery volume. At the same time, fluoroboric acid attacks most other metals and metal oxides to give soluble reaction products. While we have found that neither lead nor lead dioxide are attacked in the absence of oxygen, the generally corrosive nature of this electrolyte requires a careful selection of the battery materials of construction.

At the present time, lead-fluoroboric acid type batteries use bipolar electroplated electrodes consisting of nickel-plated steel shim stock with lead plated on one side and layers of α - and β -lead dioxide on the other. Capacity densities of the order of 7 A-sec per cm^2 of geometric electrode area are attainable. Attempts to increase this capacity by heavier plating have proved fruitless owing to adhesion or active material brittleness problems. The only successful attempts to increase cell capacity have resulted from increases in electrode plate area (3).

Lately, some work (4) has been carried out in the area of development of bonded lead dioxide electrodes possessing higher capacities and improved mechanical properties. The present paper summarizes results obtained along similar lines, based primarily on the use of electrode hot-pressing techniques.

Experimental

The raw materials were: commercially available lead dioxide powder (Fisher Scientific; particle size range: 90-100 μ); lead sheet (99% pure, 0.52 mm thickness); and 48% fluoroboric acid (Harshaw Chemical). All materials were used without preliminary purification or processing steps. The lead dioxide particles were solvent-coated with suitable thermoplastic binders and the resulting mix was comminuted and then hot-pressed onto expanded metal (*e.g.*, nickel) current collector grids.¹ The test cells were constructed using lead sheet counterelectrodes, a "back-to-back" configuration (lead dioxide cathode sandwiched between two lead anodes), and microporous polyvinyl chloride separators.

When using 2.5 by 3.8 cm electrodes with 1.5 ml of electrolyte the cells weighed about 10g each, had a volume of 2 cm^3 , and a theoretical capacity of approximately 0.5 A-hr. They were evaluated by force-discharging at constant current and recording voltage *vs.* time. Linear voltage sweeps were carried out with a Wenking Model 121 potentiostat and a Wenking SMP 66 function generator. Internal resistance measurements were based on a modification of a previously reported technique (5), using 20 μsec interruptions.

Self-discharge tests were also carried out, by maintaining a test cell at open-circuit at various temperatures for predetermined time intervals and then discharging it at the given temperature and/or at room temperature. A Conrad environmental chamber was used for all tests taking place at other than room temperature.

Results and Discussion

Figure 1 shows typical discharge curves of a fluoroboric acid test cell at various temperatures; they all exhibit well defined voltage end points and no apparent activation transients. Figure 2 exhibits the effect of discharge rate on the coulombic efficiency (*i.e.*, available capacity) of the lead dioxide electrode. For the types of electrodes evaluated there appears to be essentially no change in attainable capacity up to about 50 mA/cm^2 . Higher discharge currents result in lower capacities.

It is interesting to note that 200 mA/cm^2 corresponds to approximately the 1 min rate, at which

¹ The oxidizing characteristics of lead dioxide would seem to present a potential hazard. However, no difficulties were encountered in this work and DTA tests of the plastic-coated lead dioxide have exhibited initiation temperatures for a redox reaction which are about 30°C higher than the hot-pressing temperatures required for electrode preparation. Nevertheless, this aspect will warrant further attention prior to any development of large scale manufacturing processes.

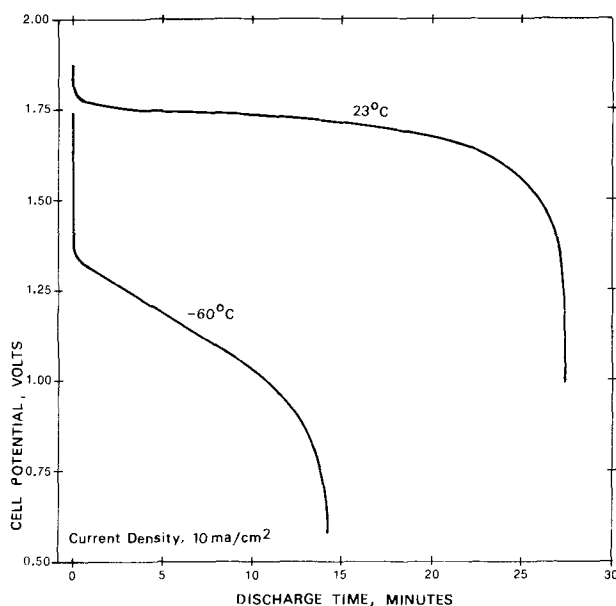


Fig. 1. Typical discharge curves for a Pb/HBF₄/PbO₂ test cell

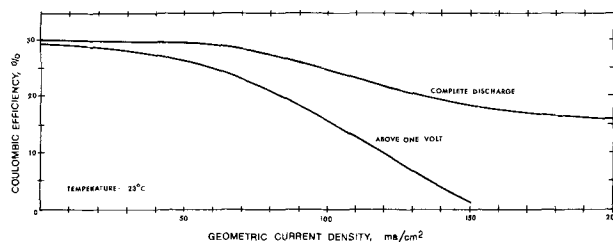


Fig. 2. Coulombic efficiency characteristics of the lead dioxide electrode in fluoroboric acid.

point the efficiency is still 16%. Furthermore, we have evidence to indicate that pulse current densities of 300 mA/cm^2 are also possible.

Figure 3 shows the effect of temperature on the coulombic efficiency of the system. At low temperatures the internal resistance accounts for the lower capacity, whereas at the higher temperatures, capacity is limited by self-discharge. Indeed, as far as this latter aspect is concerned, we note that commercially available electroplated bipolar electrodes have an activated stand capability of less than 6 min at room temperature. As opposed to that, state-of-the-art, high rate, bonded lead dioxide electrodes do not self-discharge appreciably for the first 48 hr at room temperature (Fig. 4). At a temperature of -50°C, corresponding to a variety of applications (*e.g.*, weather balloons), no significant self-discharge has been observed after 4 months of activated stand.

Figure 5 summarizes our findings regarding the activated stand capability of a bonded, high rate, lead dioxide electrode at the upper temperature extreme of 80°C. The capacity loss is rapid, about 1.33% per min, corresponding to complete self-discharge after 75 min. Similar studies were conducted at 40° and 60°C. The

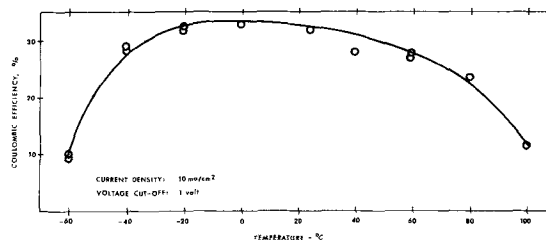


Fig. 3. Coulombic efficiency characteristics of the lead dioxide electrode in fluoroboric acid.

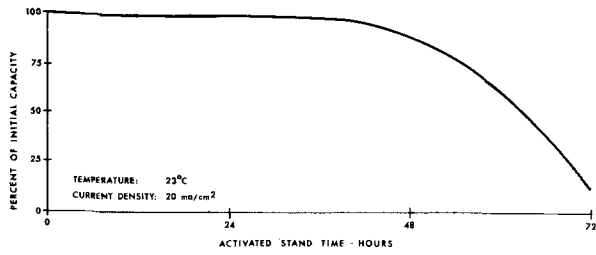


Fig. 4. Self-discharge characteristics of high rate, bonded, lead dioxide electrode in fluoroboric acid.

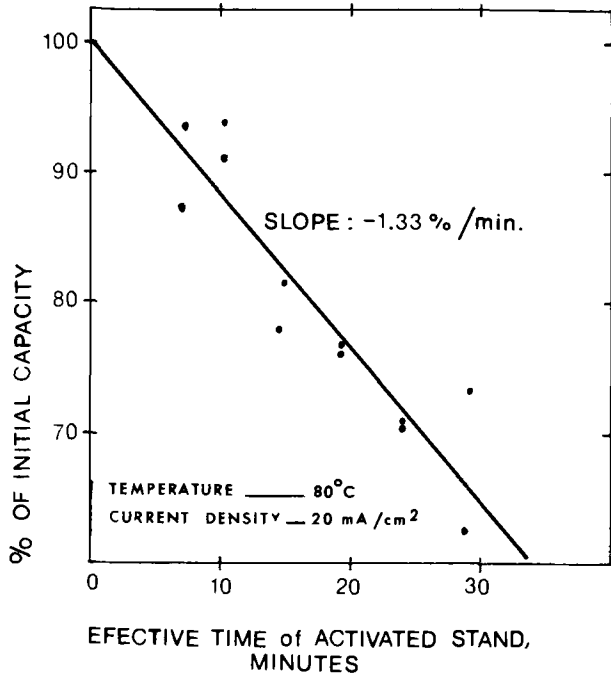


Fig. 5. Self-discharge characteristics of high rate, bonded, lead dioxide electrode in fluoroboric acid.

absolute temperature was found to be logarithmically related to the self-discharge rate with an intercept of 375 (correlation coefficient of 0.9994).

As expected, most of the loss in capacity is due to grid-active material interactions. Recent test results, based on the use of modified, low rate electrodes, not containing metallic current collector grids, have shown some promise for long activated stand lives under difficult conditions. An example in point is a 79 hr steady current discharge of 155 μA per cm^2 (which happens to be a discharge rate required by some

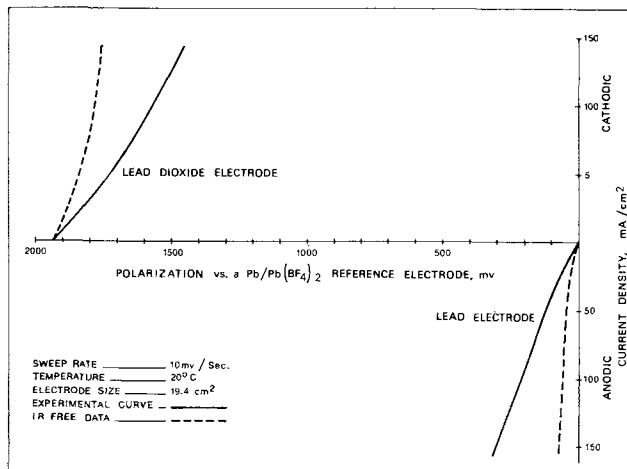


Fig. 6. Linear voltage scans for the system $\text{Pb}/\text{HBF}_4/\text{PbO}_2$

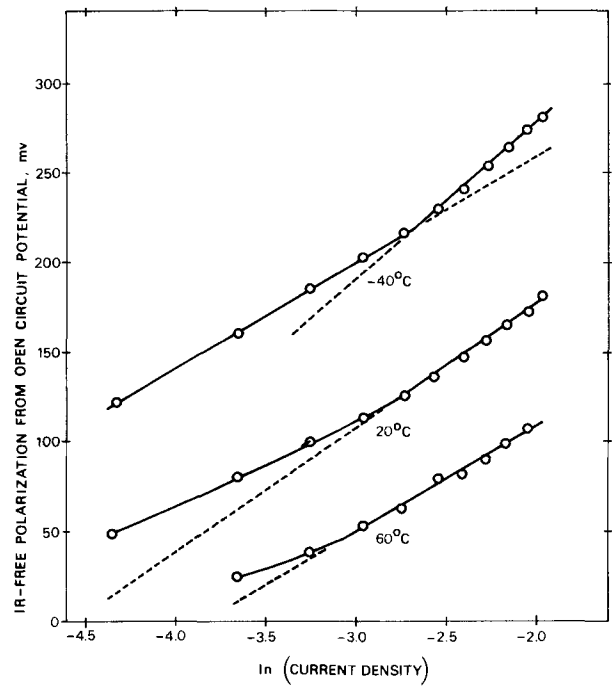


Fig. 7. Tafel plots for the lead dioxide electrode in fluoroboric acid.

applications) at 50°C, recently demonstrated in our laboratory.

A general operation aspect, noteworthy from a design standpoint, is the complete lack of gassing in this type of battery, either due to self-discharge or any other reason.

Figure 6 presents some typical linear voltage sweep data. Single electrode potentials are expressed vs. a

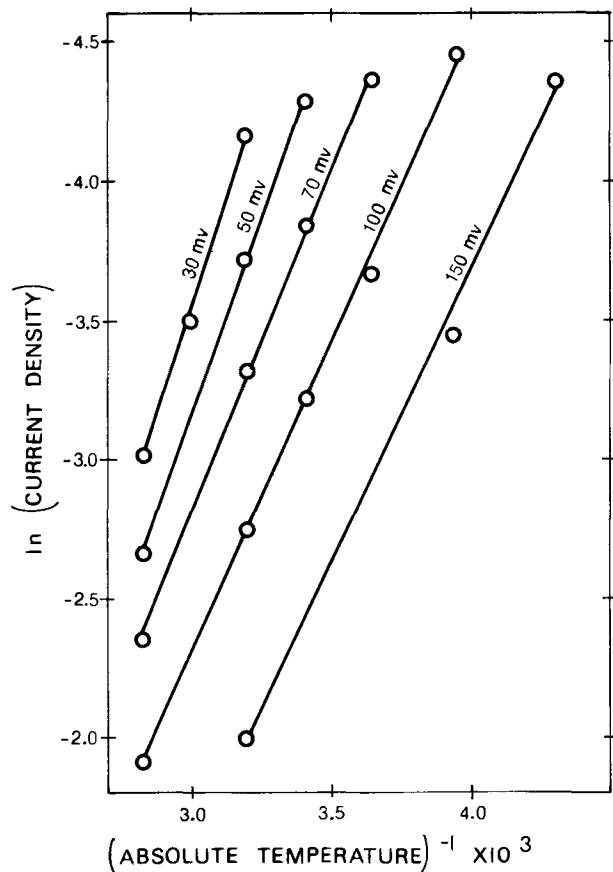


Fig. 8. Arrhenius plots for the lead dioxide electrode in fluoroboric acid.

lead-lead fluoroborate reference electrode. The scans were terminated at 3A owing to equipment limitations. Figure 7 is a Tafel plot of these data. At high temperatures essentially ideal behavior is exhibited, while at the lower temperatures, the curve is suggestive of a dissolution process (6). The Tafel slope, based on these lines, exhibits the theoretical linear temperature dependence with a slope corresponding to R/F . The calculated exchange current at 20°C is approximately 10^{-5} A/cm².

Figure 8 is an Arrhenius plot of the data yielding an activation energy of 1.1 kcal/gmole at 100 mV polarization for the linear portions of the curves (*i.e.*, the lower current regions). This very low value, together with the Tafel information, would indicate diffusion control of the reaction. However, an examination of Fig. 8 shows that the activation energy is dependent on electrode polarization. This suggests that chemical polarization also plays a role (7). The low activation energy, however, would seem to indicate that the electrode reaction proceeds with little impedance and that constructional parameters affecting the internal resistance of a cell will be the limiting factor for this system.

Conclusions

The improvements already demonstrated for the fluoroboric acid battery by the use of high capacity bonded lead dioxide electrodes of both the high rate (metallic current collector) and low rate variety are likely to increase the utility of this system for low specific energy (≤ 45 whr/kg) applications, requiring wide temperature range capabilities at low cost. One feature representing a completely new aspect of this

technology is the significantly longer activated stand life demonstrated for the present state-of-the-art lead-fluoroboric acid system.

It is therefore possible that this type of reserve battery may provide sufficiently attractive design-related characteristics to be considered as an alternative to some of the costlier systems presently in use.

Acknowledgments

The authors would like to acknowledge the able experimental assistance of John Slater who effectively contributed to the concluding portion of this work.

Manuscript submitted Nov. 3, 1971; revised manuscript received Jan. 25, 1972. This was Paper 21 presented at the Cleveland, Ohio, Meeting of the Society, Oct. 3-7, 1971.

Any discussion of this paper will appear in a Discussion Section to be published in the December 1972 JOURNAL.

REFERENCES

1. M. A. Barron, "Proc. 23rd Annual Power Sources Conf.," May 20-22, 1969, pp. 134-136.
2. F. G. Turrill and W. C. Kirchberger, "Proc. 24th Annual Power Sources Conf.," May 19-21, 1970, pp. 36-39.
3. J. P. Schrodt, W. J. Otting, J. O. Schoegler, and D. N. Craig, *Trans. Electrochem. Soc.*, **90**, 405 (1946).
4. T. J. Kilduff and E. F. Horsey, "Proc. 24th Annual Power Sources Conf.," May 19-21, 1970, pp. 30-35.
5. L. Reid, D. Cole, and I. Trachtenberg, *This Journal*, **113**, 954 (1966).
6. J. O'M. Bockris and E. C. Potter, *ibid.*, **99**, 169 (1952).
7. S. V. Gorbachev, "Soviet Electrochemistry" (Proceedings of the Fourth Conf. on Electrochemistry). Vol. 1, pp. 63-71, Consultants Bureau, N. Y. (1961).

An Ellipsometric-Electrochemical Cell: Initial Films on Titanium in Water and Methanol Solutions

Tennyson Smith* and Florian Mansfeld*

North American Rockwell Science Center, Thousand Oaks, California 91360

ABSTRACT

An ellipsometric-electrochemical cell is described for simultaneous ellipsometric and electrochemical measurements of metal samples. The unique feature of this cell is the ability to prepare in one cavity with an appropriate etch-polishing solution surfaces which within the experimental error of ellipsometric measurements approach an atomically clean state. The reaction product and etchant are washed away in a second cavity and *in situ* measurements of changes on the surface are made in a third cavity without exposing the sample to the atmosphere. It is demonstrated that Ti surfaces, which have the same optical constants as observed after ion bombardment cleaning and annealing in an ultra high vacuum system ($\sim 10^{-10}$ Torr), can be prepared in the cell. Results are reported for the initial film growth on clean Ti in aqueous HF, aqueous NaCl, aqueous methanol-HCl, and anhydrous methanol-HCl solutions as a function of applied electrochemical potential.

It is well known that obtaining and studying atomically clean metal surfaces requires a means for removing surface films in an ultra high vacuum (UHV) system (*e.g.*, ion bombardment, cleaving, scraping). The UHV system must operate in the 10^{-9} - 10^{-10} Torr range in order to maintain a clean surface for periods of minutes to hours. It would be desirable to study metal surfaces which approach cleanliness obtainable in a UHV system, but immersed in an electrolyte in an electrochemical cell. This can in some instances be accomplished in an ordinary electrochemical cell if the

metal surface contamination can be removed electrochemically and the electrolyte does not contain surface active contamination. However, for many metals (*e.g.*, Ti) air-formed oxide films cannot be removed electrochemically.

The purpose of this paper is to report our attempts to introduce atomically clean Ti surfaces to the electrolyte of interest and observe surface reactions *in situ* via ellipsometry as well as potential and current measurements. The technique involves cleaning of the surface by a suitable process (etching, electropolishing, etc.), followed by exposing this freshly cleaned surface to the electrolyte without exposing it to another environment (such as air).

* Electrochemical Society Active Member.
Key words: aqueous and anhydrous solutions, HF contamination, optical constants, polarization, ultra high vacuum.

lead-lead fluoroborate reference electrode. The scans were terminated at 3A owing to equipment limitations. Figure 7 is a Tafel plot of these data. At high temperatures essentially ideal behavior is exhibited, while at the lower temperatures, the curve is suggestive of a dissolution process (6). The Tafel slope, based on these lines, exhibits the theoretical linear temperature dependence with a slope corresponding to R/F . The calculated exchange current at 20°C is approximately 10^{-5} A/cm².

Figure 8 is an Arrhenius plot of the data yielding an activation energy of 1.1 kcal/gmole at 100 mV polarization for the linear portions of the curves (*i.e.*, the lower current regions). This very low value, together with the Tafel information, would indicate diffusion control of the reaction. However, an examination of Fig. 8 shows that the activation energy is dependent on electrode polarization. This suggests that chemical polarization also plays a role (7). The low activation energy, however, would seem to indicate that the electrode reaction proceeds with little impedance and that constructional parameters affecting the internal resistance of a cell will be the limiting factor for this system.

Conclusions

The improvements already demonstrated for the fluoroboric acid battery by the use of high capacity bonded lead dioxide electrodes of both the high rate (metallic current collector) and low rate variety are likely to increase the utility of this system for low specific energy (≤ 45 whr/kg) applications, requiring wide temperature range capabilities at low cost. One feature representing a completely new aspect of this

technology is the significantly longer activated stand life demonstrated for the present state-of-the-art lead-fluoroboric acid system.

It is therefore possible that this type of reserve battery may provide sufficiently attractive design-related characteristics to be considered as an alternative to some of the costlier systems presently in use.

Acknowledgments

The authors would like to acknowledge the able experimental assistance of John Slater who effectively contributed to the concluding portion of this work.

Manuscript submitted Nov. 3, 1971; revised manuscript received Jan. 25, 1972. This was Paper 21 presented at the Cleveland, Ohio, Meeting of the Society, Oct. 3-7, 1971.

Any discussion of this paper will appear in a Discussion Section to be published in the December 1972 JOURNAL.

REFERENCES

1. M. A. Barron, "Proc. 23rd Annual Power Sources Conf.," May 20-22, 1969, pp. 134-136.
2. F. G. Turrill and W. C. Kirchberger, "Proc. 24th Annual Power Sources Conf.," May 19-21, 1970, pp. 36-39.
3. J. P. Schrodt, W. J. Otting, J. O. Schoegler, and D. N. Craig, *Trans. Electrochem. Soc.*, **90**, 405 (1946).
4. T. J. Kilduff and E. F. Horsey, "Proc. 24th Annual Power Sources Conf.," May 19-21, 1970, pp. 30-35.
5. L. Reid, D. Cole, and I. Trachtenberg, *This Journal*, **113**, 954 (1966).
6. J. O'M. Bockris and E. C. Potter, *ibid.*, **99**, 169 (1952).
7. S. V. Gorbachev, "Soviet Electrochemistry" (Proceedings of the Fourth Conf. on Electrochemistry). Vol. 1, pp. 63-71, Consultants Bureau, N. Y. (1961).

An Ellipsometric-Electrochemical Cell: Initial Films on Titanium in Water and Methanol Solutions

Tennyson Smith* and Florian Mansfeld*

North American Rockwell Science Center, Thousand Oaks, California 91360

ABSTRACT

An ellipsometric-electrochemical cell is described for simultaneous ellipsometric and electrochemical measurements of metal samples. The unique feature of this cell is the ability to prepare in one cavity with an appropriate etch-polishing solution surfaces which within the experimental error of ellipsometric measurements approach an atomically clean state. The reaction product and etchant are washed away in a second cavity and *in situ* measurements of changes on the surface are made in a third cavity without exposing the sample to the atmosphere. It is demonstrated that Ti surfaces, which have the same optical constants as observed after ion bombardment cleaning and annealing in an ultra high vacuum system ($\sim 10^{-10}$ Torr), can be prepared in the cell. Results are reported for the initial film growth on clean Ti in aqueous HF, aqueous NaCl, aqueous methanol-HCl, and anhydrous methanol-HCl solutions as a function of applied electrochemical potential.

It is well known that obtaining and studying atomically clean metal surfaces requires a means for removing surface films in an ultra high vacuum (UHV) system (*e.g.*, ion bombardment, cleaving, scraping). The UHV system must operate in the 10^{-9} - 10^{-10} Torr range in order to maintain a clean surface for periods of minutes to hours. It would be desirable to study metal surfaces which approach cleanliness obtainable in a UHV system, but immersed in an electrolyte in an electrochemical cell. This can in some instances be accomplished in an ordinary electrochemical cell if the

metal surface contamination can be removed electrochemically and the electrolyte does not contain surface active contamination. However, for many metals (*e.g.*, Ti) air-formed oxide films cannot be removed electrochemically.

The purpose of this paper is to report our attempts to introduce atomically clean Ti surfaces to the electrolyte of interest and observe surface reactions *in situ* via ellipsometry as well as potential and current measurements. The technique involves cleaning of the surface by a suitable process (etching, electropolishing, etc.), followed by exposing this freshly cleaned surface to the electrolyte without exposing it to another environment (such as air).

* Electrochemical Society Active Member.
Key words: aqueous and anhydrous solutions, HF contamination, optical constants, polarization, ultra high vacuum.

Experimental Techniques

Materials.—The cell was constructed of glass reinforced Teflon, the electrolyte reservoirs were of glass, the etchant reservoir tanks were of Teflon, as were the tubes connecting the reservoirs with the cell. Consequently, the etchant (20% H_2SO_4 , 20% HF, 30% HNO_3 by volume) was exposed only to Teflon, while the electrolyte was exposed only to Teflon, glass, paraffin (used for sealing), the platinum counterelectrode, and the sample.

The Ti samples were cut from Ti-75A as cylinders having a slight taper. The surface to be studied was polished to a mirror finish with 600 silicon carbide paper and etched to remove surface damage. The final polishing solution consisted of 1μ alumina in a solution of 1 part ammonium hydroxide, 1 part distilled water, and 1 part 3% hydrogen peroxide. The hydrogen peroxide was added last and was fresh.

Electrolytes.—The electrolytes were prepared from reagent grade materials and bidistilled water.

The cell.—A photograph of the assembled cell is shown in Fig. 1. Figure 2 shows a side view of the Teflon cell, which contains three cavities (A, B, and C) and a Teflon slider S that holds the metal sample. When the sample is positioned at cavity A, etchant (20% H_2SO_4 , 20% HF, 30% HNO_3 by volume) can be made to flow through the cavity from its reservoir, past the sample and into the collector reservoir. After exposing the sample to the etchant for a predetermined length of time, the sample is positioned at cavity B. At cavity B the electrolyte is forced past the sample to remove etchant carried from cavity A, and is then collected in another reservoir. After thus washing the sample in cavity B for a predetermined period, it is positioned at cavity C through which the test solution is flowing for observation by ellipsometry with or without a potential applied to the specimen. The window W in Fig. 2 is used for visual inspection of the sample in cavity C. The slider S in Fig. 2 consists of a rectangular plate of Teflon S_1 bolted to a steel plate S_2 . The sample is forced into a cylindrical well (slightly smaller than the large diameter of the tapered sample) with attached bolt and nut, such that the metal surface is about 0.004 in. below the surface of the Teflon slider. This is to ensure that the metal sample will not scratch the cell surface as the sample is sliding up and down and thus cause leaks between cavities. In order to prevent leakage between cavities, the slider surface must be pressed against the cell surface with considerable pressure. To accomplish this, a plate P is

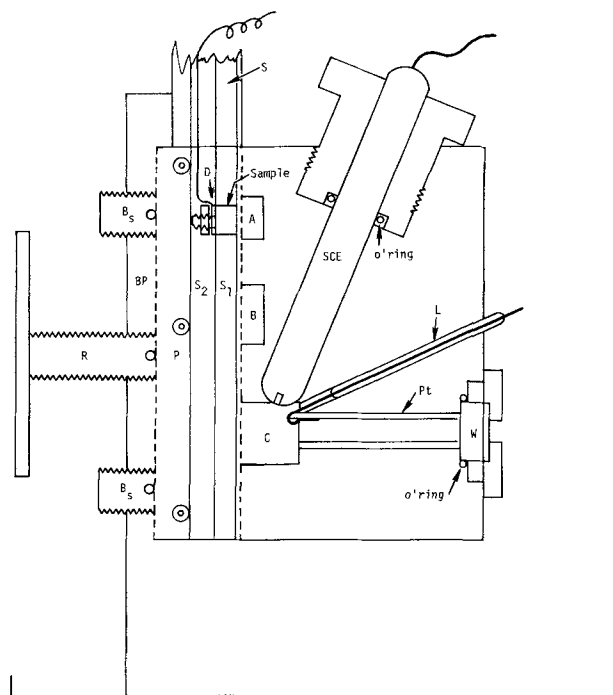


Fig. 2. Sketch of ellipsometric-electrochemical cell

spring loaded against the back plate BP, with the spring load bolts B and a wrench R. To reduce the friction between plates P and S_2 , bearings are placed in plate P or S_2 to roll on. The slider is pulled up and down with a lever and can be positioned by a notched side arm such that the sample is at the center of cavity A, B, or C.

Electrodes.—The counterelectrode consists of a platinum cylinder in the channel leading to window W. This Pt counterelectrode is spot welded to a Pt wire which had been sealed into a glass tube and inserted into the cell, as shown in Fig. 2 as L. A saturated calomel reference electrode (SCE) is inserted as shown in Fig. 2. The O-rings in the windows and around the SCE were coated with paraffin before use. For electrical connections to the sample, an insulated copper wire is spot welded to a copper washer that is placed on the sample bolt under the nut as shown at D (Fig. 2). Entrance and exit channels for the etchant, washing solution, and electrolyte are placed such that the entrance to each cavity is at the bottom of the cavity and the exit at the top. This eliminates collection of gas bubbles in the cavities. The channels for the light beam are placed such that the beam has an angle of incidence of 70° .

Ellipsometry.—A good description of ellipsometry can be found in Ref. (1). The cell was constructed to be mounted on a Rudolph ellipsometer (sensitivity 0.01°). Filters were used to isolate the 5461Å light from a mercury lamp or the 6328Å light from a He-Ne laser. The polarizer and compensator were placed before the reflecting surface and the analyzer and detector after the reflecting surface. The ellipsometer parameters Δ and ψ refer to the phase shift of the normal and parallel component of the polarized light and the arctan of the amplitude ratio of these components, respectively. The polarizer angle p and analyzer angle a are related to Δ and ψ (in zone I) by $\Delta = 2p + \pi/2$ and $\psi = a$. p and a values were averaged for the four zones to minimize alignment errors (1).

To correct for the birefringence of the windows, it would be desirable to measure p and a values with and without the windows. However, since measurement with electrolyte in the cell but without windows cannot be made, it was necessary to first measure the correction due to the windows in an unstressed state, i.e.,

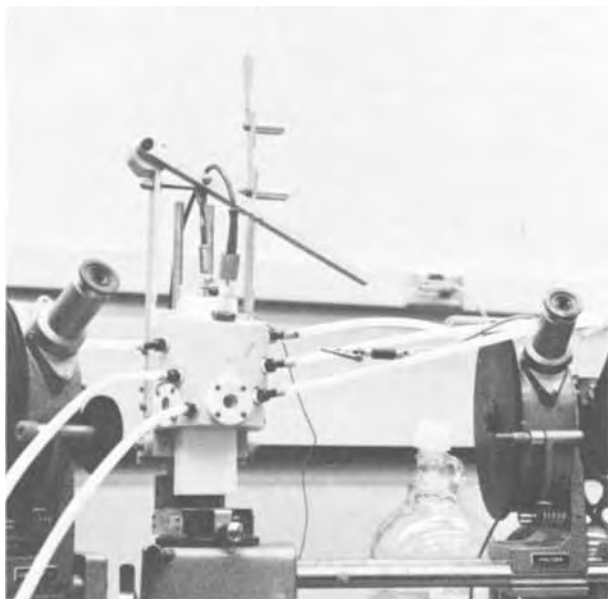


Fig. 1. Photograph of cell

Table I. Measurements to obtain window corrections

Test condition	Zone	p	a
Windows off	1	11.52	29.63
	1	11.65	29.70
	1	11.52	29.67
	1	11.63	29.57
Average value		11.58 ± 0.06	29.64 ± 0.04
	3	10.77	30.34
	2	10.65	29.39
	4	11.50	30.70
Average of 4 zones		11.25 ± 0.41	30.02 ± 0.50
Windows, no pressure (Average 4 zones)		9.15	30.48
Correction for loose windows		2.10	-0.46
CH ₃ OH flowing, windows leaking (Average 4 zones)		5.08	28.93
CH ₃ OH flowing, leak tight (Average 4 zones)		4.37	28.02
Correction for window pressure		0.71	0.91
Correction for loose windows		2.10	-0.46
Total window correction		2.81	0.45

measurement of p and a with and without the windows but with air in the cell. The results in Table I indicate that for unstressed windows a correction of $11.25^\circ - 9.15^\circ = 2.10^\circ$ must be made. A second correction is necessary for the stress induced in the windows when sufficient pressure is applied to prevent leakage of electrolyte from the cell. To obtain this correction, measurements of p and a were made with electrolyte in the cell and the windows held loosely in position (electrolyte leaking) and with enough pressure to prevent leakage. The results in Table I indicate this correction to be $5.08^\circ - 4.37^\circ = 0.71^\circ$. The total window correction is then $2.10^\circ + 0.71^\circ = 2.81^\circ$ for p . A similar calculation yields a total correction of 0.45° for a . Measurement of p and a without windows (air in cell) show that measurements can be repeated with an average deviation of about $\pm 0.05^\circ$ (see Table I).

HF contamination.—Care must be taken to be sure that none of the HF in the etching-polishing solution is carried into the working cavity (C of Fig. 2). This can occur if scratches exist in the Teflon slider or mating cell surface, or if insufficient pressure is used between these parts. A check for such leakage was made by using distilled water in the washing and working cavities and monitoring the pH of the water leaving the working cell. To show the drastic effect of small HF contamination in the electrolyte in the working cell, a series of experiments was performed with varying concentrations of HF added to distilled H₂O as test electrolyte. The resultant changes in p and a are shown as a function of time in Fig. 3a. Tests with small additions of H₂SO₄, HCl, or HNO₃ of similar concentration gave virtually no changes in p and a readings. The effect of HF must result from the strong complexing action of the F⁻ ion resulting in thick films of corrosion products. Accelerated corrosion of Ti in sulfuric acid containing fluoride ions has been reported recently (7).

Since there are only two experimental ellipsometric parameters p and a and there are three unknowns, film thickness d , index of refraction n_f , and absorption coefficient κ_f , a unique solution for d , n_f , and κ_f is not possible. It becomes necessary, therefore, to interpret p and a in terms of d and n_f for reasonable ranges of κ_f . A discussion of the problems inherent in the interpretation of the ellipsometric results in terms of thickness d and film index of refraction is given in Appendix A. A computer program (2) is used to calculate solutions for d and index of refraction of the film n_f while assuming various values of the absorption coefficient κ_f (i.e., $\kappa_f = 0, 1, 2,$ and 3). In the case of films formed in pure water, solutions for n_f and d were not found except for $\kappa_f \rightarrow 0$. In the case of films formed in the presence of HF, solutions were found for $\kappa_f \approx 0$ and 1 , but for $\kappa_f = 0$ the values of n_f were too small and d too large to be realistic. It is concluded that films formed in solutions containing HF as contamination are absorbing with $\kappa_f \sim 1$, whereas films formed in pure water are transparent with $\kappa_f \sim 0$.

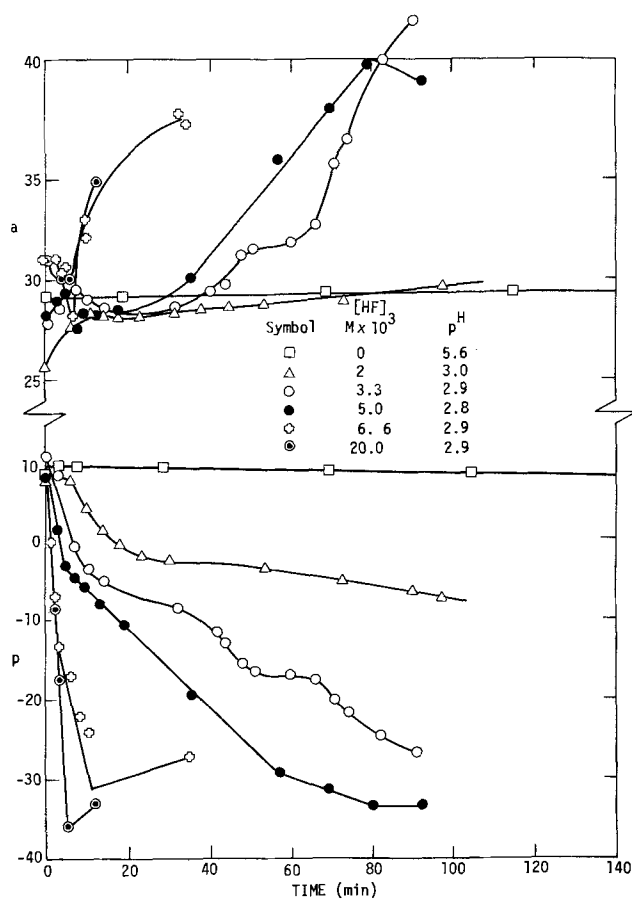
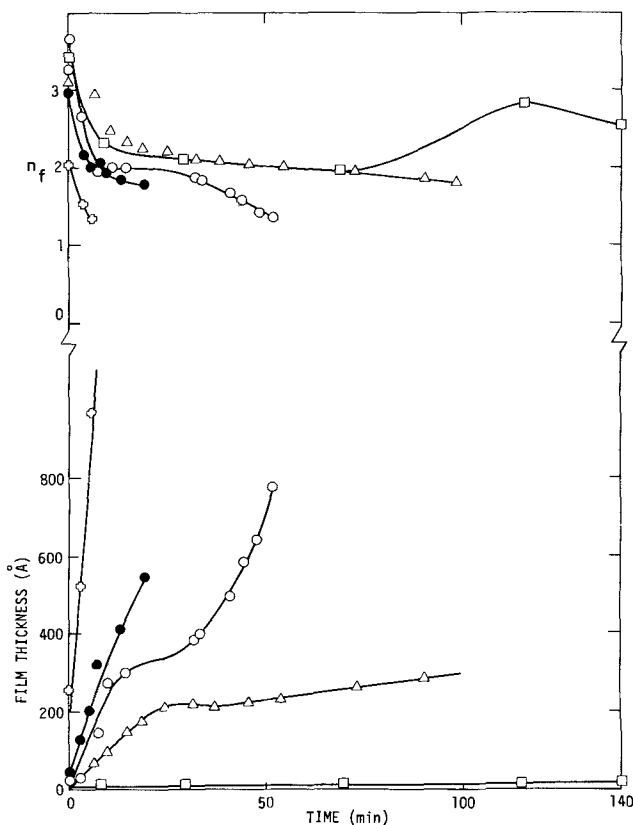
Fig. 3(a). Effect of HF contamination in distilled H₂O on ellipsometric readings (p, a).Fig. 3(b). Film thickness and index of refraction, n_f

Figure 3b shows the calculated values of film thickness d , and index of refraction n_f which corresponds to Fig. 3a, with $\kappa_f = 0$ for pure water and $\kappa_f = 1$ for HF

solutions. In distilled water, without HF addition, a film of about 14Å is formed in 100 min. The addition of HF causes very thick films to grow. The initial growth rate of these films is second order with respect to HF concentration. In every case n_f decreases and levels off as the films grow.

Experimental Results

Optical constants of cleaned surfaces.—A test of the surface cleanliness was made by comparing the optical constants obtained in the ellipsometric-electrochemical cell immediately after etching and washing, with the optical constants obtained after cleaning by ion bombardment and annealing in an ultra high vacuum (UHV) system (3). Auger spectroscopy in the UHV was used to determine the presence of contamination in the first atom layers of the Ti substrate. It was possible to prepare surfaces with less than 0.1 monolayers of Cl and S which were the only contaminants after ion bombardment and annealing at about 550°C. Zone refined polycrystalline Ti was used in the UHV system, while polycrystalline Ti-75A was used in the ellipsometric-electrochemical cell. It would be expected that the optical constants of these materials are the same. In experiments in the cell the Ti surface was cleaned by passing the etching-polishing solution¹ through cavity A for 10 sec. The specimen was then washed in cavity B for 10 sec with the test electrolyte and moved to cavity C, through which the test electrolyte was slowly flowing. The ellipsometer readings Δ and ψ were recorded as a function of time. Using the computer program (2) mentioned above the optical constants were then calculated. The initial values for various electrolytes are compared with those obtained in the UHV system in Table II. The average values of the optical constants for a freshly cleaned surface $n_s = 3.05 \pm 0.05$ and $\kappa_s = 1.20 \pm 0.06$ are close to the values obtained in the UHV system, $n_s = 3.09 \pm 0.01$ and $\kappa_s = 1.11 \pm 0.01$ for $\lambda = 5461\text{Å}$. Similar agreement is found for $\lambda = 6328\text{Å}$. This indicates that etching the Ti-75A sample in cavity A for 10 sec and washing in cavity B for 10 sec provides a surface which is approaching an atomically clean state (within the uncertainty of n_s and κ_s). The uncertainty of n_s and κ_s for experiments in the cell is about 0.05 units which corresponds to an uncertainty with respect to surface cleanliness of about 3Å effective thickness for TiO_2 as the contamination.

Electrochemical studies.—The primary purpose of the cell was to make possible simultaneous ellipsometric and electrochemical studies. Solutions used were 3.5% NaCl, CH_3OH -1N HCl "aqueous" and CH_3OH -1N HCl "anhydrous." The "aqueous" solutions were prepared by adding concentrated (37%) HCl to methanol, while the "anhydrous" solutions were prepared by

¹ The mixture of HF - HNO_3 - H_2SO_4 - H_2O removes oxide films on Ti, but also chemically polishes the surface. Effects of surface roughness on ellipsometric data are therefore not to be expected.

Table II. Optical constants of polycrystalline Ti 75A in various electrolytes compared to zone refined Ti in the ultra high vacuum (UHV)
N = number of experiments

Electrolyte	λ (Å)	Optical constants		N
		n_s	κ_s	
I. Ellipsometric-electrochemical cell				
CH_3OH	5461	3.03 ± 0.01	1.20 ± 0.01	5
CH_3OH -0.01N NaCl	5461	3.06 ± 0.18	1.30 ± 0.06	4
-0.3% H_2O				
H_2O	5461	2.96 ± 0.01	1.23 ± 0.03	8
6N HCl	5461	3.15 ± 0.01	1.08 ± 0.01	4
		3.05 ± 0.05	1.20 ± 0.06	
CH_3OH	6328	3.28	1.11	2
CH_3OH -1N HCl aq.	6328	3.31 ± 0.05	1.01 ± 0.02	20
CH_3OH -1N HCl anh.	6328	3.30 ± 0.05	1.05 ± 0.02	18
H_2O	6328	3.27 ± 0.06	1.14 ± 0.05	12
3.5% NaCl	6328	3.25 ± 0.03	1.12 ± 0.005	13
		3.26 ± 0.03	1.11 ± 0.02	
II. UHV				
5×10^{-10} Torr	5461	3.09 ± 0.01	1.11 ± 0.01	5
5×10^{-10} Torr	6328	3.16 ± 0.01	1.12 ± 0.01	5

saturation CH_3OH with HCl gas and then diluting with CH_3OH until the solution was 1N in HCl. For further details, see Ref. (4). These solutions were used since it had been shown earlier by potentiostatic polarization curves (4), that Ti is covered with a passive film in the aqueous solutions, but no such film can form in anhydrous solutions. Figure 4 shows a typical plot of the change in polarizer and analyzer readings as a function of time for potentiostatic anodic polarization of Ti-75A in aqueous 3.5% NaCl. The bars at the end of the curves at 1500 mV indicate the range of the scatter of the data. The data at each potential were obtained for a freshly cleaned and polished surface. Most of the curves increase rapidly with time, level off after about 100 sec, then slowly increase with time. Pitting occurred in aqueous CH_3OH -HCl solutions (4) when a potential of +200 mV was exceeded as indicated by a continuous rise of the anodic current. Within the scatter of the data p and a values were close to those measured in aqueous NaCl solutions where no pitting was observed. Figure 5 shows average values of the change in p (Fig. 5A) and a (Fig. 5B) after 100 sec as a function of the applied potential. Curve 1 in Fig. 5A is for Ti in 3.5% NaCl, curve 2 is for Ti in aqueous CH_3OH -1N HCl, and curve 3 is for Ti in anhydrous CH_3OH -1N HCl.

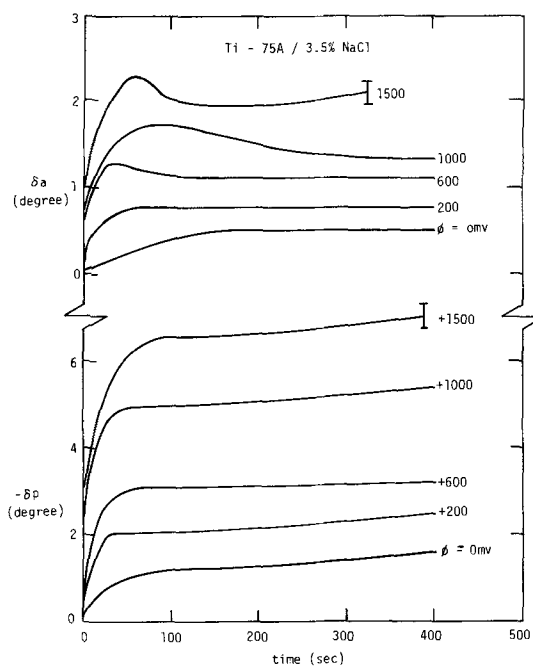


Fig. 4. Changes of ellipsometric values as a function of time and potential (vs. SCE). Ti75A, aqueous 3.5% NaCl.

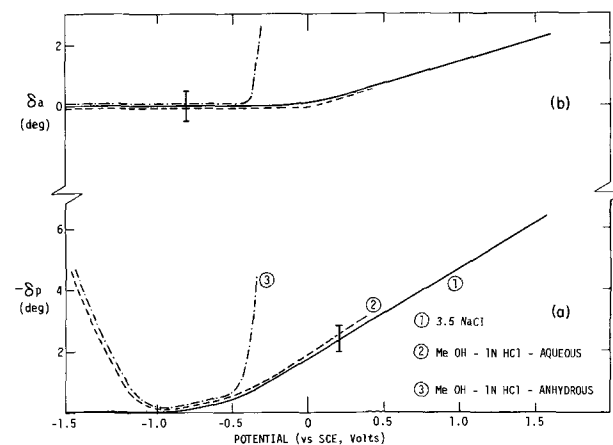


Fig. 5. Ellipsometric values after 100 sec and film thickness as a function of potential. — 3.5% NaCl, - - - CH_3OH -1N HCl-aqueous, - · - CH_3OH -1N HCl-anhydrous.

The results in Fig. 5 show that the changes of the ellipsometric parameters with potential in 3.5% NaCl are essentially the same as in aqueous CH₃OH-1N HCl for potentials noble to the rest potential which for a freshly cleaned specimen was $\sim -0.8V$. However, for Ti in anhydrous CH₃OH-1N HCl very thick films form at potentials more positive than $-0.4V$. For potentials cathodic to the rest potential ($< -0.8V$) no film is formed in 3.5% NaCl. The films that form more negative than $-0.8V$ in the methanol solutions are essentially the same in aqueous and anhydrous solutions.

Discussion

It has been shown (Table II) that it is possible to prepare by proper etching and washing in our ellipsometric-electrochemical cell Ti surfaces the cleanliness of which approaches cleanliness obtained in UHV after ion bombardment. The finding that it is possible to produce a clean surface in an environment like water is not contradicted by the results of Beck and co-workers (8), who showed that the anodic current on a freshly broken Ti surface in an electrolyte decreases to a very small value in a few milliseconds. While this can be called repassivation, it does not have to mean that the whole surface is being covered by an oxide film, but might result from blockage of the most active sites on the freshly broken surface by adsorbed oxygen as demonstrated by Frankenthal for passivation of Fe-Cr (9). Depending on the applied potential and the electrolyte, different films are formed; it was observed, however, that at least for the first 100 sec after the electrode was immersed in the electrolyte (cavity C) film growth was very slow at potentials close to the rest-potential. Our results in 3.5% NaCl at potentials noble to the rest-potential are similar to those obtained by Green and Sedricks (5) for Ti-7.76% Al who found a linear increase of the ellipsometric parameter Δ with potential. The film thickening at potentials active to $-1.0V$, reported by these authors based on some indirect evidence but not shown by ellipsometric results, was not detected in our studies.

The different behavior of Ti-75A at potentials noble to the rest-potential in anhydrous and aqueous solutions of CH₃OH-HCl can be explained based on the result obtained in a study of the effect of water on passivity and pitting of Ti (4). In aqueous CH₃OH-1N HCl enough water is present to produce a passive film, which is destroyed by pitting when the applied potential exceeds the critical pitting potential. Consequently, it was found in the present study that thin films grow in aqueous solutions at about 40 Å/V for the first 100 sec, when an anodic potential was applied. In anhydrous CH₃OH-1N HCl no passive film can be formed; thus, anodic polarization results in accelerated dissolution under charge transfer control (4). The rapid change of ellipsometric parameters in this solution is then due to accumulation of corrosion products on the surface of the test specimen.

Films formed on Ti-75A at potentials negative to the rest potential seem to be identical for aqueous and anhydrous solutions of CH₃OH-HCl. They therefore do not require water molecules for their formation. While hydride formation might take place, more experiments have to be carried out to determine the nature of these films. Potentiostatic polarization experiments in CH₃OH-HCl solutions have shown (6), that at potentials more negative than $-1.2V$ the current continuously increases at constant potential with an ever increasing rate of gas evolution. Potentiokinetic measurements show a change in slope at this potential and a marked hysteresis when the potential is decreased to more noble potentials leading to a more noble rest-potential.

Due to the difficulties mentioned above and described in Appendix A, unique values of the complex index of refraction of the films formed and their thickness cannot be obtained. However, certain conclusions

can be drawn concerning these physical parameters from the ellipsometric data in Fig. 5. In the anodic region ($\phi > -0.8V$) for films formed in NaCl or aqueous methanolic solutions (curves 1 and 2) experimental values for p and a are consistent with those calculated with a complex refractive index of $n_f \sim 2.5$ and $\kappa_f \sim 0$. These values are consistent with TiO₂ films as reported in the literature (10-13). The anodic oxide film forms at about 40 Å/V in the first 100 sec between -0.5 and $1.5V$. This is estimated from the slopes of the curves in Fig. 5 between -0.5 and $+1.5V$ and the slopes of the curves for $n_f = 2.5$, $\kappa_f = 0$ in Fig. A-1a. This is about twice the value reported (13, 14) for much larger potentials (0-200V).

In the cathodic region ($\phi < -0.8V$) the lack of a change in p and a indicates that films are not formed on Ti in the NaCl solutions. Very peculiar films are formed in aqueous and anhydrous methanol solutions in the cathodic region. The peculiarity lies in the fact that for these films the polarizer azimuth p changes dramatically but within experimental error no change in the analyzer azimuth a occurs. Figure A-1a of the appendix indicates that for transparent films (i.e., $\kappa_f = 0$) δa remains unchanged or becomes negative only for n_f slightly greater than 1 or less. However, for these values of n_f , δp is positive. Therefore, the cathodic films formed in CH₃OH-HCl cannot be transparent (nonabsorbing). Figure A-1c and d indicate that for $\kappa_f > 2$, δa is always positive, therefore cathodic films formed in CH₃OH-HCl are limited to the range of n_f and κ_f found in Fig. A-1b and in particular to values of about $n_f \sim 1-3$, $\kappa_f \sim 1$. The large absorption coefficient $\kappa_f \sim 1$ corresponds to films of metallic character (e.g., for Ti $n \approx 3$, $\kappa \approx 1$). The cathodic films formed in CH₃OH-HCl may be titanium hydride or colloidal particles of metallic Ti with some electrolyte between the particles. Further experimental data are needed to elucidate this point.

Our results also have shown that care has to be taken to avoid the presence of F⁻ ions which even in very small amounts leads to severe corrosion and film formation on Ti.

Acknowledgment

We would like to acknowledge the help of A. J. Lewin and N. G. Taylor in the design of the cell.

Manuscript submitted Nov. 15, 1971; revised manuscript received Feb. 14, 1972.

Any discussion of this paper will appear in a Discussion Section to be published in the December 1972 JOURNAL.

APPENDIX A

Since there are only two experimental ellipsometric parameters p and a and there are three unknowns, film thickness d , index of refraction n_f , and absorption coefficient κ_f , a unique solution for d , n_f , and κ_f is not possible. It becomes necessary, therefore, to interpret p and a in terms of d and n_f for reasonable ranges of κ_f . To aid this interpretation, values of p and a were computed for various values of d , n_f , and κ_f for Ti in distilled water for very thin films with $\lambda = 6328\text{\AA}$ and an angle of incidence of 70° . Figure A-1 shows plots of p and a vs. d for the values of n_f (first number) and κ_f (second number) reported in brackets on each curve. From Fig. A-1 and a knowledge of the range of values expected for n_f and κ_f , it is possible to anticipate the relative increase or decrease of p and a as the film

Table A-1. Comparison of optical constants of Ti and W to show the effect of surface contamination

Metal	Preparation	n	κ	Ref.
W	Ion bombard. 10^{-10} Torr, annealed	3.75	0.800	(13)
W	Heat treatment. 10^{-7} to 5×10^{-6} Torr	3.40	0.88	(15)
Ti	Ion bombard. 10^{-10} Torr, annealed	3.09	1.11	(13)
Ti	Polished in air	2.0	1.5	(16)

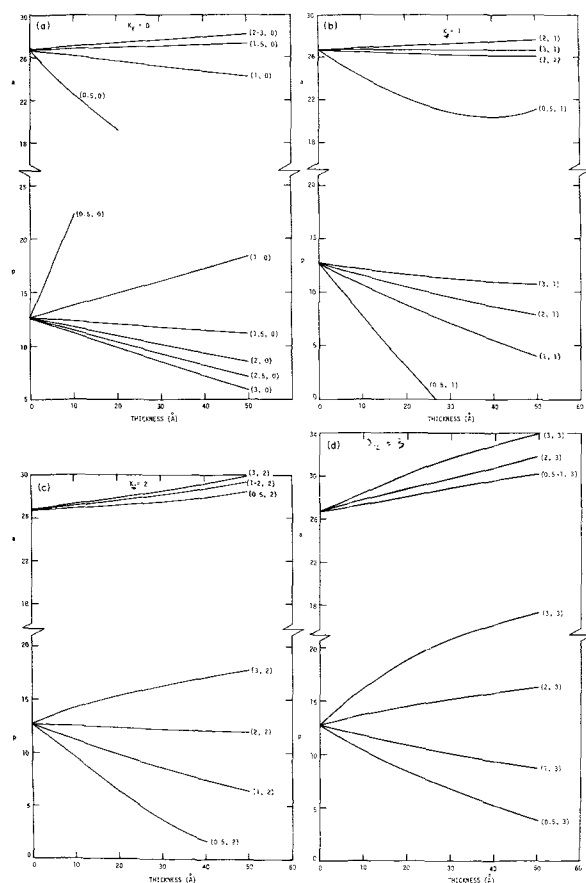


Fig. A-1. Computed values of p and a vs. film thickness d for TiO_2/Ti in water at 6328Å , for various values of the absorption coefficient of the film κ_f and refractive index of the film n_f .

grows. For example, more metallic films are expected to have lower values of n_f and higher values of κ_f . The opposite is expected for insulating films. Consequently, insulating films will always cause p to decrease and a to increase as d increases. a only decreases for very small values of n_f and κ_f , and p only increases for very small or very large values of n_f and κ_f .

It should be noted that accurate values for optical constants are difficult to obtain due to surface contamination. For example, Table A-I gives reported values for Ti and W for different preparation of the samples. Computer calculations using the exact Drude relations indicate that contamination tends to decrease n and increase κ if the ambient is gas or vacuum. Therefore, it is believed that the lower values reported for W and Ti in Table A-I resulted from surface contamination.

REFERENCES

1. F. L. McCrackin *et al.*, *J. Res. Nat. Bur. Std.*, **A**, **67**, 363 (1963).
2. F. L. McCrackin, *Nat. Bur. Std. Tech. Notes* 474, April 1969.
3. T. Smith, *J. Opt. Soc. Am.*, To be published.
4. F. Mansfeld, *This Journal*, **118**, 1412 (1971).
5. J. A. S. Green and A. J. Sedriks, *Met. Trans.*, **2**, 1807 (1971).
6. F. Mansfeld, Unpublished results.
7. M. J. Maudry and G. Rosenblatt, *This Journal*, **119**, 29 (1972).
8. T. R. Beck, M. J. Blackburn, and W. H. Smyrl, Quarterly Report No. 20, Contract NAS7-489, also Quarterly Report No. 14.
9. R. P. Frankenthal, *This Journal*, **116**, 580, 1646 (1969).
10. R. C. Menard, *J. Opt. Soc. Am.*, **52**, 427 (1962).
11. G. Hass, *Vacuum II*, 331 (1952).
12. M. Kayama, *Chem. Abstracts* 62: 12572e; *Rika Gaku Kenkyusho Hokoku*, **39**, 121 (1963).
13. T. Smith, Unpublished data.
14. M. E. Sibert, *This Journal*, **110**, 65 (1963).
15. D. W. Juenker, L. J. LeBlanc, and C. R. Martin, *J. Opt. Soc.*, **58**, 164 (1968).
16. M. M. Kirillova and B. A. Charikov, *Phys. Metals Metallorg.*, **15**, 138 (1963).

Contact Angle Measurements of Tin Sensitizing Solutions

N. Feldstein* and J. A. Weiner

RCA Corporation, David Sarnoff Research Center, Princeton, New Jersey 08540

ABSTRACT

A study of tin sensitizing solutions was made by contact angle measurements. Through the control of solution composition, *i.e.*, stannous and stannic concentrations, major improvements in the effectiveness of such sensitizers on hydrophobic surfaces have resulted. The incorporation of excess sodium chloride was found to further improve the performance of such sensitizing solutions. The presence of the stannic ions facilitates the adsorption of the stannous ions necessary for the reduction of palladium.

In the plating of dielectric substrates, a pretreatment of the substrate is essential in order to effectively deposit metals by the electroless plating technique. One of the more prevalent procedures in commercial use is the two-step immersion sequence of acidic stannous chloride solution followed by an acidic palladium chloride solution. In general, the first bath is referred to as the sensitizer solution while the second solution is the activator. The net result of this sequence is the formation of finely divided palladium nuclei which initiate the autocatalytic plating process (1,2). The

formation of the palladium metal nuclei is believed to be due to a redox reaction taking place between the adsorbed stannous ions on the surface and the palladium ions in the activating solution.

In spite of the wide commercial application of plated plastic parts, very little work has been reported regarding the chemistry of sensitizing and activating solutions. A review of this technology has been summarized by Goldie (3). Pearlstein (4) has observed variations in plating due to compositional changes of either the sensitizer or activator solutions. More recently, Cohen *et al.* (5,6), investigated the solution chemistry of the tin chloride sensitizing process. This study was based upon the Mossbauer spectroscopy of

* Electrochemical Society Active Member.

Key words: sensitizer solutions, electroless plating, contact angle measurements.

tin. Their proposed model invokes a colloidal formation based on the stannic ion with stannous ions bound onto this colloid.

Although the sensitizer compositions described in the literature are most effective for a wide variety of substrates, such solutions possess a major shortcoming whenever hydrophobic substrates are employed. Based upon work in this laboratory, it has been demonstrated that the performance of conventional-type sensitizers ($\text{SnCl}_2 \cdot n\text{HCl}$ plus colloidal Sn(IV)) (5, 6) may be greatly improved for use with hydrophobic substrates. This is achieved primarily through the proper control of the stannous-stannic concentrations.

In this investigation, a study of tin sensitizing solutions was undertaken employing contact angle measurements. Such an approach was believed to be useful since adsorption of thin films can potentially alter the resulting contact angle. Such an approach may lead to a more quantitative way by which the effectiveness of sensitizers may be evaluated. A later publication (7) will propose a mechanism for the sensitization of hydrophobic and hydrophilic substrates by tin-type solutions.

Experimental Procedures

Chemicals and solutions.—All chemicals used throughout were Baker Reagent grade; the hydrochloric acid used was Mallinckrodt electronic grade. The water used was deionized and then distilled. The following solution was used throughout this investigation

Concentrate 2.6M $\text{SnCl}_2 \cdot 2\text{H}_2\text{O}$ in concentrated HCl (37%) (Final HCl is 9.4M)

Working sensitizer solutions of different compositions were made from this concentrate.

Substrate preparation.—Cover glass plates, 2 × 2 in. (E. Leitz, Inc., New York, Cat. No. 19821), which were cleaned in a mild soap solution, rinsed and spin dried, served as substrates. These substrates were coated with commercially available photoresists to form hydrophobic surfaces for testing. A positive resist, AZ-1350 (distributed by Shipley Company, Newton, Massachusetts) was spin coated onto the glass at 5000 rpm for 60 sec. To remove solvent(s) and polymerize the resist film, a baking procedure of 200°C for 3 min was employed. For a typical negative resist, KTRF (Eastman Kodak Company) was used. The resist composition was mixed in accordance with the manufacturer's specification. This resist was spin coated at 8000 rpm for 30 sec. A baking procedure of 7 min at 200°C was employed. Teflon¹ (FEP) Type A film was also used in conjunction with this study. The film thickness chosen was 20 mils. Prior to the contact angle measurements on the Teflon, a mild soap cleanup was employed.

Substrate treatment.—Two basic procedures were employed prior to the contact angle measurements. In the first procedure (procedure "a"), drops of varied sensitizer composition were placed on the photoresist surface, and the contact angle was measured. An alternate procedure was developed (procedure "b") which resulted in a greater sensitivity in the measurements. This adopted procedure consisted of

1. Immersion of substrate into various sensitizer compositions for 1.0 min.
2. Substrates were dipped (about 2 sec) in D.I. water of 1 liter volume.
3. Substrates were rinsed in D.I. water in an overflow rinse tank (volume = 1.2 liter) with a flow rate about 4 liters/min.
4. Substrates were spin dried in air.
5. Drops of D.I. water (or palladium chloride solution consisting of 1 g/liter PdCl_2 and 1 cc/liter concentrated HCl) were placed on the photoresist surface

¹ Teflon (fluorocarbon film)—Trademark of E. I. du Pont de Nemours & Co.

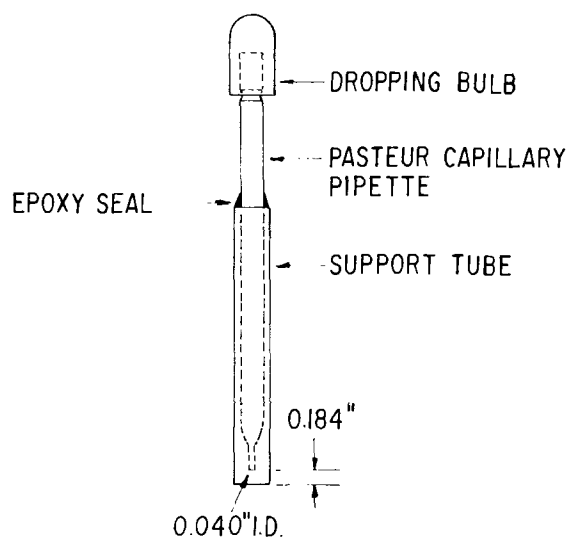


Fig. 1. Dispensing device for contact angle measurements

using a Pasteur pipette from a controlled height of 0.184 in. (See Fig. 1).

6. Contact angle was measured.

Contact angle measurements.—All measurements were made using a contact angle goniometer Model A-100 (Ramé-Hart, Inc., 43 Bloomfield Avenue, Mountain Lakes, New Jersey 07046). Due to the spreading effect, contact angles were measured as a function of time and extrapolated to time zero. A time interval of 10 min was chosen for convenience, however, no changes in the extrapolated values were noted in measurements greater than 10 min. Figure 2 shows the contact angle of sessile drops as employed in procedures "a" and "b," respectively. A least square calculation was used to derive the extrapolated values at zero time. All reported angles are the extrapolated values, and these values were found to be reproducible within $\pm 2^\circ$, except for the case of Teflon, which resulted in variations of $\pm 5^\circ$.

Surface tension measurements.—Surface tension measurements were made using a Fisher Surface Tensiometer Model 20. A 6 cm Pt-Ir ring was used for making measurements.

Results and Discussion

In the first stage of this investigation, a procedure was attempted in which the contact angle was measured by placing sensitizer drops onto the organic surface. Typical results employing this procedure showed little change upon the addition of stannic ions. Surface tension measurements of sensitizing solutions, with and without added stannic ions, resulted in variations of a few per cent. Specifically, the addition of $2.5 \times 10^{-2}\text{M}$ stannic chloride to a solution composed of 0.13M SnCl_2 and 0.47M HCl, resulted in surface tensions ranging from 68 dynes/cm to 70 dynes/cm. These minor alterations in the surface tension of the sensitizer solutions are consistent with the minor variations of contact angle. It is concluded that a different mechanism takes place, other than surface tension modification, which accounts for the variations in the effectiveness of the present sensitizers on hydrophobic-type substrates. Therefore, this approach was not further pursued.

Examination of the contact angle following the sensitization step showed a greater degree of sensitivity in comparison to the results of procedure "a". Hence, all reported angles are based upon the modified procedure (Fig. 2, procedure "b"). In the modified procedure, it was found that results within experimental error were obtained by using drops of either water or palladium chloride solutions. For convenience, the use of water drops was adopted for most of the experimental work.

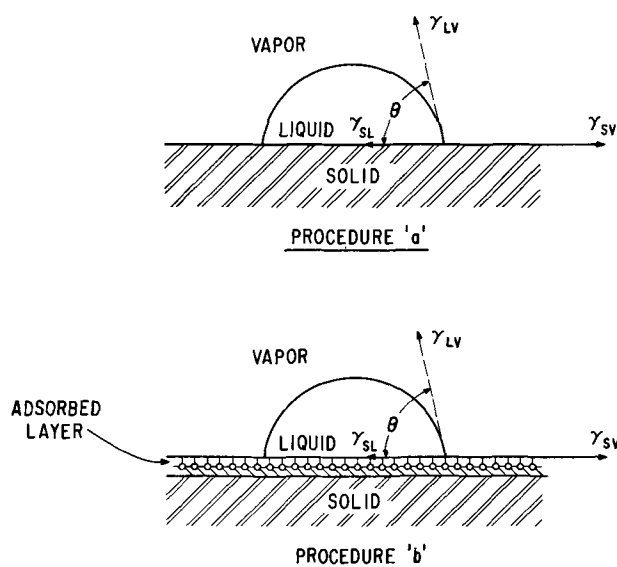


Fig. 2. Contact angle of sessile drops

In a recent study, the role of the stannic ions in conventional-type sensitizers was described. As pointed out (6), typical reagent grade stannous chloride contains approximately 5 mole per cent (m/o) stannic ions, and upon dissolution in aerated water, further oxidation yields a total of about 6 m/o of stannic ions. A model based upon the formation of colloidal stannic compound(s) has been invoked to account for the mechanism of sensitization. The stannous ions are bound onto these colloids and are presumably retained on the surface by both an adsorption- and absorption-type mechanism. Table I shows the resulting contact angle measurements of different sensitizer compositions. It is quite evident that for sensitizers 1 through 4, the contact angle is nearly the same and thus seems to be independent of composition ($\text{SnCl}_2/\text{nHCl}$ ratio) as well as the manner by which the sensitizer was prepared. It should be recalled (6) that sensitizers A, B, and C were proposed as a means for controlling the colloid present in the stannous solutions. By contrast, the incorporation of the stannic chloride solution as made in this laboratory (Table I, No. 5) shows clearly the modifications associated with such combinations, further suggesting that other mechanism(s) may take place during the sensitization process which are especially important in the case of the hydrophobic-type substrates.

Figures 3 and 4 show the variations of the contact angle due to the compositional modification of the sen-

Table I. Contact angle^(a) for typical stannous sensitizers/activators

Sensitizer/activator system	Contact angle (degrees)
1 Bell Telephone Laboratories "A" ^(b)	66
2 Bell Telephone Laboratories "B" ^(c)	67
3 Bell Telephone Laboratories "C" ^(d)	67
4 RCA ^(e)	66
5 RCA ^(f)	53
6 Catalyst 9F and Accelerator 19 ^(g)	71

^(a) AZ-1350 resist was used.

^(b) Solution prepared by dissolving 20.0g $\text{SnCl}_2 \cdot 2\text{H}_2\text{O}$ in water, adding 10.0 ml concentrated HCl and then diluting up to 1 liter with water.

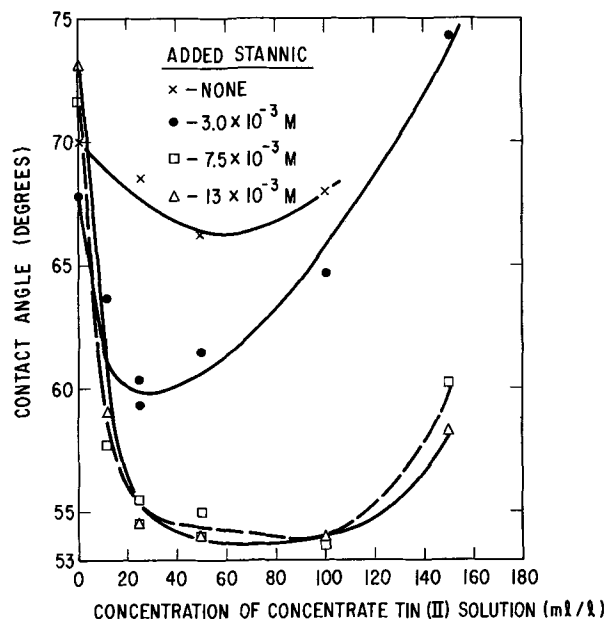
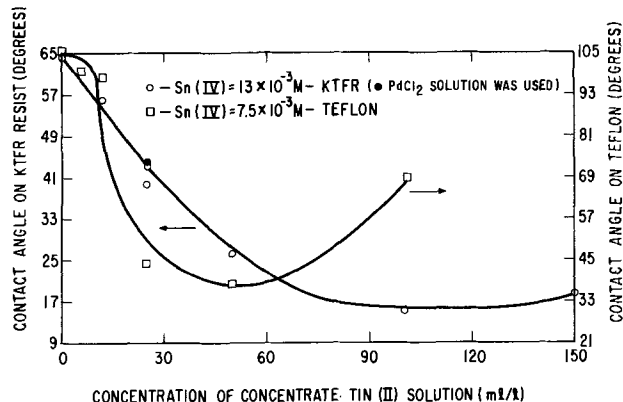
^(c) Solution prepared by dissolving 20.0g $\text{SnCl}_2 \cdot 2\text{H}_2\text{O}$ in 10.0 ml HCl and then diluting to 1 liter with water.

^(d) Solution prepared by dissolving 10.0 ml HCl in nearly 1 liter water, adding and dissolving 20.0g $\text{SnCl}_2 \cdot 2\text{H}_2\text{O}$ and then diluting to 1 liter with water.

^(e) Solution composed of 0.13M SnCl_2 in 0.47M HCl.

^(f) Same as Footnote (e) plus $7.5 \times 10^{-3}\text{M}$ SnCl_4 .

^(g) Shipley Company, Inc., Newton, Mass., Catalyst 9F was mixed with 2 parts water and 1 part HCl as suggested by supplier. Accelerator was mixed with 4 parts of water. Immersion in the above two was for 3 min each; a sufficient DI rinse was carried out between the catalyst and accelerator.

Fig. 3. Contact angle variations vs. compositional changes on AZ-1350 resist. Concentrate tin(II)—2.6M SnCl_2 , 9.4M HCl.Fig. 4. Contact angle variations vs. compositional changes. Concentrate tin(II)—2.6M SnCl_2 , 9.4M HCl.

sitizer solution. The choice of substrate materials in these figures was made because of the good reproducibility obtained in their preparation. For a constant added Sn(IV) , a sharp drop in the measured contact angle takes place upon increasing the $\text{Sn}^{2+}/\text{Sn}^{4+}$ ratio. A minimum in the contact angle is found, after which further increase in the $\text{Sn}^{2+}/\text{Sn}^{4+}$ ratio results in an increase in the contact angle. Increasing the tin (IV) concentration results in displacing the minimum towards lower values. However, a convergence is found at the higher tin (IV) concentrations. The increasing portion of the curves with excess addition of $\text{SnCl}_2/\text{nHCl}$ is due to a combination of factors: (i) increasing the hydrogen ion concentration tends to increase the measured contact angle and (ii) the large excess of stannous ions relative to the stannic ions prevents the surface adsorption of the latter ions. These factors were qualitatively tested and verified. A full account concerning the shape of these curves will be covered in a later publication.

Figure 4 shows the variations in the measured contact angle on KTRF resist and Teflon. The general trend for these cases is similar to that demonstrated in Fig. 3. Of the various materials examined, the Teflon shows the most dramatic change in contact angle with variations in the stannous/stannic ratio.

Figure 5 shows the effect(s) of added sodium chloride on the resulting contact angle. As seen from Fig. 5, the addition of this salt to a conventional-type sensitizer (0.13M SnCl_2 and 0.47M HCl) results in no appreciable effect on the measured contact angle. At the

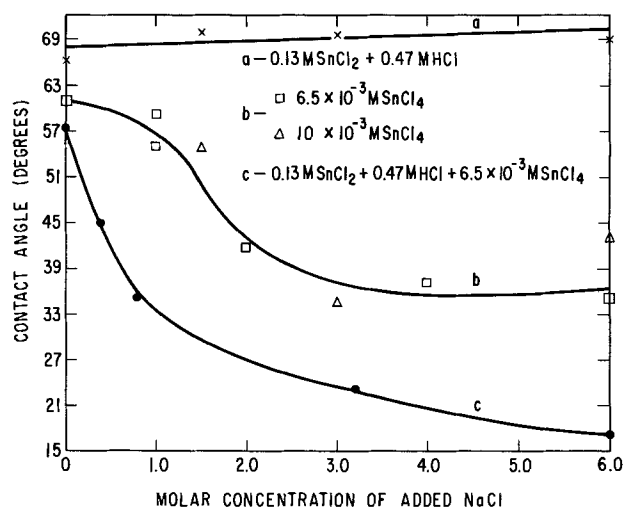


Fig. 5. Contact angle variations vs. sodium chloride concentration on AZ-1350 resist.

same time, the addition of sodium chloride to solutions containing the stannic ions alone shows a substantial decrease in the measured contact angle. Excess addition of sodium chloride to this media (6.5×10^{-3} or 1×10^{-2} M SnCl₄) results in a leveling effect. In curve c, the effect of added sodium chloride to a solution containing both the stannous and stannic ions is demonstrated. The concentrations of the stannous, stannic, and hydrochloric acid are the combined concentrations of those concentrations used for curves a and b. Although there is a general resemblance between curves b and c, the effect of sodium chloride is more pronounced in a system which combines the stannous and the stannic ions. These results are thus suggestive that an interaction exists whereby the degree of surface modification due to sensitization is altered to a greater extent. Substitution of bromide ion for the chloride resulted in the same general characteristics.

Table II provides a summary of the contact angle measurements resulting at each of the steps along the sensitization and activation sequence. As seen, the major surface modifications take place after the sensitization step. Once the surface is suitably "sensitized," very little change is noted at the conclusion of the activation step. In an alternative sequence, the process of sensitization and activation was divided into

Table II. Contact angle measurements during the different stages of pretreatment

	Two-step sequence Contact angle (degrees)	Three-step sequence Contact angle (degrees)	
AZ-1350 resist, as prepared	70	AZ-1350 resist as prepared	70
After sensitization ^(a)	53	After stannic ^(b)	59
After activation	51	After stannous ^(c)	53 ^(d)
		After activation	56

^(a) Sensitizer used composed of 0.13M SnCl₂, 7.5×10^{-3} M SnCl₄ and 0.47M HCl.

^(b) Solution composed of 7.5×10^{-3} M SnCl₄ plus 1M NaCl to compensate for the chloride content present in a combined solution.

^(c) Solution composed of 0.13M SnCl₂ and 0.47M HCl.

^(d) Deletion of the stannic immersion step gives a contact angle of 67°.

three distinct steps: (i) immersion in stannic, (ii) immersion in stannous, and (iii) immersion in palladium chloride activator solution. As seen from Table II, the major change in the contact angle is observed following the stannic immersion step with a slight change in the subsequent steps (immersion in stannous and palladium, respectively). It is interesting to note that a contact angle of 53° has resulted prior to the activation step independent of the path taken. Furthermore, upon deletion of the stannic ions, following immersion in stannous type solution, the observed contact angle is about 67°. It is thus concluded that the presence of the stannic ions provides a new mechanism (7) by which the active stannous ions are adsorbed onto the substrate. The stannic ion may be incorporated along with a conventional-type stannous sensitizer solution or used as a separate immersion step prior to conventional-type sensitization. In a subsequent publication (7), a mechanism accounting for the different modes of sensitization will be given.

Conclusion

In the plating of dielectric substrates, a pretreatment step of sensitization and activation is generally employed. Following this sequence, a catalytic layer is present which is capable of initiating electroless plating baths. In general, it is desired to have a continuous conductive metallic layer prior to an electrolytic build-up of the metallic films. There are, however, materials which do not yield a uniform metallic film. These materials are generally hydrophobic. Of the various steps prior to the electroless plating, the sensitization process controls whether the final metallic film is uniform.

In the current investigation, it has been demonstrated that contact angle measurements can quantitatively demonstrate the effectiveness of sensitizing solutions. Furthermore, controlled additions of stannic ions with or without sodium chloride provide a simple and effective way of modifying conventional sensitizers for the uniform plating of hydrophobic substrates. The role of the added stannic ions is to provide a path for the adsorption of the stannous ions. The stannous ions adsorbed on the substrate were not necessarily bound to any stannic ions in bulk solution, and, in fact, separate solutions may be used effectively, thus separating the stannous from the stannic ions.

Acknowledgments

The authors wish to thank G. L. Schnable for useful discussions and for the reviewing of this paper.

Manuscript submitted Sept. 24, 1971; revised manuscript received ca. Dec. 6, 1971.

Any discussion of this paper will appear in a Discussion Section to be published in the December 1972 JOURNAL.

REFERENCES

1. J. P. Morton and M. Schlesinger, *This Journal*, **115**, 16 (1968).
2. R. Sard, *ibid.*, **117**, 864 (1970).
3. W. Goldie, "Metallic Coatings of Plastics," Vol. I, Chap. 5, Electrochemical Publications Limited, Hatch End, Middlesex, England (1968).
4. F. Pearlstein, *Metal Finishing*, **53**, 59 (1955).
5. R. L. Cohen, J. F. D'Amico, and K. W. West, *This Journal*, **118**, 2042, (1971).
6. R. L. Cohen and K. W. West, *ibid.*, **119**, 433 (1972).
7. N. Feldstein, Unpublished results.

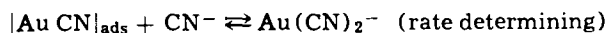
A Study of Gold Reduction and Oxidation in Aqueous Solutions

D. M. Mac Arthur*

Bell Telephone Laboratories, Incorporated, Murray Hill, New Jersey 07974

ABSTRACT

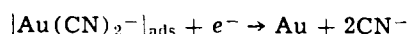
The electrochemical behavior of gold in alkaline cyanide, citrate, and phosphate buffered solutions has been studied using cyclic voltammetry and galvanostatic transients. Two reaction paths were observed. At low overvoltage the reaction goes through an adsorbed intermediate.



At larger overvoltages a direct transfer between the gold complex in solution and the metal atom was found on reduction. The reduction reaction was the same in all the solutions but in the phosphate and citrate baths the gold did not oxidize to a soluble species.

The electrodeposition of gold on various electronic devices is in widespread practice because the metal has good corrosion resistance, electrical conductivity, and bonding properties. A complete understanding of the reaction mechanism for electrodeposition would be of considerable value to the technology of gold plating but has not been achieved. The work described here was undertaken to add to our knowledge of the reaction mechanism for gold reduction and oxidation in practical gold-plating baths.

Maja (1) has reported on the alkaline gold cyanide bath which contains an excess of free cyanide and on the basis of thermodynamics and kinetic measurements concluded that reduction from alkaline solution occurs as follows¹



He also found that the oxidation reaction is



Cathro and Koch (2) used potentiostatic and galvanostatic measurements on gold oxidation in alkaline cyanide electrolytes. They concluded that gold was oxidized to $|\text{Au CN}|_{\text{ads}}$ at potentials less than -0.6V (SCE reference) and became passive in the potential range -0.6 to -0.3V through the formation of a gold oxide or basic cyanide. A second active region was found at approximately $+0.1\text{V}$ which, it was proposed, was the conversion of an adsorbed Au(I) basic cyanide to an adsorbed Au(III) basic cyanide. A third active region at $+0.4\text{V}$ was found and was passivated by the formation of Au_2O_3 . Thermodynamically the formation of gold oxides is expected to occur at potentials considerably more positive than -0.3V . Basic gold cyanides are not known to exist in alkaline cyanide solutions. It is difficult to accept therefore that a gold oxide or basic cyanide can form at a potential of -0.3V . It is also difficult to accept that an Au(III) salt can exist in contact with an aqueous cyanide solution since $\text{Au}(\text{CN})_4^-$ is known to be unstable with respect to $\text{Au}(\text{CN})_2^-$ and cyanogen in these solutions, or that steady-state currents in the range of $1\text{-}2\text{ mA/cm}^2$ can be observed for the oxidation of one adsorbed species to another. We believe, therefore, that the proposed passivation mechanisms at -0.3 and $+0.1\text{V}$ may be in error.

* Electrochemical Society Active Member.

Key words: electrodeposition, gold plating, cyclic voltammetry.

¹ The solutions of commercial significance in gold plating all contain gold predominately as the $\text{Au}(\text{CN})_2^-$ complex.

Taran and co-workers (3) have proposed that solutions with a low pH have a more easily discharged gold complex in solution and that the citrate solution, in particular, has adsorbed citrate on the gold metal surface.

These authors have proposed various reaction mechanisms. Although the solutions vary, it is difficult to accept that the reactions can be so different since the initial and final gold species are the same. In this work cyclic voltammetry and galvanostatic transient techniques are used to provide additional information on the reaction mechanisms.

Experimental

Three gold plating solutions were used in this work as follows:

Alkaline cyanide; 15.0g $\text{KAu}(\text{CN})_2$, 55.0g KCN, 5.0g KOH per liter of solution pH 12.2

Citrate; 50.0g dibasic ammonium citrate, 20.0g $\text{KAu}(\text{CN})_2$ per liter of solution pH 5.0.

Phosphate; 18.2g $\text{KAu}(\text{CN})_2$; 36.4g dibasic potassium phosphate; 9.1g monobasic potassium phosphate pH 7.0.

Reagent grade chemicals were used throughout. De-ionized water that had been passed through both cation and anion exchangers was used to prepare solutions.

Wire electrodes 0.025 in. in diameter and held in a gold-plated pin vise were used as working electrodes. These wires were about 1 in. in length and were immersed 0.5 in. into the solutions. It would be preferable to use an immersed electrode with defined area, but the problem of leakage around edges, particularly in cyclic potentiometry experiments led to the adoption of this technique. The counterelectrode was either a platinum- or gold-plated platinum wire. A saturated calomel reference electrode was used and all potentials are referred to this electrode. In the galvanostatic transient experiments, a gold wire reference electrode in the same solution was used, and its potential frequently checked against the calomel reference.

A standard potentiostatic circuit incorporating an X-Y recorder, potentiostat, and triangular wave function generator was used in the potential scan experiments. The galvanostatic transient experiments used a 24V battery supply for the cathodic transient with a potentiometer for current control and a Western Electric 276B mercury-wetted relay to switch the current. Another 3V battery was used to apply a small anodic current preceding the cathodic transient. Potentials were fed through a high impedance voltage follower and displayed on an oscilloscope which was triggered by the switching circuit.

Solutions (100 ml) were contained in a double-walled Pyrex flask with circulating water for tempera-

ture control. The temperature was $61^\circ \pm 1^\circ\text{C}$. The flask had a machined Teflon lid. All solutions were deoxygenated by bubbling N_2 through them.

Results

Cyclic Voltammetry Experiments

The alkaline cyanide bath.—Figure 1 shows a scan of the bath using a gold wire electrode. (In this preliminary scan a 0.020 in. diameter wire was used.) Two reduction regions A and B may be observed and two oxidation regions C and F are also evident. The oxidation peaks C and F were observed as distinct peaks in all scans moving in the anodic direction, but only in the first two scans were they separate when moving in the cathodic direction. As scanning was continued, peak F disappeared and the peak in the C region became complex as shown in the figure. Peaks A and B were only observed when moving from the anodic to cathodic potentials in all scans.

The areas under peaks C and F on the anodic scan were approximately 105 and 150 millicoulombs as determined by geometric integration of the curves. The double layer charging current was about $1 \mu\text{A}$ and negligible. Oxidation of a monolayer of Au would require only about 0.05 millicoulombs (using the area of the electrode as 0.20 cm^2 , assuming Au(I) was formed and taking the radius of the Au atom as 1.5\AA). The peaks correspond to oxidation of 2000-3000 monolayers. This is too large to represent a thin adsorbed layer nor can it be the formation of an insoluble film since there is no corresponding large reduction peak and the peaks do not change upon continued scanning. It will be shown that peak C is an oxidation reaction that proceeds through a surface film to a soluble product and that peak F is an oxidation reaction passivated by the formation of an oxide on the electrode. The area under peak B on the other hand is approximately 1 millicoulomb, a quantity that could correspond to an adsorbed species. Peak A will be shown to correspond to reduction of Au(CN)_2^- from solution.

Some of the details of the gold reaction are obscured in the standard solution because of the high free cyanide level (approximately 0.85M). Figure 2 shows a potential scan of a gold wire (0.025 in. diameter) in a solution of 0.2M KCN and 0.2M KOH. This solution is about one quarter the concentration in CN^- and twice the concentration OH^- of the standard bath. In Fig. 2 the solution does not contain Au(CN)_2^- to an appreciable extent. Peak A is not present, but there is some evidence of peak B at -1.0V . It is not as large as in solutions containing relatively large amounts of Au(CN)_2^- , and therefore it appears to be related to the presence of Au(CN)_2^- in solution. Peaks C and F are evident scanning in both directions and peak F shows further evidence of being complex. In addition a broad peak E on the side of the oxygen wave and a reduction peak D located just anodic to the oxidation peak F when scanning in the cathodic direction, are

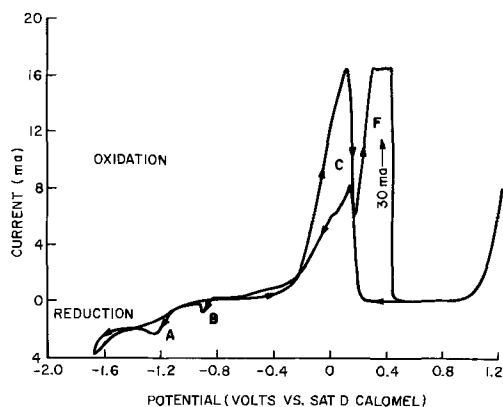


Fig. 1. Potential scan of a Au wire in the alkaline cyanide gold bath. Velocity 0.040 V/sec .

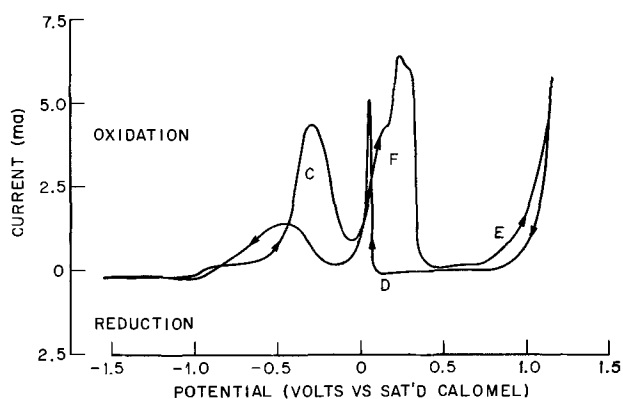


Fig. 2. Potential scan of a Au wire in 0.2M KCN and 0.2M KOH. Velocity 0.042 V/sec .

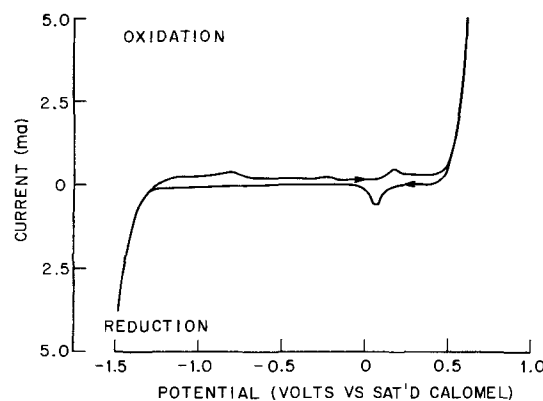


Fig. 3. Potential scan of a Au wire in 0.2M KOH

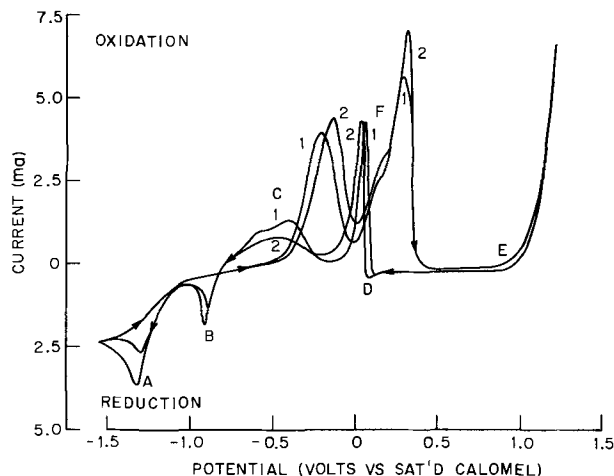


Fig. 4. Potential scans of a Au wire in 0.2M KCN, 0.2M KOH and 0.035M KAu(CN)_2 . Curve 1, 0.041 V/sec ; curve 2, 0.099 V/sec .

observed. Peak D may be seen more clearly in Fig. 4. In order to identify peak D comparison may be made to Fig. 3 which is a scan of a gold wire in 0.2M KOH only. The rest potential of the $\text{Au/Au}_2\text{O}_3$ electrode in KOH solutions has been reported (4) as about 1.1V on the hydrogen electrode scale. For the 0.2M KOH solution this would be about 0.1V on the SCE scale. The oxidation peak and the reduction peak which are close to this value in the figure may reasonably be assigned to the formation and reduction of gold oxide. By analogy it then appears reasonable to correlate peak D in the alkaline cyanide solutions with reduction of gold oxide on the electrode. Peak E is assumed to be a thickening of the gold oxide layer which is first formed at potentials closer to 0.1V.

Figure 4 shows two scans at different velocities of the same 0.2M KCN, 0.2M KOH solution to which

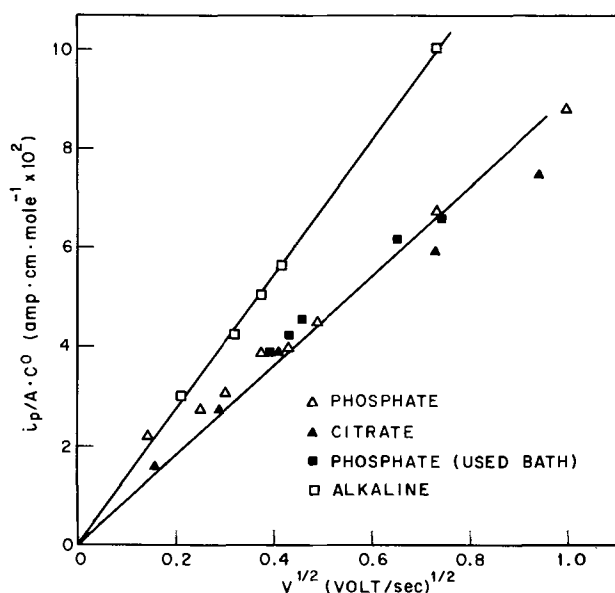


Fig. 5. Peak height as a function of the square root of the scan rate for reduction peak A.

$\text{KAu}(\text{CN})_2$ has been added to make the $\text{Au}(\text{CN})_2^-$ concentration 0.035M. The behavior of peaks A, B, C, and F as the scan rate is varied will now be discussed. At high scan rates the cylindrical geometry of the wire electrode may be approximated by planar geometry. This approximation is valid for rates determined by the inequality (5)

$$\frac{1}{r} \left(\frac{D}{nV} \right)^{1/2} < 0.2$$

which, for the wires used in this work requires that the scan rate be greater than 0.45 V/sec.² Although the effect of cylindrical geometry may be found in the shape of the recorded curves it turns out (5) that the peak height is only slightly altered, and the peak current is a linear function of the square root of the scan rate for velocities as low as 0.1 V/sec. At 61°C this function is

$$i_p = 2.57 \times 10^5 n^{3/2} A D^{1/2} C^\circ V^{1/2}$$

A plot of $i_p/A \cdot C^\circ$ as a function of $V^{1/2}$ is shown in Fig. 5 for peak A. A linear relationship was observed indicating a diffusion limited reaction which must be the reduction of the $\text{Au}(\text{CN})_2^-$ from solution. The true area of the gold wire was estimated from the peak height vs. $V^{1/2}$ plot for the oxidation of $\text{Fe}(\text{CN})_6^{4-}$ and its known diffusion coefficient in dilute chloride solution at room temperature. A roughness factor of 1.3 was determined. Using this true area of the gold wire the diffusion coefficient of $\text{Au}(\text{CN})_2^-$ in the 0.2M KOH, 0.2M KCN solution was found to be $1.8 \times 10^{-5} \text{ cm}^2 \text{ sec}^{-1}$ at 61°C. Literature sources (6) give the value of $1.60 \times 10^{-5} \text{ cm}^2 \text{ sec}^{-1}$ which is satisfactory agreement.

Peak B was found to have a constant capacity of about 1 millicoulomb in the two different alkaline cyanide solutions and for the various scan rates used. This would correspond to about 15-30 molecular layers depending on how tightly packed the atoms were. The reduction reaction would appear to have two possible paths; one through an adsorbed state (peak B) and one by direct charge transfer (peak A).

The number of coulombs passed in area C increased as the scan rate decreased. This was evident not only in the cathodic to anodic scan but in the reverse direction also. In addition the current did not increase without limit when moving in the anodic direction as would be expected for a charge transfer reaction forming directly a soluble species from a metal electrode.

These observations then are consistent with a reaction mechanism in which charge transfer forms an intermediate on the electrode and the intermediate species is solubilized in a following chemical reaction.

Cathro and Koch (2) concluded that the peak in area C was passivated by the formation of an adsorbed basic gold cyanide. The shape of the peak is not consistent with a passivation type reaction which causes an abrupt decrease in current (compare the shape of peak F and C). It is consistent with the charge transfer followed by chemical reaction mechanism in which the chemical reaction is rate limiting and the surface intermediate interferes with the charge transfer reaction.

Peak F has the characteristic shape of a passivated reaction which is depassivated upon reduction of a surface film at D. As mentioned earlier, this reduction potential corresponds to that for gold oxide which, therefore, is the passivating film. Cathro and Koch (2) observed two peaks in this area and indeed peak F does give evidence of being composed of two overlapping peaks. The number of coulombs passed in this region is much too large for the reaction to be the formation of an adsorbed layer. In addition, the observation that the number of coulombs passed does not increase with decreasing scan rate (except to a small and sometimes variable extent) suggests that the reaction is direct oxidation to a soluble species complicated by the presence of gold oxide which eventually passivates the electrode. This phenomenon has also been observed (7) for gold oxidation in acid chloride solutions and the same explanation for passivation was proposed.

The citrate bath.—Gold-plated Kovar (Fe, Ni, Co alloy) wires were used for some of the experiments in the citrate and phosphate baths. The gold was electrodeposited at about 1 mA (approximately 4 mA/cm²) from the solution before commencing the scans. In the citrate and phosphate solutions the gold is not oxidized to a soluble species because of the absence of excess CN^- or other complexing agents and the electrocoated wires were not observed to differ from the solid gold wires.

Figure 6 shows scans at three different speeds of a gold-plated Kovar wire in the citrate bath. The peak numbering scheme used in describing the results of the alkaline bath is retained here and also for the phosphate bath to be described next. A plot of $i_p/A \cdot C^\circ$ (peak A) as a function of $V^{1/2}$ is included in Fig. 5. A linear relationship was observed but the calculated diffusion coefficient was $0.88 \times 10^{-5} \text{ cm}^2 \text{ sec}^{-1}$ not in agreement with the literature value (6) of $1.67 \times 10^{-5} \text{ cm}^2 \text{ sec}^{-1}$. This lack of agreement indicates that peak A is not a simple charge transfer reaction involving reduction of a soluble species. The absence of a clearly

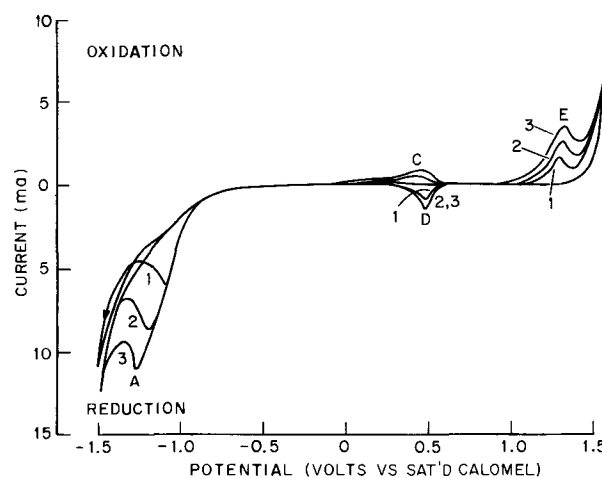


Fig. 6. Potential scans of Au plated wire in the citrate bath. Curve 1, 0.17 V/sec; curve 2, 0.52 V/sec; curve 3, 0.85 V/sec.

² A list of symbols used is included at the end of the paper.

defined peak B which is assumed to be reduction of an adsorbed intermediate suggests that this reduction path is also occurring in the potential range of peak A resulting in the low calculated value for the diffusion coefficient. More evidence to establish that this is the case was obtained from the galvanostatic transients which will be described later.

Peak C was observed to have a capacity in the range of 0.1-0.3 millicoulombs—that expected for the formation of an insoluble surface layer. From a comparison of this figure with the preceding figures, it is concluded that this is oxidation of gold to the adsorbed intermediate observed in the alkaline bath but in this case the following chemical step to a solubilized product does not occur because of the absence of excess CN^- . Peaks D and E are reduction of gold oxide and oxidation of gold, respectively.

The phosphate bath.—Figure 7 shows scans of a gold wire in the phosphate bath. The current in peak A is plotted in Fig. 5. The calculated D is $0.88 \times 10^{-5} \text{ cm}^2 \text{ sec}^{-1}$ the same as that for the citrate bath and not in agreement with the literature value (4) of $1.63 \times 10^{-5} \text{ cm}^2 \text{ sec}^{-1}$. In this bath it is also concluded that reduction through the adsorbed intermediate is occurring in the same potential range as the direct charge transfer to $\text{Au}(\text{CN})_2^-$ although evidence for peak B may be seen on the edge of the reduction wave. Peak C was observed to have capacities ranging from 0.2 to 1.1 millicoulombs indicating that in this bath oxidation proceeds to the intermediate surface state which is not solubilized.

Galvanostatic Transient Experiments

Oxidation.—Galvanostatic transients for a gold wire during oxidation in a 0.2M KOH, 0.2M KCN, and $3.58 \times 10^{-2} \text{M KAu}(\text{CN})_2$ solution were obtained in the range of 18 to 48 mA/cm^2 . A potential of 0.3 to 0.45V (peak F) was observed for the oxidation followed by a sharp potential rise to oxygen evolution at potentials greater than 1V [Fig. 8(a)]. The transition time was taken as the commencement of the sharp potential rise. For the lower current densities another plateau at about 0.1V was observed with a capacity of about 1.7 millicoulombs/ cm^2 before the potential plateau at 0.3-0.45V. The transition times include this plateau because the surface intermediate is later chemically dissolved. Figure 9 is a plot of $i\tau$ and $i\tau^{1/2}$ determined from these oxidation experiments as a function of current density. The linear $i\tau^{1/2}$ relationship is an indication that the predominate oxidation reaction is the formation of a soluble species. (If the reaction were predominately the formation of a surface film a linear $i\tau$ relationship would be observed.) For a metal oxidation reaction into solution the concentration of the metal ion at the surface is

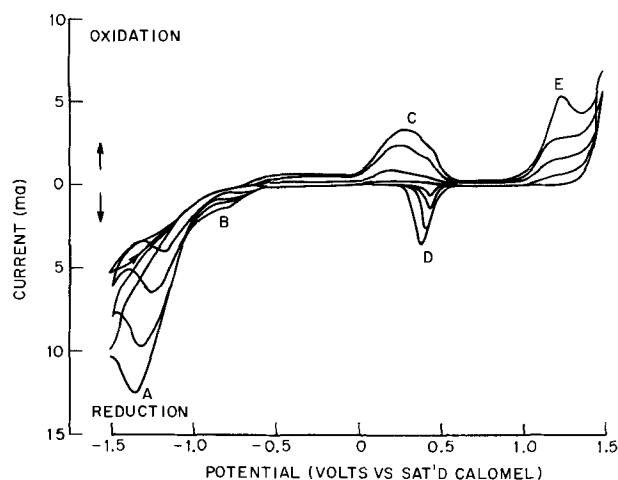


Fig. 7. Potential scans of a Au wire in the phosphate bath. Scan rates were 0.060, 0.24, 0.55, and 1.0 V/sec.

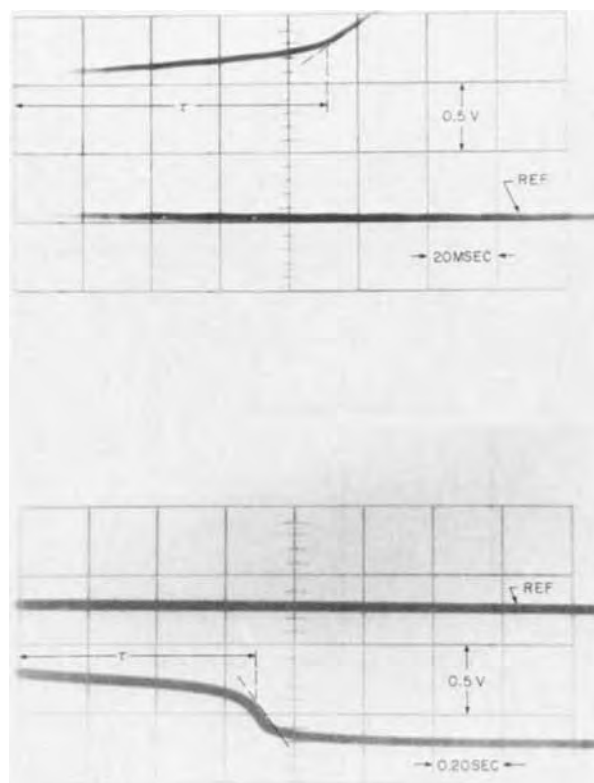


Fig. 8. (a) Upper curve, a typical potential-time transient for gold oxidation in 0.2M KOH, 0.2M KCN solution at 61°C. Current density 38 mA/cm^2 . (b) Lower curve, a typical potential-time transient for gold reduction. Wire electrode, alkaline cyanide solution 0.035M in $\text{Au}(\text{CN})_2^-$, current density 21 mA/cm^2 .

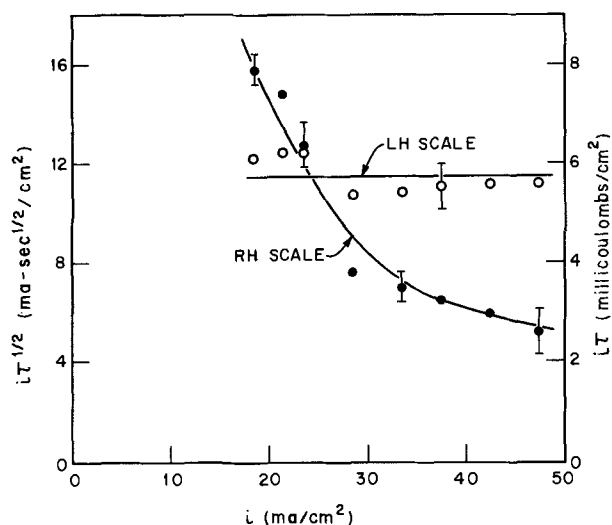


Fig. 9. Transition time curves for gold oxidation in 0.2M KOH, 0.2M KCN, and 0.2M $\text{KAu}(\text{CN})_2$.

$$C_o = \frac{2i}{nF D^{1/2}} \sqrt{t/\pi}$$

If the electrode follows Nernst behavior then the potential of the electrode increases as the logarithm of the square root of time without abrupt transition. When a passivating reaction can occur, however, as it does in this case then the potential rises to the value where passivation occurs and then increases abruptly. The concentration of the metal ion when this occurs may be designated C_o^* and is given by

$$C_o^* = \frac{2i}{nF D^{1/2}} \sqrt{t/\pi}$$

Substitution of the value 11.5×10^{-3} (Fig. 9) for $i\tau^{1/2}$ into this equation gives a value of 3.5×10^{-2} mole/l for Co^* . This value is less than the saturation value for $\text{Au}(\text{CN})_2^-$ suggesting that passivation occurs not from precipitation of gold cyanide but as a result of another reaction beginning at a potential of about 0.45V and this is the formation of gold oxide.

Reduction.—The transition time during reduction occurs when the reaction, under mass transport limited kinetics, reaches the condition that the surface concentration of the reacting species is zero. The transition time is given by

$$i\tau^{1/2} = \frac{1}{2}\pi^{1/2}nFC^0D^{1/2}$$

If the reaction is preceded by a slow chemical reaction then the $i\tau^{1/2}$ product is not constant but decreases with increasing current density. If the reaction is preceded by an adsorption step then the product $i\tau$ becomes constant at sufficiently high current densities and the $i\tau^{1/2}$ product increases. A convenient means of distinguishing these reaction mechanisms is thus available. Peters and Lingane (8) have modified transition time theory for planar electrodes to include cylindrical geometry. In the worst case considered here the correction is less than 10% for the cylindrical geometry so the unmodified theory is used throughout. A typical potential-time curve for gold reduction is given in Fig. 8(b).

The data from transition time experiments are displayed in Fig. 10. In these experiments four different solutions and three different geometries were used. Considering this, the scatter in the $i\tau^{1/2}/C^0$ values is not excessive. One set of data (the open circles) indicates a preceding adsorption step. These measurements were taken with the electrode "floating" without an applied potential before the imposition of the cathodic current. All the other data in the figure were obtained with an anodic current of from 50 to 200 μA applied to the electrode before switching to the cathodic current. In these latter experiments the formation of an oxide on the surface prevented adsorption of the intermediate reduced in peak B (Fig. 2). On reduction the thin oxide layer was rapidly reduced and then $\text{Au}(\text{CN})_2^-$ was reduced from solution. The oxide layer was thin (about 1 millicoulomb/cm²), reacted rapidly and at a potential about 0.5V anodic to the gold reduction wave so that it did not interfere in the measurements.

Experiments using the $\frac{1}{2}$ in. diameter rod consistently gave transition times less than those using the $\frac{1}{4}$ in. rod, and the wire, and with less scatter. This could be the result of a better geometry. In any event examining all the data there does not appear to be any

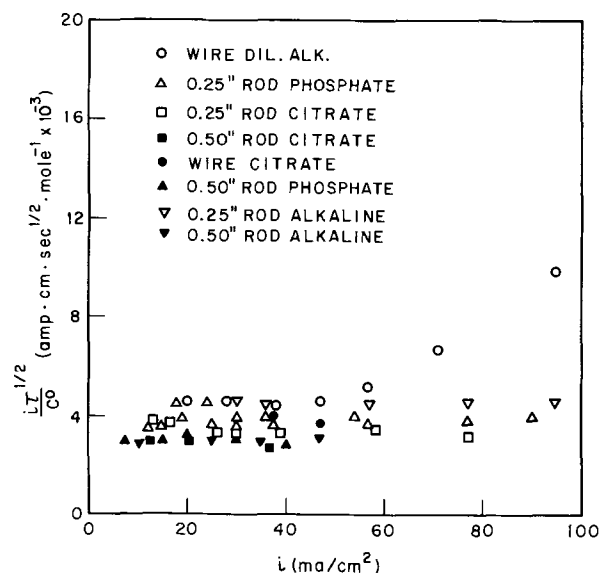


Fig. 10. Transition time plot for various Au electrodes in the citrate, phosphate, and alkaline Au plating solutions.

difference in the reduction mechanism from the three solutions and the diffusion coefficient of the reacting species is the same within the experimental error. This is expected to be the case since the reacting species is the same in all the solutions and the diffusion coefficient will vary only slightly with the activity of the ion in the solutions of different ionic strength. The average value from all the experiments with the exception of the "free floating" one provides a diffusion coefficient of 1.8×10^{-5} cm² sec⁻¹. The scatter in the data, however, place a possible error of $\pm 0.35 \times 10^{-5}$ cm² sec⁻¹ on this value.

There is sufficient agreement between this value for D and the literature values (6) for the diffusion coefficient of $\text{Au}(\text{CN})_2^-$ in alkaline cyanide, citrate, and phosphate solutions to conclude that $\text{Au}(\text{CN})_2^-$ is the reacting species and that the reason for the low D values found from the cyclic voltammetry experiment was the interference of the adsorbed intermediate in the citrate and phosphate solutions.

Summary

Oxidation of gold.—The oxidation of gold in alkaline cyanide solutions is seen to be complex. It is concluded that at low overvoltages oxidation proceeds through a surface intermediate probably $[\text{Au}(\text{CN})]_{\text{ads}}$ and that the oxidation of gold in the region -0.6 to -0.3V is limited by the dissolution of the surface intermediate. When the surface is completely covered the rate of reaction is controlled by the rate of chemical dissolution of the intermediate. In this work no true passive region was observed when the gold electrode was potentiostated at potentials less than $+0.45\text{V}$ in the alkaline cyanide bath at temperatures higher than 40°C . The chemical dissolution reaction logically must be



At higher overvoltages a complex oxidation peak (F) was observed. In agreement with Cathro and Koch (2) it is concluded that this active region is passivated by the formation of oxide on the gold surface. The capacity of the peak does not allow assignment to the oxidation of a surface film. The results indicate that in this region gold is oxidized to a soluble species. The reaction is too complex to analyze fully at this time, but two possibilities are the direct oxidation of gold to $\text{Au}(\text{CN})_2^-$ without the formation of an intermediate and the oxidation of gold to an $\text{Au}(\text{III})$ complex which presumably would react with CN^- oxidizing this and being in itself reduced to $\text{Au}(\text{CN})_2^-$.

Reduction of gold.—Two reduction paths were observed. In the alkaline cyanide bath these were evident in the cyclic voltammetry curves but in the citrate and phosphate baths they were not. One reduction path was through an adsorbed intermediate and on the basis of the oxidation results this is presumed to be $[\text{Au}(\text{CN})]_{\text{ads}}$. The other reduction path was a direct charge transfer to the soluble $\text{Au}(\text{CN})_2^-$. The two reduction paths may be expected to lead to electrodeposits differing in physical character.

Manuscript submitted April 30, 1971; revised manuscript received ca. July 29, 1971.

Any discussion of this paper will appear in a Discussion Section to be published in the December 1972 JOURNAL.

LIST OF SYMBOLS

r	radius (cm)
D	diffusion coefficient (cm ² sec ⁻¹)
n	number of electrons
V	scan rate of velocity (volts sec ⁻¹)
i_p	maximum current in a peak (A)
A	area of electrode (cm ²)
C^0	initial concentration (moles cm ⁻³)
C_s	surface concentration (moles cm ⁻³)
t	time (sec)
τ	transition time (sec)

REFERENCES

1. M. Maja, *Atti Accad. Sci. Torino: Classe Sci. Fis. Mat. Nat.*, **99**, 1111 (1965).
2. K. J. Cathro and D. F. A. Koch, *This Journal*, **111**, 1416 (1964).
3. L. A. Taran, S. I. Berezina, and G. S. Vozdvizhenskii, *Tr Kazan Khim in-ta*, **36**, 591 (1967). Foreign Language Center Trans. #3792.
4. R. Thacker and J. P. Hoar, *Electrochem. Technol.*, **2**, 61 (1964).
5. P. Delahay, "New Instrumental Methods in Electrochemistry," p. 122, Interscience (1954).
6. H. Y. Cheh, *This Journal*, **118**, 551 (1971).
7. J. N. Gaur and G. M. Schmid, *J. Electroanal. Chem.*, **24**, 279 (1970).
8. D. G. Peters and J. J. Lingane, *ibid.*, **2**, 1 (1961).

Current Distribution at the Rotating Ring-Disk Electrode

G. Neubert, E. Gorman, R. Van Reet, and K. B. Prater*

Department of Chemistry, University of Texas at El Paso, El Paso, Texas 79968

ABSTRACT

The digital simulation method is used to calculate the current densities at both the ring and disk surfaces of a ring-disk electrode when the two surfaces are at the same potential. Simulated and experimental results show that the current density at the ring is nonuniform and measurably different from that at the disk electrode, even if the current density at the disk is assumed to be uniform. In addition, a technique is presented which allows the determination of the simulation representations of the electrode radii from experimental data.

Most treatments (1-3) of rotating disk and ring-disk electrodes have assumed that the disk is a uniformly accessible surface—that is, that the current density is uniform across the entire surface of the disk electrode. Newman (4) concluded that the current density should in fact be nonuniform at applied potentials below the limiting current. Albery and Ulstrup (5) presented results of experiments at the ring-disk electrode in which observed collection efficiencies for the Br-Br₂ system deviated from those predicted by a theory based upon the assumption of uniform accessibility. This deviation was attributed to nonuniform accessibility by the authors. Marathe and Newman (6) then pointed out that the deviation observed by Albery and Ulstrup was in the wrong direction to be attributable to nonuniform current density at the disk. It seemed to us that a more reasonable explanation for the observed deviation would be that the current efficiency at the disk was less than 100%. This has recently been confirmed by Albery and Hitchman (7). In the same chapter (7) Albery and Hitchman also present new ring-disk electrode data which are in agreement with Newman's treatment. These data and the data obtained by Marathe and Newman (6) and Bruckenstein and Miller (8) leave no doubt that under certain conditions nonuniform current density prevails at the disk electrode.

In response to the Albery and Ulstrup paper (5), Marathe and Newman (6) suggested that the ring-disk electrode could be used for a quantitative study of nonuniform current distributions by applying the same potential to the disk and ring electrodes. They suggested that observed differences in the current densities at the ring and disk electrodes would be a direct measure of the nonuniformity of the current density at the disk electrode. The purpose of this paper is to present the results of digital simulation and experimental work which show that, due to the presence of the insulating gap between the ring and disk and the different boundary condition which holds there, even if the current density were uniform at the disk, a nonuniform and measurable different current density would be observed at the ring. Only in the limit as the width

of the gap approaches zero will the two current densities approach one another.

Digital Simulation

The technique for the digital simulation of the rotating ring-disk electrode has been presented previously (3). For the purposes of this study two quantities in addition to the collection efficiency (3), N , were simulated for the reversible reaction



In order to accurately model the electrodes, it was necessary to simulate the limiting current at the ring when the disk was held at open circuit potential. This was done simply by applying the boundary condition which is used for the gap to the disk as well, and applying the usual disk boundary condition to the ring. The second simulation was that of the limiting currents and current densities at the disk and the ring when the two electrodes are shorted together and the potential is such that the limiting current is passed at the disk. In the nomenclature of Ref. (3), the boundary conditions were

$$\begin{aligned} F_A(1,1) &= F_A(1,K_R) = 0.0 \\ F_B(1,1) &= F_B(1,K_R) = 1.0 \end{aligned} \quad [2]$$

The dimensionless disk current parameter, ZD , which is calculated by this technique is

$$ZD = i_d / (0.51)^{1/3} n F A_d C_A^0 D_A^{2/3} \omega^{1/2} \nu^{-1/6} \quad [3]$$

where i_d is the limiting current at the disk, n is the number of electrons transferred per molecule, F is the Faraday, A_d is the area of the disk, C_A^0 is the bulk concentration of species A , D_A is the diffusion coefficient of A , ω is the rotation rate, and ν is the kinematic viscosity. Notes that ZD is proportional to the current density at the disk.

The dimensionless ring current parameter, ZR , which is calculated by this technique (3) is

$$ZR = i_r / (0.51)^{1/3} n F A_d C_A^0 D_A^{2/3} \omega^{1/2} \nu^{-1/6} \quad [4]$$

where i_r is the limiting ring current. When ZR is multiplied by the ratio of the area of the disk to the area of the ring, A_r , a new parameter, ZRN , is generated

* Electrochemical Society Active Member.

Key words: ring-disk electrode, current distribution, uniform current density.

Table I. Dependence of current density ratio on width of gap

Width of gap ^(a)	CDR ^(b)
40	1.54
20	1.34
10	1.20
1	1.03

^(a) Arbitrary units.^(b) Current density ratio— $(i_r/A_r)/(i_d/A_d)$.

which is proportional to the average ring current density.

$$ZRN = i_r / (0.51)^{1/3} n F A_r C^{\circ} A D_A^{2/3} \omega^{1/2} \nu^{-1/6} \quad [5]$$

Note that the ratio of ZRN to ZD is the ratio of average current density at the ring to the current density at the disk when the two are shorted together. That is

$$CDR = ZRN/ZD = (i_r/A_r)/(i_d/A_d) \quad [6]$$

Thus for a given electrode, three experimentally measurable parameters were calculated (i) the ratio of the limiting ring current with the disk inactive to the limiting disk current, (ii) the collection efficiency (3), and (iii) the ratio of the average current density at the ring to the current density at the disk when the two electrodes are shorted.

Simulation Results

The simulated ratio of the average current density at the ring to the current density at the disk when the two electrodes are shorted together is presented in Table I for a series of electrodes differing only in the width of the gap. For these calculations, the radius of the disk was, in each case, 99.5 units, the width of the ring was 25 units, and the width of the gap was varied as shown in Table I. The current densities were calculated using the same boundary conditions at the ring and disk and assuming uniform current density at the disk.

As might be expected, the average ring current density approaches the disk current density as the thick-

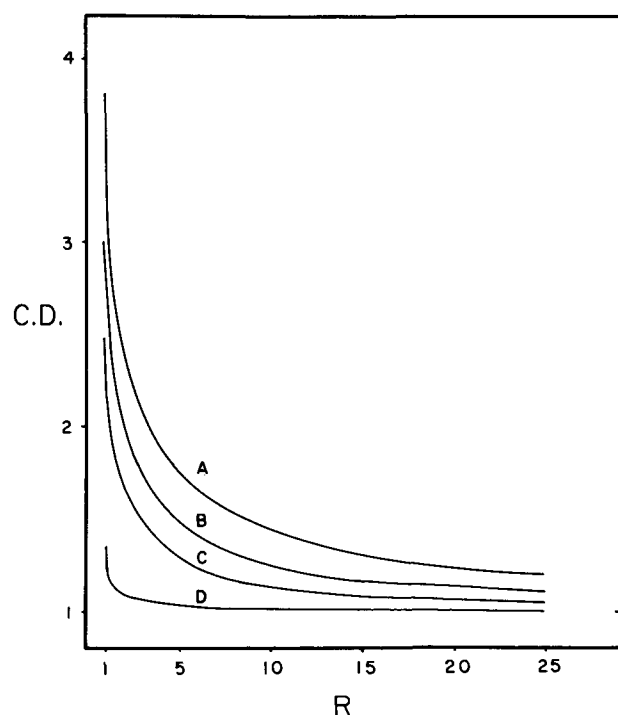


Fig. 1. Ring current density profile for electrodes in Table I. Ring and disk are shorted together. R is the distance from the inner edge of the ring. C.D. is the ring current density at each point normalized by the disk current density. The width of the gaps are: A = 40, B = 20, C = 10, D = 1.

ness of the gap approaches zero. As the gap is made wider, the average current density gets larger and would be expected to approach that for a ring electrode alone.

The current density profile for each of the electrodes is presented in Fig. 1. Again the results are as might be expected with a uniform current density being approached only as the width of the gap approaches zero.

Experimental

All chemicals were reagent grade and used without further purification. The potentiostat which was used for limiting current measurements was a Werking Model 66TS10 and the recorder was a Hewlett Packard 7004A X-Y with 17171A d-c preamp plug-ins. For collection efficiency measurements, a constant current source with a floating power supply and utilizing Analog Devices operational amplifiers was used to supply the disk current. The platinum ring-disk electrodes were obtained from Pine Instruments, Grove City, Pennsylvania, and were rotated with a Motomatic E-550 motor with feedback controller modified to operate up to 10,000 rpm which was obtained from Electro Craft, Hopkins, Minnesota. All experiments were carried out at room temperature.

Before each run, the electrodes were pretreated by rotating them in an acid dichromate solution for 60 sec, rinsing with distilled water and drying. With this procedure, limiting currents could be reproduced within $\pm 0.5\%$. Measurements of the collection efficiency were made by applying a constant current to the disk electrode and determining the limiting current at the ring.

Results and Discussion

Measurements were made on two electrodes. One, electrode A, had a relatively thin gap while the other, electrode B, had a much wider gap. The collection efficiencies of these electrodes were determined for solutions which were $1 \times 10^{-3}M$ in $K_4Fe(CN)_6$ and $2M$ in KCl. The results are presented in Table II. In all runs, the current applied to the disk was less than the limiting current.

Next, the limiting disk current, i_d , limiting ring current with the disk at open circuit, i_{r0} , and the limiting current with the disk and ring shorted together, i_{rd} , were measured in succession in the same solution. This procedure was repeated at rotation rates varying from 100 to 5000 rpm.

The ratio of i_{r0} to i_d and the collection efficiency were used to determine the radius of the outer edge of the gap, r_2 , and the radius of the outer edge of the ring, r_3 , relative to the radius of the disk, r_1 . This was done by simulating these two parameters for various values of the simulation representation of these radii, IR1, IR2, and IR3. A value of IR1 was selected and the parameters IR2 and IR3 were adjusted until the simulated values of i_{r0}/i_d and the collection efficiency were in satisfactory agreement with the experimental values. Since (3)

$$IR1 - 0.5 = r_1 \Delta r \quad [7]$$

and

$$IR2 - 0.5 = r_2 \Delta r \quad [8]$$

$$(IR2 - 0.5)/(IR1 - 0.5) = r_2/r_1 \quad [9]$$

Table II. Experimental collection efficiencies

ω ^(a)	Electrode A		Electrode B	
	N	Runs	N	Runs
500	0.569 \pm 0.005	15	0.452 \pm 0.003	17
1000	0.569 \pm 0.004	31	0.449 \pm 0.002	9
2000	0.570 \pm 0.004	14	0.450 \pm 0.003	11
3000	0.563 \pm 0.005	14	0.450 \pm 0.002	10
4000	0.563 \pm 0.004	14	0.450 \pm 0.003	8
5000	0.561 \pm 0.004	23	0.448 \pm 0.002	20
Avg.	0.566 \pm 0.005		0.450 \pm 0.003	

^(a) Rotation rate, rpm.

Table III. Experimental and simulated collection efficiencies and limiting current ratios

	Electrode A		Electrode B	
	N	i_{ro}/i_d	N	i_{ro}/i_d
Experimental	0.566 ± 0.005	3.21 ± 0.04	0.450 ± 0.003	2.56 ± 0.03
Simulated	0.566	3.20	0.448	2.56
IR1 = 83, IR2 = 92, IR3 = 159		IR1 = 83, IR2 = 104, IR3 = 151		

and similarly

$$(IR3 - 0.5)/(IR1 - 0.5) = r_3/r_1 \quad [10]$$

In a similar manner, it is found that the ratio of the area of the ring to the area of the disk, A_r/A_d is given by

$$A_r/A_d = [(IR3 - 0.5)^2 - (IR2 - 0.5)^2]/(IR1 - 0.5)^2 \quad [11]$$

Note that in order to determine r_2 and r_3 explicitly, r_1 would have to be determined independently. This is not necessary for this work. The experimental results and best fit simulation results are presented in Table III.

With satisfactory values of IR1, IR2, and IR3 determined, it was then possible to calculate the expected values of the ratio of the average current density at the ring, i_{rs}/A_r , to the current density at the disk, i_d/A_d , when the ring and disk are shorted together for each of the two electrodes for which data were available. The experimental values of i_{rs} were obtained by subtracting the measured i_d from i_{rd} , the total ring and disk current. The ratio i_{rs}/i_d when multiplied by A_d/A_r , the reciprocal of Eq. [11], yields the experimental ratio of the current densities, CDR. The agreement between the experimental and simulated current density ratios is shown in Table IV.

Conclusion

It has been shown that the current density at the ring electrode when shorted to the disk electrode is nonuniform even if the current density at the disk is uniform as it is at the limiting current. The digital simulation technique has been shown to accurately

Table IV. Experimental and simulated current density ratios

	Electrode A	Electrode B
	Experimental	1.07 ± 0.01
Simulated	1.07	1.20

calculate the average current density at the ring when the current density at the disk is uniform. It is expected that a nonuniform current density at the disk would give rise to measurably different average current densities at the ring under these conditions and that such a technique should be valuable in measuring such nonuniformity. The digital simulation of this case is now being undertaken.

Acknowledgments

The authors wish to thank the Research Corporation and the University Research Institute of the University of Texas at El Paso for financial support of this work.

Manuscript submitted Nov. 3, 1971; revised manuscript received ca. Nov. 22, 1971.

Any discussion of this paper will appear in a Discussion Section to be published in the December 1972 JOURNAL.

NOTE ADDED IN PROOF: Newman has recently obtained similar results with an essentially analytical solution. See *This Journal*, **119**, 212 (1972).

REFERENCES

- V. G. Levich, "Physicochemical Hydrodynamics," Prentice-Hall, Inc., Englewood Cliffs, N. J. (1962).
- W. J. Albery and S. Bruckenstein, *Trans. Faraday Soc.*, **62**, 1920 (1966).
- K. B. Prater and A. J. Bard, *This Journal*, **117**, 207 (1970).
- J. Newman, *ibid.*, **113**, 1235 (1966).
- W. J. Albery and J. Ulstrup, *Electrochem. Acta*, **13**, 281 (1968).
- V. Marathe and J. Newman, *This Journal*, **116**, 1704 (1969).
- W. J. Albery and M. L. Hitchman, "Ring-Disc Electrodes," Oxford University Press, London (1971).
- S. Bruckenstein and B. Miller, *This Journal*, **117**, 1044 (1970).

Electrode Kinetic Studies on Electro-Organic Syntheses Involving Carbonium Ions

I. Anodic Oxidation of Acetate Ions to Methyl Acetate

Ashok K. Vijh*

Hydro-Quebec Institute of Research, Varennes, P. Q., Canada

ABSTRACT

Anodic electrosynthesis of methyl acetate on graphite electrodes in aqueous acetate solutions is known to proceed via intermediate formation of carbonium ions. Kinetic-mechanistic aspects of this reaction have not been examined previously and an attempt has been made in the present investigation to elucidate these aspects by carrying out electrode kinetic studies. Potentiostatic Tafel plots, potentiodynamic profiles, anodic charging curves, open-circuit potential decay measurements, capacity-potential relationships, apparent heats of activation, and reaction order derivatives are reported for this system. On the basis of an analysis of these data, it has been suggested that initial discharge step is the rate-determining step (r.d.s.) in the over-all reaction. Possible explanation for the occurrence of a carbonium ion pathway, in preference to a radical one as observed for the Kolbe reaction, in the present case is also put forward.

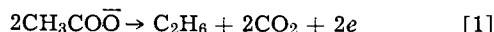
An interesting aspect of modern work in synthetic organic chemistry is the elucidation of the role of radicals and radical ions in various syntheses. This

* Electrochemical Society Active Member.

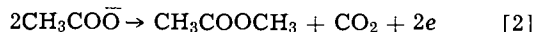
Key words: carbonium ions, electro-organic synthesis, electrode kinetics, anodic oxidation, acetate ions.

problem also arises in some electro-organic syntheses in which it has been observed that radicals (1) or carbonium ions (2) can play an important role as reactive intermediates. If one considers the anodic oxidation of acetate ions in aqueous solutions on a platinum

electrode, one observes that ethane and carbon dioxide are formed in the over-all reaction



This reaction, called the Kolbe reaction, is known to proceed in several steps and is believed (1, 2) to occur by intermediate formation of radicals. When one conducts the anodic electrolysis of the aqueous acetate solutions on a graphite electrode, however, one does not obtain the usual Kolbe products but instead, methyl acetate is formed as the major product with a yield (2) of ca. 82%. The over-all reaction in this case is



Several investigators, notably Corey and co-workers (3, 4) and Koehl (5) have presented a great deal of evidence to show that the over-all reaction in Eq. [2] involves intermediate formation of carbonium ions. In several other related anodic electrosyntheses, Ross and co-workers (2) have postulated the intermediate formation and participation of carbonium ions.

Despite a great deal of synthetic work (2-5) on electro-organic syntheses involving carbonium ions, no electrode kinetic studies seem to have been carried out. The purpose of the present series of studies is to examine the electrode kinetic features of electro-organic syntheses involving carbonium ions, on the basis of general approaches applied earlier to the Kolbe reaction (1). The aim would be to present new electrochemical evidence and an associated kinetic analysis that will seek to examine the nature of various elementary steps involved in the over-all reaction as well as the identity of the rate determining step (r.d.s.) in a likely reaction pathway. An attempt will also be made to establish the nature and role of any adsorbed reaction intermediates that might be involved in the over-all reaction. It is believed that such electrode kinetic studies will provide vital information, supplementary to the previous synthetic work (2-5), needed to formulate a kinetic-mechanistic picture of electro-syntheses involving carbonium ions. It is hoped that a somewhat better understanding of the various aspects of these electrode processes thus developed will perhaps aid in the further explorations of electro-organic syntheses involving carbonium ions.

Experimental Section

The instruments and the cell employed as well as the details on electrodes, gas purification, preparation of conductivity water, cell cleaning, etc. have been described recently (6). The general electrode kinetic approaches used in the present work were reviewed previously (1).

All electrode potentials expressed here are against a hydrogen reference electrode in the same solution. No pre-electrolysis was conducted in the present work since it was noted previously (1) that in electro-organic work pre-electrolysis tends to produce rather than remove traces of impurities.

All solutions were made from potassium acetate (Fisher, A.C.S. certified, mol. wt. 98.15), acetic acid (Fisher reagent, 99.7%), and conductivity water.

Results

Steady-state current-potential relationships.—In Fig. 1, steady-state (point-by-point) potentiostatic current-potential relationships for the anodic oxidation of acetate ions on graphite electrodes in aqueous acidic solutions have been presented. An hysteresis between the ascending and descending curves is observed which is not entirely unexpected for anodic reactions (7). A Tafel slope of ca. $2.3 \times 2RT/F$ is observed at higher anodic potentials, whereas Tafel lines showing higher slopes are indicated below 1.8V. Some rudimentary inhibition inflections, of the type discussed by Gilroy and Conway (8) may also be noted, around 0.5V on the ascending curve and around 1.3V on the descending curve.

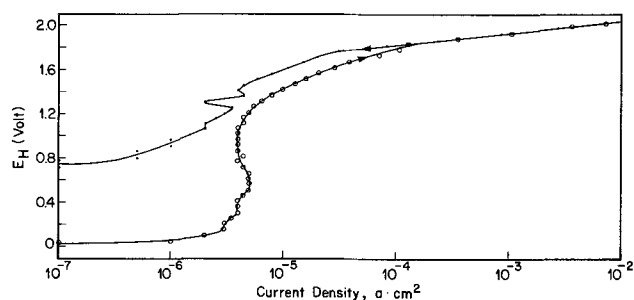


Fig. 1. Potentiostatic, steady-state (point-by-point) Tafel relationships on a graphite electrode in aqueous acetate solutions, both in the ascending and descending direction of potentials. The Tafel slope at the high anodic potentials is ca. $2.3 \times \frac{2RT}{F}$. Solution is 5N $\text{Cl}_3\text{COOK} + 1\text{N } \text{CH}_3\text{COOH}$ in water. Room temperature. Time of polarization at every point is 2 min.

curve. The change in Tafel slopes around 1.8 would indicate two parallel mechanisms (7).

Temperature effects on the rate.—In Fig. 2 (a) and 2 (b), effect of temperature on the ascending and descending, respectively, Tafel plots has been represented. Only the linear Tafel regions have been shown. It is seen that the potential at which the two Tafel lines with different slopes intersect depends on the temperature, i.e., at higher temperature the change in the slope of the Tafel line, and the associated shift over to an alternative parallel mechanism, tends to occur at lower electrode potentials. This is not at all unexpected since temperature and potential both drive

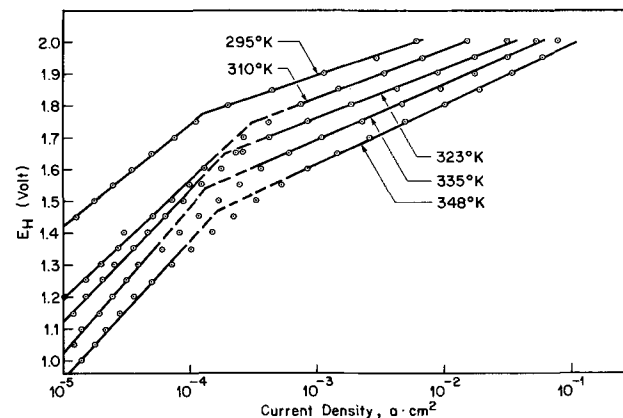


Fig. 2 (a). Tafel plots at the shown temperatures taken in the ascending direction of potentials. Graphite anode in 2N $\text{CH}_3\text{COOK} + 1\text{N } \text{CH}_3\text{COOH}$. Time of polarization at every potential is 2 min.

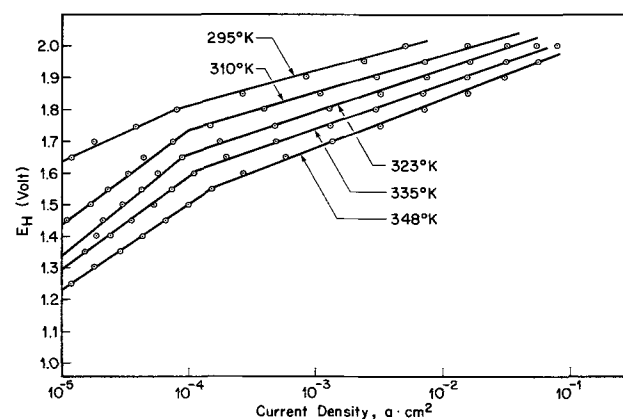


Fig. 2 (b). Same as Fig. 2 (a) but now taken in the descending direction of electrode potentials.

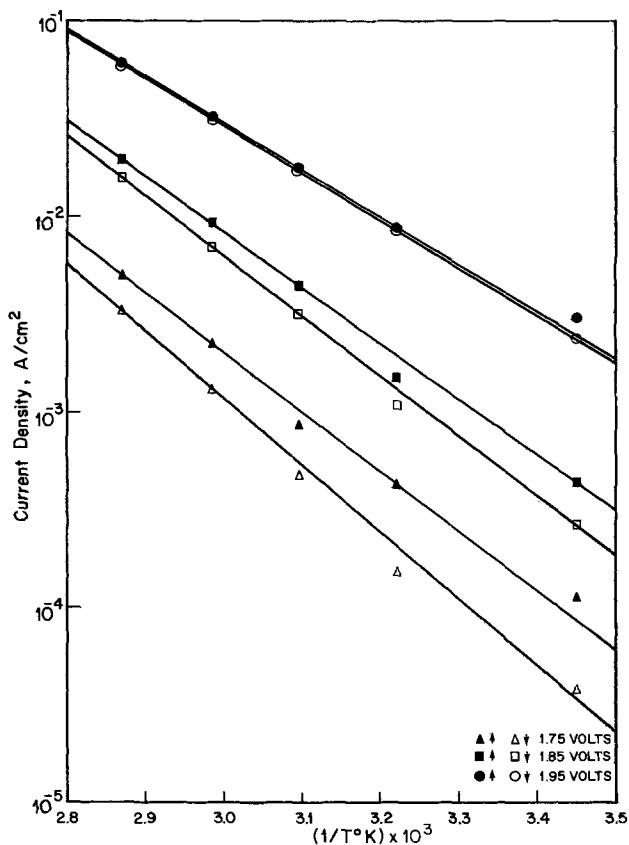


Fig. 3. The current density vs. $1/T$ (where T is the absolute temperature) plots adopted from Fig. 2 (a) and 2 (b) in order to determine the apparent heat of activation. The ΔH^* values lie between ca. 10 and 16.5 kcal depending on the electrode potential.

the reaction in the same direction, i.e., higher rates at higher values of potential or temperature.

The electrochemical Arrhenius plots at some typical electrode potentials, as derived from Fig. 2 (a) and 2 (b) have been presented in Fig. 3. It is seen that the apparent heat of activation as given by the differential, $\left(\frac{\delta \log i}{\delta (1/T)}\right)_{\eta, \psi, T, \dots}$, lies between ca. 10.6 and 16.6 kcal depending on the electrode potential.

Reaction orders.—An important parameter in the modern electrode kinetic analysis is recognized to be the electrochemical reaction order (7, 9). In the present work, the potentiostatic current-potential curves were studied at various acetate concentrations, both in the ascending [Fig. 4 (a)] and the descending [Fig. 4 (b)]

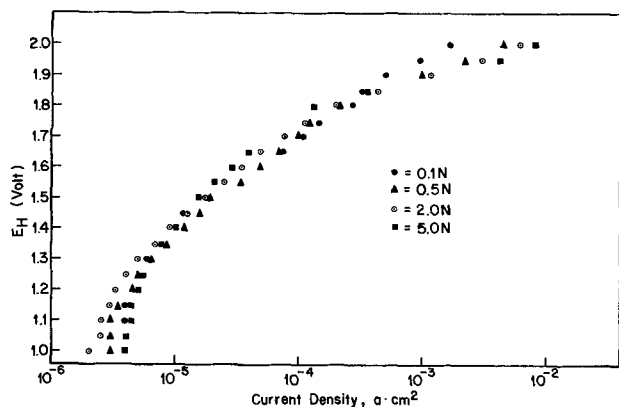


Fig. 4 (a). Tafel plots taken in the ascending direction of potentials in the following solutions: ● 0.1N $\text{CH}_3\text{COOK} + 1\text{N } \text{CH}_3\text{COOH}$; ▲ 0.5N $\text{CH}_3\text{COOK} + 1\text{N } \text{CH}_3\text{COOH}$; ◊ 2.0N $\text{CH}_3\text{COOK} + 1\text{N } \text{CH}_3\text{COOH}$; ■ 5.0N $\text{CH}_3\text{COOK} + 1\text{N } \text{CH}_3\text{COOH}$.

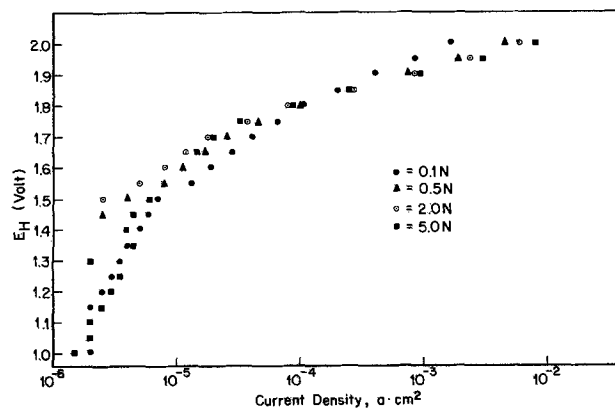


Fig. 4 (b). Same as Fig. 4 (a) but now taken in the descending direction of electrode potentials.

directions of the electrode potential. An attempt was made to deduce the reaction order derivative, $\left(\frac{\delta \log i}{\delta \log C_{\text{CH}_3\text{COO}}}\right)_{\eta, \psi, T, \dots}$, from these plots [Fig. 4 (a) and (b)] and the results are presented in Fig. 5. At lower potentials, the reaction order tends to be zero whereas at 2.0V, it is observed that

$$\left(\frac{\delta \log i}{\delta \log C_{\text{CH}_3\text{COO}}}\right)_{\eta, \psi, T, \dots} \approx 0.4$$

Potentiodynamic profiles.—No peaks were observed in the potentiodynamic profiles taken over a wide range of sweep rates. A typical potentiodynamic profile (1, 7) is shown in Fig. 6. Absence of peaks would preliminarily suggest absence of significant change in the electrode coverage in the potential range scanned as well as absence of diffusion-controlled oxidation-reduction of redox type species in the solution.

Open-circuit decays.—Open-circuit decay profiles triggered from various initial steady-state potentials show absence of any arrests. Typical results are given in Fig. 7. This would tend to confirm the conclusions deduced from the potentiodynamic profiles, namely,

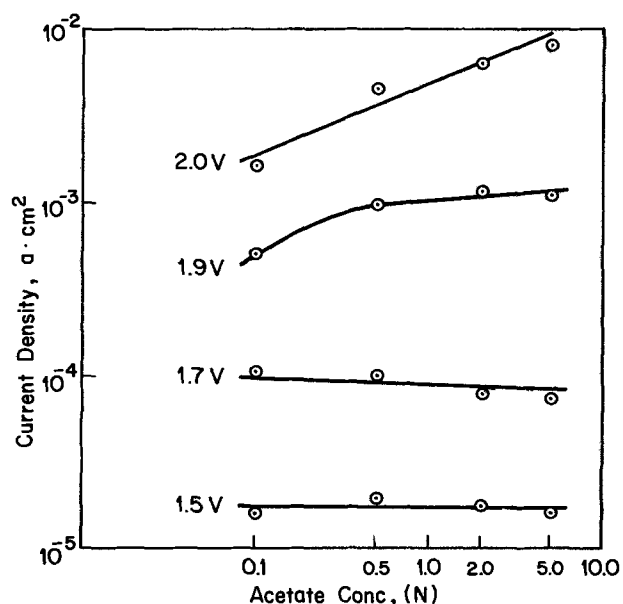


Fig. 5. Log [current density] vs. log. [acetate ion concentration] plot adopted from Fig. 4 (a). The $\left(\frac{\delta \log i}{\delta \log C}\right)$ value at 2.0V is ca. 0.4 whereas at lower potentials these values approach zero. Essentially similar results are obtained when one constructs this plot from Fig. 4 (b).

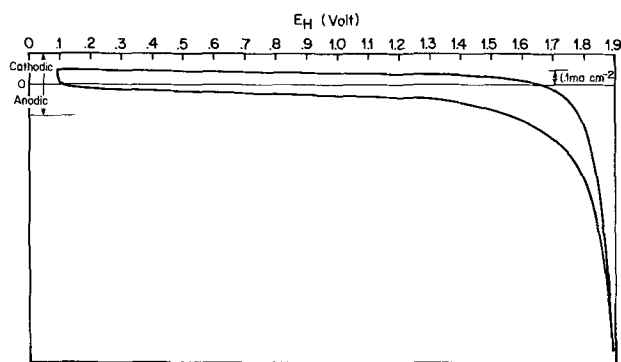


Fig. 6. A typical potentiodynamic profile on graphite in 2N $\text{CH}_3\text{COOK} + 1\text{N CH}_3\text{COOH}$. Sweep speed, 5 mV sec^{-1} . Absence of peaks may be noted. No peaks are observed even when one changes the sweep rate by several orders of magnitude.

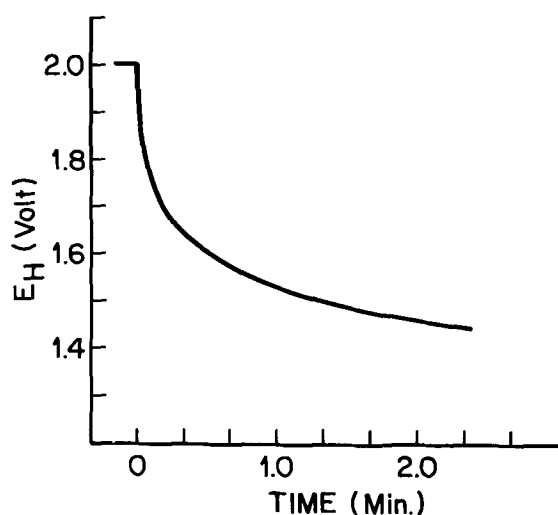


Fig. 7. A typical open-circuit potential decay profile for a graphite anode in 2N $\text{CH}_3\text{COOK} + 1\text{N CH}_3\text{COOH}$. Absence of arrests may be noted.

absence of significant electrode coverage by electroactive species in the steady state.

Charging curves.—In order to examine the possibility of coverage by adsorbed intermediates further, anodic charging curves were recorded at various current densities. Clear-cut arrests were again not observed although at low charging current densities, some incipient changes of slope in the charging curve were observed (Fig. 8). An electrode capacity-potential profile calculated from a typical charging curve (Fig. 8) is presented in Fig. 9 in which no clear-cut capacity maxima or minima, possibly diagnostic of changes of the electrode coverage during the transient, are observed. The maximum values of the differential capacity in this Fig. 9 would suggest the presence of some adsorption pseudocapacitance even when one takes into account the fact that the graphite electrodes have a very large ratio of real to geometric area (this ratio being unknown) and that such electrodes can uptake significant amounts of absorption (6). The values of differential capacity in Fig. 9, however, cannot perhaps be taken as a sufficient evidence for the presence of significant amounts of adsorbed intermediates in the steady state. A consideration of the peculiarities of the graphite electrode (6) as well as the evidence in Fig. 6-8 would tend to indicate rather strongly that the anodic formation of methyl acetate in the present study probably proceeds without involving significant coverage by the adsorbed intermediates during the steady-state electrolysis.

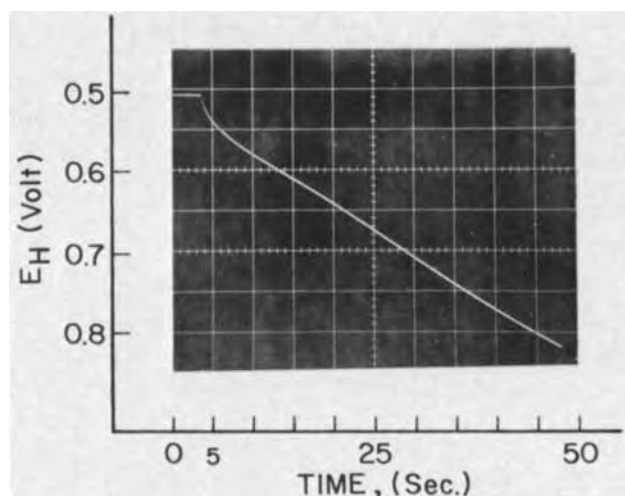


Fig. 8. An anodic charging curve (charging current density = $27.6 \mu\text{A cm}^{-2}$) triggered from the rest potential (0.5V). Graphite in 2N $\text{CH}_3\text{COOK} + 1\text{N CH}_3\text{COOH}$. Although an incipient arrest is indicated, significant coverage of the electrode during steady-state electrolysis is not concluded on the basis of discussion in the text. This incipient arrest does not become more pronounced, but rather tends to disappear, when one changes the charging current density.

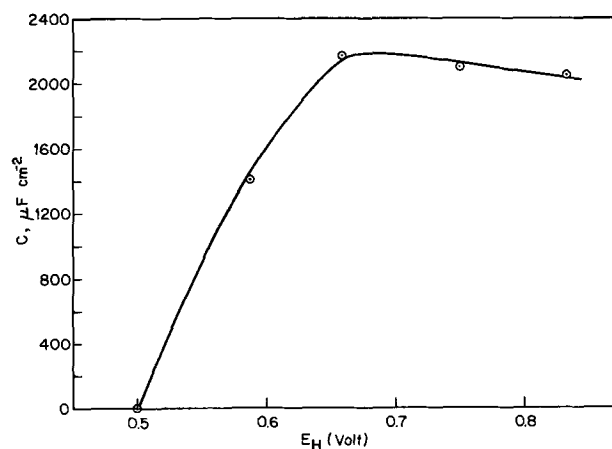
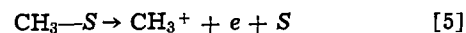
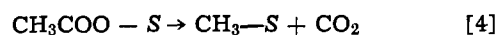


Fig. 9. A capacity-potential profile constructed from Fig. 8

Discussion

The anodic formation of methyl acetate by an overall two-electron reaction (i.e., Eq. [2]), which is known to proceed via intermediate formation of carbonium ions (2-5) may be assumed to involve the following elementary steps



Here, S, denotes the graphite electrode surface on which the reaction occurs.

A value of Tafel slope equal to $2.3 \times 2RT/F$ and absence of a significant amount of electrode coverage in the steady state, as observed in this investigation, would indicate rather unambiguously that the initial discharge step (i.e., Eq. [3]) is the likely rate-determining step (r.d.s.) in the over-all reaction (1, 7), at least above 1.8V. The rate equation for this case in concentrated solutions ($\psi \rightarrow 0$) may be written as

$$i = k(1 - \theta) C_{\text{CH}_3\text{COO}^-} e^{\beta n F / RT} \quad [7]$$

Where i is the current; θ , the electrode coverage; k , a combination of constants; $C_{\text{CH}_3\text{COO}^-}$, the concentration

of acetate ions; β , the charge transfer symmetry factor; η , the anodic over potential; F , the Faraday; R , the gas constant; and, T , the absolute temperature. Since the coverage, θ , is observed to approach zero, one may write Eq. [7] as

$$i = k C_{\text{CH}_3\text{COO}^-} e^{\beta n F / RT} \quad [8]$$

$$\text{or } \left(\frac{\delta \eta}{\delta \log i} \right) = 2.3 \times \frac{2RT}{F} = \text{Tafel slope}$$

The reaction order expected would be

$$\left(\frac{\delta \log i}{\delta \log C_{\text{CH}_3\text{COO}^-}} \right) = 1$$

This predicted reaction order, however, is not in agreement with the observed value (≈ 0.4 at high anodic potentials) and the source of this discrepancy is not clear, although some tentative explanations can be put forward (see below).

The heats of activation observed (Fig. 2, 3) are quite high (> 10 kcal mole $^{-1}$), which would qualitatively tend to support the mechanism suggested here, by analogy with the case of hydrogen evolution reaction.

On the basis of reaction order evidence (Fig. 4, 5) alone, it would appear attractive to suggest that a step subsequent to the initial discharge is perhaps the r.d.s. However, other evidence such as the Tafel slopes, lack of appreciable coverage as deduced from the transient studies, and rather high heat of activation would tend to support quite strongly the mechanistic proposal put forward here, namely, initial discharge as the r.d.s.

It appears interesting to speculate here on the possible reasons for the formation of carbonium ions, and thence methyl acetate, on graphite electrodes in contrast to the occurrence of the Kolbe reaction on platinum electrodes in the electrolysis system investigated here. Since the strength of Pt—CH $_3$ and C—CH $_3$ bonds, as estimated by the Pauling equation, is nearly identical (10), the explanation would seem to lie elsewhere. It has been pointed out by Ross (10) that the graphite electrodes possess paramagnetic centers on which the methyl radicals are probably bound ultra-strongly. If this suggestion is assumed to be correct, it is easy to see that the second electron transfer from

the adsorbed methyl radical, to give the carbonium ion, is more facile than the alternative path demanding desorptive coupling of the methyl radicals.

Although a clear-cut interpretation of the observed reaction orders seems difficult, a possible explanation may be mentioned. Fractional reaction orders of this magnitude would be expected if one invokes the presence of competing reactions, a situation consistent with the present case in which the efficiency of formation of methyl acetate is substantially less than 100%. This suggestion is particularly emphasized by the direction of the abrupt changes in slopes of the Tafel lines [Fig. 1, 2 (a) and 2 (b)], so characteristic of a change over to a parallel reaction or a parallel rate-determining step within the same reaction (7).

Acknowledgments

The author is grateful to Mr. R. Jacques for carrying out the experimental work. Dr. G. Bélanger is thanked for some discussions during the progress of the work. Thanks are also due to Dr. P. Lenfant for his interest and encouragement.

Manuscript submitted Nov. 22, 1971; revised manuscript received Dec. 28, 1971.

Any discussion of this paper will appear in a Discussion Section to be published in the December 1972 JOURNAL.

REFERENCES

1. A. K. Vijh and B. E. Conway, *Chem. Rev.*, **67**, 623 (1967).
2. S. D. Ross, *Trans. N. Y. Acad. Sci.*, **30**, 901 (1968).
3. E. J. Corey, N. L. Bauld, R. T. LaLonde, J. Casanova, Jr., and E. J. Kaiser, *J. Am. Chem. Soc.*, **82**, 2645 (1960).
4. E. J. Corey and J. Casanova, Jr., *ibid.*, **85**, 165 (1963).
5. W. J. Koehl, Jr., *ibid.*, **86**, 4684 (1964).
6. A. Bélanger, G. Bélanger, and A. K. Vijh, *This Journal*, **118**, 1543 (1971).
7. B. E. Conway "Theory and Principles of Electrode Processes," Ronald Press Co., New York (1965).
8. D. Gilroy and B. E. Conway, *J. Phys. Chem.*, **69**, 1259 (1965).
9. K. V. Vetter, "Electrochemical Kinetics," Academic Press, New York (1967).
10. S. D. Ross and M. Finkelstein, *J. Org. Chem.*, **34**, 2923 (1969).

Surface Concentration of Molybdenum in Types 316 and 304 Stainless Steel by Auger Electron Spectroscopy

G. J. Barnes, A. W. Aldag, and R. C. Jerner

School of Chemical Engineering and Materials Science, University of Oklahoma, Norman, Oklahoma 73069

ABSTRACT

Auger electron spectroscopy has been used to determine surface concentrations of Mo in Types 304 and 316 stainless steel. The technique involved Ar^+ bombardment removal of the stainless surface with alternate monitoring of the height of the 190 eV Mo peak. Surface concentrations of 14% were observed in mill-finished Type 316 containing 1.95% bulk Mo. Surface segregation of Mo was also observed in Type 304 containing 0.45% Mo impurity.

The effect of minor Mo additions on the corrosion resistance of 18-8 Type stainless steels is well established (1) and has led to increased utilization of molybdenum-bearing (2-4% Mo) stainless steels, especially in saline environments. The role of Mo in enhancing corrosion resistance has not been established because of a lack of information about the surface composition. Indeed, due to diffusion from the bulk, concentrations in the surface phase may be quite distinct from that in the bulk. Using Auger electron spectroscopy (AES), Harris (2), Haas (3), and Sickafus (4) have shown that certain thermal treatments can be used to concentrate bulk impurities at a free surface. In the case of 3340 steel, sulfur was observed (2) to concentrate at the surface after a short time at 330°C.

In the present studies, AES has been used to determine the concentration of Mo from the surface into the bulk of Types 316 and 304 stainless steel. Surface concentration of 14% was observed in mill-finished Type 316 containing 1.95% Mo. Surface segregation was also observed in Type 304 containing 0.45% Mo impurity.

Review of Auger Spectroscopy

The technique of Auger electron spectroscopy is not new (5) although its application to surface studies is relatively recent (6). The Auger electron emission process is analogous to x-ray emission from an excited atom and, in fact, the processes often occur simultaneously in a given experiment. When an inner core vacancy of an atom is neutralized by absorption of an electron from one of the outer shells either an x-ray or an Auger electron with a precise energy will be emitted from the sample (Fig. 1).

In applying AES to surface studies, the initial inner core vacancy is created by electron bombardment of the surface with 1-3 keV electrons. The secondary Auger electrons have energies typically between 0 and 1000 eV, and only those electrons coming from within a few monolayers of the surface escape with a well-defined energy (7). The Auger energy levels of many of the metals and typical surface contaminants are known and the values agree quite well with the x-ray values tabulated by Hill *et al.* (8).

The interest in Auger spectroscopy as applied to surface studies evolved from the early low energy electron diffraction (LEED) experiments of Lander (9). In analyzing the energy distribution for secondary electrons emitted by a solid surface, he attributed the small peaks to Auger transitions in the solid and suggested that the characteristic energies of these peaks could be used for qualitative surface chemical analysis. The peaks were, however, small and difficult to detect

within the broad, rather uniform background distribution. Harris (6) subsequently suggested that since the background was indeed relatively uniform, detection of Auger peaks could be greatly enhanced by electronically differentiating the energy distribution. This technique brought AES into its current prominence as a valuable tool for surface studies. Subsequent refinements were made by Palmberg (10) who demonstrated that the sensitivity for atoms at the surface could be enhanced by using a grazing incidence primary beam and that the energy resolution could be improved by replacing the old 3-grid LEED optics by a 4-grid system. Palmberg also confirmed experimentally that the low energy (<200 eV) Auger electron escape depth was of the order of 4-8Å. The minimum sensitivity for surface impurities has been estimated to be a few per cent of a monolayer (11).

More recently AES experiments are being performed independent of LEED studies. In principle, since the Auger process involves inelastic collisions with the surface, a well-defined crystal geometry as required by LEED is not a prerequisite for AES. A new cylindrical mirror analyzer (12) with a coaxial electron gun provides a simple electron optics system with precise energy discrimination. This system can be adapted to most conventional ultrahigh vacuum chambers and AES experiments performed in conjunction with other types of surface studies. An example of the Auger spectra obtained from a stainless steel surface using PEI Cylindrical Analyzer is shown in Fig. 2. The various surface components are noted on the trace.

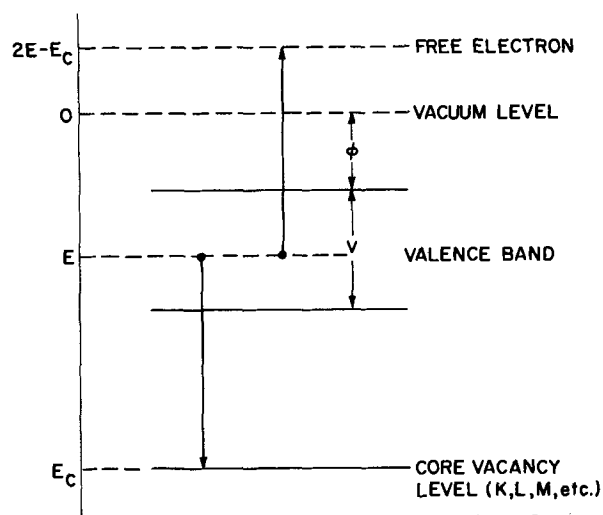


Fig. 1. Auger electron emission from an excited atom. Φ , work function, V , width of the valence band, E_c , energy of the core electron level, E , original energy of the emitted electron.

Key words: segregation, corrosion, concentration gradient.

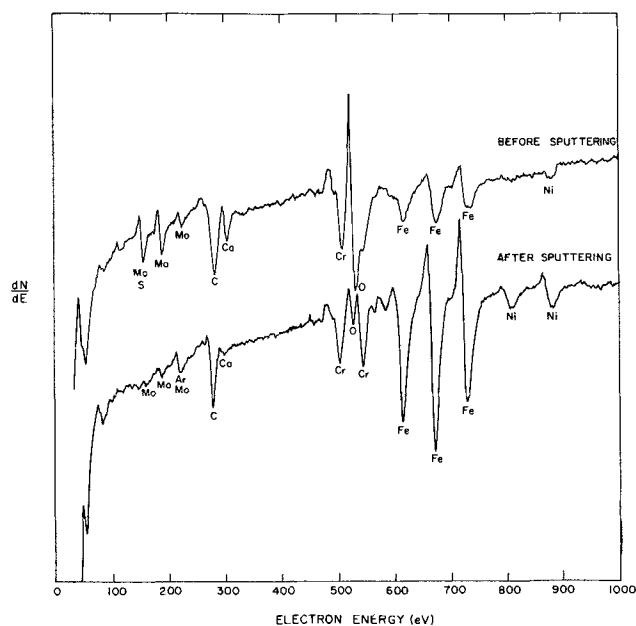


Fig. 2. (Upper) Auger electron spectrum of stainless steel before sputtering, $V_B = 2000$ eV. (Lower) Auger electron spectrum of stainless steel after sputtering, $V_B = 2000$ eV.

Experimental Procedure

Types 304 and 316 mill-finished stainless steel sheet 0.050 in. thick, was used in this investigation. Specimens were washed with detergent, rinsed in distilled water, acetone, trichloroethylene, and acetone, and then dried with a lintfree cloth. The samples were then placed in an ion and titanium sublimation-pumped vacuum chamber, which was evacuated and then baked at 250°C for 6 hr. The system was rough-pumped, oil-free, using zeolite-filled cryosorption pumps. Pressure, as indicated by a nude ionization gauge, was in the low 10^{-9} Torr range. An initial Auger spectrum was recorded and is shown in Fig. 2 (upper). This spectrum is representative of a surface cleaned in the manner described above but prior to electron or Ar^+ bombardment. The ion pump was then deactivated and Ar was admitted to a sputtering pressure of 1×10^{-4} Torr. Titanium sublimation pumps were activated during the entire sputtering sequence in order to maintain Ar purity. After sputtering for a predetermined time, usually 15 sec, the ion pump was again activated, resulting in a rapid pressure reduction into the 10^{-9} Torr range. The sample was then repositioned, by simple rotation, in front of the cylindrical mirror analyzer for Auger analysis. A spectrum was recorded next, and the sample was repositioned for additional sputtering. This sequence was repeated until the Auger spectra remained unchanged with additional sputtering. A spectrum taken after long-term sputtering is also shown in Fig. 2 (lower). It should be noted that the 190 eV Mo peak has been significantly reduced by sputtering from that in Fig. 2 (upper). The repetitive nature of several Auger spectra after long sputtering times demonstrates that the procedures used to reposition the sample were reproducible, and the spectra obtained are representative of the bulk composition (13).

Results

The Auger spectrum for pure Mo is shown in Fig. 3. The major 190 eV Mo peak (14), corresponding to a $M_5N_5N_5$ (15) transition, was used to monitor the molybdenum concentration on the stainless steel surface as a function of sputter time. Assuming a unity removal coefficient (16), sputtering times were converted to atom layers removed. The resulting concentration gradients are shown in Fig. 4. As mentioned before, the values of the Mo concentration were obtained from stainless steel spectra after various sputter-

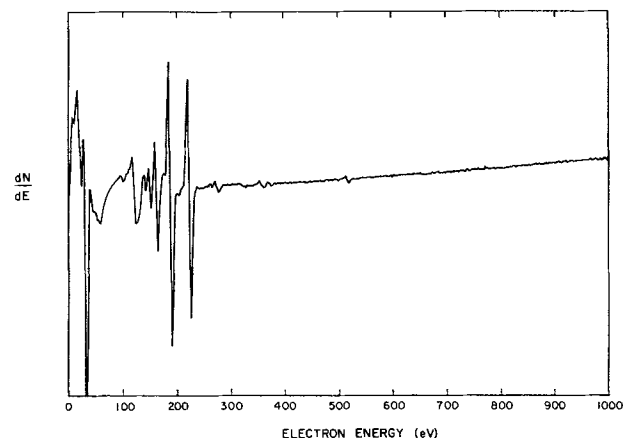


Fig. 3. Auger electron spectrum of pure molybdenum, $V_B = 2000$ eV.

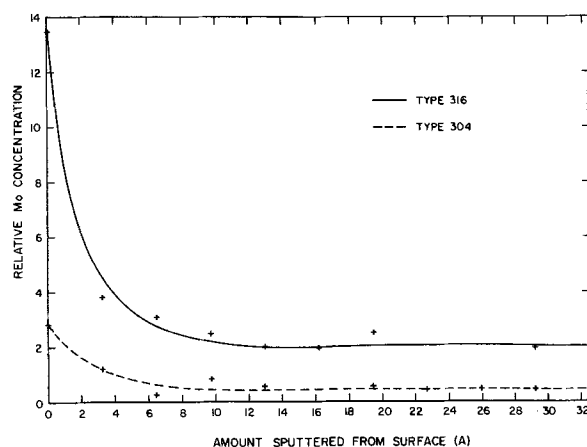


Fig. 4. Relative molybdenum concentration vs. amount of material removed in Types 304 and 316 stainless steel.

ing times. It is also assumed that the Auger spectrum obtained after long sputtering time is representative of the bulk concentration. If the Auger peak height is taken to be directly proportional to the concentration of atoms present (17), the minimum surface concentration can be estimated. These assumptions result in a surface concentration of 14-15% and 3-4% for Types 316 and 304, respectively. The initial 190 eV peak height is undoubtedly obtained from a surface which contains a carbonaceous deposit resulting from the pre-treatment and cleaning steps (18). Thus, the observed initial Mo concentration may be somewhat less than the actual values due to this overlayer.

The results shown in Fig. 4 indicate that Mo concentrates at the surface of mill-processed stainless. Surface segregation is observed even in Type 304 where Mo is present as an impurity. As the surface is removed by Ar^+ bombardment, the major Mo Auger peak decreases in height to a value representative of the bulk concentration.

Conclusions

It has been found that mill processing tends to concentrate Mo at the surface of Types 304 and 316 stainless steel. This surface segregation has been brought about in some manner by mill processing. Subsequent thermal or mechanical processing would disturb this surface concentration and in all probability result in the surface concentration of Mo being dependent on treatment. Thus any property, such as corrosion resistance, that is dependent on the presence of Mo might be altered significantly. Much of the scatter observed in corrosion tests on Types 304 and 316 stainless might be attributable to differences in molybdenum surface concentrations brought about by variations in thermal-

mechanical processing as well as other metallurgical factors.

Acknowledgment

This investigation was conducted with funds provided by National Science Foundation Grant GY 8964.

Manuscript submitted Sept. 8, 1971; revised manuscript received Dec. 17, 1971.

Any discussion of this paper will appear in a Discussion Section to be published in the December 1972 JOURNAL.

REFERENCES

1. M. G. Fontana and N. D. Greene, "Corrosion Engineering," p. 57, McGraw-Hill, New York (1967).
2. L. A. Harris, *J. Appl. Phys.*, **39**, 1428 (1968).
3. T. W. Haas and G. J. Dooley, III, *J. Metals*, **22**, 17 (1970).
4. E. N. Sickafus, *Surface Sci.*, **19**, No. 1, 181 (1970).
5. P. J. Auger, *J. Phys. Radium*, **6**, 205 (1925).
6. L. A. Harris, *J. Appl. Phys.*, **39**, 1419 (1968).
7. P. W. Palmberg and T. N. Rhodin, *ibid.*, **39**, 2425 (1968).
8. R. D. Hill, E. L. Church, and J. W. Mihelich, *Rev. Sci. Instr.*, **23**, 523 (1952).
9. J. J. Lander, *Phys. Rev.*, **91**, 1382 (1953).
10. P. W. Palmberg, *Appl. Phys. Letters*, **13**, 183 (1968).
11. R. E. Weber and W. T. Peria, *J. Appl. Phys.*, **38**, 4355 (1967).
12. P. W. Palmberg, G. K. Bohm, and J. C. Tracy, *Appl. Phys. Letters*, **13**, 254 (1969).
13. P. W. Palmberg and H. L. Marcus, *Trans. Am. Soc. Metals*, **62**, 1016 (1969).
14. D. F. Stein, R. E. Weber, and P. W. Palmberg, *J. Metals*, Feb., **39** (1971).
15. T. W. Haas, J. T. Grant, and G. J. Dooley, *Phys. Rev. B*, **1**, 1449 (1970).
16. N. Laegreid and G. K. Wehner, *J. Appl. Phys.*, **32**, 365 (1961).
17. R. E. Weber, and A. L. Johnson, *ibid.*, **40**, 1, 314-318 (1968).
18. H. Poppa and A. G. Elliot, *Surface Sci.*, **24**, 149 (1971).

Vibration Characteristics of Crystal Slicing ID Saw Blades

S. E. Forman and W. J. Rhines

Bell Telephone Laboratories, Incorporated, Whippany, New Jersey 07981

ABSTRACT

The natural frequencies and associated mode shapes have been determined for the transverse vibration of three ID saw blades commonly used for crystal wafering. The purpose of the investigation was to determine what frequencies of excitation could excite blade natural frequencies, since excessive blade transverse motion can be a cause of severe crystal and blade damage. The fundamental frequencies for the 4 in. ID-10% in. OD, the 4 in. ID-12 in. OD, and the 6 in. ID-16% in. OD blades, based on a maximum cutting edge hoop stress of 130,000 psi were found to be 780, 640, and 465 Hz, respectively. Experimental measurements have confirmed that cutting edge transverse motion exists with amplitudes up to 0.001 in. but at a frequency equal to the spinning speed, which is always an order of magnitude less than the computed natural frequency.

At the present time the most widely used method of slicing cylindrical crystal ingots into thin wafers is ID sawing. Unlike the more conventional OD saw, the ID saw is extremely thin, is clamped at its outer edge, and has diamond abrasive grit on its inner edge where the cutting is performed. In order to achieve the stiffness necessary to slice crystal ingots, the clamped blade must be placed in a highly tensioned state by one of several available tensioning devices. The basic ingot-blade-wafer system characteristic of the ID sawing process is shown in Fig. 1.

The most important functions of crystal wafering are to provide wafers with flat, parallel sides and to induce a minimum of damage to each side. In order to better understand the interaction of the blade with the ingot it is useful to determine the vibration characteristics of the blade. This allows the determination of excitation frequencies needed to cause resonance of the blade and hence large transverse displacements which could severely damage one or more of the elements in the ingot-blade-wafer system.

There is a great deal of published literature concerning the vibration characteristics of rotating disks. However, in almost every case treated the disk is clamped at its center and free around its outside edge (standard OD saw geometry). Mote presents an excellent listing of many of the theoretical and experimental investigations of vibration characteristics of these disks under various environmental conditions

(1). Rhines (2) has made a simplified calculation of the lowest natural frequency of an ID blade as a function of blade tension and blade dimensions. His results were obtained by Rayleigh's method using a one-term approximation for the fundamental mode shape.

In this paper, highly accurate approximations of the fundamental frequency and several higher frequencies are obtained using Lagrange's equations coupled with multiterm series approximations of the associated mode shapes. The calculations are made for the three blade sizes most widely used in the semiconductor industry. In addition, experimental measurements of actual blade transverse motion and its frequency of occurrence are presented.

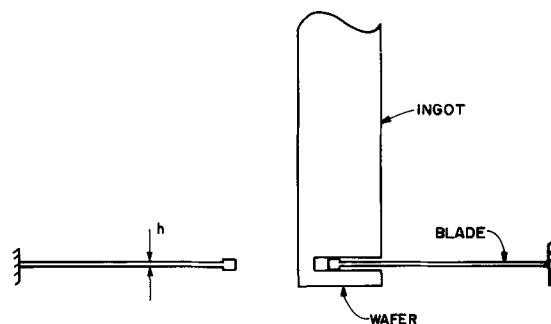


Fig. 1. Blade-ingot-wafer system

Key words: crystal wafering, ID sawing blade vibration.

mechanical processing as well as other metallurgical factors.

Acknowledgment

This investigation was conducted with funds provided by National Science Foundation Grant GY 8964.

Manuscript submitted Sept. 8, 1971; revised manuscript received Dec. 17, 1971.

Any discussion of this paper will appear in a Discussion Section to be published in the December 1972 JOURNAL.

REFERENCES

1. M. G. Fontana and N. D. Greene, "Corrosion Engineering," p. 57, McGraw-Hill, New York (1967).
2. L. A. Harris, *J. Appl. Phys.*, **39**, 1428 (1968).
3. T. W. Haas and G. J. Dooley, III, *J. Metals*, **22**, 17 (1970).
4. E. N. Sickafus, *Surface Sci.*, **19**, No. 1, 181 (1970).
5. P. J. Auger, *J. Phys. Radium*, **6**, 205 (1925).
6. L. A. Harris, *J. Appl. Phys.*, **39**, 1419 (1968).
7. P. W. Palmberg and T. N. Rhodin, *ibid.*, **39**, 2425 (1968).
8. R. D. Hill, E. L. Church, and J. W. Mihelich, *Rev. Sci. Instr.*, **23**, 523 (1952).
9. J. J. Lander, *Phys. Rev.*, **91**, 1382 (1953).
10. P. W. Palmberg, *Appl. Phys. Letters*, **13**, 183 (1968).
11. R. E. Weber and W. T. Peria, *J. Appl. Phys.*, **38**, 4355 (1967).
12. P. W. Palmberg, G. K. Bohm, and J. C. Tracy, *Appl. Phys. Letters*, **13**, 254 (1969).
13. P. W. Palmberg and H. L. Marcus, *Trans. Am. Soc. Metals*, **62**, 1016 (1969).
14. D. F. Stein, R. E. Weber, and P. W. Palmberg, *J. Metals*, Feb., **39** (1971).
15. T. W. Haas, J. T. Grant, and G. J. Dooley, *Phys. Rev. B*, **1**, 1449 (1970).
16. N. Laegreid and G. K. Wehner, *J. Appl. Phys.*, **32**, 365 (1961).
17. R. E. Weber, and A. L. Johnson, *ibid.*, **40**, 1, 314-318 (1968).
18. H. Poppa and A. G. Elliot, *Surface Sci.*, **24**, 149 (1971).

Vibration Characteristics of Crystal Slicing ID Saw Blades

S. E. Forman and W. J. Rhines

Bell Telephone Laboratories, Incorporated, Whippany, New Jersey 07981

ABSTRACT

The natural frequencies and associated mode shapes have been determined for the transverse vibration of three ID saw blades commonly used for crystal wafering. The purpose of the investigation was to determine what frequencies of excitation could excite blade natural frequencies, since excessive blade transverse motion can be a cause of severe crystal and blade damage. The fundamental frequencies for the 4 in. ID-10% in. OD, the 4 in. ID-12 in. OD, and the 6 in. ID-16% in. OD blades, based on a maximum cutting edge hoop stress of 130,000 psi were found to be 780, 640, and 465 Hz, respectively. Experimental measurements have confirmed that cutting edge transverse motion exists with amplitudes up to 0.001 in. but at a frequency equal to the spinning speed, which is always an order of magnitude less than the computed natural frequency.

At the present time the most widely used method of slicing cylindrical crystal ingots into thin wafers is ID sawing. Unlike the more conventional OD saw, the ID saw is extremely thin, is clamped at its outer edge, and has diamond abrasive grit on its inner edge where the cutting is performed. In order to achieve the stiffness necessary to slice crystal ingots, the clamped blade must be placed in a highly tensioned state by one of several available tensioning devices. The basic ingot-blade-wafer system characteristic of the ID sawing process is shown in Fig. 1.

The most important functions of crystal wafering are to provide wafers with flat, parallel sides and to induce a minimum of damage to each side. In order to better understand the interaction of the blade with the ingot it is useful to determine the vibration characteristics of the blade. This allows the determination of excitation frequencies needed to cause resonance of the blade and hence large transverse displacements which could severely damage one or more of the elements in the ingot-blade-wafer system.

There is a great deal of published literature concerning the vibration characteristics of rotating disks. However, in almost every case treated the disk is clamped at its center and free around its outside edge (standard OD saw geometry). Mote presents an excellent listing of many of the theoretical and experimental investigations of vibration characteristics of these disks under various environmental conditions

(1). Rhines (2) has made a simplified calculation of the lowest natural frequency of an ID blade as a function of blade tension and blade dimensions. His results were obtained by Rayleigh's method using a one-term approximation for the fundamental mode shape.

In this paper, highly accurate approximations of the fundamental frequency and several higher frequencies are obtained using Lagrange's equations coupled with multiterm series approximations of the associated mode shapes. The calculations are made for the three blade sizes most widely used in the semiconductor industry. In addition, experimental measurements of actual blade transverse motion and its frequency of occurrence are presented.

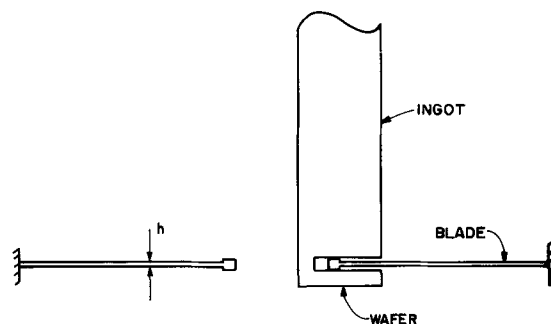


Fig. 1. Blade-ingot-wafer system

Key words: crystal wafering, ID sawing blade vibration.

Table I. Dimensions and properties of blades

Blade type	Blade dimensions 2a	2b	h
1	4	10 1/8	0.004
2	4	12	0.004
3	6	16 1/8	0.004

Blade properties

Material: AISI 301 stainless steel
 Density, $\rho = 0.725 \times 10^{-3}$ lb-sec²/in.⁴
 Young's modulus, $E = 27.6 \times 10^6$ psi
 0.2% Offset yield stress: 153,000 psi

Analysis

In-plane stress state.—Physically the blade is a thin annular stainless steel plate of inner radius a , outer radius b , thickness h , density ρ , and Young's modulus E . Material properties and typical dimensions of ID blades are given in Table I. It is assumed that the stiffness given to the blade by the tensioning device is analogous to applying a uniform radial load σ_0 to the blade's outer periphery as shown in Fig. 2. At the tensioning stress levels normally used, the contribution to the blade stiffness by the bending rigidity of the blade is negligible and the blade can be treated as an annular membrane.

The in-plane state of stress in the blade is a biaxial one consisting of the radial stress σ_r and the hoop stress σ_θ . Each of these stresses is made up of contributions from tensioning and spinning. The tensioning stresses are given by the well-known formulas (3)

$$\sigma_r = \frac{\sigma_0(1 - a^2/r^2)}{1 - a^2/b^2}$$

$$\sigma_\theta = \frac{\sigma_0(1 + a^2/r^2)}{1 - a^2/b^2} \quad [1]$$

The maximum value of stress due to tensioning is the hoop stress on the cutting edge (at $r = a$), and its magnitude is

$$\sigma_{\max} = \frac{2\sigma_0}{1 - \frac{a^2}{b^2}} \quad [2]$$

The allowable value of σ_{\max} should be sufficiently below the 0.2% offset yield stress of the blade material in order to avoid large amounts of plastic deformation. Strain gauge experiments have shown (4) that for the 4 in. ID-10 1/8 in. OD blade the current fully tensioned value of σ_{\max} ranges from 100,000 to 130,000 psi and in what follows the value of 130,000 psi will be used for all geometries. At this tensioning stress level the con-

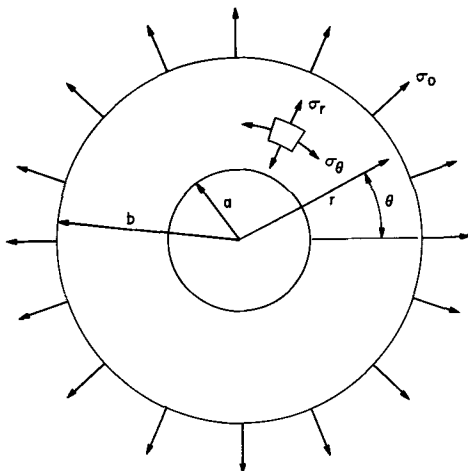


Fig. 2. Model of ID blade used for vibration analysis

tribution of spinning to the stress state is negligible for the current range of speeds used and will be ignored.

Mode shapes and associated natural frequencies.—The differential equation which governs the transverse vibration of the tensioned annular membrane described previously is (5)

$$\rho W_{,tt} - \sigma_r W_{,rr} - \sigma_\theta \left(\frac{1}{r} W_{,r} + \frac{1}{r^2} W_{,\theta\theta} \right) = 0 \quad [3]$$

where W is the transverse displacement of the membrane and partial derivatives are defined using comma notation, i.e., $W_{,r} = \partial W / \partial r$. The geometric boundary conditions are taken to be

$$W = 0 \text{ at } r = b$$

and

$$W = \text{finite at } r = a \quad [4]$$

Because of the form of the in-plane stresses σ_r and σ_θ given by Eq. [1] an exact solution to the previously described boundary value problem cannot be achieved and an approximate technique will be used.

The authors have found it convenient to use Lagrange's equations of motion coupled with a multiterm series representation of the transverse displacement. The displacement is assumed to be of the form

$$W(r, \theta, t) = \left[\sum_{j=1}^J A_j(t) \sin \frac{j\pi(b-r)}{2(b-a)} \right] \cos n\theta \quad [5]$$

where n is the number of nodal diameters, j is the number of nodal circles, and $A_j(t)$ is the set of generalized coefficients which are to be determined from Lagrange's equations of motion.

Lagrange's equations of motion for the case of free vibration are (6)

$$\frac{d}{dt} \left(\frac{\partial L}{\partial \dot{A}_i} \right) - \frac{\partial L}{\partial A_i} = 0 \quad (i = 1 \dots J) \quad [6]$$

where $\dot{A}_i = \partial A_i / \partial t$ and L is the Lagrangian $T - V$ where T is the kinetic energy and V is the potential energy of the blade. The kinetic energy is given by the formula

$$T = \frac{1}{2} \rho h \int_0^{2\pi} \int_a^b (W_{,t})^2 r dr d\theta \quad [7]$$

and the potential energy is given by

$$V = \frac{1}{2} h \int_0^{2\pi} \int_a^b \left(\sigma_r (W_{,r})^2 + \frac{\sigma_\theta}{r^2} (W_{,\theta})^2 \right) r dr d\theta \quad [8]$$

where σ_r and σ_θ are given by Eq. [1] (1).

Substituting Eq. [5], [7], and [8] into Eq. [6] and performing the indicated differentiations and integrations gives rise to the following equations of motion

$$\sum_{j=1}^J \left\{ \rho h \pi \ddot{A}_j \int_a^b r \sin \frac{j\pi(b-r)}{2(b-a)} \sin \frac{i\pi(b-r)}{2(b-a)} dr \right.$$

$$+ \frac{\sigma_0 h \pi A_j}{1 - \frac{a^2}{b^2}} \left\{ \frac{\pi^2 i j}{4(b-a)^2} \int_a^b \left(r - \frac{a^2}{r} \right) \cos \frac{j\pi(b-r)}{2(b-a)} \right.$$

$$\cos \frac{i\pi(b-r)}{2(b-a)} dr + n^2 \int_a^b \left(\frac{1}{r} + \frac{a^2}{r^3} \right) \sin \frac{j\pi(b-r)}{2(b-a)}$$

$$\left. \left. \sin \frac{i\pi(b-r)}{2(b-a)} dr \right\} \right\} = 0 \quad i = 1, 2, \dots, J \quad [9]$$

To determine the blade natural frequencies $A_i(t)$ is written in the form

$$A_i(t) = \tilde{A}_j \sin \omega t \quad [10]$$

where ω is the natural frequency of the particular mode being considered. Substituting Eq. [10] into Eq.

[9] results in an eigenvalue problem which can be written in the following matrix notation

$$[K_{ij} - \lambda M_{ij}][\tilde{A}_j] = 0 \quad \begin{matrix} i = 1, \dots, J \\ j = 1, \dots, J \end{matrix} \quad [11]$$

where

$$\lambda = \frac{\rho(b^2 - a^2)}{\sigma_0} \omega^2 \quad [12]$$

$$M_{ij} = \int_a^b \frac{r}{b^2} \sin \frac{j\pi(b-r)}{2(b-a)} \sin \frac{i\pi(b-r)}{2(b-a)} dr \quad [13]$$

$$K_{ij} = \frac{\pi^2 i j}{4(b-a)^2} \int_a^b \left(r - \frac{a^2}{r} \right) \cos \frac{j\pi(b-r)}{2(b-a)} \cos \frac{i\pi(b-r)}{2(b-a)} dr + n^2 \int_a^b \left(\frac{1}{r} + \frac{a^2}{r^3} \right) \sin \frac{j\pi(b-r)}{2(b-a)} \sin \frac{i\pi(b-r)}{2(b-a)} dr \quad [14]$$

Equation [11] can now be solved using a straightforward eigenvalue-eigenvector computer package. The individual integrals of M_{ij} and K_{ij} are also obtained numerically by a Romberg integration computer routine (7).

For each value of n the value of J is increased (starting at $J = 2$) until less than a 1% error exists between consecutive values of λ for the cases of one to six nodal circles. When this occurs the transverse deflection of a radial cross section associated with the final value of λ is graphically compared with that associated with the previous value of λ . If there appear to be no serious deviations between the two shapes then the last value of λ is taken as the correct eigenvalue. However, if there are deviations on the order of 5% or more at any point of the cross section, J is increased until the deviations are less than 5%. It was in general found that the values of λ converged more rapidly as J increased than did the deviations between mode shapes.

Results and Discussion

The values of the eigenvalue λ associated with several different mode shapes are given in Table II. Calculations have been made for the three blade geometries of Table I. The natural frequency in cycles per second is easily attained from the value of λ by the relation

$$f = \frac{1}{2\pi} \sqrt{\frac{\sigma_{max} \lambda}{2b^2 \rho}} \quad [15]$$

where σ_{max} is given by Eq. [2].

The values of the natural frequencies and sketches showing the nodal circles and nodal diameters of the associated mode shapes are given in Fig. 3, 4, and 5 for the three blade geometries. All calculations have been

Table II. Values of eigenvalue λ for various blade sizes

Nodal diam	Nodal circles					
	1	2	3	4	5	6
1. 4 in. ID-10 1/8 in. OD						
0	6.88	36.3	89.2	166	265	387
1	12.2	41.9	94.6	171	271	393
2	25.7	59.7	111	187	287	409
3	42.9	88.3	142	215	314	437
4	62.6	122	185	258	354	476
2. 4 in. ID-12 in. OD						
0	6.51	34.3	84.2	156	251	368
1	12.6	41.3	91.0	163	257	374
2	26.3	62.7	112	183	277	394
3	42.8	92.6	150	220	312	427
4	61.7	125	197	275	365	478
3. 6 in. ID-16 1/8 in. OD						
0	6.65	35.0	86.1	160	256	375
1	12.4	41.4	92.2	166	262	381
2	26.1	61.3	112	184	280	400
3	42.9	91.0	146	217	312	430
4	62	124	193	267	358	471

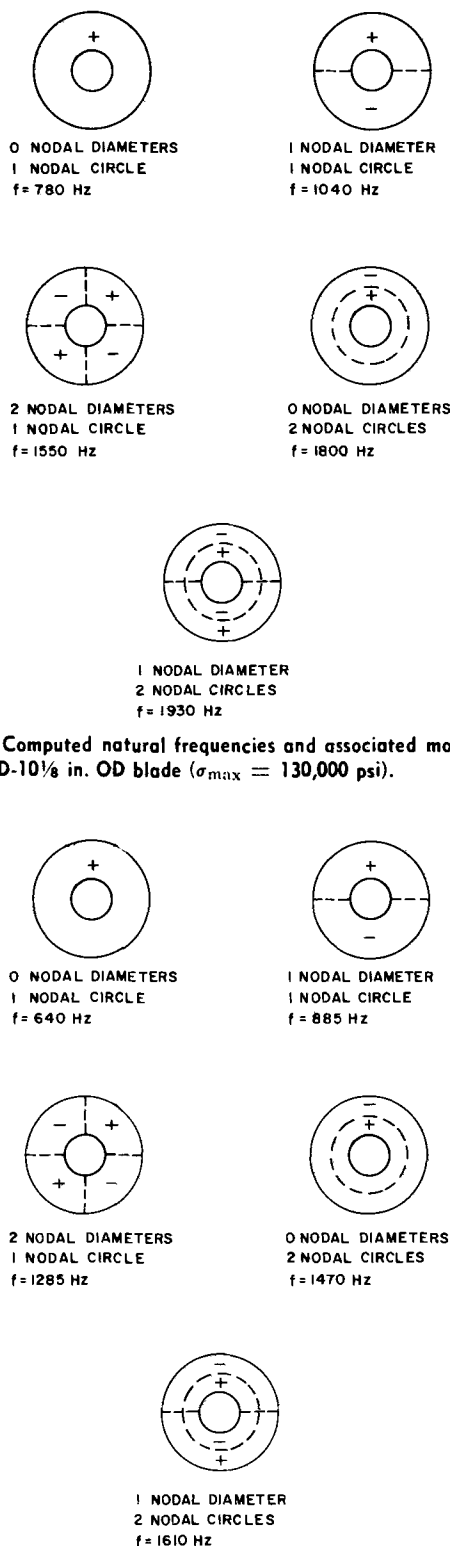


Fig. 3. Computed natural frequencies and associated mode shapes of 4 in. ID-10 1/8 in. OD blade ($\sigma_{max} = 130,000$ psi).

Fig. 4. Computed natural frequencies and associated mode shapes of 4 in. ID-12 in. OD blade ($\sigma_{max} = 130,000$ psi).

based on a maximum hoop stress of 130,000 psi. As indicated in (4), the frequencies associated with the fundamental and 2 nodal diameter-1 nodal circle modes of the 4 in. ID-10 1/8 in. OD blade have been verified experimentally to within 10%.

For the particular case of the fundamental mode, the natural frequency decreases from 780 Hz for the smallest blade size (4 in. ID-10 1/8 in. OD) to 465 Hz for the largest blade size (6 in. ID-16 1/8 in. OD). The usual spinning speeds utilized with the three blade geometries range from 30-40 Hz for the large blade and 50-70 Hz for the other two. Thus, it appears that, for

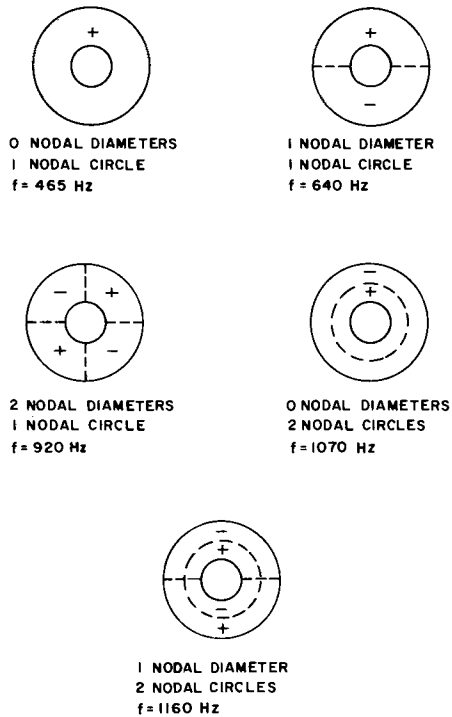


Fig. 5. Computed natural frequencies and associated mode shapes of 6 in. ID-16 1/8 in. OD blade ($\sigma_{max} = 130,000$ psi).

the range of σ_{max} mentioned earlier, spindle speed is unlikely to be a source of excitation near the fundamental mode unless its magnitude is increased at least ten times.

Typical profiles of the transverse displacement of the radial cross section of a blade are presented for several mode shapes in Fig. 6-10. The number of nodal diameters is listed on each figure and the number of nodal circles is listed on each profile. In each case the displacement has been normalized with respect to the maximum value that occurs between the inner and outer radius. The curves shown are all obtained using $J = 6$ in the series representation of the displacement for the 4 in. ID-10 1/8 in. OD blade.

For small numbers of nodal diameters the maximum value of transverse displacement always seems to occur at the cutting edge regardless of the number of nodal circles. This is due to the zero radial stress con-

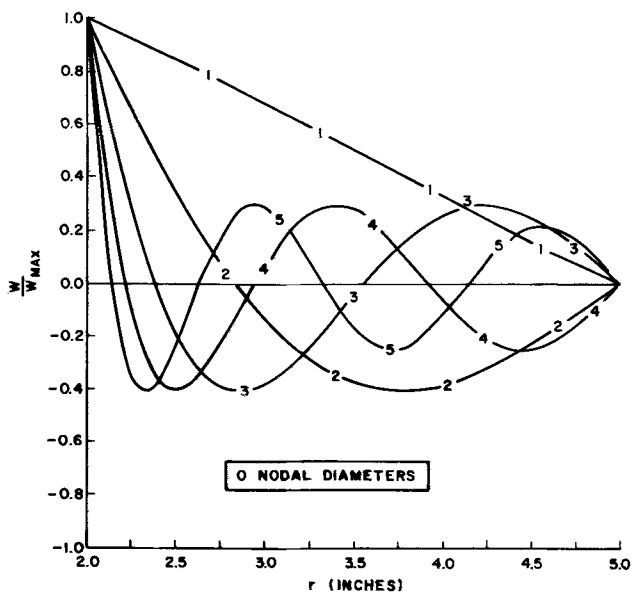


Fig. 6. Radial profiles of 4 in. ID-10 1/8 in. OD blade

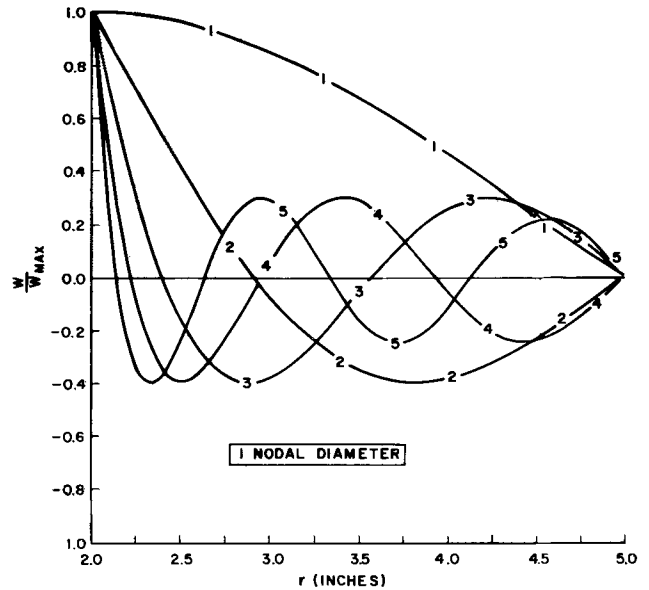


Fig. 7. Radial profiles of 4 in. ID-10 1/8 in. OD blade

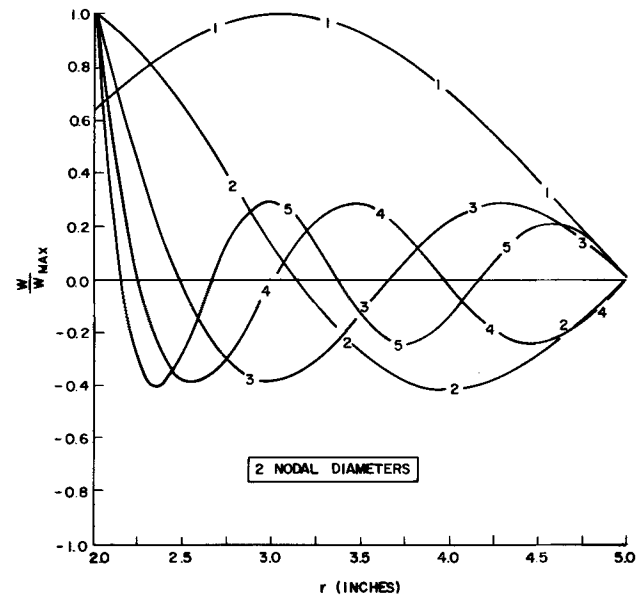


Fig. 8. Radial profiles of 4 in. ID-10 1/8 in. OD blade

dition at the inner edge. However as the number of nodal diameters increases, the maximum displacements start occurring away from the cutting edge.

Experimental measurements.—In order to determine the amplitude and frequency of cutting edge transverse motion, a displacement-measuring technique described by Yakunin and Khasdan (8) was used on a current ID slicing machine. They used an “inductive differential detector with a variable air gap.” As the air gap between the detector and blade changed, the amplitude and frequency of any transverse displacements from the initial position could be recorded. A device such as this, with a sensitivity that enables it to measure deflections as small as 0.1 ± 0.02 mils (1 mil = 0.001 in.) was used to make the measurements described here (4).

Hand rotation of the blade gave rise to transverse deflections of 0.6-0.7 mils. Spinning the blade without cutting (idling) gave rise to deflections ranging from 0.45 to 0.80 mils depending on the spinning speed. For both hand rotation and idling, the peak to peak displacement occurs once per blade revolution. During the cutting cycle, the transverse displacement spectrum still occurs once per revolution but the amplitude is

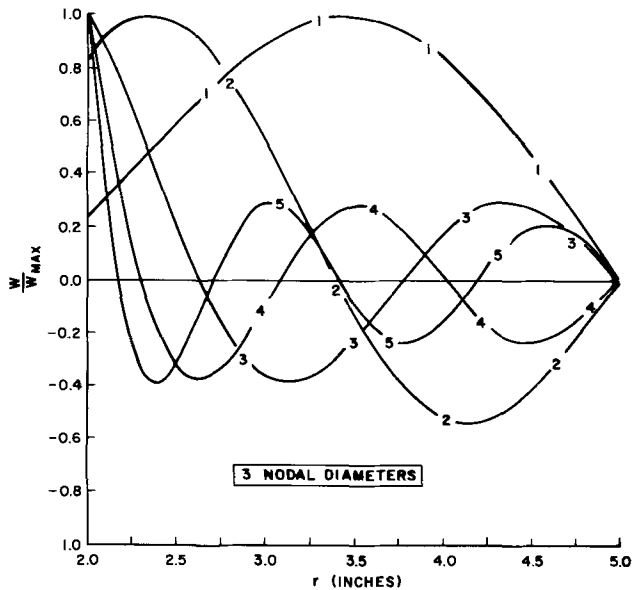


Fig. 9. Radial profiles of 4 in. ID-10 $\frac{1}{8}$ in. OD blade

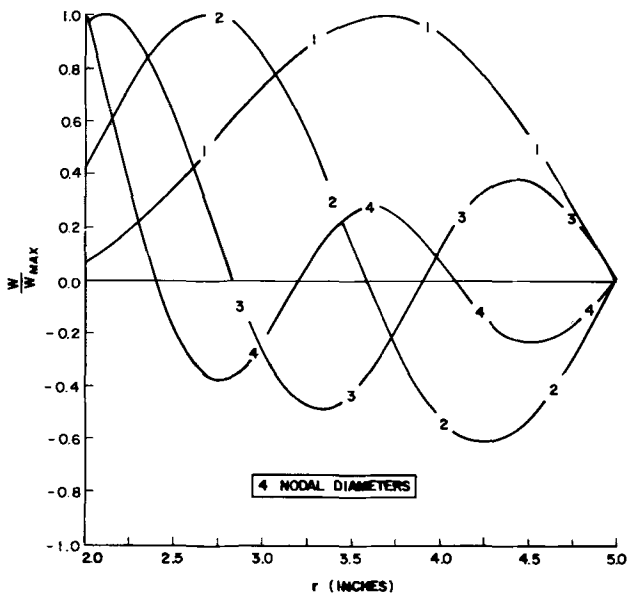


Fig. 10. Radial profiles of 4 in. ID-10 $\frac{1}{8}$ in. OD blade

altered. For a given spinning speed, the amplitude of the idling deflection decreases by 50-60% during feed and by 30-40% during retraction. It is believed that

this transverse motion is the cause of the periodic score marks often observed on wafers.

Conclusions

The natural frequencies and associated mode shapes have been determined for the transverse vibration of three ID saw blades widely used in the semiconductor industry. The purpose of the investigation was to determine what excitation frequencies need to exist in order to excite natural frequencies of the blade.

It was found that for all three blades the spinning speeds used are an order of magnitude less than the lowest natural frequency. Since the frequency is directly proportional to the square root of the maximum hoop stress, the range of current maximum hoop stresses (100,000-130,000 psi) would have to be reduced by two orders of magnitude in order for the natural frequency to be on the same order as the spinning speed. The frequency also decreased as a function of the blade surface area, but for the current blade sizes being used the natural frequency is always an order of magnitude greater than the spinning speed. In conclusion, experimental measurements indicate that under present operating conditions, cutting edge transverse motion occurs at a frequency equal to the spinning speed. There is no indication of any blade excitation which occurs at frequencies near the natural frequency.

Manuscript submitted Nov. 3, 1971; revised manuscript received ca. Feb. 1, 1972.

Any discussion of this paper will appear in a Discussion Section to be published in the December 1972 JOURNAL.

REFERENCES

1. C. D. Mote, Jr., "Effect of In-Plane Stresses on the Vibration Characteristics of Clamped-Free Discs," PhD Thesis, Univ. California, Berkeley, 1963.
2. W. J. Rhines, "Preliminary Investigation of the Vibration Characteristics of Crystal Slicing Circular Saw Blades," Internal Memorandum, Bell Telephone Laboratories, Inc.
3. C. T. Wang, "Applied Elasticity," McGraw-Hill Book Co., New York (1953).
4. S. E. Forman, "Mechanics of Crystal Wafering as Performed on ID Saws," Internal Memorandum, Bell Telephone Laboratories, Inc.
5. V. V. Bolotin, "The Dynamic Stability of Elastic Systems," Holden-Day, Inc., San Francisco (1964).
6. F. B. Hildebrand, "Methods of Applied Mathematics," 2nd ed., Prentice-Hall, Inc., Englewood Cliffs, N. J. (1965).
7. B. Carnahan, H. A. Luther, and J. O. Wilkes, "Applied Numerical Methods," John Wiley & Sons, Inc., New York (1969).
8. Y. K. Yakunin and S. M. Khasdan, *Woodworking Industry (USSR)*, Vol. 6, No. 8 and 9 (1957), CSIRO Translation No. 4065.

Mathematics of the Electrochemical Extraction of Hydrogen from Iron

Leonard Nanis* and T. K. Govindan Nambodhiri

The School of Chemical Engineering, University of Pennsylvania, Philadelphia, Pennsylvania 19104

ABSTRACT

The transient current of hydrogen removal from iron following steady-state permeation is analyzed theoretically for two limiting conditions at the input side. For the fastest possible removal ($C = 0$ at $X = 0$ and at $X = L$), the amount extracted at the potentiostated side ($X = L$) is one third of the total present at steady-state permeation described by $C_{(X)} = C_0(1 - X/L)$. Comparison of the integrated total flux and the amount given by the integral of $C_{(X)}$ indicates possible concentration dependence of hydrogen diffusivity in iron.

The study of diffusion of hydrogen through metals has attracted much interest because of its relation to the problem of hydrogen embrittlement. The electrochemical permeation technique (1) for measurement of diffusion of hydrogen in metals has been extensively employed recently (2, 3). The mathematical basis of this method was developed by McBreen *et al.* (4). This paper presents some results and conclusions concerning permeation in Armco iron based on an extension of the theory and application of permeation technique to provide additional information regarding hydrogen entry and extraction from metals.

The permeation method.—In the electrochemical permeation method, a thin membrane of the material is cathodically charged with hydrogen on one side, while the hydrogen diffusing out at the opposite side is oxidized by maintaining anodic conditions. Mathematically, this procedure provides the boundary condition

$$C = 0, \quad X = L, \quad t \geq 0 \quad [1]$$

The current needed to maintain the constant anodic potential is a direct measure of the rate at which hydrogen is diffusing out.

McBreen *et al.* (4) solved the diffusion equation (Fick's second law)

$$\frac{\partial^2 C}{\partial X^2} - \frac{1}{D} \frac{\partial C}{\partial t} = 0 \quad [2]$$

applying the pertinent initial condition

$$C = C_0(1 - X/L) \quad [3]$$

and boundary conditions to get expressions for the decay of permeation current from the steady state when the charging is stopped.

Two limiting decay transients were considered. For the fastest possible extraction, the concentration at the input side is considered to drop instantaneously to zero upon input current interruption, *i.e.*

$$C = 0, \quad X = 0, \quad t > 0 \quad [4]$$

where time is reckoned from the instant of interruption. Slowest possible extraction through the potentiostated side Eq. [1] is based on the assumption of zero flux at the input side, *i.e.*, after current interruption, the input side ($X = 0$) becomes impermeable to hydrogen, described as

$$\frac{\partial C}{\partial X} = 0, \quad X = 0, \quad t > 0 \quad [5]$$

Using Laplace transform methods, McBreen *et al.* (4) obtained for the slowest possible decay (Eq. [5], [1],

[3], and [2]), the flux in terms of the previous steady-state value (J_s) as

$$\frac{J_r}{J_s} = 1 - 2 \sum_{n=0}^{\infty} (-1)^n \operatorname{erfc} \frac{2n+1}{2\tau^{1/2}} \quad [6]$$

where $\tau = Dt/L^2$, a dimensionless time parameter.

Solving Eq. [2] with Eq. [1], [3], and [4], the fastest possible extraction gives

$$\frac{J_r}{J_s} = 1 - 2 \sum_{n=0}^{\infty} \frac{1}{\pi^{1/2}} \frac{1}{\tau^{1/2}} e^{-\frac{(2n+1)^2}{4\tau}} \quad [7]$$

It should be noted that Eq. [7] is a corrected version of a previous result (4).

The decay part of the permeation technique has been mostly neglected by previous workers. However, the decay transient is a source of additional information regarding the diffusivity and solubility of hydrogen in the membrane and of the nature of the reaction at the input metal-electrolyte interface. In particular, the time integral of flux from $X = L$ reflects the total amount of hydrogen extracted at this side and is equal to the total hydrogen in the membrane if the input side is impermeable according to Eq. [5]. The total amount at steady state ($t = 0$) is readily obtained from the product of average concentration (integral of Eq. [3]) and the volume of the permeated region of the membrane. Thus, integration of experimental decay curves of current *vs.* time should permit evaluation of the number of mols of hydrogen extracted for comparison with the prediction according to Eq. [3] using the value of C_0 , which, in turn, is obtained from the steady-state permeation current density and the diffusivity derived from the build-up transient.

When the boundary conditions are such that the decay follows Eq. [7], *i.e.*, fast decay, the amount of hydrogen extracted at the potentiostated side ($X = L$) is only a fraction of the total amount in the membrane at steady-state permeation. The remaining part of the hydrogen diffuses out through the input side ($X = 0$) in order to satisfy the boundary condition given by Eq. [4]. Hence, in order to calculate the hydrogen concentration of the membrane at steady-state permeation, it is essential to have an estimate of the relative amounts of hydrogen diffusing out at both sides of the membrane ($X = 0$ and $X = L$). The following mathematical analysis was performed to get these values.

Mathematics of fast decay.—Consider a membrane of thickness L which is charged from the side $X = 0$ and potentiostated at $X = L$ in order to maintain a zero concentration of hydrogen. During charging, a hydrogen concentration C_0 is maintained at $X = 0$. The steady-state concentration profile obtained by charging is described by Eq. [3]. This profile becomes the initial

* Electrochemical Society Active Member.

Key words: hydrogen dissolution in iron, hydrogen extraction, hydrogen diffusion, concentration-dependent diffusivity, permeation.

condition used together with the boundary conditions Eq. [1] and [4] to solve Eq. [2], with time measured from the instant of input current interruption. The solution sequence is to (i) obtain concentration of hydrogen as a function of time and position in the region $0 < X < L$; (ii) obtain the gradient of concentration at $X = 0$, $X = L$ to determine flux; and (iii) integrate each flux with respect to time over the entire range $0 < t < \infty$. Both separation of variables and Laplace transform methods were used.

Solution by the method of separation of variables.—The concentration of hydrogen within the membrane during the fast decay was obtained as

$$C = \frac{2C_0}{\pi} \sum_{n=1}^{\infty} \frac{1}{n} \sin \frac{n\pi X}{L} e^{-\frac{n^2\pi^2 Dt}{L^2}} \quad [8]$$

Differentiating Eq. [8] with respect to X gives

$$\frac{\partial C}{\partial X} = \frac{2C_0}{L} \sum_{n=1}^{\infty} \cos \frac{n\pi X}{L} e^{-\frac{n^2\pi^2 Dt}{L^2}} \quad [9]$$

Substituting $X = 0$ in Eq. [9], the gradient at the input surface is

$$\left. \frac{\partial C}{\partial X} \right|_{X=0} = \frac{2C_0}{L} \sum_{n=1}^{\infty} e^{-\frac{n^2\pi^2 Dt}{L^2}} \quad [10]$$

and for $X = L$, Eq. [9] gives the gradient as

$$\left. \frac{\partial C}{\partial X} \right|_{X=L} = \frac{2C_0}{L} \sum_{n=1}^{\infty} (-1)^n e^{-\frac{n^2\pi^2 Dt}{L^2}} \quad [11]$$

The flux F (mol cm⁻² sec⁻¹) of material diffusing across each surface is obtained from Eq. [10] and [11] with Fick's first law as

$$F = -D \frac{\partial C}{\partial X} \quad [12]$$

The total amount per unit area, Q_E , of hydrogen diffusing out at each surface is obtained by integrating the flux, F , over the entire range of time. Hence, the amount of hydrogen evolved at $X = 0$ is

$$\begin{aligned} Q_E \Big|_{X=0} &= \int_0^{\infty} F_{(X=0)} dt \\ &= \frac{-2C_0 D}{L} \int_0^{\infty} \left[\sum_{n=1}^{\infty} e^{-\frac{n^2\pi^2 Dt}{L^2}} \right] dt \quad [13] \end{aligned}$$

Integrating in Eq. [13] term by term gives a well-known convergent series as

$$Q_E \Big|_{X=0} = -\frac{2C_0 L}{\pi^2} \sum_{n=1}^{\infty} \frac{1}{n^2} = \frac{-C_0 L}{3} \quad [14]$$

In a similar fashion, Eq. [11] and [12] give

$$Q_E \Big|_{X=L} = \frac{-2C_0 L}{\pi^2} \sum_{n=1}^{\infty} \frac{(-1)^n}{n^2} = \frac{C_0 L}{6} \quad [15]$$

The sign of Q_E in Eq. [14] and [15] reflects the vectorial character of the flux with respect to the coordinate system. It is thus appropriate to consider absolute values to obtain the total amount extracted, Q_{Tot} , as

$$Q_{Tot} = |Q_E|_{X=0} + |Q_E|_{X=L} = \frac{C_0 L}{2} \quad [16]$$

The amount stored in the membrane (per unit area) at steady state before current interruption ($t < 0$) is readily determined by integration of Eq. [3] as

$C_0 L/2$ (mol cm⁻²), in agreement with Eq. [16]. Hence, the fraction of hydrogen diffusing out at $X = 0$ is

$$\frac{|Q_E|_{X=0}}{Q_{Tot}} = \frac{2}{3} \quad [17]$$

and the fraction diffusing out at $X = L$ is

$$\frac{|Q_E|_{X=L}}{Q_{Tot}} = \frac{1}{3} \quad [18]$$

Solution by Laplace transforms.—To check the results obtained as Eq. [17] and [18], Eq. [2], [3], [1], and [4] were solved using the method of Laplace transforms. The concentration of hydrogen within the membrane during fast decay is given by

$$\begin{aligned} C(x,t) &= C_0(1 - X/L) - C_0 \sum_{n=0}^{\infty} \operatorname{erfc} \left\{ \frac{2nL + X}{2\sqrt{Dt}} \right\} \\ &+ C_0 \sum_{n=0}^{\infty} \operatorname{erfc} \left\{ \frac{2L(n+1) - X}{2\sqrt{Dt}} \right\} \quad [19] \end{aligned}$$

Differentiating Eq. [19] with respect to X , and multiplying the slopes by $-D$, the flux (Eq. [12]) at $X = 0$ is

$$\begin{aligned} F \Big|_{X=0} &= \frac{DC_0}{L} \left[1 - \frac{1}{\sqrt{\pi\tau}} \left(\sum_{n=0}^{\infty} e^{-\frac{n^2}{\tau}} \right. \right. \\ &\left. \left. + \sum_{n=0}^{\infty} e^{-\frac{(n+1)^2}{\tau}} \right) \right] \quad [20] \end{aligned}$$

and the flux at $X = L$ is

$$F \Big|_{X=L} = \frac{DC_0}{L} \left[1 - \frac{2}{\sqrt{\pi\tau}} \sum_{n=0}^{\infty} e^{-\frac{(2n+1)^2}{4\tau}} \right] \quad [21]$$

Equations [20] and [21] have to be integrated with respect to τ over the range $0 < \tau < \infty$ to get the total amounts of hydrogen diffusing out at the surfaces $X = 0$ and $X = L$, respectively. Equations [20] and [21] both become infinite for $\tau = 0$. Also, for $\tau = \infty$, the integral of Eq. [20] and [21] becomes infinite because of the term of unity. Hence, with an analytic solution of the integrals not possible, a graphical integration was performed since the summations in Eq. [20] and [21] converge rapidly for numerical evaluation. The results are in good agreement (within 2%) of the values in Eq. [17] and [18]. Equations [19], [20], and [21] are useful in preparing tables and curves for short time, since Eq. [8], [10], and [11] are very slowly convergent for $\tau < 0.05$. The $n = 0$ term of Eq. [21] is sufficient even up to $\tau \leq 0.3$ and provides a simple form.

Thus, during fast decay, only one third of the total amount of hydrogen diffuses out through the potentiostated side ($X = L$), and provides a lower bounding limit, while the upper limit [$(Q_{E_{X=L}})/(Q_{E_{Tot}}) = 1$] is obtained during the slow decay because of the condition imposed by Eq. [5]. Comparison of the extracted amount of hydrogen with the value predicted from the initial concentration profile (Eq. [3]) thus provides further insight as to the nature of the boundary condition existing at $X = 0$ during decay, with Eq. [4] and [5] as limits.

Experimental Results

Hydrogen permeation experiments were performed with the potentiostat circuit as essentially described by McBreen *et al.* (4). A constant current circuit was used for the cathode input side of the membrane. Build-up and decay transients were recorded for various charging current densities in 0.2N NaOH and 0.1N H₂SO₄ catholytes for annealed Armco iron at 22°C. The anolyte was always 0.2N NaOH.

Table I. Analysis of decay transients

Annealed Armco iron; 22°C; catholyte: 0.1N H ₂ SO ₄ ; anolyte: 0.2N NaOH				
Average diffusivity, $D \times 10^5 \text{ cm}^2 \text{ sec}^{-1}$				
Charging current density, mA/cm ²	From decay			$\frac{ Q_E _{X=L}}{Q_{Tot}}$
	From build-up*	Fit to Eq. [7] (fast)	Fit to Eq. [6] (slow)	
0.021	4.84	3.86	10.48	0.334
0.064	4.16	4.23	11.21	0.326
0.194	5.52	4.63	12.68	0.280
0.409	6.60	5.34	14.50	0.266
0.841	7.66	5.78	15.70	0.258
2.13	8.45	6.40	17.20	0.243
4.27	8.31	6.22	16.90	0.235

* Numerical values for the build-up permeation-time curve may be computed by subtracting the right-hand side of Eq. [7] from unity.

By fitting the experimental build-up curves to theory (4), hydrogen diffusivity, D , and surface concentration, C_0 , were evaluated. It should be noted that there is no total agreement between theory and data over the entire build-up time span. By minimizing the misfit at different time intervals, a corresponding best fitted diffusivity may be computed. The trend suggests that diffusivity increases with hydrogen concentration. This aspect will be fully explored in forthcoming publications.

In the present computations of C_0 from the steady-state permeation current, the diffusivity value is that obtained by a best fit to the build-up theory for early time. This value of D may be seen to be the most appropriate choice since the hydrogen arriving at $X = L$ at the time of breakthrough has traversed a region free of hydrogen. At steady state, the flux at $X = L$ is given by Eq. [12] with, however, the implicit feature given in Eq. [1], namely that the local diffusivity (allowing for possible concentration dependence) corresponds to the zero concentration value. Based on this value of C_0 and the steady-state concentration profile given by Eq. [3], the total amount of hydrogen, Q_{Tot} , held within the membrane was calculated to be

$$Q_{Tot} = \frac{1}{2} C_0 V \quad [22]$$

where V = volume of the charged section of the membrane.

An estimate of the amount of hydrogen extracted at the potentiostated side ($X = L$) was obtained by measuring the area beneath the decay current-time traces and converting to equivalents of hydrogen. This value was then compared with Q_{Tot} to obtain the ratio $|Q_E|_{X=L}/Q_{Tot}$. Table I shows the results obtained for permeation from 0.1N H₂SO₄. Figure 1 shows the decay transients which were compared with the two theoretical decay curves (fast, Eq. [7], and slow, Eq. [6]) to yield average D values given in columns 3 and 4 of Table I. Also indicated in this table are the D values obtained from build-up transients, based on the best fit over all time. As mentioned previously, the diffusivity at small time was used for calculating Q_{Tot} in column 5. This value is $4.0 \times 10^{-5} \text{ cm}^2 \text{ sec}^{-1}$. Comparison of the two possible decay-fitted values with the build-up D indicates clearly that the boundary condition given by Eq. [4] is most likely. The ratio $|Q_E|_{X=L}/Q_{Tot}$ in Table I varies from the theoretical limit of 0.33 for fast decay to even smaller values. Thus, the charging at 0.021 mA/cm² follows the expected behavior and also gives the best fit over-all in Fig. 1. However, charging at higher currents produces a shift of the decay curves to shorter times, indicating an increase in D , listed in Table I. The decrease in $|Q_E|_{X=L}/Q_{Tot}$ from 0.334 to 0.235 as charging current increases brings these values into a region below the lower numerical limit calculated in Eq. [18]. This negative deviation from the

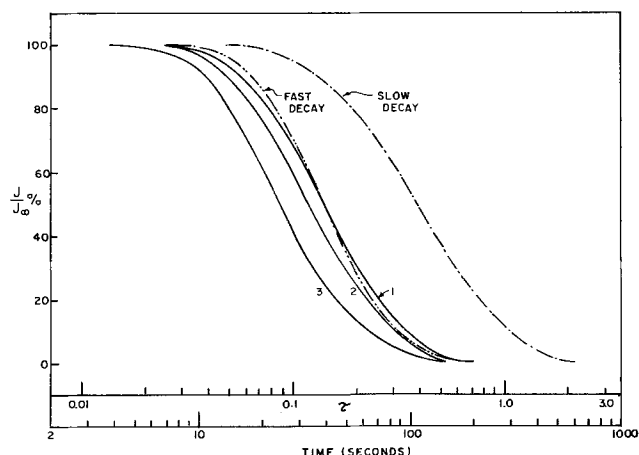


Fig. 1. Decay transients for Armco iron, 0.1N H₂SO₄. Catholyte, 22°C. Charging current densities (mA/cm²) are: curve 1, 0.021; curve 2, 0.194; and curve 3, 2.13.

limit based on constant diffusivity theory is in accord with a diffusivity which increases with increasing concentration. For such concentration dependence of D , the basic Eq. [2] and subsequent results are no longer applicable. Qualitatively, however, the concentrated region near $X = 0$ should provide a more rapid flux and an amount $|Q_E|_{X=0}$ greater than predicted by Eq. [14]. Thus, the flux and amount at $X = L$ will be less than that predicted in Eq. [15], causing the values for $|Q_E|_{X=L}/Q_{Tot}$ to be less than the theoretical constant D limit of 0.333.

During permeation experiments using 0.1N H₂SO₄ as catholyte, a cathodic protection current of 0.0215 mA/cm² was always applied to prevent corrosion of the Armco iron membrane. Permeation build-up and decays were then recorded by applying a cathodic current from a separate circuit. The response of the cathode ($X = 0$) to step current switching was sufficiently rapid so as to produce a virtually potentiostated surface when compared with the orders of magnitude greater diffusion-controlled hydrogen decay time. Thus, the boundary condition in Eq. [4] is assured.

When 0.2N NaOH catholyte was used, corrosion was not a severe problem, so that no cathodic protection was needed. Figure 2 shows decay transients observed for this case. Table II gives the D values and $|Q_E|_{X=L}/Q_{Tot}$ ratios obtained from these data. Best over-all fitting in Fig. 2 was found for the short time region for the 0.86 mA/cm² study. For lesser and greater cathodic input current densities, no clear pattern of shifting was observed as found for 0.1N H₂SO₄ (Fig. 1). In Table II, the build-up and decay determined D values

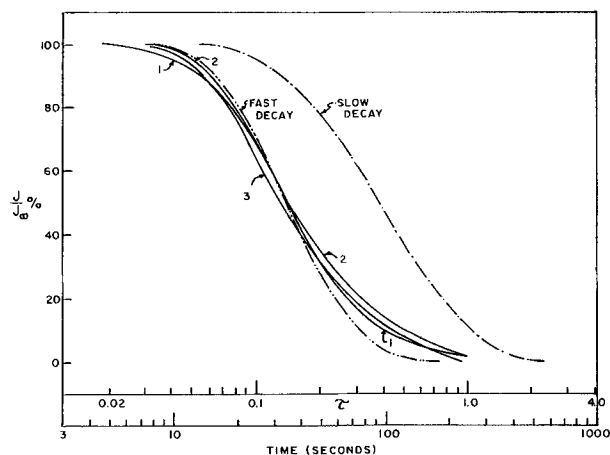


Fig. 2. Decay transients for Armco iron, 0.2N NaOH. Catholyte, 22°C. Charging current densities (mA/cm²) are: curve 1, 0.43; curve 2, 0.86; and curve 3, 4.30.

Table II. Analysis of decay transients

Annealed Armco iron; 22°C; 0.2N NaOH electrolyte				
Charging current density, mA/cm ²	Average diffusivity, $D \times 10^6 \text{ cm}^2 \text{ sec}^{-1}$			
	From build-up	From decay		$ Q_E _{X=L} / Q_{Tot}$
		Fit to Eq. (7) (fast)	Fit to Eq. (6) (slow)	
0.43	5.27	4.53	12.20	0.356
0.86	5.46	4.53	12.20	0.372
2.15	5.16	—	—	0.338
4.30	5.25	4.96	12.95	0.326

do not change appreciably with charging current, in contrast with results for 0.1N H₂SO₄ (Table I). The ratio $|Q_E|_{X=L} / Q_{Tot}$ ranges from 0.326 to 0.372, in good agreement with the lower limit of 0.333 associated with fast decay.

Discussion and Conclusions

Testing of the present decay mathematics shows unexpected lower than theoretical values for $|Q_E|_{X=L} / Q_{Tot}$ for 0.1N H₂SO₄. In combination with the shift of the build-up transients to shorter time with increased current, the data provide strong evidence for a hitherto unsuspected concentration dependence of hydrogen diffusivity in iron. The evidence suggests that D increases with increasing concentration. For 0.2N NaOH and 0.1N H₂SO₄, the fit of the decay current-time curve in comparison with the build-up curve and also the $|Q_E|_{X=L} / Q_{Tot}$ ratio values are best associated with a surface condition at $X = 0$ which corresponds to zero hydrogen concentration. From the trend of $|Q_E|_{X=L} / Q_{Tot}$ values below the constant D limit of 0.333, it is probable that, for similar charging current, the concen-

tration of hydrogen in iron is greater in the 0.1N H₂SO₄ catholyte than in the 0.2N NaOH solution.

In testing the possibility that traps may be contributing to the nonconstant diffusivity, the phenomenological diffusivity discussed by Oriani (5) should always be less than the true lattice diffusivity. As predicted (5), the true lattice diffusivity is $3.06 \times 10^{-5} \text{ cm}^2 \text{ sec}^{-1}$ at 22°C, in good agreement with the lowest values in Tables I and II, i.e., $5 \times 10^{-5} \text{ cm}^2 \text{ sec}^{-1}$. As shown, the D values increase to about $8 \times 10^{-5} \text{ cm}^2 \text{ sec}^{-1}$ with increasing current, so that trapping is an unlikely alternative to the presently suggested concentration dependence.

Acknowledgments

The financial support of the Office of Naval Research (N00014-67-A-0216-0004, School of Chemical Engineering, University of Pennsylvania) is gratefully acknowledged. The opinions and assertions contained herein are the private ones of the authors and are not to be construed as official or reflecting the views of the Navy Department.

Manuscript submitted Nov. 1, 1971; revised manuscript received Jan. 18, 1972.

Any discussion of this paper will appear in a Discussion Section to be published in the December 1972 JOURNAL.

REFERENCES

1. M. A. V. Devanathan and Z. O. J. Stachurski, *Proc. Roy. Soc.*, **A270**, 90 (1962).
2. W. Beck, J. O'M. Bockris, M. A. Genshaw, and P. K. Subramanian, *Met. Trans.*, **2**, 883 (1971).
3. C. D. Kim and A. W. Loginow, *Corrosion*, **24**, 313 (1968).
4. J. McBreen, L. Nanis, and W. Beck, *This Journal*, **113**, 1218 (1966).
5. R. A. Oriani, *Acta Met.*, **18**, 147 (1970).

Standard Potentials of Ag-AgCl Electrode and Related Thermodynamic Quantities in Dimethyl Sulfoxide-Water Mixtures from 5° to 45°C

Rabindra N. Roy, William Vernon, Alfred Bothwell, and James Gibbons

Department of Chemistry, Drury College, Springfield, Missouri 65802

ABSTRACT

EMF measurements were performed at 5°, 15°, 25°, 35°, and 45°C on the cell of the type Pt|H₂ (g, 1 atm)|HCl (m), DMSO (X), H₂O (Y)|AgCl, Ag, where X = 5, 10, and 20 w/o (weight per cent) dimethyl sulfoxide (DMSO). The standard potentials were evaluated by means of a curve-fitting program. The mean molal activity coefficients of HCl have been determined for molalities from 0.001 to 0.1 mol kg⁻¹. The cell has also been used to derive (i) the primary medium effect on HCl, (ii) the relative partial molal enthalpy (L_2) of HCl, and (iii) the thermodynamic constants ΔG° , ΔH° , and ΔS° for the transfer of HCl from water to the respective solvent compositions (X = 5, 10, and 20). The standard emf has been expressed as a function of temperature. The electrostatic contribution of the Gibbs free energy of transfer has been calculated, based on Born's model, and the results have been interpreted in terms of acid-base interactions, as well as the structure-breaking processes of the solvents.

The behavior of electrolytes in dipolar, aprotic solvent-water media such as tetrahydrofuran (THF)-water (1), 1, 2 dimethoxyethane (DME)-water (2, 3) are of interest in understanding acid-base interactions, ionic solvation, and association phenomena of solution chemistry. Mixtures of dipolar aprotic solvent (DMSO) with water (4, 5), have been found to strongly accel-

Key words: dimethyl sulfoxide, medium effect, activity coefficient, mixed solvents standard emf, thermodynamic.

ate the rates of many reactions involving nucleophiles or bases (6, 7). Although the chemistry of pure DMSO has been the subject of numerous investigations (8-10), no thermodynamic information for this electrolyte in DMSO-water mixtures (X = 5, 10, and 20), where X = weight per cent (w/o) of DMSO, has been reported to date. The present work is based on emf measurements on the cell, without liquid junction, Pt|H₂ (g, 1 atm)|HCl (m), DMSO (X), H₂O (Y)|AgCl, Ag at 5°,

15°, 25°, 35°, and 45°C. As a prerequisite to studies of acid-base equilibria, solvent effects on rates, instability constants, solubilities, and structures of solvents, we have reported the results on (i) the standard emf of the cell for $X = 5, 10,$ and $20,$ (ii) the activity coefficient of HCl, (iii) the primary medium effect, (iv) the relative partial molal enthalpy of HCl, and (v) the thermodynamic functions for the transfer of one mole of the acid from the aqueous standard state to the standard state in the mixed solvents.

Experimental

DMSO (Fisher spectroanalyzed) was used without further purification, and the label indicated the water content to be 0.02%. The solvent had a dielectric constant of 46.7 at 25°C.

An aqueous stock solution of hydrochloric acid was prepared from twice-distilled, constant-boiling acid. Analytical reagent grade acid was used to make up the constant-boiling acid. The acid was standardized by a gravimetric determination of chloride as AgCl. The average difference among replicate determinations was less than $\pm 0.03\%$. The bromide content was found to be less than 0.002 m/o (mole per cent). The distilled water used in the preparation of the solutions had a conductance of $0.7\text{--}0.8 \times 10^{-6} \text{ ohm}^{-1} \text{ cm}^{-1}$. The mixed solvents were prepared by weighing DMSO, water, and hydrochloric acid. All solutions were freshly prepared before each run. The acid concentration was known to within $\pm 0.02\%$.

The silver-silver chloride electrodes were of the thermal electrolytic type (11) and were aged in 0.1M HCl, which was deoxygenated by bubbling hydrogen. Two days after preparation, the finished electrodes were intercompared and had bias potentials usually less than ± 0.02 mV. The hydrogen electrodes were lightly coated with platinum black, according to the recommendations of Hills and Ives (12).

The purification of the hydrogen gas and other experimental details have been described previously (13).

All measurements were made with two Ag-AgCl electrodes and two hydrogen electrodes. The equilibrium was reached in about 3-4 hr after the initiation of hydrogen bubbling. The potentials of the cell were measured at 5°, 15°, 25°, 35°, and 45°C by means of a K-3 Universal Type Potentiometer which was calibrated against an Eppley standard cell. A mirror-type galvanometer with a sensitivity of ± 0.02 mV per division was used. The thermostat maintained a temperature within $\pm 0.01^\circ\text{C}$.

The emf usually was measured at 25° at the beginning, in the middle, and at the end of each run. These three readings agreed within ± 0.09 mV. The average value is given in Table I. The criterion for the attainment of equilibrium was a steady reading to the nearest 0.1 mV for a period of about 1 hr. Each emf value recorded in Table I is the average of two pairs of electrodes in the same cell. Observed values of emf have been converted to a hydrogen partial pressure of 1 atm. The dielectric constant (D) of the mixed solvent at each Celsius temperature, t , was calculated from the equations

$$\log D (X = 5) = 1.8938 - 0.00204(t - 25^\circ) \quad [1]$$

$$\log D (X = 10) = 1.8925 - 0.00204(t - 25^\circ) \quad [2]$$

and

$$\log D (X = 20) = 1.8888 - 0.00204(t - 25^\circ) \quad [3]$$

derived from the data of Tommila and Pajunen (15). The density, ρ_0 , of each of these mixtures, at different temperatures, was obtained by an interpolation and extrapolation procedure from the literature (15).

DMSO has a very low vapor pressure. In order to correct the emf to a hydrogen partial pressure of 1 atm, vapor pressures of the solvent components were assumed to obey Raoult's law, and were so calculated.

Table I. Electromotive force (volts) of the cell
Pt | H₂ (g, 1 atm) | HCl (m), DMSO (X), and H₂O (Y) | AgCl, Ag
at different temperatures

X and Y are weight percentages

$m_{\text{HCl}},^a$ moles/kg	5°	15°	25°	35°	45°
X = 5					
0.00501	0.4900	0.4929	0.4945	0.4966	0.4994
0.01001	0.4577	0.4586	0.4605	0.4617	0.4635
0.0300	0.4071	0.4064	0.4073	0.4063	0.4058
0.0400	0.3932	0.3933	0.3946	0.3929	0.3905
0.0476	0.3861	0.3853	0.3866	0.3841	0.3819
0.0601	0.3755	0.3742	0.3743	0.3732	0.3710
0.0811	0.3609	0.3600	0.3604	0.3586	0.3558
0.0922	0.3560	0.3544	0.3535	0.3521	0.3488
X = 10					
0.00500	0.4893	0.4901	0.4922	0.4933	0.4951
0.01001	0.4566	0.4566	0.4580	0.4589	0.4582
0.0400	0.3937	0.3925	0.3899	0.3875	0.3852
0.0501	0.3849	0.3818	0.3789	0.3759	0.3745
0.0601	0.3769	0.3737	0.3701	0.3666	0.3632
0.0801	0.3632	0.3599	0.3557	0.3509	0.3480
0.1001	0.3523	0.3498	0.3448	0.3403	0.3372
0.1502	0.3345	0.3320	0.3255	0.3200	0.3140
X = 20					
0.00386	0.4995	0.5010	0.5037	0.5072	0.5092
0.01001	0.4546	0.4558	0.4575	0.4586	0.4590
0.03002	0.4059	0.4056	0.4054	0.4036	0.4015
0.0400	0.3940	0.3928	0.3924	0.3894	0.3867
0.0500	0.3843	0.3827	0.3826	0.3815	0.3742
0.0601	0.3736	0.3725	0.3731	0.3694	0.3646
0.0801	0.3618	0.3603	0.3579	0.3546	0.3489
0.1001	0.3510	0.3496	0.3483	0.3431	0.3373
0.1501	0.3331	0.3305	0.3275	0.3219	0.3152

^a Accuracy of molality within 0.05%.

Results

Standard emf.—The most common method used to evaluate the standard potential involves the graphical extrapolation of some linear plot of emf of the cell against the concentration of hydrochloric acid, as in the following equations (16)

$$E'' = E + 2k \log m - 2ks_f c^{1/2} / (1 + a_0 B c^{1/2}) - 2k \log (1 + 0.002mM_{xy}) \quad [4]$$

$$= E^\circ_m + f(m)$$

where E°_m is the standard potential of the cell on the molal (m) scale, E is the observed electromotive force of the cell, c is the molarity of HCl, a_0 is the ion-size parameter, M_{xy} is the mean molecular weight, $k = 2.3026RT/F$, and B and s_f are the Debye-Hückel constants. In this paper, we report the results of E°_m determined by a theoretically justified polynomial curve-fitting program, which does not require the above information such as the ion-size parameter, the Debye-Hückel constants, the densities, and the dielectric constants of the mixed solvents. It is indeed attractive to contemplate the derivation of E°_m without the information required in the Gronwall, LaMer, and Sandved (17) extension of the Debye-Hückel theory.

Sen, Johnson, and Roy (18) and our recent papers (19-21) have convincingly demonstrated that an equation of the form

$$E + (2RT/F) \ln m = E^\circ + A_1 m^{1/2} + A_2 m + A_3 m^{3/2} + \dots \quad [5]$$

is theoretically sound and accurately expresses the standard potential.

The activity coefficient (on molal scale) can be expressed by the equation (18)

$$\ln \gamma_{\pm} = A_1' m^{1/2} + A_2' m + A_3' m^{3/2} + \dots \quad [6]$$

where coefficients in Eq. [5] and [6] are not arbitrary adjustable parameters. The form of Eq. [6] has been shown to be consistent with the theory (22).

Table II summarizes the values of the standard potentials on three scales, namely the molal (m), molar (c), and mole fraction (N) scales in DMSO-water

Table II. Standard emf of the cell; Pt | H₂ (g, 1 atm) | HCl (m), DMSO (X), H₂O (Y) | AgCl, Ag at different temperatures

X = w/o DMSO			
t/°C	E° _m	E° _c	E° _N
X = 5 (±0.0003V)			
5	0.2314	0.2310	0.0408
15	0.2255	0.2252	0.0280
25	0.2179	0.2178	0.0136
35	0.2102	0.2103	-0.0010
45	0.2036	0.2039	-0.0144
X = 10 (±0.0006V)			
5	0.2312	0.2306	0.0426
15	0.2210	0.2205	0.0274
25	0.2148	0.2145	0.0129
35	0.2093	0.2091	0.0003
45	0.2029	0.2028	-0.0130
X = 20 (±0.001V)			
5	0.2271	0.2257	0.0426
15	0.2186	0.2174	0.0274
25	0.2117	0.2096	0.0129
35	0.2076	0.2067	0.0032
45	0.1990	0.1983	-0.0120

mixtures. The values of E°_m are expressed as a function of t (°C) by the equations

5% DMSO

$$E^{\circ}_m = 0.2179 - 7.085 \times 10^{-4} (t - 25^{\circ}) - 9.782 \times 10^{-7} (t - 25^{\circ})^2 \quad [7]$$

10% DMSO

$$E^{\circ}_m = 0.2147 - 6.840 \times 10^{-4} (t - 25^{\circ}) + 5.807 \times 10^{-6} (t - 25^{\circ})^2 \quad [8]$$

20% DMSO

$$E^{\circ}_m = 0.2119 - 6.704 \times 10^{-4} (t - 25^{\circ}) + 3.300 \times 10^{-6} (t - 25^{\circ})^2 \quad [9]$$

The standard potentials on the molar and mole fraction scale, E°_c and E°_N, respectively, have been calculated by means of the relationships

$$E^{\circ}_c = E^{\circ}_m + 2k \log \rho_0 \quad [10]$$

and

$$E^{\circ}_N = E^{\circ}_m - 2k \log (1000/M_{xy}) \quad [11]$$

where ρ₀ is the density of the mixed solvent at the particular temperature, and M_{xy} is the mean molecular weight of the solvent.

The mean molal activity coefficients of hydrochloric acid, sγ_±, in DMSO-water mixtures at 25°C were computed from the equation

$$\log s\gamma_{\pm} = [E^{\circ}_m - \{E + (2RT/F) \ln m\}] / (4.6052RT/F) \quad [12]$$

using the respective values of E°_m listed in Table II. The smoothed values of {E + (2RT/F) ln m} at rounded molalities were obtained from the constants of Eq. [5] and the values of sγ_± are presented in Table III.

The primary medium effect (ion-solvent interaction) is concentration-independent and measures the change in escaping tendency of HCl in the transfer from a standard state in one solvent to a standard state in another solvent. Thermodynamically, it can be represented as

$${}^wE^{\circ}_m - {}^sE^{\circ}_m = \lim_{m \rightarrow 0} (4.6052RT/F) \log s_w\gamma_{\pm} \quad [13]$$

Table III. Mean activity coefficients (sγ_±) of hydrochloric acid in 5, 10, and 20 w/o dimethyl sulfoxide at 25°C

m _{HCl} , moles/kg	X = w/o DMSO		
	X = 5	X = 10	X = 20
0.001	0.957	0.950	0.927
0.002	0.942	0.933	0.903
0.005	0.917	0.905	0.857
0.01	0.892	0.879	0.817
0.02	0.859	0.852	0.772
0.05	0.824	0.820	0.718
0.1	0.801	0.797	0.692

Table IV. Primary medium effect (molal scale) of dimethyl sulfoxide-water mixtures on hydrochloric acid at 5°, 25°, and 45°C

X = w/o dimethyl sulfoxide			
X	5°C	25°C	45°C
5	0.0244	0.0372	0.0373
10	0.0263	0.0631	0.0435
20	0.0637	0.0983	0.0737

where the value of ^sE°_m is the same as E°_m. The superscripts w and s on E°_m represent water and the mixed solvent, respectively. The subscripts w and s on γ_± mean that γ_± is referred to unity at infinite dilution in water and in a mixed solvent, respectively. These values are presented in Table IV.

Relative partial molal enthalpy.—The relative partial molal enthalpies of HCl for 5 w/o DMSO at five different temperatures were computed with the following equations (23)

$$L_2 = \bar{H} - \bar{H}^{\circ} = \bar{H} - \bar{H}^{\circ} = -2RT^2 \delta (\ln s\gamma_{\pm}) / \delta T \quad [14]$$

The (δ ln sγ_± / δT) value required by Eq. [14] was obtained from the first derivative of the least square polynomial

$$-\log s\gamma_{\pm} = A + BT + CT^2 \quad [15]$$

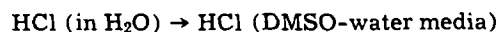
where T is the thermodynamic temperature. The constants of Eq. [15] are given in Table V, together with the standard error of the calculated values of log sγ_±.

Combination of Eq. [14] and [15] yields

$$L_2 = (2RT^2 \ln 10) (B + 2CT) \quad [16]$$

The values of L₂ are given in Table VI.

Standard Gibbs energy, entropy, and enthalpy of transfer of HCl from water to the mixed solvent.—The standard thermodynamic functions for the transfer process (t)



in three DMSO-water mixtures were calculated from the standard emf of the cell in water (16) and in the mixed solvent together with the temperature coefficients of E°_m in water and the respective mixed solvents. The Gibbs energy of transfer is defined by the equation

$$\Delta G^{\circ}_t(\text{HCl}) = {}^s\bar{G}^{\circ}_{\text{HCl}} - {}^w\bar{G}^{\circ}_{\text{HCl}} = {}^s\Delta G^{\circ}_{\text{HCl}(\text{soln})} - {}^w\Delta G^{\circ}_{\text{HCl}(\text{soln})} \quad [17]$$

where $\bar{G}^{\circ}_{\text{HCl}}$ represents the molar Gibbs energy in the

Table V. Constants of the equation $-\log s\gamma_{\pm}$ (molal scale) = A + BT + CT²

m _{HCl} , moles/kg	X = 5			Std. error
	A	B × 10 ⁴	C × 10 ⁷	
0.001	-0.02612	1.8949	-1.1646	0.0001
0.002	-0.01209	0.9731	-1.1688	0.0001
0.01	-0.01793	2.4595	-3.2742	0.0002
0.01	-0.01239	5.2685	-4.6751	0.0001
0.1	-0.15180	12.2221	-8.7866	0.0001

Table VI. Relative partial molal enthalpy (L₂)^a of hydrochloric acid in 5 w/o DMSO between 5° and 45°C

m _{HCl} , moles/kg	X = w/o DMSO				
	5°	15°	25°	35°	45°
0.001	370	389	409	428	447
0.002	481	524	568	616	656
0.01	671	718	766	816	868
0.05	791	819	845	868	889
0.1	2173	2276	2377	2475	2570

^a L₂ is expressed in J/mole. 1 thermochemical calorie = 4.1840 joules.

Table VII. Thermodynamic quantities^a (mole fraction scale) for the transfer of HCl from water to dimethyl sulfoxide-water mixtures at 25°C

X = w/o DMSO						
X	ΔG°_t	ΔG°_{el}	ΔG°_{chem}	ΔH°_t	ΔS°_t	D
5	231	6	225	-1630	-6.2	78.30
10	324	17	307	-829	-3.9	78.07
20	294	87	207	-471	-2.6	77.41

^a ΔG° and ΔH° are expressed in joules mole⁻¹ and ΔS° in joules K⁻¹ mole⁻¹.

mixed solvent (s) and water (w), respectively. The effect of the solvent on transfer Gibbs energy has been calculated on the mole fraction scale which does not contain the change of the number of solvent molecules by different solvents; therefore, it will eliminate Gibbs energy changes due to concentration changes. The pertinent relationship for the transfer Gibbs energy is given by

$$\Delta G^\circ_t = F(wE^\circ_N - sE^\circ_N) \quad [18]$$

The values of this quantity are given in Table VII

The transfer of charged particles, the hydrogen ion and chloride ion, from water to DMSO-water mixtures can be thought of in three stages: (i) desolvation of the ions in water, (ii) transfer of H⁺ and Cl⁻ to the mixed solvent (s), and (iii) resolution of the ions in the mixed solvent (s). The parameters that adequately describe the effect of this changing solvent composition on the transfer Gibbs energy are not yet well understood. It is convenient, however, to divide the transfer energy into two parts (24-26)

$$\Delta G^\circ_t = \Delta G^\circ_{el} + \Delta G^\circ_{chem} \quad [19]$$

The electrostatic term, ΔG°_{el} , represents the coulombic forces between the ionic charge and the charge distributions on the solvent molecules. All other effects, including the basicity and the difference in work required to create a cavity for the ions in the two media, contribute to the second term (24, 27). The electrostatic contributions to the transfer energy has been computed from the Born equation

$$\Delta G^\circ_{el} = (Ne^2/2) (D_s^{-1} - D_w^{-1}) (r_+^{-1} + r_-^{-1}) \quad [20]$$

where D_s and D_w represent the dielectric constants of the mixed solvent and water, respectively. The radius of the "hydrogen ion" (r_+) is taken as 2.76Å (28) and that of the chloride ion (r_-) is taken as 1.81Å (29). The values of ΔG°_{chem} have been obtained by subtracting the electrostatic free energy from the total transfer quantity. Table VII summarizes the values of these quantities.

By the application of the usual thermodynamic relationship

$$\Delta S^\circ_t = -d(\Delta G^\circ_t)/dT \quad [21]$$

to the temperature variation of E°_m , one obtains

$$\Delta S^\circ_t = F[(a + 2bT - 50b - k) - (a_w + 2b_wT - 50b_w - k_w)] \quad [22]$$

where a and b are the second and third coefficients of Eq. [7] to [9]. The values of a_w and b_w are given in the literature (16); the constant $k = (2R/F) \ln(1000/M_{xy})$, and k_w (a constant) is taken as 6.92×10^{-4} . The values of ΔS°_t are given in Table VII.

The values of the transfer enthalpy, shown in Table VII, were obtained from the relation

$$\Delta H^\circ_t = \Delta G^\circ_t + T\Delta S^\circ_t \quad [23]$$

The values of the electrostatic energy, ΔG°_{el} , may be accurate, but the experimental uncertainties in the values of ΔH°_{el} and ΔS°_{el} will be greater; hence, no attempts were made to calculate these quantities. The correct evaluation of the values of ΔG°_{el} is hampered

by the uncertainties of effective ionic radii and the variation of the dielectric constant with distance from the ionic surface (dielectric saturation). Nevertheless, the values of ΔG°_{el} (and hence ΔG°_{chem}) can be considered sufficiently significant to draw some general conclusions which are qualitatively correct.

Discussion

The values of the activity coefficient, Table III, for $X = 5, 10,$ and 20 at 25°C decrease (at a given molality) with the increasing proportions of DMSO. The general pattern of this trend is similar to that found in our other investigations, such as glycerol-water (30), isopropyl alcohol-water mixtures (31). Hydrochloric acid shows the characteristic of a strong electrolyte in the experimental DMSO-water mixtures and its behavior is very similar to that in water. An error of ± 0.09 mV in emf value corresponds to an error of ± 0.003 in the values of $\epsilon\gamma_{\pm}$.

An examination of Table IV shows that the escaping tendency of HCl is greater in DMSO-water mixtures than in pure water, because the primary medium effect of DMSO-water mixtures on HCl becomes greater with gradual addition of DMSO.

The total transfer Gibbs energy appears to be positive for all experimental solvent compositions in the DMSO-water system. Hydrochloric acid thus appears to be in a higher Gibbs energy state in the mixed solvent than in water. The positive values of ΔG°_{chem} also suggest that, as far as the acid-base reaction or solvation is concerned, the transfer of HCl from water to DMSO-water mixtures is not favored. In other words, water is more basic than the mixed solvent. The values of ΔG°_t are accurate to within ± 24 joule mole⁻¹.

The values of ΔH°_t and ΔS°_t reflect contributions from the effects of the ions on the structure of the solvents while the values of ΔG°_t provide information in regard to acid-base theory of ion solvation. The function, ΔG°_t , is a simpler one, and may not be affected by structural factors (32-34). It may also be regarded as the resultant of the other two, and more complex. Table VII shows that the values of ΔH°_t and ΔS°_t are negative, which suggests that, on the transfer process, the net amount of order created by HCl is more in the mixed solvent than in water. Hydrochloric acid thus breaks more structure in water than in DMSO-water mixtures. This is further supported with the view (35) that all structure-forming processes, including solvation of ions are exothermic and are accompanied by a decrease in entropy.

SYMBOLS

wE°_N, sE°_N	standard electrode potential in water and in a mixed solvent (mole fraction scale), volts
wE°_m, sE°_m	standard electrode potential in water and in a mixed solvent (molal scale), volts
a_0	ion-size parameter, angstroms
X	w/o DMSO in a mixture with water
$\epsilon\gamma_{\pm}$	mean ionic activity coefficient of HCl (molal scale) in a mixed solvent relative to unit value at infinite dilution in a mixed solvent (subscript, s)
D_s, D_w	dielectric constant of the mixed solvent and water, respectively
M_{xy}	mean molecular weight of the solvent kg · mole ⁻¹
r_+, r_-	radius of the cation (H ⁺) and anion (Cl ⁻), respectively, angstroms
L_2	relative partial molal enthalpy, cal/mole
E°, A_1, \dots	the constants of Eq. [5]
A, B, C	empirical constants of Eq. [15]

Acknowledgments

The authors are indebted to Dr. J. Padron for providing the facility for this experimental work and Mr. G. Moore for his technical assistance.

Manuscript submitted May 4, 1971; revised manuscript received May 26, 1971.

Any discussion of this paper will appear in a Discussion Section to be published in the December 1972 JOURNAL.

REFERENCES

- R. N. Roy and B. Sen, *J. Chem. Eng. Data*, **13**, 79 (1968).
- R. N. Roy, W. Vernon, and A. L. M. Bothwell, *ibid.*, **16**, 347 (1971).
- D. A. Johnson and B. Sen, *ibid.*, **13**, 376 (1968).
- E. Tommila and I. Palenius, *Acta Chem., Scand.*, **17**, 1980 (1968).
- C. A. Kingsbury, *J. Am. Chem. Soc.*, **87**:23, 5409 (1965).
- A. J. Parker, *Quart. Rev. (London)*, **16**, 163 (1962).
- C. D. Ritchie in, "Solute-Solvent Interactions," J. F. Coetzee and C. D. Ritchie, Editors, Marcel Dekker, New York (1969).
- H. L. Clever and E. F. Westrum, *J. Phys. Chem.*, **74**, 1309 (1970).
- M. Salomon, *This Journal*, **118**, 1392 (1969).
- G. Holleck, D. R. Cogley, and J. N. Butler, *ibid.*, **116**, 952 (1969).
- R. G. Bates, "Determination of pH," p. 281, John Wiley & Sons, Inc., New York (1964).
- G. J. Hills and D. J. G. Ives in, "Reference Electrode," p. 107, D. J. G. Ives and G. J. Janz, Editors, Academic Press, New York (1961).
- R. N. Roy and B. Sen, *J. Chem. Eng. Data*, **12**, 584 (1967).
- I. M. Kolthoff and T. B. Reddy, *This Journal*, **108**, 980 (1961).
- E. Tommila and A. Pajunen, *Suomen Kemistilehti*, **B41**, 172 (1968).
- H. S. Harned and B. B. Owen, "The Physical Chemistry of Electrolytic Solutions," 3rd ed., pp. 458, 715, Reinhold Publishing Corp., New York (1958).
- T. H. Gronwall, V. K. LaMer, and K. Sandved, *Physik. Z.*, **29**, 358 (1928).
- B. Sen, D. A. Johnson, and R. N. Roy, *J. Phys. Chem.*, **71**, 1523 (1967).
- R. N. Roy, W. Vernon, and A. L. M. Bothwell, *This Journal*, **118**, 1303 (1971).
- R. N. Roy, W. Vernon, and A. L. M. Bothwell, *J. Chem. Therm.*, **3**, 769 (1971).
- R. N. Roy, W. Vernon, and A. L. M. Bothwell, *J. Chem. Soc., (A)*, 1242 (1971).
- A. J. Dill, L. M. Itzkowitz, and O. Popovych, *J. Phys. Chem.*, **72**, 4580 (1968).
- R. A. Robinson and R. H. Stokes, "Electrolyte Solutions," 2nd revised ed., p. 34, Butterworths, London (1965).
- R. G. Bates and R. A. Robinson in, "Chemical Physics of Ionic Solutions," chap. 12, B. E. Conway and R. G. Barradas, Editors, John Wiley & Sons, Inc., New York (1966).
- O. Popovych, *Crit. Rev. Anal. Chem.*, **1**, 73 (1970).
- M. Alfenaar and C. L. deLigny, *Rec. Trav. Chim.*, **86**, 929 (1967).
- S. Goldman, P. Sagner, and R. G. Bates, *J. Phys. Chem.*, **75**, 826 (1971).
- M. Paabo, R. G. Bates, and R. A. Robinson, *ibid.*, **70**, 247 (1966).
- L. Pauling, "The Nature of the Chemical Bond," 3rd ed., pp. 464, 521, Cornell Univ. Press, Ithaca, N. Y. (1960).
- R. N. Roy, W. Vernon, and A. L. M. Bothwell, *J. Electroanal. Chem.*, **30**, 335 (1971).
- R. N. Roy and A. Bothwell, *J. Chem. Eng. Data*, **15**, 548 (1970).
- D. Feakins in, "Physico-Chemical Processes in Mixed Aqueous Solvents," p. 71, F. Franks, Editor, American Elsevier Publishing Co., New York (1967).
- R. G. Bates in, "Hydrogen-Bonded Solvent Systems," p. 49, A. K. Covington and P. Jones, Editors, Taylor and Francis, London (1968).
- F. Franks and D. J. G. Ives, *Quart. Rev. London*, **20**, 1 (1966).
- H. S. Frank and M. G. Evans, *J. Chem. Phys.*, **13**, 507 (1945).

Diffusion Kinetics at Microelectrodes

Chris R. Ito, S. Asakura, and Ken Nobe*

School of Engineering and Applied Science, University of California, Los Angeles, California 90024

ABSTRACT

The effect of the electrode size on the diffusion current of the cathodic reaction $I_3^- + 2e = 3I^-$ was investigated under transient conditions. Plane circular surfaces of platinum electrodes with diameters, d , ranging from 1.27 to 0.0127 cm were used. The diffusion current under potentiostatic conditions could be expressed as

$$i = \frac{nFA\sqrt{DC}}{\sqrt{\pi}} \left(\frac{1}{\sqrt{t}} + \frac{2M\sqrt{\pi D}}{d} \right)$$

where M is an empirical parameter which is a function of d . For $d < 0.1$ cm, $M = 1$ and the diffusion mode was equivalent to semi-infinite spherical diffusion. On the other hand, for $d > 0.3$ cm, $M = 0$, and semi-infinite linear diffusion was the controlling mode. The change in the diffusion mode occurred rather abruptly at about $d = 0.2$ cm.

Diffusion kinetics at a microelectrode often plays an important role in electrochemical processes (e.g., electroanalytical chemistry methods, electrodeposition, and electropolishing). It is known that the mass transfer processes at microconfigurations differ to a great extent from those at macroconfigurations. However, comparatively few fundamental studies have been reported on the subject. By dimensional analysis, Agar (1) determined that the mass transfer mode under steady-state conditions changed from convection control to diffusion control as the electrode size decreased. Ibl (2) applied boundary layer theory in his investigation of

the mass transfer process at thin wire electrodes. He determined that the deviation of the diffusion current at plate electrodes increased as the diameter decreased. Jacquet (3) observed the thickness of the anodic diffusion layer during electropolishing and found that it was greater over valleys than over peaks. Beacom (4) studied the thickness of the diffusion layer over small notches by the Schlieren method. Wagner (5) examined theoretically the mass transfer process at a rough surface where the surface roughness was approximated by a sine wave.

A number of papers (6) have been published on electroanalytical studies using stationary microelectrodes. However, only a few of these studies have considered

* Electrochemical Society Active Member.

Key words: chronoamperometry, tri-iodide, platinum.

Any discussion of this paper will appear in a Discussion Section to be published in the December 1972 JOURNAL.

REFERENCES

- R. N. Roy and B. Sen, *J. Chem. Eng. Data*, **13**, 79 (1968).
- R. N. Roy, W. Vernon, and A. L. M. Bothwell, *ibid.*, **16**, 347 (1971).
- D. A. Johnson and B. Sen, *ibid.*, **13**, 376 (1968).
- E. Tommila and I. Palenius, *Acta Chem., Scand.*, **17**, 1980 (1968).
- C. A. Kingsbury, *J. Am. Chem. Soc.*, **87**:23, 5409 (1965).
- A. J. Parker, *Quart. Rev. (London)*, **16**, 163 (1962).
- C. D. Ritchie in, "Solute-Solvent Interactions," J. F. Coetzee and C. D. Ritchie, Editors, Marcel Dekker, New York (1969).
- H. L. Clever and E. F. Westrum, *J. Phys. Chem.*, **74**, 1309 (1970).
- M. Salomon, *This Journal*, **118**, 1392 (1969).
- G. Holleck, D. R. Cogley, and J. N. Butler, *ibid.*, **116**, 952 (1969).
- R. G. Bates, "Determination of pH," p. 281, John Wiley & Sons, Inc., New York (1964).
- G. J. Hills and D. J. G. Ives in, "Reference Electrode," p. 107, D. J. G. Ives and G. J. Janz, Editors, Academic Press, New York (1961).
- R. N. Roy and B. Sen, *J. Chem. Eng. Data*, **12**, 584 (1967).
- I. M. Kolthoff and T. B. Reddy, *This Journal*, **108**, 980 (1961).
- E. Tommila and A. Pajunen, *Suomen Kemistilehti*, **B41**, 172 (1968).
- H. S. Harned and B. B. Owen, "The Physical Chemistry of Electrolytic Solutions," 3rd ed., pp. 458, 715, Reinhold Publishing Corp., New York (1958).
- T. H. Gronwall, V. K. LaMer, and K. Sandved, *Physik. Z.*, **29**, 358 (1928).
- B. Sen, D. A. Johnson, and R. N. Roy, *J. Phys. Chem.*, **71**, 1523 (1967).
- R. N. Roy, W. Vernon, and A. L. M. Bothwell, *This Journal*, **118**, 1303 (1971).
- R. N. Roy, W. Vernon, and A. L. M. Bothwell, *J. Chem. Therm.*, **3**, 769 (1971).
- R. N. Roy, W. Vernon, and A. L. M. Bothwell, *J. Chem. Soc., (A)*, 1242 (1971).
- A. J. Dill, L. M. Itzkowitz, and O. Popovych, *J. Phys. Chem.*, **72**, 4580 (1968).
- R. A. Robinson and R. H. Stokes, "Electrolyte Solutions," 2nd revised ed., p. 34, Butterworths, London (1965).
- R. G. Bates and R. A. Robinson in, "Chemical Physics of Ionic Solutions," chap. 12, B. E. Conway and R. G. Barradas, Editors, John Wiley & Sons, Inc., New York (1966).
- O. Popovych, *Crit. Rev. Anal. Chem.*, **1**, 73 (1970).
- M. Alfenaar and C. L. deLigny, *Rec. Trav. Chim.*, **86**, 929 (1967).
- S. Goldman, P. Sagner, and R. G. Bates, *J. Phys. Chem.*, **75**, 826 (1971).
- M. Paabo, R. G. Bates, and R. A. Robinson, *ibid.*, **70**, 247 (1966).
- L. Pauling, "The Nature of the Chemical Bond," 3rd ed., pp. 464, 521, Cornell Univ. Press, Ithaca, N. Y. (1960).
- R. N. Roy, W. Vernon, and A. L. M. Bothwell, *J. Electroanal. Chem.*, **30**, 335 (1971).
- R. N. Roy and A. Bothwell, *J. Chem. Eng. Data*, **15**, 548 (1970).
- D. Feakins in, "Physico-Chemical Processes in Mixed Aqueous Solvents," p. 71, F. Franks, Editor, American Elsevier Publishing Co., New York (1967).
- R. G. Bates in, "Hydrogen-Bonded Solvent Systems," p. 49, A. K. Covington and P. Jones, Editors, Taylor and Francis, London (1968).
- F. Franks and D. J. G. Ives, *Quart. Rev. London*, **20**, 1 (1966).
- H. S. Frank and M. G. Evans, *J. Chem. Phys.*, **13**, 507 (1945).

Diffusion Kinetics at Microelectrodes

Chris R. Ito, S. Asakura, and Ken Nobe*

School of Engineering and Applied Science, University of California, Los Angeles, California 90024

ABSTRACT

The effect of the electrode size on the diffusion current of the cathodic reaction $I_3^- + 2e = 3I^-$ was investigated under transient conditions. Plane circular surfaces of platinum electrodes with diameters, d , ranging from 1.27 to 0.0127 cm were used. The diffusion current under potentiostatic conditions could be expressed as

$$i = \frac{nFA\sqrt{DC}}{\sqrt{\pi}} \left(\frac{1}{\sqrt{t}} + \frac{2M\sqrt{\pi D}}{d} \right)$$

where M is an empirical parameter which is a function of d . For $d < 0.1$ cm, $M = 1$ and the diffusion mode was equivalent to semi-infinite spherical diffusion. On the other hand, for $d > 0.3$ cm, $M = 0$, and semi-infinite linear diffusion was the controlling mode. The change in the diffusion mode occurred rather abruptly at about $d = 0.2$ cm.

Diffusion kinetics at a microelectrode often plays an important role in electrochemical processes (e.g., electroanalytical chemistry methods, electrodeposition, and electropolishing). It is known that the mass transfer processes at microconfigurations differ to a great extent from those at macroconfigurations. However, comparatively few fundamental studies have been reported on the subject. By dimensional analysis, Agar (1) determined that the mass transfer mode under steady-state conditions changed from convection control to diffusion control as the electrode size decreased. Ibl (2) applied boundary layer theory in his investigation of

the mass transfer process at thin wire electrodes. He determined that the deviation of the diffusion current at plate electrodes increased as the diameter decreased. Jacquet (3) observed the thickness of the anodic diffusion layer during electropolishing and found that it was greater over valleys than over peaks. Beacom (4) studied the thickness of the diffusion layer over small notches by the Schlieren method. Wagner (5) examined theoretically the mass transfer process at a rough surface where the surface roughness was approximated by a sine wave.

A number of papers (6) have been published on electroanalytical studies using stationary microelectrodes. However, only a few of these studies have considered

* Electrochemical Society Active Member.

Key words: chronoamperometry, tri-iodide, platinum.

the difference between diffusion kinetics at microelectrodes and macroelectrodes.

Under transient conditions, diffusion at planar electrodes has usually been approximated by semi-infinite linear diffusion, regardless of the electrode size. Cottrell (7), Laitinen and Kolthoff (8), and Laitinen (9) showed the constancy of the product of the current and the square root of the time under potentiostatic conditions. However, Vielstich and Delahay (10) pointed out the limitations of applying semi-infinite linear diffusion to small electrodes. Lorenz (11) reported that surface roughness on the order of the diffusion layer thickness increased the transition time during galvanostatic polarization. Although Laitinen and Kolthoff (8) attempted to verify the applicability of semi-infinite spherical diffusion to spherically shaped microelectrodes, convection effects precluded these experimental measurements. Bard (12) surmised that the increase in the chronopotentiometric transition time constant at long transition times is due to spherical diffusion and natural convection. In order to predict more accurately the current-time behavior of finite planar electrodes during chronoamperometric experiments, Lingane (13) expanded the chronoamperometric constant as a power series in terms of the reciprocal of the radius and neglected the second and higher order terms. This expression was almost identical to that obtained for semi-infinite spherical diffusion, the former differing only slightly from the latter in the numerical value of the coefficient of the first-order term. The separate contributions of spherical diffusion and convection could not be determined from Bard's (12) and Lingane's (13) results and, therefore, their dependence on the electrode size could not be ascertained.

As shown in this brief review, only a few studies have been reported on diffusion kinetics at microelectrodes under transient conditions in spite of the importance for transient studies of electrode processes. In this work, the effect of the electrode size on the diffusion kinetics has been studied under transient conditions where the time did not exceed 1 sec. In order to exclude the complication resulting from a slow charge transfer process, a highly reversible redox reaction, $I_3^- + 2e = 3I^-$, was examined.

Experimental

The test cell was a 3 liter Pyrex kettle jar and a specially constructed cover with nine ground glass joints for the positioning of a thermometer, a gas bubbler for deaeration, an auxiliary electrode, a reference electrode, and five test electrodes.

The reference electrode was platinum wire. This wire was placed inside the Luggin capillary. The end of the capillary was placed as close as possible to the test electrode in order to minimize the ohmic potential drop within the electrolyte between the test and reference electrodes. The counterelectrode was a large platinum foil.

The test electrodes were of reference grade platinum and had a plane, circular surface with diameters ranging from 1.27 to 0.0127 cm. The electrodes of small diameter, 0.058, 0.0254, 0.0127 cm, were prepared by sealing the platinum wire in a glass tube of 0.6 cm diameter. The glass tubing was then sanded and polished so that only the cross section of the wire was exposed. For larger diameter wires of 0.206 and 0.129 cm, the platinum wire was sealed in glass tubing with Apiezon wax. The wire was held in the glass tubing and the melted wax was sucked up into the tubing. The electrode was sanded and polished as before. Mercury was used to make contact between the platinum and the copper lead wire. For the electrodes of 1.27 and 0.635 cm diameter, a circular piece of platinum foil was glued onto the polished cross section of an iron rod with conductive epoxy cement. Then, shrinkable Teflon was fitted around the electrode and only the platinum surface was exposed. A holder for these electrodes was

constructed of Teflon rod. Electrical contact was made by a pressure-fitted copper wire.

The electrolyte was 1N potassium iodide containing various amounts of iodine, ranging from 0.1 to 0.001M (molar). The added iodine reacted with I^- to produce I_3^- forming the I_3^-/I^- redox couple (14, 15). Before each run, the electrolyte was deaerated with pre-purified nitrogen for approximately 3 hr.

The potential was controlled and generated with a high speed potentiostat and a mercury relay. The rise time of the potential step imposed on the system was less than 10 μ sec. The current was recorded with a high speed oscillograph (frequency response of 500 Hz).

Results

In this paper, the cathodic current is taken as a positive value. A decrease in current due to the diffusion of I_3^- after the imposition of a potential step was observed. Typical current variations with time are shown in Fig. 1. The current was the function of time (t), applied potential (E), and the concentration of I_3^- (C). As can be seen in Fig. 1, the current-time curve does not shift when E is negative enough. In order to examine only the diffusion process, attention was focused on this limiting current, i . The limiting current thus obtained is plotted vs. $1/\sqrt{t}$ in Fig. 2 and 3, for all electrode diameters at $C = 0.02M$. All plots show a linear relation in the range of 0.01–1 sec. While the plots intersect the origin, $1/\sqrt{t} = 0$, $i = 0$ for large diameter electrodes, they do not for the small diameter electrodes. The following relationship was obtained

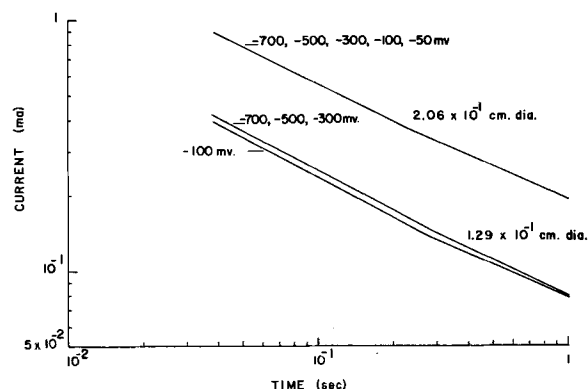


Fig. 1. Current variation with time

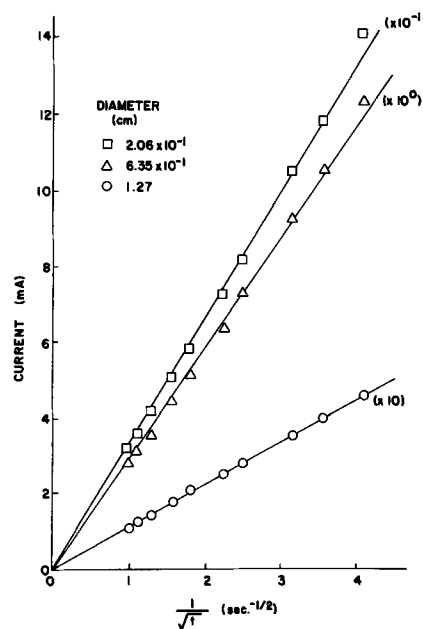


Fig. 2. Plots of current vs. $1/\sqrt{t}$ for relatively large electrodes

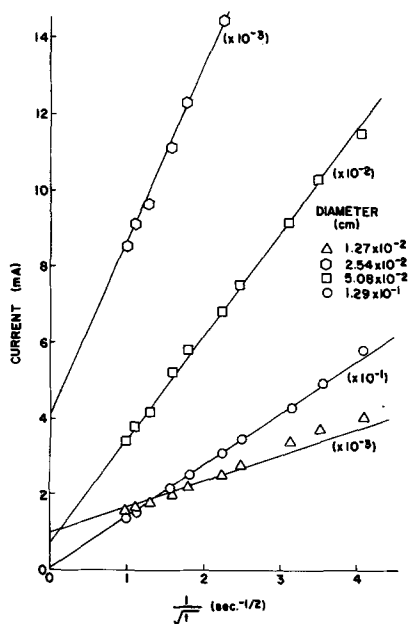


Fig. 3. Plots of current vs. $1/\sqrt{t}$ for relatively small electrodes

$$i = S(1/\sqrt{t} + f(d)) \quad [1]$$

where S is the slope of the plot and $f(d)$ is some function of the diameter. For electrodes of large diameters, $f(d)$ is zero. The slope, S , is plotted vs. the electrode diameter (d) on a log-log scale in Fig. 4. A linear relation with a slope 2 was obtained, i.e.

$$S = k_1 d^2 \quad [2a]$$

which can be rearranged to the form

$$S = k_1' (\pi/4) d^2 = k_1' A \quad [2b]$$

where A is the electrode area. The dependence of k_1' on C is shown in Fig. 5. The log of S/A is linearly related to the log of C with a slope of unity. Then, S can be expressed as

$$\frac{S}{A} = k_2 C \quad [3]$$

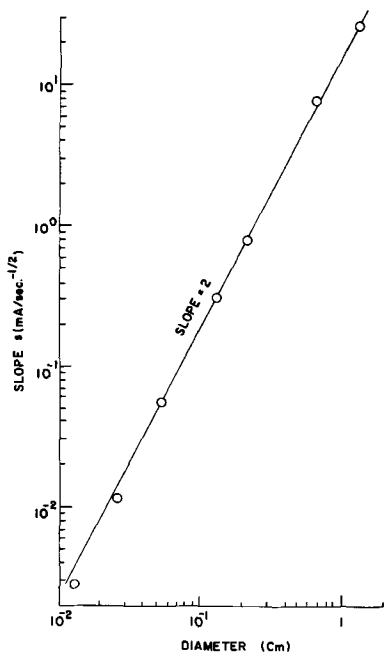


Fig. 4. Dependence of slope S on the electrode diameter

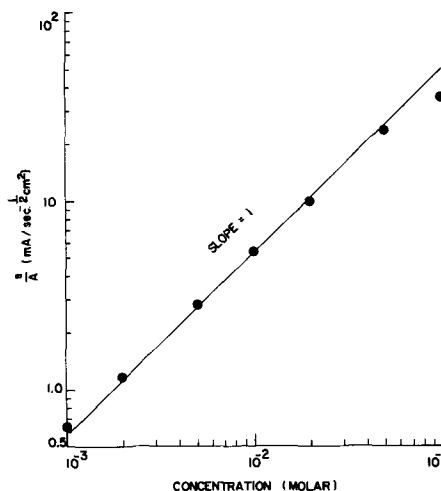


Fig. 5. Dependence of S/A on concentration

where k_2 is a constant determined experimentally ($534 \text{ A-cm-sec}^{1/2}/\text{mole}$) and is independent of C and d .

The current (i) can be extrapolated to $1/\sqrt{t} = 0$ to determine $f(d)$ as seen in Fig. 3. The extrapolated current (i_x) gives the relation

$$f(d) = i_x/S \quad [4]$$

A linear relation was obtained between i_x and d , as shown in Fig. 6, when the diameter is less than 0.129 cm , i.e.

$$i_x = k_3 d, \text{ for } d \leq 0.129 \text{ cm} \quad [5]$$

where k_3 is a function of C and independent of d . To determine the dependence of k_3 on C , $\log(i_x/d)$ is plotted vs. $\log C$ in Fig. 7. This plot gives a linear relationship with a slope of unity. Thus, a proportionality between k_3 and C was obtained and

$$i_x = k_4 d C \quad [6]$$

Equations [4] and [6] give

$$f(d) = k_4 d C / S, \text{ for } d \leq 0.129 \text{ cm} \quad [7]$$

where k_4 is a constant determined experimentally ($7.15 \text{ A-cm}^2/\text{mole}$) and is independent of d and C . Since $f(d)$ is zero for large electrode diameters, the cur-

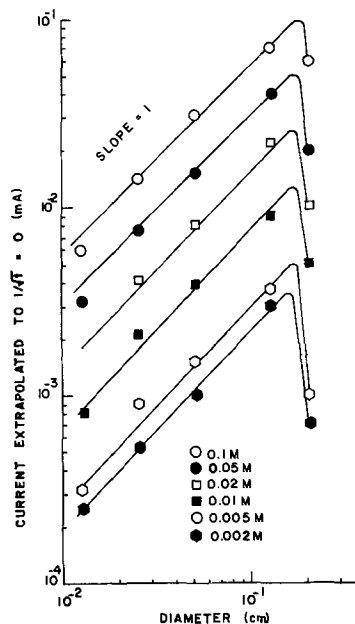
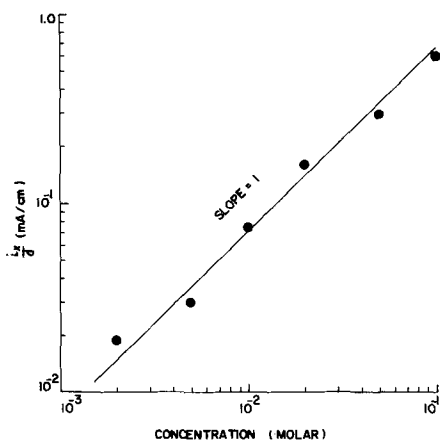


Fig. 6. Current extrapolated to $1/\sqrt{t} = 0$, i_x , vs. electrode diameter.

Fig. 7. Plots of i_x/d vs. concentration

rent (i) in Eq. [1] can be expressed empirically as

$$i = k_2 CA [1/\sqrt{t} + M(k_4/k_2)(d/A)] \quad [8]$$

where M is a function of the diameter and can have values between zero and one. The dependence of M on diameter is shown in Fig. 8. It was found that M decreased rather abruptly from unity to zero as the electrode diameter increased. This abrupt decrease occurred at about the electrode diameter of 0.2 cm.

Discussion

It is known that when a circular plane electrode is large and the polarization duration is short, mass transport at the electrode is controlled by semi-infinite linear diffusion. However, when the electrode dimension is small, mass transfer is approximated by semi-infinite spherical diffusion. The limiting current for a potential step is given by Eq. [9] for semi-infinite linear diffusion and by Eq. [10] for semi-infinite spherical diffusion (16)

$$i_{lin} = \frac{nFA\sqrt{DC}}{\sqrt{\pi}\sqrt{t}} \quad [9]$$

$$i_{sph} = \frac{nFA\sqrt{DC}}{\sqrt{\pi}} \left(\frac{1}{\sqrt{t}} + \frac{2\sqrt{D\pi}}{d} \right) \quad [10]$$

where n and F have their usual significance and A and D are the electrode area and the diffusion coefficient of I_3^- , respectively.

The current can be expressed generally for all electrode diameters examined in this study by introducing an empirical parameter M

$$i = \frac{nFA\sqrt{DC}}{\sqrt{\pi}} \left(\frac{1}{\sqrt{t}} + \frac{2M\sqrt{\pi D}}{d} \right) \quad [11]$$

In the case of $d \leq 0.1$ cm, the diffusion mode is semi-infinite spherical diffusion and $M = 1$. For $d > 0.3$ cm, $M = 0$ and semi-infinite linear diffusion is the controlling mode. The change from semi-infinite spherical to semi-infinite linear diffusion occurs around $d = 0.2$ cm. It is evident that when plane circular electrodes similar in size to those examined in this investigation are used, the change of the diffusion mode with the electrode dimensions is an important consideration.

Acknowledgment

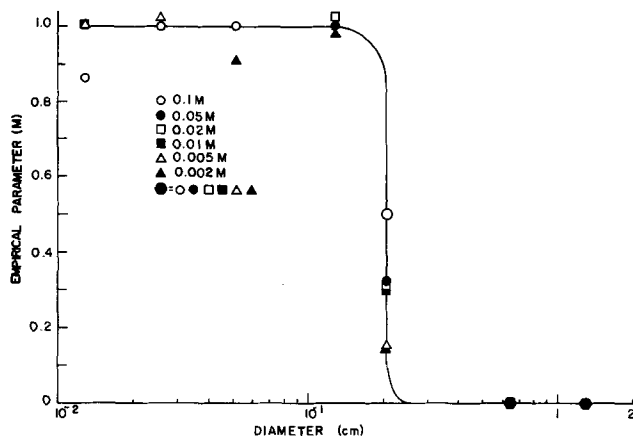
This work is part of the UCLA Engineering research program in Air Pollution.

Manuscript submitted Sept. 25, 1971; revised manuscript received Dec. 29, 1971.

Any discussion of this paper will appear in a Discussion Section to be published in the December 1972 JOURNAL.

REFERENCES

1. J. N. Agar, *Discussions Faraday Soc.*, No. 1, 26 (1947).
2. N. Ibl, *Electrochim. Acta*, **1**, 3 (1959).
3. P. A. Jacquet, *Nature*, **135**, 1076 (1935).
4. S. E. Beacom, *Plating*, **46**, 814 (1959).
5. C. Wagner, *This Journal*, **101**, 225 (1954).
6. I. M. Kolthoff and J. J. Lingane, "Polarography," 2nd ed., Vol. 1, p. 399, Interscience, New York (1952).
7. F. Cottrell, *Z. Phys. Chem.*, **42**, 385 (1902).
8. H. Laitinen and I. Kolthoff, *J. Am. Chem. Soc.*, **61**, 3344 (1939).
9. H. Laitinen, *Trans. Electrochem. Soc.*, **82**, 289 (1942).
10. W. Vielstich and P. Delahay, *J. Am. Chem. Soc.*, **79**, 1874 (1957).
11. W. Lorenz, *Z. Elektrochem.*, **59**, 730 (1955).
12. A. J. Bard, *Anal. Chem.*, **33**, 11 (1961).
13. Z. G. Soos and P. J. Lingane, *J. Phys. Chem.*, **68**, 3821 (1964); P. J. Lingane, *Anal. Chem.*, **36**, 1723 (1964).
14. J. Mellor, "A Comprehensive Treatise on Inorganic and Theoretical Chemistry," Vol. 2, p. 815, Longmans and Green Co., New York (1922).
15. J. Lingane, "Electroanalytical Chemistry," p. 141, Interscience Publishers, Inc., New York (1958).
16. P. Delahay, "New Instrumental Methods in Electrochemistry," Interscience Publishers, Inc., New York (1954).

Fig. 8. Variation of the empirical parameter M with electrode diameter.

Local Natural Convection Mass Transfer Measurements

J. R. Lloyd

University of Notre Dame, Notre Dame, Indiana 46556

and E. M. Sparrow and E. R. G. Eckert

University of Minnesota, Minneapolis, Minnesota 55455

ABSTRACT

Apparatus and experimental technique for measurements of local natural convection mass transfer on vertical and upward-facing inclined surfaces are described, and corresponding results are presented and discussed. The experiments were performed using the electrochemical technique, with Cu^{++} as the transferred ions and sulfuric acid as the supporting electrolyte. The objective of the research was to obtain highly local information. Two types of mass transfer probes were employed, the smaller of which were about $\frac{1}{4}$ mm in spanwise width, with a probe-to-probe spacing of $\frac{1}{20}$ mm. These miniature probes were used in the measurement of spanwise mass transfer variations encountered in the laminar-turbulent transition regime on inclined surfaces. Local laminar mass transfer results and instability Rayleigh numbers for vertical and inclined plates were measured by means of a set of small circular probes. All data were collected for limiting current operation, and the requisite concentration levels of Cu^{++} ions were examined and documented. In addition, the influence of cathode-to-anode orientation was investigated, as were the edge effects associated with the lateral edges of the test surface.

Electrochemical techniques have been used by numerous investigators in recent years to study mass transfer between a surface and a liquid environment, as witnessed, for instance, by a recently published summary paper by Mizushima (1). One of the attractive features of these techniques is the capability of obtaining local mass transfer results, that is, mass transfer results for a small region of the over-all surface being studied. The present concern with local measurements is motivated by the nature of the phenomenon being investigated. It has been shown by flow visualization studies (2) that for natural convection adjacent to an inclined upward-facing surface, the breakdown of the laminar regime is marked by the presence of a secondary flow. That is, superposed on the main streamwise flow, there are alternate regions of inflow and outflow distributed more or less periodically across the horizontal span of the surface. It would be expected that such an inflow-outflow pattern would give rise to a spanwise variation of surface mass transfer. The typical spanwise dimension of the inflow-outflow cells observed in this investigation is 1 mm. Therefore, to resolve the spanwise mass transfer distribution within a cell, several local measurements must be made within a span of 1 mm. Thus, it is necessary that the mass transfer probes be very small and, also, that they be very close together.

The instrumentation and experimental technique for performing highly localized measurements of the type discussed above is described here in detail. Also, representative spanwise mass transfer distributions are presented for the laminar-to-turbulent transition regime in natural convection flow on inclined surfaces.

Quite apart from the just-mentioned spanwise distributions, another type of local measurements was made which is appropriate to either the laminar or turbulent regimes. The instrumentation and technique for this measurement is also described. Local mass transfer results are presented for laminar natural convection flow on vertical and inclined surfaces. From these results, the Rayleigh number marking the breakdown of the laminar regime is identified.

A survey of the available literature failed to disclose local electrochemical mass transfer measurements characterized by probe sizes and by probe-to-probe proximities as small as those of the present investiga-

tion. Only in connection with wall shear stress measurements, where electrodes are embedded in an inert wall, have comparably small electrodes been employed (3). Representative prior studies, where either local or quasi-local electrochemical mass transfer measurements are reported, may be found in Ref. (4-6) for natural convection flow and in Ref. (7, 8) for forced convection flow.

Experimental Apparatus

An over-all schematic diagram of the experimental apparatus is pictured in Fig. 1. The electrochemical fluid, an aqueous solution of cupric sulfate and sulfuric acid, both reagent grade, was contained in a polyethylene tank ($61 \times 45.6 \times 45.6$ cm, length \times width \times height). The cupric ions play the role of the transferred ion and plate out on the cathode, thereby giving rise to concentration and density gradients in the fluid adjacent to the cathode. In turn, the density gradient creates a buoyancy force which causes the natural convection flow.

As seen in the figure, the main components of the apparatus included the cathode (which is the test surface), anode, reference electrode, circuitry, instrumentation, power source, and voltage control. These several components will now be described, starting with the test surface.

A front-face schematic of the test surface is shown in Fig. 2. As pictured therein, the test surface con-

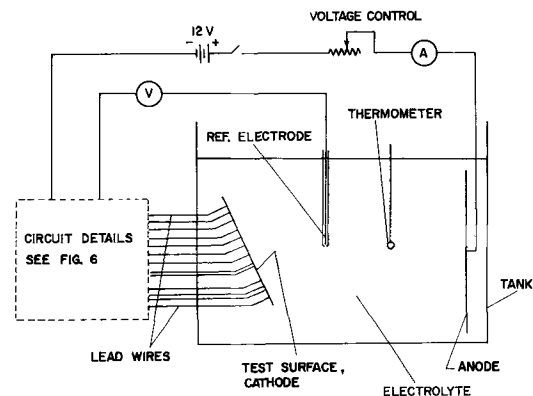


Fig. 1. Over-all schematic of the experimental apparatus

Key words: natural convection, inclined surface, mass transfer, limiting current.

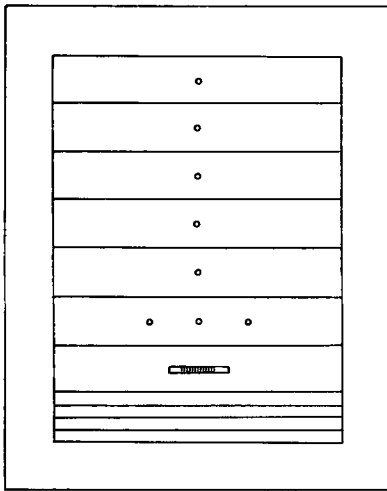


Fig. 2. Front-face view of the test surface

sisted of eleven individual segments set into an electrically passive framework. All segments were fabricated from nickel 200 and were 0.635 cm thick and 15.2 cm in spanwise width. The seven probe-bearing segments were 2.54 cm high, whereas the four uninstrumented segments, which served to vary the streamwise locations of the mass transfer probes, were 0.635 cm in height. The positions of the segments could be interchanged at will, so that their arrangement in Fig. 2 is only for illustration. The active surface had a streamwise height of 20.3 cm and a spanwise width of 15.2 cm. The width of the surrounding Teflon frame was 2.54 cm.

Six of the segments were instrumented with small circular electrodes (0.343 cm diameter) which served as local mass transfer probes for flow conditions characterized by spanwise uniformity (*i.e.*, either laminar or turbulent flow). The circular probes were situated at the centers of the respective host segments and, in one case, two supplementary probes were installed 2.54 cm to either side of the center. The installation of the circular probes is illustrated in Fig. 3, which is a schematic view of the back face of one of the host bars. The probe was electrically insulated from the host bar by a 0.0127 cm annular gap filled with epoxy. The back side of the probe and the attached end of the current-carrying lead wire were embedded in epoxy. Glyptal insulating paint was applied to the epoxy and to the entire back face of the host bar.

The seventh instrumented segment contained an ensemble of 55 very small probes whose function was to measure the spanwise mass transfer distribution in the laminar-turbulent transition regime on inclined upward-facing surfaces. The probe ensemble consisted of successive sheets of nickel 200 and of polyethylene insulation. Each probe had a spanwise dimension of 0.0254 cm, with a spacing between probes (*i.e.*, thickness of the polyethylene foil) of 0.0051 cm. In the streamwise direction, the probes were 0.318 cm in length. The end pieces of the ensemble were also of nickel 200, 0.635 cm thick, and cut in the same shape as the probes. The ensemble was held together by two nickel screws which were insulated from the probes by Teflon tubing. A photograph of the probe section is given in Fig. 4, wherein the active sensing surface is along the bottom-most edge.

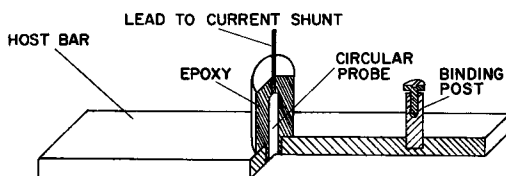


Fig. 3. Diagram showing installation of circular probes

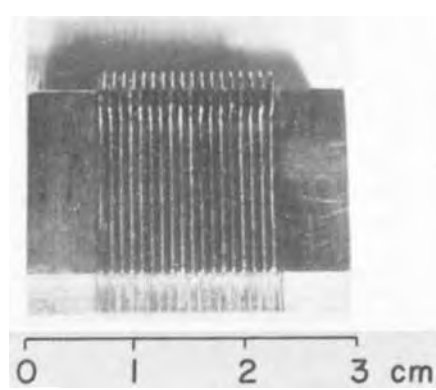


Fig. 4. Photograph of the ensemble of miniature probes

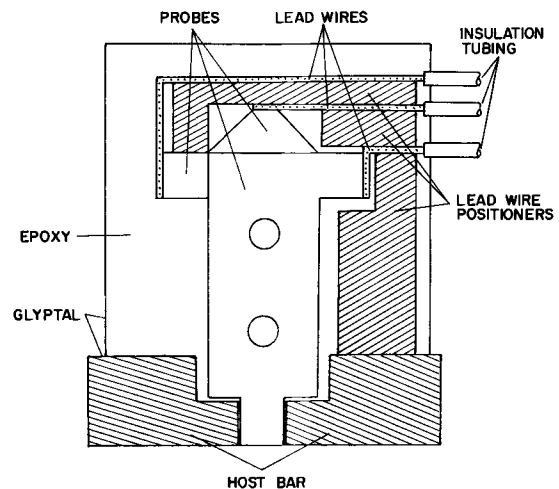


Fig. 5. Diagram showing installation of miniature probes

The assembly of the probe section and its installation in the host bar are illustrated in Fig. 5. A rectangular hole slightly larger than the face of the probe section was machined into the bar, with a clearance of about 0.02 cm being maintained. Glyptal insulating paint was poured into the gap and a coating of epoxy applied to the face of the probe section and on the hardened Glyptal filler. The hardened epoxy was carefully finished with grade 600 wet or dry Tri-M-ite paper and a fine hone, exposing the faces of all 55 probes. The probe section was held in place by a bracket mounted on the back of the host bar.

Lead wires were soldered to the probes and segregated from each other by positioners as shown in Fig. 5, the lead wires being affixed to the positioners with epoxy. The figure shows the different positions of lead wire attachment for three successive probes. The entire back side of the probe section, the positioners, and the ends of the lead wires were painted with Glyptal, embedded in epoxy, and painted again with Glyptal to ensure that no unaccounted areas were exposed to the electrolyte solution.

Each one of the eleven segments comprising the test surface was equipped with a binding post on its back face to facilitate connection to the external circuit. The posts and wire were of nickel 200. Glyptal insulating paint was applied to the binding posts, and plastic tape was wrapped around them to retard corrosion of the area of electrical contact.

The segmented test surface was housed in a Teflon frame which has already been mentioned in connection with Fig. 1. A groove was machined along the inner circumference of the frame to receive the segments, so that the exposed face of the test surface and of the frame were in the same plane. The segments themselves were carefully aligned to ensure that they presented a smooth, continuous surface to the flow, and

the alignment, once attained, was fixed by electrically isolated, thumb-tightened set screws. The Teflon frame was supported by a nickel-plated stand, which was painted with Glyptal to make it electrically and chemically neutral. The stand facilitated the positioning of the test surface at various angles of inclination. Typically, the test surface was situated about 4 cm above the floor of the tank, and its topmost edge was 15 to 20 cm beneath the surface of the electrochemical bath.

The anode was a 40-cm square copper sheet, 0.08 cm thick. For the data runs, the anode was positioned as indicated in Fig. 1. However, a number of preliminary runs were made to explore the influence of anode position on the mass transfer results, and the findings of these runs are reported in a later part of the paper.

A reference electrode was placed in the electrolyte solution to facilitate the measurement of the voltage between the fluid bulk and the test surface. The reference electrode was a 0.1 cm diameter copper wire housed in a Teflon tube. A small hole at the bottom of the tube permitted the electrolyte to contact the electrode. The reference electrode was typically positioned to the side of the test surface (about 5 cm away) and at its half-height.

External Circuitry and Instrumentation

A schematic diagram of the electric circuitry is presented in Fig. 6. A 12V automotive storage battery, supplemented by a rheostat and a trimming pot, served as the power supply. The cathode voltage was measured with a 0-1.5V, 1%, d-c Simpson panel meter. A calibrated Weston Model 901 d-c ammeter served to measure the over-all current flow through the electrolyte.

The segments which make up the cathode were tied together electrically, so that they were all of the same potential. Adjacent segments were actually in contact, but gaps are indicated in the figure in order to delineate the separate segments. A current shunt was incorporated into the circuit for each of the probes. The current shunts for the eight circular probes were 15-ohm calibrated precision resistors. For the ensemble of 55 miniature probes, 55-1%, 174-ohm calibrated precision resistors served as the current shunts.

For the steady mass transfer rates encountered under laminar flow conditions, the voltage drops across the current shunts were measured with a Leeds and Northrup K-3 potentiometer, supplemented by a low contact resistance, 24-position thermocouple selector switch. For the unsteady mass transfer rates that are characteristic of nonlaminar flows, the shunt voltage drops were read with a Dymec Digital Voltmeter. This

instrument could be programmed to read repetitively the output of a single probe at preselected intervals of time. Alternatively, it could be programmed to read successively the outputs of as many as 24 probes, with the sweeping of the 24 probes being repeated as many times as desired. To accommodate the 55 probes of the ensemble to the Dymec, they were subdivided into two sets of 24 and one set of seven. About 45 sec were required to disconnect one set and to connect another.

Experimental Technique

During the course of each data run, copper was plated out on the test surface. Removal of deposited copper and refinishing of the surface was a necessary aspect of the experimental procedure. The importance of removing the deposited copper is heightened when local mass transfer probes are used, as in the present experiments. If not removed, a build-up of deposited copper could eventually bridge over the insulation between a probe and its host bar or between adjacent probes. Such a bridging over would cause the local probe to become inoperative.

At the conclusion of each data run, the cathode and anode were water washed and carefully dried with soft paper towels, and the mass transfer probes were checked for shorts. Prior to the start of a new data run, the electrodes were painstakingly resurfaced. The resurfacing operations were performed in such a way as to ensure that the surfaces of the probes and the host bars were coplanar. First, the test surface was wiped clean of any airborne particles. Then, grade 600 wet or dry Tri-M-ite paper was used to refinish all parts of the test surface except for the ensemble of 55 miniature probes, for which a wet, very fine hone was used (to avoid shorts between adjacent probes). Immediately after the refinishing, methanol technical was freely applied to wash away small particles of copper sanding dust. Next, the epoxy insulation between the probes and their host bars was cleaned with a stiff bristle brush and methanol technical, after which all parts of the test surface were washed again with liberal amounts of methanol technical and wiped with paper gauze pads. Finally, all probes were checked to verify the absence of shorts.

The anode was also subjected to a sequence of resurfacing operations similar to those for the test surface, with grade 180 wet or dry paper being employed in the refinishing of both sides of the anode.

Prior to the initiation of the mass transfer process, the electrochemical solution was stirred to ensure uniformity of concentration and temperature, and a waiting period was allowed for the decay of motions due to stirring. No data were collected until the starting transient of the system had died away.

The data acquisition procedure for laminar and for nonlaminar conditions differed because the mass transfer rates were, respectively, steady and unsteady. Only the unsteady situation merits discussion here. The signal from any one of the circular probes was read by the Dymec Digital Voltmeter at intervals of 0.2 to 0.3 sec for a period of 3 min to determine timewise variations in the local rate of mass transfer. Alternatively, the outputs of the eight circular probes were read in succession, with the eight-probe sweep being repeated again and again. Local time averages were evaluated from instantaneous data collected from both of these measurement procedures. For the ensemble of miniature probes, the signals from the first 24 probes were read successively by the Dymec in a period of about 7 sec, and the scanning of this set of probes was repeated until about 1½ min had elapsed. Then, the second set of 24 probes was connected to the Dymec and readings were taken for 1½ min, and so forth.

The composition of the bulk solution was obtained by sampling. The concentrations of the copper ions and sulfuric acid were determined, respectively, by spectrometric and titration methods, described in Ref. (9) and (10), respectively. Vertical concentration

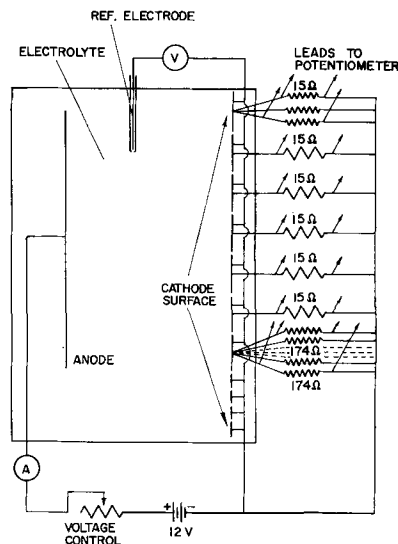


Fig. 6. Electric circuitry diagram

gradients were monitored, and data acquisition was restricted to cases where the gradient was less than 0.00007M (molar) concentration of copper ions per centimeter. No change in the mixed mean bulk concentration was detected during the course of a data run.

Limiting Current Conditions

To facilitate the evaluation of mass transfer coefficients, all final data were taken for the limiting current operating condition. This condition corresponds to a zero concentration of transferred ion (i.e., copper) at the cathode, thereby eliminating the need for concentration measurements at the test surface. Limiting current operation can be identified by a plateau in a graph of cathode current vs. cathode voltage (measured with respect to the reference electrode).

The attainment of a limiting current plateau is favored by higher concentrations of copper ions in the fluid bulk. On the other hand, the rate at which copper plates out on the test surface is also increased with higher bulk concentrations. Such higher plating rates can lead to short circuiting of the mass transfer probes. Furthermore, high plating rates enhance the rapidity at which the surface of the plated copper may become roughened, thereby causing a change in the effective surface area (11). It is relevant, therefore, to perform the experiments at the lowest bulk copper ion concentrations which are compatible with the existence of a limiting current plateau.

Figures 7 and 8 show typical current-voltage curves. The bulk copper ion concentration ranged from 0.0066 to 0.0825M for these test conditions, while the sulfuric acid concentration was about 1.5M for all cases. It is evident that limiting current plateaus do not exist for the 0.0066 and 0.0113M concentrations. On the other hand, the curves for the 0.0375 and 0.0825M concentrations indicate limiting current operation. The absence of limiting current plateaus at low copper ion concentrations has already been noted by Fenech and

Tobias (5). The cause of this behavior is not completely understood at the present.

On the basis of Fig. 7 and 8 and of other such current-voltage curves, it was established that limiting current operation could be attained for bulk copper ion concentrations above 0.03M. To ensure that all final data actually corresponded to limiting current operation, a current voltage curve such as those of Fig. 7 and 8 was mapped out for each data run. A sequence of six or seven steps was taken to define limiting current conditions. At each step, the current was monitored with a strip chart recorder, and a steady reading was approached before advancing to the next step. The length of the data acquisition period under steady limiting-current conditions varied with the type of flow observed; for laminar flow approximately 1½ min, for turbulent flow approximately 3 min, and to monitor two sets of local spanwise readings about 4 min.

Results and Discussion

Owing to the fact that all data were taken for limiting current operation and in the presence of excess supporting electrolyte, the local mass transfer coefficient k_x can be evaluated as

$$k_x = i/nFc_o \quad [1]$$

where i and c_o , respectively, denote the measured values of the current density and the concentration of copper ions in the fluid bulk. The quantities n and F are the valence of the copper ions and the Faraday number. A dimensionless representation for k_x is provided by the Sherwood number Sh_x , which is defined as

$$Sh_x = k_x x/D \quad [2]$$

in which x is the streamwise distance along the test surface, with $x = 0$ corresponding to the leading edge of the active surface.

The other dimensionless grouping relevant to the natural convection process is the Rayleigh number. In constructing the Rayleigh number appropriate to an inclined test surface, we use the component of the body force parallel to the surface (i.e., $g \cos \theta$) and indicate the presence of the inclination angle θ by the notation Ra_θ . Then, the local Rayleigh number is given by

$$Ra_{\theta,x} = [\rho g \cos \theta (\rho_o - \rho_w) x^3 / \mu^2] Sc \quad [3]$$

where Sc denotes the Schmidt number $\mu/\rho D$, and ρ_o and ρ_w are the densities in the fluid bulk and at the surface. The quantities D , ρ , and μ appearing in Eq. [2] and [3] were evaluated at the average of the concentrations at the wall and in the bulk. Typically, the wall-to-bulk fluid property variations were on the order of 1%. Detailed information about the evaluation of the fluid properties is given in Ref. (12). The property evaluations were based on data given in Ref. (5) and in Ref. (19-24).

An initial set of experiments was performed to explore the effect of cathode-to-anode orientation. Another objective of this set of experiments was to examine the influence of edge effects associated with the lateral edges of the test surface. The experiments in question were performed for laminar flow conditions and with the test surface vertical. However, instead of the configuration pictured in Fig. 2, the test surface assembly was turned through 90 degrees, so that the main line of circular probes was situated along a horizontal, each probe being at the same distance from the leading edge. Five electrically active, instrumented segments were employed, each with a central circular probe, plus Plexiglas spacer bars which were used to segregate the active segments. The active segments and spacers were arranged so that, proceeding along the horizontal span of the test surface, one encounters the 2.54 cm Teflon frame, 10.16 cm of active surface, a 2.54 cm spacer, 2.54 cm of active surface, a 5.08 cm spacer, and the Teflon frame.

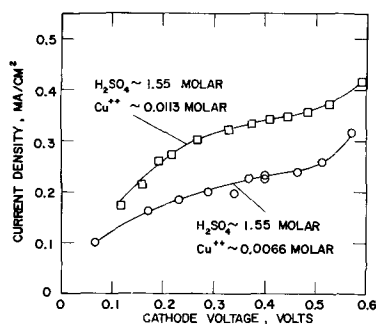


Fig. 7. Current-voltage curves at low Cu^{++} concentrations

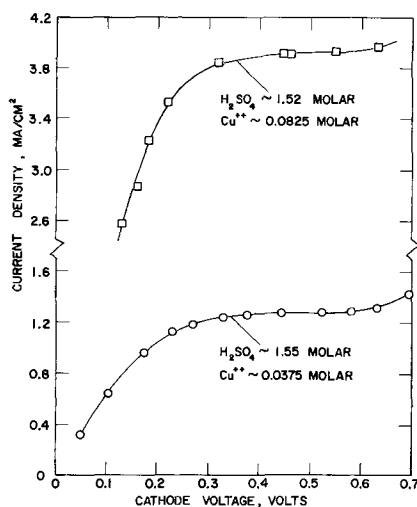


Fig. 8. Current-voltage curves showing limiting current plateaus

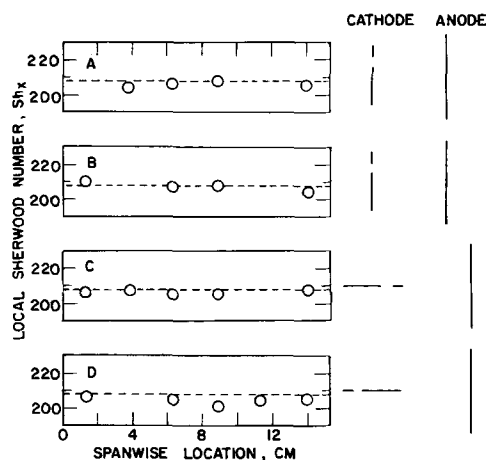


Fig. 9. Spanwise uniformity tests for laminar flow adjacent to a vertical plate.

Local Sherwood number results from four experimental runs, performed over a period of several days, are shown in Fig. 9. The dashed line appearing in each graph represents the prediction of laminar vertical plate theory corresponding to $Sc = 2000$ (13)

$$Sh_x/0.499 Ra_x^{1/4} = 1 \quad [4]$$

Adjacent to the graph for each run is a plan-view schematic indicating the positioning of the cathode and the anode. The line representing the cathode denotes the active portions of the surface, and the break in the line denotes a spacer. In runs A and B, the cathode and anode were parallel, whereas in runs C and D they were at right angles. Owing to the shorting out of a mass transfer probe, only four data points appear in the graphs for runs A and B.

Inspection of the figure indicates that the mass transfer results show no systematic variation with spanwise location, regardless of the position of the anode or of the proximity of a probe to the lateral edges of the test surface. Furthermore, the agreement of the data with laminar theory is excellent, the average deviation being about 1.6%. These findings indicate that for the conditions of the present experiments, cathode-to-anode orientation and edge effects have a negligible influence on the mass transfer results. Furthermore, the excellent agreement with theory lends confidence in the experimental technique, instrumentation, and thermophysical properties used in the data reduction.

For all subsequent experimental runs, the test surface was situated in its original configuration, and the anode was positioned parallel to the cathode and as far away as possible.

A second series of experiments was performed to determine local laminar mass transfer results for vertical and inclined surfaces and, in addition, to examine the conditions marking the breakdown of the laminar regime. The circular mass transfer probes were used in these experiments. The results are plotted in Fig. 10 with $Sh_x/0.499 Ra_{\theta,x}^{1/4}$ on the ordinate and $Ra_{\theta,x}$ on the abscissa. The motivation for the form of the ordinate variable stems from the analytical prediction for laminar natural convection mass transfer on a vertical plate, Eq. [4], which, when generalized by replacing g with $g \cos \theta$, becomes

$$Sh_x/0.499 Ra_{\theta,x}^{1/4} = 1 \quad [5]$$

Equation [5] corresponds to $Sc = 2000$, which is the typical Schmidt number of the experiments. In view of Eq. [5] and if laminar theory is obeyed, the data, when plotted using the coordinates of Fig. 10, should fall on a horizontal line having an ordinate value of unity. A particular advantage of such a presentation is that deviations from the laminar line are readily

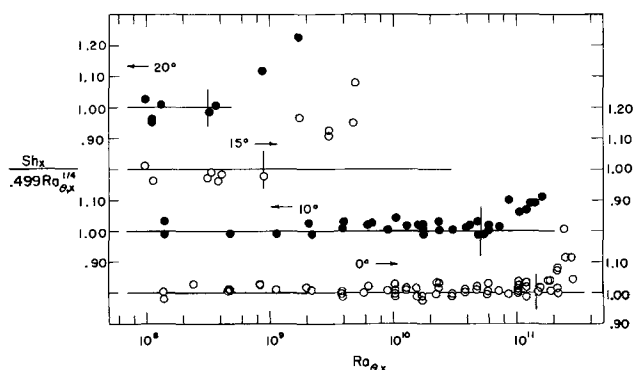


Fig. 10. Local laminar mass transfer results on vertical and inclined surfaces.

observable, thereby facilitating the identification of the onset of laminar-turbulent transition.

Results for surface inclination angles, relative to the vertical, of 0, 10, 15, and 20 degrees are plotted in Fig. 10. The data for each inclination angle are referred to a separate ordinate scale, as designated by the arrows. Results for inclination angles greater than 20 degrees are not shown in the figure since, for such angles, the flow at the lowermost probe was not laminar.

Inspection of Fig. 10 shows excellent agreement between the laminar data and the analytical prediction expressed by Eq. [5], adding further confidence in the experimental technique, instrumentation, and thermophysical properties. For the inclination angles of 0 and 10 degrees, the experimental results are generally within 3% of the prediction in the laminar range. At the 15 and 20 degree inclination angles, where there are fewer laminar data, the agreement is within 4%.

The present local mass transfer results for the vertical plate, when integrated over a streamwise length L , yield $Sh_L = 0.665 Ra_L^{1/4}$, which is in excellent agreement with the over-all measurements of Wilke, Tobias, and Eisenberg (14). On the other hand, the over-all measurements of Fouad and Ahmed (15) on vertical and inclined plates appear to lie outside the laminar regime, so that no comparisons are possible.

Next, attention may be turned to the onset of laminar-turbulent transition. One way of identifying the onset of transition is from the systematic upward departure of the data, as plotted in Fig. 10, from the horizontal lines which correspond to laminar flow. A second indication is given by the measurements of current flow. For strictly laminar conditions, the current readings were very steady. However, for Rayleigh numbers just below those at which data lift-off occurred, small fluctuations in the readings were observed. The Rayleigh numbers at which these fluctuations were first noted are indicated by short vertical lines for each angle of inclination. These Rayleigh numbers are regarded here as marking the onset of transition and are listed in Table I.

The table indicates that the transition Rayleigh number decreases with increasing angle of inclination. The drop-off is especially sharp between 10 and 20 degrees, and this might well be due to the change in the nature of the laminar instability as observed via flow visualization (16).

The transition Rayleigh numbers of Table I, which correspond to mass transfer at $Sc = 2000$, do not corre-

Table I. Rayleigh numbers at the onset of transition

θ (degrees)	$Ra_{\theta,x}$
0	1.5×10^{11}
10	5.0×10^{10}
15	9.1×10^9
20	3.5×10^9

late too well with those encountered in heat transfer experiments at Prandtl numbers in the range 0.7-5 (16). (The Schmidt and Prandtl numbers play analogous roles in the mass and heat transfer processes.) In particular, at inclination angles of 0 and 10 degrees, the $Ra_{\theta,x}$ of Table I are substantially higher than the available transition values from heat transfer studies. Thus, the Rayleigh number might not, in itself, be a sufficient criterion for transition, and there might be a separate dependence on the Schmidt (or Prandtl) number. This possibility has already been suggested by Fouad and Ibl (17). Also, it is quite possible that the natural disturbances in the fluid environment may be smaller in the mass transfer case than in the heat transfer case, thereby favoring a later transition in the former.

The transition Rayleigh number of Table I for the vertical plate falls in the range encountered in other electrochemical mass transfer experiments; however, as noted in Ref. (18), there is a substantial spread in the results from different investigations.

The last set of experiments to be reported here are those in which the array of miniature probes was used to measure spanwise mass transfer distributions on inclined surfaces in the laminar-turbulent transition regime. Some preliminary experiments for laminar flow adjacent to a vertical surface gave data which agreed very well with the analytical predictions. The deviations were only a few per cent, and this might well have been due to uncertainties in the visual determination of the electrically active surface area of the miniature probes.

Representative transition regime results for inclined surfaces are pictured in Fig. 11, which is for an inclination angle of 30 degrees relative to the vertical. The figure shows instantaneous spanwise mass transfer distributions. The ordinate is the current density, which is directly proportional to the mass transfer rate. The abscissa is the spanwise location, measured relative to the first probe in the ensemble. Data from probes 1 through 24 are plotted in the left-hand part of the figure, while data from probes 25 through 48 are shown in the right-hand part. To provide a clearer picture, dashed lines have been faired through the points for a given instant of time.

The instantaneous distributions presented in Fig. 11 were constructed from cross plots of the data collected from the successive sweeps of the probe ensemble. The time lapses between the successive instantaneous distributions are indicated in the figure, as is the Rayleigh number.

From the figure, it is seen that the instantaneous mass transfer rate varies in an oscillatory manner across the span of the plate. The amplitude of the variation is a substantial fraction of the spanwise

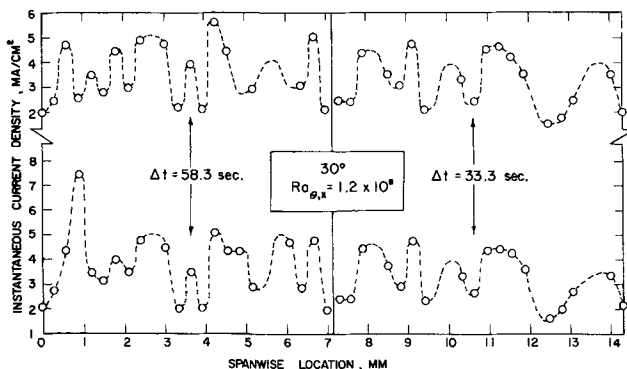


Fig. 11. Instantaneous spanwise mass transfer distributions in the laminar-turbulent transition regime.

average. The distance between adjacent peaks and valleys is on the order of 1 mm. Results similar to Fig. 11, but for other inclination angles, are available in Ref. (12).

Concluding Remarks

The miniature probes employed in the present experiments appear to have been equal to the task of resolving the spanwise variations encountered in the transition regime on inclined surfaces. The spanwise dimensions of the probes and of the insulation between the probes were the smallest that could be fabricated consistent with the avoidance of short circuits in the probe assembly prior to its use in the electrochemical solution. During the course of the experiments, the sulfuric acid in the electrochemical solution attacked the epoxy insulation, ultimately causing short circuiting of adjacent probes.

It is clear from Fig. 11 that had larger probes and/or greater probe-to-probe separation distances been employed, an accurate picture of the spanwise variations would not have been obtained.

Manuscript submitted Aug. 13, 1971; revised manuscript received Jan. 11, 1972.

Any discussion of this paper will appear in a Discussion Section to be published in the December 1972 JOURNAL.

REFERENCES

1. T. Mizushima in, "Advances in Heat Transfer," Vol. 7, T. F. Irvine and J. P. Hartnett, Editors, Academic Press, New York (1971).
2. E. M. Sparrow and R. B. Husar, *J. Fluid Mech.*, **37**, 251 (1969).
3. J. S. Son and T. J. Hanratty, *ibid.*, **35**, 353 (1969).
4. C. Wagner, *This Journal*, **95**, 161 (1949).
5. E. J. Fenech and C. W. Tobias, *Electrochim. Acta*, **2**, 311 (1960).
6. G. Schütz, *Int. J. Heat Mass Transfer*, **6**, 873 (1963).
7. A. Iribarne, A. O. Gosman, and D. B. Spalding, *ibid.*, **10**, 1661 (1967).
8. T. Mizushima, *op. cit.*, pp. 128-132 and 135-136.
9. E. B. Sandell, "Colorimetric Determination of Traces of Metals," Interscience Publishers, New York (1950).
10. I. M. Kolthoff and E. B. Sandell, "Textbook of Qualitative Inorganic Analysis," Macmillan, New York (1965).
11. N. Ibl and J. N. Schadegg, *This Journal*, **114**, 54 (1967).
12. J. R. Lloyd, "Laminar, Transition, and Turbulent Natural Convection Adjacent to Vertical and Upward Facing Inclined Surfaces," Ph.D. Thesis, Department of Mechanical Engineering, University of Minnesota (1971).
13. A. J. Ede in, "Advances in Heat Transfer," Vol. 4, J. P. Hartnett and T. F. Irvine, Editors, Academic Press, New York (1967).
14. C. R. Wilke, C. W. Tobias, and M. Eisenberg, *Chem. Eng. Prog.*, **49**, 663 (1953).
15. M. G. Fouad and A. M. Ahmed, *Electrochim. Acta*, **14**, 651 (1969).
16. J. R. Lloyd and E. M. Sparrow, *J. Fluid Mech.*, **42**, 465 (1970).
17. M. G. Fouad and N. Ibl, *Electrochim. Acta*, **3**, 233 (1960).
18. J. Selman and J. Newman, *This Journal*, **118**, 1070 (1971).
19. M. Eisenberg, C. W. Tobias, and C. R. Wilke, *ibid.*, **103**, 413 (1956).
20. G. W. Vinal and D. N. Craig, *J. Res. Nat. Bur. Std.*, **10**, 781 (1933).
21. A. F. W. Cole and A. R. Gordon, *J. Phys. Chem.*, **40**, 733 (1935).
22. W. A. James, E. A. Hollingshead, and A. R. Gordon, *J. Chem. Phys.*, **7**, 89 (1939).
23. E. A. Hollingshead and A. R. Gordon, *ibid.*, **8**, 423 (1940).
24. Landolt-Bornstein, "Physikalisch-Chemische Tabellen," 5 Auflage, **1**, 248 and 397 (1936).

Throwing Power Measurements during High Rate Nickel Dissolution under Active and Transpassive Conditions

Dieter Landolt*

Energy and Kinetics Department,
School of Engineering and Applied Science, University of California, Los Angeles, California 90024

ABSTRACT

Throwing power measurements for anodic dissolution of nickel under electrochemical machining conditions were performed in a flow channel apparatus. Acidified 1M NaCl and neutral 1M NaClO₃ solutions were chosen as examples of a nonpassivating and a passivating electrolyte. Anode and cathode potential measurements and current efficiency determinations were used for the interpretation of measured throwing power data. Current distribution at high current densities was little affected by passivation. The lower throwing power found for the passivating NaClO₃ electrolyte compared to the nonpassivating NaCl electrolyte was therefore solely due to a different dependency of dissolution efficiency on current density.

Throwing power is a concept used by electroplaters to describe the ability of a bath to yield macroscopically uniform deposits. Throwing power is usually determined experimentally in a Haring Blum cell (1) by measuring the weight change of two equipotential cathodes located at different distances from a central anode. Several empirical formulas are in use for calculating a numerical value of throwing power from such measurements. The concept of throwing power can also be applied to electrochemical machining (ECM) for characterizing the degree of "overcut" or "stray cutting" occurring during a machining operation with a given electrolyte. A low value of throwing power is desirable in ECM because "overcut" can be reduced by restricting anodic dissolution to the immediate vicinity of the cathodic tool. In analogy to the electroplating situation, the experimental determination of ECM throwing power may include the measurement of the weight loss of two equipotential anodes located at different distance from a central cathode. Such measurements have recently been reported by Brook and Iqbal (2), but their data have been criticized by Chin and Wallace (3). The latter authors propose a different experimental method based on the assumption that a logarithmic relationship between weight loss ratio and length ratio exists.

It has been mentioned in the literature that better dimensional accuracy can be obtained in ECM if passivating electrolytes such as sodium chlorate are employed (4, 5), but few pertinent data have been given so far to explain this behavior. The present study was undertaken with the aim to investigate the difference in ECM throwing power between a nonpassivating and a passivating electrolyte and to relate the measured throwing power to the more fundamental parameters, current distribution and dissolution efficiency. For this purpose weight loss determinations and electrode potential measurements for anodic dissolution of nickel were carried out with well-defined cell geometry under carefully controlled experimental conditions. Acidified sodium chloride and neutral sodium chlorate solutions were chosen as examples of a nonpassivating and a passivating electrolyte, respectively. The metal-electrolyte combinations were chosen because of their technological interest and because their electrochemical behavior had been studied previously in this laboratory. Separate experiments performed on a technical ECM machine suggested that general conclusions based on the behavior of nickel in these two electrolytes ought to be applicable to the machining of steel also (6).

Experimental

Apparatus and experimental method.—In the present study it was necessary to measure dissolution rates, electrode potentials, and throwing power under identical, well-defined conditions. Because this is difficult to accomplish in a Haring Blum type cell involving the simultaneous dissolution of two anodes, it was considered more suitable to perform subsequent experiments with a single anode at varying gap width while keeping cell voltage and temperature constant. For that purpose a flow channel cell with fixed electrodes was used in which the distance between anode and cathode was given by the thickness of a Teflon spacer inserted between two PVC cell blocks. A detailed description of the cell and the apparatus which included a discontinuously driven piston pump and a 2 liter electrolyte storage flask has been given elsewhere (7). The flow channel employed was 0.317 cm wide and 0.0534, 0.140, or 0.267 cm high. The distance between fluid inlet and upper edge of the electrodes was 7 cm. At the smallest gap width of 0.0534 cm this corresponded to 77 hydraulic diameters, sufficient to establish fully developed velocity profiles at the electrodes. At larger gap width the velocity profiles at the electrodes were not fully developed, but the conclusions of the present study are not affected by this fact.

The 0.317 cm wide and 1.02 cm long electrodes were made of nickel 200 cast into a PVC holder. Before each measurement the anodes were ground to a 400 carborundum surface finish and washed with detergent. To maintain geometry, the duration of the experiments was kept short. The maximum amount of dissolved material in any experiment corresponded to an average depth of dissolution of 69×10^{-4} cm or 13% of the smallest gap width. Length ratios needed in throwing power calculations were not corrected for this small change. All experiments were conducted at a constant volume flow rate of 16.9 ml/sec. At the smallest gap width this corresponded to a linear velocity of 1000 cm/sec. Temperature in all experiments was $25.5^\circ \pm 0.5^\circ\text{C}$. Analytical grade chemicals and distilled water were used. Special care was taken to avoid the presence of chloride ion in the NaClO₃ solution. Tests with AgNO₃ indicated that the chloride ion concentration in these solutions was below the detection limit of 10^{-4} moles/liter. The apparatus did not contain any metallic parts in contact with the solution, thus eliminating possible contamination of the solution during experiments. Effects of gas evolution and electrolyte heating on measured throwing power data were eliminated by restricting the current density to values below 15 A/cm² (8). This current den-

* Electrochemical Society Active Member.

Key words: electrochemical machining, throwing power, transpassive dissolution, nickel, sodium chlorate.

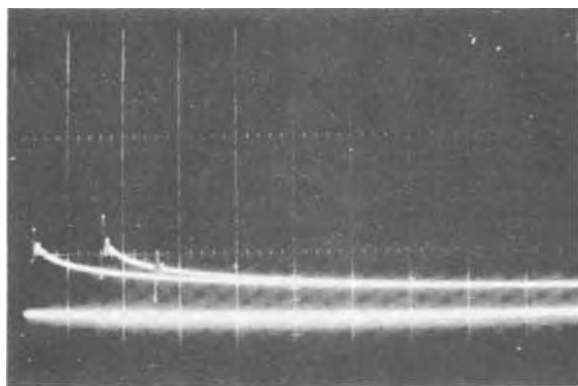


Fig. 1. Anodic potential decay transients measured in 0.9M NaCl + 0.1M HCl. Flow velocity 1000 cm/sec; potential scale 0.2 V/division; time scale 50 μ sec/division; current densities 3.6 A/cm² (left), 6.5 A/cm² (right). Horizontal line = open circuit potential.

sity is somewhat low for practical ECM, but is significantly higher than current densities used in conventional electrolysis. The experiments were therefore expected to provide a valid insight into the factors determining throwing power in high rate metal dissolution.

Throwing power measurements.—At first current vs. cell voltage curves were determined by applying a constant voltage to the cell from a constant voltage/constant current power supply¹ and recording the resulting current as a function of time on a strip chart recorder.² The same procedure was then used for throwing power measurements, except that in addition the time of the experiment was measured with a stopwatch and the total charge passed was calculated by integration of the current trace. In all experiments the anode was ground on 400 carborundum, rinsed, and dried. It was then weighed on an analytical balance to 0.1 mg accuracy and inserted into the cell. After the experiment it was quickly removed, rinsed, dried, and reweighed.

In order to compute throwing power data from separate weight loss measurements performed at different gap width voltage, temperature and time have to be identical. In the present experiments, the amount of material dissolved at the smallest gap width had to be small to preserve geometry (see above). Keeping the experimental time the same in all experiments would therefore have resulted in even smaller amounts being dissolved at the lower currents corresponding to larger gap width. To circumvent this problem, the experiments at larger gap were run for a longer time period than at the smaller gaps. A "reduced" weight loss corresponding to the time of the shortest experiment was then computed from the measured weight loss and current data.

Current-voltage curves.—When measuring potential-current curves at high current density, voltage drops between capillary tip and measuring electrode have to be eliminated. This was accomplished here in two different ways. On one hand, a constant current was applied to the cell using the power supply mentioned above. After 2 to 3 sec, the current was interrupted by means of a mercury relay and the nonohmic potential decay was monitored on an oscilloscope with a time scale of 50 μ sec/division (Fig. 1). A dynamic hydrogen reference electrode was used in these experiments. It consisted of two platinized platinum wires across which a constant current density of approximately 1 mA/cm² was applied. The potential of this electrode was periodically checked against a saturated calomel electrode.

In the second type of experiment, a constant potential was applied to the working electrode and the current was recorded as function of time. A multipurpose

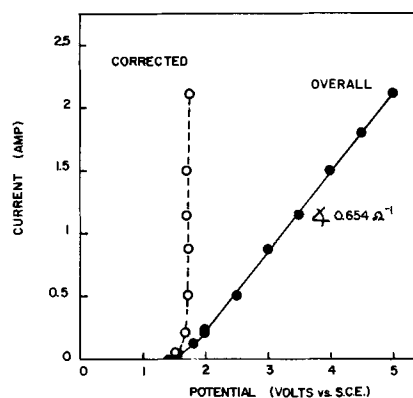


Fig. 2. Anodic current potential curve illustrating algebraic IR correction. Electrolyte 1M NaClO₃; flow velocity 1000 cm/sec; electrode area 0.322 cm².

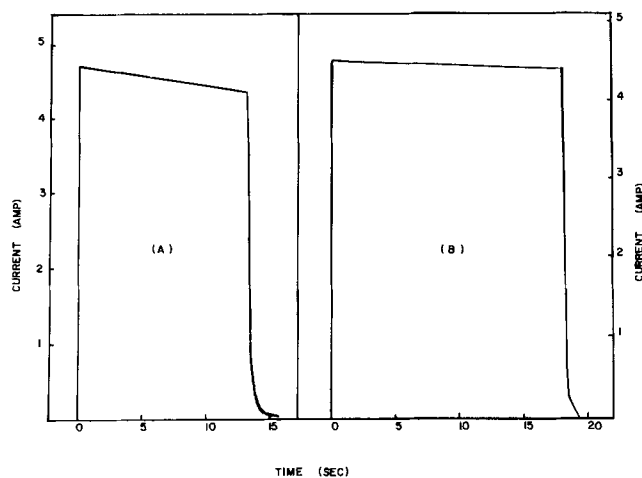


Fig. 3. Current time response to application of constant cell voltage: (A) 0.9M NaCl + 0.1M HCl, applied voltage = 9.55V; (B) 1M NaClO₃, applied voltage = 14.2V, electrode area 0.322 cm², gap 0.0534 cm, flow velocity 1000 cm/sec.

electrochemistry unit³ including potentiostat, function generator, and recorder was employed. In this case anode potentials were measured vs. a saturated calomel reference electrode. From the measured current time traces, the over-all current potential curve was plotted as illustrated in Fig. 2. At high current densities these curves exhibited a linear behavior and the effective ohmic resistance could be estimated from the slope. Using this resistance value, the IR contribution to each measured point was evaluated and subtracted from the over-all potential. Although this procedure is not accurate enough for mechanistic studies, it was sufficient for the purposes of the present investigation. All current potential measurements were performed at the smallest gap width and a temperature of 25.5° \pm 0.5°C.

Results

Typical current transients measured on application of a constant cell voltage are given in Fig. 3. They exhibit a steady decrease with time which is due to the dissolution of the anode. Initial current values measured with freshly ground anodes are plotted vs. cell voltage in Fig. 4. Weight loss experiments were performed at the voltages indicated by the dotted line (Fig. 4). The results are summarized in Table I. Throwing power data derived from these measurements are given in the first five columns of Table II. The length ratio is obtained by dividing the larger by the smaller gap width, the weight loss ratio by dividing the "reduced" weight loss corresponding to the smaller gap by that corresponding to the larger gap.

¹ Harrison Laboratories Model 6267A, 0-36V, 0-10A.

² Honeywell Elektronik Model 194.

³ Princeton Applied Research, Model 170.

Table I. Experimental weight loss determination

Electrolyte	Applied voltage (V)	Gap (cm)	Initial current density, A/cm ²		Dissolution time (sec)	Measured weight loss (mg)	Current efficiency for dissolution* (%)	Reduced weight loss (mg)**		
			Measured	Average				Individual	Average	
0.9M NaCl + 0.1M HCl	9.55	0.0534	4.7	4.72	13.5	18.7	100.2	18.7	18.9	
			4.75		13.5	19.1	101.7	19.1		
		0.140	1.83	1.84	29.1	16.6	102.4	7.70		7.71
			1.85		34.5	19.7	103.6	7.71		
		0.267	1.07	1.05	50.5	16.3	97.4	4.36		4.27
			1.03		53.5	16.5	100.6	4.17		
1M NaClO ₃	14.2	0.0534	4.55	4.55	18.0	7.3	30.2	7.3	7.43	
			4.54		18.7	7.9	31.4	7.56		
		0.140	1.78	1.79	45.0	5.7	24.0	2.28		2.28
			1.80		45.0	5.7	24.0	2.28		
		0.267	1.00	1.00	61.0	2.8	15.0	0.83		0.88
			1.00		61.2	3.2	17.1	0.94		

* Based on Ni²⁺ formation.

** Weight loss computed for the time of the shortest experiment, i.e. 13.5 sec in sodium chloride and 18.0 sec in sodium chlorate.

Numerical values of throwing power shown in the fifth column were computed by using an empirical formula which is commonly employed in the electroplating literature

$$TP = \frac{(L - M) 100}{L + M + 2} \quad [1]$$

Here L is the length ratio and M is the weight loss ratio.

For the chloride solution the calculated value of throwing power is nearly zero. This indicates that in this case the weight loss is almost inversely proportional to electrode distance (primary current distribution). In NaClO₃, on the other hand, negative values of throwing power are obtained. This means that here the weight loss at larger gap width is even less than predicted for primary current distribution. The throwing power data of Table I are also represented in Fig. 5 in the form of a "linear throwing index" plot. The "linear throwing index" is defined as the slope of the best straight line resulting from plotting the weight loss ratio vs. the length ratio. The "linear throwing index" is 1 for primary current distribution and zero for secondary current distribution. In NaClO₃, a throwing index larger than one is obtained, indicating again an even less uniform cutting rate than corresponding to primary current distribution.

Results of anode and cathode potential measurements in 0.9M NaCl + 0.1M HCl are given in Fig. 6. The black dots were derived from potential decay transients as illustrated by Fig. 1. All the other points were determined from measurements of the type illustrated in Fig. 2. The IR free potential values exhibit anodic Tafel behavior up to the highest current densities employed. Due to uncertainties in IR compensation, the points scatter considerably making an accurate determination of the Tafel slope difficult. The solid line indicated in Fig. 6 which reasonably well represents the data has a slope of 80 mV consistent with results of other nickel dissolution studies (9, 10). The cathodic data can be approximated by two logarithmic relationships with a slope of approximately 190 mV. The plateau separating the two cathodic Tafel regions is apparently due to a change in the mechanism of the hydrogen evolution reaction coinciding with the depletion of H⁺ ions near the cathode. Conditions during weight loss experiments shown in Tables I and II corresponded to the upper cathodic Tafel region. It may be

Table II. Throwing power data

Solution	Applied voltage (V)	Length ratio	Weight loss ratio	Throwing power	Current ratio	Calculated current ratio
0.9M NaCl + 0.1M HCl	9.55	5.0	4.42	0.077	4.49	4.87
		2.62	2.45	0.054	2.57	2.58
		1.91	1.81	0.058	1.75	1.89
1M NaClO ₃	14.2	5.0	8.45	-0.30	4.55	4.89
		2.62	3.26	-0.16	2.54	2.58
		1.91	2.59	-0.27	1.79	1.89

noted that potential data given here include possible concentration polarization effects since they refer to

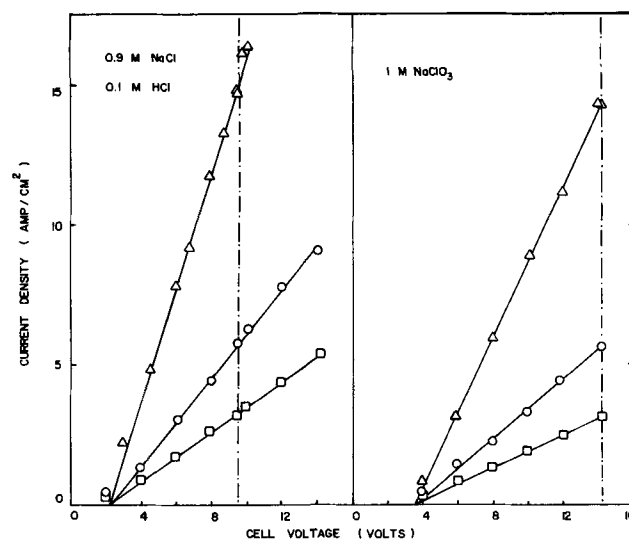


Fig. 4. Current vs. cell voltage curves for different gap width: Δ = 0.0534 cm, \circ = 0.140 cm, \square = 0.267 cm, flow rate 16.9 ml/sec.

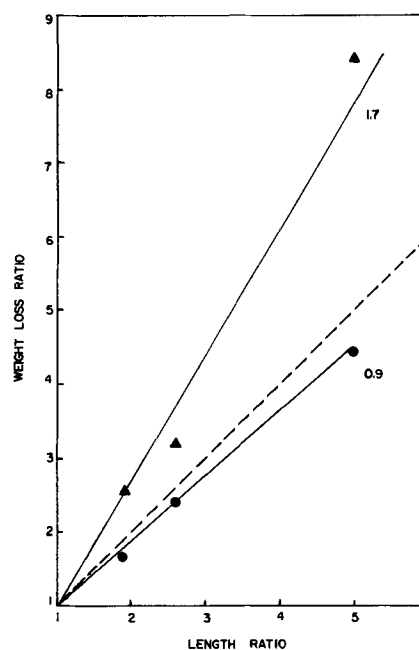


Fig. 5. Weight loss ratio as a function of length ratio for 1M NaClO₃ (Δ) and 0.9M NaCl + 0.1M HCl (\bullet). Slopes indicated represent the "linear throwing index;" broken line with slope 1 corresponds to primary current distribution.

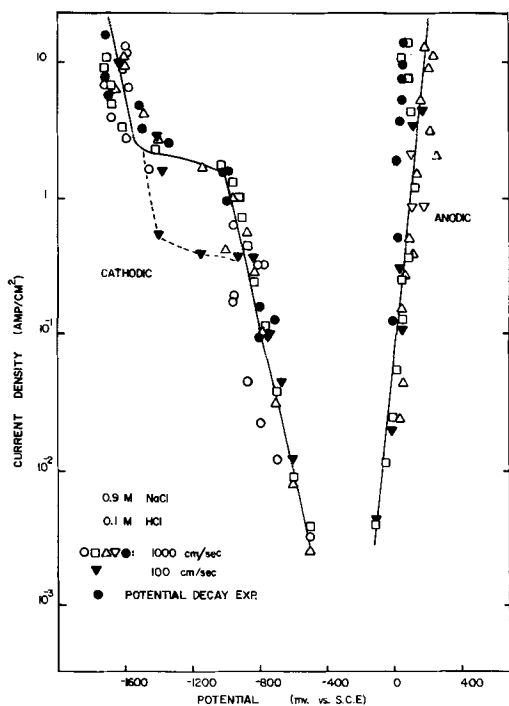


Fig. 6. Anodic and cathodic current potential curve (excluding IR drops) for nickel in 0.9M NaCl and 0.1M HCl at different flow velocity, gap = 0.0534 cm.

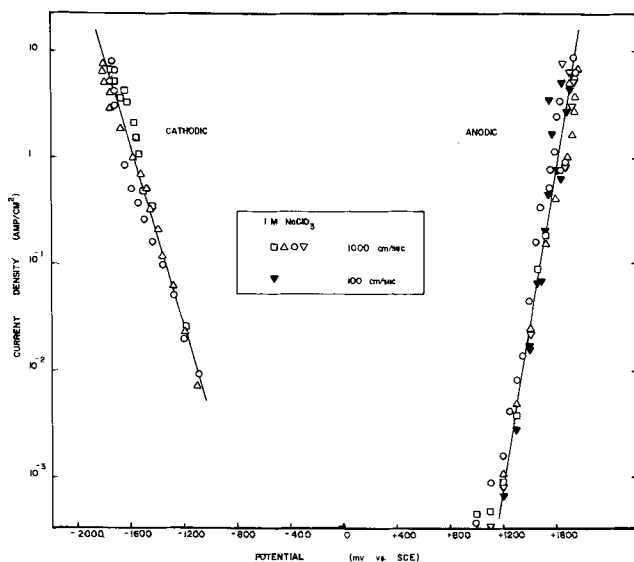


Fig. 7. Anodic and cathodic current potential curve (excluding IR drops) for nickel in 1M NaClO₃ at different flow velocity; gap = 0.0534 cm.

measurements taken at sufficiently long times to establish steady state with respect to mass transfer. This was done purposely because the aim of the measurements was not so much to establish detailed charge transfer kinetics, but to measure electrode potentials prevailing under conditions of throwing power determinations. From the data taken at different flow rate (Fig. 6) it appears, however, that anodically mass transfer did not substantially affect the polarization curve.⁴ Potential data for 1M NaClO₃ are given in Fig. 7. Again Tafel behavior is observed, the anodic and cathodic slopes being approximately 150 and 240 mV, respectively. No significant effect of flow rate on mea-

⁴ This statement holds true only within the range of measurements shown. Indeed it was observed that at a flow rate of 100 cm/sec increasing the current density above the maximum values given in Fig. 6 led to a change in the shape of the current transient and to brightening of the surface, both facts being indications of a change in dissolution mechanism.

sured anode potentials is observed. Compared to the data obtained in chloride solution, the anodic Tafel line is shifted to much higher potentials here. This is due to anodic passivation: nickel in acidified NaCl dissolves in the active mode, but it spontaneously passivates in neutral NaClO₃. The anodic current voltage curve shown, therefore, refers to transpassive behavior. Previous studies in this laboratory (9) showed that vigorous oxygen evolution occurs in the transpassive potential region.

Discussion

Numerical values of throwing power or throwing index such as given in Table II or Fig. 5 are useful for comparing different electrolytes, but they do not have much physical significance because for a given metal electrolyte combination they depend on cell dimensions and applied voltage (11, 12). In order to gain an insight into the physical parameters governing ECM throwing power, one has to consider separately current distribution and dissolution efficiency. Current distribution can be computed from a knowledge of the current-potential curve and the specific electrolyte resistance. For example, in the case of the present throwing power experiments it is possible to estimate the current ratios of Table II from measurements at a single gap width. Neglecting edge effects, the current density is given by

$$i \approx (U - \phi_t) / \rho_e l \tag{2}$$

with ρ_e = specific electrolyte resistance and ϕ_t = sum of anode and cathode potentials, U = applied cell voltage, l = gap width. From Fig. 6 and 7, ϕ_t can be approximated for NaCl and NaClO₃, respectively by

$$\phi_t(\text{NaCl}) = 1.58 + 0.27 \log i \tag{3}$$

and

$$\phi_t(\text{NaClO}_3) = 3.22 + 0.37 \log i \tag{4}$$

The magnitude of ρ_e can be estimated from cell voltage and potential data as illustrated by Fig. 8. From Eq. [2], [3], and [4], the current density for a given cell voltage and gap width is obtained and current ratios for different gap widths can be computed. Results given in the last column of Table II show good agreement between calculated and measured current ratios. It is to be noted that in the present experiments current distribution is not affected by anodic passivation. This conclusion ought to apply in ECM whenever significant concentration polarization effects are absent and a logarithmic current-potential relationship exists.

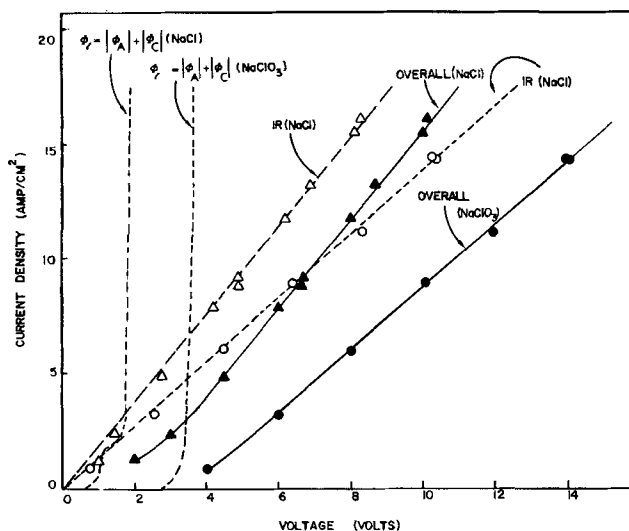


Fig. 8. Ohmic voltage drop in cell obtained by subtracting independently measured electrode potentials from cell voltage. Gap 0.0534 cm, flow velocity 1000 cm/sec; \blacktriangle cell voltage, \triangle IR in 0.9M NaCl + 0.1M HCl, \bullet cell voltage, \circ IR in 1M NaClO₃, . . . sum of anode + cathode potentials (from Fig. 6 and 7).

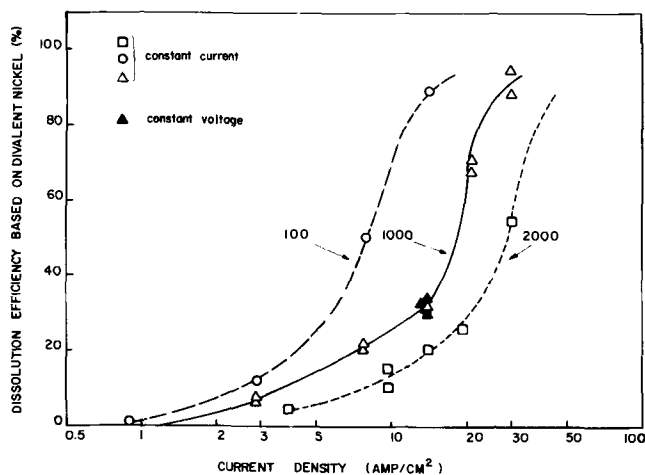


Fig. 9. Current efficiency for nickel dissolution in 1M NaClO₃ (based on Ni²⁺ formation) as a function of current density; gap 0.0534 cm, flow velocity 100, 1000, 2000 cm/sec.

Current distribution on the work piece is then determined by the magnitude of a dimensionless parameter (13)

$$P = \frac{b}{2.3 \rho_e l i} \quad [5]$$

where b is the anodic Tafel slope, ρ_e the specific electrolyte resistance, l a characteristic length, and i the current density. Primary current distribution is approximated for $P \ll 1$. Because of the high current densities employed this condition usually ought to be satisfied in ECM. For example, using the measured b and ρ_e values for NaCl and NaClO₃, respectively, with the gap width l as characteristic length the value of P in the present experiments varied between 0.0046 to 0.0041 for NaCl and between 0.0057 and 0.0051 in NaClO₃. Upon application of higher current densities, the value of P would be even smaller. It is worth noting that P does not depend on the actual anodic potential values, but only on the slope of the current voltage curve. Therefore the width of the passive potential region in a conventional potentiostatic current-voltage curve should not significantly affect current distribution under ECM conditions, contrary to some statements found in the literature (15).

The data in Table II indicate that the reason for the observed difference in throwing power between the passivating NaClO₃ and the nonpassivating NaCl lies in a different dependency of dissolution efficiency on current density. In the case of NaCl, the metal dissolution efficiency is constant, while in the case of NaClO₃ it is a strong function of current density. This is further illustrated by the data of Fig. 9, which were obtained from weight loss determinations performed at constant current density at the smallest gap width of 0.0534 cm. For comparison the weight loss data of Table I, obtained at constant voltage, are also indicated. Because of oxygen evolution, very low metal dissolution efficiencies are obtained at low current densities, but with increasing current the dissolution efficiency sharply increases. The detailed shape of the curve depends on flow rate; the higher the flow rate, the lower the dissolution efficiency at a given current

density. A similar S shaped curve for dissolution efficiency of nickel in NaClO₃ plotted vs. current density has been obtained previously in this laboratory in a different experimental cell (9). The numerical values obtained in that study were somewhat different, however, and no effect of stirring was observed. This was probably because hydrodynamic conditions were not as well defined as here. A more detailed investigation of the experimental factors affecting current efficiency for nickel dissolution in the transpassive potential region will have to be made before a mechanistic interpretation of the shape of the curves shown in Fig. 9 can be given.

The present results show clearly, however, that a discussion of how passivating electrolytes affect the dimensional control in ECM cannot be based on current potential measurements alone, but it has to include the study of reaction stoichiometry. Lower values of throwing power than theoretically possible with a nonpassivating electrolyte can indeed be obtained with a passivating electrolyte provided the current efficiency for metal dissolution is an increasing function of current density. The present study, therefore, supports and puts on a firm basis ideas advanced by other workers (6, 16, 17) who recognized the importance of the metal dissolution efficiency in obtaining good dimensional control with passivating ECM electrolytes.

Acknowledgment

Financial support of this work by the Office of Naval Research under Contract No. N00014-69-A-0200 is greatly appreciated.

Manuscript submitted Dec. 1, 1971; revised manuscript received Jan. 15, 1972.

Any discussion of this paper will appear in a Discussion Section to be published in the December 1972 JOURNAL.

REFERENCES

- H. E. Haring and W. Blum, *Trans. Am. Electrochem. Soc.*, **44**, 313 (1923).
- P. A. Brook and Q. Iqbal, *This Journal*, **116**, 1458 (1969).
- D. T. Chin and A. J. Wallace, Jr., *ibid.*, **118**, 831 (1971).
- M. A. LaBoda and M. L. McMillan, *Electrochem. Technol.*, **5**, 340 (1967).
- J. P. Hoare, M. A. LaBoda, M. L. McMillan, and A. J. Wallace, Jr., *This Journal*, **116**, 199 (1969).
- D. Landolt and J. Sutherland, UCLA Engineering Report No. 7174, October 1971.
- D. Landolt, Submitted to *Rev. Sci. Instr.*
- D. Landolt, R. H. Muller, and C. W. Tobias, *This Journal*, **117**, 839 (1970).
- M. Datta and D. Landolt, UCLA Engineering Report No. 7102, January 1971; *Corrosion Sci.*, To be published.
- M. L. Kronenberg, J. C. Bantor, E. Yeager, and F. Hovorka, *This Journal*, **110**, 1007 (1963).
- J. N. Agar and T. P. Hoar, *Discussions Faraday Soc.*, **1**, 158 (1947).
- T. P. Hoar and J. N. Agar, *ibid.*, **1**, 162 (1947).
- C. Wagner, *Plating*, **48**, 988 (1961).
- J. A. Klingert, S. Lynn, and C. W. Tobias, *Electrochim. Acta*, **9**, 297 (1964).
- J. P. Hoare, *This Journal*, **117**, 142 (1970).
- K. Chickamori and S. Ito, *Denki Kagaku*, **38**, 492 (1970).
- W. König and H. Degenhardt, "Fundamentals of Electrochemical Machining," Charles L. Faust, Editor, Electrochemical Society Inc. (1971).



Gallium Oxidation in Alkaline Solution

R. S. Perkins¹

Department of Chemistry, University of Southwestern Louisiana, Lafayette, Louisiana 70501
and

Rate Processes Institute, University of Utah, Salt Lake City, Utah 84112

The electrochemistry of gallium is important not only in practical applications, but also for theoretical considerations due to its existence as either a liquid or a solid in aqueous electrode systems.

Past studies of the anodic oxidation of Ga in alkaline solutions have been limited. It is the purpose of this study to investigate in somewhat more detail, using cyclic voltammetry, the first stages of anodic oxidation of Ga in aqueous NaOH solutions.

Experimental

A three compartment Pyrex cell was used.

Carbonate free NaOH solutions were made of reagent grade materials. Solutions were made from water doubly distilled from a basic permanganate solution.

The reference, counter, and test electrodes were each in a separate cell compartment and each were in the same solution. A closed stopcock effectively separated the reference and working compartments. An open stopcock connected the counter and working compartments. A hydrogen reference electrode and a platinum counterelectrode were used. Test electrodes of several designs were used. All test electrodes were made from gallium of 99.999% purity. In some experiments the test electrode consisted of a gallium hemisphere of 0.06 cm² geometrical area formed in one end of a U-shaped glass tube. Another design consisted of gallium forced through a 0.051 cm diameter channel in a short length of Teflon tube. The emerging gallium formed a bead of area approximately 0.008 cm². In one experiment this bead was removed and the electrode was planar with an area equal to the cross sectional area of the 0.051 cm diameter channel in the Teflon.

The gallium electrode used was prepared and installed in the cell in an atmosphere of nitrogen. After fabrication, the gallium electrode was solidified. Experiments were carried out at room temperature, approximately 25°C.

Except for the reference electrode compartment, the cell was deaerated with nitrogen.

A conventional cyclic voltammetry apparatus was used with an Exact Electronics function generator and a Wenking potentiostat. The resulting curves were displayed on an X-Y recorder.

In some experiments, current-potential curves were obtained as the gallium electrode was mechanically renewed by scraping. For this work an experimental arrangement similar to that described previously (1) was used. The Teflon mounted gallium electrode was used.

Data

The data taken was in the form of potential-current plots over the potential region of hydrogen evolution to various points of anodic oxidation. Experiments in each solution were done at a number of sweep rates as will be noted in the discussion to follow. A typical curve obtained in 1M NaOH is given in Fig. 1. It is seen to consist of a region of hydrogen evolution, a region of anodic oxidation which is composed of sev-

eral smaller regions defined by shoulders and changes of slope, and a small region of cathodic reduction which obviously represents much less charge than the corresponding region of anodic oxidation. The qualitative features of this curve do not change greatly when the sweep rate is altered.

Discussion

In these experiments the most striking feature of the data is the fact that with increasing anodic potential, the current increases without limit in the potential range studied, and this current is not due to oxygen evolution. Experiments were also performed in which the potential was adjusted to greater anodic values, and it was observed that although the current finally levelled out with increase of potential, no subsequent decrease was noted and oxygen evolution was never observed. It is reported that oxygen evolution in 1M KOH solutions does not occur until a potential of 10-30V vs. NHE is imposed on the electrode (2, 3). The absence of passivation may be explained by assuming that the product of oxidation does not form a thick film on the electrode. In view of the large amount of product formed, it must be concluded that the product of oxidation is soluble in the solution used. In this region of pH, the reaction product predicted thermodynamically is Ga₂O₃. This substance is highly soluble and forms GaO₃⁻⁻⁻ in basic solution (4). Dissolution of the electrode was observed visually at high current densities. Formation of a soluble product also explains the small amount of cathodic charge observed.

It is seen from Table I that over a relatively wide range of sweep rate, the size of the cathodic charge is fairly constant. This would indicate that the sub-

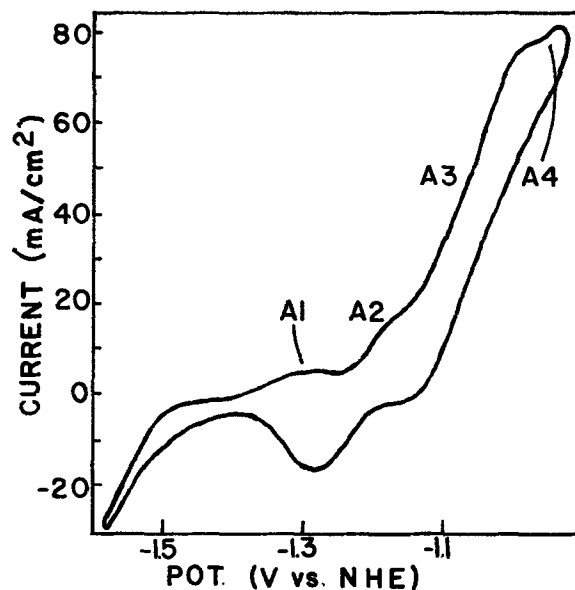


Fig. 1. Current-potential curve for spherical Ga electrode in 1M NaOH. Sweep rate = 0.47 V/sec.

¹ Present address: Department of Chemistry, University of Southwestern Louisiana, Lafayette, Louisiana 70501.

Key words: gallium, oxidation, anodic, oxide, dissolution, films.

Table I. Effect of sweep rate in 1M NaOH

Sweep rate, V/sec	Anodic charge, mcoulomb/cm ²	Cathodic charge, mcoulomb/cm ²
0.0255	123	*
0.0408	72.7	*
0.051	93.7	2.60
0.153	32.2	2.39
0.255	23.2	2.15
0.47	22.7	2.19 (Fig. 1)
0.51	20.9	2.22

* Peak too small to determine area.

stance being reduced is a thin film of oxide on the electrode.

Further evidence of a thin film of oxide on the electrode is given by the scraping experiments in which it is indicated that the reaction is retarded and by exposing fresh electrode surface, additional product may be formed. In the scraping experiments, the Ga electrode was mechanically scraped with a sharpened sapphire rod rotating at 30,000 rpm. The scraping was done at various parts of both the anodic and cathodic sweeps but not in the region of hydrogen evolution. In all regions of oxidation (A1 through A4) the anodic current is increased by scraping. The scraping does not produce a smooth curve of higher current but rather a number of transients reflecting the violent scraping conditions at the electrode. The size of the transients was not reproducible although the general effect was. Most transients were larger than the prescrape current at a given voltage by a factor of between 2 and 10. In some instances, at lower current densities, scraping increased the current by as much as a factor of fifty. As well as can be determined, the current transient is not produced until the scraping drill touches the electrode. Contact with a nonrotating drill has no effect. The transient is definitely not due to stirring of bulk solution.

An idea of the thickness of the thin film can be obtained by assuming a roughness factor of one for the test electrode and further assuming that the cathodic peak is due only to reduction of the oxide film and not due at all to reduction of soluble product in solution near the electrode. With these assumptions, a value of approximately 3.4 monolayers of Ga₂O₃, as measured in terms of layers of Ga consumed, is calculated for film thickness at the time of reduction. This agrees well with film thickness obtained by constant current discharge of passivated Ga (5).

The amount of charge equal to this film thickness on the anodic sweep corresponds to the area under the curve making up the two first parts of the oxidation peak (A1 and A2). For calculating area, the anodic boundaries of A1 and A2 were taken as vertical lines drawn down to the potential axis from the current-potential curve at the points of slope changes defining A1 and A2. Experiments were done in which the sweep was reversed after A2. This reversal hardly affected the area of the cathodic peak. It appears then, that the cathodic peak is due to the reduction of an oxide film, the formation of which is represented by A1 and A2. The first part of the oxidation peak, A1, corresponds to approximately a monolayer of coverage on the electrode. It is likely that such a monolayer would alter the electrode enough to significantly change the kinetics of a reaction. Formation of such monolayers has been studied on mercury (6). The experiments done here do not allow us to state with certainty the composition of any films formed. The initial monolayer may be Ga₂O₃, or chemisorbed oxygen, or some oxide which has not been well characterized thermodynamically.

Oxidation of gallium in 1M NaOH would appear to proceed, therefore, by an initial formation of a monolayer of oxide or oxygen with subsequent thickening of this film to about three or four layers. At this point the properties of the film become such that the rate of dissolution increases and prevents further thickening.

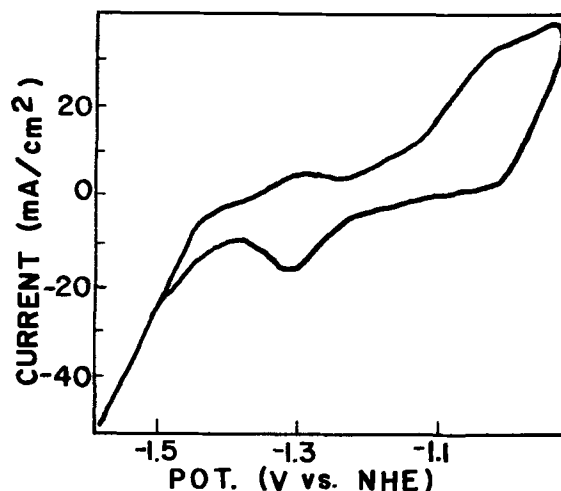


Fig. 2. Current-potential curve for planar Ga electrode in 1M NaOH. Sweep rate = 0.47 V/sec.

Further increase of potential should increase the rate of oxidation of gallium and such an increase of current is observed. As higher current densities are obtained, diffusion either through the oxide film or through the electrolyte should play a more important part in the reaction. Evidence that this is true is seen in Fig. 1 and 2. The two curves in these figures were obtained under experimental conditions which were identical except that the electrode area and shape differed. Curve 1 was obtained using a spherical electrode and curve 2 was obtained with a planar electrode. The two curves differ in that at high anodic potentials the current density obtained is higher for the spherical electrode. This is to be expected if diffusion is involved (7, 8). Evidence that the diffusion is taking place in solution is that stirring increases the anodic current as was also found by Popova and Simonova (9). The similarity of regions A1 for the two types of electrode is at variance, however, with the diffusion studies of Faizullin *et al.* (10).

Solutions of 0.1M NaOH give smaller anodic currents. Thus the limiting diffusion is that of OH⁻ and not of product ions.

The current-potential curve has another change of slope very near the anodic end of the potential sweep. The current increases more slowly with change of potential. This is probably not due to a change in product as the A3 and A4 segments are so similar. It is possibly due to a change in the nature of the oxide film on the electrode. Perhaps diffusion in the oxide begins to play a part in the rate of oxidation at this point but the data here are not extensive enough to study this further.

Acknowledgment

I would like to thank Drs. T. N. Andersen and H. Eyring for their help and encouragement. The work was supported by a Petroleum Research Fund grant.

Manuscript submitted July 15, 1971; revised manuscript received Feb. 1, 1972.

Any discussion of this paper will appear in a Discussion Section to be published in the December 1972 JOURNAL.

REFERENCES

1. R. S. Perkins, R. C. Livingston, T. N. Andersen, and H. Eyring, *J. Phys. Chem.*, **69**, 3329 (1965).
2. F. F. Faizullin and E. V. Nikitin, *Elektrokhimiya*, **2**, 112 (1966).
3. E. V. Nikitin and F. F. Faizullin, *Aspir. Rab. Kazan. Gos. Univ. Khim. Geol.*, **1967**, 44.
4. Marcel Pourbaix, "Atlas of Electrochemical Equilibria in Aqueous Solutions," Pergamon Press Inc. (1966).
5. T. I. Popova, N. A. Simonova, Z. I. Moiseeva, and N. G. Bardina, *Elektrokhimiya*, **6**, 706 (1970).
6. R. D. Armstrong, W. P. Race, and H. R. Thirsk, *J. Electroanal. Chem.*, **19**, 233 (1968).

7. W. H. Reinmuth, *J. Am. Chem. Soc.*, **79**, 6358 (1957).
 8. R. S. Nicholson and I. Shain, *Anal. Chem.*, **36**, 706 (1964).
 9. T. I. Popova and N. A. Simonova, *Elektrokhimiya*, **6**, 1125 (1970).
 10. F. F. Faizullin, E. V. Nikitin, and N. N. Guidina, *ibid.*, **3**, 120 (1967).

A Rapid and Complete Method to Remove Plutonium Contamination from Aluminum

P. L. Wallace, J. C. Walden, and J. W. Magana

Lawrence Radiation Laboratory, University of California, Livermore, California 94550

The Process

This process was first described in a German patent (1), and is used here to decontaminate aluminum parts of complex shapes. Its principal usage has been in decontaminating x-ray spectrographic cell holders. This contamination occurs when acid solutions of plutonium leak from standard liquid cells and attack the aluminum.

The process involves (i) degreasing the part in acetone, (ii) dipping it in a heated (90°C) bath for about 30 sec, (iii) rinsing the part in water, (iv) drying it, and, finally, (v) checking it for any residual contamination. All of these operations are carried out in an open front hood to prevent contamination spread.

The composition of the cleaning bath is given in Table I. It has been found important to not reuse the solution for large numbers of parts, because depletion of some components causes the reaction rate to lessen. Rinsing quickly after cleaning is mandatory, because the part will blacken rapidly otherwise. No electric current is necessary to augment the process.

Results

Parts having fixed plutonium contamination of greater than 10,000 alpha counts/min have been decontaminated to no detectable counts with the 30 sec cleaning.

Table I. Cleaning bath composition

Component	Volume (%)
Phosphoric acid	50
Nitric acid	6.5
Acetic acid	6
Sulfuric acid	25
Water	12.5

Plus 3 g/cc of crystalline nickel nitrate, $\text{Ni}(\text{NO}_3)_2 \cdot 6 \text{H}_2\text{O}$.

Key words: plutonium, aluminum, decontamination.

The surface condition after cleaning is bright and somewhat shiny. However, the patent writeup indicates that a 3 min immersion would produce a mirror-like finish. While such a finish is desirable, it does entail more metal removal than is wanted to maintain the sample holder's close tolerances.

To get a feeling for the actual amount of metal removed during processing, aluminum tubes were tested as mockups for the cell holders. The weight loss for five 20g tubing sections (4 cm long by 2.0 cm ID; 2.6 cm OD) in 30 sec (bath temperature 90°C) varied from 50 to 100 mg, depending on the amount the bath was depleted by usage. The outside diameter change on these tubes was less than 0.03 mm in each case.

Conclusions

A rapid method of decontaminating aluminum parts has been found. To date, it has made every sample holder that had been grossly contaminated available for reuse.

Acknowledgment

Thanks are due to D. M. Cheney (Argonne National Laboratories, Idaho Reactor Site) who first brought this process to one author's (P. L. Wallace) attention about 1960. The adaptation for decontamination was discovered here some 10 years later.

This work was performed under the auspices of the U. S. Atomic Energy Commission.

Manuscript submitted Nov. 3, 1971.

Any discussion of this paper will appear in a Discussion Section to be published in the December 1972 JOURNAL.

REFERENCE

1. A. Vernet, Process for Producing Shiny Surfaces on Objects Made of Aluminum and Aluminum Alloys, German Pat 804-054 (1948), UCRL-Trans. 10518 (1971).

An Electrochemical Technique for Microsectioning Silver

Nghi Q. Lam, Steven J. Rothman, and L. J. Nowicki

Materials Science Division, Argonne National Laboratory, Argonne, Illinois 60439

The electrochemical technique for removing thin uniform sections from a metallic sample consists of forming an anodic oxide layer that can be either mechanically stripped or chemically dissolved without attack of the metal substrate. This method has not been applied to silver to date; the sectioning techniques that have been used have been based on the formation of dissolvable films of silver iodide or silver bromide and their dissolution in either a 1M sodium-

Key words: anodization, silver, sectioning, stripping, surface preparation.

thiosulfate solution (1) or a solution of 1.0 g/liter KCN in water (2). In our preliminary experiments, the former solvent stained the silver surface, probably due to the formation of colloidal silver on the surface (1), and the latter solvent attacked the silver substrate at an unacceptable rate. We have therefore developed an electrochemical method of removing thin sections of silver for the determination of very small diffusion coefficients. This method has also proved useful for preparing a good surface on silver diffusion samples.

Experimental Methods and Results

Surface preparation.—Monocrystalline silver rods of 1.24 cm diam were grown from 99.999% purity silver by the Bridgman method and spark-cut into disks a few millimeters thick. After mechanical polishing through 0.3μ Al_2O_3 , the samples were chemically polished with a solution made up of 25 ml of saturated chromic acid and 3 ml of 10% HCl (3). The chemical polishing was performed by swabbing the silver surface with a cotton-tipped applicator saturated with the solution and rinsing the sample intermittently in running water. Chemical polishing in this manner for 10 min removes a layer $\sim 15\mu$ thick, which was the approximate depth of the region deformed in polishing. At the end of this polishing step, the sample was washed with distilled water and then with alcohol in an ultrasonic vibrator, and dried in warm air. After chemical polishing, a few layers approximately 200Å thick were removed from the silver surface by anodizing in an electrolyte of 0.5% KOH in water (with current density = 1.0 mA/cm^2 , time = 22 sec) and then dissolving the silver oxide in an aqueous solution of NH_4OH . This procedure helped remove submicroscopic irregularities from the surface. The entire surface obtained was optically flat and free of pits.

Sectioning.—Most of the anodizing experiments were made on a (100) face of a silver single crystal that had been irradiated for 3 days in a flux of 3×10^{12} thermal neutrons/cm²-sec. The specific activity of the crystal (^{110}Ag) was measured as 5.43×10^3 cpm/ μg , thus allowing a conversion from counts/min to micrograms of silver. A simple anodizing cell was used. The platinum foil cathode was cleaned with HNO_3 before use. Silver paint was used to fasten a copper wire to the back of the specimen for the electrical connection. The sample was masked with Tygon protective paint, so that only the preanodized surface was exposed to the electrolyte. The wire was also coated with Tygon. The electrolyte consisted of 5g KOH per liter of water. After anodizing, the silver oxide films, which, if thick enough, showed uniform interference colors, were dissolved in a solution of 1% (in volume) NH_4OH in water.

To determine whether this solvent attacks the silver, oxide layers of different thicknesses were formed on the irradiated silver crystal by anodizing with current densities of 0.17, 0.48, and 0.85 mA/cm^2 for 30 sec. The sample was then immersed in the NH_4OH solution, and the activity of the solution was counted as a function of time. Figure 1 shows that the NH_4OH solution dissolved the oxide and attacked the silver to an insignificant extent. About 5 sec were sufficient to remove an oxide layer 1000Å thick. Interference microscopy showed that the silver surface remained clean and flat after oxide removal.

The thickness of silver removed is plotted as a function of anodizing time in Fig. 2 for various current densities. The thickness removed in each anodizing-dissolution step was determined by counting the solvent for ^{110}Ag content and using the measured value of specific activity to convert to micrograms of silver. The sample was also weighed on a microbalance before and after removal of 40 sections; the difference between amounts of material removed, as measured by the two techniques, was about 9%, which is within the experimental error. The step height on a nonradioactive silver crystal, part of which was masked by a spot of Tygon paint, was measured on an interference microscope after anodizing and removing 40 sections under the same current and time conditions. The step height agreed, within the experimental error, with the thickness removed from the radioactive sample. The amount of material removed per anodization under identical conditions was reproducible to $\pm 8\%$. Less than 3% of the removed activity was found in the anodizing solution and on the cathode.

The same anodizing treatments on silver crystals of random orientation yielded the same anodic film

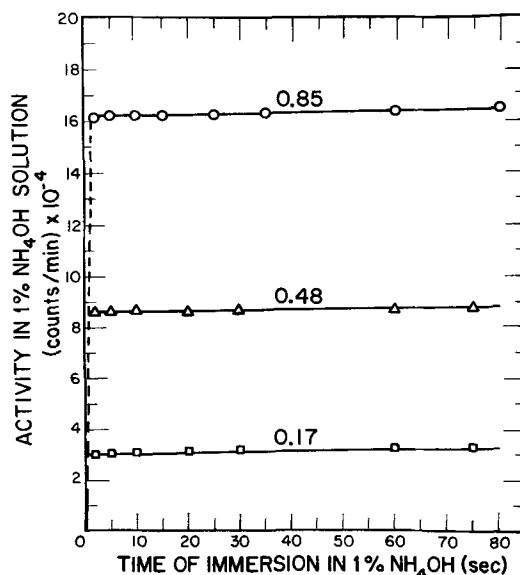


Fig. 1. Plot of ^{110}Ag activity of 1% NH_4OH solution after immersing the anodized silver sample in the solvent for various times. The different thicknesses of silver oxide were formed by anodizing for 30 sec with current densities of (\square) 0.17, (\triangle) 0.48, and (\circ) 0.85 mA/cm^2 .

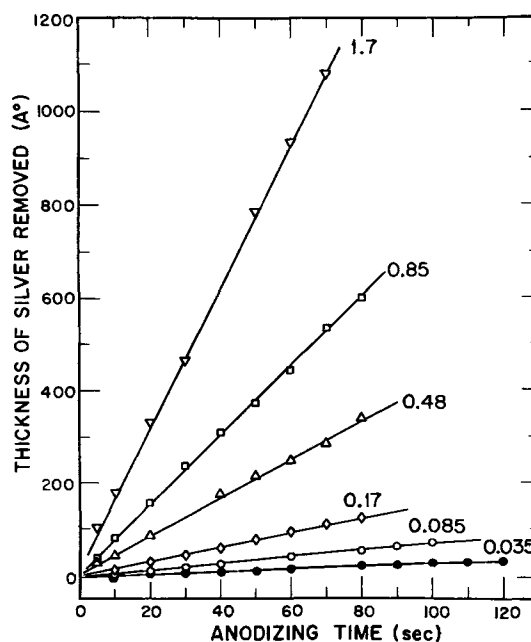


Fig. 2. Calibration of the anodizing of monocrystalline silver in an aqueous electrolyte containing 0.5% KOH. The numbers on the curves indicate the anodic current densities in units of mA/cm^2 .

thickness, indicating that the rate of anodization is orientation independent, as was observed for gold (4). The thickness of the anodized layer was found to be independent of the KOH concentration in the electrolyte. The same observation was also made by Vermilyea (5) in a study of anodic oxidation of tantalum.

The thickness of silver that was anodically oxidized in 1 sec, deduced from the slopes of the curves in Fig. 2, is shown in Fig. 3 as a function of current density. An increase in current density from 0.17 mA/cm^2 to 1.7 mA/cm^2 led to a tenfold augmentation in the anodizing rate, similar to the case of anodizing gold (4). For high current densities ($>4 \text{ mA/cm}^2$), it was better to use current pulses of $\frac{1}{2}$ -sec duration rather than constant current densities, because the oxygen evolution, which occurred shortly after establishing the current, could affect the uniformity and thickness of the oxide.

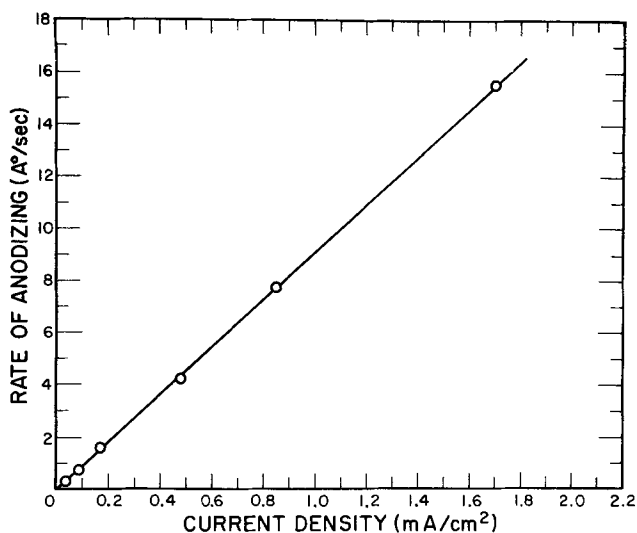


Fig. 3. Relationship between the rate of anodizing (in Å/sec) and the anodic current density (in mA/cm²). Anodizing rate = 9.1 × (current density).

Conclusions

The anodic oxidation technique can be used for removing reproducible thin sections from silver. An

aqueous solution containing 1% NH₄OH appears to be the best solvent for removing the silver oxide, inasmuch as it does not attack the silver substrate and enables one to obtain a clean surface after the dissolution. A combination of chemical polishing and anodizing-dissolution techniques can be used instead of electropolishing to prepare a flat, strain-free silver surface prior to diffusion experiments.

Acknowledgment

The authors wish to thank Dr. N. L. Peterson for his constant interest in this work.

This work was performed under the auspices of the U. S. Atomic Energy Commission.

Manuscript submitted Nov. 29, 1971; revised manuscript received Feb. 2, 1972.

Any discussion of this paper will appear in a Discussion Section to be published in the December 1972 JOURNAL.

REFERENCES

1. T. Andersen and G. Sørensen, *Rad. Effects* 2, 111 (1969).
2. R. G. Vardiman and M. R. Achter, *ORNL Report 6869* (1968); and *Trans. AIME*, 245, 178 (1969).
3. H. J. Levinstein and W. H. Robinson, *J. Appl. Phys.*, 33, 3149 (1962).
4. J. L. Whitton and J. A. Davies, *This Journal*, 111, 1347 (1964).
5. D. A. Vermilyea, *Acta Met.*, 1, 282 (1953).

Brief Communication



Transport in Non-Newtonian Flow

R. Greif, R. Kappesser, and I. Cornet*

Department of Mechanical Engineering, University of California, Berkeley, California 94720

Rendering a fluid non-Newtonian by the addition of a high molecular weight polymer alters the heat, mass, and momentum transport characteristics of the fluid (1-10). Electrochemists have long dealt with such non-Newtonian systems, for example, for achieving smoother and finer grained deposits in electrolytic metal deposition or in electrodeposition of rubber or related synthetic polymers from latices.

There have been several investigations that have dealt with the determination of the molecular diffusivity in non-Newtonian systems (3, 6, 7, 9, 10). These studies utilize mass flux measurements in conjunction with theoretical results for non-Newtonian systems to obtain the diffusivity. In these studies the relationship between the shear stress and the rate of strain is written in the form of a power-law, viz.

$$\tau_{xy} = -K \left(\frac{\partial V_x}{\partial y} \right)^n \quad [1]$$

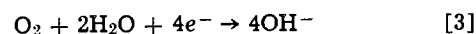
although more complex relations are possible. In contrast, the corresponding expression for the molecular flux of mass or heat is assumed to be a linear function of the concentration, or temperature, gradient so that

$$J = -D \frac{\partial C}{\partial z} \text{ or } q = -\lambda \frac{\partial t}{\partial z} \quad [2]$$

* Electrochemical Society Active Member.
Key words: transport, non-Newtonian theory, molecular flux, concentration gradient.

In this study we experimentally demonstrate the validity of the assumption that J is a linear function of the concentration gradient.

In a previous investigation (10) we determined the molecular diffusivity of oxygen in aqueous 4% sodium chloride solutions which were rendered non-Newtonian by addition of various concentrations of Polyox WSR 301 (Union Carbide), a completely water soluble polymer of ethylene oxide. The system consisted of a rotating Monel disk, which was made cathodic while the anode was a platinized-titanium wire mesh cylinder. The mass flux of oxygen diffusing to the rotating disk was determined by measuring the mass transfer limiting current for the net reaction



The mass flux is dependent on the over-all oxygen concentration difference, $\Delta C_{\text{O}_2} = C_{\text{O}_2,x} - C_{\text{O}_2,w}$. The concentration of oxygen far from the disk, $C_{\text{O}_2,x}$, was measured by Winkler analysis while the concentration at the disk surface, $C_{\text{O}_2,w}$, was taken to be zero. Equating the experimental and theoretical results for the mass flux yielded the results for the diffusivity.

A critical confirmation of the experiment and analysis was readily made by comparing the value obtained for the diffusion coefficient in the absence of Polyox with the value reported in the International Critical Tables (11). The results were in excellent agreement under this Newtonian flow condition (10).

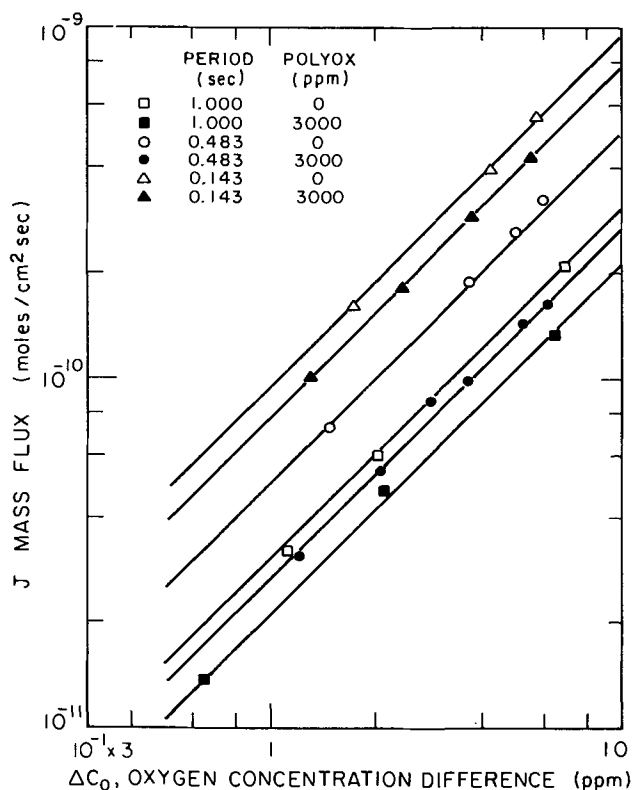


Fig. 1. Comparison of mass flux dependence on concentration gradient in Newtonian and non-Newtonian fluids.

In the analysis for the mass transport the molecular flux had been assumed to be linearly dependent on the concentration gradient (cf. Eq. [2]). We had thought that this assumption had been previously confirmed but apparently this is not so. Therefore, a series of tests was performed at different concentration differences, that is, for different values of $\Delta C_0 = C_{0,w}$. This was achieved by first bubbling nitrogen through the solution until the desired concentration of oxygen was achieved. We note that all our previous experiments had been performed at essentially a single value of $C_{0,w}$.

The experimental results are presented in Fig. 1 in terms of the mass flux vs. the oxygen concentration difference. Results are shown for the Newtonian fluid (0 ppm of Polyox) and for the non-Newtonian fluid (3000 ppm of Polyox) for three periods of rotation (Reynolds number). For a linear system, the mass flux would vary linearly with the concentration difference, and this is clearly the result shown. Note that the linear slope of 1.0 is observed for all the conditions tested, thereby demonstrating the validity of Eq. [2].

Although Eq. [1] is not required, as far as the above conclusion is concerned, the values of the coefficients, K and n are of interest. For shear stress in units of dynes/cm² and rate of strain in units of sec⁻¹, $n = 1.00$, $K = 0.0094$ for 0 wppm of Polyox and $n = 0.68$, $K = 0.88$ for 3000 wppm of Polyox (temperature of 27°C). These values were obtained from measurements we performed with a Fann U-G, Model 35, rotating cylinder viscometer. Now, the theoretical result for the mass

flux to a rotating disk in laminar flow divided by the concentration difference, that is, $J/\Delta C_0$, varies with rpm according to $(\text{rpm})^{1/n+1}$ (9, 10). Thus, an independent check is afforded by comparing the value of n obtained directly from the viscometer measurement and the value of n obtained directly from the mass flux measurement. The results are in excellent agreement (10).

Lastly it should be noted that the shear rates determined from the viscometer measurements varied from 150 to 1000 (sec⁻¹) (10). In the present experiments with a 3.65 cm diam disk, the maximum shear rates may be calculated (12, 13) and the results vary from 40 to 1200 (sec⁻¹).

Acknowledgment

The authors acknowledge with appreciation the assistance of J. A. Paterson. We also acknowledge with appreciation the support of this research by the Office of Saline Water, the Office of Naval Research, and the Sea Water Conversion Laboratory.

Manuscript submitted Nov. 5, 1971; revised manuscript received Feb. 4, 1972.

Any discussion of this paper will appear in a Discussion Section to be published in the December 1972 JOURNAL.

NOMENCLATURE

C	Concentration of diffusing species, moles/cm ³
$C_0, C_{0,w}, C_{0,x}$	Concentration of O ₂ in fluid, bulk, or at the wall, respectively, moles O ₂ /cm ³ or ppm O ₂
D	Diffusion coefficient, cm ² /sec
J	Mass flux, moles/cm ² sec
K, n	Fluid constants as in Eq. [1]
q	Heat flux, calories/cm ² sec
t	Temperature, °K
V_x	Fluid velocity in x direction, cm/sec
x, y, z	Coordinates, cm
λ	Thermal conductivity, calories/cm sec °K
τ_{xy}	Shear stress, dynes/cm ²

REFERENCES

1. A. H. P. Skelland, "Non-Newtonian Flow and Heat Transfer," John Wiley & Sons, New York (1967).
2. W. L. Wilkinson, "Non-Newtonian Fluids," Pergamon Press, New York (1960).
3. S. B. Clough, H. E. Read, A. B. Metzner, and V. C. Behn, *A.I.Ch.E. (Am. Inst. Chem. Engrs.) J.*, **8**, 346-350 (1962).
4. A. Metzner and D. Gluck, *Chem. Eng. Sci.*, **12**, 185-190 (1960).
5. A. Metzner, R. Vaughn, and G. Houghton, *A.I.Ch.E. (Am. Inst. Chem. Engrs.) J.*, **3**, 92-100 (1957).
6. G. Astarita, *Ind. Eng. Chem. Fundamentals*, **4**, 236-237 (1965).
7. G. Astarita, *ibid.*, **5**, 14-18 (1966).
8. G. Astarita, G. Marrucci, and G. Palumbo, *ibid.*, **3**, 333-339 (1964).
9. G. S. Hansford and M. Litt, *Chem. Eng. Sci.*, **23**, 849-864 (1968).
10. R. Greif, I. Cornet, and R. Kappesser, *Intern. J. Heat Mass Transfer*, To be published.
11. "International Critical Tables," McGraw-Hill Book Co., New York (1928).
12. P. Mitschka, *Collection Czech. Chem. Commun.*, **29**, 2892-2905 (1964).
13. P. Mitschka and J. Ulbrecht, *ibid.*, **30**, 2511-2526 (1965).



This Discussion Section includes discussion of papers appearing in the *Journal of The Electrochemical Society*, Vol. 118, No. 2, 4, 9, and 10; February, April, September, and October 1971.

Investigation of the Direct Reduction of Zinc Oxide in Alkaline Electrolytes

D. Drazic and Z. Nagy (pp. 255-257, Vol. 118, No. 2)

K. Schwabe, O. Hladik, and H. Oude¹: Drazic and Nagy have investigated the direct reduction of zinc oxide in alkaline electrolytes in the paper under discussion. From their experiments they conclude that our suggestion about the direct reduction of solid zinc oxide confirmed by our radiochemical investigations² and by the investigations of other authors is not true; the current efficiency of the direct reduction should be very small with respect to the reduction of the soluted zincate. We cannot agree with this opinion.

The conditions of the experiments are quite different. We have worked with a "paste electrode," that means under conditions which can be compared with a working alkaline zinc battery. The surface of the zinc oxide was very large with respect to the volume of the zincate solution. The conductivity of the zinc oxide was small compared with that of the ZnO single crystal applied by Drazic and Nagy. From the high electron conductivity of the single crystal, it is clear that it works as cathode under the conditions described by the authors, because the amount of zincate in the solution is much larger than that of ZnO in the single crystal. Up to 100 mA/cm², we have not observed any hydrogen evolution with our paste electrode; reducing zincate solution without solid zinc oxide already at 10 mA/cm² the hydrogen evolution is visible. With our paste electrode we observe H₂ evolution only if the reduction of the paste of ZnO was reduced and the formed Zn came in direct contact with the solution. The difference

¹ Forschungsinstitutes Meinsberg, Meinsberg Post 7305 Waldheim, Dresden, Germany.

² O. Hladik and K. Schwabe, *Electrochim. Acta*, 15, 635 (1970).

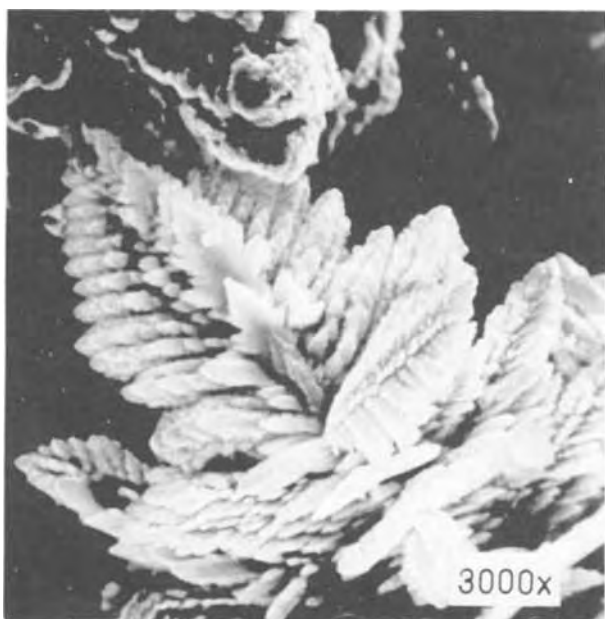


Fig. 1. Electroplated dendrites from saturated solution of potassium zincate (100 mA/cm²).

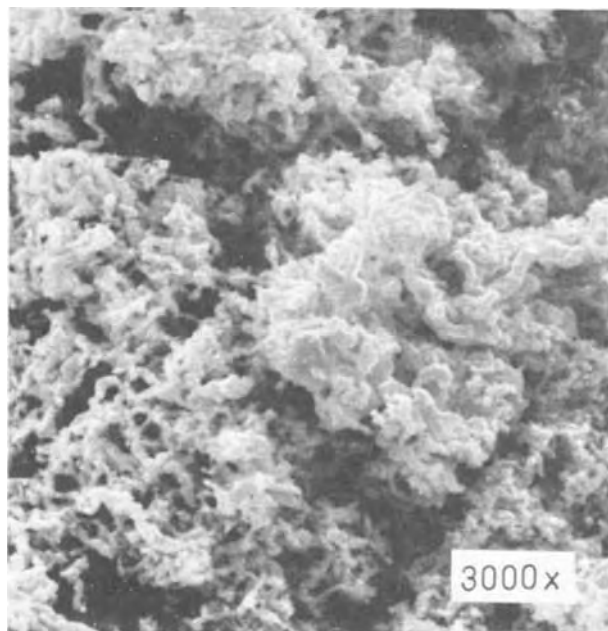


Fig. 2. Crystals electroplated from ZnO/KOH-paste (100 mA/cm²)

in the cathodic overvoltage, which the authors have found, is quite reasonable under their conditions, but not under our conditions. The structure of the zinc reduced from zincate solution is that of dendrites (Fig. 1) found also by Gerischer.³ From ZnO-paste we receive a zinc powder without macrostructure (Fig. 2) because it is formed by destruction of the ZnO lattice. We are therefore convinced, that under our conditions, similar to that of an alkaline Zn-battery, mainly the solid ZnO is reduced because our results can only be explained by this mechanism.

D. Drazic and Z. Nagy: When referring to the paper of K. Schwabe and O. Hladik⁴ we wanted to point out that the polarization curves obtained with the ZnO paste electrode in 1M and 11M hydroxide solutions can also be explained by a process other than the solid-state oxide reduction.

It is known that the polarization curves obtained with porous electrodes (ZnO paste is also a porous system) include a considerable IR voltage drop formed inside the pores, especially at higher current densities. The resulting linear current-voltage relation is particularly well pronounced in Fig. 5 of their paper.⁵ Since no IR drop corrections were made, and the authors have not discussed this matter at all, we had reasons to believe (e.g., if the resistance of the pores in ZnO paste was only 0.5 ohm, the IR drop could be as high as 500 mV at 1000 mA/cm²) that the polarization curves obtained without IR drop corrections should be similar in solutions of similar conductivities, no matter what reaction was going on inside the electrode.

Further, the results of the radiotracer measurements to which the authors refer, seem very logical, but give information only about transfer processes taking place in the bulk of the solution and have nothing to do with the electrode reaction. The results would be the same whether zincate ion or a solid-state reaction path was

³ H. Gerischer, *Surface Sci.*, 13, 265 (1969).

⁴ O. Hladik and K. Schwabe, *Electrochim. Acta*, 15, 635 (1970).

⁵ O. Hladik and K. Schwabe, *Electrochim. Acta*, 15, 635 (1970).

operative. Namely, if the zincate ion path was operative, it would be the zincate ions formed by dissolution of ZnO very close to the metallic zinc surface inside the pores which would be reacting, and not the zincate ions from the bulk of the solution.

The absence of hydrogen evolution from the paste electrode can also be explained by the dissolution-deposition mechanism: the zincate concentration within the pores is kept high by the continuous dissolution of the oxide.

Finally, referring to the question of morphology of zinc deposited within the porous electrode, we think that the nondendritic deposit cannot be considered as proof that zincate ions are not the reacting particles in the electrochemical step of the over-all deposition reaction. It has been shown⁶ that one of the necessary preconditions for dendritic growth is diffusion control of the electrode process. This condition is not fulfilled within the pores because of ready availability of zincate through the dissolution of ZnO and, therefore, no dendrites can be expected until the zincate ions from the solution layer start taking part in deposition, i.e., very close to the end of the charging process.

Hence, we still do not have any reason to believe that our conclusion about the importance of zincate ion reaction path in the charging process cannot be applied to the real situation in batteries.

The Thermodynamics and Electrode Kinetic Behavior of Nickel in Acid Solution in the Temperature Range 25° to 300°C

R. L. Cowan and R. W. Staehle (pp. 557-568, Vol. 118, No. 4)

V. Ashworth⁷ and P. J. Boden⁸: The authors have shown that the data required to construct electrochemical equilibrium diagrams for any system at a temperature other than 298°K may be readily computed by means of the empirical "correspondence principle" technique due to Criss and Cobble. However, the subsequent interpretation of these diagrams is rarely so straightforward as it might appear at first even when their intrinsic limitations are fully appreciated.

In particular, it is important to recognize that the abscissa of the diagram properly refers to the negative logarithm of the hydrogen ion activity ($-\log a_{H^+}$) which for a single solution will vary to a greater or lesser extent throughout the temperature range (i.e., $d \log a_{H^+}/dT \neq 0$). With the exception of solutions within a very limited range of hydrogen ion activity it is, therefore, invalid to use the solution pH measured at room temperature (298°K) as the reference point on the abscissa in connection with a diagram constructed for a higher or lower temperature. Fortunately it is possible to calculate the change in a_{H^+} of a solution with change in temperature and further, for a more limited number of cases, a second scale may be added to the diagram such that the use of the room temperature pH becomes permissible.

In the simplest case, as the temperature of an unbuffered aqueous solution is raised, chemically equivalent amounts of additional hydrogen and hydroxyl ions will be generated as a result of the increased dissociation of water. The ionic product of water, ($K_w(T)$), at temperature T is given by

$$K_w(T) = (a_{H^+}(298^\circ K) + x)(a_{OH^-}(298^\circ K) + x)$$

where x is the additional ion activity as a result of the temperature change from 298°K to T K. At 298°K and pH n

$$a_{H^+} = 10^{-n}$$

and

$$a_{OH^-} = 10^{-(14-n)}$$

⁶ A. R. Despic, J. W. Diggle, and J. O'M. Bockris, *This Journal*, 115, 507 (1968).

⁷ Department of Chemical Engineering, U. M. I. S. T., Manchester, England.

⁸ Department of Metallurgy, Nottingham University, Nottingham, N97, 2RD, England.

thus at temperature, T

$$K_w(T) = (10^{-n} + x)(10^{-(14-n)} + x) \quad [1]$$

and the negative logarithm of the hydrogen ion activity becomes $-\log_{10}(10^{-n} + x)$. Clearly, with a knowledge of the value of $K_w(T)$, the solution of Eq. [1] will yield the corresponding value of x for any given value of n and it becomes possible to refer the negative logarithm of the hydrogen ion activity at T to the room temperature pH. It is this former value which should be used as a reference point when employing the diagrams derived by the authors when considering unbuffered solutions. Alternatively, as shown in Fig. 1, a second scale may be added to the abscissa which conveniently relates pH (at 298°K) to the a_{H^+} at temperature. Since the room temperature pH is more commonly measured this second scale is the more convenient to use, but its asymmetry makes it imprecise for neutral and alkaline solutions. Under these circumstances its linearization, as shown in Fig. 2, becomes desirable. The asymmetry of the new abscissa derives from its logarithmic nature; briefly, although x varies symmetrically with n , reaching a maximum in the neutral pH region, the introduction of small amounts of hydrogen ion by dissociation makes a greater contribution to $-\log a_{H^+}$ at high rather than low pH values.

When a solution has some buffer capacity, the hydrogen ion activity no longer varies as the dissociation constant of water; and, although in these circumstances the use of the second scale is incorrect, calculation of the new activity is possible. Thus an aqueous solution of a weak acid (HA) will contain H_2O , HA, H^+ , A^- and OH^- , to preserve electroneutrality

$$[H^+] = [OH^-] + [A^-] \quad [2]$$

where the square brackets represent concentrations and, further, neglecting activity coefficients

$$K_w = [H^+][OH^-]$$

Thus from Eq. [2]

$$[H^+]^2 = [H^+][OH^-] + [H^+][A^-]$$

and

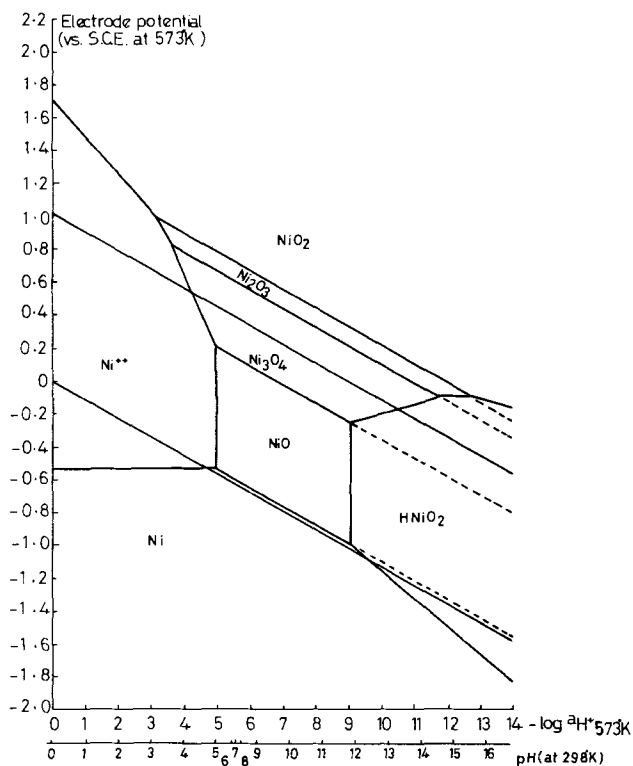


Fig. 1. Potential pH diagram calculated for nickel at 573°K

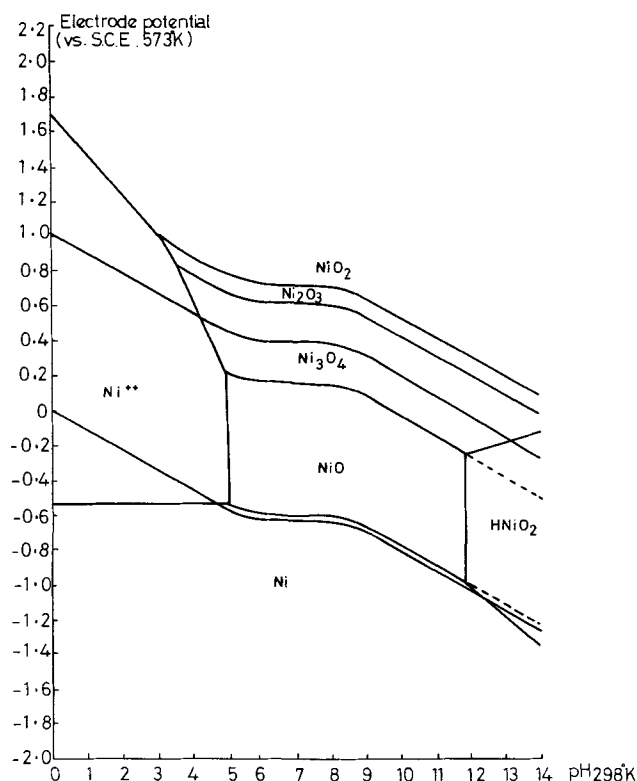


Fig. 2. Potential pH diagram calculated for nickel at 573°K with abscissa in pH units measured at 298°K.

$$2[\text{H}^+]d[\text{H}^+] = dK_w + [\text{H}^+]d[\text{A}^-] + [\text{A}^-]d[\text{H}^+]$$

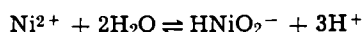
or

$$d[\text{H}^+] = \frac{dK_w + [\text{H}^+]d[\text{A}^-]}{2[\text{H}^+] - [\text{A}^-]} \quad [3]$$

That is, if some undissociated HA is present in the solution at 298°K, by raising the temperature the hydrogen ion activity will alter as a result of changes in both K_w and K_{HA} (the acid dissociation constant). In the special case where $[\text{A}^-]$ cannot change (unbuffered solutions of strong acids and in pure water), $d[\text{A}^-]$ becomes zero for a temperature rise and the value of $d[\text{H}^+]$ from Eq. [3] will coincide with the value of x given by Eq. [1]. The analogous equation to Eq. [3] for a solution containing a weak base (BOH) is given by

$$d[\text{H}^+] = \frac{dK_w - [\text{H}^+]d[\text{B}^+]}{2[\text{H}^+] + [\text{B}^+]}$$

To use the derived equilibrium diagrams correctly it becomes necessary to calculate the value of $d[\text{H}^+]$ and, hence, a_{H^+} for the buffered solution at the temperature in question. A buffered condition which may be overlooked occurs when the metal-water system generates a self-buffering situation which controls the a_{H^+} by means of displacement of a hydrolytic equilibrium. For example, in the Ni/H₂O system the equilibrium



may become important at very high temperatures and itself represent such a self-buffered system. Although the nickel ion activity ($\text{Ni}^{2+} + \text{HNiO}_2^-$) is defined, when the diagram is calculated (say at 10^{-6} kg ions/m³), the hydrogen ion activity will depend on the dissociation constant of the weak acid Ni^{2+} . Any combination of $a_{\text{Ni}^{2+}}$ and $a_{\text{HNiO}_2^-}$ which satisfies the requirement

$$a_{\text{Ni}^{2+}} + a_{\text{HNiO}_2^-} = 10^{-6} \text{ kg ions/m}^3$$

is permissible. Nevertheless, the use of Eq. [3] is equally applicable to such a system and requires only

a recognition that all solution species must be considered in calculating the variation in hydrogen ion activity.

Returning to the original paper the authors point out that, on the basis of their electrochemical equilibrium diagrams, "the range of stability of the nickel oxy-anion HNiO_2^- , increases greatly with increasing temperature." Superficially this suggests that, in mildly oxidizing alkaline solution, nickel metal will be in equilibrium with NiO at 298°K; whereas, in the same solution heated, say to 573°K, the metal will be in equilibrium with the oxy-anion. That is, in the former case the material may become passive and in the latter it may corrode. In fact such a highly alkaline solution (see the authors' Fig. 2 in the paper under discussion) will be, at best, only poorly buffered; the temperature rise will increase the a_{H^+} , and as our Fig. 2 shows, the probability is that the solution will be no more aggressive at 573°K than it was at 298°K, although both predictions may be overruled by kinetic factors. The implication of this calculation is that the temperature differential of the dissociation constant of the "acid" NiO is comparable with that for the ionic product of water. As a broad generalization it can be said that the equilibrium diagrams for the Ni/H₂O system predict that an increase in temperature will lead to an over-all increase in the stability range of NiO (from pH 9-12 at 298°K to $\text{pH}_{(298^\circ\text{K})}$ 5-12 at 573°K), the metal being resistant, to a wider range of aqueous environments at the higher temperatures. It is interesting to speculate that had the region of stability of the oxy-anion advanced to values of $-\log a_{\text{H}^+}$ approaching 7 at the higher temperature, then a test solution based on a temperature stable buffer system of pH ca. 7 at room temperature might prove to be more aggressive to Ni than an unbuffered solution of similar pH (at 298°K), the additional hydrogen ions generated in the latter case shifting the metal into a passive region.

The following analysis of the change of a_{H^+} with temperature broadly confirms the observations of Greeley, reported by the authors, that for a closed hydrogen saturated acid solution only small changes in a_{H^+} occur with increase in temperature. Nevertheless, that small change has a significant effect on $-\log a_{\text{H}^+}$ in weakly acid solutions ($\text{pH} > 4$ at 298°K). For example, we have calculated the activity of the hydrogen ion at various temperatures for the solutions used by the authors, assuming them to be effectively unbuffered (solutions of strong acids and the salts of strong acids and bases), with the results given in Table I.

Table I.

	Temperature (°K)						
	298	323	363	423	473	523	573
$-\log a_{\text{H}^+}$	1.30	1.30	1.30	1.30	1.30	1.30	1.30
	3.40	3.40	3.40	3.40	3.40	3.40	3.40
	6.30	6.24	6.04	5.75	5.60	5.55	5.55

The table shows that only in the case of the two most acid solutions does $-\log a_{\text{H}^+}$ remain constant. This effect interacts not only with the interpretation of the equilibrium diagrams but also with the authors' correction to E_{corr} . This correction was used by the authors to allow for the thermal liquid junction potential in their system and, further, to transpose their potential measurements to the standard hydrogen scale at the test temperature. The correction is valid for the two most acid solutions but, as a result of the assumption that a_{H^+} remains constant throughout the temperature range, the authors' values for E_{corr} and the arrest potentials in the least acid solution are in error by up to 86 mV $[(6.30 - 5.55) \times 2.3 RT/F]$, that is, the potentials are not all on the "same thermodynamically meaningful scale." This does not invalidate the conclusions drawn from the potential decay experiments

Table II.

Temp, °K	$E_{\text{arrest}} \text{ (V)}$		$E_{\text{Ni/NiO}}$ vs. SHE _(298°K)	$E_{\text{Ni/Ni}_3\text{O}_4}$ vs. SHE _(298°K)
	vs. SHE _(TK)	vs. SHE _(298°K)		
pH 1.3				
295	+0.240	+0.237	+0.041	+0.231
327	+0.213	+0.239	+0.036	+0.225
pH 3.4				
306	+0.078	+0.085	-0.089	+0.101
328	+0.048	+0.074	-0.102	+0.087
370	-0.075	-0.011	-0.126	+0.062
571	-0.205	+0.033	-0.241	-0.061
pH 6.3				
295	-0.204	-0.207	-0.251	-0.061
327	-0.261	-0.235	-0.289	-0.100
354	-0.335	-0.286	-0.320	-0.131
381	-0.350	-0.278	-0.350	-0.163
574	-0.500	-0.259	-0.574	-0.394

since the failure to allow for changes in a_{H^+} in correcting the arrest potentials is counteracted by the same omission in the calculation of the equilibrium potentials for the oxides.

Thermal temperature coefficients of standard electrode potential may be calculated from first principles by the method due to de Bethune *et al.*⁹ which uses entropy data determined at 298°K. For the Ni/NiO and Ni/Ni₃O₄ equilibria we have obtained coefficients of +0.097 and +0.062 mV/°K, respectively, using the entropy data given by Cowan and Staehle. In Table II we record the calculated thermal equilibrium potentials (*i.e.* with respect to a standard hydrogen electrode at 298°K) for these reactions at the pH levels investigated by the authors. In deriving these values no allowance has been made for changes in a_{H^+} with temperature in order that our calculations should be on the same basis as the reported results. The table also includes the values of the potential arrests obtained by the authors both as reported and also corrected to the standard hydrogen scale at 298°K (assuming dE°/dT for the hydrogen electrode to be 0.871 mV/°K). The calculations appear to confirm the views of the authors that in the two most acid solutions and at the highest temperature in the least acid solution the bulk oxide, if not the passive film, is Ni₃O₄; whereas, at lower temperatures in this latter solution the bulk oxide is NiO although the near correspondence between the arrest and equilibrium potentials may well be fortuitous. While it is gratifying that the equilibrium potential calculated for elevated temperatures by two entirely independent methods give rise to the same conclusions, when compared with the present experimental data it is disappointing that these potentials do not coincide when transposed to the same reference scale. The accuracy of the method used by the authors for estimating C_p at temperature has been questioned recently¹⁰ and it may be that the disagreement arises from this source although we have no reason to suppose that the entropy data used in our calculations is more accurate.

A serious limitation of the electrochemical equilibrium diagram has always been that it can only be as good as the data from which it is constructed. This restriction is magnified in the high temperature diagrams and a cautious approach to the interpretation of experimental data in terms of such diagrams seems appropriate.

M. Kesten¹¹: In the paper under discussion, Cowan and Staehle found that the active-passive transition of the metal disappeared when the temperature of the electrolyte was raised above 90°C. For the interpretation and possible explanation of this phenomenon it is worthwhile to refer to the considerable number of

⁹ A. J. de Bethune, T. S. Licht, and N. Swendeman, *This Journal*, 106, 616 (1959).

¹⁰ J. V. Dobson and H. R. Thirsk, *Electrochim. Acta*, 16, 315 (1971).

¹¹ Institut für Metallphysik, Technische Universität Berlin, 1 Berlin 15, Germany.

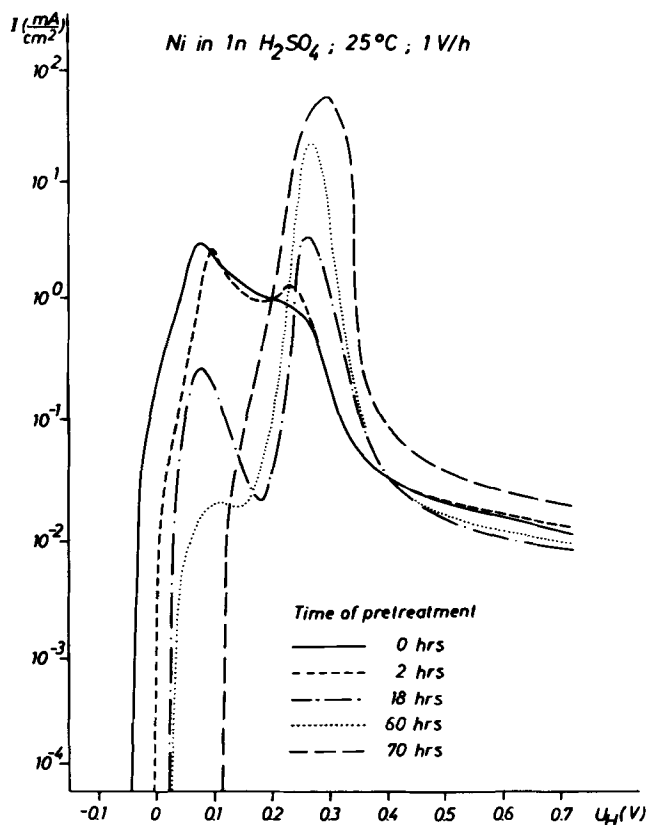


Fig. 1. Anodic polarization behavior of nickel (99.998%) in the active to noble scan mode. Before the experiment the samples have been kept in the electrolyte for different times.

recent investigations dealing with the specific influence of anions on the polarization characteristics of metals.¹²⁻²² It has been proved in these studies that anions, which are adsorbed on the surface of the metal, are apt to participate in the dissolution mechanism. Their effectiveness on the reactions taking place at the interface depends on the bonding strength between them and the surface atoms of the metal. While weakly adsorbed ions inhibit the active metal dissolution by reducing the available free surface, strongly adsorbed ions are able to accelerate the dissolution of the metal whenever they undergo chemical reactions with the surface atoms.

This kind of behavior is not only restricted to the halide ions Cl⁻, Br⁻ and J⁻. It has been found for sulfate ions as well, although, under similar conditions these ions are adsorbed to a much smaller degree.²³ Because of the necessary activation energy, the specific adsorption of anions from the electrolyte is a matter of time and temperature. According to Dreyer and Dreyer,²⁴ the time to reach a maximum coverage with sulfate ions on a Zr surface is about 10³ min at 20°C, while at 80°C this process is completed in 20 min. Besides all this, the competitive adsorption of other particles of the electrolyte (*e.g.*, OH⁻ ions or chemisorbed oxygen) can also play an important

¹² Y. M. Kolotykin, *This Journal*, 108, 207 (1961).

¹³ K. E. Heusler and G. H. Cartledge, *This Journal*, 108, 732 (1961).

¹⁴ B. Y. Konyaev and V. A. Khitrov, *Zashchita Metal.*, 2, 745 (1966).

¹⁵ Y. M. Kolotykin, *Zashchita Metal.*, 3, 131 (1967).

¹⁶ N. Y. Buné, *Zashchita Metal.*, 1, 168 (1965).

¹⁷ N. Y. Buné, *Zashchita Metal.*, 3, 50 (1967).

¹⁸ G. G. Lopovok, Y. M. Kolotykin, and L. A. Medvedeva, *Zashchita Metal.*, 2, 527 (1966).

¹⁹ W. J. Lorenz, *Corrosion Sci.*, 5, 121 (1965).

²⁰ Z. A. Iofa, V. V. Batrakov, and Kho Ngok Ba, *Protection of Metals*, 1, 44 (1965).

²¹ Z. A. Iofa, *Zashchita Metal.*, 6, 49 (1970).

²² M. Kesten and H. G. Feller, *Electrochim. Acta*, 16, 763 (1971).

²³ T. Murakowa, T. Kato, S. Nagaura, and N. Hackerman, *Corrosion Sci.*, 7, 657 (1967).

²⁴ I. Dreyer and R. Dreyer, *Z. Physik. Chem.*, 236, 107 (1967).

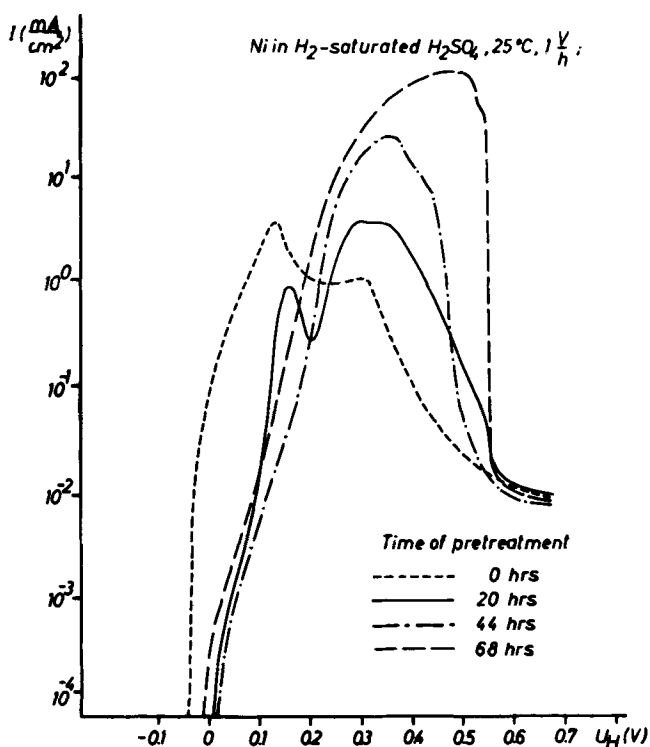


Fig. 2. Anodic polarization behavior of nickel (99.998%) in the active to noble scan mode. Consecutive runs measured with the same sample. Between the runs the sample has been kept unpolarized in the electrolyte for one day.

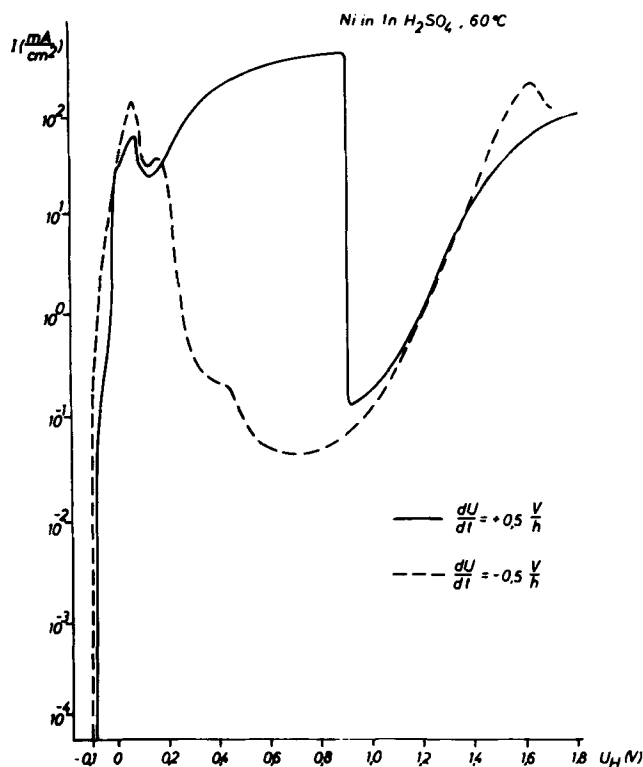


Fig. 3. Anodic polarization behavior of nickel (99.998%) in both scan modes at 60°C.

role.^{25,26} Under these circumstances the question of a pretreatment of the sample before the experiment becomes a critical factor for the interpretation of any result.

²⁵ K. Schwabe, *Electrochim. Acta*, **6**, 223 (1962).

²⁶ K. Schwabe and C. Weissmantel, *Z. Physik. Chem.*, **215**, 48 (1960).

Our recent studies, about the influence of specifically adsorbed sulfate ions on the anodic behavior of nickel,²⁷ proved that one can get very similar results to those reported by Cowan and Staehle. But instead of increasing the temperature, the adsorption conditions for the sulfate ions were changed prior to the polarization experiment. Figure 1 shows the polarization curves obtained in 1N H₂SO₄ with nickel samples pretreated differently. Before the polarization was started the samples were kept in the electrolyte at the open circuit potential for different times. With increasing time of pretreatment the amount of specifically adsorbed sulfate ions increases too. At the same time, the primary nickel dissolution is lowered considerably. On the other hand, a remarkable increase in metal dissolution is observed in a potential region where untreated samples already undergo the active-passive transition. It could be demonstrated that, in this range of second activation, the nickel dissolves because of the direct participation of the sulfate ions in the dissolution process.

The described effect increases, when hydrogen is bubbled through the solution (Fig. 2). With increasing metal dissolution the so-called passivation potential is shifted to higher values. Finally, Fig. 3 shows the polarization curve of an untreated sample measured in 1N H₂SO₄ at 60°C. It indicates that the time for getting a sufficient coverage with sulfate ions can be minimized by increasing the test temperature.

The potential of the sudden passivation of the electrode is not reproducible. Polarization curves of that kind, reported also by Cowan and Staehle, are typical for dissolution processes proceeding with high current densities. In these cases the shape of the curve no longer reflects the true relationship between the current density and the electrode potential, because of the IR drop in the potential measuring system.²⁸ From those data alone it is not possible, therefore, to decide whether an electrode is in the active or passive condition corresponding to a certain measured potential.

On the basis of the cited literature and our own experimental results the vanishing of the active-passive transition in nickel, under the condition reported by Cowan and Staehle, is not unexpected. It is a consequence of the specific adsorption of sulfate ions favored by the temperature of the electrolyte.

Polarization Behavior of Graphite in Sodium Chloride Solutions in the Presence and Absence of Ethylene

A. Bélanger, G. Bélanger, and A. K. Vijh
(pp. 1543-1545, Vol. 118, No. 9)

N. Ibl and P. M. Robertson²⁹: We are investigating, and have been for some time, the oxidation of olefins (mainly isobutylene) at various electrodes in H₂SO₄ and HClO₄ solutions, with and without the addition of mercury salts. Our results are in agreement with those of the authors. No reaction was observed at graphite anodes. Substantial oxidation takes place only at gold electrodes.³⁰ The oxidation on gold of lower molecular weight olefins, such as ethylene, has been the subject of a few recent papers.^{31, 32} On the other hand, with the system of the authors, chlorhydrin (which is an intermediate in the production of the oxide) is easily formed. We obtained, with very high current efficiency (up to 97%), ethylene and propylene chlorhydrin at graphite anodes,³³ the pH being, however, somewhat more acid than that in the experiments of Bélanger *et al.*

²⁷ M. Kesten and H. G. Feller, *Electrochim. Acta*, **16**, 763 (1971).

²⁸ J. Osterwald, *Ber. Bunsenges. Physik. Chem.*, **66**, 401 (1962).

²⁹ Technisch-chemisches Laboratorium, Swiss Federal Institute of Technology, Zurich, Switzerland.

³⁰ P. M. Robertson, H. Isler, and N. Ibl, *Chem. Ing. Tech.*, In preparation.

³¹ J. W. Johnson, S. C. Lai, and W. J. James, *Electrochim. Acta*, **15**, 1511 (1970).

³² T. N. Hartley and D. Price, *This Journal*, **117**, 448 (1970).

³³ N. Ibl and A. Selvig, *Chem. Ing. Tech.*, **42**, 180 (1970).

A. Bélanger, G. Bélanger, and A. K. Vijh: We appreciate Ibl and Robertson's comments and are gratified that their results are in agreement with ours for the comparable system. The related work on gold cited by these authors also appears of interest although clear-cut explanation of different behavior at gold and other electrodes is still an open question, notwithstanding the interpretations put forward previously.³⁴

In this context, it is perhaps relevant to point out that our recent attempts³⁵ to carry out partial anodic oxidation of methane and ethylene in liquid ammonia, with a view to prepare alkyl amines, have not been successful even when a variety of electrode material was examined.

Energetics of Single Ion Solvation in Nonaqueous Solvents and the Effects on Electrode Kinetics

M. Salomon (pp. 1609-1614, Vol. 118, No. 10)

O. Popovych³⁶: In this paper Salomon raises the known³⁷ valid objection to Izmailov's extrapolation methods of determining the solvation energies of single ions, but then proceeds to use what appears to be a slight modification of one of these methods. According to Salomon, Izmailov extrapolated as a function of reciprocal radius, r^{-1} , only the combinations $(\Delta G^{\circ}_M - \Delta G^{\circ}_H)$ and $-(\Delta G^{\circ}_H + \Delta G^{\circ}_X)$, obtaining nonlinear plots with potentially two different intercepts. What he fails to mention, however, is that Izmailov was aware of these difficulties and, therefore, recommended plotting the average of the above functions, $[(\Delta G^{\circ}_M - \Delta G^{\circ}_X)/2 - \Delta G^{\circ}_H]$, which in mathematical form is identical with Salomon's own Eq. [1] in the paper under discussion. This average function also gives linear plots and unique values for the intercept. The only discrepancy between Izmailov's and Salomon's approaches is that the former used average reciprocal radii of isoelectronic ions, whereas the latter interpolated his data points for hypothetical anions and cations of equal radii. Unfortunately, neither the essence of this modification, nor the rationale for its supposed superiority over Izmailov's approach are brought out for the benefit of the reader.

In my opinion, the same objections pertain to Salomon's as to Izmailov's methods. In both approaches, long extrapolations to infinite radius are made from data points representing a narrow range of small ions, mostly those of alkali metals and the halides. None of the ions in Salomon's plots are as large as 4-5Å (the point corresponding to $r^{-1} = 0.2$, in Fig. 1 of the paper being discussed, must be an extrapolation already). On the other hand, we found^{38, 39} that the ΔG° 's for the tetraalkyl and tetraaryl ions with radii in the 4-5Å range are determined overwhelmingly by their non-electrostatic, or neutral components, $\Delta G^{\circ}(\text{neut})$, which are not functions of r^{-1} . Salomon dismisses the whole question of $\Delta G^{\circ}(\text{neut})$ too lightly, at the same time attributing, incorrectly, to Noyes⁴⁰ an endorsement of the isoelectronic inert-gas assumption for its estimation.

Salomon's rejection of the reference-electrolyte method for the estimation of solvation-energy changes for single ions is poorly founded. It is motivated mainly by the possibility of experimental errors in the determination of solubility products, rather than by any flaws in the method itself. Certainly no chemist would seriously accept the generalization that solubility products are unreliable because of possible complications due to ion pairs, crystal solvates, complexes, and

micelles. Of these obstacles, only a slight degree of ion pairing was encountered in our work with the reference electrolytes, and it was easily corrected with the aid of conductance data. Thus, the above experimental difficulties are neither generally encountered nor are they fundamental to the evaluation of the reference-electrolyte method.

The only genuine criticism directed at the basic assumption of the reference-electrolyte method, is that cited from the work of Coetzee and Sharpe⁴¹ who deduced from NMR shifts the existence of specific solvation effects even with the large reference ions. We have shown,³⁸ however, that the differentiating effects of the several solvent pairs in question are, at the most, of the order of experimental error in the measured solvation-energy changes for the tetraphenylarsonium and the tetraphenylphosphonium reference ions. The experimental error of the ΔpK_{sp} determinations is about 0.1 kcal/mole. To my knowledge, no extrapolation method is capable of that kind of precision.

M. Salomon: The relative merits between extrapolation and reference ion methods for obtaining individual ionic contributions to free energies and/or enthalpies is indeed a complex problem as indicated by Popovych above and elsewhere.⁴² From a theoretical viewpoint there is much to be desired in either method, but there are instances in which one is to be preferred. This is true for the methanol-water systems as several inconsistencies appear in the use of solubility data (see below). In the case of careful solubility measurements, such as those reported by Cogley *et al.*⁴³ where oxygen and water were rigorously excluded from various propylene carbonate (PC) solutions, there is excellent agreement with those results obtained by the emf method (e.g., see footnote 44). For the salts NaCl and KCl, the solubility data of Cogley *et al.* give $\Delta G^{\circ}_{\text{soln}}$ values of 10.7 and 9.5 kcal/mole⁻¹, respectively; the emf data give 10.5 and 9.4 kcal/mole⁻¹, respectively, for these salts. The split into $\Delta G^{\circ}_t(\text{ion})$ values by the solubility method⁴³ and the extrapolation method⁴⁴ are gratifyingly close so that it is difficult to choose between the two.

The methanol-water systems studied by various methods^{42, 45-47} are, however, not consistent as is shown in Table V of my original paper. In this table, it should be noted that for those cases^{45, 47} where the sum $\Delta G^{\circ}_t(M^+) + \Delta G^{\circ}_t(X^-)$ are not equal to the observed⁴⁶ $\Delta G^{\circ}_t(MX)$, the results based on an extrapolation method⁴⁷ and a reference ion method⁴⁵ are similar. Both indicate that methanol is a weaker base than water. There is, however, contrary evidence^{46, 48, 49} which indicates that methanol is the stronger base and this is suggested by negative values of $\Delta G^{\circ}_t(M^+)$ for the transfer of small cations from water to pure methanol or methanol-water mixtures.

Let us consider first, Izmailov's method of extrapolation.⁴⁷ We have shown elsewhere,⁴⁹ and in my paper, that the values of $\Delta G^{\circ}_{\text{soln}}(MX)$ used by Izmailov are in error and that this accounts for the nonlinearity of his cation plot. While it is true that Izmailov does plot the average function

$$\{(\Delta G^{\circ}_M + - \Delta G^{\circ}_X -)/2 - \Delta G^{\circ}_H +\} \text{ vs. } \frac{1}{2}(\Gamma_{M^+}^{-1} + \Gamma_{X^-}^{-1}) \quad [1]$$

Popovych's statement above indicates that this procedure is in fact identical with mine. This is not the

³⁴ J. W. Johnson, S. C. Lai, and W. J. James, *Electrochim. Acta*, **15**, 1511 (1970).

³⁵ A. K. Vijh, *This Journal*, In preparation.

³⁶ Department of Chemistry, Brooklyn College of the City University of New York, Brooklyn, New York 11210.

³⁷ O. Popovych, *Critical Reviews in Analytical Chemistry*, **1**, 73 (1970).

³⁸ O. Popovych, A. Gibofsky, and D. H. Berne, *Anal. Chem.*, In preparation.

³⁹ D. H. Berne and O. Popovych, *Anal. Chem.*, In preparation.

⁴⁰ R. M. Noyes, *J. Am. Chem. Soc.*, **84**, 513 (1962).

⁴¹ J. F. Coetzee and W. R. Sharp, *J. Phys. Chem.*, **75**, 3141 (1971).

⁴² O. Popovych, *Critical Reviews in Analytical Chem.*, **1**, 73 (1970).

⁴³ D. R. Cogley, J. N. Butler, and E. Grunwald, *J. Phys. Chem.*, **75**, 1477 (1971).

⁴⁴ M. Salomon, *J. Phys. Chem.*, **74**, 2519 (1970); *J. Electroanal. Chem.*, **26**, 319 (1970).

⁴⁵ O. Popovych, *J. Phys. Chem.*, **70**, 1671 (1966); *Anal. Chem.*, **38**, 558 (1966).

⁴⁶ D. Feakins, "Physico-Chemical Processes in Mixed Aqueous Solvents," F. Franks, Editor, Elsevier, New York (1967).

⁴⁷ N. A. Izmailov, *Russ. J. Phys. Chem.*, **34**, 1142 (1960).

⁴⁸ F. Franks and D. J. G. Ives, *Quart. Rev.*, **20**, 1 (1966).

⁴⁹ C. M. Criss and M. Salomon, "Physical Chemistry of Organic Solvents," A. K. Covington and T. Dickinson, Editors, Chap. 2.4, Plenum Press, London (1972).

case as is exemplified in my paper and in the following quote from Izmailov: " $\Delta G^{\circ}_{H+} + \Delta G^{\circ}_{X-}$ can be plotted as a function of $1/r$ for the corresponding halide ions and the quantity $\Delta G^{\circ}_{H+} - \Delta G^{\circ}_{M+}$ as a function of $1/r$ for the corresponding metal ions. Both these quantities will tend, as r increases, to one value $\Delta G^{\circ}_{H+} \dots$. Determination of the limit is not very reliable since it is necessary to extrapolate from distances remote from $1/r = 0$. Since, however, the two plots tend the same limit, and $\Delta G^{\circ}_{H+} + \Delta G^{\circ}_{X-}$ is a linear function of $1/r$, it is nevertheless possible to find that limit. This is facilitated by plotting an auxiliary line, representing the means of the sums and differences, which tends to the same limit $\Delta G^{\circ}_{H+} \dots$." Thus Izmailov does not report (as Popovych suggests) average values of the intercepts for the cation and anion plots but, rather, a single one. The values of ΔG°_{H+} , which I and which Franks and co-workers (e.g., see footnotes 46 and 48) report, are averages of the cation and anion intercepts. The belief that not all components of the solvation energy vanish at $1/r \rightarrow 0$, which incidentally was discussed and considered to be negligible by Izmailov, is the essence of the difference between our two works. The statement by Popovych, that the essence or rationale for my method is not brought out for the reader, is not well founded as considerable discussion was presented. Since my method assumes that these nonvanishing components to ΔG° (ion) become equal for very large ions, there is then the question (which Popovych did not comment upon) of whether or not this is valid. The reference to Noyes' paper serves only to illustrate an alternate model which might invalidate my method and does not refer to any stand on the subject by this author.

The use of reference ions to calculate ΔG°_t (ion) values is not rejected in my paper as discussed above. There are, however, times when the use of some reference salts should be excluded as there are instances in which some extrapolations should also be excluded. In the methanol-water systems there is no data in the literature that I could find which might indicate that such salts as tetrabutylammonium tetraphenylboride (Bu_4NBPh_4) or triisobutylbutylammonium tetraphenylboride ($TAB \cdot BPh_4$) do not exhibit specific solvation or ion-ion interactions; however, there is the NMR data on similar salts studied by Coetzee and Sharp⁵⁰ which cautions one in the use of this method for the solvents under consideration here. I do not doubt that free energies based on solubility can be measured to within 0.1 kcal/mole. What I do doubt, in some cases, is the accuracy of some measurements. For example, based on the solubility of KCl in water and methanol, a value of $\Delta G^{\circ}_t(KCl)$ was obtained⁴⁵ which is ~ 1 kcal/mole lower than that obtained by the emf method (e.g., see footnote 46). This exceeds Popovych's stated accuracy by a factor of ten. There is also the question regarding the solubilities of the salts of the large reference ion in water and methanol⁴⁵ because of their in-

⁵⁰ J. F. Coetzee and W. R. Sharp, *J. Phys. Chem.*, **75**, 3141 (1971).

stability in aqueous solutions, and because of the different standard states employed. Since the salts Bu_4NBPh_4 and $TAB \cdot BPh_4$ are unstable in water, an additivity method was used⁴⁵ to obtain $\Delta G^{\circ}_t(\text{salt})$: e.g.

$$\Delta G^{\circ}_t(TAB \cdot BPh_4) = \Delta G^{\circ}_t(TAB \cdot Pi) + \Delta G^{\circ}_t(KBPh_4) - \Delta G^{\circ}_t(KPi) \quad [2]$$

where Pi = picrate ion. Equation [2] is thermodynamically correct and the accuracy of the quantity on the LHS is dependent upon that of the RHS. Assuming that oxygen and water have been rigorously excluded from the methanol solutions, a problem of different standard states can arise using solubility data. For example, in methanolic $TAB \cdot Pi$ solutions, the concentration of undissociated salt (or ion-pair?) is 0.125M compared to the free ion concentration of 0.267M. Similarly, for $Bu_4N \cdot Pi$ solutions in methanol the solvated salt (or ion-pair?) concentrations is 0.359M compared to 0.514M for the free ions.⁴⁵ Two points are of interest here: first, for solutions of such high concentrations, γ_{\pm} cannot be calculated from a simple Debye-Hückel equation^{51,52} but rather from one of the extended relations; second, is the point that the calculation of $\Delta G^{\circ}_{\text{soln}}(\text{salt})$ for the above saturated solutions (from $-2RT \ln [M_{\text{sat}} \gamma_{\pm}]$) refers to standard states of 0.125M and 0.359M of undissociated salt for $TAB \cdot Pi$ and $Bu_4N \cdot Pi$, respectively. While a constant ionic strength media is as valid a standard state, as is the zero ionic strength media, one must be consistent in employing the same standard state throughout. Since a mixing of standard states does occur in this work,⁴⁵ another source of error is introduced into the solubility data. The fact that ion-pairing has been corrected for in this work is, therefore, irrelevant to accuracy of the ΔpK_{50} results.

Finally, in answering Popovych's comments on ionic relations, I think adequate discussion has been presented in my paper and elsewhere^{46,48,49,53} where the basis of a linear $1/r$ relation is attributed to enthalpy and entropy effects. Certainly linear relations exist; or is this being questioned? If on this matter Popovych is justifying his use of reference ions of equal Stokes radii, then I can only say again that the significance of these radii is unclear. The fact that Walden's rule holds (only) for the larger ions in many solvents is misleading since it suggests a causative relationship between λ° and η : the relevant value for η in Stokes' frictional factor $6\pi\eta r_s$ is uncertain due to electrostriction, local structure-making or breaking effects, and dielectric relaxation effects which really requires the use of local rather than bulk values of η (cf. 52, 54).

⁵¹ W. J. Hamer, National Bureau of Standards Publication No. NSRDS-NBS 24, Dec. (1968).

⁵² B. E. Conway, "Physical Chemistry. An Advanced Treatise," E. Eyring, Editor, Vol. IXA, Chap. 1, Academic Press, New York (1970).

⁵³ M. Salomon, *J. Phys. Chem.*, **74**, 2519 (1970).

⁵⁴ G. J. Hills, "Chemical Physics of Ionic Solutions," B. E. Conway and R. G. Barradas, Editors, Chap. 23 (and following discussions), John Wiley & Sons, New York (1966).

Erratum

In the paper "Electrolytic Determination of Porosity in Gold Electroplates, II. Controlled-Potential Techniques" by Ronald J. Morrissey which appeared on pp. 446-450 in the April 1972 JOURNAL, Vol. 119, No. 4, on p. 447 the term $(\beta_a/\beta_a + \beta_c)$ in Eq. [2] and [4] should appear as an exponent rather than as a multiplier, so that the correct expressions should be

$$I_{\text{corr}} = C_1 A_a \frac{\beta_a}{\beta_a + \beta_c} \quad [2]$$

and

$$\frac{\Delta I}{\Delta V} = C_1 C_2 A_a \frac{\beta_a}{\beta_a + \beta_c} \quad [4]$$



Oxidation of Beta-Phase Plutonium

J. W. Lindsay, K. Terada, and M. A. Thompson

Dow Chemical U. S. A., Rocky Flats Division, Golden, Colorado 80401

ABSTRACT

Oxidation of β -phase plutonium was studied by hot-stage x-ray diffraction, microtopography, and thermogravimetry. The oxidation process was found initially to proceed by the formation of a protective sesquioxide film. Subsequently, the protective film was destroyed by blistering and the reaction rate accelerated.

Plutonium is very susceptible to oxidation. The mechanisms involved in this oxidation are complicated by the existence of six temperature-dependent allotropic modifications of the metal and a rather complex metal-oxygen relationship (1). Of the six metallic phases, the low-temperature α -phase which is stable to 112°C, has received the most attention (2-8). Under conditions of low humidity, oxidation of the α -phase appears to follow a parabolic rate law. Sackman (4) observed a series of successive parabolic weight gain curves when the reaction was allowed to proceed for extended periods of time. This behavior was thought to arise from the continued failure and regrowth of a protective sesquioxide film.

Few in-depth investigations of the reactions of higher temperature metallic phases with oxygen have been made. Schnizlein and Fischer (9), in investigating the oxidation process above 140°C reported parabolic kinetics through the β (112°-185°C), γ (185°-310°C), and δ (310°-452°C) phases. The parabolic model involves the simultaneous production of a protective inner film and an outer porous layer. Thompson (10) observed two linear stages of oxidation in the β -phase with parabolic kinetics being followed only in the γ - and δ -phases.

Both Thompson and Schnizlein observed a reduction in the rate of oxidation of δ -phase metal at about 400°C. Thompson (10) and Vesterberg and Ekbohm (11) reported an additional rate reduction occurring in the β -phase at about 160°C.

The present study was designed to investigate reaction mechanisms and kinetics associated with the oxidation of β -phase plutonium. Special attention was given to the relationship between the reaction rate, types of oxides formed, and microtopography of the resulting oxide products. Kinetic data were obtained by thermogravimetry. The types of oxides produced and the exterior oxide surface characteristics were followed by hot-stage x-ray diffraction and microscopy using conditions duplicating those in the rate studies.

Experimental Material and Procedures

Material.—Very pure electrorefined plutonium metal was used in the kinetic and mechanistic investigations. The electrorefined button was cast into an ingot and hot-rolled in the β -phase to a thickness of 0.018 in. Impurities in the resulting sheet are listed in Table I.

Key words: corrosion, alpha-Pu₂O₃, PuO₂.

Procedures.—Isothermal oxidation experiments were conducted with fresh polished samples. The samples were given a final finish with dry jeweler's rouge. The oxidation was followed thermogravimetrically on a Mettler I Thermoanalyzer enclosed in a glove box. The atmosphere used in the investigation was a 20% O₂-80% Ar mixture. Moisture was removed to less than 10 ppm by volume by passing the gas over a molecular sieve desiccant. Moisture levels were determined with a Consolidated Engineering Corporation Model 26-303 hygrometer. All runs were made at 640 Torr.

Hot-stage x-ray diffraction patterns of the initial stages of oxidation were made at various isotherms with a Picker Nuclear diffractometer fitted with a hot-stage cell. Metal samples and atmospheres were kept as closely as possible to those employed in the kinetics investigations. Hot-stage optical microscopy investigations were made using a Unitron Model HHS metallograph. Conditions were again kept as closely as possible to those employed in the thermogravimetric runs.

Results

Thermogravimetry.—Isothermal weight gain curves showing the rate of oxygen reaction with respect to time are shown in Fig. 1. The figure also shows that the over-all reaction rate increases with temperature between 120° and 175°C before decreasing to a minimum at about 190°C. Above 190°C, the rate resumes its increase with temperature. Each curve consists of two distinct stages of oxidation. This phenomenon oc-

Table I. Bulk metal impurities

Element	Impurity, ppm by weight	Element	Impurity, ppm by weight
Al	28.0	Li	0.05
As	0.7	Mg	2.0
B	0.09	Mn	9.0
Ba	0.8	N	3.0
Be	0.06	Na	2.0
C	10.0	Nd	8.0
Ca	0.9	Ni	0.6
Cd	0.8	Np	1.0
Cl	6.0	O	38.0
Co	0.04	P	0.1
Cr	2.0	Pb	0.2
Cu	0.7	Pr	4.0
F	0.2	S	0.7
Fe	7.0	Si	7.0
Gd	4.0	Ta	31.0
I	0.2	Ti	1.0
K	0.9	U	2.0
La	5.0	W	65.0
		Zn	2.0

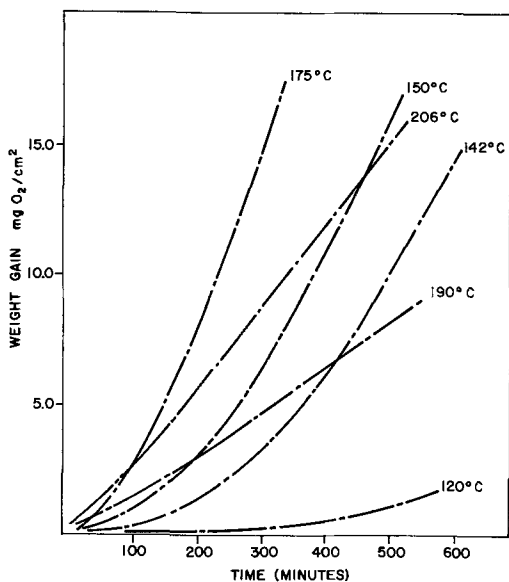


Fig. 1. Weight gain curves showing oxidation behavior from 120° to 206°C.

curves throughout the β -phase. The 206°C curve was included in Fig. 1 to show that two stages of oxidation also occur in the lower temperature region of the γ -phase. The two stages are shown more clearly in the plot of the natural logarithms of the weight change with respect to the logarithms of time for the isotherm at 142°C (Fig. 2).

The initial stage of oxidation (Fig. 3), whose duration shortens with increasing temperature, conforms reasonably well to a linear rate law. Effect of temperature on the rate of oxidation during the initial stage is shown in the Arrhenius plot in Fig. 4.

The parabolic rate preceding the linear rate, reported by Schnizlein and Fischer (9) and Larson and Cash (7) was not observed in the weight gain curves. However, weight change data at the beginning of the isothermal oxidation were lost because it required several minutes for the balance to reach equilibrium after the metal was exposed to the oxidizing gas. Figure 3 shows that when the linear rate is extrapolated to the weight gain axis, the intercepts steadily increase as the temperature rises above 150°C. This suggests that the observed linear rate is not in effect during the very early stages of reaction.

Following a brief transition period, which is best seen in Fig. 2, the reaction proceeds by an accelerating rate.

Microscopy.—Microtopographic examinations were made of the oxide surface during both the initial

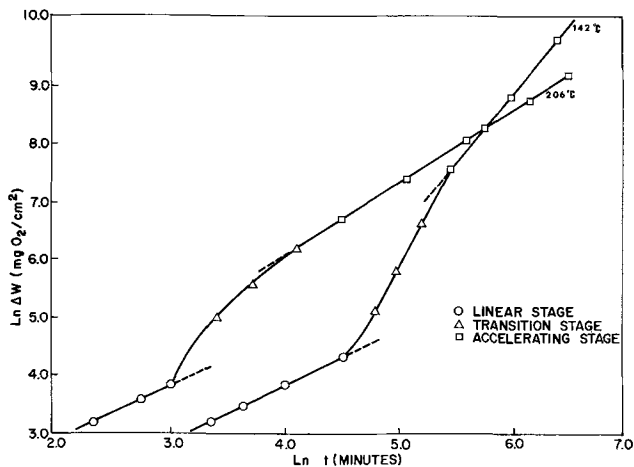


Fig. 2. Ln-Ln plot of weight gain with respect to time

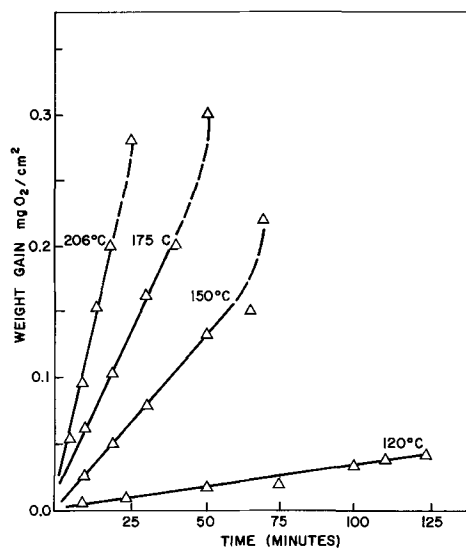


Fig. 3. Initial stage of oxidation

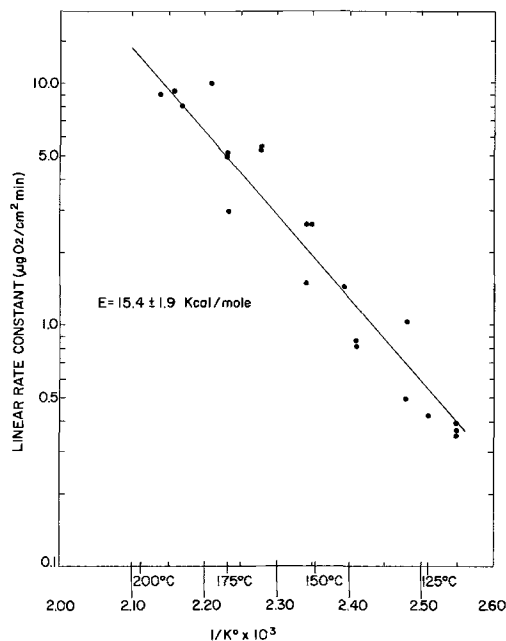


Fig. 4. Arrhenius plot of rate constants obtained from first stage of oxidation.

linear stages and the transition stages using the same conditions as those employed in the kinetic investigations. Several series of photomicrographs were taken of the surface at 750X magnification with direct and indirect illumination and at temperatures from 120° to 206°C.

During the linear stage of oxidation, an interesting pattern of oxide growth was observed. A compact, black oxide film was formed over most of the metal surface. The remaining areas consisted of dark, circular areas which formed early in the oxidation and grew larger in size and number with time. As these circular areas grew, it became apparent that they were blister-like features on the surfaces. These features eventually resulted in mounds of loose, brownish-green oxide which ultimately covered the entire surface.

Hot-stage photomicrographs taken of the oxidation process at 145°C and various time intervals are shown in Fig. 5. The photomicrographs are of representative areas of the surface and show the growth of the blister-like oxides. The light areas correspond to the compact, black oxide film, except for Fig. 5a where

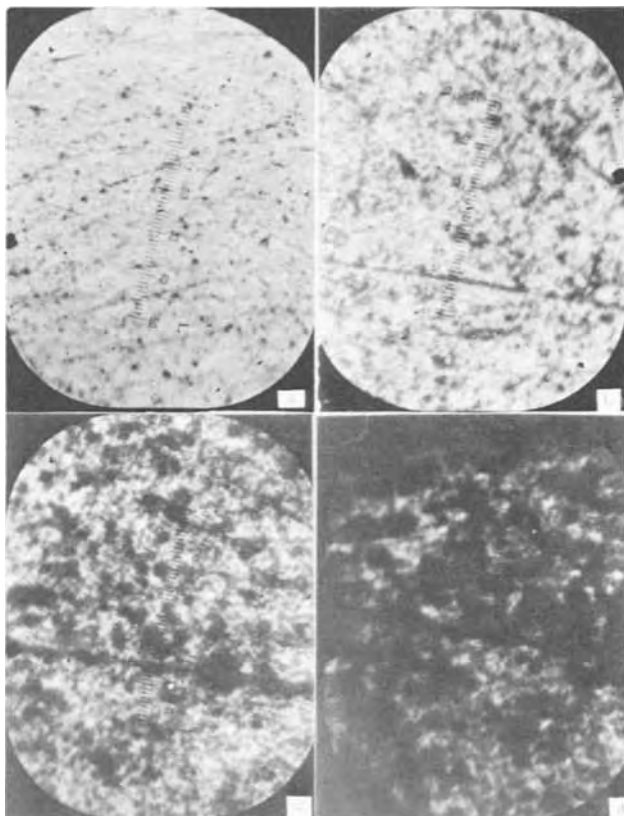


Fig. 5. Hot-stage photomicrographs (750X) of plutonium oxidation at 145°C. (a) Initial surface, (b) after 20 min, (c) after 40 min, (d) after 80 min.

the light area is the metal surface. There is no definite correlation between the spots on the initial metal surface and the dark, circular areas which develop during oxidation. Similar observations were made in other hot-stage microscopy experiments between 120° and 206°C. The rate of formation and growth of blisters increased with temperature.

X-ray diffraction.—Following several exploratory scans at each of several isotherms, it was determined that only α -Pu₂O₃ and PuO₂ were produced in the oxidation of β -phase plutonium. Progress of the formation of the two oxides was followed by scanning the α -Pu₂O₃ 2 θ peaks at 28.0° and 55.0°, and the PuO₂ 2 θ peaks at 28.1° and 56.5° (12). In addition, the strong β peak of the metal at 34.3° was periodically scanned since its presence was a good indication that loss of inner oxide layers from the diffraction scan was not due to a thicker outer film exceeding the penetration limit of the x-ray beam. Figure 6 shows the results of hot-stage x-ray diffraction and thermogravimetric experiments at 175°C. The relative areas under the 2 θ peaks of 55.0° and 56.5° for α -Pu₂O₃ and PuO₂, respectively, are plotted against time to show the change in relative amounts of the oxides during a reaction. Also plotted on the same time coordinate is the thermogravimetric data of an experiment at the same temperature. The PuO₂ shown in the graph is slightly exaggerated due to a weak α -Pu₂O₃ diffraction peak at 56.4°, but it does not mask the trend.

Alpha-Pu₂O₃ was the principal oxide formed during the early stages of reaction. The decrease in the amount of the sesquioxide occurred when the rates of PuO₂ formation and weight gain began to accelerate.

Observation of only a small change in the β -metal peak height indicated that the loss of diffraction intensity of the α -Pu₂O₃ was not due to its covering by a thick layer of PuO₂. An initial decrease in PuO₂ was observed. This phenomenon is thought to be the result of the net reduction of the dioxide by the sub-

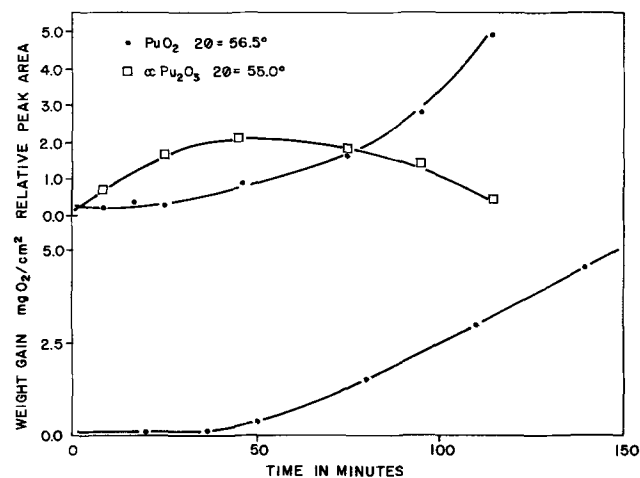


Fig. 6. Hot-stage x-ray diffraction and weight gain data for oxidation at 175°C.

strate metal to the sesquioxide (13). This reduction started at temperatures above 150°C. The same type of behavior described above was observed at other temperatures. The difference was only in the rates. X-ray diffraction analyses of samples removed from the thermogravimetric analyzer during the accelerated stage of oxidation were also made. Oxides readily removed from the sample surface with a camel's hair brush were analyzed separately from those that were more adherent to the metal. The loose oxide was all PuO₂. The slightly more adherent oxide was practically all PuO₂. These oxides were not as compact nor as adherent as the initially formed α -Pu₂O₃ film.

Discussion

Isothermal weight gain curves obtained from the oxidation of β -phase plutonium have the general form shown in Fig. 7. The different stages of the oxidation discussed in this section are indicated in the figure.

Although experimental difficulties in this work prevented the detection of the parabolic stage (A), x-ray diffraction and TGA data point to its occurrence.

The first part of the reaction definable by TGA (stage B) conformed to a linear rate. X-ray diffraction analyses demonstrated that the compact oxide formed during the early part of this stage was principally α -Pu₂O₃. The decrease of the amount of the sesquioxide as the greenish-brown PuO₂ covered the surface was the result of the reaction

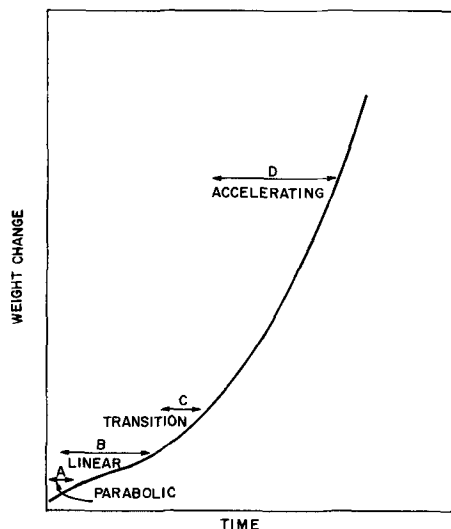
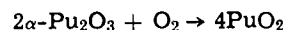


Fig. 7. Typical weight gain curve for isothermal oxidation of β -phase plutonium.

The acceleration of the oxidation rate as the sesquioxide was depleted indicated that the initial parabolic rate resulted from the formation of a protective film of α -Pu₂O₃. Microscopic examination of the α -Pu₂O₃ film surface during its formation showed localized blistering of an otherwise compact oxide film. Appearance of the blisters was observed very early in the isothermal oxidation process. The apparent linear rate was the result of a combination of the decreasing rate of oxidation due to growth of a thicker, protective sesquioxide film and an increasing rate of oxidation due to loss of areas covered by the protective film. The protective sesquioxide film was progressively replaced by less coherent and consequently less protective PuO₂.

The transition stage (C) began when the oxidation rate started to accelerate. The rate accelerated as the protective α -Pu₂O₃ was progressively depleted and replaced by nonprotective PuO₂.

During the accelerated stage (D), the oxidation reached its maximum rate. The amount of sesquioxide on the metal became undetectable by x-ray diffraction and the entire surface was covered by the greenish-brown oxide. It is interesting that the α -Pu₂O₃ did not reform under the blisters as a protective film. One possible explanation is that the conditions under which the initial oxide layer and succeeding layers were formed were quite different. The initial oxide film was formed immediately following polishing of the metal in air. During this relatively slow oxidation, the oxide formed could become the nucleus for succeeding oxide growth which could withstand higher stresses before failure. This type of oxide is contrasted to that formed where bare metal is suddenly exposed to oxygen at elevated temperatures. Support for this mechanism was obtained in a series of experiments in which metal samples were exposed to air at room temperature for 24 hr prior to oxidation. In each case, a definite delay in the accelerated oxidation rate was exhibited with high concentrations of α -Pu₂O₃ remaining for as great as four times longer.

Figure 1 shows that above 175°C, there is a minimum rate in the later stages of reaction. Thompson (10) first reported this and more recently, Vesterberg and Ekbom (11) working with moist argon, made a similar observation. However, in these earlier reports, the rate minimum was found at about 160°C, while it was observed at 190°C in this work. According to Schnizlein and Fischer (9) the accelerated rate can be eliminated by oxidation with extremely dry oxygen. One may conclude from it that the rate minimum is the result of activity of moisture on the oxide film.

Summary and Conclusions

Oxidation of β -phase plutonium metal involves several processes. Initially, there is a concurrent forma-

tion of protective α -Pu₂O₃ film and blisters in the oxide. At the beginning, the α -Pu₂O₃ grows relatively rapidly, and the blister formation and growth rate is low. With time, this is gradually reversed and eventually the entire surface is disrupted. The α -Pu₂O₃ is oxidized to PuO₂. For the period of linear reaction rate, an activation energy of 15.4 ± 1.9 kcal/mole was calculated.

As the protective sesquioxide is oxidized to a nonprotective PuO₂, the oxidation rate accelerates to a maximum. This maximum accelerated rate increased with temperature but began to decrease at about 175°C to minimum at 190°C.

Acknowledgment

The authors gratefully acknowledge the assistance of H. L. Bramlet and R. L. Meisel in the x-ray diffraction work and R. W. Loser in the computer reduction of some data. This work was performed under United States Atomic Energy Commission Contract AT(29-1)-1106.

Manuscript submitted Sept. 13, 1971; revised manuscript received Jan. 17, 1972.

Any discussion of this paper will appear in a Discussion Section to be published in the December 1972 JOURNAL.

REFERENCES

1. E. R. Gardner, T. L. Markin, and R. S. Street, *J. Inorg. Nucl. Chem.*, **27**, 541 (1965).
2. K. S. Covert and M. Kolodney, USAEC Report LA-314, June 1945.
3. E. Dempsey and A. E. Kay, *J. Inst. Metals*, **86**, 739 (1958).
4. J. F. Sackman, "Plutonium 1960," pp. 222-229, E. Grison, W. B. H. Lord, and R. D. Fowler, Editors, Cleaver-Hume, London (1961).
5. J. F. Sackman, AWRE-O-4/62 (1962).
6. J. T. Waber and E. S. Wright, "The Metal Plutonium," pp. 194-204, A. S. Coffinberry and W. N. Miner, Editors, Univ. of Chicago Press, Chicago (1961).
7. D. T. Larson and D. L. Cash, *J. Phys. Chem.*, **73**, 2814 (1969).
8. A. Tanon and H. Bordes-Page's "Plutonium 1965," pp. 603-616, A. E. Kay and M. B. Waldron, Editors, Chapman and Hall, London (1967).
9. J. G. Schnizlein and D. F. Fischer, *This Journal*, **114**, 23 (1967).
10. M. A. Thompson, USAEC Report RFP-491 (1966).
11. V. Vesterberg and L. Ekbom, "Plutonium 1970," pp. 164-170, W. N. Miner, Editor, Met. Soc., AIME, New York (1970).
12. R. N. R. Mulford and C. E. Holley, Jr., USAEC Report LA-DC-8266 (1966).
13. K. Terada, R. L. Meisel, and M. R. Dringman, *J. Nucl. Mat.*, **30**, 340 (1969).

Plutonium Oxidation in Moist Oxygen-Nitrogen Mixtures

J. L. Stakebake and L. M. Steward

Dow Chemical U. S. A., Rocky Flats Division, Golden, Colorado 80401

ABSTRACT

Plutonium oxidation studies were conducted at 90°C in dry air and moist oxygen-nitrogen mixtures using both cast and rolled plutonium. Oxidation in dry air obeyed a linear rate law with average rate constants of 0.042 and 0.050 mg/cm²hr for the cast and rolled plutonium, respectively. Both metal samples were found to oxidize faster in the moist oxygen mixtures than in moist nitrogen. Linear oxidation rates were observed in moist oxygen-nitrogen mixtures with average rate constants of 0.68 and 0.34 mg/cm²hr for the cast and rolled plutonium. In moist nitrogen oxidation followed a parabolic rate law with average rate constants of 3.60 and 1.11 mg/cm²hr^{1/2} for the cast and rolled samples, respectively. The reaction with water vapor observed during this investigation was greatly influenced by the purity of the metal as well as its metallurgical history. Samples of cast, electrorefined plutonium containing some microcracks reacted very rapidly, while for the relatively impure rolled material the reaction was somewhat slower. In all cases at this temperature, the reaction with water vapor was diffusion controlled and not reaction controlled as has been reported previously. The diffusing species is believed to be OH⁻ ions formed by the dissociative adsorption of water on plutonium dioxide.

Plutonium metal is very reactive and highly susceptible to oxidation which destroys the integrity of the metal. Two methods are known to minimize the amount of oxidation. One is by reducing the reactivity of the metal by alloying with another metal such as gallium, aluminum, or zirconium. Another is to minimize the contact of plutonium with oxidizing gases. However, taking advantage of the second method of reducing oxidation requires some understanding of the oxidation characteristics of plutonium metal. For example, plutonium oxidation is greatly enhanced by the presence of water vapor. Thompson (1) observed that an increase in water content of an oxygen atmosphere from 1.5 to 35 ppm resulted in an oxidation rate increase of about 19-38.6 μg/cm²hr at 85°C. Raynor and Sackman (2) found that the rate of oxidation at 90°C increased with increased humidity up to about 2% relative humidity. Above 2% relative humidity, increasing the water vapor content had little effect on the reaction. This effect was not observed above 215°C but at 190°C as little as 180 ppm H₂O caused the linear oxidation rate to accelerate an order of magnitude (3).

According to most of the earlier studies, the accelerating effect of water vapor on plutonium oxidation is more pronounced in inert gases than in air or oxygen. For example, Waber (4) stored two plutonium samples at 75°C and 50% relative humidity in helium and also air. After 26 hr, the extent of oxidation of the sample stored in helium was about 60 times greater than for the sample stored in air. Raynor and Sackman (5) have also studied the oxidation of plutonium in argon and air at 30°, 60°, and 90°C and 95% relative humidity. In all cases, the oxidation was faster in argon than in air. However, this difference was very small for unalloyed plutonium at 90°C. These early observations have led to the conclusion that it is better to store plutonium in "dry" air than in a "dry" inert gas in order to minimize corrosion. Under these conditions, the oxygen tends to inhibit the oxidation by water.

Unfortunately, storing plutonium in air presents a fire hazard since plutonium will burn in atmospheres containing more than 6% oxygen (6). Therefore, it is often preferable to store and handle plutonium in an inert atmosphere despite the increased susceptibility to oxidation. Since oxygen has been reported to inhibit water oxidation of plutonium, it is conceivable that low oxygen concentrations in an inert atmosphere would provide a significant amount of corrosion protection. However, almost no work has been done to evaluate

the effect of small oxygen concentrations on the oxidation rate of plutonium by water vapor in inert gases. Tanon *et al.* (7) performed some glove box oxidation experiments using various argon-oxygen mixtures. Their results showed that the rate of oxidation of plutonium in argon-oxygen mixtures was less than in argon but greater than in pure oxygen. This was true at 50° and 70°C, but no results were reported at 90°C. The scatter of the results did not permit any definite relationship to be established between the rate of oxidation and the oxygen concentration. To be able to minimize the oxidation of plutonium in semi-inert atmospheres, this relation must be established.

Experiments discussed in this paper provide information on the oxidation behavior of plutonium in reduced oxygen atmospheres at 90°C. These experiments also provide additional information on the effects of impurities on plutonium oxidation and the nature of the plutonium-water reaction.

Experimental

Apparatus.—The experimental system used for the measurement of oxidation rates is shown in Fig. 1. The principal component is a Cahn® recording electro-microbalance. This balance has an accuracy of ±5 μg. With the vacuum system incorporated into the balance system, the working pressure can be varied from 10⁻⁷ to 600 Torr. A resistance furnace controlled with a power proportioning programmer was used to heat the samples. The actual temperature of the sample was measured with a thermocouple located adjacent to the

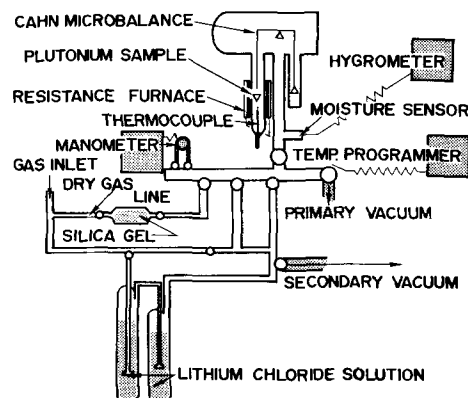


Fig. 1. Experimental apparatus

Key words: plutonium oxidation, moist oxygen-nitrogen.

Table I. Mass spectrometer analysis of two plutonium samples

Element	Rolled Pu, ppm by weight	Cast Pu, ppm by weight
Ag	3	3.0
Al	47	5.0
Am	1563	—
C	100	32.0
Cl	4	3.0
Co	2	—
Cr	86	0.5
Cu	23	0.5
F	2	0.7
Fe	430	9.0
Ga	31	5.0
In	2	—
Mg	2	0.4
Mn	17	0.6
Mo	2	—
N	5	0.5
Ni	69	2.0
Np	19	11.0
O	160	40.0
P	37	0.4
Pb	4	0.6
S	2	0.7
Si	94	5.0
Sn	2	2.0
Ta	27	7.0
Ti	2	—
U	230	25.0
W	15	270.0
Zn	26	5.0
Zr	2	—
Other	2	6.3
Total	3010	435.0

sample inside the hangdown tube. Gas mixtures were introduced into the system via a series of traps which conditioned the gas to the desired water content. Moisture levels were measured with a Panametrics® hygrometer during each run.

Samples.—Two different batches of plutonium were used for this study. One batch had been stored for about six years and was originally rolled from an electrorefined ingot. Thompson (8) used this same metal in his work and reported an average total impurity content of 870 ppm. During storage, the impurity content increased to about 3010 ppm with americium and iron being the major impurities (Table I).

Nearly all previous microbalance studies have been conducted with samples cut from rolled sheets. Recent developments, however, permitted the use of thin cast samples. The second batch of plutonium was vacuum cast from an electrorefined ingot into plates about 0.75 mm thick. Total impurities in this batch were 435 ppm (Table I).

Sample coupons were cut from bulk sheets about 0.75 mm thick so as to have a final surface area of about 0.50 cm². Each coupon was mechanically polished using 600 grit silicon carbide paper. Other techniques, such as electropolishing and a metallographic polish with 1 μ diamond paste, were also tried. The mechanical polish, however, seemed to yield the most reproducible results.

Procedure.—Immediately after polishing the samples were loaded on the balance and the system evacuated. Samples which were to be oxidized in a dry atmosphere were outgassed for 2 hr at about 1×10^{-6} Torr. Those to be run in a moist atmosphere were evacuated to 1×10^{-5} Torr. After evacuation, the temperature of the sample was increased to 90°C and the system back-filled to a pressure to 500 Torr with the reacting gas. For this study, the reacting gases were mixtures of nitrogen and 0, 3, and 21 v/o (volume per cent) oxygen and also 100% oxygen. Two moisture contents, 5 and 12,000 ppm, were used during this experiment. The 12,000 ppm moisture level was generated by passing the gas through two traps containing a saturated solution of LiCl. Purified gases were passed through a silica gel trap to obtain the 5 ppm moisture level.

Data from the plutonium oxidation runs were processed using a digital computer curve fitting program (9) to determine the best equation for the data. In many cases, it is difficult to fit the rate data exactly to any one simple rate equation, because changes during

the oxidation run are frequent. For the data from this study, the single equation which best fits the data was chosen.

Results and Discussion

Oxidation of unalloyed plutonium.—Results from this study of the oxidation of rolled and cast unalloyed plutonium are shown in Fig. 2 and 3. The pronounced effect water has on plutonium oxidation is quite evident from these runs. At 90°C oxidation was found to be faster in the moist oxygen containing atmospheres than in moist nitrogen. This observation is opposite that observed at lower temperatures where oxidation has been reported to be faster in the inert gas and any oxygen present apparently exerts an inhibiting effect on the oxidation process (5, 7).

Oxidation in dry air.—Compared to the rate observed with moisture present, plutonium oxidation in dry air was relatively slow and very reproducible. Curve A in Fig. 2 and 3 shows the results of oxidation in dry air for the rolled and the cast samples, respectively, after subtracting any inhibition time. The runs in dry air were all initially inhibited for periods up to about 200 hr. This inhibition was probably caused by the formation of a nonporous, adherent oxide film on the surface prior to the start of the experimental run. Although inhibition times for different samples varied from 32 to about 200 hr, the final oxidation rate was the same in all cases. The oxidation process in dry air followed the

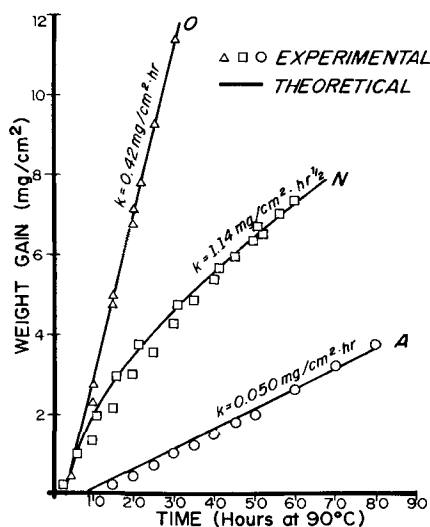


Fig. 2. Oxidation of rolled unalloyed plutonium at 90°C in dry air A, moist oxygen-nitrogen mixtures O, and moist nitrogen N.

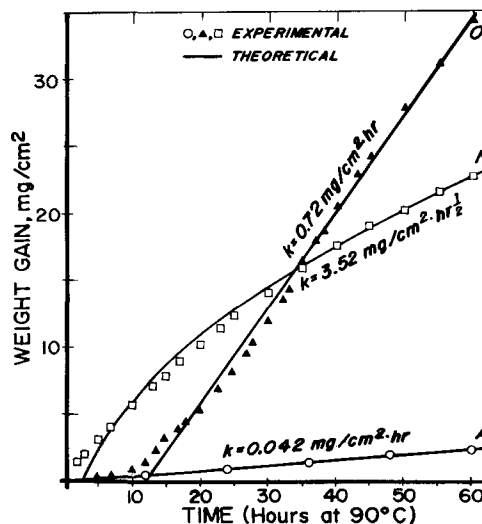


Fig. 3. Oxidation of cast electrorefined plutonium at 90°C in dry air A, moist oxygen-nitrogen mixtures O, and moist nitrogen N.

linear rate law, $x = kt + c$. The rate constant, k , was determined to be 0.050 mg/cm²hr for the rolled plutonium and 0.042 mg/cm²hr for the cast plutonium.

Data from this study were compared to the results obtained earlier by Thompson (8) under the same conditions and with the same rolled metal. At 90°C, in dry air, Thompson reported a linear oxidation rate of about 0.048 mg/cm²hr. The average rate from all runs in this study was 0.046 mg/cm²hr. On the basis of these comparisons, it appears that storage and the accompanying increase in impurities (up to at least 3000 ppm) as well as radiation damage, has no effect on the metal oxidation rate in dry air. Furthermore, the method of metal preparation, either rolling or casting, did not influence the oxidation rate appreciably.

Linear oxidation kinetics can result from several possible rate-determining processes (10). These include: phase boundary processes involving metal/oxide or oxide/oxide interfaces; diffusion through an oxide film of constant thickness; and the adsorption of oxygen. Formation of a porous oxide, resulting in a reaction at the metal/oxide interface, is probably the most commonly used explanation for linear kinetics. However, in the present experiments the initial oxide formed was not porous as evidenced by the long inhibition times.

The observed results can be explained, however, by assuming the initial reaction with the nonporous oxide film was one which formed a porous oxide. This was a rearrangement process within the oxide structure and not further oxidation. Variations in the length of the inhibition time were due to differences in the thickness of the initial nonporous layer. After formation of the porous oxide, oxidation took place at the metal/oxide interface. Adsorption as the rate-controlling step was ruled out because the reaction rate was independent of oxygen pressure. The possible reaction at an oxide/oxide interface likewise was not considered to be the primary rate-determining step since only PuO₂ was detected by x-ray diffraction at this temperature. However, this interaction cannot be completely ruled out at this time.

Oxidation in moist oxygen-nitrogen atmospheres.—The primary objective of this study was to determine the effect of oxygen on the oxidation of plutonium by water vapor. Runs were made in moist nitrogen atmospheres containing 3 and 21% oxygen and also in 100% oxygen. In all cases, the oxidation rate was faster in the oxygen-containing atmospheres than in moist nitrogen. This is opposite all previously reported results (4, 5, 7). One possible explanation is the temperature at which these runs were carried out. The majority of the evidence for a protective oxide film has been found at room temperature and that work done at 90°C showed little difference between oxidation in moist oxygen and in moist argon (5). Furthermore, it should be noted that the experimental procedures used in earlier studies provided mostly qualitative and semi-quantitative information. Because of this, a definite explanation of the effect of oxygen on plutonium oxidation by water has not been reported.

Typical results from this study are shown as curve O in Fig. 2 and 3. It is obvious from these runs that water vapor greatly accelerates the oxidation of plutonium. The protective oxide layer normally formed by oxygen during oxidation in moist atmospheres was not observed with the possible exception of the first few hours on some runs. Run O in Fig. 3 is such an example. In this case, the oxidation proceeded along the curve obtained for dry air for about 7 hr indicating water vapor was not yet taking part in the reaction. After 7 hr, the rate began increasing until the final linear rate was reached. The final linear rates obtained for the oxygen runs shown in Fig. 2 and 3 (curve O) were 0.42 and 0.72 mg/cm²hr for the rolled and cast plutonium samples, respectively. All of the runs in oxygen-containing atmospheres followed a linear rate

law with an average rate of 0.34 mg/cm²hr for the rolled plutonium and 0.68 mg/cm²hr for the cast metal. The difference in rates between the two metal samples is attributed to the difference in purity as well as the metallurgical history. This is consistent with the results reported by Raynor and Sackman (5).

Rate constants obtained for the rolled metal were compared with the 0.18 mg/cm²hr rate obtained earlier by Thompson (8) using the same metal. The rate observed in this study was about twice as fast. This increased rate was probably due to differences in the moisture content for the two studies.

Effect of oxygen partial pressure on plutonium oxidation.—The relation between oxygen pressure and the plutonium oxidation rate has not been clearly established. There has been a fairly significant pressure effect reported at higher temperatures (8, 11). This ranges from a very positive effect at about 200°C (11) to an inverse effect at 400°C (8). However, the effect appears to be minimal at room temperature. Tanon *et al.* (7) reported an inverse oxygen pressure dependence for oxidation in moist atmospheres at 50° and 70°C. The exact relationship could not be defined from their data and no results were reported at temperatures greater than 70°C.

The results from this study show a very strong positive effect at low oxygen concentrations. This is evidenced by the difference between curves O and N in Fig. 2 and 3. The exact oxygen concentration required for this effect was not determined; however, it was less than 3 v/o or a partial pressure of 15 Torr. Oxygen concentrations greater than 3 v/o produced no effect on the oxidation rate at 90°C.

Oxidation in moist nitrogen atmospheres.—Typical results from the oxidation of unalloyed plutonium in moist nitrogen are shown in Fig. 2 and 3 (curve N). At 90°C plutonium oxidation by water vapor was found to be very fast and to obey a parabolic rate law, *i.e.*, $x = kt^{1/2} + c$, as shown in Fig. 4. The rate constants for the typical runs shown in Fig. 4 were 1.14 mg/cm²hr^{1/2} for the rolled metal and 3.52 mg/cm²hr^{1/2} for the cast sample. The average rate constants for all of the runs made with these two samples were 1.11 mg/cm²hr^{1/2} for the rolled plutonium and 3.60 mg/cm²hr^{1/2} for the cast plutonium.

The products from the reaction between water and plutonium were examined by x-ray diffraction and found to be PuO₂. No PuH₂ was detected although this was not totally unexpected due to the similarity in crystal structure between PuO₂ and PuH₂. The nitride, PuN, is not expected to form under 300°C and was not detected in the products. The color of the PuO₂ formed during oxidation of the rolled plutonium was yellow-green, while the oxide formed from oxidation of the cast metal was black. This difference in color may be indicative of two different mechanisms and is discussed in more detail later.

Because of the threefold difference in reaction rate for the two types of plutonium samples, the character

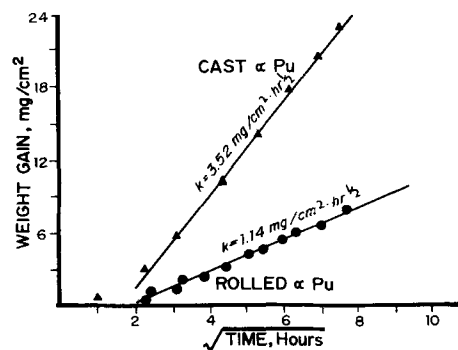


Fig. 4. Parabolic oxidation of cast and rolled plutonium at 90°C in moist nitrogen.

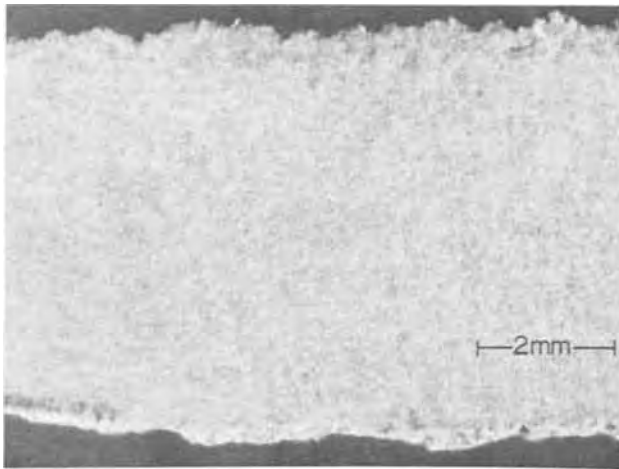


Fig. 5a. Surface of a rolled plutonium coupon following oxidation at 90°C in moist nitrogen.

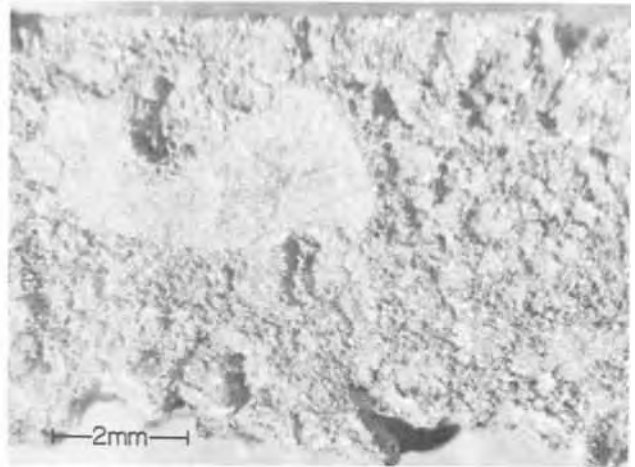


Fig. 6a. Surface of a cast plutonium coupon following oxidation at 90°C in moist nitrogen.

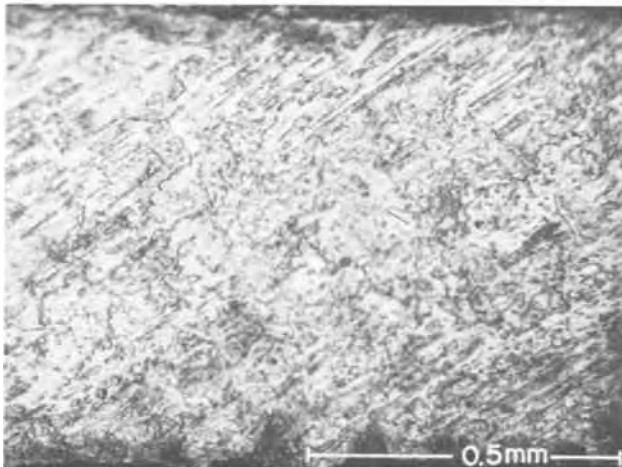


Fig. 5b. Cross section of a rolled plutonium coupon following oxidation at 90°C in moist nitrogen.

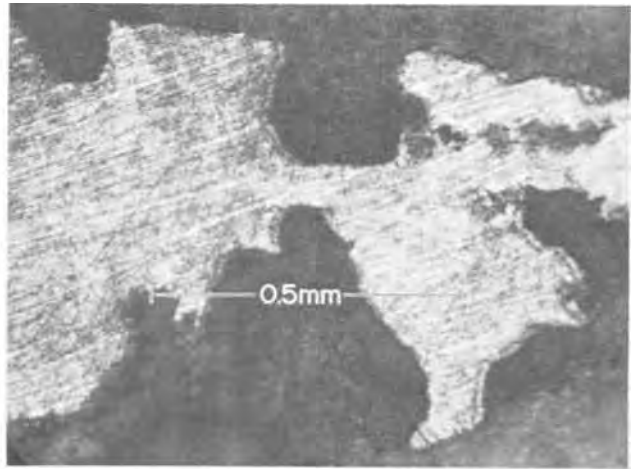


Fig. 6b. Cross section of a cast plutonium coupon following oxidation at 90°C in moist nitrogen.

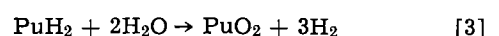
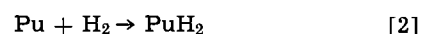
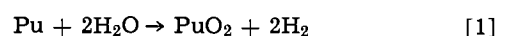
of the plutonium metal was examined in detail. Photomicrographs were taken of coupons from both the rolled and cast samples after about 25% of total oxidation in moist nitrogen. Figure 5a shows the surface of the rolled coupon after all loose oxide had been removed. The water vapor appeared to be nearly uniform with the major reaction occurring on the edges. Figure 5b is a cross-sectional view of the same coupon. Again, there was no serious pitting, indicating the reaction was fairly uniform. These surfaces are indicative of an atypical water reaction with plutonium which was probably caused by the high impurity content. Photomicrographs of the cast plutonium coupon are included as Fig. 6a and 6b. The water vapor attack on this sample was catastrophic. In Fig. 6a, severe pitting is shown on the surface and in Fig. 6b the cross-sectional view shows that some of these pits nearly penetrate the coupon. This type of attack is similar to the hydrogen reaction with plutonium and is identical to that normally expected with water vapor.

Initially, the difference in impurities appeared to be the primary reason for the different types of attack on the two samples. Further comparison of these two samples, however, provided additional reasons for the difference in rates. Metallographic examinations of the two metal samples showed the cast material to contain numerous microcracks (Fig. 7). These cracks were absent in the rolled material (Fig. 8). The microcracks in the cast specimens could account for the catastrophic type attack. In this case, moisture

could condense in the microcracks causing accelerated oxidation and subsequent breakaway.

The microcracks probably originate from internal stresses caused by cooling through the β - α phase transformation during casting. Since the rolled plutonium sample also was cooled from the γ -phase to the α -phase it might also be expected to contain microcracks. However, it was essentially free from any cracks. One reason for the lack of cracks may be the relatively high impurity content. It has been shown that impurities reduce the incidence of microcracking (12). Iron, particularly, serves as a stress-relieving agent by precipitation as Pu_6Fe in the grain boundaries. Thus, somewhat indirectly, impurities may be the major contributing factor in the two different oxidation rates.

Mechanism of water vapor attack.—Several mechanisms (13) have been proposed to explain the oxidation of plutonium by water vapor. Draley (14) proposed a hydride mechanism for the interaction of hydrogen with metals. In the case of plutonium, water reacts to form plutonium hydride which further reacts to form the oxide. That is



Waber (15) suggested that the reaction between plutonium and water vapor is under anodic control. The cathodic reaction involves the dissociation of adsorbed

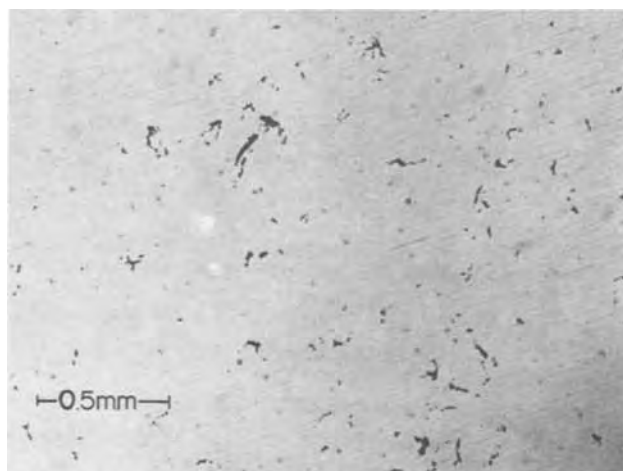


Fig. 7. Metallographic section of a cast plutonium sample

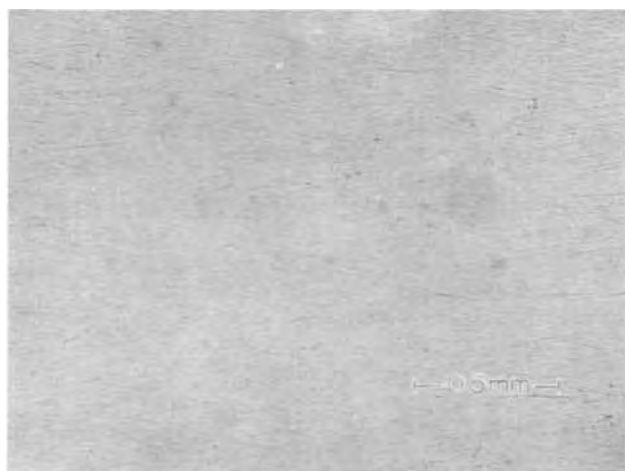
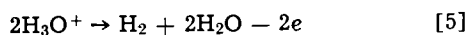
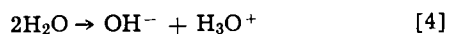
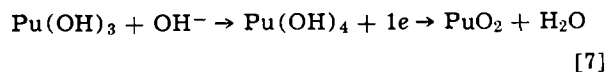


Fig. 8. Metallographic section of a rolled plutonium sample

water vapor on the oxide-covered plutonium metal. Therefore



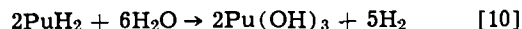
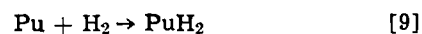
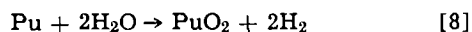
The anodic reaction takes place on the diffusion of OH^- anions to the metal/oxide interface and involves the reactions



which are said to be rate controlling. Hydrogen produced by dissociation of adsorbed water was thought to have only a minor effect on the over-all reaction rate. In this mechanism, it is assumed that the water produced at the metal/oxide interface in reaction [7] dissociates so that the reaction sequence [6] and [7] is again repeated. However, it is possible that water could react differently with the metal according to reactions [1]-[3] or that the hydrogen produced by the dissociation of the water could react directly with the metal thus producing some hydride.

Thompson (8) has proposed a compromise between the "hydride" and the "hydroxide" mechanisms. This hypothesis attempts to explain the importance of small amounts of moisture as well as the presence of hydride in the reaction products.

The reaction sequence is



with the rate-controlling step being the hydride-water reaction [10]. In the case of oxidation by water vapor in nitrogen, Eq. [11] would have to be modified to Eq. [7].

Results obtained in this study do not clearly support any of the previously proposed mechanisms. For example, the plutonium-water vapor reaction followed a parabolic rate law indicating a diffusion-controlled reaction. Previous reports, including those of Waber (15) and Thompson (8), indicated the reaction was linear and reaction controlled. The difference between these proposed mechanisms and the diffusion-controlled mechanism proposed from this work may be the temperature employed, but this has not been verified. The diffusion involved in this study was probably the diffusion of OH^- ions to the metal/oxide interface as suggested by Waber (15). This is supported by parallel studies of water adsorption on PuO_2 (16). However, in this case the diffusion was rate controlling and not the $\text{Pu} + \text{OH}^-$ reaction.

Two different plutonium dioxides appeared to be formed by reaction of the rolled and cast metal with water. Oxide resulting from oxidation of the rolled plutonium was a yellow-green while that from the cast metal was black. Black is the color which is normally observed when plutonium dioxide is formed from a hydroxide intermediate (17) or if plutonium hydride is present. Therefore, on the basis of the product formed, the reaction between the cast electrorefined plutonium and water vapor appears to follow a "hydroxide" type mechanism. Strictly on the basis of color, the reaction between the rolled plutonium and water vapor does not follow the proposed mechanism. However, color can be a function of purity and particle size so one of the mechanisms may still be applicable.

Hydrogen is a product of the plutonium-water reaction, regardless of the mechanism proposed. In these studies hydrogen has been detected in the gas phase following a reaction. Whether or not this hydrogen reacts with the plutonium is the difference between the "hydroxide" and various "hydride" mechanisms. Since hydrogen reacts so readily with plutonium, it is difficult to believe there is no hydride present. However, hydride is difficult to detect and was not found in this study. Additional work of an analytical nature is required to establish conclusively the mechanism for this reaction.

Summary and Conclusions

The oxidation of both rolled and cast unalloyed plutonium at 90°C was investigated in nitrogen-oxygen mixtures containing 12,000 ppm water vapor and also in dry air. Plutonium was found to oxidize faster in the oxygen-containing mixtures than in pure moist nitrogen. Earlier studies by other workers have shown the oxidation rates in moist air and moist argon or helium to be nearly the same or slightly faster in moist nitrogen at 90°C . It appears from this work that at about 90°C water vapor begins to exert less of an accelerating effect on the oxidation rate and oxygen assumes more of a controlling role. Because of the rapid oxidation in oxygen atmospheres at 90°C , it is apparent that there is no inhibiting effect by oxygen on the water vapor reaction. Metal purity and metallurgical history had no effect on the oxidation rate in dry air but became more important with the addition of water vapor.

The oxygen pressure dependence of this reaction became very strong at some partial pressure less than 15 Torr. The exact pressure at which this occurred was not determined. For this study there was no oxy-

gen pressure dependence observed for partial pressures between 15 and 500 Torr.

The attack by water vapor observed during this study was greatly influenced by the purity of the metal as well as its metallurgical history. Samples of cast electrorefined plutonium containing some microcracks reacted very rapidly while for the impure rolled material the reaction was somewhat slower. In all cases at this temperature, the reaction with water vapor was diffusion controlled and not reaction controlled as previously reported. The diffusing species is believed to be OH^- ions formed by the dissociation of water vapor adsorbed on the plutonium dioxide.

Acknowledgment

This work was performed under United States Atomic Energy Commission Contract AT(29-1)-1106.

Manuscript submitted Nov. 22, 1971; revised manuscript received Jan. 7, 1972.

Any discussion of this paper will appear in a Discussion Section to be published in the December 1972 JOURNAL.

REFERENCES

1. M. A. Thompson in, "Plutonium Handbook", Vol. 1, p. 155, O. J. Wick, Editor, Gordon and Breach, Science Publishers, New York (1967).
2. J. B. Raynor and J. F. Sackman, *J. Nucl. Mater.*, **23**, 302 (1967).
3. J. G. Schnizlein and D. F. Fischer, *This Journal*, **114**, 23 (1967).
4. J. T. Waber in, "Plutonium Handbook", Vol. 1, p. 153, O. J. Wick, Editor, Gordon and Breach, Science Publishers, New York (1967).
5. J. B. Raynor and J. F. Sackman in, "Plutonium 1965," p. 575, A. E. Kay and M. B. Waldron, Editors, Chapman & Hall, London (1967).
6. L. E. Musgrave, "The Effect of Water Vapor, Reduced Oxygen Concentrations, and Solvent Vapors on Plutonium Ignition," USAEC Report RFP-1376, Rocky Flats Division, Dow Chemical U.S.A. (1970).
7. A. Tanon and H. Bordes-Pages in, "Plutonium 1965," p. 603, A. E. Kay and M. B. Waldron, Editors, Chapman & Hall, London (1967).
8. M. A. Thompson in, "Plutonium 1965," p. 592, A. E. Kay and M. B. Waldron, Editors, Chapman & Hall, London (1967).
9. R. W. Loser, Unpublished data, Rocky Flats Division, Dow Chemical U.S.A. (1971).
10. P. Kofstad, "High Temperature Oxidation of Metals," p. 233, John Wiley & Sons, Inc., New York (1966).
11. J. T. Waber in, "Plutonium Handbook," Vol. 1, p. 167, O. J. Wick, Editor, Gordon and Breach, Science Publishers, New York (1967).
12. H. R. Gardner, *Trans. AIME*, **224**, 358 (1962).
13. J. L. Stakebake, *J. Nucl. Mater.*, **38**, 247 (1971).
14. J. E. Draley, *This Journal*, **104**, 329 (1957).
15. J. T. Waber, Second U. N. Geneva Conference on the Peaceful Uses of Atomic Energy, p. 204, (1958).
16. J. L. Stakebake and L. M. Steward, *J. Colloid Interface Sci.*, In press.
17. J. L. Drummond and G. A. Welch, *J. Chem. Soc.*, **1957**, 4781.

TiO₂ Film Properties as a Function of Processing Temperature

E. T. Fitzgibbons,*¹ K. J. Sladek,* and W. H. Hartwig

Departments of Electrical and Chemical Engineering, The University of Texas at Austin, Austin, Texas 78712

ABSTRACT

Thin film TiO₂ was produced at 150°C by chemical vapor deposition using hydrolysis of tetraisopropyl titanate. Films were amorphous as grown, but annealing in air caused crystallization, with anatase formed beginning at 350°C and rutile at 700°C. Density and index of refraction increased substantially with increasing anneal temperature, while etch susceptibility in HF and H₂SO₄ decreased. Comparison with literature data showed two groups of processes. One group yields films having properties that gradually approach those of rutile with increasing process temperature. The other group gives rutile directly at moderate temperatures. Deposition of amorphous film followed by etching and annealing is suggested as a means for pattern definition.

Thin film TiO₂ has been produced by anodization and thermal oxidation of Ti, evaporation of TiO₂, reactive sputtering of Ti, a variety of chemical vapor deposition (CVD) processes, and even by liquid deposition. The electrical, chemical, and physical properties of TiO₂ films exhibit considerable diversity, which arises from differences in stoichiometry and structure among films formed by different means. The present research began with the discovery of a unique low-temperature process for producing films of readily etchable amorphous TiO₂. Annealing procedures were found to convert these films to the anatase and rutile forms of the material. Film properties could then be determined for a range of well-controlled structures. One purpose of this investigation was to provide a comprehensive set of structure-property data which might serve to explain discrepancies in reported values of density, refractive index, and etch susceptibility. Another purpose was to develop a means for produc-

ing thin film TiO₂ for applications requiring pattern definition.

Titanium dioxide exists in two tetragonal structures, anatase and rutile, plus orthorhombic brookite. Rutile is the thermodynamically stable form at all temperatures investigated so far, but anatase and brookite retain their structures until heated to fairly high temperatures, at which they transform irreversibly to rutile. Reported temperatures for significant rates of conversion to rutile are 800°-1100°C for anatase and 700°-1300°C for brookite (1, 2). Theoretical densities of anatase and rutile are calculated to be 3.94 and 4.27 g/cm³, respectively, using recent values of the unit cell dimensions (1). These agree reasonably well with measured values of 3.90 and 4.23 g/cm³ (2). Average index of refraction (n) values at 0.55 μm are 2.57 for natural crystals of anatase and 2.74 for synthetic crystals of rutile (1).

While properties of bulk anatase and rutile are well established, little agreement has been reached regarding the properties of thin film TiO₂. One of the most thorough studies is due to Hass (3), who produced films both by thermal oxidation of Ti and by a CVD

* Electrochemical Society Active Member.

¹ Present address: North American Rockwell Microelectronics Company, Anaheim, California 92803.

Key words: thin films, chemical vapor deposition, titanium dioxide.

process. Evaporated Ti films were oxidized above 200°C and the resulting oxide was shown to be rutile by electron diffraction. The index of refraction of these films was 98-99% of that of bulk, single-crystal rutile for the whole range from 0.4 to 2.0 μm . In contrast, hydrolysis of TiCl_4 produced amorphous films below 280°, and anatase films above 300°C, with n values near 2.3.

Films of TiO_2 have also been produced by anodization (4, 5), reactive sputtering (6), vacuum evaporation (7), and by drying substrates which had been dipped into a titanate solution. Drying at 180°-900°C gave films with n values of 1.95-2.45 (8).

CVD processes include the $\text{TiCl}_4\text{-H}_2\text{O}$ reaction near 300°C (3), at 150°C (9), and at 800°C (10). Pyrolysis of tetraisopropyl titanate (TPT) at 300°-700°C gave amorphous and anatase films exhibiting a range in density, refractive index, and etch susceptibility (11). Reaction of TiCl_4 with O_2 gave epitaxial rutile on some substrates above 700°C and polycrystalline rutile at lower temperatures (12). In the present work the TPT- H_2O reaction was used, as described next.

Deposition Phenomena

The CVD apparatus is illustrated in Fig. 1. The two liquid feeds are evaporated from heated flasks into metered carrier gas streams. The feed streams then issue from parallel nozzles at the ends of the delivery lines, intermingle with each other and with the room air, and are directed onto the substrate, which is heated from beneath. Film growth is controlled manually by moving the substrate around under the nozzles or by moving the nozzles. By observing the sharp interference colors, the operator can manually control the thickness uniformity of the film to within 100-200Å over a 1.25-in. diameter substrate wafer.

The best temperature range for the TPT evaporator is 75°-85°C. The water evaporator temperature is not critical and films can even be grown without using the CO_2 carrier and water source; in that case, the water vapor in the ambient air is evidently sufficient to maintain the reaction. The growth dynamics appear to be the same with and without the water vapor stream and the structural, optical, and chemical properties are also the same in both cases. The only differences were observed in the reproducibility of electrical properties, and the water vapor source was used to stabilize these.

Under typical conditions, the helium flow rate was 1 l/min, the CO_2 flow rate was $\frac{1}{4}$ l/min, the TPT and water evaporators were at 75° and 90°C, respectively, and the substrate heater was at 150°C. With these parameters, a 1.25-in. substrate could be covered with a 2000Å film in 10 min.

These conditions were chosen after making a number of observations about the film quality obtained under various deposition conditions. When the TPT evaporator was too hot (90°-100°C) a milky film having diffuse interference colors resulted. Microscopic examination revealed that the film lacked coherence,

but rather was made up of tiny stacked spheres. The film had an odor of alcohol or TPT and was soft enough to be smeared with a cloth. Evidently, the TPT condensed after leaving the nozzle and the resulting film was made up of small droplets of TPT which had reacted at their outer surfaces only. Similar results were obtained with the TPT evaporator at 75°C when the He carrier flow exceeded 2 l/min, when the nozzle was closer than 1 in. from the substrate, or when the substrate temperature was below 100°C. Excessive CO_2 carrier flows ($> \frac{1}{2}$ l/min) caused a white powdery deposit, evidently due to premature hydrolysis of TPT, giving a powder product which rained down onto the substrate. The same effect occurred when the nozzle was held more than 3 in. from the substrate. In summary, the conditions chosen above were selected to avoid both incomplete and premature reaction which led to formation of films lacking coherence. Under the chosen conditions, the films were smooth and relatively hole free. No detail could be observed in the scanning electron microscopy at 20,000X, except for an occasional pinhole.

When film thicknesses of 4000-5000Å were reached during a normal deposition, cracks would appear and propagate over the film, reducing it to a field of small triangular pieces, each separated from the substrate with its points bending upward. This was observed with all the substrates described below at approximately the same film thickness. Several experiments with duplex films were performed. When a film was grown to several thousand angstroms and then later a new film was grown atop the previous one, fracture occurred when the sum of the two thicknesses fell into the 4000-5000Å range. However, when a film was grown and annealed above 350°C (to be described later) and then a new film was grown on the annealed one, fracture occurred when the second film reached 4000-5000Å. This behavior indicates that the film is deposited with an intrinsic tensile stress. Fracture may be associated with a failure of the film-substrate adhesive bond due to increased shear stress as the film thickens.

Films could be grown on any smooth object that could be heated. In the present work, different substrates were used for different experiments. Fused quartz was used for optical transmission measurements. Fused quartz covered with evaporated Pt and also polished Si were used as substrates in determining refractive index and thickness relationships by ellipsometry and interferometry. Soft glass microscope slides, as well as some of the other materials, were used in x-ray analysis. Before deposition, the fused quartz and the soft glass substrates were cleaned thoroughly in low residue detergent, were rinsed in deionized water, and were heated in air at 1000° and 350°C, respectively, to drive off surface contaminants. The Pt/quartz substrates were annealed in air at 1000°C to stabilize them, and no further cleaning was performed. The Si wafers had been commercially prepared using mechanical and electrochemical polishing and were used as supplied.

Annealing and Crystallization

Films produced by the CVD method described above underwent dramatic changes in physical and chemical properties during annealing. The changes in crystal structure are described here.

Crystalline phases were identified using an x-ray diffractometer with copper $K_{\alpha 1}$ radiation. Four types of samples were used. Powder samples were obtained by allowing the standard deposition process to continue for several hours until a thick white powdery deposit had built up; this was then scraped off and divided into samples for testing. The other three types of samples consisted of 3000-4000Å films grown on fused quartz, soft glass, and polished Si.

The powder in the as-grown condition showed no sign of crystallinity and was evidently amorphous. No

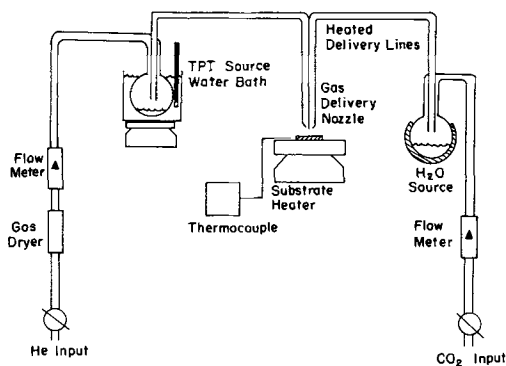


Fig. 1. Chemical vapor deposition system

Table I. Crystalline phase and anneal temperature for TiO₂ on several substrates

Anneal temperature, °C	Substrate ^b			
	Powder sample	Soft glass	Polished Si	Fused quartz
150 (as grown)	Amorphous	Amorphous	Amorphous	Amorphous
350	Amorphous + anatase	Amorphous + anatase	Amorphous + anatase	Amorphous + anatase
700	Rutile + anatase	Rutile + anatase	Rutile + anatase	Anatase
1000	Rutile	—	Rutile	Anatase

^a All anneals carried out in air.

^b Crystalline phases identified in all films showed no orientation.

crystallization occurred during aging at room temperature in air for one week. Annealing the powder for 10 min at 350°C resulted in the appearance of the two strongest diffraction peaks of the anatase form of TiO₂. A sample annealed at 700°C for 2 hr showed the five strongest anatase peaks and the three strongest rutile peaks. A 20-hr anneal at 1000°C completely converted the powder to rutile; many rutile peaks were observed, and no anatase peaks were detectable.

Table I summarizes the data for all four types of samples. In every case the as-grown material is amorphous, and material annealed at 350°C shows some anatase. However, the weakness of the anatase patterns suggested that only partial crystallization occurred at 350°C. This temperature can be regarded roughly, as an amorphous-anatase transition temperature. Additional anneals at 300°-400°C indicate that the transition is not sharp, but rather occurs over a range of about 50°C in which the extent of crystallization gradually progresses. The temperature, 700°C, appears similarly to be characteristic of the anatase-rutile transition. This transition appears to be less sharp and progresses over a range of about 300°C. An important exception is the films on fused quartz which persist in the anatase form, even after annealing at 1000°C. Somehow, the quartz-TiO₂ interface stabilizes the anatase structure, perhaps by preventing nucleation of rutile.

The present data are in accord with some of the literature data described earlier. The anatase-rutile transition occurs in bulk samples at 800°-1100°C (1, 2). In films produced by CVD or liquid dipping, a change from amorphous to anatase structures was found at 280°-300°C (3), and at 250°-350° (8). An anatase-rutile transition was observed at 800°C (3), and several investigators produced rutile directly at 800°C or above (10, 13). In contrast, rutile films were produced as low as 400°C from Ti oxidation (3) and from the TiCl₄-O₂ reaction (12).

Thickness and Index of Refraction

Changes in interference colors occurred as a result of annealing, and these indicated a change in thickness, d , and/or index of refraction, n . If a standard color chart for SiO₂ was used, the changes indicated that annealing a 150°C film at 1000°C caused an increase in d . However, measurements using an ellipsometer indicated a substantial decrease in d , accompanied by an increase in n , and indicating that a single color chart, based on fixed n , would be misleading. To obtain additional independent values of d and n , a multiple beam interferometric technique was used. Both the ellipsometer and the interferometer used the 5460Å green line of Hg.

Coated and uncoated portions of a step were used to find both d and nd with the interference method (14). The ellipsometer yields separate values of d and n (15). A cross check was provided by a color chart, which gives nd (14).

Results obtained before and after annealing at 1000°C are shown in Table II. The several methods give good agreement, and it is clear that annealing

Table II. Change in thickness and index of refraction due to annealing at 1000°C

Sample condition	Thickness, A (method) ^a	Index of refraction (method) ^a
As grown, 150°	3820 (I), 3870 (E)	1.98 (I), 2.10 (E)
Annealed, 1000°	2510 (I)	2.49 (I)
As grown, 150°	2400 (E)	2.00 (E), 1.95 (C)
Annealed, 1000°	1580 (E)	2.40 (E), 2.47 (C)
As grown, 150°	1900 (E)	2.10 (E), 2.06 (C)
Annealed, 1000°	1220 (E)	2.60 (E), 2.50 (C)

^a I = interferometer; E = ellipsometer, C = color chart plus ellipsometer-determined thickness.

causes a substantial decrease in d and increase in n .

To complete these measurements, a final series of data was obtained as a function of anneal temperature. A film was deposited on Pt/quartz and data were obtained by ellipsometry, using averages of two to four measurements. Figure 2 is a plot of resulting values of thickness and index of refraction.

The thickness shrinkage of 35% is quite remarkable in magnitude. Since the film is constrained to a fixed area, any density changes are evidently exhibited only in one dimension. One might suspect that such a violent dimensional change would set up stresses which might rupture the film. However, examination of a 1000°C annealed film in the scanning electron microscope at 20,000X showed no cracks, tears, or eruptions.

It was suspected that the shrinkage might be accompanied by a mass loss, as would be expected if the as-grown material were a hydroxide or hydrate. A hydroxide, Ti(OH)₄, would lose 31% of its initial weight if complete dehydration occurred. Several experiments were carried out in an effort to detect a weight change on annealing. In the most sensitive experiment, a sample was weighed on a vacuum microbalance and annealed *in situ*. No weight change could be detected within the experimental uncertainty of $\pm 7\%$ of the initial film weight. Although the sensitivity of this experiment was rather low, the result does rule out mass reduction as a primary cause of the volume shrinkage.

It is possible that the films are microporous and that shrinkage occurs by sintering. Swaroop (16) and Pliskin and Lehman (17) attributed densification of SiO₂ films to sintering. Sladek and Herron (18) investigated TiO₂ film growth by the TPT-H₂O reaction at 25°C, and suggested that voids are incorporated when isopropyl groups are removed from the growing film during surface reaction.

The difference between a microporous material and a "homogeneous" one of abnormally low density is only in the size of the void spaces. Our observations using the scanning electron microscope detected no pores. Qualitatively, the optical transparency and sharp interference colors of our films indicate negligible scattering by void spaces. However, both of these

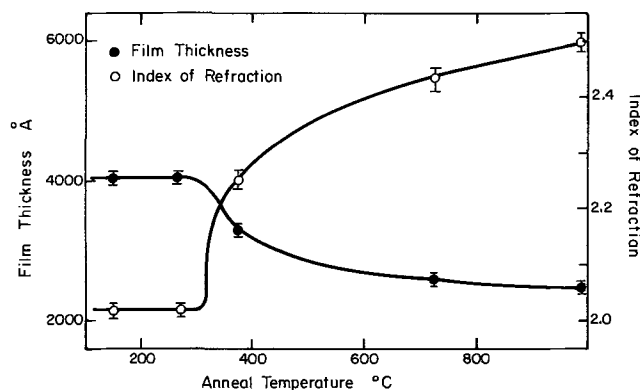


Fig. 2. Thickness and index of refraction as a function of anneal temperature. TiO₂ on Pt/quartz.

Table III. Chemical susceptibility to several etches

Anneal temperature, °C	Etch rate and behavior			
	0.5% HF	48% HF	100% H ₂ SO ₄	85% H ₃ PO ₄
150	50-75 A/sec	Very rapid	Slow at 25°C 25-40 A/sec at 50°C	Leaves residue
350	On Pt: very slow On Si: undercutting	Slow and uneven	About 15 A/sec at 50°-100°C	
700	No etching	On Pt: slow On Si: undercutting	Very slow	
1000	No etching	On Pt: slow On Si: undercutting	About 1000 A/hr at 120°C	Very slow at 120°C

observations would be insensitive to voids of size below about 200Å. We attribute the abnormally low density of the present amorphous films to voids of size somewhere in the range between atomic dimensions and about 200Å.

Susceptibility to Chemical Etch

Etch susceptibility is a prerequisite for electronic applications of TiO₂. Some past work indicates that amorphous TiO₂ is readily etched while high-temperature and hence crystalline forms are quite impervious to chemical attack. Barksdale (19) observed in 1949 that, while bulk TiO₂ is known to be slightly soluble in H₂SO₄, HF, and a few strong alkalis, material annealed near 1000°C is almost completely inert chemically.

Etchability of TiO₂ as a function of anneal temperature was determined for films grown on Si and on Pt substrates. Results are summarized in Table III. Again there is a wide, controllable gradation in properties, with the low-temperature form showing high chemical susceptibility while the 1000°C material is nearly inert. Films on Si behaved the same as those on Pt except for the 48% HF case. This etch lifted the TiO₂ off the surface of Si, evidently by dissolving a thin interfacial layer of SiO₂ and undercutting the TiO₂.

These results are in accord with data of Yokozawa *et al.* (11), who reported that their amorphous TiO₂ films etched in dilute HF at 4-60 A/sec, while anatase films etched only slowly in concentrated HF. Feuer-sanger (9) reported that his films were easily etched in 10% HF; this suggests that they were amorphous, as would be expected for a 150°C process. His high index of refraction (discussed later) is then the only property that does not agree with the present results. Harbison and Taylor (10) reported an etch rate of 700 A/min in 48% HF for material grown at 800°C. This is much higher than would be expected from our results.

Optical Absorption

An optical transmission spectrum of a 350°C annealed film is shown in Fig. 3. This was obtained by measuring the difference between the transmission of the film on fused quartz and the transmission of the fused quartz alone. We attribute the maxima and min-

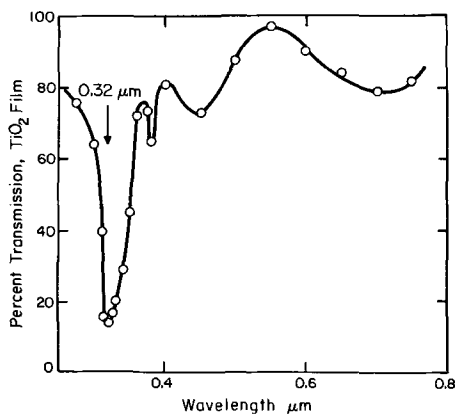


Fig. 3. Optical transmission spectrum. 2600Å film of TiO₂ annealed at 350°C.

ima above 0.35 μm to interference due to multiple internal reflection, and the strong absorption peak at 0.32 μm (3.9 eV) to an electronic transition. Transmission in an amorphous TiO₂ film was also measured and similar results were obtained, except that the strong absorption peak was much broader, although still centered at 0.32 μm. In agreement with these results, Maserjian (20) found an absorption peak at 0.32 μm with a rutile film. In contrast, however, single-crystal rutile exhibits an absorption edge (21) at 0.41 μm (3.0 eV). The cause of the discrepancy between bulk single-crystal and thin film TiO₂ is not known. However, in both this work and that of Maserjian (20) the 0.32 μm peak has been established.

Discussion

Present data on density and index of refraction are compared with literature values in Fig. 4. Since absolute values of density were not obtained in this work, it was necessary to choose a value for one condition, and 2.5 g/cm³ for the amorphous films was used, based on the results of Yokozawa *et al.* (11).

Results of two of the CVD studies (11, 13) and the liquid deposition (8) show good agreement with present data in both properties plotted. Results of Hass (3) on films formed by TiCl₄ hydrolysis and by oxidation of "TiO" (formed by evaporating Ti with O₂ present) show an increase in *n* with temperature similar to that observed here, although with somewhat higher values of *n*.

In contrast, Hass (3) obtained nearly the bulk rutile value of *n* with oxidized Ti, and Ghoshtagore and Noreika (12) found an even higher value with films formed from TiCl₄ + O₂ in the whole temperature range studied. (We have applied a small correction to their reported value of *n_D* to obtain a value applicable at 0.55 μm.) The fact that their *n* exceeds the random-orientation average for bulk rutile could have been due to preferred orientation of their films.

In summary, one group of processes produces films which show a characteristic variation in physical and

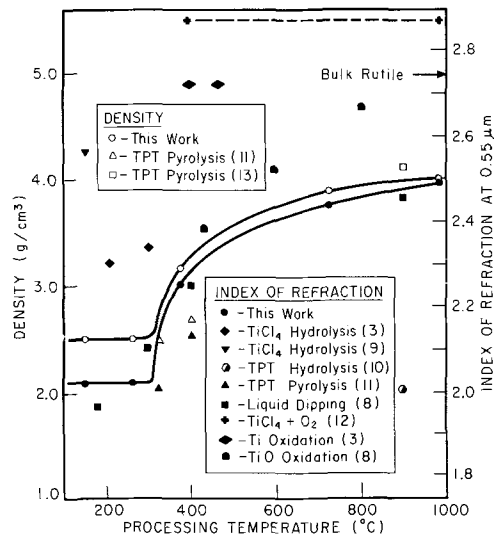


Fig. 4. Density and refractive index vs. processing temperature: a comparison with other work.

chemical properties with maximum processing temperature, whether this temperature is reached during deposition or during postdeposition anneal. These variations arise from densification and crystallization and ultimately yield material with properties approaching those of the equilibrium (rutile) bulk state. However, it is also possible to bypass these intermediate stages and obtain rutile directly at moderate temperatures.

We have found that, of the several forms produced, rutile or anatase-rutile mixtures have superior dielectric properties. The relative dielectric constant/dissipation factor at 1 kHz was about 100/0.04 for material annealed at 700°-1000°C. The sign of the surface charge of TiO₂ on Si was negative, and positive, negative and zero, values could be obtained by growing duplex TiO₂/SiO₂ films. (Details of these electrical studies will be reported later.) These properties suggest a number of applications for rutile in integrated circuit technology.

Although it is possible to produce rutile films directly, they are almost impossible to etch (Table III). In contrast, the deposition-annealing process used here could lend itself readily to the various etch steps needed for integrated circuit production. Standard photomasking techniques could be used to define a desired pattern in the as-grown film, and a later anneal would convert the material to its stable form.

The fact that the TiO₂ itself changes chemical susceptibility suggests that patterns might be defined without photoresists, if a means were found for selective conversion in desired areas. This idea has led to some further work (to be reported later) in which an electron or photon beam is used to define positive patterns in amorphous TiO₂.

In conclusion, it is possible to produce rutile films either directly or via a series of stages progressing in density, refractive index, and etch susceptibility. The present method of low-temperature deposition followed by annealing is promising for applications requiring pattern definition.

Acknowledgment

This work was supported in part by the National Aeronautics and Space Administration and in part by the Joint Services Electronics Program under Research Grant AFOSR-69-1792.

Manuscript submitted Aug. 20, 1971; revised manuscript received Jan. 20, 1972. This was Paper 10 and part of Paper 11 presented at the Washington, D.C., Meeting of the Society, May 9-13, 1971.

Any discussion of this paper will appear in a Discussion Section to be published in the December 1972 JOURNAL.

REFERENCES

1. "Kirk-Othmer Encyclopedia of Chemical Technology," Second ed.; Vol. 20, pp. 390-395 (1969).
2. G. Skinner, H. L. Johnston, and C. Beckett, "Titanium and Its Compounds", pp. 21-28, H. L. Johnston Enterprises, Columbus, Ohio (1940).
3. G. Hass, *Vacuum*, **2**, 331 (1952).
4. L. Young, "Anodic Oxide Films," Academic Press, New York (1961).
5. O. S. Heavens, *Rept. Progr. Phys.*, **23**, 1 (1960).
6. T. K. Lakshmanan, C. A. Wysocki, and W. J. Slegesky, *IEEE Comp. Parts*, **CP-11**(2), 14 (1964).
7. M. Shiojiri, *J. Phys. Soc. Japan*, **21**, 335 (1966).
8. T. N. Krylova and G. O. Bagdyk'yants, *Opt. Spectry. (USSR) (English Transl.)*, **9**, 339 (1960).
9. A. E. Feuersanger, *Proc. IEEE*, **52**(12), 1463 (1964).
10. D. R. Harbison and H. L. Taylor in "Thin Film Dielectrics," pp. 254-278, F. Vratney, Editor, Electrochem. Soc. (1969); also D. R. Harbison, Ph.D. Dissertation, Univ. of Texas at Austin (January 1969).
11. M. Yokozawa, H. Iwasa, and I. Teramoto, *J. Appl. Phys. (Japan)*, **7**, 96 (1968).
12. R. N. Ghoshtagore and A. J. Noreika, *This Journal*, **117**, 1311 (1970).
13. S. Sakurai and M. Watanabe, *Rev. Elec. Commun. Lab. (Tokyo)*, **11**, 178 (1963), as quoted by Yokozawa *et al.* (11).
14. R. M. Burger and R. P. Donovan, "Fundamentals of Silicon Integrated Device Technology," Vol. 1, pp. 78-100, Prentice-Hall, Englewood Cliffs, N. J. (1967).
15. R. J. Archer, "Manual on Ellipsometry," Gaertner Scientific Corp., Chicago (1968).
16. B. Swaroop, in "Thin Film Dielectrics," pp. 407-431, F. Vratney, Editor, Electrochem. Soc. (1969).
17. W. A. Pliskin and M. S. Lehman, *This Journal*, **112**, 1013 (1965).
18. K. J. Sladek and H. M. Herron, *I&EC Prod. Res. Dev.*, **11**, 92 (1972).
19. J. Barksdale, "Titanium. Its Occurrence, Chemistry, and Technology," Ronald Press, New York (1949).
20. J. Maserjian, "Conduction Through Thin Titanium Dioxide Films," N66-39934, Oct. 1, 1966.
21. D. C. Cronmeyer, *Phys. Rev.*, **87**, 876 (1952).

Cathodoluminescence Characteristics of Mn^{2+} -Activated Willemite (Zn_2SiO_4) Single Crystals

R. J. R. S. B. Bhalla*¹ and E. W. White

Materials Research Laboratory, Pennsylvania State University, University Park, Pennsylvania 16802

ABSTRACT

Cathodoluminescence studies were made of Mn^{2+} -activated willemite single crystals using an electron microprobe and a simple interference-type spectrometer attachment. Use of the microprobe allows single-crystal cathodoluminescence measurements to be made on comparatively small (<0.01 mm) crystals. Green cathodoluminescence emission from Mn^{2+} -activation was found to be partially polarized. The electric vector of emission was along a direction perpendicular to the c -axis of the crystals. Examination of the emission spectra in the two perpendicular polarization directions, corresponding to the analyzer direction parallel to the c -axis, and perpendicular to the c -axis, showed a difference of about 100Å in the emission peak positions. Measurements of spectra and integrated intensity of emission were also made as a function of manganese concentration. The intensity of luminescence was maximum for Mn concentration of 2.9 w/o (weight per cent). The peak position of the Mn^{2+} band was found to shift from 5160 to 5300Å as the manganese concentration increased from just a trace to about 12 w/o. The polarized cathodoluminescence emission can be explained on the basis of crystal-field theory and symmetry arguments. These arguments lead to the conclusion that the two Zn^{2+} sites in the willemite structure, which are occupied by the Mn^{2+} ions, have effective local symmetries of C_{3v} and C_1 , respectively. The emission peak shift to longer wavelengths, as the manganese concentration is increased, cannot be explained by simple crystal-field theory. A model showing emission from Mn^{2+} - Mn^{2+} pairs dominating at higher concentrations, in comparison to emission from isolated Mn^{2+} ions, is proposed to explain this shift of emission peak to longer wavelengths.

Emission spectra from oriented single crystals of impurity activated (or self-activated) phosphors can give very important clues to the site symmetry of the activator. In the past polarized emission from phosphor single crystals has been studied to determine nature and symmetry of the luminescence centers (1, 2). Thus, although the advantages of single-crystal studies were recognized for some time, such studies have been limited to very few well-known phosphors. The main reason for this is the general lack of large enough single crystals. Furthermore, almost no studies of these luminescence characteristics exist for cathode-ray excitation in single crystals. A recent communication (3) has described preliminary results for a cathodoluminescence study of oriented single crystals of Mn^{2+} -activated willemite. The main purpose of this paper is to give a detailed account of the polarized cathodoluminescence studies of Mn^{2+} -activated single crystals of willemite [$Zn_2SiO_4(Mn)$]. In addition, spectra and luminescence intensity, as a function of manganese concentration, are also measured on artificially doped single crystals of willemite.

Experimental

An applied Research Laboratory Model EMX electron microprobe was used for cathode-ray excitation of the willemite luminescence from sample areas as small as 5 μ m diameter. The electron microprobe offers the additional advantage that the luminescence emission is observed from the surface of the sample excited by the electron beam rather than observing in transmission as is generally done in conventional cathodoluminescence apparatus. The electron beam is incident normal to the specimen surface and is coaxial with the light microscope objective. The broad band luminescence spectra were recorded using a simple light spectrometer and photomultiplier readout described by Greer and White (4). A Polaroid analyzing cap was

attached to the eye piece of the probe microscope making it possible to record the luminescence emission spectra in any polarization direction. Use of this arrangement made it possible to study, individually, very small (<0.01 mm) single crystals, and micron scale inhomogeneities in larger grains with a sensitivity which is not possible with conventional cathodoluminescence apparatus.

Samples used in this study were natural willemite crystals from Franklin, New Jersey, and Tsumeb, South-West Africa. Franklin, New Jersey, specimens showed the strong green luminescence characteristic of Mn^{2+} -activated orthorhombic willemites and were found to contain 0.1-4.0% manganese in solid solution. Mn was rather uniformly distributed in the individual crystals. Other cationic impurities which have been reported in bulk chemical analyses of willemites are Fe, Mg, and Ca (5). However, probe analysis showed these impurities to be located in micron scale, highly oriented inclusions. No Fe, and only traces of Ca and Mg were detected in the willemite matrix. Absence of Fe in the willemite matrix is significant since it is known to act as a killer of luminescence in most materials. Willemite, which has only fourfold coordinated cationic sites, has a very low tolerance for Fe. In contrast to the Franklin, New Jersey, specimens, the South-West Africa willemite crystals do not luminesce green and have no detectable Mn or Fe impurities. Mn^{2+} was introduced in these crystals by solid-state diffusion at 1250°C. Selected samples were then set in Lakeside 70 and prepared as polished thin sections by grinding and polishing. Final sample surfaces were polished successively with 6, 3, 1, and $\frac{1}{4}$ μ m diamond pastes and coated with a thin layer of carbon (200-400Å) by vacuum evaporation to provide a conductive path for the electrons. This method of preparation yielded grains with many different crystallographic orientations. Grains having the desired orientations for study were selected using a polarizing light microscope and marked for convenient location in the microprobe.

* Electrochemical Society Active Member.

¹ Present address: Central Research Laboratory, American Cyanamid Company, Stamford, Connecticut 06904.

Key words: cathodoluminescence, single crystal, Mn^{2+} -activated willemite, electron microprobe, polarized emission.

Experimental Results

Polarized cathodoluminescence.—Willemite belongs to the rhombohedral crystal class and as such has two principle axes (a and c). Crystals with orientations such that the c -axis was perpendicular to the surface (a in the plane) did not show any polarization of the green Mn^{2+} emission. However, the crystals with orientations such that the surface contained the c -axis, showed partial polarization of Mn^{2+} emission. The degree of polarization, p , given by $p = (I' - I'') / (I' + I'')$, where I' and I'' are maximum and minimum intensities as the analyzer is rotated around its axis, was found to be 0.25. The electric vector of the emitted radiation was along a direction perpendicular to the c -axis.

Emission spectra of Mn^{2+} -activated willemite powders were comparable to the commercially available willemite powders and consisted of a single broad band with peak position around 5250Å (for 1% Mn). This peak shifted toward slightly longer wavelengths as the concentration of Mn increased. The peak position as well as the degree of polarization were not found to be current density dependent. Examination of the emission spectra in the two perpendicular polarization directions corresponding to the analyzer directions parallel and perpendicular to the c -axis showed a difference of about 100Å in the peak positions. This is illustrated in Fig. 1. The peak intensities were matched by lowering the electron beam current while recording the spectrum in the maximum transmission direction. The more intense spectrum, obtained with the electric vector perpendicular to the c -axis, yielded the longer wavelength peak.

Effect of Mn^{2+} concentration on cathodoluminescence.—Measurement of the variation in the green emission spectral characteristics as a function of Mn concentration were made on South-West Africa willemite crystals into which Mn^{2+} was introduced by solid-state diffusion at 1250°C. The diffusion was carried out on small transparent prismatic crystals. Selected crystals were coated with very finely powdered $MnCO_3$ and heated to 1250°C for 12 hr in a platinum crucible. Crystals treated in this way were then mounted for probe analysis as usual. Cross sections through such crystals gave a concentration gradient of Mn. The luminescence intensity and the emission spectra along with Mn, Zn, and Si concentrations were recorded at many points along the Mn gradient. These measurements established that the Mn^{2+} is introduced in the lattice at the expense of Zn^{2+} . Figure 2 shows a plot of integrated luminescence intensity as a function of Mn concentration. This measurement was made at 20 keV and sample current of 2×10^{-8} A. The spot was about 2 μ m in diameter. The intensity of luminescence is maximum for a Mn concentration of 2.9 w/o (weight per cent). This value is higher than the optimum of 1% reported

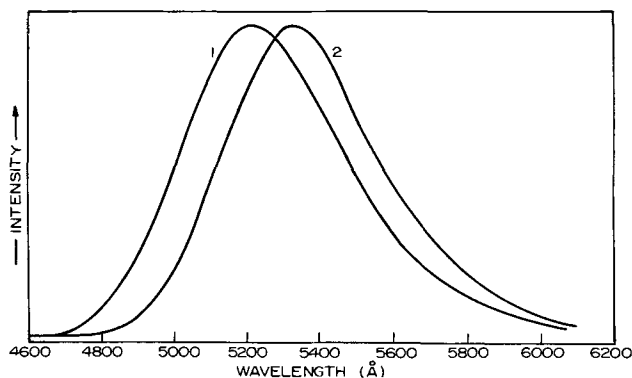


Fig. 1. Polarized cathodoluminescence spectra of Mn^{2+} in willemite. Curve 1 corresponds to the analyzer direction (electric vector) along the c -axis and curve 2 corresponds to the analyzer direction perpendicular to the c -axis. The peak intensities of the two curves are normalized to facilitate comparison of the spectra.

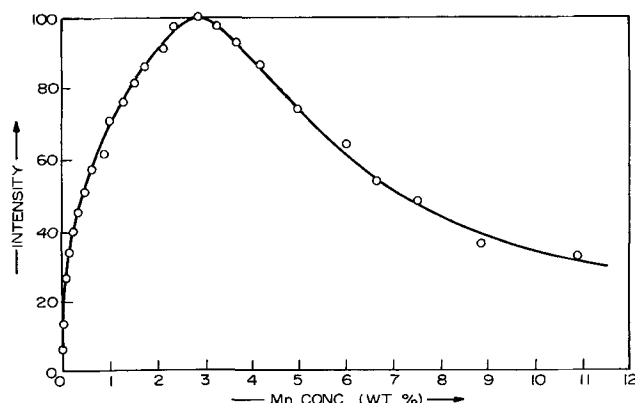


Fig. 2. Plot of integrated intensity vs. Mn concentration for a South-West Africa willemite crystal into which Mn was diffused by solid-state reaction with $MnCO_3$ at 1250°C. Measurements were made at 20 keV and a sample current of 2×10^{-8} A. The spot size was about 2 μ m diameter. No correction was made for the possible change in the photomultiplier response as the emission peak shifts to slightly longer wavelengths for higher Mn concentrations.

for powder phosphors (6). It may be pointed out that the optimum concentration is dependent on the electron beam energy which is not specified in Ref. (6). It was found that, as the Mn concentration increases, the luminescence peak position shifts toward longer wavelengths. As the concentration of Mn increases from just a trace to about 12% the peak position shifts from 5160 and 5300Å. This observation compares well with similar results reported by Leverenz (6) on powder phosphors.

Discussion of Results

For an explanation of the polarization of $Zn_2SiO_4(Mn^{2+})$ luminescence, and the spectra in the two polarization directions, it is necessary to consider only the local symmetry of the activator site. The position of the Mn^{2+} energy levels involved in this luminescence emission, with respect to the position of valence and conduction bands of willemite, is not known. However, as is usual with Mn^{2+} -activated phosphors, it is fairly certain that the transition responsible for green emission of Mn^{2+} -activated willemite is localized within the 3d shell (7, 8). Although excitation by cathode-rays may be substantially through the conduction band, the final transition giving rise to the luminescence emission takes place within the Mn^{2+} activator without any involvement of valence or conduction bands.

Mn^{2+} replaces Zn^{2+} in the crystal structure of willemite and Zn^{2+} is fourfold coordinated forming approximately a tetrahedral arrangement (9). Detailed refinement of the willemite structure has not been reported, thus the exact coordinates and distortions of the tetrahedral sites are not known. If there were no distortions in the tetrahedral Zn^{2+} sites then the symmetry of the site occupied by the activator Mn^{2+} would be T_d . The ground state of Mn^{2+} , which has $3d^5$ configuration, is 6S with symmetry 6A_1 . This state is changed very little in energy under the influence of a crystal field. The first excited term 4G in the free ion gets split up into branches 4A_1 , 4E , 4T_2 , and 4T_1 in a tetrahedral field, with 4T_1 level having the lowest energy. The transition responsible for Mn^{2+} emission is believed to be the one from $^4T_1 \rightarrow ^6A_1$ (7). Group theoretical calculations show that if the symmetry of the emitting Mn^{2+} ion were perfectly tetrahedral there would be no polarization of the emitted radiation as the transitions in x , y , and z directions are equally allowed. In the crystal structure of willemite the Zn atoms, thus also the replacing Mn atoms, are reported at general positions and have a space group symmetry of C_1 (9). Under such symmetry conditions the emitting 4T_1 level would split up into three levels and again, according to group theory, transitions from these levels

Table I. Estimated Zn-O bond lengths of the distorted tetrahedra around Zn(1) and Zn(2) positions

Bond type	Bond length (Å)
Zn(1)-O ₁	1.93
Zn(1)-O ₂	1.75
Zn(1)-O ₃	1.88
Zn(1)-O ₄	2.05
Zn(2)-O ₁	1.82
Zn(2)-O ₂	1.82
Zn(2)-O ₃	1.94
Zn(2)-O ₄	1.96

to the ground level are equally allowed in the x, y, and z directions giving no polarization. The fact that the emitted radiation is polarized leads to the conclusion (on the basis of crystal field theory arguments) that the emitting center has a local symmetry which is lower than T_d but higher than the space group symmetry C_1 .

Any lowering of perfect T_d symmetry of the center would result in splitting of the triply degenerate 4T_1 into two or three separate levels depending on the lowered symmetry of the center. Polarization properties under the reduced symmetry conditions can be understood easily on the basis of group theoretical arguments (10), if the local symmetry of the center is known. An attempt to find out the local symmetries of Zn^{2+} ions in the willemite structure was made by calculating bond lengths and the following explanation is attempted on that basis.

The willemite structure has two different distorted tetrahedral Zn^{2+} sites [herein called Zn(1) and Zn(2) sites] where Mn^{2+} can go (9, 10). Approximate distortions in these sites were determined by using the atomic coordinates given by Bragg and Zachariasen (9). Calculations of bond lengths for the two sites are tabulated in Table I. It can be seen that the Zn(1) sites are highly distorted and do not seem to have any symmetry. Thus, taking C_1 as symmetry of this site, Mn^{2+} replacing Zn^{2+} on such sites would show no polarization. However, the Zn(2) sites have three bonds which are approximately equal, with an average bond length of 1.94Å. The fourth bond has a bond length 1.82Å which is appreciably shorter than the rest. It is very likely that this site has an effective pseudosymmetry of C_{3v} , with the threefold axis along the shorter bond. Mn^{2+} replacing Zn^{2+} on this site would have the emitting triply degenerate 4T_1 level split into a doubly degenerate level, 4E , and a nondegenerate 4A_2 level. Strictly group theoretical arguments show that the transition ${}^4A_2 \rightarrow {}^6A_1$ is forbidden and the transition ${}^4E \rightarrow {}^6A_1$ is allowed in (x, y) direction, i.e., a direction perpendicular to the shorter bond length. Since this direction makes smaller angles ($\sim 35^\circ$) with the basal plane, the electric vector in the basal plane would be of greater magnitude than the component along the c-axis. This explains the observed partial polarization of emission along a direction perpendicular to the c-axis. The energy level diagrams for the emission of Mn^{2+} at the two Zn^{2+} sites are shown in Fig. 3. At Zn(1) sites (C_1 symmetry, Fig. 3b) the 4T_1 level splits into three 4A levels and these are equally allowed in x, y, and z directions, thus, contributions along the perpendicular to the c-axis are equal. The splitting is probably too small to show up in the broad band spectra. Figure 3c shows the splitting of 4T_1 level at Zn(2) sites (C_{3v} symmetry). Level 4E is placed higher than 4A_2 in the energy level diagram since the 4A_2 level is connected with the shorter bond, thus, a greater crystal field. The small shift of peak to shorter wavelengths, for the spectra along the c-axis, can be explained if the peak of Mn^{2+} band for Zn(1) is at a comparatively shorter wavelength than the peak due to Mn^{2+} at Zn(2) position.

The above model explains the observed polarization satisfactorily (observed polarization, $\phi = 0.25$, in comparison to the calculated value of 0.21). However, the symmetries of the two Zn sites can be predicted with

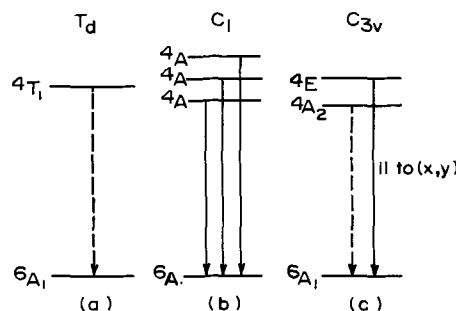


Fig. 3. Splitting of triply degenerate 4T_1 (G) level of Mn^{2+} ion under the influence of lowered symmetries. All the transitions are forbidden by spin symmetries, and for T_d symmetry the transition ${}^4T_1 \rightarrow {}^6A_1$ is also forbidden by orbital symmetry. Under C_1 symmetry all transitions are allowed but under C_{3v} symmetry only the transition ${}^4E \rightarrow {}^6A_1$ is allowed in (x,y) directions by the orbital symmetries.

more confidence only when precise atomic coordinates for willemite structure become available. All other theoretically possible lower symmetries, which can be formulated for Zn(2) sites, do not explain the observed polarization satisfactorily.

Recently Palumbo and Brown (12) have made absorption measurements on $Zn_2SiO_4:Mn$ powders and have seen complete splitting of the 4T_1 level. They did not study polarized absorption from single crystals and assignment of symmetries is not possible on the basis of their data. However, these measurements clearly show the symmetries (of one or both sites) lower than T_d . Another study of interest is that of Perkins and Sienko (11). They studied ESR spectra from Mn^{2+} -doped Zn_2SiO_4 single crystals. Their data showed the location of Mn^{2+} at two crystallographically nonequivalent zinc positions in the willemite structure. They did not elaborate on the distortions of these sites but discounted any possibility of Mn^{2+} at six coordinated sites, which would produce an associated defect also.

It may be pointed out here that the selection rules given in Fig. 3 are for electric dipole type of interactions and are allowed (or forbidden) by the symmetry of purely electronic wave functions. These rules would be somewhat relaxed by vibronic coupling, however, the intensity contributions due to vibronic coupling are usually an order of magnitude smaller than those due to purely electronic transitions.

Simple crystal-field explanation of the observed peak shift toward longer wavelengths, as the concentration of Mn^{2+} in the lattice is increased, is not possible. Increased concentration of Mn^{2+} of ionic radius 0.80Å, which replaces Zn^{2+} of ionic radius 0.74Å, causes the lattice to expand slightly (13). Thus on the basis of simple crystal field theory it would be expected that this would result in emission peak shifts toward shorter wavelengths since the field strength at the activator has been reduced (14). However, at higher concentrations it is no longer justified to consider emission from isolated Mn^{2+} ions only. With an increase in concentration, the probability that two Mn^{2+} ions would occupy immediate neighboring positions increases rapidly and the emission from these ion pairs would be expected to show up increasingly with the increase in Mn^{2+} concentration. This type of pair absorption has been found to occur in Mn^{2+} activated cubic ZnS crystals (15). An explanation of the observed shift of the green band to longer wavelengths with increasing Mn concentration can be made on the basis of pair emission concept if the model shown in Fig. 4 is considered. For simplicity, splitting of the 4T_1 level is ignored. The pair of two neighboring Mn^{2+} ions is shown to give rise to two levels, one of which is higher than the original 4T_1 level and the second level lower. A shift toward the red is expected if all the emission peak is a mixture of contributions from single ions and ion pairs. As the concentration of Mn^{2+} increases the contribution to emission intensity from ion pairs increases

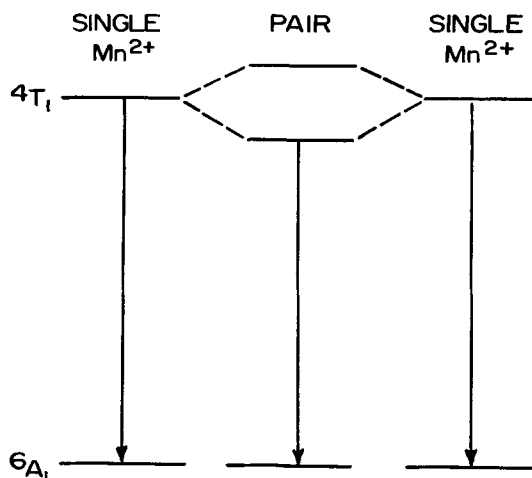


Fig. 4. Formation of ion pairs by two neighboring Mn^{2+} ions, shown for perfect T_d symmetry. The green emission peak would shift toward longer wavelengths if the emitting level for the pair is the lower level.

and the contribution from single ions decreases. This would give rise to the observed shift of emission peak wavelength.

Acknowledgment

The authors wish to thank Professors W. B. White, R. Roy, and H. K. Henisch for continued interest and many helpful discussions. Support for this work was provided by Advanced Research Projects Agency Contract No. DA-49-083-OSA-3140.

Manuscript submitted July 1, 1971; revised manuscript received Dec. 23, 1971. This was Paper 53 pre-

sented at the Los Angeles Meeting of the Society, May 10-15, 1970.

Any discussion of this paper will appear in a Discussion Section to be published in the December 1972 JOURNAL.

REFERENCES

1. P. P. Feofilov, "The Physical Basis of Polarized Emission," State Physico-Mathematical Press, Moscow (1959); Consultants Bureau, New York (1961).
2. S. Shionoya in, "Luminescence of Inorganic Solids," p. 206, P. Goldberg, Editor, Academic Press (1966).
3. R. J. R. S. B. Bhalla and E. W. White, *J. Appl. Phys.*, **41**, 2267 (1970).
4. R. T. Greer and E. W. White, *Trans. Second Nat. Conf. on Electron Probe Analysis*, Paper 51 (1967).
5. C. Palache, *U.S. Geol. Survey Prof. Paper 180* (1937).
6. H. W. Leverenz, "Introduction to Luminescence of Solids," p. 223, John Wiley & Sons, Inc., New York (1950).
7. L. E. Orgel, *J. Chem. Phys.*, **23**, 1958 (1955).
8. M. A. Konstantinova-Shlezinger, *Bull. Acad. Sci., USSR-Phys. Ser.*, **30**, 729 (1966).
9. W. L. Bragg and W. H. Zachariasen, *Z. Krist.*, **72**, 518 (1930).
10. F. A. Cotton, "Chemical Applications of Group Theory," Interscience (1963).
11. H. K. Perkins and M. J. Sienko, *J. Chem. Phys.*, **46**, 2398 (1967).
12. D. T. Palumbo and J. J. Brown, *This Journal*, **117**, 1184 (1970).
13. H. G. Jenkins, A. H. McKeag, and H. P. Rooksby, *Nature*, **143**, 978 (1939).
14. See, for example, energy level diagrams, J. S. Berkes, Materials Research Laboratory Monograph No. 2, Pennsylvania State University (1968).
15. D. S. McClure, *J. Chem. Phys.*, **39**, 2850 (1963).

Effect of Impurity Gas Additions on the Superconducting Critical Current of Vapor-Deposited Nb_3Sn

R. E. Enstrom,* J. J. Hanak, J. R. Appert,* and K. Strater¹

RCA Laboratories, Princeton, New Jersey 08540

ABSTRACT

The addition of various gaseous impurities into the process gases used in the chemical vapor deposition of superconducting Nb_3Sn has been found to alter the grain size of Nb_3Sn and thereby the critical current (I_c). Increasing concentrations of CO_2 , CO , and N_2 cause a progressive decrease in the particle size and a concomitant increase of I_c up to three times the value found for undoped specimens. In contrast, O_2 and CH_4 increase the particle size and reduce I_c . I_c is linearly dependent on the reciprocal of the grain size, $1/D$, to values of D as small as 400Å. The present work suggests that impurities serve to control the grain size, presumably by the formation of small second-phase precipitates which interfere with the growth of Nb_3Sn grains.

One of the requirements of superconducting materials used in the construction of high-field solenoids is a high critical current, I_c . Over the years it has been found that I_c is proportional to the density of flux pinning centers, which can consist of a variety of defects such as second-phase impurities, dislocations, strain, radiation damage, etc.

In order to achieve a high, current-carrying capacity with ductile metallic alloy superconductors, such as Nb-Zr and Nb-Ti, the materials are extensively cold-

worked during fabrication and are also heat-treated according to prescribed schedules. However, these conventional methods cannot be utilized with Nb_3Sn , since it is a nonductile, mechanically weak compound. In Nb_3Sn prepared by diffusion of tin into niobium, a significant increase in I_c has been achieved by the addition of small amounts (0.7%) of zirconium to the niobium (1). Zirconium presumably forms precipitates with impurities scavenged from the niobium, thereby increasing I_c . For chemically, vapor-deposited Nb_3Sn ribbon (2, 3), we reported earlier a strong dependence of I_c on the grain size (4). We have found, in turn, that the grain size can be influenced by impurities in the process gases (5). A study of the addition of various

* Electrochemical Society Active Member.

¹ Present address: RCA Electronic Components, Somerville, New Jersey 08876.

Key words: Nb_3Sn , doping impurities, particle size, critical current, superconductivity.

gases during vapor deposition has made it possible to control and obtain reproducibly high values of I_c as is described in detail in this paper.

Experimental Procedure

The Nb_3Sn -coated ribbons were prepared by the hydrogen reduction of tin and niobium chlorides using equipment and procedures previously described (3). Briefly, Nb and Sn metal sources are reacted with Cl_2 at 900° and $800^\circ C$, respectively, and the chlorides are fed along with a H_2 carrier gas into the growth zone where the Nb_3Sn is synthesized. A continuous length of metal ribbon is passed through the growth zone and heated electrically to about $1000^\circ C$, while the growth furnace is maintained at about $700^\circ C$. This temperature profile keeps the incoming metal chlorides volatile and minimizes deposition of Nb_3Sn on the walls of the quartz growth tube. To achieve a stoichiometric ratio in the vapor-grown Nb_3Sn layer (75.0% Nb), the gas phase must have a Nb:Sn chloride ratio between 1:3 and 1:4.

Since this study focused on impurity gas additions, the process gases were purified where possible. Ultra-pure hydrogen² with a total impurity content of less than 10 ppm was passed through a platinum catalyst and any water of reaction absorbed with $CaSO_4$. Helium was purified by passing the gas stream through Linde 5A and 13X molecular sieve held at $77^\circ K$. The hydrogen chloride gas used in the present study was not further purified. However, infrared analysis indicated no impurity bands to be present in the range 3-15 μm , the region where CO_2 and phosgene would appear if present. Infrared analysis of the Cl_2 showed it also to be quite pure.

The impurity gas additions studied included CO_2 , CO , CH_4 , O_2 , and N_2 and these were injected either into the hydrogen or into the chlorine stream prior to entry into the growth apparatus. CO_2 , CO , and CH_4 additions ranged from 0.01 to 1 v/o (volume per cent) of the total Cl_2 flow of 140 ml/min, while the O_2 and N_2 additions ranged up to 36 v/o. The equipment was equilibrated for $\frac{1}{2}$ hr prior to the preparation of the 30m length of ribbon used in the superconductivity tests.

The critical current was measured on 30m lengths of ribbon, silver plated to increase electrical stability (6), and wound onto a coil form to produce a small magnet. This small magnet was, in turn, placed into another superconducting magnet, at $4.2^\circ K$, and energized so that the two magnetic fields were additive and parallel to the coil axis. The current through the small sample magnet was increased to a value which quenched superconductivity, thereby causing a large increase in voltage across a pair of potential leads; this was taken as the critical current. This procedure was repeated at background fields from 0 to 40 kG to generate a curve of I_c as a function of H. Tests at higher fields were conducted at the facilities of NASA, in Cleveland, Ohio, and at the Francis Bitter Magnet Laboratory at M.I.T. Measurements of the transition temperature, T_c , for selected samples were performed as previously described (7).

The vapor-grown layers were also examined by optical and electron microscopy. In addition, the sub-grain size was determined as a function of processing using an x-ray line broadening method and procedures described earlier (4). X-ray fluorescence analyses for Nb and Sn composition on the ribbon were performed using procedures already described (3) to monitor the stoichiometry of the deposit.

Results and Discussion

Effect of doping gases on I_c .—The critical current increases by about a factor of three with the addition of CO_2 as shown in Fig. 1. Here, the undoped Nb_3Sn ribbon carries 65A at 40 kG (curve 1) and the ribbon doped with 0.25% CO_2 carries 183A (curve 6). Since the thickness of the Nb_3Sn is similar for most samples,

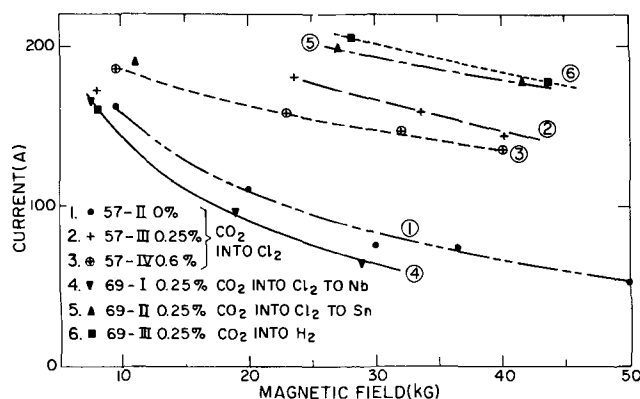


Fig. 1. Critical current as a function of total magnetic field for Nb_3Sn ribbon samples doped with CO_2 .

this corresponds to current densities, J_c , of about 2.5×10^5 and 8.0×10^5 A/cm², respectively. It may also be seen that I_c is a function of the CO_2 concentration and that the optimum value is around 0.25% for injection into the Cl_2 gas stream (curves 2 and 3).

Alternative doping gas injection sites were investigated and these results also are summarized in Fig. 1. The addition of 0.25% CO_2 to the Cl_2 stream leading to the Sn metal source (curve 5) results in an I_c (H) curve nearly equivalent to that observed for injection into the H_2 port (curve 6). However, the same concentration of CO_2 injected into the Cl_2 stream leading to the Nb metal source (curve 4) results in an I_c (H) curve somewhat below that observed for undoped Nb_3Sn ribbon. This latter result probably can be explained by gettering of the CO_2 in the Cl_2 stream by the Nb metal to form NbC and Nb_xO_y so that the CO_2 is not available to the growing Nb_3Sn layer. In contrast, CO_2 does not completely react with the Sn source at the $800^\circ C$ chlorination temperature and therefore is available to the Nb_3Sn being synthesized in the deposition chamber.

This hypothesis was confirmed by a thermodynamic analysis of the possible reactions of Sn with CO or CO_2 , which showed that the free energy change is zero at $800^\circ C$. Thus, any reaction between CO_2 and Sn would be near equilibrium, thereby allowing a substantial portion of the CO_2 to pass through unreacted. If kinetics limited the rate of reaction, an even greater fraction of CO_2 would pass through the Sn metal zone and into the Nb_3Sn deposition chamber. If CO_2 is injected into the Cl_2 stream before it is split into portions going to the Nb source and to the Sn source, then the CO_2 is gettered from the Cl_2 exiting from the Nb chamber. Accordingly there is an apparent difference in the optimum values for the amount of CO_2 injected into the gas stream at the various locations.

This effect probably explains the dependence of the I_c (H) curve on CO concentration given in Fig. 2. In-

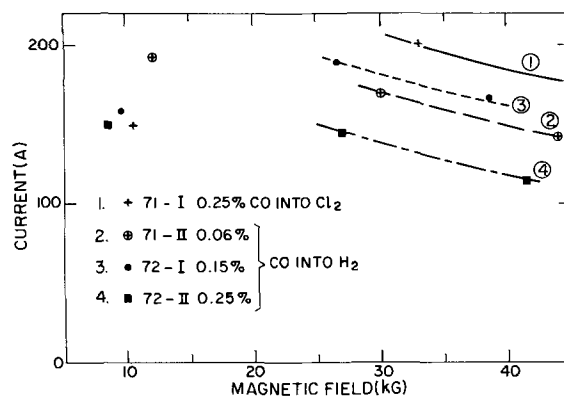


Fig. 2. Critical current as a function of total magnetic field for Nb_3Sn ribbon samples doped with CO .

² Matheson Company, East Rutherford, New Jersey.

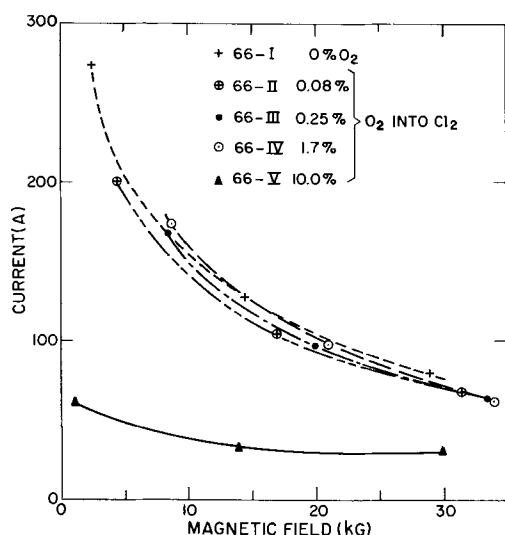


Fig. 3. Critical current as a function of total magnetic field for Nb₃Sn ribbon samples doped with O₂.

jection of the CO into the total Cl₂ stream results in a portion of the CO being gettered by the Nb metal source and the remainder, perhaps 0.18%, enters the deposition chamber. This concentration is closer to an optimum value and accordingly produces the Nb₃Sn ribbon with the highest current-carrying capability.

Thus, we have seen that both CO₂ and CO are effective in increasing I_c . In the next two series of runs, a hydrocarbon, CH₄, and O₂ were used. The results for the introduction of O₂ into the Cl₂ stream are shown in Fig. 3. Here, the undoped Nb₃Sn ribbon has the highest I_c . Increasing concentrations of O₂ result in successively lower I_c values and the value for 10% O₂, 29A at 30 kG, represents the lowest I_c observed at that magnetic field of all the various samples tested. It should be pointed out that all of the doped layers, except the 10% O₂-doped Nb₃Sn, had compositions within 1% of the correct stoichiometric ratio. The high O₂-doped sample was seriously deficient in Nb, presumably because of the formation of Nb oxides. Although these results indicate that large concentrations of O₂ should be excluded from the reactant gas stream, it is also apparent that I_c is rather insensitive to small oxygen impurity concentrations.

The results for the CH₄ doping demonstrate that CH₄ in concentrations of 0.15-0.25% is not effective in increasing the critical current. But, other results (5) show that hydrocarbon gases with a molecular weight greater than 16 (CH₄) are as effective as CO and CO₂ in increasing the I_c , presumably because they are less stable than CH₄. Therefore, since both CO and CO₂ and hydrocarbons such as ethane can successfully dope Nb₃Sn to high values of I_c , it is concluded that carbon is the principle atom responsible for the enhancement of I_c in these cases.

The next series of experiments performed with N₂ gas additions is summarized in Fig. 4. In this case, N₂ concentrations up to 36% were used to achieve values about twice as high as could be achieved with undoped Nb₃Sn. However, N₂ concentrations from 0.1 to 5% produced Nb₃Sn with I_c values not very much higher than for undoped Nb₃Sn. It should be pointed out that 99.999% pure N₂ containing less than 10 ppm hydrocarbon impurities had been used in these experiments which, when further diluted in the gas stream, should not influence I_c even at the highest flows of N₂ used. Thus, it appears that N₂ also can be used to enhance I_c . However, the use of CO₂ in conjunction with N₂ does not lead to a higher I_c than achieved with CO₂ alone, implying that the modes of enhancement are not additive.

Next, the influence of the Sn/Nb chloride ratio in the gaseous ambient was examined to determine its effect

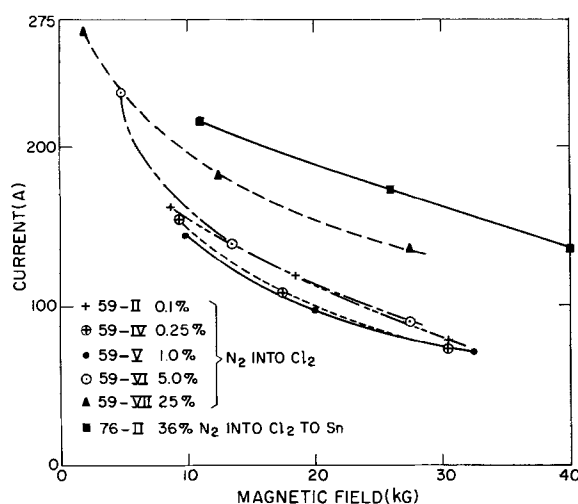


Fig. 4. Critical current as a function of total magnetic field for Nb₃Sn ribbon samples doped with N₂.

on I_c . As mentioned earlier, a Sn/Nb ratio greater than 3/1 must be used to achieve the correct stoichiometry in the vapor-grown Nb₃Sn layer; lower ratios result in Nb₃Sn with excess Nb and a lower T_c . Accordingly, ratios greater than 3/1 were examined both with and without CO₂ additions, and it was found that higher ratios produce Nb₃Sn that is up to 2.5% richer in Sn.

In Fig. 5 it is seen, in turn, that the 3 Sn/1 Nb ratio has the highest I_c (H) curve for both doped and undoped ribbons. But, CO₂ is effective in increasing the I_c at a given value of H for the three chloride ratios examined. It can be observed that the interval between the 3/1 and the 5/1 ratios is about the same for the doped and undoped series but that the 4/1 curve lies closer to the 5/1 curve for the undoped samples and closer to the 3/1 curve for the CO₂-doped Nb₃Sn. This latter result is fortunate since this allows some margin for error in the adjustment of the Sn/Nb chloride ratio while permitting a high I_c (H) relationship to be achieved.

In the standard growth process for the preparation of Nb₃Sn ribbon, the ribbon travels 15 m/hr counter-current to the gas stream and the total flow rate of chlorine to the Nb and Sn metal sources is 140 ml/min. The effect of several variations in the process on the I_c (H) curve are given in Fig. 6 and these may be compared with both CO₂- and CO-doped as well as undoped ribbon samples. It may be seen that concurrent travel of the gas and the stainless steel substrate leads to an I_c (H) curve that is about 50% lower than when a countercurrent arrangement is used. The reason for this result is not clear.

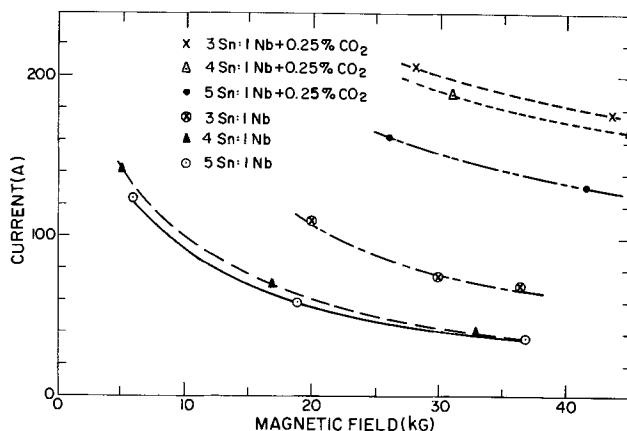


Fig. 5. Critical current as a function of total magnetic field for Nb₃Sn ribbon samples prepared with various Sn/Nb ratios in the vapor ambient.

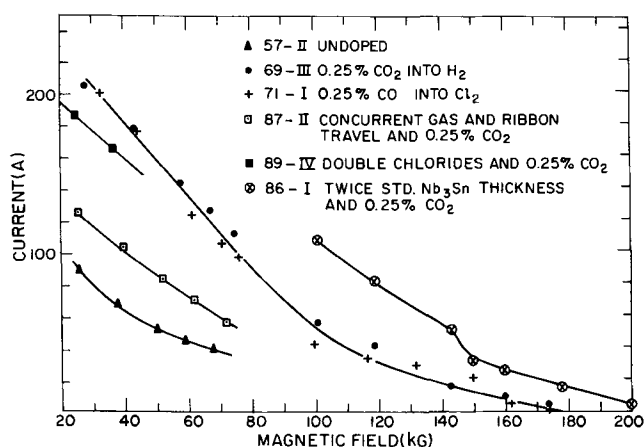


Fig. 6. Critical current as a function of total magnetic field for Nb_3Sn ribbon samples prepared under various vapor-growth conditions.

Higher partial pressures of the metal chlorides were investigated to study the effect on I_c and to increase the growth rate so that a thicker layer and thus a higher I_c could be attained for a given ribbon speed. It was found that doubling the partial pressures of the Nb and Sn chlorides by doubling the Cl_2 flow rates to the metal sources degrades the $I_c(H)$ curve somewhat, as shown in Fig. 6. Moreover, no significant increase in deposit thickness was observed. The deposit thickness was increased to twice the normal thickness, however, by decreasing the ribbon speed from 15 to 7 m/hr. I_c was thereby doubled as shown in Fig. 6, indicating that the deposit is homogeneously doped throughout its thickness. The factor-of-two higher I_c is very important, especially for the construction of magnets above about 120 kG where the I_c is dropping rapidly. In addition, the thicker Nb_3Sn has a significantly higher critical field, H_{c2} , presumably because the extra Nb_3Sn grown onto the ribbon is further removed from the metallic substrate and therefore less contaminated by diffusion of Fe, Mo, and Ni from the substrate. The nature of the interface between the Nb_3Sn and the stainless steel will be examined in another publication (8).

Impurity doping of Nb_3Sn deposits on ribbon substrates lowers the T_c onset from 17.0°K for undoped material to 15.0°K for optimally doped material. Part of this decrease is due to elastic strain built into the ribbon, as shown by an increase of T_c to 15.9°K when the substrate is etched away with nitric acid, and part is due to a large strain in the lattice introduced by the presence of the impurities. When the substrate-free deposit is annealed at 850°C for 2 hr, the T_c increases to 17.9°K which is probably due to relief of the internal strain.

Effect of doping on grain size of Nb_3Sn .—A striking change in the appearance of the Nb_3Sn from a dull, nonreflective surface to a very bright, reflective surface occurs with the introduction of CO, CO_2 , or N_2 into the gas stream. This change appeared to be associated with a reduction of the Nb_3Sn crystallite size. Accordingly, grain size measurements were made by x-ray line broadening of all specimens using techniques described in our earlier paper (4). It was found that increasing concentrations of CO_2 , CO, and N_2 decrease the Nb_3Sn grain size from $\sim 1000\text{\AA}$ (100 nm) for an undoped sample to a minimum of $\sim 370\text{\AA}$ (37 nm) for the most heavily doped samples. For O_2 and CH_4 doping, a tendency toward an increase of grain size is observed. The I_c data were converted to critical current density, J_c , and to $\alpha = J_c H$ and were plotted in Fig. 7 as a function of the inverse of the grain size, $1/D$. A similar linear dependence of J_c vs. $1/D$ was obtained up to $1/D \approx 2.5 \times 10^5 \text{ cm}^{-1}$ [grain size $\approx 400\text{\AA}$ (40 nm)] as before (4), regardless of the doping gas

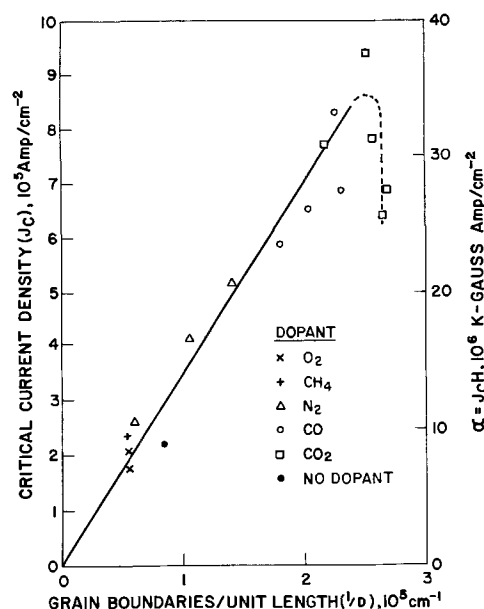


Fig. 7. Critical current density at 40 kG as a function of the reciprocal of the grain size.

used. The variable $1/D$ represents the number of pinning sites per unit distance and J_c is linearly dependent on it. The doping gas thus appears merely to provide a control over the grain size of Nb_3Sn , probably via the formation of submicroscopic precipitates such as carbides or nitrides of niobium which interfere with grain growth of Nb_3Sn .

Attempts to identify the form which the impurities take in the deposit were only partially successful. Mass spectroscopic analyses of carbon in an undoped and a CO_2 -doped deposit (0.25% CO_2 in gas phase) show 50-100 ppm and 700-2400 ppm, respectively, indicating the incorporation of carbon. This amount of carbon would be sufficient to form a second phase. But, neither x-ray nor electron diffraction techniques were able to identify the presence of phases other than Nb_3Sn . However, a transmission electron micrograph of a specimen thinned by etching showed a multitude of dark spots which could be interpreted as a fine precipitate of a second phase (9).

Conclusions

The addition of various gaseous impurities into the process gases used in the chemical vapor deposition of superconducting Nb_3Sn has been found to alter the grain size of Nb_3Sn and thereby the critical current. Increasing concentrations of impurity gases including CO_2 , CO, and N_2 have been found to cause a progressive decrease in the Nb_3Sn particle size and an increase in I_c . Additions of O_2 and CH_4 , on the other hand, tend to increase the particle size of Nb_3Sn and lower I_c . Regarding the effectiveness of doping, CO_2 and CO have been found to be the most effective since about 0.25% impurity causes up to a threefold increase of I_c compared to undoped specimens. In contrast, 36% of N_2 impurity is required to increase I_c twofold. The process is rather insensitive to oxygen impurity as 1.7% O_2 decreases I_c only 6% and large amounts of O_2 (10%) are required to decrease I_c to less than $\frac{1}{2}$ the value of undoped specimens. Since I_c scales up with deposit thickness at a given doping level, doping is a bulk effect. The increase of I_c and J_c has a similar linear dependence on the inverse of the grain size $1/D$ as reported previously (4), regardless of the type of dopant used. It appears, therefore, that the impurities serve only as a means of controlling the grain size, presumably by the formation of small, second-phase precipitates which interfere with the growth of Nb_3Sn grains.

Acknowledgments

The authors are grateful to the staffs of the M.I.T. Francis Bitter Magnet Laboratory and NASA, Cleveland, for their cooperation during the high-field superconductivity tests.

Manuscript submitted June 24, 1971, revised manuscript received Oct. 20, 1971.

Any discussion of this paper will appear in a Discussion Section to be published in the December 1972 JOURNAL.

REFERENCES

1. W. DeSorbo, *Cryogenics*, **4**, 218 (1964).
2. J. J. Hanak, "Metallurgy of Advanced Electronic Materials," p. 161, G. E. Brock, Editor, Interscience Publishers, New York (1963).

3. J. J. Hanak, K. Strater, and G. W. Cullen, *RCA Rev.*, **25**, 342 (1964).
4. J. J. Hanak and R. E. Enstrom, "Proc. Tenth International Conf. on Low Temperature Physics," Vol. IIB, p. 10, Moscow, U.S.S.R. (1967).
5. R. E. Enstrom, J. J. Hanak, F. R. Nyman, and K. Strater, U.S. Pat. No. 3,400,016, September 1968.
6. H. C. Schindler and F. R. Nyman, *RCA Rev.*, **25**, 570 (1964).
7. J. L. Cooper, *ibid.*, **25**, 405 (1964).
8. R. E. Enstrom and J. Appert, To be published.
9. M. C. Inman, "Phenomenon of Superconductivity" (Phase II), October 1966, prepared by RCA Laboratories, Princeton, N. J., for Air Force Materials Laboratory, Wright-Patterson Air Force Base, Ohio, p. 56.

Hydrogen Chloride and Chlorine Gettering: An Effective Technique for Improving Performance of Silicon Devices

R. S. Ronen and P. H. Robinson*

RCA Laboratories, Princeton, New Jersey 08540

ABSTRACT

Moderate levels of lifetime killing impurities in silicon can be removed or neutralized by a high-temperature treatment in the presence of approximately 1% gaseous hydrogen chloride or chlorine in dry oxygen. Results using bulk silicon as well as thin-film silicon on sapphire (SOS) indicate a significant improvement in the effective minority carrier lifetime. Crystal quality, doping level, oxygen content of the silicon, and surface treatment are found to be important variables. The paper describes the effect of chlorine getting on various bulk silicon and SOS devices.

It has been well documented that many high-temperature fabrication steps used in silicon device processing often result in the reduction of minority carrier lifetime (1-6), because of the redistribution of heavy metallic impurities, *e.g.*, Au and Cu, or the precipitation of such impurities on dislocations. Thus these impurities become effective recombination centers (7, 8). Heavy metal impurities were found to have states near the center of the gap (2, 5, 6, 9). Oxidation, in particular, was very detrimental to lifetime (10). Contaminants can come from a number of sources, such as the bulk and surface of the wafer or the furnace tube.

Various getting techniques to eliminate them or prevent them from generating effective traps have been reported (3, 4, 11, 12). One has been a phosphorus glass layer in contact with the Si at elevated temperatures (4, 11). A second technique uses KCN or sintered Ni in contact with the Si to prevent impurities from in-diffusing during processing (13). Oxides such as P₂O₅, B₂O₅, and V₂O₅ have also been used, as have been chlorides (BCl₃ and PCl₅), during high-temperature diffusion for the preservation of lifetime (3, 4).

Transmission electron microscopy and infrared microscopy verified the elimination of Cu precipitates from dislocations after getting treatment (14).

Recently, bulk Si as well as thin-film Si on insulators has shown a significant increase in minority carrier lifetime after heating in a dry O₂/HCl ambient (15, 18). At 950°C, the lowest temperature used for the HCl getting process, the diffusion constants of the lifetime killing impurities (Cu, Fe, Au) in Si range from 10⁻⁵ to 10⁻⁸ cm²/sec. Since Cl₂ is more reactive than HCl we

believe that it can more effectively improve lifetime; that is, getting can be done at a lower temperature, and the magnitude of the improvement would be greater for the same time and temperature using Cl₂ rather than HCl. This paper describes various results obtained with Cl₂ getting; a comparison of HCl and Cl₂ is made.

Experimental Procedure

Getting was carried out in a dry O₂ ambient either before device processing when films were being studied or after fabrication, just before metalization. A typical procedure consisted of the following steps:

1. Thorough cleaning of the wafer, to remove surface impurities.
2. Getting in a mixture of 1% Cl₂ in dry O₂ at a temperature T_g of 800° to 1150°C.
3. Annealing in dry He for 15 min at T_g to remove Cl₂ from the furnace and sample and to reduce positive oxide charge (16).
4. Hydrogen annealing for 15 min at 500°C to reduce density of interface states.

The effective minority carrier lifetime was then determined by C-V and C-t measurements (17). Getting times range from 1 to 100 hr, and the getting temperatures were either 950° or 1050°C. The lifetime improvement was found to be dependent on the time × temperature product. When junction devices were being studied, a period of 2 hr at 950°C was used so as not to alter the diffusion profile in these devices significantly.

On several occasions, oxidation prior to the admission of HCl or Cl₂ was necessary to prevent etching and pitting of the Si. The concentration of HCl or Cl₂ was kept low (~ 0.5-1%) because severe attack of the Si was observed at higher concentrations (~ 5-10%).

* Electrochemical Society Active Member.

Key words: getting, minority carrier lifetime, SOS, silicon, HCl, Cl₂.

Water vapor was removed from the oxygen gas by a dry ice trap. For SOS devices C-V measurements were not always effective because of series resistance. C-V measurements at d.c. and high frequency were employed with SOS devices to determine lifetime.

We tried different annealing techniques which included only inert gases such as N_2 , He, Ar, H_2 , as well as oxygen but no HCl or Cl_2 , at various temperatures and periods. The wafers and devices showed little or no improvement, and the O_2 treatment was in fact detrimental to lifetime in most cases. These heat-treatments were carried out under conditions identical to those used for Cl_2 .

Measuring Technique

The effective minority carrier lifetime was determined from the transient response of a depletion capacitance structure (17). To facilitate the measurement a mercury probe made contact with the SiO_2 in a circular pattern (~ 35 mil diam). A back contact was employed in the bulk Si measurements, and a circular contact around the dot for the SOS measurements. To minimize series resistance, particularly when measuring SOS, an interdigitated pattern was used, thus making the resistance smaller than the capacitive reactance.

Heiman (17) has shown that $\tau_{eff} = (T/2) (N_i/N_a)$ is an approximate solution to the recovery from deep depletion of an MOS capacitor; τ_{eff} = effective lifetime of minority carrier in depletion region, T = recovery time constant, N_i = intrinsic carrier concentration, N_a = carrier concentration of wafer under investigation. The three wave shapes shown in Fig. 1 represent recovery of an MOS capacitor with shallow surface states, with deep surface states, and with no surface states. If the transient response on the wafers is observed before and after gettering, and the response has the same shape, only one calculation of T is necessary. The second and third wave shapes were typically observed on SOS and good-quality Si, respectively.

The MOS capacitor structure used for C-t measurements is shown in Fig. 2. From the typical C-V curve shown in Fig. 3 one can calculate the doping density to within a few diffusion lengths of the surface, and effective oxide charge, and get an indication of the surface state density (19). A typical C-t curve is shown in Fig. 4. The effective minority carrier lifetime is obtained, following Heiman's method (17), without much processing; however, the results must be interpreted with care.

Comparative lifetime measurements, before and after gettering, are meaningful even though the technique assumes recombination centers at mid-gap. It was assumed that the majority carrier concentration does not change during gettering at $950^\circ C$ for 2 hr. This was shown to be valid by Hall measurements, C-V curves, and 4-point probe measurements.

For very thin SOS devices (those with planar junctions such as epitaxial bipolar transistors), the C-V

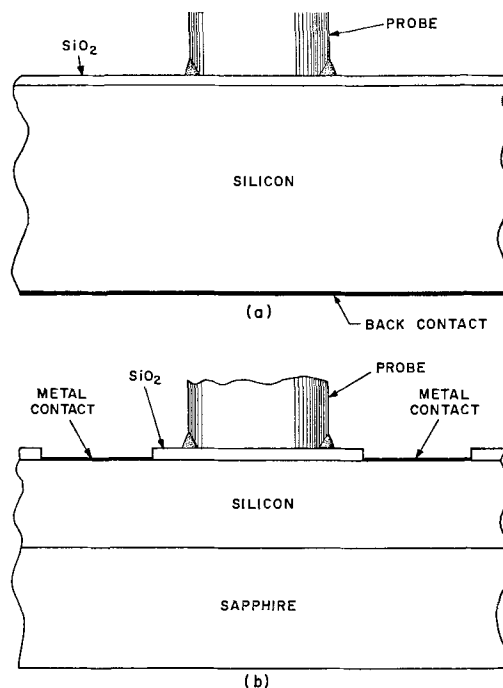


Fig. 2. Structure of MOS capacitor. a, Bulk; b, SOS

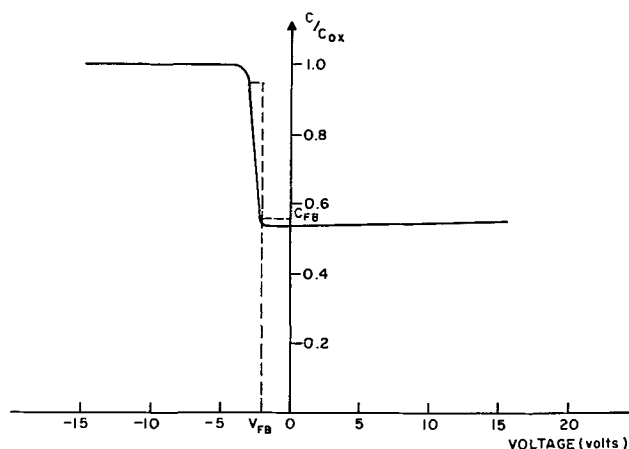


Fig. 3. Typical capacitance-voltage curve, p-type bulk silicon

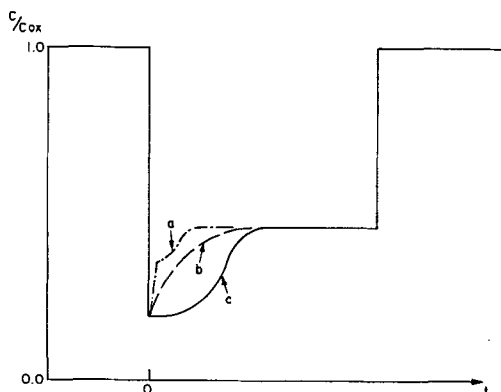


Fig. 1. Transient response of an MOS capacitor. a, Response in the presence of shallow surface states; b, response with deep surface states; c, response with no surface states.

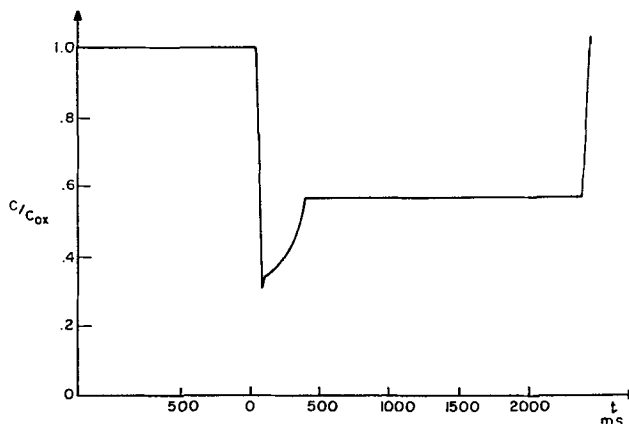


Fig. 4. Typical capacitance-time curve, bulk silicon

and pulse-capacitance measurements are difficult to make or useless; hence, other methods were used. SOS devices were evaluated by extending the logarithmic plot of the forward I-V characteristics asymptotically, determining the slope, and evaluating the zero voltage

intercept. The effective minority lifetime is then obtained, and comparison of measurements taken before and after gettering becomes meaningful. An I-V logarithmic plot exhibits a good straight line to the point where series resistance effects obscure the real junction behavior. We assume a simple junction theory of the form $I = I_0 \exp qV/nkt$ ($1 \leq n \leq 2$), with $n = 1$ for pure diffusion and $n = 2$ when recombination in the transition region is dominant (9). The slope of the linear part of logarithmic plot yields n directly, giving information about the relative magnitude of diffusion vs. recombination in the material (surface and bulk effects). The zero voltage intercept of the I-V asymptote yields a measure of the minority carrier lifetime in the depletion region of a diode. The forward diffusion current (linear part) at $V = 0$ is equated to the reverse leakage current (recombination), and the lifetime τ is calculated. This is only an approximate method, but comparison of curves before and after gettering and the absolute value of the leakage current yield very useful results. In the case of multilevel planar junctions such as SOS epitaxial bipolar transistors, high-frequency measurements of f_T vs. current, give the base transit time. The linear part of the curve depicting $[f_T]^{-1}$ vs. M is extrapolated to $M \equiv (kT/q)/I_E = 0$ (corresponding to $I_E \rightarrow \infty$, i.e., zero emitter delay time) where $f_T = D/\pi w^2$ and base transit time $T_r = w^2/2D = 1/(2\pi f_T)$. Knowing T_r and D yields the base width. The low-frequency common base current gain, when very close to unity, yields the minority carrier lifetime

$$\alpha_0 \approx 1 - \frac{1}{2} \frac{w^2}{L^2} = 1 - \frac{w^2}{2Dt} = 1 - \frac{T_r}{\tau}$$

when $\beta_0 = \alpha_0/(1 - \alpha_0) \gg 1$, we get $\tau = \beta_0 T_r$. The base width was also obtained by other techniques and found to be in close agreement with that obtained from UHF measurements.

Experimental Results

General observations.—1. Gettering is more effective on good-quality bulk crystals and thin-film SOS layers with scratch-free surfaces. Impurities introduced during processing can be eliminated or their effect significantly reduced by gettering.

2. In wafers exhibiting low lifetime due to oxygen contamination even below the sensitivity of mass spectrography ($10^{16}/\text{cc}$) improvement via gettering is marginal. The lifetime killing species is apparently bonded

to the Si differently in this case, or the SiO_2 complexes introduce deep recombination centers. This was mainly observed in thin epitaxial layers grown on sapphire.

3. Using Cl_2 , improvement was greater on n-type Si than on p-type material of comparable doping density. This indicates that the lifetime killing impurity may not reside near mid-gap in both types, an observation in agreement with Waldner and Sivo (4).

4. Up to a limit, the effectiveness of gettering increases with time and temperature. At gettering temperatures above 1000°C no further improvement was obtained after 30 hr.

5. If the Si is heavily contaminated with metal impurities or O_2 , some impurities tend to concentrate in the SiO_2 layer formed during oxidation, thus yielding large C-V shifts. Stripping the SiO_2 and regettering still results in large C-V shifts as well as charge storage effects in the oxide; this prevents meaningful C-t measurements.

6. Gettering diode structures resulted in the reduction of reverse leakage currents by several orders of magnitude. The reverse and forward I-V characteristics were also found to improve significantly.

7. Gettering MOSFET's showed only better drain diode breakdown characteristics, with no other effect on device performance observed. Metalized MOSFET's, with Al or Cr-Au, could not be gettered at the proper temperatures.

8. Mass spectrographic analyses on bulk and thin-film SOS were below the sensitivity range needed to detect changes in the Au and Cu content before and after gettering. Analysis showed a concentration of Cl_2 in the oxide after gettering 10^3 - 10^4 higher than in the bulk material. This may be responsible for tying up the impurities in the oxide at the interface.

Bulk silicon.—A series of p- and n-type [100] and [111] bulk silicon wafers were obtained from Ventron and Monsanto and were gettered with Cl_2 for different periods and temperatures, as shown in Table I. The effective lifetime after high-temperature oxidation was reduced to 100-300 nsec in most wafers and to 1-2 μsec in material that had both surfaces polished and relatively free of work damage. The [111] Ventron material, least affected by gettering, had unpolished back surfaces. The [100] n-type wafers, with both surfaces chemically polished, showed the greatest improvement; less consistent results were obtained with the [111] oriented wafers. After 16 hr of gettering no

Table I. Silicon wafers gettered with Cl_2

Manufacturer	Orientation	Type	Resistivity, ohm-cm	Process*	Original τ (if known), μsec	τ , μsec	Remarks
Ventron	[111]	P	8-11	A1	<2	0.05	Rough back
				B1		0.07	
				D1		0.07	
				E1		0	
				A1		0.1	
		N	8.5-11.5	B1	1.0	0.3-0.5	Polished back (chemically)- relatively work-damage free
				D1		1.5-2.0	
				A1		0.02	
				B1		0.02	
				D1		0.05	
Monsanto	[100]	N	10	A1	5-10	0.05	Chemically polished back
				D1		0.6	
				A2		0.04	
				E2		9.0	
				A1		0.02	
Ventron	[100]	P	10	B1	<10	1.2	Rough back
				A1		0.02	
				B1		0.02	
				A1		0.02	
Monsanto	[100]	N	10	A2	<10	1.0	Rough back
				B2		5.25	
				A2		0.3	
		P	10	B2		0.75	Relatively smooth back
				C2		0.1	
				A2		45.0	
Monsanto	[100]	N	10	A2	<10	0.5	Chemically polished back
				B2		4.5	
				A2		2.2	
				B2		5.5	

* Symbols: A, 5 min steam SiO_2 at 1050° ; B, process "A" followed by 2 hr Cl_2 gettering; C, process "A" followed by 4 hr Cl_2 gettering; D, process "A" followed by 16 hr Cl_2 gettering; E, process "A" followed by 100 hr Cl_2 gettering; 1, gettering temperature = 950°C ; 2, gettering temperature = 1050°C .

further improvement was observed in any of the wafers.

HCl gettering was studied and at 950°C was found to be slightly less effective than chlorine at the same temperature, while at high temperatures, ~ 1100°C, HCl was more effective by a factor of 2-5. Typical lifetimes were 1 μ sec for an n-type Cl₂-gettered silicon wafer, as compared with 4 μ sec for the HCl gettered one, with $T_g = 1150^\circ\text{C}$.

Cooling the bulk silicon wafers and the SOS films at 100°C/min in He or quenching them in He produced no significant difference in the results.

Results on thin-film silicon on sapphire.—The minority carrier lifetime of thin-film SOS layers as grown is typically 1-2 nsec. After high-temperature processing it is usually reduced to 0.1 nsec or less. The lifetime was found to increase to 4 nsec in 2- μ m-thick p-type layers after gettering in Cl₂ at 950°C for 2 hr. Increasing the gettering temperature to 1050°C increased the lifetime to the 10-40 nsec range. The n-type films showed a slight improvement over these p-type results, i.e., 20-50 nsec. The C-V measurements on these layers had high series-resistance contacts; to overcome this problem interdigitated geometries were used. Films $\geq 2 \mu\text{m}$ with doping densities $> 10^{16}$ were needed, since, with higher resistivity Si, the maximum depletion width can be equal to or greater than the film thickness, rendering deep-depletion measurements invalid. Typical C-V and C-t wave forms are shown in Fig. 5.

Silicon-on-sapphire epitaxial bipolar transistors.—Mesa-type epitaxial SOS bipolar transistors were gettered using either HCl or Cl₂ at 950°C for 2 hr just prior to the metalization step. Interdiffusion effects are insignificant, and measurements of the base width before and after gettering showed no change in thickness. The effect of this treatment on device performance, however, was quite dramatic. Figure 6 shows the transistor characteristics of a typical device before gettering, Fig. 7 after gettering. Low-frequency gain, β , increased by a factor of 2-10 after this treatment, and many devices with $\beta \approx 20$ were obtained (Fig. 8). A few devices with $\beta = 60$ were obtained. These most probably had very thin base regions and, hence, should make very good high-frequency transistors. A large reduction in the leakage current of emitter-base and base-collector diodes, along with an increase in the breakdown voltage, was observed. This is shown in the I-V characteristics of Fig. 9, before and after gettering. Note the different current scales on the two parts. The linear part of the forward I-V characteristics, $I = \exp$

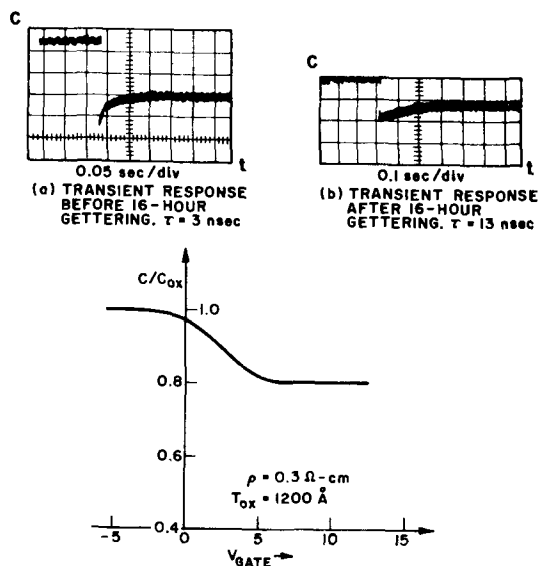


Fig. 5. Capacitance-time curves for an SOS capacitor before and after gettering; capacitance-voltage curve after gettering.

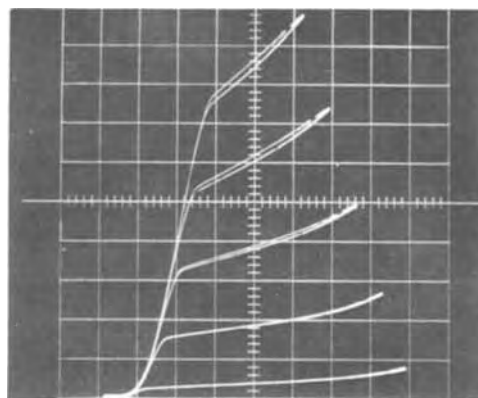


Fig. 6. Bipolar transistor before gettering. $\beta = 2$, Vertical, 1 mA/cm; horizontal, 2 V/cm; base current, 1 mA/step.

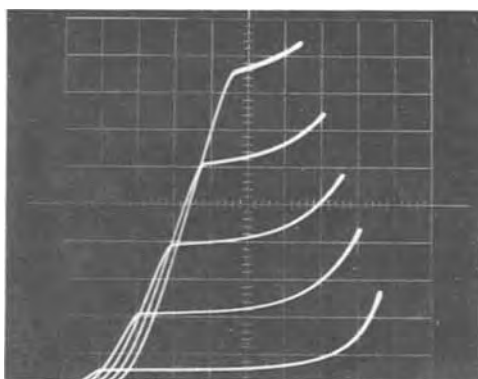


Fig. 7. Bipolar transistor after gettering. $\beta = 8$. Vertical, 2 mA/cm; horizontal, 2 V/cm; base current, 0.5 mA/step.

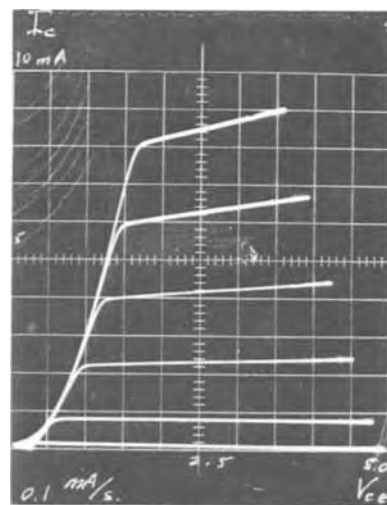


Fig. 8. Typical SOS bipolar characteristics. $\beta = 20$

(qv/nkt), exhibited $\eta < 1.4$ as compared with $\eta > 1.6$ before gettering. This result is indicative of a change in the recombination mechanism in the space charge region of the diodes (see Fig. 10).

Another measurement, that of $[f_t]^{-1}$ vs. $[I_E]^{-1}$, showed that the base transit time and the minority carrier lifetime in the base region had increased to 325 and 16 nsec, from values less than 2 and 0.1 nsec, respectively. This is shown in Fig. 11. Effective minority carrier lifetimes in SOS devices and films measured by the three different methods agree rather well.

The gettering process has significantly improved the SOS bipolar transistor.

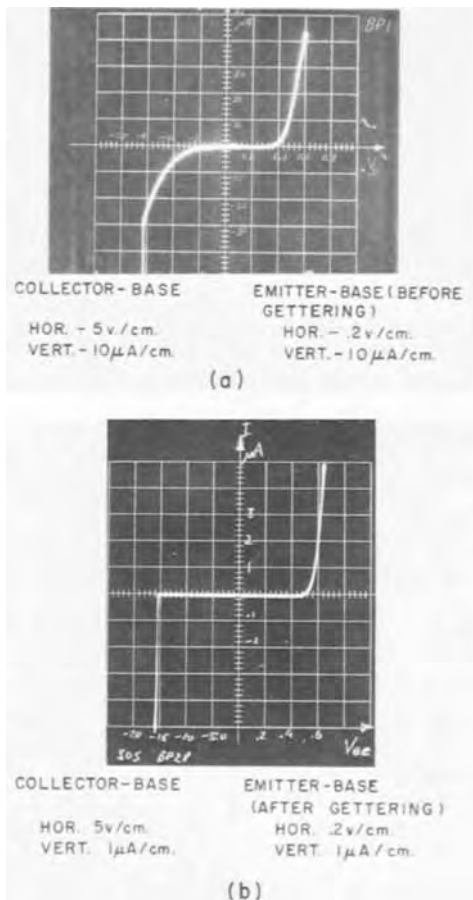


Fig. 9. Effect of gettering on the I-V characteristics of the two junctions in an SOS bipolar transistor.

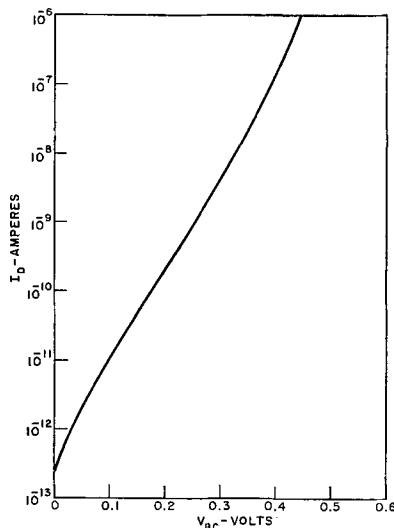


Fig. 10. Forward current voltage characteristic of base-collector junction.

Conclusions

A small amount of gaseous HCl or Cl₂ introduced during oxidation in dry oxygen significantly reduced recombination rate in both bulk Si and SOS films and devices. The mechanism whereby the lifetime is increased is still open to speculation. One possibility is the formation of volatile metallic impurity chlorides. Other mechanisms, such as Cl₂ diffusing into the Si and somehow tying up heavy or light ions, thereby neutralizing them or reducing their effectiveness as recombination centers, are also possible, as is some cleaning of the furnace. The gettering mechanism appears

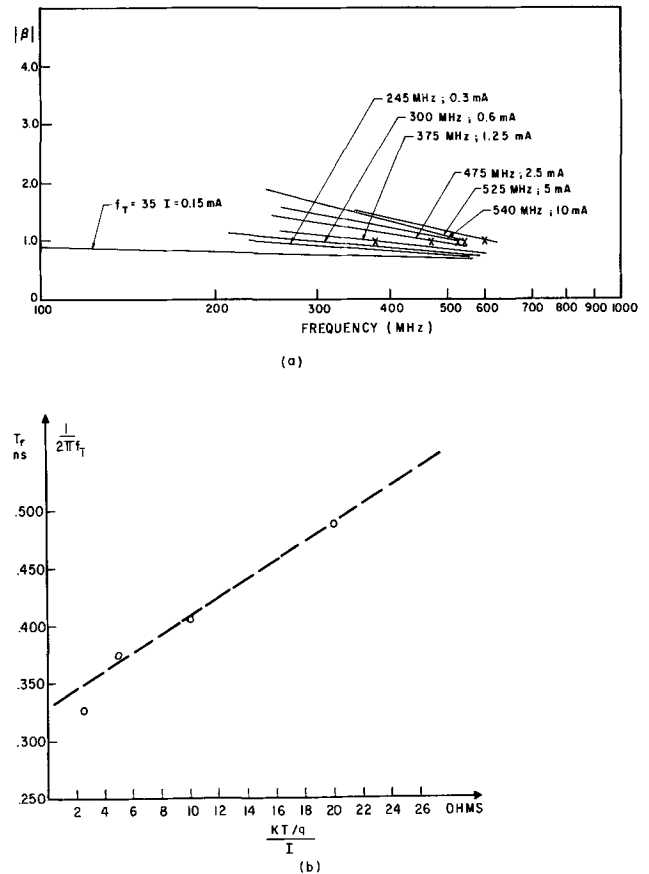


Fig. 11. High frequency behavior of SOS bipolar. (a) β vs. frequency; (b) $[t_T]^{-1}$ vs. $[I_E]^{-1}$.

to be related to the O₂ content of the starting material. Low-temperature Cl₂ is somewhat more effective than HCl, and improvements in the electrical characteristics of both diodes and bipolar transistors fabricated in SOS resulted from the gettering treatment. Because of the increase in the minority carrier lifetime due to Cl₂ and HCl gettering, bipolar transistors with average current gains of 20 have been produced.

Acknowledgments

The research reported herein was supported in part by the Air Force Avionics Laboratory, Air Force Systems Command, Wright-Patterson Air Force Base, Ohio, under Contract No. F33615-70-C-1100 and RCA Laboratories, Princeton, New Jersey. The authors would like to thank C. W. Mueller and D. Dumin for interesting discussions; also C. F. Arasim and R. O. Wance for their assistance in this study, and to S. Dierk for editorial assistance. The encouragement of both H. Steenbergen and D. Peacock of the Air Force Avionics Laboratory is highly appreciated.

Manuscript submitted March 31, 1971; revised manuscript received Dec. 8, 1971.

Any discussion of this paper will appear in a Discussion Section to be published in the December 1972 JOURNAL.

REFERENCES

1. L. M. Nijland and L. J. Van Der Pauw, *J. Elec. Control*, **3**, 391 (1957).
2. A. Goetzberger and W. Shockley, *J. Appl. Phys.*, **31**, 1821 (1960).
3. L. A. Murray and H. Lressel, *Electrochem. Technol.*, **5**, 406 (1967).
4. M. Waldner and L. Sivo, *This Journal*, **112**, 298 (1960).
5. R. N. Hall and J. H. Rocette, *J. Appl. Phys.*, **35**, 379 (1964).
6. J. E. Lawrence, *This Journal*, **112**, 796 (1965).
7. J. D. Struthers, *J. Appl. Phys.*, **27**, 1560 (1956).

8. B. I. Boltaks and I. J. Sosinov, *Z. Tekh. Fiz.*, **28**, 679 (1958).
9. C. T. Sah, R. N. Noyce, and W. Shockley, *Proc. IRE*, **45**, 1228 (1957).
10. K. D. King, Final Report, AF19 (628-303) (1963).
11. S. W. Ing, R. E. Morrison, L. L. Alt, and R. W. Aldrich, *This Journal*, **110**, 533 (1963).
12. E. J. Mets, *ibid.*, **112**, 420 (1965).
13. Y. Tokumaru, *Japan. J. Appl. Phys.*, **2**, 542 (1963).
14. J. E. Lawrence, *Trans. Met. Soc. AIME*, **242**, 484 (1968).
15. F. P. Heiman and P. H. Robinson, *This Journal*, **118**, 141 (1971).
16. B. E. Deal, A. S. Grove, and E. H. Snow, *ibid.*, **114**, 266 (1967).
17. F. P. Heiman, *IEEE Trans.*, **ED-14**, 781 (1967).
18. D. J. Dumin and W. N. Henry, *Met. Trans.*, **2**, 677 (1971).
19. K. H. Zaininger and F. P. Heiman, *Solid State Technol.*, **13**, 49 (1970).
20. D. J. Dumin, *Solid State Electron.*, **13**, 415 (1970).

Sputtered Cadmium Oxide and Indium Oxide/Tin Oxide Films as Transparent Electrodes to Cadmium Sulfide

R. R. Mehta and S. F. Vogel

International Business Machines Corporation, SDD, San Jose, California 95114

ABSTRACT

Thin films of cadmium oxide (CdO) and indium oxide/tin oxide ($\text{In}_2\text{O}_3/\text{SnO}_2$) were reactively sputtered from their respective metal or alloy targets. CdO films combine sheet resistances of less than 100 ohms/square with optical transmission greater than 45% for wavelengths greater than 5000Å, and make ohmic contacts with high-resistivity CdS films. Indium oxide/tin oxide films show optical transmission greater than 45% for wavelengths greater than 4000Å and sheet resistances of 100 to 200 ohms/square. Indium oxide/tin oxide also makes useful contacts to CdS films, but reduces the resistivity of the CdS films. A band diagram is proposed which qualitatively explains the ohmic nature of the contacts between two wide bandgap materials.

Recent interest in optoelectronic devices has led to the development of electrode materials which are transparent to light. One application of such materials is the use of transparent electrodes in a ferroelectric/photoconductor storage device (1, 2). Another application is in high-sensitivity photodetectors. There, maximum photocurrents (3, 4) are obtained when the photoconductor is sandwiched between the electrodes and the radiation is incident in the direction of the applied field, and when the thickness of the photoconductor equals the absorption length.

To be useful in high-sensitivity photodevices, the transparent electrode should have sheet resistances no larger than a few hundred ohms/square and maximum possible optical transmission. Also, the transparent electrode must make ohmic contact with the photoconductors.

In the past, thin metal films (e.g., gold, indium), have been used as the transparent electrodes. However, they have the disadvantage of lower transparency for reasonable values of sheet resistance. Some attempts have been made to use metal oxides (e.g., cadmium oxide and indium oxide) as transparent electrodes to photoconductors.

Only limited information about the basic properties of cadmium oxide is available. This is due to the unavailability of large single crystals (5). However, several papers have appeared during the past few years on studies of powdered material, sintered blocks, compressed tablets, or sputtered films (6). Some basic properties are given in the International Tables of Constants and Numerical Data (7). The effects of doping CdO by In and Cu and the effect of reduced oxygen in the reactively sputtered films have been studied by Lakshmanan (8). Electrical transport properties in single-crystal In_2O_3 have been discussed by Weiher (9). From high-temperature conductivity measurements, Weiher deduced the bandgap of indium oxide to be 3.1 eV, close to the value of 3.5 eV reported by Rupprecht (10). Recently, Fraser and Cook (11)

reported some measurements on films of indium oxide/tin oxide sputtered from oxide targets.

The first use of $\text{In}_2\text{O}_3/\text{SnO}_2$ as a transparent electrical contact with a photoconductor (CdS) was reported by Shivonen and Boyd (12). They used 82% indium/18% tin alloy sputtered in oxygen to give a transparent contact on a CdS crystal. Their films were about 200Å thick, had a resistance of 100 to 150 ohms/square, and showed very good transmittance characteristics, i.e., > 80% for $\lambda > 5000\text{Å}$. Williams (13) used thin films of In_2O_3 as transparent contacts to ZnS crystals. He also prepared $\text{In}_2\text{O}_3/\text{SnO}_2$ films by sputtering indium/tin alloy (4:1) in oxygen. However, he found that films so deposited had a high concentration of free metal and were opaque. These films had to be further heated in air at 300°-400°C to obtain transparency. The V-I curve measurements by Williams (13) indicated that the $\text{In}_2\text{O}_3/\text{SnO}_2$ films made ohmic contacts to ZnS crystals.

Our paper deals with the properties of CdO and $\text{In}_2\text{O}_3/\text{SnO}_2$ films deposited by reactive sputtering. Deposition conditions, such as the gas, the pressure, and the substrate temperature, are varied. Optical and electrical properties of these films are studied as a function of the deposition conditions. The quality of the contact to high resistivity ($> 10^7$ ohm-cm) thin polycrystalline films of CdS is investigated. Substrate and post-heat-treatment temperatures are kept below approximately 350°C to avoid diffusion of Cd or In from the oxide films into CdS.

Deposition of the CdO and $\text{In}_2\text{O}_3/\text{SnO}_2$

Two kinds of transparent electrodes were deposited by reactive sputtering of two metal targets: cadmium (14) and 82 In/18 Sn (12, 13).

The sputtering system was a diode-type MRC¹ Model SM8500 sputtering module mounted on a Norton-NRC² diffusion-pumped vacuum system Model 3116.

¹ MRC-Materials Research Corporation, Orangeburg, New York 10962.

² Norton-NRC: Now a division of Varian Associates, Palo Alto, California 94304.

Key words: transparent electrodes, cadmium oxide films, indium oxide/tin oxide films, cadmium sulfide films, reactive sputtering.

With a circular target (cathode) 5 in. in diameter, a cathode-substrate distance between 1 and 1½ in. was chosen. A magnetic field of 100 gauss produced by coils around the cathode and anode concentrated the discharge and caused relatively high deposition rates with an rf power of 200W. Substrates of Pyrex glass and tin oxide coated glass (NESA, Corning 9753) with a thin photoconductive film of CdS were placed on the heated anode. The substrate temperature was an important parameter in determining the resistivity of the films; therefore, temperature was measured directly with a fine-wire thermocouple on the surface of the substrate.

Naturally, the metal targets can be sputtered with d-c power; most indium oxide/tin oxide films were deposited with a d-c voltage of around 1.5 kV and a discharge current around 70 mA. However, sputtering with radio-frequency power (13.56 MHz) was preferred, because it allowed the use of lower gas pressures in the development stages of the work. When rf power of 200W was applied, the target assumed a self-bias of typically 1000V.

A pure oxygen atmosphere ranging in pressure from 6 to 200 μ was initially used for the sputtering of CdO. Later, an improvement in the optical transparency was obtained when an oxygen/nitrogen mixture was used. As little as 2% oxygen in nitrogen at a total gas pressure of 100 μ caused completely reactive sputtering and led to the best results with CdO. However, the In₂O₃/SnO₂ films were finally sputtered only in pure oxygen; 50/50 oxygen/nitrogen and oxygen/argon mixtures caused higher electrical resistances in the films.

CdO and In₂O₃/SnO₂ films differed appreciably in their deposition rates at otherwise equal conditions. CdO showed a rate of about 200 Å/min when sputtered in pure oxygen and 130 Å/min when sputtered in the oxygen/nitrogen mixture. Deposition times of 10 min (pure oxygen sputtering) were required to form films of satisfactory sheet resistances. The deposition rate of the In₂O₃/SnO₂ films was six times lower. Correspondingly, the deposition times were 1 hr.

After the deposition, some films were heat-treated at approximately 340°C on a hot plate for 1 hr in air. Such treatment not only reduced the electrical resistivity but also increased the optical transmission of the oxide films.

Experimental Results

Optical and electrical properties of CdO films.—Table I gives thickness, optical transmission, electrical sheet resistance, resistivity, and estimated electron density of CdO films prepared under various deposition conditions. Curves 1 and 2 in Fig. 1 show transmission as a function of wavelength for two representative films, one sputtered in 100% O₂ atmosphere and the second prepared with 2.5% O₂ in N₂ atmosphere.

These data were measured on a Cary 14 spectrophotometer. As previously reported (15), the films sput-

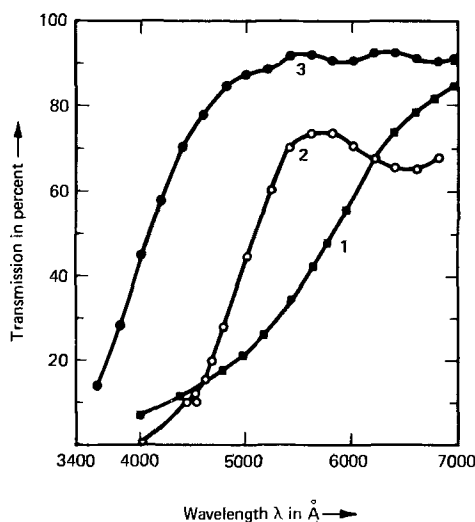


Fig. 1. Spectral transmittance of CdO and In₂O₃/SnO₂ films. Curve 1 is for CdO film No. 91 sputtered in 100% O₂ ambient; curve 2 is for CdO film No. 144 sputtered in 2.5% O₂ in N₂ ambient; curve 3 is for In₂O₃/SnO₂ film No. 214 C-1. Details of preparation are in Tables I and II.

tered in 2% O₂ in N₂ have higher transmission for shorter wavelengths. The thickness measurements on these films were made with a Sloan³ angstrometer which works on the principle of multiple beam interferometry. Sheet resistance measurements were made with a four-point probe. The mobility of electrons is assumed to be 120 cm²/V-sec (7), and the calculated value of electron concentration is listed in Table I. These values are very close to the values given by Lakshmanan.

Contact properties of CdO to CdS films.—A cadmium sulfide (CdS) film is deposited by a chemical spray process (16). In this process, a solution of cadmium acetate is mixed with a solution of thiourea to form a soluble complex. This soluble complex is directed in the form of a finely atomized spray to the surface of a heated substrate where it is decomposed to form a film of cadmium sulfide.

The substrate was a tin oxide (NESA) coated glass slide. The conducting coating of tin-oxide acted as a base (or bottom) electrode. CdO spots having an area $\sim 10^{-2}$ cm² were deposited on the CdS film. Deposition conditions were the same as for sample 144 listed in Table I, except deposition time was half that for sample 144. Indium metal spots of the same size area were deposited near the CdO spots, so that their contact quality could be compared. The V-I characteristics are always measured between the top electrode (CdO or In) and bottom tin-oxide (NESA) electrode. The measured V-I curves when the sample is illuminated

³ Sloan Instrument Corporation, Santa Barbara, California.

Table I. Details of preparation, optical and electrical properties of cadmium oxide films

Sample Number	Conditions of film deposition and subsequent heat-treatment	Thickness of films, Å	Optical transmission in % at wavelength			Sheet resistance of films, ohms per square	Resistivity of films, ohm-cm	Electron concentration in films assuming (7) $\mu = 120$ cm ² /V-sec
			4000Å	5000Å	6000Å			
91	60 μ O ₂ pressure; sputtering time of 10 min; heat-treated at 340° and 400°C for 1 hr each	2260	6.8	25.2	71.9	62.0	1.40×10^{-3}	3.72×10^{19}
98	100 μ O ₂ pressure; sputtering time of 10 min; heat-treated at 100°C for 1 hr in air	1740	2.5	10.8	59.0	26.0	4.52×10^{-4}	1.15×10^{20}
102	100 μ O ₂ pressure; sputtering time of 10 min; substrate temp 205°C; heat-treated in air for 1 hr at 340° and 400°C	1770	13.6	44.4	74.0	82.0	1.45×10^{-3}	3.60×10^{19}
140	100 μ O ₂ in N ₂ pressure; sputtering time of 10 min; max substrate temp 270°C	1220	1.2	40.0	66.0	43.0	5.75×10^{-4}	9.90×10^{19}
144	100 μ O ₂ in N ₂ pressure; sputtering time of 10 min; max temp 240°C	1275	1.2	44.4	70.8	29.0	3.7×10^{-4}	1.41×10^{20}

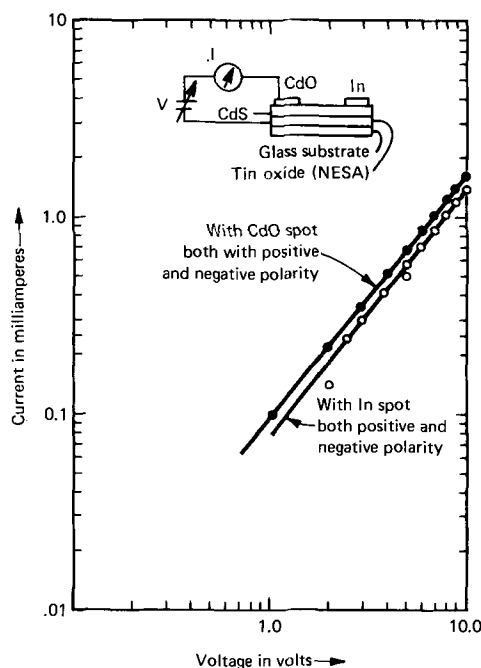


Fig. 2. Current-voltage characteristics under illumination for CdO and In spots on CdS film which is on tin oxide-coated glass substrate (NESA). Sample is illuminated through the glass substrate. Measurement configuration is also indicated.

through the glass substrate for the CdO and In spots for both polarities are shown in Fig. 2. The slope of these curves is practically constant for both polarities and both CdO and In spots. This suggests that contact quality is equally good for CdO and In, and the linearity of the curves suggests that the contacts are ohmic under the examination conditions.

A further test on this sample was carried out with the measurement of the spectral response of the photoconductor, with light incident through the NESA-coated glass substrate and through the CdO electrode. The results are depicted in Fig. 3. As expected for $\lambda < 5000\text{\AA}$, the photocurrent is about a factor of 2 smaller for light incident through the CdO spot. For $\lambda > 5000\text{\AA}$, the photocurrent is smaller by only a factor of 1.7. In this wavelength region, CdO serves as a reasonable contact to the CdS film. In the dark, there does not seem to be any change in the film resistivity as a result of CdO deposition and postdeposition heat-treatment.

Optical and electrical properties of $\text{In}_2\text{O}_3/\text{SnO}_2$ films.—Table II gives the conditions of film deposition and subsequent heat-treatment, thickness, optical transmission, sheet resistance, and resistivity of $\text{In}_2\text{O}_3/\text{SnO}_2$ films. From the table it is clear that films deposited at $300^\circ\text{--}350^\circ\text{C}$ and subsequently heat-treated at 340°C in air combine low resistivity with high optical transmission. There does not seem to be a dramatic difference in films produced by either d-c or rf sputtering. In general, higher substrate temperatures favor the lower sheet resistance and higher transmission. Curve 3 in Fig. 1 shows a transmission of film 214 C-1 as a function of wavelength.

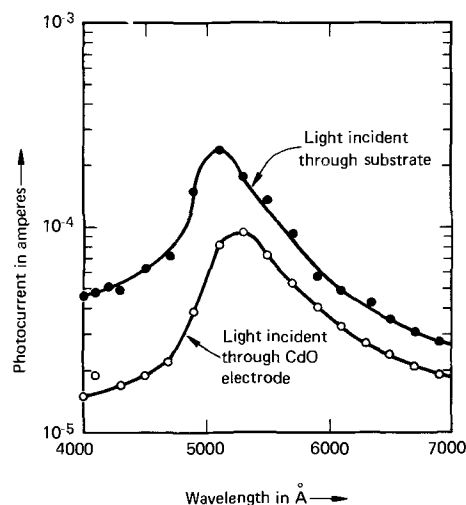


Fig. 3. Photoconductivities (constant intensity) of CdO spots on chemically sprayed CdS film, one with light incident through the contact and the other with light through the glass substrate with NESA coating. The applied voltage is 5V in both cases. Incident photon flux is about 10^{15} photons/cm² sec.

Contact properties of $\text{In}_2\text{O}_3/\text{SnO}_2$ on CdS films.—Again, the contact properties of $\text{In}_2\text{O}_3/\text{SnO}_2$ films were evaluated in conjunction with the CdS film. Electrodes of 10^{-2} cm² area were sputtered through a mask on the same kind of chemically sprayed CdS film mentioned before, which was an a NESA-coated glass substrate; NESA formed the bottom electrode for photoconductivity measurements. On the same films, In metal electrodes of the same area were evaporated between the $\text{In}_2\text{O}_3/\text{SnO}_2$ electrodes. This electrode arrangement permitted a direct comparison of contact quality of $\text{In}_2\text{O}_3/\text{SnO}_2$ and In to CdS film. The V-I characteristics are always measured between the top electrode ($\text{In}_2\text{O}_3/\text{SnO}_2$ or In) and the bottom tin oxide (NESA) electrode.

Figure 4 shows the V-I plot for this film under a photon flux density of $10^{15}/\text{cm}^2$ sec. Curves 1 and 2 show the current through the sample as a function of voltage with light incident through the $\text{In}_2\text{O}_3/\text{SnO}_2$ electrode for positive and negative applied voltages, respectively. Curves 3 and 4 show the current through the sample vs. voltage when the light is shining through the NESA for both polarities of voltage. The difference in currents for curves 1-2 and 3-4 is due to a difference in light absorption (and reflection) in the indium oxide/tin oxide films on one side and in the tin-oxide coated glass substrate in the other side of the photoconductor. These curves have a constant slope reasonably close to unity, suggesting that current is proportional to voltage. The difference between the current in positive and negative polarities for curves 1-4 is small; the reason for this difference is not understood at the present time. Curve 5 shows current through the CdS film as a function of voltage for an In metal electrode when light is shining through the tin-oxide coated glass substrate. The higher current for curves 3 and 4 compared to 5 can be interpreted

Table II. Details of preparation, optical and electrical properties of indium oxide/tin oxide films

Sample Number	Conditions of film deposition and subsequent heat-treatment	Thick-ness, Å	% Transmission at λ		Sheet resist-ance, ohms per square	Resistivity of films, ohm-cm
			5000Å	7000Å		
181 A-1	60 μ O ₂ ; d-c 1.6 kV; 95 mA; 1:09 hr; 370°C substrate temp; 340°C for 1 hr in air	—	95	89	72	—
181 B	Same conditions as 181 A-1 except no heat-treatment	1880	98	91	150	2.82×10^{-3}
191 A	100 μ O ₂ rf; 150W (indicated); 290°C substrate temp; no heat-treatment	4600	81	91	210	9.66×10^{-3}
191 B-1	Same conditions as 191 A; heat-treated in air at 340°C for 1 hr	3720	83	98	93	3.46×10^{-3}
213 E	60 μ O ₂ ; 400W; 1:30 hr dep. time; max substrate temp 371°C	—	86	90	195	—
213 C-1	Same as 213 E; heat-treated in air for 1 hr at 343°C	—	91	94	110	—
214 E	60 μ O ₂ ; 400W; 1:30 hr dep. time; max temp 377°C	—	85	90	90	—
214 C-1	Same as 214 E; heat-treated in air for 1 hr at 343°C	—	93	54	88	—

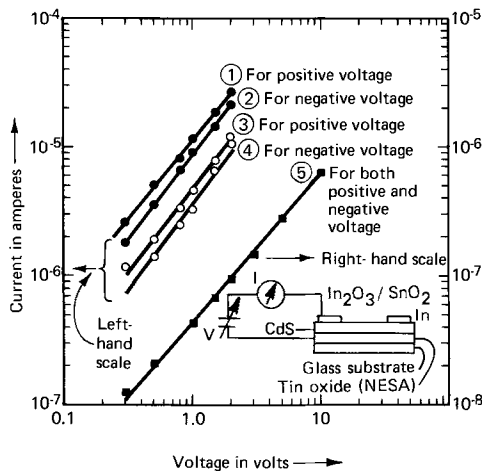


Fig. 4. Current-voltage characteristics under illumination for a CdS film which is on NESA-coated glass substrate and having both In₂O₃/SnO₂ (sample No. 214 C-1) and In as top electrodes. Incident flux for all three sets of curves is 10¹⁵ photons/cm²/sec. Curves 1 and 2 are for an In₂O₃/SnO₂ spot with light incident through the top electrode. Curves 3 and 4 are for the In₂O₃/SnO₂ spot with light incident through bottom electrode of NESA. Curve 5 is for In spot with light incident through NESA. For curves 1-4 refer to the current scale on the left. For curve 5 refer to the current scale on the right.

possibly in terms of a sensitization effect resulting from doping of the CdS by In during the sputtering and heat-treatment of indium oxide/tin oxide. This effect is similar to that reported by Shivonen and Boyd (12).

This hypothesis of sensitization is further confirmed by measuring the dark current for both In₂O₃/SnO₂ and In electrodes (Fig. 5). For In₂O₃/SnO₂ the dark currents are almost an order of magnitude larger than those obtained for In electrodes, suggesting doping by In and consequently a reduction in resistivity of the film. The In doping for In₂O₃ electrodes results from heat-treatment performed during and after deposition to obtain desired optical transmittance and sheet resistance. However, in the case of In electrodes, no heat-treatment is performed during or after evaporation of In. As a result, the film resistivity is unchanged. The difference between V-I curves for positive and negative polarities in the case of In₂O₃/SnO₂ suggests

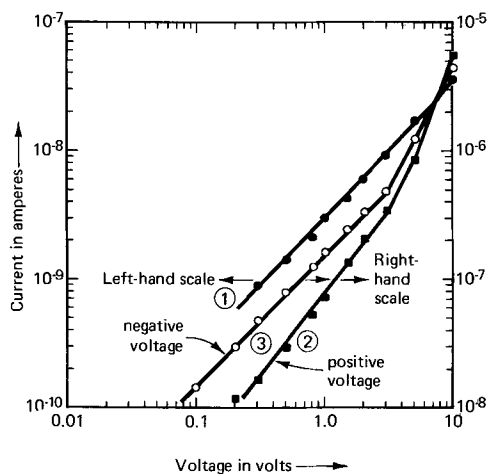


Fig. 5. Current-voltage characteristics in the dark for CdS films having electrodes of both In₂O₃/SnO₂ and In. Curve 1 is for both positive and negative voltages with In electrode. Curve 2 is for In₂O₃/SnO₂ electrode for positive applied voltages and also for In₂O₃/SnO₂ electrode for negative applied voltages. For curve 1 refer to current scale on the left, and for curves 2 and 3 refer to the scale on the right.

a barrier at the interface when no illumination is incident.

To summarize, In₂O₃/SnO₂ gives ohmic contact to CdS under illumination. However, for these 1μ thick CdS films, deposition of the transparent electrodes results in some In doping of the CdS films. This causes the CdS films to have lower dark resistivity.

Discussion—Band Model

From the above-illustrated measurements it is clear that CdO and In₂O₃/SnO₂ produce ohmic contact with CdS under present conditions of measurement. Little is known about the interface between wide bandgap materials like In₂O₃/SnO₂ and CdS. The junction between these two materials is a heterojunction. As a simple extension of the Kroger *et al.* (17) model for ohmic contact of a metal to a semiconductor, we propose a model for ohmic contact of heavily doped, wide bandgap material to an undoped, narrower bandgap material. This model is illustrated in Fig. 6. An ohmic contact is brought about by a rather thin layer (region III) of highly conducting (strongly n-type) material in the photoconductor adjacent to the electrode (region IV). This heavily doped n-type layer in the case of the CdO contact is produced by diffusion of Cd into CdS. For the In₂O₃/SnO₂, the heavily doped n-type layer is produced by the diffusion of In into CdS. Between the highly conducting part of CdS and the electrode, there may exist an exhaustion barrier (layer II) which, due to the presence of such a strongly conducting layer, is so thin that electrons may easily tunnel through it. The region of strongly conducting CdS acts as a supply of electrons for the highly resistive bulk (region IV), and the whole system acts ohmic when an electric field is applied.

Conclusions

The transparent electrode material for an electro-optic device can have a sheet resistance as high as a few hundred ohms per square. From the measurements reported here, it appears that resistances in this range can be readily achieved in sputtered cadmium or indium oxide/tin oxide films. CdO is a better material for making ohmic contact than In₂O₃/SnO₂ because it does not reduce the resistivity of the thin CdS film.

However, the optical transmission properties of CdO on CdS are less desirable compared to those of In₂O₃/SnO₂. Since CdO has an optical transmittance greater than 70% for wavelengths of 6000Å, it may form a better transparent contact to Cd(S, Se) or CdSe, with absorption edges at wavelengths longer than 6000Å. In general, the transparent electrode requirements for an electrooptic device may be met by films of either cadmium oxide or indium oxide/tin oxide.

Acknowledgments

The authors wish to thank D. E. Hill who assisted with the sputtering runs, and J. L. Wolf for making

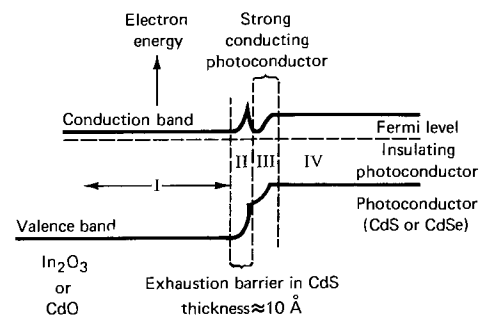


Fig. 6. Proposed band model of an ohmic contact between highly resistive n-type bulk material IV and a highly conducting transparent metal oxide electrode I. Region III is a thin layer of strongly n-type semiconductor, and region II is an exhaustion barrier due to the difference in work function between electrode I and material III.

the thickness, optical, and electrical measurements. The authors are indebted to Mr. D. W. Chapman for his encouragement throughout this work and for giving helpful suggestions on the manuscript.

Manuscript submitted Aug. 3, 1971; revised manuscript received Dec. 6, 1971.

Any discussion of this paper will appear in a Discussion Section to be published in the December 1972 JOURNAL.

REFERENCES

1. A. H. Meitzler, J. R. Maldonado, and D. B. Fraser, *Bell System Tech. J.*, July/August, p. 953 (1970).
2. S. A. Keneman, G. W. Taylor, A. Miller, and W. H. Fonger, *Appl. Phys. Letters*, **17**, No. 4, 173 (1970).
3. G. W. White, *Phil. Mag.*, **27**, 370 (1914).
4. Y. T. Shivonen and D. R. Boyd, *Bull. Am. Phys. Soc.*, **5**, 105 (1960).
5. R. Haul and D. Lust, *J. Appl. Phys. Suppl.*, **33**, No. 1, 487 (1962).
6. J. S. Preston, *Proc. Roy. Soc.*, 449 (1950); C. Helwig, *Z. Physik*, **132**, 621 (1952); L. Holland and G. Siddal, *Vacuum*, **11**, No. 4, 375 (1953); V. K. Miloslavskii and A. I. Ranyuk, *Soviet Optics and Spectroscopy*, 536 (1960); F. Lappe, *Z. Physik*, **137**, 380 (1954); R. W. Wright, *Proc. Phys. Soc.*, **64A**, 350 (1951); R. W. Wright and J. A. Bastin, *This Journal*, **71**, 109 (1958).
7. "International Tables of Constants and Numerical Data," **12**, Pergamon Press (1961).
8. T. K. Lakshmanan, *This Journal*, **110**, 548 (1963).
9. R. L. Weiher, *J. Appl. Phys.*, **33**, 2834 (1962).
10. G. Rupprecht, *Z. Physik*, **139**, 504 (1954).
11. D. B. Fraser and H. D. Cook, Paper 29 presented to Electrochemical Soc. Meeting, May 1971.
12. Y. T. Shivonen and D. R. Boyd, *Rev. Sci. Instr.*, **31**, 992 (1960).
13. V. A. Williams, *This Journal*, **113**, 234 (1966).
14. L. Holland, "Vacuum Deposition of Thin Films," Chapman and Hall (1961).
15. J. Stuke, *Z. Physik*, **137**, 401 (1954).
16. R. R. Chamberlin and J. S. Skarman, *This Journal*, **113**, 86 (1966).
17. F. A. Kroger, G. Diemer, and H. A. Glassens, *Phys. Rev.*, **105**, 297 (1956).

Coprecipitation of Ga₂O₃ in the Liquid-Phase Epitaxial Growth of GaP

M. Kowalchik, A. S. Jordan, and Mildred H. Read

Bell Telephone Laboratories, Incorporated, Murray Hill, New Jersey 07974

ABSTRACT

Coprecipitation of β -Ga₂O₃ has been observed in O-doped GaP epitaxial films grown by liquid-phase epitaxy under isothermal conditions at an average growth temperature of $\sim 1040^\circ\text{C}$. The coprecipitation seems to be independent of cooling rate and of the source of O [Ga₂O₃ powder, bulk Ga₂O₃, or glassy Zn(PO₃)₂]. The coprecipitation of β -Ga₂O₃ could be prevented either by imposing a temperature gradient over the ampoule (to enhance vapor transport via Ga₂O) or by reducing the amount of O added to the Ga-rich solution in an isothermal system to $\sim 2.5 \times 10^{-2}$ a/o (atom per cent). The latter result is interpreted as giving the solubility at $\sim 1040^\circ\text{C}$ of Ga₂O₃ in Ga saturated with GaP and is used to obtain an estimate of the eutectic valley in the ternary Ga-P-Ga₂O₃ system.

GaP red light-emitting diodes (LED's) have become devices of technological importance in the last decade. The early work of Starkiewicz and Allen (1) demonstrated that the presence of both Zn and O as dopants in the GaP crystals is needed for the generation of red light at room temperature. In the case of solution growth (SG) (2, 3) and sealed-tube liquid-phase epitaxy (LPE) (4, 5), the concentration of Zn added to the Ga-GaP solutions by different investigators to maximize the electroluminescent or photoluminescent efficiency varies from 0.03 (5) to 0.14 a/o (atom per cent) (4). Because of vaporization losses the Zn additions in open-tube LPE (6, 7) are higher [0.15 (7) to 0.20 a/o (6)]. At these Zn concentrations in the Ga-GaP solutions the resulting crystals are expected to contain (8) Zn at concentrations less than 10^{18} cm⁻³ (at a typical growth temperature of $\sim 1040^\circ\text{C}$); hence, the deleterious effect of Auger recombination (9) on efficiency is avoided.

However, the doping requirements for maximizing the efficiency by means of O additions (in the form of Ga₂O₃) are less well understood. In particular, in open-tube LPE "best" devices have been reported for 0.15 (7) and 0.4 a/o O (6). In sealed-tube growth (SG or LPE) maximum efficiencies have been found over a surprisingly wide range of O additions, specifically between 0.03 (2) and 1.05 a/o O (5). The solubility of Ga₂O₃ in liquid Ga (10) is only ~ 0.03 a/o O at

$\sim 1040^\circ\text{C}$; hence, the reasons for much exceeding this solubility limit in closed-tube LPE systems were not immediately obvious.

The initial objective of this study is to explain the disparate results on the O-doping of GaP. In the next section it is shown that in a nonisothermal, closed-tube LPE system the loss of O from the tipping solution via the vaporization of Ga₂O is responsible for the high optimum O concentration (5), exceeding the solubility limit (10). Our experiments demonstrate that when more than ~ 0.025 a/o O is added to the Ga-GaP solution in an isothermal, sealed-tube LPE growth system at $\sim 1040^\circ\text{C}$, coprecipitation of Ga₂O₃ takes place along with the GaP epitaxial growth. The major objective of this study is to identify, characterize, and explain these precipitates. In particular, the coprecipitation of Ga₂O₃ with GaP (or its absence in a nonisothermal system) is shown to be consistent with thermodynamic information for the Ga-Ga₂O₃ binary system. Moreover, by interpreting the coprecipitation results by means of a ternary phase diagram, the oxygen concentration along the eutectic valley in the Ga-P-Ga₂O₃ system is estimated.

Experimental Procedure and Results

The usual LPE growth of GaP by Nelson's method (11) involves a cooling rate of approximately $10^\circ\text{C}/\text{min}$. To achieve such a relatively large cooling rate many LPE systems utilize furnaces with a small thermal mass which do not possess an isothermal zone

Key words: light-emitting diodes, oxygen solubility, crystal growth, compound semiconductors, phase diagrams.

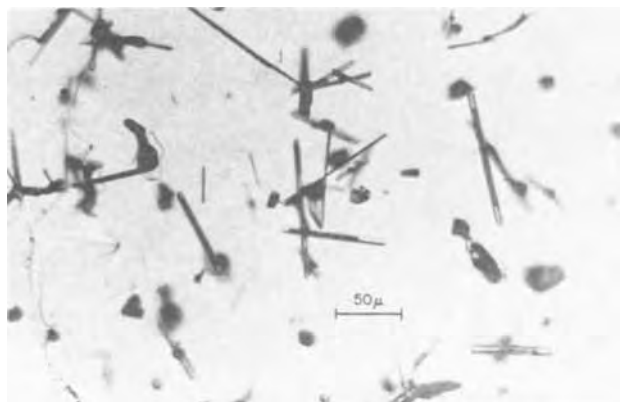
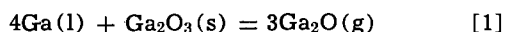


Fig. 1. Transmission photomicrograph of needle-shaped β -Ga₂O₃ precipitates in the GaP matrix grown from a solution containing 1.05 a/o O (added as Ga₂O₃) and 0.05 a/o Zn. The solution was cooled from \sim 1050° to \sim 600°C at a rate of \sim 10°C/min.

over the entire length of the ampoule used for crystal growth. It has been found (12) for a small thermal mass furnace with a viewing port (typical of those used to make efficient LED's) that there may be a decrease in temperature of about 25°C between the Ga-rich melt and the seal-off area (4) at a nominal LPE growth temperature of \sim 1040°C. Because of the reversible reaction of Ga and Ga₂O₃ to produce Ga₂O(g) according to



a temperature difference causes a drop in the equilibrium partial pressure of Ga₂O(g) (20 Torr for a temperature difference of 25°C at \sim 1040°C) (13, 14). The reversible nature of this reaction is demonstrated by the observed condensation of Ga₂O₃ and Ga at the cool (seal) end of the capsule during an LPE run.

In order to minimize the loss of Ga₂O₃ via this vapor transport, all the experiments reported herein have been conducted in nearly isothermal furnaces. In the initial phase of this study a furnace (without a viewing port) with a \sim 4°C difference along the sealed capsule was used. The 10 cm long quartz capsule, similar in construction to capsules described by previous workers (4, 5), enclosed a quartz boat which contained the GaP substrate at one end, near the seal-off plug, and the solution of Ga-GaP-dopants¹ at the other end. The plug serving as the seal was placed tightly against the boat, after evacuation to 10⁻⁶ Torr, to minimize the capsule volume.

In a typical run the sealed ampoule, containing the substrate and solution doped with 1.05 a/o O added as Ga₂O₃ and 0.05 a/o Zn [serving as a reference dopant concentration in comparison with published values (5)], was heated to 1065°C and held for 30 min to achieve saturation. An LPE layer was then grown by tipping the furnace and capsule assembly at 1050°C and cooling at a rate of \sim 10°C/min to 600°C. By monitoring thermocouples attached to either end of the capsule, it was determined that the temperature difference was minimal (less than 4°C in this series of experiments) throughout the LPE cycle. After completing a run, excess Ga₂O₃ was found only on the top of the solution, indicating negligible vapor transport. Examination of the typically \sim 50 μ m thick epitaxial layer by optical reflection and transmission microscopy disclosed the presence of a needle-like second phase embedded in the GaP matrix. In Fig. 1 we show a transmission photomicrograph of this second phase in the LPE layer. Note that the thin needles are found at all levels between surface and growth interface and

are occasionally as long as 100 μ m. That the needles are not an etching artifact due to reaction of the GaP with HNO₃, frequently used to digest the Ga, is shown by the fact that they are also seen without etching. Additional experiments have shown that an undoped or a Zn-doped solution did not result in needles in the LPE layer but a solution doped with Ga₂O₃ alone (1.05 a/o O) did. Moreover, when a sharp temperature gradient was imposed along the capsule, by extending the length of the ampoule with a quartz spacer placed between the end of the boat and the seal and cooling with a stream of N₂, no needles were observed in the LPE layer, even at 1.05 a/o O additions. Not unexpectedly, after this run a mixture of Ga droplets and Ga₂O₃ was found on the seal and no excess Ga₂O₃ appeared on the surface of the Ga solution.

Microscopic examination of the as-received Ga₂O₃ powder at 800X showed a few needles, 5-10 μ m long. These needles were similar in shape although not in size to the ones found in the LPE layers. This similarity strongly suggested that precipitation of the monoclinic, high-temperature β form of Ga₂O₃ had occurred in the epitaxial films. The precipitates were conclusively identified by a wide-film, modified, Debye-Scherrer x-ray diffraction method (15). With the flat LPE layer and substrate stationary at 16° to the beam, an x-ray photograph of the epitaxial film was generated. A typical photograph (Fig. 2) for a run with 1.05 a/o O addition shows the curved lines of polycrystalline β -Ga₂O₃ superimposed on the single-crystal GaP pattern. In addition, an examination of the β -Ga₂O₃ precipitate-rich layer by the Direct Image Mass Analyzer (DIMA) (16) exhibits a strong O-signal when sputtered in an oxygen beam. As viewed by the DIMA, a β -Ga₂O₃ needle is represented by a bright elongated image which is much more intense than the background O signal detected from the GaP matrix.

After this positive identification of β -Ga₂O₃ precipitates, a number of changes were made in the experimental apparatus and procedure. In place of the conventional quartz tipping boat, we utilized a slider (17) assembly, fabricated from Al₂O₃ (G.E.-Lucalox). It was anticipated that the use of Al₂O₃ would eliminate the observed reaction between Ga and quartz to form Ga₂O(g) (13). In addition, a new furnace with a variation of only 1°C over the capsule was introduced. Figure 3 is a schematic of the quartz sealed assembly, located in the isothermal zone of the furnace. As in the earlier experiments, the Ga-rich solution, here contained in an opening cut through the moving slider, was tipped onto the GaP substrate. With the slider, however, growth could be terminated at will at any temperature by tipping the slider to its

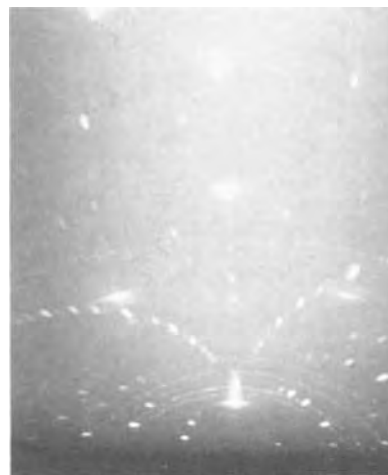


Fig. 2. X-ray photograph of precipitates and matrix. Note the spotty curved lines of polycrystalline β -Ga₂O₃ superimposed on the monocrystalline GaP pattern.

¹ The source materials used for these experiments were phosphine-grown polycrystalline GaP (Monsanto), Ga₂O₃ powder (Alusuisse), and Zn (United Minerals), all with 99.9999% nominal purity. The n-type GaP substrates, cut from liquid encapsulation Czochralski (LEC) grown ingots, were mechanically polished on the phosphorus (B) face.

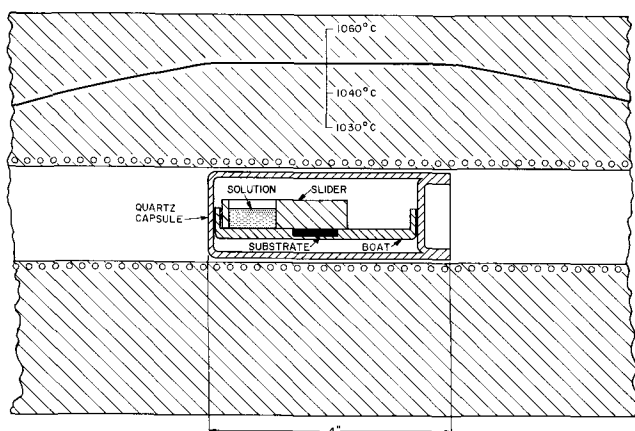


Fig. 3. Slider assembly and its relation to the temperature profile of the furnace (schematic). The slider and boat are made of Al_2O_3 (G.E.-Lucalox).

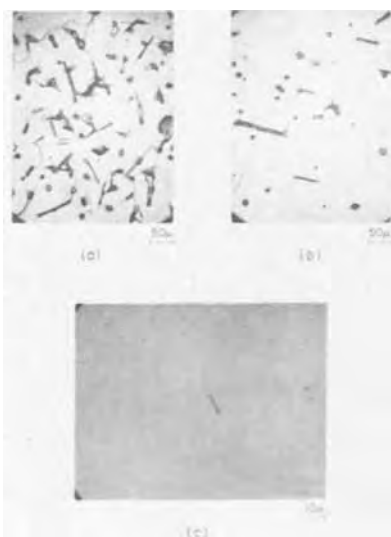


Fig. 4. Effect of decreasing Ga_2O_3 additions to the solution on the density of $\beta\text{-Ga}_2\text{O}_3$ precipitates. The transmission photomicrographs (a), (b), and (c) correspond to 0.45, 0.075, and 0.03 a/o O additions, respectively. All three crystals were grown by cooling the solution from $\sim 1050^\circ$ to 1035°C at a rate of $1^\circ\text{C}/\text{min}$.

initial position, resulting in the removal of the excess solution from the substrate.

In this manner GaP LPE layers were grown, with 0.45, 0.075, and 0.03 a/o O additions as Ga_2O_3 to the solution, between 1050° and 1035°C at a cooling rate of $1^\circ\text{C}/\text{min}$. Transmission micrographs of these crystals (Fig. 4) show a strong reduction in the concentration of $\beta\text{-Ga}_2\text{O}_3$ precipitates with decreasing Ga_2O_3 additions to the solution. The precipitates completely disappear, as viewed at $800\times$, between 0.027 and 0.021 a/o O additions to the solution.

Experiments performed by cooling from 1050° to 1020°C at a rate of $2^\circ\text{C}/\text{min}$ also resulted in Ga_2O_3 precipitation, demonstrating that the precipitation is apparently unaffected by cooling rate between 1° and $10^\circ\text{C}/\text{min}$. It should be noted that when the solution was cooled to 1020°C even an O addition of only 0.025 a/o gave rise to a few precipitates. Finally, we changed the source of O from Ga_2O_3 powder to bulk Ga_2O_3 ² or glassy $\text{Zn}(\text{PO}_3)_2$ (18). Both of these additions to the Ga-GaP solution yielded precipitates.

Discussion

The presence of precipitates in GaP is not unique among III-V compounds. For example, Eckhardt (19)

² Bulk polycrystalline Ga_2O_3 was pulled by W. Grodkiewicz of Bell Laboratories by the Czochralski method under ~ 3 atm of argon pressure.

has observed precipitates of $\alpha\text{-Ga}_2\text{O}_3$ [the low-temperature form (20)] less than $3\ \mu\text{m}$ in size in Czochralski- and Bridgman-grown GaAs. Recently, Kressel *et al.* (21) have identified by electron diffraction Ga_2Te_3 precipitates in GaAs which they attributed to precipitation from solid solution. However, several observations indicate that the $\beta\text{-Ga}_2\text{O}_3$ second phase in the GaP LPE layers is not the result of solid-state precipitation. First, as seen in Fig. 1, there is no distinct orientation relationship between the precipitates and the matrix. Second, the precipitates are obviously too large to originate from a supersaturated solid solution. Third, precipitates were observed in epitaxial layers grown by relatively slow cooling rates in the narrow temperature range tipping experiments ($1^\circ\text{C}/\text{min}$, $1050^\circ\text{-}1035^\circ\text{C}$; $2^\circ\text{C}/\text{min}$, $1050^\circ\text{-}1020^\circ\text{C}$), wherein the excess Ga solution was removed from the film prior to withdrawal from the furnace. It is unlikely that the rate of solid-solution precipitation is rapid enough to account for the formation of precipitates in these experiments, since precipitation would have to take place during the short time required to cool the crystal to room temperature.

Therefore, it is concluded that the $\beta\text{-Ga}_2\text{O}_3$ precipitates are the consequence of the coprecipitation of Ga_2O_3 with GaP from a Ga-rich solution supersaturated with respect to both Ga_2O_3 and GaP. Thus, the tipping experiments conducted between 1050° and 1035°C , showing that the precipitates completely disappear between 0.027 and 0.021 a/o O additions, can be interpreted as giving the solubility of O in liquid Ga also saturated with GaP to be ~ 0.025 a/o O at $\sim 1040^\circ\text{C}$. Hence, when O is added to the tipping solution in excess of ~ 0.025 a/o in a sealed isothermal system at a mean growth temperature of $\sim 1040^\circ\text{C}$, the presence of precipitates in the epitaxial film results from supersaturation with respect to two solid phases. Conversely, the absence of precipitates in GaP grown in a nonisothermal system indicates that the solution became unsaturated due to the loss of excess oxide via $\text{Ga}_2\text{O}(\text{g})$ transport according to Eq. [1].

The coprecipitation can be more readily discussed in terms of a schematic ternary liquidus isotherm at $\sim 1040^\circ\text{C}$ for the Ga-P- Ga_2O_3 system, shown in Fig. 5, which was drawn in analogy with the Ga-As-Si system (22, 23). The work of Foster and Scardefield (10) gives the solubility of Ga_2O_3 (or O) in Ga between 1000° and 1200°C . The present tipping experiments show a small ($\sim 20\%$) reduction in the O solubility at

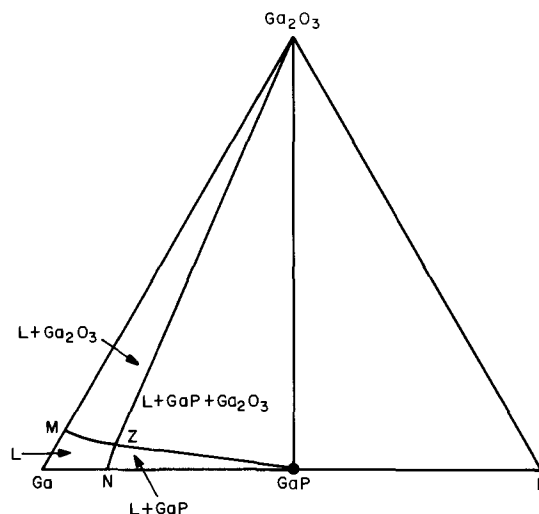


Fig. 5. Schematic 1040°C liquidus isotherm for the Ga-P- Ga_2O_3 system. Points M, N, and Z are the 1040°C solubilities of Ga_2O_3 in Ga (~ 0.01 m/o) (10), P in Ga (2.5 a/o) (24), and the ternary eutectic point of Ga_2O_3 (~ 0.008 m/o), respectively. The compositions within the triangle are not drawn to scale; the mole fraction of Ga_2O_3 dissolved in Ga is more than two orders of magnitude smaller than the atom fraction of P saturating Ga.

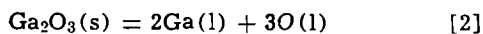
~1040°C when the solution is also saturated in GaP. In Fig. 5 points M and N, respectively, represent the binary solubilities of Ga₂O₃ (~0.01 m/o) (10) and P (~2.5 a/o) (24) in Ga at ~1040°C, and point Z is the ternary eutectic point at which the solution, saturated with Ga₂O₃ (~0.008 m/o Ga₂O₃ or ~0.025 a/o O) and P, is in equilibrium with GaP and β-Ga₂O₃. According to the schematic liquidus isotherm, as long as the Ga₂O₃ additions to the solution vary along the curve N-Z, O-doped GaP but not β-Ga₂O₃ will precipitate. However, over-all solution compositions which are located within the Z-GaP-Ga₂O₃ tie triangle yield a liquid of composition Z in equilibrium with both solid phases, permitting their coprecipitation.

There are two phenomena, consistent with Fig. 5, which may lead to precipitation. The first one is mechanical in nature, due to the closeness in density between Ga and Ga₂O₃³ at the tipping temperature. Accordingly, at ~1040°C the Ga₂O₃ powder is either suspended in the liquid solution or it sinks to the vicinity of the substrate. However, the possibility that most of the observed precipitates originate directly from suspended particles which have never dissolved is discounted because only 5% of the as-received powder consists of needles, and even these are about a factor of 10 shorter than the precipitates. Therefore, we suggest that the small excess oxide particles,⁴ suspended in the O- and GaP-saturated solution, may serve as nucleation sites for the growth of the observed β-Ga₂O₃ needles during the second phenomenon (coprecipitation) which is of chemical origin. During LPE growth, as the temperature decreases, the ternary eutectic point (point Z in Fig. 5) moves toward the Ga corner of the phase diagram, corresponding to an increasing supersaturation of the liquid with respect to GaP and Ga₂O₃ which results in the coprecipitation of both solid phases.

Since we would expect the number of nucleation sites to be proportional to the amount of excess oxide added to the solution (above point Z), the preceding interpretation is consistent with Fig. 4, showing an increasing amount of precipitates with increasing Ga₂O₃ additions in LPE layers grown under otherwise identical conditions. It should be noted that the presence of oxide nuclei is not a prerequisite for coprecipitation, especially when an LPE layer is grown over a wider temperature range. For example, when a solution of composition Z (0.025 a/o O) was cooled to 1020°C instead of 1035°C, the resulting epitaxial film contained a few precipitates.

Although at ~1040°C the solubility of Ga₂O₃ in Ga saturated with GaP is only a little less than the reported solubility of Ga₂O₃ in liquid Ga alone, it is by no means assured that at higher temperatures, corresponding to larger phosphorus concentrations in the solution, the difference between binary and ternary solubilities will remain small. An approximate thermodynamic calculation can be performed to yield the variation of the O solubility in the ternary system as a function of temperature. Here we consider ternary solubility at the ternary eutectic point Z, illustrated in Fig. 5, which is an invariant point at a set temperature, T. The variation of Z with T gives the ternary eutectic valley.

The dissolution of Ga₂O₃ in Ga or in Ga saturated with P can be represented by the reaction



where O represents the oxygen dissolved in the liquid. Under the conditions of Foster and Scardefield's binary

³ At ~30°C the density of liquid Ga (25) (6.09 g/cc) is greater than that of β-Ga₂O₃ (20) (5.88 g/cc). However, at 1040°C the measured density of Ga (25) (5.48 g/cc) is smaller than the estimated density of β-Ga₂O₃ (~5.65 g/cc) which is based on an extrapolation of the linear expansion coefficients of Al₂O₃-Ga₂O₃ solid solutions (26) to pure Ga₂O₃.

⁴ Because of the brittleness of bulk Ga₂O₃ and the reaction of Zn(PO₃)₂ with Ga to form Ga₂O₃, the presence of oxide particles suspended in the melt cannot be excluded even when O was added in one of these forms.

solubility measurements (10), the binary activities, $a_{i,b}$, of the designated species in the liquid are given by $a_{Ga,b} = x_{Ga,b}\gamma_{Ga,b} \approx 1$ and $a_{O,b} = x_{O,b}\gamma_{O,b}$, where $x_{i,b}$ and $\gamma_{i,b}$ are the atom fraction and activity coefficient of species i , and b refers to the binary system. However, a comparison of the Ga-Ga₂O₃ (10) and Ga-P (24) binary data shows that the mole fraction of Ga₂O₃ dissolved in Ga is more than two orders of magnitude smaller than the atom fraction of P saturating Ga, indicating that the activity of Ga in the ternary system cannot be taken as unity. As the activity of Ga₂O₃ is unity, the equilibrium constant, K , for Eq. [2] becomes

$$K = a_{Ga,t}^2(x_{O,t})^3(\gamma_{O,t})^3 \approx (x_{O,b})^3(\gamma_{O,b})^3 \quad [3]$$

where the subscript t refers to the ternary system. Rearranging Eq. [3] gives

$$\ln \frac{x_{O,b}}{x_{O,t}} = \ln \gamma_{O,t} - \ln \gamma_{O,b} + 2/3 \ln(x_{Ga,t}\gamma_{Ga,t}) \quad [4]$$

As there are no thermodynamic data for the liquid phase, we assume regular binary and ternary solution behavior (27). Assuming in addition to $x_{Ga,b} \approx 1$ that $x_{O,t} \ll x_{P,t}$ and $x_{Ga,t} + x_{P,t} \approx 1$, we find approximate expressions for the activity coefficients⁵ which when substituted into Eq. [4] yield

$$\ln \frac{x_{O,b}}{x_{O,t}} \approx \left(\frac{1 - x_{Ga,t}}{RT} \right) \left[-\omega_{Ga-O} + \omega_{P-O} + \frac{\omega_{Ga-P}}{3} (2 - 5x_{Ga,t}) \right] + 2/3 \ln x_{Ga,t} \quad [5]$$

where the ω_{ij} 's are the ternary interchange energies.

To evaluate Eq. [5] we take ω_{Ga-P} from the work of Thurmond (24) and since $x_{P,t} + x_{Ga,t} \approx 1$, $x_{Ga,t}$ can be approximated by its value along the Ga-P liquidus curve (24). However, ω_{Ga-O} and ω_{P-O} are both unknown. The simplest assumption is to set $\omega_{P-O} = 0$ (ideal solution), since at the high temperatures of interest P-O liquids do not exist. By substituting the ratio $x_{O,b}/x_{O,t}$ ($3 \times 10^{-2}/2.5 \times 10^{-2}$) in units of atom per cent at ~1040°C into Eq. [5], we obtain $\omega_{Ga-O} \approx -25$ kcal/mole. The negative deviation from Raoult's law implied by this value is considered reasonable in comparison, for instance, with the Cu(1)-O system. Recent thermodynamic measurements (28) yield $\omega_{Cu-O} \approx -6.3$ kcal/mole at 1100°C. By using the estimated value of ω_{Ga-O} and keeping $\omega_{P-O} = 0$, $\ln(x_{O,b}/x_{O,t})$ can be readily calculated from Eq. [5] up to the melting point of GaP. A combination of this ratio with the Ga-Ga₂O₃ solubility curve of Foster and Scardefield (10) gives the variation of $x_{O,t}$ along the Ga-P-Ga₂O₃ eutectic valley, shown in Fig. 6.

Although in Fig. 6 the departure of $x_{O,t}$ from $x_{O,b}$ becomes pronounced at higher temperatures, below about 1100°C only a small error is made by using the binary solubility curve (10) instead of the ternary eutectic valley. Because of the calculated maximum there is only about a factor of 2 increase in the ternary oxygen solubility between ~1100°C and the melting point of GaP. The sections of the eutectic valley at high and low temperatures are shown as dashed lines because they are based on portions of the binary solubility curve which were found by extrapolating the published curve. Moreover, if $\omega_{P-O} \neq 0$, according to Eq. [5] this would influence $x_{O,t}$ only at high $x_{P,t}$ corresponding to high temperatures.

The estimate shown in Fig. 6 does not eliminate the need for further experimental work to establish the eutectic valley of the system Ga-P-Ga₂O₃. Such information in conjunction with thermodynamic analysis of the type presented here would greatly aid the understanding of this technologically important ternary system. Unfortunately, even if the Ga-P-Ga₂O₃ eutectic

⁵ The expressions are: $RT \ln \gamma_{O,b} \approx \omega_{Ga-O}$, $RT \ln \gamma_{O,t} \approx x_{Ga,t}\omega_{Ga-O} + (1 - x_{Ga,t})\omega_{P-O} - x_{Ga,t}(1 - x_{Ga,t})\omega_{Ga-P}$, and $RT \ln \gamma_{Ga,t} \approx (1 - x_{Ga,t})\omega_{Ga-P}$.

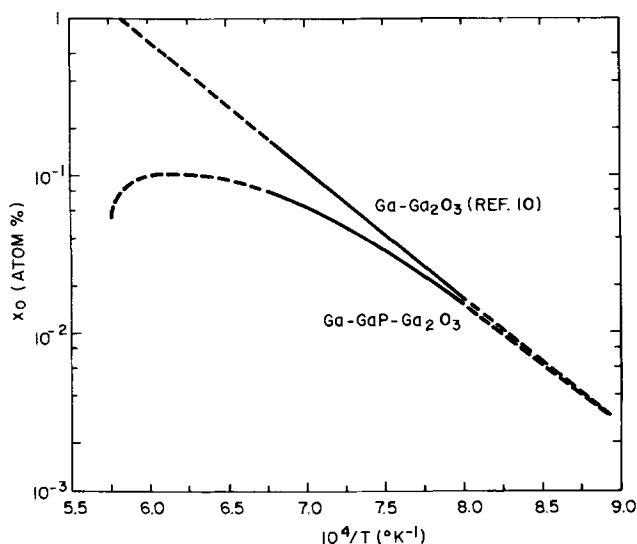


Fig. 6. Estimated eutectic valley for the Ga-P-Ga₂O₃ ternary system and its relation to the solubility of Ga₂O₃ in Ga (10). The plot is given in terms of a/o O vs. reciprocal temperature. Note that Ga₂O₃ can only coprecipitate with GaP at O concentrations above the loop.

valley were known, independent experimental work would be required to give the equilibrium concentration of O dissolved in GaP crystals. However, one can predict on thermodynamic grounds that GaP in equilibrium with liquid compositions along the eutectic valley (Fig. 5, point Z; Fig. 6) contains the maximum amount of oxygen which can be dissolved at each temperature. Liquid compositions above Z result in precipitation of a second phase, β -Ga₂O₃, without an increase in the equilibrium oxygen concentration in the GaP crystal.

Of course, GaP epitaxial films which are free of precipitates may be grown in a nonisothermal LPE system even when a large excess of Ga₂O₃ is added to the solution, initially moving the over-all liquid far above Z. The loss of O from the growth solution via the vaporization and transport of Ga₂O according to Eq. [1] explains not only the absence of β -Ga₂O₃ needles in LPE layers grown in a nonisothermal system but also the disparity in reported optimum O additions [0.03 (2) and 1.05 a/o O (5) for SG and LPE, respectively]. Our preliminary experiments demonstrate that efficient diodes can be fabricated in an isothermal LPE system without excessive O additions to the solution. Using the slider (Fig. 3), a nearly precipitate-free p-type layer was grown at $\sim 1040^\circ\text{C}$ onto an n-type LPE and LEC structure from a solution containing 0.03 a/o O in the form of Zn(PO₃)₂ and 0.045 a/o Zn. The annealed and encapsulated diodes exhibited red electroluminescent (EL) efficiencies as high as 2.7%, which we consider promising since the dopant concentrations have not yet been optimized. This figure is within about a factor of two of the best reported values of 4.5% (29) and 6% (30) for similar structures which were grown from solutions containing a large excess of Ga₂O₃ but presumably under nonisothermal conditions [tipping in a small thermal mass furnace (29) and dipping, (30) respectively].

The effect of the concentration of β -Ga₂O₃ precipitates on EL efficiency of devices has not been examined in detail. However, point contact EL efficiency measurements were made on mesa diodes taken from a relatively precipitate-free and from a heavily precipitated area (such as shown in Fig. 2) of a p-type LPE film grown on a 2.5 cm long n-type LEC substrate from a solution containing 1.05 a/o O added as Ga₂O₃ and 0.05 a/o Zn. The EL efficiencies were as much as 15 times higher for the diodes prepared from the clean segment than for the ones made from the heavily precipitated area. We think that the reduction in effi-

ciency is very likely due to the difficulty of achieving suitable contact with a heavily precipitated p-type layer. But a small concentration of precipitates may not have any significant effect on the EL efficiency. Indeed, we speculate that such small concentrations of precipitates may be present in the LED's reported in the literature but have been overlooked because of their negligible effect on diode performance. Finally, recent measurements of Glorizova et al. (31) show that the 100°K hole mobility of Zn, O-doped SG GaP drops precipitously when more than 0.03 a/o O is added to the melt as Ga₂O₃. Since we have also seen Ga₂O₃ precipitates in SG platelets, the results of Glorizova et al. (31) may be related to scattering by a second phase.

Acknowledgments

We would like to express our appreciation to F. A. Trumbore for many helpful discussions and suggestions in the course of this work. We are also grateful to C. D. Thurmond for several discussions and advice. Useful discussions with R. H. Saul, M. E. Weiner, and S. Wagner are also acknowledged. We thank L. R. Dawson for the DIMA work.

Manuscript submitted Aug. 9, 1971; revised manuscript received Dec. 13, 1971. This was RNP 250 presented at the Atlantic City Meeting of the Society, Oct. 4-8, 1970.

Any discussion of this paper will appear in a Discussion Section to be published in the December 1972 JOURNAL.

REFERENCES

1. J. Starkiewicz and J. W. Allen, *J. Phys. Chem. Solids*, **23**, 881 (1962).
2. M. Gershenzon, F. A. Trumbore, R. M. Mikulyak, and M. Kowalchik, *J. Appl. Phys.*, **36**, 1528 (1965).
3. R. A. Logan, H. G. White, and F. A. Trumbore, *Appl. Phys. Letters*, **10**, 206 (1967).
4. K. K. Shih, M. R. Lorenz, and L. M. Foster, *J. Appl. Phys.*, **39**, 2747 (1968).
5. R. H. Saul, J. Armstrong, and W. H. Hackett, Jr., *Appl. Phys. Letters*, **15**, 229 (1969).
6. I. Ladany, *This Journal*, **116**, 993 (1969).
7. F. A. Trumbore, M. Kowalchik, and H. G. White, *J. Appl. Phys.*, **38**, 1987 (1967).
8. A. S. Jordan, *This Journal*, **118**, 781 (1971).
9. See, for example, K. P. Sinha and M. DiDomenico, Jr., *Phys. Rev.*, **B1**, 2623 (1970).
10. L. M. Foster and J. Scardefield, *This Journal*, **116**, 494 (1969).
11. H. Nelson, *RCA Rev.*, **24**, 603 (1963).
12. L. Derick, Personal communication.
13. C. N. Cochran and L. M. Foster, *This Journal*, **109**, 144 (1962).
14. C. D. Thurmond and C. J. Frosch, *This Journal*, **111**, 184 (1964).
15. Mildred H. Read, 27th Annual Diffraction Conference, Pittsburgh, November 1964.
16. J. V. DiLorenzo, R. B. Marcus, and R. Lewis, *J. Appl. Phys.*, **42**, 729 (1971); J. V. DiLorenzo, *This Journal*, **118**, 1645 (1971).
17. M. B. Panish and S. Sumski, *J. Appl. Phys.*, **41**, 3195 (1970).
18. A. S. Jordan, L. Derick, R. Caruso, and M. Kowalchik, Paper 49 presented at Electrochem. Soc. Meeting, Houston, Texas, May 7-11, 1972.
19. G. Eckhardt, *J. Appl. Phys.*, **33**, 1016 (1962).
20. I. A. Sheka, I. S. Chaus, and T. T. Mityureva, "The Chemistry of Gallium," p. 32, Elsevier Publishing Co., Inc., New York (1966).
21. H. Kressel, F. Z. Hawrylo, M. S. Abrahams, and C. J. Buiocchi, *J. Appl. Phys.*, **39**, 5139 (1968).
22. M. B. Panish, *This Journal*, **113**, 1226 (1966).
23. F. E. Rosztoczy, "Proceedings of the International Conference on the Physics and Chemistry of Semiconductor Heterojunctions and Layer Structures," Vol. 1, p. 333, Akademiai Kiado, Budapest (1971).
24. C. D. Thurmond, *J. Phys. Chem. Solids*, **26**, 785 (1965).
25. K. E. Spells, *Proc. Phys. Soc.*, **48**, 299 (1936).
26. H. P. Kirschner, *J. Am. Ceram. Soc.*, **52**, 379 (1969).
27. I. Prigogine and R. Defay, "Chemical Thermodynamics," p. 257, Longmans Green and Co., London (1954).

28. C. R. Nanda and G. H. Geiger, *Met. Trans.*, **1**, 1235 (1970).
 29. W. H. Hackett, Jr. and R. H. Saul, Abstract 81, Extended Abstracts of the Los Angeles Meeting of the Electrochemical Society, May 10-15, 1970.
 30. B. P. Johnson and R. M. Potter, *Bull. Am. Phys. Soc., Ser. II*, **16**, 433 (1971).
 31. R. I. Glorizova, V. M. Grachev, L. I. Kolesnik, and L. I. Marina, *Sov. Phys., Semicond.*, **4**, 1363 (1971).

Mass Spectrometric Studies of Vapor-Phase Crystal Growth

II. GaN

Vladimir S. Ban

RCA Laboratories, Princeton, New Jersey 08540

ABSTRACT

A mass spectrometer has been coupled to an open-tube, vapor-phase, crystal growth apparatus in order to study vapor-phase processes leading to the deposition of GaN crystals. Studies of the HCl and Cl₂ reactions with gallium showed that GaCl_(g) is the only gallium chloride formed. Studies of NH₃ decomposition showed that very little NH₃ decomposes under given experimental conditions, but this can be changed by the presence of W and Pt. Thermochemical data were collected or calculated for all species detected in the system. The reaction mechanisms leading to the deposition of GaN are discussed. It is concluded that the reaction controlling the deposition of GaN can be written as



Comparison of the experimentally determined vapor composition with one predicted from the available thermochemical data showed that important deviations from the thermochemical equilibrium occur in our system.

Gallium nitride has a direct energy bandgap of 3.39 eV (1) and is therefore an interesting material for electronic applications. Recently, single-crystalline epitaxial films of GaN were successfully prepared by means of the open-tube, vapor-transport method (1). The apparatus and technique used were very similar to those used previously in the preparation of other III-V compounds (2).

The chemistry of vapor-phase processes leading to the deposition of GaN was not completely understood. For this reason, we undertook studies of some fundamental aspects of the GaN deposition. In particular, the following processes were studied: (a) the transport of Ga with HCl and Cl₂ in the temperature range of 700°-900°C; (b) the thermal decomposition of NH₃ in the same temperature range as affected by various catalysts; and (c) the reactions leading to the deposition of GaN and the influence of temperature on the rate of this reaction. The influence of the replacement of H₂ by He as a carrier gas was also studied. Furthermore, the thermochemistry of the deposition system is discussed and the experimentally determined composition of the vapor phase is compared with the composition predicted from the chemical equilibrium calculations.

In order to determine the composition of the vapor phase under a variety of experimental conditions, we coupled a time-of-flight mass spectrometer to the vapor-growth tube. With the mass spectrometer, we could directly identify species present in the vapor phase and determine their relative abundances.

Experimental Procedure and Results

The mass spectrometer-vapor growth tube system is shown schematically at the top of Fig. 1. Details of this system and the sampling technique have been described in Part I of this series (3), which reports a study of the GaAs_xP_{1-x} system. The present experiments were done in a similar fashion to those described in Part I. However, the temperature gradients, concentrations of reacting gases, and flow rates were

chosen to be similar to those employed (1) in growth of GaN epitaxial layers. GaN was also deposited on the walls of the reactor in the course of our experiments.

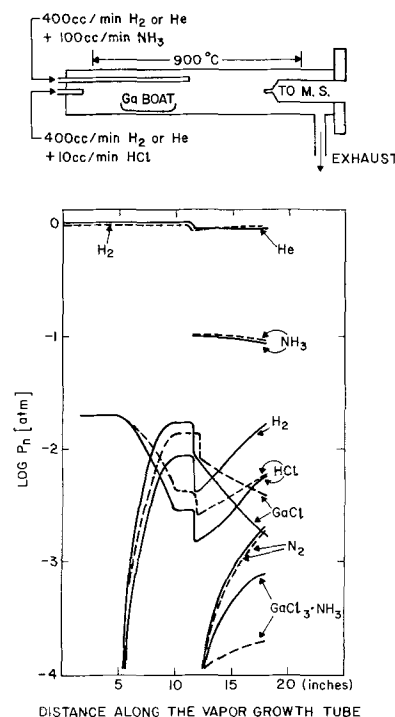
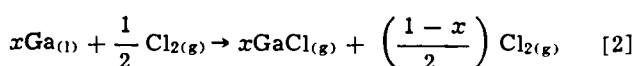
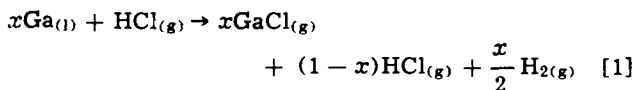


Fig. 1. Mass spectrometric determination of the variation of partial pressures of species along the growth tube during epitaxial growth of GaN. The apparatus and experimental conditions are schematically represented in the upper part of the drawing. (Dotted lines give pressures when H₂ is the carrier, solid lines when He is the carrier. Kinks in the pressure curves at 12 in. are caused by the additional volume of gas introduced at that point by the NH₃ inlet tube. These curves are drawn from the determination of initial and final partial pressures of vapor species.)

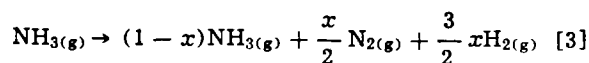
Occasionally, even the sampling capillary became clogged with GaN deposit.

Halogen transport of Ga.—The HCl transport of Ga in the temperature range of 400°–800°C was discussed in Part I (3). This time we also examined the Cl₂ transport of Ga as well as the influence of the carrier gas (H₂ vs. He) on the HCl transport efficiency. The boat containing gallium was 12.5 cm long; 25 cm² of the liquid gallium surface was exposed to the gas phase. With the chosen flow rates (500 cm³/min H₂ or He + 10 cm³/min HCl or Cl₂), the gas stream velocity was about 3.5 cm/sec. It was found that HCl and Cl₂ react with Ga according to the following reactions



where x = mole fraction of HCl or Cl₂ reacting. Values of x for various experimental conditions are given in Table I. These values were obtained by changing the position of the HCl or Cl₂ inlet, which could be placed either upstream or downstream from the boat containing Ga. The mass spectrometer signal due to HCl (or Cl₂) was first measured with the inlet placed downstream, so that the halogen species could not react with Ga. A second measurement was made with the inlet placed upstream, so that a portion of the halogen did react. Since the second signal was due to the unreacted HCl (or Cl₂), its ratio to the first signal was equal to $(1-x)$. The mass spectra also showed that the monochloride (GaCl) was the only gallium chloride species resulting from the halogen-gallium interaction.

Decomposition of NH₃.—It is important to know to what extent ammonia is decomposed into nitrogen and hydrogen, because GaN cannot be deposited by direct reaction between GaCl and N₂. Ammonia is a thermodynamically unstable gas (4) at temperatures usually employed in the growth of GaN crystals, and over 99.5% of incoming NH₃ would decompose if equilibrium were achieved under our experimental conditions. However, it is known that thermal decomposition of NH₃ is a sluggish reaction. It can be accelerated with various catalysts, e.g., Pt and W (5). Normally, the walls of the growth tube are made of quartz, but sometimes, in order to prevent the deposition of a permanent layer of the insoluble GaN on the reactor wall, a removable tungsten or graphite liner is placed in the tube. This could change the composition of the gaseous phase. We therefore studied the influence of various materials on the decomposition of NH₃, which can be described by the following equation



where x = mole fraction of NH₃ decomposing. A foil of Pt, W, or graphite (25 cm² in each case) could be placed in and removed from the growth tube. Mass spectrometer signals due to NH₃ and N₂ were measured with and without the foil in the system. The values of

Table I. Mole fractions of HCl_(g) or Cl_{2(g)} reacting with Ga_(l) according to Eq. [1] and [2], respectively

P_{HCl} or $P_{\text{Cl}_2} = 2.0 \times 10^{-2}$ atm, total flow rate = 510 cm³/min, Ga surface area = 25 cm²

T, °C	Mole fraction (x) of Cl ₂ or HCl		
	Cl ₂ in He	HCl in He	HCl in H ₂
700	0.78	0.79	0.70
800	0.78	0.83	0.72
900	—	0.86	—

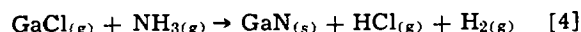
Table II. Mole fraction of NH_{3(g)} decomposing according to Reaction [3]

$P_{\text{NH}_3} = 2.0 \times 10^{-1}$ atm, total flow rate = 500 cm³/min, catalyst surface area = 25 cm²

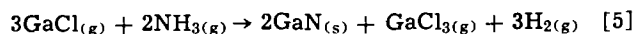
Catalyst and carrier gas	Mole fraction (x) of NH ₃				
	700°C	800°C	850°C	900°C	950°C
Quartz, H ₂	0	—	0.02	—	0.03
Quartz, He	0	—	0.02	—	0.04
Graphite, H ₂	0	0.02	—	0.02	—
Graphite, He	0	0.03	—	0.04	—
Pt, H ₂	0	0.02	—	0.02	0.02
Pt, He	0	0.10	—	0.23	0.35
W, H ₂	0	0.04	0.10	0.22	0.47
W, He	0	0.11	0.25	0.40	0.54

x computed from these measurements in the temperature range of 700°–950°C are given in Table II. In these experiments, a mixture of 100 cm³/min of NH₃ with 400 cm³/min of He or H₂ was passed through the tube. The influence of the carrier gas on the extent of decomposition is also depicted in Table II. When no catalyst was present, no more than about 4% of the NH₃ was decomposed at temperatures as high as 950°C. This was estimated from the increase in the N₂ signal at the elevated temperatures in comparison with N₂ background signal at room temperature.

Deposition reactions.—In analogy with the deposition of other III-V compounds, one can postulate two thermodynamically feasible reactions which might lead to the deposition of GaN



and



In order to test for the occurrence of these reactions, we monitored mass spectrometrically the pressures of GaCl, HCl, and GaCl₃ in the system before and after the introduction of NH₃. In these experiments Ga was transported with HCl. A decrease in the GaCl signal and an increase in the HCl signal after the introduction of NH₃ indicated that Reaction [4] does indeed occur. No GaCl₃ was detected, but we discovered a [GaCl₂ · NH₃]⁺ ion in the mass spectra. The most probable parent molecule is GaCl₃ · NH₃, whose existence at reasonably high temperatures has been reported (6). It is known that metal trihalides lose a halogen atom when ionized by the electron beam, giving a MX₂⁺ ion as the most prominent peak in the mass spectrum (7). From the intensity of the peak we estimate that the partial pressure of GaCl₃ · NH₃ was between 1 and 5 × 10⁻⁴ atm. From these results we concluded that Reaction [5] also occurs in our system, producing GaCl_{3(g)} which then reacts with NH₃ to form the observed ammonia complex.

The increase in P_{HCl} and the decrease in P_{GaCl} due to the reaction of GaCl with NH₃ at 900°C are listed in Table III. Values of P_{GaCl} and P_{HCl} after the reaction between HCl and gallium were known from the gallium transport experiments, initial P_{NH_3} was 1.0 × 10⁻¹ atm and the total flow in the system was 1.0 l/min. The carrier gas was either H₂ or He. Values of P_{GaCl} and P_{HCl} after the reaction with NH₃ were calculated from the respective changes in mass spectrometric intensities of these species.

We used the same procedure to measure the consumption of GaCl as a function of temperature be-

Table III. Changes in P_{GaCl} and P_{HCl} due to reactions with NH₃

$P_{\text{NH}_3} = 1.0 \times 10^{-1}$ atm, total flow rate = 1.0 l/min, T = 900°C

	He carrier	H ₂ carrier
	Initial P_{GaCl} (atm)	8.5 × 10 ⁻³
Final P_{GaCl} (atm)	1.7 × 10 ⁻³	3.8 × 10 ⁻³
Initial P_{HCl} (atm)	1.5 × 10 ⁻³	2.5 × 10 ⁻³
Final P_{HCl} (atm)	5.8 × 10 ⁻²	5.7 × 10 ⁻²

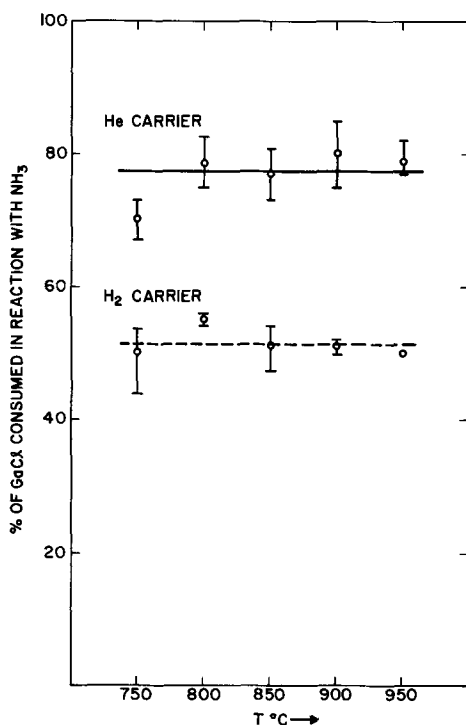


Fig. 2. Percentage of incoming $\text{GaCl}_{3(g)}$ consumed in reaction with $\text{NH}_{3(g)}$ at various temperatures. Initial partial pressures (in atm): P_{H_2} or $P_{\text{He}} = 9 \times 10^{-1}$, $P_{\text{NH}_3} = 1 \times 10^{-1}$, $P_{\text{GaCl}_3} = 8 \times 10^{-3}$. Total flow = 1 l/min, reaction time = 4 sec.

tween 750° and 950°C. The results are presented in Fig. 2. The extent of GaCl consumption was not markedly temperature dependent, but it was significantly greater for He as the carrier gas than for H₂. In these experiments the reactor walls were graphite lined.

Thermochemical Data

By means of our mass spectrometric measurements, we determined qualitatively and quantitatively the species present in the vapor phase and also specified the reactions occurring in the system. These results combined with reliable thermochemical data for all species in the system make possible a meaningful discussion of the chemistry of the vapor-phase deposition.

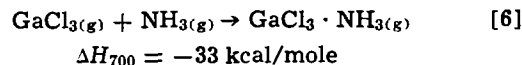
For this purpose the most useful data are the standard free energies of formation ΔF°_f of all species in the temperature interval of interest. Knowledge of ΔF°_f permits one to calculate the standard free energies of reaction ΔF°_r for reactions occurring in the system, and from these to find values of equilibrium constants K_p and values of equilibrium partial pressures for the vapor species.

In Table IV we list values of ΔF°_f for species in the system at $T = 1173^\circ\text{K}$, the temperature at which epitaxial layers of GaN are usually grown. Data for $\text{GaCl}_{3(g)}$ and $\text{GaCl}_{3(s)}$ were taken from a recent paper by Kirwan (8). $\text{GaCl}_{3(g)}$ is not present in the system as such, but data for it are necessary to compute the ΔF°_f for $\text{GaCl}_3 \cdot \text{NH}_{3(g)}$. Data for $\text{HCl}_{(g)}$ and $\text{NH}_{3(g)}$ were taken from JANAF Tables (4).

Table IV. Values of ΔF°_f (free energy of formation) at $T = 1173^\circ\text{K}$ for species present in the GaN deposition system

Species	ΔF°_f (kcal/mole)	Reference
$\text{HCl}_{(g)}$	-24.3	(4)
$\text{GaCl}_{(g)}$	-28.9	(8)
$\text{GaCl}_{3(g)}$	-71.5	(8)
$\text{NH}_{3(g)}$	+19.9	(4)
$\text{GaCl}_3 \cdot \text{NH}_{3(g)}$	-55.6	Calculated from data in (7) and (9)
$\text{GaN}_{(s)}$	+6.2	Calculated from data in (10) and (11)

The value for ΔF°_f of $\text{GaCl}_3 \cdot \text{NH}_{3(g)}$ was determined from ΔH data given by Friedman and Taube (6)



The ΔS for reactions of this type (i.e., $\text{M}_{(g)} + \text{X}_{(g)} \rightarrow \text{MX}_{(g)}$) is usually around -22 eu (9). Using the expression $\Delta F^\circ_r = \Delta H^\circ_r - T\Delta S^\circ_r$, one finds for the above reaction $\Delta F^\circ_r = -4 \text{ kcal/mole}$ at $T = 1173^\circ\text{K}$. Since

$$\Delta F^\circ_r = \Delta F^\circ_f \text{ GaCl}_3 \cdot \text{NH}_{3(g)} - (\Delta F^\circ_f \text{ NH}_{3(g)} + \Delta F^\circ_f \text{ GaCl}_{3(g)})$$

one finds $\Delta F^\circ_f \text{ GaCl}_3 \cdot \text{NH}_{3(g)} = -55.6 \text{ kcal/mole}$ at $T = 1173^\circ\text{K}$.

Marina and Nashel'skii (10) estimate ΔS_f and C_p of $\text{GaN}_{(s)}$. Their values are based on the corresponding thermochemical data for the elemental Group IV semiconductors which are well known. The ΔH_f of GaN at 298°K is -26.4 kcal (11). This value is based on experimental work done by Hahn and Juza (12), and applied to the reaction



The above data permit one to calculate ΔF°_f for $\text{GaN}_{(s)}$; at 1173°K $\Delta F^\circ_f = 6.2 \text{ kcal/mole}$.

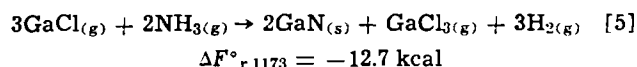
Discussion

Our studies of Ga transport, which are summarized in Table I, showed that between 70 and 80% of the introduced HCl participates in the transport reaction, in good agreement with the values determined in Part I (3). Replacement of H₂ with He as a carrier gas improved the efficiency of the HCl transport, and the HCl/He mixture was more efficient than the Cl₂/He mixture, but the differences in values were not very significant. More important, in all cases chemical equilibrium was not established, since according to the thermochemical data in Ref. (8), practically all the HCl and Cl₂ introduced should have reacted with Ga. It was shown in Part I (3) that the relatively high flow rates employed in our growth systems are responsible for the observed deviations from equilibrium in the transport reaction.

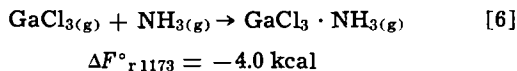
Table II shows the influence of various catalysts on the thermal decomposition of NH₃. The metals tungsten and platinum are significantly more efficient catalysts than the nonmetals graphite and quartz (reactor walls). However, below 700°C very little decomposition occurred, regardless of the catalyst. Furthermore, the influence of the carrier gas was quite pronounced. The decomposition proceeded more readily in the presence of He than in the presence of H₂, particularly in the case of platinum; in the presence of He significant amounts of NH₃ decomposed on platinum, while virtually no decomposition occurred in the presence of H₂. This is possibly due to some interaction of H₂ with platinum which changes the catalytic activity of Pt and therefore inhibits the decomposition of NH₃.

Studies of NH₃ decomposition, as summarized in Table II, indicated that the reactor wall materials and the carrier gas are factors with a significant influence on the composition of the gas phase in the growth system. Frequently, only the vapor species directly participating in the reactions in a system are considered in predicting the vapor-phase composition. Secondary factors, such as those mentioned, are often neglected. Such neglect can lead to serious errors in estimates of the vapor-phase composition.

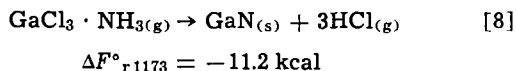
Combining thermochemical data and the mass spectrometric results one can now discuss the chemistry of the deposition system. Besides the direct reaction of GaCl with NH₃ (Reaction [4]), there are other routes leading to the deposition of GaN. One possible sequence of reactions is



The resultant $\text{GaCl}_{3(g)}$ then reacts with $\text{NH}_{3(g)}$ to form the observed $\text{GaCl}_3 \cdot \text{NH}_{3(g)}$ complex



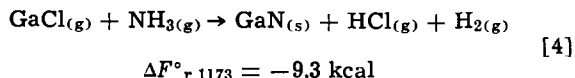
This complex is thermodynamically unstable with respect to the following reaction



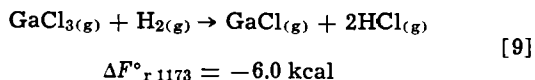
Indeed, $\text{AlN}_{(s)}$ has been deposited by decomposing the analogous complex $\text{AlCl}_3 \cdot \text{NH}_{3(g)}$ (13). Recently, the thermal decomposition of a $\text{GaBr}_3 \cdot 4\text{NH}_3$ complex has been used for the deposition of GaN films (14).

Our results also permit us to say something about the kinetics of the above reactions. Reactions [4] and [5] are fairly fast; e.g., 80% of introduced $\text{GaCl}_{(g)}$ reacts with $\text{NH}_{3(g)}$ in 4 sec¹ when He is used as the carrier gas, 50% when H_2 is the carrier. Reaction [6] must be fast also, because no unreacted $\text{GaCl}_{3(g)}$ was detected. On the other hand, Reaction [8] is slower than [6], because an appreciable amount of $\text{GaCl}_3 \cdot \text{NH}_{3(g)}$ exists in the vapor phase.

Summation of Eq. [5], [6], and [8] yields the overall controlling equilibrium for the deposition of $\text{GaN}_{(s)}$



An alternative reaction path is also thermodynamically feasible. The resultant $\text{GaCl}_{3(g)}$ (Reaction [5]) can undergo reduction by $\text{H}_{2(g)}$

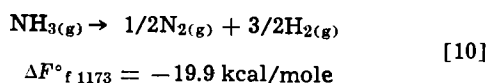


The $\text{GaCl}_{(g)}$ then reacts with $\text{NH}_{3(g)}$ according to Reaction [5] and contributes to the deposition of $\text{GaN}_{(s)}$.

Summation of Reactions [5] and [9] leads again to Eq. [4] which therefore establishes the controlling equilibrium for both complex reaction paths as well as for the direct GaCl-NH_3 reaction. Most likely, the direct Reaction [4] is the biggest contributor to the deposition of GaN, because partial pressures of reactants GaCl and NH_3 are much higher than partial pressures of either GaCl_3 or $\text{GaCl}_3 \cdot \text{NH}_3$.

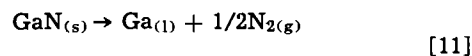
From the value of $\Delta F^\circ_r = -9.3$ kcal for Reaction [4] the corresponding value of the equilibrium constant $K_{(4)} = 55$. This value of $K_{(4)}$ suggests that in the case of the H_2 carrier the partial pressure $P_{\text{H}_2} = 9 \times 10^{-1}$ atm is sufficiently high to prevent all $\text{GaCl}_{(g)}$ from reacting with $\text{NH}_{3(g)}$ ($P_{\text{NH}_3} = 1 \times 10^{-1}$ atm). When He is used as the carrier gas (i.e., $P_{\text{H}_2} \approx 10^{-3}$ atm) more $\text{GaCl}_{(g)}$ reacts (Fig. 2). However, in neither case was the equilibrium reached.

Figure 1 shows the partial pressures of various gaseous species along the tube for the cases of H_2 and He as the carrier gas. The pressure curves were drawn from the determination of the initial and final partial pressures of vapor species; no experimental data were obtained for the intervening points. It is usually assumed that in vapor-phase deposition apparatus thermochemical equilibrium is established throughout the system. Our results show that this is not the case in the GaN deposition system. From the thermochemical data in Table IV it is obvious that the following reactions would occur readily if equilibrium were achieved under our experimental conditions



and

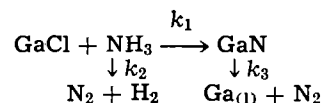
¹ Value of the reaction time (4 sec) was determined from the known gas stream velocity and the known distance between the NH_3 inlet tube and the mass spectrometer sampling capillary.



$$\Delta F^\circ_{f1173} = -6.2 \text{ kcal/mole}$$

The decomposition of $\text{NH}_{3(g)}$ has already been discussed. Lorenz and Binkowski have shown (16) that while the decomposition of $\text{GaN}_{(s)}$ does occur at temperatures over 600°C, the rate of this reaction is very slow. Therefore, due to the kinetic limitations, the above reactions do not proceed in this system and the thermochemical equilibrium is not established. On the other hand, the deposition of $\text{GaN}_{(s)}$ is a fast process.

Indeed, the very fact that $\text{GaN}_{(s)}$ can be deposited under our experimental conditions is the result of the fortuitous kinetics. The deposition and the deposition-opposing processes can be represented by the following scheme



where k_1 , k_2 , and k_3 are rate constants of corresponding processes. One succeeds in depositing $\text{GaN}_{(s)}$ only because the fact that $k_1 \gg k_2, k_3$ leads to the favorable deviations from the thermochemical equilibrium. Due to these deviations the reacting NH_3 is present in sufficiently high concentrations and the decomposition of the deposited $\text{GaN}_{(s)}$ is practically negligible.

Significant deviations from the equilibrium situation were also detected in our earlier work on the $\text{GaAs}_x\text{P}_{1-x}$ system (3).

Conclusions

The main results of mass spectroscopic studies of the GaN deposition system are:

1. Both Cl_2 and HCl react readily with $\text{Ga}_{(l)}$ in the temperature interval 700°-900°C. $\text{GaCl}_{(g)}$ was the only gallium chloride produced in these reactions.

2. NH_3 does not undergo significant decomposition under the experimental conditions present in our deposition system. The influence of various catalysts and the carrier gas (He vs. H_2) on the decomposition of NH_3 was studied and reported.

3. On the basis of mass spectrometric results and collected thermochemical data we discussed the feasibility of various reaction mechanisms which lead to the deposition of GaN. The over-all reaction-controlling equilibrium can be written as



4. The ability to deposit GaN under our experimental conditions rests on the fact that reactions of decomposition of NH_3 and GaN are much slower than the GaN deposition reaction. The resulting favorable deviation from the thermochemical equilibrium leads to the net accumulation of GaN, although it is actually a metastable phase at the temperatures employed.

Acknowledgments

The author would like to thank T. Zrebiec for technical assistance. Enlightening discussions with D. Richman, R. Enstrom, M. Ettenberg, and J. Tietjen are gratefully acknowledged.

Manuscript submitted Aug. 11, 1971; revised manuscript received Dec. 15, 1971.

Any discussion of this paper will appear in a Discussion Section to be published in the December 1972 JOURNAL.

REFERENCES

- H. P. Maruska and J. J. Tietjen, *Appl. Phys. Letters*, **15**, 327 (1969).
- J. J. Tietjen and J. A. Amick, *This Journal*, **113**, 724 (1966).
- V. S. Ban, *ibid.*, **118**, 1473 (1971).
- JANAF Tables of Thermochemical Data, D. R. Stull, Editor, Dow Chemical Co., Midland, Mich. (1965), and quarterly supplements; now available as PB-168370 from the Clearinghouse for Federal Scientific and Technical Information, Springfield, Va.

5. C. N. Hinshelwood, "The Kinetics of Chemical Change," The Clarendon Press, Oxford (1940).
6. H. L. Friedman and H. Taube, *J. Am. Chem. Soc.*, **72**, 2236 (1950).
7. J. W. Hastie and J. L. Margrave, *High Temp. Sci.*, **1**, 481 (1969).
8. D. J. Kirwan, *This Journal*, **117**, 1572 (1970).
9. L. Brewer *et al.*, "The Chemistry and Metallurgy of Miscellaneous Materials," p. 185, L. L. Quill, Editor, McGraw-Hill Co., New York (1950).
10. L. I. Marina and A. Ya. Nashel'skii, *Russ. J. Phys. Chem. (English Transl.)*, **43**, 963 (1969).
11. D. D. Wagman, W. H. Evans, V. B. Parker, I. Halow, S. M. Bailey, and R. H. Schumm, *Nat. Bur. Std. Tech. Note* 270-3 (1968).
12. H. Hahn and R. Juza, *Z. Anorg. Allgem. Chem.*, **244**, 111 (1940).
13. A. J. Noreika and D. W. Ing, *J. Appl. Phys.*, **39**, 5578 (1968).
14. T. L. Chu, *This Journal*, **118**, 1200 (1971).
15. M. R. Lorenz and B. B. Binkowski, *This Journal*, **109**, 24 (1962).

Thermodynamic Analysis of the III-V Alloy Semiconductor Phase Diagrams

III. The Solidus Boundary in the $\text{Ga}_{1-x}\text{Al}_x\text{As}$ Pseudobinary System

L. M. Foster,* J. E. Scardefield, and J. F. Woods

IBM T. J. Watson Research Center, Yorktown Heights, New York 10598

ABSTRACT

The solidus boundary in the $\text{Ga}_{1-x}\text{Al}_x\text{As}$ pseudobinary system was determined by a technique which employs the electron microprobe to analyze the primary phase of compositions equilibrated in the two-phase field. The solid solutions in this system appear to be essentially ideal over the entire composition range, since the experimental solidus boundary is in good agreement with that calculated with the assumption of ideal solid and liquid solutions. This is consistent with the hypothesis that an alloy whose two components have the same lattice parameter will obey Raoult's law of mixing.

Of all the III-V compound semiconductors, alloys between GaAs and AlAs offer some of the most attractive features. Direct radiative transitions with high quantum efficiencies are permitted up to about 40 m/o (mole per cent) AlAs, corresponding to red (ca. 6800Å) light emission. The alloys are particularly amenable to preparation by liquid-phase epitaxy from gallium-rich solutions (1), and high quality, single-crystal GaAs substrates are readily available. A primary consideration in the early choice of $\text{Ga}_{1-x}\text{Al}_x\text{As}$ for exploitation was the almost perfect lattice parameter match between GaAs and AlAs ($a_{\text{GaAs}} = 5.653\text{Å}$; $a_{\text{AlAs}} = 5.662\text{Å}$) (2). Because of this lattice match, strain-free layers of $\text{Ga}_{1-x}\text{Al}_x\text{As}$ of high metallurgical quality could be deposited by epitaxial techniques onto GaAs substrates. Moreover, the lattice parameter match avoids the introduction of carrier trapping states at the interface between the epitaxial layer and the GaAs.

The authors recently suggested (3) that the degree of match between the lattice parameters of the two III-V compounds forming an alloy might also determine in part the homogeneity and general "quality" of bulk crystals of the alloy. This is a consequence of the absence of lattice strain that would otherwise be introduced when alloys are formed from components of different sizes. This strain makes a contribution to the excess free energy of mixing, which causes a departure of the phase boundaries in the $T-x$ phase diagram from their positions for ideal solutions.

In the earlier investigation, Foster and Woods (3) determined the degree of nonideality of the three homologous alloy systems, $\text{Ga}_x\text{In}_{1-x}\text{Sb}$, $\text{Ga}_x\text{In}_{1-x}\text{As}$, and $\text{Ga}_x\text{In}_{1-x}\text{P}$, in which the lattice parameters of the two components differ by 6.10, 6.92, and 7.38%, respectively. The excess free energy of mixing found for the three solid alloys correlated with the lattice parameter

mismatch, increasing from the antimonide to the arsenide to the phosphide.

In a separate study (4) it was shown that in the $\text{GaSb}_{1-x}\text{As}_x$ system, where the lattice mismatch is still greater (7.52%), the excess free energy of mixing is also greater than for the other systems.

Although the relationship between the lattice parameter mismatch and the nonideality of a system is not known in detail, and probably cannot be simply described in terms of elastic strain, it was predicted that a vanishing mismatch would be accompanied by a vanishing excess free energy of mixing. The assumption that the $\text{Ga}_{1-x}\text{Al}_x\text{As}$ system was ideal, because of the very good parameter match, had been made by others (5, 6), and this was largely supported by calculation of the Ga-Al interaction parameter from solubility data in the gallium-rich corner of the Ga-Al-As ternary. The liquidus data at low temperatures could be fit quite well using an interaction parameter of zero. The fit was poorer at the highest temperature (1100°C), however.

The present investigation to determine the solidus boundary in the $\text{Ga}_{1-x}\text{Al}_x\text{As}$ system was undertaken in order to test the hypothesis that this pseudobinary system is ideal, with data obtained in the same manner as for the earlier systems (3).

Experimental

The procedure employed to obtain the solidus boundary has been described by Foster and Scardefield (7). In brief, referring to Fig. 1, a finely ground (to pass 200 mesh) mixture of the two components is pressed into a pellet and held at a constant temperature T within the two-phase region of the pseudobinary diagram for a sufficient time to become equilibrated. It will then consist of solid solution particles whose composition is given by the solidus at T , suspended in a liquid whose composition is given by the liquidus at this temperature. After the equilibrated sample is quenched, the solid solution particles can be readily

* Electrochemical Society Active Member.

Key words: phase diagrams, compound semiconductors, solution theory.

Table I. Solidus data in the $\text{Ga}_{1-x}\text{Al}_x\text{As}$ system

Temp, °C	x_{AlAs} , mole fraction
1273	0.200
1313	0.368
1350	0.480
1435	0.680
1490	0.748
1563	0.835
1602	0.879
1653	0.926

identified visually and are analyzed with an electron microprobe. The entire solidus curve is generated by equilibrating a sufficient number of samples in the two-phase region over the temperature range between the melting points of the pure components.

The method of encapsulating the pressed sample pellets for equilibration at high temperatures is shown in Fig. 1 of Ref. (7). For the present experiments, a pyrolytic boron nitride crucible was preferred over the alumina one shown there because of the greater ease of removal of the sintered pellet after quenching. It was determined that 48 hr at temperature was sufficient for equilibration, as indicated by flat plateaus in the composition *vs.* distance plots of the microprobe data [see Ref. (7)].

For samples of high AlAs content it was necessary to maintain a film of kerosene over the polished surface until just before insertion into the microprobe vacuum in order to prevent reaction with air or moisture.

Results and Discussion

Eight experimental points were determined. The data are given in Table I and plotted in Fig. 1. The samples for the four highest temperature points were equilibrated in a different furnace from that used for the lower four. The displacement of one set relative to the other probably reflects a small error in temperature measurement in one of the furnaces and is not considered significant. The melting point of GaAs (1240°C) was taken from Lichter and Sommelet (8). The melting point of AlAs (1770°C) was determined in this laboratory by R. J. Chicotka.

The continuous curves of Fig. 1 are the ideal liquidus and solidus boundaries calculated from [1] and [2] below (Eq. 13 and 14, Ref. 3).

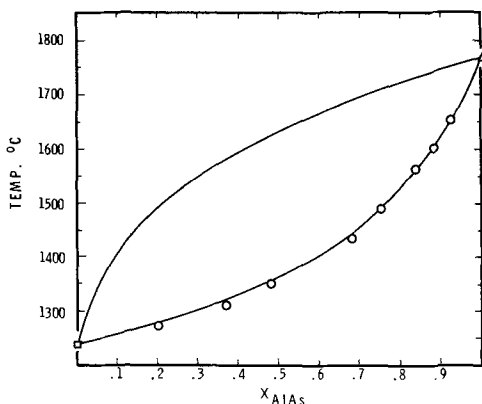


Fig. 1. GaAs-AlAs pseudobinary system. ○ This work; □ Ref. (8); △ R. J. Chicotka, personal communication. — Ideal boundaries calculated from [1] and [2] (see text).

$$x_{id}^l = \{1 - \exp[-L_1(T - T_1)/RTT_1]\} / \{\exp[-L_2(T - T_2)/RTT_2] - \exp[-L_1(T - T_1)/RTT_1]\} \quad [1]$$

$$x_{id}^s = \{1 - \exp[L_1(T - T_1)/RTT_1]\} / \{\exp[L_2(T - T_2)/RTT_2] - \exp[L_1(T - T_1)/RTT_1]\} \quad [2]$$

where the heat of fusion of GaAs, L_1 , is taken to be 25.18 kcal/mole, as measured by Lichter and Sommelet (8). There are no experimental heat of fusion data for AlAs. The ideal curves were calculated with the entropy of fusion of AlAs assumed equal to that of GaAs; i.e., $S_f = L_1/T_1 = 16.64$ eu, and $L_2 = 16.64 \times 2043 = 34.0$ kcal/mole. This, of course, is very approximate; however, plots with the entropy of fusion of AlAs taken 0.5 eu higher or lower were essentially indistinguishable from those of Fig. 1. x_{id}^l and x_{id}^s in [1] and [2] are the mole fractions of AlAs in the liquid and solid, respectively. T_1 and T_2 are the melting temperatures of pure GaAs and AlAs.

It appears from Fig. 1 that the solidus in this system is very nearly ideal. This cannot be established unequivocally in the absence of data for the liquidus, since deviations from Raoult's law in the liquid would affect the solidus curve as well as the liquidus curve. [The liquidus data that are available (5, 6) are not at sufficiently high temperature for extrapolation onto the GaAs-AlAs tie line to give the liquidus in the pseudobinary.] According to our calculations, however, in order for such deviations to shift the solidus for a nonideal solid to the position calculated for an ideal solid, the liquid would have to be even less ideal than the solid. In the four systems studied previously (3, 4) the liquids were all more ideal than the solids. If this character is assumed for the $\text{Ga}_{1-x}\text{Al}_x\text{As}$ system, it can be concluded that both liquid and solid phases in this system are ideal. This strengthens the hypothesis (3) that, in a III-V semiconductor alloy, departure from Raoult's law of mixing is closely associated with the degree of lattice mismatch between the two components of the alloy.

Acknowledgment

The authors wish to thank R. J. Chicotka for supplying the AlAs and J. D. Kupsis for performing the electron microprobe analyses.

Manuscript submitted Dec. 2, 1971; revised manuscript received Jan. 31, 1972.

Any discussion of this paper will appear in a Discussion Section to be published in the December 1972 JOURNAL.

REFERENCES

1. J. M. Woodall, H. Rupprecht, and W. Reuter, *This Journal*, **116**, 899 (1969).
2. S. M. Ku and J. F. Black, *J. Appl. Phys.*, **37**, 3733 (1966).
3. L. M. Foster and J. F. Woods, *This Journal*, **118**, 1175 (1971).
4. L. M. Foster and J. F. Woods, *ibid.*, **119**, 504 (1972).
5. M. Ilegems and G. L. Pearson, "Gallium Arsenide," p. 3, C. I. Pearson, Editor, Inst. of Phy. and the Physical Soc., London (1969).
6. M. B. Panish and S. Sumski, *J. Phys. Chem. Solids*, **30**, 129 (1969).
7. L. M. Foster and J. E. Scardefield, *This Journal*, **117**, 534 (1970).
8. B. D. Lichter and P. Sommelet, *Trans. AIME*, **245**, 1021 (1969).

The Effect of Mask Edges on Dopant Diffusion into Semiconductors

C. F. Gibbon, E. I. Povilonis, and D. R. Ketchow

Bell Telephone Laboratories, Incorporated, Murray Hill, New Jersey 07974

ABSTRACT

A series of masked diffusions of Sn into GaAs and B into Si has been made through masks having stripe openings ranging in width from 20 mils (508 μm) down to 0.1 mils (2.5 μm). For Sn diffusion into GaAs from a pyrolytically deposited, doped SiO_2 source the junction depth depends strongly on mask opening width. It increases with decreasing mask opening size, passes through a maximum as large as 3 times the unmasked value and then decreases slightly at the smallest opening widths. These results are shown to be consistent with the presence of an accelerated diffusion at the mask edge. This "pull-down" of the junction at the mask edge overlaps at narrow mask openings and produces the increase in junction depth. Diffusion of boron through an SiO_2 mask opening also results sporadically in the production of a junction profile which suggests that diffusion is accelerated at the mask edge with an accompanying change in junction depth with mask opening size. It is shown that the effect appears in a variety of diffusion source systems. Three possible mechanisms by which mask edges could affect diffusion of dopants into semiconductor substrates are described. Some tentative explanations of the observed effects have been made on the basis of these mechanisms.

Although diffusion into semiconductors is often studied on unmasked slices, in practice most diffusions for device applications are masked to produce a planar pattern. In carrying out diffusions of Sn into GaAs the authors have observed that the junction depth obtained with a diffusion done through a mask opening is frequently much deeper than that obtained under identical circumstances in an unmasked slice. It is clear, therefore, that diffusions through mask openings are not necessarily identical to diffusions into unmasked slices done under the same conditions. At least three factors could cause enhanced penetration in the case of the masked diffusions; they are strain effects, source film edge effects, and indiffusion of impurities from the mask. These three factors are discussed below.

Strain effects.—In many cases, as for instance when using SiO_2 masks on Si, the mask has a significantly different coefficient of expansion than the substrate. Stresses are then present at the mask/substrate interface at any temperature different from the temperature of formation or deposition of the mask. When a strip of the mask is removed for diffusion, it is conceivable that the elastic strain in the vicinity of the mask edge could be relieved by the generation of a dislocation network along the mask edge. This generation might not occur until later when the slice is heated for diffusion and the yield stress diminished by the increase in temperature. It has been shown (1) that mechanical deformation can accelerate or retard diffusion in silicon depending on the dopant type. Thus one might expect to find some enhancement or retardation of diffusion along the mask edge in a semiconductor substrate due to thermal strain effects.

Source film edge effects.—If the diffusion is done by driving the dopant into the substrate from a finite, predeposited, thin film source, then the effective source film thickness can change considerably near the mask edge. (See Fig. 1; the walls of the mask opening are shown as vertical in this illustration although they are generally at some angle to the surface due to undercutting.) At the mask edge the thickness of the film will increase due to the deposition of the film source on the side walls of the mask opening and also due to filleting of the corner if the source viscosity is low enough that it will flow under the influence of the source film surface tension. This effect will be im-

portant only in those cases where the source film is sufficiently thin or the diffusivity of dopant in the film sufficiently high that the finite thickness of the source becomes important in the diffusion kinetics.

In-diffusion from mask.—The mask itself can operate as a source of impurities during diffusion. This is particularly true for diffusions of certain dopants into compound semiconductors such as GaAs where pyrolytically deposited SiO_2 films intentionally doped with phosphorus are used as masks (2). The phosphorus is needed to decrease the diffusivity of dopants in the mask medium but, of course, it could diffuse into the substrate itself. Therefore, along the mask edge the diffusion of the dopant could be altered by the presence of the in-diffusing impurity which has the mask as its source. If the impurity is electrically active it can produce a field which may either retard or accelerate the dopant depending on the relative charge and the difference in size of the diffusion coefficients of the two species (3). If the ions are substitutional and of considerably different size then strain effects might also produce an interaction between them, and an alteration of their diffusion coefficients. Thus again some variation in diffusion properties near the mask edge might be expected.

In this work it is shown that the differences in diffused junction depths between masked and unmasked substrates is related to an apparent dopant diffusion acceleration effect associated with mask edges. Several features of this mask enhanced diffusion effect make it of interest. First as noted below, in the case of boron diffusion into silicon from certain sources it is sporadic,

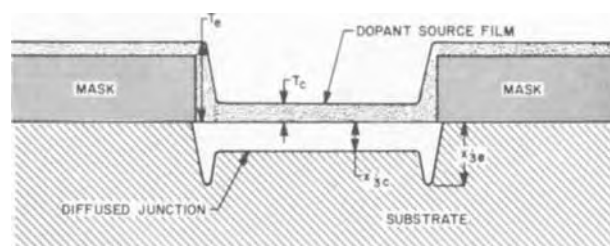


Fig. 1. Hypothetical diagram of diffusion source distribution around a mask opening and resulting junction profile; T_c and T_e are the center and edge thicknesses of the source film; and x_{jc} and x_{je} are the center and edge junction depths.

• Key words: diffusion, silicon, gallium arsenide, masking.

occurring unpredictably for silicon substrates processed with nominally identical procedures in the same or different facilities. It thus represents a possible source of diminished control over diffused elements. Second, the effect gives a variation in the junction depth with mask opening size which makes monitoring diffused layer properties with separate test chips difficult. And third, the mask edge effect, when present, creates a junction profile with a point under the mask edge (see Fig. 1) which could be a source of altered reverse bias breakdown in diodes. [The overlapping effects of the mask edges for small ($\leq 10 \mu\text{m}$) mask openings produces what appears to be simply a deeper junction than would be produced on an unmasked slice without the edge-associated pull-down.]

Experimental

In order to investigate the existence and magnitude of mask opening effects on diffusion, a mask having openings from 20 mils ($508 \mu\text{m}$) to 0.1 mil ($2.5 \mu\text{m}$) wide was made and a series of diffusions was done into slices having this configuration etched into their masks. Diffusions were done with Sn through phosphorus-doped SiO_2 masks into GaAs and with B through thermally grown SiO_2 into Si.

The gallium arsenide substrates into which Sn diffusions were done were p-type boat-grown ingots having a base doping $p = 5 \times 10^{16}/\text{cm}^3$. The polished and etched slices were cleaned and phosphorus-doped SiO_2 masks deposited on them. After application of photoresist, exposure through the mask and etching, approximately 3000\AA of tin-doped SiO_2 was deposited as a diffusion source from a forming gas stream passed through a solution of ethylorthosilicate plus 2 volume per cent (v/o) tetramethyl tin. The dopant was then driven-in for 1 hr in forming gas at 1050°C . This tin diffusion system has been discussed in detail by Gibson and Ketchow (4). The specimens were angle lapped, stained, and photographed after diffusion.

The boron diffusions were done into silicon wafers, 8 mils thick, cut from a 10-12 ohm-cm, n-type, phosphorus-doped, $\langle 111 \rangle$ oriented silicon ingots, 0.850 in. in diameter. Three of these were float zone ingots and one Czochralski. These wafers had one side silica-sol polished, and it is into this side that the diffusions were performed.

Both sides of the substrate were either wet or dry oxidized to $10,000\text{\AA}$ (the oxide on the back side is retained throughout processing). The dry oxidations were done at 1200°C and the wet oxygen oxidations at 1050°C . A boron diffusion is then performed into the substrate wafer through the mask openings. Diffusion sources utilized included boron nitride, boron tribromide, boron-doped oxide films, and low energy boron ion implantations.

Several different BN source systems were used, but in each case a 10-20 min predeposition in an inert gas ambient at $870^\circ\text{--}900^\circ\text{C}$ was followed by a 60-70 min drive-in in 10% O_2 in N_2 at $1135^\circ\text{--}1150^\circ\text{C}$. (These parameters were constant for each system, the ranges refer to all systems utilized.) The BBr_3 source diffusion included a predeposition in 0.2% O_2 in N_2 at 875° or 1140°C and a drive-in in 10% O_2 in N_2 at $1135^\circ\text{--}1140^\circ\text{C}$. A control wafer, without any oxide mask, was usually diffused simultaneously with the oxide-masked substrate wafer. The sheet resistance of the diffused layer on the control wafer was measured with a 4-point-probe. Both the control wafer and the substrate wafer were angle-lapped, stained, and the junction depths of the diffusion measured and photographed with an interferometer. In studying the photomicrographs of the angle laps one should keep in mind that the diffused region is distorted by the magnification of distances perpendicular to the surface by a factor of 20 over those parallel to the surface. Surface concentrations were determined from sheet resistance and junction depth data using Irvin's curves (5).

Tin Diffusion into GaAs

Results

Figures 2 and 3 show the junction depths obtained after diffusion of Sn in GaAs as a function of mask opening size. The data are given for two different mask thicknesses: 1600 and 4800\AA . The junction depth in an unmasked slice given the same treatment was $0.9 \mu\text{m}$. The diffusion depth starts near this value for the center of the widest mask opening and increases with decreasing mask opening. It reaches a maximum of nearly three times the unmasked depth in the neighborhood of 20-50 μm mask opening width. It then decreases slightly. The thickness of the mask seems to have little effect. Near the edge of the phosphorus-doped SiO_2 mask the junction depths are deeper than at the center when the mask opening is larger than $50 \mu\text{m}$. This mask edge "pull-down" effect is clearly visible in Fig. 4, which shows photomicrographs of four diffused stripes of various widths in a specimen with a 1600\AA phosphorus-doped SiO_2 mask. The junction outline is given a peculiar dish out appearance by this mask edge effect. It can be seen that the apparent increase in center junction depth with decreasing opening width is due to the overlapping of the two-edge effects.

Discussion

The first of the mechanisms postulated in the beginning of this paper by which diffusion might be altered by the presence of the mask edge is the presence of a deformed region due to the difference in the thermal expansion coefficient of the oxide and GaAs substrate.

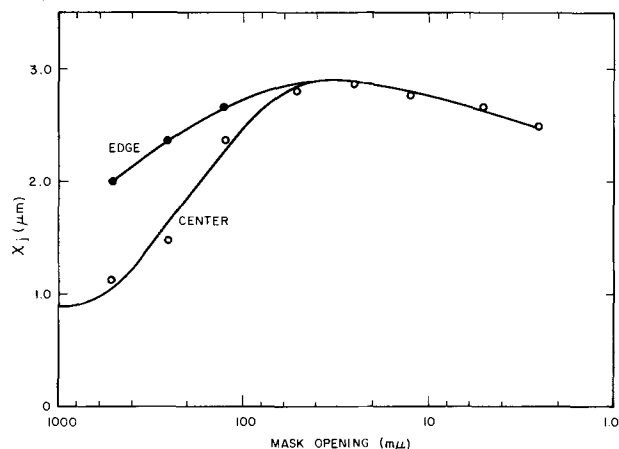


Fig. 2. The junction depth as a function of mask opening size for tin diffusion into GaAs with a 1600\AA P-doped SiO_2 mask. Measurements from both the center and near the mask edge are shown.

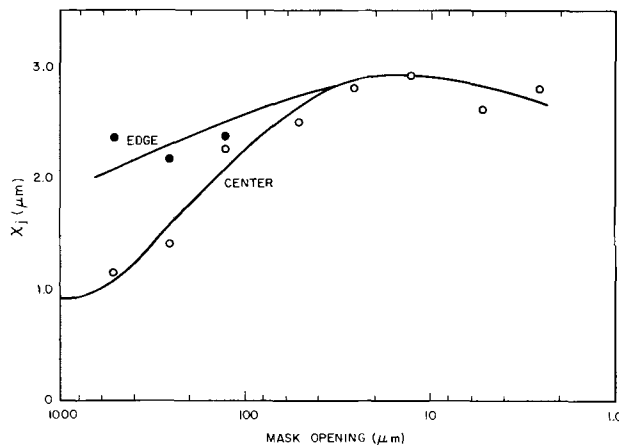


Fig. 3. The junction depth as a function of mask opening size for a 4800\AA mask.

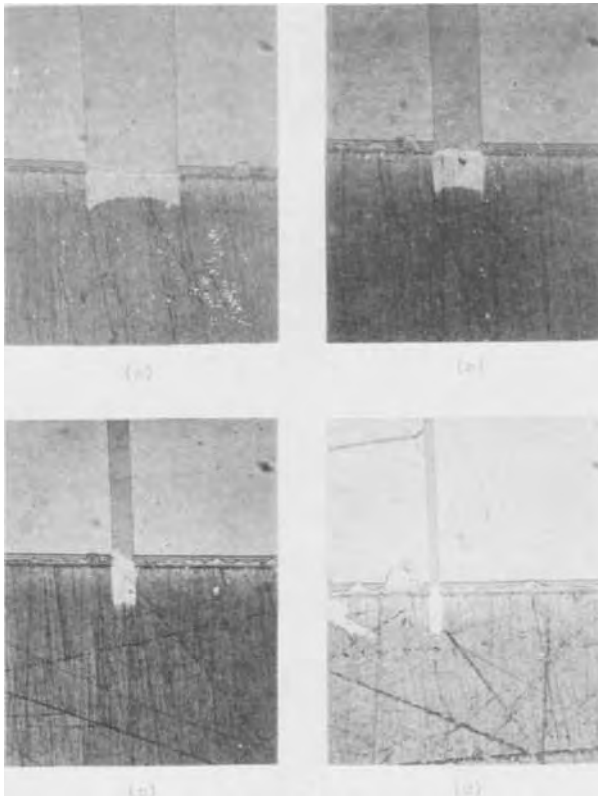


Fig. 4. Photomicrographs of angle-lapped slices of GaAs showing pull-down of diffusion near the phosphorus-doped SiO_2 mask edge; mask opening width (a) 10 mils, (b) 5 mils, (c) 1 mil, and (d) 0.5 mils.

The thermal expansion coefficient of the phosphorus-doped SiO_2 mask is not known; however, the expansivity of pure SiO_2 is low, about $6 \times 10^{-7}/^\circ\text{C}$, while that of GaAs is nearly $60 \times 10^{-7}/^\circ\text{C}$. The general tendency is for a marked increase, up to an order of magnitude, in the thermal coefficient of expansion of silicate glasses as other compounds are added to SiO_2 . For instance, borosilicate glasses have an expansivity around $40 \times 10^{-7}/^\circ\text{C}$. Thus the expansion coefficient of the mask is probably, but not certainly, less than GaAs, and interface stresses may develop when the masked substrate is heated above the deposition temperature. This stress could conceivably alter the diffusivity of the tin in the substrate and produce the observed pull-down at the mask edge.

The second effect postulated was variations in the source film thickness due to the presence of the mask walls (see Fig. 1). The possible extent of this effect can be estimated from Eq. [A4], which is developed in the Appendix, that is

$$R^2 = \left(\frac{x_{je}}{x_{jc}} \right)^2 = \frac{4Dt}{(x_{jc})^2} \ln \frac{T_e}{T_c} + 1 \quad [\text{A-4}]$$

In this case x_{jc} for a wide mask opening is about 1.0×10^{-4} cm, D is approximately 5×10^{-13} cm^2/sec (4), t is 3.6×10^3 sec and it seems reasonable to assume that the largest difference one could postulate between T_e and T_c is about the thickness of the mask, so T_c is 3×10^{-5} cm and T_e is about 8×10^{-5} cm. If these values are used to find R from Eq. [A4], one finds

$$R = 1.2$$

This is less than the value of 2.0-2.5 which can be seen from Fig. 2 and 3 to hold for R at large mask openings. The difference of about 0.2 μm between center and edge junction depth predicted is one-fifth the observed difference of 1.0-1.5 μm . Thus source thickness variations appear unlikely to be the major source of the mask edge junction pull-down.

The third possibility for the origin of this effect is the coupling of the Sn diffusion flux to a flux of some impurity which diffuses in from the mask. In these experiments, the mask is doped with phosphorus, and thus it is possible that there is some in-diffusion of P. Very little is published on the subject of phosphorus diffusion in GaAs, but it is known from the work of Stone (6) that a surface concentration of P around $10^{20}/\text{cm}^3$ can be produced from 1 atm of phosphorus pressure at 1000°C . Stone estimates the diffusion coefficient of phosphorus in GaAs to be 10^{-12} to 10^{-13} cm^2/sec at 700°C - 800°C . Thus phosphorus may be present in the GaAs under the mask at 1050°C , the drive-in temperature utilized in the present work. The mechanism by which the phosphorus might couple with the tin diffusion to accelerate it is not clear. The phosphorus probably substitutes isoelectronically for arsenic on the arsenic sublattice, and thus it appears that the electronic effects would be small. Phosphorus with a tetrahedral covalent radius of 1.10Å (7) is smaller than the arsenic it replaces which has a corresponding value of 1.18Å. Since the covalent radius of Sn is larger than Ga, 1.40Å as compared to 1.26Å, if tin diffuses substitutionally it could be accelerated by a gradient in strain energy since the strain field associated with it would be opposite in sign to that associated with the phosphorus impurity.

In summary the junction depth variation with mask opening size is a result of junction pull-down along the mask edge. It appears that this acceleration of diffusion at the mask edge is due either to strain effects related to differences in the thermal coefficient of expansion of the substrate (GaAs) and the mask (P-doped SiO_2), or to in-diffusion of phosphorus. A more definitive understanding of this effect will require further investigation.

Boron Diffusion into Silicon

Results

Figure 5 shows the variation in junction depth with mask opening size for a silicon slice diffused with the BN system (note the suppressed zero in this figure). Assuming the diffusion to be approximately Gaussian, calculation of the surface concentration from the sheet resistance and junction depth of an unmasked test slice gives $C_s = 3 \times 10^{19}/\text{cm}^3$.

Here, as in the case of Sn diffusion into GaAs, the junction depth varies with mask opening size and this effect is seen in the inset angle lap photographs in Fig. 5 to be associated with a junction pull-down at the mask edge. The enhancement in junction depth

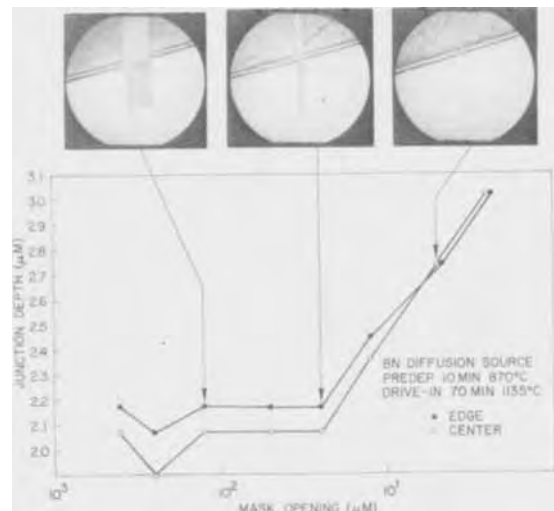


Fig. 5. Typical enhancement in junction depth vs. mask opening size for boron diffused into silicon using a source layer predeposited from oxidized BN disks.

for the smallest mask opening size is considerably greater than the individual enhancement along either edge which suggests that the effect combines super-linearly when the mask edges come in close proximity. It might be suggested that the general increase in junction depth is due to a nonuniform diffusion across the slice, however no such effect was seen on accompanying unmasked test slices, and it recurred in the same way on a number of identical masked slices.

It should be noted though that silicon slices were diffused which had none of the mask edge effect or junction depth dependence on mask opening size seen here. The occurrence, or nonoccurrence, was always uniform across a slice: the slice either showed the mask-edge pull-down or it did not. Identical slices were diffused in similar BN source systems by different operators with similar results: very roughly half the time the mask edge acceleration was seen in four different systems.

A number of variables were examined in detail to try to locate the origin of the sporadic appearance of the mask-edge effect. These included the orientation of the mask opening channels on the (111) slice surface, and the growth ambient and temperature of oxidation of the mask oxide. These variables were selected because it was felt they might influence the strain distribution around the mask edge. None of these variables detectably influenced occurrence of the mask-edge effect.

Another variable examined was the ingot source of the substrate. The slices utilized in this work were cut from four nominally identical ingots. Most of the experiments (86 slices) were carried out on slices from two ingots, one float zone and one Czochralski, in which the mask-edge effect occurred; in the other two (float-zone ingots from which 17 wafers were processed) no mask-edge pull-down was observed. Thus the occurrence of the effect may be contingent on the value of some property in the substrate; however, it was not possible to determine what this feature was. There was no clear relationship, for instance, between ingot growth type and the presence of the enhanced mask-edge diffusion.

For a single system, slices were diffused with a series of predeposition times in order to vary the final surface concentration. Table I lists the results of this experiment. The mask-edge acceleration appears to occur more frequently at higher concentrations. The sporadic nature of the mask-edge effect thus appears to be related to variations in the surface concentration between individual diffusions and to some differences in substrate properties. Although the list of variables examined seems reasonably exhaustive, other undefined variations from slice to slice may influence the appearance of this effect.

The effect appeared much less frequently and with a much smaller influence on junction depth in the case of diffusions from a source glass deposited from BBr_3 . Figure 6 shows a typical case where some mask-edge

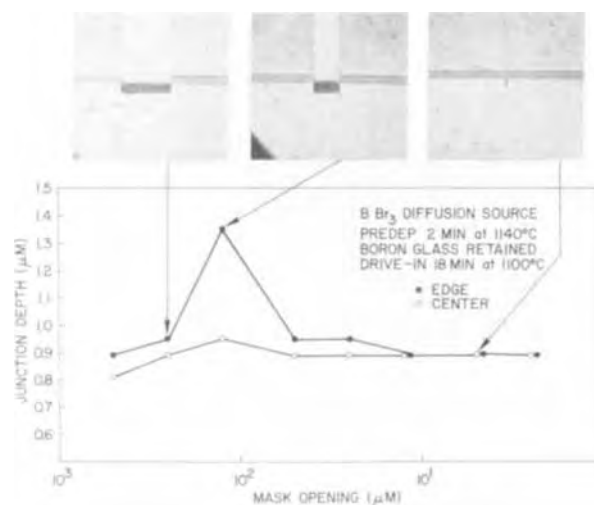


Fig. 6. Junction depth vs. mask opening size for diffusion source predeposited from BBr_3 .

effect was apparent. In this system, the mask-edge effect did not appear uniformly across the slice, also other irregularities away from the mask edge occasionally appeared. Table II lists results of a series of diffusions done with different conditions to produce different surface concentrations. There is in this case little evidence of dependence on surface concentration.

Several other sources of boron were used for boron diffusion in this study. Diffusions from these sources also show the mask-edge acceleration effect. It was called to the authors' attention that an apparent mask-edge acceleration of diffusion is occasionally observed in integrated circuits in which a p-layer is diffused from a boron ion-implantation (8). In an effort to independently reproduce this effect, $5 \times 10^{12}/\text{cm}^2$ and $5 \times 10^{13}/\text{cm}^2$ implantations of boron were made at room temperature at 30 keV. The boron was then diffused in a 10% O_2 in N_2 ambient for 1 hr and 5 hr at 1150°C. Evidence of mask-edge acceleration could be detected in the 5 hr but not the 1 hr diffusions (see Fig. 7). The fact that such an effect is observed in these diffusions strongly suggests that filleting of a chemical source film is not the origin of the mask-edge effect.

Another experiment performed which indicated that the influence of mask-edge filleting is not the source of mask-edge acceleration was the diffusion of boron from channels of boron-doped SiO_2 pyrolytically deposited from silane, diborane, and oxygen at 350°C. No oxide mask, as such, is present in this case. Boron-doped SiO_2 was deposited uniformly over the slice and then all of it was removed except for stripes which were parallel bars forming a pattern just the negative of the mask pattern previously used. The slice was driven-in in N_2 at 1100°C. As seen in Fig. 8 a channel edge acceleration appeared among these slices. (Some lateral diffusion along the unprotected surface also occurred.) Again, this result points away from source

Table I. Diffusions from a BN source

Time (min)	Predep. Temp. (°C)	Time (min)	Drive-in Temp. (°C)	Mask-edge effect	Surface conc. (No./cm ²)
1	870	60	1135	No	1×10^{19}
1	870	60	1135	No	1×10^{19}
1	870	60	1135	No	1×10^{19}
5	870	60	1135	No	6×10^{18}
5	870	60	1135	No	6×10^{18}
5	870	60	1135	No	6×10^{18}
5	870	60	1135	No	6×10^{18}
10	870	60	1135	No	1×10^{19}
10	870	60	1135	Yes	1×10^{19}
10	870	60	1135	Yes	1×10^{19}
20	870	60	1135	Yes	3×10^{19}
20	870	60	1135	Yes	3×10^{19}
20	870	60	1135	Yes	3×10^{19}
20	870	60	1135	Yes	3×10^{19}
100	870	60	1135	No	9×10^{19}
100	870	60	1135	No	9×10^{19}
100	870	60	1135	Yes	9×10^{19}

Table II. Diffusions from a BBr_3 source

Time (min)	Predep. Temp. (°C)	Time (min)	Drive-in Temp. (°C)	Evidence of mask-edge effect	Surface conc. (No./cm ²)
20	875	30	1135	Yes	6×10^{18}
20	875	30	1135	No	6×10^{18}
20	875	60	1135	No	7×10^{18}
20	875	60	1135	No	7×10^{18}
20	875	60	1135	No	7×10^{18}
20	875	60	1135	No	9×10^{18}
1	875	60	1135	Yes	9×10^{18}
1	875	60	1135	No	3×10^{18}
10	875	60	1135	No	3×10^{18}
10	875	60	1135	No	3×10^{18}
100	875	60	1140	No	1×10^{20}
100	875	60	1140	No	1×10^{20}
10	1140	10	1135	Yes	4×10^{20}
10	1140	10	1135	No	4×10^{20}

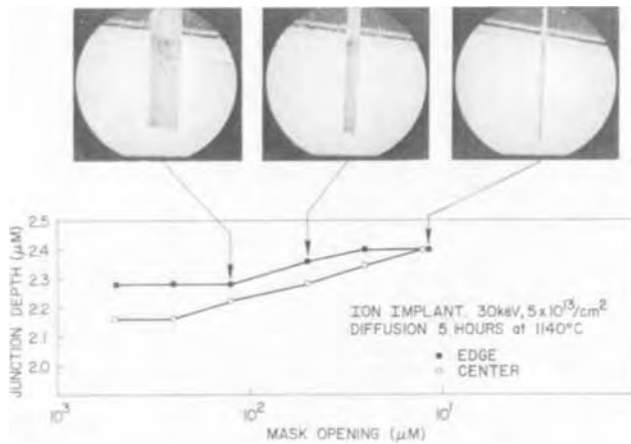


Fig. 7. Junction depth vs. mask opening size for a diffusion from an ion implanted source (Total dose = $5 \times 10^{15}/\text{cm}^2$; implantation energy = 30 keV; diffusion 5 hr at 1140°C).

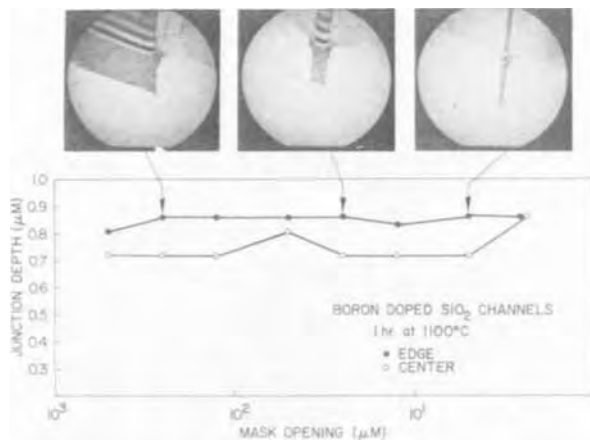


Fig. 8. Junction depth vs. channel width for boron diffusion from an unmasked stripe of deposited B-doped SiO_2 .

accumulation at the mask edge as the origin of the apparent acceleration.

In summary, this study reveals the presence of a sporadic mask-edge diffusion phenomenon for boron diffusion into silicon. It does not depend on the type or thickness of the masking silica film used nor does it appear to be related to the facility in which the oxide film is formed. No consistent pattern has occurred regarding the mask-edge effect with any of the variations of the many parameters of predeposition and drive-in of the boron impurity which were studied, although there is some suggestion that the pull-down occurs more frequently for higher surface concentrations in the BN system. The possibility of a dependence on silicon ingot source from which the various substrate wafers were cut was found. No influence of the orientation of the channel patterns on the slice surfaces was discerned.

Discussion

The mask-edge effect as has just been seen has a very elusive origin. Its presence in slices diffused from ion implanted sources and B-doped SiO_2 channels eliminates source filleting as a primary cause of it. As noted before some diffusion masks used on compound semiconductors are heavily doped to decrease the permeability of the mask material to the dopant and this may influence in-diffusion near the mask edge. However, the diffusion masks used on silicon are thermally grown SiO_2 which is generally very lightly doped (by accumulation of base doping from the substrate), and, therefore, the influence of impurities in-diffusing from the mask seems unlikely to have a

strong influence on subsequent diffusion through openings made in the mask. (The fact that oxidation conditions do not have a critical influence on the appearance of the mask-edge effect supports this conclusion.)

Thus the presence of strain at the mask edge, due to the thermal expansivity mismatch seems the most prominent potential cause of the mask-edge effect. It should be pointed out, however, that x-ray topography has failed to reveal dislocations associated with mask edges in any of the boron diffused slices studied (9). (Dislocations have been observed to be generated at a mask edge (10); however, this appears to be associated with diffusions in which the surface is nearly saturated with the dopant, a condition not generally fulfilled in the present work.) This indicates that any strain effects which are active must be related to elastic strain fields with no influence of plastic deformation. This is a rather surprising observation since mechanical strain effects on diffusion in silicon are generally associated with the generation of dislocations (1). The random appearance of the pull-down strongly suggests that the conjunction of several factors may be required to precipitate its occurrence. The magnitude of the strain field surrounding the mask edge could be a very sensitive function of a number of factors (oxidation temperature, orientation, oxidation ambient, diffusion ambient, and substrate preparation); thus a strain field of appropriate sign and magnitude may be present only in a limited number of cases even where the procedure is nominally the same.

Elastic strain effects if present at the mask edge can influence diffusion in two ways. First there can be the direct influence of the strain field on the diffusion flux itself (11). Second the strain field can alter the equilibrium concentration of point defects and thus potentially influence the diffusion coefficient. Other somewhat more subtle effects of the presence of the mask may be the source of the diffusion acceleration, however. Perhaps, for instance, the transient flow of vacancies of the slice during cooling of the slice from the diffusion furnace may be influential.

Summary and Conclusions

1. An effect of mask opening size on diffusion into semiconductor substrates could arise from a number of sources: (i) strain effects at the mask edge; (ii) source film filleting at the mask edge; and (iii) in-diffusion of impurities from the mask.

2. It has been found that, in the diffusion of GaAs with Sn from Sn-doped SiO_2 through openings in P-doped SiO_2 masks, the junction depth depends strongly on the mask opening size. Examination of the photomicrographs of angle laps of the junctions suggests that the observed variation was due to a diffusion acceleration associated with the mask edge. An approximate calculation shows that this pull-down is probably not due to the presence of a thicker source film along the mask edge. Thus enhancement in the diffusion flux at the mask edge due either to mask-edge strain effects or to the simultaneous in-diffusion of phosphorus from the mask appears to be the origin of the effect.

3. In diffusions of boron into silicon the apparent mask edge associated diffusion acceleration is not associated exclusively with any particular diffusion source system; it appears sporadically in all systems examined including BN, BBr_3 , B-doped predeposited SiO_2 channels, and ion-implanted sources.

4. The effect appears in diffusion systems where mask-edge source filleting could not be its origin. Thus mask-edge strain is indicated as a likely source of the apparent diffusion acceleration.

5. Since no dislocations can be associated with the mask edges in x-ray topographic studies of these slices it appears that the effect might be related to elastic strain. However exact delineation of the mechanism of enhanced diffusion will require further study.

Acknowledgments

J. V. Dalton, T. E. Saunders, P. N. Pappas, and K. R. Gardener each prepared several diffused slices for us. The ion-implanted diffusion sources were produced for us under the supervision of R. A. Moline. G. R. Weber deposited the B-doped oxide films.

We are grateful to G. A. Rozgonyi who took and interpreted several x-ray topographs for us.

Manuscript submitted July 26, 1971; revised manuscript received Feb. 7, 1972.

Any discussion of this paper will appear in a Discussion Section to be published in the December 1972 JOURNAL.

APPENDIX

The only case considered is that where the diffusion is sufficiently long that the source film has begun to deplete. In that case we will approximate the source film as an instantaneous source having a surface concentration of C_0T (atoms/cm²) where C_0 is the dopant concentration in the source film and T its thickness. For an instantaneous source

$$C = \frac{Q}{\sqrt{\pi Dt}} e^{-\frac{x^2}{4Dt}} \quad [\text{A-1}]$$

where C is the concentration at position x and time t . Q is the source surface concentration and D is the dopant diffusion coefficient. Then, if Q is associated with C_0T , the junction depth, x_j , is related to T by

$$\ln \left(\frac{C_s \sqrt{\pi Dt}}{C_0} \right) = \ln T - \frac{(x_j)^2}{4Dt} \quad [\text{A-2}]$$

where C_s is the concentration of dopant in the substrate. If the film thickness at the mask edge is T_e , and at the mask center is T_c , then the junction depth at the edge (x_{je}) and center (x_{jc}) should be related by

$$(x_{je})^2 - (x_{jc})^2 = 4Dt \ln \frac{T_e}{T_c} \quad [\text{A-3}]$$

or, dividing by $(x_{jc})^2$

$$(R)^2 - 1 = \frac{4Dt}{(x_{jc})^2} \ln \frac{T_e}{T_c} \quad [\text{A-4}]$$

where R is the ratio between the junction depth at the edge and the center. Since

$$(x_{jc})^2 = 4Dt \ln \frac{C_0 T_c}{C_s \sqrt{\pi Dt}} \quad [\text{A-5}]$$

we have

$$(R)^2 - 1 = \frac{1}{\ln (C_0 T_c / C_s \sqrt{\pi Dt})} \ln \frac{T_e}{T_c} \quad [\text{A-6}]$$

Thus the center to edge ratio should increase with increasing background doping in the substrate, diffusion coefficient, and time. It should decrease with increasing doping concentration in the source film and increasing source film thickness.

REFERENCES

1. J. E. Lawrence, *Brit. J. Appl. Phys.*, **18**, 405 (1967).
2. D. Flatley, N. Goldsmith, and J. Scott, Paper 69 presented at Electrochem. Soc. Meeting, Toronto, May 3-7, 1964.
3. R. J. Jaccodine, *Appl. Phys. Letters*, **11**, 370 (1967).
4. C. F. Gibbon and D. R. Ketchow, *This Journal*, **118**, 975 (1971).
5. J. C. Irvin, *Bell System Tech. J.*, **41**, 387 (1962).
6. L. E. Stone, *J. Appl. Phys.*, **33**, 2795 (1962).
7. L. Pauling, "The Nature of Chemical Bond," Cornell University Press (1960).
8. K. Gardner, Private communication.
9. G. Rozgonyi, Private communication.
10. G. H. Schwuttke and J. M. Fairfield, *J. Appl. Phys.*, **37**, 4394 (1966); J. M. Fairfield and G. H. Schwuttke, *This Journal*, **115**, 415 (1968).
11. P. G. Shewmon, "Diffusion in Solids," p. 23, McGraw-Hill Book Co., New York (1963).

Silicon Cleaning with Hydrogen Peroxide Solutions: A High Energy Electron Diffraction and Auger Electron Spectroscopy Study

R. C. Henderson*

Bell Telephone Laboratories, Incorporated, Murray Hill, New Jersey 07974

ABSTRACT

HEED and Auger electron spectroscopy have been used to evaluate silicon cleaning by sequential immersions in basic and acidic peroxide solutions. It was determined that an oxide film 13-15Å thick was left after the cleaning. This film contained boron at a surface concentration estimated at 10^{13} - 10^{14} B/cm². The carbide contamination that results upon heating to 800°C in ultrahigh vacuum was dramatically reduced when compared to wafers cleaned with other techniques. Wafers cleaned with the same process except for a final HF etch had no detectable boron in the surface oxide, formed relatively large amounts of surface silicon carbide at 800°C, and suffered extensive surface roughening with 1100°C heating in vacuum. The protective mechanism of the peroxide cleaning is thought to be due to formation of a thin nearly carbon free oxide layer that volatilizes when the wafers are heated in ultrahigh vacuum. It is recommended that experiments requiring a solvent type cleaning and the heating of Si in ultrahigh vacuum should use this cleaning method.

When a silicon wafer is heated to 800°C in ultrahigh vacuum, the silicon decomposes carbon-containing adsorbates to form β -SiC particle protuberances (1-2). These particles can play a significant role as evident

by their effect on silicon epitaxy experiments (3, 4). A thorough chemical precleaning is desirable since it is thought that this step is the dominating source of the carbon contamination (2).

A recent study has appeared evaluating the use of basic and acidic peroxide solutions in sequential steps

* Electrochemical Society Active Member.

Key words: silicon cleaning, Auger electron spectroscopy, HEED.

for silicon cleaning (5). The work to be reported here presents the results of high-energy electron diffraction (HEED) and Auger electron spectroscopy experiments on wafers cleaned by this method and heated in ultra-high vacuum. Particular emphasis in this study has been placed on the desirability of HF as a final processing step. This emphasis was motivated by results indicating HF (i) enhances the carbon contamination (6), (ii) is a source of metal contamination (5), and (iii) is associated with the creation of stacking faults on (100) surfaces following oxidation (7).

The wafers used in these experiments were "Syton" polished (111) samples. The HEED optics and vacuum apparatus have been described previously (2). The Auger electron spectra were obtained using a coaxial cylindrical analyzer manufactured by the PHI Electronics Company. The detailed wafer processing, referred to here as peroxide cleaning, is presented in the Appendix. After loading, pump-down, and bakeout wafers were subjected to various heat-treatments in pressures not greater than 1×10^{-9} Torr. HEED diffraction patterns and Auger electron spectra were recorded after the samples had cooled to room temperature.

Some samples were examined by ellipsometry before being loaded in the vacuum station. In all cases the surface film found after cleaning was 13-15Å thick. A 1 min etch in concentrated HF reduced this thickness to 8-9Å.

Auger electron spectra obtained from a boron-doped wafer ($10^{15}/\text{cm}^3$) cleaned with the peroxide method and before any heat-treatment are presented in Fig. 1. In addition to the carbon, SiO, and O peaks, there is a peak at 180 eV. According to tabulated values this peak could be due to the chlorine $L_{3}M_{23}M_{23}$ or the boron $KL_{2}L_{2}$ Auger transitions (8). No peaks were observed in the region 2200-2400 eV where the KLL chlorine peaks would be expected. Accordingly, the 180 eV peak is ascribed to boron. (From the peak size one would estimate the surface concentration to be 10^{13} - $10^{14}/\text{cm}^2$.)

Figure 2 shows the data obtained from the same wafer described above after heating at 500°C for 10^3 sec, heating at 900°C for 10^3 sec, and then rapid cooling to room temperature. No significant data changes were observed after the 500°C heat-treatment. However, it is evident that after the 900°C treatment the peaks due to Si have changed dramatically in a manner described before (8) and that the O and B have been reduced to values below their detection limits (which is expected to be 10^{12} - $10^{13}/\text{cm}^2$). A small quantity of carbon remains. Confirming these observations, it is easy to calculate from SiO vapor pressure data (9) and the density of SiO_2 that at 900°C in vacuum the

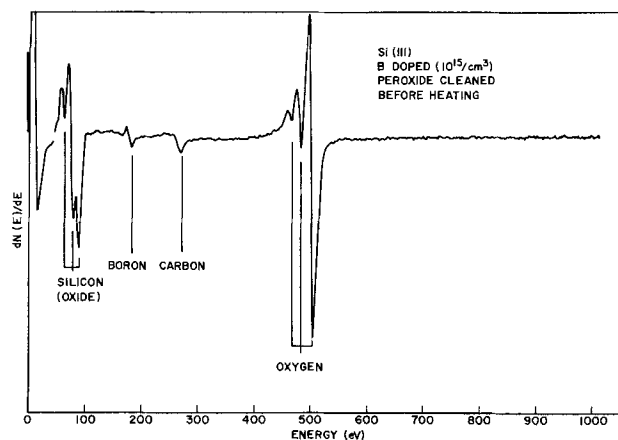


Fig. 1. Auger electron spectra from a wafer cleaned as detailed in Appendix and before any heat-treatment of the sample.

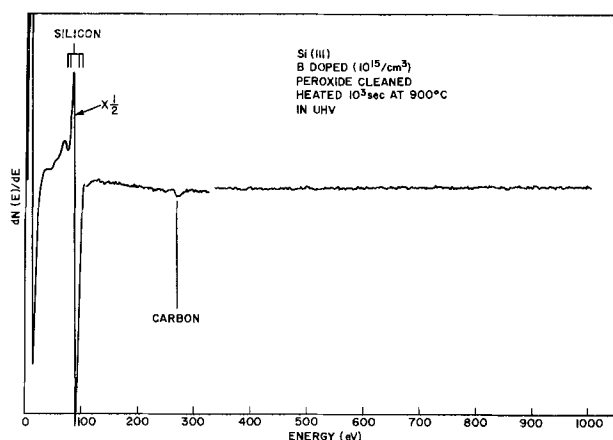


Fig. 2. Auger electron spectra from the wafer in Fig. 1, but after heating at 500°C for 10^3 sec, heating at 900°C for 10^3 sec and then cooling to room temperature.

observed 15Å of oxide would have evaporated in less than 10^3 sec.

The HEED diffraction pattern obtained from the same wafer after heating to 900°C is shown in Fig. 3A. The notable feature here is the extremely weak diffraction spots due to β -SiC. (The small streaks distributed on semicircular arcs are the Si(111)-7 surface structure described previously) (2). By way of contrast, note the plentiful amount of carbide evident in the pattern in Fig. 3B. The sample had been treated

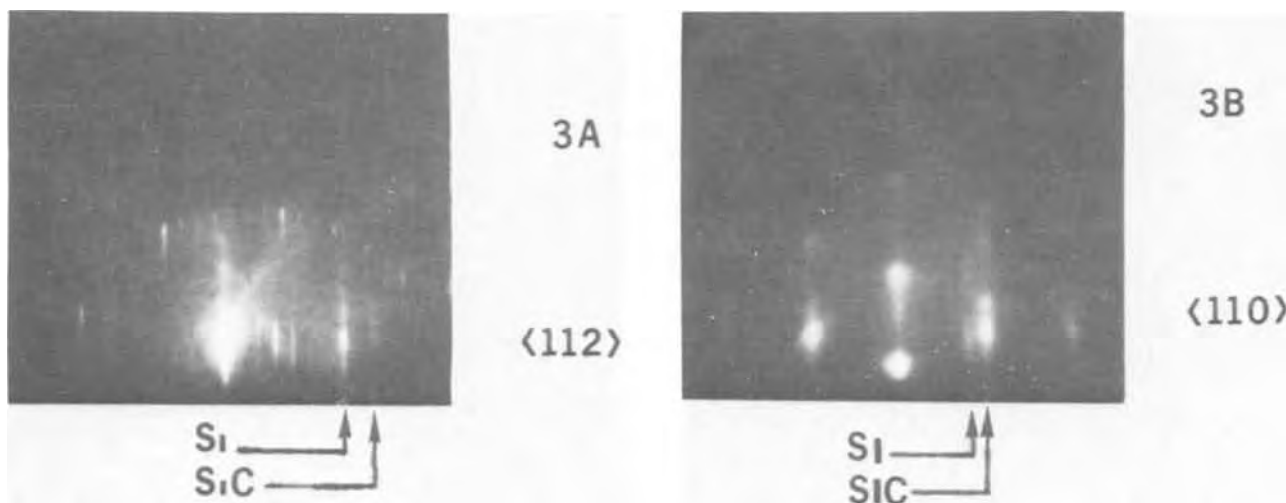


Fig. 3. A. HEED diffraction pattern from the wafer described in Fig. 2. B. HEED diffraction pattern from a wafer cleaned and heated as in Fig. 2 except for a final HF etch.

in the same manner as that of Fig. 3A, except that after the peroxide cleaning the wafer was dipped for 1 min in concentrated HF.

The experiments described above were repeated with phosphorus-doped ($\sim 10^{16}/\text{cm}^3$) and antimony-doped ($\sim 10^{15}/\text{cm}^3$) wafers. The results were identical.

In all these experiments there was no observable difference in the HEED or Auger data if the final wafer heating was in the range $900^\circ\text{--}1100^\circ\text{C}$. Lower temperatures, however, did not rid the surface of oxide within the 10^3 sec. Higher temperatures ($\geq 1150^\circ\text{C}$) leave no observable carbide (2).

To confirm that the 180 eV peak was indeed boron, a peroxide cleaned wafer was heated to 1100°C for 1×10^3 sec. Subsequently, the surface concentration was obtained by a capacitance inverse doping technique (10). The data showed 3×10^{17} B atoms/ cm^3 within 0.1μ of the surface. This number is to be expected based on the diffusion solution from a thin film source using the diffusion constant of boron at 1000°C (4×10^{-13} cm^2/sec) and a surface concentration of 1×10^{13} B atoms/ cm^2 . The excellent agreement supports the conclusion of boron contamination.

The boron concentration was the one particular uncontrolled variable noted with this cleaning technique. With some wafers no boron was detected at all. On the other hand, consistency was observed for a given batch of samples, all cleaned at the same time although of varying dopant types or crystal faces. This fact implies that the contamination arises from the Pyrex glassware utilized or possibly the cleaning solutions themselves.

Wafers given a final HF etch after being peroxide cleaned differed in several respects from the data presented above. In the first place, no boron Auger peak was detected with these samples. Secondly, as evident from Fig. 3B, significantly greater amounts of carbide were formed when the wafer was heated. Finally, HF-etched wafers unaccountably often exhibit a matte-type finish due to surface roughening after being heated to $\sim 1100^\circ\text{C}$. For the most part, this effect does not occur with the peroxide cleaned wafers.

These latter results confirm earlier HEED experiments that demonstrate HF enhanced carbon contamination (6). In the early work wafers were cleaned by heating to 1200°C in vacuum until the surface was carbide free (presumably by solid-state diffusion of the carbon). A comparison was made between those wafers that were subsequently exposed to atmosphere and etched in HF and those that were just exposed to atmosphere. After heating to 800°C in vacuum the resulting diffraction patterns were quite similar to Fig. 3B and 3A, respectively.

Another comparison may be made to wafers cleaned by vapor etching in HCl gas at a substrate temperature of 1100°C until $10\mu\text{m}$ of Si has been removed. After loading the wafer into the vacuum station no carbon is detectable with the Auger electron spectrometer and only a faint trace of carbide is detectable with HEED after heating to 900°C (11). This latter technique is the most successful approach observed to date with respect to carbon. However, as a method the elevated temperature and the relatively large amount of Si removal required for successful cleaning, limit its applicability.

It is thought that the peroxide cleaning process produces a relatively small amount of carbide contamination by the following mechanism: After processing the 15A of film remaining is silicon oxide that is relatively free of carbon-containing compounds. The oxide acts as a passivating and protective layer with respect to carbon adsorbates. At 900°C the oxide becomes relatively volatile. Since the majority of the adsorbates are physisorbed to the oxide, they are carried away during the sublimation process when the wafer is heated.

In contrast the surface that emerges from HF etch is particularly reactive. In addition to oxygen, the surface will also take up carbon compounds either from the HF directly or from the atmosphere. The resulting oxide film has relatively large amounts of carbon in contact with native silicon. When heated, the silicon attacks these compounds and yields copious amounts of SiC. Moreover, it is seen that carbon codeposited within this oxide phase is the major source of contamination rather than from the background gases of the vacuum station as had been previously supposed (1).

Previous HEED experiments have examined wafers cleaned by iodine passivation (12) or other etchants. Judging the amount of carbide from the intensity of the SiC diffraction spots, these experiments all show that the peroxide method is the most successful solvent type precleaning approach observed to date with respect to carbon. On the other hand, based on the discussion above, any method that would leave $\sim 15\text{A}$ of carbon-free oxide should serve equally as well.

Preferential local thermal etching is thought to be the mechanism that causes the surface roughening with high-temperature vacuum heating. The results obtained above suggest that this roughening is associated with the amount of silicon carbide contamination.

The boron incorporation is not surprising due to the known strong affinity of boron for the oxide phase (13). As noted above, this surface boron acts as a thin film diffusion source when these wafers are heated, and the Pyrex cleaning glassware is suspected to be the boron source. Although the boron can be eliminated by HF etching, this has undesirable effects with regard to carbon or metallic contamination. Consequently, it is recommended that the peroxide method described here be used, but modified by using quartz ware for the cleaning solutions.

It is also evident that the peroxide method does not completely eliminate the carbide resulting from heating the wafers. Moreover, vacuum ambient exposures of 10^{-4} Torr \cdot sec are sufficient that heat-treated "clean" silicon surfaces became carbon contaminated (2). Hence, some sort of *in situ* cleaning (e.g., argon sputtering) is desirable to obtain a rigorously clean surface or to rejuvenate one that has been treated in vacuum. In any case, since it is difficult to get rid of the carbide, the relatively small amount formed with the peroxide cleaning is advantageous.

A summary of the HEED and Auger electron spectroscopy results regarding the peroxide process are:

1. An oxide film 15A thick is left after the cleaning. This film can contain appreciable amounts of boron presumably due to the use of Pyrex glassware.
2. Wafers heated in vacuum after this processing are considerably reduced in the carbide contamination when compared to other cleaning methods.
3. Etching with HF as a final processing step enhances the carbon contamination.
4. Surface roughening that occurs with 1100°C vacuum heating is largely reduced.
5. The protective mechanism of the cleaning process is thought to be due to the formation of a thin carbon-free oxide layer that volatilizes when the wafers are heated in ultrahigh vacuum.

In light of the desirability of reducing the carbide contamination, the peroxide cleaning method is recommended for experiments that require heating of Si in vacuum and where the high temperature and large amount of surface removal by the HCl vapor etching method cannot be tolerated. Etching with HF as a final step should be avoided. Quartz ware for containing the cleaning solutions should be used to avoid the boron contamination. Although these recommendations are particularly directed to Si vacuum experiments the information contained in this report should be useful for IC processing as well.

Acknowledgments

The author wishes to thank Rohe Helm who assisted in setting up the Auger electron spectrometer and obtaining some of the data. Thanks are also due to R. Kaiser who obtained the ellipsometry data and M. Hanes who obtained the doping profile. Miss B. Kerns provided the detailed peroxide cleaning specifications.

Manuscript submitted Nov. 4, 1971; revised manuscript received Jan. 13, 1972. This was Paper 188 presented at the Cleveland, Ohio, Meeting of the Society, Oct. 3-7, 1971.

Any discussion of this paper will appear in a Discussion Section to be published in the December 1972 JOURNAL.

APPENDIX

Peroxide Cleaning Specifications

1. Scrub polished wafer with acetone and then with 0.2% Triton X-100 solution. Rinse with filtered deionized water. Flush wet surface with absolute ethyl alcohol. Keeping slice surfaces wet transfer to a quartz holder in methyl alcohol.
2. Place holder and slices in a solution of NH_4OH - H_2O_2 - H_2O maintained at 80°C for 10 min, insuring that the holder is beneath the liquid surface at all times. Agitate during this period. (The solution is to be made up fresh prior to use and is to have the following composition:
1 part NH_4OH —reagent grade
1 part H_2O_2 —Superoxol, unstabilized
4 parts H_2O —18 megohm, $0.2\ \mu\text{m}$ filtered
Mix NH_4OH and H_2O and bring to temperature. Three minutes prior to use add H_2O_2 .)
3. Overflow rinse with grade O or better deionized water for 2 min.
4. Rinse in cascade, 30 sec in each compartment. Agitate.

5. Place holder in a suitable container of fresh 49% HF for 2 min with agitation.
6. Rinse as in steps 3 and 4.
7. Place holder in a beaker of freshly prepared 4 to 1 to 1 HCl - H_2O_2 - H_2O at 80°C for 10 min. Agitate by hand. (Mix HCl and H_2O and bring to temperature. Three minutes before use add H_2O_2 .)
8. Rinse as in steps 3 and 4.
9. Blow dry with filtered N_2 .

REFERENCES

1. I. H. Khan and R. N. Summergrad, *Appl. Phys. Letters*, **11**, 12 (1967).
2. R. C. Henderson, R. B. Marcus, and W. J. Polito, *J. Appl. Phys.*, **42**, 1208 (1971).
3. B. A. Joyce, J. H. Neave, and B. E. Watts, *Surface Sci.*, **15**, 1 (1969).
4. D. J. D. Thomas, *Phys. Status Solidi*, **13**, 359 (1966).
5. W. Kern and D. A. Puotinea, *RCA Rev.*, **31**, 187 (1970).
6. R. C. Henderson and W. J. Polito, Unpublished results.
7. C. M. Drum and W. Van Gelder, Paper 234RNP presented at Electrochem. Soc. Meeting, Atlantic City, N. J., October 4-8, 1970.
8. C. C. Chang, in "Modern Methods of Surface Analysis," Peter Mark and Jules D. Levine, Editors, p. 53, North-Holland Publishing Company, Amsterdam (1971).
9. J. J. Lander and J. Morrison, *J. Appl. Phys.*, **33**, 2089 (1962).
10. J. A. Copeland, *IEEE Trans. Electron Devices*, **ED-16**, May 1969.
11. R. C. Henderson and Rohe F. Helm, *Surface Sci.*, To be published.
12. R. Lieberman and D. Klein, *This Journal*, **113**, 956 (1966).
13. A. S. Grove, "Physics and Technology of Semiconductor Devices," p. 74, John Wiley & Sons, Inc. New York (1967).

Thermodynamic Calculations of the Ge-H-Cl System

V. J. Silvestri*

IBM Thomas J. Watson Research Center, Yorktown Heights, New York 10598

ABSTRACT

The partial pressures of the gas species GeCl_4 , GeCl_2 , GeHCl_3 , HCl , and H_2 in equilibrium with Ge solid have been calculated in the temperature range 400° - 1223°K at chlorine to hydrogen ratios ranging from 10^{-4} to 10. The theoretical efficiency for the deposition of germanium as applied to an open tube epitaxial system is discussed. Comparisons are made to the Si-H-Cl system.

In conjunction with growth rate and surface morphology studies in the GeCl_4 - H_2 system, thermodynamic calculations giving theoretical maximum Ge deposition rates were made and compared with specific experimental Ge growth rate data (1). The purpose of this report is to separately, but more extensively describe the calculations and to display the pertinent features of the Ge-H-Cl equilibrium in a more general way. Comparable calculations have been reported by Lever (2) for the analogous Si-H-Cl system.

Equilibrium considerations in an open tube vapor growth system are useful (i) to determine a maximum yield for the system, (ii) for certain mass transport limited systems (3, 1) to predict deposition rates, and (iii) as a general guide for optimizing a process.

Assumptions.—The present analysis considered the gas species GeCl_4 , GeCl_2 , GeHCl_3 , HCl , and H_2 in equilibrium with Ge solid.¹ The important assumptions

* Electrochemical Society Active Member.

Key words: thermodynamics, germanium-hydrogen-chlorine system.

¹ Gas species such as GeH_2Cl_2 , GeH_3Cl , GeH_4 , and GeCl were not considered in the calculations, since it has been shown by Lever (2) that in the analogous Si-H-Cl system that the corresponding Si species were minor constituents.

which were made for the calculations were:

1. The above gas species are the pertinent species.
2. All chlorine containing species are confined to the gas phase in equilibrium with solid Ge.
3. It was assumed that all gas species obey ideally Dalton's and the Ideal gas law.
4. Certain assumptions were also made with regard to the constancy of ΔH°_T and ΔS°_T for specific equilibria and these shall be cited appropriately below.

Variables.—The phase rule requires that a system having three components (Ge, H, and Cl), and consisting of two phases will have three degrees of freedom. Since these calculations were made specifically with reference to an open tube epitaxial deposition system, practical considerations lead to the following choice of independent variables: (i) total pressure, where for these calculations $P_T = 1$ atm, since in most open tube systems this approximation is valid, (ii) temperature T , and (iii) the chlorine to hydrogen ratio, Cl/H , which is a conserved quantity in the gas phase.

Equilibrium.—For a given temperature the reaction chamber would contain the five gas species in equilib-

rium with Ge solid. Among the five species considered to be present in the system, three independent equilibria may be written with their associated equilibrium constants, K , where P_x is the partial pressure of the species x .



$$K_1 = \frac{(P_{\text{GeCl}_4})(P_{\text{H}_2})^2}{(P_{\text{HCl}})^4} \quad [1]$$



$$K_2 = \frac{(P_{\text{GeCl}_2})(P_{\text{H}_2})}{(P_{\text{HCl}})^2} \quad [2]$$



$$K_3 = \frac{(P_{\text{GeHCl}_3})(P_{\text{H}_2})}{(P_{\text{HCl}})^3} \quad [3]$$

Thermodynamic data.—The calculations made use of the above equations along with the appropriate van't Hoff expressions of the form

$$\log K = -\frac{\Delta H}{2.303 RT} + \frac{\Delta S}{2.303 R} \quad (R \text{ is the gas constant})$$

relating the equilibrium constant with temperature T written below

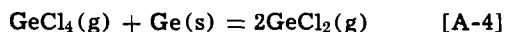
$$\log K_1 = \frac{6730}{T} - 8.02 \quad [1a]$$

$$\log K_2 = \frac{-465}{T} + 1.12 \quad [2a]$$

$$\log K_3 = \frac{7580}{T} - 7.45 \quad [3a]$$

The linear relationship for $\log K_1$ (Eq. [1a]) is the best fit of K_1 values for a number of temperatures in the temperature interval 400°–1100°K. The K_1 values were calculated from room temperature enthalpy and entropy of formation data for Ge(s), H₂(g), HCl(g) (4), and GeCl₄(g) (5) corrected for higher temperatures using the tables of Kelley (6).

Sedgwick's (7) equilibrium data, Eq. [4a], for the reaction



$$\log K_4 = \frac{-7660}{T} + 10.25 \quad [4a]$$

was used along with Eq. [1a] to obtain Eq. [2a]. The reported K_4 data for reaction, Eq. [A-4], was extrapolated to include the entire range of the calculations.

Thermodynamic data for GeHCl₃ is not known, and the room temperature enthalpy and entropy of formation were estimated by linear interpolation for the series GeH₄, GeH₃Cl, GeH₂Cl₂, GeHCl₃, and GeCl₄. This procedure is based on the assumption that bond energies are additive in generating the above series. Approximations of this type have been found to be valid in the analogous carbon series, and were used in estimating heats for the Si series (2). Using this method, ΔH°_{298} for GeHCl₃ was estimated at $-90 \text{ kcal} \pm 10 \text{ kcal}$ from the room temperature enthalpy of GeCl₄ and the reported enthalpy of 21.6 kcal for GeH₄ (8). An interpolated room temperature entropy of 75.6 eu was used for GeHCl₃, since the linear assumption was found to hold well for the above series for calculated values of GeH₄, GeHCl₃, and GeCl₄ as reported by Kelley (9). Equation [3a] was obtained assuming that ΔH°_{298} and ΔS°_{298} for reaction, [A-3], is constant over the temperature range of the calculations.

Because of the large uncertainty in the thermodynamic constants for GeHCl₃ the enthalpy of formation was varied in the calculations using values of -100 and -85 kcal . The effect of these enthalpy value

changes on the calculations shall be discussed later. Equation [3a] has been written using a -100 kcal enthalpy value for GeHCl₃(g). Dalton's law and Ideal gas law—from Dalton's law we have that the total pressure

$$P_T = P_{\text{GeCl}_4} + P_{\text{GeCl}_2} + P_{\text{GeHCl}_3} + P_{\text{H}_2} + P_{\text{HCl}} = 1 \text{ atm} \quad [5]$$

Conservation of Cl, H, Ge in the system.—The following conservation equations have been written in terms of partial pressures which are convenient to the calculations, since it has been assumed that the partial pressures of each species is related to its molar density in the system by the Ideal gas law $PV = nRT$. The following summations may be written

$$P_{\text{Cl}} = 4P_{\text{GeCl}_4} + 2P_{\text{GeCl}_2} + 3P_{\text{GeHCl}_3} + P_{\text{HCl}} \quad [6]$$

$$P_{\text{H}} = 2P_{\text{H}_2} + P_{\text{GeHCl}_3} + P_{\text{HCl}} \quad [7]$$

$$P_{\text{Ge}} = P_{\text{GeCl}_4} + P_{\text{GeCl}_2} + P_{\text{GeHCl}_3} \quad [8]$$

From Eq. [6–8] we can readily evaluate the various component ratios, such as

$$\text{Cl/H} = \frac{P_{\text{Cl}}}{P_{\text{H}}}, \quad \frac{\text{Ge}}{\text{Cl}} = \frac{P_{\text{Ge}}}{P_{\text{Cl}}}, \quad \text{and} \quad \frac{\text{Ge}}{\text{H}} = \frac{P_{\text{Ge}}}{P_{\text{H}}}$$

A convenient ratio to consider in this case is the Cl/H ratio. This ratio is an independent variable controlled experimentally, and is conserved in the gas phase. Thus the chlorine to hydrogen ratio at equilibrium, Cl(e)/H(e), is equal to the chlorine to hydrogen ratio at input, Cl(i)/H(i), and

$$\frac{4P_{\text{GeCl}_4}}{2(1 \text{ atm} - P_{\text{GeCl}_4})} = \frac{\text{Cl(i)}}{\text{H(i)}} = \frac{\text{Cl(e)}}{\text{H(e)}} \quad [9]$$

where P_{GeCl_4} is the partial pressure of the GeCl₄ in the gas stream, and $(1 \text{ atm} - P_{\text{GeCl}_4}) = P_{\text{H}_2}$.

Since we are interested in evaluating an efficiency for the system which describes the amount of dissolution of Ge in the gas phase or deposition of Ge from the gas at equilibrium, the Ge(e)/Cl(e), the Ge to chlorine ratio at equilibrium corresponding to a particular Cl(i)/H(i) must also be evaluated. The change in the Ge/Cl ratio from the input value can then be written in terms of an efficiency factor, α , as defined by Sedgwick (9) where

$$\alpha = \frac{\frac{\text{Ge(i)}}{\text{Cl(i)}} - \frac{\text{Ge(e)}}{\text{Cl(e)}}}{\frac{\text{Ge(i)}}{\text{Cl(i)}}} \quad [10]$$

The $\frac{\text{Ge(i)}}{\text{Cl(i)}}$ at input refers to the input gas consisting of GeCl₄ and hydrogen, and is therefore 0.25.

The factor, α , which is a function of T , and Cl/H, where total pressure is assumed constant may change from 1 through 0 to negative values. Thus a positive value of α predicts germanium deposition ($\alpha = 1$ indicating 100% Ge deposition from the gas phase); $\alpha = 0$ to no net deposition, since $\frac{\text{Ge(i)}}{\text{Cl(i)}} = \frac{\text{Ge(e)}}{\text{Cl(e)}}$; and negative values of α to various degrees of etching.

Method of calculation.—The calculations described below for the Ge-H-Cl employed a parametric approach which has been described in detail by Darken (10) and Lever (2). In such an approach one specifies a partial pressure ratio at equilibrium which allows one to calculate many sets of numerical values of the equilibrium partial pressures which are consistent with the values of the equilibrium constants and the total pressure. By evaluating $\frac{\text{Cl(e)}}{\text{H(e)}}$ and using Eq. [9] one can relate these solutions to a particular $\frac{\text{Cl(i)}}{\text{H(i)}}$.

For these calculations the quantity $P_{HCl}/P_{H_2} = X$ was chosen.

By substituting for the partial pressures in Eq. [5] in terms of the appropriate K , X , and P_{HCl} from Eq. [1-3] one obtains

$$(P_{HCl})^2 [K_1 X^2 + K_3 X] + P_{HCl} \left[K_2 X + 1 + \frac{1}{X} \right] - 1 = 0$$

This quadratic equation can be readily solved for P_{HCl} by specifying a value for X for a given temperature, and employing Eq. [1a-3a]. The other partial pressures and component ratios of interest may then be readily evaluated.

Results and Discussion

Calculations of partial pressures of all species, the $Ge(e)/Cl(e)$ and Cl/H ratios, and α were made in the temperature range 400°-1223°K for a total pressure of 1 atm. The computer calculations were made using an APL program on IBM System 360.

The results are graphically displayed in Fig. 1-9. In Fig. 1-4, the partial pressures of the different species together with the $Ge(e)/Cl(e)$ ratio have been plotted as a function of temperature for specific Cl/H ratios. For increasing Cl/H it is noted that in general the formation of $GeHCl_3$, $GeCl_2$, and $GeCl_4$ is favored, hence we note an increase in the equilibrium $Ge(e)/Cl(e)$ ratio. Exclusive of H_2 which is nearly always at an atmosphere, HCl is consistently the major vapor species. Normal operating conditions for epitaxial deposition systems are generally at inputs using Cl/H ratios in the 0.001 range and at temperatures of 759°C or higher (Fig. 2). It will be noted that the major chlorine containing species under these conditions are HCl and $GeCl_2$. For any given Cl/H condition (Fig. 1-4) we note that increasing temperature causes

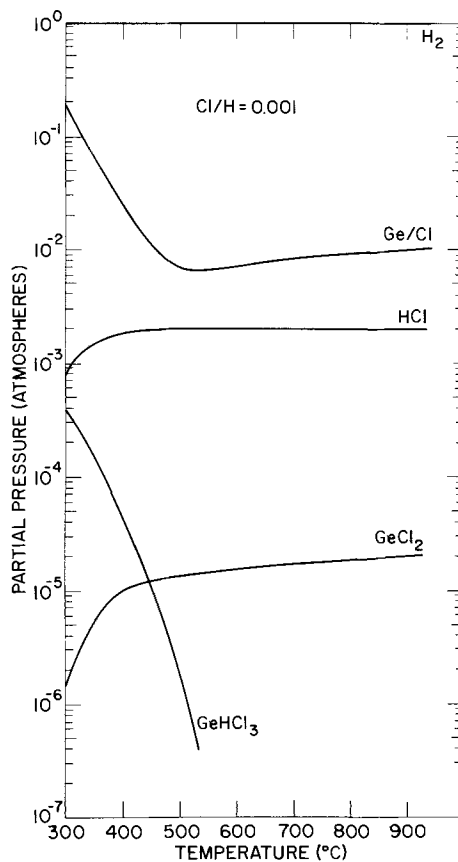


Fig. 2. Partial pressures of the various gas species vs. temperature at a total pressure of 1 atm at a chlorine/hydrogen ratio of 0.001.

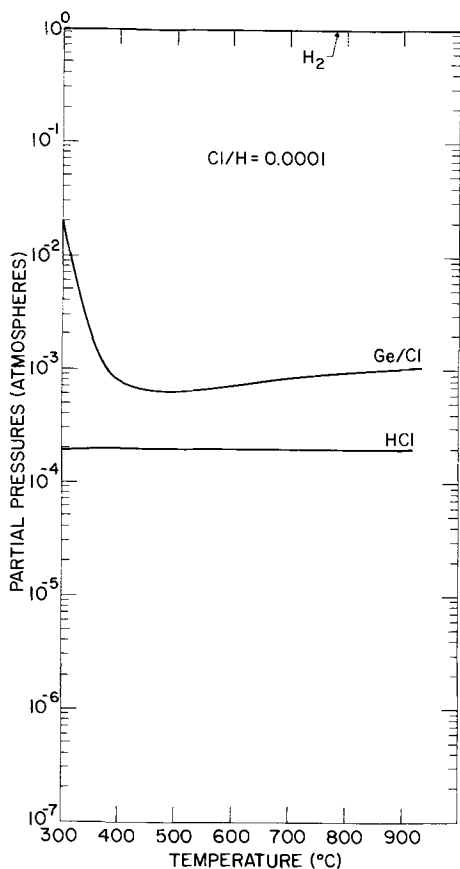


Fig. 1. Partial pressures of the various gas species vs. temperature at a total pressure of 1 atm at a chlorine/hydrogen ratio of 0.0001.

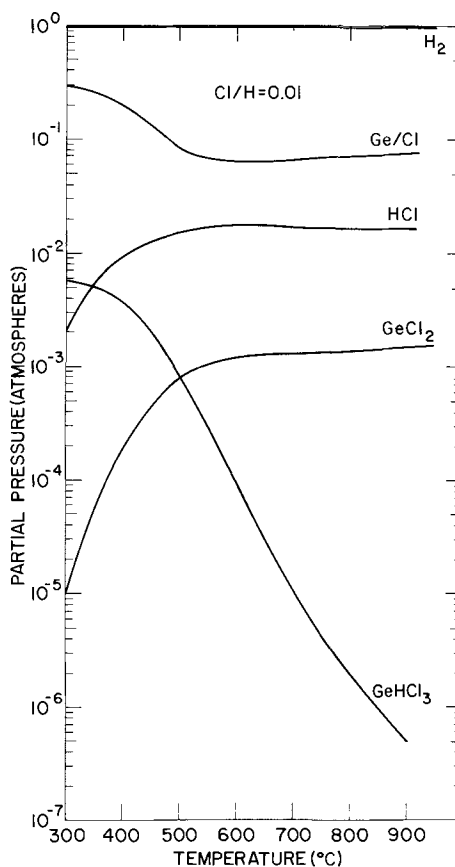


Fig. 3. Partial pressures of the various gas species vs. temperature at a total pressure of 1 atm at a chlorine/hydrogen ratio of 0.01.

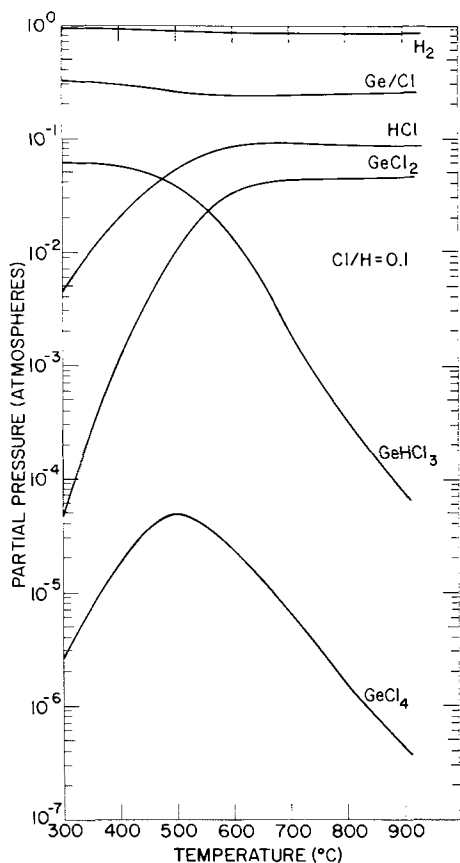


Fig. 4. Partial pressures of the various gas species vs. temperature at a total pressure of 1 atm at a chlorine/hydrogen ratio of 0.1.

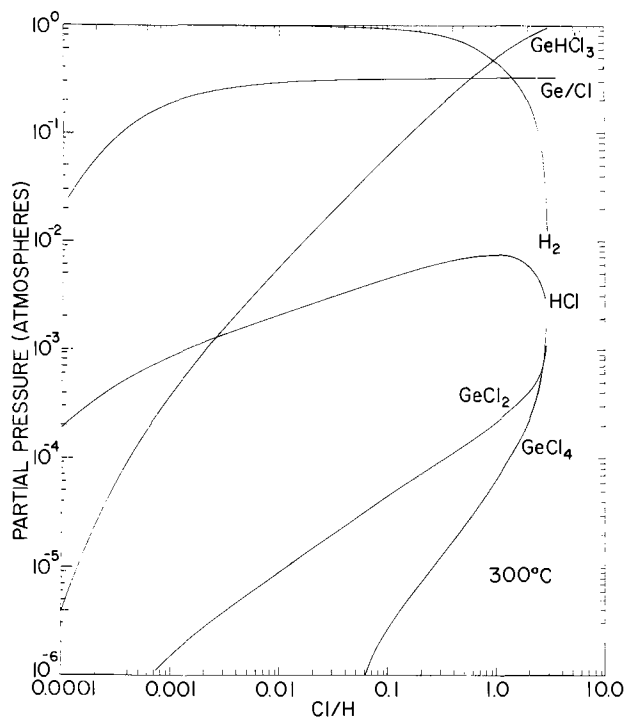


Fig. 5. Partial pressures of the various gas species vs. Cl/H ratio at a temperature of 300°C. Total pressure = 1 atm.

a reduction of GeHCl_3 pressure and an increase in GeCl_2 and HCl pressure.

In Fig. 5 and 6 the composition of the gas phase, in terms of partial pressure, is plotted for two temperatures, 300° and 800°C, respectively as a function of Cl/H ratio. For the lower temperature (Fig. 5) it can

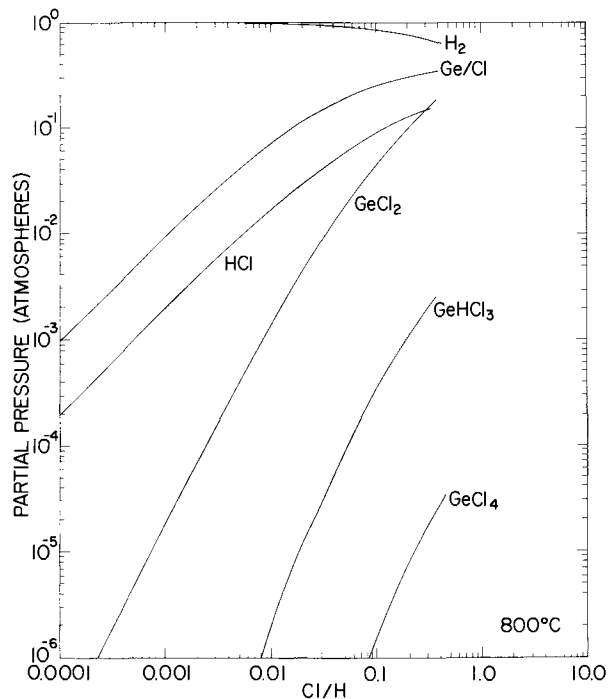


Fig. 6. Partial pressures of the various gas species vs. Cl/H ratio at a temperature of 800°C. Total pressure = 1 atm.

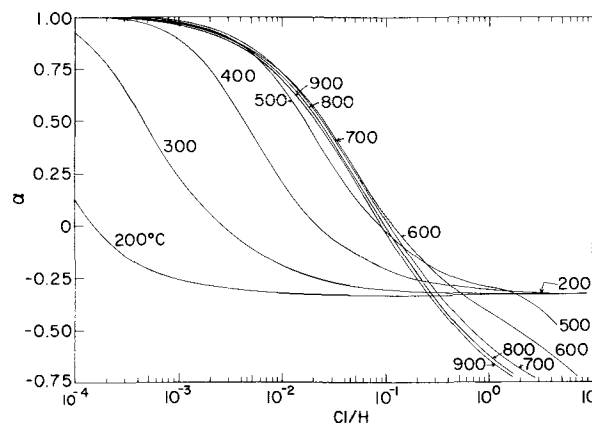


Fig. 7. Efficiency factor, α vs. Cl/H ratio for different temperatures at a total pressure of 1 atm.

be clearly seen that GeHCl_3 dominates the system as the major Ge bearing gas species, while at the higher temperature (Fig. 6) GeCl_2 is dominant. Since the formation of any Ge bearing species leads to etching, one can consider the etching to be primarily due to the formation of GeHCl_3 at lower temperatures and at higher temperatures to the formation of GeCl_2 .

In Fig. 7 the efficiency factor, α , has been plotted vs. the Cl/H ratio for specific temperatures. As might be expected from the previous figures, etching is favored ($\alpha < 0$) for all temperatures at high Cl/H input ratios. The trend of all curves toward 100% efficiency, $\alpha = 1.0$, at low Cl/H ratios correspond to a complete reduction of all Ge bearing species ($\text{Ge}(e)/\text{Cl}(e) = 0$), to form HCl and H_2 . For Cl/H values < 0.1 one observes that for the temperature interval 500°-900°C there is little change in α resulting from temperature variation. This is more clearly seen in Fig. 8 where α is plotted as a function of temperature for specific Cl/H inputs. The convergence of curves to a value of -0.33 is the result of the dominant trend for GeHCl_3 to form at low temperatures and high Cl/H ratios.

The effect of varying the enthalpy value of GeHCl_3 from -100 kcal to -85 kcal in the calculation as discussed earlier, are summarized in Fig. 9. In Fig. 9 the

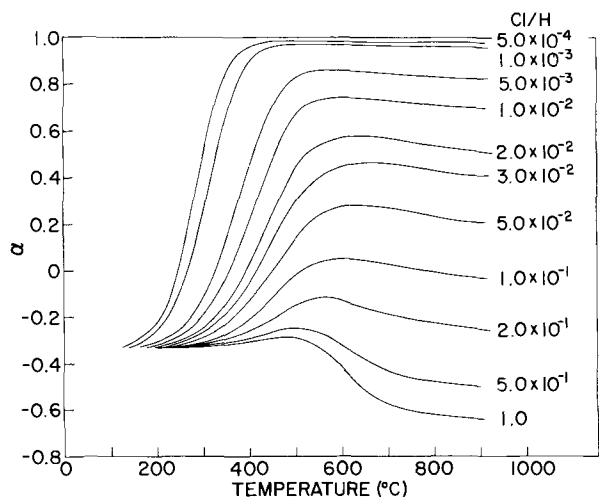


Fig. 8. Efficiency factor, α vs. temperature at different Cl/H ratios at a total pressure of 1 atm.

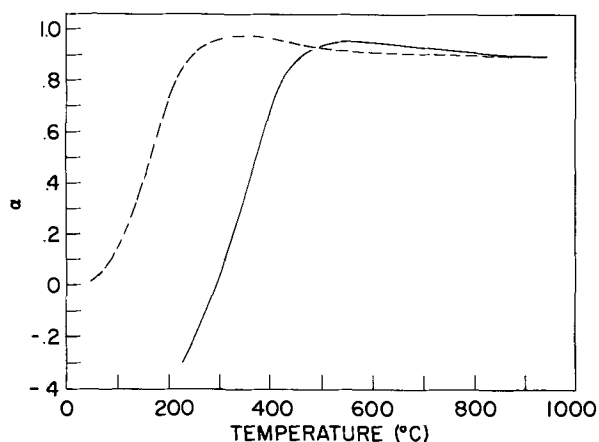


Fig. 9. Efficiency factor, α vs. temperature calculated using two room temperature enthalpy values for GeHCl_3 . Cl/H = 2.2×10^{-3} ; ---, (-85 kcal); —, (-100 kcal).

efficiency factor, α , is plotted vs. temperature for a Cl/H ratio of 2.2×10^{-3} using the indicated enthalpy values for GeHCl_3 . It will be noted that at temperatures $< 500^\circ\text{C}$, α becomes highly sensitive to the en-

thalpy value chosen. For the general calculations the more negative enthalpy value was used.

The Ge-H-Cl system is analogous to the Si-H-Cl system (2) with respect to the role that the corresponding gas species SiHCl_3 and GeHCl_3 , and SiCl_2 and GeCl_2 have on the dissolution or deposition rate. The general trends in both systems are:

1. That increased concentration of Ge or Si bearing vapor species reduces efficiency.
2. That in certain temperature intervals there is little variation of the Ge/Cl or Si/Cl ratios and hence efficiency. This results from increased formation of $(\text{M})\text{Cl}_2$ vapor species being balanced by the reduction of $(\text{M})\text{HCl}_3$ species where M can be either Ge or Si.
3. In the temperature intervals where significant variations of Ge/Cl or Si/Cl ratios occur, they are associated with the increased concentration of either $(\text{M})\text{HCl}_3$ or $(\text{M})\text{Cl}_2$.

Acknowledgments

The author wishes to gratefully acknowledge the helpful discussions with R. F. Lever, S. A. Papazian, and T. O. Sedgwick, and the programming assistance of W. J. Mesimer, M. E. Cowher, and S. A. Chan.

Manuscript submitted Nov. 15, 1971; revised manuscript received Jan. 10, 1972.

Any discussion of this paper will appear in a Discussion Section to be published in the December 1972 JOURNAL.

REFERENCES

1. V. J. Silvestri, *This Journal*, **116**, 81 (1969).
2. R. F. Lever, *IBM J. Res. Develop.*, **8**, 460 (1964).
3. T. O. Sedgwick, *This Journal*, **111**, 1381 (1964).
4. O. Kubaschewski and E. Evans, "Metallurgical Thermochemistry," Pergamon Press, New York (1968).
5. D. F. Evans and R. E. Richards, *J. Chem. Soc.*, **1952**, 1292-4.
6. K. K. Kelley, Bureau of Mines Bulletin, 584, U.S. Government Printing Office, Washington, D.C. (1961).
7. T. O. Sedgwick, *This Journal*, **112**, 496 (1965).
8. S. R. Gunn and L. G. Green, *J. Phys. Chem.*, **65**, 779 (1961).
9. K. K. Kelly and E. G. King, Bureau of Mines Bulletin, 592, U.S. Government Printing Office, Washington, D.C. (1961).
10. L. S. Darken and R. W. Gurry, "Physical Chemistry of Metals," p. 218, McGraw-Hill Book Co., New York (1953).

Some Properties of Vapor Deposited Ge₃N₄ Films and the Ge₃N₄-Ge Interface

Takehisa Yashiro

Musashino Electrical Communication Laboratory,
Nippon Telegraph and Telephone Public Corporation, Musashino-shi, Tokyo, Japan

ABSTRACT

Germanium nitride films were deposited on germanium substrates heated to 400°-600°C by vapor phase reactions of germanium tetrachloride and ammonia. The properties of these films, such as the dissolution rate and the dielectric constant, were determined as a function of deposition temperature. The masking against Sb and As was also investigated. The films exhibited an instability related to trapping at room temperature but Na⁺ ion migration was not observed under bias-temperature stress. A hysteresis of the C-V curves for metal-nitride-semiconductor structures was noted. The amount of the hysteresis depended on deposition temperatures; a deposition temperature of 550°C resulted in the smallest hysteresis. By heat-treatment in NH₃, the magnitude of the hysteresis of the samples deposited at low temperature could be diminished while the interface state densities increased.

A method for depositing Ge₃N₄ films by vapor phase reaction of germanium tetrachloride and ammonia has been reported by Nagai and Niimi (1). They investigated the physical and chemical properties of the films formed at temperatures between 400° and 600°C and reported that the films deposited at these temperatures were amorphous. When the films were kept at or above 600°C in H₂, Ar, or N₂, they were reduced or decomposed. They were crystallized by heat-treatment above 700°C in NH₃ (2).

In this study, the physical properties of the nitride films and the electrical properties of the Ge₃N₄-Ge interface were investigated as a function of deposition temperature of the nitride films. It has been found that the electrical characteristics of the Ge₃N₄-Ge interface vary with deposition temperature. It became clear that germanium nitride can be utilized as a diffusion mask for Sb and As into germanium.

Experimental

Germanium wafers used for these studies were (111) surface oriented, p-type, in the range of 0.2-3 ohm·cm. The wafers were etched in an acid containing 25 parts by volume of HF, 25 of HNO₃, and 0.75 of acetic acid with 0.2 Br₂ dissolved, and washed in distilled water. Germanium nitride was formed by reacting germanium tetrachloride and ammonia in a horizontal quartz tube with an inside diameter of 4.5 cm. The germanium tetrachloride vapor was transported to the rf-heated substrates by bubbling hydrogen through the saturator at 0°C. This gas was mixed with pure hydrogen and then with ammonia near the rf-heated substrates, as reported by Nagai and Niimi (1). Ammonia was dried by passing it through a cold trap kept at -30°C. The relative flow rates were as follows: H₂ 600 mliter/min; NH₃ 200 mliter/min; H₂ through germanium tetrachloride 200 mliter/min. Depositions were carried out at 400°-600°C.

Metal-nitride-germanium (MNS) capacitor structures for electrical measurements were formed by vacuum evaporation of either aluminum or gold on the surface of the nitride film through the mask. The area of the electrodes ranged from 3.0 × 10⁻⁴ to 4.5 × 10⁻⁴ cm².

Results and Discussion

Physical Properties

Dielectric constant and etch rate.—The thickness of the nitride films used for this experiment was 1540-1620Å and was measured by multiple beam interfer-

Key words: germanium, germanium nitride, passivation.

ometry on mechanically polished test slices. The field plates of circular dots 200μ in diameter were formed by photolithography. The capacitance of germanium nitride films was measured at 1 MHz by applying a large negative d-c bias to the field plates so that the p-type germanium surface was accumulated. From these values, the dielectric constant of germanium nitride films was calculated. The results, shown in Table I, indicate that the dielectric constant is almost independent of deposition temperature.

Since the etch rate is sensitive to the structural properties of the films, the value in H₃PO₄ at 110°C was measured as a function of deposition temperatures. The results are also shown in Table I. It is noted that at lower substrate temperatures the etch rate increases. The increase in the etch rate for the lower deposition temperatures is thought to be due to the increase of unsaturated bonds of germanium in the germanium nitride (3-5).

Diffusion masking.—When the germanium nitride film was kept at or above 600°C in H₂, Ar, or N₂, the film was reduced or decomposed (1). However, since the film was stable to 650°C in NH₃, the masking properties of the germanium nitride film on germanium were investigated in NH₃. The diffusion was carried out in an open tube system. The source material was metallic Sb kept at 525°C or As at 350°C. Because of the low diffusion constant of acceptor elements (Ga, In, B) in germanium, they were excluded from this experiment.

Nitride films 1200Å thick were deposited at 500°-550°C on the surface of chemically etched 0.2-3 ohm·cm p-type wafers in which circular dots 100μ in diameter or rings 160μ in outside diameter and 80μ in inside diameter were opened for diodes. During the diffusion process, the germanium wafers were kept at 600°C for 1-5 hr.

The results were determined by two methods: (i) the diode characteristic measurement and (ii) the hot probe method after removing the nitride film. A typical diode curve obtained by As diffusion is shown in Fig. 1. From these results, it is concluded that ger-

Table I. Dielectric constant and etch rate of Ge₃N₄

Deposition temperature (°C)	Dielectric constant	Etch rate in H ₃ PO ₄ at 110°C (Å/sec)
600	7.8	23
550	8.0	38
500	8.0	44
450	7.9	75

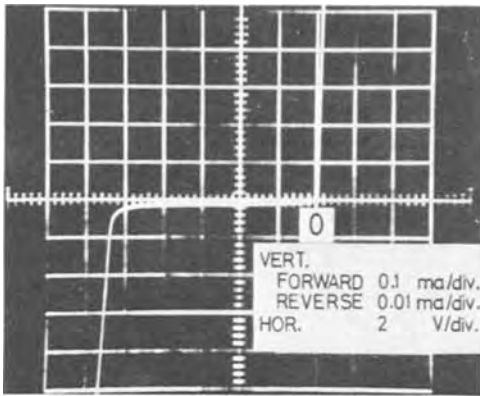


Fig. 1. Current-voltage characteristics of the germanium diode of the ring type. The substrate is $0.3 \text{ ohm}\cdot\text{cm}$ and the masking film was deposited at 500°C . The diffusion depth and surface concentration are 2.1μ and $2 \times 10^{19} \text{ cm}^{-3}$, respectively.

manium nitride films 1200\AA thick can be used as masks against the diffusion of Sb and As into germanium.

Electrical Properties

Interface properties.—The C-V curves of as-deposited Ge_3N_4 -Ge structures were obtained at room temperature and 1 MHz. Typical examples are shown in Fig. 2. The scanning speed of the bias was 4 V/sec. The theoretical curve in the absence of surface charge and interface state (6) is also shown in the figure. Hysteresis was observed for all samples investigated and its extent depended on the deposition temperature. The deposition below 500°C resulted in large hysteresis. The smallest hysteresis was obtained on the sample deposited at 550°C . The shape of the C-V curves deposited below 500°C depended on the scanning speed of the bias. The low scanning speed showed that the curve becomes flatter. On the other hand, the deposition at 600°C showed a distortion as compared to the theoretical curve, i.e., the very gradual decrease of capacitance with the bias voltages. This phenomenon would indicate a continuous distribution of states in the forbidden gap of germanium (7). The "knee" (8) or "plateau" (9) observed in the SiO_2 -Ge systems were not observed on as-deposited samples.

The direction of the hysteresis in this experiment is opposite to that which is caused by the polarization of insulators in metal-insulator-semiconductor structures (10, 11). Such a phenomenon can be explained if charges move across the Ge_3N_4 -Ge interface and are trapped (12). Since the hysteresis is thought to be related to the bulk properties of the nitride film near the

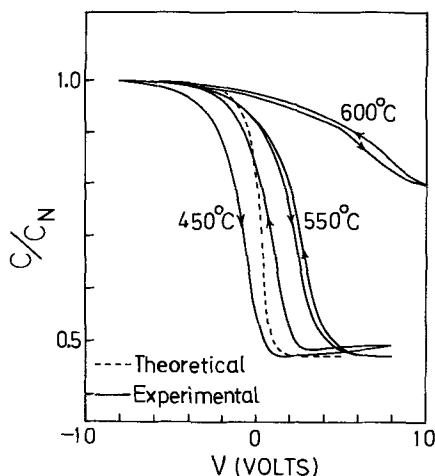


Fig. 2. C-V curves for MNS structures measured at 1 MHz showing the effect of deposition temperatures of the nitride. (p-type, $0.45 \text{ ohm}\cdot\text{cm}$; film thickness 1300\AA ; electrode Al.)

Ge_3N_4 -Ge interface, the nitride film deposited at lower temperatures may be incompletely nitrified (13-15), i.e., there will be unsaturated bonds or vacancies in germanium nitride as suggested by the fast etching rates in H_3PO_4 . On the other hand, as the origin of the interface states could be due to unsaturated bonds very near the semiconductor-insulator interface (16, 17), the high-temperature deposition is thought to make unsaturated bonds at the interface.

Heat-treatment.—It was observed that heat-treatment in NH_3 affects the shape of C-V curves, i.e., the magnitude of the hysteresis and slope variation. In this investigation, three wafers on which germanium nitride was deposited at 400° or 450°C showing the large hysteresis and two wafers on which germanium nitride was deposited at 550°C showing the smallest hysteresis, were divided into many pieces and each piece was treated at a given temperature in NH_3 . Then, gold electrodes were evaporated through the metal mask.

Typical C-V curves measured at room temperature are shown in Fig. 3. The samples were cut from the same wafer deposited at 450°C and then heat-treated at various temperatures for 30 min. The measuring frequency of 1 MHz was affected slightly by the frequency response of the interface states, so that the curves were obtained at 50 MHz to prevent the interface states from following the a-c signal. The voltages were applied from left to right. A feature of the Ge_3N_4 -Ge interface after annealing is that increasing the treatment temperature causes the curves to become flatter because the interface states continuously distribute energy throughout the bandgap (7). Sedgwick (8) and Sedgwick *et al.* (18, 19) reported the appearance of a "plateau" or "knee" in the C-V curves in the SiO_2 -Ge systems after annealing in H_2 or N_2 containing H_2 above 600°C due to monoenergetic acceptor states at the interface. They reported that the acceptor states are located at the center of the Ge energy gap. However, since the samples of Fig. 3 were heat-treated in NH_3 between 500° and 650°C , the plateau related to hydrogen was not observed. The other feature of the shape of C-V curves after annealing is the decrease in the extent of hysteresis. The polarization-type hysteresis observed by Iwauchi *et al.* (20) in the Al_2O_3 -Ge structure after annealing in N_2 was not observed in the Ge_3N_4 -Ge structure.

In Fig. 4, the interface state density N_{SS} at zero surface potential and the extent of hysteresis $\Delta N_{FB}'$ are shown. The samples in the figure were obtained from the same wafer deposited at 450° or 550°C and heat-treated at various temperatures. N_{SS} was calculated

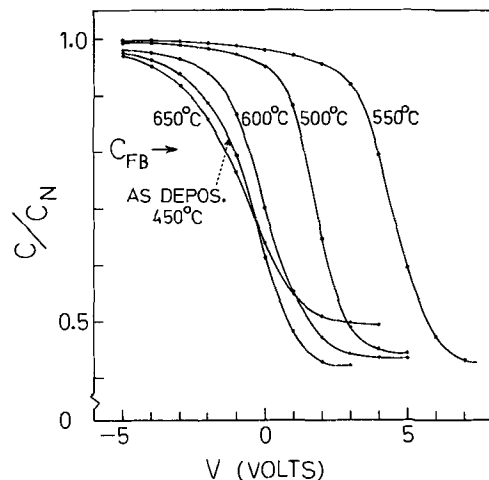


Fig. 3. C-V curves measured point by point and at 50 MHz for the samples after heat-treatment at various temperatures in NH_3 for 30 min. (p-type, $0.45 \text{ ohm}\cdot\text{cm}$; film thickness 1150\AA ; electrode Au.)

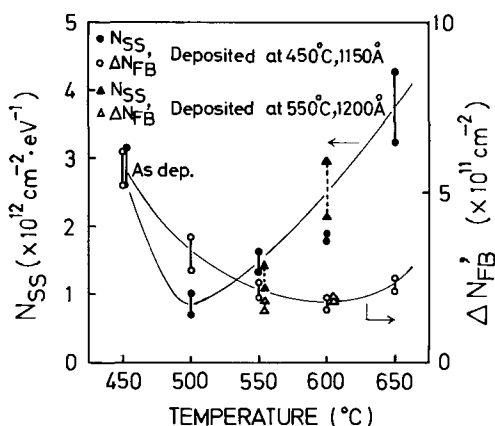


Fig. 4. Change of N_{SS} and $\Delta N_{FB}'$ after annealing at various temperatures for 30 min. The sample deposited at 450°C was the same as that in Fig. 3. The sample deposited at 550°C was 0.7 ohm-cm, 1200Å. N_{SS} and $\Delta N_{FB}'$ after annealing at 550°C for the sample deposited at 550°C were about the same.

from the C-V curves measured at 50 MHz by the following equation (21, 22)

$$N_{SS} = \frac{C_N}{q} \frac{d\Delta V(\psi_s)}{d\psi_s}$$

where C_N is the capacitance of the nitride film, $\Delta V(\psi_s)$ is the difference between the measured and ideal C-V curves, and ψ_s is the germanium surface potential. $\Delta N_{FB}'$ was calculated by $\Delta N_{FB}' = C_N \cdot \Delta V_{FB}' / q$ and $\Delta V_{FB}'$ was obtained as the difference of V at the theoretical flat-band capacitance when V was swept from positive to negative and from negative to positive values by a constant applied field swing of about -8×10^5 to $+8 \times 10^5$ V/cm. The C-V curves used to obtain $\Delta N_{FB}'$ were measured at 1 MHz and automatically plotted on an X-Y recorder by the voltage sweep of 4 V/sec. The reason for the primed $\Delta N_{FB}'$ is that the capacitance does not correspond to a true flat band condition because of the capacitive contribution of the interface state charges as stated above. The experimental results shown by bars are the upper and the lower limits of more than three measurements on the same piece.

As seen in the figure, N_{SS} and $\Delta N_{FB}'$ are reduced by heat-treatment at 500°C for the samples deposited at 450°C. Above 550°C, $\Delta N_{FB}'$ was found to decrease with increasing treatment temperature to 600°C, while N_{SS} increased uniformly. On the other hand, the reduction of $\Delta N_{FB}'$ was not clearly observed on the samples deposited at 550°C in the temperature range investigated. N_{SS} does not change at 550°C but increases at 600°C. The increasing trend of N_{SS} at 600°C is the same as that of 450°C deposited samples. These trends of N_{SS} and $\Delta N_{FB}'$ after annealing were reproducible. Only one of an anomalous curve shape observed is shown in Fig. 5. The C-V curve in this figure is similar to that of the other heat-treated samples with

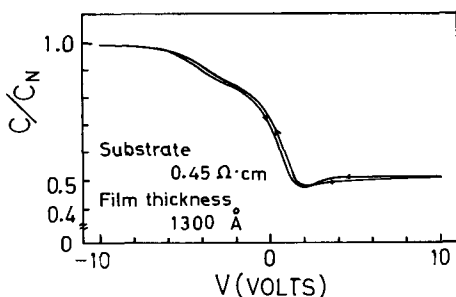


Fig. 5. C-V curve measured at 1 MHz showing a "break" after annealing at 600°C for 1 hr in NH_3 . Germanium nitride was deposited at 400°C.

regard to the increase of the interface states and the decrease of the extent of hysteresis, but a "break" appears in the curve. This result was not reproducible. The reason for the appearance of the break is not clear at the present time.

To investigate the reason for the change of N_{SS} or $\Delta N_{FB}'$, the sample deposited at 450°C was annealed at 350°C in H_2 or at 530°C in Ar for 30 min. Annealing in H_2 at high temperature was excluded because of the reduction of germanium nitride. It was found that annealing in H_2 or Ar did not reduce N_{SS} or $\Delta N_{FB}'$ compared to as-deposited structures. Therefore, the effect of annealing in NH_3 appears to be that nitrogen atoms fill unsaturated bonds in germanium nitride and reduce the hysteresis. At the same time, the reaction of germanium and nitrogen proceeds at the interface and the increase of N_{SS} results. This reaction at the interface between germanium nitride and germanium was also observed by Nagai (2).

Ion migration.—An instability related to metal-silicon dioxide-silicon structures is alkali ion migration within silicon dioxide as reported by Snow *et al.* (23). It is observed as a displacement of C-V curves along the voltage axis when the voltages are applied to the metal electrode above 150°C. The direction of the displacement is opposite to the applied voltages and the extent is a function of applied voltage, temperature, and time.

In this investigation, germanium wafers covered with 1300Å of germanium nitride were first rinsed in a solution of NaCl (0.1%) and then aluminum electrodes 200μ in diameter were deposited. The contamination of NaCl was confirmed by the microscopic observation prior to the deposition of the electrodes.

Initially, C-V curves were obtained at room temperature. The samples were then treated at 200°C, +2V on the field plate for 10 min and were cooled rapidly to room temperature with the voltage applied. Thereafter, C-V curves were traced again. The applied field during this treatment was smaller than the threshold field required for trapping of electrons (8.5×10^5 V/cm). The result of these bias-temperature treatments is shown in Fig. 6. A displacement of about 0.5V in the positive direction was observed. However, since this displacement is opposite to that of ion migration, we concluded that Na^+ ions do not migrate appreciably within the germanium nitride films.

Trapping.—When positive or negative voltages exceeding some critical values are applied to the field plate at room temperature, the shift of C-V curves in the positive or negative direction, respectively, has been observed by many investigators (12, 14, 24-27). The direction of this displacement is opposite to that caused by ion migration. The reason for this displace-

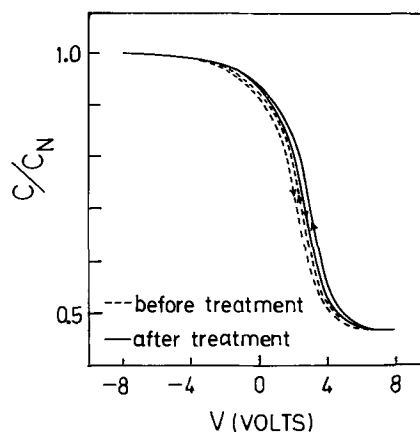


Fig. 6. Bias-temperature treatment for intentionally NaCl-contaminated Al- Ge_3N_4 -Ge structures.

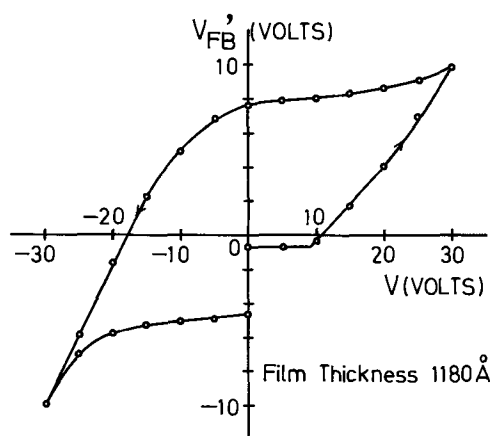


Fig. 7. Shift of V_{FB}' (see text) as a function of applied bias for 30 sec.

ment is thought to be due to trapping or releasing of carriers in the insulator.

It was found that the trapping occurs in the metal-germanium nitride-germanium system. A measurement of V_{FB}' vs. applied voltage is shown in Fig. 7. The meaning of the primed V_{FB} is the same as that given in the section on Heat-treatment. From these results, it was determined that the threshold field of the displacement is 8.5×10^5 V/cm for the positive bias.

By a combination of photon radiation and C-V measurement, trap levels in germanium nitride were investigated. It was found that there are deep and shallow electron traps in germanium nitride (28). Therefore, the positive shifts in this investigation would be caused by trapping of electrons.

Conclusion

Physical and electrical properties of germanium nitride and the germanium nitride-germanium interface were investigated. It became clear that germanium nitride can be used as a mask against the diffusion of Sb and As at 600°C in NH_3 . Na^+ ion migration was not observed by bias-temperature treatments at 200°C . The dielectric constant of germanium nitride was about 8.0 and was not significantly affected by the deposition temperatures. The etch rate depended on deposition temperature and is in the range of 23-75 Å/sec in H_3PO_4 at 110°C . The hysteresis of C-V curves was observed for all the samples and was a function of the deposition temperature. A small hysteresis in the C-V curves was obtained on samples deposited at 550°C . At lower deposition temperature the hysteresis was larger. The magnitude of the hysteresis could be reduced by heat-treatment in NH_3 while interface state density increased. The extent of the hysteresis and the interface state density for as-deposited samples at 550°C and for samples deposited below 500°C and then heat-treated at 550°C were about the same. An instability in germanium nitride due to trapping

of electrons was observed. Germanium nitride is unstable as compared with silicon nitride and is reduced or decomposed above 600°C in H_2 , Ar, or N_2 . However, the reverse characteristics of the germanium diodes that utilized germanium nitride as a diffusion mask and as passivation film were good.

Acknowledgments

The author wishes to thank Professor T. Niimi of Keio University and Mr. Igarashi for helpful suggestions throughout the work. He is also grateful to Mr. Nagai and Mr. Shibata for their discussions and Mr. Yano for his preparation of germanium nitride films.

Manuscript submitted July 20, 1971; revised manuscript received ca. Dec. 7, 1971.

Any discussion of this paper will appear in a Discussion Section to be published in the December 1972 JOURNAL.

REFERENCES

- H. Nagai and T. Niimi, *This Journal*, **115**, 671 (1968).
- H. Nagai, *Electrical Communication Laboratory Tech. J.*, **20**, 929 (1971) (in Japanese).
- T. L. Chu, C. H. Lee, and G. A. Gruber, *This Journal*, **114**, 717 (1967).
- K. E. Bean, P. S. Gleim, and R. L. Yeakley, *ibid.*, **114**, 733 (1967).
- V. Y. Doo, D. R. Kerr, and D. R. Nichols, *ibid.*, **115**, 61 (1968).
- R. Lindner, *Bell System Tech. J.*, **41**, 803 (1962).
- B. E. Deal, E. L. MacKenna, and P. L. Castro, *This Journal*, **116**, 997 (1969).
- T. O. Sedgwick, *J. Appl. Phys.*, **39**, 5066 (1968).
- T. Yashiro, *Japan. J. Appl. Phys.*, **8**, 740 (1970).
- E. H. Snow and B. E. Deal, *This Journal*, **113**, 263 (1966).
- Y. Haneta and Y. Matsukura, *Japan. J. Appl. Phys.*, **6**, 1176 (1967).
- S. M. Hu, D. R. Kerr, and L. V. Gregor, *Appl. Phys. Letters*, **10**, 97 (1967).
- T. Sugano, K. Hirai, K. Kuroiwa, and K. Hoh, *Japan. J. Appl. Phys.*, **7**, 122 (1968).
- D. M. Brown *et al.*, *This Journal*, **115**, 311 (1968).
- M. T. Duffy and A. G. Revesz, *ibid.*, **117**, 372 (1970).
- B. E. Deal, M. Sklar, A. S. Grove, and E. H. Snow, *ibid.*, **114**, 266 (1967).
- P. V. Gray and D. M. Brown, *Appl. Phys. Letters*, **8**, 31 (1966).
- T. O. Sedgwick and J. A. Aboaf, *IEEE Trans. Electron. Devices*, **ED-15**, 1015 (1968).
- T. O. Sedgwick, J. A. Aboaf, and S. Krongelb, *IBM J. Res. and Develop.*, **14**, 2 (1970).
- S. Iwauchi and T. Tanaka, *Japan. J. Appl. Phys.*, **10**, 260 (1971).
- A. G. Revesz and K. H. Zaininger, *RCA Rev.*, **29**, 22 (1968).
- Y. Haneta, *Japan. J. Appl. Phys.*, **8**, 929 (1969).
- E. H. Snow, A. S. Grove, B. E. Deal, and C. T. Sah, *J. Appl. Phys.*, **36**, 1664 (1965).
- S. M. Hu, *This Journal*, **113**, 693 (1966).
- T. L. Chu, T. R. Szedon, and C. H. Lee, *Solid-State Electron.*, **10**, 897 (1967).
- B. E. Deal, P. J. Fleming, and P. L. Castro, *This Journal*, **115**, 300 (1968).
- C. A. T. Salama, *ibid.*, **117**, 913 (1970).
- T. Yashiro, *Japan. J. Appl. Phys.*, **10**, 1691 (1971).

Crystal Growth and Isothermal Annealing of $Pb_{1-x}Sn_xTe$ Alloys

G. Dionne

Hydro-Québec Institute of Research, Varennes, Quebec, Canada

and J. C. Woolley

University of Ottawa, Ottawa, Ontario, Canada

ABSTRACT

Single crystal ingots of $Pb_{1-x}Sn_xTe$ alloys have been grown using the Bridgman technique. A study of the crystal perfection revealed that in most cases the bulk of each ingot consists of a highly perfect single crystal with no detectable grain boundaries. In addition, the "as-grown" material is highly homogeneous in both alloy composition and carrier concentration, and is free from metal precipitates. A simplified isothermal annealing technique has been used to obtain various carrier concentrations in $Pb_{1-x}Sn_xTe$ alloy samples with $x = 0.06, 0.13,$ and 0.21 . The carrier concentration in these alloys, equilibrated at the liquid + solid/solid solution boundary, has been determined for several annealing temperatures.

The alloys $Pb_{1-x}Sn_xTe$ and several other IV-VI compounds and alloys have much in common in that they have the same cubic rocksalt structure, have similar phase diagrams, can be prepared by similar methods, and their carrier concentrations can be controlled in a similar manner. These systems are often represented by the symbol MN to generalize the discussion (1), M representing the group IV elements and N the group VI elements. The use of the stoichiometric formulas MN (i.e., with the number of M atoms exactly equal to the number of N atoms) to represent these compounds and alloys is only approximate. At finite temperatures, the free energy of the crystal may be lowered by the introduction of atomic point defects, such as vacancies, and in general the compound is stable over a range of composition, called the homogeneity range, which sometimes does not include the stoichiometric composition. In undoped PbTe, SnTe, and their alloys the carrier concentration is a direct measure of the deviation from stoichiometry because the point defects, responsible for this deviation, supply practically all extrinsic carriers. While intrinsic effects and ionized impurities may also contribute to the total carrier concentration, for materials prepared from pure elements and not deliberately doped, these contributions are usually very small at low temperatures (1). In the present work, the lowest carrier concentration investigated was about 10^{17} cm^{-3} . At the temperature of the Hall measurements (77°K), the intrinsic carrier concentration will not exceed $2.2 \times 10^{13} \text{ cm}^{-3}$ for any of the three alloy compositions investigated here (2). The alloys were prepared from elements of high semiconductor purity. While the impurity content was not directly determined, as will be shown in Fig. 3 the present alloys had higher mobilities than similar alloys prepared elsewhere (3), and the latter had total p-type impurities of approximately $1 \times 10^{17} \text{ cm}^{-3}$ as found by mass spectrometry. Thus in the present work, it is reasonable to assume that the carrier concentration is a direct measure of the nonstoichiometry of the alloy except perhaps at the lowest carrier concentration values. It has been found for SnTe that each tin vacancy produces 2 holes (4-6). Brebrick (6) indicates that the hole to vacancy ratio c varies smoothly with x in these alloys and is closer to unity in the Pb-rich alloys. Thus in the present work, the value of c has been assumed to lie between 1 and 2.

Key words: nonstoichiometry, carrier concentration, IV-VI alloys, single crystals, semiconductors.

Growth and Characterization

The furnace used to grow all the crystals is shown schematically in Fig. 1, together with a typical temperature profile. The furnace consisted of a high and a low temperature section which were independently controlled. The two sections were separated by a water-cooled jacket which permitted the establishment of a steep temperature gradient. The quartz ampoule, containing the melt, was held in a mullite tube which was driven slowly in the direction of the low temperature zone. The driving mechanism was built to provide three speeds: 1.1, 3.4, and 10.4 cm/day. In addition, the furnace could be tilted as shown in Fig. 1. The temperature gradient, at the temperature of freezing, was always greater than $50^\circ\text{C}/\text{cm}$.

The melts were prepared by mixing the elements in stoichiometric proportion. Lead, tin, and tellurium, all six 9's grade, were obtained from Cominco Ltd., Montreal. Lead and tin were available in the form of rods,

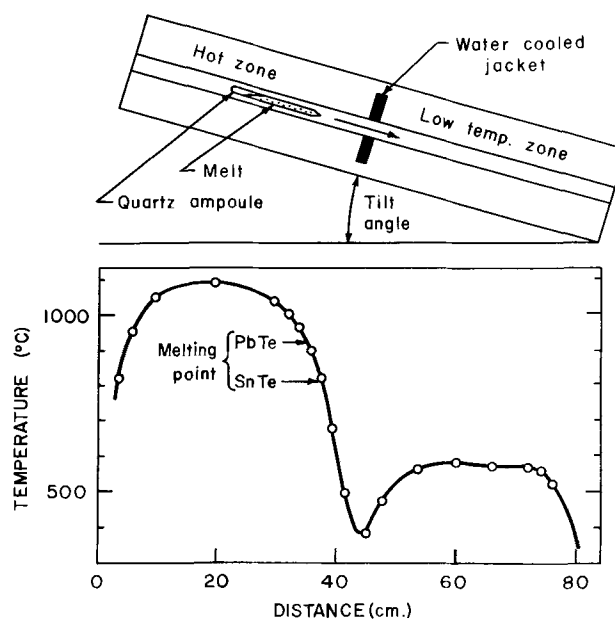


Fig. 1. Schematic of the furnace used for crystal growth and its temperature profile.

Table I. Starting composition, weight, 1st to freeze composition, and carrier concentration of $Pb_{1-x}Sn_xTe$ alloys grown by the step-freeze technique

Ingot No.	Starting x	Weight, g	1st to Freeze x	Hole carrier concentration at 77°K, cm^{-3}
2	0.2	50	0.12	$2-4 \times 10^{19}$
3	0.4	50	0.27	$7-15 \times 10^{19}$
4	0.6	50	0.45	$2-4 \times 10^{20}$
5	0.8	75	0	5×10^{20}
6	0.1	100	0.05	1.2×10^{19}
7	0	67	0	7×10^{19}
8	0.3	100	0.18	4×10^{19}

approximately 12 mm in diameter, from which sections were cut and the oxide skin removed, with a steel blade, just before use. The elements were sealed under vacuum in a 13 mm inside diameter quartz ampoule, one end of which was made conical. The ampoule was then introduced in the hot zone of the step-freeze furnace and left there, at a temperature higher than 1000°C, for at least 1 day for complete mixing. The melt was driven through the steep temperature gradient at a speed of 3.4 cm/day, the conical tip being the first to freeze.

Table I lists the $Pb_{1-x}Sn_xTe$ ingots grown using the above procedure. Ingots 2 to 4 were grown with the furnace in the horizontal position, while ingots 5 to 8 were grown with a tilt angle of 45° (Fig. 1). The main advantages of the tilted position are the following: (i) since the melt completely fills the ampoule, as shown in Fig. 1, large cross sections of crystal are obtained; (ii) there is no transport of material, through the vapor phase, over already grown material as there is in the horizontal set-up; (iii) there is no need to seal the quartz ampoules close to the material, thus oxidation during the sealing operation can be avoided.

The alloy compositions were determined using the results of Bis and Dixon (7) which showed that the lattice parameter a_0 depends upon both composition x and carrier concentration p (i.e., nonstoichiometry), but that for a fixed value of p , a_0 varies linearly with x . Thus the composition of each sample was found by measuring the carrier concentration and the lattice parameter for the sample and then using the data in Fig. 2 of Bis and Dixon (7). Composition values determined in this way were accurate to better than 1%. The lattice parameters were determined from Debye-Scherrer powder photographs taken with $CuK\alpha$ radiation and using a standard 114.6 mm diameter camera.

The $\left(\frac{\cos^2\theta}{\sin\theta} + \frac{\cos^2\theta}{\theta}\right)$ extrapolation method was used to determine a_0 . To remove any internal stress, produced during the grinding operation, the alloy powder samples to be used for the x-ray work were annealed for about 10 hr at a temperature no higher than 250°C. The accuracy of the lattice parameter so determined was $\pm 0.0005\text{\AA}$.

The starting compositions and the first-to-freeze compositions, listed in Table I, are consistent with the phase diagrams for $Pb_{1-x}Sn_xTe$ determined by Wagner and Woolley (8). As expected from this phase diagram, the growing material is always richer in PbTe than the melt. As growth slowly proceeds, the melt becomes more and more depleted of PbTe and hence a composition gradient exists along the length of the ingot. However, the composition gradient is very small in the first quarter to freeze due to the relatively small separation between the liquidus and solidus curves at a given temperature. In ingot No. 2, for example, the composition varied by less than 2% in the first quarter of the ingot to freeze.

Table I also lists the range of carrier concentrations measured in these ingots. The higher the SnTe content of the alloys, the higher are the carrier concentrations. This is due to an increasing deviation from stoichiometry as we go from PbTe to SnTe. When grown from stoichiometric melts, $Pb_{1-x}Sn_xTe$ alloys are always

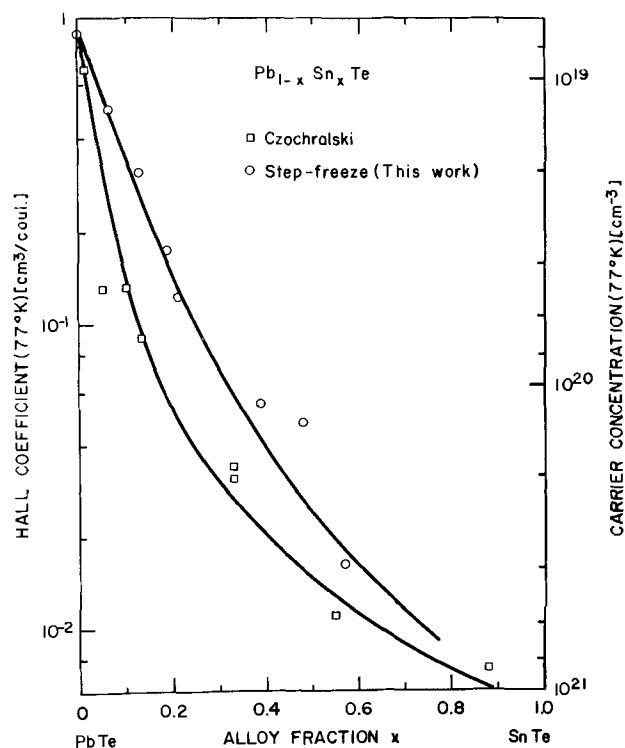


Fig. 2. Hall coefficient as a function of alloy composition in the "as-grown" $Pb_{1-x}Sn_xTe$ alloys.

tellurium rich, and this excess tellurium is accommodated in the lattice by lead and/or tin vacancies, which ionize to produce p-type carriers. That the alloys grown from stoichiometric melt are tellurium rich is clearly seen in SnTe rich ingots, for which the last to freeze is always a small amount of pure tin. Brebrick (4) showed that the point defects in SnTe were tin vacancies and that the carrier-to-vacancy ratio was approximately 3. But Brebrick calculated the carrier concentration using $p = 1/R_0e$, in which R_0 is the low field Hall constant and e is the electronic charge. When using the correct expression for the carrier concentration, $p = r/R_0e$, with the values for r given by Tsu *et al.* (9), the carrier-to-vacancy ratio becomes 2. This agrees with the intuitive notion that an ionized divalent (Sn^{++}) vacancy produces exactly 2 carriers. The increase of carrier concentrations from PbTe to SnTe is almost a hundredfold for ingots grown from stoichiometric melts (see Table I), suggesting that tin vacancies are more easily generated than lead vacancies.

Several circular disks cut from ingots No. 6 and No. 8 were lapped with coarse powder to produce microcleavages over the surface of the disks. By using a distant source of light, any small angle grain boundaries could be detected with a high degree of accuracy by observing the reflection from the numerous {100} microcleavage planes. A detailed examination revealed that the ingots were single crystal over their whole length with small grain boundaries predominantly in a small first-to-freeze region and near the surface of the ingots. With each circular disk so treated, the examination showed that more than 50% of its volume was single crystal with no detectable grain boundary, while the remaining volume had small angle grain boundaries present, the angles varying from about 2° to 5°. With ingots No. 6 and No. 8, x-ray back reflection photographs were taken at 3 mm intervals across a diameter of a face cut parallel to the long axis of the ingot with normal incidence of the x-ray beam. These x-ray photographs confirmed some of the above observations concerning the single crystal character and the crystal perfection of the material.

The "as-grown" material was homogeneous. First, metallographic examination showed no voids, no cracks,

and no sign of metal precipitation. We believe that the small growth rate (3.4 cm/day) and the steep temperature gradient at the freezing interface ($> 50^\circ\text{C}/\text{cm}$) were responsible for the absence of metal precipitation and cellular substructure frequently observed in $\text{Pb}_{1-x}\text{Sn}_x\text{Te}$ ingots (10). Second, x-ray diffraction (Debye-Scherrer powder photographs) indicated that the alloys were single phase and of good alloy homogeneity, in all cases the α_1, α_2 doublet being resolved in the high angle lines. Third, resistivity measurements taken at two different positions along the samples, indicated that the "as-grown" material was homogeneous in carrier concentration. Several samples were measured in this way at temperatures between 4.2°K and room, and, in all cases, the two resistivity measurements agreed to better than 1% at every temperature.

Values of Hall coefficient and Hall mobility are plotted in Fig. 3 and 4. For comparison, the results of Czochralski-grown (3) single crystals are also shown. It is seen that the alloys grown by the Bridgman method in this laboratory have fewer carriers and higher mobilities. The higher mobility for a given alloy composition is probably due to the corresponding lower carrier concentration.

Isothermal Annealing

For the heat treatments, a constant temperature furnace was needed. In order to satisfy this requirement for several temperatures, an annealing furnace was constructed with two concentric furnace tubes, each with a particular type of winding. The outer heater consisted of a wire element very closely wound near each end of the furnace, and gradually more spaced towards the center of the furnace. The temperature profile of this outer heater alone thus peaked at each end and showed a minimum at the center. The inner heater was wound with a constant spacing between the turns and hence its temperature profile showed a broad maximum at the center of the furnace. For all temperatures at which the furnace was used, it was possible to find current settings on the two heaters which gave a resultant temperature variation with position of less than $\pm 1^\circ\text{C}$ over at least 15 cm. The

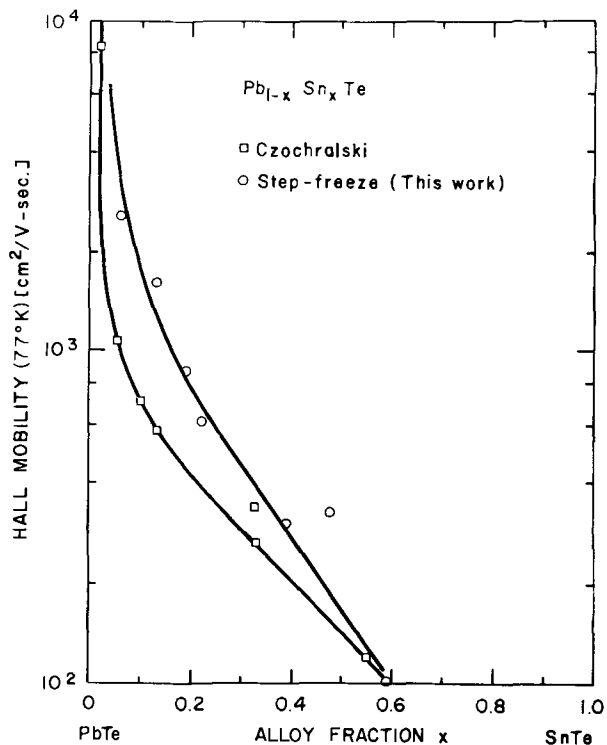


Fig. 3. Hall mobility as a function of alloy composition in the "as-grown" $\text{Pb}_{1-x}\text{Sn}_x\text{Te}$ alloys.

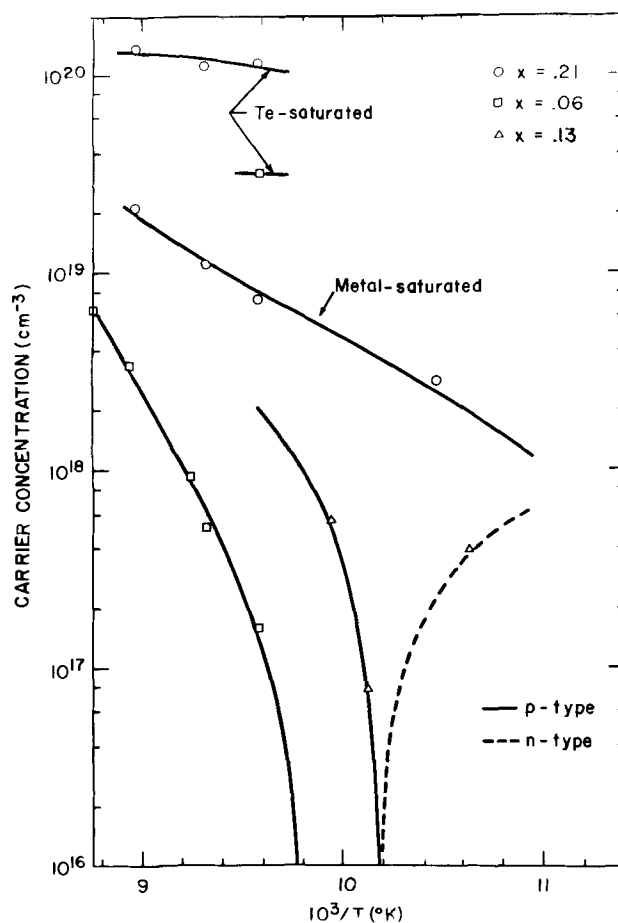


Fig. 4. Carrier concentration ($1/R_0e$) at 77°K as a function of isothermal annealing temperature for $\text{Pb}_{1-x}\text{Sn}_x\text{Te}$ alloys.

furnace temperature was maintained constant with time by a proportional control acting on the outer heater. For each annealing temperature, the appropriate value of the current in the inner heater was found by trial and error. The stability of the temperature over long periods of time was $\pm 2^\circ\text{C}$.

The explanation of the method used to control the deviation from stoichiometry in $\text{Pb}_{1-x}\text{Sn}_x\text{Te}$ requires a knowledge of the various phase diagrams used to describe nonstoichiometry in MN systems. A general review of this information has been given by Strauss and Brebrick (1). These diagrams suggest several methods by which nonstoichiometry (or carrier concentration) can be controlled. For example, the carrier concentration can be controlled by fixing the temperature and the partial vapor pressure P_{N_2} over solid MN. However, this is a technique that requires special furnaces to control the two variables P_{N_2} and T . Another more practical method was first used by Brebrick and Allgaier in PbTe (11). The technique involved the equilibration under isothermal conditions of a relatively large Pb-rich PbTe charge with a sample of PbTe . The charge and the sample were enclosed in a sealed quartz ampoule, the volume of which was made small enough to prevent any change of composition of the sample by volatilization. When equilibrium is reached, the PbTe sample lies on the Pb-rich solidus line and is made to retain that phase by fast quenching to room temperature. For alloys of the system $\text{Pb}_{1-x}\text{Sn}_x\text{Te}$, this technique would require the preparation of metal rich charges having the same Pb-Sn ratios as those of the samples to be annealed. Here a simplified annealing technique has been used.

This technique is based on the same principle as that of Brebrick and Allgaier (1, 11). If the MN system is closed and contains all three phases (liquid, solid, and vapor), it has only one degree of freedom, and hence fixing the temperature fixes the equilibrium

composition of each phase. Thus, if the composition of the charge and sample combined lies in the liquid-solid region, the solid composition and the liquid composition are fixed by the values of the solidus and liquidus lines at the annealing temperature, and the partial pressure P_{N_2} in equilibrium with the system is fixed by that temperature. When the above condition is satisfied, the composition of the sample changes by solid-state diffusion until, at equilibrium, it reaches the M-saturated or N-saturated solidus line depending on whether the charge is M-rich or N-rich. By varying the annealing temperature, solid specimens can be equilibrated to various nonstoichiometry values, corresponding to various carrier concentrations or compositions.

The simplification of the present annealing technique over those used elsewhere (11, 12) is in the use of minute charges of pure N or pure M only. Since the only requirement is that the composition of the sample and charge combined lie between the solidus and the liquidus curve at the annealing temperature, the amount of M or N needed is given by

$$\text{atoms of M or N} > \left\{ p \text{ (sample)} - p \text{ (at the solidus line)} \right\} V/c \quad [1]$$

in which p is the carrier concentration, V the volume of the sample, and c is the number of carriers per vacancy, c lying between 1 and 2. For example, consider a PbTe sample, with 2×10^{19} holes cm^{-3} and of dimensions $0.1 \times 0.3 \times 1.0 \text{ cm}^3$, which is to be equilibrated at a temperature for which the Pb-saturated solidus line is at the stoichiometric composition. The number of atoms of pure Pb required is given by Eq. [1] and is $> 6/c \times 10^{17}$. Thus only a little over $0.2/c$ mg of pure lead, introduced in the quartz ampoule with the PbTe sample, is necessary to equilibrate the sample to the stoichiometric composition. The exact amount is not critical and in general more than the amount calculated from Eq. [1] can be used to allow for the uncertainty in the exact value of c and to ensure that the composition of the charge and the sample together is well into the liquid-solid region. At the start of the annealing, the Pb charge is liquid. The excess tellurium in the sample is transferred (*via* vapor phase) to the charge until the charge has collected enough Te to cross the liquidus line. Then, the charge will be partly liquid and partly solid until equilibrium is reached. At equilibrium, the sample is lead saturated and lies on the solidus line. If the amount of pure lead used is so large as to prevent the charge from reaching the liquidus line before the sample reaches the solidus line, then surface melting of the sample will occur to provide the extra Te needed by the charge to reach the liquidus line. Thus, in order to prevent melting of the sample, an upper limit to the amount of pure Pb used as a charge is determined by the position of the liquidus line in the T-x projection [Fig. 1 of Ref. (1)]. This limit is given by

$$\text{atoms of M} < \frac{\Delta pV}{c} \left(\frac{1-x}{x} \right) \quad [2]$$

$$\text{atoms of N} < \frac{\Delta pV}{c} \left(\frac{x}{1-x} \right) \quad [3]$$

in which $\Delta pV/c$ is the right hand side of Eq. [1] and x is the composition of the appropriate liquidus at the annealing temperature. For example, in PbTe $x = 0.1$ at 700°C for the Pb-rich liquidus. From Eq. [2], we find $9(\Delta pV/c)$ as the upper limit to the number of atoms in the Pb charge.

For the $\text{Pb}_{1-x}\text{Sn}_x\text{Te}$ alloy samples, the charges used for N- and M-saturation were pure tellurium and a mixture of lead with tin respectively. The mixtures of lead with tin, at 5 atomic per cent (a/o) intervals, were prepared by melting the elements together at a high temperature and then quenching rapidly. For M-

saturation, the mixture having the closest Pb-Sn ratio to that of the $\text{Pb}_{1-x}\text{Sn}_x\text{Te}$ sample to be equilibrated was used. It was not necessary to have exactly the same Pb-Sn ratio in both the charge and the sample because the charge was minute and could not produce an appreciable change in composition x of the much larger $\text{Pb}_{1-x}\text{Sn}_x\text{Te}$ sample. The charges were weighed using a precision balance, and ranged in weight from 0.1 to 1.3 mg. Each sample and its charge were encapsulated in a small quartz ampoule, which was evacuated and backfilled with $1/3$ atmosphere of argon to minimize thermal etching of the specimens (12). After the specimens had been equilibrated, the quartz ampoules containing the samples were rapidly quenched in water.

The main advantage of the present annealing technique are: (i) the preparation of the charge is simple and the equality of its Pb-Sn ratio to that of the sample is not as critical a requirement as it was in previous techniques (11, 12); (ii) the sample and the small charge can easily be separated inside the quartz ampoule and hence no complications such as a "tube within a tube" (12) are necessary to keep them separated; (iii) owing to the small size of the quartz ampoules, it is easier to have the whole ampoule in a region of constant temperature in the furnace. This is desirable to prevent transport of the sample, through the vapor phase, to colder regions of the ampoule; (iv) the small size of the quartz ampoule permits higher quenching rates. Fast quenching is desirable to prevent internal precipitation (1).

The results of the annealing experiments using the above technique are given in Table II for several compositions of $\text{Pb}_{1-x}\text{Sn}_x\text{Te}$ alloys. The first column gives the sample number. The second column indicates the nature of the charge (M for Pb-Sn mixture, and Te for tellurium), the amount of which was determined using Eq. [1-3] assuming a suitable value for c , and which varied from 0.1 to 1.3 mg for a typical sample volume of $0.15 \times 0.3 \times 1.0 \text{ cm}^3$. The third, fourth, and fifth column give the thickness in mm, the annealing temperature in degrees centigrade, and the annealing time in days, respectively.

The annealing times chosen should be sufficiently long for equilibration. The values of interdiffusion coefficients necessary for the calculation of equilibration times are not available for the various carrier concentrations, alloy compositions, and temperatures used in the present work. However, if the smallest of the two interdiffusion coefficients determined for PbTe

Table II. Results of isothermal saturation annealing experiments obtained from $\text{Pb}_{1-x}\text{Sn}_x\text{Te}$ alloys grown by the step-freeze technique. All carrier concentrations are p-type unless indicated (n) for n-type

Sample No.	Charge	Thickness, mm	Temp. ($^\circ\text{C}$)	Annealing time (days)	Hole carrier concentration at 77°K , cm^{-3}	Carrier mobility at 77°K $\text{cm}^2/\text{V-sec}$.
(a) Composition $x = 0.06$						
6-0	None				1.25×10^{19}	2,560
6-1	Te	1.02	771	4	3.20×10^{19}	860
6-6	M	1.56	869	4	6.41×10^{18}	4,670
6-5	M	1.3	845	8	3.33×10^{18}	7,370
6-4	M	1.1	810	4	8.00×10^{17}	12,870
6-3	M	1.4	800	6	5.06×10^{17}	14,300
6-2	M	1.42	771	4	1.56×10^{17}	14,920
(b) Composition $x = 0.21$						
8-1	None				5.10×10^{19}	612
8-3	Te	1.6	842	2 3/4	1.32×10^{20}	164
8-5	Te	1.34	771	4	1.17×10^{20}	188
8-6	Te	1.34	800	6	1.10×10^{20}	211
8-2	M	1.76	842	2 3/4	2.14×10^{19}	1,660
8-7	M	1.43	800	6	1.08×10^{19}	3,270
8-4	M	1.68	771	4	7.11×10^{18}	4,750
8-8	M	1.5	680	30	2.88×10^{18}	9,550
(c) Composition $x = 0.13$						
2-2	None				2.00×10^{19}	1,600
2-2.1	M	1.0	734	2	5.65×10^{17}	15,000
2-2.4	M	1.0	712	3	7.9×10^{18}	16,000
2-2.3	M	1.0	667	7	$3.9 \times 10^{17(n)}$	40,600

(13) is assumed to apply for the alloys, the annealing times used here were more than sufficient for equilibrium to be reached in all cases. For example, the interdiffusion coefficient for the annealing temperature of sample 8-8 is 5×10^{-8} so that it would be equilibrated after 1.1 day which is about 25 times less than the annealing time used for that sample.

As with the "as-grown" material, the homogeneity of the annealed samples were checked by measurement of electrical resistivity and Hall effect. Since during the finite quenching time following the annealing, some diffusion may take place near the surface and produce a change in carrier concentration in a thin surface layer, the annealed samples were lapped on all 6 faces to remove about 100μ of material before the Hall and conductivity measurements were made. The homogeneity in carrier concentration, which indicates whether or not equilibration was attained during annealing, was checked by measuring the resistivity at two positions along each specimen. All samples with 21% SnTe and 6% SnTe were measured in this way at temperatures from 77°K to room and in every case the agreement between the two measurements was better than 1%. However at temperatures lower than 77°K, samples No. 6-3 and No. 6-2 showed drastic changes in resistivity and Hall coefficient. It should be pointed out that for these samples with low carrier concentration and high mobility, large surface effects are not unlikely and hence the observed resistivity anomalies need not be due to bulk material inhomogeneities. For all the annealed samples, including No. 6-2, and No. 6-3, metallographic examination revealed no sign of precipitation, supporting the assumption that during quenching either no retrograde solidus line was crossed, or, if such a line was crossed, it was at too low a temperature for precipitation to occur.

Values of carrier concentration ($p \approx 1/R_0e$) and Hall mobility ($R_0\sigma$) determined at 77°K are given in the sixth and seventh columns of Table II. The variation of p with annealing temperature is also shown in Fig. 4. Similar curves were obtained by Calawa *et al.*

(12) in $Pb_{1-x}Sn_xTe$ and the general agreement between the two sets of results is good. However, our 13% SnTe curve shows a crossover temperature (from p-type to n-type) significantly higher than that reported by Calawa *et al.* (12) for the same composition. This difference could be due to the presence of ionized impurities, in addition to ionized vacancies, which would be n-type in our material or p-type in the material of Calawa *et al.*

Acknowledgment

This work constitutes part of a thesis submitted to the University of Ottawa by G. Dionne in partial fulfillment of the requirements of the Ph.D. degree in Physics.

Manuscript submitted Nov. 3, 1971; revised manuscript received Jan. 24, 1972.

Any discussion of this paper will appear in a Discussion Section to be published in the December 1972 JOURNAL.

REFERENCES

1. A. J. Strauss and R. F. Brebrick, *J. Phys. Colloque C-4*, suppl. 29, 21 (1968).
2. I. Melngailis, *ibid.*, 29, 84 (1968).
3. J. W. Wagner and R. K. Willardson, *Trans. TMS-AIME*, 242, 366 (1968).
4. R. F. Brebrick, *J. Phys. Chem. Solids*, 24, 27 (1963).
5. B. B. Houston, R. S. Allgaier, J. Babiskin, and P. G. Siebenmann, *Bull. Am. Phys. Soc.*, 9, 60 (1964).
6. R. F. Brebrick, *J. Phys. Chem. Solids*, 32, 551 (1971).
7. R. F. Bis and J. R. Dixon, *J. Appl. Phys.*, 40, 1918 (1969).
8. J. W. Wagner and J. C. Woolley, *Mater. Res. Bull.*, 2, 1055 (1967).
9. R. Tsu, W. E. Howard, and W. Esaki, *Phys. Rev.*, 172, 779 (1968).
10. J. F. Butler and T. C. Harmon, *This Journal*, 115, 67C (1968).
11. R. F. Brebrick and R. S. Allgaier, *J. Chem. Phys.*, 32, 1826 (1960).
12. A. R. Calawa, T. C. Harman, M. Finn, and P. Youtz, *Trans. TMS-AIME*, 242, 374 (1968).
13. L. Goldstein, *Compt. Rend Acad. Sci., Paris*, 268, 686 (1969).

Technical Notes



Preparation and Properties of Hexaferrite Films

R. C. Taylor* and V. Sadagopan*

IBM Thomas J. Watson Research Center, Yorktown Heights, New York 10598

Polycrystalline hexaferrite films have been prepared both by RF sputtering and chemical vapor deposition (CVD) techniques for possible semi-transparent photomask (STP) applications. Among the three hexaferrite compositions investigated, the $PbFe_{12}O_{19}$ films prepared by the CVD technique appear particularly interesting for STP applications in view of their satisfactory combination of hardness, optical transmission characteristics, and etchability. Hexaferrite films also have a potential application in the area of magnetic bubble domain devices.

The fabrication and utilization of masks is a significant aspect of the manufacture of integrated cir-

cuits. It is recognized that the quality of the circuits is largely dependent on the quality of the masks. The lack of transparency of current materials used for contact mask fabrication, such as chromium and photographic emulsions, makes it very difficult to visually align the mask with the structures underneath it, especially when the ratio of opaque to clear area is large. Recently, a number of new materials that are transparent in the visible region and opaque in the ultraviolet around 4000Å have been suggested for STP applications (1, 2, 3). The favorable optical characteristics of these materials permit the accurate visual alignment of the mask and make it possible to use much finer structures for contact printing. The general material requirements for STP applications are: (a)

* Electrochemical Society Active Member.

Key words: chemical vapor deposition, magnetoplumbite, optical transmission spectra.

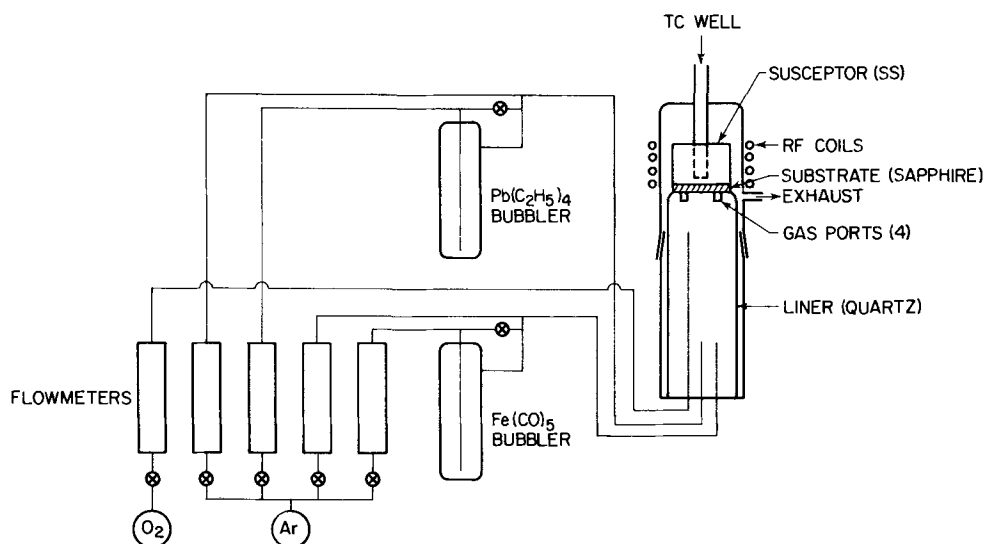


Fig. 1. Apparatus for the deposition of $\text{PbFe}_{12}\text{O}_{19}$ films by the chemical vapor deposition technique.

zero transmission in the region below 3500\AA to facilitate masking; (b) transmission of greater than 30% at 5890\AA to permit visual alignment; (c) easy etchability in solvents compatible with photoresist processing; and (d) reasonable hardness to provide durability. In the light of the above requirements, we have examined a variety of transition metal oxides in addition to those screened by Sinclair *et al.* (1). Among these, thin films of GaFeO_3 , prepared by sputtering techniques, and hexaferrite of the composition $\text{PbFe}_{12}\text{O}_{19}$ (magnetoplumbite), prepared by the CVD method, appear to be promising for STP applications. We present here the details of the CVD method of preparation of $\text{PbFe}_{12}\text{O}_{19}$ and its optical transmission characteristics and compare the optical properties of the latter with those of other hexaferrite films with compositions such as $\text{BaFe}_3\text{Ga}_4\text{O}_{19}$ and $\text{BaFe}_{8.5}\text{Al}_{3.5}\text{O}_{19}$.

Polycrystalline films of magnetoplumbite have been vapor deposited onto single crystal sapphire substrates by pyrolysis of iron pentacarbonyl and tetraethyl lead in the presence of oxygen. The structure of the films was examined by standard x-ray diffraction techniques.

The apparatus for the chemical vapor deposition of magnetoplumbite is shown schematically in Fig. 1. The reactants, tetraethyl lead and iron pentacarbonyl, are contained in two quartz bubblers which are painted black to prevent photodecomposition of the reactants into free organic radicals and $\text{Fe}(\text{CO})_9$. Each source bubbler is connected to two flowmeters, one for metering the transport argon flow and one for the argon diluent flow. The reactant and oxygen vapors feed into a vertical quartz reactor. The quartz liner inside of the reactor is tapered at the top to support the substrate and contains four slits below the substrate which serve as gas exhaust ports. A stainless steel susceptor is in contact with the upper surface of the substrate and is RF heated. The thermocouple well goes almost to the bottom of the susceptor to monitor the substrate temperature. The substrate is mounted at the top of the reactor to prevent wall deposits from falling onto it. In a typical deposition of $\text{PbFe}_{12}\text{O}_{19}$ onto a C-axis sapphire substrate, the reactant bubblers are kept at room temperature and the substrate is heated to 400°C . Argon flow is regulated to $50\text{ cm}^3/\text{min}$ through the tetraethyl lead bubbler, and $7\text{ cm}^3/\text{min}$ through the iron pentacarbonyl bubbler, resulting in transport rates of 6×10^{-5} moles/hr $\text{Pb}(\text{C}_2\text{H}_5)_4$ and 7×10^{-4} moles/hr $\text{Fe}(\text{CO})_5$. The oxygen flow rate is $50\text{ cm}^3/\text{min}$. Under these conditions, a film of approximately 1000\AA thickness is deposited in 3-4 hr. The films are polycrystalline with the standard hexaferrite structure. Attempts at film orientation by post-deposition annealing at 1000°C resulted in decomposition with the loss of PbO and a residual deposit of Fe_2O_3 on the substrate.

The effect of substrate temperature on the rate of PbO deposition by the oxidation of $\text{Pb}(\text{C}_2\text{H}_5)_4$ has been studied. The results are shown in Fig. 2. The shape of the curve shows the usual effects of kinetic control at low temperature, diffusion limitation at intermediate temperature, and gas-phase reactant depletion at higher temperature. These results were combined with those of MacChesney (2) and Carlton (4) for $\text{Fe}(\text{CO})_5$ to arrive at the approximate deposition conditions.

Thin films of other hexaferrite compositions ($\text{BaFe}_3\text{Ga}_4\text{O}_{19}$ and $\text{BaFe}_{8.5}\text{Al}_{3.5}\text{O}_{19}$) for possible STP applications have been prepared by standard RF sputtering techniques starting from either a powder target or a bulk pressed disk. The films were prepared both in argon and in oxygen atmospheres. The details of the sputtering parameters and their effect on the structure, orientation, deposition rate, and composition of the films will be presented elsewhere.

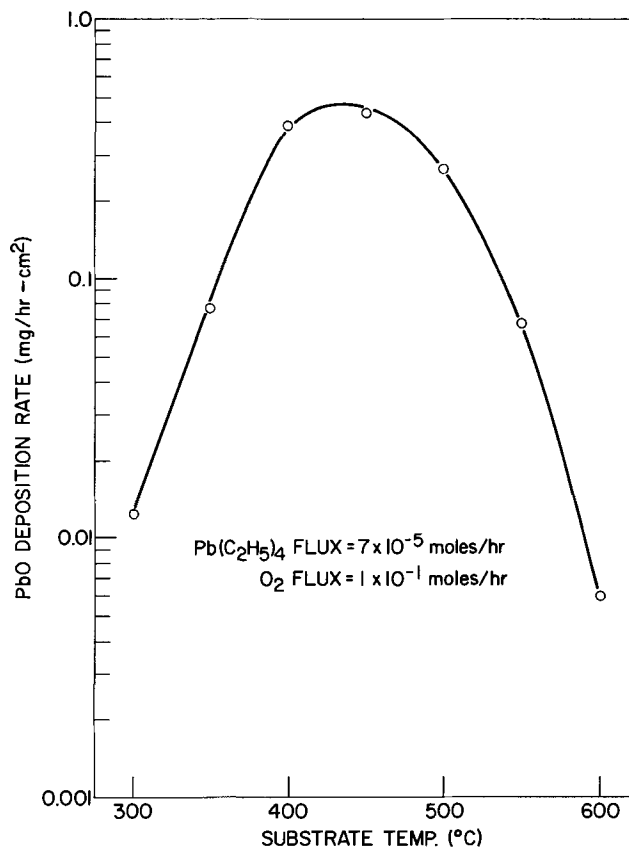


Fig. 2. Deposition rate of PbO vs. substrate temperature ($^\circ\text{C}$)

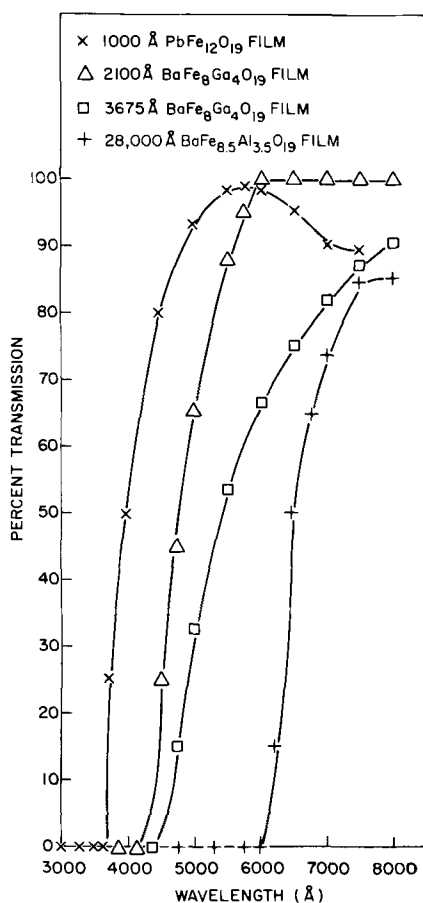


Fig. 3. Optical transmission vs. wave length of selected hexaferrite compositions; 1000Å $\text{PbFe}_{12}\text{O}_{19}$ film was prepared by CVD method; 3675Å $\text{BaFe}_8\text{Ga}_4\text{O}_{19}$ and 28,000Å $\text{BaFe}_{8.5}\text{Al}_{3.5}\text{O}_{19}$ films were prepared in argon atmosphere in contrast to the 2100Å $\text{BaFe}_8\text{Ga}_4\text{O}_{19}$ film which was prepared in oxygen atmosphere. A 2800Å argon-sputtered $\text{BaFe}_{8.5}\text{Al}_{3.5}\text{O}_{19}$ film had transmission features similar to the data presented in this figure.

All the deposited films adhered well to the substrates and could not be scratched by a stainless steel needle. Their durability is thus satisfactory although no quantitative measurement of their abrasion resistance was made. The films with thickness greater than 2000Å were free from pinholes. The optical transmission characteristics of the different hexaferrite compositions are presented in Fig. 3. The data shows that the hexaferrite films sputtered in argon ambient have a broad absorption edge in contrast to the sharp absorption edge exhibited by films sputtered in oxygen ambient. The broad absorption edge of argon-sputtered films is interpreted to arise from oxygen nonstoichiometry in such films. Among the three hexaferrite compositions investigated, $\text{BaFe}_{8.5}\text{Al}_{3.5}\text{O}_{19}$ films are not trans-

parent in the 5890Å (see-through) region (Fig. 3) and, hence, are not considered useful for STP applications. On basis of their favorable optical spectra, the vapor deposited $\text{PbFe}_{12}\text{O}_{19}$ and sputtered $\text{BaFe}_8\text{Ga}_4\text{O}_{19}$ films qualify for use in STP technology. The sputtered films, however, are remarkably resistant to chemical attack by acids that are compatible with photolithographic processing. On the other hand, vapor deposited $\text{PbFe}_{12}\text{O}_{19}$ films are readily and uniformly etched by dilute HCl (9%) at room temperature at the rate of 300 Å/min. The observed differences in the etching behavior of sputtered and vapor deposited hexaferrite films are attributed to differences in morphology of the deposits unique to the individual film fabrication techniques (2). The ease with which vapor deposited $\text{PbFe}_{12}\text{O}_{19}$ films dissolve in dilute HCl is, however, not an adequate criterion for its selection as a STP mask. An etched pattern could still be ragged if the rate of etching were distinctly different in different crystallographic directions. Etched test patterns have been obtained with satisfactory resolution. It is believed that the slow rate of deposition of $\text{PbFe}_{12}\text{O}_{19}$ is partially responsible for the uniform etching. Thus, slow deposition might be an advantage rather than a handicap for this material.

In summary, on the basis of their adequate hardness, favorable optical absorption characteristics, satisfactory etchability, and ease of fabrication, the vapor deposited films of $\text{PbFe}_{12}\text{O}_{19}$ are considered to be of particular interest for STP applications in the manufacture of semiconductor integrated circuits. Further, the optical and etching characteristics of $\text{PbFe}_{12}\text{O}_{19}$ films compare favorably with those of vapor deposited films of Fe_2O_3 , the only other material that, so far, has met the stringent criteria for masks capable of real time visual alignment. In addition to their potential usefulness for STP applications, the hexaferrites would be of considerable interest in the area of magnetic bubble domain devices if deposition conditions and substrate materials were modified in order to give single crystal films.

Acknowledgments

The authors are indebted to W. J. Haag for technical assistance in film growth and to E. A. Giess for fabrication of hexaferrite targets used in the sputtering part of the study.

Manuscript submitted Sept. 21, 1971; revised manuscript received Feb. 14, 1972.

Any discussion of this paper will appear in a Discussion Section to be published in the December 1972 JOURNAL.

REFERENCES

1. W. R. Sinclair, M. V. Sullivan, and R. A. Fastnacht, *This Journal*, **118**, 341 (1971).
2. J. B. MacChesney, P. B. O'Connor, and M. V. Sullivan, *ibid.*, **118**, 776 (1971).
3. V. Sadagopan *et al.*, Unpublished results.
4. H. E. Carlton and W. M. Goldberger, *J. Metals*, **17**, 611 (1965).

The Detection of Silicon-Oxynitride Layers on the Surfaces of Silicon-Nitride Films by Auger Electron Emission

H. G. Maguire and P. D. Augustus

Allen Clark Research Centre, The Plessey Company Limited, Caswell, Towcester, Northants., England

Considerable attention has been paid recently to the properties of silicon nitride films as the diffusion mask and gate dielectric since the advent of the insulated-gate field-effect transistor, and a great amount of effort directed toward the investigation of these films for semiconductor device applications. There are many purposes for which dielectric films may be used in devices but for most practical device applications it is normally desirable to achieve a single-phase film in order to avoid possible inhomogeneous properties associated with mixtures. In order to possess uniform properties, these films should be amorphous in structure, impervious to contaminants to reduce instability effects, and be compatible with the substrate for acceptable mechanical and electrical characteristics. Previous work (1) concerning films intermediate in composition between silicon nitride and silicon dioxide has not been clear in distinguishing between the solid solution and mixture possibilities. Recent work, however, using electron diffraction (2) indicates that the silicon nitride and silicon dioxide end members form a continuous series of solid solutions rather than mixtures. Generally, a variation in the gas composition during deposition (3, 4) influences the stoichiometry of the nitride layers which will cause the electrical and optical properties to vary.

Apart from the electron diffraction work mentioned above, there does not appear to have been any investigation using microscopic techniques on these films. However, recently, backscattering and channeling effect measurements with MeV ^4He ions have been used to analyze the composition as a function of depth of oxide and nitride layers on silicon (5). The composition was determined to be stoichiometric for high ratios of NH_3 to SiH_4 used in the deposition reaction but, for lower ratios, departures from this were found. Previously these techniques had been used to analyze ion implanted layers (6-8) and surface contamination (9), and α -particle backscattering from a radioactive source such as ^{242}Cm has also been used in chemical analyses of surfaces (10).

In view of the importance of nitride films in MNS and MNOS device fabrication, the present investigation of the surfaces onto which metal electrodes, normally aluminum, are to be deposited was undertaken using the techniques of Auger emission spectroscopy and low-energy electron diffraction. Using Auger electron emission, the surface of the sample to be studied is bombarded by primary electrons of several keV of energy while the energy distribution of the secondary and backscattered electrons is observed. Within this energy distribution, Auger electrons are observed with energies characteristic of the atoms from which they arise (11, 12). The low energies of the Auger electrons (below 1 keV) ensure that the observed effects arise from atoms very near the surface and the Auger method is particularly sensitive for the detection of the lighter elements on solid surfaces.

Experimental

The variables of importance which affect the deposition rate of Si_3N_4 and its subsequent properties are the composition and flow rate of the reactant mixture and the substrate temperature. In this work all deposi-

tions were carried out on Si substrates at a temperature of 900°C with ammonia as the major constituent in the reaction mixture. The flow rate of silane was 5 ml/min, while that of ammonia was 500 ml/min. The flow rate of the nitrogen carrier gas was 30 liter/min. Using these mixtures, the reaction kinetics taking place during the pyrolytic formation of Si_3N_4 films is quite complicated and the possible reactions that may occur have already been considered in some detail (1).

Of the many films of varying thicknesses that were grown under identical conditions, two were selected, one having a growth time of 1.5 min and the other 2.5 min, giving films of thicknesses 610 and 1010 Å, and refractive indices of 1.88 and 1.95, respectively. These quantities were determined using ellipsometry.

The Auger spectrometer used, which was modified from a LEED system (13-15), consisted of three-grid electron optics constructed in these laboratories, with the electron gun producing a beam current of about $1\ \mu\text{A}$ at normal incidence to the specimen. The specimens used were typically $1\ \text{cm} \times 5\ \text{mm} \times 0.2\ \text{mm}$ thick and were resistively heated while held in tantalum clips. A modulating frequency of 2 kHz was used throughout, and detection of the Auger signal was carried out by recording the second harmonic which yielded the derivative of the energy distribution, $dN(E)/dE$. Peak-to-peak modulation varied from 15V for detection in the higher energy range down to 3V in the lower energy range. All the observations described here were made using incident beam energies of not more than 1.5 keV.

After initial pumpdown from atmospheric pressure and overnight bakeout, a working pressure of 5×10^{-10} Torr was achieved which never exceeded 2×10^{-8} Torr during initial outgassing of the specimen. Temperatures were measured using an optical pyrometer with appropriate corrections made for emissivity and transmission through the viewport.

Both sides of the specimen were subjected to examination, and for comparison the first derivative of the energy distribution of secondary electrons from Si_3N_4 and Si is shown in Fig. 1. The peaks at 522 and 495 eV are due to oxygen and are attributed to the $\text{KL}_{2,3}\text{L}_{2,3}$ and $\text{KL}_{1,1}$ transitions, respectively (16). The peaks occurring at 389 and at 362 eV are the $\text{KL}_{2,3}\text{L}_{2,3}$ transition of nitrogen and its associated plasmon. The peak at 270 eV is the $\text{KL}_{2,3}\text{L}_{2,3}$ transition of carbon which is found on most samples freshly inserted into the UHV chamber and is increased by contamination from residual hydrocarbons during bakeout.

The remaining peaks below 100 eV from both sides of the specimen are due to silicon and reflect the effect of chemical binding. The spectrum from clean silicon which has been adequately discussed elsewhere (17-19) and will not be considered further, is shown in the upper trace of Fig. 2.

Heating the specimen at 1140°C for 5 min was sufficient to remove the oxygen from the silicon side of the specimen, but only a slight reduction in the oxygen peak was detectable on the nitride side from which practically all the carbon had desorbed. The same heat treatment for a further 20 min followed by argon ion bombardment ($1\ \mu\text{A}$ at 500V for 30 min) removed the nitrogen and remaining carbon from the silicon side,

Key words: Auger, LEED, plasmon, ellipsometry.

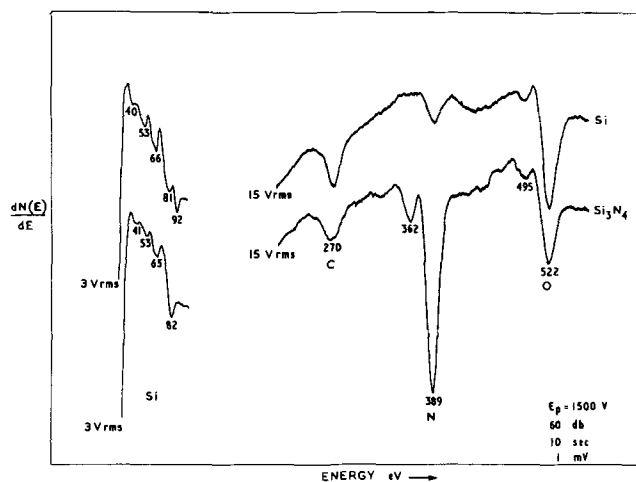


Fig. 1. The first derivative of the energy distribution of secondary electrons from Si (upper trace) and Si_3N_4 (lower trace) for the as-inserted specimen showing the presence of C and O on both sides of the specimen, together with the degraded spectrum of silicon.

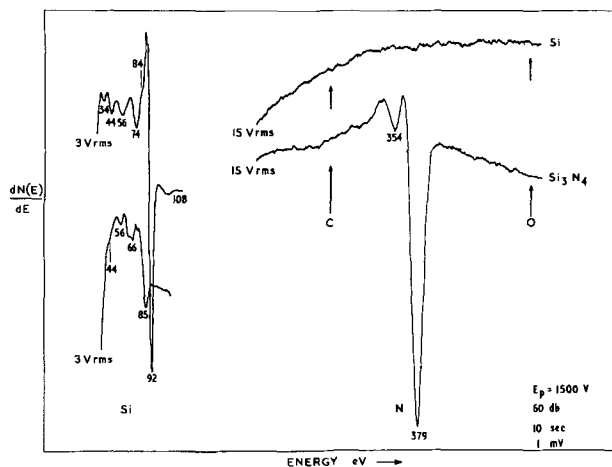


Fig. 2. The same specimen as in Fig. 1 but showing clearly the effect of the desorption of C and O from both sides of the specimen.

and was accompanied on the nitride side by an increase in the nitrogen peak.

Further heating for up to 2 hr was necessary in order to dislodge the remaining oxygen with an increase in the magnitude of the nitrogen peak to a final steady value. The silicon spectrum from the silicon side (Fig. 2) now has the character normally associated with "clean" silicon while that from the nitride has changed with the desorption of carbon and oxygen, and reflects the effect of chemical binding in the nitride.

Measurements of the thickness of the layers by ellipsometry after removal from the UHV chamber showed that they had decreased by about 30Å, and that the refractive index had increased to just over 2.0. This may be compared to a value of about 1.99 obtained with a reactant molar ratio $\text{O}_2/\text{SiH}_4 = 0$ (4).

Both specimens were scanned on a Perkin-Elmer 337 infrared spectrometer at room temperature, before and after the above-mentioned heat-treatment in UHV. No shift was found for either of the samples in the broad absorption band characteristic of the stretching of the Si-N bond. However, the absorption peaks differed for the two films; that for the thinner film occurring at about 870 cm^{-1} and that of the thicker film at about 840 cm^{-1} . Evidently the small amount of oxygen we are dealing with here limits severely any useful comparison using infrared techniques.

We have at all stages monitored the surfaces for LEED patterns and after the initial heat-treatment ob-

tained a good, clear (7×7) pattern on the silicon side. No patterns were obtained at any time from the nitride layer.

Summary and Conclusions

Amorphous layers of silicon nitride of varying thickness have been deposited on silicon substrates by the pyrolysis of silane with ammonia. Care was taken to exclude likely sources of oxygen contamination. Using Auger emission spectroscopy, we have examined the surface of these layers and of silicon on the reverse side for comparison.

Initial heating of the specimen at 1080°C for about 40 sec was sufficient to desorb the oxygen from the silicon surface but only produced a slight reduction in the size of the oxygen peak from the nitride. Further heating at 1140°C did not result in a decrease in the oxygen signal. This then would suggest that on top of the silicon nitride layer is another layer consisting of silicon oxynitride, $\text{Si}_x\text{O}_y\text{N}_z$, and further that it is about 30Å thick, as deduced by ellipsometry. It is possible that this film is more common than had been previously realized in which case one would not have a strictly metal-nitride interface but a metal ($\text{Si}_x\text{O}_y\text{N}_z$ -nitride) interface. The effect of this on film characteristics is noticeable. One notices immediately a rise in the refractive index once all the oxynitride layer has been removed by prolonged heating in ultrahigh vacuum. The differing values reported in the literature for the refractive index for zero oxygen to silane ratios may in fact be due to the presence of just such a layer. It is expected that the presence of an oxynitride layer on the nitride will influence the value of the dielectric constant but it would appear that here it is the ratio of ammonia to silane in the formation of the nitride layer that is more important. It would also be of interest to investigate the effect of these films on the I-V and C-V characteristics bearing in mind the stronger polarity dependence of the oxynitride over the nitride.

Though every precaution was taken to ensure an oxygen free system, the only plausible explanation for the presence of oxygen is as an impurity in one of the reactor gases. The fact that oxygen occurs only in the top 30Å would suggest possible contamination of the nitrogen carrier gas with water and/or oxygen, remembering, of course, that after the flow of the silane and ammonia is stopped, the specimen is left to cool with the nitrogen still on, during which time the surface of the layer remains at a sufficiently elevated temperature to react with the oxygen to form an oxynitride. Under these circumstances it would be difficult to avoid formation of such a layer at all.

In conclusion we may consider the mechanism by which the oxygen is desorbed. Assuming that oxygen on the surface from the interior is not an important factor since oxygen exchange between the surface and the bulk at temperatures below 1000°C is an exceedingly slow process (20), then removal of oxygen from the silicon is facilitated by evaporation of silicon monoxide which does not form associated molecules (21). As far as removal of oxygen from the nitride by total depletion of the oxynitride is concerned, we would tentatively suggest that silicon released from the rapid pyrolysis of silane results in a nitride layer containing excess silicon. Formation of the oxynitride then proceeds as suggested above, with the subsequent removal of oxygen by evaporation of silicon monoxide formed by the reaction of this excess silicon with the oxygen in the oxynitride layer. This process would require diffusion of the excess silicon from the nitride to react with oxygen to form volatile silicon monoxide but at a much slower rate than happens on the reverse side where silicon is readily available; hence the extended period of heating necessary to bring about removal of oxygen.

Acknowledgments

Thanks are due to The Plessey Company Limited for permission to publish these findings and to R. Oakley who prepared the specimens and carried out the ellipsometric measurements.

Manuscript submitted March 29, 1971; revised manuscript received Oct. 25, 1971.

Any discussion of this paper will appear in a Discussion Section to be published in the December 1972 JOURNAL.

REFERENCES

1. D. M. Brown, P. V. Gray, F. K. Jeumann, H. R. Philipp, and E. A. Taft, *This Journal*, **115**, 311 (1968).
2. N. C. Tombs, F. A. Sewell, and J. J. Cromer, *ibid.*, **116**, 862 (1969).
3. G. A. Brown, W. C. Robinette, and H. G. Carlson, *ibid.*, **115**, 949 (1968).
4. T. L. Chu, J. R. Szedon, and C. H. Lee, *This Journal*, **115**, 318 (1968).
5. J. Gyulai, O. Meyer, J. W. Mayer, and V. Rodriguez, *Appl. Phys. Letters*, **16**, 232 (1969).
6. L. Erikson, J. A. Davies, N. G. Johansson, and R. W.

- Mayer, *J. Appl. Phys.*, **842** (1969).
7. J. W. Mayer and O. J. March, "Applied Solid State Science," Vol. 1, p. 239, Academic Press Inc., New York (1969).
8. E. Bøgh, *Can. J. Phys.*, **46**, 653 (1968).
9. D. A. Thompson, H. D. Barber, and W. D. MacIntosh, *Appl. Phys. Letters*, **14**, 102 (1969).
10. J. H. Patterson, A. L. Turkevich, and E. Franzgrote, *J. Geophys. Res.*, **70**, 1311 (1965).
11. J. J. Lander, *Phys. Rev.*, **91**, 1382 (1953).
12. L. A. Harris, *J. Appl. Phys.*, **39**, 1419 (1968).
13. R. E. Weber and W. T. Peria, *ibid.*, **39**, 2425 (1968).
14. P. W. Palmberg and T. N. Rhodin, *ibid.*, **39**, 2425 (1968).
15. E. J. Scheibner and L. N. Tharp, *Surface Sci.*, **8**, 247 (1967).
16. J. A. Beardon and A. F. Burr, *Rev. Mod. Phys.*, **39**, 125 (1967).
17. N. J. Taylor, *Surface Sci.*, **15**, 169 (1969).
18. H. E. Bishop and J. C. Riviere, *ibid.*, **17**, 462 (1969).
19. H. G. Maguire and P. D. Augustus, *J. Phys. C. Solid State Phys.*, **4**, 174 (1971).
20. J. J. Lander and J. Morrison, *J. Appl. Phys.*, **33**, 2089 (1962).
21. W. Brewer and F. T. Greene, *J. Phys. Chem. Solids*, **2**, 286 (1957).

DISCUSSION SECTION



This Discussion Section includes discussion of papers appearing in the *Journal of The Electrochemical Society*, Vol. 118, No. 2, 9, and 12; February, September, and December 1971.

Observation of Mixed Thermoelectric Power in ThO₂

N. M. Tallan and I. Bransky (pp. 345-349, Vol. 118, No. 2)

D. S. Tannhauser¹: In the paper by Tallan and Bransky, and in a previous one by Ruka, Bauerle, and Dykstra,² the change of thermoelectric power of an ionically conducting oxide is measured when the atmosphere surrounding the sample is changed. The materials are ThO₂ in the paper being discussed, and (ZrO₂)_{0.85}(CaO)_{0.15} in the paper by Ruka *et al.*² The atmosphere varies from pure oxygen through mechanically diluted oxygen to mixtures of CO₂/CO and H₂O/H₂. The change of thermoelectric power, referred to that measured in an arbitrary standard atmosphere, is then plotted against the difference between physical quantities, which are called in these papers the partial molar entropies of oxygen, and which are calculated for the atmospheres involved. Agreement between experiment and theory is good.

It is the purpose of this note to point out that the use of the term "partial molar entropy" in these papers is wrong. This does not affect the validity of the papers but we believe it is worthwhile to point this out since the use of thermodynamic concepts in an incorrect way can be misleading and has often led to the wrong results.

According to Darken and Gurry³ the definition of the partial molar entropy of component *j* in a multi-component mixture is

$$\bar{S}_j = \left(\frac{\partial S'}{\partial n_j} \right)_{T,P,n_{i \neq j}} \quad [1]$$

Here *S'* is the total entropy of the mixture, *n_j* is the

¹ Department of Physics, Technion—Israel Institute of Technology, Haifa, Israel.

² R. J. Ruka, J. E. Bauerle, and L. Dykstra, *This Journal*, **115**, 497 (1968).

³ L. S. Darken and R. W. Gurry, "Physical Chemistry of Metals," p. 238, McGraw Hill Book Co., New York (1953).

molar fraction of component *j*, and *T* and *P* are temperature and pressure of the mixture.

Darken and Gurry³ then derive the following relation (their Eq. [10-23]) between the chemical potential and the partial molar entropy

$$\left(\frac{\partial \mu_j}{\partial T} \right)_{P,n_i} = -\bar{S}_j \quad [2]$$

In Eq. [2] the derivative with respect to temperature is calculated with all *n_i* as well as *P* constant. This derivative has a real physical meaning for a mechanical mixture of components, *i.e.*, components which do not react with each other, since there one can actually vary the temperature while keeping *P* and all *n_i* constant.

For a chemical mixture in equilibrium this derivative does not have a physical meaning. It implies clamping of the composition of the mixture (*e.g.*, CO₂, CO, and O₂) while the temperature is varied at constant pressure; and this clamping is not compatible with chemical equilibrium. However, the definition of Eq. [1] as well as the relation given in Eq. [2] still holds.

Tallan and Bransky show that the heterogeneous part α_{het} of the thermoelectric power $\alpha = \alpha_{\text{het}} + \alpha_{\text{hom}}$ of an oxide conducting by O⁼ ion diffusion can be expressed as

$$\alpha_{\text{het}} = -\frac{1}{q} \left[\frac{1}{2} \frac{\partial \mu(\text{O}_i^=)_{\text{oxide}}}{\partial T} - \frac{1}{4} \frac{\partial \mu(\text{O}_2)_{\text{gas}}}{\partial T} - \frac{\partial \mu(e^-)_{\text{Pt}}}{\partial T} \right] \quad [3]$$

They then calculate the change with oxygen partial pressure of α , after assuming that α_{hom} is independent of oxygen partial pressure and that the only term in α_{het} that depends on oxygen partial pressure is the second term on the right of Eq. [3]. This gives the equation

$$\alpha_{\text{gas 1}} - \alpha_{\text{gas 2}} = \frac{1}{49} \frac{\partial \mu(\text{O}_2)_{\text{gas 1}}}{\partial T} - \frac{1}{49} \frac{\partial \mu(\text{O}_2)_{\text{gas 2}}}{\partial T} \quad [4]$$

Equation [4] is verified by plotting experimental values for $\Delta\alpha$ against calculated values of $\Delta\partial\mu(\text{O}_2)_{\text{gas}}/\partial T$. The latter are calculated by the use of the equation

$$-\frac{\partial\mu(\text{O}_2)}{\partial T} = 2 \left[\bar{S}^\circ(\text{CO}_2) - \bar{S}^\circ(\text{CO}) - R \ln \frac{P(\text{CO}_2)}{P(\text{CO})} \right] \quad [5]$$

which is valid for a chemical gas mixture in which the ratio $P(\text{CO}_2)/P(\text{CO})$ is independent of temperature.

Tallan and Bransky as well as Ruka, who apparently did the same calculation, call the derivative in Eq. [5] the partial molar entropy and denote it by $\bar{S}(\text{O}_2)_{\text{gas}}$. This, as stated above, is not correct, since the derivative is calculated for conditions in which the partial pressure, and, therefore, the molar fraction of oxygen, is a function of temperature.

The original theory of the thermopower of chemical cells was developed by Holtan, Mazur and de Groot.⁴ After Eq. [38] of their paper, they introduce ΔS as the change of entropy due to the heterogeneous electrode reaction, but they do not call this term the partial molar entropy. We repeat again that the calculations in the paper discussed here and in the paper by Ruka *et al.*² are correct, but the use of the expression "partial molar entropy" is misleading.

Equation [4] can, incidentally, be interpreted in a manner which is more familiar to electrochemists: we can write

$$\alpha_{\text{gas}} - \frac{1}{4} \frac{\partial\mu(\text{O}_2)_{\text{gas}}}{\partial T} = \text{constant}$$

and after multiplying by dT this equation gives

$$V_a - V_b = \frac{1}{4} [\mu(\text{O}_2)_a - \mu(\text{O}_2)_b] + \text{constant}$$

which, except for the constant term, is the equation of an electrochemical cell with different oxygen activity on its two sides a and b. The constant nonzero term, generated by the temperature gradient, comes from the entropies of transport of ions in the electrolyte and electrons in the platinum electrode which are assumed in Tallan and Bransky's paper and in the paper by Ruka *et al.*,² to be independent of oxygen pressure.

Phosphorescence Decay of Calcium Oxide Activated by Yttrium

L. M. Schwarz, J. M. Voutay-Poncet, and J. Janin
(pp. 1512-1514, Vol. 118, No. 9)

W. Lehmann⁵: This paper is misleading as it implies luminescence in calcium oxide due to "activation" by yttrium, i.e., to traces of yttrium dissolved in the CaO lattice. We have looked into this system as well as into many other combinations of CaO with various other impurities. To set the matter clear, neither we nor the authors of this paper⁶ have observed any luminescence in CaO clearly attributable to yttrium. Yttrium may possibly have an influence on the trap distribution in CaO and, thus, on the decay characteristic of phosphorescence of CaO activated by whatever else it might be. However, yttrium is no activator of luminescence in calcium oxide in the commonly used sense.

L. M. Schwarz: Dr. Lehmann's comment is right. The choice of the word "activated" is wrong. The system CaO(Y) has no fluorescence. Nevertheless the CaO samples we have examined are very phosphorescent and thermoluminescent at all temperatures. The addition of small quantities of certain elements like Ga, Y, Hf, etc., increases the phosphorescence and then

⁴ H. Holtan, Jr., P. Mazur, and S. R. De Groot, *Physica*, **19**, 1109 (1953).

⁵ Westinghouse Research Laboratories, Pittsburgh, Pennsylvania 15235.

⁶ Personal communication by L. M. Schwarz.

allows the study of its decay during a very long period. That is the only purpose of this paper.

Dielectric Breakdown in Electrolytic Capacitors

F. J. Burger and J. C. Wu (pp. 2039-2042, Vol. 118, No. 12)

S. E. Libby⁷: Determination of the breakdown voltage of tantalum samples, when anodized in simple aqueous electrolytes at room temperature, was carried out. Several series of electrolytes were used. In each electrolyte series, the anion and its concentration was held constant and the cation species was varied, thereby varying the resistivity of the electrolyte solutions.

Tantalum samples were 2 × 2 cm flags with an integral tab 0.5 × 2 cm. The samples were cut from capacitor grade foil 0.001 in. thick. The samples were prepared for anodization by vapor degreasing trichloroethylene, washing in warm detergent solution, and rinsing in deionized water. Anodization was carried out using a constant current of 0.005 A/cm². The electrolyte was controlled at 25° ± 1°C and strongly stirred to avoid local heating effects.

Breakdown voltage was defined as the voltage at which the first observable deviation from linearity occurred in the voltage-time plot as recorded by a chart recorder with 10 V/in. scale factor. A VTVM with 11 megohm input impedance was used as a preamplifier to reduce loading effects. The measured breakdown voltage was corrected for IR drop in essentially the same manner as that used by Burger and Wu.

The following summary of an electrolyte series using acetate as the anion (Table I) serves to indicate the nature of the results obtained. Each electrolyte in the series was prepared in such a manner that the concentration of the acetate ion was 0.010M. Seven to ten determinations of breakdown voltage were carried out in each electrolyte.

Other series having different anions (Cl⁻ and NO₃⁻) and different anion concentrations (0.01 to 0.5M) were also used and the results were consistent: for a given anion and anion concentration, the breakdown voltage was constant and not dependent on the electrolyte resistivities.

It is obvious that these results do not remotely resemble those reported by Messrs. Burger and Wu. I can in no way account for the disagreement unless it is due to my use of electrolytes which are simple compared to those which they employed.

F. J. Burger and J. C. Wu: There are major differences in experimental technique which may account for discrepancies between our results and those of S. E. Libby. For example, he uses a current density ten times our own which was 0.5 mA/cm², also his temperature is 25°C, compared to our 85°C, his choice of acetate as the electrolyte bears a likely responsibility. Not all of our electrolytes are complicated, indeed electrolytes K, M, and O, as described in our paper, are quite simply dilute aqueous solutions containing 0.1, 0.03, and 0.01 parts by weight of phosphoric acid, respectively.

The conclusion at this stage must, therefore, be that some anomalies occurred in Mr. Libby's formation experiments which prevented the full potential of breakdown voltages from being attained. His voltages are from about 120 to 160V below what might have

⁷ Pownal Center, Vermont 05261.

Table I.

Electrolyte	Resistivity at 25°C	Mean breakdown voltage	Standard deviation
HC ₂ H ₃ O ₂	705 ohm-cm	343V	7.0V
KC ₂ H ₃ O ₂	1020 ohm-cm	350V	4.2V
Cu(C ₂ H ₃ O ₂) ₂	1900 ohm-cm	345V	5.5V

been predicted from electrolyte resistivities as supplied by him, in accordance with our experience.

The empirical linear relationship between breakdown voltage and log of electrolyte resistivity, as described by us, should be looked upon as a limiting relationship in the sense that the observed breakdown voltages have been found to be the highest attainable, provided no side reactions occur that interfere with the formation process. In the case of aluminum, we have singled out certain corrosion reactions as exam-

ples of the interference mechanisms. Anomalies of a different kind are known to occur in the tantalum system, *e.g.*, characterized by the production of the so called "gray" oxide. Whereas in the case of tantalum it has been found relatively easy to develop electrolyte systems and discover conditions that ensure trouble free anodization, this has been much less successful in the case of metals such as Nb and Zr; this latter point was briefly mentioned in our paper.



The Specific Conductance and NMR Spectra of Fused Pyridinium Salts

David S. Newman,* Walter Rohr, and Duane Kirklin

Department of Chemistry, Bowling Green State University, Bowling Green, Ohio 43403

and H. D. Frame

Department of Chemistry, Southwestern State College, Weatherford, Oklahoma 73096

ABSTRACT

The specific conductance of pyridinium HCl, N-methylpyridinium chloride, N-methylpyridinium bromide, 4-methylpyridinium bromide, and pyridinium bromide, was measured as a function of temperature. The NMR spectra of the first three fused salts were also measured over the same temperature ranges. Correlations between conductance data and spectral data were found to exist.

The experimental results indicate that the "friction" between the chloride and pyridinium ion is greater than between the bromide and the pyridinium ion. The positive charge of the pyridinium ion seems to be localized on the nitrogen. In the pyridinium HCl system the labile proton is probably contributing to the conductivity.

The present investigation focuses its attention on a series of fused pyridinium salts with the intention of correlating a transport property, the conductance, with a spectral property. The pyridinium salts were chosen for study for a variety of reasons. They are potentially very important as the conducting media in high-temperature batteries. They are useful solvents for synthetic purposes and for investigations of the structure of complex ions (1). They are low-melting, noncorrosive to Pyrex, stable over a relatively wide temperature range, and easily synthesized. Because of their low melting points, many of the pyridinium salts are accessible to study by NMR techniques as well as by more conventional means. The intriguing possibility of obtaining direct correlations between transport properties and spectral properties, therefore, presents itself.

This kind of correlation between a structural property and a transport property, though very useful, has been made in only a limited number of fused-salt systems and then only fairly crudely. For example, there is a rough correlation between ion size and mobility. The reason why the literature lacks such correlations is that transport properties result from a combination of short and long range forces, but a typical transport property experiment does not give the individual contribution of each kind of force. Spectral measurements predominately elucidate short range forces except when lattice vibrations are being studied so that both kinds of measurement on the same system under similar conditions are thus necessary to remove ambiguity and characterize the melt. The salts studied, and their melting points, are shown in Fig. 1.

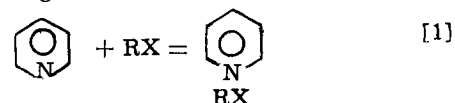
Experimental

Synthetic methods.—Each of the salts was synthesized in fundamentally the same way based on the

* Electrochemical Society Active Member.

Key words: fused salts, conductance, organic melts, NMR spectroscopy.

method first described by Rozdhestvenskii and Brode (2). The appropriate anhydrous gas, acting as a Lewis acid, reacted with pyridine [in the case of (IV), 4-methylpicoline] which acted as a Lewis base. The equation describing the neutralization reaction is



Reagent grade pyridine was dried over BaO and then distilled. The dried distilled pyridine was mixed with anhydrous reagent grade ether to form a 40% pyridine solution. The anhydrous halide gas was then

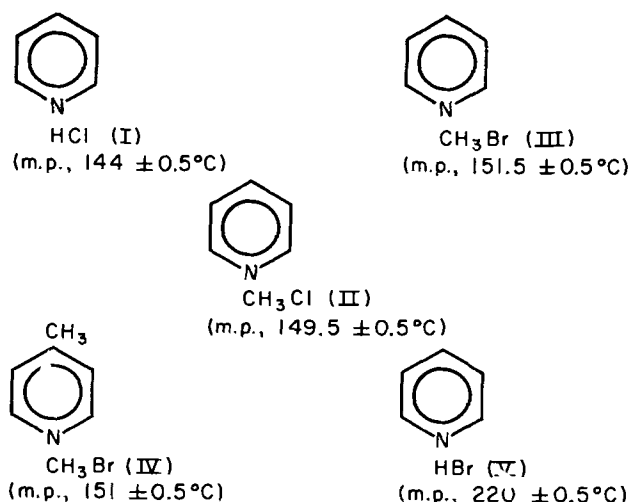


Fig. 1. (I) pyridinium HCl; (II) N-methylpyridinium chloride; (III) N-methylpyridinium bromide; (IV) 4-methyl-N-methylpyridinium bromide; (V) pyridinium HBr.

bubbled through this solution. After about 45 sec, white crystals of salt became visible. The reaction takes place in pure pyridine, but the yields of salt are better and the subsequent purification processes are easier using the pyridine-ether mixture. The reaction is slightly exothermic so the reaction flask was placed in an ice bath.

After the salt had formed, the excess ether and pyridine were removed, first by decantation and then by evaporation from a rotatory solvent evaporator. The resulting salt was identified by its infrared spectrum in a KBr pellet and by its melting point.

All transfer operations were carried out in a dry box or glove bag because the salts are hygroscopic.

Conductance measurements.—The specific conductance, κ , of each salt was measured with an Industrial Instruments bridge at 1000 Hz. The salts were contained in a Pyrex capillary cell. Cylindrical platinum electrodes were used.

The advantages of this type of cell over conventional cells for fused salt conductance measurements are many (3), but the most important advantage is that the cell constant does not vary significantly as function of temperature. The major portion of the salt's resistance occurs in the capillaries which increase in both diameter and length as the temperature is raised. A Teflon stopper, machined to fit the outer half of a 29/42 ground-glass joint, served as the top of the cell. Three holes were drilled in the Teflon stopper. Two of them were for the electrode compartments and the third was for a gas outlet tube. Using a Teflon top, rather than a glass top, made it much easier to remove the salt after an experiment and substantially increased the life span of the cell. A small hole in each of the glass tubes above the capillaries allowed trapped air and other gases to escape, thereby facilitating the rise of the fused salt into the capillary.

Dow-Corning 710 silicone oil was used as the heat transfer medium in the constant temperature bath. This oil has a flash point of 300°C. The temperature was regulated to $\pm 0.2^\circ\text{C}$. The cell constants were measured at 25°C using a 1 Demal-KCl solution. They ranged from 150 to 1500 cm^{-1} depending on the diameter of the capillaries used.

A minimum of two series of conductance measurements of each of the salt samples were made. Conductance readings were taken at 10° intervals over a temperature range bounded at one end by the melting point of each salt and at the other by the boiling point or the decomposition point of those salts that showed signs of decomposition. The system was allowed to stabilize at each temperature for 20 min. The readings at the highest temperature were taken first, then the next highest, etc. The process was then repeated. A second sample of the salt was treated in the same fashion.

NMR spectroscopy.—The NMR spectra were obtained using the variable temperature probe of a Varian A56/60A NMR machine. A sample of salt was transferred into an NMR tube in a dry box. Both hexamethyldisilane and hexamethyldisiloxane were tested as reference materials. The disilane was selected because of its higher melting point. In the subsequent discussion all chemical shifts of fused pyridinium salts will refer to this material. To correct to TMS, an addition of 3.83 Hz is required.

The NMR tubes were sealed under a partial vacuum and then removed from the dry box. The filled tubes were next placed in the oil bath. The bath temperature was raised to just over 200°C, the upper temperature limit of the NMR machine, or until the salt began to decompose noticeably. The bath temperature was then lowered to below the melting point of the salt being studied. This thermal cycling was repeated several times to assure the stability of the particular salt sample and to minimize the chance of a tube exploding in the NMR machine. After cycling, the NMR spectrum of

each salt was taken, as a function of temperature, from just below 200°C to its melting point. N-methylpyridinium chloride showed signs of decomposition at approximately 180°C so this temperature was set as an upper limit for this salt. The NMR machine was allowed to stabilize for at least 15 min at each selected temperature. In most instances sharp spectra could be obtained well below the normal melting points of the salts which implies they are easily supercooled.

Results

The conductance data measured as a function of temperature are shown in Table I. The complete NMR spectrum of (I), measured with a sweep width of 1000 Hz at 156°C, is shown at the bottom of Fig. 2. The ring protons are emphasized using the slower sweep (250 Hz) at the top of Fig. 2. The entire spectrum is offset 100 Hz.

The chemical shifts of the ring protons as well as the chemical shift of the R group attached to the nitrogen are listed for all three compounds in Table II. The chemical shifts of the α , β , and γ hydrogens of (III), dissolved in DMSO, are also listed, with an asterisk, in the table for comparison (4).

The coupling constant, $J_{\beta\gamma} = \delta_\gamma - \delta_\beta$, was essentially the same for all four systems and had a value of 3.6 Hz with a variation of ± 0.1 Hz. This consistency in $J_{\beta\gamma}$ indicates that the coupling is intramolecular and not affected by the external field.

The NMR spectrum of (V) could not be obtained because of the high melting point of this salt. The NMR spectrum of (IV) will be discussed in a subsequent paper.

Discussion

Conductance.—Focusing attention on the conductance data, several points can be made. The salts are very good conductors. Also, the principal charge carrier is the anion. This can be seen, in the absence of reliable transference numbers, by comparing the conductance of (III) and (IV) in Table I. These data compared the N-methylpyridinium ion with the 4-methylpyridinium ion because Br^- is the anion in both salts. The values of κ are nearly the same, despite differences in both size and electron density of the cations, because the more mobile species is the Br^- . The small difference that does exist in κ is also in the expected direction with (III) being the better conductor. The difference in conductance between compounds (II) and (III) in Table I further substantiates the notion that the anion is the principal charge carrier in these salts. Here, the same cations are being compared so any difference in conductance is most likely due to differences in anion size. The conductance difference is in the right

Table I. Specific conductance parameters

$$(\text{ohm}^{-1} \text{cm}^{-1}) = a + bT (^\circ\text{K})$$

Salt	— (a)	(b × 10 ³)	(σ × 10 ³) [*]	Temperature range, °K ^{**}	No. of data
PyHCl	0.5511	1.554	1.6	425-474	12
N-methyl PyCl	0.5722	1.565	1.7	419-463	8
N-methyl PyBr	0.4816	1.303	0.5	433-473	7
4-methyl N-methyl PyBr	0.5017	1.349	0.3	433-464	10
PyHBr	0.5888	1.556	1.1	504-536	9

^{*} σ is the rms deviation (in κ) of the experimental points from the calculated straight line.

^{**} Temperature range of measurements.

Table II. Chemical shifts in ppm

Compound	α	β	γ	R
pyr HCl (I)	9.45	8.55	9.05	14.71
N-methylpyr HCl (II)	9.83	8.70	9.20	4.99
N-methylpyr Br (III)	9.70	8.63	9.13	5.00
N-methylpyr Br (III) [*]	8.80	8.02	8.49	

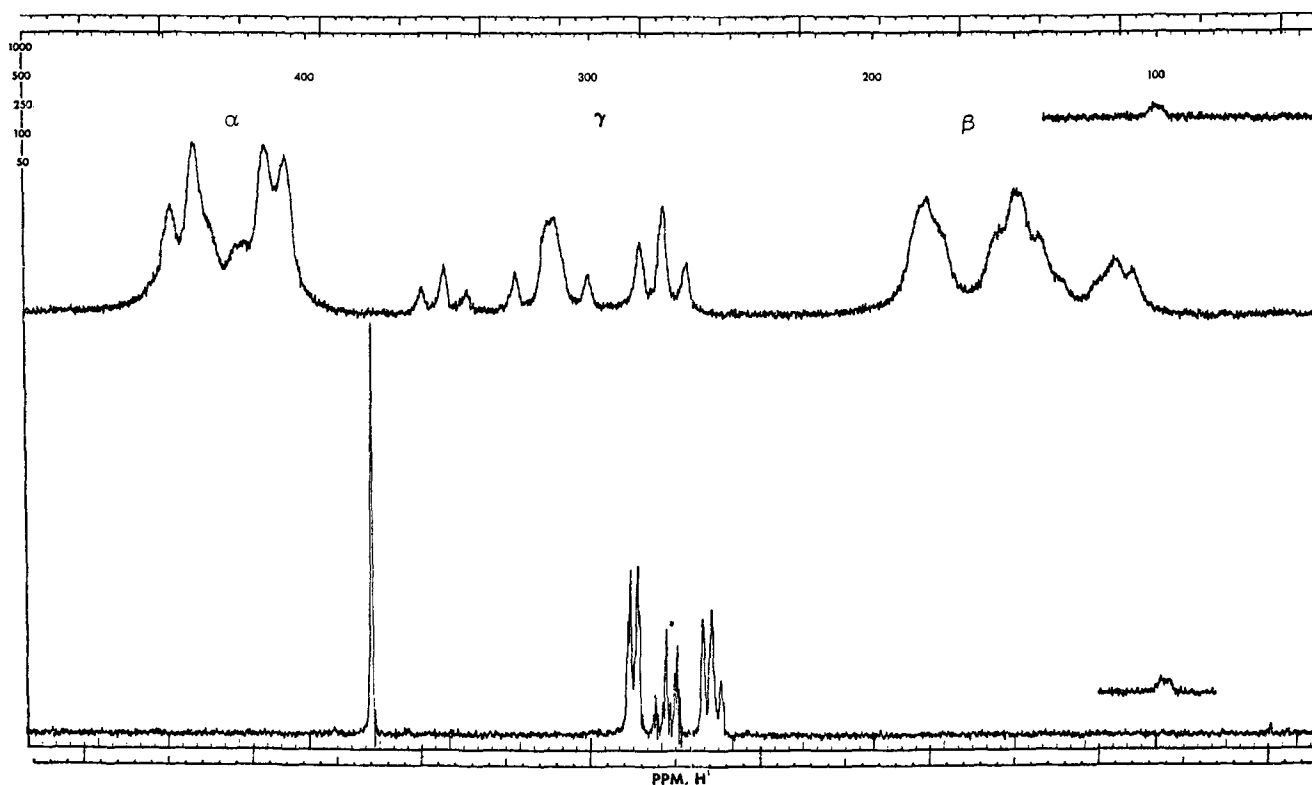


Fig. 2. NMR spectra of fused pyridinium HCl at 156°C, offset 100 Hz

direction with the Cl^- being a better conductor than the Br^- . The size of this difference is predictably larger than in the previous case because these ions carry most of the current. Since the salts are all somewhat alike, it is probable that they have similar glass transition temperatures. Therefore, comparison of conductances at the same temperatures is reasonable.

The conductance data for (I) as a function of temperature is within approximately 1% of the results published by Easteal and Angell (5). The conductance data for (II) is about 10% higher than that of Wallace and Bruins (6). A partial explanation for this discrepancy is that these authors were not especially interested in quantitative results and so used a dipping type conductivity cell which is ill suited to fused salt work. The electrodes spread apart as the temperature is raised, thereby decreasing the conductance of the salt relative to its true value based on a cell constant measured at room temperature. Their cell constant was also too small (7,8). This meant that, with the bridge employed, fairly imprecise results were obtained. A combination of these factors can easily account for the difference in the two sets of conductance data. There does not seem to be conductance data for the other fused salts in the literature.

NMR spectroscopy.—All five salts are basically AB_2X_2 systems and their spectra are extremely complex (9). The major features of the spectra are those expected for this system and are shown in Fig. 2. The α hydrogens show a nitrogen broadened doublet, the γ hydrogen appears as a triplet of triplets, and the β hydrogens give a triplet. The fine structure of the spectra will not be discussed further.

The positions of the α , β , and γ peaks were virtually independent of temperature. That is, the spectra of a given salt, taken at 10° intervals, were superimposable. This indicates no substantial change in molecular structure or aggregation as a function of temperature and probably indicates that these salts are completely dissociated in the melt even at the lowest molten temperatures.

The sharp downfield spike in the pyridinium HCl spectrum indicates a rapid exchange of protons be-

tween equivalent nitrogen sites. A similar sharp, upfield spike appeared in the spectra of (II) and (III) indicating that the methyl group is also exchanging rapidly. The position of the methyl peak seemed to be independent of the anion.

The most important differences in the spectra of the ring protons become apparent when salts (II) and (III) are compared. The three sets of protons in the chloride are all further downfield than the equivalent protons in the bromide. This indicates the interaction between the chloride and the N-methylpyridinium ion is stronger than the interaction between the bromide and the same ion. This is certainly reasonable because the chloride has a higher charge to volume ratio than does the bromide.

Correlations between NMR spectra and conductance.

—In the chloride melt the α protons are 0.13 ppm down field, relative to the protons of the bromide, whereas the β and γ protons are only 0.07 ppm down field. This implies that, as the halide ion passes by the N-methylpyridinium ion, it spends, on the average, more time in the vicinity of the nitrogen than at the opposite end of the ion. This concept leads to the likelihood that the positive charge is localized on the nitrogen atom rather than spread over the entire ion. If the charge were delocalized, the chemical shifts of the three sets of protons in the chloride salt would be about equal, relative to the same protons in the bromide salt, because the halide would pass by the center of the ion.

At this point it is useful to discuss the interaction between the halide ions and the pyridinium ion in terms of "interionic friction." The concept of friction originated in the works of Onsager and Kirkwood but the particular form of the idea that is meaningful here arose from equations of the form (10, 11)

$$\vec{F}_i = \sum_k^N \Gamma_{ik} X_k (\vec{v}_i - \vec{v}_k) \quad [2]$$

where \vec{F}_i is the force on component i , X_k the mole fraction of component k , the \vec{v}_i are the average velocities

Table III. Per cent difference in κ between chlorides and bromides in several "anion conductors"

Salts	$\Omega^{-1} \text{ cm}^{-1}$ at M.P.	Per cent difference	Best estimate for anion transference numbers
PbCl ₂	1.43	65	(0.75)
PbBr ₂	0.58		
CsCl	1.12	34	(0.60)
CsBr	0.84		
BaCl ₂	2.03	36	(0.75)
BaBr ₂	1.18		
(II)	0.115	28	> (0.75)
(III)	0.090		

of the components, and the Γ_{ik} are the friction coefficients. The Γ_{ik} are called friction coefficients because they encompass the proportionality between i relative to species k and \vec{F}_i when species i is in the environment of species k . For a particular value of \vec{F}_i and X_k , in Eq. 2, $(\vec{v}_i - \vec{v}_k)_1$ can only be less than $(\vec{v}_i - \vec{v}_k)_2$ if $(\Gamma_{ik})_1$ is greater than $(\Gamma_{ik})_2$. In other words, there must be more friction between species i and k in system 1 than in system 2. In the absence of detailed information about changes in the wave functions of the species as they pass one another, this phenomenological description is necessary.

The friction between the chloride or the bromide and the cation probably causes an unusually small percentage difference in the conductance of (II) and (III) relative to inorganic salts with the same two anions. The average drift velocity of the halides is reduced because of this interionic "friction" but the velocity of the chloride is reduced more than the velocity of the bromide. Stating it somewhat differently, there is more friction between anion and cation in the organic chloride melt than in the organic bromide melt but there is more friction in both of them than in "hard" salts. Presumably, the greater polarizability of the N-methylpyridinium ion relative to a metal ion causes the excess friction.

The plausibility of these conjectures can be further substantiated by observing the data shown in Table III. In this table the percentage difference in conductances for hard salts, in which the anion is the principal carrier, are compared (12). The number in parenthesis is the best estimate of the transference numbers (13). The data have not been corrected for this factor making them minimum per cent differences. Even so, the per cent difference between chloride and bromide is smallest in the pyridinium salts.

Another interesting correlation can be made. The conductance of (I) and (II) compares the N-methylpyridinium ion with the pyridinium ion, the Cl⁻ being common to both. These conductances should be closer together. The same anion is carrying the major share of the current which implies that the salts should show nearly the same per cent difference in κ as (III) and (IV) where the N-methylpyridinium ion is being compared with the 4-methyl N-methylpyridinium ion, the bromide ion being common to both. A reasonable ex-

planation is that the pyridinium HCl is an abnormally good conductor because the labile proton, which appears in the spectrum of fused pyridinium HCl and in aqueous solutions of pyridinium salts (14), is contributing to the conductance.

Errors.—The conductance data is accurate to nearly $\pm 1\%$. This figure takes into account the precision and accuracy of the bridge, $\pm 0.2\%$, the ability to regulate temperature, $\pm 0.2^\circ$, impurities in the salts $\sim 0.5\%$, and a small amount of decomposition and hydrolysis. The NMR data have about the same accuracy. The chemical shifts seem accurate to ± 0.02 ppm. The variable temperature probe of the NMR machine can regulate temperature to $\pm 2^\circ$ which is not nearly as good as the temperature regulation of the bath. However, the peak positions are not very temperature sensitive. While impurities have less effect on the spectra than on κ , there are more "noise" and machine "stability" problems at elevated temperatures.

Acknowledgments

The authors thank the staff of Argonne National Laboratory and the Atomic Energy Commission for the use of the NMR machine. The authors also thank the Faculty Research Committee of Bowling Green State University for its generous support.

This paper is based partly on work performed under the auspices of the U. S. Atomic Energy Commission.

Manuscript submitted Aug. 23, 1971; revised manuscript received Jan. 28, 1972. This was Paper 177 presented at the Washington, D.C., Meeting of the Society, May 9-13, 1971.

Any discussion of this paper will appear in a Discussion Section to be published in the June 1973 JOURNAL.

REFERENCES

1. D. M. Gruen and R. L. McBeth, *J. Phys. Chem.*, **63**, 393 (1959).
2. M. S. Rozhdestvenskii and L. M. Brode, *J. Appl. Chem. USSR*, **10**, 722 (1937).
3. G. J. Janz, "Molten Salt Handbook," Academic Press Inc., New York (1967).
4. A. K. Sheinkman, L. M. Kapkan, L. G. Gahk, E. V. Titov, S. N. Baranov, and A. N. Yost, *Dokl. Akad. Nauk USSR*, **193**, 366 (1970).
5. A. J. Easteal and C. A. Angell, *J. Phys. Chem.*, **74**, 3987 (1970).
6. R. A. Wallace and P. F. Bruins, *This Journal*, **114**, 209 (1967).
7. R. A. Wallace and P. F. Bruins, *ibid.*, **114**, 212 (1967).
8. R. A. Wallace, Ph.D. Thesis, University Microfilms, Inc., Ann Arbor, Mich. (1963).
9. J. A. Pople, W. G. Schneider, and H. J. Bernstein, "High Resolution Nuclear Magnetic Resonance," McGraw-Hill Book Co., Inc., New York (1959).
10. A. Klemm, *Z. Naturforsch.*, **8a**, 397 (1953).
11. R. W. Laity, *J. Phys. Chem.*, **63**, 80 (1959).
12. G. Blander, "Molten Salts," Interscience Publishers, Inc., New York (1964).
13. B. Sundheim, "Fused Salts," McGraw-Hill Book Co., Inc., New York (1964).
14. M. Cocivera, *J. Phys. Chem.*, **72**, 2515 (1968).

Chloroaluminate Equilibria in $\text{AlCl}_3\text{-NaCl}$ Melts

Armand A. Fannin, Jr., Lowell A. King, and David W. Seegmiller

Frank J. Seiler Research Laboratory (AFSC) and Department of Chemistry,
United States Air Force Academy, Colorado 80840

ABSTRACT

Equilibrium constants were calculated for reactions governing the species present at 175°C in molten mixtures of aluminum chloride and sodium chloride. The equilibria postulated pertain to formation of the complex ions AlCl_4^- , Al_2Cl_7^- , and $\text{Al}_3\text{Cl}_{10}^-$ from Cl^- , AlCl_3 , and Al_2Cl_6 . The constants were derived from potentials exhibited by concentration cells of the type $\text{Al}/\text{AlCl}_3(N)$, $\text{NaCl}/\text{AlCl}_3(N')$, NaCl/Al , and from vapor pressures over pure AlCl_3 and molten $\text{AlCl}_3\text{-NaCl}$ mixtures. Measurements were made throughout the concentration range $N = 0.498\text{-}0.71$. The possibilities of using these concentration cells as high energy density batteries are considered.

Aluminum-chlorine formation cells utilizing molten mixtures of AlCl_3 and NaCl as the electrolyte are being investigated in this laboratory for use as high energy density batteries. An essential part of the program has been the determination of the activities of the aluminum species in the electrolyte. Several investigators have presumed the aluminum to be distributed among various chloroaluminate species in such melts, and have made calculations based on this presumption. Øye and Gruen (1) calculated equilibrium constants governing the formation of chloroaluminate ions in $\text{AlCl}_3\text{-NaCl}$ melts at 190°C in the composition region $0.536 \leq N \leq 0.658$. They used the vapor pressure data of Dewing (2) as the basis of their calculation. Trémillon and Letisse (3) introduced the solvent system definitions of acid and base (chloride ion acceptor and donor, respectively) for NaAlCl_4 melts, and determined the value of the solvent dissociation constant at 175°C. They performed a potentiometric titration of Cl^- over the composition range of $0.498 \leq N \leq 0.502$ by the strong acid Al_2Cl_7^- , which was produced coulometrically. A similar technique was employed to measure equilibrium constants by Boxall, Jones, and Osteryoung (4) over the composition range $0.50 \leq N \leq 0.70$ and the temperature range 175°-355°C. Torsi and Mamantov (5) potentiometrically measured the same dissociation constant in the temperature range 175°-400°C and the composition range $0.498 \leq N \leq 0.503$. They varied the composition of their melt by adding known weights of AlCl_3 to the salt mixture. Morrey and Moore (6) calculated equilibrium constants governing the formation of chloroaluminate ions in $\text{AlCl}_3\text{-KCl}$ melts at 725°C by measuring the distribution of uranium(III) between the two phases $\text{UCl}_3(1)$ and $\text{AlCl}_3\text{-KCl}(1)$.

A wide variety of additional properties of aluminum halide-Group I metal halides melts has been investigated. Boston (7) recently reviewed these studies.

A convenient way to measure activities is to use a concentration cell of the type $\text{Al}/\text{AlCl}_3(N)$, $\text{NaCl}/\text{AlCl}_3(N')$, NaCl/Al where the activities of aluminum in solution and the observed cell voltage are related by the equation

$$E = \sum_i \frac{RT}{z_i F} \ln \left(\frac{a_i}{a_i'} \right) + E_J \quad [1]$$

Experimental

Concentration cells.—A variety of concentration cells was built. All had in common an aluminum wire immersed in each of two different electrolytes contained in compartments connected by a porous barrier. Glass frits, asbestos wicks, Fiberglas mats, and thin Pyrex membranes were used as barriers in the several cells. Electrolytes were molten mixtures of aluminum chlo-

ride and sodium chloride, with the aluminum chloride content ranging from $N = 0.498$ to 0.71. These compositions correspond, respectively, to a saturated solution of NaCl and to a point where the vapor pressure of AlCl_3 over the electrolyte was too difficult to contain with our cell design.

Most of the cells were made of Pyrex glass in two basic designs. One version was a typical H-cell, with the porous barrier in the connecting arm. Some of the electrolyte compartments were simply closed with cork stoppers through which the aluminum wire electrodes passed. However, because of the extreme reactivity of aluminum chloride with moisture and because of the relatively high vapor pressures over AlCl_3 -rich electrolytes, the H-cells usually were completely sealed with tungsten wire lead-throughs for electrical connections. Tungsten did not touch the melts; the aluminum wire electrodes were mechanically bound to the tungsten in the vapor phase region of the cells.

In experiments where the aluminum chloride content of either of the electrolytes exceeded approximately $N = 0.55$, the vapor pressure of the electrolytes tended to force the melt through the barrier (Pyrex membranes were not used with the H-cell design). To eliminate this problem, a second capillary was used to connect the vapor phase regions of the two arms of the H-cell. Electrolyte composition changes due to vapor transfer were extremely slow and did not present a problem.

The other basic cell design was comprised of a small tube, one end of which terminated in a Pyrex bubble. This tube was ring-sealed into a larger closed-ended tube equipped with a side arm. The side arm and the remaining end of the small tube were sealed, with tungsten lead-throughs provided as in the first design.

All cells were loaded with powdered electrolyte at room temperature in a glove box. The glove box atmosphere was nitrogen recirculated through a molecular sieve. The dew point was below -60° (less than 15 ppm H_2O). All of the sealed cells were equipped with side arms connected to each electrolyte compartment. Weighed amounts of powdered electrolyte were added to the compartments, the cells evacuated, and the side arms sealed off. The composition of an electrolyte could be changed by breaking the side arm, adding the required salt, and resealing the cell. Loading and changing the compositions of electrolytes in cells which were closed with cork stoppers were simpler.

Chemicals.—"Baker Analyzed" reagent grade 0.032 in. aluminum wire was used as electrodes. The reported impurities totaled less than 0.2%. The principal impurities were silicon and iron. "Baker Analyzed" reagent grade sodium chloride was heated in air to just below its melting point for 24 hr, then ground to a powder inside a glove box immediately before use. "Baker Analyzed" aluminum chloride was purified by a crystal growth method described elsewhere (8). The

Key words: aluminum chloride, concentration cell, battery, molten salt.

crystals were ground to a powder immediately before use by means of a Chemical Rubber Company Micro-Mill which was located inside the glove box.

Apparatus.—The concentration cells were immersed in a well-stirred bath of the ternary eutectic $\text{NaNO}_3\text{-NaNO}_2\text{-KNO}_3$. Bath temperature was measured with a Chromel-Alumel thermocouple calibrated at the melting point of Sn-Pb eutectic (9) and was maintained by a temperature controller. Voltages of the cells which utilized Pyrex membranes were measured with a Data Technology Corporation Model 370 digital voltmeter and the voltages of the remaining cells were measured with a L&N Type K-3 potentiometer and Type 9834 electronic d-c null detector.

Results and Discussion

The ratio of activities of aluminum in the two electrolytes of a concentration cell can be calculated by Eq. [1] and the observed cell voltage. Many binary molten halide systems are approximately ideal mixtures if the species are correctly identified (10). The aluminum chloride-alkali metal chloride system appears to be no exception (11). If the aluminum system were to behave ideally and the activity of Al^{III} were proportional to N , the expected cell voltages from Eq. [1] would reach a maximum of 0.03V with electrolyte

Table I. Concentration cell voltages

Cell No.	N^*	N^a	E
1	0.507	0.508	0.0014
		0.553	0.0915
		0.595	0.1421
		0.640	0.190
2	0.508	0.678	0.2272
		0.531	0.05045
		0.569	0.09955
		0.586	0.1192
		0.608	0.1418
		0.619	0.1556
		0.630	0.1661
		0.652	0.1893
		0.658	0.1943
		0.676	0.2131
3	0.506	0.504	-0.0195
		0.517	0.0281
		0.533	0.0655
		0.546	0.0864
		0.560	0.1067
		0.574	0.1240
		0.579	0.1322
		0.598	0.1531
		0.611	0.1665
		0.624	0.1826
		0.635	0.1914
		0.666	0.2261
		0.698	0.2519
		0.701	0.240
		0.529	0.0442
4	0.514	0.553	0.0900
		0.597	0.1407
		0.642	0.1760
		0.583	0.121
		0.701	0.0682
		0.658	0.0252
		0.622	-0.0126
		0.546	-0.0897
		0.498	-0.5553
		0.689	0.09138
5	0.625	0.660	0.06190
		0.619	0.01934
		0.582	-0.01682
		0.566	-0.0339
		0.549	-0.0529
		0.518	-0.1083
		0.501	-0.190
		0.498	-0.54
		0.681	-0.0151
		0.617	-0.0802
6	0.598	0.555	-0.1415
		0.530	-0.1522
		0.498	-0.591, -0.583
		0.688	-0.00740
		0.632	-0.0616
		0.586	-0.1080
		0.538	-0.1560
		0.517	-0.2025
		0.509	-0.2299
		0.633	-0.1550
7	0.699	0.614	0.1345
		0.582	0.1076
		0.558	0.0792
		0.528	0.0223
		0.525	0.014
		0.498	-0.42
		0.540	0.0402
		0.681	-0.0151
		0.617	-0.0802
		0.555	-0.1415
0.530	-0.1522		
8	0.707	0.688	-0.00740
		0.632	-0.0616
		0.586	-0.1080
		0.538	-0.1560
		0.517	-0.2025
		0.509	-0.2299
		0.633	-0.1550
		0.614	0.1345
		0.582	0.1076
		0.558	0.0792
9	0.509	0.528	0.0223
		0.525	0.014
		0.498	-0.42
		0.540	0.0402
		0.681	-0.0151
		0.617	-0.0802
		0.555	-0.1415
		0.530	-0.1522
		0.498	-0.591, -0.583
		0.688	-0.00740

* Listed in the order in which data were taken.

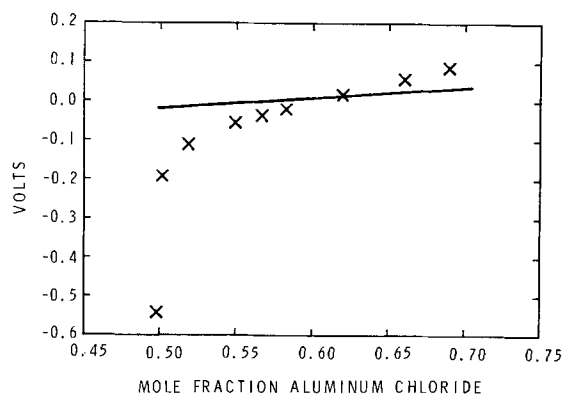
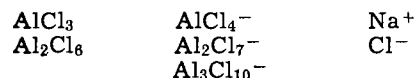


Fig. 1. Concentration cell voltages, cell No. 6. —, Predicted for ideal mixing; X, observed.

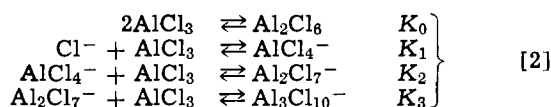
compositions corresponding to the extreme maximum and minimum values which we used. This value includes in E_j the term involving the two sodium ion activities, but no other junction effects.

The voltages observed on nine cells in which electrolyte composition was varied are given in Table I. The results for a typical cell, No. 6, are shown in Fig. 1 and are compared with the results expected for ideal mixing. Two significant features are apparent. The experimental points on the upper half of the figure span over 0.3V and are an order of magnitude larger than the ideal values. This behavior was reproducibly observed on all cells, as long as the aluminum chloride mole fraction in both electrolytes exceeded $N = 0.500$. The other notable feature of these cells is a sharp increment of approximately 0.4V obtained whenever the composition of aluminum chloride in one of the electrolytes was reduced to below $N = 0.500$. This behavior also was reproducibly obtained in a number of cells, including some cited in Table I.

The following species have been reported (1, 11, 12) to exist in aluminum chloride-sodium chloride melts



A reasonable set of reactions linking these anions and molecular species follows

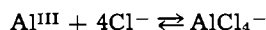


Aluminum chloride in the vapor phase exists almost exclusively as the dimer Al_2Cl_6 at temperatures below 400°C (13). From the JANAF Tables (14) one may calculate the vapor dimerization constant. Using that value and the vapor pressure of pure aluminum chloride (15) it is possible to calculate K_0 . At 175°C , $K_0 = 2.9 \times 10^7$. (See Appendix I for the method of calculation.)

Equation [2] is written in terms of AlCl_3 , even though Al_2Cl_6 is the dominant neutral species in solution over virtually the entire composition range studied. That choice was made primarily because it led to simpler algebra, and because measurements in the literature customarily are expressed in terms of the apparent mole fraction of monomer, which is our N . As may be seen in the Appendixes, the actual calculations were made in terms of Al_2Cl_6 . In any case, the equilibrium constants of Eq. [2] are related by the factor K_0 to an equivalent set of equilibria written in terms of Al_2Cl_6 .

If it is assumed that Na^+ is the only current-carrying species, and that the concentration of the electrochemically active aluminum species is in equilibrium with the aluminum-containing species cited above, the Nernst equation can be written for this type of con-

centration cell. For convenience, the equilibrium chosen was



The term E_J in Eq. [1] becomes $-(RT/F)\ln(a_{\text{Na}^+}/a_{\text{Na}^+(\text{ref.})})$, since other contributions to E_J were small enough compared to experimental errors to be neglected. Within experimental error, the cells with Pyrex membranes yielded the same potentials as did cells of the other designs when the same concentration of electrolyte was employed in the two different cells.

The activity coefficients of Na^+ , AlCl_4^- , and Cl^- are not known precisely. The most important term in the Nernst equation is the one involving the activity of Cl^- . The concentration of Cl^- remained very small over the entire composition range which was studied. Boxall and Johnson (16) showed that the activity coefficients of dilute solutes remain constant as their concentrations change. The concentrations of Na^+ and of AlCl_4^- were too large to make this assumption; however, the concentrations of these species did not vary greatly over the composition region studied, and unless relatively enormous changes in activity coefficients occurred, little error was introduced by replacing activity ratios by mole fraction ratios.

Accordingly, the Nernst equation for a concentration cell with transference then becomes

$$E = \frac{-RT}{3F} \left[4\ln \left(\frac{X_{\text{Cl}^-}}{X_{\text{Cl}^-(\text{ref.})}} \right) - \ln \left(\frac{X_{\text{AlCl}_4^-}}{X_{\text{AlCl}_4^-(\text{ref.})}} \right) + 3\ln \left(\frac{X_{\text{Na}^+}}{X_{\text{Na}^+(\text{ref.})}} \right) \right] \quad [3]$$

If the model of Eq. [2] is correct, and if the concentration of any one of the participating species (except Na^+) can be determined precisely as a function of over-all melt composition, the constants K_1 , K_2 , and K_3 can be determined. A composition range in which concentrations are relatively easy to determine lies in the immediate vicinity of the $N = 0.500$ point, since E changes rapidly and $X_{\text{AlCl}_4^-}$ and X_{Na^+} remain nearly constant.

Suitable experimental data for this composition range are those of Torsi and Mamantov (5). Their experiment was performed by adding very small increments of aluminum chloride to one arm of a concentration cell. The composition of the variable arm of the cell was thus increased in small steps from an initial composition of $N = 0.498$ to a final composition of $N = 0.503$. Their experimental cell voltages, when plotted vs. composition, displayed typical titration curve behavior. The titration data was treated by means of the equilibrium expression

$$K = \frac{K_2}{K_1} = \frac{X_{\text{Cl}^-} X_{\text{Al}_2\text{Cl}_7^-}}{(X_{\text{AlCl}_4^-})^2} \quad [4]$$

and the simplified Nernst equation

$$E = \frac{-4RT}{3F} \ln \left(\frac{X_{\text{Cl}^-}}{X_{\text{Cl}^-(\text{ref.})}} \right) \quad [5]$$

At the equivalence point

$$\frac{K_2}{K_1} = \frac{(X_{\text{Cl}^-})^2}{(X_{\text{AlCl}_4^-})^2} \quad [6]$$

Equation [5] can be expanded to a theoretical equation of the form (see Appendix II for derivation)

$$E = \frac{-4RT}{3F} \ln A + B \quad [7]$$

where

$$A = (0.5) (-C + [C^2 + 0.0245 K_2/K_1]^{1/2}) = n_{\text{Cl}^-}$$

$$C = \frac{w - x}{133.34}$$

$$B = 0.05149 \ln m_{\text{Cl}^-(\text{ref.})} - 0.2162$$

The Torsi and Mamantov data were fit to Eq. [7] by a grid technique. Trial values of the ratio K_2/K_1 were substituted into Eq. [7] and least squares fit values of x and C were computed. The equilibrium constant ratio was varied until an apparent minimum occurred in the standard deviation of the fit. The best fit values of the three parameters, K_2/K_1 , x , and m_{Cl^-} are given in Table II, and are compared with the results calculated by Torsi and Mamantov, who used a graphical procedure. The ratio K_2/K_1 at 175°C was calculated to be $(7.8 \pm 0.6) \times 10^{-8}$.

The composition range where K_2 most conveniently may be evaluated extends approximately from $N = 0.55$ to 0.70 . The majority of the data given in Table I were taken in this composition range. Some of the remaining data were taken with one arm of the cell saturated with NaCl . This common reference point allowed the data from this laboratory to be combined with those of Torsi and Mamantov. The voltage-composition data for each cell appeared to fall on individual curves generated by cubic polynomials, as long as the composition of the electrolyte to which AlCl_3 or NaCl increments were added remained above $N = 0.51$. Therefore, these concentration cell data (excluding the saturated NaCl points) were least squares fit to Eq. [8], which is mathematically equivalent to transforming each of the least squares cubic polynomials for individual concentration cells to a (arbitrary) common reference

$$E = b_1(N - N') + b_2(N^2 - N'^2) + b_3(N^3 - N'^3) \quad [8]$$

The resulting values of b_1 , b_2 , and b_3 are listed below, immediately following Eq. [12].

The value of K_2 was obtained in the following manner: The concentrations of the various species required in Eq. [3] were calculated by an iterative technique from Eq. [2]. The value of K_2 was obtained by curve matching Eq. [8] with Eq. [3], the latter obtained by substituting the known values of K_0 , K_2/K_1 , and various trial values of K_2 and K_3 into Eq. [2]. Unfortunately, it was not possible to match directly the experimental data with the calculated curve from Eq. [3] in lieu of using Eq. [8]. That was because the individual cells

Table II. Titration curve parameters; $\text{AlCl}_3\text{-NaCl}$ at 175°C

Parameter	Least squares calculation ^a	Torsi and Mamantov calculation (5)	Trémillon and Létisse (3)
$K = \frac{K_2}{K_1}$	$(7.8 \pm 0.6) \times 10^{-8}$	$(8 \pm 2) \times 10^{-8}$	$(1.3 \pm 0.2) \times 10^{-7b}$
$m_{\text{Cl}^-(\text{ref.})}^c$	0.039 ± 0.002	0.038^d	0.049 ± 0.002
x , mass of AlCl_3 added to reach equivalence point ^e	$0.075 \pm 0.002g$	$0.076 \pm 0.002g^d$	

^a Probable errors calculated from uncertainties in weights and voltages reported by Torsi and Mamantov (5) and the appropriate partial derivatives.

^b Converted to mole fraction basis from their molality value.

^c The reference electrolyte is NaAlCl_4 saturated with NaCl (5).

^d G. Mamantov, private communication; graphical method used, not explicitly calculated in Ref. (5).

^e $N = \frac{1 + 0.095885(w - x)}{2 + 0.095885(w - x)}$; $N = 0.5$ at equivalence point since $w = x$.

all employed different reference concentrations. It therefore was necessary to resort to some mathematical treatment such as represented by Eq. [8], which converted the cell data to a common reference concentration.

The experimental data did not lie in the composition range which would be well suited for evaluation of K_3 . However, an upper limit of approximately 10^3 may be placed on K_3 , since trial values of K_3 appreciably larger than that produce significant deviations from experimental results even in the composition range which was explored.

An alternate evaluation of K_2 is possible using measurements of vapor pressures over $\text{AlCl}_3\text{-NaCl}$ melts. Several studies of vapor pressure have been reported (2, 17-21). Of these, the most reliable data appeared to be those reported by Narita, Ishikawa, and Midorakawa (20), since no residual gases were present during the measurements, and melt analyses were made after the pressure measurements. Their pressure values, taken at seven melt compositions between $N = 0.54$ and 0.75 , yield a value of K_2 similar to the value obtained by the electrochemical measurements. In the composition range $N = 0.591$ to 0.657 , the pressure-derived $K_2 = (5.5 \pm 0.5) \times 10^4$ at 175°C . The method of calculation is given elsewhere (22).

Davey, Floyd, and Marcantonio (21) examined vapor pressure measurements of several other workers (2, 17, 18). They resolved the inconsistencies between the data of Rogers (18) and those of Dewing (2) by correcting the heat capacity term in the equations reported by Dewing. From these data, Davey, Floyd, and Marcantonio (21) derived empirical equations from which vapor pressures over $\text{AlCl}_3\text{-NaCl}$ melts can be calculated. These pressures in the composition range $N = 0.52$ to 0.60 yield a K_2 of $(1.5 \pm 0.3) \times 10^4$.

Øye and Gruen (1) derived an equilibrium constant from Dewing's vapor pressures (2). The constant calculated by Øye and Gruen is equivalent to K_0/K_2^2 in the present work. At 175°C , $K_0/K_2^2 = 0.05$, which is in good agreement with the value at 190°C of 10^{-2} obtained by Øye and Gruen.

It also is possible to predict the correct voltages of concentration cells with transference from the vapor pressure data of Narita, Ishikawa, and Midorakawa (20). From theoretical free energy calculations and the Gibbs-Duhem relationship one can derive the expression

$$E = \frac{-RT}{3F} \int_N^{N'} t_{\text{Na}^+} \left(\frac{2N+1}{1-N} \right) \left(\frac{1}{N} + \frac{d \ln \gamma_N}{dN} \right) dN \quad [9]$$

where t_{Na^+} is the transport number of Na^+ and γ_N is the apparent activity coefficient of AlCl_3 , and is defined by

$$\gamma_N = \frac{X_{\text{AlCl}_3}}{N} = \frac{(X_{\text{Al}_2\text{Cl}_6}/K_0)^{1/2}}{N} \quad [10]$$

A least squares empirical polynomial for $d \ln(\gamma_N)/dN$ was obtained from Eq. [10] and the vapor pressures (15, 20). The only current carrying species was assumed to be Na^+ . Voltages obtained on integration of Eq. [9] are compared with the measured values on Fig. 2.

The derivation of Eq. [9], and a description of the calculations made from vapor pressures may be found elsewhere (22).

The experimentally determined values of the equilibrium constants are summarized in Table III. The cell voltage data of the present work and that of Torsi and Mamantov (5) are given by the empirical Eq. [11] and the theoretical Eq. [12]

$$E = b_0 + b_1N + b_2N^2 + b_3N^3 \quad [11]$$

$$0.51 \leq N \leq 0.71$$

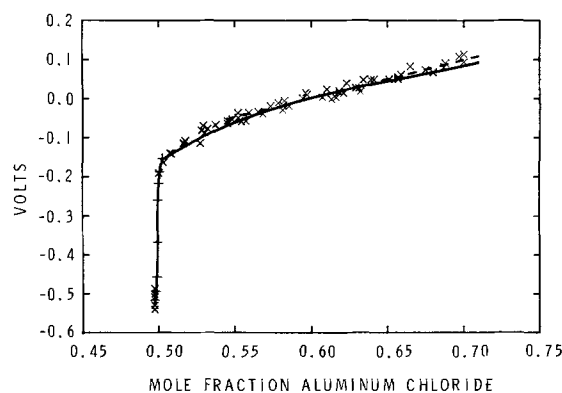


Fig. 2. Comparison of concentration cell voltages with calculated values. —, Calculated from empirical Eq. [11] and [12]; ---, calculated from vapor pressure measurements. Observed values: X, present work; +, Torsi and Mamantov (5).

$$E = \frac{-4RT}{3F} \ln \left\{ \frac{1-2N}{1-N} + \left[\left(\frac{1-2N}{1-N} \right)^2 + \frac{4K_2}{K_1} \right]^{1/2} \right\} + D \quad [12]$$

$$0.498 \leq N \leq 0.504$$

where $b_0 = -6.9028536$, $b_1 = 30.0446$, $b_2 = -44.3122$, $b_3 = 22.3541$, and $D = -0.7454$, and the reference electrode composition $N' = 0.600$.

The derivation of Eq. [12] is described in Appendix II. Figure 2 compares the experimental data and the results obtained from empirical equations. The curve calculated from Eq. [11] begins to move away slightly from the experimental voltages at $N > 0.65$. It is not clear whether this divergence, if real, was due to failure to take activity coefficients properly into account, or whether it reflected the increased participation of $\text{Al}_3\text{Cl}_{10}^-$ as an aluminum-containing species at high N .

The values of K_1 and K_2 imply a very tightly bound Al^{III} , and therefore sharply enhanced electrochemical oxidation at aluminum anodes in the sense that the free energy change at the anode is much more negative in $\text{AlCl}_3\text{-NaCl}$ melts than in the presence of pure aluminum chloride. Moreover, the effect of the equilibria is to complex the aluminum to a degree markedly dependent on melt composition. This, in turn, gives rise to the unusually large concentration cell voltages. The composition range in which this behavior was observed is quite broad; although to achieve the 0.4V increment, the composition of the two arms of a cell must lie on opposite sides of the $N = 0.500$ point. These effects can be seen more clearly in Fig. 3, which illustrates the distribution of the various species in melts. The concentrations were obtained from calculations analogous to those used for concentration distributions in polyprotic acid equilibria. According to the model, the principal aluminum-containing species is AlCl_4^- when $N < 0.63$, and is Al_2Cl_7^- beyond that composition. The reaction involving K_3 , i.e. the formation of $\text{Al}_3\text{Cl}_{10}^-$, was not included in the calculations.

The calculations were straight forward but rather complicated, and involved an iterative solution of an

Table III. Values of equilibrium constants (mole fraction basis) at 175°C

K_0	2.9×10^7
K_1	$(3.2 \pm 0.5) \times 10^{11a}$
K_2	$(2.5 \pm 0.2) \times 10^{10a}; (5.5 \pm 0.5) \times 10^{10b}; (1.5 \pm 0.3) \times 10^{10c}$
K_3	$\leq 10^3$

^a Calculated from the least squares treatment for K_2/K_1 from the data of Torsi and Mamantov (5) and the present concentration cell data.

^b From vapor pressures. See text and Ref. (20).

^c From vapor pressures. See text and Ref. (22).

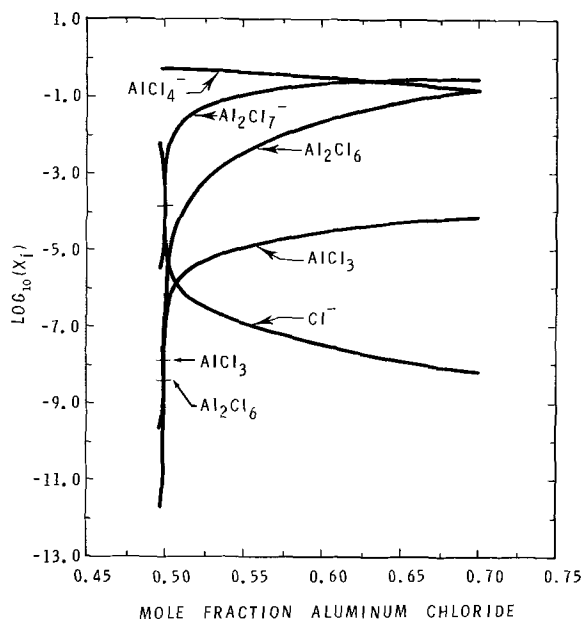


Fig. 3. Concentration of species in $\text{AlCl}_3\text{-NaCl}$ melts. (—) Indicates $\log_{10} X_i$ at $N = 0.500$.

equation in $X_{\text{Al}_2\text{Cl}_6}$ raised to integral and half-integral powers. The calculations are given in detail in Appendix III. Table IV gives the calculated values of $X_{\text{Al}_2\text{Cl}_6}$ and X_{Cl^-} at selected N . From these, all other concentrations at composition N may be calculated easily. The concentrations shown in Fig. 3 assume activity coefficients of unity. Even if the activity coefficients are not unity, the indicated concentrations are very nearly correct, the error being in the reported values of K_1 and K_2 .

Concentration cell behavior similar to that obtained in the aluminum chloride systems should be observable whenever there is a series of very stable complexes to consume the anode metal. Whether or not any such cells would display voltages as high as those encountered with aluminum remains to be seen. There is at least one possibility already in the literature; beryllium concentration cells utilizing molten $\text{BeF}_2\text{-LiF}$ electrolytes have been reported to yield potentials greater than 0.22V (23).

Curve matching was done by overlaying curves plotted by a Hewlett-Packard 9100B programmable calculator and plotter. All other data reduction was done with the aid of a Wang 720B programmable calculator.

APPENDIX I

The value of K_0 was calculated as follows
Let

Table IV. Concentration of dimer and of chloride at 175°C

N	$-\log_{10}(X_{\text{Al}_2\text{Cl}_6})$	$-\log_{10}(X_{\text{Cl}^-})$
0.4980	11.3689	2.3992
0.4985	11.1190	2.5233
0.4990	10.7683	2.6978
0.4995	10.1776	2.9923
0.5000	8.4487	3.8560
0.5005	6.7184	4.7218
0.5010	6.1263	5.0188
0.5015	5.7741	5.1957
0.5020	5.5227	5.3223
0.5030	5.1665	5.5022
0.5040	4.9122	5.6311
0.5060	4.5509	5.8153
0.5080	4.2917	5.9486
0.5100	4.0885	6.0539
0.5150	3.7125	6.2513
0.5200	3.4386	6.3981
0.5300	3.0374	6.6193
0.5400	2.7376	6.7912
0.5600	2.2848	7.0660
0.5800	1.9377	7.2930
0.6000	1.6563	7.4906
0.6200	1.4250	7.6644
0.6400	1.2344	7.8170
0.6600	1.0765	7.9515
0.6800	0.9443	8.0713
0.7000	0.8317	8.1797

$$y^\circ_{\text{AlCl}_3} = p^\circ_{\text{AlCl}_3}/P^\circ \quad \text{and} \quad y^\circ_{\text{Al}_2\text{Cl}_6} = p^\circ_{\text{Al}_2\text{Cl}_6}/P^\circ$$

$$X_{\text{AlCl}_3} = p^\circ_{\text{AlCl}_3}/P^{\text{T}}_{\text{AlCl}_3} \quad \text{and} \quad X_{\text{Al}_2\text{Cl}_6} = p^\circ_{\text{Al}_2\text{Cl}_6}/P^{\text{T}}_{\text{Al}_2\text{Cl}_6}$$

Then

$$K_0 = \frac{X_{\text{Al}_2\text{Cl}_6}}{(X_{\text{AlCl}_3})^2} = \frac{y^\circ_{\text{Al}_2\text{Cl}_6} P^\circ / P^{\text{T}}_{\text{Al}_2\text{Cl}_6}}{(y^\circ_{\text{AlCl}_3} P^\circ / P^{\text{T}}_{\text{AlCl}_3})^2} \quad [\text{AI-1}]$$

$$P^{\text{T}}_{\text{AlCl}_3} = p^\circ_{\text{AlCl}_3} + 2p^\circ_{\text{Al}_2\text{Cl}_6} = P^\circ + p^\circ_{\text{Al}_2\text{Cl}_6}$$

$$P^{\text{T}}_{\text{Al}_2\text{Cl}_6} = p^\circ_{\text{Al}_2\text{Cl}_6} + (P^\circ - p^\circ_{\text{Al}_2\text{Cl}_6})/2 = (P^\circ + p^\circ_{\text{Al}_2\text{Cl}_6})/2$$

By definition

$$K_p P^\circ = \frac{y^\circ_{\text{Al}_2\text{Cl}_6}}{(1 - y^\circ_{\text{Al}_2\text{Cl}_6})^2} \quad [\text{AI-2}]$$

Upon substitution into Eq. [AI-1], one obtains

$$K_0 = 2K_p P^\circ (1 + y^\circ_{\text{Al}_2\text{Cl}_6}) \quad [\text{AI-3}]$$

Equation [AI-2] then is solved for the physically realizable value of $y^\circ_{\text{Al}_2\text{Cl}_6}$, and that value substituted into Eq. [AI-3] yields K_0 . For all practical purposes $y^\circ_{\text{Al}_2\text{Cl}_6} = \text{unity}$ at 175°C.

The vapor pressure equation of Smits and Meijering (15) yields $P^\circ = 1145.5$ Torr. This value is high enough that the nonideality of the gas should be taken into account. The Dieterici equation (24) was used in the form

$$(P^\circ \exp [a/\tilde{V}RT])(\tilde{V} - b) = RT \quad [\text{AI-4}]$$

Equation [AI-4] was solved for the ideal \tilde{V} , using

$$a = 4bRT_{\text{critical}}$$

$$b = \tilde{V}_{\text{critical}}/2$$

where T_{critical} and $\tilde{V}_{\text{critical}}$ are from Denisova and Basikova (25).

An ideal pressure, $P^\circ_{\text{ideal}} = 1206.3$ Torr, calculated from $P^\circ_{\text{ideal}} = RT/\tilde{V}$, was the value used in Eq. [AI-2] and [AI-3] to calculate K_0 .

APPENDIX II

The theoretical Eq. [7] was derived as follows: From Eq. [2] one can derive the equations

$$n_{\text{AlCl}_3} = \left(\frac{n_t}{K_1 n_{\text{Cl}^-}} \right) n_{\text{AlCl}_4^-}$$

$$n_{\text{Al}_2\text{Cl}_6} = \left(\frac{K_0 n_t}{K_1^2 (n_{\text{Cl}^-})^2} \right) (n_{\text{AlCl}_4^-})^2$$

$$n_{\text{Al}_2\text{Cl}_7^-} = \left(\frac{K_2}{K_1 n_{\text{Cl}^-}} \right) (n_{\text{AlCl}_4^-})^2 \quad [\text{AII-1}]$$

The amount of AlCl_3 added by Torsi and Mamantov (5) is related to the species present in the electrolyte by the equation

$$\frac{w}{133.34} = n_{\text{AlCl}_3} - n^\circ_{\text{AlCl}_3} + 2n_{\text{Al}_2\text{Cl}_6} - 2n^\circ_{\text{Al}_2\text{Cl}_6} + n_{\text{AlCl}_4^-} - n^\circ_{\text{AlCl}_4^-} + 2n_{\text{Al}_2\text{Cl}_7^-} - 2n^\circ_{\text{Al}_2\text{Cl}_7^-} \quad [\text{AII-2}]$$

where

$$n_{\text{AlCl}_4^-} - n^\circ_{\text{AlCl}_4^-} + n_{\text{Al}_2\text{Cl}_7^-} - n^\circ_{\text{Al}_2\text{Cl}_7^-} = n^\circ_{\text{Cl}^-} - n_{\text{Cl}^-} \quad [\text{AII-3}]$$

and $n^\circ_{\text{AlCl}_3}$, $n^\circ_{\text{Al}_2\text{Cl}_6}$, and $n^\circ_{\text{Al}_2\text{Cl}_7^-}$ are near enough to zero to be neglected. By substituting Eq. [AII-1] and [AII-3] into Eq. [AII-2], neglecting the vanishingly small terms, and rearranging, one obtains the cubic polynomial

$$(n_{\text{Cl}^-})^3 + \left(\frac{w}{133.34} - n^\circ_{\text{Cl}^-} \right) (n_{\text{Cl}^-})^2 - \left(\frac{K_2 (n_{\text{AlCl}_4^-})^2}{K_1} + \frac{n_t n_{\text{AlCl}_4^-}}{K_1} \right) n_{\text{Cl}^-} - \frac{2K_0 n_t (n_{\text{AlCl}_4^-})^2}{K_1^2} = 0 \quad [\text{AII-4}]$$

The term immediately preceding the equality sign in Eq. [AII-4] is small enough that it may be neglected without introducing any significant error. Equation [AII-4] then will reduce to a quadratic in n_{Cl^-} . The equation will further simplify if $K_2 \gg 1$ by noting that

$$\frac{K_2(n_{AlCl_4^-})^2}{K_1} \gg \frac{n_t \cdot n_{AlCl_4^-}}{K_1}$$

Therefore

$$(n_{Cl^-})^2 + \left(\frac{w}{133.34} - n_{Cl^-} \right) n_{Cl^-} - \frac{K_2(n_{AlCl_4^-})^2}{K_1} = 0 \quad [AII-5]$$

Equation [AII-5] may be derived more directly by neglecting the term $2n_{Al_2Cl_6}$ in Eq. [AII-2].

On substitution of Eq. [AII-6] into Eq. [AII-5] and reducing the latter into the standard form for finding the roots of a quadratic equation we obtained Eq. [AII-7]

$$n_{Cl^-} = \frac{x}{133.34} \quad [AII-6]$$

$$n_{Cl^-} = (0.5) \left(-\frac{w-x}{133.34} + \left[\left(\frac{w-x}{133.34} \right)^2 + \frac{4K_2(n_{AlCl_4^-})^2}{K_1} \right]^{1/2} \right) \quad [AII-7]$$

From Eq. [5]

$$B = \frac{4RT}{3F} \ln n_{Cl^-}(\text{ref.}) \quad [AII-8]$$

Torsi and Mamantov (5) added aluminum chloride to 0.0782 moles of $NaAlCl_4$. On converting from moles to molality units, Eq. [AII-8] becomes

$$B = \frac{4RT}{3F} \ln [0.015 m_{Cl^-}(\text{ref.})] \quad [AII-9]$$

Equations [AII-7] and [AII-9] together yield Eq. [7].

From the definition of N

$$\frac{w-x}{133.34} = \left(\frac{2N-1}{1-N} \right) n_{AlCl_4^-} \quad [AII-10]$$

Since $n_{AlCl_4^-}$ is very nearly equal to n_{AlCl_3} in the immediate vicinity of $N = 0.5$, Eq. [AII-7] reduces to

$$n_{Cl^-} = \frac{n_{AlCl_4^-}}{2} \left(\frac{1-2N}{1-N} + \left[\left(\frac{1-2N}{1-N} \right)^2 + \frac{4K_2}{K_1} \right]^{1/2} \right) \quad [AII-11]$$

From Eq. [5], [AII-9], and [AII-11], one may derive Eq. [12], an expression analogous to Eq. [7], but written in terms of N . Changing N' , the reference arm of the cell, corresponds to changing the value of D in Eq. [12]. The term, D , for $N' = 0.6$ was obtained in the following manner: For each of the cells No. 5, 6, 7, and 9, the voltage was calculated which would exist between the actual reference composition used and 0.6. This increment was added to the measured voltage between the reference used and saturation. The average of these sums, $-0.5294V$, was used to obtain the constant term, D , in Eq. [12].

APPENDIX III

From Eq. [2] one can derive the equations

$$\begin{aligned} X_{AlCl_3} &= (X_{Al_2Cl_6}/K_0)^{1/2} \\ n_{AlCl_4^-} &= K_1 n_{Cl^-} (X_{Al_2Cl_6}/K_0)^{1/2} \\ n_{Al_2Cl_7^-} &= K_2 n_{AlCl_4^-} (X_{Al_2Cl_6}/K_0)^{1/2} \end{aligned} \quad [AIII-1]$$

These quantities were substituted into the equations for aluminum mass balance and for charge balance

$$N = 2n_{Al_2Cl_7^-} + n_{AlCl_4^-} + n_{AlCl_3} + 2n_{Al_2Cl_6} \quad [AIII-2]$$

$$n_{Na^+} = n_{Al_2Cl_7^-} + n_{AlCl_4^-} + n_{Cl^-} \quad [AIII-3]$$

On expressing the quantities $n_{Al_2Cl_7^-}$ and $n_{AlCl_4^-}$ in Eq. [AIII-2] and [AIII-3] in terms of $X_{Al_2Cl_6}$ and n_{Cl^-} from Eq. [AIII-1], one obtains

$$N = [2K_2(X_{Al_2Cl_6}/K_0)^{1/2} + 1] K_1 n_{Cl^-} (X_{Al_2Cl_6}/K_0)^{1/2} + n_{AlCl_3} + 2n_{Al_2Cl_6} \quad [AIII-4]$$

$$n_{Na^+} = \left\{ [K_2(X_{Al_2Cl_6}/K_0)^{1/2} + 1] K_1 (X_{Al_2Cl_6}/K_0)^{1/2} + 1 \right\} n_{Cl^-} \quad [AIII-5]$$

On eliminating n_{Cl^-} in a simultaneous solution of Eq. [AIII-4] and [AIII-5], one can derive the equation

$$(Y-2)K_1K_2X_{Al_2Cl_6}/K_0 + (Y-1)K_1(X_{Al_2Cl_6}/K_0)^{1/2} + Y = 0 \quad [AIII-6]$$

where

$$Y = \frac{N - n_{AlCl_3} - 2n_{Al_2Cl_6}}{n_{Na^+}} \quad [AIII-7]$$

The total number of moles in solution is defined by

$$\begin{aligned} n_t &= 2n_{Na^+} + n_{AlCl_3} + n_{Al_2Cl_6} \\ n_t &= \frac{2n_{Na^+}}{1 - X_{AlCl_3} - X_{Al_2Cl_6}} \end{aligned} \quad [AIII-8]$$

By substitution of Eq. [AIII-8] into Eq. [AIII-7], and rearrangement, one obtains

$$Y = \frac{N}{1-N} - \frac{2(X_{Al_2Cl_6}/K_0)^{1/2} + 4X_{Al_2Cl_6}}{1 - (X_{Al_2Cl_6}/K_0)^{1/2} - X_{Al_2Cl_6}} \quad [AIII-9]$$

Equation [AIII-6] was solved for $X_{Al_2Cl_6}$ at various values of N , and then n_{Cl^-} could be obtained from Eq. [AIII-5]. From these two values and Eq. [AIII-8] and [AIII-1] all of the species compositions could be expressed as mole fractions. Figure 3 was constructed from these calculations.

SYMBOLS

a_i	thermodynamic activity of the i th species
A^{III}	electrochemically active species of aluminum in 3^+ oxidation state
E	electromotive force
E_j	any voltage difference in a concentration cell associated with the junction between the two cell compartments
F	the faraday constant
K_i	equilibrium constant for the i th chemical reaction
K_p	vapor phase dimerization constant
\ln	natural logarithm
m_{Cl^-}	molality of chloride ion
n_i	number of moles of i th species
n_t	total number of moles in system
n_i^0	initial number of moles of i th species
N	apparent mole fraction $AlCl_3$ (the over-all mole fraction of aluminum chloride in the $AlCl_3$ - $NaCl$ electrolyte)
P	vapor pressure of $AlCl_3$ - $NaCl$ melts
$p^{\circ}_{AlCl_3}$	partial pressure of monomeric $AlCl_3$ in vapor over pure aluminum chloride
$p^{\circ}_{Al_2Cl_6}$	partial pressure of dimeric Al_2Cl_6 in vapor over pure aluminum chloride
P°	vapor pressure of pure aluminum chloride
$P^{\Gamma}_{AlCl_3}$	hypothetical vapor pressure of pure aluminum chloride if vapor existed solely as monomeric $AlCl_3$
$P^{\Gamma}_{Al_2Cl_6}$	hypothetical vapor pressure of pure aluminum chloride if vapor existed solely as dimeric Al_2Cl_6
R	universal gas constant
T	temperature in degrees Kelvin
\tilde{V}	ideal molar volume of aluminum chloride vapor
w	weight of aluminum chloride added to melt
x	weight of aluminum chloride added to melt to just reach the equivalence point
X_i	mole fraction of i th species in melt
$y^{\circ}_{AlCl_3}$	mole fraction of monomeric $AlCl_3$ in vapor over pure aluminum chloride
$y_{Al_2Cl_6}$	mole fraction of dimeric Al_2Cl_6 in vapor over $AlCl_3$ - $NaCl$ melts

$y^\circ_{\text{Al}_2\text{Cl}_6}$ mole fraction of dimeric Al_2Cl_6 in vapor over pure aluminum chloride
 z_i number of equivalents per mole of the i th species

Manuscript submitted Sept. 27, 1971; revised manuscript received March 6, 1972. This was Paper 49 presented at the Cleveland Meeting of the Society, Oct. 3-7, 1971.

Any discussion of this paper will appear in a Discussion Section to be published in the June 1973 JOURNAL.

REFERENCES

- H. A. Øye and D. M. Gruen, *Inorg. Chem.*, **3**, 836 (1964).
- E. W. Dewing, *J. Am. Chem. Soc.*, **77**, 2639 (1955).
- B. Trémillon and G. Letisse, *J. Electroanal. Chem.*, **17**, 371 (1968).
- L. G. Boxall, H. L. Jones, and R. A. Osteryoung, Colorado State University, Personal communication, 1972.
- G. Torsi and G. Mamantov, *Inorg. Chem.*, **10**, 1900 (1971).
- J. R. Morrey and R. H. Moore, *J. Phys. Chem.*, **67**, 748 (1963).
- C. R. Boston in "Advances in Molten Salt Chemistry," Chap. 3, J. Braunstein, G. Mamantov, and G. P. Smith, Editors, Plenum Press, New York (1971).
- D. W. Seegmiller, G. W. Rhodes, and L. A. King, *Inorg. Nucl. Chem. Letters*, **6**, 885 (1970).
- M. Hansen, "Constitution of Binary Alloys," 2nd ed., p. 1106, McGraw-Hill Book Co., New York (1958).
- H. Bloom, "The Chemistry of Molten Salts," p. 65ff, W. A. Benjamin, New York (1967).
- R. H. Moore, J. R. Morrey, and E. E. Voiland, *J. Phys. Chem.*, **67**, 744 (1963).
- G. Torsi, G. Mamantov, and G. M. Begun, *Inorg. Nucl. Chem. Letters*, **6**, 553 (1970).
- G. E. Vrieland and D. R. Stull, *J. Chem. Eng. Data*, **12**, 532 (1967).
- "JANAF Thermochemical Tables," Dow Chemical Co., Midland, Mich. (1967).
- A. Smits and J. L. Meijering, *Z. Physikal. Chem. Abt. B.*, **41**, 98 (1938).
- L. G. Boxall and K. E. Johnson, *Trans. Faraday Soc.*, **67**, 1433 (1971).
- I. I. Naryshkin, *J. Phys. Chem. (USSR)*, **13**, 690 (1939).
- L. Rogers, Unpublished work cited in Ref. (21).
- N. V. Galitskii, *Russ. J. Inorg. Chem.*, **13**, 1607 (1968).
- T. Narita, T. Ishikawa, and R. Midorikawa, *Denki Kagaku*, **36**, 300 (1968).
- T. R. A. Davey, J. M. Floyd, and P. J. Marcantonio, Paper presented before the Meeting of American Institute of Metallurgical Engineers, New York, March 1971.
- A. A. Fannin, Jr., L. A. King, and D. W. Seegmiller, Frank J. Seiler Research Laboratory Technical Report SRL-TR-71-0018 (1971).
- J. Braunstein, K. A. Romberger, and R. Ezell, *J. Phys. Chem.*, **74**, 4383 (1970).
- J. O. Hirschfelder, C. F. Curtiss, and R. B. Bird, "Molecular Theory of Gases and Liquids," p. 250, John Wiley & Sons, Inc., New York (1954).
- N. D. Denisova and A. P. Baskova, *Zh. Fiz. Khim.*, **43**, 2353 (1964).

A Description of the Discharge Mode of Porous $\text{Ag}/\text{Ag}_2\text{O}$ Electrodes at Low Temperatures in KOH

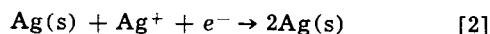
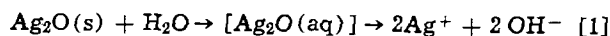
E. G. Gagnon*¹ and L. G. Austin*

Department of Material Sciences, The Pennsylvania State University, University Park, Pennsylvania 16802

ABSTRACT

Further results are presented on the anodic discharge of electroformed and pressed powder electrodes of $\text{Ag}/\text{Ag}_2\text{O}$ in eutectic KOH (aq) solution at low temperatures. It is concluded that the results are consistent with a mechanism $\text{Ag}_2\text{O}(\text{s}) + \text{H}_2\text{O} \rightarrow [\text{Ag}_2\text{O}(\text{aq})] \rightarrow 2\text{Ag}^+ + 2\text{OH}^-$, $\text{Ag}(\text{s}) + \text{Ag}^+ + e^- \xrightarrow{\text{slow}} 2\text{Ag}(\text{s})$. Loss of capacity at low porosity, high current density, and low temperature may be due to deposition of solid phases in the electrolyte.

In a previous publication (1), the loss of performance of $\text{Zn}/\text{KOH}/\text{silver oxide}$ cells at low temperatures was found to be predominantly due to increased polarization on the silver-silver oxide cathode. The discharge of porous $\text{Ag}/\text{Ag}_2\text{O}$ electrodes in 31 w/o (weight per cent) aqueous KOH at temperatures down to -60°F was studied by galvanostatic techniques; the general pattern of results is illustrated in Fig. 1 and shows five distinct regions of discharge, a, b, c, d, e, and f. It was suggested that the results are generally consistent with a mechanism



This paper gives additional data and discussion on this system.

Experimental

The experimental arrangement and methods for fabricating porous $\text{Ag}/\text{Ag}_2\text{O}$ electrodes have been de-

scribed elsewhere (1-3). Some of the electrodes were electroformed and were provided by Harry Diamond Laboratories; others were fabricated from Ag and Ag_2O powder using pressed powder techniques. The physical characteristics of some of these electrodes are shown in Table I.

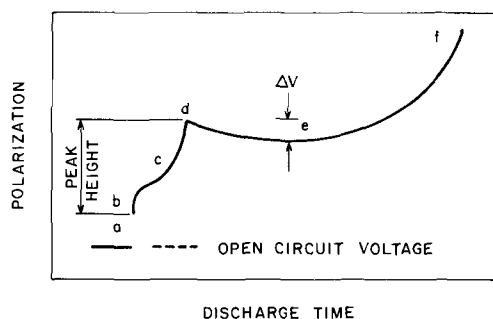


Fig. 1. Illustration of the normal discharge behavior of porous $\text{Ag}/\text{Ag}_2\text{O}$ electrodes at low temperature.

* Electrochemical Society Active Member.

¹ Present address: Electrochemistry Department, Research Laboratories, General Motors Corporation, Warren, Michigan 48090.

Key words: polarization, surface area, mass transport.

Table I. Description of electrodes

Designation	Weight per cent Ag	Weight per cent Ag ₂ O	Thickness (mm)	Porosity (%)
PP 18	9.95	90.05	0.34	14
PP 17	9.95	90.05	0.28	14
PP 28	9.95	90.05	0.35	62
PP 85	49.9	50.1	0.41	63
PP 73	49.8	50.2	0.34	19
PP 114	75.0	25.0	0.38	66
HDL	50.0	50.0	0.25	70
F 19	50.0	50.0	0.34	19
F 63	50.0	50.0	0.44	63

An electrode was mounted in a Teflon holder, with one face of about 1/3 cm² exposed to the electrolyte and a current collector press-fitted against the sealed back of the electrode. A Hg/HgO/KOH reference electrode with Luggin capillary was used. Ohmic polarization at various stages of discharge were obtained using a Hg-wetted relay for rapid make-and-break of the circuit and an oscilloscope, and hereafter will be referred to as IR polarization.

Results

In previous work (1) it was suggested that the length of the discharge plateau at c was due to a layer of abnormally active surface Ag₂O, corresponding to roughly a monolayer over the silver surface. This material discharges at lower polarizations (region c) than the bulk Ag₂O used in electrode preparation (region e). To test this hypothesis, electrodes PP 28, 85, 114 were prepared with approximately the same porosity and thickness but varying amounts of silver powder of specific surface 0.4 m²/g. These electrodes were allowed to equilibrate with electrolyte and then were galvanostatically discharged. The discharge time of plateau c vs. the amount of silver is shown in Fig. 2; the length of the step at c was roughly proportional to the weight of Ag present in the electrode at the beginning of the experiment. The slope of the line is about 4 sec/0.04g of Ag, which is equivalent to 0.24 m-coulomb/cm² Ag. These results indicate that whatever was stripped off the surface of the electrode was present on a Ag surface and had a thickness of about one monolayer.

As mentioned in an earlier paper (1), the length of plateau c is increased by anodic preforming, if the electrode is then immediately discharged after anodizing. The result is shown in Fig. 3. As might be expected, the amount of abnormally active Ag₂O formed (as indicated by the length of plateau c) is roughly proportional to the coulombs of anodization. Note that the anodization potential does not reach the Ag₂O/AgO potential, and the material cannot therefore be AgO. Figure 4 shows the result if the Ag₂O/AgO potential is exceeded; a peak b' is introduced between region b and c on the cathodic discharge curve. This is most likely a nucleation polarization effect associated with the transformation of AgO → Ag₂O. If, on the other hand, the anodized electrode is allowed to stand for 20 min and then discharged, the peak b' disappears. This indicates that the AgO which was formed during anodic charge had been removed on stand at open cir-

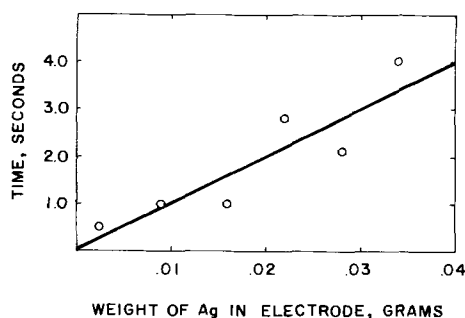
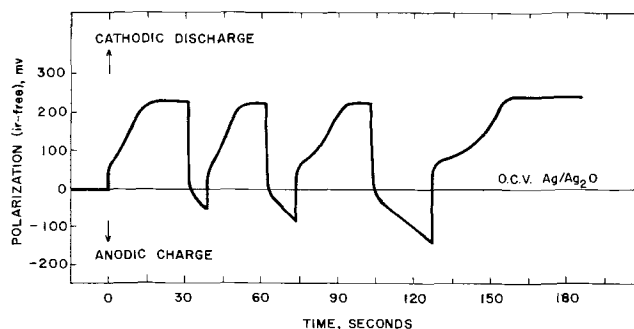
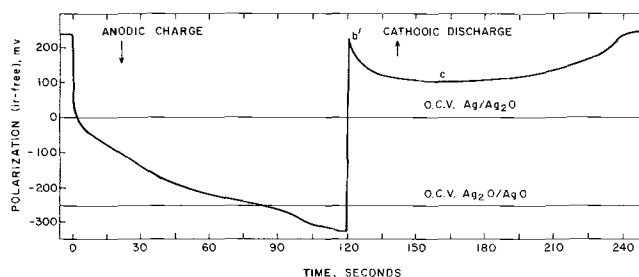


Fig. 2. Plot of time at plateau c vs. weight of Ag in electrode

Fig. 3. Effect of anodic charging on the galvanostatic discharge of HDL electrodes at low temperature; anodic charging stopped and reversed before the electrode passed through the Ag₂O/AgO potential.Fig. 4. Effect of anodic charging on the galvanostatic discharge of electrodes at low temperature; anodic charge stopped and current reversed after the electrode passed through the Ag₂O/AgO potential.

cuit. Presumably, after the brief charging period, the electrode was made up of Ag, the bulk Ag₂O used in the electrode preparation, and recently formed AgO and [Ag₂O], where the brackets indicate that the actual structure is not known. Since the electrode cannot be at both the Ag/Ag₂O and the Ag₂O/AgO potentials simultaneously, it is likely that at open-circuit conditions, the following reaction occurred, Ag + AgO → Ag₂O, so that when the cathodic current was switched back on, only Ag and Ag₂O were present in the electrode. Finally, anodized electrodes allowed to stand in electrolyte for 12 hr reverted to a length of plateau c the same as that without anodization, showing the unstable nature of the abnormally active material.

Considering the peak voltage ΔV at d, Fig. 5 shows the value of ΔV as a function of the amount of silver in the pressed-powder electrodes (top curve). The amount of silver in electroformed electrodes was also varied by partially discharging electrodes to different degrees at a low current density of 6 mA/cm²; they were then discharged at 30 mA/cm² and -52°F, ΔV measured, and the results plotted in Fig. 5 (bottom curve). The correspondence between ΔV and amount of

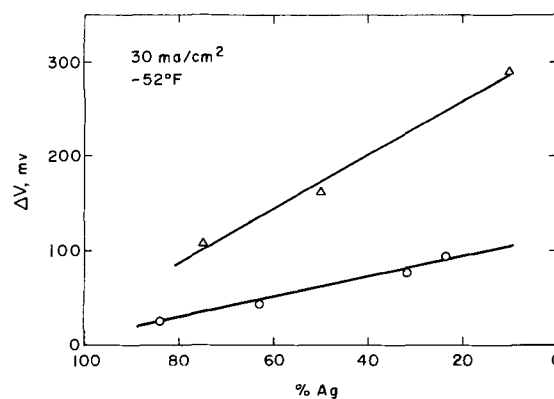


Fig. 5. Plot of ΔV vs. % Ag in the electrode: Δ pressed powder electrodes; ○ electroformed electrodes.

silver indicates that high silver area reduces the peak voltage difference ΔV ; it was also shown that the peak voltage is not primarily due to ohmic polarization. This eliminates the possibility that the polarization overshoot is caused (1) by a slow rate of solution of Ag₂O(s), and implies that it is due in some way to the Ag(s) + Ag⁺ + e⁻ → 2Ag(s) step in the mechanism.

The peak overshoot at d occurs regardless of whether the test electrode is an electroformed (HDL) or a pressed powder electrode. When the current was shut off after the peak region at d and then suddenly re-applied within seconds, the voltage returned to the same value without going through a peak. This behavior is evident in Fig. 3. However, if the electrodes were allowed to stand at open-circuit conditions for some time before the current was switched back on, a peak formed which was much more pronounced than the initial peak. This type of behavior has been noted with other oxide electrode systems, such as β -PbO₂ in H₂SO₄, MnO₂ in H₂SO₄, and Ti₂O₃ in alkaline media (4), at room temperature conditions.

Results from our previous studies (1,5) indicated that the process occurring in the major discharge plateau e was due to a simple, one-electron charge-transfer process, probably Ag(s) + Ag⁺(aq) + e⁻ → 2Ag(s). It was reasoned that if the area of the Ag was reduced significantly by fabricating electrodes with large particles of Ag, the performance of the electrode would be drastically reduced. Pressed powder electrodes were fabricated using a standard Ag₂O powder (approximately 1 μ) and silver powders of different particle sizes (Handy and Harmon). The electrodes fabricated with silver powders of approximately 1 μ in diameter were found to be strong and could be handled easily without the electrode crumbling. Electrodes made up with silver powders $\geq 20\mu$ were fragile and difficult to handle. Polarization curves for these electrodes had the same characteristic shape as described earlier. Figure 6 shows oscilloscopic traces for the a, b, c, d, e portions of discharge. In general, electrodes made with 1 μ Ag powder gave about the same type of results as the HDL electrodes, and performed much better than the electrode fabricated with the larger 149 μ Ag powder (see Table II).

Electrodes made with the larger particles of Ag displayed higher polarization peaks and larger IR polarization than did electrodes fabricated with 1 μ size Ag. After about 40 sec of discharge, the IR polarization had decreased to ~ 70 mV, of the same order as the HDL and pressed electrodes made up with 1 μ size Ag particles.

At low temperatures, there is a region f, after the plateau region, where the polarization increases rap-

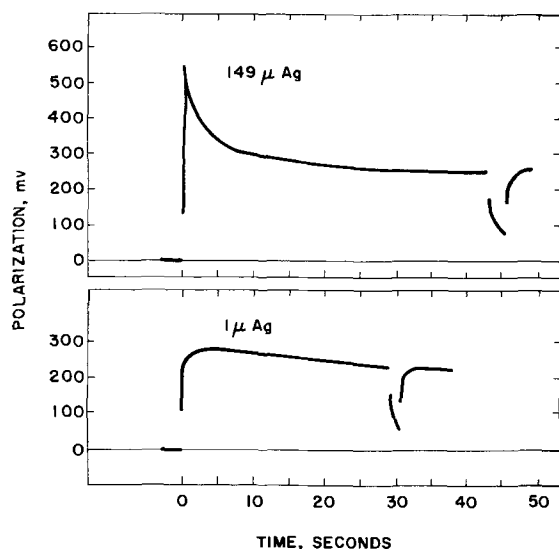


Fig. 6. Initial portions of the oscilloscopic traces of polarization vs. time of pressed powder electrodes varying in Ag particle size.

Table II. Effect of particle size of Ag on discharge of pressed powder electrodes at 30 mA/cm² and -52°F

Particle size of Ag (μ)	d Peak height (mV)	ΔV (mV)	IR polarization (mV)	
			Initial	Steady
1	280	65	100	70
149	560	310	170	70

idly as the electrode approaches complete discharge. To test whether the discharged electrode builds up a relatively impermeable (product) layer which gives rise to IR or mass transport effects, experiments were carried out using HDL electrodes that had been completely discharged at 200 mA/cm² (A) or 10 mA/cm² (B) and then placed as the outer-face in a 20-mil stack, giving a total stack thickness of 30 mil. In another arrangement (C), the outside electrode in the stack was a porous Ag electrode of the type used in the electroformation (1) of the HDL electrodes. Each stack was discharged at 30 mA/cm² and the results compared to a 20-mil stack of HDL electrodes having no discharged electrode at its face (D). The results of these tests are shown in Fig. 7 plotted as polarization (corrected for IR loss between test and Luggin tip) vs. discharge time. Initially, the polarization difference between electrodes D and C is that expected from the outer layer acting as a barrier to ion flow (ohmic effect). As discharge progresses and when discharge is nearly completed (in region f), the presence of the outer layers in A, B, C causes a large deviation from D, and the effect is not solely an ohmic effect. The higher the rate of discharge prior to using as an outer layer, the higher the polarization; e.g., A is worse than B is worse than C.

Earlier work showed that an electrode of 0.25 mm thickness and 70% porosity discharged at -52°F does not show marked effects of distributed reaction until currents in excess of 30 mA/cm² are used. However, lower porosity forces the electrode into the distributed reaction region, since the effective conductance of electrolyte in the porous system is approximately proportional to porosity squared (6). Low porosity ($\sim 14\%$) electrodes (PP 17 and 18) made up with 90% Ag₂O:10% Ag gave large initial peaks d at room temperature (130 mV) and at -52°F (850 mV). The peak for the 14% porosity electrode was about 350 mV greater, at -52°F, than that obtained for the 60% porosity electrode (PP 28). A low porosity (19%) pressed powder electrode (PP 73, Table I) was discharged at 30 mA/cm², then placed as the outside electrode in a two-electrode stack where the inside electrode had the same physical characteristics as PP 73. This two-electrode stack was then discharged at 30

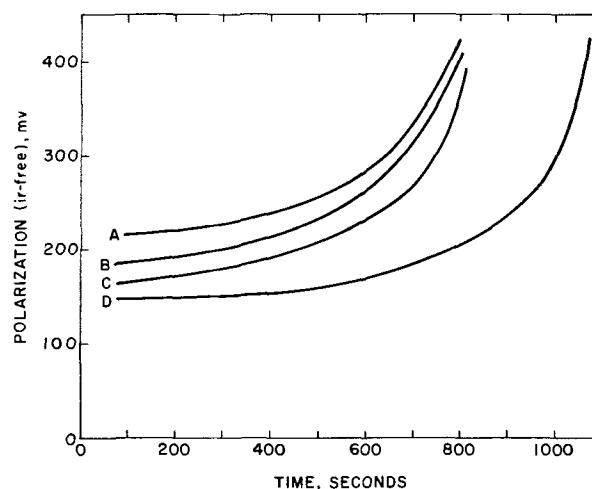


Fig. 7. Effect on polarization vs. time for stacks of HDL electrodes with an outer layer that had been previously discharged.

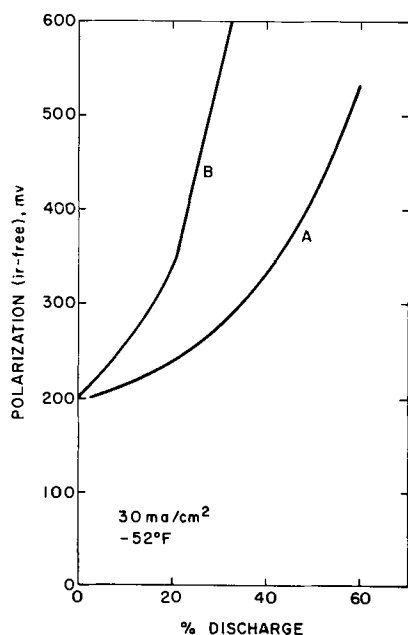


Fig. 8. Polarization vs. per cent discharge for low porosity electrodes.

mA/cm². Figure 8 shows the results for the discharge of a single PP 73 electrode (B, top curve) compared to the stack containing the discharged outer electrode (A, bottom curve). It can be seen that these low porosity electrodes give high polarization even at low states of discharge. Further, the results show that the use of a discharged electrode as the outer layer in a stack causes the polarization to increase much more rapidly than the electrode without the outer layer of discharged material.

At room temperature, discharge of 19 and 63% porosity, pressed powder, electrodes (F19 and F63, Table I) occurred with little polarization over most of the discharge (see Fig. 9); there was no difference in polarization up to 50% of discharge, at which time the polarization of the 19% porosity electrode started to increase faster than the 63% porosity electrode. As the electrodes approached 80% discharge, both gave rapidly increasing polarization (region f). At -52°F, the low porosity electrode gave high polarization and

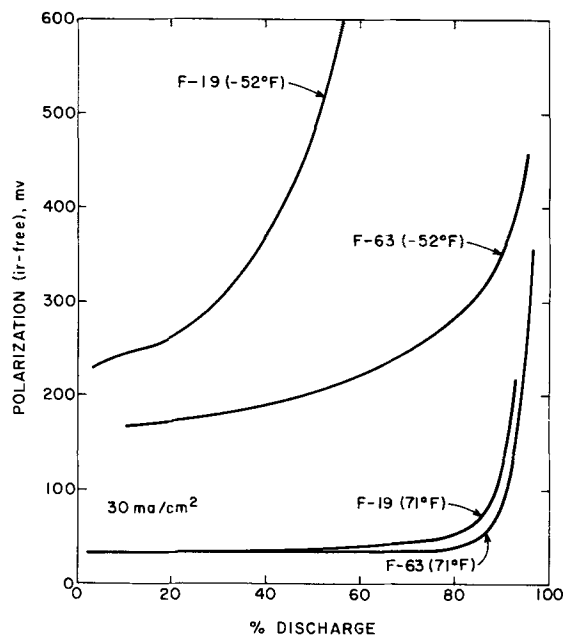


Fig. 9. Polarization vs. per cent discharged for different porosity electrodes at different temperatures.

the electrode reached 600 mV before the electrode was 60% discharged.

Discussion of Results

Explanation of discharge regions.—Region a.—For the electroformed HDL electrodes, this region represents the IR polarization which is due primarily to the electrolyte path between the surface of the test electrode and the tip of the Luggin capillary (1). For the pressed powder electrodes, however, this region varied with the physical properties of the pressed powder electrode. For example, electrodes made up with 90% Ag₂O and 10% Ag were found to have high initial IR polarization, which decreased to normal values before the electrode was 5% discharged. This effect was also noticed with high porosity (>80%) pressed powder electrodes (1). On the other hand, when pressed powder electrodes of 60% porosity were made with equal amounts of Ag and Ag₂O of about 1μ size, the initial IR observed was the normal value. It is concluded that in this case there is intimate contact of particles in the matrix leading to negligible electronic resistance, whereas smaller proportions of Ag to Ag₂O, or larger silver particles, or very high porosity, give significant contact resistance. As silver is deposited during charge, it grows as crystallites on existing silver, and these form conductivity bridges between the silver particles in the matrix. Thus, contact resistance becomes negligible after some discharge, or is initially negligible for an electroformed electrode. The formation of Ag crystallites on existing Ag is consistent with the kinetic model which proposes that the Ag₂O forms Ag⁺, which is then deposited in new locations where it can receive an electron, thus growing from pre-existing conductive Ag matrix.

Region b.—When the time scale in this region is expanded using faster sweep times (millisecond) on the oscilloscope, the voltage-time trace can then be used to estimate the double layer capacity of the electrode from $C = i/(dV/dt)$, providing faradaic current is small compared to the applied current. For a porous system, it is possible to get spurious results due to distributed capacity, but the mathematical treatment by Austin (3) gives a method of calculating the operating conditions for which correct results may be obtained. He concludes that the apparent capacity approaches the true capacity when $t \geq (1/3)\rho CL$, where ρ is the effective specific resistance of the electrolyte in the porous system (ohm-cm); C is the capacitance per plane area of electrode (farads/cm²), and L is the electrode thickness (cm). Distributed reaction produces a curvature in the initial portion of the potential-time trace (typically for about 7 msec for the HDL electrodes). Using the subsequent straight line portion gave an average capacity of 6300 μF for HDL electrodes containing 0.14g Ag. Taking the true capacity of Ag to be about 50 μ/cm² (7), this gives a double-layer capacity area of 0.4 m²/g, compared to the BET area of 0.7 m²/g. The double-layer capacity of bulk Ag₂O is much less than that of Ag, and if all of the silver surface were covered by a thick film of Ag₂O, the electroformed electrode would show a very small double layer capacity. If, however, electroforming of fine Ag powder produces discrete, fresh crystallites of Ag₂O which do not block the remaining silver surface, then the double-layer capacity of a 50% Ag:50% Ag₂O electrode would be that of the remaining silver, which is less than the total BET area. This is in accordance with the data.

Region c.—This region is the discharge of abnormally reactive material, which discharges at lower polarization than the bulk Ag₂O. The quantity of abnormal material at equilibrium with electrolyte (at open circuit) is proportional to the silver area and corresponds to roughly 0.24 mcoulombs/cm² of internal area. Electroforming increases the quantity of abnormally reactive material [Ag₂O], but the quantity reverts to the equiv-

alent of a few millicoulombs per square centimeter on standing in contact with electrolyte. Presumably this material is surface Ag₂O or AgOH in an amorphous form which is less stable than an ordered Ag₂O crystallite.

Region d.—The polarization decrease, ΔV , between the peak at d and the plateau at e is greater for a lower proportion of silver area, for lower temperature, for lower porosity, and for higher current density. In some cases, part of this decrease was directly due to lowered IR loss as a conducting network of silver was formed during discharge. It should be noted that a decreasing resistance not only reduces IR polarization but also indicates that silver area not previously in contact with the general matrix [and, therefore, not taking part in the reaction $\text{Ag}^+ + \text{e}^- \rightarrow \text{Ag}(\text{s})$] may be brought into play, thus lowering activation polarization. However, significant ΔV was found where the resistance did not change before and after the peak at d, and the peak at d is re-established when the electrode is allowed to stand at open circuit in contact with electrolyte. It is concluded that ΔV contains a major component of nucleation polarization from the nucleation of silver deposition sites.

Region e.—In addition to the discussion of this region given before (1,5) the additional work shows that polarization in this region is less for higher specific silver areas, indicating that the rate-determining step is the reaction $\text{Ag}(\text{s}) + \text{Ag}^+ + \text{e}^- \rightarrow 2\text{Ag}(\text{s})$.

Region f.—At lower currents and higher temperatures, an extended plateau region at e is seen, followed by sudden development of region f. As current is increased, or temperature decreased and/or the porosity of the electrode is decreased, region f starts at a lower per cent of discharge and is more spread out. Also, the use of discharged outer layers (Fig. 7 and 8) forces the polarization to reach higher values (in region f) than with electrodes not having the discharged outer layers. It does not seem possible to explain these effects solely on the basis of decreased reaction surface area, or increased hindrance to ionic and diffusional transfer due to reaction products blocking the pores. Gomis *et al.* (8) have shown that NiOOH/KOH/Cd cells discharged at -60°C gave only 10-20% of their rated capacity; the discharge behavior of the positive nickel electrode has similarities to that presented here for Ag/Ag₂O. The loss in capacity was attributed to the formation of ice and/or hydrates such as KOH·2H₂O, etc., blocking the pores of the electrodes. On discharge of Ag₂O, water is consumed and OH⁻ ions are formed; hence, water is the reactant which must be transported from the bulk of the electrolyte through the pores of the electrode to the interior, and hydroxyl ions must be transported from the interior of the electrode to the bulk electrolyte. The effect of discharge is thus to increase the concentration of the electrolyte in the interior of the electrode, which may lead to sufficient deviation from the eutectic composition to give crystal deposition.

Some idea of the magnitude of possible concentration changes occurring in the electrode can be obtained as

follows. The diffusion coefficient of water at room temperature is about (2) (10^{-5}) cm²/sec; assuming that the diffusion coefficient decreases with temperature in approximately the same ratio as the specific resistance of the electrolyte increases, the diffusion coefficient of water at -52°F is roughly 0.2×10^{-5} cm²/sec. The concentration changes occurring across a 10-mil HDL electrode at 30 mA/cm² at -52°F can be crudely approximated using "rate per unit area" $\simeq (D\Delta C/L)$, giving $\Delta C = 2.2\text{M}$. Lower porosity, lower temperature, increased depth of discharge, and the presence of added outer layers would all aggravate the concentration change. Thus, the concentration of the electrolyte at the back interior of the electrode at almost complete discharge should be about 9.4M (38 w/o KOH). From the phase diagram of the H₂O/KOH system (9) it follows that one or more hydrates might be deposited within the pores of the electrode under these conditions.

Such deposition may cause radical increases in polarization by (i) slowing the rate of dissolution of Ag₂O, (ii) slowing mass transport of dissolved silver to the conductive matrix, and (iii) causing electrolyte IR polarization effects due to pore blockage.

Acknowledgments

We gratefully acknowledge the National Science Foundation for financial assistance, and Handy and Harmon, New York, for generously supplying different types of silver powders.

We gratefully acknowledge the expertise of Warren T. Piver, Department of Chemical Engineering, North Carolina State University at Raleigh, in preparing some of the porous electrodes used in this work.

Manuscript submitted Oct. 4, 1971; revised manuscript received Feb. 11, 1972.

Any discussion of this paper will appear in a Discussion Section to be published in the June 1973 JOURNAL.

REFERENCES

1. E. G. Gagnon and L. G. Austin, *This Journal*, **118**, 497 (1971).
2. E. G. Gagnon, Ph.D. Thesis, The Pennsylvania State University, University Park, Pennsylvania (1970).
3. L. G. Austin, "Fuel Cells," NASA SP-120, Washington, D. C. (1971).
4. H. B. Mark and W. C. Vosburgh, *This Journal*, **103**, 616 (1961).
5. L. G. Austin and E. G. Gagnon, *Am. Inst. Chem. Eng.* **17**(s), 1057 (1971).
6. L. G. Austin, "Handbook of Fuel Cell Technology," C. Berger, Editor, Prentice Hall, Inc., Englewood Cliffs, N. J. (1968).
7. J. McCullum, R. W. Hardy, and R. F. Redmond, Technical Report AFAPL-TR-66-31, Battelle Memorial Institute, April (1966).
8. J. P. Gomis, J. C. Jarrousseau, and B. Monnerot, "Proc. 23rd Annual Power Sources Conference," p. 120 (1969).
9. R. W. Schult and W. T. Stafford, Contract No. STL/TR-60-0000-0934, Space Technology Laboratories, Inc., Los Angeles, Calif., Feb. 1960.

Corrosion Kinetics of Iron in Acid Sulfate Solutions

Effects of Impurities in the Metal

Sidney Barnartt*,¹

Edgar C. Bain Laboratory for Fundamental Research,
United States Steel Corporation, Research Center, Monroeville, Pennsylvania 15146

ABSTRACT

The kinetics of anodic iron dissolution and cathodic hydrogen evolution have been studied during the corrosion of four grades of iron: zone-refined, iron with 0.5 Mn (a/o) or 0.15 Ti added, and Ferrovac E. The titanium, which caused second-phase particles to accumulate on the surface, and manganese had little effect on iron-dissolution rates, but both additions inhibited hydrogen evolution significantly. Zone-refined iron yielded constant Tafel slopes: $b_a = 0.067 \pm 0.002$, $b_c = -0.11$ to $0.12V$. Impurities caused b_a and b_c to drift to more positive values during corrosion. A new method of analyzing anodic transients is recommended, and this analysis shows that the usual steady-state polarization curve is an unreliable indicator of reaction mechanism.

When iron corrodes in acid solutions at low pH, the corrosion rate is the same as the rate of anodic iron dissolution



and is also the same as the rate of cathodic hydrogen evolution



The reverse reaction of either [1] or [2] occurs at an insignificant rate at low pH. The rate of reaction [1], expressed as current I_1 at potential ϵ , is known to follow the Tafel equation which may be written as $\epsilon - \epsilon^\ddagger = b_a \log(I_1/I^*)$, where b_a is the anodic Tafel slope and ϵ^\ddagger is a reference potential. Since it is convenient to refer polarized potentials to the corrosion potential ϵ^* , the rate equation for reaction [1] takes the form

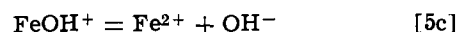
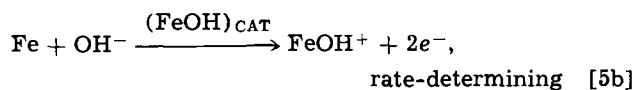
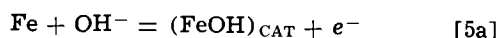
$$\epsilon - \epsilon^* = b_a \log(I_1/I^*),$$
$$\text{or } I_1/I^* = \exp\left[\frac{2.303}{b_a}(\epsilon - \epsilon^*)\right] \quad [3]$$

A similar relation may be written for reaction [2], which is also known to follow the Tafel equation. When current is applied to change the potential of a corroding electrode, the measured current I is just $\pm(I_1 - I_2)$, and is given by

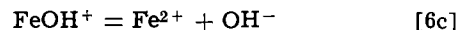
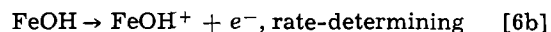
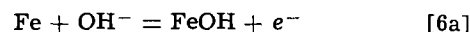
$$I/I^* = \pm \left\{ \exp\left[\frac{2.303}{b_a}(\epsilon - \epsilon^*)\right] - \exp\left[\frac{2.303}{b_c}(\epsilon - \epsilon^*)\right] \right\} \quad [4]$$

Here the cathodic Tafel slope b_c is always a negative number, b_a always positive, and the negative sign in front of the braces applies only when $(\epsilon - \epsilon^*)$ is negative.

Experimental determinations of the cathodic Tafel slope for purified iron have given values close to $b_c = -2.303 RT/0.5F$ (or $-0.118V$), which is in accord with (but does not itself establish) a slow H^+ -discharge mechanism for the hydrogen evolution reaction (1). Experimental determinations of b_a , however, have varied significantly. There are two theoretical values which are most frequently found experimentally. One of these is $b_a = 2.303 RT/2F$ (or $0.030V$), predicted by the Heusler mechanism (4-6) for reaction [1]



This mechanism, involving adsorbed FeOH as a catalyst, has found independent support (7, 8). The other theoretical value is $b_a = 2.303 RT/1.5F$ (or $0.039V$), predicted by the mechanism of Bockris, Drazic, and Despic (1-3)



This mechanism also has independent experimental support (9-11). The experimental methods of various authors who obtained the results $b_a = 0.03$ or $0.04V$ were all based on steady-state polarization data. The discrepancies in the steady-state data may have been caused by impurities in the electrolyte (1, 9), by impurities or high dislocation densities in the metal (11-13), and by rather large differences in the electrolysis time required to reach steady state [e.g., 5 sec for zone-refined iron vs. 20 min for Armco iron (11)].

In the present work, some effects of impurities in annealed iron on the kinetics of both iron dissolution and hydrogen evolution are investigated. Also, the validity of steady-state galvanostatic measurements is studied. The results lead to new recommendations for obtaining charge-transfer polarization data from galvanostatic potential-time curves. Minor impurities in the iron are found to inhibit the hydrogen-evolution reaction significantly. Impurities can also cause the Tafel slopes to change slowly as corrosion proceeds.

Experimental

Metals.—Four relatively pure grades of iron were studied: a high-purity zone-refined iron,² a zone-refined iron to which 0.5 Mn [atomic per cent (a/o)] was added (14), an "interstitial-free" iron gettered with 0.15 Ti,¹ and commercial Ferrovac E iron. Each material, obtained as rod, was cleaned by a standardized procedure consisting of chemical polishing in concentrated H_3PO_4 : 50% H_2O_2 (2:1 parts by volume) for 8 min, lightly etching in 6M H_2SO_4 for 3 min, then thorough rinsing in redistilled water and pure acetone. The metal was first reduced to 8 mm diameter by swaging with carefully cleaned dies. It was then re-cleaned and wire-drawn with molybdenum disulfide lubricant to 2.7 mm diameter, followed by centerless

² Prepared in the Fundamental Research Laboratory, United States Steel Corporation.

* Electrochemical Society Active Member.

¹ Present address: Technicon Instruments Corporation, Tarrytown, New York 10591.

Key words: corrosion, iron, impurity effects, electrode kinetics, Tafel slopes.

Table I. Impurity content, hydrogen anneal, and grain size of the four grades of iron

Metal: Atomic % Fe:	Fe(z-r) 99.97	Fe(z-r, 0.5 Mn) 99.4	Fe(0.15 Ti) 99.7	Ferrovac E 99.8
Analysis, a/o (nr = not reported)				
Mn	nr	0.50	<0.03	0.001
Ti	nr	nr	0.15	nr
Co	0.0012	0.0001	<0.005	0.005
Ni	0.0012	0.0011	0.005	0.01
Cr	0.0006	0.0005	0.004	<0.01
Cu	0.00003	0.002	<0.004	0.003
C	0.0056	0.005	0.020	0.09
N	0.0028	0.0016	0.004	<0.002
Si	0.0016	0.0020	0.016	0.012
S	<0.00002	0.0005	0.009	0.005
O	0.007	0.005	nr	0.002
P	0.0001	0.0009	0.004	0.005
Al	nr	0.003	0.006	nr
Other:	0.001 Na 0.0005 Cl 0.0003 Ge 0.0002 K 0.0001 Ca	0.006 B 0.002 Mg <0.001 Ca <0.001 Zn	0.0002 Pb 0.005 V 0.005 Nb 0.003 Mo 0.003 W 0.002 B 0.001 Zr	0.003 W 0.0006 Mo <0.004 V
Hydrogen anneal	600°C, 2 hr	700°C, 2 hr	800°C, 1 hr	900°C, 2 hr
Mean grain diameter (μm)	50	60	20	100

grinding and honing to obtain straight rods 2.4 mm in diameter. From these rods electrodes were cut to a length of 5 cm with one end hemispherical and the other end threaded. After recleaning the electrodes were annealed in very dry purified hydrogen, as shown in Table I which also lists the metal analysis. No second phase was seen microscopically in annealed specimens of the zone-refined iron and Fe (z-r, 0.5 Mn). Small particles of a second phase were present in the Ferrovac E, presumably iron oxide, and in the Fe (0.15 Ti), presumably a Ti(C,N) phase.

Solutions.—The solutions studied were 1M NaHSO₄ and 1M H₂SO₄ at 25°C. They were made from reagent grade chemicals and redistilled water and were purified by passage through acid-washed activated charcoal (15). The reversible hydrogen electrode potentials, on the standard hydrogen electrode (SHE) scale, were -0.028V in the sodium bisulfate ($\text{pH} = 0.48$) and -0.003V in the sulfuric acid solution ($\text{pH} = 0.05$).

Cell.—The cell, shown schematically in Fig. 1, was designed so that only the three metal electrodes and Pyrex glass contacted the electrolyte. The test electrode t (also the similar auxiliary electrode a) was threaded tightly into a bare Ferrovac E holding rod which fit snugly into the Teflon stem T of a sealable Teflon-glass valve v (Lab Crest valve, Fischer and Porter Company). The bottom edges of the two valves, and the top edges of the three Teflon sleeves used to

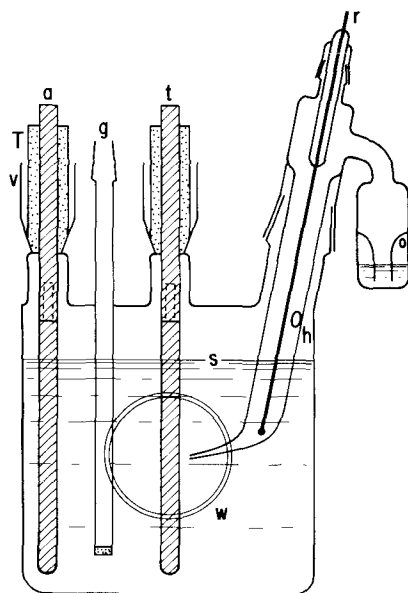


Fig. 1. Schematic diagram of cell

seal the standard-taper joints, were the only Teflon areas exposed to the vapor phase. It was found in preliminary experiments that contact of the iron electrodes in the liquid phase with Teflon or glass insulators must be completely avoided, for this induced trenching attack along the metal-insulator-solution contact line and affected the corrosion kinetics. The simple electrode arrangement of Fig. 1 always yielded uniform corrosion with no evidence of localized pitting or trenching.

The two cylindrical iron electrodes were 2 cm (17 \times electrode radius) apart and were immersed to a depth 3.5 cm below solution level s (total solution depth 3.8 cm). With this geometry, the difference between the current density at the center of the test electrode and the mean current density was expected to be acceptably small. The capillary tip (diameter d) of the reference compartment was positioned about 3d from the test electrode; measurement of the tip to electrode distance, facilitated by the optical window w, permitted accurate IR drop corrections. The hydrogen reference electrode r was a platinumized platinum wire in the same electrolyte. A hydrogen atmosphere was maintained in the cell. Purified hydrogen entered the cell at g and passed through hole h into the reference compartment before exiting through a bubbler. Hydrogen flow was turned off 3 min before a potential-time curve was recorded; preliminary measurements showed no change in reference potential during this 3-min period.

Just before being inserted in the cell, the iron test specimen was first chemically polished by a 3-min immersion in H₃PO₄-H₂O₂, and then etched 3 min in 6M H₂SO₄ followed by 1 min in 0.5M HNO₃. This precleaning procedure yielded reproducible corrosion behavior.

Electrode polarization measurements.—Galvanostatic pulses were applied from a constant-current source (Model 225, Keithley Instruments, Inc.), which was switched rapidly from a dummy load to the cell by use of a mercury-wetted contact relay (Type HG 3A1008, C. P. Clare Company). Potential-time curves were recorded on a storage oscilloscope (Tektronix 564 with 3A9 vertical amplifier and 3B3 time base) and photographed. Corrosion potentials were measured with a high-impedance millivoltmeter (Orion Model 801) standardized from a K3 potentiometer (L&N).

Polarization curves at a specified corrosion time t^* (corresponding to corrosion current density i^* and potential ϵ^*) were obtained by applying a series of anodic and cathodic constant-current pulses, each of duration 0.5-2 sec, with sufficient time between pulses to permit the potential to return to the same value of ϵ^* within $\pm 10^{-3}\text{V}$. By limiting the magnitude of the applied current so that the polarized electrode potential remained within the range $\epsilon^* \pm 0.06\text{V}$, reproducible and hystere-

sis-free polarization curves were obtained, as described in detail in a preliminary report of the present work (16). These polarization curves were analyzed by a three-point method developed for the pre-Tafel region (17), a method which yields i^* , b_a , and b_c with good precision (16).

Results and Discussion

Potential-time curves.—The four grades of iron studied all had regular cathodic behavior: during a short constant-current pulse the potential rose smoothly from the corrosion potential to a steady value, and on opening the circuit it decayed smoothly back to ϵ^* .

Anodic galvanostatic behavior was more complex, and here proper interpretation of the ϵ - t curves was crucial for obtaining consistent values of i^* and b_a . In the first 30 hr or so of corrosion each of the four metals yielded anodic ϵ - t curves similar to those in Fig. 2A and B. These curves exhibit the characteristic $\Delta\epsilon$ maximum ($\Delta\epsilon_m$) reported by Heusler (4) and later authors. However, the curves are not in accord with Heusler's finding that the total potential change on opening the circuit ($\Delta\epsilon_{oc}$) is equal to $\Delta\epsilon_m$. For the four grades of iron studied here $\Delta\epsilon_{oc}$ was always smaller than $\Delta\epsilon_m$ if the curve contained an appreciable peak.

As corrosion proceeds, the rise to a maximum $\Delta\epsilon$ becomes sharper (compare Fig. 2A and 2B), an effect associated with a large increase in the current required to produce a given change in potential. The existence of the anodic peak persisted through 75 hr of corrosion with Fe(z-r), Fe(z-r, 0.5 Mn), and Fe(0.15 Ti). With Ferrovac E, however, the sharp peak disappeared after 40 hr of corrosion, Fig. 2D, within the restricted range $\Delta\epsilon \leq 0.06V$ of this study (but peaks still appeared at higher applied currents).

The anodic curves, whether the usual peaked ones or the peakless Ferrovac E curves, exhibited a drop in potential to a value less than ϵ^* at the end of the anodic pulse. In the case of peakless curves (Fig. 2D) the value of $\Delta\epsilon_{oc}$ was independent of pulse time over a wide range, 0.5-5 sec, and was the same as the extrapolated value $\Delta\epsilon_{t=0}$. In the case of peaked curves where $\Delta\epsilon_{oc} < \Delta\epsilon_m$, the value of $\Delta\epsilon_{oc}$ was again essentially constant as illustrated in Fig. 2C, which shows consecutive pulses of 1 and 8 sec. The examples of ϵ - t curves given in Fig. 2 all refer to 1M NaHSO₄ solution, but the same general behavior was found in 1M H₂SO₄.

These facts led to the interpretation depicted in Fig. 3, in which the general transient is considered to be the

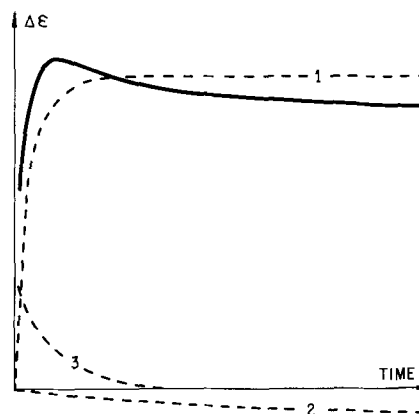


Fig. 3. The three additive components (broken curves) of the anodic transient (solid curve). Curve 1. Charging of the double layer at constant current I . Curve 2. Shift of corrosion potential ($I = 0$) with time. Curve 3. Superpolarization.

sum of three effects: double layer charging (curve 1), ϵ^* shift (curve 2), and the superpolarization effect (curve 3). According to Roiter *et al.* (18) superpolarization is not characteristic of the charge-transfer process since it can be made to disappear. The present work is in agreement with this, in that all four grades of iron exhibited decreasing superpolarization after long corrosion times. With these metals, the superpolarization at any t^* decayed to a negligible value within about 0.1 sec.

It is concluded that $\Delta\epsilon_{oc}$ obtained from half-second pulses contains no superpolarization component and is a valid measure of the desired charge-transfer controlled potential. This conclusion was tested in the following way. A pair of pre-Tafel cathodic and anodic polarization curves, corresponding to a given corrosion time t^* of the system Fe(z-r)/1M NaHSO₄, was analyzed by the three-point method using anodic $\Delta\epsilon_m$ data; the values of i^* , b_a , and b_c so obtained showed wide variations. When the corresponding $\Delta\epsilon_{oc}$ anodic data were substituted, the resulting values of b_a and b_c were constant within $\pm 3\%$. Similar results were found at other corrosion times, both for NaHSO₄ and H₂SO₄ solutions. These results show that our $\Delta\epsilon_{oc}$ measurements are in agreement with an I - ϵ relation of the form of Eq. [4], whereas the $\Delta\epsilon_m$ measurements (to which the "nonsteady-state" data in the literature correspond (4, 20) are inconsistent with Eq. [4].

Based on these results, we recommend $\Delta\epsilon_{oc}$ as the most reliable measurement of charge-transfer polarization for the iron-acid system. Steady-state potential measurements, on the other hand, cannot be readily interpreted. During steady-state measurements there occur significant and variable shifts in the reference corrosion state (in potential ϵ^* and current I^*). Such measurements violate the theoretical principle that all points on a true polarization curve, whether in the Tafel or pre-Tafel region, must correspond to a single reference corrosion state. Because of this violation no attempt was made in the present work to establish steady-state anodic polarization curves. Clearly the slope of an approximately linear steady-state Tafel region can differ appreciably from the true charge-transfer slope. Thus a steady-state measurement of b_a is unreliable as a criterion for distinguishing between proposed iron-dissolution mechanisms.

All of the results to follow were based on $\Delta\epsilon_{oc}$ measurements. All measured currents were converted to current densities by use of the geometrical electrode area.

Dependence of ϵ^* , i^* , b_a , and b_c on corrosion time.—Corrosion parameters for a typical 72 hr experiment with the system Fe(z-r)/1M NaHSO₄ are summarized in Fig. 4. The corrosion potential, recorded as a function of time, showed a characteristic slow rise before leveling off. The potential rise was not greatly changed

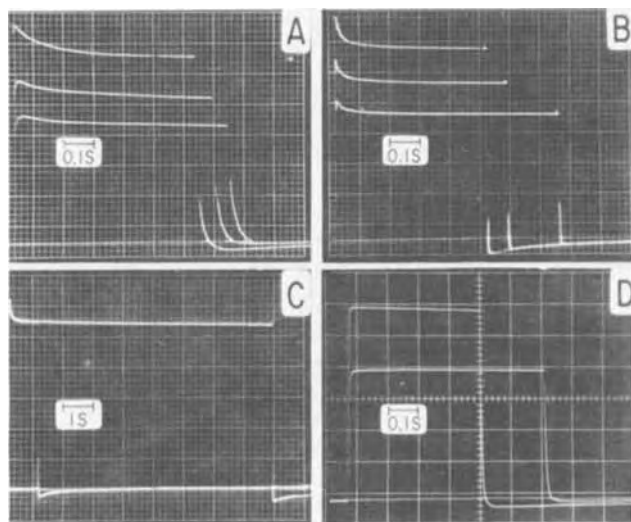


Fig. 2. Constant-current anodic pulses, iron in 1M NaHSO₄, vertical scale 10 mV per major division, horizontal trace $\epsilon = \epsilon^*$. A: Fe(z-r) at $t^* = 5.5$ hr; 1.5, 2.5, and 5 Am⁻². B: Fe(z-r) at $t^* = 23$ hr; 40, 60, and 90 Am⁻². C: Fe(z-r) at $t^* = 71.5$ hr; 60 Am⁻². D: Ferrovac E at $t^* = 42$ hr; 15 and 30 Am⁻².

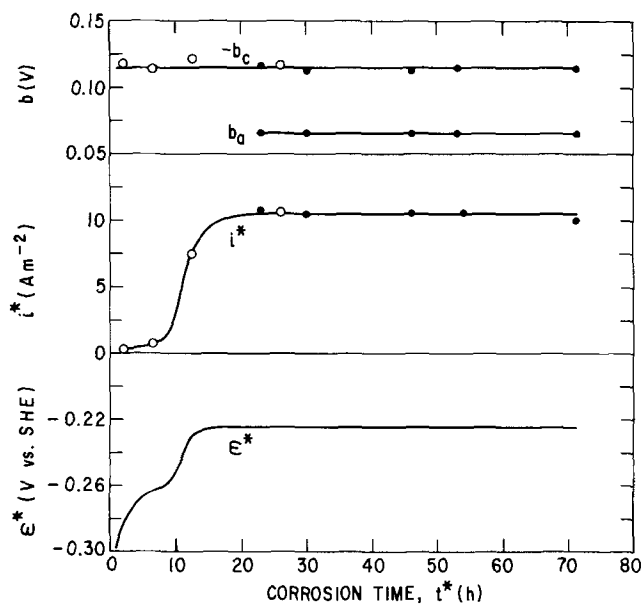


Fig. 4. Variations of corrosion potential, corrosion current, and Tafel slopes with corrosion time, Fe(z-r) in 1M NaHSO₄. ●, By three-point analysis; ○, from cathodic Tafel line.

by using other etching pretreatments of the electrode. Also, if the electrode were allowed to corrode until ϵ^* leveled off, and were then removed, re-etched, and replaced in the cell, ϵ^* reverted almost to its initial value and the rising portion of the ϵ^* - t^* curve was qualitatively reproduced.

Polarization curves (i - ϵ) covering the potential range $\epsilon^* \pm 0.06V$ were determined periodically by application of anodic and cathodic pulses, and these pre-Tafel curves were analyzed by the three-point method to obtain i^* , b_a , and b_c . In the particular case of zone-refined iron, however, this procedure was usable only after ϵ^* leveled off. At shorter times ϵ^* shifted too rapidly: a shift of more than 3 mV during the interval required to obtain the two polarization curves led to appreciable errors in i^* and the two Tafel slopes. Fortunately it was possible in the early corrosion period to obtain linear cathodic Tafel lines, over the limited range ($\epsilon^* = 0.09$ - $0.14V$), by applying a minimum number (four to five) of cathodic pulses. In this way b_c and i^* were evaluated. Such data, shown as open circles in Fig. 4, agreed well with data obtained by the three-point method where the two methods overlapped. During the period after ϵ^* leveled off, ϵ^* varied less than ± 0.5 mV during measurement of the two polarization curves, and the latter were readily analyzed to yield b_a as well as b_c and i^* .

Figure 4 shows that b_c remained substantially constant over the entire corrosion period. Also b_a was constant where it was evaluated, namely after ϵ^* had leveled off. Initially i^* was remarkably small, about two orders of magnitude less than the final steady current.

The other zone-refined metal, Fe(z-r, 0.5 Mn), gave curves showing all the same general trends as in Fig. 4. The Fe(0.15 Ti) metal, however, differed in showing changing Tafel slopes during the initial period of changing ϵ^* and i^* (Fig. 5). Both b_a and b_c drifted to larger (more positive or less negative) values, before becoming constant in the steady corrosion condition. Figure 5 shows that ϵ^* drifted more slowly for Fe(0.15 Ti) than it did for the zone-refined metals during the early corrosion period, so that it was possible to obtain pre-Tafel polarization curves with little hysteresis and to evaluate b_a after 5 hr of corrosion.

The steady corrosion conditions achieved by the three metals just discussed are compared kinetically in Fig. 6. Shown here are the calculated "partial" log i - ϵ relations for anodic iron dissolution and cathodic hydrogen evolution. These lines are established by the

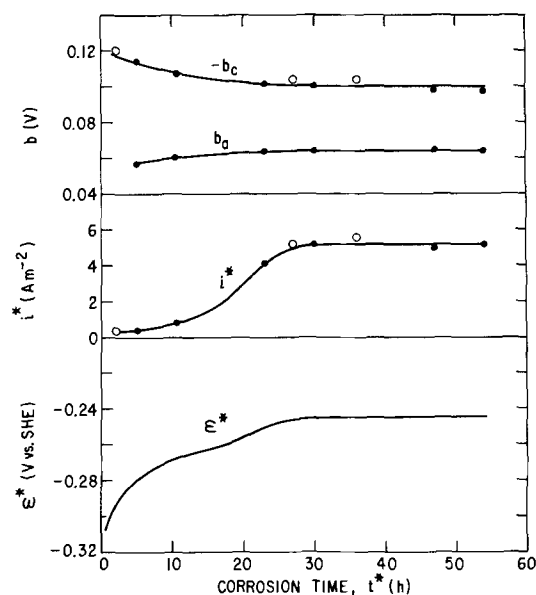


Fig. 5. Variations of corrosion potential, corrosion current, and Tafel slopes with time, Fe(0.15 Ti) in 1M NaHSO₄. ●, By three-point analysis; ○, from cathodic Tafel line.

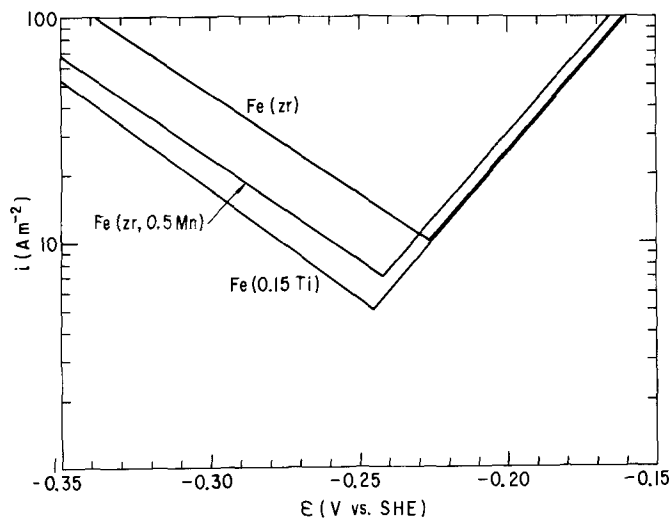


Fig. 6. Steady reaction rates of anodic iron dissolution and cathodic hydrogen evolution in 1M NaHSO₄ as functions of potential, $t^* > 30$ hr.

values of i^* , b_a , and b_c , determined from the measured polarization curves by the three-point analysis. The intersection of the anodic and cathodic lines gives the values of ϵ^* and i^* . The addition of manganese or titanium primarily reduced the hydrogen evolution rate at a given potential, manganese having a smaller effect than titanium (with its accompanying minor impurities). The reduction in hydrogen evolution rate is associated with a shift of ϵ^* to a less noble potential and with a reduction in corrosion rate.

A summary of all of the long-time corrosion data obtained for the four metals studied is presented in Table II. The data on zone-refined iron in the two solutions studied (pH 0.05 and 0.48) are in accord with the well-known effect that increasing acidity reduces the rate of the iron-dissolution reaction at a given potential. These data also exhibit an increase in hydrogen-evolution rate with increasing acidity, in conformity with the slow-discharge mechanism of hydrogen evolution.

Table II and Fig. 6 show that manganese or titanium additions to iron had no effect on b_a in the steady- ϵ^* region. Our measured range $b_a = 0.065$ - $0.069V$, based on $\Delta\epsilon_{oc}$ measurements, is remarkably close to the range 0.065 - $0.070V$ obtained by Bockris, Drazic, and Despic

Table II. Mean kinetic parameters for iron corrosion in 1M NaHSO₄, corrosion time 30-70 hr

Metal	Solution	ϵ^* (V vs. SHE)	i^* (A m ⁻²)	b_a (V)	b_c (V)
Fe(z-r)	1M NaHSO ₄	-0.226	10	0.065	-0.112
	1M H ₂ SO ₄	-0.198	15	0.069	-0.120
Fe(z-r, 0.5 Mn)	1M NaHSO ₄	-0.242	7	0.066	-0.110
	1M NaHSO ₄	-0.245	5	0.065	-0.102
Ferrovac E	1M NaHSO ₄	-0.29 ^a	7	0.074	-0.100
	1M H ₂ SO ₄	-0.25 ^b	15	0.078	-0.113

^a After 70 hr corrosion, ϵ^* decreasing slowly.

^b After 47 hr corrosion, ϵ^* decreasing slowly.

(1) from $\Delta\epsilon_m$ measurements in sulfate solutions at low pH (1-2). In these low pH solutions their steady-state values were in the range $b_a = 0.045-0.054V$, appreciably higher than the value 0.039V required by the Bockris *et al.* mechanism. Many other authors have obtained approximately $b_a = 2.303 RT/F$ (or 0.059V) from $\Delta\epsilon_m$ measurements in various electrolytes (20). Whether our larger value 0.067 ± 0.002 , as determined from $\Delta\epsilon_{oc}$ data, is significant mechanistically or whether the difference from the value 0.059V is attributable to small amounts of surface impurities cannot be settled yet (see below).

Ferrovac E exhibited a major difference from the other metals listed in Table II, in that a steady corrosion potential was not reached even after 75 hr of corrosion, although the values of i^* , b_a , and b_c all leveled off. A typical set of corrosion-time data is plotted in Fig. 7. The initial portion of the ϵ^*-t^* curve was similar to that for the other metals, but as the corrosion current approached its final value ϵ^* went through a maximum and thereafter decreased considerably. The existence of a maximum in the ϵ^*-t^* curve for annealed Ferrovac E was reported by Akiyama, Patterson, and Nobe (11) but without interpretation. The kinetic significance of this maximum is revealed upon plotting the calculated partial anodic and cathodic log $i-\epsilon$ relations as a function of corrosion time, Fig. 8. These data show that, after the maximum ϵ^* is passed, the iron-dissolution rate continues to increase whereas hydrogen evolution reaches a maximum rate (for any given potential) and then decreases continuously. Even though both the iron-dissolution and hydrogen-evolution rates are changing continuously, i^* becomes apparently constant after 40 hr of corrosion (Fig. 7).

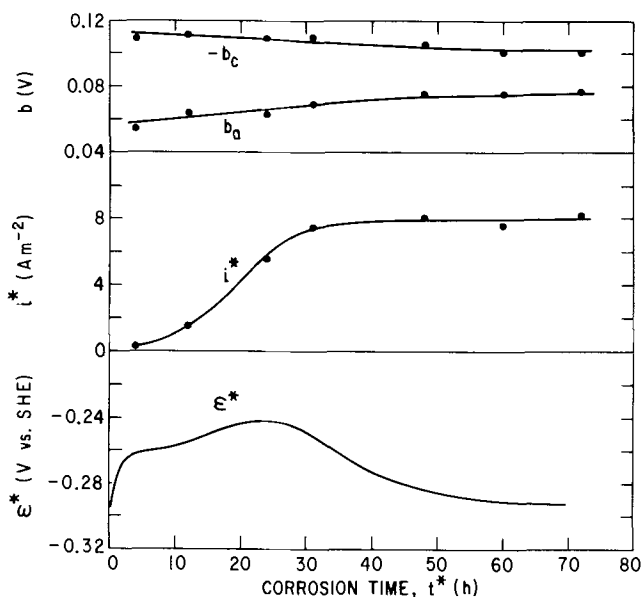


Fig. 7. Variations of corrosion potential, corrosion current, and Tafel slopes with time, Ferrovac E iron in 1M NaHSO₄.

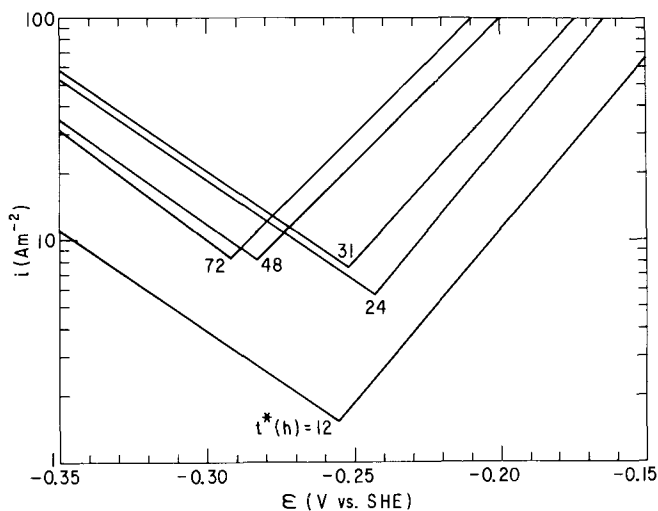


Fig. 8. Movement of the anodic and cathodic Tafel lines with corrosion time, Ferrovac E in 1M NaHSO₄.

A major kinetic effect of impurities in the metals studied here is a reduction in the hydrogen-evolution rate at a given potential. In Fe(0.15 Ti) and Ferrovac E the impurities also induce slow changes of Tafel slope as corrosion proceeds, causing b_a and b_c to increase with time from their initial values of approximately $b_a = 0.06V$ and $b_c = -0.12V$. It is reasonable to suppose that slowly developing impurity effects arise from an enrichment of impurities on the corroding metal surface. This has been demonstrated recently by Cartledge (19) for iron containing 0.1% by weight technetium, where the corroded surface layer was shown by β -emission measurements to be highly enriched in technetium. It remains a possibility that even the two zone-refined metals could have suffered some surface-impurity enrichment by the time of the first b_a measurement (Fig. 4), and that a rise of b_a similar to that shown in Fig. 5 for Fe(0.15 Ti) could have occurred during the initial corrosion period.

Surface analysis.—Surface morphology of the corroded metals was studied by scanning electron microscopy. One typical example of the surface appearance of each of the four metals is shown in Fig. 9. In all cases crystallographic etching was observed. Some relatively flat facets were found on Fe(z-r), Fe(0.15 Ti), and Ferrovac E, but on Fe(z-r, 0.5 Mn) all crystal surfaces had the distinctive roughness seen in Fig.

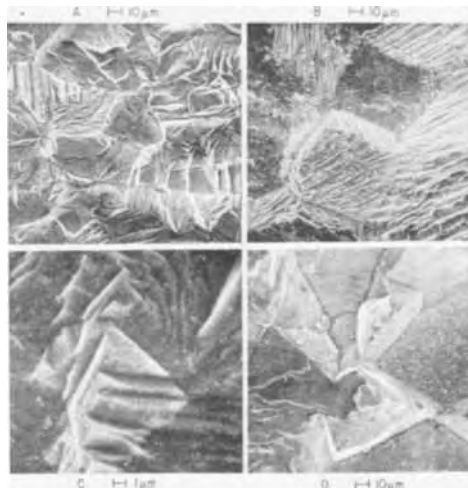


Fig. 9. Scanning electron micrographs of iron surfaces after corrosion in 1M NaHSO₄ for the following times: A, Fe(z-r), 50 hr; B, Fe(z-r, 0.5 Mn), 52 hr; C, Fe(0.15 Ti), 70 hr; D, Ferrovac E, 30 hr.

9B. No pitting and no preferential grain-boundary attack occurred on any of the metals.

Second-phase particles were not discernible on corroded surfaces of the two zone-refined metals, which showed no internal second phase. Also no second-phase particles were seen on corroded Ferrovac E; oxide particles present inside the metal would be expected to dissolve during the corrosion process. Second-phase particles were present on corroded Fe(0.15 Ti), as shown in Fig. 9C where they appear as irregular white specks. These were proven to be titanium-rich particles, in the scanning electron microscope, by having the electron beam stationary and focused at the center of the particle, then analyzing emitted x-rays with an energy-dispersion x-ray analyzer.

Microprobe analyses of corroded surfaces of the Fe(z-r, 0.5 Mn) metal showed a manganese content slightly lower than that of the uncorroded surface. Since the analysis was considered reliable to $\pm 5\%$ and the difference between the corroded and uncorroded surfaces was less than 5%, these results were inconclusive with respect to changes in surface manganese content. Similarly, no conclusive evidence was found for surface depletion or enrichment of other impurities on corroded zone-refined iron or Ferrovac E by analyzing long-count x-ray spectra.

Undoubtedly traces of impurity equivalent to less than a monolayer could influence the kinetic behavior of the iron surface, but such traces are not readily detectable by the x-ray method employed, which samples the surface to a depth of roughly 2000Å. More sensitive techniques will be needed, such as the radio-tracer method already mentioned (19) and methods based on removing sub-monolayer amounts, analyzing either the material removed (as by mass spectrometer) or the newly created surface (as by Auger spectroscopy).

Conclusions

1. The most reliable measure of charge-transfer polarization from anodic galvanostatic transients is the total potential fall, $\Delta\epsilon_{oc}$, at the end of a short current pulse.

2. The $\Delta\epsilon_{oc}$ data yield an anodic Tafel slope of 0.067V for zone-refined iron in sulfate solutions at low pH. This is higher than the commonly observed steady-state values. The steady-state Tafel slope is subject to error from drift in the reference corrosion state, hence it is not a good indicator of the reaction mechanism. This weakens the present experimental

support of each of the two popular iron-dissolution mechanisms.

3. Trace impurities in the iron can reduce cathodic hydrogen-evolution rates considerably while having little effect on anodic iron-dissolution rates.

4. Impurities can cause both the anodic and cathodic Tafel slopes to drift to more positive values as corrosion proceeds.

Acknowledgment

The author is indebted to Drs. W. H. Hu, W. C. Leslie, and E. T. Turkdogan for supplying the bulk metals used in this study, to Drs. W. H. Hu and G. Langford for assistance in specimen preparation, and to Dr. J. L. Bombard and his group for scanning electron microscopy and microprobe analysis.

Manuscript submitted Dec. 2, 1971; revised manuscript received March 10, 1972.

Any discussion of this paper will appear in a Discussion Section to be published in the June 1973 JOURNAL.

REFERENCES

1. J. O'M. Bockris, D. Drazic, and A. R. Despic, *Electrochim. Acta*, **4**, 325 (1961).
2. J. O'M. Bockris and D. Drazic, *ibid.*, **7**, 293 (1962).
3. J. O'M. Bockris and H. Kita, *This Journal*, **108**, 676 (1961).
4. K. E. Heusler, *Z. Elektrochem.*, **62**, 582 (1958).
5. K. F. Bonhoeffer and K. E. Heusler, *Z. Physik. Chem. N.F.*, **8**, 390 (1956).
6. K. E. Heusler and G. H. Cartledge, *This Journal*, **108**, 732 (1961).
7. W. J. Lorenz, H. Yamaoka, and H. Fischer, *Ber. Bunsenges. Physik. Chem.*, **67**, 932 (1963).
8. C. Voigt, *Electrochim. Acta*, **13**, 2037 (1968).
9. E. J. Kelly, *This Journal*, **112**, 124, 1255 (1965).
10. J. J. Podesta and A. J. Arvia, *Electrochim. Acta*, **10**, 171 (1965).
11. A. Akiyama, R. E. Patterson, and K. Nobe, *Corrosion*, **26**, 51 (1970).
12. W. J. Lorenz and G. Eichkorn, *Ber. Bunsenges. Physik. Chem.*, **70**, 99 (1966).
13. G. Eichkorn, W. J. Lorenz, L. Albert, and H. Fischer, *Electrochim. Acta*, **13**, 183 (1968).
14. W. C. Leslie, F. J. Plecity, and J. T. Michalak, *Trans. Met. Soc. AIME*, **22**, 691 (1961).
15. S. Barnartt, *Can. J. Chem.*, **47**, 1661 (1969).
16. S. Barnartt, *Corrosion*, **27**, 467 (1971).
17. S. Barnartt, *Electrochim. Acta*, **15**, 1313 (1970).
18. V. A. Roiter, W. A. Juza, and E. S. Polujan, *Acta Physicochim. URSS*, **10**, 389 (1939).
19. G. H. Cartledge, *This Journal*, **118**, 1752 (1971).
20. G. M. Florianovich, L. A. Sokolova, and Y. M. Kolytyrkin, *Elektrokhimiya*, **3**, 1027 (1967).

Dissolution Potentials and Activation Energies of InSb Single Crystals

M. E. Straumanis* and Lih-da Hu

Departments of Metallurgical and Chemical Engineering and Graduate Center for Materials Research, University of Missouri-Rolla, Rolla, Missouri 65401

ABSTRACT

The rest (or corrosion) and dissolution potentials of InSb single crystals in HCl were determined. There is no potential difference (within error limits) between the inverse {111} faces in pure HCl. A difference of up to 44 mV and more develops as soon as the InSb electrode is anodically dissolved. The potential becomes less noble in the sequence In{111}, {100}, {110}, Sb{ $\bar{1}\bar{1}\bar{1}$ }. The Tafel relationship is observed over three decades of current density. With additions of FeCl₃, FeCl₂, K₃Fe(CN)₆, K₄Fe(CN)₆, H₂C₄H₄O₆ to 2N HCl, the anodic potentials of both inverse {111} faces are shifted to more active values; the ϵ'_H of In{111} is always nobler than that of Sb{ $\bar{1}\bar{1}\bar{1}$ }. There are indications that the various potentials observed are a function of current density within the pores of a protective layer, Sb₄O₅Cl₂. The apparent activation energy, ca. 20 kcal/mole, of the anodic dissolution reaction is nearly the same on all crystallographic planes of InSb. The rate of anodic dissolution of Sb{111} in pure 2N HCl is 3-7 times larger than that of the inverse face at the same potential.

In a previous publication (1) the anodic dissolution reaction of InSb single crystals in HCl was described and the cited literature can be found there. However, no potential measurements were made. The anodic potentials obtained for a InSb single crystal electrode under various conditions of corrosion or dissolution are reported here.

The construction of the electrode and the type of contact with the crystal were similar to that of GaAs (2); the potentials were measured against a normal calomel electrode using a salt bridge (~3.5N KCl) and a Luggin capillary. The data were reduced to the standard hydrogen scale. The measurements were performed with a precision potentiometer and the potential (ϵ')-current density, i , curves were obtained by potentiostatic and galvanostatic methods. Purified N₂ was introduced into the reaction vessel containing the electrodes.

The n-type, undoped single crystals were obtained from the Monsanto Company (St. Louis, Missouri) and were grown in the [111] direction by the Czochralski or the gradient-freeze technique. The impurity level was less than 1 ppm, the carrier concentration was 8×10^{15} atoms·cm⁻³, mobility 1.7×10^5 cm²·V⁻¹·sec⁻¹, and the resistivity 0.005 ohm·cm; 670 etch pits·cm⁻² were developed on the {111} planes. The surface area subjected to the electrolyte was between 0.35-0.82 cm² for the various electrodes.

Results

Rest potentials.—The potential readings were taken as soon as possible after the electrode was chemically pre-etched with CP-4 (1). Then the next reading was made after 5 min and subsequent readings after 15 min intervals. No anodic current was applied.

The results are summarized in Fig. 1. Figure 1 shows that:

1. The ϵ'_H 's of the inverse {111} faces in the same concentration of HCl are approximately equal, $\Delta\epsilon'_H \sim 10$ mV; however In{111} has a slightly more noble potential than does Sb{ $\bar{1}\bar{1}\bar{1}$ }.
2. For both inverse {111} faces, the higher the normality of HCl, the less noble is the ϵ'_H .
3. Time has no particular influence on ϵ'_H ; steady potentials are usually obtained after 15 min of immersion.
4. The potentials are reproducible within ± 10 mV.

*Electrochemical Society Active Member.

Key words: InSb, dissolution potentials, activation energies, Tafel lines.

Significant potential changes occurred in the presence of Fe³⁺, added as FeCl₃ to the HCl. The potentials of the inverse {111} faces differed by as much as ~40 mV; the In{111} faces were always more positive than the Sb{ $\bar{1}\bar{1}\bar{1}$ }. However, the behavior of the InSb electrode in the presence of Fe³⁺ employing no anodic current required further investigation.

Anodic potential-current density relationship in 2N HCl.—The anodic potential measurements were carried out as previously described (1, 2). The platinized platinum electrode serving as the cathode was coupled with the InSb electrode. During each run, the time, milliammeter and potentiometer readings were recorded. The readings were taken after 5 min at each milliammeter setting. All current densities were plotted against the measured anodic potential (SHE). The oxygen was excluded (N₂ atmosphere).

The separation of the dissolution potentials into those characteristic of the In{111} and Sb{ $\bar{1}\bar{1}\bar{1}$ } faces occurred even at low anodic current densities. The potentials were in the vicinity of those of InSb in 2N HCl as shown in Fig. 1. At a current density of 3×10^{-3} mA/cm² the difference was about 12 mV. This increased with increasing current density (Fig. 2). It is evident from Fig. 2 that:

1. The ϵ'_H of the four different faces becomes less noble in the sequence: In{111}, {100}, {110}, Sb{ $\bar{1}\bar{1}\bar{1}$ }.

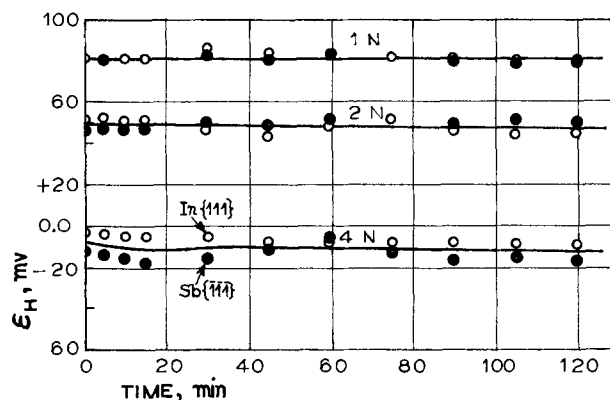


Fig. 1. Rest potentials, ϵ'_H of InSb single crystals in various concentrations of HCl (reagent grade) at 25°C. ○—In{111} and ●—Sb{111} faces.

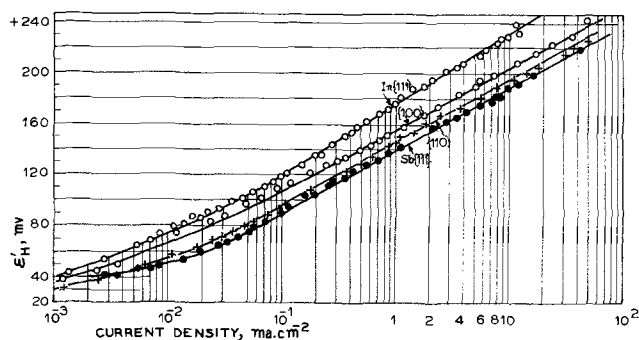


Fig. 2. Anodic dissolution potentials ϵ'_H of InSb vs. log of current density i of the single crystal planes In{111}, Sb{111}, {110}, and {100} at 25°C. 2N HCl.

The potential difference between the inverse 111-faces approaches 30 mV at 3×10^{-2} mA/cm² and 44 mV at 10 mA/cm².

2. All four anodic polarization curves obey the Tafel relation over about three decades of current density (3×10^{-2} to 30 mA/cm²).

3. Within this range of current density the latter three faces give parallel Tafel lines with a slope of ~ 48 mV/log i , while the first line has a slope of ~ 56 mV/log i . However, significant departures from these potentials occur upon addition of oxidizers or reducers to the HCl.

ϵ'_H -log i relationship in 2N HCl in the presence of Fe^{3+} .—The results of these measurements are summarized in Fig. 3, where the Tafel lines of InSb in pure 2N HCl are redrawn to show the influence of Fe^{3+} . The Tafel region occurs only between 1 and 10 mA/cm². Clearly, in the presence of Fe^{3+} ions, the potentials of both inverse {111} faces are shifted to more active values by approximately the same amount (~ 33 mV in 0.0004M and 37 mV in 0.002M solutions of Fe^{3+}). The slope of the Tafel line of In{111} in both solutions is 62 mV/log i and that of Sb{111} is about 58 mV/log i .

Similar measurements were also performed by adding $FeCl_2$ solutions to the 2N HCl. As the solutions were prepared in air, part of the Fe^{2+} ions oxidized

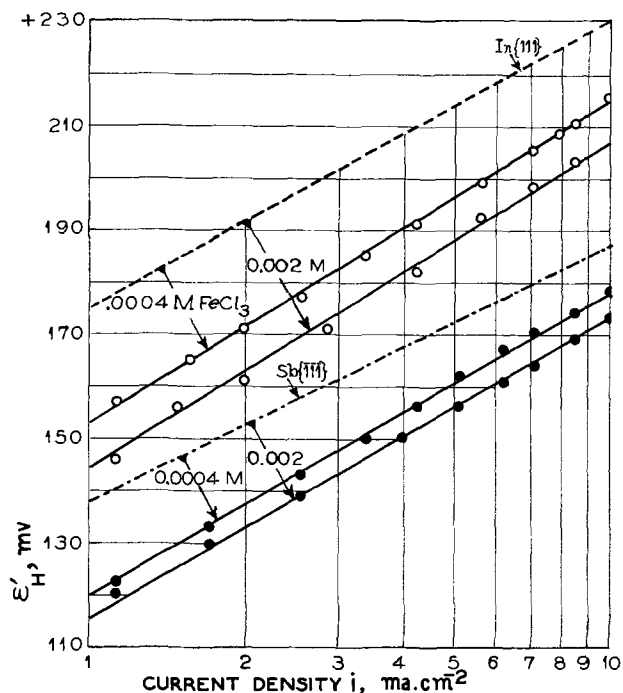


Fig. 3. ϵ'_H of the inverse {111} faces of InSb vs. log i in 2N HCl in presence of Fe^{3+} at 25°C. Dashed lines — ϵ'_H in pure 2N HCl.

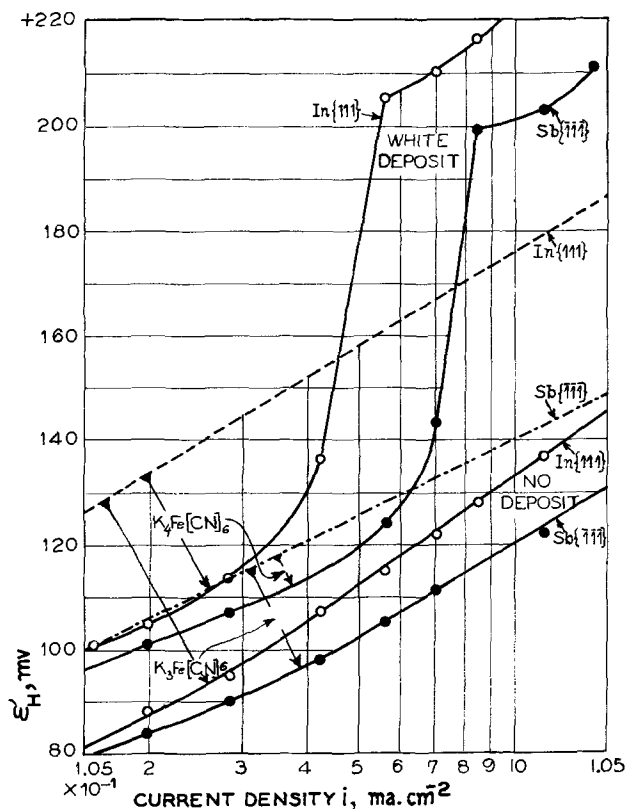


Fig. 4. ϵ'_H of the inverse {111} planes of InSb vs. log i in 2N HCl in presence of 0.00125M solutions of $K_4[Fe(CN)_6]$ and of $K_3[Fe(CN)_6]$. Dashed lines — ϵ'_H in pure 2N HCl.

to Fe^{3+} and, therefore, the results obtained resembled those with Fe^{3+} . There was a shift of potentials to more active values; however, the polarization lines were not as parallel as shown in Fig. 3.

The influence of $K_4[Fe(CN)_6]$ and of $K_3[Fe(CN)_6]$ on the anodic potential.—The ϵ'_H -log i curves in the presence of potassium ferro and ferri cyanides are shown in Fig. 4. The influence of the cyanides was observed even below 1 mA/cm². The potentials of the inverse {111} planes shifted to more active values, the action of $K_3[Fe(CN)_6]$ being stronger. No deposit was observed on the anodes when $K_3[Fe(CN)_6]$ was added. However, a white sediment appeared on both inverse faces in the presence of $K_4[Fe(CN)_6]$ at current densities above 0.4 mA/cm². In all the measurements the potential of the In{111} face was more positive than that of the Sb{111}. Evidently the potential changes were connected with the formation and presence of deposits on the anodic surfaces. This possibility was checked by trying to remove chemically the oxide layer which is formed on Sb (of the InSb) in HNO_3 .

Potentials of InSb in HNO_3 in the presence of tartaric acid.—It is known that antimony oxide dissolves in $H_2C_4H_4O_6$ yielding water-soluble, antimony-tri-tartrate. Polarization curves of the InSb{111} inverse planes are reproduced in Fig. 5. They show that, indeed, at low anodic current densities (up to 0.3 mA/cm²), the potentials of both faces coincide. A possible explanation is offered in the discussion. The Tafel relationship is nevertheless partially fulfilled.

Activation energies.—The chosen temperature of the water bath, containing the U-vessel with the InSb and Pt electrodes, was maintained at $\pm 0.2^\circ C$. Purified N_2 was bubbled slowly through the electrolyte (HCl). Figure 6 shows the curves obtained for the inverse {111} planes of InSb. As can be seen, the anodic dissolution potential ϵ'_H for both inverse {111} planes becomes less noble with increasing temperature and the Tafel lines exist over three decades of i . The slopes differ slightly: 55.6 mV/log i for In{111} and 47.1 for

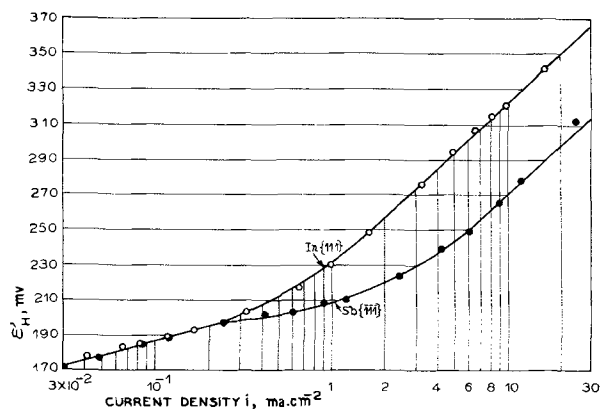


Fig. 5. ϵ_H of the inverse $\{111\}$ planes of InSb vs. log of anodic current density in 1N HNO_3 -1N $\text{H}_2\text{C}_4\text{H}_4\text{O}_6$ at 25°C.

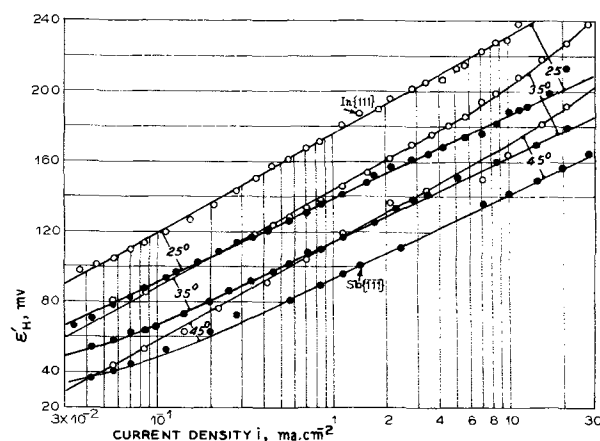


Fig. 6. ϵ_H of In $\{111\}$ and Sb $\{111\}$ vs. log i in 2N HCl at three temperatures. Galvanostatic measurements.

Sb $\{111\}$. The In $\{111\}$ faces are always nobler than the inverse by ~ 36 , 27, and 20 mV at 25°, 35°, and 45°C respectively.

Current density measurements for four different crystal planes of InSb, were plotted against T^{-1} (Fig. 7).

The apparent activation energies E_a were calculated (Table I) from the slopes of the lines (Fig. 7).

Discussion

As InSb consists of two elements, it is interesting to see what the dissolution potentials of the latter are relative to that of InSb. In Fig. 8 the respective potentials are plotted vs. log i .

Figure 8 reveals that the dissolution potentials of the inverse $\{111\}$ faces are close to that of Sb and at a current density of 1 mA/cm² there is no difference within experimental error limits. However, metallic Sb starts to passivate at about 15 mA/cm², whereas the Sb $\{111\}$ face remains active at higher current densities and the Tafel relationship results over nearly 3½ decades of log i . Evidently In, which passes simultaneously into solution (1), prevents the formation of a tight, adherent Sb-oxychloride protective layer on the InSb. In fact a thicker layer can be removed easily with a soft brush (1). Metallic In, which displays a

Table I. E_a for the anodic reactions on various planes of InSb in 2N HCl

Plane	E_a galvanost. kcal/mole	E_a potentiost. kcal/mole
In 111	24.0	21.3
Sb 111	21.3	20.3
110	—	18.5
100	—	—
	Average	20.05

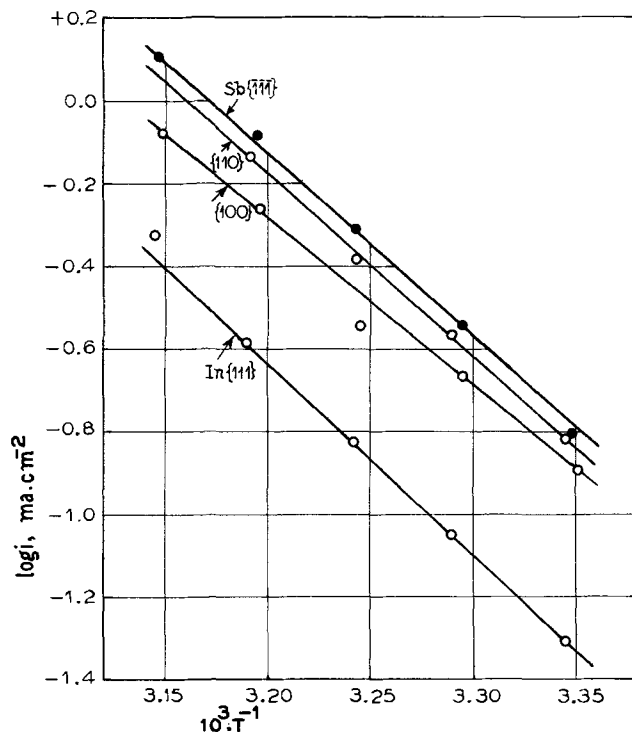


Fig. 7. Arrhenius plot of the anodic dissolution of four planes of InSb single crystals in 2N HCl.

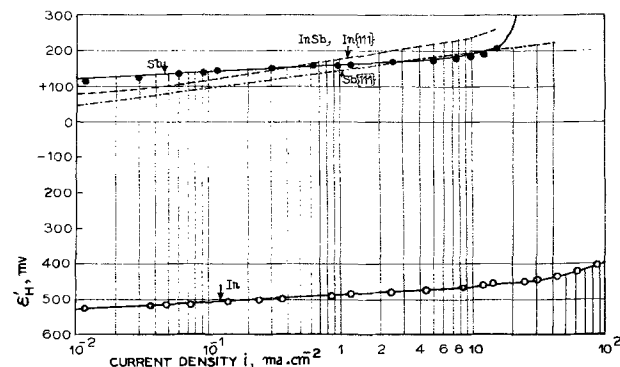


Fig. 8. ϵ_H of metallic In, metallic Sb (both 99.999% pure) and of the inverse faces of InSb vs. log i in 2N HCl, 25°C.

very negative potential in 2N HCl (Fig. 8) loses much of its free energy by combining with Sb. Thus, the In in InSb might be in a form which is more electropositive than the Sb. At high anodic current densities part of the latter accumulates on the surface and is embedded in the oxychloride layer (anodic disintegration of Sb). This results in a lower electron number for InSb [Ref. (1), Fig. 6].

For immersion of InSb into pure 2N HCl, where the corrosion rate is very low [Ref. (1), Table I], the protective layers formed on all crystallographic faces are evidently of the same consistency and adherence. Therefore, there is little, if any, potential difference between the inverse $\{111\}$ faces and the potential is strongly dependent on the pH of the solution (Fig. 1) as it is for a pure Sb electrode (3, 4).

However, as soon as an anodic current is applied, the oxychloride layer is at least partially removed from the various faces of the InSb crystal. The difference in valency of the two constituents now comes into play and this can be noticed, especially on the inverse $\{111\}$ planes. The potential difference between these planes is the greatest among those investigated and the potentials become more negative in the order: In $\{111\}$, $\{100\}$, $\{110\}$ and Sb $\{111\}$ (Fig. 2). Explanations of this difference have been offered by other authors (5, 6). GaAs in KOH behaves similarly (2) (Fig. 3).

If now at the same current density various crystallographic planes exhibit different anodic potentials (Fig. 2), it can be assumed (if InSb behaves like a metal) that this is due to the difference in the structure of the protective films. During anodic dissolution both inverse {111} planes of InSb are covered with a Sb-oxychloride film (1), but this film may be, for unknown reasons, more dense and/or more adherent to the In{111} rather than to the Sb{ $\bar{1}\bar{1}\bar{1}$ } plane. Moreover, it is also probable that In (within the InSb structure), due to the loss of free energy, is present in a different form, than in a metal, and now has less ability to go into solution. Both assumptions contribute to the presence of a more noble potential on the In{111} than on the Sb{ $\bar{1}\bar{1}\bar{1}$ } face, especially under conditions of anodic dissolution. The other planes should exhibit intermediate values. This anodic behavior, as a current density effect, requires a smaller pore size on the In{111} face which results in a higher current density within the pores and a steeper Tafel line will be obtained (Fig. 2). When the anodic current is decreased, the quality of the previous oxide film on the faces will be restored and consequently the potential difference between the inverse {111} planes will diminish (Fig. 2) and finally approach zero (Fig. 1).

Therefore, agents which partially remove the Sb-oxide film from the InSb electrode should also decrease the potential difference between the inverse planes. This is the case when InSb is dissolved in 1N HNO₃ containing tartaric acid (Fig. 5). At low current densities the oxide film is thin on both planes, since the newly formed Sb-oxide easily dissolves in tartaric acid. However, at current densities above 0.3 mA · cm⁻² the thickness of the film increases so much that the dissolution of the film is not rapid enough and a separation of the potentials occurs. The film on the In{111} should be denser. This follows from the inclination of the Tafel lines: at low current densities—26 mV/log *i* and above 4 mA · cm⁻² ~ 92 mV/log *i*. Furthermore the potential of InSb in 1N HNO₃ is much more positive than in HCl (compare Fig. 2 and 5) caused partially by the difference in the composition and properties of the layers. Denser oxide or hydroxide films are formed in HNO₃ because of the oxidizing action of the acid.

Increasing the concentration of a nonoxidizing acid (e.g., HCl) should decrease the thickness of the surface oxide layers, which results in a more negative potential, as shown in Fig. 1.

Similar to the behavior of the Sb electrode, the potential of the InSb electrode is very easily disturbed by oxidizing and reducing agents, and it is difficult to understand this disturbance. For instance (Fig. 3), minute amounts of FeCl₃ added to 2N HCl shift the potential of both inverse {111} planes to less noble values, the shift increasing with increasing concentration of the Fe³⁺ ions. Nevertheless the Tafel line relationship persists and the In{111} planes are always nobler than the inverse. Evidently Fe³⁺ ions are adsorbed by the oxychloride layer, changing its properties, increasing its pore size, which results in a lower pore current density and in a more active potential.

The action of K₄Fe(CN)₆ and of K₃Fe(CN)₆ additions is still more complicated. In both cases the potential of the anode becomes more negative relative to the dissolution potentials in pure 2N HCl (see Fig. 4). Again the In{111} is more noble than the inverse face.

If the InSb is anodically dissolved in a 2N HCl-0.00125M K₄Fe(CN)₆ solution, then at current densities higher than 0.4 mA · cm⁻² the formation of a white colloidal layer is observed on both inverse {111} planes. The layer can be removed by rinsing with water. No deposit was observed in a 2N HCl-0.00125M K₃Fe(CN)₆ solution, even at current densities above 10 mA · cm⁻². According to Mellor (7) K₄Fe(CN)₆ forms a white precipitate with In³⁺ but K₃Fe(CN)₆ does not. This was confirmed experimentally. Thus the jump in the

curves (Fig. 4) is explained as the onset of the precipitate formation. At about 1 mA · cm⁻² the precipitate is already so dense that one can see it readily. Thus this surface layer causes a strong polarization, which does not occur for K₃Fe(CN)₆, because the salt formed is water soluble and the slope of the Tafel lines above 0.6 mA · cm⁻² is ~ 70 mV for In{111} and 60 mV for Sb{ $\bar{1}\bar{1}\bar{1}$ }.

With increasing temperature the dissolution potentials become more negative (Fig. 6) partially because of thermodynamic reasons and also due to the decrease of the anodic current density within the pores (widening of the pores with increasing temperature).

Since the slopes of the Tafel lines fluctuate mostly between 40 and 60 mV/log *i*, the possibility of a one electron charge transfer as a rate-determining step is not excluded. Nevertheless, the rate of dissolution in pure 2N HCl of Sb{ $\bar{1}\bar{1}\bar{1}$ } at the same potential is 3-7 times larger than that of the inverse face, in agreement with the concept of pore width. Evidently, the effective current density (within the pores) is the same on all the faces. However, as the pores of the protective layer on Sb{ $\bar{1}\bar{1}\bar{1}$ } are larger, a stronger current results from this face.

The apparent activation energies (Table I) for the anodic reactions on various planes of InSb are the same within the error limits, suggesting that the reactions (1) are all the same, independently of the plane chosen for the anode. However, the *E*_a value of ~ 20 kcal/mole is relatively high for a dissolution reaction. A similar value of 16.7 kcal/mole was also obtained for the anodic dissolution reaction of the compound GaAs in KOH (2). Much lower activation energies were found for metals simply dissolving in acids, e.g., 5.3 ± 0.5 kcal for Hf dissolving in 1N HF or in a mixture of HF and HCl (8) and 3.8 to 4.2 kcal for Zr in 0.2N HF or 0.1N HF + 1.0N HCl respectively (9). However, when the oxygen content of Zr was increased up to 7% b.w., the *E*_a increased to 5.9 kcal. Simultaneously the rate of dissolution decreased, evidently the dissolved oxygen tightly bound by the Zr atoms hampered the reaction rate with the acid.

As InSb exhibited a much lower dissolution rate (1), a higher activation energy should be expected for this reaction, because it is chiefly the value of *E*_a which determines the rate (10), even of an anodic dissolution process. The activation energy of ~ 20 kcal/mole was, therefore, expected. Thus a high activation energy of dissolution of InSb (and of GaAs) in comparison with that of pure metals is characteristic of the former and corresponds to its reaction sluggishness.

Acknowledgments

The authors are grateful to Dr. W. J. James, Professor of Chemistry and Director of the Graduate Center for Materials Research, for assisting with the present manuscript, and to the New Enterprise Division of the Monsanto Company in St. Louis, especially to Mr. J. B. McNeely, for donation of the InSb single crystals.

This is Contribution No. 135 from the Graduate Center for Materials Research.

Manuscript submitted Nov. 11, 1971; revised manuscript received March 6, 1972.

Any discussion of this paper will appear in a Discussion Section to be published in the June 1973 JOURNAL.

REFERENCES

1. M. E. Straumanis and Lih-da-Hu, *This Journal*, **118**, 433 (1971).
2. M. E. Straumanis, J. P. Krumme, and W. J. James, *ibid.*, **115**, 1050 (1968).
3. H. T. S. Britton and R. A. Robinson, *J. Chem. Soc.*, **1931**, 458.
4. H. T. S. Britton, "Hydrogen Ions," Vol. I, Van Nostrand, Princeton (1956).
5. H. C. Gatos and M. C. Lavine, *This Journal*, **107**, 427 (1960).

6. H. C. Gatos and M. C. Lavine, *J. Phys. Chem. Solids*, **14**, 169 (1960).
7. J. W. Mellor, "A Comprehensive Treatise of Inorganic and Theoretical Chemistry" Vol. V, pp. 393-397; Vol. IX, pp. 378-388 and 503-509, Longmans, Green & Co., London (1922).
8. W. J. James, J. W. Johnson, and M. E. Straumanis, *Z. Physik. Chem.*, **27**, 199 (1961).
9. W. J. James, W. G. Custead, and M. E. Straumanis, *Corrosion Sci.*, **2**, 237 (1962).
10. A. J. Rutgers "Physical Chemistry," p. 627, Interscience Publishers, New York (1953).

The Effect of Two-Dimensional Nucleation on the Rate of Electrocrystallization

Ugo Bertocci

Solid State Division, Oak Ridge National Laboratory, Oak Ridge, Tennessee 37830

ABSTRACT

The effect of random two-dimensional nucleation on current-potential curves, valid for epitaxial electrodeposition on single-crystal faces, has been examined employing a specific model for nucleation and surface step motion. Computations have been performed for the electrodeposition of silver and copper: for the first metal the results are in reasonable agreement with some experimental data concerning two-dimensional nucleation on close-packed surfaces. In the case of copper the agreement with experimental results seems to be less satisfactory. The influence of assumptions, such as the type of surface step distribution, on the rate of electrocrystallization has been examined and discussed. Computer simulations of potentiostatic transients have also been carried out, and some effects of suppressing nucleation in the vicinity of steps have been investigated.

From computer-simulated experiments on the influence of two-dimensional nucleation and step motion on the rate of crystal growth (1), formulas have been obtained which allow one to estimate the relative importance of random nucleation and step density on the growth rate. The purpose of the present paper is to apply these results to the case of electrocrystallization processes, attempting to evaluate current-potential curves for the deposition of metals on close-packed and vicinal surfaces of single-crystal electrodes.

Models and Methods of Calculation

In the epitaxial growth of a single crystal by electrocrystallization, the current density i depends on the density and velocity of the steps moving on the surface

$$i = \frac{zFh_{(hkl)}}{V_m} V \theta \quad [1]$$

where z is the number of electrons exchanged, $h_{(hkl)}$ is the height of a crystal layer in the $[hkl]$ direction, V_m the molar volume, and V and θ the step velocity and step density. If the dependence of the current density on the overvoltage η has to be found, it is necessary to express V and θ as a function of overvoltage. The step velocity can be considered in general to depend on η and θ and an expression will be derived later (Eq. [13]). Steps on the surface can be due to misorientation with respect to a close-packed plane (the step density due to misorientation is indicated as ζ) or to the interplay between two-dimensional nucleation rate R_n and step velocity V . The formula relating these quantities is (1)

$$\theta = \sqrt[3]{\frac{2R_n}{V} + \zeta^3} \quad [2]$$

and our purpose is to obtain the dependence of R_n and V , and therefore θ , on the overvoltage.

According to nucleation theory (2), R_n is given by the product of the concentration of critical nuclei, which are formed by aggregating adatoms over the

close-packed portions of the surface, the rate of addition of single adatoms to the critical nucleus, and the Zeldovich nonequilibrium factor

$$R_n = Z n_{cr} \omega \quad [3]$$

Since two-dimensional nucleation is considered here, nuclei are assumed to be cylindrical in shape, their height being one atom layer. The concentration of critical nuclei is

$$n_{cr} = NA \exp \left(-\frac{\Delta G^\ddagger + \Delta G_q + \Delta G_s}{kT} \right) \quad [4]$$

where N is Avogadro's number and A the concentration of unaggregated adatoms (in mol/cm²); ΔG^\ddagger is the free energy for the formation of a nucleus

$$\Delta G^\ddagger = -\frac{\pi h_{(hkl)} \gamma^2 V_m}{\Delta \mu} \quad [5]$$

where γ is the surface energy and $\Delta \mu$ is the decrease in free energy in the crystallization process. ΔG_q is the contribution to the free energy due to the distribution of nuclei on the various sites of the substrate. The number of such sites is equal to $Nd_{(hkl)}$ where $d_{(hkl)}$ is the surface density of the close-packed layer (hkl) (in mol/cm²).

$$\Delta G_q = \frac{kT}{A} \left[d_{(hkl)} \ln \left(\frac{d_{(hkl)} - A}{d_{(hkl)}} \right) + A \ln \left(\frac{A}{d_{(hkl)} - A} \right) \right] \quad [6]$$

Calling K the ratio $d_{(hkl)}/A$ where K is a constant greater than 1, Eq. [6] becomes

$$\Delta G_q = kT \ln \left[\frac{A}{d_{(hkl)}} \left(\frac{K-1}{K} \right)^{K-1} \right] \quad [7]$$

The free energy of separation, as defined by Lothe and Pound (3), is

$$\Delta G_s = kT \ln (\sqrt{2\pi i_{cr}}) \quad [8]$$

where i_{cr} is the number of atoms in the critical nucleus.

The Zeldovich nonequilibrium factor is (4, 5)

$$Z = \left(\frac{\Delta G^\ddagger}{4\pi kT i_{cr}^2} \right)^{1/2} \quad [9]$$

The rate of addition ω of adatoms to the nucleus is the product of the number of adatoms per unit surface NA , the circumference of the critical nucleus $-2\pi\gamma V_m/\Delta\mu$, and the velocity of an adatom on the surface which is equal to the surface diffusion coefficient D_s divided by the length of a jump $\alpha_{(hkl)}$ between two rest positions on the (hkl) plane. Therefore

$$\omega = - \frac{2\pi\gamma V_m N A D_s}{\alpha_{(hkl)} \Delta\mu} \quad [10]$$

Combining Eq. [3]-[10], the nucleation rate is obtained

$$R_n = \sqrt{\frac{(-\Delta\mu)}{2RT}} \left(\frac{K}{K-1} \right)^{K-1} \frac{N A D_s (-\Delta\mu)}{\pi V_m \alpha_{(hkl)} \gamma} \exp\left(\frac{\pi h_{(hkl)} \gamma^2 V_m}{kT \Delta\mu} \right) \quad [11]$$

It should be noted that if $K \gg 1$, $[K/(K-1)]^{K-1}$ approaches the value e .

In the following, calculations are performed only for the (100) and (111) surfaces of a fcc metal. In this case, given the atomic radius E , the molar volume $V_m = 4\sqrt{2} NE^3$, $h_{(100)} = \sqrt{2} E$, $h_{(111)} = 2\sqrt{2}/\sqrt{3} E$, $\alpha_{(100)} = 2E$, and $\alpha_{(111)} = 2/\sqrt{3} E$. The formulas employed are therefore

for (100)

$$R_n = \sqrt{\frac{(-\Delta\mu)}{RT}} \left(\frac{K}{K-1} \right)^{K-1} \frac{A D_s (-\Delta\mu)}{16\pi E^4 \gamma} \exp\left(\frac{8\pi\gamma^2 E^4 N}{kT \Delta\mu} \right)$$

for (111)

$$R_n = \sqrt{\frac{3(-\Delta\mu)}{RT}} \left(\frac{K}{K-1} \right)^{K-1} \frac{A D_s (-\Delta\mu)}{16\pi E^4 \gamma} \exp\left(\frac{16\pi\gamma^2 E^4 N}{\sqrt{3} kT \Delta\mu} \right) \quad [12]$$

The nucleation rate depends on the adatom concentration A . In order to evaluate it, a particular model describing the electrocrystallization process has to be chosen. Here the model employed assumes that the adatom concentration is always the equilibrium one in the immediate vicinity of a step (6). For the sake of simplicity it will be assumed that the electrode charge-transfer reaction involves only one electron: $M \rightleftharpoons M^+ + e^-$, that is $z = 1$.

The adatom concentration as a function of the distance x from a surface step between two parallel steps which are a distance l apart is

$$A(x, l, \eta) = A_{eq} \left[\exp\left(-\frac{F\eta}{RT} \right) - \left(\exp\left[-\frac{F\eta}{RT} \right] - 1 \right) \frac{\cosh(\lambda[l/2 - x])}{\cosh(\lambda l/2)} \right] \quad [13]$$

where

$$\lambda = \sqrt{\frac{i_0}{F D_s A_{eq}}} \exp\left[\frac{(1-\beta)F\eta}{2RT} \right] \quad [14]$$

Here η is the overvoltage (excluding concentration polarization), i_0 is the exchange current density, and β is the symmetry factor (in the computations β is taken as 0.5).

The expression $\Delta\mu$ which occurs in the formula for the nucleation rate is given by

$$\Delta\mu = RT \ln \frac{A_{eq}}{A(x, l, \eta)} \quad [15]$$

where A_{eq} is the equilibrium adatom concentration.

According to the same model, the step velocity V can also be expressed as a function of the overvoltage η and step spacing l

$$V(\eta, l) = \frac{2}{d_{(hkl)}} \sqrt{\frac{i_0 D_s A_{eq}}{F}} \left[\exp\left(\frac{(1-\beta)F\eta}{2RT} \right) - \exp\left(-\frac{(1+\beta)F\eta}{2RT} \right) \right] \tanh\left(\frac{\lambda l}{2} \right) \quad [16]$$

The average nucleation rate $\bar{R}_n(\eta, l)$ for a surface covered with parallel steps with step spacing l can be found by introducing [13] and [15] in [11] and integrating

$$\bar{R}_n(l, \eta) = \frac{1}{l} \int_0^l R_n[A(x, l, \eta)] dx \quad [17]$$

The system formed by Eq. [2], [16], and [17] can be solved, giving the rate of growth (and therefore the current density) as a function of the overvoltage η and the step density due to misorientation ζ , if the effect of random nucleation is supposed to be equivalent to an increase of step density above the value ζ producing, however, a uniform step distribution. Then all steps are supposed to be spaced at a constant distance l , and $\theta = 1/l$. Therefore

$$i = \frac{F h_{(hkl)}}{V_m} V(\theta, \eta) \sqrt{\frac{2\bar{R}_n(\theta, \eta)}{V(\theta, \eta)} + \zeta^3} \quad [18]$$

The computational procedure consists of calculating $A(x, l, \eta)$ from [13] at several distances from a step, employing the results for the numerical integration of [17]. Evaluation of [2] with the calculated values of \bar{R}_n and V will give a new value for θ , and [18] can be solved by successive approximations.

Random nucleation, whether or not steps due to misorientation are present, obviously generates a surface where steps are not arranged in a uniform manner. This is visualized, for instance, in Fig. 1 which represents a misoriented surface on which random patches are

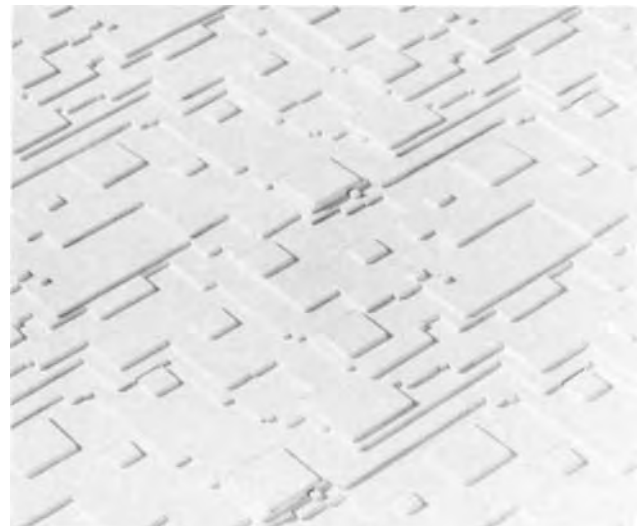


Fig. 1. Appearance of a single-crystal surface produced by computer simulation of crystal growth. Random two-dimensional nucleation superimposed to growth by step motion.

growing, as it was generated in a computer run. It is interesting, therefore, to have an idea of the influence of a nonuniform step distribution on the rate of growth. An approximate solution for such a case can be obtained in the following way: from the results obtained for a uniform distribution, if the value of $(R_n)_\infty$, the nucleation rate at infinite distance from a step, is compared with the average value $\bar{R}_n(l)$, it is found that to a good approximation

$$\bar{R}_n(l) = (R_n)_\infty \left(1 - \frac{2f(\eta)}{\lambda l} \right) \quad \text{for } l \geq \frac{2f(\eta)}{\lambda}$$

$$\bar{R}_n(l) = 0 \quad \text{for } l < \frac{2f(\eta)}{\lambda} \quad [19]$$

Equation [19] corresponds to assuming that nucleation is completely suppressed at distances less than $f(\eta)/\lambda$ from a step, elsewhere being equal to $(R_n)_\infty$. The function $f(\eta)$ represents, in units of diffusion distance $1/\lambda$, how far from a step nucleation is prevented. That a step function such as [19] describes the influence of step spacing is not surprising: the nucleation rate is greatly affected by relatively small changes in adatom concentration. Several experiments have shown the existence of the threshold value in $\Delta\mu$ below which the rate of nucleation is negligibly small. Computations carried out with many different sets of parameters have shown that the function $f(\eta)$ is very insensitive to variations of i_0 , D_s , or A_{eq} , and it is independent of step distance until l is so small that the average nucleation rate for that step spacing is small with respect to $(R_n)_\infty$.

By means of the simplification afforded by [19], it is possible to obtain the expression for the average nucleation rate as a function of the average step density θ when the spacings between steps are distributed exponentially, according to the distribution function $n(l) = \theta^2 \exp(-\theta l)$

$$R_n(\theta) = (R_n)_\infty \theta^2 \int_{2f(\eta)/\lambda}^{\infty} \left[l - \frac{2f(\eta)}{\lambda} \right] \exp(-\theta l) dl = (R_n)_\infty \exp\left(-\frac{2f(\eta)}{\lambda} \theta\right) \quad [20]$$

The limited validity of [19] has little effect on the accuracy of [20], since areas of small step spacing contribute very little to the average nucleation rate.

The average step velocity $V(\theta)$ can also be obtained by integration of the product of [16] and the step distribution function

$$V(\theta) = \frac{V_\infty \theta}{\lambda} \left[\Psi\left(\frac{\theta}{2\lambda} + \frac{1}{2}\right) - \Psi\left(\frac{\theta}{2\lambda}\right) - \frac{\lambda}{\theta} \right] \quad [21]$$

where V_∞ , the step velocity for infinite step spacing, is obtained from [16] by setting the value of the hyperbolic tangent term to 1. The function Ψ is the derivative of the logarithm of the gamma function. The computational procedure is analogous to that described above, introducing [20] and [21] in [2] and [18], instead of [16] and [17].

Potentiostatic Transients

The concepts and computational methods employed in the simulations which led to obtain formula [2] for the steady-state rate of growth are very similar to those used by Bewick, Fleischmann, and Thirsk (7) to simulate the initial potentiostatic transients. These authors found that the growth rate underwent damped oscillations, in some cases of considerable amplitude. It was interesting to see if these results could be confirmed, and to what extent the amplitude of the oscillation might depend on the intrinsic limitations of the computer model. Accordingly, initial transients were computed using two different simulated surface areas having a ratio 6.25.¹

¹ The surfaces were represented by arrays having 32400 and 5184 places, respectively. For the details of the simulation method, see Ref. (1).

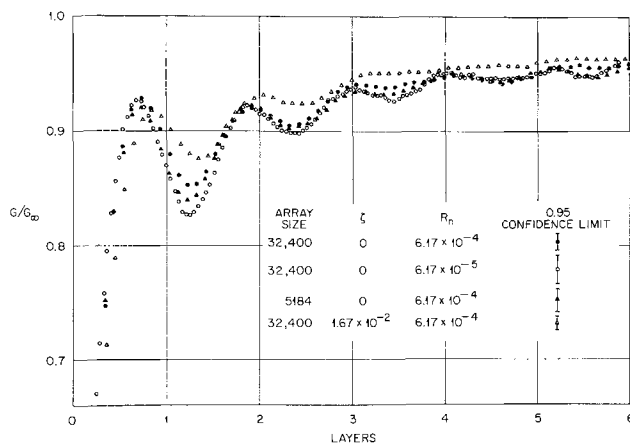


Fig. 2. Initial transient of the growth rate. Constant nucleation rate.

If the results are plotted as ratio of the growth rate over the asymptotic growth rate vs. the number of layers grown, the curves obtained are substantially independent of surface size as well as ratio between nucleation rate and step velocity. The results are shown in Fig. 2. It can be seen that damped oscillations are indeed produced, the maximum amplitude being about 10% of the asymptotic rate. The oscillations decrease rapidly and only four or five can be detected with some degree of certainty.

If comparison is made with experimental results for potentiostatic transients starting from a smooth surface (7), the simulated oscillations are smaller in amplitude and more rapidly damped. However, an important difference between the computer simulations and the analytical models describing electrocrystallization (such as the one employed in the preceding section) is that in the latter the nucleation probability is thought to decrease in the vicinity of a step if the supersaturation of the crystallizing species is a function of the distance from a step. In order to test if variations in the nucleation rate can be responsible for the large and persistent oscillations, a computer simulation was carried out in which nucleation was prevented close to a step, up to the third nearest neighbor place. This caused the initial oscillations to be larger and more persistent, as shown in Fig. 3.

Obviously, the simulation is but a crude approximation of the phenomena occurring on real surfaces. The extent of the surface on which nucleation is reduced because of steps depends on the value of the diffusion distance and this can conceivably be large. The computer simulations, however, show that if the nucleation rate depends on step density, large periodic oscillations of the current density during a potentiostatic transient can be generated.

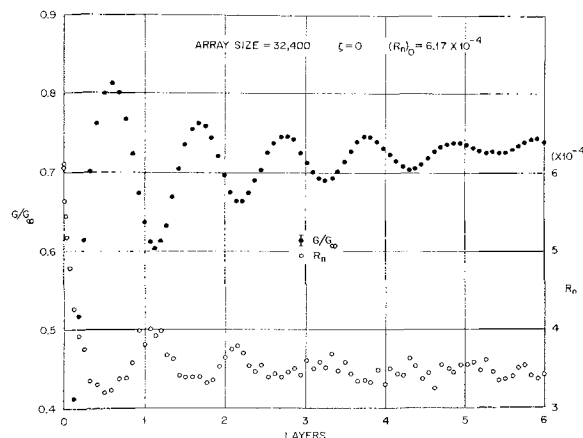


Fig. 3. Initial transient of the growth rate. Variable nucleation rate.

Results of the Computations

Computations according to the formulas given above have been carried out. Their purpose is two-fold: on one side they give examples by means of which the significance of different assumptions, such as uniform or exponential step distribution, can be assessed. On the other hand the best estimates for the parameters necessary to carry out the computations have been chosen so that comparison with experiment, whenever possible, could give some indication of the validity of the models employed here.

Calculations have been performed for copper and silver, considering a one electron over-all charge-transfer reaction. This, for Cu, would correspond to deposition from halide or ammonia solutions.

Silver.—For this metal, Budevski and co-workers (8) have derived a value for the surface energy from the time necessary to form the first nucleus as a function of the overvoltage. However, such a calculation involves the assumption that a steady-state condition is instantaneously achieved. Of the two possible reasons for a delay in the onset of steady state, the non-ideal behavior of the potentiostat can be considered negligible: because of the small surface area of the electrode, of the order of $2 \cdot 10^{-4}$ cm², the adatom concentration can be brought to the value corresponding to overvoltages between -10 and -20 mV in times much shorter than those required to form the first nucleus. However, even when the adatom concentration is stationary, an initial transient in the nucleation rate occurs because of the finite time necessary to aggregate adatoms in clusters of various sizes up to the critical nucleus. The solution of this problem is obtained by integrating the Frenkel-Zeldovich equation (4, 9). The expression for the nucleation rate as a function of time is (10)

$$R_n(t) = R_n(\infty) \left[1 + 2F \left(\frac{t}{\tau} \right) \right] \quad [22]$$

where $R_n(\infty)$ is given by [11] and

$$F \left(\frac{t}{\tau} \right) = \sum_{i_n}^{\infty} (-1)^n \exp \left(-n^2 \frac{t}{\tau} \right) = \frac{1}{2} - \sqrt{\frac{\pi\tau}{t}} \exp \left(-\frac{\pi^2\tau}{4t} \right) \sum_{o_n}^{\infty} \exp \left(-n(n+1) \frac{\pi^2\tau}{t} \right) \quad [23]$$

The two expressions for $F(t)$ can be obtained from each other by means of Jacobi's imaginary transformation (11). The time constant τ is given by

$$\tau = - \frac{8kT}{\pi^2\omega \left(\frac{\partial^2\Delta G}{\partial i^2} \right)_{i=i_{cr}}} \quad [24]$$

where ω is given by [10]

and

$$\left(\frac{\partial^2\Delta G^{\ddagger}}{\partial i^2} \right)_{i=i_{cr}} = \frac{\Delta\mu^3}{2\pi h_{(hkl)} V_m \gamma^2} \quad [25]$$

For a (100) surface of a fcc metal therefore

$$\tau_{(100)} = \frac{16\sqrt{2}}{\pi^2} \frac{RTE^2\gamma}{F^2 A_{eq} D_s \eta^2} \exp \left(\frac{F\eta}{RT} \right) \quad [26]$$

since $A = A_{eq} \exp(-\Delta\mu/kT)$, and $N\Delta\mu = F\eta$ all over the surface when no steps are present.

The steady-state nucleation rate can be evaluated by integration of [22]

$$1 = S \int_0^t R_n(t) dt \quad [27]$$

where S is the surface area and t the time necessary for the formation of the first nucleus. The integral [27] obtained from the left-hand side expression in [23] has

been reported in the literature (10). When t/τ is small, however, the right-hand side expression in [23] converges more rapidly. Integral [27] becomes

$$1 = S \cdot R_n(\infty) \tau G(t/\tau) \quad [28]$$

where

$$G \left(\frac{t}{\tau} \right) = 4\sqrt{\pi} \left\{ \sum_0^{\infty} \exp \left[- \left(n + \frac{1}{2} \right)^2 \frac{\pi^2\tau}{t} \right] - \pi^{3/2} \left(n + \frac{1}{2} \right) \operatorname{Erfc} \left[\left(n + \frac{1}{2} \right) \pi \sqrt{\frac{\tau}{t}} \right] \right\} \quad [29]$$

From [28] it can be seen that for a given overvoltage the value of $G(t/\tau)$ depends only on γ , since A_{eq} and D_s drop out of the product $R_n(\infty)\tau$. The time necessary to form the first nucleus, therefore

$$t = \tau G^{-1} \left(\frac{t}{\tau} \right) \quad [30]$$

decreases linearly with an increase of the product $A_{eq}D_s$, besides being strongly dependent on γ . Figure 4 shows a comparison between calculated values of $\log t$ vs. $1/\eta$ and Budevski's experimental points (8). The range of γ values which produce agreement is very small, variations being of the order of few per cent. The value of the product $A_{eq}D_s$, which gives the best fit is $2 \cdot 10^{-19}$ mol/sec, and can be increased or decreased by a factor of 3.

Another comparison between calculated and experimental values can be made: The time necessary to form a monolayer from a single nucleus at the overvoltage of 6 mV was found to be about 3.5 sec for a circular electrode of 150 μ m diameter (8). Therefore, the step velocity in these conditions can be estimated as being between 20 and 50 μ m/sec. The velocity of an isolated step can be obtained from [16] letting $\tanh(\lambda l/2) = 1$. The velocity increases with the square root of the product $i_0 A_{eq} D_s$, so involving parameters whose values have already been chosen for the best fit in the nucleation rate. If a value of $5 \cdot 10^{-18}$ A·mol/cm² sec is chosen for $i_0 A_{eq} D_s$, a velocity of 17 μ m/sec is obtained.

Bachmann and Vetter (12) have reported values of 2 and 5.4 A/cm² for the exchange current density of (100) Ag in 0.1 and 0.5M AgClO₄ solutions respectively. They also found a crystallization capacitance of the order of 300-500 μ F/cm² corresponding to about 10^{-10} mol/cm² for the surface adatom concentration. As expected for a symmetry factor β close to 0.5, i_0 increases approximately with the square root of the concentration in solution. Therefore, in a 6M solution

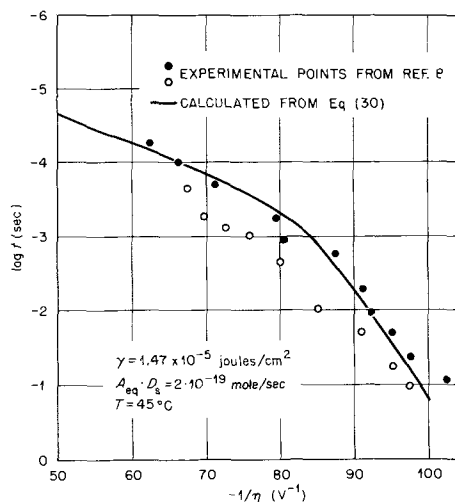


Fig. 4. Comparison between experimental and calculated values for the time necessary to form the first nucleus.

at 45°C as Budevski employed, it is not unreasonable to assume i_0 to be as high as 25 A/cm².

In order for the product $i_0 A_{eq} D_s$ to be $5 \cdot 10^{-18}$, a value of $2 \cdot 10^{-9}$ cm²/sec for D_s should be chosen. No reliable values for D_s are available in the literature, and estimates range between 10^{-7} and 10^{-10} cm²/sec. With such values, the product $A_{eq} D_s$ becomes $2 \cdot 10^{-19}$ mol/sec, which allows a good fitting of the experimental data concerning the nucleation rate.

Steady-state current density as a function of overvoltage and misorientation could be calculated also, once the various parameters have been chosen. However, in such conditions transport in solution would become the slowest process and both crystallization and charge-transfer would no longer be rate determining.

Copper.—Experimental data concerning the electrochemical behavior of Cu in monovalent copper solutions are scarce and tend to indicate that some of the assumptions used in developing the present treatment may not be applicable, chief among them the hypothesis of equilibrium at a step, particularly for (100) orientations (13). Computations therefore have been performed principally in order to show the effect of conditions such as the step distribution or to indicate broadly the limits of validity of the formulas. Nevertheless, the choice of the values of the parameters involved in the computations has been made according to the best evidence available. In this way it is hoped that when comparison with existing data is possible, some conclusions can be drawn from the degree of agreement between experimental and calculated values.

In order to obtain values for A_{eq} , which were not available in the literature, galvanostatic pulses at low current density for the system Cu/Cu⁺ 0.1M, KCl 2M, HCl 1M at 23.5°C were recorded. Single crystals having (100) and (111) orientation were used as electrodes. Surface preparation and other experimental methods have been described (13, 14). Anodic and cathodic constant current pulses between 50 and 300 μ A/cm² were superimposed to small bias currents between +3 and -3 μ A/cm², so that the overvoltage at the beginning of the pulse could be varied about 10 mV above and below the equilibrium value. Oscilloscope sweep rates ranged between 2 and 50 msec/cm. The slopes of the voltage-time curves were measured at regular time intervals and plotted as $\log(d\eta/dt)$ vs. time.

A detailed interpretation of the results is complicated, since in certain current density and time ranges the plots are not straight lines. However, for (111) surfaces a reliable extrapolated value $(\partial\eta/\partial t)_{t=0}$ could be obtained. Figure 5 reports the values of the electrode capacitance

$$C = \frac{i}{\left(\frac{\partial\eta}{\partial t}\right)_{t=0}} = \frac{i}{C_{dl} + \frac{F^2 A}{RT}} \quad [31]$$

(i = current density) plotted as a function of the bias overvoltage. Equation [31] shows the relationship between C and the adatom concentration A (15). It was found that the capacitance tends to increase at lower electrode potentials, which can be interpreted as being due to changes in adatom concentration under the assumption that the small bias currents caused negligible charge-transfer overvoltage. Then

$$A(\eta) = A_{eq} \exp\left(-\frac{F\eta}{RT}\right) \quad [32]$$

if the double layer capacitance C_{dl} is known, the equilibrium adatom concentration A_{eq} can be derived from [31] and [32]. The straight line in Fig. 5 is calculated assuming $C_{dl} = 30 \mu$ F/cm² and from these data A_{eq} for (111) copper is estimated as $4 \cdot 10^{-11}$ mol/cm². For (100) surfaces the capacitance was about 30μ F/cm²,

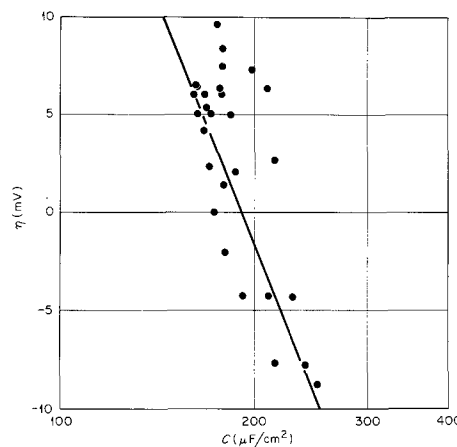


Fig. 5. Electrode capacitance vs. initial overvoltage for Cu in Cu⁺ 0.1M, KCl 2M, HCl 1M.

and independent of the potential, and it can only be concluded that A_{eq} cannot be deduced from these experiments. Its upper value could be tentatively set at 10^{-12} mol/cm².

From the examination of the first milliseconds of the galvanostatic transients, as well as from steady-state polarization curves, the exchange current density can be estimated to be between 1 and 10 mA/cm² both on (111) and (100). Considering that the Cu⁺ activity in these solutions is of the order of 10^{-8} M, such a value is compatible with the high i_0 for this reaction found in cupric solutions (16) where Cu⁺ activity is of the order of 10^{-4} M.

In vacuum the surface energy of Cu is approximately 1.4 times that of Ag (17); accordingly, a value of $2 \cdot 10^{-5}$ j/cm² for Cu in contact with an electrolytic solution has been chosen. It should be noted, however, that other authors (18) have estimated a value more than 10 times larger.

The available information indicates that the exchange current density as well as the surface energy, should not be strongly dependent on orientation. In the case of γ , the value of which affects nucleation rate very strongly, only differences from 1 to 4% were observed for copper in vacuum (19). For the surface diffusion coefficient, however, calculations by Haruyama (20) and more recently by Wynblatt and Gjostein (21) indicate large differences between (111) and (100) surfaces, which would lead to diffusion coefficients of 10^{-5} cm²/sec for (111) and 10^{-8} cm²/sec for (100) at room temperature. An interesting point is that, according to these authors, on copper (100) vacancy migration could be more important than adatom migration, since both energy of formation and energy of migration are significantly lower for vacancies than for adatoms. Vacancy migration could effectively reduce the differences in surface diffusion coefficient between the two close-packed surfaces. The effect of considering a metal-solution interface, instead of a metal in vacuum for which the calculations are valid, is very difficult to estimate: a reduction of a factor of 10 for D_s has been suggested (18). For our purposes only the product $A_{eq} D_s$ has to be determined. According to the preceding discussion, the product could range between 10^{-17} and 10^{-19} for (111) and between 10^{-19} and 10^{-21} mol/sec for (100). These are the values used in the computations.

Figures 6 and 7 show some steady-state current-potential curves for (100) and (111). In the first case, the lower value of $A_{eq} D_s$ would give a qualitative agreement with experimental data (13) if a misorientation of 0° were taken. The actual electrodes, however, because of slight misorientation and the presence of dislocations, had at least an average step density corresponding to a misorientation of 30' of arc. The agreement with the curve calculated for this misorientation is less satisfactory. The main cause of the discrepancy

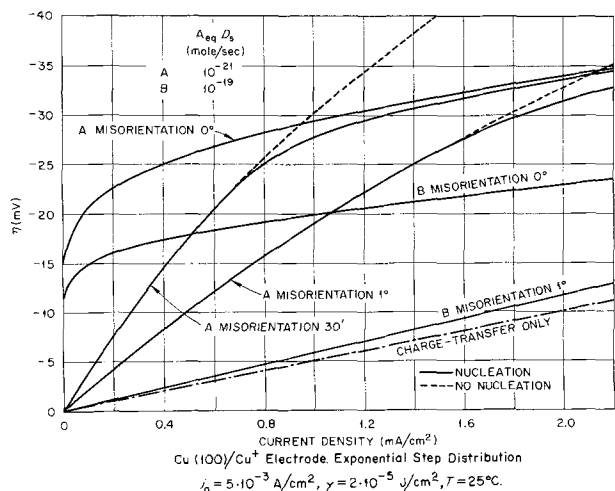


Fig. 6. Current-potential curves calculated for the Cu(100)/Cu⁺ electrode. Exponential step distribution. $i_0 = 5 \cdot 10^{-3} \text{ A/cm}^2$, $\gamma = 2 \cdot 10^{-5} \text{ J/cm}^2$, $T = 25^\circ\text{C}$.

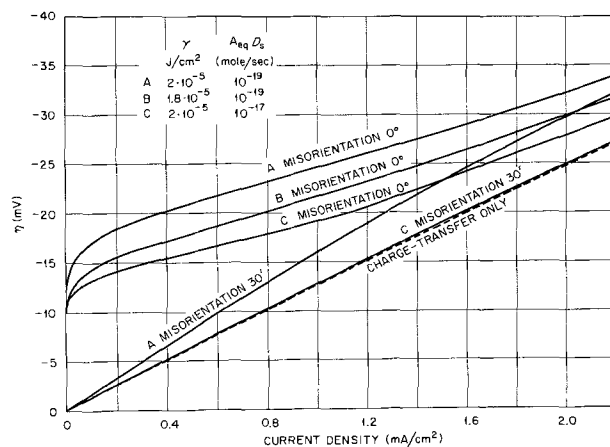


Fig. 7. Current-potential curves for the Cu(111)/Cu⁺ electrode. Exponential step distribution. $i_0 = 2 \cdot 10^{-3} \text{ A/cm}^2$, $T = 25^\circ\text{C}$.

is probably that the assumption of equilibrium for adatoms in the immediate vicinity of a step is not satisfied for these surfaces, the motion of the steps being hindered by adsorption (22).

The curves for both (100) and (111) show that even in the presence of small misorientations the influence of the nucleation rate on current density is felt only beyond -25 mV . The range of conditions where two-dimensional nucleation is rate-determining is shown to be rather restricted.

Some calculated values are reported in Tables I and II. It can be seen that the choice of the step distribution affects step velocity and step density, the two parameters which determine the rate, in opposite ways. As nucleation rate is higher for the exponential distribution, the step density is increased and this is very pronounced at small misorientations. The average step velocity, on the contrary, is slowed down, since many of the steps are close together. The two effects tend to compensate each other, so that the current density is in many cases only slightly influenced by the distribution. In Table I, calculated for a surface 15' from (100), the radius of the critical nucleus and the num-

ber of atoms in it are also given. The numbers indicate that the assumption of a circular nucleus is probably justified for overvoltages up to -30 mV .

Table II shows the effect of step distribution on current density, step velocity, step density, and nucleation rate for surfaces near (111). Depending on how close the surface is to (111), the choice of the distribution can lead to an increase or a decrease of the current density.

Discussion

The purpose of this work was to apply nucleation theory to the case of electrocrystallization and to indicate how values accessible to measurement, such as current density, could be calculated. Since experimental values for many of the parameters involved in the calculations are not known with certainty, comparison with experiment is often difficult. However, it must be borne in mind that in electrochemistry comparisons between theoretical expectations and experimental data have sometimes not been performed for lack of a clear understanding of the way such calculations might be carried out. This work is intended to illustrate methods for this purpose.

For the calculation of nucleation rates, both pre-exponential and exponential factors have been de-

Table I. Cu/Cu⁺ electrode orientation 15' from (100)

$T = 25^\circ\text{C}$, $\gamma = 2 \cdot 10^{-5} \text{ J/cm}^2$, $i_0 = 5 \text{ mA/cm}^2$, $A_{eq}D_s = 10^{-21} \text{ mol/sec}$

η , mV	Step Distrib.	Curr. density, mA/cm ²	Avg. nucl. rate, N/cm ² sec	Avg. step spacing, Å	Avg. step velocity, 10 ⁻⁶ cm/sec	ρ_{cr} , Å	i_{cr} , atoms
-5	Uniform	0.069	$8.0 \cdot 10^{-20}$	414	1.16	29.5	418
	Exponential	0.065	$8.7 \cdot 10^{-20}$	414	1.11		
-10	Uniform	0.145	$1.3 \cdot 10^{-1}$	414	2.45	14.7	104
	Exponential	0.138	$1.4 \cdot 10^{-1}$	414	2.33		
-15	Uniform	0.230	$2.4 \cdot 10^5$	414	3.88	9.8	46
	Exponential	0.218	$2.5 \cdot 10^5$	414	3.68		
-20	Uniform	0.326	$4.0 \cdot 10^8$	413	5.49	7.4	26
	Exponential	0.309	$4.2 \cdot 10^8$	412	5.20		
-30	Uniform	1.19	$5.8 \cdot 10^{11}$	194	9.37	5.0	12
	Exponential	1.14	$7.0 \cdot 10^{11}$	175	8.14		
-40	Uniform	3.54	$7.4 \cdot 10^{12}$	98	14.1	4.0	8
	Exponential	3.68	$1.7 \cdot 10^{13}$	66	9.9		

Table II. Effect of step distribution on current density, step velocity, step density, and nucleation rate

Cu(111)/Cu⁺ electrode. $T = 25^\circ\text{C}$, $\gamma = 2 \cdot 10^{-5} \text{ J/cm}^2$, $i_0 = 2 \text{ mA/cm}^2$, $A_{eq}D_s = 10^{-10} \text{ mol/cm}^2$

η , mV	Misorientation = 0°				Misorientation = 30'			
	i_{exp}	V_{exp}	θ_{exp}	$(R_n)_{exp}$	i_{exp}	V_{exp}	θ_{exp}	$(R_n)_{exp}$
	i_{unit}	V_{unit}	θ_{unit}	$(R_n)_{unit}$	i_{unit}	V_{unit}	θ_{unit}	$(R_n)_{unit}$
-5	1.00	1.00	1.00	1.00	0.83	0.83	1.00	∞
-10	1.00	1.00	1.00	1.00	0.84	0.84	1.00	∞
-15	0.99	0.98	1.01	1.01	0.85	0.85	1.00	∞
-20	1.04	0.84	1.24	1.58	0.85	0.85	1.00	∞
-25	1.25	0.62	2.03	5.15	0.86	0.86	1.00	10^{62}
-30	1.28	0.48	2.67	9.12	0.87	0.86	1.01	10^{42}
-40	1.19	0.36	3.28	12.9	0.91	0.78	1.17	10^{36}

duced from the theory. In view of the continuing controversies (23) involving uncertainties of several orders of magnitude, it is encouraging that the computations are in good agreement with the best set of data existing in the electrochemical literature (8).

In order to estimate the influence of two-dimensional nucleation on current density, a formula derived from computer simulations has to be employed. This formula is admittedly empirical, but its approximate validity can be demonstrated (24), and it has been shown that the value of numerical coefficient which is the result of the averaging procedure, is rather insensitive to the details of the model (1). The same computer simulation which had been used for deducing the formula has provided here a way to explain the transient behavior of potentiostatic curves, providing an argument in favor of interpreting some electrocrystallization data as influenced by surface diffusion.

In many problems concerning electrocrystallization processes, the step velocity, and therefore the reaction rate, are evaluated for a uniform step density distribution. Although uniform step spacing can be stable for certain step-interaction functions, it has been proved that under a wide range of conditions such a distribution is unstable (25) and the assumption would be unjustified. In this paper an attempt has been made to evaluate the influence of a different step spacing distribution. It has not been shown that the exponential distribution is closer to the experimental conditions, and the ways whereby a nonuniform distribution can be attained have not been discussed. The calculations, however, have shown that the average step velocity, and therefore the current density, are sometimes strongly dependent on the distribution. The effect of releasing the constraint of uniform step spacing is in general a decrease of the current density, unless nucleation is rate determining; the current density also becomes less dependent on orientation. The last point could contribute to explaining why, in a number of cases, little dependence of current density on orientation was observed.

Acknowledgment

This research was sponsored by the United States Atomic Energy Commission under contract with the Union Carbide Corporation.

Manuscript submitted Nov. 1, 1971; revised manuscript received Feb. 10, 1972.

Any discussion of this paper will appear in a Discussion Section to be published in the June 1973 JOURNAL.

REFERENCES

1. U. Bertocci, *Surface Sci.*, **15**, 286 (1969).
2. J. P. Hirth and G. M. Pound, "Progress in Material Science," Vol. 11, Macmillan, New York (1963); G. M. Pound, M. T. Simnad, and Ling Yang, *J. Chem. Phys.*, **22**, 1215 (1954).
3. J. Lothe and G. M. Pound, *J. Chem. Phys.*, **36**, 2080 (1962).
4. J. B. Zeldovich, *Acta Physicochim. URSS*, **18**, 1 (1943).
5. J. P. Hirth, *Acta Met.*, **7**, 755 (1959).
6. W. Lorenz, *Z. Elektrochem.*, **57**, 382 (1953); *Z. Naturforsch.*, **9A**, 716 (1954); A. R. Despic and J. O'M. Bockris, *J. Chem. Phys.*, **32**, 389 (1960).
7. A. Bewick, M. Fleischmann, and H. R. Thirsk, *Trans. Faraday Soc.*, **58**, 2200 (1962).
8. E. Budevski, W. Bostanoff, T. Witanoff, Z. Stoinoff, A. Kotzawa, and R. Kaischew, *Electrochim. Acta*, **11**, 1697 (1966).
9. F. C. Collins, *Z. Elektrochem.*, **59**, 404 (1955); S. Toschev and I. Gutzow, *Phys. Status Solidi*, **21**, 683 (1967); D. Kashchiev, *Surface Sci.*, **14**, 209 (1969).
10. S. Toschev and I. Markov, *J. Cryst. Growth*, **3**, 4, 436 (1968).
11. A. Erdélyi, Editor, "Higher Transcendental Functions," Vol. II, p. 370, McGraw-Hill Book Co., New York (1953).
12. K. J. Bachmann and K. J. Vetter, *Z. Physik. Chem. N. F.*, **51**, 98 (1966).
13. U. Bertocci, *This Journal*, **113**, 605 (1966).
14. L. H. Jenkins, *ibid.*, **117**, 630 (1970).
15. H. Gerischer, *Z. Elektrochem.*, **62**, 256 (1958).
16. E. Mattson and J. O'M. Bockris, *Trans. Faraday Soc.*, **55**, 1586 (1959).
17. H. Udin, A. J. Shaler, and J. Wulff, *Trans. AIME*, **185**, 186 (1949).
18. H. Kita, M. Enyo, and J. O'M. Bockris, *Can. J. Chem.*, **39**, 1670 (1961).
19. W. M. Robertson and P. G. Shewmon, *Trans. AIME*, **224**, 804 (1962).
20. S. Haruyama, *J. Electrochem. Soc. Japan*, **33**, 181 (1965).
21. P. Wynblatt and N. A. Gjostein, *Surface Sci.*, **12**, 109 (1968).
22. U. Bertocci, *ibid.*, **9**, 18 (1968).
23. W. G. Courtney, *J. Phys. Chem.*, **72**, 421 (1968).
24. R. D. Armstrong and J. A. Harrison, *This Journal*, **116**, 328 (1969).
25. W. W. Mullins and J. P. Hirth, *J. Phys. Chem. Solids*, **24**, 1391 (1963); L. D. Hulett and F. W. Young, Jr., *This Journal*, **113**, 410 (1966); R. L. Schwöebel and E. J. Shipsey, *J. Appl. Phys.*, **37**, 3682 (1966).

Electrohydrodimerization Reactions

II. Rotating Ring-Disk Electrode, Voltammetric and Coulometric Studies of Dimethyl Fumarate, Cinnamionitrile, and Fumaronitrile

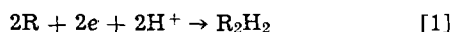
V. J. Puglisi and Allen J. Bard*

Department of Chemistry, The University of Texas at Austin, Austin, Texas 78712

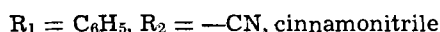
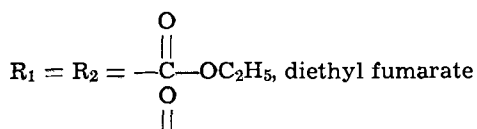
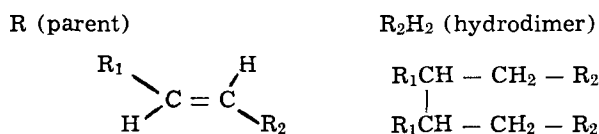
ABSTRACT

The reduction of the activated olefins dimethyl fumarate, cinnamionitrile, and fumaronitrile in tetra-*n*-butylammonium iodide-dimethylformamide solutions at a platinum electrode has been studied by rotating ring-disk electrode (RRDE) voltammetry, cyclic voltammetry, and coulometry. The results indicate that each compound undergoes a one-electron reduction to the anion radical which then undergoes a dimerization reaction. Rate constants for this dimerization reaction were found to be 110 (dimethyl fumarate), 880 (cinnamionitrile), and 7×10^5 (fumaronitrile) 1/mole-sec. Evidence of some bulk polymerization reaction was obtained from the coulometric results.

The general equation for electrohydrodimerization (or electrolytic reductive coupling) of an activated olefin, R, is shown in Eq. [1]



The first paper in this series (1) dealt with the determination of the mechanism of this reaction for diethyl fumarate reduction in dimethylformamide (DMF) solutions. Results of



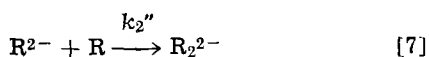
double potential-step chronoamperometry experiments showed that the reduction proceeded by coupling of the electrogenerated radical anions (mechanisms I)



rather than by reaction of the radical anion with parent and subsequent electron transfer (mechanism II)



[and variations of this mechanism (2)] or initial formation of a dianion (mechanism III)



We assume throughout that protonation can occur at any stage of the reaction sequence, ultimately leading to R_2H_2 , but that the protonation steps are not rate determining.

* Electrochemical Society Active Member.

Key words: reductive coupling, electrochemical dimerizations, rotating disk electrode, coulometry, cyclic voltammetry.

In this paper we extend the study of the mechanism of electrohydrodimerization to the compounds dimethyl fumarate, cinnamionitrile, and fumaronitrile, with special emphasis on the application of rotating ring-disk electrode (RRDE) techniques, which have been shown to be particularly useful in distinguishing among mechanisms I, II, and III (2). Previous studies of these compounds [(3-6) and references therein] have verified that hydrodimers are the major products of the electroreduction. Since the lifetimes of the electrogenerated intermediates for these compounds span the range of millisecond to second, these studies also provide a useful test of the application of RRDE techniques over a wide range of reaction rates.

Experimental

Reagents.—Dimethylformamide (DMF), obtained from Baker Chemical Company, was purified by the method of Faulkner and Bard (7) and was stored under He. Solvent purity was ascertained by voltammetric analysis of a DMF solution of tetrabutylammonium iodide (TBAI). Southwestern Analytical Chemical's polarographic grade TBAI was used as received. Fumaronitrile (Aldrich Chemical Company) was sublimed twice prior to use. Dimethyl fumarate, twice sublimed, and cinnamionitrile, used as received, were obtained from K. and K. Laboratories, Inc. All reagents were stored over Drierite.

Apparatus.—A Model 170 Electrochemistry System (Princeton Applied Research Corporation, Princeton, New Jersey) was employed throughout the study. A regulated power supply was used as a constant current source. The current was determined by measuring the potential developed across a 10 kohm ($\pm 0.025\%$) resistor with a digital multimeter. The electrochemical cell and dispensing vessel are shown in Fig. 1. The platinum Teflon rotating ring-disk electrode, having a disk radius (r_1) of 0.187 cm and inner (r_2) and outer (r_3) ring radii of 0.200 and 0.332 cm, respectively, was constructed by Pine Instrument Company, Grove City, Pennsylvania. The N-value for this electrode was determined from the geometry and by experimental measurements on electrochemical systems unperturbed by reactions of the disk generated species (e.g., azobenzene) and was found to be 0.555 ± 0.001 . The electrode was rotated using a Motomatic Model E-550 motor and controller (Electrocraft Corporation, Hopkins, Minnesota). Electrical contact to the shaft was made using two sets of silver graphalloy brush and leaf assemblies. A platinum wire spiral served as the auxiliary electrode. The reference electrode was either a saturated calomel electrode (SCE) (coulometric experiments only) or a silver wire spiral (Ag-RE). The working electrode in the coulometric experiments was

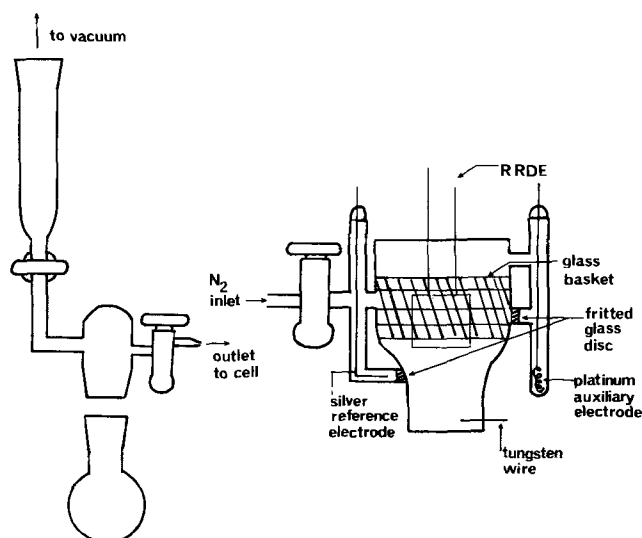


Fig. 1. Electrochemical cell and dispensing vessel

either a mercury pool or a platinum wire gauze. Cyclic voltammograms were recorded on a Tektronix, Type 564 storage oscilloscope. All experiments were carried out at 24°C. Dissolved oxygen was removed from the solution by the freeze-pump-thaw technique. The dispensing vessel was then brought to atmospheric pressure with He. The solution was transferred to the electrochemical cell, which was continually being flushed with N₂, by the introduction of positive N₂ pressure. It was convenient to fill each compartment of the electrochemical cell separately. All experiments were conducted with a continuous stream of N₂ flowing over the solution surface. Impurities in the cinnamionitrile appeared as a irreversible reduction wave at the foot of the main cinnamionitrile reduction wave. This small wave was removed by carrying out exhaustive electrolysis at a potential on the plateau of this wave. The cinnamionitrile reduction current, after electrolysis of the impurity, equaled, within experimental error, the sum of the impurity and cinnamionitrile reduction currents prior to the pre-electrolysis. Limiting disk current (*i*_{d,1}) rotation rate (ω) relationships were determined at several different potentials on the limiting current plateau. These *i*_{d,1} values were determined both from voltammograms obtained at scan rates of 5 and 10 mV/sec and from currents obtained by stepping to potentials corresponding to the limiting current region. In all collection efficiency measurements a constant current was applied to the disk while the ring was maintained at a controlled potential. The ring was adjusted to a potential such that the ring current (*i*_r) was zero at the current sensitivity to be used in the measurement of *i*_r, when the disk current (*i*_d) equaled zero; this potential was always at a value where any radical anion being produced at the disk would undergo mass transfer controlled electrochemical oxidation at the ring. This procedure for measuring *i*_r allowed the accurate determination of even very small values of *i*_r, and is most useful for studying short-lived disk generated species.

Results

Dimethyl fumarate.—Rotating disk electrode (RDE) voltammograms (*i*_d vs. *E*_d) taken at slow scan rates (5–10 mV/sec) for millimolar solutions of dimethyl fumarate in DMF–0.1M TBAI at ω -values of 47.6–200 sec⁻¹ exhibit a reduction wave with *E*_{1/2} = –0.75V vs. Ag-RE followed by a dip in *i*_d after development of a well-developed plateau. This dip develops into a second reduction wave on addition of water (6). The discussion of all results here are limited to processes occurring at the first reduction wave. Values of the Levich constant, *i*_{d,1}/ $\omega^{1/2}C$, for different values of ω and *C* are given in Table I. Although the values of the Levich

Table I. Typical rotating-disk electrode data for the first reduction waves^a

Concentration, <i>C</i> (mM)	Limiting disk current, <i>i</i> _{d,1} (μA)	Rotation rate, ω (sec ⁻¹)	<i>i</i> _{d,1} / $\omega^{1/2}C$
A. Dimethyl fumarate			
3.00	149	47.6	7.19
3.30	158	47.6	6.96
3.54	168	47.6	6.90
4.45	207	47.6	6.75
6.20	213	27.0	6.61
	276	47.6	6.45
	330	67.2	6.48
	398	98.6	6.48
	491	149	6.48
	568	202	6.45
B. Cinnamionitrile			
1.25	58.0	47.6	6.72
2.12	99.0	47.6	6.77
2.50	122	47.6	7.07
	140	67.2	6.83
	167	98.6	6.75
	198	149	6.49
	227	202	6.39
	252	253	6.34
	276	305	6.32
3.13	138	47.6	6.39
3.26	153	47.6	6.80
11.3	497	47.6	6.38
C. Fumarionitrile			
0.42	29.4	202	4.93
0.92	63.3	202	4.84
1.92	125	202	4.59
2.18	67	47.6	4.45
	81	67.2	4.53
	98	98.6	4.54
	119	149	4.47
	130	179	4.44
	136	202	4.39
3.18	191	202	4.24
3.94	226	202	4.04

^a The solutions were all 0.1M TBAI in DMF. The RDE radius was 0.187 cm.

constant are independent of ω , in accordance with the Levich equation [8], there is a small decrease of *i*_{d,1}/ $\omega^{1/2}C$ with increasing concentration.

$$i_{d,1} = 0.62 n F A D^{2/3} \nu^{-1/6} \omega^{1/2} C \quad [8]$$

This decrease is probably caused by a small contribution from a polymerization reaction consuming parent material. This polymerization is more strongly reflected in coulometric experiments, where controlled potential reduction of millimolar solutions of dimethyl fumarate at potentials on the plateau of the first reduction wave (–1.625V vs. SCE) yields an *n*_{app} value (*n*_{app} = number of faradays per mole of electroactive substance) of 0.62. Similar *n*_{app} values were found for diethyl fumarate (1).

To obtain information about the mechanism of the reaction, RRDE experiments were undertaken, and the variation of the kinetic collection efficiency, *N*_K, where

$$N_K = |i_r/i_d| \quad [9]$$

*i*_r and *i*_d are the ring and disk currents, respectively, as a function of the disk current, expressed as CONI, at different values of ω and *C* was determined

$$CONI = i_d/i_{d,1} \quad [10]$$

Typical results are shown as the points in Fig. 2. The trend of *N*_K with CONI, i.e., *N*_K decreasing with increasing CONI, has been shown to be characteristic of mechanism I (given in Eq. [2] and [3]) and excludes mechanisms II (it is possible that a nuance of mechanism II [see (2) case II_d, Fig. 6] could exhibit, for some values of equilibrium and rate parameters, this same trend. However, in that case *N*_K would vary as the square of the bulk concentration and the *N*_K vs. 1-CONI trends could also be different for different concentrations of parent R), and III (2), as well as first order decomposition of R^{•-}. Note these other reactions of R^{•-} may be occurring in parallel with the dimerization of R^{•-} (Eq. [3]), but dimerization must be the predominant pathway. The experimental points

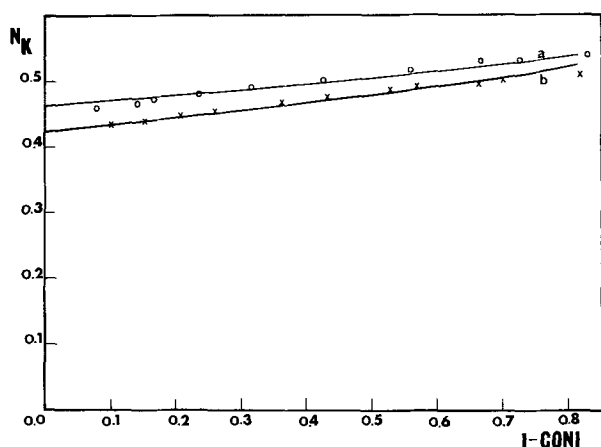


Fig. 2. Collection efficiency (N_K) vs. $1-CONI$ for a 6.20 mM dimethyl fumarate solution at rotation rates (ω) of 67.2 (o) and 47.6 (x) radians sec^{-1} . Solid lines are theoretical curves corresponding to mechanism I and (a) $XKTC = 0.16$ and (b) $XKTC = 0.25$, where $XKTC = (0.51)^{-2/3} \nu^{1/3} D^{-1/3} C \omega^{-1} k_2$.

were fit by simulating mechanism I for different values of $XKTC$, the dimensionless simulation

$$XKTC = (0.51)^{-2/3} \nu^{1/3} D^{-1/3} C \omega^{-1} k_2 \quad [11]$$

variable defined in Eq. [11]. For example, the line in Fig. 2 corresponds to an $XKTC$ value of 0.25. Values of $XKTC$ obtained by this method at different C and ω are given in Table II, along with the normalized parameter ($XKTC$)(ω)/ C . Values of k_2 were calculated from this parameter and the diffusion coefficient determined from $i_{d,1}$ and Eq. [8]; the average value of k_2 obtained from this data is $1.1 \pm 0.1 \times 10^2$ liters/mole-sec. This value can be compared to the dimerization

Table II. Calculated rate constants for reactions of radical anions obtained from RRDE results^a

ω (sec^{-1})	Concentration, C (mM)	$XKTC^b$	($XKTC$)(ω) ^b C	k_2 (liter/c mole-sec)	k_2' (liter/d mole-sec)
A. Dimethyl fumarate					
47.6	3.54	0.10	1.34×10^3	0.9×10^2	
	4.45	0.17	1.82	1.2	
	6.20	0.25	1.92	1.3	
67.2	3.54	0.06	1.14	0.8	
	6.20	0.16	1.73	1.1	
	4.45	0.08	1.77	1.2	
98.6	6.20	0.10	1.59	1.1	
			Avg. 1.59×10^3	1.1×10^2	
	B. Cinnamionitrile				
47.6	1.25	0.35	1.33×10^4	8.8×10^2	
	2.12	0.60	1.37	9.1	
	3.13	0.88	1.34	8.9	
	3.26	0.91	1.33	8.8	
	3.67	1.01	1.33	8.8	
	7.46	2.25	1.44	9.6	0.6×10^2
	11.3	2.95	1.24	8.2	0.6×10^2
67.2	1.25	0.25	1.33	8.8	
	2.12	0.41	1.29	8.6	
	3.13	0.58	1.24	8.2	
	3.26	0.69	1.33	8.8	
	3.26	0.47	1.42	9.4	
98.6	1.25	0.25	1.33	8.8	
	2.12	0.27	1.26	8.3	
	3.13	0.46	1.45	9.6	
	3.26	0.47	1.42	9.4	
	3.67	0.46	1.24	8.2	
	4.72	0.61	1.27	8.4	
		0.77	1.41	9.4	
		Avg.	1.33×10^4	8.8×10^2	0.6×10^2
C. Fumarionitrile					
201	0.42	24.5	1.2×10^7	7×10^6	10×10^6
	0.42	28.5	1.4	8	10
	0.82	50.0	1.1	6	6
	1.92	92	1.0	5	6
	3.18	180	1.0	5	2
	3.94	150	0.8	4	3
				1.1×10^7	6×10^6

^a The solutions were all 0.1M TBAI in DMF. The RRDE had $r_1 = 0.187$ cm, $r_2 = 0.200$ cm, and $r_3 = 0.332$ cm.

^b $XKTC = (0.51)^{-2/3} \nu^{1/3} D^{-1/3} C \omega^{-1} k_2$, $\nu = 0.00849$ cm^2/sec .

^c For reaction $2R^- \rightarrow R^{2-}$.

^d For reaction $R^- + R \rightarrow R_2^-$.

rate found previously for diethyl fumarate by double potential step chronoamperometry of about 34 liters/mole-sec.

Cinnamionitrile.—The rotating disk electrode voltammogram for cinnamionitrile shows a reduction wave with $E_{1/2} = -1.21V$ vs. Ag-RE. The limiting current for this wave conforms closely to the Levich equation for different values of both ω and C (Table I). A second reduction wave with a height about 1.5 times that of the first wave, occurs at $-1.83V$ vs. Ag-RE. Controlled potential coulometric analysis at the first wave shows n_{app} values of 0.96 ± 0.10 for cinnamionitrile concentrations of 1 to 11 mM. The coulometric n_{app} value near one, the existence of a second reduction wave even without the addition of water, and the lack of dependence of $i_{d,1}/\omega^{1/2}C$ on C suggest that polymerization reactions are absent during reduction of cinnamionitrile under these conditions.

RRDE experiments involving determination of N_K with $CONI$ were also carried out; typical results are shown in Fig. 3. Again the behavior is characteristic of mechanism I, and best fit values of $XKTC$ and k_2 are listed in Table II. The average value of k_2 for dimerization of cinnamionitrile was $8.8 \pm 0.1 \times 10^2$ liter/mole-sec. For concentrations of cinnamionitrile of 7.5 mM or higher a better fit to the experimental data was obtained by carrying out the simulation with the inclusion of some reaction of R^- by the reaction of Eq. [4]. Simulations of this scheme, simultaneous occurrence of mechanisms I and IIa (2), assuming only R^- was oxidized at the ring, gave the same k_2 values as found at lower concentrations and k_2' values of 0.6×10^2 liters/mole-sec.

Fumarionitrile.—RDE voltammetry of fumarionitrile exhibits a reduction wave at $E_{1/2} = -0.68V$ vs. Ag-RE and a dip in the limiting current where a second reduction wave is expected. Values of the Levich constant listed in Table I are quite constant with ω , but show a strong dependence on concentration. The coulometric n_{app} values for reduction of 1 to 3 mM solutions at the first reduction wave are 0.44 ± 0.02 . These results suggest some polymerization of fumarionitrile occurs. The Levich constant for fumarionitrile is smaller than expected, based on the values for dimethyl fumarate and cinnamionitrile. Similar results are found by cyclic voltammetry (Table III). Although this result could be ascribed to polymerization, the constancy with ω and with time, as well as the trend with C lead to an explanation based on some fumarionitrile in a dimeric form in rapid equilibrium with monomeric form. This point will be discussed more fully in a later communication.

The anion radical of fumarionitrile is the least stable of the compounds studied here. For example, no

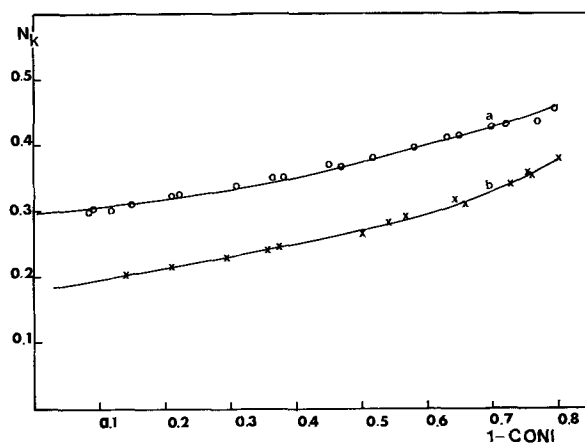


Fig. 3. Collection efficiency (N_K) vs. $1-CONI$ at $\omega = 47.6$ radian sec^{-1} for a 3.00 (o) and 7.46 (x) mM cinnamionitrile solution. Solid lines are theoretical curves corresponding to mechanism I and (a) $XKTC = 0.88$ and (b) $XKTC = 2.25$.

Table III. Cyclic voltammetric data and calculated rate constants^a

Scan rate v (V/sec)	i_{pc}^b $v^{1/2}C$	i_{pa} i_{pc}	τ^c	ω^d	k_2^e (liter/ mole-sec)
A. Dimethyl fumarate ($C = 4.46$ mM)					
0.05	91	0.33			
0.10	98	0.39			
0.20	100	0.43			
0.50	99	0.58	0.68	2.4	1.9×10^5
1.00	97	0.74	0.34	0.84	1.3×10^5
2.00	100	0.78	0.17	0.60	1.9×10^5
5.00	91	0.98			
10.0	86	1.02			
20.0	82	1.04			
(C = 6.20 mM)					
0.05	90	0.35			
0.10	95	0.38			
0.20	97	0.43			
0.50	101	0.54	0.68	4.2	1.8×10^5
1.0	90	0.72	0.34	2.1	1.1×10^5
2.0	77	0.76	0.17	1.0	1.1×10^5
5.0	91	0.89	0.25	0.42	1.4×10^5
					Avg. 1.6×10^5
B. Cinnamionitrile ($C = 3.46$ mM)					
0.05	94	0.31			
0.10	93	0.33			
0.20	91	0.39			
0.50	89	0.49	0.60	4.5	8.5×10^4
1.0	86	0.56	0.30	2.2	8.0
2.0	83	0.70	0.15	1.1	8.0
5.0	82	0.84	0.06	0.34	7.0
10.0	78	0.95			
20.0	82	1.00			
					Avg. 7.9×10^4
C. Fumaronitrile ($C = 1.76$ mM)					
0.05	55.3				
0.10	53.6				
0.20	51.9				
0.50	50.6				
1.0	51.4				
2.0	50.8				
10.0	50.3				
20.0	49.6				

^a Solutions contained 0.1M TBAI and DMF. The platinum working electrode area was 0.11 cm².

^b i_{pc} = cathodic peak current for first reduction wave (μ A), v = scan rate (V/sec), C = concentration (mM).

^c $\tau = (E_{\lambda} - E^{\circ})/v$, where E_{λ} is the switching potential, E° is the formal electrode potential, and v is the scan rate.

^d $\log \omega = \log 2k_2C\tau + 0.034(a\tau - 4)$, $a = (nF/RT)v$ [see Ref. (8)].

^e Note that Nicholson *et al.* (8) define the rate constant for reaction in Eq. [3] in terms of loss of R⁻, i.e., $d[R^-]/dt = -k_{2N}[R^-]^2$, while we define k_2 in terms of formation of the dimer $d[R_2^{2-}]/dt =$

$$\frac{-1}{2} \frac{d[R^-]/dt}{[R^-]^2} = k_2. \text{ Therefore, } k_2 = \frac{1}{2} k_{2N}.$$

reversal wave is observed in cyclic voltammograms for scans of up to 500 mV/sec (see below) and only very small ring currents are measured during generation of R⁻ at the disk. However, by using the technique of adjustment of E_r to a potential where $i_r = 0$ for $i_d = 0$, and then determining i_r at high current sensitivity for increasing i_d values, precise values of i_r could be determined. Typical results of N_K vs. $CONI$ for a 0.92 mM fumaronitrile solution are given in Fig. 4; note the small N_K values. As in the case of cinnamionitrile, the trend is clearly that of mechanism I, but a best fit to the data is obtained by assuming a small contribution (ca. 1-2%) for mechanism IIa. A summary of results for different concentrations of fumaronitrile are shown in Table II. The somewhat larger scatter in the data probably reflects the larger deviation in determining small N_K values, as well as a greater perturbation of the measurements by the polymerization reaction. Assuming the data at the lowest concentration is the least perturbed, we can give the following estimated rate constants

$$k_2 = 7 \times 10^5 \text{ liters/mole-sec, } k_2' = 10^4 \text{ liters/mole-sec.}$$

Cyclic voltammetry experiments.—Cyclic voltammetric experiments were undertaken to obtain additional evidence pertaining to the proposed mechanism and to confirm the RRDE simulations. Typical cyclic voltammograms of the three compounds are shown in Fig. 5. Cyclic voltammetric treatments of dimerization reactions like that in mechanism I have been given by

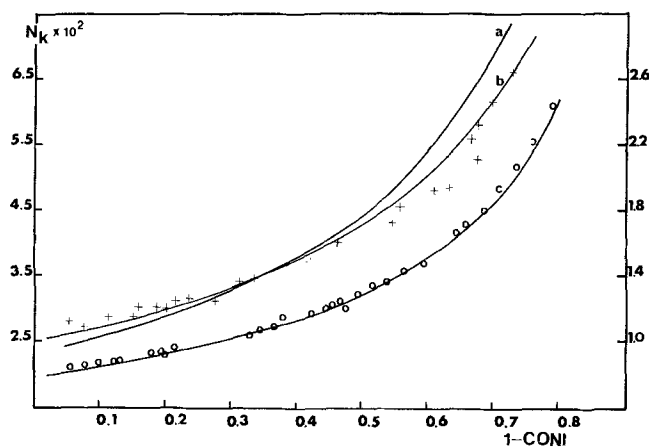


Fig. 4. Collection efficiency (N_K) vs. $1-CONI$ at $\omega = 202$ radians/sec for 0.92 (o) and 1.92 (+) mM fumaronitrile solutions. Solid lines are theoretical curves corresponding to (a) mechanism I, $XKTC = 133$, (b) mechanism I, $XKTC = 92$, and mechanism IIa, $XKTC = 1.0$, considered as parallel paths, and (c) simultaneous consideration of mechanism I, $XKTC = 50$, and mechanism IIa, $XKTC = 0.5$. The right scale applies to curves a and b whereas, the left to curve c.

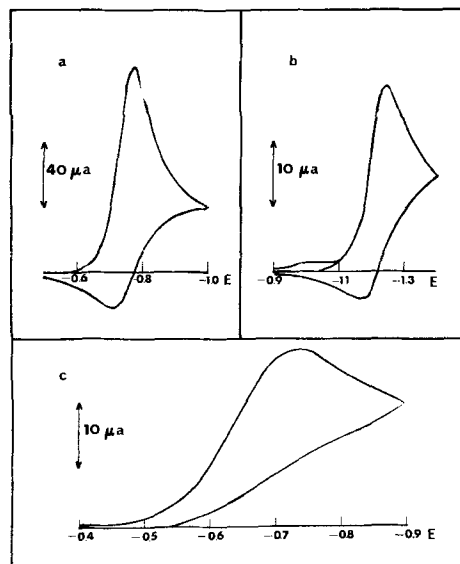


Fig. 5. Cyclic voltammograms at 100 mV/sec. of (a) 4.45 mM dimethyl fumarate, (b) 1.09 mM cinnamionitrile. Note the small impurity wave prior to the cinnamionitrile reduction wave. This wave was removed upon pre-electrolysis at $-0.98V$ vs. Ag-RE, and (c) 1.92 mM fumaronitrile solution.

both Nicholson and co-workers (8) and Saveant and co-workers (9). Second order ECE reactions, such as shown in mechanism II, have also been considered (9). Qualitatively, both mechanisms show i_{pa}/i_{pc} ratios [i_{pa} and i_{pc} are anodic (reversal) and cathodic peak currents, respectively] which increase with increasing scan rate, v . However, the mechanisms differ in the behavior of the current function $i_{pc}/v^{1/2}C$ with scan rate (1, 9). For the EC dimerization (mechanism I) $i_{pc}/v^{1/2}C$ decreases with increasing v , while the ECE process (mechanism II) shows the opposite trend. Typical cyclic voltammetric data for the three compounds are given in Table III. The current function trend characteristic of mechanism I can be discerned in the data for cinnamionitrile and fumaronitrile, while the data for dimethyl fumarate shows this trend at faster scan rates, but is considerably more scattered. A similar trend has also been observed for diethyl fumarate (1). If one assumes that mechanism I is occurring, then the i_{pa}/i_{pc} values can be employed to calculate the dimerization rate constant, k_2 , following

the procedure of Nicholson *et al.* (8). This procedure was carried out for dimethyl fumarate and cinnamionitrile in the region where i_{pa}/i_{pc} is most sensitive to variations in k_2 . The i_{pa} values for fumaronitrile were too small to allow precise calculations from cyclic voltammetric data. The results and some intermediate factors used in the calculations are shown in Table III. The k_2 values obtained for dimethyl fumarate and cinnamionitrile are 1.6×10^2 and 7.9×10^2 liters/mole-sec, respectively.

Discussion

The results obtained here support the previous studies (1) and point to the major pathway in the electrohydrodimerization of these compounds as involving initial production of the anion radical followed by a coupling step. Other aspects of the mechanism, the protonation steps, the nature of the polymerization reaction, and the reactions at the later waves, which sometimes lead to secondary radicals (10), still await elucidation.

In examining the results, we see that dimethyl fumarate, which undergoes dimerization at the slowest rate of the three compounds, shows the most scatter in the k_2 value calculated from RRDE results and only fair agreement with that obtained by cyclic voltammetry. Several factors contribute to this. Because the radical ion disappearance is slow on the RRDE time scale, N_K values are close to those for an unperturbed collection efficiency, and the observed slopes are rather insensitive to small changes in $XKTC$. Moreover, the small value of k_2 necessitates use of high dimethyl fumarate concentrations, which increases the polymerization side reaction.

The RRDE results for cinnamionitrile fall into the sensitive N_K vs. $CONI$ region for our electrode and the reaction is unperturbed by polymerization. The k_2 values determined by RRDE measurements over a wide range of C and for differing ω show good precision and agree very well with the value determined by cyclic voltammetry. This good agreement between a steady-state and transient technique also is suggestive of lack of involvement of adsorption of parent or intermediates in the reaction mechanism.

The fumaronitrile RRDE experiments were performed near the upper limit of determinable k_2 values with our RRDE. For this reaction, for concentrations of 0.4 to 4 mM, N_K values of only 0.020-0.006 ($CONI = 1$) were found. For both the cinnamionitrile and fumaronitrile reactions the data suggest some contribution from a reaction of the anion radical with parent, although in both cases this contribution was relatively small. It is interesting that even this small contribution can be noticed and accounted for in the analysis of the data, although other processes removing anion radical, such as a first order ECE reaction leading to RH_2 , may also account for the small deviations from a close fit to mechanism I.

Acknowledgment

The support of the Robert A. Welch Foundation and the National Science Foundation (GP 6688X) are gratefully acknowledged. We also thank Dr. Ira B. Goldberg for helpful suggestions.

Manuscript submitted Dec. 17, 1971; revised manuscript received March 20, 1972.

Any discussion of this paper will appear in a Discussion Section to be published in the June 1973 JOURNAL.

REFERENCES

1. W. V. Childs, J. T. Maloy, C. P. Keszthelyi, and A. J. Bard, *This Journal*, **118**, 874 (1971).
2. V. J. Puglisi and A. J. Bard, *This Journal*, **119**, 833 (1972).
3. M. Baizer, *This Journal*, **111**, 215 (1964).
4. T. Asahara, M. Seno, and M. Tsuchiya, *Bull. Chem. Soc. Japan*, **42**, 2416 (1969).
5. M. Baizer and J. D. Anderson, *This Journal*, **111**, 223 (1964).
6. J. Petrovich, M. Baizer, and M. Ort, *ibid.*, **116**, 749 (1969).
7. L. R. Faulkner and A. J. Bard, *J. Am. Chem. Soc.*, **90**, 6284 (1968).
8. M. L. Olmstead, R. G. Hamilton, and R. S. Nicholson, *Anal. Chem.*, **41**, 225 (1969).
9. C. P. Andrieux, L. Nadjo, and J. M. Saveant, *J. Electroanal. Chem.*, **26**, 147 (1970).
10. I. Goldberg and A. J. Bard, Unpublished experiments, Univ. of Texas, 1971.

Rotating Ring-Disk Electrodes

IV. Dimerization and Second Order ECE Reactions

Vincent J. Puglisi and Allen J. Bard*

Department of Chemistry, The University of Texas at Austin, Austin, Texas 78712

ABSTRACT

Digital simulation techniques have been employed to compute the steady-state currents at the rotating ring-disk electrode (RRDE) as functions of a rate parameter exhibiting explicit dependence on concentration of parent species (A) and rotation rate and also as functions of the flux at the disk for those cases in which the disk generated product (B) undergoes a following dimerization EC reaction ($2B \rightarrow$ products) or a second order ECE reaction ($B + A \rightarrow C$, where C may be electroactive at the disk potential) and nuances thereof. Diagnostic criteria are given for using RRDE results to distinguish among possible reaction mechanisms and working curves are provided to allow calculation of the rate constants of the homogeneous reactions.

The rotating ring-disk electrode (RRDE) has been used to study electrogenerated intermediates which react by different schemes (1). Past papers in this series (2-4) have discussed the use of digital simulation techniques to treat the currents at the disk and the ring of the RRDE and discussed methods for

extracting kinetic information about the reactions of the disk-generated species. In this paper results of the digital simulation of reaction mechanisms in which the disk generated species can couple with itself (dimerization) or with the parent compound are presented. Many examples of actual electrode reactions which proceed by mechanisms such as these can be given; particular current interest centers around reductive coupling reactions of activated olefins or elec-

* Electrochemical Society Active Member.

Key words: digital simulation, hydrodimerization reactions, rotating disk electrode, electrode reactions.

trohydrodimerizations [see (5-6) and references contained therein].

The following mechanisms are considered:

I. *Dimerization EC (electrochemical-chemical)*—Species B, which is generated at the disk electrode by



dimerizes to a nonelectroactive product



At the ring electrode A is regenerated from B by the reaction



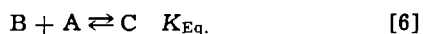
II. *Second order ECE*.—Species B, produced at the disk as in Eq. [1], reacts with parent



where C is immediately reduced at the disk



At the ring electrode either (a) B alone is oxidized, as in Eq. [3], or (b) both B and C are oxidized. Nuances of ECE mechanism IIa (7-8) consider (c) the irreversible reaction represented in Eq. [4] or (d) the reversible reaction



followed by an irreversible oxidation-reduction charge transfer reaction



III. *Second order EC*.—Species B, produced at the disk as in Eq. [1], reacts with parent to form a nonelectroactive product



Again at the ring B oxidizes to A via Eq. [3].

Note that these three mechanisms represent possible paths from A to a coupled product (X, Y, or Z). The treatment below is aimed at computing how the collection efficiency, N_K ,

$$N_K = |i_r/i_d| \quad [9]$$

where i_r and i_d are the ring and disk currents, respectively, varies with concentration of parent, C, rotation rate, ω , i_d , and the rate constants of the reactions consuming B and at establishing criteria for distinguishing between these mechanisms. The application of the RRDE to the elucidation of the mechanism of electrohydrodimerization of dimethyl fumarate, cinnamionitrile, and fumarionitrile is demonstrated in the accompanying paper (9).

Digital Simulation

The general approach to the simulations and the notation to be used has been described in the previous communications (2-4). Two different types of experiments were simulated. In the first the disk was assumed to be held at a potential where the concentration of A at the disk surface was always zero and for mechanism II, the concentration of C at the disk surface was also zero. A second simulation concerned a constant current maintained at the disk, so that the flux of A (or the sum of the fluxes of A and C in mechanism II) was held constant at the disk. In both cases the boundary condition at the ring electrode was that the concentration of B was zero at the ring. In mechanism IIb, the concentration of C was also held at zero at the ring surface. Surface boundary conditions for the different experiments and mechanisms considered are given in Table I. As in previous simulations, the results are specific for the particular RRDE geome-

Table I. Surface boundary conditions

Mechanism	Boundary conditions ($x = 0$)		
	$t < 0$	$t \geq 0$	
	Disk and ring	Disk	Ring
A. Controlled disk potential			
I	$C_A = C_A^0$ $C_B = 0$	$C_A = 0$ $C_B = C_A^0$	$C_A = C_A'$ $C_B = 0$
IIa	$C_A = C_A^0$ $C_B = 0$ $C_C = 0$	$C_A = 0$ $C_B = C_A^0$ $C_C = 0$	$C_A = C_A'$ $C_B = 0$ $C_C = C_C'$
IIb	$C_A = C_A^0$ $C_B = 0$ $C_C = 0$	$C_A = 0$ $C_B = C_A^0$ $C_C = 0$	$C_A = C_A'$ $C_B = 0$ $C_C = 0$
IIc	$C_A = C_A^0$ $C_B = 0$ $C_C = 0$	$C_A = 0$ $C_B = C_A^0$ $C_C = 0$	$C_A = C_A'$ $C_B = 0$ $C_C = C_C'$
IId	$C_A = C_A^0$ $C_B = 0$ $C_C = 0$	$C_A = 0$ $C_B = C_A^0$ $C_C = 0$	$C_A = C_A'$ $C_B = 0$ $C_C = C_C'$
III	$C_A = C_A^0$ $C_B = 0$	$C_A = 0$ $C_B = C_A^0$	$C_A = C_A'$ $C_B = 0$
B. Controlled disk current			
I	$C_A = C_A^0$ $C_B = 0$	$D_A \left(\frac{\partial C_A}{\partial x} \right)_{x=0} = \frac{i}{nFA}$ $-D_B \left(\frac{\partial C_B}{\partial x} \right)_{x=0} = \frac{i}{nFA}$	$C_A = C_A'$ $C_B = 0$
IIa	$C_A = C_A^0$ $C_B = 0$ $C_C = 0$	$D_A \left(\frac{\partial C_A}{\partial x} \right)_{x=0} + D_C \left(\frac{\partial C_C}{\partial x} \right)_{x=0} = \frac{i}{nFA}$ $-D_B \left(\frac{\partial C_B}{\partial x} \right)_{x=0} = \frac{i}{nFA}$	$C_A = C_A'$ $C_B = 0$ $C_C = C_C'$
IIb	$C_A = C_A^0$ $C_B = 0$ $C_C = 0$	$D_A \left(\frac{\partial C_A}{\partial x} \right)_{x=0} + D_C \left(\frac{\partial C_C}{\partial x} \right)_{x=0} = \frac{i}{nFA}$ $-D_B \left(\frac{\partial C_B}{\partial x} \right)_{x=0} = \frac{i}{nFA}$	$C_A = C_A'$ $C_B = 0$ $C_C = 0$
IIc	$C_A = C_A^0$ $C_B = 0$ $C_C = 0$	$D_A \left(\frac{\partial C_A}{\partial x} \right)_{x=0} + D_C \left(\frac{\partial C_C}{\partial x} \right)_{x=0} = \frac{i}{nFA}$ $-D_B \left(\frac{\partial C_B}{\partial x} \right)_{x=0} = \frac{i}{nFA}$	$C_A = C_A'$ $C_B = 0$ $C_C = C_C'$
IId	$C_A = C_A^0$ $C_B = 0$ $C_C = 0$	$D_A \left(\frac{\partial C_A}{\partial x} \right)_{x=0} + D_C \left(\frac{\partial C_C}{\partial x} \right)_{x=0} = \frac{i}{nFA}$ $-D_B \left(\frac{\partial C_B}{\partial x} \right)_{x=0} = \frac{i}{nFA}$	$C_A = C_A'$ $C_B = 0$ $C_C = C_C'$
III	$C_A = C_A^0$ $C_B = 0$	$D_A \left(\frac{\partial C_A}{\partial x} \right)_{x=0} = \frac{i}{nFA}$ $-D_B \left(\frac{\partial C_B}{\partial x} \right)_{x=0} = \frac{i}{nFA}$	$C_A = C_A'$ $C_B = 0$

try considered. The electrode under consideration here had $IR_1 = 94$, $IR_2 = 100$, and $IR_3 = 166$, where IR_1 , IR_2 , and IR_3 are the number of simulation boxes necessary to represent the radius of the disk electrode, and the radii to the inner and outer edge of the ring electrode, respectively; these values yield a collection efficiency in the absence of kinetic perturbations of 0.555. Values of i_d , i_r , and N_K were calculated as functions of the dimensionless parameter $XKTC$ in the controlled

$$XKTC = (0.51)^{-2/3} \rho^{1/3} D^{-1/3} C_A^0 \omega^{-1} k_2 \quad [10]$$

potential simulation and as functions of $XKTC$ and the flux at the disk in the constant disk current simulation. Because a basic assumption of mechanism II is that species C is more easily reduced than species A, it was first necessary to establish in the constant current simulation if the total flux at the disk, as defined by the current, was greater or less than the maximum flux possible for species C. If greater, a fraction of the total current was allocated sufficient to maximize the concentration gradient of C at the disk surface

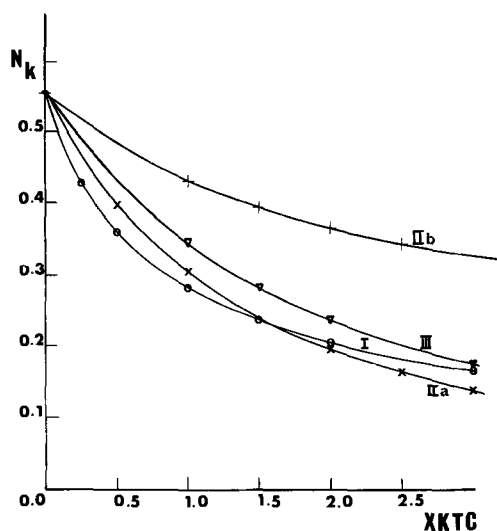


Fig. 1. Collection efficiency (N_K) vs. $XKTC$ for the EC dimerization mechanism (I), the ECE radical-parent coupling mechanisms (IIa and IIb), and the EC radical-parent coupling mechanism (III).

[FC(1,1) = 0] while the remaining current diminished the concentration of A. If less, a finite concentration of C remained at the surface and the concentration of A was not altered by the passage of current. In every instance the diffusion coefficients of species A, B, and C were assumed equal, although provision is included in the program for introducing a different value for each species.

Results

Controlled disk potential results.—The results of simulations where the disk potential is maintained on the limiting current plateau for reaction [1] and the ring maintained at a potential where [3] occurs at the mass transfer controlled rate are shown in Fig. 1. [Mechanisms IIc and IId are not shown in Fig. 1 because of N_K 's dependence on two parameters (equilibrium constant and rate constant) instead of one for the mechanisms as shown but qualitatively they would show the same sort of behavior.] All curves yield a value of $N_K = N = 0.555$ as $XKTC$ approaches 0 (k_2C approaches 0, or ω approaches infinity) and all show a similar decrease of N_K with increasing $XKTC$. While these N_K - $XKTC$ curves are indicative of kinetic perturbations and could be used to determine k_2 values once the mechanism is known, they are clearly not very useful in distinguishing among the various mechanisms under consideration. Further, the dependence of the disk limiting current on $XKTC$ (Table II) is of value only in distinguishing case III from cases I and II. Case II, categorized as an ECE type, is unlike the simple ECE case in that n , the number of electrons per molecule of starting material, A, electrolyzed, equals one independent of the rotation rate. Case III, however, undergoes a change in n from $n = 1$ to $n = 2$ with increasing rotation rate and thus, exhibits a dependence of disk limiting current with varying $XKTC$ values.

Controlled disk current results.—Experiments involving disk currents at values below the limiting one are more diagnostic in deciding among the various reaction schemes under consideration here, because the relative fluxes of A and B from the disk can be varied. Simulations in this case are of N_K at different values of the relative disk current, $CONI$, where

$$CONI = i_d/i_{d,1} \quad [11]$$

and $i_{d,1}$ is the limiting disk current, and for different values of $XKTC$. In this case a separate N_K vs. $CONI$ curve must be given for each value of $XKTC$. Results for the mechanisms under consideration here are given in Fig. 2-7. Note that for a first order decomposition

Table II. Dependence of disk limiting current on $XKTC$

Mechanism	$XKTC$	N_K	ZR ^a	ZD ^b
I	0.5	0.360	0.279	0.776
	1.0	0.281	0.218	0.776
	1.5	0.235	0.183	0.776
	2.0	0.205	0.159	0.776
	3.0	0.165	0.128	0.776
IIa	0.0	0.556	0.432	0.776
	1.0	0.305	0.236	0.776
	2.0	0.194	0.151	0.776
	3.0	0.135	0.105	0.776
IIb	1.0	0.430	0.333	0.776
	2.0	0.366	0.284	0.776
	3.0	0.326	0.253	0.776
	4.0	0.298	0.231	0.776
	6.0	0.260	0.202	0.776
	8.0	0.234	0.182	0.776
III	1.0	0.344	0.236	0.688
	2.0	0.235	0.151	0.643
	3.0	0.170	0.104	0.615
	4.0	0.128	0.076	0.596
	5.0	0.100	0.058	0.581
	8.0	0.052	0.029	0.551

$$^a ZR = \frac{i_r}{(0.51)^{1/3} n F A_d C_A^0 D_B^{2/3} \omega^{1/2} \nu^{-1/6}}$$

$$^b ZD = \frac{i_d}{(0.51)^{1/3} n F A_d C_A^0 D_A^{2/3} \omega^{1/2} \nu^{-1/6}}$$

of B, N_K is independent of $CONI$, at a given value of XKT , because both the velocity of the following reaction and the amount of B reaching the ring are proportional to disk current. The trend of N_K with $CONI$ is

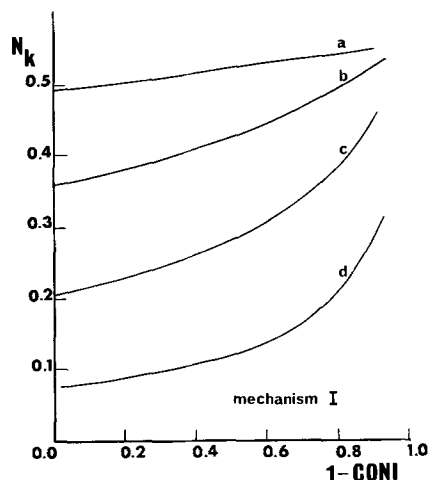


Fig. 2. Collection efficiency (N_K) vs. $1-CONI$ for mechanism I and $XKTC$ equal to (a) 0.1, (b) 0.5, (c) 2.0, and (d) 10.0, where $CONI = i_d/i_{d,1}$ and $XKTC = (0.51)^{-2/3} \nu^{1/3} D^{-1/3} \omega^{-1} k_2 C$.

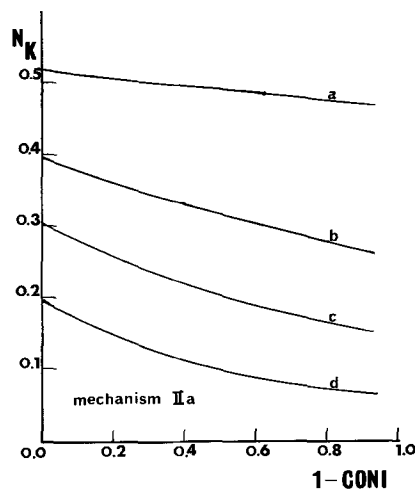


Fig. 3. Collection efficiency (N_K) vs. $1-CONI$ for mechanism IIa and $XKTC$ equal to (a) 0.1, (b) 0.5, (c) 1.0, and (d) 2.0.

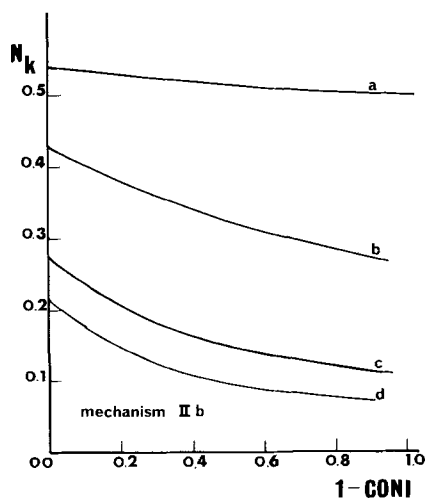


Fig. 4. Collection efficiency (N_K) vs. $1-CONI$ for mechanism IIb and $XKTC$ equal to (a) 0.1, (b) 1.0, (c) 5.0, and (d) 10.0.

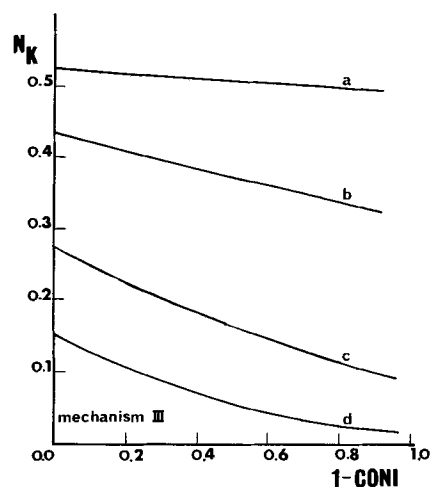


Fig. 7. Collection efficiency (N_K) vs. $1-CONI$ for mechanism III and $XKTC$ equal to (a) 0.1, (b) 0.5, (c) 2.0, and (d) 5.0.

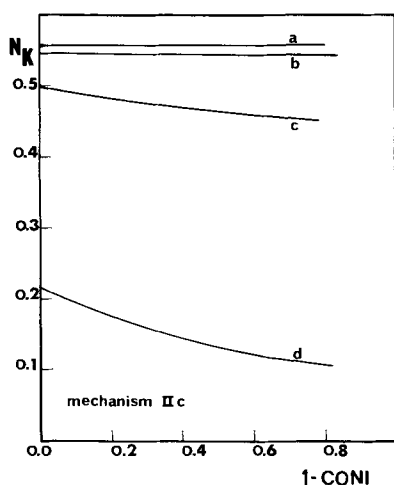


Fig. 5. Collection efficiency (N_K) vs. $1-CONI$ for mechanism IIc, $XKTC_2$ equal to 1000 and $XKTC_1$ equal to (a) 0.001, (b) 0.010, (c) 0.10, and (d) 1.0, where $XKTC_1$ and $XKTC_2$ describe the reactions represented in Eq. [4] and [7], respectively.

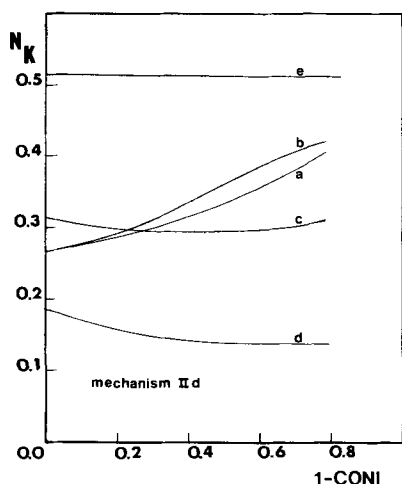


Fig. 6. Collection efficiency (N_K) vs. $1-CONI$ for mechanism II d and (a) $CK = 10^{-4}$, $XKTC = 10^5$; (b) $CK = 10^{-3}$, $XKTC = 10^4$; (c) $CK = 10^{-2}$, $XKTC = 10^3$; (d) $CK = 10^{-1}$, $XKTC = 10^2$, and (e) $CK = 10^{-3}$, $XKTC = 10^3$.

qualitatively different for cases I and IIa (or IIb, IIc, III). For mechanism I, the dimerization EC reaction, the velocity of the following reaction only depends on B concentration. Hence, as i_d becomes smaller ($CONI$ approaches 0), the B concentration at the disk de-

creases and the kinetic perturbation of the following reaction becomes less. Hence, for case I, $N_K \rightarrow N$ as $CONI \rightarrow 0$ and N_K approaches its minimum value as $CONI \rightarrow 1$. For cases IIa, IIb, IIc, or III, which involve coupling with the parent, the rate of the following reaction is a function of both A and B concentration at the disk. Hence, as i_d approaches $i_{d,1}$ ($CONI$ approaches 1) the A concentration decreases and the following reaction rate decreases. For these cases N_K approaches its maximum value at a given value of $XKTC$ as $CONI \rightarrow 1$. As $CONI$ approaches 0, the concentration of A is essentially constant and the reaction of B approaches pseudo-first order conditions. When product C is also electroactive at the ring electrode (mechanism IIb), the trend is the same as for mechanism IIa but the N_K values are larger because i_r is larger. Although case II d exhibits qualitatively different behavior depending on the value of the equilibrium constant for [6] and the rate constant for [7] as shown in Fig. 6, some trends are evident. For values of CK ($CK =$ bulk concentration of A \times equilibrium constant (K) for reaction [6]) greater than or equal to 0.10 and $XKTC$ values resulting in collection efficiencies in the normal working range for the simulated RRDE ($0.02 < N_K < 0.54$), N_K approaches its maximum value as $CONI \rightarrow 1$. As $CONI \rightarrow 0$, the concentration of C is essentially constant and the reaction consuming B approaches pseudo-first order behavior. For CK values less than or equal to 0.001 (e.g., $K = 1$ when $C = 1$ mM), the N_K variation with $CONI$ is qualitatively similar to case I because the velocity of the following reaction assumes an over-all second order dependence on B concentration. Transitional behavior, exemplified by curves b, c, and e (Fig. 6), occurs at intermediate values of CK . Quantitatively, the behavior of case II d differs from that of case I, for all values of CK , because the product of the appropriate dimensionless simulation parameters for case II d (i.e., CK and $XKTC$), which defines the velocity of the reactions consuming species B (and thus the magnitude of N_K) has a squared dependence on the bulk concentration of A, whereas for case I, the reaction velocity is described by only one dimensionless simulation rate parameter, $XKTC$.

Discussion

The results show that the RRDE should be useful in studying different mechanisms of following reactions. Since RRDE studies involving steady-state N_K measurements are relatively free from adsorption and double layer charging effects, the experimental results will be subject to fewer complications than transient methods. Digital simulation methods are capable of treating rather complex reaction schemes involving higher order chemical reactions. Variations of the mechanisms considered here, such as the simultaneous

occurrence of two of the reaction paths, can be treated by straightforward extensions of the described programs. For example, in studies of hydrodimerization reactions with the RRDE (9) it was sometimes necessary to consider the possibility of parallel reaction pathways of the intermediate radical ion (equivalent to substance B here) by both coupling and ECE mechanisms. The results in that work provide experimental confirmation of these theoretical results.

Acknowledgment

The support of the Robert A. Welch Foundation and the National Science Foundation (GP6688X) are gratefully acknowledged.

Manuscript submitted Dec. 17, 1971; revised manuscript received March 20, 1972.

Any discussion of this paper will appear in a Discussion Section to be published in the June 1973 JOURNAL.

REFERENCES

1. W. J. Albery and M. L. Hitchman, "Ring-Disc Electrodes," Oxford University Press, London (1971).
2. K. B. Prater and A. J. Bard, *This Journal*, **117**, 207 (1970).
3. *Ibid.*, 335 (1970).
4. *Ibid.*, 1517 (1970).
5. W. C. Childs, J. T. Maloy, C. P. Keszthelyi, and A. J. Bard, *ibid.*, **118**, 874 (1971).
6. M. M. Baizer, J. P. Petrovich, and D. A. Tyssee, *ibid.*, **117**, 173 (1970).
7. M. D. Hawley and S. W. Feldberg, *J. Phys. Chem.*, **70**, 3459 (1966).
8. L. Nadjo and J. M. Saveant, *J. Electroanal. Chem.*, **33**, 419 (1971).
9. V. J. Puglisi and A. J. Bard, *This Journal*, **119**, 829 (1972).

Electrochemical Reduction of Allopurinol

P. K. De and Glenn Dryhurst

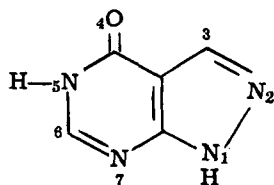
Department of Chemistry, University of Oklahoma, Norman, Oklahoma 73069

ABSTRACT

Allopurinol (1H-pyrazolo [3,4-d] pyrimidin-4-ol) is electrochemically reduced at the dropping mercury electrode by way of a single polarographic wave. Above pH 2, the electrode reaction is a $2e-2H^+$ reduction of allopurinol to give 6,7-dihydroallopurinol as the sole product. At lower pH (i.e., pH 0) the single polarographic wave involves $4e$ and is due to reduction of allopurinol to 2,3,6,7-tetrahydroallopurinol. Under the conditions of prolonged electrolysis, however, the latter product slowly decomposes to give 4-carbamido-5-aminopyrazoline (2,3). The mechanism of these reactions have been elucidated by polarography, coulometry, cyclic voltammetry at the pyrolytic graphite electrode, mass electrolysis and isolation of products. The products have been identified by u.v., IR, NMR, mass spectrometry, and elemental analysis.

Pyrazolo [3,4-d] pyrimidines have found considerable application in clinical biochemistry as carcinostatic agents. Allopurinol (1H-pyrazolo [3,4-d] pyrimidine 4-ol) is a well-known inhibitor of the enzyme xanthine oxidase (1), and, hence, inhibits the formation of uric acid by oxidation of purines in organisms containing this enzyme (2, 3). This property of allopurinol makes it possible to use lower doses of otherwise highly toxic 6-thiopurine in the treatment of leukemia (4). Allopurinol also substantially alters pyrimidine metabolism (5).

Because of the importance of understanding the oxidation-reduction behavior of biologically important compounds which interact with oxidation-reduction enzymes, we have begun a detailed and systematic study of the electrochemistry of the allopurines. The structure of allopurinol and the numbering employed in this paper is that used in "Chemical Abstracts," and is shown below.



Experimental

Chemicals.—Allopurinol was obtained from Aldrich and was found to be chromatographically homogeneous. The other chemicals were of reagent grade. Argon (Linde) used for deoxygenating was equili-

brated with water; no other purification was necessary. Buffer solutions used had an ionic strength of 0.5M except sulfuric and acetic acid solutions which were 1M in strength.

Apparatus.—The electrochemical apparatus has been described elsewhere (6-8). All potentials are referred to the SCE at 25°C. The dropping mercury electrode had normal m and t values.

Ultraviolet absorption spectra were recorded on a Perkin Elmer-Hitachi Model 124 spectrophotometer. Infrared spectra were recorded on a Beckman IR-8 using KBr pellets. NMR spectra were recorded on Varian Model T-60 spectrometer. Mass spectra were recorded on a Hitachi Model RMU-6E spectrometer.

Coulometry and macroscale electrolysis.—For coulometry a measured volume (usually 100 ml) of background solution was introduced into the working electrode compartment of a three compartment cell. This solution was electrolyzed at the appropriate potential until an electronic current integrator gave a constant and small count. Then a weighed amount of allopurinol was introduced into the working electrode compartment sufficient to make the solution ca. 1 mM. After dissolution electrolysis was recommenced at the same potential, stirring rate, and flow rate of argon. Many macroscale electrolyses were carried out in the same fashion except that solutions were ca. 5-6 mM in allopurinol and an integrator was not employed. Completion of the electrolysis was confirmed by disappearance of the characteristic u.v. absorption and polarographic wave of allopurinol, and by characteristic cyclic voltammetric behavior at the pyrolytic graphite electrode.

Key words: 1H-pyrazolo [3,4-d] pyrimidin-4-ol, bioelectrochemistry, 6,7-dihydroallopurinol, 2,3,6,7-tetrahydroallopurinol.

In order to reduce contamination of the products of macroscale electrolysis with KCl (from salt bridges and SCE reference electrode), a two-compartment cell was frequently employed, one compartment for the working electrode, one for a platinum gauze counter-electrode. These two compartments were separated by a fine sintered glass disk and an agar-acetic acid salt bridge. Such salt bridges were made by heating 4g of agar with 40 ml of water until a homogeneous solution was obtained. Then, 40 ml of 2M HOAc was added and the solution cooled to room temperature when a stable gel was formed. The reference electrode was a Beckman fiber-tip SCE inserted into the working electrode compartment.

Chromotropic acid test for formaldehyde.—Aliquots of 0.2 to 0.6 ml of electrolysis solution were transferred to 25 ml volumetric flasks and diluted to 1 ml with water. Then 1 ml chromotropic acid solution (0.6g of the disodium salt of chromotropic acid in 20 ml water added to 180 ml of concentrated H_2SO_4) was added and the volume made up with concentrated H_2SO_4 . The flasks were heated for an hour on a steam bath, cooled to room temperature, and the absorbance measured at 570 nm against a water blank carried through the same procedure. A calibration curve was prepared with standard formaldehyde solution. Allopurinol itself does not respond to this test.

Estimation of formaldehyde in argon stream from electrolysis cell.—In order to decide if free formaldehyde is liberated upon electrochemical reduction of allopurinol, an electrolysis was carried out in a cell with the working electrode compartment sealed with a rubber stopper provided with inlet and outlet tubes for argon. After bubbling the argon through the electrolyzing solution it was passed sequentially through three gas bubbling towers containing distilled water, 0.1M sodium sulfite, and chromotropic acid reagent solution. After completion of the reduction the contents of the three towers were analyzed for formaldehyde by the chromotropic acid method (see above). The sodium sulfite solution gave a positive formaldehyde test when the electrolysis was carried out in 1M H_2SO_4 . Using 1M HOAc as the supporting electrolyte solution, no formaldehyde could be detected in any of the trap solutions. In 1M H_2SO_4 one mole of formaldehyde was determined per mole of allopurinol reduced, approximately 10-15% in the sodium sulfite trap and 85-90% by direct application of the chromotropic acid procedure to an aliquot of the electrolysis solution. The same quantity of formaldehyde was detected for an electrolysis in 1M HOAc, all in the electrolysis solution.

Isolation of acetic acid reduction product.—After the completion of a mass electrolysis, the solution was freeze-dried. The resultant white solid was separated from small amounts of potassium chloride (from reference electrode and salt bridges) by extracting with absolute methanol. This, on crystallization from chloroform and methanol, formed white crystals melting at 115°-120°C which were very very soluble in water and gave a positive test for acetate (14). The IR and NMR spectra of this compound clearly indicated that it was an acetate salt. In order to isolate the free base, the freeze-dried white solid was dissolved in methanol and passed through a column (30 cm × 1 cm) of basic alumina. The column was eluted with methanol and five 15 ml fractions were collected. The first fraction was contaminated with some KCl and the other fractions, upon evaporation of the methanol, gave pure 6,7-dihydroallopurinol as evidenced by IR, NMR, and u.v. spectra, and elemental analysis. The free base is a white crystalline compound, sparingly soluble in water, having a mp of 210°C. Elemental analysis: found, C = 43.23%, H = 4.36%, N = 40.32%; theory, C = 43.47%, H = 4.35%, N = 40.58%. The yield of pure product was ca. 80%.

The free base could also be isolated by passing an aqueous solution of the acetic acid product through a basic ion-exchange resin (Dowex 2-X8 in OH⁻ form). On eluting with water, KOH (from KCl contaminating the sample) eluted first followed by the base. After evaporation of the water, the sample was dissolved in methanol and passed through a small basic alumina column. The resultant product was analytically pure.

Reduction of allopurinol, in McIlvaine buffer pH 2.2, gave the same product. Isolation of the product from such a buffer was carried out by first freeze-drying the product and extracting with absolute methanol, evaporating the methanol and extracting again. This methanol extract was then passed through a Florosil column and eluted with methanol. A 60% yield of 6,7-dihydroallopurinol was obtained.

Isolation of sulfuric acid reduction product.—After complete electrolysis of a 6 mM solution of allopurinol in 1M H_2SO_4 , the solution was treated with a slight excess of saturated barium hydroxide solution. The precipitated barium sulfate was removed by filtration and then the clear solution was treated with carbon dioxide to remove excess of barium. The barium carbonate was removed by filtration and the clear solution was freeze-dried. The resultant solid obtained was separated from the KCl present and then recrystallized from chloroform and methanol. The reduction product was a canary yellow solid, mp 125°-30°C which was very soluble in water.

Thin layer chromatography.—A 2 mg/ml solution of the isolated electrolysis products and allopurinol itself, in water, were employed. Approximately 100 μ l of these solutions were spotted onto thin-layer plates. The most definitive data, which is quoted below, was obtained with a silica gel support (Eastman Chromogram 6060 with fluorescent indicator) and n-propanol-water (70-30) as solvent. The reduction product isolated from acetic acid, and McIlvaine buffer pH 2.2, was chromatographically homogeneous and had an R_F value of 0.75 (fluorescence). Allopurinol had an R_F of 0.85. Neither allopurinol nor its reduction product formed in acetic acid gave a positive test with Ehrlich reagent (for ureido groups) on a thin layer plate. The product isolated from sulfuric acid gave a single spot (fluorescence), $R_F = 0.7$; this spot when sprayed with Ehrlich reagent gave a bright yellow color.

Results and Discussion

Polarography.—Allopurinol gives a single polarographic reduction wave in solutions between pH 0-8. At low pH, the wave is very close to background discharge, but at pH above ca. 4, it becomes well defined and easy to measure. In 1M H_2SO_4 (pH 0), and in acetate buffer pH 4.7, the limiting current appeared to be entirely under diffusion control as evidenced by the drop-time dependence of the wave and its temperature coefficient (2.1%/°C at pH 4.4). The wave rapidly decreased in height above pH 6 and disappears above pH 8.

In 1M H_2SO_4 , the diffusion current constant ($I = i_1/Cm^{2/3}t^{1/6}$) is about 10, but decreases at higher pH so that between pH 2.3-6, it has an average value of close to 4 (Fig. 1, section A). Over this latter pH range, the magnitude of the diffusion current constant indicates a 2e polarographic process. The half-wave potential of allopurinol shifts linearly more negative with increasing pH (Fig. 1, section B), and is described by the equation $E_{1/2} = -1.118 - 0.067 \text{ pH}$.

Voltammetry at PGE.—Allopurinol shows a single reduction peak at the stationary pyrolytic graphite electrode (PGE) between pH 0-6. Generally the peak is so close to the onset of background discharge that, often, it merely forms an inflection; and hence, it is not possible to measure meaningful peak current values. In as far as it could be determined, the variation of peak potential at PGE is given by $E_p = -0.85 - 0.120 \text{ pH}$.

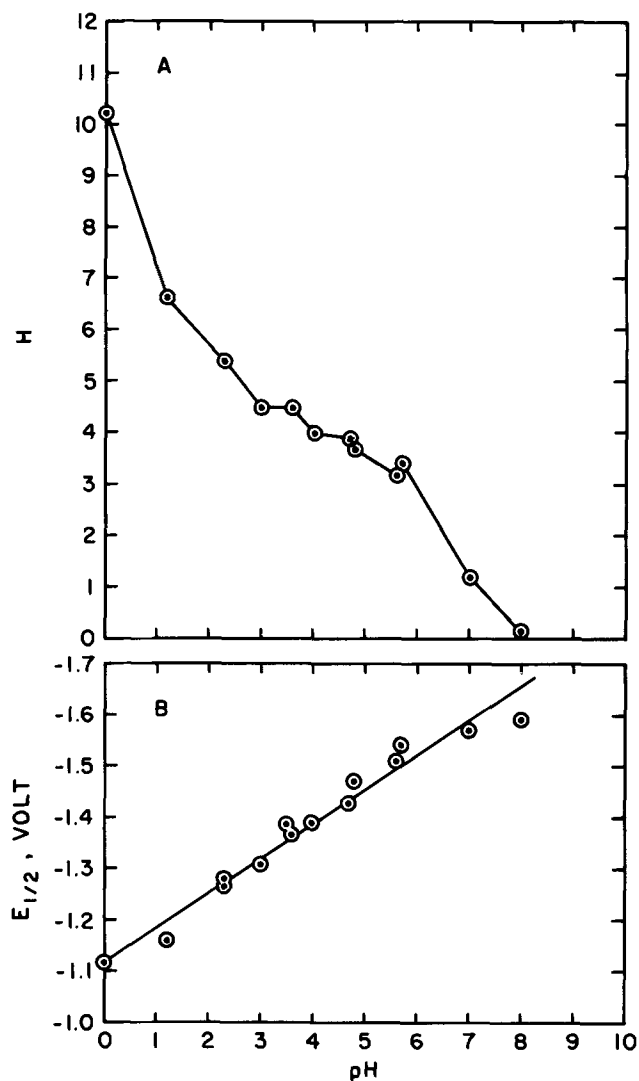


Fig. 1. A, Variation of the polarographic diffusion-current constant with pH and; B, variation of $E_{1/2}$ with pH for allopurinol.

Coulometry and macroscale electrolysis.—Because of the closeness of the voltammetric reduction peak at PGE to the background discharge, it was not possible to obtain meaningful n values at this electrode. Preliminary studies of the controlled potential electrolysis of allopurinol, at a mercury electrode in a number of background electrolytes, revealed that either allopurinol or its reduction product considerably lowers the hydrogen overpotential. Thus, owing to considerable catalytic hydrogen reduction, large apparent electron numbers were obtained when coulometry was performed at potentials corresponding to the crest of the polarographic waves. Accordingly, in order to circumvent this problem, coulometry was carried out by only partially electrolyzing at potentials on the rising portion of the wave. In 1M H_2SO_4 , the n value was found to be 4.0 ± 0.2 ; whereas, in 1M HOAc, McIlvaine (pH 4.0) and acetate (pH 4.7), the values of n were 1.8 ± 0.1 , 2.0 ± 0.2 , and 2.2 ± 0.2 , respectively.

Following the initial coulometry, extensive electrolysis in 1M H_2SO_4 and 1M HOAc were carried out; detailed spectra were obtained and cyclic voltammetry performed during, and at the completion of, the electrolysis. These two electrolyte systems were selected because they were representative of media in which the $4e$ and $2e$ processes occur. In addition, both H_2SO_4 and HOAc are relatively easily removed, hence, allowing product isolation.

Electrolysis in 1M HOAc.—After complete reduction of allopurinol in 1M HOAc, the u.v. absorption spectrum of the product ($\lambda_{max} = 266$ nm and $\lambda_{max} = 240$

nm) was quite different to that of allopurinol ($\lambda_{max} = 250$ nm). The solution gave a positive test for formaldehyde (9), one mole of reduced allopurinol giving rise quantitatively to one mole of formaldehyde. However, attempts to bubble formaldehyde out of the reduced solution were not successful indicating that a product is formed that yields formaldehyde only under the extremely acidic conditions of the chromotropic acid-formaldehyde reaction.

Cyclic voltammetry of allopurinol at the PGE showed one cathodic peak [peak I_c very close to background discharge, $E_p = -1.55$ V to -1.60 V (Fig. 2, section A)]. Once having scanned this cathodic peak, two well-defined anodic peaks were obtained, $E_p = 0.40$ V and 0.80 V (peaks I_a and II_a Fig. 2, section A). Peak II_a was always larger than peak I_a . Cyclic voltammetry of reduced allopurinol indicated that on the first scan toward negative potential at a clean electrode there were no cathodic peaks. However, on the first scan toward positive potentials, two anodic peaks were observed whose peak potentials corresponded exactly with peaks I_a and II_a (Fig. 2, section B). Peak I_a was always much smaller than peak II_a and occasionally was not observed at all. Having scanned anodic peaks I_a and II_a , a large cathodic peak at the same potential as cathodic peak I_c was observed (Fig. 2, section B).

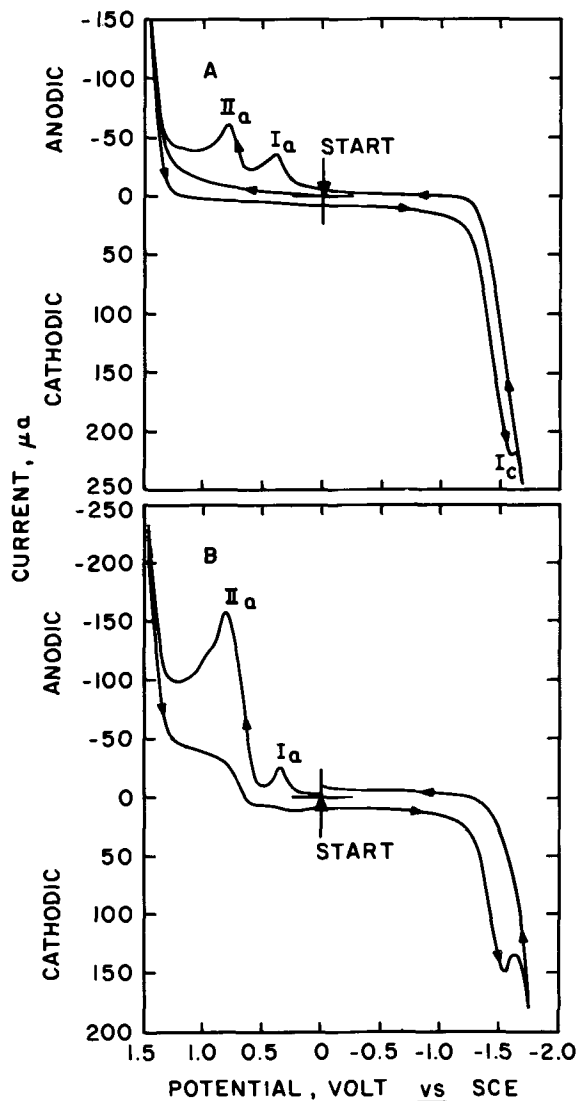


Fig. 2. A, Cyclic voltammogram of 4 mM allopurinol in 1M HOAc at PGE; scan pattern: $0.0V \rightarrow 1.45V \rightarrow -1.70V \rightarrow 1.45V \rightarrow 0.0V$. B, Cyclic voltammogram at PGE of product of complete electrochemical reduction of 4 mM allopurinol at mercury in 1M HOAc. Scan pattern: $0.00V \rightarrow 1.45V \rightarrow -1.75V \rightarrow 0.00V$; scan rate: 200 mV/sec.

After completely reducing a solution of allopurinol, reverse coulometry was carried out on the product solution using a large PGE and applying a potential of 0.9V, i.e., sufficient to completely oxidize the product giving rise to anodic peaks I_a and II_a . Under these conditions allopurinol was quantitatively recovered as evidenced by u.v. and polarographic analysis. An average value of $2.2e$ was obtained for reverse coulometry.

Electrolysis in 1M H_2SO_4 .—The u.v. absorption spectrum of the product of reduction of allopurinol in 1M H_2SO_4 ($\lambda_{max} = 245$ nm and 202 nm) was somewhat different than that of allopurinol at the same pH ($\lambda_{max} = 252$ nm and 210 nm). When a fairly concentrated solution (4–8 mM) was electrolyzed, it took ca. 16 hr for complete removal of allopurinol (u.v. spectrum, polarography). However, often the u.v. spectrum revealed a distinct shoulder at 270 nm in addition to the peaks described earlier; the shoulder gradually disappeared with time. During and after completion of the electrolysis, formaldehyde could be detected in the solution; one mole of formaldehyde was produced for every mole of allopurinol reduced. Some formaldehyde could be bubbled out of the solution and trapped in sodium sulfite solution (see Experimental). This indicates that part of the product formed in the $4e$ reduction of allopurinol in 1M H_2SO_4 decomposes giving formaldehyde.

Cyclic voltammetry at the PGE of allopurinol showed no oxidation peak if the first voltage sweep was towards positive potential. However, on sweeping toward negative potentials, a single cathodic peak (peak I_c), $E_p = -1.30$ V, is observed (Fig. 3, section A). Having scanned this peak, two anodic peaks are observed on the next cycle toward positive potential (peaks I_a and II_a), $E_p = 0.35$ V and 0.75V, respectively. After complete reduction, cyclic voltammetry of the product at PGE reveals no cathodic peaks on the initial scan toward negative potential at a clean electrode. However, the first sweep toward positive potential shows three peaks at $E_p = 0.34$ V, 0.75V, and 0.95V (Fig. 3, section B). The first two peaks correspond to peaks I_a and II_a observed on cyclic voltammetry of allopurinol. The most positive third peak will be designated as peak III_a . Further cyclic voltammetric experiments on the reduced solution revealed that cathodic peak I_c could be observed if peaks I_a and II_a were first scanned.

When cyclic voltammetric scans were made at various times throughout the course of a controlled potential electrolysis in 1M H_2SO_4 , it was found that, in the early stages, anodic peaks I_a and II_a were of nearly equal height and peak III_a was absent. As the electrolysis progressed peak III_a appeared. In order to further investigate the relationship of anodic peaks I_a , II_a , and III_a to cathodic peak I_c , the solution obtained after complete reduction of allopurinol was reoxidized at a large PGE at potentials corresponding to each of the oxidation peaks. After complete removal of peaks I_a and II_a by such oxidation, only ca. 65% of the original allopurinol was regenerated and peak III_a remained. Further oxidation at potentials of peak III_a did not form any more allopurinol. Accordingly, the species responsible for III_a was considered to be a product of breakdown or rearrangement of the species giving rise to peak I_a .

Characterization of isolated electrolysis products.—**Acetic acid.**—A product could be isolated by solvent extraction and column chromatography as an acetate salt or free base (see Experimental). Infrared spectra of allopurinol, the reduction product acetate salt, and the free base are shown in Fig. 4, sections A, B, and C, respectively. Thang and Delbarre (10) assigned the 1695 cm^{-1} band of allopurinol to $>C=N$. The inflection on this band at ca. 1650 – 1660 cm^{-1} corresponds to the

O
||
amide carbonyl—C—NH— absorption. The intense band at 1580 cm^{-1} is cyclic $C=C$ and around 3000 cm^{-1}

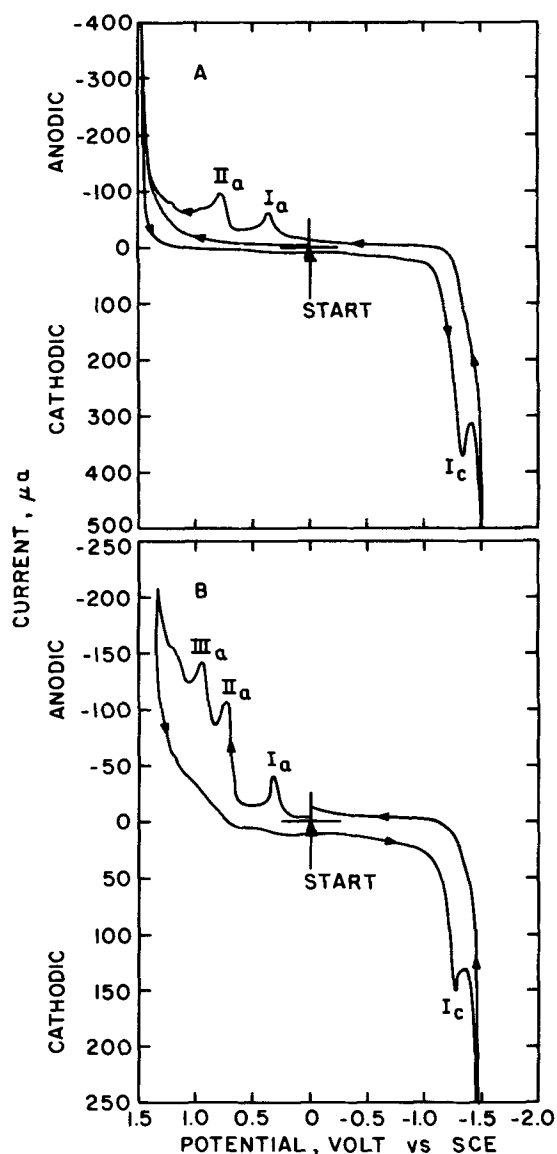


Fig. 3. A, Cyclic voltammogram of 6 mM allopurinol in 1M H_2SO_4 at PGE; scan pattern: 0.00V \rightarrow 1.45V \rightarrow -1.50V \rightarrow 1.45V \rightarrow 0.00V. B, Cyclic voltammogram at PGE of product of complete electrochemical reduction of allopurinol at mercury in 1M H_2SO_4 . Scan pattern: 0.00V \rightarrow 1.40V \rightarrow -1.45V \rightarrow 0.00V; scan rate: 200 mV/sec.

various N—H stretches are observed. On reduction, the $>C=N$ absorption is decreased (shoulder at ca. 1700 cm^{-1}) and the amide carbonyl, 1650 cm^{-1} , becomes prominent. The cyclic $-C=C$ band remains at 1580 cm^{-1} . Two small bands at 1450 cm^{-1} and 1360 cm^{-1} in the reduction products may be attributed to $>CH_2$ bending. The acetate salt (Fig. 4, section B) gives a typical carboxylate band at 1405 cm^{-1} (11).

NMR spectra of allopurinol, and the acetate-free product in deuterated dimethyl sulfoxide, are shown in Fig. 5, sections A and B, respectively. This solvent was used because the compounds were not sufficiently soluble in D_2O . Allopurinol shows two singlet peaks at 7.95 δ and 8.10 δ . The latter is associated with the hydrogen at C_6 , the former with the hydrogen at C_3 (12). These assignments are made by analogy with the NMR spectrum of hypoxanthine (6-oxypurine) in the same solvent (13). The reduction product has no NMR peak at 8.10 δ ; but one at 7.8 δ , which is ascribed to the C_3 proton, remains. In addition, a triplet centered around 4.35 δ appears (Fig. 5, section B) typical of a methylene group which must be located at C_6 . For this methylene group $\delta H_1 = 4.35$ ppm and $\delta H_2 = 4.41$ ppm, $JH_1H_2 = 8$ Hz. The three broad peaks at 3.40 δ , 6.20 δ ,

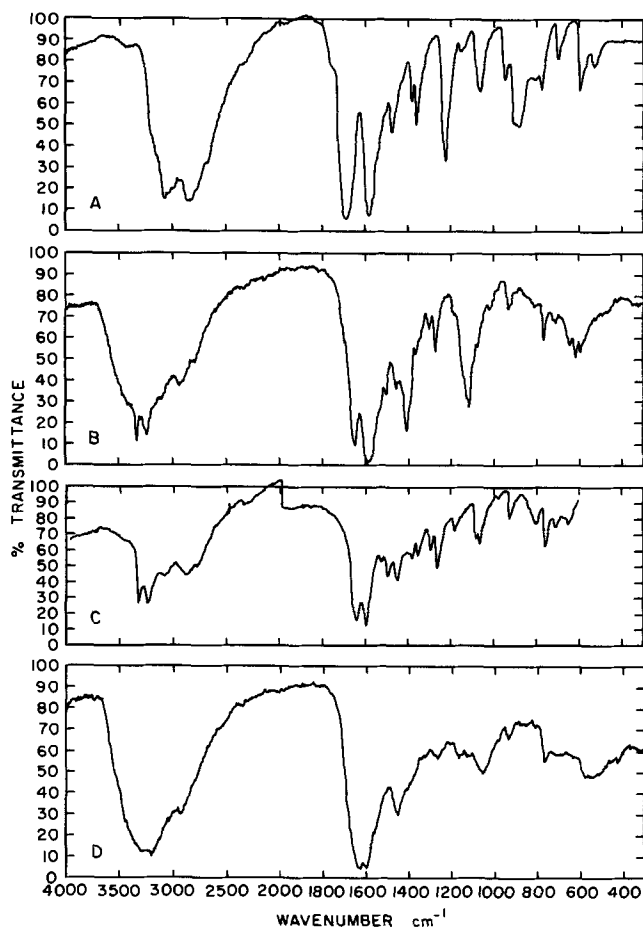


Fig. 4. Infrared spectra (KBr) of A, allopurinol; B, the acetate salt of the electrochemical reduction product of allopurinol at Hg in 1M HOAc; C, the acetate free base from B; and D, the product of electrochemical reduction of allopurinol at Hg in 1M H₂SO₄.

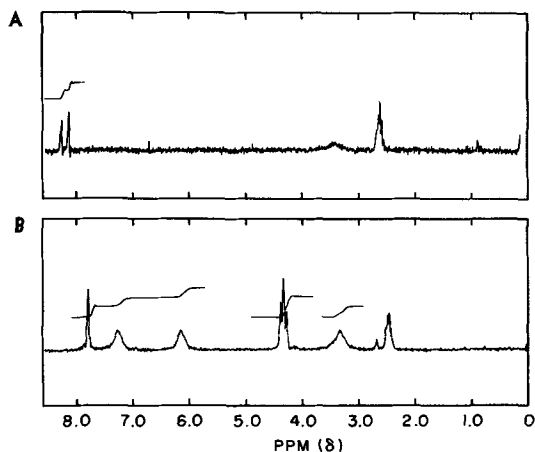


Fig. 5. 60 MHz NMR spectrum of A, allopurinol; and B, the product of electrochemical reduction of allopurinol in 1M HOAc (acetate-free base). Solvent: deuterio dimethylsulfoxide.

and 7.35 δ are for hydrogens associated with three N-atoms of the reduced product. Integration of the peaks centered at 7.8 δ , 7.35 δ , 6.20 δ , 4.35 δ , and 3.4 δ , reveal a proton ratio of 1:1:1:2:1. In view of this evidence the compound is clearly 6,7-dihydroallopurinol.

The mass spectrum of the free base shows a molecular ion of $m/e = 138$ (Fig. 6) which is that expected for 6,7-dihydroallopurinol. The base peak ($m/e = 110$) corresponds to the primary fragment $C_4H_4N_3O^+$ by loss of $\cdot NCH_2$ ($m/e = 28$) from the molecular ion. Subsequent loss of CO and a proton results in the fragment $C_3H_3N_3^+$ ($m/e = 81$) as proposed by Chalmers *et al.* (15). A mechanism illustrating the

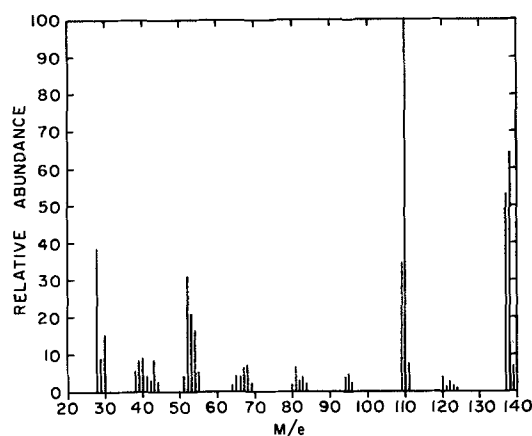


Fig. 6. Mass spectrum of the product of electrochemical reduction of allopurinol at Hg in 1M HOAc; Source temperature: ca. 200°C; ionizing voltage: 12 eV.

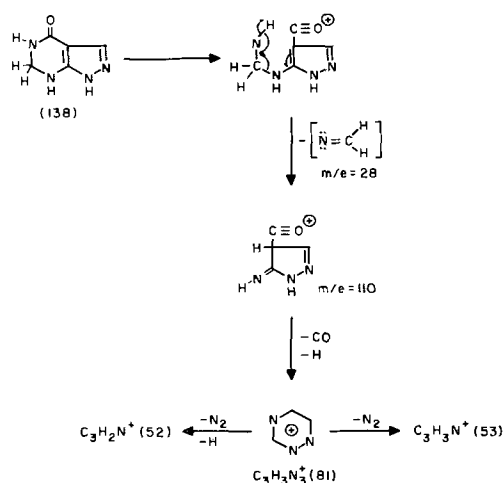


Fig. 7. Proposed mass spectroscopic fragmentation mechanism for 6,7-dihydroallopurinol.

probable formation of the major fragments in mass spectrometry is shown in Fig. 7.

Elemental analysis (see Experimental), IR, NMR, and mass spectroscopic data all support the view that the product of reduction of allopurinol at $pH > 2$ is 6,7-dihydroallopurinol.

Sulfuric acid.—Thin layer chromatography under a variety of conditions failed to indicate that more than one product was formed in sulfuric acid. Cyclic voltammetry and reverse coulometry, however, support the view that two products are formed, one which could be reoxidized to allopurinol and one which could not. Thin layer chromatography, however, did support

the view that a ureido group (—C(=O)—NH_2) was present because of the intense yellow spot developed with Ehrlich reagent. The two products of reduction could never be satisfactorily separated. However, the infrared spectrum of the reduction product (Fig. 4, section D) did reveal the presence of $>N\text{—}H$ groups by broad absorption around 3200 cm^{-1} . Two very close bands at 1640 cm^{-1} and 1600 cm^{-1} are compatible with the presence of amide, carbonyl, and cyclic $>C=C$ groupings, respectively. Also, the very pronounced peak at 1455 cm^{-1} is indicative of the presence of a methylene group (11).

Mass spectra of the sulfuric acid product show the existence of a molecular ion of $m/e = 140$. This lends support for a tetrahydroallopurinol in the reduction product.

Mechanism.— $pH > 2$.—The value of diffusion-current constant and coulometry support a 2e process

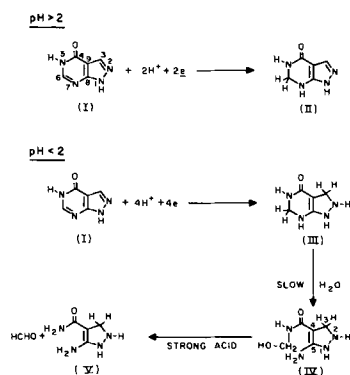
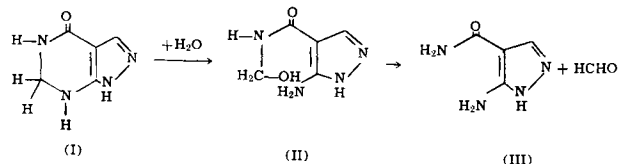


Fig. 8. Proposed scheme for the electrochemical reduction of allopurinol at mercury electrodes.

above a pH 2. IR, NMR, and mass spectra indicate that the product is 6,7-dihydroallopurinol. The reaction can be written as a straightforward $2e-2H^+$ reduction of allopurinol (I, Fig. 8) to 6,7-dihydroallopurinol (6,7-dihydro-4-hydroxy-[3,4-d] pyrimidine) (II, Fig. 8). Under cyclic voltammetric conditions at the PGE the appearance of anodic peaks I_a and II_a (Fig. 2, section A), after having scanned the cathodic peak I_c of allopurinol, suggests that at the PGE some additional electrochemical or chemical reduction of the dihydroallopurinol to tetrahydroallopurinol occurs. The latter compound gives rise to peak I_a . However, in view of the fact that peak I_a is so small, or nonexistent after coulometry of allopurinol at mercury, suggests that at the latter electrode little or no further reduction occurs. The closeness of allopurinol peak I_c to the background discharge in 1M HOAc at the PGE, suggests that considerable hydrogen ion reduction could accompany the electrochemical reduction; and the dihydro derivative could be partially reduced to a tetrahydro derivative by reduction with hydrogen. Similar behavior was observed at higher pH at mercury and graphite electrodes to that in 1M HOAc. In view of the $2e$ nature of the reduction process at high pH, the mechanism must be essentially identical to that observed in acetic acid.

The fact that the reduced form of allopurinol in 1M HOAc gives a positive test for formaldehyde, under the conditions of the chromotropic acid reaction, is explained by hydrolysis of 6,7-dihydroallopurinol (I, Eq. [1]) to the corresponding alcohol (II, Eq. [1]). This would yield formaldehyde and the pyrazolamine (III, Eq. [1]). This process is identical to that observed with all purines reduced at the C_2-N_3 position under similar conditions (16). In the electrolysis solution the conditions are such that the reaction (Eq. [1]) does not proceed to any extent and formaldehyde cannot be bubbled out of the solution.



[1]

The decrease in height of the allopurinol reduction wave above ca. pH 6, and disappearance above pH 8, is related to the fact that, at pH 8 and above, allopurinol undergoes a rapid degradation to 3-amino-4-carbamidopyrazole (17). The latter compound is not polarographically reducible.

pH < 2.—Below pH 2 the limiting current for polarographic reduction of allopurinol increases and at pH 0 involves $4e$. Infrared spectra indicate that both $-C=N$ groupings have been reduced and that $>CH_2$ groups

are present. Mass spectra support the view that a tetrahydroallopurinol is present. These observations support the view that at low pH allopurinol (I, Fig. 8) is reduced in a $4e - 4H^+$ process to 2,3,6,7-tetrahydroallopurinol (III, Fig. 8). This is the sole product when the electrolysis time is short as is evidenced by the fact that only two anodic peaks, peaks I_a and II_a of equal height, appear on cyclic voltammetry of the product at the PGE. Since the product isolated from acetic acid ($2e$) dissolved in 1M H_2SO_4 gives only peak II_a , it is clear that peak I_a is due to oxidation of 2,3,6,7-tetrahydroallopurinol to 6,7-dihydroallopurinol. Correspondingly, peak II_a is due to oxidation of the 6,7-dihydro compound to allopurinol.

After complete reduction in sulfuric acid, peak III_a appears in addition to peaks I_a and II_a . The products responsible for peaks I_a and II_a can be reoxidized back to allopurinol; but that responsible for III_a cannot. Also, the u.v. spectrum of the somewhat more concentrated solution of allopurinol (4-8 mM) shows a shoulder at 270 nm, in addition to the peaks at 245 nm and 202 nm, which are observed after electrolysis of a more dilute solution (1-2 mM). The nature of the product responsible for cyclic voltammetric peak III_a and the u.v. absorption at 270 nm can be inferred from the TLC and estimation of formaldehyde. Thus, spraying the single spot observed by TLC with Ehrlich reagent gives a positive test for the ureido group

$\begin{matrix} O \\ || \\ (-C-NH_2) \end{matrix}$. In addition, after prolonged electrolysis approximately 0.1-0.15 mole of formaldehyde/mole of allopurinol reduced can be bubbled out of the solution (the remaining 0.85-0.9 mole of formaldehyde is found in solution under the conditions of the chromotropic acid reaction). This evidence suggests that the product of $4e$ reduction, i.e., 2,3,6,7-tetrahydroallopurinol (III, Fig. 8), slowly decomposes to a compound having a ureido group and formaldehyde. The fact that the product still absorbs at ca. 270 nm suggests the basic chromophore in the allopurinol system, $-C_8=C_9-C_4=O$ is still present. Accordingly, it is proposed that the tetrahydroallopurinol (III, Fig. 8) slowly hydrolyzes to the 4-substituted-2,3-dihydro-5-aminopyrazole (IV, Fig. 8; note numbering change for pyrazole derivatives). This is a reaction very similar to that proposed for breakdown of tetrahydropurines (16). Compound IV (Fig. 8) appears to readily cleave in the presence of concentrated acid to give formaldehyde and 4-carboxamido-5-aminopyrazole (2,3) (V, Fig. 8). The latter species would be expected to give a strong ureido test with Ehrlich reagent and to absorb in the u.v. region owing to the $-C=C-C=O$ chromophore. The nature of the product of peak III_a , which is presumably due to oxidation of compound V (Fig. 8), is not known although it is certainly not allopurinol.

Acknowledgment

The authors would like to thank the National Science Foundation which helped support the work described.

Manuscript received June 1, 1971; revised manuscript received March 14, 1972.

Any discussion of this paper will appear in a Discussion Section to be published in the June 1973 JOURNAL.

REFERENCES

- G. B. Elion, A. Kovenski, and G. H. Hitchings, *Biochem. Pharmacol.*, **15**, 863 (1960).
- M. Frey-Wettstein, G. Pedio, and K. Giger, *Schweiz. Med. Wochschr.*, **97**, 148 (1967).
- W. N. Kelly and J. B. Wyngaarden, *J. Clin. Invest.*, **49**, 602 (1970).
- R. W. Rundles, J. B. Wyngaarden, G. H. Hitchings, G. B. Elion, and H. R. Silberman, *Trans. Assoc. Am. Physicians*, **76**, 126 (1963).
- W. N. Kelly and T. B. Beardmore, *Science*, **169**, 388 (1970).
- G. Dryhurst and P. J. Elving, *This Journal*, **115**, 1014 (1968).

7. G. Dryhurst, *ibid.*, **116**, 1097 (1969).
8. G. Dryhurst, *ibid.*, **116**, 1411 (1969).
9. G. Dryhurst, "Periodate Oxidation of Diol and Other Functional Groups. Analytical and Structural Applications," p. 141, Pergamon Press, Inc., New York (1970).
10. K. V. Thang and F. Delbarre, *Compt. Rend.*, **268**, 525 (1969).
11. J. R. Dyer, "Applications of Absorption Spectroscopy of Organic Compounds," Prentice-Hall, Inc., Englewood Cliffs, N. J. (1965).
12. J. A. Montgomery and H. J. Thomas, *J. Organometal. Chem.*, **31**, 1411 (1966).
13. W. C. Coburn, M. C. Thorpe, J. A. Montgomery, and K. Hewson, *J. Organometal. Chem.*, **30**, 1110 (1965).
14. F. Feigl, "Spot Tests in Organic Analysis," 5th Ed., p. 343, Elsevier Publishing Co., Amsterdam (1956).
15. R. A. Chalmers, R. Pasker, H. A. Simmonds, W. Snedden, and R. W. E. Watts, *Biochem. J.*, **112**, 527 (1969).
16. D. L. Smith and P. J. Elving, *J. Am. Chem. Soc.*, **84**, 1412 (1962).
17. P. D. Gressel and J. F. Gressel, *J. Pharm. Sci.*, **57**, 335 (1968).

The Thermodynamic Properties of the Zn-Sn-Cd-Bi Liquid Quaternary Solutions

W. Ptak and Z. Moser

Polish Academy of Sciences, Institute for Metal Research, Reymonta 25, Kraków, Poland

ABSTRACT

The emf method employing concentration cells with liquid electrodes and electrolyte for the determination of zinc activity in the quaternary system Zn-Sn-Cd-Bi has been used. Experiments were conducted on seventy-five liquid alloys of different mole fractions, with zinc liquid reference electrodes, over the temperature range 714°-877°K. The results were compared with calculated data obtained using Krupkowski's formulas. The zinc isoactivity plots made for constant tin concentration show good agreement between the experimental and theoretical results. Krupkowski's formulas also enable the calculation of the activity coefficients of the remaining components of the quaternary system, namely, tin, cadmium, and bismuth.

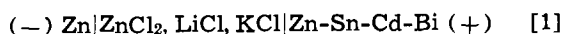
Measurements of the electromotive force of concentration cells using liquid electrodes and liquid electrolyte has been applied successfully to the determination of the thermodynamic properties of multicomponent liquid metal solutions. This method is particularly suitable for investigating low-melting alloys where the proper electrolyte can be found easily, e.g., zinc alloys. Experimental investigations on liquid zinc alloys for binary and multicomponent metal solutions (1-2) and in dilute solutions (3-6) were carried out. Research work on multicomponent solutions requires both extensive experimental data and the application of specific methods for the interpretation of the experimental results. In the investigations reported here, on the quaternary Zn-Sn-Bi-Cd solutions, Krupkowski's method (7) was applied for the calculation of activity coefficients of alloy components. The experimental data of zinc activity obtained by the emf measurements of concentration cells are compared with a_{Zn} values calculated from Krupkowski's formulas (7). For the thermodynamic analysis of multicomponent systems in Krupkowski's method, the dependences of activity coefficients of respective binary alloys are sufficient. From among the different methods applicable for the interpretation of experimental results, Krupkowski's method was chosen which, on the basis of binary data, enables the full thermodynamic description of the multicomponent system. The good agreement between the a_{Zn} values obtained from the emf measurements and the theoretical activity data from Krupkowski's formulas led to the choice of this method for the calculation of the integral molar thermodynamic functions of the liquid Zn-Sn-Cd-Bi solutions (8).

Experimental Method

For the determination of the thermodynamic properties of liquid quaternary solutions the emf method of

Key words: concentration cell, liquid quaternary system, zinc isoactivity plots.

concentration cells was chosen. This method enabled the evaluation of the partial thermodynamic functions of one component. In our case it was zinc, which also formed the reference electrode in the concentration cell



The experimental arrangement is shown in Fig. 1. The basic element was the quartz tube which contained a large amount of molten electrolyte composed of lithium, potassium, and zinc chlorides. This quartz tube, drawn separately on Fig. 1, had a water-cooled cover. The tungsten wires in glass shields went through the cover in the center of which was the Pt-Pt-10% Rh thermocouple mounted in molten electrolyte. There was a special tube for the inlet and outlet of argon which was passed through a heated column of copper turnings and over phosphorus pentoxide to remove water and oxygen. Six tubes made of high-melting glass with orifices on the lower part were suspended from the cover. These tubes contained the liquid alloys in which the tungsten wires were submerged. When the cover with the tubes was transferred to the quartz vessel the liquid electrolyte entered the tubes containing the alloys. In this manner contact was obtained between the liquid metals and electrolyte.

The cells were operated in a high heat capacity resistance furnace which had three windings to enable the proper regulation of the temperature along the axis of the furnace. In addition, a block of heat resistant steel was placed in the furnace to maintain a constant temperature gradient in the cells. The thermocouple was connected to the temperature regulator in this block. The voltage of each winding was adjusted experimentally to maintain a uniform temperature distribution. The outer jacket of the furnace was water-cooled to keep heating conditions constant. Temperature deviation after several hours did not exceed $\pm 1^\circ\text{C}$.

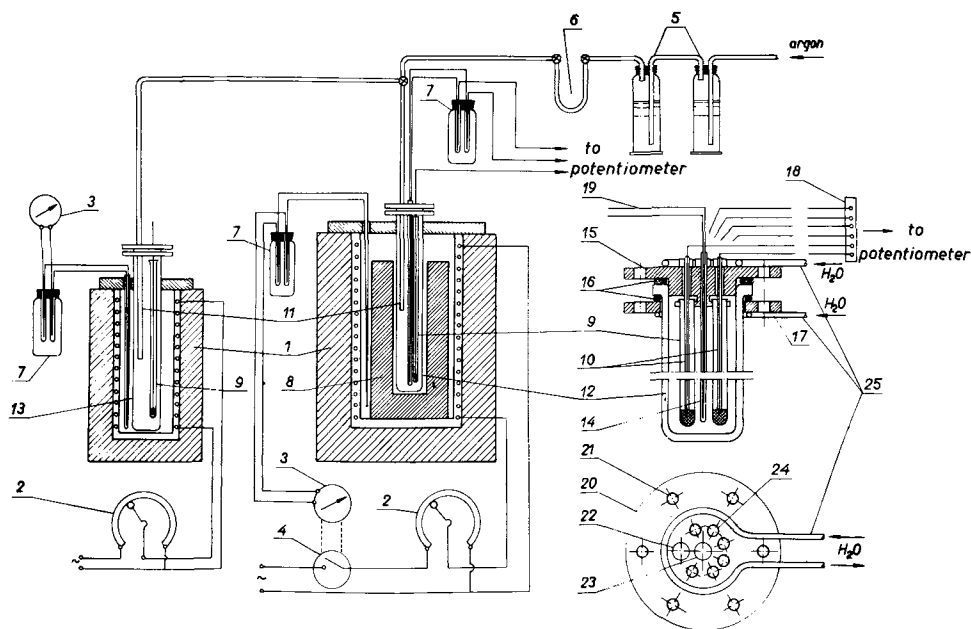


Fig. 1. Schematic diagram of the experimental arrangement for the investigation of the thermodynamic properties of liquid metal solutions: 1, resistance furnaces; 2, autotransformers; 3, galvanometers; 4, regulator of temperature; 5, gas purifier with concentrated H_2SO_4 ; 6, U-tube with P_2O_5 ; 7, thermostats; 8, steel block for thermostating; 9, supramax tubes for alloys; 10, tungsten electrodes; 11, inlet and outlet of argon; 12, measuring quartz tube; 13, tube for melting samples; 14, tube for thermocouple; 15, cover of quartz tube; 16, rubber seal; 17, bottom cover; 18, outlet of electrodes to potentiometer; 19, outlet of thermocouples to potentiometer; 20, upper view of the quartz tube cover; 21, orifices for cover screws; 22, orifice for argon inlet; 23, orifice for thermocouple; 24, orifices for tubes containing liquid metals; 25, inlet for water-cooling system.

In the second furnace shown also in Fig. 1, the alloys were heated to a molten state in argon before being put into the quartz tube. This took several seconds. The same prepared electrolyte could be used several times. With this arrangement five alloys could be measured simultaneously.

Experimental Results

The emf values of the concentration cells [1] were used for the direct calculation of activity, the activity coefficient, the partial molar heat of solution, and the partial molar entropy of zinc in the Zn-Sn-Cd-Bi quaternary solutions.

The activity and the chemical potential of zinc were calculated from the following formulas

$$\Delta\bar{G}_{\text{Zn}} = -zEF \quad [2]$$

$$\Delta\bar{G}_{\text{Zn}} = RT \ln a_{\text{Zn}} \quad [3]$$

where $\Delta\bar{G}_{\text{Zn}}$ = change in chemical potential of zinc, a_{Zn} = activity of zinc, E = emf of cell [1] in volts, z = valence (in the case of zinc = 2), and F = Faraday's constant in cal/volt.

The measurements were performed for 75 alloys with different concentrations of the components. The zinc concentrations were varied from 0.1 to 0.6 in steps of 0.1 mole fractions. In a similar manner the concentrations of the other components were changed. The first column of Table I gives the concentrations of the components used in the experiments.

The next factor which was taken into account was temperature. The range of temperature was limited both by the melting point of zinc and by the pressure of such metals as zinc and cadmium. The emf values were measured at 714°, 757°, 805°, 842°, and 877°K. At the highest temperatures the cadmium vapor pressure over the pure metal is about 100 Torr, which could result in some change of composition by cadmium vaporization. This process may be decreased by a several centimeter layer of molten electrolyte. In addition, the vapor pressure of cadmium in the alloys is lower than in pure cadmium. These two factors prevented detection of the change in cadmium concentration by means of chemical analysis.

Experimental errors may result from side reactions between zinc chloride which is present in the electrolyte and the components of the alloys. Taking into account the affinity of metals to chlorine, we can find the similar position of zinc and cadmium in this series. Zinc has a higher affinity to chlorine and therefore was chosen as the reference electrode. At lower zinc concentrations, side reactions may influence the emf values and the activity of the zinc in the solution. Wagner (9) evaluated an error of 0.5% in zinc activity in the zinc-cadmium alloy when $X_{\text{Zn}} = 0.1$ and $X_{\text{Cd}} = 0.9$ at 783°K as the result of side reactions.

In our experiments this error is smaller. Side reactions have no influence on the measurements of the other components such as tin and bismuth.

The accuracy of the emf measurements of cell [1] was evaluated at ± 0.05 mV, and greater errors are possible at lower zinc concentrations. The metal used in these experiments was of minimum purity 99.99%. The composition of the electrolyte was LiCl, 57 m/o (mol per cent); KCl, 38 m/o; and ZnCl_2 , 5 m/o.

The experimental results are given in Table I. The total emf error of the cells was 4-7%. The binary Zn-Bi system is partly immiscible in the liquid state. The obtained experimental results enabled the determination of the range of immiscibility in the liquid state in quaternary solutions (10).

The activity coefficients of zinc in quaternary solutions were calculated from the formula

$$\gamma_{\text{Zn}} = \frac{a_{\text{Zn}}}{X_{\text{Zn}}} \quad [4]$$

where X_{Zn} = zinc concentration in mole fractions and γ_{Zn} = activity coefficient of zinc.

Comparison between Experimental and Theoretical Results

The thermodynamic properties of zinc in the ternary systems Zn-Bi-Sn, Zn-Sn-Cd, and Zn-Cd-Bi have been reported in Ref. (11), (12), and (13), respectively. These solutions form the ternary limiting values for the Zn-Sn-Cd-Bi quaternary system. For the determination of the activity coefficients and activities of metals in quaternary solutions we used Krupkowski's formu-

Table II. Values of functions $\omega(T)$ and m for binary solutions

System	m	$\omega(T)$	Ref.
Zn-Sn	1.10	$\frac{1081}{T} + 0.79 (2.303 \log T - 1) - 5.61$ (16)	
Zn-Cd	1.87	$\frac{392}{T}$ (17)	
Zn-Bi	1.05	$\frac{687}{T} - 0.29$ (18)	
Cd-Sn	1.60	$\frac{537}{T} + 0.27 (2.303 \log T - 1) - 2.04$ (19)	
Sn-Bi	1.55	$\frac{49.3}{T}$ (20)	

monograph that the deviation of these solutions from ideal ones with reference to the values of the activity coefficients is smaller than 15%. Therefore, we can assume that these solutions may be treated with some approximation as the ideal ones.

The data from Table II and Krupkowski's scheme (14) enabled us to give the formulas for the activity coefficients *vs.* temperature over the whole range of concentration in quaternary solutions in the following form

$$\begin{aligned} \log \gamma_{Zn} = & -\omega_{1,2}(1 - X_{Zn})^{-0.9} X_{Zn} X_{Sn} \\ & + \omega_{1,2}(1 - X_{Zn})^{-0.9} X_{Sn} - \omega_{1,3}(1 - X_{Zn})^{-0.33} X_{Zn} X_{Cd} \\ & + \omega_{1,3}(1 - X_{Zn})^{-0.33} X_{Cd} - \omega_{1,4}(1 - X_{Zn})^{-0.95} X_{Zn} X_{Bi} \\ & + \omega_{1,4}(1 - X_{Zn})^{-0.95} X_{Bi} - \omega_{2,3}(1 - X_{Cd})^{-0.4} X_{Cd} X_{Sn} \\ & - \omega_{2,4}(1 - X_{Sn})^{-0.45} X_{Sn} X_{Bi} \quad [8] \end{aligned}$$

The equations for activity coefficients of tin, cadmium, and bismuth are summarized in the Appendix.

The respective relations of energy coefficients $\omega(T)$ are from Table II, and the numbers in the equations for the activity coefficients correspond to the different metals, namely: 1-Zn, 2-Sn, 3-Cd, and 4-Bi. The activity coefficients of zinc at 714°, 805°, and 877°K were calculated from formula [8] and the activity values of zinc were calculated from formula [4].

The activity data were used for plotting the zinc isoactivity curves. In Fig. 2-5 the zinc isoactivities at 714°K are given. The constant tin concentration was varied from $X_{Sn} = 0.1$ to $X_{Sn} = 0.4$ in steps of 0.1. In Fig. 2 and 3 the dashed regions correspond to immiscibility

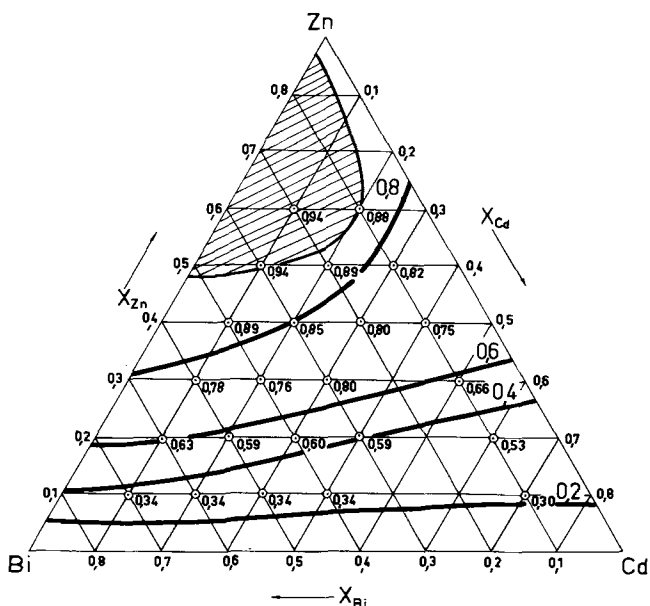


Fig. 2. Isoactivity curves of zinc, continuous lines, and the experimental values of zinc activity in a Zn-Sn-Cd-Bi system, $X_{Sn} = 0.1$ at 714°K.

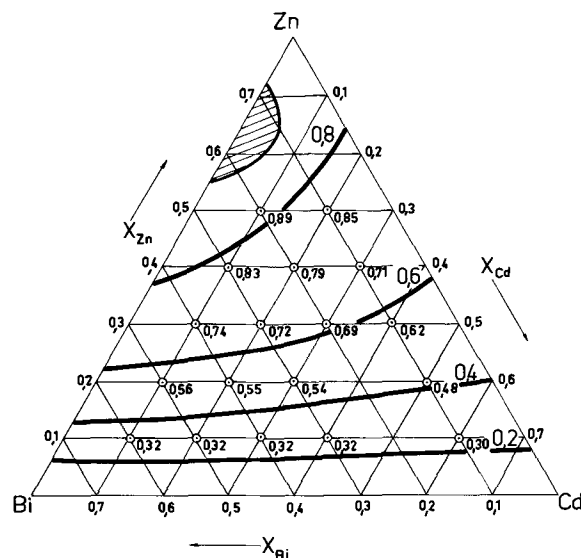


Fig. 3. Isoactivity curves of zinc, continuous lines, and the experimental values of zinc activity in a Zn-Sn-Cd-Bi system, $X_{Sn} = 0.2$ at 714°K.

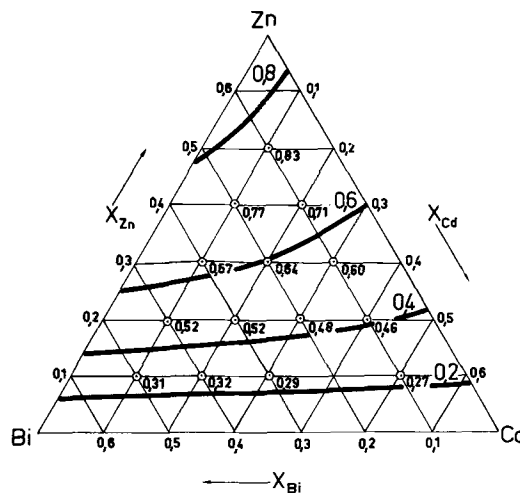


Fig. 4. Isoactivity curves of zinc, continuous lines, and the experimental values of zinc activity in a Zn-Sn-Cd-Bi system, $X_{Sn} = 0.3$ at 714°K.

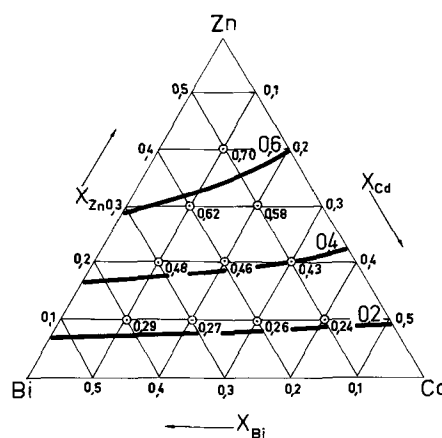


Fig. 5. Isoactivity curves of zinc, continuous lines, and the experimental values of zinc activity in a Zn-Sn-Cd-Bi system, $X_{Sn} = 0.4$ at 714°K.

bility in the liquid state (10). In a similar manner, Fig. 6-9 illustrate the zinc activities at 805°K for the same constant tin concentrations.

The immiscibility in the liquid state exists only for $X_{Sn} = 0.1$ (Fig. 6). Finally Fig. 10-13 give the zinc

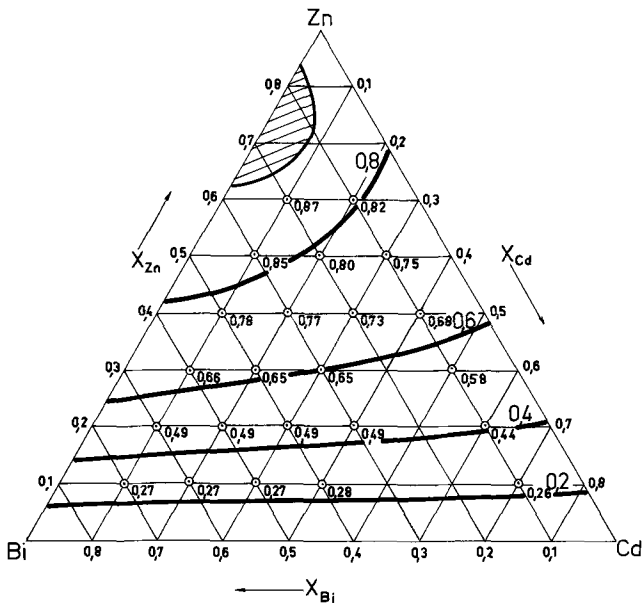


Fig. 6. Isoactivity curves of zinc, continuous lines, and the experimental values of zinc activity in a Zn-Sn-Cd-Bi system, $X_{Sn} = 0.1$ at $805^\circ K$.

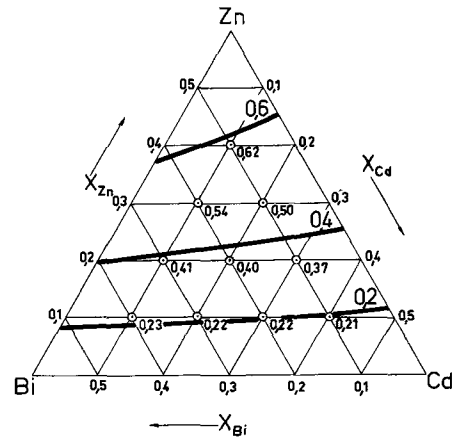


Fig. 9. Isoactivity curves of zinc, continuous lines, and the experimental values of zinc activity in a Zn-Sn-Cd-Bi system, $X_{Sn} = 0.4$ at $805^\circ K$.

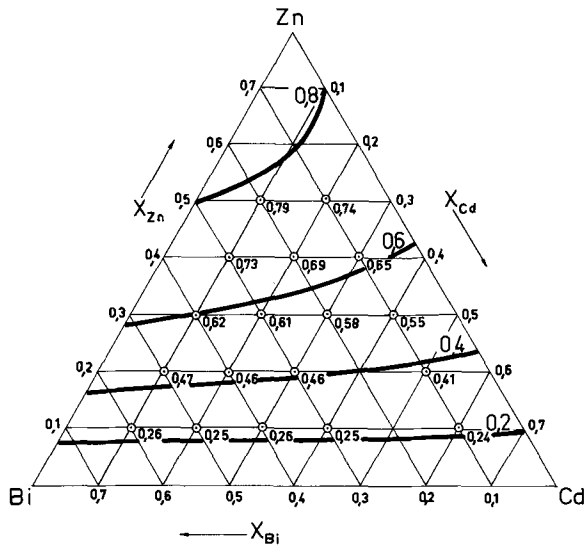


Fig. 7. Isoactivity curves of zinc, continuous lines, and the experimental values of zinc activity in a Zn-Sn-Cd-Bi system, $X_{Sn} = 0.2$ at $805^\circ K$.

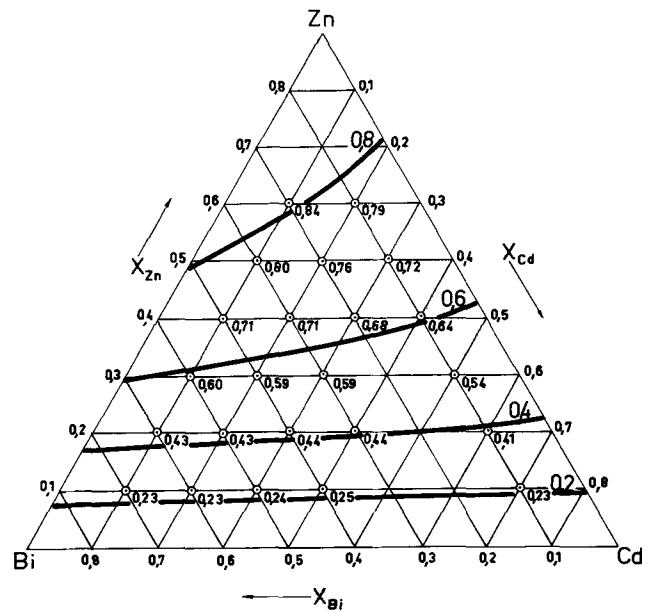


Fig. 10. Isoactivity curves of zinc, continuous lines, and the experimental values of zinc activity in a Zn-Sn-Cd-Bi system, $X_{Sn} = 0.1$ at $877^\circ K$.

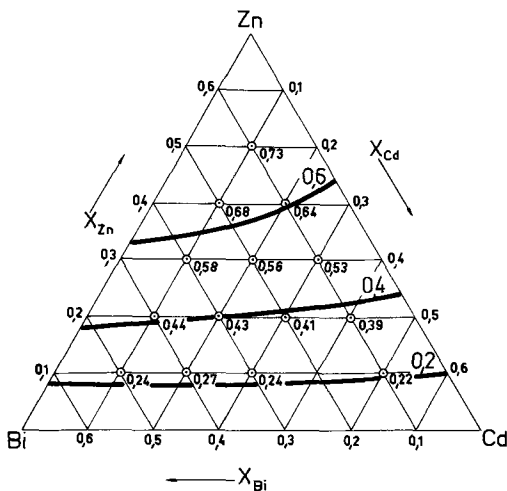


Fig. 8. Isoactivity curves of zinc, continuous lines, and the experimental values of zinc activity in a Zn-Sn-Cd-Bi system, $X_{Sn} = 0.3$ at $805^\circ K$.

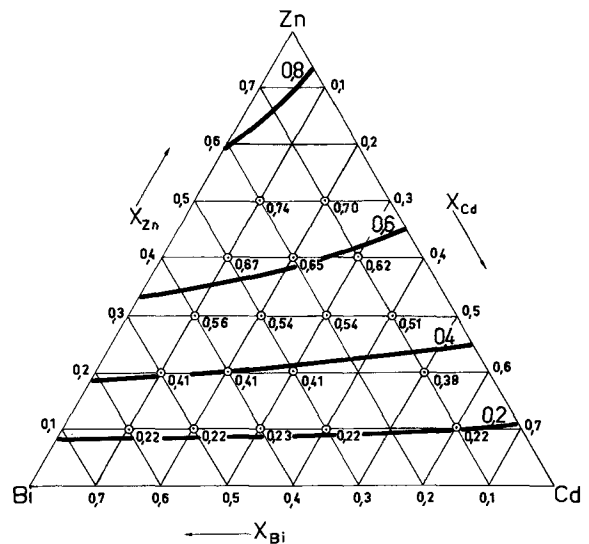


Fig. 11. Isoactivity curves of zinc, continuous lines, and the experimental values of zinc activity in a Zn-Sn-Cd-Bi system, $X_{Sn} = 0.2$ at $877^\circ K$.

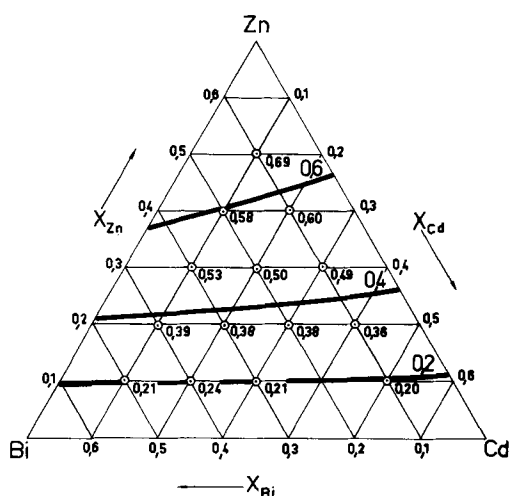


Fig. 12. Isoactivity curves of zinc, continuous lines, and the experimental values of zinc activity in a Zn-Sn-Cd-Bi system, $X_{Sn} = 0.3$ at $877^\circ K$.

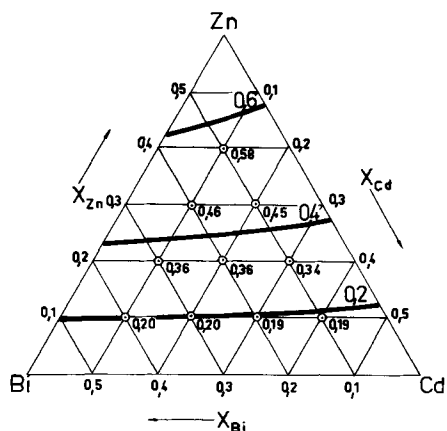


Fig. 13. Isoactivity curves of zinc, continuous lines, and the experimental values of zinc activity in a Zn-Sn-Cd-Bi system, $X_{Sn} = 0.4$ at $877^\circ K$.

isoactivities at $877^\circ K$. Figures 2-13 were plotted for zinc isoactivities $a_{Zn} = 0.2$ to 0.8 in steps of 0.2 . The experimental activity values from Table I are also given on these figures.

While comparing the isoactivity curves with the experimental data we see that good agreement is obtained at 805° and 877° . Deviations in this case do not exceed 8% , while the greater deviations are observed at lower temperatures. In general we can state that the experimental data obtained in this paper are higher than those calculated from Krupkowski's method. The agreement would be better if the influence of the liquid Bi-Cd solutions showing negative deviations from Raoult's law were considered. Then the energy coefficient $\omega(T)$ appearing in formulas [5] and [6] would be negative and the component of formula [8] $-\omega_{3,4}(1 - X_{Cd})^{m_{3,4}-2}X_{Cd}X_{Bi}$ would result in the increase of the $\log \gamma_{Zn}$ values and in better agreement between experimental data and those calculated from Eq. [8]. The data from the literature summarized by Hultgren *et al.* (22) on the liquid Bi-Cd system allow us to consider it as ideal and not ascribe to it negative or positive deviations from Raoult's law. Such an assumption is based on γ_{Cd} values obtained from emf measurements which oscillate about unity.

Discussion

It was shown for the second time in the investigations of the liquid Zn-Sn-Cd-Bi solutions that it is possible to apply Krupkowski's method for the calculation of partial and integral thermodynamic functions of components. The first papers dealt with

research on the liquid Zn-Sn-Cd-Pb system (23, 24, 25). As in the case of the results shown in this paper good agreement was obtained between the experimental data and those calculated from Krupkowski's formulas. These formulas were used for the interpretation of experimental data for liquid metal solutions over the wide range of concentrations of components. For example, the investigations on the liquid Zn-In-Pb alloys when $X_{Zn} > 0.1$ molar fraction (26), a systematic comparison between Krupkowski's (14) and Darken's (27) method was carried out and very similar results from both methods were obtained. We suppose that Krupkowski's method can be applied successfully in the case of binary, ternary, and quaternary solutions and this was verified experimentally. In the case of multicomponent systems this method is also promising.

The fundamental assumption of Krupkowski's method consists in the additivity of thermodynamic properties of multicomponent systems given by formula [7] on the basis of the properties of binary systems. When for the components j, k in solutions j, k the activity coefficients are given by formulas [5] and [6], then the respective terms of the sum [7] are the following

for $i = j$

$$[\log \gamma_j]_{j,k} = -\omega_{j,k}(1 - X_k)^{m_{j,k}-2}X_jX_k + \frac{\omega_{j,k}}{m_{j,k}-1} [1 - (1 - X_k)^{m_{j,k}-1}] \quad [9]$$

for $i = k$

$$[\log \gamma_k]_{j,k} = -\omega_{j,k}(1 - X_k)^{m_{j,k}-2}X_jX_k + \omega_{j,k}(1 - X_k)^{m_{j,k}-2}X_j \quad [10]$$

for $i \neq k$
 $i \neq j$

$$[\log \gamma_i]_{j,k} = -\omega_{j,k}(1 - X_k)^{m_{j,k}-2}X_jX_k \quad [11]$$

Equation [11] shows the influence of thermodynamic properties of j,k solutions on the activity coefficient of the remaining components i in multicomponent system. Formula [7] and others of the type [9], [10], and [11] enable the establishment of the dependence of the activity coefficient of the component in the multicomponent system. It should be added that a detailed analysis of Krupkowski's method has been given (28).

Acknowledgment

The authors are indebted to Mr. Z. Panek for technical assistance in measurements and calculations.

Manuscript submitted June 1, 1971; revised manuscript received Jan. 14, 1972.

Any discussion of this paper will appear in a Discussion Section to be published in the June 1973 JOURNAL.

REFERENCES

1. W. Ptak and Z. Moser, *Arch. Hutnictwa*, **13**, 33 (1968).
2. W. Ptak, Z. Moser, and L. Zabdyr, *Rev. Roumaine Chim.*, **14**, 851 (1969).
3. Z. Moser, *Bull. Acad. Pol. Sci., Sér. Sci. Tech.*, **17**, 27 (1969).
4. Z. Moser, *Arch. Hutnictwa*, **14**, 371 (1969).
5. Z. Moser, *Bull. Acad. Pol. Sci., Sér. Sci. Tech.*, **18**, 51 (1970).
6. Z. Moser, *Met. Trans.*, **2**, 2175 (1971).
7. A. Krupkowski, *Bull. Acad. Pol. Sci. et Lett.*, **1**, 15 (1951).
8. W. Ptak, Z. Moser, and J. Wypartowicz, *Arch. Hutnictwa*, **16**, 229 (1971).
9. C. Wagner and A. Werner, *This Journal*, **110**, 326 (1963).
10. W. Ptak and Z. Moser, *Bull. Acad. Pol. Sci., Sér. Sci. Tech.*, **19**, 71 (1971).
11. W. Ptak and Z. Moser, *Arch. Hutnictwa*, **11**, 289 (1966).
12. W. Ptak and Z. Moser, *ibid.*, **12**, 81 (1967).
13. W. Ptak and Z. Moser, *ibid.*, **12**, 363 (1967).
14. A. Krupkowski, "Principles of Thermodynamics

and Their Application in Metallurgy and Science of Metals," Państwowe Wydawnictwo Naukowe, Kraków (1958).

15. A. Krupkowski, *Freiberger Forschungsh.*, **B-67**, 101 (1962).
16. W. Ptak, *Arch. Hutnictwa*, **5**, 169 (1960).
17. W. Ptak, *Arch. Górnictwa-Hutnictwa*, **2**, 71 (1954).
18. W. Ptak and Z. Moser, *Arch. Hutnictwa*, **11**, 207 (1966).
19. W. Ptak, *ibid.*, **4**, 335 (1959).
20. W. Seltz and F. J. Dunkerley, *J. Am. Chem. Soc.*, **64**, 1392 (1942).
21. J. F. Elliott and J. Chipman, *Trans. Faraday Soc.*, **47**, 138 (1951).
22. R. Hultgren, R. L. Orr, Ph. D. Anderson, and K. K. Kelley, "Selected Values of Thermodynamic Properties of Metals and Alloys," John Wiley & Sons, New York-London (1963).
23. W. Ptak and Z. Moser, *Trans. Met. Soc., AIME*, **242**, 558 (1968).
24. W. Ptak and Z. Moser, *Bull. Acad. Pol. Sci., Sér. Sci. Tech.*, **9**, 17 (1967).
25. W. Ptak and Z. Moser, *Arch. Hutnictwa*, **13**, 373 (1968).
26. Z. Moser and K. Fitzner, In preparation.
27. L. Darken, *J. Am. Chem. Soc.*, **2**, 2909 (1950).
28. W. Ptak, "Księga Jubileuszowa dla uczczenia zastug naukowych," Aleksandra Krupkowskiego, 413, Warszawa (1965).

APPENDIX

Equations for activity coefficients of tin, cadmium, and bismuth have the following form

$$\begin{aligned} \log \gamma_{\text{Sn}} = & -\omega_{1,2}(1 - X_{\text{Zn}})^{-0.9}X_{\text{Zn}}X_{\text{Sn}} \\ & + 10.000\omega_{1,2}[1 - (1 - X_{\text{Zn}})^{0.1}] \\ & - \omega_{1,3}(1 - X_{\text{Zn}})^{-0.33}X_{\text{Zn}}X_{\text{Cd}} \\ & + \omega_{1,4}(1 - X_{\text{Zn}})^{-0.95}X_{\text{Zn}}X_{\text{Bi}} \\ & - \omega_{2,3}(1 - X_{\text{Cd}})^{-0.4}X_{\text{Cd}}X_{\text{Sn}} \\ & + 1.667\omega_{2,3}[1 - (1 - X_{\text{Cd}})^{0.6}] \\ & - \omega_{2,4}(1 - X_{\text{Sn}})^{-0.45}X_{\text{Sn}}X_{\text{Bi}} + \omega_{2,4}(1 - X_{\text{Sn}})^{-0.45}X_{\text{Bi}} \end{aligned} \quad [12]$$

$$\begin{aligned} \log \gamma_{\text{Cd}} = & -\omega_{1,2}(1 - X_{\text{Zn}})^{-0.9}X_{\text{Zn}}X_{\text{Sn}} \\ & - \omega_{1,3}(1 - X_{\text{Zn}})^{-0.33}X_{\text{Zn}}X_{\text{Cd}} \\ & + 3.333\omega_{1,3}[1 - (1 - X_{\text{Cd}})^{0.67}] \\ & - \omega_{1,4}(1 - X_{\text{Zn}})^{-0.95}X_{\text{Zn}}X_{\text{Bi}} - \omega_{2,3}(1 - X_{\text{Cd}})^{-0.4}X_{\text{Cd}}X_{\text{Sn}} \\ & + \omega_{2,3}(1 - X_{\text{Cd}})^{-0.4}X_{\text{Sn}} - \omega_{2,4}(1 - X_{\text{Sn}})^{-0.45}X_{\text{Sn}}X_{\text{Bi}} \end{aligned} \quad [13]$$

$$\begin{aligned} \log \gamma_{\text{Bi}} = & -\omega_{1,2}(1 - X_{\text{Zn}})^{-0.9}X_{\text{Zn}}X_{\text{Sn}} \\ & - \omega_{1,3}(1 - X_{\text{Zn}})^{-0.33}X_{\text{Zn}}X_{\text{Cd}} \\ & - \omega_{1,4}(1 - X_{\text{Zn}})^{-0.95}X_{\text{Zn}}X_{\text{Bi}} \\ & + 20.000\omega_{1,4}[1 - (1 - X_{\text{Zn}})^{0.05}] \\ & - \omega_{2,3}(1 - X_{\text{Cd}})^{-0.4}X_{\text{Cd}}X_{\text{Sn}} \\ & - \omega_{2,4}(1 - X_{\text{Sn}})^{-0.45}X_{\text{Sn}}X_{\text{Bi}} \\ & + 1.818\omega_{2,4}[1 - (1 - X_{\text{Sn}})^{0.55}] \end{aligned} \quad [14]$$

Deuterium Labeling by Electrochemical Reactions

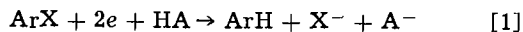
John R. Cockrell¹ and Royce W. Murray*

Department of Chemistry, University of North Carolina, Chapel Hill, North Carolina 27514

ABSTRACT

The extent to which d₁-labeled isomeric anisoles and toluene result from electrolysis of the corresponding iodoaromatics in deuterium-containing solvent media has been explored. Solvent mixtures of D₂O and unlabeled acetonitrile or dimethoxyethane give products of excellent isotopic purity when lithium perchlorate serves as supporting electrolyte. Use of tetraethylammonium as supporting electrolyte cation gives appreciable percentages of unlabeled product.

The electrochemical reduction products of many classes of organic compounds contain hydrogen which was abstracted from the solvent medium during the electrochemical reaction. An example is the reduction of an aromatic halide, which generally proceeds by the reaction (1)



HA is the solvent, a supporting electrolyte component, or an acidic additive. If this reaction is carried out in a medium where HA is replaced by a deuterium source DA, a labeled product ArD will result. Such an experiment offers two possibilities. One is the electro-synthesis of ArD in high isotopic purity if DA acts as the exclusive donor. Failing such exclusivity, isotopic analysis of the ArH,ArD product mixture provides a quantitative assessment of the degree to which other components of the electrochemical solvent medium can serve as hydrogen donors in the electrode reaction. This report explores these two points for the aromatic halide reduction, using the isomeric (*o*, *m*, *p*) iodoanisoles and *o*-iodotoluene as examples.

There have been several previous publications dealing with electrochemical deuterium labeling. Throop and Tökés (2) contributed the sole electrochemical study, in which steroid carbonyl functions were reduced at constant current at lead electrodes in dioxane/D₂O/D₂SO₄ solvent. The labeling efficiency was high, and some polydeutero product also resulted. Webb, Mann, and Walborsky (3), seeking information on hydrogen donor sources, reduced (+)-1-bromo-1-methyl-2,2-diphenylcyclopropane in CD₃CN/N(C₂H₅)₄Br to obtain 75% deuterium label on the 1-carbon. Barger and Coleman (4) examined the potential dependence of the extensive hydrogen-deuterium exchange which propane and benzene undergo at a Pt fuel cell electrode in D₂O/D₃PO₄ medium.

The choice of the deuterium-containing solvent medium is obviously crucial if a high labeling efficiency is to be sought in reaction [1]. The following considerations apply in this choice. A per-deutero solvent clearly offers assurance of high labeling efficiency; for organic solvents this entails costly reagents. If an acidic additive DA is to be used in an otherwise unlabeled solvent, a suitable level of DA acidity and concentration includes the opposing factors of sufficiently low acidity and concentration to avoid direct electrochemical discharge of deuterium, and suffi-

* Electrochemical Society Active Member.

¹ Present address: Ivorydale Technical Center, Proctor and Gamble Company, Cincinnati, Ohio 45200.

Key words: deuterium, electro-synthesis, iodoanisole, isotopic labeling, supporting electrolyte.

ciently high concentration to avoid interference from ubiquitous H₂O impurity in the solvent. In this study, we chose to employ the very weakly acidic donor D₂O in gross amounts, mixed with unlabeled acetonitrile or dimethoxyethane (DME). The choice of supporting electrolyte is shown to be equal in importance to that of the solvent.

Experimental

Chemicals.—Spectrograde and "anhydrous" acetonitrile, tetraethylammonium perchlorate (Et₄NClO₄), *o*-, *m*-, and *p*-iodoanisoles, *o*-iodotoluene, and 1,2-dimethoxyethane were obtained from Eastman, anhydrous reagent LiClO₄ from G. F. Smith Company, D₂O (99.9% isotopic purity) from Columbia Organic Chemicals, and CD₃DN from Bio-Rad. All were used as received. Solutions were prepared under nitrogen in a closed system to avoid external water contamination. The Et₄NClO₄ was vacuum-oven dried at 60°C for 24 hr.

Apparatus.—The electrolysis cell followed the design of Harrar and Shain (5), consisting of two concentric cylinders terminating in medium and fine frits and nested in a beaker cell containing a stirred mercury pool. The three compartments thus provided, namely, the (lower) sample compartment with pool electrode, sample solution, and reference electrode, the (middle) salt bridge compartment containing sample solution, and the (upper) auxiliary electrode compartment containing the large Pt gauze auxiliary electrode and sample solution, were closed to the atmosphere by appropriate sleeves and o-rings and were filled with solution to equal, concentric levels to minimize intercompartment mixing. The sample compartment had provision for inserting a dropping mercury electrode for polarographic assessment of appropriate electrolysis potentials and for closed system removal of product solution, and had a volume of either 50 (mainly used) or 250 ml of sample solution in contact with the mercury pool electrode. Further details of cell construction can be provided upon request.

The electrolysis potentiostat utilized either a Wenking Model 61R or a Kepco Model 120-5M operational power supply as control amplifier and conventional associated operational amplifier circuits. The electrolysis required approximately 30 min for completion.

Gas chromatographic product isolations were accomplished with a Varian Autoprep unit (3/8 in. × 20 ft Dowex-11 column) or an F & M Model 30 chromatograph (1/8 in. × 2 meter column containing 10% SE-30/chromosorb, for anisole, or 25% TCEP/chromosorb, for toluene). The chromatographically purified labeled product was analyzed for isotopic purity using a Hitachi-Perkin Elmer Model RMU-6E or an AEI Model MS-902 mass spectrometer.

Procedure.—Following polarographic assessment of appropriate control potential for preparative electrolysis, a small-scale electrolysis was conducted to provide a product solution for ultraviolet spectrophotometric comparison to the expected authentic (unlabeled) product. Then a larger scale electrolysis was conducted and the pure product isolated for mass spectrometric analysis. The electrolysis was continued until the current had decayed to background levels. In the case of iodotoluene, a spontaneous reaction (unknown products) occurred with the open-circuit mercury pool. This reaction was circumvented by applying the control potential to the working electrode in contact with supporting electrolyte solution prior to injection of the iodotoluene sample. In the case of *m*-iodoanisole, the solution developed a yellow-orange color during electrolysis. A high-melting red-brown precipitate obtained during solvent stripping could not be identified. This side reaction was not apparently deleterious to the labeling reaction.

To remove the supporting electrolyte prior to the gas chromatographic product isolation, the sample and about one-half of the organic portion of the solvent,

plus some D₂O, were stripped off with a 12-in. unpacked glass column. One milliliter injections were used with the Autoprep chromatograph. In the analytical-scale F & M chromatograph, several 100 μl injections of distillate were required for collection of sufficient anisole from the SE-30 column. The anisole eluted (80°C) from this column after about 30 min, following the large solvent peak, and was captured in a glass wool-packed capillary maintained at dry ice temperature. After sufficient sample (several microliters) had been collected in the capillary, it was sealed for subsequent introduction into the mass spectrometer. In the case of toluene, 500 μl injections into the TCEP column gave a toluene peak resolved from and just preceding the large solvent peak which was collected as above.

In the mass spectral isotope analysis, the labeled parent ion peak M_{d1} was corrected for contributions from the C¹³ peak of d₀ unlabeled product and the C¹³ (M-1)_{d1} peak. The parent ion peak for unlabeled product, M_{d0}, was corrected for the (M-1)_{d1} contribution. The per cent deuteration was calculated from these corrected peak heights as 100 M_{d1}/(M_{d1} + M_{d0}) and is believed accurate to ±1%. No d₂-labeled products could be detected in any of the isotopic analyses.

Many of the electrolysis and analysis experiments were performed in duplicate; the per cent deuteration was found in these replicates to be reproducible to within ±1%.

Results and Discussion

The results of labeling experiments using a variety of solvent media are presented in Table I. The results of Experiments 1, 2, and 8-11 show that an excellent level of d₁ labeling efficiency can be obtained electro-synthetically. The D₂O/DME/LiClO₄ mixture proved in the few experiments run in this medium to be superior to the several D₂O/acetonitrile mixtures tested. These isotopic purities compare favorably with previous chemical syntheses of d₁-anisoles, where the isomeric d₁-forms have been prepared in 90% purity by Grignard conversion of bromoanisoles (6), and *p*-d₁-anisole was obtained at essentially 100% purity from catalytic D₂/Pd/charcoal reduction of *p*-bromoanisole (7). Other standard chemical methods for halide-reductive labeling, such as CH₃COOD/Zn, LiAlD₄, and NaBD₄ reductions (8) and tributyl stannane-d₁ reactions (9), appear not to have been applied to the anisoles but should provide comparable results.

While no attempt was made in these studies to isolate more than the few milligrams of product required for mass spectral analysis, a more exhaustive gas chromatographic isolation could be expected to yield at least 50 mg of pure product (corresponds to 50%

Table I. Deuterium labeling efficiencies from reduction of aromatic iodides in various media

Exp.	Solvent medium ^a	Reactant	% d ₁ Product
1	60/40 ^b D ₂ O/DME/0.5M LiClO ₄	<i>o</i> -C ₇ H ₇ OI (0.02M)	99.0
2	50/50 D ₂ O/DME/0.5M LiClO ₄	<i>o</i> -C ₇ H ₇ I (0.02M)	≥96.0
3	35/65 D ₂ O/AN/0.5M LiClO ₄	<i>o</i> -C ₇ H ₇ I (0.02M)	87.0
4	35/65 D ₂ O/AN/0.5M LiClO ₄	<i>o</i> -C ₇ H ₇ OI (0.02M)	76.0
5	10/90 D ₂ O/AN/0.5M LiClO ₄	<i>o</i> -C ₇ H ₇ OI (0.01M)	94.0
6	10/90 D ₂ O/AN/0.5M LiClO ₄	<i>o</i> -C ₇ H ₇ OI (0.025M)	94.0
7	25/75 D ₂ O/AN/0.5M LiClO ₄	<i>o</i> -C ₇ H ₇ OI (0.02M)	95.5
8	60/40 ^b D ₂ O/AN/0.5M LiClO ₄	<i>o</i> -C ₇ H ₇ OI (0.02M)	95.8
9	60/40 ^b D ₂ O/AN/0.5M LiClO ₄	<i>m</i> -C ₇ H ₇ OI (0.02M)	94.0
10	60/40 ^b D ₂ O/AN/0.5M LiClO ₄	<i>p</i> -C ₇ H ₇ OI (0.02M)	93.5
11	60/40 ^b D ₂ O/AN/0.5M LiClO ₄	<i>o</i> -C ₇ H ₇ I (0.02M)	96.0
12	60/40 ^b D ₂ O/AN/0.5M LiClO ₄	<i>o</i> -C ₇ H ₇ OI (0.02M)	99.1
13	10/90 D ₂ O/AN/0.5M LiClO ₄	<i>o</i> -C ₇ H ₇ OI (0.02M)	91.5
14	20/80 D ₂ O/AN/0.5M LiClO ₄	<i>o</i> -C ₇ H ₇ OI (0.02M)	91.5
15	60/40 D ₂ O/AN/0.5M Et ₄ NClO ₄	<i>o</i> -C ₇ H ₇ OI (0.02M)	84.0
16	60/40 D ₂ O/AN/0.5M Et ₄ NClO ₄ , 0.5M LiClO ₄	<i>o</i> -C ₇ H ₇ OI (0.02M)	84.0

^a DME, AN, and AN_a are 1,2-dimethoxyethane, spectrograde acetonitrile, and "anhydrous" acetonitrile, respectively. Ratios are volumes.

^b Highest volume fraction of D₂O with retention of adequate sample solubility.

recovery from 50 ml of 0.02M d_1 -anisole solution). Experiments 3 and 4 show that use of more concentrated sample solutions for production of larger quantities can lead to lowered isotopic purity. This is a disadvantage as compared to the chemical synthetic approaches. The electrochemical experiments in this study were unbuffered, and the use of appropriately labeled buffers or of pD-statting during electrolysis may increase the usable sample concentration levels.

The results of Table I also allow some conclusions as to the source(s) of hydrogen abstracted (from species other than D_2O) during the electrode reaction.

The first point which must be inspected is the level of H_2O contamination of the D_2O label source. The mole percentage of H_2O in the original D_2O is insignificant (0.1%). The H_2O level in the spectrograde acetonitrile is 100 mmole or less. This H_2O level in 60/40, 35/65, 25/75, 20/80, and 10/90 D_2O /acetonitrile mixtures corresponds to 0.33, 0.57, 0.80, 1.00, and 2.00 mole per cent H_2O (with respect to D_2O). These levels are too small to account for more than a small fraction of the total hydrogen impurity in the d_1 -labeled materials prepared in these mixtures. Karl Fischer titrations of solutions of $LiClO_4$ and Et_4NClO_4 in acetonitrile showed no detectable increase in the water level from residual moisture in the dried supporting electrolytes. The results in so-called anhydrous (titration-grade) acetonitrile Experiments 13 and 14, were inferior to those in untreated spectrograde solvent, indicating the presence of a more potent hydrogen donor impurity in the former.

In the $D_2O/CH_3CN/LiClO_4$ mixtures, the acetonitrile itself, rather than impurity H_2O , must then provide the source of hydrogen impurity in the labeled product. Higher proportions of acetonitrile (Experiments 5-7 compared to 8) yield slightly more hydrogen impurity. A more definitive demonstration is provided by use of per-deutero-acetonitrile in Experiment 12 (compare to Experiment 8). The results of Wawzonek *et al.* (9) and Webb *et al.* (3) have shown, in controlled potential electrolysis experiments, that acetonitrile does undergo hydrogen loss in certain electrode reactions. It is interesting in the present results that acetonitrile can compete, albeit at a minor level, with the D_2O as a proton source.

Use of tetraethylammonium rather than lithium salts as supporting electrolyte bears the consequence of rather substantial hydrogen impurity in the labeled product (see Experiment 15). Webb, Mann, and Walborsky (3) have shown that proton abstraction from the tetraethylammonium cation occurs in the reduction of a bromocycloalkane from acetonitrile solvent. They present evidence that this proton abstraction occurs indirectly; the carbanion electrochemically derived from the alkyl halide primarily attacks the solvent, the resulting CH_2CN^- secondary base reacting with the tetraethylammonium species. This indirect pathway is not dominant in the iodoanisole reaction,

however; the reactive base from iodoanisole reduction clearly attacks the tetraethylammonium cation directly and more readily than it does the acetonitrile solvent (compare Experiments 8 and 15). Indirect attack of tetraethylammonium by OD^- to yield HOD can also be ruled out, owing to the high dilution of the latter species by the D_2O , as a major source of hydrogen introduction into the anisole product. The possibility that any ion pairing effect of lithium ion distorts the comparison of Experiments 8 and 15 is likewise ruled out, by Experiment 16, which shows that the addition of $LiClO_4$ causes no change in the hydrogen impurity level observed in the presence of tetraethylammonium cation.

The above results show, in summary, that:

1. Reductive electrochemical synthesis of deuterium-labeled organic compounds can lead to labeled materials of very high isotopic purity in small quantities.

2. Use of isotopic labels can lead to better understanding of electrode reaction mechanisms and, in particular, to recognition of components of the solvent medium which must be controlled if one wishes to minimize sources of acidic reactivity toward electrode reaction products or intermediates.

Acknowledgment

This research was sponsored by the Air Force Office of Scientific Research under grant AFOSR-69-1625. J.R.C. also acknowledges support from a National Defense Education Act Fellowship. Mass spectral isotopic analyses were carried out with helpful advice from Professor M. M. Bursey and with the assistance of the Research Triangle Region Mass Spectroscopy Facility, sponsored by National Institutes of Health Special Biotechnology Grant PR-330.

Manuscript submitted Nov. 3, 1971; revised manuscript received Jan. 31, 1972.

Any discussion of this paper will appear in a Discussion Section to be published in the June 1973 JOURNAL.

REFERENCES

1. C. K. Mann and K. K. Barnes, "Electrochemical Reactions in Nonaqueous Solvents," Marcel Dekker, Inc., New York (1970).
2. L. Throop and L. Tökés, *J. Am. Chem. Soc.*, **89**, 4789 (1967).
3. J. L. Webb, C. K. Mann, and H. M. Walborsky, *ibid.*, **92**, 2042 (1970).
4. H. J. Barger and A. J. Coleman, *J. Phys. Chem.*, **72**, 2285 (1968); **74**, 880 (1970); **75**, 3715 (1971).
5. J. E. Harrer and I. Shain, *Anal. Chem.*, **38**, 1148 (1966).
6. D. P. N. Satchell, *J. Chem. Soc.*, **1956**, 3911.
7. D. Jerina, G. Guroff, and J. Daly, *Arch. Biochem. Biophys.*, **124**, 612 (1968).
8. G. A. Russell and G. W. Holland, *J. Am. Chem. Soc.*, **91**, 3968 (1969).
9. S. Wawzonek, E. W. Blaha, R. Berkey, and M. E. Runner, *This Journal*, **102**, 235 (1955).

The Bockris-Swinkels Isotherm and Low-Coverage Electrosorption of Monocarboxylic Acids on a Copper Cathode

R. S. Salter, P. Seto, and A. J. Sukava

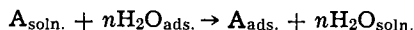
Department of Chemistry, University of Western Ontario, London, Ontario, Canada

ABSTRACT

A theoretical analysis of equations pertaining to the electrosorption of normal monocarboxylic acids on a copper cathode indicates that, at surface coverages approaching zero, the net free energy of adsorption of the polar carboxyl group depends on the number of adsorbed water molecules displaced per molecule of adsorbing additive, while the free-energy contribution of the hydrocarbon part of the molecule is independent of this number. Accordingly, the carboxyl and hydrocarbon parts of the molecule appear to be specifically and nonspecifically adsorbed, respectively. A coverage-dependent interaction parameter or apparent free energy is inherent in the Bockris-Swinkels isotherm and is proportional to the fractional surface coverage as the coverage approaches zero, with the proportionality constant also dependent on the solvent displacement number. An equation is derived relating the solvent displacement number to other physical properties of the adsorbate. The results seem consistent with a condensation mechanism of physical adsorption.

Studies of the effects of normal monocarboxylic acids on the cathode overpotential during electrodeposition of copper from acid sulfate electrolyte have shown (1, 2) that specific adsorption free energy contributions due to the individual structural units of such additive molecules can be calculated from overpotential increment and additive concentration data. A coverage-dependent apparent free energy, assumed to be due to lateral interaction, is also calculable (2), with results similar to those obtained for the adsorption of butanoic and 2-methyl-propanoic acids on mercury (3). Theoretical considerations indicate that the lateral interaction arises primarily from dipole-dipole effects in the adsorbed phase (2).

The present paper deals with the electrosorption of monocarboxylic acids in general terms, with restriction to very low or near-zero coverages. The blocking equation (1, 2, 4) and an appropriate form of the Bockris-Swinkels isotherm (2, 5) are assumed applicable, and some pertinent and useful information is derived based on this assumption. Special attention is given to the relationship between the various free energy components and the solvent displacement number n , the number of adsorbed water molecules displaced per molecule of additive in the adsorption "reaction" (5)



Theory

Calculation of θ , the fraction of cathode surface covered by adsorbed additive, from the overpotential increment $\Delta\eta$ caused by such additive, assumes the applicability of the blocking equation (1, 4)

$$\theta = 1 - \exp(-\Delta\eta/b) \quad [1]$$

where b is the Tafel slope. Obviously, this equation can only be applied to the so-called Tafel region where charge transfer is rate determining (6, 7), and only if the presence of adsorbed additive does not alter the charge-transfer kinetics of the cathode process, that is, only if the additive merely increases the true current density at the electrode surface.

For normal monocarboxylic acids as additives, the coverage θ can then be related to the individual adsorption free energy contributions of the various parts of the adsorbed molecule by writing the Bockris-Swinkels version of the Langmuir isotherm (5) (derived for adsorption involving solvent displacement) in the appropriate form (2)

$$\frac{\theta}{(1-\theta)^n} = \frac{\{ \theta + n(1-\theta) \}^{n-1}}{n^n} \exp \left[\frac{-\Delta G^\circ_P - x\Delta G^\circ_{CH_2} - g(\theta)}{RT} \right] \quad [2]$$

In Eq. [2], C is the concentration of additive, x is the number of methylene groups in the additive molecule, including the terminal methyl, and n is the solvent displacement number. ΔG°_P and $\Delta G^\circ_{CH_2}$ denote the standard free energy contributions of the polar carboxyl group and each methylene group respectively,¹ while the coverage-dependent parameter $g(\theta)$ is a Frumkin-like interaction term definable as an apparent standard free energy (8) due to lateral forces between the adsorbed molecules.

Values of $g(\theta)$ have been calculated (2) for adsorbed straight-chain monocarboxylic acids from cathode overpotential increments in accordance with Eq. [1] and [2]. The results are in reasonable agreement at low coverages with values calculated from theory, assuming only dipole-dipole interaction and neglecting dispersion effects [see Fig. 6 of Ref. (2)]. Accordingly, for these compounds, $g(\theta)$ can be treated to a first approximation as a dipole-dipole interaction energy only, provided the surface coverage is not too high.

Experiments with low concentrations of the straight-chain monocarboxylic acids from propanoic to octanoic inclusive have also shown (2) that, in the adsorption of these compounds on a copper cathode during electrodeposition under galvanostatic control, the free energy term $\Delta G^\circ_{CH_2}$ is independent of surface coverage. Therefore, since change in coverage gives rise to change in cathode potential under galvanostatic conditions, then, within the limitations of the data, $\Delta G^\circ_{CH_2}$ can be treated as independent of potential. For this reason, any potential dependence of the free energy of adsorption of short-chain normal monocarboxylic acids is considered in this paper to be incorporated in the term ΔG°_P , primarily.

Since the cathode overpotential in galvanostatic experiments is determined by the concentration and nature of any surface-active additive, as well as by the apparent current density, the temperature, and the composition of the standard electrolyte apart from the

¹ While this division of the standard free energy of adsorption into separate contributions from the carboxyl and methylene groups follows from experimental data in this instance (2), it should be noted that the same division would arise in a purely theoretical manner if Traube's rule is assumed to apply to the adsorption from solution of compounds in a homologous series such as the straight-chain monocarboxylic acids.

Key words: theory, isotherm, blocking, homologous, additives.

additive, then, assuming the adsorption of the carboxyl group to be potential dependent, the value of ΔG°_P in Eq. [2] varies with additive concentration in such experiments. By extrapolating the galvanostatic data to zero additive concentration, i.e., to zero surface coverage, a limiting value of ΔG°_P is obtained which corresponds to a potentiostatic state arbitrarily determined and fixed by the experimental current density, the temperature, and the composition of the standard electrolyte. Purely mathematical equivalents of such an extrapolation can be derived by applying Eq. [1] and [2] to low surface coverages and considering the limiting case as the coverage approaches zero.

Proportionality of $\Delta\eta$ and C at low surface coverage.—Experiments have shown (2) that the cathode-overpotential increment caused by adsorbed monocarboxylic acid is proportional to the concentration of the additive if the surface coverage (or additive concentration) is sufficiently low. This proportionality can be shown to follow as a direct consequence of Eq. [1] and [2].

As θ approaches zero, $\Delta\eta$ and $g(\theta)$ also approach zero, and Eq. [1] and [2] become, respectively

$$\theta = \Delta\eta/b \quad [3]$$

and

$$\theta = nKC \quad [4]$$

where K is given by

$$K = \frac{1}{55.5} \exp \left[\frac{-\Delta G^\circ_P - x \cdot \Delta G^\circ_{CH_2}}{RT} \right] \quad [5]$$

Obviously, for a given additive at a fixed apparent current density and temperature, K is fixed at near-zero coverages since ΔG°_P takes on its limiting zero-coverage value as determined by the arbitrary experimental conditions, and since $\Delta G^\circ_{CH_2}$, being independent of coverage (2), is assumed to be independent of potential. Equations [3] and [4] then give, in the limit

$$(\Delta\eta/C)_{C \rightarrow 0} = nbK \quad [6]$$

showing that the initial slope of the $\Delta\eta$ vs. C curve is fixed for any monocarboxylic acid and for any fixed value of n .

Substituting Eq. [5] into [6], and writing the result in logarithmic form, gives

$$\ln(\Delta\eta/C)_{C \rightarrow 0} = \left[\ln \frac{nb}{55.5} - \frac{\Delta G^\circ_P}{RT} \right] - \frac{\Delta G^\circ_{CH_2}}{RT} \cdot x \quad [7]$$

Therefore, as has been shown by experiment [see Fig. 3 of Ref. (2)], the logarithm of the initial slope varies linearly with the number of methylene groups in a normal monocarboxylic acid molecule.

Equation [7] leads to some interesting observations, assuming that Eq. [1] and [2], on which it is based, are both valid. Obviously, in the electrosorption of normal monocarboxylic acids on copper, the methylene-group contribution to the free energy, given by the slope in Eq. [7], is independent of the solvent displacement number n . On the other hand, the carboxyl-group contribution can only be found from the intercept in [7] if n is known, and consequently, it appears that adsorption of these compounds on copper from aqueous solution must occur in a manner such that adsorbed water molecules are displaced only by the carboxyl group. The free energy of adsorption of the carboxyl group, ΔG°_P , is then, presumably, a net free energy, the algebraic sum of the actual free energy of adsorption of this group and the free energy of desorption of n moles of water. It follows that a distinction can be made between the carboxyl-group and methylene-group effects as specific and nonspecific adsorption, respectively. Further, to be consistent with the significance of x in Eq. [7], the hydrocarbon chain of an adsorbed monocarboxylic acid molecule probably lies parallel to or along the copper surface, and presumably on top of undisplaced, adsorbed water molecules.

Proportionality of $g(\theta)$ and θ at low surface coverage.—Experimental data and calculations reported by different workers (2, 3, 5, 9) appear to indicate that, in any adsorption, the coverage-dependent energy parameter $g(\theta)$ becomes proportional to the surface coverage at coverages approaching zero, with the proportionality constant having some nonzero value. This proportionality follows as a consequence of the adsorption isotherm, Eq [2].

Solving Eq. [2] for $g(\theta)$, and introducing Eq. [5], gives, after rearrangement

$$g(\theta)/RT = \ln \frac{nKC}{\theta} + n \ln(1 - \theta) - (n - 1) \ln \left\{ 1 - \frac{n - 1}{n} \cdot \theta \right\} \quad [8]$$

which applies at all values of θ . Straightforward substitution of power-series expressions for the logarithms in the second and third terms in [8], followed by division through by θ and taking the limit as θ approaches zero, gives

$$\frac{1}{RT} \left[\frac{g(\theta)}{\theta} \right]_{\theta \rightarrow 0} = \left[\frac{1}{\theta} \ln \frac{nKC}{\theta} \right]_{\theta \rightarrow 0} + \frac{1}{n} - 2 \quad [9]$$

where the first term on the right is indeterminate in view of [4]. Equation [9] permits direct calculation of the zero-coverage slope of the $g(\theta)$ vs. θ curve, requiring only that the indeterminate quantity be found.

For sufficiently low values of θ , and assuming the blocking theory to be valid, Eq. [6] can be applied to give, on substitution from [1]

$$nKC = -\ln(1 - \theta) = \theta + \frac{\theta^2}{2} + \frac{\theta^3}{3} + \dots$$

which applies only when surface coverage is sufficiently low to make $\Delta\eta$ proportional to C . With this substitution for nKC , the first term in [9] becomes, after further substitution of power series and simplification

$$\frac{1}{\theta} \ln \frac{nKC}{\theta} = \left(\frac{1}{2} + \frac{\theta}{3} + \frac{\theta^2}{4} + \dots \right) - \frac{1}{2\theta} \left(\frac{\theta}{2} + \frac{\theta^2}{3} + \dots \right)^2 + \dots$$

which, for the zero-coverage limit, is

$$\left[\frac{1}{\theta} \ln \frac{nKC}{\theta} \right]_{\theta \rightarrow 0} = \frac{1}{2} \quad [10]$$

Equations [9] and [10] then give the slope of the $g(\theta)$ vs. θ curve at coverages approaching zero as

$$\left[\frac{g(\theta)}{\theta} \right]_{\theta \rightarrow 0} = \left(\frac{1}{n} - \frac{3}{2} \right) RT \quad [11]$$

The nonzero value of $g(\theta)$ at all nonzero values of θ as given by Eq. [11] is a characteristic inherent in the Bockris-Swinkels isotherm. It is consistent with the expected nature of any physical adsorption at near-zero coverages. To attain their lowest possible free-energy state at such coverages, molecules of adsorbate would be expected to achieve a degree of lateral interaction by locating adjacent to each other in oriented and clustered array, in a manner analogous to ordinary condensation. This condensation mechanism of adsorption would be similar to the formation of so-called coherent islands as found in the case of long-chain monocarboxylic acids at the air-solution interface (10). The adsorbed phase would not be expected to exist as randomly spaced individual and separately adsorbed molecules.

Solvent displacement number and physical properties of the adsorbate.—If localized adsorption is assumed with lateral interaction due mainly to dipole effects (2, 5), then, according to theory (5), the molal value of $g(\theta)$ can be given in terms of coverage θ and dipole interaction U_{dip} , by

$$g(\theta) = \phi \theta N U_{\text{dip}} \quad [12]$$

where N is the Avogadro number and where ϕ , a constant, depends on the manner in which the adsorbed molecules are arrayed and oriented on the surface (5). The molecular contribution to the dipole interaction is given by (5)

$$U_{\text{dip}} = -\frac{\mu_D^2}{\epsilon r^3} \quad [13]$$

where μ_D is the dipole moment, ϵ the dielectric constant of the medium (the primary electrode layer), and r the average distance between adjacent dipoles in the adsorbed phase. Consequently, an equation can be written relating the solvent displacement number n directly to the parameters on the right in [13] by substituting [12] and [13] into [11] to give, for sufficiently low coverages

$$\left[\frac{3}{2} - \frac{1}{n} \right] kT = \frac{\phi \mu_D^2}{\epsilon_{\theta \rightarrow 0} r^3} \quad [14]$$

where k is the Boltzmann constant and where the zero-coverage value of ϵ is specified to conform to the requirements of Eq. [11]. [It should be noted that the dielectric constant of the primary electrode layer has been considered to vary with coverage (5, 11, 12)].

The quantities n , μ_D , ϵ , and r in Eq. [14] are not accurately known. In particular, widely different values of ϵ have been considered appropriate at zero coverage, e.g., 80 (5), 15 (11), 6 (12), and 1 (13), depending on the adsorbate, the mode of adsorption, and the proximity of the dipole to the surface (13). However, assuming the validity of Eq. [14], at least as an approximation, and noting that n , ϕ , μ_D , and r are presumably determined by the fixed dimensions and structure of the adsorbate molecules, then $\epsilon_{\theta \rightarrow 0}$ is likewise also fixed and determined primarily by these molecules themselves, even at coverages approaching zero. This conclusion is consistent with the view that clustering of adsorbed molecules occurs at near-zero coverages, according to the condensation concept, as has been stated in connection with Eq. [11].

Furthermore, it is of interest to note the value of $\epsilon_{\theta \rightarrow 0}$ as calculated from reasonable estimates of the parameters in Eq. [14] for adsorbed monocarboxylic acids. If n is taken as about 2.2 [estimated from the cross-sectional area of the hydrocarbon chain relative to the projected area of the water molecule (3)], r as about 4.9 Å [estimated for close-packed array from the cross-sectional dimensions of the hydrocarbon chain (5)], and μ_D as about 1.5 Debye [taken as an average for short-chain monocarboxylic acids (14)], and if localized adsorption, hexagonal array, and antiparallel orientation are assumed, i.e. if $\phi = 4.5$ (5), then $\epsilon_{\theta \rightarrow 0}$ for these compounds is about 2.1 at 25°C. For parallel orientation, with $\phi = 9.24$ (5), $\epsilon_{\theta \rightarrow 0}$ would be about 4.3. These values of $\epsilon_{\theta \rightarrow 0}$ may be compared with the liquid-state value of about 2.5 for pure monocarboxylic acids (15).

Condensation concept of adsorption.—The argument that the nonzero slope of the $g(\theta)$ vs. θ curve given by Eq. [11] is consistent with a condensation mechanism of adsorption finds support in a simple calculation based on Eq. [12] and [13], according to which the initial zero-coverage slope of the $g(\theta)$ vs. θ curve would be zero if the adsorption occurred by a random distribution of separate molecules.

If such a random distribution of individual adsorbate molecules is assumed, then ϵ and r in Eq. [13]

would be functions of θ , the coverage. This assumption is implicit in the belief that the dielectric "constant" of the primary cathode layer varies linearly with coverage (5, 11, 12), according to which one would write for monocarboxylic acids adsorbed from aqueous solution

$$\epsilon = 6 - 3.5 \theta$$

where the zero-coverage ϵ -value of 6 is assumed to be that of pure water in the primary cathode layer (12) and that at full coverage, taken as 2.5, is the value for pure liquid monocarboxylic acids (15). Then, since the coverage dependence of r would be given by (9, 16)

$$r = q \cdot \theta^{-1/2}$$

where q is a constant,² Eq. [12] and [13] would give, for separate-molecule adsorption with dipole-dipole interaction assumed predominant

$$\frac{g(\theta)}{\theta} = -\phi N \mu_D^2 q^{-3} \left[\frac{\theta^{3/2}}{6 - 3.5 \theta} \right]$$

Obviously, as θ approaches zero, this would become

$$\left[\frac{g(\theta)}{\theta} \right]_{\theta \rightarrow 0} = 0$$

in contrast to the behavior inherent in the Bockris-Swinkels isotherm as given by Eq. [11].

Acknowledgments

Helpful discussions with Dr. W. J. Meath, Chemistry Department, University of Western Ontario, and the financial support of the National Research Council, Ottawa, and the Department of University Affairs of Ontario, are gratefully acknowledged.

Manuscript submitted March 24, 1971; revised manuscript received Dec. 29, 1971.

Any discussion of this paper will appear in a Discussion Section to be published in the June 1973 JOURNAL.

² This simple relation between r and θ arises from a basic statistical relationship according to which the average distance between randomly distributed and separately adsorbed molecules is given by the square root of the average over-all surface area per molecule. Since this area is inversely proportional to the coverage, the r vs. θ relation follows as given.

REFERENCES

1. A. K. P. Chu and A. J. Sukava, *This Journal*, **116**, 1188 (1969).
2. R. O. Loutfy and A. J. Sukava, *ibid.*, **118**, 216 (1971).
3. K. M. Joshi, M. R. Bapat, and S. W. Dhawale, *Electrochim. Acta*, **15**, 1519 (1970).
4. R. W. Hansen and B. H. Clampitt, *J. Phys. Chem.*, **58**, 908 (1954).
5. J. O'M. Bockris and D. A. L. Swinkels, *This Journal*, **111**, 736 (1964).
6. J. O'M. Bockris and A. Damzanovic, "Modern Aspects of Electrochemistry," Vol. 3, pp. 224-346, J. O'M. Bockris and B. E. Conway, Editors, Butterworths, London (1964).
7. E. Mattson and J. O'M. Bockris, *Trans. Faraday Soc.*, **55**, 1586 (1959).
8. B. E. Conway, "Theory and Principles of Electrode Processes," Chap. 5, Ronald Press (1965).
9. R. G. Barradas and B. E. Conway, *Electrochim. Acta*, **5**, 319 (1961).
10. N. K. Adam, "The Physics and Chemistry of Surfaces," Chap. 2, Dover (1968).
11. L. Pospisil and J. Kuta, *Coll. Czechoslov. Chem. Commun.*, **34**, 3047 (1969).
12. J. O'M. Bockris, M. A. V. Devanathan, and K. Müller, *Proc. Roy. Soc., London*, **274A**, 55 (1963).
13. T. N. Andersen and J. O'M. Bockris, *Electrochim. Acta*, **9**, 347 (1964).
14. A. L. McClellan, "Tables of Experimental Dipole Moments," W. H. Freeman and Co., London (1963).
15. A. A. Maryatt and E. R. Smith, "Tables of Dielectric Constants of Pure Liquids," National Bureau of Standards Circular 514 (1951).
16. E. A. Blomgren and J. O'M. Bockris, *J. Phys. Chem.*, **63**, 1475 (1959).

Linear Models and the Kinetics of Thermally Activated Currents and Voltages

B. Gross¹

*Escola de Engenharia de São Carlos, Departamento de Física,
Avenida Dr. Carlos Botelho, 1465; São Carlos, Estado de São Paulo, Brazil*

ABSTRACT

Experimental results from thermally activated measurements can be analyzed by different methods. In view of the difficulty of obtaining precise solutions of the differential equations describing the transport and trapping of charge carriers in solid dielectrics, various linearized theories have been developed. In the present paper the isothermal theory of conventional models is generalized and a nonisothermal model theory is established. Current transients generated by heating in short-circuit and voltage-transients generated by heating in open-circuit are discussed. It is found that under nonisothermal conditions the concept of equivalency of models must be severely restricted and that the assumptions of charge invariance and absence of current reversals, implicit in many existing theories, cannot be taken for granted. One concludes that the interpretation of thermal activation measurements without the knowledge of the structure of the system under consideration and the underlying physical mechanism leads to ambiguities.

The measurement of thermally stimulated currents has become an important tool for the investigation of relaxation processes in solid dielectrics (1). When the temperature of a polarized dielectric is increased, depolarization currents are generated and current peaks are observed which are indicative of the successive release of charge carriers or dipoles from fixed positions. But the quantitative interpretation of results is still open to discussion since procedures based on existing theories (2) have recently been questioned by several authors (3).

The method of thermal activation is an extension of the isothermal methods of analysis previously used in the practice of dielectric measurements. The isothermal behavior of solid dielectrics has been adequately described with the help of electrical models in which temperature appears as a time-independent parameter. It can be expected that model theory will be equally useful for the discussion of nonisothermal behavior. It is the purpose of the present paper to generalize isothermal model theories by introduction of temperature as a time-dependent variable and to study nonisothermal transitions of linear models. Results show the limitations of some of the assumptions inherent in existing theories and give a comprehensive treatment of temperature-induced electrical transients. They indicate that the measurement of thermally stimulated voltages is complementary to that of thermally stimulated currents and suggest them as a new experimental approach to the problem. The concept of equivalence of models is found to lose validity. Therefore the selection of a particular model can no longer be dictated by the convenience of mathematical description but must be determined by the physics of the relaxation system.

Concepts of Nonisothermal Model Theory

Assumptions.—The paper deals with the theory of linear electrical relaxation processes in solid dielectrics with a finite, discrete spectrum of activation energies. It discusses electrical transients in charged or polarized systems after the external source of electrical energy has been disconnected. Conductivity glow curves are not included. The characteristic variables are current, voltage, and temperature which might all be functions of time. Temperature shall, however, vary slowly enough to ensure no departure from spatial uniformity

¹ Present address: Sternwartestrasse 55, Vienna, Austria A-1180.
Key words: electrets, thermally stimulated currents, thermally stimulated voltages, linear electrical model theory (nonisothermal).

throughout the sample. Phase transitions and irreversible processes like aging are excluded. The activation energies are considered as temperature-independent physical constants. Physical systems are represented by linear electrical models with lumped elements composed of resistors and capacitors. Changes of temperature shall not affect the arrangement of the elements of a model but only their values. These shall be state variables. The link between physical system and model is established by means of conventional rate theory.

Isothermal and nonisothermal theories.—Conventional theory, as it has been applied to relaxation processes (4), considers current transients caused by voltage changes and voltage transients caused by current changes at different, but constant temperatures; therefore it is an isothermal theory. It leads to differential equations with constant coefficients. Thermally activated processes involve nonisothermal transitions during which system parameters are time-dependent functions. They are no longer described by differential equations with constant coefficients. The formalism must therefore be generalized. A suitable starting point is found in model theory. Thus the present nonisothermal theory uses the method of network analogs to discuss current transients caused by temperature changes at constant (i.e., zero) voltage and voltage transients caused by temperature changes at constant (i.e., zero) current.

Models.—Many different models have been used to discuss molecular relaxation processes (5). Here we shall discuss in detail only two representative models: the Maxwell model, given by a parallel arrangement of branches, each containing a series connection of resistor and capacitor; and the Wagner-Voigt model, given by a series arrangement of loops, each containing a parallel connection of resistor and capacitor.

State variables.—How does a given model react to a change of temperature? The model structure, i.e., the particular arrangement of elements that characterizes the model, must remain the same if the model concept is to be meaningful at all under nonisothermal conditions, but the values of the elements become variables.

A priori the value P of a circuit element can depend on temperature $T(t)$, its time derivatives $dT/dt, d^2T/dt^2, \dots$, and explicitly on time t . In this case one would have $P[T(t), dT/dt, \dots, t]$. To develop a theory one

must specify the type of functional dependence. If P depended explicitly on time, the system would undergo irreversible modifications, e.g., aging. If P depended on any time derivative of temperature, it could assume different values for the same value of T and lead to "thermal hysteresis." Here we shall not consider these effects and assume that at any time P is uniquely determined by the value of T at that time. This definition makes P a state variable which is written $P[T(t)]$. A system composed of elements whose values are state parameters goes through a succession of equilibrium states during a change of temperature.

Charge invariance.—Most theories of thermally stimulated currents implicitly assume that the time integral over the short-circuit current from zero to infinity is independent of the function $T(t)$ during the discharge interval and defines the initial "charge of the system." In a preceding paper we have called this the principle of charge invariance and derived from it a theory of nonisothermal effects (6). But charge invariance is not an assumption of the present theory. Rather it will be shown that it does not always apply and is a criterion which allows one to distinguish between different models.

Current and Voltage Measurements

In electric network and model theory a parallelism exists between the treatment of short-circuit currents and open-circuit voltages. Past experience in the field of electrets, closely related to that of thermally activated relaxation processes, has shown that a combination of current (7) and voltage (8) measurements is necessary to understand nonisothermal conduction and polarization effects (9), but recent studies of thermally activated processes have relied exclusively on current measurements. Introduction of the method of voltage measurements is an important complement of current measurements. No analytical treatment is complete that does not discuss both methods on the same level.

Thermally stimulated currents.—The dielectric is charged at a high temperature, cooled to a low temperature, and short-circuited. After a suitable period of quiescence it is reheated in short-circuit. A depolarization current is observed.

Thermally stimulated discharge voltage.—The treatment is the same as before up to the moment of the short-circuit. Then, while the voltage source is removed, the dielectric remains in open-circuit. A slow low-temperature voltage decay sets in. The discharge is accelerated by reheating. In the presence of several relaxation processes with different activation energies a stepwise voltage curve should be observed (Fig. 1, part III).

Thermally stimulated return voltage curves.—The experimental conditions are the same as for the measurement of thermally stimulated currents, until the beginning of the reheating. Then, instead of leaving the system in short-circuit and measuring currents, one removes the short-circuit and measures voltages. A return voltage is observed; the voltage recovery proceeds stepwise when charge release is governed by multiple activation energies; eventually the increase of the intrinsic conductivity of the dielectric causes the voltage to drop to zero (Fig. 1, part IV).

Thermally Stimulated Currents

Maxwell model.—The differential equation.—The Maxwell model is represented in Fig. 2. The values of the resistors and capacitors are state variables, thus $R_i = R_i[T(t)]$ and $C_i = C_i[T(t)]$. Their products $R_i C_i = \tau_i[T(t)]$ are also state variables; under isothermal conditions they are the time-constants of the system. The short-circuit current J is given by the sum of the branch currents J_i , thus

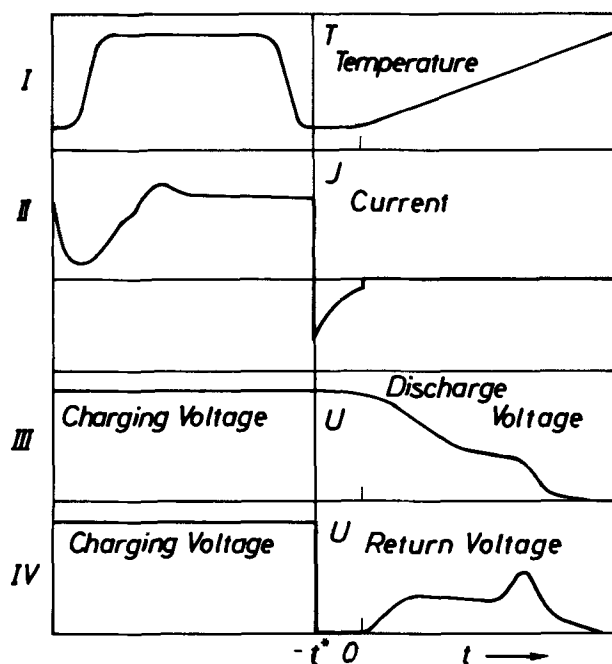


Fig. 1. Thermally activated voltages. I, Temperature; II, Current; III, Discharge voltage curve; IV, Return voltage curve. $t < -t^*$: polarization period; $-t^* < t < 0$: short-circuit; $0 < t$: open-circuit. Time scale in hours.

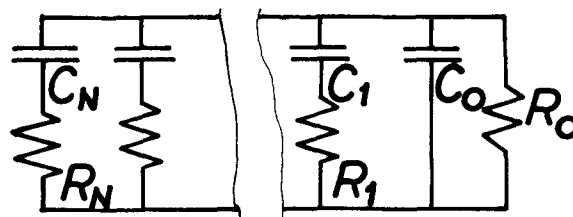


Fig. 2. Maxwell model

$$J_1(T, t) = \sum_1^N J_i(T, t) \quad [1]$$

where N is the number of branches. The voltage across a resistor R_i is $R_i J_i$ and that across a capacitor C_i is $(1/C_i) \int_0^t J_i dt$. In short-circuit the sum of both voltages must be zero and therefore

$$R_i C_i J_i + \int_0^t J_i dt = 0, \quad i = 1, 2, \dots, N \quad [2]$$

Introducing τ_i and differentiating with regard to time one has

$$dJ_i/dt + J_i(1/\tau_i + d \ln \tau_i/dt) = 0, \quad i = 1, 2, \dots, N \quad [3]$$

Let us introduce the notations

$$I_i(t_1, t_2) = \int_{t_1}^{t_2} (\tau_i[T(s)])^{-1} ds \quad [4]$$

and

$$q_i(t_1, t_2) = q_i(0) \exp(-I_i(t_1, t_2)) \quad [4a]$$

one obtains the solution

$$J_i(T, t) = (\tau_i[T(t)])^{-1} \cdot q_i(0, t) \quad [5a]$$

The quantities $q_i(0) = J_i(0) \cdot \tau_i(0)$ are integration constants which depend on the initial conditions at $t = 0$.

The coefficients of J_i in the differential Eq. [3] can be written explicitly in the form $k_i = (1/\tau_i)(1 + (d\tau_i/dT)(dT/dt))$. They contain the time derivatives of the temperature and therefore are not state variables. If

the temperature is constant, $dT/dt = 0$ and $k_1 = (1/\tau_1) = \text{const}$. This gives the well-known differential equations of the isothermal theory. If one were to take these equations as the starting point and generalize them by allowing T to become a function of time, one would miss the term containing dT/dt .

Charge invariance.—By noting that

$$dq_i(t_1, t_2)/dt_2 = -q_i(t_1, t_2)/\tau_i [T(t_2)] \quad [4b]$$

one can write Eq. [5a] as

$$J_i(T, t) = -dq_i(0, t)/dt \quad [5b]$$

The current is therefore a total differential. Since T and τ_i are always finite, the value of the integral I_1 in Eq. [4] becomes infinite when t_2 becomes infinite and the exponential goes to zero. Integration over time between an arbitrary time t_0 and ∞ gives therefore

$$\int_{t_0}^{\infty} J_i[T(t), t] dt = q_i(0, t_0) \quad [6]$$

The integral on the left side contains the arbitrary function $T(t)$ in the time interval $t_0 < t < \infty$, but the value of this integral, given by the expression on the right side, depends only on the values of the function $T(t)$ in the time interval $0 < t < t_0$ and on the initial conditions at $t = 0$. Therefore the value of the time integral over the current between t_0 and ∞ is inde-

pendent of T in the interval. Since $J = \sum_1^N J_i$ the same conclusions apply also to the total discharge current J . Taking in particular $t_0 = 0$ one has

$$\int_0^{\infty} J[T(t), t] dt = q(0), T(t) \text{ arbitrary} \quad [7]$$

This equation represents a very particular situation. To each temperature function $T(t)$, $0 < t < \infty$, belongs a particular discharge current $J[T(t), t]$; different heating rates give different discharge currents. There is no *a priori* reason to assume that the time integral over these different currents has always the same value, but Eq. [7] shows that this indeed is the case. The depolarization charge $q(0)$ is a constant which depends only on the state of the system at $t = 0$, *i.e.*, on temperature and voltage during the interval $t < 0$ which precedes the reheating period. This property of the integral [7] allows one to introduce a single value for the depolarization charge without specifying the temperature as a function of time during the discharge.

Activation energies.—The relaxation variables τ_i can be related to the characteristic constants of the physical system with the aid of rate theory. In isothermal theory, the relaxation time is related to temperature by the equation $\tau = (1/\nu) \exp(u/kT)$. The temperature dependence of the frequency factor ν is small compared to that of the exponential factor and usually is neglected; u is an activation energy. In usual applications T is considered to be a parameter; in the present case where the system undergoes a temperature excursion, it is a time-dependent function. We generalize the rate equation by introducing T as a function of time, but suppose that within the limited temperature interval considered here the activation energies are temperature-independent constants. This assumption excludes the occurrence of phase transitions. Thus the constant relaxation times of the isothermal theory are replaced by the relaxation variables

$$\tau_i [T(t)] = (1/\nu_i) \exp(u_i/kT(t)) \quad [8a]$$

The activation temperatures are defined by

$$T_i = u_i/k \quad [8b]$$

The definition of the products $R_i C_i$ as state variables allows one to identify them with the functions τ_i defined by Eq. [8a] and to write

$$R_i C_i = (1/\nu_i) \exp(u_i/kT(t)) \quad [8c]$$

Linear heating rate.—Inversion of the function $T(t)$ gives time as a function of temperature and allows one to introduce the latter as the independent variable. In most experiments heating rate is constant and temperature is a linear function of time, *i.e.*, $T = T_0 + \beta t$. Inversion gives

$$t = (T - T_0)/\beta \quad [9]$$

Introduction of Eq. [8a] and [9] into Eq. [4] gives the current as a function of temperature alone

$$J_i(T) = J_i(0) \exp(-u_i(1/kT - 1/kT_0)) - (\nu_i/\beta) \int_{T_0}^T \exp(-u_i/kT) dT \quad [10]$$

This is the equation for first order kinetics on which many authors (1) have based their analysis of thermally stimulated currents. Their treatment is therefore equivalent to the introduction of a Maxwell model (6). Implicitly it involves the validity of charge invariance as shown in Eq. [7].

Wagner-Voigt model.—**Differential equation.**—The Wagner-Voigt model is shown in Fig. 3a. Resistors R_i , capacitors C_i , and their products τ_i will again be state variables. The external voltage U is equal to the sum of the loop voltages U_i . In short-circuit one has $U = 0$ and therefore

$$\sum_1^N U_i(T, t) = 0 \quad [11]$$

The current through a resistor R_i is U_i/R_i and through a capacitor it is $d(C_i U_i)/dt$; the total current is therefore $d(C_i U_i)/dt + U_i/R_i$. Inspection of Fig. 3a shows that all currents have the same value and are equal to the external current J . This gives the system of equations

$$J(T, t) = U_i/R_i + U_i dC_i/dt + C_i dU_i/dt, \quad i = 1, 2, \dots, N \quad [12]$$

which shows that the value of the current in each loop is the same. We shall give the analytical solution for a two-loop four-element model and subsequently discuss qualitatively the behavior of a multi-element model for very slow heating rate.

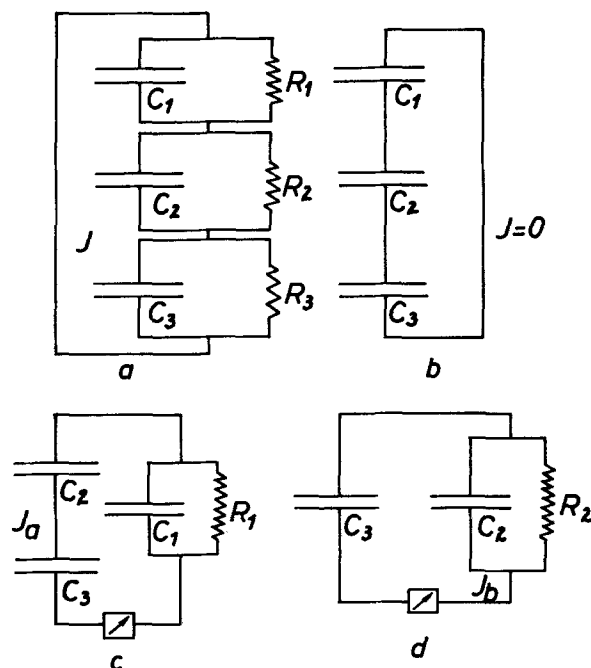


Fig. 3. Wagner-Voigt model. a, Three-loop model; b, Idealized model, low temperature; c, Idealized model, intermediate temperature; d, Idealized model, high temperature.

Analytical solution for four-element model.—With $N = 2$, Eq. [11] gives $U_1 = -U_2$ and Eq. [12] gives

$$(1/R_1 + 1/R_2)U_1 + U_1 d(C_1 + C_2)/dt + (C_1 + C_2)dU_1/dt = 0 \quad [13]$$

Introducing $1/R = 1/R_1 + 1/R_2$, $C = C_1 + C_2$, $\tau = RC$, $q(0) = U[T(0), 0] \cdot C[T(0)]$, and the integral

$$I(0, t) = \int_0^t ds/\tau[T(s)] \quad [14]$$

also defining

$$q(0, t) = q(0) \exp(-I(0, t)) \quad [14a]$$

and noting that

$$q(0, t) = -\tau[T(t)] \cdot dq(0, t)/dt \quad [14b]$$

one obtains

$$U_1(T, t) = C^{-1}[T(t)] \cdot q(0, t) = -R[T(t)] \cdot dq(0, t)/dt \quad [15a]$$

and

$$\begin{aligned} dU_1(T, t)/dt &= -C^{-2} \cdot (dC/dt) \cdot q(0, t) + C^{-1} \cdot dq(0, t)/dt \\ &= (C^{-2} \cdot (dC/dt) \cdot \tau + C^{-1}) \cdot dq(0, t)/dt \end{aligned} \quad [15b]$$

Introducing Eq. [15a, b] into [12] gives the current

$$J(T, t) = -F(T, t) \cdot dq(0, t)/dt \quad [16a]$$

with

$$F(T, t) = R/R_1 - C_1/C + \tau d(C_1/C)/dt \quad [16b]$$

A comparison of these equations with the corresponding equations for the Maxwell model shows significant differences.

Nonvalidity of charge invariance.—The current given by Eq. [16a, b] is not a total differential due to the presence of the front-factor F . After partial integration one has

$$\begin{aligned} \int_0^\infty J[T(t), t] dt &= -F(0) \cdot q(0) \\ &+ \int_0^\infty q(0, t) \cdot (dF(T, t)/dt) dt \end{aligned} \quad [17a]$$

The term on the right side depends on the initial conditions at $t = 0$ and on the values of the function $T(t)$ in the discharge interval $0 < t < \infty$. Each temperature function $T(t)$ gives a different value for the time integral over the depolarization current. Charge invariance does not apply and instead of Eq. [7] one has

$$\int_0^\infty J[T(t), t] \neq \text{const}, T(t) \text{ arbitrary} \quad [17b]$$

Thus the externally measured depolarization charge of an always identically charged dielectric need not always be the same. One must distinguish between the "released" charge and the "internal" charge. The first is defined as the time integral over the short-circuit discharge current; the second is represented by the amount of charge stored in the capacitors of the model. In the Maxwell model the capacitors are not shunted by resistors. During the discharge the entire "internal" charge flows through the external circuit and the integral over the external current is independent of temperature conditions during the discharge. In the Wagner-Voigt model all capacitors are shunted by resistors. During the discharge only a fraction of the "internal" charge flows through the external circuit while the rest disappears by "internal" leakage. The relation between the two fractions depends on the values of the resistors and therefore on the temperature during the discharge. This excludes the existence of a temperature invariant charge value $q(0)$.

Activation energies.—The values of the four model elements define the relaxation variables $\tau_1 = R_1 C_1$ and $\tau_2 = R_2 C_2$ which are linked with the activation energies u_1 and u_2 by the rate Eq. [8a-c]. But the output current does not separate into two components one containing only τ_1 and the other only τ_2 but is given by a single component containing the complex function τ and, explicitly, the values of the model elements. Formally τ can be represented by a rate equation, but the corresponding activation energy value u is not related to any elementary relaxation mechanism. Therefore if the thermally stimulated current were to be analyzed by one of the conventional methods (1, 2), one would obtain an energy value which is not one of the constants of the system; it could not readily be interpreted on a molecular basis, e.g., as a trap depth.

Current reversals.—The term F in Eq. 16 can change its sign in consequence of the temperature dependence of the resistive values R_1 and/or capacitive values C_1 . We shall consider here only the resistive effect since the temperature dependence of the capacitive values is usually small. With $d(C_1/C)/dt = 0$, the direction of the current is determined by the sign of the term $R/R_1 - C_1/C$. We have $C_1/C < 1$ and $R/R_1 < 1$. These inequalities hold in every case. Consider a situation in which, at high T , $R_2 \ll R_1$, making $R/R_1 \ll 1$, while at low temperature, $R_2 \gg R_1$, making $R/R_1 \simeq 1$. Then, as T goes from low to high a value of T can be reached at which $R/R_1 \simeq C_1/C$. Below this temperature, $R/R_1 - C_1/C$ is positive; above it, negative. Therefore the current reverses its direction. Such current reversals, which would be impossible in the case of a Maxwell model, can occur only when the temperature dependence of the R values is very different, e.g., when the dielectric contains two phases with widely different physical characteristics.

Qualitative discussion of multi-element systems.—It is instructive to discuss qualitatively the behavior of a multi-element model under the assumption that (i) the heating rate is low and (ii) activation temperatures are widely spaced. The first condition might present experimental difficulties because low heating rates give low amplitudes of current peaks.

The behavior will be discussed with the aid of the three-loop model shown in Fig. 3. Loops relax one after the other at successively higher temperatures T_1, T_2, \dots . The main temperature-sensitive elements will again be the resistors; the temperature dependence of the capacitors is supposed to be small. As long as the temperature is considerably below the first activation temperature T_1 , all resistors are blocking, all capacitors remain charged. This is shown in Fig. 3b which is obtained from Fig. 3a by omitting R_1, R_2, R_3 (a blocking resistor is an open-circuit). When the temperature reaches the neighborhood of T_1 , the first loop discharges since R_1 becomes conducting. This is shown in Fig. 3c which is obtained from Fig. 3b by adding R_1 in the appropriate place. A current transient is produced; its relaxation time which is also its approximate duration can be read from the figure and is found to be $\tau_a = R_1(C_1 + C_2 C_3 / (C_2 + C_3))_{T_1}$. After the temperature goes beyond T_1 , the resistor R_1 becomes conducting and practically short-circuits the capacitor C_1 . Eventually the temperature reaches the neighborhood of T_2 and the remaining capacitors C_2 and C_3 discharge through R_3 . This is shown in Fig. 3d which is obtained from Fig. 3c by adding R_2 and deleting the discharged loop R_1, C_1 (the conducting resistor R_1 is considered equivalent to a short-circuit). The relaxation time and approximate duration of the new transient is seen to be $\tau_b = R_2(C_2 + C_3)_{T_2}$. Since $\tau_a > \tau_1(T_1)$ and $\tau_b > \tau_2(T_2)$, the "all or nothing" approximation used to describe the discharge characteristics of the loops is justified by the exponential term in the rate Eq. [8]. This equation maps a logarithmic variation of temperature into a linear variation of time. Therefore the transition

from "nonconducting" to "conducting" occurs within a small temperature interval.

The idealized models shown in Fig. 3b, 3c, and 3d terminate in single capacitors. For this reason they are charge-invariant. Indeed, if U is the capacitor voltage, the output current is $J = d(CU)/dt$. Integration gives

$\int_0^\infty J dt = -C(0)U(0)$. Thus the time integral over the current is independent of the function $T(t)$ during the discharge and depends exclusively on the initial charge of the capacitor.

The behavior of the system is also shown in the diagram of Fig. 4. It gives temperature as a function of time for two constant heating rates. The duration of the current transients which are observed when the temperature goes through one of the values $T_1, T_2 \dots$ is indicated on the time axis by the values τ_a, τ_b, \dots . If the heating rate is low as in Fig. 4a, the time intervals covered by the τ_a, τ_b, \dots do not overlap and the output current can be resolved into independent linearly superposing components. If the heating rate is high as in Fig. 4b, the intervals on the time axis do overlap and separate treatment of transients is not justified.

Thermally Stimulated Open-Circuit Voltages

The difficulty of eliciting from current measurements the desired information in the case of a Wagner-Voigt model suggests as an alternative the resort to voltage measurements. It will now be shown that the current measurements in the case of a Maxwell system have their counterpart in voltage measurements in the case of the Wagner-Voigt model.

Wagner-Voigt model.—Differential equation.—The open-circuit is defined by the condition that the output current is zero. Introduction of $J(T,t) = 0$ into Eq. [12] gives for the loop voltages U_i the equation

$$dU_i/dt + U_i(1/\tau_i + d \ln C_i/dt) = 0, i = 1, 2, \dots, N \quad [18]$$

which has the solution

$$U_i(T,t) = C_i^{-1}[T(t)] \cdot q_i(0,t) \quad [19]$$

The open-circuit output voltage

$$U(T,t) = \sum_1^N U_i(T,t) \quad [20]$$

is the sum of N independent terms each of which contains only one of the variables τ_i . Therefore voltage curves in the case of the Wagner-Voigt model can be analyzed in the same way as current curves in the case of the Maxwell model. The voltages $U_i(0)$ are loop voltages at the beginning of the open-circuit. They are integration constants which depend on the initial con-

ditions and are different for discharge and return voltage curves.

Discharge voltage curves.—For $t = 0$, the terminal voltage is approximately equal to the charging voltage U_0 and the initial values $U_i(0)$ are approximately equal to the loop voltages at the end of the charging period. Subsequently the terminal voltage decreases stepwise from U_0 to 0, the amplitude of each step being $U_i(0)$.

Return voltage curves.—When the circuit is opened at $t = 0$ the terminal voltage is zero. This gives $\sum_1^N U_i(0) = 0$. The short-circuit removes from each capacitor the charge $U_0C(0)$ where $1/C(0) = \sum_1^N 1/C_i(0)$.

Therefore, if $U_i(0_-)$ are the voltage values immediately before the short-circuit, their values afterward are given by $U_i(0)C_i(0) = U_i(0_-)C_i(0) - U_0C(0)$. (This treatment neglects the loss of charge during the low-temperature period in which the system remains in short-circuit). The loop voltages $U_i(0_-)$ immediately before the short-circuit depend on the polarization conditions. Thermal activation produces a stepwise voltage recovery shown schematically in Fig. 1, IV. A detailed discussion goes beyond the scope of the present paper and will be given elsewhere. It might be mentioned however, that isothermal voltage recovery has been discussed extensively by Gross (8).

Maxwell model.—The sum of all branch currents must be zero while the terminal voltages of all branches must be the same and equal to $U(T,t)$. Thus the short-circuit Eq. [1] and [2] must be replaced by

$$\sum_1^N J_i(T,t) = 0 \quad [21]$$

and

$$U(T,t) = R_i J_i + (1/C_i) \int_0^t J_i dt = 0, i = 1, 2, \dots, N \quad [22]$$

The analytical solution of these equations is difficult even in the case of $N = 2$. An approximate treatment for low heating rate is possible along the same lines as above. But a detailed discussion seems not warranted before experimental results on thermally stimulated voltages are known.

Discussion

The need for combined experimental techniques.—Our conclusions underline the fact that results of measurements by the method of thermal activation cannot always be taken at face value. This does not detract from the value of the method as a searching tool but suggests only that a critical review is necessary and that one should not rely on a single type of measurement, i.e., currents alone or voltages alone, but try to combine both to see which is best suited in each physical situation. In addition, independent methods of analysis such as the sectioning technique (10), where feasible, might give valuable additional evidence. Assumptions such as charge invariance or the exclusion of current reversals should not be taken for granted. Their range of validity can be explored by performing measurements with different heating rates and different thermal treatment during polarization. The interpretation of peaks in curves of thermally stimulated currents or voltages depends on the particular physical model on which the analysis is based. Some knowledge about the structure of the system is necessary to obtain physically meaningful results.

Equivalence of models.—In isothermal theory it is proved that a specified physical behavior, i.e., a given response function, can be represented by means of a Maxwell model or a Wagner-Voigt model; under iso-

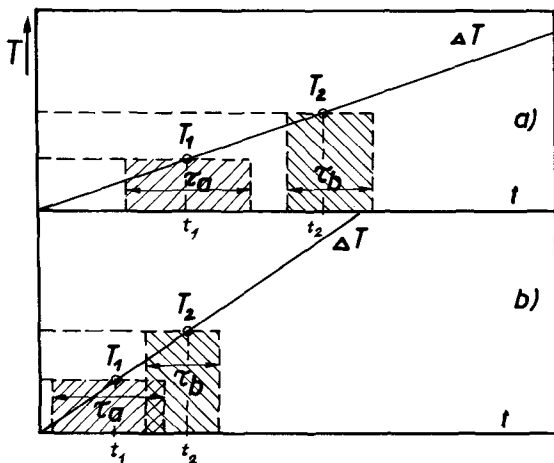


Fig. 4. Influence of heating rate, Wagner-Voigt model. a, Low heating rate; b, High heating rate.

thermal conditions these models are equivalent. The previous discussion has proved that under nonisothermal conditions the properties of these models are different. A Maxwell model is always charge-invariant, it does not admit current reversals, and its output current is always given by the superposition of independent components. None of these properties is found with a Wagner-Voigt model. Therefore these models are no longer equivalent when exposed to temperature transients. Under nonisothermal conditions the theory of equivalent models, which is one of the mainstays of the conventional theory of linear systems, loses validity. Therefore experiments involving temperature changes help to distinguish between isothermally equivalent models and thus can remove the degeneracy inherent in isothermal theory. A model that uniquely describes the behavior of a physical system has physical significance and a theory involving such models ceases to be formal.

Maxwell model and uniform volume polarization.—

In view of the great variety of possible physical situations, one might ask how far it is meaningful to select two particular models as we have done here. We believe this is justified because these models describe correctly frequently encountered physical situations.

The Maxwell model represents a dielectric volume polarization caused by hindered dipole orientation or by the displacement of charge carriers over microscopic distances within a dielectric matrix which contains irregularly distributed traps. Orientation of dipoles and displacement of charge carriers proceeds out of phase with the applied field. The rate constants which describe the time lag are functions of temperature. The electric displacement field is $D = \epsilon E + P$ where E is the field strength, ϵ the dielectric constant, and P the "persistent" component of the polarization. In the presence of different types of dipoles or traps with different depths the polarization P is given by the sum over components P_i , i.e., $P = \sum P_i$. The current is $J = adD/dt$ where a is the electrode area. Assuming first order kinetics one has $dP_i/dt = -P_i/\tau_i$. The short-circuit current, with $E = 0$, is therefore $J = adP_i/dt$ and the released charge is $q = aP_i(0)$. These equations describe the behavior of a Maxwell model. They were introduced at the beginning of the century by Pellat (11) and since then have been frequently rediscovered and used to describe the effects of dielectric absorption.

Wagner-Voigt model and interfacial polarization.—

The Wagner-Voigt model applies to inhomogeneous dielectrics. In its simplest form it describes the behavior of a three-layer capacitor where the central layer represents the bulk of the dielectric and the two external layers represent the dielectric-electrode interfaces which have electrical properties different from those of the center section. Application of an external electric field produces what has been called interfacial polarization. When the temperature dependence of the dielectric-electrode interface is very different from that of the bulk material current reversals can occur; also the system is not charge invariant.

More complex situations exist where neither of these models is satisfactory. Release of charge carriers from traps might be described by a Maxwell model in the case of slow retrapping and by a Wagner-Voigt model in the case of fast retrapping.

Acknowledgments

The present paper is based on lectures given by the author in July and September 1970 at Centraal Laboratorium, Toegepast Natuurwetenschappelijk Onderzoek (T.N.O.), Delft, Netherlands, and at Northern Electric Research and Development Laboratories, Ottawa, Canada. The author wishes to thank Dr. M. Perl-

man for reading and commenting on the manuscript, and Drs. J. van Turnhout and J. van den Eikhoff for preparation of a summary of his lectures given at T.N.O. and the Brazilian Nuclear Energy Commission for concession of a research grant.

Manuscript submitted June 18, 1971; revised manuscript received Nov. 11, 1971.

Any discussion of this paper will appear in a Discussion Section to be published in the June 1973 JOURNAL.

LIST OF SYMBOLS

C	capacitance (F)
D	electric displacement (C/m ²)
E	electric field strength (V/m)
k	Boltzmann constant (J K ⁻¹)
k _i	coefficient of differential equation (s ⁻¹)
J	current (A)
N	number of branches of Maxwell model, number of loops of Wagner-Voigt model
P	generalized circuit element
P	dielectric polarization (component not in phase with the electric field strength) (C/m ²)
q	charge (C)
R	resistance (ohm)
s	parametric time (s) in Eq. [4] and [14]
t	time (s)
T	absolute temperature (Kelvins or K)
u	activation energy (J)
U	voltage (V)
β	heating rate (K/s)
ε	dielectric constant (F/m)
γ	frequency factor (s ⁻¹)
τ	relaxation time (s)

[] Square brackets are used extensively to denote an implicit functional dependence, e.g., τ[T(t)] means that the relaxation time τ of an elementary RC circuit is a function of temperature T which in turn is a function of time, generally through the heating rate β in Kelvins per second.

REFERENCES

1. C. Bucci, F. Fieschi, and G. Guidi, *Phys. Rev.*, **148**, 816 (1966); I. J. Saunders, *J. Phys. C., Solid State Phys.*, **2**, 2181 (1969); A. C. Lilly, Jr., L. L. Stewart, and R. M. Henderson, *J. Appl. Phys.*, **41**, 2007 (1970); R. A. Creswell and M. M. Perlman, *J. Appl. Phys.*, **41**, 2365 (1970); J. van Turnhout, *Polymer J. (Japan)*, **2**, 173 (1971).
2. C. F. J. Garlick and A. F. Gibson, *Proc. Phys. Soc.*, **60**, 574 (1948); K. H. Nichols and J. Woods, *Brit. J. Appl. Phys.*, **18**, 1045 (1967).
3. P. Land, *J. Phys. Chem. Solids*, **30**, 1693 (1969); P. Kelly and P. Braeunlich, *Phys. Rev.*, **B1**, 1583, 1596 (1970).
4. K. W. Wagner, *Elektrotech. Z.*, **36**, 135, 163 (1915); A. V. Tobolsky and R. D. Andrews, *J. Chem. Phys.*, **11**, 1251 (1943); F. Schwarzl and A. V. Staverman, *J. Appl. Phys.*, **23**, 838 (1952); A. V. Tobolsky, *J. Appl. Phys.*, **27**, 673 (1956); B. Gross, *J. Appl. Phys.*, **40**, 3397 (1969).
5. D. R. Axelrad, *Advan. Mol. Relaxation Processes*, **2**, 41 (1970).
6. I. L. Hopkins, *J. Polymer Sci.*, **28**, 631 (1958); B. Gross, *This Journal*, **115**, 376 (1968); B. Gross, *Appl. Optics, Suppl. 3: Electrophotography*, 176 (1969).
7. B. Gross and L. F. Denard, *Phys. Rev.*, **67**, 253 (1945).
8. B. Gross, *Z. Physik*, **107**, 217 (1937), *Phys. Rev.*, **57**, 57 (1940), **62**, 383 (1942).
9. B. Gross, *J. Chem. Phys.*, **17**, 866 (1949); G. Wiseman and G. Feaster, *J. Chem. Phys.*, **26**, 521 (1957); M. M. Perlman and J. L. Meunier, *J. Appl. Phys.*, **36**, 420 (1965); D. E. Tilley, *J. Appl. Phys.*, **38**, 2543 (1967).
10. B. Gross, Report TO 144, Northern Electric, Ottawa, Canada, September (1970).
11. H. Pellat, *Compt. Rend. (Paris)*, **128**, 1312 (1899); *Ann. Chim. Phys.*, **18**, 150 (1899); *J. de Physique*, **9**, 313 (1903).

The Anodic Behavior of Some Materials in Liquid Ammonia in Presence and Absence of Methane or Ethylene

Ashok K. Vijh*

Hydro-Quebec Institute of Research, Varennes, P. Q., Canada

ABSTRACT

Results on the anodic behavior of platinum, palladium, nickel, cobalt, graphite, lead, and sodium-tungsten bronze electrodes in liquid ammonia at -73°C in the absence and presence of either CH_4 or C_2H_4 are reported. The experiments consist of potentiostatic current-potential relationships, potentiodynamic profiles, and product analysis. The aim of these studies was to attempt anodic synthesis of CH_3NH_2 from CH_4 (or C_2H_4) and ammonia, which could not be achieved. The measurements obtained appear to have some qualitative significance, however, in relation to electrochemical behavior of materials in liquid ammonia in general and with regard to their anodic dissolution and oxidation of ammonia in particular. The characteristic features of these data are reported together with their possible qualitative significance.

Although electrosyntheses of organic compounds have been carried out for decades (1) by various investigators, a noticeable resuscitation (2-5) of interest has recently occurred in this area. It has recently (3) been suggested that a possible electrolytic conversion of low molecular weight-hydrocarbons to pure alkyl amines would perhaps offer an electrosynthetic procedure amenable to commercial exploitation. Although functionalization of low molecular weight hydrocarbons, especially paraffins is generally considered as difficult and achievable only under rather drastic conditions, by virtue of lack of reactivity of paraffins, it was regarded, nevertheless, of interest to explore the possibility by an electrochemical procedure. This problem was approached by attempting to anodize various electrocatalytic materials in liquid ammonia in the presence of an appropriate hydrocarbon. An attempt was made to explore whether it was possible to prepare alkyl amines by means of an hypothetical reaction of the type



Experimental Procedures

The experimental details for the work reported here are as follows.

Instruments and circuits.—The instruments employed are: Wenking potentiostat (No. 7713 68FR 0.5); Tacussel milliammeter Type MAL 284, and, in some runs, a precision resistor used in conjunction with Tacussel digital voltmeter (high input impedance) as the current measuring arrangement; Honeywell X-Y recorder, Type 550M; Tacussel function generator, Type GSTP2; General Radio decade resistor box. The potential measurements were recorded on the Tacussel digital voltmeter; vapor phase chromatograph (Victoreen, Series 400 supplied by Fischer Scientific). Conventional potentiostatic and potentiodynamic circuits were employed (6, 7).

Materials and electrodes.—All electrode materials, except the sodium-tungsten bronze, were spectroscopic grade and were in either wire or rod or plate configurations. The sodium-tungsten bronze samples were obtained from outside this laboratory and were prepared by the electrolytic method and contained an uncontrolled (up to 100 ppm) amount of platinum impurity. The sodium content of the various bronze samples was somewhat different, a fact that did not seem to influence the results to be reported here which have only a qualitative significance in any case. All electrodes (except the platinized-platinum used in the reference compartment) were mounted in heat-

shrinkable Teflon tubing as described previously (8). The counterelectrodes were made of spectroscopic grade graphite rod. A hydrogen reference electrode was employed.

The electrolyte consisted of nonaqueous (probably only nominally nonaqueous since an elaborate dry box was not used although all precautions were taken to exclude moisture as far as possible) liquid ammonia containing 10% (by weight) of dry ammonium perchlorate (Fischer Certified high purity reagent). The ammonia was 99.99% and was obtained from Matheson. The He gas used in the working compartment (when CH_4 or C_2H_4 was not being bubbled) was of 99.998% purity (supplied by Matheson) and was dried by passage over suitable traps in a gas purification line. The methane used was 99% pure (supplied by Union Carbide) and the C_2H_4 employed had a purity of 98.5% and was supplied by Liquid Air.

The low temperatures were maintained by immersing the cell in a Dewar flask containing isopropyl alcohol and solid carbon dioxide mixture.

The column material for the v.p.c. was Chromosorb-P 60/80 mesh whereas the liquid phase consisted of 21% Polyethyleneimine. The carrier gas was helium. The Chromosorb-P material was intended to detect both methyl amine and dimethyl amine: the latter could, it was thought, possibly have been formed as a side product.

Cell and cleaning.—A three compartment Pyrex cell was used with the working and the counter compartments separated by a coarse fritted disk. The cell was provided with the usual gas inlets and outlets and all the connections to the cell from the gas lines were made by means of glass-to-glass joints. The use of grease was absolutely avoided. The cell could be closed to the atmosphere by means of appropriate stopcocks. A positive pressure of He (or CH_4 or C_2H_4 as the case may be) was always maintained inside the cell in order to minimize the possibility of diffusion of atmospheric moisture into the electrolyte solution. The cell was cleaned with chromic acid and repeatedly soaked and washed in deionized and doubly distilled water (both distillations being carried out over alkaline permanganate in Pyrex glass stills; before distillations, the deionized water was passed over suitable (proprietary) adsorbent columns designed to remove traces of organic matter) and subsequently thoroughly dried over night in an oven.

All electrodes except graphite were washed in chromic acid and subsequently soaked and washed in doubly distilled water, followed by thorough drying in an oven in a Pyrex tray. The graphite electrodes were cleaned in boiling trichloroethylene (to remove

* Electrochemical Society Active Member.

Key words: anodic behavior, liquid ammonia, methane, ethylene.

organics which are generally believed to adhere tenaciously to graphite electrodes) and dried.

Purification of gases.—The hydrogen gas for the reference compartment was "Electrolytic, Grade A" and was deoxygenated by passage over a palladium catalyst ("Deoxo") and further purified by passage through activated charcoal and activated alumina, both at liquid air temperature. Helium, methane, and ethylene were passed over molecular sieves and other traps in order to remove any moisture that may be present in them.

General experimental procedures.—The steady-state, potentiostatic current-potential relationships were obtained by stopping for 2 min at every value of electrode potential. The potentiodynamic profiles were obtained at various sweep rates.

Results and Discussion

Anodic behavior in the absence of CH_4 or C_2H_4 .—Anodization of Pt, Ni, and Co in liquid ammonia led to a visible anodic dissolution which was evident from the characteristic coloration (yellow for Pt, blue for Ni, and pale greenish blue for Co) produced in the solution. In some cases, e.g., on platinum, a yellow coating, probably a loosely attached precipitated corrosion product, was observed on the electrode surface. The formation of colored corrosion products in liquid ammonia on anodization of transition metals such as Pt, Ni, and Co is not entirely unexpected because of the pronounced tendency of ions of these metals to undergo coordination complex formation in liquid ammonia. The current associated with the anodization of various materials in liquid ammonia under He atmosphere must, however, be attributed only partially to anodic dissolution since part of it must arise from the anodic oxidation of ammonia itself, especially, on the more catalytic metals such as platinum. This was qualitatively confirmed by adding small amounts of water to the "nonaqueous" solution which gave rise to a noticeable decrease in current at a given potential, presumably owing to passivation of platinum and consequent decrease in the anodic dissolution current; the residual current, however, was still appreciable and is believed to have arisen from anodic oxidation of ammonia. The relative contribution of anodic dissolution and anodic oxidation of ammonia to the current at a given potential in the nonaqueous solution (under He atmosphere) was not examined, however, in any details since this aspect was not of interest in the present study. No visible signs of anodic dissolution were noted on Pd, graphite, and sodium-tungsten bronze electrodes. It may be added that the lead electrodes underwent complete disintegration as soon as the anodization in liquid ammonia was commenced. No measurements could, therefore, be made on this particular electrode material.

Anodic behavior in the presence of CH_4 or C_2H_4 .—Subsequent to the investigation of the anodic behavior of various materials under He atmosphere, experiments were conducted to establish whether introduction of methane or ethylene, bubbling vigorously under atmospheric pressure, had any effect on the current-potential curves. The main observations are as follows:

1. In the presence of methane, the rate at a given potential shows some decrease on graphite, platinum, palladium, and the sodium-tungsten bronze electrodes. On cobalt and nickel, however, the rate stays unaffected.

2. In presence of ethylene, the current at a given potential shows some increase on nickel whereas on cobalt, platinum, palladium, and graphite the rate stays either unaffected or exhibits some variations only in certain regions of potential. On palladium a character-

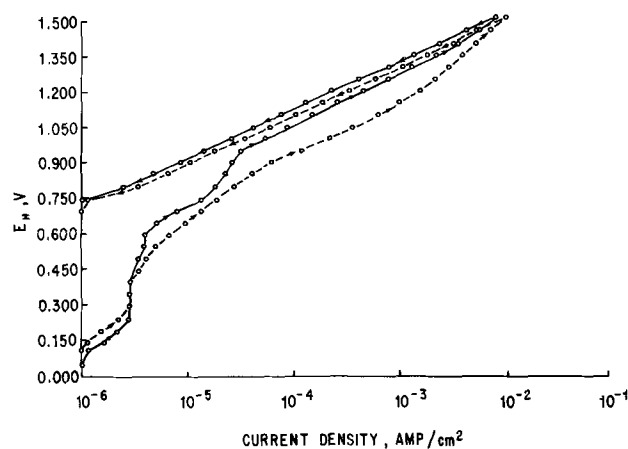


Fig. 1. Steady-state potentiostatic current-potential relationships on graphite in liquid ammonia in the absence (-----) and presence (——) of methane.

istic inhibition inflection, of the type discussed by Gilroy and Conway (9), is observed around 0.9V.

The general features of the polarization curves, from which the above qualitative observations have been deduced, may perhaps be best conveyed by considering some typical Tafel plots obtained in the absence and presence of either CH_4 or C_2H_4 . In Fig. 1, the steady-state potentiostatic Tafel plots have been presented which show that anodic oxidation of ammonia (corresponding to the total current under He atmosphere in this case since no visible signs of anodic dissolution or disintegration were observed) proceeds at rather high rates on graphite and the presence of methane in the reaction chamber tends to decrease the rate. On cobalt, anodization in liquid ammonia in presence and absence of methane leads virtually to the same current-potential relationship (Fig. 2). The current observed in this case must, of course, be attributed to the oxidation of ammonia as well as the cobalt electrode itself (to form soluble complexes) as indicated earlier. On a typical case of a sodium-tungsten bronze electrode, it appears that high anodic potentials are needed to effect moderate oxidations of ammonia (dissolution of this electrode being assumed absent since no visible signs were observed to indicate otherwise) and even these oxidation rates are drastically diminished by the presence of methane in the vicinity of the electrode (Fig. 3). Rather noticeable reduction of rate in presence of methane would indicate that methane is strongly adsorbed on the electrode surface to give a species which is not easily oxidized off, even under high anodic polarizations.

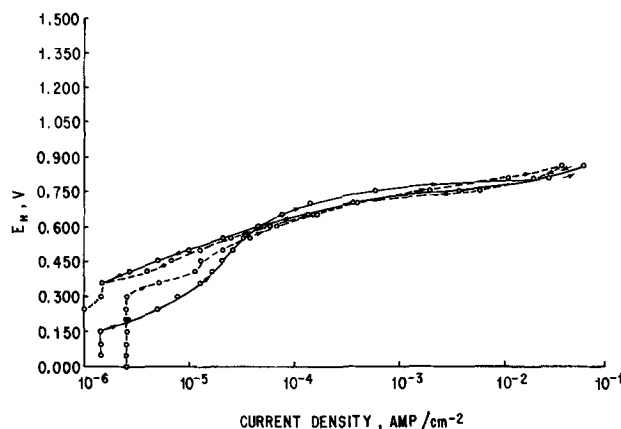


Fig. 2. Steady-state potentiostatic current-potential relationships on cobalt in liquid ammonia in the absence (-----) and presence (——) of methane.

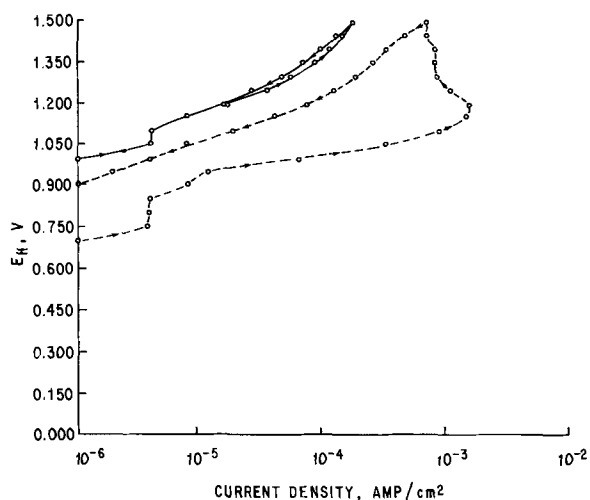


Fig. 3. Steady-state potentiostatic current-potential relationships on a sodium-tungsten bronze (containing a trace impurity of platinum) electrode in liquid ammonia in the absence (-----) and presence (——) of methane.

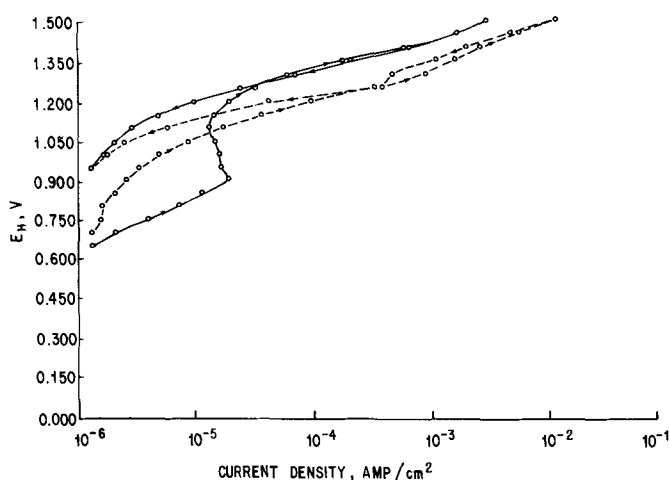


Fig. 4. A typical steady-state current-potential relationship, obtained potentiostatically, on palladium in liquid ammonia in the absence (-----) and presence (——) of ethylene.

Some characteristic cases of anodic behavior in liquid ammonia in presence of ethylene may also be considered. On palladium (Fig. 4) at low overpotentials presence of ethylene leads to an increase of rate and a characteristic inhibition inversion (9), whereas at high anodic potentials a decrease in rate is observed. This would indicate that the palladium electrode is not altogether unreactive in presence of ethylene in liquid ammonia, even though the elusive methyl amine or related side products were not indicated to be formed. Typical polarization curves representative of the anodic behavior of platinum in liquid ammonia in the presence and absence of ethylene are shown in Fig. 5. In the anodic polarization curves of nickel in liquid ammonia, rather high oxidation rates were observed at low overpotentials, both in presence and absence of ethylene, undoubtedly arising largely from the anodic dissolution of nickel.

Potentiodynamic profiles.—Extensive potentiodynamic profiles (6, 7) were obtained on various electrodes at a number of sweep rates. No peaks (either activation or diffusion controlled) or inhibition inflections could be observed. Some typical potentiodynamic profiles are shown in Fig. 6. It is clear that no significant information can be deduced from this type of profiles (Fig. 6).

General significance of the Tafel plots.—Although detailed mechanistic proposals or quantitative analyses

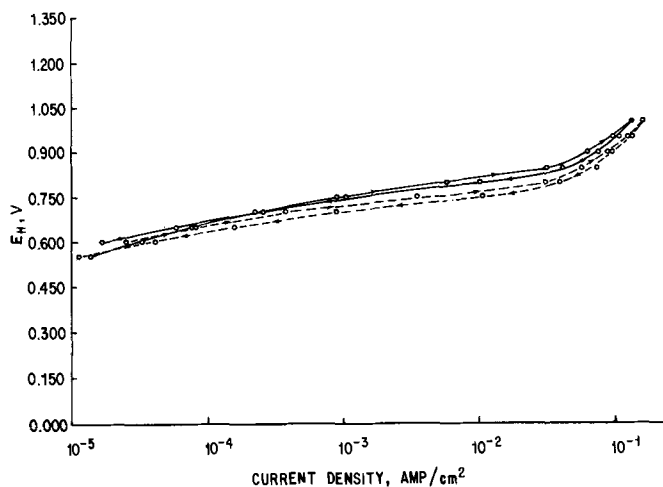


Fig. 5. A typical, potentiostatic current-potential relationship on platinum in liquid ammonia in the absence (-----) and presence (——) of ethylene.

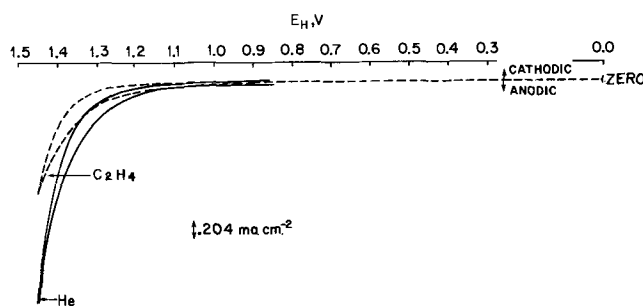


Fig. 6. Potentiodynamic current-potential relationships on palladium in liquid ammonia in the absence and presence of ethylene. The sweep rate is 48.3 mV sec⁻¹. Absence of peaks or other details may be noted.

cannot be put forward on the basis of data reported here, some general salient features of the Tafel plots may, however, be pointed out. First, a large hysteresis between the ascending and descending potentiostatic current-potential curves (Fig. 1, 3, 4) observed in some cases would indicate presence of surface films or irreversibly absorbed surface species. Second, presence of surface films on the electrode is indirectly indicated by the magnitude of Tafel slopes which in most cases (cf. Fig. 5, however) are higher than $2.3 \times 2RT/F$ which is equal to ca. 73 mV at the temperature of the experiments, namely, -73°C . That anomalously high Tafel slopes can often arise from the presence of solid films on the electrode surface has been discussed previously (6, 9, 10) and need not be elaborated upon here.

Acknowledgments

The author is grateful to Mr. R. Jacques for skillful assistance in experimental work. Thanks are due to Dr. G. Bélanger and Mr. A. Bélanger for making some contributions to this work. Dr. P. Lenfant is thanked for his interest in this work.

Manuscript submitted Oct. 18, 1971; revised manuscript received Jan. 18, 1972.

Any discussion of this paper will appear in a Discussion Section to be published in the June 1973 JOURNAL.

REFERENCES

1. M. J. Allen, "Organic Electrode Processes," Chapman and Hall (1958).
2. F. Goodridge, *Chem. Proc. Eng.*, March, 121 (1966).
3. T. Dickinson and P. J. Ovenden, *Chemistry in Britain*, pp. 260 (1969).
4. N. L. Weinberg and H. R. Weinberg, *Chem. Rev.*, **68**, 449 (1968).
5. M. Fleischmann and D. Pletcher, *Platinum Metals Rev.*, **113**, 46 (1969).

6. A. K. Vijh and B. E. Conway, *Chem. Rev.*, **67**, 623 (1967); A. K. Vijh, Ph.D. Thesis, Ottawa University, Ottawa (1966).
7. N. D. Greene, "Experimental Electrode Kinetics," Rennselaer Polytechnic Press (1965).
8. A. K. Vijh and R. S. Alwitt, *J. Chem. Educ.*, **46**, 121 (1969); R. S. Alwitt and A. K. Vijh, *This Journal*, **117**, 413 (1970); A. Bélanger, G. Bélanger, and A. K. Vijh, *ibid.*, **117**, 1615 (1970).
9. D. Gilroy and B. E. Conway, *J. Phys. Chem.*, **69**, 1259 (1965); B. E. Conway, "Theory and Principles of Electrode Processes," Ronald Press Co., New York (1965).
10. A. K. Vijh, *J. Phys. Chem.*, **73**, 506 (1969).

Behavior of Carbon Electrodes in Aqueous and Nonaqueous Systems

Richard E. Panzer*

Electrochemistry Research Section (Code 134.16), Mare Island Naval Shipyard, Vallejo, California 94592

and Philip J. Elving*

Department of Chemistry, The University of Michigan, Ann Arbor, Michigan 48104

ABSTRACT

Cyclic voltammetry was used to investigate the surface phenomena and general electrochemical behavior encountered when glassy carbon and pyrolytic graphite are used as indicator electrodes in aqueous and nonaqueous (acetic acid, acetonitrile, dimethylformamide, and pyridine) media for inorganic (ferrocyanide and ferrocene) and organic (quinone) compounds. Factors evaluated included effects of method of preparation of the graphite, different resurfacing methods including magnitude of the induced electrostatic charge and surface regularity, interplanar adsorption of electroactive solutes, presence of surfactant, acidity, and potential ranges, and potential scanning procedures used.

The limitations of the dropping mercury electrode (DME) for the electrochemical oxidation of many organic and inorganic compounds are well known. Since it cannot be used beyond a potential of about +0.4V with respect to the saturated calomel electrode (SCE), electrochemists have turned to solid electrodes. Surface adsorption effects on platinum electrodes are well documented, and, since organic compounds are so troublesome in this respect, electrochemists have searched for some material which would be more satisfactory for electrooxidation of organic compounds, with interest focusing on carbon electrodes.

The present investigation is concerned with the nature of the surface phenomena observed when carbon materials are used as indicator electrodes in voltammetric techniques, particularly in respect to the nature of the changes which occur in nonaqueous solutions. The investigation was restricted to pyrolytic graphite and glassy carbon, since these are most readily prepared and their behavior as electrodes is apparently not so heavily dependent upon the origin of and preparation from the raw materials.

Since the pyrolytic graphite electrode (PGE) or the glassy carbon electrode (GCE), and nonaqueous solvents are increasingly being combined in electrochemical studies, numerous questions require answers, e.g., what are the best ways for encasing the sides of the PGE to prevent diffusion of the solution between layers, what is the effect of surface roughness, what are the optimum methods of resurfacing, what is the nature of the surface exposed by resurfacing, is the solvent as well as organic and inorganic ions adsorbed, what is the relation of chemical structure of the adsorbate and its adsorption, and what are the effects of surfactants on the electrode surface?

Consequently, the present studies are concerned with methods of encasing the electrodes, effects of resurfacing methods on the behavior of the electrode, micro-

scopic examination of electrode surfaces, magnitude of the electrostatic charge induced by resurfacing methods, and physical variations between pyrolytic graphite from various sources and the relation of these to electrochemical behavior, as well as investigation of the interplanar adsorption of ferrocyanide in aqueous solution and of ferrocene in nonaqueous systems, the behavior of the quinone redox system with respect to electrode characteristics, the effect of a surfactant on electrode behavior in two solvent systems, and the effect of changes in acidity in aqueous and nonaqueous solutions. In all of these studies, correlation of the electrode surface character with its electrochemical behavior was emphasized. The principal electrochemical technique used was cyclic voltammetry.

Experimental

The cyclic voltammetry system used is based on operational amplifier units and has been described (1). The usual scan or polarization rate was 100 mV/sec. In conformity with normal voltammetric practice, cathodic (reduction) currents are shown as positive and anodic (oxidation) currents as negative. Peak heights were determined by running straight lines along the ascending and base portions of each voltammogram and using the vertical distances of the resulting points of intersection from the cathodic and anodic peaks.

Electrochemical cells.—In addition to three-compartment cells with a water jacket integral with the cell, which have been described (2), a triangular three-compartment design incorporating draincocks in the connection sections (Fig. 1), which could be immersed in a thermostat bath, was used in the aqueous investigations. The connection sections, which were attached to the compartments with O-ring joints, allowed changing the background electrolyte solution rapidly or continuously, if desired. The compartments were separated by fine frit Pyrex disks. The reference electrode was placed in one side compartment with the indicator and counterelectrodes in the center and other

* Electrochemical Society Active Member.

Key words: adsorption, cyclic voltammetry, graphite, surface phenomena.

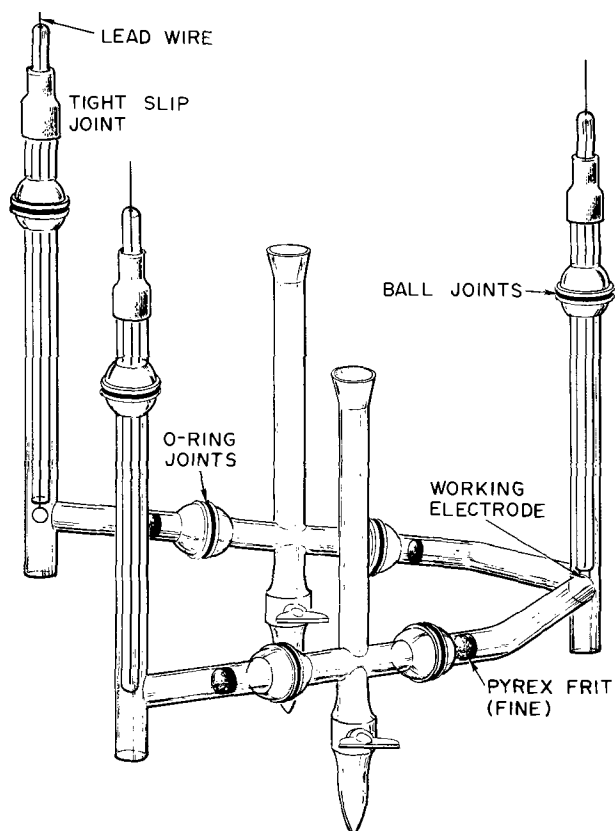


Fig. 1. Three-compartment cell with flushable bridges. For clarity, O-ring joint clamps are not shown.

side compartment, adjacent to each other. A fine Pyrex glass frit with an agar-saturated KCl plug on the reference electrode side separated the reference and indicator electrode compartments.

For nonaqueous work, special three-compartment cells were designed to fit inside a 2000 ml resin reactor vessel (Pyrex No. 6947) in such a manner that the cell compartments were directly under each of the three 24/40 S.T. joints of the vessel cover (Fig. 2). Electrodes were then mounted in gas- and vacuum-tight slip joints, which allowed their immersion in the electrolyte as required. The center 34/45 joint of the cover was reduced to 24/40, into which was inserted the inlet spout for the cell solutions. A specially modified separatory funnel with a gas bypass and a 12/19 S.T. joint in its top was used for mixing the nonaqueous solutions and deoxygenating them prior to passing them into the cell compartments (Fig. 3). In this way, the background electrolyte solution for the whole cell could be deaerated with oxygen-free, dry argon gas prior to its introduction. The solution of the electroactive species was then prepared, deoxygenated, and passed into the indicator electrode compartment. At the start of a run, the electrodes were inserted into the appropriate slip joints, and the whole vessel evacuated to a pressure of about 10^{-6} atm; the vessel was then filled with argon and the evacuation-gas addition process repeated several times. Finally, the vessel was filled with argon, the deoxygenated electrolyte solutions were introduced into the cell compartments, the electrodes were dipped into their respective solutions, and a steady stream of argon was passed through the cell and vented through an oil-filled bubbler. Because of the slight back pressure caused by the bubbler, it is necessary to fasten the tapered joints with springs and to clamp the cover tightly. Since the cover could not be slid off because of the electrodes and solution feed tube dipping down into the vessel, a special gas- and vacuum-tight gasket was formed on the vessel flange with General Electric RTV 102 silicone rubber; this allowed the cover and

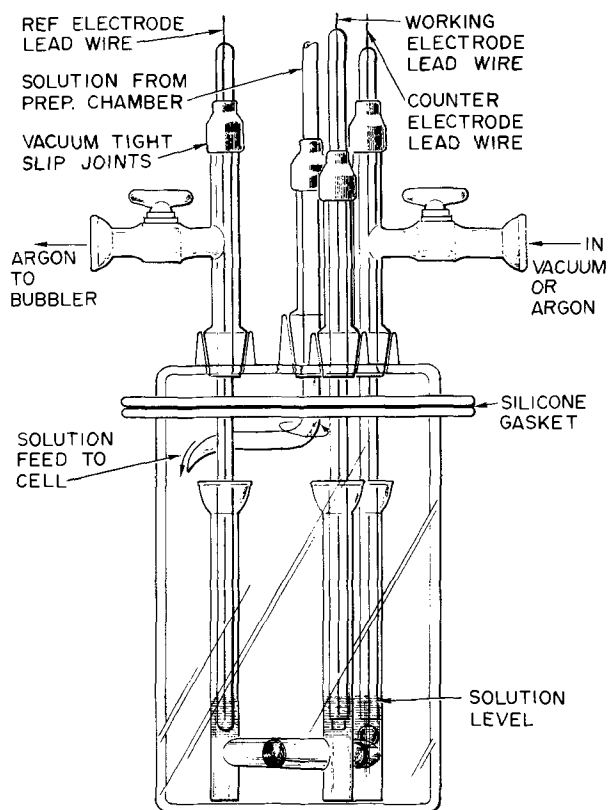


Fig. 2. Three-compartment cell in gas- and vacuum-tight jacket

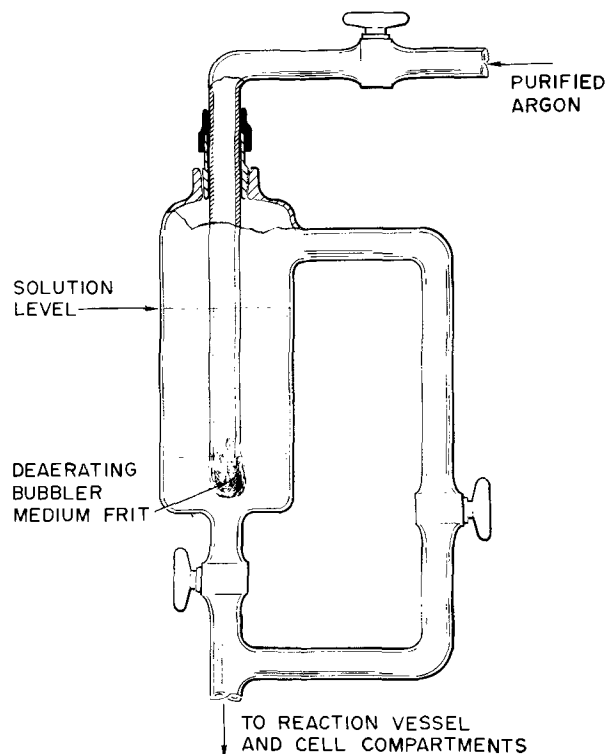


Fig. 3. Solution preparation, deaerating and feed assembly. This unit connects to the reaction vessel as shown in Fig. 2.

electrodes to be lifted directly off, without sliding or sticking, when the clamp was loosened.

The vessel itself was immersed in a bath, which was placed in a fume hood and through which water at 25°C was circulated.

Graphite electrodes.—Electrode materials were pyrolytic graphite from several sources and glassy carbon from the Tokai Electrode Manufacturing Company of Tokyo. The latter material, obtained in the form of 5

mm diameter rods, was turned down to 4 mm; it is difficult to machine, since it tends to chip and fracture due to its glassy structure. The pyrolytic graphite electrodes were 4 mm diameter rods, machined from larger pieces. Material obtained from the General Electric Company (GE) appeared to have a taper structure, i.e., it was thicker at one end than the other, and retained this structure when cleaved; this indicated that it was formed on a mandrel, perhaps for an exhaust nozzle. Pyrolytic graphite from High Temperature Materials Company (HTM or HT) was in the form of 0.5 in. thick plates; it was uniform in thickness, as was the pyrolytic graphite (Pyroid) from Space Age Materials Corporation (a division of the Charles Pfizer Company). Since Pyroid became available to us only late in the investigation, it was used only in dimethylformamide solutions.

Besides the taper structure mentioned, the graphite structures also varied in grain size. The GE material had large and small hemispheres (2-5 mm diameter) in a random pattern across its surface. The HTM and Pyroid graphites were more uniform in grain size, averaging 1-2 mm diameter. Such criteria are not really a prime consideration, since Coy (3) has shown that the macroscopic structure of these materials extends down into the microscopic structure. Of interest was the observation that the HTM and Pyroid graphites tended to be slightly harder, more dense, and less easily cleaved for resurfacing than the GE graphite.

The 4 mm diameter electrodes (projected area = 0.126 cm²) were sealed into a 300 mm length of 6 mm OD Pyrex tubing, using either Epoxy-Patch, a filled epoxy material from Hysol Corporation, or melted polyethylene. The epoxy material makes a good seal and, when slightly warmed, will flow to give a smooth coating; it is impervious to the solvents used in the present work and has been used in liquid ammonia, acetone, hexamethylphosphoramide, and many other solvents with no observable deterioration. However, the epoxy was too hard to cleave when this was done to renew the electrode surface; consequently, electrodes intended for cleaving were mounted with melted polyethylene.

Reference electrodes.—Reference electrodes in the aqueous studies were saturated calomel electrodes (SCE) prepared in the usual manner.

Reference electrodes used in nonaqueous studies were all based on a silver system. Where a stable soluble silver salt could be used, the electrode was Ag/0.1M Ag⁺ in the solvent with background (supporting) electrolyte. In some solvents, a Ag/AgCl, Cl⁻ (0.1M LiCl) half-cell was used. All of the reference half-cells were prepared in a microcracked configuration, which has been extensively used by one of the authors (4) and is adapted from Perley's controlled crack electrode (5). These high impedance electrodes require the routine use of a follower (unity-gain amplifier), since so little current can be drawn through them.

When a glass tube-crack assembly is cleaned, dried and ready for use, the reference half-cell silver system is placed in the tube to a depth of 2 cm; contact is made with a silver wire which is sealed at the open end of the tube with epoxy cement to prevent leakage or evaporation of the solution.

The potentials of the various reference half-cells used were placed on a common basis by measuring each of them against the aqueous SCE (Table I). Although such a measurement includes an unknown junction potential, the latter is probably very small in most cases; Nelson (6), who investigated this topic, makes the point that such junction potentials are not as large as commonly believed. Electrodes were prepared in batches of 5 or 6; their potentials checked against one another for stability and reproducibility to within a few millivolts, which is within the experimental error of the potential measurements.

Table I. Reference electrode potentials

Electrode system-solvent	Potential, ^(a) V
Ag/Ag ⁺ in CH ₃ CN	-0.016
H ⁺ /H ₂ (NHE), aq.	0.000
SCE, aq.	+0.249
Ag/AgCl, Cl ⁻ in HOAc	+0.253
Ag/Ag ⁺ in pyridine	+0.304
Ag/AgCl, Cl ⁻ in DMF	+0.754

^(a) Potentials are according to the 1953 Stockholm Convention and were measured vs. an aqueous saturated calomel electrode (SCE) at 27.5°C and converted to read vs. the normal hydrogen electrode (NHE).

Chemicals.—Ferrocene was used as a standard redox material at 1 mM concentration, since it is readily soluble in the solvents used and produced sharp reversible voltammograms in all of the systems studied. Consequently, since the primary purpose of the present study was to characterize the electrode surfaces, complications due to the electroactive species were minimized at the outset. In addition, ferrocene had been previously characterized voltammetrically in pyridine (7), which allowed comparison to be made. The ferrocene was recrystallized several times from purified dry acetonitrile, then dried under vacuum at 50°C. Initial efforts with cobalticene were abandoned, since the compound proved to be only slightly soluble in some of the solvents to be used.

All other chemicals used were of reagent grade. The argon was dried by passage through Linde 4A molecular sieves.

Solvents.—Reagent grade solvents were dried or purified further, depending on the solvent. Pyridine, which was zone fractionally crystallized (2), had very low levels of water and electroactive impurities; pyridine (reagent grade) was also used only after drying over molecular sieves. In the present investigations, there seemed to be little difference between the two solvents, since the potentials used were not in the same range as those utilized when interferences from electroactive impurities were noted (2).

Acetonitrile (Matheson Nanograde) and N,N-dimethylformamide (reagent grade) were dried over molecular sieves. Glacial acetic acid (reagent grade), freshly opened as needed, was rapidly transferred to solution mixing vessels to prevent moisture acquisition.

Electrode Surface and Resurfacing

Initial studies included microscopic examination and physical characterization of the electrode materials, and determination of the effects of resurfacing the electrodes.

Electrode resurfacing.—Pyrolytic graphite (PG) electrodes are commonly resurfaced by grinding with a rotating disk of 600 mesh SiC paper or by full layer cleavage; both are sometimes followed by vigorous rubbing on filter paper (8). Resurfacing or even machining glassy carbon (GC) generally results in fractures and chipping caused by the brittle nature of the material. Resurfacing of GC (rarely necessary) is best done by polishing with successively finer abrasives, finishing with 0.5μ alumina on Microcloth (A. Buehler Company). Giles, Harrison, and Thirsk (9) have also used the metallurgical polishing method for GC electrodes. However, Sunahara and Ishizuka (10) used "emery paper 80", which undoubtedly provided microscratches on the GC surface, not a mirror finish as is obtained by using the alumina polishing compound.

Following various treatments, the electrode surfaces were observed with 100× magnification. Cleaved PG generally had a complete new surface across the plane of the electrode, but the existence of a partial layer can allow occlusion of material under it. Use of a hand lens for inspection of the renewed PG surface provided a means of quickly checking that cleavage produced a completely fresh disk.

Microscopic examination revealed large differences in the surfaces as prepared by the different methods and, as it turned out, predicted the observed electrochemical behavior. There was no evidence that the epoxy compounds or polyethylene used to seal the carbon material to the glass tube were smeared across the electrode surface during resurfacing. Occasionally, a few particles of SiC or sealant would appear after the grinding operation; these were removed by wiping with a tissue, which also removed loose particles of carbon. However, a peculiar phenomenon was observed when these resurfaced PG electrodes were used in cyclic voltammetry. Loose carbon had initially been removed by wiping with a tissue, rinsing with acetone, pyridine or ethanol (depending on the solvent system in use), or rubbing with Whatman No. 1 filter paper. Nevertheless, after the electrode had been subjected to several charge-discharge cycles, a deposit of carbon appeared on the white epoxy rim around the PG. Occasionally, this deposit was very heavy but it was never present prior to the voltammetric cycling.

Grinding with 600 mesh SiC paper produced a flat surface on both the PGE and GCE, although the latter material is much harder. However, under $100\times$ magnification, one could observe microfine scratches over the entire GC surface; these were found to be responsible for the very high residual currents in voltammetry. For example, electrodes treated with 600 mesh SiC paper gave a residual current of $70\ \mu\text{A}$, but, when the electrodes were lapped with $0.5\ \mu$ alumina, the residual current was only about $0.5\ \mu\text{A}$.

One can visualize the effect of grinding the PG by considering the result of slicing an onion across some section of the sphere; a large number of planes (skin and onion layers) is exposed. In the case of the PG cones, the layers are quite porous, allowing large amounts of solvent to penetrate the layers. Since the macro structure is essentially duplicated in the micro structure, it is obvious why the grinding operation can lead to a greatly enlarged surface area compared to that produced by cleaving.

Charge accumulation on electrode surface.—The dust particle effect indicated that a high charge was localized on the electrodes. A Keithley Model 610B electrometer, which has a very high input impedance and indicates charge directly in coulombs, was utilized to measure the charge; its output was fed into a potential-time recorder to provide a record of the change during the experiment. For comparison with the PGE and GCE, the charge was measured for a mercury pool electrode of $7\ \text{mm}^2$ surface area, which was contained in a U-tube arm immersed in electrolyte solution. The solution used in these charge measurements was $0.5M$ KCl; cells were thermostated at 25°C ; a Pt wire was used as counterelectrode.

The electrode to be measured was treated in the desired manner and then connected to the electrometer prior to insertion in the electrolyte solution. Changes in the charge were followed over a period of about 1500 sec (Table II). Noteworthy is the extremely high initial charge on the ground PGE; the other electrodes had a much lower initial charge which slowly increased due to the capacitance effects of the solution and effects from reaction of the electrode surface and

adsorbed species. The charge on the ground GCE identified the source of the high residual current voltammetrically observed on this electrode; the microscopic (600-grain) scratches are the locale for both the charge and the residual current. The initial charge on the mercury electrode, which corresponds to $2.8\ \mu\text{coulombs/cm}^2$ and which does not increase appreciably for several minutes, is presumably due to halide adsorption. The contribution from the grid current of the electrometer (maximum of $2 \times 10^{-8}\ \mu\text{coulombs/sec}$) is negligible.

Open circuit potentials.—Significant variations were found in the open circuit potentials (OCP) of the various materials in $0.5M$ KCl solution (Table III). The significance of an OCP is that it indicates the sum of the preparative background effects on the electrode surface; the OCP will be a function of variations due to crystal structures, strains, and growth sites. The variation in OCP parallels that of the charge measurement (Table II).

The effect of any significant difference between PGE surfaces fabricated from the mandrel and deposition sides of the graphite can be obviated by always using the same side for the electrode surface. From a structural standpoint, one would expect the mandrel side to be only as smooth as the original substrate surface itself; the deposition side is a function of the whole pyrolysis process, including the inclusion of dirt and soot. For these reasons, the variations between the GE and HTM PG electrodes may be significant. The HTM material is produced in flat plates, while the GE material is cut from a tapered and somewhat variable density block of unknown origin (cf. Experimental section).

Behavior in Aqueous Media

Initial voltammetric investigations were conducted with an aqueous $1\ \text{mM}$ $\text{K}_4\text{Fe}(\text{CN})_6$ solution ($0.5M$ KCl as supporting electrolyte) to determine the differences in behavior of the indicator electrode materials and the tendency for the electroactive species to be adsorbed in the PG layers, thus causing a memory effect due to entrapped material.

The special cell, designed so that fresh KCl solution could be run through periodically to remove diffused mercury ions from the SCE or diffused iron species, was arranged in a double, two-electrode configuration, i.e., the SCE in the middle compartment and the ferrocyanide solution were one set, and the SCE and a $0.5M$ KCl solution in the third leg constituted the other set. In operation, the electrode being investigated was placed in the deoxygenated ferrocyanide solution and cycled several times until the voltammogram had reached a steady trace. The electrode was then removed, rinsed quickly but thoroughly with distilled water to remove iron species adhering to the outer surfaces, and placed in the deoxygenated KCl solution in the third compartment. Cycling was promptly repeated across the redox potential range of ferrocyanide with the recorder set at high sensitivity; any interlayer adsorbed electroactive species would then produce a current peak at $+0.28V$.

In all cases where the ground PGE was used, small but distinctive peaks were observed, indicating a carryover of ferrocyanide. Such peaks were not observed on the cleaved PGE, except in one case where

Table II. Charge on electrodes on insertion and after standing in aqueous $0.5M$ KCl solution

Material electrode ^(a)	Charge on electrode, $\mu\text{coulombs}$			
	Initial	After 50 sec	After 500 sec	After 1500 sec
Glassy carbon	0.5	1.0	7.8	18.5
GE PG (cleaved)	2.6	3.3	5.3	8.4
GE PG (ground)	4.6	8.0	16.5	31.0
Hg pool	0.20	0.28	0.64	2.17

^(a) GE PG = General Electric pyrolytic graphite.

Table III. Open circuit potentials of graphite electrodes in aqueous $0.5M$ KCl solution

Electrode material	Potential, V, vs. SCE	
	Initial	After 1500 sec
Glassy carbon	-0.12	-0.77
GE PG (ground) ^(a)	+0.76	-0.29
GE PG (cleaved)	+0.25	-0.7

^(a) A large positive charge also appears on the ground electrode.

a partial layer of the cleaved graphite was inadvertently left in place. As a general rule, the retention on the ground surface (and its interlayers) was ten to twenty times greater than the worst case observed with the cleaved surface. On glassy carbon, there was never any detectable carry over of iron species.

Initial current phenomena.—Of particular interest is the fact that, when an indicator electrode is connected to the recording system via a follower (unity gain) vs. the SCE and then immersed in the cell solution, positive potentials and anodic currents are observed, which are greatest on the ground PGE, far less on the cleaved PGE, and practically nil on GC or polished platinum electrodes.

The typical curve of Fig. 4 illustrates the high initial current on electrode immersion and the decreased cathodic peak on the first voltage scan. The cathodic peak on the initial scan is always the lowest and is an indication of the amount of ferricyanide formed on the electrode when the charged electrode is immersed in the ferrocyanide solution. No correlation appeared between the first cathodic peak height and the charge on the electrode or the time of immersion prior to initiating the sweep toward more negative potential. Thus, cathodic peak 1 in Fig. 4 is that due to the reduction of ferricyanide formed as indicated, while cathodic peak 2 is that due to the ferricyanide formed during anodic peak 1.

Effect of surfactant.—The effects of adding small quantities of a wetting agent to the aqueous ferrocyanide solution depend on the electrode material (Fig. 5). The cleaved graphite and the GC electrodes were

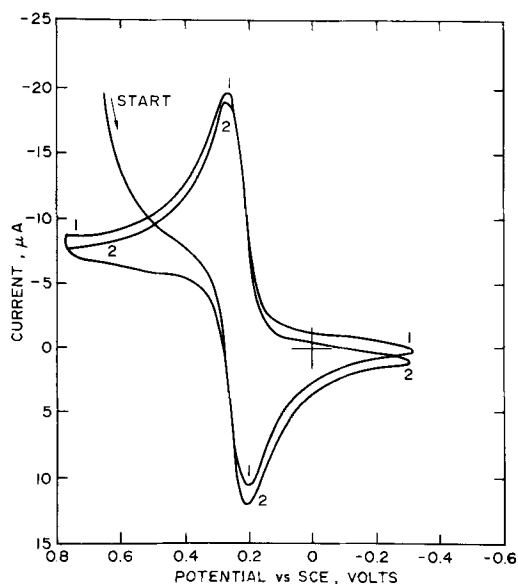


Fig. 4. Cyclic voltammogram for 1 mM $K_4Fe(CN)_6$ in 0.5M KCl aqueous solution. Effect of initial anodic current.

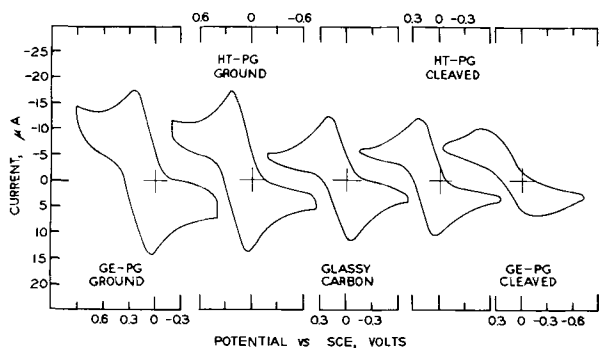


Fig. 5. Cyclic voltammogram for 1 mM $K_4Fe(CN)_6$ in 0.5M KCl aqueous solution. Effect of 0.002% Triton X-100 on curve shapes on different electrodes.

greatly influenced by the presence of 0.002% Triton X-100; the peaks were suppressed and shifted in potential, and the voltammograms generally flattened. By contrast, the ground surface graphite electrodes were not noticeably affected; only when a 0.01% Triton level had been reached did suppression of the peak current become obvious. These observations support the suggestion that the ground PG surfaces have a very much larger effective area than either the cleaved PG or GC surfaces. The surfactant drastically suppresses electroactivity on the latter materials because it is rapidly adsorbed across a large portion of the total available electrode area.

Effect of pH.—The effect of pH on electrode behavior was studied by adjusting the pH of the ferrocyanide solution by suitable buffering (Fig. 6 and 7 present typical curves). Some effects were common, to some degree, to all electrodes and are evidently due to variation in the nature of the electroactive species caused by the pH change. The most obvious of these is the very sharp and heightened current peak at pH 1.8; the effect was extreme on the ground PGE from both sources, but was much less on the cleaved PGE. By comparison, the GCE showed a sharper peak at pH 1.8 but the variation with pH was not as extreme as on the PGE.

At higher pH, the reversibility of the $Fe(CN)_6^{3-}/Fe(CN)_6^{4-}$ couple was much reduced on the cleaved PGE compared to that on the ground PGE. The values of i_p and E_p in Table IV provide a quantitative summary of the observed shifts. The shift in E_p for both cathodic and anodic processes to more negative potential with increasing pH (Table IV) results from the acid-anion equilibria involving ferrocyanic and ferricyanic acids.

Effect of electrode area.—The data on the commonly used PGE (projected area = 0.126 cm²) were compared with those on ground and cleaved PGE of 0.196 cm² area from Rosen's work (11) (Fig. 8, Table V). The sharper peaks resulting from the ground surface

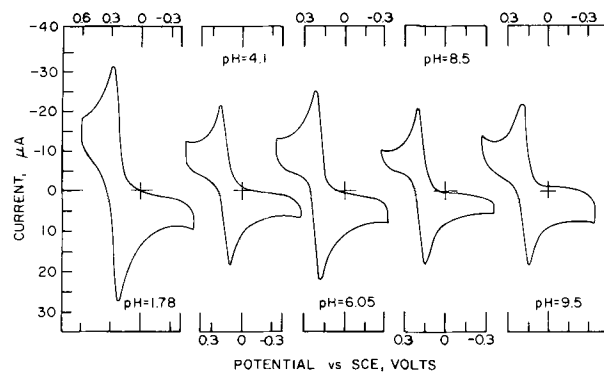


Fig. 6. Effect of pH on cyclic voltammograms for 1 mM $K_4Fe(CN)_6$ in 0.5M KCl aqueous solution. Ground pyrolytic graphite electrode (High Temperature Materials Company).

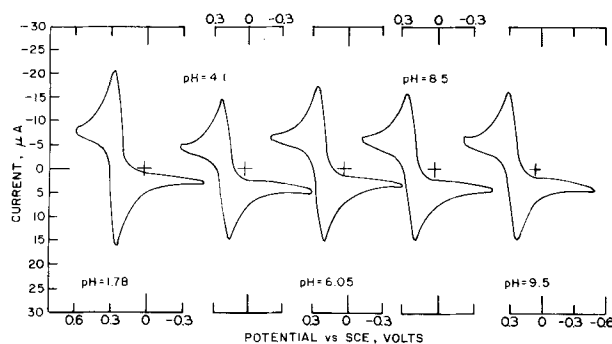


Fig. 7. Effect of pH on cyclic voltammograms for 1 mM $K_4Fe(CN)_6$ in 0.5M KCl aqueous solution. Cleaved pyrolytic graphite electrode (High Temperature Materials Company).

Table IV. Variation of current and potential with pH for ferrocyanide oxidation on carbon electrodes^(a)

Electrode type	pH of ferrocyanide solution				
	1.78	4.1	6.05	8.5	9.5
High-Temp. PG (ground)					
Anodic: E_p	0.30	0.26	0.26	0.26	0.25
i_p	30.3	20.0	24.5	21.2	20.2
Cathodic: E_p	0.23	0.19	0.19	0.17	0.19
i_p	29.3	19.8	25.0	21.0	20.2
High-Temp. PG (cleaved)					
Anodic: E_p	0.30	0.26	0.27	0.26	0.26
i_p	21.8	17.3	19.3	18.3	17.5
Cathodic: E_p	0.24	0.18	0.19	0.18	0.18
i_p	21.3	17.0	18.8	17.8	17.5
Gen. Elec. PG (ground)					
Anodic: E_p	0.30	0.26	0.26	0.27	0.26
i_p	30.0	21.0	25.3	18.0	18.0
Cathodic: E_p	0.23	0.18	0.19	0.18	0.19
i_p	27.0	21.0	25.6	19.8	17.5
Gen. Elec. PG (cleaved)					
Anodic: E_p	0.32	0.26	0.30 ^(b)	0.28	0.30
i_p	17.3	13.8	19.2	18.5	12.5
Cathodic: E_p	0.22	0.14	0.17 ^(c)	0.15	0.13
i_p	17.0	13.0	18.3	17.8	11.8
Glassy carbon					
Anodic: E_p	0.31	0.28	0.29	0.28	0.29
i_p	19.5	15.5	16.2	17.5	14.8
Cathodic: E_p	0.23	0.16	0.16	0.17	0.14
i_p	19.5	16.5	16.5	17.6	15.0

^(a) Potentials are in volts and are positive with respect to the aqueous SCE. Currents are in μA . PG = pyrolytic graphite.

^(b) Potential became more positive until the seventh scan.

^(c) Potential became more negative until the seventh scan.

Table V. Effect of area on ground and cleaved pyrolytic graphite electrodes^(a)

Electrode area, cm^2	Electrode preparation	Anodic peak			Cathodic peak		
		$E_{p/2}$, V	E_p , V	i_p , μA	$E_{p/2}$, V	E_p , V	i_p , μA
0.126	Cleaved	0.21	0.25	23.5	0.23	0.19	23.2
	Ground	0.18	0.33	33.7	0.24	0.12	29.2
0.196	Cleaved	0.21	0.33	28.4	0.22	0.17	25.5
	Ground	0.19	0.26	31.8	0.25	0.17	33.0

^(a) Data are for 1 mM ferrocyanide in aqueous 0.5M KCl solution.

as compared to the cleaved surface are the most obvious characteristics. However, these ground surfaces could not be resurfaced as reproducibly as could the cleaved surfaces. Most of the variation in peak height is due to the much larger residual current on the ground electrode.

The peak currents do not show the expected proportionality to the electrode area. Theoretical peak currents in cyclic voltammetry for reversible systems can be calculated from the equation (12)

$$i_p = 2.72 \times 10^5 n^{3/2} A D^{1/2} C^0 v^{1/2} \quad [1]$$

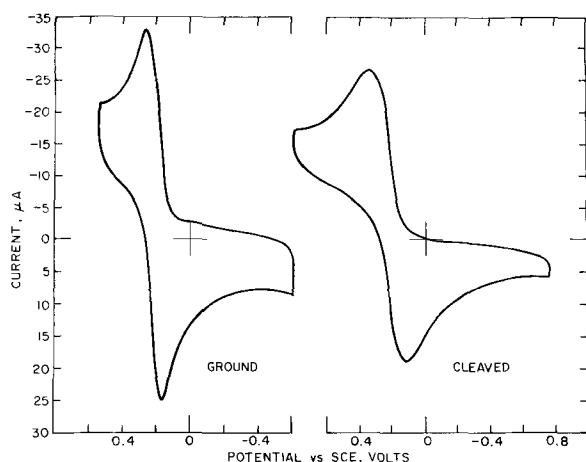


Fig. 8. Cyclic voltammograms for 1 mM $\text{K}_4\text{Fe}(\text{CN})_6$ in 0.5M KCl aqueous solution. Pyrolytic graphite electrodes of 0.196 cm^2 projected area.

where i_p is the current in amperes, n the electron change, A the electrode area in cm^2 , D the diffusion coefficient in cm^2/sec and C^0 the concentration of the diffusing species in moles/ cm^3 , and v the scan rate in V/sec. At $v = 100$ mV/sec, calculated $i_p = 27.0$ μA for the electrode of 0.126 cm^2 and 41.14 μA for $A = 0.196$ cm^2 (a value of 0.60×10^{-5} cm^2/sec was used for D). Although the projected area was used with no allowance for surface roughness, it seems that the cleaved surface more nearly follows the expected current relationship, but the differences in cathodic and anodic E_p values are much greater on the cleaved electrode than on the ground electrode. For a reversible couple, a separation of 58 mV is expected for a one-electron change, which is about that observed on the ground electrodes in both cases. Based on the half-peak potential, $E_{p/2}$, the reversibility does not appear to vary as greatly as does that based on the E_p data.

Effects of multiple scans and initial potential direction.—The effects of multiple scans and of starting the scan in either potential direction from the zero of the SCE reference electrode were investigated and significant differences were observed.

Figure 9 shows the curves obtained on HT pyrolytic graphite and on glassy carbon. When ground PG electrodes are used, an initial high anodic peak is seen, independent of the direction of scan. If the scan is started toward positive potential, i_p is progressively less on subsequent scans and, at times, does not reach a constant level after five or six scans. On the other hand, if the scan is initially toward negative potential, although no reduction peak results from the ferrocyanide solution, the first anodic peak is high by about 2.5 μA but subsequent scans tend to superimpose; even after 25 cycles, there is often not more than 0.25 μA variation. The general effect is much less pronounced on (polished) GC electrodes; voltammograms have very sharp peaks and subsequent curves retrace the first scan. The evidence suggests that an initial cathodic scan (toward negative potential) tends to neutralize the positive surface charge on the ground electrode, thus lowering the anodic peak height on the first sweep and leading to more reproducible peak currents.

Beilby (13) has stated that, if the voltage scan is allowed to go too far positive, irreversible changes can occur on the PGE surface. Consequently, in the present

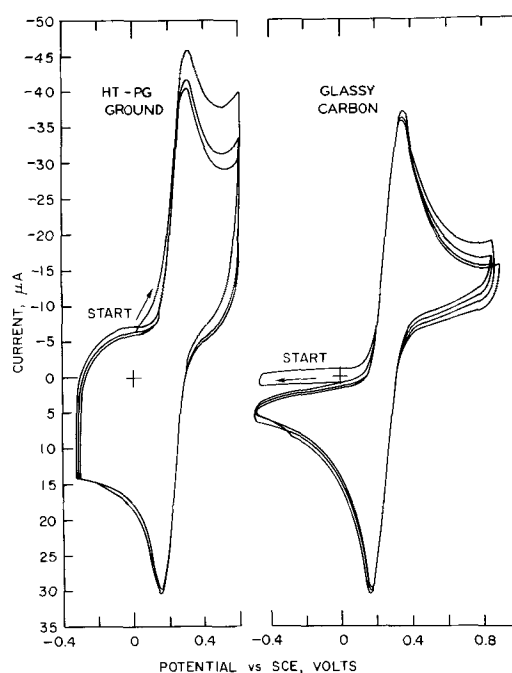


Fig. 9. Effects of repetitive scans and initial potential direction on glassy carbon and pyrolytic graphite electrodes for 1 mM $\text{K}_4\text{Fe}(\text{CN})_6$ in 0.5M KCl aqueous solution.

study, the scan was not allowed to go more than a fraction of a volt beyond the peak potential observed on either cathodic or anodic scans. The effects of starting the scan in the cathodic direction provide additional evidence for the presence of a positively charged surface. Although the latter has been called an "oxidized surface" (14), its reduction must occur at a very low potential judging by the increased height of the ferrocyanide anodic peak. A more likely explanation, as discussed, is the presence of positive static charges induced by the grinding of the surface.

Summary.—In aqueous voltammetry under a given set of conditions, cleaved pyrolytic graphite surfaces provide a lower peak current as well as a much lower residual current. These surfaces cause the $\text{Fe}(\text{CN})_6^{3-}/\text{Fe}(\text{CN})_6^{4-}$ couple to appear less reversible, i.e., the separation between the anodic and cathodic peaks is greater and the peaks themselves are more rounded. The ground PG electrodes produce sharper, more reversible peaks, but they retain electroactive species within the layers and the surface is not reproducible on resurfacing. More will subsequently be said on the latter point.

The significance of these studies in aqueous solutions is that they provide a comparison of the behavior of a well characterized electrochemical system on the various carbonaceous electrodes. From the results obtained, large differences in the performance of the electrodes might be expected when they are utilized in nonaqueous systems.

Behavior in Nonaqueous Media

Investigations in nonaqueous solutions were also designed to determine the effects of resurfacing methods on electrode behavior. Although every effort was made to eliminate water and oxygen from the solutions prior to their introduction into the electrochemical cell, "complete" elimination of these ubiquitous impurities is problematical. Even if solutions are handled in the best available inert atmosphere dry box, there remains a possibility of surface contamination due to water levels in the solvents on the order of 10^{-9} moles/cc. A situation of diminishing returns arises as the requirements of experimentation tend toward levels of oxygen and moisture which are below the presently detectable limits for these substances. A common error in nonaqueous investigations is the use of so-called spectrophotometric grade solvents without further purification. Although such solvents may have no interfering bands in a given spectrum range, they may contain quite large amounts of impurities (including water), if these materials do not absorb significantly in the given spectral range.

A recent paper (15) points out that the water levels in many purified solvents—even in some "as received" materials—do not interfere with electrochemical investigations conducted in them. On the other hand, the present work indicates that much depends on the potential range used, the stand (rest) time of the electrode in contact with solutions, and the rates of reaction of water with the solvent, solutes, or other electroactive species. It is, indeed, true, as pointed out (15), that much more than simple electrostatics is involved in solute-solvent interactions. It is important to recognize these factors; although there is obviously no such thing as a totally anhydrous nonaqueous solvent, the limits of water which can be tolerated will depend on many experimental factors.

Behavior in Pyridine

In order to determine the effects of electrode resurfacing on the redox voltammetry of an organic compound, quinone was used as the electroactive species in 0.1M tetraethylammonium perchlorate (TEAP) solutions in pyridine. The previously reported (2) pre-wave occurring at -1.72V in pyridine, which has not been sufficiently purified to remove a proton-releasing substance, did not interfere, as the potential scan was

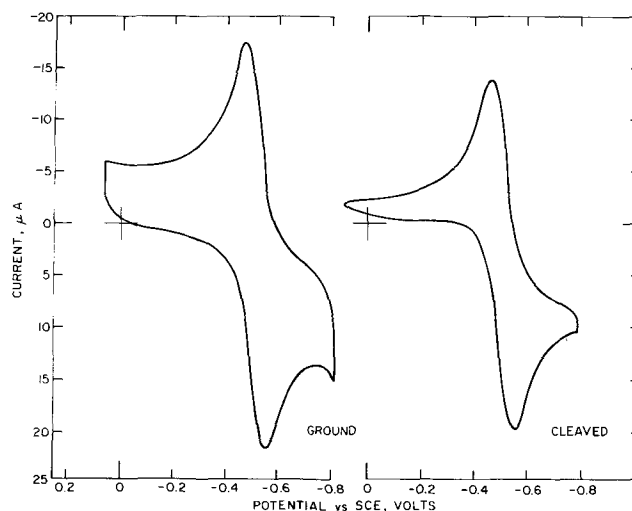


Fig. 10. Cyclic voltammograms on pyrolytic graphite electrodes of 1 mM quinone in pyridine (0.1M TEAP).

reversed just after the first reduction peak was reached, i.e., at about -0.8V . The reproducibility on ground or cleaved General Electric PGE was evaluated by resurfacing the electrode a number of times and reinserting it each time in the cell system for another cyclic scan, which was started toward negative potential. The initial peaks on cleaved electrodes varied from subsequent ones by less than $0.25\ \mu\text{A}$; a series of cleaved electrode voltammograms were almost superimposable, e.g., Fig. 10. However, the first sweep on the ground electrodes was often erratic; the anodic and cathodic peaks were variable in height by as much as $2.5\ \mu\text{A}$ between the first and succeeding scans, and also between first scans on resurfaced electrodes. This variation amounted to 10-15%, since i_p was often around $20\ \mu\text{A}$.

For pyridine solutions (0.1M LiClO_4) of ferrocene, the ground electrode—as in aqueous solutions—provides a very high first peak on multiple scan voltammograms; subsequent scans have a very reproducible cathodic peak, but the anodic peaks decrease with each succeeding scan. (It should be emphasized that a shift in E_p has never been observed with successive scans; variations are always in lowered i_p .)

Adding pyridinium nitrate to a solution of ferrocene in LiClO_4 -pyridine has no noticeable effect on voltammograms taken with cleaved electrodes; curves were entirely reproducible with i_p and E_p constant for 0.5 to 10 mM acid (Fig. 11). Voltammograms taken with the ground PGE on pyridinium nitrate addition are not much different until about 10 mM is reached, at which concentration the first scan overshoot is only about $0.5\ \mu\text{A}$, compared to previously seen overshoots of 2.5-5.0 μA (Fig. 14).

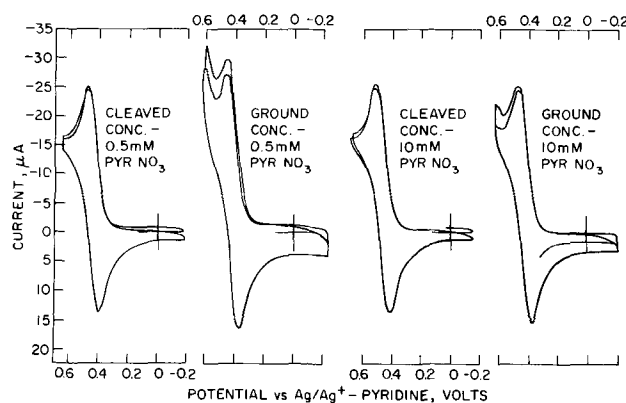


Fig. 11. Effect of added pyridinium nitrate on cyclic voltammograms on pyrolytic graphite electrodes of 1 mM ferrocene in pyridine (0.1M LiClO_4).

The ratio of the anodic and cathodic peak heights is approximately unity, indicating that the ferrocene/ferrocenium couple is reversible in LiClO_4 -pyridine solutions.

Equation [1] was used to calculate i_p values for the ferrocene oxidation peak on a cleaved General Electric PGE in LiClO_4 -pyridine solutions. At a scan rate of 50 mV/sec, the observed i_p for the ferrocene oxidation peak on a General Electric PGE in LiClO_4 -pyridine solution, based on a series of highly reproducible voltammograms, corresponds to a diffusion coefficient of $8.34 \times 10^{-6} \text{ cm}^2/\text{sec}$ when the projected electrode area is used in Eq. [1].

Behavior in Acetonitrile

The results for 1 mM ferrocene in acetonitrile solution (0.1M LiClO_4) on PG cleaved and ground electrodes are very similar to those obtained in pyridine. The ground surfaces had a very large positive charge in acetonitrile. When the electrode was first inserted in the solution, a positive potential of $E_p = +0.37$ and an anodic i_p of ca. 200 μA were observed. Consequently, the scan was started toward more negative potential. The scan produced a low cathodic peak since the electrode had been only briefly immersed in the solution before the scan began and there was very little time for the production of much oxidized material on the electrode surface. The scan, on being reversed toward positive potential after the first low cathodic peak, produced a very high first anodic peak, indicating that the charge phenomenon on the electrode was not completely eliminated during the initial scan towards more negative potential or that the amount of ferricinium ion produced by the inherent positive (anodic) electrode potential and charge was larger than that which was reduced on the initial scan.

Notable on all of the voltammograms on all electrode materials are the very sharp anodic and cathodic peaks, and the high degree of reversibility, *e.g.*, the ratio of the anodic and cathodic peak heights is almost exactly unity and the difference between the peak potentials is 70 mV or less. Although these characteristics hold true for all electrode surfaces, the curves on glassy carbon are much more definitive, as the electrode area is most nearly that of the projected geometrical area, 0.126 cm^2 ; a typical run is shown in Fig. 12. The curves from the cleavage graphite surfaces are much "cleaner"

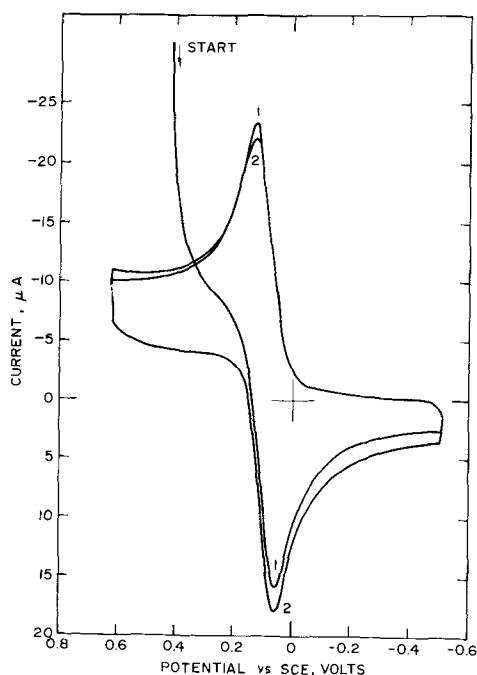


Fig. 12. Voltammograms on glassy carbon electrode of 1 mM ferrocene in acetonitrile (0.1M LiClO_4).

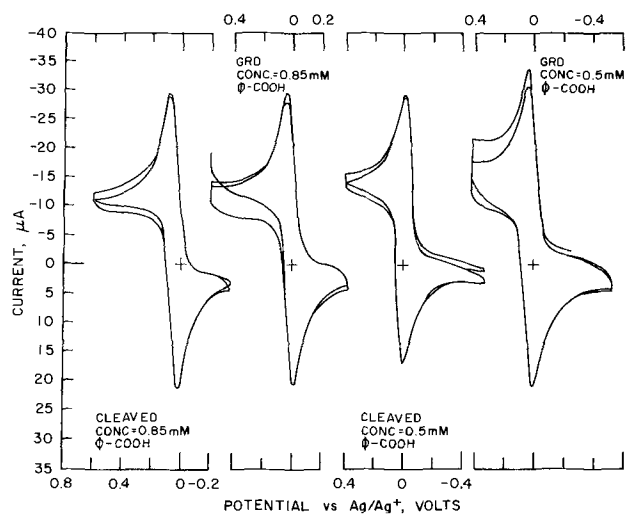


Fig. 13. Effect of added benzoic acid on cyclic voltammograms on pyrolytic graphite electrodes of 1 mM ferrocene in acetonitrile (0.1M LiClO_4).

than those from the ground surfaces; the peak heights for the latter are 15-20% higher, indicating the greater area of the ground surface. Using Eq. [1] and glassy carbon electrode data, the diffusion coefficient of ferrocene is calculated to be $4.26 \times 10^{-5} \text{ cm}^2/\text{sec}$. On the glassy carbon electrode, a plot of i_p vs. $v^{1/2}$ results in a straight line, indicating that the ferrocene electrode reaction is diffusion controlled.

When benzoic acid (0.5 to 1.05 mM) was added to ferrocene (Fig. 13), the only change seemed to be a lessening of the first scan overshoot for solutions of higher benzoic acid content. The peaks were sharper and successive traces were exactly superimposed on the first. A proton-rich environment evidently reduces the effect of the charge phenomenon on the ground and cleaved electrodes.

Behavior in Acetic Acid

In glacial acetic acid, many of the previously observed variations between the ground and cleaved PG and GC electrodes were somewhat leveled out, *e.g.*, initial overshoots on the first scan were much less, generally amounting to about 0.5 μA . Typical curves are shown in Fig. 14. Reproducibility of the ground electrodes was best in this solvent compared to the other systems utilized. For 1 mM ferrocene solution, i_p was 16.5 μA on the ground graphite electrode, and 16.25 μA on the cleaved electrode and on glassy carbon. If the glassy carbon surface is considered to be essentially the projected area, the closeness of the peak current values indicates that the effects of grinding are considerably lessened by the solvent.

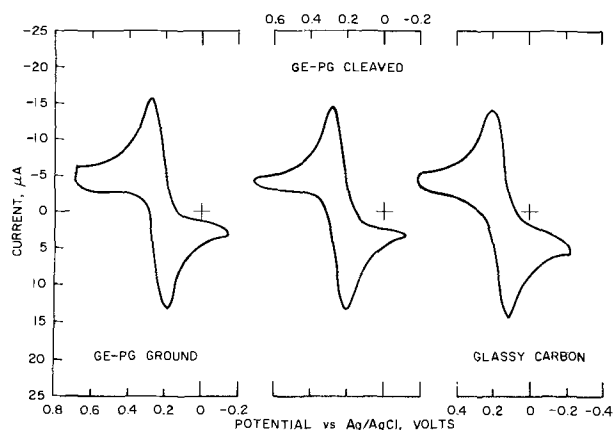


Fig. 14. Voltammograms of 1 mM ferrocene in acetic acid (0.1M LiClO_4).

All peak currents are much less in this solvent than in the other solvents. If the peak currents are assumed to be proportional to the square root of the diffusion coefficient (cf. Eq. [1]) and if the only change in diffusion coefficient in going from one solvent to another is that due to solvent viscosity (η), the currents would be inversely proportional to $\eta^{1/2}$ and the product $i_p \eta^{1/2}$ would be expected to be constant. The viscosities at 25° of the solvents used in the present study are acetonitrile 0.35, dimethylformamide 0.80, pyridine 0.88, water 0.89, and acetic acid 1.16 centipoise; the corresponding value of $\eta^{-1/2}$, based on water, are acetonitrile 1.60, DMF 1.04, pyridine 1.01, water 1.00, and acetic acid 0.88.

In acetonitrile, i_p values of around 30 μA are commonly observed; in acetic acid, i_p is about 16.3 μA . The ratio of 1.84 is in excellent agreement with the $\eta^{-1/2}$ ratio of 1.82.

A light blue color appeared in the ferrocene-acetic acid solution after it had stood for about 10 days. A voltammogram of this solution showed the peaks due to the ferrocene electrode reaction, but i_p was about 25% less and the potentials were about 25 mV more positive; the latter may be partially due to a shift in the reference electrode potential on standing, since the Ag/AgCl electrode does not have long term stability in HOAc.

Behavior in Dimethylformamide

On all of the electrodes (except glassy carbon) used in this solvent system (1 mM ferrocene; 0.1M LiClO₄), the first scan overshoot was about 1-2 μA over the average peak current, which is small compared to behavior in acetonitrile and pyridine. The Pyroid PGE, either ground or cleaved, did not provide reproducible traces on successive scans; it also tended to give a higher i_p than GE or HTM material at a given scan rate, occasionally as much as 4 μA greater. This would indicate that the Pyroid has a greater effective surface area than the others.

Generally, the ferrocene couple is less reversible in DMF than in the other solvents used, e.g., i_p (anodic) was about 1.3 μA higher than i_p (cathodic) for all electrodes. Peak potential separation was 70 to 80 mV, i.e., anodic $E_p = 0.84\text{V}$ and cathodic E_p is 0.76 for all electrodes. These values are comparable to that of 0.88V for the ferrocene oxidation potential previously obtained in DMF (NaClO₄ and TEAP as supporting electrolytes) (16).

Addition of Triton X-100 caused extremely erratic behavior and poor reproducibility on successive scans. Higher surfactant concentrations eventually reduced the peak height, shifted the anodic potential in a more positive direction and the cathodic peak to a more negative direction, and caused rounding of the peaks.

The variation in performance between the three types of PGE is more obviously seen in Fig. 15. The

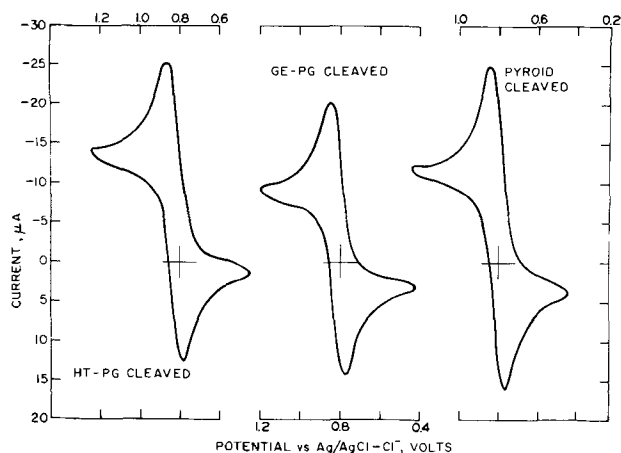


Fig. 15. Voltammograms on different types of pyrolytic graphite for 1 mM ferrocene in dimethylformamide (0.1M LiClO₄).

voltammograms on HTM electrodes provide clean superimposable curves with minimum residual current and sharp peaks with a very slight overshoot on the first scan and constancy on those following. Even on ground resurfaced HTM electrodes, the electrochemical behavior is better than in the other types. The General Electric material is second best and the Pyroid material is least satisfactory. Some of the variations observed are due to differences in the "cone" structure of the individual graphites, as these differences are manifested by variations in cone size, hardness, uniformity, etc. Generally, all the electrodes made from HTM material, used either in the present work or in subsequent work, have provided a much more uniform surface when they have been cleaved or ground for each resurfacing. Low power magnification shows considerable variation between various electrodes of General Electric and Pyroid material, especially in cone size and in the previously mentioned density gradients of the GE graphite. Some of the variations observed in electrode behavior are undoubtedly due to these uncontrollable physical variations in the electrode material itself.

Discussion

A thorough review of the literature (17) and unreported research results indicate that the most likely phenomena involving alteration of the surface of graphite, which would account for the variation in performance of graphite electrodes are the following:

1. Chemisorbed oxygen: This may exist by itself or may serve as an attractive site for H₂O molecules.

2. Tenaciously held water: This is of importance when the graphite is used in nonaqueous solvents.

3. Oxidation sites: Carbon-oxygen reaction sites and complexes may be localized at stress regions.

4. Carbon-oxygen surface compounds: acidic or basic organic compounds such as quinoids, quinhydrones, phenols, and carbonyls are definite possibilities, depending upon the conditions of formation. Additionally, under special conditions sulfate surface effects, hydrogen-bonded interlayer groupings, and free radicals may be involved (18, 19).

5. Mellitic acid derivatives: Pyromellitic acid-chloroquinone, pentacarboxylchlorobenzene and similar compounds could be produced under moderately oxidizing conditions (20, 21).

6. Lamellar compounds or their residues: These include bisulfates or other species, which in themselves are difficult to reduce or oxidize, and which are formed when graphite electrodes are subjected to strong oxidizing conditions.

7. Surface films: Constituting a broad field, these films encompass any of the previously listed effects, as well as some unknown effects peculiar to the dense structure of pyrolytic graphite.

Presently, no single agent of those listed appears to account for the observed phenomena on pyrolytic graphite. One distinct possibility is that exposure to air and moisture may spontaneously produce surface species. The investigator is then faced with the necessity of conducting all operations in an inert atmosphere or, at least, of handling the graphite in a sealed system or a vacuum.

Plock (22) has conducted rather extensive evaluations of the effect of pH and ligand changes on the usable potential ranges of glassy carbon, pyrolytic graphite, and platinum wire electrodes. Notable is the fact that the usable potential range of the GCE and PGE shift about 0.3V more negative at pH 8 to 11 and, with some organic materials such as diisopropylamine, the range was narrowed down significantly. There seems little correlation between Plock's results and the present results, except that the effect of the high pH in both cases is to restrict the range and behavior of the carbonaceous electrodes.

Concurrently with these investigations, Rosen (11) investigated certain aqueous systems, using pyrolytic graphite electrodes. Numerous questions as to the na-

ture of the PGE surface had been raised by earlier observations (14), e.g., very slow changes in the activity of the surface, rather poor reproducibility under a wide variety of resurfacing, usage or storage in air, and extremely irreproducible double layer capacitance measurements.

Electrode resurfacing.—It is clear from the results of the present investigation that resurfacing a pyrolytic graphite electrode by grinding produces a nonreproducible electrode surface. The admonition of Miller and Zittel (24) that the PGE should be resurfaced not by grinding but only by cleaving and then only when absolutely necessary, is well taken. The use of ground electrodes for studies of the electrolytic oxidation of organic compounds may lead to the deposition of oxidation products which are not readily removed. Should such be the case, the material can be removed with a nitric-sulfuric acid mixture as recommended by Meites (25). Due to the strong adsorption of chromium compounds on electrode surfaces, they are not easily removed and may interfere in subsequent use of the electrode; consequently, chromate solutions should not be used to clean electrodes.

The surface of the glassy carbon electrode can be readily stripped of deposits by brief immersion in the acid mixture and normally requires little surface treatment beyond returning the applied potential to the zero point. The latter suggestion of Zittel and Miller (26) has been verified in the present study. If necessary, the glassy carbon electrode is readily repolished with 0.5μ alumina. The glassy carbon can be imbedded in an epoxy such as the Hysol material, resulting in a very sturdy electrode structure, to which connection may be made via a mercury drop on the back side.

It is instructive to relate the present results with those previously reported. The present investigations indicate that the surface charge on a PG electrode is extremely high when resurfacing is done by grinding, but much less when resurfacing is done by cleaving the c planes of the graphite to yield a new plane.

Mamantov *et al.* (27) have reported that two types of films are produced on PGE surfaces when they are subjected to chemical or electrochemical oxidation. Investigations by Kekedy, Markay, and Dragoi (28) on the pretreatment of PG electrodes established that the surfaces obtained after oxidation with nitric acid, chromic acid, or KMnO_4 , or after reduction with ferrous ammonium sulfate could be characterized via chronopotentiometry. Using ferri/ferrocyanide and $\text{V(V)}/\text{V(IV)}$, they found that reproducible chronopotentiograms of the former system were only obtained on untreated electrodes, whereas V(V) could only be reduced on chemically reduced or oxidized, or untreated electrodes, and not at all on cathodically reduced electrodes. The over-all electrode process for vanadium redox systems on the electrodes was irreversible, but this effect was lessened on oxidized surfaces. No explanation was given.

Rosen (11) summarizes many investigations aimed at the delineation of the electrode reactions of oxygen and hydrogen on the PGE; he calls attention to the work of Morcos (29), who showed that the reduction of oxygen to peroxy ion proceeds much more readily on the edge planes of the PGE than on the cleaved planar surface. Grinding exposes a large number of edge planes of the truncated cones of the graphite layers. The cleaved surfaces are uniformly reproducible and provide in nonaqueous solution far better voltammograms than do the ground electrodes. The existence of the large anodic charge, shown by a high potential and peak current when the electrode is inserted into aqueous or nonaqueous solution, indicates that the anodic charge is more likely a static charge phenomenon than an oxidation. The requirement that the scan be started toward the cathodic (negative) direction in order to overcome it, indicates that, while some of the electroactive species is indeed oxidized by the charge phenomenon (first cathodic peak), some of

the charge does not oxidize the Fe(II) species. This may be due to shielding of inner layers of the graphite or to some other effect arising as a consequence of the unique structure of the pyrolytic graphite.

The work of Boehm *et al.* (30) has provided a definitive view of the types of oxidized sites occurring on carbon. These include phenolic, carboxylic, lactone, and ketonic types of oxygen compounds and may include hydrogen bridging between adjacent carbon-oxygen sites on the neighboring carbon hexagons. In the present work, one can visualize what might occur when the PGE is resurfaced in air by grinding. The grinding mechanism removes carbon by breaking bonds between adjacent atoms and between planes. In the case of pyrolytic graphite with its conical structures protruding from the surface, grinding will break vastly greater numbers of adjacent carbon bonds than if the planes are merely cleaved apart. The energy of breaking these bonds is partially dissipated as heat. However, the surface area is vastly increased and, since all the surface atoms have unbalanced charges ("free valencies") in the direction away from the bulk of the carbon, the surface energy must likewise be vastly increased. Inasmuch as the grinding is conducted in the air, the combination of heat and surface energy on the carbon atoms provides an optimum environment for oxidation of the carbon by atmospheric oxygen to form the various types of C-O compounds postulated by Boehm *et al.* (30). These occur on adjacent carbon atoms on the edges of the hexagonal planes of the graphite. Depending on the sites available, there may be bridging between adjacent groups and hydrogen bonding when OH groups are present. Obviously, if the PGE cone edges are vastly increased by the grinding, these compounds should form more readily and thus interfere with the reduction of other electroactive species when used in voltammetric studies.

From the standpoint of the surface charges produced on resurfacing, we determined these to be on the order of 5-10 μC , which is equivalent to 40 to 80 $\mu\text{C}/\text{cm}^2$ of projected PGE area. Such a large positive charge on the graphite surface may lead to the adsorption of anions. When the electrode is scanned towards negative potential in pyridine, an inflection is observed which appears to be a reduction. This may actually be due to the removal of the adsorbed anions, which requires that additional negative charges (electrons) be put on the electrode and results in an inflection as observed. These negative charges are also relevant to the observed levels of open circuit potential. When the electrodes are ground in air, oxidation of the carbon atoms on the edge planes would be expected to occur to form various types of C-O groupings, depending on the -C-C-C- environment. Unfortunately, we have not yet been able to determine the effect of resurfacing the PGE in an inert, dry atmosphere and using it quickly thereafter in the dry-box atmosphere. However, such a procedure may only prove that static charges predominate or that the dry-box atmosphere with less than a part per million of water and oxygen still has too much of these species present for definitive results.

It seems likely that much of the problem of measuring double layer capacity of PGE (14) may be traceable to the charges and surface oxidation compounds produced by the grinding or cleavage of the electrodes.

A technique, which might shed further light on the nature of the surface compounds on the PGE, involves exposing a new layer of material, while the electrode is connected to the measuring circuit, to determine the "potential of zero charge" (31). If the charge on a PGE could be neutralized by several scans and the electrode then cleaved under the solution while potential and current are measured, the results may indicate the nature of the newly exposed carbon planes. Such an

operation could be conducted in a dry-box atmosphere under a highly purified nonaqueous solution.

The proposed technique for the identification of surface functional groups on active carbon by infrared reflection spectroscopy (32) may be applicable to surfaces such as pyrolytic graphite, glassy carbon, and other opaque electrode surfaces.

Acknowledgments

The authors thank the Naval Ordnance Laboratory, Corona, for the Fellowship awarded to R.E.P. under the NOLC Educational Program and the National Science Foundation for research support given to P.J.E. R.E.P. extends his gratitude to W. C. Spindler at NOLC, whose encouragement through the years is deeply appreciated.

Manuscript submitted Aug. 20, 1971; revised manuscript received Jan. 21, 1972.

Any discussion of this paper will appear in a Discussion Section to be published in the June 1973 JOURNAL.

REFERENCES

- D. A. Hall, M. Sakuma, and P. J. Elving, *Electrochim. Acta*, **11**, 337 (1966).
- D. A. Hall and P. J. Elving, *Anal. Chim. Acta*, **39**, 141 (1967).
- W. J. Coy, *J. Am. Ceram. Soc.*, **45**, 223 (1962).
- R. E. Panzer and G. E. McWilliams, "Nonaqueous Solvent Electrochemistry," NOLC Report 689, Naval Ordnance Laboratory, Corona, Calif., Oct. 15, 1966.
- G. A. Perley, *Trans. Electrochem. Soc.*, **92**, 504 (1947).
- I. V. Nelson, *Diss. Abst.* 64-8509, University Microfilms, Ann Arbor, Mich. (1964).
- W. R. Turner and P. J. Elving, *Anal. Chem.*, **37**, 467 (1965).
- U. Eisner, Private communication.
- R. D. Giles, J. A. Harrison, and H. R. Thirsk, *J. Electroanal. Chem.*, **20**, 47 (1969).
- H. Sunahara and T. Ishizuka, *Rev. Polarog. (Kyoto)*, **14**, 176 (1967).
- M. Rosen, Ph.D. Dissertation, University of Michigan (1968).
- R. S. Nicholson and I. Shain, *Anal. Chem.*, **36**, 706 (1964).
- A. Beilby, Private communication.
- H. H. Bauer, M. S. Spritzer, and P. J. Elving, *J. Electroanal. Chem.*, **17**, 299 (1968).
- J. R. Jezorek and H. B. Mark, *J. Phys. Chem.*, **74**, 1627 (1970).
- J. B. Headridge, M. Ashraf, and H. L. H. Dods, *J. Electroanal. Chem.*, **16**, 114 (1968).
- R. E. Panzer and P. J. Elving, Work being prepared for publication.
- G. R. Hennig, *J. Chim. Phys.*, **58**, 12 (1961).
- G. R. Hennig, *Proc. Conf. Carbon, Penn. State*, (1961), **5**, 143 (1962).
- H. H. Heller, *Trans. Electrochem. Soc.*, **87**, 501 (1945).
- S. Wawzonek and D. S. P. Eftax, *This Journal*, **104**, 494 (1957).
- C. E. Plock, Report No. RFP-1221, Dow Chemical Co., Golden, Colo., (1968); under Contract AT (29-1)-1106 with U.S.A.E.C.
- R. N. Adams, Paper 146 presented at Electrochem. Soc. Meeting, San Francisco, May 9-13, 1965.
- F. J. Miller and H. E. Zittel, *Anal. Chem.*, **35**, 1866 (1963).
- L. Meites, "Polarographic Techniques," Interscience Publishers, New York (1955).
- H. E. Zittel and F. J. Miller, *Anal. Chem.*, **37**, 200 (1965).
- G. Mamantov, D. R. Freeman, F. J. Miller, and H. E. Zittel, *J. Electroanal. Chem.*, **9**, 305 (1965).
- L. Kekedy, F. Makkay, and a. Dragoi, *Studia Univ. Babeş-Bolyoi, Ser. Chemia*, **13**, 63 (1968).
- I. H. Morcos, Ph.D. Dissertation, Western Reserve University (1966).
- N. P. Boehm, E. Diehl, W. Heck, and R. Sappok, *Angew. Chem.*, **76**, 742 (1964).
- T. N. Andersen, J. L. Anderson, and H. Eyring, *J. Phys. Chem.*, **73**, 3562 (1969).
- J. S. Mattson, H. B. Mark, and W. J. Weber, *Anal. Chem.*, **41**, 355 (1969).

Technical Notes



The Electrolytic Fluorination of Anthracene Derivatives

I. 9, 10-Diphenylanthracene

C. J. Ludman, E. M. McCarron, and R. F. O'Malley*

Department of Chemistry, Boston College, Chestnut Hill, Massachusetts 02167

Electrochemical acetoxylation, methoxylation, and cyanation, believed to occur by attack of the appropriate nucleophilic anion on radical cations and/or dications formed at the anode, have been reviewed (1). A similar route to fluorine derivatives of aromatic hydrocarbons seemed logical if a suitable solvent-electrolyte system were available.

Acetonitrile, with a useful anodic range of at least +3.0V vs. SCE (2), depending upon the anion present, was chosen as the solvent. The salt tetramethylammonium dihydrogen trifluoride $(\text{CH}_3)_4\text{NF} \cdot 2\text{HF}$ (3) was prepared and characterized. It is soluble in acetonitrile.

Knunyants and his group have used triethylammonium fluoride in acetonitrile (4) for the anodic fluorination of naphthalene, and tetraethylammonium trihydrogen tetrafluoride (5) for the anodic fluorination of naphthalene and 1-fluoronaphthalene. Earlier, Schmidt (6, 7) had described the anodic fluorination of 1,1-diphenylethylene, by electrolysis in potassium hydrogen fluoride solutions in glacial acetic acid, and silver fluoride solutions in acetonitrile, but with very low yields.

The anodic formation of cationic species from polyaromatic hydrocarbons and related compounds has been investigated extensively in a number of laboratories and is the subject of a recent lengthy review (1). The compound 9,10-diphenylanthracene DPA was chosen because of the stability of its radical cation (8, 9, 10). It has been shown to react with water (10) to form 9,10-diphenyl-9,10-dihydroxy-9,10-dihydroan-

* Electrochemical Society Active Member.

Key words: fluorination, electrolysis, polyarenes, radical-cations.

thracene. The use of H_2F_3^- ion, as a nucleophile for reaction with the cationic species of DPA, is the basis of the work described here.

Experimental

Apparatus.—The controlled potential electrolysis was conducted in a cell constructed from a 500 ml Pyrex resin flask, fitted with a side arm made from a 24/40 outer joint. A medium porosity frit inserted at the juncture of the flask and a side arm separated the reference electrode compartment from the electrolysis compartment. A platinum cylindrical gauze anode (5 cm long and 1.5 cm in diameter) and a platinum foil cathode (11.25 cm²) were suspended in the resin flask through the ground joints in the cover; no diaphragm was used to separate them. The potential of the anode *vs.* the SCE reference was controlled by an Anotrol Model 4100 research potential controller.

Before performing the electrolyses, RPE voltametric curves were obtained with a Sargent micro-platinum electrode (S-30420) rotated at 600 rpm by a Sargent synchronous motor (S-76485). A conventional Pyrex H-cell, with the electrode compartments separated by medium porosity frits, contained the acetonitrile solution of salt and organic substrate and the SCE reference electrode. The current-voltage curves were obtained on a Sargent Model XV polarograph, without solution resistance compensation.

Melting points were determined on a Mel Temp apparatus and are uncorrected. Infrared and ultraviolet spectra were recorded on Perkin-Elmer spectrophotometers, Models 137 and 202, respectively. The NMR spectra were recorded on a Varian Model HA-60 spectrometer.

Chemicals.—Matheson, Coleman, and Bell chromatography quality acetonitrile was used without further purification. Tetramethylammonium dihydrogen trifluoride was prepared as described previously (3). The 9,10-diphenylanthracene was from K & K Laboratories, Inc.

Elemental analyses were performed by Galbraith Laboratories, Inc., Knoxville, Tennessee. Molecular weight determinations were made by R. Sacher, U. S. Army Natick Laboratories, Natick, Massachusetts, on a Mechrolab vapor pressure osmometer, Model 301A.

Electrochemical Synthesis.—The RPE examination of DPA in 0.40M $(\text{CH}_3)_4\text{NF} \cdot 2\text{HF}$ in acetonitrile gave a value of 1.27V *vs.* SCE for its $E_{1/2}^{\text{ox}}$.

Because of the relatively low solubility of DPA in acetonitrile, it was added in portions from time to time during the electrolysis. A total of 1.00g (3.03 mmole) was added to 95 ml of 0.40M $(\text{CH}_3)_4\text{NH}_2\text{F}_3$ in acetonitrile. The current of 0.50A was observed after the addition of each portion of 9,10-diphenylanthracene and fell to 0.030A before the next addition. The electrolysis was allowed to proceed for 11 hours at which time the current had decreased to 0.015A. An atmosphere of nitrogen was maintained throughout the electrolysis.

A white precipitate formed in the vicinity of the anode. After filtration, washing with acetonitrile, and recrystallization from benzene it melted with decomposition at 229°–229.5°.

Analysis.—Calculated for $\text{C}_{26}\text{H}_{18}\text{F}_2$: C, 84.78; H, 4.90; F, 10.32. Found: C, 84.70; H, 5.30; F, 10.30. Molecular Weight: Calculated 368; Found, 391. The yield was 0.48g, 43% based on the mass of starting material. The ultraviolet spectrum had a primary absorption at λ_{max} 219 ($\epsilon = 58,000$) and four secondary absorptions at λ_{max} 242 ($\epsilon = 221$), λ_{max} 239 ($\epsilon = 206$), λ_{max} 231 ($\epsilon = 134$), and λ_{max} 223 ($\epsilon = 64$) were observed. A 56.4 MHz F^{19} NMR spectrum in benzene at 78° showed a single peak at 4.86 ppm upfield from 1-fluoronaphthalene.

A sample of 9,10-difluoro-9,10-diphenyl-9,10-dihydroanthracene was synthesized by the action of anhydrous HF on 9,10-dihydroxy-9,10-diphenyl-9,10-dihydroanthracene, prepared by the method of Awad,

Fateen, and Zayed (11). Its properties were identical to those of the product of the electrochemical synthesis.

Efforts to fluorinate naphthalene by electrolysis in acetonitrile solutions of $(\text{CH}_3)_4\text{NF} \cdot 2\text{HF}$ failed because the anode was quickly coated.

Results and Discussion

That the fluorinated product of the electrolysis was 9,10-difluoro-9,10-diphenyl-9,10-dihydroanthracene, mp 229° (dec), was consistent with the elemental analysis, molecular weight, ultraviolet spectrum, and F^{19} NMR spectrum. A comparison of the ultraviolet spectrum with the spectrum of 9,10-diphenylanthracene showed a marked decrease in resonance. A similar decrease in resonance was shown by 9,10-dihydroxy-9,10-dihydro-9,10-diphenylanthracene. The presence of but a single peak in the F^{19} NMR spectrum supported the predicted structure, since it showed that each of the two fluorine atoms had the same environment.

The same compound was prepared by a chemical synthesis. The treatment of 9,10-dihydroxy-9,10-dihydro-9,10-diphenylanthracene with anhydrous HF gave a white solid which had the same melting point, elemental analysis, infrared spectrum, and ultraviolet spectrum. No experiment was performed which would indicate whether the *cis*- or the *trans*-form of the 9,10-difluoro compound had been formed.

The controlled potential electrolysis was conducted at a potential (1.65V *vs.* SCE) sufficiently higher than $E_{1/2}^{\text{ox}}$ of DPA (1.27 *vs.* SCE) to assure the formation of sufficient radical cations to react with the H_2F_3^- anions. The potential was sufficiently lower than the decomposition potential of the solvent-electrolyte system to preclude interference from fluorine atoms formed by oxidation of the anions. Evidence that the anions are oxidized at the decomposition potential has been obtained (12).

It is not clear whether dicationic species were formed in significant quantities to be effective in the formation of the fluorine-containing product formed. The more important mechanism involved in the anodic fluorination is probably that proceeding through two one-electron transfers, as depicted in Fig. 1.

Whether fluorinations of a wide variety of substances is possible by this method is under investigation.

Acknowledgment

This work was supported by the Advanced Research Projects Agency and administered by the Air Force Office of Scientific Research, Office of Aerospace Research, under grant AF AFOSR-910-65, Lt. Col. C. J. Donovan, monitor.

Manuscript submitted Nov. 1, 1971; revised manuscript received March 8, 1972.

Any discussion of this paper will appear in a Discussion Section to be published in the June 1973 JOURNAL.

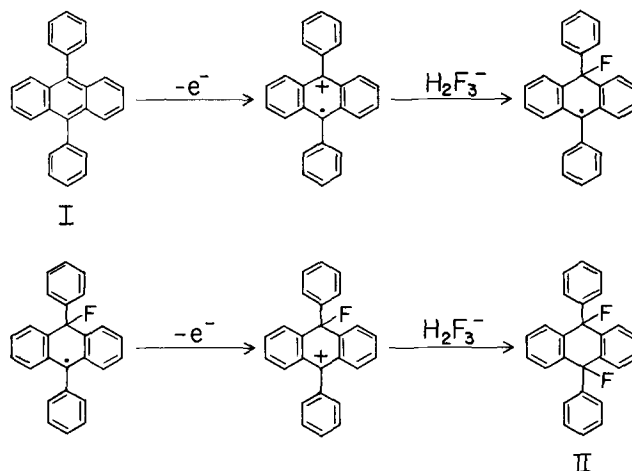


Figure 1.

REFERENCES

1. N. L. Weinberg and H. R. Weinberg, *Chem. Rev.*, **68**, 449 (1968).
2. M. Fleischmann and D. Pletcher, *Tetrahedron Letters*, 6255 (1968).
3. J. Domijan, C. J. Ludman, E. M. McCarron, and R. F. O'Malley, *Inorg. Chem.*, **8**, 1534 (1969).
4. I. L. Knunyants, I. N. Rozhkov, A. V. Bukhtiarov, M. M. Gol'din, and R. V. Kudryavtsev, *Izv. Akad. Nauk SSSR Ser. Khim.*, 1207 (1970).
5. I. N. Rozhkov, A. V. Bukhtiarov, N. D. Kuleshova, and I. L. Knunyants, *Dokl. Akad. Nauk SSSR*, **193**, 1322 (1970).
6. H. Schmidt and H. D. Schmidt, *J. Prakt. Chem.*, **2**, 250 (1955).
7. H. Schmidt and H. Meinert, *Angew. Chem.*, **72**, 109 (1960).
8. R. E. Visco and E. A. Chandross, *J. Am. Chem. Soc.*, **86**, 5350 (1964).
9. M. E. Peover and B. S. White, *J. Electroanal. Chem.*, **13**, 93 (1967).
10. R. E. Sioda, *J. Phys. Chem.*, **72**, 2322 (1968).
11. W. I. Awad, A. K. Fateen, and M. A. Zayed, *J. Org. Chem.*, **26**, 2112 (1961).
12. J. D. Domijan, Ph.D. dissertation, Boston College, 1969.

Integration of Gibbs-Duhem Equation Along Phase Boundaries in Multicomponent Systems

N. A. Gokcen and E. T. Chang

Chemical Thermodynamics Section, Laboratories Operation,
The Aerospace Corporation, El Segundo, California 90245

The experimental data on the partial molar property of one component may be used to calculate all the remaining partial molar properties of a multicomponent system by integrating the Gibbs-Duhem equation. The methods of integration have been presented and discussed in detail in a previous paper (1) and summarized by Pitzer and Brewer (2). These methods consist of graphical integration along a restricted path on which the system is univariant, i.e., an adequate number of restrictions is imposed on the variables of state at constant temperature and pressure so that the path of integration is along one independent variable. We wish to point out in this communication that these restrictions may also be the coexistence of an adequate number of phases, and to show that it is possible to compute the numerical values of the integrand by a new method. The results are useful in checking the thermodynamic data and the compositions of coexisting phases.

The degrees of freedom or the number of independent variables for a system of p phases and c components at constant temperature and pressure is $c - p$; therefore the univariant condition prevails when $p = c - 1$. We illustrate the required mathematical treatment for $c = 3$ and $p = 2$, for which the Gibbs-Duhem relation is

$$-X'_1 d\bar{G}_1 = X'_2 d\bar{G}_2 + X'_3 d\bar{G}_3 \quad [1]$$

$$-X''_1 d\bar{G}_1 = X''_2 d\bar{G}_2 + X''_3 d\bar{G}_3 \quad [2]$$

where X_i is the mole fraction, \bar{G}_i , the partial molar Gibbs energy, or the chemical potential, and the primes denote the phases. The chemical potential of a component in various coexisting phases is the same; hence, we do not need primes over \bar{G}_i . We assume that the data on \bar{G}_1 exists from which we proceed to obtain \bar{G}_2 and \bar{G}_3 . The algebra of determinants may be used to solve for the unknown terms $d\bar{G}_2$ and $d\bar{G}_3$ in Eq. [1] and [2]; thus

$$d\bar{G}_2 = -(D_{13}/D_{23}) d\bar{G}_1 \\ = [(X''_1 X'_3 - X'_1 X''_3)/(X'_2 X''_3 - X''_2 X'_3)] d\bar{G}_1 \quad [3]$$

where the determinants D_{ij} are given by

$$D_{23} = \begin{vmatrix} X'_2 & X'_3 \\ X''_2 & X''_3 \end{vmatrix} \quad \text{and} \quad D_{13} = \begin{vmatrix} X'_1 & X'_3 \\ X''_1 & X''_3 \end{vmatrix} \quad [4]$$

Key words: Gibbs-Duhem, integration, multicomponent, multiphases.

The determinant D_{13} is obtained from D_{23} by substituting the coefficients of $-d\bar{G}_1$ in Eq. [1] and [2] in the first column of D_{23} . Likewise

$$d\bar{G}_3 = -(D_{21}/D_{23}) d\bar{G}_1 \quad [5]$$

In general, for c components and $c - 1$ phases, the determinant in the denominator is

$$D_{23 \dots c} = \begin{vmatrix} X'_2 & X'_3 & \dots & X'_c \\ \cdot & \cdot & \cdot & \cdot \\ \cdot & \cdot & \cdot & \cdot \\ X_2^{(c-1)} & X_3^{(c-1)} & \dots & X_c^{(c-1)} \end{vmatrix} \quad [6]$$

When $c = 2$ and $p = 1$, it is evident that the ratio of determinants in Eq. [3] becomes X'_1/X'_2 and we obtain the following well-known relationship for a binary system

$$d\bar{G}_2 = -(X'_1/X'_2) d\bar{G}_1 \quad [7]$$

Equation [3] may be integrated graphically by plotting D_{13}/D_{23} vs. \bar{G}_1 along the path of coexisting phases and measuring the area under the curve. The experimentally measurable property is $(\bar{G}_i - G_i^\circ)$ where G_i° is the molar Gibbs energy of pure i in a condensed state at one atmosphere, and $(\bar{G}_i - G_i^\circ)$ may be used instead of \bar{G}_i in integrating Eq. [3]. This property may be obtained by measuring the emf of an appropriate cell or by determining the partial pressure of component i . Since $\bar{G}_i - G_i^\circ = RT \ln a_i$, where R is the gas constant in appropriate units, T the temperature in K , \ln the natural logarithm, and a_i the activity of i , it is possible to convert Eq. [3] into the following form

$$\ln a_2 - \ln a_3 \text{ (at } X_1 = \alpha) = - \int_{X_1=\alpha}^{X_1} (D_{13}/D_{23}) d \ln a_1 \quad [8]$$

The equation corresponding to $\ln a_3$ can readily be obtained by interchanging the subscripts 2 and 3 in Eq. [8]. We emphasize that the method by which the integrand D_{13}/D_{23} can be computed constitutes a new and convenient procedure.

We illustrate the usefulness of Eq. [8] by the published data summarized in Landolt-Börnstein (3) for the system benzene-water-ethanol, C_6H_6 - H_2O - C_2H_5OH at $64.9^\circ C$, as listed in Table I. The published values of a_i were calculated (3) from $a_i = P_i/P_i^*$ where P_i is the partial pressure of i over a selected pair of coexisting liquids obtained from the measured values of total pressure and the vapor composition, and P_i^* is the

Table I. Activities in two ternary systems. X_i and a_i are mole fraction and activity of component i , respectively. They refer to two coexisting phases on the same horizontal line. Phases are identified by superscripts over X_i . Experimental data are from a summary in Landolt-Börnstein (3).

System 1—Component 1: C ₆ H ₆ ; 2: H ₂ O; 3: C ₂ H ₅ OH; at 64.9°C											
C ₆ H ₆ -rich phase			H ₂ O-rich phase			Experimental			Calculated		
X ₁ [']	X ₂ [']	X ₃ [']	X ₁ ^{''}	X ₂ ^{''}	X ₃ ^{''}	a ₁	a ₂	a ₃	a ₂	a ₃	
0.819	0.040	0.141	0.006	0.833	0.161	0.931	0.883	0.390	(0.883)*	(0.390)*	
0.664	0.104	0.232	0.021	0.754	0.225	0.910	0.859	0.415	0.861	0.432	
0.555	0.164	0.281	0.048	0.675	0.277	0.899	0.851	0.424	0.851	0.448	
0.486	0.2055	0.3085	0.067	0.635	0.298	0.892	0.854	0.429	0.845	0.456	
0.330	0.331	0.339	0.133	0.536	0.331	0.878	0.859	0.437	0.833	0.471	
0.299	0.3575	0.3485	0.146	0.516	0.338	0.872	0.856	0.439	0.828	0.476	
0.257	0.397	0.346	0.173	0.486	0.341	0.864	0.847	0.440	0.821	0.484	

System 2—Component 1: H ₂ O; 2: C ₃ H ₅ OH; 3: CCl ₄ ; at 65.4°C											
H ₂ O-rich phase			CCl ₄ -rich phase			Experimental			Calculated		
X ₁ [']	X ₂ [']	X ₃ [']	X ₁ ^{''}	X ₂ ^{''}	X ₃ ^{''}	a ₁	a ₂	a ₃	a ₂	a ₃	
0.9675	0.032	0.0005	0.018	0.032	0.950	0.958	0.240	0.979	(0.240)*	(0.979)*	
0.952	0.047	0.001	0.030	0.056	0.914	0.942	0.348	0.941	0.321	0.969	
0.939	0.060	0.001	0.038	0.078	0.884	0.939	0.362	0.937	0.363	0.964	
0.930	0.068	0.001	0.055	0.110	0.835	0.939	0.351	0.943	0.387	0.949	
0.925	0.073	0.002	0.060	0.120	0.820	0.925	0.398	0.927	0.401	0.947	
0.923	0.075	0.002	0.062	0.125	0.813	0.941	0.348	0.943	0.407	0.946	
0.899	0.099	0.002	0.112	0.223	0.665	0.926	0.560	0.860	0.520	0.911	

* Lower integration limit of left side in Eq. [8], same as corresponding experimental value. It is this limit and the convenience in computations that dictate numbering the components. In general, a component is labeled 1 if the experimental data for activity are available for that component.

vapor pressure over pure component i . The activity a_i of each component i is the same in each set of coexisting phases as required by thermodynamics. The data in Table I for the phase relationship are shown in Fig. 1 where the coexisting phases are indicated by the tie-lines. The path of integration for Eq. [8] is along the phase boundary curve where the system is univariant. The lower integration limits in Eq. [8] are taken as the values of a_1 and a_2 at $X_1 = \alpha = 0.819$. The last two columns in Table I contain the values of a_2 and a_3 calculated by Eq. [8]; and they are in poor agreement with the corresponding experimental values of a_2 and a_3 . Significant errors could hardly be ascribed to the vapor pressure measurements, but the analytical errors in the gas, and particularly in the coexisting liquids, are largely responsible for the disagreement between the experimental and the calculated values of a_2 and a_3 . This conclusion is based on the following simple analysis. The expression for $-(D_{13}/D_{23})$ in Eq. [3] and [8] is given by $(X''_1 X'_3 - X'_1 X''_3)/(X'_2 X''_3 - X''_2 X'_3)$. The numerator and the denominator in this expression contain the difference of two terms, and each term is a product of two mole fractions; therefore, small errors in the mole fractions of liquids cause large errors in D_{13}/D_{23} .

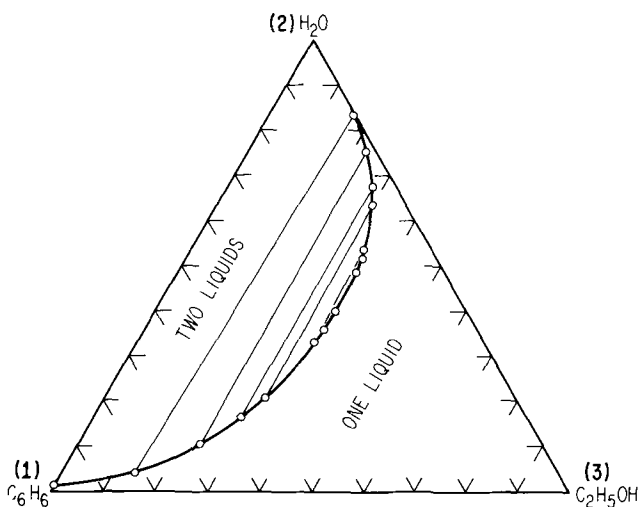


Fig. 1. Ternary system benzene-water-ethanol at 64.9°C; 1, 2, and 3 are component designations. Thin lines are tie-lines joining coexisting phases. Phase boundary curve is univariant. Data are from a summary in Landolt-Börnstein (3).

Similar calculations have also been made by using Eq. [8] and the published values (3) of a_1 for the system water-propanol-carbon tetrachloride, H₂O-C₃H₅OH-CCl₄ at 65.4°C. The results are also listed in Table I. The calculated values agree fairly well with the experimental values for this system. It is, therefore, evident that Eq. [8] provides an excellent check on the consistency of data for a_1 at the phase boundaries.

Equation [8] may also be used in computing the activities in a frequently encountered system, as illustrated by Fig. 2, where the components 2 and 3 are liquids and the component 1 is a solid which dissolves limited amounts of 2 and 3. If the data are available for $\bar{G}_1 - G_1^\circ$ the integration may be carried out as described; however, if there are no data but X_1 , for the solid is greater than 0.9, it is reasonable to assume that for the solid solution Raoult's law is obeyed, i.e., $a_1 = X_1$. The liquid and solid phases may be designated by (') and (") respectively, and the equality of \bar{G}_1 in both phases may be used to obtain

$$G_1^\circ + RT \ln a'_1 = G_1'' + RT \ln X''_1$$

This equation may be rearranged into

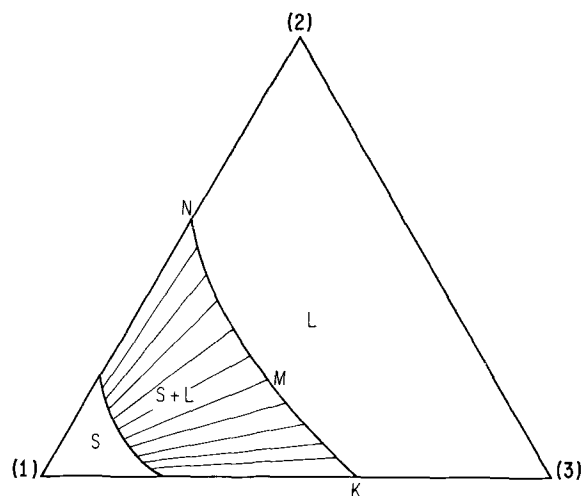


Fig. 2. Hypothetical ternary system formed by pure solid component 1, and pure liquid components 2 and 3. Solid solution is S, liquid solution, L, and thin lines are tie-lines joining coexisting solid and liquid phases. Line KMN shows composition of liquid phase in equilibrium with solid phase.

$$G_1^{\circ} - G_1^{\circ\prime} = -RT \ln (a'_2/X''_1) \quad [9]$$

where the left side is the standard Gibbs energy of fusion which is usually available in convenient tables for simple components (4-6); therefore, a'_1 may be calculated along the liquidus line KMN since X''_1 is also known. From the values of a_1 , it is then possible to calculate the values of a'_2 by Eq. [8], and a'_3 by an equation obtained by interchanging the subscripts 2 and 3 in Eq. [8].

Acknowledgment

This work was conducted under U. S. Air Force Space and Missiles Systems Organization (SAMSO), Contract F04701-71-C-0172.

Manuscript submitted Aug. 9, 1971; revised manuscript received March 16, 1972.

Any discussion of this paper will appear in a Discussion Section to be published in the June 1973 JOURNAL.

REFERENCES

1. N. A. Gokcen, *J. Phys. Chem.*, **64**, 401 (1960).
2. G. N. Lewis and M. Randall, "Thermodynamics," revised by K. S. Pitzer and L. Brewer, 2nd edition, Chap. 34, McGraw-Hill Book Co., Inc., New York (1961).
3. Landolt-Börnstein Tables, 6 Auflage, II Band, 2. Teil, pp. 726, 735, J. Springer, Berlin (1960).
4. R. Hultgren, L. R. Orr, P. D. Anderson, and K. K. Kelley, "Selected Values of Thermodynamic Properties of Metals and Alloys," John Wiley & Sons, Inc., New York (1963).
5. D. R. Stull *et al.*, "JANAF Thermochemical Tables," Clearinghouse for Federal Scientific and Technical Information, U.S. Department of Commerce, Washington, D. C. (1965).
6. D. R. Stull, E. F. Westrum, Jr., and G. C. Sinke, "The Chemical Thermodynamics of Organic Compounds," John Wiley & Sons, Inc., New York (1969).



On the Mechanism of Low-Temperature Oxidation (23°-450°C) of Polycrystalline Nickel

M. J. Graham and M. Cohen*

Division of Chemistry, National Research Council of Canada, Ottawa, Ontario, Canada K1A 0R9

ABSTRACT

The oxidation of "clean" nickel has been investigated from 24° to 450°C at oxygen pressures of 5×10^{-3} to 6×10^{-1} Torr. Ultra-high vacuum techniques made it possible to start oxidation on specimens free of oxide and surface impurities such as C, Si, and S. Oxygen uptake was measured manometrically with a capacitance gauge of submonolayer sensitivity. Initial rapid oxygen adsorption (and place exchange) on nickel was followed by slower oxidation obeying a logarithmic rate law over the thickness range 8-30 Å. Growth of thicker films was in accord with a parabolic rate law, transport through the oxide occurring predominantly via easy diffusion paths. The value of 41 kcal·mole⁻¹ calculated from an Arrhenius plot of the parabolic rate constants from 300° to 450°C is an approximate measure of the activation energy for growth via leakage paths. A $p^{1/6}$ dependence of the parabolic growth rate on oxygen pressure was found at 450°C.

Nickel oxidation is considered to be one of the simpler systems of study since only one oxide, NiO, is produced, and partly for this reason has been the subject of numerous investigations (1). NiO, a p-type semiconductor, grows by the outward movement of nickel cations and electrons via vacancies and holes. At high temperatures, say >1000°C, parabolic growth is generally observed. However, at moderate temperatures (around 500°C), a variety of experimental kinetics have been reported. These include parabolic (2), two stage logarithmic (3, 4), and logarithmic followed by quartic (5) rates of oxidation. It may be that differences in material purity, surface preparation, and pretreatment could account for the variation in experimental data, and the present work on well-characterized surfaces was undertaken in an attempt to resolve some of the discrepancies and, if possible, to present a simplified model for the low-temperature oxidation of nickel.

Experimental

Apparatus.—The oxidation apparatus is shown schematically in Fig. 1. It is an improved design of an earlier manometric system (6), having ultra-high vacuum capabilities (pressures $<3 \times 10^{-10}$ Torr after bakeout at 250°C) and employing a sensitive capacitance gauge to follow the pressure decrease with time during oxidation. The gauge was an M.K.S. Instruments 90H-1, held at 30°C by a temperature controller (Type 1090-1). With the exception of the quartz specimen chamber the apparatus was all metal and contained a working volume of about 1 liter. At oxidation pressures $\sim 5 \times 10^{-3}$ Torr, sub-monolayer adsorption was readily measured. During pressure measurements, the reference side of the capacitance gauge was pumped with an 8 liter · sec⁻¹ ion pump. Specimen heating was by a tube furnace (hot zone variation of $\pm 2^\circ\text{C}$) around the quartz tube.

* Electrochemical Society Active Member.

Key words: kinetics, pressure dependence, manometric apparatus.

Specimen material.—Zone-refined nickel sheet (0.02 cm thick) supplied by Materials Research Corporation was used. It was analyzed to be 99.998% nickel, containing as impurities (in ppm atomic): C, 2; O, 3; F, <0.1; Na, 0.2; Mg, 0.5; Si, 0.7; Cl, 0.2; K, 0.2; Cr, 0.6; Fe, 6; S, not detected.

Gases.—Spectroscopically standardized oxygen (<70 vpm impurities) and hydrogen (<14 vpm impurities) were used (Baker Chemical Company).

Specimen preparation.—Coupons, 0.02 by 1 cm and from 2 to 4 cm long, were degreased, chemically polished for 30 sec at 85°C in a mixture of 30% volume nitric acid, 10% sulfuric acid, 10% phosphoric acid, and 50% acetic acid, and then electropolished for 2 min at 23°C in a 4-volume sulfuric acid:3-volume water mixture at a current density $\sim 0.5 \text{ A} \cdot \text{cm}^{-2}$. Chemical polishing removed about 5 μm and electropolishing 8

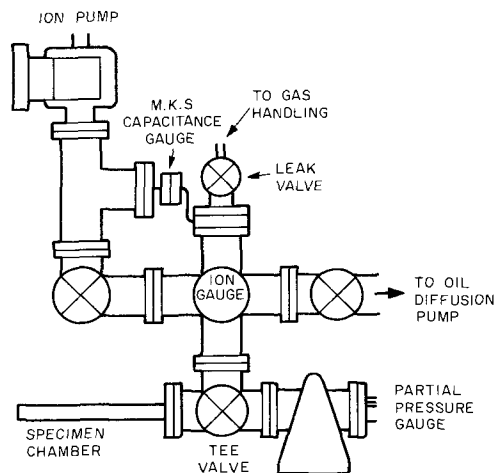


Fig. 1. Manometric oxidation system

μm of material. The specimen was then placed on a platinum support in the quartz tube of the oxidation system.

Oxidation.—After bakeout, the following procedures were carried out.

(i) When the system had cooled, 1 Torr oxygen was admitted for 1 hr to saturate the walls of the system; this minimized surface adsorption during a subsequent oxidation experiment.

(ii) To decrease the carbon impurity concentration the specimen was heated to 700°C and enough oxygen admitted to produce $\sim 100\text{\AA}$ of NiO. During continued annealing of the film in vacuum, CO evolved. [Gas analyzed by an A.E.1 Minimax partial pressure gauge (Fig. 1)]. In some experiments the capacitance gauge was used to follow the pressure increase in the system due to CO formation, presumably by the reaction: $\text{C} + \text{NiO} \rightarrow \text{CO} + \text{Ni}$, and corresponded after $2\frac{1}{2}$ hr at 700°C to the removal of >1 ppm of C from the specimen.

(iii) The remaining oxide was reduced with 1 Torr hydrogen at 600°C . Gas was admitted for 5 min, pumped out, and the system refilled with fresh hydrogen.

(iv) Hydrogen was pumped out and the temperature set to the oxidation temperature. When thermal equilibrium was established and the pressure was $\sim 5 \times 10^{-9}$ Torr, the oxidation was performed. The "tee" valve (Fig. 1) was first closed and the initial oxygen dose size measured before oxidation of the specimen began. In this way, when the tee valve was opened the extremely rapid initial uptake by the specimen could be determined. Calibration runs without specimens at each experimental temperature measured the small uptake on the walls of the system. Oxidation pressures ranged from 5×10^{-3} to 6×10^{-1} Torr; pressures quoted are average values and during the course of oxidation were adjusted to $\sim 25\%$ above (by admitting more oxygen), and allowed to fall $\sim 25\%$ below these values.

Surface and oxide examination.—To ensure that no contamination had occurred, surfaces pretreated as above and oxidized at low temperatures were analyzed for impurities by x-ray emission techniques (7). Replicas of oxide surfaces and stripped oxide films were examined by electron microscopy.

Results

The kinetic curves for the oxidation of polycrystalline nickel ($\sim 120 \mu\text{m}$ average grain diameter) from room temperature to 450°C in 5×10^{-3} Torr oxygen are shown in Fig. 2. Uptake is expressed as μg oxygen

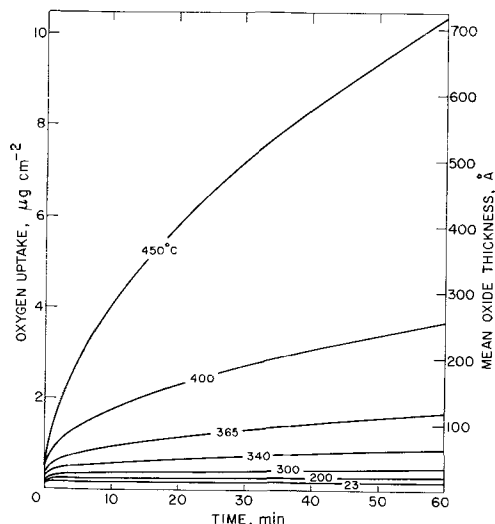


Fig. 2. Oxidation of polycrystalline nickel from 23° to 450°C in 5×10^{-3} Torr oxygen.

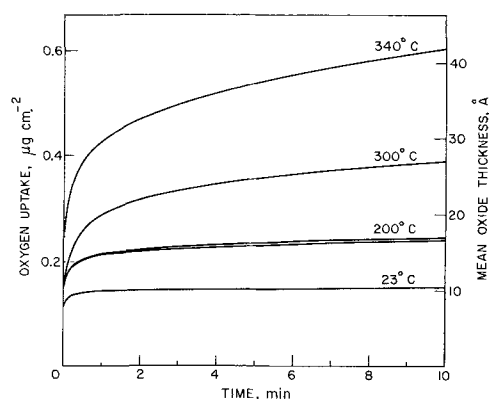


Fig. 3. Early stages of oxidation of polycrystalline nickel up to 340°C in 5×10^{-3} Torr oxygen; expansion of data in Fig. 2.

cm^{-2} . Mean oxide thicknesses are also given and have been calculated assuming a roughness factor of 1 and an NiO density of 6.75 ($1 \mu\text{g}$ oxygen cm^{-2} equivalent to 69.2\AA of NiO). Uptakes are low up to 340°C and the early stages of oxidation are better observed in the expanded plot of Fig. 3. Duplicate experiments were carried out at most temperatures; the reproducibility of oxidation is indicated by the two runs at 200°C .

As seen in Fig. 3, an initial extremely rapid oxidation is followed by a transition to a period of lower oxidation rate. At room temperature an uptake of $0.15 \mu\text{g}$ oxygen cm^{-2} is approached, equivalent to a limiting oxide thickness of about 10\AA . At 200°C a continuing uptake is measured and the data are found to follow a direct logarithmic law of the form, $x = A \ln t + B$, where x is the oxygen uptake (thickness) and t the oxidation time (see Fig. 4). Thin film data (up to $\sim 30\text{\AA}$) at higher temperatures also follow a logarithmic law; the duration of the log dependence diminishes with temperature and at 340°C (as seen in Fig. 4) applies for only the first 2 min of oxidation. Thicker films ($>30\text{-}40\text{\AA}$), as illustrated by data at 340° and 400°C in Fig. 5, grow in accordance with a parabolic rate law.

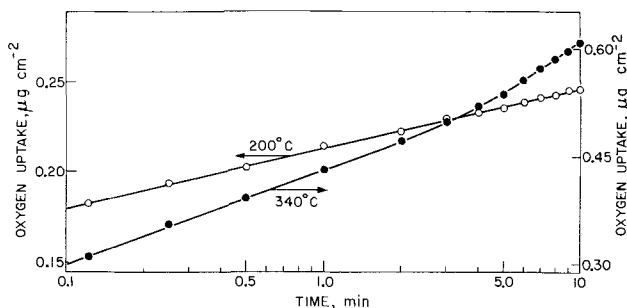


Fig. 4. Logarithmic plot of data from oxidation of a polycrystalline nickel at 200° and 340°C .

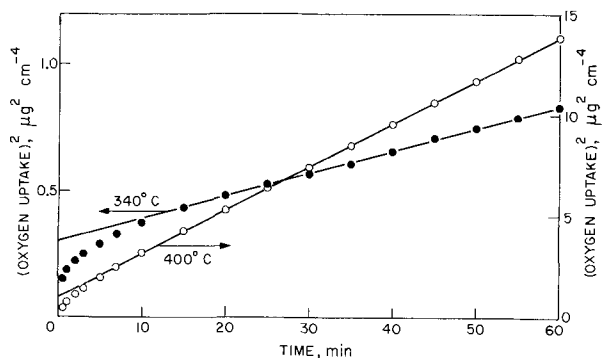


Fig. 5. Parabolic plot of data from oxidation of polycrystalline nickel at 340° and 400°C .

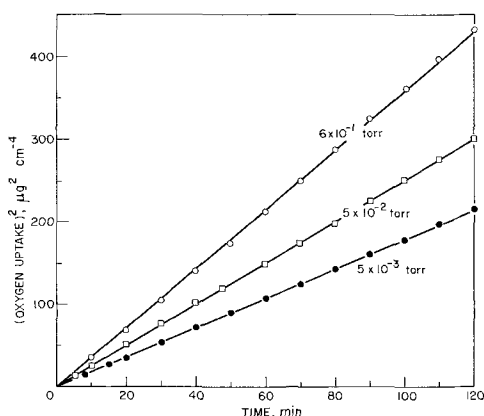


Fig. 6. Parabolic plots of data from the oxidation of polycrystalline nickel at 450°C in 5×10^{-3} , 5×10^{-2} , and 6×10^{-1} Torr oxygen.

To examine the effect of pressure on the kinetics, oxygen uptakes at 450°C were measured at three different pressures: 5×10^{-3} , 5×10^{-2} , and 6×10^{-1} Torr. In Fig. 6 the data are plotted parabolically and a good relationship is observed. Expressing the rate constant, K_p , proportional to $(\text{oxygen pressure}, p)^{1/n}$, the value of n can be obtained by plotting $\log_{10} K_p$ against $\log_{10} p$. From Fig. 7 the data fit a reciprocal slope of $n = 6$ much better than one of $n = 4$. Although only three orders of magnitude of pressure could be covered with the present gauge, a $p^{1/6}$ relationship would seem to be applicable, at least over the present range of study.

Discussion

The oxidation may be considered to proceed in three stages. Initial adsorption (and place exchange) is followed by slower oxidation obeying a logarithmic law (from oxide thicknesses 8–30 Å), and if the temperature is sufficiently high for further thickening to occur, this continued growth obeys a parabolic rate law.

Initial stage.—Evaporated metal films have been used extensively for measurements of sticking coefficients (8), heats of adsorption (9, 10), and surface potentials (11, 12) of oxygen on nickel from -196° to 150°C . On nickel single crystals, electron diffraction techniques have identified sub-monolayer structures (13–16). If nickel and other metals such as Fe, Co, and Ti are exposed to oxygen at room temperature, more than a monolayer of oxygen is rapidly adsorbed with an unchanging heat of adsorption. The heats of adsorption measured are similar to heats of formation of the oxide (9), and coverage values on nickel at saturation correspond to about two to three oxygen atoms per surface metal atom (9, 10). The present data at room temperature give an instantaneous uptake

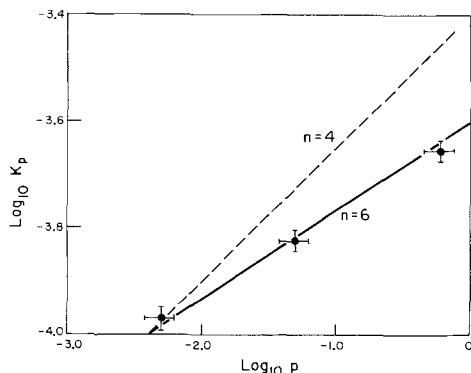


Fig. 7. Logarithm of parabolic rate constants for oxidation of polycrystalline nickel at 450°C plotted against logarithm of oxidation pressure. The bars on the data indicate the considered errors. Lines drawn have reciprocal slopes $n = 6$ and $n = 4$.

approaching a coverage value of three. It is considered that rearrangement of the initial adsorbed layer occurs by a process of rapid place exchange (17, 18), resulting in the formation of nickel oxide.

Logarithmic growth.—Continued growth on the initial oxide occurs much more slowly and the present data follow a logarithmic rate law from ~ 8 –30 Å, as illustrated by results at 200° and 340° in Fig. 4.

Previous work on nickel oxidation in this thickness range has also indicated logarithmic growth (19, 20), and many theories have been developed to account for logarithmic kinetics (21–27). Besides the difficulty in deciding whether thin film data follow a direct or indirect logarithmic law (the present results fit the former better), the absence of other information such as the pressure dependence and the effect of electric fields on thin film growth, makes it difficult to favor a particular process (either electron or ionic transport, or chemisorption at the outer oxide surface) as the rate-determining step.

Parabolic growth.—For oxide thicknesses above 30–40 Å the data follow parabolic kinetics (see Fig. 5 and 6).¹ As mentioned earlier various rate laws have been previously reported for nickel oxidation at 400°–500°C including parabolic (2), two stage logarithmic (3, 4), and logarithmic followed by fourth power (5). We would consider that the variety of results arise from the development of structurally different oxides whose formation has been influenced by the nature of the starting surface. In this intermediate temperature range where grain boundary diffusion is an important factor, a change in oxide grain size with oxidation time could cause a continued decrease in the apparent parabolic rate constant (28), accounting for deviation from parabolic kinetics. The initial oxide grain size and epitaxy will depend on the nature (both chemical and physical) of the surface prior to oxidation. Impurities such as carbon and sulfur tend to segregate at the nickel surface (29, 30) and the influence of carbon and silicon on the oxide epitaxy has been reported (31). Also, the presence of a prior oxide film affects subsequent oxide morphology and growth, a point which is demonstrated in the following paper (32). The oxide-free starting surfaces in this work are considered to be clean; the experimental procedure resulted in surface impurity concentrations of sulfur, silicon, and iron below the limit of detection of the x-ray emission technique (7), which is about 5% of a monolayer. Carbon impurity levels were also usually as low, although with decreasing oxidation temperature there was an increased probability of carbon contamination due to cracking of the $<10^{-9}$ Torr background carbon monoxide.

Oxides produced on these "clean" and flat nickel surfaces were not well oriented; thinner oxides (a few hundred angstroms thick) exhibited preferred orientation, but with increasing thickness tended to become more polycrystalline. In addition, oxide grain size increased with temperature, from ~ 100 Å at 300°–340°C to ~ 1000 Å at 450°C. The many grain boundaries, and perhaps subgrain boundaries present in these oxide films are considered to be paths for easy nickel diffusion (33, 34), the anisotropy of oxidation in the thin-film range reflecting a varying density of these high-diffusivity paths (35). Because of structural changes of the oxide with temperature, the activation energy of 41 kcal·mole⁻¹ calculated from the parabolic rate constants over the temperature range 300°–450°C (see Fig. 8) is considered to be only an approximate measure of the activation energy for growth via leakage paths.²

¹ Good parabolic behavior was maintained in the longest oxidation experiment performed—64 hr at 450°C (oxide thickness $\sim 1 \mu\text{m}$).

² As will be seen in the following publication, a line of slope 37 kcal·mole⁻¹ may be drawn through the present data and rates of oxidation from 500° to 700°C. This value, while again probably not an accurate measure of the activation energy for growth via leakage paths because the structure of the oxide is changing with temperature, is significantly less than values ≥ 52 kcal·mole⁻¹ representative of lattice diffusion through nickel oxide (32).

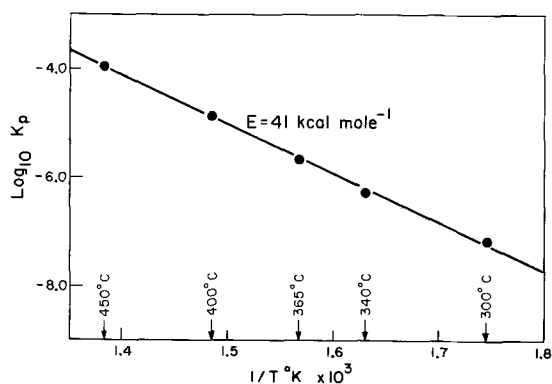


Fig. 8. Logarithm of parabolic rate constants for oxidation of polycrystalline nickel from 300° to 450°C in 5×10^{-3} Torr oxygen plotted against (absolute temperature) $^{-1}$.

Pressure dependence of parabolic growth.—The degree of ionization of nickel vacancies in NiO has been a matter for discussion (36). From electrical conductivity measurements at high temperatures (around 1000°C), both singly ionized (37-39) and doubly ionized vacancies (40-42) have been proposed as the predominant defect. The present results of the effect of oxygen pressure (5×10^{-3} to 6×10^{-1} Torr) on the oxidation rate at 450°C as seen in Fig. 7, fit a $p^{1/6}$ dependence, consistent with the formation and movement of doubly charged cation vacancies.

Acknowledgment

The authors thank Dr. D. Caplan for helpful discussion. This was paper N.R.C.C. No. 12444.

Manuscript submitted Nov. 29, 1971; revised manuscript received Feb. 15, 1972.

Any discussion of this paper will appear in a Discussion Section to be published in the June 1973 JOURNAL.

REFERENCES

- G. C. Wood, I. G. Wright, and J. M. Ferguson, *Corrosion Sci.*, **5**, 645 (1965).
- W. J. Moore and J. K. Lee, *Trans. Faraday Soc.*, **48**, 916 (1952).
- H. H. Uhlig, J. Pickett, and J. MacNairn, *Acta Met.*, **7**, 111 (1959).
- J. C. Rocaries and M. Rigaud, *Scripta Met.*, **5**, 59 (1971).
- K. Haufler, L. Pethe, R. Schmidt, and S. R. Morrison, *This Journal*, **115**, 456 (1968).
- M. J. Graham, S. I. Ali, and M. Cohen, *ibid.*, **117**, 513 (1970).
- P. B. Sewell, D. F. Mitchell, and M. Cohen, *Develop. Appl. Spectr.*, **7A**, 61 (1969).
- A. M. Horgan and D. A. King, *Surface Sci.*, **23**, 259 (1970).
- D. Brennan, D. O. Hayward, and B. M. W. Trapnell, *Proc. Roy. Soc. (London)*, **A256**, 81 (1960).
- D. Brennan and M. J. Graham, *Discussions Faraday Soc.*, **41**, 95 (1966).
- C. M. Quinn and M. W. Roberts, *Trans. Faraday Soc.*, **60**, 899 (1964).
- T. A. Delchar and F. C. Tompkins, *Proc. Roy. Soc. (London)*, **A300**, 141 (1967).
- L. H. Germer and A. U. MacRae, *J. Appl. Phys.*, **33**, 2923 (1962).
- R. L. Park and H. E. Farnsworth, *J. Chem. Phys.*, **40**, 2345 (1964).
- A. U. MacRae, *Surface Sci.*, **1**, 319 (1964).
- P. B. Sewell and M. Cohen, *Appl. Phys. Letters*, **7**, 32 (1965).
- M.A.H. Lanyon and B. M. W. Trapnell, *Proc. Roy. Soc. (London)*, **A227**, 387 (1955).
- D. D. Eley and P. R. Wilkinson, *ibid.*, **A254**, 327 (1960).
- W. E. Campbell and U. B. Thomas, *Trans. & J. Electrochem. Soc.*, **91**, 623 (1947).
- K. Haufler and B. Ilshner, *Z. Electrochem.*, **58**, 382 (1954).
- N. F. Mott, *Trans. Faraday Soc.*, **36**, 472 (1940).
- N. Cabrera and N. F. Mott, *Rept. Progr. Phys.*, **12**, 163 (1948-49).
- T. B. Grimley and B. M. W. Trapnell, *Proc. Roy. Soc. (London)*, **A234**, 405 (1956).
- A. T. Fromhold, Jr. and E. L. Cook, *Phys. Rev.*, **158**, 600 (1967).
- I. M. Richie and G. L. Hunt, *Surface Sci.*, **15**, 524 (1969).
- F. P. Fehlner and N. F. Mott, *Oxid. of Metals*, **2**, 59 (1970).
- D. E. Davies, U. R. Evans, and J. N. Agar, *Proc. Roy. Soc. (London)*, **A225**, 443 (1954).
- E. A. Gulbransen and K. F. Andrew, *This Journal*, **101**, 128 (1954).
- E. N. Sickafus, *Surface Sci.*, **19**, 181 (1970).
- J. M. Blakely, J. S. Kim, and H. S. Potter, *J. Appl. Phys.*, **41**, 2693 (1970).
- L. B. Garmon, Ph.D. Thesis, Univ. of Virginia (1966).
- M. J. Graham, G. I. Sproule, D. Caplan, and M. Cohen, *This Journal*, **119**, 883 (1972).
- J. M. Perrow, W. W. Smeltzer, and R. K. Ham, *Acta Met.*, **15**, 577 (1967).
- J. M. Perrow, W. W. Smeltzer, and J. D. Embury, *ibid.*, **16**, 1209 (1968).
- J. V. Cathcart, G. F. Petersen, and C. J. Sparks, Jr., *This Journal*, **116**, 664 (1969).
- Z. M. Jarzebski and S. Mrowec, *Oxid. of Metals*, **1**, 267 (1969).
- H. H. Baumbach and C. Wagner, *Z. Physik. Chem.*, **B24**, 59 (1934).
- I. Bransky and N. M. Tallan, *J. Chem. Phys.*, **49**, 1243 (1968).
- J. T. Cox and C. M. Quinn, *J. Mater. Sci.*, **4**, 33 (1969).
- S. P. Mitoff, *J. Chem. Phys.*, **35**, 882 (1961).
- S. Pizzini and R. Morlotti, *This Journal*, **114**, 1179 (1967).
- Y. D. Tretyakov and R. A. Rapp, *Trans. AIME*, **245**, 1235 (1969).

The Effect of Surface Preparation on the Oxidation of Nickel

M. J. Graham, G. I. Sproule, D. Caplan, and M. Cohen*

Division of Chemistry, National Research Council of Canada, Ottawa, Ontario, Canada K1A 0R9

ABSTRACT

A study was made of the effect of surface preparation and pretreatment on the oxidation of zone-refined nickel from 500° to 700°C. "Clean," hydrogen-reduced surfaces, maintained essentially free of impurities such as S, Si, Fe, and C, oxidized at a faster rate than air-exposed electropolished or etched annealed nickel. At 700°C, the rapid rate, arising from a high leakage path density in the oxide, resulted in the formation of voids at the metal-oxide interface. The oxidation rate of electropolished and etched specimens was strongly dependent on substrate orientation and this anisotropy, responsible for a slower average oxidation rate, reflected varying contributions of leakage path diffusion. Very thin oxides, as on nickel orientations near (112) after electropolishing, formed primarily by lattice diffusion and the parabolic rate constant at 600°C was $\sim 10^4$ lower than for the thickest oxides. Correlation with other studies in the laboratory indicates that the activation energy for the growth of NiO on Ni is ≥ 52 kcal·mole⁻¹ for lattice diffusion and approximately 37 kcal·mole⁻¹ for leakage path diffusion.

A previous paper described the kinetics of oxidation from room temperature to 450°C (1) of polycrystalline nickel free of oxide and surface impurities. Oxides formed were fine grained and nickel diffusion via grain boundaries was considered to be the major transport process. Differences in kinetics and oxide structure were found on extending the work up to 700°C. The parabolic rate constant changed with time and oxide-metal separation was evident. This paper discusses these results together with the effect of different surface preparations (either sulfuric acid electropolish or nitric acid etch) on the oxidation of nickel surfaces.

Experimental

Zone-refined polycrystal and single-crystal nickel specimens were used. Analysis of the 99.998% polycrystalline sheet (0.02 cm thick) has been given previously (1). Single crystals were spark machined from rods of similar purity; contamination from cutting was eliminated by the removal of 100 μ m of nickel by chemical polishing (1).

Oxidations were performed in a manometric system (1) using two distinctly different starting procedures:

(a) "Hot-bare" oxidations were performed on surfaces free of prior oxide; i.e., the oxide film present after electropolishing in H₂SO₄ was reduced in hydrogen before admitting oxygen to the specimen at temperature. Starting surfaces were also free of impurities such as S, Si, Fe, and C. (See Ref. (1) for further details of procedure.)

(b) "Furnace-raised" oxidations involved heating the electropolished or etched specimen to the oxidation temperature in the presence of oxygen.

(i) Electropolishing was in a 4-volume H₂SO₄:3-volume H₂O mixture for 2 min at room temperature, which removed ~ 8 μ m of material. Prior to electropolish, polycrystalline specimens were chemically polished for 30 sec (removing 5 μ m of nickel).

(ii) Etching was for 30 sec in 5% HNO₃ which removed ~ 200 Å of nickel. Before etching, specimens were chemically polished and then electropolished for 30 sec.

Characterization of the oxide films was carried out by reflection electron diffraction, x-ray emission analysis, transmission and scanning electron microscopy, and metallography.

* Electrochemical Society Active Member.
Key words: kinetics, oxide morphology.

Results

Hot-bare oxidation.—Oxidation of polycrystalline nickel sheet at 0.5 Torr¹ was performed at 500°, 600°, and 700°C for times up to 70 hr.

Oxygen uptake and (oxygen uptake)² for the first 20 hr of oxidation at 500° and 600°C are shown in Fig. 1 and 2. At both temperatures good parabolic plots are obtained. Instantaneous parabolic rate constants K_p , expressed as $2w \cdot dw/dt$ (twice the oxygen uptake times the rate of uptake) were determined and as seen in Table I also demonstrate that K_p changes little with time.

At 700°C, the oxidation showed poor reproducibility, as illustrated by the three runs shown in Fig. 3. Differences occur after the first hour of oxidation, run 1 exhibiting an abrupt change in oxidation rate. Run 2 is plotted on parabolic coordinates in Fig. 4 where it is seen that K_p for this experiment is also decreasing with time, falling from 7.6×10^{-2} mg²cm⁻⁴hr⁻¹ at 0.1 hr to 2.3×10^{-2} mg²cm⁻⁴hr⁻¹ at 20 hr (see also Table I).

Figure 5 shows the structure of oxide films formed at 700°C. Oxide of run 3 (Fig. 3) comprises only one

¹ Pressures quoted are average values and during oxidation were adjusted to $\sim 25\%$ above and allowed to fall to $\sim 25\%$ below these values.

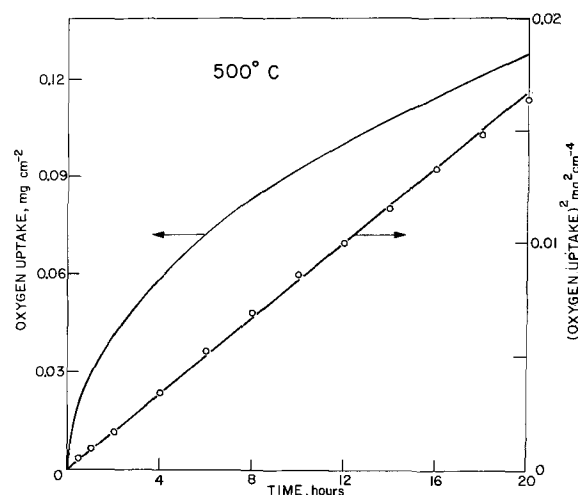


Fig. 1. Hot-bare oxidation of polycrystalline nickel at 500°C and 0.5 Torr oxygen.

Table I. Parabolic rate constants for hot-bare and furnace-raised nickel oxidations at 0.5 Torr oxygen

Specimen preparation and run number	Temperature, °C	Parabolic rate constant,* mg ² cm ⁻⁴ hr ⁻¹ at			
		0.1 hr	2hr	10 hr	20 hr
Hot bare	500	9.2×10^{-4}	7.8×10^{-4}	7.8×10^{-4}	7.7×10^{-4}
Hot bare	600	$\sim 1.1 \times 10^{-2}$	1.1×10^{-2}	9.5×10^{-3}	8.7×10^{-3}
Hot bare (3)	700	9.0×10^{-2}	5.3×10^{-2}	—	—
Hot bare (2)	700	7.6×10^{-2}	5.9×10^{-2}	3.5×10^{-2}	2.3×10^{-2}
Hot bare (1)	700	8.0×10^{-2}	2.7×10^{-2}	8.3×10^{-3}	8.3×10^{-3}
Cold-rolled, electropolished (4)	700	—	5.2×10^{-2}	4.0×10^{-2}	3.3×10^{-2}
Annealed 700°C, electropolished (5)	700	—	3.1×10^{-2}	2.4×10^{-2}	1.9×10^{-2}
Annealed 700°C, etch (6)	700	—	1.3×10^{-2}	9.5×10^{-3}	7.2×10^{-3}

* K_p calculated from slope of uptake curve, as $2w \cdot dw/dt$.

layer [see Fig. 5(a)]. Examination of oxide sections of runs 1 and 2 however revealed the presence of a double-layer oxide. In run 2 the major portion of the scale was one layer [Fig. 5(d,f)], but a few areas of duplex oxide were evident [Fig. 5(e,g)]. Oxide of run 1, which exhibited the marked reduction in oxidation rate, was duplex on all areas [Fig. 5(b)]. The duplex oxide, resulting from loss of oxide contact, comprises an inner layer bridged to the finer grained first-formed oxide. The difference in grain size is clearly evident in Fig. 5(c).

Effect of surface pretreatment on oxidation.—Comparison at 700°C of hot-bare run 2 with furnace-raised oxidation of (i) cold-rolled nickel, electropolished in sulfuric acid (run 4), (ii) annealed nickel, electropolished in sulfuric acid (run 5), and (iii) annealed nickel, etched in nitric acid (run 6) is shown in Fig.

6. The cold-rolled nickel was annealed in vacuum at 700°C after cleaning by chemical polishing and electropolishing. Run 4 oxidizes at a similar rate to hot-bare run 2, which is higher than for annealed, electropolished polycrystalline nickel and annealed, etched polycrystalline nickel surfaces.

Analysis of the kinetic data showed that for furnace-raised oxidation runs 4-6, K_p decreased with time. As seen in Table I, changes are not as marked as for hot-bare experiments, K_p falling at most by a factor of 2 over 20 hr of oxidation. Because of the relatively slow heating to 700°C (~ 4 min), oxidation rates at 0.1 hr are not very reliable and have been omitted from the table. The reproducibility of furnace-raised oxidations, as indicated by a repeat of run 5, was found to be about $\pm 3\%$ over 20 hr.

The anisotropy of oxidation at 700°C became more marked as the oxidation rate decreased for runs in Fig. 6, and two extreme cases are shown in Fig. 7. The oxide on hot-bare run 3 [Fig. 7(a,b)] is of uniform thickness over the specimen, whereas the slowest oxidizing run 6 exhibits the greatest variation in oxide thickness with substrate orientation [Fig. 7(c,d)]. The small grained structure of the thick oxides [Fig. 7(b,d)], together with the enhanced oxidation over metal grain boundaries for run 6 [Fig. 7(d)] is indicative of oxide growth via easy diffusion paths through the mismatched oxide.

The early stages of oxidation of the various pretreated surfaces were determined at 600°C. As in Fig. 8, hot-bare nickel oxidizes at the fastest rate, and electropolished polycrystalline nickel oxidizes more slowly initially than etched nickel. After a time, however, an increase in the oxidation rate of electropolished nickel is observed, resulting eventually in a cross-over of the curves; at greater oxide thicknesses etched nickel oxidizes at the slower rate, consistent with the data at 700°C. The data, of course, represent

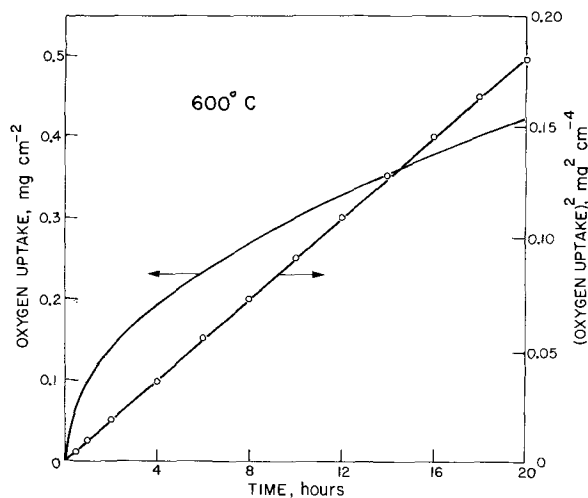


Fig. 2. Hot-bare oxidation of polycrystalline nickel at 600°C and 0.5 Torr oxygen.

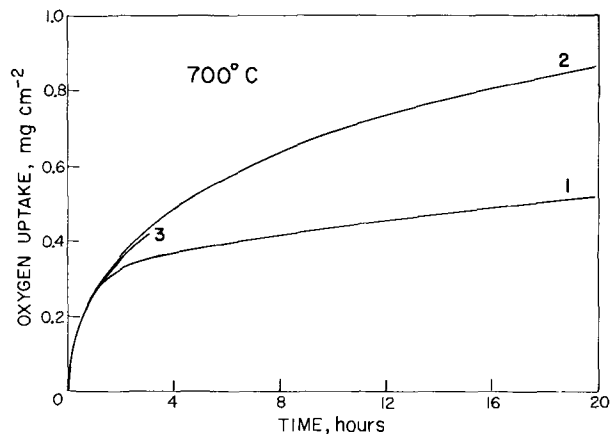


Fig. 3. Hot-bare oxidation of polycrystalline nickel at 700°C and 0.5 Torr oxygen showing nonreproducibility of oxidation.

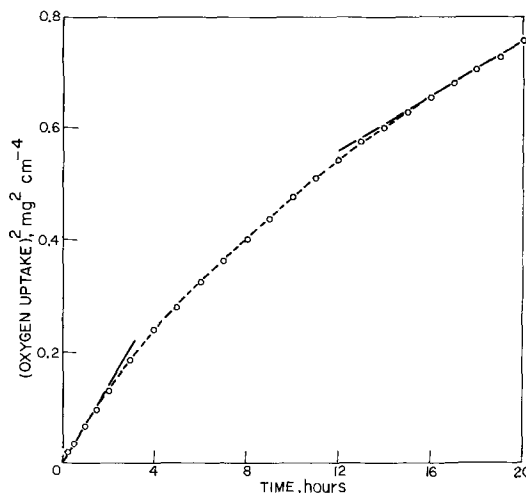


Fig. 4. Plot of (oxygen uptake)² vs. time at 700°C for data of hot-bare run 2, showing deviation from parabolic behavior.

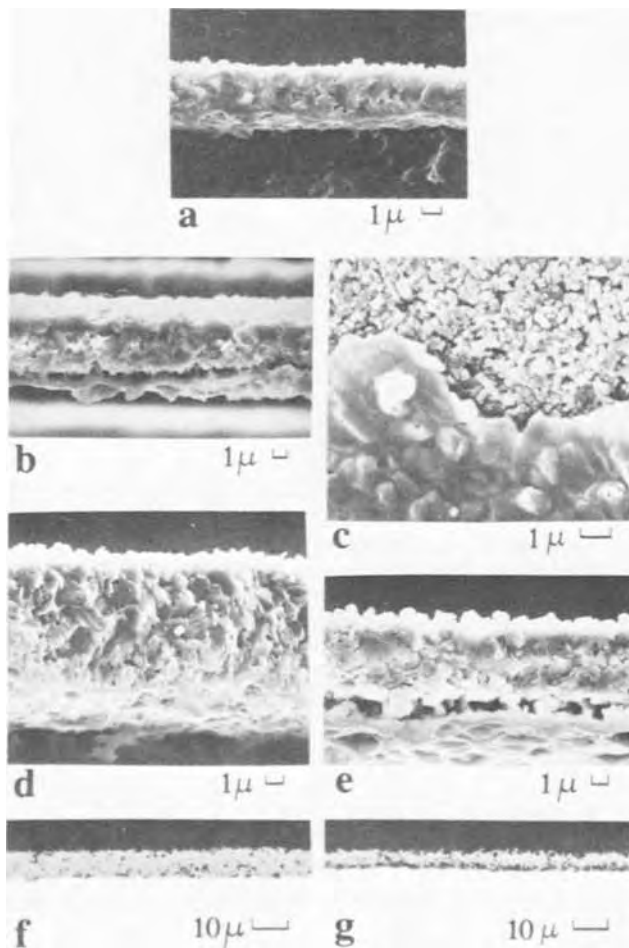


Fig. 5. Structure of oxides formed during hot-bare oxidation at 700°C. (a) Scanning electron micrograph showing cross section and undersurfaces of single-layered oxide of run 3. (b) Scanning electron micrograph showing duplex oxide scale of run 1; loss of oxide contact resulted in the formation of the inner thin layer of oxide. (c) Scanning electron micrograph showing undersurface of the double-layered oxide of run 1; the finer grained oxide (top) was the first formed and the coarser grained oxide (bottom) nucleated after loss of contact of the initial oxide. (d) Scanning electron micrograph showing cross section and undersurface of single-layered oxide of run 2; majority of oxide of run 2 comprised one layer. (e) Scanning electron micrograph showing one of the few duplex oxide areas of run 2. (f), (g) Metallographic cross sections correlating with scanning electron micrographs (d) and (e) respectively, showing single-layered and double-layered oxide of run 2.

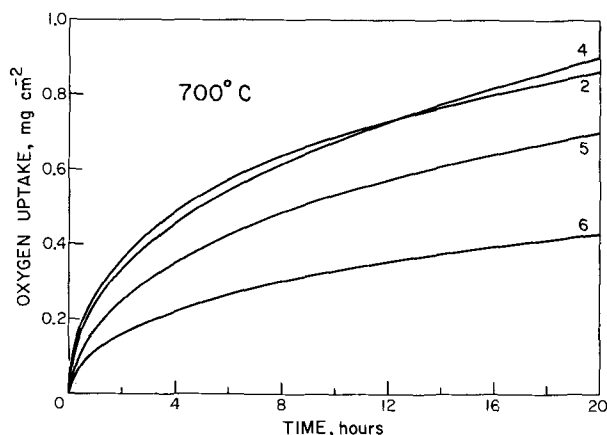


Fig. 6. Effect of pretreatment on the oxidation of polycrystalline nickel at 700°C and 0.5 Torr oxygen. Run 2, hot-bare oxidation; run 4, furnace-raised, cold-rolled, and electropolished; run 5, furnace-raised, annealed, and electropolished; run 6, furnace-raised, annealed, and etched.

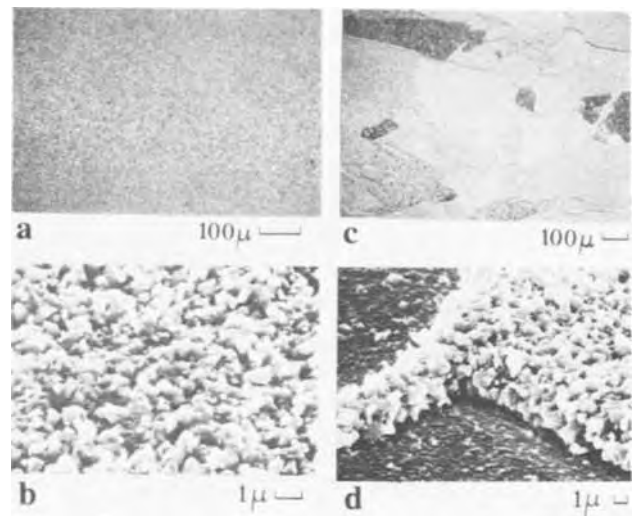


Fig. 7. Scanning electron micrographs of outer oxides formed on polycrystalline nickel at 700°C. (a) and (b), hot-bare run 3; (c) and (d), furnace-raised and etched run 6. Note marked variation in oxide thickness in run 6 (c) compared with uniform oxide of run 3 (a), and thickening of oxide over metal grain boundaries in run 6 (d).

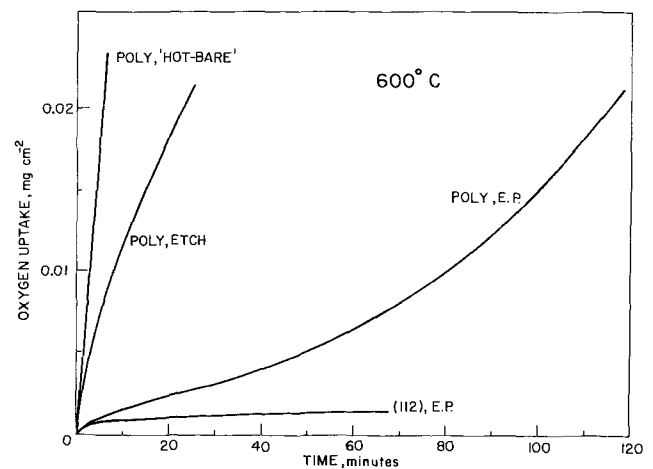


Fig. 8. Effect of surface pretreatment on the early stages of oxidation of nickel at 600°C. Hot-bare oxidation of polycrystalline nickel in 0.5 Torr oxygen; furnace-raised oxidation of etched and electropolished polycrystalline nickel in 0.1 Torr oxygen; furnace-raised oxidation of electropolished (112) nickel in 5×10^{-3} Torr oxygen.

an average oxidation rate of different nickel substrate orientations. Oxidation of a single-crystal hemisphere at 600°C illustrated the marked anisotropy of oxidation, showing that orientations close to (112) after electropolishing in H_2SO_4 oxidize at a very low rate (as low as any orientations after an HNO_3 etch). The oxidation curve for (112) electropolished nickel at 600°C is included in Fig. 8 showing that only $\sim 100\text{\AA}$ of oxide had formed after 1 hr; the data fit a parabolic rate law and the resulting rate constant of $1.7 \times 10^{-6} \text{ mg}^2\text{cm}^{-4}\text{hr}^{-1}$ is about 10^4 lower than for hot-bare oxidations of polycrystalline nickel at 600°C.

Discussion

We shall first consider the hot-bare oxidations, then compare the effect of different surface pretreatments and finally correlate the data with other studies (1, 2).

Hot-bare oxidations.—At 500° and 600°C the data obey a parabolic rate law (Fig. 1 and 2), the instantaneous rate constant changing little with time (see Table I). In hot-bare oxidations, the initial oxide forms extremely rapidly and contains many mismatch boundaries which act as easy diffusion paths for nickel [cf. Fig. 7(b)]. At 700°C, this rapid oxidation rate leads to varying degrees of oxide separation from the metal, and hence the poor reproducibility of runs in Fig. 3. Separation was never observed at lower temperatures.

Oxide separation from the metal is due to void formation at the metal-oxide interface, probably as a result of condensation of inward moving cation vacancies. Presumably, for the first hour of oxidation at 700°C insufficient voids are nucleated to greatly reduce the oxidation rate, but when the oxide is $\sim 2 \mu\text{m}$ thick, the combination of high vacancy flux, high oxide hot strength, and low oxidation pressure³ leads to more complete interfacial detachment. The first-formed oxide continues to grow over unseparated areas, and where loss of contact has occurred an inner oxide layer develops on the metal, producing a duplex scale [Fig. 5(b,e)]. The hot-bare procedure (1) removed most of the carbon impurity from the metal but sufficient remains to provide CO in the void for transporting oxygen between the outer and inner oxide layers [cf. (4)]. The formation of pockets of CO could also contribute to the production of voids at the interface. Examination of the under surface of the duplex oxide by SEM [Fig. 5(c)] showed the first formed oxide to have a much smaller grain size than the new inner layer, and by transmission electron diffraction that the latter grains were well-oriented blocks consistent with the slow growth rate anticipated from the low oxidation potential within the void.

Effect of surface pretreatment on oxidation.—Differences in oxidation rate with surface pretreatment (Fig. 6, 8) may be explained by the formation of varying proportions of oxide high in leakage paths. High oxidation rates are observed in hot-bare run 2 and furnace-raised, cold-rolled electropolished nickel run 4 (Fig. 6), because oxide on all substrate orientations is growing by leakage path diffusion.³ Little variation in oxide thickness is found over these specimens [cf. Fig. 7(a)], with the exception of some separated grains on run 2. The lower oxidation rates in furnace-raised runs with annealed nickel [runs 5, 6 in Fig. 6] demonstrate how pretreatment and the prior oxide affect the leakage path population in the oxide overgrowth. This effect is strongly dependent on the metal orientation, as illustrated by the variation in oxide thickness over the specimen [see Fig. 7(c)]. Some oxide grains are very thin, while others are as thick as those for cold-rolled metal (run 4); run 6 (etched annealed nickel) has the highest proportion of thin grains and consequently the lowest average oxidation rate. The thinnest grains are considered to grow primarily by lattice diffusion.

In all oxidations at 700°C the parabolic rate constant, K_p , decreased with time (see Table I). Explanations proposed (5) are (i) a continuing decrease in the effectiveness of easy diffusion paths because of growth

³ Void formation and the effect of external gas pressure in suppressing oxide separation have been considered for the oxidation of iron (3). Oxidations were faster at 760 Torr than 10³ Torr because voids formed at the Fe₃O₄-Fe interface were squashed closed by higher pressure. Similar considerations could apply for nickel oxidation, the present pressures of 0.5 Torr being insufficient to collapse interfacial voids.

³ The increased oxidation rate of cold-worked over annealed iron (5) and nickel (2) has been considered in detail. For iron oxidation an additional factor was that extra sinks in cold-worked metal facilitated vacancy annihilation suppressing void formation at the metal-oxide interface. Interfacial voids are not generally observed on oxidizing annealed nickel (e.g., runs 5, 6), and the enhanced oxidation rate of cold-rolled nickel (run 4) is primarily due to the production of an oxide high in leakage paths. However, a few thick grains on runs 5, 6 did show evidence of earlier separation as in hot-bare experiments [Fig. 5(b,e)]. Here the oxidation rate and thus the vacancy flux is at a maximum. Since no voids could be found on cold-rolled run 4 where the oxidation rate was as high, one may conclude that residual cold work in nickel has also prevented minor void formation.

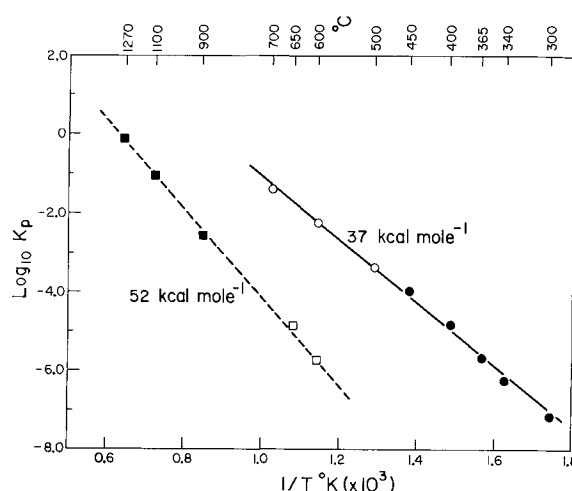


Fig. 9. Arrhenius plot for nickel oxidation from 300° to 1270°C and 5×10^{-3} Torr oxygen pressure. \circ , This work; hot-bare oxidation rates plotted have been obtained by reducing rates of oxidation at 0.5 Torr according to a $p^{1/6}$ dependence (1). \bullet , Previous work (1); hot-bare oxidation rates at 5×10^{-3} Torr oxygen. \square , This work; furnace-raised oxidation of electropolished (112) nickel at 5×10^{-3} Torr. \blacksquare , Caplan et al. (2); cold-insertion oxidation rates were obtained from thickness measurements of the thinnest oxides formed in 760 Torr oxygen, and have been reduced by a $p^{1/6}$ dependence in order to compare with data at 5×10^{-3} Torr oxygen.

of the small oxide grains, and (ii) increasing separation of oxide from the metal. This latter effect gives rise to the abrupt decrease in rate in hot-bare run 1 (Fig. 3) and is a contributing factor in hot-bare run 2. However, oxide separation was minor in runs 3-6 (not observed in runs 3, 4 and only to a small extent in runs 5, 6) and grain growth of the thicker oxide is probably the main reason for the falling K_p in these experiments.

An example of extremely slow oxidation, where the leakage path density in the oxide is approaching a minimum, is on (112) nickel after electropolish (see Fig. 8). Reflection electron diffraction showed the electropolished film (prior oxide) to be well epitaxed and the slow oxidation rate is associated with the retention of the original epitaxy during growth at 600°C. The breakaway characteristics of polycrystalline electropolished nickel in Fig. 8 indicate modification, to varying degrees, on different substrate orientations of the initial epitaxed, protective film and growth of a more polycrystalline oxide high in leakage paths. Subsequent differences in oxidation rate of electropolished or etched surfaces are explained by varying ratios of oxide growing by lattice and leakage path diffusion.

Parabolic rate constants and activation energies.—Differences in K_p approaching 10^4 between hot-bare experiments on polycrystalline nickel, and furnace-raised oxidation of (112) electropolished nickel at 600°C (see Fig. 9) show the marked increase in rate resulting from leakage path diffusion. Leakage path diffusion strongly predominates in all hot-bare oxidations and the low activation energy in Fig. 9 is consistent with this view. A single line of activation energy 37 kcal \cdot mole⁻¹ may be drawn through the present hot-bare rates of oxidation from 500° to 700°C and previous hot-bare data from 300° to 450°C (1). This value only approximates the true activation energy for growth via leakage paths because of structural changes in the oxide with temperature (e.g., the degree of preferred orientation is greater at low temperatures, the oxide grain size increases with temperature, and any contributions from subgrain boundaries decreases with temperature) but it is significantly less than the 52 kcal \cdot mole⁻¹ slope drawn through other data in Fig. 9, considered to represent lattice

diffusion. This latter line correlates present rates of oxidation of (112) electropolished nickel at 600° and 650°C with rates of formation of the thinnest oxide grains at 1270°, 1100°, and 900°C (2). In both cases, essentially single-crystal oxides are produced and the number of grain and subgrain boundaries which could act as easy diffusion paths is approaching a minimum. The low rates of oxidation are governed by bulk diffusion of nickel through the NiO lattice, the activation energy for the process being $\cong 52 \text{ kcal} \cdot \text{mole}^{-1}$.

Acknowledgment

This was paper N.R.C.C. No. 12445.

Some Properties and Electrical Instabilities in RF Sputtered Niobium Oxide Films

Mao-Chieh Chen*

Research Laboratories, General Motors Corporation, Warren, Michigan 48090

ABSTRACT

Niobium oxide films were prepared by rf sputtering in an oxygen atmosphere and various electrical properties were investigated. Forms of ionic instability in the oxide layer were studied in relation to changes in the flat-band voltage during MOS capacitance measurements. As sputtered, the films exhibited the presence of both highly mobile positive and negative ionic charges. When annealed at 800°C in a helium or an oxygen atmosphere, the films exhibited only positive ionic charge. Inclusion of a small amount of trichloroethylene in the oxygen annealing process resulted in oxide films essentially free from ionic instability.

Dielectric films deposited on semiconducting substrates serve many functions in microelectronics technology. Amorphous silicon dioxide films have been used extensively for this purpose and are still the most commonly used dielectrics. However, the diversified requirements of solid-state devices cannot be fulfilled by silicon dioxide films alone. Silicon dioxide is known to have a porous structure, a low dielectric constant, and to be permeable to ionic migration. These problems have therefore prompted the investigation of other oxide and nitride dielectrics, such as the transition-metal oxides (TiO_2 , Ta_2O_5 , and Nb_2O_5).

Niobium oxide (Nb_2O_5) films exhibit desirable resistivity, permittivity, and thermal stability characteristics and are attractive for use in such applications as high-resolution silicon vidicons (1, 2). The high dielectric constant permits a reduction in the area occupied by a capacitor in an integrated circuit. It is also possible to fabricate high value capacitors for uses such as decoupling (3). Dielectric constants of 41 for anodically grown amorphous Nb_2O_5 (4), and as high as 100 for the crystalline phase have been reported (5, 6). In recent years, there have been published reports of niobium oxide thin films prepared by halogen transport reactions (5) and by vapor deposition (1, 7). However, only the vapor-deposited niobium oxide has been investigated by metal-oxide-semiconductor (MOS) techniques (1, 7). A positive oxide charge below $5 \times 10^{11} \text{ cm}^{-2}$ for a 1000Å oxide was reported (1, 7), and a slow trapping type hysteresis was observed (1). Vapor-deposited niobium oxide and anodic niobium oxide films have been reported to be amorphous (1). Vapor-deposited niobium oxide begins to crystallize at a temperature higher than 1200°C, while the anodic

Manuscript submitted Nov. 29, 1971; revised manuscript received Feb. 15, 1972.

Any discussion of this paper will appear in a Discussion Section to be published in the June 1973 JOURNAL.

REFERENCES

1. M. J. Graham and M. Cohen, *This Journal*, **119**, 879 (1972).
2. D. Caplan, M. J. Graham, and M. Cohen, Submitted to *This Journal*.
3. D. Caplan, M. J. Graham, and M. Cohen, *Corrosion Sci.*, **10**, 1 (1970).
4. C. T. Fujii and R. A. Meussner, *This Journal*, **111**, 1215 (1964).
5. D. Caplan and M. Cohen, *Corrosion Sci.*, **6**, 321 (1966).

oxide requires only 500°-600°C (4). In contrast to this, niobium oxides deposited by the halogen transport method tend to be polycrystalline because of the high deposition temperature. In the present case, rf sputtered (in oxygen atmosphere) niobium oxides are polycrystalline, although the substrate temperature was maintained at 150°C.

The current trend in research in this class of materials is to improve the preparation techniques and to understand the fundamental nature of materials, the parameters that influence their behavior, and the effect of associated processes. In this study, the MOS capacitance technique was employed. Along with the experimental procedure, the observed dielectric properties, oxide surface charges, and results of bias-temperature stress tests on the niobium oxide MOS structure are reported and discussed.

Experimental Technique

Polished and (111) oriented silicon wafers were used in the fabrication of the test samples. For surface charge study, epitaxial n-type wafers of 10 ohm-cm resistivity were used as substrates. On the other hand, low-resistivity (0.0014-0.0026 ohm-cm) p-type wafers were used for investigation of the dielectric properties of the sputtered niobium oxide films. Prior to oxide deposition, the silicon wafers were cleaned in a 1:1:1 solution of acetone, isopropyl alcohol, and trichloroethylene, and rinsed in ultrasonically agitated, flowing, deionized water. The niobium oxide films were then deposited by rf sputtering.

A conventional diode-type rf sputtering system was employed for this purpose. The rf generator operating at 13.56 MHz was used as the source of power which was coupled to the target electrode through a tunable MRC (Material Research Corporation) matching network to ensure matching between the coaxial trans-

* Electrochemical Society Active Member.

Key words: dielectric, instabilities in RF sputtered niobium oxide films.

mission line impedance and the sputtering system load impedance. The cathode used was a ceramic niobium pentoxide (Nb_2O_5) (nominal purity 99.99%) disk 5 in. in diameter and $\frac{1}{4}$ in. thick. It was metalized on one side and bonded to a flat water-cooled aluminum disk which formed part of the vacuum chamber wall through a system of vacuum seals and an insulating ring. A metal shield surrounded the exposed areas of the water-cooled aluminum disk at a spacing of 0.5 cm in order to prevent sputtering from this region. The substrate was set on a grounded plate which was situated about 4 cm below the cathode. Most of the depositions were performed in a pure oxygen atmosphere at pressures of 18–20 mTorr and with 0.8 W/cm^2 input power density. By proper tuning, the reflected power was kept to zero, practically, and the rate of deposition was about 30 \AA/min . The support plate was preheated so that nominal substrate temperatures were maintained at about 150°C throughout the entire sputtering process. The deposition was also performed in argon and argon-oxygen mixtures. It turns out that the leakage current of the MOS structure increases as the percentage of oxygen in the argon discharge decreases. In general, the niobium oxide films sputtered in a pure argon atmosphere showed such high conductance that no proper MOS behavior could be observed. It has been reported that chemical reduction of oxides was observed during rf sputtering (8, 9). As a result, the oxide conductivity arises from oxygen deficient niobium oxide. To prevent this, oxygen has to be replenished during the deposition.

Annealing treatments were carried out in two different atmospheres: in helium and in a trichloroethylene/oxygen atmosphere, both at 800°C for 2 hr. In the former case, the wafers were set in a furnace through which helium gas (1.5 liters/min) was flowing. In the latter case, a small amount of trichloroethylene (C_2HCl_3) was introduced into an oxygen gas stream before admission into the annealing furnace (10). Helium flowing at 0.05 liter/min was bubbled through a trichloroethylene solution before being mixed with the oxygen stream of 1.5 liters/min. It should be noted that no special precautions as to the cleanliness of the annealing furnace were taken.

Aluminum gate electrodes were applied to the oxide films by means of thermal evaporation and photomasking (using KMER as photoresist). Gate areas were $3.44 \times 10^{-3} \text{ cm}^2$ (26 mil diameter aluminum dot). Individual devices were diced out, and die and lead bonded to TO-5 headers using ultrasonic bonders.

MOS Device Characteristics

Dielectric relaxation.—The frequency dependence of the loss tangent and capacitance, with sample temperature as the parameter, is shown in Fig. 1(a) and (b), respectively. These data were obtained in small a-c signal measurements on a film sputtered with 0.8 W/cm^2 input power density on a low-resistivity (0.0014–0.0026 ohm-cm) p-type silicon substrate and are reproducible. The oxide is about 5000 \AA thick and is an as-sputtered film. It can be seen that as the temperature is increased, the loss peak shifts to higher frequencies. The corresponding capacitance is roughly inversely proportional to the frequency for the aluminum-niobium oxide-silicon structure. If the logarithm of the frequency corresponding to the dielectric loss peak is plotted against reciprocal temperature (Arrhenius plot), a straight line results as in Fig. 2, implying that there is an exponential dependence of the relaxation times on temperature, $\tau = \tau_0 \exp(E/kT)$. The activation energy, E , of the dispersion process is found to be 1.135 eV. In a Cole-Cole diagram (11), shown in Fig. 3, the data points fall on an arc and thus indicate dielectric dispersion. However, two features of the diagram are to be noted. First, the data points obtained at lower frequencies (right part of the diagram) tend to deviate from the arc. This representation, together with the rising trend of loss

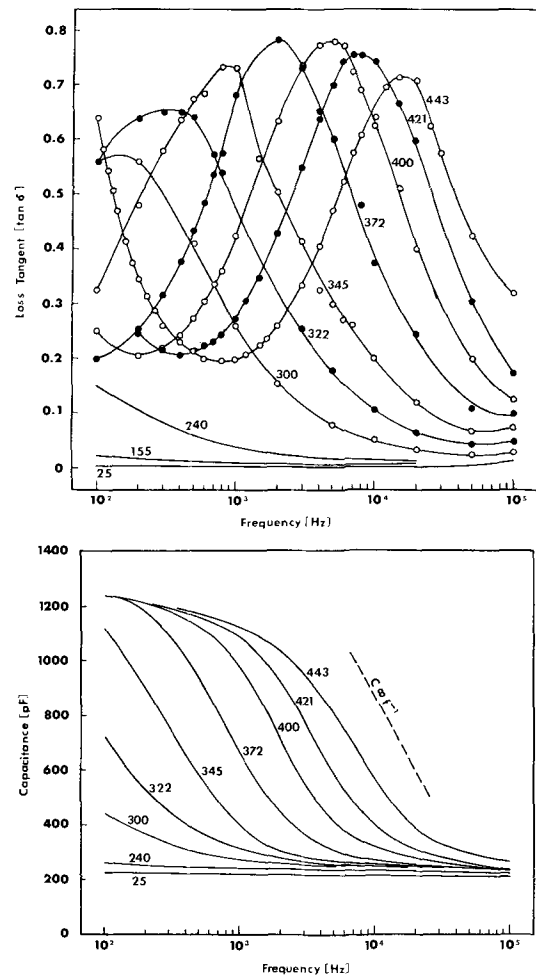


Fig. 1. Loss tangent (a) and capacity (b) behavior as a function of frequency at different temperatures. The number on each curve shows the temperature (in $^\circ\text{C}$) at which each measurement was made.

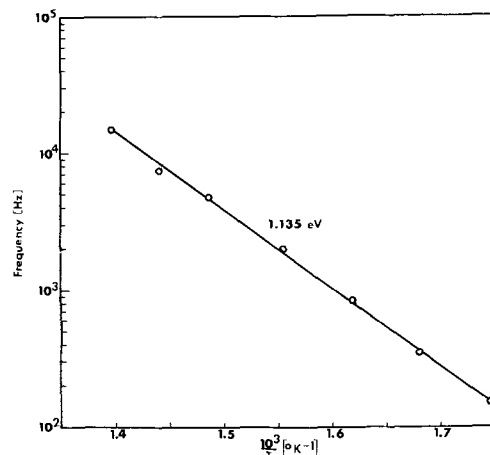


Fig. 2. Loss peak frequency as a function of reciprocal temperature (Arrhenius plot).

tangent at lower frequencies as is evident from Fig. 1, points to the existence of another well-separated dispersion region which is beyond the available frequency range. Second, the arc of the Cole-Cole diagram is displaced downward. A polydispersion with several closely distributed relaxation times (12) would explain the phenomena. It is widely accepted that the dielectric constant can be expressed, in this case, as

$$\epsilon(\omega) - \epsilon_\infty = \frac{\epsilon_0 - \epsilon_\infty}{1 + (i\omega\tau)^\beta}$$

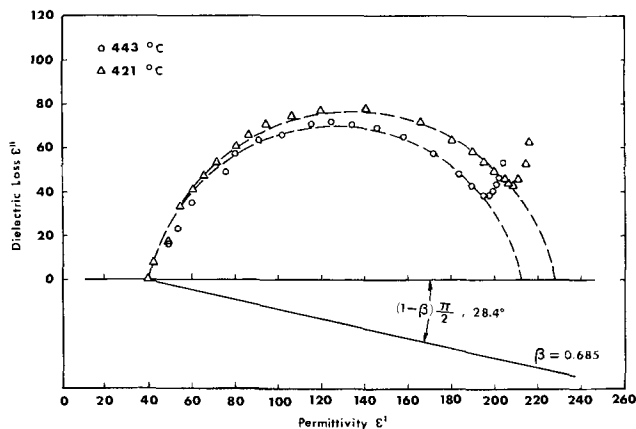


Fig. 3. Cole-Cole diagram for niobium oxide with aluminum and silicon (0.0014-0.0026 ohm-cm p-type) electrodes at 443° and 421°C.

where β represents a measure of deviation from the mono-disperse system, and its meaning is shown in Fig. 3; and ϵ_0 and ϵ_∞ are the values of permittivity at zero and infinite frequencies, respectively. The value of β was determined to be 0.685.

MOS capacitance and effective surface charges.—The capacitance-voltage curves of MOS structures shown in Fig. 4 are typical ones representing niobium oxide as sputtered in a pure oxygen atmosphere at power densities of 0.32, 0.80, and 1.25 W/cm², respectively, as well as the 800°C annealed specimens. The film thickness for the respective sample is tabulated in Table I. These curves indicate that the total surface charge, as measured from the flat-band voltage of the C-V characteristics, increases with sputtering power density. Similar observations of the deterioration of the silicon surface properties in using high power densities were also reported by Hu and Gregor (13) and Salama (14). The measured dielectric constant of the sputtered niobium oxide appears to increase with sputtering power density, ranging from 18 at a power density of 0.32 W/cm² to 33 at 0.8 W/cm² and to 58 at 1.25 W/cm². Low film density related to low power density has been reported (13, 14). However, densification by a factor of 3 is unlikely, and the low dielectric constant observed at low power densities may arise from compositional difference.

The typical C-V curves of C₂HCl₃/O₂, He, and O₂ annealed samples are also shown in Fig. 4. These were annealed from the samples sputtered at the power density of 0.80 W/cm². It is seen that these annealed samples exhibit a steeper slope in their C-V curves. This reveals, therefore, that the annealing effect has

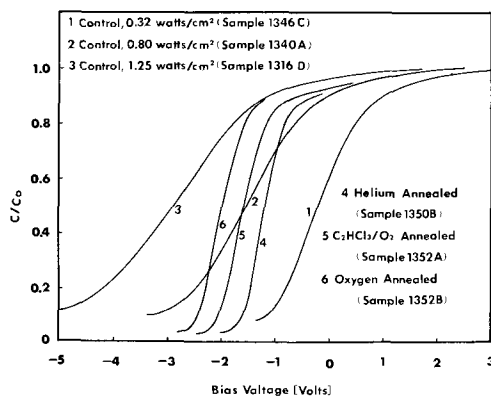


Fig. 4. Experimental MOS C-V characteristics of rf sputtered niobium oxide measured at 300°K and 1 MHz. The substrates are (111) oriented epitaxial n-type silicon wafers of 10 ohm-cm resistivity. Annealing was performed at 800°C for 2 hr from the samples sputtered at the power density of 0.80 W/cm².

Table I. Effective surface charge density for various niobium oxide specimens

Annealing is performed at 800°C for 2 hr

Sample No.	Effective surface charge density (No./cm ²)	Thickness (Å)	Sputtering power density (W/cm ²)	Sample preparation
1346C	(0.68-2.0) × 10 ¹¹	2240	0.32	Control
1316D	(2.0-3.0) × 10 ¹²	4250	1.25	Control
1340A	(6.85-9.75) × 10 ¹¹	3480	0.80	Control
1350A	(7.20-11.20) × 10 ¹¹	4050	0.80	Control
1346D	(8.55-10.0) × 10 ¹¹	3850	0.80	Control
1340B	(1.02-1.18) × 10 ¹²	3480	0.80	Annealed in C ₂ HCl ₃ /O ₂
1352A	(1.75-1.81) × 10 ¹²	5830	0.80	Annealed in C ₂ HCl ₃ /O ₂
1350B	(1.75-1.84) × 10 ¹²	4050	0.80	Annealed in He
1352B	(2.77-2.82) × 10 ¹²	5830	0.80	Annealed in O ₂

reduced the fast interface states. The dielectric constants as obtained from their MOS capacitance measurements were 120, 93, and 143 for the C₂HCl₃/O₂, He, and O₂ annealed samples, respectively. The drastic increase in the dielectric constant is not understood. Values of the dielectric constant around 120 have been reported for the H-modification, polycrystalline films of Nb₂O₅ (5). Investigation of the pre- and post-annealed samples, using a scanning electron beam microscope with 15,000X and 30,000X magnification, clearly showed different patterns. The unannealed samples showed a smooth, amorphous-like surface, while the annealed samples revealed clear crystalline structure. However, x-ray diffraction pattern analysis indicated that for both samples crystalline phases are deposited, and both patterns are identical. Unfortunately, positive identification was not possible with available ASTM¹ data.

The effective oxide surface charge density for the various oxide specimens was evaluated from the flat-band voltage. The results are tabulated in Table I. These data were obtained from at least five randomly selected samples in each case. It is seen that the as-sputtered films have a larger dispersed distribution of their effective surface charge than those of the annealed films. On the other hand, the annealed films have a little higher effective surface charge density.

Ionic instabilities.—The films, as deposited and unannealed, exhibited a high degree of ionic instability even at room temperature. In order to investigate the fast ionic movement under applied bias, a 60 Hz sine wave voltage was used to sweep the device voltage, and the C-V curve was displayed on the oscilloscope. After the initial curve was obtained, the sweeping voltage was then turned off, and a d-c bias was applied to the device for a predetermined period of time. The d-c bias was then removed, and the sweeping voltage was applied to generate the C-V curve, which was displayed on the oscilloscope and a picture taken. The above process was quickly manipulated in a few seconds in order to minimize any recovery effect. Figure 5(a) and (b) are pictures showing the shifting of the C-V curves under positive and negative bias stress, respectively. The film exhibits more negative flat-band voltage after positive stress and more positive flat-band voltage after negative stress. This depicts the movements typical of ionic migration in the oxide and also clearly indicates the presence of a fairly large negative charge density in the layer (15). Similar phenomena of ionic instabilities were reported in pyrolytically deposited SiO₂ films (16). After 2 hr of stress, the rapid charge movements were further detected by short-circuiting the devices. Figure 5(c) and (d) shows the results, indicative of a highly mobile charge species. This high mobility of charge species has caused some difficulty in the recording of the C-V curves because of the disturbance of the 60 Hz sweeping voltage, particularly when the flat-band

¹ American Society for Testing and Materials, 1916 Race St., Philadelphia, Pennsylvania.

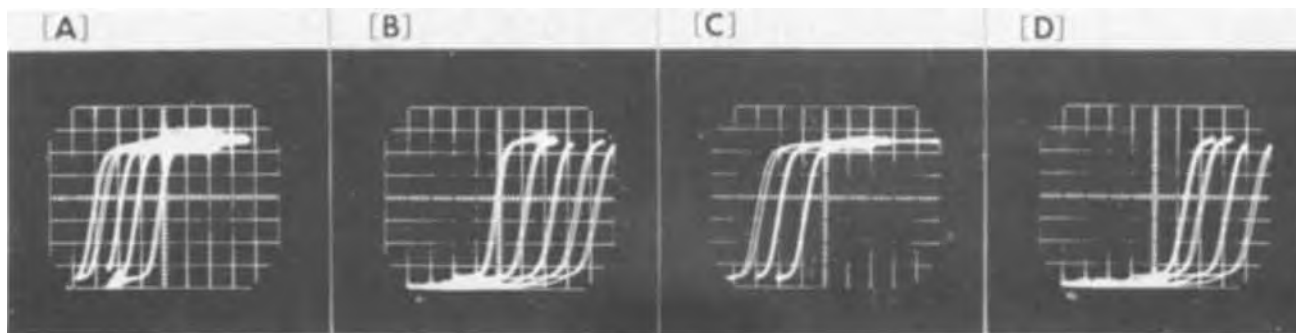


Fig. 5. Capacitance vs. voltage curves for unannealed devices showing rapid charge movement after bias at room temperature. Applied voltages are represented by the horizontal axis, 4 V/division. The numbers stated below in each case correspond to the curves from left to right in sequence in each picture. The double line in each curve results from the hysteresis. (a) +5V stress: 120, 60, 25, 9, and 0 min, respectively. (b) -5V stress: 0, 9, 25, 60, and 120 min, respectively. (c) Rapid charge movement after stress in (a): initial, 4, and 25 min. (d) Rapid charge movement after stress in (b): 120, 50, and 9 min and the initial curve.

voltage had shifted to a nearly saturated value after hours of stress. Superimposing the sweeping voltage on the d-c bias voltage, however, slows down and reduces the flat-band movement, because the positive and the negative half cycles of the sine wave do not produce the same effect during the process of bias stress.

Figure 6 depicts the dependence of the excess charges induced in the silicon ($Q_s = C_0 \Delta V$) on the time of polarization at -1.5×10^5 V/cm bias as well as the time dependence of the recovery charge drift when the devices were short-circuited after hours of negative bias. It is seen that the number of the negative charges and their mobility increase with decreasing power density. It also shows that during both bias and recovery driftings, the Q_s is proportional to $t^{1/2}$ at some initial period, and then approaches a saturation value, similar to sodium ionic transport phenomena in insulating films (15). The presence of the negative ionic species is believed to be partly due to oxygen ions which are generated in oxygen glow discharges, and partly due to the drive in of energetic species of unknown origin under the influence of the anode field. When the oxide is deposited under low power density, the dis-

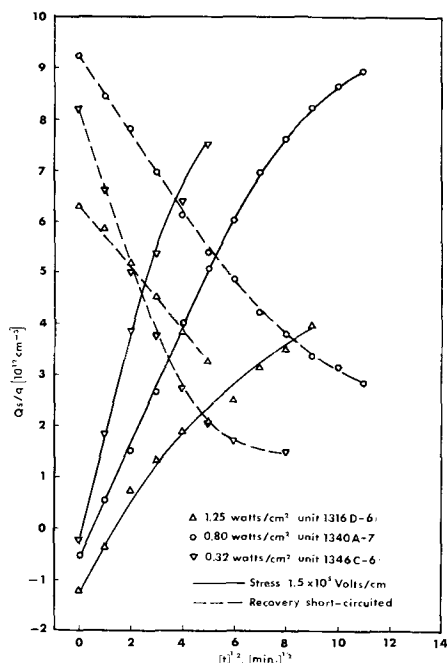


Fig. 6. Dependence of the excess charges induced in the silicon on the time of polarization at room temperature for the rf sputtered niobium oxide MOS devices under -1.5×10^5 V/cm stress, as well as the time dependence of the recovery charge drift when the devices were short-circuited after hours of the negative bias. Niobium oxides sputtered in three different power densities are shown.

charge voltage level is correspondingly low. There are more low-energy slow electrons in the plasma which favor the electron attachment process when they collide with oxygen molecules. The process in which O^- ions are formed through $O_2 + e \rightarrow O^- + O$ has been studied by Lozier (17), Hagstrum (18), Craggs *et al.* (19), and Chanin *et al.* (20). The negative oxygen ions may diffuse through the plasma and be adsorbed on the substrate and the deposited oxide layer. The presence of the negative oxygen ions has been reported by Wu and Formigoni (21) and Chen (22) in low-voltage, high-pressure d-c sputtering conditions.

Annealing effects.—All annealing was carried out at 800°C and shows prominent effects on the ionic instabilities. The specimens annealed in the helium and oxygen atmospheres show essentially the same characteristics: the devices are quite stable under negative bias-temperature (BT) stress, however, the positive bias stress still reveals a great amount of instability. On the other hand, the C_2HCl_3/O_2 annealed samples show a quite stable feature in response to both positive and negative BT stress.

Figure 7 shows the C-V curves of oxygen-annealed specimens under successive stressing conditions as well as the recovery movement. No practical instability was observed under negative BT stress up to 200°C . Although the stress at 300°C made the curve shift a small amount in the negative direction along the voltage axis, this is due to carrier-injection-extraction mechanism (21-28) and is not due to ionic migration. Under positive bias, rapid ionic migration still occurs at room temperature, and a test at 100°C showed a substantial increase of mobility of the ionic species.

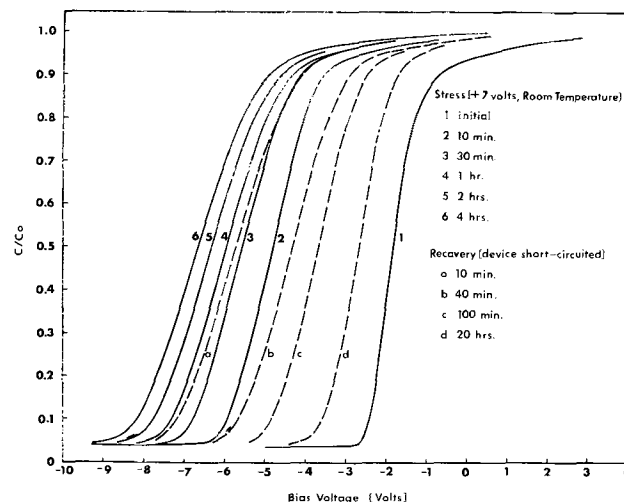


Fig. 7. MOS C-V characteristics of oxygen-annealed sample under successive positive bias at room temperature, as well as the recovery movement.

The total amount of oxide surface charges determined from the saturated flat-band voltage shift is about the same as those of the unannealed sample. From this observation, it is evident that the negative ions have essentially been eliminated through some kind of reaction at elevated temperatures. It also implies that the positive ions are distributed in a region near the metal-oxide interface. The positive ions are believed to be charged alkali ions, most likely sodium ions, which contribute to the instability under positive bias and are obviously unaffected by heat-treatment. The existence of the positively charged oxygen vacancies, produced by the reaction of aluminum with SiO_2 at the metal-oxide interface, was proposed by Thomas and Young (29). However, it is unlikely the oxygen vacancies will apply to our case, which is contrary to the assumption that oxygen inhibits vacancy formations (29). Careful examination in Fig. 7 also reveals an instability characterized by a change in slope of the C-V curve. However, it is seen mostly recovered when the C-V curve shifts back toward its original pre-stressed position. Hofstein (23) has reported a similar phenomenon and pointed to the generation of donor-type fast interface states as the source. However, for a clear understanding of the present reported phenomena, further investigation should be pursued.

The specimens which were annealed in $\text{C}_2\text{HCl}_3/\text{O}_2$ atmosphere, show the elimination of mobile ionic species in the oxide. The results of the BT test are shown in Fig. 8 which depicts the flat-band voltage vs. temperature with the gate stressing voltage as the parameter. The BT stress was carried out at a given bias and temperature for 30 min, and then cooled to room temperature before the C-V curves were taken. It is seen that the positive bias results in a shift of flat-band voltage in the positive direction along the voltage axis, while the negative bias results in a shifting in the negative direction. Unlike the ionic migration, prolonged short-circuit and high-temperature treatment of the devices showed only little or no recovery of the shifted C-V curves. This is a clear indication of the electron injection-extraction mechanism (21-28). This slow trapping instability was found to be thermally activated (23). The phenomena shown in Fig. 8 is, therefore, to be expected because of the decreasing slow-trapping time constant at higher temperatures, similar to those observed in the Al_2O_3 MOS structure (22). It is not known whether the slow trapping instability is present in the unannealed sample. The ionic-type instability of the corresponding unannealed sample is so large that it makes the observation of the small slow trapping instability infeasible.

The removal of the positive ionic species from the oxide by the introduction of C_2HCl_3 vapor might be expected. It is believed that the pyrolytic product, chlorine, acts as a gettering agent for sodium and other ionic contaminants during the annealing process. Presumably the chlorine reacts with the metallic ions to form volatile chlorides which are removed as a gas (10,30). Comparison of the results obtained on

thermally grown SiO_2 oxide prepared in C_2HCl_3 and CCl_4 gettering processes indicated that the chlorine is responsible for the gettering of metallic ions, while the presence of hydrogen catalyzes the gettering process as well as annealing out some fixed oxide surface charges (31). Further effort, however, is required to clarify this point.

As shown in Table I, the annealed samples show higher effective surface charge density than those of their corresponding unannealed samples. Among the annealed samples, the $\text{C}_2\text{HCl}_3/\text{O}_2$ annealed sample shows a little less effective surface charge density than the O_2 annealed specimen. These observations should be understandable because elimination of the negative ions in the oxide layer by annealing treatment implies the increase of the effective positive surface charges. This charge density is further reduced with the elimination of the positive ionic species through the $\text{C}_2\text{HCl}_3/\text{O}_2$ annealing process.

Summary and Conclusions

The niobium oxide films prepared by rf sputtering in an oxygen atmosphere are observed to be polycrystalline. The oxide films display a polydispersion of relaxation time. A drastic increase in the effective dielectric constant of the oxide films was observed after annealing treatment, but the mechanism is not known.

The unannealed films exhibited the effects of rapid charge movement at room temperature, indicative of both positive and negative ionic charges in the oxide layer. The negative charges are believed to be partly due to oxygen ions generated in oxygen glow discharges, and all of them can be eliminated by annealing treatment in helium or oxygen atmosphere. The positive charges are likely to be sodium ions which can be gettered during the oxygen annealing process by the inclusion of a small amount of trichloroethylene. Although the effective surface charge densities for the pre- and post-annealed samples do not reveal any remarkable difference, the various annealing treatments do reduce the interface states. A small amount of carrier injection-trapping polarization effect is present in the trichloroethylene-processed niobium oxide MOS structures which are essentially free from ionic instability.

Acknowledgments

The author wishes to thank C. M. Hoyland and A. Fritz for their technical assistance, and J. W. Hile and M. H. Brooks for various suggestions and encouragement. Thanks are also due to T. P. Schreiber and A. Forster for the scanning electron microscopic and the x-ray diffraction analyses, respectively.

Manuscript submitted Nov. 11, 1971; revised manuscript received March 6, 1972.

Any discussion of this paper will appear in a Discussion Section to be published in the June 1973 JOURNAL.

REFERENCES

1. C. C. Wang, K. H. Zaininger, and M. T. Duffy, *RCA Rev.*, **31**, 728 (1970).
2. M. H. Crowell and E. F. Labuda, *Bell System Tech. J.*, **48**, 1481 (1969).
3. N. Schwartz and R. W. Berry, "Physics of Thin Films," Vol. 2, G. Hass and R. Thun, Editors, Academic Press, New York (1964).
4. L. Young, "Anodic Oxide Films," Academic Press, New York (1961).
5. H. R. Brunner, F. P. Emmenegger, M. L. A. Robinson, and H. Röttschi, *This Journal*, **115**, 1287 (1968).
6. F. P. Emmenegger and M. L. A. Robinson, *J. Phys. Chem. Solids*, **29**, 1673 (1968).
7. M. T. Duffy, C. C. Wang, A. Waxman, and K. H. Zaininger, *This Journal*, **116**, 234 (1969).
8. J. L. Vossen and J. J. O'Neill, Jr., *RCA Rev.*, **29**, 149 (1968).
9. R. E. Jones, H. F. Winters, and L. I. Maissel, *J. Vacuum Sci. Technol.*, **5**, 84 (1968).
10. M. C. Chen and J. W. Hile, *This Journal*, **119**, 223 (1972).

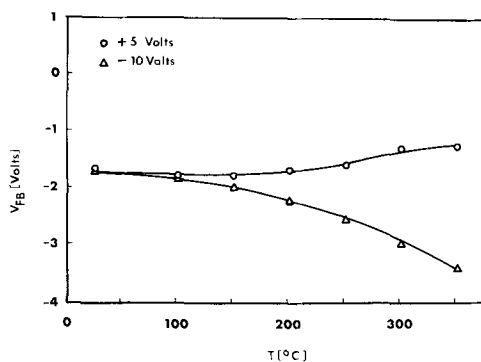


Fig. 8. Flat-band voltage vs. temperature with gate voltage as parameter for the $\text{C}_2\text{HCl}_3/\text{O}_2$ annealed samples.

11. K. S. Cole and R. H. Cole, *J. Chem. Phys.*, **9**, 341 (1941).
12. Y. Ishibashi, A. Sawada, and Y. Takagi, *J. Phys. Soc. Japan*, **28**, 1488 (1970).
13. S. M. Hu and L. V. Gregor, *This Journal*, **114**, 826 (1967).
14. C. A. T. Salama, *ibid.*, **117**, 913 (1970).
15. E. H. Snow, A. S. Grove, B. E. Deal, and C. T. Sah, *J. Appl. Phys.*, **36**, 1664 (1965).
16. P. M. Dunbar and J. R. Hauser, *This Journal*, **117**, 674 (1970).
17. W. W. Lozier, *Phys. Rev.*, **46**, 268 (1934).
18. H. D. Hagstrum, *Rev. Mod. Phys.*, **28**, 185 (1951).
19. J. D. Craggs, R. Thorburn, and B. A. Tozer, *Proc. Roy. Soc. (London)*, **A240**, 473 (1957).
20. L. M. Chanin, A. V. Phelps, and M. A. Biondi, *Phys. Rev.*, **128**, 219 (1962).
21. S. Y. Wu and N. P. Formigoni, *J. Appl. Phys.*, **39**, 5613 (1968).
22. M. C. Chen, *This Journal*, **118**, 591 (1971).
23. S. R. Hofstein, *Solid-State Electron.*, **10**, 657 (1967).
24. Y. Miura and Y. Matukura, *Japan. J. Appl. Phys.*, **5**, 180 (1966); **6**, 582 (1967).
25. E. Ferriou and B. Pruniaux, *This Journal*, **116**, 1008 (1969).
26. S. Nishimatsu, T. Tokuyama, and M. Matsushita, "Thin Film Dielectrics," p. 338, F. Vratny, Editor, Electrochem. Soc., Princeton, N. J. (1969).
27. T. L. Chu, J. R. Szedon, and C. H. Lee, *Solid State Electron.*, **10**, 897 (1967).
28. S. M. Hu, D. R. Kerr, and L. V. Gregor, *Appl. Phys. Letters*, **10**, 97 (1967).
29. J. E. Thomas, Jr. and D. R. Young, *IBM J. Res. Develop.*, **8**, 368 (1964).
30. P. H. Robinson and F. P. Heiman, *This Journal*, **118**, 141 (1971).
31. M. C. Chen, Unpublished.

Thermally Stimulated Currents and Voltages and Dielectric Properties

Martin M. Perlman

Department of Physics, Collège militaire royal de Saint-Jean, Saint-Jean, Québec, Canada

ABSTRACT

Experimental techniques for charging and observing thermally stimulated currents and voltages (TSC and TSV) in polymers and crystals are described and an outline is given of the theory of the processes. The polymers are corona charged, and trapping takes place near one surface. In an attempt to determine the microscopic nature of the traps, a study is made of a polyolefin series of ten polymers. Charge storage is shown to take place mainly along the chains themselves and through caging between neighboring molecules. In addition, the corona itself may produce changes in the polymers to create primary trapping sites. Charge storage stability is a function of electronegativity of the ions, symmetry along the chains, and packing density. The crystal work consists of a study of impurity-vacancy (I-V) dipoles in doped alkali halides, such as KCl:Sm⁺⁺, Eu⁺⁺, Yb⁺⁺, and Ca⁺⁺. The dipoles are field polarized. Analysis of the thermally stimulated dipolar peaks yields relaxation times, activation energies, and dipole concentrations. Other I-V dipole phenomena that may be studied with these techniques are described. A comparison is made between information obtainable from TSC and the more normal dielectric constant-loss tangent measurements, and we conclude that TSC is a valuable aid in the characterization of insulators. These studies also yield information on the basic electrical conduction mechanisms in insulators. The paper concludes with suggestions for further work and practical applications.

In this paper, I am advertising an experimental technique that has not been fully exploited, and am presenting some intriguing possibilities that are offered by thermally stimulated current (TSC) and voltage (TSV) measurements. The over-all purpose is to make clear the processes responsible for dipole polarization and for electron, hole, and ionic trapping in dielectrics, and to determine the parameters associated with these processes: lifetimes and activation energies for dipole polarization and escape probabilities and depths for trapping. Hopefully one may also be able to identify the microscopic nature of the dipoles and traps, and to clarify the electrical conduction mechanism in insulators.

Work on polymers and on single crystals is described, and results obtainable from TSC measurements are compared with those from the more normal dielectric constant, loss tangent, and conduction measurements. Finally, some ideas for future work in this field are presented.

Theory

In this method, a previously charged dielectric is heated at a uniform rate, and the resulting short-

Key words: thermally stimulated currents, nature of charge traps in polymers and dipoles in crystals, characterization of insulators.

circuit current (or open-circuit voltage) is measured as a function of temperature (1). An electrical "spectrum" consisting of a series of peaks (or steps) is obtained.

We (2-4) recently developed a theory to account for the shape of the TSC peaks from materials charged near one surface and thermally stimulated in the absence of any external field. The result is given in Eq. [1].

$$j = A \exp \left[-E_a/kT - B \int_{T_0}^T \exp(-E_a/kT) dT \right] \quad [1]$$

Here, j is the externally measured current, T is the absolute temperature, E_a is the trap depth, and A , B , and k are constants. The temperature dependent expression in brackets is identical to that obtained by Bucci (5) for dipolar decay. Equations [2] and [3] give the values of A and B in the two cases

Near surface trapping

$$A = (n_{t_0} e \delta)^2 (\mu \tau) / (2 \epsilon d \tau_0), \quad B = 2 / (\beta \tau_0) \quad [2]$$

Dipolar decay

$$A = N p^2 E_C / (k T C \tau_0), \quad B = 1 / (\beta \tau_0) \quad [3]$$

Here, N and n_{t_0} are the charge concentrations, $(\mu \tau)$ the

charge mobility-free lifetime product, δ the depth of penetration of charge, τ_0 the inverse of the trap escape frequency, p the dipole moment, E_C and T_C the polarizing field and temperature, and the other quantities have their usual meaning (2-4).

Equation [1] can be written in the form of Eq. [4]

$$\ln \left[\left(\int_t^\infty j dt \right) / j \right] = \ln \tau = \ln \tau_0 + E_a/kT \quad [4]$$

Thus the parameters E_a and τ_0 may be determined from a straight line semilog plot of the remaining charge divided by the current at a particular temperature vs. the inverse of that temperature. Alternatively, these parameters may be determined from the low-temperature tail of Eq. [1] using

$$\ln j \stackrel{\approx}{=} \ln A - E_a/kT \quad [5]$$

(The use of Eq. [1] assumes monomolecular kinetics, Eq. [5] gives the parameters independent of any assumptions as to kinetics, provided that a particular E_a has been isolated in cases where there are multi-energy levels.)

Equations [6] and [7] (6) are used to determine n_{t_0} , $\mu\tau$, and δ

$$n_{t_0} = (Q/\epsilon dS) (2d/\delta); (\mu\tau) = \epsilon(\delta/d) (\delta S/Q) \quad [6]$$

$$\delta = 2d(Q/S)/(\sigma + Q/S) \quad [7]$$

Here d , S , and ϵ are the surface area, thickness, and dielectric constant of the sample, respectively, Q is the total released charge, and σ is the externally measured charge density prior to warming.

Experimental

Thermally stimulated current spectra obtained from corona-charged Mylar and FEP Teflon have previously been published (2, 4). There are many TSC peaks and the spectra are complex. Typical thermally stimulated voltages [or net surface charge decays measured using the vibrating electrode technique (7)] obtained from corona-charged polystyrene, polypropylene, and medium- and high-density polyethylene are shown in Fig. 1. Note the TSV steps. (TSV in general shows less detail than TSC; one does not always obtain a stepwise decrease for each corresponding TSC peak.) The spectra require a cleaning technique to separate the individual peaks (or steps). Briefly, the sample is partially discharged by heating to a temperature just beyond that of the first maximum (emptying the low temperature trap), then lowered and raised again just beyond that of the second maximum, etc. Appropriate normalization and subtraction yields the isolated peaks (8).

Typical fits to a cleaned isolated peak following Eq. [1] and [4] are illustrated in Fig. 7 and 8 of Ref. (8).

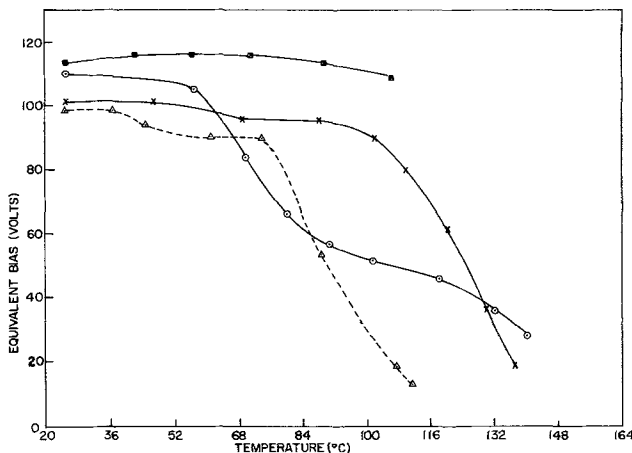


Fig. 1. Thermally stimulated charge decay. □, Polystyrene; ○, polypropylene; X, △, polyethylene, high and medium density.



Substituted polyolefins	A	B	D	E
Polyethylene (PE) high density	H	H	H	H
Polyvinyl chloride (PVC)	H	H	Cl	H
Polyvinyl fluoride (PVF)	H	H	F	H
Chlorinated polyvinylchloride (Cl/PVC)	H	H	Cl	H
Polyvinylidene fluoride (PVF ₂)	H	H	F	F
Polypropylene (PP)	H	H	CH ₃	H
Polystyrene (PS)	H	H	C ₆ H ₅	H
Polytetrafluoroethylene (PTFE) "Teflon"	F	F	F	F
Polyfluoroethylene propylene (PFEP) "Teflon"	F	F	CF ₃ , F	F
Polytrifluorochloroethylene (PTFCE) "Aclar"	F	F	Cl	F

Polystyrenes with SO₃H end groups, also C filled (16%)
 Polyethylenes with different crystallinities; branching

As a further check on the parameters obtained from the isolated peaks, a completely independent method of analysis was used. Here, the sample was heated to a series of temperatures (e.g., 50, 55, 60 . . . °C) each separated by rapid cooling. The low-temperature tail of Eq. [1] is a single exponential as shown in Eq. [5]. Hence Arrhenius plots give the activation energy over the complete temperature range (8). The activation energies obtained from the plateaus in a $\ln E_a$ vs. T_{max} plot agree well with those determined from the overall fits to the peaks. How well this technique works depends on the number of peaks and the extent of their overlap.

Polymers

Apparatus.—The moving polymer film (~1 mil thick) was corona charged in air, and the net surface charge density immediately monitored, using a vibrating electrode to pick up an a-c signal, and a field-canceling bias to null the received signal (2). The polymer film traversed rollers, metalized side down and grounded, 0.5 mm beneath a knife edge held at -6 kV.

The samples were coated with conducting paint electrodes. Depolarization was carried out in ovens fitted with SCR temperature programers. Heating rates were linear and typically 1°C/min. The apparatus in Fig. 2 enables simultaneous TSC and TSV measurements on two samples. The TSC is automated using a data acquisition system consisting of a multiplexer, analog-digital converter, and interface to a teletype that records current, temperature, time, and scale factor of the electrometer, and punches these values out on paper tape. The paper tape is then converted to cards, and all calculations are performed with the aid of a Control Data 3300 computer.

Results and discussion.—In an attempt to determine the nature of the charge storage traps, we studied the polyolefin series shown in Table I. In addition we used a polystyrene series with end group substitution and

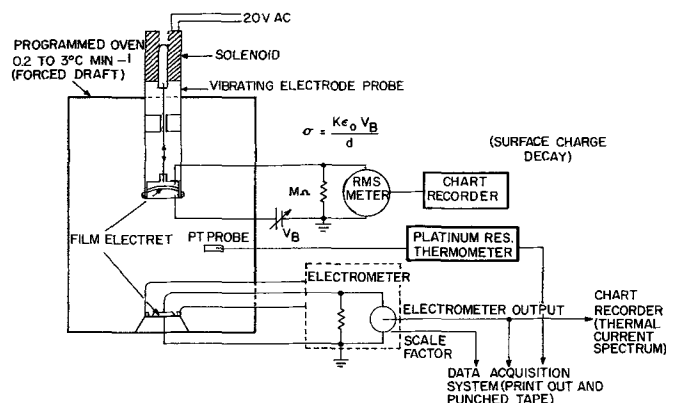


Fig. 2. Thermally stimulated current (TSC) and charge decay (TSCD) apparatus.

Table II. Thermally stimulated currents

Polymer	Link	Peaks (T_{max}), °C	T_g , °C	E_a , eV	τ_0 , sec	$n\tau_0 (\times 10^{15})$, cm ⁻³	$\mu\tau (\times 10^{-9})$, cm ² V ⁻¹
Teflon (PTFE)	—CF ₂ —CF ₂ —	100, 115, 135, 160, 207	127	1.4, —, —, 1.4, 1.5	10 ⁻¹⁶ –10 ⁻¹²	1.2–2.8	0.8–1.8
Polythene (HD)	—CH ₂ —CH ₂ —	53, 69, 98	(70)	1.7, 1.3, 1.2	10 ⁻²³ –10 ⁻¹⁴	3–16	1.1–2.0
Polystyrene	—CH ₂ —CH— ϕ	45, 65, 100	100	—, —, 1.3	10 ⁻¹⁵	2.5	1.0
Polypropylene	—CH ₂ —CH— CH ₃	48, 68, 93, 111	—	1.2, 2.3, 1.4, 1.9	10 ⁻²² –10 ⁻¹⁶	0.4–11	0.2–6.4
Aclar	—CF ₂ —CFCl—	42, 53, 79, 105	45	1.9, 1.7, 1.6, 1.6	10 ⁻²⁶ –10 ⁻²²	0.3–1.2	2.2–9.7
Cl/PVCl	—CHCl—CHCl—	42, 65, 92	—	—	—	—	—
PVF ₂	—CH ₂ —CF ₂ —	40, 65, 100	(65, 97)	—	—	—	—
PVCl	—CH ₂ —CHCl—	34	68	1.0	—	5	0.7
PVF	—CH ₂ —CHF—	29	—	1.5	10 ⁻²⁰	4.7	0.5

carbon filled, as well as polyethylenes of different crystallinity. A complete paper on this work will be published shortly (9). The results of the TSC measurements and the constants associated with the various traps are shown in Table II. Untrapping occurs at thermal energies of the same order as required by molecular motion or phase transitions in polymer structure. The temperature maximum of some of the peaks correlate well with the known glass transition temperatures (T_g) of the polymers. The bracketed temperatures are those where molecular motion is known to take place from elastic constant measurements.

First of all we should say that the traps are not due to chemical impurities, for the same peaks have been observed in a variety of the same materials, supplied by different manufacturers, and also made from resin into film.

Charge storage in polymers can take place on three structural levels: the so-called primary, secondary, and tertiary levels. At the primary level, the traps are on the molecular chains themselves, the charge is stored at atomic sites. At the secondary level, electrons can become caged within groups of atoms in neighboring molecules and are held there due to the charge affinity of these groups. To release charge at the primary level requires individual atomic motions, while at the secondary level it is dependent on the motion of groups of atoms. At the tertiary level, charge may be stored in both crystalline and amorphous regions of the polymer, or at boundaries (1). Charge release in this case depends on main chain motion.

Table III lists the polymers in order of decreasing charge stability together with the temperature at which the externally measured charge vanishes in a thermally stimulated charge decay measurement. From this table we may conclude the following.

Charge storage stability at the primary level, i.e., along the molecular chains, is determined by both the electronegativity of the ions and symmetry along the chains. In the first four polymers listed, the fluorine, hydrogen, phenyl, and methyl groups are in order of decreasing electronegativity. Since chlorine has an electronegativity between that of F and H one might expect that Aclar in which one Cl has been substituted for a Teflon F might lie between Teflon and polyethylene. Instead it lies fifth in the table. Here we feel

Table III. Charge stability

Polymer	Symbol	Link	$T (\sigma = 0)$, °C
1 Polytetrafluoroethylene	PTFE	—CF ₂ —CF ₂ —	230
2 Polyethylene (high density)	PE(HD)	—CH ₂ —CH ₂ —	145
3 Polystyrene	PS	—CH ₂ —CH— ϕ	130
4 Polypropylene	PP	—CH ₂ —CH— CH ₃	130
5 Aclar	AC	—CF ₂ —CFCl—	125
6 Polyethylene (medium density)	PE(MD)	—CH ₂ —CH ₂ —	115
7 Chlorinated polyvinyl chloride	Cl/PVCl	—CHCl—CHCl—	90
8 Polyvinylidene fluoride	PVF ₂	—CH ₂ —CF ₂ —	85
9 Polyvinyl chloride	PVCl	—CH ₂ —CHCl—	55
10 Polyvinyl fluoride	PVF	—CH ₂ —CHF—	35

that the relatively large C-Cl bond (1.63Å compared with 1.06Å for C-H and 1.33Å for C-F) introduces a distortion in the symmetry along the chains that makes for poorer charge stability. The same thing happens on comparing PVCl and PE where one Cl has been substituted for an H.

Similarly substituted fluorine and chlorine polyolefins have similar electret charge stability. A single substitution of a fluorine or chlorine atom for hydrogen in PE (PVF and PVCl) produces a poor charge storer. A second substitution (PVF₂ and Cl/PVCl) produces greater storage stability. Complete substitution in the case of PTFE produces a very stable electret. Disturbing the symmetry by substitution of the trifluoromethyl group (PFEP) in PTFE and the methyl group (PP) in PE also reduces charge stability.

Charge storage stability at the secondary level, i.e. caging between neighboring molecules, is better the higher the packing density and the lower the branching. Teflon of highest packing density heads the table and high density (HD) PE is much better than MD which is in turn better than LD.

PS with a sulfonic end group (SO₃H) proved to be as stable as PS, and no additional traps were evident in the TSC spectra. PS and Mylar, both of which contain the phenyl group have almost identical TSC spectra. PE of high crystallinity (HC) is much more stable than PE of low crystallinity (LC). The high-temperature TSC peak at ~100°C in HC does not appear in LC. We attribute this to a loss of the charge storage site at the chain folds as the chains unfold in going from HC to LC. We made an attempt to determine the effect of charge storage at interfaces by doping PS with carbon but were unable to charge the material. The film was highly conductive and arced through under the corona.

While the above provide a fairly consistent picture of the observed phenomena, other possibilities should not be overlooked. The corona itself may produce changes in the polymer to create primary trapping sites.

All films were negatively corona charged. Negative ions are most probably trapped within some tens of monolayers at the polymer surface. The ion may combine chemically with the polymer or it may transfer an electron to the polymer. Depth of penetration measurements were made using the capacitance *vs.* frequency technique, described by Badian *et al.* (10). Estimates could also be obtained from Eq. [7]. Our experiments show that the charge penetrates to a depth of about 5% of the film thickness, assuming that the spatial distribution is uniform. Thus the "transferred" or "free" electrons can be trapped within the bulk, as well as at the surface.

It has been established that at least two chemical changes take place in the surface layer of a polymer exposed to a corona in air (11, 12). One is the formation of double bonds ($>C=C<$), and the other is the chemical combination of oxygen to form a carbonyl group ($>C=O$). These are present in densities as great as or greater than the charge density formed in the polymer. The double bonding (unsaturation) occurs before the reaction with oxygen (can also be O⁻, O₃, etc.) (13). The electrons or ultraviolet light in

the corona can initially break the carbon-carbon bond, and supply enough energy for the H-atom rearrangement necessary in the >C=C< bond formation. It is then very easy, but at the surface only, to have a reaction with oxygen occur. Charge storage at the primary level might then take place on the double bond and carbonyl groups (13).

Electron trapping on molecular oxygen that has diffused in from the atmosphere is another possibility, as previously found in thermoluminescence measurements on polyethylene by Partridge (14), and more recently by Bousted (15).

The untrapping of charge may be a dual process that arises from both a lowering of trap depth with molecular motion plus thermal excitation of the charge out of the trap. Since charge release in these polymers is so intimately connected with molecular motion, it may be that some of the activation energies mentioned are not those due to charge affinity of various atoms, or groups of atoms, but rather are to be associated with molecular vibration and rotation.

Crystals

Apparatus.—We are at present also growing alkali halide crystals such as KCl by pulling from the melt using the Czochralski technique. KCl powder (mixed with dopant) sits in a porcelain crucible and is melted in a furnace. A seed is attached to a chuck which is simultaneously rotated and pulled from the melt at about 1/4 in./hr. The crystals are grown in an Argon gas atmosphere, and provision is made for water cooling the various parts of the furnace. A temperature controller is used to lower the temperature slowly enough to avoid rapid surface crystallization of the melt. We have successfully grown crystals of pure KCl and KCl doped with Ca^{++} , Sm^{++} , Eu^{++} , and Yb^{++} .

A typical cryostat that enables one to charge using fields, as well as irradiate with electrons, or ultraviolet light, is shown in Fig. 3.

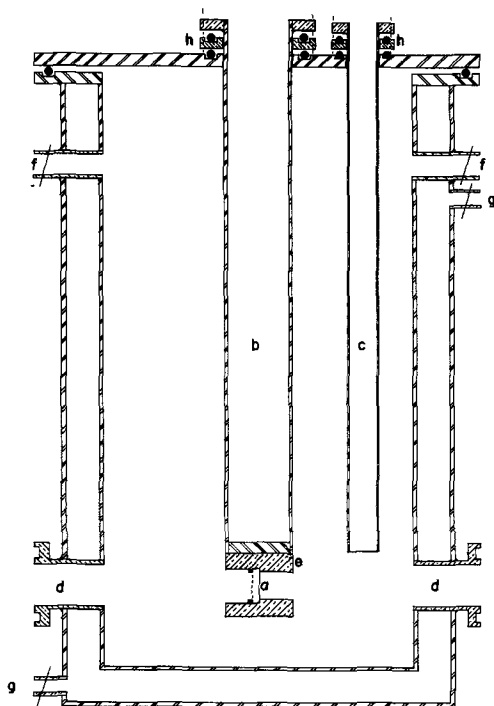


Fig. 3. Stainless steel cryostat. a, Crystal; b, liquid nitrogen and heater finger; c, liquid N_2 trap; d, ports for uv or electron irradiation; e, copper block; f, ports for vacuum or inert gas; g, ports for water; h, heat insulation.

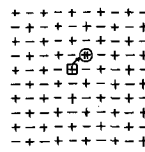
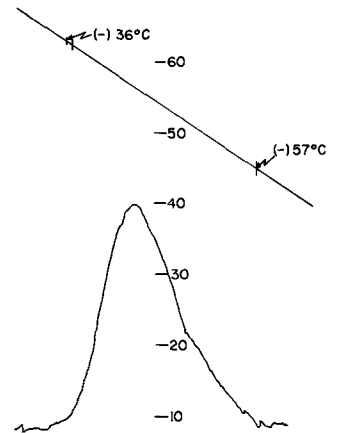


Fig. 4. Divalent impurity and associated positive ion vacancy in a fcc alkali halide. The dipole moment (arrow) is along a (100) direction. KCl: Sm^{++} ; $N = 4 \times 10^{16}/\text{cm}^3$, $\beta = 6^\circ/\text{min}$, $E_p = 11.8 \text{ kV/cm}$, $T_{\text{max}} = -47^\circ\text{C}$, $\tau_0 = 1.5 \times 10^{-14} \text{ sec}$, $E_a = 0.70 \text{ eV}$.



Results and Discussion.—If during the growth of an alkali halide crystal from the melt, one dopes with doubly charged divalent ions (such as Sm^{++}), (e.g., adding SmCl_2 to KCl) the divalent ion enters the lattice substitutionally (for K^+). To preserve charge neutrality, another positive ion must leave the lattice. The most likely place for this to occur is in the neighborhood of the impurity, thus forming a system of impurity-vacancy (I-V) dipoles, as in Fig. 4.

If one polarizes these dipoles by applying an external field to the crystal at a particular temperature, lowers the temperature with the field still applied, removes the field, and warms the crystal, one obtains a peak in the measured external current as a function of temperature. This is the so-called ITC or ionic thermal current peak (5). A typical recorder trace (KCl: Sm^{++}) is shown in Fig. 4.

Here, the polarizing field was 11.8 kV/cm, the heating rate during thermal stimulation, $6^\circ\text{C}/\text{min}$, and the temperature maximum at which the peak appeared, -47°C . Note the extremely low dipolar concentration. One can in fact detect currents a factor of 10 lower than this, i.e., detect impurities to 1 part in 10^8 .

Figure 5 shows overlapping Ca^{++} , and Sm^{++} I-V dipole peaks. The calcium is an unwanted impurity that is present in any inexpensive reagent powder, such as those supplied by Baker and Fisher. It is made

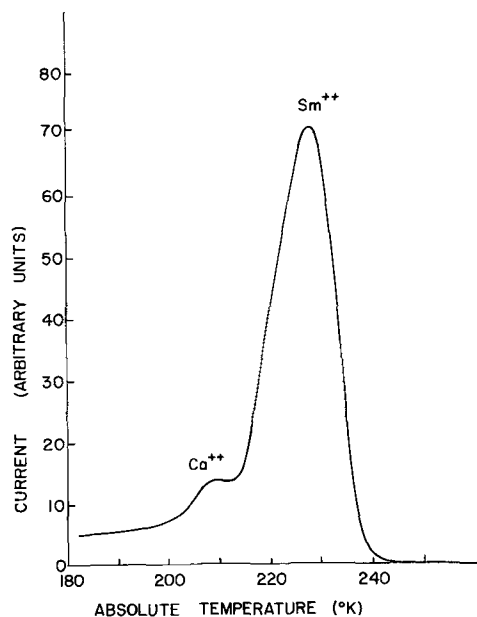


Fig. 5. Overlapping Ca^{++} and Sm^{++} I-V dipole peaks

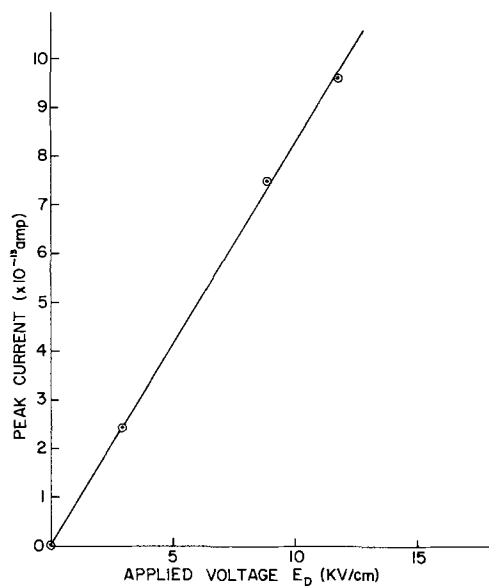


Fig. 6. Current maximum as a function of polarizing field for KCl:Sm⁺⁺.

negligible (relative to the Sm⁺⁺ peak) by waiting a few days for the dipoles to aggregate (see ahead).

The theory of the dipolar peaks is summarized by Eq. [1] and [3]. Equation [3] shows that the current maximum should be a linear function of applied field if we are dealing with a dipolar phenomenon, and not, e.g., space charge. Accordingly, we first measured the current maximum as a function of polarizing field. A linear relationship identified the peaks as dipolar. A typical example for KCl:Sm⁺⁺ is given in Fig. 6.

The activation energies and the relaxation times for dipolar relaxation were determined with the aid of a computer, by the initial rise (Eq. [5]), Bucci (5) (Eq. [4]), and Cowell and Woods (2, 16) techniques and are listed in Table IV. The activation energy for KCl:Ca⁺⁺ is a bit larger than that determined by Chiba *et al.* (17) (0.66 eV), from dielectric absorption measurements. The constants for KCl:Sm⁺⁺, KCl:Eu⁺⁺, and KCl:Yb⁺⁺ have not been previously measured. Table IV also lists values for KCl:Be⁺⁺, Sr⁺⁺, and Cd⁺⁺ for comparison purposes. The activation energy can be associated microscopically with one or more of the following processes: the barrier to rotation of the vacancy around the impurity, impurity-vacancy interchange, movement of the vacancy from nearest neighbor positions to next nearest neighbor, or vice versa (18).

We have a particular interest in rare-earth doped alkali halides using Sm⁺⁺, Eu⁺⁺, and Yb⁺⁺ for it turns out that these doubly valent ions can be made singly valent by irradiation with x-rays, and that the reaction is reversible under annealing or irradiation

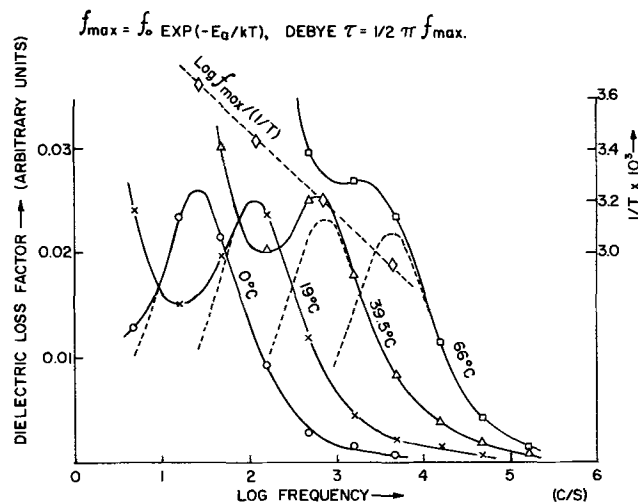


Fig. 7. Dielectric absorption at various temperatures for sodium bromide with calcium impurity.

with uv. Thus the electret can be switched on and off, with possible application to memory elements.

The thermal current method used on single crystals allows one to investigate the production, concentration, and motion of defects in solids. The I-V dipoles diffuse to form higher aggregates (often trimers) of negligible dipole moment. Qualitative aggregation rates for the various dipoles are given in Table IV. If one anneals the crystals at fixed temperatures for increasing times, and measures the decreasing released polarization charge on warming, the kinetics of the aggregation, and the activation energy for defect motion, can be determined. One can even study chemical reactions taking place in a solid matrix. If one dopes KCl, for example, with both Ca and OH, the precipitation of Ca(OH)₂ in the solid matrix can be followed (19), because it leads to dipole destruction that is measurable with ITC.

Since impurities can be identified with enormous sensitivity (compared with other methods of analysis such as E.P.R.), we expect that the method will eventually be used commercially for this purpose. Very little work has as yet been carried out using ITC.

TSC vs. $\tan \delta$, ϵ' Measurements

For many years now, people have been characterizing insulators by measuring dielectric constant (ϵ') and loss tangent ($\tan \delta$) as a function of frequency (f) and temperature (T). A typical example is shown in Fig. 7. One usually measures $\tan \delta$ vs. f at a series of temperatures, and then makes an Arrhenius plot of $\ln f_{\max}$ vs. $1/T$ from which the activation energy E_a , f_0 , and the Debye relaxation time τ for a single relaxation process, may be determined. While much valuable information has been obtained, the latter suffers from two inherent disadvantages. If more than one relaxation process is present in a dielectric, this manifests

Table IV. Dipole parameters for KCl:X⁺⁺

	m	r , Å	T_M , °K	E , eV	τ_0 , sec	R
a. Ca ⁺⁺	40.1	0.99	215	0.70 ± 0.01	(3.0 ± 1.9) × 10 ⁻¹⁵	Days
a. Sm ⁺⁺	150	1.13†	227	0.70 ± 0.03	(2.7 ± 2.5) × 10 ⁻¹⁴ (range 10 ⁻¹⁸ -10 ⁻¹⁶)	Very long
a. Eu ⁺⁺	152	1.13†	224	0.68 ± 0.01	(3.7 ± 1.0) × 10 ⁻¹⁴	Very long
a. Yb ⁺⁺	173	1.00†	215	0.67 ± 0.01	(1.1 ± 0.6) × 10 ⁻¹⁴	Very long
b. Be ⁺⁺	9	0.31	133	0.24	10 ⁻⁸	Minutes
			161	0.45	5 × 10 ⁻¹³	
b. Sr ⁺⁺	87.6	1.13	217	0.657 ± 0.002	10 ⁻¹³	Days
c. Cd ⁺⁺	112	0.97	220	0.67 ± 0.01	—	Hours

* Legend: m = atomic weight, r = ionic radius, T_M = temperature maximum of peak, E = activation energy, τ_0 = inverse of jumping probability, R = qualitative aggregation rate at room temperature, † = X⁺⁺, a = this work, b = Bucci (5), c = Capelletti (24).

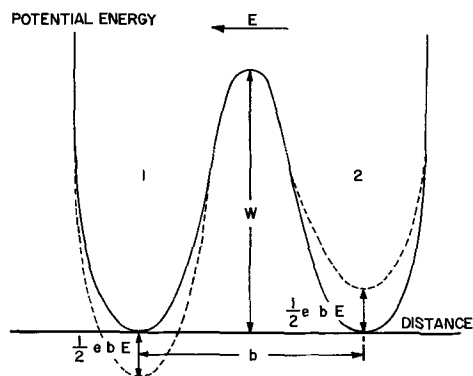


Fig. 8. Bistable model. Debye equations

$$\epsilon' = \epsilon_{\infty} + \frac{(\epsilon_s - \epsilon_{\infty})}{1 + \omega^2\tau^2}, \epsilon'' = \frac{(\epsilon_s - \epsilon_{\infty})\omega\tau}{1 + \omega^2\tau^2}, \tan \delta = \epsilon''/\epsilon'$$

TSC gives Debye τ and Np^2/kTc . Here, $(\epsilon_s - \epsilon_{\infty})/4\pi = Np^2/kTc$, ϵ_{∞} from $P(O) = (\epsilon_{\infty} - 1)E/4\pi$. ϵ' , ϵ'' , $\tan \delta$ then determined.

itself as a broadening in the Debye curve ($\tan \delta$ vs. frequency). In addition, the dipole orientation losses usually occur on top of a background loss due to conductivity. Thus it is very difficult (usually impossible) to sort out the individual relaxation processes.

We feel that TSC measurements (without external bias) provide a better characterization of insulators than ϵ' , $\tan \delta$ measurements. They produce a peak for each relaxation process, and conductivity does not interfere. If there is an overlap of a few peaks, they may be easily separated. In addition, very small dipole concentrations can be detected. ($\sim 10^2$ - 10^3 times more sensitive than loss measurements). This should effectively mean that we can measure very low $\tan \delta$'s, i.e., those associated with bond moments and the motion of small chain segments.

Indeed ϵ' and $\tan \delta$ may be determined by combining TSC measurements with d-c response. The Debye equations together with the constants obtainable from TSC measurements are shown in Fig. 8. Also illustrated is the bistable model in which the dipole has two equivalent positions 180° apart. The application of an electric field E modifies the depth of the potential wells so that with the field the jump probability from 2 to 1 is greater than that from 1 to 2, and a net polarization results. Using this model, $(\epsilon_s - \epsilon_{\infty})$ may be determined from the TSC constant Np^2/kTc . The Debye τ is also known from TSC. ϵ_{∞} may be obtained from the zero time polarization response of the dielectric to an applied step. Thus ϵ' , ϵ'' , and hence $\tan \delta$ are determined. Our feeling is that all of the old dielectric absorption measurements could profitably be combined with TSC to isolate the microscopic mechanisms.

In order to achieve success with the above technique, one would need a fairly ideal dielectric with a small number of relaxations. The TSC measurements must be made over a temperature range that includes all of the relaxation mechanisms. In many practical dielectrics in which there are multirelaxation processes, it may be impossible to thermally clean and separate the quasi-continuous spectra.

Electrical Conduction Mechanism in Insulators

The thermal current technique offers a key to the comprehension of the fundamental microscopic mechanisms responsible for charge storage and release, such as dipolar phenomena, electron, hole, and ionic traps, space charge, etc. It is these phenomena that govern electrical conduction in dielectrics, for example, since trap hopping is often invoked as a conduction mechanism, a knowledge of trap parameters is desirable. Thus, a study of charge storage yields valuable information about electrical conduction. An understand-

ing of the processes responsible for electrical conduction in dielectrics is of course essential in any and all applications of insulators. Different forms of excitation, i.e. charging (such as corona to supply ions, electron, x-ray and ultraviolet irradiation to supply electrons and holes, d-c fields to orient dipoles) may be used on the same dielectric to characterize it electrically as much as possible.

The origin of each of the TSC peaks may be determined by performing current-voltage measurements at a series of fixed temperatures, in addition to TSC. This procedure has recently been followed by Jonscher (20) on thin film silicon oxide. There are four distinct regions of different slope in the I-V curves. An activation energy may be determined for each region from Arrhenius plots of $\ln I$ vs. $1/T$ at constant V . By comparing these energies with those obtained from initial rise calculations on the TSC peaks of silicon oxide, Jonscher was able to say which of the peaks were ionic, electronic, due to space charge, etc.

Using different forms of excitation and thermally stimulated currents and voltages, studies may be made of the effect on the electrical properties of plastic additives in polymers such as Polythene or PVC, with a view toward improving the electrical characteristics of these insulators (for use in cables, condensers, breakers, etc.), or toward finding others to replace them. Discharges occurring in insulation provide copious supplies of carriers that are trapped, changing the subsequent insulation resistance and breakdown properties. This phenomenon may also be studied by the proposed methods.

The TSC spectra are unique to the insulators under study. They are fingerprints of them and are sensitive to impurities, additives, discharges, humidity, i.e., to any chemical or morphological change. They provide a sensitive analytical tool that could be used to guide the production of insulators with fixed electrical properties.

We feel that TSC will eventually develop into an electrical spectroscopy and have practical application to electrical quality control.

Future Work

In conclusion, I would like to say a few words about other possible applications of TSC.

In 1967 Sinencio *et al.* (21) irradiated solution-grown orthorhombic S crystals with uv, and found that electron and hole trap filling was confined to the penetration volume of the radiation ("near surface") independent of the application of a bias during irradiation. In other words, carriers were not drawn into the bulk of the specimen by a field applied during irradiation. On the other hand if a bias were applied during subsequent thermal stimulation either carrier (depending on bias polarity) could be drawn from the "near surface" region, and separate electron and hole TSC spectra were obtained. Both electron and hole peaks occurred at $\sim 175^\circ\text{K}$. To show that these were different, growth curves (i.e., peak height vs. filling time) studies were made on the two peaks, and indeed they exhibited different kinetic behavior. More studies of this type are needed.

Recently, Gross (22) examined a number of dielectric models which, although equivalent at constant temperature, were shown to be nonequivalent nonisothermally. He found that if the total released charge was independent of heating rate, the Maxwell model applied, and the TSC measurement was the significant one, for each cleaned peak could then be associated with a single relaxation process. If, on the other hand, the released charge varied with heating rate, the Wagner-Voigt model applied and the TSV measurement was the significant one. Figure 9 shows the TSC and TSV to be expected for the same trap depth.

The processes responsible for conduction in thin (thousand Angstrom) films (such as silicon oxide, tantalum oxide, aluminum oxide) used in integrated

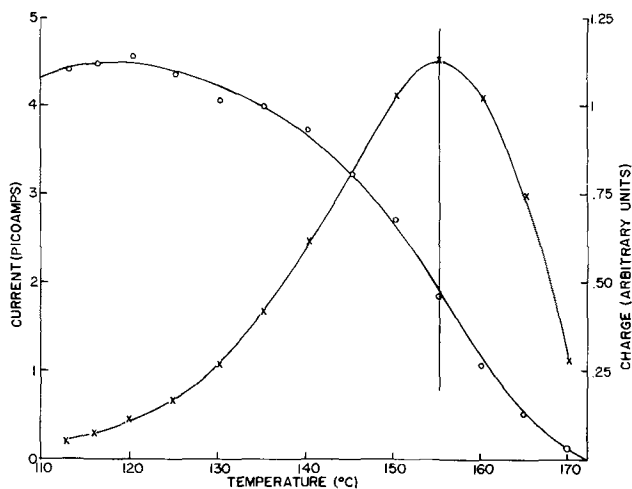


Fig. 9. Thermally stimulated current and charge decay for the same trap depth (FEP Teflon, $E_a = 1.36$ eV).

circuits are the same as those responsible for conduction in all dielectrics, with the possible addition of tunneling. Thus TSC studies on thin films should prove valuable. Recently, Weisberg and Schade (23) have shown how the use of a Schottky barrier can extend the use of TSC to low-resistivity semiconductors such as silicon. No work has as yet been reported on thermal currents from ferroelectrics, which should be very large.

Some practical applications of this work are the following: There has recently been a need for a high-temperature, radiation resistant plastic to use in cable wrapping. Kapton (a du Pont product) satisfies the first criterion. One measure of the second is whether it is a poor or good charge storer, a question that was easily answered by running a TSC spectrum. There are many practical applications for charge storage devices. We have developed a microphone now marketed by Sony in tape recorders and broadcast mikes, and soon to be used by Bell Canada in the microphones of all telephone handsets. There are two other uses for charged polymers in communications that represent large savings over equipment now in use, but are commercially confidential for the moment. Other possible applications are in air filters, memory elements, high-voltage and a-c generators, motors, meters, radiation dosimeters, precipitators, phono cartridges, relays, voltmeters, electrometers, explosion initiators, vibration transducers, electrostatic lenses, etc.

Acknowledgments

The author is indebted to R. A. Creswell and Dr. M. A. Kabayama of Bell-Northern Research Labora-

tories, Ottawa, Ontario, Canada for the experimental work on the polymers, and helpful discussions, respectively, and to Dr. S. Unger of our laboratory for the experimental work on the crystals. This work was supported by the Defense Research Board of Canada under Grant 9512-31.

Manuscript submitted May 3, 1971; revised manuscript received Feb. 3, 1972.

Any discussion of this paper will appear in a Discussion Section to be published in the June 1973 JOURNAL.

REFERENCES

1. T. Takamatsu and E. Fukada, *Polymer J.*, **1**, 1010 (1970).
2. R. A. Creswell and M. M. Perlman, *J. Appl. Phys.*, **41**, 2365 (1970).
3. M. M. Perlman and R. A. Creswell, *ibid.*, **42**, 531 (1971).
4. M. M. Perlman and R. A. Creswell, Annual Report of Conference on Electrical Insulation, p. 30 (1970).
5. C. Bucci, R. Fieschi, and G. Guidi, *Phys. Rev.*, **148**, 816 (1966).
6. G. Sessler, To be published, *Journal of Applied Physics* (1972).
7. C. Reedyk and M. M. Perlman, *This Journal*, **115**, 49 (1968).
8. M. M. Perlman, *J. Appl. Phys.*, **42**, 2645 (1971).
9. R. A. Creswell, M. M. Perlman, and M. A. Kabayama, *Polymer Preprints*, **72**, (1), 206 (March 1971).
10. L. Badian, B. Ai, R. Lacoste, and C. Mayoux, *Compt. Rend.*, **261**, 2181 (1965).
11. D. J. Carlsson and D. M. Wiles, *Can. J. Chem.*, **48**, 2397 (1970).
12. C. Mayoux and Y. Teisseyre, *C. R. Acad. Sc. Paris*, **271**, Ser. B., 665 (1970).
13. R. A. Creswell, B. I. Gribbon, M. A. Kabayama, and M. M. Perlman, *Telesis (Canada)*, **2**, (1), 21 (1971).
14. R. H. Partridge, *J. Polymer Sci.*, **A3**, 2817 (1965).
15. I. Bousted, *Nature*, **225**, 846 (1970).
16. T. Cowell and J. Woods, *Brit. J. Appl. Phys.*, **18**, 1045 (1967).
17. Y. Chiba, K. Ueki, and M. Sakamoto, *J. Phys. Soc. Japan*, **18**, 1092 (1963); **20**, 1284 (1965).
18. R. W. Dreyfus, *Phys. Rev.*, **121**, 1675 (1961).
19. N. Januzzi and S. Mascarenhas, in "Electrets and Related Electrostatic Charge Storage Phenomena," p. 41, L. M. Baxt and M. M. Perlman, Editors, Electrochemical Society, Princeton, N. J. (1968).
20. A. K. Jonscher, *This Journal*, **116**, 217C (1969).
21. F. S. Sinencio *et al.*, *Phys. Letters*, **A 26**(2), 70 (1967).
22. B. Gross, Northern Electric Co., Ottawa, Ont., Canada, Internal Report T0145 (1970).
23. L. R. Weisberg and H. Schade, *J. Appl. Phys.*, **39**, 5149 (1968).
24. R. Capelletti and E. De Benedetti, *Phys. Rev.*, **165**, 981 (1968).

The Oxidation of Thin Copper Films Condensed in the Presence of Various Residual Gases

Lawrence O. Brockway and Irving M. Adler

Department of Chemistry, The University of Michigan, Ann Arbor, Michigan 48104

ABSTRACT

(100) copper films were prepared by vapor deposition in the presence of hydrogen, water, or air in the pressure range from 10^{-8} to 10^{-4} Torr. The films were annealed and oxidized under constant conditions and were examined at various stages by electron microscopy and diffraction. A reproducible decrease in the Cu_2O grain density was observed when hydrogen was the residual gas: a ten-fold increase in p_{H_2} , in the range between 3×10^{-4} to 4×10^{-6} Torr, resulted in a decrease of 6.4×10^6 grains cm^{-2} . The appearance of wide stacking faults in unannealed copper films and the occurrence of (121) oxide grains also was observed.

Over the past decade several studies have shown that significant variations in the physical properties of thin vapor-deposited metal films can be produced by residual gases present in the film-deposition chamber during film formation. These include observations on electrical resistivity, superconductivity, magnetization, and epitaxy (1-8). No study has appeared on the possible influence of the residual gases on the chemical behavior of vapor-deposited metal films. The present investigation looks at the influence of various gases present during condensation on the texture and oxidation behavior of thin, (100) copper films.

Experimental

Copper was condensed at a rate of about 8 Å/sec to a thickness of about 900 Å on single-crystal substrates of sodium chloride held near 340°C. The principal change from previous experiments on copper in this laboratory (9) was a reduction in the residual pressure to 10^{-8} Torr. This allowed backfilling with gases whose effect on the copper film was to be tested as a function of total pressure and composition. The gases used were hydrogen, water, and air with total pressures ranging from 4×10^{-8} to 3×10^{-4} Torr. Gas compositions were determined in each case with a residual gas analyzer.

Annealing was carried out in a glass line containing a heated Vycor section with a stream of hydrogen at 1 atm and 630°C. The film was treated either (a) for 10 min while still on the NaCl substrate (substrate-anneal), or (b) for 15 min after being removed from the NaCl and mounted on a 1/8 in. diam copper support grid (grid-anneal). For the substrate-annealed films the subsequent exposure to water during the film stripping and mounting was followed by a further treatment in hydrogen (1 atm, 425°C, 10 min) in order to remove oxide formed during the grid-mounting process.

All oxidations were performed under a single set of conditions: 1.0×10^{-3} Torr of oxygen at 525°C for 5 min. Since the conditions for annealing and oxidizing were fixed, variations observed in the oxidized films were attributed to the changes in the gas pressures and compositions during the condensation of the copper.

Observations were made at various stages in the treatment of the films by transmission electron microscopy and diffraction using a Philips EM 75 and a Jeolco 6A microscope. The specimens were examined for the occurrence of stacking faults and dislocations, for the identification of the oxidation products, for the determination of the crystallographic orientation (epitaxy) of both the copper film and the cuprous

oxide, and for the average size and separation (or density on the film) of the cuprous oxide grains.

Results

The copper film crystallized in a single orientation having the (100) plane parallel to the film surface (except for an occasional area on some films with the (310) plane extended; the (310) areas amounted to much less than 1% of the total). The unannealed film showed many dislocations and twins (Fig. 1) and a pronounced thickness variation with the appearance of islands separated by narrow canals. Annealing on the substrate at 630°C reduced the thickness variations and eliminated the twins; grid-annealing at 630°C was not as effective. Substrate-annealing always produced the perpendicular network of stacking faults previously reported (9). For the first time we found wide stacking faults in unannealed films but they were very rare; the area of faulted plane was less than that in substrate-annealed films by a factor of 2×10^{-5} .

The structure and texture of the copper films before oxidation were not influenced in any detectable way by changes in the conditions of condensing the copper.

The oxidation experiments were performed on both substrate- and grid-annealed films by immediately following the exposure to hydrogen (in the reduction treatment at 425°C or the annealing treatment at 630°C) with an exposure to oxygen.

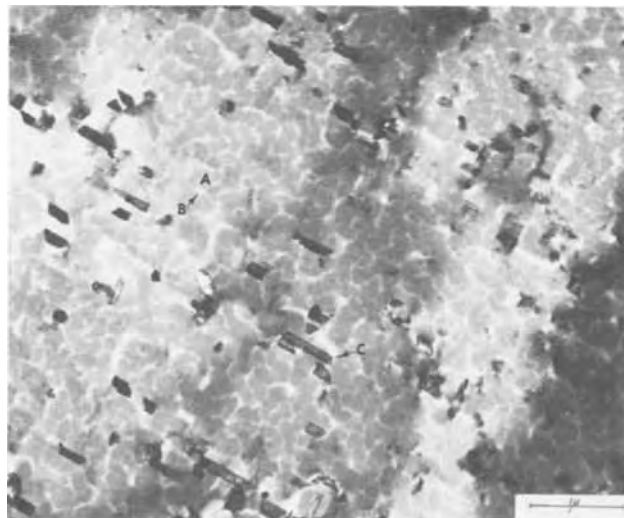


Fig. 1. Electron micrograph of unannealed copper film. The unannealed film contains islands (A) separated by narrow canals (B) and many twin lamellae (C).

Key words: films, copper, oxidation, epitaxy.

Table I. Shapes and epitaxies of Cu₂O grains

□	A: (100) Cu ₂ O	(100) Cu
	[110] Cu ₂ O	[110] Cu
△	A': (100) Cu ₂ O	(100) Cu
	[110] Cu ₂ O	[110] Cu
▽	B: (110) Cu ₂ O	(100) Cu
	[110] Cu ₂ O	[110] Cu
△	C: (111) Cu ₂ O	(100) Cu
	[110] Cu ₂ O	[110] Cu
▽	D: (121) Cu ₂ O	(310) Cu
	[111] Cu ₂ O	[131] Cu

Cuprous oxide grains were formed, but in none of the micrographs or diffraction patterns was there any distinction between grains formed on substrate-annealed or grid-annealed films. Five distinct shapes with four epitaxies were observed (Table I); no variations of even a few degrees in the crystallographic orientations were detected in the diffraction patterns. Three of these shapes (A, B, C,) have been observed previously. The D grains (illustrated in Fig. 2) have a (121) plane of the oxide parallel to the copper and occur only on the (310) areas of copper; accordingly, oxidation of (310) copper yields (121) cuprous oxide.

In relative abundance the B(110) and C(111) types account for about 98% of all oxide grains, with B somewhat more prevalent in most areas. The A and A' type, both (100) orientation, make up the remainder with the A type more common. A typical micrograph is given in Fig. 3. No correlation between the occurrence of the different grain types and gas composition during condensation of the copper was observed.

The number of oxide grains appearing on an oxidized film was counted in fifteen to thirty different areas, each representing $6.9 \times 10^{-7} \text{ cm}^2$ (corresponding to the field of view in the electron microscope used). The results are reported as densities in grains cm^{-2} together with the standard deviation from the mean value for the areas measured. The oxide densities observed for the four distinct gas compositions are listed in Table II.

The first four entries represent primarily water at three pressures (1.8×10^{-8} , 3.6×10^{-6} , and 1.2×10^{-5} Torr) and laboratory air (N₂ and O₂) at 3.0×10^{-5} . There is no apparent relation between pressure and oxide density; indeed, the single value of 2.5×10^7 grains cm^{-2} falls within the range of the standard deviations of all four values. Even when the partial pressures of the individual species (H₂O, N₂, O₂, CO₂)



Fig. 2. Electron micrograph of (121) oxide grains



Fig. 3. Electron micrograph of substrate-annealed, oxidized copper film. The (100)-type (A), (110)-type (B), and (111)-type (C) grains are all present in this area of the oxidized film.

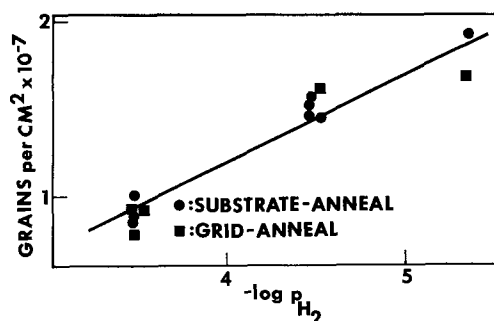


Fig. 4. Influence of hydrogen pressure on oxide density

were compared with the oxide densities, no correlation appeared.

The case of hydrogen used as a backfill is quite different. The consistency of the results at each pressure used is better; the standard deviations average to less than a sixth of those for the other gases. In addition, the oxide densities change systematically with the hydrogen pressures as shown in Fig. 4, where the individual results for thirteen oxidized films are shown. The line in the figure represents the relation

$$D \text{ (grains cm}^{-2}\text{)} \times 10^{-7} = -0.641 \log p_{\text{H}_2} - 1.33$$

in the range of hydrogen pressure from 3×10^{-4} to 4×10^{-6} Torr. It is clear that hydrogen backfilling has a pronounced, reproducible influence on the surface density of Cu₂O grains produced on subsequent oxidation of the copper.

Discussion

The presence of hydrogen during the condensation of the copper onto the NaCl substrate has some effect whereby a tenfold increase in the pressure of hydrogen decreases the density of oxide grains subsequently formed by $6.4 \times 10^6 \text{ cm}^{-2}$ or about 20 to 50% in the range studied. We note that during the condensation of copper the substrate surface was bombarded with

Table II. Influence of gas composition on oxide density

Backfill	$-\log p_{\text{ave}}$	Major component	Average density (grains cm^{-2}) $\times 10^{-7}$
None	7.321	H ₂ O	2.55 ± 0.51
Water	5.446	H ₂ O	3.25 ± 0.79
Water	4.917	H ₂ O	2.48 ± 0.71
Air	4.523	N ₂	2.15 ± 0.55
Hydrogen	5.370	H ₂	1.79 ± 0.18
Hydrogen	4.519	H ₂	1.55 ± 0.07
Hydrogen	3.503	H ₂	0.91 ± 0.08

H₂ molecules at a rate ranging from 0.83 to 63 times the rate of arrival of copper atoms. It is easy to suppose that some of this hydrogen may be retained or trapped interstitially; however, the fact that the disturbing effect of hydrogen persists through either of the annealing treatments, where the copper is exposed to a 10⁹ greater pressure of hydrogen at a higher temperature, casts doubt on interstitial trapping as the mechanism for transmitting the influence on the later oxidation. It is true that the total hydrogen bombarding the film during its condensation is 10⁶ greater than the saturated concentration at 1 atm and 630°C (10), but the loss by diffusion (11) during the later heating under vacuum would produce a final equilibrium concentration of hydrogen far less than that under a pressure of 1 atm and at 630°C.

A more plausible possibility for the direct effect of hydrogen present during the condensation of copper is that the number of vacancy sites in the copper structure increases with the pressure of hydrogen. It is possible to calculate (12-14) the distortions in the copper lattice around such point defects, and we suggest that the changes in lattice energy produced by these distortions have an influence on the density of oxide nucleation sites occurring in the subsequent reaction with oxygen. The occurrence of vacancy sites in metal crystals grown in the presence of hydrogen is supported by an observation of Kokotailo (15) who found a decrease in the unit cell size of platinum crystallites grown in hydrogen as compared with those grown in air, nitrogen, or argon; he ascribed the lattice shrinkage of ¾% to vacancy sites induced by the hydrogen.

A consideration of the density of oxide nucleation sites is based on suggestions made by Benard (16). Three stages occur in the growth of oxide on metals at low oxygen pressures: (i) an incubation period during which the concentration of oxygen on and in the metal builds up to some critical value, (ii) the simultaneous appearance of isolated oxide nuclei, which then grow laterally until a continuous oxide layer is formed, and (iii) the thickening of the layer in a fashion which is uniform over the surface of the film. In step (ii), where our principal interest lies, Benard noted that the density of isolated oxide nuclei increases with the pressure of oxygen and called the area associated with one nucleus the "zone of influence," supposing that the oxygen bombarding this pressure-dependent area can contribute to only one nucleus. Observations by Brockway and Rowe (9) showed that for oxygen pressures from 10⁻¹ to 10⁻³ Torr the first oxide nuclei appearing on copper at 525°C were distributed uniformly with the density in grains cm⁻² equal to 5.5 × 10⁹ × p_{O₂} (Torr). The proportionality to pressure means that the number of oxygen molecules bombarding the "zone of influence" (area per oxide nucleus) is independent of the pressure and equal to 4.0 × 10¹⁰ molecules per second.

We suggest now that the stresses in the copper due to the hydrogen-induced vacancy sites reduce the effectiveness of oxygen bombardment for oxide nucleation and that a larger number of oxygen molecules per second must be supplied for each nucleus formed. Therefore, the copper films formed in the presence of hydrogen and subsequently oxidized require a larger surface area to contribute to the formation of a single oxide nucleus and the density of oxide nuclei is reduced. Without being able to make a quantitative prediction, we note that an increase in the hydrogen pressure from 10⁻⁵ to 10⁻⁴ Torr decreases the oxide

grain density by 40%; in the absence of the hydrogen effect, a 40% decrease in the oxygen pressure would have the same result.

Summary

Copper films exhibiting the (100) epitaxy were prepared by condensation onto heated, single-crystal, sodium chloride substrates. The distinguishing feature of the present work lay in backfilling the film-deposition chamber with hydrogen, water, or air in the pressure range from 10⁻⁸ to 10⁻⁴ Torr. In every case specimens of the copper films were annealed and oxidized under the same conditions used in previous investigations, and the effect of the residual gases was tested by examining the films with the techniques of electron diffraction and microscopy.

No effect of the residual gases could be detected in the epitaxy or annealing characteristics of the copper films or in the shape and epitaxy of the Cu₂O grains formed on subsequent oxidation. A pronounced reproducible effect on the surface density of Cu₂O grains was observed when hydrogen was present during the condensation of the copper. We suggest that the presence of hydrogen during the growth of the copper crystal increases the number of vacancy sites in the metal, which have an inhibiting effect on the subsequent nucleation of oxide grains.

Two other observations in this study of thin single-crystal copper were the occasional appearance of wide stacking faults in unannealed films and the formation of limited areas of copper film with the (310) epitaxy on which Cu₂O grains grew with a (121) epitaxy.

Acknowledgments

We wish to acknowledge support provided for Mr. Adler by the Allied Chemical Industrial Fellowship and by the Union Carbide Summer Fellowship.

Manuscript submitted May 3, 1971; revised manuscript received Feb. 21, 1972.

Any discussion of this paper will appear in a Discussion Section to be published in the June 1973 JOURNAL.

REFERENCES

1. H. L. Caswell, *J. Appl. Phys.*, **32**, 105 (1961).
2. H. L. Caswell, *ibid.*, **32**, 2641 (1961).
3. C. A. Newugebauer, "Vacuum Symposia," Vol. 8, p. 924, L. E. Preuss, Editor, Pergamon Press, New York (1962).
4. J. D. Blades, J. Gerber, and C. T. Thompson, *ONR Symposium Rept. ACR-50*, p. 121 (1960).
5. J. F. Marchant and A. Venema, *Philips Res. Rept.*, **14**, 427 (1959).
6. E. Ruedl, *Vacuum*, **7**, 8, 56 (1957-1958).
7. S. Ino, D. Watanabe, and S. Ogawa, *J. Phys. Soc. Japan*, **19**, 881 (1964).
8. J. W. Matthews, *J. Vacuum Sci. Technol.*, **3**, 133 (1956).
9. L. O. Brockway and A. P. Rowe, "Fundamentals of Gas-Surface Interactions," p. 147, H. Saltzburg, Editor, Academic Press, New York (1967).
10. A. Sieverts, *Z. Metallk.*, **21**, 37 (1929).
11. S. Dushman and J. M. Lafferty, "Scientific Foundations of Vacuum Technology," 2nd ed., p. 572, John Wiley & Sons, New York (1962).
12. H. Kanzaki, *J. Phys. Chem. Solids*, **2**, 24 (1957); **2**, 107 (1957).
13. P. H. Miller and B. R. Russell, *Phys. Rev.*, **23**, 1163 (1952); **24**, 1248 (1953).
14. J. D. Eshelby, *J. Appl. Phys.*, **25**, 255 (1954).
15. G. T. Kokotailo, Private communication.
16. J. Bénard, F. Grønlund, J. Oudar, and M. Duret, *Z. Electrochem.*, 799 (1959).

Optical Properties of Rare Earths in Germanate Hosts

Mohan Munasinghe^{*,1}

Ceylon Institute of Scientific and Industrial Research, Colombo 7, Ceylon

ABSTRACT

The luminescence characteristics of barium magnesium germanate crystal and glass matrices doped with the rare earths Eu^{3+} , Tb^{3+} , and Nd^{3+} have been investigated. Tb^{3+} to Eu^{3+} energy field transfer is indicated in the crystal but not in the glass. A partial crystal field splitting for the principal Nd^{3+} states in crystal is given. Results of the quenching of Nd^{3+} emission by iron impurity yields a value of $\sim 14\text{\AA}$ for the range of the neodymium-iron quenching interaction, based on a simple model. Relevant physical properties and results from a study of devitrification of the glass are used to examine the structure of the two hosts.

Rare earths are now widely used as dopants in both crystal and glass host matrices to produce fluorescence in the visible and infrared regions of the spectrum (1-3). Hence the study of the luminescence properties of these materials has become important in the search for more versatile solid-state lasers. The results of an investigation of the optical properties of the rare earths europium, terbium, and particularly neodymium in barium magnesium germanate crystal and glass hosts are presented in this paper.

Experimental Procedure

Glass samples of rare-earth doped $\text{Ba}_2\text{MgGe}_2\text{O}_7$ were prepared by melting down and stirring a stoichiometric mixture of the required composition in a platinum crucible. After mixing thoroughly at $\sim 1300^\circ\text{C}$ the mixture was rapidly cooled through the temperatures for maximum crystallite nucleation and growth rate by pouring it into a molybdenum crucible immersed in liquid nitrogen. Final cooling from $\sim 700^\circ\text{C}$ down to room temperature was carried out in a preheated oven at a slower average rate of $\sim 1^\circ\text{C}/\text{min}$, to prevent straining and cracking of the glass. Relatively large (i.e., 7 cm radius by 1 cm thickness) and strain-free pieces of clear glass could be prepared in this way. A top seeded solution method (4) was used to prepare the single crystals of doped $\text{Ba}_2\text{MgGe}_2\text{O}_7$. K^+ charge compensators were provided in all the melts. The samples were cut and polished to a standard size of approximately $5 \times 6 \times 7 \text{ cm}^3$.

The standard experimental setup shown in Fig. 1 was used for fluorescence and excitation studies. 1 kW mercury and xenon lamps were the chief light sources. Excitation spectra were recorded with the aid of a monochromator and suitable filters to pump in different regions of the spectrum. For emission spectra, the pumping light was passed through a 10-cm thick, saturated solution of CuSO_4 to attenuate wavelengths

above $\sim 5500\text{\AA}$. For Tb^{3+} and Eu^{3+} doped samples, an additional filter was used when necessary to cut off exciting radiation above $\sim 4000\text{\AA}$.

Cary 14R and Beckman IR12 double beam spectrophotometers were used for absorption measurements in the ranges 2500-20,000 \AA and 1.7-5 μ , respectively. Rare earth concentrations in crystalline samples were deduced from chemical analysis and absorption data. Further details of the experimental procedure may be found elsewhere (5, 6).

Results and Discussion

Tb^{3+} and Eu^{3+} data.—Figures 2 and 3 are the emission spectra of Tb^{3+} and Eu^{3+} in $\text{Ba}_2\text{MgGe}_2\text{O}_7$ crystal at 80°K . Both emission and absorption peaks of these rare earths in the crystalline host were broadened and reduced in intensity as the temperature was increased from 80° to 300°K . The main Tb^{3+} emission is seen to occur from the $^5\text{D}_3$ state, i.e., $< 4500\text{\AA}$.

For a crystal sample codoped with $\sim 1\%$ atomic fraction² each of Tb^{3+} and Eu^{3+} the intensities of Tb^{3+} emission lines were found to be at least ten times weaker than the intensities of corresponding lines from a crystal doped with $\sim 1\%$ atomic fraction of Tb^{3+}

² Atomic fraction = $N_a/(N_a + N_h) \approx N_a/N_h$ when $N_h \gg N_a$ and where N_a = density of rare earth activator ions and N_h = density of Ba^{2+} host matrix cation which is replaced by activator ions.

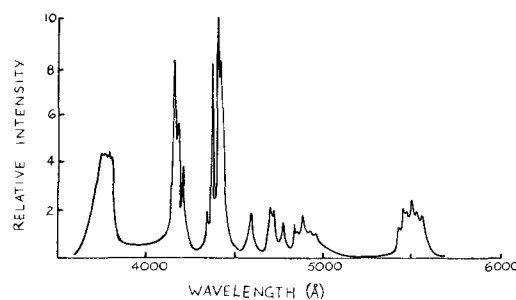


Fig. 2. Emission spectrum of Tb^{3+} in $\text{Ba}_2\text{MgGe}_2\text{O}_7$ crystal at 80°K .

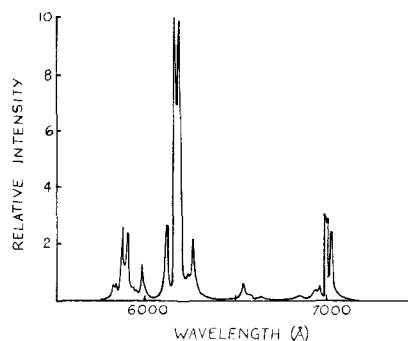


Fig. 3. Emission spectra of Eu^{3+} in $\text{Ba}_2\text{MgGe}_2\text{O}_7$ crystal at 80°K .

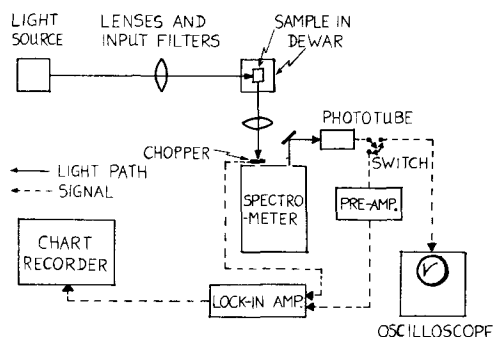


Fig. 1. Block diagram of basic fluorescence apparatus

* Electrochemical Society Student Associate.

¹ Present address: Electrical Engineering Department, McGill University, Montreal 110, P.Q., Canada.

Key words: luminescence, fluorescence, emission, rare earth, neodymium.

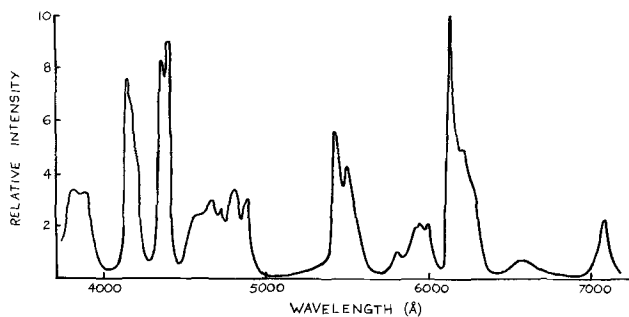


Fig. 4. Emission spectrum of Ba₂MgGe₂O₇:2% Tb³⁺ :2% Eu³⁺ glass at 80°K.

only. No significant enhancement of Eu³⁺ emission was observed from the doubly doped sample when compared with a crystal doped with ~1% Eu³⁺ only. Energy transfer from Tb³⁺ to Eu³⁺ may be the cause of the quenching of Tb³⁺ emission in the codoped sample (7).

No quenching of Tb³⁺ emission was seen in the equivalently doped glass host. The fluorescent spectrum of a doubly doped glass sample was found to be a superposition of the spectra in glass of the individual Eu³⁺ and Tb³⁺ activators. Temperature-insensitive inhomogeneous broadening, which is typical for rare earths in a glass matrix, can be seen for the absorption and emission spectra (Fig. 4) of barium magnesium germanate glass codoped with ~2% atomic fraction each of Tb³⁺ and Eu³⁺. In general, broad energy bands in the spectra of the glass samples were not significantly shifted with respect to corresponding groups of lines in the crystal spectra.

Nd³⁺ data.—Absorption and fluorescent spectra of Nd³⁺ in both hosts exhibited the same general characteristics as those of the other two rare earths, i.e., reduction of widths and intensification of lines with decreasing temperature for the crystal samples and inhomogeneously broadened bands, indicating variations of the crystal field at typical Nd³⁺ sites in the glass samples.

Small shifts in the positions of crystal lines occurred with changes in temperature. For a tetragonal crystal such as Ba₂MgGe₂O₇ the coefficients of thermal expansion along the c and a axes are different. The resultant changes in the symmetry as well as intensity of the crystal field at activator sites is likely to lead to small shifts in the energy levels as the temperature is varied. Table I gives the dependence of wavelength on temperature for a typical Nd³⁺ line. While room-temperature broadening is due to lattice phonons, the residual component of broadening at 5°K is probably caused by the presence of neighboring K⁺ charge compensators at some of the activator sites. Nd³⁺ spectra in both types of host are discussed at greater length elsewhere (5).

All observed transitions in the crystal host were predominantly electric dipole in nature since the σ and axial (or δ) spectra were identical (8). Electric quadrupole transitions which are ~10³ weaker may be ruled out. Transitions in the glass are comparable in strength to those in the crystal host. Figure 5 gives a partial

Table I. Temperature dependence of the wavelength and halfwidth of one of the ⁴F_{3/2} → ⁴I_{9/2} transitions in Ba₂MgGe₂O₇:0.45% Nd³⁺ crystal

	300°K	80°K	5°K
Wavelength (Å)	9325	9318	9315
Halfwidth (Å)	38	12	5

Error: ±1Å for wavelength measurements.
±0.5Å for halfwidth measurements.

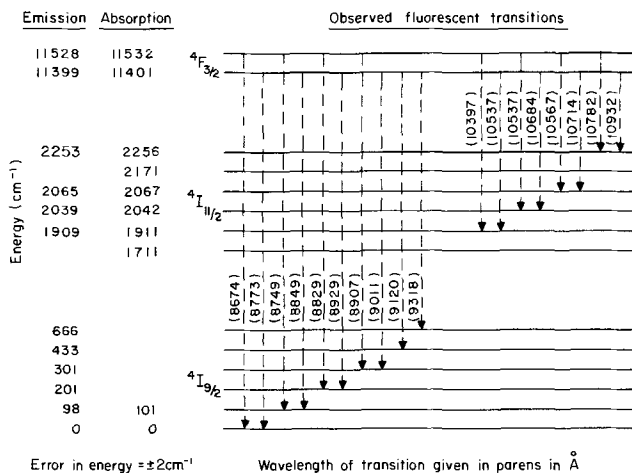


Fig. 5. Observed splittings of Nd³⁺ energy levels in Ba₂MgGe₂O₇ crystal at 80°K.

crystal field splitting at 80°K for the ⁴F_{3/2}, ⁴I_{9/2}, and ⁴I_{11/2} states of Nd³⁺ in Ba₂MgGe₂O₇, deduced from the crystal spectra. The splitting of the ⁴F_{3/2} state is seen to be ~130 cm⁻¹ at 80°K. For variations in activator concentration up to 2% atomic fraction, shifts in these energy levels were found to be <2 cm⁻¹.

The absorption cross section for various Nd³⁺ lines was found to be independent of activator concentration. Thus Beer's law is obeyed for Nd³⁺ absorption in both types of host indicating constant oscillator strength for these transitions (9). Excitation spectra revealed that the energy absorbed directly by the matrix (i.e., for excitations below the absorption edge ~2800Å) is not transferred to the activator ions (7). Concentration quenching of emission was strong in the glass but practically nonexistent in the crystal for Nd³⁺ concentrations up to 2% atomic fraction. This and other related concentration- and temperature-dependent phenomena may be attributed to two predominant types of resonant energy transfers between Nd³⁺ ions in the glass: (a) a Peterson-Bridenbaugh type quenching energy transfer, and (b) a resonant cross relaxation (2, 5, 10-12), shown in Fig. 6a and b.

Since the intensity of Nd³⁺ emission was also found to be a sensitive function of impurity iron concentration, emission from a series of glass samples doped with both neodymium and iron was studied. The iron concentration was varied while the neodymium concentration of all the samples was fixed at 0.5% atomic fraction. Earlier studies (5) showed that Nd³⁺-Nd³⁺ interaction effects, which could complicate the analysis of the results, are negligible at these relatively low activator concentrations. Figure 7 shows the typical absorption spectrum of one such sample. The characteristic spectrum of Nd³⁺ in glass is evident, superposed over broad iron bands. The Nd³⁺ emission spectrum of this sample (and others in the series) is identical to that of the corresponding glass sample not containing iron, except for a reduction in intensity of emission due to the iron impurity. The emission per

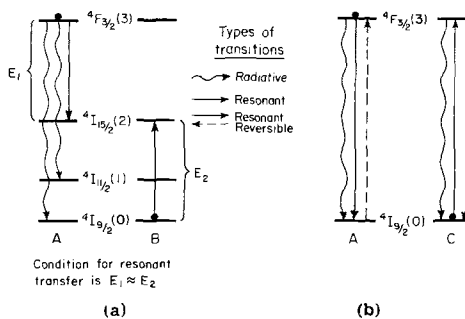


Fig. 6. Energy transfer of Nd³⁺ in Ba₂MgGe₂O₇ crystal

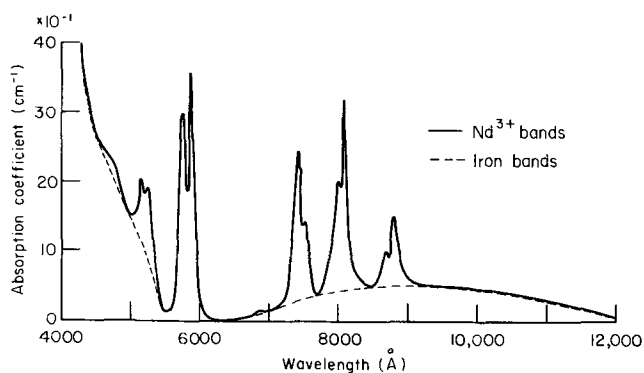


Fig. 7. Absorption spectrum of Ba₂MgGe₂O₇:0.5% Nd³⁺ :0.5% iron glass at 80°K.

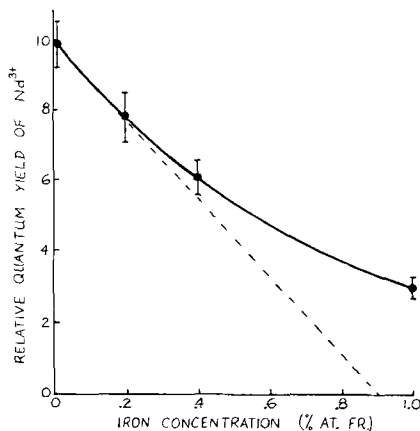


Fig. 8. Relative emission intensity per Nd³⁺ ion vs. iron concentration in Ba₂MgGe₂O₇ glass at 300°K.

Nd³⁺ activator is plotted as a function of iron concentration in Fig. 8. We may obtain an estimate for the range of the neodymium-iron quenching interaction from the following simple model.

We hypothesize that if an activator is located less than a critical distance R_q away from an impurity iron atom, emission from it is totally quenched. Otherwise the Nd³⁺ ion fluoresces normally. Thus each iron atom effectively poisons a spherical volume $V_q = 4\pi R_q^3/3$ around itself. The Nd³⁺ concentration is constant and we assume that both the neodymium and iron are uniformly distributed throughout the host matrix. Therefore at low concentrations, the ratio of the number of quenched Nd³⁺ ions to the total number of Nd³⁺ ions present would be equal to the total poisoned volume per unit volume of the sample. This ratio may be written as

$$r = n_i V_q$$

where n_i = number of impurity iron atoms per unit volume.

The mean intensity of emission per Nd³⁺ ion would be proportional to the number of unquenched activators. Since absorption measurements show that the energy absorbed per Nd³⁺ ion is independent of iron concentration, the mean quantum yield may be written as

$$\eta_{avg} = \eta_0 (1 - n_i V_q)$$

where η_0 = the quantum yield when no iron is present.

It should be noted that we obtain a linear relationship between η_{avg} and n_i only if the iron concentration is low enough such that there is no significant overlap of the poisoned volumes of adjacent iron atoms. In fact, as n_i increased, this effect would tend to decrease the negative slope of the η_{avg} vs. n_i curve and flatten it out. Hence the linear relationship holds for small values of n_i only. These deductions from our model are consistent with the data shown in Fig. 8.

Now 1% atomic fraction of iron corresponds to a concentration of $\sim 1 \times 10^{20}$ atoms per cm³ of the sam-

ple. Therefore, from the intercept on the x axis made by the tangent to the linear portion of the curve (i.e., at low iron concentrations) we get

$$V_q = 1 / (0.9 \times 10^{20})$$

This yields the final result $R_q \approx 14\text{Å}$, where R_q is the range of the quenching interaction between neodymium and iron based on this simple model.

A study of the devitrification of barium magnesium germanate glass was attempted to provide some insight into fundamental differences between the two hosts. Some preliminary results are given below.

Several glass samples containing 4% atomic fraction of Nd³⁺ were annealed on a hot stage mounted on a polarizing microscope. Emission from the samples was monitored at various stages of the devitrification process using the apparatus of Fig. 1. Crystallites of linear dimensions up to 100 μ were observed after annealing at $\sim 850^\circ\text{C}$ for about 10 min. Further growth could not be observed visually due to increasing opacity of the sample. At this stage of devitrification of the sample (i.e., 10 min at $\sim 850^\circ\text{C}$), there was no detectable change in its fluorescent spectrum. Another sample annealed at 750°C for 6 hr became completely opaque and marblelike in appearance. The emission spectrum of this sample, obtained by scattering from the surface, is shown in Fig. 9. It shows typical broad bands of Nd³⁺ emission from glass, on which are superposed some sharp lines characteristic of Nd³⁺ emission from the crystal. This implies that only certain areas of the glass have reverted to the normal Ba₂MgGe₂O₇ crystal structure, although the sample was opaque.

Ba₂MgGe₂O₇ is isomorphous with Ca₂MgSi₂O₇ (13, 14) (i.e., it has the akermanite structure) in the crystalline state. The MgO₄ and GeO₄ tetrahedra are arranged in a sheetlike pattern parallel to the (001) plane, while BaO bonds link adjacent sheets together. A typical Ba²⁺ site in which Nd³⁺ activators are incorporated substitutionally (5) is shown in Fig. 10. The eight nearest neighbor oxygen atoms are arranged approximately in the form of an Archimedean antiprism around the cation.

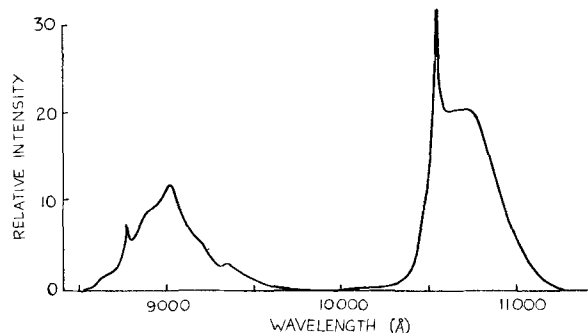


Fig. 9. Emission spectrum of partially devitrified Ba₂MgGe₂O₇: 4% Nd³⁺ glass at 300°K.

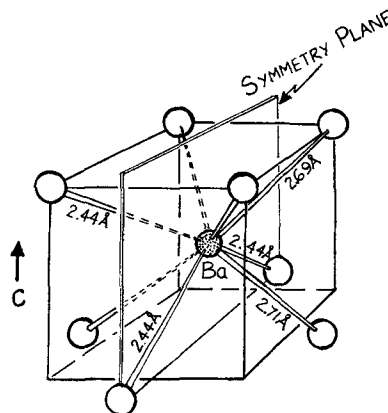


Fig. 10. Ba²⁺ antiprism site in Ba₂MgGe₂O₇ crystal

The densities of all crystal and glass samples were found to agree within 0.5%, indicating very little differences in the packing density. Small variations in the densities of glass samples may be attributed to the difficulty of reproducing exactly the method of preparation for each batch of samples. The density of the $\text{Ba}_2\text{MgGe}_2\text{O}_7$ crystal samples (4.737 g/cm^3) was identical to the figure calculated from the lattice parameters: $a = 8.835\text{\AA}$, $c = 5.545\text{\AA}$. These values were determined from x-ray measurements using oriented plates (a, c, and 110), which gave high intensity, higher order reflections (15). The values of the lattice constants and the x-ray diffraction powder pattern are similar to those reported elsewhere (14).

It was not possible to grow crystals which contained more than ~2% atomic fraction of activator concentration even though the melt itself contained much higher concentrations of activator. Thus it would not be possible for the whole of a glass sample which contained 4% atomic fraction of Nd^{3+} to devitrify into the normal $\text{Ba}_2\text{MgGe}_2\text{O}_7$ crystal structure. Furthermore since the melting point of $\text{Ba}_2\text{MgGe}_2\text{O}_7$ is $\sim 1300^\circ\text{C}$, the fluidity of the glass is low at 750°C . The Nd^{3+} site symmetry varies in the glass, which is probably microheterogeneous (16, 17). Hence by annealing at this temperature only those localized portions of the glass which contained less than 2% atomic fraction of activator and were structurally closest to the crystal's atomic configuration could recrystallize, leaving areas of high activator concentration and high disorder relatively unchanged. This may be part of the reason for the composite spectrum observed in Fig. 9.

Summary

The advantages of the comparative study of crystal and glass hosts of identical chemical composition using rare earth fluorescence as a probe have been discussed at greater length elsewhere (5). The technique can be extended to other hosts and activators as well.

In this paper, we have used the technique to investigate differences in behavior between the crystalline and glassy states of the barium magnesium germanate host, and to study activator-activator and activator-impurity interactions. Some conclusions have been drawn regarding the structure of the two types of host. The drastic quenching effects of iron impurity on the emission intensity of neodymium has also been demonstrated.

Acknowledgments

The experimental work was carried out while the author was at the Materials Science Center, Massa-

chusetts Institute of Technology, and supported by the Office of Naval Research.

The contributions of the following members of the Crystal Physics Laboratory, Massachusetts Institute of Technology are gratefully acknowledged: Dr. Arthur Linz for encouragement, advice and helpful criticisms, Mr. J. Kalnajs for the gathering of x-ray and spectroscopic data, and Mr. V. Belruss for growing all the crystals. Thanks are also due to Mrs. Sria Munasinghe for typing and correcting this manuscript, and colleagues in the Ceylon Institute of Scientific and Industrial Research for helpful discussions.

Manuscript submitted Dec. 3, 1971; revised manuscript received Feb. 7, 1972. This was Paper 44 presented in part at the Washington, D. C., Meeting of the Society, May 9-13, 1971.

Any discussion of this paper will appear in a Discussion Section to be published in the June 1973 JOURNAL.

REFERENCES

1. Z. J. Kiss and R. J. Pressley, *Proc. IEEE*, **54**, 1236 (1966).
2. E. Snitzer, *ibid.*, **54**, 1249 (1966).
3. G. O. Karapetyan and A. L. Reishakrit, Translated from *Izv. Akad. Nauk. SSSR, Neorgan. Materialy*, **3**, 217 (1967).
4. V. Belruss, J. Kalnajs, A. Linz, and R. C. Folweiler, *Mater. Res. Bull.*, **6**, 899 (1971).
5. M. Munasinghe and A. Linz, *Phys. Rev.*, **B**, **4**, 3833 (1971).
6. M. Munasinghe, "Rare Earth Fluorescence in Barium Magnesium Germanate Crystal and Glass Hosts," S.M. & E.E. Thesis, Elec. Eng. Dept., M.I.T. (1969).
7. L. G. Van Uitert, "Luminescence of Inorganic Solids," p. 465, P. Goldberg, Editor, Academic Press, New York (1966).
8. B. DiBartolo, "Optical Interactions in Solids," p. 414, John Wiley & Sons, Inc., New York (1968).
9. D. W. Harper, *Phys. Chem. Glasses*, **5**, 11 (1964).
10. L. G. Van Uitert and L. F. Johnson, *J. Chem. Phys.*, **44**, 3514 (1966).
11. Yu K. Voronko, A. A. Kaminskii, and V. V. Osiko, *Sov. Phys. JETP*, **22**, 295 (1966).
12. L. G. De Shazer and L. G. Komai, *J. Opt. Soc. Am.*, **55**, 940 (1965).
13. W. A. Deer, R. A. Howie, and J. Zussman, "Rock Forming Minerals—Vol. 1: Ortho- and Ring Silicates," p. 237, John Wiley & Sons, Inc., New York (1962).
14. H. Koelmans and C. M. C. Verhagen, *This Journal*, **106**, 677 (1959).
15. J. Kalnajs, Measurements made at the Crystal Physics Laboratory, M.I.T. (1967).
16. C. Hirayama and D. W. Lewis, *Phys. Chem. Glasses*, **5**, 44 (1964).
17. C. Hirayama, *ibid.*, **7**, 52 (1966).

Eu^{+2} Emission in Ternary Alkaline Earth Aluminum Fluorides

Mary V. Hoffman*

Lighting Research Laboratory, General Electric Company, Nela Park, Cleveland, Ohio 44112

ABSTRACT

The ternary systems $\text{MF}_2\text{-MF}_2\text{-AlF}_3$ where $\text{M} = \text{Ca, Sr, or Ba}$, were examined for compatibility triangles and compounds. The compounds SrCaAlF_7 and BaCaAlF_7 were found, each with three polymorphs. The β - and γ -forms in the SrCaAlF_7 compound could be quenched. The two low-temperature (α) forms show strong line emission at 358 to 360 nm with Eu^{+2} activation, resulting from absorption into the 5d states and emission from the ${}^6\text{P}_{7/2}$ levels to the ${}^8\text{S}_{7/2}$ ground state. The β - and γ -forms of SrCaAlF_7 contain a band emission and a much weaker line.

Divalent Eu activation in alkaline earth aluminum fluorides has been found to give two types of emission,

* Electrochemical Society Active Member.

Key words: luminescence, spectra, Eu^{+2} activation, alkaline earth aluminum fluoride compounds.

the band emission normally associated with Eu^{+2} 5d to 4f transitions, and line emission from transitions within the 4f⁷ configuration. A general description of both types has been reported (1), and a more detailed

description of the line emissions has also been published (2).

The binary compounds in the systems MF_2-AlF_3 ($M = Ba, Sr, \text{ or } Ca$) have been described (1). The work on the single-crystal growth and characterization of one of these compounds, $SrAlF_5$, will be published (3). Of the three MF_2-MF_2 systems used in these ternaries, two have complete solid solution at high temperatures. In the CaF_2-BaF_2 system, this solid solution exists only above $915^\circ C$ (4, 5) while for BaF_2-SrF_2 , only the temperature range close to the liquidus has been reported (6). In the CaF_2-SrF_2 system, solid solution has been assumed but not verified (7).

This paper extends this work into the ternary systems $MF_2-MF_2-AlF_3$, and includes the compatibility triangles, the compounds and polymorphic forms, and the optical data with Eu^{+2} activation. It also includes some additional data on one binary compound in the BaF_2-AlF_3 system.

Experimental

The procedures used for the preparation, firing, and characterization of the compounds in the ternary systems and the optical measurements made were similar to those previously described (1, 2). Compositions in the ternary regions were usually formulated by combining a binary alkaline earth aluminum fluoride compound in the precipitated form and an alkaline earth fluoride, and were prepared both with and without Eu^{+2} . The use of the activation permitted comparisons of spectral distributions run at 10 Å/in. scan and 0.5Å spectral band width (SBW) to detect the presence of the several different line emitting compounds in two- and three-phase regions. In all of the systems, identification of the phases present and the validity of the joins and the triangles were verified by using identical compositions prepared by several methods and by a combination of the identification methods, x-ray diffraction, spectral measurements, and the petrographic microscope. X-ray diffraction data for the ternary compounds are given in the Appendix.

Results

Compound formation.—Compositions in MF_2-MF_2 systems were prepared by firing in HF at $800^\circ C$. In the CaF_2-BaF_2 and SrF_2-BaF_2 systems, the x-ray diffraction patterns showed only the end member fluorides. The SrF_2-BaF_2 system is probably analogous to the CaF_2-BaF_2 system in having complete solid solution below the liquidus and a lower limit of stability. This limit was not established in this work. In the SrF_2-CaF_2 system, complete solid solution was found after firings at $800^\circ C$, with the lattice parameters changing linearly with composition (Table I).

The data on transitions and melting points for most of the MF_2-AlF_3 compounds have been given (1). One compound, $Ba_9Al_2F_{24}$, has been examined in more detail by differential thermal analysis (DTA). Two heat effects were found at 770° and $820^\circ C$ which are probably due to polymorphic inversions, and melting was found to occur at $915^\circ C$. Samples obtained by rapid cooling showed that the form stable above $770^\circ C$ could not be quenched, but a change in the x-ray diffraction pattern was obtained on a sample which was cooled rapidly from $850^\circ C$. This pattern resembled BaF_2 , but microscopic examination showed a highly

Table I. SrF_2-CaF_2 system

Composition, m/o		a_0^*
SrF_2	CaF_2	
100	—	5.797
67	33	5.684
50	50	5.628
33	67	5.571
—	100	5.458

* Based on the 220 line.

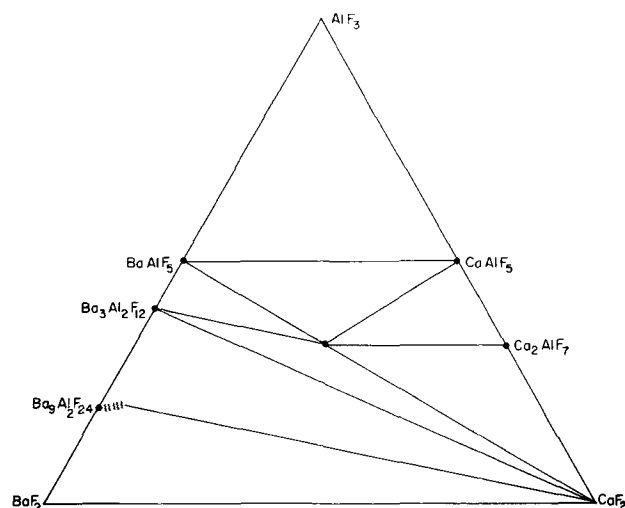


Fig. 1. Compatibility triangles in the system $CaF_2-BaF_2-AlF_3$ at $750^\circ C$.

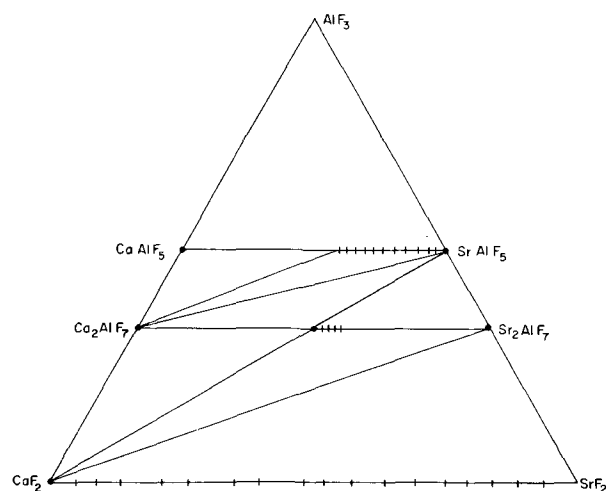


Fig. 2. Compatibility triangle in the system $CaF_2-SrF_2-AlF_3$ at $750^\circ C$.

uniform anisotropic crystalline form. When $Ba_9Al_2F_{24}$ was prepared with Eu^{+2} , reflectance measurements showed weak absorption at 250 nm, but no significant emission was found from this composition with any of the heating and quenching treatments.

Ternary systems.—The compatibility triangles found for these ternary systems at $750^\circ C$ are shown in Fig. 1, 2, and 3. The system $CaF_2-BaF_2-AlF_3$ is the least complex, and contains one ternary compound at $BaCaAlF_7$, and a limited amount of solid solution in $Ba_9Al_2F_{24}$, based on a shift in observed d spacings. The system $CaF_2-SrF_2-AlF_3$ also contains a single ternary compound, at $SrCaAlF_7$, with a small amount of solid solution toward Sr_2AlF_7 possible. Along the $SrAlF_5-CaAlF_5$ join, solid solution was found between $SrAlF_5$ and $Sr_{0.6}Ca_{0.4}AlF_5$ (1).

In the system $SrF_2-BaF_2-AlF_3$, two regions of solid solutions were found. One extends from $SrAlF_5$ almost completely along the join to $Sr_{0.15}Ba_{0.85}AlF_5$. The solid solution of Sr in $BaAlF_5$ is limited to less than 2 m/o (mole per cent) (1). The second solid-solution region extends from $Ba_9Al_2F_{24}$ along the join toward SrF_2 and also toward a composition of approximately $3BaF_2:2SrF_2:2AlF_3$, as evidenced by shifts in the observed d spacings. The exact region and nature of this solid solution was not investigated further.

The two ternary compounds were examined by DTA, and heat effects which are attributed to the transitions of three polymorphic forms were found in each compound (Table II).

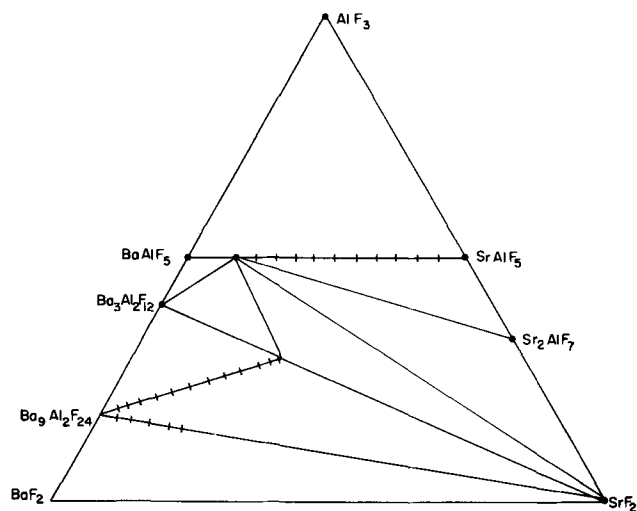


Fig. 3. Compatibility triangles in the system $\text{SrF}_2\text{-BaF}_2\text{-AlF}_3$ at 750°C .

In SrCaAlF_7 , all three forms have been obtained. These were prepared by firing in the HF atmosphere, close to the melting point, for several hours, then holding in the desired stability region in flowing nitrogen. These inversions are slow to occur in both the heating and cooling direction, so that firing times of up to 16 hr were needed to completely convert the material to a pure phase. The presence of a second phase was usually caused by insufficient firing time rather than re-inversion on cooling. The quick cooling required to retain the β - and γ -phases were limited by the bulk of the tubular platinum furnace used for HF firings, which required 5-10 min to cool to below 500°C . This cooling rate was sufficient to retain the β - and γ -forms.

In the BaCaAlF_7 compound, only the α -form has been obtained, with no evidence of the β - or γ -form being quenched with rapid cooling. In order to obtain faster cooling than available in the HF furnace and to maintain the controlled atmosphere, samples containing Eu^{2+} were sealed in 5 mm Pt tubing under nitrogen, and quenched in water from 735° and 800°C . Optical measurements from both quenchings agreed with the emission spectra of $\alpha\text{-BaCaAlF}_7\text{:Eu}^{2+}$ and x-ray diffraction showed the α -form as the probable phase.

Quaternary solid solution.—The compositional series between SrCaAlF_7 and BaCaAlF_7 were also prepared and examined by x-ray diffraction, by DTA, and by emission spectra for possible solid solution. Samples were prepared with 0.02 Eu^{2+} from mixtures of BaAlF_5 , SrAlF_5 , and CaF_2 . These were fired in HF above the melt point and then refired below the α -to- β inversion temperature. X-ray diffraction patterns showed neither a discernable shift in d spacings nor evidence of the presence of the end member compounds. With more than about 15 m/o substitution, the patterns showed broadened lines inconsistent with the sharp patterns obtained for the end members. DTA data obtained on these samples were not incompatible with a solid-solution series. With substitution of up to 15% Ba in SrCaAlF_7 , the transition temperatures for the two inversions were raised and the inversions became more rapid, showing solid solution to at least this composition.

Table II. Ternary compounds

Heat effect transition	Temperature, $^\circ\text{C}$ SrCaAlF_7	Temperature, $^\circ\text{C}$ BaCaAlF_7
$\alpha \rightarrow \beta$	487 ± 5	716 ± 4
$\beta \rightarrow \gamma$	670 ± 5	744 ± 4
Melting point	775 ± 10	816 ± 3

Luminescence.—The four structures which can be obtained in the two ternary compounds all show emission with Eu^{2+} with the two low-temperature polymorphs showing predominantly line emissions at 358-360 nm.

BaCaAlF_7 .—The $\alpha\text{-BaCaAlF}_7$ structure shows more intense line emission than found in any of the previously reported fluoride compounds (1). The spectra at two resolutions are shown in Fig. 4, taken at 25°C in which the single line is shown to resolve into four lines of similar intensities. When measured at 78°K , and with time resolved spectra, more than eight lines are discernable in this same wavelength region. The excitation spectra (Fig. 5) shows broad band absorption into the 5d level of Eu^{2+} . The excitation and emission mechanism follows that found for the binary fluorides, that is, excitation from the $^8\text{S}_{7/2}$ ground state to the $4f^65d$ states, followed by emission from the $^6\text{P}_{7/2}$ and $^6\text{P}_{5/2}$ levels to the $^8\text{S}_{7/2}$ ground state (2). The phosphor is also excited by cathode rays and by x-rays.

Optimum Eu^{2+} concentration was found to be between 0.001 and 0.10 of Eu^{2+} , but the matrix will accept at least 0.40 Eu^{2+} , calculated as substituting in the Ba^{2+} site, with no evidence found for the formation of a second phase by x-ray diffraction. No changes in spectra were found for much lower activator concentrations, while the high concentrations showed splitting of lines which could be resolved at 0.5 SBW at room temperature.

SrCaAlF_7 .—The three polymorphs of SrCaAlF_7 show emission with Eu^{2+} , but only one is predominantly line emission. The α -form closely resembles that of BaCaAlF_7 at 25°C , differing in the position of the four emission lines but containing more 5d-4f emission

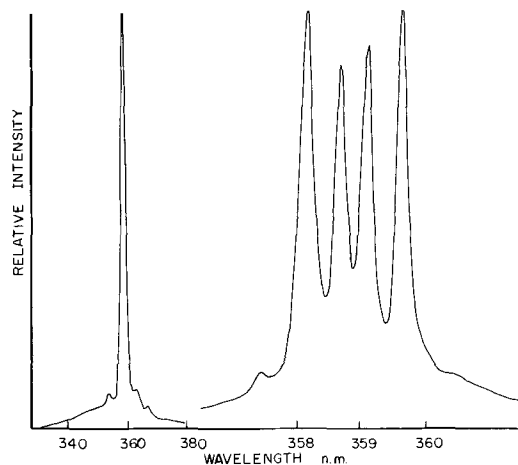


Fig. 4. Spectral distribution, $\alpha\text{-BaCaAlF}_7\text{:0.02 Eu}^{2+}$. Left curve, 5Å SBW; right curve, 0.5Å SBW; 2537Å excitation.

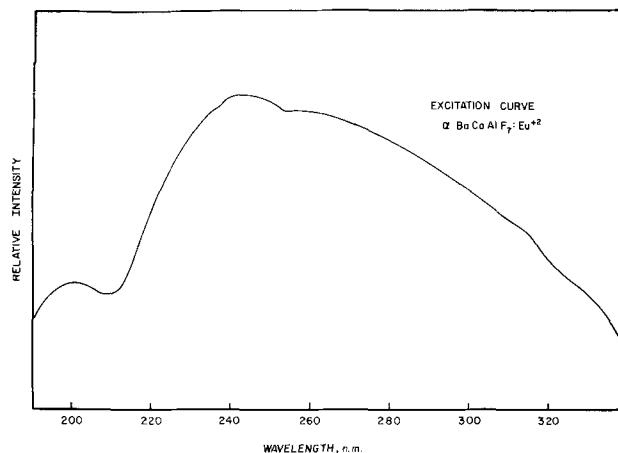


Fig. 5. Excitation curve, $\alpha\text{-BaCaAlF}_7\text{:0.02 Eu}^{2+}$

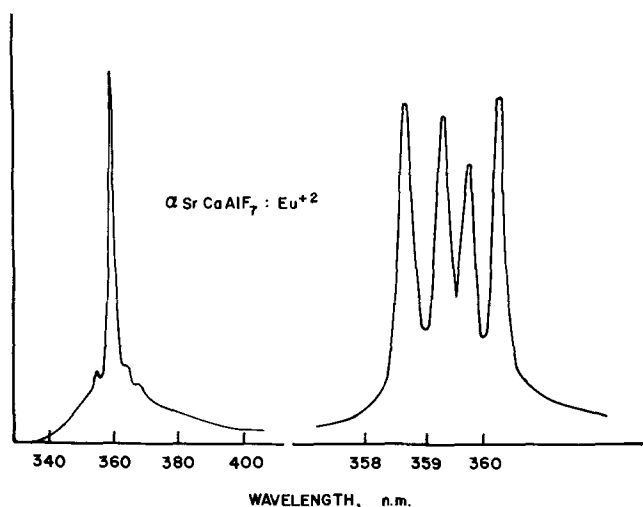


Fig. 6. Spectral distribution, α -SrCaAlF₇:0.02 Eu²⁺. Left curve, 5Å SBW; right curve, 0.5Å SBW; 2537Å excitation.

(Fig. 6). At 78°K and with time resolved spectroscopy, only six lines can be resolved, with the remaining lines either too weak or overlapping too closely to be resolved.

The maximum Eu²⁺ content which could be incorporated in the α -form was 0.16 Eu²⁺ substituted for Sr²⁺. Above this level, new x-ray diffraction lines appeared which were not attributed to either the β - or γ -forms.

The β - and γ -forms of SrCaAlF₇ show a mixed emission of predominantly bands peaking between 380 and 400 nm with a line positioned at 358 nm (Fig. 7 and 8). The line differs from the α -form in that little or no structure is resolved. At 78°K, the β -form shows some resolution into four shoulders, but the line of the γ -form is symmetrical.

Ba_{1-x}Sr_xCaAlF₇.—The similarities of the spectra of the α -forms of BaCaAlF₇ and SrCaAlF₇ are the main evidence that solid solution could exist along this compositional series, since unambiguous x-ray diffraction data could not be obtained. Samples were prepared with a final firing in the α stability range, and spectra were run on the expanded scale of 10 Å/in. over the four lines of the major emission between 355 and 360 nm. Each of the four lines was broadened, but the line position of each showed an apparent shift as shown in Fig. 9. The spectra were sufficiently narrow to permit detection of the two outside lines of the two end members if present in a mixture of the two phases. While measurements of the spectra at 25°C and without further scale expansion are insufficient to differentiate

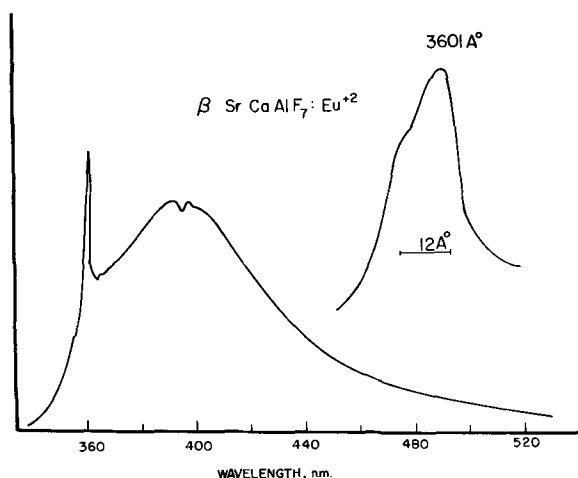


Fig. 7. Same as Fig. 6 for β -SrCaAlF₇:0.02 Eu²⁺

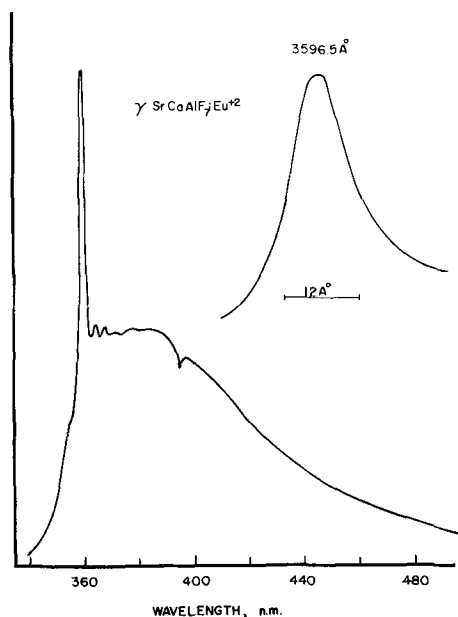


Fig. 8. Same as Fig. 6 for γ -SrCaAlF₇:0.02 Eu²⁺

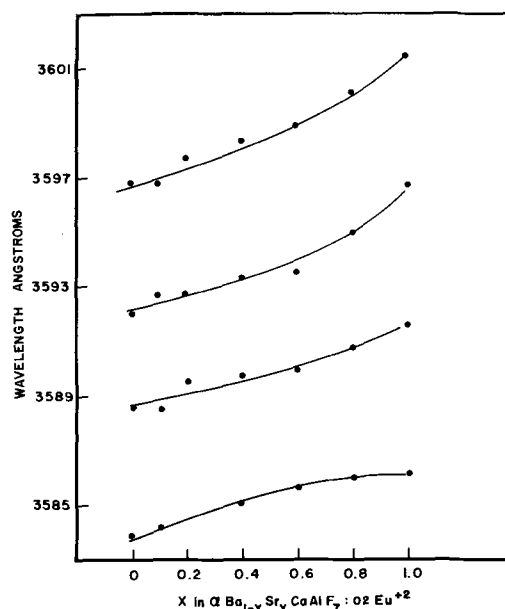


Fig. 9. Shift in position of line emissions with composition. Measured at 0.5Å SBW and 25°C.

between a broadened, shifted emission line and a change in intensity of several overlapping lines, the absence of the strong lines of each end member would indicate that a solid solution is probable and that the line positions are affected by it.

Intensity measurements.—The relative intensities of these fluorides are shown in Table III for 2537Å excitation. These are based on the spectral distributions shown in Fig. 4, 6, 7, and 8, and compare the peak

Table III. Relative intensities, Eu²⁺ emission*

Phosphor matrix	Line	Peak height band	Wavelength, nm
α -BaCaAlF ₇	1000		
α -SrCaAlF ₇	420		
β -SrCaAlF ₇	58	48	390
γ -SrCaAlF ₇	52	25	380
SrAlF ₅	350		
Sodium salicylate		50	415

* Measured at 5Å SBW. Activator content, 0.02 Eu²⁺ per formula.

Table IV. Comparison of barium silicate: Pb and α -BaCaAlF₇:Eu⁺²

Phosphor	Test condition	Relative response
Barium silicate: Pb	7 kV, 3 μ A/cm ²	30.2
α -BaCaAlF ₇ :Eu ⁺²	7 kV, 3 μ A/cm ²	14.3

height of the line as measured at 5Å SBW, or of the band emission taken at its peak, to sodium salicylate, which is used as an arbitrary standard at 50 units peak heat at 415 nm. The spectral distribution of SrAlF₅:Eu⁺² has been similarly measured and a quantum efficiency of 65% was determined (1). The quantum efficiencies of the ternary fluorides, which contain considerably less 5d-4f emission than SrAlF₅:Eu⁺², were not measured.

Under cathode-ray excitation, α -BaCaAlF₇ gives the same line emission and has been compared with barium silicate:Pb, which is a band emitter with a peak at 360 nm and a width at half height of 39 nm (Table IV). The measurements compared the emission in the ultraviolet region using a Corning 7-54 filter and an EMI 9524B (S11 Type response) photomultiplier.

Summary

The ternary systems MF₂-MF₂-AlF₃ (M = Ba, Sr, Ca) contain a compound only with Ca, and, at the 1:1:1 ratio, SrCaAlF₇ and BaCaAlF₇. Each has three polymorphic forms. The α -form of each accepts Eu⁺² and shows 4f-4f line emission at 358 to 360 nm. As with the similar compounds in the binary alkaline earth aluminum fluoride systems, the emission consists of a group of lines which can be resolved into more than eight lines and a varying amount of 5d-4f emission. The high-temperature structures, which can be quenched only in the strontium compound, contain more band emission and have a line which cannot be resolved into its structure at liquid nitrogen temperature. The phosphors are excited by cathode-ray and x-ray excitation as well as 2537Å ultraviolet. The peak height of the Eu⁺² line in α -BaCaAlF₇ is the highest obtained in any compound showing this type of emission.

Acknowledgments

The author is pleased to acknowledge the help of Lynne Wichert in preparation and measurements on the samples, of Dr. R. A. Hewes and Bobbie Burts for the spectral measurements, of Jeanette Cooper and Dean McClellan for x-ray diffraction work, and of Dr. T. F. Soules for many discussions on the optical properties.

APPENDIX

2 θ *	d	I	2 θ *	d	I
α -SrCaAlF ₇			β -SrCaAlF ₇		
23.8	3.74	70	22.95	3.87	15
24.4	3.65	40	24.3	3.66	42
25.6	3.47	70	24.75	3.59	40
26.1	3.41	70	25.10	3.54	45
28.0	3.18	45	26.1	3.41	95
28.2	3.16	30	28.2	3.16	100
28.45	3.14	45	29.2	3.06	60
29.4	3.035	100	30.5	2.93	30
31.15	2.96	35	30.85	2.89	45
33.8	2.65	18	32.25	2.77	9
39.55	2.27	85	34.6	2.59	15
40.15	2.22	30	39.6	2.27	30
45.4	1.99	30	41.05	2.19	20
46.1	1.97	40	41.5	2.174	28
46.5	1.95	30	45.3	2.00	45
48.7	1.87	20	45.9	1.97	30
50.05	1.82	25	46.6	1.95	45
			47.8	1.90	25
			48.0	1.89	30
γ -SrCaAlF ₇			α -BaCaAlF ₇		
18.7	4.74	15	21.3	4.17	20
22.3	3.98	10	21.7	4.09	45
24.3	3.66	55	22.2	4.00	30
26.15	3.40	100	23.4	3.81	80
27.9	3.195	20	25.1	3.54	100
28.2	3.16	25	27.4	3.25	20
28.45	3.13	28	28.5	3.14	50
29.1	3.066	18	28.9	3.09	50
29.35	3.04	25	29.7	3.02	30
30.95	2.88	55	30.7	2.91	30
34.65	2.59	10	33.3	2.69	50
41.6	2.17	28	37.8	2.38	20
45.5	1.99	48	38.3	2.35	30
46.05	1.97	40	39.9	2.26	55
46.45	1.95	28	40.8	2.21	35
49.9	1.83	25	43.5	2.08	30
			44.4	2.04	40
			45.5	1.99	45
			46.0	1.97	30
			48.0	1.90	30

* Data on 2 θ values are for CuK α_1 radiation.

Manuscript submitted Sept. 30, 1971; revised manuscript received Jan. 28, 1972. This was Paper 43 presented at the Washington, D. C., Meeting of the Society, May 9-13, 1971.

Any discussion of this paper will appear in a Discussion Section to be published in the June 1973 JOURNAL.

REFERENCES

1. M. V. Hoffman, *This Journal*, **118**, 933 (1971).
2. R. A. Hewes and M. V. Hoffman, *J. Luminescence*, (3), 261 (1971).
3. J. P. Meehan and E. J. Wilson, To be published.
4. N. Rolin and M. Clausier, *Rev. Int. Haute Temp. et Refract.*, t-4, p. 39 (1967).
5. B. M. Zhigarnovskii and E. G. Ippolitov, *Izv. Akad. Nauk, SSSR, Neorgan. Materialy*, **5**, 1558 (1969).
6. R. H. Nafziger, *J. Am. Ceram. Soc.*, **54**, 467 (1971).
7. Z. A. Mateiko and G. A. Bukhalova, *Zhur. Neorgan. Khim.*, **6**, 1728 (1961).

Solid-Gas Phase Equilibria and Thermodynamic Properties of Cadmium Selenide

A. Gary Sigai*¹ and Heribert Wiedemeier

Department of Chemistry, Rensselaer Polytechnic Institute, Troy, New York 12181

ABSTRACT

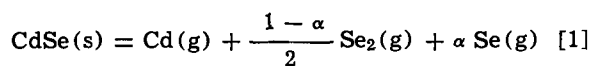
The investigation of the solid-gas phase equilibrium of CdSe revealed that at about 400°C CdSe sublimes initially by losing selenium to form nonstoichiometric CdSe_{1-x}, where $x \approx 0.002$; the resulting compound CdSe_{1-x} sublimes congruently. Since existing thermodynamic data for CdSe are either incomplete or show significant differences, the high-temperature thermodynamic properties of CdSe were reinvestigated using the Knudsen effusion technique. With the heat capacity function for CdSe(s) ($C_p = 12.36 + 1.45 \times 10^{-3} T$ eu [320°-760°K]) measured for the first time in this work and with tabulated thermochemical data, the vapor pressure measurements were evaluated in terms of the standard heat of formation [$\Delta H^\circ_{298} = -35.7 \pm 1.0$ kcal/mole (third-law evaluation)] and the absolute entropy [$S^\circ_{298} = 19.8 \pm 1.2$ eu (second-law evaluation)] of CdSe(s). Previous investigations are reviewed and compared with present results.

Several investigations of the mode of vaporization (1-3) and high-temperature thermodynamic properties (1, 4-8) of CdSe have been performed because of its potential use in solid-state devices and their importance for the growth of single crystals from the vapor phase. However, the precise mode of vaporization of CdSe is still uncertain and existing thermodynamic data are incomplete or show significant discrepancies. An experimentally determined heat capacity function of CdSe has not been reported prior to this work.

A knowledge of the equilibrium vapor pressure of CdSe is important since earlier investigations of CdSe (9-11) and other II-VI compounds (12) have demonstrated that these types of materials generate native point defects which are electrically active and play a substantial role in determining the electrical and optical properties of these compounds. Therefore, it is essential to define the conditions of preparation and any subsequent treatment of the specimen with respect to the equilibrium partial pressures of the components for a reliable interpretation of electrical and optical measurements.

Solid-Gas Phase Equilibria

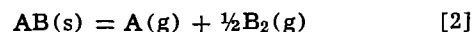
General form of vaporization reaction.—Mass spectrometric data (1) and vaporization studies on CdSe in the presence of excess elemental Cd or Se in the gas phase (7) indicate that CdSe(g) and higher molecular weight species than Se₂(g) are negligible under present experimental conditions. Therefore, the congruent sublimation of CdSe can be described by the reaction



where α is the degree of dissociation of Se₂(g). Wiedemeier and Goyette (13) have developed a calculational technique to compute α for this type of reaction from Knudsen data and the dissociation energy of the chalcogen species. With a dissociation energy for Se₂(g) of 75.7 kcal/mole (14) and with experimental data of the CdSe sublimation to be presented later, α was found to be less than 0.1% over the entire temperature range of this investigation. Therefore, monatomic cadmium and diatomic selenium are the only predominant species in the gas phase. This is in agreement with earlier mass spectrometric work (1).

Congruency of cadmium selenide sublimation.—It has usually been assumed that II-VI compounds sub-

lime congruently according to the reaction



Although early investigations (1, 4, 5) indicated the above mode of sublimation for CdSe, later studies (2, 3) suggested that the sublimation of CdSe is not completely congruent. Reisman (2) found that stoichiometric CdSe sublimes at about 400°C to form a selenium-rich gas phase and a selenium-deficient nonstoichiometric solid residue. Berkowitz and Chupka (3) conclude from mass spectrometric studies that stoichiometric CdSe does not sublime congruently. They observed that cadmium vaporizes preferentially and that the intensity ratio of Cd to Se₂ changes with time. Since a precise knowledge of the gas-phase composition is germane to the evaluation of Knudsen data and since reported results are not concordant, reinvestigation of the congruency of sublimation of CdSe was required.

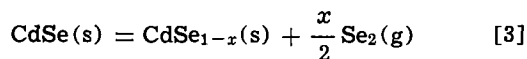
For this purpose stoichiometric CdSe (as determined by wet chemical analysis and x-ray diffraction techniques described below) was prepared from high-purity elements by direct sublimation and by vapor transport (15) with iodine. The CdSe was loaded into a Knudsen cell of fused silica and heated under high vacuum ($<10^{-6}$ Torr) slowly until a weight loss was detected at about 450°C. The cell was kept at this temperature until no further weight loss occurred. X-ray analysis revealed that the condensed sublimate was elemental selenium and that the residue was CdSe. Within the limits of experimental error ($\pm 0.001\text{\AA}$) there was no difference in the lattice parameters of CdSe before and after the heat-treatment. From the amount of vaporized selenium the change in stoichiometry of CdSe was found to be about 0.2 m/o (mole per cent) which is below the detection limits of the x-ray diffraction technique. These results were confirmed repeatedly on both sublimed and vapor-transported material. The presence of unreacted, elemental selenium in the starting material can be safely excluded because of the method of preparation and the fact that there was no weight loss or condensate at temperatures around 250°C where elemental selenium has a measurable vapor pressure. After the preferential vaporization of selenium at around 450°C had stopped, the temperature was increased until measurable sublimation occurred again at about 600°C. X-ray diffraction patterns and lattice parameters of the starting material, residue, and sublimed material show that the selenium-deficient CdSe sublimes congruently within the limits of detectability. In addition, it should be noted that the results of this investigation presented

* Electrochemical Society Active Member.

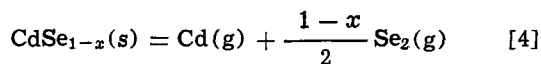
¹ Present address: RCA Laboratories, Princeton, New Jersey 08540.
Key words: equilibrium vaporization, thermodynamic properties, CdSe.

in Fig. 2 demonstrate that there is no measurable trend in the present data which would be expected for further changes in stoichiometry. Reisman *et al.* (2) reported final Cd/Se molar ratios ranging from 1.005 to 1.013 after heat-treatment of initially stoichiometric CdSe under various conditions.

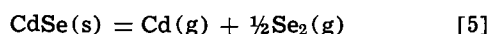
The above observations indicate strongly that stoichiometric CdSe vaporizes initially according to the reaction



and that the nonstoichiometric phase sublimes congruently according to the reaction



A rigorous evaluation of Knudsen data should be based on Reaction [4]. Thermochemical calculations show that the effect of the above deviation in stoichiometry on the evaluation of data according to the reaction



is negligibly small. For simplicity all experimental data presented in this work are evaluated on the basis of the "stoichiometric" Reaction [5].

The significance of this particular mode of vaporization of CdSe is that Reaction [3] is not time independent; the selenium partial pressure decreases during the initial phase of the vaporization according to Reaction [3]. If stoichiometric CdSe is heated rapidly to 600°C and above, both Reactions [3] and [4] occur simultaneously. This results in erroneous partial pressures and subsequently derived thermodynamic data. This may, in part, explain some of the observed discrepancies mentioned earlier. In order to obtain reliable Knudsen data CdSe must be vacuum annealed to constant weight prior to vapor pressure measurements to establish the steady-state conditions.

For the calculation of total pressures from experimental Knudsen data the Knudsen equation modified by Pashinkin (16, 17) was used in the form

$$P_t = \frac{3m(2\pi RT)^{1/2}}{at(M_{\text{Se}_2}^{1/2} + 2M_{\text{Cd}}^{1/2})} \text{ (atm)} \quad [6]$$

where P_t is the equilibrium total pressure in atmospheres, m the weight loss in grams, T the absolute temperature, a is the effective orifice area in square centimeters, t the time in seconds, and M the molecular and atomic weight, respectively, of the effusing species.

The equilibrium constant, K_p , for Reaction [5] is given by

$$K_p = P_{\text{Cd}} P_{\text{Se}_2}^{1/2} \quad [7]$$

Since the total pressure is the sum of the partial pressures

$$P_t = P_{\text{Cd}} + P_{\text{Se}_2} \quad [8]$$

and since

$$P_{\text{Cd}} = 2P_{\text{Se}_2} \quad [9]$$

Eq. [8] and [9] can be combined with [7] to yield

$$K_p = \frac{2\sqrt{3}}{9} P_t^{3/2} \quad [10]$$

Experimental

Preparation of starting material.—Cadmium selenide was prepared by vapor transport (15) of elemental Cd (99.999%) and Se (99.999%) with iodine and by direct sublimation of stoichiometric ratios of the elements in the temperature gradient 950° → 875°C and with iodine concentrations of 1–3 mg/cm³ tube volume for the vapor transport. Wet chemical analysis by EDTA titration (18) [$\text{Cd}(\text{exp}) = 58.5 \pm 0.5\%$; $\text{Cd}(\text{theor}) = 58.74\%$] and x-ray diffraction patterns [$a_0(\text{exp}) = 4.298\text{\AA}$, $c_0(\text{exp}) = 7.014\text{\AA}$; $a_0(\text{lit.}) =$

4.2985Å, $c_0(\text{lit.}) = 7.0150\text{\AA}$] (19) verified that both materials were stoichiometric within the limits of experimental error and had the wurtzite structure. However, these analytical methods are not sensitive enough to detect the above discussed small deviation from stoichiometry.

Heat capacity measurements of CdSe.—For the heat capacity measurements a 300 mg sample of CdSe, prepared by direct sublimation and vacuum annealed to constant weight, was pressed into a 6 mm diameter pellet at a pressure of 13 kbar. A packing density of about 0.96 was achieved. The pellet was then hermetically sealed in an aluminum capsule with a minimum free volume and placed in the DSC cell attachment of a du Pont 900 Thermal Analyzer. During the runs the DSC cell was purged with high-purity dry nitrogen at a flow rate of 0.3 liter/min. A heating rate of 5°/min was used and high-purity alumina served as a reference material. Measurements were recorded in 5° intervals between 50° and 490°C for three separate runs and then averaged. There was no detectable reaction between the sample and the container after completion of the runs.

Knudsen effusion measurements.—The Knudsen effusion measurements on CdSe were carried out with a Cahn RH microbalance which recorded the weight loss of the sample as a function of time. The Knudsen cell was suspended by a tungsten wire and enclosed in a fused silica tube. A single-zone high-temperature Kanthal furnace with a constant temperature zone ($\pm 1^\circ\text{C}$) of about 6 cm length was maintained at the desired temperature using a West Instrument Controller. The temperature was measured with a Pt/Pt-10% Rh thermocouple in a fixed position on the outside wall of the silica tube, with the hot junction and center of the crucible at the same level. The temperature difference between the outside position and the inside of the Knudsen cell was determined under experimental conditions over the entire temperature range. The thermocouples were calibrated with an NBS secondary standard Pt/Pt-10% Rh thermocouple. The system was evacuated by means of an oil diffusion and mechanical pump. During operation the residual pressure monitored by a Veeco ionization gauge was 10^{-6} Torr or less.

The Knudsen cell made of fused silica was 25 mm in height; the maximum outside diameter was 12 mm and the maximum inside diameter 8 mm. The cell was tapered to fit conveniently into a tungsten wire basket. The effective orifice area of the cell was determined by calibration with high-purity vacuum distilled zinc under pressure conditions corresponding to the actual Knudsen measurements. The vapor pressure of zinc is well established (20). With the vapor pressure function of Barrow *et al.* (21) and experimental Knudsen data for the zinc vaporization an effective orifice area of $1.215 \times 10^{-3} \text{ cm}^2$ was obtained.

Prior to the CdSe Knudsen measurements, the material was vacuum annealed to obtain the congruently vaporizing nonstoichiometric composition. In run No. I, about 1.5g of material prepared by chemical transport and in run No. II, about 800 mg of CdSe prepared by direct sublimation were used in these studies.

Results and Discussion

Heat capacity of CdSe.—The results of the heat capacity measurements are represented in Fig. 1. The estimated error in the heat capacity is less than 3%. The heat capacity as a function of temperature is given by the equation

$$C_p = 12.36 + 1.45 \times 10^{-3} T \text{ (cal/deg} \cdot \text{mole)} \quad [11]$$

for the temperature range 320°–760°K. The error involved in using only a two-term expansion is well below other errors of the measurements. The total error in using Eq. [11] between 298°K and the upper tem-

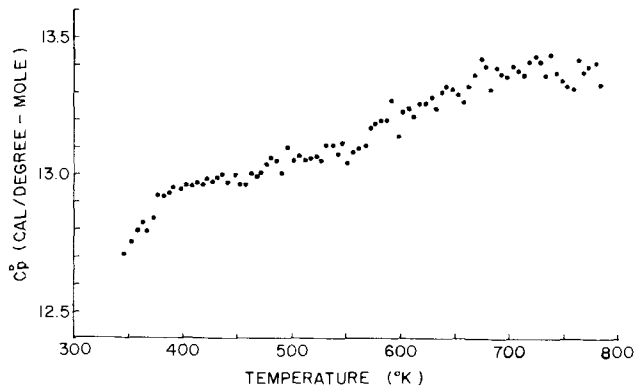


Fig. 1. Heat capacity of cadmium selenide (CdSe_{1-x}) as a function of temperature.

perature limit of the Knudsen studies is less than 0.3 kcal.

Knudsen effusion measurements.—The numerical results of the Knudsen measurements are listed in Tables I and II. The first two columns contain the temperature in degrees Kelvin and the weight loss in grams per hour. The errors in these quantities are less than 2° and 2×10^{-5} g, respectively. Values of the total pressure are given in the third column. Log K_p values and standard Gibbs free energies for Reaction [5] are given

Table I. Vapor pressures, free energies, and heats of sublimation of $\text{CdSe}(s)$ according to Reaction [5]

Run No. I, CdSe prepared by chemical transport, orifice area = 1.215×10^{-3} cm²

T, °K	m/hr, $\text{g} \times 10^{-4}$	P_t , atm $\times 10^{-6}$	$-\text{Log } K_p$	ΔG°_T , kcal/mole	ΔH°_{298} , kcal/mole
866	0.791	1.07	9.3725	37.16	79.5
879	1.13	1.54	9.1353	36.76	79.7
879	1.20	1.63	9.0962	36.57	79.5
893	1.90	2.60	8.7918	35.93	79.5
893	2.05	2.81	8.7423	35.74	79.3
911	3.55	4.91	8.3779	34.93	79.3
926	5.30	7.39	8.1117	34.38	79.5
926	4.90	6.83	8.1625	34.60	79.7
936	6.80	9.53	7.9548	34.04	79.6
936	7.00	9.81	7.9267	33.96	79.5
948	9.40	13.26	7.7308	33.52	79.6
948	9.20	12.98	7.7447	33.58	79.7
959	13.2	18.68	7.5076	32.96	79.6
978	22.4	32.09	7.1550	32.01	79.5
978	22.4	32.09	7.1550	32.01	79.5
978	23.2	33.24	7.1319	31.91	79.4
992	32.0	46.17	6.9183	31.39	79.5
992	34.0	49.06	6.8787	31.22	79.5
992	33.2	47.90	6.8939	31.29	79.4
1003	50.4	73.33	6.6169	30.53	79.4
1009	50.4	73.35	6.6164	30.54	79.5
1009	51.0	74.23	6.6086	30.51	79.4

Average: 79.5 ± 0.2

Table II. Vapor pressures, free energies, and heats of sublimation of $\text{CdSe}(s)$ according to Reaction [5]

Run No. II, CdSe prepared by sublimation of the elements, orifice area = 1.215×10^{-3} cm²

T, °K	m/hr, $\text{g} \times 10^{-4}$	P_t , atm $\times 10^{-6}$	$-\text{Log } K_p$	ΔG°_T , kcal/mole	ΔH°_{298} , kcal/mole
888	1.60	2.18	8.9056	36.19	79.5
903	2.65	3.65	8.5716	35.41	79.5
903	2.62	3.61	8.5790	35.44	79.5
920	4.40	6.12	8.2350	34.68	79.5
935	6.80	9.53	7.9462	34.00	79.5
952	10.4	14.70	7.6639	33.36	79.6
965	15.0	21.35	7.4203	32.77	79.7
977	21.6	30.94	7.1788	32.10	79.6
978	21.6	30.95	7.1788	32.12	79.6
989	28.2	40.63	7.0012	31.67	79.7
999	37.0	53.59	6.8210	31.19	79.7
1013	52.8	77.01	6.5847	30.53	79.7
1013	52.8	77.01	6.5847	30.53	79.7
1013	53.2	77.59	6.5800	30.51	79.6
1020	64.0	93.67	6.4570	30.15	79.6
1035	92.8	136.80	6.2104	29.42	79.5
1035	92.4	136.20	6.2134	29.43	79.5

Average: 79.6 ± 0.1

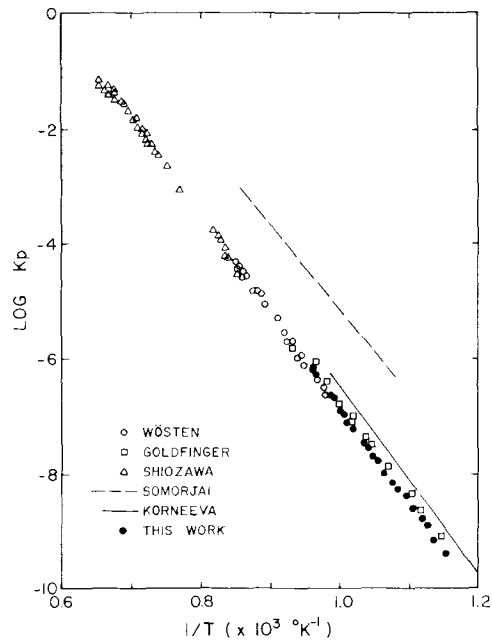


Fig. 2. Plot of $\log K_p$ vs. $1/T$ data of the sublimation of cadmium selenide obtained in this work and by other investigators.

in the fourth and fifth columns, respectively. The calculations were carried out on an IBM 360 computer. Based on experimental errors, the errors in P_t are less than 6%. The accuracy of ΔG°_T values is better than ± 0.5 kcal/mole. The last column in Tables I and II gives values for the third-law heat of reaction, ΔH°_{298} . For the third-law evaluation absolute entropies of $\text{Cd}(g)$ (40.07 eu) and $\text{Se}_2(g)$ (60.2 eu) from Kelley (22) and of $\text{CdSe}(s)$ (obtained from a second-law evaluation of the data discussed below) and heat capacities of $\text{Cd}(g)$ (4.97 eu) (23) and $\text{Se}_2(g)$ [$8.73 + 0.32 \times 10^{-3}T - 0.34 \times 10^{-5}T^2$ (eu)] (23), and the heat capacity of $\text{CdSe}(s)$ measured in this work (Eq. [11]) were used. The average value of the third-law heat of reaction is $\Delta H^\circ_{298} = 79.5 \pm 0.2$ kcal/mole. The error in this quantity is estimated at about 1 kcal/mole. The high degree of reproducibility of the individual third-law results indicates that experimental errors connected with the heat capacity, temperature measurements, and weight loss determinations are small.

The experimental data obtained in this work are shown in Fig. 2 compared to those of other investigations. The numerical results of a linear least-squares treatment of our data and of a conversion of second-law results of other investigators to 298°K are listed in Table III. For these calculations heat capacities of

Table III. Compilation of second-law heats and entropies of sublimation of $\text{CdSe}(s)$ for the reaction: $\text{CdSe}(s) = \text{Cd}(g) + \frac{1}{2} \text{Se}_2(g)$, at experimental temperature and at 298°K obtained in this work and by other investigators

Investigator	Temperature range, °K	ΔH°_T , kcal/mole	ΔS°_T , eu	ΔH°_{298} , ^a kcal/mole	ΔS°_{298} , ^a eu
Wösten (4)	1020-1170	78.7	47.7	81.9	52.8
Goldfinger (1)	870-1050	73.9	46.4	76.5	50.9
Shiozawa (7)	1070-1470	77.6	46.8	81.6	52.5
Somorjai (5)	920-1170	68.8	45.6	—	—
Korneeve (6)	810-1010	75.2	45.7	77.6	50.0
[corrected by Pashinkin (24)]					
Run No. I	866-1009	77.1	46.8	—	—
Run No. II	888-1035	76.2	45.2	—	—
Run No. I & II, second-law	866-1035	77.0	45.9	79.5	50.4
Run No. I & II, third-law	866-1035	—	—	79.5	—

^a These values were derived using the C_p -function of $\text{CdSe}(s)$ determined in this work.

Cd(g) (23) and Se₂(g) (23) and the above measured C^o_p-function of CdSe(s) were used. The values of the second-law heat and entropy of sublimation based on the combined data of runs No. I and II are 77.0 ± 0.8 kcal/mole and 45.9 ± 0.7 eu at 950°K. On being converted to 298°K, these values become 79.5 ± 1.4 kcal/mole and 50.4 ± 1.2 eu, respectively.

The data of Somorjai (5) deviate strongly in terms of vapor pressures from the results of the present and other investigations. This could be due to the use of closed systems in Somorjai's methods (5). A slight excess of an elemental component can cause serious errors in closed systems, especially at low pressures. The lower values for the heat of sublimation observed by Korneeva (6) and Goldfinger (1) could be due to a possible interference of Reaction [3]. However, in view of the sensitivity of the second-law method to experimental errors the results of Korneeva (6) [corrected by Pashinkin (24)] and of Goldfinger (1) are considered in general agreement with the present work. The same applies to the results of Wösten (4) and Shiozawa (7). The slightly larger values found by these authors (4,7) could be explained by the increased degree of dissociation of Se₂(g) at higher temperatures which was not considered by Wösten and Shiozawa.

The heat of formation and absolute entropy of CdSe(s) obtained in this work are listed in Table IV. These values were derived from the heats and entropy of sublimation at 298°K (Table III) on the basis of Reaction [5]. The heat of formation of CdSe(s) based on the heat of sublimation of cadmium (26.75 kcal/mole) (25) and on the heat of formation of Se₂(g) (34.12 kcal/mole) (25) is $\Delta H^{\circ}_{298} = -35.7 \pm 0.2$ kcal/mole. The error in this quantity is about 1 kcal/mole. The absolute entropy of CdSe(s) based on the absolute entropy of Cd(g) (40.07 eu) (22) and the absolute entropy of Se₂(g) (60.2 eu) (22) is $S^{\circ}_{298} = 19.8 \pm 1.2$ eu. In Table IV are also listed the heats of formation and absolute entropies of CdSe(s) calculated from the corresponding values (Table III) of other investigations. The value of Terpilowski (8) was taken directly from the literature without further correction. Although this value (-34.6 kcal/mole) (8) is based on an estimated C^o_p-function of CdSe(s) it is in closer agreement with the result obtained in this work than values computed from other investigations. Possible reasons for the larger deviations have been discussed above.

Summary

The original purpose of this investigation was to determine accurate vapor pressures through direct weight loss measurements employing the Knudsen effusion technique. In order to evaluate experimental data it was necessary to establish the mode of vaporization and to determine the heat capacity of cadmium selenide at elevated temperatures. Additional information was obtained through a second- and third-law evaluation of data, namely, the heat of formation and the absolute entropy of cadmium selenide.

Table IV. Compilation of computed heats of formation and absolute entropies of CdSe(s) at 298°K using the tabulated values of ΔH°_{298} and ΔS°_{298} from Table III

$-\Delta H^{\circ}_{298}$, kcal/mole	S°_{298} , eu	Investigator	Technique	Refer- ence
38.1	17.4	Wösten	Transpiration	4
32.7	19.3	Goldfinger	Knudsen, second law	1
37.8	17.3	Shiozawa	"Boiling point" method	7
33.8	20.2	Korneeva (cor- rected by Pashinkin)	Knudsen, second law	6, 24
34.8 ^a	18.6 ^a	Terpilowski	EMF cell	8
35.7	19.8	This work	Knudsen, second law	
35.7		This work	Knudsen, third law	

^a Taken directly from the literature without correcting the C^o_p-function of CdSe(s).

A preferential loss of selenium during the initial heating of CdSe has been observed in this work, resulting in a deviation in stoichiometry. After the congruently vaporizing phase has been established, evaluation of experimental data in terms of thermochemical properties based on Reaction [4] or [5] leads to identical values within the limits of error. However, if the steady-state vaporization conditions are not established prior to actual vapor pressure measurements, erroneous partial pressures and thermochemical values are obtained. This could possibly explain the discrepancy in previously published results.

General trends and chemical considerations indicate possible inconsistencies in the heats of formation of other II-VI compounds. Similar deviations from stoichiometry on heating as observed for CdSe could occur in related systems. In order to resolve these uncertainties a precise determination of the mode of vaporization of these compounds is desirable.

Acknowledgments

The authors are pleased to acknowledge the support of this work by the National Science Foundation and by the National Aeronautics and Space Administration. This paper is based in part on a thesis submitted by one of the authors (A.G.S.) to the Graduate School of Rensselaer Polytechnic Institute in partial fulfillment of the requirements for the Ph.D. degree.

Manuscript submitted Aug. 16, 1971; revised manuscript received Feb. 4, 1972.

Any discussion of this paper will appear in a Discussion Section to be published in the June 1973 JOURNAL.

REFERENCES

- P. Goldfinger and M. Jeunehomme, *Trans. Faraday Soc.*, **59**, 2851 (1963).
- A. Reisman, M. Berkenblit, and M. Witzten, *J. Phys. Chem.*, **66**, 2210 (1962).
- J. Berkowitz and W. A. Chupka, *J. Chem. Phys.*, **45**, 4289 (1966).
- W. J. Wösten, *J. Phys. Chem.*, **65**, 1949 (1961).
- G. A. Somorjai, *ibid.*, **65**, 1059 (1961).
- I. V. Korneeva, V. V. Sokolov, and A. V. Novoselova, *Russ. J. Inorgan. Chem. (English Transl.)*, **2**, 117 (1960).
- L. R. Shiozawa and J. M. Jost, Report No. ARL65-98 to Aeronautical Research Laboratories, Office of Aerospace Research, USAF (1965).
- J. Terpilowski and E. Ratajczak, *Bull. Acad. Polon. Sci., Ser. Sci. Chim.*, **12**, 355 (1964).
- H. Tubota, H. Suzuki, and K. Hirakowa, *J. Phys. Soc. Japan*, **15**, 1701 (1960).
- H. Tubota, *Japan. J. Appl. Phys.*, **2**, 259 (1963).
- L. R. Shiozawa, J. L. Barrett, S. S. Derlin, G. P. Chotkerys, and J. M. Jost, Report No. ARL62-365 to Aeronautical Research Laboratories, Office of Aerospace Research, USAF (1962).
- F. A. Kröger, "Chemistry of Imperfect Crystals," Chap. 16, North-Holland Publishing Co., Amsterdam (1964).
- H. Wiedemeier and W. J. Goyette, *J. Chem. Phys.*, **48**, 2936 (1968).
- P. Budininkas, R. K. Edwards, and P. G. Wahlbeck, *ibid.*, **48**, 2867 (1968).
- H. Schäfer, "Chemical Transport Reactions," Academic Press, New York (1964).
- A. S. Pashinkin, *Russ. J. Phys. Chem. (English Transl.)*, **38**, 1461 (1964).
- A. S. Pashinkin, *Zh. Fiz. Khim.*, **40**, 2611 (1966).
- H. Flaschka, *Chem. Anal.*, **42**, 56 (1953).
- M. Aven and J. S. Prener, "Physics and Chemistry of II-VI Compounds," Chap. 3, p. 128, John Wiley & Sons, Inc., New York (1967).
- R. Hultgren, R. L. Orr, P. D. Anderson, and K. K. Kelley, "Selected Values of Thermodynamic Properties of Metals and Alloys," p. 319, John Wiley & Sons, Inc., New York (1963).
- R. F. Barrow, P. G. Dodsworth, A. R. Downie, E. A. N. S. Jefferies, A. C. P. Pugh, F. J. Smith, and J. M. Swinstead, *Trans. Faraday Soc.*, **51**, 1354 (1955).

22. K. K. Kelley and E. G. King, *U.S. Bur. Mines, Bull.* 592, 24, 82 (1961).
 23. K. K. Kelley, *U.S. Bur. Mines, Bull.* 584, 35, 158 (1960).
 24. A. S. Pashinkin, *Russ. J. Inorgan. Chem. (English Transl.)*, 7, 1367 (1962).
 25. D. R. Stull and G. C. Sinke, *Advan. Chem. Ser.*, 18, 64, 180 (1956).

Devitrification Characteristics of the Semiconductor System



N. S. Platakis and H. C. Gatos*

Department of Metallurgy and Materials Science and Department of Electrical Engineering,
 Massachusetts Institute of Technology, Cambridge, Massachusetts 02139

ABSTRACT

The devitrification kinetics in the system $(1 - x)\text{As}_2\text{Se}_3 \cdot x\text{Sb}_2\text{Se}_3$ were studied as a function of temperature (69°-183°C) and composition ($x = 0.1-0.5$). The activation energy of the linear growth rates of relatively large rectangular platelet-like crystals in the vitreous matrix was found to be 38 kcal/mole for $x = 0.1$ and 50 kcal/mole for $x = 0.3, 0.4,$ and 0.5 . Along the long dimension of the platelets the growth rate was found to be three times greater than that along the short dimension. Along this long dimension the growth rate increased about three orders of magnitude in going from $x = 0.1$ to $x = 0.5$. The number of crystals formed in the vitreous matrix per unit area increased with increasing Sb_2Se_3 content. The chemical composition of the crystals formed by devitrification was found to be different than that of the surrounding matrix. Quantitative electron microprobe analysis and scanning electron microscopy showed that the Sb content was higher in the crystals than in the surrounding matrix. Crystals grown directly from the melt (by slow cooling) were even richer in Sb than the neighboring matrix. X-ray diffraction results showed that the materials with low Sb_2Se_3 content crystallized in the system of As_2Se_3 (monoclinic) whereas materials relatively rich in Sb_2Se_3 crystallized in the Sb_2Se_3 system (orthorhombic). In alloys of intermediate composition both systems were present. In materials in which the monoclinic structure predominated the devitrification rates and the associated activation energies were found to increase with the Sb_2Se_3 content; whereas they were composition independent in materials in which the orthorhombic structure predominated.

Although the devitrification of oxide glass systems has been extensively investigated, devitrification studies on chalcogenide systems have been very limited. The rate of devitrification of bulk As_2Se_3 (1) and $\text{As}_2\text{Se}_3\text{Ge}_y$ (2) has been successfully studied as a function of temperature by means of resistivity and density changes and it was found to increase with increasing temperature. As_2Se_3 films could not be devitrified, whereas Sb_2Se_3 and $\text{As}_2\text{Se}_3\text{Sb}_2\text{Se}_3$ were readily devitrified on exposure to an electron beam. The nucleation rate was found to be temperature independent, while the growth rate was reported to increase with increasing temperature (3). Selenium is by far the most studied amorphous semiconductor not only because of its relative simplicity, but also because of its important role in xerography and electronic devices.

In recent years amorphous-crystalline transformations and the associated changes in electrical properties have received intensive attention as they are believed to be directly related to the memory switching phenomena observed in amorphous semiconductor systems. With the emerging potential of this type of phenomena the basic aspects of the vitreous state and its relationship to the crystalline state are now the subject of world-wide fundamental studies.

The present system was chosen because one of its constituents, As_2Se_3 , adopts primarily the amorphous state, whereas Sb_2Se_3 is primarily a crystalline material. The tendency of their solutions to transform from the amorphous to the crystalline state increases with increasing Sb_2Se_3 content, providing a wide range of

devitrification characteristics. Furthermore, these materials were found to exhibit switching and memory-switching phenomena.

Experimental

Sample preparation.—Devitrification was carried out by heating the amorphous samples at constant temperature on the stage of a microscope. The microscope's 450W xenon lamp (white light) served as the heat source. The temperature was measured with Chromel-Alumel thermocouples (25 μ diameter wire) imbedded in the samples. Imbedding of the thermocouples into the samples was carried out by means of a hot stage especially designed for this purpose (Fig. 1). Vitreous material of the desired composition (prepared as described elsewhere) (4, 5) was sealed under vacuum in a quartz ampoule which then was placed into the furnace. A thermocouple was positioned into a shallow quartz vessel placed below the ampoule. While the furnace was brought to the desired temperature, the system was repeatedly evacuated and flushed with high-purity argon; then argon was allowed to flow under slightly positive pressure. The tip of the quartz tube was broken by means of a rotating blade and the molten material was cast into the quartz vessel into which the thermocouple was fixed. Fast quenching (of the order of seconds) was achieved by water-cooling the metal plate on which the quartz vessel was resting, by increasing the argon flow prior to casting, and by positioning a heat-reflecting blade between the opening of the furnace and the quartz vessel. Fast quenching was important in ensuring homogeneous vitreous samples and preventing the reaction of the thermocouple with the molten material.

* Electrochemical Society Active Member.

Key words: chalcogenide semiconductors, amorphous semiconductors, devitrification of chalcogenide semiconductors $(1 - x)\text{As}_2\text{Se}_3 \cdot x\text{Sb}_2\text{Se}_3$.

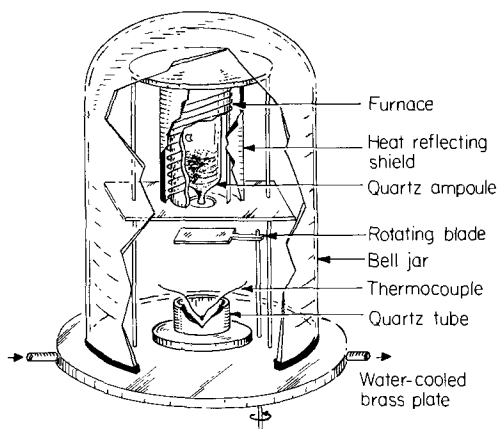


Fig. 1. Schematic diagram of the hot stage for imbedding thermocouples into the vitreous samples.

The samples were removed from the quartz vessel, mounted in plastic, and ground with a 0.25μ particle abrasive until the thermocouple junctions appeared on the surface. The samples were 12 mm in diameter and approximately 4 mm thick. Amorphous, single-phase samples with the composition $x = 0, 0.1, 0.2, 0.3, 0.40,$ and 0.45 were successfully prepared as confirmed by powder x-ray diffraction, interference contrast optical microscopy, and scanning electron microscopy. Samples with $x = 0.5$ were amorphous but, toward their center, clusters of individual small crystals were present as shown in Fig. 2.

Heating procedure.—The white light beam of a microscope lamp, serving as the heat source, was focused on the desired area of the sample which was kept in an ultrapure argon atmosphere. The cross section of the impinging beam was about 0.3 mm^2 . By focusing the beam on the thermocouple it was found that a constant temperature was achieved in less than 1 min; even for periods of several days the temperature remained constant within less than 0.5°C . Upon turning off the beam the sample reached room temperature in less than 1 min. Moving the sample and positioning the thermocouple in various parts of the beam's cross section led to no detectable temperature variation. The ratio of the illuminated area to the area of the thermocouple junction was about 150/1. By changing the aperture diaphragm setting any temperature in the range of $23^\circ\text{--}190^\circ\text{C}$ could be chosen. Once the desired temperature was established, areas far removed from the thermocouple were illuminated for

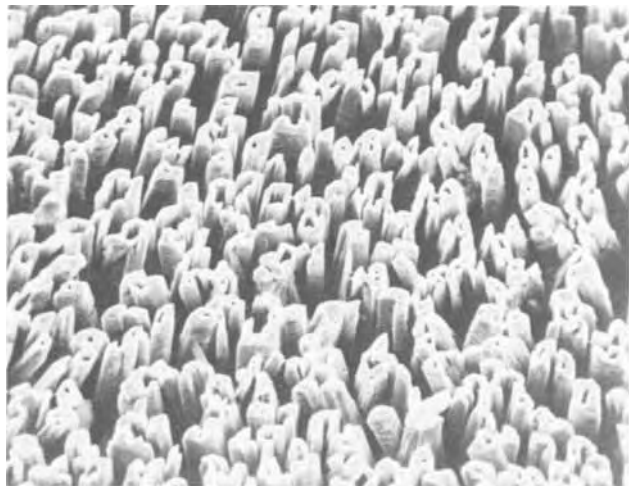


Fig. 2. Scanning electron micrograph of crystals formed while attempting to imbed the thermocouple in a sample of the composition $0.5\text{As}_2\text{Se}_3 \cdot 0.5\text{Sb}_2\text{Se}_3$. Vitreous matrix was etched with a KOH solution (370X).

nucleation and crystal growth observations. In this way any possible effects of the thermocouple on the stability of its adjacent sample areas were avoided. It was assumed that the temperature at any area illuminated by the beam was the same as that registered by the thermocouple when illuminated by the same beam. Heat losses through the thermocouple were considered negligible in view of its very small size. Since the rates of devitrification were very small (of the order of $10^{-5} \mu/\text{sec}$) it was assumed that the latent heat of crystallization caused no appreciable thermal fluctuations. The present method of heating for devitrification studies has the distinct advantage of allowing the direct observation of the devitrification process and crystal growth.

Devitrification was confined to the area illuminated (1/400 of the total sample); accordingly, several experiments could be carried out on the same sample. The self-consistency of the results as a function of temperature indicates that devitrification was heat-rather than photon-induced.

Morphology and chemical composition of the devitrified material.—The morphology of the crystals formed in the amorphous matrix was examined after several microns of the matrix material were removed by etching in an aqueous solution of KOH. The crystalline material was attacked only slightly by this solution. Scanning electron microscopy (in the secondary electron mode) was used for examining the morphology of the crystals. For studying chemical composition changes in the crystalline-amorphous matrix system an electron beam microanalyzer was used and a scanning electron microscope (in the x-ray mode) equipped with a silicon detector and a multiple-stage x-ray counter. A thin gold film was evaporated on the samples to prevent electrostatic charging and serve as a heat sink. For quantitative chemical analysis standards were used in conjunction with a computer program.

Results and Discussion

Early stage of devitrification.—The time required for the first crystal to become visible under a 570X magnification was determined as a function of temperature and composition. The results are plotted in Fig. 3 and summarized in Table I. It is seen that the (apparent) activation energy for the early stages of devitrification is approximately the same for all compositions except for that with $x = 0.1$ for which it is significantly smaller. Apparently the ease of devitrification decreases abruptly at the As_2Se_3 -rich composition range. In all cases the number of crystals forming per unit

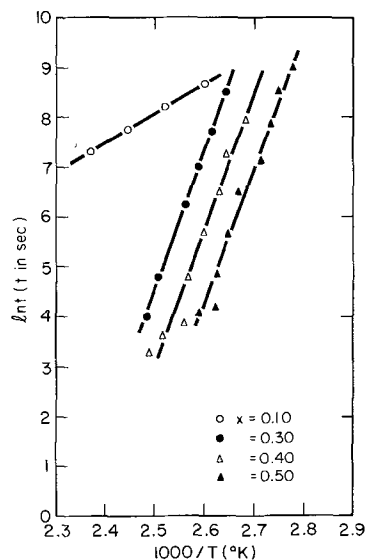


Fig. 3. Temperature dependence of the time required for the first crystal to appear during devitrification.

Table I. Activation energies (ΔH) of the early stages of devitrification. A is the pre-exponential factor

Composition	A, sec	ΔH , kcal/mole	Temperature range, °K
0.9As ₂ Se ₃ ·0.1Sb ₂ Se ₃	1.5 × 10 ⁻⁸	11.6	384-421
0.7As ₂ Se ₃ ·0.3Sb ₂ Se ₃	0.52 × 10 ⁻²⁰	55.9	378-402
0.6As ₂ Se ₃ ·0.4Sb ₂ Se ₃	3.6 × 10 ⁻²⁰	55.6	373-397
0.5As ₂ Se ₃ ·0.5Sb ₂ Se ₃	1.7 × 10 ⁻²⁰	54.0	360-386

area was small (of the order of 10/mm² for materials with $x = 0.1$, and 10⁴/mm² for the rest of the studied compositions) but under the present conditions (relatively low magnification) no observations could be made regarding the initial stages of nucleation. The time intervals presented here include the incubation period, the formation time of the nucleus, and its growth to approximately 5 μ in diameter.

Crystal growth rates.—The crystal growth rates in the vitreous matrix following the initiation of crystal formation were determined as a function of temperature and composition. For the initiation of crystals an area of the sample, away from the thermocouple, was heated at 190°C with the light beam until well-defined crystallites were formed. Heating for about 3 min in the case of $x = 0.1$ and for a few seconds in the cases of $x = 0.3-0.5$ produced individual crystallites measuring approximately 10 × 20 μ as shown in Fig. 4. Devitrification was arrested upon removing the light beam. No crystallites were formed outside the illuminated area. The beam was focused on the thermocouple, its intensity was adjusted to correspond to the desired temperature, and then brought to the areas where the individual crystals were earlier formed. The temperature range used was relatively narrow to avoid high growth rates which were difficult to measure. The crystal growth rates were determined by measuring the crystal dimensions before, during, and after the growth period from large magnification photographs. These photographs were taken at low beam intensity corresponding to room temperature where no crystal growth took place.

The measured growth rates along the length and width of the crystals for the composition with $x = 0.4$



Fig. 4. Typical crystals formed by heating for a few seconds at 190°C; composition 0.6As₂Se₃·0.4Sb₂Se₃ (615X).

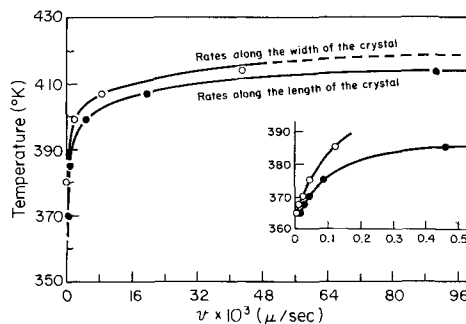


Fig. 5. Temperature dependence of crystal growth rates in a vitreous matrix of 0.6As₂Se₃·0.4Sb₂Se₃.

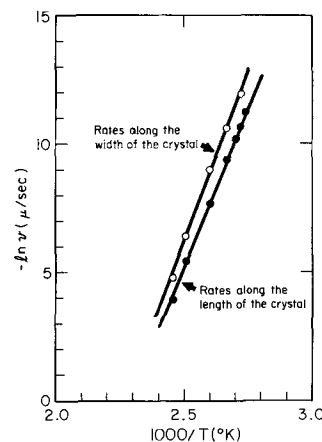


Fig. 6. Crystal growth rates in a vitreous matrix of 0.6As₂Se₃·0.4Sb₂Se₃.

are plotted as a function of temperature in Fig. 5. Their exponential dependence on temperature is shown for the same composition in Fig. 6. The activation energies and the corresponding pre-exponential factors for all compositions studied are summarized in Table II. For direct comparison, the growth rates of the various compositions were calculated for three temperatures (from the data of Table II) and are presented in Table III. Apparently, the temperature ranges employed lie below the temperature range in which the growth rates decrease with increasing temperature (6). As seen in Table II, the activation energy as well as the pre-exponential factor increase sharply in going from the composition with $x = 0.1$ to that with $x = 0.3$ and remain fairly constant for the compositions with $x = 0.3, 0.4$, and 0.5 . This behavior is identical to that of the activation energy associated with the early stages of devitrification (Table I). The values of the two types of activation energies are also similar except in the material with $x = 0.1$. The relatively low

Table II. Activation energies (ΔH) of crystal growth in a vitreous matrix. A is the pre-exponential factor. Subscripts 1 and 2 refer to growth along the length and along the width of the crystal, respectively

Composition	ΔH_1 , kcal/mole	ΔH_2 , kcal/mole	A ₁ , μ/sec	A ₂ , μ/sec	Temperature Range, °K
As ₂ Se ₃	31.2 (1)	—	—	—	—
0.9As ₂ Se ₃ ·0.1Sb ₂ Se ₃	37.8	—	2.8 × 10 ¹⁰	—	398-456
0.7As ₂ Se ₃ ·0.3Sb ₂ Se ₃	49.7	52.3	7.3 × 10 ²⁴	7.7 × 10 ²⁵	329-405
0.6As ₂ Se ₃ ·0.4Sb ₂ Se ₃	48.9	52.5	2.2 × 10 ²⁴	9.9 × 10 ²⁵	365-414
0.5As ₂ Se ₃ ·0.5Sb ₂ Se ₃	49.3	53.0	5.2 × 10 ²⁵	2.2 × 10 ²⁷	347-386

Table III. Dependence of crystal growth rate on composition calculated from the results of Table II. v_1 is the rate along the length of the crystal and v_2 is the rate along the width of the crystal

Composition	$v_1 = A_1 e^{-\Delta H_1/RT}$ (μ/sec)			$v_2 = A_2 e^{-\Delta H_2/RT}$ (μ/sec)		
	353°K	373°K	403°K	353°K	373°K	403°K
0.9As ₂ Se ₃ ·0.1Sb ₂ Se ₃	1.11×10^{-7}	1.99×10^{-6}	8.88×10^{-5}	—	—	—
0.7As ₂ Se ₃ ·0.3Sb ₂ Se ₃	1.24×10^{-6}	5.54×10^{-5}	8.15×10^{-3}	3.21×10^{-7}	1.75×10^{-5}	3.34×10^{-3}
0.6As ₂ Se ₃ ·0.4Sb ₂ Se ₃	1.17×10^{-6}	4.91×10^{-5}	6.67×10^{-3}	3.11×10^{-7}	1.72×10^{-5}	3.35×10^{-3}
0.5As ₂ Se ₃ ·0.5Sb ₂ Se ₃	1.56×10^{-5}	6.76×10^{-4}	9.56×10^{-2}	3.38×10^{-6}	1.95×10^{-4}	3.99×10^{-2}

activation energy (11.6 kcal/mole) found for the early stage of devitrification of the composition $x = 0.1$ is perhaps associated with the nucleation (including incubation) rather than the growth process. It appears that at low Sb₂Se₃ concentrations the devitrification characteristics of As₂Se₃ are modified by Sb₂Se₃ whereas at the compositions with $x \cong 0.3$, the characteristics of $(1 - x)\text{As}_2\text{Se}_3 \cdot x\text{Sb}_2\text{Se}_3$ are affected only slightly, if at all, by a change in composition. Similarly, the energy gap of the composition with $x = 0.5$ is approximately the same as that for pure Sb₂Se₃ (5, 7).

Powder x-ray diffraction results showed that As₂Se₃-rich materials crystallize in the monoclinic system, the crystallographic system of As₂Se₃, while materials relatively rich in Sb₂Se₃ crystallize in the orthorhombic, the Sb₂Se₃ crystallographic system. In intermediate compositions both systems were present. The exact compositions at which the transition from the monoclinic to the mixed system and to the orthorhombic occur were not determined. However, in materials with $x = 0.2$ the monoclinic system predominated (the orthorhombic could hardly be detected), whereas in those with $x = 0.3$ both systems were equally pronounced. Materials with $x \leq 0.1$ and $x \geq 0.45$ crystallized in the monoclinic and orthorhombic systems, respectively. A related behavior has been reported for the system Sb₂Se₃-Sb₂Te₃ (8). These results indicate that the devitrification as well as the electrical and optical parameters in the present system are composition dependent when the monoclinic structure predominates and independent of composition when the orthorhombic structure predominates.

It is of interest to note that an activation energy of 31.2 kcal/mole has been reported (1) for the devitrification of pure As₂Se₃ which was already more than 50% devitrified. This activation energy corresponds to the growth activation energies measured in the present study and is in good agreement with the value estimated from the compositional dependence of the growth activation energy established in this study. Furthermore, the activation energy of viscous flow of pure As₂Se₃, which is believed to be relevant to the devitrification process, was found to be 37 kcal/mole (1) and is consistent with the present results.

Crystal morphology compositional changes.—The crystals formed in the vitreous matrix with $x = 0.1$ had a dendritic-like appearance and grew in blade-type shape as shown in Fig. 7. The morphology of the crystals was not temperature dependent. On the other hand, in all other compositions the shape of the crystals was found to be temperature dependent. They were rectangular single crystals (as confirmed by transmission electron diffraction patterns) and maintained their general morphology during the growth provided the growth rates were kept relatively low (Fig. 4). At higher growth rates (in the range of 120°-150°C) a number of elongated small crystals grew from the original single crystal. Figure 8 is a scanning electron microscope photograph of a crystal, the last part of which was grown at high temperatures; the surrounding vitreous matrix was etched away in an aqueous KOH solution. Near the softening temperature range of the vitreous materials, the growth rate was

very fast (it could not be measured under the present experimental conditions) leading to clusters of elongated crystals as shown in Fig. 9. A similar behavior

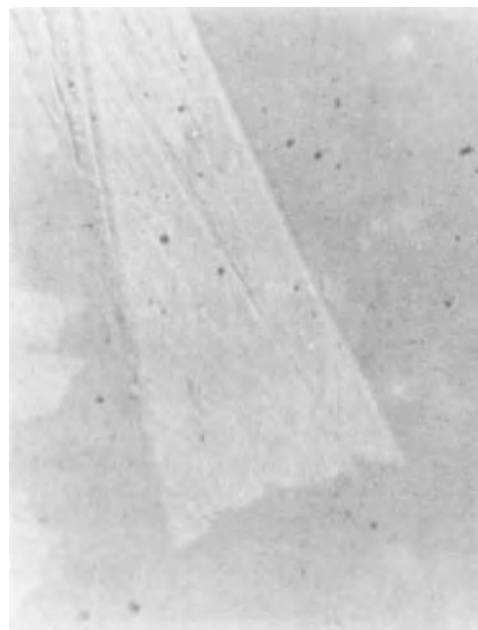


Fig. 7. Photomicrograph of crystals grown in a vitreous sample with the composition 0.9As₂Se₃·0.1Sb₂Se₃. The sample was not etched (615X).

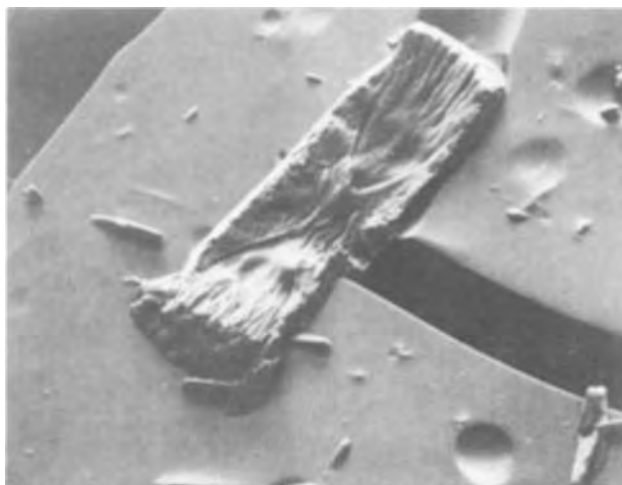


Fig. 8. Scanning electron microscope photograph of one of the crystals shown in Fig. 4, whose last part was grown at a higher temperature, after etching the specimen in a KOH solution (190X).

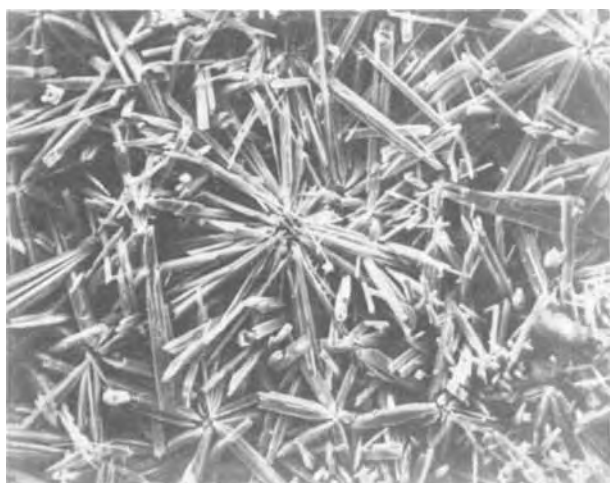


Fig. 9. Scanning electron micrograph of crystals grown in a vitreous matrix ($0.6\text{As}_2\text{Se}_3 \cdot 0.4\text{Sb}_2\text{Se}_3$) heated by illumination at 190°C . The sample was etched in a KOH solution (370X).

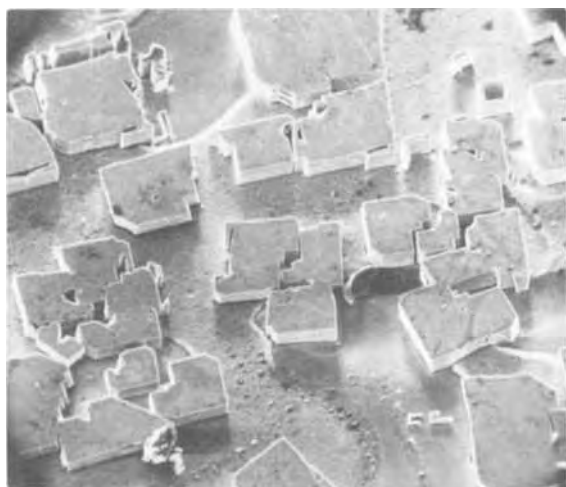


Fig. 10. Scanning electron micrograph of crystals formed in a vitreous matrix ($0.6\text{As}_2\text{Se}_3 \cdot 0.4\text{Sb}_2\text{Se}_3$) during slow cooling from the melt. Surface of the sample across the longitudinal axis of the ingot. The samples were etched in a KOH solution (165X).

was observed during crystallization directly from the melt by slow cooling. Figures 2 and 10 show crystals grown by cooling from 750°C to room temperature in several minutes and several hours, respectively.

The chemical composition of crystals grown during devitrification and that of the surrounding vitreous matrix were studied, employing scanning electron microscopy (in the x-ray mode). Homogeneous materials with $x = 0, 0.1, 0.2, 0.3, 0.4, 0.45,$ and 0.5 were prepared and used as standards. X-ray spectra (AsK_α , SeK_α , and SbL_α lines) were taken on the samples along a line traversing along a crystal, the crystal-matrix interface, and the matrix. A computer program was used for normalizing and reducing the data.

The results obtained with crystals formed by devitrification (illumination heating) of vitreous matrices having original compositions $x = 0.1$ and 0.4 and with crystals grown directly from a melt with $x = 0.4$ by slow cooling are summarized in Fig. 11. It is seen that in all cases the crystals were richer in Sb than the surrounding vitreous matrix and that the Sb content in the crystals decreased in going from the center of the crystal toward the interface. The Sb content in the vitreous-crystal interface was lower than in the crystals and the vitreous matrix. The difference in Sb content between the crystals and the surrounding vitreous matrix is far more pronounced in the crystals grown from the melt than in crystals grown by illumination

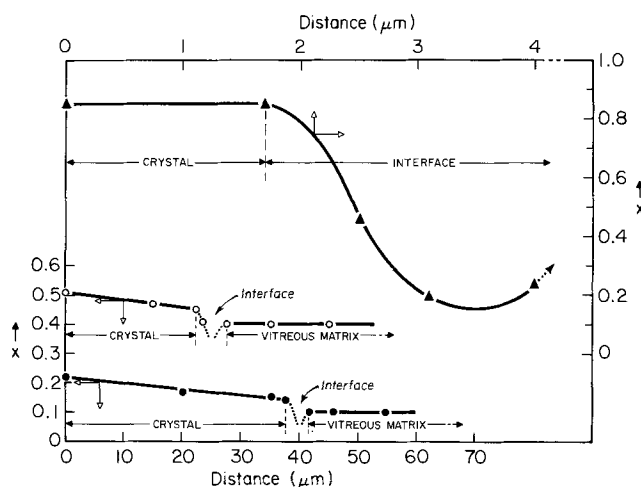


Fig. 11. Composition profile along crystals and into the vitreous matrix. \blacktriangle = matrix composition $x = 0.4$ (crystal formed upon slow cooling of melt); \bullet = matrix composition $x = 0.1$; \circ = matrix composition $x = 0.4$; in the two latter cases crystals were formed by illumination heating.

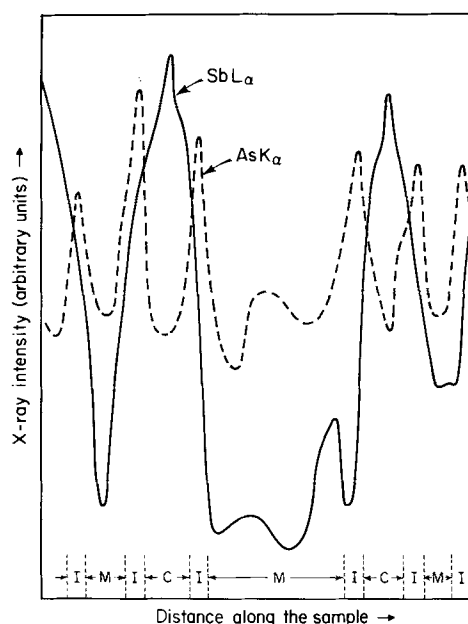


Fig. 12. Electron microanalyzer tracing of arsenic and antimony distribution along the path pp of Fig. 14; the areas indicated as C, I, and M correspond to crystal, interface, and matrix, respectively.

heating. It is apparent that Sb_2Se_3 -rich compositions nucleate preferentially, consistent with the present results on nucleation and growth as a function of composition. Accordingly, the crystal-matrix interface is somewhat depleted in Sb_2Se_3 and enriched as As_2Se_3 . Figure 12 is an electron microanalyzer scan along a sample shown in Fig. 13. It is clearly seen that the Sb content decreases and the As content increases significantly at the crystal-matrix interfaces. The higher Sb concentration and the Sb concentration gradient in the crystals are also clearly seen. Figures 14 and 15 are x-ray images obtained from the same area of a sample (similar to that shown in Fig. 13) using as signal the SbL_α (Fig. 14) and AsK_α lines (Fig. 15). The light areas in Fig. 14 correspond to the crystals and the dark areas to the vitreous matrix, clearly showing the increased Sb content in the crystals. In Fig. 15 the dark areas correspond to the crystals. Although the As segregation is not as well pronounced as the segregation of Sb (in Fig. 14) the crystals are clearly evident. Also the increased As concentration in the interface regions can be readily seen.

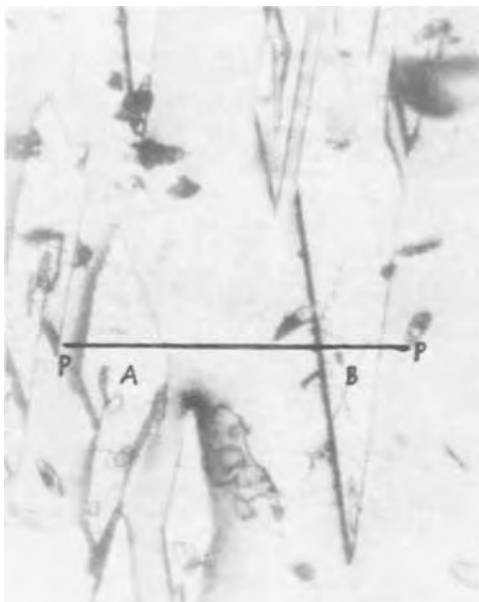


Fig. 13. Microphotograph of an unetched sample cut along the longitudinal axis of ingot cooled slowly from the melt (615X).



Fig. 14. X-ray image of an area of the specimen of Fig. 13, obtained with an electron microanalyzer using as signal the SbL_{α} line.

Attaching electrodes on thin samples of these materials (of the order of 30μ) or on flash evaporated films, memory switching (9) could be readily observed with switching time of the order of nanoseconds. The switching time is many orders of magnitude smaller than the time necessary to establish crystalline conduction paths through the vitreous matrix. Similarly, the resistance of the device in the "On" state is about four orders of magnitude smaller than that expected even if the entire device were in the crystalline state. These facts and the fact that appreciable compositional changes take place in the devitrified areas raise serious questions regarding the view that memory switching is directly related to reversible crystalline filament formation. A study of the memory switching characteristics as a function of composition and of the related amorphous-crystalline transformation is now in progress in our laboratory.

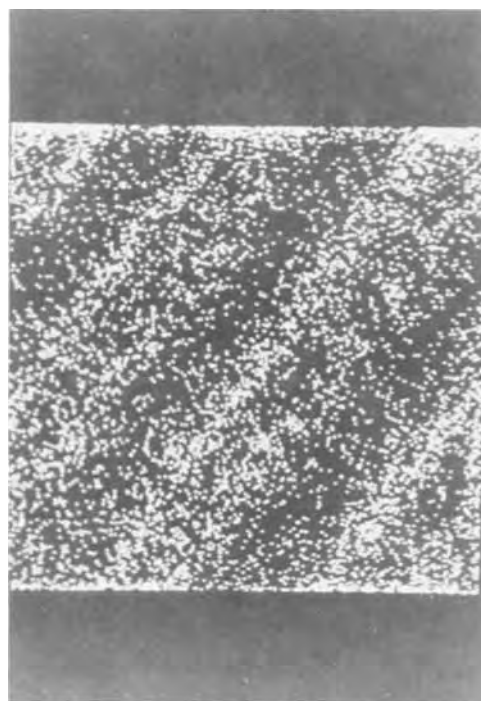


Fig. 15. X-ray image of the same area as in Fig. 14, using as signal the AsK_{α} line.

Summary

The activation energies of devitrification for the early stage of crystal formation and for the subsequent stage of growth were determined as a function of composition in the system $(1-x)As_2Se_3 \cdot xSb_2Se_3$. They were found to be similar for both stages except in materials with $x = 0.1$. This difference is believed to be associated with the nucleation rather than the growth process. The dependence of the activation energies and pre-exponential factors on composition were found to be identical.

Crystals grown in As_2Se_3 -rich materials had a dendritic-like appearance and grew in a blade-type shape. Their morphology was temperature independent. On the other hand, the morphology of the crystals, grown in Sb_2Se_3 -rich materials was temperature dependent; in this case the crystals were rectangular single-crystal platelets at low temperatures and had dendritic-type forms at higher temperatures (120° - $150^{\circ}C$). When devitrification took place near the softening temperature range, then, clusters of elongated single crystals were formed.

The chemical composition of the crystals was found to be different than that of the surrounding matrix. Crystals grown during devitrification were 20-100% richer in Sb than the matrix, depending on the original composition of the parent vitreous matrix.

X-ray diffraction measurements showed that low Sb_2Se_3 content alloys crystallize in the monoclinic system (that of As_2Se_3) while those with high Sb_2Se_3 content crystallize in the orthorhombic system (that of Sb_2Se_3). The transition from one system to the other is gradual, and both systems co-exist in a composition range whose exact limits were not determined. However, in alloys with $x = 0.2$ the orthorhombic system was present only in traces, while in those with $x = 0.3$, both systems were present in approximately equal amounts. Materials with $x \leq 0.1$ and $x \geq 0.4$ were crystallized exclusively in the monoclinic and orthorhombic system, respectively. The devitrification characteristics, the electrical and optical behavior of these materials are composition dependent when the monoclinic system predominates and composition independent when the orthorhombic system predominates. The devitrification rates, at least in the present sys-

tem, are far too slow when compared with the switching time of electrical switching in these materials. Accordingly, questions are raised regarding the view that amorphous-crystalline transformations are directly responsible for memory switching in these materials.

Acknowledgments

The authors are indebted to the Advanced Research Projects Agency and the National Science Foundation for financial support.

Manuscript submitted Nov. 29, 1971; revised manuscript received Feb. 14, 1972.

Any discussion of this paper will appear in a Discussion Section to be published in the June 1972 JOURNAL.

REFERENCES

1. E. V. Shkol'nikov, "Solid State Chemistry," p. 132, Z. U. Borisova, Editor, Consultants Bureau Translation, New York (1966).
2. R. L. Myuller and E. V. Shkol'nikov, "Solid State Chemistry," p. 306, Z. U. Borisova, Editor, Consultants Bureau Translation, New York (1966).
3. M. D. Coutts and E. R. Levin, *J. Appl. Phys.*, **38**, 4039 (1967).
4. N. S. Platakis, H. C. Gatos, and A. F. Witt, *This Journal*, **116**, 510 (1969).
5. N. S. Platakis, "Semiconducting Properties of the System $(1-x)\text{As}_2\text{Se}_3 \cdot x\text{Sb}_2\text{Se}_3$ in Its Amorphous and Crystalline State," Ph.D. Thesis, M.I.T., May 1970.
6. See for example H. Rawson "Inorganic Glass-Forming Systems," p. 34, Academic Press, New York (1967).
7. N. S. Platakis, V. Sadagopan, and H. C. Gatos, *This Journal*, **116**, 1436 (1969).
8. W. Procarione and C. Wood, *Phys. Status Solidi*, **42**, 871 (1970).
9. See for example N. F. Mott, *Contemp. Phys.*, **10**, 125-138 (1969).

Measurements of the Absolute Radiative Efficiency of Cathodoluminescent Phosphors

V. D. Meyer

The Bayside Research Center of GTE Laboratories Incorporated, Bayside, New York 11360

ABSTRACT

The absolute efficiency of cathodoluminescent phosphors has been measured as a function of voltage and current density. The results are in good agreement with the highest values previously reported. Changes of slope in the luminance vs. voltage curves indicate that changes in the voltage dependence may occur at x-ray excitation potentials; these observations are related to results reported by others for x-ray excitation of scintillation crystals. The indications are that it may not be possible to assume that the intrinsic efficiency is independent of the kinetic energy of the incident electron beam unless the energy exceeds the K x-ray levels of the host.

The absolute radiative efficiency of a phosphor is the energy given off in the form of radiation¹ divided by the energy incident upon the phosphor. The absolute value of the radiative conversion efficiency of phosphors under cathode ray excitation has been measured by Brill (1), Brill and Klasens (2) (BK) and more recently by Ludwig and Kingsley (3) (LK). At high accelerating voltages (20 kV), the highest efficiency (0.25) was measured by BK for the phosphor ZnS:Ag,Al. Since they approximate their error to be 15%, the efficiency may be as low as 0.212 or as high as 0.288. Estimates of the maximum attainable efficiency calculated by several authors (4-7) when only unavoidable energy losses are accounted for range from 0.22 to 0.26 for ZnS:Ag,Al. All these estimates are based on the assumption that excitation by cathode rays leads directly to the formation of electron-hole pairs.

Measured efficiencies increase as the accelerating voltage of the exciting electron beam is increased and appear to become constant at high accelerating voltages. The increase with accelerating voltage has been interpreted (2, 3) by using Gergely's (8) formulation which accounts for surface effects. Bieringer (9) has also formulated a relationship which accounts for the so-called "dead-layer" and his predicted voltage dependence agrees with the measured change in brightness as the accelerating voltage is increased. Since

surface effects may result from contamination or effects inherent to an interface, it is desirable to measure the variation with voltage using a clean surface. It would be interesting to determine if utilization of modern vacuum technology would yield higher measured efficiencies by reducing surface contamination.

The efficiency 0.08 ± 0.012 reported by Brill (1) for the National Bureau of Standards phosphor NBS 1021, $\text{Zn}_2\text{SiO}_4:\text{Mn}^{2+}$, exceeds by a significant amount the measured value, 0.047, recently reported by LK (3). This is especially significant because variations produced by different phosphor synthesis procedures and techniques are not involved in comparing these results, since investigators used phosphor from the same lot, i.e., NBS 1021.

In this paper we report measurements of the absolute radiative efficiency of cathodoluminescent phosphors, using an oil-free vacuum system in order to minimize surface contamination, with special emphasis on the efficiencies of ZnS:Ag,Al and $\text{Zn}_2\text{SiO}_4:\text{Mn}^{2+}$. Other phosphors including several rare-earth activated materials have also been measured.

In the course of our measurements, we found indications of changes in efficiency at energies corresponding to electronic energy levels of the host material in the x-ray region. Due to the relative insensitivity of thermopiles and the possibility of surface charging, we found it impossible to demonstrate these changes by measuring the efficiency. In order to more carefully study the voltage dependence near x-ray levels, we have instead measured the luminosity using a sensitive photomultiplier under several experimental conditions in which the possibility of surface charging could be

Key words: luminescence, cathode-ray, sulfide, rare-earth.

¹The term radiation used here is meant to include radiation in the visible, near ultraviolet and near infrared regions of the spectrum. It does not include x-ray or thermal radiation. Obviously the measured efficiency includes only those wavelengths which can be detected by the thermopile. In our case this would be limited by the transmission of a quartz window.

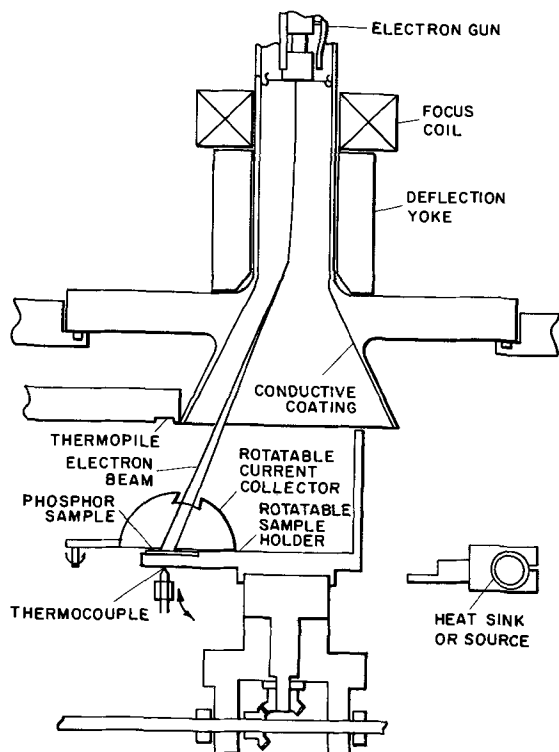


Fig. 1. Schematic diagram of apparatus. Current collector is rotated into position to measure current, and rotated out to permit measurement of emitted radiation by the thermopile. Sample holder can be rotated 180° to make contact with a heat sink or source which hangs on a hollow tube.

minimized or eliminated. These measurements are reported in the section on Voltage Dependence near X-Ray Levels.

Experimental

General description.—A schematic diagram of the apparatus is shown in Fig. 1. The electron beam generated in the electron gun is focused and scanned at normal television rate. (Field-scanning frequency of 60 Hz and frame-scanning frequency of 30 Hz.) The raster size at the screen can be varied from larger than the screen size down to spot size. The screen contains four slots for the prepared samples and by magnetic coupling the sample holder can be rotated in order to position the desired sample directly below the thermopile. The thermopile was sealed into a vacuum-tight case by the manufacturer (Charles M. Reeder Company). The quartz window of the thermopile is positioned 6.86 cm directly above the sample. Prior to sealing the thermopile into the vacuum system with a conflat flange seal, it was calibrated against a National Bureau of Standards Standard Lamp. The vacuum-pumping system consists of a VacSorb roughing pump and a Vaclon pump supplemented by a titanium sublimation pump. Pressures of 2×10^{-8} Torr are regularly obtained after overnight pumping and the pressure during operation is approximately 3×10^{-8} Torr.

A measurement of the screen current only is not a valid measure of the total beam current since secondary electrons may not be detected. To insure measurement of the total beam current, a current collector is added. This consists of a cup which, when rotated into position over the sample, forms with the screen a hemispherical enclosure with a square opening to permit the incident beam to enter.

When the sample holder is rotated 180° from the measuring position, it comes into contact with a heat sink which hangs on a hollow tube. To heat or cool the phosphor samples, a heater can be inserted into the tube, or liquid nitrogen can be poured into the tube.

Sample preparation.—Phosphor samples were prepared by settling the powder onto 1 in.² aluminum

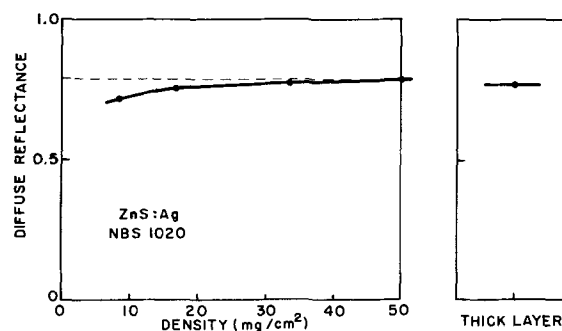


Fig. 2. Diffuse reflectance for various coating densities and for a thick layer.

plates using a silicate binder. To insure sufficient coverage of the metal slide by the phosphor powder, thick phosphor layers were prepared. However, in preparing thick layers, the possibility of the phosphor surface charging becomes more likely. Therefore, it is desirable to add just enough phosphor to obtain sufficient coverage. Our approach to this problem was to assume that diffuse reflectance from a sample with sufficient coverage should be very nearly the same as that for a thick, lightly packed powder. Figure 2 shows that diffuse reflectance for various settling weights of the phosphor ZnS:Ag (NBS 1020) and also the diffuse reflectance for the same phosphor in the form of a packed powder. We note that at a coating density of 50 mg/cm² the diffuse reflectance is nearly the same as that for the thick powder. This and additional evidence, given later, led us to choose 50 mg/cm² as the proper coating density. Since the particle sizes of the important cathodoluminescent phosphors are of the same order of magnitude, we have assumed this coating density to be sufficient for most phosphors.

Experimental procedure.—The intrinsic efficiency of a phosphor under cathode ray excitation can be expressed as follows²

$$\eta_i = \frac{2\pi r^2 CE}{I_0 V_0 (1 + R_\infty)}$$

In order to measure the intrinsic efficiency, η_i , therefore, it is necessary to know: r , the distance from the phosphor to the thermopile and C , the calibrated thermopile sensitivity in W/V cm²; it is also necessary to measure: (i) E , the emf generated by the thermopile, (ii) I_0 , the incident beam current, (iii) V_0 , the accelerating voltage, and (iv) R_∞ , the reflection coefficient of the phosphor sample.

With the accelerating voltage set at a measured value, a phosphor sample is rotated into position directly beneath the thermopile, and the raster size is adjusted to insure that the largest dimension (the diagonal of the raster) is less than one fifth² of the distance from the phosphor to the thermopile. The hemisphere current collector is rotated into position and the total current is recorded. Immediately thereafter, the collector is rotated out and the emf generated by the thermopile is recorded. The reflection coefficient of each sample as a function of wavelength is measured using a Cary 14 Spectrometer, and the reflection coefficient at the wavelength corresponding to the peak of the emission is used to calculate the intrinsic efficiency.

Efficiency Measurements

Phosphor thickness.—Bril and Klasens (2) have shown that the intrinsic efficiency can be written as

$$\eta_i = \frac{2\eta_m(\infty)}{(1 + R_\infty)}$$

² In order for the inverse square relationship to be valid, and therefore the equation for intrinsic efficiency to be applicable, the distance from the source must be at least five times the maximum dimension of the source. See I.E.S. Lighting Handbook, 3rd ed., pp. 9-29, Illuminating Engineering Society, New York, N. Y. (1962).

where $\eta_m(\infty)$ is the measured efficiency uncorrected for the loss due to imperfect reflection by a very thick sample. The above equation results from assuming that the depth of penetration of the electron beam is very small compared to a thickness within which reabsorption of the emitted light becomes significant. It is further assumed that half of the light is emitted up (back toward the electron beam) and the other half is emitted downward. Of the half emitted downward, a certain fraction which depends upon the reflection coefficient is reflected back toward the detector. R_∞ is the reflection coefficient for an infinitely thick layer. In order for this equation to be validly applied therefore, the reflection coefficient of the phosphor sample should be equal to that of a thick powder layer of the same material.

We have measured the efficiency at various settling weights and applied corrections for the reflection coefficient of the individual samples. We call this corrected efficiency η_c

$$\eta_c = \frac{2\eta_m}{1 + R}$$

As the thickness, t , increases η_c approaches η_i , i.e., $(\eta_c)_{t \rightarrow \infty} \rightarrow \eta_i$. The efficiency at various settling weights is shown in Fig. 3 together with the efficiency measured for a thick powder of the same phosphor ZnS:Ag (NBS-1020). This result agrees with our conclusion from reflectance measurements, that 50 mg/cm² is sufficient to provide not only complete coverage but enough thickness to produce a reflectance nearly the same as that for a very thick powder layer; therefore at this settling weight η_c is very nearly equal to η_i .

Beam current.—At high current densities some phosphors become "nonlinear" (saturate), and the efficiency measured at high current densities is degraded. To avoid such reduction in efficiency it is necessary to establish the current density at which such effects occur; therefore, the efficiency was measured as a function of current density for all the phosphors. Nonlinearity is most pronounced in the case of the II-VI sulfides, and Fig. 4 shows the variation with current density for ZnS:Ag (NBS 1020). Nonlinearity becomes significant at currents above approximately 0.5 μ A. (This corresponds to an average current density of approximately 0.5 μ A/cm² since the raster size is approxi-

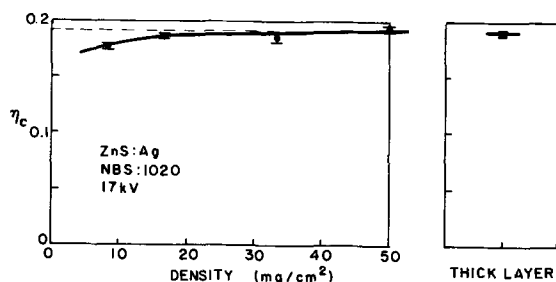


Fig. 3. Efficiency corrected for reflectance properties at various coating densities and for a thick layer.

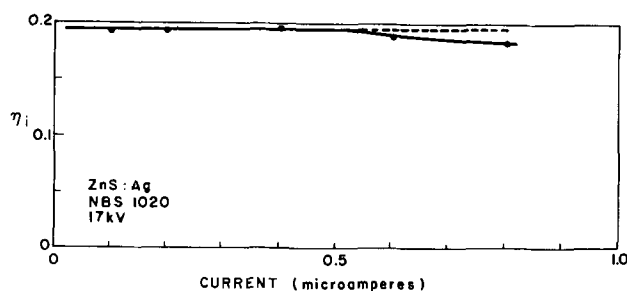


Fig. 4. Efficiency for various beam currents. The raster size is approximately one square centimeter. Nonlinearity becomes significant beyond 0.5 μ A/cm².

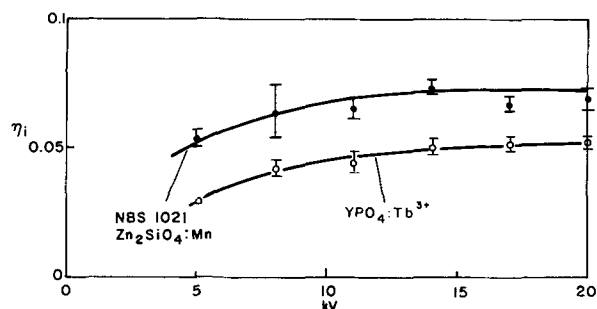


Fig. 5. Voltage dependence of intrinsic efficiency for green-emitting $\text{Zn}_2\text{SiO}_4:\text{Mn}^{2+}$ and $\text{YPO}_4:\text{Tb}^{3+}$.

mately one square centimeter.) In order to be certain that the current density was less than that at which nonlinearity becomes significant, our measurements for the true efficiency were made at 0.1 μ A.

Voltage dependence.—Typical efficiency measurements as a function of accelerating voltage are shown in Fig. 5. Table I shows the measured efficiencies and the voltage at which the maximum was measured for several phosphors. The phosphors have been listed according to emitted color, i.e., blue first then green then red. Similar phosphors have been grouped together. The deviations listed in Table I are the deviations found for the number of measurements indicated and the average deviation over all samples at high voltage was 0.004. Mean deviations are indicated by error bars in the figure. Some of the samples show indications of surface charging at high voltages, usually at 17 to 20 kV. We have chosen to have the measurements extend from 5 to 20 kV; surface effects become pronounced below 5 kV and Brill's measurements show that the measured efficiencies do not increase appreciably beyond 20 kV for most phosphors. In some cases it is possible that the maximum efficiency has not been reached at 20 kV, and in other cases charging effects might be suspected when the apparent maximum is found at relatively low voltage.

Effect of heat treatment.—Several of the phosphor samples were heated in the vacuum system at approximately 100°C for several hours and then allowed to cool to room temperature. The results obtained with and without this heat treatment are summarized in Table II. The heating apparently reduces the charging effect and in some cases a slight but detectable increase in efficiency is observed. Figure 6 shows the case in which the largest increase occurred after the heat treatment. While our results indicate that the heating has reduced charging, it apparently has not removed surface contaminants since the efficiencies measured at low voltages (5 kV) did not increase after being heated.

Comparison with other measurements of efficiency.—The agreement among the various investigators is in

Table I. Measured efficiencies, η_i

Phosphor	η_{Max}	kV at η_{Max}	Times measured
NBS 1020 ZnS:Ag	0.204 \pm 0.005	20 ^(a)	15
Str ₃ (PO ₄) ₂ :Eu ²⁺	0.055 \pm 0.004	14	6
Str ₅ (PO ₄) ₃ Cl:Eu ²⁺	0.044 \pm 0.002	14	6
(Zn,Cd)S:Ag			
Source A	0.154 \pm 0.004	20 ^(a)	4
Source B	0.198 \pm 0.002	20 ^(a)	6
(Zn,Cd)S:Cu,Al			
Source A	0.168 \pm 0.004	11	6
Source B	0.171 \pm 0.004	17	6
Source C	0.184 \pm 0.005	20 ^(a)	6
YPO ₄ :Tb ³⁺	0.052 \pm 0.002	20 ^(a)	6
NBS 1021 Zn ₂ SiO ₄ :Mn	0.074 \pm 0.002	14	4
YVO ₄ :Eu ³⁺	0.057 \pm 0.006	14	6
YVO ₄ :Eu ³⁺ ,Bi ³⁺	0.065 \pm 0.002	17	6
Y ₂ O ₃ :Eu ³⁺	0.080 \pm 0.005	14	6
Y ₂ O ₂ S:Eu ³⁺	0.098 \pm 0.000	17	6
(Cd,Zn)S:Ag ⁺	0.143 \pm 0.005	17	6

^(a) Twenty kilovolts or more.

Table II. Effect of heat treatment

Phosphor	Without heating		After heating	
	η_i	kV at Max	η_i	kV at Max
NBS 1020 ZnS:Ag	0.204 \pm 0.002	20 ^(a)	0.208 \pm 0.001	20 ^(a)
ZnS:Ag,Al	0.215 \pm 0.008	11	0.212 \pm 0.003	20 ^(a)
Cubic ZnS:AgCl	0.162 \pm 0.009	14	0.190 \pm 0.002	20 ^(a)
Hex. ZnS:Ag,Cl	0.168 \pm 0.003	17	0.181 \pm 0.004	17

^(a) Twenty kilovolts or more.

Table III. Comparison of efficiency measurements

Phosphor	η (Bril)	η (Ludwig, Kingsley)	η (Meyer)
ZnS:Ag,Al	0.25 \pm 0.039		0.212 \pm 0.003
ZnS:Ag NBS 1020	0.21 \pm 0.032		0.204 \pm 0.005
ZnS:Ag		0.196	
Zn ₂ SiO ₄ :Mn NBS 1021	0.08 \pm 0.012	0.047	0.074 \pm 0.002
(Zn,Cd)C:Ag (green)		0.21	0.154 to 0.198
YVO ₄ :Eu	0.06	0.060 to 0.067	0.057 \pm 0.006
Y ₂ O ₃ :Eu	0.075	0.065	0.080 \pm 0.005 ^(c)
Y ₂ O ₂ S:Eu		0.13 ^(a)	0.098 \pm 0.000 ^(b)

^(a) RCA 334-256 lot 84,89,90, 4.0 m/o Eu by analysis.

^(b) RCA 334-256A lot 169,170, 4.3 m/o Eu by analysis.

^(c) 5.7 m/o Eu by analysis.

general very good; however, there are a few exceptions. Table III presents a comparison of our results with efficiencies measured by others. For the phosphors NBS 1020 and 1021, our results agree with Bril's within his experimental error. The LK value of ZnS:Ag is listed separately in Table III since they apparently did not measure NBS 1020.

The measured efficiency of ZnS:Ag,Al is compared with Bril's results in Table III. Since this is not a National Bureau of Standards phosphor, we cannot be sure that the measurements were made on identical samples (phosphors vary significantly from one lot to another). In spite of this we find that our results agree with Bril's within his experimental error at high voltages. When we compared the voltage dependence of this phosphor with that reported by BK we found that our values were slightly higher at low voltages, but slightly lower at high voltages. These apparent differences in the measured voltage dependence could be the result of a reduction of surface contamination in the improved vacuum system.

One case in which there appears to be a definite disagreement is for the phosphor Zn₂SiO₄:Mn²⁺, NBS 1021. Since this is a National Bureau of Standards phosphor, we can be certain that the phosphor lot used by all the investigators is identical. Any differences then can only result from differences of measurement or preparation of test samples. Our results lie between those reported by Bril and those reported by Ludwig and Kingsley; our value, however, lies within the experimental error reported by Bril, but does not agree with LK results. There are two plausible reasons for this discrepancy. The sample density, 8-14 mg/cm², used by LK was considerably less than we found necessary. For our measurements of NBS 1021 at a coating density of 33 mg/cm² we measured an efficiency of 0.062 which is already considerably less than 0.074

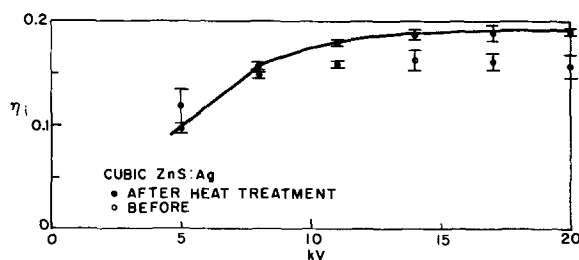


Fig. 6. Voltage dependence of intrinsic efficiency for cubic ZnS:Ag before and after being heated in vacuum.

measured at a coating density of 50 mg/cm². One might expect then that at 14 mg/cm² the measured value could be much lower. A second possible error could result in the case of this particular phosphor from using a modulation technique. LK used a lock-in amplifier at a frequency of 25 Hz. During this period (40 msec) the detector received a square wave pulse for half (20 msec) of the period so that from the end of one pulse to the beginning of another 20 msec elapsed. During that time the green emission from Zn₂SiO₄:Mn²⁺ decays to approximately 10% of its brightness during excitation. Since the synchronous technique measures only the modulation there is a possibility of error for this slowly decaying phosphor.

Our measurements for Y₂O₃:Eu are somewhat higher than those of LK, but agree fairly well with Bril's value. This might result from the lighter coating density used by LK. On the other hand, for Y₂O₂S:Eu the LK value is higher than our measured value. Part of these inconsistencies may be attributed to differences in the phosphor samples or in the preparation of test samples.

Voltage Dependence near X-Ray Levels

Results

In other measurements of efficiencies we have noticed indications of changes in efficiency as the accelerating voltage increases beyond the value corresponding to x-ray levels of the host material. To more carefully study the voltage dependence, measurements have been made using a sensitive photomultiplier in place of the thermopile, and experimental conditions which minimize or eliminate charging have been used.

To eliminate charging effects, measurements of the voltage dependence of cathodoluminescence using cathode ray tubes having aluminized phosphor screens have been made. In these measurements, the luminance was measured over a wide voltage range at a constant current density. The accelerating voltage is corrected for loss in the aluminum layer by using the Thomson-Whiddington relationship and the range of electrons in aluminum films as measured by Feldman (10). The results for ZnS:Ag are shown in Fig. 7 and the K x-ray absorption edges of zinc and sulfur are indicated. There is an obvious change of slope which appears to occur near the zinc level. A similar curve for YPO₄:Tb³⁺ (Fig. 7) shows no change of slope in the region of 10

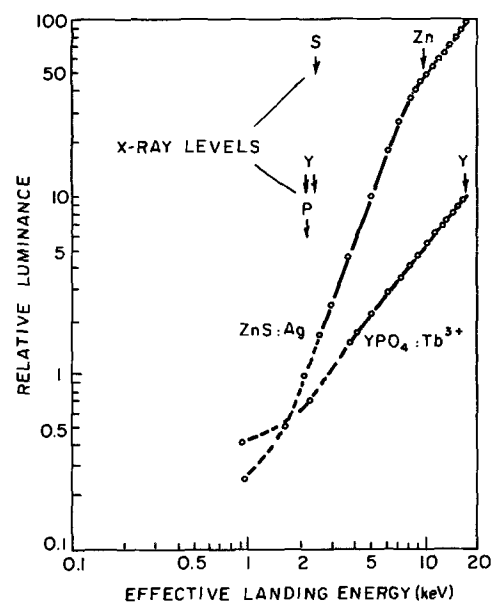


Fig. 7. Voltage dependence of luminance for ZnS:Ag and YPO₄:Tb³⁺. The voltage scale is corrected for energy lost in penetrating through 2000Å of aluminum. At low voltages, the dashed curve indicates possibility of large error since correction applied to the voltage is almost as large as the measured voltage.

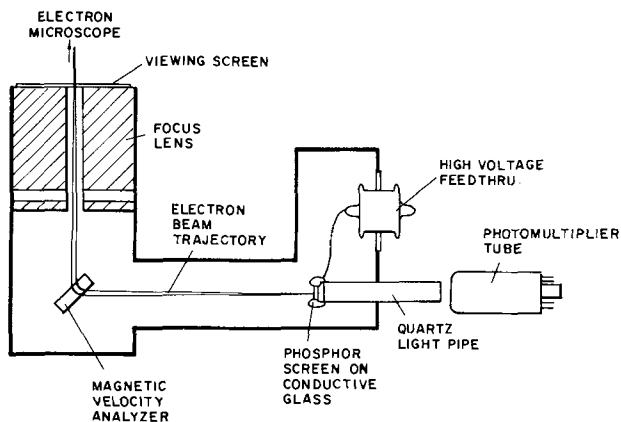


Fig. 8. Schematic representation of modification added to electron microscope.

kV. Since a correction has been applied, the voltage scale may be shifted. At low voltages the error in the corrected value of the accelerating voltage can be quite large, since the correction becomes as large as the applied potential. The curves are dashed to indicate that changes in slope suggested by points in this region are questionable.

One of the difficulties in measuring the change in brightness with accelerating voltage is the stringent requirement that the current must be maintained constant. This requires a readjustment at each accelerating voltage in the normal cathode ray tube. In order to eliminate this possible source of error, another method was used to measure the voltage dependence. In this case, an electron microscope which had been modified for other studies (11) was used (see Fig. 8). A hole was drilled in the viewing screen and a focusing lens and magnetic velocity analyzer were added. With the analyzer and focusing coil set properly the electron beam was deflected through 90° and focused onto a phosphor screen deposited on conductive glass and attached to the end of a quartz light pipe leading to a sensitive photomultiplier tube. The potential of the phosphor screen was determined by a separate highly regulated high-voltage power supply. With the electron beam current and voltage adjusted to a convenient value, the effective accelerating voltage of electrons exciting the phosphor screen (the potential difference between phosphor screen and electron source—the effective landing voltage) could be varied without changing the beam current simply by altering the potential applied to the phosphor screen. Since the phosphor screen was large ($\frac{1}{2}$ in. diam) compared to the focused electron beam spot (<0.005 in.) and since the photomultiplier viewed the entire screen (2 in. diam active photocathode), small changes in position on the screen or in spot size produced by changes in screen potential, even over large voltage changes, did not change the current delivered to the screen.

With a ZnS:Ag phosphor screen and the electron beam in the microscope accelerated to 7 kV, the potential of the phosphor screen was varied from 1 to 5.5 kV (i.e., the effective landing voltage varied from 8 to 12.5 kV). The relative photomultiplier response over this range is shown in a log-log plot in Fig. 9, curve A. A change of slope appears to occur near the indicated Zn K ionization level. To determine if the change of slope results from a change inherent in the apparatus as a result of the voltage applied to the phosphor screen, or is due to some characteristic of the phosphor itself, the beam voltage in the microscope was reduced to 6 kV and the voltage applied to the phosphor screen was varied from 2 to 5.5 kV. The relative photomultiplier response over this range is shown in curve B of Fig. 9. The change of slope again occurs at the same effective accelerating voltage. We conclude therefore that the change of slope occurs at a characteristic voltage difference between the phosphor screen and

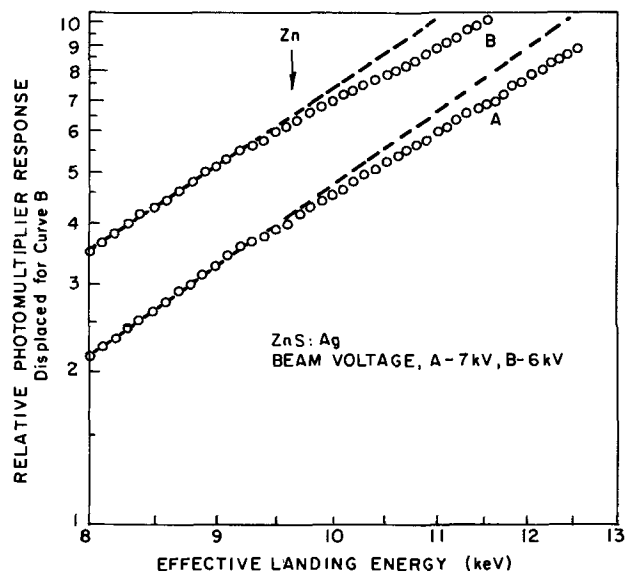


Fig. 9. Voltage dependence of luminance for ZnS:Ag. The effective accelerating voltage varied from 8 to 12.5 kV. In case A the beam voltage was 7 kV and a potential of 1-5.5 kV was applied to the phosphor screen. For case B, beam voltage = 6 kV, phosphor screen voltage = 2-5.5 kV.

the electron source (effective landing voltage) and not as a result of change in electron trajectory, focus, etc. which might result from changing the potential difference between the phosphor screen and the surrounding metal case which is at ground potential.

Similar measurements for a single crystal of CaWO_4 covered on the electron beam side with a thin film of aluminum are shown in Fig. 10. With the beam voltage set at 18 kV, the retarding voltage on the crystal was first increased from -1 kV to -10 kV in 500V steps and then reduced from -10 kV back to -1 kV. Thus two points appear at each effective landing potential giving an estimate of the scatter in the data. The two curves show two series of such measurements. There is a definite change of slope which appears to occur in the region of the tungsten L_1 , L_2 , and L_3 absorption edges. Since the aluminum film was very thin and the effective landing voltage was high, correction for energy loss in the aluminum film was small and made no detectable difference in the voltage at which the change of slope appears to occur. However, if the effective landing voltage is reduced much further the

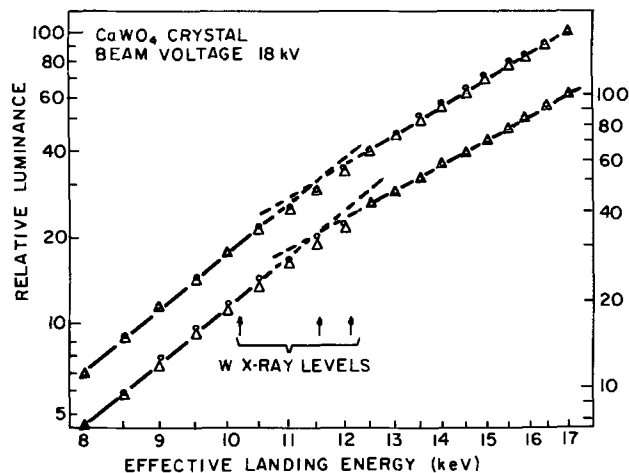


Fig. 10. Voltage dependence of luminance for CaWO_4 single crystal. Two series of measurements are shown. In each series the two points at each voltage are values obtained on consecutive measurements. Beam voltage = 18 kV, retarding potential of -1 to -10 kV.

correction becomes significant. Therefore, to observe lower lying x-ray absorption edges, a similar experimental arrangement was used, except that the metal film on the electron beam side of the CaWO_4 crystal was evaporated through a mask to provide a slot slightly larger than the beam size. That is, the metal covered the crystal except in the region where the beam landed. To minimize the possibility of surface charging the beam current was reduced to the minimum level necessary to obtain a usable signal. Visual examination of the spot showed no distortion or enlarging of the spot. With the beam voltage set at 12 kV and the retarding potential varied from -5.5 to -10 kV, the results shown in Fig. 11 were obtained. Each point in this figure is the average of three measurements and the root-mean-square deviation is indicated by the error bars. Two series of measurements are represented by the two curves, one at 500V intervals and another at finer intervals. Changes of slope are repeatedly found in the regions of the Ca and W x-ray excitation potentials. The changes can be further demonstrated by dividing the luminosity by the kinetic energy of the exciting electron beam. This quantity which is proportional to the efficiency is shown in Fig. 12. It is apparent that changes in slope occur at or near the Ca x-ray excitation potential although the change is less obvious at the W level.

Changes in slope of the brightness vs. accelerating voltage curve have been reported previously; however, to our knowledge, they have not been correlated with excitation potentials of x-ray levels. Brown (12) measured the brightness of willemite ($\text{Zn}_2\text{SiO}_4:\text{Mn}^{2+}$) at low and intermediate voltages. In his Fig. 4 he shows that the brightness varies as the second power of the accelerating voltage from 200 to 800V and then suddenly increases more rapidly. The K absorption edge for oxygen is located at approximately 500 eV. Nottingham (13) also measured the brightness of willemite as a function of accelerating voltage, but at slightly higher voltages than Brown. In his Fig. 15 Nottingham shows a plot of the logarithm of brightness vs. the logarithm of the accelerating voltage. There is a change of slope at approximately 1500V. The K x-ray level of silicon is located at about 1.8 keV, and zinc levels are located at 1.2, 1.05, and 1.02 keV.

The idea that the efficiency of producing luminescence is not the same from different energy levels in the x-ray region has been demonstrated by others (14-16) using photon excitation. In their Fig. 6 Aitken,

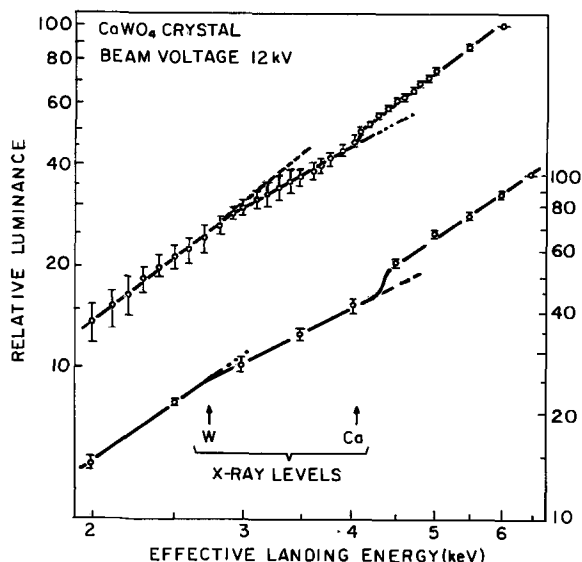


Fig. 11. Voltage dependence of luminance for CaWO_4 single crystal. Two series of measurements are shown. Each point is the average of three measurements and the root-mean square deviation is indicated by the error bars. Beam voltage = 12 kV, retarding potential of -5.5 to -10 kV.

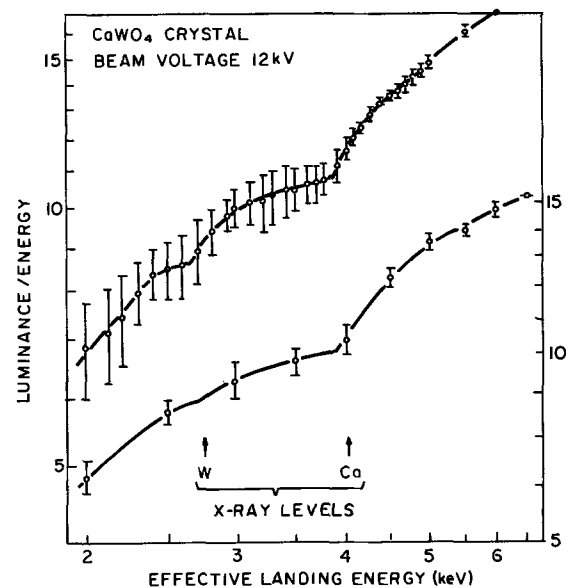


Fig. 12. Voltage dependence of luminance divided by kinetic energy for CaWO_4 single crystal. Conditions are the same as in Fig. 11.

et al. (14) show the response curve for single crystal CsI(Tl) . Not only do these results reveal discontinuities at the iodine and cesium L- and K-shell absorption edges, but they also show that between absorption edges the response is a function of the energy. After the L-shell absorption edge (between 5 and 6 keV) there is an increase of approximately 30% in the response as the energy increases to 20 keV. It might be claimed that this is a result of a nonluminescent surface which becomes less significant as the energy is increased. However, at lower energies, the response decreases by approximately 20% as the energy increases from 4 keV to approximately 6 keV. This certainly is not a result of surface effects but must be attributed to a change in the intrinsic efficiency as the energy increases. The energy dependence of the x-ray response curves for NaI(Tl) scintillation crystals have been reported by Engelkeimer (15) and by Kaiser, Baker, McKay, and Sherman (16). They find that the response is significantly nonlinear with changes occurring at energies which correspond to iodine absorption edges. These results also show that the response is not constant until the energy is much greater than that of the absorption edge having the highest energy. In addition, Kaiser *et al.* (16) show a postulated electron response curve which shows a change of slope at the K edge of iodine (33 keV).

Discussion

The referenced studies of x-ray excitation have demonstrated that for scintillation crystals: (i) there is a discontinuity in the efficiency at an x-ray absorption edge, (ii) the intrinsic efficiency is a function of the energy, and (iii) postulated electron response curves are nonlinear with a change of slope occurring in the region of the voltage corresponding to an x-ray edge. The change of slope is not abrupt, but more gradual than that observed by high energy photon excitation. It should be noted in addition that the change in slope does not result solely from the discontinuity at the absorption edge; it also results from the changes in efficiency just before and after the edge. The location of the change of slope therefore may not coincide exactly with the x-ray absorption edge.

We suggest that for phosphors other than scintillation crystals, one cannot be certain that the efficiency is constant unless the accelerating voltage is much larger than the K ionization energy. We expect to find, therefore, a constant efficiency only at high accelerating voltages for materials like ZnS , Zn_2SiO_4 , etc. (the K ionization energy of Zn is 9.66 keV); but at lower volt-

ages, as the accelerating voltage is increased and passes through the ionization energy of an x-ray level, we might expect to observe a small change in the measured efficiency and a change in the energy dependence. We expect to find, as in the postulated electron response curves for scintillation crystals a change of slope which is gradual rather than abrupt. Since the luminance is proportional to the efficiency multiplied by the kinetic energy of the electron beam, we expect to observe changes in slope of luminance *vs.* accelerating voltage plots at x-ray excitation potentials similar to those in Fig. 7-12.

It is not suggested that surface effects are unimportant, but the data indicate that x-ray level effects may be superimposed on the surface effect in the voltage dependence curves; therefore, it cannot be assumed that the intrinsic efficiency is constant unless the excitation energy exceeds the largest K x-ray energy of the host material.

Summary

Our measurements of efficiency show that the estimated maximum attainable efficiency has not been exceeded but has very nearly been reached for II-VI sulfides. The over-all agreement with previous measurements is generally good, and best agreement is found with the higher of previously reported values. For the NBS phosphor No. 1021, $Zn_2SiO_4:Mn^{2+}$, our results are within Brill's experimental error but do not agree with the lower value measured by Ludwig and Kingsley.

Heating the phosphor samples in vacuum prior to measurement, has reduced the charging effect at high voltages. Measurements of luminance and efficiency over a wide range of accelerating voltages together with an examination of previously reported results has led us to conclude that in some cases there may be a change in efficiency when the incident energy is increased and passes through an x-ray level of the host material. The intrinsic efficiency of a cathodoluminescent phosphor cannot therefore be assumed to be constant unless the incident energy exceeds the largest K x-ray absorption energy of the host.

Acknowledgments

It is a pleasure to acknowledge the assistance of C. Creter in making the measurements and of J. Rapp in designing the apparatus.

Manuscript submitted July 13, 1971; revised manuscript received March 1, 1972.

Any discussion of this paper will appear in a Discussion Section to be published in the June 1973 JOURNAL.

REFERENCES

1. A. Brill, in "Luminescence of Organic and Inorganic Materials," H. P. Kallmann and G. N. Spruch, Editors, pp. 479-493, John Wiley & Sons, Inc., New York (1962).
2. A. Brill and H. A. Klasens, *Philips Res. Rept.*, **7**, 401 (1952).
3. G. W. Ludwig and J. D. Kingsley, *This Journal*, **117**, 348 and 353 (1970).
4. V. Meyer, *J. Appl. Phys.*, **41**, 4059 (1970).
5. V. L. Levskin, Y. M. Popov *et al.*, "Soviet Researches on Luminescence." Trans. (Trudy). P. N. Lebedev, Phys. Inst. XXIII Part II, "Investigations of the Cathodoluminescence of Zinc Sulfide and Certain Other Cathodoluminophors," Chap. 1 (1964) English translation by Consultants Bureau Enterprises Inc., 227 West 17th Street, N. Y. 10011.
6. J. P. Davey, Ph.D. dissertation, University of Cambridge (1964).
7. G. F. J. Garlick, "Luminescence of Inorganic Solids," P. Goldberg, Editor, Chap. 12, Academic Press, New York (1966).
8. G. Gergely, *J. Phys. Chem. Solids*, **17**, 112 (1960).
9. R. J. Bieringer, *Phys. Rev.*, **142**, 550 (1966).
10. C. Feldman, *ibid.*, **117**, 455 (1960).
11. T. Emma, V. Meyer, and R. Simon, To be published.
12. T. B. Brown, *J. Opt. Soc. Am.*, **27**, 186 (1937).
13. W. B. Nottingham, *J. Appl. Phys.*, **8**, 762 (1937).
14. D. W. Aitken, B. L. Beron, G. Yenicay, and H. R. Zullinger, *IRE Trans. Nucl. Sci.*, **NS-14**, 468 (1967).
15. D. Engelkeimer, *Rev. Sci. Instr.*, **27**, 589 (1956).
16. W. C. Kaiser, S. I. Baker, A. J. Mac Kay, and I. S. Sherman, *IRE Trans. Nucl. Sci.*, **NS-9**, 22 (1962).

Comparison of Infrared and Activation Analysis Results in Determining the Oxygen and Carbon Content in Silicon

Chris Gross and Gianni Gaetano

NASA Langley Research Center, Hampton, Virginia 23365

and T. N. Tucker* and J. A. Baker

Dow Corning Corporation, Hemlock, Michigan 48626

ABSTRACT

The oxygen and carbon content of several silicon single crystals have been measured using ^3He activation techniques and are compared with values determined from infrared absorption measurements. The oxygen and carbon content of these crystals as determined from the activation analysis ranged from <0.05 to 28 ppm and <0.05 to 7 ppm, respectively. The infrared absorption measurements gave results that agreed with the activation analysis to within ~40%.

Infrared absorption spectrophotometry has been used to determine the oxygen and carbon content of monocrystalline silicon (1-3). This method is particularly attractive because it has a sensitivity in the ppba (parts per billion atomic) range and it is inexpensive, quick, and nondestructive. However, questions regard-

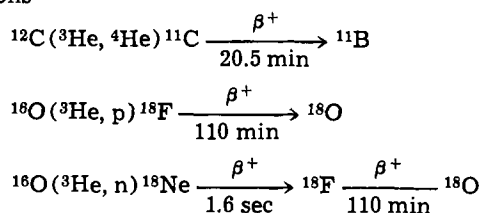
ing the accuracy of this technique for measuring the total oxygen and carbon content can arise because only interstitial oxygen and substitutional carbon, with absorption bands at 1130 and 607 cm^{-1} , respectively, can be detected. Agreement between results of IR spectrophotometry and charged particle activation analysis for oxygen determination has been reported to vary between near identical to a factor of 2 (4-6), while an agreement within 30% has been obtained among IR,

* Electrochemical Society Active Member.

Key words: activation analysis, spectroscopic analysis, infrared spectroscopy, carbon impurities, oxygen impurities, silicon purity, helium 3 ions, semiconductor silicon.

mass spectroscopy, and variation in lattice parameters for carbon (3). However, chemical methods do not correlate with IR measurements for carbon determination in silicon. The IR method indicates that carbon is present in semiconductor grade silicon in concentrations in the ppma range or less, while chemical methods indicate that carbon is always present in silicon in concentration greater than 50 ppma (7-14).

Because of the importance of the IR absorption method and the questioning of its accuracy, we felt that a systematic comparison of this method with a sensitive and precise method, such as activation analysis, for a wide range of oxygen and carbon contents was warranted. Activation with ^3He ion, utilizing the reactions



was chosen because sensitivity in the ppba for both oxygen and carbon can be obtained (4-6) at relatively low energies where interferences from spallation products are negligible (15).

Experimental Procedure

Sample preparation.—Pulled-crucible and float-zoned silicon single crystals, obtained from commercial sources, and specially prepared low oxygen-carbon and carbon-doped crystals were used in this study. The commercial crystals were representative of semiconductor-grade silicon used for transistor and nuclear detector manufacturing. The low oxygen-carbon crystals were obtained by float-zone refining of ultrapure polycrystalline deposited rods. A carbon-doped crystal was prepared by vacuum-zone refining a low oxygen-carbon crystal that was painted with a mixture of acetone and spectroscopic-grade graphite (3).

The crystals were cut into cylinders 2 cm in diameter, 1 cm thickness, and polished to a surface flatness of less than 2μ for IR measurements. Slices 2 mm thick, adjacent to those used in activation analysis, were similarly cut and polished and were used in the IR carbon content determination. A 1 min etch in a semiconductor grade HF:HNO₃ mixture was given to each sample prior to activation to clean the surfaces. Reference samples of oxygen and carbon with the same dimensions as the silicon samples were prepared from high-purity quartz and carbon.

Infrared measurements.—Measurements of the 1100 cm⁻¹ and 607 cm⁻¹ absorption bands due to interstitial oxygen and substitutional carbon, respectively, were made at room temperature using a Beckman IR-12 double-beam grating infrared spectrophotometer. Silicon crystals containing less than 50 ppba oxygen and 200 ppba carbon (as determined by activation analysis) and of the same thickness as the unknown samples were placed in the reference beam to suppress the silicon lattice bands particularly intense in the 607 cm⁻¹ carbon line region. Using this differential technique, only the differences in absorption due to the presence of impurities in the unknown samples are recorded. With 1 cm thick samples, the same as used in the activation analysis experiment, a 50 ppba detection limit at 300°K was achieved for the oxygen content determination.

For the carbon content determination, instead of using the same samples later tested by activation analysis, adjacent 2 mm thick polished silicon slices were used in the IR measurement. This was necessary since the strong two-phonon lattice band and reflectivity losses reduce the incident energy to about 5% of its initial value, leaving the instrument in an energy-limited condition. With extreme care, it was possible

to obtain an acceptable signal-to-noise ratio with a detection limit of 200 ppba at 300°K. For both impurities, measurement accuracy was better than 2% for concentrations in the range of 1 ppma or greater.

Calibration coefficients taken from the literature (1, 2) (1.1×10^{17} per cm³ for carbon and 4.5×10^{17} per cm³ for oxygen) were utilized in computing the oxygen and carbon content.

Activation analysis.—Activation of the samples was performed at the ORNL Asynchronous Cyclotron. Because of the difficulty of obtaining a low energy $^3\text{He}^+$ beam, an extracted 25.6 MeV $^3\text{He}^+$ beam was reduced to 16.6 MeV by the use of 27.4 mg/cm² of aluminum and 23.6 mg/cm² of silicon placed immediately in front of the sample. By removing 50 μ from the sample's irradiated surfaces, the energy was further reduced to 13.9 MeV, which was chosen to give near-optimum sensitivity without producing significant interference from reactions such as Si(^3He , X)C¹¹ and Si(^3He , X) ^{18}F . The beam was collimated to 1 cm in diameter immediately in front of the sample holder which was water cooled and electrically insulated from ground. An electrometer was used to measure and to integrate the beam intensity.

Each of the silicon samples was irradiated at an intensity of 1 μA for 1000 sec, while the standard samples were irradiated at 0.01 μA for 10 sec. Prior to counting, 50 μ of the silicon sample's irradiated surface was removed by grinding and etching to eliminate errors arising from surface contamination. Similarly, a 50 μ thick slice of silicon was placed in front of the reference samples during irradiation to correct for the removal of material from the silicon samples. In addition, the ^{30}P activity produced by $^{28}\text{Si}(^3\text{He}, \text{p})^{30}\text{P}$ of these slices was extrapolated back to the end of the irradiation time, and was used to determine whether errors were introduced in the beam-current measurements by the quartz sample, since it is an insulator. For purpose of comparison, several samples were activated twice.

A standard β^+ -pair spectrometer, using two 3×3 in. NaI(Tl) crystals and having window widths set from 0.40 to 0.55 MeV with a coincidence resolving time of 50 nanoseconds, was used to measure the ^{11}C and ^{18}F activity. A ^{22}Na source was used to calibrate the spectrometer. Recording of the sample's activity was not started until about 40 min after irradiation to allow the 2.5 min half-life activity of ^{30}P to decay to a level where there was negligible pile-up error. The coincidence count rate was recorded by a 400 channel multiscaler with a 1 min period per channel during the first 2 hr and then with a 10 min period per channel every hour for the next 8 hr. The β^+ activities of the reference samples were counted for a period of four times their respective reaction's half-lives. The impurity concentrations were then calculated by the usual comparison method (16).

In this method, the use of reference samples of quartz and carbon, containing a known amount of the same unknown atom species that were activated in the samples, established a reference datum which eliminated most of the errors associated with the determination of reaction cross section, detector geometry, and detector efficiency (16). Assuming equal isotopic distribution of impurities in both silicon and reference samples, and neglecting the small error associated with particle removal from the beam by competing nuclear reactions, the unknown atom concentration, N_x , was calculated from the formula

$$N_x = \frac{A_x \phi_s R_s \bar{\sigma}_s (1 - e^{-\lambda t_s}) e^{-\mu_s d_s}}{A_s \phi_x R_x \bar{\sigma}_x (1 - e^{-\lambda t_x}) e^{-\mu_x d_x}} N_s \quad [1]$$

where A is the β^+ activity at the end of the irradiation period, ϕ the intensity of the ^3He beam, R the range of the ^3He ions, $\bar{\sigma}$ the average reaction cross section, λ the decay constant, t the irradiation time, μ the attenuation coefficient for annihilation radiation, d the

Table I. Computed values of radiation cross sections for silicon, carbon, and quartz samples used in activation analysis

Material	Range of 13.5 MeV ^3He ion (g/cm 2)	Average cross section for ^{18}F production (millibarns)	Average cross section for ^{11}C production (millibarns)	Attenuation coefficients for 0.511 MeV gamma rays (cm 2 /g)
Silicon	0.0315	242	221	0.0870
Carbon	0.0249	—	243	0.0841
Quartz	0.0282	222	—	0.0841

sample thickness, and N_s the standard sample concentration of the atoms to be measured. The x and s subscripts refer to parameters associated with the silicon and standard samples, respectively. The average radiation cross sections were calculated by numerical integration (17, 18) using values taken from the literature (19-21). Their computed values for 13.5 MeV ^3He ions are given in Table I along with the ranges and the attenuation coefficients.

Results and Discussion

The β^+ activities as a function of time for three silicon samples containing 22 ppma of oxygen, 4.4 ppma of carbon, and less than 20 ppba of either oxygen or carbon are shown in Fig. 1. Activity data of this type were least-square fitted (using fixed half-lives of 2.5, 20.5, and 110 min for ^{30}P , ^{11}C , and ^{18}F , respectively) to determine the activity of each component and its associated statistical error at the end of the irradiation period. Substituting these values, along with those in Table I and other measured quantities (ϕ , t , d), into Eq. [1], the amounts of oxygen and carbon present in the silicon samples were calculated and are listed in Tables II and III. The corresponding impurity concentrations obtained by the infrared absorption measurements are also listed in Tables II and III. The detectable limit of 20 ppba for the activation analysis is based on twice the one coincidence/min background and on the measured count rate of 100 coincidences/min taken 1 hr after the end of the irradiation period. This corresponds to oxygen or carbon concentration of 1 ppma.

The values listed in Table II show that infrared spectrophotometry gives oxygen concentrations that

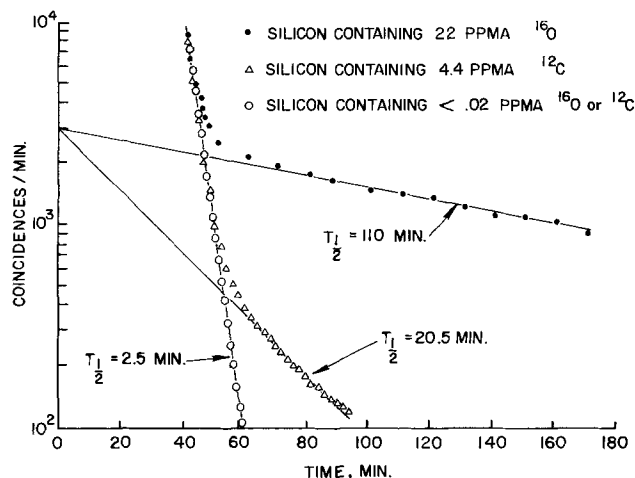


Fig. 1. Decay curves for activated silicon samples containing 22 ppma oxygen, 4.4 ppma carbon, and less than 0.02 ppma oxygen or carbon. (The 2.5 min half life is ^{30}P .)

are consistently 30% lower in the case of Czochralski-grown crystals, while for the float-zone crystals, neither method detected oxygen in concentrations greater than 50 ppba. The values listed in Table III show that infrared spectrophotometry gives carbon concentrations that are consistently higher than those obtained by activation analysis.

The difference in the results of the two methods is not thought to arise from errors in activation analysis for the following reasons: (i) surface contamination errors were completely eliminated by the removal of 50 microns of material from the irradiated surface (4); (ii) interference from such reactions as $\text{Si}(^3\text{He}, \text{X})^{11}\text{C}$, $\text{Si}(^3\text{He}, \text{X})^{18}\text{F}$, and $^{16}\text{O}(^3\text{He}, 2\alpha)^{11}\text{C}$ for 13.5 MeV ^3He ions were calculated to be negligible (15); (iii) the error associated with particle channeling has been shown to be insignificant (22); (iv) beam energy determination, etched layer thickness uncertainty, reference sample densities, and so forth were calculated to be no more than 10% for all samples; (v) interference arising from the possible presences of impuri-

Table II. Comparison of oxygen content in silicon as determined by activation analysis and infrared absorption techniques

Type	Resistivity (ohm-cm)	Growth method	Oxygen content (ppm)		Ratio $N_{\text{IR}}/N_{\text{ACT}}$
			Activation analysis	Infrared absorption	
N*	10	Czochralski	28 ± 0.2	20	0.71
P*	25	Czochralski	22 ± 0.1	16	0.73
N	4	Czochralski	2.4 ± 0.09	1.8	0.75
P	25	Czochralski	0.9 ± 0.05	0.6	0.66
N	55	Floating-Zone	<0.02	<0.05	—
N	13	Floating-Zone	0.04 ± 0.02	<0.05	—
P	20,000	Floating-Zone	<0.02	<0.05	—

* Samples which were activated twice or more.

Table III. Comparison of carbon content in silicon as determined by activation analysis and infrared absorption techniques

Type	Resistivity (ohm-cm)	Growth method	Carbon content (ppm)		Ratio $N_{\text{IR}}/N_{\text{ACT}}$
			Activation analysis	Infrared absorption	
N*	10	Czochralski	7.0 ± 0.3	9.1	1.30
N*	90	Floating-Zone†	4.4 ± 0.09	6.3	1.43
N*	13	Floating-Zone†	3.4 ± 0.08	4.8	1.41
P	20,000	Floating-Zone	0.7 ± 0.06	0.8	—
N	15	Floating-Zone	<0.05	<0.3	—
N	10	Czochralski	3.6 ± 0.1	4.8	1.33
N	10	Czochralski	0.9 ± 0.08	1.2	—

* Samples which were activated twice or more.

† Carbon doped.

ties such as Al, Na, N, Be, B, F, Ne, were thought to be insignificant either because of the technology involved in the silicon crystal refining or because of their high-threshold energy values; (vi) the counting statistics errors associated with those samples in Tables II and III which were used for comparison purpose were found to be less than 5%; (vii) the total experimental error as deduced from those samples that were irradiated two times or more, has been estimated to be less than 10% for the compared values.

The difference between results from IR and activation analysis then can be attributed to any one or to a combination of the following possibilities: (i) errors in published infrared absorption coefficients, (ii) infrared experimental errors arising from slit width dependence on narrow absorption peaks, (iii) inability of the IR method to detect impurities present in configurations other than those possessing known absorption bands, (iv) nonuniform distribution of the impurity atoms throughout the crystal.

For carbon, possibility (iii) is not plausible, since activation analysis results were consistently lower than the corresponding IR values, leaving (i), (ii), and (iv) as probable causes for the discrepancy. For oxygen, only possibilities (i) and (iii) appear to be the probable causes of the 30% difference between IR and activation analysis values, since (ii) and (iv) are not plausible because of the oxygen broad adsorption peak and the fact that activation on both sides of several samples yielded the same oxygen concentration within 10%, respectively.

In view of the above, we feel that the differences between the two methods are real and that the spectrophotometric method underestimates the carbon concentration by $29 \pm 15\%$ and overestimates the oxygen concentration by $37 \pm 15\%$.

The ranges of oxygen and carbon concentrations measured for the silicon crystals obtained from commercial sources are in general agreement with other activation analysis results (4, 5, 15, 23). However, the results obtained for the carbon content are in disagreement with chemical analysis results. The carbon content of the crystals analyzed was of the order of a few ppma or less, which is much smaller than the concentrations of 50 ppma or greater that have been measured by chemical methods. Because of the inherent reliability of the activation analysis method, it is felt that the chemical analysis techniques used to date grossly overestimate the carbon content in silicon.

Conclusions

Agreement between results obtained by infrared spectrophotometry and those obtained by the activation analysis method has been found to be consistent within $\sim 40\%$ in determining the oxygen and carbon impurities concentration in silicon. The carbon content of semiconductor grade silicon was found to be of the

order of a few ppma, which is in disagreement with chemical analysis results.

Manuscript submitted April 29, 1971; revised manuscript received Dec. 30, 1971.

Any discussion of this paper will appear in a Discussion Section to be published in the June 1973 JOURNAL.

REFERENCES

1. W. Kaiser, P. H. Keck, and C. F. Lange, *Phys. Rev.*, **101**, 1264 (1956).
2. R. C. Newman and J. F. Willis, *J. Phys. Chem. Solids*, **26**, 373 (1965).
3. J. A. Baker, T. N. Tucker, N. E. Moyer, and R. C. Buschert, *J. Appl. Phys.*, **39**, 4365 (1968).
4. G. I. Aleksandrova, A. M. Demidov, G. A. Kotel'nikov, G. P. Ploshakova, G. V. Sukhov, D. Ya. Choporov and G. I. Shmanenhova, *At. Energ. (USSR)*, **23**, No. 2, 106 (1967).
5. H. L. Rook and E. A. Schweikert, *Anal. Chem.*, **41**, 941 (1969).
6. E. A. Schweikert and H. L. Rook, *ibid.*, **42**, 1525 (1970).
7. M. Balkanski, W. Nazarewicz, and E. DaSilva, *Compt. Rend. Acad. Sci. (Paris)*, **251**, 1277 (1960).
8. L. Oucet and C. Cornet, "A New Method for the Determination of Microquantities of Carbon in Semiconductor," in "Ultrapurification of Semiconductor Materials," Boston, April (1961) The Macmillan Co., New York.
9. K. Sato, *Solid-State Electron.*, **7**, 743 (1964).
10. N. Schink, *ibid.*, **8**, 767 (1965).
11. W. Schroder, "Reinstoffprobleme," Vol. 1, p. 577, E. Rexer, Editor, Akademie-Verlag, Berlin (1966).
12. P. Rai-Choudhury and A. J. Noreika, *This Journal*, **115**, 68C, (1968).
13. E. Schuster and K. Wolleben, *Z. Anal. Chem.*, **240**, 175 (1968).
14. W. Bonsels and J. L. Lambert, in "Semiconductor Silicon," Rolf R. Haberecht and Edward L. Kern, Editors, pp. 89-96, The Electrochemical Society Softbound Symposium Series, New York (1969).
15. T. Nozaki, Y. Yatsurugi, and N. Akiyama, *J. Radioanal. Chem.*, **4**, 87 (1970).
16. D. M. Lee, C. V. Stanfacher, and S. S. Markowitz, *Anal. Chem.*, **42**, 994 (1970).
17. E. Ricci and R. L. Hahn, *ibid.*, **40**, 54 (1968).
18. P. Cziffra and M. J. Moravcsih, "A Practical Guide to the Method of Least Squares," UCRL-8523, Oct. 17, 1958.
19. S. S. Markowitz and J. D. Mahony, *Anal. Chem.*, **34**, 329 (1962).
20. D. R. F. Cochran and J. D. Knight, *Phys. Rev.*, **128**, 1281 (1962).
21. W. H. Barkas and M. J. Berger, "Tables of Energy Losses and Ranges of Heavy Charged Particles," NASA SP-3013 (1964).
22. E. Ricci, "Influence of Channeling in Customary ^3He Activation Analysis," Proc. Modern Trends in Activation Analysis, NBS Spec. Publ. 312, Vol. II, 785 (1969).
23. T. Nozaki, Y. Yatsurugi, and N. Akiyama, *This Journal*, **117**, 1566 (1970).

Origin of the High Resistance Region at the Epitaxial GaAs Layer-Substrate Interface

Fumio Hasegawa

Central Research Laboratories, Nippon Electric Company, Ltd., Kawasaki, Japan

ABSTRACT

In order to find the reason for the high resistance region which appears at the interface between a vapor-grown epitaxial GaAs layer and the substrate, epitaxial layers were grown by changing the substrate temperature or arsenic pressure in the reaction system. Heat-treatment of substrates was also examined under a hydrogen atmosphere or in a flow of GaCl/As₄/H₂. A high resistance layer occurred even when the growth was initiated after the reaction had reached a steady state. While mere heat-treatment in hydrogen changed the surface carrier density only slightly, the heat treatment in the flow of GaCl/As₄/H₂ changed the region within a few microns from the surface of undoped substrates to almost semi-insulating. The experimental results seem to indicate that the high resistance region is formed on GaAs surface or at the interface if the gas etching slightly overcomes the growth in a reaction system. Results of photoresponse and photoluminescence measurements on the high resistance region are also presented.

The epitaxial growth by the AsCl₃/Ga/H₂ vapor transport method is the most common and useful one for GaAs epitaxy. In that method, however, the auto-doping effect cannot be avoided if heavily Te- or S-doped substrates are used (1). On the other hand, when the substrate is Si- or Sn-doped, undoped, or Cr-doped semi-insulating, an anomalous high resistance region appears at the interface between the epitaxial layer and the substrate (2, 3).

The occurrence of this high resistance region is a basic problem in obtaining an epitaxial layer with a uniform doping profile and has been studied by many workers (2-10). But the problem has not entirely been solved as yet. The purpose of this paper is to clarify the origin of the occurrence of the high resistance region.

The occurrence of the high resistance region has been interpreted by either of the following two things: (i) formation of As vacancy or Si-As vacancy center due to arsenic deficiency at the beginning of the growth (2-7), (ii) impurity contamination at the interface due to improper cleaning or diffusion from the substrate (8-10). Wolfe *et al.* (2) have first found the problem in an epitaxial layer on a Si-doped substrate and attributed it to the amphoteric property of Si in GaAs. We have independently found (3, 4) the problem and attributed it to some defects formed at the interface during the initial stage of the growth. Recently, Shaw (5) has shown that when a Ga source covered with GaAs crust was heated in hydrogen, the crust dissolved in Ga and AsCl₃ supply of several minutes was necessary to recover the Ga source with crust. Some investigators (2, 6) have reported that the occurrence of the high resistance region could be suppressed by saturating the Ga source with arsenic or by adding excess arsenic pressure. These results seem to support the first reason. On the other hand, Blakeslee *et al.* (8) and Nakashima *et al.* (9) found the copper at the interface by the measurements of radioactive copper or photoluminescence. DiLorenzo *et al.* (10) have found Si, K, and many other impurities at the interface by a Direct Image Mass Analyzer, although its quantity (10²¹ cm⁻³) is deemed surprisingly large. But, distribution of impurities such as copper is generally influenced by the distribution of the defect (11), and hence, existence of impurities may be related with the defect formation.

In the present work, in order to avoid the deficiency of arsenic, the growth with the Ga source covered by

GaAs crust was tried. But the occurrence of the high resistance layer could not be eliminated. Furthermore, several phenomena which cannot be explained by arsenic vacancies were found. This paper will present such experimental results and give some speculations for the origin of the high resistance region. Some defects other than arsenic vacancy or Si at the As site seem to be necessary to interpret the achieved experimental results.

Experimental

Epitaxial layers of GaAs were grown by using the Ga/AsCl₃/H₂ vapor transport method (1). A schematic diagram of the growth apparatus is shown in Fig. 1. It has two zones. One is the main reaction zone in which the Ga source and the substrate are placed. The other is a zone where AsCl₃ is decomposed to arsenic metal and where the arsenic vapor pressure of the reaction system is controlled.

The epitaxial growth procedure is the same as the one previously reported (1) unless specially mentioned. When one wants to reduce the arsenic vapor pressure in the reaction system, the sliding furnace is placed apart from the main furnace as shown in Fig. 1, and AsCl₃ is decomposed at 860°C before it reaches the main reaction zone. The decomposed arsenic metal deposits at the low temperature region between the main furnace and the sliding furnace. To increase the arsenic vapor pressure, the temperature of the deposited arsenic metal is raised by the sliding furnace (400° ~ 450°C). Growth rate was reduced to less than half the normal growth rate when AsCl₃ was decomposed at 860°C before it reaches the main reaction zone.

In order to suppress the growth on the substrate until the reaction reaches a steady state, a special substrate holder having a cover was provided. This holder is shown in Fig. 2 and will be described in detail in the following section.

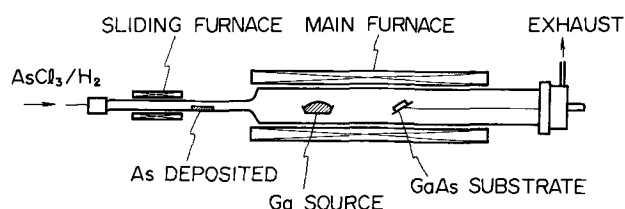


Fig. 1. Reaction system of GaAs vapor epitaxial growth. A sliding furnace is provided to decompose AsCl₃ before it reaches the main reaction zone.

Key words: GaAs, vapor growth, AsCl₃, carrier density profile, high resistance region, deep acceptor.

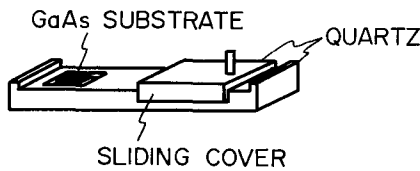


Fig. 2. A special substrate holder is provided in order to initiate growth after the reaction has reached a steady state; the holder is made of high purity quartz.

The carrier density profiles (net donor density profiles) were measured by the differential capacitance voltage method. In some cases, a plotting apparatus was used. Measurements of photoluminescence were performed by using excitation with a 50 mW He-Ne laser, a spectrometer (Spex 1702), and a detector with an RCA 7102 photomultiplier.

Experimental Results and Discussion

Initiation of growth under steady state.—Shaw (5) has reported that, when a Ga source covered with GaAs crust was heated to the operation temperature, a portion of GaAs crust dissolved into Ga and several minutes of $AsCl_3$ supply was necessary to completely recover the Ga liquid with GaAs crust. In order to initiate substantial growth on a substrate after a Ga source is completely covered with GaAs crust and the reaction has reached a steady state, a substrate holder made of high purity quartz as shown in Fig. 2 was prepared. On the top surface of the quartz plate, a small hollow in which the substrate is put is provided. The hollow can be closed tightly with a sliding cover which can be moved by a connecting rod from the outside of the reaction tube.

The growth procedure is as follows: The substrate is placed in the hollow. The temperature of the reaction system is elevated to growth temperature while the hollow is not covered. Then, the hollow is shut and $AsCl_3/H_2$ is admitted. After the reaction has reached a steady state, the cover is removed and growth on the substrate is begun. It was verified experimentally that the growth on the substrate was negligible while the hollow was covered.

Figure 3 shows doping profiles of the epitaxial layers grown by the method mentioned above, by changing the interval from the beginning of the flow of $AsCl_3$ to the beginning of the growth on the substrate (5, 10, 15 min). The used substrates are Si-doped and are from the same ingot. No correlation between the magnitude of the high resistance region at the interface

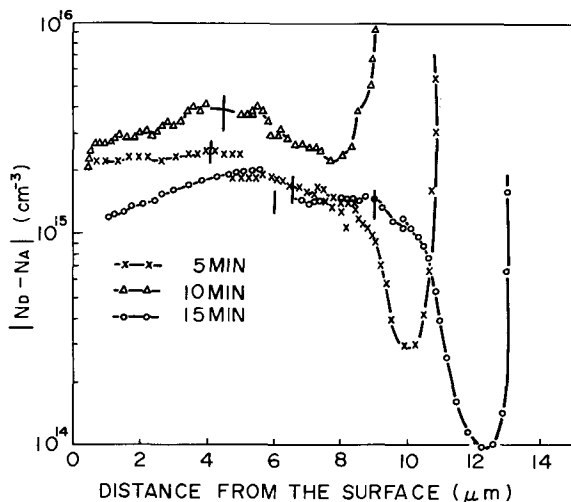


Fig. 3. Carrier density profiles of epitaxial layers grown by using the substrate holder shown in Fig. 2. The interval between the beginning of the flow of $AsCl_3/H_2$ and the beginning of the substantial growth on the substrate was changed. Substrates are heavily Si-doped.

and the interval the hollow is covered can be found in the figure. The same experiment was repeated several times, but no correlation could be found and the high resistance region could not be avoided. It has been reported (5) that the crust completely reformed in 5.3 min after $AsCl_3$ was admitted, even when the Ga source was heated for 30 min under hydrogen flow. Then, the above results seem to indicate that the high resistance region sometimes appears at the interface, even if the growth is initiated after the Ga source is completely covered with GaAs crust or the reaction has reached a steady state.

On the other hand, there is an experimental fact that the excessive pressure of arsenic can eliminate the occurrence of the high resistance region. In the next section, it will be shown that this experimental result does not necessarily imply that the deficiency of arsenic is the cause of the high resistance region.

Occurrence of a low resistance layer with excessive arsenic pressure.—Figure 4 shows the carrier density profile of an epitaxial layer grown on a Si-doped substrate by adding excessive arsenic pressure (about 3 mm Hg) from the beginning of growth as shown in the inset of Fig. 4. Instead of the high resistance region, a low resistance region is seen near the substrate in this sample as if the autodoping effect has occurred. The reason for the occurrence of this low resistance layer was thought at first to be the deficiency of Ga due to the excessive arsenic pressure (6). If this is the case, it seems that the carrier density in the whole region of the epitaxial layer shown in Fig. 4 should be greater than that of normally grown layers. But, the surface carrier density is not particularly greater than that of normally grown undoped layers.

In order to study the effect of arsenic pressure on the doping profile, the arsenic pressure of the reaction system was raised in the midst of growth. The resulting carrier density profile is shown in Fig. 5. The first half of the growth is carried out in a normal way and a high resistance layer appears near the substrate. From the mid point of the growth, the temperature of the arsenic zone was raised to 420°C, as shown in the inset of Fig. 5. A low resistance layer appeared only at the beginning of the temperature elevation of the arsenic zone, and the profile of that region resembled closely the one of the low resistance region seen in the epitaxial layer grown on a semi-insulating substrate with excessive arsenic pressure (6). This fact indicates that the appearance of the low resistance region is not peculiar to the beginning of growth, but is peculiar to the beginning of the temperature elevation of the arsenic zone. In addition, the agreement of the carrier density before and after the addition of excessive arsenic pressure seems to indicate that the

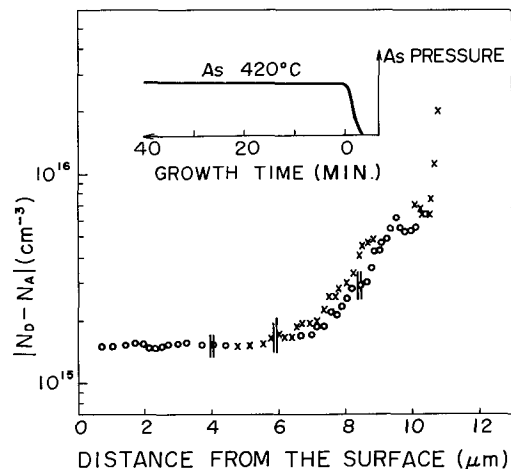


Fig. 4. Carrier density profile of the epitaxial layer grown with excessive arsenic pressure. The temperature of the arsenic zone was raised at the beginning of growth.

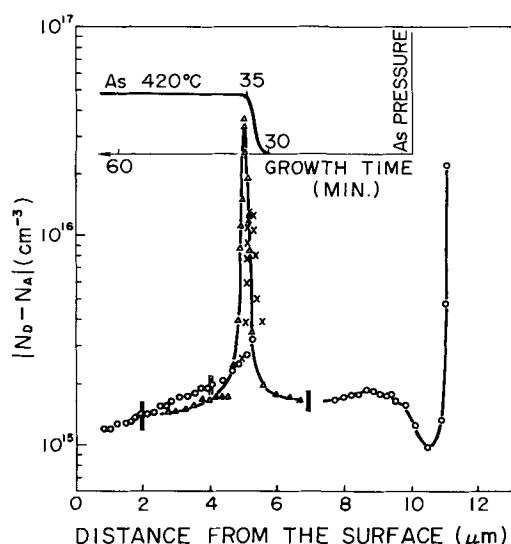


Fig. 5. Carrier density profile of the epitaxial layer grown with excessive arsenic pressure. The temperature of the arsenic zone was raised in the midst of growth as shown in the inset.

arsenic partial pressure itself does not greatly affect the carrier density of the grown layer.

If the occurrence of the high resistance region is due to the deficiency of arsenic, a high resistance region should appear even at the midst of a grown layer if the supply of arsenic is decreased. This was examined by decomposing AsCl_3 at 860°C with the sliding furnace shown in Fig. 1. The result is shown in Fig. 6. No high resistance region is seen at the point where the arsenic pressure of the reactor is lowered. (No high resistance region is seen even at the epitaxial layer-substrate interface in Fig. 6. This is due to the rough measurements of the interface, because the main concern is about the mid point of the epitaxial layer.) Another layer was grown also under low arsenic pressure, by decomposing AsCl_3 at 860°C before it reaches the main reaction zone during the growth period. The carrier density was almost the same as usual, although the growth rate was smaller than half the usual one. This fact also indicates that the carrier density is not directly controlled by the arsenic vapor pressure in the reaction system.

The occurrence of the low resistance layer shown in Fig. 5 can explain the following two facts without conflict: (i) Addition of excessive arsenic pressure could suppress the occurrence of the high resistance layer. (ii) The carrier density of the grown layer was not affected by the arsenic pressure. Disappearance of

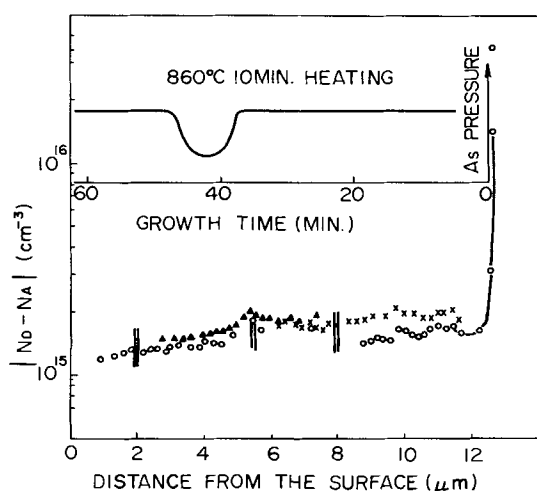


Fig. 6. Carrier density profile of the epitaxial layer which was grown by reducing the arsenic supply during growth as shown in the inset.

the high resistance region might be due to compensation of acceptors with the donors doped at the beginning of the heating of the arsenic zone, rather than due to the effect of the arsenic pressure.

Doping profiles obtained by changing the substrate temperature during growth.—The initiation of growth after the steady state of the reaction has been reached (or Ga source is completely covered with crust) seems to be a fascinating method to avoid the occurrence of the high resistance region. This was examined by changing the substrate temperature instead of using the special substrate holder mentioned previously. The substrate temperature was maintained at 800° or 850°C at the beginning of the growth (source temperature was 850°C). After AsCl_3 had flowed for 5 min, the substrate temperature was slowly lowered to 750°C . The resulting doping profiles are shown in Fig. 7 (The substrates are Si-doped). Growth rate decreased rapidly when the substrate temperature was above 800°C (5), and no growth or slight gas etching occurred at 850°C . Therefore, growth must begin after the reaction has reached a steady state (without deficiency of arsenic), when the substrate temperature is lowered from 800° or 850°C . But both of the doping profiles have a dip in the carrier density profile at the interface, in addition to a low resistance layer which is due to a higher substrate temperature than usual [carrier density increases with increase of the substrate temperature (12)]. The dip in the carrier density profile was larger when the substrate was lowered from 850° rather than from 800°C .

In order to clarify the effect of substrate temperature on the occurrence of the dip in the carrier density profile as seen in Fig. 7, the substrate temperature was changed in the mid point of the growth. The doping profiles of the grown layers are shown in Fig. 8. The substrate temperature was changed as shown in the inset of the figure (source temperature was 830°C in this case). When the substrate temperature was raised to 800°C (dotted line), only a low resistance layer was seen. But, when the substrate temperature was raised to 830°C (the same as the source temperature), a dip in carrier density profile (or a high resistance layer) appears in addition to the low resistance layer, similar to the profiles shown in Fig. 7. These facts also indicate that the occurrence of the dip in the carrier density profile as seen in Fig. 7 or Fig. 8 is due neither to the deficiency of arsenic nor to contamination with impurities.

The occurrence of the high resistance layer seen in Fig. 7 and 8 can be understood if it is presumed that the high resistance layer occurs when a substrate is heat-treated under the condition that the gas etching

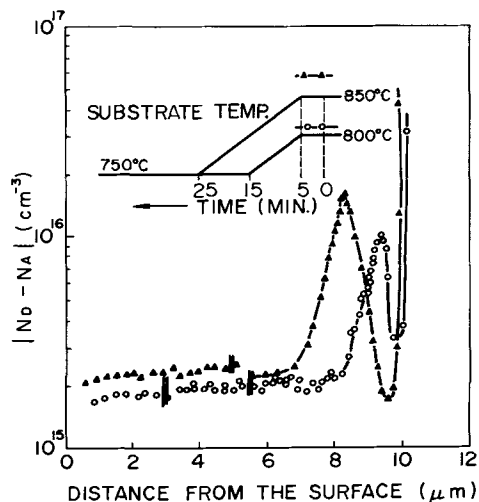


Fig. 7. Carrier density profiles of the epitaxial layers grown by changing the temperature of the substrate at the initial stage of growth as shown in the inset.

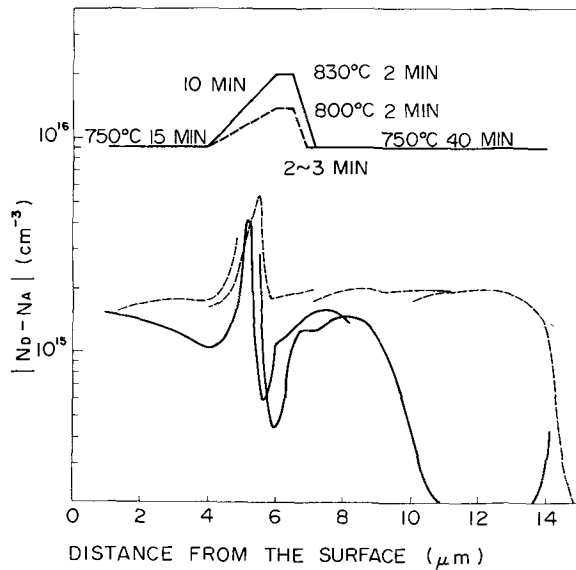


Fig. 8. Carrier density profiles of the epitaxial layers grown by changing the substrate temperature in the midst of growth as shown in the inset.

slightly overcomes the growth (this is further considered in the next section). In Fig. 8, only a low resistance layer appeared when the substrate temperature was raised to 800°C. In this case, no gas etching occurred. On the other hand, when the substrate temperature was raised to 830°C, the same as the source temperature in this case, a slight gas etching occurred and a high resistance layer would appear [the gas etching was examined by covering a portion of a substrate surface with a small quartz plate (1)]. The reason for the appearance of the high resistance layer when the substrate temperature is lowered from 800°C shown in Fig. 7 is not well understood, but a slight gas etching might occur at initial stage of reaction when arsenic is absorbed by a Ga source (5) and substantial growth is inhibited.

Change of surface carrier density by heat treatment in GaCl/As₄/H₂ or in H₂.—As described in the previous section, it is quite probable that the occurrence of the high resistance region is associated with slight gas etching. But no change in surface carrier density is observed when normal gas etching is performed. In order to clarify the phenomena at the state when growth balances with the gas etching, a heat treatment was carried out in a flow of GaCl/As₄/H₂.

Undoped bulk GaAs with a carrier density of about $1.3 \times 10^{16} \text{ cm}^{-3}$ was used. The sample was placed on the substrate holder in the epitaxial growth tube with a Ga source saturated with As. The sample was heat-treated in a flow of AsCl₃/H₂ (therefore, GaCl/As₄/H₂) or of only hydrogen (200 cc/min). The temperatures of the Ga source and of the substrate were 850°C. The surface carrier density profiles after the heat-treatment for 30 min in a hydrogen atmosphere are shown in Fig. 9. Sample VEF-10-4 (▲) was heat-treated without the Ga source and in a just washed reaction tube. The other two samples (VEF-10-11, VEF-8-4) were heat-treated with Ga source and after several epitaxial growths. The carrier density of the former sample was clearly decreased at the surface as reported by Muñoz *et al.* (13). But the change in the carrier density was found within only about 1.0 μm from the surface. Decrease of the surface carrier density in the other two samples is not clear. This may be due to suppression of arsenic evaporation from the surface of the sample because of the existence of the Ga source saturated with arsenic and deposited GaAs or As. These facts indicate that the surface carrier density of the substrate is not greatly changed before growth in the usual epitaxial growth procedure.

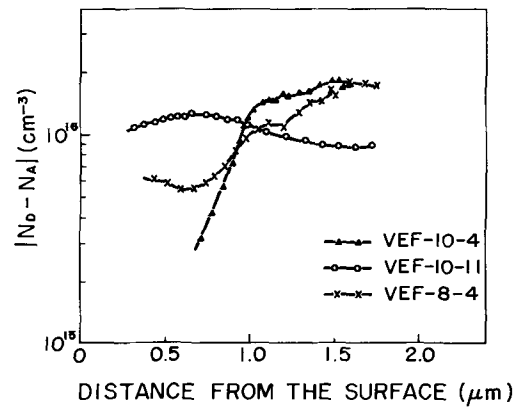


Fig. 9. Surface carrier density profiles of undoped bulk GaAs heat-treated in a hydrogen atmosphere at 850°C for 30 min. VEF-10-4, without Ga source; VEF-8-4 and VEF-10-11; with Ga source saturated with arsenic.

When the heat-treatment was performed with the flow of AsCl₃/H₂, the surface of the sample changed to almost semi-insulating in contrast to the case of the heat-treatment in hydrogen. The representative surface carrier density profiles are shown in Fig. 10. One (shown by ○) was heat-treated for 30 min in the flow of GaCl/As₄/H₂, and the other (indicated by ▲) is the one heat-treated in hydrogen for about 15 min after the same heat-treatment in the flow of GaCl/As₄/H₂. It was confirmed that a slight gas etching occurred during the heat-treatment and, when the etched layer was thick the surface high resistance layer was thin. Since the drastic change of the surface carrier density occurred in the atmosphere of GaCl/As₄/H₂ (precisely speaking, GaCl, GaCl₃, HCl, As₄, and H₂) and under a slight gas etching, it is reasonable to think that Ga was removed from the GaAs surface in a fairly high arsenic partial pressure and some defect, for example, such as Ga vacancy, was formed at the surface. Muñoz *et al.* (13) also reported that, when a sufficient arsenic pressure was applied during the heat-treatment, surface carrier density was decreased due to formation of Ga vacancy.

The surface carrier density of the sample VEF-8-5 (indicated by ▲) is higher than other's and the surface high resistance region is thicker. This seems to be due to evaporation or arsenic from the surface and diffusion of the defects into the substrate by the further 15 min of heat-treatment in hydrogen.

Since the surface high resistance layer was thin when the etched depth was large, the fact that there

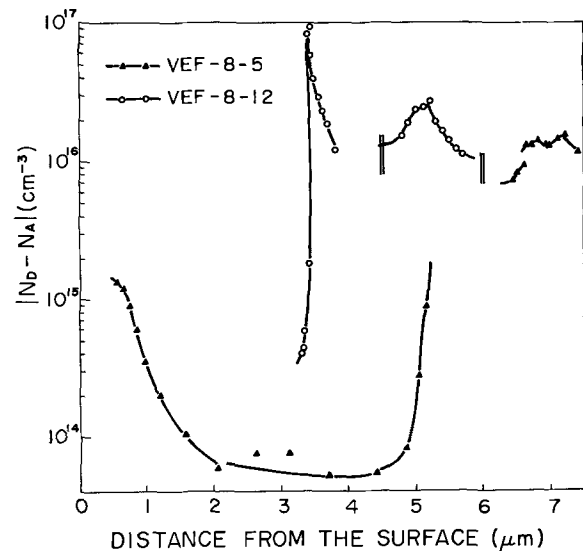


Fig. 10. Surface carrier density profiles of undoped bulk GaAs heat-treated in the flow of GaCl/As₄/H₂ at 850°C for 30 min.

was no formation of the surface high resistance layer by a normal gas etching must be due to the speed of gas etching being higher than the diffusion speed of the defects. But, when the reaction at the substrate is changed from gas etching to growth, the gas etching balances with the growth at some moment, and at that time, acceptors related to the defects may be induced to form a high resistance layer. In a usual growth procedure, too, a slight gas etching might occur while arsenic is absorbed in the Ga source (5) and substantial growth is inhibited. This way of thinking can explain two experimental results (4, 14, 15) which could not be explained hitherto. One is the high resistance layer found in the substrate. We have reported (4) that a high resistance layer appeared inside the substrate when a doped thin epitaxial layer was grown on an undoped substrate. The other is difference of the effect of gas etching among different investigators. When the reaction is slowly moved from gas etching to growth, the high resistance layer appears at the interface (2, 3). But Hirao *et al.* (14) and Nozaki *et al.* (15) have reported that the appearance of the high resistance layer was suppressed by a special way of gas etching. Each way differs in the transition speed from gas etching to growth. In the former way, gas etching balances with growth for a while due to a slow transition. In the latter way, the transition must be too fast for the defect to appear.

Photoresponse and photoluminescence of the surface high resistance layer.—In previous investigations (6, 16), deep energy levels of 0.5–0.6 eV above the valence band have been found in the high resistance region at the epitaxial layer substrate interface from measurements of photoresponse, capacitance, or Hall constant. Photoresponse due to similar deep centers was found in the high resistance layer at the surface as shown in Fig. 10. Such deep centers that were considered to be the cause of the high resistance layer were not observed by photoluminescence measurements.

The photoresponse measured on a reverse current of a Schottky barrier made on the surface high resistance layer is shown in Fig. 11. A broad response around 1300 m μ is observed in addition to the response of band to band transition. This result implies that many deep centers of about 0.5 eV above the valence band exist in the high resistance layer. A dotted line shows photoresponse of a Schottky barrier on an etched surface from which the high resistance layer has been removed. Extrinsic photoresponse as large as the one observed on the high resistance layer is not observed. Therefore, the extrinsic photoresponse shown by the solid line is peculiar to the surface high resistance layer, and the deep centers of about 0.5 eV above the valence band edge must be the acceptor centers in-

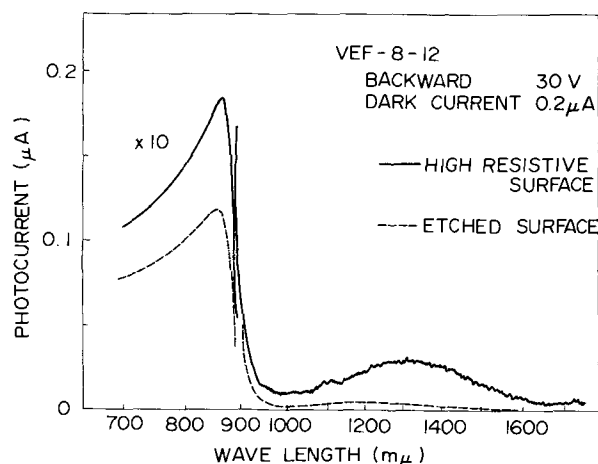


Fig. 11. Photoresponse for the reverse current of Schottky barrier diodes; solid line—Schottky barrier on the high resistive surface as shown in Fig. 10; dotted line—Schottky barrier on an etched surface.

duced on the surface. (These deep centers are obviously not the ones due to Si at the As site.)

The extrinsic photoresponse shown in Fig. 11 is quite similar to that of the high resistance region at the epitaxial layer-substrate interface [see Fig. 11 of Ref. (16)]. Therefore, the acceptors in the surface high resistance layer are probably the same as the acceptors in the high resistance region at the epitaxial layer-substrate interface.

Measurement of photoluminescence spectra is generally a convenient method to determine the energy level in semiconductors. Nakashima and Hirao (9) have observed a peak of 1.36 eV due to Cu_{Ga} at the grown layer-substrate interface, and they attributed the problem to the contamination of the substrate surface with copper. On the other hand, Iwasaki and Sugibuchi (7) have made the same measurement, and have found the peak of 1.40 eV peculiar to the interface, and they attributed the problem to a Si-As vacancy complex.

In order to find the acceptor levels in the surface high resistance region, photoluminescence spectra were measured in this study too. Results are shown in Fig. 12. Samples are from undoped bulk GaAs ($n \sim 1.3 \times 10^{16} \text{ cm}^{-3}$). One is as grown, another (VEF-8-6) is the one heat-treated in hydrogen at 850°C for 30 min and whose surface carrier density is little changed. Still another (VEF-8-12) is the one heat-treated in the flow of $\text{GaCl}/\text{As}_4/\text{H}_2$ and whose surface is almost semi-insulating as shown in Fig. 10. As-grown GaAs shows a peak of 1.36 eV due to the first level of Cu_{Ga} acceptors, in addition to the band edge emission. For the sample (VEF-8-6) heat-treated in hydrogen, a strong peak appears at 1.40 eV, which can be attributed to a Si-As vacancy complex. (The amplitude is scale reduced to one twentieth in this spectrum for ease of comparison with the others.) On the other hand, the sample (VEF-8-12) heat-treated in the flow of $\text{GaCl}/\text{As}_4/\text{H}_2$, shows very weak photoluminescence over the wavelength range measured.

Since the surface carrier density was only slightly decreased by heat-treatment in hydrogen, centers for the peak at 1.40 eV do not seem to be responsible for the surface high resistance layer shown in Fig. 10. From the fact that the surface high resistance layer shows only very weak photoluminescence, the acceptor centers responsible for the surface high resistance layer should be nonradiative or be too deep to be observed in the photoluminescence measurement. This result agrees with the fact that an extrinsic photoresponse appears around 1300 m μ in a reverse current of a Schottky barrier formed on the high resistance layer.

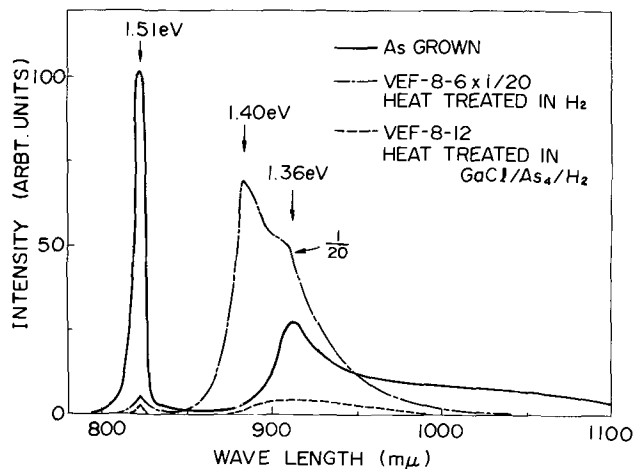


Fig. 12. Photoluminescence spectra of the surface of heat-treated GaAs. Solid line—As-grown bulk GaAs, VEF-8-12—heat-treated in a flow of $\text{GaCl}/\text{As}_4/\text{H}_2$, VEF-8-6—heat-treated in a flow of hydrogen.

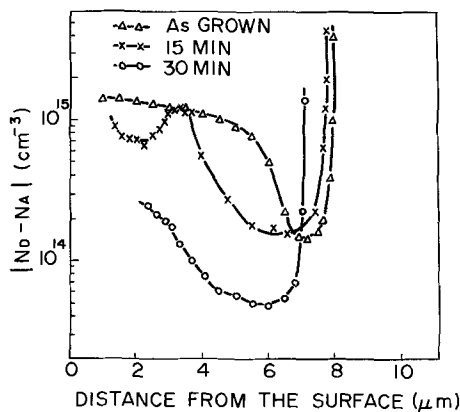


Fig. 13. Change of the high resistance region by a heat-treatment

Since the substrate is unintentionally heat-treated before growth, a photoluminescent peak of 1.40 eV may be found at the interface (7). The distribution of substitutional copper is affected by the Ga vacancy distribution (11), and hence the peak attributable to copper (9) or copper itself (8) may be found at the interface. But these seem to be not the real reason for the high resistance region from the facts shown in this study.

Change of the high resistance region by heat-treatment.—Effect of a heat-treatment on the dip in the carrier density profile was studied in order to see the diffusion of acceptors in the high resistance region. Figure 13 shows the carrier density profiles of an epitaxial layer before and after heat-treatment at 850°C for 15 min or at 850°C for 30 min. The high resistance region spreads with the heat-treatments. The diffusion constant of the acceptors was estimated to be about 10^{-11} cm²/sec \sim 10^{-10} cm²/sec from the profiles in Fig. 13, if the profile of the diffused impurities was assumed to be a complementary error function. Muñoz *et al.* (13) estimated the diffusion constant of the acceptors induced at the surface by a heat-treatment to be about 10^{-12} cm²/sec for P_{As} (arsenic pressure) \geq 50 Torr and about 10^{-10} cm²/sec for $P_{As} <$ 50 Torr. These values are considered to be comparable to ours if one considers the relatively low accuracy of the measurements and the derivation. Diffusion speed of the acceptors induced at the surface by the heat treatment with GaCl/As₄/H₂ shown in Fig. 10 is the same order of magnitude as the one derived from Fig. 13.

Summary

Occurrence of the high resistance layer in epitaxial GaAs has been interpreted hitherto by (i) arsenic vacancies or Si at the As site (2-7), or by (ii) impurity contamination (8-10).

In the present paper, several experimental results that cannot be explained by the above two reasons

were shown: (i) The high resistance layer appeared even when the growth was initiated after the reaction has reached a steady state. (ii) A high resistance layer occurred even within the grown layer when growth is slightly overcome by gas etching during the growth. (iii) The surface of undoped GaAs was changed to almost semi-insulating by a heat treatment in a flow of GaCl/As₄/H₂. (iv) Deep energy levels in the surface high resistance layer were about 0.5 eV above the valence band (the same as the one at the interface).

From these results, the occurrence of the high resistance layer presented here is considered to be due to formation of some defect, such as Ga vacancy, which might appear on the surface of the substrate when growth is balanced with or is slightly overcome by gas etching. This way of thinking can explain some of the phenomena that has not been explained hitherto.

Acknowledgments

The author wishes to thank S. Kikuchi for giving various facilities in the epitaxial growth, H. Iwasaki for his help in the measurement of photoluminescence, and T. Saito, Y. Seki, and K. Sekido for their stimulating discussions on this subject.

Manuscript submitted Sept. 24, 1971; revised manuscript received Feb. 5, 1972.

Any discussion of this paper will appear in a Discussion Section to be published in the June 1973 JOURNAL.

REFERENCES

1. F. Hasegawa and T. Saito, *Japan. J. Appl. Phys.*, **7**, 1342 (1968).
2. C. M. Wolfe, A. G. Foyt, and W. T. Lindley, *Electrochem. Technol.*, **6**, 208 (1968).
3. F. Hasegawa and T. Saito, *Japan J. Appl. Phys.*, **7**, 1125 (1968).
4. F. Hasegawa and T. Saito, *ibid.*, **7**, 1540 (1968).
5. D. W. Shaw, *J. Cryst. Growth*, **8**, 117 (1971).
6. T. Saito and F. Hasegawa, *Japan. J. Appl. Phys.*, **10**, 197 (1971).
7. H. Iwasaki and K. Sugibuchi, *Appl. Phys. Letters*, **18**, 420 (1971).
8. A. E. Blakeslee and J. E. Lewis, Paper 121 presented at Electrochem. Soc. Meeting, New York, May 4-9, 1969.
9. H. Nakashima and M. Hirao, *Japan. J. Appl. Phys.*, **9**, 1495 (1970).
10. J. V. DiLorenzo, R. B. Marus, and R. Lewis, *J. Appl. Phys.*, **42**, 729 (1971).
11. R. N. Hall and J. H. Racette, *ibid.*, **9**, 379 (1970).
12. J. V. DiLorenzo and A. E. Machala, Paper 177 presented at Electrochem. Soc. Meeting, Cleveland, Ohio, Oct. 3-7, 1971.
13. E. Munoz, W. L. Snyder, and J. L. Moll, *Appl. Phys. Letters*, **16**, 262 (1970).
14. M. Hirao and H. Nakashima, Proc. 2nd Conf. on Solid State Devices, Tokyo, 1970, p. 46.
15. T. Nozaki and T. Saito, *Japan. J. Appl. Phys.*, **11**, 110 (1972).
16. F. Hasegawa, *ibid.*, **9**, 639 (1970).

Preparation and Properties of Nonheat-Treated Single Crystal Cu_2S -CdS Heterojunctions

P. F. Lindquist¹ and R. H. Bube

Department of Materials Science, Stanford University, Stanford, California 94305

ABSTRACT

The photoelectronic properties of single-crystal Cu_2S -CdS heterojunctions have been investigated. The heterojunctions were formed on the A or B faces of conducting CdS single crystals by dipping in a cuprous chloride solution at 75°C. No separate heat-treatment was given. The cells typically had monochromatic quantum efficiencies greater than 10% in the region 0.5-0.9 μ . The photoresponse is due to carrier pair generation in the Cu_2S , with transfer of electrons across the interface into the CdS. The forward current at and below room temperature is dominated by tunneling of electrons through interface states. A general band diagram of the heterojunction is discussed. Consistent differences in the behavior of A and B face samples were noted with respect to the growth kinetics of the Cu_2S , the maximum photovoltage at 300°K, the I-V characteristics, and the junction capacitance. The effect of uniaxial stress on the capacitance of A and B face samples suggests a piezoelectric mechanism.

The Cu_2S -CdS p-n heterojunction has been the subject of a considerable research effort over the past decade because of its promise as an efficient thin-film solar cell. At present, these cells typically produce 0.5V on open circuit and 20 mA/cm² on short circuit in sunlight, with efficiencies in the range 5-8%. The history of the development of the thin-film Cu_2S -CdS cell has been summarized by Shirland (1).

Numerous investigations have attempted to clarify the mechanism of the photoresponse of the Cu_2S -CdS junction, particularly the "extrinsic" response at wave lengths longer than the CdS band edge. Mechanisms proposed to account for this photoresponse include: a postulated p-n homojunction in the CdS with an impurity band of copper centers (2), generation of holes in the CdS at native imperfections (3, 4) or at diffused-in impurity centers (5, 6), and absorption in the Cu_2S with transfer of photoexcited electrons into the CdS (7-13). The latter process is now thought to account for the major portion of the photoresponse of relatively efficient cells.

The thin-film Cu_2S -CdS cells require a postfabrication heat-treatment to develop the maximum efficiency. This heat-treatment also gives rise to transient and secondary-light-source effects in the photoresponse which are not observed in the nonheat-treated junctions (13). These effects, also observed in heat-treated single-crystal cells, have been attributed to the trapping of holes in deep centers in the CdS depletion region near the junction (13).

This paper is concerned with the properties of Cu_2S -CdS heterojunctions fabricated from single crystals of CdS, with no heat-treatment after formation of the junction. These devices did not exhibit the transient effects mentioned above. It is shown that relatively efficient single-crystal cells can be produced without the heat-treatment step. The heterojunctions were formed on either the A or B basal plane of the CdS. While the basic properties of the cells were similar for the two orientations, certain consistent differences attributed to the polarity of the CdS structure were observed. These differences are discussed, and a model for the photovoltaic behavior of the heterojunction is described.

Experimental

Fabrication of heterojunctions.—The Cu_2S -CdS heterojunctions were formed by immersing single crystals of CdS in a saturated aqueous solution of cuprous chloride at 75°C for times ranging from 2 to 8

hr. The CdS was thereby converted to Cu_2S by a displacement reaction, the thickness of the Cu_2S increasing with time in the solution. The CdS crystals, grown by sublimation in a moving temperature gradient, had an average resistivity of 1 ohm-cm. The high conductivity was a consequence of nonstoichiometry; no intentional impurities were added.

Rectangular bars approximately 1 × 5 mm in area and 0.5-1 mm thick were cut from the CdS crystals. The large faces were normal to the c-axis within about 5° as determined by x-ray back-reflection Laue patterns. The A face [Cd, (0001)] and B face [S, (0001)] were distinguished by etching in concentrated HCl (14). These faces were mechanically polished with 0.3 μ alumina on silk. Ohmic indium contacts were diffused at both ends of the crystal, on the face opposite the one subsequently dipped in the CuCl solution. The face to be dipped was either left in the as-polished condition or was etched for 2 min in a solution of KMnO_4 in sulfuric acid at room temperature (15).

The crystal bars to be dipped were mounted on glass slides with black wax so that only the top surface of each crystal was exposed to the solution. The solution consisted of 0.2M CuCl, 0.2M $\text{NH}_2\text{OH} \cdot \text{HCl}$ (hydroxylamine hydrochloride), and 0.5M KCl in water, to which several drops of dilute HCl were added to give an initial pH of about 3. The hydroxylamine hydrochloride inhibited the oxidation of the cuprous ions to the cupric state, and the KCl increased the solubility of the CuCl by promoting the formation of complex ions (16).

The barrier-forming displacement reaction was carried out in a 500 ml Pyrex crystallizing dish, sealed with an argon atmosphere over the solution to inhibit oxidation. The dish was placed in a drying oven, the temperature of which was maintained at 75° ± 1°C for the required time. The reacted crystals were then removed from the solution, demounted from the glass slides, rinsed with TCE, acetone, distilled water and methanol, dried and stored in a dessicator until ready for measurements. The samples discussed in this paper were not given a heat-treatment after formation of the junction.

Measurements.—I-V characteristics were recorded on Polaroid film using a Tektronix Type 575 transistor curve tracer. Point-by-point measurements of the dark forward and reverse characteristics over at least 5 decades of current were also made.

The spectral response of photocurrent and photovoltage was measured using a Bausch and Lomb grating monochromator with a tungsten ribbon light source. The slits were set to give a dispersion of 6.6 μm . The

¹ Present address: Hewlett-Packard Laboratories, Palo Alto, California 94300.

Key words: photovoltaic, heterojunction, Cu_2S -CdS, capacitance, piezoelectric.

output of the monochromator was focused on the sample with a condensing lens and was incident on the junction through the CdS. The edges of the samples were masked with black wax to minimize absorption of noncollimated light. The light intensity at the sample position was measured as a function of wavelength with a Perkin-Elmer thermopile. The spectral response data were normalized to the photon flux at 600 mμ, which was 5.8×10^{14} photons/cm²-sec, with an estimated uncertainty of $\pm 20\%$.

The intensity dependence of photovoltage and photocurrent were measured using a beam of unfiltered tungsten light of integrated intensity 280 mW/cm² (hereafter referred to as intensity I_0) with a series of neutral density filters.

The short-circuit photocurrent was measured with a Keithley 149 microvoltmeter across a 1% 100 ohm resistor in series with the sample. The open-current photovoltage was measured with a Keithley 610A electrometer (input impedance of 10^{14} ohms).

Measurements of the junction capacitance as a function of bias voltage were made with a Boonton 75-D capacitance bridge with a 77-2A range extender. The operating frequency of the bridge was 1 MHz with a signal level of about 20 mV peak to peak. Bias voltage was supplied by an external source.

The temperature dependence of the dark I-V characteristics and the photoresponse in white light were measured with the samples mounted in an evacuated chamber at the end of an Air Products Cryo-Tip cooling device operating on the Joule-Thomson principle. Photocapacitance measurements, the results of which are reported elsewhere (17), were also performed using this apparatus.

Capacitance-voltage curves were measured at room temperature for two samples under uniaxial stress. The stress was applied by means of a steel plunger which passed through two guides and rested in a copper block which contacted the crystal. The stress was parallel to the plane of the junction, in the direction of the CdS a-axis.

Results

Growth characteristics of the Cu₂S layer.—The Cu₂S layer was observed to form more rapidly on the A face of CdS than on the B face by about a factor of three. The layer thickness was measured optically using a micrometer stage and a filar eyepiece. The thickness was generally uniform over the sample area. Figure 1 shows thickness vs. time at the reaction temperature of 75°C for the two crystal faces. The thickness varies as t^n , with n slightly greater than unity, in both cases.

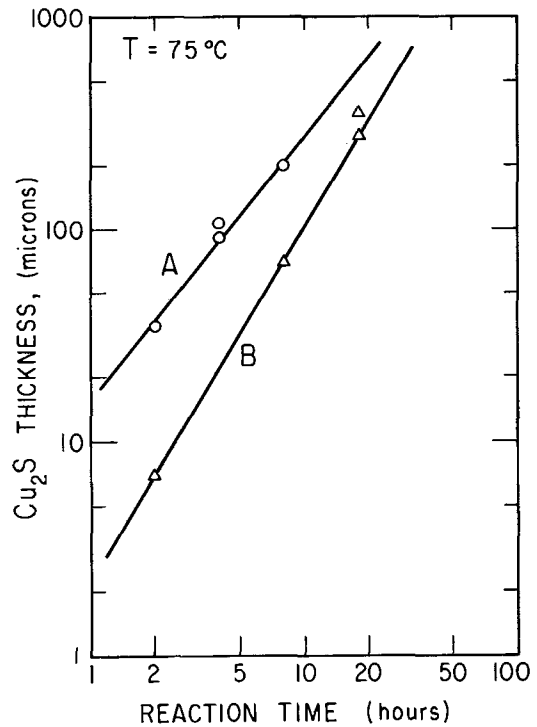


Fig. 1. Thickness of Cu₂S layer as a function of dipping time at 75°C for A and B faces of CdS.

The nearly linear time dependence suggests that the growth rate is controlled by the interface reaction rather than by diffusion through the Cu₂S layer, for which thickness proportional to the square root of time would be expected. Microscopic examination of the Cu₂S layers revealed numerous cracks perpendicular to the interface, which permitted continual passage of the cuprous ion solution to the CdS. The grown layers were confirmed to be primarily Cu₂S (chalcocite) by x-ray powder patterns.

Four-point probe measurements on a number of Cu₂S layers grown from CdS in aqueous solution gave p-type resistivities in the range 6×10^{-4} to 3×10^{-3} ohm-cm. This corresponds to a range in hole density of 10^{21} to 2×10^{20} cm⁻³, assuming a mobility of 10 cm²/V-sec (18).

Diode characteristics.—Figure 2 gives Polaroid traces of the dark and light-generated I-V curves for two

Table I. Summary of properties of Cu₂S-CdS heterojunctions prepared from 1 ohm-cm CdS

Sample	Cu ₂ S thickness, μ	$t_{Cu_2S}/t^{(a)}$	Geometrical area, cm ²	$J_{sc}^{(b)}$ mA/cm ²	$V_{oc}^{(b)}$ mV	R_s , ohms	C/A , ^(c) 10 ⁴ pf/cm ²	G/A , ^(c) 10 ⁵ μV/cm ²
2-A (P)	35	0.062	5.20×10^{-2}	6.73	450	13.7	6.70	1.30
2-A (P + E)	35	0.068	5.33	6.20	455	8.6	6.14	1.26
2-B (P)	10	0.014	7.61	5.58	470	8.2	5.38	0.91
2-B (P + E)	10	0.012	7.28	6.18	475	5.8	5.32	0.61
4-A (P)	93	0.101	3.38	4.00	420	7.0 ^(d)	8.37	1.96
4-A (P + E)	108	0.212	6.40	4.45	400	7.0 ^(d)	7.64	1.94
8-A (P)	199	0.221	4.29	3.62	400	5.7	12.15	0.56
8-A (P + E)	210	0.261	3.49	3.15	400	5.3	11.88	0.76
8-B (P)	68	0.124	4.22	5.45	445	5.0	4.80	0.31
8-B (P + E)	69	0.093	4.36	4.35	465	5.9	4.16	0.23

Sample	J_0 , 10 ⁻⁸ A/cm ²		ψ , V		Low voltage		High voltage	
	Low V	High V	I-V	C-V	α , ^(e) V ⁻¹	η ^(f)	α , V ⁻¹	η
2-A (P)	—	0.96	0.62	0.4	—	—	29.1	1.3
2-A (P + E)	1030	6.2	0.9	0.5	10.7	3.6	24.8	1.55
2-B (P)	5.5	0.18	0.7	0.7	20.2	1.9	29.9	1.3
2-B (P + E)	9.2	0.14	0.68	0.7	16.5	2.3	31.1	1.2
4-A (P)	—	3.0	—	0.3	—	—	27.4	1.4
4-A (P + E)	—	47	—	0.25	—	—	23.5	1.6
8-A (P)	93	7.7	0.65	0.6 ^(g)	19.2	2.0	26.8	1.4
8-A (P + E)	—	8.6	0.65	0.6 ^(g)	—	—	24.2	1.6
8-B (P)	130	3.8	0.8	0.7	11.9	3.2	24.0	1.6
8-B (P + E)	920	3.2	0.7	0.8	11.3	3.4	24.8	1.55

(a) $t = t_{Cu_2S} + t_{CdS}$.
 (b) White tungsten light, 280 mW/cm².
 (c) Corrected for series resistance.
 (d) Assumed value.
 (e) Forward characteristic exp (αV).
 (f) Forward characteristic exp ($qV/\eta kT$).
 (g) From extrapolation of $1/C$, not $1/C^2$.

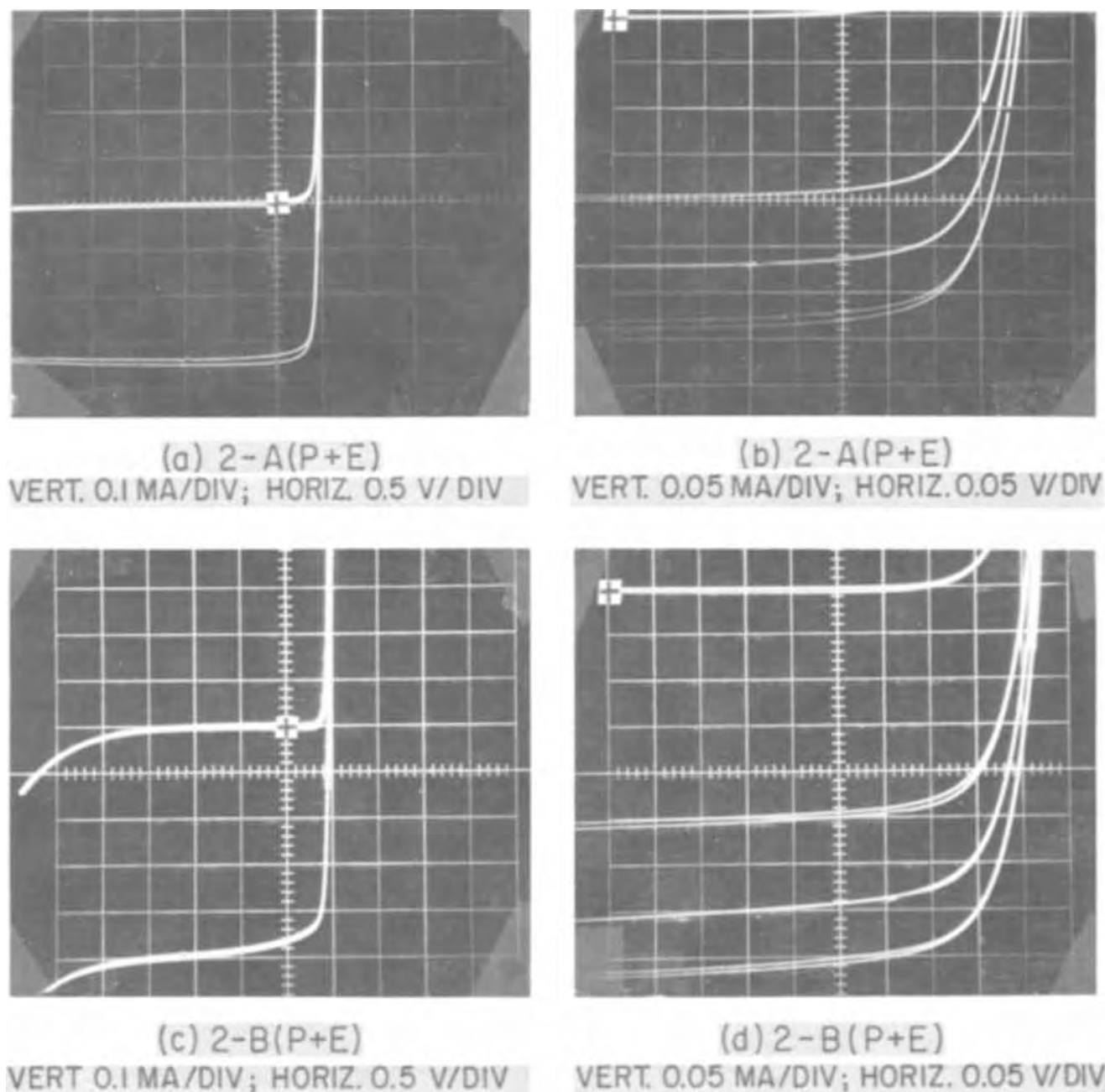


Fig. 2. Dark and light-generated I-V characteristics for samples 2-A(P+E) and 2-B(P+E)

samples. The uppermost curve in each photograph is the dark characteristic. The bottom curves are the light-generated characteristics in unfiltered tungsten light of 280 mW/cm^2 integrated intensity (I_0). The two intermediate curves in (b) and (d) are for lower intensities of white light. These characteristics are typical of those observed in a series of ten samples, 6 A-face and 4 B-face. A tabulation of data for these samples appears in Table I.

The "fill factors" of the light I-V curves (ratio of the area of the maximum power rectangle to the product $I_{sc} \times V_{oc}$) are about 70%. The open-circuit voltage of the B-face sample is somewhat greater than that of the A-face sample, and the reverse characteristic of the B-face sample is "softer." These features were generally observed for corresponding pairs of A and B-face samples (see Table I).

Photoresponse.—Figure 3 presents the spectral response of short-circuit current for two A-face samples. The curves have been normalized to a photon flux of $5.8 \times 10^{14} \text{ cm}^{-2} \text{ sec}^{-1}$ assuming a linear dependence of photocurrent on light intensity at each wavelength. At this intensity, a current density of 10^{-5} A/cm^2 corre-

sponds to a quantum efficiency of slightly greater than 0.1 electrons/photon. These spectral response curves show the typical relatively flat response from 0.5 to 0.9μ associated with the most efficient Cu_2S -CdS cells. The curves for the B-face samples were identical in shape to those in Fig. 3.

Figure 4 shows two spectral response curves replotted as the square root of photocurrent vs. photon energy. The long-wavelength edge of the response is a straight line on this plot, the slope of which changes abruptly below 1.2 eV. This behavior is similar to that of the absorption coefficient of Cu_2S , measured by Marshall and Mitra (19). The basic mechanism of the long-wavelength response of the Cu_2S -CdS heterojunction is optical absorption in the Cu_2S followed by emission of the photoexcited electrons into the CdS. The small response at energy lower than 1.2 eV is due to the phonon absorption branch of the indirect absorption coefficient of Cu_2S .

The intensity dependence of open-circuit photovoltage in white tungsten light was measured for each sample. The photovoltage decreased only slightly with decreasing intensity down to two orders of magnitude

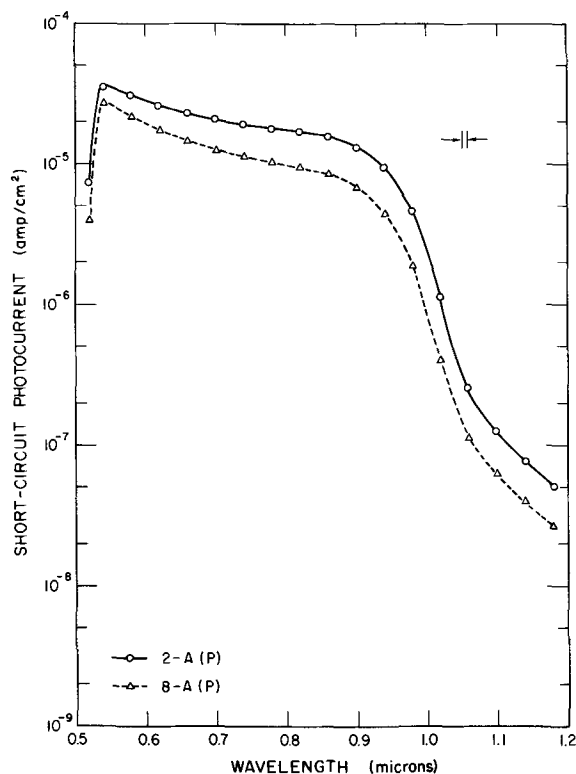


Fig. 3. Spectral response of short-circuit photocurrent for samples 2-A(P) and 8-A(P).

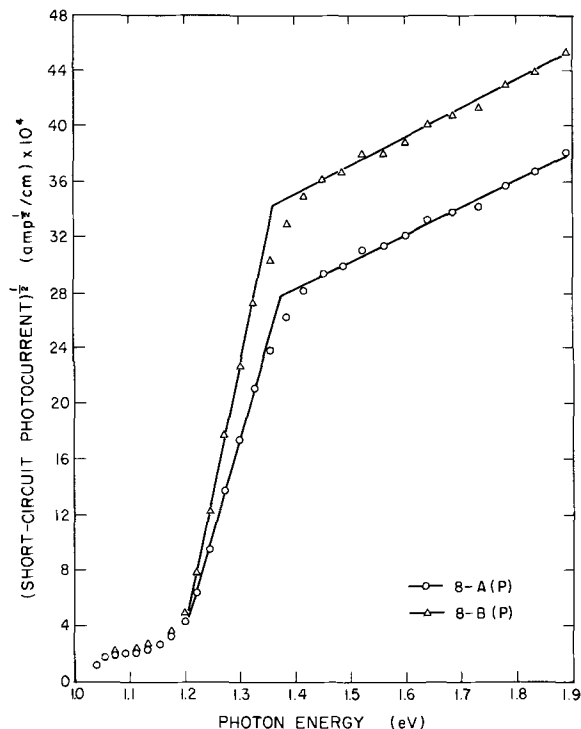


Fig. 4. Square root of short-circuit photocurrent vs. photon energy for samples 8-A(P) and 8-B(P).

below the maximum, and then dropped off more rapidly with decreasing intensity, finally becoming proportional to intensity. The same qualitative behavior was observed for all samples, both A and B face. The magnitude of the photovoltage at a fixed low intensity varied considerably from sample to sample, however, and was correlated with the crystal face and also with the surface treatment of the CdS prior to junction formation [polished (P) or polished and etched (P + E)]. This correlation is illustrated in Fig. 5, which plots the

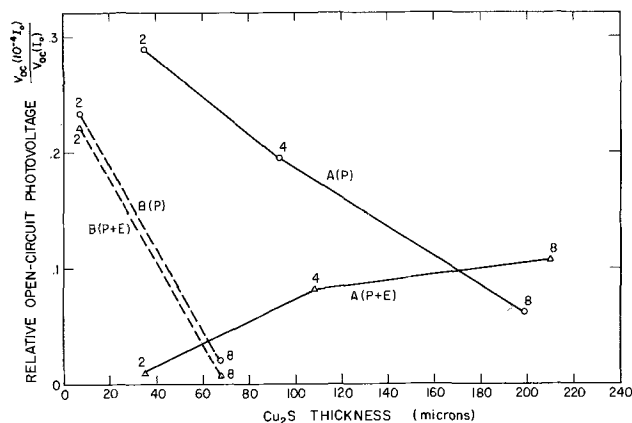


Fig. 5. Dependence of relative open-circuit photovoltage at intensity $10^{-4} I_0$ on thickness of Cu₂S and surface condition. ($I_0 = 280 \text{ mW/cm}^2$ white tungsten light.)

relative open-circuit voltage at intensity $10^{-4} I_0$ against Cu₂S thickness and surface condition. The numbers accompanying the points denote the dipping time in hours. The values of Cu₂S thickness are those appearing in Table I. For the B-face samples, the low-intensity V_{oc} drops with increasing Cu₂S thickness (dipping time), with very little difference between corresponding polished and polished + etched samples. A significant difference between the polished and etched A-face samples is observed, however. For the shortest dipping time, the polished A-face sample gives a much higher V_{oc} at low intensity than does the corresponding etched sample. The difference between polished and etched A-face samples decreases with increasing layer thickness and reverses for the 8-hr samples.

Figure 6 shows a correlation between the relative open-circuit photovoltage at low intensity and the "saturation" current density J_0 (the value obtained by extrapolating the dark, forward characteristic, $\log J$ vs. V , to $V = 0$). The values of J_0 are listed in Table I [from "low-V" column, where indicated (20)]. This

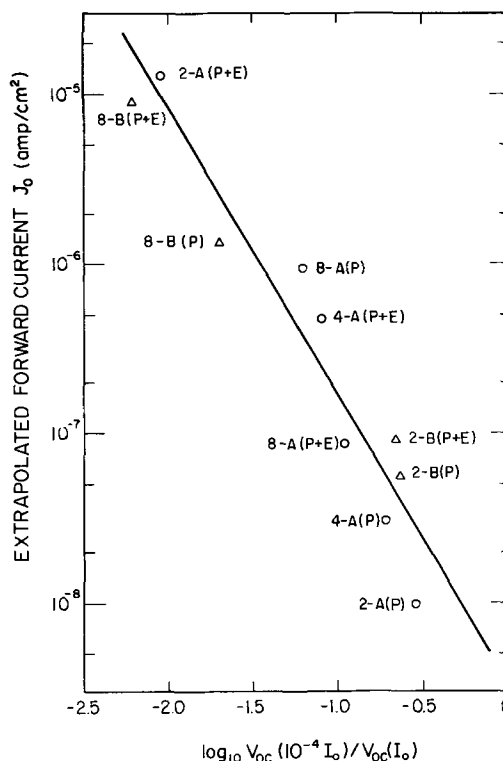


Fig. 6. Relation between low-intensity open-circuit photovoltage and dark forward current extrapolated to $V = 0$.

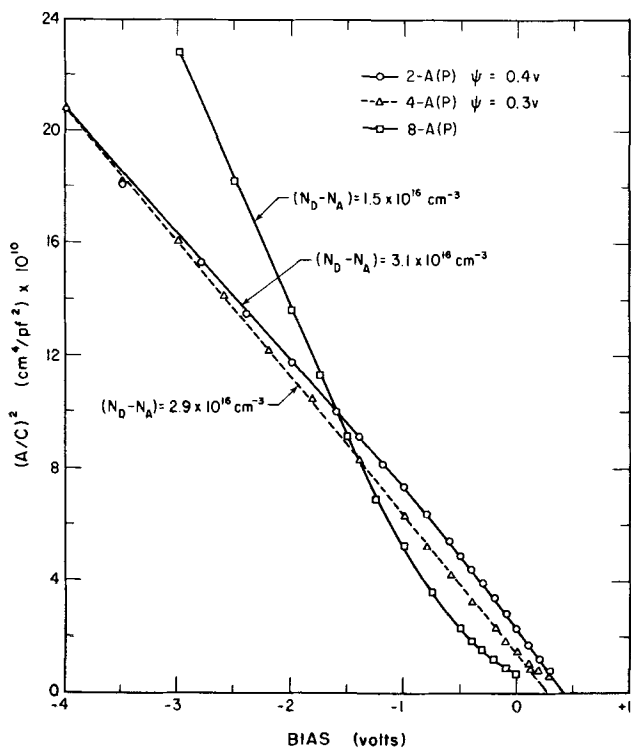


Fig. 7. $1/C^2$ vs. voltage for three A-face samples

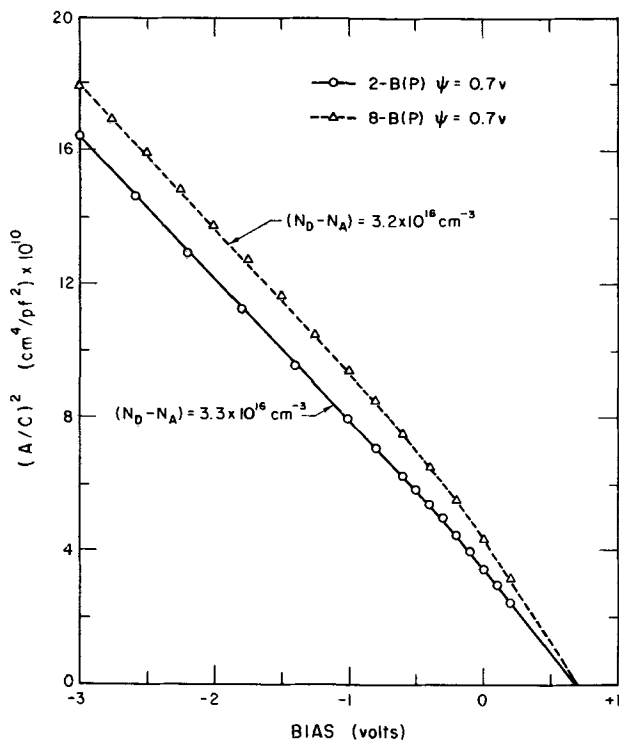


Fig. 8. $1/C^2$ vs. voltage for two B-face samples

plot indicates that a high value of V_{oc} at low intensity is associated with a low value of J_0 . From Fig. 5 it may be inferred that etching the CdS surface before dipping increases the saturation (or leakage) current, J_0 , of the resulting cell, and that the effect is especially pronounced for A-face samples dipped for short times. The etching had no noticeable effect on either the growth rate of the Cu_2S layer or the photocurrent response curves.

Capacitance-voltage curves.—Plots of $1/C^2$ vs. bias voltage at room temperature are given for three A-face and two B-face samples in Fig. 7 and 8, respectively. The values of capacitance were corrected for the effect

of series resistance by the relationship

$$C = C' / \{ (1 - R_s G')^2 + (R_s \omega C')^2 \} \quad [1]$$

where C' and G' are the measured values of capacitance and conductance, R_s is the series resistance, and ω is the angular frequency. Values of R_s were obtained by pulsing the forward characteristic, and are tabulated in Table I.

For the thinnest Cu_2S layers, the $1/C^2 - V$ plots were linear for both A- and B-face samples, with a slight increase in slope in the forward and low reverse bias region. The values of net donor density in the CdS, $N_D - N_A$, agreed with the measured conductivity of the initial CdS crystals. With increasing thickness of the Cu_2S , the $1/C^2 - V$ plots for A-face samples developed a pronounced upward concavity at low bias, whereas the plots for B-face samples became slightly more concave downward. Values of the capacitance per unit area at zero bias and the intercept voltage ψ from $1/C^2 - V$ data are given for each sample in Table I. For comparison, values of ψ obtained by extrapolating the series-resistance-limited forward characteristics to zero current (21) are also shown. The quantity ψ obtained by either of these techniques is a rough measure of the diffusion potential of the junction.

Temperature Dependence.—The forward I-V characteristic and the photoresponse in white light were measured between 300° and $100^\circ K$ for a number of samples. Figures 9 and 10 present typical results for an A-face sample. The behavior of A- and B-face samples were qualitatively similar.

Figure 9 shows the forward I-V characteristic at various temperatures. The data fit an expression of the form

$$J(V, T) = J_0(T) e^{\alpha V} \quad [2]$$

where α is independent of temperature. For the case shown, the average value of α was $31.4 V^{-1}$. Values of α for all the samples, based on room temperature data only, are given in Table I. The temperature-independent slope of the forward characteristic suggests a tunneling mechanism for the forward current. If the

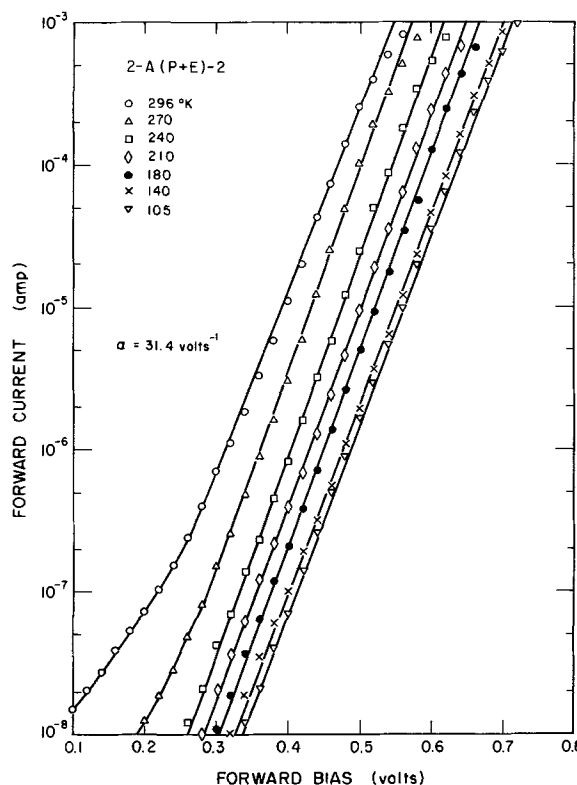


Fig. 9. Forward I-V characteristic in the dark as a function of temperature for sample 2-A(P+E)-2.

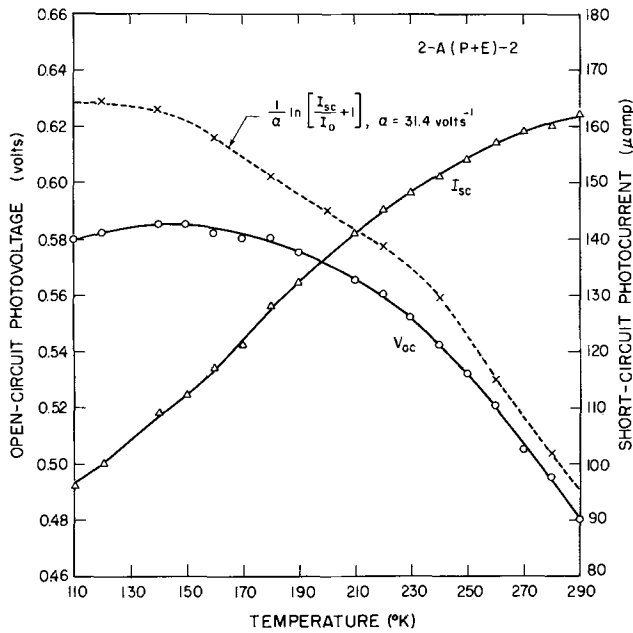


Fig. 10. Short-circuit photocurrent and open-circuit photovoltage in white tungsten light (280 mW/cm²) vs. temperature for sample 2-A(P+E)-2. Calculated curve for photovoltage is also shown.

values of current at a fixed voltage from Fig. 9 are plotted against 1/T, it is found that near 300°K, J₀(T) is apparently thermally activated with an energy of 0.26 eV. (A similar plot for the B-face samples gave an average activation energy of about 0.45 eV.) At lower temperatures J₀(T) becomes increasingly independent of temperature, with no variation below about 120°K.

Figure 10 illustrates the temperature variation of the open-circuit photovoltage and short-circuit photocurrent in unfiltered tungsten light. The short-circuit current decreases by about 30% from room temperature to 100°K, approximately linearly. The open-circuit voltage increases by about 12% over the same temperature range. The increase in photovoltage is nearly linear with decreasing temperature near 300°K, but the curve bends over at lower temperatures and passes through a broad maximum at 150°K. This behavior can be understood in terms of the relationship between open-circuit voltage and short-circuit current for an idealized photovoltaic cell

$$V_{oc} = \frac{1}{\alpha} \ln \left[\frac{J_{sc}}{J_0} + 1 \right] \quad [3]$$

where α and J₀ are defined by Eq. [2]. The right side of this expression is plotted in Fig. 10 (dashed line), using the experimental values of J_{sc} and J₀ vs. T and the value of α from Fig. 9, 31.4V⁻¹. The dashed curve is slightly higher than the experimental V_{oc} at all temperatures but has the same general shape. The positive deviation of the calculated curve is attributed to a finite shunt resistance in the actual cell. The plot of (1/α) ln [(J_{sc}/J₀) + 1] demonstrates that the "fold-over" in V_{oc} with decreasing temperature is a consequence of the temperature independence of J₀ at low temperature.

Effect of uniaxial stress.—The capacitance as a function of bias was measured at room temperature for two specially prepared samples, one A- and one B-face, with and without uniaxial stress applied parallel to the plane of the junction (parallel to the CdS a-axis). These samples were prepared from 5 ohm-cm CdS, with the Cu₂S layer about 10μ thick in each case. Figure 11 gives plots of 1/C² vs. V for the A-face sample, both with stress applied (2.55 kg/mm²) and after removal of the stress. Figure 12 shows similar data for the B-face sample, with the stress in this case

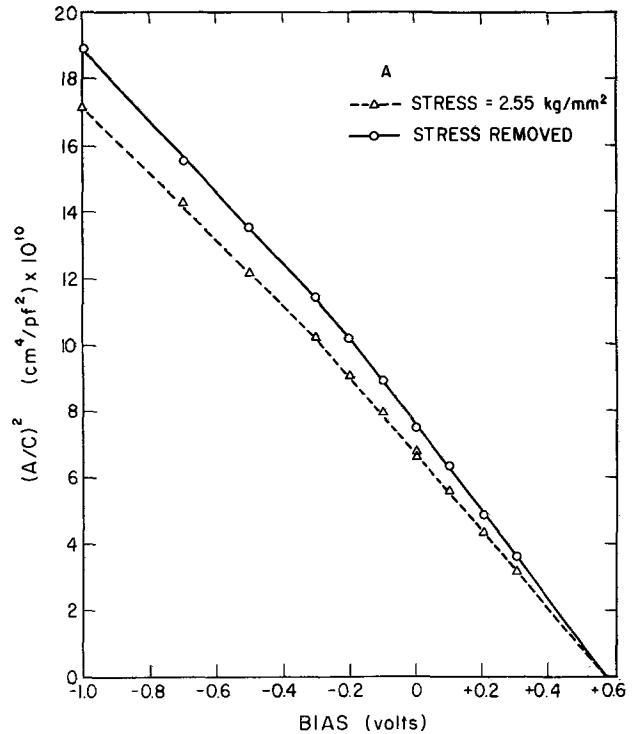


Fig. 11. Effect of uniaxial stress (2.55 kg/mm² nominal) on the 1/C²-V plot for an A-face sample. Capacitance values were corrected for series resistance.

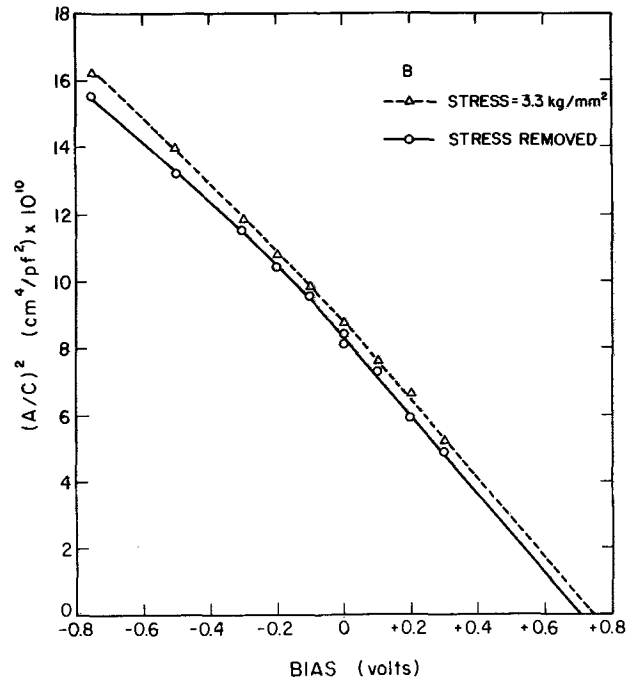


Fig. 12. Effect of uniaxial stress (3.3 kg/mm² nominal) on the 1/C²-V plot for a B-face sample. Capacitance values were corrected for series resistance.

equal to 3.3 kg/mm². For the A-face sample, the capacitance is increased by the applied stress for all values of bias; the opposite effect is observed for the B-face sample.

Discussion

Band diagram.—The general properties of the Cu₂S-CdS heterojunction can be described in terms of the energy band profile given in Fig. 13. The Cu₂S is shown as a degenerate p-type semiconductor with (indirect) band gap of 1.2 eV. The Fermi level lies roughly 0.05 eV below the valence band edge for a hole density of

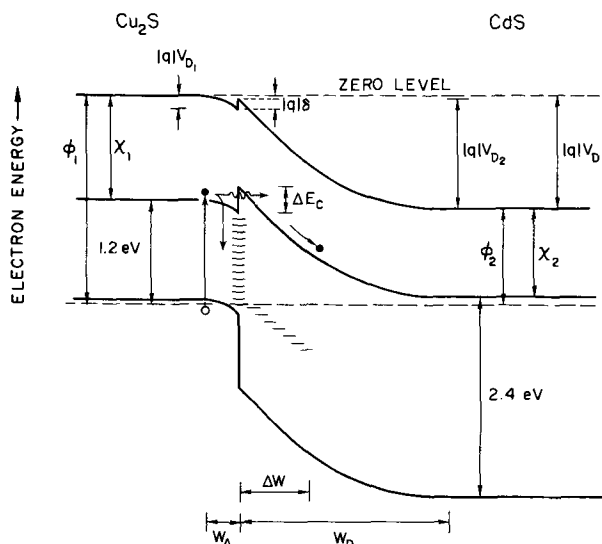


Fig. 13. Band diagram for the Cu_2S - CdS heterojunction, showing deep acceptor levels and interface states. Carriers photoexcited in the Cu_2S may cross into the CdS and contribute to the photocurrent, or may recombine through interface states.

10^{20} cm^{-3} . The CdS has a (direct) band gap of 2.4 eV. A quasi-continuum of interface states arising from the severe lattice mismatch is postulated (22).

A positive discontinuity or "spike" in the conduction band is also indicated. Such a spike may arise as a result of the difference in electron affinities of Cu_2S and CdS , and also if an electrostatic dipole of the proper sense exists at the interface. The magnitude of the spike is given by

$$\Delta E_c = \chi_1 - \chi_2 - |q|\delta \quad [4]$$

or

$$\Delta E_c = |q|(V_{D1} + V_{D2}) + (\phi_2 - \chi_2) - (\phi_1 - \chi_1) \quad [5]$$

χ is the electron affinity, δ the interface dipole (positive or negative), V_D the diffusion potential, and ϕ the work function. In this case, subscript 1 refers to Cu_2S and subscript 2 to CdS . In the case of 1 ohm-cm CdS , $(\phi_2 - \chi_2)$ is approximately 0.1 eV. With $(\phi_1 - \chi_1)$ for Cu_2S about 1.25 eV (band gap plus 0.05 eV between valence band edge and Fermi level), a total diffusion potential ($V_{D1} + V_{D2}$) greater than 1.15V is required for a positive discontinuity. This spike has been postulated as part of a model to account for the transient and secondary illumination effects observed in heat-treated cells (13), and is discussed elsewhere in relation to photocapacitance phenomena (17).

The existence or nonexistence of the conduction band spike cannot be proven from the measured values of ψ given in Table I. The general relationship between the quantity ψ , obtained by extrapolating a plot of $1/C^2$ vs. V from low reverse or forward bias to zero, and the total diffusion potential $V_{D1} + V_{D2}$, has been given by Donnelly and Milnes (23)

$$\psi = V_{D1} + V_{D2} - \frac{Q^2}{2q(\epsilon_1 N_1 + \epsilon_2 N_2)} \quad [6]$$

where Q is the net interface charge per unit area, N_1 and N_2 are the net impurity densities on the two sides of the junction, and ϵ_1 and ϵ_2 are the respective dielectric constants. It is reasonable to assume that the large lattice mismatch (about 5%) between oriented Cu_2S formed on the basal plane of CdS gives rise to a significant density of charged imperfections at the interface (22, 24). Thus the value of ψ may be somewhat lower than the true diffusion potential.

The values of ψ determined by the extrapolation of the series-resistance limited forward I-V characteristic to zero current are also expected to be lower than the true diffusion potential in this case, since the forward

current is apparently dominated by tunneling rather than by emission over the total barrier.

Photoresponse.—The photoresponse of the junction under short-circuit conditions can be understood in terms of Fig. 13 as follows: light incident from the CdS side is absorbed in the Cu_2S , generating non-equilibrium densities of electrons and holes. The absorption coefficient of Cu_2S varies from about 10^4 cm^{-1} at 1.2 eV to about 10^5 cm^{-1} at 2.2 eV (18). The diffusion length of electrons in Cu_2S has been measured by a light microprobe technique to be in the range $1-4 \times 10^{-5} \text{ cm}$ (25). Thus most of the incident radiation which reaches the Cu_2S through the CdS is absorbed within a diffusion length in the Cu_2S . The photoexcited electrons must cross the interface into the CdS in order to contribute to the photocurrent. Some are lost due to recombination via the interface states, as indicated in Fig. 13. If a conduction band spike exists, the electrons must either tunnel through or be thermally excited over the barrier in order to enter the CdS . The absence of transient and secondary-illumination effects in efficient, nonheat-treated junctions at room temperature suggests that the spike width cannot be modulated as in the case of the heat-treated cells (13).

Deep levels in the CdS depletion layer.—A number of deep levels located about midway in the CdS band gap are also shown in Fig. 13. The existence of these levels in the nonheat-treated cells has been deduced primarily from photocapacitance data (17). The distance, ΔW , over which these deep acceptor levels are distributed in the CdS depletion region can be estimated from capacitance-voltage curves. The plots of $1/C^2$ vs. V for samples 2-A(P), 2-B(P), and 8-B(P), Fig. 7 and 8, show a change in slope at low reverse and forward bias. If the density of ionized donors in the CdS depletion region is assumed to have a step decrease near the interface of magnitude ΔN_D and width ΔW , then it can be shown that (26)

$$V^* = (V_{D1} + V_{D2}) + \frac{q}{2\epsilon} \left[1 - \frac{\Delta N_D}{N_A + N_D} \right] \Delta N_D (\Delta W)^2 \quad [7]$$

where V^* is the intercept voltage obtained by extrapolating the $1/C^2 - V$ plot from the linear, high reverse-bias region, and $(V_{D1} + V_{D2})$ is the total diffusion potential of the junction. (N_A in this case refers to the acceptor density on the p-type side.) If it is assumed that $(V_{D1} + V_{D2})$ is given approximately by the value of ψ obtained by extrapolation of $1/C^2$ from the low-bias region of steeper slope, and that $\Delta N_D \approx N_D$ so that ΔW is an "intrinsic" layer, then for $N_A \gg N_D$ we obtain as an upper limit

$$\Delta W \approx \left[\frac{2\epsilon}{qN_D} (V^* - \psi) \right]^{1/2} \quad [8]$$

For each of the two-hour samples of Fig. 7 and 8, $V^* - \psi$ is about 0.2V. Taking $N_D = 3 \times 10^{16} \text{ cm}^{-3}$ and $\epsilon = 10\epsilon_0$, where ϵ_0 is the permittivity of free space, we find $\Delta W = 860 \text{ \AA}$. For sample 8-B(P) (Fig. 11), $V^* - \psi$ is about 0.4V, giving $\Delta W = 1200 \text{ \AA}$, which is about half the depletion layer width at zero bias. The A-face samples show a rapid increase in junction capacitance with increasing Cu_2S thickness (see Table I), resulting in $1/C^2 - V$ plots which are concave upward for the two thicker samples (Fig. 7). Values of ΔW were not obtained for the thicker-layer A-face samples because of this effect. At least part of the increase in capacitance may be due to a nonplanar interface between the Cu_2S and the CdS for A-face samples which becomes more pronounced with longer reaction time. Goodman (27) has shown that this results in a voltage-dependent effective junction area which gives rise to a concave-upward $1/C^2 - V$ plot when the nominal geometrical area is assumed. The influence of

stress on the charge profile of the junction may also contribute to this effect, as discussed later.

The deep centers are most likely diffused in copper levels incorporated during formation of the Cu₂S layer. The penetration depths estimated above from capacitance data are much greater than those expected from available data for bulk diffusion of copper in CdS (28). It is therefore suggested that the motion of the copper is assisted by dislocations formed in the CdS near the advancing Cu₂S interface which accommodate the lattice mismatch. Oldham and Milnes (29) have shown that for a lattice mismatch of about 4%, the interfacial dislocations are formed in a crossed grid with spacing of the order of 200Å, the thickness of the grid being less than a typical depletion layer width.

Forward current.—The temperature-independent slope of the forward I-V characteristic suggests that the forward current is due to tunneling of electrons from the CdS conduction band through the interface states to the Cu₂S valence band. The different thermal activation energies for the forward current at a fixed voltage for A- and B-face samples near 300°K indicate a possible difference in interface state density and distribution in energy in the two cases.

Uniaxial stress effect.—The results of the capacitance measurements under applied stress for the A- and B-face samples can be interpreted in terms of the piezoelectric properties of CdS. The capacitance of the A-face sample was observed to increase slightly under compressive stress applied along the a-axis, with the opposite behavior for the B-face sample. From the piezoelectric properties of the wurtzite lattice, it can be shown (30, 31) that a compressive stress applied along the a-axis gives rise to an electric field ϵ_p , directed from the A toward the B face parallel to the c-axis, with magnitude

$$\epsilon_p = \frac{P_3}{\epsilon} = \frac{d_{31}\sigma_1}{\epsilon} \quad [9]$$

where P_3 is the component of polarization charge per unit area parallel to the c-axis, d_{31} is the appropriate element of the piezoelectric tensor, σ_1 is the compressive stress applied along the a-axis, and ϵ is the dielectric constant. For CdS, $d_{31} = -5.18 \times 10^{12}$ coulombs/newton (30). This polarization field is neutralized by the mobile conduction electrons in the bulk of the crystal, but adds to or subtracts from the built-in field in the depletion region of a p-n junction formed on the B or A face of the CdS, respectively. The effect is illustrated in Fig. 14, which shows the charge density profile and electric field in the depletion layer, with and without stress, for both A and B faces. An intrinsic region of width ΔW is assumed. In the A-face case, the stress-induced field ϵ_p acts in opposition to the electric field due to the space charge on the CdS side of the junction. The electric field profile with compressive stress applied is given by the dashed line. The discontinuity in field at the Cu₂S-CdS interface implies a net positive charge on the interface states (assumed neutral in the absence of external stress). The stress narrows the depletion layer in the CdS from W_D to W_D' . From similar triangles

$$W_D' = \Delta W \left(\frac{\epsilon_p}{\epsilon_m} \right) + W_D \left(1 - \frac{\epsilon_p}{\epsilon_m} \right) \quad [10]$$

ϵ_m , the maximum field, is given by

$$\epsilon_m = \frac{qN_A W_A}{\epsilon} = \frac{qN_D (W_D - \Delta W)}{\epsilon} \quad [11]$$

for the case illustrated (differences in the dielectric constants of the two materials are ignored). Since $N_A \gg N_D$ for the Cu₂S-CdS junction, the depletion layer width W_A in the Cu₂S is negligible compared to W_D , the width in the CdS. Consequently, we define the capacitance

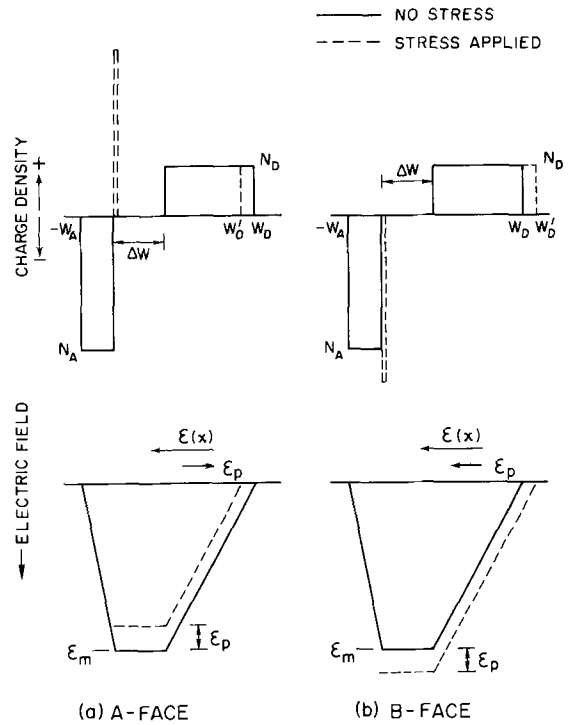


Fig. 14. Change in charge density and electric field profiles due to applied stress for A- and B-face samples.

$$C_0 = \frac{\epsilon A}{W_D}, \quad C_0 + \Delta C = \frac{\epsilon A}{W_D'} \quad [12]$$

The fractional change in capacitance due to applied stress, for the A-face case, is

$$\left(\frac{\Delta C}{C_0} \right)_A = \frac{W_D}{W_D'} - 1 = \left[1 - \frac{\epsilon_p}{\epsilon_m} \left(1 - \frac{\Delta W}{W_D} \right) \right]^{-1} - 1 \quad [13]$$

The increment ΔC is positive. Using Eq. [10] and [12], this can be written in the form

$$\left(\frac{\Delta C}{C_0} \right)_A = \frac{K\sigma_1}{1 - K\sigma_1} \quad [14]$$

where $K = d_{31}/qN_D W_D$ and σ_1 is the stress normal to the c-axis, negative for compression.

For the B-face case (Fig. 14b), a similar treatment gives

$$\left(\frac{\Delta C}{C_0} \right)_B = - \frac{K\sigma_1}{1 + K\sigma_1} \quad [15]$$

The capacitance increment is negative. The electric field discontinuity at the interface implies a net negative charge in the interface states.

For the two samples for which are shown in Fig. 11 and 12, the calculated values of K were $\approx 10^{-1}$. Using the values of nominal stress, Eq. [14] and [15] predict an effect larger by an order of magnitude than observed. At least part of the discrepancy may be attributed to a decrease in d_{31} due to a high density of dislocations in the CdS near the interface. Chubachi *et al.* (32) observed a decrease in d_{31} from 5.18 to 2.32 (10^{-12} coulombs/newton) as the dislocation density in CdS increased from 3×10^4 to 1.5×10^7 cm⁻². Additional factors may be an overestimation of the actual stress applied to the junction and an oversimplified model.

Equations [14] and [15] predict that the magnitude of the capacitance change for the A-face junction increases more rapidly with stress than that for the B-face. This is also consistent with the existence of net charge at the interface when the samples are under

stress. The dependence of capacitance on interface state charge density Q can be expressed as (23)

$$C = A(V_{D1} + V_{D2} - BQ^2)^{-1/2} \left(1 + K \frac{dQ}{dV} \right) \quad [16]$$

for zero bias, where A , B , and K depend on doping and dielectric constants and $V_{D1} + V_{D2}$ is the diffusion potential. (The above expression neglects a possible dipole.) Thus for both cases illustrated in Fig. 14 the capacitance would tend to increase under stress due to the induced interface state charge, independent of the change in capacitance resulting from widening or narrowing of the depletion layer by the polarization field (Eq. [14], [15]). In the as-formed junctions without externally applied stress, the piezoelectric effect may influence the junction capacitance through the elastic interfacial strain between the Cu_2S and CdS , and also through the stress fields associated with interfacial dislocations. For example, Table I indicates that with increasing relative thickness of the Cu_2S layer (and corresponding increase in interface stress), the zero-bias capacitance for B-face samples decreases, while that for A-face samples increases by a relatively greater amount.

Conclusions

The fabrication and properties of nonheat-treated single-crystal Cu_2S - CdS heterojunctions have been described. The major portion of the photovoltaic response arises from light absorption within a diffusion length in the Cu_2S , with transfer of the photoexcited electrons across the interface into the CdS . A large density of interface states exists due to the mismatch strain between the two materials when the Cu_2S is formed on the CdS basal planes. A density of deep acceptors comparable to the net donor density in the CdS occurs in a fraction of the CdS depletion region near the interface.

Differences between A- and B-face samples were observed with respect to Cu_2S growth rate, open-circuit photovoltage, I-V characteristics, and changes in junction capacitance under applied stress. The latter was analyzed in terms of a simple model involving the piezoelectric properties of CdS .

Acknowledgment

This research was sponsored by the National Aeronautics and Space Administration through Lewis Research Center, Cleveland, Ohio.

Manuscript submitted May 27, 1971; revised manuscript received Nov. 11, 1971.

Any discussion of this paper will appear in a Discussion Section to be published in the December 1972 JOURNAL.

REFERENCES

1. F. A. Shirland, *Advan. Energy Conversion*, **6**, 201 (1966).
2. H. G. Grimmeiss and R. Memming, *J. Appl. Phys.*, **33**, 2217 (1962).
3. N. Duc Cuong and J. Blair, *ibid.*, **37**, 1660 (1966).
4. W. Palz and W. Ruppel, *Phys. Status Solidi*, **6**, K161 (1964).
5. T. Shitaya and H. Sato, *Japan. J. Appl. Phys.*, **7**, 1348 (1968).
6. R. R. Chamberlin and J. S. Skarman, *Solid-State Electron*, **9**, 819 (1966).
7. A. E. Potter, Jr., and R. L. Schalla, "Mechanism of CdS Film Cell," NASA Technical Note, NASA TN D-3849 (1967).
8. E. R. Hill and B. G. Keramidas, *Rev. Phys. Appl.*, **1**, 189 (1966).
9. I. V. Egorova, *Sov. Phys.-Semiconductors*, **2**, 266 (1968).
10. R. J. Mytton, *Brit. J. Appl. Phys.*, **1**, 721 (1968).
11. L. R. Shiozawa, G. A. Sullivan, and F. Augustine, Proc. Seventh Photovoltaic Specialists Conference, 39 (1968).
12. B. Selle, W. Ludwig, and R. Mach, *Phys. Status Solidi*, **24**, K149 (1967).
13. W. D. Gill and R. H. Bube, *J. Appl. Phys.*, **41**, 3731 (1970).
14. E. P. Warekois, M. C. Lavine, A. N. Mariano, and H. C. Gatos, *ibid.*, **33**, 690 (1962); **37**, 2203 (1966).
15. J. E. Rowe and R. A. Forman, *ibid.*, **39**, 1917 (1968).
16. M. C. Sneed, J. F. Maynard, and R. C. Brasted, "Comprehensive Inorganic Chemistry," Vol. II, p. 76, D. Van Nostrand Co. (1954).
17. P. F. Lindquist and R. H. Bube, *J. Appl. Phys.*, To be published.
18. B. Selle and J. Maeger, *Phys. Status Solidi*, **30**, K153 (1968).
19. R. Marshall and S. S. Mitra, *J. Appl. Phys.*, **36**, 3882 (1965).
20. Where two values are given for J_0 in Table I, the $\log J$ vs. V plot showed a break point from a smaller to a larger slope with increasing voltage. The first value is from extrapolation of the low-voltage segment ("low-V" column).
21. W. E. Howard and A. B. Fowler, *ibid.*, **39**, 1533 (1968).
22. W. G. Oldham and A. G. Milnes, *Solid-State Electron.*, **6**, 121 (1963).
23. J. P. Donnelly and A. G. Milnes, *IEEE Trans.*, **ED-14**, 63 (1967).
24. J. Singer and P. A. Faeth, *Appl. Phys. Letters*, **11**, 130 (1967).
25. W. D. Gill and R. H. Bube, *J. Appl. Phys.*, **41**, 1694 (1970).
26. C. van Opdorp, *Solid-State Electron.*, **11**, 397 (1968).
27. A. M. Goodman, *J. Appl. Phys.*, **34**, 329 (1963).
28. G. A. Sullivan, *Phys. Rev.*, **184**, 796 (1969).
29. W. G. Oldham and A. G. Milnes, *Solid-State Electron.*, **7**, 153 (1964).
30. D. Berlincourt, H. Jaffe, and L. R. Shiozawa, *Phys. Rev.*, **129**, 1009 (1963).
31. G. Arlt and P. Quadflieg, *Phys. Status Solidi*, **25**, 323 (1968).
32. N. Chubachi, K. Iinuma, and Y. Kikuchi, *J. Appl. Phys.*, **42**, 962 (1971).

A High Production System for the Deposition of Silicon Nitride

V. D. Wohlheiter and R. A. Whitner

Western Electric Company, Inc., Allentown, Pennsylvania 18103

ABSTRACT

Amorphous silicon nitride is well known as a barrier to the penetration of alkali metal contaminants into junctions of semiconductor devices and as a gate dielectric for MIS devices. This paper discusses the operating characteristics of a production system for the deposition of silicon nitride by the ammonolysis of silicon tetrachloride in a hot wall furnace, and the characteristics of the resulting films.

The protective film (1700-2500Å) for bipolar devices can be deposited at a rate of 120 wafers/hr. For MIS work, where film thickness directly affects device threshold voltage, better uniformity can be achieved by modifying the wafer placement and operating procedures. The nitride films are amorphous with an index of refraction of approximately 1.95; the surface-state density is in the order of 10^{12} ; and the etch rate in buffered hydrofluoric acid¹ is 1 ± 2 Å/min.

This paper describes the design of a production system for the deposition of silicon nitride and some of the characteristics of the films produced.

Amorphous silicon nitride was introduced into the manufacture of beam lead chips to act as a contamination barrier, as has been reported in the literature (1). The system was designed to meet the following specifications for the barrier film: thickness, 1750-2500Å; etch rate, 11 ± 3 Å/min in buffered HF at 23°C; sodium penetration (2), 92% removed after etching 50Å. The etch rate has been specified to fall within a normally achievable range that will allow the silicon nitride to pass the sodium penetration test; i.e., when the etch rate in buffered hydrofluoric acid increases, the probability of sodium penetration increases (3). The etch rate is directly related to the amount of oxygen in the silicon nitride; and because the presence of oxygen weakens the nitride barrier to alkaline contaminants, the etch test is sufficient to provide some indication as to the quality of silicon nitride. The actual testing procedure for sodium penetration will be discussed later.

Initially, silicon nitride was deposited in either a carousel or a barrel-type epitaxial reactor. However, the need for large production numbers (greater than 50 wafers/hr) suggested that an alternate system be developed due to the high cost of reactors and the relatively long cycle time. It was decided to develop a system using a standard diffusion furnace to deposit silicon nitride. Table I compares the reactor statistics with the goals of the proposed furnace system.

Table I

	Reactor	Furnace
Cost (installed)	\$50K (min)	\$18K
Turn-around time	60 min	25 min
Capacity/run	25 wafers	50 wafers

These figures are based on data when the study began four years ago. A capacity ratio of 3:1 (furnace wafers to reactor wafers) and a cost ratio of 1:8 for the furnace system have been obtained.

In the initial furnace operation, the effort was directed toward producing a satisfactory nitride film. This was done using a streamlined quartz boat with the wafers lying flat. Several conclusions were drawn from this work: (i) the gases must be absolutely dry

Key words: thin films, contamination barrier, chemical vapor deposition (CVD), sodium penetration, diffusion furnace CVD, silicon integrated circuits.

¹ The etch rate of thermally grown silica in buffered hydrofluoric acid is 1000 Å/min.

to meet the etch rate requirements; (ii) the uniformity of the film depends strongly on the geometry of the system; (iii) the zone of uniform deposition depends strongly on the bulk gas volume, i.e., gas velocity; and (iv) a deposition rate of about 100 Å/min appeared optimum. To achieve volume output, it was necessary to place wafers in a stand-up position; and the next phase of development was concentrated on obtaining uniform films on at least four rows of standing wafers. The need for a high volume of nitrogen carrier flow had been suggested by previous work with boron doping systems and, in this case, solved the uniformity problem. The details of the design and operation of the system reflect the need to use and accommodate a high volume and high velocity of bulk gas.

Description of the System

The most recent systems consist of a standard, two-tube diffusion furnace with a quartz tube, a dry nitrogen supply, bottled ammonia, and a cooler for a flask of silicon tetrachloride. A cross-sectional view is shown in Fig. 1. The upper tube is used to preheat the bulk flow of nitrogen which reduces the heat load on the deposition furnace and, therefore, allows a longer uniform temperature zone. Other preheat schemes could also be used, such as a double walled tube. Typical operating conditions are: quartz tube size, $2\frac{5}{8} \times 3\frac{1}{4}$ in. (66 × 83 mm); carrier N₂, 135 liters/

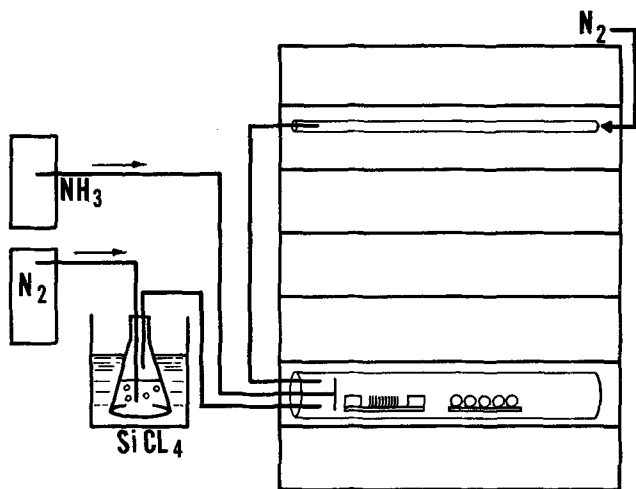


Fig. 1. Cross-sectional view of the silicon nitride deposition system.

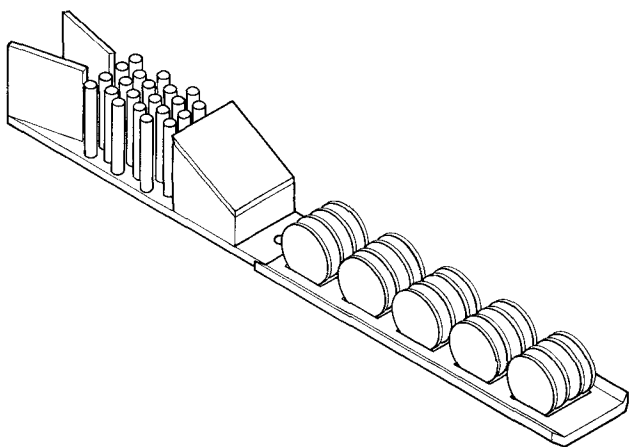


Fig. 2. The quartz gas diffuser and silicon boat containing silicon wafers.

min;² NH₃, 0.4 liters/min;² SiCl₄ at 10°C, 0.150 liter/min N₂ bubbled;² temperature, approximately 900°C.

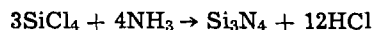
The temperature of the silicon tetrachloride was controlled with a constant temperature bath so that the vapor pressure was constant and a specific amount was vaporized by the bubbling nitrogen. The temperature of the SiCl₄ cooler and the flow rate of the nitrogen through the silicon tetrachloride were experimentally determined and set to yield a deposition rate of 100 Å/min. The constant temperature baths now being used do not use water as the bath media for the silicon tetrachloride. Water can react violently if the flask were to be broken in the cooling chamber. The silicon tetrachloride utilized is an epitaxial grade while the ammonia is anhydrous and instrument grade.

During initial development the amount of moisture present in the ammonia was found to be critical. Excess oxygen and water will cause a silicon oxy-nitride to be deposited; therefore, anhydrous 99.999% pure ammonia was chosen. The silicon oxynitride can be identified by its much higher etch rate in buffered hydrofluoric acid. The flow rate of ammonia was set to provide an excess of ammonia to insure complete reaction of the silicon tetrachloride. The ratio of ammonia to silicon tetrachloride (NH₃/SiCl₄) used was 16.6/1. The ammonia was introduced directly into the hot zone to avoid the possibility of alternate silicon tetrachloride-ammonia reactions taking place at lower temperatures.

Figure 2 is a drawing of the baffle section and paddle design now in use. The baffle section is quartz and is used to improve deposition uniformity, both by deflecting the gas flow and by heating the reaction components. The boat which holds the wafers parallel to the gas flow is high purity silicon and was chosen because of the ease of cleaning in concentrated hydrofluoric acid, the absence of devitrification, and the accuracy achieved in machining. The silicon boat may be placed on a quartz carrier on wheels and allows automatic insertion and withdrawal from the deposition system with its attendant reproducibility.

In operation, the wafers are loaded on the silicon boat and the boat pushed into the furnace before the ammonia and silicon tetrachloride are introduced. The boat is usually preheated, and the ammonia turned on a minute or so before the silicon tetrachloride is introduced. If the reaction gases are introduced before the

wafers are heated, a hazy deposit forms on the cold wafers. The ammonia is introduced first to prevent the possibility of depositing silicon from the breakdown of silicon tetrachloride. The ammonolysis of silicon tetrachloride which forms silicon nitride is a complicated series of reactions. Simply stated, it is



The excess hydrogen chloride creates a favorable condition according to subsequent investigation by MacKenna *et al.* (4), who showed that the hydrogen chloride can act as a getter for any sodium ions present in the deposition cycle. After depositing the desired thickness, the ammonia and silicon tetrachloride are turned off and the wafers withdrawn.

Film Properties

Because the primary purpose of this film is that of a silicon nitride barrier, the thickness uniformity is not as stringent as that required for MIS work. The specifications for the barrier application are typically 2100 ± 400 Å, while the thickness variation from a routine run of at least 60 wafers averages ±200 Å. Usually, the deposits are uniform in any row but may vary from row to row depending upon the nitrogen flow and the wafer to wafer spacing. Rainbow effects, depicted in Fig. 3 with the edge toward the gas flow receiving a heavier deposit, are noted when the bulk nitrogen flow is too low or when the wafer to wafer spacing is too small, less than 0.214 in. Each shaded area represents a thickness variation of about 300 Å; and since homogenous films of this thickness range exhibit light interference, this variation causes an apparent color difference in the various areas of the wafer. With this low flow, less than 3 ft³/min, the last rows also tend to have thin deposits. The bulk nitrogen flow is from left to right in Fig. 3. However, if the bulk nitrogen flow is too high, the first wafer row becomes thinner than the subsequent rows due to the incomplete reaction of the silicon tetrachloride and ammonia. The amount of silicon tetrachloride influences the deposition rate; but if the gas stream is kept fairly dilute, the uniformity is not affected greatly. The baffle section and boat design also influence uniformity. The baffle section (Fig. 2) has an upper deflection plate which helps to direct the flow down towards the bottom of the wafers to help reduce the thin area above the slot mark.

The results of varying the processing parameters were investigated to properly evaluate the deposition system. The effects of changes in source bubbler rates and deposition temperatures, upon both the deposition and etch rates, were examined. In addition, a comparison of the film quality with other deposition systems was made by etching the films in buffered hydrofluoric acid and phosphoric acid. Results are presented in the following paragraphs.

To investigate the effects of varying system parameters, silicon tetrachloride was bubbled at three different rates, and each of these rates was repeated in the 850°-950°C deposition temperature range at 25°C steps. The results are shown in Fig. 4. The deposition rate showed an increase with both increased deposition temperature and bubbler rates.

As mentioned previously, the nitride film requirements are a thickness of 2100 ± 400 Å and an etch rate in buffered hydrofluoric acid of 11 ± 3 Å/min. Figures 5 and 6 represent typical data for 45 runs showing a plot of average thickness and average etch

² Flowrates are based on data supplied by the Brookes Instrument Division of the Emerson Electric Company.

Fig. 3. Silicon wafers with nonuniform thickness of silicon nitride.



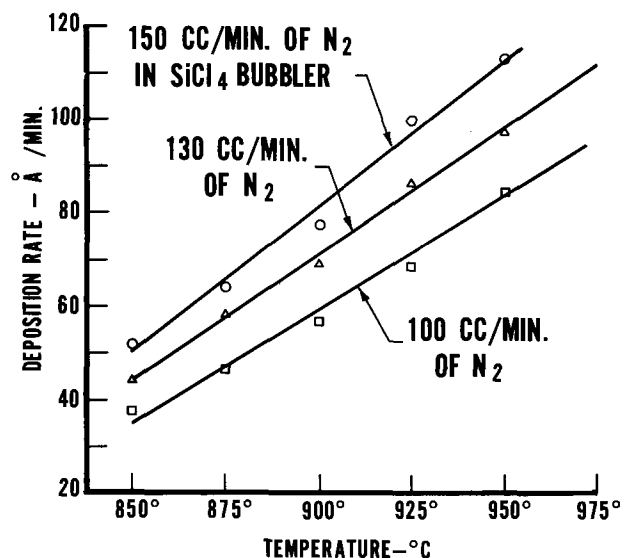


Fig. 4. Deposition rate vs. furnace temperature for several bubbler rates of nitrogen in silicon tetrachloride at 10°C.

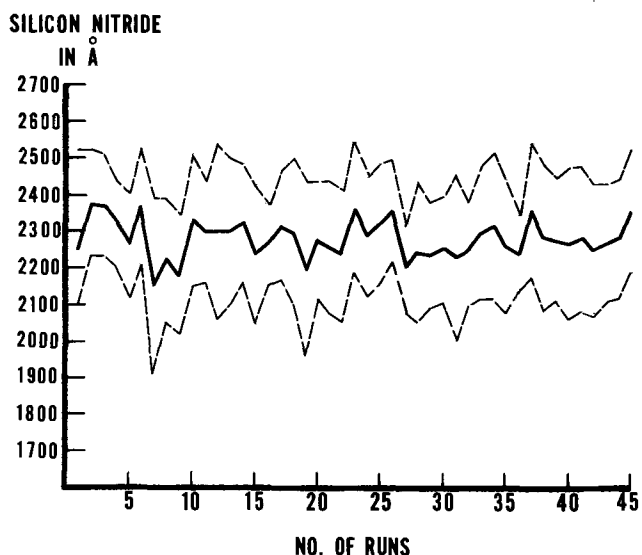


Fig. 5. Thickness of silicon nitride vs. deposition runs

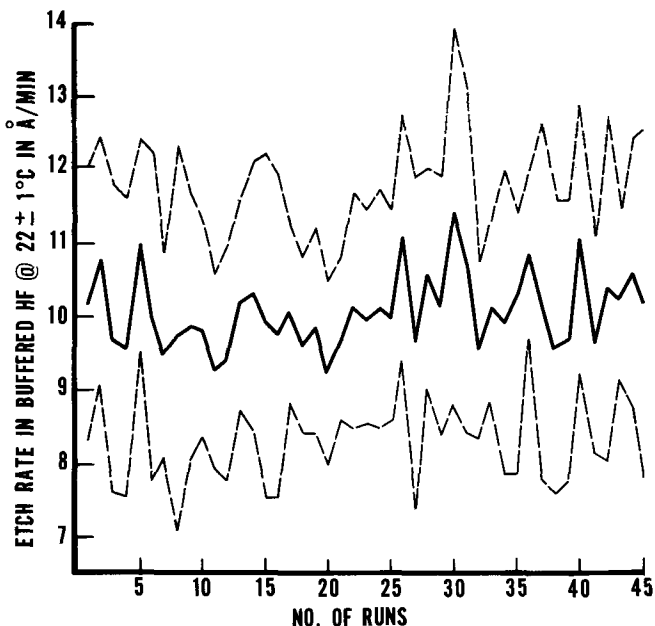


Fig. 6. Etch rate of silicon nitride in buffered hydrofluoric acid vs. deposition runs.

rate with their 2σ limits, respectively. A sample of five wafers, one from each row, was used to calculate the value. The maximum variation of average thickness between runs was less than 250Å and etch rate variation was less than 2 Å/min.

Because silicon nitride is used as a mask against buffered hydrofluoric acid, and is etched in hot phosphoric acid, the etch rate as a function of deposition temperature was measured in these etching solutions. Over the increasing deposition temperature range investigated, the etch rate in buffered hydrofluoric acid decreased slightly. This has been shown to be caused by an increase in the density of the silicon nitride (5). Figure 7 is a plot of this data. The information presented in Fig. 8 shows that the silicon nitride etch rate in boiling phosphoric acid at 180°C also decreases with increasing deposition temperature. The rates in phosphoric acid compare favorably with those reported by VanGelder and Hauser (6).

The index of refraction has been measured over a three month period and found to be in the range of 1.94-2.00. The measurements were made, with an ellipsometer at $\lambda = 5460\text{Å}$, of silicon nitride deposited upon blank silicon wafers. The density of silicon nitride

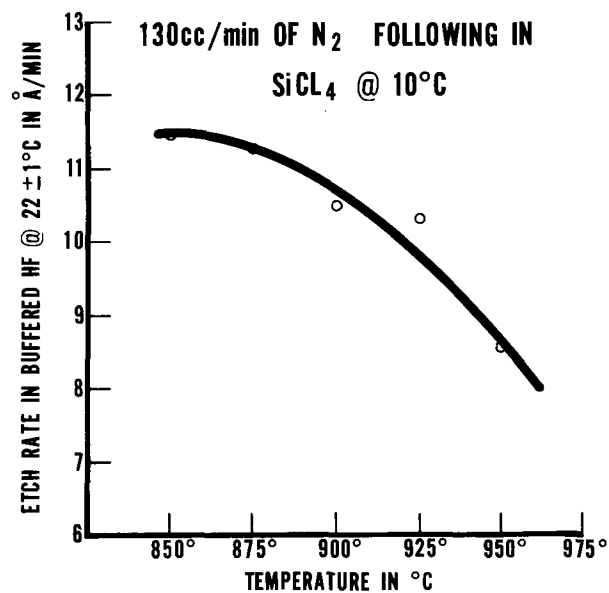


Fig. 7. Etch rate of silicon nitride in buffered hydrofluoric acid vs. deposition temperature.

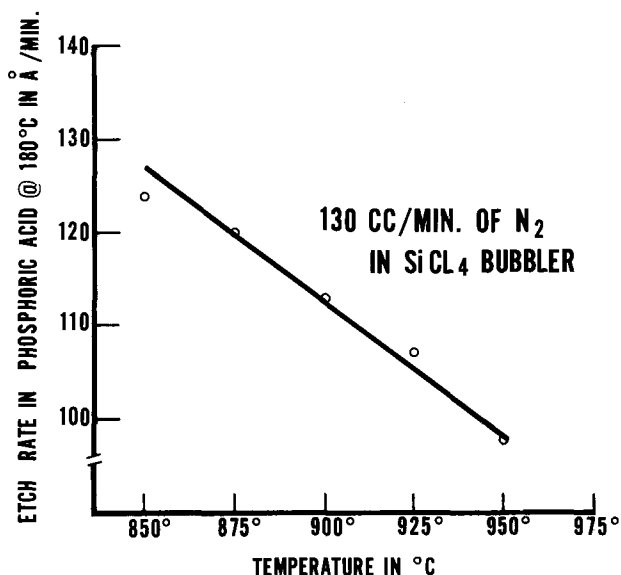


Fig. 8. Etch rate of silicon nitride in boiling phosphoric acid at 180°C vs. deposition temperature.

was determined by a weighing technique to be approximately 2.9 g/cc. Silicon nitride was deposited on polished silicon wafers which had been previously weighed. The area covered by the nitride was measured and the average thickness measured. The wafers were reweighed and the density calculated. The wafers were etched clean of silicon nitride and reweighed to verify the previous reading.

Using the deposition systems described, limited studies have been conducted on MOS properties of silicon nitride on silicon. Our results indicated the surface state density, N_{ss} , to be in the order of $10^{12}/\text{cm}^2$ and the capability to consistently deposit films in the 300Å range. This is comparable to that reported by Chu *et al.* (7) and Doo *et al.* (8). However, we have not studied charge storage effects or other properties presently considered important for gate dielectrics.

Sodium Penetration Testing

A radioactive tracer technique (3) is used to test the effectiveness of silicon nitride as a barrier to sodium penetration. Radioactive sodium in the form of sodium chloride is evaporated onto the film in a vacuum, heated to 600°C for 22 hr, and diffusion allowed to take place. Using a scintillation detector, a count of the gamma radiation from the Na^{22} is obtained for the surface and following each etch step to develop a profile. If after 50Å have been removed only 8% of the original concentration remains, it is implied that the film is a reliable barrier against sodium. The films deposited in this system consistently pass this test. A less sophisticated method of evaluating silicon nitride is by actually subjecting devices to a sodium chloride solution (10g NaCl/100 ml H_2O) during a certain baking period of 300°C for 8 hr, and then testing the semiconductor devices for high leakage currents.

Conclusion

An operating high production system for the deposition of silicon nitride using the ammonolysis of silicon

tetrachloride has been described. The unit has the capability of at least 60 wafers/run.

From the data presented, it has been shown that the system has repeatability and reliability over a large number of runs with silicon nitride varying less than $\pm 250\text{Å}$ within the run. The assembly costs are relatively inexpensive, and the actual operation is quite simple and reliable.

Acknowledgments

We are grateful for the technical discussions with R. E. Caffrey, V. E. Hauser, R. Berman, and E. B. Slutski of the Bell Telephone Laboratories; to Mrs. Kay Locke for performing many sodium penetration tests; and to D. H. Wyker and J. S. Pitsko for the valuable experimental assistance.

Manuscript received July 30, 1971; revised manuscript received Jan. 10, 1972. This was Paper 91 presented at the Washington, D.C., Meeting of the Society, May 9-13, 1971.

Any discussion of this paper will appear in a Discussion Section to be published in the June 1973 JOURNAL.

REFERENCES

1. T. M. Buck, F. G. Allen, J. V. Dalton, and J. D. Struthers, *This Journal*, **114**, 862 (1967).
2. J. V. Dalton, "Sodium Drift and Diffusion into Silicon Nitride Films," RNP presented at Electrochem. Soc. Meeting, Cleveland, May 1-6, 1966.
3. J. V. Dalton and J. Drobek, *This Journal*, **115**, 865 (1968).
4. E. MacKenna, V. Rodriguez, and P. Kodama, Paper 146 presented at Electrochem. Soc. Meeting, Atlantic City, Oct. 4-9, 1970.
5. J. T. Milek, "Silicon Nitride for Microelectronics Applications," Part 1, p. 21, IFI/Planum Data Corp., New York (1971).
6. W. VanGelder and V. E. Hauser, *This Journal*, **114**, 869 (1967).
7. T. L. Chu *et al.*, *Solid-State Electron.*, **10**, 897 (1967).
8. V. Y. Doo, D. R. Kerr, and D. R. Nichols, *This Journal*, **115**, 63 (1968).

Dislocation Etch for (100) Planes in Silicon

F. Secco d' Aragona

Dow Corning Corporation, Solid State Research and Development, Hemlock, Michigan 48626

ABSTRACT

A new etch composed of a dilute aqueous solution of an alkali dichromate and hydrofluoric acid, for suitably revealing dislocations and other lattice defects in (100) planes of silicon, is reported. The etch is fast (typically 5 min), brings out both lineage (low angle grain boundaries) and slip lines, and works over a wide range of resistivities for n- and p-type material. The application of the etch is not restricted to (100) planes; dislocation etch pits are formed on all crystallographic orientations. The same etching characteristics were found with dilute aqueous solutions prepared from various chromium compounds and hydrofluoric acid.

The two etches primarily used to reveal dislocations in silicon are the Dash etch (1) and the Sirtl etch (2). The Dash etch yields deep etch pits on any surface independent of its crystallographic orientation. It has, however, the drawback of requiring long etching periods (4 to 16 hr) and is sensitive to oxygen impurity concentration.

The fast working Sirtl etch is almost exclusively used as a preferential etch for crystallographic defects in silicon but fails to produce pits on (100) planes and on planes close to (100) orientation [e.g., (115)]. Mounds are formed instead, resulting in a rough sur-

face and loss of detail. Using a modified Sirtl etch, a correlation between mounds and dislocations has been reported recently (3). However, the effectiveness of the etch is hindered due to the formation of numerous mounds of various sizes which do not appear to be related to dislocations.

In view of the previous difficulties, an effort was made to develop an improved dislocation etch for (100) planes of silicon. Such an etch should meet the following minimum requirements: (i) well-defined (deep) etch pits must be developed at the emergence points of all dislocations, including slip and lineage arrays; (ii) the etch must work for a wide range of resistivities and for n- and p-type material; (iii) the etch must

Key words: silicon crystals, etchants, dislocations, crystal imperfections.

work in a reasonably short time and be sensitive only to crystallographic defects (avoid surface roughness and formation of artifacts). An etch containing a dilute aqueous solution of an alkali dichromate and hydrofluoric acid was found which meets the above requirements. Moreover, the etch is isotropic in that it appears to reveal dislocations on surfaces of all orientations.

Experimental

Before etching, the silicon wafer is chemically polished. This step is important because a rough or dirty surface will automatically cause a poor etching. Any modification of the $\text{HNO}_3\text{-CH}_3\text{COOH-HF}$ polishing mixture leading to a shiny surface can be used. A commercial polishing solution of the composition $\text{HNO}_3/\text{CH}_3\text{COOH/HF}$ (3:2:2) was used in our experiments. After 2-3 min, the polishing solution is rapidly flushed away with water. Particular care should be taken not to touch the wafer with the fingers or gloves, as this can result in subsequent anomalous etching effects. The standard dislocation etch recommended consists of one part by volume of a 0.15 molar solution of $\text{K}_2\text{Cr}_2\text{O}_7$ in distilled H_2O and two parts HF (49%). The etchant was tested on (100) wafers cut from dislocated crystals of different resistivities and type. The resistivity range was from 0.01 to 10,000 ohm-cm. P-type (doped with boron) and n-type (P, As, Sb) crystals were examined.

An etching time of 20 min is necessary to bring out dislocation pits of a size suitable for counting purposes in crystals with resistivities between 1 and 10,000 ohm-cm. Agitation strongly reduces the etching time. By using ultrasonic agitation, it can be lowered to 5 min. Ultrasonic agitation also leads to an improved surface appearance, avoiding bubble formation, and is, therefore, recommended. Lower resistivity wafers require longer etching periods of the order of 10-15 min with agitation. After a few minutes of etching, the etch changes to a brown-green color. This is due to the formation of Cr^3 cations and does not seem to affect the strength of the solution significantly.

The bulk etching rate was determined from thickness measurements at etching intervals of 10 min for dislocated and dislocation-free wafers in the resistivity range 4-300 ohm-cm, p- and n-type. Thickness measurements were made with a precision micrometer on a circular zone of approximately 8 mm diam in the center of the wafer. The wafer was held vertically and the etch temperature was kept between 25° and 30°C.

Results

A dark field view of a (100) Czochralski wafer etched 5 min is shown in Fig. 1. Perpendicular slip lines, which are dense near the periphery and less pronounced toward the center, are visible. Figure 2 shows a (100) wafer cut from a float-zoned crystal of $\langle 111 \rangle$ orientation. The white irregular lines, mostly radiating from the center of the wafer, are lineage or low angle grain boundaries. A closer view of the etch pits forming slip and lineage is given in Fig. 3.

In order to demonstrate that each etch pit corresponds to a dislocation, an x-ray topograph of a (100) wafer was compared to an optical image of the etch pattern of the same wafer (Fig. 4a and b). Superimposing a magnified view of the topograph to the etch pattern resulted in Fig. 4c which shows that a one-to-one correspondence between etch pits and dislocations does exist.

The effect of the etch is not restricted to (100) planes. An optical micrograph showing the shape of the dislocation pits on four different planes is given in Fig. 5. The shape of the pits varies from elliptical to circular. This indicates a basically nonpreferential character of the etch. The pits exhibit shapes no longer dictated by crystal symmetry, as in the case of the Sirtl etch, but instead they develop a pattern due to the pursuit of defects down into the crystal. When the dislocation line is perpendicular to a certain crystallographic plane, a

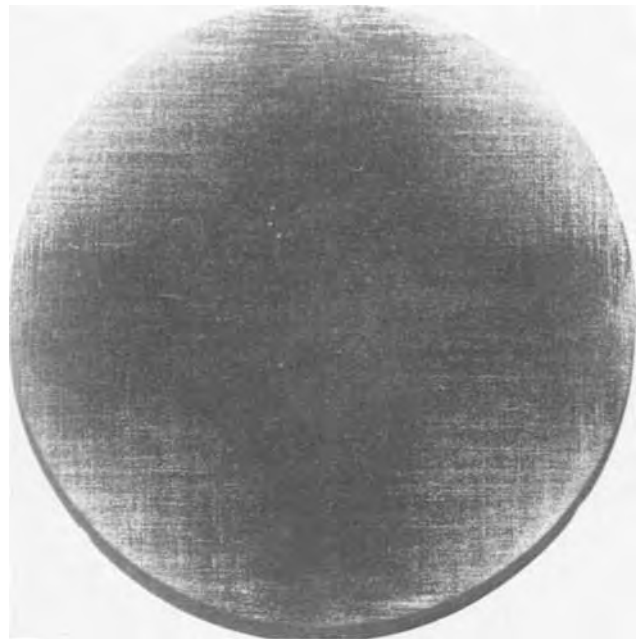


Fig. 1. Slip lines on a (100) Czochralski wafer, p-type (boron) with $\rho \approx 300$ ohm-cm; etching time, 5 min.

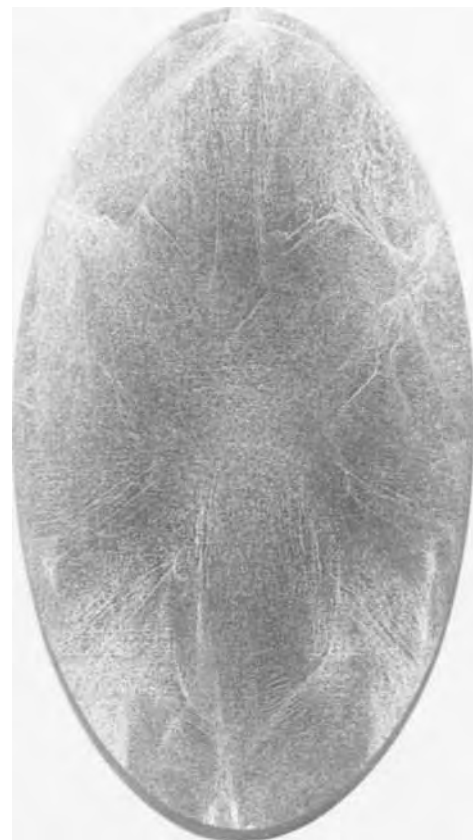


Fig. 2. Low angle grain boundaries (lineage) on a (100) wafer cut from a float zone crystal of $\langle 111 \rangle$ orientation, n-type (phosphorous) with $\rho \approx 1000$ ohm-cm; etching time, 5 min.

circular pit will form as a result of the symmetrical circular strain around the dislocation. As expected, more circular pits are present on (110) planes. These are probably due to dislocations aligned in the $\langle 110 \rangle$ direction meeting the surface under an angle of 90°. On the other planes, the orientation of the elliptical pits is mostly random and determined by the angle the dislocation line makes with the surface. Variation in

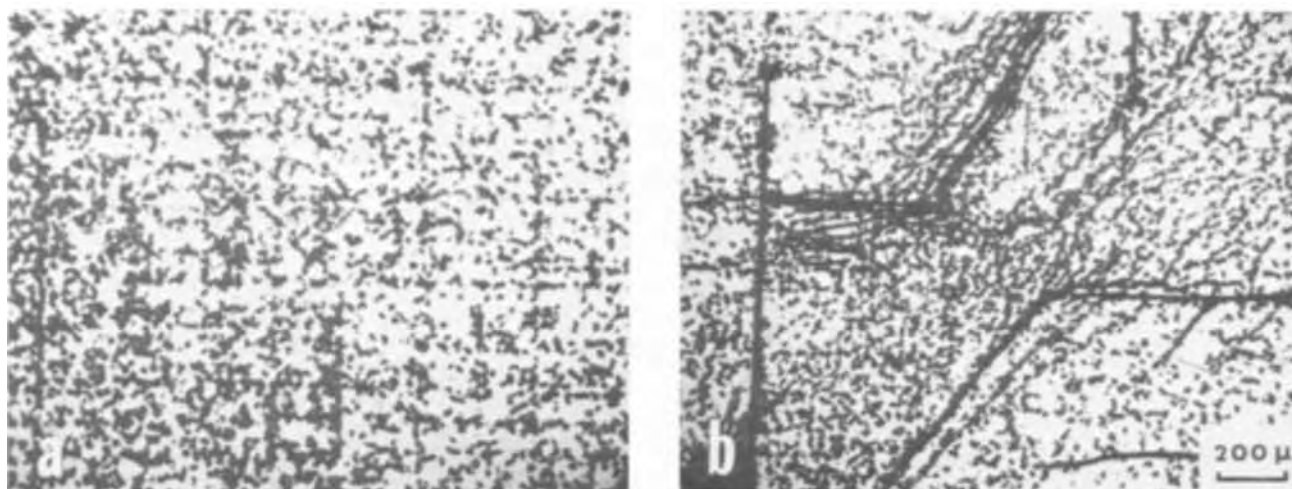


Fig. 3. Magnified view of the etch pits of the slip lines (a) and low angle grain boundaries (b)

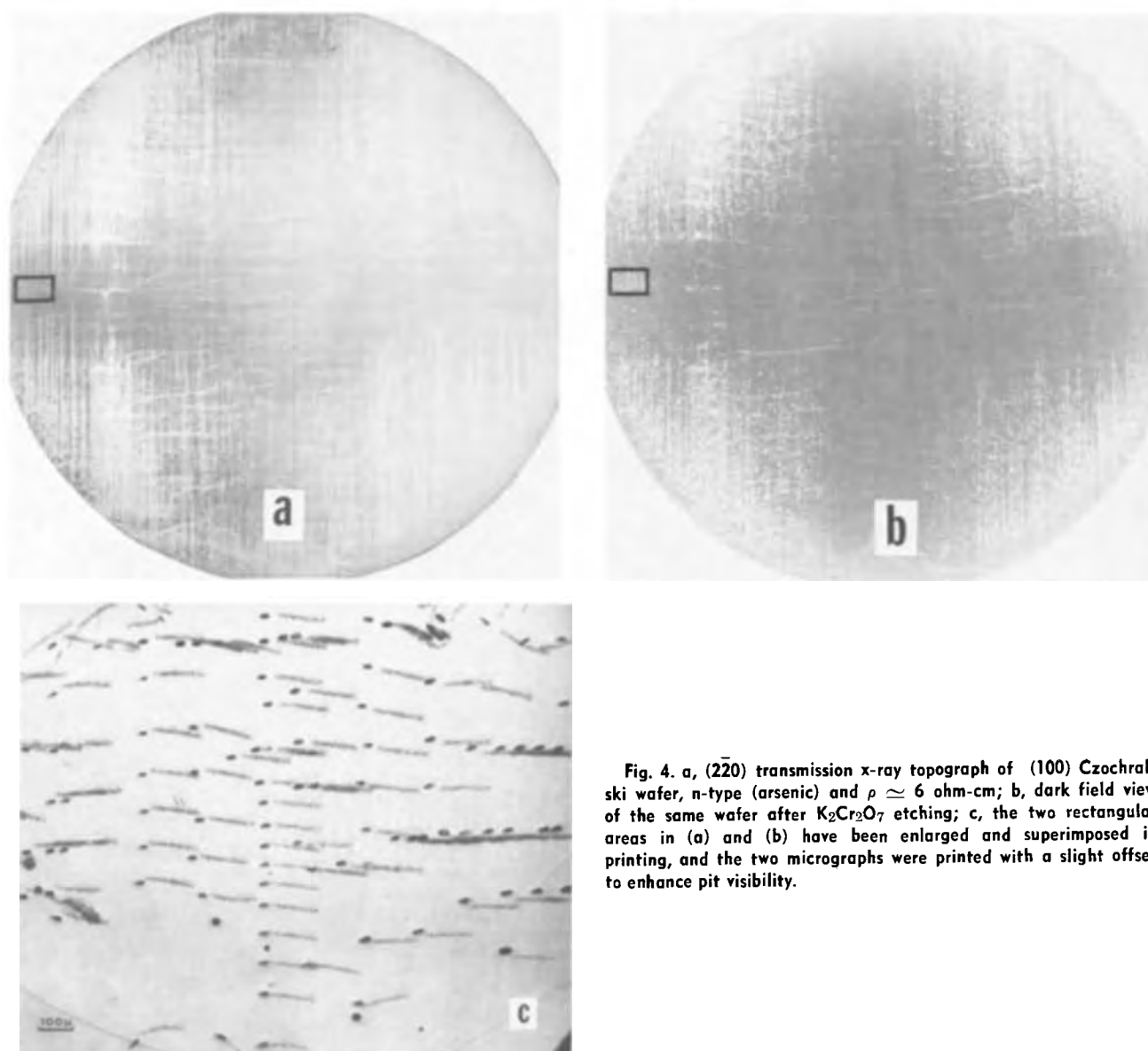


Fig. 4. a, $(\bar{2}20)$ transmission x-ray topograph of (100) Czochralski wafer, n-type (arsenic) and $\rho \approx 6$ ohm-cm; b, dark field view of the same wafer after $K_2Cr_2O_7$ etching; c, the two rectangular areas in (a) and (b) have been enlarged and superimposed in printing, and the two micrographs were printed with a slight offset to enhance pit visibility.

pit shapes at dislocations in germanium, when the ratio of HF to HNO_3 is varied, was reported by Faust (4).

When dislocation-free crystals grown by the float zone method are Sirtl etched, swirls of shallow triangular pits are usually seen on (111) planes. These pits are thought to be due to vacancy clusters (5) and

have been extensively described (6). Due to the non-preferential character of the dichromate etch, the same defects cause shallow circular pits and their shape does not vary with the orientation of the silicon slice.

A typical curve for the bulk etching rate of the standard mixture is represented in Fig. 6. The etching

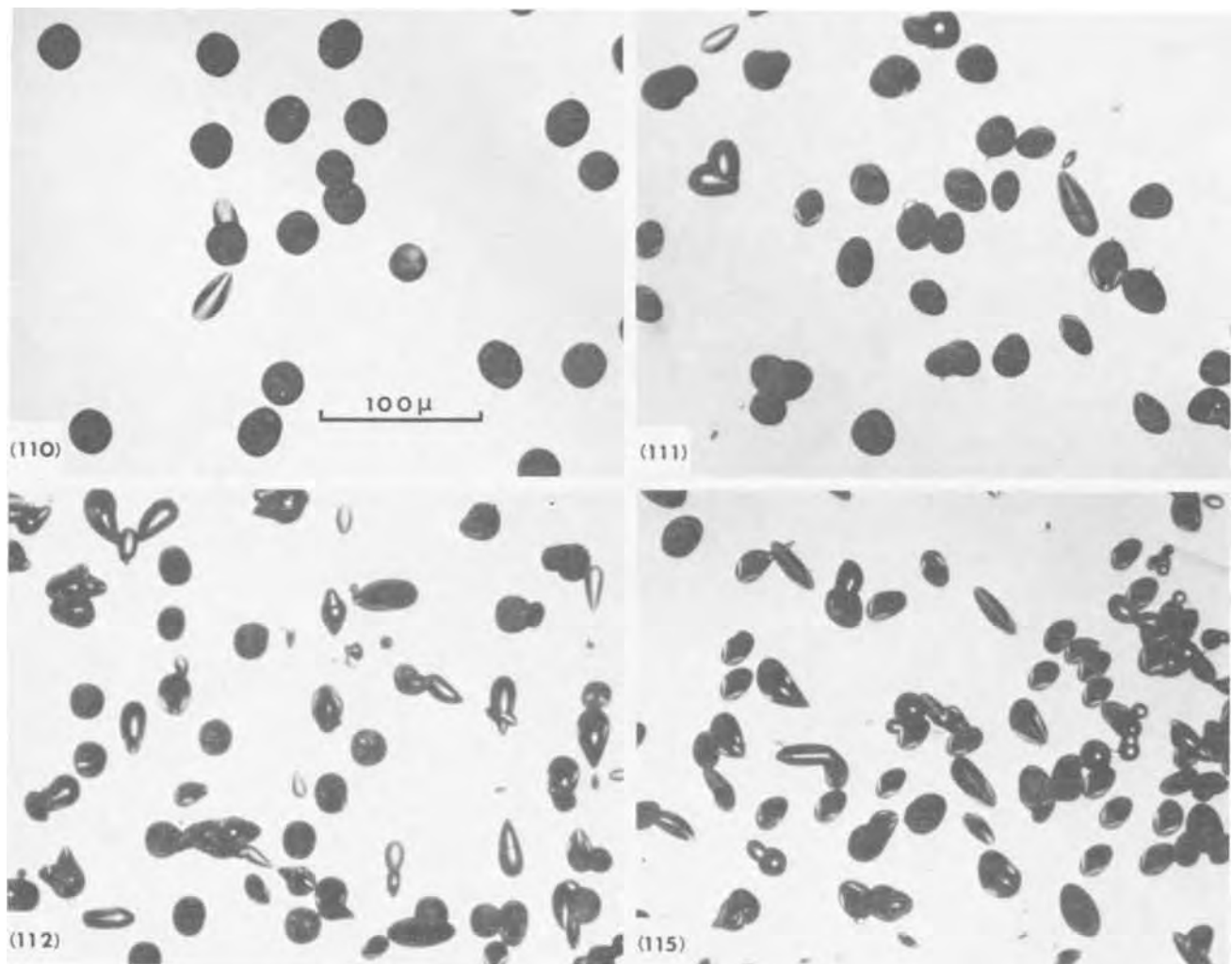


Fig. 5. Appearance of dislocation pits on (110), (111), (112), and (115) planes

rate is linear and equal to approximately $1.5 \mu/\text{min}$. No appreciable variation in etching rate exists between dislocated and dislocation-free crystals. Other lattice defects such as, for example, the hillocks of the swirl pattern (6), stacking faults, twin boundaries, etc., are also revealed by the etch.

The results reported above refer to a dilute (0.15M) aqueous solution of $\text{K}_2\text{Cr}_2\text{O}_7$ and HF. Etch pits with properties similar to those described may be formed also by using $\text{Na}_2\text{Cr}_2\text{O}_7$ as the oxidizing agent. At first it was thought that the presence of alkali ions in the recommended standard etch causes the better orientation-insensitive etching compared with the CrO_3 -HF

system. However, this concept was disproved when similar results were obtained substituting $(\text{NH}_4)_2\text{Cr}_2\text{O}_7$ or CrO_3 for the alkali dichromate. The main difference between the standard Sirtl etch and the etch described in this paper is a decrease in the content of Cr cations in the present etch accompanied by an increase in the acidity of the solution. These two factors together probably play the most important role in accounting for the different etching characteristics.

Acknowledgment

The author is deeply grateful to E. Sirtl and T. F. Ciszek for many helpful comments during the course of this work.

Manuscript submitted Dec. 20, 1971; revised manuscript received March 3, 1972. This was Paper 60 presented at the Houston Meeting of the Society, May 7-11, 1972.

Any discussion of this paper will appear in a Discussion Section to be published in the June 1973 JOURNAL.

REFERENCES

1. W. C. Dash, *J. Appl. Phys.*, **27**, 1193 (1956).
2. E. Sirtl and A. Adler, *Z. Metallk.*, **52**, 529 (1961).
3. C. E. Hallas and E. Mendel, *J. Appl. Phys.*, **42**, 477 (1971).
4. J. W. Faust, "The Surface Chemistry of Metals and Semiconductors," H. C. Gatos, Editor, p. 151, John Wiley & Sons, Inc., New York (1960).
5. A. J. R. de Kock, *Appl. Phys. Letters*, **16**, 100 (1970).
6. F. Secco d'Aragona, *Phys. Status Solidi* (a), **7**, 577 (1971).

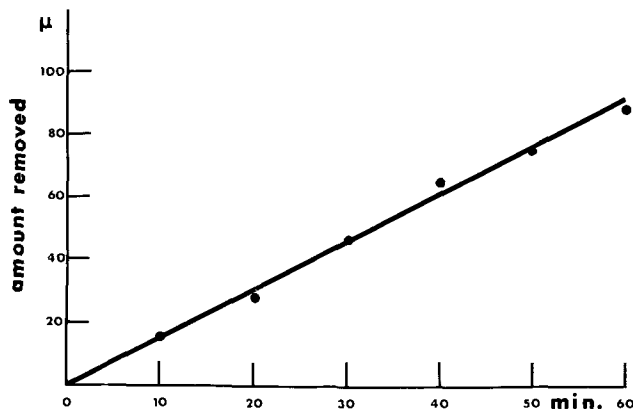


Fig. 6. Etching rate for the dichromate etch

Properties of Vapor-Deposited Aluminum Arsenide

A. G. Sigai,* M. S. Abrahams, and J. Blanc

RCA Laboratories, Princeton, New Jersey 08540

ABSTRACT

Single crystalline epitaxial AlAs layers having donor concentrations as low as $2 \times 10^{17} \text{ cm}^{-3}$ and room temperature mobilities of $294 \text{ cm}^2/\text{V-sec}$ were deposited on GaAs substrates by an open tube vapor-growth technique. The effects of various reaction liners on the purity and electrical properties of the deposited layers are considered. Optical absorption measurements show that in addition to the fundamental absorption edge at about 2.17 eV, a weaker absorption is observed at about 0.96 eV ($1.3 \mu\text{m}$) which is associated with deviations in stoichiometry. The magnitude of this peak depends on the aluminum to arsenic ratio in the gas phase. The observed bending of the epitaxial layer and measured dislocation densities in the AlAs are found to be consistent with previous models dealing with dislocation morphology and the occurrence of bending in epitaxially prepared heterojunction structures.

Because of the large energy gap of AlAs (2.17 eV) and its close lattice and thermal match with GaAs, this material is of potential interest for a variety of electro-optic devices. Alloys of AlAs and GaAs have already provided a multitude of useful devices including visible electroluminescent diodes and injection lasers. However, little is known about the properties of AlAs because its synthesis is complicated by the high reactivity of aluminum compounds at normal growth temperatures which makes high purity single-crystal growth difficult. Also, the reported hygroscopic nature (1) of this material presents difficulties in subsequent physical measurements.

Recently, the preparation of AlAs by an open tube continuous flow vapor growth system has been reported (2). In this system, aluminum is transported as a chloride by reaction of aluminum with HCl, and arsenic is provided by the thermal decomposition products of arsine. Unlike gallium and indium chlorides, the aluminum chlorides have been found to attack quartz reaction tubes. Consequently, protective liners must be used to minimize contamination during growth.

In the present work, the effects of various reaction liners on the purity and electrical properties of the deposited layers are considered. In addition, the optical and structural properties of layers employing this vapor growth technique are determined.

Vapor Growth Apparatus

The basic growth apparatus and technique have been described in detail previously (2) and, therefore, will not be described in detail here. The growth system, shown in Fig. 1, consists of a quartz tube which accommodates either an alumina or carbon liner. Within the liner, a series of alumina or carbon boats is used to contain the aluminum source metal. An alumina or carbon plug with several holes is placed at the end of the liner to provide a high velocity of gaseous aluminum chloride exiting the liner. This was found to be essential for significant epitaxial deposition, since the aluminum chloride and arsine react to form AlAs immediately at the points where the two gases begin to mix, independent of the mixing temperature or concentrations of the reacting species. Without the high gas velocity the AlAs would otherwise form at a point too close to the exit of the alumina liner to properly position a substrate.

In some experiments, a tungsten liner (not shown) is used in the deposition region, in addition to the alumina liner, plug, and boats, to further reduce the attack of the quartz by the aluminum chloride. In other experiments, all the alumina components were replaced with high purity carbon, as shown in Fig. 1, and the

tungsten liner was replaced by a uniform carbon coating which was formed by the pyrolysis of electronic grade acetone at 1000°C . The GaAs substrates were supported by a carbon substrate holder on the end of a carbon-coated quartz growth rod.

The AlAs layers were deposited at 1000°C on undoped GaAs substrates oriented 3° from the {100} plane. The substrates were chemically polished in a 5:1:1 $\text{H}_2\text{SO}_4:\text{H}_2\text{O}_2:\text{H}_2\text{O}$ solution for 1 hr followed by a 1 min polish in a 1% bromine-methanol solution just prior to growth. With nominal flow rates of 0.8 liters/min of 3% AsH_3 in H_2 and 2.3 liters/min of 1% HCl in H_2 , growth rates of 1 to 2 mils/hr were realized.

The carbon components (boats, plug, and liner) were chemically cleaned and baked prior to initial use. The chemical cleaning consisted of an immersion in aqua regia for 5 hr followed by a 24 hr reflux in deionized triply-distilled water. The carbon was then fired in air at 280°C for 3 hr after which it was fired in hydrogen at 1000°C for 4 hr. Just prior to their use in the growth assembly, the carbon components were re-heated in vacuum at 1500°C for 4 hr to remove adsorbed gases and other volatile constituents.

General Properties of Deposited Layers

The AlAs epitaxial layers were single crystalline as confirmed by the Laue back-reflection x-ray technique and were typically between 3 to 5 mils thick, although layers as thick as 15 mils have been deposited. The AlAs deposit initially appeared metallic, but on contact with air, developed uniform interference colors. After the appearance of a few fringes, very little further reaction with the atmosphere was observed. Electrical measurements on several samples (to be discussed later) stored in dry air were repeatable and reproducible several weeks later. This suggests that the reported rapid deterioration of this material (1) occurs only on the surface and that the properties of the bulk are maintained appreciably longer. The stability of the layers appeared to depend on the nature of the ambient and the crystalline quality of the deposit.

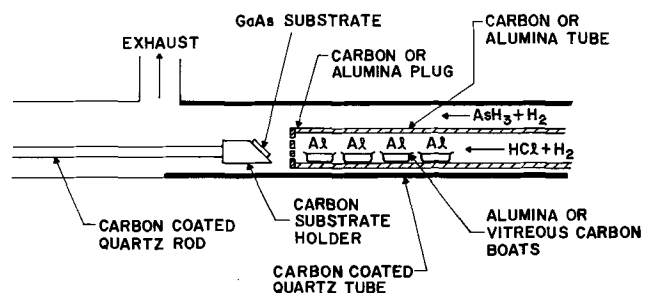


Fig. 1. Apparatus used for the vapor growth of AlAs

* Electrochemical Society Active Member.

Key words: epitaxial AlAs layers, vapor growth AlAs, optical absorption, electrical properties, dislocation structure.

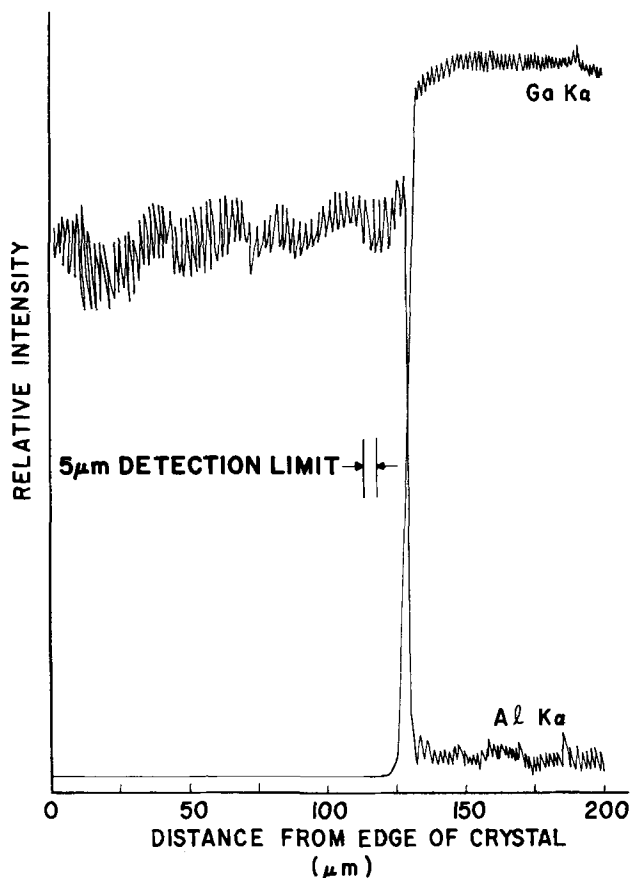


Fig. 2. The relative intensities of the Ga K_{α} and Al K_{α} wavelengths as a function of distance from the edge of the crystal along the growth direction determined on the $\{110\}$ plane.

Of key importance for proper interpretation of the electrical, optical, and structural properties presented here is the extent of interaction between the AlAs and the GaAs at the epitaxy-substrate interface after several hours growth at 1000°C . Therefore, a sample was cleaved parallel to a $\{110\}$ plane (*i.e.*, perpendicular to the growth direction) and examined by electron microprobe analysis. Using separate spectrometers, the relative Ga and Al concentrations were determined by monitoring the Ga and Al K_{α} intensities, respectively. The results were made quantitative by using polished single crystalline AlAs and GaAs as standards. The results of the analysis are presented in Fig. 2. The Ga intensity has been corrected for fluorescence of the As K_{α} on the AlAs side of the junction. The random variation in intensity observed for the Al K_{α} is believed to be due to variations in surface topography rather than in concentration, since complementary variations in the Ga K_{α} intensity are not observed. Clearly, the amount of interdiffusion, if it exists at all, is less than $5\ \mu\text{m}$, which is the limit of detection under the experimental conditions used.

Structural Properties

One question important for potential device fabrication is the degree of strain which may be present in an AlAs epitaxial layer which has been deposited on a GaAs substrate. For thick (> 5 mils) as-grown AlAs layers deposited on undoped substrates, the epitaxy-substrate composite is typically bowed strongly toward the GaAs substrate. Furthermore, during routine processing of relatively thin (3 mil) layers, the AlAs frequently cleaved into several pieces upon removal of the GaAs substrate. Both observations suggest the presence of large strain in these layers, which at first appears to be inconsistent with the reported (3) similarities of the room temperature lattice parameters ($a_{0\text{AlAs}} = 5.6610\text{\AA}$, $a_{0\text{GaAs}} = 5.6533\text{\AA}$) and thermal expansion coefficients ($\alpha_{\text{AlAs}} = 5.2 \times 10^{-6}$, $\alpha_{\text{GaAs}} = 6.6 \times$

10^{-6}). In fact, the excellent lattice and thermal match has been thought to play an important role in the excellent device performance of (Ga,Al)As electro-optic devices.

Both observations, however, can be explained on the basis of previous models dealing with the dislocation morphology (4) and the occurrence of bending (5) in epitaxially prepared heterojunction structures. According to these models, an orthogonal array of misfit dislocations will form at or near the heterojunction due to the difference in lattice parameter between the substrate and epitaxial layer. When the misfit dislocations bend out of the plane of growth, they give rise to inclined (4) dislocations whose density is n_I . As shown in earlier work (5), the edge components of the inclined dislocations produce a bending moment in the crystal if the extra half-planes of these dislocations are parallel to each other.

A value of $n_I = 1 \times 10^6\ \text{cm}^{-2}$ is calculated (4) by using the lattice parameters (3) appropriate to the growth temperature of 1000°C . Using this value for n_I , the calculated (5) radius of curvature of an isolated AlAs layer is 17 cm. This radius of curvature is in reasonable agreement with the value of 10 cm measured from a bowed layer of AlAs that had been isolated from its substrate. A similarly grown sample was examined by transmission electron microscopy; the value of n_I here was found to equal $7 \times 10^6\ \text{cm}^{-2}$. Furthermore, the transmission electron micrograph of the dislocations in the AlAs layer, shown in Fig. 3, indicates that the inclined dislocations do tend to align, which is consistent with the proposed model (5). [Direct observation of the sense of bending of the inclined dislocations in III-V compounds will be published in due course (6).] Also, the layer would be expected (5) to bend toward the GaAs as observed. The difference between the calculated and measured values of n_I most likely arises from the uncertainty in the lattice parameters. The values of the lattice constant at 1000°C for AlAs and GaAs are $5.6899 \pm 0.0005\text{\AA}$ and $5.6906 \pm 0.0005\text{\AA}$, respectively. Within the specified limits, the calculated value of n_I may vary by a factor of 4.

Further electron microscopical studies were performed on $\{110\}$ cross-sectional planes which are normal to the $\{100\}$ plane of growth. Examination of these specimens revealed the presence of an interfacial layer about $1\ \mu\text{m}$ thick at the position of the original

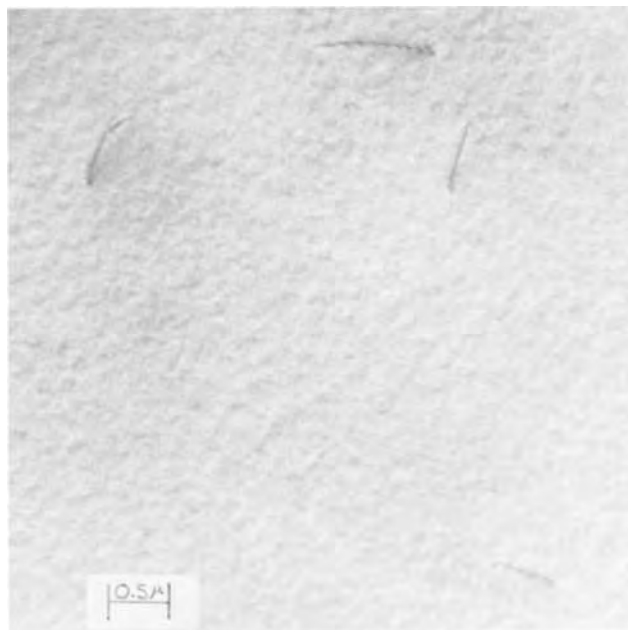


Fig. 3. Transmission electron micrograph showing inclined dislocations in AlAs.

growth interface. Although the interfacial layer has not been identified, the bond strengths of the interfacial layer must be substantially different from either GaAs or AlAs. This is based on the observation that during thinning of the GaAs/AlAs interface on the {110} plane by ion bombardment for TEM studies, the etch rates of the various layers in the GaAs-interface-AlAs composite were significantly different. Practically all of the GaAs substrate was removed, clearly delineating the interface before any appreciable thinning of the interface occurred. Furthermore, a good deal of the AlAs was completely removed before the interface was thinned sufficiently for transmission of the 100 keV electron beam. It is believed that this layer has little direct effect on the bending of the composite epitaxial layer-substrate sandwich. This is because the similarity of GaAs and AlAs cause approximately equal and opposite effects at the respective interfaces. However, stacking faults with a density of $3 \times 10^6 \text{ cm}^{-2}$ were also present in the AlAs. The presence of faults is unexpected since the substrate surface was free of work-damage (7) and since both the substrate and epitaxial layer contained no second-phase particles (8). This high stacking fault density may well be due to the presence of the interfacial layer. It should be noted that the lattice spacing of the intermediate layer normal to the growth direction must be close to that of both AlAs and GaAs, since it would otherwise give rise to higher values of n_1 than are actually observed.

The effect of strain due to differential thermal expansion was also calculated (3, 9), resulting in an expected radius of curvature of 47 cm. Any effect of the intermediate layer was neglected. This radius is clearly too large to account for the observed bending.

In view of the uncertainty in the lattice constants, the presence of a high density of stacking faults, and the presence of an interfacial layer of unknown composition, the conclusions drawn above dealing with the inclined dislocations and the radii of curvature are undoubtedly simple-minded. Nonetheless, application of this model to this system satisfactorily accounts for our observations of dislocation densities and bending.

Electrical Properties

As-grown AlAs layers.—The electrical properties of the vapor deposited AlAs were determined by standard Hall measurements on layers which were first removed from the substrate. Ohmic contacts were made by ultrasonically bonding indium and by annealing at 700°C for 5 min in a hydrogen atmosphere. Thicknesses greater than 3 to 4 mils were required to avoid cracking the layers. Table I summarizes the electrical properties of several AlAs layers which were vapor-deposited with various modifications to the growth system. Also included is the impurity analysis of each sample, determined either by mass or emission spectrographic techniques. In the first series of runs employing only the alumina boats, liner, and plug, the layers were found to be unintentionally doped n-type

and show high concentrations of Si. This is to be expected based on the high reactivity of Al-compounds at high temperature and the use of a quartz reaction tube. Note also the correlation between the free electron concentration (from Hall measurements) and the concentration of Si (from mass and emission spectrographic analyses), suggesting Si as the predominant electrically active impurity. This is consistent with the observation that Si is the predominant donor impurity in many other III-V compounds prepared by similar vapor growth techniques (10).

Based on this hypothesis, a second series of runs was carried out employing an outer tungsten liner in the deposition zone to further reduce the observed attack of the quartz reaction tube. The tungsten liner was used in addition to the alumina components and liner in the source zone. Runs 3·23 and 3·24 in Table I clearly show a reduction of Si contamination by an order of magnitude with a corresponding reduction in the measured free electron concentration. Even with the tungsten liner, trace amounts of Fe, Cu, and Mg were present. These could originate from the alumina plug and boats since they contained 0.05% SiO₂, 0.1% Fe₂O₃, as well as a multitude of other trace impurities.

In a third series of experiments, efforts were made to reduce the Si contamination even further by replacing the tungsten liner with a pyrolytic carbon coating on the quartz reaction tube in the source and deposition zones and by replacing the alumina boats, plug, and liner with carbon components. The results in Table I show that the free electron concentration was reduced to $2 \times 10^{17} \text{ cm}^{-3}$ with reduced amounts of Fe, Cu, and Mg. However, some reaction with the carbon and quartz was observed which may have been related to pinhole cracks in the carbon coating. This may also account for the relatively high Si concentration in these samples compared to other III-V compounds grown by this technique.

In Fig. 4 the mobility of the unintentionally doped n-type vapor-deposited samples are plotted as a function of electron concentration. Although no simple curve is apparent, a general trend of increasing mobility with decreasing carrier concentration is observed. The carrier concentration of $2 \times 10^{17} \text{ cm}^{-3}$ and mobility value of 294 cm²/V-sec represent the lowest concentration and highest room temperature mobility values obtained for our vapor-grown AlAs.

P-type doping.—It has been demonstrated previously (11) that Zn can be satisfactorily diffused into vapor-deposited AlAs layers to form p-n junctions which emit near bandgap radiation at room temperature. However, it is also of interest to examine the feasibility of growing p-n junctions *in situ*. Therefore, using a doping arrangement similar to that described by Tietjen (12) for GaAs and GaP, Zn vapor was introduced into the reaction tube during growth. Although a very high Zn concentration ($>10^{-3} \text{ atm}$) was obtained in the gas phase, mass spectrometric analyses of several layers revealed that only about 1 ppm Zn was incorporated into the AlAs, which is not sufficient

Table I. Impurity analysis and electrical properties of vapor-deposited aluminum arsenide

Alumina components		Analysis technique	Element (ppma)*			
Run No.	$n \text{ (cm}^{-3}\text{)}$		Si	Fe	Cu	Mg
2·18	1.4×10^{18}	Mass spec.	110	1.7	0.6	1.0
2·25	6.4×10^{18}	Mass spec.	200	1.2	1.0	0.6
3·2	4.0×10^{18}	Emission spec.	30-300	1-10	0.1-1	1-10
3·19	1.9×10^{18}	Emission spec.	5-50	0.6-6	1-10	0.3-3
Alumina components with tungsten liner in deposition zone						
3·23	3.6×10^{17}	Emission spec.	2-20	1-10	0.3-3	N.D.
3·24	5.3×10^{17}	Emission spec.	1-10	N.D.	0.03-0.3	1.5-15
Carbon components with carbon coating of quartz tube						
8·20	2.0×10^{17}	Emission spec.	1-10	N.D.	N.D.	0.03-0.3

* 1 ppma = $5 \times 10^{16} \text{ cm}^{-3}$.
N.D.—Not detected.

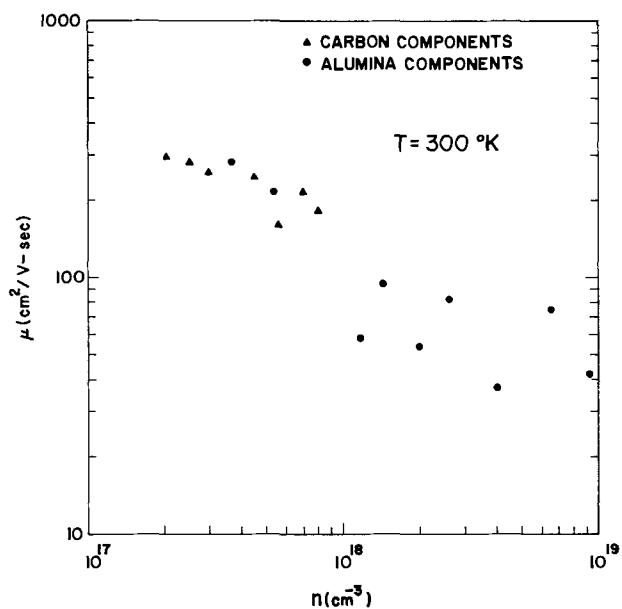


Fig. 4. The variation of electron mobility with free electron concentration for unintentionally doped AlAs. Si is believed to be the electrically active impurity.

to overcompensate the background donor concentration. This inability to obtain p-type AlAs during growth may be related to the presumably high vapor pressure of Zn required for its incorporation into the AlAs at the growth temperature of 1000°C. For example, since the vapor pressure of Zn in the gas phase is introduced at only 10^{-3} atm compared to an equilibrium vapor pressure of Zn at the growth temperature of >1 atm, very little Zn would be expected to be incorporated. Although the activity of Zn in AlAs has not been considered, it is not expected that this would significantly alter these conclusions. These results further suggest that it may also be difficult to incorporate Zn or other volatile dopants at high-growth temperatures into other III-V compounds employing this vapor-phase growth technique.

Optical Properties

For optical absorption measurements, several vapor-deposited AlAs layers were polished flat and parallel on both sides using a chemical-mechanical polish technique with a ½% bromine-methanol solution. Layers at least 5 mils thick were required for the measurements and polishing procedure, since thinner layers inevitably cleaved as the GaAs/AlAs interface was approached. Layers polished in this manner were typically mirror smooth and transmitted orange light. However, a few minutes after exposure to the atmosphere the surface developed blue interference fringes, indicative of oxidation. To avoid appreciable oxidation, layers were stored and transported in trichloroethylene after polishing. Optical measurements were made using a Carey 14 double-beam spectrophotometer which had been thoroughly purged with high purity dry nitrogen prior to use. No apparent change in either the optical density or the general shape of the absorption curve was observed during several scans of the same sample. The absorption coefficient was calculated using the simple relation

$$\alpha = 1/t \ln (I_0/I)$$

where t is the thickness and I_0 and I are the initial and transmitted photon intensities, respectively. Although values of α obtained in this manner could be in considerable error in the region of long wavelengths due to neglecting reflection considerations, the relative values of α are quite reliable. Furthermore, values of α thus obtained were partially corrected for reflectance

and other unaccounted-for absorption losses by subtracting the absorption which was present at wavelengths greater than that of the absorption edge and which remained relatively constant with wavelength. The values thus obtained were used for the subsequent evaluations.

The absorption coefficient of the AlAs layers were found to follow the relation

$$\alpha = K(h\nu - E_G)^m$$

with $m = 2$ for an indirect energy band structure. The energy gap was then determined from a plot of $\alpha^{1/2}$ vs. $h\nu$ with α extrapolated to zero. Analysis of several AlAs samples in this manner have yielded a value of the energy gap at room temperature of 2.17 ± 0.02 eV, which is in excellent agreement with previously published values of 2.15 eV (13) and 2.16 eV (14).

In addition to the fundamental absorption edge, Yim (13) has reported a weaker absorption peak at $1.3 \mu\text{m}$ in vapor-grown AlAs, which he suggested was associated with deviations in stoichiometry. Since this peak had never been observed in vapor-grown samples prepared in the present investigation or in AlAs grown by other techniques (14, 15), efforts were made to determine the existence of such an absorption peak. Several samples were grown using various HCl flow rates over the aluminum source and various flow rates of AsH_3 in order to change the aluminum to arsenic ratio in the gas phase. The absorption curves of these samples are presented in Fig. 5. It can clearly be seen that a peak does indeed exist at $1.3 \mu\text{m}$ and that the intensity of this peak depends on the HCl/ AsH_3 flow rates, and, in turn, on the aluminum to arsenic ratio in the gas phase. This may be the reason why these deviations had not been apparent earlier in melt-grown AlAs (14) or in aluminum-rich (Ga,Al)As layers grown by liquid phase epitaxy (15). These findings demonstrate that the stoichiometry of the material can be controlled during vapor-phase growth by adjusting the Al/As ratio in the gas phase. Similar deviations in stoichiometry have been observed in other vapor-grown III-V compounds such as AlP (16), and, recently, GaAs (17) and Ga(As,P) (18). In the later works (17, 18), the deviations in stoichiometry have been found to have a profound effect on the luminescence properties of the vapor-deposited layers.

Summary and Conclusions

The epitaxial deposition of AlAs layers using the Al/HCl/ AsH_3 vapor-phase growth technique requires many precautions to prevent serious contamination of the grown layers. After examination of several methods for reducing the attack of the quartz reaction tubes, the highest purity layers ($n = 2 \times 10^{17} \text{ cm}^{-3}$ with $\mu = 294 \text{ cm}^2/\text{V-sec}$) were found to be obtained in an all carbon component system. However, the residual

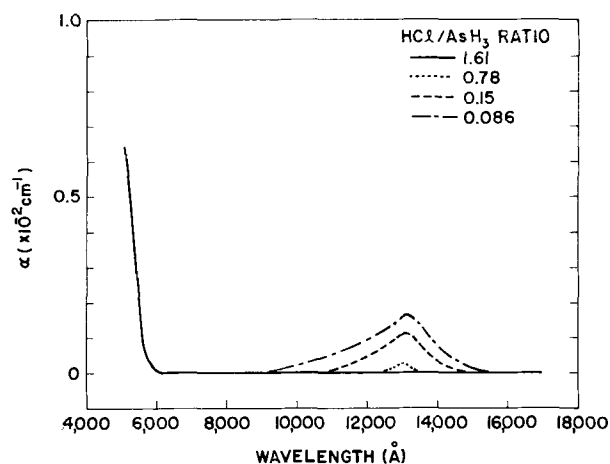


Fig. 5. The optical absorption spectra of several AlAs layers grown under various HCl/ AsH_3 flow rates.

impurity content is still higher than that desired for reproducible control of the electrical properties. The electrically active impurity is thought to be silicon.

P-type layers could not be grown *in situ* by doping with Zn vapor presumably due to the high residual donor concentration and the difficulty with which the Zn is incorporated into the layer at the high growth temperature. Deviations in stoichiometry are suggested by the presence of a 1.3 μm peak in the optical absorption spectra of AlAs grown in an arsenic-rich atmosphere. However, this can easily be controlled by adjusting the Al/As ratio in the gas phase.

Despite the apparent thermal and lattice match between the AlAs epitaxial layer and the GaAs substrate, bending of the heterojunction structure occurs toward the GaAs with a radius of curvature of 10 cm. This observation can be explained on the basis of earlier models in which inclined dislocations, formed by misfit dislocations bending out of the growth plane, produce a bending moment if the extra-half planes of these dislocations are parallel to each other. The calculated inclined dislocation density, $1 \times 10^6 \text{ cm}^{-2}$, is in good agreement with the measured value of $7 \times 10^6 \text{ cm}^{-2}$.

An interfacial layer was found between the AlAs and GaAs. Although this layer was not identified, it is thought that it gives rise to an unexpected stacking fault density of $3 \times 10^6 \text{ cm}^{-2}$.

Acknowledgments

The authors wish to acknowledge E. Bertin, C. Buiocchi, W. Harrington, H. Whitaker, and T. Zamerowski for assistance in various phases of the research. They are also grateful to Drs. R. Enstrom, H. Kressel, C. Nuese, D. Redfield, and D. Richman for valuable discussions and review of this manuscript.

This research was supported by the National Aeronautics and Space Administration, Langley Research

Center, Hampton, Virginia under Contract NAS 12-538 and by RCA Laboratories.

Manuscript submitted Dec. 1, 1971; revised manuscript received March 1, 1972. This was Paper 204RNP presented at the Washington, D.C., Meeting of the Society, May 9-13, 1971.

Any discussion of this paper will appear in a Discussion Section to be published in the June 1973 JOURNAL.

REFERENCES

1. H. M. Manasevit, *This Journal*, **118**, 647 (1971).
2. M. Ettenberg, A. G. Sigai, A. Dreeben, and S. Gilbert, *ibid.*, **118**, 1355 (1971).
3. M. Ettenberg and R. Paff, *J. Appl. Phys.*, **41**, 3926 (1970).
4. M. S. Abrahams, L. R. Weisberg, C. J. Buiocchi, and J. Blanc, *J. Mater. Sci.*, **4**, 223 (1969).
5. M. S. Abrahams, L. R. Weisberg, and J. J. Tietjen, *J. Appl. Phys.*, **40**, 3754 (1969).
6. M. S. Abrahams, J. Blanc, and C. J. Buiocchi, To be published.
7. M. S. Abrahams and C. J. Buiocchi, *J. Phys. Chem. Solids*, **28**, 927 (1967).
8. M. S. Abrahams and J. J. Tietjen, *ibid.*, **30**, 2491 (1969).
9. S. Timoshenko, *J. Opt. Soc. Am.*, **11**, 233 (1925).
10. D. R. Bosomworth, R. S. Crandall, and R. E. Enstrom, *Phys. Letters*, **28**, 320 (1968).
11. C. J. Nuese, A. G. Sigai, M. Ettenberg, J. J. Gannon, and S. L. Gilbert, *Appl. Phys. Letters*, **17**, 90 (1970).
12. J. J. Tietjen and J. A. Amick, *This Journal*, **113**, 724 (1966).
13. W. M. Yim, *J. Appl. Phys.*, **42**, 2854 (1971).
14. M. R. Lorenz, R. Chicotka, and G. D. Pettit, *Solid State Commun.*, **8**, 693 (1970).
15. H. Kressel, Private communication.
16. D. Richman, *This Journal*, **115**, 45 (1968).
17. A. Y. Cho and I. Hayashi, *Solid-State Electron.*, **14**, 125 (1971).
18. C. E. E. Stewart, *J. Crystal Growth*, **8**, 259 (1971).

Optical Response in the Photoselective Metal Deposition (PSMD) Imaging System

J. F. D'Amico,* F. A. Litt, and M. A. DeAngelo

Western Electric Company, Engineering Research Center, Princeton, New Jersey 08540

ABSTRACT

The optical response of a representative PSMD imaging system, stannous chloride sensitized polyimide film, was determined by exposing sensitized substrates to ultraviolet radiation and measuring the resulting decrease in catalytic activity for electroless copper deposition. This activity was determined by measuring light transmission through the deposited metal and substrate.

The imaging reaction photoresponse was measured in the 200-400 nm wavelength range. The sensitivity was found greatest at 200 nm, decreasing monotonically with wavelength. The upper limit for useful imaging in air occurred in the vicinity of 350 nm. The imaging reaction rate was also found proportional to $I^{0.7}$, where I is the incident light intensity. This intensity dependence was found over the entire range of measured wavelengths. An explanation of the system's optical behavior in terms of light-generated electron-hole pairs is offered.

A process for generating metal patterns on dielectric substrates using uv light exposure in combination with electroless (chemical) plating has been reported in a recent patent (1) and in several recent papers (2-7). This process, known as photoselective metal deposition (PSMD), combines conventional electroless plating technology with an imaging procedure added

to the conventional two-step process between sensitization (immersion in aqueous SnCl_2) and activation (immersion in aqueous PdCl_2). Where exposed to the uv radiation, the sensitized substrate becomes non-catalytic in the subsequent metalization procedure. The imaging system is, thus, a positive working one since it generates a replica of the photomask.

The papers cited above contain a general description of the PSMD process and its potential capabilities and uses. In this paper we shall focus on the system's

* Electrochemical Society Active Member.

Key words: photoimaging, pattern generation, ultraviolet photochemistry, electroless plating.

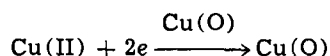
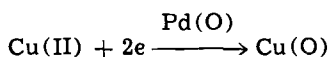
optical characteristics as they relate to the formation of images. Accordingly, we have provided a detailed description and analysis of a specific (but also representative) imaging system: hydrated stannous oxide¹ as sensitizer and, following activation with aqueous palladium chloride, deposited electroless copper. The scope of this paper is limited to effects of the incident radiation, and accordingly, all procedures relating to the substrate preparation and the image development have been arbitrarily fixed. In a future paper, we will report on the role of ambient conditions and substrate preparations in the PSMD system.

We have determined the extent of photoconversion in our system *vs.* incident light wavelength and intensity, using as a basis for analysis the degree of metalization with electroless copper under a fixed set of development parameters. In effect, we have used the imaging reaction itself as an analytical device for evaluation of the extent of reaction. This somewhat indirect procedure has been necessary because a direct quantitative analysis of the sensitizer reaction, Sn(II) → Sn(IV), is not feasible in this range using available methods.

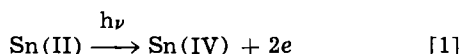
The techniques involving image development, which will be described in detail in this paper, can be used to provide basic information related to the PSMD photoreaction. In addition, they provide the PSMD user with necessary information for the design and operation of practical imaging systems.

Method of Analysis

As previously described (6, 7), the electroless metalization process can be summarized in the following reactions



where the electrons in the electroless copper reactions are provided by a reducing agent in the bath, formaldehyde in this case. The PSMD imaging step consumes Sn(II) in the exposed areas by the reaction



the electron transfer in reaction [1] being made to ambient oxygen.

The divalent tin is deposited on the substrate by immersion into a dilute solution of stannous chloride and then a water rinse. As deposited, the sensitizer appears mainly as a hydrated SnO/SnO₂ mixture, with the tetra- to divalent tin ratio (7) close to 2/1. Some aspects of the structure and chemistry of the sensitizer deposit have been studied using Mössbauer techniques and are reported in Ref. (7). The metallic palladium microdeposits generated by the Sn(II)-Pd(II) redox reaction provide catalytic sites for initiation of the electroless metal deposition (9).

On polyimide, a substrate opaque in the ultraviolet, it is not possible to monitor reaction [1] by spectrophotometry. We can, however, follow the photoconversion by taking the sensitized/exposed substrate through the remaining steps in the metalization process and measuring the optical density of the metal deposit as an indicator of the density of active sensitizer sites. While the ratio of metal atoms to active sensitizer atoms depends on the development procedures, we can use the amount of copper deposited as an index of the degree of tin oxidation by maintaining all sensitizing, washing, and plating procedures constant.

While the tin conversion that corresponds, for instance, to 50% reduction in the optical density of the copper deposit is not known, we are assured that in two experiments which give the same density reduction, that the fractions of the Sn(II) consumed in each via reaction [1] are equal.

In using this method, we have selected an electroless plating time brief enough to ensure that the copper layer remains optically transparent; otherwise, changes in optical density would not be readily detectable. We shall indicate the extent of the sensitizer reaction by the ratio D/D_0 , where D is the optical density of the metal deposit over the exposed sensitizer and D_0 is that over the unexposed region.

Experimentally, we have imaged a narrow beam of monochromatic light of known intensity on a sensitized polyimide specimen for a precisely specified time; we have then developed the beam image in electroless copper and measured light transmission through the plated specimen. This method is possible because the polyimide is transparent over a portion of the visible range. In this way, we have obtained T and T_0 , the light transmission through the copper deposits in the exposed and unexposed regions, respectively. The transmissions T and T_0 have been defined relative to the light transmission through a blank substrate which is used to set the value of $T = 100\%$ on a microphotometer. Thus, $T = 100\%$ corresponds to the measured transmission through a polyimide film devoid of all deposits. The respective light transmissions have then been used to determine the optical density ratio D/D_0 , where

$$D = \log(1/T) \quad \text{and}$$

$$D_0 = \log(1/T_0)$$

At present, we are not in a position to state the exact relationship between the deposited copper optical density D (or D_0) and the concentration of active tin atoms from which the deposit was initiated. It is sufficient in the present discussion that D (and D_0) *vs.* light exposure merely be a sensitive single valued index of the tin oxidation. Further discussion of the use of the optical density measurements to characterize the sensitizer activity is given in Appendix A.

At each wavelength, we have fitted a smooth curve to plots of D/D_0 *vs.* light exposure E ,² with light intensity I as a parameter ($E(\lambda) \equiv I(\lambda) \cdot t$, where t is exposure time). From such plots, we have determined $E_{1/2}$, where $E_{1/2} \equiv$ light energy required to reduce D/D_0 from 1.0 to 0.5. This energy will be used to indicate the relative reaction sensitivity at the given wavelength.

Experimental

Sensitizer-substrate system.—The PSMD process has made use of several sensitizer solutions on a variety of substrates. The solution used in the work reported here consisted of 10g SnCl₂ · 2H₂O and 10 ml conc HCl dissolved in one liter of deionized water. The substrate was a 2 mil polyimide film (du Pont KAPTON®).

Stannous chloride-based sensitizer solutions undergo ostensible changes in their appearance on standing in air; they become increasingly cloudy with time and eventually form a readily visible colloid mixture of stannous and stannic oxide (6-8). They also undergo color changes, going from colorless to yellow as they age. Such changes in solution properties produce changes in the sensitizer deposit (7), principally the total weight deposited and the Sn(II)/Sn(IV) ratio.

In the work reported here, we have used a sensitizer system whose properties change relatively slowly with time. In our case changes in the sensitizer properties over the duration of about 8 hr were not significant. Using solutions freshly prepared each day, we were able to ignore the time dependence and still sensitize the substrate reproducibly.

¹ The general form of the sensitizer deposit following immersion in the conventional SnCl₂ · 2H₂O - HCl solutions and a water rinse. For further details, see Ref. (7, 8).

² The customary procedure for characterizing photographic sensitizers is to plot density *vs.* log E rather than E as we have done here.

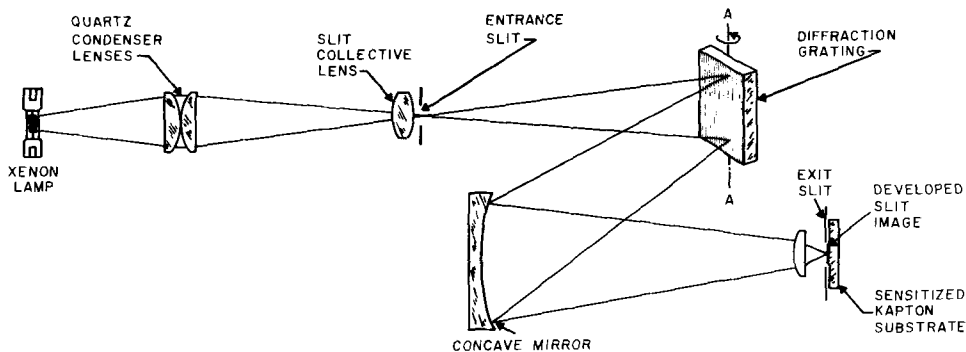


Fig. 1. Exposure system

Substrate preparation, sensitization, and development.—The polyimide substrate was cut into 1.5 in. \times 3 in. specimens which were treated for 10 min in 24°C 10N NaOH, then rinsed an equal time in running deionized water. Specimens were then sensitized by a 3 min immersion in the sensitizer solution (no agitation), then immediately rinsed for one minute in flowing deionized water. Following a gentle drying in a jet of N_2 , specimens were immediately exposed to monochromatic uv light, as described below.

Following exposure, specimens were immersed for 30 sec in a solution of 1g $PdCl_2$ and 10 ml conc HCl dissolved in 2 liters of deionized water (no agitation). Finally, after being rinsed in flowing deionized water for 30 sec, specimens were electroless³ copper plated for 1.50 min.

Exposure system.—The sensitized specimens were exposed to uv light by means of the optical system shown schematically in Fig. 1. A 900W high pressure xenon lamp, mounted in a Christie UF Xenolite housing with uv quartz condenser lenses was used as a light source; a Bausch & Lomb high intensity monochromator with a uv-visible grating (No. 33-86-07, dispersion 7.4 nm/mm) was used to form monochromatic light images. Sensitized specimens were placed directly against the exit slit so that a contact print of the slit outline was produced. Measurement of light intensity at the slit was made by removing the specimen and placing the entrance slit of an Eppley laboratory-type linear thermopile in the same position.

The exit slit width was 2.5 mm, giving a wavelength spread of 18.5 nm across the slit image. Measurements in the wavelength range 200-400 nm were made in 25 nm intervals. For measurements above 340 nm, a glass filter was inserted into the optical train ahead of the monochromator. This filter, transparent above 320 nm but essentially opaque below 300 nm, was used to prevent any possible leakage of 180-200 nm radiation through the monochromator due to second order diffraction from the grating.

Determination of optical density.—After exposure and development of the slit image in the electroless copper solution, light transmissions T and T_0 through exposed and unexposed regions, respectively, were measured using a Jarrell-Ash Model 21-050 recording microphotometer and optical densities of the respective regions were computed. The measuring procedure is illustrated in Fig. 2. Specimens to be measured were mounted in the microphotometer carriage between two glass plates, then scanned as indicated to obtain the recorded transmission trace.

In all measurements, the point $T = 1.0$ (i.e., 100% transmission) was adjusted to correspond to the reading of the instrument through cleaned but unsensitized and undeveloped polyimide substrate. The $T = 0.0$ point was adjusted for the condition where the light beam was completely blanked off.

The transmission trace in Fig. 2 is typical, a dip in transmission at the uppermost slit edge (relative to specimen orientation in the electroless bath) being ob-

served. This dip was found to be highly reproducible for specimens which were reproducibly positioned in the electroless bath. This effect was also more pronounced at greater exposure, suggesting that it may be the result of differences in plating rates in the exposed *vs.* the unexposed regions, in conjunction with local convection in the plating cell. In view of the effects just mentioned, variations in the copper deposit produced by light intensity and/or wavelength gradients across the slit image were not significant.

To minimize variations in copper deposition, we maintained exactly reproducible procedures and plating geometry during image development. Special fixtures were used to ensure accurate specimen placement in the bath, and fresh solutions of electroless solution were prepared daily. In addition, slit images were kept small (relative to over-all specimen size) and limited to one per specimen. With these precautions, transmission measurements reproducible within the error limits of the microphotometer could be obtained.

Results

Exposures were made at nine wavelengths in the 200-400 nm interval. At each wavelength values of D/D_0 were plotted *vs.* exposure E with light intensity I as a parameter. Figure 3 shows representative results for light of 250 nm wavelength. In this figure, we observe the anticipated reduction in D/D_0 as exposure is increased. We also observe a systematic increase in the curve slope (i.e., the sensitivity) as light intensity is reduced. The behavior noted in Fig. 3 for the reaction at 250 nm was found at all other wavelengths. Control experiments established that the dark reaction was not significant over the times used in the experiment, so that the changes in slope are indeed due to the light intensity variations.

Values of $E_{1/2}$ at each wavelength have been determined from plots such as those in Fig. 3. In Fig. 4 we have summarized our results by plotting $E_{1/2}$ *vs.* I with wavelength as a parameter. Each point in this figure is derived from one D/D_0 *vs.* E line. Representa-

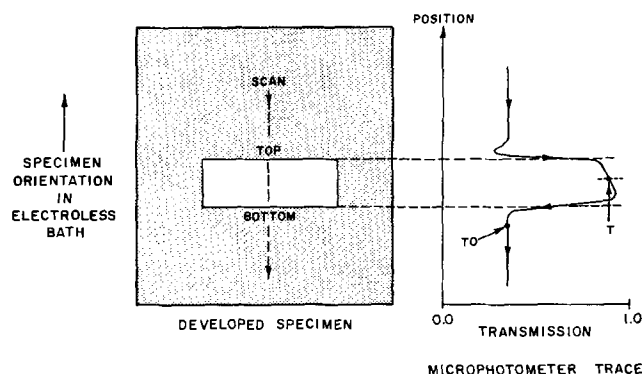


Fig. 2. Measurement of light transmission of slit images

³ Fresh Enthone 400, prepared as recommended by the manufacturer, was used in all our experiments. All plating was done under room ambient conditions.

Table I. Slope of $\log E_{1/2}$ vs. $\log I$ plots as a function of wavelength

Wavelength (nm)	$d(\log E_{1/2})/d(\log I)$
200	0.199 ± 0.043
225	0.245 ± 0.003
250	0.309 ± 0.015
275	0.275 ± 0.012
300	0.284 ± 0.025
325	0.300 ± 0.009
350	0.383 ± 0.026
375	0.349
400	0.326

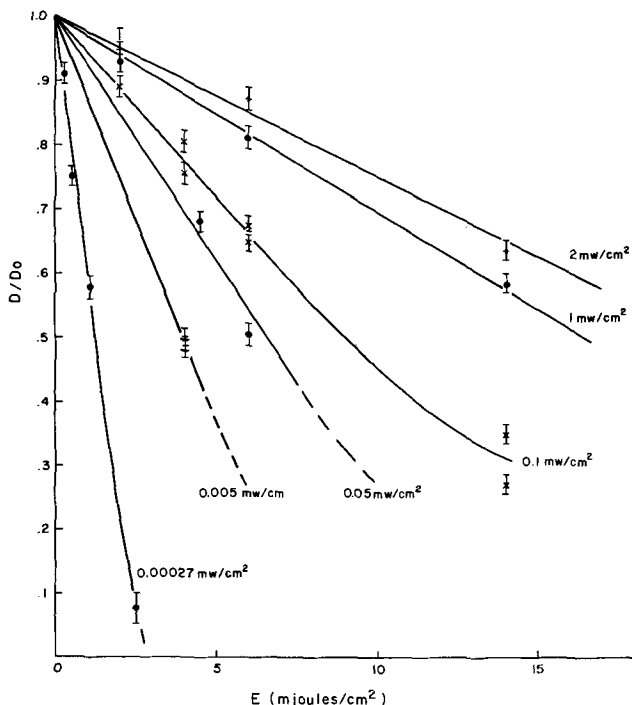


Fig. 3. Optical density vs. light exposure E at 250 nm (light intensity as a parameter).

average deviations for the individual determinations are also shown in both figures.

We have used a linear least squares analysis to fit our $E_{1/2} - I$ data at each wavelength. The slopes of the individual lines at each wavelength (and also their standard errors) are presented in Table I. The results in Table I suggest that, within experimental accuracy, the lines have a common slope. This hypothesis was tested by application of a multiple correlation analysis, from which a correlation coefficient of 0.9980 was obtained. Thus we conclude that the observed differences in slope are not statistically significant.

On the assumption of a common slope at all λ , we have fitted all data, Fig. 4, to a single expression re-

lating $E_{1/2}$ to I and λ

$$\ln E_{1/2} = 0.3931 - (0.0148 \pm 0.0037)\lambda + (0.00007 \pm 0.00000)\lambda^2 + (0.3013 \pm 0.0105) \ln [1000 I] \quad [2]$$

In Eq. [2] the units for $E_{1/2}$, I , and λ are mj/cm^2 , mW/cm^2 , and nm , respectively. Error estimates here are standard errors from the regression analysis. From Eq. [2], the common slope $d(\ln E_{1/2})/d(\ln I)$ ($=d(\log E_{1/2})/d(\log I)$) is 0.30 ± 0.01 . A typical photoresponse (or action spectrum) for the reaction, $E_{1/2}$ vs. λ , is shown in Fig. 5 at $I = 0.2 \text{ mW}/\text{cm}^2$.

Discussion

Sensitization reaction.—Dependence on light intensity.—In Fig. 3, we note that D/Do is not a unique function of E but also depends upon I . This differs from many photographic systems which obey a “reciprocity law” with regard to light exposure (10); in these, the extent of image development depends on the product $I \cdot t$ but not on I separately.

It will be useful at this point to look more closely at Eq. [2] since this relationship sheds some light on the reaction mechanism. To interpret Eq. [2], we first postulate a rate expression for the imaging reaction, presumed to be an oxidation of a stannous tin species to the stannic form. Thus

$$\frac{d[\text{Sn (II)}]}{dt} = -k \cdot I^n \cdot A \quad [3]$$

where A is a time-independent function of $[\text{Sn (II)}]$ and $[\text{Sn (IV)}]$, and t is the exposure time. Equation [3] may be integrated from initial conditions to a degree of oxidation that reduces D/Do to 0.5

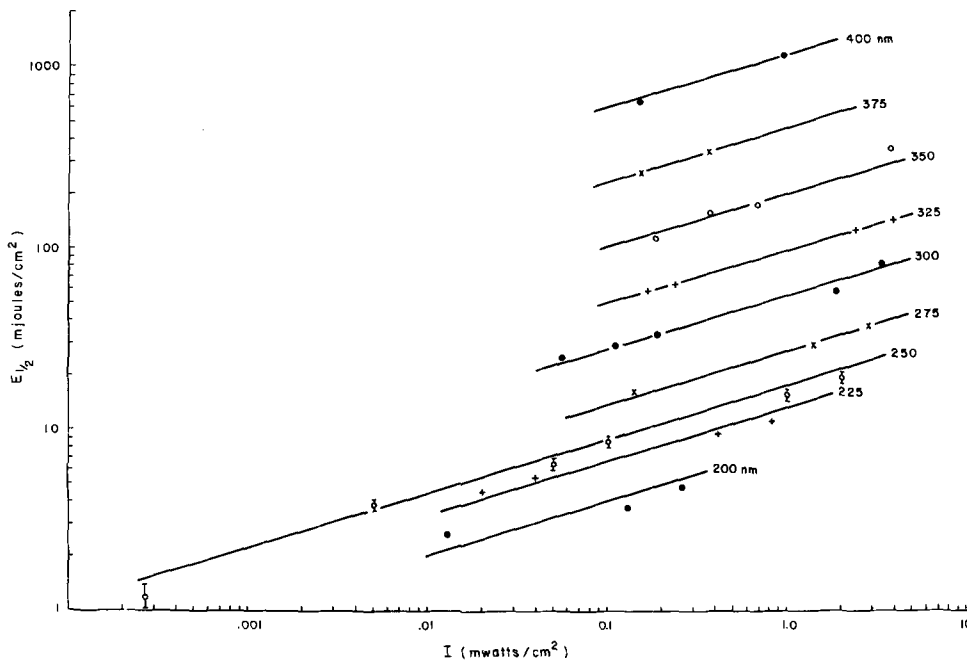


Fig. 4. $E_{1/2}$ vs. light intensity (wavelength as a parameter).

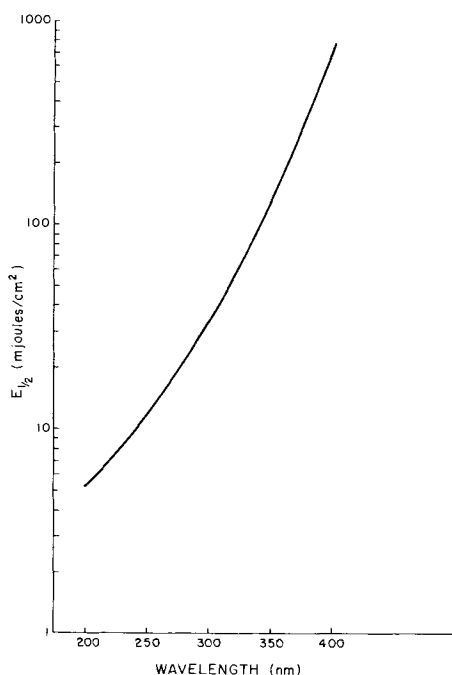


Fig. 5. $E_{1/2}$ vs. wavelength ($I = 0.2 \text{ mW/cm}^2$)

$$\int_{[\text{Sn(II)}]_0}^{[\text{Sn(II)}]_{1/2}} \frac{d[\text{Sn(II)}]}{A} = -k \cdot I^m \int_0^{t_{1/2}} dt$$

Defining $-B$ as the integral on the left, then $B = k \cdot t_{1/2} \cdot I^m$ and is a constant characteristic only of the sensitizing and developing procedures. Recalling that $E_{1/2} = I \cdot t_{1/2}$, then

$$E_{1/2} = \frac{B}{k} \cdot I^{(1-m)}$$

The slopes in Fig. 4 are, therefore, equal to $1 - m$, with $m = 0.70$. Thus $d[\text{Sn(II)}]/dt \sim I^{0.70}$, an intensity dependence similar to that observed in other solid-state photoconductors (11, 12). From elementary steady-state kinetics (13), this type of intensity dependence suggests that the reaction proceeds by a mechanism requiring the presence of a transient carrier species (for example, electrons or holes). This species would decay via a reaction step which is of higher order in this species than is the reaction step of the tin oxidation. Thus, for example, the tin oxidation step could be first order in the concentration of mobile electrons while the decay rate of these species could have a term proportional to the square of their concentration. As an example, if n denotes the concentration of mobile electrons and p the corresponding concentration of mobile holes generated as a result of incident light of intensity I , then the net rate of the electron (or hole) carrier generation can be expressed as

$$\frac{dn}{dt} = \alpha I - \beta n \cdot p = \alpha I - \beta n^2$$

since $n = p$ in an intrinsic photoconductor. If n_0 denotes the equilibrium value of n (or p) for a given steady I , then $\alpha I - \beta n_0^2 = 0$ and, thus, $n_0 \sim I^{0.5}$. Thus, if $d[\text{Sn(II)}]/dt \sim n_0$, we would expect that $d[\text{Sn(II)}]/dt \sim I^{0.5}$. An intensity dependence I^m , where $\frac{1}{2} < m < 1$, in this case suggests the presence of traps, e.g., defects or impurities. These can readily modify the mean carrier lifetime and thereby shift the equilibrium carrier density n_0 and p_0 at any given I . The value of m obtained in any given system depends upon the number and energy distribution of the trapping levels (14).

An alternative explanation for an $I^{0.7}$ dependence is that the carriers are participating in a mixture of mono- and bimolecular processes. This dependence, however, would be observed only as transition between

high and low light levels and should occur over a small range in intensity (11, 14). This appears not to be the case for our data, at least at 250 nm.

In our model for the SnO-SnO₂ sensitizer layer, we are postulating that the role of the light is to generate electron-hole pairs, one or both of which would be relatively mobile in the sensitizer layer and could either recombine (a second order process) or participate in the tin oxidation (a first order process). The light intensity dependence of the imaging reaction which we have reported above refers to a specific sensitizer/substrate system. For other systems, we might expect differences in both the over-all system response (as characterized by $E_{1/2}$) and in the light intensity dependence (as characterized by m). Experiments using alternate sensitizer and substrate systems are now in progress.

Dependence on ambient conditions.—From previous work⁴ and our own experiments in progress, the ambient conditions during light exposure are known to affect the reaction rate. However, the measurements presented in this report were made under conditions of constant ambient, within the capability of local temperature and humidity controls. Room temperature was maintained at $24^\circ \pm 2^\circ\text{C}$ while relative humidity was maintained in the range 40-50%. Throughout the course of experimentation, we maintained a check on the repeatability of the measurements in order to insure that ambient variations were not significant. Our data show that ambient fluctuations within the above limits did not introduce a significant source of variation in these experiments. Ambient effects outside the above ranges are being measured and will be treated in a future paper.

Photoresponse and reaction quantum efficiency.—In Fig. 5, $E_{1/2}$ is observed to increase by more than two orders of magnitude over the measured wavelength range, the minimum light energy requirement occurring at 200 nm. The light absorption spectrum for a chemically similar sensitizer on quartz (15, 16) shows the absorption greatest at 200 nm, steadily decreasing with increasing wavelength. The possibility is thus suggested that the behavior of the photoresponse is merely a reflection of the wavelength dependence of the absorption. If this were so, then the quantum efficiency of the basic reaction, i.e., the amount of photo-oxidation per photon absorbed by the sensitizer, would be constant over the entire wavelength interval. We estimate however, that the quantum efficiency is not wavelength independent but decreases monotonically from a value of about 0.6 at 200 nm to about 0.06 at 400 nm for the data presented in Fig. 5. Thus, while absorption accounts for much of the action spectrum, other factors must also be contributing to the observed behavior.

Using sensitizer absorption data on quartz (16), we can make an order of magnitude estimate of the quantum efficiency Φ of the primary reaction. In this case, Φ is defined as the number of active stannous atoms converted per light photon absorbed. The absorption data is taken as approximate because of known differences in the sensitizer films due to differences in sensitizing solutions and substrates used.

In order to estimate Φ , we need estimates of: (i) the number of active tin atoms per unit area of the sensitizer film, (ii) the optical absorption of the film, and (iii) the number and efficiency of alternate light absorbing processes which may or may not promote the reaction. The details of our estimate of Φ are given in Appendix B. The result for $\lambda = 250 \text{ nm}$ is $\Phi \sim 0.5$, a value not inconsistent with the photoelectronic model proposed earlier. Quantum efficiencies for photoconduction in germanium phototransistors (12), by way of comparison, are typically 3 or 4.

PSMD energy requirements compared to other imaging processes.—For the purpose of comparison, the

⁴ Most pertinent on this topic are Ref. (6, 7, 15).

Table II. Energy requirements for imaging in selected systems (values for typical exposure/development conditions)

System	Energy to obtain a developable image (mj/cm ²)
PSMD: Sensitizer/substrate as described in report; exposure at 254 nm, 0.2 mW/cm ²	22
Shipley AZ-1350 positive photoresist	98*
Eastman KPR-2 negative photoresist	76*
Eastman KOR negative photoresist	1-5*
Silver halide-medium speed	0.001†

* M. S. Htoo, *Phot. Sci. Eng.*, 12, 169 (1968).

† B. H. Carroll, "Photographic Systems For Engineers," 2nd Ed., p. 17, SPSE, Washington, D. C. (1969).

light energy requirements of the PSMD process and other imaging systems are given in Table II. We have selected the energy at 254 nm to characterize PSMD since low-pressure mercury lamps (whose output is primarily at this wavelength) are the most common light sources used at the present time. In terms of our data, the energy for full image development is approximately twice the value of $E_{1/2}$.⁵ We note in Table II that the PSMD system which we have discussed here has a photographic speed comparable to that of conventional photoresists.

Summary

For the sensitizer-substrate system described in this report, the imaging reaction sensitivity is greatest at 200 nm and steadily decreases with wavelength. The useful wavelength range for image generation was found to be 200 nm to about 350 nm. Reaction rate was also found proportional to light intensity to the 0.7 power. The observed light-dependent properties are consistent with a photoelectric model for the reaction, the light absorbed by the sensitizer serving to generate electrons and holes, one or both of which promote the oxidation.

Acknowledgments

The authors gratefully acknowledge J. T. Kenney and D. J. Lando for valuable technical discussions. We also acknowledge J. D. Nohe and K. L. Morton for information and assistance in the microphotometer transmission measurements; D. A. Green for x-ray fluorescence measurements of tin and palladium on polyimide films; and R. P. Thayer for the statistical regression analysis.

Manuscript submitted Nov. 1, 1971; revised manuscript received Feb. 2, 1972.

⁵ We have assumed here, for simplicity, that D/D_0 vs. E remains linear as D/D_0 goes to zero. This is not quite the case as seen in Fig. 3.

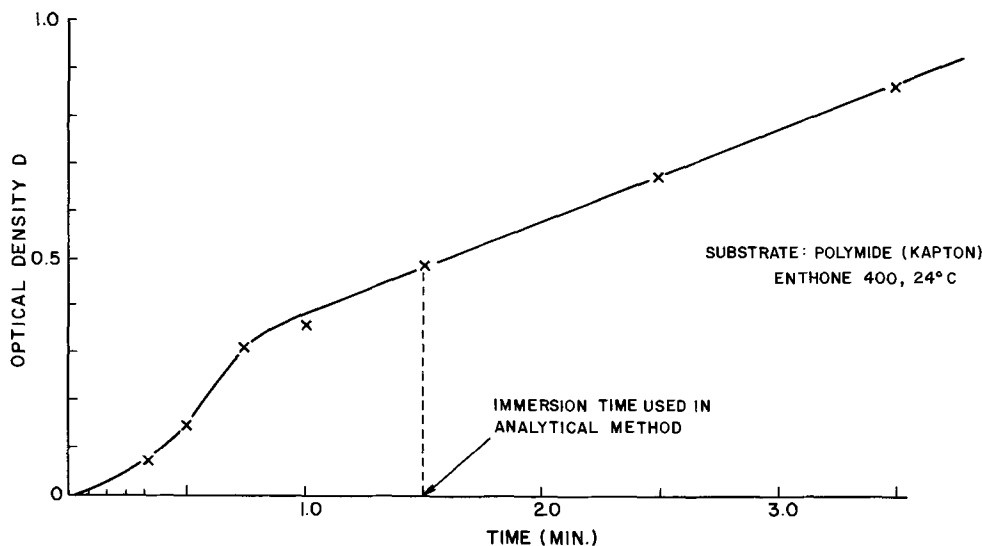


Fig. A-1. Optical density of copper deposit vs. immersion time in electroless bath.

Any discussion of this paper will appear in a Discussion Section to be published in the June 1973 JOURNAL.

APPENDIX A

Characterization of Sensitizer Activity by Optical Density Determinations

Sensitizer activity (i.e., the rate at which a sensitized substrate initiates electroless metal deposition) has been characterized by measuring optical density D through the deposited copper film and substrate. The results of a representative series of microphotometer measurements of D vs. immersion times, in the electroless bath, are presented in Fig. A-1. The D vs. time plot is seen to be linear for times greater than about 45 sec.

Our value of D_0 , the optical density of an unexposed substrate after a total immersion time of 1.5 min, is also indicated in this figure. For $D = D_0 = 0.48$, the copper thickness is estimated to be on the order of 200-300 Å (17).

The rate of metal deposition from an electroless bath (under reasonably constant conditions) should also be constant, once the catalytic surface has been completely covered by the depositing metal. (This rate is determined by the characteristic catalytic activity of the deposited metal itself, plus solution parameters such as temperature and ion concentrations.) In our system, complete surface coverage occurred after about 45 sec, as observed by scanning electron microscopy by G. W. Kammlott, Bell Telephone Laboratories, Murray Hill, New Jersey, and by the electron microscopy studies of R. Woods of our laboratory. For depositions of greater than 1 min duration (for the unexposed substrate), therefore, the linear D vs. time range also corresponds to a linear change in copper weight vs. time. Thus, the copper deposit after a brief initial period follows Lambert's law, D proportional to the thickness of the copper film. This is not an unexpected result.

When the sensitized specimens are exposed to uv light, their catalytic activity is reduced depending on the degree of exposure. For partial exposures, the substrates can still be metalized, but the time for complete coverage with copper is extended due to the reduced catalytic activity. This process is depicted schematically in Fig. A-2. As exposures $E_2 > E_1 > E_0 = 0$ are used, the initial growth of the electroless deposits are slowed, and the net result is that after the fixed immersion time T , the optical densities show a monotonic (though not necessarily linear) decrease vs. exposure.

Of course, once the surface is completely metalized with copper, then further deposition occurs at a rate which is characteristic of the bath parameters, and not the sensitizer activity. Thus the slopes are constant at long times and are independent of the light exposure.

APPENDIX B

Estimate of Quantum Efficiency for the Photo-Oxidation Reaction

The quantum efficiency for the photo-oxidation reaction will be denoted by Φ , where

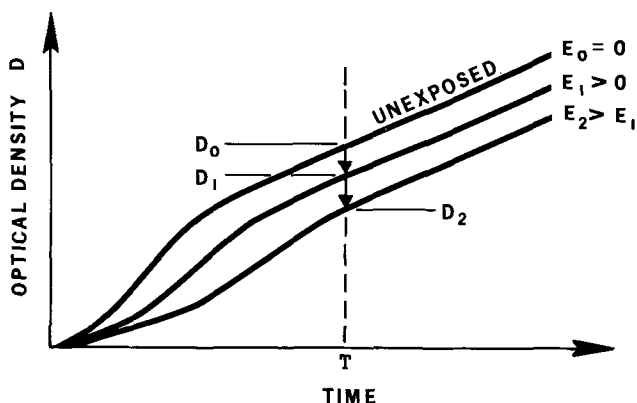


Fig. A-2. Optical density of copper deposit vs. immersion time in electroless bath (light exposure E as a parameter).

ϕ = number of Sn (II) atoms reacted per photon absorbed by the sensitizer film.

The determination of ϕ was carried out using a substrate of uv grade quartz which was sensitized using a solution containing 10g of $\text{SnCl}_2 \cdot 2\text{H}_2\text{O}$ and 0.8 ml conc HCl in 100 ml of deionized water [for details, see Ref. (15)]. Immediately following sensitization, the optical density D of the unexposed deposit was measured from 200-400 nm on a Cary 14 spectrophotometer, using the double beam mode with a duplicate quartz specimen as the blank. The specimen was then exposed to uv radiation from a low-pressure mercury lamp, then remeasured on the spectrophotometer. The exposure was sufficient for complete oxidation of the Sn(II) to Sn(IV) [a typical spectrophotometer plot vs. exposure is given in Ref. (6)]. A duplicate substrate was also sensitized, then dipped in aqueous PdCl_2 solution, followed by a water rinse. After this procedure, the remaining palladium atoms are due only to reaction with Sn(II) and can, thus, be used to determine the initial Sn(II) in the sensitizer deposit. A determination of total tin in the sensitizer was also made, both analyses by x-ray fluorescence (16).

In this case we have assumed a one-to-one correspondence between Sn(II) and the deposited Pd, and found a surface density of 1.8×10^{15} Sn(II) atoms/cm². We will assume that all of these are reacted when the deposit becomes noncatalytic.

The light energy required for reaction of all species is approximately $2E_{1/2}$. At 250 nm, for $I = 0.2 \text{ mW/cm}^2$, $E_{1/2}$ on polyimide is $\sim 11 \text{ mJ/cm}^2$. Here we are using the photoresponse (Fig. 5) and assuming the changes in substrate and in sensitizer do not appreciably alter the energy requirements of the reaction.

The fraction f of $2E_{1/2}$ absorbed by the sensitizer is $1 - 10^{-D}$, where D is the optical density of the sensitizer layer.

This optical density has been measured on the same quartz specimens from which the atom concentrations were determined. At 250 nm, D initially was 0.078. After prolonged light exposure this value had dropped

to 0.042, the absorption of the completely photoconverted film. The average of these D values will be taken as representative of the mean light absorption, \bar{D} . Thus $\bar{D} = 0.060$ and $f = 1 - 0.87 = 0.13$.

The total energy absorbed by the sensitizer in reacting the tin atoms is $2E_{1/2} \cdot f = 2.86 \text{ mJ/cm}^2 = 2.86 \times 10^4 \text{ ergs/cm}^2$.

Each photon at 250 nm has an energy $h\nu$ of 7.94×10^{-12} ergs, so that the total number of photons absorbed, $2E_{1/2} \cdot f/h\nu$, is $3.6 \times 10^{15}/\text{cm}^2$.

Therefore

$$\phi = \frac{1.8 \times 10^{15}}{3.6 \times 10^{15}} = 0.50 \text{ at } I = 0.2 \text{ mW/cm}^2$$

If we compute the range of ϕ over the light intensity values measured at 250 nm, we find ϕ to vary from 4.1 at $I = 0.0002 \text{ mW/cm}^2$, $E_{1/2} = 1.4 \text{ mJ/cm}^2$ to 0.3 at $I = 2.0 \text{ mW/cm}^2$, $E_{1/2} = 23 \text{ mJ/cm}^2$.

REFERENCES

1. M. A. DeAngelo and D. J. Sharp, U.S. Pat. 3,562,005, Feb. 9, 1971.
2. D. J. Sharp, Paper 262 presented at the New York Meeting of the Society, May 4-9, 1969.
3. D. J. Sharp, J. F. Henrickson, J. F. D'Amico, and J. T. Kenney, Paper 136 presented at the Detroit Meeting of the Society, Oct. 5-9, 1969.
4. D. J. Sharp, J. F. Henrickson, J. F. D'Amico, and J. T. Kenney, Paper presented at the 23rd Annual Conference, Photographic Science and Engineering (SPSE), New York, May 1970.
5. D. J. Sharp, *Plating*, **58**, 786 (1971).
6. J. F. D'Amico, M. A. DeAngelo, J. F. Henrickson, J. T. Kenney, and D. J. Sharp, *This Journal*, **118**, 1695 (1970).
7. R. L. Cohen, J. F. D'Amico, and K. West, *This Journal*, **118**, 2042 (1971).
8. R. L. Cohen and K. West, Paper 107 presented at the Cleveland, Ohio, Meeting of the Society, Oct. 3-7, 1971.
9. Electroless metallization using sensitizer solutions chemically similar to ours has been described in detail by R. Sard, *This Journal*, **117**, 864 (1970).
10. See, for example, C. E. K. Mees and T. H. James, "The Theory of the Photographic Process," 3rd Ed., Chap. 4, The Macmillan Co., New York (1966).
11. C. Kittel, "Introduction to Solid State Physics," p. 515, John Wiley & Sons, Inc., New York (1956).
12. J. N. Shive, "The Properties, Physics and Design of Semiconductor Devices," p. 142, Van Nostrand, New York (1959).
13. See, for example, S. W. Benson, "Foundations of Chemical Kinetics," Chap. III, McGraw-Hill Book Co., New York (1960).
14. A. Rose, "Concepts in Photoconductivity and Allied Problems," p. 38, Interscience, New York (1963).
15. P. Sewall, Masters Thesis, Lehigh University, June 1969.
16. J. F. D'Amico and M. A. DeAngelo, Unpublished research.
17. Estimated from measurements of D (at 633 nm) vs. weight of deposited copper, J. F. Henrickson, Unpublished research.

Thermodynamic Properties of Solutions of Group IV Metals Dissolved in Liquid Sodium

I. Sodium-Lead and Sodium-Germanium Solutions

P. Hubberstey

Department of Chemistry, University of Nottingham, Nottingham NG7 2RD., Great Britain

and A. W. Castleman, Jr.

Brookhaven National Laboratory, Upton, New York 11973

ABSTRACT

An emf cell technique was used to measure the thermodynamic properties of Pb-Na solutions at temperatures ranging from 245° to 500°C and compositions between 2.35 and 16.79 atomic per cent (a/o) Pb. The results, while in general agreement with earlier work, reveal that the deviations from ideal solution behavior cross over from negative to positive at low Pb concentrations. This property has not been previously reported for the Pb-Na system. Sodium activity measurements, which were made as a function of decreasing temperature, display a marked change in slope upon transition to a two-phase region. The resulting liquidus-line is in agreement with the published phase diagram. A study of the change in sodium activity as a function of temperature was also made for saturated solutions of Ge in Na. The results show that the solubility of Ge in Na is represented by the equation

$$\ln S_{Ge} = 2.657 - 4837/T$$

Thermodynamic properties of sodium solutions of the Group IV metals tin and lead have been reported for a wide range of intermediate solute compositions, but only limited data are available for both the dilute and concentrated regions. We employed an emf technique to measure the partial molar excess free energy of mixing and related enthalpy and entropy values for liquid sodium solutions containing less than 20 atomic per cent (a/o) solute and report the results in a two-part series. The results for solutions of lead and germanium in liquid sodium are presented in this first paper, while the second one comprises a detailed discussion of the tin-sodium system.

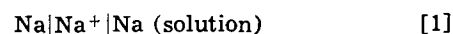
The thermodynamic properties of solutions of lead in liquid sodium have been investigated by three previous groups. Lantratov *et al.* (1, 2) reported data over the concentration range 10 to 95 a/o lead; the data of Hauße and Vierk (3) extends from 6 to 66 a/o lead, whereas that of Porter and Feinleib (4) extends from 59.9 to 94.9 a/o lead. Hultgren *et al.* (5) critically reviewed the available information and concluded that the thermodynamic properties of these solutions were best represented by the data of the first group of authors; they computed their selected values accordingly. Examining the concentration ranges investigated in the earlier studies clearly shows that there is a paucity of data at the two extremes of concentration, particularly for dilute solutions. Consequently, we chose the dilute region for detailed investigation. A further impetus for studying the properties of dilute solutions was provided by our continuing interest (6-11) in the nature of solutes dissolved in liquid metals at concentrations where interactions between the solute atoms are less important than those between the solute and solvent.

No previous investigations of the thermodynamic properties of solutions of germanium in liquid sodium have been published. The Ge-Na results reported in the present paper are preliminary, but are of considerable value because they provide information on the limited solubility of germanium in liquid sodium, for which no other data are available.

Key words: solution thermodynamics, sodium-lead solutions, sodium-germanium solutions, emf.

Experimental

The cell.—The electrochemical cell used in this investigation is represented by the cell reaction



The measured emf, E , is related to the difference in chemical potential of the sodium at the two electrodes by the equation

$$\mu_{\text{Na}} - \mu^\circ_{\text{Na}} = -EF \quad [2]$$

where μ°_{Na} and μ_{Na} are the chemical potentials of pure sodium and sodium in the solution, respectively, and F is the Faraday. It is implicitly assumed that one electron is transferred during the reaction. By definition

$$\mu_{\text{Na}} = \mu^\circ_{\text{Na}} + RT \ln a_{\text{Na}} \quad [3]$$

where a_{Na} represents the activity of the sodium component of the solution. Hence

$$RT \ln a_{\text{Na}} = -EF \quad [4]$$

Pure liquid sodium at the temperature and pressure of the cell is chosen as the standard state. Therefore, the excess partial molar free energy of sodium, $\Delta\overline{G}_{\text{Na}}^E$, is given by

$$\Delta\overline{G}_{\text{Na}}^E = RT \ln \gamma_{\text{Na}} \quad [5]$$

where γ_{Na} , the activity coefficient of the sodium in the solution, is related to its activity and mole fraction x_{Na} , by the expression

$$\gamma_{\text{Na}} = a_{\text{Na}}/x_{\text{Na}} \quad [6]$$

Hence

$$\Delta\overline{G}_{\text{Na}}^E = -(EF + RT \ln x_{\text{Na}}) \quad [7]$$

Apparatus.—The electrochemical cells were constructed of Pyrex. Pyrex was chosen because it is suitable as a selective cation electrolyte for sodium transfer via cell Reaction [1]. Basically, the cell, shown in Fig. 1, consisted of two reservoirs, A and B, linked by a pressure equalizing capillary D. The inner reservoir (1.5 cm diam, 20 cm long) extended into the outer reservoir (4.5 cm diam, 2.5 cm long) to a depth of 2 cm. A loading tube C (1.5 cm diam, 10 cm long), through which the metals could be introduced, was

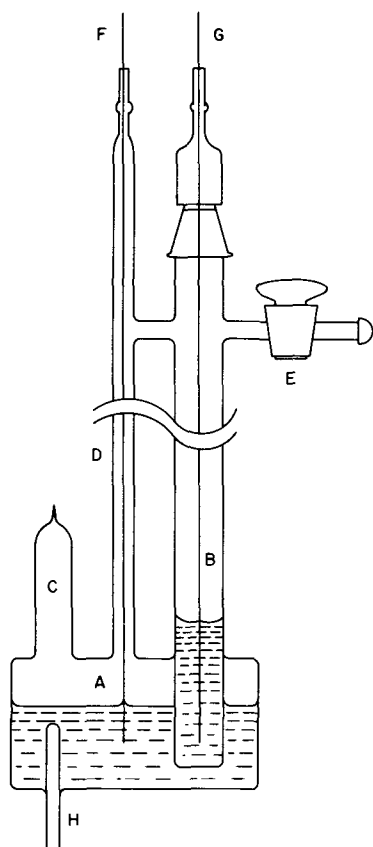


Fig. 1. The electrochemical cell. A,B—reservoirs; C—loading tube; D—equalizing capillary; E—evacuation port stopcock; F—outer reservoir electrode; G—inner reservoir electrode.

attached to the top of reservoir A. A ground joint was fitted to the top of the cell to allow access to the inner reservoir. Provision was made for evacuation of the cell through both port E, and the vacuum connection at the top of reservoir B. Stainless steel rods (ASME Type 316), known to be chemically resistant to attack towards sodium at temperatures $\geq 600^\circ\text{C}$ (12) were used as electrodes. The outer reservoir electrode, F, was fitted through a glass-to-metal seal at the top of the capillary section; the other electrode, G, was also fitted through a glass-to-metal seal and was introduced into the cell through the ground glass connection located above reservoir B.

During operation, the cell was mounted in a 1.5 kW wire wound resistance furnace which had a maximum operating temperature of 600°C . A Honeywell Electronik 18 proportional-band controller was used for accurate temperature control, the maximum variation being $\pm 0.5^\circ$ at 500°C . The temperature of the cell was measured by means of a Chromel-Alumel thermocouple inserted in the thermocouple well, H (also shown in Fig. 1). The emf resulting from Reaction [1] was measured using a Keithley 602 high impedance electrometer in conjunction with a Doric digital voltmeter.

Materials.—The sodium used in the experiments was obtained from the J. T. Baker Company and was specified to have a purity of 99.9%. In order to effect a further reduction in impurity level, the sodium was pipetted from a stock source heated to $\approx 120^\circ\text{C}$. At this temperature, the maximum concentration of dissolved nonmetals is ca. 10 ppm. The lead, 99.9% purity, was obtained from the General Chemical Division of the Allied Chemical Corporation. Ultrapure single crystals of germanium were prepared at Brookhaven National Laboratory and were used without further purification.

Procedure.—Prior to loading, the cell was cleaned with a concentrated solution of chromic acid, thoroughly outgassed by evacuation to a pressure of

10^{-5} mm Hg, and baked at 500°C for several hours. It was then transferred under vacuum to a special high purity vacuum glove-box chamber in which the metal additions were made. The helium atmosphere of the glove-box was continually circulated through a cryogenic purification system, the total volume of the box being replenished every 1.5 min. The concentrations of oxygen and water vapor measured in the recirculating helium stream were less than 1 and 0.1 ppm, respectively.

The solutions were prepared in the outer reservoir; their compositions being determined by weighing the individual components before addition. After introduction of the metals, the cell was evacuated to ≈ 300 Torr and the loading tube C (Fig. 1) was sealed off. The cell was then placed inside the furnace and heated overnight at $\approx 25^\circ\text{C}$ above the estimated liquidus-temperature corresponding to the solution under investigation. During this time period, both the dissolution process and the aging of the cell were accomplished. Subsequently, the emf of the cell was measured at 25° intervals, up to a maximum temperature of 500°C . The temperature was then decreased from 500° to 300°C , during which period measurements were also generally taken at 25°C intervals. However, as the temperature approached the estimated liquidus-line, the measurements were recorded at 5°C intervals. The heating and cooling cycles were always repeated a second time.

Results and Discussion

The lead-sodium system.—The temperature dependence of the excess partial molar free energy of solution for sodium was investigated for solutions containing up to 16.79 a/o lead. Measurements were made over the temperature range from the respective liquidus temperature to 500°C . Representative plots of $\overline{\Delta G_{\text{Na}}^E}$ vs. T are shown in Fig. 2 for solutions containing 2.35, 5.08, 10.01, and 14.61 a/o lead, respectively. The experimental results were obtained during two heating and cooling cycles over a period of 48 hr. Considering the temperature cycles and their duration, as well as the very low emf produced by these cells and the concomitant expanded ordinate scale required in plotting the results, the indicated scatter of the data is quite reasonable.

Since

$$\overline{\Delta G_{\text{Na}}^E} = \overline{\Delta H_{\text{Na}}} - T\overline{\Delta S_{\text{Na}}^E} \quad [8]$$

curves of $\overline{\Delta G_{\text{Na}}^E}$ vs. T can be used to deduce the corresponding enthalpy, $\overline{\Delta H_{\text{Na}}}$, and excess entropy, $\overline{\Delta S_{\text{Na}}^E}$. Numerical values of $\overline{\Delta H_{\text{Na}}}$ and $\overline{\Delta S_{\text{Na}}^E}$ were computed by means of a least squares analysis. These values are plotted as a function of composition in Fig. 3. As the concentration of lead in the solution increases, the partial molar enthalpy of sodium rises to a maximum at

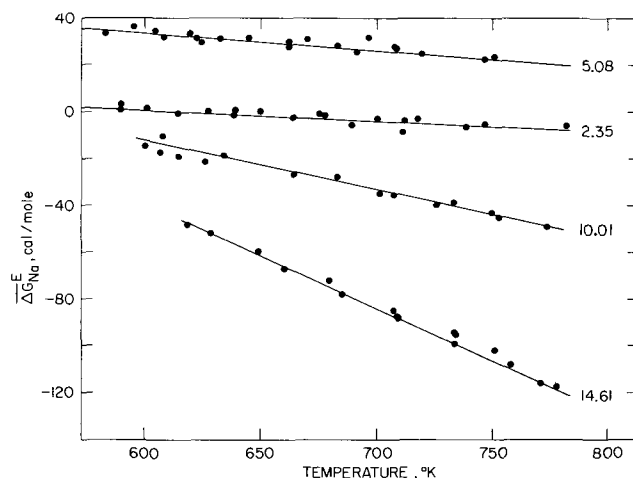


Fig. 2. Typical curves of $\overline{\Delta G_{\text{Na}}^E}$ vs. temperature derived from the emf data using Eq. [7].

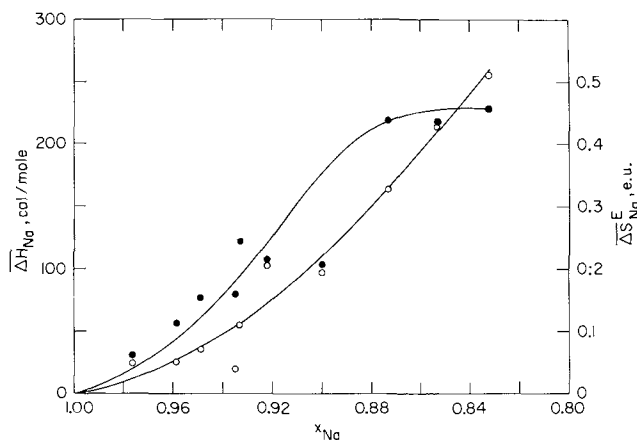


Fig. 3. Plots of the enthalpy and excess partial molar entropy of solution, for the sodium component, vs. sodium composition. The ΔH_{Na} is represented by the closed points while the ΔS_{Na}^E values are shown by open circles.

≈ 14 a/o lead. However, the entropy increases continually throughout the composition range investigated. These results are indicative of an initial positive deviation from ideality followed by a pronounced negative deviation thereafter. The fact that there is a positive deviation from ideality at low composition is borne out both by the sodium activity coefficients calculated from emf's measured at compositions of 2.35 and 5.08 a/o Pb, and by the sodium activity coefficients derived from the corresponding averaged enthalpy and entropy values obtained from Fig. 3. Consequently, we believe this observation to be a real property of the system.

The thermodynamic properties for the complete composition range have been tabulated by Hultgren *et al.* (5). These were based on the data of Lantratov *et al.* (1, 2) noting that the results reported by Hauffe and Vierk (3) were in approximate agreement. A comparison of the results obtained in this study with the earlier work shows generally good agreement in terms of the over-all picture, the basic difference being our observation of an initial region where the deviation from the properties of an ideal solution is positive. This positive deviation was not observed by either of the two previous investigators, undoubtedly due to their lack of substantive results over the concentration range 0 to 15 a/o lead. The lowest concentration investigated by Lantratov *et al.* (1, 2) was 10 a/o lead; Hauffe and Vierk's measurements for solutions containing 6 and 13 a/o lead were in conflict with the former result. It should also be noted that sodium solutions of thallium (3), cadmium (13), and tin (14) also exhibit initial positive deviations before crossing over to negative deviations from ideality at progressively higher solute compositions.

If, in simple terms, the behavior of the thermodynamic properties of these solutions is considered to be attributable to the two factors, size and electronic structure difference of the component metals, then it is possible to rationalize the observations. We follow the arguments of Wagner (15) who has accounted for the behavior of the partial molar enthalpy of silver solutions of tellurium in terms of the electronic structures. Thus, in the present system, the addition of sodium to a sodium-rich solution will simply involve an increase in the number of electrons in the conduction band. The corresponding contribution to the free energy term will be negligible; the dominant factor will be the size difference of the component metals which may give rise to small positive deviations from ideality. On the other hand, in more concentrated solutions, the extra electrons provided by sodium will tend to localize on the lead atoms forming loosely bound pseudo-ionic salt intermetallic compounds (Na_4Pb , $NaPb$, etc.). The corresponding free energy term will be strongly exothermic. This very large factor will dominate at higher

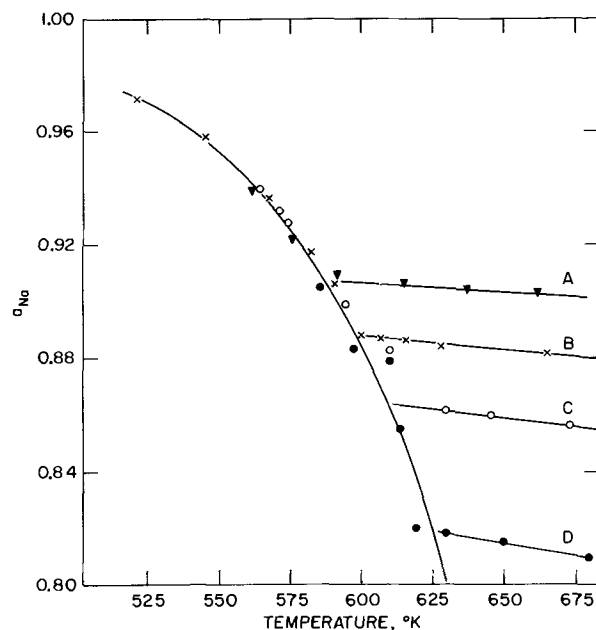


Fig. 4. Plot of the sodium activity as a function of temperature for Pb-Na solution. Curve A (triangles) was obtained with a solution having an initial lead composition of 7.79 a/o, B (crosses) 10.01 a/o, C (open circles) 12.65 a/o, and D (closed circles) 14.61 a/o.

concentrations, eventually giving rise to a negative deviation from ideality.

Additional experiments were carried out to extend the measurements of the sodium activity to temperatures low enough where the onset of a two-phase region might be observed. A plot of the temperature dependence of the sodium activity for the lead-sodium system is shown in Fig. 4. In the homogeneous liquid phase, the temperature coefficient of the activity is approximately constant. However, in the two-phase region it constantly changes because of the continued depletion of lead with decreasing temperature. The transition from the single to the two-phase region is marked by an abrupt discontinuity in the activity-temperature curve as seen in Fig. 4. Since this transition corresponds to the liquidus phase boundary, these data lead to an estimate of the liquidus-line for the sodium-lead phase diagram. As shown in Fig. 5, the results obtained by this analysis are in reasonable agreement with the phase diagram compiled by Hansen (16).

The germanium-sodium system.—The temperature dependence of the sodium activity for saturated solu-

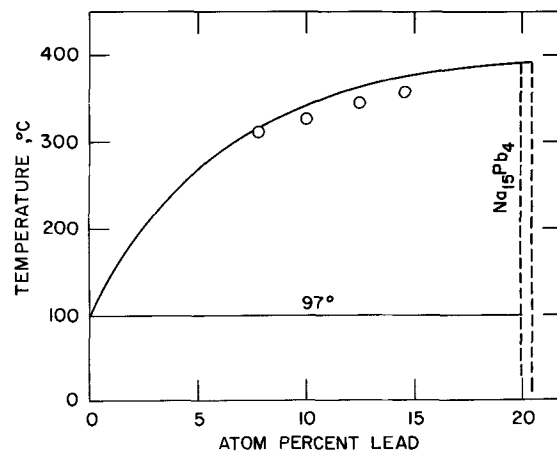


Fig. 5. A comparison of the phase diagram given by Hansen (13) for compositions up to 20 a/o Pb with the points (open circles) obtained from the emf measurements obtained in the present study.

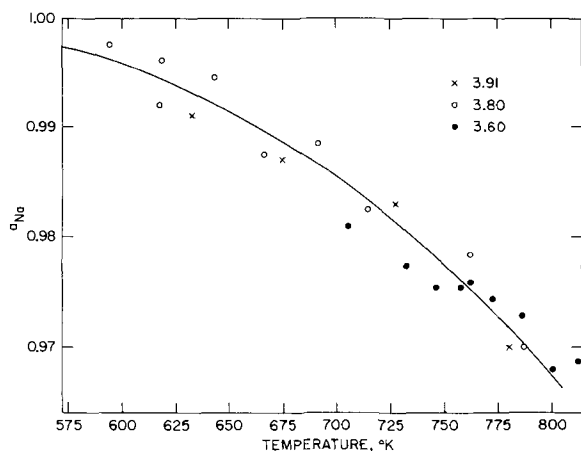


Fig. 6. Plot of the sodium activity vs. temperature for saturated solutions of Ge in Na. The experimental measurements were made with solutions of the following compositions: crosses, 3.91 a/o Ge; open-circles, 3.80 a/o Ge; closed-circles, 3.60 a/o Ge.

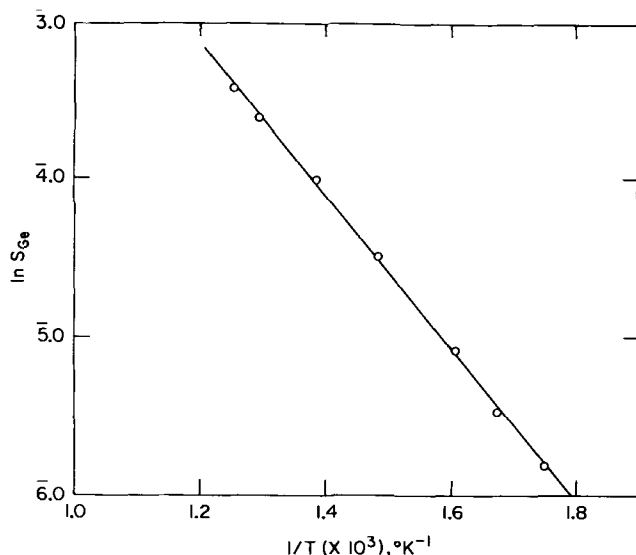


Fig. 7. Plot of $\ln S_{\text{Ge}}$ vs. reciprocal temperature. The germanium solubility is expressed in terms of mole fraction.

tions of germanium in liquid sodium is shown in Fig. 6. This curve is plotted on the basis of emf measurements made over the temperature range 300° to 550°C using cells containing 3.60, 3.80, and 3.91 a/o germanium. These Ge concentrations were found to be high enough to maintain a saturated solution even at 550°C. Other experiments were carried out with dilute solutions of germanium in liquid sodium corresponding to compositions of 1.03, 1.78, and 2.34 a/o Ge at temperatures sufficiently high for a homogeneous liquid phase to be attained (ca. 360°, 420°, and 470°C, respectively). Although the resulting activities could be differentiated from those obtained with saturated solutions, the accuracy of the data was insufficient to ascertain the exact temperature of the activity discontinuity corresponding to the point of complete solubility. This was due to the very small magnitudes and differences in the measured emf values.

Although the present Ge-Na results are of a preliminary nature, they are of value since they give a very good estimate of the temperature dependence of the solubility of germanium in liquid sodium. To our knowledge, there is no previous data available for this property of the Ge-Na system. Over the temperature range considered, 300° to 550°C, the mole fraction of sodium in the liquid phase does not decrease below 0.967. As a first approximation, we can take the sodium

activity coefficient to be nearly unity over this relatively small composition range. This is justifiable since, for the corresponding composition range in the Pb-Na system $\gamma_{\text{Na}} \leq 1.00^5$ at 400°C and for Sn-Na solutions, $\gamma_{\text{Na}} \leq 1.00^9$ when $x_{\text{Na}} = 0.967$ (14). With the assumption of unit activity, the mole fraction of germanium in the saturated solution, S_{Ge} , can be calculated from the activity-temperature data. A plot of the resulting $\ln S_{\text{Ge}}$ vs. $1/T$ is a straight line as shown in Fig. 7. The equation of the line is

$$\ln S_{\text{Ge}} = 2.657 - 4.837/T \quad [9]$$

where T is the absolute temperature in degrees Kelvin.

The enthalpy, $\Delta H_{\text{Ge}}(\text{sol})$, and entropy, $\Delta S_{\text{Ge}}(\text{sol})$, of solution can be computed from the solubility data using the relationship

$$\ln S_{\text{Ge}} = -\frac{\Delta H_{\text{Ge}}(\text{sol})}{RT} + \frac{\Delta S_{\text{Ge}}(\text{sol})}{R} \quad [10]$$

where R is the molar gas constant. The calculated values of the enthalpy and entropy of solution are 9.61 kcal/mole and 5.28 eu, respectively.

Acknowledgment

The authors would like to thank Messrs. J. G. Davis and H. R. Munkelwitz for assistance in performing the experiment.

This work was performed under the auspices of the United States Atomic Energy Commission.

The experimental work was done at the Brookhaven National Laboratory during a postdoctoral appointment held by Dr. P. Hubberstey.

Manuscript submitted Aug. 9, 1971; revised manuscript received Feb. 2, 1972.

Any discussion of this paper will appear in a Discussion Section to be published in the June 1973 JOURNAL.

REFERENCES

1. A. F. Alabyshev, M. F. Lantratov, and A. G. Morachevskii, *Usp. Khim.*, **27**, 921 (1958).
2. M. F. Lantratov, *Russ. J. Inorg. Chem.*, **4**, 927 (1959).
3. K. Hauffe and A. L. Vierk, *Z. Elektrochem.*, **53**, 151 (1949).
4. B. Porter and M. Feinleib, *This Journal*, **103**, 300 (1956).
5. R. Hultgren, R. L. Orr, P. D. Anderson, and K. K. Kelley, "Selected Values of Thermodynamic Properties of Metals and Alloys," pp. 868-871, John Wiley and Sons, New York (1963).
6. A. W. Castleman, Jr., and J. J. Conti, *Phys. Rev.* **A2**, 1975 (1970).
7. I. N. Tang, A. W. Castleman, Jr., and H. R. Munkelwitz, "The Transport of Fission-Product Cesium from Sodium" in *Advances in Chem. Series 93, Radionuclides in the Environment* 71-82, ACS, Washington (1970).
8. A. W. Castleman, Jr., I. N. Tang, and R. A. Mackay, "Fission Product Behavior in Sodium Systems," in *Alkali Metal Coolants*, IAEA, Vienna 729-41 (1967).
9. A. W. Castleman, Jr., and I. N. Tang, "Fission Product Vaporization from Sodium Systems," ANL-7520, I, 540-8 (1968).
10. C. C. Addison, G. K. Creffield, P. Hubberstey, and R. J. Pulham, *J. Chem. Soc. (A)*, 1482 (1969).
11. C. C. Addison, G. K. Creffield, P. Hubberstey, and R. J. Pulham, *ibid.*, 1393 (1971).
12. "Liquid Metals Handbook," U.S. AEC Publication NAVEXOS, P-733 (Rev.), 144 (1952).
13. K. Hauffe, *Z. Elektrochem.*, **46**, 348 (1940).
14. P. Hubberstey and A. W. Castleman, Jr., *This Journal*, **119**, 967 (1972).
15. C. Wagner, "Thermodynamics of Alloys," pp. 45-47, Addison-Wesley Press, Cambridge, Mass. (1952).
16. M. Hansen, "Constitution of Binary Alloys," 2nd ed., pp. 997-1000, McGraw Hill Book Co., New York (1958).

Thermodynamic Properties of Solutions of Group IV Metals Dissolved in Liquid Sodium

II. Sodium-Tin Solutions

P. Hubberstey

Department of Chemistry, University of Nottingham, Nottingham NG7 2RD, Great Britain

and A. W. Castleman, Jr.

Brookhaven National Laboratory, Upton, New York 11973

ABSTRACT

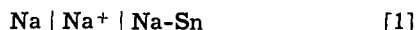
Using an emf technique, the thermodynamic properties of dilute sodium solutions containing tin were measured over the temperature range 300° to 500°C. Results are reported for solution compositions ranging from 0.82 to 19.04 atomic per cent (a/o) tin, thereby, completing the requisite studies to detail the thermodynamic properties for this system over the entire range of composition. The results, in agreement with earlier findings for the Cd-, Tl-, and Pb-Na systems, show that the deviations from ideal solution behavior cross over from negative to positive at low Sn concentrations. Sodium activity measurements, which were made as a function of decreasing temperature, display a marked change in slope upon transition to a two-phase region. Appropriate measurements, made as a function of temperature for the two-phase region, give 13.07 kcal/mole for the enthalpy and 15.65 eu for the entropy of solution. The standard enthalpy and entropy of formation for the compound Na₄Sn were also determined; the values are -20.65 kcal/mole and -9.63 eu, respectively.

The thermodynamic properties of sodium solutions containing tin have been investigated by several authors. Delmarskii and Kolotin (1) have measured the excess thermodynamic functions for the sodium component over the composition range 11 to 75 a/o Sn and temperatures ranging from 723° to 923°K. The results of less comprehensive studies have been reported by Hauffe and Vierk (2) and Alabyshev *et al.* (3) in terms of the excess free energy of sodium in Na-Sn solutions. Their studies have covered the composition ranges from 5 to 73 a/o and 13 to 91 a/o tin, respectively, but each study was only made at a single temperature. Hultgren *et al.* (4) critically reviewed the data in 1963 and calculated selected values using the results of Delimarskii and Kolotin. However, at that time there was a paucity of data for both dilute and concentrated solutions, and the excess thermodynamic functions compiled for these regions were somewhat uncertain.

More recently, Yuan and Kröger (5) have reported the results of a study of concentrated tin solutions in liquid sodium thereby completing the work needed to detail the thermodynamic properties for the high concentration region. We have made an extensive investigation of the dilute concentration region below 20 a/o Sn and report the results herein.

Experimental

The cell and experimental procedure.—The electrochemical cell used in this investigation is represented by the cell reaction



Pyrex has been shown to be a suitable material for selective sodium cation transfer (2, 5, 6) and it was used for the electrolyte in this study. The design of the cell, the ancillary equipment, and the experimental procedure have been described in detail in an earlier paper (6). Briefly, the procedure was as follows: After the cell was charged with the component metals, it was heated overnight at $\approx 25^\circ$ above the estimated liquidus of the solution under investigation. This effected both

the necessary aging of the cell and the complete dissolution of the tin in the liquid sodium. The emf of the cell was then measured as a function of increasing and decreasing temperature, the cycle being carried out twice.

The measured emf, E , is related to the excess partial molar free energy of the sodium, $\overline{\Delta G_{\text{Na}}^E}$, and mole fraction of sodium in the solution, x_{Na} , by the relationship

$$\overline{\Delta G_{\text{Na}}^E} = -(EF + RT \ln x_{\text{Na}}) \quad [2]$$

where F is the Faraday and T is the absolute temperature.

Materials.—The sodium used in the experiments was obtained from the J. T. Baker Company and was specified to have a purity of 99.9%. A further reduction in impurity level was effected by pipetting the sodium from a stock source heated to $\approx 120^\circ\text{C}$. At this temperature, the maximum concentration of dissolved nonmetals is *ca.* 10 ppm. The tin, purity 99.9%, was obtained from the General Chemical Division of the Allied Chemical Corporation and used without further purification.

Results and Discussion

The temperature dependence of the excess partial molar free energy of sodium was investigated for solutions containing up to 19.04 a/o tin. Measurements were made over the temperature range extending from the respective liquidus temperature to 500°C. Representative plots of $\overline{\Delta G_{\text{Na}}^E}$ vs. temperature are shown for tin compositions of 16.64, and 19.04 a/o in Fig. 1 and 0.82 and 10.20 a/o in Fig. 2. The experimental scatter of the data is reasonable considering the small magnitude and range of the measured emf, *i.e.*, the minimum and maximum emf values measured for the 19.04 a/o tin solution were 14.10 and 15.48 mV, respectively.

Since

$$\overline{\Delta G_{\text{Na}}^E} = \overline{\Delta H_{\text{Na}}} - T\overline{\Delta S_{\text{Na}}^E} \quad [3]$$

the corresponding enthalpy, $\overline{\Delta H_{\text{Na}}}$, and entropy, $\overline{\Delta S_{\text{Na}}^E}$, are readily deduced from these plots. The actual numerical values were computed using a least squares

Key words: solution thermodynamics, sodium-tin solutions, emf.

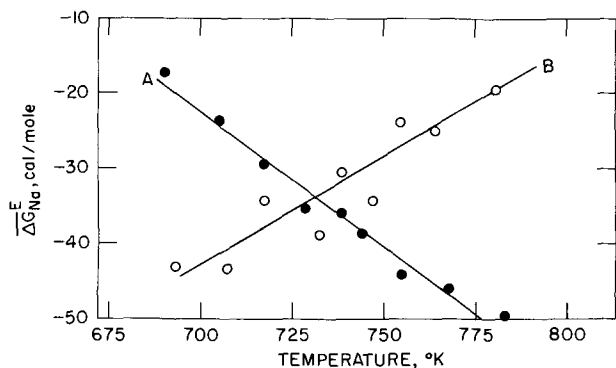


Fig. 1. Plot of partial molar excess free energy of mixing for sodium vs. temperature. A and B represent least-squares lines fitted to data obtained for solutions of composition 16.64 and 19.04 a/o tin, respectively.

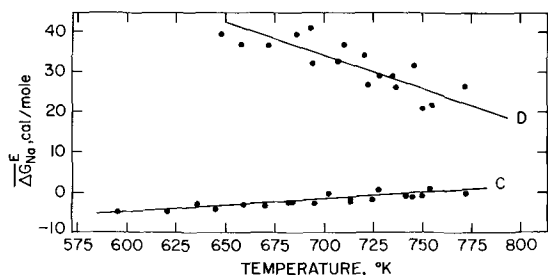


Fig. 2. Plot of partial molar excess free energy of mixing for sodium vs. temperature. C and D represent least-squares lines fitted to data obtained for solutions of composition 0.82 and 10.20 a/o, respectively.

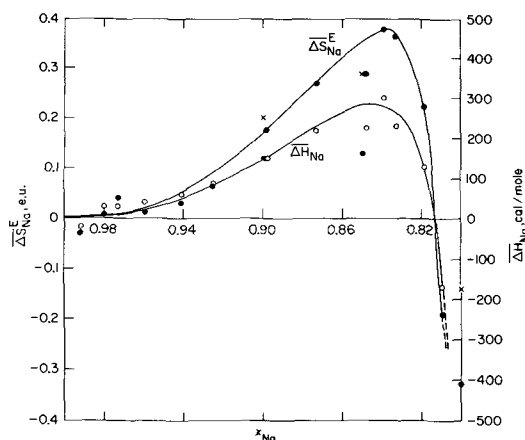


Fig. 3. Partial molar enthalpy and excess entropy of mixing plotted vs. composition [open circles, $\overline{\Delta H}_{Na}^E$, present results; open circles plus crosses, $\overline{\Delta H}_{Na}^E$, Ref. (4); closed circles, $\overline{\Delta S}_{Na}^E$, present results; crosses, $\overline{\Delta S}_{Na}^E$, Ref. (5)].

analysis. The $\overline{\Delta H}_{Na}^E$ and $\overline{\Delta S}_{Na}^E$, so obtained, are plotted as a function of composition in Fig. 3. The figure also includes data taken from the compilation of Hultgren *et al.* (4), based on the data available in 1963. It is readily seen that, in general, the present results are in good agreement with the assessments made by Hultgren *et al.*; the latter were, of course, based on rather sparse data for the regions of dilute concentration.

It can be seen from Fig. 3 that the enthalpy and entropy increase with increasing tin concentration up to ca. 16 a/o at which point both functions reach a maximum. A further increase in tin concentration leads to a decrease in the thermodynamic functions; they ultimately pass through zero and subsequently exhibit large negative values. These variations are indicative of an initial positive deviation from the properties of an ideal solution ($\gamma > 1$) followed by a pronounced negative deviation ($\gamma < 1$).

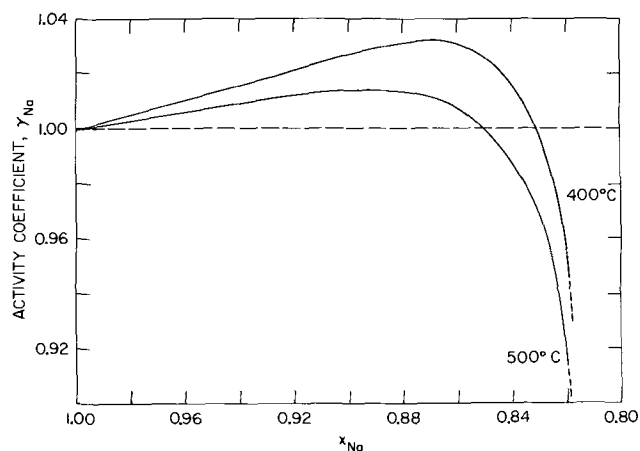


Fig. 4. Sodium component activity coefficient plotted vs. sodium composition for temperatures of 400° and 500°C. The activity coefficients, calculated from the average $\overline{\Delta H}_{Na}^E$ and $\overline{\Delta S}_{Na}^E$ values given in Fig. 3, show a crossover from values less than unity (negative deviation from ideal solution behavior) to greater than unity (positive deviations) at progressively lower tin compositions.

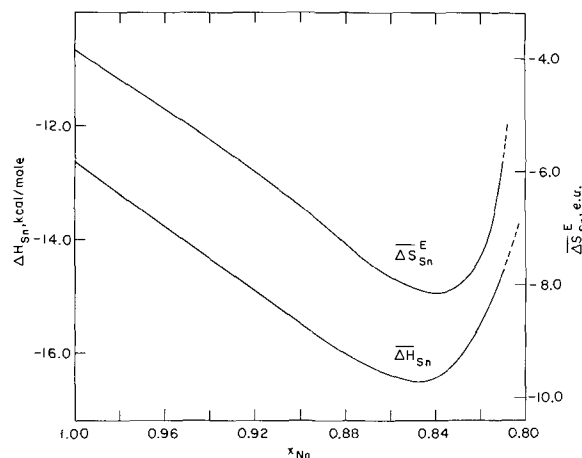


Fig. 5. Plot of the partial molar enthalpy and excess entropy of solution for the tin component.

The activity coefficient-composition isotherms at 400° and 500°C, derived from the average enthalpy and entropy functions given in Fig. 3, are shown in Fig. 4. Although the initial positive deviations are small, the trends discussed above are readily discernible. Similar observations have been reported for solutions of thallium (2), cadmium (7), and lead (6) in sodium. This type of behavior has been rationalized in terms of the size and electronic structure differences of the solute and solvent for the case of Pb-Na solutions (6) and the same arguments are applicable for the Sn-Na system as well.

As shown in Table I, the selected data of Hultgren *et al.* agree very closely with the present results. Therefore, it was deemed reasonable to select the corresponding value of $\overline{\Delta H}$ and $\overline{\Delta S}^E$ for the tin component and employ a Gibbs-Duhem integration to calculate the excess thermodynamic properties of tin from the properties measured for sodium. The resulting partial molar enthalpy and excess partial molar entropy of solution are plotted as a function of composition in Fig. 5. For dilute solutions, these functions decrease

Table I.

Author	Partial molar functions at $x_{Na} = 0.90$	
	$\overline{\Delta H}_{Na}^E$ (cal./mole)	$\overline{\Delta S}_{Na}^E$ (e.u.)
Hultgren <i>et al.</i>	150	0.20
Present work	146	0.17

Table II.

T° (C)	γ_{Sn} (infinite dilution) $\times 10^4$
300	1.11
325	1.77
350	2.70
375	4.00
400	5.77
425	8.07
450	11.04
475	14.83
500	19.50

regularly with increasing tin concentration. As the concentration increases, both functions pass through a minimum and then increase rapidly. Since the excess thermodynamic functions of tin are approximately linearly dependent on composition below 10 a/o, it is possible to estimate its activity coefficient at infinite dilution. Values are tabulated as a function of temperature in Table II.

Experiments were also carried out to study the temperature dependence of the sodium activity of these solutions for the temperature range extending from the single- into the two-phase region. The results are shown in Fig. 6. For the region where the solution is single phase, the temperature coefficient of the activity is approximately constant. The boundary between the regions is characterized by an abrupt change in the temperature coefficient of the activity; at this point, activity commences to increase much more rapidly with decreasing temperature. The temperature dependence of the activity for the two-phase region, when correlated with the composition of the solutions, gives a good measure of the liquidus-line for the corresponding region of the phase diagram. The liquidus temperature determined in these experiments is compared in Fig. 7 with the phase diagram given by Hansen (8). The agreement between the two is excellent.

The enthalpy, $\Delta H_{Sn}(sol)$, and entropy, $\Delta S_{Sn}(sol)$, of tin dissolved in liquid sodium are related to the solubility of the tin, S_{Sn} , by the equation

$$\ln S_{Sn} = -\frac{\Delta H_{Sn}(sol)}{RT} + \frac{\Delta S_{Sn}(sol)}{R} \quad [4]$$

where R is the molar gas constant and T , the absolute temperature. The solubility of tin in liquid sodium, calculated from the liquidus determined in the present study, is given as a function of temperature in Fig. 8. The equation of the straight line relating the solubility to temperature, is

$$\ln S_{Sn} = -\frac{6579}{T} + 7.874 \quad [5]$$

The corresponding enthalpy and entropy of solution, which were computed by means of a least squares analysis, are 13.07 kcal/mole and 15.65 eu, respectively.

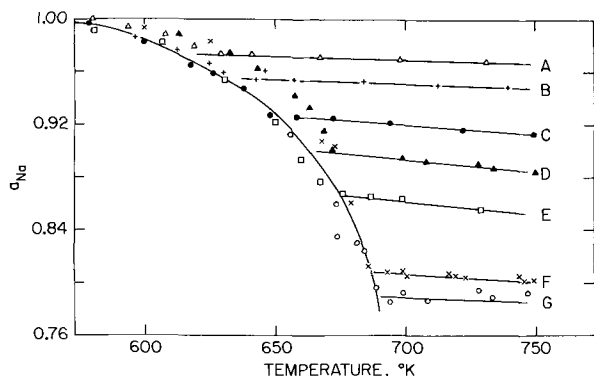


Fig. 6. Sodium activity vs. temperature showing the transition from a single-phase to a two-phase solution at progressively lower temperatures. The respective solution compositions in a/o tin are as follows: A—5.92, B—7.46, C—10.20, D—12.72, E—15.15, F—18.12, and G—19.04.

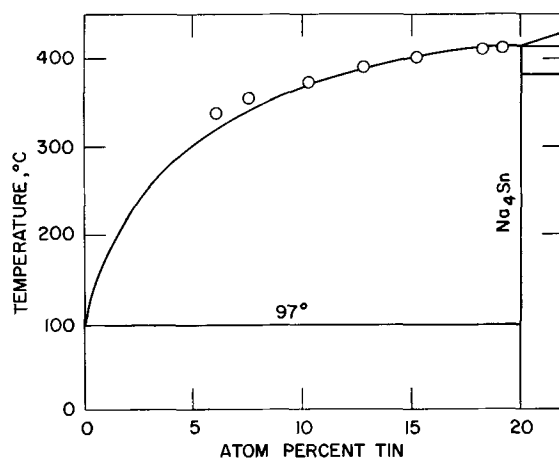


Fig. 7. Comparison of the phase diagram taken from Ref. (8) with the liquidus determined in the present study. Present results shown by the open circles.

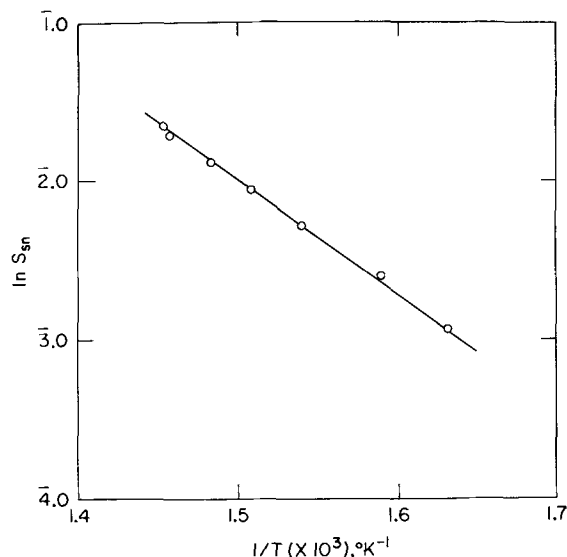


Fig. 8. Natural logarithm of the solubility of tin in sodium plotted vs. reciprocal absolute temperature.

These values are compared with those published by Lamprecht *et al.* (9) in Table III. The present results were determined over the temperature range 340°-415°C whereas those of Lamprecht *et al.* were measured for the temperature range 100°-260°C.

A consideration of the phase diagram (8) (also see Fig. 7) indicates that the compound Na_4Sn does not exhibit appreciable solid solubility. Thus the solid phase which precipitates when solutions containing up to 20 a/o tin are cooled, constitutes the pure intermetallic compound Na_4Sn . The activity of the sodium in a particular solution is measured directly at the liquidus temperature; the corresponding activity of tin can be calculated from the values of ΔH_{Sn} and ΔS_{Sn}^E compiled above.

Since the activity of the compound is unity for the chosen standard states, the free energy of formation of Na_4Sn can be calculated directly from the data and the relationships



Table III.

	$\Delta H_{Sn}(sol)$ kcal/mole	$\Delta S_{Sn}(sol)$ cal/dg/mole
Present investigation	13.07	15.65
Ref. (9)	10.76	10.78

Table IV.

T (°C)	$-\Delta G_f$ (kcal/mole)
340	14.73
360	14.54
380	14.40
400	14.21
415	13.97

and

$$\Delta G^{\circ}_f = -RT \ln K_{eq} \quad [7]$$

$$= -RT \ln (a_{Na_4Sn}/a^4_{Na} \cdot a_{Sn}) \quad [8]$$

where ΔG°_f is the free energy of formation of Na_4Sn from the pure elements.

Standard free energies of formation of Na_4Sn between 340° and 415° were calculated and the values are given in Table IV. The standard enthalpy and entropy of formation of Na_4Sn were determined by a least squares analysis of the temperature dependence of the free energy function; the respective values are -20.65 kcal/mole and -9.63 eu.

Acknowledgments

The authors thank Messrs. J. R. Davis and H. R. Munkelwitz for assistance in performing the experiments and I. N. Tang for helpful discussions during the course of this work.

This work was performed under the auspices of the United States Atomic Energy Commission.

The experimental work was done at the Brookhaven National Laboratory during a postdoctoral appointment held by Dr. P. Hubberstey.

Manuscript submitted Aug. 9, 1971; revised manuscript received Feb. 2, 1972.

Any discussion of this paper will appear in a Discussion Section to be published in the June 1973 JOURNAL.

REFERENCES

1. Y. K. Delimarskii and A. Kolotin, *Zh. Fiz. Khimii*, **28**, 1169 (1954).
2. K. Hauffe and A. L. Vierk, *Z. Elektrochem.*, **53**, 151 (1949).
3. A. F. Alabyshev, M. F. Lantratov, and A. G. Morachevskii, *Usp. Khim.*, **27**, 921 (1958).
4. R. Hultgren, R. L. Orr, P. D. Anderson, and K. K. Kelley, "Selected Values of Thermodynamic Properties of Metals and Alloys," pp. 873-877, John Wiley and Sons, New York (1963).
5. D. Yuan and F. A. Kröger, *J. Phys. Chem.*, **73**, 2390 (1969).
6. P. Hubberstey and A. W. Castleman, Jr., *This Journal*, **119**, 963 (1972).
7. K. Hauffe, *Z. Elektrochem.*, **46**, 348 (1940).
8. M. Hansen, "Constitution of Binary Alloys," 2nd ed., pp. 1004-1006, McGraw Hill Book Co., New York (1959).
9. G. J. Lamprecht, P. Crowther, and D. M. Kemp, *J. Phys. Chem.*, **71**, 4209 (1967).

Thermodynamic Properties of Ternary Refractory Carbides

III. Relations between Thermodynamic Properties, Bonding, and Compressibility

M. Hoch and S. Yamauchi

Department of Materials Science and Metallurgical Engineering, University of Cincinnati, Cincinnati, Ohio 45221

ABSTRACT

The high-temperature thermodynamic data previously obtained on ternary carbides having the sodium-chloride structure are correlated with the bonding and mechanical properties of these carbides. The metal-metal bonding on the metal sublattice in the carbide is found to be the same as in the binary body-centered cubic metals. The variation of the carbon-carbon and metal-carbon interaction energies is interpreted to mean that the metal-carbon bonds are localized bonds. From the dependence of metal-carbon interaction energy on composition at elevated temperatures the compressibility of the carbides was calculated. The values obtained agree to within a factor of two with values derived from room temperature measurements of mechanical properties. The results show that the metal-carbon bond is responsible for the carbide properties and that the metal-metal and carbon-carbon bonds play a minor role.

In a previous paper (1), Hoch investigated the pairwise interaction energies in binary compounds having the sodium-chloride structure. As pointed out in that paper, these energies show a certain regularity. Their values for zirconium, hafnium, and niobium carbide are reproduced in Table I together with the values for uranium carbide which were derived later (2). (The nomenclature in this paper has been changed: 1 refers to zirconium, 2 to hafnium, niobium, or uranium, and 3 to carbon.)

In subsequent papers, Jun and Hoch (3) and Hoch, Hapase and Yamauchi (4) studied the activities of the components in the single phase, NaCl type structure in zirconium-niobium-carbon (3) zirconium-uranium-

carbon (4), and zirconium-hafnium-carbon (4). From these data they derived the pairwise interaction energies, or their differences, between the various atoms. The present paper will attempt to interpret the thermodynamic results and will calculate the compressibility from these pairwise interaction energies.

Table I. Energy terms in binary carbides

Material	E_{33} , kcal/mole	$E_3 + E_{13} + E_{23}$ ($E_3 + E_{23} + E_{33}$), kcal/mole
ZrC	28 ± 3	-35.2 ± 4
HfC	15 ± 8	-47 ± 10
UC	0	-28.1 ± 1.6
NbC	15.2 ± 2.5	-28.6 ± 2.5

Key words: ternary carbides, thermodynamic properties of carbides, bonding in carbides, compressibility of carbides.

The paper of Jun and Hoch (3) indicated that the carbon-carbon interaction energy in the ternary zirconium-niobium-carbide, $Zr_xNb_{1-x}C_y$ varied parabolically with composition and was given by

$$E_{33} = 15.62 + 9.37x - 29.50(1 - x)x \quad \text{kcal/mole}$$

(Note that x here refers to the relative amount of Zr, and y refers to the carbon/metal ratio. Some authors use x for the latter purpose in describing monocarbides, e.g., ZrC_x .)

This result, in itself, suggests that the bonding in the system is localized because a parabolic variation with composition requires that carbon atoms be "attached" to niobium and to zirconium, according to an analysis by Jun and Hoch (3).

The model used for the statistical thermodynamic derivation of the activity has been discussed earlier (11, 12) and needs only to be summarized here. The standard state for all elements is the pure, condensed element at the temperature in question. The atoms are assumed to be distributed randomly over the available sites, as in a regular solution, since the error introduced is very small. [First assuming ordered, and, later, randomly distributed atoms, Hoch *et al.* calculated only a 10% change in the pairwise interaction in the case of NbO (11)].

The grand partition function was then set up with only pairwise interaction energies, E_{ij} , neglecting the additional terms which reflect the influence of nearby atoms.

The model also neglects the small amount of Schottky defects present, and therefore is only valid when $1 - y \gg \delta$, the concentration of Schottky defects.

Experimental Results and Discussion

Table II presents the metal-to-metal distances in pure elements as calculated from Darken and Gurry (5) and those in the carbides as determined during the previous investigations of this series. Those figures reveal that the metal-metal distance in the carbides is about 10% greater than the metal-metal distance in the pure bcc metals.

In addition, Table II gives the metal-metal interaction energy on the metallic sublattice as determined in three cases and also as calculated from the binary metal phase diagrams. These data show that the interaction energy on the metal sublattice in the carbide is approximately 2 kcal/mole larger than that in the bcc metal phase. This small difference of 2 kcal/mole can be attributed mostly to the transformation of the bcc structure to a fcc structure and to the expansion

Table II.

A. Metal-metal interaction energy [$E_{12} - \frac{1}{2}(E_{11} + E_{22})$] in binary body-centered cubic metal alloys and on the metal sublattice in ternary carbides

System	$E_{12} - \frac{1}{2}(E_{11} + E_{22}), \text{ kcal/mole}$		
	bcc metal	fcc carbide sublattice	Difference carbide-metal
Zr-Hf-C	≥ 0	1.86 ± 0.3	1.86 ± 0.5
Zr-U-C	4.4 ± 0.2	6.7 ± 0.6	2.30 ± 0.8
Zr-Nb-C	4.9 ± 0.3	6.5 ± 0.3	1.60 ± 0.5
			Avg: 1.92 ± 0.6

B. Metal compressibility and metal-metal distance in body-centered cubic metals and face-centered cubic sublattice in carbides

System	$P = 1/\beta$ (10^{12} dyn/cm^2)	Distance in A		
		bcc metal	fcc carbide sublattice	Difference carbide-metal
Zr	0.90 (13)	3.11	3.32	0.21
Hf	1.10 (13)	3.07	3.29	0.22
Nb	1.64 (13)	2.86	3.17	0.31
U		3.00	3.52	0.52

Avg: 0.31 ± 0.10

Table III. Dependence on composition of [$E_{13} - E_{23}$] in ternary carbides

System	$E_{13} - E_{23}$
Zr-Nb-C	$E_{13} - E_{23} = (1.08 \pm 0.11) - (16.15 \pm 0.44)x \text{ kcal/mole}$
Zr-U-C	$E_{13} - E_{23} = (8.5 \pm 0.05) - (23.6 \pm 0.2)x \text{ kcal/mole}$
Zr-Hf-C	$E_{13} - E_{23} = (9.6 \pm 0.8) - (7.8 \pm 0.2)x \text{ kcal/mole}$

of the metal-metal distance. Thus, we conclude that the metal to metal bonding in the carbides is the same as in the pure metallic systems.

Another result obtained during the previous investigations (3, 4) was that the value of [$E_{13} - E_{23}$], the difference in bonding energy between the zirconium-carbon bond and the other metal-carbon bond, was found not to be constant but to vary with composition. The equations obtained for [$E_{13} - E_{23}$] are given in Table III. This variation suggests that localized metal to carbon bonds get compressed or expanded as the composition changes.

To explain the behavior of the carbides, it is necessary to look at a potential energy vs. distance diagram (Fig. 1). Since the lattice parameters of the various carbides are similar, the amount of compression or expansion of each metal-carbon bond is small, and our attention can be restricted to the bottom of the potential well. Although the carbon-carbon bond and the metal-metal bond contribute to the total cohesive energy, we assume that the metal-carbon bond is primarily responsible for the force constants (i.e., shape of the potential) near the equilibrium separation. That is, the carbon-carbon and metal-metal bonds are assumed to be independent of separation for small displacements. Then, by subtracting off the (constant) energies of the other two bonds, we can write the two metal-carbon interaction energies as

$$E_{13} = \alpha_1(r - r_1)^2 + E^{\circ}_{13} \quad [1]$$

$$E_{23} = \alpha_2(r - r_2)^2 + E^{\circ}_{23} \quad [2]$$

where E°_{13} and E°_{23} are the metal-carbon interaction energies in the binary carbides, r_1 and r_2 are the metal-carbon distances in the binary carbides, r is the average metal-carbon distance in a ternary carbide (obtained from lattice parameters), and E_{13} and E_{23} are the metal-carbon interaction energies in the ternary carbide. The coefficients α_1 and α_2 are related to the compressibilities of the two carbides. As the compressibilities of the carbides are not very different at room temperature (see Table III), we assume, as a first approximation, that they are not very much different at 2500°K, and thus, set $\alpha_1 \approx \alpha_2 \approx \alpha$. So we finally obtain

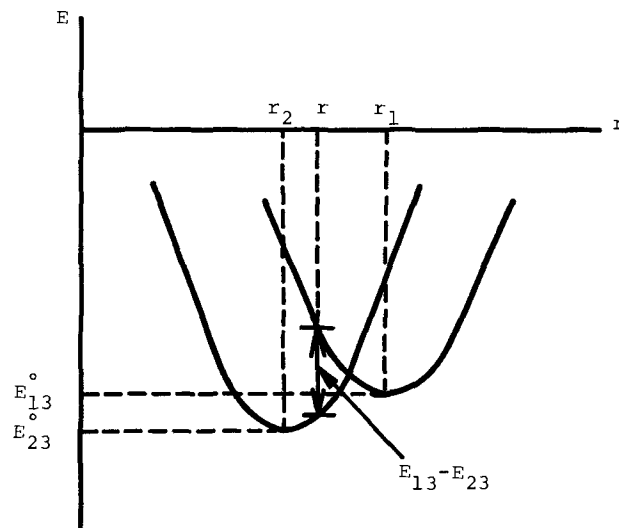


Fig. 1. Schematic potential-distance curves for two metal-carbon bonds.

$$E_{13} - E_{23} = \alpha(r_2 - r_1)[2r - (r_1 + r_2)] + E^{\circ}_{13} - E^{\circ}_{23} \quad [3]$$

The lattice parameters in the ternary carbides at constant carbon content vary linearly with metal composition (3, 4)

$$r = r_2 + x(r_1 - r_2) \quad [4]$$

Combining Eq. [3] and [4], we have

$$E_{13} - E_{23} = E^{\circ}_{13} - E^{\circ}_{23} - 2\alpha(r_1 - r_2)^2(x - 0.5) \quad [5]$$

This equation indicates that $[E_{13} - E_{23}]$ should be equal to $[E^{\circ}_{13} - E^{\circ}_{23}]$ when $x = 0.5$. These values, which were calculated from the thermodynamic data on ternary carbides in Table III and from binary data in Table I, are presented in Table IV. The agreement between the two sets of values is within a factor of two. In using the data in Table I, it was assumed that $E_3 + E_{33}$ was the same for all the carbides investigated. This term represents the energy required to take a carbon atom from its standard state (graphite), put it on the carbon sublattice, and then cause it to form a bond with another carbon atom.

The value of α , which is related to the compressibility of the carbide, can now be calculated from the variation of $[E_{13} - E_{23}]$ with composition using Eq. [5]. We can also calculate α using the method of Slater (6) to treat the cohesive energy of metals. With the choice of a Morse potential, Slater (6) obtains a relation which can be put in a form appropriate for our treatment

$$\alpha = N_0 c r_0 (9/2) P \quad [6]$$

where N_0 is Avogadro's number; r_0 is the nearest-neighbor distance; P is the bulk modulus $= 1/\beta$, where β is the compressibility; and c is a constant, such that the volume per molecule is $c r_0^3$ and $c = 2$ in the NaCl type structure. The results of both calculations are shown in Table V.

Looking at Table V-B, α appears to be the same within a factor of two for all the carbides used in the present investigation; thus, the earlier assumption that α_1 and $\alpha_2 = \alpha$ seems to be justified. It must be kept in mind, however, that the values of α in Table V-B were obtained from data taken at room temperature on polycrystalline materials. The values presented in Table

V-A are from thermodynamic data taken at 2500°K and represent values for single crystals.

The results derived from thermodynamic measurements and from room temperature compressibility are of the same order of magnitude. The average value of α for zirconium-carbide and niobium-carbide is 8×10^{21} cal/cm²mole and compares with the value of 5.6×10^{21} cal/cm²mole obtained from high-temperature thermodynamic measurements for Zr-Nb-C. Similarly, the average value for zirconium-carbide and uranium-carbide is 5.9×10^{21} cal/cm²mole, compared with 4.8×10^{21} cal/cm²mole obtained from high-temperature thermodynamic measurements on Zr-U-C. The value of 43.5×10^{21} cal/cm²mole for α in the Zr-Hf-C system can be disregarded because $(r_1 - r_2)^2$ is very small, giving a very uncertain value to α .

Comparison is possible with the results of Speck (7), who measured elastic constants of polycrystalline NbC_{0.97} having 95% theoretical density. At room temperature, he found the compressibility was 3.05×10^{12} dyn/cm², which corresponds to $\alpha = 5.3 \times 10^{21}$ cal/cm²mole. However, his values decrease more rapidly with increasing temperature than the thermodynamic data of Table V-A would indicate.

The agreement, within a factor of two, between calculated compressibility values and experimentally measured ones shows that the assumption used here is correct: the carbon-metal bond determines the properties (such as bonding, mechanical properties, etc.) of the refractory carbides, and that the metal-metal and carbon-carbon bonds play a minor role. (The small role the metal-metal bond plays in the control of properties of carbides was already indicated as the metal-metal interaction is the same in the fcc carbide and the pure bcc metals.)

The bulk moduli of the carbides is at least, by a factor of two larger than that of the metals (Tables II and V) and thus the compressibility is lower. Such a large difference in bulk moduli can only be expected if the controlling factor is the metal-carbon bond. An enhanced metal-metal bond in the carbides (compared to the pure metals) could not account for the difference in bulk modulus.

Acknowledgment

This research was supported in part by the Air Force Materials Laboratory (MAYA), Wright-Patterson Air Force Base, Ohio 45433, under Contract No. F33615-67-C-1565.

Manuscript submitted Sept. 29, 1969; revised manuscript received Jan. 10, 1972. This was Paper 120 presented at the Detroit Meeting of the Society, Oct. 5-9, 1969.

Any discussion of this paper will appear in a Discussion Section to be published in the June 1973 JOURNAL.

REFERENCES

1. M. Hoch, "Phase Stability in Metals and Alloys," P. S. Rudman, J. Stringer, and R. I. Jaffee, Editors, p. 419, McGraw Hill Book Co., New York (1967).
2. M. Hoch, E. F. Juenke, and L. H. Sjudahl, "Thermodynamics of Nuclear Materials," 1967, p. 497, International Atomic Energy Agency, Vienna (1968).
3. C. K. Jun and M. Hoch, *This Journal*, **118**, 1498 (1971).
4. M. Hoch, M. G. Hapase, and S. Yamauchi, *ibid.*, **118**, 1504 (1971).
5. L. S. Darken and R. W. Gurry, "Physical Chemistry of Metals," pp. 50-56, McGraw-Hill Book Co., New York (1953).
6. J. C. Slater, "Introduction to Chemical Physics," p. 452, McGraw-Hill Book Co., New York (1939).
7. D. A. Speck, *Cer. Bull.*, **48**, 397 (1969).
8. R. Chang and L. J. Graham, *J. Appl. Phys.*, **37**, 3778 (1966).
9. H. L. Brown, P. E. Armstrong, and C. P. Kempter,

Table IV. Calculation of $E^{\circ}_{13} - E^{\circ}_{23}$ in ternary carbides

System	$E^{\circ}_{13} - E^{\circ}_{23}$, kcal/mole	
	Data from Table III $E_{13} - E_{23}$ at $x = 0.5$	Data from Table I $[E_3 + E_{13} + E_{33}] - [E_3 + E_{23} + E_{33}]$
Zr-Nb-C	-7.0 ± 0.5	-6.6 ± 5
Zr-U-C	-3.3 ± 0.2	-7.1 ± 4.5
Zr-Hf-C	$+5.5 \pm 0.8$	11.8 ± 10.8

Table V. Evaluation of α

A. From thermodynamic data at 2500°K

System	Slope (kcal/mole)	$(r_1 - r_2)^2 A^2$	α (10^{21} cal/cm ² mole)
Zr-Nb-C	-16.1	0.0144	5.6
Zr-U-C	-23.6	0.0169	4.8
Zr-Hf-C	-7.8	0.0009	43.5

B. From the compressibility $\alpha = N_0 c r_0 (9/2) (1/\beta)$

System	$P = (1/\beta)$ (10^{12} dyn/cm ²)	r_0 (Å)	α (10^{21} cal/cm ² mole)
ZrC	2.2 (9)	2.35	7.0
NbC	3.0 (10)	2.23	9.0
UC	1.4 (11)	2.48	4.7
HfC	2.42 (10)	2.32	7.5

- J. Chem. Phys.*, **45**, 547 (1966).
 10. C. P. Kempter, *J. Less-Common Metals*, **10**, 294 (1966).
 11. M. Hoch, A. S. Iyer, and J. Nelken, *J. Chem. Phys.*, **23**, 1463 (1962).
 12. M. Hoch, *Trans. Met. Soc.*, **230**, 138 (1964).
 13. W. J. McGregor Tegart, "Elements of Mechanical Metallurgy," McMillan, New York (1966).

Technical Notes



A Scanning Electron Microscope Investigation of Etching Phenomena in GaP Electroluminescent Diodes

W. H. Hackett, Jr., T. E. McGahan, R. W. Dixon, and G. W. Kammlott

Bell Telephone Laboratories, Incorporated, Murray Hill, New Jersey 07974

Chemical etching is commonly used in semiconductor device fabrication as a convenient method for thinning, polishing, and shaping material, as well as for junction delineation (1). Moreover, the formation of complicated device structures from III-V compounds is greatly aided by the use of preferential etching. Several authors have demonstrated preferential etching for p-type material in Ge (2, 3), Si (5, 6), and GaAs (6, 7) using a variety of electrolytes which include solutions of NaOH, HF, and HF-HNO₃. More recently, solutions of NaOH have been similarly applied to several additional III-V semiconductor systems (8), including GaAs_x, P_{1-x}InP, In_xGa_{1-x}P, and Al_xGa_{1-x}As.

The p-type preferential etching is usually achieved under conditions in which the p region is the anode in the electrolyte. For these conditions it has been shown that the current density is generally much higher at the (p-region)-electrolyte interface (analogous to a forward-biased p-n junction) than at the (n-region)-electrolyte interface (analogous to a reverse-biased p-n junction), and is related to the participation of holes in the conduction process (9). Since the semiconductor etching rate is proportional to the current density at the semiconductor-electrolyte interface, etching is highly preferential for p-type material.

In addition, there have also been a few early reports of anodic n-type preferential etching in Ge, using solutions of NaOH, KOH, HCl, and NaCl (2, 10, 11). In this case, the n-region is the anode in the electrolyte and the p-region is either the cathode or is floating. Here electrical conduction of holes is relatively poor in the reverse direction of the p-n junction when compared to the (n-region)-electrolyte interface. This poor conduction tends to block dissolution of the p-region with respect to the n-region.

It is the purpose of this paper to describe several observations of similar n-type and p-type preferential etching in GaP, which have been made with the scanning electron microscope (SEM) during our investigations of the near-junction properties of GaP electroluminescent diodes (12, 13). For example, it has been found that a 3:1:1 solution of H₂SO₄:H₂O₂:H₂O, which is used to remove surface damage for red-emitting diodes (14), is highly preferential for p-type GaP and is electrochemically controllable under conditions in which the p-region is the anode in the electrolyte. Solutions of HF-HNO₃ (15) and NaOH (16) have also been found useful for p-type preferential etching in GaP. It has also been observed that, using a solution

of HF:H₂O₂, the photoetching delineation of GaP p-n junctions (17) is due to preferential etching of the p-region. Finally, a complementary preferential etchant for n-type GaP is reported, in which the n-region is the anode in an electrolyte consisting of a solution of NaOCl-HCl.

Experimental Results and Discussion

Several properties of these etchants have been investigated on assembled GaP red-emitting diodes using the SEM. With its high resolution, large depth of field, and versatile detection system [which includes secondary emission, cathodoluminescence (CL), and specimen current (SC) modes], this instrument has been found to be ideally suited for this purpose. For example, etch steps are easily seen without cleaving the device for optical examination and direct observations of etching isotropy are possible. Detailed weight measurements are not necessary. In addition, the location of the p-n junction may be unambiguously obtained using the voltage contrast in the secondary emission, the CL, or the SC modes. For more quantitative information, such as absolute etching rates and detailed current-voltage characteristics of the respective semiconductor-electrolyte interfaces, additional care may be taken to mask electrical contacts, agitate the electrolyte, and provide uniform current densities. These precautions were not taken here and, therefore, the results are considered to be of a preliminary and semiquantitative nature.

Preferential etching of p-type GaP (3:1:1 solution H₂SO₄:H₂O₂:H₂O).—The red-emitting GaP electroluminescent diodes are diced structures which have been fabricated and assembled on Au-plated TO-18 headers. Figure 1a is a secondary emission image of such a diode, and illustrates its general appearance. The junction structure consists of an n-type Czochralski substrate, a Te-doped n-type epitaxy layer grown on the {111} P-face, and a Zn,O-doped p-type epitaxy layer grown on the n-layer (18). The two layers are approximately 25-30μ thick. Prior to assembly, appropriately doped Au contacts were evaporated and sintered onto the junction material, after which the material was slurry-cut into 0.4 mm × 0.4 mm dice. The wire bonded to the top surface of the diode in Fig. 1a is the electrical contact to the p-type epitaxy layer on the {111} P-face of the crystal.

The etching characteristics of a 3:1:1 solution of H₂SO₄:H₂O₂:H₂O were first investigated because it has been used in this laboratory to remove slurry-cutting induced surface damage from assembled diodes (14).

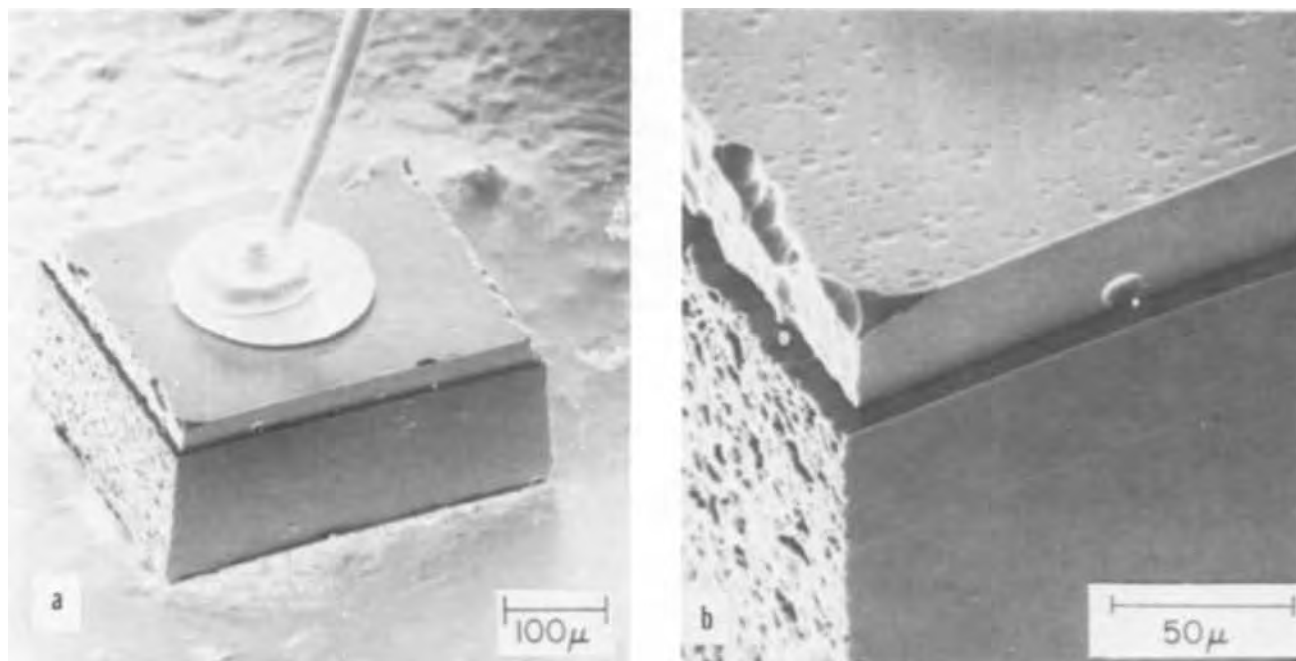


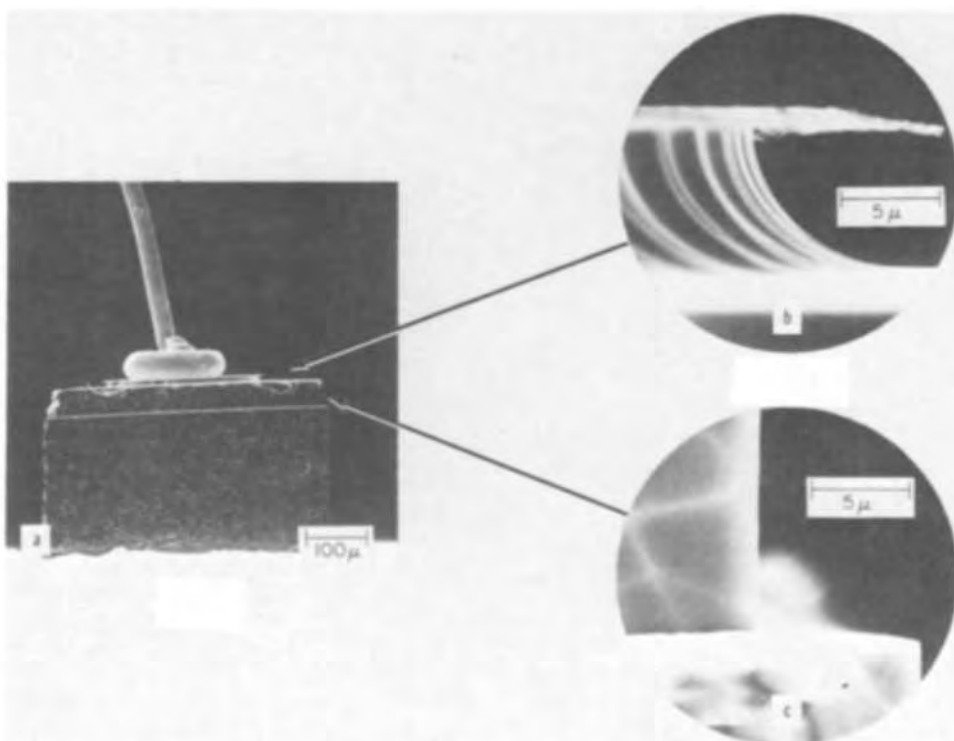
Fig. 1 a. Secondary emission image of a GaP red-emitting diode, which is a diced structure consisting of an n-type Czochralski substrate (bottom), a ~ 25 micron n-type epitaxy layer (center), and a ~ 30 micron p-type epitaxy layer (top). This diode has been etched resulting etching step at the junction, as shown. Etching is also evident near the p-contact, in addition to a faint delineation of the (n-Czochralski)-(n-epitaxy) interface. b. A magnified view of the corner of the same diode. In addition to the features described above, etch pits are clearly discernable on the top surface of the p-region.

For example, after diodes were etched in a freshly prepared solution for 5 min at 60°C , they typically exhibited a step at the p-n junction as a result of preferential etching of the p-region. Figures 1a and 1b show such a diode after 20 min of etching. In this case, the front surface of the die had been polished prior to assembly in order to provide more quantitative data. The coincidence of the etching step with the p-n junction is confirmed by the voltage-contrast at the junction, and has been independently verified using the CL mode (which determines the location of the red-emitting p-region) and the SC mode (which de-

termines the locus of efficient beam-induced junction current) (13).

To make a quantitative estimate of the etch rate, the diode was repositioned so that both the p-n junction plane and the polished surface were parallel to the viewing direction as shown in Fig. 2. In addition, from this perspective, a comparison can be made of relative etch rates in different crystallographic directions. In this case the etching step at the junction is approximately 8.6μ wide and the etch rate is $0.42\mu/\text{min}$ in directions perpendicular to the $\langle 111 \rangle$ axis (*i.e.*, the etching step has the same width for all four slurry-

Fig. 2 a. Secondary-emission image of the same diode as in Fig. 1, but with both the junction plane and the polished surface parallel to the viewing direction for a better perspective. Here the etching step at the p-n junction and the undercutting at the p-contact are clearly defined. b. Magnified view of the material removed at the p-contact. The thin top layer is the evaporated and sintered contact, and the rest is p-type semiconductor. c. Magnified view of the etching step at the p-n junction.



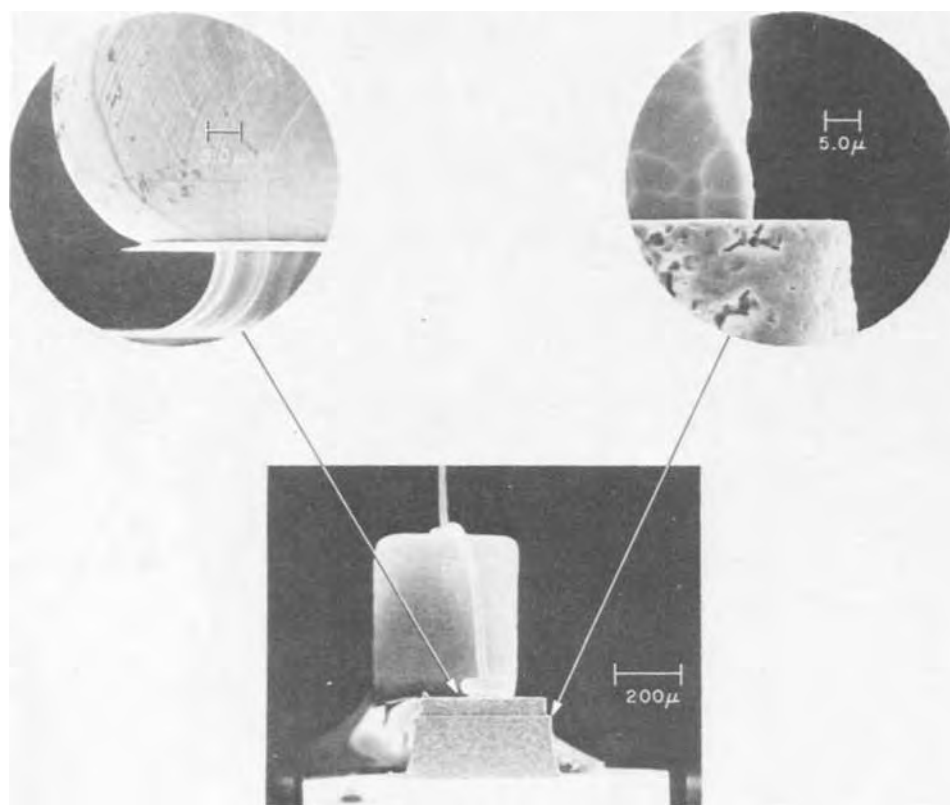


Fig. 3. Secondary emission image of a GaP red-emitting diode, which has been etched in the 3:1:1 solution under conditions in which the p-region was the anode in the electrolyte. The diode has been etched for 20 min at 60°C, using 5 mA electrode current.

cut faces). Also, as shown by the etching about the p-contact, the etching rate along the $\langle 111 \rangle$ axis is within 20% of this value. Thus, the etching in the p-region appears to be approximately isotropic. The taper at the step forms an angle of 6 degrees, with respect to the junction plane, which can be used to estimate the relative etching rates for the n- and p-material, viz., $p\text{-rate}/n\text{-rate} = \cot 6^\circ \cong 9.4$. These results confirm that the etching is highly preferential to p-type material.

To further define the characteristics of this etchant, an assembled diode was immersed in the electrolyte with the p-region biased positive with respect to a stainless or platinum electrode, which is similar to procedures reported previously (2-8). Typical results are shown in Fig. 3 for a diode etched for 20 min at 60°C, and for 5 mA electrode current. In this case, the preferential etching has been enhanced to the extent that the angle of the step relative to the junction plane is nearly zero. This enhanced preferential etching for p-type material is generally consistent with the respective characteristics of n- and p-type semiconductor-electrolyte interfaces (*i.e.*, a positive potential across the p-electrolyte interface conducts current easily, while a similar potential across the n-electrolyte interface results in only limited current densities) (9).

In this case, approximately 12.8μ of p-material have been removed, at an etching rate of $0.64\mu/\text{min}$. From the relative magnitudes of the etching step, and the etching under the p-contact on the top surface, it is concluded that the etching is still isotropic for the p-region even though there has been no attempt made to keep the current density uniform at the semiconductor-electrolyte interface. There was also no unusual attack at the contact-GaP interface. Approximately 0.6-0.8V were required to produce the 5 mA electrode current, but no detailed current-voltage relationships were determined in this preliminary characterization.

With the present diode-electrode configuration, the current density is probably somewhat nonuniform over the p-electrolyte interface. In addition, it is likely that the etching rate is slightly inhibited by gas evolution and the formation of by-products at the semi-

conductor surface since no special precautions were used to promote mixing of the solution near the interface. Nonetheless, the enhanced p-type preferential etching under these anodic conditions is amply demonstrated.

For completeness, a similar diode was also immersed in the electrolyte for 20 min at 60°C, but with the p-region biased negatively with respect to the electrode. Under these conditions, the preferential etching was suppressed. No undercutting of the contact was visible, and there was no measurable etching step. Very little etching of either p- or n-type material was evident. These observations are consistent with the general current-voltage characteristics of the p-electrolyte interface and demonstrate the electrochemical control of the preferential etch.

The HF:H₂O₂ photoetch.—A solution of HF:H₂O₂ has often been used as a photoetch to delineate p-n junctions in GaP (17). In order to better understand the cause of this delineation, a slurry cut diode similar to those previously discussed was selected. One surface was polished with Linde A and then etched in hot aqua regia to remove any remaining surface damage prior to assembly. The topography at this surface near the junction plane was smooth, as expected for the assembled diode, without any etch step at the junction indicating that hot aqua regia does not selectively etch n- or p-type GaP. When this diode was subsequently photoetched for 90 sec, at 24°C in a 1:1 solution of HF:H₂O₂, a step approximately $\frac{1}{2}\mu$ wide resulted at the p-n junction due to preferential etching of the p-region. At present, the origin of the dominant etching mechanism is not clear, although it may be simply a preferential dissolution of the p-region caused by a photoinduced voltage at the p-n junction. It is evident, however, that the junction delineation results from preferential etching of the p-region.

Preferential etching of n-type GaP.—We also report here what we believe to be the first successful attempt to preferentially etch n-type GaP. In this case the n-region was the anode in an electrolytic solution of NaOCl and HCl (which is unstable under acid conditions), and a stainless steel or platinum electrode was

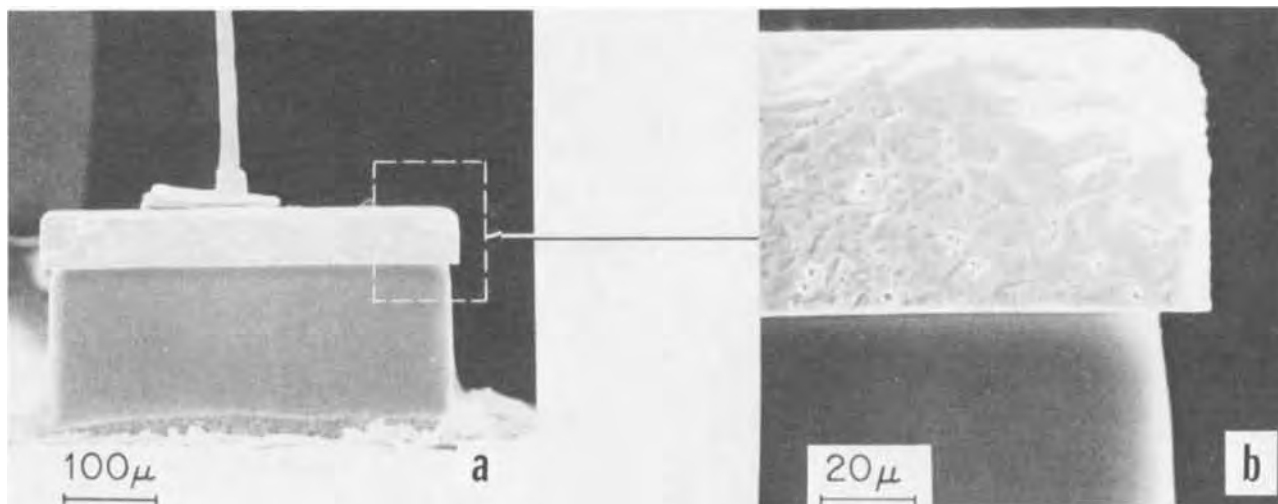


Fig. 4. Secondary emission image of a GaP red-emitting diode, which has been n-preferentially etched in an electrolyte consisting of a solution of NaOCl and HCl. In this case, the n-region was the anode in the electrolyte.

the cathode. This procedure takes advantage of the relatively poor conduction of holes in the reverse direction of the p-n junctions, and, thus, preferentially removes n-type GaP from assembled diodes while having no appreciable effect on the p-type material.

Figure 4 shows the result of electrochemically etching an assembled diode for 5 min at 24°C in an etchant consisting of a 7:1 ratio of (5.25% wt solution of NaOCl): (HCl). The electrode current was 5 mA. The abrupt step at the p-n junction is now indicative of n-type preferential etching. The fact that no detectable angle exists between the junction plane and the etching step indicates that very little or none of the p-type material has been removed. Note that somewhat more n-material has been removed near the p-n junction than further away. From this and similar observations it is believed that the etch rate is highest where the doping concentration is highest (near the junction $N_D - N_A \sim 2 \times 10^{18} \text{ cm}^{-3}$) and decreases in more lightly doped material (the bulk of the n-substrate has $N_D - N_A \sim 2 \times 10^{17} \text{ cm}^{-3}$) (18). (The preferential etching was suppressed when the applied potential was reversed.) The etch rate of this solution, nominally 2 μ/min , is considerably faster than that of 3:1:1 for p-material. Also the gold n-contact is somewhat attacked by this etch.

While no attempt has been made to optimize this etch, or to investigate its characteristics in detail, its discovery does demonstrate the feasibility of n-type preferential etching in GaP. The existence of such solutions complements the growing number of p-type preferential etchants for this material.

Summary and Conclusions

Several interesting observations of preferential etching of GaP electroluminescent diodes have been made using the SEM. Specifically, two electrochemically controllable etchants have been found, one for p-type material, and one for n-type material. Although the detailed anodic characteristics have not been determined for the respective n- and p-type semiconductor-electrolyte interfaces, one would expect, on the basis of the anodic preferential etching characteristics, that they are similar to those for Ge and Si. Also, it has been determined that a commonly used photoetch is,

in fact, a preferential etch for p-type material. These and similar preferential etchants have potentially important uses in the technology of GaP light-emitting diodes, where it is desirable to economically fabricate sophisticated structures (19).

Acknowledgment

The authors are indebted to R. H. Saul for helpful discussions and comments on the manuscript.

Manuscript received Dec. 2, 1971.

Any discussion of this paper will appear in a Discussion Section to be published in the June 1973 JOURNAL.

REFERENCES

1. V. A. Myamlin and Yu. V. Pleskov, "Electrochemistry of Semiconductors," Chap. 5, Plenum Press, New York (1967).
2. M. Sparks, U.S. Pat. 2,656,496 (1953).
3. R. W. Jackson, *J. Appl. Phys.*, **27**, 309 (1956).
4. C. S. Fuller, U.S. Pat. 2,740,700 (1956).
5. C. S. Fuller and J. A. Ditzenberger, *J. Appl. Phys.*, **27**, 550 (1956).
6. B. A. Joyce, *Solid-State Electron.*, **5**, 102 (1962).
7. Yu. V. Pleskov, *Dokl. Akad. Nauk SSSR*, **143**, 1399 (1962).
8. C. J. Nuese and J. J. Gannon, *This Journal*, **117**, 1094 (1970).
9. W. H. Brattain and C. G. B. Garrett, *Bell System Tech. J.*, **34**, 129 (1955).
10. E. Billig and J. J. Dowd, *Nature*, **172**, 115 (1953).
11. J. I. Pankove, *RCA Rev.*, **16**, 398 (1955).
12. W. H. Hackett, Jr., *J. Appl. Phys.*, **42**, 3249 (1971).
13. W. H. Hackett, Jr., R. W. Dixon, and G. W. Kamm-lott, 1971 Device Research Conference, University of Michigan.
14. N. E. Schumaker and G. A. Rozgonyi, *This Journal*, To be published.
15. R. F. Scott and L. A. Koszi, Private communication.
16. R. L. Meek and N. E. Schumaker, *This Journal*, To be published.
17. M. R. Lorenz and M. Pilkuhn, *J. Appl. Phys.*, **37**, 4094 (1966).
18. W. H. Hackett, Jr. and R. H. Saul, Paper 81 presented at the Los Angeles Meeting of the Society, May 10-15, 1970.
19. N. E. Schumaker, M. Kuhn, and R. A. Furnanage, *IEEE Trans. Electron. Dev.*, **ED-18**, 627 (1971).

Diffusion from a Thin Layer into a Semi-Infinite Medium with Concentration Dependent Diffusion Coefficient

M. Ghezzi*

General Electric Corporate Research and Development Center, Schenectady, New York 12301

It is well known in the literature (1) that the Boltzmann transformation is the most suitable method for solving the diffusion equation with concentration dependent diffusion coefficient when the boundary conditions satisfy certain requirements. In particular, this transformation may be applied when the surface concentration of the indiffused medium is invariant with time, for example, in the predeposition process used in silicon device manufacturing (2). The Boltzmann transformation yields, in this case, a convenient formula for determining the diffusion coefficient as a function of concentration when the diffusion profile has been experimentally determined. The opposite is more difficult and, in order to compute the diffusion profile from the diffusion coefficient, an iterative method must be followed (1).

When the diffusing substance is subject to a redistribution within the indiffused medium, the Boltzmann transformation may not be applied because the surface concentration decreases with time which implies a time dependence of the concentration separate from the ratio of penetration depth to square root of diffusion time postulated by Boltzmann. A very important case of concentration redistribution in a semi-infinite medium with an impermeable boundary is represented by diffusion of impurities from a superficial thin layer of this medium into its bulk. An example is provided in silicon device processing by the so-called drive-in diffusion, which is used for adjusting the concentration profile to the device specifications after the predeposition step (2).

The purpose of this note is to show the potential inherent in the transformation approach even in the case of concentration redistribution within a semi-infinite medium, provided that the Boltzmann transformation is replaced by a suitable modification in accordance with the different boundary conditions. As the main interest of this work consists of a demonstration of the method, the mathematical treatment was kept as simple as possible, at the expense of its utility in solving actual diffusion problems, by limiting the investigation to a diffusivity dependence on the ratio of concentration to surface concentration instead of on concentration alone.

Theory

By calling Q the total amount of impurities per unity of surface in the indiffused medium, the assumption of an impermeable boundary results in the constancy of Q with time. Thus, the relationship

$$Q = \int_0^{\infty} N(x,t) dx \quad [1]$$

imposes a condition on the functional dependence of the impurity concentration, $N(x,t)$; on the time, t ; and the penetration depth, x . As Q must have a finite value, Eq. [1] requires that at any time

$$N(x,t) = 0 \text{ for } x \rightarrow \infty \quad [2]$$

Besides, the initial concentration profile will be represented as a delta function

$$N(x,t) \neq 0 \text{ for } x = 0, t = 0 \quad [3a]$$

$$N(x,t) = 0 \text{ for } x > 0, t = 0 \quad [3b]$$

The Boltzmann's transformation may be represented by

$$N(x,t) = G(x/\sqrt{t}) \quad [4]$$

with G satisfying the diffusion equation and the boundary conditions.

Application of Eq. [4] to [1] shows a time dependence of Q given by

$$Q = \sqrt{t} \int_0^{\infty} G(x/\sqrt{t}) d(x/\sqrt{t}) \quad [5]$$

which contradicts the hypothesis of an impermeable boundary.

Comparison of Eq. [5] with [1] shows that the required time independence of Q is easily achieved by the following transformation

$$N(x,t) = F(x/\sqrt{t})/\sqrt{t} \quad [6]$$

which gives for Q the value

$$Q = \int_0^{\infty} F(x/\sqrt{t}) d(x/\sqrt{t}) \quad [7]$$

Assuming that the diffusion coefficient D is concentration dependent, the diffusion equation may be written for a one-dimensional geometry (1)

$$\frac{\partial N}{\partial t} = \frac{\partial}{\partial x} \left(D(N) \frac{\partial N}{\partial x} \right) \quad [8]$$

Replacing N in Eq. [8] with its expression given by Eq. [6], and performing a change of coordinates from (x,t) to (η,t) , where η is defined by

$$\eta = x/\sqrt{t} \quad [9]$$

the diffusion equation becomes

$$\begin{aligned} & -\frac{1}{2t\sqrt{t}} \frac{d}{d\eta} [\eta \cdot F(\eta)] \\ & = \frac{1}{\sqrt{t}} \frac{\partial}{\partial \eta} \left[D \left(\frac{F(\eta)}{\sqrt{t}} \right) \cdot \frac{1}{t} \cdot \frac{dF(\eta)}{d\eta} \right] \end{aligned} \quad [10]$$

which simplifies to

$$-\frac{1}{2} \frac{d}{d\eta} [\eta \cdot F(\eta)] = \frac{\partial}{\partial \eta} \left[D \left(\frac{F(\eta)}{\sqrt{t}} \right) \cdot \frac{dF(\eta)}{d\eta} \right] \quad [11]$$

The need for Eq. [11] to be self-consistent imposes a limitation on D which must depend on η alone for avoiding the situation in which the solution for F would depend both on \sqrt{t} and η in contradiction with the assumption used in the derivation of Eq. [11].

As the surface concentration at time t , $N(0,t)$ is equal to

$$N(0,t) = F(0)/\sqrt{t} \quad [12]$$

this specification on D is satisfied by adding the limitative hypothesis that D be a function of the ratio $N(x,t)/N(0,t)$, which is equivalent to assume $D(F(\eta)/F(0))$.

Equation [11] is immediately integrated between η and ∞ , yielding the first order differential equation

* Electrochemical Society Active Member.
Key words: diffusion theory, Boltzmann's transformation, concentration dependent diffusion coefficient.

$$-\frac{1}{2}\eta F(\eta) = D \left(\frac{F(\eta)}{F(o)} \right) \cdot \frac{dF(\eta)}{d\eta} \quad [13]$$

The passage from Eq. [11] to Eq. [13] is possible because

$$\lim_{\eta \rightarrow \infty} (\eta \cdot F(\eta)) = \lim_{\eta \rightarrow \infty} \left(D \left(\frac{F(\eta)}{F(o)} \right) \cdot \frac{dF(\eta)}{d\eta} \right) = 0 \quad [14]$$

as Eq. [7] requires that $F(\eta)$ be of order greater than one in $1/\eta$ in order to yield a finite Q .

Equation [13] may be integrated between $\eta = o$ and η after proceeding to a variable separation between the two members of the equation. This results in the relationship

$$\int_1^{F(\eta)/F(o)} \frac{D(\xi) d\xi}{\xi} = -\frac{1}{4}\eta^2 \quad [15]$$

where $\xi = F/F(o)$.

The constant, $F(o)$, can be determined from Eq. [7] after a suitable modification of this equation as shown below.

Changing the integration variable from η to ξ by means of Eq. [13], Eq. [7] becomes

$$Q = 2F(o) \int_0^1 \frac{D(\xi) d\xi}{\eta(\xi)} \quad [16]$$

where it was taken into account that according to Eq. [2] and [6] $\xi = 0$ and $\eta \rightarrow \infty$.

Replacement of $\eta(\xi)$ in Eq. [16] with its expression given by Eq. [15], yields this formula for $F(o)$

$$F(o) = Q \left/ \int_0^1 \frac{D(\xi) d\xi}{\sqrt{\int_\xi^1 \frac{D(\rho)}{\rho} d\rho}} \right. \quad [17]$$

where ρ is defined as ξ .

A check of the validity of the above equations is provided by computing the concentration profile for the case $D = D_o$, with D_o a constant.

Integration of Eq. [15] yields immediately

$$F(\eta) = F(o) \exp(-\eta^2/4D_o) \quad [18]$$

which is equivalent, according to Eq. [6] and [9], to

$$N(x,t) = N(o,t) \exp(-x^2/4D_o t) \quad [19]$$

Application of Eq. [17] gives the value of $F(o)$

$$F(o) = Q/\sqrt{D_o} \cdot \int_0^1 \frac{d\xi}{\sqrt{\ln(1/\xi)}} \quad [20]$$

As the definite integral in Eq. [20] is equal to $\sqrt{\pi}$ (3), Eq. [19] becomes the familiar gaussian distribution function

$$N(x,t) = \frac{Q}{\sqrt{\pi D_o t}} \exp(-x^2/4D_o t) \quad [21]$$

Example

Let us assume that

$$D(N(x,t)/N(o,t)) = D_o[1 + k(N(x,t)/N(o,t))] \quad [22]$$

which corresponds to a linear dependence of D on the ratio of concentration to surface concentration with slope $k \cdot D_o$, where D_o is the intrinsic diffusivity, and k a real positive number.

From Eq. [15], [12], and [6], the expression of D given by Eq. [22] yields, after integration, the formula

$$\frac{x}{2\sqrt{D_o t}} = \sqrt{k \left(1 - \frac{N(x,t)}{N(o,t)} \right) - \ln \frac{N(x,t)}{N(o,t)}} \quad [23]$$

which is the normalized version of the diffusion profile.

In Fig. 1 a plot of the profiles, corresponding to different values of k , shows that an increase in k

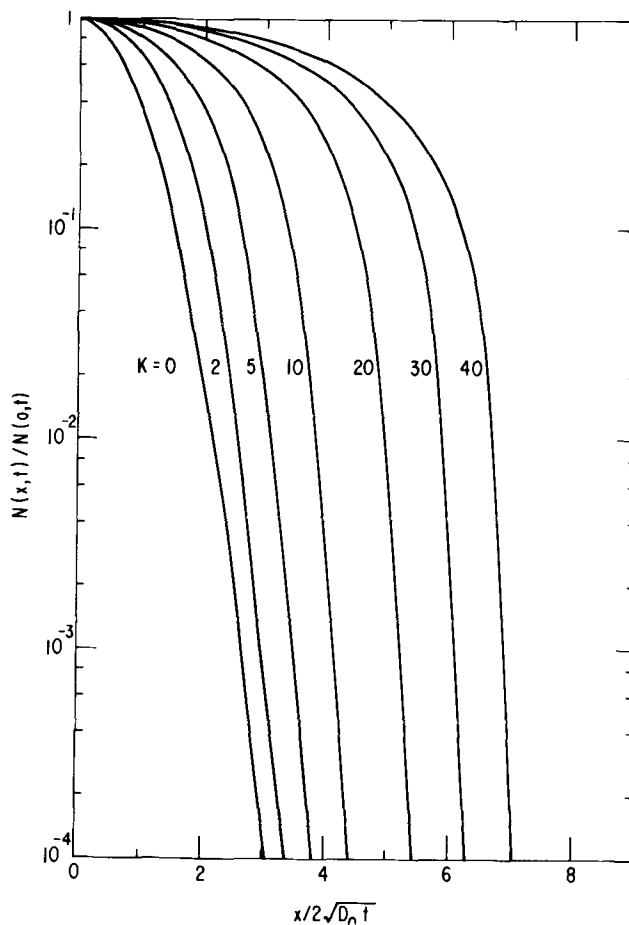


Fig. 1. Normalized diffusion profiles for a diffusion coefficient $D = D_o[1 + k(N(x,t)/N(o,t))]$ with $k = 0, 2, 5, 10, 20, 30, 40$, in the case of planar diffusion into a semi-infinite medium limited by an impermeable boundary. The solute is concentrated before diffusion in a very thin layer adjacent to the boundary.

flattens the initial part of the profile and introduces a sharper concentration drop in the profile tail. The profile for $k = 0$ is represented by the gaussian error function, while the profiles for higher values of k correspond to an enhanced diffusion. In particular, the profile for $k = 30$ was included in Fig. 1 for making the example more realistic; because in high concentration arsenic diffusions into silicon, the ratio of maximum diffusivity to intrinsic diffusivity is about 30 for a wide temperature range (950°-1150°C) according to Kennedy and Murley (4).

The profiles of Fig. 1 are expressed in normalized form. So as to determine the actual profiles the surface concentration at time t , $N(o,t)$, must be computed through a numerical integration of Eq. [17].

Conclusion

A modified version of the Boltzmann transformation method was used for obtaining an exact solution of the diffusion equation in a semi-infinite medium, limited by a plane impermeable boundary with finite source initially close to this boundary, and with the diffusion coefficient dependent on the ratio of concentration to surface concentration. The general solution was verified for a constant diffusion coefficient by yielding the gaussian error function. Calculation of the profiles corresponding to a diffusion coefficient linearly dependent on the ratio of concentration to surface concentration was used for illustrative purposes.

Manuscript submitted Dec. 8, 1971; revised manuscript received March 8, 1972.

Any discussion of this paper will appear in a Discussion Section to be published in the June 1973 issue of the JOURNAL.

REFERENCES

1. J. Crank, "The Mathematics of Diffusion," p. 148 ff., Oxford University Press, Clarendon, England (1956).
2. A. S. Grove, "Physics and Technology of Semiconductor Devices," p. 43 ff., John Wiley & Sons, New York (1967).
3. R. C. Weast, Editor, "Handbook of Chemistry and Physics," 50th ed., p. A-198, Chemical Rubber Publishing Co., Cleveland, Ohio (1969).
4. D. P. Kennedy and P. C. Murley, *Proc. IEEE*, 59, 335 (1971).

Erratum

In the paper "Diffusion of ^{51}Cr in NiO Single Crystals" by M. S. Seltzer which appeared on pp. 802-805 in the May 1971 JOURNAL, Vol. 118, No. 5, in converting from natural logarithms to base 10 logarithms the dif-

fusion coefficients were multiplied by the factor 2.303 when they should have been divided by this factor. Therefore, to get the correct diffusivities in Fig. 2 and 3, one must divide by $(2.303)^2$.



Stress Corrosion Cracking of 18% Cr Ferritic Stainless Steels

R. T. Newberg* and H. H. Uhlig*

Department of Metallurgy and Materials Science,
 Massachusetts Institute of Technology, Cambridge, Massachusetts 02139

ABSTRACT

Stress corrosion cracking of ferritic 18% chromium stainless steels in $MgCl_2$ solution depends on nickel content (0-8%) as well as on heat-treatment and cold work. Maximum susceptibility occurs at 2% Ni; alloyed manganese has a small effect; molybdenum can be detrimental. Rolling direction has little or no effect on failure times of ferritic 18-8, contrary to failure by hydrogen cracking, indicating different mechanisms of failure. Whether or not failure occurs depends on the relation of critical to corrosion potentials for all but the lowest nickel alloys. Hence galvanic couples can be useful or damaging. The results are not readily explained in terms of electrochemical dissolution or brittle oxide films. A mechanism is favored based on adsorption of Cl^- ions on appropriate surface imperfection sites.

The relatively good resistance or complete immunity of ferritic stainless steels, e.g. AISI Type 430, to stress corrosion cracking (s.c.c.) in hot aqueous chloride solutions was pointed out by Scheil *et al* (1) as early as 1943. Later tests showed that ferritic alloys containing small amounts of Ni, e.g. 12% Cr, 2% Ni-Fe; or 28% Cr, 5% Ni, 1.7% Mo-Fe, exposed to $MgCl_2$ boiling at 154°C either failed or showed surface cracks (2). Copson (3) presented data showing that additions of Ni to 15-26% Cr-Fe stainless steels at first increased, then decreased their susceptibility to s.c.c. in boiling 42% $MgCl_2$ resulting in maximum susceptibility between 0 and 8% Ni. Riedrich and Kohl (4) established that minimum resistance of austenitic alloys containing 16% Cr, 9% Mn appeared at about 4-5% Ni, with Mn having little effect on susceptibility, but with copper, at a given weight per cent, being more damaging than Ni.

Uhlig, White, and Lincoln (5, 6) found that a low C, low N, 18% Cr, 8% Ni stainless steel, ferritic (or martensitic) as quenched from 1050°C, was resistant to cracking in $MgCl_2$ boiling at 154°C (>250 hr) whereas a similar alloy when austenitic as quenched (containing higher C and N), failed in short times (0.2-1.4 hr). The structure rather than C and N content was responsible for the difference as was shown by the parallel observed resistance to s.c.c. of originally austenitic 18-8 alloys subsequently transformed to ferrite by cold working at liquid N_2 temperatures (5, 6). A higher Ni alloy, e.g., 20% Ni stainless steel, which did not transform, became less rather than more resistant after cold rolling. Bond and Dundas (7) reported that 18% Cr-Fe ferritic stainless steels annealed at 815°C for 1 hr did not crack in $MgCl_2$ boiling at 140°C if the Ni content was below about 1% and similarly if the Cu content was below 0.5%. For resistance to s.c.c., the total Ni plus $3 \times$ Cu content, they stated, should preferably be below 0.9%. Small alloying additions of Mo (1-5%) had no effect, but 2% Mo combined with small amounts of Ni, Cu, or Co induced susceptibility.

It is the purpose of the present investigation to extend the available information on susceptibility to s.c.c. of the ferritic 18% Cr stainless steels containing from 0 to 8% Ni. It appears particularly desirable to know more about possible mechanisms that can account for the relative resistance of some ferritic-type stainless steels (body-centered cubic) and the comparable lack of resistance of austenitic alloys (face-centered cubic) of a similar or even the same composition.

Experimental Procedure

Alloys were vacuum melted by high frequency in dense pure alumina crucibles, followed by casting in purified argon by drawing up the melt into 7 or 9 mm diameter Vycor tubing and water quenching. Ingots were homogenized in argon at 1050°C for 24 hr, then cold-rolled to strip about 0.041-in. thick. Starting materials were electrolytic iron deoxidized at 1150°C for 2 hr in dry H_2 and decarburized at 760°C for 48 hr in wet H_2 . Carbonyl Ni was furnished by courtesy of the

Table I. Composition of ferritic stainless steels

Alloy	Weight per cent			% Addition
	% Cr	% Ni	% C	
17% Cr-Fe (Type 430) (Commercial)	17.38		0.095	
16% Cr-Fe	15.8		0.0013	
18% Cr, 0.2% Ni-Fe	18.19	0.17	0.005	
18% Cr, 0.6% Ni-Fe	18.31	0.57	(0.004)	
18% Cr, 1.1% Ni-Fe	18.31	1.10	(0.003)	
18% Cr, 1.5% Ni-Fe	17.81	1.50	0.003	
17% Cr, 2% Ni-Fe (A)	16.9	2.27	0.003	
18% Cr, 2% Ni-Fe (B)	17.81	2.07	<0.001	
(C)	18.40	2.19	0.009	
18% Cr, 3% Ni-Fe	17.93	3.01	(0.004)	
18% Cr, 5% Ni-Fe (A)	18.1	5.01	0.005	
(B)	18.35	5.02	0.007	
18% Cr, 8% Ni-Fe (A)	18.27	8.43	0.001	
(B)	18.33	8.36	0.002	
16% Cr, 2% Mo-Fe	16.2		0.001	2.00
17% Cr, 2% Ni, 2% Mo-Fe	17.3	2.26	0.003	1.97
16% Cr, 8% Ni, 2% Mo-Fe	16.0	7.72	0.0015	2.24
19% Cr, 1.1% Ni, 1.6% Mn-Fe	18.73	1.10	0.002	1.61
18% Cr, 3% Ni, 1.5% Mn-Fe	17.89	2.88	(0.004)	1.53
18% Cr, 3% Ni, 3% Mn-Fe	18.19	2.84	0.0052	3.02

* Numbers in parentheses were estimated from first and last split heat.

* Electrochemical Society Active Member.

Key words: critical potential, alloyed molybdenum, alloyed nickel, stress-sorption cracking, NaOH solutions, nitrate solutions, magnesium chloride solutions.

International Nickel Company and pure Cr was purchased from the Electrometallurgical Company. Molybdenum was Johnson-Matthey spectroscopic grade; Mn was electrolytic grade. Chemical analyses of the cold-rolled strip are listed in Table I. Duplicate alloys A and B of the 5 and 8% Ni, and triplicate alloys A, B, and C of the 2% Ni compositions, were prepared to furnish additional test specimens; they performed similarly for any one category of composition within the experimental variations of the tests.

Specimens measuring $1\frac{3}{4} \times 3/16 \times 0.041$ in. ($4.5 \times 0.5 \times 0.1$ cm) were sheared from the cold-rolled strip with the long dimension in the rolling direction, unless otherwise specified. They were either tested as such (cold-rolled 80% reduction in thickness), or water quenched from 1050°C (water quenched), or heated to 1050°C and subsequently annealed at 815°C for 1 hr in argon followed by air-cooling (annealed). In all cases, specimen surfaces were abraded with wet No. 120C silicon carbide paper followed by No. 0 emery paper. They were then degreased, and pickled in 15 v/o (volume per cent) HNO_3 -5 v/o HF at 90°C for 5 min.

Specimens were bent beyond the elastic limit to a span of $1\frac{5}{8}$ in. (4.1 cm), transferred by means of a notched gauge to insulated holders of the test apparatus, and adjusted to a final span of $1\frac{7}{16}$ in. (3.7 cm), avoiding springback. They were held at constant flow stress by means of a compressed spring. When tests were conducted under constant applied potential, a Ni wire or one of the same composition alloy as the specimen was spot welded to one end of the specimen and enclosed with Teflon tubing. A saturated calomel electrode at room temperature was located in a side arm containing MgCl_2 solution nearest the point of maximum bending and separated from the boiling MgCl_2 solution by a fritted glass disk. Auxiliary electrodes of graphite were located in two arms on either side of the specimen, also separated by fritted glass disks. The test apparatus employing MgCl_2 solution boiling at 130°C has been depicted in a former publication (8). Because of variations in batches of MgCl_2 as received, all solutions were prepared from salt obtained by thorough mixing of several batches. Tests were run to a maximum of 200 hr; controlled potential runs normally ran to only 50 hr because of chemical changes in the solution resulting from electrolysis. The critical potential for a given alloy was obtained by plotting failure times vs. controlled potentials for 10 to 15 specimens. Typical plots of this kind were presented in an earlier publication (9).

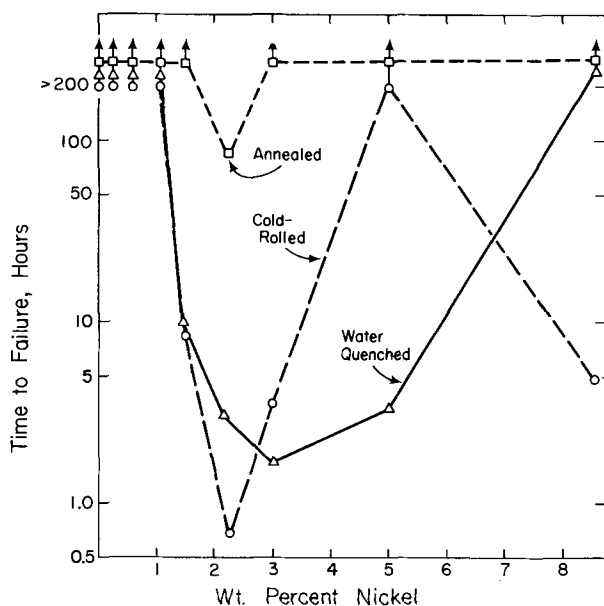


Fig. 1. Effect of alloyed nickel in 18% chromium stainless steels on stress corrosion cracking in MgCl_2 , 130°C.

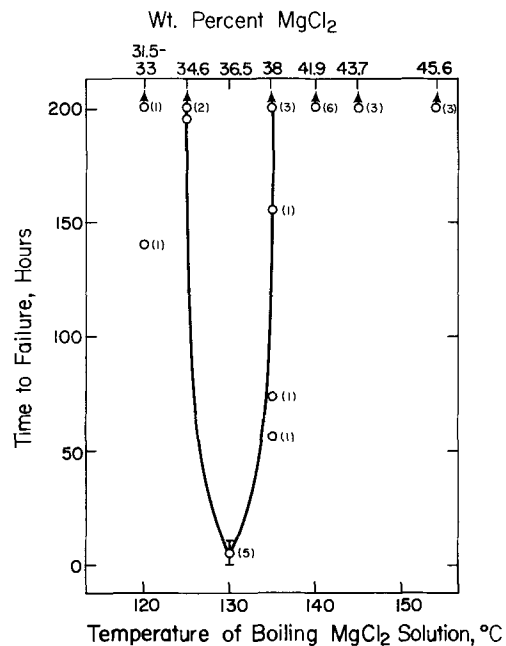


Fig. 2. Effect of MgCl_2 concentration on stress corrosion cracking of cold-rolled ferritic 18-8 stainless steel, boiling temperatures.

Failure Times

Cracking times of 16-18% Cr stainless steels as a function of Ni content are shown in Fig. 1. Each point represents the average of three or more tests. Most cracks followed predominantly transgranular paths, as far as could be determined, but with some evidence of partial intergranular cracking in some alloys such as the water-quenched 1.5-5% Ni compositions. No failures were observed up to 1% Ni within 200 hr, whether the alloys were cold-rolled, quenched, or annealed. At 1.5% Ni, the cold-rolled and quenched alloys failed, but the annealed alloys still resisted cracking above 200 hr. At about 2% Ni, susceptibility became maximum, and the alloy failed in short times typical of the behavior of austenitic 18-8 stainless steels. The annealed alloy remained more resistant than the quenched or cold-rolled alloy. At 5% Ni, both the annealed and cold-rolled alloys (stressed parallel to rolling direction) were resistant (>200 hr), but the quenched alloy failed. At 8% Ni, the alloy failed only in the cold-rolled condition, but this behavior turned out to be peculiar to 130°C. The same alloy, for example, as had been reported previously (5, 6) did not fail within 200 hr in MgCl_2 boiling at 154°C, nor did it fail at 140° or 145°C. It failed in relatively longer times at 120°, 125°, and 135°C as shown in Fig. 2. A commercial austenitic 18-8 alloy, on the other hand, cold-rolled 35% reduction in thickness, failed in shorter times the higher the temperature. Cracking times were 29, 0.3, 0.2, and 0.1 hr in MgCl_2 solutions boiling at 120°, 130°, 140°, and 154°C respectively (10).

The ferritic 16-18% Cr stainless steels containing less than 8% Ni failed in about the same times in MgCl_2 at 130° or 154°C with the exception of the quenched 5% Ni alloy which was resistant at 154°C. The Ni-free 16% Cr-Fe alloy did not fail by cracking at either temperature, but was observed to undergo pitting corrosion in long-time tests, which in the extreme caused failure by creep of the spring-loaded specimen.

It was of interest to learn whether direction of applied stress had an effect on failure times of the cold-rolled ferritic 18-8 stainless steel in MgCl_2 at 130° or 154°C. Five specimens at 130°C stressed parallel to the rolling direction failed in 4.9 ± 1.0 hr, whereas four specimens stressed at right angles to the rolling direction failed in 2.4 ± 0.3 hr. This difference of cracking times is not considered to be of great significance. At 154°C, cold-rolled ferritic 18-8 did not fail within at least 200 hr whether stressed parallel or at right angles

Table II. Effect of alloyed Ni, Mn, and Mo on cracking times in MgCl₂, 130°C

Alloy	Time to failure, hr		
	Water quenched from 1050°C	Cold-rolled 80% reduction in thickness	Annealed 815°C, 1 hr
16% Cr-Fe	>200 [3]*	>200 [3]*	>200 [3]
18% Cr, 1.1% Ni-Fe	>200 [3]	>200 [3]	>200 [3]
19% Cr, 1.1% Ni, 1.6% Mn-Fe	>200 [3]	>200 [3]	>200 [3]
18% Cr, 3% Ni-Fe	1.6 ± 0.5 [3]	3.6 ± 0.3 [5] (Parallel) 1.4 ± 0.4 [3] (Perpendicular)	>200 [3]
18% Cr, 3% Ni, 1.5% Mn-Fe	3.2 ± 1.4 [4]	3.1 ± 0.6 [3]	90 ± 9 [3]
18% Cr, 3% Ni, 3% Mn-Fe	3.2 ± 1.1 [4]	2.8 ± 1 [3]	33 ± 3 [3]
18% Cr, 5% Ni-Fe		>200 [3] (Parallel) 2.2 ± 0.4 [3] (Perpendicular)	
16% Cr, 2% Mo	>200 [3]	5.6 ± 4 [3]	>200 [3]
17% Cr, 2% Ni, 2% Mo-Fe	2.0 ± 0.2 [2]	2.0 ± 0.2 [3]	2.0 ± 0.4 [3]
18% Cr, 8% Ni-Fe	>200 [3]	4.9 ± 1 [5] (Parallel) 2.4 ± 0.3 [3] (Perpendicular)	>200 [3]
16% Cr, 8% Ni, 2% Mo-Fe } Ferritic	1.4 ± 0.4 [3]	73 ± 23 [3]	7 ± 2 [3]

* The number in brackets is the number of specimens tested.

to the rolling direction. By way of contrast, the same alloy stressed parallel to the rolling direction was resistant to hydrogen cracking (>200 hr) when cathodically polarized in 5% H₂SO₄ + As₂O₃, but failed in short time (0.1 hr) when stressed perpendicular to the rolling direction (11). This marked difference of behavior can be taken as evidence that crack nuclei and fracture paths associated with hydrogen cracking, and which are oriented by cold rolling, are not the same nuclei and fracture paths associated with stress corrosion cracking. Obviously the mechanisms of the two types of fracture are not the same.

The effect of small alloying additions of Mo or Mn to 16-18% Cr-Fe alloys was usually either inconsequential or in the direction of increasing susceptibility. Some of the relevant data are tabulated in Table II. Included are data on the effect of rolling direction on failure times of the 3, 5, and 8% Ni alloys showing that an appreciable effect is observed only with the 5% Ni alloy. Manganese tends to make the 3% Ni alloy, as annealed, more susceptible; it has no measurable effect on the 1.1% Ni alloy. The quenched and cold-rolled alloys are unaffected. Riedrich and Kohl (4) found that 9-18% Mn in quenched alloys containing 5-16% Cr were resistant to cracking in MgCl₂ at 154°C provided that Ni was below 1.5-2% and Cu below 0.7%. Two per cent Mo addition is not damaging (Table II), in accord with conclusions of Bond and Dundas (7), except for the cold-rolled state in which the Mo alloy fails. For the annealed alloy, molybdenum combined with 2% Ni is worse than Ni alone. The combination of 2% Mo with 8% Ni makes s.c.c. properties of the ferritic alloy worse except perhaps for the cold-rolled alloy. A few 2% Ni stainless steels were made up with additions of 0.08-0.15% Sn, or with 0.5% Zr but these elements had no marked effect on time to cracking in MgCl₂.

Tests in 35% NaOH + 0.1% PbO boiling at 126°C showed that both the cold-rolled 16% Cr-Fe and the cold-rolled 17% Cr, 2% Ni-Fe alloys were resistant to cracking for at least 300 hr. The former alloy showed evidence of superficial intergranular corrosion which appeared to be independent of stress. The two alloys also did not fail by s.c.c. within 200 hr in 60% Ca(NO₃)₂, 3% NH₄NO₃ solution boiling at 110°C. These results confirm similar data reported earlier by Bond, Marshall, and Dundas (12).

Critical Potentials

A specific potential below which s.c.c. of 18-8 stainless steel is inhibited in boiling MgCl₂ or CaCl₂ solutions has been reported by several investigators (8, 9, 13-15). For cold-rolled commercial austenitic 18% Cr, 8% Ni alloy (35% reduction in thickness) in MgCl₂ boiling at 130°C, the observed value is -0.145V (SHE) (9) and for the quenched alloy it is -0.130V (16). With increasing amounts of alloyed Ni, this value becomes more noble, reaching -0.10V for a cold-rolled stainless steel containing 21% Cr, 34.8% Ni (8). Whenever the prevailing steady-state corrosion potential of

the alloy (measured for the stressed or unstressed alloy) is noble to the critical potential, which is the normal situation for austenitic 18-8 immersed in boiling MgCl₂ solution, cracking can and does take place. But at higher Ni compositions (>26%), the corrosion potential tends to be less noble than the critical potential and hence cracking is no longer observed (maximum test period: 200 hr).

In evaluating the present ferritic alloys, the same relation of corrosion potential to critical potential describes whether or not cracking takes place. For example, although the stressed cold-rolled low-nickel alloys (<1.5%) and the 5% Ni alloy did not fail on immersion in boiling MgCl₂ solution, cracking was observed nevertheless whenever the alloys containing >0.2% Ni were anodically polarized above a specific critical potential. Cracking of the 0.2% Ni alloy was uncertain because of simultaneous pitting. A critical potential was also typical of the higher Ni compositions (1.5-8%) which failed spontaneously in immersion tests, but which required cathodic polarization in order to inhibit cracking. The Ni-free alloy and the annealed or quenched 0.2-1.1% Ni alloys were exceptions in that they did not crack in either immersion tests or when anodically polarized; when polarized they tended to thin and pit instead. For this reason, a critical potential for s.c.c. cannot be assigned to these particular alloys.

The corrosion and critical potentials for various cold-rolled alloys are plotted in Fig. 3. The steady-state corrosion potentials, as measured 48 hr after immersion for unstressed specimens, lie below the critical values up to and including 1.1% Ni; these alloys do not fail when unpolarized. The indicated critical potential of -0.26V for the 0.2% Ni alloy is uncertain, for reasons mentioned earlier, but neither pitting nor cracking occurs below this value of potential. Above 1.1% Ni, the corrosion potential continues to shift with increasing Ni in a noble direction,

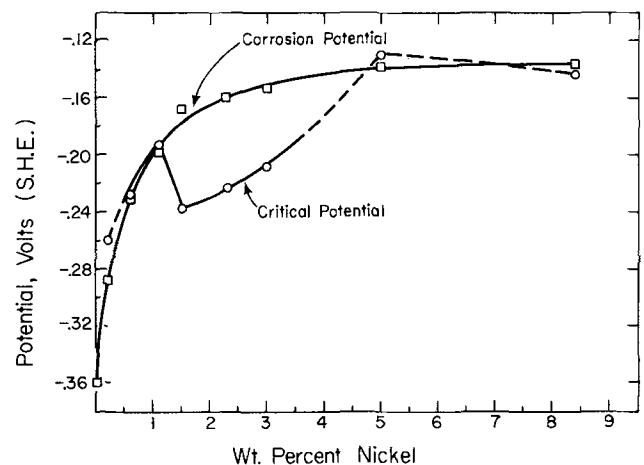


Fig. 3. Effect of alloyed nickel in cold-rolled 18% chromium stainless steel on critical and corrosion potentials, MgCl₂, 130°C.

Table III. Effect of cold work and heat-treatment on critical potentials for s.c.c. of ferritic stainless steel in $MgCl_2$, 130°C

Alloy	Condition	$\phi_{crit.}$ (SHE), V	$\phi_{corros.}$ (SHE), V	Difference ($\phi_{corros.} - \phi_{crit.}$)	Time to failure (hr)*
17% Cr, 2% Ni	Cold rolled	-0.225	-0.160	+0.065	0.7 ± 0.1 [5]
	Quenched	-0.185	-0.150	+0.035	3.1 ± 1.2 [6]
	Annealed	-0.185	-0.160	+0.025	88 ± 33 (4)
18% Cr, 5% Ni	Cold rolled	-0.130	-0.140	-0.010	>200 (3)
	Quenched	-0.185	-0.135	+0.050	3.3 ± 0.4 [3]
18% Cr, 8% Ni	Cold rolled	-0.145	-0.135	+0.010	4.9 ± 1 [5]
	Quenched	-0.100	-0.130	-0.030	>200 (3)

* The number in brackets is the number of specimens tested.

Table IV. Effect of galvanic coupling on stress corrosion cracking of stainless steels in $MgCl_2$, 130°C

Alloy	$\phi_{crit.}$, V	Coupled to equal area of	$\phi_{corros.}$, V	Failure time, hr	
				Uncoupled	Coupled
17% Cr, 2% Ni (Cold rolled)	-0.225	16% Cr-Fe	-0.360	0.7	>200
18% Cr, 8% Ni (Cold rolled)	-0.145	17% Cr-Fe (Commercial)	-0.225	4.9	>200

but the critical potential takes a sudden drop corresponding to observed failures of the 1.5-3% Ni alloys. At 5% Ni, the corrosion potential is 10 mV active to the critical potential and hence this alloy as cold rolled and unpolarized does not fail. At 8% Ni, the corrosion potential is 10 mV noble to the critical potential and the alloy fails. However, when the latter alloy is quenched from 1050°C, the corrosion potential becomes 30 mV active to the critical potential and now the alloy does not fail. Corresponding potentials for the quenched 2-8% Ni stainless steels are given in Table III. Cold rolling of the 2 and 8% Ni alloys, it will be noted, shifts the critical potential in the active direction corresponding to greater susceptibility to s.c.c. The reverse situation, however, applies to the 5% Ni alloy. To make certain this was not an experimental accident, a second alloy of the same approximate composition (Table I) was prepared, but the critical potential of this alloy as cold rolled, -0.140V, was still noble to the observed value for the alloy as water quenched, -0.185V, in agreement with the sequence of values shown in Table III for alloy B. As is discussed later, this alloy is an exception probably because its behavior is sensitive to rolling direction.

Failure of the cold-rolled ferritic 18-8 in $MgCl_2$ at 130°C but not at 154°C is also explained by the relative potentials at either temperature. At 130°C, the corrosion potential is noble to the critical potential by 10 mV and the alloy fails (Table III), but at 154°C, the corrosion potential, -0.095V (SHE), is active to the critical potential, -0.060V, by 35 mV and the alloy does not fail. In other words, in summary, whether a susceptible stainless steel, either austenitic or ferritic in structure, fails spontaneously by s.c.c. in a given chloride environment depends on the relative order of corrosion and critical potentials.

For the few alloys that were studied, molybdenum additions to the ferritic alloys tended to shift the corrosion potential in the noble direction more so than the critical potential. However, more data are needed in order to reach any general conclusions.

Galvanic Coupling

The necessity of a corrosion potential noble to the critical potential for spontaneous s.c.c. suggested the important conclusion that galvanic coupling should in principle induce or inhibit cracking of any susceptible alloy. Two such couples are listed in Table IV. Both the cold-rolled 2 and 8% Ni alloys, which normally fail in short times, do not fail when coupled to a ferritic stainless steel which polarizes them to a potential that is active to their critical potentials. It was shown previously (8) that pure nickel coupled to stressed 18-8 austenitic stainless steel inhibits failure in $MgCl_2$ solution at 130°C because nickel with a more active corrosion potential (-0.18V) in this solution polarizes the couple to a value more active than the measured critical potential (-0.145V) of 18-8.

Discussion

Annealing at 815°C for 1 hr improves resistance to transgranular stress corrosion cracking of the ferritic stainless steels containing up to 8% Ni. This heat-treatment is also effective for improving resistance of ferritic stainless steels to intergranular corrosion (not requiring stress) and is usually recommended for this purpose. Annealing in this instance probably reduces Cr concentration gradients established in the vicinity of carbide precipitates localized at grain boundaries (17-19). Whether C (or N) in the small amounts that are normal to the present alloy series is responsible for transgranular s.c.c. is not established by the present or any previous data. Stress corrosion cracks may follow paths other than the grain boundaries where carbides tend to concentrate, suggesting that susceptibility has no obvious relation to carbides or associated Cr concentration gradients. In addition, the low solubility of C in the b.c.c. ferritic lattice argues against any important role played by C, but tests on C-free alloys are probably needed to resolve the question. The beneficial effect of annealing is likely related to reduced imperfection density, as is discussed later.

Additions of small amounts of Ni to 15-18% Cr-Fe account for alpha and gamma phases in equilibrium at both annealing and quenching temperatures as the phase diagrams of Fig. 4 show (20). A consequent two-phase structure is observed under the microscope for 2-5% Ni alloys (Fig. 5). Both phases are ferritic, consisting of the b.c.c. structure, as was proved for the present alloy series by x-ray determinations, but they differ in Cr and Ni content. The two-phase structure is not required for susceptibility to s.c.c. because a still lower 1.5% Ni composition which is single phase (as shown by microstructure) nevertheless fails when cold

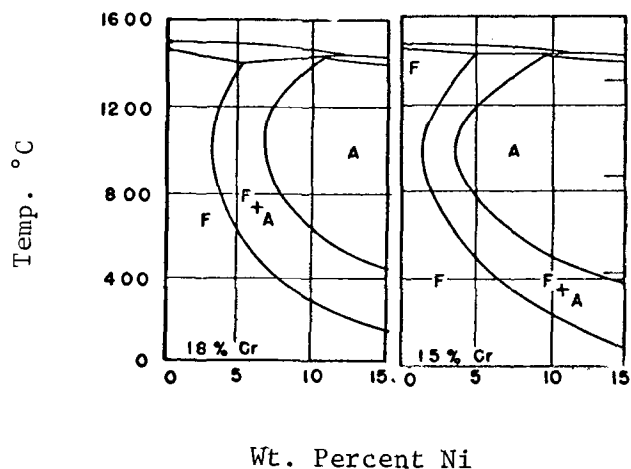


Fig. 4. Phase diagrams for 15 and 18% chromium stainless steels containing alloyed nickel (F = ferrite, A = austenite).

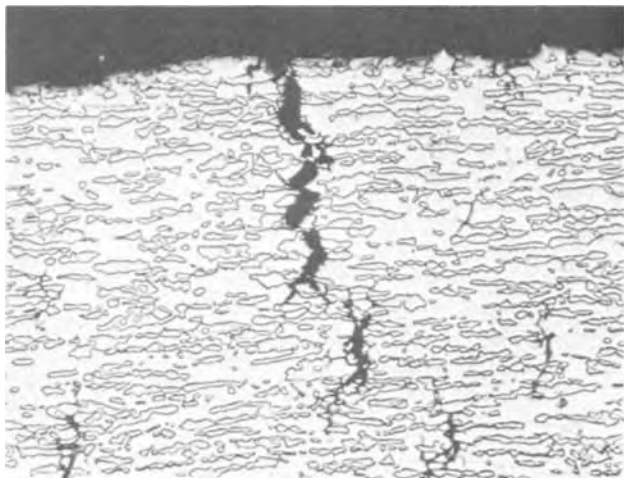


Fig. 5. Stress corrosion cracking in water-quenched 18% chromium, 2% nickel stainless steel, $MgCl_2$, $130^\circ C$, showing largely transgranular cracks. Magnification X175.



Fig. 6. Stress corrosion cracking in water-quenched 18% chromium, 1.5% nickel stainless steel, $MgCl_2$, $130^\circ C$, showing both transgranular and intergranular cracks. Magnification X90.

rolled or quenched (Fig. 6). The resistant 8% Ni alloy is single-phase martensite as quenched.

Increased corrosion of test specimens at the base of a notch, supposedly brought about by small alloyed nickel additions, is not likely to account for initiation of cracks nor their propagation. For one thing, cold work, if it has an effect at all, usually increases the corrosion rate, but cold-worked specimens do not crack in appreciably shorter times compared to the quenched alloys except for the 8% Ni alloy. For the latter alloy, failure occurs at $130^\circ C$ but not at $154^\circ C$, despite cold working. Cold working of the 5% Ni alloy actually improves resistance to s.c.c. Second, if the critical potential is the potential below which the corrosion rate is severely limited or is zero (open-circuit anode potential), it is impossible to have a corrosion cell in which the observed corrosion potential is active to such a potential. The corrosion potential for any corrosion cell must always be noble to the open-circuit anode potential. Since this expected relation is not observed for the present alloys, the critical potential must have another interpretation, as has been discussed previously (8, 9).

Fracture of a supposed oxide film rich in nickel or any other element is also an unlikely mechanism because the low-Ni alloys fail independent of time of anodic polarization during which an oxide film can form provided the polarized potential is above and not below the critical value. And the higher Ni alloys which fail spontaneously continue to fail when cathodically polarized unless the polarized potential is below the critical value. Stainless steels containing more than 45% Ni, or none, do not fail at all whether or not they are polarized. Furthermore, either cold-rolled or quenched 1.5-3% Ni alloys fail spontaneously but only the quenched and not the cold-rolled 5% Ni, and the cold-rolled but not the quenched 8% Ni alloys fail, which would require unusual oxide properties to account for such varied behavior.

It seems more likely that Ni influences the imperfection structure of the plastically deformed alloy, allowing damaging Cl^- ions to adsorb on appropriate imperfection sites located at the alloy surfaces and to reduce metal bond strength. Such adsorption favors both crack initiation and crack growth (stress sorption cracking) (21). Whether or not adsorption occurs depends not only on a favorable imperfection array, but also on a favorable electrical field; in other words, the required adsorption takes place only above but not below a well-defined critical potential. The effect of Ni on the imperfection structure of the alloy presumably increases with Ni content, but the affinity of surface imperfections for Cl^- ions diminishes with Ni content (negative free energies of formation are in the order: $CrCl_2 > FeCl_2 > NiCl_2$). Bergen (22) showed, for example, that surface migration of radioactive Cl^- ions toward the region of maximum stress (highest imperfection density) in an austenitic 18% Cr stainless steel decreases as Ni content increases from 9.9 to 33%. These two opposing tendencies probably account for maximum susceptibility of 18% Cr-Fe stainless steels to cracking in chloride solutions at 2% Ni. In other media, e.g., OH^- and NO_3^- solutions, a parallel affinity of imperfection sites does not exist regardless of Ni content, and hence s.c.c. is not observed. Accordingly, annealing of the present alloys at $815^\circ C$ leads to greater observed resistance to failure in $MgCl_2$ solution, probably because imperfections favorable to s.c.c. are annealed out, or their subsequent formation in the strained alloy is inhibited.

The effect of Ni on susceptibility to s.c.c. in $MgCl_2$ solution is also clearly seen in parallel properties of Ni-Fe alloys. Copson (23) showed that iron itself did not fail, but alloys containing up to 8.7% Ni did fail, and there was again no failure at the next higher Ni contents of 28 and 42%. Royuela and Staehle (24) showed similarly that stressed Ni-Fe alloys failed in $MgCl_2$ up to and including 25 a/o (atom per cent) Ni, but not at higher Ni compositions. Present data obtained in $MgCl_2$ at $130^\circ C$ showed that low-carbon Ni-Fe alloys undergo s.c.c. at 4.6 and 11.9% Ni (failure time: 6 and 17 hr, respectively); they did not fail at 2.3 and 3.5% Ni (>200 hr) or at still lower Ni contents, but with some tendency toward pitting and increased general corrosion for the lowest Ni alloys. Nickel alone, therefore, and not chromium or the passivity it confers, is apparently responsible for the observed susceptibility of the ferritic Cr-Fe-Ni stainless steels. Chromium may shift the range of Ni content within which the alloys are susceptible, but cracking can occur without it. A suitable imperfection array, the alloy composition, and the make-up of the environment, in turn, determine the critical potential above which Cl^- ions can adsorb attended by crack initiation and below which they desorb without subsequent cracking. These factors may also shift the corrosion potential in relation to the critical potential and thereby influence the possibility of spontaneous cracking.

Additional cold work of the 8% Ni alloy is necessary to shift the critical potential below the corrosion po-

Table V. Critical and corrosion potentials in $MgCl_2$, 130°C of 18-8 stainless steel quenched from 1050°C

	$\phi_{crit.}$ (SHE), V	$\phi_{(corros.)}$ (SHE), V (48 hr)	Failure time, hr
Ferritic (18.3% Cr, 8.4% Ni, 0.001% C)	-0.100	-0.130	>200
Austenitic (18.8% Cr, 9.2% Ni, 0.06% C)	-0.130	-0.090	1.4 ± 0.1

tential, accompanied by spontaneous cracking. Any predicted effect of cold work on behavior of the 2 and 5% Ni alloys is complicated by their two-phase structure. Susceptibility of the latter compositions depends both on the relative susceptibility of each phase, and the degree to which the two phases are interspersed. If the resistance of one phase is much greater than the other because of composition differences, cold work would then increase the difficulty of crack propagation through the more susceptible phase. This situation probably accounts for the observed resistance of the cold-worked 5% Ni alloy stressed parallel to the rolling direction. When the alloy is stressed perpendicular to the rolling direction, cracks through the more susceptible phase meet fewer barriers interposed by elongated grains of the resistant phase, and hence the alloy fails (Table II). The 2 and 3% Ni alloys, on the other hand, are less affected by cold work probably because the two phases are both susceptible to s.c.c., and hence their relative dispersion by cold work has little effect on rate of crack propagation. Direction of rolling of the 3% Ni alloy is not of great consequence (Table II).

In addition to an effect of alloyed Ni, lattice structure of the alloy apparently also plays a part in the formation of favorable imperfection sites. As mentioned earlier, the corrosion potential of a quenched ferritic 18-8 is 30 mV active to its critical potential, hence the alloy does not fail. To the contrary, the corrosion potential of a quenched austenitic 18-8 is 40 mV noble to its critical potential and the alloy fails within a short time (Table V). It appears, therefore, that surface imperfections generated by straining a quenched austenitic 18-8 are better adsorption sites for damaging Cl^- ions than are comparable imperfections generated in a quenched ferritic alloy of the same approximate composition. Accordingly, the critical potential for austenitic 18-8 is 30 mV active to that for the ferritic alloy. The corrosion potential, on the other hand, which is determined by the electrochemical polarization characteristics of the corroding alloy, including effects of surface (sometimes visible) oxide films (8) is more noble for the austenitic compared to the ferritic 18-8. The effect of lattice structure on both critical and corrosion potentials explains, therefore, why ferritic 18-8 is resistant but austenitic 18-8 is susceptible to s.c.c.

Conclusions

1. Ni-free 16-18% Cr stainless steels are resistant to s.c.c. in boiling $MgCl_2$ solution (130° and 154°C), in boiling 35% NaOH + 0.1% PbO (126°C), and in boiling calcium nitrate-ammonium nitrate solution (110°C). Addition of 2% Ni makes the alloy susceptible to failure in $MgCl_2$ solution but not in the other media.

2. Maximum susceptibility to s.c.c. in $MgCl_2$, 130°C, is observed at 2% Ni. Alloys containing less than about 1% Ni are resistant whether cold rolled, annealed, or water quenched. Alloys containing >2% Ni annealed at 815°C, 1 hr, are resistant.

3. Cold-rolled ferritic 18-8 fails in $MgCl_2$ boiling at 130°C but not at 154°C. Susceptibility to s.c.c. is not dependent on rolling direction, contrary to a dependence when failure is by hydrogen cracking.

4. Whenever the prevailing corrosion potential is noble to the critical potential for s.c.c., but not otherwise, the alloys fail spontaneously. This relation applies to the behavior of galvanic couples and also accounts for the resistance of cold-rolled ferritic 18-8 in $MgCl_2$ at 154°C but not at 130°C, and to the resistance of the quenched ferritic but not of the quenched austenitic 18-8.

5. Alloyed Mn in 16-18% Cr-Fe alloys has but little effect on susceptibility; alloyed Mo can be damaging.

6. The present results are not readily explained by electrochemical dissolution of metal atoms at the base of a notch, or by rupture of oxide or passive films. They are more successfully explained by adsorption of damaging Cl^- ions on appropriate defect sites favored by alloyed Ni which reduce bond strength of strained metal atoms at a notch or incipient crack (stress sorption cracking).

Acknowledgment

The authors are pleased to acknowledge support of this research by the Office of Saline Water, United States Department of the Interior.

Manuscript submitted Nov. 22, 1971; revised manuscript received Feb. 24, 1972. This was Paper 51 presented at the Cleveland Meeting of the Society, Oct. 3-7, 1971.

Any discussion of this paper will appear in a Discussion Section to be published in the June 1973 JOURNAL.

REFERENCES

1. M. Scheil, O. Zmeskal, J. Waber, and F. Stockhausen. *Welding J.*, Res. Supplement (October 1943).
2. M. Scheil in "Corrosion Handbook," p. 180, H. H. Uhlig, Editor, John Wiley & Sons, Inc., New York (1948).
3. H. Copson, "Physical Metallurgy of Stress Corrosion Fracture," p. 247, T. Rhodin, Editor, Interscience Publishers, New York (1959).
4. G. Riedrich and H. Kohl, *Berg-Hüttenmänn. Monatsh.*, **108**, 1 (1963).
5. H. Uhlig, R. White, and J. Lincoln, Jr., *Acta Met.*, **5**, 473 (1957).
6. H. Uhlig and R. White, *Trans. Am. Soc. Metals*, **52**, 830 (1960).
7. A. Bond and H. Dundas, *Corrosion*, **24**, 344 (1968).
8. H. Lee and H. Uhlig, *This Journal*, **117**, 18 (1970).
9. H. Uhlig and E. Cook, *ibid.*, **116**, 173 (1969).
10. E. Cook, Jr., M. S. Thesis, Department of Metallurgy and Materials Science, M.I.T. (1968).
11. J. Marquez, I. Matsushima, and H. Uhlig, *Corrosion*, **26**, 215 (1970).
12. A. Bond, J. Marshall, and H. Dundas, Spec. Tech. Pub. No. 425, p. 116, Am. Soc. Test. Materials, Philadelphia (1967).
13. S. Brenner, *Jernkont. Ann.*, **144**, 560 (1960).
14. S. Barnartt and D. van Rooyen, *This Journal*, **108**, 222 (1961).
15. M. Smialowski and M. Rychik, *Corrosion*, **23**, 218 (1967).
16. R. Newberg and H. Uhlig, Unpublished data.
17. H. H. Uhlig, "Corrosion and Corrosion Control," 2nd Ed. p. 308, John Wiley & Sons, Inc., New York (1971).
18. A. Bond, *Trans. Met. Soc. AIME*, **245**, 2127 (1969).
19. R. Hodges, *Corrosion*, **27**, 119 (1971).
20. "The Making, Shaping and Treating of Steel," 8th Ed., p. 1114, Harold E. McGannon, Editor, United States Steel Corp., Pittsburgh (1964).
21. H. Uhlig in "Physical Metallurgy of Stress Corrosion Fracture," p. 1, T. Rhodin, Editor, Interscience Publishers, New York (1959); also in "Fundamental Aspects of Stress Corrosion Cracking," p. 86, R. Staehle et al., Editors, Nat. Assoc. of Corros. Engrs., Houston (1969).
22. C. Bergen, *Corrosion*, **20**, 269f (1964).
23. H. Copson in "Physical Metallurgy of Stress Corrosion Fracture," p. 260, T. Rhodin, Editor, Interscience Publishers, New York (1959).
24. R. Staehle in "Fundamental Aspects of Stress Corrosion Cracking," p. 247, R. Staehle et al., Editors, Nat. Assoc. of Corros. Engrs., Houston (1969).

The Anodic Deposition of Oxide Films on Platinum from Ferrous Sulfate Solutions

J.-L. Leibenguth¹ and Morris Cohen*

National Research Council of Canada, Division of Chemistry, Ottawa, Ontario, Canada

ABSTRACT

A study has been made of the effect of pH and Fe^{++} ion concentration on the anodic deposition from ferrous sulfate solutions of ferric oxide type films on a platinum substrate. Examination of the deposition kinetics and film composition was made. The rate of deposition was increased by increases in pH and ferrous ion concentration. The films were mainly $\gamma\text{-FeOOH}$ but also contained small amounts of water, Fe^{++} , and sulfate ions. The proportion of sulfate decreased markedly with an increase in pH. It was concluded that the film is deposited mainly by the diffusion and oxidation of a complex hydroxy ferrous ion with some contribution from a sulfate containing ion. The relationship of these films to anodically formed passive films is discussed.

It was shown in previous work that hydrated iron oxide films can be deposited on both iron (1, 2) and platinum (3) by the anodic oxidation of ferrous ion dissolved in borate solutions. The films contained quite large amounts of boron and appeared to be a mixture of hydrated iron and boron oxides. It was not possible to obtain electron diffraction patterns from the films.

In this paper the deposition of films on platinum from sulfate solution is described. The sulfate ion is not as strong a complexing agent as borate ion, and it was believed that purer and more crystalline-hydrated iron oxide films could be obtained. The effect of pH on the rate of deposition and composition of the film was also studied.

Experimental

The electrolytic cell with its accompanying storage vessels, gas deaerating and bubbling system, and electrical devices were the same as described previously (2, 3). High-purity tank argon, further purified by passage through a copper column, was used as both purging and stirring gas. The volume of the solution was 30 cc.

Platinum specimens were 1×5 cm with handles 0.2×2 cm cut from smooth sheet. Reactive metals in the platinum were removed by alternate cycles of oxidation and treatment in hot 6*N* HCl. After this the specimens were heated to 800°C and pumped to a vacuum of 10^{-8} Torr. Hydrogen (1 Torr) was then introduced and heating continued for 6 hr at 800°C. Reflection electron diffraction after this treatment gave only a few broad weak rings characteristic of smooth polycrystalline platinum. The potential of clean specimens was -640 mV vs. SCE on cathodic polarization at $10 \mu\text{A}/\text{cm}^2$. Contaminated specimens exhibited much more negative potentials.

Anodic deposition.—All anodic oxidation experiments were carried out at a constant potential of $+300$ mV vs. SCE. The supporting electrolyte was a 0.15*N* (in SO_4^{--}) solution of $(\text{NH}_4)_2\text{SO}_4$ to which NH_3 was added to adjust the initial pH. The iron was added to the solution in the form of ferrous ammonium sulfate. Both solutions were deaerated separately before mixing in order to avoid oxidation of the ferrous ion. The cell was flushed with deaerated electrolyte to remove oxygen from the system. Current density vs. time was recorded and the curves integrated by planimeter to obtain coulombs. The ferrous concentration of the solution was measured before and after the experiments. Specimens were weighed before and after anodic deposition to $\pm 2 \mu\text{g}$ on a Mettler M5 balance.

* Electrochemical Society Active Member.

¹ Present address: Institut de Chimie, Université Louis Pasteur, Strasbourg, France.

Key words: iron oxide, passivity, anodic deposition.

Examination of the deposited films.—In order to determine the sulfate content of the film, S^{35} isotope in the form of sulfate ions was added to some of the solutions. The procedures and precautions for this measurement have been published previously (4).

The crystal structure of the oxide was examined by reflection electron diffraction and x-ray diffraction. Using a Debye Scherrer Camera and chromium $K\alpha$ radiation the x-ray diffraction technique required films at least 400–500 Å thick (5) to give patterns.

Some of the specimens were cathodically reduced at a current density of $10 \mu\text{A}/\text{cm}^2$ in a borate buffer solution of pH 8.4.

A number of the film-covered specimens were heated in an oxidizing atmosphere (air or oxygen at 1 Torr) at 400°–500°C or in vacuum over a range of temperatures. In the case of the vacuum heating the evolved gases were monitored with a mass spectrometer. The specimens were examined by diffraction and chemical analysis after heating.

Many of the films were dissolved in HCl for chemical analysis. Normally, warm 1*N* HCl was used. For specimens which had been heated to 800°C hot 6*N* HCl was required for dissolution of the film. Total iron was determined by the o-phenanthroline method and ferrous iron by $\alpha\text{-}\alpha'$ bipyridyl. Blanks were run in all cases to correct for iron in the reagents.

Results

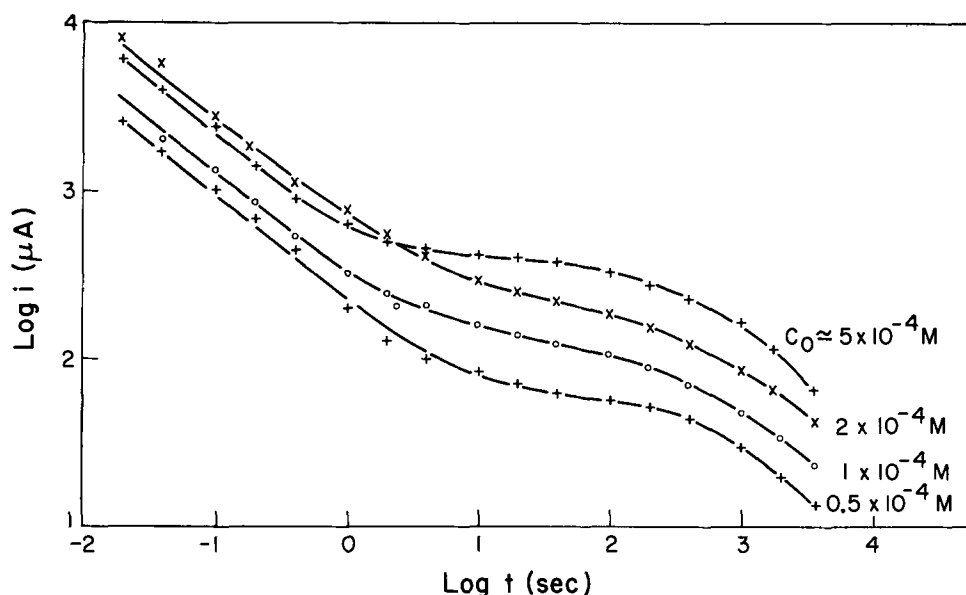
Formation of Films

Two series of deposition experiments were carried out. In the first the solutions started at the same pH but contained various concentrations of ferrous ion. Results from this type of experiment are shown in Fig. 1. In the second series the initial iron concentration was the same and the pH was varied. The shape of the log current-log time curves were similar to those shown in Fig. 1, with the initial deposition rate being greatest at the higher pH's. A plot of coulombs vs. time for this type of experiment is shown in Fig. 2. These curves are similar to those observed using borate solutions (3).

In all cases there is a rapid drop in current density within the first 10 sec. This decrease is considered to be due to the buildup of a continuous resistant film. The charge passed during this initial stage is of the order of 1 to 2×10^{-9} eq./cm². Assuming the film composition to be $\text{FeO}(\text{OH})$ with a density 4.3 the thickness of this initial continuous film is less than 25 Å.

During the steady-growth region the slowly decreasing rate of deposition is a rather complex function of film thickness, Fe^{++} concentration in the solution, and pH of the solution during deposition. The electrolyte is a poor buffer in the pH range used in these experi-

Fig. 1. Effect of initial Fe^{++} concentration on deposition current. Initial pH ≈ 7.0 .



ments, and there is some decrease in pH during the experiment. This decrease is negligible at pH 8.0 but is 0.3 at a pH of 6.6. In general the rate of deposition increases with increases in either Fe^{++} concentration or pH.

Current efficiency for formation.—The amount of film deposited was determined by weighing the platinum specimens before and after deposition. This weight was converted to equivalents on the basis of a film composition of FeOOH ($n_{\text{FeOOH}} = \mu\text{g} \times 1.125 \times 10^{-8}$). The amount of iron used to form the film was determined by before and after analysis of Fe^{++} in the solution. It was converted to equivalents of FeOOH , and is referred to in the tables as Q_i .

These results were compared with Q_e , the number of coulombs passed (also expressed as equivalents and based on the reaction $\text{Fe}^{++} \rightarrow \text{FeOOH}$ and are shown in Tables I and II for either constant initial iron concentration or constant pH. There is excellent agreement between Q_i and Q_e in all cases. The weights of the films are all too high if based on pure FeOOH as the composition of the deposited film. The effect of time of deposition (or thickness of deposit) is shown in Table III. Once again there is good agreement between Q_i and Q_e (indicating a high current efficiency for deposition) and also an overweight of films in all

cases. The overweight ratio, n_{FeOOH}/Q_e , decreases as the film thickens.

Sulfur content of films.—The amount of sulfur in the films, probably present as SO_4^{--} ion, was determined by the use of S^{35} as a tracer (4). The effect of initial pH on the amount of sulfur in the film is shown in Fig. 3. There is a marked decrease in the per cent sulfate content of the film as the pH increases. The effect of

Table I. Comparison of film weight, quantity of electricity, and iron used in oxidation experiments at various pH's

pH	Film weight, μg	n_{FeOOH} ($\times 10^{-8}$)	Quantity of electricity Q_e ($\times 10^{-6}$)	Iron used Q_i ($\times 10^{-6}$)	n_{FeOOH}/Q_e	Q_i/Q_e
6.6	199	2.24	1.94	2.01	1.16	1.040
	194	2.18	1.925	1.95	1.13	1.015
7.0	413	4.65	4.08	4.05	1.14	0.993
	399	4.49	3.98	4.00	1.13	1.005
7.5	522	5.87	5.23	5.32	1.12	1.017
	515	5.79	5.23	5.27	1.11	1.007
8.0	524	5.895	5.30	5.30	1.11	1.000
	500	5.625	5.19	5.165	1.08	0.996

n -Equivalents calculated from weight. Q_i -Equivalents calculated from Fe^{++} depletion. Q_e -Equivalents calculated from coulombs used.

Table II. Comparison of film weight, quantity of electricity, and iron used in oxidation experiments at various initial iron concentrations

Initial pH = 7						
Approximate initial Fe^{++} concentration, mols/liter	Film weight, μg	n_{FeOOH} ($\times 10^{-8}$)	Quantity of electricity Q_e ($\times 10^{-6}$)	Iron used Q_i ($\times 10^{-6}$)	n_{FeOOH}/Q_e	Q_i/Q_e
0.5×10^{-4}	103	1.16	0.96	0.89	1.21	0.930
1×10^{-4}	189	2.13	1.63	1.63	1.30	1.000
2×10^{-4}	315	3.54	3.00	3.025	1.18	1.010
5×10^{-4}	525	5.91	5.21	5.04	1.13	0.967

Table III. Comparison of film weight, quantity of electricity, and iron used in oxidation experiments of various times

Time, min	Film weight, μg	n_{FeOOH} ($\times 10^{-8}$)	Quantity of electricity Q_e ($\times 10^{-6}$)	Iron used Q_i ($\times 10^{-6}$)	n_{FeOOH}/Q_e	Q_i/Q_e
90	346	3.89	3.33	3.32	1.17	0.997
24	167	1.88	1.58	1.56	1.19	0.989
8.5	92	1.035	0.81	0.82	1.27	1.006
1.5	33	0.37	0.22	0.21	1.70	1.023
0.75	24	0.27	0.14	0.15	1.97	1.109

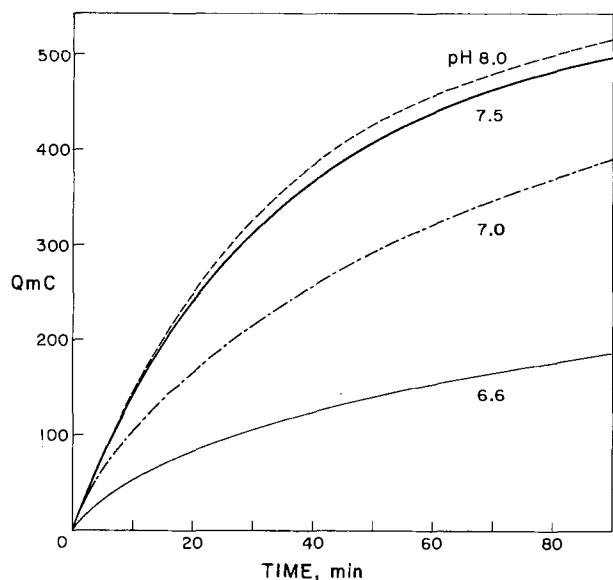


Fig. 2. Effect of pH on deposition rate. Initial $[\text{Fe}^{++}] \approx 2 \times 10^{-4}$ M.

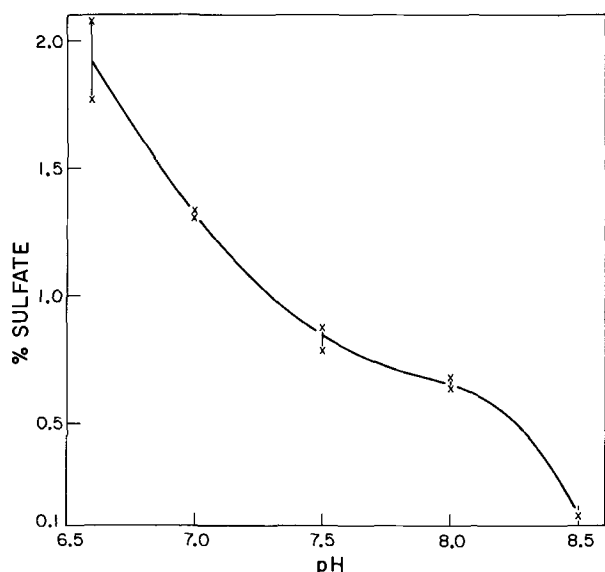


Fig. 3. Effect of pH on per cent (weight) of sulfur (as SO_4^{--}) in film. Initial $Fe^{++} \approx 2 \times 10^{-4}$ M. Time 90 min.

initial Fe^{++} ion concentration is not nearly as dramatic, (Table IV). There is a small increase in per cent sulfate at the higher initial Fe^{++} ion concentrations. This may be partly related to the thickness of the film. As shown in Table V, there is a definite increase in the ratio as the film thickens. This latter increase is probably enhanced by the lowering of pH during deposition at pH 7.

Fe⁺⁺ content of films.—Some of the deposited films were dissolved in 1N HCl and the resulting solutions analyzed for total iron and ferrous ion. In all cases a small amount of Fe^{++} (<5%) was found to be present in the films. The total iron found by dissolving the films is in good agreement with the total iron calculated from the current-time curves (Q_e). Some results are shown in Table VI. The per cent of ferrous ion in the films appears to decrease as the thickness of the films increases (due to either higher initial pH or Fe^{++} ion concentration in the depositing solution).

Structure of films.—As deposited.—The films were examined by both x-ray diffraction and electron diffraction. No patterns were obtained by x-ray diffraction—which would indicate that either the films were too

Table IV. Sulfate content of films deposited at various initial iron concentrations

Approximate initial iron concentration	Sulfate, m μ g	Film weight (μ g)	$\frac{Q_{SO_4^{--}}}{Q_e}$, %
0.5×10^{-4}	1.14	103	1.10
1×10^{-4}	2.02	189	1.07
2×10^{-4}	3.97	315	1.26
5×10^{-4}	6.98	525	1.33

Initial pH = 7.

Table V. Sulfate content of films of various thicknesses

Coulombs $\times 10^{-6}$	Film weight, μ g	Sulfate, μ g	$\frac{\text{Sulfate}}{\text{Film wt.}} \times 100$
3.33	348	5.30	1.53
1.58	167	2.78	1.66
0.81	92	1.06	1.15
0.22	33	0.31	0.94
0.14	24	0.11	0.46

Initial pH = 7.

thin and/or the crystal size too small to be detected by x-rays. Good patterns corresponding to γ -FeOOH were obtained with electron diffraction.

On heating.—When the specimens were heated in air or oxygen water was driven off and the γ -FeOOH was converted (at 500°C or higher) to α -Fe₂O₃. If the specimen was first heated *in vacuo* and then air or oxygen admitted a cubic oxide structure was observed by electron diffraction. Chemical analysis of the dissolved oxide showed the presence of only a small amount of Fe^{++} in the oxide. The bulk of the cubic oxide was probably γ -Fe₂O₃. Heating in vacuum gave quite variable results which were highly dependent on the pre-treatment of the platinum. Unless great care was taken to purify the platinum with respect to both carbon and traces of other elements a proportion of the deposited oxide was reduced to iron and dissolved in the platinum. This reduction was mainly caused by carbon, and mass spectrometry of the gases evolved on heating showed the formation of both CO and CO₂. The dissolved iron in the platinum could be removed by heating in oxygen and then dissolving the resultant surface oxide in acid. Electron diffraction results from an "as deposited" specimen and a vacuum heated specimen are shown in Fig. 4.

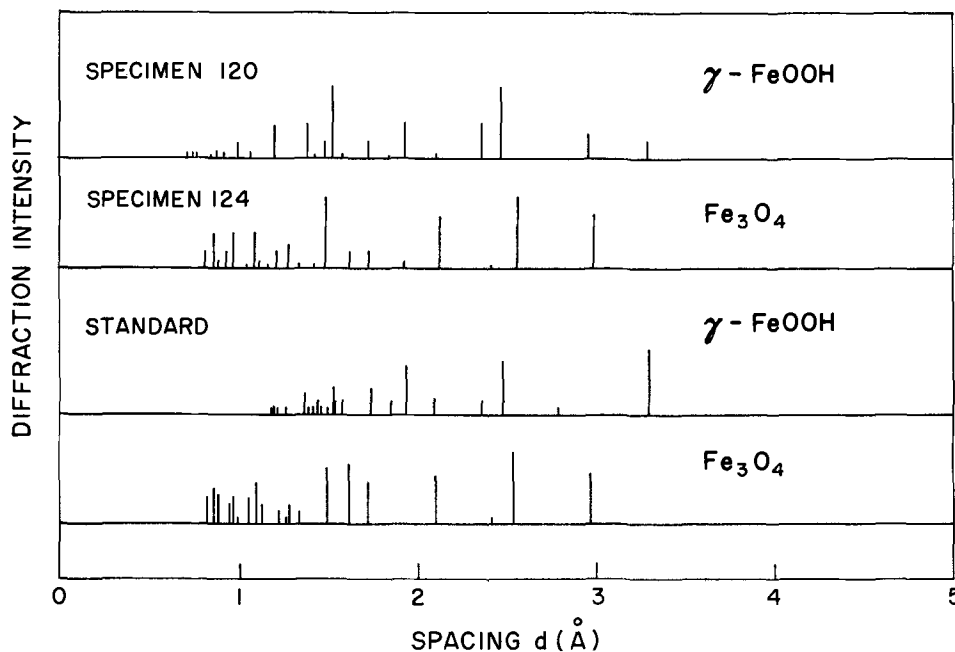


Fig. 4. Electron diffraction patterns of deposited films compared to standard patterns of Fe₃O₄ (γ -Fe₂O₃) and FeOOH. Specimen 120—as deposited. Specimen 124—heated *in vacuo* and then exposed to oxygen. Temp. < 500°C.

Table VI. Fe⁺⁺ content of films

pH	Initial Fe ⁺⁺ equivalent liter	Q _e	Q _{Fe⁺⁺}	$\frac{Q_{Fe^{++}}}{Q_e} \times 100$
6.6	2×10^{-4}	1.93×10^{-6}	0.075×10^{-6}	3.9
7.0	0.5×10^{-4}	0.96	0.045	4.6
7.0	1	1.63	0.06	3.9
7.0	5	5.21	0.15	2.8

Cathodic Reduction

Some of the films were cathodically reduced in the deaerated borate-boric acid buffer at a constant current density of $10 \mu\text{A}/\text{cm}^2$. The potential-time curves showed two arrests, with a rather sharp inflection point between the two. When the final steady potential of -860 mV (vs. SCE) was reached no further reduction of the film to ferrous iron in solution took place, although it was obvious that some film remained on the specimen. If at that stage the solution was changed, without exposure of the specimen to oxygen, the cathodic-reduction potential dropped rapidly to -860 mV with no reduction of the film. However, if the specimen was exposed to air before the second cathodic reduction step, the film was further reduced. By running a series of reductions with intermediate exposure to air it was possible to reduce the film to an equivalent thickness of about 20-30Å. Electron diffraction examination of the film after each reduction gave a pattern corresponding to $\gamma\text{-FeOOH}$, the same as that of the originally deposited film. An example of a series of cathodic reductions on one specimen, with intermediate exposure to air, is given in Fig. 5.

When a clean platinum specimen is treated cathodically at $10 \mu\text{A}/\text{cm}^2$ in the borate buffer solution a steady potential of -640 mV is reached. The cathodic process is the evolution of hydrogen. If, however, there is iron in the solution the potential of the specimen drops to about -800 mV . The specimen becomes covered with a thin film which is soluble in HCl and corresponds to an iron oxide thickness about 20Å. This would indicate that the potential -860 mV corresponds to hydrogen evolution on deposited iron.

The estimation of the exact quantity of ferrous ion produced by cathodic reduction of these thick films is complicated by the reoxidation and deposition of some of the ferrous iron at the anode. There is also some

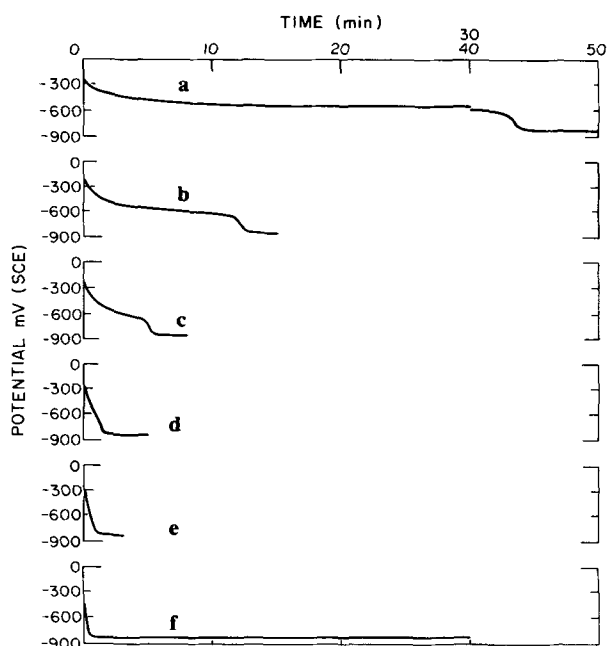


Fig. 5. Successive cathodic reduction of film with intermediate exposure to air.

precipitation on the walls of the vessel. Hence one analysis for reduced iron requires the dissolution of this deposited and precipitated iron in dilute HCl. Some of the ferrous ion is reduced to metallic iron at the cathode and the ease of hydrogen evolution on this iron accounts for the cessation of cathodic reduction of the remaining film. By taking these factors into consideration it has been possible to balance deposition equivalents and cathodic reduction equivalents.

Discussion

As can be seen in Fig. 1 and 2, films are deposited from the sulfate solutions with much the same current and coulomb-time characteristics as in the deposition from borate solutions. However, the films differ considerably in terms of both chemical composition and physical structure.

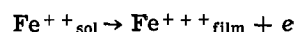
Composition of deposited films.—The major portion of the film has a composition corresponding to FeOOH. However all films formed under the range of conditions studied in this work contain varying small amounts of water, sulfate, and Fe⁺⁺ ions. The per cent of water decreases as the film thickens (Table III). The per cent of sulfate decreases as the pH increases. At constant pH the per cent of sulfate is independent of thickness. At constant pH the per cent of Fe⁺⁺ decreases with thickness.

Properties of deposited films.—In contrast to the "amorphous" films deposited from borate solution the films deposited from the nearly neutral sulfate solutions are mainly crystalline $\gamma\text{-FeOOH}$. They also contain small amounts of water, sulfate, and ferrous ions.

When the films are heated, they lose both water and sulfur and, depending on the conditions of heating, can be converted to either $\gamma\text{-Fe}_2\text{O}_3$ or $\alpha\text{-Fe}_2\text{O}_3$. The films which were converted to $\gamma\text{-Fe}_2\text{O}_3$ contain small amounts of Fe⁺⁺ ion, probably present in the films before heating. If the platinum supporting electrode contained carbon or other available reducing agents (due to inadequate pretreatment), the deposited films were converted on heating to Fe₃O₄ with some dissolution of iron into the platinum.

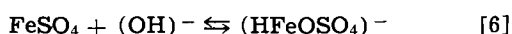
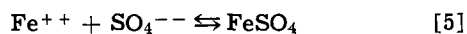
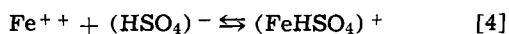
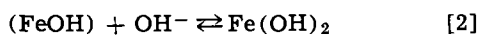
None of the deposited films could be completely cathodically reduced in a single step. Although the residual film gave the diffraction pattern of $\gamma\text{-FeOOH}$ cathodic reduction to dissolved Fe⁺⁺ in solution had ceased and the potential had dropped to -860 mV (vs. SCE). If the specimen were then exposed to air further cathodic reduction could take place. A cathodic potential of less than -800 mV could be obtained with platinum on which iron had been electrochemically deposited. This would indicate that the cathodic reduction of $\gamma\text{-FeOOH}$ ceased when sufficient iron had been deposited from Fe⁺⁺ in solution to either cover the $\gamma\text{-FeOOH}$ and/or produce an alternate current carrying path to the underlying platinum. In any case the preferred cathodic reaction became hydrogen evolution. Exposure of the partially reduced film to air resulted in the oxidation of the finely divided deposited iron, and further reduction of the deposited oxide became possible. A more detailed study of cathodic reduction of deposited $\gamma\text{-FeOOH}$ will be presented in a subsequent paper.

Mechanism of deposition.—Under all the conditions used in this study the films were deposited with approximately 100% current efficiency with respect to the nominal reaction.



The rate of deposition at constant potential was dependent on both the hydroxyl ion (pH) and Fe⁺⁺ ion concentration. The concentration of sulfate in the film decreased as the pH increased. These observations are all consistent with the concept that the film is formed by the direct oxidation of ferrous containing

species in the solution. Some of the possible ionic equilibria are as follows



The equilibria tend to go from [1] to [3] and [4] to [6] as the pH increases. However the hydroxyl ion complexes are more stable than the sulfate ion complexes, and one would expect that the ratio of oxidation of ferrous ion from the hydroxyl complexes to oxidation from the sulfate complex would increase as the hydroxyl ion concentration increases. This is confirmed by the results shown in Fig. 3.

The rate of oxidation will depend on the rate of arrival of the ferrous ion complex at the anode. This rate was shown to be dependent on both Fe^{++} ion and hydroxyl ion concentration, which would indicate that the major portion of the current is being carried by hydroxyl ion complexes. This also follows from the relatively small amount of sulfate in the film even at the lowest pH tested. The greater ease of migration of the less positively charged hydroxy complex in the diffusion layer probably accounts for both the rate effect of pH and the formation of FeOOH rather than Fe_2O_3 .

As was the case with deposition from borate, there is a very rapid decrease in current during the deposition of the first 20-30Å of oxide. This is probably due to the relatively high resistance of the $\text{FeO}(\text{OH})$ film.²

² Assuming an electronic resistance of 10^{14} ohms/cm² for FeOOH a 30Å film would add a resistance of 30×10^8 ohms to the original low solution resistance. This would be quite sufficient to account for the large decrease in current.

It would appear that the deposition rate at constant pH is dependent on both Fe^{++} complex ion concentration and the thickness of the film.

Implications for anodic passivity.—From this and the previous work it is clear that the possibility of film formation from Fe^{++} in solution must be considered in any study of the anodic passivity of iron, particularly in nearly neutral solutions. If the initial conditions are such that corrosion of iron takes place to any significant degree before the onset of passivity some of the passive film will contain some γ - FeOOH , as well as the anhydrous oxides. It will also contain any anionic species of the solution which may be co-deposited with the iron. Hence the anodic passive behavior becomes very dependent on the method of bringing the specimen into the "passive potential" region. Any sequence which allows an initial corrosion to Fe^{++} ion, such as a slow or stepwise potential rise will automatically lead to a change in the over-all composition of the passive film (and probably its thickness). The incorporation of foreign anions in the film will also have a strong modifying effect on the stability of the final film. In all cases where deposition is possible, anodic passivation will result in the formation of a film containing several chemical species.

Manuscript submitted Nov. 29, 1971; revised manuscript received March 27, 1972.

Any discussion of this paper will appear in a Discussion Section to be published in the June 1973 JOURNAL.

REFERENCES

1. M. Nagayama and M. Cohen, *This Journal*, **110**, 670 (1963).
2. V. Markovac and M. Cohen, *ibid.*, **114**, 674 (1967).
3. V. Markovac and M. Cohen, *ibid.*, **114**, 678 (1967).
4. M. E. Bednas, J. L. Leibenguth, and D. S. Russell, *Electrochem. Technol.*, **6**, 11 (1968).
5. J. Wilkinson and L. Calvert, *J. Sci. Instr.*, **39**, 87 (1962).

A Study of Passivity Phenomena by Using O^{18} Tracer Techniques

J. Siejka* and C. Cherki

Groupe de Physique des Solides de l'École Normale Supérieure,
Tour 23, 9 Quai Saint-Bernard, Paris 5ème, France

and J. Yahalom¹

Technion, Israel Institute of Technology, Department of Materials Engineering, Haifa, Israel

ABSTRACT

A 1N solution of H_2SO_4 in O^{18} -enriched water was used to study the passivity of nickel by means of nuclear microanalysis. The fixation of the first monolayer of oxygen coming from the water was shown to have a decisive effect on the passive nature of the metal; however, further thickening to a maximum of five layers also influences the anodic current through an ion transfer mechanism. The oxygen loss rate of the passive layer, measured in open circuit and under polarization near steady-state conditions, was found to be equal to $\sim 10^{13}$ atoms/cm²-sec. The current efficiency for passive film formation was calculated and found to be low. It is suggested that passive layer growth occurs at the metal-film interface.

Investigations of the passivity of metal such as nickel, iron, chromium, and their alloys, by electrochemical (1) or optical (2) methods, have displayed the role

* Electrochemical Society Active Member.

¹ Present address: Bell Telephone Laboratories, Murray Hill, New Jersey 07974.

Key words: corrosion, dissolution, nuclear microanalysis, O^{18} tracing, nickel, passivation, passive film thickness, polarization, sulfuric acid.

played by oxygen in the mechanism of the formation of passive layers (3) as well as in the dissolution processes (4). A certain number of models, often controversial, have been proposed on the basis of this experimental evidence (5-11). Differences among them are partly caused by a lack of quantitative experimental data on the oxygen content in passive layers, and on its behavior.

In this work, we carried out a microanalysis of the oxygen isotopes by means of nuclear reactions [$O^{16}(d,p)O^{17*}$ and $O^{18}(p,\alpha)N^{15}$] to study the oxygen content of passive films formed on nickel in 1N H_2SO_4 . The method of nuclear microanalysis which has been developed in our laboratory for the purpose of studying the anodic oxidation of "valve" metals (12-14) and of semiconductors (15), allows one to determine the number of O^{16} and O^{18} atoms/cm² present near the surface of the material with an experimental error of about 1% for coverages as low as one monolayer. Thus, the above method, which has been described in detail elsewhere (16, 17), provides a powerful means for studying passivity phenomena.

Nickel was chosen on account of experimental data available from previous investigations (1, 5, 6, 18). We undertook to study: (i) the relationship between the potential or current and the quantity of oxygen fixed on the metal surface (first results on this point have been presented in Ref. (19)), (ii) the behavior of passive layers under polarization and in open circuit, and (iii) the current efficiency for layer formation.

Experimental

Application of O^{18} tracing.—The high sensitivity of nuclear microanalysis for the determination of minute amounts of O^{16} makes it very useful for the study of passivity films. However, the method cannot be applied directly since measurements are not performed *in situ*: the samples to be analyzed must be transferred from the passivation cell to the scattering chamber which is connected to the Van de Graaff accelerator. During transfer in the ambient atmosphere, some oxygen may be thermally fixed on the passivated samples, therefore changing the total content on the metal surface. In order to determine precisely the quantity of oxygen, attached to the metal, that originates from the solution, we resorted to the O^{18} tracing techniques described here.

All experiments were performed in a 1N H_2SO_4 degassed solution in ordinary water (" S_{016} " solution), or in water enriched to about 10% in O^{18} (" S_{018} " solution). Labeled water was purified under vacuum in order to eliminate impurities introduced during the process of enrichment. This method of purification has been described previously in Ref. (14). The isotopic composition of hydrogen in the O^{18} enriched water was normalized to natural abundance.²

The S_{018} solution was prepared by introducing labeled water into highly pure 95% H_2SO_4 of normal isotopic oxygen content. It was established by investigations on O^{18} labeling of oxygenated compounds that no isotopic exchange occurs at room temperature between the water and sulfate anions at acid concentrations similar to those used in the present experiments (20). This was furthermore confirmed by a control study of the labeling level of the water in S_{018} by the tantalum oxidation technique (21). The absence of exchange means that any O^{18} detected at the surface of the nickel actually comes from the water.

In order to remove air, purified dry nitrogen was passed through the solutions for at least 3 hr before immersing the specimen and during the experiment. On account of the high cost of the enriched solution, a special small-capacity cell was used, of about 12 cm³. Since most of the experiments were performed in the passive range, the contamination of the electrolyte by nickel was kept at a minimum.

The time during which the samples to be analyzed were in actual contact with the ambient atmosphere was reduced to a minimum (~5 min). In order to avoid the exchange of oxygen between O^{18} enriched samples and the atmosphere, the samples were stored in dry oxygen at $-45^\circ C$ between the end of the polarization and the beginning of analysis with the accelerator. Preliminary experiments showed that under

such storage conditions, the oxygen exchange can be disregarded. Nevertheless, some oxygen exchange could have occurred just when oxygen from the atmosphere is fixed on the surface, when the sample is taken out from the enriched solution. Such an effect would decrease the quantities of oxygen 18 measured on the metal surface. We have based the interpretation of our results on the assumption that this effect is negligible.

Preparation of samples.—Nickel plates of 99.99% purity were used. The samples were carefully degreased in acetone under ultrasonic vibration and then electrochemically polished for 10 min at room temperature, in stirred 54.5% sulfuric acid at 400 mA/cm². After polishing, the sample was carefully rinsed in triple-distilled water and kept under vacuum. Just before experiment, the samples were repolished for 1 min under the same conditions. The quantity of oxygen remaining on the surface varied from sample to sample, but lay within the limits $(6 \pm 1.5) \times 10^{15}$ atoms/cm². The effectiveness of the polishing procedure has been discussed in detail in Ref. (19).

The experiments were performed with a Tacussel potentiostat (Model PRT 2000 C) and potentials were measured with a high impedance Keithley voltmeter (Model 610 B). All potentials are expressed on the hydrogen scale. The experiments were carried out at $22^\circ \pm 1^\circ C$.

Experimental procedure.—The sample was left unpolarized for 5 min during which its potential stabilized at -60 mV. Then, cathodic polarization at -450 mV was applied for 5 min. As shown below, this procedure removed practically all the initial oxide. Polarization was then switched off for 5 min; the potential immediately rose to values near zero, decreased gradually, and stabilized at -100 mV. This phenomenon is presumably related to the expulsion of hydrogen which might be present near the surface of the metal. A positive potential was then applied by means of the potentiostat. On completing the process, the polarized samples were removed under polarization, and immediately plunged into triple-distilled water of natural isotopic composition. Preliminary experiments verified that this process stops dissolution of the passive layer and does not involve isotopic exchange of oxygen. After rinsing, samples were dried and stored in dry air at $-45^\circ C$.

Nuclear measurements.—The analytical techniques for O^{16} and O^{18} determinations were routine, as quoted above, except for the following point. Adsorbed elements may be desorbed under bombardment due to ionization by the beam during the measurements. In the case of nickel, this problem arose and was avoided by continuously changing the impact point of the 0.2 μA beam, which has a diameter of 1 mm. The scanning speed was 0.2 mm/sec. Moreover, the use of three 3-cm² detectors, with a total solid angle of detection of 0.3 steradian, enabled us to keep the duration of bombardment short while getting sufficiently accurate results. It was observed that this procedure eliminates any detectable desorption of oxygen.

Results and Interpretations

The results of nuclear microanalysis yield the number of O^{18} atoms/cm² (N_{O18}) and the number of O^{16} atoms/cm² (N_{O16}) in the film. The number of oxygen atoms coming from the water, \hat{N}_{O18} , may be obtained by dividing N_{O18} by the water enrichment (ratio of O^{18} to total oxygen in the water), i.e., by normalizing the results. Moreover, by subtracting \hat{N}_{O18} from the total oxygen detected on the metal surface ($N_{O16} + N_{O18}$) we can obtain ΔN_{O16} , the number of oxygen atoms coming from sources other than the water of the solution.

² Normalized O^{18} enriched water produced at the Weizmann Institute, Rehovot, Israel. The natural abundance of O^{18} is 0.204%.

As conditions for preparation of sample surfaces were rigorously the same for all experiments, the roughness factor can be considered to be a constant. Like most authors, we take it to be equal to unity. This implies that the absolute values for quantities of oxygen as given below are in fact, upper limits of the true values. Nevertheless, we would point out that certain values (such as the relative rates of oxygen loss which are obtained from the slopes of curves showing oxygen loss transients) are independent of the roughness factor if the latter is constant for all samples.

O¹⁸ contents in passive layers formed in labeled solutions.—We have studied the quantity \hat{N}_{O18} attached to the surface of nickel as a function of the potential V_{ox} in solutions of S₁₈. Below the region of passivity, polarization was stopped upon stabilization of the current. In the region of passivity, polarization was switched off at potentials when the current density I dropped to 20 $\mu\text{A}/\text{cm}^2$. This value appeared to be the best compromise between the need for rapid experiments (owing to the very high cost of O¹⁸ solution and the need to reduce solution loss, etc.) and the desire to approach steady-state conditions. The time required to reach this final current density depends on the potential. It is, for example, 140 sec for $V_{ox} = 640$ mV and 750 sec for $V_{ox} = 1040$ mV. We preferred to predetermine the final current density rather than the duration of passivation, in order for the experimental conditions to be similar to those which give a linear relationship between film thickness and formation potential in anodic oxidation of "valve" metals. In fact, in the latter case, there exists an empirical relationship at constant temperature between I and V_{ox} (14)

$$I = A \exp B \frac{V_{ox}}{d} \quad [1]$$

where d is film thickness and A and B are constants.

The number of atoms (\hat{N}_{O18}) at the surface of the metal as a function of polarization potential applied to the sample is given typically in Fig. 1. It should be noted that repeated experiments at 1040 mV result in a scatter of 5% or less in the values for the O¹⁸ levels. The salient observations are:

1. No oxygen coming from the water was fixed at the surface of the nickel below the passive region.
2. The relationship between \hat{N}_{O18} and V_{ox} is approximately linear in the passive region.
3. The maximum number of oxygen atoms (\hat{N}_{O18}) in the passive region is never more than $(6.3 \pm 0.4) \times 10^{15}$ atoms/cm², which corresponds approximately to 5 monoatomic layers of oxygen, assuming that one atom

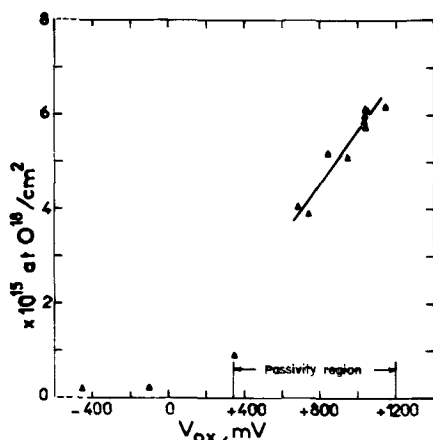


Fig. 1. Normalized O¹⁸ content (\hat{N}_{O18}) as a function of applied potential V_{ox} for samples for which polarization was stopped at a final current density $I = 20 \mu\text{A}/\text{cm}^2$ [from Ref. (19)].

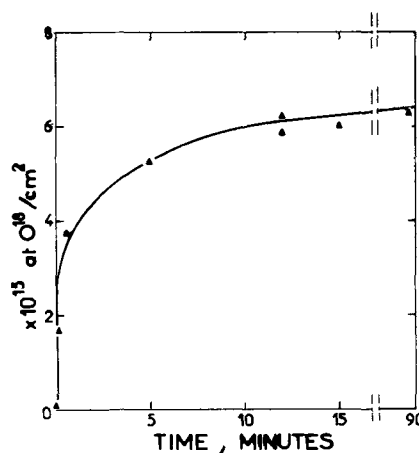


Fig. 2. \hat{N}_{O18} as a function of time for $V_{ox} = 1040$ mV [from Ref. (19)].

of Ni is bound to one atom of oxygen, or to 10Å of nickel oxide if a NiO structure with density 7.45 g/cm³ is assumed.

In a second series of experiments, we have studied the quantity of \hat{N}_{O18} attached to the surface of nickel as a function of polarization time for a constant potential V_{ox} . In Fig. 2, \hat{N}_{O18} is plotted as a function of time for $V_{ox} = 1040$ mV. It is shown that the rate of oxygen pickup decreases rapidly with time. The formation of a first layer of $\sim 1.2 \times 10^{15}$ atoms/cm² takes place in about 10 sec. Subsequently several minutes are required to quintuplicate the quantity of oxygen and to reach a value which does not change appreciably for long polarization periods. Within the margin of error, it can be considered that at this applied potential ($V_{ox} = 1040$ mV), the growth of the passivation layer is negligible after a time (t_f) of 10-12 min, even though the current density, which at t_f is about 20 $\mu\text{A}/\text{cm}^2$, continues to decrease slightly for $t > t_f$ and does not actually stabilize until several hours later.

A quasi-exponential decrease of the current densities is observed during the formation of the passive films at constant potential. It was interesting to relate the number of oxygen atoms, \hat{N}_{O18} , attached to the metal surface (Fig. 2) to the corresponding values of the current density. We observed that the relationship between $1/\hat{N}_{O18}$ and current densities was neither linear (ohmic conduction) nor logarithmic (high-field conduction) over the whole range of current densities investigated. On the other hand a high-field conduction process may be expected to occur (1, 7, 10) in passive layers exceeding the monolayer coverage (unit-cell thickness). It might also be expected that the mechanism of ionic transport is different depending on whether the thickness of surface coverage is of the order of or less than unit cell. Our results show that the \hat{N}_{O18} values exceed the equivalent of a unit-cell thickness for current densities lower than $\sim 60 \mu\text{A}/\text{cm}^2$. In this range a logarithmic law

$$1/\hat{N}_{O18} = K \text{Log } I + K_0 \quad [2]$$

may be assumed. The results are illustrated in Fig. 3 for the whole range of current densities. They show indeed that Eq. [2] is followed up to current densities around 60 $\mu\text{A}/\text{cm}^2$. The much faster variation of $1/\hat{N}_{O18}$ with I above this value is discussed below.

Behavior of oxygen in the passivity layers.—Attempts were made to investigate the mechanisms of ionic transport near the steady-state conditions. The existence of a steady state was studied and discussed

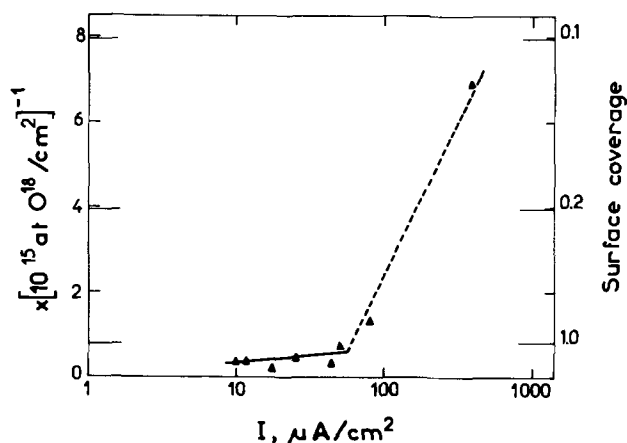


Fig. 3. Inverse of normalized O^{18} content ($1/\hat{N}_{\text{O}^{18}}$) as a function of the logarithm of the current density I for $V_{\text{ox}} = 1040$ mV. Also shown is an ordinate depicting the surface coverage (deduced from $\hat{N}_{\text{O}^{18}}$ values).

in a series of papers (1, 3, 6, 22-24). Two principal hypotheses have been proposed:

1. The steady state would be due to the balance between the rate of chemical dissolution of the film (rate which would be independent of the potential) and its rate of anodic formation (6, 7).

2. The growth would be stopped when the layer has a thickness sufficient to reduce the average gradient of the electrochemical potential of oxygen to such a value that the rate of inward oxygen penetration becomes negligible. This means that a quasi-stationary state is obtained when the electrochemical equilibrium of oxygen is reached (25).

Two series of experiments were carried out to study the rate of the loss of oxygen O^{18} attached to the surface of the samples, when the latter are held in the solution without polarization for various times. The samples were first polarized in $\text{S}_{\text{O}^{18}}$ at 1040 mV with a final current density of $20 \mu\text{A}/\text{cm}^2$. In the first series of experiments, the samples were held in the $\text{S}_{\text{O}^{18}}$ solution used to prepare them, whereas for the second series, the experiments were repeated under identical conditions of film formation, but dissolution took place in an $\text{S}_{\text{O}^{16}}$ solution.

Typical results obtained in both cases are shown in Fig. 4. The error ranges given for the curves are due to irreproducibility of the initial passive layers. The experimental points indicated by circles represent losses of O^{18} in the $\text{S}_{\text{O}^{18}}$ solution and those indicated by squares represent the O^{18} losses in the $\text{S}_{\text{O}^{16}}$ solution. It seems that the rate of oxygen loss is about the same for $\text{S}_{\text{O}^{16}}$ and $\text{S}_{\text{O}^{18}}$. This would indicate, first of all, that isotopic exchange phenomena of oxygen between the solutions and the passivity film are negligible as compared to the rate of oxygen 18 loss by dissolution. In fact, isotopic exchange should have been more rapid than dissolution for these phenomena to be distinguished in the curves of Fig. 4. By maximizing the effect of film irreproducibility, the initial rate of oxygen 18 loss v_{10} and the corresponding errors may be estimated from the curves of Fig. 4 and is presented in Table I.

In a further series of experiments, the oxygen 18 losses under polarization were studied. Samples were

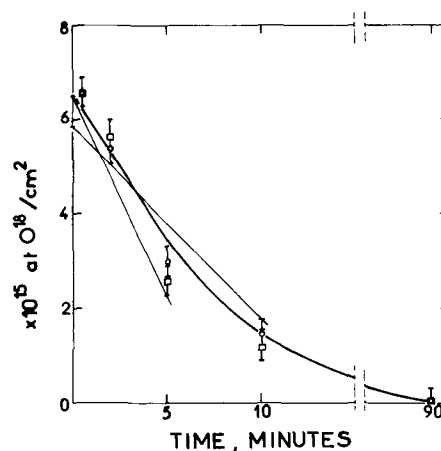


Fig. 4. $\hat{N}_{\text{O}^{18}}$ as a function of time of dissolution in open circuit for samples polarized in $\text{S}_{\text{O}^{18}}$ at 1040 mV down to a final current density $I = 20 \mu\text{A}/\text{cm}^2$. \circ , Dissolution in $\text{S}_{\text{O}^{18}}$ solution; \square , dissolution in $\text{S}_{\text{O}^{16}}$ solution. Straight lines correspond to the minimum and maximum initial slope, i.e. oxygen loss rate.

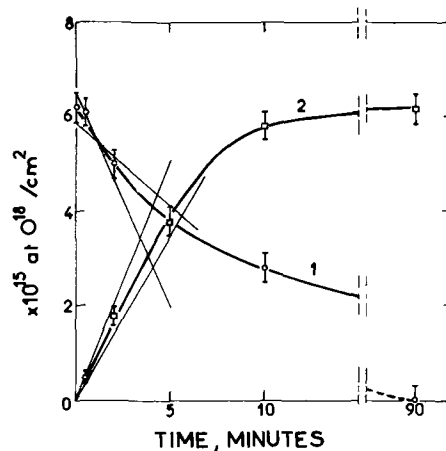


Fig. 5. $\hat{N}_{\text{O}^{18}}$ loss (curve 1) or uptake (curve 2) as a function of time of polarization at 1040 mV. Curve 1: samples polarized in $\text{S}_{\text{O}^{18}}$ at 1040 mV, then repolarized under the same conditions in $\text{S}_{\text{O}^{16}}$ solution. Curve 2: the reverse. Straight lines correspond to the minimum and maximum values of oxygen loss and uptake.

initially formed down to $20 \mu\text{A}/\text{cm}^2$ in $\text{S}_{\text{O}^{18}}$ at 1040 mV and then immersed in $\text{S}_{\text{O}^{16}}$ and kept at the same potential. After a sharp rise, the current leveled off in about 1 min to the final current value in $\text{S}_{\text{O}^{18}}$ and continued to decrease at the same rate as in the case of an uninterrupted formation. Curve 1, in Fig. 5, shows a decrease of O^{18} in the second solution as a function of time. The value for the initial rate of oxygen 18 loss v_{10} , which was obtained from this curve, is presented in Table I. We then performed an experiment in an inverse sequence, i.e., the passivity was first induced in $\text{S}_{\text{O}^{16}}$ under the previous conditions down to $20 \mu\text{A}/\text{cm}^2$; the samples were then immersed and polarized in $\text{S}_{\text{O}^{18}}$. The uptake of O^{18} at the surface of nickel as a function of time is shown on curve 2 of Fig. 5. The initial rate of O^{18} uptake v_{up} is represented in Table I.

Table I. Initial rate of oxygen 18 loss*

v_{10} , Oxygen 18 loss in open circuit from Fig. 4		v_{1p} , Oxygen 18 loss under polarization from Fig. 5, curve 1		v_{up} , Oxygen 18 uptake under polarization from Fig. 5, curve 2	
Atoms/cm ² -sec	$\mu\text{A}/\text{cm}^2$	Atoms/cm ² -sec	$\mu\text{A}/\text{cm}^2$	Atoms/cm ² -sec	$\mu\text{A}/\text{cm}^2$
$[1 \pm 0.4] \times 10^{18}$	3.2 ± 1.1	$[1 \pm 0.5] \times 10^{18}$	3.3 ± 1.5	$[1.4 \pm 0.4] \times 10^{18}$	4.5 ± 1.1

* Samples prepared at $V_{\text{ox}} = 1040$ mV (HE), $I_{\text{ftn}} = 20 \mu\text{A}/\text{cm}^2$.

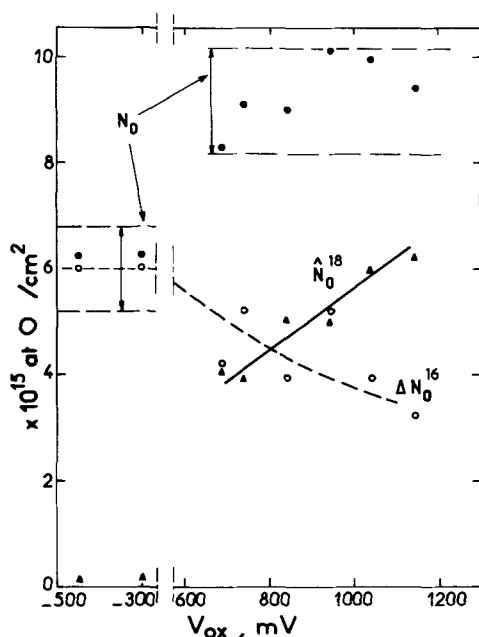


Fig. 6. Oxygen contents on polarized samples as a function of potential V_{ox} . \circ , ΔN_{O16} ; \blacktriangle , \hat{N}_{O18} (see Fig. 1); \bullet , $N_O = N_{O16} + N_{O18}$, i.e. total oxygen content. The arrows indicate the range of values of total oxygen content measured directly, on samples prepared in S_{016} solution.

For similar reasons as before, a large degree of error is involved in the estimation of v_{lp} and v_{up} . However, from the values in Table I, it can be deduced that the initial rates of oxygen 18 loss are the same in open circuit and under polarization, v_{1o} , v_{1p} , although it seems that v_{up} is slightly higher than v_{1p} .

Origin of oxygen coming from other sources.—The amount of oxygen in the film coming from sources other than the water (ΔN_{O16}) was measured for a number of cases (Eq. [3])

$$\Delta N_{O16} = N_{O18} + N_{O16} - \hat{N}_{O18} \quad [3]$$

In principle, three sources may be assumed as possible contributors of oxygen: (i) the initial layer of O^{16} that remains on the metal in the solution after cathodic treatment; (ii) incorporation of SO_4^{2-} anions; and (iii) oxygen uptake from the atmosphere (oxidation or adsorption) during transfer of samples from the polarization cell to the accelerator.

Figure 6 shows ΔN_{O16} as a function of potential for samples polarized in S_{018} at the final current density $I = 20 \mu A/cm^2$. The content \hat{N}_{O18} for these samples is also given in Fig. 6 which includes results from Fig. 1. Figure 7 shows results of ΔN_{O16} obtained on samples for which losses of O^{18} in open circuit, in S_{018} and

S_{016} , had been studied (see Fig. 4). \hat{N}_{O18} as a function of time is shown. It is seen from Fig. 6 and 7 that the total quantity of oxygen analyzed N_O remains practically constant ($9 \pm 1.5 \times 10^{15}$ atoms/cm²) for the quantities of $\hat{N}_{O18} \cong \sim 2 \times 10^{15}$ atoms/cm² and slightly decreases for the surfaces free of oxygen coming from the solution ($\hat{N}_{O18} \approx 0$). The arrows indicate the range of values of oxygen contents measured in S_{016} solution. Details of these experiments are presented in Ref. (19). It appears that, at some stage between the initial preparation of the specimen and its final analysis, any deficiency in oxygen picked up from the water is supplemented by oxygen from another source.

Since the O^{18} content was shown before to be determined only by the polarization conditions, it turns out that the additional oxygen depends on the O^{18} content

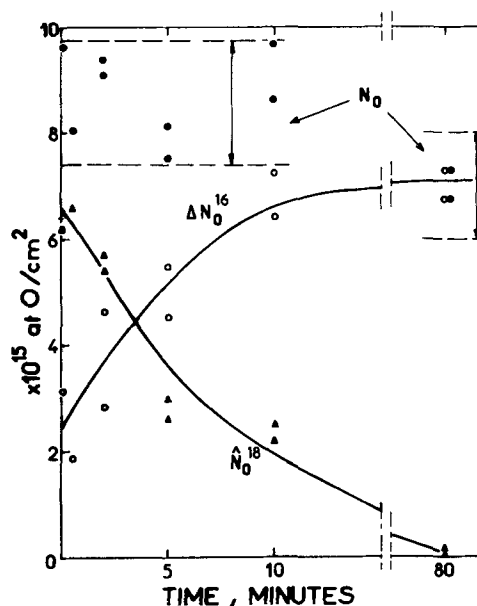


Fig. 7. Oxygen contents during the dissolution in open circuit (see Fig. 4). \circ , ΔN_{O16} ; \triangle , \blacktriangle (curve 2), \hat{N}_{O18} dissolution in S_{018} and S_{016} , respectively; \bullet , $N_O = N_{O16} + N_{O18}$, i.e., total oxygen content. The arrows as in Fig. 6.

and not vice versa. This would rule out the assumption that the additional oxygen originates from an initial film which remained on the film despite cathodic polarization. It is also difficult to consider a mechanism by which sulfate ions should combine more heavily with a thinner passive film.

Of the three possible sources, the most likely one seems to be the outer atmosphere during the transfer of samples.

From the above, it should follow that if indeed the outer atmosphere is contributing the extra oxygen, the total film formed in air is $(3 \text{ to } 5) \times 10^{15}$ atoms/cm² thicker than the passive film.

Components of the current.—In the absence of redox systems other than the natural redox system of water in the solution studied, the current I is entirely ionic. This point, emphasized by several authors, was demonstrated for iron in $1N H_2SO_4$ by Franck and Weil (26). Most authors assume that the same is true for nickel. The current density I passing through the film-solution interface at any instant may hence consist of two components: I_{ox} , the part of the current which contributes to passive layer growth and I_{dis} , the dissolution current, so that

$$I = I_{ox} + I_{dis} \quad [4a]$$

while

$$I_{dis} = I_{cat} + I_{ch} \quad [4b]$$

as I_{dis} includes the current density I_{cat} of direct dissolution of cations and I_{ch} , which is the amount of oxide dissolved chemically, expressed in terms of the equivalent charge required to have formed it (per unit area, per unit time).

Attempts were made to deduce the components of the current from the N_{O18} measurements. On the basis of the literature data (6, 18, 24, 27) and of our results (see preceding heading) we assume that the transfer of oxygen 16 ions at the passive film-solution interface due to the SO_4^{2-} fixation on the metal surface can be neglected compared to the oxygen transfer from the water (O^{18}). This assumption is reasonable (13, 24) for low current densities ($I = 20 \mu A/cm^2$) but could be incorrect for high current densities. Details of this phenomenon will be studied in the near future, both by O^{18} tracing and by direct nuclear analysis of sulfur.

We present here the results for two ranges of values of I :

(i) $I = 20 \mu\text{A}/\text{cm}^2$

The difference between v_{up} and v_{lp} should give the over-all rate of growth of the passive layer at $I = 20 \mu\text{A}/\text{cm}^2$. However, in view of the inaccuracy in the results, it is not possible to estimate this difference. Considering the values of v_{up} and v_{lp} , it can be stated that the maximum value for over-all growth rate of the passive layer at $I = 20 \mu\text{A}/\text{cm}^2$ is 1.3×10^{13} atoms/ $\text{cm}^2 \cdot \text{sec}$. This corresponds to a maximum value of I_{ox} equal to $4.2 \mu\text{A}/\text{cm}^2$ (if we assume that two charges are attached to each oxygen atom), i.e., a maximum value of current efficiency for passive film formation, R , of 21%. From these two observations, it may be inferred that I_{dis} lies within the limits

$$15.8 \mu\text{A} \leq I_{\text{dis}} \leq 20 \mu\text{A}/\text{cm}^2 \quad [5]$$

The value of v_{lp} taken from Fig. 5 contains the rate of O^{18} loss by dissolution and the rate of O^{18} loss by isotopic exchange with the solution. This implies that the values of v_{lp} are in fact upper bounds of I_{ch} . This means that $I_{\text{ch}} \leq 4.8 \mu\text{A}/\text{cm}^2$ (see Table II). It should follow that the current density of electrochemical dissolution of cations I_{cat} amounts to at least $11 \mu\text{A}/\text{cm}^2$ or 55% of I . These data are shown in Table II.

(ii) $20 \mu\text{A}/\text{cm}^2 < I < 800 \mu\text{A}/\text{cm}^2$

The total current efficiency for the formation of passive films, from the start of polarization until $t = t_f$ (for which $I = 20 \mu\text{A}/\text{cm}^2$) can be measured, under the assumptions indicated above, by comparing the charge passed through the circuit and $N_{\text{O}18}$ measured at t_f .

In fact [see Ref. (14)], the number of oxygen atoms per square centimeter coming from the water and fixed in the layer at time t is $N_{\text{O}18}(t)$

$$\begin{aligned} N_{\text{O}18}(t) - N_{\text{O}18}(0) &= K \int_0^t I_{\text{ox}}(\theta) d\theta \\ &= K \int_0^t R(\theta) I(\theta) d\theta \end{aligned} \quad [6]$$

where $R(t)$ is the current efficiency for passive film formation at any instant t

$$R(t) = \frac{I_{\text{ox}}(t)}{I(t)} \quad [7]$$

and where the constant K is equal to 0.312×10^{19} atoms of oxygen per coulomb if we assume that the oxygen is fixed in the films in the form O^{2-} .

On the other hand, the number Q of coulombs per square centimeter

$$Q = \int_0^t I(\theta) d\theta \quad [8]$$

consumed during polarization allows one to determine the current efficiency for passive film formation from the following relation, deduced from [6]

Table II. Components of the current deduced from $N_{\text{O}18}$ measurements for samples prepared at $V_{\text{ox}} = 1040 \text{ mV}$ (HE)

Near the steady-state conditions $I = 20 \mu\text{A}/\text{cm}^2$	From the start of polarization ($t_0 = 5 \text{ sec}$) to the steady-state region ($t_f = 12 \text{ min}$) $\sim 800 \mu\text{A}/\text{cm}^2 > I > 20 \mu\text{A}/\text{cm}^2$
$I_{\text{ox}}(\text{max}) = 4.2 \mu\text{A}/\text{cm}^2$	$Q = \int_{t_0}^{t_f} I(\theta) d(\theta) \quad (\text{Eq. [8]})$ $R = (6 \pm 1) \%$ $Q_{\text{dis}} = (94 \pm 1) \% \text{ of } Q$ $Q_{\text{ch}} \sim 10\% \text{ of } Q$ $Q_{\text{cat}} \sim 84\% \text{ of } Q$
$R(\text{max}) = 21\%$	
$I_{\text{dis}}(\text{min}) = 15.8 \mu\text{A}/\text{cm}^2$	
$I_{\text{ch}}(\text{max}) = 4.8 \mu\text{A}/\text{cm}^2$	
30% of I_{dis}	
24% of I	
$I_{\text{cat}}(\text{min}) = 11 \mu\text{A}/\text{cm}^2$	
70% of I_{dis}	
55% of I	

* Calculated for $I_{\text{ch}} = 4.8 \mu\text{A}/\text{cm}^2$.

$$R = \frac{1}{K} \frac{dN_{\text{O}18}}{dQ} \quad [9]$$

Experimental measurements of this quantity can be used to determine I_{ox} by means of Eq. [7].

The very high current during the first few seconds of polarization was not recorded by the experimental system. The total current efficiency for passive film formation was therefore measured between $t = 5 \text{ sec}$ and $t = t_f$, using the difference between $N_{\text{O}18}$ found at these times, respectively. We obtained $R = 6 \pm 1\%$ at $V = 1040 \text{ mV}$, which leaves $94 \pm 1\%$ for the losses. If the layer dissolution current (I_{ch}) measured at $I = 20 \mu\text{A}/\text{cm}^2$ is assumed to be constant during the entire layer formation, it would only account for at most 10% of the total losses measured between $t = 5 \text{ sec}$ and t_f : this, in turn, implies that electrochemical dissolution of cations constitutes at least 84% of the losses during layer formation. These data are shown in Table II.

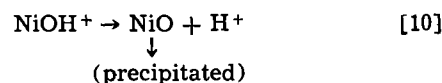
Discussion

The results obtained clearly show the existence of two different kinetic regions of fixation of oxygen coming from water. As shown in Fig. 3, fixation of the first monolayer in the region of high passivity potential ($V_{\text{ox}} = 1040 \text{ mV}$) is accompanied by a large drop in current. Thus, to go from a surface coverage of about 10% ($1/\hat{N}_{\text{O}18} \sim 8 \times 10^{-15} \text{ cm}^2/\text{atom}$) to a total coverage ($1/\hat{N}_{\text{O}18} \sim 0.8 \times 10^{-15} \text{ cm}^2/\text{atom}$), one observes experimentally a current drop of one order of magnitude, whereas to pass from a coverage by a single monoatomic layer to a formation of approximately five monoatomic layers, the current only changes from $I \sim 60 \mu\text{A}/\text{cm}^2$ to $I \sim 10 \mu\text{A}/\text{cm}^2$. Moreover, Fig. 1 clearly shows that the metal is virtually stripped of oxygen coming from water after cathodic polarization and stabilization of the solution ($V_{\text{ox}} = -100 \text{ mV}$), in agreement with ellipsometric observations of Sato (28), Bockris *et al.* (5), and Reddy and Rao (29).

According to the Tafel curve drawn from the results of Sato and Okamoto (18), the theoretical value of the initial current on application of $V_{\text{ox}} = 1040 \text{ mV}$ would be about $\sim 10^4 \text{ A}/\text{cm}^2$. Therefore, for the fixation of a monoatomic layer totally covering the surface ($1/\hat{N}_{\text{O}18} \sim 0.8 \times 10^{-15} \text{ cm}^2/\text{atom}$ and $I \sim 60 \mu\text{A}$), there is a current drop of eight orders of magnitude if initial limitation by diffusion in the solution is not considered. This conclusion, similar to that drawn by Frankenthal (9, 10, 22) on passivation of iron and Fe-Cr alloys, suggests that the fixation of the first monoatomic layer of oxygen coming from water plays a fundamental role in the passivation process. This hypothesis is consistent with the assumption we have made above, namely, that the incorporation or electrochemical decomposition of SO_4^{2-} anions is not of great or of decisive importance in the process of passivation on the metal surface.

To explain this effect, Frankenthal supposes that for short times at high potential (that is, before fixation of the monoatomic layer with total coverage), there exists a mechanism of preferential dissolution-adsorption and a mechanism of anodic dissolution by direct activated transfer of the surface ions of the metal in the solution.

Bockris, Reddy, and Rao (5) suggested, to explain the formation of the first layer of passivation, another mechanism called dissolution-precipitation. In this model, it is assumed that when the concentration of NiOH^+ increases to above the saturation value, which is determined by the solubility product of NiO , precipitation of NiO occurs in the area around the surface, by the reaction



Frankenthal does not find this model convincing, since if the prepassive film is converted entirely into passivation film, then the former must also be of monomolecular dimensions, which is most unlikely for a precipitate. Moreover, Sato and Okamoto point out that the oxide film deposited from the solution according to Reaction [10] is expected to have a porous character; this would lead to the formation of a layer whose great thickness would be easily detectable by the present measuring method. However, this is not the case, and thus we are inclined to think that the adsorption mechanism would be more probable than the precipitation mechanism, under our experimental conditions.

The second point to be discussed concerns the behavior of passivity films in the slow kinetic region, *i.e.*, when the film thickness deduced from N_{O18} measurements exceeds one monoatomic layer. The results in Fig. 1 allow us to assume the existence of a linear relationship between film thickness and potential, for a final constant current density which is close to the steady state ($I = 20 \mu\text{A}/\text{cm}^2$). Between 640 and 1040 mV, the thickness varies from 3 to 5 monoatomic layers. The linearity between N_{O18} and V_{ox} in the passive range is in agreement with the ellipsometric observations of Sato (28); under similar conditions, he observed a linear increase in passive film thickness with increasing potential.

Bockris *et al.* (5) did not observe any variation of thickness with potential in the passivity region; the thickness was reported to remain constant, to the order of 70-100Å. It should be noted that the solution used by Bockris *et al.* (0.01N $\text{H}_2\text{SO}_4 + 0.5\text{M K}_2\text{SO}_4$) was less acidic than the present 1N H_2SO_4 .

According to Frankenthal (9, 10, 22) the steady state would not be reached until formation of an oxide film of more than unit cell thickness, anodic dissolution and film formation proceeding by field-assisted ionic transport through the oxide. This conclusion seems to be in agreement with our results. In fact, the linear variations of $1/\hat{N}_{O18}$, at low current densities, with $\log I$ (Fig. 3) and of \hat{N}_{O18} with V_{ox} (Fig. 1) can be interpreted in terms of a high-field conduction process. Moreover, the change of mechanism of oxygen fixation is observed, when the "thickness" of passive film deduced from N_{O18} measurements, exceeds one unit cell.

From the above, it should follow that a high-field conduction process is most likely when the thickness of the film exceeds that of one unit cell.

The results obtained permit us to define precisely the nature of the mechanisms involved in this growth region. We shall first examine the principal mechanisms proposed in the literature (3, 6, 7, 23). In order to explain the potential-independence of the final current I_f in the passivity region under steady-state conditions, two reactions schemes have been presumed possible: (a) the direct transfer of Ni^{++} from the passivation layer to the solution; (b) a transfer by an intermediary complex of the NiOH^+ . Transfers (a) and (b) would be independent of the electrode potential and controlled solely by the potential difference across the oxide-solution interface, which would be maintained at an equilibrium value dependent on the pH for the reaction $(\text{O}^{2-})_{\text{film}} + 2\text{H}^+ = \text{H}_2\text{O}$ (7). The results of Sato and Okamoto (6) suggest that the second type of transfer would be dominant. It should be noted that this transfer would produce a rate of oxygen loss $v_{f_0} = 0.63 \times 10^{13}$ atoms/cm²·sec for $I_f = 2 \mu\text{A}/\text{cm}^2$, value observed on the nickel in 1N H_2SO_4 at 25°C (6). For our part, we measured, for the quasi-stationary state ($I = 20 \mu\text{A}/\text{cm}^2$) a rate of oxygen 18 loss (v_{1p}) equal to $(1 \pm 0.5) \times 10^{13}$ atoms/cm²·sec (see Table I). We should add that v_{1p} although higher corresponds, within the margin of experimental error, to v_{f_0} , if we take into consideration that v_{1p} was measured not at 2 but at 20 $\mu\text{A}/\text{cm}^2$.

As shown by our results the oxygen 18 losses are independent of potential ($v_{10} = v_{1p}$, Table I). Thus, it is reasonable to assume that I_{ch} , deduced from O^{18} measurements (v_{1p}) is due to the same process that produces I_f . This means that I_{ch} , as well as I_f , are a result of transfer mechanism (b).

Vetter (7) and Sato (6) implicitly assume all of the metal dissolution to be due to mechanism (b). According to our findings, it appears that the equivalent current I_{ch} , due to mechanism (b) represents at most 24% of the total current crossing the film-solution interface at $I = 20 \mu\text{A}/\text{cm}^2$. This leads us to consider that, in addition to reaction (b), reaction (a) takes place, even though the transfer mechanism of metal cations toward the interface cannot be precisely defined. It should be recalled that Novakovsky *et al.* (25) suppose transfer (b) to be completely blocked and dissolution to be due to transfer (a). Our findings imply the existence of both types of transfer for $I = 20 \mu\text{A}/\text{cm}^2$. It is logical to assume that whenever the current decreases and tends toward a limiting value ($I_f = 2 \mu\text{A}/\text{cm}^2$), mechanism (a) is blocked and dissolution of the metal occurs only by mechanism (b), *i.e.*, the limiting value of I_{ch} is 2 $\mu\text{A}/\text{cm}^2$.

Mobility of ionic carriers during formation of passive layers near steady-state conditions.—Another problem we attempt to elucidate was the determination of the interface at which the oxidation reaction, *i.e.*, film growth, takes place near the steady-state conditions. As shown in Fig. 2 the growth of passive layer is practically stopped when the current densities drop below 20 $\mu\text{A}/\text{cm}^2$, although the equivalent current of layer dissolution (I_{ch}) is within the range 2-4.2 $\mu\text{A}/\text{cm}^2$ (see above). From the above, it should follow that the equivalent current for new layer formation is equal to I_{ch} (dynamic equilibrium).

The existence of an electrochemical dissolution of cations (I_{cat} is at least 55% of I) provides experimental evidence for the mobility of cations. *A priori*, this could imply that growth would occur at the oxide-solution interface. If this were the case, the processes of dissolution and oxygen fixation would both occur on the external interface and the internal layer would not be in direct contact with the solution, which will imply that the increase in oxygen in Fig. 5 (v_{up}) could have occurred only by isotopic exchange and diffusion. However, as indicated by the results in Fig. 4, these phenomena are negligible in comparison with dissolution. On the basis of these results, we therefore suppose that the increase in O^{18} measured in Fig. 5 (v_{up}) is due to growth rather than to isotopic exchange phenomena. Thus, the formation of new layers can only take place at the metal-passive layer interface by migration of oxygen coming from the solution. This pattern of growth was proposed by Novakovsky (23) to explain the passivation of iron and also by Hoar and Mott (30) for porous growth of aluminum during anodic oxidation in acids. Moreover, in accordance with Novakovsky (23), one can explain the absence of passive film formation at the passive layer-solution interface, in spite of the large cation flow across this interface, by a decrease in chemical potential of the cations resulting from formation of bonds with oxygen in the oxide. The same reasoning was used to explain the presence of the current of electrochemical dissolution of cations during anodic oxidation of aluminum in aqueous solutions of ammonium citrate (14) or sulfuric acid (31).

Stability of passive layers.—As shown by the results, the passive layers are not stable and reoxidize in air. This seems to confirm our conclusions according to which the "thickness" of the passive layer in the solution is determined by the equilibrium between the rates of layer formation and dissolution. When the specimen is removed from solution, the rate of dissolution of the layer is virtually zero. On the other hand, the equilibrium thickness of passive layer formation in

the presence of adsorbed water and gaseous oxygen should be higher than in the N_2 -purged H_2SO_4 due to a higher oxygen redox potential. The new equilibrium requires an increase in layer thickness, which we observed (ΔN_{O16}). The passive layer is not thermodynamically reversible, in agreement with Frankenthal (22). Dissolution (Fig. 4) requires about 30 min, whereas the electrode potential goes down to the initial value after ~ 30 sec.

Conclusions

The conclusions based essentially on the measurements of the quantities of the oxygen coming from the water (O^{18}) may be summed up as follows. The first layer of oxygen fixed on the metal surface is found to have a decisive effect on the passive nature of metal and causes the anodic current density to decrease by several orders of magnitude. When the layer thickness due to the fixation of oxygen coming from water exceeds the size of one "unit cell," the current is probably limited by "field-assisted ionic transfer phenomena." A linear relationship exists between the thickness of the layer and its formation potential, for the same final current value.

The current efficiency for passive layer formation was found to be very small. The current of cations crossing the oxide-solution interface consists of the current of direct transfer of cations, plus the current equivalent to the dissolution of oxide. The latter is equal to the current at the "steady-state condition" and to the dissolution current of the layer when it is in an open circuit.

It seems that the formation of a new layer takes place at the metal-oxide interface via migration of oxygen ions from the water. The thickness of the passive layer depends on the dynamic equilibrium between the rates of formation and of dissolution.

It was found that the passive layers are unstable and reoxidize in air, and that the rate of isotopic oxygen exchange is lower than the rate of dissolution, both in open circuit and under passivation potential. And finally, the passive layers are not thermodynamically reversible and the value of the electrode potential in an open circuit is not related to the presence of the layer.

Acknowledgments

The authors wish to thank Dr. G. Amsel for his numerous comments and suggestions during this work. They are grateful to Mr. B. Agius for enlightening discussions and for help during the experiments. The technical assistance of Mr. A. Laurent was much appreciated. This work was supported by the Centre National de la Recherche Scientifique, (RCP No. 157), the DRME, and the DGRST.

Manuscript submitted Sept. 24, 1971; revised manuscript received April 10, 1972.

Any discussion of this paper will appear in a Discussion Section to be published in the June 1973 JOURNAL.

REFERENCES

1. T. P. Hoar, in "Modern Aspects of Electrochemistry," Vol. 2, Chap. IV, p. 262, Butterworth Scientific Publications, New York (1959).
2. J. Kruger, *This Journal*, **110**, 654 (1963).
3. T. P. Hoar, *ibid.*, **117**, 17C (1970).
4. J. Epelboin and M. Keddam, *ibid.*, **117**, 1052 (1970).
5. J. O'M. Bockris, A. K. N. Reddy, and B. Rao, *ibid.*, **113**, 1133 (1966).
6. N. Sato and G. Okamoto, *ibid.*, **110**, 605 (1963).
7. K. J. Vetter, *ibid.*, **110**, 597 (1963).
8. H. Nagayama and M. Cohen, *ibid.*, **110**, 670 (1963).
9. R. P. Frankenthal, *ibid.*, **114**, 542 (1967).
10. R. P. Frankenthal, *ibid.*, **116**, 580 and 1646 (1969).
11. H. H. Uhlig, *Z. Electrochem.*, **62**, 626 (1958).
12. G. Amsel and D. Samuel, *J. Phys. Chem. Solids*, **23**, 1707 (1962).
13. G. Amsel, C. Cherki, G. Feuillade, and J. P. Nadai, *ibid.*, **30**, 2117 (1969).
14. J. Siejka, J. P. Nadai, and G. Amsel, *This Journal*, **118**, 727 (1971).
15. M. Croset, E. Petreanu, D. Samuel, G. Amsel, and J. P. Nadai, *ibid.*, **118**, 717 (1971).
16. G. Amsel, J. P. Nadai, E. D'Artemare, D. David, E. Girard, and J. Moulin, *Nucl. Instr. Methods*, **92**, 481 (1971).
17. G. Amsel, C. Cherki, M. Croset, D. Dieumegard, B. Maurel, J. P. Nadai, C. Ortega, S. Rigo, and J. Siejka, *Collection Czech. Chem. Commun.*, **36**, 883 (1971).
18. N. Sato and G. Okamoto, *This Journal*, **111**, 897 (1964).
19. J. Siejka, C. Cherki, and I. Yahalom, Paper presented at 3rd Internat. Symposium on Passivity, Cambridge, England, July 6-10, 1970; *Electrochim. Acta*, **17**, 161 (1972).
20. T. C. Heoring and J. W. Kennedy, *J. Am. Chem. Soc.*, **79**, 56 (1957).
21. G. Amsel, M. Croset, C. Ortega, and S. Rigo, "A High Sensitivity Isotopic Oxygen Analysis of Water by Anodic Oxidation," To be published.
22. R. P. Frankenthal, *Electrochim. Acta*, **16**, 1845 (1971).
23. V. M. Novakovsky, *ibid.*, **10**, 353 (1965).
24. L. Young, "Anodic Oxide Films," Academic Press, London and New York (1961).
25. V. M. Novakovsky and Y. A. Likhachev, *Electrochim. Acta*, **12**, 267 (1967).
26. U. F. Franck and K. G. Weil, *Z. Electrochem.*, **56**, 814 (1953).
27. G. Gilli, P. Borea, F. Zucchi, and G. Trabonelli, *Corrosion Sci.*, **9**, 673 (1969).
28. N. Sato, K. Kudo, and T. Noda, *ibid.*, **10**, 785 (1970); and N. Sato, Private communication.
29. A. K. N. Reddy and B. Rao, *Can. J. Chem.*, **47**, 2693 (1969).
30. T. P. Hoar and N. F. Mott, *J. Phys. Chem. Solids*, **19**, 95 (1959).
31. C. Cherki and J. Siejka, "Porous Oxidation of Aluminium in Acid Solution Studied by O^{18} Tracing," To be published.

Kinetics of Iron Corrosion in Concentrated Acidic Chloride Solutions

E. McCafferty*¹ and Norman Hackerman*²

Department of Chemistry, The University of Texas, Austin, Texas 78700

ABSTRACT

The kinetics of active iron dissolution at 25°C has been studied in deaerated 1*N* and 6*N* chloride solutions for hydrogen ion concentrations of 0.1-6.0*N*. For 1*N* chloride solutions with $[H^+] \leq 3N$, the dissolution reaction is described by anodic Tafel slope $b_a = 60$ mV and electrochemical reaction order with respect to hydrogen ion activity $z_{H^+} = -1$. These parameters are characteristic of a dissolution mechanism in which chemisorbed halide ions interact with adsorbed hydroxyl ions in a two-electron rate-determining step. For 6*N* chloride solutions, this mechanism holds only over a narrower $[H^+]$ region up to 0.24*N*, in which $z_{H^+} = -1$. With increased $[H^+]$, z_{H^+} is zero; and for $[H^+] > 2.4N$, $z_{H^+} = +2$, indicating that the hydrogen ion (and no longer the hydroxyl ion) catalyzed the dissolution reaction. A positive value of z_{H^+} ensues for synergistic adsorption of hydrogen ions on the halide ion covered surface. A formal detailed dissolution mechanism is proposed, giving $z_{H^+} = +2$ and $z_{X^-} > 0$, in agreement with experiment. Alternate dissolution mechanisms including one-electron transfer schemes are discussed.

The kinetics and mechanism of iron dissolution in acids has been the subject of numerous investigations (1). Previous mechanistic studies in chloride solutions, however, have been with total chloride concentrations of 1*N* or less. Studies in this laboratory on organic corrosion inhibitors have commonly used concentrated HCl (3 to 6*N*) to provide a high uninhibited dissolution rate. The purpose of the present communication is to report recent investigations on the mechanism of iron dissolution in these deaerated, concentrated acidic chloride solutions.

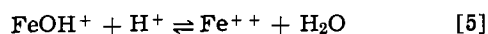
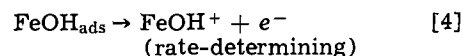
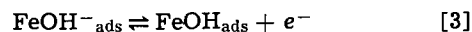
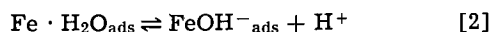
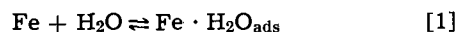
An important result is that with 6*N* chloride solutions at sufficiently low pH, synergistic effects between adsorbed anions and hydrogen ions in solution impose a different dissolution mechanism than is operative with more dilute chlorides. The difference in the mode of dissolution is that H^+ ions and not OH^- ions catalyze the anodic reaction, as is the case for 1*N* chloride solutions (2). Similar synergism has been recognized before between adsorbed halide ions and organic corrosion inhibitors (3-5).

The current work also bears on electrochemical processes which occur in microscopic corrosion pits growing on passive or oxide-covered iron surfaces. This application to pitting corrosion stems from the composition of local electrolyte within corrosion pit interiors. There have been many reports (6-9) that the local pH within growing pits and other "occluded corrosion cells" (10) is acidic, even when the bulk solution is neutral. An accumulation of chloride ions within the pit has been often postulated (6, 11, 12), although not yet experimentally verified. In addition, active pits are thought to be oxygen-free (7, 13). Thus the uniform dissolution of iron in deaerated concentrated acidic chlorides can serve as a scaled-up model of localized corrosion within active corrosion pits. Macroscopic models which simulate corrosion pits and other related forms of "occluded cell" corrosion have been used from the early 1940's (14) to the present (13, 15). The approach taken, however, has been the thermodynamic rather than kinetic one with emphasis on factors such as resultant pH and electrode potential, solution composition, and the like.

In order to relate the present work to previous kinetic studies, it will be helpful to briefly outline

prior work which bears on the present problem. It is generally recognized that there are two main types of dissolution mechanisms for active iron, depending on the nature of the solution anion. For solutions of weakly adsorbable anions, such as sulfate or perchlorate, dissolution proceeds through the dissociation of chemisorbed water molecules at the iron surface. Surface active anions, such as halide ions, on the other hand, are believed to participate directly in the dissolution process by adsorption at the metal surface.

Two different reaction mechanisms have been proposed for the anodic dissolution of iron in acidic sulfates and perchlorates (in the absence of halides). The more generally accepted Bockris-Kelly (16, 17) mechanism is



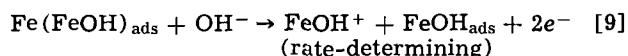
This sequence is characterized by the parameters

$$b_a = \left(\frac{\partial E}{\partial \log i_a} \right)_{a(H^+)} = \frac{2}{3} \cdot \frac{2.303 RT}{F} = 40 \text{ mV} \quad [6]$$

and

$$z_{H^+} = \left(\frac{\partial \log i_a}{\partial \log a(H^+)} \right)_E = -1 \quad [7]$$

A second group of investigators (18-20) has observed $b_a = 30$ mV and $z_{H^+} = -2$.³ In the Heusler mechanism which yields this set of parameters, Eq. [4] above is replaced by



Recent work (21, 22) has suggested that either mechanism can be followed, depending on the surface microstructure. A low density of grain boundaries and other imperfections favored the Bockris-Kelly mechanism, while a high density of imperfections yielded the Heusler mechanism.

³ Felloni (20) observed $z_{H^+} = -1.5$ rather than -2.0 and explained the fractional order on the basis of a Freundlich adsorption isotherm.

* Electrochemical Society Active Member.

¹ Present address: Metallurgy Division, Naval Research Laboratory, Washington, D. C. 20390.

² Present address: Department of Chemistry, Rice University, Houston, Texas 77001.

Key words: iron, corrosion, active dissolution, dissolution mechanisms, reaction orders, acids, chloride solutions.

As is well known, a salient feature of the above mechanisms is direct participation of hydroxyl ions in the dissolution process in bulk electrolytes which are acidic. The involvement of OH^- ions at the iron/acid interface was first suggested by Bonhoeffer and Heusler (23) to explain the experimental observations that at the same electrode potential, the rate of iron dissolution in acid solutions was less than that in basic solutions (24) and decreased in acid solutions with decreasing pH (25). The generation of OH^- ions in acid solutions is presumed to occur by dissociation of water molecules at the electrode surface (1, 17-27). In addition, the reaction mechanisms are directed toward production of the species FeOH^+ , which results from the hydrolysis of ferrous salts and "is present in significant concentrations even in relatively acid media" (28).

In the presence of the chloride ion, which is more surface active than SO_4^{2-} or ClO_4^- (4, 29), there is competitive adsorption between chloride and hydroxyl ions (30). Chloride adsorption will tend to prevail at high chloride activity and low pH; and accordingly, the dissolution mechanism will be different than in the Bockris-Kelly or Heusler cases. Fisher, Lorenz, and co-workers (2, 22, 31) have observed a change from Heusler parameters to the following for $\text{pH} < 1.5 - 2$

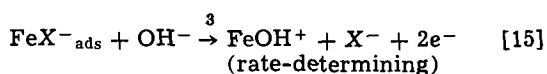
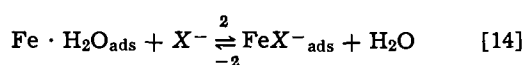
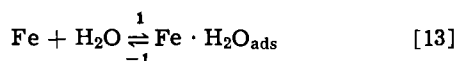
$$b_a = \left(\frac{\partial E}{\partial \log i_a} \right)_{a(\text{H}^+), a(\text{X}^-)} = \frac{2.303 RT}{F} = 60 \text{ mV} \quad [10]$$

$$z_{\text{H}^+} = \left(\frac{\partial \log i_a}{\partial \log a(\text{H}^+)} \right)_{E, a(\text{X}^-)} = -1 \quad [11]$$

$$z_{\text{X}^-} = \left(\frac{\partial \log i_a}{\partial \log a(\text{X}^-)} \right)_{E, a(\text{H}^+)} = -1 \quad [12]$$

Felloni (20) reports $b_a = 60 \text{ mV}$ (53 to 70) and $z_{\text{H}^+} \cong -1$ (-1.09 to -0.83) for $\text{pH} < 2$, with Bockris-Kelly parameters for $\text{pH} > 2$ for 1N chlorides. Arvia and Podesta (32) have proposed a reaction mechanism for chlorides analogous to Eq. [1]-[5], but their own data shows $b_a = 60 \text{ mV}$ (53 mV) for $\text{pH} = 1.78$ (33).

The following reaction sequence was first proposed by Lorenz, Yamaoka, Fisher (31) and developed in later publications (2, 22) to account for Eq. [10]-[12]



followed by Eq. [5]. Equations [13]-[15] will be referred to herein as the LYF mechanism for the sake of abbreviation. In this sequence, chemisorbed X^- ions displace adsorbed water molecules and then interact with adjacently adsorbed hydroxyls. It is necessary that the hydroxyl ion in Eq. [15] be adsorbed at a vacant site in order to give the required reaction order $z_{\text{X}^-} = -1$ (as $\theta_{\text{X}^-} \rightarrow 1$).

Other pertinent reaction mechanisms proposed in the literature will be considered after the present results have been presented. As mentioned earlier, kinetic studies have been lacking in more concentrated chloride solutions. An understanding of such systems is necessary before extension can be made to systems more complicated in composition (e.g., with organic inhibitors) or in geometry (corrosion pits, crevices, or stress-corrosion cracks).

Experimental

Experimental techniques have been described previously (34). In brief, the iron electrodes were Mallinckrodt analytical grade wire (99.5% Fe, 0.01% C, 0.03% Mn, 0.001% P, < 0.001% Si, 0.01% S). The wire was

Table I. Corrosion parameters for iron in concentrated hydrochloric acid

Normality HCl	i_{corr} ($\mu\text{A}/\text{cm}^2$)	Tafel slopes (mV)		E_{corr} (mV SCE)	γ_{\pm}	$\gamma_{\pm} \cdot m_{\text{H}^+}$
		b_a	$-b_c$			
1	48	70	110	-513	0.81	0.83
3	238	75	115	-492	1.37	4.38
4.8	837	70	110	-463	2.61	13.91
6	1982	70	110	-450	4.18	28.76

inserted through a close-fitting hole in a Teflon holder which fit into a standard tapered glass joint at the end of the electrode assembly. Electrical contact was made by means of mercury inside the tubing.

The wires were cut to a length of 2.0 cm to give a projected surface area of 0.227 cm^2 . Before use, an electrode was degreased with spectroscopic grade pentane and then electropolished at $85 \text{ mA}/\text{cm}^2$ for 2 min in a 4/1 mixture of HClO_4 : CH_3COOH . The electrode was then washed with double-distilled water and inserted into the polarization cell, which was the usual three-electrode type with provision for deaeration. Solutions were deaerated for at least 8 hr with helium passed through charcoal at -195°C and then through a solution identical to that being studied to minimize vapor loss of solution in the polarization cell. Polarization measurements were made galvanostatically with a 90V battery and series of variable resistors, as described earlier (34). Steady open-circuit potentials were established in 1-8 hr, the longer times being required for the more dilute solutions. For a given applied anodic current, a steady potential was usually observed in 2-5 min.

All solutions were prepared from reagent grade chemicals and double-distilled water prepared in a Barnstead still. Polarization measurements were made in three types of solutions: (i) 1-6N HCl, (ii) solutions with varying pH for 1N constant chloride ion concentration, and (iii) solutions with varying pH for 6N constant chloride ion concentration. In the last two types of solutions, the base electrolyte was HCl with either LiCl additions to increase the chloride ion concentration, or HClO_4 additions to increase the acidity.

Results

Hydrochloric acid.—Polarization curves for iron in concentrated HCl are shown in Fig. 1; kinetic parameters are summarized in Table I. The open-circuit cor-

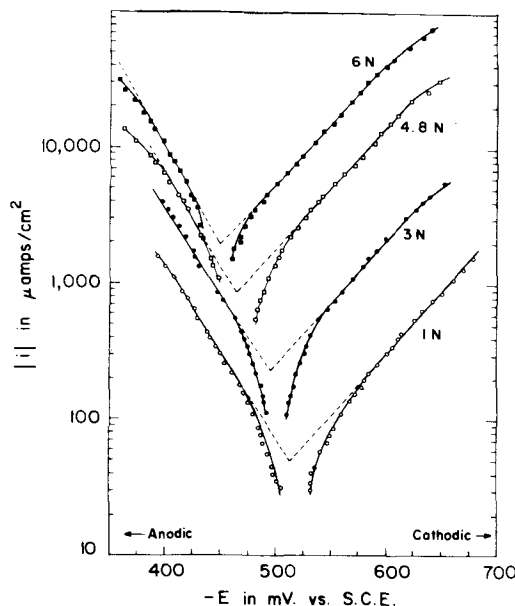


Fig. 1. Polarization curves for iron in hydrochloric acid of various concentrations at 25°C .

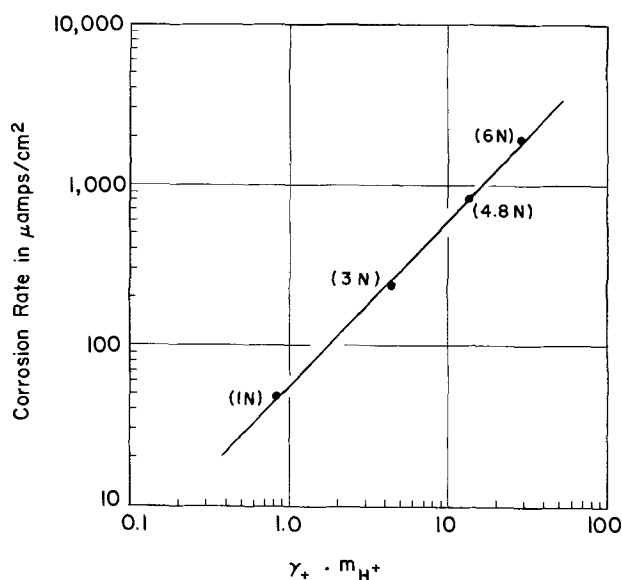


Fig. 2. Open-circuit corrosion rate of iron in hydrochloric acid as a function of hydrogen ion activity.

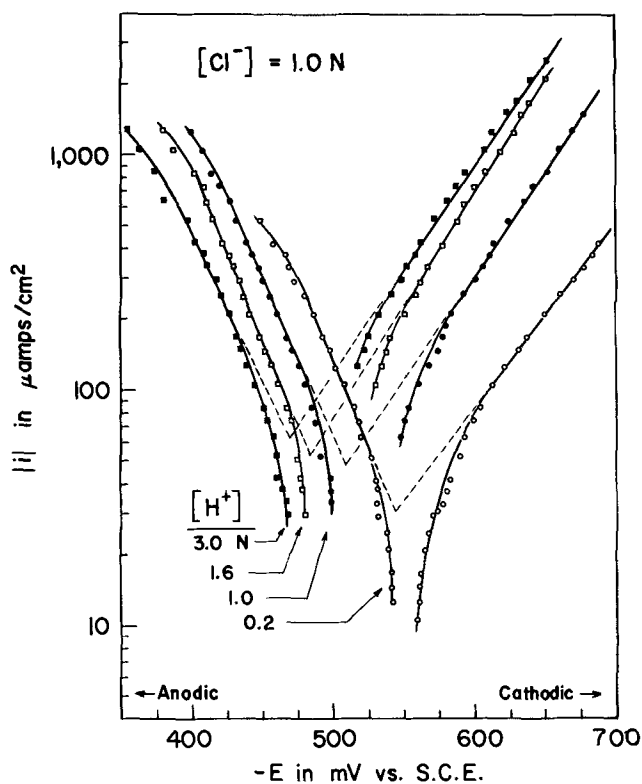


Fig. 3. Polarization curves for iron in 1N chloride solutions of varying acidity.

rosion rate of iron is a linear function of hydrochloric acid activity, as shown in Fig. 2. A similar linear dependence over a smaller activity range (1-8 molal) has been reported previously (35).

Activities plotted in Fig. 2 and listed in Table I are based on activity coefficients taken from Harned

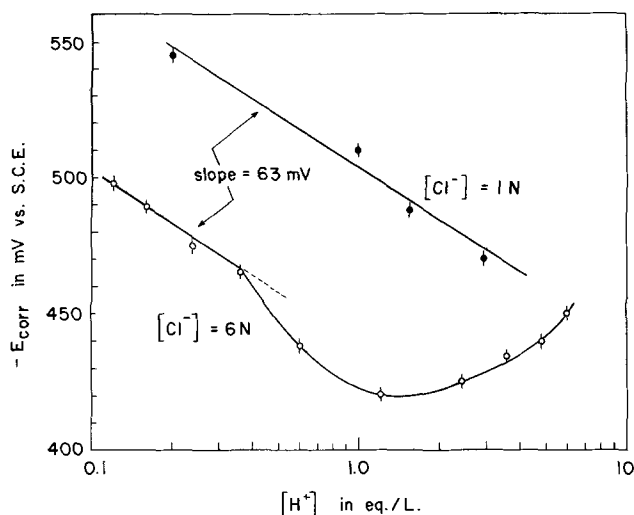


Fig. 4. Variation in the open-circuit corrosion potential with acidity for two different chloride ion concentrations.

and Owen (36). The activity of HCl a_{HCl} is given by $a_{HCl} = a_+ a_- = a_{\pm}^2$. As usual, $a_i = \gamma_i m_i$, where γ_i is the molal activity coefficient. Definition of the mean molal activity coefficient as $\gamma_{\pm}^2 = \gamma_+ \gamma_-$ gives $a_{\pm} = \gamma_{\pm} \cdot m_{HCl}$.

Little information on the dissolution mechanism can be inferred from Fig. 2, however, in that each of the three variables E , pH , and $[Cl^-]$ is different for each solution. Accordingly, solutions of constant chloride ion concentration were used.

1N chloride solutions.—Figure 3 shows anodic and cathodic polarization curves for iron in 1N chloride solutions of varying hydrogen ion concentration. The effect of decreased acidity is to shift the open-circuit corrosion potential E_{corr} to more negative potentials. The change in mixed potential with hydrogen ion concentration is: $(\partial E_{corr} / \partial pH) = -63$ mV, as shown in Fig. 4. Values of -51 mV (20) and -56 mV (37) have been reported previously.

Tafel slopes for 1N chloride solutions are listed in Table II. The cathodic Tafel slopes are the usual 120 ± 10 mV/decade (17). The anodic Tafel slopes are 65-70 mV/decade, in nominal agreement with the value of 60 mV, required by Eq. [10] (if $\alpha = 0.46-0.40$, rather than 0.50).

Figure 5 shows evaluation of the electrochemical reaction order with respect to the hydrogen ion. Our results gave z_{H^+} to be -0.7 rather than the theoretical value of -1.0 required by Eq. [11]. Mean molal activity coefficients γ_{\pm} of HCl with and without LiCl additions were calculated from Debye-Huckel theory using the equation (38)

$$\log \gamma_{\pm} = \frac{-0.354}{1 + A\sqrt{2C_T}} + B(2C_1) + B'(2C_T - 2C_1) - \log(1 + 0.036 m_T) \quad [16]$$

where C_T is the total molar concentration of the solution; C_1 the molar concentration of acid; m_T the total molality; and A , B , and B' are 0.747, 0.0864, and 0.0875, respectively. Activity coefficients for the HCl-HClO₄ mixtures were interpolated from the data of Storokin *et al.* (39). The electrochemical reaction order z_{H^+} for the cathodic reaction was $\sim +1$, as required by the usual mechanism of hydrogen evolution (17).

Table II. Corrosion parameters for iron in 1N chloride solutions

[H ⁺]	Solution (eq./liter)	$-E_{corr}$ (mV SCE)	i_{corr} ($\mu A/cm^2$)	b_a (mV)	$-b_c$ (mV)	m_{H^+}	γ_{\pm}	$\gamma_{\pm} \cdot m_{H^+}$
0.20	0.20 HCl + 0.80 LiCl	545	32	65	130	0.20	0.823	0.168
1.00	1.00 HCl	510	48	70	115	1.02	0.820	0.838
1.59	1.00 HCl + 0.59 HClO ₄	487	55	65	110	1.67	0.959	1.62
2.96	1.00 HCl + 1.96 HClO ₄	470	66	75	115	3.31	1.58	5.24

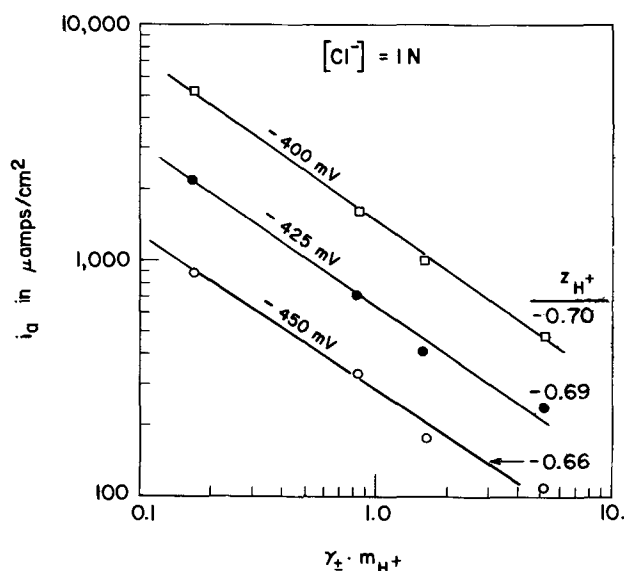


Fig. 5. Evaluation of the electrochemical reaction order

$$z_{H^+} = \left(\frac{\partial \log i_a}{\partial \log \alpha_{(H^+)}} \right)_{E, \alpha(X^-)} \text{ for } 1N \text{ chloride solutions.}$$

Thus, the anodic dissolution of Mallinkrodt iron wire is adequately described by the LYF mechanism, *i.e.*, Eq. [13]-[15] for solutions 1N in Cl^- with H^+ concentration up to 3N. For hydrogen ion concentrations above 3N, anodic Tafel slopes of 95 ± 5 mV/decade, rather than 60 mV, were observed. In these solutions, the high concentration of ClO_4^- ions may cause a change in reaction mechanism, but this aspect will not be considered here. The effect was the same if H_2SO_4 was used instead of $HClO_4$.

6N chloride solutions.—Representative polarization curves for solutions 6N in chloride ion with varying acidity are shown in Fig. 6 and 7. Polarization parameters are listed in Table III. Again, the cathodic Tafel slopes are 120 ± 10 mV. As with the 1N chloride solutions, the anodic Tafel slopes are generally 60-75 mV

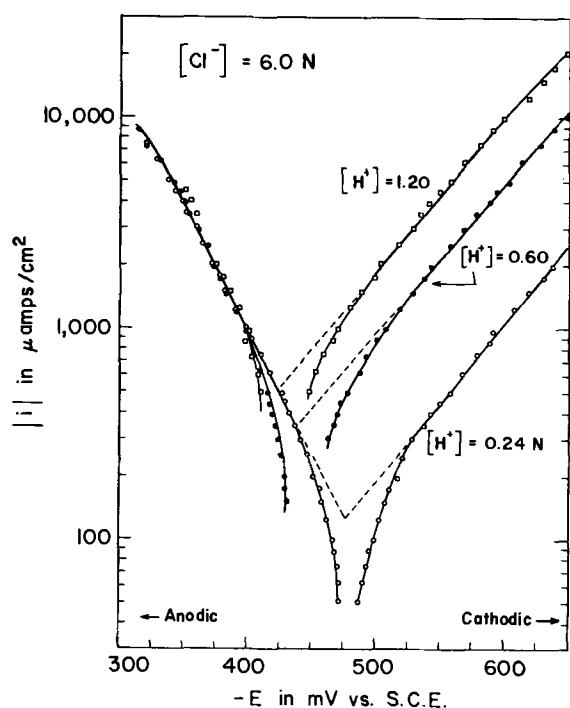


Fig. 6. Polarization curves for iron in 6N chloride solutions (for acidities where $z_{H^+} = 0$).

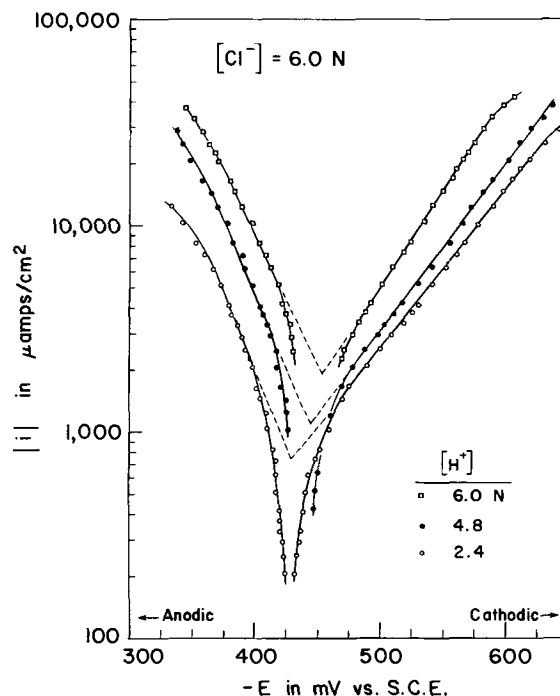


Fig. 7. Polarization curves for iron in 6N chloride solutions (for acidities where $z_{H^+} = +2$).

in accord with a 2-electron transfer (60 mV) mechanism of dissolution, if $\alpha = 0.50$ to 0.40.

Unlike the 1N chloride solutions, however, the corrosion potential does not shift uniformly with hydrogen ion concentration (see Fig. 4). This behavior suggests that the dissolution mechanism is not the same over the entire range of hydrogen ion concentrations shown.

This change in mechanism is evident in evaluation of z_{H^+} , as shown in Fig. 8, in which $\log i_a$ is plotted as a function of H^+ activity. Mean molal activity coefficients γ_{\pm} of hydrochloric acid in HCl-LiCl mixtures were calculated from Eq. [16] and are summarized in Table III.

As seen in Fig. 8, with increased proton activity, z_{H^+} equals in turn ca. -1 , 0 , and $+2$ (see Table IV). These changes in z_{H^+} with proton activity indicate changes in the dissolution mechanism with increased acidity.

For the lower H^+ activities, the kinetic parameters point to the LYF mechanism of iron dissolution. The experimental value of $z_{H^+} = -0.9$ compares well with the theoretical value of -1.0 , but the experimental Tafel slopes for these concentrated LiCl solutions are some 20 mV higher than the theoretical 60 mV value. However, the third kinetic parameter, the electrochemical reaction order with respect to halide ion was evaluated to be: $z_{X^-} = -1$, as required by Eq. [12]. This evaluation was based on but two data points, and is intended to show the trend rather than to be an exact value (See Table IV).

Table III. Corrosion parameters for iron in 6N chloride solutions

N HCl*	$-E_{corr}$ (mV SCE)	i_{corr} (μA / cm^2)	b_a (mV)	$-b_c$ (mV)	m_{HCl}	γ_{\pm}	$\gamma_{\pm} \cdot m_{H^+}$
0.12	498	106	80	130	0.14	4.094	0.57
0.16	488	127	85	130	0.18	4.090	0.74
0.24	475	128	85	135	0.27	4.093	1.11
0.36	465	145	75	130	0.36	4.089	1.47
0.60	438	317	80	140	0.68	4.085	2.78
1.20	420	529	75	140	1.37	4.071	5.58
2.40	425	748	60	135	2.74	4.046	11.09
3.60	435	925	60	120	4.11	4.024	16.53
4.80	440	1057	55	125	5.50	3.996	21.98
6.00	450	1982	70	115	6.84	3.977	27.20

* LiCl additions were used to maintain constant chloride ion concentration.

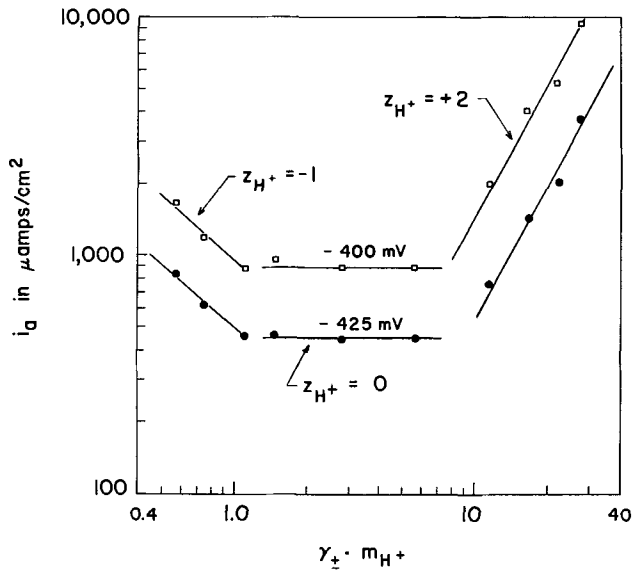


Fig. 8. Evaluation of the electrochemical reaction order

$$z_{H^+} = \left(\frac{\partial \log i_a}{\partial \log a_{(H^+)}} \right)_{E, a_{(X^-)}}$$
 for 6N chloride solutions.

With increased proton activity, there is a region in which $z_{H^+} = 0$, i.e., the anodic current density at constant electrode potential is independent of pH. At even higher proton activities, there is a synergistic effect between halide anions chemisorbed at the iron surface and hydrogen ions in solution. Hydrogen ions are electrostatically attracted toward the iron surface covered with Cl^- anions (3-5) and catalyze the dissolution reaction, as indicated by the positive value of z_{H^+} . In addition, evaluation of z_{X^-} based again on a limited amount of data gave $z_{X^-} = +0.62$ and $+0.91$ for two different electrode potentials (see Table IV).

Figure 9 shows evaluation of the electrochemical reaction order for the cathodic reaction. The hydrogen evolution reaction is first order in H^+ over the entire activity range studied, in agreement with Kelly (17).

Discussion

Mechanism of dissolution.—The following mechanism of dissolution is proposed to account for $z_{H^+} = +2$

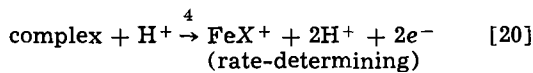
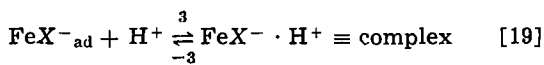
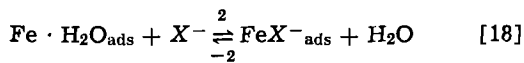
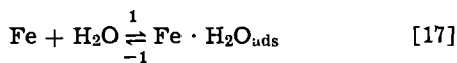


Table IV. Summary of electrochemical reaction orders

[Cl ⁻] (eq./liter)	[H ⁺] (eq./liter)	$z_{H^+} = \left(\frac{\partial \log i_a}{\partial \log a_{(H^+)}} \right)_{E, a_{(X^-)}}$	
		E = -400 mV	E = -425 mV
6.00	0.12-0.24	-0.90	-0.89
6.00	0.24-1.20	0	0
6.00	2.40-6.00	+1.82	+1.87
[Cl ⁻] (eq./liter)	[H ⁺] (eq./liter)	$z_{X^-} = \left(\frac{\partial \log i_a}{\partial \log [X^-]} \right)_{E, [H^+]}$	
		E = -400 mV	E = -425 mV
1.0-6.0	0.20	-0.85	-0.86
3.0-6.0	3.00	+0.91	+0.62

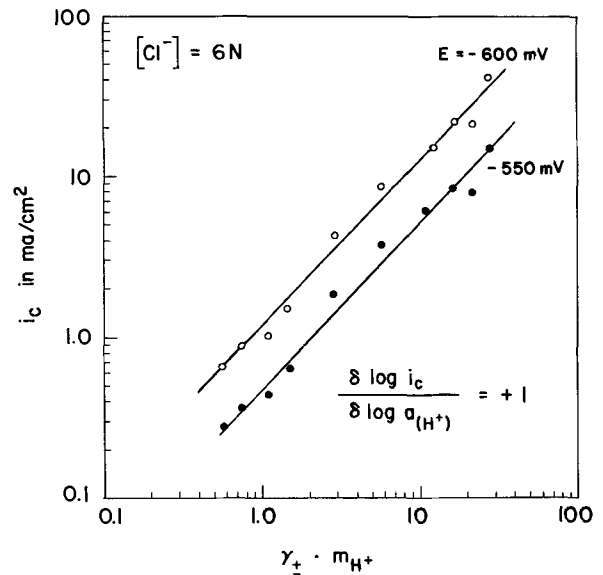
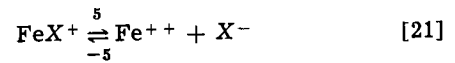


Fig. 9. Evaluation of the electrochemical reaction order

$$z_{H^+} = \left(\frac{\partial \log i_c}{\partial \log a_{(H^+)}} \right)_{E, a_{(X^-)}}$$
 for the cathodic reaction in 6N chloride solutions.



where FeX^+ represents a ferrous ion which is part of the metal surface but not the metal lattice.

The formal rate expression for the above sequence is derived as follows. The anodic current density is

$$\frac{i_a}{F} = 2 \bar{k}_4 \beta \theta_{\text{complex}} a_{(H^+)} \quad [22]$$

where

$$\bar{k}_i = k_i \exp(\pm \alpha n F E / RT) \quad [23]$$

with E the electrode potential, n the number of electrons transferred, α the transfer coefficient, and the plus and minus signs refer to the anodic and cathodic processes, respectively. The factor β is given by: $[FeX^+ \cdot H^+] = \beta \theta_{\text{complex}}$, where θ_{complex} is the fractional coverage (of the anodic surface) of the complex. These notations follow Kelly (17).

This system of equations [17]-[21] is described by

$$\beta \frac{d\theta_w}{dt} = \bar{k}_1(1 - \theta_T) - \bar{k}_{-1} \beta \theta_w - \bar{k}_2 \beta \theta_w a_{(X^-)} + \bar{k}_{-2} \beta \theta_{X^-} \quad [24]$$

$$\beta \frac{d\theta_{X^-}}{dt} = \bar{k}_2 \beta \theta_w a_{(X^-)} - \bar{k}_{-2} \beta \theta_{X^-} - \bar{k}_3 \beta \theta_{X^-} a_{(H^+)} + \bar{k}_{-3} \beta \theta_{\text{complex}} \quad [25]$$

$$\beta \frac{d\theta_{\text{complex}}}{dt} = \bar{k}_3 \beta \theta_{X^-} a_{(H^+)} - \bar{k}_{-3} \beta \theta_{\text{complex}} - \bar{k}_4 \beta \theta_{\text{complex}} a_{(H^+)} \quad [26]$$

where θ_w and θ_{X^-} are the fractional coverages of $Fe \cdot H_2O_{ads}$ and FeX^-_{ads} , respectively; and $\theta_T = \theta_w + \theta_{X^-} + \theta_{\text{complex}} \cong 1$. In the steady-state approximation, $\beta \frac{d\theta_i}{dt} = 0$. Simultaneous solution of Eq. [24]-[26] and [22] then yields

$$\frac{i_a}{F} = 2 k_4 \beta^2 a_{(H^+)}^2 \frac{k_1 k_2 k_3 a_{(X^-)}}{(k_1 + k_{-1} \beta) k_{-2} k_{-3} + k_1 k_2 a_{(X^-)} [k_{-3} + k_3 a_{(H^+)}]} \cdot \exp\left(\frac{FE}{RT}\right) \quad [27]$$

with $\alpha = 1/2$ and $\bar{k}_4 a_{(H^+)} \ll \bar{k}_{-3}$. The simultaneous equations also yield

$$\theta_{X^-} = \frac{k_1 k_2 k_{-3} a_{(X^-)}}{(k_1 + k_{-1\beta}) k_{-2} k_{-3} + k_1 k_2 a_{(X^-)} [k_{-3} + k_3 a_{(H^+)}]} \quad [28]$$

and

$$\theta_{\text{complex}} = \frac{k_1 k_2 k_3 a_{(H^+)} a_{(X^-)}}{(k_1 + k_{-1\beta}) k_{-2} k_{-3} + k_1 k_2 a_{(X^-)} [k_{-3} + k_3 a_{(H^+)}]} \quad [29]$$

If $\theta_{X^-} \gg \theta_{\text{complex}}$, it follows that $k_{-3} \gg k_3 a_{(H^+)}$ and Eq. [27] reduces to

$$\frac{i_a}{F} = 2\beta^2 \frac{k_4 k_3}{k_{-3}} a_{(H^+)}^2 \frac{k_1 k_2 a_{(X^-)}}{(k_1 + k_{-1\beta}) k_{-2} + k_1 k_2 a_{(X^-)}} \cdot \exp\left(\frac{FE}{RT}\right) \quad [30]$$

This expression yields $b_a = 60$ mV and

$$z_{H^+} = \left(\frac{\partial \log i_a}{\partial \log a_{(H^+)}}\right)_{E, a_{(X^-)}} = +2 \quad [31]$$

as required by experiment. Equation [30] also gives

$$z_{X^-} = \left(\frac{\partial \log i_a}{\partial \log a_{(X^-)}}\right)_{E, a_{(H^+)}} = \frac{(k_1 + k_{-1\beta}) k_{-2}}{(k_1 + k_{-1\beta}) k_{-2} + k_1 k_2 a_{(X^-)}} \quad [32]$$

With $\theta_{X^-} \gg \theta_{\text{complex}}$, θ_{X^-} is given as $k_1 k_2 a_{(X^-)} / [k_1 k_2 a_{(X^-)} + (k_1 + k_{-1\beta}) k_{-2}]$ so that $z_{X^-} = 1 - \theta_{X^-}$, and goes from 1 to 0 as θ_{X^-} goes from 0 to 1. Thus, $z_{X^-} > 0$ and not -1 , as in the LYF case for more dilute halide solutions, i.e., Eq. [13]-[15]. Evaluation of z_{X^-} based on a limited amount of data gave $z_{X^-} > 0$ for two different electrode potentials at $[H^+] = 3.0$ eq./liter (see Table IV).

Activity of water.—The above derivation and its application has assumed that the water activity a_w is constant. To be rigorous, the factor a_w should be included in terms k_1 and k_{-2} arising from steps [17] and [18]. In addition, the water activity would affect electrochemical reaction orders, e.g.

$$z_{H^+} = \left(\frac{\partial \log i_a}{\partial \log a_{(H^+)}}\right)_{E, a_{(X^-)}, a_w} \quad [33]$$

The water activity is given by (35)

$$\ln a_w = -\frac{2m\phi}{55.1} \quad [34]$$

where ϕ is the osmotic coefficient of HCl + LiCl mixtures of total molality m . Values of ϕ for mixtures of $m = 4$ were calculated from osmotic coefficients of pure LiCl and pure HCl in water using relationships developed by Harned (40, 41). Results are given in Table V. Appropriate data were not available to make these calculations at $m = 6.8$. But Table V shows that for concentrated chlorides, the activity of water a_w is

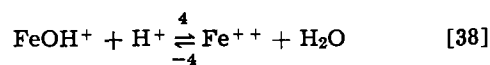
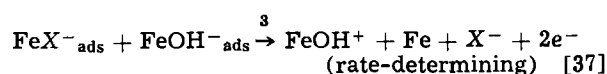
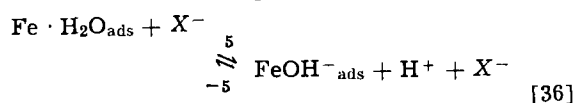
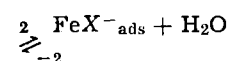
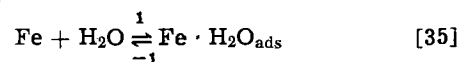
Table V. Activity of water in the system LiCl-HCl-H₂O at total molality $m = 4.0$

m_{HCl}	ϕ	a_w
0	1.449	0.812
0.1	1.452	0.811
0.5	1.462	0.810
1.0	1.474	0.809
2.0	1.494	0.806
3.0	1.510	0.804
4.0	1.519	0.803

virtually constant in the system LiCl-HCl-H₂O. Thus, the water activity does not complicate diagnosis of the reaction mechanism.

Competitive adsorption.—That different dissolution mechanisms are followed within the 6N chloride level for high and for low proton activities is due to competitive adsorption between OH⁻ and X⁻ ions. At the higher acidities, OH⁻ adsorption is not favored and the dissolution precursor will not be FeOH⁺, as in the LYF mechanism. Instead, adsorption of X⁻ predominates, and the corrosion reaction is catalyzed by H⁺ ions electrostatically attracted to the negative halide-covered surface (3-5).

This competitive adsorption can be emphasized by rewriting the LYF mechanism of corrosion, Eq. [13]-[15] as follows



The anodic current density is

$$\frac{i_a}{F} = 2\bar{k}_3\beta\theta_{\text{OH}^-}\theta_{X^-} \quad [39]$$

and, at equilibrium

$$\beta \frac{d\theta_w}{dt} = \bar{k}_1(1 - \theta_T) - \bar{k}_{-1}\beta\theta_w - \bar{k}_2\beta\theta_w a_{(X^-)} + \bar{k}_{-2}\beta\theta_{X^-} - \bar{k}_5\beta\theta_w a_{(X^-)} + \bar{k}_{-5}\beta\theta_{\text{OH}^-} a_{(H^+)} a_{(X^-)} = 0 \quad [40]$$

$$\beta \frac{d\theta_{X^-}}{dt} = \bar{k}_2\beta\theta_w a_{(X^-)} - \bar{k}_{-2}\beta\theta_{X^-} - \bar{k}_3\beta\theta_{\text{OH}^-}\theta_{X^-} = 0 \quad [41]$$

$$\beta \frac{d\theta_{\text{OH}^-}}{dt} = \bar{k}_5\beta\theta_w a_{(X^-)} - \bar{k}_{-5}\beta\theta_{\text{OH}^-} a_{(H^+)} a_{(X^-)} - \bar{k}_3\beta\theta_{\text{OH}^-}\theta_{X^-} = 0 \quad [42]$$

Solution of Eq. [40]-[42] subject to $v_3 \ll v_{-5}$, $v_3 \ll v_{-2}$, and $\theta_T \cong \theta_w + \theta_{X^-}$ gives

$$\frac{i_a}{F} = 2\beta^2 \frac{k_1^2 k_2 k_3 k_5 k_{-2} a_{(X^-)}}{[(k_1 + k_{-1\beta}) k_{-2} + k_1 k_2 a_{(X^-)}]^2 k_{-5} a_{(H^+)}} \exp\left(\frac{FE}{RT}\right) \quad [43]$$

with $\alpha = 1/2$. Equations [43] yields $b_a = 60$ mV, $z_{H^+} = -1$, and $z_{X^-} = -1$ (as $\theta_{X^-} \rightarrow 1$), in accord with Eq. [10]-[12]. But in addition, the simultaneous Eq. [40]-[42] can also be solved for the surface coverage of hydroxyl ions FeOH⁻_{ads}. The result

$$\theta_{\text{OH}^-} = \frac{k_1 k_5 k_{-2}}{k_{-5} a_{(H^+)} [(k_1 + k_{-1\beta}) k_{-2} + k_1 k_2 a_{(X^-)}]} \quad [44]$$

shows that the coverage of adsorbed hydroxyl ions depends upon the bulk concentrations of both bulk H⁺ and X⁻. For a given chloride level, θ_{OH^-} decreases with increasing acidity. The present experimental results infer that for $[X^-] = 6N$, corrosion does not pro-

ceed through $\text{FeOH}^-_{\text{ads}}$ when $[\text{H}^+] > 2.4N$. For a given acidity, θ_{OH^-} is the higher for lower chloride concentrations. At $[\text{H}^+] = 2.4N$, for example, corrosion of iron in 1N chlorides proceeds through $\text{FeOH}^-_{\text{ads}}$ and not $\text{FeX}^+_{\text{ads}}$, as in 6N chloride (compare Fig. 5 and 8).

Another improvement in rewriting the LYF scheme is that the sequence [35]-[38] shows clearly the origin of chemisorbed hydroxyls to be the dissociation of adsorbed water molecules. The LYF mechanism is ambiguous in this regard in that the hydroxyl ion is represented as a free solution species, i.e., Eq. [15]. In fact the hydroxyl "ion" must be adsorbed at a vacant site to give $z_{\text{X}^-} = -1$ (as $\theta_{\text{X}^-} \rightarrow 1$). That is in the LYF scheme, Eq. [13]-[15], it is necessary to write

$$\frac{i_a}{F} = 2\bar{k}_3\beta\theta_{\text{X}^-}a_{(\text{OH}^-)}(1 - \theta_{\text{X}^-}) \quad [45]$$

and

$$\beta \frac{d\theta_{\text{X}^-}}{dt} = \bar{k}_2\beta\theta_{\text{w}}a_{(\text{X}^-)} - \bar{k}_{-2}\beta\theta_{\text{X}^-} - \bar{k}_3\beta\theta_{\text{X}^-}a_{(\text{OH}^-)}(1 - \theta_{\text{X}^-}) = 0 \quad [46]$$

with

$$\beta \frac{d\theta_{\text{w}}}{dt} = \bar{k}_1(1 - \theta_{\text{T}}) - \bar{k}_{-1}\beta\theta_{\text{w}} - \bar{k}_2\beta\theta_{\text{w}}a_{(\text{X}^-)} + \bar{k}_{-2}\beta\theta_{\text{X}^-} = 0 \quad [47]$$

When $v_3 \ll v_{-2}$, and $\theta_{\text{T}} = \theta_{\text{w}} + \theta_{\text{X}^-} \cong 1$, the resulting expression for i_a is similar to Eq. [43] except that $k_1k_3/k_{-5}a_{(\text{H}^+)}$ is replaced by $(k_1 + k_{-1}\beta)a_{(\text{OH}^-)}$. Both forms yield Eq. [10]-[12].

Identity relations.—Internal consistency can be checked through the following identity (17, 42) which relates several experimental variables

$$\left(\frac{\partial \log i_a}{\partial \log a_{(\text{H}^+)}} \right)_{E, a_{(\text{X}^-)}} = - \frac{\left(\frac{\partial E}{\partial \log a_{(\text{H}^+)}} \right)_{i_a, a_{(\text{X}^-)}}}{\left(\frac{\partial E}{\partial \log i_a} \right)_{a_{(\text{H}^+)}, a_{(\text{X}^-)}}} \quad [48]$$

With $E = \eta + E_{\text{corr}}$

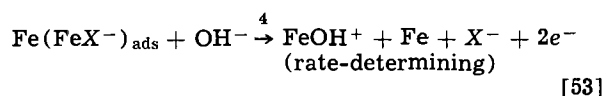
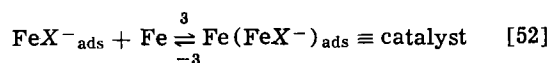
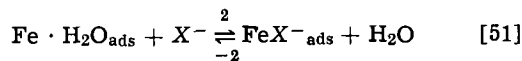
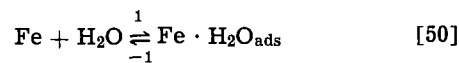
$$z_{\text{H}^+} = - \frac{1}{b_a} \left\{ \left(\frac{\partial \eta}{\partial \log a_{(\text{H}^+)}} \right)_{i_a, a_{(\text{X}^-)}} + \left(\frac{\partial E_{\text{corr}}}{\partial \log a_{(\text{H}^+)}} \right)_{a_{(\text{X}^-)}} \right\} \quad [49]$$

Figure 10 shows η and E_{corr} as functions of proton activity, and Table VI evaluates the identity from the experimental data.

Discussion of other possible mechanisms.—The observation that hydrogen ions catalyze iron dissolution at high $[\text{H}^+]$ and $[\text{Cl}^-]$, i.e., $z_{\text{H}^+} = +2$, is new. For the more familiar case of OH^- participation with $z_{\text{H}^+} = -1$, mechanisms other than LYF, i.e., Eq. [13]-[15] or the modified form, Eq. [35]-[38], have been proposed and are discussed briefly below.

Lorenz (2) has suggested that an $\text{Fe}(\text{FeX}^-)_{\text{ads}}$ catalyst participates in the 60 mV mechanism at low pH

similarly to the $\text{Fe}(\text{FeOH})_{\text{ads}}$ catalyst of the Heusler mechanism. The reaction scheme is



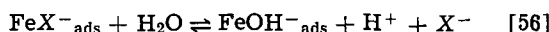
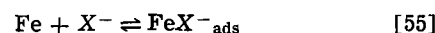
followed by Eq. [5]. If this mechanism proceeds completely analogously to the $\text{Fe}(\text{FeOH})_{\text{ads}}$ catalyst mechanism; Eq. [8] and [9], then the OH^- in step [53] must react directly with the $\text{Fe}(\text{FeX}^-)_{\text{ads}}$ surface catalyst. The resulting rate equation which we derive is

$$\frac{i_a}{F} = 2\beta \frac{k_3k_4a_{(\text{OH}^-)}}{k_{-3}} \cdot \frac{k_1k_2a_{(\text{X}^-)}}{(k_1 + k_{-1}\beta)k_{-2} + k_1k_2a_{(\text{X}^-)}} \cdot \exp\left(\frac{FE}{RT}\right) \quad [54]$$

with $\theta_{\text{X}^-} = k_1k_2a_{(\text{X}^-)}/[(k_1 + k_{-1}\beta)k_{-2} + k_1k_2a_{(\text{X}^-)}]$. Necessary assumptions required to give Eq. [54] are $v_{-3} \gg v_4$ and $\theta_{\text{T}} \cong \theta_{\text{w}} + \theta_{\text{X}^-}$. Equation [54] gives $b_a = 60$ mV and $z_{\text{H}^+} = -1$, as required, but not $z_{\text{X}^-} = -1$. As θ_{X^-} goes from 0 to 1, z_{X^-} goes from 1 to 0, and is never negative, in disagreement with the experimental data (2, 22, 31). To get $z_{\text{X}^-} = -1$, the OH^- ion in Eq. [53] must not react directly from solution with the "catalyst" $\text{Fe}(\text{FeX}^-)_{\text{ads}}$, but is required to first adsorb at the surface at vacant sites, as was the case with Eq. [15] in the LYF mechanism. The corresponding rate equation will not be detailed here, as the derivation is similar to the LYF case. With the same assumptions outlined following Eq. [54] plus $k_3 \cong k_{-3}$ the amended rate expression will give $z_{\text{X}^-} = -1$ as $\theta_{\text{X}^-} \rightarrow 1$. Now, however, the catalytic effect has been removed; and the mechanism is essentially the same as Eq. [13]-[15] except that an unnecessary additional step has been interposed between the adsorption of halide ions and their reaction with hydroxyl ions.

One possible drawback of the mechanisms proposed by Lorenz, Yamaoka, and Fisher (31) and in the present work is the two-electron transfer step. This aspect will be considered after several one-electron transfer mechanisms have first been discussed.

Arvia and Podesta (32) have recently proposed a mechanism involving two successive one-electron transfers similar to the Bockris-Kelly mechanism in the absence of halide ions, i.e., Eq. [1]-[5]. The Arvia and Podesta scheme is



followed by Eq. [3]-[5]. The rate expression derived by Arvia and Podesta yields $b_a = 40$ mV and $z_{\text{X}^-} = 0$. The first result is in disagreement with much evidence (including the present work) that $b_a = 60$ mV for pH

Table VI. Evaluation of Eq. [46]

No. of runs	z_{H^+}	(A) $\left(\frac{\partial \eta}{\partial \log a_{(\text{H}^+)}} \right)_{i_a, a_{(\text{X}^-)}}$	(B) $\left(\frac{\partial E_{\text{corr}}}{\partial \log a_{(\text{H}^+)}} \right)_{a_{(\text{X}^-)}}$	(C) b_a	$z_{\text{H}^+} = - \frac{(A) + (B)}{(C)}$
3	-0.9	0 mV	+72 mV	85 mV	-0.85
4	0.0	-76 mV	+79 mV	79 mV	+0.04
4	+1.8	-43 mV	-65 mV	61 mV	1.77

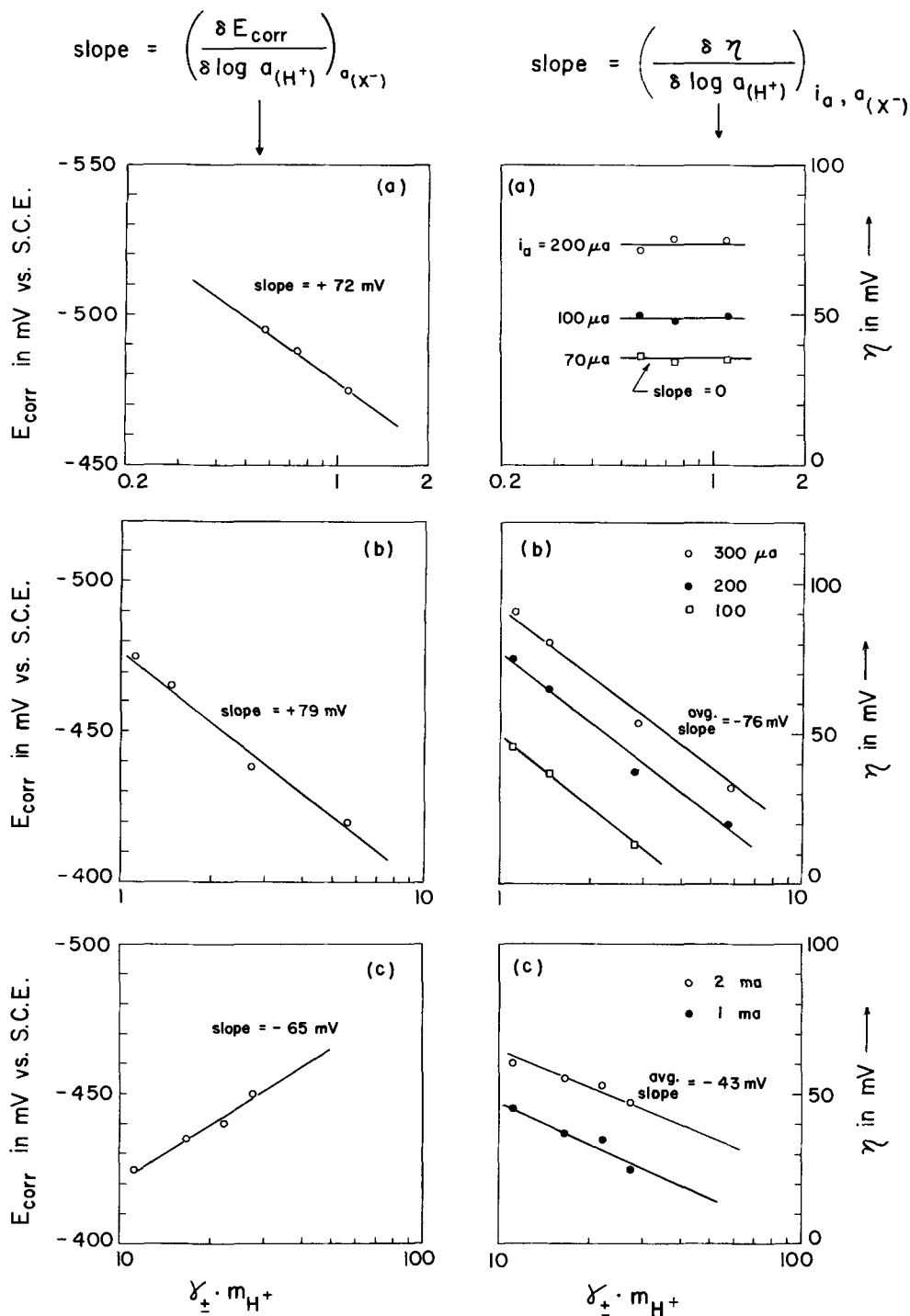
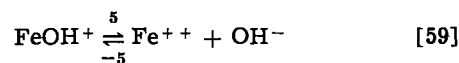
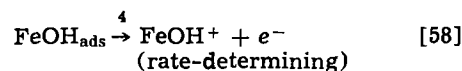
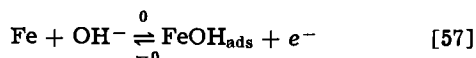


Fig. 10. Evaluation of $\left(\frac{\partial E_{\text{corr}}}{\partial \log a_{(\text{H}^+)}} \right)_{a_{(\text{X}^-)}}$ and $\left(\frac{\partial \eta}{\partial \log a_{(\text{H}^+)}} \right)_{i_a, a_{(\text{X}^-)}}$ for 6N chlorides in the region where (a) $x_{\text{H}^+} = -1$, (b) $x_{\text{H}^+} = 0$, and (c) $x_{\text{H}^+} \cong +2$.

less than 1.5-2 (2, 20, 22, 31). As mentioned previously, Podesta and Arvia (33) themselves earlier listed $b_a \cong 60$ mV (54 mV) for pH = 1.78 and $[\text{Cl}^-] = 2M$. The prediction that $x_{\text{X}^-} = 0$ is also in disagreement with experiments (20, 22, 31) and with the general observation that halide ions inhibit acid dissolution of iron (4). Thus, the above mechanism is not without drawbacks.

A recent attempt to extrude a 60 mV Tafel slope from consecutive single-electron transfer steps has been made by Asakura and Nobe (43) on the basis of Temkin adsorption. To examine their approach, it is helpful to first reconstruct the mathematics. These authors wrote the Bockris-Kelly mechanism for dissolution in alkaline solutions as



The above sequence is of interest to the present work as the halide ion X^- could conceivably play the role of OH^- in Eq. [57]-[59]. Asakura and Nobe consider the species FeOH_{ads} to follow Temkin rather than Langmuir adsorption. Thus

$$\frac{i_a}{F} = \bar{k}_0' (1 - \theta_{\text{OH}}) a_{(\text{OH}^-)} e^{-[\Delta G_1 + \gamma f(\theta) RT]/RT} + \bar{k}_{-0}' \beta \theta_{\text{OH}} e^{-[\Delta G_{-1} - (1-\gamma) f(\theta) RT]/RT} + \bar{k}_4' \beta \theta_{\text{OH}} e^{-[\Delta G_3 - (1-\delta) f(\theta) RT]/RT} \quad [60]$$

where \bar{k}_i has the same meaning as before and is given here as $\bar{k}_i e^{-\Delta G_i / RT}$, with γ , δ , and $f(\theta)$ the Temkin parameters. See Ref. (43, 44). The steady-state expression for FeOH_{ads} is

$$\beta \frac{d\theta_{\text{OH}}}{dt} = \bar{k}_0(1 - \theta_{\text{OH}})a_{(\text{OH}^-)}e^{-\gamma f(\theta)} - \bar{k}_{-0}\beta\theta_{\text{OH}}e^{(1-\gamma)f(\theta)} - \bar{k}_3\beta\theta_{\text{OH}}e^{(1-\delta)f(\theta)} = 0 \quad [61]$$

With $v_{-0} \gg v_4$, the above expression was solved for $f(\theta)$

$$f(\theta) = \ln \left[\frac{\bar{k}_0}{\bar{k}_{-0}} a_{(\text{OH}^-)} \right] \quad [62]$$

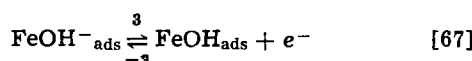
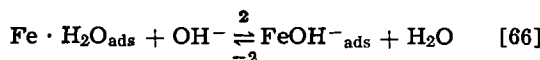
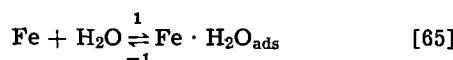
assuming $\ln \theta_{\text{OH}}/(1 - \theta_{\text{OH}})$ to be negligible at intermediate coverages compared to $f(\theta)$ (45). The current density follows as

$$\frac{i_a}{F} = 2\bar{k}_4\beta\theta_{\text{OH}} \left[\frac{\bar{k}_0}{\bar{k}_{-0}} a_{(\text{OH}^-)} \right]^{(1-\gamma)} \quad [63]$$

Recall that $\bar{k}_i = k_i e^{\pm \alpha nFE/RT}$. With both α and γ taken as $1/2$, Eq. [63] gives

$$\frac{i_a}{F} = 2 \left(\frac{k_0}{k_{-0}} \right)^{1/2} k_4\beta\theta_{\text{OH}}a_{(\text{OH}^-)}^{1/2} \cdot \exp \left(\frac{FE}{RT} \right) \quad [64]$$

Although this expression apparently yields $b_a = 60$ mV, it should be noted that θ_{OH} was not solved explicitly in terms of k . Moreover, the reaction sequence [57]-[59] fails to consider that the electrode surface is water-covered and that adsorption of solution anions is a replacement reaction [46]-[48]. If Eq. [57] is rewritten as

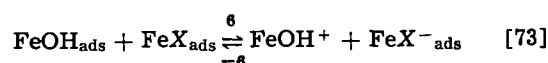
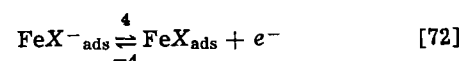
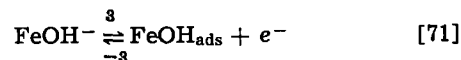
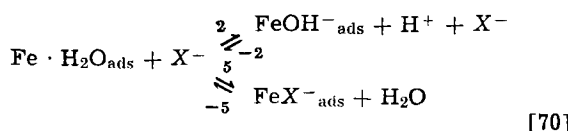
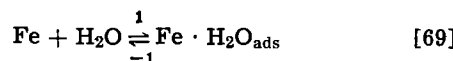


followed by Eq. [58] and [59], a different Tafel slope ensues. The result is

$$\frac{i_a}{F} = 2k_4\theta_{\text{OH}} \left(\frac{k_1}{k_{-1}} \right)^{1/2} \cdot \exp \left(\frac{FE}{2RT} \right) \quad [68]$$

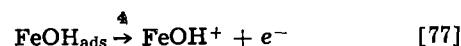
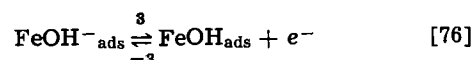
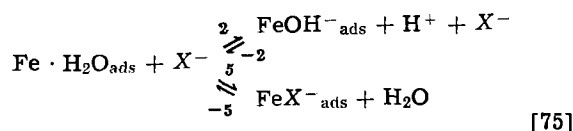
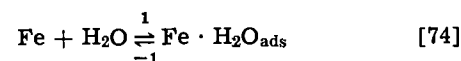
The necessary conditions are $v_{-3} \gg v_4$ and $e^{f(\theta)} \gg \theta_{\text{W}}/(1 - \theta_{\text{T}})$. Solution of steady-state kinetics for Eq. [65]-[67] and [58] is similar to the Asakura-Nobe case with the addition that the Temkin parameter $f(\theta)$ vanishes from the exponential for step [67] which involves adsorbate-adsorbate interaction rather than an adsorption or desorption step. The fact that Eq. [68] yields $b_a = 120$ mV when Eq. [64] is modified only to account for the precoverage of the electrode by adsorbed water casts doubt that 60 mV Tafel slopes can be explained on the basis of Temkin adsorption in the Bockris-Kelly mechanism.

Another one-electron transfer scheme which will not explain the experimental results involves a disproportionation reaction similar to that considered by Lovrecek and Marincic (49) for cadmium dissolution. Suppose

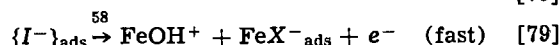
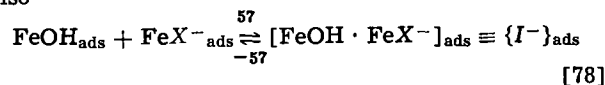


If step 6 is rate-determining, the back reaction should be discounted. With $v_{-3} \gg v_6$ and $v_{-4} \gg v_6$, and $\theta_{\text{T}} = \theta_{\text{W}} + \theta_{\text{X}^-}$, the resulting rate equation gives $z_{\text{H}^+} = -1$, $z_{\text{X}^-} = -1$ (as $\theta_{\text{X}^-} \rightarrow 1$), but $b_a = 30$ mV. If step 3 is rate-determining, the -3 reaction is ignored. With $v_3 \ll v_6$ and $v_3 \ll v_{-2}$ and θ_{T} as before, the resulting rate expression will give the correct values of z_{H^+} and z_{X^-} , but will also give $b_a = 120$ mV rather than 60 mV. If step 4 is rate-determining, similar considerations give not only $b_a = 120$ mV, but also z_{H^+} and $z_{\text{X}^-} = 0$, all of which are inconsistent with experimental data.

One mechanism with successive one-electron transfers does have some merit, however, as it can explain some but not all of the present results. This mechanism involves Eq. [1]-[3] of the Bockris-Kelly mechanism in parallel with the formation of a surface complex between FeOH_{ads} and the halide ion



Also



This scheme is the same as that given by Kelly for the effect of the benzoate anions on iron dissolution in sulfuric acid (50). Here X^- plays the role of Bz^- in Ref. (50). The resulting rate equation is

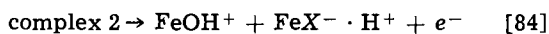
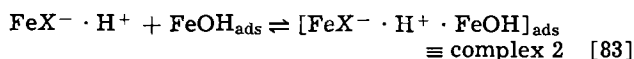
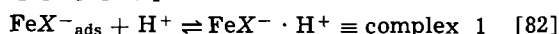
$$\frac{i_a}{F} = 2\beta \frac{k_1 k_2 k_3 k_4}{k_{-2} k_{-3} a_{(\text{H}^+)}} \cdot \frac{k_{-5}}{k_1 k_5 a_{(\text{X}^-)} + k_{-5}(k_1 + k_{-1}\beta)} \exp \left(\frac{3FE}{2RT} \right) + 2\beta^2 k_{57} \frac{k_1 k_2 k_3 k_{-5}}{k_{-2} k_{-3} a_{(\text{H}^+)}} \cdot \frac{k_1 k_5 a_{(\text{X}^-)}}{[k_1 k_5 a_{(\text{X}^-)} + k_{-5}(k_1 + k_{-1}\beta)]^2} \exp \left(\frac{FE}{RT} \right) \quad [80]$$

with the necessary conditions being $\bar{k}_{58} \gg \bar{k}_{-57}$, $v_{-3} \gg v_4 + v_{58}$, and $\theta_{\text{T}} \approx \theta_{\text{W}} + \theta_{\text{X}^-}$. For details see Ref. (50). With $\theta_{\text{X}^-} = k_1 k_5 a_{(\text{X}^-)} / [k_1 k_5 a_{(\text{X}^-)} + k_{-5}(k_1 + k_{-1}\beta)]$, the first term on the right hand side of Eq. [80] can be recast as $i_{a, \theta_{\text{X}^-} = 0} \cdot (1 - \theta_{\text{X}^-})$, as noted by Kelly (50), so that Eq. [80] can be abbreviated as

$$i_a = i_{a, \theta_{\text{X}^-} = 0} (1 - \theta_{\text{X}^-}) + i_a^* \quad [81]$$

If $v_{58} \gg v_4$, then $i_a = i_a^*$ and Eq. [80] yields Eq. [10]-[12]. It may be noted that if the desorption of the halide ion is the slow step ($k_{58} \ll k_{-57}$), the ensuing Tafel slope will revert to 40 mV.

If the electrostatic attraction of H^+ ions for FeX^-_{ads} is considered, the reaction mechanism may be modified to be Eq. [74]-[77] plus



With $\bar{k}_{84}a_{(H^+)} \gg \bar{k}_{-83}$, $\theta_T \cong \theta_W + \theta_{X^-}$, $v_{-3} \gg v_4 + v_{84}$, and $v_{84} \gg v_4$, the result is

$$\frac{i_a}{F} = 2\beta^2 \frac{k_{83}k_{82}}{k_{-82}} \cdot \frac{k_1k_2k_3k_{-5}}{k_{-2}k_{-3}} \cdot \frac{k_1k_5a_{(X^-)}}{[k_1k_5a_{(X^-)} + k_{-5}(k_1 + k_{-1}\beta)]^2} \cdot \exp\left(\frac{FE}{RT}\right) \quad [85]$$

which gives $b_a = 60$ mV, $z_{H^+} = 0$, and $z_{X^-} = -1$ (as $\theta_{X^-} \rightarrow 1$). The first two parameters correspond to the middle region of Fig. 8 (z_{X^-} was not determined experimentally).⁴ However, this system of parallel reactions cannot be extended to explain synergistic dissolution where $z_{H^+} = +2$. To get $z_{H^+} = +2$, it is necessary that a total of three hydrogen ions participate in steps [82] and [83], e.g., three H^+ ions could be electrostatically attracted to FeX^-_{ads} . This occurrence seems unlikely. It should be noted that the number j of H^+ ions (if any) participating in step [84] is unimportant as the term $\bar{k}_{84}(\beta\theta_{\text{complex 2}})a_{(H^+)^j}$ is recast in terms of \bar{k}_{83} in the steady-state solutions of the dissolution kinetics for Eq. [74]-[77] together with [82]-[84].

Thus, at present it is difficult to interpret the total experimental results reported herein without invoking the concept of the two-electron transfer step. According to one point of view (51), the probability of two electrons tunneling simultaneously between the metal and an ion is low enough to be prohibitive. However, this question still remains open as the theoretical treatment of electron tunneling at the electrode/solution interface in the presence of "adsorbed" species is not yet well-developed. The rate constant is given by (52)

$$k = \frac{k_B T}{h} \chi_e \exp\left(\frac{-E^*}{RT}\right) \quad [86]$$

with χ_e the probability of electron tunneling. Thus, a lower probability of tunneling ($\chi_e < \chi_e^2$) could be coupled with a lower activation energy E^* (possibly caused by adsorbed chloride) to give a rate comparable to a higher probability coupled with a higher activation energy.

The two-electron transfer step has in fact been shown to be possible for Tl(I)-Tl(III) exchange in solution (52), and is thought possible when the reaction is catalyzed by a platinum black surface (53). Within the past year, two-electron transfer steps have been proposed for the dissolution of tungsten in NaOH (54) and for zinc in water-propanol mixtures (55). To cite another case, Timmers, Sluyters-Rehbach, and Sluyters (56) are of the opinion that Zn^+ is not a stable intermediate at the zinc amalgam electrode, which instead reacts in a two-electron step. Hampson and co-workers (57) have recently proposed that for PbO_2 in alkali, the charge transfer at low overvoltage is a two-electron transfer step.

Summary

An important feature of the present results is that iron dissolution at high $[H^+]$ and $[Cl^-]$ is promoted by hydrogen ions rather than by hydroxyls. A detailed mechanism has been proposed involving electrostatic attraction of H^+ ions to chemisorbed halide ions. Various reaction mechanisms which have appeared in the

literature have been discussed and have been shown to be either inadequate or inapplicable.

Acknowledgment

The authors are grateful to the Robert A. Welch Foundation of Houston, Texas, for financial support of this work.

Manuscript submitted Sept. 24, 1971; revised manuscript received March 24, 1972.

Any discussion of this paper will appear in a Discussion Section to be published in the June 1973 JOURNAL.

REFERENCES

1. For a recent review, see: G. M. Florianovich, L. A. Sokolova, and Ja. M. Kolotyrlin, *Soviet Electrochem.*, **3**, 1027 (1967).
2. W. J. Lorenz, *Corrosion Sci.*, **5**, 121 (1965).
3. T. Murakawa and N. Hackerman, *ibid.*, **4**, 387 (1964).
4. N. Hackerman, E. S. Snavelly, Jr., and J. S. Payne, Jr., *This Journal*, **113**, 677 (1966).
5. (a) T. Murakawa, S. Nagaura, and N. Hackerman, *Corrosion Sci.*, **7**, 79 (1967); (b) T. Murakawa, T. Kato, S. Nagaura, and N. Hackerman, *ibid.*, **8**, 463 (1968).
6. N. D. Greene and M. G. Fontana, *Corrosion*, **15**, 25t (1959).
7. G. J. Schafer, J. R. Gabriel, and P. K. Foster, *This Journal*, **107**, 1002 (1960).
8. Ja. M. Kolotyrlin, *Corrosion*, **19**, 261t (1963).
9. B. F. Brown, C. T. Fujii, and E. P. Dahlberg, *This Journal*, **116**, 218 (1969).
10. B. F. Brown, *Corrosion*, **26**, 249 (1970).
11. N. D. Greene and G. Judd, *ibid.*, **21**, 15 (1965).
12. D. A. Vermilyea, *This Journal*, **118**, 529 (1971).
13. M. Pourbaix, CEBELCOR Rt. 127 May (1965); also "Electrochemical Aspects of Stress-Corrosion Cracking," paper presented at the NATO Conference on the Theory of Stress Corrosion Cracking in Alloys, Ericeira, Portugal, March 29-April 2, To be published in proceedings.
14. E. D. Parsons, H. H. Cudd, and H. L. Lochte, *J. Phys. Chem.*, **45**, 1339 (1941).
15. M. Pourbaix, *Corrosion*, **26**, 431 (1970).
16. J. O'M. Bockris, D. Drazic, and A. R. Despic, *Electrochim. Acta*, **4**, 325 (1961).
17. E. J. Kelly, *This Journal*, **112**, 124 (1965).
18. K. E. Heusler, *Z. Elektrochem.*, **62**, 529 (1958).
19. C. Voigt, *Electrochim. Acta*, **13**, 2037 (1968).
20. L. Felloni, *Corrosion Sci.*, **8**, 133 (1968).
21. F. Hilbert, Y. Miyoshi, G. Eichkörn, and W. J. Lorenz, *This Journal*, **118**, 1919 (1971).
22. G. Eichkörn, W. J. Lorenz, L. Albert, and H. Fisher, *Electrochim. Acta*, **13**, 183 (1968).
23. K. F. Bonhoeffer and K. E. Heusler, *Z. Elektrochem.*, **61**, 122 (1957).
24. B. Kabanov, R. Burstein, and A. Frumkin, *Discussions Faraday Soc.*, **1**, 259 (1947).
25. K. F. Bonhoeffer and K. E. Heusler, *Z. Phys. Chem. N.F.*, **8**, 390 (1956).
26. T. Hurlen, *Acta Chem. Scand.*, **14**, 1533 (1960).
27. K. A. Christiansen, H. Hoeg, K. Michelson, G. Bech Nielson, and H. Nord, *ibid.*, **15**, 300 (1961).
28. J. O'M. Bockris and A. Damjanovic in "Modern Aspects of Electrochemistry," Vol. 3, p. 268, J. O'M. Bockris and B. E. Conway, Editors, Butterworths, London (1964).
29. T. Murakawa, T. Kato, S. Nagaura, and N. Hackerman, *Corrosion Sci.*, **7**, 657 (1967).
30. K. E. Heusler and G. H. Cartledge, *This Journal*, **108**, 732 (1961).
31. W. J. Lorenz, H. Yamaoka, and H. Fisher, *Ber. Bunsenges. Phys. Chem.*, **67**, 932 (1963).
32. A. J. Arvia and J. J. Podestá, *Corrosion Sci.*, **8**, 203 (1968).
33. J. J. Podestá and A. J. Arvia, *Electrochim. Acta*, **10**, 171 (1965).
34. E. McCafferty and N. Hackerman, *This Journal*, **119**, 146 (1972).
35. A. C. Makrides, N. M. Komodromos, and N. Hackerman, *ibid.*, **102**, 363 (1955).
36. H. S. Harned and B. B. Owen, "The Physical Chemistry of Electrolytic Solutions," p. 716, 751, Reinhold Publishing Co., New York (1958).
37. M. Stern, *This Journal*, **102**, 609 (1955).
38. J. E. Hawkins, *J. Am. Chem. Soc.*, **54**, 4480 (1932).

⁴ In a two-electron transfer scheme, $z_{H^+} = 0$ ensues for Eq. [17], [18] followed by $FeX^-_{ads} \rightarrow FeX^+ + 2e^-$ and then Eq. [21].

39. A. V. Storonkin, M. D. Lagunov, and V. I. Belokoskov, *Russ. J. Phys. Chem.*, **40**, 1501 (1966).
40. H. S. Harned, *J. Phys. Chem.*, **67**, 1739 (1963).
41. H. S. Harned, *ibid.*, **64**, 112 (1960).
42. G. E. F. Sherwood and A. E. Taylor, "Calculus," p. 483, Prentice Hall, New York (1954).
43. S. Asakura and K. Nobe, *This Journal*, **118**, 19 (1971).
44. B. E. Conway and E. Gileadi, *Trans. Faraday Soc.*, **58**, 2493 (1962); also "Modern Aspects of Electrochemistry," Vol. 3, p. 381, J. O'M. Bockris and B. E. Conway, Editors, Butterworths, London (1964).
45. D. O. Hayward and B. M. W. Trapnell, "Chemisorption," p. 176, Butterworths, Washington (1964).
46. T. N. Andersen and J. O'M. Bockris, *Electrochim. Acta*, **9**, 347 (1964).
47. J. O'M. Bockris and D. A. J. Swinkels, *This Journal*, **111**, 736 (1964).
48. E. Gileadi, "Electrosorption," p. 1 ff. Plenum Press, New York (1967).
49. B. Lovrecek and N. Marincic, *Electrochim. Acta*, **11**, 237 (1966).
50. E. J. Kelly, *This Journal*, **115**, 1111 (1968).
51. J. O'M. Bockris and A. K. N. Reddy, "Modern Electrochemistry," Vol. 2, p. 1082, Plenum Press, New York (1970).
52. I. Ruff, *J. Phys. Chem.*, **69**, 3183 (1965).
53. I. R. Jonasson and D. R. Stranks, *Electrochim. Acta*, **13**, 1147 (1968).
54. Th. Heumann and N. Stolice, *ibid.*, **6**, 1635 (1971).
55. M. H. Miles and H. Gerischer, *This Journal*, **118**, 837 (1971).
56. B. Timmer, M. Sluyters-Rehbach, and J. H. Sluyters, *J. Electroanal. Chem.*, **14**, 181 (1967).
57. J. P. Carr, N. A. Hampson, and R. Taylor, *Ber. Bunsenges. Phys. Chem.*, **74**, 557 (1970).

Kinetics of the Deposition of Inert Particles from Electrolytic Baths

N. Guglielmi*

Laboratori di Ricerca Tecnologica, Ing. C. Olivetti & C. S.p.A., Ivrea, Italy

ABSTRACT

To explain the peculiarities shown by the codeposition of inert particles from electrolytic baths, a mechanism based on two successive adsorption steps is proposed. In the first step the particles are loosely adsorbed, and they are in equilibrium with the particles in suspension. In the second step the particles are irreversibly adsorbed. Making a few elementary hypotheses about the mechanism that governs the two steps it is possible to deduce a general expression relating the concentration of the embedded particles to the suspension concentration and the electrode overpotential. This relationship is verified experimentally.

The possibility of codepositing inert particles from electrolytic baths in order to obtain composite layers of a metal matrix containing finely dispersed inert particles has long been known (1, 2). In more recent years this technique has received increasing attention in view of the interesting possibilities it offers, for example, the electrodeposition of layers characterized by desirable properties like wear and abrasion resistance, the electroforming of dispersion-hardened alloys, and so on (3, 4).

Although the technique has been considerably developed from the practical point of view, the theoretical details of the deposition mechanism have not received particular attention, and are actually far from being well understood. The problem is to give a physical explanation of the deposition of the "inert" particles together with the metal ions, and to justify the influence of the principal parameters acting on the process, which have been shown to be the current density and the particle concentration in the bath. In Fig. 1 a typical example of codeposition curves is shown. The nonlinear dependence on concentration, even in very diluted suspensions, and the pronounced dependence on current density, can be noted.

Two different phenomena can be taken into account to explain the observed deposition: electrophoresis and adsorption. Both possibilities can be supported by some arguments and contradicted by others.

An electrophoretic effect could explain the observed dependence on current density, but some difficulty would arise as far as the nonlinear concentration dependence is concerned. In every case a fundamental

objection must be advanced against the possibility of an electrophoretic effect in a medium of very high ionic strength such as a plating bath.

On the other hand, the striking similarity of the curves in Fig. 1 with the well known adsorption isotherms undoubtedly supports a mechanism based on an adsorption effect. But such an hypothesis is contradicted by the very low value of the coverage where the surface appears to be saturated. In addition, it can be shown that a simple adsorption mechanism cannot give a satisfactory explanation for the observed dependence on current density.

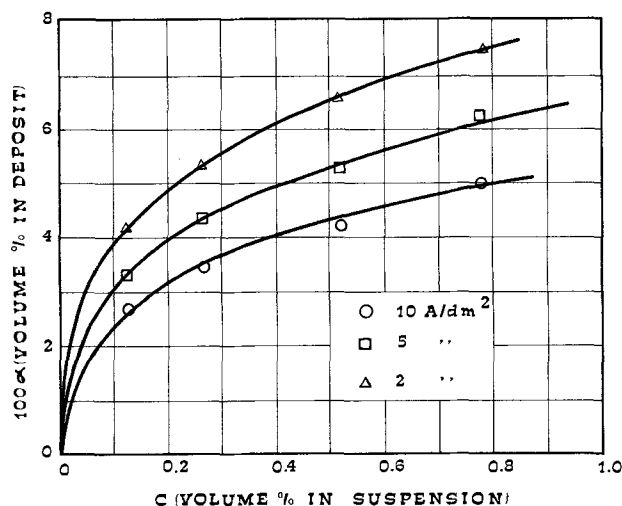


Fig. 1. Codeposition of TiO_2 particles from nickel sulfamate bath

* Electrochemical Society Active Member.

Key words: composite deposits, deposition mechanism, inert particles.

To find a solution for the above dilemma we make use of the evident complementary relationship existing between the two mechanisms just discussed and advance a hypothesis in which both are taken into account in such a way as to eliminate the contradictions.

The proposed mechanism is based on two consecutive adsorption steps. The first step is postulated to be substantially physical in character and to produce a layer of loosely adsorbed particles with a rather high coverage. The second adsorption step is thought to be field assisted, therefore substantially electrochemical in character, and produces a strong adsorption of the particles onto the electrode. The strongly adsorbed particles are then progressively submerged by the growing metal.

As to the physical meaning of the two adsorption steps, it can be inferred that in the first the inert particles are still coated by a thin layer of adsorbed ions and solvent molecules, which substantially screens the interaction between the electrode and the particles. In the second step the electrical field existing at the interface helps to uncover the particles, so producing a stronger, field-assisted adsorption. There is an evident analogy between the two postulated stages of adsorption for the particles and the adsorption of ions respectively in the outer and inner Helmholtz planes of the electrode.

It can be shown that the postulated mechanism is not affected by the above-mentioned objections, and makes it possible to justify both current density and nonlinear concentration dependence of the deposition process. In the following a quantitative treatment of the proposed model is developed and subjected to experimental verification.

Mathematical Treatment

The previously outlined model is schematically shown in Fig. 2. The steps of loose adsorption, strong adsorption, and embedding have been represented as progressing from the top to the bottom of the figure, but are obviously randomly distributed over the whole surface of the electrode. The minimum approach distance of the loosely adsorbed particles, which has molecular dimensions, has been markedly exaggerated. We define the loose adsorption coverage, σ , and the strong adsorption coverage, ϑ , respectively as

$$\sigma = S_1/S \quad \vartheta = S_s/S \quad [1]$$

where S , S_s , S_1 are the total electrode area, and respectively the area overshadowed by strongly adsorbed and partially embedded particles and by loosely adsorbed particles.

The dependence of σ on the concentration C of suspended particles can be deduced in much the same way as the classical Langmuir adsorption isotherm (5), the difference being that only a fraction $(1 - \vartheta)$ of the surface area is really available for the establishment of the equilibrium. It is easily seen that such a limitation can be taken into account by introducing a factor

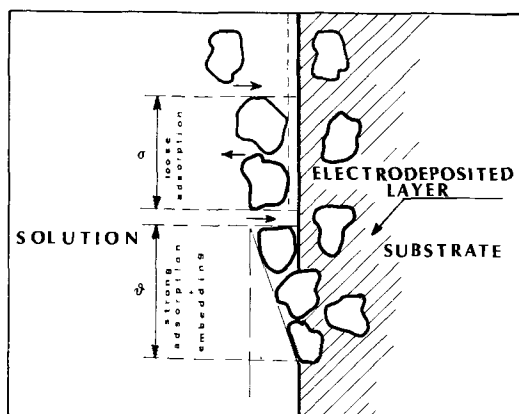


Fig. 2. Scheme of the two-step deposition process

$(1 - \vartheta)$ into the classical expression of the isotherm and therefore

$$\sigma = \frac{kC}{1 + kC} (1 - \vartheta) \quad [2]$$

where the constant k depends essentially on the intensity of the interaction between particles and electrode.

The dependence on σ of the strong adsorption rate is obviously linear. To take into account the postulated field dependence of the process, we introduce an exponential rate factor $v_0 e^{B\eta}$ where η is the overpotential related to the metal deposition process, while v_0 and B are constants.

Such a factor has a strict analogy with the Tafel exponential governing the electrode processes at high overpotentials, and it is compatible with an adsorption mechanism implying a field-assisted activated state.

As to the apparently arbitrary dependence on η , which is here introduced for convenience, it can be noted that, if an exponential dependence on field intensity at the interface is accepted, every magnitude linearly related to such field intensity, and therefore also η , can be inserted in the exponential if the constants v_0 and B are properly adjusted. We can therefore write for the strong adsorption rate, taking Eq. [2] into account

$$dV_p/dt = \sigma v_0 e^{B\eta} = v_0 e^{B\eta} (1 - \vartheta) \frac{kC}{1 + kC} \quad [3]$$

where dV_p/dt is the volume of particles strongly adsorbed on 1 cm^2 of electrode surface per second.

The volume dV_m/dt of metal electrodeposited on 1 cm^2 of electrode surface per second can be deduced from Faraday's law

$$dV_m/dt = \frac{Wi}{nFd} \quad [4]$$

where F is the Faraday constant, W the atomic weight of the electrodeposited metal, d the density of the same, n the valence, and i the current density.

If the particle concentration in the deposit is expressed as volume fraction α , it is easily seen that the total volume (metal + particles) deposited on 1 cm^2 of electrode surface per second can be expressed as

$$dV/dt = \frac{dV_m}{dt(1 - \alpha)} = \frac{Wi}{nFd(1 - \alpha)} \quad [5]$$

On the other hand, the current density i is related to the overpotential by the Butler-Vomer equation (6), which at high field approximation can be written in the Tafel form

$$i = (1 - \vartheta) i_0 e^{A\eta} \quad [6]$$

where the factor $(1 - \vartheta)$ takes into account the area really available for electrodeposition. Inserting Eq. [6] in Eq. [5] we get

$$dV/dt = \frac{Wi_0 e^{A\eta} (1 - \vartheta)}{nFd(1 - \alpha)} \quad [7]$$

The volume fraction α of particles in the deposit can be related, in a stationary condition, to the rates of strong adsorption dV_p/dt and total deposition dV/dt

$$\alpha = \frac{dV_p/dt}{dV/dt} \quad [8]$$

Substituting Eq. [3] and [7] in Eq. [8] and rearranging, we arrive at a general expression, relating the volume fraction of the embedded particles to the suspension concentration and the electrode overpotential

$$\frac{\alpha}{1 - \alpha} = \frac{nFdv_0}{Wi_0} \cdot e^{(B-A)\eta} \cdot \frac{kC}{1 + kC} \quad [9]$$

This equation summarizes all the principal features of the inert particle codeposition. The depen-

dence on concentration is proportional, but not identical with the adsorption isotherm factor [2] and therefore the observed apparent saturation of the electrode at low values of θ can be explained by the related high values of σ . The parameters v_0 and B , related to the particles' deposition, play a symmetrical role with the parameters i_0 and A related to the metal deposition. In particular, α increases or decreases with η depending on the relative values of A and B . In the restricted case of low values of α the factor $(1 - \alpha)$ can be dropped and Eq. [9] can be rearranged in the following form

$$\frac{C}{\alpha} = \frac{Wi_0}{nFdv_0} \cdot e^{(A-B)\eta} \cdot \left(\frac{1}{k} + C \right) \quad [10]$$

If the expression constituting the left-hand side is plotted against C for different values of η , it represents a sheaf of straight lines having the common intersection on the point $1/k$ of the C axis and a slope equal to the factor outside the parenthesis

$$tg\phi = \frac{Wi_0}{nFdv_0} \cdot e^{(A-B)\eta} \quad [11]$$

Equation [10] should be tested by deposition experiments at constant potential; however it also has an approximate validity at constant current, as long as the factor α is small. In this approximation, $i/i_0 \approx e^{A\eta}$ and the following substitutions can be made in order to express $tg\phi$ as a function of i

$$i_0 e^{(A-B)\eta} = i_0 e^{A\eta(1-B/A)} = i_0 B/A i^{(1-B/A)} \quad [12]$$

Substituting the last expression in Eq. [11] and taking the logarithms we get

$$\log tg\phi = \log \frac{Wi_0 B/A}{nFdv_0} + (1 - B/A) \log i \quad [13]$$

which shows linear dependence of $\log tg\phi$ on $\log i$.

If we plot $tg\phi$ against i in logarithmic coordinates we obtain a straight line having a slope $(1 - B/A)$ and a value at $i = 1$ ($\log i = 0$) equal to the argument of the first term appearing in the right-hand side of Eq. [13].

Experimental

The apparatus and the experimental techniques used to obtain the deposits have been described elsewhere (7). The plating solution was a normal sulfamate bath of the following composition:

Nickel sulfamate	400 g/liter
Nickel chloride	5 g/liter
Boric acid	30 g/liter
Antipit agent	0.5 g/liter
pH	4 ± 0.2
Temperature	$50^\circ\text{C} \pm 2^\circ\text{C}$

To this bath were added variable amounts of the following powders: (i) TiO_2 , C. Erba S.p.A. reagent grade, mean size $1 \mu\text{m}$, density 3.84. (ii) SiC , Elektroschmelzwerk GmbH, mean size $2 \mu\text{m}$, density 3.21. All deposits were obtained at constant current. The analyses were performed by gravimetric methods.

Results and Discussion

In Fig. 3 the experimental results of Fig. 1, concerning Ni- TiO_2 deposits, are plotted according to Eq. [10]. The experimental points can be satisfactorily grouped on a sheaf of straight lines converging at a negative point on the abscissa, as required by the above-developed theory.

The common intercept on the C axis has a value -0.19 , which can be equated to $-1/k$ giving 5.3 for the adsorption constant k . Such a constant is dimensionally a pure number, being the inverse of a dimensionless per cent concentration.

For particles of reasonably regular shape, the volume fraction α has nearly the same value as the sur-

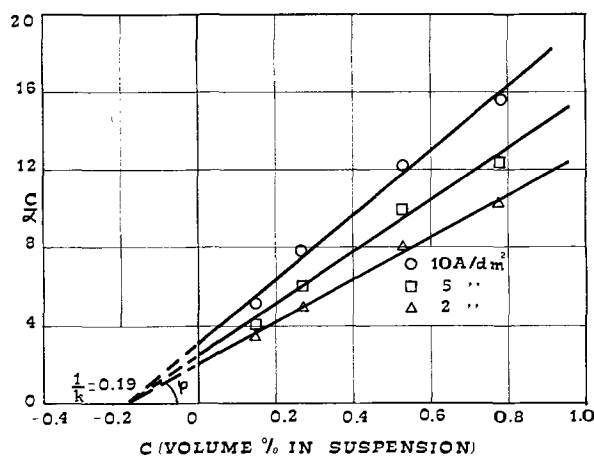


Fig. 3. Codeposition of TiO_2 particles according to Eq. [10]

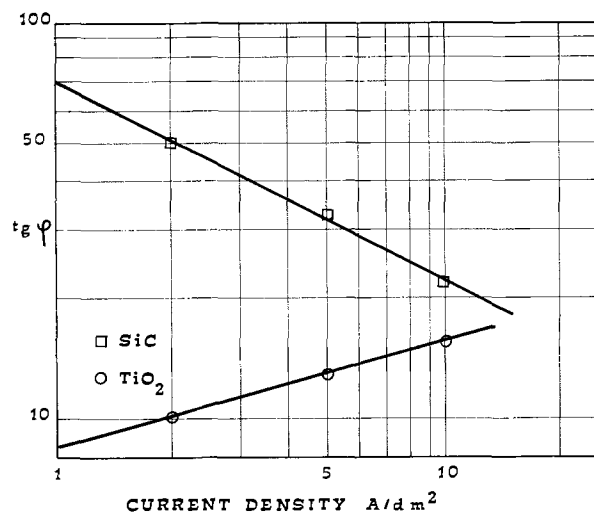


Fig. 4. Slope ($tg\phi$) dependence on current density

face fraction θ . It is therefore possible, knowing k and θ , to compute σ by means of Eq. [2]. In Table I the computed concentrations are listed at a fixed current density. All the values being given as percentages it is possible to compare surface and volume concentrations on a common scale. The values 100α , as noted above, are also indicative of the surface concentration of strongly adsorbed particles.

It can easily be seen that the concentration of loosely adsorbed particles is greater by two orders of magnitude than the concentration of suspended particles, and that also in very diluted suspensions a prevailing fraction of the electrode surface is screened, so justifying the premature saturation of the surface experimentally observed. The substantially lower concentration of strongly adsorbed particles shows that the second adsorption step is relatively slow. In Fig. 4 the logarithms of the slope $tg\phi$ of the lines in Fig. 3, are plotted against $\log i$. The values are well grouped on a straight line with a slope 0.35. Equating this value to $(1 - B/A)$ according to Eq. [13] it is possible to express B in terms of A

$$B = 0.65A \quad [14]$$

A similar analysis has been carried out on Ni-SiC

Table I. Per cent concentration of TiO_2 particles at 5 A/dm^2

C (%)	100σ (%)	100α (%)
0.13	40.8	3.5
0.26	55.2	4.3
0.52	69.5	5.2
0.78	75.5	6.2

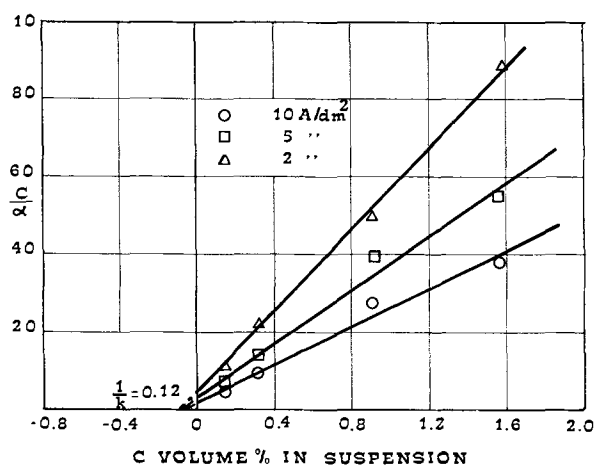


Fig. 5. Codeposition of SiC particles according to Eq. [10]

deposits on the basis of the experimental results plotted in Fig. 5 in the same way as those of Fig. 3. Also in this case the points group well on a sheaf of straight lines converging to a negative point on the C axis. The constant k is substantially higher than in the previous case, having a value 8.3. By use of such a value the surface concentration of loosely adsorbed particles can be computed, obtaining the results reported in Table II for $i = 5 \text{ A/dm}^2$. The loose adsorption of SiC particles is notably greater than that of TiO_2 particles and can lead to an almost complete saturation of the surface.

Figure 4 shows the dependence of $\text{tg}\phi$ on current density for Ni-SiC deposits. The slope of the straight line is negative with a value -0.51 which gives the following expression for the constant B

$$B = 1.51A \quad [15]$$

We note that if $B > A$ there is an increase of α when current density is increased while in the case $B < A$ there is a corresponding decrease. TiO_2 and SiC particles in sulfamate baths illustrate the two cases.

The very high coverage by loosely adsorbed particles observed on the electrode points out the problem of the interference of these particles with the electrodeposition of metal ions. Since the metal layers are

Table II. Per cent concentration of SiC particles at 5 A/dm^2

C (%)	100σ (%)	100α (%)
0.16	55.7	1.9
0.31	70.8	2.1
0.93	86.5	2.3
1.56	90.2	2.8

compact and uniformly deposited it must be concluded that the interference is not so important. It can be argued that the particles, gigantic in respect to ionic dimensions, do not block the arrival of ions to the electrode surface, in a similar way as a disconnected row of irregular big stones does not stop a stream of water. It seems probable that by means of electrode polarization measurements a better insight into this problem could be obtained.

Conclusions

The experimental data agree well with the proposed codeposition mechanism based on a two-step adsorption process. In this model the deposition of inert particles depends on three parameters (k , v_0 , B). All these can be computed by means of the relations [10] and [13] once the constants i_0 and A , obtainable by overpotential measurements in the plating solution, are known.

The strong dependence of particle codeposition on solution composition, observed by many authors, can easily be justified in the present model since the behavior of the particles depends strictly on the structure of the layer of molecules and ions adsorbed on their surface, and indirectly on the composition of the solution.

A separate determination of the three parameters k , v_0 , and B at different compositions could probably give more detailed information on the effective action of the various solution components. Research in this direction is presently being carried out by our laboratory and will be the subject of a later paper.

Acknowledgment

The stimulating support, and permission for publication given by Dr. F. Foa, is gratefully acknowledged.

For valuable experimental assistance I am indebted to Mr. G. Cerbone and G. Icardi.

Manuscript submitted June 22, 1971; revised manuscript received ca. Jan. 4, 1972.

Any discussion of this paper will appear in a Discussion Section to be published in the December 1972 JOURNAL.

REFERENCES

1. F. M. Sautter, *This Journal*, **110**, 557 (1963).
2. R. V. Williams and P. W. Martin, *Trans. Inst. Metal Finishing*, **42**, 182 (1964).
3. E. C. Kedward and B. Kiernan, *Metal Finishing J.*, **13**, 116 (1967).
4. V. P. Greco and W. Baldauf, *Plating*, **55**, 250 (1968).
5. J. H. de Boer, "The Dynamical Character of Adsorption," Chap. V, pp. 54-58, Clarendon Press, London (1953).
6. J. O'M. Bockris and A. K. M. Reddy, "Modern Electrochemistry," Vol. II, Chap. 8, pp. 883-894, Plenum Press, New York (1970).
7. N. Guglielmi and G. Icardi, *La Metallurgia Italiana*, **62**, 420 (1970).

The Role of U.V. Light in the Inhibition of Electroless Deposition

S. L. Chow, N. E. Hedgecock, M. Schlesinger,
and J. Rezek

Department of Physics and Department of Engineering Materials,
University of Windsor, Windsor, Ontario, Canada

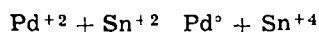
ABSTRACT

Ultraviolet light has been shown to be effective in inhibiting the electroless deposition of Cu, Ni, and Co if applied after sensitization, and of Ni and Co after activation. Electron microscopic techniques are applied to investigate these phenomena. It is concluded that structural changes in the sensitizing and activating agents induced by the u.v. light are connected with the inhibition of metal deposition.

Thin metal films deposited by the electroless process have attracted the interest of a number of workers recently. This is largely so because of the considerable technical potential that this kind of film has. One of the rather interesting characteristics that these films have is the relative ease with which they can be deposited. Although quite a number of chemical systems for metal deposition have been developed (1), little is understood about the actual mechanisms which govern the physical chemistry of these systems.

We have investigated previously (2) the nucleation and growth of thin electroless Ni-P deposits. Sard has carried out (3) similar studies on electroless copper deposits. The nucleation of electroless Co-P deposits has been studied to some extent by Frieze, Sard, and Weil (4).

An important property of electroless systems is their ability to deposit metals selectively. This has been demonstrated by Sharp and co-workers (5) who desensitized portions of a surface with u.v. radiation. The same effect has been observed by other workers [see, for example, Ref. (6)]. In an effort to further elucidate the process of sensitization prior to deposition, Cohen *et al.* (6) used Mossbauer spectroscopy to study tin sensitizer deposits formed on Kapton films (du Pont polyimide). On the basis of these and other results, they have concluded that the sensitizer is present as a colloid in the sensitizing bath and is adsorbed on the substrate when it is dipped. They also suggested that the photosensitive substance contains more Sn^{+4} than Sn^{+2} . The Sn^{+2} is oxidized by exposure either to air or to the Pd activation bath. In the Pd bath the process



presumably leads to the formation of a Pd layer on the substrate. This surface supposedly provides catalytic sites for deposition of the electroless metal. Ultraviolet irradiation is assumed to inhibit the metal growth by simply oxidizing the Sn^{+2} to Sn^{+4} prior to the Pd bath, hence, preventing the formation of a palladium layer.

No previous studies have been reported of the effect of u.v. irradiation on the palladium activated surface. Working with Ni and Co, we have found that u.v. light is effective in inhibiting the electroless deposition even if it is applied after activation. This, we shall show, renders the model of Cohen *et al.* (6) rather incomplete. Based on some experimental evidence, we claim that the u.v. introduces structural changes in the catalytic sites. As a result of those changes electroless deposition becomes impossible.

Experimental

Although our main interest in this work has been a study of the premetalizing stages, the complete proc-

Key words: films, crystallization, irradiation, structure, electroless.

esses for electroless deposition of nickel, copper and cobalt were used in the investigation. The chemical solutions employed for deposition of the three metals were as given in the literature (2-4). All chemicals were supplied by Fisher or Canlab, and were used without further purification.

Microscope slide glasses coated on both sides with Formvar (4g polyvinylformal in 1 liter of ethylene dichloride) were used as substrates. The Formvar was floated off the glass in distilled water.

The samples were examined with a Hitachi HU-12 electron microscope. The effect of irradiation on the microstructure of the sensitized and activated surfaces was investigated by examining samples in the microscope, removing them for irradiation, and then re-examining the same samples.

In investigating the effect of u.v. irradiation on the metal deposition, Formvar coated glass substrates were immersed in the sensitizing (or sensitizing and activating) solutions and then irradiated, on one side only, with u.v. light. The opacity of the glass prevented irradiation of the other side. Continuation of the deposition process resulted in normal deposition on the non-irradiated side, showing that any inhibition of deposition on the other side was directly due to the irradiation.

The u.v. irradiation was carried out using an Oriel 50W mercury lamp at a distance of about 5 cm from the sample.

Results

In Fig. 1 we present transmission electron micrographs of Formvar coated surfaces: a, sensitized (1 min) and rinsed ($\frac{1}{2}$ min); and b, sensitized (1 min), rinsed ($\frac{1}{2}$ min), activated (1 min), and rinsed ($\frac{1}{2}$ min). In accordance with Sard's observation, the product of the sensitization process appears to consist of particles of approximately 20Å diameter, agglomerated into dense clumps an order of magnitude or so larger. The clumps themselves are randomly distributed on the surface. The activated surface shows particles of about 50Å in size. This is presumably (3) a deposit of metallic palladium.

In Fig. 2, the corresponding diffraction patterns are shown. Figure 2a, for the sensitized surface, is a pattern which seems to be characteristic of SnO_2 (3). The pattern for the sensitized and activated surface is seen in Fig. 2b. It is rather difficult to attribute these diffuse patterns to any one symmetry or chemical compound. One might expect a more distinctive pattern from the activated layer since a palladium layer would be expected in accordance with Bravais' law to form with the close packed planes {111} parallel to the substrate surface. We assume that the lack of a distinctive pattern is due to the small particle size.

Figure 3 shows the effect of ultraviolet irradiation on the a, sensitized, and b, sensitized and activated

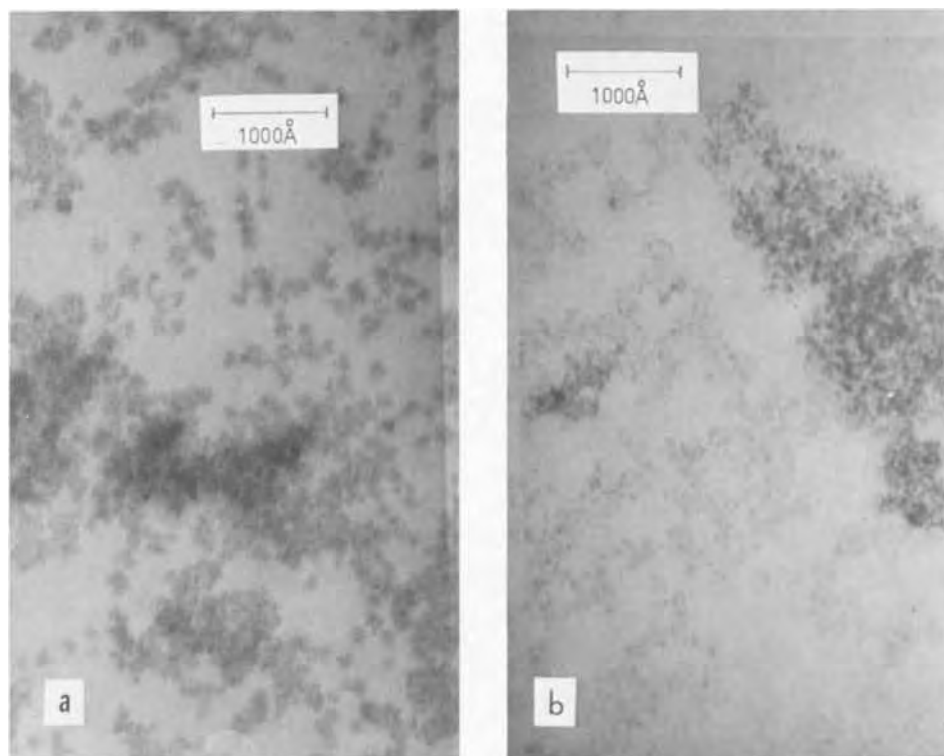


Fig. 1a. Transmission electron micrograph of a Formvar coated surface sensitized in SnCl_2 for 1 min and rinsed for $\frac{1}{2}$ min in distilled water; 1b, Transmission electron micrograph of a Formvar coated surface after sensitization as in (a) and subsequent activation for 1 min (in PdCl_2) followed by a $\frac{1}{2}$ min rinse.

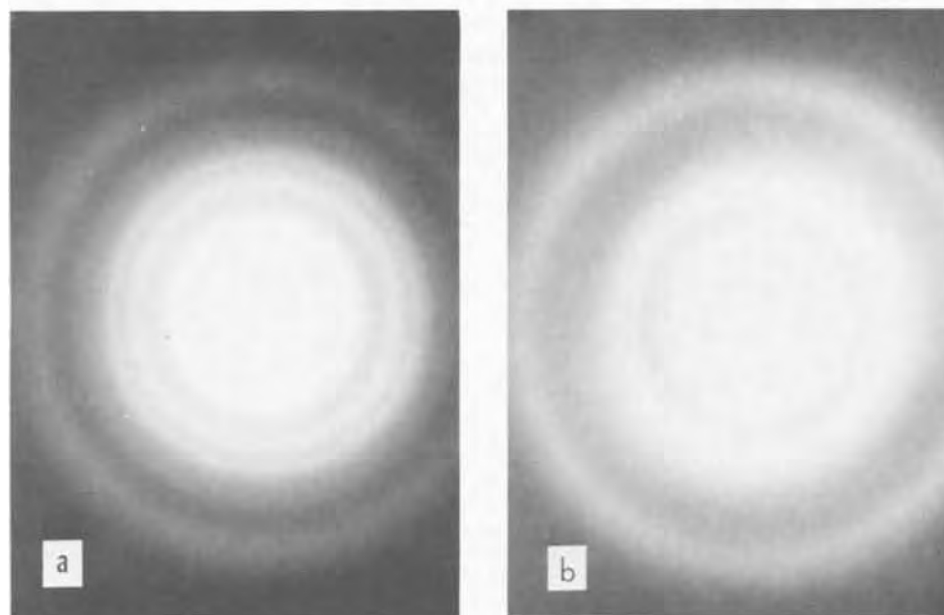


Fig. 2a. Electron diffraction pattern exhibited by the sample corresponding to Fig. 1a—electron beam energy 100 keV; 2b, electron diffraction pattern exhibited by the sample corresponding to Fig. 1b—electron beam energy 100 keV.

Formvar surfaces. The electron diffraction patterns obtained before (I) and after (II) 50 min of u.v. illumination are shown for each case. We have found that the u.v. treatment is effective at both stages in inhibiting the deposition of nickel and cobalt. In the case of copper, however, u.v. light is effective only after the sensitization stage. The significance of the difference in behavior between copper on the one hand and nickel and cobalt on the other is discussed below.

Figure 4 shows micrographs and corresponding diffraction patterns of Co-P films at early stages of growth. These results show clearly that the deposit is initially amorphous, and that the extent of crystallization and the size of the individual crystallites increase with deposition time. Other factors, such as the pH of the metalizing bath, influence the degree of crystallization and are being currently investigated by us.

Discussion

Working with electrolessly deposited copper, Cohen *et al.* (6) have found that u.v. irradiation after sensitization is sufficient to inhibit metal deposition. This they explained in terms of the oxidation of Sn^{+2} to Sn^{+4} by the u.v. light. The Sn^{+2} is essential for the formation of the metallic Pd deposit in the activation stage (see above). It is plain that this cannot be accepted as the complete explanation of the role of u.v. in inhibiting growth since, for Co or Ni, u.v. light is effective in inhibiting metal deposition even after the Pd bath.

Based on the results presented in Fig. 3, we believe that an explanation of the influence of u.v. light must also include crystalline structure changes. While more experimental work is needed before a complete model

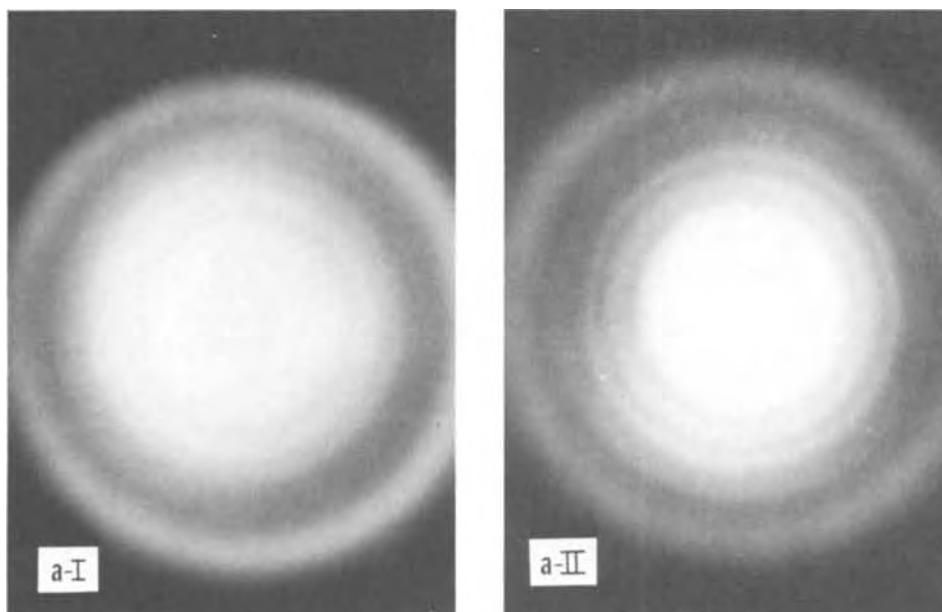


Fig. 3a—I. Electron diffraction pattern of sensitized Formvar (no u.v.); Electron beam energy 100 keV. 3a—II. Diffraction pattern for the same sample as in 3a—I after 50 min u.v. illumination.

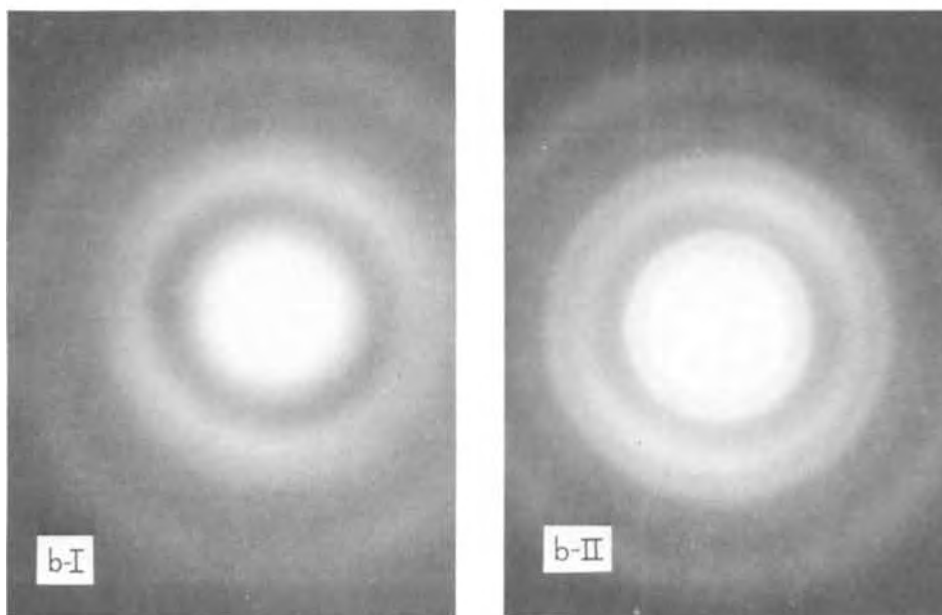


Fig. 3b—I. Electron diffraction pattern of activated Formvar (no u.v.); Electron beam energy 100 keV. 3b—II. Diffraction pattern for the same sample as in 3b—I after 50 min u.v. illumination.

can be drawn, one can argue in the following qualitative way.

The effect of irradiation on the diffraction patterns of both the sensitized and activated layers is to increase the degree of crystallization. This is a consistent trend which was observed in many samples prepared under various conditions. In the case of the sensitized layer, this may well be associated with the oxidation of a divalent tin compound to form SnO_2 ; but it is also clear that the degree of crystallization is also increased by the irradiation. The situation is similar for the activated layer. It is harder to envisage a chemical change in metallic palladium resulting from irradiation, although, it is tempting to suggest an oxidation to a divalent state by analogy with the oxidation of the tin compound. In any event, again a higher degree of crystallization definitely results from the irradiation.

The fact that deposition of nickel and cobalt is inhibited by irradiation of the activated layer, while copper is deposited with no discernible change in the rate of deposition, is particularly interesting. This disparity in behavior cannot be explained simply in terms of the crystal structure of the metals involved. Pal-

ladium is face-centered cubic, and it is reasonable to suppose that other metals with the same crystal structure could form epitaxially on the palladium. Both copper and nickel are face-centered cubic; cobalt is normally hexagonal close packed. Hence, on this basis one would expect cobalt rather than copper to behave differently.

The difference most probably lies in the fact that the chemistry of the nickel and cobalt deposition processes is closely related, and involves phosphorus, which is incorporated into the deposited layer. For copper, however, no hypophosphite is used in the metalizing solution, and it is known that hydrogen is incorporated into the deposited film. This difference might be the reason for an initially liquid-like structure for both Ni(2) and Co (see Fig. 4). In carrying this point somewhat further it may be speculated that, under such circumstances, an increased crystallinity in the Pd prior to metalizing might well inhibit the deposition of Ni and Co. The present state of knowledge of the detailed chemistry of the processes is inadequate to provide any further explanation.

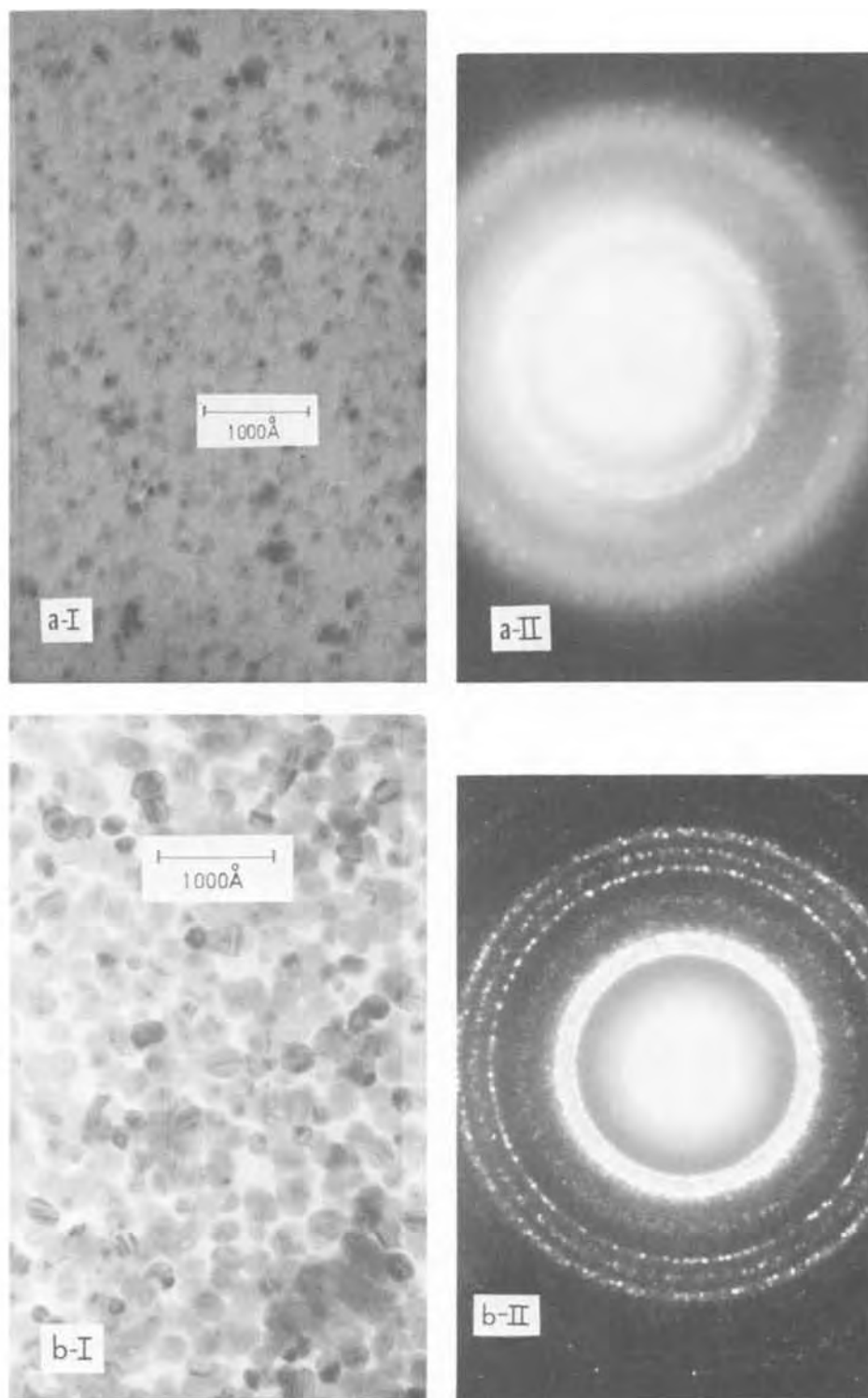


Fig. 4. Electron micrographs and corresponding electron diffraction patterns for Co-P films at early growth stage. a—I. 2 min in metalizing solution (micrograph). a—II. 2 min in metalizing solution (diffraction pattern). b—I. 4 min in metalizing solution (micrograph). b—II. 4 min in metalizing solution (diffraction pattern).

Acknowledgments

This work was supported in part by a National Research Council of Canada grant to M. Schlesinger. The skillful technical assistance of Mr. B. Sears is gratefully acknowledged.

Manuscript submitted Feb. 17, 1972; revised manuscript received April 10, 1972.

Any discussion of this paper will appear in a Discussion Section to be published in the June 1973 JOURNAL.

REFERENCES

1. W. Goldie, "Metallic Coating of Plastics," Electrochemical Publications Ltd., Middlesex, England (1968).
2. J. P. Marton and M. Schlesinger, *This Journal*, **115**, 16 (1968).
3. R. Sard, *ibid.*, **117**, 864 (1970).
4. A. S. Frieze, R. Sard, and R. Weil, *ibid.*, **115**, 587 (1968).
5. J. F. D'Amico, M. A. DeAngelo, J. F. Henrickson, J. T. Kenney, and D. J. Sharp, *ibid.*, **118**, 1695 (1971).
6. R. L. Cohen, J. F. D'Amico, and K. W. West, *ibid.*, **118**, 2042 (1971).

Two-Layer Printed Wirings on Mylar Foil

A. Politycki

Siemens AG, Forschungslaboratorien München, 8000 München 80, Balanstrasse 73, West Germany

ABSTRACT

Two-layer wirings with a total thickness of only 15 μm could be prepared by chemically metalizing a 5 μm Mylar foil, electrodeposition of copper and photoetching. It was possible to produce plates of the outer dimensions 170 \times 360 mm. Resistances of the metal lines (100 μm width and 5 μm thickness) were equal to within $\pm 5\%$ of an average value. Matrices of this sort may be used for various purposes, e.g., as drive line systems for low-current plane magnetic film memories.

For the realization of plane magnetic film memories, suitable drive line systems are necessary to operate the magnetic elements. It has proved advantageous to apply flexible printed wirings in front of the memory plane. They may be produced by photoetching of commercial copper-clad polyester or polyimide foils, as was done by Bittmann *et al.* (1). In commercial copper-clad laminates, which are now available in great variety (2), the separation between the two metallic sheets amounts to more than 20 μm . The distance of the lines from the magnetic elements has a very great influence on the intensity of the necessary drive current. In order to develop a low-current planar magnetic film memory it was, therefore, necessary to have a line matrix with a very small separation of the lines on both sides of the support. It was the purpose of the present work to produce a two-layer wiring matrix with a total thickness of 15 μm .

A Mylar foil of 5 μm thickness was chosen as the substrate, which was to be chemically metalized without using adhesives. The thin metal film was to be reinforced by electrodeposited copper so that the line pattern could then be etched.

The main problem was the poor adherence of the metal to the Mylar due to the lack of chemical bonding forces on the mechanically smooth surface. Without adhesives, Mylar foils have only been coated with metal films of less than 0.3 μm thickness (3, 4).

In preparation for metalization, the specimens were dipped into a hot solution of sodium hydroxide for 5 min. By this means, a surface layer of about 1 μm thickness was dissolved and the remaining foil was roughened. It was useful to mechanically vibrate the frame during this hot dip. After activation in solutions of tin chloride and palladium chloride the Mylar was ready for metalization. Chemically deposited copper or nickel resulted in unsatisfactory adherence. Satisfactory adherence was achieved, however, when chemically deposited films of silver, which had been aged, were reinforced by copper.

Without aging, the peel strength of etched silver/copper lines was very poor, but an increase was noticed when the silver film was heated for several hours at 100°C. A second heat-treatment after the electrodeposition of copper resulted in a further small improvement. This adherence, though not very strong, proved satisfactory, since all parts of the memory matrix were to be held together by compression. Figure 1 shows a micrograph of this type of double-coated Mylar foil. The silver film, having a thickness of only 200 nm, cannot be observed, whereas the copper deposit on both sides of the insulating material is clearly visible. The separation of the two metallic planes is 4 μm . In comparison to this, the separation of the two metallic sheets of a commercial copper-clad foil ranges between 20 and 30 μm .

For reasons of corrosion resistance and soldering technique, it was preferred to have the lines coated

with gold. A reversed photomask was, therefore, applied, and the noble metal was electrolytically deposited onto the unprotected areas. This was performed by applying a commercial, neutral gold bath, which operated at 75°C and had a yield of nearly 100%. The gold layer of 2 μm thickness served as an etching mask for the production of the line pattern on both sides of the foil. Etching was carried out using a solution of chromium oxide in sulfuric acid. To complete the removal of the silver, an intermediate treatment in a solution of sodium thiosulfate was used. Figure 2 shows a matrix with the outer dimensions of 160 \times 200 mm. The word lines are seen on the upper side of the foil in a vertical position. They begin near the edge of the frame and extend to the opposite strip

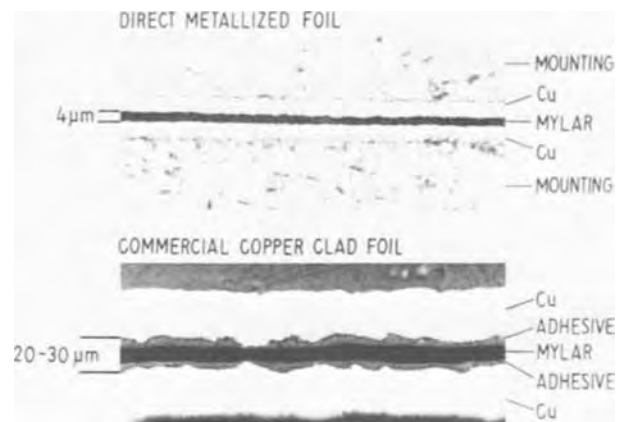


Fig. 1. Micrographs of coated Mylar foils

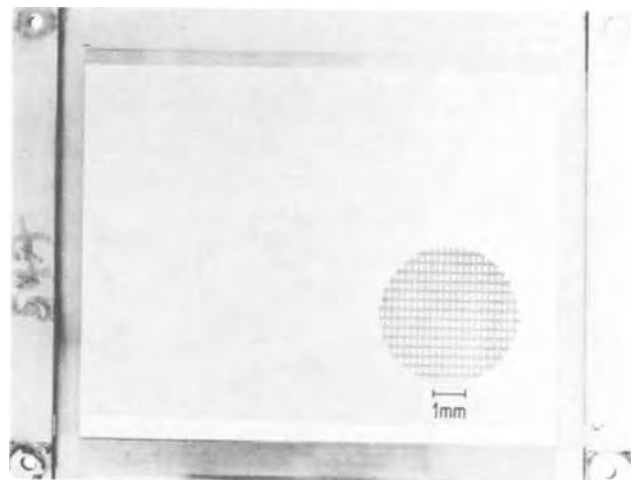


Fig. 2. Line matrix for a low current memory device. Outer dimensions, 160 \times 200 mm; width of the word lines, 100 μm ; digit lines 200 μm .

Key words: magnetic film memory, chemical metalization, electrodeposition, photoetching.

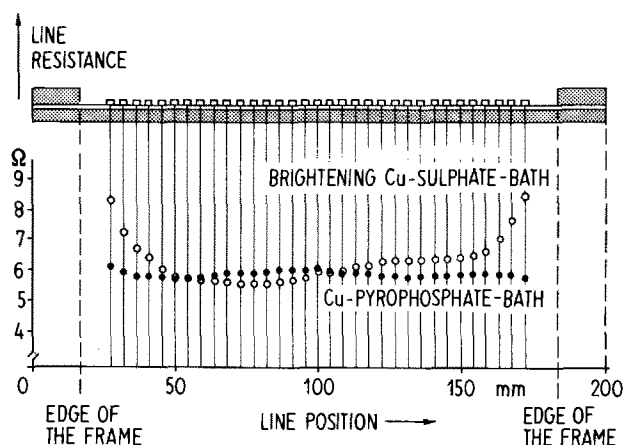


Fig. 3. Resistance of word lines as a function of the position in the matrix.

below. On the reverse side, the digit lines cover the foil in a horizontal position. It was necessary that all resistances of the lines should be equal to within $\pm 5\%$ of an average value. We were, therefore, obliged to check the resistance of every line. This was performed automatically by a motor driven contact and a strip-chart recorder. Figure 3 shows typical resistance values for the x-lines of two different matrices. Over the middle of the plate, whose copper deposit was produced by a brightening CuSO_4 bath (open circles), the resistances were constant to within ± 0.5 ohm. Near the edge of the frame, however, the values increased considerably. It was observed that a reduced

thickness of the copper deposit was the cause of the increased resistances, due to a screening effect of the frame. The throwing power of the applied brightening copper sulfate bath was not good enough. The effect did not appear, when the deposition of the metal was performed in a copper pyrophosphate electrolyte and the values shown in the other curve (filled circles), were obtained. The tolerances prescribed for the resistances of the lines were thus achieved.

Having overcome the main problems, it was possible to produce plates with the outer dimensions of 170×360 mm, which were needed for a memory model. The results concerning the function of this memory device have been published recently (5).

Acknowledgments

The author gratefully acknowledges the advice of Dr. K. U. Stein and the assistance of L. Bernowitz, O. Hingerl, and U. Jacob.

Manuscript submitted Sept. 13, 1971; revised manuscript received Jan. 10, 1972. This was Paper 30 presented at the Washington, D. C., Meeting of the Society, May 9-13, 1971.

Any discussion of this paper will appear in a Discussion Section to be published in the June 1973 JOURNAL.

REFERENCES

1. E. E. Bittmann, L. J. Arndt, and I. W. Hart, *IEEE Trans. Magnetics*, **3**, 476 (1967).
2. F. Beldon, "Proc. EIPC Conference on Flexible Circuitry," 41 (1970), Europ. Inst. of Printed Circuits, Gemsenstr. 2, 8006 Zurich, Switzerland.
3. J. Moradzadeh, *This Journal*, **112**, 891 (1965).
4. J. S. Judge, J. R. Morrison, and D. E. Speliotis, *ibid.*, **113**, 547 (1966).
5. K. U. Stein, *IEEE Trans. Magnetics*, **3**, 912 (1969).

Double Layer Capacity Measurement in Dilute Solution: A New Technique

M. Babai,* N. Tshernikovski, and E. Gileadi*

Institute of Chemistry, Tel-Aviv University, Ramat-Aviv, Israel

ABSTRACT

An instrument is described that can automatically plot the capacitance-potential curve of polarizable electrodes. The instrument is suitable for operating with solid electrodes and in dilute solutions, using positive feedback for IR correction. Several illustrations of its applicability are given and its limitations discussed.

Measurement of the impedance of the ionic double layer at mercury and at solid electrodes is of major importance for the understanding of double layer structure, electrosorption, and electrode kinetics. The methods of measurement may be classified in two groups, namely, the a-c and the pulse techniques.

The a-c group includes the well-known bridge method which was developed to a high degree of accuracy by Grahame (1) and applied widely for the dropping mercury electrode. It is the most accurate method for impedance measurement. However, its time-consuming character limits its use to electrodes whose impedance is independent of time and mostly to liquid metal electrodes. Another method is the so-called a-c polarography developed by Breyer and Gutmann (2) in which a small sinusoidal signal is superimposed on a slowly varying triangular potential sweep. In modern a-c polarography a phase-sensitive unit is in-

corporated that yields separately the "in-phase" and the "out-of-phase" (quadrature) components of the double layer impedance. Recently, Tshernikovski and Gileadi (3) have replaced the sinusoidal by a small triangular signal. As long as the impedance measured is mainly capacitive, the response to a small triangular wave is a square wave whose amplitude is proportional to the capacity. Rectification of the resulting square wave by a proper sampling technique allows one to obtain directly the whole capacitance vs. potential curve, as in a-c polarography.

Pulse techniques include repetitive square wave, single pulse, and the coulometric method. The first two have been developed by Hackerman and co-workers (4) and applied mostly to the study of double layer capacitance at solid electrodes. These two methods are usually simpler and faster than the a-c techniques, but provide results of much lower accuracy. The coulometric method developed by Delahay, De Levie, and Giuliani (5) permits double layer measurements in very dilute solutions.

* Electrochemical Society Active Member.

Key words: capacitance meter, double layer, solid electrode, dilute solutions.

Until recently, all methods neglected the ohmic potential drop (IR) due to the resistance in solution between the working electrode and the tip of the Luggin capillary connected to the reference electrode. This potential drop can be compensated for by adding a positive feedback loop to a conventional potentiostat. De Levie and Husovsky (6) have used this mode of IR compensation in a modern version of an a-c polarograph with phase sensitive detection, developed by them. In the present communication, an instrument similar to that of Tshernikovski and Gileadi (3), in which an IR compensation loop and a modern sampling unit have been incorporated, is described. This instrument allows quick and accurate measurements of the double layer capacity at concentrations down to $3 \times 10^{-4}M$.

Circuit Description

A small triangular signal (1-25 mV) is produced internally by a triangular wave generator shown in the upper section of Fig. 1. This signal is fed to the input of a conventional potentiostat having a positive feedback loop for IR correction (7) (operational amplifiers 1-3 in Fig. 1). Total compensation for large series resistance (very dilute solutions) is impossible because the whole circuit then tends to go into oscillations. This difficulty was also realized by De Levie and Husovsky (6) who had to use *a-posteriori* corrections when the total ionic strength in solution was below 0.01M. Figures 2b and 2c show the uncorrected and the corrected forms of the square wave, respectively, obtained with the present instrument, compared to the theoretical waveform which would be expected for a pure capacitor (Fig. 2a). Comparison of Fig. 2a and 2c shows that after a certain fraction of the period (marked by arrows) the current becomes constant and equal to that obtained for an ideal capacitor of the same magnitude. It is in this portion of the wave that one should sample the current to minimize errors due

to IR drop and its incomplete compensation. The shorter the sampling time, the smaller the error due to the above effect as seen from Fig. 2c. In addition to sampling, a clamping circuit was used to isolate d-c currents, which may originate in the instrument itself or in slow Faradaic processes, from being included in the output of the sampling unit. Eliminating the d-c level of the signal by a capacitor is not suitable because the final state is established only after several cycles. The clamping circuit described below has the advantage of reaching it in the first cycle.

The switching circuit includes two FET gates, one of which is open while the other is closed. Their opening and closing is synchronized with the square wave output of the potentiostat (after IR compensation) as shown in Fig. 3. The part of the switching circuit which controls the FET gates is shown in Fig. 4. Pulses are fed to A and B (cf. Fig. 4) from two comparators (amplifiers 5 or 7 and 6). One of them is controlled by the square wave (Fig. 3a) and the other by the triangular wave (Fig. 3b). The gate will open when both A and B in Fig. 4 are negative (or positive for the second FET in Fig. 1). Owing to the fact that the triangular wave is anti-phase with the square wave (Fig. 3a, 3b), they must be fed to opposite inputs of the corresponding comparators. The exact moment at which the gate will be opened is determined by the adjustable d-c level at the second input of the comparators which are synchronized with the triangular wave.

Performance

Measurements on dummy cells with capacitors in the range of 0.1-5 μF in series with resistors from 10 ohms to 10 kohms indicate proper correction for the series resistance up to frequencies of 4×10^3 Hz. Phase shifts in the positive feedback loop limit the upper frequency range. There is no instrumental limitation on the lowest frequency which can be employed. This will tend to be limited by electronic noise on the one hand and by the purity of the chemical

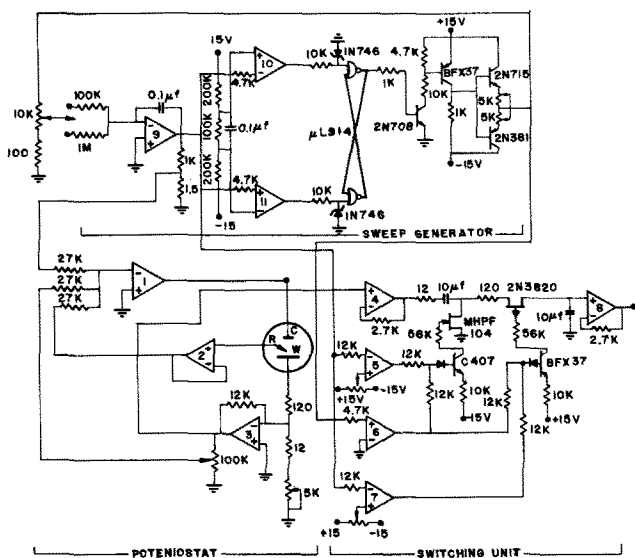


Fig. 1. Electronic circuit. Amplifiers 1-3 and 9, Date Device D-5; amplifiers 4-8 and 10-11, STS-709.

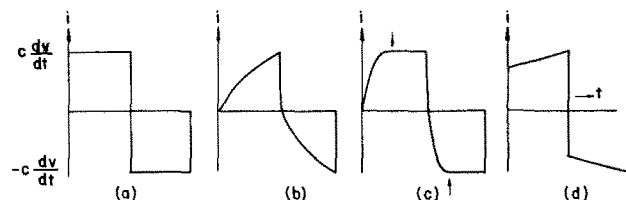


Fig. 2. Schematic representation of response of capacitors and resistors to triangular signal. (a) Pure capacitor, (b) capacitor and resistor in series, (c) as in (b) but following IR compensation, (d) capacitor and resistor in parallel.

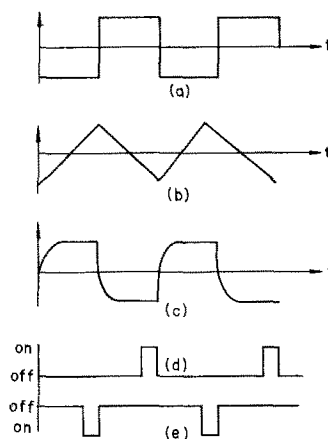


Fig. 3. Relation between the opening and closing of the FET gates and other signals in the instrument. (a) Square wave input, (b) triangular wave generated by square wave, (c) resulting square wave (after IR correction), (d) clamping gate trigger, (e) sampling gate trigger.

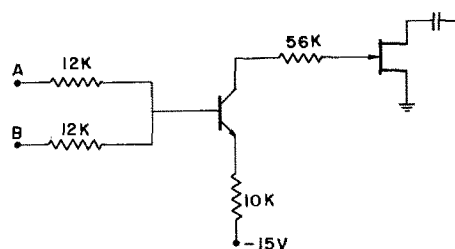


Fig. 4. Circuit controlling the FET gate

system (which determines the magnitude of the undesirable Faradaic currents) on the other hand.

The proper IR compensation is determined by viewing the square wave signal at the negative input of amplifier 4 (Fig. 1). The resistance of the potentiometer in the positive feedback loop is increased gradually, until the waveform changes from a shape such as in Fig. 2b to one resembling that in Fig. 2c. If the constant part of the square wave is longer than the sampling time (10% of the period in the present work), total compensation has been achieved. When the instrument capability is exceeded, such compensation cannot be achieved for any setting of the potentiometer, unless the frequency is decreased. Overcompensation drives the instrument into large amplitude oscillations. This should be avoided when working with solid electrodes since the surface of the electrode is likely to change in an irreversible manner.

The absolute value of the measured capacitance is obtained by calibration with a dummy cell consisting of calibrated capacitors and a variable series resistor. The dummy cell is connected directly to the working electrode terminal of the instrument and through 100-ohm resistors to the counter and reference electrode terminals. After measurement with the electrochemical cell the system is switched to the dummy cell. A capacitance similar to that of the real cell is chosen and the series resistance is changed (without changing the IR compensation) until a proper square wave is seen. The recorder reading in this position is calibrated in terms of the known value of the calibrated capacitor in the dummy cell.

The data of Grahame (8) for 0.01M NaF are compared in Fig. 5 with those obtained with the present instrument. The agreement is particularly good if it is remembered that our results were taken on a hanging mercury drop while those of Grahame are for a dropping mercury electrode. The whole C vs. E plot in Fig. 5 was obtained in a few minutes by applying a slow linear potential sweep from an external function generator (introduced to the summing point of amplifier 1 in Fig. 1). In Fig. 6 the comparison to Grahame's data (9) is made for a 1 mM solution of KCl at a frequency of 200 Hz. Here a dropping mercury electrode was used and the capacitance value was read off the recorder trace at a fixed time in the drop life, so that every mercury drop yielded a single point. In this dilute solution the IR compensation had to be readjusted in different ranges of potential, where there is a substantial change in capacity, to obtain best results. The agreement with Grahame's results for the same system is seen to be very good over the whole potential region. In Fig. 7 the capacitive component of the double layer impedance on a gold electrode in 0.3 and 1 mM solutions of HClO_4 are shown. For this purpose a gold rod was press-mounted in a Teflon plug in such

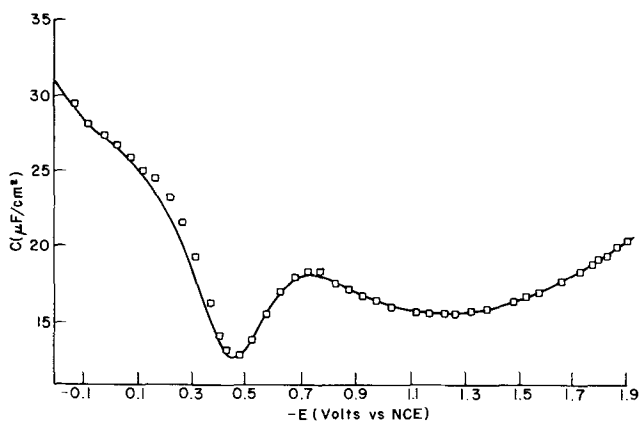


Fig. 5. Capacitance/potential plot for hanging mercury drop in 0.01N NaF at 25°C (solid line). Frequency 500 Hz, amplitude 12 mV. Sweep rate 20 mV/sec. Points are taken from data by Grahame (9).

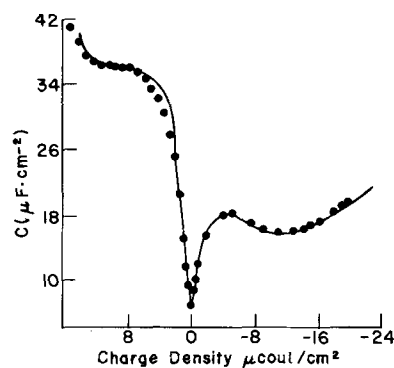


Fig. 6. Capacitance/charge plot in 10^{-3}M KCl at 25°C on a dropping mercury electrode. Frequency 200 Hz, amplitude 12 mV. Solid line taken from data by Grahame (4).

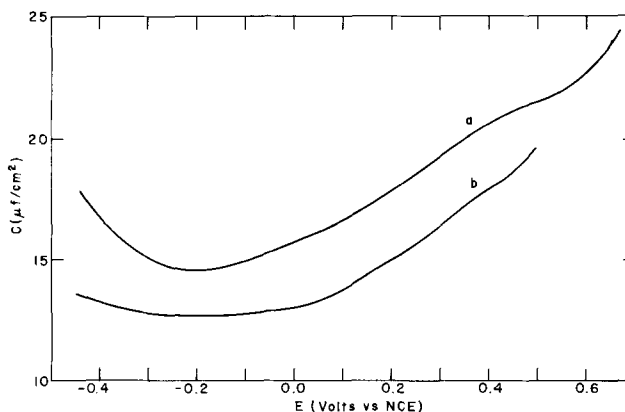


Fig. 7. Capacitance/potential plot on a gold disk electrode in (a) 10^{-3}M HClO_4 , (b) $3 \times 10^{-4}\text{M}$ HClO_4 . Frequency 200 Hz, amplitude 12 mV. Sweep rate 3 mV/sec.

a way that the gold surface was equiplanar with the bottom face of the Teflon. Thus the electrode in contact with the solution was a gold disk of well-defined dimensions (diameter 2 mm). The electrodes were polished using aluminum oxide, particle size 0.05μ on a Slyvat cloth. Solutions were deaerated by bubbling high purity helium. The results obtained for 1 mM solution generally agree with those reported by Schmid and Hackerman (10) who employed the single current-pulse technique.

Correction for Faradaic Current

The existence of Faradaic currents due to incomplete polarizability of the (solid) electrode under the desired experimental conditions, may be considered as a parallel resistance in the equivalent circuit representation of the ionic double layer impedance. The error introduced by this factor in the measured capacity is reduced by increasing the frequency and adjusting for optimum IR compensation. The shape of the square wave at the output of the potentiostat is shown for such a case in Fig. 2d. The error resulting from the Faradaic current can be readily estimated from the shape of the signal on the oscilloscope. The true capacitance C is related to the measured capacitance C_m through the equation

$$C = C_m \frac{i_{\min}}{(1 - P)i_{\max} + P i_{\min}}$$

where P is the fraction of the half-cycle during which sampling is made, i_{\min} and i_{\max} are the values of the current at the beginning and at the end of the half-cycle, measured on a curve such as Fig. 2d. Thus, as long as $(i_{\max} - i_{\min})/i_{\min}$ is relatively small a good estimate of the correction required to the measured capacity due to Faradaic reaction can be obtained.

Conclusions

The instrument described herein is best suited for double layer capacity measurements at highly polarizable electrodes. Correction for a small Faradaic current is possible, but the existence of electrochemical reactions at a high rate make measurements impossible. The dependence of the capacitance on potential or time can be plotted continuously. Measurements can be extended to very dilute solutions (lowest concentration used was $3 \times 10^{-4}M$) by incorporating a positive feedback loop. Measurements in $10^{-3}M$ KCl solution on Hg showed excellent agreement with the best literature data obtained by the bridge technique, but the instrument may find more applications for measurements on solid electrodes, where it can follow the slow drift in the values of double layer capacity with time. It can also be conveniently used to obtain the capacitance/potential curve during cycling with a triangular wave.

The advantage of a circuit applying a triangular wave over that applying the sine wave is that the occurrence of a series resistance is easily detected by the deviation of the resulting a-c current from square wave shape. Moreover, with the sampling method described above complete compensation for the series resistance is not necessary, thus measurements at higher frequencies and/or higher solution resistances are possible. The numerical value of the capacitance is obtained directly at the recorder output of the instrument and no *a posteriori* correction need be applied.

Acknowledgment

Financial support of this work by the Ford Foundation under Grant No. 6/C/IV is gratefully acknowledged. The authors also wish to thank Mr. S. Flash for building the capacitance meter.

Manuscript submitted Feb. 25, 1972; revised manuscript received March 24, 1972.

Any discussion of this paper will appear in a Discussion Section to be published in the June 1973 JOURNAL.

REFERENCES

1. D. C. Grahame, *J. Am. Chem. Soc.*, **71**, 2975 (1949); Tech. Report No. 6 ONR, May (1951).
2. B. Breyer and F. Gutmann, *Trans. Faraday Soc.*, **42**, 645, 650 (1946).
3. N. Tshernikovski and E. Gileadi, *Electrochim. Acta*, **16**, 579 (1971).
4. J. J. McMullen and N. Hackerman, *This Journal*, **106**, 341 (1959); J. S. Riney, G. M. Schmid, and N. Hackerman, *Rev. Sci. Instr.*, **32**, 588 (1961).
5. P. Delahay, R. De Levie, and A. M. Giuliani, *Electrochim. Acta*, **11**, 1141 (1966).
6. R. De Levie and A. A. Husovsky, *J. Electroanal. Chem.*, **20**, 181 (1969).
7. E. B. Brown, T. G. McCord, D. E. Smith, and D. D. DeFord, *Anal. Chem.*, **38**, 1119 (1966).
8. D. C. Grahame, Tech. Report No. 14 ONR (1954).
9. D. C. Grahame, A. Higinbottom, and F. Deane, "Trans. Symp. Electrode Proc., Philadelphia," p. 197, E. Yeager, Editor (1961).
10. G. M. Schmid and N. Hackerman, *This Journal*, **109**, 243 (1962).

Electrochemical Reactions with Consecutive Charge-Transfer Steps: Steady-State and Time-Dependent Behavior under Charge-Transfer and Diffusion Control

K. J. Bachmann

Bell Laboratories, Murray Hill, New Jersey 07974

ABSTRACT

Electrochemical reactions involving consecutive charge-transfer steps as expressed by the reaction schema



are considered assuming that the only irreversible processes are charge-transfer and diffusion and that disproportionation of the intermediate reaction products does not occur. An arbitrary number of n consecutive steps is assumed where feasible, but detailed discussion is restricted to the experimentally best understood case of a two-step reaction. A general description is given of the steady-state current density-overvoltage characteristics and for the current density vs. time curves in potentiostatic single-pulse experiments and for the variation of overvoltage with time in galvanostatic single-pulse experiments, respectively.

In recent years much attention has been devoted to studies of multistep electrochemical reactions mainly because of the increasing interest in organic electrochemistry where the over-all electrode reaction frequently consists of a sequence of chemical and charge-transfer reaction steps. Polarographic techniques have been particularly useful for studying reactions of this type partly because of the experimental advantages connected to the DME but, also, because an advanced theoretical concept of the effect of various combina-

tions of chemical and electrochemical reactions was earlier available for d-c polarography than for other electrochemical methods. We refer here to the well-known publications of Koutecky and Brdicka (1-3) and to the fundamental paper of Koutecky and Koryta (4) in which a general theory of polarographic kinetic currents was worked out by reducing all transport problems involving fast chemical reactions to a diffusion problem that may be solved by the usual means of a Laplace transformation or by the method of the dimensionless parameters (5). Tables of the appropriate boundary conditions and dimensionless parameters for a large variety of types and

* Electrochemical Society Active Member.

Key words: consecutive reactions, Tafel lines, potentiostatic and galvanostatic single-pulse method.

combinations of one chemical reaction and one charge-transfer step have been provided in Ref. (4). More recently the theoretical consideration of multistep electrode reactions was extended to other experimental methods, as, for example, a-c polarography, cyclic voltammetry, controlled-potential electrolysis, chronocoulometry, chronoamperometry and voltammetry on rotating disk and ring disk electrodes. An extensive review of the literature in this field up to 1966 has been given by Bewick and Thirsk (6) but considerable progress has been made since then, especially with respect to a-c and nonsteady-state type techniques.

The theory of a-c polarography was extended by Hung and Smith (7) and McCord and Smith (8-10), respectively, to include systems with two consecutive charge-transfer steps and coupling of a first-order chemical reaction to a preceding or subsequent charge-transfer reaction. Also, McCord and Smith (11) presented a general theory of second harmonic a-c polarography for the case of homogeneous chemical reactions coupled to a single heterogeneous charge-transfer step. Sluyters and Sluyters-Rehbach (12) considered the potential dependence of the kinetic parameters that determine the admittance of an electrode solution interface where the charge-transfer reaction is combined with first-order chemical reactions including reactant adsorption and catalytic reactions.

Because of their importance in organic electrochemistry much effort was made developing the theory with respect to electrode reactions following the ECE mechanism. The d-c polarographic current-potential relation was discussed by Sobel and Smith (13) and the changes in current density and reactant concentrations with time under the conditions of controlled-potential analysis were considered by Karp and Meites (14) and Harrison and Shoemith (15). Nicholson and Shain (16) examined the characteristics of cyclic voltammograms assuming that both charge-transfer reactions occur at the same equilibrium potential. The effect of a separation in the equilibrium potentials was later discussed by Polcyn and Shain (17). The special case of the intermediate chemical reaction being reversible was studied by Mastragostino, Nadjo, and Saveant (18) who also considered disproportionation as an alternative reaction path which may be distinguished from a reaction of the ECE type by a variation of the peak C.D. larger than proportional to the concentration. A discussion of the implication of uncompensated ohmic drop and double-layer charging in cyclic voltammetry with fast sweep rates as employed in investigations of multistep electrochemical reactions was given by Imbeau and Saveant (19). The effect of a disproportionation reaction onto the limiting C.D. obtained on a DME and a RDE was examined by Kastening (20) and Holub (21), respectively. Koopman (22) presented a theoretical treatment of double-step chronocoulometry for ECE reactions involving a chemical surface reaction assuming a linear adsorption isotherm for the reactants. Further references on the application of the various aforementioned methods in studies of the kinetics of organic electrode reactions may be found in the excellent reviews of Adams (23) and in the book of Frumkin and Eshler (24), an English translation of which has been recently published.

Aside from their relevance to organic electrochemistry, consecutive charge-transfer processes also have been recognized as being important in many metal/metal-ion systems and metal-ion redox electrodes. Classical examples are the copper/copper(II) and the thallium(I)/thallium(III) systems for which a consecutive mechanism of the type



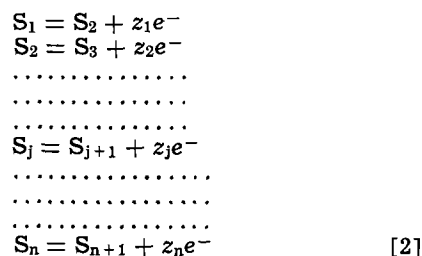
($S_1 = \text{Cu}, \text{Tl}^+$; $S_2 = \text{Cu}^+, \text{Tl}^{2+}$; $S_3 = \text{Cu}^{2+}, \text{Tl}^{3+}$) was

proposed in the earlier literature (25, 26). While this mechanism was confirmed for the Cu/Cu²⁺ electrode by recent investigations of various authors (27, 30) the results of Vetter and Thiemke (26) for the Tl⁺/Tl³⁺ electrode appear to be somewhat in question by later work of Catherino and Jordan (31), Ulstrup (32), and Jonasson and Stranks (33). Extensive investigations of Losev and co-workers (34-38) resulted in a three-step mechanism for the In/In³⁺ and the Bi/Bi³⁺ electrode reactions. These results are supported by the work of Armstrong *et al.* (34) on the anodic dissolution of indium in alkaline solutions and by studies of Lovrecek and Mekljavic (40) for the electrochemical behavior of bismuth amalgam electrodes. Recently a mechanism according to Eq. [1] was proposed by Gaiser and Heusler (41, 42) for the Zn/Zn²⁺ and the Cd/Cd²⁺ electrodes assuming strong adsorption of the intermediate monovalent ions ($S_2 = \text{Zn}_{\text{ads}}^+$ and Cd_{ads}^+ , respectively) on the surface of the electrode. A two-step mechanism for the Cd/Cd²⁺ electrode was also concluded by Despic *et al.* (43) who studied the faradaic impedance of a Cd-amalgam electrode; but no adsorption effects were incorporated in their analysis.

In the author's opinion, only for the Cu/Cu²⁺ electrode sufficient experimental evidence is available for convincingly stating a consecutive charge-transfer mechanism.¹ All the other above-mentioned examples appear to be somewhat indeterminate and need further consideration, particularly since the major part of the arguments in favor of consecutive mechanisms was based on interpretations of steady-state C.D. *vs.* overvoltage curves in terms of Tafel lines, which as demonstrated below can easily lead to ambiguous results. Also, the outcome of nonsteady-state type experiments is far from being understood when adsorption of the reactants is of importance since in this case, as shown by Delahay and co-workers (49, 50), charging of the double layer cannot be approximated by an *a priori* separable capacitive current. The problems which arise in a theoretical treatment of electrochemical reactions under such conditions were recently discussed by Rangarajan (51) but multistep reactions have not yet been considered in this context. In this paper we restrict ourselves to systems for which the influences of adsorption-desorption processes can be neglected. Both the steady-state and nonsteady-state behavior of electrodes characterized by a consecutive charge-transfer mechanism are described.

Steady-State Current Density-Overvoltage Characteristics

For a general description the consecutive charge-transfer reactions are expressed by the reaction scheme



where the symbol S_1 stands for the most reduced substance of the electrochemical systems, S_j is an intermediate substance, and S_{n+1} is the most oxidized substance. In the following discussions all parameters related to S_1, S_2, \dots, S_j , and S_n , respectively, are noted by the subscripts 1, 2, \dots, j , and n , respectively (for

¹ In another paper (44) new experimental results on the Cu/Cu²⁺ electrode will be presented which support this mechanism. Note that in nonaqueous solvents the reaction $\text{Cu} = \text{Cu}^{2+} + 2e^-$ occurs in two well separated steps (45, 47) but disproportionation of the Cu⁺ in aqueous solutions is assumed in Ref. (45-47). A recent investigation of Hampson and Latham (48) on the dependence of the exchange C.D. on Cu²⁺ concentration did not confirm the participation of Cu⁺ in nitrate solution.

example c_1 = concentration of S_1 , D_4 = diffusion constant of S_4). Also we label the current density carried by the ν th charge-transfer reaction as i_ν , i.e., the current density carried by the first step as i_1 , etc. In analogous fashion the exchange current densities and charge-transfer coefficients related to the ν th reaction are denoted as $i_{\nu,0}$ and α_ν , respectively. If the first charge-transfer step, Eq. [1], is a redox reaction, then $z_1 = 1$. However, if it is a metal/metal-ion charge-transfer reaction, where a metal ion of charge z_1 crosses the double layer, then $z_1 \geq 1$. In this case Reaction [2] would be a redox reaction in which the metal ion S_2 created in Reaction [1] changes its valency by 1. Since we do not consider here adsorption-desorption processes which may be associated with partial charge-transfer steps, and also, exclude purely chemical reactions, $z_\nu = 1$ for all $\nu > 1$. It is assumed that the only irreversible processes are charge-transfer and diffusion and that disproportionation of the intermediate substances S_j does not occur. The electrode surface is considered to be an infinite plane, so that diffusion takes place in direction x perpendicular to the interface. Also the assumption is made that prior to the flow of an external current the electrode is in equilibrium with respect to all charge-transfer reactions and that a large excess of supporting electrolyte is present. Anodic current densities i and overvoltage η are taken to be positive. The total current density flowing through the electrode is given by

$$i_t = \sum_{\nu=1}^n i_\nu \quad [3]$$

where i_ν is the current density carried by the ν th charge-transfer reaction.

By Volmer's equations i_ν is related to the concentrations of S_ν and $S_{\nu+1}$ at the interface

$$i_\nu = i_{\nu,0} \cdot \frac{c_\nu(x=0)}{c_{\nu,0}} \cdot \exp\left(\frac{\alpha_\nu z_\nu F}{RT} \eta\right) - i_{\nu,0} \frac{c_{\nu+1}(x=0)}{c_{\nu+1,0}} \exp\left(-\frac{[1-\alpha_\nu]z_\nu F}{RT} \eta\right) = i_{\nu,+} \frac{c_\nu(x=0)}{c_{\nu,0}} - i_{\nu,-} \frac{c_{\nu+1}(x=0)}{c_{\nu+1,0}} \quad [4]$$

Also, by combining Fick's law with Faraday's law we get $n + 1$ equations relating the gradient of the concentration of the $n + 1$ substances S_ν to the C.D.'s of the reaction steps in which S_ν is created and used up, respectively

$$\frac{dc_\nu}{dx} = \frac{i_\nu}{z_\nu F D_\nu} - \frac{i_{\nu-1}}{z_{\nu-1} F D_\nu} \quad \text{at } x = 0 \quad [5]$$

We assume that under steady-state conditions a diffusion layer of constant width δ is established and that in the bulk of the solution, i.e., at $x \geq \delta$, the equilibrium concentrations $c_{\nu,0}$ are maintained. If no chemical reactions occur in the diffusion layer the concentration gradients may be written as

$$\frac{dc_\nu}{dx} = -\frac{c_\nu(x=0) - c_{\nu,0}}{\delta} \quad \text{at } 0 \leq x \leq \delta \quad [6]$$

$$\frac{dc_\nu}{dx} = 0 \quad \text{at } x \geq \delta \quad [7]$$

Let

$$\frac{c_\nu}{c_{\nu,0}} = y_\nu \quad (\nu = 1, 2, \dots, n + 1) \quad [8]$$

and substitute [6] and [4] into [5] to get

$$\alpha_\nu y_\nu - 1 y_{\nu-1} + \alpha_{\nu+1} y_{\nu+1} + \alpha_{\nu,\nu+1} y_{\nu+1} = 1 \quad [9]$$

where

$$\alpha_{\nu,\nu-1} = -\frac{z_\nu}{z_{\nu-1}} \cdot \frac{i_{\nu-1,+}}{i_{\nu,1}} \quad [10]$$

$$a_{\nu,\nu} = 1 + \frac{i_{\nu,+}}{i_{\nu,1}} + \frac{z_\nu}{z_{\nu-1}} \cdot \frac{i_{\nu-1,-}}{i_{\nu,1}} \quad [11]$$

$$a_{\nu,\nu+1} = -\frac{i_{\nu,-}}{i_{\nu,1}} \quad [12]$$

and $i_{0,+} = i_{0,-} = i_{n+1,+} = i_{n+1,-} = 0$. The quantity

$$i_{\nu,1} = \frac{z_\nu F D_\nu c_{\nu,0}}{\delta} \quad [13]$$

is the formal diffusion-limited C.D. for substance S_ν . In matrix notation, the set of $n + 1$ nonhomogeneous linear equations with $n + 1$ unknowns y_ν ($\nu = 1, 2, \dots, n + 1$) defined by Eq. [9] may be represented as

$$[a]\{y\} = \{1\} \quad [14]$$

where

$$[a] = \begin{pmatrix} a_{11} & a_{12} & 0 & \dots & \dots & 0 \\ a_{21} & a_{22} & a_{23} & 0 & \dots & 0 \\ 0 & a_{32} & a_{33} & a_{34} & \dots & 0 \\ \dots & \dots & \dots & \dots & \dots & \dots \\ 0 & \dots & \dots & a_{nn-1} & a_{nn} & a_{nn+1} \\ 0 & \dots & \dots & a_{n+1n} & a_{n+1n+1} & \dots \end{pmatrix} \quad [15]$$

is the $(n + 1)$ by $(n + 1)$ coefficient matrix and $\{y\}$ and $\{1\}$ are column vectors of order $(n + 1)$. Since the determinant of $[a]$ does not vanish, the solutions to Eq. [9] and [14] are obtained explicitly by premultiplication of Eq. [14] by the inverse coefficient matrix $[a]^{-1}$

$$\{y\} = [a]^{-1}\{1\} \quad [16]$$

i.e., the value of x_ν is determined by the sum of the elements of the ν th row of the adjoint of $[a]$ divided by det. $[a]$.

$$i_t = \sum_{\nu=1}^n i_\nu = \sum_{\nu=1}^n i_{\nu,+} y_\nu - \sum_{\nu=1}^n i_{\nu,-} y_{\nu+1} \quad [17]$$

represents in conjunction with Eq. [16] the general form of the C.D.-overvoltage characteristics in case of an electrode reaction involving an arbitrary number of n consecutive charge-transfer steps under both charge-transfer and diffusion control.

For a two-step reaction Eq. [17] reduces to

$$i_t = i_1 + i_2 \quad [18]$$

$$i_1 = \frac{i_{1,+}}{i_{1,+} + i_{1,1}} \cdot (i_{1,1} + i_{1,-} \cdot Q) - i_{1,-} \cdot Q \quad [19]$$

$$i_2 = i_{2,+} \cdot Q - \frac{i_{2,-}}{i_{2,-} + i_{3,1}} \cdot (i_{3,1} + i_{2,+} \cdot Q) \quad [20]$$

where

$$Q = \frac{c_2}{c_{2,0}} = \frac{1 + \frac{i_{1,1}}{z_1 i_{2,1}} \cdot \frac{i_{1,+}}{i_{1,+} + i_{1,1}} + \frac{i_{3,1}}{i_{2,1}} \cdot \frac{i_{2,-}}{i_{2,-} + i_{3,1}}}{1 + \frac{i_{1,1}}{z_1 i_{2,1}} \cdot \frac{i_{1,-}}{i_{1,+} + i_{1,1}} + \frac{i_{3,1}}{i_{2,1}} \cdot \frac{i_{2,+}}{i_{2,-} + i_{3,1}}} \quad [21]$$

and

$$i_{1,1} = \frac{z_1 F D_1 c_{1,0}}{\delta} \quad [22]$$

$$i_{2,1} = \frac{F D_2 c_{2,0}}{\delta} \quad [23]$$

$$i_{3,1} = \frac{F D_3 c_{3,0}}{\delta} \quad [24]$$

assuming $z_1 = z$ and $z_2 = 1$.

For large anodic overvoltage the diffusion-limited C.D. $i_{1,+}$ is given by

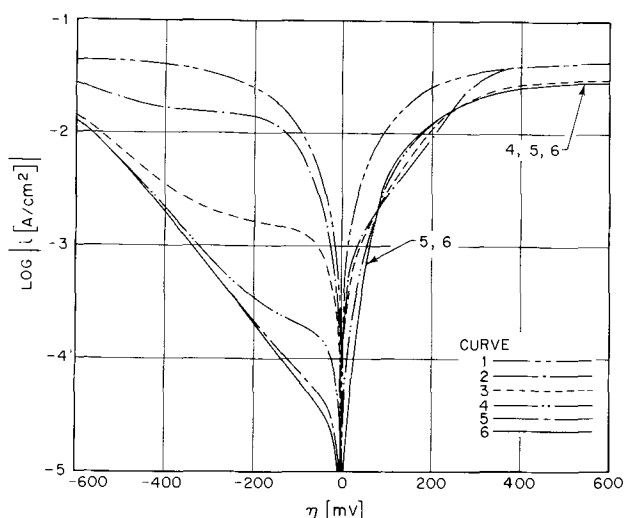


Fig. 1. Curves $\log |i|$ vs. overvoltage η , varied parameters $i_{2,0}$ and $i_{2,1}$.

Curve 1: $i_{1,0} = i_{2,0} = 10^{-3}$ A/cm²; $z = 1$; $\alpha_1 = 0.3$; $\alpha_2 = 0.7$; $D_1 = D_2 = D_3 = 1.5 \times 10^{-5}$ cm² sec⁻¹; $c_{1,0} = c_{2,0} = c_{3,0} = 10^{-5}$ mole/cm³; $i_{1,1} = i_{2,1} = i_{3,1} = 1.5 \times 10^{-2}$ A/cm².

Curve 2: as curve 1 but $i_{2,0} = 10^{-5}$ A/cm².

Curve 3: as curve 2 but $c_{2,0} = 10^{-6}$ mole/cm³; $i_{2,1} = 1.5 \times 10^{-3}$ A/cm².

Curve 4: as curve 2 but $c_{2,0} = 10^{-7}$ mole/cm³; $i_{2,1} = 1.5 \times 10^{-4}$ A/cm².

Curve 5: as curve 2 but $c_{2,0} = 10^{-8}$ mole/cm³; $i_{2,1} = 1.5 \times 10^{-5}$ A/cm².

Curve 6: as curve 2 but $c_{2,0} = 10^{-9}$ mole/cm³; $i_{2,1} = 1.5 \times 10^{-6}$ A/cm².

$$i_{1,+} = \lim_{\eta \rightarrow \infty} i_t = \frac{1}{z} \{ (z+1) i_{1,1} + z i_{2,1} \} \quad [25]$$

While for large cathodic overvoltage the diffusion-limited C.D. $i_{1,-}$ is given by

$$i_{1,-} = \lim_{\eta \rightarrow \infty} i_t = - \{ (z+1) i_{3,1} + z i_{2,1} \} \quad [26]$$

However, if $i_{2,0} = 0$ then $i_{+,1} = i_{1,1}$ and $i_{-,1} = -z i_{2,1}$, and if $i_{1,0} = 0$ then $i_{+,1} = i_{2,1}$ and $i_{-,1} = -i_{3,1}$, i.e., the quantities $i_{1,1}$, $i_{2,1}$, $i_{3,1}$ are the diffusion-limited C.D.'s as expected if only either one of the two reactions would occur. As demonstrated in Fig. 1 only under certain special conditions the individual values of $i_{1,1}$, $i_{2,1}$, and $i_{3,1}$ may be derived from the C.D. overvoltage characteristics.

Clearly $\lim_{i_{1,1} \rightarrow \infty} Q = 1$ and $i_t = (i_{1,+} + i_{2,+}) -$

$(i_{1,-} + i_{2,-})$, i.e., under pure charge-transfer control the Tafel lines would be determined by both reactions and if $i_{1,0} \neq i_{2,0}$ by the reaction with the larger exchange C.D. in both the anodic and the cathodic branch. If one considers the more likely special case $i_{1,1} = i_{3,1} \rightarrow \infty$ but with $i_{2,1} \rightarrow 0$ then $Q \rightarrow (i_{1,+} + i_{2,-}) / (i_{1,-} + i_{2,+})$ and Eq. [18] becomes identical with the expressions derived by Vetter (52). For $\eta \gg 0$, $i_t \approx 2i_{1,+}$ while for $\eta \ll 0$, $i_t \approx -2i_{2,-}$, i.e., here the anodic Tafel lines depend on Reaction [1] while the cathodic Tafel lines yield the parameters of Reaction [2]. A detailed evaluation of Vetter's method of determining kinetic parameters from the steady-state C.D.-overvoltage characteristics in the Tafel regime was undertaken by Hurd (53) on the basis of digitally simulated curves. However, no rigorous treatment of the interaction of charge-transfer and diffusion was given and transport phenomena were neglected in extending Vetter's theory to an unlimited number of consecutive charge-transfer reactions.

Losev, Gorodetskii, and Molodov (54, 57) have recently published a number of papers in which the special case of a three-step reaction is discussed. Their

work does not add any new information to the previously published results of Vetter (52) and Hurd (53) but, in my opinion, it is wrong in a fundamental assumption. While Vetter recognized that the steady-state continuity condition $i_\nu = i_{\nu+1}$, is satisfied only if diffusion of the intermediate substances can be neglected and Hurd restricts his extension of Vetter's work to pure charge-transfer control, Losev *et al.* state explicitly [for example in Ref. (55)] that this condition is always satisfied even at high concentrations of the intermediate products and assuming exchange of these substances with the bulk via diffusion. This is obviously not true since under such conditions the bulk solution represents an additional source or sink from which the equivalent mass flow at the interface may be balanced in steady state even if $i_\nu \neq i_{\nu+1}$.

For a demonstration of the properties of the C.D.-overvoltage characteristics in the general case of mixed diffusion and charge-transfer control for all three substances involved in a two-step reaction a family of $\log |i|$ vs. overvoltage curves has been generated via digital simulation on the basis of Eq. [18]-[21] assuming $i_{1,0} \gg i_{2,0}$, $i_{1,1} = i_{3,1} \approx 15 i_{1,0}$ but $i_{2,1} \ll i_{2,0}$ and $\alpha_1 = 0.3$ and $\alpha_2 = 0.7$. If $i_{1,1}$ and $i_{2,1}$ are finite and $i_{1,0} \neq i_{2,0}$, a situation may occur where the Tafel line for the reaction with lower exchange C.D. exists but the Tafel line for the faster reaction step is masked by the over-all diffusion limited C.D. This behavior which according to Vetter and Abend [*loc. cit.*, p. 380 Ref. (26)] may be realized in the case of the $\text{Sn}^{2+}/\text{Sn}^{4+}$ redox couple, is demonstrated by curve 6 in Fig. 1. Extrapolation of the cathodic Tafel line to $\eta = 0$ yields $2i_{2,0}$ and its slope is governed by $(1 - \alpha_2)$. A pseudo Tafel line may be considered in the anodic branch at low η yielding also $i_{2,0}$ [compare Mohilner (58)]. Although $i_{1,1}$ exceeds $i_{1,0}$ by a factor of 15, no true anodic Tafel line is observable in curve 6. Curves 5 to 2 were calculated with the same parameters as curve 6 except that $i_{2,1}$ was increased by a factor of 10 from curve to curve. For curve 5, $i_{2,1} \approx i_{2,0}$ and the slope of the cathodic "Tafel line" decreases which experimentally may not be recognized as a deviation from the true Tafel line at $i_{2,1} \ll i_{2,0}$. If $i_{2,1} \gg i_{2,0}$ the cathodic C.D. tends to show $i_{2,1}$ as a separate step in the C.D.-overvoltage characteristic. In this case neither the parameters of Reaction [1] nor those of Reaction [2] can be derived. Even worse, curve 3 shows an "apparent Tafel line" in the anodic branch, but extrapolation of this linear section to $\eta = 0$ yields an intermediate value between $i_{2,0}$ and $i_{1,0}$. This demonstrates that interpretation of the steady-state C.D.-overvoltage characteristics on the basis of "Tafel lines" becomes an ambiguous affair if the two exchange C.D.'s differ very much and $i_{2,1}$, although much less than $i_{1,1}$ and $i_{3,1}$, has a value comparable or larger than the smallest exchange C.D.

It should be mentioned here that a more general consideration of the steady-state C.D. vs. overvoltage curve in the vicinity of the equilibrium potential which involves an arbitrary number of charge-transfer steps and chemical reactions in series was given by Mauser (59), subsequently extended by Riddiford (60) to include transport control and more complex coupling between the partial reactions. However, with increasing complexity of the reaction path, separation of the various consecutive steps on the basis of an interpretation of the steady-state C.D.-overvoltage characteristics becomes more and more impractical and other experimental techniques offer a better chance for successfully deriving the kinetic parameters. An especially promising approach seems to be investigations with a ring disk electrode that have been theoretically evaluated in a series of papers by Alberly *et al.* (61) [compare Ref. (6) for the earlier literature]. Also, the utilization of nonsteady-state type experiments, demonstrated in the following section, may be of advantage.

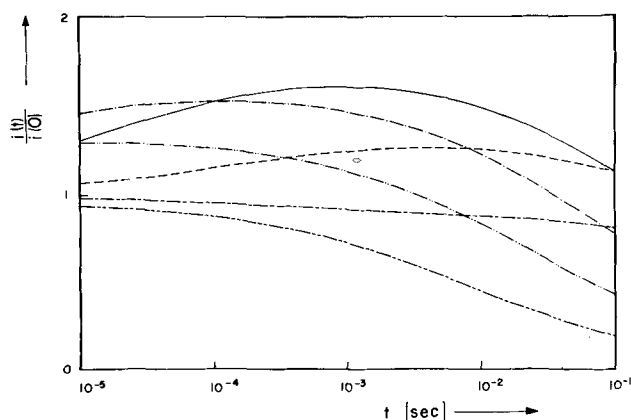


Fig. 2. Current densities $i(t)$, expressed as fractions of the initial current densities $i(0)$, as a function of time t .

Parameters: $i_{1,0} = 10^{-3}$ A/cm²; $i_{2,0} = 10^{-5}$ A/cm²; $\alpha_1 = 0.3$; $\alpha_2 = 0.7$; $z = 1$; $D_1 = D_2 = D_3 = 1.5 \times 10^{-5}$ cm²/sec; $c_{1,0} = c_{3,0} = 10^{-5}$ mole/cm³; $c_{2,0} = 10^{-8}$ mole/cm³ (compare curve 5 Fig. 1).

$\eta = 80$ mV ---; $\eta = 100$ mV - · - ·; $\eta = 150$ mV —; $\eta = 200$ mV - - - -; $\eta = 250$ mV - · · - ·; $\eta = 300$ mV - · · · · - ·.

Current Density vs. Time Curves in Potentiostatic Single-Pulse Experiments

Analysis of single-pulse potentiostatic transients for pure metal/metal-ion and for alloy/metal-ion electrodes under charge-transfer and diffusion control in case of an electrode reaction involving two consecutive charge-transfer steps was presented in two preceding papers (62, 63).² As shown, the current density vs. time is of the form

$$i(t) = A \cdot f(t) + B \cdot g(t) \quad [27]$$

where $f(t)$ is a function which decreases in the time interval $[0, \infty]$ monotonically from 1 to 0, while $g(t)$ is zero at the beginning of the overvoltage pulse and at infinite time, but positive in between. A and B are constants, A being always of same sign as η . The sign of B may be the same as the sign of A if $i_{1,0} \neq i_{2,0}$ and $c_{2,0}D_2 < c_{1,0}D_1$; $c_{3,0}D_3$. In this case a characteristic delayed maximum occurs in the $i(t)$ -transient at $\eta < 0$ if $i_{1,0} < i_{2,0}$ and at $\eta > 0$ if $i_{1,0} > i_{2,0}$. It turns out that these conditions, for which potentiostatic single-pulse experiments reveal a property which is specific for consecutive charge-transfer reactions and which depends quite sensitively on the values of the kinetic parameters, are identical with those for which interpretation of steady-state data is particularly difficult. For example, taking the kinetic parameters and bulk concentrations which were chosen for the calculation of curve 5 in Fig. 1, an anodic overvoltage regime $85 \text{ mV} < \eta < 295 \text{ mV}$ exists for which sign $A = \text{sign } B = \text{sign } \eta$. Figure 2 shows a family of curves $i(t)/i(t=0)$ vs. time t calculated with the same parameters on the basis of Eq. [27] and with the amplitude of the overvoltage pulse as varied parameter. For $\eta = 80 \text{ mV}$ and $\eta = 300 \text{ mV}$, i.e., 5 mV outside the limits of η for which sign $B = \text{sign } \eta$, the usual monotonically falling function is observed. In accordance with the properties of the C.D. vs. time curves discussed in Ref. (62, 63) at 100, 150, 200, and 250 mV delayed maxima appear. Note that due to limitations by convection and by the finite rise time of electronic potentiostats the electrode process can be described in terms of the model discussed in this paper only within a time range $10^{-5} \leq t \leq 1 \text{ sec}$. Therefore, the delayed maximum in the

² The general case of n consecutive charge-transfer reactions was considered by Koutecky (2) assuming pure diffusion control. Note that in a chronoamperometric study of the reduction of *p*-nitrosophenol Alberts and Shain (64) discussed the ECE case but with different b.c. as used in Ref. (62, 63) since only one substance was assumed to be present at $t = 0$ in their treatment.

$i(t)$ transient for $\eta = 250 \text{ mV}$ would not be recognized in an experiment.

Overvoltage vs. Time Curves in Galvanostatic Single-Pulse Experiments

Since experiments under galvanostatic conditions require much less involved apparatus than those performed under potentiostatic conditions the galvanostatic single-pulse method frequently has been favored in studies on the nonsteady-state behavior of electrode systems although its theoretical analysis is more complicated than the potentiostatic case. This is due to the fact that in boundary condition Eq. [5], the desired function $\eta(t)$ occurs in the exponentials and double-layer charging has to be considered.

In case of a single-step electrode reaction the function $\eta(t)$ was derived by Berzins and Delahay (15) under the assumptions that the total C.D. may be separated into capacitive C.D. i_c and faradaic C.D. i_f and that a linear relationship exists between i_f and η . These assumptions hold only approximately and require that the charge stored in the double layer due to changes in the excess of substances which attend in the charge-transfer reaction is negligible and that the overvoltage is limited to $|\eta| \lesssim 1 \text{ mV}$ [compare Ref.

(49, 50) and Kojiman *et al.* (66)]. Nevertheless, the classical formula derived by Berzins and Delahay for the overvoltage vs. time curve in galvanostatic single-pulse experiments has found many useful applications.

Very little is known yet on the nonsteady-state behavior under galvanostatic conditions in case of consecutive charge-transfer reactions. Plonski (67) considered the $\eta(t)$ curve in case of a reaction of the type $M \rightleftharpoons M^{z_1+} + z_1e^-$ and $M^{z_1+} \rightleftharpoons M^{z_2+} + (z_2 - z_1)e^-$ where M stands for a pure metal. However, mass transport was neglected in this treatment, which in the opinion of the author, is an unrealistic assumption unless strong adsorption of the intermediate ion and the existence of a very large concentration of the most oxidized ion in solution are assumed. In the latter case, however, other problems arise, a discussion of which is outside the scope of the present paper. We consider here the $\eta(t)$ curve for the reaction being controlled by both charge-transfer and diffusion with no restrictions on the bulk concentrations and diffusion constants of all substances involved, but do not include adsorption so that the aforementioned assumptions made in Ref. (65) may be utilized in a treatment of the two-step case.

It can be shown that under these conditions the desired expression for the overvoltage as a function of time is

$$\eta(t) = iR_D \cdot \{K_1\theta_1(t) + K_2\theta_2(t) + K_3\theta_3(t) + K_4\sqrt{t} + K_5\} \quad [28]$$

where

$$R_D = \frac{RT}{zF i_{1,0}} + \frac{RT}{F i_{2,0}} \quad [29]$$

is the charge-transfer resistance and

$$\theta_\mu = \exp\left(\frac{t}{\tau_\mu}\right) \cdot \text{erfc} \sqrt{\frac{t}{\tau_\mu}}, \quad \mu = 1, 2, 3 \quad [30]$$

The constants $K_1 \dots K_5$ may be written in terms of the time constants τ_1, τ_2, τ_3 , and $\tau_D = R_D \cdot C_D$

$$K_1 = \frac{\tau_1^2(\tau_D - \sqrt{\tau_2\tau_3})}{\tau_D^2(\sqrt{\tau_1} - \sqrt{\tau_2})(\sqrt{\tau_1} - \sqrt{\tau_3})} \quad [31]$$

$$K_2 = \frac{\tau_2^2(\tau_D - \sqrt{\tau_1\tau_3})}{\tau_D^2(\sqrt{\tau_2} - \sqrt{\tau_1})(\sqrt{\tau_2} - \sqrt{\tau_3})} \quad [32]$$

$$K_3 = \frac{\tau_3^2(\tau_D - \sqrt{\tau_1\tau_2})}{\tau_D^2(\sqrt{\tau_3} - \sqrt{\tau_1})(\sqrt{\tau_3} - \sqrt{\tau_2})} \quad [33]$$

$$K_4 = \frac{2}{\sqrt{\pi}} \cdot \left\{ \frac{K_1}{\sqrt{\tau_1}} + \frac{K_2}{\sqrt{\tau_2}} + \frac{K_3}{\sqrt{\tau_3}} \right\} \quad [34]$$

$$K_5 = - (K_1 + K_2 + K_3) \quad [35]$$

The time constants are related to the kinetic parameters and bulk concentrations by a cubic equation

$$(\sqrt{\tau})^3 - \frac{\Delta}{\epsilon} (\sqrt{\tau})^2 + \frac{\sigma}{\epsilon} \sqrt{\tau} - \frac{1}{\epsilon} = 0 \quad [36]$$

where

$$\epsilon = \frac{F}{RTc_D} \cdot i_{1,0} i_{2,0} \cdot \left\{ \frac{1}{zF\sqrt{D_1}c_{1,0}} + \frac{(z+1)^2}{zF\sqrt{D_2}c_{2,0}} + \frac{z}{F\sqrt{D_3}c_{3,0}} \right\} \quad [37]$$

$$\Delta = \frac{i_{1,0} i_{2,0}}{zF^2\sqrt{D_1}D_2D_3c_{1,0}c_{2,0}c_{3,0}} \cdot (c_{1,0}\sqrt{D_1} + c_{2,0}\sqrt{D_2} + c_{3,0}\sqrt{D_3}) + \frac{1}{\tau_D} \quad [38]$$

and

$$\sigma = \frac{i_{1,0}}{2F\sqrt{D_1}c_{1,0}} + \frac{i_{1,0}}{2F\sqrt{D_2}c_{2,0}} + \frac{i_{2,0}}{F\sqrt{D_2}c_{2,0}} + \frac{i_{2,0}}{F\sqrt{D_3}c_{3,0}} \quad [39]$$

Details on the derivation of Eq. [28] and its application to the interpretation of experimentally obtained $\eta(t)$ -curves are discussed in another paper (44).

Summary

A general description of the steady-state C.D.-overvoltage characteristic is derived for electrochemical reactions involving an arbitrary number of consecutive charge-transfer steps as expressed by the equation

$$S_\nu = S_{\nu+1} + z_\nu e^{-\nu} \quad \nu = 1, 2, \dots, n \quad [1]$$

assuming both charge-transfer and diffusion control. A detailed discussion of the properties of plots of $\log |i|$ vs. η is given for reactions involving two charge-transfer steps and it is demonstrated via digital simulation that interpretation of the steady-state C.D.-overvoltage characteristics in terms of Tafel lines becomes ambiguous if the exchange C.D.'s differ in magnitude and the formal diffusion-limited C.D. for the intermediate product becomes comparable or larger than the smallest exchange C.D.

As demonstrated under these conditions characteristic delayed maxima appear in the C.D. vs. time curve obtained in potentiostatic single-pulse experiments which, therefore, are a very useful supplement to steady-state type measurements. Also, a general expression is given for the variation of overvoltage with time in galvanostatic single-pulse experiments which is interpreted in terms of the charge-transfer resistance and of three characteristic time constants.

Acknowledgments

The author would like to thank J. H. Wernick for many helpful suggestions and for his interest in this work.

Manuscript submitted Dec. 2, 1971; revised manuscript received April 10, 1972. This was Paper 152 presented at the Cleveland Meeting of the Society, Oct. 3-7, 1971.

Any discussion of this paper will appear in a Discussion Section to be published in the June 1973 JOURNAL.

REFERENCES

1. J. Koutecky and R. Brdicka, *Collection Czech. Chem. Commun.*, **12**, 337 (1947).

2. J. Koutecky, *ibid.*, **18**, 11, 183, 311 (1953).
3. R. Brdicka, *Z. Elektrochem.*, **64**, 16 (1960).
4. J. Koutecky and J. Koryta, *Electrochim. Acta*, **3**, 318 (1961).
5. J. Koutecky, *Czech. J. Phys.*, **2**, 50 (1953).
6. A. Bewick and H. R. Thirsk in "Modern Aspects of Electrochemistry," Vol. 5, J. O'Bockris and B. E. Conway, Editors, Academic Press, New York (1969).
7. H. L. Hung and D. E. Smith, *J. Electroanal. Chem.*, **11**, 237 (1966); **11**, 425 (1966).
8. T. G. McCord and D. E. Smith, *Anal. Chem.*, **41**, 116 (1969).
9. T. G. McCord, H. L. Hung, and D. E. Smith, *J. Electroanal. Chem.*, **21**, 5 (1969).
10. D. E. Smith and T. G. McCord, *Anal. Chem.*, **40**, 474 (1968).
11. T. G. McCord and D. E. Smith, *ibid.*, **40**, 1967 (1968); *J. Electroanal. Chem.*, **26**, 61 (1970).
12. M. Sluyters-Rehbach and J. H. Sluyters, *J. Electroanal. Chem.*, **26**, 237 (1970).
13. H. R. Sobel and D. E. Smith, *ibid.*, **26**, 271 (1970).
14. S. Karp and L. Meites, *ibid.*, **17**, 253 (1968).
15. J. A. Harrison and D. W. Shoosmith, *ibid.*, **28**, 301 (1970).
16. R. S. Nicholson and I. Shain, *Anal. Chem.*, **37**, 178 (1965).
17. D. S. Polcyn and I. Shain, *ibid.*, **38**, 370 (1966).
18. M. Mastragostino, L. Nadjo, and J. M. Saveant, *Electrochim. Acta*, **13**, 721 (1968).
19. J. C. Imbeaux and J. M. Saveant, *J. Electroanal. Chem.*, **31**, 183 (1971).
20. B. Kastening, *ibid.*, **24**, 417 (1970).
21. K. Holub, *ibid.*, **30**, 71 (1971).
22. R. Koopmann, *Ber. Bunsenges. Physik. Chem.*, **72**, 32 (1968).
23. R. N. Adams, *Accounts Chem. Res.*, **2**, 175 (1969); "Electrochemistry at Solid Electrodes," Marcel Dekker, New York (1969).
24. A. N. Frumkin and A. B. Eshler, "Progress in Electrochemistry of Organic Compounds," Plenum Press, New York (1971).
25. E. Mattson and J. O'M. Bockris, *Trans. Faraday Soc.*, **55**, 1586 (1959); L. N. Nekrasov and N. P. Berezina, *Dokl. Akad. Nauk SSSR*, **142**, 855 (1962).
26. K. J. Vetter and G. Thiemke, *Z. Elektrochem.*, **64**, 805 (1960); K. J. Vetter, "Elektrochemische Kinetik," p. 376, Springer Verlag, Berlin (1961).
27. O. R. Brown and H. R. Thirsk, *Electrochim. Acta*, **10**, 383 (1965).
28. U. Bertocci, *ibid.*, **11**, 1261 (1966).
29. V. V. Losev, L. E. Sribnyi, and A. I. Molodov, *Elektrokhimiya*, **2**, 1431 (1966).
30. C. Wagner, *Electrochim. Acta*, **14**, 971 (1969).
31. H. A. Catherino and J. Jordan, *Talanta*, **11**, 1959 (1964).
32. J. Ulstrup, *Electrochim. Acta*, **13**, 535 (1968).
33. I. R. Jonasson and D. R. Stranks, *ibid.*, **13**, 1147 (1968).
34. V. V. Losev and A. P. Pchel'nikov, *Elektrokhimiya*, **4**, 264 (1968); **6**, 41 (1970).
35. A. I. Molodov, G. N. Markosyan, A. P. Pchel'nikov, and V. V. Losev, *ibid.*, **4**, 1233 (1968).
36. V. V. Gorodetskii, A. G. Alenina, and V. V. Losev, *ibid.*, **5**, 227 (1969).
37. V. V. Gorodetskii and V. V. Losev, *ibid.*, **7**, 631 (1971).
38. V. V. Losev, *Electrochim. Acta*, **15**, 1095 (1970).
39. R. D. Armstrong, A. B. Suttie, and H. R. Thirsk, *ibid.*, **13**, 1 (1968).
40. B. Lovrecek and I. Mekljavic, *ibid.*, **14**, 301 (1969).
41. L. Gaiser and K. E. Heusler, *ibid.*, **15**, 161 (1970).
42. K. E. Heusler and L. Gaiser, *This Journal*, **117**, 762 (1970).
43. A. R. Despic, D. R. Jovanovic, and S. P. Bingulac, *Electrochim. Acta*, **15**, 459 (1970).
44. U. Bertocci and K. J. Bachmann, To be published.
45. I. M. Kolthoff and J. F. Coetzee, *J. Am. Chem. Soc.*, **79**, 1852 (1957).
46. K. W. Boyer and R. T. Iwamoto, *J. Electroanal. Chem.*, **7**, 458 (1964).
47. R. R. Bessette and J. W. Olver, *ibid.*, **21**, 525 (1969).
48. N. A. Hampson and R. J. Latham, *Trans. Faraday Soc.*, **66**, 3131 (1970).
49. P. Delahay, *J. Chem. Phys.*, **70**, 2067 (1966); **70**, 2373 (1966); P. Delahay and C. G. Susbielles, *ibid.*, **70**, 3150 (1966); P. Delahay, K. Holub, G. Tessari, and P. Delahay, *ibid.*, **71**, 2612 (1967).

50. P. Delahay and K. Holub, *J. Electroanal. Chem.*, **16**, 131 (1968); K. Holub, *ibid.*, **17**, 277 (1968); C. G. Susbielles and P. Delahay, *ibid.*, **17**, 289 (1968).
51. S. K. Rangarajan, *ibid.*, **25**, 344 (1970).
52. K. J. Vetter, *Z. Naturforsch.*, **7a**, 328 (1952); **8a**, 832 (1953).
53. R. M. Hurd, *This Journal*, **109**, 327 (1962).
54. V. V. Losev, A. I. Molodov, and V. V. Gorodetski, *Electrochim. Acta*, **12**, 475 (1967).
55. V. V. Losev and V. V. Gorodetski, *Elektrokhimiya*, **3**, 1061 (1967).
56. V. V. Losev, V. V. Gorodetski, and A. I. Molodov, *Collection Czech. Chem. Commun.*, **32**, 2917 (1967).
57. V. V. Losev and V. V. Gorodetski, *Elektrokhimiya*, **4**, 1103 (1968).
58. D. M. Mohilner, *J. Phys. Chem.*, **68**, 623 (1964).
59. H. Mauser, *Z. Elektrochem.*, **62**, 419 (1958).
60. A. C. Riddiford, *J. Chem. Soc.*, **1960**, 1175.
61. W. J. Albery, M. L. Hitchman, and J. Ulstrup, *Trans. Faraday Soc.*, **64**, 2831 (1968); **65**, 1101 (1969).
62. K. J. Bachmann and U. Bertocci, *Electrochem. Acta*, **15**, 187 (1970).
63. K. J. Bachmann, *This Journal*, **118**, 226 (1971).
64. G. S. Alberts and I. Shain, *Anal. Chem.*, **35**, 1859 (1963).
65. T. Berzins and P. Delahay, *J. Am. Chem. Soc.*, **77**, 6448 (1955).
66. D. J. Kooijman, M. Sluyters-Rehbach, and J. H. Sluyters, *Electrochim. Acta*, **11**, 1197 (1966).
67. I. H. Plonski, *This Journal*, **116**, 945 (1969).

The Electrosorption of Pentane on Bright Platinum Electrodes

A. R. Blake, A. T. Kuhn,¹ and J. G. Sunderland

The Electricity Council Research Centre, Capenhurst, Chester, England

ABSTRACT

The kinetics of pentane adsorption on bright Pt electrodes were studied in 1N sulfuric acid at 85°C over the potential range +0.1 to +0.4V RHE. The process is shown to be activation controlled. The adsorption process is analyzed in terms of the number of electrons per site for the adsorbed species, which are separated into cathodically desorbable and nondesorbable material.

The literature devoted to the anodic adsorption and oxidation of hydrocarbons is extensive (1-14) and a variety of studies based on steady-state experimental data and nonsteady-state have been investigated. Various techniques have long been available for the measurement of coverage of adsorbed species on solid electrodes. Thus galvanostatic and potential step techniques (multipulse potentiodynamic, MPP) (8-12) terminating in a potential ramp or constant current, have been employed. Through the work of Brummer (2-6), Shropshire (7), Gilman (8-11), and Cairns (12) this concept has been advanced by linking measurements of the anodic charge with measurements of free surface area, determined under identical conditions of electrode pretreatment, adsorption potential, and time. From these two determinations may be calculated a value of ν , the number of electrons (2-6) required to oxidize the adsorbate per platinum site. A further refinement enables the adsorbate to be characterized in terms of adsorbed species which can be cathodically desorbed (θ_{des}) and those which cannot ($\theta_{\text{non-des}}$).

Brummer *et al.* (4) studied the kinetics of hexane adsorption in 85% phosphoric acid at a temperature of 130°C using the technique of MPP followed by a constant current transient. They found that the process under these conditions was essentially diffusion controlled. This paper reports on the adsorption of pentane at lower temperatures and in dilute acid where the adsorption process might be expected to become activation controlled and the adsorbate to exist in a highly reduced state. The results confirm this and also reveal a number of interesting features which would of necessity be obscured under diffusion-controlled conditions.

Experimental

The technique of MPP has been described elsewhere (8-11), as have the methods in which this is followed

¹Present address: University of Salford, Salford 5, Lancashire, England.

Key words: electrosorption, pentane.

by a galvanostatic charging process (3-6) (either anodic or cathodic). The generation of the potential program was achieved with a pulse generator designed in these laboratories (15), the output of which was fed into a Chemical Electronics, 1.6A potentiostat. The constant current was obtained by the use of suitable value tin oxide resistors in series with the cell to drop 90V from a stabilized d-c source to obtain the desired current. Substitution of the potential sequence for the constant current was achieved by rapid switching using a mercury-wetted relay (Elliot EB2). The relay change over from potential control to a constant current mode was achieved in 800 μsec by over-running the relay for a short time; the relay coil was activated by a pulse from the pulse generator. Potential-time transients were recorded photographically on a Tektronix 502A oscilloscope, via a type-O operational amplifier.

The three compartment cell, with a bubbling hydrogen reference electrode was housed in a separate chamber in the third compartment. Purified hydrogen was obtained by passing through a heated Pd/Ag thimble. Argon was used as a purge gas, and was Air Products prepurified grade. Further purification to remove any trace hydrocarbons was achieved by passing the gas through molecular sieve, glass spheres, and glass wool cooled to 142°K. All gas outlets were via bubble traps containing water. The cell was provided with presaturators for the hydrogen electrode and each gas purge stream.

Solutions of 1N H₂SO₄ were prepared by dilution of B.D.H. Aristar sulfuric acid with triply distilled water, followed by potentiostatic pre-electrolysis with a platinized platinum electrode (40 cm² geometric area) at 0.7V for 48 hr and 0.2V for 48 hr with gas stirring. After use the pre-electrolysis electrode was raised into the gas space above the electrolyte. The level of dissolved impurities was determined with anodic and cathodic charging curves in an argon-stirred system after 10 msec adsorption time at 0.2 and 0.3V and again after 300 sec using the potential program shown in Fig. 1A. The length of the potential arrests indicated

the level of dissolved impurities, and runs showing more than 8% change of arrest time were abandoned.

Pentane was Phillips Research Grade (99.99% minimum purity) and was introduced into the anode compartment with the argon purge gas. The partial pressure of the pentane was controlled by maintaining constant temperature in a water bath ($\pm 0.1^\circ\text{C}$) the pentane being passed into the cell via a heated tube maintained at the cell temperature before being introduced into the presaturator. A constant cell temperature was achieved by thermostating in an air oven at 85°C ($\pm 0.2^\circ\text{C}$).

The counterelectrode was a 10 cm^2 platinized electrode. The working electrode, which was a flamed platinum wire (Johnson-Matthey) 1 cm long and 0.0254 cm^2 diameter ($R.F. = 1.95$) was inserted through a Teflon cap at the bottom of the cell so that it was in close proximity to the Luggin capillary. Results are expressed in terms of "real area" derived from hydrogen atom charging (2) and potentials refer to the hydrogen electrode in the same electrolyte.

Results

Variation of charge as a function of current density.—As in all adsorption studies, it is essential to ensure that the anodic (Q_{ox}) and cathodic (Q_H) charges are determined at a current density in the region where Q_{ox} or Q_H are substantially independent of current density. This was verified as outlined below. The potential sequence of Fig. 1A was used to make these measurements, at 0.2 V , for three adsorption times 20, 60, and 100 sec. For the anodic component Q_{ox} (Fig. 2A), the variation was $\pm 15\ \mu\text{C cm}^{-2}$. Similar current density constancy was observed by Brummer (2, 4) for propane and hexane. A current density of 60 mA cm^{-2} was used for routine measurements.

Since it has been shown that much of the adsorbed pentane is readily desorbed at potentials below 0.1 V , it is essential to ensure that the hydrogen deposition charging process is completed before cathodic desorption can occur. The constancy of charge at several cathodic current densities over the range $20\text{--}160\text{ mA cm}^{-2}$ is shown in Fig. 2B and is seen to vary by only $\pm 9\ \mu\text{C cm}^{-2}$. A current density of 120 mA cm^{-2} was used for routine measurements.

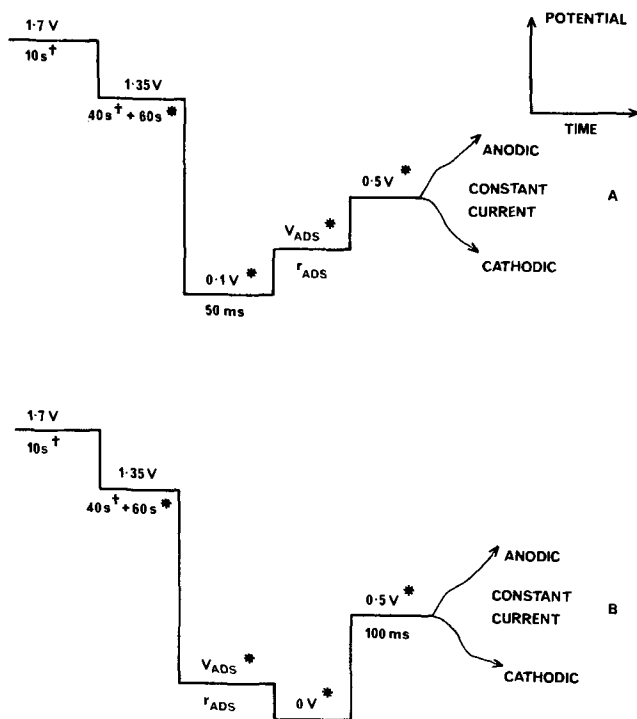


Fig. 1. Potential sequences used in galvanostatic estimations of the anodic charge and electrode coverage. + Stirred, * quiescent.

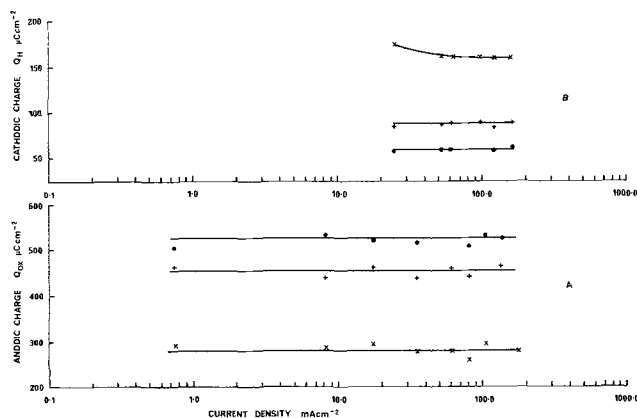


Fig. 2. Adsorption of pentane at 0.2 V and 85°C . X 20 sec, + 60 sec, and ● 100 sec.

Adsorption as a function of time.—The anodic charges Q_{ox} vs. the adsorption time for $0.1\text{--}0.4\text{ V}$ are plotted in Fig. 3 and 4. Potential sequence shown in Fig. 1A was again used to obtain these data. The data shown are for 85°C and a pentane partial pressure of 611 mm . Stirring had relatively little effect on the rate of adsorption; the rate remaining essentially unaffected.

Experiments on the effect of the partial pressure of pentane were also carried out; as expected the rate of adsorption was lower at the lower partial pressure. The partial pressures employed were 611 and 183 mm . At the higher partial pressure, the anodic charge corresponding to 300-sec adsorption time was approximately 25% higher than that observed at the lower partial pressure.

Similarly for the above, coverages $\theta_{H.C.}$ have been determined. $\theta_{H.C.}$ is defined by

$$\frac{Q_{H^S} - Q_H}{Q_{H^S}}$$

where Q_{H^S} is the number of coulombs cm^{-2} required to form a monolayer of hydrogen on the electrode, and Q_H is the charge required to fill the sites available for

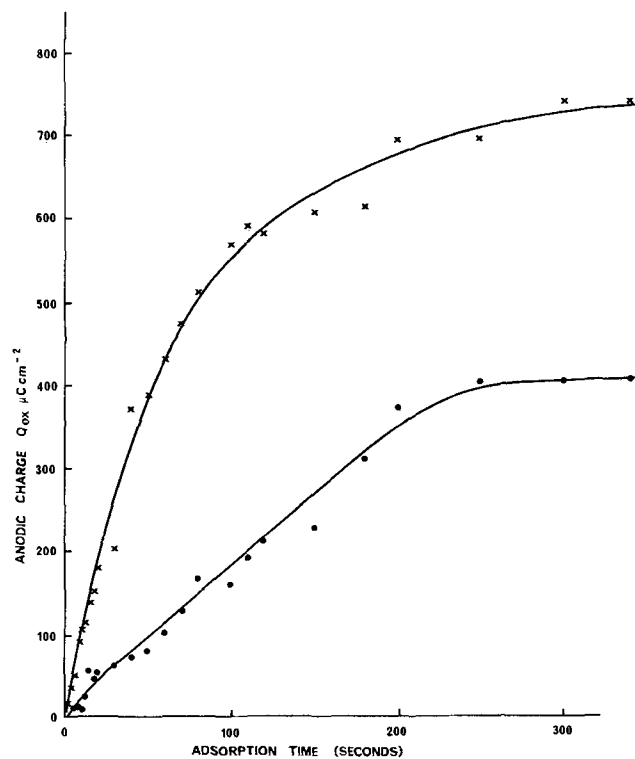


Fig. 3. Quiescent adsorption of C_5H_{12} at 85°C . ● 0.1 V , X 0.2 V

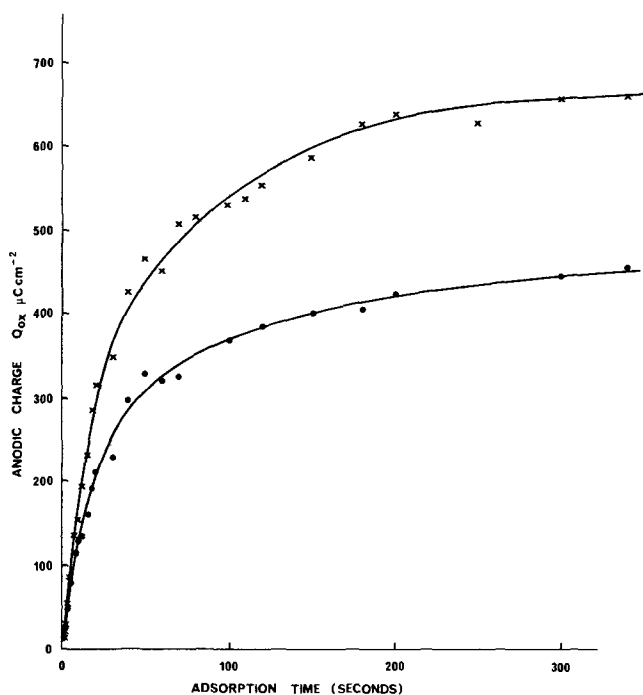


Fig. 4. Quiescent adsorption of C_5H_{12} at $85^\circ C$. X 0.3V, ● 0.4V

hydrogen adsorption in the absence and presence of pentane, respectively.

A typical plot of coverage as a function of adsorption time, for the total adsorbate θ_{TOT} and the cathodically nondesorbable $\theta_{N.D.}$ species, is shown in Fig. 5 for adsorption at 0.2V. Similar behavior was observed at 0.3 and 0.4V. However, at 0.1V, the cathodically nondesorbable species was not detected.

Variation of the anodic charge with electrode coverage.—Variation of the anodic charge Q_{ox} with electrode coverage $\theta_{H.C.}$ during the adsorption of hydrocarbon has been investigated as a function of potential. It has been separated into two components, for the cathodically desorbable species, CH- α , Fig. 6 shows this. Figure 7 shows the complementary cathodically nondesorbable species O-type. A combination of potential sequence shown in Fig. 1A and 1B was employed to determine the two adsorbed species. Sequence 1A was used to determine the charge corresponding to the total adsorbate and sequence 1B to determine that associated with cathodically nondesorbable species. Subtraction of the cathodically nondesorbable charge from the total charge was used to construct Fig. 6.

Adsorption at infinite time as a function of potential.—The adsorption isotherm, in terms of Q_{ox} , at maxi-

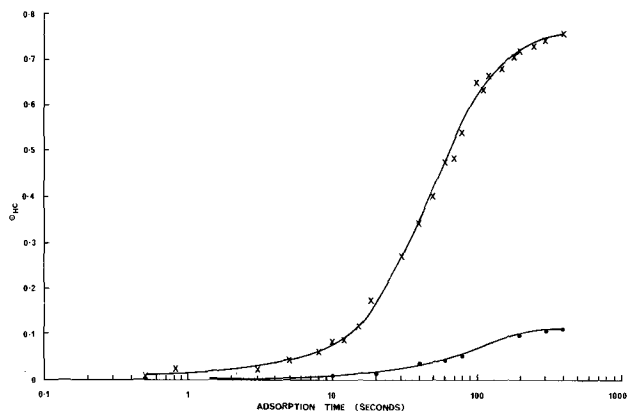


Fig. 5. Quiescent adsorption of C_5H_{12} . Electrode coverage θ at 0.2V. X Total coverage, ● coverage with cathodically nondesorbable species.

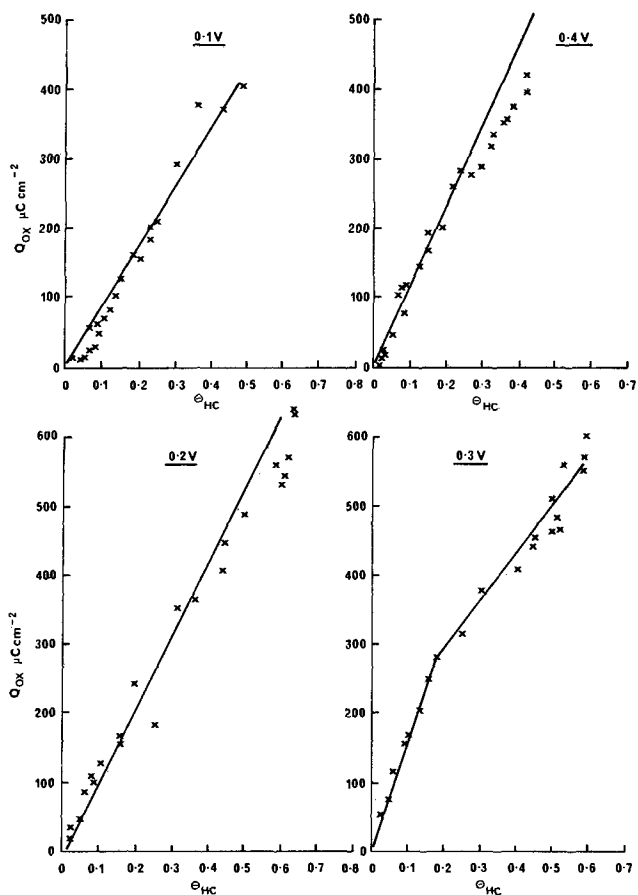


Fig. 6. Q_{ox} vs. $\theta_{H.C.}$ for cathodically desorbable species as a function of potential, $85^\circ C$.

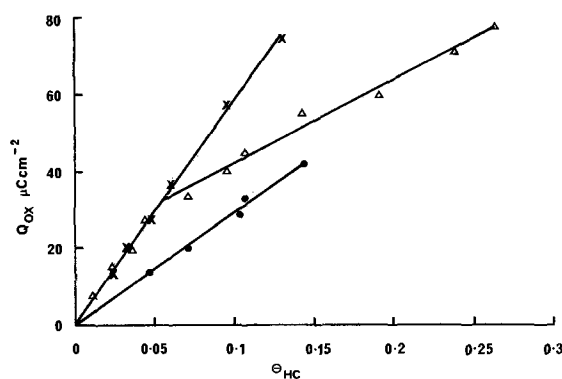


Fig. 7. Q_{ox} vs. $\theta_{H.C.}$ for cathodically nondesorbable species as a function of potential, $85^\circ C$. X 0.2V, Δ 0.3V, ● 0.4V.

mum coverage as a function of potential is shown in Fig. 8.

Discussion

Kinetics of adsorption of pentane from H_2SO_4 at $85^\circ C$.—The adsorption of hexane (4) has been shown to be diffusion controlled at $130^\circ C$ and it was thought that pentane, at a lower temperature and in a higher concentration, might also be expected to adsorb under diffusional control. However, although classical $\tau^{1/2}$ plots could readily be fitted to the experimental data, diffusional controlled adsorption was not thought to be the predominant process for the following reasons:

1. If diffusional controlled adsorption were operative, potential dependence on the rate would not be expected to occur.
2. Stirring should have a profound effect on the rate of adsorption. In fact, the rate remains essentially unaffected.
3. If diffusional controlled kinetics are operative, the linear region would only be expected to hold over

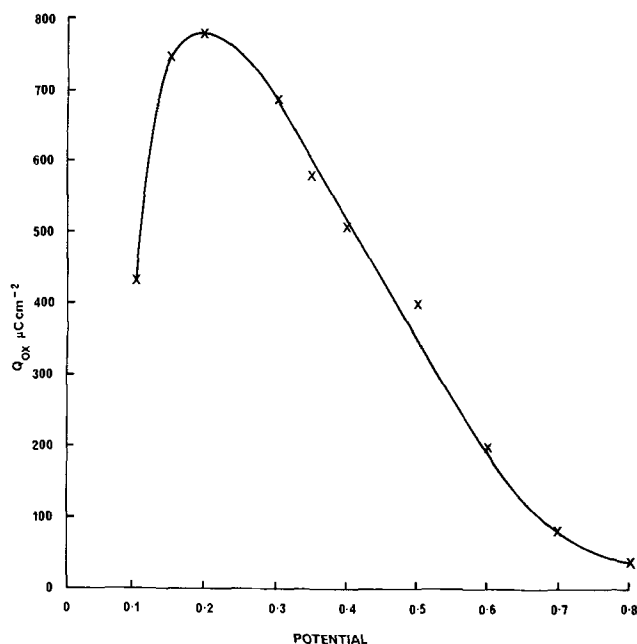


Fig. 8. Variation of the maximum anodic charge with potential

a short time, *c.f.*, Cairns (12) and Brummer (2-4) not as is observed in this case, a linear region extending up to about 70 sec.

4. The strongest evidence against diffusion-controlled adsorption is the time before adsorption becomes significant, which is referred to as the "induction period."

Confirmation that diffusion-controlled adsorption was not operative at any stage of the adsorption process was obtained by analyzing the diffusion equation for pentane diffusing to a cylindrical electrode under potentiostatic control, over the range of

$$Q_{ox} = \int_0^{\tau} (f) d\tau \quad [1]$$

where Q_{ox} is the anodic charge and therefore is a measure of the number of moles of pentane adsorbed on the electrode, and τ is the adsorption time in seconds.

The solution of the diffusion equation requires a knowledge of the solubility of pentane (C_s) under our experimental conditions. This is not available in the literature. Solubility data (17-19) for several hydrocarbons are shown in Fig. 9.

It is noted that the solubility/temperature relationship is parallel over the temperature range 25°-90°C. On this basis, the reported solubility at 25°-90°C has been extrapolated to 85°C. By this method a value of $C_s = 2.36 \times 10^{-7}$ moles cm^{-3} is obtained. Since adsorption in our case lay in the mid region 1-100 sec the complete solution of the diffusion equation [1] is necessary; (see Appendix). This was carried out on a Univac 1108 computer and the solution plotted in Fig. 10 together with the corresponding experimental values of Q_{ox} and τ for each potential.

It is seen that in all cases the experimental values fall well below the theoretical curve. The evidence presented above clearly shows that the adsorption rate is activation controlled. This is in accord with the findings of Gilman (8) and Flannery (14) for ethane and butane, respectively.

In view of the complex chain of reactions involved, it was not thought appropriate to analyze the data in terms of the equilibrium relationships (Langmuir or Temkin). It has, however, been analyzed in terms of a Langmuir-type relationship (20), relating the rate of adsorption to the available surface of the electrode ($1 - \theta_{H.C.}$).

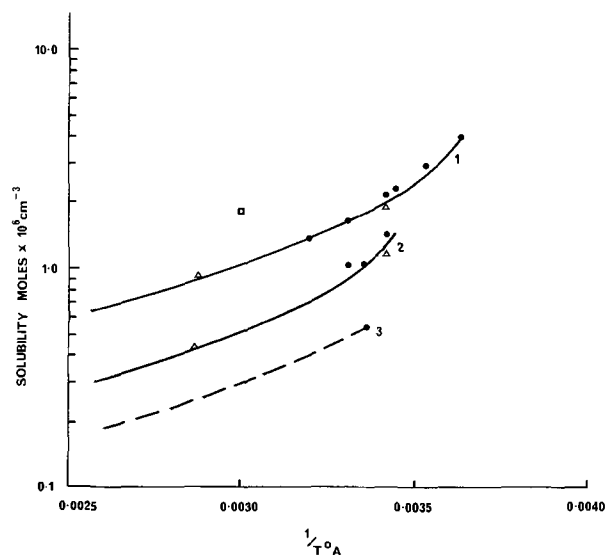


Fig. 9. Solubility of several hydrocarbons as a function of the reciprocal of the temperature. 1 Ethane, 2 butane, 3 pentane (extrapolated to 85°C). Data indicated is taken from following: ● Ref. (17, 18); Δ Ref. (19); □ Ref. (8).

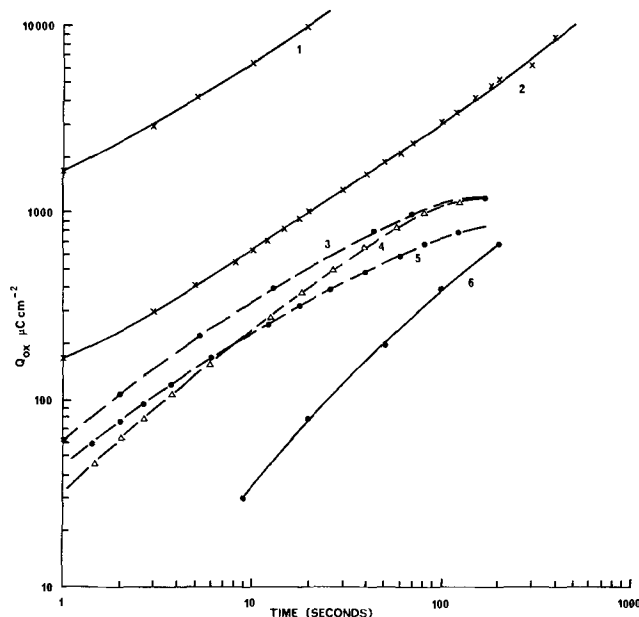


Fig. 10. Graphical solution of diffusion equation. Curves 1 and 2 relate to the theoretical relationship for the charge per unit area to the adsorption time. Curve 1: $C = 2.36 \times 10^{-7}$ moles cm^{-3} . Curve 2: $C = 1 \times 10^{-7}$ moles cm^{-3} . Curves 3-6 relate to the experimental data: 3, 0.3V; 4, 0.2V; 5, 0.4V; 6, 0.1V.

$\theta_{H.C.}$ is the electrode coverage with pentane at time τ .

Using the Langmuir relationship in terms of $\theta_{H.C.}$ the rate equation is

$$\frac{d\theta_{H.C.}\tau}{d\tau} = kC(1 - \theta_{H.C.}\tau)^m \quad [2]$$

where $\theta_{H.C.}$ = coverage with hydrocarbon, defined by the expression

$$\theta_{H.C.} = \frac{Q_{H^{\infty} org} - Q_{H^{\tau} org}}{Q_{H^{\infty} org}} \quad [3]$$

$Q_{H^{\infty} org}$ = hydrogen charge at infinite time: in $\mu\text{C cm}^{-2}$

$Q_{H^{\tau} org}$ = hydrogen charge at time τ : in $\mu\text{C cm}^{-2}$

m = reaction order in available surface

k and C = constants

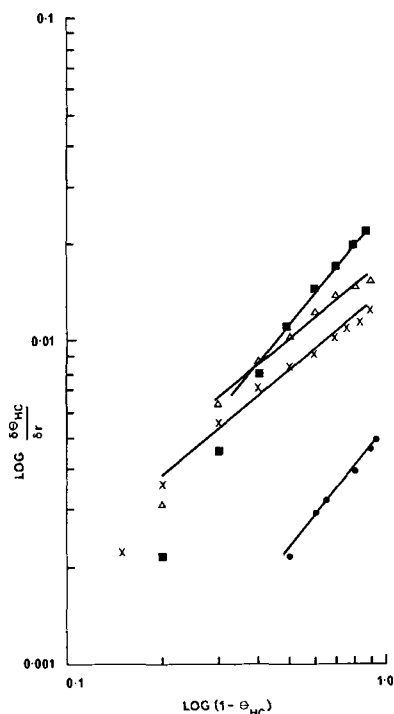


Fig. 11. Rate of electrode coverage vs. available electrode surface. ● 0.1V, X 0.2V, Δ 0.3V, □ 0.4V.

Plot of $\log d\theta_{H.C.}/d\tau$ against $\log (1 - \theta_{H.C.})$ (Fig. 11) showed that the reaction was predominantly first order in available surface suggesting that the first step in the adsorption in terms of free surface is rate controlling.

A study of the kinetics of the formation of the cathodically nondesorbable species does not appear to have been attempted before since diffusional controlled adsorption has generally been operative. A simple attempt at analysis is presented below.

Plotting the rate of formation of the nondesorbable species $d\theta_{N.D.}/d\tau$ as a function of available electrode area $(1 - \theta_{des}) \times \theta_{des}$ results in a linear relationship at 0.3 and 0.4V. However, at 0.2V the relationship breaks down; this is probably due to the presence of significant coverage with hydrogen (21).

The result for 0.4V is plotted in Fig. 12 and indicates that the formation of O-type is first order in available surface, as well as θ_{des} ; thus supporting the hypothesis that the nondesorbable species is derived from the cathodically desorbable species. The Q_{ox} vs. τ plots, Fig. 3 and 4, indicate a significant induction period before measurable adsorption occurs at 0.1V. This is potential dependent the longest "induction" period

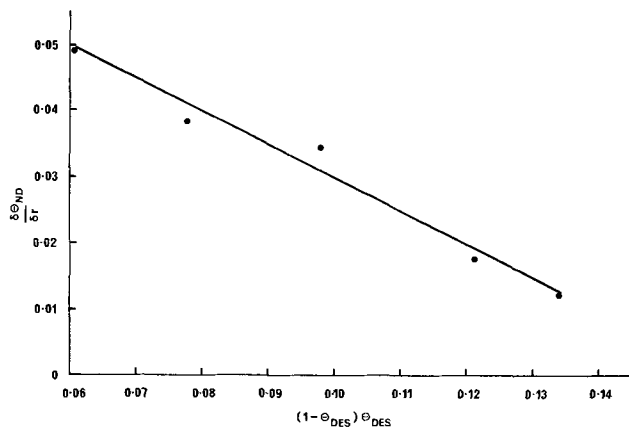


Fig. 12. Relationship between the rate of formation of non-desorbable material to available electrode area 0.4V.

being at 0.1V subsequently reducing as the potential is made more anodic. It is likely that adsorbed hydrogen plays a part in controlling the length of the "induction period." This is explained by assuming that a replacement mechanism is involved and that the replacement of hydrogen by hydrocarbon is significantly slower than the subsequent rate-controlling adsorption step. The absence of a significant induction period at 0.3 and 0.4V gives strong support to this assumption. Similarly, it was found that on lowering the temperature to 30°C the "induction period" was increased by about a factor of ca. 3 at 0.2V. Reducing the concentration of pentane also resulted in an increase in the "induction period" again consistent with the proposed replacement mechanism.

Adsorbed species.—Two distinct types of adsorbed species are present on the electrode, one cathodically desorbable and the other cathodically nondesorbable. This finding is similar to that of Brummer for the adsorption of propane and hexane on platinum. Brummer designated the species CH- α and O-type (and CH- β), respectively, and the same nomenclature is used here. The CH- α species has been found in our experiments to be always predominant. The CH- α species (except at 0.1V where adsorbed hydrogen results in anomalously low values) gives on oxidation an average $[e]$ value of 5.2. It is noted that at 0.3V possibly a second CH- α species is present. Although two lines have been drawn through the experimental points, the significance is questionable. On account of the high value of 5.2 "electrons per site" it is suggested that the adsorbed species is uncracked.

A simple model of pentane adsorbed on a platinum (100) face is a close-packed array (Fig. 13) would result in an $[e]$ value of 5.4, i.e., 27 electrons for total oxidation to carbon dioxide and water. Considering the simplest case where hydrogen is not co-adsorbed, e.g., 0.3V, it is possible to calculate the number of molecules of pentane adsorbed on 1 cm² of platinum. The experimental value at 0.3V for the CH- α species to 6.6×10^{14} molecules cm⁻² compares with the expected theoretical value of 8.8×10^{14} molecules cm⁻². These values are felt to be in close agreement in view of the fact that screening of the available electrode surface, which is inferred from the data shown in Fig. 6, occurs, which reflects a somewhat higher theoretical value since the electrode coverage will be higher than is in fact the case. In addition, not all the surface is available for adsorption since the Pt-Pt and C-C bond lengths are not identical and therefore a lower value still would be expected for the theoretical value.

The O-type species oxidizes, yielding values of 3 and 1.5 electrons per site and are probably oxygenated species, as suggested by Brummer (3, 4, 6) and Cairns (12). The $[e]$ value decreases with increasing potential (Fig. 13) which is consistent with the formation of a more highly oxidized species at high potentials.

Conclusions

Pentane has been shown to adsorb under predominantly activation-controlled conditions and the adsorption process is first order in available electrode surface at all the potentials studied. At low potentials an induction period is observed which is thought to be connected with a hydrogen replacement stage.

The majority of the pentane is adsorbed in an uncracked state (CH- α) and is readily cathodically desorbable. The cathodically nondesorbable O-type forms only a small proportion of the adsorbate and becomes more highly oxidized with increasing potential. The formation of O-type species is shown to be first order in the available electrode surface.

APPENDIX

The mathematical relationship for relating the diffusion of hydrocarbon in an infinite region surrounding a cylindrical electrode, radius a , where the diffusion coefficient, D , and the concentration in the bulk

electrolyte, C_s , are given is related to the current per unit area of electrode by

$$i = \frac{4nFD C_s}{\pi^2 a} \int_0^\infty \frac{\exp\left(-\frac{Dt}{a^2} z^2\right) dz}{z(J_0^2(z) + Y_0^2(z))}$$

Carslaw and Jaeger (22) give the formula for the heat flow in the corresponding heat problem as

$$f = \frac{4KV}{\pi^2 a} \int_0^\infty \frac{\exp\left(-\frac{Kt}{a^2} z^2\right) dz}{z(J_0^2(z) + Y_0^2(z))}$$

where $z = a, u$ and $V \equiv C_s, X \equiv D, K \equiv nFD$.

To carry out the numerical analysis of the integral given above for all times the asymptotic series (first four terms) for $0 \leq T \leq 0.3$ are employed. For $T > 0.3$ the following is integrated numerically

$$q = \frac{4nFDC_s}{\pi^2 a} \int_0^t \int_0^\infty \frac{\exp\left(-\frac{Dt}{a^2} z^2\right) dz \cdot dt}{z(J_0^2(z) + Y_0^2(z))} \\ = \frac{4nFC_s a}{\pi^2} \int_0^\infty \frac{(te^{-Te^2}) dz}{z^3 J_0^2(z) + Y_0^2(z)}$$

To carry out this integrand it is found that for $T > 0.3, z > 3.6, 1 - e^{-z^2 T}$ is a monotonic increasing function and equal to 0.99 to an approximation of $\pm 1\%$,

and that $\frac{1}{a(J_0^2(z) + Y_0^2(z))}$ is a monotonically decreasing function and equal to 1.58 to an approximation of $\pm 1\%$. Consequently

$$\int_{3.6}^\infty \frac{(1 - e^{-z^2 T}) dz}{z^3 (J_0^2(z) + Y_0^2(z))} \simeq 0.99 \times 1.58 \int_{3.6}^\infty \frac{dz}{z^2} \\ = \frac{0.99 \times 1.58}{0.36} = 0.4345$$

Now for modified integral limits

$$0 < \alpha < \frac{0.2}{T^{1/2}}, \quad \frac{1 - \exp^{-z^2 T}}{z^2} \simeq \frac{(1 - \alpha^2 T)}{4} T$$

to within 1%, and for

$$0 < \alpha \leq 0.2 : Y_0 \simeq 0.07 + \frac{2}{\pi} J_0 \ln(z)$$

$$\therefore z(J_0^2(z) + Y_0^2(z)) \\ \simeq z(J_0^2(z)) \left(1 + \left(-0.07 + \frac{2}{\pi} \ln(z)\right)^2\right)$$

$$\therefore q = \frac{4nFC_s a}{\pi^2} \left\{ \frac{\left(1 - \frac{\alpha^2 T}{4}\right) T}{\left(1 - \frac{\alpha}{4}\right)} \int_0^\alpha \frac{dz}{z \left(1 + \left(-0.07 + \frac{2}{\pi} \ln(z)\right)^2\right)} \right. \\ \left. + \int_\alpha^{3.6} \frac{(1 - e^{-z^2 T}) dz}{z^3 (J_0^2(z) + Y_0^2(z))} \right\} + 0.4345$$

where α is a minimum at $(0.2, 0.2/T^{1/2})$. Now

$$\int_0^\alpha \frac{dz}{z \left(1 + \left(-0.07 + \frac{2}{\pi} \ln(z)\right)^2\right)} \\ = \frac{\pi}{2} \left[\frac{\pi}{2} + \tan^{-1} \left(-0.07 + \frac{2}{\pi} \ln \alpha\right) \right]$$

in the range $-\pi/2$ to $\pi/2$.

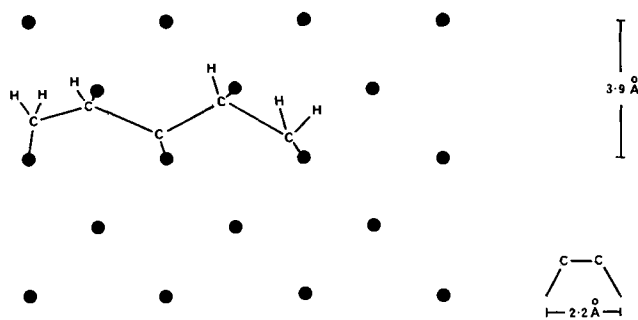


Fig. 13. Model of platinum lattice with pentane dissociatively adsorbed on the surface. ● Pt atom.

The integral between α and 3.6 was integrated numerically using the Simpsons rule procedure SIMINI given in the Univac Mathpack (23) with a relative error setting of 0.001. The integrand was evaluated (24) using

$$2 \leq z \leq 3.6 \frac{1}{z(J_0^2(z) + Y_0^2(z))} = 1.59 \\ \text{(better than } \pm 1\%)$$

$$0 \leq z \leq 2 \quad J_0(z) = 1 - 2.25 \left(\frac{z}{3}\right)^2 \\ + 1.26562 \left(\frac{z}{3}\right)^4 - 0.31639 \left(\frac{z}{3}\right)^6$$

$$Y_0(z) = \frac{2}{\pi} \ln\left(\frac{z}{2}\right) J_0(z) + 0.367467 \\ + 0.605594 \left(\frac{z}{3}\right)^2 - 0.743504 \left(\frac{z}{3}\right)^4 + 0.253 \left(\frac{z}{6}\right)^6$$

The following numerical values were then substituted into the above expressions: $D = 2.15 \times 10^{-5} \text{ cm}^2 \text{ sec}^{-1}$ (25); $a = 0.0127 \text{ cm}$; $n = 27$. The curves shown on the graph of experimental results Fig. 13 are for $C_s = 10^{-7}$ and $2.34 \times 10^{-7} \text{ moles cm}^{-3}$.

Acknowledgments

The authors wish to thank Dr. R. Hodgkins for the solution of the diffusion equation and Dr. D. Gilroy for helpful discussions.

Manuscript submitted Dec. 8, 1971; revised manuscript received April 4, 1972.

Any discussion of this paper will appear in a Discussion Section to be published in the June 1973 JOURNAL.

REFERENCES

1. J. O'M. Bockris et al., *J. Electroanal. Chem.*, **6**, 401 (1963).
2. S. B. Brummer, J. I. Ford, and M. J. Turner, *J. Phys. Chem.*, **69**, 3424 (1965).
3. S. B. Brummer and M. J. Turner, *ibid.*, **71**, 2825 (1967).
4. S. B. Brummer and M. J. Turner, *ibid.*, **71**, 3494 (1967).
5. A. H. Taylor and S. B. Brummer, *ibid.*, **72**, 2856 (1968).
6. A. H. Taylor and S. B. Brummer, *ibid.*, **73**, 2397 (1969).
7. J. A. Shropshire and H. H. Horowitz, *This Journal*, **113**, 490 (1966).
8. S. Gilman, *Trans. Faraday Soc.*, **61**, 2546 (1965).
9. S. Gilman, *ibid.*, **61**, 2561 (1965).
10. S. Gilman, *ibid.*, **62**, 466 (1966).
11. S. Gilman, *ibid.*, **62**, 481 (1966).
12. E. J. Cairns and A. M. Breitenstein, *This Journal*, **114**, 764 (1967).
13. L. W. Niedrach, *ibid.*, **113**, 645 (1966).
14. G. Aronowitz and R. J. Flannery, *ibid.*, **116**, 938 (1969).
15. W. E. Roberts and J. A. Sunderland, To be published.
16. J. Timmermans, "Physico-Chemical Constants of Pure Organic Compounds," p. 32, Elsevier Publishing Co., New York (1950).

17. C. McAuliffe, *J. Phys. Chem.*, **70**, 1268 (1966).
18. W. F. Claussen and M. F. Polglase, *J. Am. Chem. Soc.*, **74**, 4817 (1952).
19. L. R. Griffith and D. R. Rhodes, *Am. Inst. Chem. Engrs.*, 32-39 (1963).
20. M. J. D. Low, *Chem. Rev.*, **60**, 267 (1960).
21. M. W. Breiter, *Trans. Faraday Soc.*, **61**, 749 (1965).
22. H. S. Carslaw and J. C. Jaeger, "Conduction of Heat in Solids," Oxford Press (1959).
23. Univac Mathpack 1108UP4051 Rev. 1.
24. M. Abramowitz and T. A. Stegun, "Handbook of Mathematical Functions," Dover Press (1965).
25. P. A. Witherspoon and D. N. Saraf, *J. Phys. Chem.*, **69**, 3752 (1965).

Thermodynamic and Physical Properties of Molten Sodium Polysulfides from Open-Circuit Voltage Measurements

Nirmal K. Gupta* and Ragnar P. Tischer*

Scientific Research Staff, Ford Motor Company, Dearborn, Michigan 48121

ABSTRACT

The open-circuit voltage of the cell Na/ β -alumina/Na₂S_x/pyrolytic graphite has been measured as a function of temperature and sodium-polysulfide composition. From these data, differential free energy, entropy, and enthalpy values for the potential-determining reaction and the differential free energy of formation for various polysulfide compositions were calculated. The partial differential enthalpy (\bar{H}_1) of adding Na to the polysulfide melt is -47.6 kcal/mol independent of melt composition and temperature. The solubility of sulfur in sodium pentasulfide was determined between 280°-390°C, and the Na₂S-S phase diagram of Pearson and Robinson was revised in the Na₂S₂-S range and extended to show the Na-rich border of the miscibility gap.

So far very little has been known about the electrochemistry of the Na-S system in the molten state. With the application of β -alumina and related structures of high sodium ion conductivity, direct electrochemical investigation of this system became possible. The application in the Na-S battery makes a more detailed knowledge of the electrochemical behavior of the system highly desirable.

As a first step in a program to gather such knowledge, the open-circuit voltage of the cell Na/ β -alumina/Na₂S_x melt/graphite has been measured as a function of temperature and of the composition of the melt. The data obtained in conjunction with recent DTA measurements by Oei (1) of this laboratory permit a revision to be made of the Na₂S-S phase diagram by Pearson and Robinson (2). The use of open-circuit voltage (OCV) measurements for the determination of a phase diagram has the distinct advantage that one can wait an unlimited time (at least theoretically) for equilibrium to be reached. This is quite important in a system with such strong tendency for undercooling as the Na-S system. The limits of the miscibility gap, for instance, cannot be determined by the usual method of analyzing the phases, because the two phases will not separate, at least under natural gravity, when kept at temperature for three weeks.

From the open-circuit voltages a variety of thermodynamic values can be calculated hitherto not available in literature. A search revealed only a few heats of formation for sodium polysulfides in the solid state at room temperature and in liquid ammonia (3, 4).

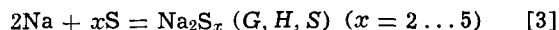
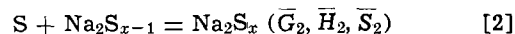
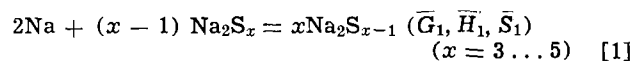
Theoretical Considerations

Na₂S₂-S phase diagram. Sulfur solubility in Na₂S₅.—For the purpose of determining the solubility of sulfur in Na₂S₅ as a function of temperature, two sets of data were needed. One set of data consisted of OCV mea-

surements as a function of Na-polysulfide composition at various temperatures. The other set was obtained by measuring OCV using a Na-polysulfide melt in equilibrium with sulfur at the same temperatures. The plot of OCV *vs.* composition extrapolated to the OCV of the S-saturated melt at the same temperature yields the composition of this melt. The S-solubility in Na₂S₅ as a function of temperature forms the Na-rich boundary of the miscibility gap in the Na₂S-S phase diagram.

Liquidus line.—The liquidus line, including the melting points of the Na-polysulfides that exist as definite compounds in the solid state, and the melting points and compositions of eutectics can be determined from the OCV *vs.* temperature curves.

Thermodynamic properties.—The Gibbs free energy, enthalpy, and entropy for the three reactions involved are symbolized as follows



The (barred) partial molar quantities are differential energies and entropies of adding Na or S to a large excess of polysulfide melt such that the over-all polysulfide composition does not change. Subscript 1 represents Na and subscript 2 represents S.

Calculation of \bar{G}_1 , \bar{G}_2 and G .—The OCV of the cell is determined by Reaction [1]. Sodium is ionized or discharged at the sodium electrode and passes through the Na-ion conducting ceramic to or from the melt.



The sulfur electrode transfers electrons and responds to the reaction



* Electrochemical Society Active Member.

Key words: free energy of formation, phase diagram.

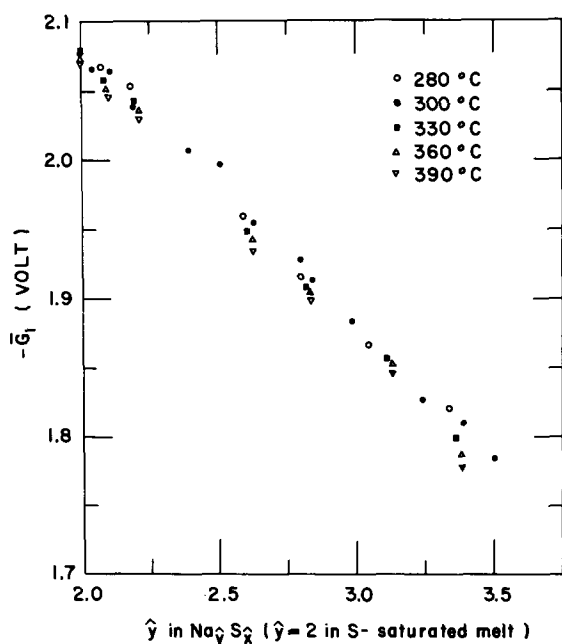


Fig. 1. \bar{G}_1 as a function of \hat{y} at various temperatures, indicating that $d\bar{G}_1/d\hat{y} = \text{constant}$.

We have here the rare case of a redox system with the oxidized and the reduced form of an atom present in one and the same ion (cp. I_3^- in aqueous solution). The OCV (difference of reversible potentials) is related to \bar{G}_1 by

$$-\bar{G}_1 = FE$$

where F = Faraday constant and E = open circuit voltage.

The value of \bar{G}_2 is calculated from \bar{G}_1 by using the Gibbs-Duhem relation

$$\hat{y} d\bar{G}_1 + \hat{x} d\bar{G}_2 = 0$$

where 2 and \hat{x} are the stoichiometric numbers of Na and S in Na_2S_x ; $\hat{y} = 2\hat{x}/\hat{x}$ with $\hat{x} = \text{constant}$ = stoichiometric number of S in Na_2S_x in equilibrium with free sulfur. \hat{x} is a function of temperature.¹

Dividing this by $d\hat{y}$ and integrating with respect to \hat{y} while having \hat{x} constant, we obtain

$$\int_0^{\hat{y}} \eta \frac{d\bar{G}_1}{d\eta} d\eta + \hat{x} \int_0^{\hat{y}} \frac{d\bar{G}_2}{d\eta} d\eta = c$$

A plot of $-\bar{G}_1$ vs. \hat{y} at constant \hat{x} shows that in this system at any temperature within the range of interest $d\bar{G}_1/d\hat{y}$ is also a constant (Fig. 1). Hence

$$\bar{G}_2 = -\frac{\hat{y}^2}{2\hat{x}} \frac{d\bar{G}_1}{d\hat{y}} + c$$

The value of the constant c is calculated by introducing the data for a reference polysulfide composition in which a small addition or removal of sulfur does not cause a free energy change, i.e., $\bar{G}_2 \equiv 0$. Such a reference composition is given by the sodium-rich boundary of the miscibility gap, because there the melt is in

¹ Stoichiometric numbers can be used conveniently for this calculation because the Gibbs-Duhem equation is homogeneous.

equilibrium with sulfur. As we have set $x = \hat{x}$ at this composition, we have

$$c = \frac{\hat{y}^2}{2\hat{x}} \frac{d\bar{G}_1}{d\hat{y}} = \frac{2}{\hat{x}} \frac{d\bar{G}_1}{d\hat{y}}$$

since here $\hat{y} = 2$, or

$$\bar{G}_2 = \frac{1}{2\hat{x}} \frac{d\bar{G}_1}{d\hat{y}} (4 - \hat{y}^2)$$

where $2 \leq \hat{y} \leq \hat{x}$. The value of G is then calculated from the relation

$$G = 2\bar{G}_1 + x\bar{G}_2$$

It should be noted that the G -values are based on one mole of Na_2S_x whereas \bar{G}_1 and \bar{G}_2 are for one atom of Na and S, respectively.

Calculation of the entropy term.—The value of \bar{S}_1 can be calculated from the temperature dependence of \bar{G}_1 , i.e.

$$(\partial\bar{G}_1/\partial T)_p = -\bar{S}_1$$

Calculation of \bar{H}_1 .—Making use of the thermodynamic relation

$$\bar{G}_1 = \bar{H}_1 + T(\partial\bar{G}_1/\partial T)_p$$

substituting $-\bar{G}_1 = FE$ and rearranging, we get

$$[(\partial E/\partial T)_p - E/T] = (1/T)\bar{H}_1/F$$

so that a plot of $(\Delta E/\Delta T - E/T)$ vs. $1/T$ has a slope equal to \bar{H}_1/F .

Experimental Procedure

Material preparation.—The Na_2S_4 obtained from Alpha-Inorganics contained traces of S and C_2H_5OH as impurities. It was purified by shaking with spectrograde CS_2 (Matheson-Coleman & Bell) at room temperature followed by vacuum drying at $70^\circ C$ over P_2O_5 for one week. The purified Na_2S_4 was stored in a dry box (under helium) until used.

Na_2S was prepared from the hydrate by the conventional method (5). The high-purity sulfur (99.999%) obtained from American Smelting and Refining Corporation was used without further purification.

Na_2S_5 was synthesized by mixing Na_2S and S in the stoichiometric proportions and heating at $500^\circ C$ for 1 hr in a Vycor tube sealed under vacuum. Any excess sulfur was removed by shaking Na_2S_5 with spectrograde toluene at $25^\circ C$ followed by vacuum drying over P_2O_5 .

The various Na_2S_x compositions were prepared by taking appropriate amounts of two of the following compounds: Na_2S , Na_2S_4 , Na_2S_5 , and S, and heating at $500^\circ C$ for 4 hr in a Vycor tube sealed under vacuum. The melt was cooled and all the solid was transferred to the cell.

Cell construction.—*Pyrolytic graphite electrode.*—Pyrolytic graphite (p.g.) rods ($1/4$ in. diam x 6 in.) obtained from Union Carbide were shaped to a pencil point as shown in Fig. 2. A high-purity titanium wire, of 0.062 in. diam and with 0-80 thread at one end, was threaded into the p.g. This assembly was enclosed in a Vycor tube and the p.g. was degassed at $900^\circ C$ for 4 hr with continuous evacuation. The Vycor tube was subsequently allowed to shrink over the p.g. tip by heating. The titanium wire was sealed into the Vycor tube close to the p.g. rod by careful heating followed by slow annealing. The tip of the electrode was ground flat and polished to expose the cross section of the p.g.; and the whole assembly was immersed in distilled

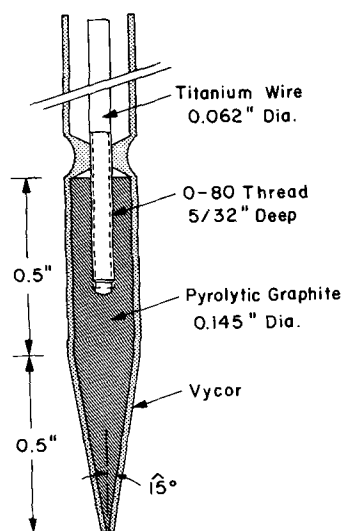


Fig. 2. Pyrolytic graphite microelectrode

water to check for leakage. After testing for 12 hr, the other end of the Vycor tube was also shrunk onto the titanium wire. A vacuum-tight Vycor-to-titanium seal was made at this end by using Torr-seal low vapor pressure resin supplied by Varian Associates. No creepage of the polysulfide melt was detected along the p.g.-Vycor interface.

The Cell.—Figure 3 shows the Pyrex cell used. Sodium (99.999% pure) was filtered through a Pyrex fritted disk and introduced into the β -alumina tube. The connecting Pyrex tube A was then sealed at B under vacuum. Electrical contact was made by using a tungsten wire sealed in Pyrex.

A calibrated Chromel-Alumel thermocouple was used to measure the temperature of the melt. The Na_2S_x was introduced into the cell in an atmosphere of dry nitrogen. The cell was then evacuated and sealed at C at room temperature to avoid changes in the composition of the melt at high temperature due to sulfur evaporation.

The cell construction was such that the polysulfides came in contact with Pyrex, Vycor, p.g., and β -alumina ceramic only.

Voltage measurements.—A Keithley 660A differential d-c voltmeter was used to measure the thermocouple emf and the open-circuit voltage between the Na-reference electrode and the S/S= electrode. The correction for thermo emf between the two electrodes was negligible (< 1 mV at all temperatures).

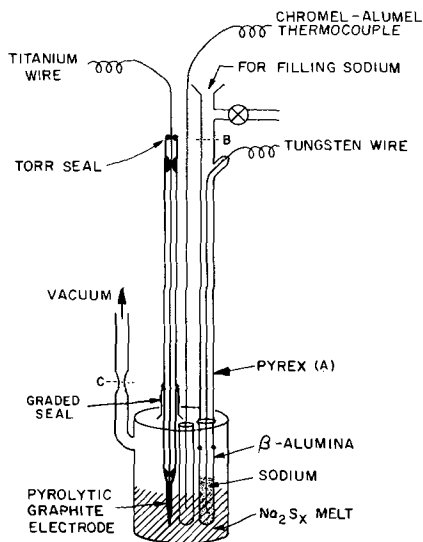


Fig. 3. Pyrex cell

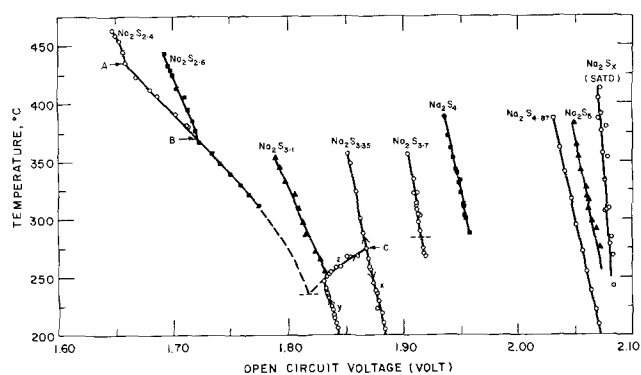


Fig. 4. Open-circuit voltage vs. temperature data

Results and Discussion

Solubility and phase diagram.—Figure 4 shows the OCV vs. temperature data for various polysulfide compositions studied. For all compositions, the OCV increases with decreasing temperature. In the case of the $\text{Na}_2\text{S}_{2.4}$ and $\text{Na}_2\text{S}_{2.6}$ compositions, the OCV increases until a break occurs (A and B, respectively) due to the separation of solid Na_2S_2 phase out of the melt. The curves further on coincide for both starting compositions. The shape of this curve is determined by the change in the OCV due to the changing composition of the melt with temperature, because solid Na_2S_2 phase precipitates, and by the changing temperature. The points A and B lie on the liquidus curve in the Na_2S -S phase diagram.

In melts that contain a larger amount of sulfur, e.g., $\text{Na}_2\text{S}_{3.35}$ composition, no such break occurs in the cooling curve. A supercooling by as much as 100°C (stable for more than three days) has been observed in this case, before the melt solidifies. It should be noted that supercooling has been observed in all the melt compositions studied above $\text{Na}_2\text{S}_{2.6}$ composition. The supercooling tendency increases with increasing length of the sulfur chain present in the polysulfide ions. The point C corresponding to the liquidus line, in such a case, is determined by reheating the solid. A hysteresis loop (xyz) is observed as expected. The OCV decreases as the temperature is raised until the liquidus line (z) is reached. A break in the OCV vs. temperature curve (y) occurs and the OCV increases owing to changing composition of the melt along the liquidus line in the Na_2S -S phase diagram. At the second break (C), the heating curve leaves the liquidus line. After the solid phase has disappeared, the original cooling curve is retraced.

The composition of a eutectic that exists between Na_2S_2 and Na_2S_4 composition is also determined from the $\text{Na}_2\text{S}_{3.35}$ data. According to Pearson and Robinson (2), and Oei (1), the melting point of this eutectic is 235°C . If we extrapolate the OCV vs. temperature data obtained along the liquidus line (z) for $\text{Na}_2\text{S}_{3.35}$ composition to 235°C , we find that the composition of the eutectic corresponds to Na_2S_3 . A second-order least square approximation was used for this extrapolation. Pearson and Robinson (2) reported a composition close to $\text{Na}_2\text{S}_{3.24}$.

Consistent results could not be obtained by this method between Na_2S_4 and Na_2S_5 because the cell was not equipped for stirring to overcome the severe undercooling in this region.

The sulfur solubility in Na_2S_5 is determined from the OCV vs. composition relationship at fixed temperatures taken from Fig. 4, and the OCV's of sulfur-saturated melt shown in Fig. 5. The data in Fig. 5 were obtained using polysulfide melts with excess sulfur. The curve (D) was obtained on cooling the melt. The straight line (U) was obtained on heating after allowing the Na_2S_5 to crystallize out of molten sulfur by cooling. The hysteresis loop is formed because of the

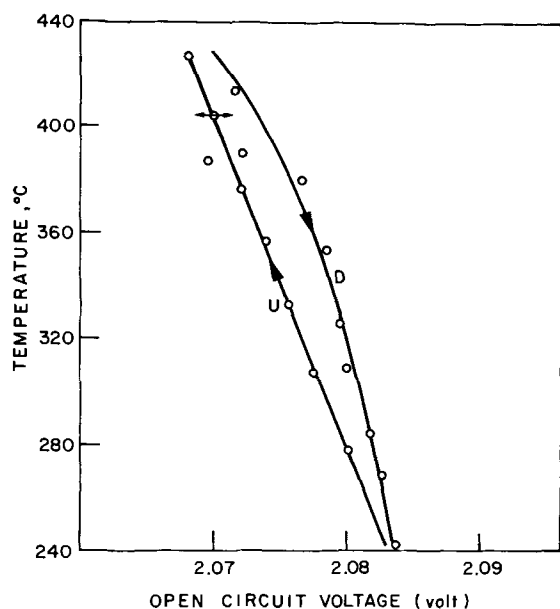


Fig. 5. OCV vs. temperature data for Na-polysulfide melt containing excess sulfur.

formation of supersaturated melt on cooling. These supersaturated melts have proved to be very stable. The OCV values at each point on the curve did not change even after waiting for 24 to 72 hr. The straight line shows the OCV of polysulfide melts in equilibrium with sulfur as a function of temperature. The composition of such melts at various temperatures is obtained by plotting the data from the straight line in Fig. 5 and the OCV vs. composition data obtained from Fig. 4. Such plots are shown in Fig. 6, which depicts the OCV vs. composition data at five different temperatures. The horizontal lines correspond to the data obtained from straight line U in Fig. 5. As explained earlier in the theoretical section, the line passing through the points of intersection forms the Na-rich boundary of the miscibility gap (Table I). The accuracy with which the S-solubility can be determined by this method is of the order of $\pm 0.02\%$ total sulfur.

The almost linear dependence of the OCV on composition does not permit any decision as to the potential-determining reaction. The range of compositions accessible in this system is so small that any logarithmic plot is linear with good approximation. But the

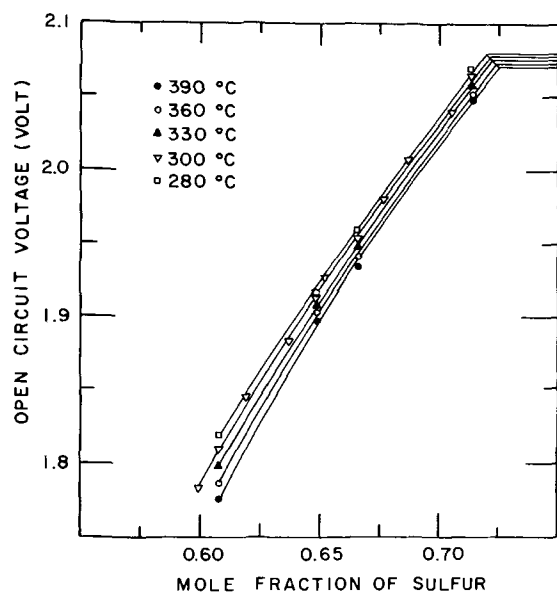


Fig. 6. OCV vs. composition at various temperatures

Table I. Sulfur-saturated melt composition at various temperatures

Temp, °C	Sulfur (wt %)
280	78.28
300	78.33
330	78.40
360	78.48
390	78.50

slope (RT/nF) of reasonable logarithmic plots yields an n of 0.25. This suggests that the oxidized form S and the reduced form S^- in the sulfur/sulfide redox couple cannot be treated as separate entities.

Figure 7 shows the Na-S phase diagram constructed using the Na-rich boundary of the miscibility gap (line A) and the points (solid) on the liquidus line obtained from the data in Fig. 4. The open circles show the data points obtained by Oei (1) using DTA and other analytical methods. The thin line (B) shows the Na_2S -S phase diagram as published by Robinson and Pearson (2) in 1930. The S-rich boundary of the miscibility gap has not yet been determined. The miscibility gap does not close at the top because sulfur boils at 444.6°C under atmospheric pressure. Whereas the DTA data by Oei and the OCV data presented in this paper agree very well, there is a discrepancy with the diagram obtained by Pearson and Robinson (2). This may be attributed to an uncertainty in the polysulfide compositions caused by the analytical method used by Pearson and Robinson and/or the supercooling associated with polysulfide melts with a S/Na ratio $\cong 1.3$. Pearson and Robinson obtained all their data from cooling curves. Figure 8, which is an enlarged view of a portion of the Na-S phase diagram, shows that the S-solubility limit does not pass through Na_2S_5 at its melting point. This clearly indicates that some sulfur dissolves in liquid Na_2S_5 down to solidification. No attempt was made to determine the solubility of sulfur in solid Na_2S_5 . Establishment of equilibrium, being very sluggish in the melt, can be expected to be considerably more so in the solid state.

Thermodynamic properties.—Table II lists the values of $-\bar{G}_1$ and $-\bar{G}_2$ calculated from the experimental data. At any temperature, $-\bar{G}_1$ decreases with de-

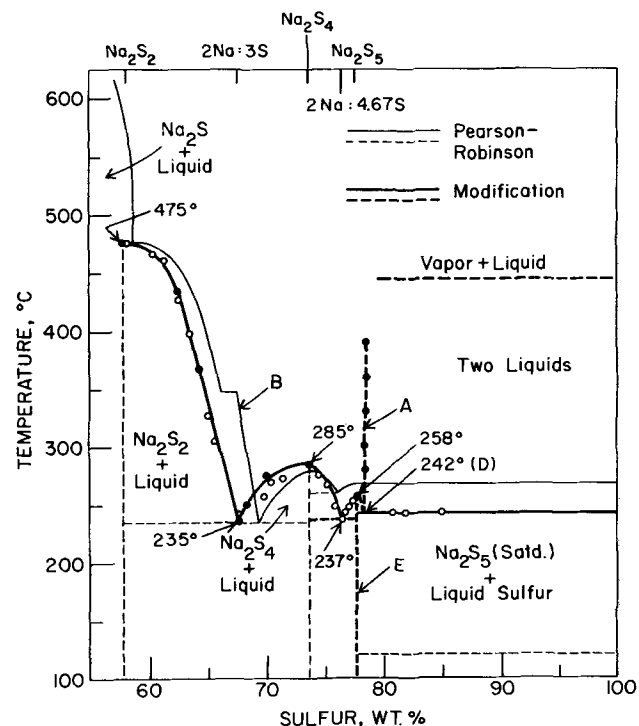


Fig. 7. Na_2S -S phase diagram. ● Data from this work, ○ data from Oei (1).

Table II. Gibbs free energy for sodium polysulfides obtained from open-circuit voltage measurements

Polysulfide composition (molten)	$-\bar{G}_1$, kcal					$-\bar{G}_2$, kcal				
	280°C	300°C	330°C	360°C	390°C	280°C	300°C	330°C	360°C	390°C
Na ₂ S ₅	47.6	47.5	47.4	47.3	47.2	0.09	0.18	0.20	0.24	0.27
Na ₂ S ₄	45.2	45.2	45.0	44.9	44.8	1.13	1.24	1.28	1.33	1.40
Na ₂ S _{3.7}	44.3	44.2	44.0	43.9	43.7	1.62	1.74	1.78	1.85	1.92
Na ₂ S _{3.1}	42.0	41.7	41.5	41.2	40.9	3.06	3.20	3.26	3.36	3.47
Na ₂ S ₃		41.2					3.54			
Na ₂ S _{2.6}			39.0 (440°C)					No data		
Na ₂ S _{2.4}			38.3 (440°C)					No data		

creasing S content of the melt, whereas the $-\bar{G}_2$ value increases. The \bar{G}_2 values for the Na₂S_{2.4} and Na₂S_{2.6} compositions were not calculated because of difficulties in determining the composition of the S-saturated polysulfide melt (needed as a reference point) close to the boiling point of S with any accuracy.

Figure 9 shows plots of $-(\Delta E/\Delta T - E/T)$ vs. $1/T$. For all the compositions investigated, the relationship is linear and all the lines have practically the same negative slope. Such a constancy in the value of \bar{H}_1 (-47.6 ± 0.7 kcal/mole) means that the same reaction is potential determining over the entire temperature and composition range. This reaction is the addition of Na to the polysulfide melt (Eq. [1]).

Table III shows the values of the total free energy (G) for the formation of the polysulfide, and \bar{H}_1 and \bar{S}_1 for adding Na to the polysulfide melt (Eq. [1]). Since the variation of \bar{G}_1 with temperature for any polysulfide composition is small, the values of S , \bar{S}_2 , H ,

Table III. Thermodynamic data for sodium polysulfides calculated from open-circuit voltage measurements

Polysulfide composition (molten)	$-G$, kcal					$-\bar{H}_1$	$-\bar{S}_1$
	280°C	300°C	330°C	360°C	390°C	kcal	cal °K ⁻¹
Na ₂ S ₅	95.7	96.0	95.8	95.7	95.7	47.8	4.1 ± 1
Na ₂ S ₄	95.0	95.3	95.1	95.1	95.1	48.2	3.8 ± 2
Na ₂ S _{3.7}	94.6	94.9	94.6	94.6	94.6	46.3	4.9 ± 1.5
Na ₂ S _{3.1}	93.5	93.4	93.1	92.9	92.6	47.6	10.0 ± 2.5
Na ₂ S ₃		93.1					
Na ₂ S _{2.6}			No data			47.8	24.6
Na ₂ S _{2.4}			No data			47.8	24.6
Na ₂ S ₂ (solid)		89.6 (?)					

and \bar{H}_2 could not be calculated accurately from the data. The accuracy of the G values is of the order of ± 0.1 kcal/mole. The free energy of formation of solid Na₂S₂ at 235°C was arrived at by making use of the fact that molten Na₂S₃ and solid Na₂S₂ are in thermodynamic equilibrium at the melting point of Na₂S₂-Na₂S₄ eutectic.

Acknowledgment

The authors are grateful to Ford Motor Company for giving permission to publish this work and wish to thank Dr. J. V. Petrocelli, Dr. N. Weber, and Dr. R. W. Minck for many helpful and clarifying discussions.

Manuscript submitted Aug. 6, 1971; revised manuscript received March 21, 1972. This was Paper 344 presented at the Los Angeles Meeting of the Society, May 10-15, 1970.

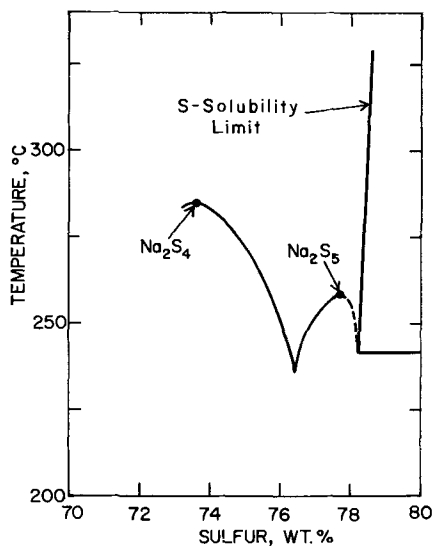
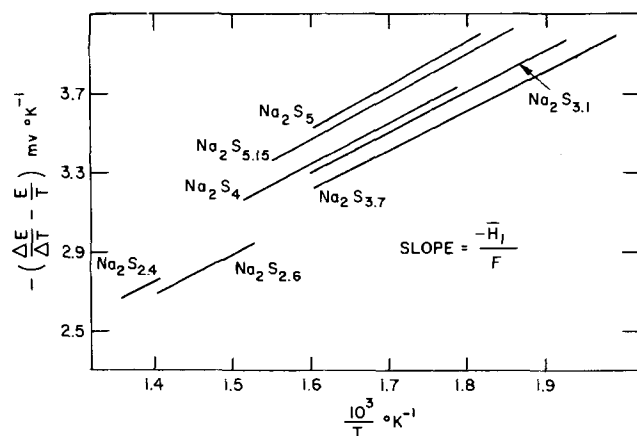
Any discussion of this paper will appear in a Discussion Section to be published in the June 1973 JOURNAL.

LIST OF SYMBOLS

E	open-circuit voltage
F	Faraday constant
G	Gibbs free energy
H	enthalpy
S	entropy
T	absolute temperature
—	an overbar denotes differential partial energies and entropies
1	subscript for Na
2	subscript for S
x	stoichiometric number for S
\hat{x}	stoichiometric number for S in Na ₂ S _{\hat{x}} in equilibrium with free S
\hat{y}	$2\hat{x}/x$
η	integration variable for \hat{y}

REFERENCES

- D. G. Oei, Paper presented at the ACS Meeting in Los Angeles, Spring 1971.
- T. G. Pearson and P. L. Robinson, *J. Chem. Soc.*, **132**, 1473 (1930).
- "Handbook of Chemistry and Physics," 51st ed., D-70 (1970-1971).
- Charles A. Kraus and John A. Ridderhoff, *J. Am. Chem. Soc.*, **56**, 79 (1934); Landolt-Börnstein, II, 4, p. 202, Springer-Verlag, Berlin-Göttingen-Heidelberg (1961).
- Georg Brauer, "Handbook of Preparative Inorganic Chemistry," 2nd ed., Translated by Scripta Technica, Inc., Reed F. Riley, Translation Editor, Academic Press, New York (1963-1965).

Fig. 8. Na₂S-S phase diagram (magnified view)Fig. 9. Plot for various compositions of $-(\Delta E/\Delta T - E/T)$ vs. $1/T$

A Calomel Cell and the Fugacity of Hydrogen

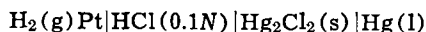
W. R. Howell, Jr.,¹ J. H. Woodson, and H. A. Liebhafsky*

Department of Chemistry, Texas A&M University, College Station, Texas 77843

ABSTRACT

By use of recent data for hydrogen as a real gas, it has been shown that there is no need to introduce changes in the activities of condensed phases to explain the electromotive forces measured when the partial pressure of hydrogen in a calomel cell (0.1N HCl as electrolyte) is increased up to 1035 atm at 25°.

In a classic investigation (1, 2) it was found at 25° that the emf, ϵ , of the cell



increased more rapidly than required by the Nernst equation when the partial pressure p of hydrogen, varied up to 1035 atm, was used in the calculation. The departure of hydrogen from ideal behavior was of course mainly responsible, and all but 2.3 mV of the difference at 1000 atm was accounted for by using a simple equation of state for this gas in a treatment based on the volume change attending the cell reaction. The residual difference was attributed in the main to an effect of hydrogen dissolved at high pressure on the partial molar volume of hydrochloric acid. Calculations reported here, which are based on recent data (3-6), show that this assumption is no longer necessary. Extensive preliminary calculations indicated the results of Michels *et al.* (5, 6) to be best for our purposes.

Two sets of final calculations were made. In the first, the increment $\Delta\epsilon$ resulting from an increase of p above 1 atm (101325 N/m²) was obtained for each such increase from the familiar equation

$$\Delta\epsilon = (0.029580\text{V})\log f_p/f_1 \quad [1]$$

which contains the fugacity quotient for the two partial pressures in question. The fugacities were obtained from

$$\ln f/p = (14.38P)/RT + (0.006671P^2)/2RT \quad [2]$$

where P is the pressure in atmospheres for a hydrogen Pv isotherm experiment; R has the value 82.056 cm³ · atm/kmol, and T is the temperature in Kelvins. The calculation assumes that P may be substituted for p , the partial pressure of hydrogen in the cell, when the two pressures are equal. This assumption is tantamount to saying that the water vapor present does not change the fugacity of hydrogen. The first virial coefficient is the value of B for 25° in Ref. (6); the second is that of $(C - B^2)/RT$ for the same temperature.

In addition, a differential calculation was needed. This is based on three thermodynamic relations

$$d \ln f = (pv/RT) d \ln p$$

$$(v = \text{molar volume of H}_2) \quad [3]$$

$$\epsilon^a = \epsilon^* + (RT/2F) \ln f$$

$$(a \text{ denotes actual gas}) \quad [4]$$

$$\epsilon^i = \epsilon^* + (RT/2F) \ln p$$

$$(i \text{ denotes ideal gas}) \quad [5]$$

which lead to

$$(\delta\epsilon)_n = \epsilon_n^a - \epsilon_n^i = (RT/2F) (\ln f_n - \ln p_n) \quad [6]$$

or

$$(\delta\epsilon)_n = (0.029580\text{V}) (\log f_n - \log p_n) \quad \text{at } 25^\circ\text{C} \quad [7]$$

as the "departure from ideality" for the n 'th cell. Experimental values of $(\delta\epsilon)_n$ may be plotted against $\log p_n$ and measured slopes, $d(\delta\epsilon)/d \log p$, taken from the resulting curve. These may be compared with slopes calculated from

$$d(\delta\epsilon) = (0.029580\text{V}) (pv/RT - 1) d \log p \quad (p = P) \quad [8]$$

Equation [8] results from Eq. [3] and [7] applied to a pair of cells with partial pressures of hydrogen only slightly different. Equations [7] and [8] thus permit a direct intercomparison of two kinds of measured quantities: emf and Pv isotherms.

In Eq. [4] and [5], ϵ^* is the emf of the cell at unit fugacity of hydrogen. We have used $\epsilon^* = 0.39375\text{V}$, a value based on the first measured result of Ref. (7), Table I, corrected to 0.1N HCl by use of activity coefficients in Tables III and IV.

The data to this point are given in Table I.

The complexity of the calomel cell, uncovered (7) since 1924, could be responsible for the Δ 's in Table I. It is gratifying to see that they show no dependence on p , and that they are smaller and opposite in sign to the 2.3 mV mentioned above.

Figure 1 shows the plot of $(\delta\epsilon)_{\text{meas}}$ vs. $\log p$. Table II gives the comparison of the measured slopes from Fig. 1 with calculated values from Eq. [8] at five pressures at which isotherms were measured. The agreement is satisfactory. The fugacity of hydrogen is thus the only variable needed to explain the variation of ϵ with p in the cell under consideration. The measured emf's give no evidence of any net change in the activities of the condensed phases. In particular, they show no effect of the difference of electrolyte composition in the regions near anode and near cathode even at a hydrogen partial pressure that exceeds 1000 atm (10⁸ N/m²).

LIST OF SYMBOLS

f_p fugacity of hydrogen at partial pressure p , atm

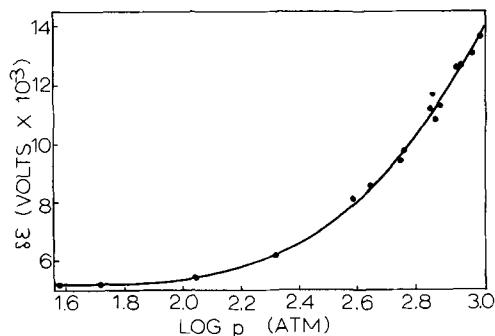


Fig. 1. "Departure from ideality" of measured emf. Greatest vertical deviation from the curve is 0.5 mV. $\delta\epsilon$ is expressed in millivolts.

* Electrochemical Society Active Member.

¹ Present address: Dow Chemical Company, Texas Division, Freeport, Texas 77541.

Key words: hydrogen fugacity, electrochemical cell, partial pressure.

Table I. Data for a hydrogen/calomel cell at various partial pressures of hydrogen at 25°C
All emf's in millivolts

p (atm)	f (atm)	ϵ_{meas} (mV)	All emf's in millivolts		Δ^a (mV)	ϵ^t (mV)	$(\delta\epsilon)_{\text{meas}}^b$ (mV)
			$(\Delta\epsilon)_{\text{meas}}$ (mV)	$(\Delta\epsilon)_{\text{calc}}$ (mV)			
1.00	1.0006	399.0	0.0	0.0	0.0	393.8	+5.2
37.8	38.7	445.6	46.6	46.9	-0.3	440.4	5.2
51.6	53.2	449.6	50.6	51.0	-0.4	444.4	5.2
110.2	117.8	459.6	60.6	61.3	-0.7	454.2	5.4
204.7	232.2	468.3	69.3	70.0	-0.7	462.1	6.2
386.6	495.2	478.4	79.4	79.7	-0.3	470.3	8.1
439.3	583.9	480.4	81.4	81.8	-0.4	471.9	8.5
556.8	805.7	484.4	85.4	86.0	-0.6	475.0	9.4
568.8	830.4	485.0	86.0	86.3	-0.3	475.2	9.8
701.8	1133.7	489.1	90.1	90.3	-0.2	477.9	11.2
717.8	1174.2	489.9	90.9	90.8	+0.1	478.2	11.7
731.8	1210.3	489.3	90.3	91.2	-0.9	478.5	10.8
754.4	1270.2	490.3	91.3	91.8	-0.5	478.9	11.4
862.2	1583.8	493.2	94.2	94.6	-0.4	480.6	12.6
893.9	1685.6	493.8	94.8	95.4	-0.6	481.1	12.7
974.5	1966.7	496.3	97.3	97.4	-0.1	482.2	14.1
1035.2	2201.4	497.5	98.5	98.9	-0.4	482.9	14.6

$$^a \Delta = (\Delta\epsilon)_{\text{meas}} - (\Delta\epsilon)_{\text{calc}}$$

$$^b (\delta\epsilon)_{\text{meas}} = \epsilon_{\text{meas}} - \epsilon^t$$

Table II. Comparison of calculated and measured slopes.
See Fig. 1

p (atm)	$\frac{0.029580}{(pv/RT - 1)}$	$(d(\delta\epsilon)_{\text{meas}}/dp)$
83.1	0.00149	0.000700
208.8	0.00386	0.00459
395.7	0.00752	0.00856
624.6	0.0120	0.0131
1026.1	0.0198	0.0179

f_1	fugacity of hydrogen at $P = 1$ atm, atm
p	partial pressure of hydrogen in the cell, atm
P	hydrogen pressure for Pv isotherm, atm
R	universal gas constant, S.I. value = 8.3143 J/kmol. In Eq. [2], $R = 82.056 \text{ cm}^3 \cdot \text{atm}/\text{kmol}$
T	temperature, Kelvins
v	molar volume of hydrogen, $\text{cm}^3 \text{ mol}^{-1}$
$\Delta\epsilon$	calculated emf, V
ϵ^a	emf for actual gas, V
ϵ^*	standard electrode potential, V
$(\delta\epsilon)_n$	"departure from ideality" for n 'th cell, V

Acknowledgment

We thank the Robert A. Welch Foundation for supporting this work. WRH expresses his appreciation to

the National Science Foundation for the support of a NSF Traineeship.

Manuscript submitted Feb. 9, 1972; revised manuscript received March 28, 1972.

Any discussion of this paper will appear in a Discussion Section to be published in the June 1973 JOURNAL.

REFERENCES

- W. R. Hainsworth and D. A. MacInnes, *J. Am. Chem. Soc.*, **44**, 1021 (1922).
- W. R. Hainsworth, H. J. Rowley, and D. A. MacInnes, *ibid.*, **46**, 1437 (1924).
- W. E. Deming and L. E. Shupe, *Phys. Rev.*, **40**, 848 (1932).
- C. E. Holley, W. J. Worlton, and R. K. Zeigler, Los Alamos Scientific Reports, LA-2271, TID-4500, 14th ed. (1959).
- A. Michels, W. DeGraaff, T. Wassenaar, J. M. H. Leveit, and P. Louwerse, *Physica*, **25**, 25 (1959).
- A. Michels, W. DeGraaff, and C. A. Ten Seldam, *ibid.*, **26**, 393 (1960).
- G. J. Hills and D. J. G. Ives, *J. Chem. Soc.*, **1951**, 305.

Electrochemical Studies of Zinc Tetraphenylporphin

J. G. Lanese¹ and George S. Wilson*

Department of Chemistry, University of Arizona, Tucson, Arizona 85721

ABSTRACT

The reduction of zinc (II) tetraphenylporphin (ZnTPP) in dimethylformamide (DMF) was investigated. The products of electron transfer and associated chemical reactions were studied by polarography, cyclic voltammetry, thin-layer controlled potential coulometry and spectroscopy, and epr. Reduction proceeds initially as a series of two reversible one-electron steps. After the second and subsequent steps, however, proton abstraction from the solvent medium occurs which, in turn, determines the reaction path. Characteristics of the porphyrin ring reactions are studied and compared with those of porphyrin free bases.

In recent years, there has been considerable interest in the area of porphyrin chemistry. The background and implications of these studies have been discussed

in a previous paper, and a scheme for the electrochemical reduction of tetraphenylporphin (TPP) in aprotic medium (DMF) proposed (1). The present study was carried out as a continuation of the previous work (1, 2) in order to examine the effect of a central metal atom on the reactivity of the porphyrin ring in aprotic medium. The compound used for the

* Electrochemical Society Active Member.

¹ Present address: Stiefel Research Institute, Oak Hill, New York 12460.

Key words: zinc tetraphenylporphin, optical spectra, coulometry, cyclic voltammetry, aprotic solvent.

study was zinc tetraphenylporphin, ZnTPP. Of particular interest is the manner in which the central metal atom will influence ring reduction and associated chemical reactions without undergoing reduction itself.

The chemical reduction of ZnTPP in THF to yield the anion radical ZnTPP^- and the chlorin, ZnTPC, has been reported by Closs and Closs (3). Seely and co-workers (4, 5) have reported the photochemical reduction of ZnTPP and zinc porphin to the respective chlorins in benzene and ethanol. The polarography of ZnTPP has been studied by Clack and Hush (6) while Felton and Linschitz (7) have reported polarography and epr spectra of electrochemical reduction products of TPP, ZnTPP, and ZnTPC in DMSO. The present study involves the detailed examination of porphyrin reactions by spectral and electrochemical methods.

Experimental

Materials.—ZnTPP was prepared from tetraphenylporphin by the method described by Adler *et al.* (8). The product was purified by column chromatography on neutral alumina eluted with benzene and recrystallized from chloroform.

The solvent, dimethylformamide (DMF), and the supporting electrolyte, tetraethyl ammonium perchlorate (TEAP), were purified as described elsewhere (2). Purification of degassing nitrogen has also been described (2).

Apparatus and methods.—Polarographic and cyclic voltammetric data were obtained using the apparatus described previously (2). A conventional hanging mercury drop electrode (HMDE) was employed. For measurements at very negative potentials, however, the electrode tip was inverted. This prevented the drop from falling off in regions of low mercury surface tension. All potential measurements were made with respect to an aqueous saturated calomel electrode (SCE) at $25^\circ \pm 0.1^\circ\text{C}$.

Near infrared and visible spectra were obtained with a Cary 14R spectrophotometer used in conjunction with a thin-layer cell of approximately 0.07 mm path length utilizing a gold minigrad electrode (2). Spectra of products produced were also obtained during the thin-layer cyclic voltammetric studies.

For thin-layer cell controlled potential coulometry, reductions and oxidations were carried out in the thin-layer cell using the polarographic apparatus and integrating the resultant current-time curve. The volume of the thin-layer cell was determined by coulometric determination of a solution of the disodium salt of anthraquinone 2,6 disulfonate of known concentration in 0.1M HCl. Current-time curves were corrected for cell edge diffusion. The current quickly decays to a small but constant value which is due to electrolysis at both ends of the cell. If this constant value is subtracted from the current-time curve, excellent agreement between known systems is obtained.

Epr spectra were generated *in situ* in the cavity of a Varian E-3 epr spectrometer in a cell similar to that described by Visco (9).

Results

Polarography and cyclic voltammetry.—The reduction of ZnTPP gives four diffusion controlled waves. A typical polarogram is shown in Fig. 1. Data for these waves are listed in Table 1. When corrected for drop time, the four wave heights are in the ratio of 1:1:1.2:1.5. No prewaves were observed. A poorly defined wave follows the second wave and will be discussed subsequently. The polarographic data for ZnTPP indicate that the first two waves are a result of one electron steps to form the anion radical (ZnTPP^-) and the dianion (ZnTPP^{2-}) respectively. The third and fourth waves result from irreversible, multiple electron processes. All four waves give cur-

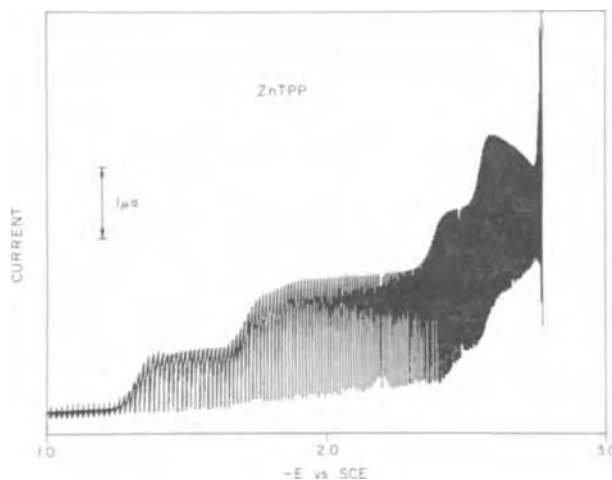


Fig. 1. Polarogram of $3.2 \times 10^{-4}\text{M}$ ZnTPP in DMF, 0.1M TEAP

rents which are linearly proportional to concentration over the range of about 5×10^{-5} to $1 \times 10^{-3}\text{M}$.

The effect of proton donor addition was studied by introducing water or benzoic acid into the aprotic medium. Above 1.3% (v/v), water and 0.03% benzoic acid, the first and second waves merged to form one long poorly defined wave somewhat lower in height than the sum of the first two waves. The small wave which initially followed the second wave became more prominent. The third and fourth waves became poorly defined as many new overlapping processes began to occur in this region.

The polarographic data are confirmed by cyclic voltammetry using the conventional polarographic cell (Fig. 2). At moderate scan rates (about 0.1 V/sec), the first two processes show cathodic and anodic peak separation indicative of a reversible one electron step (Fig. 2A). At slower scan rates, the anodic peak associated with the second step disappears and a new anodic peak appears at about -0.5V (Fig. 2B). This latter process corresponds to the oxidation of the product formed by the chemical reaction of the dianion (ZnTPP^{2-}).

When the potential is scanned at less than 0.1 V/sec, an additional reduction process appears at -1.9V (Fig. 2C) with cathodic and anodic peaks at -1.88 and -1.82V respectively. This process coincides in potential with the small polarographic wave noted above. When the scan is held at -1.9V , the oxidation peak (-1.82V) disappears and a small oxidation peak appears at -1.2V . The latter is in addition to the previously described peak at -0.5V . The sequence of events occurring when the electrode is polarized at -1.9V might be characterized as an ECECE mechanism. The first electrochemical step is reversible and involves the formation of the porphin dianion (ZnTPP^{2-}) from the anion radical. This is followed by rapid protonation to form the phlorin anion (ZnTPPH^-). Analysis of the cyclic voltammetric data yields a pseudo first order rate constant for the protonation of about 1 sec^{-1} as calculated by the method of Nicholson and Shain (10). The second electrochemical step involves the one-electron reduction of the

Table I. Polarographic data for zinc tetraphenylporphin^(a)

Wave	$E_{1/2}$ (E vs. SCE)	Slope ^(b)
1	-1.31	53
2	-1.71	65
3	-2.32	43
4	-2.53	27

^(a) Data obtained in purified DMF 0.1M TEAP.

^(b) Slope = $E_{1/4} - E_{3/4}$.

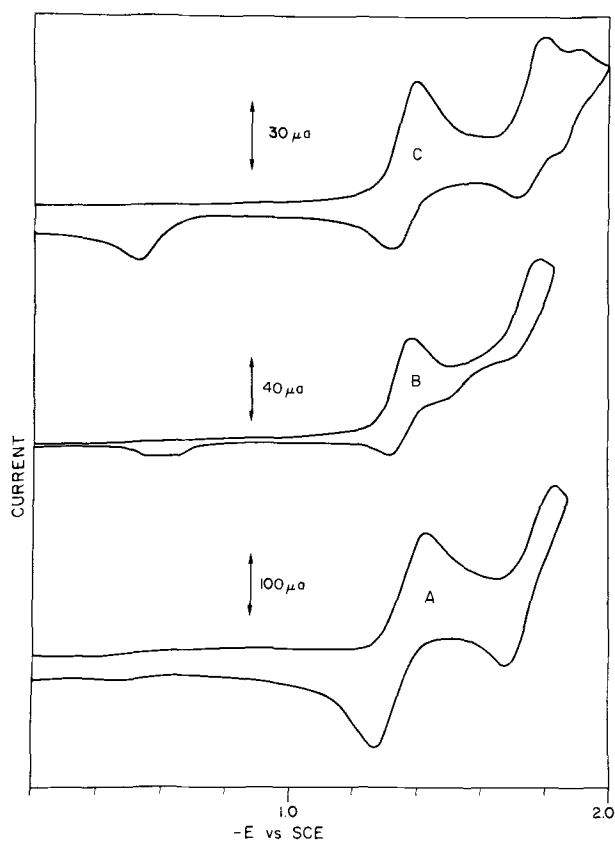


Fig. 2. Cyclic voltammetry of $1.5 \times 10^{-3} \text{M}$ ZnTPP in DMF, 0.1M TEAP at the HMDE. Scan rates: A, 0.178 V/sec; B, 0.033 V/sec; C, 0.033 V/sec.

phlorin anion to form the phlorin dianion (ZnTPPH^{2-}). This assignment is verified by cathodic-anodic peak separation and by the coulometric data to be presented subsequently. The second chemical step and the electron transfer process associated with it are quite slow as described below.

The third and fourth cyclic voltammetric processes are irreversible and occur at -2.38 and -2.55V respectively. At scan rates greater than 0.008V/sec , the third wave merges into the fourth. When the potential is scanned through all four waves, interpretation becomes complex due to the many oxidation peaks which result from large numbers of reactions of the reduction products with protons.

Thin-layer Electrochemistry.—Figures 3 and 4 show the spectra of the species formed in the thin-layer cell. Table II summarizes the spectral data between 350 and 1000 nm. When the ZnTPP is reduced at -1.35V , the anion radical ZnTPP^- is formed (3). This product may be reversibly oxidized back to the parent compound, ZnTPP. Electrolysis at -1.75V yields a compound giving the spectrum of Fig. 3. The product

Table II. Spectra of zinc tetraphenylporphin and its reduced species

Species	λ_{max} (nm)	$\epsilon \times 10^{-4}$
ZnTPP	405 (s)	5.49
	425	65.4
	515	0.305
	555	1.96
	595	0.85
ZnTPP^-	455	12.1
	680 (s)	0.63
	710	1.20
	790	0.45
	905	1.01
ZnTPPH^-	457	9.5
	825	2.4
ZnTPPH^{2-}	458	5.0
	510	2.0
$\text{ZnTPPH}_{c+1}^{(4-c-1)-}$	790	4.0
	620	4.1
$\text{ZnTPPH}_{(c+1-d)}^{(4-n-c-1+d)-}$	680	6.0

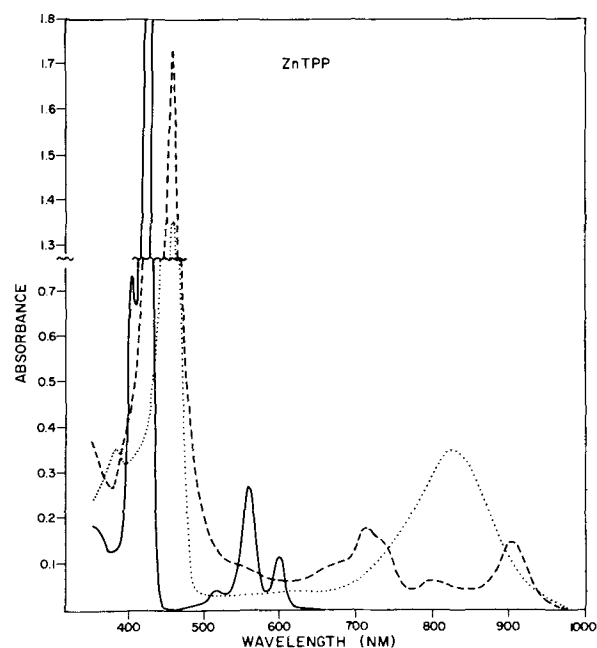


Fig. 3. Spectra of ZnTPP and reduction products in DMF, 0.1M TEAP in thin layer cell. Concentration— $1.5 \times 10^{-3} \text{M}$ ZnTPP (—). ZnTPP^- (---), ZnTPPH^- (.....).

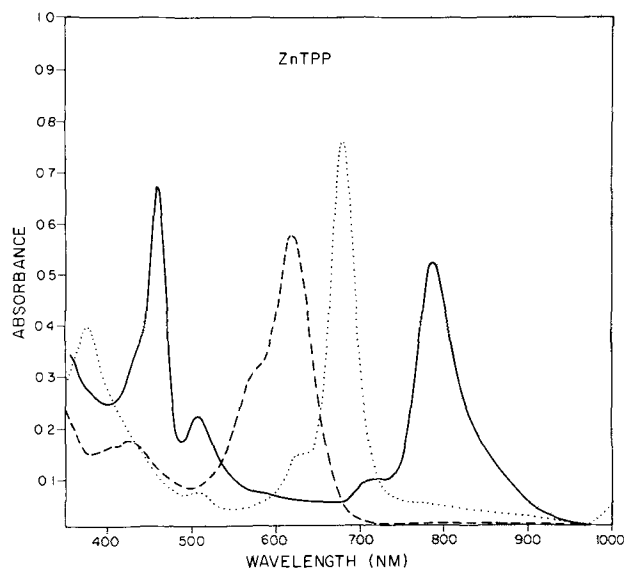


Fig. 4. Spectra of ZnTPP reduction products in DMF, 0.1M TEAP in thin layer cell. Concentration— $1.5 \times 10^{-3} \text{M}$. ZnTPPH^{2-} (—), $\text{ZnTPPH}_{(c+1)}^{(4-c-1)-}$ (---), $\text{ZnTPPH}_{(c+1-d)}^{(4-n-c-1+d)-}$ (.....).

ZnTPPH^- is identified from its similarity to the spectrum of Closs and Closs (3) who obtained bands at 457 and 810 nm in THF. This anion is irreversibly oxidized to the parent compound at -0.45V . At a potential of -1.90V , the phlorin anion is converted by a one-electron reversible reduction to ZnTPPH^{2-} as described above. The product is oxidized back to the phlorin anion at -1.8V . If the potential is held at -1.9V , the reduction product ZnTPPH^{2-} is converted to $\text{ZnTPPH}_{c+1}^{(4-c-1)-}$ by a one-electron process. This conversion is slow, requiring about an hour to go to completion. The conversion can be followed spectrally, and two isosbestic points are exhibited at 535 and 678 nm. These observations suggest that the rate of conversion is controlled by a slow chemical step involving a proton, isomerization, or both, and also that only two species are observed.

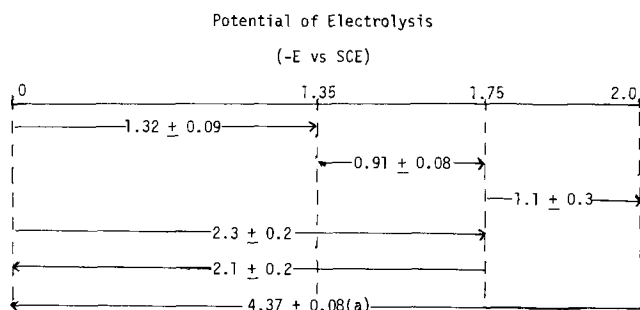


Fig. 5. Results of coulometric studies.—Number of electrons involved in oxidations and reductions by stepping between various potentials. a—Oxidation performed after holding at -2.0V for 1 hr.

The $\text{ZnTPPH}_{c+1}^{(4-c-1)-}$ is oxidized to a spectrally distinct intermediate, $\text{ZnTPPH}_{(c+1-d)}^{(4-n-c-1+d)-}$ at -1.2V , then to the phlorin anion, ZnTPPH^- .

Figure 5 summarizes the results of the thin-layer coulometric studies. A potential step from 0 to -1.35V results in the formation of ZnTPP^- as confirmed spectrally. The N_{app} values are somewhat greater than the expected value of unity and this is probably due to the presence of reducible impurities in the solvent. The step from -1.35 to -1.75V converts the ZnTPP^- to ZnTPPH^- . Oxidation of this product back to the parent compound at 0V confirms the assignment of oxidation state. The conversion of ZnTPPH^- to ZnTPPH^{2-} (-1.75 to -2.0V) requires about 1.1 electrons/mole. Because the chemical reaction following electron transfer is slow, it is possible to obtain the coulometric data and phlorin dianion spectrum before further electron transfer can occur at the applied potential (-2.0V). If the potential is held long enough for complete reaction to occur, about 4 electrons are required to convert the resulting product

($\text{ZnTPPH}_{c+1}^{(4-c-1)-}$) back to the parent compound. This means that the conversion of the phlorin dianion

to $\text{ZnTPPH}_{c+1}^{(4-c-1)-}$ must be a one-electron process. It is not known at present whether this latter step involves proton addition, but such a possibility is quite likely. In each of the controlled potential thin-layer electrolyses described above, the products were confirmed by spectral measurements. Typical electrolyses are completed in about 20 sec for an effective solution volume of approximately 20 microliters.

Typical thin-layer cyclic curves are shown in Fig. 6. Curve A shows the reversible reduction to ZnTPP^- at -1.3V and the irreversible reduction to ZnTPPH^- at -1.7V . The ZnTPPH^- is oxidized back to the parent at -0.45V . The reduction at -1.85V (Fig. 6B) to ZnTPPH^{2-} is reversible as the dotted line indicates. The double peak in the -0.4 to -0.7V range is attributed to the oxidation of the phlorin anion and a presumably isoelectronic form of the phlorin anion to the parent compound ZnTPP . This latter conclusion is based on the area and potential of the oxidation peak.

EPR studies.—*In situ* generation of ZnTPP^- confirms its paramagnetic character. A single line with a width between inflection points of 22 gauss is obtained. This is clearly distinguished from the spectrum obtained at -1.95V which is considerably narrower (6.4 gauss) and possesses hyperfine structure. The spectrum appears possibly consistent with that expected for a phlorin dianion (11).

Conclusions

Figure 7 shows a scheme for the reduction of ZnTPP which is consistent with the experimental observations. Acid-base reactions play an important role in determining the path of the electron transfer reactions. In

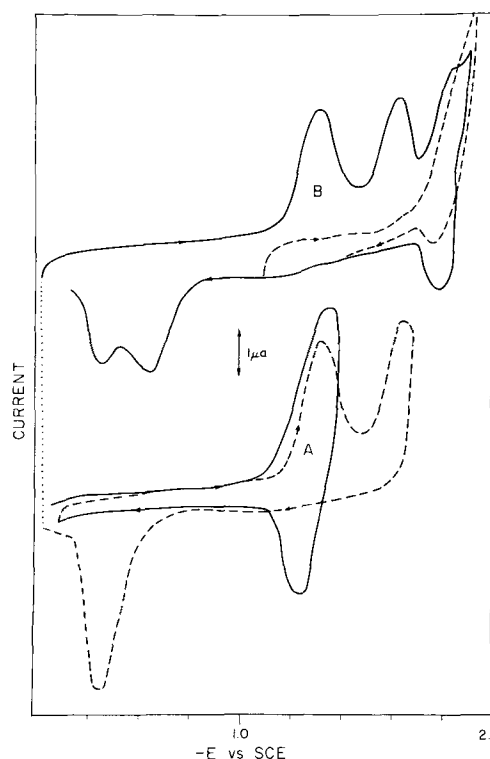


Fig. 6. Typical thin layer cyclic voltammetry. Approximately 10^{-4}M ZnTPP in DMF, 0.1M TEAP. Scan rate, $0.05\text{V}/\text{min}$.

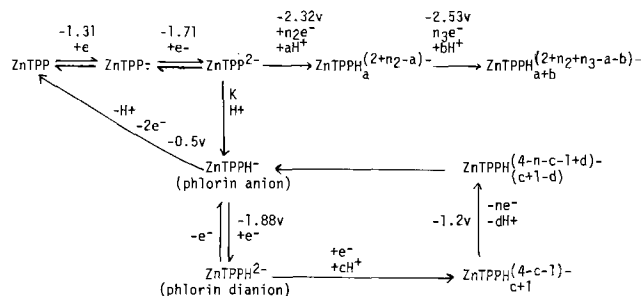


Fig. 7. Scheme for the electrochemical reduction of ZnTPP in DMF, 0.1M TEAP.

this regard, the insertion of zinc(II) as a central metal atom produces some significant differences in porphyrin ring reactions. For example, the dianion of the porphyrin free base (TPP^{2-}) is quite stable in DMF (1) and in contrast to ZnTPP^{2-} does not undergo the above-described protonation reaction to form the phlorin anion. Porphyrin electrochemical reduction has been shown to be followed by electrophilic attack on the methine bridge positions between the pyrrole rings (12). In this case, the result would be saturation of one of the bridge positions. Such a process is favored by increased electron density in the bridge position. The manner in which central metal atom substitution might influence bridge electron density is the subject of continuing study.

Phlorin anion oxidation to the parent porphyrin is similar for both ZnTPPH^- and the corresponding TPPH^- . In neither case is there evidence of neutral radical (ZnTPPH^{\cdot}) formation during the oxidation. There is also no evidence of chlorin formation from the phlorin anion in this medium. ZnTPPH^- is reduced in a one-electron reversible step to form the paramagnetic phlorin dianion. The latter species reacts slowly, probably with a proton, and a further one-electron reduction occurs at the same potential as the reduction of ZnTPPH^- . Some porphyrin-free base phlorin anions may well proceed by a similar mechanism, but if this

is so, the phlorin dianion is unstable, protonates rapidly, and the over-all irreversible process involves an apparent two-electron step (2).

Reduction beyond the two-electron level is complicated by the varying extent of acid-base reactions with reduced forms. It is clear on the basis of potentials that beyond the formation of the phlorin anion, the polarography-cyclic voltammetry conditions are not the same as the thin-layer experiment. This is due to the difference in time scale between the various experiments which allows varying degrees of protonation to occur.

Acknowledgment

The support of the National Science Foundation (GP-9484) and a University Science Development Program Grant from the National Science Foundation to the University of Arizona are gratefully acknowledged.

Manuscript submitted Sept. 27, 1971; revised manuscript received March 6, 1972. This was Paper 131 presented at the Washington, D.C., Meeting of the Society, May 9-13, 1971.

Any discussion of this paper will appear in a Discussion Section to be published in the June 1973 JOURNAL.

REFERENCES

1. G. Peychal-Heiling and G. S. Wilson, *Anal. Chem.*, **43**, 550 (1971).
2. G. Peychal-Heiling and G. S. Wilson, *ibid.*, **43**, 545 (1971).
3. G. L. Closs and L. E. Closs, *J. Am. Chem. Soc.*, **85**, 818 (1963).
4. G. R. Seely and K. Talmadge, *Photochem. and Photobiol.*, **3**, 195 (1964).
5. G. R. Seely and M. Calvin, *J. Chem. Phys.*, **23**, 1068 (1955).
6. D. W. Clack and N. S. Hush, *J. Am. Chem. Soc.*, **87**, 4238 (1965).
7. R. H. Felton and H. Linschitz, *ibid.*, **88**, 1113 (1966).
8. A. D. Adler, F. R. Longo, F. Kampas, and J. Kim, *J. Inorg. Nucl. Chem.*, **32**, 2443 (1970).
9. R. E. Visco, Ph.D. Thesis, University of Illinois, Urbana, Ill. (1962).
10. R. S. Nicholson and I. Shain, *Anal. Chem.*, **37**, 190 (1965).
11. N. S. Hush and J. R. Rowlands, *J. Am. Chem. Soc.*, **89**, 2976 (1967).
12. H. H. Inhoffen, *Pure Appl. Chem.*, **17**, 443 (1968).

Anodic Films and ECM Dimensional Control: A Study of Steel Electrodes in Solutions Containing Na_2SO_4 and NaClO_4

Der-Tau Chin*

Electrochemistry Department, Research Laboratories, General Motors Corporation, Warren, Michigan 48090

ABSTRACT

The relationship between the passive film and the dimensional control of electrochemical machining (ECM) has been demonstrated experimentally with the behavior of steel electrodes in neutral Na_2SO_4 and NaClO_4 solutions. Potentiostatic transient measurements were first made with a mild steel rotating spherical electrode to reveal the mechanism of passivity, and the results were then compared to those obtained with rotating rods under actual ECM conditions. It is found that passivation is initiated by the formation of a salt layer resulting from supersaturation of dissolution products in the immediate vicinity of the anode. The rate of film formation is diffusion controlled, and the ECM dimensional control achieved by passivity of this kind is convection dependent. The results also indicate that this anodic film of the dissolution-precipitation type can serve only as partial protection for the metal surface during ECM.

One of the major problems associated with electrochemical machining (ECM) is that of obtaining satisfactory dimension control of a desired machining configuration. In practice, this is done by designing a proper shape for the cathode in order to give a required contour on the anode. The cathode (tool) design must rely on various process variables, e.g., electrolyte properties, fluid flow effects, current and temperature distributions in the electrode gap (1-5). Among the parameters, the most important factor for achieving successful dimensional control is the choice of electrolyte. For instance, the use of NaCl solution in the ECM of steel brings about extensive stray cutting at sites located some distance from the machining surface facing the cathode, whereas under the same conditions the highly localized action of NaClO_3 gives excellent dimensional control (6, 7). Additions of Na_2SO_4 have been claimed to improve the ECM performance of NaCl solutions (8). Recently, NaClO_4 has been reported to give dimensional control similar to that obtained with NaClO_3 (9, 10).

To explain why the use of different electrolytes results in different machining characteristics, Hoare, LaBoda, McMillan, and Wallace (11, 12) propose a film theory based on steady-state polarization measurements. According to them, to achieve good ECM dimensional control, the electrolyte used must be able to passivate the metal at certain anodic potentials. During ECM, metal is removed most heavily from the surface of the anode directly facing the cathode. This portion of the anode is called the cutting area or the high current density area where the voltage gradient across the electrode gap is high, and the dissolution is assumed to take place in the transpassive state. At places on the anode located well away from the cutting area, the distance to the cathode is large, and the IR drop in the solution lowers the metal/solution interfacial potential difference to values corresponding to the passive state. A passive film, therefore, is formed, resulting in little or no metal removal at these places.

Consequently, it is necessary to understand the nature of passivity to achieve further development of the ECM process. In a previous report (13), the mechanism of film formation was described for steel in NaCl

* Electrochemical Society Active Member.

Key words: passivation of mild steel, rotating spherical electrode.

and NaClO_3 solutions. That investigation employed potentiostatic transient measurements with a rotating disk electrode (RDE). In the present work, the study has been extended to Na_2SO_4 and NaClO_4 solutions. Since a steel RDE would recede into the support and upset the flow characteristics during metal dissolution, a steel rotating spherical electrode (RSE) was used instead. The concept of a RSE is to replace the disk electrode on the RDE with a hemispherical head electrode. The hemispherical head merely reduces in diameter during the dissolution; this change does not alter the flow characteristics. A mathematical theory for the use of the RSE has been reported elsewhere (14).

To compare the transient results with the ECM behavior of steel in the electrolytes, experiments were also made under actual ECM conditions using a rotating steel rod, a stationary cathode, and a narrow gap space. Similar to the rotating rod experiment described by Dyke, Gurklis, and Faust (15), the method has the advantage of avoiding the complexity of pumping electrolyte at high pressures, while still providing a high rate of electrolyte flow in the electrode gap. This paper describes the results of these investigations.

Experimental

Potentiostatic transient studies.—A RSE was used for the study of anodic transients on steel in Na_2SO_4 and NaClO_4 electrolytes. With slight modifications, the electrode construction was similar to the one reported in an earlier mass transfer study (16). It consisted of a replaceable, mild steel hemispherical head electrode,¹ a cylindrical Teflon support, and a stainless steel holder. The head electrode was 0.317 cm in radius, and was mounted on one end of the Teflon support, 1.9 cm OD \times 9 cm long. The other end of the support was attached to the stainless steel holder, which was machined to fit snugly into the spindle shaft of a high speed rotator. The electrolytic cell was an acrylic container, 15 cm ID \times 15 cm high, having a platinum cathode on the bottom. The RSE was extended down from the rotator into the cell, and the spacing between the anode and the cathode was kept at 3 cm. A saturated calomel electrode immersed in a Luggin capillary tube was used as the reference electrode. To avoid disturbing the flow characteristics, the capillary tip was placed on the downstream of the electrolyte flow around the spherical electrode.

Procedures for the transient measurement were described in a previous report (13). For each run, the surface of the mild steel anode was degreased in isopropanol, cleaned in dilute HCl, and rinsed in distilled water. The clean RSE was then transferred to the cell filled with the test electrolyte, and was installed on the rotator. The electrode was further treated cathodically at -1.2V vs. SCE to remove any remaining trace of oxides on the surface. After the cathodic treatment, the system was permitted to rest for several minutes to allow the anode potential to return to the steady-state value at open circuit. A constant potential pulse was then applied to the anode, and the current transient was recorded on a Sanborn 296 recorder. A Magna 4700M potentiostat was used to control the anode potential.

The solutions used were 1M Na_2SO_4 and 4M NaClO_4 ; the pH of these solutions varied from 5 to 7 at room temperature. Before the start of each test, the solution was presaturated with nitrogen, and during the run, a nitrogen atmosphere was maintained by passing the gas through the cell. All the experiments were performed at a constant temperature of $24^\circ \pm 1^\circ\text{C}$.

ECM tests.—The ECM test was made with an uncoated steel rod rotating in the test electrolyte above a stationary cathode with a narrow gap space between them. Figure 1 illustrates the arrangement. The hydrodynamic condition within the electrode gap, studied by

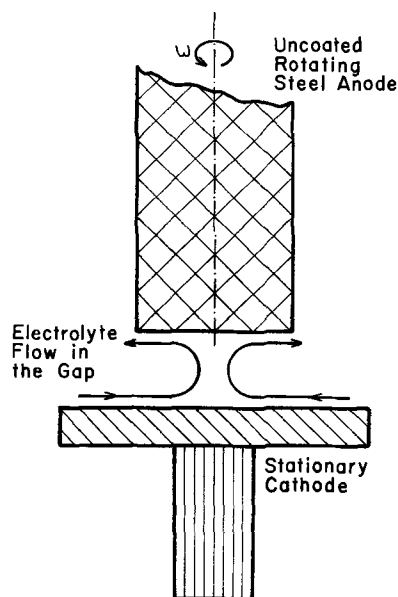


Fig. 1. Schematic diagram of ECM tests with a rotating rod

Mellor, Chapple, and Stokes (17), is characterized by flow of electrolyte into the gap near the stationary cathode and a swirling outward-flowing boundary layer on the tip of the rotating rod. Between the two there is a core flow (toward the anode) rotating with a constant angular velocity. The Reynolds number is calculated by $\text{Re} = \omega g^2 / \nu$, where ω is the angular velocity of the rotating rod, g , the electrode gap; and ν , the kinematic viscosity of the electrolyte. It has been found by these investigators that the flow becomes turbulent when the Reynolds number is greater than 100.

In the present study an SAE 5160H steel rod, 0.635 cm diameter \times 10 cm long, was used as the anode. It was mounted on the high speed rotator, and extended down into a 5 liter glass jar filled with the test electrolyte. The tip of the anode faced a stationary copper cathode, 1.27 cm diameter, as shown in Fig. 1. A jack was used to support the glass jar, and the anode-cathode gap space could be varied by adjusting the height of the jack. An initial gap of 0.085 cm was used for all the tests. After applying a selected angular velocity to the rotator, the tip of the steel rod was electrochemically machined at constant current for a given period of time. The current was controlled by a Magna 4700M potentiostat. Current density values were based on the cross-sectional area of unmachined rod (0.317 cm^2). The voltage drop across the cell was recorded on a Sanborn 296 recorder. No attempt was made to adjust the electrode gap space during the ECM. The rod was weighed before and after machining to determine the amount of metal removal, and the computation for current efficiency was based on ferrous ion as the dissolution product. The solutions used were: 1.5-3M NaClO_4 , 1M Na_2SO_4 , 3M NaClO_3 , and a mixed electrolyte containing 0.5M Na_2SO_4 and 1.5M NaClO_4 . All experiments were performed at a constant temperature of $24^\circ \pm 1^\circ\text{C}$.

Results and Discussion

Steady-state polarization curves.—Before the transient measurements, steady-state current/potential curves were first determined for the steel RSE in the test electrolyte. Figures 2 and 3 give the results of the measurements in 1M Na_2SO_4 and 4M NaClO_4 , respectively. For comparison, a polarization curve of steel in 4M NaClO_3 is also plotted in Fig. 3 as the dashed line.

The current density in sodium sulfate electrolyte is given for three different anode revolution rates in Fig. 2. The data points obtained at zero (black dots) and 400 rpm (triangles) exhibit three distinct potential

¹ Composition of the mild steel: Fe, 98.4%; Mn, 0.98%; S, 0.29%; C, 0.10%; P, 0.06%; Si, 0.005%.

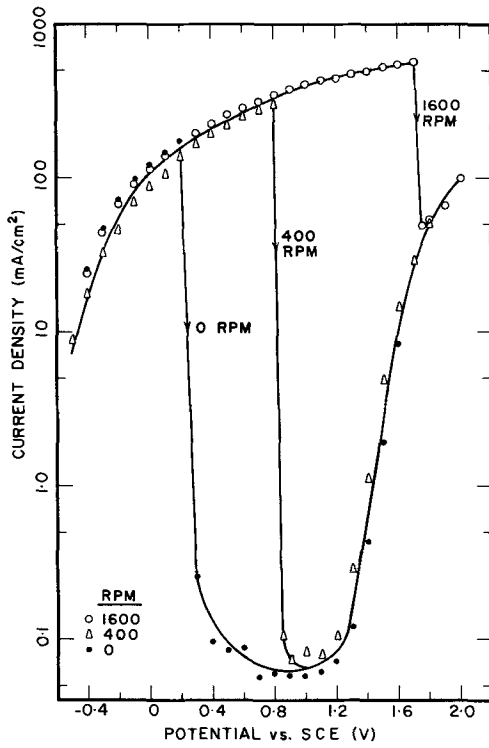


Fig. 2. Steady-state polarization curves in 1M Na₂SO₄

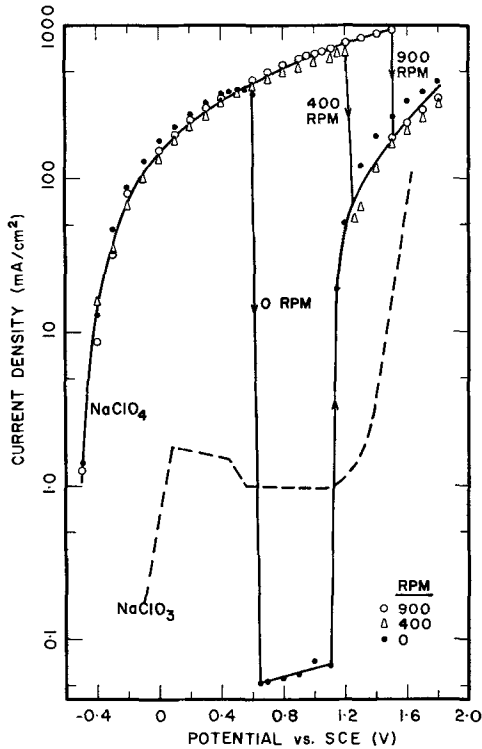


Fig. 3. Steady-state polarization curves in 4M NaClO₄. For comparison, a steady-state polarization curve obtained in 4M NaClO₃ is also plotted as the dashed line; this curve is independent of the speed of rotation.

states, i.e., active dissolution, passive and transpassive regions. The current density does not seem to vary with the rotational speed; however, the critical potential at the point where the transition from the active to the passive region takes place is shifted in the noble direction as the speed of rotation increases. Consequently, the span of passive potentials diminishes with increasing speeds. At 1600 rpm, no passive region was observed, and the current density dropped directly from the active dissolution state to the transpassive

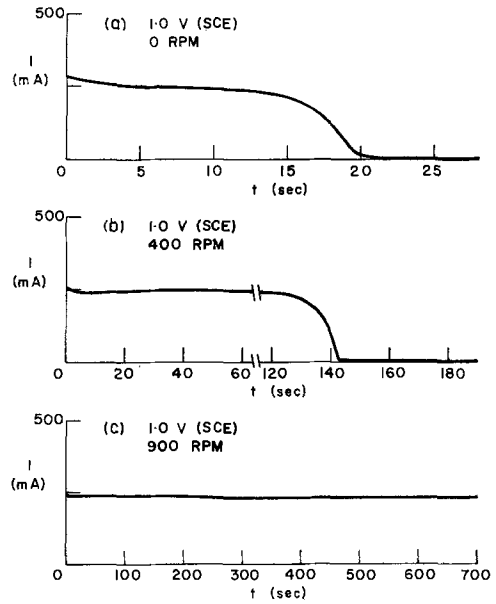


Fig. 4. Typical current transient in 1M Na₂SO₄ solution

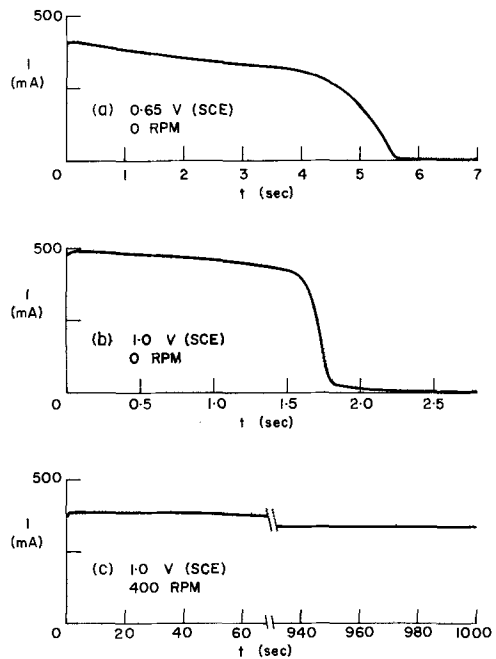


Fig. 5. Typical current transient in 4M NaClO solution

state at 1.7V vs. SCE. Figure 3 shows that the same phenomena occur in sodium perchlorate solution, and that the effect of electrode rotation on passivity appears to be greater than was found in Na₂SO₄. The dissolution product was ferrous compounds in the form of greenish-black precipitates in the sulfate electrolyte, and black precipitates in the sodium perchlorate electrolyte.

Anode transients at passive potentials.—Typical results of a potential pulse in the passive region are shown in Fig. 4 and 5 for Na₂SO₄ and NaClO₄, respectively. These curves are characterized by an initial constant current plateau followed by a rapid drop to the steady state. The magnitude of the plateau current, *I_p*, corresponds to the magnitude of the active dissolution current on the steady-state polarization curve. Evidently, the plateau current represents the iron dissolution rate prior to the passivation, and the current drop is caused by decreasing dissolution due to spreading of an anode film over the electrode surface. At a constant potential, the time required for passivation to

occur becomes longer as the rate of anode rotation increases. In Na_2SO_4 , for instance, the passivation time increases from 20 sec at zero rpm to 145 sec at 400 rpm (Fig. 4a and b). At 900 rpm, no current drop occurs over a period of 700 sec after the potential pulse (Fig. 4c); the slight decrease in current observed in Fig. 4c is due to reduction of the electrode size as the iron dissolves. The effect of rotation is even greater in NaClO_4 solution, as shown in Fig. 5b-c, where no current drop takes place at an anode revolution rate of 400 rpm. Also at a constant rotational speed, Fig. 5a and b shows that the current transient period decreases with increasing anode potentials.

Onset of passive films.—Both the steady-state and the transient results demonstrate that the passivation of mild steel in Na_2SO_4 and NaClO_4 is of the dissolution-precipitation type. Transient behavior of this kind has also been found to occur during the anodic dissolution of steel in NaCl solution (13), iron in sulfuric acid (18-20), and copper in hydrochloric acid (21). For these systems the passivity is attributed to formation of a salt layer of reaction products on the anode surface. During ECM of copper in H_2SO_4 and NaClO_3 solutions, the work of Cooper, Landolt, Muller, and Tobias (22, 23) also reveals the presence of a salt layer on the anode.

In the present study, ferrous compounds are found to be the dissolution product. Evidently, the initial stage for the passivity of steel in Na_2SO_4 and NaClO_4 electrolytes involves precipitation on the metal surface of a ferrous salt. The current density during the active dissolution is high (Fig. 2 and 3), and the concentration of dissolution products in the vicinity of the anode is likely to increase to a value required for the precipitation (24, 25). The time required to attain such a concentration is represented by the duration of the initial plateaus on the transient curves. Once the precipitate starts to form on the electrode surface, it appears to impede the dissolution reaction, causing the current to drop rapidly as shown in Fig. 4 and 5 (26). The longer time for the onset of passivation observed at faster anode revolution rates implies that diffusion of reaction products away from the electrode is the rate-determining step for the film formation process. Because of a non-*in-situ* technique used presently, the composition of the salt layer is not known. However, judging from the greater convection dependence for the passivity of steel in NaClO_4 solution as compared to Na_2SO_4 solution, and from the higher solubility in water of $\text{Fe}(\text{ClO}_4)_2 \cdot 6\text{H}_2\text{O}$ as compared to $\text{FeSO}_4 \cdot 7\text{H}_2\text{O}$ (26.4g Fe/100 ml for the perchlorate as against 3.14g Fe/100 ml for the sulfate) (27), it is probable that the salt film is a layer of hydrated ferrous perchlorate in NaClO_4 , and hydrated ferrous sulfate in Na_2SO_4 .

Passivation of iron has been studied galvanostatically by Serra and Feliu (28) in neutral Na_2SO_4 solutions, and by Snavely and Hackerman (29) in a nearly neutral sulfate solution. Serra and Feliu measured the duration of passivating time as a function of applied current densities, and the results were in accordance with a kinetic model for the dissolution-precipitation process (24). Snavely and Hackerman's mass balance data also indicate that dissolution of iron is a necessary step to achieve passivity. These results give supporting evidence that the passivating of mild steel in concentrated Na_2SO_4 and NaClO_4 solutions starts with a salt layer.

The mechanism may be further confirmed by comparing the transient data with Muller's dissolution-precipitation theory (18). Under potentiostatic conditions, the current-time relation during the precipitation of reaction products is given by

$$t = C_1 + C_2 \left(-\frac{1}{I_p - I} + \frac{1}{I_p} \ln \frac{I_p - I}{I_p} \right) = C_1 + C_2 f(I) \quad [1]$$

where I_p is the constant plateau current; I , the current

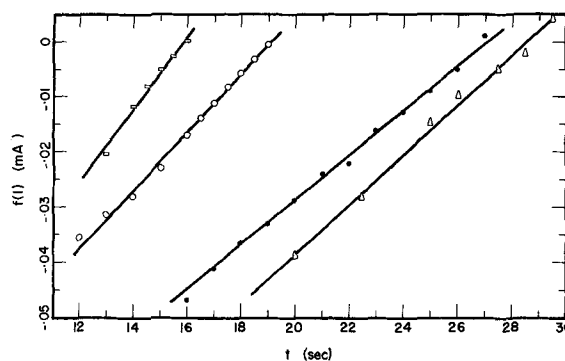


Fig. 6. Comparison with Muller's dissolution-precipitation model for current transients in 1M Na_2SO_4 at 0 rpm.

	E vs. SCE (V)	I_p (mA)	C_1 (sec)	C_2 (mA sec)
□	1.1	280	15.9	151
○	1.0	270	19.1	188
●	0.9	258	27.1	248
△	0.8	245	28.6	222

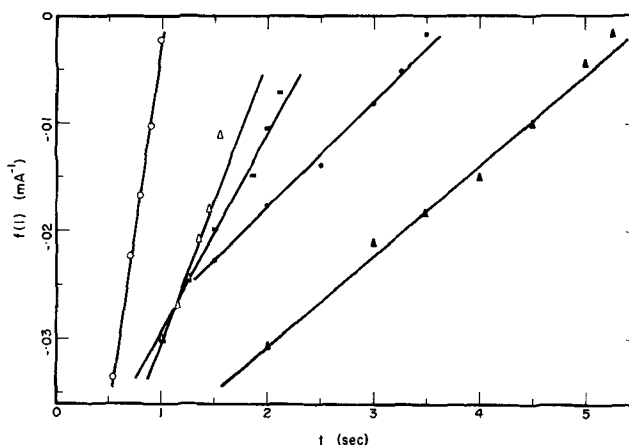


Fig. 7. Comparison with Muller's dissolution-precipitation model for the current transients in 4M NaClO_4 at 0 rpm.

	E vs. SCE (V)	I_p (mA)	C_1 (sec)	C_2 (mA sec)
○	1.1	530	1.0	14
△	1.0	500	2.1	38
■	0.85	480	2.6	54
●	0.7	425	3.8	102
▲	0.65	390	5.7	120

in the drop period; and C_1 and C_2 are constants for a given transient. Accordingly, a plot of $f(I)$ vs. t would be expected to be linear with a slope equal to $1/C_2$ and an intercept at $t = C_1$. The constant C_1 , is therefore a measure of the passivating time, and C_2 is inversely related to the rate of current drop. Figure 6 shows a set of such plots for various potentiostatic transients in Na_2SO_4 solution at zero rpm. The same plots for the perchlorate data are given in Fig. 7. It is seen that agreement between the theory and the experimental data is reasonably good. The accompanying table in each figure lists the magnitude of the plateau currents as well as values of C_1 and C_2 computed from the transient data. These tables indicate that the higher the dissolution rate (represented by the plateau current), the less in the passivating time (C_1), and the faster is the rate of film spreading ($1/C_2$) over the electrode surface.

Results of ECM tests.—Since the dissolution-precipitation type of film formation is limited by the diffusion of reaction products away from the anode, dimensional control is expected to be convection-dependent for the

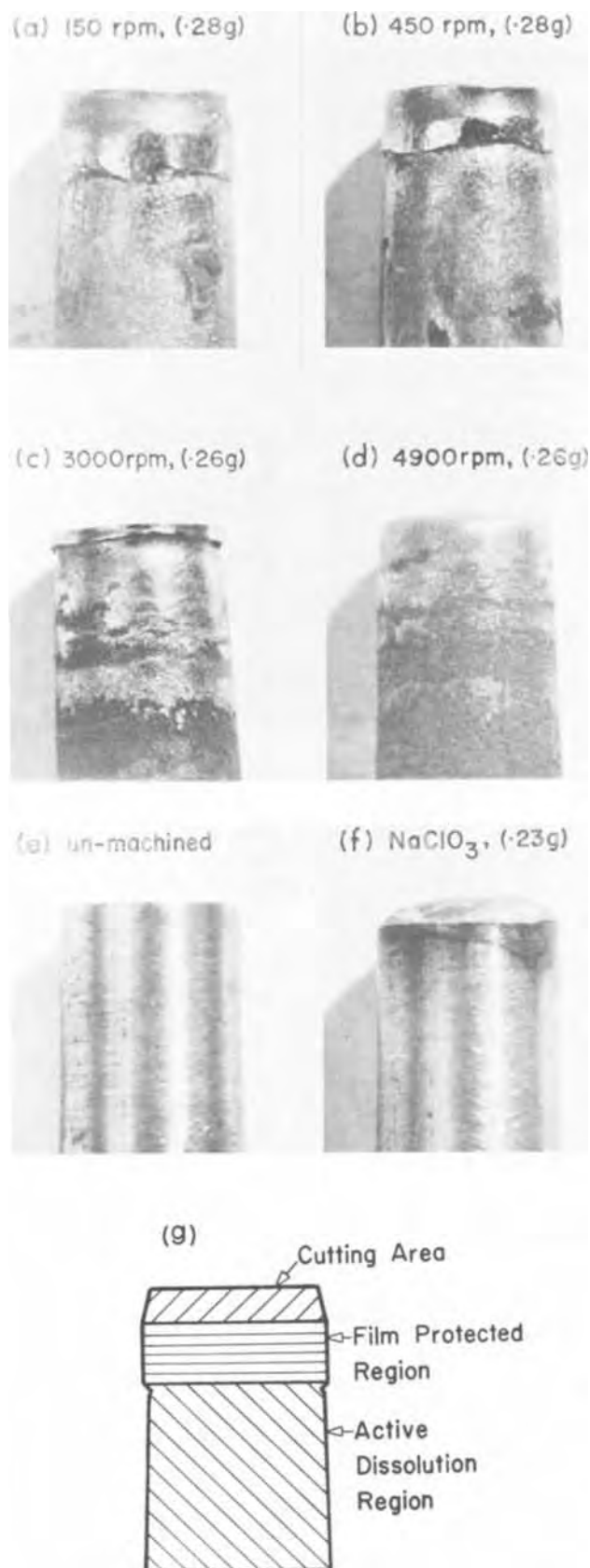


Fig. 8. Photomicrographs of steel rod-ends electrochemically machined in (a-d) 3M NaClO₄; (e) an un-machined rod; (f) 3M NaClO₃; (g) is a schematic diagram showing various current density regions.

ECM of steel with electrolytes containing Na₂SO₄ and NaClO₄.

To test the validity of this prediction, actual ECM experiments were made with rotating steel rods. Fig-

ure 8a-d shows a set of photomicrographs of rod-ends that have been electrochemically machined for 2 min in 3M NaClO₄ solution at various rotational speeds. The applied current density for the tests was 15.8 A/cm² (102 A/in.²), based on the cross-sectional area of the steel rod. The amount of metal removal in each run is indicated in the brackets; the average current efficiency based on Fe going into the solution as Fe⁺⁺ ions was 100%. Also given in Fig. 8 are photomicrographs of an un-machined rod (Fig. 8e), and of a rod-end that has been electrochemically machined in 3M NaClO₃ solution (Fig. 8f). The current density for the chlorate run was also 15.8 A/cm²; however, for the sake of comparison, the machining time was made longer in order to give approximately the same amount of metal removal. The dimensional control obtained with NaClO₃ is excellent; the metal removal took place only at the very end of the steel rod. For the perchlorate, it varies from fair to poor with increasing speed of rotation, and the agreement with the prediction is apparent.

Figure 8g illustrates three distinct current density regions for rod-ends electrochemically machined in NaClO₄ solutions. During the machining, the metal is removed most heavily from the tip of the rod opposite the stationary cathode. This region is called the cutting area (or the high current density area) as shown in the diagram. Next to the cutting area is a film-protected region, where the distance to the cathode is larger, and hence the IR drop in the solution lowers the metal/solution interfacial potential difference to the value corresponding to the passive state on the steady-state polarization curves. A protective film, therefore, is formed on the surface, resulting in only a slight amount of metal removal in the region; the mirror-like bright surface is probably caused by dissolution through the film as suggested by the mechanism of electropolishing (30). Further away from the cathode is an active dissolution region, where the IR drop is large enough to lower the interfacial potential difference to the value corresponding to the active region on the polarization curves. The groove-cut at the end of this zone is caused by the peak current density near the critical potential. In accordance with the results of the potentiostatic studies, the film-protected region diminishes in size as the speed of rotation increases (Fig. 8a-d). At 4900 rpm, the film-protected region has completely disappeared, and the cut resembles those obtained with NaCl solutions.

Figure 3 indicates that the current density for the active dissolution of mild steel in NaClO₃ is two orders of magnitude smaller than that in NaClO₄. In addition, the current density in NaClO₃ has about the same order of magnitude in both the active and the passive regions. Since chlorate ion is a strong oxidizing agent in the anodic process (31), iron is readily passivated due to the formation of a stable oxide film on the surface. As a consequence, the surface of the steel rod during ECM with NaClO₃ is well protected except at the cutting area directly facing the cathode. On the other hand, perchlorate ion is a weak oxidizing agent (32) so that the passivation must rely on the dissolution of iron to form a salt layer on the anode surface. At sufficiently high potentials, the inner portion of this salt layer in contact with the metal may be converted into a more protective oxide film as suggested by polishing of the surface in the film-protected regions (Fig. 8). Since the passivity is preceded by the high rate active dissolution, the passive film of the dissolution-precipitation type can give only partial protection to the metal surface. This limitation appears to impede the usefulness of NaClO₄ for the ECM of steel.

Comparison of the ECM results and the basic studies for Na₂SO₄ is not possible, for the Na₂SO₄ electrolyte did not cut steel under the ECM experimental conditions. The current efficiency for metal removal was found to be less than 10%. Apparently in the sulfate,

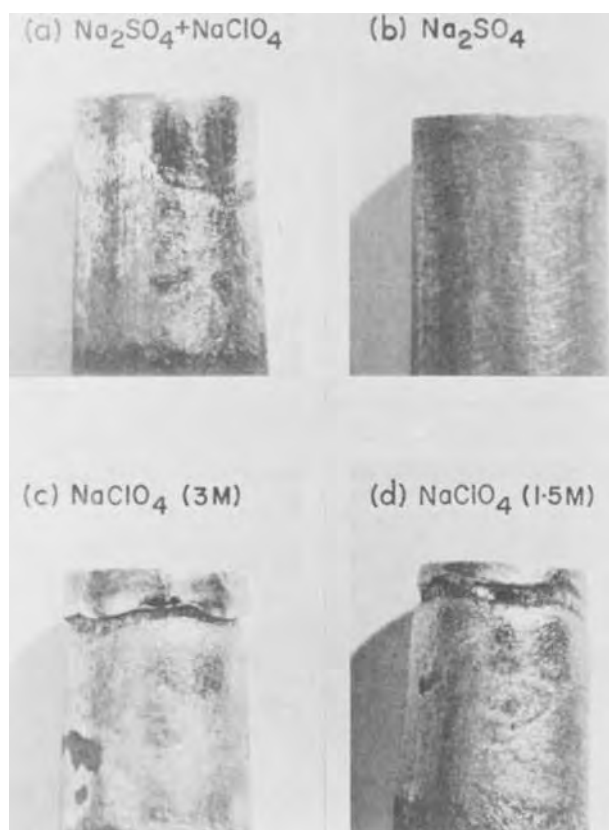


Fig. 9. Photomicrographs of steel rod-ends machined by ECM at 1000 rpm in (a) mixed Na_2SO_4 and NaClO_4 solution; (b) 1M Na_2SO_4 ; (c) 3M NaClO_4 ; (d) 1.5M NaClO_4 .

the electrolysis of water is the favored reaction at the transpassive potentials. Therefore, the effect of passivation by sulfate ions on the ECM of steel could be studied only by mixing Na_2SO_4 with other electrolytes such as NaClO_4 . Since the passive film formed with Na_2SO_4 is less subject to convection influence, it was thought that by adding Na_2SO_4 to the NaClO_4 solution, one might promote salt layer formation, and thus improve the ECM dimensional control at a given flow rate. To test the assumption, ECM experiments were carried out in an electrolyte containing 0.5M Na_2SO_4 and 1.5M NaClO_4 . A current density of 14.5 A/cm^2 (93 A/in.^2) was used for the tests. In spite of the presence of sulfate ions, the current efficiency based on $\text{Fe} \rightarrow \text{Fe}^{++}$ was found to be 100%. Figure 9a is a photomicrograph of a steel rod-end that has been electrochemically machined in the mixed electrolyte for 5 min at an anode rotational speed of 1000 rpm. For comparison, photomicrographs of rod-ends obtained with 1M Na_2SO_4 , 3M NaClO_4 , and 1.5M NaClO_4 are also given in Fig. 9. It is seen that while Na_2SO_4 gives little cutting on the steel rod, stray cutting takes place in the active dissolution region with NaClO_4 solutions. Addition of Na_2SO_4 to the NaClO_4 electrolyte appears to widen the film-protected area, and thus improves the ECM dimensional control.

Summary

In summary, correlation between the formation of passive films and dimensional control has been demonstrated experimentally by the ECM of steel in electrolytes containing NaClO_4 and Na_2SO_4 . It is found that the passivity of mild steel in the electrolytes originates

in the formation of a salt layer resulting from supersaturation of dissolution products near the anode. The rate of film formation is diffusion-controlled, and the ECM dimensional control achieved by this kind of passivation is convection-dependent. This passive film of the dissolution-precipitation type can provide only partial protection for the metal surface during the ECM process.

Manuscript submitted Oct. 12, 1971; revised manuscript received Feb. 1, 1972.

Any discussion of this paper will appear in a Discussion Section to be published in the June 1973 JOURNAL.

REFERENCES

1. D. T. Chin and A. J. Wallace, Jr., *This Journal*, **118**, 831 (1971).
2. J. F. Thorpe and R. D. Zerkle, *Int. J. Mach. Tool Des. Res.*, **9**, 131 (1969).
3. J. Hopenfeld and R. R. Cole, *J. Eng. Ind. Trans. ASME*, **88**, 455 (1966); **91**, 755 (1969).
4. C. L. Faust, *Trans. Inst. Metal Finishing*, **41**, 1 (1964).
5. N. D. G. Mountford, *ibid.*, **40**, 171 (1963).
6. M. A. LaBoda and M. L. McMillan, *Electrochem. Technol.*, **5**, 341 (1967).
7. M. L. McMillan and M. A. LaBoda, *ibid.*, **5**, 346 (1967).
8. J. W. Cuthbertson and T. S. Turner, *Production Engr.*, **45**, 270 (1966).
9. J. P. Hoare, K. W. Mao, and A. J. Wallace, Jr., *Corrosion*, **27**, 211 (1971).
10. K. W. Mao, *This Journal*, **118**, 1876 (1971).
11. J. P. Hoare, M. A. LaBoda, M. L. McMillan, and A. J. Wallace, Jr., *ibid.*, **116**, 201 (1969).
12. J. P. Hoare, *ibid.*, **117**, 142 (1970).
13. D. T. Chin, *ibid.*, **118**, 174 (1971).
14. D. T. Chin, *ibid.*, **118**, 1434 (1971).
15. D. E. L. Dyke, J. A. Gurklis, and C. L. Faust, in "Fundamentals of Electrochemical Machining," pp. 279-299, C. L. Faust, Editor, The Electrochemical Society, Inc., Princeton, N. J. (1971).
16. D. T. Chin, *This Journal*, **118**, 1764 (1971).
17. G. L. Mellor, P. J. Chapple, and V. K. Stokes, *J. Fluid Mech.*, **31**, 95 (1968).
18. W. J. Muller, *Trans. Faraday Soc.*, **27**, 737 (1931).
19. J. H. Bartlett, *Trans. & J. Electrochem. Soc.*, **87**, 521 (1955).
20. A. Pigeaud and H. B. Kirkpatrick, *Corrosion*, **25**, 209 (1969).
21. R. S. Cooper, *This Journal*, **103**, 307 (1956).
22. J. Cooper, R. H. Muller, and C. W. Tobias, in "Fundamentals of Electrochemical Machining," pp. 300-315, C. L. Faust, Editor, The Electrochemical Society, Inc., Princeton, N. J. (1971).
23. D. Landolt, R. H. Muller, and C. W. Tobias, *This Journal*, **118**, 40 (1971).
24. A. K. N. Reddy, M. A. V. Devanathan, and J. O'M. Bockris, *J. Electroanal. Chem.*, **6**, 61 (1963).
25. R. D. Armstrong, J. A. Harrison, and H. R. Thirsk, *Corrosion Sci.*, **10**, 679 (1970).
26. U. Ebersback, K. Schwabe, and K. Ritter, *Electrochim. Acta*, **12**, 927 (1967).
27. C. D. Hodgman, R. C. Weast, C. W. Wallace, and S. M. Selby, Editors, "Handbook of Chemistry and Physics," Chemical Rubber Publishing Co., Cleveland (1954).
28. M. Serra and S. Feliu, "Proc. 6th Meeting Intern. Comm. Electrochem. Thermodynam. and Kinetics," p. 360, Poitiers, France (1954).
29. E. S. Snavely, Jr. and N. Hackerman, *Can. J. Chem.*, **37**, 268 (1959).
30. T. P. Hoar and J. A. S. Mowat, *Nature*, **165**, 64 (1950).
31. M. C. Sneed, J. L. Maynard, and R. C. Brasted, "Comprehensive Inorganic Chemistry," Vol. III, p. 164, Van Nostrand, New York (1954).
32. T. Moeller, "Inorganic Chemistry," p. 443, John Wiley & Sons, Inc., New York (1952).

Rotating Spherical Electrode: A Perturbation Theory for Schmidt Number Corrections

Der-Tau Chin*

Electrochemistry Department, Research Laboratories, General Motors Corporation, Warren, Michigan 48090

ABSTRACT

Using a method of singular perturbation, the theory of the rotating spherical electrode has been extended to include the correction terms for convective diffusion at small Schmidt numbers. The resulting rate equation expressed in the form of an asymptotic series permits a good approximation of the transfer rate for $Sc \cong 1$. Within this region the accuracy of the theory increases with increasing Schmidt numbers; the maximum error, occurring at $Sc = 1$, is less than 5%.

In a previous paper (1), a theory has been reported for laminar mass transfer on a rotating spherical electrode (RSE). The result for a hemispherical electrode can be expressed in dimensionless form as

$$Sh = 0.474 Re^{1/2} Sc^{1/3} \quad [1]$$

where Sh is the average Sherwood number, Re is the Reynolds number based on the electrode radius, and Sc is the Schmidt number. An experimental study over the range of Schmidt numbers between 920 and 37,000 (2) has shown that this expression is valid for Reynolds numbers less than 15,000. For Reynolds numbers larger than 15,000, the flow becomes turbulent, and the laminar theory is no longer valid.

Equation [1] represents only the asymptotic behavior of the transport process occurring at large Schmidt numbers. It has an inherent error on the order of $Sc^{-1/3}$. At Schmidt numbers considerably less than 1000, the use of the equation would yield a great error.

This paper describes an extension of the theory to include the correction terms for convective diffusion at lower Schmidt numbers. A method of singular perturbation for large Sc is used, and the resulting differential equations are solved either analytically, or numerically on an IBM 360 digital computer. The solutions combine to give an asymptotic expansion which permits a good approximation of the rate of transfer for $Sc \cong 1$.

Theoretical

Perturbation analysis.—Throughout this analysis we shall confine ourselves to a domain specified by a set of spherical polar coordinates, r , θ , and ψ . The coordinate, r , is measured radially outward from the center of the spherical electrode, θ is an angle measured from the pole of rotation, and ψ is the azimuth. It is assumed that sufficient inert electrolyte is present such that the migration flux of the diffusing ion in the electric field can be neglected. The spherical electrode has a radius, r_0 , and is rotating with an angular velocity, ω , in a solution of constant properties. The boundary layer equations of fluid motion and convective diffusion have been given elsewhere (1) and are not repeated here. It has been shown that by introducing a transformation

$$\eta = \left(\frac{\omega}{\nu} \right)^{1/2} (r - r_0) \quad [2]$$

on the radial distance, r , and by expanding the concentration of the diffusing ion in a power series of θ

$$C = C_\infty + (C_0 - C_\infty)$$

$$\{\Phi_1(\eta) + \theta^2\Phi_3(\eta) + \theta^4\Phi_5(\eta) + \dots\} \quad [3]$$

the equation for the convective diffusion can be trans-

formed into the following set of ordinary differential equations

Zeroth-order equation

$$\left(-0.51023\eta^2 + \frac{1}{3}\eta^3 - 0.10265\eta^4 + \dots \right) \frac{d\Phi_1}{d\eta} = \frac{1}{Sc} \frac{d^2\Phi_1}{d\eta^2} \quad [4]$$

First-order equation

$$\begin{aligned} & \left(0.52762\eta^2 - \frac{1}{2}\eta^3 + 0.20231\eta^4 + \dots \right) \frac{d\Phi_1}{d\eta} \\ & + \left(-0.51023\eta^2 + \frac{1}{3}\eta^3 - 0.10265\eta^4 + \dots \right) \frac{d\Phi_3}{d\eta} \\ & + 2 \left(0.51023\eta - \frac{1}{2}\eta^2 + 0.20531\eta^3 + \dots \right) \Phi_3 \\ & = \frac{1}{Sc} \frac{d^2\Phi_3}{d\eta^2} \quad [5] \end{aligned}$$

Boundary conditions

$$\begin{aligned} & \text{at } \eta = 0, \quad \Phi_1 = 1, \quad \Phi_3 = 0 \\ & \text{at } \eta \rightarrow \infty, \quad \Phi_1 = \Phi_3 = 0 \end{aligned} \quad [6]$$

The exact solutions to these differential equations are not possible. However, for electrochemical applications one always speaks of a system of large Sc (usually larger than 50). This implies that an asymptotic representation of the concentration profile may be obtained by carrying out successive perturbations of the parameter, Sc . The details of this perturbation technique have been described (3-4), and are not discussed here. Following the procedure of a singular perturbation method, we introduce a stretched coordinate

$$Z = Sc^{1/3}\eta \quad [7]$$

for the diffusion domain, and assume that the dimensionless concentrations, Φ_1 and Φ_3 , can be represented by the following asymptotic expansions in a power series of Sc

$$\begin{aligned} \Phi_1(Z, Sc) = & \phi_{11}(Z) + Sc^{-1/3}\phi_{12}(Z) \\ & + Sc^{-2/3}\phi_{13}(Z) + Sc^{-1}\phi_{14}(Z) + \dots \quad [8] \end{aligned}$$

$$\begin{aligned} \Phi_3(Z, Sc) = & \phi_{31}(Z) + Sc^{-1/3}\phi_{32}(Z) \\ & + Sc^{-2/3}\phi_{33}(Z) + Sc^{-1}\phi_{34}(Z) + \dots \quad [9] \end{aligned}$$

Substituting these expressions into Eq. [4]-[5], and equating the terms having the like powers of Sc , we have

Zeroth-order equations

* Electrochemical Society Active Member.

Key words: mass transfer, convective diffusion, limiting current.

$$\frac{d^2\phi_{11}}{dZ^2} + aZ^2 \frac{d\phi_{11}}{dZ} = 0 \quad [10]$$

$$\frac{d^2\phi_{12}}{dZ^2} + aZ^2 \frac{d\phi_{12}}{dZ} = \frac{1}{3} Z^3 \frac{d\phi_{11}}{dZ} \quad [11]$$

$$\frac{d^2\phi_{13}}{dZ^2} + aZ^2 \frac{d\phi_{13}}{dZ} = \frac{1}{3} Z^3 \frac{d\phi_{12}}{dZ} - 0.10265Z^4 \frac{d\phi_{11}}{dZ} \quad [12]$$

First-order equations

$$\frac{d^2\phi_{31}}{dZ^2} + aZ^2 \frac{d\phi_{31}}{dZ} - 2aZ\phi_{31} = 0.52762Z^2 \frac{d\phi_{11}}{dZ} \quad [13]$$

$$\begin{aligned} \frac{d^2\phi_{32}}{dZ^2} + aZ^2 \frac{d\phi_{32}}{dZ} - 2aZ\phi_{32} &= 0.52762Z^2 \frac{d\phi_{12}}{dZ} \\ &- \frac{1}{2} Z^3 \frac{d\phi_{11}}{dZ} + \frac{1}{3} Z^3 \frac{d\phi_{31}}{dZ} - Z^2\phi_{31} \quad [14] \end{aligned}$$

$$\begin{aligned} \frac{d^2\phi_{33}}{dZ^2} + aZ^2 \frac{d\phi_{33}}{dZ} - 2aZ\phi_{33} &= 0.52762Z^2 \frac{d\phi_{13}}{dZ} \\ &- \frac{1}{2} Z^3 \frac{d\phi_{12}}{dZ} + 0.20231Z^4 \frac{d\phi_{11}}{dZ} + \frac{1}{3} Z^3 \frac{d\phi_{32}}{dZ} \\ &- 0.10265Z^4 \frac{d\phi_{31}}{dZ} - Z^2\phi_{32} + 0.41062Z^3\phi_{31} \quad [15] \end{aligned}$$

where the convection constant, $a = 0.51023$. The new boundary conditions are

$$\begin{aligned} \text{at } Z = 0, \quad \phi_{11} = 1, \quad \phi_{12} = \phi_{13} = \phi_{3i} = 0 \\ \text{at } Z \rightarrow \infty, \quad \phi_{1i} = \phi_{3i} = 0 \end{aligned} \quad [16]$$

with the dummy index, $i = 1, 2, 3$. It should be noted that the terms of the "zeroth-" and the "first-order" equations are not referred to the parameter perturbations of Sc , but to the coordinate perturbation of θ . This arrangement is necessary in order to avoid confusion in the text.

Equation [10] and its boundary conditions represent the famous Levich problem (5) of the rotating disk electrode (RDE), and we may immediately write down the solution in the form

$$\phi_{11} = 1 - 0.62045 \int_0^Z \exp\left(-\frac{a}{3} Z^3\right) dZ \quad [17]$$

Equation [13] has been solved by Chin (1); a solution that satisfies the prescribed boundary conditions can be expressed as

$$\phi_{32} = 0.12832Z \exp\left(-\frac{a}{3} Z^3\right) \quad [18]$$

Equations [17] and [18] are the first terms in the series expansions of Eq. [8] and [9], respectively. They can be termed as the basic solution for the convective diffusion at the RSE, for together they characterize an asymptotic rate of ionic transfer when Sc approaches infinity. At finite Sc , the accuracy of the theory may be improved by successively solving the rest of the differential equations for ϕ_{12} , ϕ_{13} , ϕ_{32} , and ϕ_{33} . Such attempts are described in the next two sections.

Exact solutions of ϕ_{12} and ϕ_{13} .—Equations [11] and [12] differ from Eq. [10] by only a perturbed quantity on the right-hand side. Since the equations are of the first order in $d\phi_{1i}/dZ$, the function, ϕ_{12} , may be solved analytically in terms of ϕ_{11} , and the function, ϕ_{13} , in terms of ϕ_{12} and ϕ_{11} . To solve for ϕ_{12} , we first substitute Eq. [17] into Eq. [11]

$$\frac{d^2\phi_{12}}{dZ^2} + aZ \frac{d\phi_{12}}{dZ} = -\frac{0.62045}{3} Z^3 \exp\left(-\frac{a}{3} Z^3\right) \quad [11a]$$

Equations [11a] and [16] can be integrated at once to give the following solution

$$\begin{aligned} \phi_{12} = 0.62045 \int_0^Z \left(0.29801 - \frac{1}{12} Z^4\right) \\ \exp\left(-\frac{a}{3} Z^3\right) dZ \quad [19] \end{aligned}$$

Similarly, by substituting Eq. [17] and [19] into Eq. [12], carrying out the integration and making use of the prescribed boundary conditions, we have

$$\begin{aligned} \phi_{13} = 0.62045 \int_0^Z \left(0.056335 + 0.024834Z^4 \right. \\ \left. + 0.020531Z^5 - \frac{1}{288} Z^8\right) \exp\left(-\frac{a}{3} Z^3\right) dZ \quad [20] \end{aligned}$$

Now the first three terms in the asymptotic expansion of ϕ_1 have been obtained; these functions are plotted in Fig. 1 on arithmetic scales. It is seen that for large Z , the second and third terms of the series are becoming increasingly important with increasing Z . All the functions become zero for $Z > 4$; this gives us a rough idea of the extent of the concentration boundary layer on the RSE. In the next section these solutions are used where required for the appropriate terms in the first-order equations.

Numerical solutions of ϕ_{32} and ϕ_{33} .—Equations [14] and [15] have been integrated numerically on an IBM 360 digital computer. A fourth-order Runge-Kutta method (6) is used. In view of the extent of the concentration boundary layer as shown in Fig. 1, the integration is carried out over the range, $0 \leq Z \leq 5$, with an increment of 0.05. The boundary value problems described in Eq. [16] are solved by a trial-and-error method. Briefly, the method consists of: (i) integrating Eq. [14], for example, from $Z = 0$ to $Z_\infty = 5$ with a trial value of $d\phi_{32}/dZ$ at $Z = 0$; and (ii) repeating the integration with a new trial value until the boundary condition at Z_∞ is satisfied. In this way Eq. [14] is first integrated, and the values of ϕ_{32} and $d\phi_{32}/dZ$ are stored in the computer for the successive

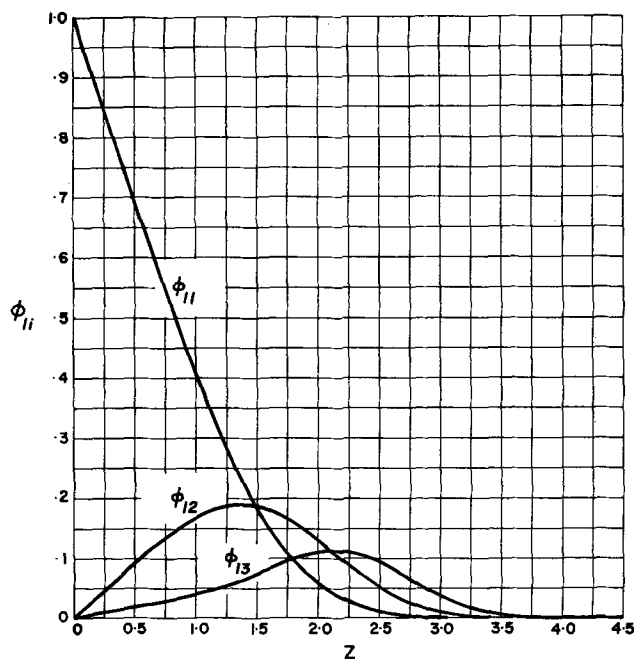


Fig. 1. Zeroth-order concentrations

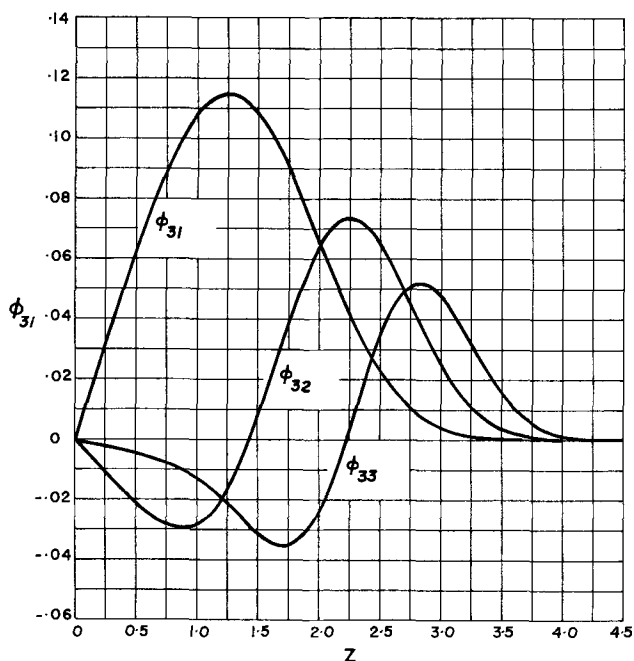


Fig. 2. First-order concentrations

integration of Eq. [15]. The results for ϕ_{32} and ϕ_{33} are expressed graphically in Fig. 2; also plotted in the figure is a curve for ϕ_{31} as calculated from Eq. [18]. The derivatives of ϕ_{32} and ϕ_{33} at $Z = 0$ are found as

$$\left[\frac{d\phi_{32}}{dZ} \right]_{Z=0} = -0.043437 \quad [21]$$

$$\left[\frac{d\phi_{33}}{dZ} \right]_{Z=0} = -0.009456 \quad [22]$$

Rate of transfer at the electrode.—Now we shall relate the results of the previous analysis to the rate of ionic transfer on the RSE, for this is the principal interest for electrochemical applications. The local mass flux at the electrode surface is related to the concentration gradient by

$$j = -D \left[\frac{\partial C}{\partial r} \right]_{r=r_0} = k (C_0 - C_*) \quad [23]$$

Here k is the mass transfer coefficient. The local Sherwood number, Sh_{loc} , defined as kr_0/D , can now be evaluated from the following equation

$$Sh_{loc} = Re^{1/2} Sc^{1/3} \left\{ 0.62045 \left[1 - \frac{0.29801}{Sc^{1/3}} - \frac{0.05633}{Sc^{2/3}} \right] - 0.12832 \theta^2 \left[1 - \frac{0.33851}{Sc^{1/3}} - \frac{0.07369}{Sc^{2/3}} \right] \right\} \quad [24]$$

The average Sherwood number, Sh , can be obtained by integrating Sh_{loc} over the spherical surface; the result is

$$Sh = \left[\frac{Kr_0}{D} \right] = Re^{1/2} Sc^{1/3} \left\{ 0.62045 \left[1 - \frac{0.29801}{Sc^{1/3}} - \frac{0.05633}{Sc^{2/3}} \right] - 0.12832 \left[1 - \frac{0.33851}{Sc^{1/3}} - \frac{0.07369}{Sc^{2/3}} \right] \frac{2(\cos\theta - 1) + 2\theta\sin\theta - \theta^2\cos\theta}{1 - \cos\theta} \right\} \quad [25]$$

Here K is the average mass transfer coefficient. Equation [25] represents the dimensionless mass transfer rate to a spherical electrode having an active surface

specified by the angle θ . For a hemispherical electrode or a sphere whose entire surface is subject to the mass transfer, we have $\theta = \pi/2$, and Eq. [25] can be simplified to

$$Sh = 0.47396 Re^{1/2} Sc^{1/3} (1 - 0.28549 Sc^{-1/3} - 0.05097 Sc^{-2/3}) \quad [26]$$

The average diffusion current density, I , on the electrode is related to the average mass transfer coefficient, K , by

$$I = nFK (C_* - C_0) \quad [27]$$

Thus Eq. [26] can be rearranged in dimensional form as

$$I = 0.47396 nF (C_* - C_0) D^{2/3} \nu^{-1/6} \omega^{1/2} \left[1 - 0.28549 \left(\frac{D}{\nu} \right)^{1/3} - 0.05097 \left(\frac{D}{\nu} \right)^{2/3} \right] \quad (\text{for } \theta = \pi/2) \quad [28]$$

Discussion of Results

The results presented in Fig. 1 and 2 would allow one to calculate the concentration profile on the RSE. For electrochemical applications, the rate equation expressed in the form of Eq. [25]-[28] could be used for determining diffusivity of the diffusing ion, and for electrode kinetic studies. It is seen that Eq. [26] differs from Eq. [1] by two correction terms inversely proportional to $Sc^{1/3}$ and $Sc^{2/3}$. The present theory would, therefore, extend the application of the RSE to electrolytes with smaller Schmidt numbers, for the inherent error is now on the order of Sc^{-1} , as compared to $Sc^{-1/3}$ for Eq. [1]. The exact error is not easy to determine unless the perturbation is further carried out for the functions, θ_{14} and θ_{34} , in the asymptotic expansion of Eq. [8] and [9]. One could, however, estimate the approximate error by comparing with point-solutions given in the literature. For the case of a rotating sphere, Banks (7) has computed numerically the thermal boundary layer at Prandtl numbers equal to 0.7 and 1.0. Since the Prandtl number is equivalent to the Schmidt number used in mass transfer, we may substitute $Sc = 0.7$ and 1.0 into Eq. [26], and arrive at

$$Sh/Re^{1/2} = 0.258 \quad \text{for } Sc = 0.7 \quad [29]$$

$$Sh/Re^{1/2} = 0.314 \quad \text{for } Sc = 1.0$$

The comparative values given by Banks' computation are 0.25 at $Sc = 0.7$, and 0.30 at $Sc = 1.0$. The agreement is excellent considering that the successive perturbation is supposedly for large Schmidt numbers.

Figure 3 is a log-log plot of $Sh/Re^{1/2}$ vs. Sc for a rotating sphere or hemispherical electrode. The thick solid curve is calculated from Eq. [26]. The dashed straight line is given by Eq. [1]. Banks' results at $Sc = 0.7$ and 1.0 are represented by the crosses. For comparison, the rotating disk theory (8) is also given in the figure as the thin solid curve. It is seen that the $0.474 Sc^{1/3}$ dependence given by Eq. [1] represents a limiting behavior for $Sc \rightarrow \infty$. Banks' results show the magnitude of transfer rates in the neighborhood of $Sc = 1.0$. Equation [26] obviously represents a curved portion that smoothly connects the two limits. Therefore, one may speak with confidence that the rate equations given by Eq. [25]-[28] are valid for $Sc \geq 1$. Since the accuracy of the asymptotic expansion is increasing with increasing Schmidt numbers, the maximum error would occur at $Sc = 1$, where the deviation from Banks' numerical result is only 4.8%, an error that is permitted by most experimental techniques. If one assumes that the error is proportional to Sc^{-1} as suggested by Eq. [8] and [9], it would then be reduced to 0.5% at $Sc = 10$, and 0.05% at $Sc = 100$. On the

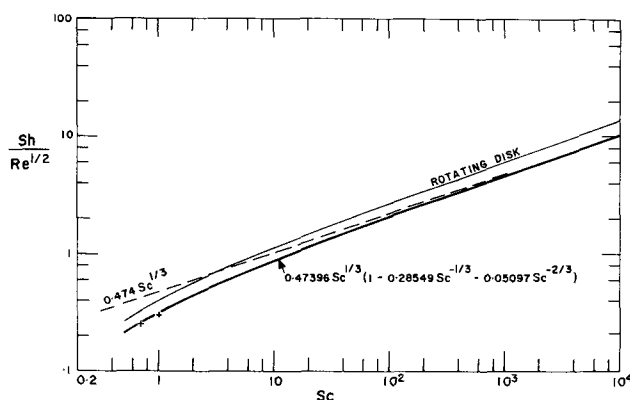


Fig. 3. $Sh/Re^{1/2}$ vs. Sc for a rotating sphere or hemispherical electrode. The thick solid curve is the result of the present analysis, Eq. [26]. The dashed straight line is calculated from Eq. [1] given by the previous theory. Banks' point-solutions at $Sc = 0.7$ and 1.0 are represented by the crosses. For comparison, the rotating disk theory is also given in the figure as the thin solid curve.

other hand, Eq. [1], which represents only the first term in the asymptotic expansion, can lead to an error of 3% at $Sc = 1000$. With the two additional correction terms, the accuracy of the theory has been greatly enhanced.

Figure 3 shows that the curve for the RDE is nearly parallel to the curve given by Eq. [26]. As discussed in the previous paper (1), the rotating disk can be treated as a special case of the RSE by merely setting $\theta = 0$. Thus, making use of Eq. [25], the present analysis gives

$$Sh_D = 0.62045 Re^{1/2} Sc^{1/3} (1 - 0.29801 Sc^{-1/3} - 0.05633 Sc^{-2/3}) \quad [30]$$

where the subscript, D, signifies the transfer process occurring on the disk electrode. The Schmidt number correction on the RDE has been treated by Newman (9, 10). Using the present notation, his result can be expressed as

$$Sh_D(\text{Newman}) = \frac{0.62048 Re^{1/2} Sc^{1/3}}{1 + \frac{0.2980}{Sc^{1/3}} + \frac{0.14514}{Sc^{2/3}} + 0(Sc^{-1})} \quad [31]$$

Using the binomial theorem, Eq. [31] can be expanded to

$$Sh_D(\text{Newman}) = 0.62048 Re^{1/2} Sc^{1/3} [1 - 0.2980 Sc^{-1/3} - 0.05634 Sc^{-2/3} + 0(Sc^{-1})] \quad [31a]$$

Thus, Newman's expression is essentially the same as our result for the disk electrode, Eq. [30]. The difference in the fifth decimal digits can be attributed to the truncation error in the numerical computations.

Based on the above discussions, we may conclude that the rate equations expressed in the asymptotic series of Eq. [25]-[28] would give an accurate estimate of the mass transfer rate on the RSE for $Sc \geq 1$. Within this region the accuracy of the equations in-

creases with increasing Schmidt numbers; the maximum deviation that occurs at $Sc = 1$, is less than 5%.

SYMBOLS

a	dimensionless constant, 0.51023
C	concentration of diffusing species, g-mole/cm ³
D	diffusivity, cm ² /sec
F	Faraday constant, coulomb/g-equiv
I	current density, A/cm ²
i	dummy index, 1, 2, 3, . . .
j	local rate of mass flux at the electrode surface, g-mole/cm ² sec
k	local mass transfer coefficient defined in Eq. [23], cm/sec
K	average mass transfer coefficient, cm/sec
n	number of electrons transferred in electrochemical reaction, g-equiv/g-mole
r	radial coordinate, cm
r_0	radius of spherical electrode, cm
Re	Reynolds number defined as $r_0^2 \omega / \nu$, dimensionless
Sc	Schmidt number defined as ν / D , dimensionless
Sh	average Sherwood number defined as Kr_0 / D , dimensionless
Sh_{loc}	local Sherwood number defined as kr_0 / D , dimensionless
Z	dimensionless radial distance defined as $Sc^{1/3} \eta$

Greek Symbols

η	dimensionless radial distance defined as $(\omega / \nu)^{1/2} (r - r_0)$
θ	latitude coordinate, rad
ν	kinematic viscosity, cm ² /sec
ψ	azimuthal coordinate, rad
ϕ_{1i}	zeroth order concentrations defined by Eq. [8], dimensionless
ϕ_{2i}	first-order concentrations defined by Eq. [9], dimensionless
Φ_i	dimensionless concentrations defined by Eq. [2]
ω	angular velocity, rad/sec

Subscripts

D	transfer process on a rotating disk
o	electrode surface
∞	bulk of solution

Manuscript submitted Oct. 12, 1971; revised manuscript received Feb. 11, 1972.

Any discussion of this paper will appear in a Discussion Section to be published in the June 1973 JOURNAL.

REFERENCES

- D. T. Chin, *This Journal*, **118**, 1434 (1971).
- D. T. Chin, *ibid.*, **118**, 1764 (1971).
- M. Van Dyke, "Perturbation Methods in Fluid Mechanics," Academic Press, New York (1964).
- M. D. Kruskal, in "Mathematical Models in Physical Sciences," pp. 17-48, S. Drobot, Editor, Prentice-Hall, Englewood Cliffs, N. J. (1963).
- V. G. Levich, "Physicochemical Hydrodynamics," Prentice-Hall, Englewood Cliffs, N. J. (1962).
- M. J. Romanelli, in "Mathematical Methods for Digital Computers," pp. 110-120, A. Ralston and H. S. Wilf, Editors, John Wiley & Sons, Inc., New York (1960).
- W. H. H. Banks, *ZAMP*, **16**, 780 (1965).
- M. Litt and G. Serad, *Chem. Eng. Sci.*, **19**, 867 (1964).
- J. Newman, *J. Phys. Chem.*, **70**, 1327 (1966).
- J. Newman, in "Advances in Electrochemistry and Electrochemical Engineering," Vol. 5, pp. 87-135, C. W. Tobias, Editor, Interscience, New York (1967).



Charging Method for Batteries, Using the Resistance-Free Voltage as Endpoint Indication

K. V. Kordesch*

Union Carbide Corporation Research Laboratory, Cleveland, Ohio 44101

The methods for charging batteries vary in many respects, depending on the type of batteries, their construction, and their application. However, all methods need to detect the fully charged state to avoid damage to the battery by overcharging.

The endpoint of charging may be determined by measuring the cell voltages, volume of gas evolved, pressure, and heat development; and by employing sensing electrodes, coulometers, or control cells.

The mode of charging can be "rapid charging," "tapered-step charging," "constant current," "constant voltage," or even "computer controlled"—depending on the type of the battery concerned and its use in a specific circuit or application.

Ni-Cd batteries and lead-acid batteries have been the most extensively investigated systems in accord with their wide range of use. Fast charging has been considered recently as essential for some users; in this method of charging, the endpoint detection has become more important from the safety standpoint. Even a short overcharge at high current can have catastrophic results.

In the case of sealed Ni-Cd batteries operating on the oxygen recombination cycle, the start of overcharge at high rates results in an increase in temperature and pressure which can be easily detected. However, their reliable use as control parameters depends on special construction of the batteries. As an example, commercially available small batteries can now be overcharged at the 1 C rate and can safely use inexpensive thermal cutoff devices like snap action switches or thermistors (1).

For other batteries which are not designed for rapid oxygen recombination, pressure sensing, or the use of auxiliary electrodes, the cell voltage is still the commonly used means of detecting the state-of-charge.

When a voltage control method is used under load conditions, the voltage drop caused by the resistive components of the cell (contacts, electrode current collector, electrolyte, etc.) influences the "terminal voltage" readings, often in an uncontrollable way. Gas evolution, concentration gradients in the electrolyte, and temperature effects are variables which are difficult to control or predict. If included in the control signal, they may cause large errors, especially under fast-charging conditions.

The Resistance-Free Measuring Principle

Several methods of determining the ohmic resistance of an operating galvanic cell are known: the use of temperature-compensated a-c bridge circuits; interrupting the current and determining the immediate voltage rise on the oscilloscope screen; and superimposing a-c on the d-c. load are some examples of methods which can be applied to finished cells. Luggin capillaries and auxiliary reference electrodes in proper positions can, of course, be used in test cells.

* Electrochemical Society Active Member.
Key words: battery-charging method, resistance-free voltage, state-of-charge detection, fast charging.

For practical evaluation in the field, directly indicating interrupter circuits have been developed which allow reading of the electrode polarization values (on discharge) or electrode overvoltages (on charge) without incurring the voltage drop across the internal resistance ("resistance polarization") of the cell. The measurements are independent of electrode spacing and, in case reference electrodes are used, insensitive to the reference positioning.

Figure 1 is a schematic diagram showing what the term "resistance elimination" means in connection with the use of an interrupter technique.

Figure 2 shows a simple double-throw switch circuit used to demonstrate the circuit principle (2). In the right position, the battery is charged (or discharged); in the left position, the voltage is measured. Due to the "slow" speed of electrochemical (mass transport dependent) processes, the average load condition is essentially maintained while the current is interrupted for voltage measurements. Only the "fast"

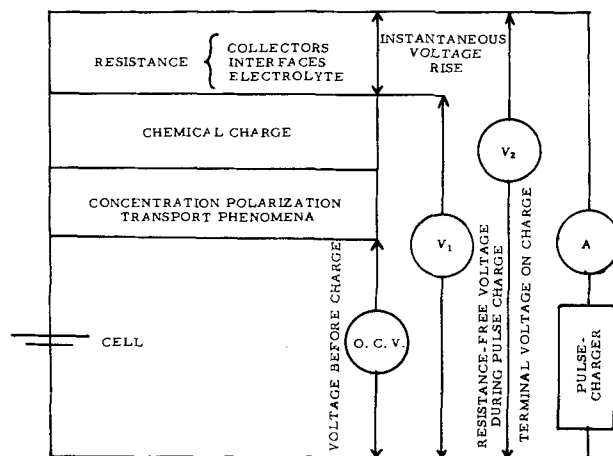


Fig. 1. Schematic diagram picturing the various types of "over-voltages" occurring in a galvanic cell during charging.

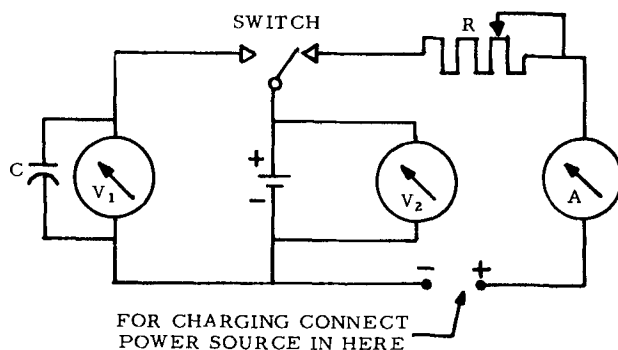


Fig. 2. Principle of a pulse current circuit for reading of the resistance-free voltage.

(electronic) voltage change across ohmic resistance components is eliminated (voltmeter 1). The battery is an excellent current integrator and the ammeter in the circuit reads the average current, as voltmeter 2 reads the average (terminal) voltage.

It should be noted that every interrupter method includes a time element of uncertain "recovery" of the voltage, depending on how the voltage was observed. Nearly instantaneous (10^{-8} sec) voltage changes can be followed with a very fast oscilloscope, while a technical interrupter circuit operated from the 60-cycle a-c line averages the potential for 1/120 sec after the interruption (unless a special bridge circuit is used; see Fig. 4).

A more practical circuit for battery charging which bypasses the need for mechanical contacts is shown in Fig. 3. Its operation is very similar to that of the circuit described in the literature in 1960 except that solid-state components are used for automatic current regulation (3).

This circuit has found wide use in the practice of battery testing; it has been incorporated in instruments designed to determine the state-of-charge of secondary batteries by combining charge and discharge tests (4, 5).

The replacement of square-wave pulses by sine-wave pulses does not change the response of the batteries; also the D'Arsonval meter movements of the voltmeter and ammeter indicate the same average value. (Note that average means $1/\pi$ with sine-wave pulses and $1/2$ with square-wave pulses of equal length.) Difficulties with slow reacting electrodes have been realized (6) but could be circumvented by operating at higher frequencies or by restricting the voltage sensing period to a small fraction of the off-current phase, as near to the interruption point as possible.

Figure 4 shows the oscilloscope traces of a charge pulse through a cell. The timing of the voltage sensing periods is indicated. The voltages are stored in capacitors and read on conventional high-resistance meters.

Charge Control with Resistance-Free Endpoint Sensing

There are many ways of producing the resistance-free signal and feeding it back to the charge-controlling SCR. In Fig. 3 is an example, showing an operational amplifier receiving the resistance-free voltage signal from the gating circuit—which is biased by the preset full-charge voltage—feeding it to the current controlling SCR circuit. The out of phase relationship between the secondary windings is important.

The circuit of Fig. 3 can be modified to operate a self-locking switch for complete shutdown, or may contain a bypass resistor for trickle-charge, or it could employ an additional control signal from a temperature sensor built into the battery. Increasing temperature lowers the preselection point of constant voltage charging circuits; therefore, this correction is an important one.

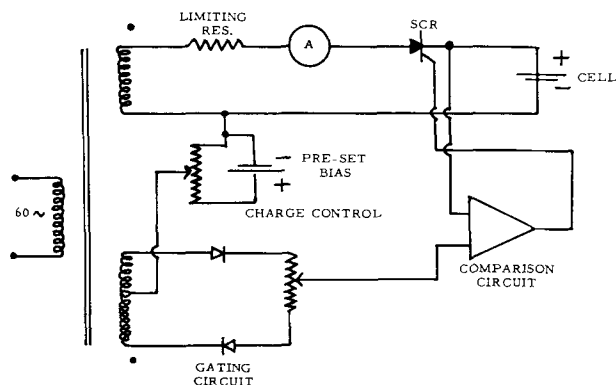


Fig. 3. Battery charger with resistance-free voltage control

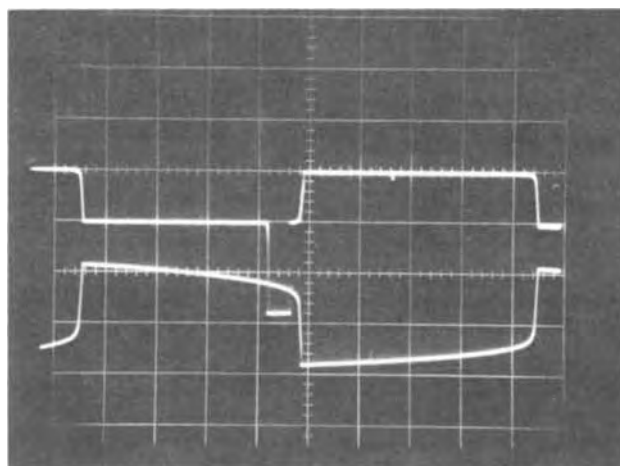
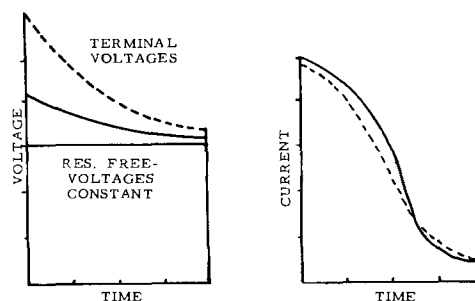


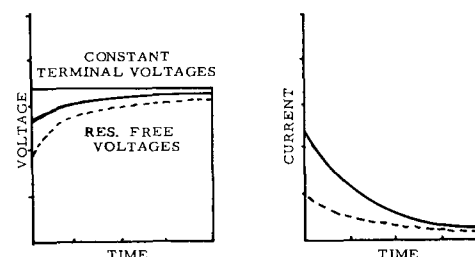
Fig. 4. Voltage-current diagram of a battery on pulse charge (60 cycles). Upper part of oscilloscope picture: Voltage trace (+ direction). Lower part: Current trace (- direction) indicating "window" in the early portion of the open-circuit period at which voltage readings are taken. The battery is in a very low state-of-charge, otherwise the curvature of the voltage curve would not be observable. (Zero line for voltage is off picture.)

An interesting circuit achieving essentially the same effect as the circuit of Fig. 2 is described in a General Electric Company patent (7); in this case a magnetic flux-controlled reed switch acts in response to the temperature-compensated battery voltage only during the intermediate period between current pulses, thereby eliminating the voltage drop on the ohmic resistance components from the signal.

Figure 5 indicates the differences between "terminal voltage" sensing and "resistance-free voltage" sensing, if one charges batteries with different internal resistance. If the charging circuit is set to a preselected voltage, the charge acceptance changes considerably and far more charging can be accomplished in the same time period if the resistance-free voltage is kept constant instead of the terminal voltage. Differences in internal resistance of old and new cells do not affect the charge acceptance if such cells are connected in series. It also does not matter too much if



a) High Rate Charge Acceptance with Resistance-Free Constant Voltage Setting



b) Low Rate Charge Acceptance with Constant Terminal Voltage Setting

Fig. 5. Different charge acceptance of batteries with low (—) and high (---) internal resistance.

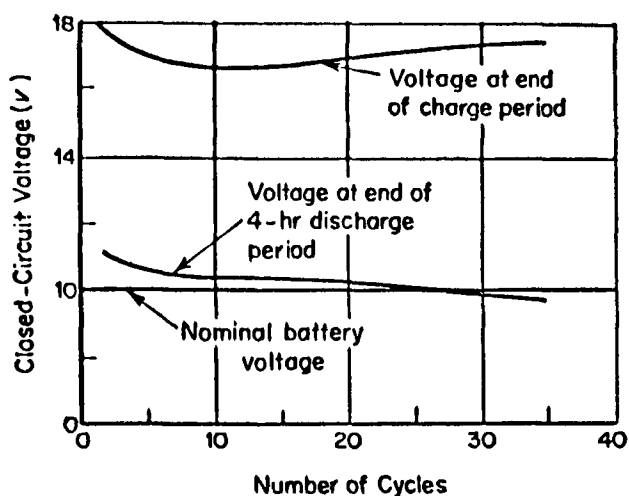


Fig. 6. Voltage characteristics of alkaline-manganese secondary battery.

the intercell connections vary somewhat. The situation becomes even more pronounced if cells are charged in parallel.

In Fig. 5, only general examples are shown. However, with all cell types the charge characteristics obtained during resistance-free charging are more reproducible and more suitable for rapid charging than are terminal voltage measurements.

Figure 6 shows the variability of the end-of-charge voltage of an alkaline MnO_2 -zinc cell dependent on the number of cycles (1). The change is to a large extent due to the increase in the internal cell resistance. Considering that a higher charge current (with a higher voltage rise) may be used, the value of the resistance-free voltage determination is obvious. In the case of the battery shown in Fig. 6 the resistance-free charge voltage would be 16.5V.

Extremely high-charge currents can only be used when the batteries are properly constructed: thin plates, good current collection, narrow spacing are essential features. High-charge currents are not objectionable; in some cases (Ni-Cd) the efficiency of charging increases with the charge rate (8). The charge acceptance and gassing rates of lead-acid batteries are functions of the charge rates, and multistep charging control is more precisely controlled with resistance-free voltage sensing. Also, the detection of "voltage steps" in the charge curves, *e.g.*, as observed with mixed depolarizer cells like MnO_2 -Ni oxide/zinc cells (9), is more accurate when not obscured by resistance phenomena.

Following the circuitry shown in Fig. 3, a resistance-free battery charger with an output of 12V-16A was built. The resistance-free voltage endpoint could be set with an accuracy of ± 10 mV.

This battery charger was capable of bringing a lead-acid battery of 12.5 A-hr capacity to 80% of the

fully charged condition in 30 min if a resistance-free voltage setting of 2.40 is used.

D-size Ni-Cd cells could be brought up to 75% of capacity in 15 min at a voltage setting of 1.48V. Silver-zinc cells require a setting of 2.00V and could be recharged even faster.

Summary and Conclusions

These results are preliminary in nature and require more experience before the resistance-free charging method can be recommended generally. However, it is evident that this method provides an improved way of determining the endpoint of charging electrically.

Especially in view of the future need for faster recharging of many consumer batteries for portable equipment and probably also for electric vehicles, fast-pulse charging will be required. As an example, a four-passenger city car will need a 20 kWhr-capacity battery for operating over a distance of 100 to 150 miles. Recharging such a battery (of *e.g.*, 200V) in half an hour will require a 300A charging capability for each vehicle at a "power station" which must then be supplied by a high voltage line to satisfy more customers at a time.

The fact that resistance-free charging can accommodate batteries (of the same type) in various conditions and of various ages simultaneously is probably the biggest advantage.

Acknowledgments

The author is indebted to Mr. Gunars Sprogis, Electronic Engineer, at the Parma Technical Center for construction of the Resistance-Free Battery Charger mentioned in this paper and to Mr. A. Marko, Wright Air Force Development Center, Dayton, Ohio, for advice on circuitry.

Manuscript submitted Sept. 30, 1971; revised manuscript received March 3, 1972.

Any discussion of this paper will appear in a Discussion Section to be published in the June 1973 JOURNAL.

REFERENCES

1. Union Carbide Corporation, "Eveready" Battery Application and Engineering Data, Handbook, issued by Consumer Products Division, 1971 edition.
2. K. V. Kordesch and A. Marko, U.S. Pat. 2,662,211 (1953).
3. K. V. Kordesch and A. Marko, *This Journal*, **107**, 480 (1960).
4. K. V. Kordesch and F. Kornfeil, U.S. Pat. 2,864,055 (1958).
5. M. Lurie, H. N. Seiger, and R. C. Shair, *Power Sources Conference* **17**, 110 (1963).
6. E. J. Cairns and H. A. Liebhafsky in "Fuel Cells and Fuel Cell Batteries," pp. 323-338, John Wiley & Sons, Inc., New York (1968).
7. F. H. Mullersman, U.S. Pat. 3,531,706 (1970).
8. W. N. Carson, Jr. and R. L. Hadley, *Power Sources 2*, 6th International Symposium, Brighton, 1968, pp. 181-197, D. H. Collins, Editor, Pergamon Press (1970).
9. K. V. Kordesch, U.S. Pat. 3,288,642 (1966).

Density and Electrical Conductivity of Molten LiI-LiCl-KI Eutectic

N. P. Yao*,¹

Atomics International, A Division of North American Rockwell Corporation, Canoga Park, California 91304

A low-melting salt mixture which possesses a high electrical conductivity, a large decomposition potential, and is chemically stable, will provide a useful electrolyte medium in several areas of molten salt electrochemical technology. The eutectic mixture 59 mole per cent (m/o) LiI-8.5 m/o LiCl-32.5 m/o KI (melting point 264°C) reported by Johnson and Foster (1) is one of the lowest melting ternary alkali-halide systems known to date.

This low-melting and lithium-rich salt electrolyte is being utilized in some high temperature battery systems with a lithium anode (2, 3). It was observed that the potassium ions in this melt would not interfere with the lithium electrode reaction in these systems (4).

In this work the density and the electrical conductivity of molten LiI-LiCl-KI eutectic are reported over a temperature range of 273°-454°C.

Experimental

Chemicals.—Anhydrous, polarographic grade LiI and LiCl were supplied in 200g ampoules by Anderson Physics Laboratory, Champaign, Illinois. "Baker analyzed" KI was vacuum dried over a 2 week period at gradually increasing temperatures up to 250°C and at 13 μ Hg pressure. The eutectic mixture (59 m/o LiI-8.5 m/o LiCl-32.5 m/o KI) was prepared by weight, fused, and filtered through a 25 μ glass frit in an argon gas-filled dry box. The melt was colorless and clear. The melting point of the eutectic mixture from the cooling curve was 264° \pm 0.5°C, in agreement with the literature value (1). "Baker analyzed" KCl, which was used in preparing the standard aqueous solution for cell constant determination, was recrystallized twice from redistilled water. The salt was dried *in vacuo* at 300°C for 120 hr. "Baker analyzed" KNO₃, which was used in the volume calibration of the pycnometer, was dried *in vacuo* at 250°C for 100 hr.

Apparatus and procedure.—The fused silica capillary cell for the conductivity measurements, containing four bright tungsten electrodes and a 1.5 mm ID capillary, was previously described by Grantham and Yosim (5). The cell used in this work had a capillary length of about 25 cm in a spiral form. The a-c conductivity determinations were made with a Leeds and Northrup No. 1666 Jones bridge which had been calibrated against secondary NBS standards. The capacitance and impedance of the cell were balanced during measurements by a variable capacitor in the bridge. The a-c signal was supplied by a Hewlett-Packard Model 200 CD audio oscillator in conjunction with a Newcomb amplifier; the signal null was detected with a General Radio Type 1231-B amplifier. The conductivity of the LiI-LiCl-KI solution was found to be frequency independent from 1 to 50 kHz. The cell constant obtained with 1 Demal standard KCl solutions (6) at 25°C was 1528.0 \pm 0.6 cm⁻¹ determined with two separately prepared KCl solutions. The calculated cell constant varied by less than 0.03% in the temperature range of 25°-455°C. The cell constant redetermined after the experimental run did not show any change.

After proper amount of LiI-LiCl-KI eutectic salt was added to the conductivity cell in the argon gas

dry box, the cell was sealed under vacuum. Conductivity measurements were made after the cell had been heated in a furnace at approximately 270°C for a few hours. The measurements were made at increasing temperatures with periodic rechecks of the previous points. Each measurement was taken 30 min after the thermal equilibrium was attained. The data were reproducible to within 0.03%; the values reported are the average of at least three determinations. The temperature of the solution was measured with a calibrated Alumel-Chromel thermocouple in contact with the cell capillary wall in conjunction with a Leeds and Northrup Millivolt Potentiometer. A temperature difference of only 0.2°C occurred over the length of the capillary.

Density measurements were made in a fused silica pycnometer which incorporated two thermocouple wells for temperature measurements. The volume of the pycnometer was calibrated with double distilled water at 25°C and with molten KNO₃ (7) at 422°C. The average volume based on four measurements at each temperature was 18.65 cm³ at 25°C and 18.71 cm³ at 422°C. The volume expansion is in agreement with the calculated thermal expansion for the pycnometer of about 0.4% in the same temperature range. The pycnometer was heated in a small insulated furnace in the argon gas dry box and the maximum temperature difference in the solution was 0.5°C. The uncertainty in the individual measurement was about 0.3%; the values reported are the average of at least three determinations.

Results

The specific conductivity of molten LiI-LiCl-KI (59 m/o-8.5 m/o-32.5 m/o) eutectic over a temperature range of 273°-454°C is given in Table I. The curve shown in Fig. 1 represents the computer-fitted, least squares equation ($\sigma = 0.009$) and can be represented by

$$\kappa = -1.708 + 1.197 \times 10^{-2}t - 1.009 \times 10^{-5}t^2 \quad [1]$$

where κ is specific conductivity in ohm⁻¹cm⁻¹ and t is temperature in °C.

Table I. Specific conductivity of LiI-LiCl-KI eutectic vs. temperature

t (°C)	κ (ohm ⁻¹ cm ⁻¹)
273.0	0.785 ₁
276.5	0.823 ₆
281.8	0.861 ₇
286.5	0.898 ₂
288.3	0.905 ₂
292.3	0.933 ₂
294.0	0.945 ₅
300.0	0.984 ₄
306.0	1.011 ₄
311.0	1.049 ₆
311.8	1.053 ₆
318.0	1.086 ₈
328.0	1.135 ₅
335.0	1.172 ₇
345.5	1.223 ₂
361.0	1.299 ₁
371.5	1.342 ₈
394.4	1.437 ₅
412.0	1.512 ₇
420.2	1.525 ₁
422.3	1.533 ₅
431.5	1.572 ₁
437.4	1.599 ₈
447.5	1.640 ₀
454.2	1.665 ₇

* Electrochemical Society Active Member.

¹ Present address: Heliotek, Division of Textron Inc., P. O. Box 4158, Sylmar, California 91342.

Key words: LiI-LiCl-KI eutectic, density, electrical conductivity.

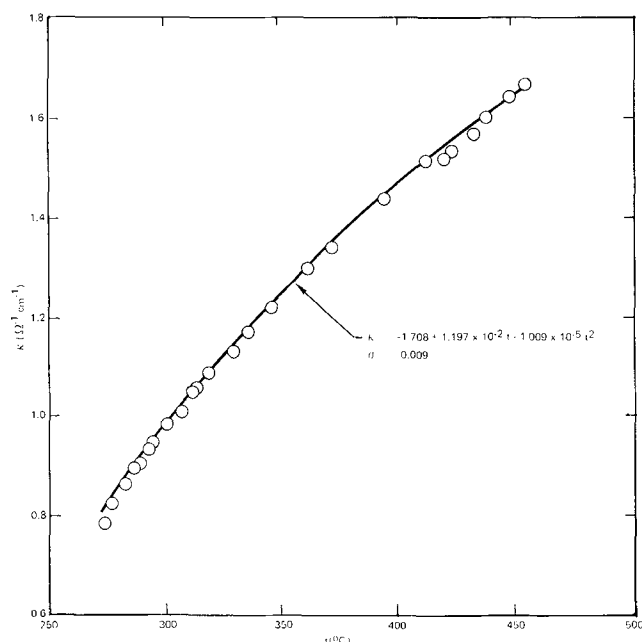


Fig. 1. Specific conductance vs. temperature for molten LiI-KI-LiCl eutectic.

Four density data, over a temperature range of 274°-437°C, are represented by a linear equation ($\sigma = 0.007$)

$$\rho = 3.214 - 7.850 \times 10^{-4}t \quad [2]$$

Surprisingly, the density values (in g/cm³) conform approximately (to within 0.5%) the additivity rule of molar volume although the densities of LiI, LiCl, and KI had been extrapolated from the reported values (8) at above the melting points of the salt components.

The specific conductivity-temperature relationship, Eq. [1], and the density-temperature relationship, Eq. [2], were both used in calculating equivalent conductances, Λ , the logarithms of which were examined for curvature when plotted vs. $1/T$ (°K). The densities at the three temperatures, i.e., 273.0°, 447.5°, and 454.2°C, were calculated from Eq. [2].

The curvature exhibited in the plot of specific conductance vs. temperature (Fig. 1) persisted in the log Λ vs. $1/T$ (K°) plot. Therefore, the three parameter equation, Vogel-Tammann-Fulcher (VTF), successfully employed by Angell (9) for glass-forming melts has been fitted to the present data using a computer program (10). The least squares representation of the data ($\sigma = 0.008$) is

$$\ln \Lambda = A - \frac{1}{2} \ln T - \frac{k}{T - T_0}$$

$$= 8.652 - \frac{1}{2} \ln T - \frac{377}{T - 348} \quad [3]$$

where Λ is in cm²/ohm-equivalent and T is in degrees Kelvin. The three parameters, A , k , and T_0 (the zero mobility temperature) are respectively 8.652, 377°K, and 348°K.

The zero mobility temperature T_0 for the glass-forming Ca(NO₃)₂ + KNO₃ molten salt mixtures was reported (9) to vary from 237°K for pure KNO₃ to 330°K for a 45% Ca(NO₃)₂ mixture. The T_0 value for the LiCl + KCl eutectic was reported (9) to be 320°K. The present data are in the range of $1.6 T_0 \leq T \leq 2.1 T_0$ based on the value of $T_0 = 348$ °K for the LiI-LiCl-KI eutectic. Since Eq. [3] is strictly applicable for temperature $\leq 1.7 T_0$, the value $T_0 = 348$ °K for the present eutectic must be considered tentative.

The Arrhenius coefficient for equivalent conductance, E_A , can be evaluated from the derivative of the analytic representation, Eq. [3], as follows

$$E_A = -R \frac{\delta \ln \Lambda}{\delta (1/T)} = -\frac{1}{2} RT + 377R \left(\frac{T}{T - 348} \right)^2 \quad [4]$$

The E_A decreases with increasing temperature; from about 5.1 kcal/mol at 273°C to about 2.0 kcal/mol at 454°C.

Manuscript submitted March 17, 1971; revised manuscript received March 15, 1972.

Any discussion of this paper will appear in a Discussion Section to be published in the June 1973 JOURNAL.

REFERENCES

1. C. E. Johnson and M. S. Foster, *This Journal*, **116**, 1612 (1969).
2. E. J. Cairns, H. Shimotake, and A. K. Fischer, "Lithium/Chalcogen Electrochemical Cells for Energy Storage," *Argonne Review*, Oct. 1969.
3. N. P. Yao, L. A. Heredy, and R. C. Saunders, *Secondary Lithium-Sulfur Battery*, in *Proc. Sixth Advances in Battery Technology Symposium*, So. California-Nevada Section of the *Electrochem. Soc.*, Dec. 4, 1970, in press.
4. N. P. Yao, T. A. Heredy, and R. C. Saunders, *This Journal*, **118**, 1039 (1971).
5. L. F. Grantham and S. J. Yosim, *J. Chem. Phys.*, **38**, 1671 (1963).
6. G. Jones and B. C. Bradshaw, *J. Am. Chem. Soc.*, **55**, 1780 (1933).
7. G. P. Smith and G. F. Petersen, *J. Chem. Engr. Data*, **6**, 493 (1961).
8. A. Klemm, Table III in "Molten Salt Chemistry," M. Blander, Editor, p. 564, Interscience Publishers, New York (1964).
9. C. A. Angell, *J. Phys. Chem.*, **70**, 2793 (1966).
10. C. T. Moynihan, *ibid.*, **70**, 3399 (1966).

Recovery of Chlorine from Waste Gas—Fundamentals

Fumio Hine* and Masaki Yasuda

Nagoya Institute of Technology, Nagoya 466, Japan

One to two per cent of the total production of chlorine by electrolysis, accounting for about 50,000 tons a year in Japan and about 100,000 tons in the United States, is being wasted. Chlorine should be recovered from such waste gases. Some processes, such as the absorption-desorption method with a chlorinated solvent, have developed, but compara-

tively few of practical application have been announced. Here a new electrochemical process with the depolarized cathode, called electrochemical recovery of chlorine, is described.

Electrochemistry of the Process

The electrolytic solution consisting of HCl and CuCl₂ is electrolyzed with the chlorine depolarized cathode. The process resembles the Kyoto-type HCl cell investigated by the same author (1).

* Electrochemical Society Active Member.
Key words: chlorine recovery, chloride electrolysis, depolarized cathode, diffusion-limiting current.

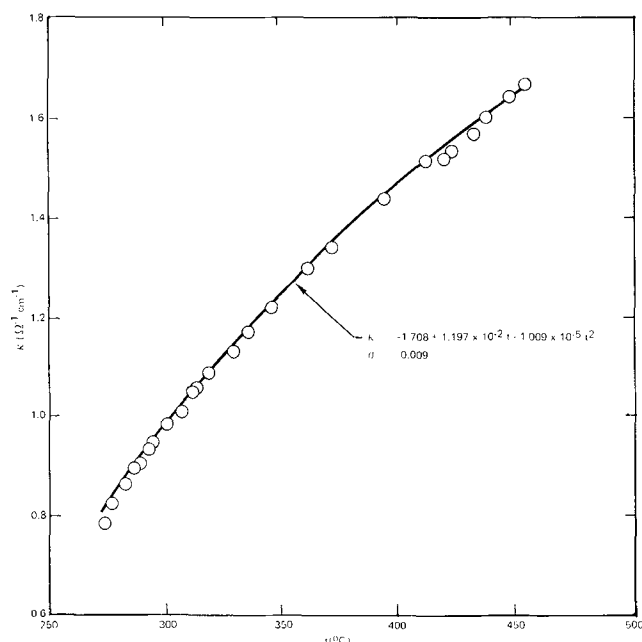


Fig. 1. Specific conductance vs. temperature for molten LiI-KI-LiCl eutectic.

Four density data, over a temperature range of 274°-437°C, are represented by a linear equation ($\sigma = 0.007$)

$$\rho = 3.214 - 7.850 \times 10^{-4}t \quad [2]$$

Surprisingly, the density values (in g/cm^3) conform approximately (to within 0.5%) the additivity rule of molar volume although the densities of LiI, LiCl, and KI had been extrapolated from the reported values (8) at above the melting points of the salt components.

The specific conductivity-temperature relationship, Eq. [1], and the density-temperature relationship, Eq. [2], were both used in calculating equivalent conductances, Λ , the logarithms of which were examined for curvature when plotted vs. $1/T$ (°K). The densities at the three temperatures, i.e., 273.0°, 447.5°, and 454.2°C, were calculated from Eq. [2].

The curvature exhibited in the plot of specific conductance vs. temperature (Fig. 1) persisted in the $\log \Lambda$ vs. $1/T$ (K°) plot. Therefore, the three parameter equation, Vogel-Tammann-Fulcher (VTF), successfully employed by Angell (9) for glass-forming melts has been fitted to the present data using a computer program (10). The least squares representation of the data ($\sigma = 0.008$) is

$$\begin{aligned} \ln \Lambda &= A - \frac{1}{2} \ln T - \frac{k}{T - T_0} \\ &= 8.652 - \frac{1}{2} \ln T - \frac{377}{T - 348} \end{aligned} \quad [3]$$

where Λ is in cm^2/ohm -equivalent and T is in degrees Kelvin. The three parameters, A , k , and T_0 (the zero mobility temperature) are respectively 8.652, 377°K, and 348°K.

The zero mobility temperature T_0 for the glass-forming $\text{Ca}(\text{NO}_3)_2 + \text{KNO}_3$ molten salt mixtures was reported (9) to vary from 237°K for pure KNO_3 to 330°K for a 45% $\text{Ca}(\text{NO}_3)_2$ mixture. The T_0 value for the LiCl + KCl eutectic was reported (9) to be 320°K. The present data are in the range of $1.6 T_0 \leq T \leq 2.1 T_0$ based on the value of $T_0 = 348^\circ\text{K}$ for the LiI-LiCl-KI eutectic. Since Eq. [3] is strictly applicable for temperature $\leq 1.7 T_0$, the value $T_0 = 348^\circ\text{K}$ for the present eutectic must be considered tentative.

The Arrhenius coefficient for equivalent conductance, E_A , can be evaluated from the derivative of the analytic representation, Eq. [3], as follows

$$E_A = -R \frac{\delta \ln \Lambda}{\delta (1/T)} = -\frac{1}{2} RT + 377R \left(\frac{T}{T - 348} \right)^2 \quad [4]$$

The E_A decreases with increasing temperature; from about 5.1 kcal/mol at 273°C to about 2.0 kcal/mol at 454°C.

Manuscript submitted March 17, 1971; revised manuscript received March 15, 1972.

Any discussion of this paper will appear in a Discussion Section to be published in the June 1973 JOURNAL.

REFERENCES

1. C. E. Johnson and M. S. Foster, *This Journal*, **116**, 1612 (1969).
2. E. J. Cairns, H. Shimotake, and A. K. Fischer, "Lithium/Chalcogen Electrochemical Cells for Energy Storage," *Argonne Review*, Oct. 1969.
3. N. P. Yao, L. A. Heredy, and R. C. Saunders, *Secondary Lithium-Sulfur Battery*, in *Proc. Sixth Advances in Battery Technology Symposium*, So. California-Nevada Section of the *Electrochem. Soc.*, Dec. 4, 1970, in press.
4. N. P. Yao, T. A. Heredy, and R. C. Saunders, *This Journal*, **118**, 1039 (1971).
5. L. F. Grantham and S. J. Yosim, *J. Chem. Phys.*, **38**, 1671 (1963).
6. G. Jones and B. C. Bradshaw, *J. Am. Chem. Soc.*, **55**, 1780 (1933).
7. G. P. Smith and G. F. Petersen, *J. Chem. Engr. Data*, **6**, 493 (1961).
8. A. Klemm, Table III in "Molten Salt Chemistry," M. Blander, Editor, p. 564, Interscience Publishers, New York (1964).
9. C. A. Angell, *J. Phys. Chem.*, **70**, 2793 (1966).
10. C. T. Moynihan, *ibid.*, **70**, 3399 (1966).

Recovery of Chlorine from Waste Gas—Fundamentals

Fumio Hine* and Masaki Yasuda

Nagoya Institute of Technology, Nagoya 466, Japan

One to two per cent of the total production of chlorine by electrolysis, accounting for about 50,000 tons a year in Japan and about 100,000 tons in the United States, is being wasted. Chlorine should be recovered from such waste gases. Some processes, such as the absorption-desorption method with a chlorinated solvent, have developed, but compara-

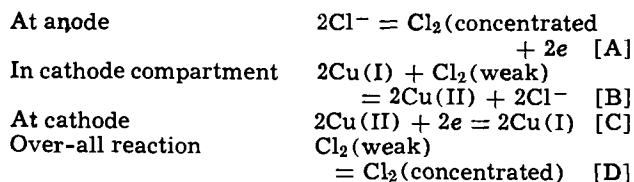
tively few of practical application have been announced. Here a new electrochemical process with the depolarized cathode, called electrochemical recovery of chlorine, is described.

Electrochemistry of the Process

The electrolytic solution consisting of HCl and CuCl_2 is electrolyzed with the chlorine depolarized cathode. The process resembles the Kyoto-type HCl cell investigated by the same author (1).

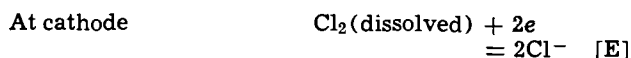
* Electrochemical Society Active Member.
Key words: chlorine recovery, chloride electrolysis, depolarized cathode, diffusion-limiting current.

The anode reaction is the evolution of chlorine from Cl^- ion (reaction [A]). Waste or weak chlorine is sent to the cathode compartment, where dissolved chlorine reacts with cuprous chloride complex ions to give cupric ions (reaction [B]). Cupric ions are cathodically reduced into cuprous by reaction [C], which has been studied in detail in the previous paper (2). The over-all reaction is, thus, represented by reaction [D] as follows



where Cu(I) and Cu(II) are the cuprous and cupric chloro complex ions, probably CuCl_2^- and CuCl_3^- , respectively (2).

The solubility of chlorine in the mixed solution consisting of HCl and CuCl_2 is considerably larger than that of oxygen (3), and the reaction rate of chlorine at the cathode is high in comparison with that of the dissolved oxygen. Thus the side reaction [E] would occur in parallel with reaction [C] at the working cathode



The reversible potentials for the anodic and cathodic processes [A] and [C] are close to each other when reaction [C] is coupled with reaction [B], a fast reaction, therefore, the decomposition voltage for the over-all reaction [D] is small enough, say about 0.1V or less, depending on such operating conditions as electrolyte composition and temperature. The cell voltage is estimated from the polarization data to be about 1.3V at 10 A/dm^2 and 1.7V at 20 A/dm^2 . It will be discussed in detail in the future.

The anode process [A] has been discussed previously as a part of studies on the Kyoto-type HCl cell (4). Therefore, the present work will emphasize the cathodic processes represented by reactions [B], [C], and [E] at the surface of the chlorine-depolarized electrode.

Experimental Procedure

The rotating graphite disk cathode of 1 cm^2 was placed at the center of the glass cell of about 1 liter capacity. A graphite anode was inserted into the anode compartment, which was separated from the cathode compartment by a sintered glass diaphragm. The Luggin probe connected to the calomel reference elec-

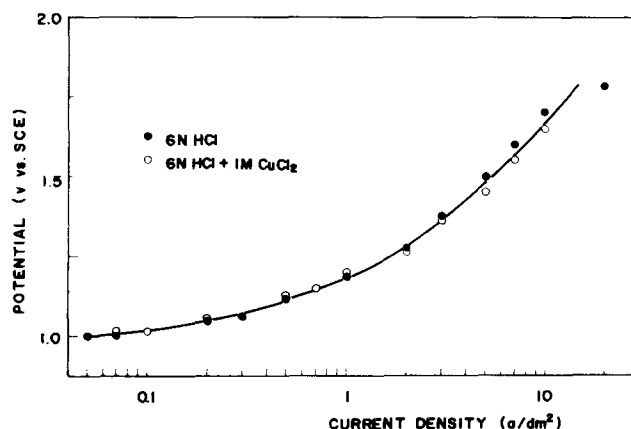


Fig. 1. Potential vs. current density curves of graphite anode in HCl and mixed solution of HCl + CuCl_2 at 40°C.

trode was located 1 mm from the center of the working cathode. The IR drop between the working cathode and the Luggin probe was calibrated by means of the current-interruption technique (5).

The electrolytic solution was made up with reagent grade HCl and CuCl_2 . Since the limiting current density for the cathodic reduction of cupric ions was independent of the HCl concentration, 6N HCl was generally used and 3N HCl was also sometimes employed, while the CuCl_2 concentration was varied over a wide range. The temperature and the moisture of the gas mixture, consisting of chlorine and nitrogen, were brought to equilibrium with the cell liquor before measurements were made.

Results and Discussion

An example of the anodic polarization curves is shown in Fig. 1. It is clear that the potential is almost independent of CuCl_2 in the electrolyte. It disagrees somewhat with the data in the paper on the Kyoto Process (4), although it has not yet been clarified.

Figure 2 shows the polarization curves for rotating graphite cathode at 500 rpm in a 6N HCl under various conditions. In a deaerated solution with nitrogen (rectangular points), only the hydrogen evolution reaction takes place at less noble potential ranges. Since the rate of the cathodic reduction of dissolved oxygen is slow, an almost similar curve is obtained even in an aerated solution (triangular points).

On the other hand, the static potential is considerably noble in the solution containing chlorine (circular points). The cathodic potential tends to become more negative with increase in the current density, the lim-

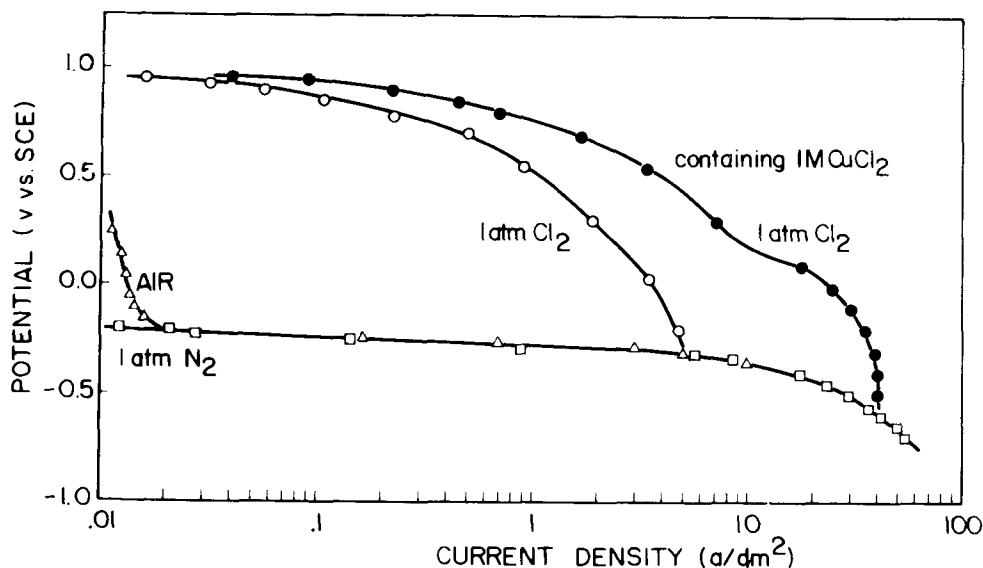


Fig. 2. Polarization curves of graphite cathode in 6N HCl at 40°C under various conditions (500 rpm).

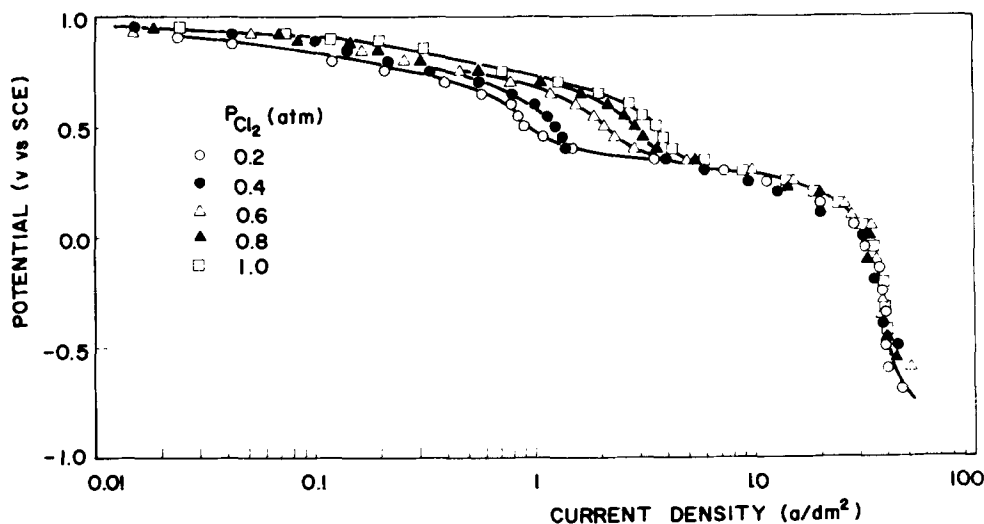


Fig. 3. Potential vs. current density curves in a mixed solution consisting of 6N HCl and 1M CuCl₂ at 40°C and 500 rpm.

iting current density for dissolved chlorine being relatively large.

It is interesting that two current density arrests appear in cupric chloride solution saturated with chlorine (closed points): these are, diffusion-limiting current densities for chlorine and cupric ions.

The first current density arrest in Fig. 3 varies with the chlorine partial pressure, and is proportional to the partial pressure, whereas the second is independent of it.

The two limiting current densities depend greatly on the rotational speed of the working cathode. The results obtained are summarized in Fig. 4. The dotted line is a plot of the current density and rotational speed at +450 mV vs. SCE, and shows that the former is independent of the CuCl₂ concentration. The current density in the mixed solution is smaller than in HCl solution at the same potential, probably due to the small solubility of chlorine in the mixed solution (3, 6).

At -400 mV vs. SCE, the current density depends on the rotational speed, as shown by the solid lines in Fig. 4. The limiting current density at this point is also proportional to the CuCl₂ concentration. With these results, it can be concluded that the first current density arrest is the diffusion-limiting current density for dissolved chlorine, and the second is for cupric

chloride, and hence, the next equation is obtained

$$i_L = k_1(p_{Cl_2})/\bar{\omega} + k_2(a_{Cu(II)})/\bar{\omega} \quad [1]$$

where i_L = limiting current density at -400 mV vs. SCE; k_1 and k_2 are constants for the cathodic reduction of chlorine and cupric chloride, respectively, at -400 mV; p_{Cl_2} = partial pressure of chlorine; $\bar{\omega}$ = rotational speed.

It is clear that the first term of the right hand side in Eq. [1] is much smaller than the second term from experimental data such as Fig. 5, Eq. [2] can be obtained

$$i_L = k_2(a_{Cu(II)})/\bar{\omega} \quad [2]$$

This would be the maximum current density for cell operation.

Because k_2 involves the diffusion coefficient and the viscosity of the solution, it would be a function of the operating temperature. At less noble potentials, the limiting current density increases with temperature, on the other hand, the current density at +0.5V at high temperature is smaller than at low temperature because of the difference in the solubility of chlorine. The limiting current density at -0.4V depends linearly on the operating temperature as shown in Fig. 5, thus

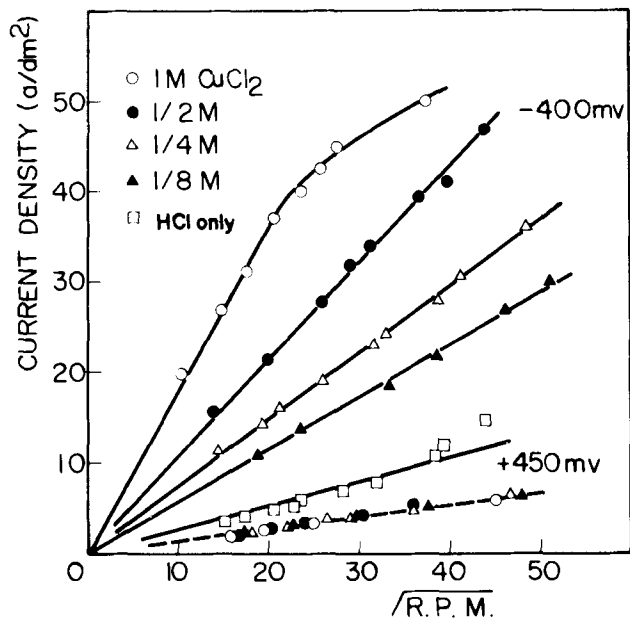


Fig. 4. Current density vs. rotating speed at constant potentials in 3N HCl containing CuCl₂ at 40°C. ($p_{Cl_2} = 1$ atm).

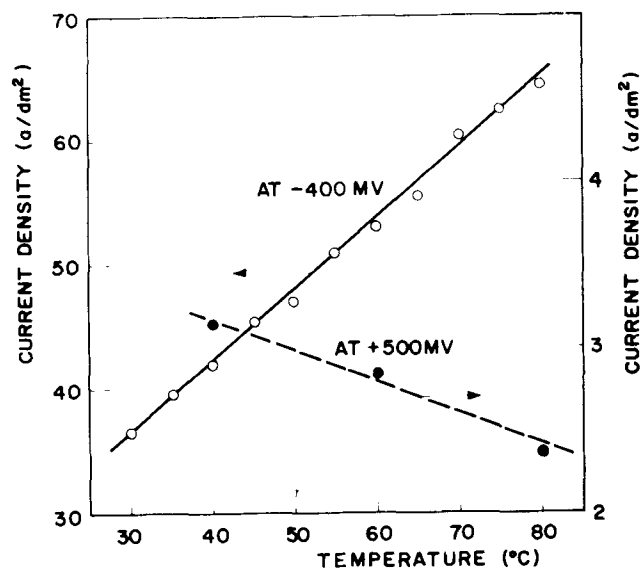


Fig. 5. Limiting current density vs. temperature in a mixed solution consisting of 6N HCl and 1M CuCl₂ under $p_{Cl_2} = 1$ atm and 500 rpm. Closed points at 500 mV represent the limiting current density of Cl₂ dissolved, whereas open points are of Cl₂ plus Cu(II) at -400 mV.

the cell should be operated at high temperature. The maximum current density might be a function of the Reynolds number as well as the operating temperature. Therefore, it should be investigated further, for development and scale-up of this process, from a chemical engineering point of view.

Conclusion

An electrochemical process for recovery of chlorine from waste gas has been developed. Fundamental studies on this process, emphasizing the cathodic reaction, have been made. Since the limiting current density for dissolved chlorine is small, the rate of the over-all cathodic process is almost controlled by the diffusion current for cupric chloride in the electrolyte. The higher the concentration and the temperature, the larger the current density obtained. The flow velocity of the electrolyte near the working cathode is also an important factor because the cathode reaction is controlled by diffusion (7).

Acknowledgment

The author wishes to thank Masatoshi Higuchi for his experimental work.

This process has been filed in Japan: Patent Numbers 594783 and 601453.

Manuscript submitted Jan. 24, 1972; revised manuscript received April 10, 1972.

Any discussion of this paper will appear in a Discussion Section to be published in the June 1973 JOURNAL.

REFERENCES

1. F. Hine, S. Yoshizawa, K. Yamakawa, and Y. Nakane, *Electrochem. Technol.*, **4**, 555 (1966).
2. F. Hine and K. Yamakawa, *Electrochim. Acta*, **15**, 769 (1970).
3. F. Hine and S. Inuta, *Bull. Chem. Soc. Japan*, **42**, 914 (1969).
4. F. Hine and K. Yamakawa, Paper 258, presented at Electrochem. Soc. Meeting, Los Angeles, May 10-15, 1970.
5. E. Yeager and F. Ludwig, 153 Nat'l. Meeting, ACS, Div. of Fuel Chem., Vol. 11, No. 1, p. 10, Miami, April 9-14, 1967.
6. F. Hine and S. Inuta, *Bull. Chem. Soc. Japan*, **41**, 71 (1968).
7. F. Hine and K. Yamakawa, *Electrochim. Acta*, **13**, 2119 (1968).

A Time-Dependent Solvation Number for Ions in Solution

J. O'M. Bockris*¹ and P. P. S. Saluja*²

Electrochemistry Laboratory, University of Pennsylvania, Philadelphia, Pennsylvania 19104

The concept of a solvation number for ions in solution existed for many decades but was associated with difficulties arising from a lack of accepted and sufficiently sharp definition. However, a primary solvation number was defined (1) as the number of water molecules per ion which had lost their own translational freedom and exhibited those of the ion. A certain number of experimental methods (1) seem to give a quantity relatively independent of the method, while from the nature of the concordant methods one may comprehend that they might be expected to yield solvation numbers corresponding to the definition ("The solvation number of an ion is the number of water molecules which have lost their own degrees of translational freedom and have those of the ion.")

However, the concept was not clear in the absence of an expression of the model in "dynamic" terms (2). A quantitative version of this model has recently been developed (3). It is wished to present it here in a qualitative way.

The suggestion is to interpret the concept of primary solvation number in terms of the residence time of the water molecules around the ions. Upon the arrival of an ion at a given site in the solution, it acts electrostatically on the surrounding solvent molecules to orient them toward an optimal energetic position. In the limiting case of small ions of high valency (e.g., Mg^{+2}), all of the first, and perhaps some of the second, shell of water molecules, will be oriented into a relatively incompressible solvent sheath around the ion. At the other extreme, with large ions and low valency (e.g., I^-), none of the water molecules will be thus oriented and they will continue to remain in

the solvent structure while the ion remains in its position before it jumps to the next site in solution.

The primary solvation number may be defined as the number of water molecules which are attached to the ion for a sufficiently long time so that they move with the ion from a given position in the solution to its next site. Thus, whether a water molecule, which is a coordination water molecule for the ion, is also a part of its solvation sheath depends³ upon: (i) the time the ion waits at a given site in solution ($\tau_{ion, wait}$); and (ii) the time the water molecule takes to orient around from its position in the solvent to come into a position of minimum energy in respect to the ion ($\tau_{water, orient}$).

To test this model, it is necessary to have a method which distinguishes between the solvation number due to cation and anion, for most methods of determining primary solvation water molecules give rise only to the sum of these. Such a method has been recently developed (3) by combining Passynski's method for the determination of the total amount of incompressible solvent water molecules around the ion with the measurements of ionic vibration potential which measures the difference in the masses of the cation and anion. We have given (3) reasons which suggest that the two methods measure the same quantity. The compressibility method gives the sum, the other method gives the difference, of the solvation numbers of cation and anion. In Fig. 1, some of these solvation numbers are plotted as a function of ionic radius.

These concepts may be tested. If they are correct, in a plot of $\tau_{ion, wait}/\tau_{water, orient}$ against solvation number, the solvation number would tend to zero if the ratio is small; and if $\tau_{ion, wait}/\tau_{water, orient}$ is large, the solva-

* Electrochemical Society Active Member.

¹ Present address: Flinders University, Adelaide, Australia.

² Present address: Cornell University, Department of Chemistry, Ithaca, New York 14850.

Key words: solvation number, coordination number, ion-wait time, water-orientation time, solvational coordination, nonsolvational coordination.

³ The coordination water molecules which are part of the solvation sheath around an ion are defined as "solvational" coordination water (SCW) molecules. The remaining water molecules (equal to total coordination number minus SCW molecules) are defined as "nonsolvational" coordination water (NSCW) molecules in the solvational model presented here.

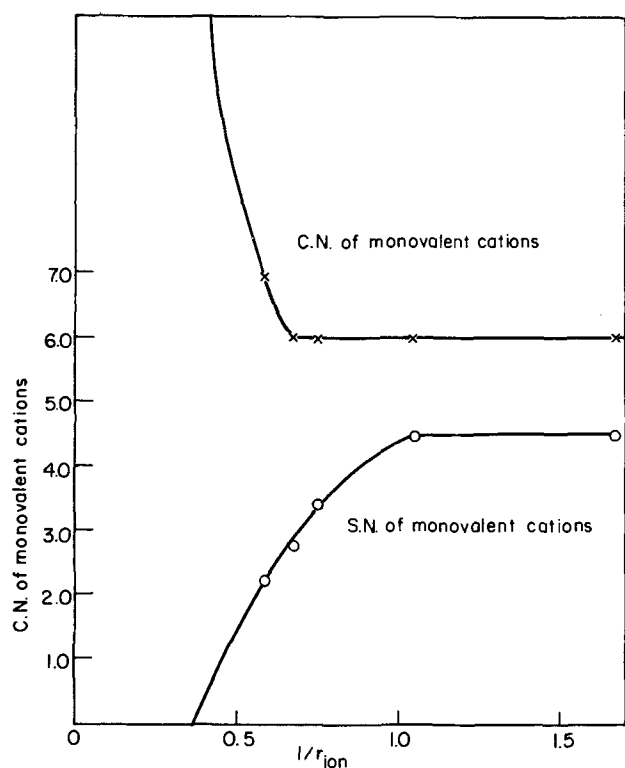


Fig. 1. S.N. and C.N. of alkali metal cations plotted as reciprocal function of cations radius.

tion number will tend to be equal to the coordination number. In Fig. 2, such a graph is shown and is seen to be consistent with the concept presented.

These ideas thrust light upon the relationship between the coordination number, as recently obtained from a systematic analysis of x-ray measurements (4), and the solvation number (see Fig. 1). These quantities are not equal, although they tend to become equal for small ions and high valency.

This work stresses the invalidity of the older concept (6) of assuming that the coordination number round an ion is always 4 or 6; it is seen that in fact a coordination number is an experimental quantity, and may vary continuously from about 4 to about 9 (4, 7) depending upon the size of the ion.

Acknowledgment

We would like to thank our sponsors, the Office of Saline Water, U.S. Department of the Interior, for support under Contract No. 14-01-0001-1467, and Dr. W. MacCoy for discussion of the work which led to the concept presented here.

Manuscript submitted Nov. 22, 1971.

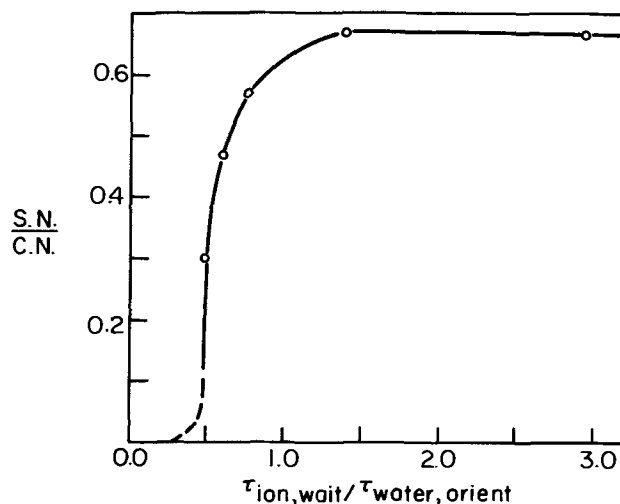


Fig. 2. S.N./C.N. plotted against $\tau_{ion, wait}/\tau_{water, orient}$ for monovalent ions.

Any discussion of this paper will appear in a Discussion Section to be published in the June 1973 JOURNAL.

REFERENCES

1. J. O'M. Bockris, *Quart. Rev. (London)*, **3**, 173 (1949).
2. J. O'M. Bockris and A. K. N. Reddy, "Modern Electrochemistry," Vol. 1, pp. 117-132, Plenum Press, New York (1970).
3. J. O'M. Bockris and P. P. S. Saluja, *J. Phys. Chem.*, In press.
4. R. M. Lawrence and R. F. Kruh, *J. Chem. Phys.*, **47**, 4758 (1967); R. M. Lawrence, Ph.D. thesis, University of Arkansas, (1965); W. Bol, G. J. A. Gerrits, and C. L. vanPanthaleon van Eck, *J. Appl. Cryst.*, **3**, 486 (1970).
5. J. O'M. Bockris and P. P. S. Saluja, *J. Phys. Chem.*, In press.
6. A list of authors, who assume that the coordination number round an ion is always 4 or 6 (independent of ionic size), is given below: J. D. Bernal and R. H. Fowler, *J. Chem. Phys.*, **1**, 515 (1933); D. D. Eley and M. G. Evans, *Trans. Faraday Soc.*, **34**, 1093 (1938); K. J. Laidler and C. Pegis, *Proc. Roy. Soc.*, **A241**, 80 (1957); A. D. Buckingham, *Disc. Faraday Soc.*, **24**, 151 (1957); H. F. Halliwell and S. C. Nyburg, *Trans. Faraday Soc.*, **59**, 1126 (1963); G. Somsen, J. Coops, and M. W. Tolks, *Rec. Trav. Chim.*, **82**, 231 (1963); **84**, 985 (1965); K. J. Laidler and J. S. Muirhead-Gould, *Trans. Faraday Soc.*, **63**, 944 (1967); L. Weeda and G. Somsen, *Rec. Trav. Chim.*, **86**, 263 (1967); **85**, 159 (1966); D. F. C. Morris, *Struct. Bonding*, **4**, 63 (1968); D. K. Ross, *Aust. J. Phys.*, **21**, 597 (1968); R. E. Burton and J. Daly, *Trans. Faraday Soc.*, **66**, 1281 (1970); W. E. Morf and W. Simon, *Helv. Chim. Acta*, **54**, 794 (1971).
7. H. G. Hertz, *Angew. Chemie (Intl. Edn.)*, **9**, 124 (1970); *Ber. Bunsenges. Physik. Chem.*, **75**, 572 (1971); **75**, 183 (1971); **74**, 666 (1970).



Electrochemical Synthesis of Ferromagnetic Fe_3S_4

S. Yamaguchi* and T. Moori

National Institute for Researches in Inorganic Materials, 2-29-3 Hon-Komagome, Bunkyo, Tokyo, Japan

Water was bubbled with nitrogen at room temperature to remove air and was then saturated with hydrogen sulfide gas. A small amount of calcium chloride was added to augment the electrical conductivity. The concentrations of H_2S and of $\text{CaCl}_2 \cdot 2\text{H}_2\text{O}$ and the pH were 0.0145 mol/liter, 0.007 mol/liter, and 4.6, respectively.

Two sheets of iron were employed as electrodes. The size was about $0.1 \times 100 \times 100 \text{ mm}^3$. An electrolysis was carried out with the current density 0.6 mA/cm^2 at about 80°C for 7 hr. The bath was replenished occasionally with the electrolyte prescribed in order to keep its concentration constant. About 0.5g of black iron sulfide was deposited in the neighborhood of the cathode. The bath containing the deposit was aged at about 100°C for 30 min. The black sediment having experienced this hydrothermal treatment became ferromagnetic and crystalline. It was attracted sensitively to a hand magnet, and was also subjected to crystallographic analysis by electron diffraction. The diffraction pattern obtained from the specimen is shown in Fig. 1. Figure 2 is a reference pattern from pure Fe_3S_4 of spinel type (1). The result of analysis of Fig. 1 is given in Table I, which verifies that the iron sulfide produced here corresponds mainly to greigite (space group: $\text{Fd}\bar{3}\text{m}$, spinel type, lattice constant: 9.875\AA).

* Electrochemical Society Active Member.

Key words: electrolysis, ferromagnetic, Fe_3S_4 , synthesis.

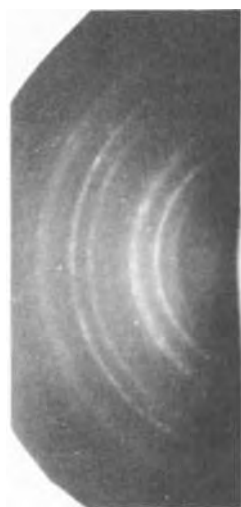


Fig. 1. Electron diffraction pattern from Fe_3S_4 produced electrochemically. Wavelength of the electrons, 0.04075\AA ; camera length, 50 cm; positive enlarged 2.3 times.

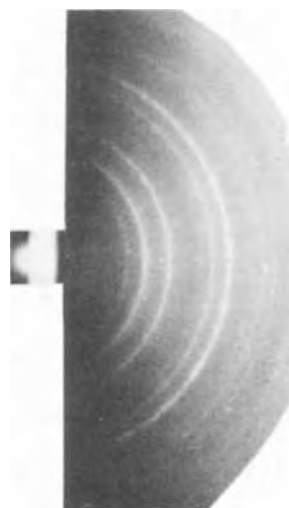


Fig. 2. Reference pattern of pure Fe_3S_4 .

Table I. Result of analysis of Fig. 1

(d , interplanar spacings; I , intensity of reflections; a_0 , lattice constant calculated.)

d (Å)	hkl	I	a_0 (Å)
5.702	111	1	9.876
3.491	220	5	9.875
2.977	311	10	9.875
2.815	222	1	9.876
2.469	400	8	9.876
2.015	422	1	9.872
1.900	333	6	9.873
1.746	440	9	9.877
			Mean 9.875 ± 0.003

Acknowledgment

The present authors would like to thank Dr. T. Yamauchi, Director of the National Institute for Researches in Inorganic Materials, Tokyo, for the help he has given us throughout this study.

Manuscript submitted June 3, 1971.

Any discussion of this paper will appear in a Discussion Section to be published in the June 1973 JOURNAL.

REFERENCES

1. R. W. G. Wyckoff, "Crystal Structures," Vol. 3, p. 79, Interscience Publishers, New York (1965); S. Yamaguchi and T. Katsurai, *Kolloid-Z*, **170**, 147 (1960); B. J. Skinner, R. C. Erd, and F. S. Grimaldi, *Am. Mineralogist*, **49**, 543 (1964).



Selective Photoetching of Gallium Arsenide

F. Kuhn-Kuhnenfeld

Wacker-Chemitronic, Burghausen, Germany

ABSTRACT

Etching of GaAs in an oxidizing etchant under intense local illumination was found to be selective and, moreover, to be a powerful method for the characterization of this material. A flat bottom hole is etched into the illuminated surface region of n-type GaAs, whereas a mesa structure forms on p-type material. Thus, it is possible to determine the conductivity type of very small surface areas. Height and depth of those structures both decrease with increasing doping level. Striations, precipitates, and decorated dislocation lines are revealed with excellent resolution even in undoped or semi-insulating samples. By measuring photovoltages between an illuminated and a dark GaAs electrode in $\text{H}_2\text{SO}_4\text{-H}_2\text{O}_2\text{-H}_2\text{O}$ -solution, the surface photovoltaic effect was shown to be the origin of selective photoetching.

Various techniques have been employed to characterize the homogeneity of dopant distribution in GaAs. Among these are infrared transmission (1, 2), schlieren images (3), cathodoluminescence (4, 5), photoluminescence (6), x-ray topography (7), transmission electron microscopy (8), ion analyzer (9), and etching (10-14).

Etching methods are the ones most frequently used for delineating striations and growth profiles; they are best suited for routine work because of their simplicity and their good resolution. On the other hand, etching has been considered a purely qualitative method (15), and little is known about the mechanisms involved. In dealing with pulsed anodic etching Dickhoff (13) has assumed that current density is higher at zones of higher conductivity and dissolution there proceeds faster. Winteler and Zimmerli (16) used Dickhoff's etching technique on GaAs, but did not find correlation in every case between etch figures and Schottky diode isoconcentration-lines. While distinct bright and dark striation zones are easily obtained by pulsed anodic etching of GaAs, the difference seems to be one of roughness rather than of depth. There are, of course, other striation etching techniques (14) that are clearly based on locally different etch rates; but no decisive answer has been given to the question of whether striation valleys or striation ridges coincide with regions of higher than average resistivity. An analogous problem has been solved, however, in the study of cathodoluminescence (4, 5).

Selective photoetching, as described in the present paper, is not only accessible to semi-quantitative interpretation, but is also much more sensitive than conventional etching techniques. Resolution is improved, and striations are revealed even in undoped or semi-insulating samples, regardless of surface orientation. So far, etched striations in undoped GaAs could hardly be detected at all (1, 14), whereas for semi-insulating material only the method of Plaskett and Parsons (12) was available and only on $\{211\}$ -planes. Finally, this selective photoetching is the only method for the

absolute determination of conductivity type on a microscopic scale. Selective photoetching is not just etching under illumination, which is a widely used procedure. It is essential that only part of the etched surface be intensely illuminated, a fact that was first recognized by Haisty (17). Haisty's experiments, however, were performed in dilute electrolytes, with comparatively weak illumination, so that striations could not be developed.

Etching Procedure

Polished GaAs samples¹ were mounted on a quartz disk of 2 in. diam. The disk was then put into a small petri dish filled with the etchant. Best results were obtained with a solution of 3 parts H_2SO_4 , 1 part 30% H_2O_2 , and 1 part H_2O at a temperature of 30°C; but a solution of 1 volume per cent (v/o) bromine in methanol was also successfully used. Due to the intense color of the etchant, however, much light is absorbed in the layer of liquid covering the sample.

The petri dish was then placed on the stage of a Zeiss Universal microscope, where the light of the illuminator (HBO 200 mercury lamp) could be projected onto a sharply confined area of the GaAs surface. The diameter of this area was adjustable between 0.5 and 5 mm by means of an iris diaphragm. The long working distance of 9 mm necessary for this type of experiment was provided by a special objective lens (Epiplan 4X POL). A heat protection filter served to make sure that IR radiation was minimized.

Short etch and exposure times of typically 5 min were sufficient for maximum resolution. It did not matter if the GaAs sample was kept in the etchant for a limited time before exposure, but it was quite important that the etching action be stopped at the same time as the illumination. This was accomplished by submerging the petri dish and its contents into a water vessel, which was kept ready next to the microscope.

An interesting feature of photoetching by means of a microscope is that one can clearly see what is going on during the exposure. Not only can striations and

Key words: compound semiconductors, striations, dislocations, selective etching, etch mechanism.

¹ Most of the GaAs samples were grown at Wacker-Chemitronic by the III-V group of B. K. Bienert.

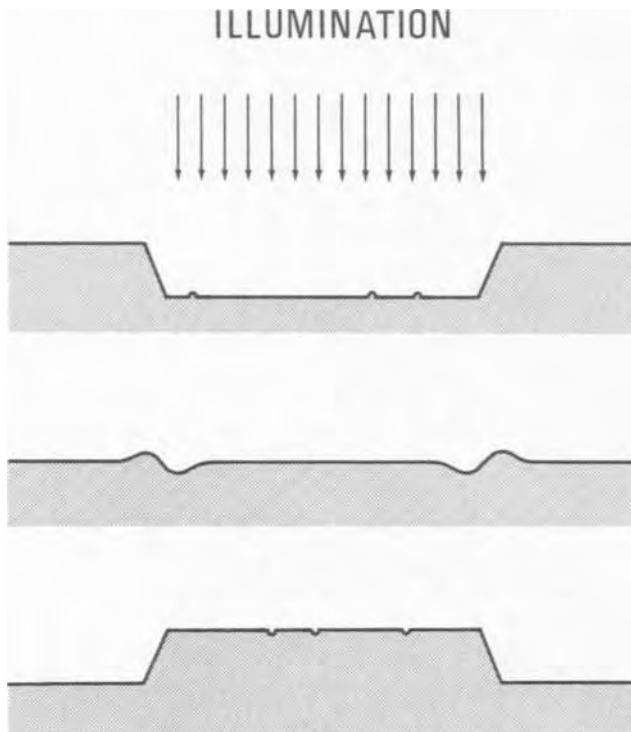


Fig. 1. Schematic diagram of photoetching effect on n-type (top), semi-insulating (middle), and p-type GaAs (bottom).

dislocations be observed while being revealed, but also occasional artifacts. It is fascinating to see some small particle move slowly across the sample surface, leaving behind an extended masking trail. A certain type of small cone is readily identified as the result of masking by tiny gas bubbles. Misinterpretation can, thus, be easily avoided.

Photoetching Results

A flat bottom hole is etched into the illuminated surface region of n-type GaAs, whereas a mesa structure forms on p-type samples (Fig. 1 and 2). The outline of such a photoetched structure is the same as that of the illuminated area, which again is an image of the diaphragm aperture (a regular dodecagon in this special case). If the diaphragm is replaced by a transparent slide, the GaAs surface may be shaped in a desired manner.

A flat bottom hole photoetched into n-type GaAs is shown in Fig. 2 (depth = 3 μm). Striations are shallow in comparison, but they still can be resolved

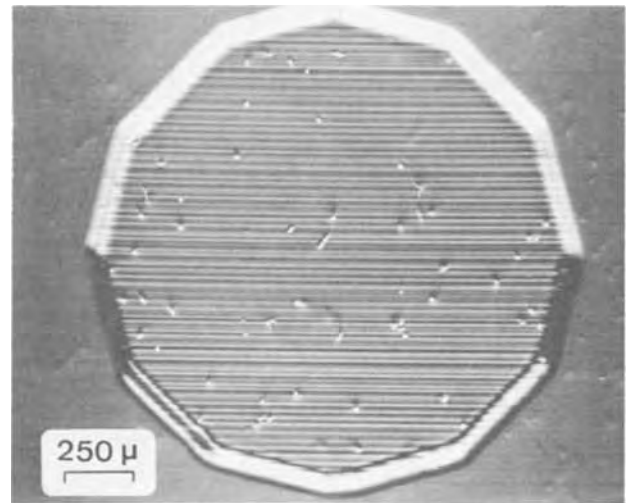


Fig. 2. Exposed 100-surface area of Sn-doped ($n = 8 \times 10^{17} \text{ cm}^{-3}$) CZ-GaAs, photoetched with $\text{H}_2\text{SO}_4\text{-H}_2\text{O}_2\text{-H}_2\text{O}$.

quantitatively by the interference microscope (Fig. 3 and 4). Worm-like lines are identified as dislocations by photoetching a 111(A)-surface, where most of these lines meet at or start from etch pits.

In many cases, the vertical dimension of etched dislocation lines is smaller than 200 \AA , so they do not show up in the etch profile (Fig. 4). In Nomarski contrast, however, such lines with a vertical extension of no more than some 10 monolayers cannot only be discerned, but one can also safely distinguish between protruding and recessed dislocation lines by comparing their bright-dark sequence with that of known structures, e.g., scratches. As a rule dislocations are elevated on n-type, and deepened on p-type GaAs; i.e., they are of the opposite sign as that of the dodecagon itself. This behavior is indicated in Fig. 1. Exceptions to the rule were found in two Cr-doped samples where the chromium content was not large enough to make them semi-insulating. Although these samples were of a low resistivity n-type, dislocation lines were deepened just as in genuine semi-insulating GaAs. An explanation might be that the chromium content was used up in forming a Cottrell atmosphere around dislocations, rendering the rest of the crystal essentially undoped.

Measured widths of etched dislocation lines were found to vary between less than 1 μm up to more than 50 μm . (If exposure time is kept short, there is no danger of measuring "memories" of dissolved dislocations.) In some crystals with resistivities between 10

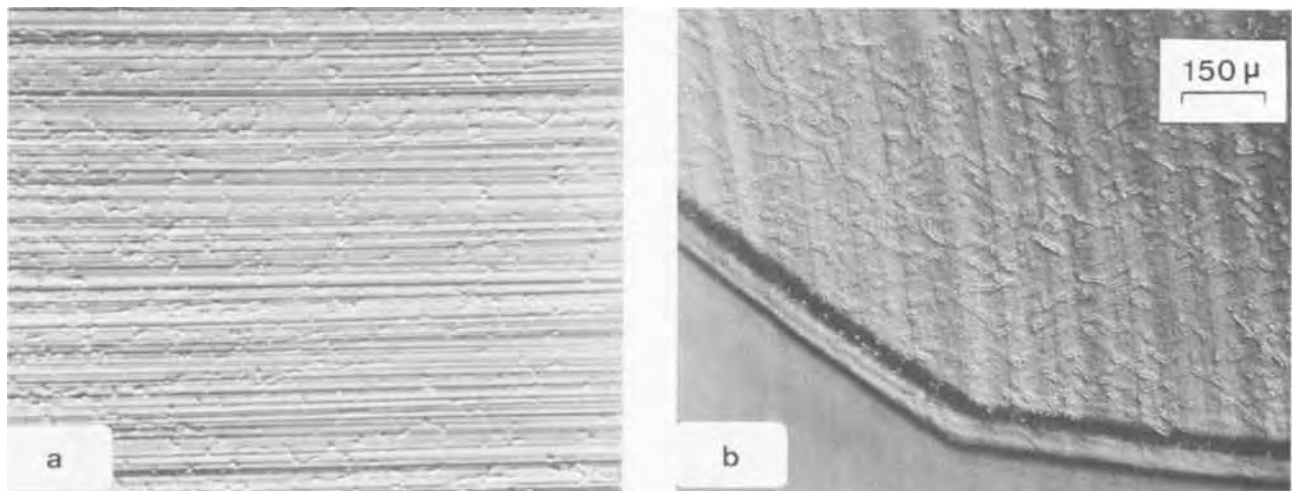


Fig. 3. Photoetched 100-surface of GaAs showing striations and dislocation lines: a, Zn-doped ($p = 8 \times 10^{18} \text{ cm}^{-3}$) FZ-GaAs; b, Te-doped ($n = 1 \times 10^{18} \text{ cm}^{-3}$) CZ-GaAs.

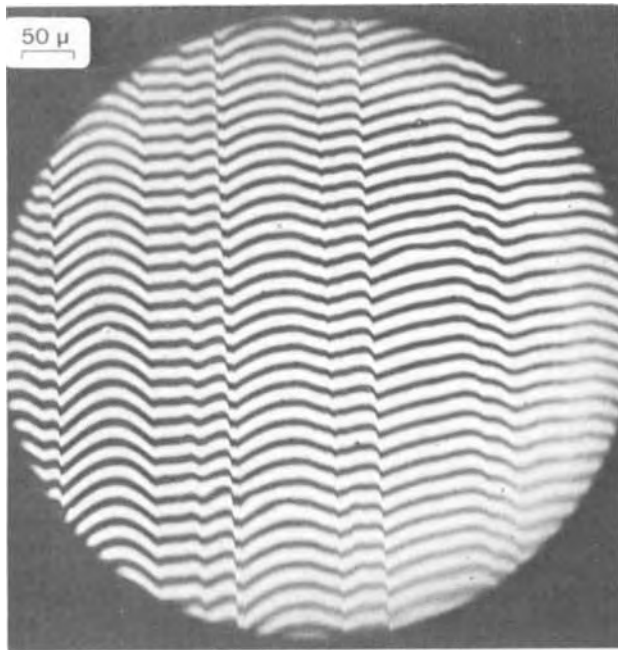


Fig. 4. Interference photomicrograph ($\lambda/2 = 270$ nm) of etch profile representing striations.

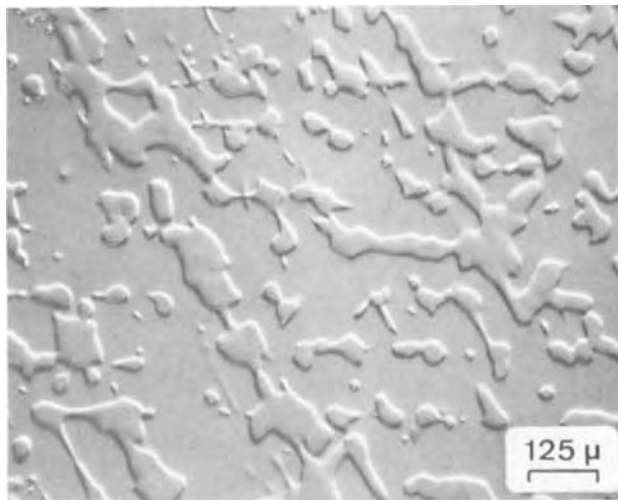


Fig. 5. Photoetched 111B-surface of undoped 200 ohm cm GaAs

and 1000 ohm-cm the width of the etched dislocation lines was comparable to their visible length (Fig. 5). Such structures might be at least one of the reasons for the rather low mobilities usually encountered in this resistivity range. In these and several other cases, dislocation cores and halos could be distinguished; details of this kind have been described earlier by Shaw and Thornton in their cathodoluminescence work (5).

In order to obtain a relation between etch rate and doping level, meticulous care had to be employed in preparing the $H_2SO_4-H_2O_2-H_2O$ -solution, since the method of preparation and the time elapsed since preparation of the etchant were found to have considerable influence on the etching rate. (The method of preparing the etchant is not critical, as long as only qualitative information is required.) Cold sulfuric acid was added dropwise to the cooled hydrogen peroxide solution in such a way that the temperature did not rise above $25^\circ C$. Subsequently, the H_2O_2 -content of the etchant was controlled by means of permanganate titration. Measured heights (+) and depths (-) of illuminated dodecagons relative to their unilluminated surroundings are listed in Table I. These photoetching rates agree well with the general impression gained

Table I. Etch differences between illuminated and dark regions of photoetched GaAs samples. Exposure time 10 min.

Sample	Type	Carriers, cm^{-3}	Mobility, $cm^2/Vsec$	Relative height	
				1st run μm	2nd run μm
1	n	9×10^{17}	3400	-2.45	-2.25
2	n	2×10^{17}	3100	-4.75	-5.25
3	n	8×10^{16}	3900	-4.1	-4.1
4	p	2×10^{17}	240	+3.9	+3.3
5	p	7×10^{16}	90	+2.8	+2.6

from the results on more than 300 GaAs samples; the absolute value of the etch difference increases with the decreasing doping level as long as the carrier concentration is not lower than about $10^{17} cm^{-3}$.

From Fig. 6 it can be seen that the photoetching rate is strongly dependent on the incident light intensity. Because of the considerable "chemical" etch rate of GaAs in an oxidizing etchant, low light intensities will have no noticeable influence. Illumination in these experiments was, therefore, selected for sufficient intensity so that the etch rate of n-GaAs was more than doubled by the influence of light. (Accurate measurements were restricted to the step height between the illuminated and the unilluminated area.)

Light intensity cannot, however, be increased indefinitely. If the etch rate is too fast, numerous small pyramids of random orientation suddenly form on the illuminated surface area of n-type samples after several seconds or minutes of photoetching. These pyramids look exactly like the ones observed by Yeh and Blakeslee (18) that have been identified by Kyser and Millea (19) as As_2O_3 precipitated from the super-saturated etchant. This explanation makes it clear why pyramids of this type also used to develop on samples with very fast etch rates (e.g., sample 2 in Table I), or during attempts to photoetch flat bottom holes deeper than $20 \mu m$ by prolonged exposure.

Photovoltage Measurement

Photoetching in dilute electrolytes has been described by Haisty (17) as an electrochemical process being driven by surface photovoltage. By separating illuminated and unilluminated surface regions, and by measuring the open circuit voltage (and short circuit current) between them, it could be shown that this picture also applies to the present case of photoetching in an oxidizing etchant.

Photovoltage measurements were designed so as to simulate photoetching. For this reason, another part

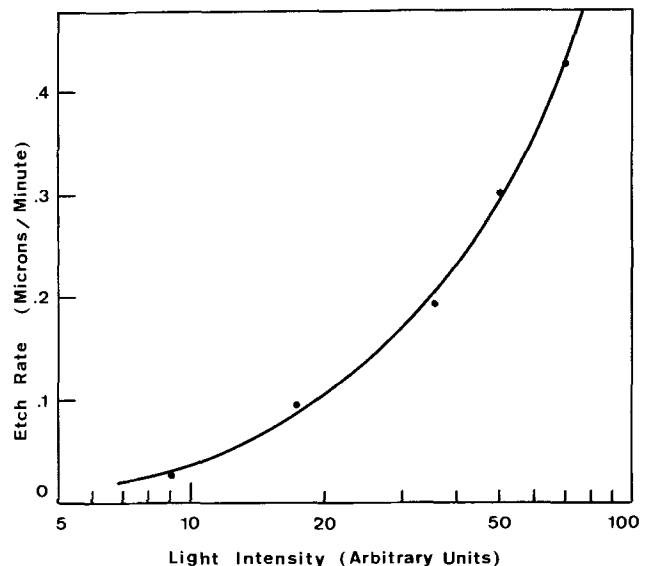


Fig. 6. Photoetching rate of Te-doped GaAs ($n = 4 \times 10^{17} cm^{-3}$) in $H_2SO_4-H_2O_2-H_2O$ (3:1:1) as a function of light intensity.

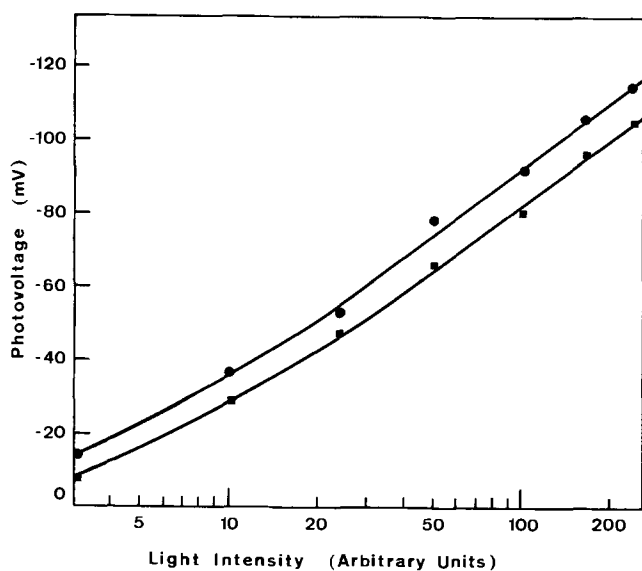


Fig. 7. Photovoltage of p-type GaAs electrodes as a function of light intensity (●, $p = 2 \times 10^{18} \text{ cm}^{-3}$; ■, $p = 4 \times 10^{18} \text{ cm}^{-3}$).

of the same slice or of an adjacent slice of GaAs was chosen as the counterelectrode. This was of great advantage since galvanic elements or other related voltages turned out to be negligible as compared to the photovoltage. Large area back contacts were applied to the electrodes so that the contact resistance was less than 1 ohm. For this purpose, numerous small dots of conductive silver paint were individually formed by capacitor discharge and then connected with each other and the leads. Subsequently, both GaAs electrodes were mounted on the same quartz block with a silicone resin,² leaving only those surface regions exposed to the etchant that were to be illuminated later. The quartz disk was then put into a petri dish just as described above. Initially, a Solartron voltmeter ($R_i = 10^{10}$ ohms) was used for measuring photovoltages, but as the typical source resistance was less than 100 ohms, a digital multimeter was also found adequate.

Photovoltage response to light intensity changes was instantaneous, which shows that photoetching is not influenced by thermal effects. Actually, no indication of temperature increase was observed when a thermocouple was illuminated in the same way. This is consistent with a temperature increase of less than 0.1°C as calculated by rough estimate.

As a result of these measurements in $\text{H}_2\text{SO}_4\text{-H}_2\text{O}_2\text{-H}_2\text{O}$ (3:1:1) solution, the unilluminated electrode was found to be positive in the case of n-type and negative in the case of p-type electrodes (Fig. 7). Contrary to Haisty's results (17), when he measured a large photovoltage on n-type and "essentially none" on p-type GaAs, photovoltages here were opposite in sign but comparable in value.

In the plot of photovoltage vs. logarithm of light intensity I , straight lines are obtained for large light intensities where the photovoltage is larger than kT/e (Fig. 7). This dependence may be described by the empirical formula for the photovoltage V_{ph}

$$V_{\text{ph}} = n \frac{kT}{e} \ln \frac{I}{I_0} \quad [1]$$

where n is a factor close to unity and I_0 an experimentally determined constant. No signs of saturation of the photovoltaic effect were observed in either n- or p-type GaAs in spite of a light intensity that pre-

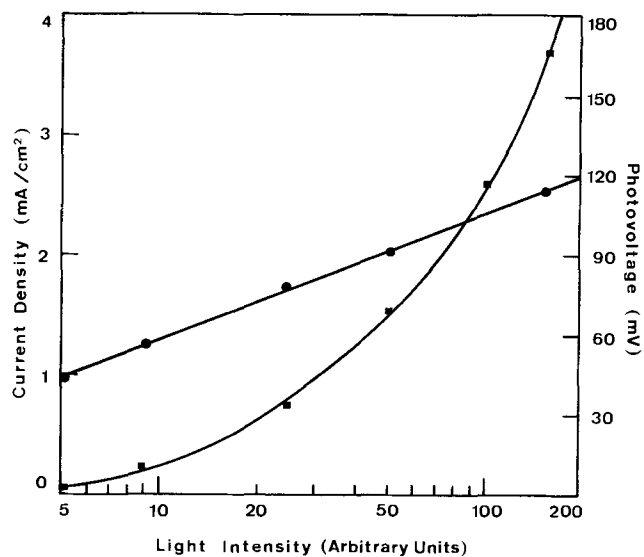


Fig. 8. Photovoltage (●) and short circuit current (■) vs. light intensity; same crystal as in Fig. 6, but different sample geometry.

sumably exceeded the one of Haisty (17) and that of Goldbach and Graff (20) by a factor of 100.

In Fig. 8, finally, photovoltage and short circuit current between two n-GaAs electrodes are plotted together vs. the light intensity incident on the smaller electrode. (The current curve has not been corrected for source resistance.) The short circuit current is very small at low light intensity; its increase with illumination is steep but still less than linear. A nearly linear dependence was obtained, however, when an external voltage of 0.3V or more was applied to the electrodes so that the illuminated n-GaAs electrode was positively biased.

Discussion

The photovoltage measurements described above have shown conclusively that selective photoetching in an oxidizing etchant is the result of the surface photovoltaic effect. This photovoltaic effect is based upon the separation of light-induced hole-electron pairs in the built-in electric field of the semiconductor surface.

A detailed account of the surface photovoltaic effect has been given by Goldbach and Graff (20). In their experiments on n-type GaAs, the illuminated surface was positive with respect to the bulk (the same can be concluded from the present results) and the photovoltage was a logarithmic function of light intensity similar, not only to Eq. [1], but also to the familiar formula describing the photovoltage of a silicon p-n junction (21). Goldbach and Graff have also determined the dependence of surface photovoltage on the carrier concentration; the photovoltage of n-type GaAs was found to decrease with increasing carrier concentration in a well defined way, so that surface photovoltage measurements could be used successfully for the contactless routine determination of carrier concentration (20). This dependence also provides the explanation for the etching results of Table I.

One necessary requirement for the surface photovoltaic effect is the existence of an electric field in the surface layer of the semiconductor. Depletion layers are the rule for GaAs of usual surface preparation (20), which means that the bands are bent upwards near the surface of n-type, and downwards near the surface of p-type GaAs. This original band-bending gives rise to a photovoltage of opposite sign that will eventually compensate it if the generation rate is high enough. The present photovoltage measurements in $\text{H}_2\text{SO}_4\text{-H}_2\text{O}_2\text{-H}_2\text{O}$ have shown that such a saturation

² Wacker Elastasil 07.

does not occur at photovoltages up to 0.12V in either n- or p-type GaAs. This result is consistent with a large density of deep surface states, and a surface Fermi level fixed near the middle of the gap. By means of the contact potential method, Atalla (22) has obtained a surface Fermi level pinned at about 0.76 eV above the valence band. Since this result was from GaAs samples cleaved in an ultra high vacuum, a direct comparison is, of course, impossible. Still, a semiconductor surface in the process of being carried off by a chemical etchant is easily reproducible and, in this respect, not inferior to a vacuum cleaved surface.

Photovoltage measurement in an oxidizing etchant is especially straightforward as compared to the small signal measurement in the air where capacitive coupling and phase-sensitive detecting have to be used (20). While the main function of the etchant is that of a translucent contact, the etchant also determines the density and distribution of surface states. The photovoltaic and photoetching behavior of GaAs in other ambients may, indeed, be very different (17) if the surface Fermi level is fixed near one band edge or if the density of surface states is low so the bands will be flat. On the other hand, the exact position of the Fermi level will be of little influence as long as the electric field strength is sufficient to collect virtually every generated charge carrier.

If an increased generation rate (e.g., illumination) leads to an increase of photovoltage, then an increased recombination rate must have the reverse effect. Lifetime and diffusion length are, therefore, to be considered primary reasons for the different photovoltages (and photoetching rates) encountered in different GaAs samples, provided that the surface recombination is not too high. Wittry and Kyser (23) have obtained a normalized surface recombination velocity (LS/D) of about 20; such a value would, indeed, drown the bulk recombination. Hilsum and Holeman (24), on the other hand, have reported a value of less than unity. In the present case of a semiconductor surface exposed to a polishing etchant, the surface recombination velocity should be especially low. The surface photovoltage is, however, not only an implicit but also a direct function of the carrier concentration; the carrier concentration has an additional direct influence as it enters into the expression for the space charge layer width. A rigorous theoretical treatment will be difficult because the optical absorption length, the diffusion length of minority carriers, and the width of the space charge layer are all of the same magnitude so that no simplification or neglect can be made. The existing theory of Goldbach and Graff (20) is, in fact, only in qualitative agreement with the experiment. The situation is somewhat more favorable with p-type GaAs where the diffusion length clearly exceeds the other two parameters.

Due to the surface photovoltaic effect, the illuminated surface area of an n-type sample is charged positively and, thus, becomes the anode of an electrochemical cell. The etching rate of this illuminated area is enhanced by anodic oxidation whereas the unilluminated area is etched more slowly than in the absence of illumination. The rate of photoetching is determined by the ion current flowing from the anode to the cathode portions of the surface (see Fig. 6 in comparison to Fig. 8).

This ion current will be sustained by the surface photovoltage but is also determined by the total series resistance of the following circuit: (i) the IR of the space-charge layer below the illuminated surface (this resistance will be small if the light intensity is high, otherwise the number of generated hole-electron pairs will limit the current); (ii) the GaAs bulk resistance; (iii) the resistance of the space-charge barrier below the large unilluminated surface area (this surface barrier will be biased in forward direction by the surface photovoltage); (iv) the resistance of the GaAs-

etching solution interface; (v) the ohmic resistance of the etchant; (vi) the resistance of the interface between the etching solution and the illuminated GaAs surface.

It will require further work to clarify the exact role of each resistance in this seemingly complex sequence. In the usual case of intensely illuminated n-type GaAs, the photocurrent is mainly limited at the (unilluminated) cathode. This can be seen by alternately illuminating the larger and the smaller one of two otherwise equal n-GaAs electrodes; the photocurrent is several times greater when the smaller electrode is illuminated. Although the cathode area is important for the total photocurrent, this does not lead to qualitative changes of etched structures within the illuminated surface area. The resistance of the large unilluminated electrode can be minimized by applying an additional negative bias, i.e., by reducing the cathode barrier (and, at the same time, increasing the anode barrier). This does not necessarily mean that the semiconductor space-charge layer is the sole reason for the cathodic barrier; Gerischer and Mattes (25) have been able to show that a considerable part of the voltage drop at a GaAs cathode can be across the Helmholtz double layer. In any case, a few tenths of a volt are sufficient to make the increase of the short circuit current nearly linear with illumination, as is characteristic of a p-n photodiode. This short circuit current is then essentially equivalent to the net generation rate within the illuminated surface barrier and can, therefore, not be increased beyond the saturation value even if the applied voltage is further increased.

The photovoltaic nature of photoetching makes it clear that zones of higher carrier concentration are etched as striation ridges on n-type GaAs and as striation valleys on p-type GaAs. For the case of n-type material, this conclusion disagrees with Dickhoff's model (13) but is in line with observations on other semiconductors. Vieweg-Gutberlet (26) reports that the chemical etching rate of heavily doped n-type silicon is distinctly slower than that of slightly doped samples. (According to Vieweg's technique, silicon samples are etched for several hours at ordinary room light.) A similar dependence has been recently obtained by Lichtensteiger, Witt, and Gatos (27) on InSb. They found that the "etching rate is a sensitive function of dopant concentration (it decreases with increasing Te concentration)." This may also be due to photoetching; but as comparable results of p-type semiconductors are not available, the possibility that the chemical etching attack is hampered by high dopant concentrations cannot be excluded either.

In semi-insulating GaAs, the anode and cathode are rudimentary (Fig. 1). Because of the high bulk resistivity, a sizable ion current can flow only at the contours of the illuminated area where anode and cathode sites are in immediate proximity to each other. Striations and dislocation lines within the illuminated area can still be recognized in most cases as an extremely shallow relief. The fine structure of the photoetched contour consists of a ridge and a ditch running parallel to each other. From the contour width, the sample resistivity may be roughly estimated. In semi-insulating material with n-type conductivity, the ditch will form on the illuminated side (Fig. 1). More than 20 semi-insulating samples (the conductivity type of which has been established by Hall effect measurement) were photoetched for comparison. The correct conductivity type was obtained in every single case. Apart from these, a "photoetching conductivity type" could be ascribed to a number of other semi-insulating samples where Hall effect results had been ambiguous. In semi-insulating GaAs, the Demer effect may possibly interfere with the photovoltaic effect. If this is the case, high resistivity p-type GaAs would appear to be high resistivity n-

type; no experimental evidence of this kind has been found, however.

Not the least merit of this selective photoetching is that it is a comparatively simple technique and requires little expenditure. It gives, nevertheless, a plastic and reliable picture of the homogeneity and perfection of GaAs.

Acknowledgments

The author is indebted to Professor H. J. Queisser for a critical review of the manuscript; to D. Reimann for many helpful discussions; to Miss C. Schreyer for performing the etching.

Manuscript received Feb. 3, 1972.

Any discussion of this paper will appear in a Discussion Section to be published in the June 1973 JOURNAL.

REFERENCES

- G. Ziegler and H. J. Henkel, *Z. Angew. Phys.*, **19**, 401 (1965).
- M. E. Drougard and J. B. Gunn, *This Journal*, **111**, 155C (1964).
- H. Salow and K. W. Benz, *Z. Angew. Phys.*, **19**, 157 (1965).
- H. C. Casey, Jr., *This Journal*, **114**, 153 (1967).
- D. A. Shaw and P. R. Thornton, *J. Mater. Sci.*, **3**, 507 (1968).
- C. Solbrig, Private communication.
- E. D. Jungbluth, *This Journal*, **112**, 580 (1965).
- E. S. Meieran, *J. Appl. Phys.*, **36**, 2544 (1965).
- A. M. Huber and G. Champier, Third International Symposium on Gallium Arsenide and Related Compounds, Aachen (1970).
- M. H. Pilkuhn and H. Rupprecht, *Trans. AIME*, **230**, 296 (1964).
- J. C. Marinace, *This Journal*, **110**, 1153 (1963).
- T. S. Plaskett and A. H. Parsons, *ibid.*, **112**, 954 (1965).
- J. A. M. Dickhoff, *Philips Tech. Rev.*, **25**, 441 (1963/64).
- G. R. Cronin, G. B. Larrabee, and J. F. Osborne, *This Journal*, **113**, 292 (1966).
- F. Vieweg-Gutberlet, *Solid-State Electron.*, **12**, 731 (1969).
- H. R. Winteler and U. Zimmerli, Unpublished.
- R. W. Haisty, *This Journal*, **108**, 790 (1961).
- T. H. Yeh and A. E. Blakeslee, *ibid.*, **110**, 1018 (1963).
- D. F. Kyser and M. F. Millea, *ibid.*, **111**, 1102 (1964).
- G. Goldbach and K. Graff, *Wiss. Ber. AEG-Telefunken*, **42**, 156 (1969).
- R. Wiesner, *Halbleiterprobleme*, **3**, 59 (1956).
- M. M. Atalla, "Mikroelektronik," Vol. 2, p. 123, Oldenbourg, Munich (1967).
- D. B. Wittry and D. F. Kyser, *J. Appl. Phys.*, **38**, 375 (1967).
- C. Hilsum and B. Holeman, Proceedings of the International Conference on Semiconductor Physics, Prague (1960).
- H. Gerischer and I. Mattes, *Z. Physik. Chem.*, **49**, 112 (1966).
- F. Vieweg-Gutberlet, Private communication.
- M. Lichtensteiger, A. F. Witt, and H. C. Gatos, *This Journal*, **118**, 1013 (1971).

A Limitation of the Pulsed Capacitance Technique of Measuring Impurity Profiles

A. R. LeBlanc, D. Dale Kleppinger, and J. P. Walsh

IBM Components Division, Essex Junction, Vermont 05452

ABSTRACT

This paper reports the results of an investigation of a limitation of the pulsed-capacitance technique for measuring impurity profiles in semiconductors (1). The limitation arises from the neglect of the majority carriers in the derivation of the previously published equation. The results, for the mathematically tractable example of a uniform profile, show that there is a minimum depth at which the technique is accurate and that this depth is a function of impurity concentration—decreasing with increasing concentration. This is a fundamental limitation of the technique as opposed to an instrumentation limitation.

A technique for determining impurity profiles in semiconductors using MOS capacitors has recently been described by Van Gelder and Nicollian (1). Their technique, based on the depletion approximation, utilizes the high-frequency capacitance of a capacitor biased in the depletion condition by short duration voltage pulses to obtain plots of $1/C^2$ vs. gate voltage. The slopes of these curves are expected to be proportional to the impurity concentration at the edge of the space charge layer. One simple check on the range of validity of the technique is to calculate the impurity profile of a uniformly doped substrate using the final equations of their paper. This calculation is straight forward since the capacitance of an MOS capacitor with uniform doping has a well-known, exact, closed-form solution (2).

The differential capacitance of a uniformly doped semiconductor space charge region is (2)

Key words: pulsed MOS measurements, silicon impurity distribution, C-V measurements, impurity profile, technique limitation.

$$C_s = \frac{dQ_s}{d\psi_s} = \frac{\epsilon_s}{L_D} \frac{(1 - e^{-\beta\psi_s}) + \frac{n_{po}}{p_{po}} (e^{\beta\psi_s} - 1)}{F\left(\beta\psi_s, \frac{n_{po}}{p_{po}}\right)} \quad [1]$$

where ϵ_s is the permittivity of silicon, β is q/KT , ψ_s is the semiconductor surface potential relative to the bulk of the semiconductor, p_{po} is the equilibrium hole concentration in the bulk of the semiconductor, n_{po} is the equilibrium electron concentration in the bulk of the semiconductor, L_D is the extrinsic Debye length in the semiconductor, and

$$F\left(\beta\psi_s, \frac{n_{po}}{p_{po}}\right) = \left[e^{-\beta\psi_s} + \beta\psi_s - 1 + \frac{n_{po}}{p_{po}} (e^{\beta\psi_s} - \beta\psi_s - 1) \right]^{1/2} \equiv F \quad [2]$$

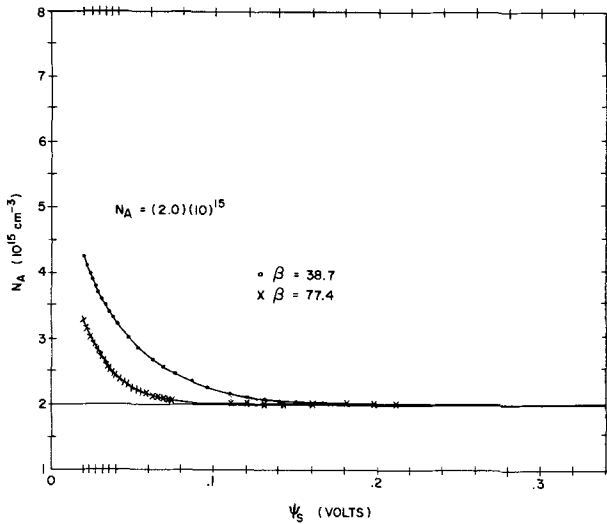


Fig. 1. The calculated impurity concentration as a function of surface potential for $\beta = 38.7$ and 77.4 , and an assumed uniform concentration of $2 \times 10^{15} \text{ cm}^{-3}$.

The total measured capacitance of the MOS capacitor is

$$C = \frac{C_o C_s}{C_o + C_s} \quad [3]$$

where C_o is the oxide capacitance.

The relationship between gate voltage and the capacitance measured in deep depletion that yields the impurity profile is given by Van Gelder and Nicollian (1) as

$$N(W) = \frac{2}{q \epsilon_s \frac{d}{dV} \left(\frac{1}{C^2} \right)} \quad [4]$$

$$N(W) = \frac{-C^3}{q \epsilon_s \left(\frac{C_o}{C_o + C_s} \right)^2 \frac{\beta \epsilon_s}{L_D F^2} \left\{ F \left(e^{-\beta \psi_s} + \frac{n_{po}}{p_{po}} e^{\beta \psi_s} \right) - \frac{1}{2F} \left[1 - e^{-\beta \psi_s} + \frac{n_{po}}{p_{po}} (e^{\beta \psi_s} - 1) \right]^2 \right\} + \frac{\epsilon_s}{L_D C_o F} \left[1 - e^{-\beta \psi_s} + \frac{n_{po}}{p_{po}} (e^{\beta \psi_s} - 1) \right]} \quad [11]$$

which for purposes of calculation is more conveniently written as

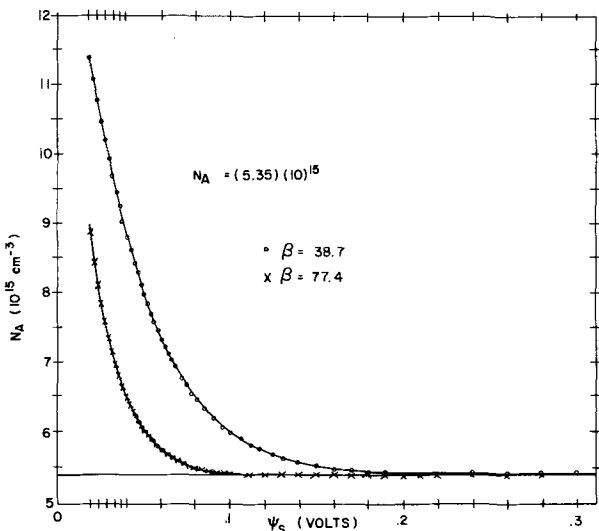


Fig. 2. The calculated impurity concentration as a function of surface potential for $\beta = 38.7$ and 77.4 , and an assumed uniform concentration of $5.35 \times 10^{15} \text{ cm}^{-3}$.

$$N(W) = \frac{-C^3}{q \epsilon_s \frac{dC}{dV}} \quad [5]$$

where V is the applied voltage. The derivative in Eq. [5] is given by

$$\frac{dC}{dV} = \frac{dC}{d\psi_s} \frac{d\psi_s}{dV} \quad [6]$$

From Eq. [1] and [3]

$$\frac{dC}{d\psi_s} = \left(\frac{C_o}{C_s + C_o} \right)^2 \frac{\beta \epsilon_s}{L_D F^2} \left\{ F \left(e^{-\beta \psi_s} + \frac{n_{po}}{p_{po}} e^{\beta \psi_s} \right) - \frac{1}{2F} \left[1 - e^{-\beta \psi_s} + \frac{n_{po}}{p_{po}} (e^{\beta \psi_s} - 1) \right]^2 \right\} \quad [7]$$

The voltage drop across the MOS capacitor is

$$V = \frac{-Q_s}{C_o} + \psi_s = \frac{\epsilon_s E_s}{C_o} + \psi_s \quad [8]$$

where the electric field at the silicon surface is

$$E_s = \frac{2}{\beta L_D} F \left(\beta \psi_s, \frac{n_{po}}{p_{po}} \right) \quad [9]$$

Differentiating Eq. [8] yields

$$\frac{d\psi_s}{dV} = \frac{1}{1 + \frac{\epsilon_s}{L_D C_o F} \left[1 - e^{-\beta \psi_s} + \frac{n_{po}}{p_{po}} (e^{\beta \psi_s} - 1) \right]} \quad [10]$$

Finally, combining Eq. [5], [6], [7], and [10] yields

$$N(W) = \frac{-C^3}{q \epsilon_s \left(\frac{C_o}{C_o + C_s} \right)^2 \frac{\beta \epsilon_s}{L_D F^2} \left\{ F \left(e^{-\beta \psi_s} + \frac{n_{po}}{p_{po}} e^{\beta \psi_s} \right) - \frac{1}{2F} \left[1 - e^{-\beta \psi_s} + \frac{n_{po}}{p_{po}} (e^{\beta \psi_s} - 1) \right]^2 \right\} + \frac{\epsilon_s}{L_D C_o F} \left[1 - e^{-\beta \psi_s} + \frac{n_{po}}{p_{po}} (e^{\beta \psi_s} - 1) \right]} \quad [11]$$

Equation [11] gives the doping level as a function of surface potential. The depth of the space charge region can be approximated by using the depletion approximation to obtain

$$W = \sqrt{\frac{2\epsilon_s \psi_s}{q N_A}} \quad [12]$$

The impurity concentration as a function of surface potential is plotted in Fig. 1, 2, and 3 using Eq. [11] for doping concentrations of 2×10^{15} , 5.35×10^{15} , and $8 \times 10^{15} \text{ cm}^{-3}$, respectively. In each figure curves are plotted for temperatures of 150° and 300°K . At surface potentials between 0 and 0.10V, these curves predict levels larger than the assumed uniform doping.

For surface potentials less than 0.1V, the pulsed technique for profile measurements appears to be in significant error.

Equations [11] and [12] have been combined to plot impurity concentrations as a function of depletion layer depth in Fig. 4, 5, and 6 for the same uniform doping levels and temperatures that were used in Fig. 1, 2, and 3. Again, accuracy of the technique is better for more heavily doped substrates and at lower temperatures. However, at depths shallower than 2000Å, the predictions of the technique deviate substantially from the assumed profile.

For analysis of the equations at surface potentials close to or at zero, the series approximation to the dif-

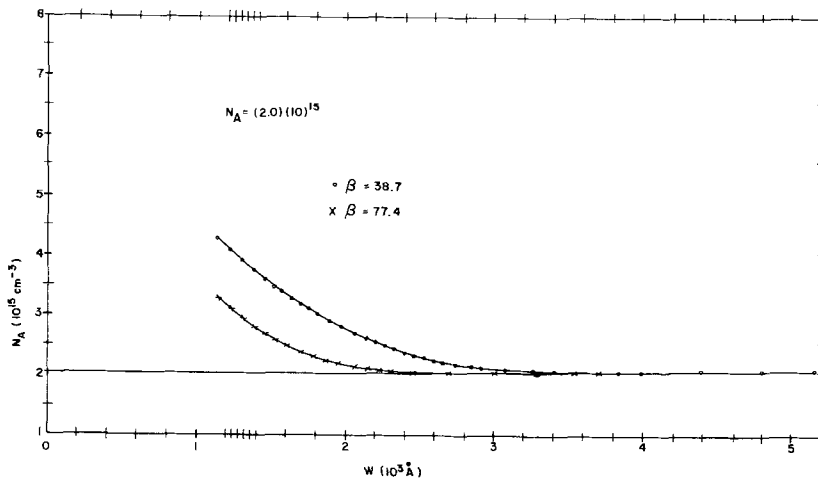


Fig. 4. The calculated impurity concentration as a function of the depletion layer depth for \$\beta = 38.7\$ and \$77.4\$, and an assumed uniform concentration of \$2 \times 10^{15} \text{ cm}^{-3}\$.

ferential capacitance can be utilized. This approach leads to

$$C_s = \frac{\epsilon_s}{L_D} \frac{\sum_0^\infty \frac{(\beta\psi_s)^i}{(i+1)!} \left[(-1)^{i+2} + \frac{n_{po}}{p_{po}} \right]}{\left\{ \sum_0^\infty \frac{(\beta\psi_s)^i}{(i+2)!} \left[(-1)^{i+2} + \frac{n_{po}}{p_{po}} \right] \right\}^{1/2}} \quad [13]$$

$$\frac{dC_s}{d\psi_s} = \frac{\epsilon_s}{L_D} \left\{ \frac{\left[\sum_0^\infty i \frac{\beta^i \psi_s^{i-1}}{(i+1)!} \left((-1)^{i+2} + \frac{n_{po}}{p_{po}} \right) \right]}{\left[\sum_0^\infty \frac{\beta^i \psi_s^i}{(i+2)!} \left((-1)^{i+2} + \frac{n_{po}}{p_{po}} \right) \right]^{1/2}} \right. \\ \left. \frac{\left[\sum_0^\infty \frac{\beta^i \psi_s^{i-1}}{(i+1)!} \left((-1)^{i+2} + \frac{n_{po}}{p_{po}} \right) \right] \left[\sum_0^\infty i \frac{\beta^i \psi_s^{i-1}}{(i+2)!} \left((-1)^{i+2} + \frac{n_{po}}{p_{po}} \right) \right]}{2 \left[\sum_0^\infty \frac{\beta^i \psi_s^i}{(i+2)!} \left((-1)^{i+2} + \frac{n_{po}}{p_{po}} \right) \right]^{3/2}} \right\} \quad [15]$$

where \$i\$ is the summation index. At \$\psi_s = 0\$, this formulation reduces to

$$C_s|_{\psi_s=0} = \frac{\sqrt{2} \epsilon_s}{L_D} \left(1 + \frac{n_{po}}{p_{po}} \right)^{1/2} \quad [14]$$

which extends Sze's (2) equation (Eq. [21], p. 432) to the case where \$n_{po}/p_{po}\$ is not negligible with respect to unity.

Equation [13] enables us to write the following expression

which can be used in Eq. [6]. At \$\psi_s = 0\$, Eq. [15] reduces to

$$\left. \frac{dC_s}{d\psi_s} \right|_{\psi_s=0} = \frac{\epsilon_s}{L_D} \left\{ \frac{\left(\frac{\sqrt{2} \beta}{3} \right) \left(-1 + \frac{n_{po}}{p_{po}} \right)}{\left(1 + \frac{n_{po}}{p_{po}} \right)^{1/2}} \right\} \quad [16]$$

The remaining factor in Eq. [6], \$d\psi_s/dV\$, can be calculated from

$$V = V_{ox} + \psi_s \quad [17]$$

and

$$dQ = C_{ox} dV_{ox} = CdV \quad [18]$$

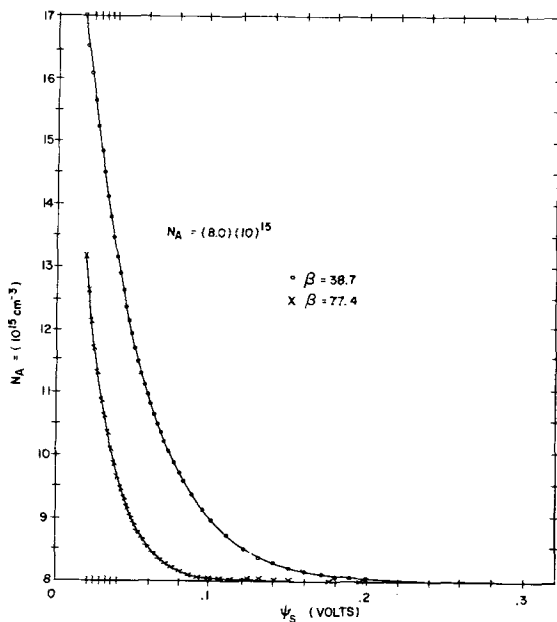


Fig. 3. The calculated impurity concentration as a function of surface potential for \$\beta = 38.7\$ and \$77.4\$ and an assumed uniform concentration of \$8 \times 10^{15} \text{ cm}^{-3}\$.

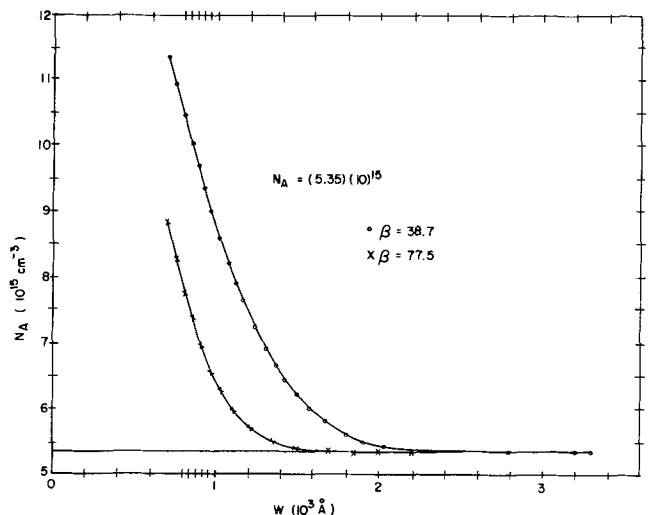


Fig. 5. The calculated impurity concentration as a function of the depletion layer depth for \$\beta = 38.7\$ and \$77.4\$, and an assumed uniform concentration of \$5.35 \times 10^{15} \text{ cm}^{-3}\$.

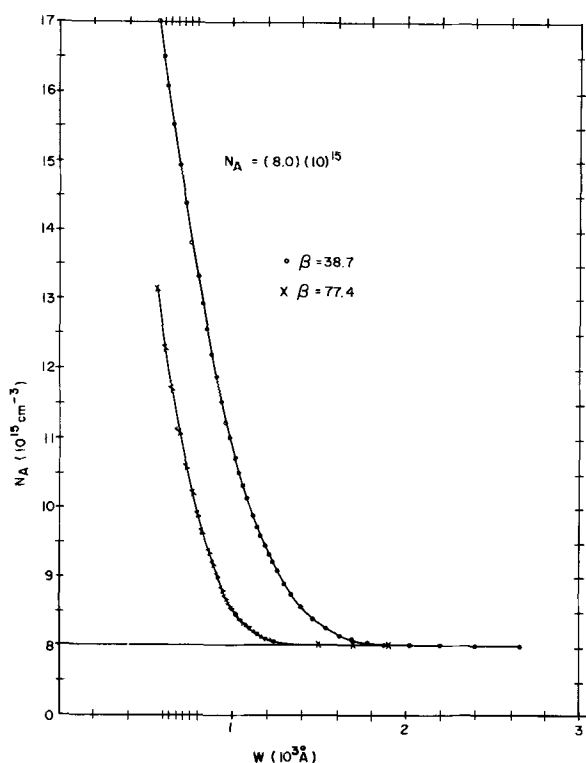


Fig. 6. The calculated impurity concentration as a function of the depletion layer depth for $\beta = 38.7$ and 77.4 , and an assumed uniform concentration of $8.0 \times 10^{15} \text{ cm}^{-3}$.

Thus

$$\frac{d\psi_s}{dV} = 1 - \frac{C}{C_0} = \frac{C_0}{C_0 + C_s} \quad [19]$$

Equations [15] and [19] show that the factors that enter the denominator of Eq. [5] through Eq. [6] are nonzero for all ψ_s , including $\psi_s = 0$ (cf. Eq. [16]). Therefore, Eq. [5] will predict a well-behaved $N(W)$.

However, using Eq. [14] and [16] to evaluate N at $\psi_s = 0$ results in

$$N(0) = 3N_A \quad [20]$$

which contradicts our assumption of uniform doping.

In summary, the technique of Van Gelder and Nicollian (1) does not properly predict the profile for small values of ψ_s since, as they acknowledge, the free carriers that they have neglected become important. They state that this occurs for $\psi_s \approx 0.05\text{V}$. Our calculations, which include the free carriers, are useful in visualizing this effect for the case of uniform doping. Figures 1, 2, and 3 show that at 0.05V the predicted profile is in error by 30-50% for the doping levels shown. [Figures 4, 5, and 6 show that the usable minimum depth decreases (improves) as the substrate doping increases. Thus, the technique is usable nearer the surfaces of more heavily doped substrates.]

Furthermore, the limitation related to interface states which Van Gelder and Nicollian point out can be mitigated by increasing the a-c measurement frequency and decreasing the amplitude of the signal. However, by using the example of uniform doping, we have shown that the contributions of the free carriers provide an underlying limitation on the minimum depth at which the impurity concentration can be usefully determined by this technique. This limitation exists even in the absence of the effects of interface states.

Acknowledgment

The authors wish to thank Arnold Berman for a discussion on the approach used and Paul Hwang for computer programming support.

Manuscript submitted Jan. 4, 1972; revised manuscript received April 13, 1972.

Any discussion of this paper will appear in a Discussion Section to be published in the June 1973 JOURNAL.

REFERENCES

1. W. Van Gelder and E. H. Nicollian, *This Journal*, **118**, 138 (1971).
2. S. M. Sze, "Physics of Semiconductor Devices," Wiley-Interscience, New York (1969).

Vapor Deposition and Properties of Binary Arsenosilicate Glass Films

J. Wong

General Electric Corporate Research and Development, Schenectady, New York 12301

ABSTRACT

The deposition characteristics of an argon-diluted $\text{SiH}_4\text{-AsCl}_3\text{-O}_2$ reaction system for the chemical vapor deposition of binary arsenosilicate glass films have been studied systematically as a function of substrate temperature and flow rates of the reactants. Film composition in the range 0 to 20 mole per cent (m/o) As_2O_3 can be controlled reproducibly at deposition rates as high as 1000Å min^{-1} . Properties such as composition uniformity, etch rate, d-c dielectric strength, and moisture resistance have been measured and their compositional dependence determined.

In an earlier communication (1) the chemical vapor deposition of binary arsenosilicate glasses in the range 0-20 mole per cent (m/o) As_2O_3 from a one-liquid source system consisting of argon-diluted mixtures of SiH_4 , O_2 , and AsCl_3 vapor has been described. Preliminary heat treatments of these binary films deposited on silicon showed that the so-far reported "glass damage" in the process of solid-to-solid state

Key words: CVD, arsenic diffusion sources into silicon.

diffusion of arsenic into silicon (1-3) is strongly dependent on the composition of the arsenosilicate films; the higher the concentration of As_2O_3 , the lower the temperature required to bring about the damage.

The object of the present paper is twofold: (i) to investigate systematically deposition characteristics such as deposition rate and chemical composition of the deposited films for the $\text{SiH}_4\text{-O}_2\text{-AsCl}_3\text{-Ar}$ system as a function of substrate temperature and flow rates of

the reactant gases; and (ii) to determine film properties such as composition uniformity, etch rate, d-c dielectric strength, and moisture resistance, that are important in the consideration of using arsenosilicate glass films as n-type solid-state diffusion sources into silicon in the planar technology for constructing microelectronic devices and circuits.

Experimental

Materials.—One ohm-cm p-type¹ (100)-oriented silicon wafers, 2.5 cm in diameter and 0.5 cm thick were used as substrates for film deposition. These were heavily etched in a conc. HNO₃-conc. HF solution (3:1 by volume) and rinsed thoroughly in distilled water prior to deposition. The silane source used was semiconductor grade obtained from the Matheson Company as a calibrated 1% mixture in argon. Ultrapure AsCl₃ liquid from Alpha Inorganics was used. All other etching solutions, e.g., HNO₃, HCl, HF, and NH₄F were either reagent or semiconductor grade.

Deposition apparatus.—The gas-flow system and vertical reactor used in the present study have been described elsewhere (1). The temperature of the hot stage in the vertical reactor was controlled to $\pm 5^\circ$ at 300°C and $\pm 10^\circ$ at 450°C during deposition. All flowmeters were calibrated with the respective gases or mixtures using two Brooks flow calibrators having capacities of 0-70 cc and 0-1000 cc. Except for the dielectric measurements, all films studied were of the order of 8000 Å thick.

Furnace for heat-treatment.—A conventional horizontal diffusion furnace consisting of an electrically heated fused quartz tube having a projecting side arm for sample loading was used. Purified argon was used to purge the system at a few cc min⁻¹ while not in use, and at 470 cc/min (~ 1 ft³ hr⁻¹) while a sample was being heat-treated. The temperature of the constant temperature zone (1½ in. long) was controlled to within 3°C or better at 1100°C. Typical heat-treatment times were of the order of 10 min.

Growth rate and etch rate measurements.—For convenience, both the growth rate of films during deposition and the etch rate were performed by visual observation of the color of the glass film under a daylight fluorescent lamp. The color chart of Pliskin and Conrad (4) for thermally grown SiO₂ was used to evaluate the thickness of the films. The actual thickness of the arsenosilicate film may be 5% lower than the one obtained by color because of the higher refractive indices of arsenosilicate glasses (~ 1.55 , depending on composition, compared to a value of 1.46 for thermal SiO₂). For deposition rate determinations, the color of the film and hence its thickness was recorded continuously with time during the deposition while the samples were in the reactor. The deposition rates were calculated from the slopes of these growth curves. For etch rate measurements, the initial thickness of the film was noted from deposition. The film was totally immersed into the etchant with constant agitation (by means of forceps holding the wafer) for a given period of time, then rinsed in distilled water dried with acetone. The magnitude of the slope of the dissolution curve gives the etch rate.

Because of the strong dependence of etch rate on the composition of the glass in a given etching solution, three solutions were used in order to make high As₂O₃ content glasses measurable within the time scale of the experiment. A buffered HF (BHF) solution consisting of a mixture of conc. NH₄F solution and conc. HF (10:1 by volume) was used for glasses varying from 0-6 m/o As₂O₃. A second solution consisting of a 1:10 (by volume) mixture of the above BHF solution and distilled water was used for glasses varying from 0-16 m/o As₂O₃, and a third 1:100 BHF:H₂O solution

was used for glasses having concentration greater than 14 m/o As₂O₃. Overlappings of glass composition allowed the etch rates of the same glass to be compared in different solutions.

Determination of film composition.—The composition of as-deposited films were determined nondestructively from the infrared spectra by calculating the optical density ratio of the As-O band at 930 cm⁻¹ and the Si-O band at 1060 cm⁻¹ and using a predetermined IR ratio-composition calibration curve (1). A Perkin-Elmer 457 double beam spectrophotometer was used to record the IR spectra. Reflection loss due to the silicon substrate were compensated for in the reference beam by a silicon wafer of the same resistivity and type.

Dielectric strength.—For dielectric strength measurements glass films of about 2000 Å thick and of various compositions were deposited on n-type silicon wafers. MOS capacitors were constructed and consisted of a 5000 Å top layer of sputtered Mo that was delineated by standard lithographic techniques to a pattern of 0.45 mm diameter circular dots. The current-voltage characteristics of these capacitors at room temperature were measured with a Tektronix transistor curve tracer. Twenty capacitors were measured per sample. The reported strength for each sample is the arithmetic average of these 20 maximum voltages without breakdown divided by the film thickness measured ellipsometrically.

Results

Deposition rate and film composition.—Two parameters are of interest in the preparation of multicomponent films by chemical vapor deposition. These are the deposition rate and film composition. For the deposition of binary arsenosilicate glasses using the SiH₄-AsCl₃-O₂-Ar reaction system, the above parameters were studied systematically as a function of the substrate temperature during deposition and flow rates of the reactant and carrier gases.

In Fig. 1 the amount of As₂O₃ incorporated into the film is plotted as a function of substrate temperature at two different O₂ flow rates while the flow rates of the remaining gases were held constant. The composition is little or not affected by the O₂ flow rate (for which the molar ratio of O₂ to total SiH₄ and AsCl₃ was always greater than 10:1). The deposition rate, however, is strongly dependent on the O₂ flow rate as shown in Fig. 2 in which an Arrhenius-type plot of log deposition rate vs. reciprocal absolute temperature (of the substrate) is given.

In Fig. 3, the deposition rate is plotted as a function of the flow rate of Ar into the AsCl₃ liquid at substrate temperatures of 300°, 350°, and 450°C while the flow rates of the Ar carrier gas and SiH₄ were held constant. Note the lower flow rate of O₂ used at 300°C. At all three temperatures, the deposition rate increases initially with increasing AsCl₃ introduced into the reactor and decreases at higher Ar flow rates into AsCl₃. The chemical composition of the resultant film shows a similar but more systematic trend as shown in Fig. 4. The concentration of As₂O₃ in the glass increases initially with the amount of AsCl₃ introduced into the reactor and decreases again at high Ar flow rates into the AsCl₃ source. An interesting feature is that the lower the substrate temperature, the greater is the amount of As₂O₃ incorporated into the glass film. The dotted line in Fig. 4 is the film composition calculated from the molar ratio of AsCl₃ to SiH₄ in the reaction mixture assuming stoichiometric oxidation of both reactants.

The deposition parameters were also studied as a function of SiH₄ flow rate at 450°C and at constant flow rates of Ar, O₂, and Ar into AsCl₃. The deposition rate increases monotonically with SiH₄ flow rate as shown in Fig. 5a while the As₂O₃ content decreases monotonically as shown in Fig. 5b. The dotted line in

¹ For dielectric strength measurements, n-type wafers of similar resistivity and orientation were used.

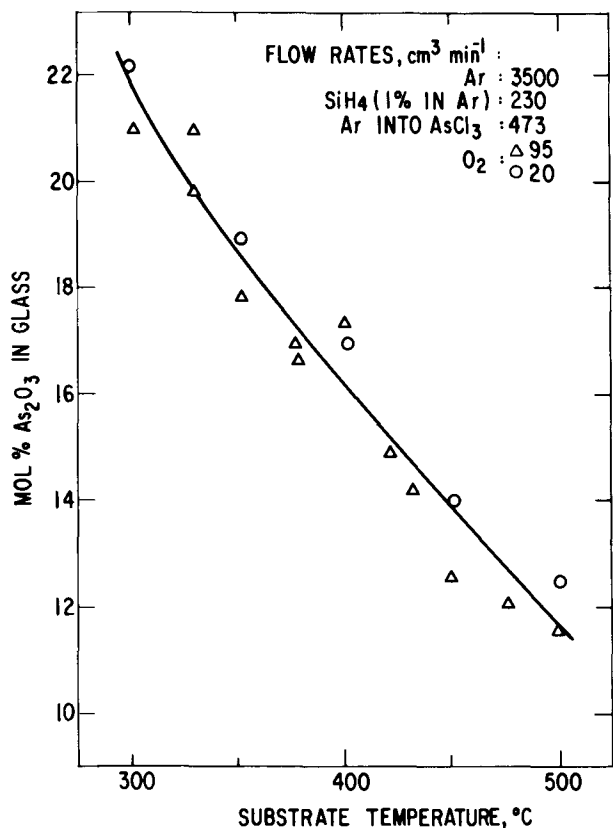


Fig. 1. Glass composition vs. substrate temperature at two given sets of flow rates of reactants.

Fig. 5b represents the film composition calculated from the molar concentration of SiH_4 and AsCl_3 in the reaction mixture assuming stoichiometric oxidation of each component.

Etch rate.—In Fig. 6, the etch rate of as-deposited arsenosilicate films is plotted as a function of As_2O_3 content in the films in various HF solutions. In a standard buffered HF (BHF) solution glasses in the range 0-6 m/o As_2O_3 deposited at a substrate temperature

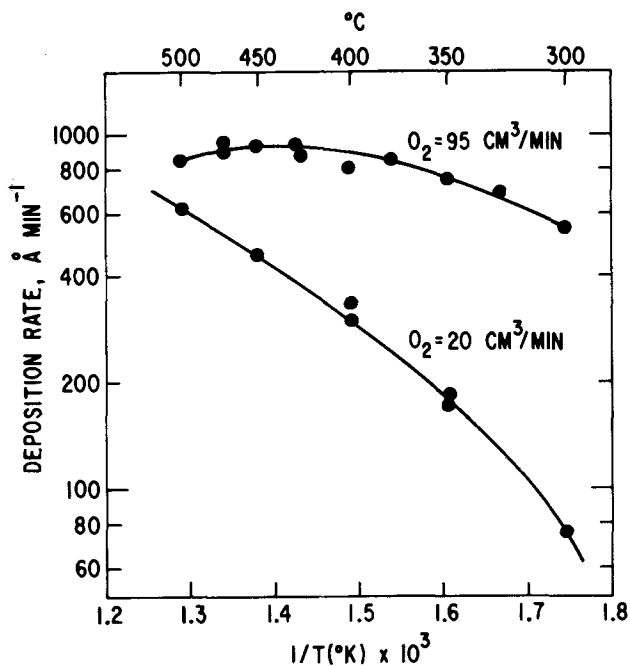


Fig. 2. Deposition rate vs. reciprocal temperature of substrate at two flow rates of O_2 . All other flow rates are given in Fig. 1.

of 450°C show an approximate twofold decrease in the etch rate in going from as-deposited films [curve (a), Fig. 6] to the same films after heat-treatment in Ar at 800°C for 10 min [curve (b), Fig. 6]. Of interest, too, is the dependence on the substrate temperature during deposition of the etch rate in a 1:100 (by volume) solution of BHF and water of as-deposited films. Films deposited at 300°C [curve (e), Fig. 6] have higher etch rates and a greater etch rate dependence on film composition than those deposited at 450°C [curve (f), Fig. 6].

Composition uniformity.—The composition uniformity of as-deposited films have been studied as a function of film thickness (i.e., layer uniformity) as well as the position along a diameter across the film surface

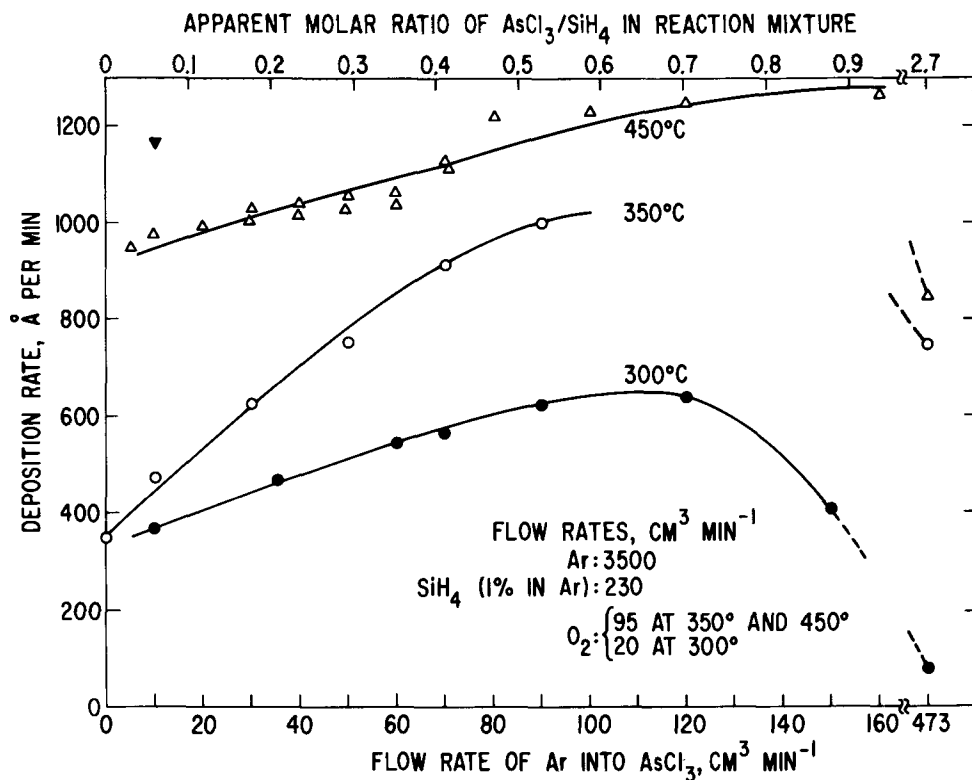


Fig. 3. Deposition rate vs. flow rate of Ar into AsCl_3 liquid source at various substrate temperatures, all other flow rates being held constant at a given temperature. The apparent molar ratio of $\text{AsCl}_3/\text{SiH}_4$ is calculated from the flow rates assuming saturation of AsCl_3 in Ar and from the known vapor pressure (10 mm Hg) (5) of AsCl_3 at room temperature. The \blacktriangledown point is for Ar flow rate of 1750 cc min^{-1} at 450°C , all other flow rates being invariant.

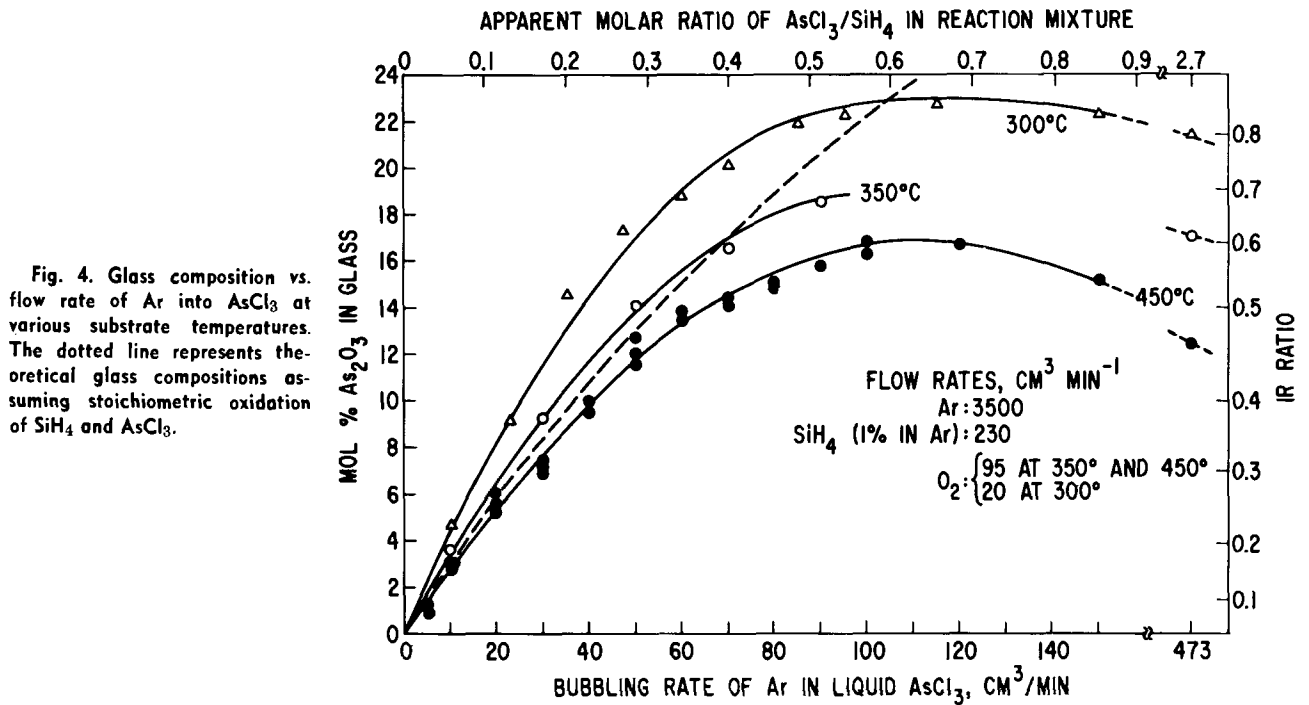


Fig. 4. Glass composition vs. flow rate of Ar into $AsCl_3$ at various substrate temperatures. The dotted line represents theoretical glass compositions assuming stoichiometric oxidation of SiH_4 and $AsCl_3$.

(i.e., point uniformity). The layer uniformity was studied using the technique of IR spectroscopy by following the absorbance ratio of the As-O band at 930 cm^{-1} and the Si-O band at 1060 cm^{-1} as the films were etched progressively in the appropriate HF solution

depending on film composition given in Fig. 6. The results are plotted in Fig. 7 as IR absorbance ratio for these two bands vs. film thickness (measured visually by color) at various over-all composition of the as-deposited films ranging from 21.5 to 1.5 m/o As_2O_3 . Films with over-all compositions of 9.6-21.5% As_2O_3 were richer in As_2O_3 during the initial stage of deposition (the first 5000Å or so) as shown by the progressive increase of the IR ratio as the films were etched down. The possibility of a preferential etching of the SiO_2 component in the 1:100 BHF or 1:10 BHF

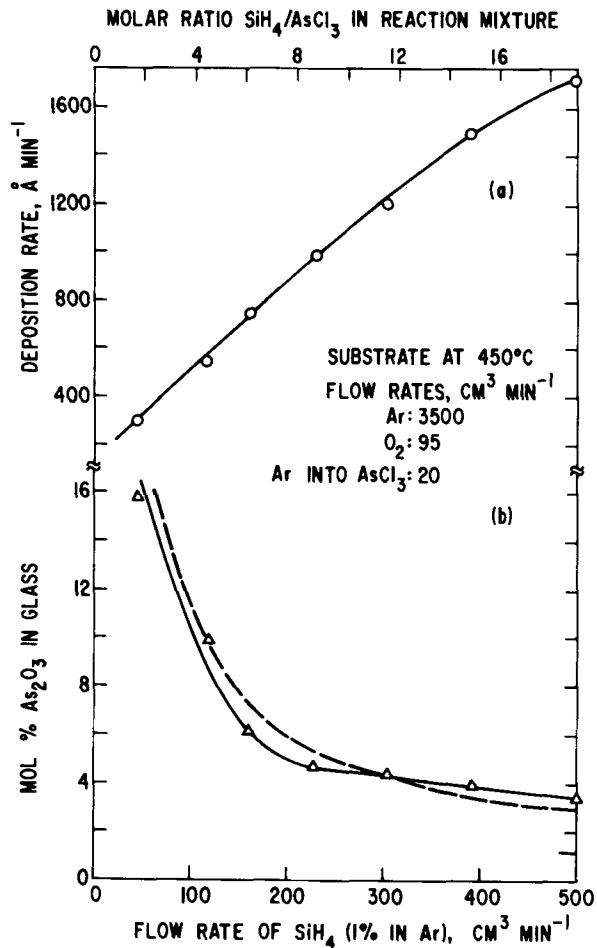


Fig. 5. (a) Deposition rate and (b) glass composition vs. flow rate of SiH_4 at $450^\circ C$. All other flow rates were held constant. The dotted line represents theoretical glass composition assuming stoichiometric oxidation of SiH_4 and $AsCl_3$.

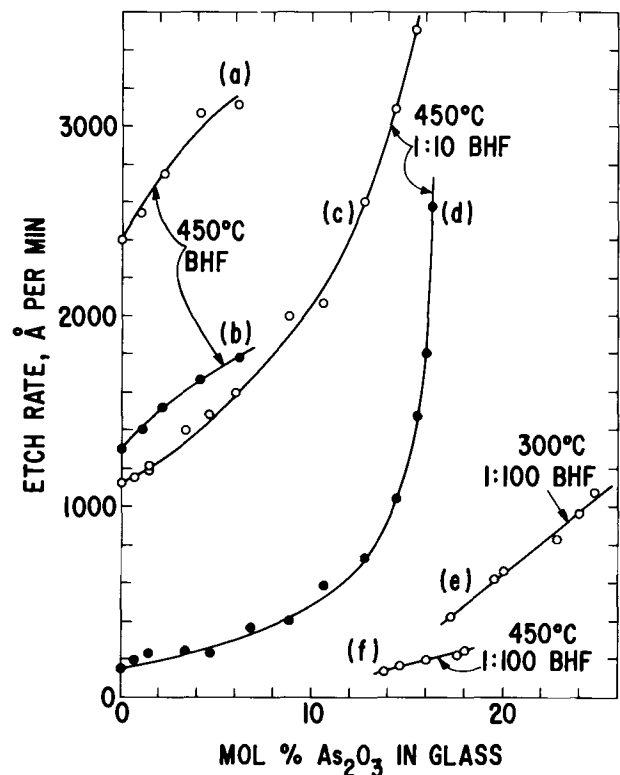


Fig. 6. Etch rate of as-deposited (open circles) and heat-treated (closed circles) arsenosilicate films vs. glass composition in various HF solutions. All heat-treatments performed at $800^\circ C$ in Ar for 10 min.

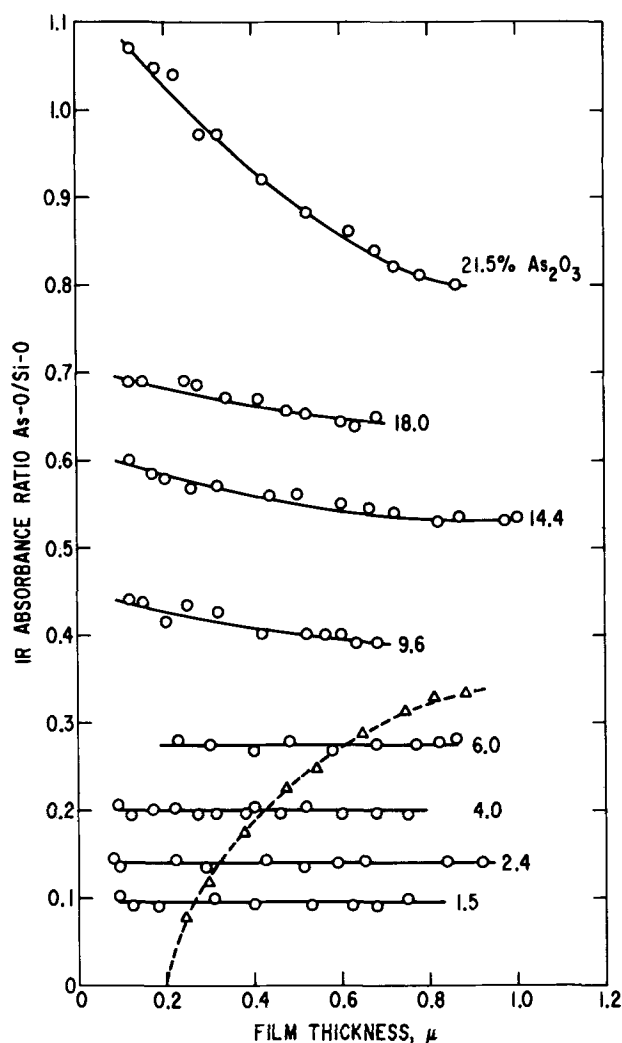


Fig. 7. Layer uniformity of as-deposited glass films at various over-all compositions determined from the IR ratios of the as-deposited films using a previously published calibration curve (1). The triangles are data for a binary film deposited on a layer of 2000Å SiO₂ on silicon.

solution can be ruled out because (i) if preferential etching in these dilute aqueous HF solutions were to take place, As₂O₃ and not SiO₂ would be leached out first because of the much higher solubility of As₂O₃ in H₂O, and (ii) in a control experiment in which a layer of pure SiO₂ (2000Å) had been deposited prior to the deposition of the binary film, the IR ratio dropped progressively to zero (triangles in Fig. 7), as expected, in the absence of preferential etching of the SiO₂ component, as the top binary film was etched down.

To examine composition uniformity across the glass surface, the amounts of As and Si in the glass films were analyzed by the technique of x-ray microprobe operated in the scanning mode. The x-ray beam was focused down to 1μ in diameter and the scan rate was set at 2.5 mm min⁻¹. The beam was allowed to probe the sample for 10 sec after which 8 sec were allowed for computation (by an on-line computer). Under the above scanning conditions each point in Fig. 8 represents the average composition over a length of 420μ of the sample and the separation between successive points is of the order of 320μ, the distance traversed by the x-ray beam in 8 sec during which the previous point data were being computed. Within the instrumental error, composition is quite uniform across the as-deposited films in the over-all composition range of 3.8 to 22 m/o As₂O₃.

In order to examine the composition uniformity further on a microscopic scale, the action of conc. HCl

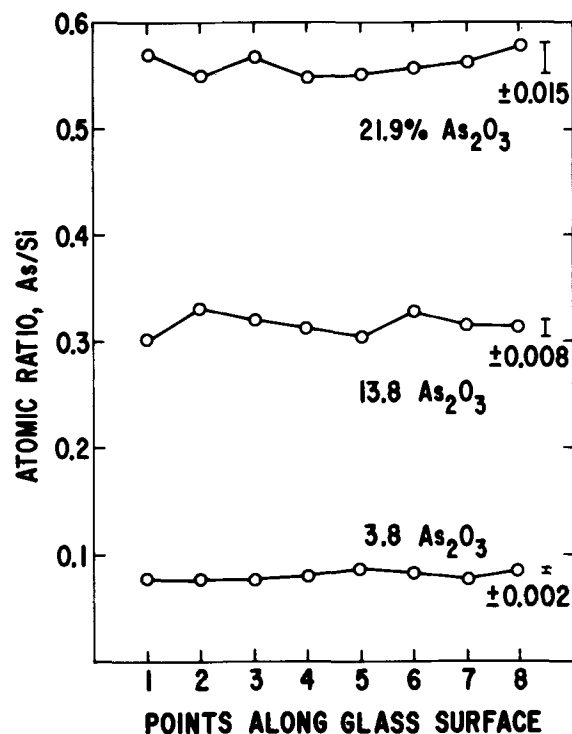


Fig. 8. Point uniformity of as-deposited glass films at various over-all composition. Analysis by x-ray microprobe. The bars denote instrumental errors.

on the as-deposited binary arsenosilicate films was studied as a function of As₂O₃ content in the glass. Changes in the films were followed by infrared spectroscopy. The results are given in Table I. Films with 19 m/o As₂O₃ or more showed preferential leaching of the As₂O₃ component in a matter of minutes upon immersion in conc. HCl. An example is given in Fig. 9 for a film containing 21.5 m/o As₂O₃ as-deposited. A progressive decrease in the As-O absorbance at 930 cm⁻¹ was observed after 1 min in conc. HCl at room temperature. After 2 hr the As-O intensity was markedly reduced with the simultaneous appearance of the OH band at 1625 and 3300 cm⁻¹. The film appeared optically continuous immediately after the 20 hr conc. HCl treatment, but was found to craze completely 3 months later. Control experiments indicated that pure As₂O₃ powders (crystalline) dissolve spontaneously in conc. HCl while a film of as-deposited CVD SiO₂ was not at all affected by the acid in 20 hr (Table I).

Dielectric strength.—The dielectric strength of as-deposited arsenosilicate glass films is plotted in Fig. 10 as a function of As₂O₃ content in the film and decreases monotonically with increase in As₂O₃ concentration. The strength of pure SiO₂ agrees quite well with those reported in the literature (6-8) for CVD SiO₂

Table I. Action of conc. HCl on as-deposited films containing various mole per cent As₂O₃

m/o As ₂ O ₃ in as-deposited film	Substrate temp. during deposition.	Action of conc. HCl
0 (Pure SiO ₂)	450°	No action after 20 hr.
4.5	300°	No action after 21 hr.
12.5	450°	No action after 48 hr.
16.0	450°	No action after 22 hr.
19.0	350°	No action after 1 hr; As ₂ O ₃ leached out after 65 hr, and OH bands at 1625 and 3300 cm ⁻¹ appeared in the IR spectrum.
21.5	300°	As ₂ O ₃ leached out progressively after 1 min. More markedly after 20 hr—see Fig. 9.

Fig. 9. Infrared spectra of a 21.5 m/o As_2O_3 glass (8000Å thick) treated for various times in conc. HCl.

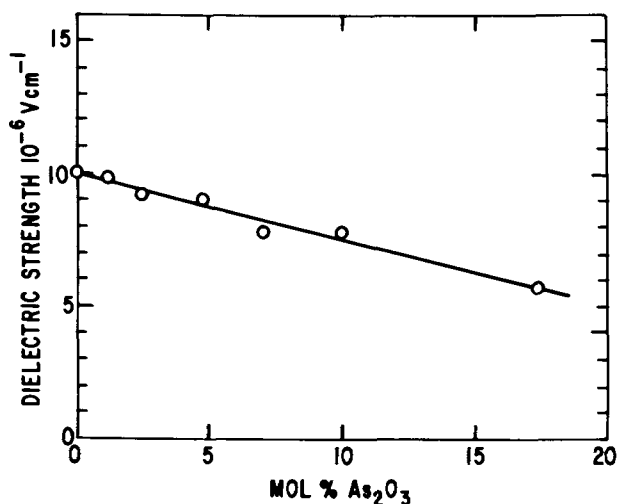
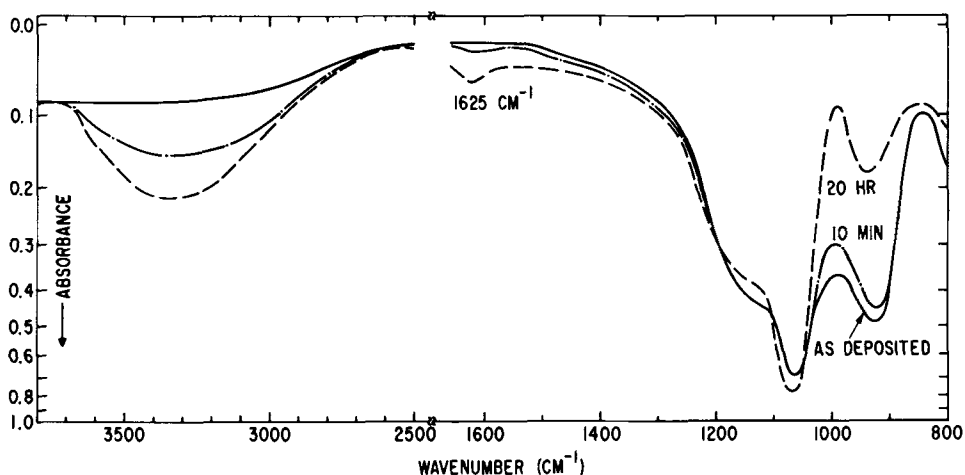


Fig. 10. Dielectric strength at room temperature of as-deposited films vs. composition.

deposited from SiH_4 and O_2 on silicon substrate at 500° and 400°C.

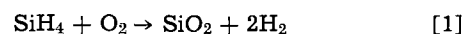
Moisture resistance.—In order to study water attack on the as-deposited binary glasses, films containing various amounts of As_2O_3 were exposed in controlled atmospheres of 30, 80, and 100% relative humidity at room temperature.² The water uptake by the films was followed by IR spectroscopy in the OH absorption regions at 1630 cm^{-1} and 3300 cm^{-1} , while the vibrational spectrum of the glass in the range 1400–250 cm^{-1} was used to follow any intrinsic change in the arsenosilicate structure. The results are given in Table II. Films with 8.8 m/o As_2O_3 or less suffer no moisture at-

² These constant humidities were generated in the closed space of a desiccator using saturated solutions of $\text{CaCl}_2 \cdot 6\text{H}_2\text{O}$, $(\text{NH}_4)_2\text{SO}_4$ (9) and distilled water respectively.

tack at low humidity over a period of 570 hr (see column 2 of Table II). At higher humidities (80–100%) slight water uptake in these films were detected after 100 hr or so; but the vibration bands of the arsenosilicate was not shifted at all. A film with 19 m/o As_2O_3 absorbed water even at a low humidity after 65 hr. The vibration bands of the arsenosilicate were progressively shifted (intensity as well as frequency) with increasing humidity and time. Figure 11(a) shows the progressive increase in intensity and frequency of the Si-O band at 1060 cm^{-1} and decrease in intensity of the As-O band at 930 cm^{-1} with time in a 100% relative humidity. After 2500 hr, the surface of the film appeared frosted. A micrograph of the frosted surface is shown in Fig. 12(a). A parallel, but more drastic, test of water uptake was performed in boiling distilled water. As-deposited films with 16 m/o As_2O_3 or less showed no water absorption and no change in the infrared spectrum after an hour immersion in boiling water. Films with 19 m/o As_2O_3 and up, however, showed OH absorption and spectral change in the infrared [Fig. 11(b)], and complete crazing in a matter of minutes of immersion [Fig. 12(b)]. The action of boiling water on these binary films containing various amounts of As_2O_3 is quite similar to that of conc. HCl shown in Table I.

Discussion

Deposition reactions.—At low temperatures, 240°–450°C, the oxidation of silane is shown by Strater (10) to follow the reaction



stoichiometrically. Furthermore the deposition rate of CVD SiO_2 was lowered when the same reaction mixture was diluted with hydrogen instead of an inert carrier gas such as Ar or N_2 (11). These two studies show clearly that H_2 is the gaseous reaction product in the oxidation of SiH_4 and not H_2O as was assumed earlier by Goldsmith and Kern (12), presumably on

Table II. Moisture attack on as-deposited glass films in various controlled atmospheres

m/o As_2O_3	Relative humidity		
	30%	80%	100%
0.8	No attack after 570 hr.	After 144 hr H_2O absorption at 1625 and 3400 cm^{-1} detected. The Si-O band at 1060 cm^{-1} and As-O band at 930 cm^{-1} were not shifted.	Water absorption detected after 100 hr. Spectrum of glass unaffected up to 2500 hr.
2.0	No attack after 570 hr.	After 144 hr H_2O absorption at 1625 and 3400 cm^{-1} detected. The Si-O band at 1060 cm^{-1} and As-O band at 930 cm^{-1} were not shifted.	Water absorption detected after 100 hr. Spectrum of glass unaffected up to 2500 hr.
4.0	No attack after 570 hr.	After 144 hr H_2O absorption at 1625 and 3400 cm^{-1} detected. The Si-O band at 1060 cm^{-1} and As-O band at 930 cm^{-1} were not shifted.	Water absorption detected after 100 hr. Spectrum of glass unaffected up to 2500 hr.
8.8	No attack after 570 hr.	After 144 hr H_2O absorption at 1625 and 3400 cm^{-1} detected. The Si-O band at 1060 cm^{-1} and As-O band at 930 cm^{-1} were not shifted.	Water absorption detected after 100 hr. Spectrum of glass unaffected up to 2500 hr.
19.0	After 65 hr H_2O absorption at 1630 and 3300 cm^{-1} detected. No change in the IR bands of the glass.	After 144 hr, there is progressive change in the IR spectrum. cf. Fig. 11(a).	Progressive change in the IR spectrum [see Fig. 12(a)]. Glass surface became frosted [see Fig. 12(a)].

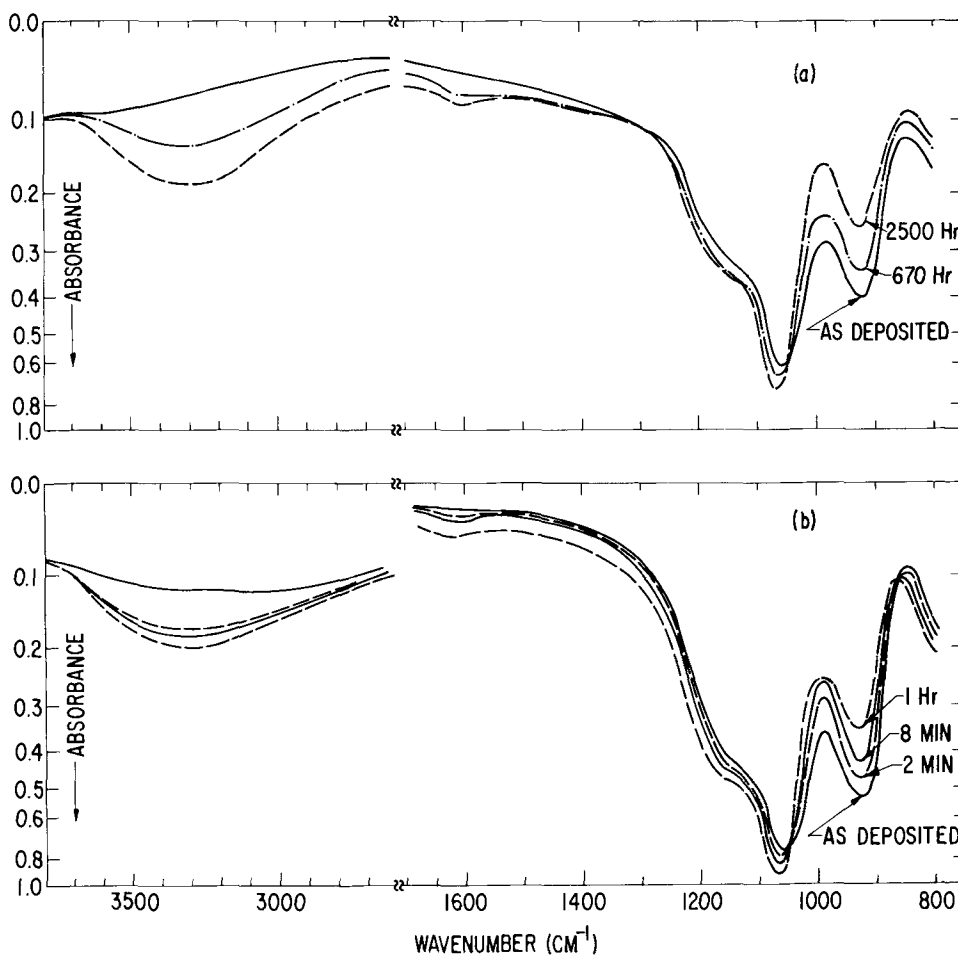
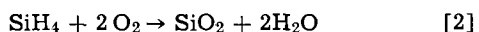


Fig. 11. Infrared spectra of a 19 m/o As_2O_3 film (8000Å thick) treated for various times in (a) 100% relative humidity (room temperature) and (b) boiling distilled water.

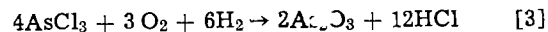
the basis that the free energy change for the reaction



has a larger negative value ($-300 \text{ kcal mole}^{-1}$) than reaction [1] ($-215 \text{ kcal mol}^{-1}$) (13) at the deposition temperature.

In the $(\text{C}_2\text{H}_5\text{O})_4\text{Si}-\text{AsCl}_3-\text{O}_2$ system used previously for the deposition of binary arsenosilicate glasses (2, 3) the oxidation of AsCl_3 appeared to be initiated by the hydrolysis of AsCl_3 by the water produced in the thermal pyrolysis of $(\text{C}_2\text{H}_5\text{O})_4\text{Si}$ to form $\text{As}(\text{OH})_3$ which was then thermally decomposed to yield the trioxide. The as-deposited film, however, contained an appreciable amount of "water" as shown in the IR spectrum (3). In our present one-liquid source SiH_4-

AsCl_3-O_2 system, however, hydrolysis of the AsCl_3 vapor is unlikely because H_2 and not H_2O is produced in the oxidation of SiH_4 . The oxidation of AsCl_3 however may be initiated in the presence of H_2 as follows



Hydrochloride gas was detected as a reaction product in the effluent gas. Control experiments showed that no film formation occurred when an argon-diluted mixture of AsCl_3 and O_2 was passed over the heated silicon substrate in the range $300^\circ-500^\circ\text{C}$. It appears therefore that the deposition of the binary $\text{As}_2\text{O}_3-\text{SiO}_2$ mixture is the result of the intermediate reaction given in Eq. [1] and [3] and can be represented by an over-all stoichiometric reaction

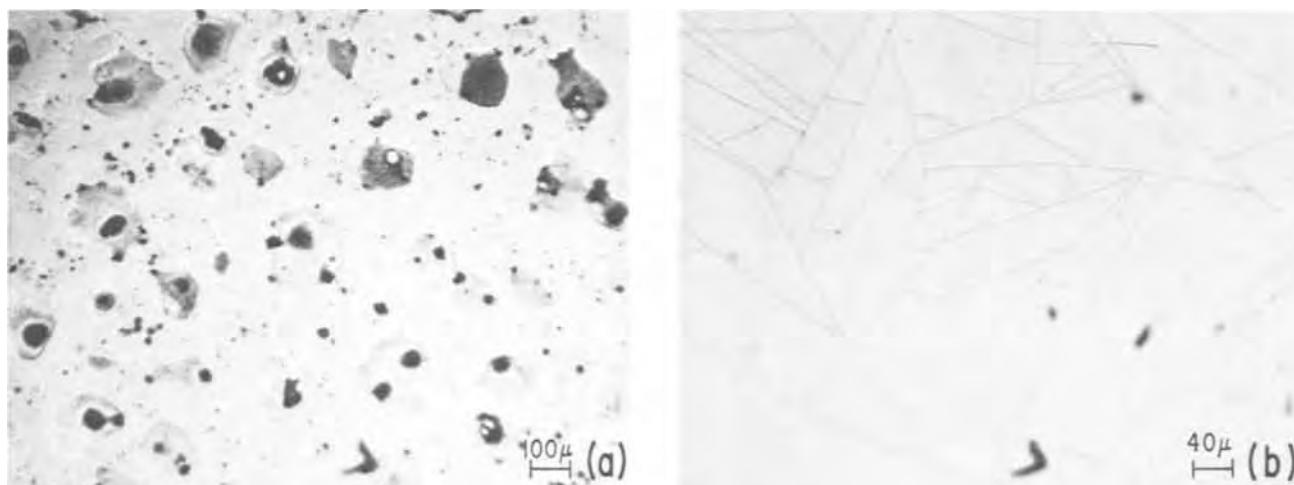
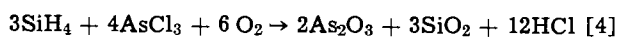


Fig. 12. Micrographs of film surface of a 19 m/o As_2O_3 film after exposing (a) 2500 hr in 100% humidity at room temperature (magnification: 69X) and (b) 1 hr in boiling distilled water (magnification: 170X).



The final composition of the deposited film depends, of course, on the molar ratio of the reaction gases in the reaction mixture. However, no OH absorption was detected in the 2.7μ region of the IR spectrum of any of the deposited films.

Film composition.—In the presence of excess O_2 , the film composition was found to be independent of the O_2 flow rate at constant flow rates of both SiH_4 and AsCl_3 (Fig. 1). The amount of As_2O_3 incorporated into the glass film decreases with increase in substrate temperature. This suggests a decrease in the sticking coefficient (14) of the As_2O_3 component with an increase in substrate temperature, which in turn can be rationalized in view of the short liquidus range of As_2O_3 (m.p. 313° and b.p. 460°C) and hence high vapor pressure in the range 300° – 500°C of investigation (15).

The composition dependence on substrate temperature during deposition is further illustrated by the data given in Fig. 4 in which the composition of the deposited films was plotted vs. the Ar flow rate into the AsCl_3 source at substrate temperatures of 300° , 350° , and 450°C . At any given set of flow rates of reactant gases, the amount of As_2O_3 incorporated into the film decreases with increase in substrate temperature. At each temperature, however, the As_2O_3 content in glass increases with initial increase in the flow rate of Ar into AsCl_3 at constant flow rate of SiH_4 , reaches a maximum at about 100 cc min^{-1} and decreases as the Ar carrier gas into AsCl_3 is further increased. This behavior, which is independent of the substrate temperature during deposition, appears to arise as a result of undersaturation of the Ar carrier gas at high flow rates into the AsCl_3 liquid source, and not as a result of changes in the reaction mechanism. Hence, the term "apparent molar ratio" is used for the upper horizontal scale in Fig. 4.

Under saturation conditions, the observed composition in the deposited glass follows quite closely the theoretical value (dotted line in Fig. 4) calculated from the molar ratio of AsCl_3 to SiH_4 in the reaction mixture, assuming stoichiometric oxidation of the reactants. A similar conformity is found between the experimental and calculated [dotted line in Fig. 5(b)] compositions for films deposited at 450°C with varying SiH_4 flow rate at constant flow rates of the remaining reactant gases. Furthermore, the oxidation rate of SiH_4 to SiO_2 is quite independent of the amount of co-deposited As_2O_3 as shown by the constancy of the IR absorbance of the Si-O band at 1060 cm^{-1} in a series of film deposited at 450°C and at constant time of deposition and flow rates of all reactant gases while the flow rate of Ar into the AsCl_3 liquid source was being varied in the saturation range (5 – 100 cc min^{-1}) (19).

Deposition rate.—In general, the deposition rate measured as the time rate of growth of film thickness of binary arsenosilicate films using the present one-liquid source system increases with increase flow rate of O_2 (Fig. 2), AsCl_3 (in the saturation range, Fig. 3) and SiH_4 (Fig. 5a) and with a decrease in the flow rate of the carrier gas (the \blacktriangledown point in Fig. 3).

In a chemical vapor deposition process, the over-all observed deposition rate is governed by both the chemical reaction rate and the rate of physical processes such as condensation-evaporation (sticking coefficient) nucleation and growth. When the reaction rate is the limiting factor, i.e., chemical rate \ll physical rate, the deposition rate at a given temperature may be given by

$$\text{dep. rate} \sim k [\text{SiH}_4]^m [\text{AsCl}_3]^n [\text{O}_2]^p \quad [1]$$

where the square brackets denote concentrations of the respective reactants, k is the rate constant, and m , n , and p are positive exponents, fractional or integral. From the data in Fig. 5(a) which shows the deposition rate at 450°C as a function of SiH_4 flow rate while the

flow rates of AsCl_3 , O_2 , and Ar carrier gas were held constant, a plot of $\log(\text{dep. rate})$ vs. $\log(\text{SiH}_4 \text{ flow rate})$ gives a slope of 1.0 ± 0.1 which is the value of m under the above deposition conditions.

The temperature dependence of deposition rate shown in Fig. 2 at two O_2 flow rates is interesting. At both O_2 concentrations, the $\log(\text{dep. rate})$ vs. reciprocal temperature plot is non-Arrhenius implying a temperature dependence of the "over-all activation energy," which is larger at low O_2 concentration.

At a given set of reactant flow rates, a reduction of the carrier gas flow rate from 3500 cc min^{-1} to 1750 cc min^{-1} gave rise to an increase of deposition rate from 990 \AA min^{-1} to 1180 \AA min^{-1} . Similar observations have been reported in the chemical vapor deposition of SiO_2 from the SiH_4 - O_2 - N_2 system (10) and boron from the BCl_3 - H_2 -He system (20). In the latter system, Gruber (20) found that the deposition rate of boron varies inversely with the square of the carrier gas partial pressure.

Film Properties

Nature of as-deposited films.—A knowledge of the basic chemical nature and compositional uniformity of vapor-deposited binary films is a very important prerequisite to the understanding of their properties such as etch rate, dielectric strength, moisture resistance, and heat-treatment characteristics. Preliminary x-ray diffraction studies showed that the binary As_2O_3 - SiO_2 films are amorphous in nature (3,21). Until recently (18) it was not clear whether vapor-deposited binary silicate glasses such as the borosilicates (16,17) and phosphosilicates (17) are really true chemical mixtures like the bulk materials prepared by quenching homogeneous mixtures from the liquid state, or mechanical mixtures of the end components matrix-isolating one another. In a recent study, advantages have been taken of the ability of the SiH_4 - B_2H_6 - O_2 -Ar reaction system to allow vapor deposition of binary borosilicate film from 0-100 m/o B_2O_3 , whereby the vibrational spectra of these mixtures could be studied by IR absorption spectroscopy across the whole composition range. From an analysis of the spectral distributions of the Si-O-Si, B-O-Si, and B-O-B bonds as a function of composition and comparison with those from a simple random distribution model, Tenney and Wong (18) showed that vapor-deposited binary borosilicates are true chemical mixtures, at least in the range 0-60 m/o B_2O_3 , with the formation of Si-O-B linkages, and not mechanical mixtures of B_2O_3 and SiO_2 .

Although such a 3-center bond distribution analysis is not possible in the narrow composition region (0-20 m/o As_2O_3) of the As_2O_3 - SiO_2 system, some indirect experimental findings are of interest. In the IR spectrum of pure crystalline As_2O_3 (22,23) strong absorption bands are found at 351 , 493 , 815 cm^{-1} and relatively weaker bands at 914 and 1044 cm^{-1} . In the vitreous state (24), the strong band 815 cm^{-1} broadens and absorption in the 1050 cm^{-1} region is merely observable. In vapor-deposited arsenosilicate films, a distinct and relative strong band at 930 cm^{-1} appeared as shown in Fig. 9. This band has been attributed by Arai and Terunuma (3) to a red shift of the very weak band of 1044 cm^{-1} for pure As_2O_3 , although from intensity consideration a blue shift of strong pure As_2O_3 band at 815 cm^{-1} is more probable. Notwithstanding the dynamical origin of this band at 930 cm^{-1} , it is worth noting that this band is not present in the pure As_2O_3 spectrum, and that its intensity varies proportionally with the amount of As_2O_3 incorporated into the glass found by chemical analysis (1). These two observations imply that As-O oscillators in the mixture are in a different chemical environment than in pure As_2O_3 , and that vapor-deposited As_2O_3 - SiO_2 films are not likely mechanical mixtures of the end components. The conclusion is further substantiated in the HCl etching results (Table I) which shows that no

preferential leaching of As_2O_3 occurs until the composition is exceeded by 16 m/o As_2O_3 . If the mixtures were mechanical, the pure As_2O_3 component (which is very soluble in conc. HCl) would be leached out preferentially regardless of film composition.

The composition appears to be uniform from point to point across the film surface as shown in Fig. 8. Good layer compositional uniformity can be obtained only with low As_2O_3 films (Fig. 7). For the deposition of high As_2O_3 -content films, there seems to be a change in the over-all reaction kinetics and/or a change in the sticking coefficient of As_2O_3 as the film grows. In light of the variation of the IR ratio with film thickness in high As_2O_3 -content glass, it is estimated that the previously published calibration curve (1) of IR ratio vs. m/o As_2O_3 is accurate to within 2 m/o As_2O_3 in the over-all composition range of 9.6-18.0 m/o As_2O_3 . Above 20 m/o As_2O_3 , deviations of as much as 4 m/o As_2O_3 may be expected for films less than 5000Å thick. Films having 6.0 m/o As_2O_3 and less have very good layer uniformity as shown by the bottom four curves in Fig. 7.

Etch rate, moisture resistance, and dielectric strength.

—Having gained an insight into the chemical nature and composition uniformity of the as-deposited binary films, the composition dependence of etch rate, moisture resistance, and dielectric strength can easily be rationalized in terms of the corresponding properties of the end components. The monotonic increase in etch rate in various HF solutions with increase in As_2O_3 -content in these films is no doubt due to the relatively higher solubility of the pure As_2O_3 end component, which dissolves even in pure water. When heat-treated for 10 min in Ar at 800°C, the etch rate drops to a half or more of its as-deposited value, but the monotonicity with composition still persists (Fig. 6). The phenomenon is often attributed to the so-called "densification" effect (25, 26) which, in the case of CVD SiO_2 , is accompanied by increases in the film density and refractive index when films deposited at low temperatures are heat-treated above the deposition temperature.

In view of the large differences in thermal and evaporation characteristics of pure As_2O_3 and SiO_2 , the decrease in absorbance of the As-O band at 930 cm^{-1} upon heat-treating as-deposited arsenosilicate films (27) appears to suggest a change in composition due to evaporation loss of the As_2O_3 component. Detailed spectral and chemical analyses (27), however, show that structural change and not composition variations are responsible for the observed shifts in band frequency and maximum absorbance in the resultant heat-treated films. The decrease in film etch rate upon heat-treatment is, therefore, one of structural origin. Besides the effects of structural changes, the deposition history also affects the film etch rate. For instance, as shown in Fig. 6, films deposited at 300°C are etched at a higher rate than those deposited at 450°C in a given etching solution.

Film deterioration by moisture attack is also strongly dependent on composition as well as the relative humidity (see Table II). With increase in humidity and time of exposure, water pickup can be detected in low

As_2O_3 content films as shown by the appearance of the OH bands at 3300 cm^{-1} and 1630 cm^{-1} in the IR spectrum (Fig. 11). The absorbed "water" is strongly held in the glass lattice and cannot be removed even when the moist films are heated to 800°C as indicated by the persistence of the OH bands in the resultant spectrum. Prolonged exposure of a high As_2O_3 film (19 m/o) in a 100% R.H. atmosphere led to drastic film deterioration indicated by a pronounced change in both the Si-O and As-O absorption [Fig. 11(a)] as well as visual frosting of the film as shown in Fig. 12(a). The moisture attack in this case must involve a conversion of the As_2O_3 component to some arsenic compounds which does not absorb in the IR at 930 cm^{-1} . This may be contrasted in the case of the boiling water attack in which As_2O_3 can conceivably be leached out of the film giving rise to a decrease in intensity of the As-O band at 930 cm^{-1} [Fig. 11(b)] (27).

The d-c dielectric strength for as-deposited SiO_2 from silane oxidation has been reported by various authors (6-8, 12), with values ranging from 2.5 to 12.0 $\times 10^6$ V cm^{-1} under different deposition conditions, oxide thickness, and the capacitor structure. These are collected in Table III. Despite the diversity of results for the strength reported for CVD SiO_2 , the systematic decrease in dielectric strength of as-deposited arsenosilicate films with increase As_2O_3 content is noteworthy (Fig. 10). The tendency of dielectric breakdown whether thermal or electrical (28) must no doubt increase with the As_2O_3 concentration in the binary film.

Conclusions

The deposition characteristics of binary arsenosilicate glass films using the present one-liquid SiH_4 - AsCl_3 - O_2 -Ar system have been studied systematically as a function of reactant flow rates and substrate temperature. Film composition and deposition rates have been evaluated reproducibly under various sets of deposition variables. High deposition rates (500-1200 Å/min) at relatively lower substrate temperatures (300°-500°C) are the main advantage of the present system over the so-far reported two-liquid source systems based on $(\text{C}_2\text{H}_5\text{O})_4\text{Si}$ and AsCl_3 (2, 3, 29-31). In addition, the deposited films are relatively free from water contamination, which is not a byproduct of the SiH_4 oxidation (10). Furthermore, the film composition is not restricted in a narrow region of high As_2O_3 concentration, but can be monitored at will and controllably in the range 0-20 m/o As_2O_3 or higher. This enables film properties such as composition uniformity, etch rate, dielectric strength, and moisture resistance to be studied systematically as a function of chemical composition.

Acknowledgments

The author would like to thank E. A. Taft and R. J. Connery for measuring film thicknesses by ellipsometry and for constructing the MOS capacitors in the dielectric strength measurements respectively. Encouragement by M. Garfinkel in various aspects of this work and his constructive comments on the manuscript are gratefully appreciated.

Table III. Reported dielectric strength for as-deposited SiO_2 from $\text{SiH}_4 + \text{O}_2$

Deposition history	Oxide thickness, Å	Capacitor structure	Dielectric strength in 10^6 V cm^{-1}	Reference
325°C at 760 Å/min	10,000	PdAu-SiO ₂ -Si	2.5	Goldsmith and Kern (12)
475°C at 2500 Å/min	10,000	PdAu-SiO ₂ -Si	3.4	Goldsmith and Kern (12)
400°C at 6000 Å/min	—	Al-SiO ₂ -Si-Al	8.5	Deal et al. (17)
400°C	1,000-12,000	Al-SiO ₂ -Si	12.0	Hammond and Bowers (8)
400°C	—	Al-SiO ₂ -Al	5.0	—
450°C at 950 Å/min	2,000	Metal*-SiO ₂ -Si	9.0	Barry (6)
		Mo-SiO ₂ -Si	10.0	Present work

* Metal unspecified.

Manuscript submitted Oct. 22, 1971; revised manuscript received March 17, 1972.

Any discussion of this paper will appear in a Discussion Section to be published in the June 1973 JOURNAL.

REFERENCES

- J. Wong and M. Ghezzeo, *This Journal*, **118**, 1540 (1971).
- H. Teshima, Y. Tarui, and O. Takeda, *Bull. Electrochem. Lab. Japan*, **33**, 631 (1969).
- E. Arai and Y. Terunuma, *J. Appl. Phys. (Japan)*, **9**, 691 (1970).
- W. A. Pliskin and E. E. Conrad, *IBM Journal*, **8**, 43 (1964).
- D. R. Stull, *Ind. Eng. Chem.*, **39**, 540 (1947).
- M. L. Barry in "Second International Conference on Chemical Vapor Deposition," John M. Blocher, Jr. and James C. Withers, Editors, p. 595, The Electrochemical Society Softbound Symposium Series, New York (1970).
- B. E. Deal, P. J. Fleming, and P. L. Castro, *This Journal*, **115**, 300 (1968).
- M. L. Hammond and G. M. Bowers, *Trans. AIME*, **242**, 546 (1968).
- Handbook of Chemistry and Physics*, 41st edition, Chem. Rubber Publishing Co. (1960).
- K. Strater, *RCA Rev.*, **29**, 618 (1968).
- T. L. Chu, J. R. Szidon, and G. A. Gruber, *Trans. AIME*, **242**, 532 (1968).
- N. Goldsmith and W. Kern, *RCA Rev.*, **28**, 153 (1967).
- JANAF Interim Thermochemical Tables, The Dow Chemical Co., Midland, Mich. (1960).
- K. L. Chopra, "Thin Film Phenomena," pp. 138-149, McGraw Hill Book Co., New York (1969).
- I. Karutz and I. N. Stranski, *Z. Anorg. Allgem. Chem.*, **292**, 330 (1957).
- W. Kern and R. C. Heim, *This Journal*, **117**, 568 (1970).
- D. M. Brown and P. R. Kennicott, *ibid.*, **118**, 293 (1970).
- A. S. Tenney and J. Wong, *J. Chem. Phys.*, **56**, 5516 (1972).
- Fig. 3 in J. Wong and M. Ghezzeo, *This Journal*, **118**, 1540 (1971).
- P. E. Gruber in "Second International Conference on Chemical Vapor Deposition," John M. Blocher, Jr. and James C. Withers, Editors, p. 25, The Electrochemical Society Softbound Symposium Series, New York (1970).
- S. F. Bartram, Private communication (1971).
- A. Bertoluzza, G. B. Bonino, and C. Castellari, *Lincei, Rend. Sci. Fis. Mat. Nat.* **XLIV**, 397 (1968).
- A. M. Bishay and S. Arafa, *J. Am. Ceram. Soc.*, **49**, 423 (1966).
- R. V. Adams, *Phys. Chem. Glasses*, **2**, 101 (1961).
- W. A. Pliskin and H. S. Lehman, *This Journal*, **112**, 1013 (1965).
- W. A. Pliskin, D. R. Kerr, and J. A. Perr, *Phys. Thin Films*, **4**, 257 (1967).
- J. Wong, To be published.
- N. Klein, *This Journal*, **116**, 963 (1969).
- D. B. Lee, *Solid-State Electron.*, **10**, 623 (1967).
- A. Cuccia, G. Shrank, and G. Queirolo, in "Semiconductor Silicon," Rolf R. Haberecht and Edward L. Kern, Editors, p. 506, The Electrochemical Society Softbound Symposium Series, New York (1969).
- P. C. Parekh, D. R. Goldstein, and T. C. Chan, *Solid-State Electron.*, **14**, 281 (1971).

Thermal Stresses in CVD Films: The Case of Binary Arsenosilicate Glasses

J. Wong

General Electric Corporate Research and Development, Schenectady, New York 12301

ABSTRACT

The heat-treatment characteristics and surface morphology of binary arsenosilicate glass films vapor-deposited on silicon have been studied systematically as a function of temperature and film composition. Initial heat-treatments in Ar at 800°C and up indicated that the thermal stresses generated in the film arising from a mismatch of expansion coefficient with the silicon substrate are largely responsible for the observed film detachment from the substrate. The higher the As₂O₃ content in the glass, the lower is the temperature required to bring about the detachment. However, when the amount of As₂O₃ in the deposited film is substantially reduced [to 0.5 mole per cent (m/o) As₂O₃] film detachment can be eliminated altogether even at temperatures as high as 1100°C. Prolonged heat treatments of these low As₂O₃ films yield very uniformly diffused N⁺ layers in silicon.

Binary silicate glass films are of considerable importance in recent years as solid-to-solid state diffusion sources into silicon for the formation of p-n junctions in the planar technology for fabricating micro-electronic devices and circuits (1-10). The use of binary arsenosilicate glasses as n-type diffusion sources has recently been demonstrated by Lee (6) who prepared vitreous films of As₂O₃-SiO₂ on silicon from a two-liquid-source system based on (C₂H₅O)₄Si and AsCl₃ by a CVD technique. Subsequent studies by various authors (7-10) showed that glasses prepared from this two-liquid-source system suffer severe "glass damage" when heated to the diffusion temperatures. The glass damage introduces undesirable characteristics into the resultant diffused layers and appears to offer a stumbling block to the use of arseno-

silicate glasses as arsenic diffusion sources in the silicon technology.

In the present paper, advantage has been taken of the ability of the SiH₄-AsCl₃-O₂-Ar reaction system to allow vapor deposition of binary arsenosilicate glass films of various compositions in the range 0-20 mole per cent (m/o) As₂O₃ (11), whereby initial stages of glass damage due to heat-treatment could be followed by optical and scanning electron microscopy as a function of film composition and temperature. Furthermore, it is hoped that suitable glass compositions in this binary system can be located so that the use of arsenosilicate glasses as n-type solid-state diffusion sources into silicon may be revived in the semiconductor industry.

Experimental

Binary arsenosilicate glass films were prepared on silicon wafers by a CVD technique using argon-diluted

Key words: surface morphology, film detachment.

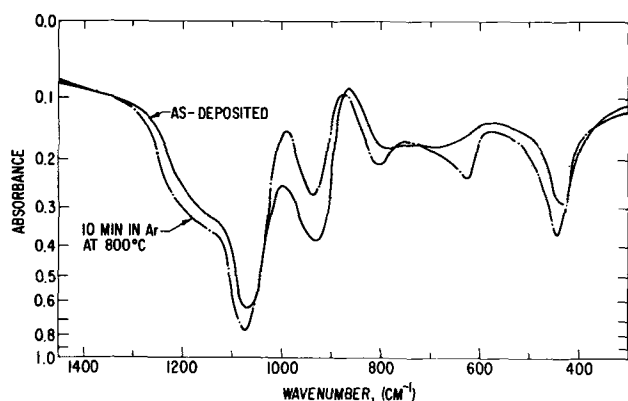


Fig. 1. IR spectra of a 14.4 m/o As_2O_3 film before and after heat-treatment in Ar at 800°C for 10 min. Film was deposited at 450°C .

mixtures of $\text{SiH}_4\text{-AsCl}_3\text{-O}_2$ at 450°C . Details of the deposition procedure and composition determination of as-deposited films from the infrared spectra have been reported elsewhere (11, 12). All films studied were 8000\AA thick. A horizontal quartz-tube furnace was used to heat-treat the deposited films in a flowing atmosphere of argon. Typical heat-treatment times were of the order of 10 min. Surface morphology of heat-treated films was examined by the technique of scanning electron microscopy.

Results and Discussion

Changes in the film structure and surface morphology due to an initial short-time heat-treatment at temperatures above deposition temperature were followed by IR spectroscopy and optical microscopy respectively. When heat-treated at 800°C for 10 min in a flowing argon atmosphere, glasses having various amounts of As_2O_3 showed the following general behavior in the IR absorption: (i) a blue shift of the silica bands from 1060 cm^{-1} to 1080 cm^{-1} , 790 cm^{-1} to 800 cm^{-1} , and 430 cm^{-1} to 450 cm^{-1} , all accompanied by an increase of band maximum absorbance; (ii) a blue shift of the As-O band at 930 cm^{-1} to 940 cm^{-1} accompanied by a decrease of band maximum absorb-

Table I. Spectral changes in arsenosilicate films due to heat-treatment at 800°C in Ar for 10 min

m/o As_2O_3 in as-deposited glass ^(a)	Absorbance of Si-O band at 1060 cm^{-1}		Absorbance of As-O band at 930 cm^{-1}		IR ratio ^(c)	
	As-dep. ^(b)	H.T. ^(b)	As-dep.	H.T.	As-dep.	H.T.
4.0	0.93	1.20	0.18	0.185	0.197	0.153
14.4	0.57	0.66	0.30	0.18	0.53	0.274
22.0	0.54	0.80	0.44	0.17	0.82	0.216

^(a) Film thickness (top to bottom): 0.82 , 0.70 , and 0.90μ respectively.

^(b) As-dep. and H.T. denote as-deposited and heat-treated, respectively.

^(c) IR ratio = ratio of the absorbance of the As-O band to that of the Si-O band.

ance; and (iii) the appearance of a well-defined band at 630 cm^{-1} . An example of these effects for a glass containing 14.4 m/o As_2O_3 is shown in Fig. 1. The systematic results are tabulated in Table I. Detailed chemical and spectral analyses of the combined Si-O and As-O bands in the region $1400\text{-}800\text{ cm}^{-1}$ of the infrared as a function of thermal history of CVD arsenosilicate films show that structural changes and not composition variations are responsible for the observed shifts in band frequency and maximum absorbance in the heat-treated film (13).

Films containing 20 m/o As_2O_3 and higher appear frosty when heat-treated at 800°C in Ar. Microscopic examinations showed that the frostiness was actually due to the appearance of very circular fringes arranged in a somewhat random manner over the entire film. Systematic heat-treatment at various temperatures in Ar for 10 min showed that the temperature required to bring about the appearance of these circular fringes is strongly dependent on the composition of the as-deposited film; the higher the concentration of As_2O_3 in the film, the lower the heat-treatment temperature is necessary to produce the fringes. Micrographs of these fringes are shown in Fig. 2 for various composition films heat-treated at the respective temperature to produce frostiness. With low enough As_2O_3 -content ($0.5\text{ m/o As}_2\text{O}_3$) films, fringe formation can be avoided even when heat-treated at temperatures as high as

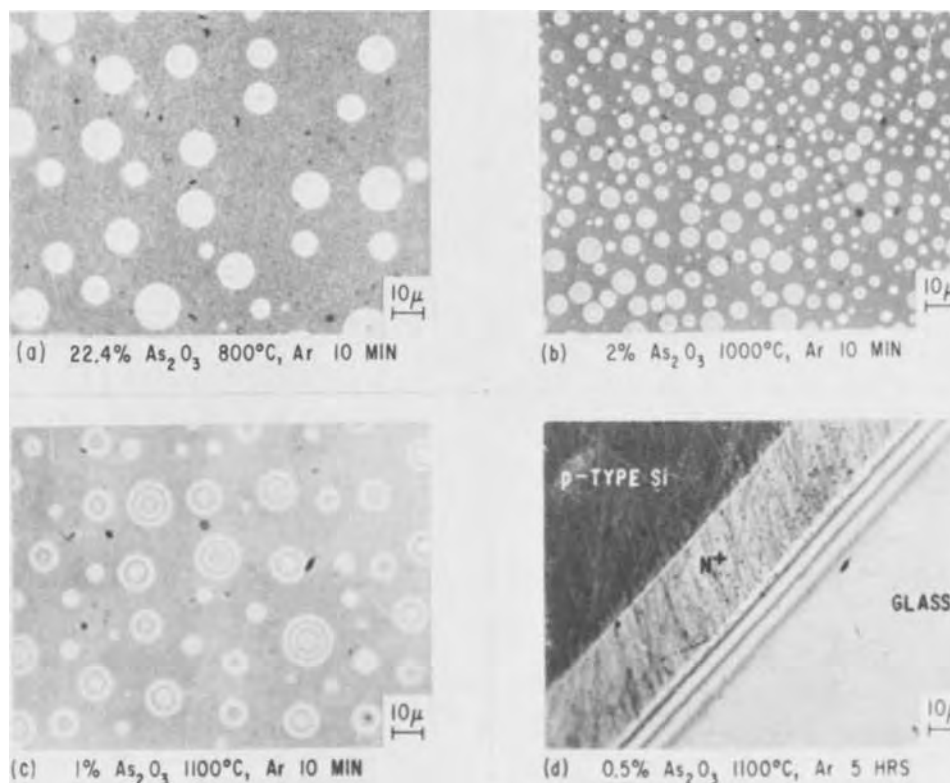


Fig. 2. Micrographs of film surfaces after heat-treatment.

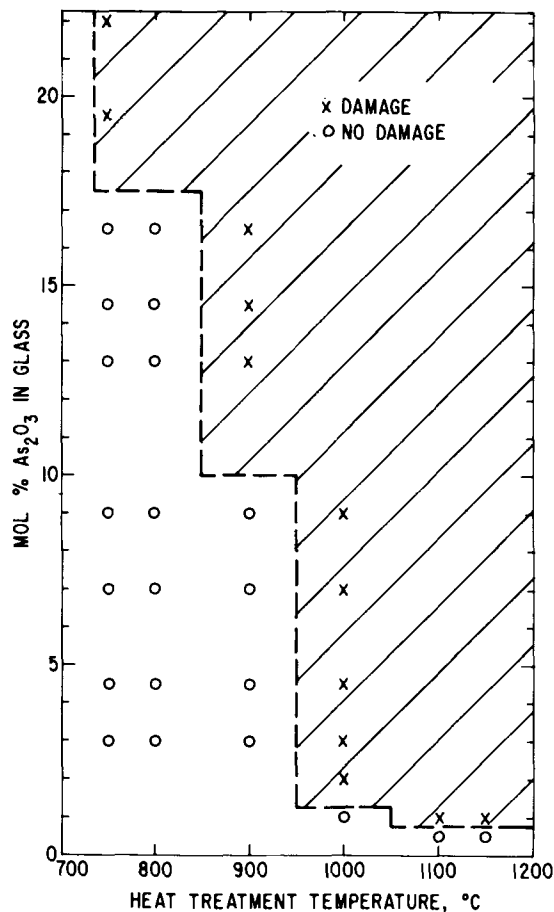


Fig. 3. Glass composition vs. temperature of circular fringe formation due to heat-treatment in Ar for 10 min.

1100°C for a period of 5 hr. The net result is the formation of a very uniform N^+ diffused layer (see Fig. 2d) as reported earlier (11). The boundary separating the compositions which give rise to circular

fringe formation at various heat-treatment temperatures is given in Fig. 3. These circular fringes are found to be very reproducible and their appearance or otherwise at a given heat-treatment temperature can be predicted quite accurately once the chemical composition of the film is determined. Heat-treating a given composition glass in the temperature range covered by the shaded area shown in Fig. 3 will always induce fringe formation.

Optically, these very circular fringes suggest regions of optical discontinuity between the silicon substrate and the glass film. Indeed, direct observation using scanning electron microscopy reveals that these fringes are actually regions of circular convex domes (Fig. 4) of the glass film heaving off from the silicon substrate under a biaxial compressive stress.

To elucidate the mechanism of fringe formation of vapor-deposited arsenosilicate films on silicon, we examine the thermal component of the stress in the glass film, arising from the difference in the thermal expansion coefficients of the film and the substrate and follow its magnitude and sign with the deposition and heat-treatment histories. The thermal stress generated in a thin film deposited on a thick substrate is given by (14)

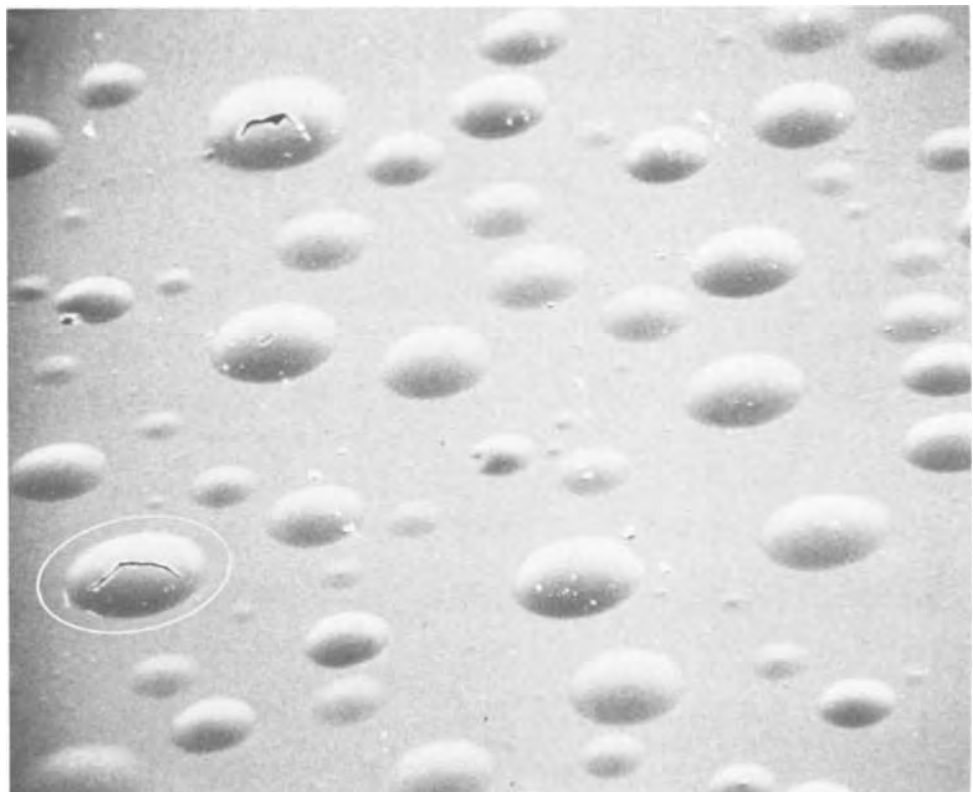
$$S_{th} = (\alpha_f - \alpha_s) \Delta T E_f \quad [1]$$

where α_f and α_s are the average coefficients of expansion for film and substrate, ΔT is the difference in temperature of the substrate during film deposition and measurement, and E_f is the Young's modulus of the film. S_{th} is positive when the film is under a tensile stress, and negative when it is under a compressive stress.

Consider the case where $(\alpha_f - \alpha_s)$ is positive, i.e., the expansion coefficient of the glass is greater than that of the silicon substrate. Assume also that the intrinsic component of the stress¹ in the deposited film is negligible compared with the thermal component at all temperatures under consideration. We examine

¹ The intrinsic stress constitutes the second component to the total stress but its origin is not well understood at present (14). Its contribution to the total stress is by no means trivial in certain cases. In our thermal cycling experiments, however, it is expected that the thermal stress plays a major role in the observed mechanical phenomenon as will be evidenced in later discussion.

Fig. 4. Scanning electron micrograph of a 14.0 m/o As_2O_3 film after 10 min heat-treatment at 800°C in Ar. Film was deposited at 450°C. Magnification: 500X.



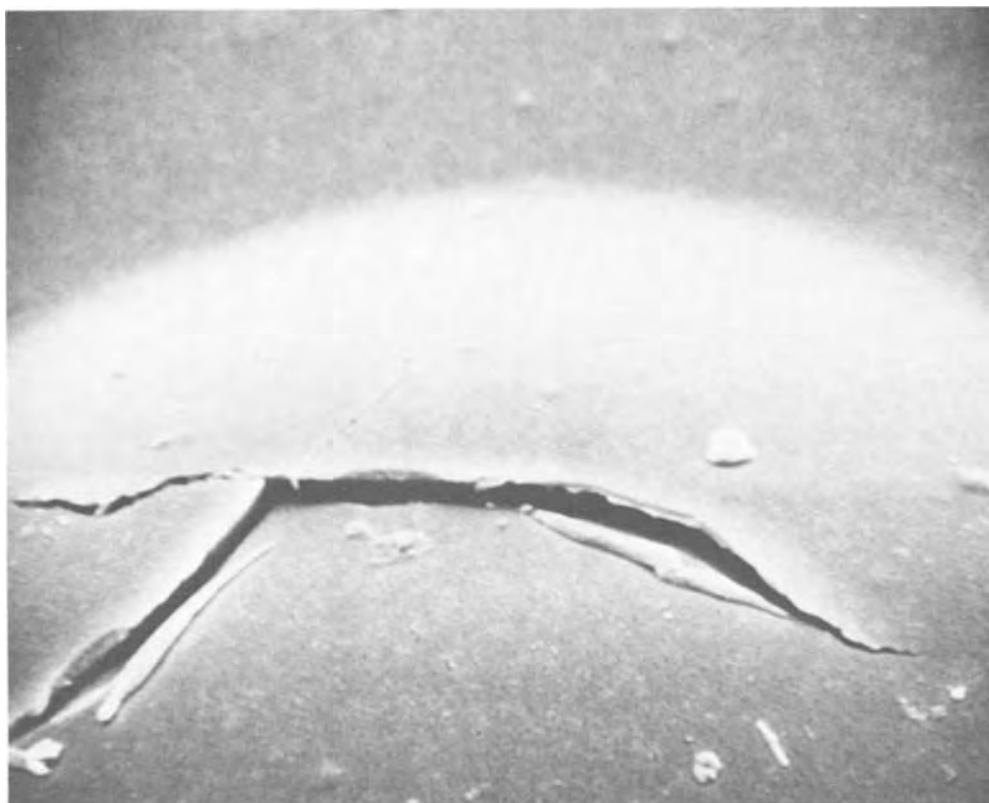


Fig. 5. Scanning electron micrograph of a cracked convex dome (circled in Fig. 4) showing relief of the biaxial compressive stress. Magnification: 500X.

the stress history of the film in the following temperature cycle. When the film is deposited at the deposition temperature, the thermal stress in the film is zero because ΔT is zero. When cooled to room temperature, the film will contract more than the substrate because of its higher expansivity, but is restrained from doing so by the substrate. A biaxial tensile stress is thus generated in the film upon cooling. Upon heat-treatment, this biaxial tensile stress is progressively reduced as the sample is heated to the deposition temperature from room temperature. At temperatures above the deposition temperature the film will expand more than the substrate, but again is restrained from doing so. In this case, S_{th} is negative because ΔT is negative, and a biaxial compressive stress is thus set up in the film. When this compressive stress is high enough, stress relief will take place to cause film buckling from the substrate as shown in Fig. 4, which in turn gives rise to the colored fringes observed under the microscope (Fig. 2).

The buckling due to a biaxial, thermal, compressional mechanism is further substantiated by a more detailed examination of the heat-treated glass surface by scanning electron microscopy at a higher magnification. In Fig. 5, a micrograph of a ruptured circular convex dome circled in Fig. 4 is further magnified 10 times. Crackings occur along two perpendicular lines, showing clearly the biaxial compressional mechanism (14). The detachment of the film from the silicon substrate as a result of the convex dome formation is shown in Fig. 6 which is a scanning electron micrograph of a diamond-scribed edge of the same sample.

In light of the present systematic study on the initial heat-treatment characteristics of vapor-deposited arsenosilicate glass films on silicon as a function of glass composition and heat-treatment temperature, the so-called "glass damage" encountered in all the early works (7-10) on high As_2O_3 concentration glass may be understood. Arai and Terunuma (9), for instance, working with 25-31 m/o As_2O_3 glasses found that heat-treatments at $1000^\circ C$ and up always cause surface damage to the glass, and that the lowest temperature for damage increases with increase in deposition temperature. The latter dependence can

easily be explained in terms of the thermal stress history of the film. The higher the deposition temperature, therefore, the higher the temperature of heat-treatment is required to generate a biaxial compressive stress large enough to initiate film detachment from the silicon surface, i.e., in order to keep ΔT constant in Eq. [1]. Raising the temperature and/or prolonging the period of heat-treatment, will further

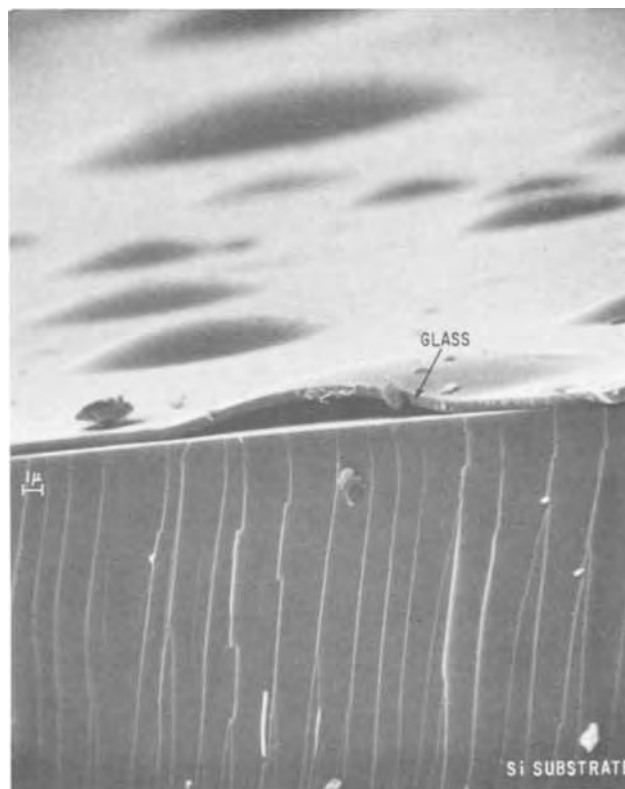


Fig. 6. Scanning electron micrograph of a diamond-scribed edge of the same film shown in Fig. 4 and 5. Magnification: 2000X.

bring about rupture of the film (Fig. 5) and even devitrification (9). The film loses its glassy appearance and acquires a dull, frosty metallic look.

Teshima and co-workers (7) found that glass damage may conceivably be reduced if a layer of 900Å SiO₂ is sandwiched between the binary glass and the Si substrate. Frosting of some kind was still observed in the glass film after heat-treatment at 1150°C.

However, as the amount of As₂O₃ is reduced in the glass film, a better expansion-coefficient match with silicon can be obtained. This automatically reduces the magnitude of the factor ($\alpha_f - \alpha_s$) in the stress expression, and thus in order to bring about the detachment under a large enough compressive stress, a higher heat-treatment temperature (i.e., larger ΔT) is required. Thus a monotonic increase in the allowable heat-treatment temperature is expected with decrease in As₂O₃ content in the film and this is found experimentally as shown in Fig. 3.

Conclusion

Results on the compositional dependence in the surface morphology of CVD arsenosilicate films on silicon substrate at the initial stage of heat-treatment in Ar at various temperatures show that the thermal compressive stress generated at these elevated temperatures are largely responsible for the observed film detachment from the substrate. These observations help to give an insight into the "glass-damage" problem associated with higher As₂O₃ content films, at least during the initial stage of heat-treatment.

When the As₂O₃ content in the films is reduced substantially to about 0.5 m/o, glass damage can be eliminated altogether and prolonged heat-treatment will yield very uniformly diffused N⁺ layers of As in Si. The diffusion characteristics of As from these low As₂O₃ glasses into the silicon will be given in a subsequent paper (15).

Acknowledgments

The author would like to thank Prof. J. W. Mitchell for the enlightening discussion on film properties and

for his constructive comments. Thanks are due to M. Ghezzi and M. F. Ciccarelli for preliminary microscopic examinations of the heat-treated films and for the SEM analysis respectively. Encouragement by M. Garfinkel in various aspects of this work and his constructive comments on the manuscript are gratefully appreciated.

Manuscript submitted Oct. 22, 1971; revised manuscript received March 17, 1972.

Any discussion of this paper will appear in a Discussion Section to be published in the June 1973 JOURNAL.

REFERENCES

1. A. W. Fisher, J. A. Amick, H. Hyman, and J. H. Scott, Jr., *RCA Rev.*, **29**, 533 (1968).
2. M. L. Barry and P. Olofsen, *This Journal*, **116**, 854 (1969).
3. M. L. Barry, *ibid.*, **117**, 1405 (1970).
4. T. Okabe and E. Tarukawa, *Suppl. Jap. J. Appl. Phys.*, **40**, 24 (1971).
5. D. M. Brown and P. R. Kennicott, *This Journal*, **118**, 293 (1971).
6. D. B. Lee, *Solid-State Electron.*, **10**, 623 (1967).
7. H. Teshima, Y. Tarui, and O. Takeda, *Bull. Electrochem. Lab. Japan*, **33**, 631 (1969).
8. A. Cuccia, G. Shrank, and G. Queirolo, in "Semiconductor Silicon," Rolf R. Haberecht and Edward L. Kern, Editors, p. 506, The Electrochemical Society Softbound Symposium Series, New York (1969).
9. E. Arai and Y. Terunuma, *Japan. J. Appl. Phys.*, **9**, 691 (1970).
10. P. C. Parekh, D. R. Goldstein, and T. C. Chan, *Solid-State Electron.*, **14**, 281 (1971).
11. J. Wong and M. Ghezzi, *This Journal*, **118**, 1540 (1971).
12. J. Wong, *ibid.*, **118**, 1071 (1972).
13. J. Wong, To be published.
14. K. L. Chopra, "Thin Film Phenomena," Chap. 5, McGraw Hill Book Co., New York (1969).
15. J. Wong and M. Ghezzi, *This Journal*, Accepted for publication.

Backscattering Studies of Anodization of Aluminum Oxide and Silicon Nitride on Silicon

M. Kamoshida¹ and J. W. Mayer

California Institute of Technology, Pasadena, California 91109

ABSTRACT

Anodic oxidation of amorphous and polycrystalline aluminum oxides and amorphous silicon nitride deposited by chemical reactions on silicon were investigated by use of 2 MeV ⁴He⁺ ion backscattering spectra and optical microscope examination. In anodization, the oxide layer was formed underneath the original aluminum oxide film and on the top surface of the silicon nitride layer. For a fixed current, the anodic voltage characteristics for aluminum oxide exhibited breakdown effects. After breakdown the aluminum oxide became nonuniform, and was removed at later stages of anodization, leaving a silicon oxide layer. For 700°C-grown aluminum oxide, irregular surfaces were formed after all stages of anodization while for 830°C-grown aluminum oxide, the oxide layer formed at later stages was similar in thickness and uniformity to those of anodically grown silicon oxide layers on bare silicon. The anodic voltage characteristics for silicon nitride did not exhibit breakdown. Backscattering data showed linear dependences on anodizing time of the decrease in amount of nitrogen and increase in amount of oxygen, suggesting that the nitrogen was replaced by oxygen during anodization. A similar mechanism was proposed by Schmidt and Wonsidler, and by Tripp.

Recently silicon nitride and aluminum oxide films have been investigated to fabricate high reliability

devices such as beam-lead, sealed-junction devices (1), or memory devices such as MNOS memory (2) or MAS memory (3). Analysis of profiles of MeV particles backscattered from dielectric films have been also described as a nondestructive method to study films

¹ Permanent address: Nippon Electric Co., Ltd., Kawasaki, Japan.

Key words: anodization, anodization of Si, Al₂O₃ films, backscattering analysis.

of silicon oxide, silicon nitride, or multilayer structures with silicon oxide and silicon nitride (4-6). More recently, the composition of sputtered silicon nitride was determined by both nuclear reactions and backscattering techniques as a function of the nitrogen content of the reactive atmosphere (7). Backscattering techniques were also used to investigate aluminum oxide films deposited onto silicon by hydrolysis of aluminum trichloride (8-10). Films grown at temperatures of 700°C or less are amorphous and contain residual chlorine [contents of 2 atomic per cent (a/o)] uniformly distributed throughout the film. Films grown at 800°C or above are polycrystalline and contain less than 0.02 a/o of chlorine. Both films are stoichiometric in composition. Influence of heat-treatment on the film properties was also investigated (11). In oxidizing atmosphere, oxygen diffuses through aluminum oxides deposited at 700° and 830°C, and new oxides were grown underneath the original aluminum oxides. A mixture of aluminum, silicon, and oxygen was found at the interface of the aluminum oxide and thermally grown new oxide.

Anodic oxidation of silicon previously covered with aluminum oxide should be attractive for comparison with thermally oxidized specimens. Schmidt and Wonsidler (12) suggested that in the anodization of polycrystalline alpha-alumina on silicon in aqueous borate solution, growth of new oxide occurred at the oxide-silicon interface. This is in contrast with anodic oxidation of silicon nitride where the oxide layer is formed on the top surface. The data of Schmidt and Wonsidler (12), and Tripp (13) indicate that the nitrogen is replaced by oxygen.

In the present work anodic oxidation of silicon covered with aluminum oxides formed by chemical reaction, at 700°C (amorphous) and at 830°C (polycrystalline), was investigated using MeV $^4\text{He}^+$ backscattering techniques and optical microscope examination. These results were compared with backscattering data from anodically oxidized silicon nitride films.

Experimental Procedure

Aluminum oxide and silicon nitride films were deposited from the vapor state by the reaction (14) of aluminum trichloride, carbon dioxide, and hydrogen, and by the silane-ammonia reaction (15) onto the surface of silicon wafers, respectively. As previously described (8-11), before the deposition the substrate silicon wafers were mechanically-chemically mirror polished to obtain a sharp interface between the deposited insulator films and the silicon surfaces. Prior to the start of deposition, wafers were rinsed with dilute hydrofluoric acid to keep to a minimum silicon oxide on the surface. Temperatures of the silicon surfaces during deposition were 700° and 830°C for aluminum oxide, and 950°C for amorphous silicon nitride films. Substrates used were n-type, 3.5~6.5 ohm-cm Si(111) for aluminum oxide and p-type, 3~5 ohm-cm Si(100) for silicon nitride.

The detailed descriptions of the other growth parameters for both films are found in Tsujide *et al.* (16) and in Kobayashi *et al.* (17) (in our case, the reactor pressure was 1 atm), respectively. The thicknesses of 700°C- and 830°C-grown aluminum oxide and silicon nitride were 1900, 1600, and 480Å, respectively. Original film thicknesses were measured by ellipsometry.

Nonaqueous systems (18) of N-methylacetamide were used for the electrolyte to which were added 0.97 weight per cent (w/o) of KNO_3 and 1.9 w/o of deionized water. Anodizations were performed using a regulated d-c power supply capable of delivering 0-400V and 0-75 mA, and were performed under illumination following the work of Schmidt *et al.* (19). An open 40 ml Teflon beaker with a hole in the bottom (where the electrolyte anodized the sample) was used and electrical contact to the silicon wafer was made

by pressing a metal (the area of which is larger than the anodic area of silicon) to the back of the silicon wafer (20). No particular precautions were taken to keep the temperature of electrolyte constant. No subsequent heat-treatment was made. Backscattering data indicated that the thickness of the 700°C-grown film (which was attacked by water) did not change if the film was immersed in the electrolyte for 30 min.

The Kellogg Laboratory 3-MV accelerator was used; typical $^4\text{He}^+$ target currents were 15~20 nA at 2 MeV incident ion energy. Particles backscattered through a laboratory angle of 168° were detected in a 25 mm² surface barrier detector (12 cm distance). Standard electronics, including a pulse pile-up rejection system, fed pulses to a 400-channel pulse height analyzer. Analyzer dead time was never greater than 3%. Energy resolution was about 15 keV.

Results

Relation between anodic voltage and anodizing time.

—Typical characteristics of anodic voltage vs. anodizing time under a condition of a fixed current, 9.2 mA/cm², are shown in Fig. 1. Sections a, b, c, and d correspond to data obtained from the samples whose original structures were bare silicon, silicon nitride on silicon, 700°C-grown aluminum oxide on silicon, and 830°C-grown aluminum oxide on silicon, respectively. The anodic characteristic obtained from silicon nitride on silicon has a similar shape (monotonic increase) as that observed from bare silicon. In the case of silicon covered with the 700°C-grown aluminum oxide film, the characteristic curve was divided into three regions: in region 1 continuous breakdown was observed (the ratio of the peak to valley in the breakdown characteristics depended on the sample); in region 2 irregular characteristics were found; and next, monotonically stable characteristics were obtained in region 3. Many spots, whose diameters were of the order of

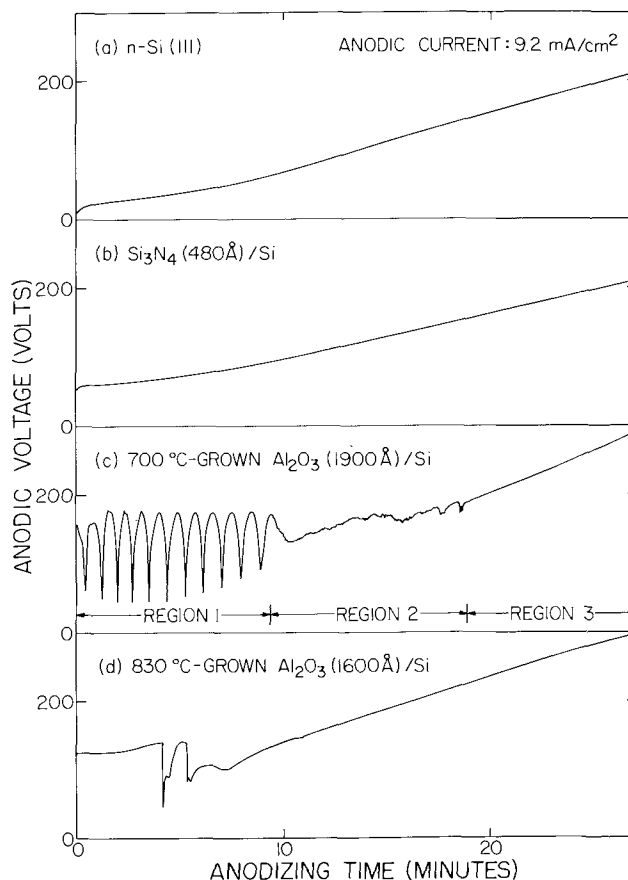


Fig. 1. Typical relations between anodic voltages and anodizing times at a fixed current of 9.2 mA/cm² for different samples.

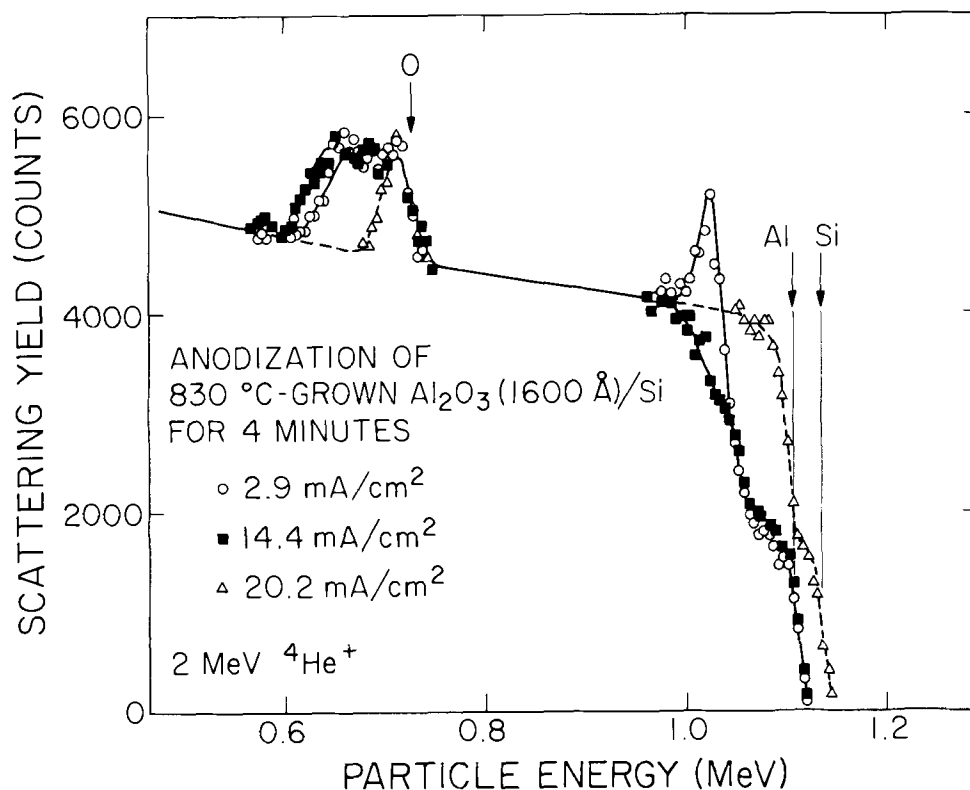


Fig. 2. Spectra of 2 MeV ${}^4\text{He}^+$ ions backscattered from 1600Å-thick aluminum oxide films deposited at 830°C and anodized for 4 min; inserted arrows indicate the energies of 2 MeV- ${}^4\text{He}^+$ ions backscattered from each element.

1 μ , were observed by optical microscopy on the surface of the aluminum oxide in region 1. After the characteristic change to region 2, the surface of the sample became nonuniform in a microscopic view. Even after the transition to the monotonic characteristic, optical microscope examination still showed surface irregularities.

Only two or three spikes (the spike shape was sharper in a thicker film) were observed in the case of 830°C-grown aluminum oxide on silicon. Before the first breakdown spike the film surface was uniform, but after the breakdown surface nonuniformity was observed. This nonuniformity did not remain (under optical microscope examination) at the stage corresponding to region 3 of 700°C-grown film, and the surface appeared like that of anodized bare silicon. Similar features of breakdown and surface nonuniformities of 700°C- and 830°C-grown films were found in the anodization over the range of current densities from 2.9 to 20.2 mA/cm². In the former case, the time between breakdown became shorter with increasing current densities and there was little change of the voltage of the top level of breakdown characteristic; in the latter case the breakdown was observed above current densities of 9 mA/cm² (up to 9 mA/cm² the characteristic change was monotonic).

Backscattering data on 830°C-grown aluminum oxide films.—Figure 2 shows spectra of particles backscattered from 1600Å-thick aluminum oxide films deposited at 830°C and anodized for 4 min at 2.9, 14.4, and 20.2 mA/cm². The spectrum (circular points) for the sample anodized at 2.9 mA/cm² [which resembled closely that for an as-grown sample (8, 10, 11)] has the following major features: (i) the energy of the leading edge in the region of higher energy coincides with the energy of particles scattered from aluminum at the surface; (ii) the step corresponds to aluminum in the aluminum oxide; (iii) the peak (at ~ 1.0 MeV) is generated by the overlap of the trailing edge of the spectrum of aluminum in aluminum oxide with the leading edge of the substrate silicon spectrum; and (iv) the peak at low energies (0.6 to 0.8 MeV) corresponds to oxygen in the aluminum oxide layer. After an anodization of 14.4 mA/cm² (filled square plots),

the position of the leading edge of this spectrum remains unchanged but the overlap peak disappears and the width of oxygen peak increases reflecting an increase in the oxide layer thickness. Since the leading edge of aluminum spectrum does not change, the new oxide layer must be formed underneath the original aluminum oxide. After the sample was anodized at 20.2 mA/cm² (open triangle plots, corresponding to region 3 in Fig. 1c), the leading edge of the spectrum shifted to the energy corresponding to silicon at the surface and the width of oxygen peak was markedly reduced. This spectrum corresponds to that of a silicon oxide film on silicon with a thickness about 1/3 of the original aluminum oxide film thickness. This indicates that the original aluminum oxide film has been removed.

Similar results were found in anodization of 830°C-grown films on silicon at constant current (see Fig. 1d). Figure 3 shows the backscattering spectra for an as-grown film of thickness of 1600Å and samples anodized at 9.2 mA/cm² for 7 min (shortly after breakdown) and 28 min (monotonically increasing voltage). In the spectrum for the sample anodized for 7 min (filled squares) the spectrum leading edge at higher energy is at the position characteristic for aluminum, and the overlap peak has disappeared. The width of the oxygen peak exhibits a slight increase. The spectrum for the sample anodized for 28 min (open triangle points) has a leading edge corresponding to that of silicon and the width of oxygen peak decreases, *i.e.*, aluminum oxide film absent. Note that the edge of the step at 1.06 MeV (corresponding to the oxide-silicon interface) is much steeper than that of the sample anodized for 7 min. This suggests that an irregular interface is present in the sample anodized for 7 min. Visual examination also indicates the surface irregularity.

Spectra for a silicon sample with 830°C-grown film (open triangle points) and for a bare silicon sample (filled triangle points), both of which were anodized at 9.2 mA/cm² to the same final anodic voltage of 307V, are given in Fig. 4. The two spectra coincide closely indicating that two silicon oxide films are nearly identical in thickness and composition. Visual exam-

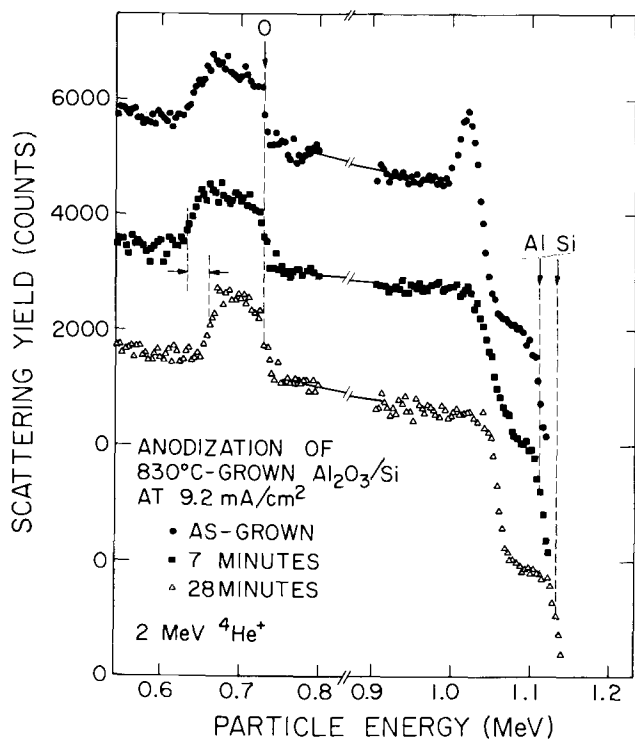


Fig. 3. Backscattering spectra obtained from anodized specimens of 1600Å-thick, polycrystalline aluminum oxide deposited at 830°C on silicon; the spectra are shifted vertically (2000 counts) for clarity.

ination indicates that both films are uniform in thickness. After anodic oxidation to the region where the voltage increases monotonically, the films are easily dissolved in hydrofluoric acid.

Backscattering data on 700°C-grown aluminum oxide films.—Figure 5 shows backscattering data of a 700°C-grown aluminum oxide of thickness of 1900Å on silicon at each anodizing stage shown in Fig. 1c, i.e., after 5.5 min (region 1), 13.5 min (region 2), and 28 min (region 3) at a fixed current density of 9.2

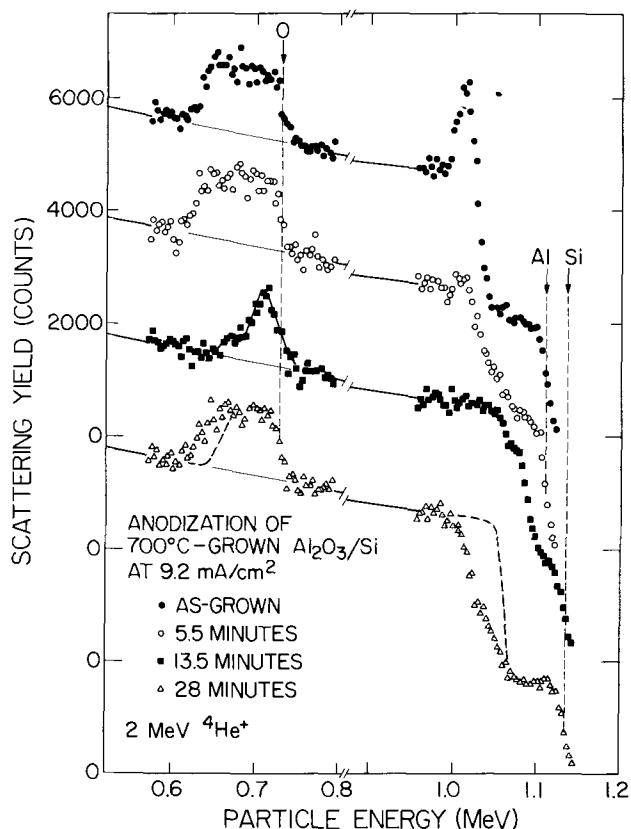


Fig. 5. Typical set of backscattering spectra indicating the anodizing time dependence obtained from 700°C-grown, 1900Å-thick amorphous aluminum oxide on silicon. Estimated silicon spectra are drawn under each oxygen spectrum with light solid curve. Dashed spectrum superposed on the data of 28 min anodization corresponds to the spectra of 29 min anodization of an 830°C-grown aluminum oxide as shown in Fig. 3. Final anodic voltages of both samples are nearly equal (~300 V).

mA/cm². In region 1 (circular points, after 5.5 min) the height of the overlap peak decreased and only small increase is noted in the width of oxygen peak.

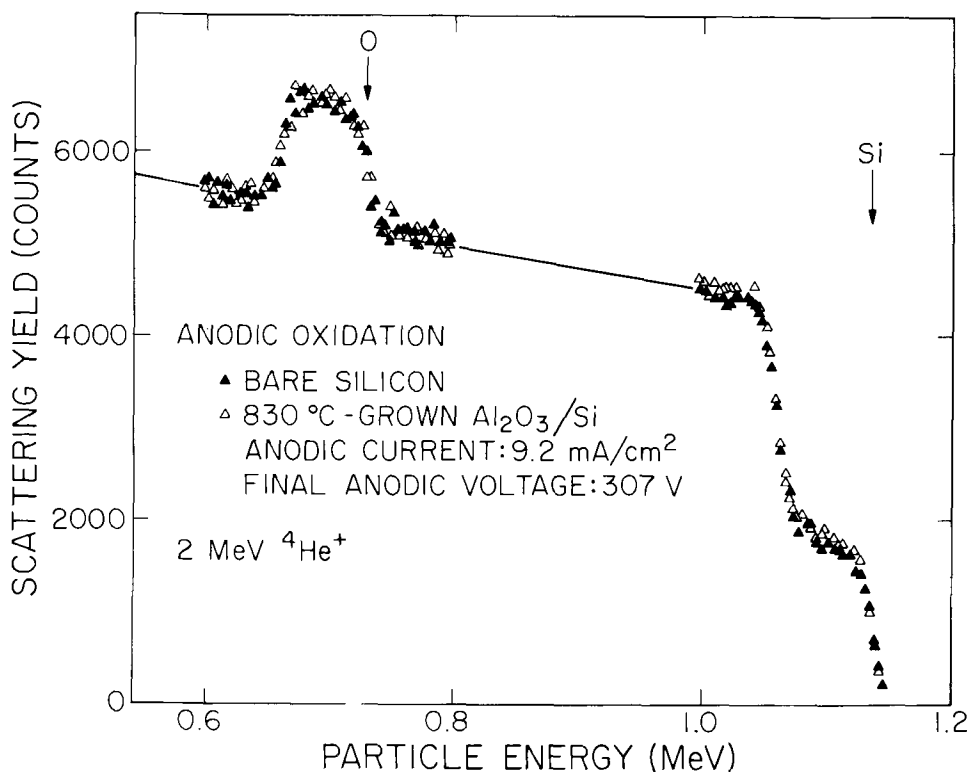


Fig. 4. Backscattering spectra (2 MeV- $^4He^+$) obtained from an 830°C-grown, 1600Å-thick aluminum oxide on silicon and bare silicon anodized under the same anodic conditions except the anodizing period; within statistics, the two spectra are identical.

After anodization for 13.5 min (filled squares, region 2 in Fig. 1c) the leading edge of the spectrum shifted to the position of silicon edge, the overlap peak disappears, and oxygen peak becomes narrower and exhibits step-like tail. This indicates that much of the aluminum oxide layer has been removed and that the remaining oxide layers are nonuniform in thickness. The slope of the leading edge suggests that some aluminum oxide is present on the predominantly silicon oxide surface. The spectrum for the sample anodized for 28 min (open triangle plots) shows an increase in the width of oxygen peak. Comparison with the spectrum (dashed line), for anodized 830°C-grown aluminum oxide film on silicon, indicates that the slope of the spectrum for the 700°C-grown film in the region around 1.07 MeV is less steep than that for 830°C-grown film. This indicates that the oxide layer is nonuniform as was also suggested by visual observation of the surfaces. Width of oxygen peak is also wider than that of 830°C-grown film on silicon anodized for 28 min.

Chlorine spectra corresponding to this sequence of anodized 700°C-grown films are of thickness of 1900Å given in Fig. 6. Anodic current density was 9.2 mA/cm². For the as-grown film (filled points) the amount of chlorine is about 2 a/o (8). The chlorine spectra exhibit a step in the leading edge due to the presence of the two chlorine isotopes (³⁵Cl and ³⁷Cl). Previous analysis (10) indicated that the chlorine is distributed uniformly throughout the film. After anodization for 5.5 min (circular points), the shape of the chlorine spectrum exhibits some change. Because of the non-uniform nature of the film after anodization, the shape of the chlorine spectrum varied somewhat for different positions of incidence of the analysis beam. However, one can note an increase of the tail in the spectrum in the region between 1.13 MeV and 1.16 MeV. In studies of chlorine spectra anodized for a fixed period and increased current densities, there was a decided trend

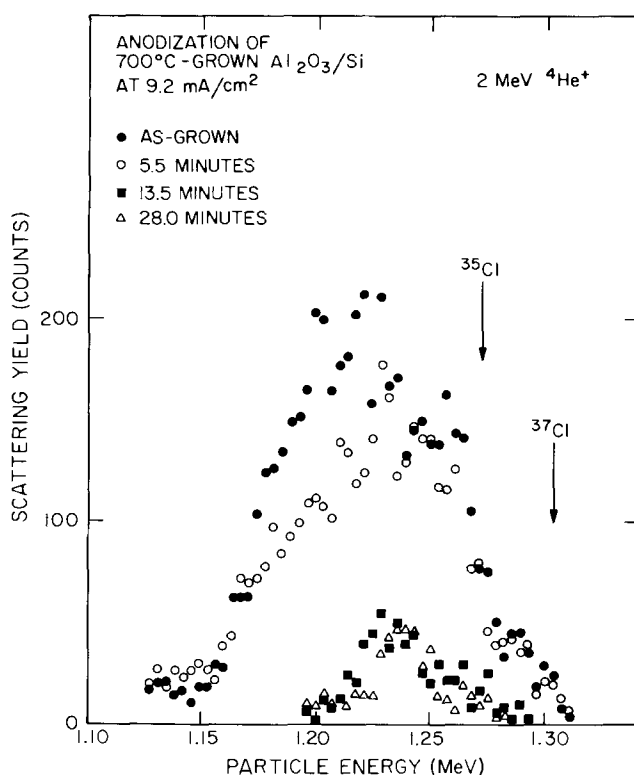


Fig. 6. Chlorine spectra corresponding to the sequence of anodized 700°C-grown aluminum oxide (1900Å). In as-grown film the amount of residual chlorine was 2 a/o. The data obtained after anodizations at 9.2 mA/cm² for 5.5 min, 13.5 min, and 28 min, correspond to the samples in regions 1, 2, and 3 in Fig. 1c.

towards an increase in amount of chlorine in this region towards the tail of the spectrum.

After anodization for 13.5 min (filled squares in Fig. 6) the total amount of chlorine is 10% of its value in the as-grown film. After further anodization (open triangle plots) the amount of chlorine remained at about 10% of the original value. The leading edge of residual chlorine spectrum did not exhibit an appreciable shift, and the width of the chlorine spectrum is narrower, indicating that the chlorine is confined to a region close to the surface. Under a fixed anodizing period condition with varying anodic current densities, similar features were observed.

Anodization of silicon nitride.—For comparison with aluminum oxide, the anodization of silicon nitride layers on silicon was investigated. Typical spectra of 2 MeV ⁴He⁺ particles backscattered from a 480Å-thick as-grown silicon nitride film, deposited on silicon, and the sample anodized at 8.7 mA/cm² for 15 min (the final anodic voltage was 132V) are shown in the inset of Fig. 7 drawn by solid and dashed curves, respectively. Shapes of these spectra are similar to those described previously by Meyer *et al.* (4) with specimens of Si₃N₄/Si and SiO₂/Si₃N₄/Si structures. After anodization, an oxygen signal appeared in the spectrum and the nitrogen peak was shifted and decreased.

Because of the large difference in mass between nitrogen and oxygen, the backscattering spectra near

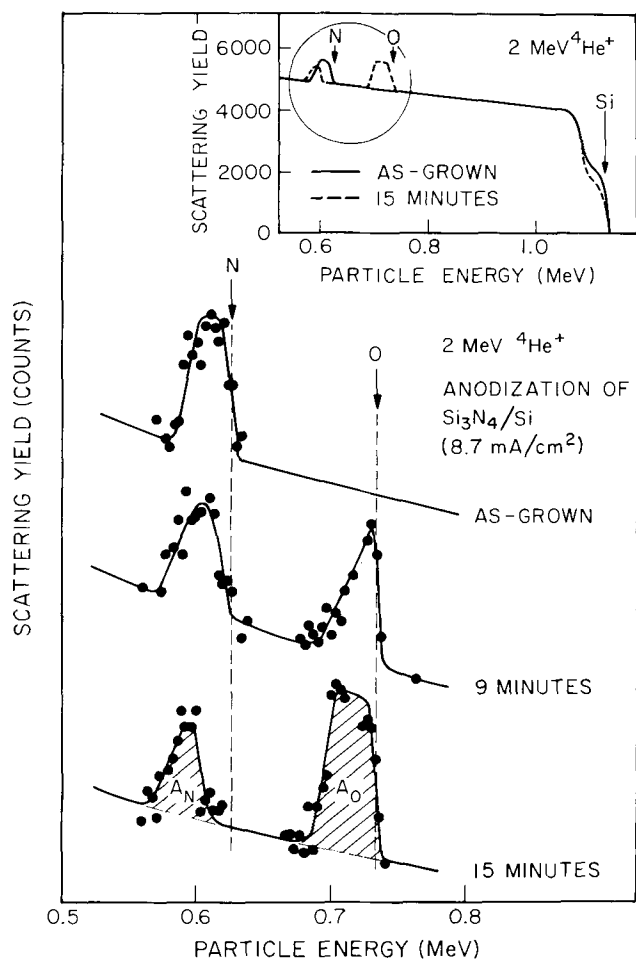


Fig. 7. Spectra of 2 MeV He⁺ particles backscattered from anodized silicon nitride previously deposited on silicon. Inset shows the spectra obtained from an as-grown, 480Å-thick silicon nitride on silicon and the sample anodized at 8.7 mA/cm² for 15 min drawn by solid and dashed curves, respectively. The main body of the figure shows backscattering spectra near the energies of oxygen and nitrogen edges (the area surrounded with a circle in inset) obtained from as-grown and anodized samples. Samples are tilted through an angle of 45° with respect to the incident beam.

the energies of nitrogen and oxygen can be used to analyze the formation of the silicon oxide layer. The parts surrounded with a circle in the inset of Fig. 7 are enlarged in Fig. 7 itself, where the spectrum obtained from a 9 min-anodized specimen is also shown. The shaded areas, A_N and A_O , are the total signal from the nitrogen and oxygen, respectively. From these data the following information was obtained: (i) the shift to lower energy of the nitrogen edge and generation of oxygen peak indicate that the oxide layer is formed on the top of silicon nitride; and (ii) a replacement of nitrogen in silicon nitride with oxygen is suggested by the fact that the amount of nitrogen (A_N) decreases as the amount of oxygen (A_O) increases.

From the quantitative point of view, if the nitrogen was replaced with oxygen, the decrease in the nitrogen signal between successive anodizations (t_1 and t_2) should be linearly related to the increase in the oxygen signal or

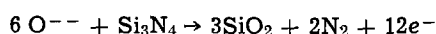
$$\frac{A_N(t_1) - A_N(t_2)}{\sigma_N f} = K_1 \frac{A_O(t_2) - A_O(t_1)}{\sigma_O f} \quad [1]$$

where σ_N and σ_O are scattering cross sections of nitrogen and oxygen, respectively; and f is a factor determined by the target to detector geometry. The factor K_1 indicates the ratio of amounts of nitrogen to oxygen converted during anodization. If the amount of silicon in the layer remains unchanged, then $K_1 = 2/3$ since two nitrogen atoms are replaced by three oxygen atoms, and

$$\frac{A_N(t_1) - A_N(t_2)}{A_O(t_2) - A_O(t_1)} = K_1 \frac{\sigma_N}{\sigma_O} = K_2 \quad [2]$$

where the constant K_2 equals 0.49 for the σ_N/σ_O value of 0.733 in this scattering geometry. In Fig. 7 the following values are observed: $K_2 = 0.39$ and 0.48 for $t_1 = 0$ (i.e., as-grown) to $t_2 = 9$ min; and $t_1 = 9$ min to $t_2 = 15$ min, respectively. These results are within the experimental error considering the problems in background subtraction and counting statistics. This suggests that the nitrogen was replaced by oxygen and agrees with the results of destructive investigations by Schmidt and Wonsidler (12) and Tripp (13).

Figure 8 shows time dependences of spectrum areas of nitrogen and oxygen. If the following relation



is assumed (13), that there are linear relations between anodic time and variations in amounts of nitrogen and oxygen for a fixed anodic current. Then, the following equations should hold

$$\left. \begin{aligned} A_O(t) &= at \\ A_N(t) &= bt + c \end{aligned} \right\} \quad [3]$$

where a , b , and c are constant. From Eq. [2]

$$-b/a = K_2 = 0.49 \quad [4]$$

In Fig. 8, the solid line was obtained from the experimental values of oxygen spectrum areas (cross points) and the slope of the dashed line was calculated on the basis of Eq. [4]. The decrease in the nitrogen areas tended to follow the estimated dashed line. This result also suggests that the nitrogen in silicon nitride was replaced by oxygen. Some of the scatter about the dashed line could arise from differences in the original film thickness.

Anodic time dependences on anodic voltage, and on the fractional amount of remaining silicon nitride, are shown in Fig. 9. The remaining amounts of silicon nitride (filled points) were evaluated from the areas of spectra of nitrogen and oxygen as follows

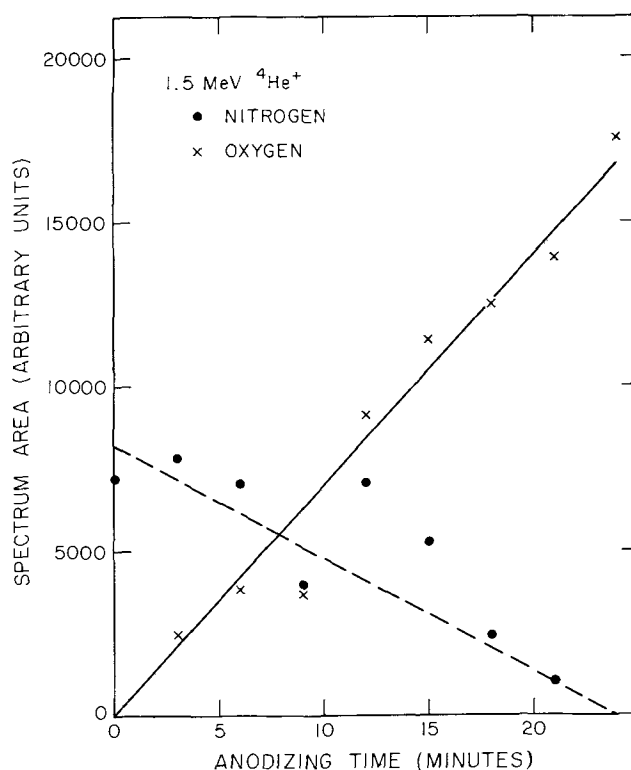


Fig. 8. Relations between anodizing times and spectrum areas of oxygen (cross points) and nitrogen (filled points) obtained by using 1.5 MeV $^4He^+$ particles. Original thickness of silicon nitride was 480\AA . Solid line was fixed to experimental data and the slope of dashed line was calculated.

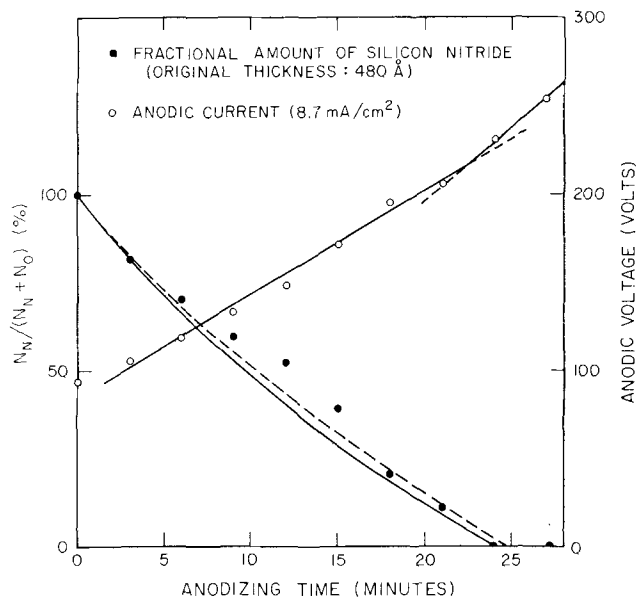


Fig. 9. Relations between anodic voltage and fractional amounts of nitrogen and oxygen in the film vs. anodization time. Solid curve shows calculated from linear relations in Fig. 8, and dashed curve shows Tripp's data [Fig. 3 in Ref. (13)]. The anodic voltages were observed under a condition of fixed current of 8.7 mA/cm^2 ; original film thickness was 480\AA .

$$\frac{N_N}{N_N + N_O} = \frac{\frac{A_N(t)}{\sigma_N f}}{\frac{A_N(t)}{\sigma_N f} + \frac{A_O(t)}{\sigma_O f}} = \frac{1}{1 + \frac{A_O(t)}{A_N(t)} \cdot \frac{\sigma_N}{\sigma_O}} \quad [5]$$

where the values of $N_N = A_N(t)/\sigma_N f$ and $N_O = A_O(t)/\sigma_O f$ correspond to the fractional amounts of nitrogen and oxygen in the dielectric films, respectively.

If we use the linear relation of time on the fractional amounts of nitrogen and oxygen, Eq. [5] should be hyperbolic. In Fig. 9 the solid curve shows the values calculated from the linear relations in Fig. 8. The experimental data (filled points) followed such a relation. One of the reasons of deviation is the presumed different thicknesses of original films. Although the electrolyte was different than in our case, because of the similar thickness of the original silicon nitride (500Å) and the current density (7.5 mA/cm²), Tripp's data [Fig. 3 in Ref. (13)] is also used for comparison in Fig. 9 (dashed curve). In both cases, about 500Å-thick silicon nitride changed to silicon dioxide after 24 ± 1 min. As shown in Fig. 9, the slope of the time dependence of anodic voltage changed at the time corresponding to the disappearance of the nitrogen peak.

Conclusions

The anodic oxidations of 700°C- and 830°C-deposited films of aluminum oxide on silicon have general features in common. In the initial stages of anodization, breakdown phenomena are noted. A visual examination of the surface reveals that the surfaces are irregular. Backscattering spectra show an increase in the width of oxygen peak but the leading edge of the spectrum does not shift (i.e., it corresponds to the aluminum edge) indicating that a silicon oxide layer is formed underneath the original aluminum oxide film. For a longer period of anodization (or higher current densities) the width of oxygen spectrum exhibits a marked decrease, and the leading edge of the spectrum shifts to that of the silicon spectrum edge. At this stage the overlying aluminum oxide film has been removed and, for 830°C-grown films, the width of the oxygen peak and the shape of the silicon spectrum coincide with those for the bare silicon samples anodized to the same voltage. For these high temperature-grown films, once the aluminum oxide film has been removed, the growth of anodic oxide layer follows that for a bare silicon sample. This offers the possibility of a new selective etching technique of polycrystalline aluminum oxide which is similar to the technique for silicon nitride suggested by Schmidt and Wonsidler (12). The as-grown 830°C-deposited aluminum oxide films are only slightly etched by hydrofluoric acid (8), however, after the anodic oxidation the films are easily dissolved with hydrofluoric acid.

One of the major differences between the anodization of 700°C- and 830°C-deposited films is the marked irregularity of the surfaces of the low temperature films. This may follow from the large number of breakdowns observed in the initial stages of anodization for these films. Even in the region where the anodic voltage shows a monotonic increase with anodizing time, the surfaces of the low temperature films are still irregular. The leading edge of the chlorine spectra for these films are not appreciably shifted during anodization. This, again, points out that a new oxide layer is formed underneath the original aluminum oxide layer. The tail that appears in the chlorine spectrum along with the residual chlorine (≈10% of the original amount after anodization) might indicate that chlorine is drifted by the applied anodizing field into the underlying oxide layer. However, because of the nonuniform nature of the film after anodization, one cannot exclude the possibility that some of the original aluminum oxide has been retained.

The result of anodic oxidation of aluminum oxide films is similar to that of thermal oxidation (11) in that the new oxide layer is grown underneath the original film. However, for thermal oxidation there is a strong adherence of the aluminum oxide layer to the newly formed oxide. This might be due to the mixing of silicon and aluminum that was noted for the thermally oxidized sample. In anodized samples, the film irregularity and anodic voltage peaks might imply

that the oxide growth takes place initially in localized regions where breakdown phenomena could provide easy paths for oxidation of the underlying silicon. At later stages, the removal of the aluminum oxide would lead to larger area regions.

For silicon nitride, backscattering data indicate that the oxide layer is formed on top of the nitride layer, i.e., the silicon nitride films act as a substrate that is anodized, in agreement with the data of Tripp (13) and Schmidt and Wonsidler (12). The basic difference is the replacement of nitrogen by oxygen. In this respect it should be noted that it is possible (due to statistics involved in background subtraction) that some (<10%) of the nitrogen remains when the anodization reaches a stage where the oxide layer just reaches the silicon. Complete disappearance of the nitrogen might occur at a later point when the substrate silicon is oxidized. Thermal oxidation of silicon nitride also proceeds by growth of the oxide layer on top of the nitride layer (21). In this case the silicon nitride masks against the diffusion of oxygen (22).

Acknowledgments

We wish to thank Nippon Electric Company, Ltd., Dr. S. Nakanuma for his encouragement, and Iida and Inoue for providing the deposited samples. We also thank R. Gorris for his preparation of equipment of anodic oxidation. This work was supported in part by Air Force Cambridge Research Laboratories and the Office of Naval Research.

Manuscript submitted Nov. 15, 1971; revised manuscript received March 17, 1972.

Any discussion of this paper will appear in a Discussion Section to be published in the June 1973 JOURNAL.

REFERENCES

1. M. P. Lepselter, *Bell Lab. Record*, **44**, 298 (1966).
2. J. T. Wallmark and J. H. Scott, *RCA Rev.*, **30**, 335 (1969); B. C. Ross and J. T. Wallmark, *ibid.*, 366.
3. S. Nakanuma, T. Tsujide, R. Igarashi, K. Onoda, T. Wada, and M. Nakagiri, *IEEE J. Solid-State Circuits*, **SC-5**, 203 (1970).
4. O. Meyer, J. Gyulai, and J. W. Mayer, *Surface Sci.*, **22**, 263 (1970).
5. J. Gyulai, O. Meyer, J. W. Mayer, and V. Rodriguez, *Appl. Phys. Letters*, **16**, 232 (1970).
6. J. Gyulai, O. Meyer, J. W. Mayer, and V. Rodriguez, *J. Appl. Phys.*, **42**, 451 (1971).
7. M. Croset, S. Rigo, and G. Amsel, *Appl. Phys. Letters*, **19**, 33 (1971).
8. M. Kamoshida, I. V. Mitchell, and J. W. Mayer, *ibid.*, **18**, 292 (1971); There is an erratum, Figs. 1 and 2 should be interchanged to correspond to the proper captions.
9. I. V. Mitchell, M. Kamoshida, and J. W. Mayer, *Phys. Letters*, **35A**, 21 (1971).
10. I. V. Mitchell, M. Kamoshida, and J. W. Mayer, *J. Appl. Phys.*, **42**, 4378 (1971).
11. M. Kamoshida, I. V. Mitchell, and J. W. Mayer, *ibid.*, Accepted for publication.
12. P. F. Schmidt and D. R. Wonsidler, *This Journal*, **114**, 603 (1967).
13. T. B. Tripp, *ibid.*, **117**, 157 (1970).
14. V. Y. Doo and P. J. Tsang, Paper 16 presented at the New York Meeting of the Society, May 4-5, 1969.
15. V. Y. Doo, D. R. Nichols, and G. A. Silvey, *This Journal*, **113**, 1279 (1966).
16. T. Tsujide, S. Nakanuma, and Y. Ikushima, *ibid.*, **117**, 703 (1970).
17. K. Kobayashi, Y. Haneta, and S. Nakanuma, *J. Electrochem. Soc. Japan*, **37**, 87 (1969).
18. E. F. Duffek, C. Mylroie, and E. A. Benjamin, *This Journal*, **111**, 1042 (1964).
19. P. F. Schmidt and W. Michel, *ibid.*, **104**, 230 (1957).
20. N. G. E. Johansson, J. W. Mayer, and O. J. Marsh, *Solid-State Electron.*, **13**, 317 (1970).
21. I. Franz and W. Langheinrich, *ibid.*, **14**, 499 (1971).
22. V. Y. Doo, *IEEE Trans. Electron Devices*, **ED-13**, 561 (1966).

The Influence of Anodic Coatings on Slip in Aluminum

P. Mehdizadeh¹ and R. J. Block

Department of Chemical Engineering and Materials Science,
The University of Oklahoma, Norman, Oklahoma 73069

ABSTRACT

Aluminum single crystals were anodized and deformed in tension. Thick coatings inhibited slip of the surface except where cracking or buckling had occurred. Strengthening of the crystal depended upon the thickness but was controlled by the residual stress of the coating.

When anodized aluminum is deformed the coating accommodates deformation of the substrate primarily by cracking. The various modes of film behavior on single crystal and polycrystalline substrates have been discussed in previous papers (1-3) and have been a source of interest for some time (4-7). In the present paper the effect of the coating upon near surface slip is discussed.

Experimental

Reynolds 99.999+ % aluminum was grown into single crystals by a modification of the Bridgman technique using high purity graphite molds. Long crystals of round cross section (for tensile testing) and square cross section (to facilitate surface examination) were produced and cut into specimens of shorter length. The specimens were numbered according to a scheme which assigned the prefix R or S depending on whether the crystal was round or square and two numbers following to indicate the crystal and specimen numbers. The orientations of the crystals are shown in Fig. 1. Prior to testing the crystals were annealed, electropolished in perchloric acid-alcohol, stripped of any residual films in a chromic-phosphoric acid bath, and then anodized. The techniques were identical to those used in previous studies (1, 2).

Oxide films were formed in boric acid buffered to a pH of 5.5. The film formation current was either maintained at less than 0.2 mA/cm² or kept slightly above 2.0 mA/cm² until the required voltage was achieved. Thereafter, the voltage was maintained until the current decayed to a terminal value usually in the neighborhood of 0.01 mA/cm².

Previous experiments (8-10) showed that residual stresses in similar anodically formed coatings depended upon film thickness and the rate of formation. However, the literature leaves some uncertainty about the magnitude and even the sign of the residual stresses which could be expected with the electrolyte used in the present work. Experiments with pH 9-10 ammonium borate solutions (8, 10) produced 150 to 3000 Å coatings which were in residual compression when the formation current density was less than 0.5 mA/cm², and predicted tensile stresses with current densities in excess of 1 mA/cm². It was also reported that the current density at which stress reversal occurred appeared to increase with decreasing solution pH. In all cases however, the residual stresses were reported to become more compressive with increasing film thickness.

Results and Discussion

After sufficient extension, anodized coatings of 1300 Å and thicker always cracked at approximately 90° to the tension axis. The cracks completely encircled the specimen. The spacings between these circumferential cracks became quite uniform, rapidly reaching an equilibrium value which depended upon the coating thickness. Thinner coatings cracked along slip plane traces as well as forming a circumferential

crack pattern similar to thicker films. Figure 2 shows the relationship between tensile elongation and crack density for anodic coatings of three different thicknesses formed at the low rate. The specimens used were annealed polycrystalline wires and round single crystals of comparable orientation to those of Fig. 1. Similar behavior has been reported previously by Edeleanu and Law (4) for sulfuric acid (cellular type) coatings and was predicted and analytically treated by Grosskreutz and McNeil (11) and Grosskreutz (12).

Once the limiting crack density had been reached, further extension served only to open the cracks. Figure 3 shows this behavior with a 3000 Å coating on a single crystal substrate. The appearance of the sur-

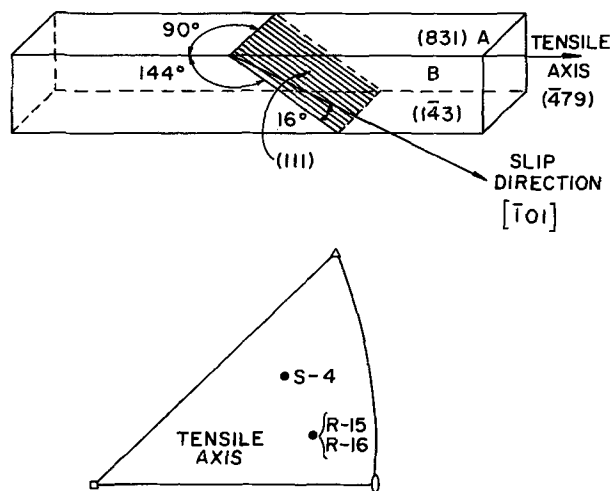


Fig. 1. Stereographic and geometric representations of the crystal orientations.

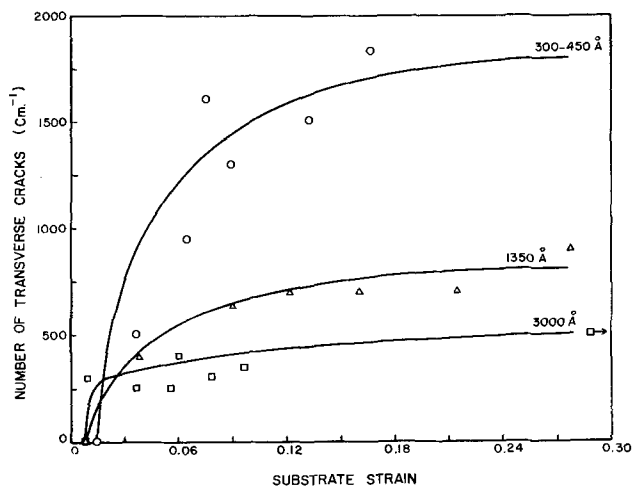


Fig. 2. Density of transverse cracks vs. strain for anodic coatings of various thicknesses formed at 0.2 mA/cm².

¹ Present address: Continental Oil Company, Ponca City, Oklahoma 74601.

Key words: anodized aluminum, residual film stress, slip lines, plastic deformation.

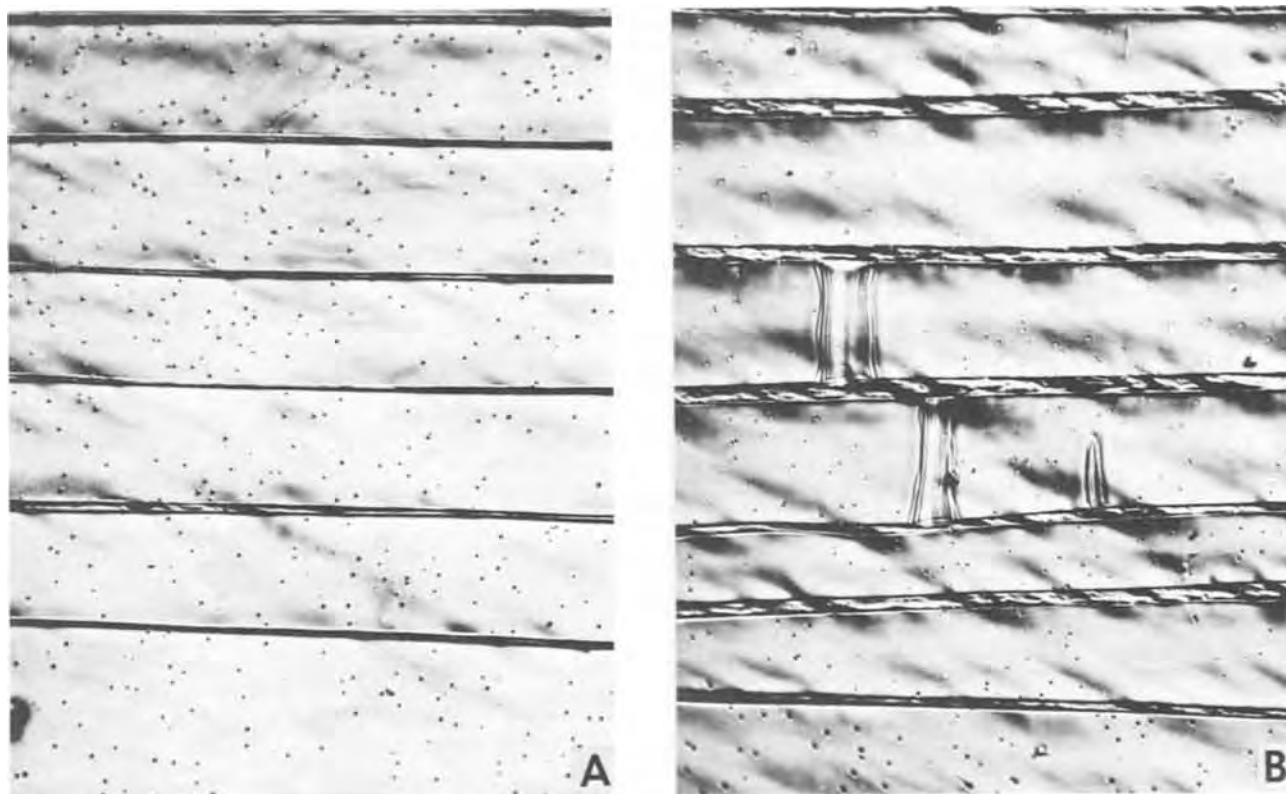


Fig. 3. Widening of transverse cracks in a 3000Å coating, face B of crystal S-4-4 is shown: a, 5.6% elongation; b, 10.5% elongation. The vertical structures in b are buckles in the coating. (X1000).

face in this figure, which is typical of a large number of specimens, may be used to illustrate several aspects of the interaction of the coating with the deformation processes in the underlying crystal.

One of the most striking features of Fig. 3 is the absence of sharp slip lines in areas where the film remained intact. The appearance of the surface immediately suggests that the coating has influenced deformation of the near surface region of the crystal suppressing or severely altering the ordinary slip processes. Cracks in the coating after 10.5% elongation are seen to be as much as 3 or 4 times larger than they were after 5.6% strain, indicating that deformation had taken place preferentially in the substrate material beneath and immediately adjacent to the cracks.

The short diagonal markings within the cracks of Fig. 3a appear to be large slip steps in the substrate crystal. Upon continued extension these were seen to enlarge further and lead out into the regions between cracks where marked undulations of the surface had developed. This deformation obviously involves the operation of a number of slip systems in a rather complex manner. The few vertical structures in Fig. 3b are the result of buckling of the coating (2) and illustrate the appearance of a coating which has become detached from the substrate.

The photomicrographs of Fig. 4 also demonstrate the ability of an anodic film to suppress slip at the coating-substrate interface. In the associated experiment, a crystal with a 3000Å coating was extended 10% and marked with two microhardness indentations (Fig. 4a). The coating was then chemically removed as evidenced by the disappearance of the interference fringes in the buckled areas. There are no sharp slip plane traces where the coating had remained intact (Fig. 4b). However, further extension by 3% produced a single set of sharp slip steps which tended to form at many of the deep slip lines within the cracks (Fig. 4c). The inclination of these slip lines corresponds to the trace of the primary slip plane in the specimen surface. Slip lines within the buckled

areas have slightly different inclinations because, once film detachment occurred, the underlying surface material then deformed while the surrounding material was still constrained by the coating.

Adherent surface coatings often have been regarded as effective barriers to dislocation egress from within the crystal (13-15). Although recent work (16) has shown that this is not necessarily true for all coating-substrate combinations, in the present system thick oxide coatings on aluminum seem to have a pronounced influence upon deformation, at least at the surface. This leads one to expect a correspondingly large effect upon the mechanical properties of coated crystals. A series of tensile tests of anodized and uncoated specimens yielded the results shown in Fig. 5 and 6. The strengthening influence of the coating may be seen to depend upon both its thickness and its state of residual stress. The latter factor was shown to be of primary importance in the strengthening of copper single crystals by electroplated metal coatings (16). However, it appears that differences exist in the mechanisms through which residual stresses act to produce strengthening in these two systems. Metal coatings on copper crystals produced large effects only where cracking occurred either prior to or during deformation. Relaxation of the substrate crystal adjoining the cracks produced a layer of dislocations which impeded the motion of primary glide dislocations toward the surface. In the present case, it appears that the aluminum oxide coating itself is capable of directly inhibiting slip at the surface. Where cracks occurred, prominent primary slip lines appeared suggesting that the strengthening had been reduced in these regions.

A coating in a state of residual tension induces compressive stresses in the substrate crystal. These stresses should inhibit the motion toward the surface of dislocations having a Burgers' vector component which is normal to the surface. The absence of slip lines beneath the coating indicates that dislocations were prevented from reaching the interface. Recent experiments (17) indicated that the pH 5.5 boric acid

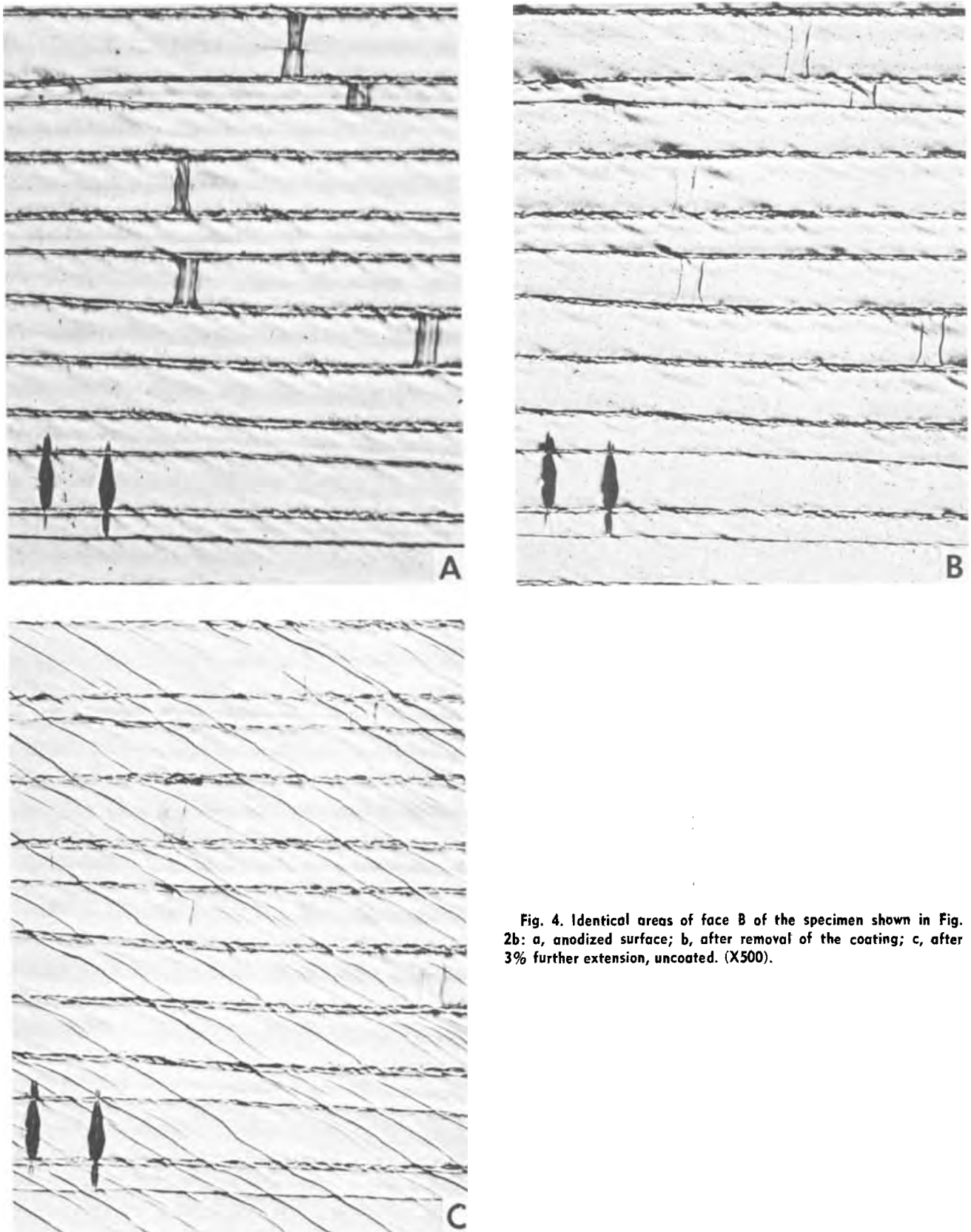


Fig. 4. Identical areas of face B of the specimen shown in Fig. 2b: a, anodized surface; b, after removal of the coating; c, after 3% further extension, uncoated. (X500).

solutions used in the present work produced coatings which were in compression even when they were formed at 2.0 mA/cm^2 . The tensile stresses induced in the substrate crystal would be expected to act in the direction of coaxing dislocations toward the surface rather than repelling them. Consistent with this view the increase in strength, induced by the coatings of low residual compression (shown in Fig. 6), was

much greater than with the more highly compressed film (shown in Fig. 5).

The magnitudes of the strengthening produced by anodized coatings become more impressive when one considers that the deformation of aluminum crystals should be relatively insensitive to conditions at the surface. Coatings exert their strongest influence during stage I deformation (18). Aluminum crystals with

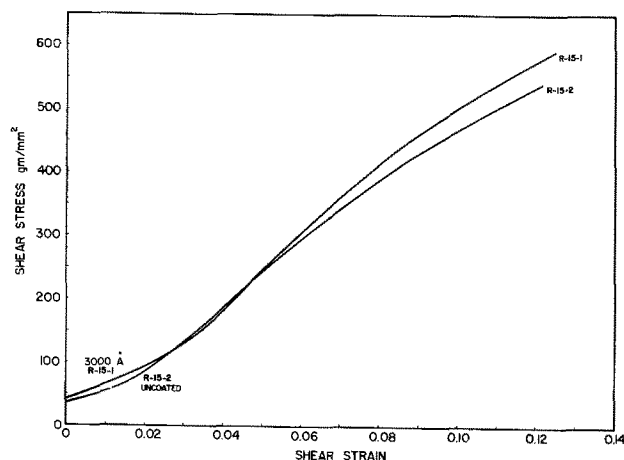


Fig. 5. The effects of a 3000Å coating formed at 0.2 mA/cm², upon the mechanical properties of an aluminum single crystal.

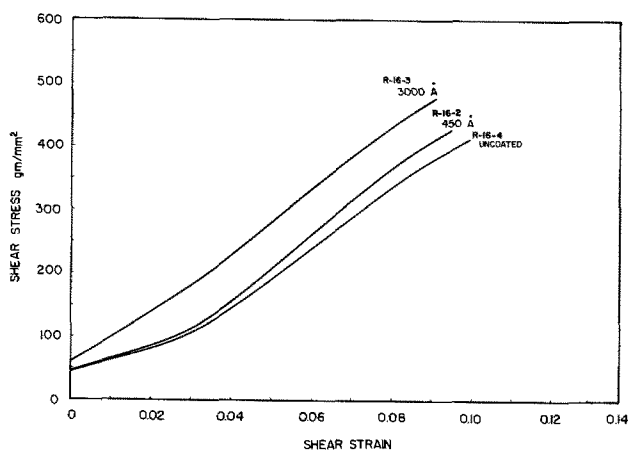


Fig. 6. The strengthening produced by a 3000Å (and 450Å) coating formed at 2.0 mA/cm².

their characteristically short, easy glide regions should not provide a system which is particularly sensitive to surface film effects. It is well known that, in aluminum, interpretation of bulk deformation behavior

from the appearance of slip lines on the surface is unreliable (19-21). Slip line patterns characteristic of single slip persist long after the end of stage I, indicating that the surface and interior harden at very different rates.

Acknowledgements

This work was funded by the U.S. Atomic Energy Commission [Contract AT-(40-1)-3401] whose support is gratefully acknowledged, and is based upon a thesis for the degree Doctor of Philosophy.

Manuscript submitted July 26, 1971; revised manuscript received March 10, 1972.

Any discussion of this paper will appear in a Discussion Section to be published in the June 1973 JOURNAL.

REFERENCES

1. N. J. Cochrane and R. J. Block, *This Journal*, **117**, 225 (1970).
2. R. J. Block, *ibid.*, **117**, 788 (1970).
3. R. J. Block and P. Mehdizadeh, To be published.
4. C. Edeleanu and T. J. Law, *Phil. Mag.*, **7**, 573 (1962).
5. S. F. Bubar and D. A. Vermilyea, *This Journal*, **113**, 892 (1966).
6. S. F. Bubar and D. A. Vermilyea, *ibid.*, **114**, 882 (1967).
7. J. C. Grosskreutz, *ibid.*, **116**, 1232 (1969).
8. D. H. Bradhurst and J. S. Ll. Leach, *Trans. Brit. Ceram. Soc.*, **62**, 793 (1963).
9. D. A. Vermilyea, *This Journal*, **110**, 345 (1963).
10. D. H. Bradhurst and J. S. Ll. Leach, *ibid.*, **113**, 1245 (1966).
11. J. C. Grosskreutz and M. B. McNeil, *J. Appl. Phys.*, **40**, 355 (1969).
12. J. C. Grosskreutz, *This Journal*, **117**, 940 (1970).
13. C. S. Barrett, P. M. Aziz, and I. Markson, *Trans. Met. Soc. AIME*, **197**, 1655 (1953).
14. J. Takamura, *Mem. Fac. Eng. Kyoto Univ.*, **18**, 255 (1956).
15. I. R. Kramer and L. J. Demer, *Progr. Mater. Sci.*, **9**, 131 (1961).
16. R. M. Johnson and R. J. Block, *Acta Met.*, **16**, 831 (1968).
17. R. J. Block and S. R. Perryman, To be published.
18. R. J. Block and M. Metzger, *Phil. Mag.*, **19**, 599 (1969).
19. D. Kuhlman-Wilsdorf, J. H. Vander Merwe, and H. Wilsdorf, *ibid.*, **43**, 632 (1952).
20. N. A. McKinnon, *ibid.*, **46**, 1150 (1955).
21. L. M. Clarebrough and M. E. Hargreaves, *Progr. Metal Phys.*, **8**, 1 (1959).

The Suppression of Ionic Contamination During Silicon Nitride Deposition

E. MacKenna* and P. Kodama

Research and Development Laboratory,
Fairchild Camera and Instrument Corporation, Palo Alto, California 94304

ABSTRACT

Electrical instabilities have been generally noted in MNOS structures incorporating SiH₄-type Si₃N₄ deposits but not in MNOS structures incorporating SiCl₄-type Si₃N₄ deposits. It is concluded that the SiCl₄ process for Si₃N₄ deposition has a built-in gettering capability for removing ionic contaminants which is not available from the SiH₄ process. It is proposed that the gettering capability arises from the presence of chloride ions. This premise was verified by purposely adding a source of chloride ions either prior to or during deposition of SiH₄-type Si₃N₄.

Many investigators (1-5) have demonstrated that thin (0.1μ) amorphous layers of silicon nitride (Si₃N₄)

* Electrochemical Society Active Member.
Key words: silicon nitride (Si₃N₄), MNOS, ionic contamination, hydrogen chloride (HCl), gettering.

can be used as barriers against the diffusion of impurity ions such as sodium. Indeed, Dalton and Drobek (6) published data demonstrating the ability of Si₃N₄ layers to mask against the diffusion of sodium at temperatures as high as 600°C. Deal *et al.* (7) have also

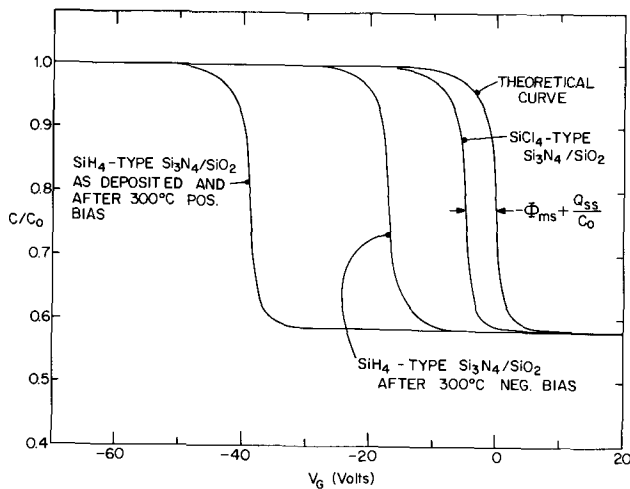


Fig. 1. Capacitance-voltage curves for a theoretical MIS capacitor, a SiCl₄-type Si₃N₄ MNOS capacitor, and a contaminated SiH₄-type Si₃N₄ MNOS capacitor as deposited and after 300°C stressing with -2.5×10^5 V/cm. [(111) p-type Si C_B $\approx 1.2 \times 10^{16}$ cm⁻³].

shown that these films act as barriers to the diffusion of hydrogen ions at temperatures as high as 550°C. Other authors (8-10) have discussed some of the advantages of MNOS as compared with MOS processing. However, because Si₃N₄ films are effective barriers to the diffusion of ionic contaminants, it is important that all sources of contamination are removed from device structures prior to Si₃N₄ deposition.

After elevated temperature processing in an oxidizing ambient, ionic contaminants such as sodium are generally located near the air-oxide interface (11). Various etching and phosphosilicate glass gettering techniques can be used to remove these sources of contamination (12). However, we have observed that the Si₃N₄ process itself can also act as a source of contamination.

During an investigation designed to study the effects of various process parameters on the electrical and physical properties of Si₃N₄ films, one anomaly was repeatedly observed. When Si₃N₄, deposited from silane and ammonia mixtures, was deposited over thermally oxidized silicon, electrical instabilities were generally noted. As shown in Fig. 1, the nature of the instability was such that it caused a negative shift (more negative turn-on voltages) to the flat-band voltages of MNOS capacitors. Application of negative fields on the order of 2.5×10^5 V/cm at 300°C caused a positive shift (less negative turn-on voltages) in the flat-band voltage. However, the flat-band voltage could not be recovered to the value corresponding to the fixed surface-state charge density (Q_{ss}/q) known to be present at the oxide-silicon interface. This fact, plus the observation that no field dependent drift of the C-V characteristics was observed, ruled out the possibility of Si₃N₄ structural polarization as being the cause of the instability.

Conductivity differences between the nitride and oxide layers, as discussed by Frohman-Bentchkowsky and Lenzlinger (13), were ruled out as being responsible for the instabilities noted because: (i) the capacitance-voltage curves were already shifted close to saturation in the negative voltage direction after Si₃N₄ deposition; (ii) application of fields on the order of $\pm 10^7$ V/cm at room temperature caused negligible shifts in the capacitance-voltage curves; (iii) application of fields on the order of $+5 \times 10^5$ V/cm or -2.5×10^5 V/cm at 300°C resulted in significant flat-band voltage shifts; and (iv) because conductivity measurements made on MNS (metal-nitride-silicon) capacitor structures indicated that the deposited Si₃N₄ was fairly nonconductive. Typically, conductivities less

than 2×10^{-15} mho/cm were measured at fields of 4.5×10^6 V/cm and these values were in agreement with measurements made on silicon tetrachloride type Si₃N₄ films which did not exhibit the instability.

Trapping could also be ruled out since the observed shifts under elevated temperature positive and negative biases were opposite to those expected for hole or electron trapping in the oxide at the oxide-silicon interface, and also due to the thickness of the underlying oxide layers themselves. All evidence pointed to some type of relatively mobile ionic species as being responsible for the instabilities noted. The lack of complete recovery of the C-V characteristics under negative bias at 300°C could be accounted for by assuming that the species is mobile only in the oxide layer and could not penetrate the Si₃N₄ layer. Repeated 300°C stressing under positive and negative biases yielded the same total magnitude of C-V drift indicating that the contamination species was consistently mobile. The magnitude of the instability was completely unpredictable from run to run, or even within any one run, and could not be correlated with any of the process parameters being studied which also strongly suggested some form of ionic contamination.

Experimental

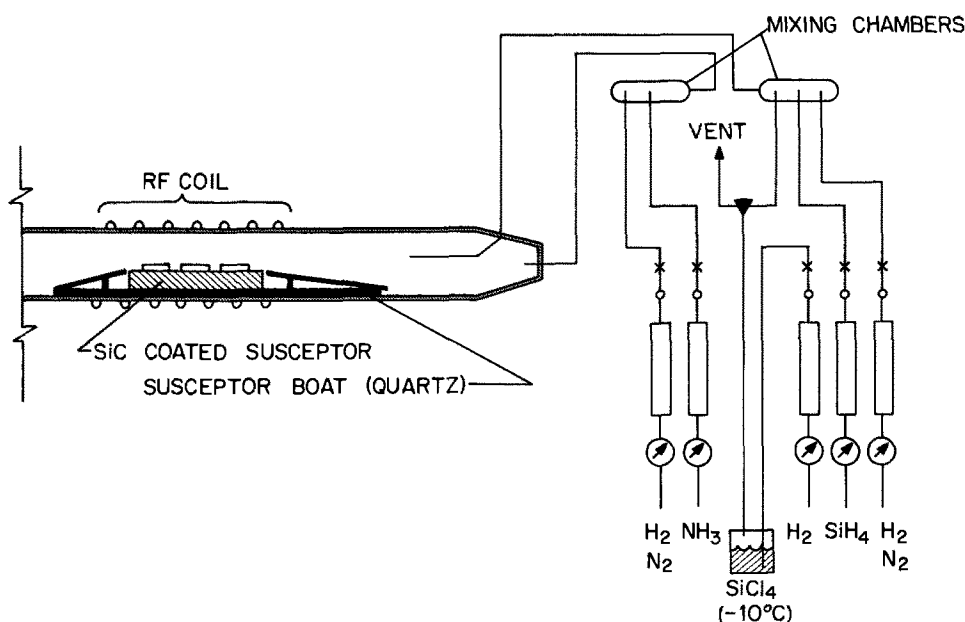
Chemically etched 1-3 ohm-cm p-type (111) Czochralski grown single-crystal silicon substrates, 1 in. in diameter, were thermally oxidized at 1200°C in dry oxygen immediately after etching and served as the primary test vehicle. The oxide thicknesses in all cases, except as noted, were 2000Å. Control wafers indicated that the conditions of oxidation yielded a fixed surface-state charge density, Q_{ss}/q , of 2×10^{11} charges cm⁻² and a nondetectable amount of mobile ionic contamination, Q_o/q ; that is, less than 4×10^{10} charges cm⁻².

Figure 2 shows a schematic of the deposition apparatus. The Si₃N₄ was deposited in an rf-heated horizontal system utilizing the reaction of silicon tetrachloride (SiCl₄) or silane (SiH₄) with ammonia (NH₃) in hydrogen or nitrogen ambients. The quartz reaction chamber has a 1¼ in. by 2¼ in. rectangular cross section and a volume of 1 liter. During the course of the investigation, total flow rates of from 3 to 6 liter/min were used. The Si₃N₄ thickness was normally 1000Å and deposited at 850°C (SiH₄ process) or 900°C (SiCl₄ process). The total flow rate and amounts of reacting gases were adjusted to yield deposition rates of from 100 to 150 Å/min. All deposits employed NH₃:SiCl₄ or SiH₄ ratios of 20:1 and 200:1, respectively; and all deposits appeared to be stoichiometric as determined by refractive index (1.99 to 2.00 at 6328Å) and etch rate measurements (3 to 5 Å/sec in 49% HF at 24°C - 0.7 to 1 Å/sec in H₃PO₄ at 153°C) and from previously conducted experiments evaluated by the technique discussed in Ref. (14).

Hydrogen and nitrogen were supplied from liquid sources through 316 stainless steel lines. The SiCl₄ used was supplied by Texas Instruments, Inc., and was contained in a quartz flask held at -10°C. The hydrogen carrier gas was bubbled through this flask and served to transport the SiCl₄ into the reaction chamber. The NH₃ used was Matheson ultra-high purity grade. Five per cent SiH₄ in nitrogen and 5% SiH₄ in hydrogen mixtures, also supplied by Matheson, were used during this investigation. Both sources of SiH₄ were analyzed for sodium by reacting the SiH₄ in a quartz combustion chamber, collecting the residue, and analyzing this using atomic absorption and flame spectrophotometric techniques (15). No evidence of sodium contamination in either source of SiH₄ was found.

As shown in Fig. 2 all gas lines, except the SiH₄ and SiCl₄ lines, leading to the mixing chambers were common for both types of Si₃N₄ deposits. The quartz reaction tube and susceptor support were fabricated from high purity quartz in our facilities. Care was exercised

Fig. 2. Schematic of deposition apparatus used for depositing SiCl_4 and SiH_4 -type Si_3N_4 .



to eliminate any external source of contamination; nevertheless, preliminary evaluations as shown in Fig. 1 indicated that an electrical instability could be induced in the underlying oxide of MNOS device structures during the Si_3N_4 deposition process.

Electrical Measurements

Most of the electrical evaluations for this investigation employed the well known capacitance-voltage (C-V) technique (16). Early in the investigation, it was noted that if contamination was present after Si_3N_4 deposition, most of it would be located close to the oxide-silicon interface. Therefore the C-V curves were already shifted close to saturation and it was convenient to monitor the contamination levels using a gold ball probe (the gold ball serving as the capacitor field plate) immediately after deposition of the Si_3N_4 without waiting for subsequent aluminum metalization and annealing steps. For these measurements any dielectric on the backside was removed with hydrofluoric acid, and a drop of water was used to insure good backside contact between the silicon and the contact plate. The standard procedure was to monitor each run by making C-V measurements at five different locations on each wafer immediately after deposition. If no obvious C-V displacement was observed, it was necessary to metalize the structure and to stress it at elevated temperatures (300°C) with positive and negative biases applied to the field-plate to determine if any mobile contamination was present. Subsequently, all wafers were metalized and additional C-V measurements were obtained at room temperature, and after elevated temperature (300°C) bias stressing, to verify the results obtained with the gold probe. Excellent correlation between the gold probe and metalized C-V data was obtained in all cases.

In this paper, data will be expressed in terms of Q_o/q , the effective number of contamination charges per cm^2 at the oxide-silicon interface. These levels of contamination were obtained from experimental C-V curves after subtracting out the flat-band voltage component due to the metal-semiconductor work function (Φ_{ms}) and the value of the fixed surface-state charge density, Q_{ss}/q , at the oxide-silicon interface. The resulting values of ΔV (in volts), along with the effective oxide thickness ($x_{o[eff]}$) in microns, was then inserted into Eq. [1] [according to Ref. (16)] and the contamination levels computed

$$\frac{Q_o}{q} \text{ (#/cm}^2\text{)} = \frac{2.16 \times 10^{10} \Delta V \text{ (volts)}}{x_{o[eff]} \text{ (microns)}} \quad [1]$$

The constant 2.16×10^{10} includes values for the dielectric constant of the oxide layer (K_o), the permittivity of free space (ϵ_o), and appropriate scaling factors for ΔV given in volts and $x_{o[eff]}$ in microns.

Results

Silane-type Si_3N_4 deposits.—Initially, contamination levels on the order of 5×10^{11} to 10^{12} cm^{-2} were observed. However, occasionally, instability levels on the order of 10^{13} cm^{-2} were found. Experimentally, it was noted that the magnitude of the instability was considerably reduced when nitrogen was substituted for hydrogen as the carrier gas during deposition. As shown in Table I, contamination levels dropped significantly when nitrogen was employed as the carrier gas. This was very puzzling at first; however, as will be shown later, a very simple explanation is possible based on the work of Burgess and Donega (17). They studied the out-diffusion of sodium from quartz furnace tubes in various atmospheres and showed that the reaction of hydrogen with quartz resulted in a marked increase in sodium vapor pressure.

Since previous data, obtained in similar systems employing silicon tetrachloride as the source of silicon, did not show the type of electrical instability seen in the SiH_4 -type deposits, it was decided to make SiCl_4 -type Si_3N_4 deposits in the same system as had been used for the SiH_4 -type deposits. No mobile ionic species were observed in MNOS capacitor structures fabricated from wafers used in these runs. Therefore, a series of consecutive Si_3N_4 deposits were made using either SiCl_4 or SiH_4 as the source of silicon. Table II shows typical C-V data from these runs. These data were obtained from consecutive runs without any cleaning of the deposition apparatus between runs. It

Table I. $\frac{Q_o}{q}$ associated with SiH_4 -type Si_3N_4 deposits

Deposition ambient	$\frac{Q_o}{q} \times (10^{-11} \text{ cm}^2)$
Hydrogen	7 to 11
Hydrogen	11 to 14
Hydrogen	7 to 24
Hydrogen	34 to 72
Hydrogen	14 to 25
Hydrogen	8 to 11
Nitrogen	1 to 2
Nitrogen	1 to 10
Nitrogen	1 to 33
Nitrogen	1 to 2
Nitrogen	<0.4 (none)
Nitrogen	2 to 4

Table II. $\frac{Q_0}{q}$ associated with SiH₄ and SiCl₄-type Si₃N₄ deposits

Run number	Si ₃ N ₄ -type	$\frac{Q_0}{q} \times (10^{-11} \text{ cm}^2)$
IS-303	SiCl ₄	<0.4 (none)
IS-304	SiH ₄	4 to 8
IS-305	SiCl ₄	<0.4 (none)
IS-306	SiH ₄	0.4 to 9
IS-307	SiH ₄	2 to 8
IS-308	SiCl ₄	<0.4
IS-309	SiCl ₄	<0.4
IS-310	SiCl ₄	<0.4
IS-311	SiCl ₄	<0.4

is noted that whenever SiCl₄ was used as the source of silicon, there was no detectable contamination in the MNOS structures subsequently fabricated on these wafers. However, whenever SiH₄ was used as the source of silicon, contamination was observed. Based on the data collected to this point, two ionic contaminants were considered as possible candidates for the contaminating species: sodium or an active species of hydrogen. Sodium was considered because of its prevalence and because of its previous history as an ionic contaminant in semiconductor processing. Hydrogen was considered based on the work of Balk (18) and Deal *et al.* (7).

In 1965, Balk proposed that adsorbed moisture at the oxide metal interface of MOS structures could react at elevated temperatures (on the order of 500°C) with aluminum or other reactive metals to form an active species of hydrogen which then migrates to the oxide-silicon interface and annihilates the fast surface-states. Recently (7) it has been shown that for MNOS structures, a SiH₄-type Si₃N₄ deposit results in lower fast surface-state densities at the oxide-silicon interface than does a SiCl₄-type Si₃N₄ deposit. It is speculated that a greater amount of active hydrogen is generated when the SiH₄ molecule breaks down than is available from the hydrogen carrier gas used in the SiCl₄-type deposits. In this study only electrical instabilities were associated with SiH₄-type deposits, and the magnitude of the instability was greater when hydrogen was used as the carrier gas than when nitrogen was used; therefore, active hydrogen was considered along with sodium as a possible candidate for the contaminating species.

Since all components except for the SiH₄ and SiCl₄ sources were common to both types of deposits, it was felt that either the SiH₄ had to be contributing contamination to the deposition ambient or the SiCl₄ process provided a chemical species capable of gettering or bonding with the contaminating species. The major chemical species present in the SiCl₄-type deposit, which is not present in the SiH₄-type deposit, is the chloride ion. Therefore, it was decided to add hydrogen chloride (HCl) to the SiH₄ deposition ambient to see if it would be effective in removing the source of contamination. Table III shows the results.

Since, as mentioned above, the magnitude of the instability was greater in a hydrogen ambient, for this experiment hydrogen carrier gas was employed. Run

Table III. $\frac{Q_0}{q}$ associated with SiH₄-type Si₃N₄ deposits with and without added HCl

Run	Si ₃ N ₄ deposition ambient	$\frac{Q_0}{q} \times (10^{-11} \text{ cm}^2)$
IS-486	SiH ₄ in H ₂	1 to 7
IS-487	SiH ₄ in H ₂ + 3 cc/min HCl	20 to 38
IS-488	SiH ₄ in H ₂ + 8 cc/min HCl	3 to 7
IS-489	SiH ₄ in H ₂ + 30 cc/min HCl	<0.4 (none)
IS-490	SiH ₄ in H ₂ + 30 cc/min HCl	<0.4
IS-491	SiH ₄ in H ₂	4 to 5
IS-492	SiH ₄ in H ₂	2 to 4
IS-493	SiH ₄ in H ₂ + 30 cc/min HCl	<0.4

number 486 was made to obtain a rough estimate of the level of contamination associated with the SiH₄-type Si₃N₄ deposits at that time. As seen in Table III the contamination level was not as high as it had been previously, as can be seen by comparing it with data in Table I. Run number 487 was the first run wherein HCl was purposely added to the gas mixture. Only a small amount of HCl, approximately 3 cc/min, was used. From the C-V results, it is apparent that this amount of HCl was not significant enough to affect the contamination levels present. There is no explanation as to why the contamination level increased; however, based on previous history little significance need be attached to the level of contamination seen in this run.

The results from run number 488 indicate that 8 cc/min of HCl had little or no effect on the level of contamination. Therefore, in run number 489, the HCl concentration was increased until faint signs of ammonium chloride formation in the gas phase could be observed. The C-V results from this run indicated that all of the contamination had been either gettered or otherwise complexed. Therefore, the run conditions were repeated with the same results. Two additional SiH₄ in H₂-type Si₃N₄ deposits were then made in an attempt to recontaminate the furnace. As seen by the data of Table III, only a moderate amount of contamination was present; however, run number 493 again indicated that 30 cc/min of HCl was capable of gettering or complexing the ionic contamination present.

Heat-treatment with additions of HCl.—The above results demonstrated that the addition of HCl to the SiH₄ deposition ambient removed the ionic species normally seen in SiH₄-type Si₃N₄ deposits. However, the question still remained as to whether it was necessary to form ammonium chloride in order to eliminate the contaminating species. Therefore, an experiment was conducted to see if an HCl heat-treatment by itself was capable of removing the source of instability. Table IV shows C-V data obtained from this experiment. Although the amount of contamination present in the reactor during the above experiment was small, it is again seen that the added HCl was effective in removing the contamination present. The fact that contamination could be removed during a hydrogen plus HCl heat-treatment at 850°C (Table IV) indicated

Table IV. $\frac{Q_0}{q}$ associated with various types of heat-treatments and Si₃N₄ deposition ambients

Run	Heat-treatment and deposition ambient at 850°C	$\frac{Q_0}{q} \times (10^{-11} \text{ cm}^2)$
IS-523	H ₂ heat-treatment (H.T.)	3 to 5
IS-524	H ₂ + 30 cc/min HCl (H.T.)	<0.4 (none)
IS-525	H ₂ + 30 cc/min HCl (H.T.)	<0.4
IS-526	H ₂ + 30 cc/min HCl (H.T.)	<0.4
IS-527	H ₂ (H.T.)	2 to 5
IS-528	H ₂ + 30 cc/min HCl (H.T.)	<0.4
IS-529	H ₂ (H.T.)	4 to 5
IS-530	H ₂ (H.T.)	2 to 5
IS-531	H ₂ + 30 cc/min HCl (H.T.)	<0.4
IS-532	H ₂ + 30 cc/min HCl (H.T.) + SiH ₄ -type Si ₃ N ₄	<0.4
IS-533	H ₂ + 30 cc/min HCl (H.T.) + SiH ₄ -type Si ₃ N ₄	<0.4
IS-534	H ₂ + 30 cc/min HCl (H.T.) + SiH ₄ -type Si ₃ N ₄	<0.4
IS-535	H ₂ + 30 cc/min HCl (H.T.) + SiH ₄ -type Si ₃ N ₄	<0.4
IS-536	SiH ₄ -type Si ₃ N ₄	0.5 to 6
IS-537	SiH ₄ -type Si ₃ N ₄	0.6 to 2
IS-538	SiH ₄ -type Si ₃ N ₄	2 to 4
IS-539	SiH ₄ -type Si ₃ N ₄	2 to 6
IS-540	H ₂ + 30 cc/min HCl (H.T.) + SiH ₄ -type Si ₃ N ₄	<0.4
IS-541	H ₂ + 30 cc/min HCl (H.T.) + SiH ₄ -type Si ₃ N ₄	<0.4
IS-542	H ₂ + 30 cc/min HCl (H.T.) + SiH ₄ -type Si ₃ N ₄	<0.4
IS-543	H ₂ + 30 cc/min HCl (H.T.) + SiH ₄ -type Si ₃ N ₄	<0.4
IS-544	SiH ₄ -type Si ₃ N ₄	1 to 5

that the ammonium chloride reaction is not necessary for removal of the contamination. Runs number 532 and 539 demonstrated that the contamination could actually be removed by introducing HCl prior to Si_3N_4 deposition. Therefore, it appears that it is not necessary to have HCl flowing during the actual Si_3N_4 deposition process to remove the source of contamination. This suggests that the contamination associated with the SiH_4 -type Si_3N_4 deposits was not necessarily associated with the SiH_4 source itself, but that it was probably coming from some component of the reactor.

Sodium contaminated wafers.—Up to this time, we have conjectured that either electrically active hydrogen or sodium might be the contaminating species. The results reported above demonstrated that it is possible to use an HCl heat-treatment prior to SiH_4 -type Si_3N_4 deposition and still remove the source of ionic contamination. This suggests that active hydrogen was not the cause of the instability. That is, it was possible to obtain contamination-free SiH_4 -type Si_3N_4 deposits by employing the predeposition heat-treatment with HCl; and yet, active hydrogen is available when the SiH_4 molecule reacts. Of course, one could speculate that enough residual chloride ions are available during the Si_3N_4 deposition process to complex the active hydrogen; however, this possibility seems remote since typical deposition times were from 5-8 min, more than enough time to remove all traces of residual chloride. To verify that chloride ions are capable of gettering or complexing sodium ions, an additional experiment was carried out. Sample preparation for this experiment was as outlined previously, except that the wafers to be contaminated had an oxide which was 1000Å thick rather than the standard 2000Å. Each run included one purposely contaminated wafer and one uncontaminated wafer. Contamination was achieved by immersing the oxidized wafers in a solution containing 460 ppm of sodium. The contaminated wafers were then blown dry and given a 30 min heat-treatment in nitrogen at 550°C in order to diffuse the sodium close to the silicon dioxide-silicon interface. Gold probe C-V measurements were then made at five different locations on each wafer. The negative shift of the reference voltage after the heat-treatment was used to establish the minimum amount of electrically active sodium present. Table V shows typical gold probe C-V data obtained from the contaminated wafers after the 550°C heat-treatment. By referring to Table V it can be seen that, although the contamination levels were not uniform across a wafer, there were relatively large amounts of contamination in all wafers. One sodium contaminated wafer, along with an uncontaminated reference wafer, were then subjected to one of three different Si_3N_4 deposition processes.

Process I consisted of depositing 0.1μ of Si_3N_4 from SiH_4 and NH_3 in hydrogen ambient at 850°C. Process II consisted of a 10 min heat-treatment in a hydrogen plus HCl ambient at 900°C followed by a Process I Si_3N_4 deposition. Process III consisted of a 0.1μ Si_3N_4 deposit at 900°C using SiCl_4 plus NH_3 in a hydrogen ambient.

Table VI shows typical gold probe C-V data obtained from these wafers after Si_3N_4 deposition. From Table

Table V. $\frac{Q_0}{q}$ associated with sodium contaminated SiO_2 layers after a 30 min heat-treatment in N_2 at 550°C

Wafer	Structure	$\frac{Q_0}{q} \times (10^{-11} \text{ cm}^2)$
Na 1	460 ppm Na/0.1μ SiO_2/Si	25 to 130
Na 2	460 ppm Na/0.1μ SiO_2/Si	46 to 87
Na 3	460 ppm Na/0.1μ SiO_2/Si	49 to 79
Na 4	460 ppm Na/0.1μ SiO_2/Si	55 to 72
Na 5	460 ppm Na/0.1μ SiO_2/Si	46 to 70
Na 6	460 ppm Na/0.1μ SiO_2/Si	68 to 98

Table VI. $\frac{Q_0}{q}$ associated with Si_3N_4 deposits made on sodium contaminated wafers

Wafers	Structure	$\frac{Q_0}{q} \times (10^{-11} \text{ cm}^2)$
640 A	0.1μ $\text{Si}_3\text{N}_4(\text{SiH}_4)/0.2\mu \text{SiO}_2/\text{Si}$	24 to 27
640 B	0.1μ $\text{Si}_3\text{N}_4(\text{SiH}_4)/\text{Na}2/0.1\mu \text{SiO}_2/\text{Si}$	18 to 31
641 A	0.1μ $\text{Si}_3\text{N}_4(\text{SiH}_4)/0.2\mu \text{SiO}_2/\text{Si}$	14 to 21
641 B	0.1μ $\text{Si}_3\text{N}_4(\text{SiH}_4)/\text{Na}4/0.1\mu \text{SiO}_2/\text{Si}$	22 to 37
642 A	0.1μ $\text{Si}_3\text{N}_4(\text{SiCl}_4)/0.2\mu \text{SiO}_2/\text{Si}$	<0.4 (none)
642 B	0.1μ $\text{Si}_3\text{N}_4(\text{SiCl}_4)/\text{Na}1/0.1\mu \text{SiO}_2/\text{Si}$	<0.4
643 A	0.1μ $\text{Si}_3\text{N}_4(\text{SiCl}_4)/0.2\mu \text{SiO}_2/\text{Si}$	<0.4
643 B	0.1μ $\text{Si}_3\text{N}_4(\text{SiCl}_4)/\text{Na}3/0.1\mu \text{SiO}_2/\text{Si}$	<0.4
644 A	$\text{H}_2 + \text{HCl}(\text{H.T.}^*)$ then 0.1μ $\text{Si}_3\text{N}_4(\text{SiH}_4)/0.2\mu \text{SiO}_2/\text{Si}$	<0.4
644 B	$\text{H}_2 + \text{HCl}(\text{H.T.}^*)$ then 0.1μ $\text{Si}_3\text{N}_4(\text{SiH}_4)/\text{Na}5/0.1\mu \text{SiO}_2/\text{Si}$	<0.4
645 A	$\text{H}_2 + \text{HCl}(\text{H.T.}^*)$ then 0.1μ $\text{Si}_3\text{N}_4(\text{SiH}_4)/0.2\mu \text{SiO}_2/\text{Si}$	<0.4
645 B	$\text{H}_2 + \text{HCl}(\text{H.T.}^*)$ then 0.1μ $\text{Si}_3\text{N}_4(\text{SiH}_4)/\text{Na}6/0.1\mu \text{SiO}_2/\text{Si}$	<0.4

* Heat-treatment.

VI it is again seen that those runs which used either SiCl_4 as a source of silicon during the Si_3N_4 deposition, or those runs which had an HCl heat-treatment prior to a SiH_4 -type Si_3N_4 deposition, resulted in contamination-free structures. Alternatively, for SiH_4 runs which did not have the HCl heat-treatment, considerable amounts of contamination were found in the structures after Si_3N_4 deposition. The data presented in Table VI indicate that both the SiCl_4 -type Si_3N_4 deposition process and the HCl heat-treatment prior to SiH_4 -type Si_3N_4 deposition process were capable of gettering the purposely added sodium contamination.

Discussion

From the experimental results obtained, it is concluded that the contaminating ionic species was sodium rather than an active species of hydrogen. However it is felt that the possibility of active hydrogen giving rise to electrical instabilities in an MNOS structure, fabricated with SiH_4 -type Si_3N_4 deposits, should not be completely dismissed especially if relatively large amounts of SiH_4 are employed. Earlier experiments involving hydrogen heat-treatments on MNOS structures, employing palladium field plates, indicated that active hydrogen could give rise to electrical instabilities in MNOS structures (7).

Although sodium metal itself has a boiling point (892°C) close to the temperatures employed for Si_3N_4 deposition, it has been repeatedly verified that the ionic contamination, assumed to be sodium in all cases and known to be sodium in some, is generally located close to the oxide-silicon interface rather than at the oxide-silicon nitride or oxide-air interface after a SiH_4 -type Si_3N_4 deposition or heat-treatment. Results from SiCl_4 -type Si_3N_4 depositions, and from heat-treatments wherein HCl was added to the heat-treatment or deposition ambient, suggest that the chloride ion provides a definite gettering action in the removal or complexing of the ionic species. Two possibilities exist to explain these results: (i) the chloride ion reacts with sodium ions to form electrically inactive species or (ii) the chloride ions tend to react with the sodium ions to form a volatile sodium chloride species which is removed from the reaction chamber in the exhaust gases.

As mentioned previously, in the absence of a chloride-containing atmosphere during the Si_3N_4 deposition, most of the contamination tends to accumulate at the Si-SiO₂ interface of $\text{Si}_3\text{N}_4/\text{SiO}_2/\text{Si}$ structures. Further, since the vapor pressure of sodium chloride at temperatures of from 850° to 900°C is only on the order of 1 mm Hg, one might therefore expect that the primary role of the chloride ion is to complex the contaminants forming electrically inactive species

rather than to form a volatile compound. Recently, Robinson and Heiman (19) have reported on a technique using HCl to getter sodium and other metal impurities in an oxidizing ambient at 1100°-1200°C. Their model assumes that HCl serves to form volatile metal chlorides. Although it is not clear which model plays the dominant role, our data seem to be in agreement with theirs indicating that chloride ions have the capability of gettering or complexing ionic contaminants from MOS structures.

It should be pointed out, however, that if there is no contamination present, stable MNOS devices can be fabricated using SiH₄-type Si₃N₄ deposits. However, if a source of contamination is present, there is no species available from the SiH₄ reaction which is capable of gettering the source of contamination. Apparently such a source of contamination existed in the quartz components of our experimental reactor which explains why, in the early stages of our investigation, larger instabilities were noted with hydrogen used as a carrier gas than with nitrogen. It is proposed that the hydrogen tends to etch the quartz releasing the source of contamination into the deposition ambient. Burgess and Donega (17) have studied the out-diffusion of sodium from a hot wall quartz furnace using atomic absorption techniques. Their work showed that the reaction of hydrogen with the hot quartz surface resulted in a marked increase in the sodium vapor pressure present in the furnace chamber. Further, their data indicated that the level of sodium contamination drops when hydrogen is replaced by a nitrogen ambient.

Conclusions

It is concluded that the SiCl₄ process for Si₃N₄ deposition has a built-in gettering capability for removing ionic contaminants from device structures during Si₃N₄ deposition which is not available in the SiH₄ process. It is proposed that the gettering capability arises from the presence of chloride ions. This premise was verified by purposely adding a source of chloride ions either prior to or during SiH₄-type Si₃N₄ depositions.

Acknowledgments

The authors would like to thank B. E. Deal and M. L. Barry for helpful discussions and encouragement given during the course of these investigations. We would also like to express our thanks to M. L. Barry for suggesting the HCl experiments.

Manuscript submitted July 1, 1971; revised manuscript received Feb. 12, 1972. This was Paper 146 presented at the Atlantic City Meeting of the Society, Oct. 4-8, 1970.

Any discussion of this paper will appear in a Discussion Section to be published in the June 1973 JOURNAL.

REFERENCES

1. N. C. Tombs *et al.*, *Proc. IEEE*, **54**, 87 (1966).
2. V. Y. Doo, *IEEE Trans. Electron Devices*, **ED-13**, 561 (1966).
3. S. M. Hu, *This Journal*, **113**, 693 (1966).
4. T. L. Chu, C. H. Lee, and G. A. Gruber, *ibid.*, **114**, 717 (1967).
5. S. M. Hu and L. V. Gregor, *ibid.*, **114**, 826 (1967).
6. J. V. Dalton and J. Drobek, *ibid.*, **115**, 865 (1968).
7. B. E. Deal, E. L. MacKenna, and P. L. Castro, *ibid.*, **116**, 997 (1969).
8. B. E. Deal, P. J. Fleming, and P. L. Castro, *ibid.*, **115**, 300 (1968).
9. D. M. Brown, P. V. Gray, F. K. Heumann, H. R. Philipp, and E. A. Taft, *ibid.*, **115**, 311 (1968).
10. M. J. Grieco, F. L. Worthing, and B. Schwartz, *ibid.*, **115**, 525 (1968).
11. E. H. Snow and B. E. Deal, *ibid.*, **113**, 263 (1966).
12. D. R. Kerr, J. S. Logan, P. J. Burkhardt, and W. A. Pliskin, *IBM J. Res. Develop.*, **8**, 376 (1964).
13. D. Frohman-Bentchkowsky and M. Lenzlinger, *J. Appl. Phys.*, **40**, 3307 (1969).
14. J. Gyulai, O. Meyer, J. W. Mayer and V. Rodriguez, *Appl. Phys. Letters*, **16**, 232 (1970).
15. B. Yurash and B. E. Deal, *This Journal*, **115**, 1191 (1968).
16. A. S. Grove, B. E. Deal, E. H. Snow, and C. T. Sah, *Solid-State Electron.*, **8**, 145 (1965).
17. T. E. Burgess and H. M. Donega, *This Journal*, **116**, 1313 (1969).
18. P. Balk, Paper 111 presented at the Buffalo Meeting of the Society, Oct. 10-14, 1965.
19. P. H. Robinson and F. P. Heiman, *This Journal*, **118**, 141 (1971).

Kinetics of Thermal Growth of Ultra-Thin Layers of SiO₂ on Silicon

Part II. Theory

R. Ghez and Y. J. van der Meulen*

IBM Thomas J. Watson Research Center, Yorktown Heights, New York 10598

ABSTRACT

The thermally activated growth of oxide on silicon as a function of time obeys a linear-parabolic relationship, the linear part of which stems from interface limited reactions. In Part I of this paper, it has been reported that this linear part cannot result from a single rate-limiting reaction step, because the order of the over-all reaction rate differs for different substrate orientations at a fixed temperature and varies for a given orientation as a function of temperature. A kinetic model for the reaction between silicon and oxygen at the Si-SiO₂ interface is now presented to account for the experimental data ($d_{\text{SiO}_2} \leq 300\text{\AA}$, $T_{\text{ox}} = 700^\circ\text{-}1000^\circ\text{C}$, $p_{\text{O}_2} = 0.01\text{-}1.0\text{ atm}$). Two parallel, competing reactions are postulated to occur. In the first of these, molecular oxygen reacts directly with silicon to form silicon dioxide and atomic oxygen; the second reaction involves the dissociation of O₂. The atomic oxygen thus formed, may either react with silicon or recombine to molecular oxygen. An analysis of the data shows that a difference in the activation energies (i.e., 1.91 vs. 0.58 eV) associated with these competing reaction steps is responsible for the shift in their relative importance as a function of temperature.

It is generally recognized that the measurement of oxidation kinetics does not allow a unique determination of the reaction mechanism. For example, logarithmic growth (i.e., the oxide thickness increases with the logarithm of time) can result from chemisorption (1), from field-assisted diffusion (2, 3), and from surface-controlled reactions (4). However, the oxidant pressure dependence of the growth rate, i.e., the order of the reaction, may furnish further insight into the reaction mechanism (5).

A number of investigations of the kinetics of silicon oxidation, in dry oxygen as a function of oxidant pressure, have been made under widely varying conditions. Law (6) has observed, close to room temperature, an exponential growth rate in the 1-2 monolayer region with a square root dependence on oxygen pressure in the 10⁻⁴-10⁻² Torr range. At higher temperatures (850°-1200°C) and greater oxide thicknesses ($L > 350\text{\AA}$), others (7-11) have observed that the kinetics are essentially of a mixed linear-parabolic type

$$\frac{L^2}{k_{\text{par}}} + \frac{L}{k_{\text{lin}}} = t$$

where k_{par} and k_{lin} are the rate constants, the first one increasing linearly with O₂ pressure. In this thickness range, the linear dependence is thought to arise from an interface reaction limited mechanism while the parabolic one is attributed to a diffusion-controlled process through the growing oxide.

Part I of this paper, by one of the present authors (12), described an ellipsometric study of the formation of thin SiO₂ layers ($L < 300\text{\AA}$), on $\langle 111 \rangle$ and $\langle 100 \rangle$ oriented silicon wafers, at temperatures (T) from 700° to 1000°C and oxygen partial pressures (p_{O_2}) from 0.01 to 1.0 atm. After a fast initial increase in thickness, the growth was found to be linear in time except for a slight parabolic perturbation indicating the onset of diffusion-controlled growth. The results reported in Fig. 4 of Part I have been replotted in normalized form in Fig. 1a and 1b. It can be seen that the linear rate constant depends on the oxygen partial pressure and the temperature, as well as on the silicon orienta-

tion. The pressure dependence of k_{lin} tends towards a $p^{1/2}$ behavior at lower temperatures; at higher temperatures, the trend is towards a linear pressure dependence for both orientations. The first order pressure dependence of the linear rate constant reported at 1200°C (10) is consistent with these data. Although the controversy (9, 13, 14, 15) over the ionic nature of the diffusing species remains unresolved, earlier work (10) shows that k_{par} exhibits a first order pressure dependence. Since dissociation of oxygen at the outer interface, together with the subsequent transport of the atomic species, necessarily gives rise to a non-first order pressure dependence of k_{par} , the evidence indicates that a molecular species (e.g., O₂ or O₂⁻) is transported across the amorphous oxide film.

Based on extensive measurements, Deal and Grove (10) proposed a kinetic scheme for the oxidation of silicon. For their model, they assume the incorporation of molecular oxygen at the gas-oxide interface followed by its transport through the oxide and direct reaction of this single oxidant species with the silicon. Consequently, the pressure dependence for all three steps should be linear. The experimental results reported in Part I of this study do not support this model since the pressure dependence of the linear rate constant was found to vary as described above. To account for this discrepancy, the present article proposes a more general kinetic treatment which incorporates two parallel, competing processes at the Si-SiO₂ interface. This scheme includes the one proposed by Deal and Grove as a special case, and it will be seen that their mechanism is valid as a limiting case at high temperatures.

Theory

Kinetic model.—Consider a growing oxide film of thickness L (Fig. 2). It is assumed that neutral molecular oxygen (O₂) is transported across the film, which implies that field and space charge effects are neglected as is ionization of the oxidant at the outer gas-oxide interface.¹ It also means that for atomic species,

¹ The existence of a fast initial mechanism is apparent in the data of Part I of this study, Fig. 3. This might be explained in terms of one of the theories previously mentioned (2-5) although there is not sufficient data to warrant such a test. It should be pointed out that the high Si-SiO₂ work function difference ($\approx 3.2\text{ eV}$) precludes any significant electron tunneling except for the very first stages of the oxidation process. The formation of charged oxygen species on the surface is, therefore, rather improbable.

* Electrochemical Society Active Member.

Key words: Si, SiO₂, oxidation, linear rate constant, interface reactions.

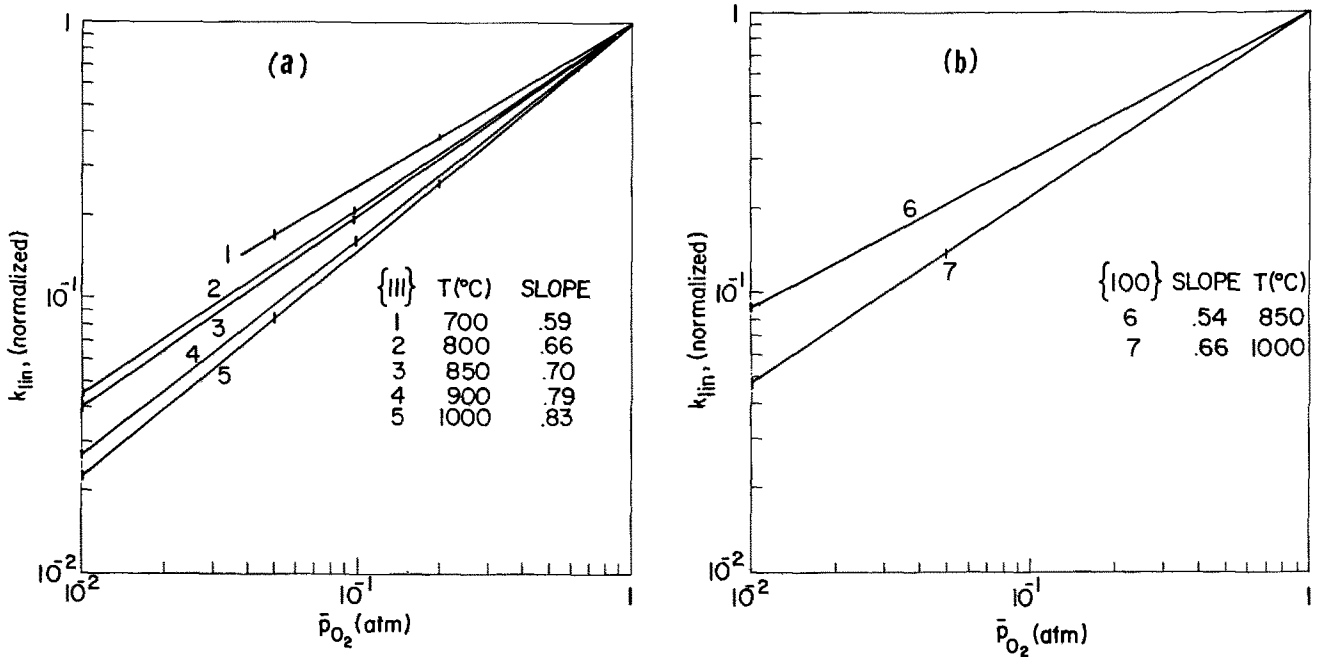


Fig. 1. Normalized plot of log k_{lin} vs. log p_{O_2} : a, $\langle 111 \rangle$ orientation; b, $\langle 100 \rangle$ orientation

which are known not to contribute significantly to the oxygen transport (8, 10), the product of the effective diffusion coefficient and the concentration gradient is negligible although dissociation and association of molecular and atomic oxygen species can occur throughout the layer. The system is also thought to be in a quasi-stationary state, i.e., the reactant concentrations are essentially constant during the relaxation times of the reactions involved.

The oxygen flux, F_o , across the O₂-SiO₂ interface is approximated by

$$F_o = h (C^* - C_o) \quad [1]$$

where h is a transfer coefficient which may include an adsorption activation energy, C_o is the actual molecular oxygen concentration in the solid at $x = 0$ (Fig. 2), and C^* is the equilibrium concentration related to the partial pressure through Henry's law

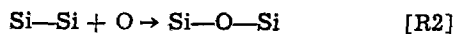
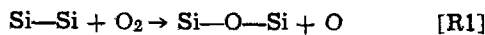
$$C^* = K \bar{p}_{O_2} \quad [2]$$

Under the above assumptions the flux across the oxide is derived from Fick's first law

$$F = D (C_o - C_L) / L \quad [3]$$

where C_L is the oxidant concentration at $x = L$, and D is the diffusion coefficient.

At the SiO₂-Si interface, the following reactions are postulated to occur



The formulation of the first two reactions is not stoichiometric in SiO₂ but is intended merely to indicate that in reaction [R1] an oxygen molecule reacts with a Si-Si bond, whereas in reaction [R2] the attacking species is an oxygen atom.²

These reactions are now considered kinetically. If v_1 , v_2 , and v_3 are the reaction velocities of reactions [R1-R3], respectively, the time dependence of the oxygen species concentrations at the SiO₂-Si interface ($x = L$) can be expressed mathematically (16) as

$$\frac{d}{dt} [\text{O}]_L = v_1 - v_2 + 2v_3 \quad [4a]$$

$$\frac{d}{dt} [\text{O}_2]_L = F_L - v_3 - v_1 \quad [4b]$$

where F_L is the oxidant flux at $x = L$. Equation [4b] indicates that the neighborhood of the SiO₂-Si interface is an open system; thus, the quantity of available molecular oxygen depends on the flux F_L as well as on the reactions [R1] and [R3]. The assumption of quasi-stationary state implies that

$$\frac{d}{dt} [\text{O}]_L, \frac{d}{dt} [\text{O}_2]_L \cong 0 \quad [5]$$

Thus one obtains

$$v_1 - v_2 + 2v_3 = 0 \quad [6]$$

and

$$F_L = v_1 + v_3 \quad [7]$$

Mathematically, F_o and F_L given by Eq. [1] and [7] are boundary conditions for the diffusion equation of which Eq. [3] is the first integral. Thus

$$F = F_o = F_L \quad [8]$$

When C_o is eliminated from Eq. [1] and [3], one obtains

$$F = h' (C^* - C_L) \quad [9]$$

where the diffusion coefficient has been imbedded in the variable

² It is possible to formulate alternative reaction equations. The scheme chosen, however, has two advantages, i.e., different attacking oxidant species are taken into account and their reaction with the silicon is considered in terms of breaking Si-Si bonds.

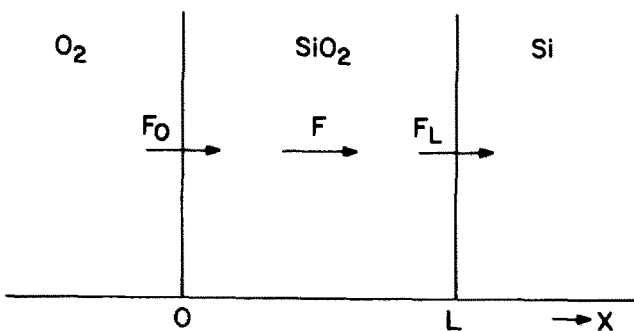


Fig. 2. Schematic representation of the O₂/SiO₂/Si system

$$h' = h/(1 + hL/D) \quad [10]$$

Any further reduction in the equations can only take place under the assumption of some functional relation between reaction velocities and concentrations. Because the reactions [R1-R3] are considered to be elementary steps (17), the reaction velocities must have the form

$$v_1 = k_1 [O_2]_L \quad [11a]$$

$$v_2 = k_2 [O]_L \quad [11b]$$

$$v_3 = k_3 [O_2]_L - k_{-3} [O]_L^2 \quad [11c]$$

where the subscript -3 in k_{-3} refers to the reverse reaction. The reverse reactions in Eq. [11a] and [11b] are neglected because of the large thermodynamic stability of SiO_2 relative to that of the reactants. Notice that Eq. [11a] and [11b] together represent the reaction velocity considered by Deal and Grove (10). From Eq. [6] and [11a-c], one finds that

$$2k_{-3} [O]_L^2 + k_2 [O]_L - (k_1 + 2k_3) [O_2]_L = 0 \quad [12]$$

Combining Eq. [7], [9], [11a], and [11c], and bearing in mind that $[O_2]_L \equiv C_L$, one obtains

$$F = (k_1 + k_3) C_L - k_{-3} [O]_L^2 = h' (C^* - C_L) \quad [13]$$

which yields

$$C_L = \frac{h' C^* + k_{-3} [O]_L^2}{k_1 + k_3 + h'} \quad [14]$$

Elimination of $[O_2]_L$ between Eq. [12] and [14] results in

$$(k_1 + 2h') k_{-3} [O]_L^2 + k_2 (k_1 + k_3 + h') [O]_L - h' (k_1 + 2k_3) C^* = 0 \quad [15]$$

which is a quadratic equation for $[O]_L$ in terms of the only accessible parameter C^* . Elimination of C_L between Eq. [13] and [14] yields an expression for the flux in terms of $[O]_L$; the latter concentration is the positive solution of Eq. [15]. The growth rate of the oxide film is then

$$\frac{dL}{dt} = \Omega F = \frac{\Omega h'}{k_1 + 2h'} \left\{ k_1 C^* + \frac{k_2}{2k_{-3} (k_1 + 2h')} [-k_2 (k_1 + k_3 + h')] + (k_2^2 (k_1 + k_3 + h')^2 + 4(k_1 + 2h') \cdot h' k_{-3} (k_1 + 2k_3) C^*)^{1/2} \right\} \quad [16]$$

where Ω is the volume of oxide formed per transported O_2 molecule. As is seen from Eq. [16], the order of the reaction, i.e., the dependence of the growth rate on the exponent of p_{O_2} and thus of C^* (cf. Eq. [2]), lies between the limits 1/2 and 1. It will be seen later that these limiting orders can be achieved for certain ranges of the temperature dependent kinetic coefficients.

Thickness-time dependence.—In this section the rate Eq. [16] is integrated to give the dependence of the oxide film thickness on oxidation time and pressure. To simplify Eq. [16], the following dimensionless variable is introduced

$$\xi' = \frac{(k_1 + k_3 + h')}{h'} \quad [17]$$

or, using Eq. [10]

$$\xi' = 1 + \frac{k_1 + k_3}{h} \left(1 + \frac{hL}{D} \right) \quad [18]$$

Notice that ξ' is always greater than 1. If one defines

four additional parameters

$$\lambda = 1 + 2k_3/k_1 \quad [19a]$$

$$\mu = k_2^2/2k_{-3} \quad [19b]$$

$$A = 2k_1 C^*/(1 + \lambda) \quad [19c]$$

$$B = 4k_1 k_{-3} \lambda C^*/k_2^2 (1 + \lambda) \quad [19d]$$

which satisfy the relation

$$A\lambda = \mu B \quad [20]$$

Eq. [16] becomes

$$\frac{d\xi'}{dt} = \frac{k_1 (1 + \lambda)}{2D} \frac{dL}{dt} = \frac{\Omega k_1 (1 + \lambda)^3}{8D} \frac{A (\xi' + \lambda) + \mu [-\xi' + (\xi'^2 + 2B (\xi' + \lambda))^{1/2}]}{(\xi' + \lambda)^2} \quad [21]$$

Let t_0 correspond to the approximate end of the fast initial oxidation when $L = L_0$ and $\xi' = \xi'_0$; if one integrates Eq. [21] from time t_0 to a variable time, t , one gets

$$\frac{\Omega k_1 (1 + \lambda)^3 (t - t_0)}{8D} = \int_{\xi'_0}^{\xi'} \frac{(\xi + \lambda)^2 d\xi}{A (\xi + \lambda) + \mu [-\xi + (\xi^2 + 2B (\xi + \lambda))^{1/2}]} \quad [22]$$

The right-hand side of Eq. [22] is an Abelian integral which can be solved by standard substitutions. Alternatively, however, using Eq. [20] it is possible to reduce the integrand to

$$\frac{1}{A} \left\{ \xi + \frac{\lambda}{2\lambda - B} [(\xi + B)^2 + B(2\lambda - B)]^{1/2} - (\xi + B) \right\} \quad [23]$$

the integral of which is readily obtained from tables (18). In either case, one finally obtains

$$\frac{\Omega k_1 (1 + \lambda)^3 (t - t_0)}{8D} = \frac{1}{2A} \left\{ \xi^2 + \frac{\lambda}{2\lambda - B} (\xi + B) \cdot (R - (\xi + B)) - \lambda B \ln |R - (\xi + B)| \right\}_{\xi'_0}^{\xi'} \quad [24]$$

where R represents the radical expression in Eq. [22] and [23]. As before, Eq. [18] relates L to ξ' .

Discussion

In the preceding section, a kinetic scheme led to expressions for the oxygen flux, Eq. [16], and the oxide thickness, Eq. [24]. In this section the general pressure dependence of the growth rate is first examined. Then the conditions under which linear growth occurs are discussed and compared to the experimental data reported in Part I of this study. The various cases involving diffusion limited growth are discussed in the Appendix.

Incorporating Eq. [2] into the general rate equation, [16], one gets

$$\frac{dL}{dt} = \frac{\Omega \xi' \mu}{(2 + k_1/h')^2} \{ \alpha' p - 1 + (1 + 2\beta' p)^{1/2} \} \quad [25]$$

where

$$\alpha' = \frac{2k_{-3} k_1 K}{k_2^2} \cdot \frac{2 + k_1/h'}{1 + k_1/h' + k_3/h'} \quad [26]$$

$$\beta' = \frac{2k_{-3} (2k_3 + k_1) K}{k_2^2} \cdot \frac{2 + k_1/h'}{(1 + k_1/h' + k_3/h')^2} \quad [27]$$

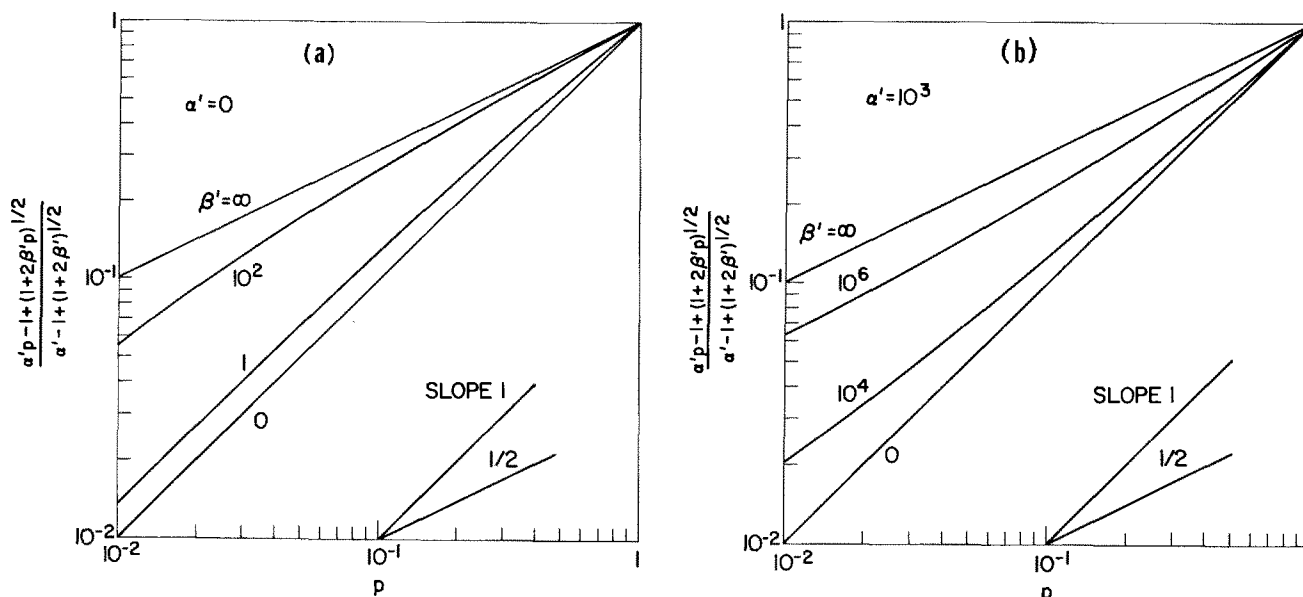


Fig. 3. Normalized plot of Eq. [25] for different values of β' : a, $\alpha' = 0$; b, $\alpha' = 10^3$

Figure 3 shows normalized graphs of the growth rate vs. the oxygen partial pressure for various pairs of values of α' and β' . The values chosen serve to indicate the possible variation in the apparent order of the reaction and it is seen that a continuous transition between the limiting cases of half power and linear pressure dependence is possible. Moreover, the deviation from linearity in the curves between $p = 0.01$ and 1.0 atm is small and, in our case, falls outside the experimental reach. It should be noted that the coefficients h' , ξ' , α' , and β' depend on the thickness L , making it difficult to fit Eq. [25] to the experimental results. The analysis becomes considerably more simple in the case of purely linear growth which takes place in sufficiently thin films.

Linear growth occurs when the surface (O_2 -SiO₂) and the interface (SiO₂-Si) reactions are rate limiting. It is observed if, and only if, the right-hand side of Eq. [21] and [25] is independent of L . In view of Eq. [18], this condition is met if

$$\frac{hL}{D} \ll 1 \tag{28}$$

for all experimentally observed values of L . In this case h' reduces to h and one may define

$$\xi = 1 + (k_1 + k_3)/h \tag{29}$$

Defining parameters α and β , equal to α' and β' of Eq. [26] and [27], in which the primes have been dropped, the linear growth rate is

$$\frac{dL}{dt} = \frac{\Omega \xi \mu}{(2 + k_1/h)^2} \{ \alpha p - 1 + (1 + 2\beta p)^{1/2} \} \tag{30}$$

The pressure dependence of the linear rate constant is the same as that of the general rate constant, therefore, Fig. 3 also depicts Eq. [30]. The coefficients α and β are now independent of the thickness, allowing a comparison with the experimental values of the linear rate constant. Note that the expressions for α and β contain six unknown reaction rate constants, each of which follows the Arrhenius law. Comparing Fig. 3 with Fig. 1, it is already seen that the experimental results are qualitatively described by the proposed scheme.

Further analysis of Eq. [30] depends on the values of the pressure and the temperature. On the basis of the physical processes involved, several limiting cases can be distinguished:

Assume the limiting process to occur at the O_2 -SiO₂ interface.—Then $\xi \gg 1$ and Eq. [30] now reduces to

$$\frac{dL}{dt} = \Omega h C^* = \Omega K h p \tag{31}$$

a result that is indeed expected and entails a linear pressure dependence. It conflicts, however, with the present experimental results and this case must, therefore, be eliminated from further consideration.

Assume the limiting process to occur at the SiO₂-Si interface.—Then $\xi \cong 1$ and Eq. [30] now reduces to

$$\frac{dL}{dt} = \frac{\Omega}{2} \left\{ k_1 C^* + \frac{\mu}{2} \left[-1 + \left(1 + \frac{4}{\mu} (k_1 + 2k_3) C^* \right)^{1/2} \right] \right\} \tag{32}$$

The general form of Eq. [30] is thus maintained and the observed pressure dependence of the linear rate constant can be fully explained on the basis of reactions at this interface only.

Equation [32] allows further discussion.

Assume that the process described by reaction [R1] can be neglected.—Now Eq. [32] reduces to

$$\frac{dL}{dt} = \frac{\Omega \mu}{4} (-1 + (1 + 2\gamma p)^{1/2}) \tag{33}$$

where

$$\gamma = \frac{8k_3 k_{-3} K}{k_2^2} \tag{34}$$

Equation [33] is still characterized by a mixed pressure dependence (cf. Fig. 3a).

Assume that $k_3 \cong 0$.—This simplifies Eq. [32] to

$$\frac{dL}{dt} = \frac{\Omega}{2} \left\{ k_1 K p + \frac{\mu}{2} \left[-1 + \left(1 + \frac{4}{\mu} k_1 K p \right)^{1/2} \right] \right\} \tag{35}$$

while maintaining a mixed pressure dependence. Further analysis of this case shows, however, that both for small and for large values of the parameter $\left(\frac{k_1 K}{\mu} \right)$, a first order pressure dependence is obtained; and even for intermediate values of this parameter

$$\frac{dL}{dt} \propto p^x \quad [36]$$

where $0.9 \leq x \leq 1.0$. This subcase, therefore, results in a rather unsatisfactory solution.

Assume that the process described by reaction [R2] can be neglected.—Now Eq. [36] can be written as

$$\frac{dL}{dt} = \Omega F = \frac{\Omega}{2} k_1 K p \quad [37]$$

It is seen that this case is precluded on basis of the first order pressure dependence.

Assume that the processes described by reaction [R3] are negligible.—This simply reduces Eq. [32] to

$$\frac{dL}{dt} = \Omega k_1 C^* = \Omega K k_1 p \quad [38]$$

This is exactly the linear situation described by Deal and Grove (10) for short oxidation times; again, it does not exhibit the required pressure dependence.

Summarizing the case of linear growth, it was seen that several combinations of rate-limiting steps give rise to the observed pressure dependence of the linear rate constant. At this time it cannot be concluded unambiguously which of the steps in the proposed reaction scheme is associated with the part that is linear in pressure, as either reaction [R1] or reaction [R3] could be responsible. It is clear, however, that the part following a half power dependence stems from the reaction of atomic oxygen with silicon at the SiO₂-Si interface.

In discussing the differences found between samples of different surface orientation, we will use an approach similar to the one of Ligenza (19) who, using high pressure steam as an oxidant, observed that the oxide growth was linear in time and in steam pressure and depended strongly on the silicon orientation ($k_{(110)} > k_{(311)} > k_{(111)}$). This orientation effect was assumed to stem from the different number of bonds accessible to the oxidant per unit area. Although no experiments were reported using (100) material, it was calculated that this orientation should have the highest activation energy for oxidation, as well as the smallest surface density of available reaction sites. The approach used is valid because the rate of growth of the oxide film, *i.e.*, the silicon oxidation rate, is proportional to the number of accessible bonds per unit area at a given time. Some basic shortcomings of Ligenza's approach, which cannot be remedied easily, are that the surface planarity is thought to be ideal regardless of orientation, lattice relaxations at the oxide-semiconductor interface are not considered, and various surface defects (*e.g.*, dislocations) cannot be taken into account. A more practical objection is that the existing treatment does not take into account the fact that for the (111) orientation, in which we are interested, two different kinds of atoms can be distinguished on the basis of their position with respect to the surface. One type is connected to the underlying atoms by three bonds at an angle of 19°25' with the surface, the other type is connected by only one bond at an angle of 90°. If this is properly accounted for one may expect an over-all reaction rate of the following form to be operative

$$\frac{1}{k} = \frac{1}{k_T} + \frac{1}{3k_B}$$

where k_T refers to the reaction rate with the three angled bonds and k_B to the reaction rate with the perpendicular bond. In (100) oriented material, on the other hand, all surface atoms are equivalent and are connected to the substrate by two covalent bonds that make an angle of 35°16' with the surface. Thus in this case a single reaction rate can be used. The fact that

our experimental results show that $k_{lin(111)} > k_{lin(100)}$ indicates that k_B is sufficiently large to preserve the sequence deduced by Ligenza. All other experimental conditions being equal, our results also show that, for oxidation on (100) oriented substrates, the order of the reaction is lower. This reflects the higher degree of steric hindrance for this direction for which direct reaction with molecular oxygen is apparently less favored than for the (111) orientation. This difference between the two orientations contrasts with the one found for the etch rates in wet ambients where the close packed (111) surface is less reactive (20).

Using the variable metric method (21), numerical values for the constants in Eq. [32] were calculated for the <111> orientation from the experimental data with the help of an IBM 360/91 computer. Reflecting the greater experimental precision, relatively more weight was given to data points representing higher growth rates. A minimum value of the following expression was sought

$$\sum_T \sum_P \left(\left(\left(\frac{dL}{dt} \right)_{calc} / \left(\frac{dL}{dt} \right)_{meas} \right) - 1 \right)^2 \cdot \left(\frac{dL}{dt} \right)_{meas}^{1/4}$$

This procedure gave a very satisfactory fit to the experimental points and resulted in

$$\left(\frac{dL}{dt} \right)_{calc} / \left(\frac{dL}{dt} \right)_{meas} = 1.00 \pm 0.05$$

Expressing the activation energies in electron volts, it was found that

$$\Omega \mu = 4.72 \exp(-2.07/kT) \text{ cm min}^{-1}$$

$$k_1 K / \mu = 1.75 \exp(0.16/kT) \text{ atm}^{-1}$$

$$k_3 K / \mu = 8.12 \times 10^{-6} \exp(1.49/kT) \text{ atm}^{-1}$$

The solubility of molecular oxygen in vitreous silica is approximately constant over the temperature range involved (700°-1000°C), which means that in Henry's law the exponential term containing the enthalpy of solution, $\exp(-\Delta H/RT)$, varies approximately as T at these temperatures, thus a single value of $K = 7.5 \times 10^{16} \text{ cm}^{-3} \text{ atm}^{-1}$ can be used (22). Estimating $\Omega = 4.44 \times 10^{-23} \text{ cm}^3$, one calculates

$$k_1 = 2.47 \times 10^6 \exp(-1.91/kT) \text{ cm min}^{-1}$$

$$k_3 = 1.15 \times 10^1 \exp(-0.58/kT) \text{ cm min}^{-1}$$

$$\mu = 1.06 \times 10^{23} \exp(-2.07/kT) \text{ cm}^{-2} \text{ min}^{-1}$$

$$\lambda = 1 + 2k_3/k_1 = 1 + 9.3 \times 10^{-6} \exp(1.33/kT)$$

$$\frac{2\lambda}{B} = 1.14 \exp(-0.16/kT)$$

$$\cdot \{1 + 4.65 \times 10^{-6} \exp(1.33/kT) p_{O_2}^{-1}\}$$

Table I shows typical values of these parameters. The activation energy of k_1 (1.91 eV) is very similar to the value reported by Deal and Grove (10) (1.99 eV).³

³ Using the same procedure to fit Eq. [33] to the results yields a value of 1.89 eV for this activation energy. In this case, however, the over-all agreement between calculation and experiment is less satisfactory.

Table I. Typical values of the kinetic coefficients, k_1 and k_3 , and the parameters λ and $2\lambda/B$ for <111> Si

T (°C)	k_1 (cm min ⁻¹)	k_3 (cm min ⁻¹)	λ	$2\lambda/B$ (atm ⁻¹)
700	3.21×10^{-4}	1.14×10^{-2}	72.4	6.22
800	2.68×10^{-3}	2.18×10^{-2}	17.3	1.85
900	1.56×10^{-2}	3.72×10^{-2}	5.78	0.79
1000	6.86×10^{-2}	5.84×10^{-2}	2.70	0.49

Knowledge of the equilibrium constant for reaction [R3] in the gas phase is not sufficient to calculate k_{-3} since the solubility of atomic oxygen in vitreous silica is unknown. Although k_3 has been calculated, a separate determination of either k_{-3} or k_2 is impossible, since they only occur combined in μ . It is seen that λ decreases with increasing temperature, reflecting the fact that reaction [R1] becomes dominant.

Summary

A model describing the oxidation kinetics of silicon in oxygen has been developed to account for the experimentally observed nonlinear pressure dependence of the linear rate constant. Based on earlier literature it was assumed that molecular oxygen is transported through the oxide, giving rise to a linear pressure dependence of the parabolic rate constant. The essential feature of this model is to allow for two parallel, competing reaction processes at the SiO₂-Si interface. In the first process, O₂ reacts with Si-Si bonds forming Si-O-Si and O; in the second one, O₂ dissociates prior to reaction with Si. The former process is dominant at high temperatures, the latter becomes more important at lower temperatures. A comparison with the experimental data for <111> oriented material made it possible to calculate some of the rate constants involved.

Acknowledgments

The authors express their gratitude to P. Balk for a number of illuminating discussions concerning reaction kinetics. They are indebted to J. M. Eldridge and A. Reisman for critically reviewing the manuscript.

Manuscript submitted Jan. 24, 1972; revised manuscript received March 20, 1972.

Any discussion of this paper will appear in a Discussion Section to be published in the June 1973 JOURNAL.

APPENDIX

In the general case, the growth law [24] affords a discussion of thick film growth kinetics for which diffusion effects are important. The following discussion will show that the growth kinetics remain essentially of the mixed linear-parabolic type. Inspection of Eq. [24] shows that its form depends critically on the relative magnitude of 2λ and B . This is not surprising since, in the limit $\lambda \rightarrow 1$, reaction [R1] completely dominates reaction [R3]; whereas, for $\lambda \rightarrow \infty$, the converse is true. The ratio $2\lambda/B = (k_2/k_1)^2 (k_1 + k_3)/k_{-3}C^*$ provides a more stringent condition since it depends on the ratio k_1/k_2 . For example, even when $\lambda \gg 1$, the process [R2-R3] will dominate over [R1] only if $k_2 > k_1$, which implies that $2\lambda/B > 1$. Table I shows that $B < 2\lambda$ holds at low temperatures, whereas, $B > 2\lambda$ is satisfied at high temperatures, the transition point occurring at roughly 865°C. The growth law [24] can now be cast into the following form

$$2\Omega C^* (k_1 + k_3)^2 (t - t_0)/D = \xi'^2 - \xi_0'^2 + \lambda B (S - S_0) \quad [A1]$$

or in terms of the thickness L , related to ξ' by Eq. [18]

$$2\Omega DC^* (t - t_0) = L^2 - L_0^2 + 2D(1/h + 1/(k_1 + k_3))(L - L_0) + (D/(k_1 + k_3))^2 \lambda B (S - S_0) \quad [A2]$$

where S is defined as

$S =$

$$\begin{cases} \eta [(\eta^2 + 1)^{1/2} - \eta] - \ln [(\eta^2 + 1)^{1/2} - \eta] & \text{if } B < 2\lambda \\ \zeta [\zeta - (\zeta^2 - 1)^{1/2}] - \ln [\zeta - (\zeta^2 - 1)^{1/2}] & \text{if } B > 2\lambda \end{cases} \quad [A3]$$

Table II. Typical values of the kinetic coefficients λB , $(k_1 + k_3)/D$, and $(k_1 + k_3)/h$ for <111> Si

T (°C)	D (cm ² min ⁻¹)	λB	$(k_1 + k_3)/D$ (cm ⁻¹)	$(k_1 + k_3)/h$
700	0.15×10^{-7}	1680	8.04×10^5	7.06×10^{-5}
1000	3.89×10^{-7}	30	3.26×10^5	7.62×10^{-4}

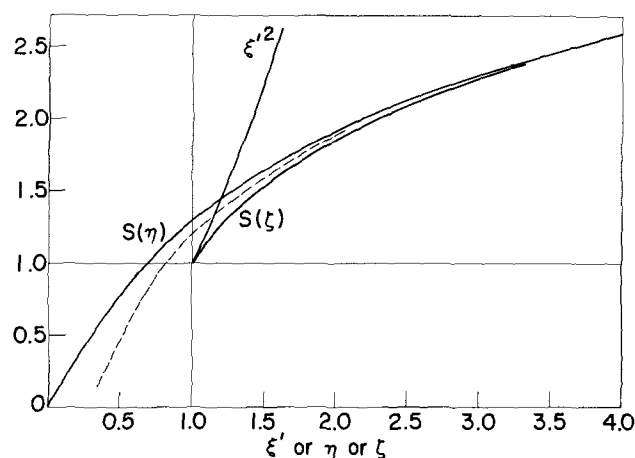


Fig. 4. Comparison of the parabolic and logarithmic terms ξ'^2 and S as given in Eq. [A1].

and is a function of the arguments

$$\begin{cases} \eta = (\xi' + B)[B(2\lambda - B)]^{-1/2} & \text{if } B < 2\lambda \\ \zeta = (\xi' + B)[B(\lambda - 2B)]^{-1/2} & \text{if } B > 2\lambda \end{cases} \quad [A4]$$

Equation [A2] shows that the oxidation kinetics are of mixed linear-parabolic type with a correction term S which will be discussed presently. The expression S_0 in Eq. [A1] and [A2] is obtained by evaluating S , given by Eq. [A3] and [A4] at $\xi' = \xi_0'$. Notice that ζ is always greater than 1 and that the logarithmic terms in S can be expressed as inverse hyperbolic functions. The relative importance of the function, S , for thick films can be seen in the following way. Using numerical values for h ($\cong 10^8 \mu/h$) (10) and D (21), together with the results as given in Table I, an estimate of $(k_1 + k_3)/D$ and $(k_1 + k_3)/h$ can be made; the result for a "low" and a "high" temperature is given in Table II. From Eq. [18], one finds that

$$\xi'(700^\circ\text{C}) \cong 1 + 8 \times 10^5 L \text{ cm}$$

$$\xi'(1000^\circ\text{C}) \cong 1 + 3.3 \times 10^5 L \text{ cm}$$

and from Eq. [A4] that

$$\eta(700^\circ\text{C}) \cong 0.46 + 0.15 \times 10^5 L \text{ cm}$$

$$\zeta(1000^\circ\text{C}) \cong 1.54 + 0.42 \times 10^5 L \text{ cm}$$

It follows that, for $L \leq 1000 \text{ \AA}$, ξ' , η , and ζ are of the same order of magnitude. The functions ξ'^2 , $S(\eta)$, and $S(\zeta)$ are plotted in Fig. 4. Although the functions S initially increase linearly with L , thus contributing to the linear growth which was discussed previously, their behavior is logarithmic for larger thicknesses. More precisely, their asymptotic behavior is

$$S \sim 0.5 + \ln(2(\eta \text{ or } \zeta)) \quad [A5]$$

and is presented as a dashed curve in Fig. 4. Thus, except perhaps for very low temperatures when λB becomes very large, the correction term, S , is negligible in the thick film region.

Summarizing the general case, the growth kinetics described by Eq. [A2] are of mixed linear-parabolic type with a logarithmic correction for large L . The parabolic rate constant is identical to the one derived by Deal and Grove (10).

LIST OF SYMBOLS

C_0, C_L	concentrations of diffusing species at the SiO ₂ -O ₂ and SiO ₂ -Si interface, respectively
C^*	equilibrium concentration of O ₂ (Henry's law)
D	diffusion coefficient
F	flux of diffusing species
L	oxide thickness
t	oxidation time
h	transfer coefficient at the SiO ₂ -O ₂ interface
v_n	reaction velocity of the n'th reaction
k_n, k_{-n}	forward and reverse rate constants for the n'th reaction
K	Henry's constant (cf. Eq. [2])
p_{O_2}, p	oxygen partial pressure

Ω volume of SiO_2 formed per transported molecule O_2

In general, a prime added to a symbol implies that diffusion effects are explicitly included.

REFERENCES

1. P. T. Landsberg, *J. Chem. Phys.*, **23**, 1079 (1955).
2. N. Cabrera and N. F. Mott, *Rep. Progr. Phys.*, **12**, 163 (1948).
3. T. B. Grimley and B. M. W. Trapnell, *Proc. Roy. Soc.*, **A234**, 405 (1956).
4. I. M. Ritchie and G. L. Hunt, *Surface Sci.*, **15**, 524 (1969).
5. O. Kubaschewski and B. E. Hopkins, "Oxidation of Metals and Alloys," Butterworths, London (1962).
6. J. T. Law, *J. Phys. Chem. Solids*, **4**, 91 (1958).
7. M. O. Thurston and K. D. Kang, Armed Services Technical Report AD 294657 (1962).
8. P. J. Burkhardt and L. V. Gregor, *Trans. AIME*, **236**, 299 (1966).
9. P. J. Jorgensen, *J. Chem. Phys.*, **37**, 874 (1962).
10. B. E. Deal and A. S. Grove, *J. Appl. Phys.*, **36**, 3770 (1965).
11. S. J. Laverty and W. D. Ryan, *Intern. J. Electron.*, **26**, 519 (1969).
12. Y. J. van der Meulen, *This Journal*, **119**, 530 (1972).
13. D. O. Raleigh, *This Journal*, **113**, 782 (1966).
14. P. J. Jorgensen, *ibid.*, **114**, 820 (1967).
15. T. Nakayama and F. C. Collins, *ibid.*, **113**, 706 (1966); **114**, 167 (1967).
16. I. Prigogine and R. Defay, "Chemical Thermodynamics," Longmans and Green, London (1954).
17. K. J. Laidler, "Chemical Kinetics," McGraw-Hill, Book Co., New York (1965).
18. H. B. Dwight, "Tables of Integrals and Other Mathematical Data," MacMillan Co., New York (1965).
19. J. R. Ligenza, *J. Phys. Chem.*, **65**, 2011 (1961).
20. R. G. Rhodes, "Imperfections and Active Centers in Semiconductors," MacMillan Co., New York (1964).
21. R. Fletcher and M. J. D. Powell, *Computer J.*, **6**, 163 (1963).
22. F. J. Norton, *Nature*, **191**, 701 (1961).

A Quantitative Calculation of the Growth Rate of Epitaxial Silicon from SiCl_4 in a Barrel Reactor

E. Fujii, H. Nakamura, K. Haruna, and Y. Koga

Central Research Laboratory, Hitachi Ltd., Kokubunji, Tokyo, Japan

ABSTRACT

A model is proposed for the epitaxial growth of silicon in a vertical reactor where the reactant gas flows parallel to silicon wafers. It is assumed that the growth rate of deposited silicon is mass-transport controlled, and the equilibrium reaction is $\text{SiCl}_4 + 2\text{H}_2 = \text{Si} + 4\text{HCl}$. The model considers the profiles of the gas velocity and the temperature of the reactant gas, and also a decrease of the concentration along the gas flow. The growth rates at various positions along the susceptor are calculated under the conditions of substrate temperatures 1100°-1300°C, wall temperatures 300°-850°C, reactant gas flow rates 40-120 liters/min, and concentrations of SiCl_4 to H_2 0.004-0.008 in mole ratio. The growth rate is expressed as a function of the dimensions of the reaction chamber, and susceptor and of process variables such as the concentration, the gas flow rate, and the temperature. Using the function, the sensitivity analysis of process variables to the growth rate is investigated. Good agreement between the theory and the experimental result of the growth rate is obtained.

This paper describes quantitatively the growth rate of epitaxial silicon layer in a vertical reactor using reasonable approximations to the silicon epitaxial process.

Several theoretical models have been proposed to explain the epitaxial growth rate of silicon by the hydrogen reduction of chlorosilane, either in a vertical reactor where the reactant gas is passed vertically, or in a horizontal reactor where the reactant gas is passed horizontally. These theories are mainly divided into three types: thermodynamic, boundary-layer, and parallel plate.

Steinmaier (2) and Seki *et al.* (3) treated the $\text{SiCl}_4\text{-H}_2$ and the $\text{SiH}_4\text{-H}_2$ systems, respectively, using the first theory. The equilibrium compositions of the component in the gas phase were calculated. A hypothetical silicon partial pressure in terms of the partial pressures of each component was related to the growth rate or the etching rate of silicon. Lever (4) made a thermodynamic calculation of the Si-H-Cl system in detail. Sedgwick (5) proposed the quasi-equilibrium model which consists of the theoretical effective concentration factor α used also by Lever and of an apparatus factor β . In general the thermodynamical analysis can

provide information about the actual mechanism of a reaction system only when the process is under sufficiently low flow rate, which is required for the system to be in equilibrium.

The second theory, the boundary-layer theory by Bradshaw (6), is applied only to vertical reaction chambers. It is assumed that there is a boundary layer of a relatively static gas adjacent to the silicon surface. The growth rate is limited by diffusion of reactants and by-products across the boundary layer. Eversteyn (7) proposed a stagnant layer model analogous to the boundary-layer theory. The stagnant layer thickness is assumed to be constant along the susceptor, but in reality the thickness of such a stagnant or boundary layer is generally not uniform but varies in the direction of gas flow. It is doubtful that the stagnant layer thickness in the case of the SiH_4 system equals that of the TiO_2 system that was used to estimate the stagnant layer thickness.

The third theory, the parallel plate theory by Shepherd (8), is applied to the horizontal reaction chamber. Two assumptions are made here: that the gas velocity profile is a fully developed parabola and that the gas temperature profile is a linear gradient along the distance normal to the gas flow.

Key words: silicon epitaxy from SiCl_4 , epitaxy in a barrel reactor, calculation of epitaxial growth rate, controlled mass transport, chemical vapor deposition.

The above theories, however, do not involve the decrease of concentration of the reactant due to the silicon deposition in the direction of the gas flow. Rundle (1) proposed the model in which the decrease of the concentration of the reactant is considered. The model is applied to the horizontal reactor by assuming that the gas velocity and the temperature are constant throughout the reaction chamber. Bradshaw (6) and Rundle (1) attempted to determine the dependence of the growth rate on the substrate temperature, on the flow rate, and on the distance along the gas flow.

In the present paper two main factors are considered: the decrease of concentration and the dimensions of a reaction chamber. A coaxial cylindrical tube is used to simulate the vertical reactor where the reactant gas flow is directed parallel to the silicon substrates. In addition to the above-mentioned two factors the gas velocity and the temperature profiles in the reaction chamber are considered in this mode. The continuity equation in such a model is solved under various process conditions. The growth rate of silicon in the direction of gas flow and the process characteristics are calculated and compared with experimental values. Furthermore, sensitivity analysis of the process parameters and the reactor dimensions to the growth rate are discussed.

Theory

The apparatus designed to perform the growth of the deposited silicon layer by the hydrogen reduction of silicon tetrachloride is shown schematically in Fig. 1. The continuity equation for a gaseous reactant is

$$\frac{dC}{dt} = -\text{div}(VC - D \text{grad } C) \quad [1]$$

where C is the concentration of the reactant, V is the gas velocity, and D is the diffusion coefficient of the reactant. The reaction of silicon deposition is usually carried out at the substrate temperature between 1100° and 1300°C to produce good single crystalline films. By calculating velocities from the equations by Bird (9) under the typical epitaxy condition the mean velocity component of the gas in the radial direction caused by the natural convection (5 cm/sec) is neglected com-

paring with that in the axial direction (50 cm/sec). The $(Gr)^{1/2}/Re (=u/v)$ is applied as a parameter of critical ranges for the free, the combined, and the forced convection flows, where Gr and Re are Grashof and Reynolds numbers, respectively, and u and v show perpendicular and parallel velocity components in the axial direction, respectively. Takahashi (10) and Sugawara (11) reported that vortex or spiral flow vanishes when the range of Gr/Re^2 is less than 1-4 or 3-7, respectively. The $Gr^{1/2}/Re$ in this experiment of silicon epitaxy is 0.1 and is included in the range of vortex vanishment. The Reynolds number for the epitaxial process is not greater than 100 under typical operating conditions, therefore, the gas flow is assumed to be laminar. The velocity profile of the gas in the reactor is approximated to the following equation for an isothermal system as given by Bird (9) (Appendix I).

$$V_z = V(r) = \frac{2\bar{V}}{1 + \left(\frac{d_1}{d_2}\right)^2 - \frac{1 - \left(\frac{d_1}{d_2}\right)^2}{\log_e\left(\frac{d_2}{d_1}\right)}} \left[1 - \left(\frac{r}{d_2}\right)^2 + \frac{1 - \left(\frac{d_1}{d_2}\right)^2}{\log_e\left(\frac{d_2}{d_1}\right)} \log_e\left(\frac{r}{d_2}\right) \right] \quad [2]$$

$V(r)$ is the gas velocity at a distance r from the center of the coaxial cylindrical tube, \bar{V} is the average gas velocity, d_1 and d_2 are the inner and the outer radii, respectively.

The gas temperature profile perpendicular to the direction of the gas flow is to be determined only by thermal conduction, because the reactant gas does not absorb heat and the gas flow is laminar. Any contribution of natural convection to the heat conduction is neglected. The gas temperature in the direction of the gas flow is taken to be constant. The gas temperature profile is as follows (9)

$$T(r) = T_1 - \frac{T_1 - T_2}{\log_e\left(\frac{d_2}{d_1}\right)} \cdot \log_e\left(\frac{r}{d_1}\right) \quad [3]$$

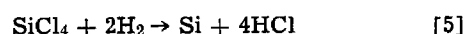
$T(r)$ is the gas temperature at a distance r from the center of the susceptor and T_1 and T_2 are the substrate and the reactor wall temperatures, respectively.

The diffusion coefficient in the binary system is calculated from Fujita's equation (12) which gives nearly equal value as that from Arnold's (13) or Hirschfelder's (14) equation. Fujita's equation is

$$D_{12} = \frac{0.00070 \cdot \left(\frac{1}{M_1} + \frac{1}{M_2}\right)^{1/2} \cdot T^{1.833}}{\left(\left(\frac{Tc_1}{Pc_1}\right)^{1/3} + \left(\frac{Tc_2}{Pc_2}\right)^{1/3}\right)^3} \quad [4]$$

where subscripts 1 and 2 refer to the gaseous components 1 and 2, respectively, Tc is the critical temperature, and Pc is the critical pressure. Using Eq. [4] the diffusion coefficients of H_2 - $SiCl_4$ and HCl - $SiCl_4$ are calculated to be 5.734 and 1.258 (cm^2/sec), respectively, at 1500°K and 760 Torr. The diffusion coefficient in the multicomponent gas system is calculated by Wilke's equation (15).

The over-all deposition reaction can be expressed by



because the concentration of chlorosilane to hydrogen is below 0.01 in mole ratio (Appendix II). The con-

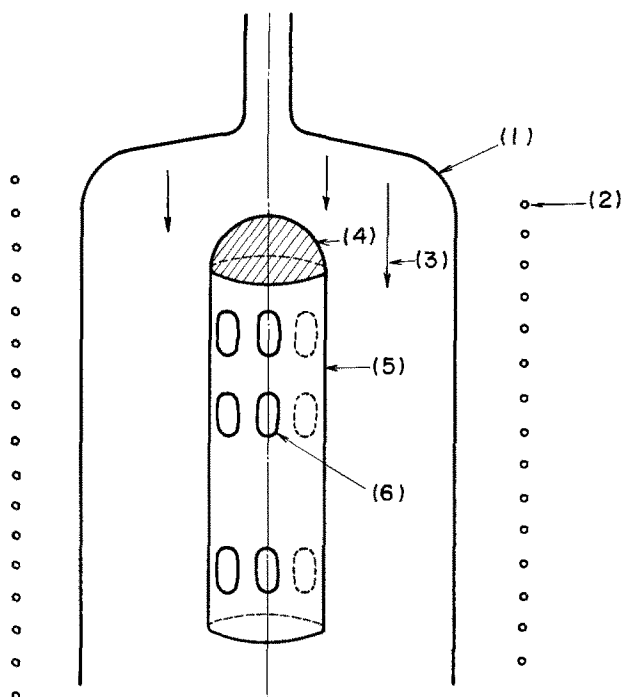


Fig. 1. Apparatus for silicon epitaxial reactor: (1) quartz tube, (2) induction coil, (3) input gas, (4) quartz cap, (5) graphite susceptor, (6) silicon substrate.

tinuity equation [1] for the steady state under the assumptions described above becomes

$$D \frac{\partial^2 C}{\partial r^2} + \left(\frac{D}{r} + \frac{\partial D}{\partial r} \right) \frac{\partial C}{\partial r} + D \frac{\partial^2 C}{\partial Z^2} - V \frac{\partial C}{\partial Z} = 0 \quad [6]$$

It is assumed that the reaction is completed at the silicon surface under the mass-transfer controlled condition, and therefore the concentration of chlorosilane at this surface is zero. No decrease of the concentration at the reactor wall is assumed. The concentration gradient at the reactor wall is taken to be zero. The boundary conditions of Eq. [6] become

$$\frac{\partial C}{\partial r} = 0 \quad \text{at } r = d_2 \quad [7]$$

and

$$C = 0 \quad \text{at } r = d_1 \quad [8]$$

Equation [6] is solved using the boundary conditions, and $\partial C/\partial r$ is obtained. The flux of the reactant to the substrate ($r = d_1$), J , is

$$J = \left(D \frac{\partial C}{\partial r} \right) \Big|_{r=d_1} \quad [9]$$

Expressing the growth rate G in microns per minute, the following equation can be obtained

$$G = 6.00 \cdot 10^5 \cdot \frac{M}{\rho} \cdot \left(D \frac{\partial C}{\partial r} \right) \Big|_{r=d_1} \quad [10]$$

where M is the atomic weight of silicon (28.09 g/mole), and ρ is the density of silicon (2.33 g/cm³).

Solution of continuity equation.—It is assumed that the concentration of the reactant may be expressed as

$$C(r, z) = C_r(r) \cdot C_z(Z) \quad [11]$$

where $C_r(r)$ and $C_z(Z)$ are the radial and the axial components of concentration, respectively.

Mass transport in the reactor is described by considering the three layers for the radial direction, as shown in Fig. 2. In the central region, the reactant is assumed to be carried by the gas flow caused by a

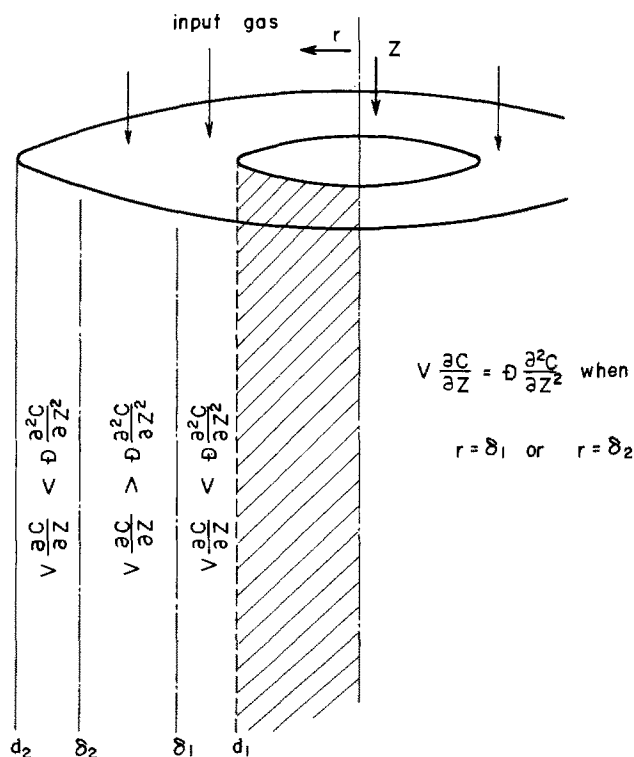


Fig. 2. Mass transport in the reactor

pressure gradient. In the neighborhood of the reactor wall and the susceptor, the gas velocity is low because of interaction of the gas with the wall and the susceptor. In this case the reactant is carried by the diffusion resulting from the concentration gradient.

The three divided layers of the radial direction are now considered in turn:

(a). $\delta_1 < r < \delta_2$.—In this region the term $D \frac{\partial^2 C}{\partial Z^2}$ in

Eq. [6] can be neglected in comparison with $V \frac{\partial C}{\partial Z}$ except near δ_1 and δ_2 . Equation [6] with Eq. [11] gives

$$\frac{1}{C_z} \cdot \frac{\partial C_z}{\partial Z} = \frac{1}{V_z(r) \cdot C_r} \cdot \left(D \frac{\partial^2 C_r}{\partial r^2} + \left(\frac{\partial D}{\partial r} + \frac{D}{r} \right) \frac{\partial C_r}{\partial r} \right) = -\beta \quad [12]$$

$$\beta : \text{constant} \quad [13]$$

The following two equations are obtained from Eq. [12] and [13]

$$C_z = a \cdot e^{-\beta z} \quad a : \text{constant} \quad [14]$$

and

$$\frac{d^2 C_r}{dr^2} + \left(\frac{1}{D} \frac{dD}{dr} + \frac{1}{r} \right) \frac{dC_r}{dr} + \frac{1}{D} \cdot \beta \cdot V_z(r) \cdot C_r = 0 \quad [15]$$

(b). $\delta_2 < r < d_2$ or $d_1 < r < \delta_1$.—In this region the term $V_z \frac{\partial C}{\partial Z}$ can be neglected in comparison with $D \frac{\partial^2 C}{\partial Z^2}$ except near δ_1 and δ_2 . Thus, Eq. [6] leads to

$$-\frac{1}{C_z} \frac{\partial^2 C_z}{\partial Z^2} = \frac{1}{C_r} \left(\frac{\partial^2 C_r}{\partial r^2} + \frac{1}{D} \left(\frac{\partial D}{\partial r} + \frac{D}{r} \right) \cdot \frac{\partial C_r}{\partial r} \right) = -\beta'^2 \quad [16]$$

$$\beta' : \text{constant} \quad [17]$$

Equation [16] and [17] lead to

$$C_z = a' \cdot e^{-\beta' z} \quad a' : \text{constant} \quad [18]$$

and

$$\frac{d^2 C_r}{dr^2} + \left(\frac{1}{D} \frac{dD}{dr} + \frac{1}{r} \right) \frac{dC_r}{dr} + \beta'^2 \cdot C_r = 0 \quad [19]$$

From Eq. [14] and [18], Eq. [11] is given by

$$C = C_r \cdot e^{-kz} \quad k : \text{constant} \quad [20]$$

The δ_1 and δ_2 approximate the inner and the outer radii, respectively. For example

$$\delta_1 = d_1 + (\sim 10^{-3} \text{ cm})$$

and

$$\delta_2 = d_2 - (\sim 10^{-3} \text{ cm})$$

in the case of flow rate 100 liters/min with the above mentioned dimensions, (cf. Appendix III). The regions $\delta_2 < r < d_2$ and $d_1 < r < \delta_1$ can practically be neglected. Thus Eq. [6] and [20] are written as

$$\frac{d^2 C_r}{dr^2} + \left(\frac{1}{D} \frac{dD}{dr} + \frac{1}{r} \right) \frac{dC_r}{dr} + \frac{1}{D} \cdot \beta \cdot V_z \cdot C_r = 0 \quad [21]$$

$$C = C_r \cdot e^{-\beta z} \quad [22]$$

The β is not only the separation constant of the variables r and z as shown in Eq. [12], but also a parameter of the concentration decrease in the direction of gas flow from Eq. [22]. Substituting Eq. [22] in Eq. [7] and [8], the boundary conditions become

$$\frac{dC_r}{dr} = 0 \quad \text{when } r = d_2 \quad [23]$$

and

$$C_r = 0 \quad \text{when } r = d_1 \quad [24]$$

In order to solve the second order differential Eq. [21] for $C_r(r)$ ($r_1 < r < r_2$) by the Runge-Kutta-Gill method, C_r and dC_r/dr at $r = d_1$ or $r = d_2$ must be given. A method of solving Eq. [21] is to derive C_r at $r = d_2$ and to use Eq. [23]. Equation [21] is to be solved so that the boundary condition Eq. [24] is satisfied. In this method dC_r/dr at $r = d_1$ instead of C_r at $r = d_2$ can be derived, and Eq. [21] is solved under the boundary condition Eq. [23].

Derivation of dC_r/dr at $r = d_1$.— \bar{C}_0 and \bar{C}_L indicate the mean concentration at $z = 0$ and $z = L$, respectively. Z denotes a distance from the top of the susceptor in the axial direction. The mean concentration at $z = 0$ is given by

$$\bar{C}_0 = \frac{\int_{d_1}^{d_2} C_0 \cdot 2\pi r \cdot dr}{\int_{d_1}^{d_2} 2\pi r \cdot dr} = \frac{P \cdot C_M}{\bar{T} \cdot R \cdot (1 + C_M)} \quad (\text{mole/cm}^3) \quad [25]$$

while the mean temperature in the reactor is given by

$$\bar{T} = \frac{\int_{d_1}^{d_2} T \cdot 2\pi r dr}{\int_{d_1}^{d_2} 2\pi r dr} = T_1 - \frac{d_2^2(T_1 - T_2)}{d_2^2 - d_1^2} + \frac{T_1 - T_2}{2 \log \frac{d_2}{d_1}} \quad (^\circ\text{K}) \quad [26]$$

where R is 82.06 cm³ atm/(deg mole), P is the pressure in the reactor, and C_M is the mole ratio of chlorosilane to hydrogen at the entrance of the reactor. From Eq. [22] and [25] the relation between \bar{C}_0 and \bar{C}_L becomes

$$\bar{C}_L = \bar{C}_0 \cdot e^{-\beta L} \quad [27]$$

The mole numbers of the feeding gas per second is written as

$$\pi \cdot (d_2^2 - d_1^2) \cdot \bar{V} \cdot \bar{C}_0 \quad [28]$$

and that of the effluent gas per second is

$$\pi \cdot (d_2^2 - d_1^2) \cdot \bar{V} \cdot \bar{C}_L \quad [29]$$

The reaction gas, which is passed through the feed pipe with pressure P_0 , temperature T_0 , and flow rate F , expands in a reactor with pressure P and mean temperature \bar{T} . The gas volume through the reactor per second is $1000/60 \cdot \bar{T}/T_0 \cdot P_0/P \cdot F$. Thus the mean velocity of gas in the cross section is given by

$$\bar{V} = \frac{\text{gas flow per second}}{\text{cross-sectional area of the reactor tube}} = \frac{16.67 \cdot F \cdot \bar{T} \cdot P_0}{\pi \cdot (d_2^2 - d_1^2) \cdot T_0 \cdot P} \quad [30]$$

where F is the total gas flow (in l/min) at T_0 ($^\circ\text{K}$) and P_0 (Torr), P_0 and T_0 are the pressure, 919 Torr and the temperature, 298 $^\circ\text{K}$ of the reactant gas before entering into the reactor, respectively. The mole numbers of the deposited silicon between $z = 0$ and $z = L$ is given by

$$\int_0^L \left(D \frac{\partial C}{\partial r} \right) \Big|_{r=d_1} \cdot 2\pi d_1 \cdot dZ \quad [31]$$

Equations [27] through [31], lead to

$$\frac{dC_r}{dr} \Big|_{r=d_1} = \beta \cdot \frac{\bar{C}_0 \cdot \bar{V} \cdot (d_2^2 - d_1^2)}{2d_1 \cdot D|_{r=d_1}} \quad [32]$$

Derivation of C_r at $r = d_2$.—Experimentally in SiCl₄-H₂ systems the reaction gas decomposes near the silicon substrate and silicon does not deposit on the reaction wall. Therefore, it is assumed that there is no deposition on the walls of the reaction chamber. C_r is given by the ideal gas law

$$C_r = \frac{P \cdot C_M}{T_2 \cdot R \cdot (1 + C_M)} \quad [33]$$

Given a proper initial value into the unknown parameter β , C_r and dC_r/dr becomes constant, and Eq. [21] is solved. In the case that a boundary condition is not satisfied, β is varied recursively for Eq. [21] to be satisfied. Equation [21] with boundary conditions (Eq. [24] and [32]) should be solved subjected to the boundary condition (Eq. [23]). It is difficult, however, to obtain a solution to satisfy Eq. [23] owing to the inclusion of the unknown β in Eq. [32]. Furthermore, the optimum β has not been found. In the case when Eq. [21] with the initial conditions (Eq. [23] and [33]) is solved to satisfy the boundary condition (Eq. [24]), the solution as well as the optimum β are obtained fairly easily. The wall temperature which cannot be measured exactly is involved in Eq. [33]. The sensitivity of the wall temperature to the growth rate is, however, low as will be described later. The calculation in the next paragraph is made by this method where the initial conditions at $r = d_2$ are assumed. The growth rate and β are obtained with good accuracy by dividing the radius into 100 increments.

Results and Discussion

The calculation of the growth rate based on the model.—The calculation of the growth rate based on the model is made for various diffusion coefficients in many gas systems and for various process parameters such as substrate temperature, reactor wall temperature, concentration, and gas flow rate. The apparatus dimensions used in the above calculation are as follows: the silicon carbide coated graphite susceptor is about 30 cm long and about 11 cm in diameter, and the quartz tube reactor is about 17 cm in diameter. Figure 3 shows the results of the calculations of the growth rate along the susceptor for the various gas compositions. Three kinds of reaction gas system are considered. The first system is, SiCl₄-H₂, where the main reactant gas is hydrogen and chlorosilane diffuses into hydrogen, the second system is, HCl-SiCl₄, where hydrogen is stagnant, and the third system is, H₂-HCl-SiCl₄, where chlorosilane diffuses into the mixture gas of hydrogen and hydrogen chloride. The

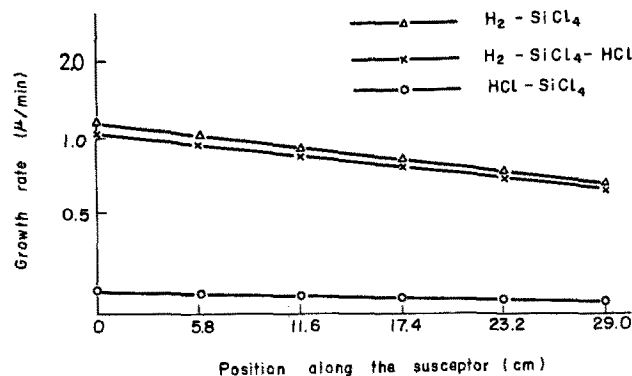


Fig. 3. Logarithm of the growth rate as a function of the diffusion coefficient in various gas components. Substrate temperature 1200 $^\circ\text{C}$, wall temperature 850 $^\circ\text{C}$, mole fraction 0.005, flow rate 80 liters/min (calculated).

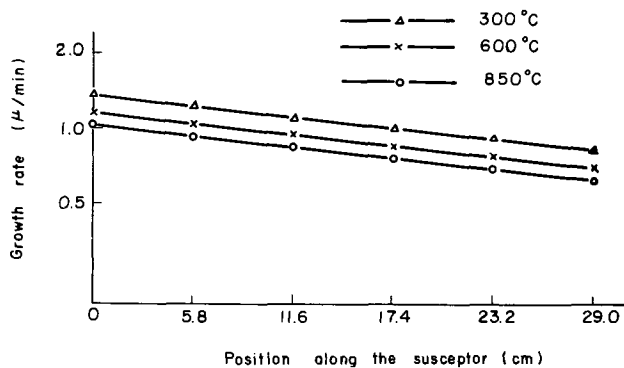


Fig. 4. Logarithm of the growth rate as a function of the wall temperature. Substrate temperature 1200°C, mole fraction 0.005, flow rate 80 liters/min (calculated).

growth rate increases linearly with the diffusion coefficient. The diffusion coefficient used in the following calculations is that for the H_2 -HCl-SiCl₄ system, which, we think, should express the epitaxial reaction better than the other gas systems, because the reaction gas consists of the one shown in Eq. [5]. Plots of the growth rate vs. the position along the susceptor are shown in Fig. 4 at three temperatures of the reactor wall: 300°, 600°, and 850°C. As the wall temperature increases, the growth rate decreases. This is explained by the following: as the wall temperature increases, the temperature difference between the substrate and the wall becomes smaller, hence the concentration gradient is less steep and the growth rate becomes lower.

Figure 5 indicates the calculated growth rate at the substrate temperatures, 1100°, 1200°, and 1300°C. The growth rate is slightly dependent on the substrate temperature.

The formulation of the growth rate based on the model.—The growth rate in the axial direction is formulated by calculations as a function of the dimensions of the reactor and the susceptor and the various process parameters. The following equation is obtained from Eq. [10] and [22]

$$G_{z=z} = 6.00 \times 10^5 \frac{M}{\rho} \cdot \left(D \frac{\partial C_r}{\partial r} \right) \Big|_{r=d_1} \cdot e^{-\beta z} = G_{z=0} \cdot e^{-\beta z} \quad [34]$$

One parameter is varied leaving other parameters constant. It is calculated how $G_{z=0}$ and β are varied by changing the parameter. Thus the following equations are obtained

$$G_{z=0} = 3.004 \cdot 10^5 \cdot \left(\frac{d_2^2 - d_1^2}{d_2} \right)^{-1.020} \cdot \frac{C_M}{1 + C_M} \cdot A \cdot T_1^{1.213} \cdot T_2^{-0.38} \quad [35]$$

$$\beta = 4\pi \cdot 10^2 \cdot \left(\frac{d_2^2 - d_1^2}{d_1 \cdot d_2} \right)^{-1.043} \cdot A \cdot \frac{T_0}{P_0} \cdot T_1^{0.852} \cdot T_2^{-0.0165} \cdot \frac{1}{F} \quad [36]$$

where $G_{z=z}$ is the growth rate at a distance Z cm from the top of the susceptor in μ /min. $G_{z=0}$ is the growth rate at the top of the susceptor in μ /min. The relation between diffusion coefficient D and A is $D = A \cdot T^{1.833}$ similar to Eq. [4]. A becomes 7.975×10^{-6} in the HCl-SiCl₄-H₂ system (SiCl₄/H₂ = 0.005). A is nearly independent of mole ratio, temperature, and pressure and is dependent on gas characteristics.

The growth rate on a tilted susceptor.—A tilted susceptor makes the gas flow rate increase due to the de-

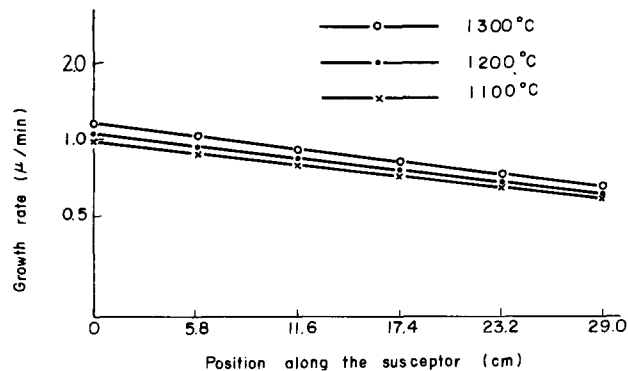


Fig. 5. Logarithm of the growth rate as a function of the substrate temperature. Wall temperature 850°C, mole fraction 0.005, flow rate 80 liters/min (calculated).

crease of the cross-sectional area of a reactor. The increase of the gas flow rate is calculated at each point along the susceptor.

θ is an angle of tilting of the susceptor. The cross-sectional area at a distance Z from the top of the susceptor becomes $\pi \cdot (d_2^2 - (d_1 + Z \tan \theta)^2)$ as shown in Fig. 6.

The correction factor of the gas flow rate is written as

$$F = \frac{\pi \cdot (d_2^2 - d_1^2)}{\pi \cdot (d_2^2 - (d_1 + Z \tan \theta)^2)} \quad [39]$$

The growth rate on the tilted susceptor is obtained by substituting Eq. [39] for F in Eq. [36].

Comparison of the theory and experiment.—The apparatus used to prepare epitaxial layers by the hydrogen reduction of tetrachlorosilane is shown in Fig. 1. The (111) face silicon substrate is 2 in. in diameter, approximately 200 μ thick, and of low resistivity (<0.02

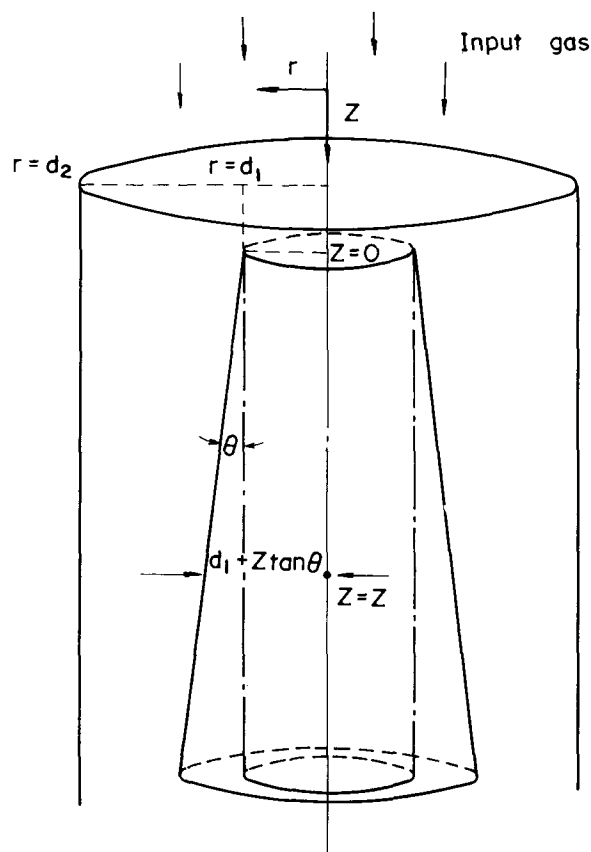


Fig. 6. Schematic view of the cross-sectional area for a horizontal reactor with the tilted susceptor.

ohm-cm). The substrate temperature has been measured with an optical pyrometer and corrected for the emissivity of the silicon. Layer thickness of about 10μ is used for the determination of the growth rate by the infrared interference method.

Silicon deposition is experimentally started at the quartz cap. But an exact growth rate on the amorphous quartz cap is not measurable. A length of the cap (6 cm) is much shorter than that of the susceptor (30 cm), therefore, the deposited quantity on the cap is small. An approximation is made that the silicon deposition is started at 6 cm in front of the top of the susceptor. The approximation expresses an experimental fact better than assuming the deposition on the cap being neglected. The following figures compare the experimental growth rate (dotted line) with the calculated (full line) under inclusion of the deposition on the cap.

Figures 7 and 8 show the growth rate at 23 cm from the quartz cap. Figure 7 gives the dependence of the growth rate on the mole ratio of SiCl_4 to H_2 . It will be seen that the growth rate is directly proportional to the mole ratio with reasonable accuracy. The flow rate of hydrogen is varied from 60 to 150 l/min. The result is shown in Fig. 8. The growth rate increases with the flow rate, but the growth rate decreases over the flow

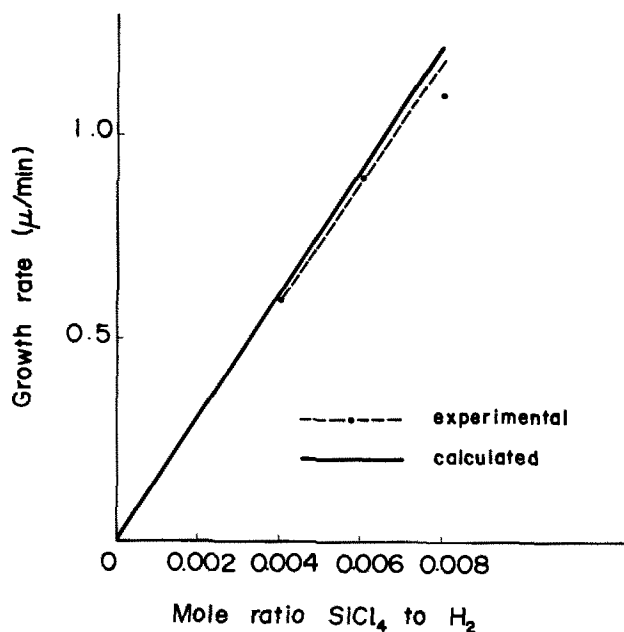


Fig. 7. The growth rates as a function of the mole ratio of SiCl_4 to H_2 . Substrate temperature 1200°C , wall temperature 850°C , flow rate 120 liters/min.

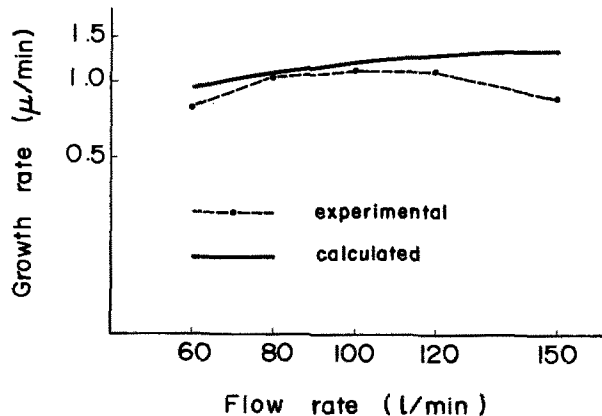


Fig. 8. The growth rates as a function of the flow rate of hydrogen. Substrate temperature 1200°C , wall temperature 850°C , mole ratio 0.008.

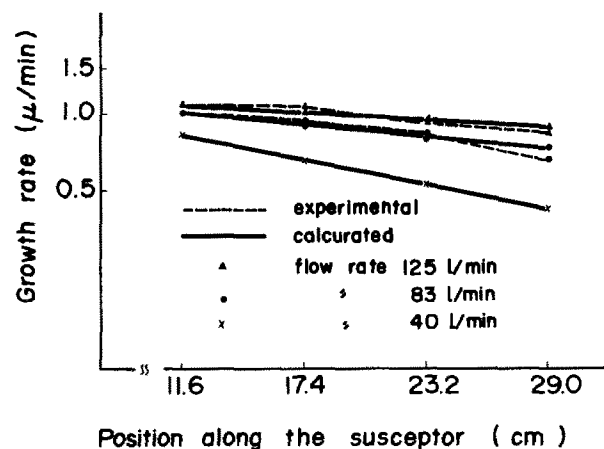


Fig. 9. The growth rates as a function of the position along the susceptor for the flow rates of 83 and 125 liters/min. Substrate temperature 1200°C , wall temperature 850°C , mole ratio 0.006.

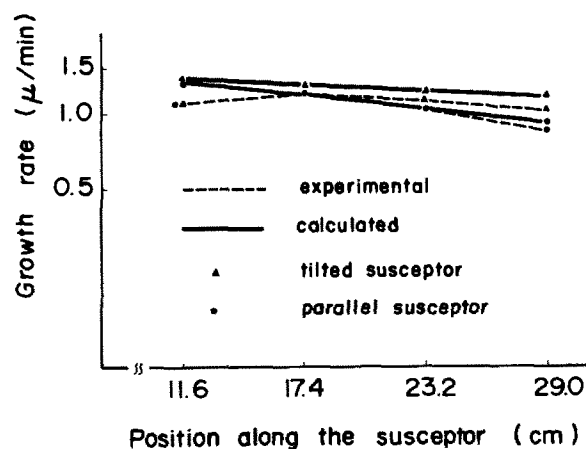


Fig. 10. The growth rates on a nontilted and a tilted susceptors as a function of the position along the susceptor. Substrate temperature 1200°C , wall temperature 850°C , flow rate 80 liters/min, mole ratio 0.008.

rate 120 liters/min. This is explained by the following: in such a great flow rate the reaction [5] is in non-equilibrium and most reaction gas passes through unchanged, so that the growth rate becomes low. Figure 9 shows the growth rate in the direction of gas flow in two flow rates under constant mole ratio. As the flow rate increases, the uniformity of the thickness of the deposition layer along the susceptor becomes considerably better.

Figure 10 compares the uniformity of the thickness in the axial direction on a tilted susceptor with that on a nontilted susceptor. An angle of tilting of the susceptor is 3° . The growth rate at the latter half of the tilted susceptor increases by 10-20% compared with that of the nontilted susceptor. The small decrease of the growth rate near the top of the susceptor in experiment is thought to be due to the reactant gas which is not yet well heated. Comparison of the theoretical result with experimental data gives good agreement.

Sensitivity analysis.—Sensitivity analysis of the process parameters to the growth rate in silicon epitaxy will now be discussed. This analysis is made in order to obtain a constant growth rate. Influence of the growth rate by the variation of the process parameters is known from the analysis. The variation of the growth rate is calculated in such a case that the dimensions of the reactor and the susceptor and the process parameters deviate by 10% from the following conditions, $T_1 = 1200^\circ\text{C}$, $T_2 = 850^\circ\text{C}$, $C_M = 0.005$, $F = 80$ liters/min.

Table I. Relative variation of the growth rate with 10% deviation of the dimensions and the process variables

Dimensions and process variables		$\Delta G/G$ ($Z = 15$)
Substrate temperature	(T_1)	9.5%
Wall temperature	(T_2)	-3.8%
Concentration (mole fraction)	(C_1)	10.1%
Flow rate	(F)	3.1%
Temperature of the feeding gas	(T_0)	-3.5%
Pressure of the feeding gas	(P_0)	3.5%
Constant term in diffusion coefficient	(A)	7.0%
Inner radius	(d_1)	7.2%
Outer radius	(d_2)	-16.7%

The following equations are applied

$$\Delta G = \left(\frac{\partial G}{\partial X} \right) \Big|_{z=15} \cdot \Delta X \quad [37]$$

and

$$\Delta X = \frac{1}{10} X \quad [38]$$

where X is one of the process parameters and dimensions. The variation G changes with a position on the susceptor. Table I gives the result for the relative variation of the growth rate, $\Delta G/G$, at the center of the susceptor, $z = 15$ cm. According to the analysis, parameters such as T_1 , C , A , d_1 , and d_2 have relatively high sensitivity. The minus sign in Table I means that the growth rate decreases with the increase of the variable. A is determined by the gas components in the system. If the three components system is the case, the deviation of A is dependent on the mole fraction SiCl_4 , H_2 , and HCl , and this is within a few per cent. The fluctuation of T_1 , d_1 , and d_2 are experimentally controllable within 5%. The control of the concentration depends on the hydrogen quantity passed into the tetrachlorosilane and the main hydrogen quantity which is carried into the reactor directly. The concentration is also varied by the hydrogen pressure and the temperature of water to control the vaporization of tetrachlorosilane. From the sensitivity analysis the control of the concentration is found to be the most important factor in order to obtain the constant growth rate.

Conclusion

The silicon epitaxial process is performed in a coaxial cylindrical tube. The growth rate is investigated under many process conditions. The growth rate is derived as a function of the apparatus dimensions and the process variables. From the sensitivity analysis the control of the reactant concentration is the most important factor in order to produce a constant growth rate on the substrate. The change in the concentration proportionally contributes to the change in the growth rate. For the purpose of obtaining the uniformity in thickness of deposition layer on the over-all susceptor it is necessary not only to increase the gas flow rate beyond 80 liter/min but also to raise the angle of tilting of the susceptor more than 3° in the present apparatus.

Acknowledgment

The authors wish to thank Mr. K. Sugawara and Mr. H. Tochikubo for many suggestions regarding this work and to acknowledge Mr. Y. Nakazawa in acquiring the experimental data. They are particularly in-

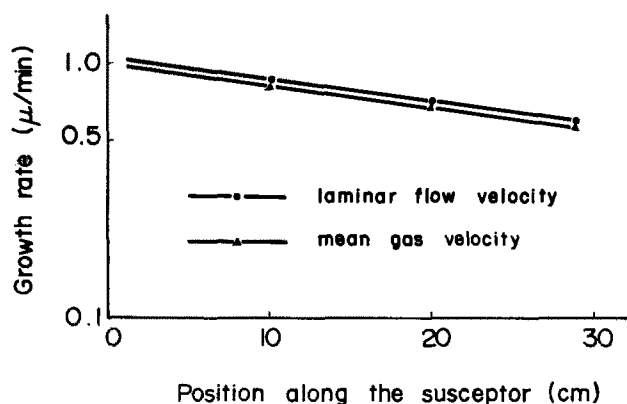


Fig. 11. Growth rates as a function of the position along the susceptor for two velocity profiles (calculated).

debted to Mr. R. Takahashi and Dr. F. Inose for their encouragement and helpful discussions.

Manuscript submitted Feb. 10, 1971; revised manuscript received Nov. 6, 1971.

Any discussion of this paper will appear in a Discussion Section to be published in the December 1972 JOURNAL.

APPENDIX I

Velocity Profile

An equation of the velocity profile in a nonisothermal system cannot be found and the derivation of the equation is troublesome. The growth rate is calculated in the case of mean velocity and laminar flow velocity in an isothermal system as shown in Fig. 11. Hence growth rate hardly depends on the velocity profile. As a result of the calculation of the growth rate, the velocity profile has little influence on growth rate; the velocity profile in an isothermal system is used.

APPENDIX II

Mole Fraction of the Gaseous Species in $\text{SiCl}_4\text{-H}_2$ System

The gaseous species involved in the $\text{SiCl}_4\text{-H}_2$ system are assumed to be mainly SiCl_4 , SiHCl_3 , SiCl_2 , SiH_2Cl_2 , HCl , and H_2 . The mole fraction of these gases are calculated in the same way as Lever (4) did and his equilibrium constants are used. Table II shows the mole fractions for several values of mole ratio of SiCl_4 to H_2 at 1500°K and 1.0 atm.

In the case of mole ratio of SiCl_4 to $\text{H}_2 < 0.01$, the mole fraction except H_2 and HCl is neglected.

APPENDIX III

Calculation of δ_1 and δ_2

The δ_1 and δ_2 are determined under the following conditions: flow rate of reaction gas of 100 liters/min, substrate temperature of 1200°C , wall temperature of 850°C , and susceptor length of 30 cm.

By Eversteyn (7) reactor efficiency is 35% when the mean velocity is over 50 cm/sec.

Mean concentration $\bar{C}_{z=z}$ and $\bar{C}_{z=0}$ are as follows from Eq. [20]

$$\bar{C}_{z=z} = \frac{\int_{d_1}^{d_2} C_r \cdot e^{-KZ} \cdot 2\pi r dr}{\int_{d_1}^{d_2} 2\pi r \cdot dr} \quad \bar{C}_{z=0} = \frac{\int_{d_1}^{d_2} C_r \cdot 2\pi r dr}{\int_{d_1}^{d_2} 2\pi r dr}$$

Table II. Mole fractions of $\text{SiCl}_4\text{-H}_2$ system at 1500°K , 1 atom

SiCl_4/H_2	SiHCl_3	SiCl_4	SiCl_2	HCl	H_2	SiH_2Cl_2
0.003	7.068×10^{-6}	1.375×10^{-7}	1.343×10^{-4}	1.162×10^{-2}	0.9882	9.527×10^{-6}
0.005	3.084×10^{-5}	9.850×10^{-7}	3.596×10^{-4}	1.894×10^{-2}	0.9806	2.531×10^{-5}
0.007	7.961×10^{-5}	3.506×10^{-6}	6.785×10^{-4}	2.591×10^{-2}	0.9733	4.739×10^{-5}
0.010	2.114×10^{-4}	1.299×10^{-5}	1.306×10^{-3}	3.575×10^{-2}	0.9626	9.020×10^{-5}
0.020	1.234×10^{-3}	1.397×10^{-4}	4.282×10^{-3}	6.365×10^{-2}	0.9304	2.859×10^{-4}

where $\bar{C}_{z=z}$ and $\bar{C}_{z=0}$ are the mean concentrations at z cm from the top of a susceptor and at the top of a susceptor, respectively. Consequently it leads to the following equation

$$\frac{\bar{C}_{z=z}}{\bar{C}_{z=0}} = e^{-Kz}$$

From that this ratio is equaled to 0.35 and $Z = 30$ cm. The K becomes 3.50×10^{-2} . The following result is obtained from Eq. [20]

$$-v \frac{\partial C}{\partial Z} - D \frac{\partial^2 C}{\partial Z^2} = K \cdot C_r \cdot e^{-Kz} (v - DK)$$

The velocity profile is calculated from Eq. [2]. Therefore δ_1 and δ_2 , that is to say, r at $-v \frac{\partial C}{\partial Z} = D \frac{\partial^2 C}{\partial Z^2}$ lead to $\delta_1 = d_1 + 1.0 \times 10^{-3}$ cm and $\delta_2 = d_2 - 2.0 \times 10^{-3}$ cm. Accordingly the area of $d_1 < r < \delta_1$ and $\delta_2 < r < d_2$ are neglected.

REFERENCES

1. P. C. Rundle, *Intern. J. Electronics*, **24**, 405 (1968).
2. W. Steinmaier, *Philips Res. Rept.*, **18**, 75 (1963).
3. H. Seki *et al.*, *Jap. J. Appl. Phys.*, **4**, 645 (1965).
4. R. F. Lever, *IBM J. Res. Develop.*, **8**, 460 (1964).
5. T. O. Sedgwick, *This Journal*, **111**, 1381 (1964).
6. S. E. Bradshaw, *Intern. J. Electronics*, **21**, 205 (1966).
7. F. C. Eversteyn *et al.*, *This Journal*, **117**, 925 (1970).
8. W. H. Shepherd, *ibid.*, **112**, 988 (1965).
9. R. B. Bird, "Transport Phenomena," John Wiley & Sons, Inc., New York (1960).
10. R. Takahashi, K. Sugawara, Y. Nakazawa, and Y. Koga, Paper 192 presented at Electrochem. Soc. Meeting, Los Angeles, May 10-15, 1970.
11. K. Sugawara, H. Tochikuba, R. Takahashi, and Y. Koga, Paper 193 presented at Electrochem. Soc. Meeting, Los Angeles, May 10-15, 1970.
12. J. Fujita, *Kagaku Kikai*, **15**, 234 (1951).
13. J. H. Arnold, *Ind. Eng. Chem.*, **22**, 1091 (1930).
14. J. O. Hirschfelder, *Chem. Rev.*, **44**, 205 (1949).
15. C. R. Wilke, *Chem. Eng. Prog.*, **46**, 95 (1950).

Plane Defect at the Interface and Dislocations in Epitaxially Grown GaAs

Seigô Kishino and Shinya Iida

Central Research Laboratory, Hitachi Ltd., Kokubunji, Tokyo, Japan

ABSTRACT

Lattice defects in vapor-grown GaAs on GaAs substrates were studied by an x-ray diffraction technique, *i.e.*, by using the Lang method. It was found that a plane defect was introduced at the epitaxial layer-substrate interface due to a lattice parameter difference between the epitaxial layer and the substrate. This difference depends on the impurity concentration difference between layer and substrate. Examination by x-ray topography also revealed that the plane defect was introduced for the liquid-phase epitaxy of GaAs due to an impurity concentration difference between layer and substrate. Dislocations induced in the epitaxial layer grown by the vapor phase technique were also studied by utilizing an x-ray topographic technique. Two kinds of dislocations were identified: a 30° dislocation, and a pure edge dislocation having Burger's vectors of $\frac{1}{2} a \langle 110 \rangle$.

To study the relationship between crystal imperfections and the performance of semiconductor devices, is of present technological importance. In the growth of the GaAs crystal, epitaxially grown either by the vapor-phase or liquid-phase epitaxy technique, lattice defects such as stacking faults (1-3) and dislocations (4) are commonly observed, and they can be detrimental to the performance of the devices involved (5). Dislocations induced in the epitaxial layer have been observed by the chemical etching method (4); however, the type of dislocation has not been clarified. Damage introduced at the epitaxial layer-substrate interface was also observed (6, 7); but, here too, the origin of the defects was not clarified.

In this paper, lattice defects introducing a plane defect at the interface and dislocations in the epitaxial layer, were observed by an x-ray diffraction technique in a manner so that the origin of the defects was clarified. In the past, the Borrmann method (8) or a reflection method (9) has been used to investigate the lattice defects of III-V compound semiconductors such as GaAs, GaP, and $\text{GaAs}_{1-x}\text{P}_x$ crystals. In this report, however, the conventional Lang method has been used and the product $\mu_0 \cdot t$ —where μ_0 and t are the linear absorption coefficient and the thickness of the specimen respectively—is made to be 1 unless especially noted.

Key words: gallium arsenide, epitaxial growth, dislocations, x-ray diffraction.

Experimental

Sample preparation.—Wafers were cut in the (001) orientation from horizontally boat-grown (Te-doped) GaAs crystals. The slices were lapped mechanically, and chemically etched by using an etch solution of H_2SO_4 , H_2O_2 , and H_2O in the ratio 3:1:1. The preparation method of the epitaxial wafers used here is described elsewhere (10). Briefly, a method that utilizes the vapor transport of GaAs with AsCl_3 and H_2 mixed gas in an open flow system was used. Substrate and source temperatures were kept at 770° and 870°C respectively. Hydrogen gas with a flow rate of 150 cc/min was bubbled through an AsCl_3 reservoir which was kept at 0°C . A growth rate of $0.6 \mu\text{m}/\text{min}$ on the (001) surface was obtained by using this method. Thicknesses of the epitaxially grown layers were about $150 \mu\text{m}$.

Specimen 1 was made from a wafer whose surface was nearly parallel to a (001) plane as schematically shown in Fig. 1. This wafer is a Sn-doped ($n = 1 \times 10^{17} \text{ cm}^{-3}$) crystal epitaxially grown on a Te-doped ($n = 1 \times 10^{18} \text{ cm}^{-3}$) substrate. The surface of the wafer was beveled at about 5° to the epitaxially grown surface, and the total thickness of the specimen was about $45 \mu\text{m}$. Figures 1(a) and (b) are respectively sectional and planar views of the specimen. The substrate-epitaxial layer interface is included in the middle part of the specimen as shown in Fig. 1(b).

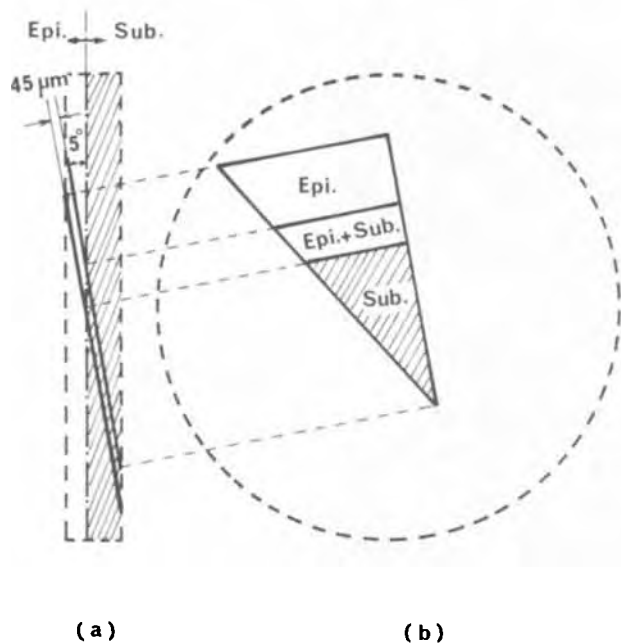


Fig. 1. Sectional (a) and planar (b) figures of specimen 1

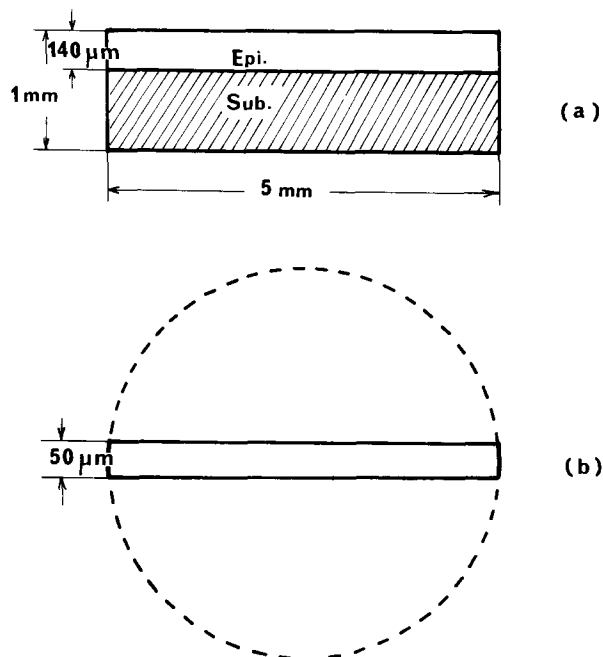


Fig. 2. Schematic diagram of method used for obtaining the section of epitaxially grown GaAs wafer. (a) Planar figure of the specimen. (b) Sectional figure of the specimen.

Specimen 2 was prepared from a Te-doped ($n = 1 \times 10^{18} \text{ cm}^{-3}$) crystal epitaxially grown on a Te-doped ($n = 1 \times 10^{16} \text{ cm}^{-3}$) substrate. The shape of the specimen is shown in Fig. 2, in which the (001) wafer was cleaved, and the specimen was thinned down to a thickness of about $50 \mu\text{m}$, by mechanical polishing and chemical etching with the etch solution described above. Specimen 3 was made from a Te-doped ($n = 1 \times 10^{16} \text{ cm}^{-3}$) crystal epitaxially grown on a Te-doped ($n = 1 \times 10^{16} \text{ cm}^{-3}$) substrate. There is no doping concentration difference between the substrate and the epitaxial layer in this specimen. The shape of the specimen was similar to that of specimen 3.

X-ray topographs.—Standard microfocus x-ray equipment was used, operated at 50 kV and 1 mA. The images were recorded on $50 \mu\text{m}$ Ilford nuclear plates at approximately 15 hours' exposure. Repre-

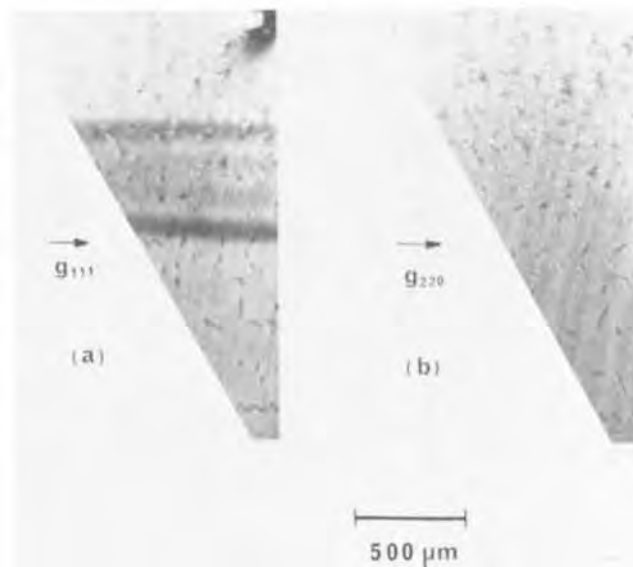


Fig. 3. X-ray topographs of specimen 1. Figures (a) and (b) are topographs with (111) $\text{MoK}\alpha_1$ and (220) $\text{MoK}\alpha_1$ diffractions respectively.

sentative x-ray topographs taken from specimen 1 are shown in Fig. 3(a), and (b). Figures 3(a) and (b) are x-ray topographs taken with (111) and (220) $\text{MoK}\alpha_1$ diffractions. X-ray interference fringes are visible in Fig. 3(a) but invisible in Fig. 3(b), revealing that visibility of the interference fringes depends on the diffraction plane used. When diffraction planes such as (220), (040), (220), and (400) were used, these being perpendicular to the (001) plane which is parallel to the surface of the epitaxial layer, the interference fringes were invisible. Conversely, they were visible when diffraction planes other than those described above—for example (202), (111), and (211)—were used. From these experimental results, the direction of the fault vector of the plane defect was determined to be [001].

Specimen 2, whose surface is (220), was also examined by the x-ray diffraction technique. X-ray topographs taken from specimen 2 are shown in Fig. 4, 5, and 6. Burger's vector directions of dislocations are rather conveniently determined by the following technique (11). Use of the criterion

$$\cos \angle (g b) = \begin{cases} 0 & \text{minimum contrast} \\ 1 & \text{maximum contrast} \end{cases} \quad [1]$$

where g is the diffraction vector and b is the fault vector, permits complete determination of the fault vector direction. From the x-ray topographs shown in Fig. 4, 5, and 6, three Burger's vector directions are determined. Those dislocations are expressed diagrammatically with the signs α , β , and γ in Fig. 7. Dislocations α have a minimum contrast in Fig. 5(a) and (b) and a maximum contrast in Fig. 4(c). Dislocations β have a minimum contrast in Fig. 4(a) and a maximum contrast in Fig. 6(b). Dislocations γ have a minimum contrast in Fig. 4(b) and a maximum contrast in Fig. 6(a). Relations between the diffraction vectors and the image contrasts are summarized in Table I, including the results obtained with (202) and (022) diffractions which are not shown. Employing the results shown in Table I, Burger's vector directions of dislocations α , β , and γ are determined to be $\frac{1}{2} a [1\bar{1}0]$, $\frac{1}{2} a [01\bar{1}]$, and $\frac{1}{2} a [10\bar{1}]$ respectively. The glide planes of the dislocations α , β , and γ are determined to be (110), (111), and (111) since images of the dislocations α , β , and γ vanished almost completely in those topographs obtained from (220), (111), and (111) diffraction planes respectively. From the data given by

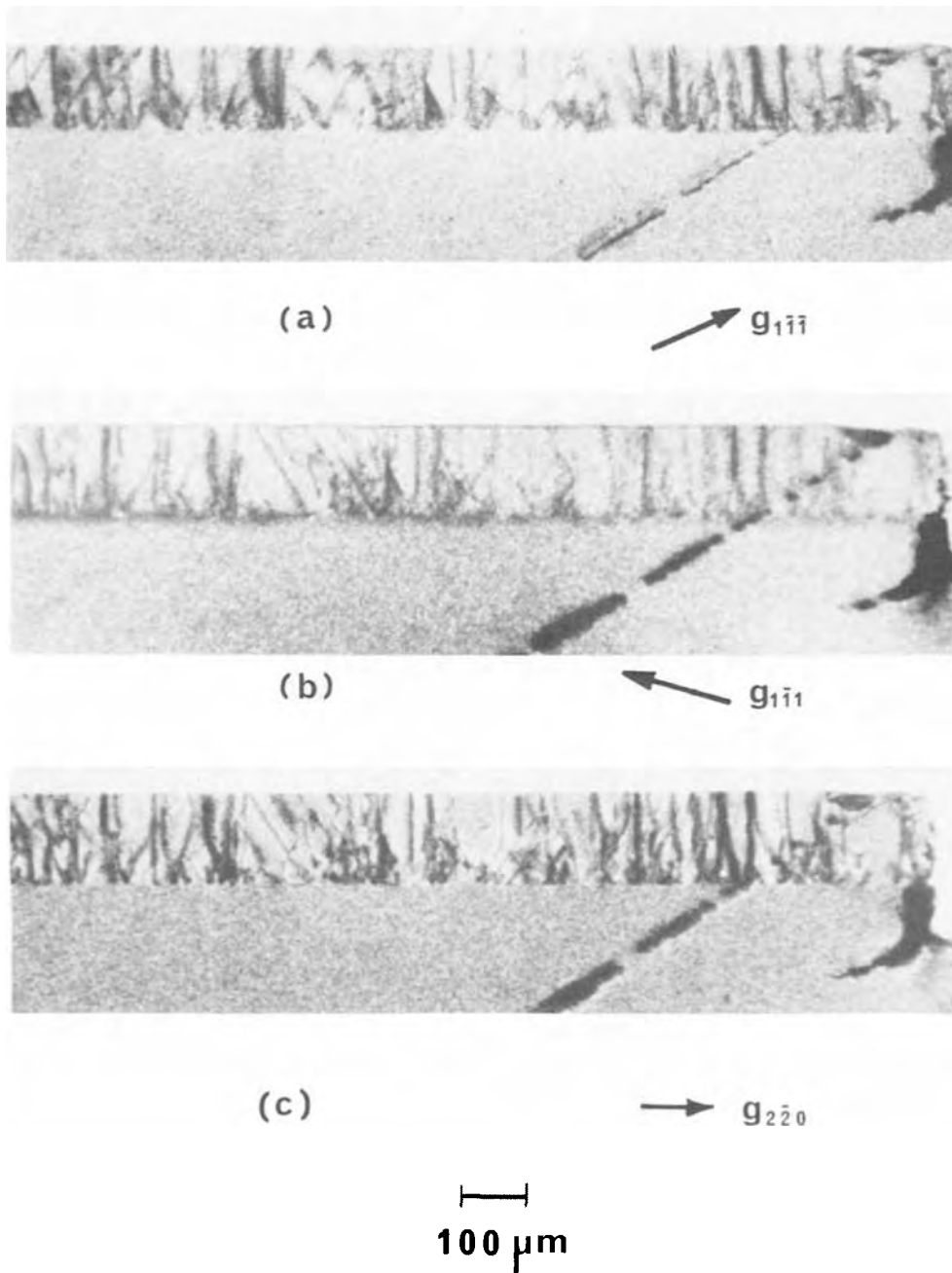


Fig. 4. X-ray topographs taken from specimen 2 (I). Figures (a), (b), and (c) are x-ray topographs with $(1\bar{1}\bar{1})$, $(\bar{1}\bar{1}\bar{1})$, and $(2\bar{2}0)$ $AgK_{\alpha 1}$ diffractions respectively.

Hornstra (12) in which dislocations with $\frac{1}{2} a \langle 110 \rangle$ Burger's vector are enumerated in a diamond cubic type crystal, the three dislocations described above are determined as follows. Dislocations α are "dislocations of Type VIII," pure-edge dislocations. On the other hand, dislocations β and γ are "dislocations of Type IV," mixed-type dislocations in which the angle between the dislocation axis and Burger's vector direction is 30° , and the glide plane is $\{111\}$.

The plane defect already shown in Fig. 3 was also observed in specimen 2. Since the plane defect was

laid perpendicularly to the surface of the specimen in this case, this was observed as line-shaped images at the epitaxial layer-substrate interface as shown in Fig. 5. The image assumes maximum contrast in Fig. 5(a) and minimum contrast in Fig. 4(c). The direction of the fault vector is similar to that of specimen 1. The image contrast of the plane defects shown in Fig. 4(a), 6(a), and (b), are opposite that shown in Fig. 4(b). They do not have a minimum contrast as shown in Fig. 4(c), because these images are not caused by the strain field as in the case of dislocation; rather, they are caused by a phase transition of x-ray waves.

The x-ray topograph taken from specimen 3 is shown in Fig. 8. Figures 8(a) and (b) are a topograph taken with (004) $AgK_{\alpha 1}$ diffraction and a corresponding optical photograph respectively. Though the diffraction plane is similar to that used in the case of Fig. 5(a), where the plane defect is observed as line-shaped images at the interface, no image contrast exists in the x-ray topograph shown in Fig. 8(a). If the plane defect is introduced due to an impurity concentration difference between layer and substrate, it is reasonable to think that the plane defect vanishes

Table I. Relation between diffraction vectors and image contrasts

Diffraction vector	Maximum contrast			Minimum contrast		
	α	β	γ	α	β	γ
$\bar{2}\bar{2}0$	yes					
$20\bar{2}$						yes
$20\bar{2}$			yes			
$0\bar{2}\bar{2}$				yes		
$0\bar{2}\bar{2}$		yes				
$1\bar{1}\bar{1}$				yes		
$1\bar{1}\bar{1}$						yes
$11\bar{3}$				yes		
004				yes		

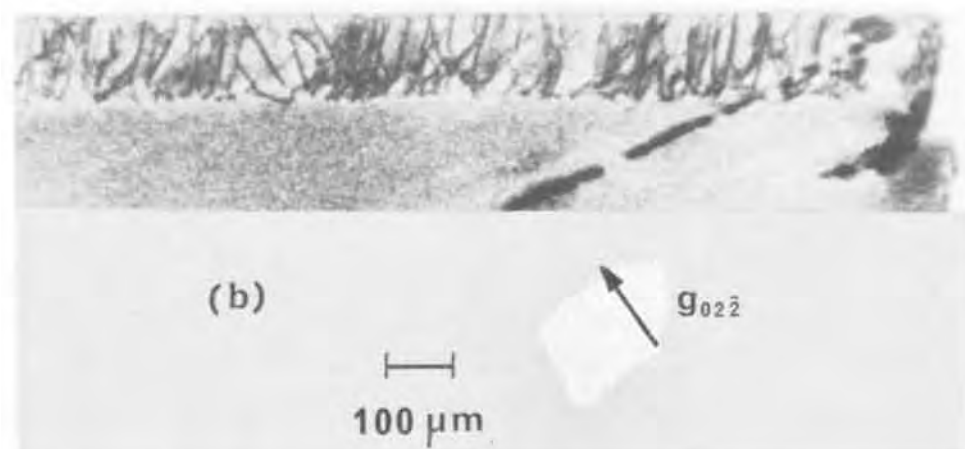
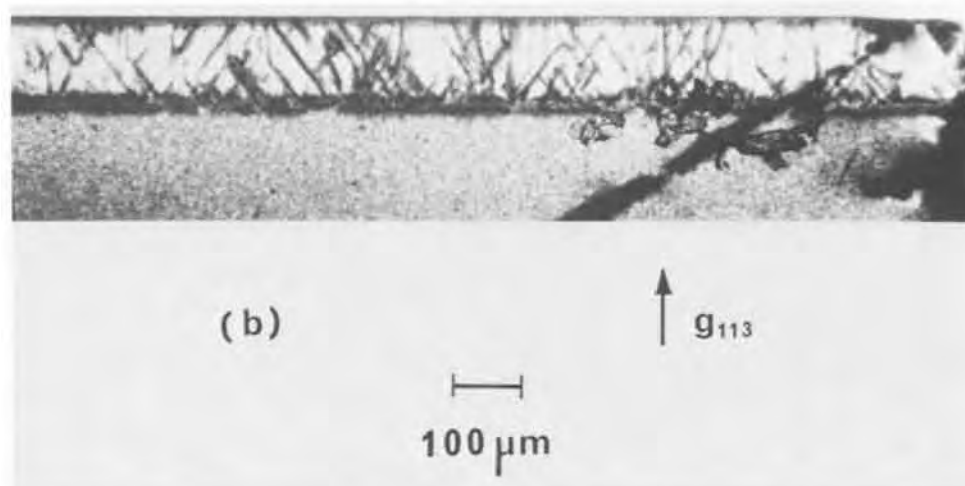
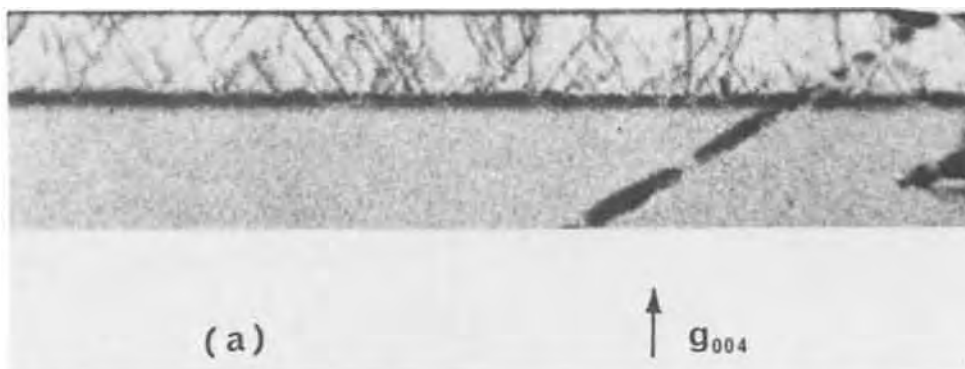


Fig. 5. X-ray topographs taken from specimen 2 (II). Figures (a) and (b) are x-ray topographs with (004) and (113) $\text{AgK}\alpha_1$ diffractions respectively.

Fig. 6. X-ray topographs taken from specimen 2 (III). Figures (a) and (b) are x-ray topographs with $(20\bar{2})$ and $(02\bar{2})$ $\text{AgK}\alpha_1$ diffractions respectively.

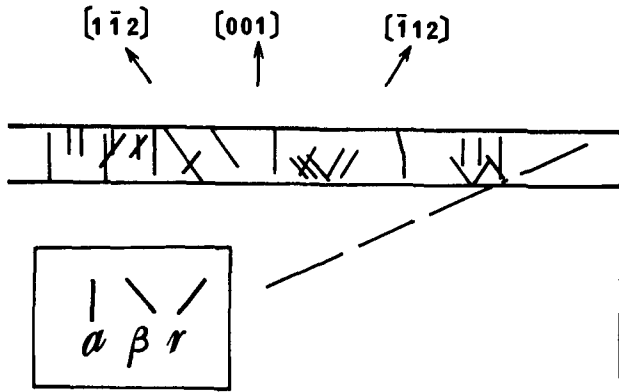


Fig. 7. Schematic diagram of dislocations observed by x-ray topographs. Signs α , β , and γ reveal dislocations in which directions of the dislocation axis are parallel to $[001]$, $[\bar{1}12]$, and $[112]$ respectively.

in this specimen, since specimen 3 has the same impurity concentration difference in the epitaxial layer and the substrate.

Results and Discussions

Types of dislocations induced in the epitaxial layer of GaAs single crystal differ from those of dislocations introduced in the homoepitaxy of Si (13) and the heteroepitaxy of Ge-GaAs (14), in which dislocations are introduced at the epitaxial layer-substrate interface by adding an extra half-plane to the portion with a smaller lattice parameter in order to compensate for the lattice parameter difference between them. On the other hand, such dislocations have not been observed in the homoepitaxy of GaAs.

When the impurity is doped in the GaAs crystal, the lattice parameter of the host crystal also increases (15); thus, the lattice strain at the interface must be

released in the homoepitaxy of GaAs when the impurity concentration differs between layer and substrate. The lattice strain in this case was released by the plane defect at the epitaxial layer-substrate interface, and consequently dislocations of different types such as 30° or pure-edge dislocations were introduced. The formation mechanism of dislocations such as a 30° or a pure edge cannot be simply explained by strain at the interface due to the impurity difference between layer and substrate. Local strain at the interface may be released by the formation of these dislocations; however, the strain-release mechanism is not clear at present.

When a p-n junction was formed from Zn diffusion into epitaxially grown n-type $\{100\}$ $\text{GaAs}_{1-x}\text{P}_x$ wafers, two types of dislocations—in which dislocation lines are parallel to $\langle 100 \rangle$ and $\langle 211 \rangle$ directions respectively—were observed from irregularity of the diffusion front (16). These dislocations may correspond to the 30° and the pure-edge type dislocations observed here. Concerning the 30° dislocations, Stringfellow (17) also observed them in $\text{GaAs}_{1-x}\text{P}_x$ crystal and offered an explanation about these dislocations in connection with the growth mechanism. The present experiment presented no explicit relation between the growth rate and the formation of 30° dislocation.

It was clarified that the plane defect was introduced at the interface when there was an impurity concentration difference between layer and substrate, as already shown. At the vapor phase epitaxy, we showed that the plane defect was not introduced at the interface if there was no impurity concentration difference between layer and substrate, as already shown in Fig. 8. This defect also may be expected in the liquid phase epitaxy of GaAs crystal, when there exists an impurity concentration difference between layer and substrate. Further studies of a sample similar to specimen 2 will be described subsequently. The sample used here has triple layers of liquid phase

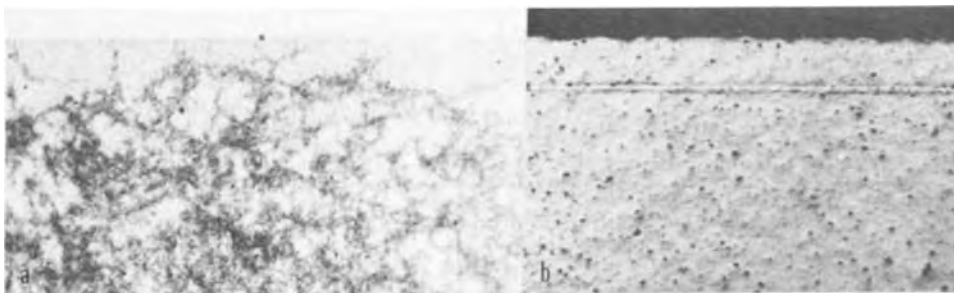


Fig. 8. X-ray topograph (a, left) and corresponding optical photograph (b, right) of specimen 3 which has no impurity concentration difference between layer and substrate.

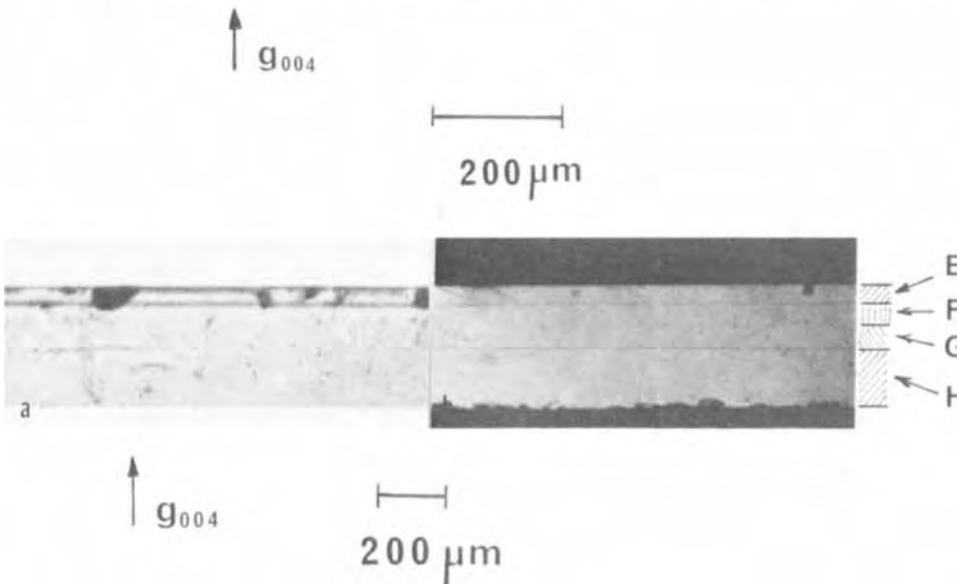


Fig. 9. X-ray topograph (a, left) and corresponding optical photograph (b, right) of sample grown by the liquid phase epitaxial technique in which the epitaxial layers are composed of triple layers E, F, and G. Impurity concentration of E, F, G, and H are $1 \times 10^{19} \text{ cm}^{-3}$, $1 \times 10^{16} \text{ cm}^{-3}$, $1 \times 10^{16} \text{ cm}^{-3}$, and $5 \times 10^{15} \text{ cm}^{-3}$ respectively.

epitaxy—namely, E, F, and G. The impurity (Te) concentrations of E, F, and G are $1 \times 10^{19} \text{ cm}^{-3}$, $1 \times 10^{16} \text{ cm}^{-3}$, and $1 \times 10^{16} \text{ cm}^{-3}$ respectively; that of substrate H is $5 \times 10^{15} \text{ cm}^{-3}$. The x-ray topograph and the optical photograph of this sample are reproduced in Fig. 9 (a) and (b) respectively. The x-ray topograph was taken with (004) $\text{AgK}_{\alpha 1}$ diffraction, permitting the plane defect to be observed as line-shaped images at each interface in the x-ray topograph, when the plane defects described above are introduced at each interface. It is clear that the plane defect is not introduced at the interface in the case of liquid phase epitaxy, when no lattice parameter difference exists with the preceding epitaxial layer. Further studies will be reported in the near future.

Acknowledgments

The authors wish to express their thanks to Dr. H. Kusumoto for his encouragement, to Messrs. M. Hirao, Y. Takeda, and K. Ito for their helpful support, and to Messrs. H. Sato, M. Tamura, and Y. Yoshihiro for their valuable discussions. They also express their thanks to Mr. M. Nakamura for providing GaAs wafers epitaxially grown by the liquid phase epitaxy technique.

Manuscript submitted July 30, 1971; revised manuscript received March 27, 1972.

Any discussion of this paper will appear in a Discussion Section to be published in the June 1973 JOURNAL.

REFERENCES

1. M. S. Abrahams and C. J. Buiocchi, *J. Phys. Chem. Solids*, **28**, 927 (1967).
2. M. S. Abrahams and J. J. Tietjen, *ibid.*, **30**, 2941 (1969).
3. M. S. Abrahams and C. J. Buiocchi, *J. Appl. Phys.*, **41**, 2358 (1970).
4. M. S. Abrahams and C. J. Buiocchi, *ibid.*, **36**, 2855 (1965).
5. "Semiconductor Silicon," R. R. Haberecht and E. L. Kern, Editors, pp. 585-653 and references therein, The Electrochemical Society Softbound Symposium Series, New York (1969).
6. G. A. Rozgonyi and S. E. Haszko, *This Journal*, **117**, 1562 (1970).
7. C. Schiller, *Solid-State Electron.*, **13**, 1163 (1970).
8. E. D. Jungbluth, *This Journal*, **112**, 580 (1965).
9. E. S. Meieran, *ibid.*, **114**, 292 (1967).
10. S. Iida, H. Sato, M. Hirao, and Y. Takeda, *J. Electrochem. Soc. Japan*, **37**, 186 (1969).
11. G. H. Schwuttke and H. Rupprecht, *J. Appl. Phys.*, **37**, 167 (1966).
12. J. Hornstra, *J. Phys. Chem. Solids*, **5**, 129 (1958).
13. Y. Sugita, M. Tamura, and K. Sugawara, *J. Appl. Phys.*, **40**, 3089 (1969).
14. G. O. Krause and E. C. Teague, *Appl. Phys. Letters*, **10**, 251 (1967).
15. J. Black and P. Lublin, *J. Appl. Phys.*, **8**, 2462 (1964).
16. D. A. Grenning and A. H. Herzog, *ibid.*, **39**, 2783 (1968).
17. G. B. Stringfellow and P. E. Greene, *ibid.*, **40**, 502 (1969).

Technical Notes



Electrolytic Etching of GaN

J. I. Pankove

RCA Laboratories, Princeton, New Jersey 08540

With the advent of visible electroluminescence (1) in GaN, new developments will be forthcoming in the technology of this material. This note marks a new step in our ability to process GaN.

Heretofore, the only known etchants for GaN were molten sodium hydroxide, potassium hydroxide, or potassium pyrosulfate (2) at about 800°C . This process, done at elevated temperatures, attacks the insulating substrate (Al_2O_3) on which the GaN is grown. The hot solvent also attacks any masking material that would be used to confine the region to be etched. Hence, it is nearly impossible to control the area from which the material is to be removed by the above chemical etches. The etching of GaN films at lower temperatures was reported by Chu (3). In this case, the film was immersed in a 50% aqueous solution of NaOH at 5° to 90°C . However, when this technique was used on our single crystal layers grown by a different vapor transport method (4), no attack could be detected. It is possible that the films of Ref. (3), although dense, were somewhat porous and, therefore, more fragile than our thicker material.

We have etched GaN electrolytically in 0.1N NaOH by anodizing the crystal to which an indium contact was attached by soldering. If the crystal is immersed in a bath of NaOH, a white layer of gallium hydroxide

forms which seems to block further etching. This mechanical interference was overcome by using a jet of electrolyte which flushed away any solid reaction by-

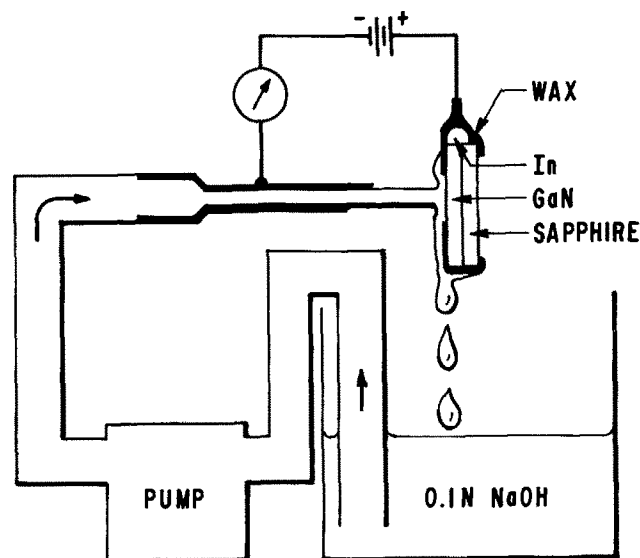


Fig. 1. Set-up for jet electrolytic etching of GaN

Key words: Jet etching, device processing, compound semiconductors, electroluminescence, surface preparation.

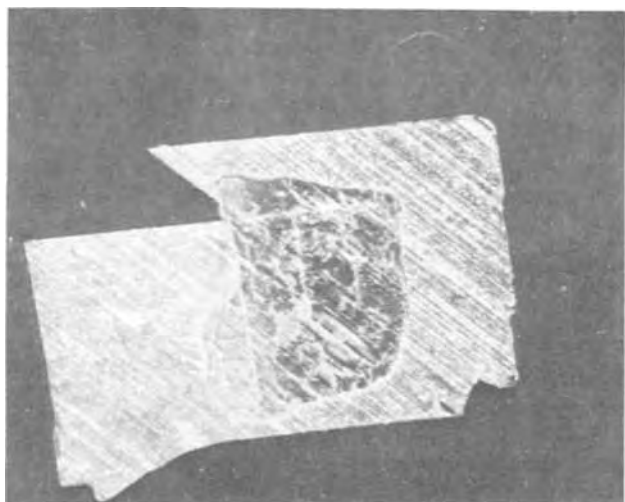


Fig. 2. Photograph of etched GaN on a sapphire substrate; the dark region is the etched unmasked portion of the crystal.

product. The experimental arrangement is shown in Fig. 1. The electrolyte is pumped through a Tygon tube to a hypodermic needle connected to the negative terminal of d-c power supply. The jet strikes the exposed region of the partially masked crystal forming the anode. The potential was adjusted to draw a current of about 2 mA. Figure 2 shows that etching proceeded as expected in the unmasked area. In this case, piceine wax was used to mask the crystal.

This electrolytic etching technique was also used to separate a layer of Zn-doped insulating GaN, grown on undoped conducting n-type GaN from the sapphire substrate. The n-type region was connected to the positive terminal of the power supply. The electrolyte jet was played on the specimen's cleaved edge which exposed the three regions: the sapphire substrate, the

n-type layer, and the insulating layer. Only the conducting n-type region was dissolved, thus, freeing the insulating GaN layer. Because of the tremendous stresses generated immediately after growth by the large differential thermal expansion between GaN and the sapphire substrate, the freed insulating layer tends to break up into flakes. When the insulating GaN layer is thick (0.5 mm), larger pieces can be obtained.

Blue-green electroluminescence from the i-n transition was seen. This rather bright luminescence is observed when the applied potential is sufficiently large to permit current flow through the i-n transition in addition to the etching current along the n-type region.

The use of electrolyte etching to produce self-supporting layers of single crystal GaN may provide us with the ideal substrate for growing strain-free material, namely, a single crystal of GaN. By concentrating the current with finer electrodes, it should be possible to etch intricate patterns (5). The use of this technique for polishing surfaces or revealing dislocations has not been explored.

Acknowledgments

The author wishes to thank E. A. Miller for growing the GaN, J. E. Berkeyheiser for technical assistance, and G. S. Lozier for a valuable discussion.

Manuscript submitted Feb. 1, 1972; revised manuscript received March 29, 1972.

Any discussion of this paper will appear in a Discussion Section to be published in the June 1973 JOURNAL.

REFERENCES

1. J. I. Pankove, E. A. Miller, and J. E. Berkeyheiser, *RCA Rev.*, **32**, 383 (1971); and *J. Luminescence*, **5**, 84 (1972).
2. H. H. Whitaker, Private communication.
3. T. L. Chu, *This Journal*, **118**, 1200 (1971).
4. H. P. Maruska and J. J. Tietjen, *Appl. Phys. Letters*, **15**, 327 (1969).
5. "The Electrochemistry of Semiconductors," p. 290, P. J. Holmes, Editor, Academic Press, New York (1962).

The Growth of Ge-GaAs and GaP-Si Heterojunctions by Liquid Phase Epitaxy

Ferenc E. Rosztochy* and William W. Stein*¹

Varian Associates, Palo Alto, California 94303

The purpose of this paper is to discuss the feasibility and practicality of growing heterojunction epitaxial layers from eutectic solutions. As practical examples for this technique, the growth of germanium-gallium arsenide and galliumphosphide-silicon heterojunctions will be described.

Eutectic epitaxy is based on the discovery that seeded single crystal layers can be obtained from eutectic liquid compositions of ternary solutions (1). Since, by definition, the liquid is in equilibrium with two solids, theoretically either of them can be used as substrates. Depending on which solid is used, one can talk about heteroepitaxy or homoepitaxy.

If the solution of a ternary system, such as A-B-C, is cooled to room temperature with a starting composition D (as seen in Fig. 1), the composition first stays constant in the liquid; then, reaching the saturation point for compound AB, AB starts to precipitate and the composition of the liquid gradually changes

to E and then to F. In Fig. 1 the A-F-B line represents the eutectic valley of the system. At F the liquid is in

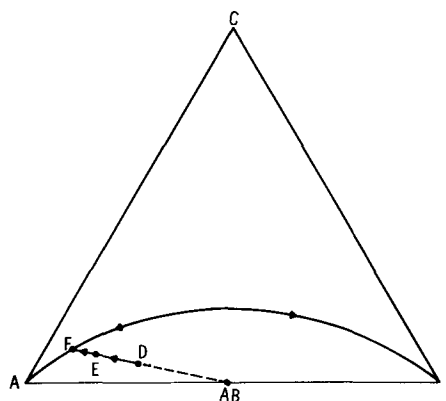


Fig. 1. A schematic ternary phase diagram (similar to the phase diagram of the Ga-As-Si system; A:Ga, B:As, C:Si).

* Electrochemical Society Active Member.

¹ Present address: ITT, Fort Wayne, Indiana 46800.

Key words: heterojunctions, epitaxy, liquid phase.

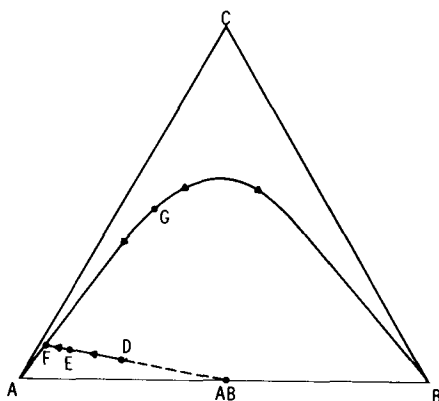


Fig. 2. A schematic ternary phase diagram (similar to the phase diagram of the Ga-As-Ge system; A:Ga; B:As; C:Ge).

equilibrium with both solids AB and C. When the liquid is further cooled, AB and C will coprecipitate and the liquid composition will vary along the eutectic line to A.

In the case of liquid-phase epitaxy, the layers of AB are grown along a line like D-E. It was assumed that on reaching F, the eutectic composition, the further growth of the single-crystal layer would virtually stop due to the coprecipitation of the other material. In the case of the Ga-As-Si system, it has been shown recently that the crystal growth did not stop but actually continued, and a Si-doped GaAs layer continued to grow while the composition of the liquid varied along the eutectic line (2).

Ge on GaAs

The Ga-As-Ge ternary system has a schematic phase diagram similar to Fig. 2 (3). When a solution with composition D was cooled to room temperature, the first grown epitaxial GaAs layer on the GaAs substrate was covered with an epitaxial layer of Ge.

Figure 3a presents the photograph of a nitric acid-stained angle lap of the wafer. The angle laps were made on a 10° block. The structure consists of n-type GaAs single crystal substrate, covered with an approximately $20\ \mu\text{m}$ thick p-type epitaxial layer of GaAs, highly doped with Ge; and on the top of this is an approximately $2\ \mu\text{m}$ thick p-type epitaxial layer of Ge saturated with both Ga and As at the growth temperature.

The complete uniform coverage of the GaAs growth, with a layer of epitaxial Ge from a eutectic solution that is saturated relative to both GaAs and Ge, is attributed to the phase diagram (3). While the melt is cooled from composition F to room temperature along the eutectic line (Fig. 2), the "precipitate" is more than 95% Ge. Once the GaAs surface, in contact with a melt supersaturated relative to Ge, becomes seeded with Ge, it suddenly covers the whole surface area in a very short time.

If a eutectic melt, saturated with both GaAs and Ge, is brought in contact with a single crystal GaAs substrate and cooled, then an epitaxial heterojunction, p-type Ge on n-type GaAs, can be grown. A melt was prepared by heating 0.45g Ga, 1.7g Ge, and 0.30g GaAs to 850°C . It was brought in contact with a GaAs substrate at 814°C and was cooled to 803°C at which point the melt was wiped off the wafer. For more details on the experimental procedure, see Ref. (4). Figure 3b presents the photograph of the nitric-acid stained angle lap of this wafer. There is an approximately $23\ \mu\text{m}$ p-type epitaxial Ge layer on the n-type GaAs substrate. There is no epitaxial GaAs regrowth on this wafer. The Ge layer was identified by use of the electron beam microprobe. It was doped with Ga and As on the order of one atomic per cent (a/o) each.

For liquid phase epitaxy, a few per cent solubility of the source material in the solvent at the growth temperature is usually preferred. To grow epitaxial heterojunctions from eutectic solution the selection of a solvent in which the substrate crystal has a much

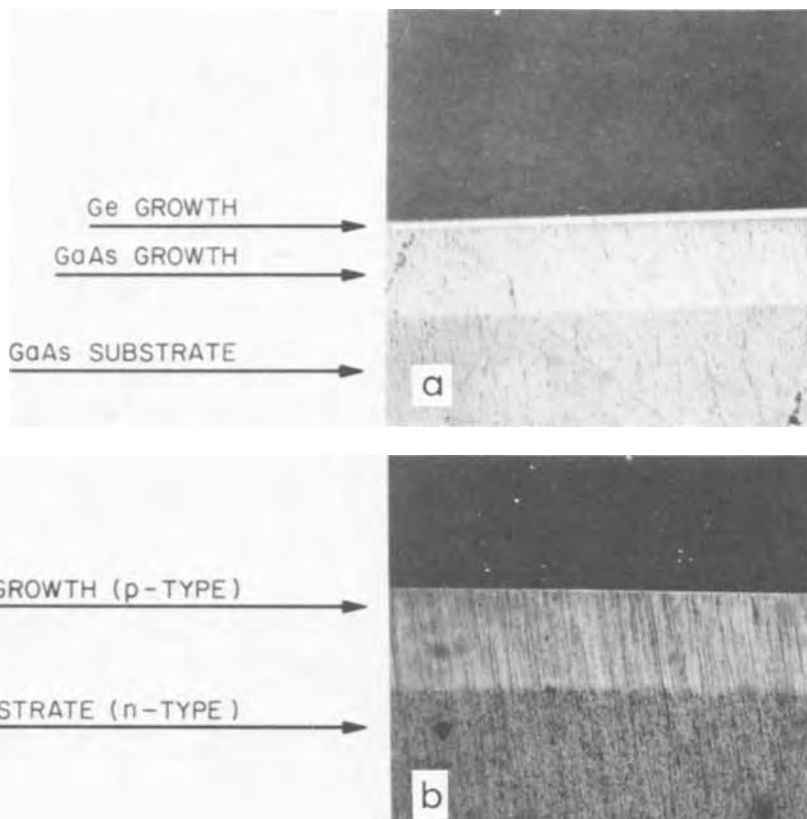


Fig. 3. Nitric acid stained angle lap of Ge growth on GaAs substrates.

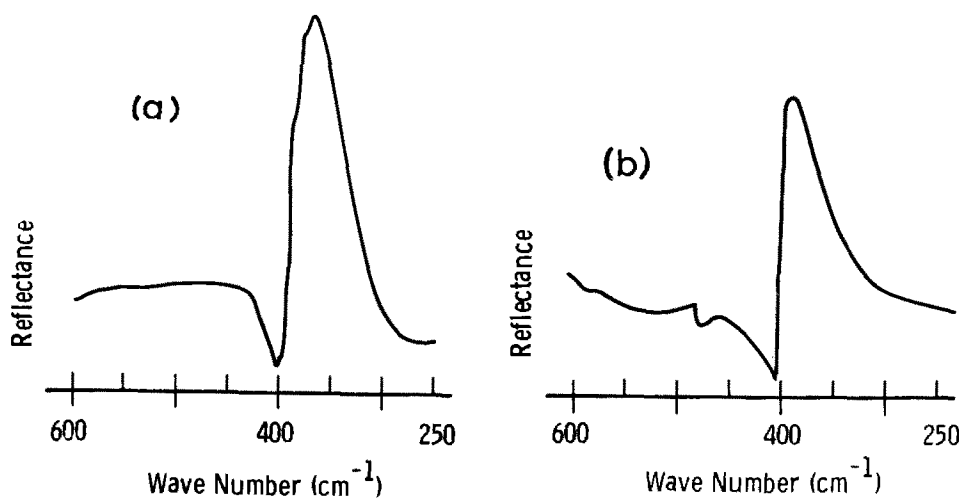


Fig. 4. a, Infrared reflection spectrum of the epitaxially grown GaP; b, infrared reflection spectrum of single-crystal, bulk GaP.

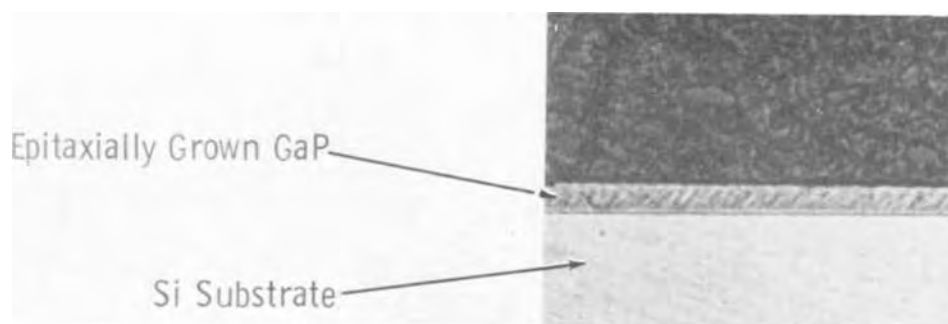


Fig. 5. Cleaved and stained cross-section of epitaxial GaP on Si substrate.

lower solubility at the growth temperature than the source material is also recommended.

GaP on Si

For device application one of the most interesting combinations is to grow epitaxial GaP on Si substrates. Using Ga as the solvent, we could not get a good epitaxial growth of GaP. We attribute the difficulty to the relatively high solubility of Si in Ga under growth conditions.

We turned our attention to quaternary systems to find the right solvent to grow GaP on Si. Based on solubility data, a number of metals appeared more favorable than Ga as a solvent. Based on thermodynamic data, lead and tin were selected. The solubility of GaP relative to the solubility of Si is relatively high in both; and the solubility of Pb and Sn in GaP crystals is relatively low.

Using a graphite boat, flowing ultra-pure dry hydrogen, and using an experimental setup similar to Nelson's design (5), a saturated solution of GaP in Pb was prepared by thoroughly mixing 13g Pb and 0.3g GaP at 950°C. After keeping the boat at 950°C for 60 min the system was quenched, subsequently saturated with Si at 950°C, and quenched again. The Si substrate was placed in the other end of the boat, the system was heated to 950°C and kept there for 30 min, then the furnace was tipped and the melt was brought in contact with the substrate. It was cooled to 800°C in 60 min and then the melt was removed from the seed. An epitaxial layer approximately 10 μm thick was grown. It was examined by x-ray and the Laue photographs proved it was epitaxial single crystal. It was identified by electron beam microprobe as GaP on Si.

The same technique and experimental setup was used to grow epitaxial layers from Sn solutions. Five grams of Sn with 0.5g of GaP were heated to 850°C to prepare a saturated solution, then it was saturated with Si. The melt was brought in contact with (111)-

or (100)-oriented Si substrates at 845°C and was cooled to 650°C in 3 hr. The epitaxial layers were on the order of 10 μm thick. The epitaxial layers were identified as GaP using an infrared spectrophotometer and measuring the Reststrahlen frequency around 25 μm . As can be seen in Fig. 4, the infrared reflection spectra of the epitaxial layers (Fig. 4a) were very similar to those of pure melt-grown GaP (Fig. 4b). Figure 5 is a photograph of a cleaved and stained GaP-Si heterojunction.

The disadvantage of this technique is that the epitaxial GaP layers were degenerately doped with Si and Pb or Sn. For most device applications an additional epitaxial layer of GaP would have to be grown by a different technique.

To summarize, a new technique called eutectic epitaxy has been described. It has been used to grow GaAs-Ge and GaP-Si heterojunctions. Its potential application to grow other heterojunctions is suggested.

Acknowledgments

Helpful suggestions and discussions with R. L. Bell and G. A. Antypas are gratefully acknowledged. The aid of S. V. Szeremy in the growth of the epitaxial layers is also gratefully acknowledged.

Manuscript submitted March 9, 1971; revised manuscript received April 3, 1972.

Any discussion of this paper will appear in a Discussion Section to be published in the June 1973 JOURNAL.

REFERENCES

1. F. E. Rosztochy, *This Journal*, **115**, 328C (1968).
2. F. E. Rosztochy, Abstract 526, p. 516, *Electrochem. Soc. Extended Abstracts*, Fall Meeting, Montreal, Oct. 6-11, 1968.
3. M. B. Panish, *J. Less-Common Metals*, **110**, 416 (1966).
4. F. E. Rosztochy, F. Ermanis, I. Hayashi, and B. Schwartz, *J. Appl. Phys.*, **41**, 264 (1970).
5. H. Nelson, *RCA Rev.*, **24**, 603 (1963).

Epitaxial Growth of Silicon from Dichlorosilane

Anders Lekholm

Microwave Institute Foundation, S-100 44 Stockholm 70, Sweden

Epitaxial silicon has found many important applications in solid-state devices. These applications may be divided into two groups: components that exploit the unique feature of epitaxy to produce layers of any desired doping on higher doped contact regions, and components that have abrupt transitions in the doping profile as an integrated part of the device.

In components where sharp steps in the impurity density distribution are required, it is necessary to minimize the Dt product of diffusion coefficient and time in the growth step. Since it is impossible to increase the growth rate above a few $\mu\text{m}/\text{min}$ (and thus decrease time) in the silicon tetrachloride process, the natural solution to this problem is to decrease the growth temperature. This is also a very effective way of decreasing the Dt product because the diffusion coefficient of most impurities in silicon decreases about one order of magnitude for every 100°C decrease in temperature.

Of the different methods available for low temperature epitaxial growth of silicon, thermal decomposition of silane has attracted most interest. Growth temperatures as low as 800°C are reported (1). To obtain high growth rates special schemes, such as water-cooled reaction vessels, have to be used to avoid gas phase decomposition and fallout of polycrystalline silicon on the wafers. Improved growth techniques have resulted in growth rates of $5 \mu\text{m}/\text{min}$ at 1000°C (2). Further increase in the growth rate is possible if the hydrogen carrier gas is substituted by helium. Using this scheme, growth rates of $3 \mu\text{m}/\text{min}$ at 900°C are reported (1).

In a production system one must, however, make a choice between the simplicity of the silicon tetrachloride process and the better results (in terms of Dt product) of the more complicated silane process.

This paper presents results from epitaxial growth of silicon from dichlorosilane. It allows high growth rates at substantially lower temperatures than silicon tetrachloride. Unlike silane, dichlorosilane is relatively stable in the gas phase and problems with premature gas phase pyrolysis are small or nonexistent.

For the experiments described, an epitaxial system with vertical gas flow and a rotating rf-heated carbon susceptor was used. The susceptor diameter is 12.5 cm and is designed to carry seven $1\frac{1}{4}$ in. diam silicon wafers. The total gas flow in all runs was 27 liters/min. The system was originally designed to use silicon tetrachloride; however, no alterations were made for these dichlorosilane experiments.

The temperature of the silicon wafers was measured with an optical pyrometer or an electro-optic, IR detector and was corrected for emissivity and for absorption losses in the quartz of the bell jar. The gas flow rates were monitored with flowmeters calibrated for the gases used. The thicknesses of the epitaxial layers were determined from infrared interference measurements.

Great care was taken to obtain reproducible results from run to run. In order to improve the temperature measurements, the susceptor was etched clean between each experimental run and was again coated with silicon in a standardized run before the next silicon wafer was processed. At high growth rates this procedure was necessary. The silicon on the susceptor would then exhibit a large-grain polycrystalline surface and, after a few runs, the uncertainty in the tem-

perature readings increased rapidly in an unpredictable way.

The growth rate as a function of mole concentration of dichlorosilane in hydrogen is shown in Fig. 1. The growth temperature was 1110°C . No attempts were made with higher growth rates than those shown in the graph. At growth rates above $5\text{--}7 \mu\text{m}/\text{min}$ small fluctuations in temperature or gas composition had a strong influence on the epitaxial layer quality. Above a growth rate of $10 \mu\text{m}/\text{min}$ dendritic growth occasionally occurred at a few spots on the susceptor resulting in ladder-like nests of dendrites about $100 \mu\text{m}$ long.

The temperature dependence of the growth rate is shown in Fig. 2. The growth rate is proportional to the dichlorosilane concentration for all temperatures studied, indicating a first order reaction. From the plot, an apparent activation energy of 13 kcal/mole is calculated. This value is greater than that found by other workers. Benzing *et al.* (3, 4) have reported an activation energy of 5.8 kcal/mole for this reaction. The latter value has been corroborated by Van Hoy (5).

The high value of the activation energy this author obtained, independent of the mentioned works, may be due to the different types of epitaxial systems used. In the vertical system used by the author, control of the reacting gas composition is good, while in a horizontal system as used by Benzing *et al.* (3), the gas composition gradually changes along the length of the susceptor.

For the concentrations and temperatures studied, epitaxial growth of high quality layers was achieved. The final surface finish was observed in a differential interference contrast microscope and was found to be comparable with that of the etch-polished (6, 7) substrates. Layers were grown at temperatures as low as 1000°C , but these showed a much higher concentration of stacking faults, which were probably due to the inefficiency of the hydrogen etching of silicon dioxide in this temperature range. Some layers, grown at

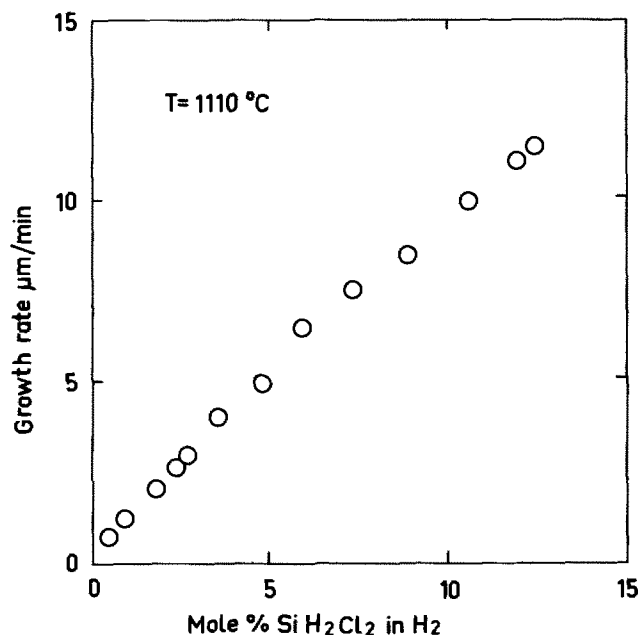


Fig. 1. Growth rate of epitaxial silicon as a function of mole concentration of dichlorosilane in hydrogen at 1110°C .

Key words: impurity distribution, redistribution of dopants, low temperature epitaxy.

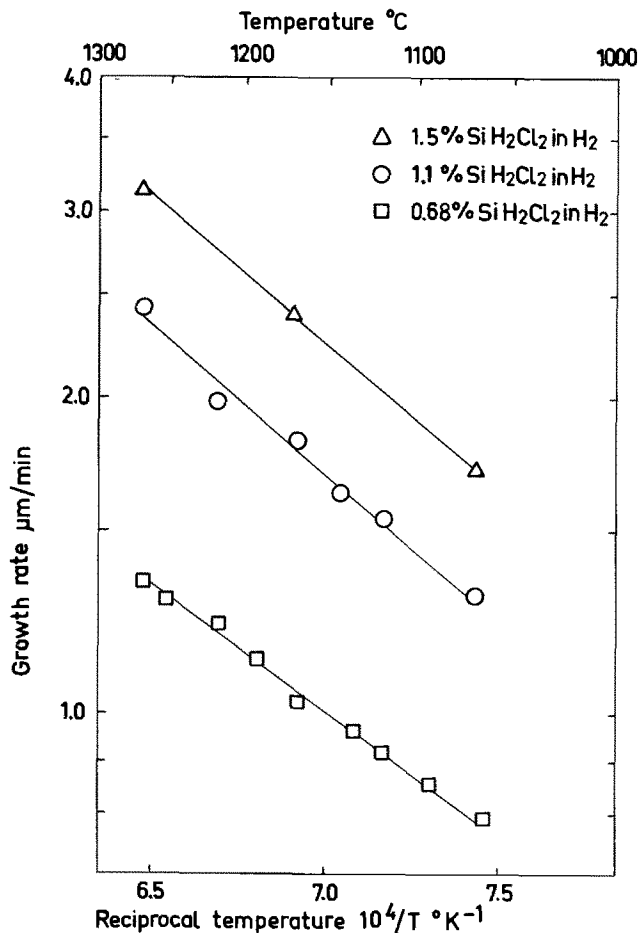


Fig. 2. Temperature dependence of the epitaxial growth for different concentrations of dichlorosilane in hydrogen.

1100°C and higher temperatures, were completely free of stacking faults (8).

The impurity density distribution at the substrate interface was determined from capacitance measurements on mesa diodes formed by diffusion and etching (9). Lightly doped layers were grown on 0.01 ohm-cm boron or antimony doped substrates. As an example, an antimony doped substrate with a 5 μm thick epitaxial layer, which was grown at 1080°C with a growth rate of 1.2 $\mu m/min$, had a step in the impurity distribution from the layer doping of $5 \cdot 10^{14} cm^{-3}$ to $1 \cdot 10^{17} cm^{-3}$ in a distance of about 0.1 μm . This result agrees well with the calculated out-diffusion from the substrate.

The similarities between epitaxy from silicon tetrachloride and dichlorosilane offers an interesting possibility to study the differences between epitaxial growth from a highly reversible reaction (silicon tetrachloride) and from an irreversible reaction (dichlorosilane). Grossman (10) and Thomas *et al.* (11, 12) have proposed that, in the reversible reaction of silicon tetrachloride and silicon in a hydrogen ambient, a thin surface layer of the silicon substrate is transferred into the gas phase and later redeposited. As a consequence of this, the impurity density distribution at the substrate-epitaxial layer interface will be more

diffuse than predicted by diffusion theory.

To test this hypothesis, lightly doped layers were grown from dichlorosilane and silicon tetrachloride under identical growth conditions. Growth rates of about 3 $\mu m/min$ at about 1230°C, were used in order to operate close to equilibrium in the silicon tetrachloride reaction. The back side of the substrates were sealed with a thermally grown layer of silicon dioxide to prevent the escape of impurities into the gas stream. The substrates were doped with boron or antimony to 0.01 ohm-cm. No differences in the impurity density distribution of the interfacial region was observed within the experimental error. There are two possible explanations for this result. Either the hypothesis is false, or the reaction kinetics are the same for the two growth processes. The latter assumption was tested by using other carrier gases than hydrogen in the dichlorosilane process. Experiments with nitrogen and argon as carriers showed that the growth rate at 1100°C was proportional to the dichlorosilane concentration but 30-40% lower than for dichlorosilane in hydrogen. This experiment, and the linear growth rate in Fig. 1, prove that epitaxial growth of silicon from dichlorosilane is a highly irreversible reaction. As a consequence of this, one can conclude that the interfacial region impurity distribution may be explained by diffusion theory alone as has been proposed by Grove *et al.* (13).

Acknowledgment

I wish to thank Peter Weissglas for his keen advice and many stimulating discussions.

Manuscript submitted Feb. 15, 1972; revised manuscript received April 4, 1972.

Any discussion of this paper will appear in a Discussion Section to be published in the June 1973 JOURNAL.

REFERENCES

1. D. Richman, Y. S. Chiang, and P. H. Robinson, *RCA Rev.*, **31**, 613 (1970).
2. D. C. Gupta and J. L. Porter, *NBS Special Publication* 337, 66 (1970).
3. W. C. Benzing, A. E. Ozias, and H. B. Bradley, *Abstracts*, p. 184, Electrochem. Soc. Extended Abstracts, Spring Meeting, Washington, D.C., May 9-13, 1971.
4. W. C. Benzing, A. E. Ozias, and I. M. Helmer, "The Rate of Epitaxial Film Growth from Dichlorosilane", Applied Materials Technical Report.
5. M. Van Hoy, "Dichlorosilane Epitaxial Layers for Integrated Circuits," presented at the 71st National Meeting of the American Institute of Chemical Engineers, Feb. 20-23, 1972.
6. E. Mendel and K-H. Yang, *Proc. IEEE*, **57**, 1476 (1969).
7. L. H. Blake and E. Mendel, *Solid-State Technology*, **13**, 42 (1970).
8. A. Lekholm, "Growth of Epitaxial Silicon for Microwave Devices," Internal Report, Microwave Institute Foundation.
9. A. S. Grove, "Physics and Technology of Semiconductor Devices," Chap. 6, John Wiley and Sons, Inc., New York (1967).
10. J. J. Grossman, *This Journal*, **110**, 1065 (1963).
11. D. Kahng, C. O. Thomas, and R. C. Manz, *ibid.*, **110**, 394 (1963).
12. C. O. Thomas, D. Kahng, and R. C. Manz, *ibid.*, **109**, 1055 (1962).
13. A. S. Grove, A. Roder, and C. T. Sah, *J. Appl. Phys.*, **36**, 802 (1965).

Formation of MgO Crystals in Anodic γ -Al₂O₃ Formed on Aluminum-3% Magnesium Alloy

A. J. Brock* and M. A. Heine

Metal Research Laboratories, Olin Corporation, New Haven, Connecticut 06504

During the high temperature oxidation of Al-Mg alloys the initial protective film of amorphous γ -Al₂O₃ is degraded and a much less protective film consisting entirely of MgO, or of both MgO and amorphous γ -Al₂O₃, is formed (1). Previous workers investigating the oxidation behavior of Al-Mg alloys (2, 3) provided little information concerning the breakdown of the initial film of amorphous γ -Al₂O₃ although De Broukère (4) did consider that MgO could possibly result from the reduction of γ -Al₂O₃ by magnesium. Accordingly, the present work was conducted to study the formation of MgO in barrier-type anodic oxides formed on Al-3% Mg alloy. This follows similar studies of the formation of crystalline γ -Al₂O₃ under anodic oxide films formed on high purity aluminum (5).

The alloy composition was 3.05% Mg, 0.0006% Si, 0.0028% Fe, <0.0005% Cu, and <0.0005% Mn. The alloy, after hot and cold rolling to 0.04 cm thick sheet, was solution treated at 600°C for 8 hr followed by quenching into water. Specimens measuring 4 × 1 cm were degreased in benzene, rinsed in methanol, etched in a solution of 3% sulfuric acid and 3% chromic acid at 70°C for 20 min, rinsed in water, then methanol, and stored in a desiccator for 24 hr to allow the formation of a uniform air-formed oxide film some 20Å thick. The etching procedure results in a slightly scalloped surface which is smooth on a microscale and suitable for studying by means of electron microscopy. Specimens were then anodized in a solution of 3% ammonium tartrate at pH 7.0. The voltage across the cell was increased manually to 10V in such a fashion that the current surge never exceeded 5 mA/cm². The current was allowed to decay at this voltage for 5 min.

* Electrochemical Society Active Member.

Key words: oxidation, anodic films, γ -Al₂O₃, MgO, solid-state reaction.

Specimens showing a residual current density greater than 25 μ A/cm² were rejected. Capacitance measurements revealed that the anodic oxide was 137Å thick, assuming a dielectric constant of 8.5. The unanodized portions of the specimens were cut off leaving one cut edge unanodized.

Following anodizing, the specimens were heated at 350°C for periods of 3 and 20 hr in a quartz tube through which purified argon was flowing at a rate

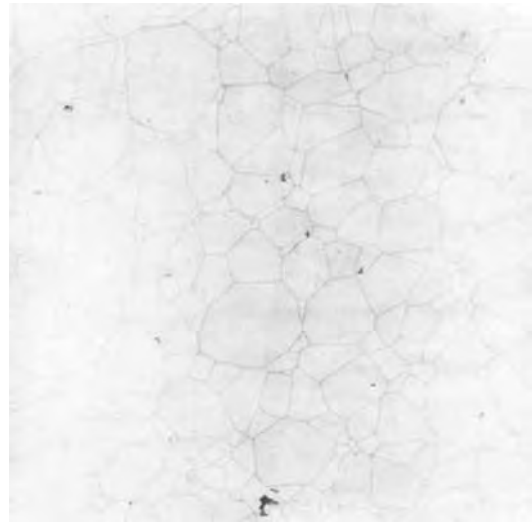


Fig. 1. Transmission electron micrograph of 10V anodic oxide film formed on aluminum-3% magnesium alloy (magnification 16,000X).

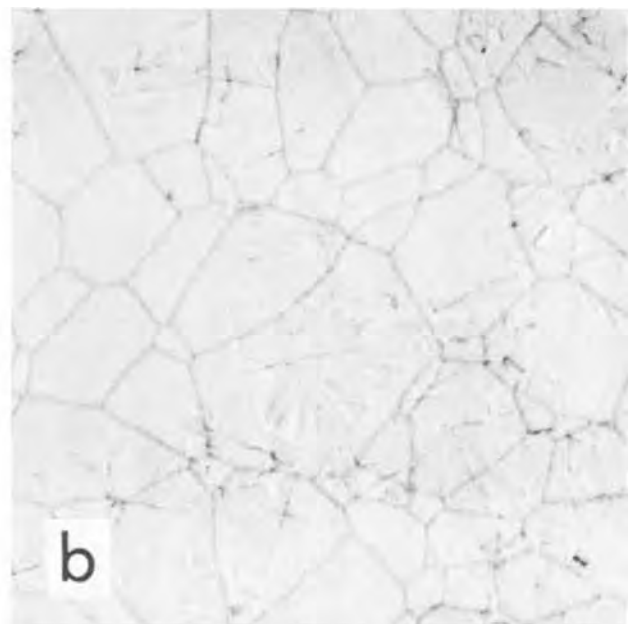
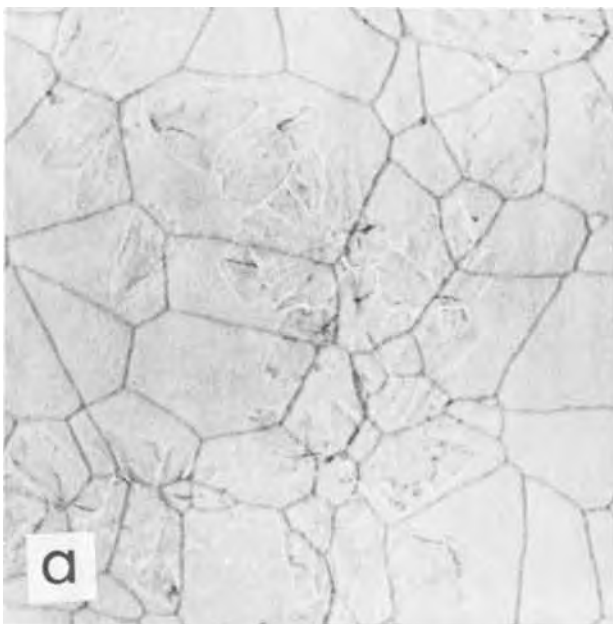


Fig. 2. Transmission electron micrographs of anodic oxide films after exposure at 350°C for 3 hr in: a, purified argon; b, oxygen at 76 Torr (magnification 45,000X).

of approximately 1 liter/hr. The argon, initially 99% pure, was further purified by passing it through a column of copper turnings at 380°C and then through a dry ice-cooled cold trap. This resulted in an oxygen concentration of about 1 ppm. Other specimens were heated for 3 hr in oxygen at 76 Torr.

The various films on the aluminum-3% Mg alloy were stripped by immersion in 10% mercuric chloride in methanol and examined by transmission electron microscopy. Figure 1 shows a transmission electron micrograph of the anodic film before heating in argon. The network seen in the micrograph is characteristic of the etched surface of the alloy. Figure 2a is a transmission electron-micrograph of the anodic oxide which had been stripped from the aluminum alloy after heating for 3 hr at 350°C in argon. This micrograph depicts the presence of crystals which transmission electron diffraction experiments revealed to be MgO. Elemental aluminum was never detected in these oxides. Figure 2b is a similar electron micrograph of an anodic oxide which had been stripped from the aluminum alloy after heating for 3 hr in oxygen. The crystal frequency and coverage is similar to that observed in

Fig. 2a. In both cases the contrast between the aluminum and magnesium oxides is quite poor because their electron scattering powers are virtually identical.

Figure 3a is a transmission electron micrograph of the anodic oxide stripped from the alloy after heating at 350°C for 20 hr in argon. In this case, coverage of MgO crystals is substantially complete. Weight measurements, made before and after heating the anodized specimens in argon for 20 hr, indicated a small weight loss of 3 μ g from each specimen. This doubtless results from loss of magnesium through volatilization from the unanodized edge of the specimen. Gravimetric measurements made on specimens heated for 20 hr in oxygen, where crystal coverage was also complete, indicated no significant change in weight. In this case, magnesium loss from the unanodized edge would be minimized because of the formation of the thermal oxide film. From knowledge of the rate of oxidation of Al-3% Mg alloy at 350°C (1), a weight gain of 0.06 μ g would be expected on the unanodized edge which is beyond the sensitivity of the microbalance.

The electron micrograph, Fig. 3b, is of a carbon-platinum replica of the oxide-gas interface of the

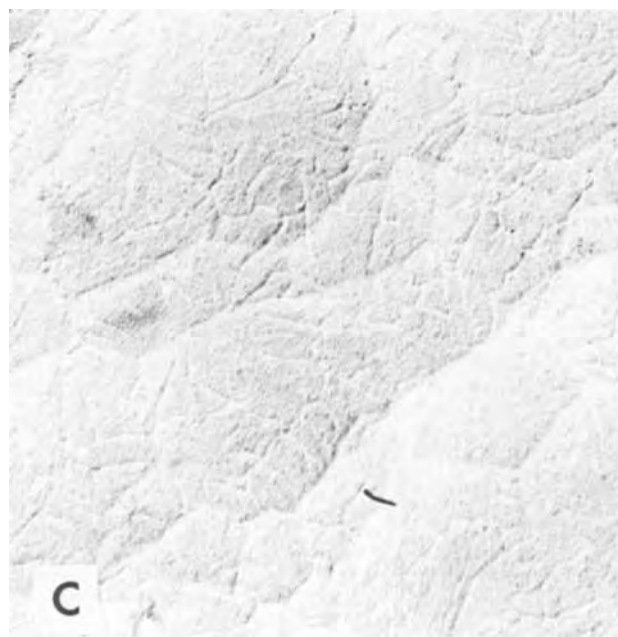
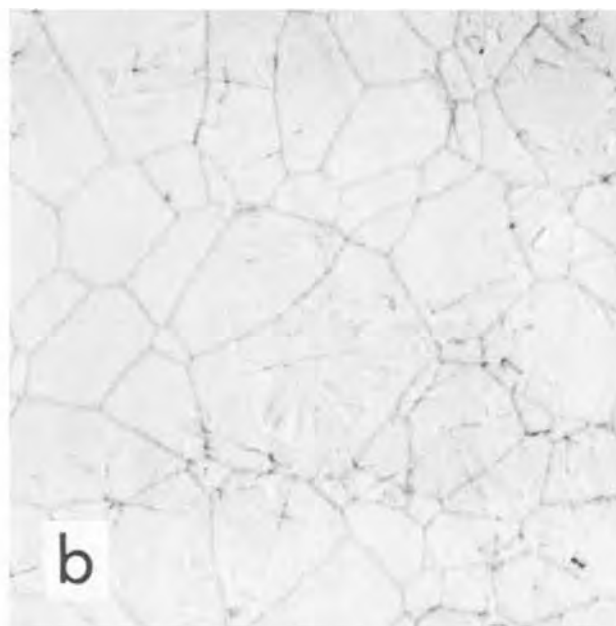
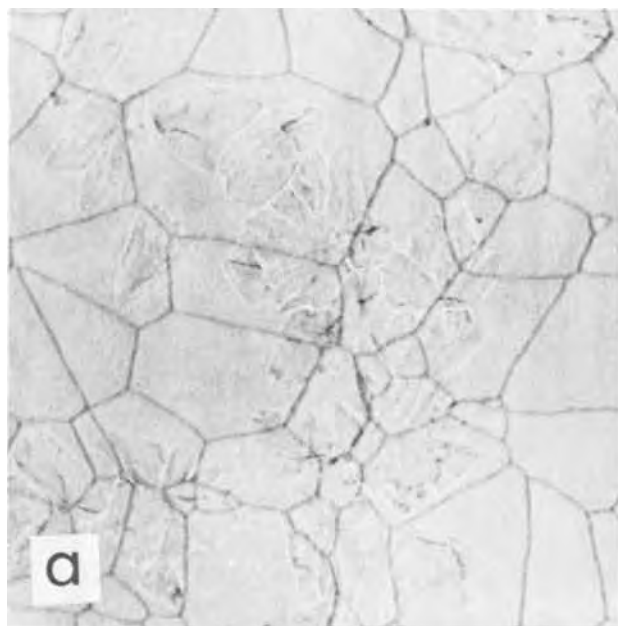


Fig. 3. Nature of the anodic oxide after exposure to argon at 350°C for 20 hr : a, transmission electron micrograph; b, positive platinum-carbon replica of oxide-gas interface; c, positive platinum-carbon replica of metal-oxide interface (magnification 45,000X).

Table I. Capacitance and resistance of anodic oxides formed on Al-3% Mg alloy before and after heating in purified argon at 350°C

Nature of film	Capacitance ($\mu\text{F}/\text{cm}^2$)	A-C resistance at 1 kHz ($\text{ohm}\cdot\text{cm}^2$)
Anodized	0.548	25,200
Anodized 3 hr in argon	0.590	18,700
Anodized 20 hr in argon	0.735	10,100
Anodized 20 hr in argon 1700 min in chromate solution	1.31	2,170

anodic film after heating in argon for 20 hr. It shows details similar to those of the etched alloy surface and does not reveal the presence of MgO crystals. Figure 3c is an electron micrograph of a replica taken from the underside of a similar stripped oxide film and depicts details of the oxide-metal interface. Here the edges of the MgO crystals are clearly visible. Accordingly, Fig. 3b and 3c show that the MgO nucleates and grows at the alloy-oxide interface.

To further clarify the position of the MgO crystals, capacitance-loss measurements were made at 1 kHz on anodized specimens before and after heating in purified argon for 3 and 20 hr, and also after thinning the heated films to the maximum degree in sodium chromate solution at pH 7. This technique has been described in detail previously (6). Figure 4 shows the transmission electron micrograph of the anodic oxide heated in argon for 3 hr and after immersion in chromate solution for 1700 min after which time film thinning had ceased. Contrast between the magnesium and aluminum oxides improves as the thickness of the latter is decreased.

It is clear from Fig. 4 that thinning occurred in a uniform manner and that the underlying crystals of MgO were not attacked. Electron optical examination of a replica of the outer surface of a fully thinned film did not reveal the presence of MgO crystals; instead the surface appeared identical to that shown in Fig. 3b. The results of the capacitance loss-measurements are shown in Table I.

The anodic film formed on the Al-3% Mg alloy has a high resistance, comparable with that of a similar film formed on pure aluminum. After heating for 3 hr in

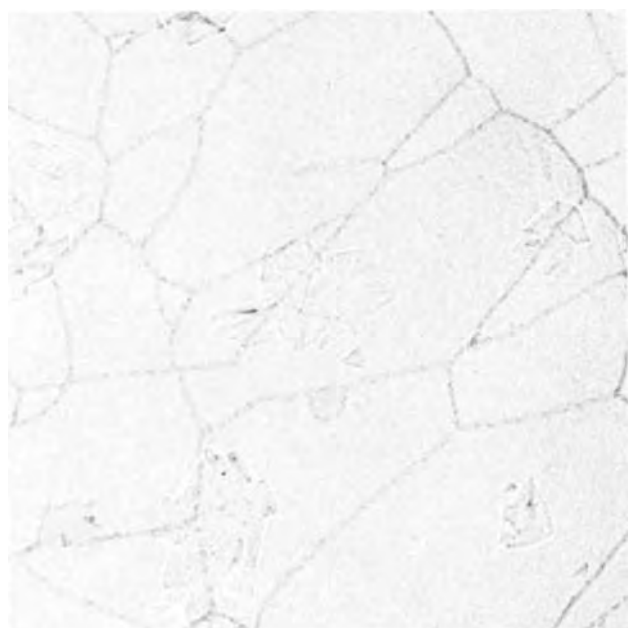


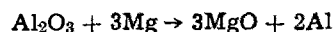
Fig. 4. Transmission electron micrograph of anodic oxide film after heating in argon at 350°C for 3 hr and after immersion in chromate solution for 1700 min (magnification 45,000X).

argon the resistance of the film decreases due to the presence of MgO which is a lossy dielectric. The corresponding increase in capacitance results from loss of alumina by its reaction with Mg to form MgO. After heating for 20 hr in argon, at which time crystalline coverage was complete, a further decrease in resistance and in capacitance was observed. Taking a dielectric constant of 8.5 for amorphous $\gamma\text{-Al}_2\text{O}_3$, and assuming that the remaining alumina had remained unchanged while heating in argon and also that the layer of MgO does not significantly contribute to the capacitance and resistance values, the capacitance measurements indicate that 36Å of $\gamma\text{-Al}_2\text{O}_3$ were consumed. From the densities of $\gamma\text{-Al}_2\text{O}_3$ and MgO of 3.69 g/cm^3 , and 3.53 g/cm^3 respectively, this corresponds to the formation of a layer of MgO crystals 38Å thick.

After fully thinning such a film in chromate solution, the capacitance increased to 1.31 $\mu\text{F}/\text{cm}^2$ indicating that 57Å of anodic $\gamma\text{-Al}_2\text{O}_3$ remain. The MgO crystals, accordingly, are positioned within this inner region which is in good agreement with the other results.

It is known that the anodic film formed on Al-3% Mg alloy contains the same ratio of aluminum to magnesium as exists in the metal (7). In order to ascertain if the magnesium in the oxide participates in the formation of MgO, anodic films were stripped from the alloy and heated in argon at 350°C for 20 hr. Examination of these films by electron microscopy did not reveal the presence of MgO, while transmission electron diffraction showed only the characteristic pattern of amorphous $\gamma\text{-Al}_2\text{O}_3$.

These results indicate that the crystals of MgO result from a solid-state reaction between the amorphous $\gamma\text{-Al}_2\text{O}_3$ and Mg from the underlying alloy according to the equation



Such a reaction is to be expected at 350°C on the basis of free energy consideration (8). An alternative explanation, that the crystalline MgO results from the reaction between Mg and oxygen, would require the inward diffusion of oxygen ions through the anodic film. Such a mechanism is responsible for the formation of crystalline $\gamma\text{-Al}_2\text{O}_3$ at 425° to 575°C under anodic oxide films formed on high purity aluminum (5). The rate of formation of the crystals of $\gamma\text{-Al}_2\text{O}_3$ is very sensitive to oxygen pressure. The insensitivity of the rate of formation of the MgO crystals to oxygen pressure argues against such an explanation in the present work. Moreover, the reaction between Mg and oxygen would require a weight gain which was not observed.

The solid-state reaction described above also results in the formation of elemental aluminum which was never detected by transmission electron diffraction experiments. However, it is possible that during the reduction, Al and Mg diffuse in opposite directions through the MgO crystallites. This would result in the aluminum returning to the alloy. Alternatively, the aluminum might have been formed in a colloidal dispersed state which would not be detectable by electron diffraction. The slight volume increase accompanying the solid-state reaction would result in the MgO crystal protruding very slightly into the metal phase but growing primarily into the oxide phase as was observed in this work.

The above results clearly demonstrate that MgO results from the solid-state reaction between magnesium and amorphous $\gamma\text{-Al}_2\text{O}_3$. Such a reaction doubtless occurs at an early stage during the thermal oxidation of Al-Mg alloys. In this case, however, the initial protective film of amorphous $\gamma\text{-Al}_2\text{O}_3$ is only some 20 to 30Å thick. Consequently, depending on the conditions of oxidation, it can be completely reduced by magnesium to MgO and elemental aluminum, as will be shown in subsequent papers (1).

Acknowledgments

The authors wish to thank the Aluminum Group of the Olin Corporation for their support of this work and for their permission to publish the results.

Manuscript received Nov. 15, 1971; revised manuscript received March 20, 1972.

Any discussion of this paper will appear in a Discussion Section to be published in the June 1973 JOURNAL.

REFERENCES

1. A. J. Brock and M. A. Heine, To be published.
2. W. W. Smeltzer, *This Journal*, **105**, 67 (1958).
3. R. A. Hine and R. D. Guminski, *J. Inst. Metals*, **89**, 417 (1960-61).
4. L. De Brouckère, *ibid.*, **71**, 131 (1945).
5. A. F. Beck, M. A. Heine, E. J. Caule, and M. J. Pryor, *Corrosion Sci.*, **7**, 1 (1967).
6. M. A. Heine and M. J. Pryor, *This Journal*, **110**, 1205 (1963).
7. A. J. Brock, Ph.D. Thesis, University of Manchester, England (1965).
8. J. Benard, "L'Oxydation des Metaux," p. 272, Gauthier-Villars et Cie, France (1962).



On the Electrochemistry of Porous Zinc Electrodes in Alkaline Solutions

Z. Nagy^{*1} and J. O'M. Bockris^{*2}

Electrochemistry Laboratory, University of Pennsylvania, Philadelphia, Pennsylvania 19104

ABSTRACT

Porous zinc electrodes were discharged galvanostatically in aqueous potassium hydroxide solutions. The morphology of the zinc oxide film formed was investigated with a scanning electron microscope. The current distribution in the porous electrode, and its dependence on current density, was determined by microslicing the electrode after discharge and chemical analysis. The oxide film had a porous, "carpet-like" structure, consisting of long needle crystals with occasional sidearms. The formation of this type of film can be explained by a dissolution-precipitation mechanism. The current distribution in the porous electrode, and its dependence on current density could also be explained, based on a model of oxide film consisting of a thin, high resistance compact film, beneath the porous oxide.

The behavior of porous electrodes is an important topic in electrochemistry since many practical electrode reactions (particularly those of energy conversion and storage) take place in porous matrices. The basic question is the distribution of current (and potential) in the porous body. The theory of porous electrodes has evolved to a considerable sophistication during the last decade. While the mathematics is complicated, analytical solutions have been obtained for a number of cases taking into account the *IR* drops in the electrolyte and the metal matrix, the diffusional processes of reactants and products, the kinetics of the charge transfer reaction, and the wetting characteristics of the metal by the electrolyte. A recent summary of these theories is available (1). None of these early theories have, however, taken into consideration the structural changes taking place in the porous matrix during the electrode process (e.g., the anodic dissolution of a metal and the formation of insoluble reaction products) which are very common in electrochemical energy storage systems. Two recent theoretical papers began work in this area. The first one (2) treats the effects of structural changes due to the anodic dissolution of the matrix without product precipitation. The other (3) considers slightly soluble reactants and products on an inactive conducting matrix, and treats the structural effects as changes in mass transport parameters of the active materials. Both of these treatments result in differential equations solvable only numerically.

The experimental determination of current distribution can be carried out in three ways: (i) the measurement of potential distribution by using numerous probes along the electrode, as was carried out with MnO_2 electrodes (4), (ii) the direct measurement of the distribution by using sectioned electrode, and mea-

suring the current separately to each section as was reported for MnO_2 (5), and the $Pb/PbSO_4$ system (6) and, (iii) sectioning the electrode after the experiment and analysis of the products as was recently carried out with cadmium electrode (7). The first two methods allow repeated cycling of the electrode while carrying out *in situ* measurements, and the determination of time dependence of the distribution is also possible, but the technique itself may interfere with the normal operation of the porous electrode thereby distorting the results. The third method is free of this objection, but it is limited to one observation per electrode, and is applicable only for processes with solid reaction products.

The zinc-zinc oxide alkaline electrode is an important system for which current distribution studies have not been reported as yet. This is surprising considering the fact that it is one of the more promising electrodes for high energy and power density energy storers (8, 9). Oxide film formation and passivation have been investigated by many workers on flat zinc electrodes in alkaline solutions. Recent reviews are available (10, 11). There is a controversy in the literature whether the passive film is formed directly on the surface or by a dissolution-precipitation mechanism (11-19). Recent results (11, 17-19) indicate, however, that there are two kinds of film formed during anodization of zinc in an alkaline solution. One, a precipitated film, appears before passivation occurs; while the second film, forming beneath it, is the cause of passivation. Correspondingly, the prevailing hydrodynamic conditions have been shown to have a strong influence on the formation of the films, and that the quiescent conditions inside a porous electrode will favor the precipitated oxide. Further, it has been shown by cathodic reduction studies (20), that the direct, solid-state, reduction of zinc oxide is energetically unfavorable compared to the dissolution-zincate reduction mechanism. Numerous reports also appeared (21-29) on the anodic behavior and passivation of porous zinc electrode in alkaline solutions, as a function of current density,

* Electrochemical Society Active Member.

¹ Present address: Diamond Shamrock Chemical Company, Painesville, Ohio 44077.

² Present address: Flinders University, Adelaide, Australia.

Key words: porous electrode, Zn/ZnO , oxide film morphology, current distribution, effect of current density.

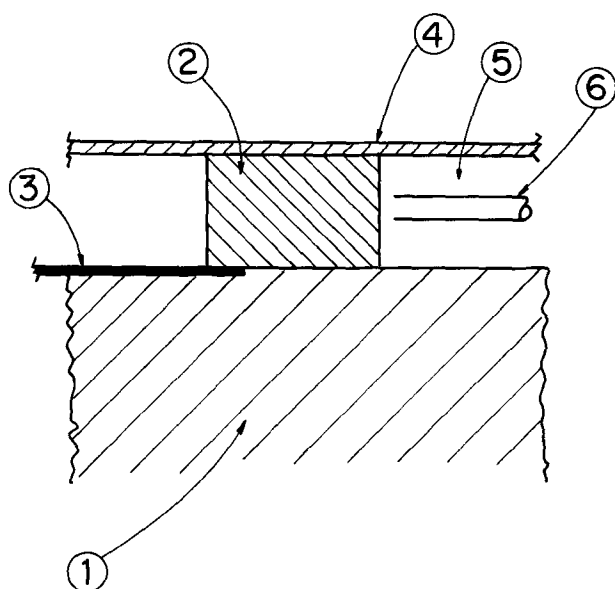


Fig. 1. Schematic of the experimental setup. 1, Teflon body; 2, porous zinc electrode; 3, current contact; 4, glass cover; 5, channel to counterelectrode; 6, Teflon Luggin.

temperature, solution composition, and porosity of the electrode, but in none has the question of current distribution within the electrode been studied.

Experimental

Porous zinc electrodes were discharged galvanostatically in alkaline zincate electrolytes. The morphology of zinc oxide formed was examined with a scanning electron microscope. The penetration of current, and its dependence on current density, were determined at the end of the process by microslicing the electrode and chemical analysis. All tests were carried out at room temperature.

The cell.—The basic concept of the cell is illustrated in Fig. 1. The porous zinc pellet was pressfitted into the solution channel of the Teflon cell body, and the assembly covered tightly with a glass sheet. Current contact to the porous electrode was made using a 0.0075 cm thick zinc foil. The solution channel on the other side of the porous electrode led to a counterelectrode chamber, the counterelectrode was a platinum wire spiral immersed in KOH-ZnO slurry. The Teflon tubing Luggin led to a reference chamber holding a calomel electrode. Details of the cell design are given elsewhere (30).

Preparation of the porous electrodes.—The test electrodes were prepared from 99.9999% pure zinc powder (United Mineral and Chemicals Corporation) with a particle size less than 0.015 cm (-100 mesh). The powder was compressed into a 0.3 cm diameter, 0.1 cm thick pellet in a suitable mold, using a pressure of 8400 psi. The porosity of the electrodes was determined, from their calculated density, as 30%.

The electrolyte solutions.—High purity potassium hydroxide-zincate solutions were prepared with a technique described before (31). For all but one experiment, a solution composition of 2M KOH and 0.1M zincate was used. In one case, the solution was 8M KOH containing 0.5M zincate.

Experimental procedure.—After assembling the cell, it was blown free of air with purified nitrogen, and the solution was introduced by applying vacuum on the outlet side of the channel. Filling of the electrode could be observed with a microscope through the glass cell cover: if bubbles were observed the evacuation and filling was repeated. A constant current was applied, using an Elron galvanostat, in the range of 4-100

mA/cm² apparent current density (calculated on the geometric area) for a time duration of 2-40 hr. The electrode potential was measured with a Beckman digital pH meter. At the end of the test, the cell was opened, and the porous electrode transferred into ethyl alcohol. It was washed several times with fresh alcohol to remove all water and potassium hydroxide. Finally, it was dried in a vacuum desiccator, where it was stored for further examination.

Observation of oxide morphology.—Some electrodes were examined with a scanning electron microscope (JSM-U3, JOELCO, Japan) to determine the shape of the oxide particles formed during the discharge. Only the top surface (facing the glass cover in the cell) was examined.

Determination of current penetration.—Some electrodes were microsliced under a microscope, equipped with a calibrated scale, using stainless steel blades. First a 1 mm wide section was cut out longitudinally (in the direction of current flow), from the middle of the electrode to avoid the influence of edge effects. This 3 × 1 × 1 mm piece was then further cut into six, 0.5 mm wide, parts. The ZnO and Zn content of each part was then determined as follows. The oxide was dissolved in a solution of 1M NH₄OH and 1M NH₄Cl. This solution dissolves the oxide but attacks the zinc only negligibly during the 5 min contact time (32). The solution was then filtered and analyzed for zinc with an EDTA titration (33). The remaining zinc was dissolved in hydrochloric acid and the solution analyzed for zinc as above.

Results

Morphology of the oxide film.—Scanning electron microscopic investigation was carried out on electrodes discharged at 4 and 40 mA/cm² current densities with a charge range of 4 to 18 mA-hr. In the interior of the electrode, a very porous "carpet-like" oxide film, consisting of long needle crystals, was found on the zinc grains. Examples are shown in Fig. 2. The appearance of the film was the same everywhere in the interior of the electrode, independently of distance from the solution, current density, and depth of discharge, within the limits of the experiments. On areas less densely populated with growth, occasionally side arms were observed on the needles (Fig. 3). At the edge of the electrode, toward the electrolyte, the film was more compact as shown in Fig. 4. An experiment was carried out using an 8M KOH solution, and produced similar results (Fig. 5).

Current penetration into the porous electrode.—This experiment was carried out at five current densities ranging from 5 to 80 mA/cm². The duration of discharge was also varied so as to keep the total charge used constant, at a value of 25% over-all conversion of the porous electrode. From the chemical analysis of the sliced electrodes, the average conversion of zinc to zinc oxide was calculated for each section. The results are plotted in Fig. 6-10, as a function of distance from the electrolyte. The measured overpotentials are given in Table I.

Discussion

The morphology of the oxide film.—The dendritic appearance of the oxide, with all the needles pointing towards the solution, suggests the following mechanism for its formation. The dissolving zinc supersaturates

Table I. Overpotentials after one minute of polarization

Current density (mA/cm ²)	Overpotential (mV)
5	4
10	10
20	14
40	23
80	39

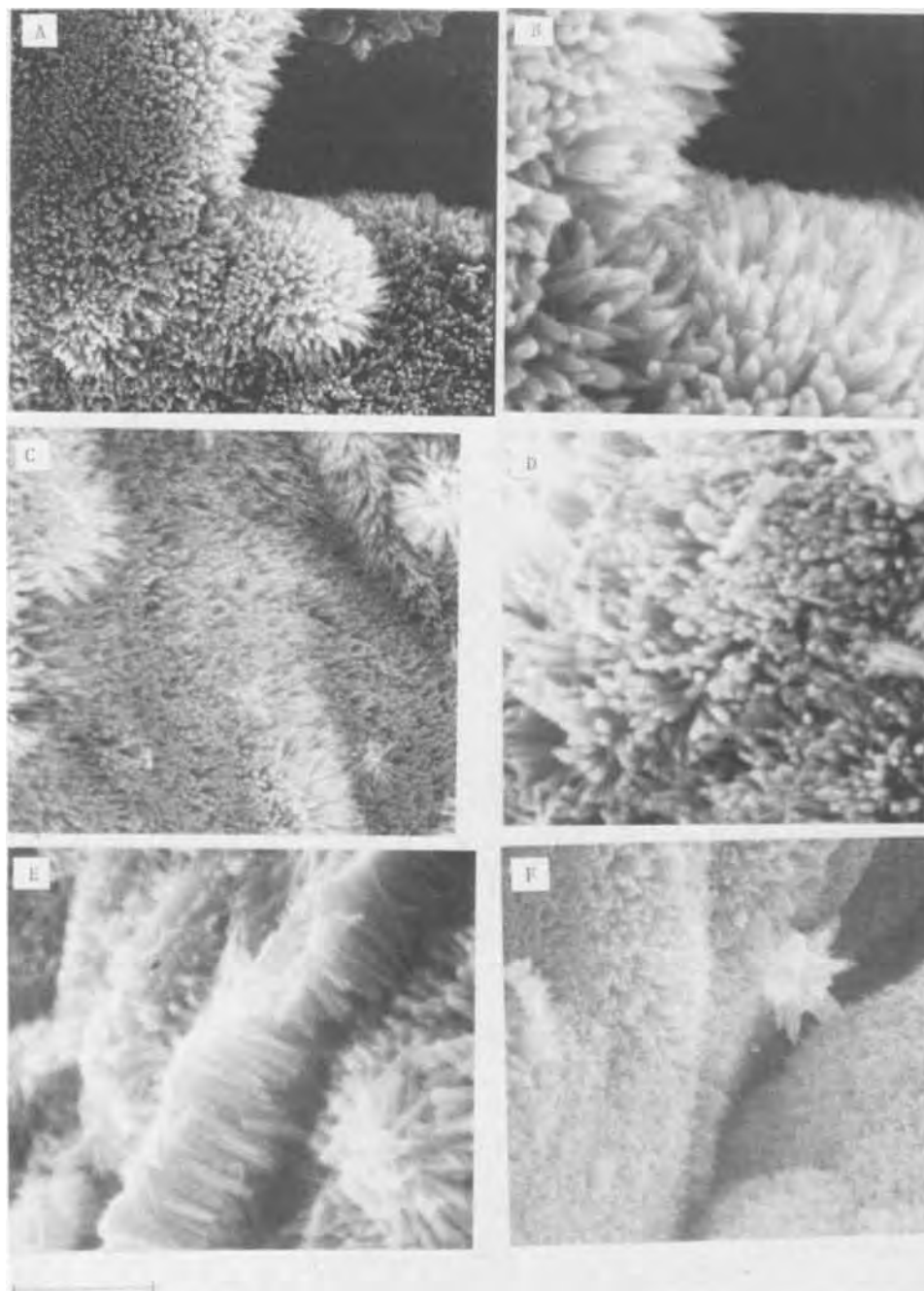


Fig. 2. Examples of SEM pictures of oxide film. A, B: 40 mA/cm², 25% discharge; C, D, E: 4 mA/cm², 25% discharge; F: 4 mA/cm², 44% discharge. Mark represents 3 μ for A, C and F; and 1 μ for B, D, and E.

the solution in zincate [the stability of highly supersaturated zincate solutions is known (21)] until a concentration is reached when oxide nucleation suddenly begins. This will happen at the surface of the metal where the zincate concentration is the highest. Once nucleation occurred, crystallization will proceed very fast from the supersaturated solution and a concentration gradient is set up, creating a diffusion layer. If the radius of curvature of some of the nuclei is small enough, to allow spherical diffusion to take over, conditions for dendritic growth are fulfilled (34, 35). Apparently, due to the simultaneous nucleation of a large number of crystals, many nuclei will have the required small radius of curvature resulting in a dense, carpet-like, appearance of the film. The observation of occasional side branches (Fig. 3) supplies strong evidence for this mechanism. This mechanism is analogous to the dendritic solidification of a cylindrical mass of molten metal (36). Figure 2E affords a side view of the film which peeled off the zinc grain.³

³ Peeling was observed only occasionally. From the present data it could not be decided whether this occurred during the electrode process, or afterwards during the vacuum drying.

Current distribution.—There is strong evidence to indicate that the reaction in a porous zinc electrode proceeds through the soluble zincate intermediate. Anodic studies on planar zinc electrodes have shown, that under hydrodynamic conditions most resembling that of the porous electrode, the oxide film was formed by a dissolution-precipitation mechanism (11, 17-19). The morphology of the zinc oxide film (see above) also supports this mechanism. Further, cathodic studies (20) have proven that the direct (solid-state) reduction of ZnO does not contribute in measurable amount to the over-all reaction. The first step in the discharge mechanism of a porous zinc electrode is, therefore, the electrochemical formation of zincate, a study of which reaction was reported earlier (31). The exchange current density of the reaction being high (80 mA/cm² for the solution concentration used in these experiments), the activation overpotential in the present case can be considered to be in the linear current density-overpotential range for all, except the highest, current density used, and even for the highest one it can be used as a good approximation (cf. also Table I). This considerably simplifies the problem. The sophisticated, and

mathematically complex, theories which use the Butler-Volmer equation (or the high overpotential approximation) in the description of the porous electrode behavior [cf. Bockris and Srinivasan (1)], can be now reduced to their simplest form, taking the linear relation between current and potential. This simple theory was considered earlier by Euler and Nonnenmacher (37) (without considering any structural changes during the reaction), and their equations will be used as a basis of approach for the present problem.

The porous electrode is considered as a network of series and parallel resistors as shown in Fig. 11. The current flowing through the metallic phase is $i_1(x)$, and that in the solution phase, $i_2(x)$. Current transfer between the two phases (through the surface resistance $1/\kappa$) results in faradaic reaction, the value of which is expressed as: di_1/dx , at any point x along the porous electrode. The current densities, and the potentials (E_1 in the metallic, and E_2 in the solution phase) are functions of distance (x) obeying the following relations

$$\frac{dE_1}{dx} = -\frac{1}{\sigma_m} i_1(x) \quad [1]^4$$

$$\frac{dE_2}{dx} = -\frac{1}{\sigma_{sol}} i_2(x) \quad [2]^4$$

$$\frac{di_1}{dx} = \kappa[E_2(x) - E_1(x)] \quad [3]$$

$$\frac{di_1}{dx} = -\frac{di_2}{dx} \quad [4]$$

Combining Eq. [1] through [4] gives the final differential equation

$$\frac{d^4 E_1}{dx^4} - \kappa \left(\frac{1}{\sigma_m} + \frac{1}{\sigma_{sol}} \right) \frac{d^2 E_1}{dx^2} = 0 \quad [5]$$

The following boundary conditions are relevant to the present problem

$$\begin{aligned} i_1(x=0) &= 0; & i_1(x=L) &= i \\ i_2(x=0) &= i; & E_2(x=0) &= 0 \end{aligned}$$

where L is the over-all length of the porous electrode and i ($=i_1$, at $x=L$) is the total current density. The solution for the distribution of the faradaic current (di_1/dy) as a function of fractional distance ($y=x/L$) is given by

$$\frac{di_1}{dy} = \frac{i \cdot \sigma_{sol} \cdot \nu}{(\sigma_{sol} + \sigma_m) \sinh \nu} \left[\frac{\sigma_m}{\sigma_{sol}} \cosh \nu(1-y) + \cosh \nu y \right] \quad [6]$$

where

$$\nu = L \cdot \sqrt{\kappa \frac{\sigma_{sol} + \sigma_m}{\sigma_{sol} \sigma_m}} \quad [7]$$

Note, that in accord with the linear i - η restriction the surface resistance ($1/\kappa$) was considered constant, independent of potential. In the general sense the surface resistance can include not only the faradaic resistance but also the electrical resistance of any film formed on the surface as shown schematically in Fig. 12 for a single pore.

⁴ The metallic and solution conductivities (σ_m , σ_{sol}) used in Eq. [1] and [2] are not equal to the corresponding bulk values. They represent the respective contributions of the metallic and solution phases to the over-all conductivity of the solution filled porous electrode. For an electrode having $p\%$ porosity their values can be estimated, as a first approximation, as

$$\begin{aligned} \sigma_m &= (\sigma_m^{bulk}) \frac{100-p}{100}, \text{ and} \\ \sigma_{sol} &= (\sigma_{sol}^{bulk}) \frac{p}{100} \end{aligned}$$

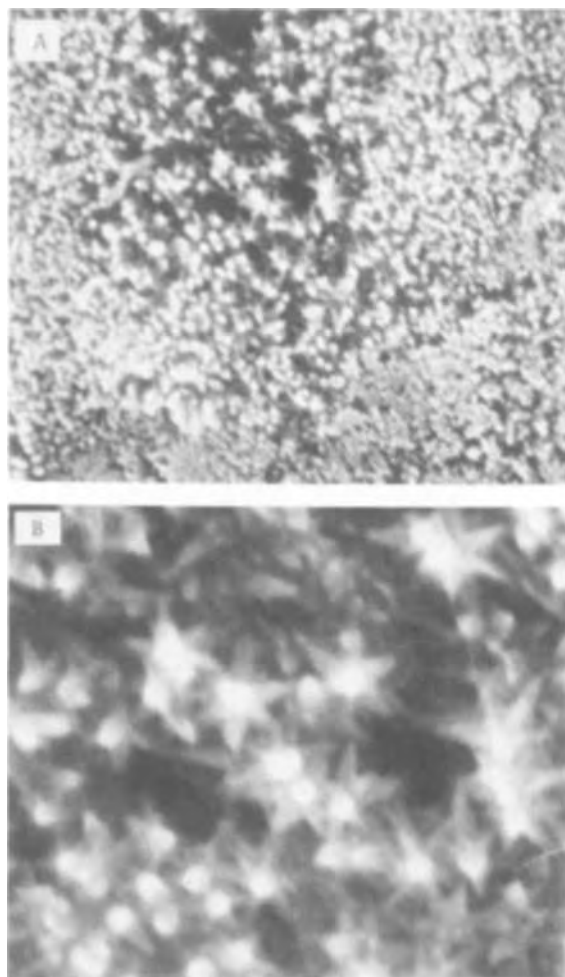


Fig. 3. Appearance of sidearms. 40 mA/cm², 28% discharge. Mark represents 3 μ for A, and 1 μ for B.

In the derivation of Eq. [6] σ_{sol} , σ_m , and κ were taken as constants, independent of distance within the electrode and time of discharge. In the case of an electrode where structural changes occur during the process, these assumptions have to be re-examined.

For the present electrode process the values of σ_{sol} , σ_m , and κ are known for the beginning of the process.⁵ If these are substituted in Eq. [6] it can be shown that the current will drop off very quickly with distance, reaching 10% of the over-all current value at $y=0.11$. This prediction, that practically all the faradaic current will go to a layer only one tenth of the electrode's depth, is not in agreement with the experimental data (Fig. 6-10) showing much greater penetration. The structural changes, dissolution of zinc, and precipitation of ZnO from the saturated zincate solution will have to be taken into account.

The dissolution of zinc will increase the resistance of the metallic phase ($1/\sigma_m$). However, since the experiments were limited to 25% conversion, the effect of this decrease in σ_m will be negligible on the current distribution, considering that the specific conductivity of the metal is six orders of magnitude greater than that of the solution.

The precipitation of ZnO will have two effects: (i) it will plug up the pores, decreasing σ_{sol} , and (ii) it will cover the surface of zinc, decreasing κ . The first effect (decrease of σ_{sol}) will not cause the current to

⁵ $\sigma_{sol} = 0.32 \times 0.3$; $\sigma_m = 1.7 \times 10^6 \times 0.7$, where the values are corrected for 30% porosity. $\kappa = 575 \times 6.15$, where 575 is the area in cm² of one cm³ of porous electrode (calculated for a 100 μ average particle diameter), and 6.15 is the reciprocal of the faradaic resistance.

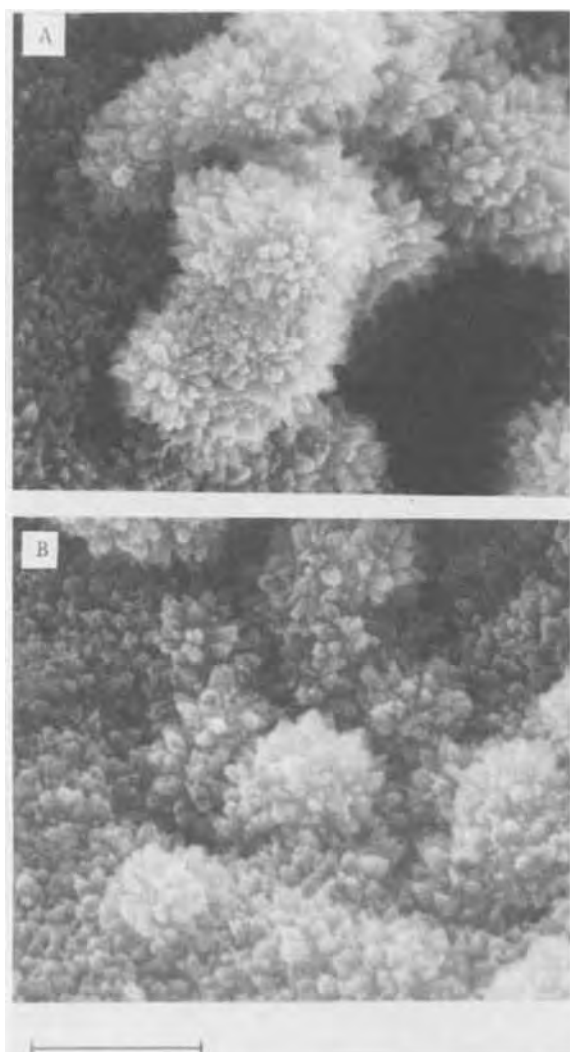


Fig. 4. Film at the edge of electrode. 40 mA/cm². Discharge: 25% for A, and 44% for B. Mark represents 3 μ .

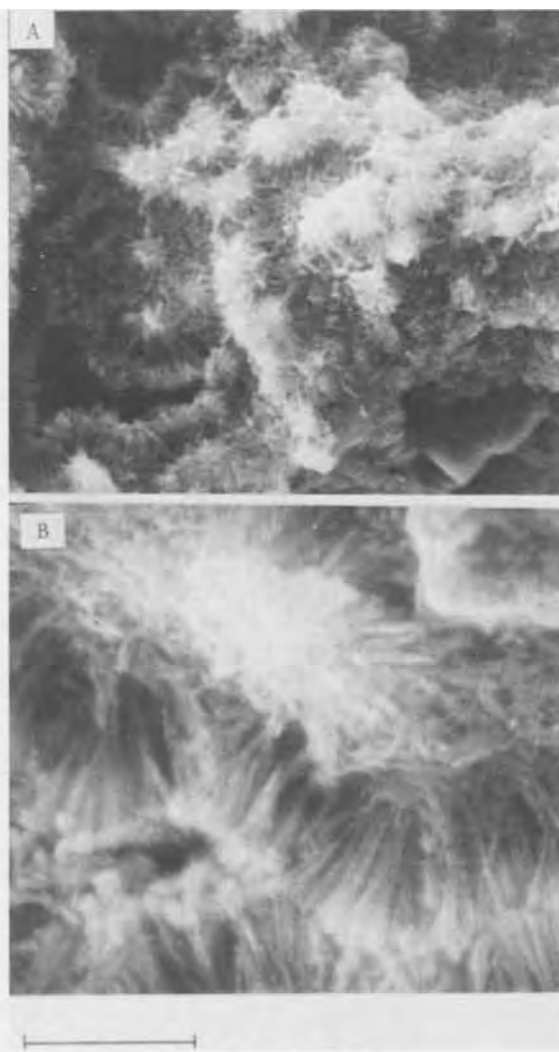


Fig. 5. Film formed in 8M KOH. 100 mA/cm², 31% discharge. Mark represents 10 μ for A, and 3 μ for B.

penetrate more deeply into the electrode. On the contrary, it can be seen, considering Fig. 11, that a decrease in σ_{sol} will cause the current to transfer, from the solution to the high conductivity metallic phase, closer to $x = 0$. This can be shown also numerically, using Eq. [6]. Taking a decreased σ_{sol} (corresponding to a porosity of 15% only) the 10% current level will now be reached at $y = 0.08$. It can be calculated that during the discharge of the present electrodes, the average porosity decreases from 30 to 20%.⁸ Therefore, this effect will change the current distribution only slightly and in the direction to make it less in agreement with the experimental results.

There remains only the possibility that $1/\kappa$ represents not only the faradaic resistance, but, in fact overwhelmingly, a film caused resistance arising from the oxide formation. Immediately after the anodic current begins, during the free dissolution of the metal, κ can be considered constant. Then the oxide precipitation will suddenly decrease κ . The value of κ will continuously decrease, after the precipitation, due to the thickening of the film. The time of precipitation can be estimated as follows. The total volume of the electrolyte in the pores of the electrode is 2.1×10^{-3} cm³. The solubility of ZnO in 2M KOH solution is 0.33M (38) and, considering that 0.1M zincate is present in the original solution, it can be calculated that a charge of 0.026 mA-hr is needed to saturate all the electrolyte

⁸ This was calculated for 25% discharge taking into consideration the density difference between Zn and ZnO (7.14 and 5.6, respectively).

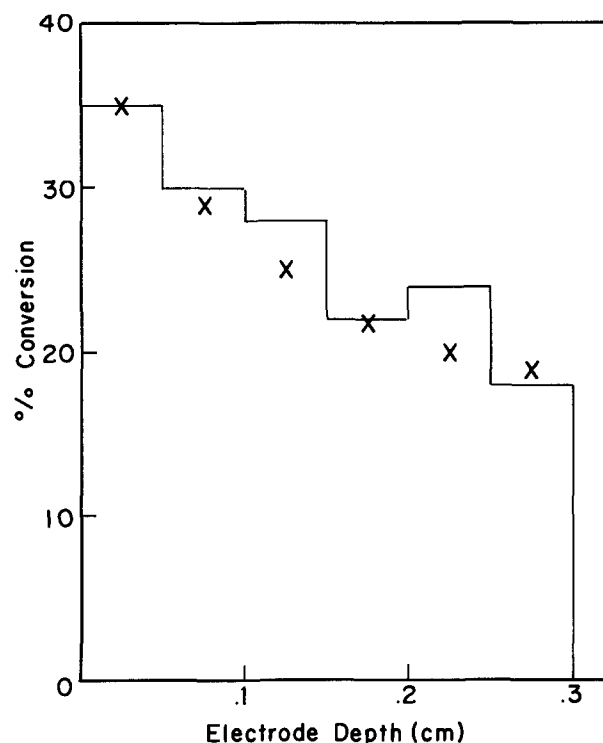


Fig. 6. Per cent conversion as function of distance. 5 mA/cm². x: values calculated with $\kappa = 0.6$.

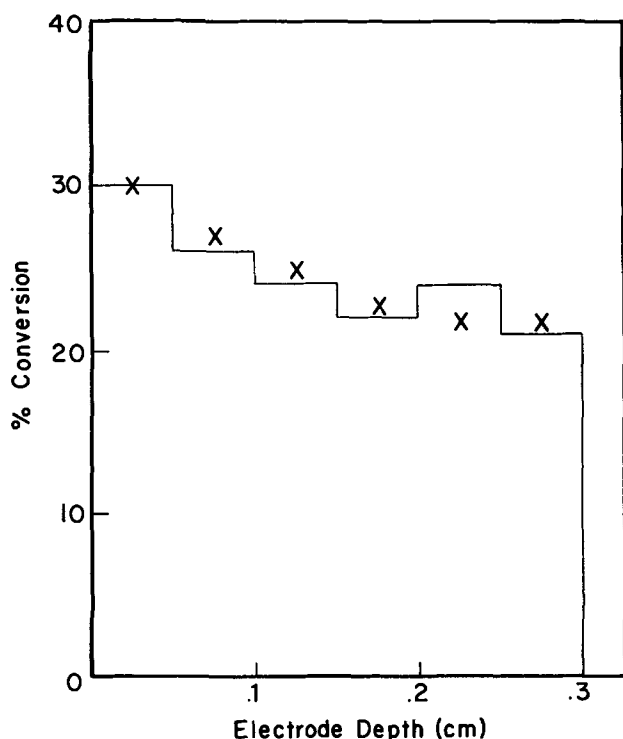


Fig. 7. Per cent conversion as a function of distance. 10 mA/cm². x: values calculated with $\kappa = 1.25$.

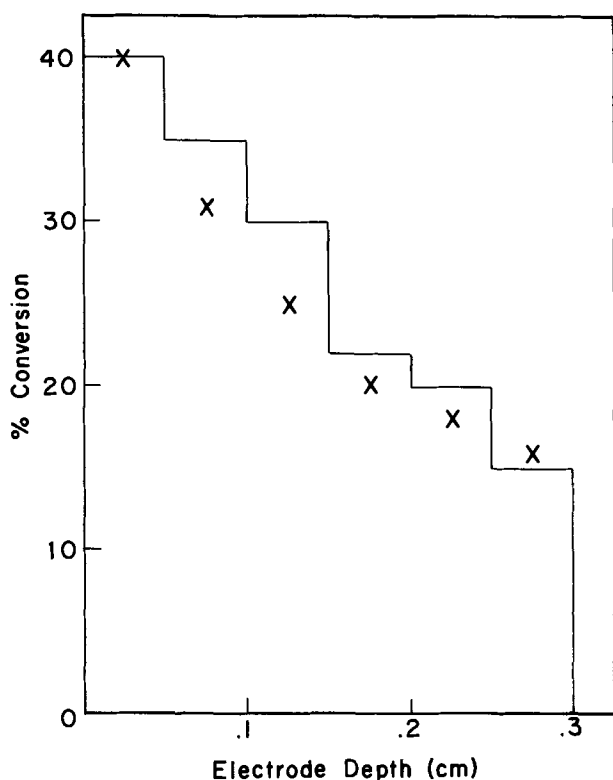


Fig. 8. Per cent conversion as a function of distance. 20 mA/cm². x: values calculated with $\kappa = 2.0$.

within the pores. This charge is negligible as compared to the total charge of 8 mA-hr used in these experiments, and therefore, it can be considered that film precipitation will occur everywhere in the electrode, instantaneously, at the beginning of discharge.⁷ The

⁷ Actually, at the beginning, practically all the current will go to the first one tenths of the electrode depth (as was shown earlier using Eq. [6] with the initial values of conductances), causing precipitation in this area and shifting the current to the next layer in the electrode until the solution becomes saturated there, and so on. This process sweeps across the electrode in a time duration negligible as compared to the total time of the experiment.

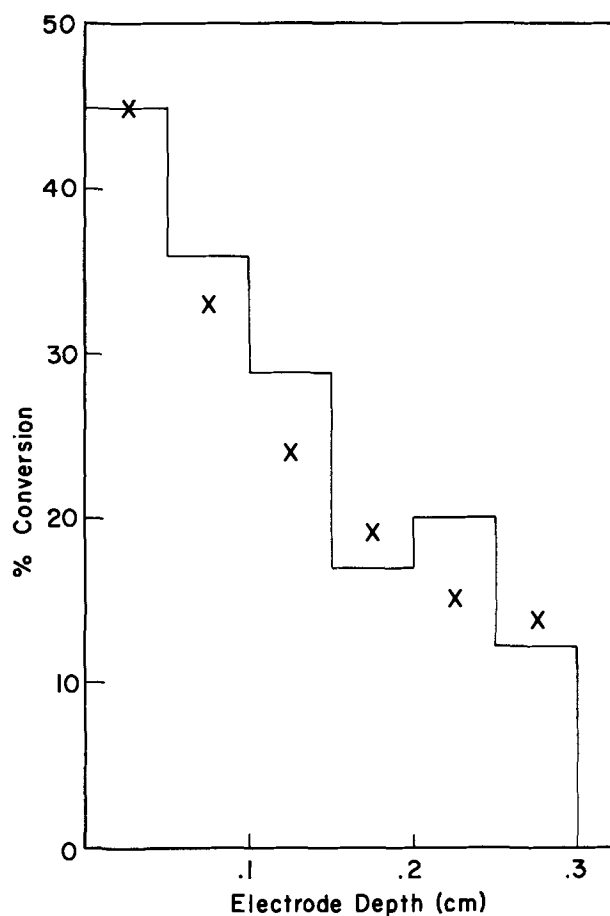


Fig. 9. Per cent conversion as a function of distance. 40 mA/cm². x: values calculated with $\kappa = 3.0$.

film then will thicken in time, causing κ to decrease further. As a first approximation, this change in time will be smoothed out, and an average κ will be considered in the following way.

An attempt was made to fit Eq. [6] to the experimental data (Fig. 6-10) with a suitable selection of the value of κ .⁸ Reasonable agreement was obtained with the κ 's indicated. These values, and their current dependence can then be examined to determine whether they are physically realistic, and whether their dependence on current density can be theoretically explained.

To arrive at an expected approximate dependence of κ on current density, the following extension of the present model for the operation of the porous electrode is used. The film is formed by precipitation from a saturated solution formed by galvanostatic dissolution of the metal, under conditions, when the reaction products can be removed only by diffusion. Under these conditions, the time of precipitation is related to the current density as

$$i t^{1/2} \approx \text{const} \quad [8]$$

The resistance of the film, on the other hand, will be proportional to its thickness, which depends on the total charge represented by the film

$$1/\kappa \approx \text{const} \cdot i \cdot t \quad [9]$$

Therefore, the dependence of " κ ," the surface conductivity, on current can be approximated from [8] and [9] as

$$\kappa \approx \text{const} \cdot i \quad [10]$$

predicting a linear relation, which in fact was observed (Fig. 13).

⁸ In these calculations, σ_m was taken as $1.7 \times 10^5 \times 0.7$ and σ_{sol} as 0.32×0.2 . A decreased solution conductivity was used to account for the plugging of pores by ZnO.

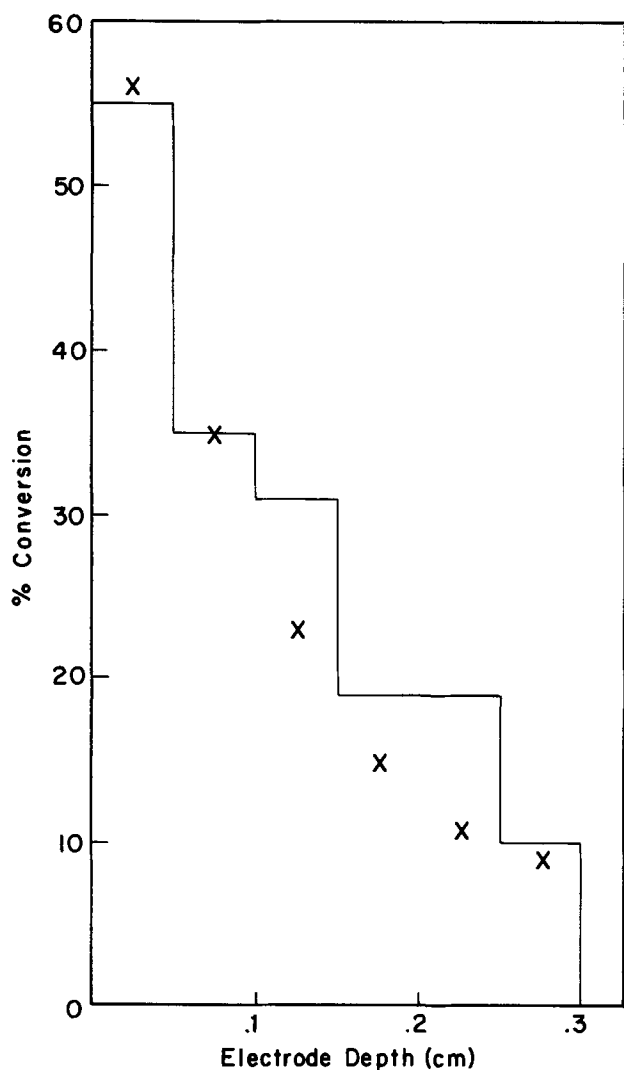


Fig. 10. Per cent conversion as a function of distance. 80 mA/cm². x: values calculated with $\kappa = 5.5$.

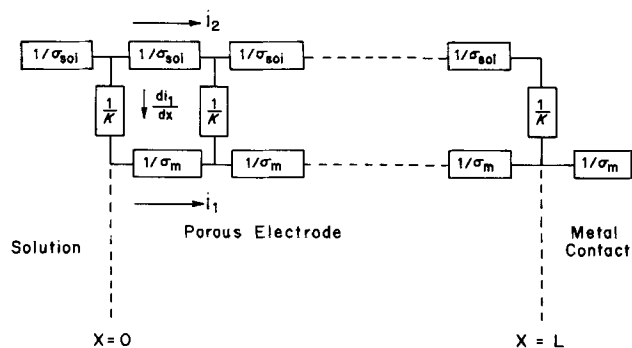


Fig. 11. Schematic representation of the porous electrode

The actual values of "κ" can also be compared to resistances calculated for different model of the film. The surface resistance ($1/\kappa$) is a sum of the terms: the faradaic resistance, the resistance of the porous zinc oxide film, and the resistance of any continuous film beneath the porous film. Assuming a surface area of 575 cm²/cm³ (calculated for an average particle size of 100μ) the surface resistance values giving the best fits to the experimental data range between 100 and 1000 ohms cm². Such a high value cannot be explained either by the decrease of apparent i_0 due to decrease of free area, or by the resistance of the porous film based on the observed film structures. It seems, therefore, that the assumption of the existence of a "com-

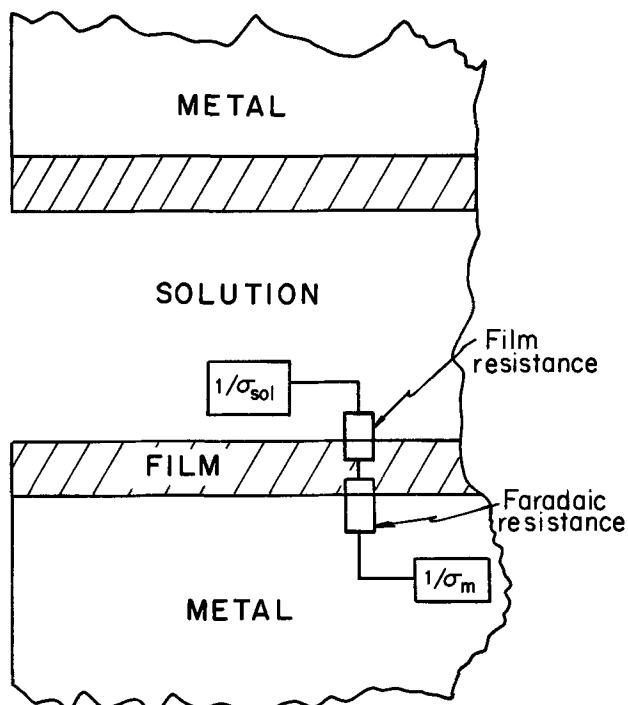


Fig. 12. Schematic representation of a single pore

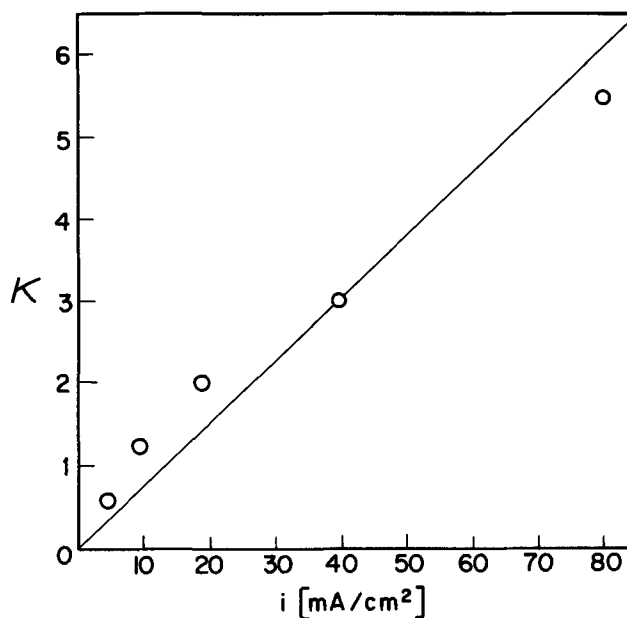


Fig. 13. Dependence of film conductivity on current density

compact" film underneath the "porous" one is necessary to explain the data. This is in agreement with the duplex films recently found on planar electrodes (11, 17-19). Since the specific resistance of zinc oxide can vary from 10⁻³ to 10¹⁷ ohm cm (39, 40) depending on stoichiometry of the oxide and on impurities, a very thin film could account for the observed resistances.

The resistance of the film will increase as the film thickens. While this will make the current distribution more uniform, it will also increase the IR losses in the electrode. This accounts for the decrease of the useful voltage of the battery as the discharge proceeds. This model, therefore, suggests a possible way to enhance the uniformity of current distribution in the porous electrode, namely the increase of oxide film resistance (possibly by suitable alloying of the zinc). This will, however, increase the IR losses, and the two effects will have to be optimized. On cathodic charging, the high resistance, compact film is expected to be reduced

fast, thereby altering the total resistance of the film and making the current distribution less uniform (as compared to that during discharge). On repeated cycling, this difference of the anodic and cathodic current distributions may cause physical distortion of the electrode structure.

The present results can be compared with the current penetration observation of Breiter (28). In that study, processes occurring in a porous zinc electrode were investigated using potential sweep technique. It was concluded that only a small portion of the interior of the electrode was active. Considering that the sweeps lasted a few minutes only, the result is in agreement with the present model, since the film formation may not have penetrated across the whole electrode during the experiments.

Acknowledgments

Our thanks are due to Mr. R. White for his help and advice during the electronmicroscopic work.

Financial assistance by the National Science Foundation (Grant No. NSF-GK-16550), and the A.R.P.A. Program in Materials Science (University of Pennsylvania) is gratefully acknowledged.

Manuscript submitted Dec. 7, 1971; revised manuscript received April 12, 1972.

Any discussion of this paper will appear in a Discussion Section to be published in the June 1973 JOURNAL.

REFERENCES

1. J. O'M. Bockris and S. Srinivasan, "Fuel Cells: Their Electrochemistry," Chap. 5, McGraw-Hill Book Co., New York (1969).
2. R. C. Alkire, E. A. Grens, and C. W. Tobias, *This Journal*, **116**, 1328 (1969).
3. J. S. Dunning, D. H. Bennion, and J. Newman, *ibid.*, **118**, 1251 (1971).
4. R. J. Brodd, *Electrochim. Acta*, **11**, 1107 (1966).
5. J. J. Coleman, *This Journal*, **98**, 26 (1951).
6. L. S. Sergeeva and I. A. Selitskii, *Zh. Fiz. Khim.*, **39**, 204 (1965).
7. P. Bro and H. Y. Kang, *This Journal*, **118**, 519 (1971).
8. S. U. Falk and A. J. Salkind, "Alkaline Storage Batteries," John Wiley & Sons, New York (1969).
9. A. Fleischer and J. J. Lander (Editors), "Zinc-Silver Oxide Batteries, John Wiley & Sons, New York (1971).
10. F. Jolas, *Electrochim. Acta*, **13**, 2207 (1968).
11. R. W. Powers and M. W. Breiter, *This Journal*, **116**, 719 (1969).
12. B. N. Kabanov, *Electrochim. Acta*, **6**, 253 (1962).
13. M. A. V. Devanathan and S. Lakshmanan, *ibid.*, **13**, 667 (1968).
14. R. D. Armstrong and G. M. Bulman, *J. Electroanal. Chem.*, **25**, 121 (1970).
15. M. N. Hull, J. E. Ellison, and J. E. Toni, *This Journal*, **117**, 192 (1970).
16. M. N. Hull and J. E. Toni, *Trans. Faraday Soc.*, **67**, 1128 (1971).
17. R. W. Powers, *This Journal*, **116**, 1652 (1969).
18. R. W. Powers, *ibid.*, **118**, 685 (1971).
19. M. W. Breiter, *Electrochim. Acta*, **16**, 1169 (1971).
20. D. Drazic and Z. Nagy, *This Journal*, **118**, 255 (1971).
21. T. P. Dirkse, *ibid.*, **102**, 497 (1955).
22. V. N. Flerov, *Zh. Prikl. Khim.*, **32**, 132 (1959).
23. A. I. Oshe, I. I. Astakhov, Z. Ya. Nikitina, I. F. Reznik, and V. S. Bagotskii, *ibid.*, **34**, 2254 (1961).
24. Z. P. Arkhangelskaya, G. P. Andreeva, and M. N. Mashevich, *ibid.*, **41**, 118 (1968).
25. Z. P. Arkhangelskaya, G. P. Andreeva, and M. N. Mashevich, *ibid.*, **41**, 1736 (1968).
26. G. N. Reshetova, L. A. Afanasjeva, and Z. P. Arkhangelskaya, *ibid.*, **43**, 843 (1970).
27. Z. P. Arkhangelskaya, M. N. Masevich, and G. P. Andreeva, *ibid.*, **43**, 1248 (1970).
28. M. W. Breiter, *Electrochim. Acta*, **15**, 1297 (1970).
29. R. N. Elsdale, N. A. Hampson, P. C. Jones, and A. N. Strachan, *J. Appl. Electrochem.*, **1**, 213 (1971).
30. Z. Nagy and D. Drazic, *Chem. Instr.*, **4**, 53 (1972).
31. J. O'M. Bockris, Z. Nagy, and A. Damjanovic, *This Journal*, **119**, 285 (1972).
32. N. Marincic and P. Bro, Paper 368 presented at Electrochem. Soc. Meeting, Montreal, Oct. 6-11, 1968.
33. F. J. Welcher, "The Analytical Uses of EDTA," p. 149, Van Nostrand, Princeton (1958).
34. J. L. Barton, and J. O'M. Bockris, *Proc. Roy. Soc.*, **268A**, 485 (1962).
35. J. W. Diggle, A. R. Despic, and J. O'M. Bockris, *This Journal*, **116**, 1503 (1969).
36. E. P. Polushkin, "Structural Characteristics of Metals," Elsevier Publishing Co., New York (1964).
37. J. Euler and W. Nonnenmacher, *Electrochim. Acta*, **2**, 268 (1960).
38. W. F. Linke, "Solubilities," 4th ed. Vol. II, p. 1676, ACS, Washington (1965).
39. M. A. Seitz and D. H. Whitmore, *J. Phys. Chem. Solids*, **29**, 1033 (1968).
40. G. Heiland, E. Mollwo, and F. Stockmann, "Solid State Physics," Vol. 9, p. 191, Academic Press, New York (1959).

Thermal Conductivity Measurements of Nickel-Cadmium Aerospace Cells

Part II: Component Conductivities

E. W. Brooman* and J. McCallum*

Battelle Columbus Laboratories, Columbus, Ohio 43201

ABSTRACT

Thermal conductivities have been determined for the positive and negative electrodes from various 20 A-hr sealed, nickel-cadmium cells. The average value obtained for the discharged positives is 0.0014 ± 0.0001 (cal/cm²/sec) (C/cm). The average value obtained for the discharged negatives is 0.0020 ± 0.0001 (cal/cm²/sec)/(C/cm). The thermal conductivities of the three separator materials studied, nonwoven, calendered, and uncalendered nylon, and nonwoven polypropylene, are a function of porosity, electrolyte absorption, and amount of compression. Dry, uncalendered nylon felt, about 82% porous, compressed to about 72% porosity, has a conductivity of about 0.00014. Dry, calendered nylon felt, about 62% porous, reduced to about 49% porosity on compression, has a conductivity of about 0.00021. Dry polypropylene wettable paper, about 46% porous, reduced to about 34% porosity on compression, has a conductivity of about 0.00016 (cal/cm²/sec)/(C/cm). As electrolyte is added to the separator materials, the conductivity initially increases relatively little compared with the conductivity of the electrolyte itself. However, as the separator pores become filled with electrolyte then conductivity values approaching that of the electrolyte may be obtained.

Part I of this paper (1) described thermal conductivity values obtained for four types of 20 A-hr, nickel-cadmium aerospace cells. Thermal resistance networks were set up to explain the variations in conductivity observed between the four types of cells. Only semi-quantitative correlation was obtained between the networks and the measurements, and one reason for this lack of precise agreement was attributed to the lack of reliable conductivity data for the materials comprising the cell elements. This present paper describes new experimental conductivity reference data for some of the principal components of the cells. Investigated were the conductivities of positive and negative electrodes from various types of the 20 A-hr cells described previously (1), and the conductivities of three separator materials as a function of electrolyte content. The three separator materials chosen were a nonwoven polypropylene, and a nonwoven nylon felt in the calendered and uncalendered conditions. These materials are candidate separator materials for use in sealed aerospace cells.

Experimental

Positive and negative electrodes from the 20 A-hr aerospace cells described previously (1), and samples from the manufacturers of the separator material (2), were used in this investigation. The basic experimental arrangement and procedures for the thermal conductivity measurements have been described elsewhere (1,2). Briefly, the thermal comparison method was used with an acrylic block as the reference material. To prevent carbonation of the wetted electrodes or separator materials resulting from exposure to the air, and to prevent drying out of these components during the measurements, the components were sealed in envelopes fabricated from about 0.003 cm thick polyethylene film. The contribution of the film to the measured over-all conductivity was calculated each time, and an appropriate correction made to the experimental results.

For the conductivity measurements of positive or negative electrodes, the complete electrodes from the 20 A-hr cells, from manufacturers II, III, and IV were

used after cell disassembly. The tabs were trimmed off, and the edges of the electrodes were inspected for any sharp protuberances which might have punctured the polyethylene envelopes.

For the conductivity measurements of the nylon and polypropylene separator materials, three or six pieces of material, depending on thickness, each about 10.0 × 5.0 cm, were cut and folded in half. These pieces were then interwoven to give a stack of six or twelve layers, each about 5.0 × 5.0 cm, before being sealed into the polyethylene envelopes. In the experiments where known amounts of electrolyte were added up to saturation, the required amount of electrolyte was added to the central layers of separator so that the electrolyte migrated to the outermost surfaces by capillary action. This procedure ensured that the separator materials were wetted throughout the stacks.

Results and Discussion

Positive and negative electrodes.—As the charge reaction of a nickel-cadmium cell is endothermic (3, 11), which may be or may not be offset by Joule heating effects depending on the charging rate and internal resistance of the cell; or offset by heat evolved in side reactions such as the evolution and recombination of oxygen) the thermal conductivity of the charged electrodes is relatively less important than the discharged-electrode conductivities. It is usually during discharge that the most heat is generated which, subsequently, has to be dissipated. Also, differences in thermal conductivity between 50% charged and discharged cells are less than 8% (2). For these reasons the conductivity values for discharged positive and negative electrodes only, are given in Table I. These conductivities were measured in a direction normal to the plane of the

Table I. Thermal conductivity of discharged positive and negative electrodes taken from 20 A-hr cells

Cell type	Thermal conductivity, cgs units	
	Positive electrodes	Negative electrodes
Manufacturer II	0.00135	0.00199
Manufacturer III	0.00151	0.00228
Manufacturer IV	0.00147	0.00187

* Electrochemical Society Active Member.

Key words: thermal conductivity of nickel electrodes, thermal conductivity of cadmium electrodes, thermal conductivity of separator materials.

Table II. Physical properties of the separator materials studies

Separator material	Thickness, cm	Apparent density, ^(a) g/cm ³	Apparent porosity, ^(b) per cent
Nonwoven nylon felt, maximum loft	0.038	0.166	82
Nonwoven nylon felt, maximum calendaring	0.015	0.431	62
Nonwoven "wetable" paper	0.0076	0.483	46

^(a) Based on weight and volume measurements.
^(b) Assuming bulk densities of 1.14 and 0.90 g/cm³ for nylon and polypropylene, respectively.

electrodes (x-direction), and the units are (cal/cm²/sec)/(C/cm), which, hereinafter, are referred to as cgs units in the text.

Because of the similarity of the conductivities for all positive or all negative electrodes investigated, even though they were fabricated using different manufacturing techniques, as a first approximation a value of 0.0014 ± 0.0001 cgs units may be taken for the thermal conductivity of discharged nickel-hydroxide positive electrodes. A value of 0.0020 ± 0.0001 cgs units may be taken for the conductivity of discharged cadmium negative electrodes.

Separator materials.—The properties assigned by the manufacturers, or determined independently for the three separator materials chosen for this investigation, are given in Table II.

Dry separator materials.—The measured thermal conductivity of dry separator materials is a function of the bulk conductivity of the materials, the as-supplied porosity, and the amount of compression in the conductivity measuring apparatus. Thermal conductivities for bulk nylon materials average about 0.00055 cgs units, and an average value for bulk polypropylene is about 0.00026 cgs units (4).

Table II gives the apparent porosity of each of the fabricated materials. These porosities were based upon the weights and the uncompressed volumes of the materials. Upon assembly in the conductivity measuring apparatus, the materials were reduced in thickness, hence, apparent porosity by about 35, 25, and 18%, respectively. Therefore the actual porosities of the materials during measurement were of the order 72, 49, and 34%, respectively, assuming that the pore volume decreased while the volume of solid remained the same.

The range of anticipated conductivities for the dry separator materials can be estimated from Eq. [1] and [2], using the average bulk conductivity values mentioned above and assuming a thermal conductivity of 0.000062 cgs units for dry air.

$$k_{max} = \theta k_s + (1 - \theta) k_d \quad [1]$$

$$k_{min} = \frac{k_s k_d}{\theta k_d + (1 - \theta) k_s} \quad [2]$$

Equation [1] gives the maximum conductivity based on a simple parallel conduction thermal model. Equation [2] gives the minimum conductivity based on a simple series conduction model. In both Eq. [1] and [2], k_s refers to the bulk conductivity of the separator material, and k_d refers to the conductivity of dry air. The volume fraction of the separator material is de-

noted by θ , hence $(1 - \theta)$ is the porosity of the material.

Table III gives the estimated maximum and minimum conductivities for the separators using Eq. [1] and [2], and assuming that the compressed porosity value given is correct. The arithmetic mean of the maximum and minimum values calculated is seen to correspond very well with the measured values for both the nylon and the polypropylene materials.

Pratt (5) gives a discussion of heat transmission in fibrous materials, and states that, for some materials in the density range 0.283-0.531 g/cm³, the "geometric" mean, Eq. [3], of the bulk material and air gives good agreement with measured values

$$k_{mean} = k_s^\theta \times k_d^{(1-\theta)} \quad [3]$$

The densities for nylon (max calendaring) and the polypropylene fall within the above density range (see Table II); therefore, using Eq. [3] with $\theta = 0.51$ and $\theta = 0.66$ for the nylon and polypropylene, respectively, the dry conductivity of the nylon is predicted to be 1.89×10^{-4} cgs units and that of the polypropylene to be 1.60×10^{-4} cgs units. These "geometric" mean values differ only slightly from the arithmetic means given in Table III.

In general, therefore, the conductivity of a dry, porous separator material can be predicted to a first approximation by taking the arithmetic mean of the limiting values calculated from Eq. [1] and [2], or the geometric mean from Eq. [3]. However, good agreement using Eq. [3] is said to occur only if the density lies in the range 0.283-0.531 g/cm³. An average value from Eq. [1] and [2] implies that heat transfer is occurring by both parallel and series paths formed by the separator and air. Values of about 0.00055, 0.00026, and 0.000062 cgs units should be used for the conductivity of bulk nylon, polypropylene, and dry air.

Wetted separator materials.—When the separator materials are wetted with electrolyte, the apparent thermal conductivity increases but cannot exceed the conductivity of the electrolyte itself if convection effects are absent. The International Critical Tables (6) give values for the thermal conductivity of several KOH solutions of different strengths. Interpolation of these data yields a value of 0.00135 cgs units for 30% KOH, compared with a value of 0.00140-0.00145 cgs units for pure water. Therefore, for the particular electrolyte in question (30% KOH), the measured conductivity of any of the separator materials investigated is not expected to exceed about 0.00135 cgs units.

The apparent conductivity value obtained for a wetted separator will be some function of (i) the porosity of the material; (ii) the conductivity of the bulk separator material; (iii) the electrolyte conductivity and amount of electrolyte available for absorption by the separator; and (iv) the electrolyte absorption value of the separator material (Table IV). In most applications, the porosity, the electrolyte absorption value, and the conductivity of the separator materials will be invariant. For a given application the conductivity of the electrolyte is also invariant. Even in unsealed flooded cells or vented cells, where there is the possibility of carbonation of the electrolyte, the over-all conductivity of the electrolyte will not change much because the thermal conductivity of potassium

Table III. Calculated conductivity values for the nonwoven dry separator materials

Separator material	Apparent uncompressed porosity	Estimated compressed porosity	Conductivity, cgs units × 10 ⁻⁴			
			Calculated maximum	Calculated minimum	Arithmetic mean	Measured
Nylon felt, maximum loft	82%	72%	1.99	0.82	1.40	1.4
Nylon felt, maximum calendaring	52%	49%	3.10	1.13	2.11	2.1
Polypropylene wettable paper	46%	34%	1.93	1.25	1.59	1.6

Table IV. Electrolyte absorption values for the nonwoven separator materials studied

Material	Electrolyte absorption, g, KOH/g separator		Amount of 30% KOH required to saturate separator materials, ml/g
	With prior drying	Without drying	
	Nylon felt, maximum loft	5.95	
Nylon felt, maximum calendaring		1.78	1.39
Polypropylene wettable paper		0.48	0.37

carbonate solutions is similar to that of hydroxide solutions (6).

Thus, for any given application, the thermal conductivity of the wetted separator is fixed for a given cell electrolyte content. If the separator materials are not saturated with electrolyte, there is the possibility that changes in electrolyte content (due to cycling, orientation, and so on) may change the apparent conductivity. Changes in internal cell pressure may be responsible for changes in separator electrolyte content. Such changes in pressure can result from gas evolution or from changes in the volume of active materials on cycling, for example. Forces acting on the electrodes in nickel-cadmium cells are known to be sufficient to buckle 0.058 cm electrodes because this has been observed during cell disassembly (7). Any change in the shape or volume of the electrodes could result in electrolyte being displaced from the separator, giving a lower apparent thermal conductivity. Migration of active materials into the separator would also result in the displacement of electrolyte.

For a maximum effective thermal conductivity, the separators should be saturated with electrolyte. In fabricating sealed cells where gas recombination is important, however, this may not always be desirable because a saturated separator impedes the diffusion of the oxygen evolved during cycling to the negative electrodes where recombination occurs. In practice, therefore, the actual separator electrolyte content must be a compromise between that dictated by good thermal design and that dictated by the chemistry and operating profile of the cell.

The electrolyte absorption capability of a separator material is defined as the quotient of the weight of electrolyte absorbed and the dry weight of the separator (8). The procedure given in Ref. (8) was used to determine the electrolyte absorption of the separator materials listed in Table II, and the results are given in Table IV. These data were required for the experiments to investigate the effect of separator wetting on thermal conductivity. The electrolyte absorption figure given in Table IV defines the amount of electrolyte (30% KOH) present in the uncompressed, saturated separator materials. It should be noted that this method of measurement is somewhat arbitrary because individual observers may use different criteria for the absence of excess electrolyte after wiping the saturated separator materials across the glass plate.

Table V lists the conductivity values obtained for the separator materials wetted to various extents with the 30% potassium hydroxide electrolyte. These data, when plotted in Fig. 1, show similarity in behavior between the nylon and the polypropylene materials. The thermal conductivity of these separator materials remains relatively small, compared with the conductivity of the electrolyte, until nearly all the pore volume is filled. As the pore volume becomes filled, and the possibility of excess electrolyte in the polyethylene bags used in the measurements exists, then the conductivity value obtained can vary appreciably according to whether or not the excess electrolyte can provide a thermal-short across or around the apparatus. If a thermal-short (continuous electrolyte path) exists, then conductivity values are obtained for the wetted

Table V. Thermal conductivities of various nonwoven separator materials as a function of electrolyte content

Separator material	Electrolyte content		Thermal conductivity, cgs units ^(c)
	ml/g ^(a)	% ^(b)	
Nylon felt, maximum loft	0.00	0.0	0.00014
	1.60	57	0.00032
	2.45	87	0.00081
Nylon felt, maximum calendaring	0.00	0.0	0.00021
	0.50	59	0.00038
	0.65	77	0.00039
	0.74	87	0.00043
	0.78	92	0.00059
Wettable polypropylene paper	0.97	114	0.00117
	0.00	0.0	0.00016
	0.37	64	0.00042

^(a) ml 30% KOH/g dry separator.

^(b) Percentage of pore volume filled in compressed separator.

^(c) For comparison the thermal conductivity of 30% KOH is taken as 0.00135 cgs units.

separators which more closely resemble that of the electrolyte alone (0.00135 cgs units).

The maximum thermal conductivity calculated from Eq. [1], assuming all the pores are filled with electrolyte, is 0.00063 cgs units for the polypropylene material and about 0.00094-0.00113 cgs units for the nylon materials. The corresponding minimum conductivities calculated from Eq. [2] are 0.00036 and 0.00077-0.00096 cgs units, for the polypropylene and maximum calendared and maximum loft nylons, respectively. If the arithmetic mean of k_{max} and k_{min} is taken for the expected measured conductivity, as was done for the dry separators, then the predicted values are 0.00050, and 0.00085-0.00105 cgs units. Inspection of Fig. 1 shows that the value obtained by extrapolation of the polypropylene data to 100% pores filled is 0.00057 cgs units. Similarly, extrapolation of the data for the two nylons gives values of 0.00080 and 0.00102 cgs units. Reasonable agreement, therefore, exists between the predicted and measured values for the saturated separator materials if a parallel-series conduction model is used which gives the arithmetic mean of Eq. [1] and [2] as the over-all conductivity.

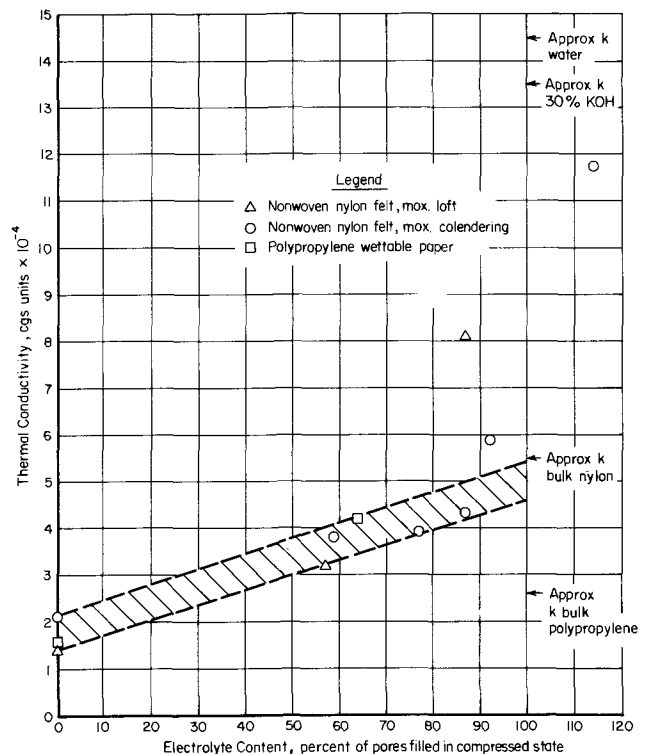


Fig. 1. Thermal conductivity of various separator materials as a function of electrolyte content.

Table VI. Calculation of tortuosity factor, t , for the wetted and dry separator materials

Material	Condition	Equation for tortuosity factor, t	t
Polypropylene wettable paper	Dry	$1.6 \times 10^{-4} = \frac{1.93 \times 10^{-4}}{t_1}$	$t_1 = 1.21$
	Wetted	$5.7 \times 10^{-4} = \frac{6.30 \times 10^{-4}}{t_2}$	$t_2 = 1.11$
Nylon felt, maximum calendaring	Dry	$2.1 \times 10^{-4} = \frac{3.10 \times 10^{-4}}{t_3}$	$t_3 = 1.48$
	Wetted	$8.0 \times 10^{-4} = \frac{8.40 \times 10^{-4}}{t_4}$	$t_4 = 1.18$
Nylon felt, maximum loft	Dry	$1.4 \times 10^{-4} = \frac{1.99 \times 10^{-4}}{t_5}$	$t_5 = 1.42$
	Wetted	$10.2 \times 10^{-4} = \frac{11.3 \times 10^{-4}}{t_6}$	$t_6 = 1.11$

Another possible model for the thermal conductivity of separator materials is a collection of parallel pores having an unknown tortuosity factor. The tortuosity of both the wetted and dry separator materials should be identical for the same amount of compression, so that the measured conductivity would be equal to the calculated conductivity for the parallel mode from Eq. [1] divided by the tortuosity factor, t . Table VI gives the calculated values of t for the wetted and dry separator materials investigated. The calculations show reasonable agreement for the tortuosity of the wet and dry polypropylene material. The agreement is not as good for the nylon materials. However, as expected, the tortuosity factor for the felted nylon materials is greater than that of the less porous polypropylene material.

From another viewpoint, Krischer and Esdorn (9) summarize the four processes of heat transfer in a damp, porous or granular solid as follows: (i) heat transfer in the solid, k_s ; (ii) heat transfer in the liquid, k_e ; (iii) heat transfer by molecular conduction and as latent heat in air contained in pores with damp walls, $k_d + k_v$; (iv) molecular heat conduction in pores with dry walls, k_a . Krischer and Esdorn then constructed a model in which the above four processes were in parallel with each other; and then this network of parallel processes was in series with another network comprising each of the four processes above in series (5). While this model gave satisfactory agreement between theoretical and experimental values for certain lightweight concretes, it does not give good agreement for the wetted separator materials under consideration.

The separator materials under investigation must, therefore, be considered as consisting of fibers compacted together in a very open structure. In a discussion of the effect of moisture on the conductivity of porous insulating materials Joy proposed the following arrangements or models (10): (i) series arrangement—minimum conductivity with liquid located in layers perpendicular to the direction of heat flow; (ii) parallel arrangement—maximum conductivity with liquid forming continuous paths that bypass the less conducting air pockets; (iii) bead arrangement—liquid uniformly distributed through the material as small beads and considered as a dispersed phase; (iv) foam arrangement—material surrounded by liquid films which connect as in a foam so that liquid forms an irregular continuous phase. Joy found that the experimental data, when compared with the theoretical data, indicated the possibility of more than one of the above arrangements being applicable to a given amount of moisture. As discussed below, the present study indicates that one of two of the above arrangements probably predominates according to the electrolyte content of the separator material.

Joy's series arrangement (i) is thought not to apply as the predominant conductivity determining factor for separator materials. This is because there are no

markedly planar surfaces in the separator material. Even if the electrolyte were concentrated at the separator/electrode interface (i.e., under the action of thermal gradients (5) which are known to be small from the temperature differences observed in the conductivity measurements) a planar film need not be stable because of the capillary forces deriving from the porous electrode and separator material surfaces. Joy's bead arrangement (iii) is possible if the separator materials are not easily wettable and are relatively thick. Since the separator materials in this study are readily wettable, the existence of beads is unlikely. Thus the parallel arrangement, (ii), and the foam arrangement, (iv), appear most appropriate for describing the conductivity of wetted separators. These latter two arrangements appear to be related to each other in that the foam arrangement probably is more descriptive at low electrolyte contents, wherein pore walls are wetted while the parallel arrangement is more descriptive at higher electrolyte contents, wherein some, if not all, of the pores are completely filled. However, there is probably no well-defined transition between the two arrangements.

In summary, in sealed aerospace cells, because of the requirements for oxygen diffusion through the separator, the pores in the separator are probably only 60 to 80% filled with electrolyte. Therefore, Fig. 1 shows that a typical conductivity value for such a material is about 0.0004 cgs units.

Use of the measured conductivity data.—If the measured and calculated conductivity data from this work, namely:

Positive electrodes;	$k_x = 0.0014$ (measured)
	$k_y = 0.03$ (calculated)
Negative electrodes;	$k_x = 0.0020$ (measured)
	$k_y = 0.03$ (calculated)
Wetted separator;	$k_x = 0.0004$ (measured)
	$k_y = 0.0004$ (estimated)

are used in the thermal resistance networks for the four types of 20 A-hr nickel-cadmium cells described previously (1, 2), reasonable agreement is found between predicted and measured cell conductivities (2), as shown in Table VII. Knowing the dimensions of a cell and its components and their composition, it is now possible to calculate cell conductivities. Similarly, if the dimensions of a battery and its components, and their composition are known, then the heat transfer

Table VII. Predicted and measured cell conductivities

Cell type	k_x , cgs units		k_y , cgs units	
	Predicted	Measured	Predicted	Measured
I	0.0028	0.0027	0.0067	0.0071
II	0.0021	0.0038	0.0065	0.0067
III	0.0025	0.0026	0.0047	0.0056
IV	0.0024	0.0086	0.0036	

properties of that battery can be calculated and used to optimize thermal design.

Conclusions

To fill an apparent void in the literature, experimental thermal conductivity data have been obtained for discharged nickel hydroxide positive, and cadmium negative electrodes, and for three types of separator material considered for use in nickel-cadmium aerospace cells.

In the direction perpendicular to the plane of the electrodes the average value obtained for discharged positive electrodes is 0.0014 ± 0.0001 cgs units. The average value for discharged negative electrodes is 0.0020 ± 0.0001 cgs units. Measurements were not made in the parallel direction, but a calculated value of about 0.03 cgs units for the positives or negatives appears to be consistent with the measured and predicted cell conductivities.

The thermal conductivities of the three separator materials studied, nonwoven calendered and uncalendered nylon, and nonwoven polypropylene, are a function of the respective bulk conductivities, porosities, and electrolyte absorption values. The conductivity of a dry separator material may be estimated by taking the arithmetic mean of the values determined from Eq. [1] and [2] using values of 0.00055, 0.00026, and 0.00062 cgs units for the bulk conductivity of nylon, polypropylene, and dry air, respectively. Experimental values of 0.00014, 0.00021, and 0.00016 cgs units were obtained for dry noncalendered nylon felt about 72% porous after compression; dry calendered nylon felt about 49% porous after compression; and dry polypropylene wettable paper about 34% porous after compression, respectively.

As the electrolyte content of the separators is increased, the thermal conductivity increases up to about 0.0004 cgs units for a pore filling (60-80%) thought to be representative for sealed aerospace cells. The thermal conductivity of saturated separator materials (100% pores filled with electrolyte) can approach that of the electrolyte itself (0.00135 cgs units).

Acknowledgments

This work was performed under Wright-Patterson Air Force Contract Number F3316-69-C-1537 as part of supporting studies to elucidate and devise "Failure Mechanisms and Accelerated Life Tests of Nickel-Cadmium Batteries." The authors wish to thank Mr. G. H. Miller, Project Monitor, for his continued interest in these studies.

Manuscript submitted Feb. 3, 1972; revised manuscript received April 13, 1972.

Any discussion of this paper will appear in a Discussion Section to be published in the June 1973 JOURNAL.

REFERENCES

1. E. W. Brooman and J. McCallum, *This Journal*, **118**, 1518 (1971).
2. E. W. Brooman and J. McCallum, "The Thermal Conductivity of Sealed Nickel-Cadmium Cells," Technical Report No. AFAPL-TR-71-75 Feb., 1972, Wright-Patterson AFB Contract No. F33615-69-C-1537.
3. W. H. Metzger, Jr. and J. M. Sherfey, *Electrochem. Technol.*, **2**, 285 (1964).
4. *Modern Plastics Encyclopedia (1968)*, Modern Plastics, **45** (1A), 38, 43 (1967).
5. A. W. Pratt, "Heat Transmission in Low Conductivity Materials," in "Thermal Conductivity," Vol. 1, Chap. 6, R. P. Tye, Editor, Academic Press, London (1961).
6. *International Critical Tables*, Vol. 5, p. 229, McGraw-Hill Book Co., Inc., New York (1929).
7. E. W. Brooman, Unpublished (1971).
8. "Characteristics of Separators for Alkaline Silver Oxide Zinc Secondary Batteries: Screening Methods," J. E. Cooper and A. Fleischer, Editors, Air Force Aero Propulsion Laboratory Special Publication, Sept. 1965.
9. O. Krischer and H. Esdorn, *Forsch. Gebiete Ingenieurw.*, **22**, 1 (1956).
10. F. A. Joy, "Thermal Conductivity of Insulations Containing Moisture," in "Symposium on Thermal Conductivity Measurement and Applications of Thermal Insulations," ASTM STP 217, American Society for Testing and Materials, p. 65, Philadelphia, Pa. (1957).
11. S. Gross, *Energy Conversion*, **9**, 55 (1969).

Effect of Chloride on the Anodic Dissolution of Titanium in Methanolic Solutions

E. P. Parry and D. H. Hern

North American Rockwell Science Center, Thousand Oaks, California 91360

ABSTRACT

A study of the polarographic characteristics of the Ti(IV)-Ti(III) couple in methanolic solutions containing various concentrations of HCl and LiCl has been the basis for the determination of the oxidation state of titanium during dissolution in these media. The Ti(IV) and Ti(III) complexes have been shown to have the same number of chloride ligands. It is also shown that titanium dissolves with an apparent oxidation number (n_{app}) between 3 and 4, with the value approaching 3 at high chloride concentrations. The acidity appears to have little effect at acidities greater than 0.10M. It is also shown that Ti(IV) in methanol solutions containing a high chloride ion concentration oxidizes Ti to form Ti(III). The nature of the complexes of titanium ion in solution and their effect on the titanium dissolution is discussed.

Considerable interest currently exists in the stress corrosion cracking mechanism of titanium and its alloys in methanol (1-4). However, very little is known about the chemistry of titanium dissolved in methanolic solutions. The importance of solution chem-

istry cannot be overlooked in mechanistic interpretations, and while electrochemical work has been reported (5, 6), very few studies about the nature of the titanium complexes present in solution have been made.

Studies of anodic dissolution of titanium have been reported. Thirsk and co-workers (7) have studied

Key words: oxidation state, polarography, solution formal potentials, solution equilibria.

the anodic dissolution of titanium in aqueous sulfuric acid solutions and have concluded, on the basis of some indirect evidence, that titanium is oxidized only to the +3 state during dissolution. On the other hand, Franz and Göhr (8) and Pourbaix (9) indicated that TiO_2 is formed when titanium dissolves anodically in aqueous sulfuric acid solutions which provides evidence that at least some Ti^{+4} is obtained. Franklin and Seklemian (10) have electrochemically oxidized titanium in a number of nonaqueous solvents with and without complexing agents present and have found oxidation numbers between 3 and 4. Johnson and Shreir (11) have found that in 3M $AlCl_3$ in diethyl ether titanium anodically dissolves to give $Ti(III)$.

When titanium was chemically oxidized in various aqueous acids (i.e., concentrated sulfuric, hydrochloric, hydrofluoric, and hydrochloric-acetic), Franklin and Seklemian found that $Ti(III)$ is formed. Recent work by Harkins (12) showed that methanol vapor reacts directly with oxide free titanium to give $Ti(OCH_3)_4$.

Menzies and Averill (13) have studied the dissolution of titanium in anhydrous methanol solutions containing hydrogen chloride. They report that titanium dissolves with an oxidation state of 3.0 independent of chloride ion or hydrogen ion concentration, potential of the specimen, water content up to 1% and several other parameters. On the basis of the independence of the titanium oxidation state upon the chloride ion concentration, they postulated a dissolution reaction involving adsorption of chloride at the electrode surface.

In a program aimed at developing a better understanding of the role of solution chemistry in titanium corrosion and stress-corrosion cracking in methanol solutions, results for the anodic dissolution of titanium in methanol have been obtained which differ from those of Menzies and Averill (13). Preliminary results are presented here which suggest that the concentration of chloride ion is of considerable importance in determining the oxidation state of anodically dissolved titanium, and indicate the important role of chloride as a complexing agent.

Experimental

A multipurpose electrochemical instrument, using operational amplifiers designed and built in this laboratory, was used both for dissolution as well as for the electrochemical measurements. A glass cell was employed having a Teflon stopper, suitably bored for electrode access. Evaporated cryogenic nitrogen was used for oxygen purging after purification by passage through copper sponge in a tube furnace at approximately 400°C. The nitrogen was presaturated with methanol before bubbling into the cell containing the solution.

A low leakage, high-impedance aqueous saturated calomel electrode was used throughout this investigation. These electrodes have nominal leak rates of approximately 25 μ liters/hr. For a 4 to 6 hr run, this changes the water and chloride content only by a negligible amount. For determination of oxidation states, the usual dropping mercury electrode (DME) having m and t values of 5.4 mg/sec and 7.05 sec, respectively, was used. In some cases, a Kemula hanging mercury drop electrode was employed. For the recording of polarization curves, a cell having a Luggin capillary placed within 2 mm of the specimen, was used. The anode and cathode compartments were not separated in this cell.

To integrate the current during potentiostatic runs to obtain the total coulombs, the voltage, measured by passing the current through a standard resistor, was integrated using a Vidar Model 241 (12470) voltage to frequency converter and a C.M.C. Model 726 BN counter. The titanium electrodes for dissolution were rods $\frac{1}{4}$ in. in diameter and 1 in. long, fitted into a Stern Makrides holder (14). The area of the electrode was 5.4 cm^2 . Each electrode was degreased in boiling

benzene for 5 min, then pickled in an acid mixture of 30% HNO_3 -20% H_2SO_4 -20% $HF-H_2O$ for 30-45 sec. The electrode was then thoroughly washed in water, then in methanol, and inserted into the cell. Both Ti 75A and arc melted titanium specimens were used. The Ti 75A material has up to 4000 ppm of impurities, including about 2000 ppm of iron. The arc melted titanium has a typical analysis of less than 400 ppm of all metallic impurities.

Mallinkrodt "Nanograde" methyl alcohol was used without further purification or treatment. Analysis for water in this solvent gave values of approximately 0.02%. To make anhydrous acid solutions of methanol, anhydrous hydrogen chloride gas was passed into a given volume of methanol for a period of time to prepare a stock solution. Standardization of this solution was made by taking aliquots, diluting with water, and titrating with base. Subsequent solutions were made by appropriate dilution of this stock solution with methanol. Analysis of typical solution containing 0.02M HCl , showed a water content of approximately 0.05%. Reagent grade lithium chloride was added to some of the solutions to adjust the chloride concentration. Solutions were made both in which the salt was carefully dried just before use, as well as from the salt in the "as-received" condition from a freshly opened bottle.

The conductivity of the solutions of interest was determined by measuring the current and phase angle resulting from application of 1000 cycle a.c. to common conductivity cells, having cell constants near 0.4 or 0.01 depending on the conductivity measured.

The anhydrous stock titanium tetrachloride solution was prepared by adding reagent grade liquid $TiCl_4$ to an anhydrous methanol-0.1M hydrogen chloride solution slowly with stirring. The titanium content of the solution was then checked against the amount added by a complexometric titration (15). A back titration was performed, using cupric ion at pH of 5.5 and pyrocatechol violet as indicator.

In some experiments, the total titanium content of the solutions was determined using atomic absorption spectroscopy. The above standardized stock solution was used for calibration. To decrease ionization and, therefore, to increase sensitivity and linearity of the calibration plot, a large excess of alkali metal ion must be present. We found that sodium ion is better than the recommended potassium ion for this purpose.

Results

Because polarography is a convenient tool to monitor the titanium oxidation state upon dissolution, and may also yield information about the titanium ion complexes in solution, some discussion of the polarographic behavior of titanium ions in methanol-hydrogen chloride is desirable.

In HCl concentrations greater than 0.01M, titanium (IV) reduction to $Ti(III)$ appears reversible by ordinary polarography. Reversibility was evaluated by the standard technique of using the slope of the E vs. $\log i_d - i/i$ plot ($0.059^{-1} V^{-1}$) and by the fact that the reduction wave for the (IV) complex and oxidation wave of the (III) complex have the same half-wave potential. Additional work done with a stationary mercury drop electrode and a fast potential scan suggests that the electrode reaction for the $Ti(IV)$ - $Ti(III)$ couple in this medium may be quasi-reversible. With ordinary polarography, however, the wave can be considered to be reversible.

Figure 1 shows the polarographic wave for a solution which is $2 \times 10^{-4}M$ in $Ti(IV)$ in a methanolic solution containing 0.01M HCl and 0.2M $LiCl$. The half-wave potential of the $Ti(IV)$ reduction wave in this solution is $-0.35V$ vs. SCE. The half-wave potential shifts approximately 18 mV in a positive direction with a tenfold increase in chloride content. This shift, however, is not corrected for ionic strength effects. The diffusion plateau is well-defined and the limiting current is

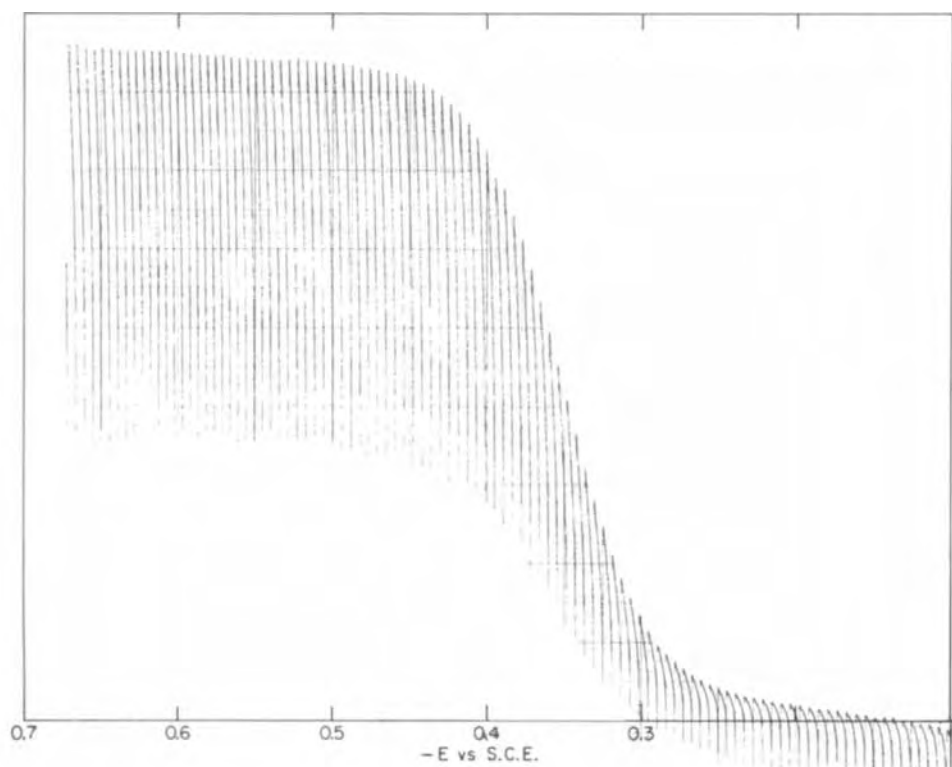


Fig. 1. Polarogram showing reduction of $2 \times 10^{-4}M$ Ti(IV) in methanol solution containing 0.01M HCl and 0.20M LiCl.

diffusion controlled. Using the Ilkovic equation, the diffusion coefficient of the Ti(IV) complex is calculated to be 1.0×10^{-5} cm²/sec. The magnitude of the diffusion current is proportional to the concentration of Ti(IV) from 4 to at least 40 parts per million (ppm) Ti(IV). The temperature coefficient of the diffusion current is 3% per degree over the temperature range from 15° to 30°C.

The Ti(III) species is easily oxidized by air to the Ti(IV) complex. The diffusion coefficient of Ti(III) is more difficult to obtain using the Ilkovic equation because the Ti(III) salts available were partially air oxidized and did not completely dissolve in methanol, and so the concentration was not accurately known. In order to determine the diffusion coefficient of Ti(III), a polarogram of a solution containing a mixture of Ti(III) and Ti(IV), but where the Ti(III) wave was at least 80-90% of the total, was obtained. The total wave height [Ti(III) + Ti(IV)] was measured. The solution was air oxidized to give a solution of only Ti(IV), but where the total titanium concentration was the same. The diffusion current was again measured. Our experimental results showed that these total diffusion currents were the same. Such a technique becomes less precise the more Ti(IV) contamination in the originally measured solution. No mathematical evaluation of the accuracy which can be obtained by this method under these experimental conditions has been done. However, the reproducibility is about $\pm 10\%$ for the diffusion coefficient of Ti(III).

At acid concentrations smaller than 0.01M, the wave becomes irreversible. Addition of water to a 0.01M, HCl solution in methanol shifts the half-wave potential to more negative values (Fig. 2). Although at 5% water content the normal polarographic wave has the reversible slope, some unusual electrochemical behavior is noted. This will be discussed in more detail in a subsequent publication. Because of the well-defined nature of the wave, the ratio of Ti(IV) to Ti(III) in any solution can be determined readily from the polarographic wave. At potentials well anodic of the half-wave potential on the diffusion current plateau, where Ti(III) is oxidized, the concentration of Ti(III) can be determined. Similarly, at potentials cathodic of the half-wave potential on the diffusion plateau of Ti(IV)

reduction, the concentration of Ti(IV) can be determined (see Fig. 3).

The apparent oxidation number (n_{app}) of the titanium species after anodic dissolution, for any mixture of Ti(IV) and Ti(III), can be obtained by application of the easily derived expression

$$n_{app} = \frac{3|i_{anod}| + 4|i_{cath}|}{|i_{anod}| + |i_{cath}|}$$

where $|i_{anod}|$ and $|i_{cath}|$ represent the absolute values of the anodic and cathodic diffusion currents, respectively. The polarographic technique can also be used to monitor the titanium oxidation state during the dissolution process. A direct measurement of the n_{app} values is thus possible which may be more precise than the coulometric technique. In this latter technique, because of the high oxidation state, a given relative error in the determination of total titanium concentration will cause a relative error four times as large in the n_{app} value.

To acquire some indication as to the effect of neglecting IR corrections in the medium, the conductivities of a methanol solution 0.02M in anhydrous HCl and one 0.02M in HCl, 0.48M in LiCl were measured. The conductivities were 2.1×10^{-3} and 1.3×10^{-2} ohm⁻¹

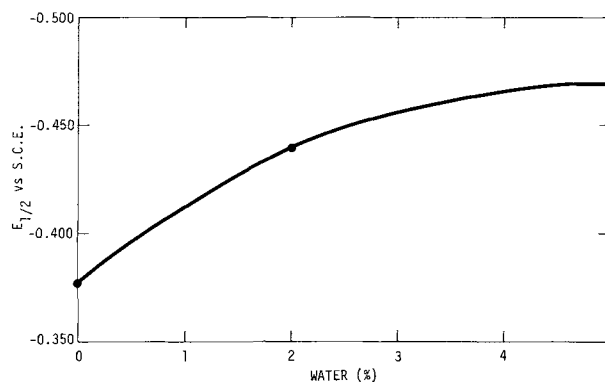


Fig. 2. Variation of normal polarographic half-wave potential with added water content in methanol solution containing 0.01M HCl.

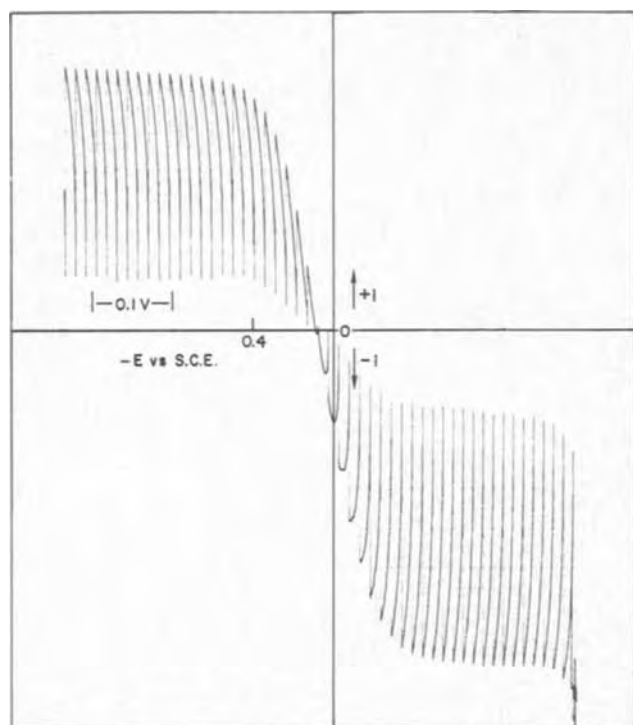


Fig. 3. Polarogram of solution after electrochemical dissolution of arc melted titanium specimen in methanol solution containing 0.02M HCl and 0.18M LiCl.

cm^{-1} , respectively. These values are both greater than would be found for an aqueous solution 0.01M in KCl.

After potentiostatic dissolution of a piece of arc melted titanium at -0.15V vs. SCE in a methanol solution containing 0.18M LiCl and 0.02M anhydrous HCl, the solution gave the polarographic behavior shown in Fig. 3. In this dissolution experiment, anodic and cathodic compartments were not separated. Both titanium (III) and (IV) species are formed upon dissolution. The $E_{1/2}$ value for the mixed polarographic wave is the same as that found for a solution where Ti(IV) was directly dissolved in another portion of this methanol-chloride medium. The same polarographic behavior and ratio of cathodic and anodic wave heights were obtained both when the indicator electrode (DME) was put directly into the cell in which the titanium was being dissolved (*in situ* technique), and when the polarographic measurement was made on an aliquot of the dissolution solution placed in a separate cell.

Although Ti(III) is very sensitive to air oxidation, it was shown that partial oxidation did not cause the mixture of oxidation states. After oxygen removal, it was found that the Ti(IV)/Ti(III) ratio was independent of time of purging, indicating no oxidation was caused by oxygen impurity in the purging gas. Moreover, simple calculations show that the amount of

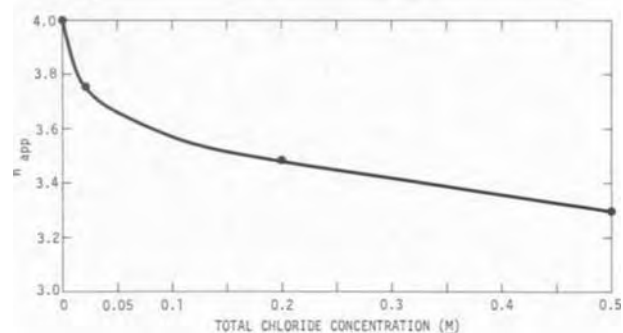


Fig. 4. Effect of chloride ion concentration on apparent oxidation number for electrochemical dissolution of titanium in methanol solutions.

oxygen which was found in the nitrogen after purification (1 ppm or less) was not sufficient to account for the oxidation.

In this same dissolution experiment, the coulombs expended were measured and the total concentration of titanium was determined using atomic absorption spectroscopy. After passing 58 coulombs and dissolving 0.166 moles of Ti, an average n_{app} value for the titanium in the solution was found to be 3.60. The polarographic data gave a value of 3.44. In other experiments, similar differences were found between coulometric and polarographic results with the polarographic result generally being lower. The reason for this discrepancy is not completely understood at present, but may be caused by less than 100% current efficiency in the oxidation process.

The *in situ* polarographic technique was used to determine the average oxidation state (n_{app} values) of titanium after dissolution at constant potential in solutions containing various concentrations of chloride. The results are given in Table I. The value of n_{app} is shown as a function of chloride ion concentration in Fig. 4. Dissolution in the absence of chloride was performed in 0.02N sulfuric acid in methanol. All data were obtained in a cell in which the cathodic and anodic compartments were separated by a glass frit. However, results for the oxidation state were the same for a cell with or without separated compartments. Both Ti 75A and arc melted titanium specimens gave similar results. The value of n_{app} also appears to be independent of electrode condition (*i.e.*, whether cold worked or annealed).

Results indicating the effect of acid concentration at constant chloride concentration are shown in Fig. 5. The results suggest that acidity has little effect on the n_{app} values, particularly at acid concentrations greater than 0.1M.

If a piece of titanium is placed into methanol containing 0.1M TiCl_4 -0.48M LiCl-0.02M anhydrous HCl, a reaction occurs in which Ti(III) is formed. The titanium metal and Ti(IV) react according to

Table I. Effective n_{app} number for electrochemically oxidized titanium

Run	Medium	n_{app}	Electrode	Potential (V vs. SCE)	Remarks
1.	0.02M HCl-methanol, with $\sim 0.05\%$ water.	3.75	Annealed 75A	+0.05	
2.	0.02M HCl-methanol, with $\sim 0.05\%$ water.	3.73	Ti 75A	-0.15	
3.	0.02M HCl-methanol, with $\sim 0.05\%$ water.	3.72	Arc melted titanium	-0.15	
4.	0.02M HCl-methanol, with $\sim 0.05\%$ water.	3.66	Annealed 75A	-0.15	
5.	0.02M HCl, 0.48M LiCl in methanol, with about 0.5% water.	3.30	Annealed	-0.15	Electrode pitted
6.	0.02M HCl, 0.48M LiCl in methanol, with about 0.5% water.	3.30	Arc melted titanium	-0.15	Electrode pitted
7.	0.02M HCl, 0.48M LiCl in methanol, with 0.08% water.	3.20	Arc melted titanium	-0.15	Active dissolution, no pitting
7a.	0.02M HCl, 0.48M LiCl in methanol, with $\sim 0.5\%$ water.	3.34	Arc melted titanium	+0.30	Pitting occurred
8.	0.02M HCl, 0.18M LiCl in methanol, with $\sim 0.2\%$ water.	3.48	Arc melted titanium	-0.15	No pitting
9.	0.1M HCl, 0.1M LiCl in methanol, with $>0.05\%$ water.	3.30	Arc melted titanium	-0.15	No pitting
10.	0.1M HCl	3.44	Arc melted titanium	-0.15	No pitting
11.	0.2M HCl in methanol, with $\sim 0.06\%$ water.	3.35	Arc melted titanium	-0.15	
12.	1.0M HCl in methanol, with 3% water.	3.20	Arc melted titanium	+0.10	Electrode in passive region—severe pitting occurred

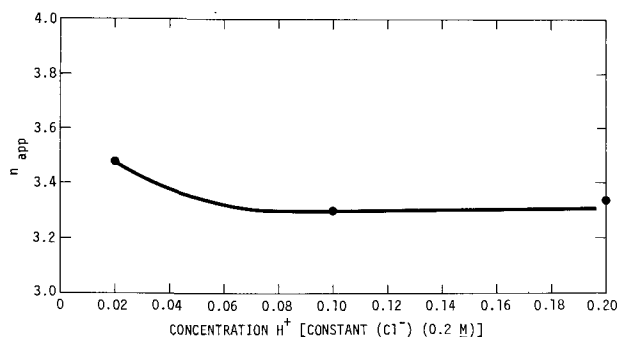
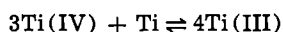


Fig. 5. Effect of hydrogen ion concentration on apparent oxidation number for titanium dissolution in methanol solution.



Arc melted titanium, Ti 75A, Ti-6Al-4V, and Ti 50A have all, in time, shown significant reaction. With Ti 75A, Ti-6Al-4V, and others, the effective n_{app} number of the titanium in solution, after several hours reaction, is approximately 3.1, indicating that the reaction goes to the right almost completely. The high concentration of chloride appears to be essential to this reaction. At considerably lower concentrations of chloride and of Ti(IV), the reaction either does not go or was too slow for our observation (8 hr). While all titanium specimens tried underwent this reaction in time, the rate of the reaction varied considerably. A specimen of Ti 75A which was not annealed after machining and only moderately etched in the $\text{HNO}_3\text{-H}_2\text{SO}_4\text{-HF}$ mixture, underwent rather rapid reaction, generating considerable blue color within 1 hr. On the other hand, an arc melted specimen, which was not annealed, but was etched the same way, appeared not to react. When the unannealed specimen was heavily etched in the etchant (10 min or longer), it would react. An arc melted specimen which was annealed, but only very lightly etched, reacted, but very slowly (color appears after 4 to 5 hr). The rate of the reaction appears to have a rather complex dependency on the oxide film on the specimen, surface cold work, and perhaps on the microstructure of the alloy. Experiments are planned to elucidate the important parameters in this reaction.

During both chemical and electrochemical dissolution with an active electrode, it was found that a black deposit formed on the electrode or flaked off into solution. The amount increased with time. This material was identified as $\alpha\text{-Ti}$ by x-ray diffraction as also found by Menzies and Averill (13).

In the initial work involving both electrochemical and chemical dissolution in the presence of lithium chloride, no special effort was made to dry the presumably anhydrous salt from a freshly opened bottle, since it was reported previously, by Menzies and Averill (13) that a water content less than 1% in methanol-HCl solutions "did not affect the oxidation state, the amount or nature of disintegration product, or the surface features of the titanium specimen after dissolution." However, Mansfeld (6) showed subsequently that as little as 0.6% water gives rise to a passive region in the titanium polarization curve in a methanol-HCl solution. The use of lithium chloride, that was not carefully dried and handled, gave solutions which contained from 0.3 to 0.5% water, as determined by a Karl Fischer titration. The n_{app} value obtained with these solutions was the same as that obtained in a solution containing 0.02-0.04% water, in agreement with the findings of Menzies and Averill. However, contrary to their data, we found that upon using the initial solutions wherein approximately 0.5% water was present in the methanol solution which contained 0.02M HCl and 0.48M LiCl, the electrode showed rather severe pitting after both chemical and electro-

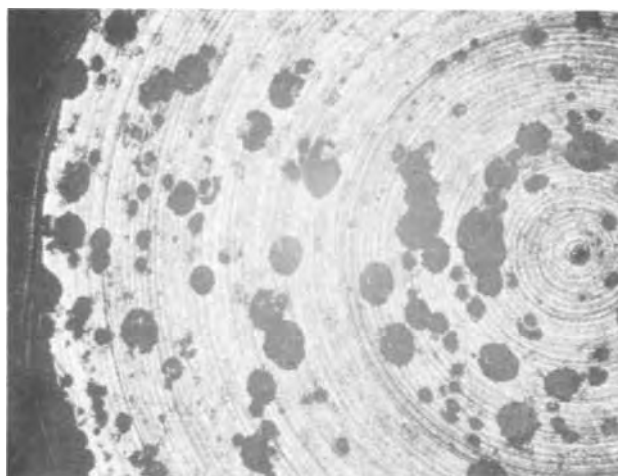


Fig. 6. Micrograph showing Ti-6A-4V specimen after 72 hr contact with methanol solution containing 0.1M TiCl_4 , 0.02M HCl and 0.48M LiCl, water content about 0.5%. Magnification 32X.

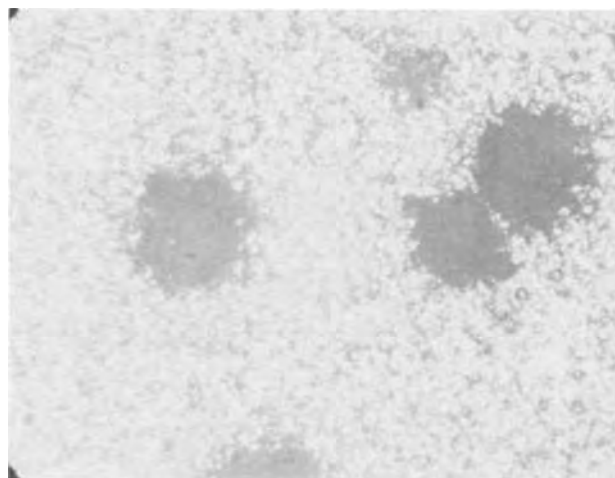


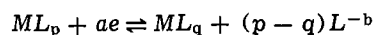
Fig. 7. Micrograph showing Ti 75A specimen after 17.5 hr electrochemical dissolution at -0.15V in methanol solution containing 0.02M HCl and 0.48M LiCl, water content about 0.5%. Magnification 100X.

chemical dissolution. The pits, micrographs of which are shown in Fig. 6 and 7, are typical of the classical pits formed by localized attack on a passive surface. The potential of the specimen in both methods of dissolution was more noble than the pitting potential [see Mansfeld (6)]. The potential of the specimens during dissolution in the work of Menzies and Averill was not specified, since they used galvanostatic techniques.

Discussion

Even though methanol has a fairly low dielectric constant (32.6), it is still a relatively good ionizing solvent (16). Thus 0.01M HCl is about 85% ionized in methanol. It can also be shown by consideration of the autoprotolysis constant of methanol, that the concentration of methoxide ion is much too small to be considered as a significant ligand for the Ti species. The important ligands for both Ti(IV) and Ti(III) species, therefore, consist of chloride, water (where present), and methanol, as shown below.

The polarographic behavior gives a reasonable amount of information concerning the nature of titanium complexes. For a reversible polarographic wave, the difference in the number of ligands attached to the ions of higher and lower oxidation states can be obtained. Thus, for a reaction



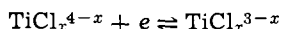
the half-wave potential of the polarographic wave, as a function of the ligand concentration, C_L , would be given by (17)

$$E_{1/2} = E^{01} - \frac{(p - q)}{a} 0.0591 \log C_L$$

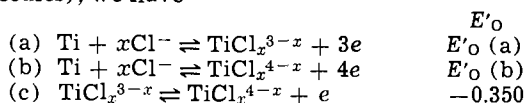
where E^{01} is a term involving both the formal potential (E'_o) of the reaction, and the diffusion coefficients of oxidized and reduced species. In the above reaction, the charge on the complex ions is omitted for simplicity. If, in the reduction of a chloro complex of Ti(IV) to a chloro complex of Ti(III), ($p - q$) is 1 [i.e., if the Ti(III) complex has one less chloride than the Ti(IV) complex], the half-wave potential should shift by 60 mV per decade change in chloride ion concentration. If the difference in the number of chloride ligands between the Ti(IV) and Ti(III) species were even greater, then a proportionately greater shift would occur. Since the experimental shift of half-wave potential per decade change in chloride ion concentration was found to be 18 mV, it indicates that either polymeric titanium species are present in the solution and involved in the electrode reaction, or the small shift is caused by a change of the ionic strength of the solution with increased chloride ion concentration. Because the diffusion coefficients obtained for titanium (IV) and (III) ions in methanol are very close to those found for typical ions in aqueous solution (e.g., PJ^{++} in 0.1M KCl: $D = 0.98 \times 10^{-5}$ cm²/sec), polymerization does not seem likely. The small shifts obtained are typical of ionic strength effects and, although experiments would have been desirable at constant ionic strength, the likelihood is great that the change in ionic strength is responsible for the small shift in half-wave potential that is noted. Thus, it is concluded that the Ti(IV) and Ti(III) complexes in these solutions have the same number of chloride ligands.

Both Ti(IV) and Ti(III) are octahedral and have sixfold coordination. The six ligand positions are either occupied by chloride ion or solvent. From the above rationale, we know that both Ti(III) and Ti(IV) have the same number of chloride ligands, but we are unable to say if all ligands are chloride or only some chloride ions are present, with solvent molecules playing an important role in the coordination sphere. The fact that methanol is a strong base towards first row transition metals [as shown by a number of previous studies (18)] suggests that methanol could compete quite successfully with chloride ion as a coordinating ligand. We thus speculate that both titanium species have methanol and chloride ion coordinated in the complex in the "anhydrous" solutions, but the data we have available at present do not permit detailed elucidation of the nature of the titanium species.

Because both Ti(IV) and Ti(III) have the same number of chloride ligands, the reaction representing the polarographic reduction can be written as



The reversible polarographic half-wave potential in a given medium gives the formal potential for the above reaction, since the diffusion coefficients are the same (18). This value has been shown to be $-0.35V$ in a methanolic solution containing 0.02M HCl and 0.18M LiCl. If we now consider the reactions in a solution of ionic strength of 0.2 (neglecting coordinating solvent molecules), we have



We can now calculate an expression relating the formal potentials for reactions (a) and (b) from the formal potential of reaction (c). Such calculations require that the free energies be used. Thus, we have

$$\Delta F_{(c)} = \Delta F_{(b)} - \Delta F_{(a)}$$

where $\Delta F = (-nFE'_o)$. Substitution of the appropriate values of n and solving we obtain the expression

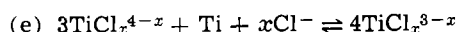
$$E'_{O(b)} = -\frac{0.350}{4} + \frac{3}{4} E'_{O(a)} \text{ (volt)}$$

which gives the relationship between the formal potentials of the reactions (a) and (b). This indicates a very small difference between the formal potentials of reactions (a) and (b). For example, if $E'_{O(a)}$ were $-0.500V$, $E'_{O(b)}$ would equal $-0.463V$. This suggests an explanation for the mixture of oxidation states found in the dissolution experiments.

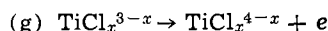
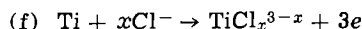
As described earlier, the reaction



has been shown to occur and to go nearly to completion. Because the same number of chloride ions are found in the Ti(IV) and Ti(III) complexes, the equation representing the observed oxidation of titanium by titanium tetrachloride can be written



Inspection of this equation suggests the reason for requiring large concentrations of chloride ion and Ti(IV) for the reaction to go from left to right. Consideration of the two half-reactions



which comprise reaction (e), and recognizing that the free energy for reaction (e) is considerably negative, we determine that the formal potential of reaction (f) is significantly more negative than $-0.350V$. However, with the data available we are unable to specify the value of the formal potential of this half-reaction.

The change in n_{app} value with chloride ion concentration seems unusual, since both the Ti(III) and Ti(IV) complexes contain the same number of chloride ligands. However, half-reactions (a) and (b) (see above) have different dependencies on the chloride ion concentration, as can be seen by consideration of the Nernst expression for the two half-reactions

$$E = E'_{O(a)} + \frac{0.06}{3} \log \frac{[TiCl_x^{3-x}]}{[Cl^-]^x} \text{ (volts)}$$

and

$$E = E'_{O(b)} + \frac{0.06}{4} \log \frac{[TiCl_x^{4-x}]}{[Cl^-]^x} \text{ (volt)}$$

In addition, because of the different charge on the complex ion, these expressions will also be affected differently by ionic strength.

While the Ti(IV)-Ti(III) couple is polarographically reversible, the dissolution of titanium is an activated process where the kinetics of the processes must be considered as well as the thermodynamics. The independence of the n_{app} value over a wide potential range was not evaluated, but the data (see Table I) do not indicate any significant dependence over a limited potential range. This would suggest that the log current-voltage curves for oxidation of Ti to the Ti(III) and Ti(IV) states, respectively, are essentially parallel over the potential range covered.

It has been generally assumed for titanium oxidation in aqueous sulfuric acid media, that titanium dissolves to give Ti(III) from an active surface and Ti(IV) from a passive surface (19) although there is no agreement on this point (7). Our data indicate that in methanol solutions containing chloride, the apparent oxidation number is independent of whether the electrode actively dissolves or dissolves under passive conditions where pitting occurs. For example, comparison of runs 5 and 6 with 7 shows that no significant difference is found in the n_{app} values for an electrode where extensive pitting occurred (runs 5 and 6), and where only

active dissolution was found (run 7). For solutions having the composition of run 12, a significant passive region exists (6) where pitting occurs, with the ratio of passive dissolution to dissolution by pitting estimated to be smaller than 1 to 100. Under these conditions, the n_{app} value is consistent with that which would be found under comparable conditions with an active electrode (compare run 12 and Fig. 4).

The use of the *in situ* technique might raise the question as to the effect of the presence of mercury in the solution on the dissolution process. It should be pointed out that mercury metal does not come directly in contact with the titanium specimen during the dissolution experiment. Thus, no alloy effect is possible. Moreover because the reversible potential of the Ti(IV-III) couple is more negative than mercury dissolution in this medium, the oxidation of mercury metal by Ti(IV) is thermodynamically unreasonable. No other reactions would appear to be feasible. Added evidence is found in the observation that the *in situ* determination of n_{app} during dissolution and the determination of n_{app} on a separate aliquot gave the same value within experimental error, although it was more difficult to prevent air oxidation upon removal of a separate aliquot.

The results reported here for the dissolution valence of titanium are not in agreement with those of Menzies and Averill (13) (M&A). Their data indicate that titanium dissolves with a valence of three independent of chloride ion, hydrogen ion, water content to 1%, etc. However, these results are in general agreement with those of Franklin and Seklemian (10) where titanium was electrochemically dissolved in a number of non-aqueous solvents to give an oxidation number between three and four (although methanol was not specifically studied).

To resolve unequivocally the difference in results between this work and that of M&A is not possible at this time because details of their experiments are not given. However, it is possible, based on their data, to indicate what the probable differences are. It does not appear to be caused by differences in water content, rate of stirring or small differences in the experimental set-up. Their analytical technique for determination of Ti is not described in sufficient detail to evaluate. Careful examination of their paper indicates that the biggest and most consistent difference between this work and that of M&A is the total coulombs passed. They used a galvanostatic technique and passed 900 coulombs. Their cell volume is not given but purely from inspection of the figure, it can be assumed to be about 50 ml. Under these conditions they would have slightly over 0.06M Ti in solution after the dissolution. As shown above, at this concentration of Ti(IV) a reaction with the Ti metal to give Ti(III) appears possible, particularly if the solution stood with the electrode in place after being exposed to air following dissolution. This reaction would lower the value of n . Such a hypothesis needs to be tested.

Our results indicate that the oxidation state is highly dependent on the complexation of the titanium ions. Thus, the dissolution process is influenced significantly by the type and nature of the complex ions in solution. The electrochemical behavior of titanium in various nonaqueous media and its passivation characteristics are of considerable current interest. While it cannot be

denied that short-lived intermediates and surface reactions play a vital role in the metal dissolution behavior and passivation processes, the bulk properties and the electrochemical behavior of soluble couples may be of importance. We have, for example, some very preliminary indication at the present time that the presence of small amounts of water in these HCl methanol solutions gives rise to an additional Ti(III) species which appears short-lived. Because titanium begins to passivate in this medium with small amounts of water present, the formation of this different species may be related. Solution chemistry and the nature of both short- and long-lived species during metal dissolution may thus be of importance, not only in understanding passive behavior, but also stress-corrosion cracking.

Acknowledgment

The authors express their thanks to Drs. F. Mansfeld and I. Goldberg for many helpful discussions during this study.

Manuscript submitted Feb. 3, 1972; revised manuscript received May 15, 1972.

Any discussion of this paper will appear in a Discussion Section to be published in the June 1973 JOURNAL.

REFERENCES

1. B. S. Hickman, H. L. Marcus, and J. C. Williams, Paper presented at International Symposium on Stress Corrosion Mechanisms in Ti Alloys, Jan. 27-29, 1971, Atlanta, Ga. (See also other papers at this Symposium.)
2. R. J. Ambrose and J. Kruger, *Corrosion Sci.*, **8**, 119 (1968).
3. M. C. Scully and D. T. Powell, *ibid.*, **10**, 718 (1970).
4. A. J. Sedriks and J. A. S. Green, *Corrosion*, **25**, 324 (1969).
5. M. Levy and D. W. Seitz, Jr., *Corrosion Sci.*, **9**, 341 (1969).
6. F. Mansfeld, *This Journal*, **118**, 1412 (1971).
7. R. D. Armstrong, J. A. Harrison, H. R. Thirsk, and R. Whitfield, *ibid.*, **117**, 1003 (1970).
8. D. Franz and H. Göhr, *Ber. Bunsenges. Phys. Chem.*, **67**, 680 (1963).
9. M. Pourbaix, *Corrosion*, **25**, 267 (1969).
10. T. C. Franklin and H. V. Seklemian, *J. Inorg. Nucl. Chem.*, **12**, 181 (1959).
11. A. J. Johnson and L. L. Shreir, *Corrosion Sci.*, **5**, 269 (1965).
12. I. R. Leith, J. W. Hightower, and C. G. Harkins, *Corrosion*, **26**, 377 (1970); C. G. Harkins, Preprint, International Symposium on Stress Corrosion Mechanisms in Ti Alloys, Jan. 27-29, 1971, Atlanta, Ga.
13. I. A. Menzies and A. F. Averill, *Electrochim. Acta*, **13**, 807 (1968).
14. M. Stern and A. C. Makrides, *This Journal*, **107**, 782 (1960).
15. F. J. Welcher, "The Analytical Uses of Ethylenediaminetetraacetic Acid," p. 184, D. Van Nostrand Co., Princeton, N. J. (1961).
16. G. Charlot and B. Tremillon, "Chemical Reactions in Solvents and Melts," p. 278, Pergamon Press, New York (1969).
17. I. M. Kolthoff and J. J. Lingane, "Polarography," Vol. 1, 2nd ed., p. 218, Interscience, New York (1952).
18. R. S. Drago and K. F. Purcell, in "Non Aqueous Solvent Systems," T. C. Waddington, Editor, p. 238 ff, Academic Press, New York (1965).
19. N. D. Tomashov and L. P. Verscinina, *Electrochim. Acta*, **15**, 501 (1970).

Anodic Dissolution and Selective Etching of Gallium Phosphide

R. L. Meek* and N. E. Schumaker

Bell Telephone Laboratories, Incorporated, Murray Hill, New Jersey 07974

ABSTRACT

Current voltage curves and the effective dissolution valence have been determined for GaP electrodes in 3N NaOH solution. At electrode potentials of a few volts the current density for p-type ($N_A \sim 4(10)^{17} \text{ cm}^{-3}$) is a factor of 10^4 greater than for n-type ($N_D \sim 4(10)^{17} \text{ cm}^{-3}$) electrodes. This difference allows selective removal of p material from p-n structures. Application of this selective etching to the fabrication of mesa structures for GaP light emitting diodes, and to junction delineation, is discussed. At large current densities, 6 charges are transferred per dissolved GaP molecule in distinction to the 3 transferred charges found previously in alkaline solution at low ($< 2 \text{ mA cm}^{-2}$) current densities.

As III-V compound semiconductor device technology is advanced, it becomes desirable to apply some of the electrochemical processing and evaluation techniques which have proven useful for silicon and germanium (1-3) to those materials. The present paper discusses anodic dissolution and selective etching of gallium phosphide.

In comparison to germanium and silicon, the electrochemistry of the III-V compounds has not been widely studied. The occurrence and nature of surface films (4, 5) and the morphology of the etched surface (5, 6) have been determined for InSb. Several authors have discussed the electrochemistry (7-12) and Nuese and Gannon have described selective etching (13) of GaAs. Memming (14, 15) has studied GaP, but not at the rather large anodic current densities desired for etching and shaping operations.

Experimental

Current density-potential relations were determined in the apparatus of Fig. 1. The electrolyte was 3N aqueous NaOH maintained at 20°C although the exact temperature is not critical. Measurements were made in the dark and potentials are relative to the saturated calomel reference electrode. The samples were of (111) orientation, and both the Ga (111) and P-($\bar{1}\bar{1}\bar{1}$) faces were studied. The faces were distinguished by their chemical etching characteristics in Cl_2 saturated methanol. This and equivalent techniques are ultimately traceable to x-ray evidence. N-type samples were Se doped and p-type samples were Zn doped to a level of about $4(10)^{17} \text{ cm}^{-3}$ and were cut from LEC (Liquid Encapsulated Czochralski) pulled ingots. Ohmic contacts on p-type (n-type) were prepared by evaporating and alloying gold containing 1% Be (2% Si). Surfaces were chemically or mechanically polished, as applicable, before use as electrodes. The number of electronic charges passing through the external circuit per dissolved atom was determined by integrating the current for a certain time and measuring the weight loss with a microbalance.

Results

Current density vs. potential data are summarized in Fig. 2. As expected, n-type ($N_D = 3.5(10)^{17} \text{ cm}^{-3}$) shows current saturation. The value is about $20 \mu\text{A cm}^{-2}$. The p-type material of about the same doping level, $N_A = 4.4(10)^{17} \text{ cm}^{-3}$, is readily dissolved and large currents ($\sim 100 \text{ mA cm}^{-2}$) are drawn at a few volts.

For both n- and p-type the rest potential is more positive for the Ga face. This is in line with Gatos' (6)

* Electrochemical Society Active Member.

Key words: anodic dissolution, selective etching, gallium phosphide, semiconductor electrochemistry, light emitting diodes.

observation that the (111) face of III-V compounds is less reactive than the ($\bar{1}\bar{1}\bar{1}$) face. The J-V curves cross, however, somewhere below the lowest current densities measured. This simply shows that the potential drop across the interface, including both the semiconductor and electrolyte space charge potentials, is different for the two surfaces. Since the arrangement of surface atoms is manifestly different (6), this is not unexpected and depends on the details of the kinetics involved. Below about 0.5 mA/cm^2 the data follow a Tafel slope of about 90 mV/decade (see insert in Fig. 2), rather different from the 120 mV/decade found by Memming and Schwandt (14). It is not wise to attach too much significance to such a Tafel slope since it is the slope on a plot of surface potential vs. current density which determines the surface carrier concentration. The electrode potential also includes the (variable) Helmholtz potential.

It is seen that, for p-type, the Ga face draws a larger current density at a given electrode potential than does the P-face. Note that plotting current den-

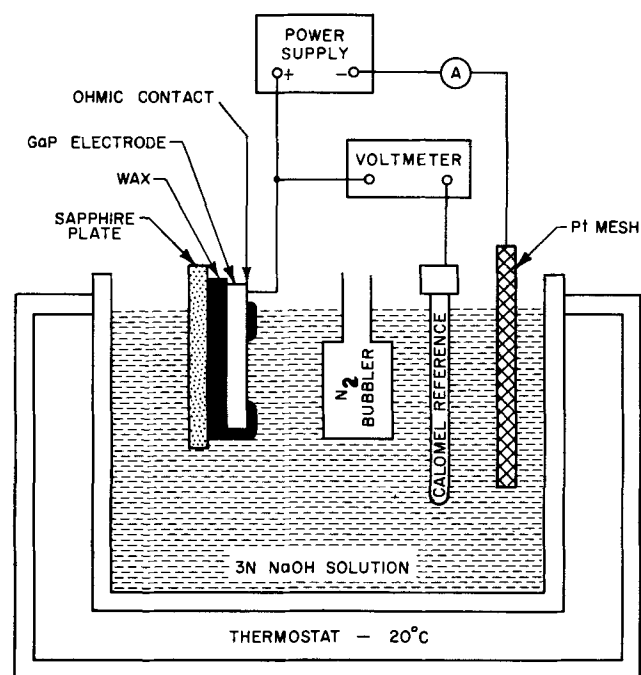


Fig. 1. Schematic of electrolyte cell used for current-voltage determinations. The reference electrode is positioned so as to minimize the contribution of the IR drop in solution.

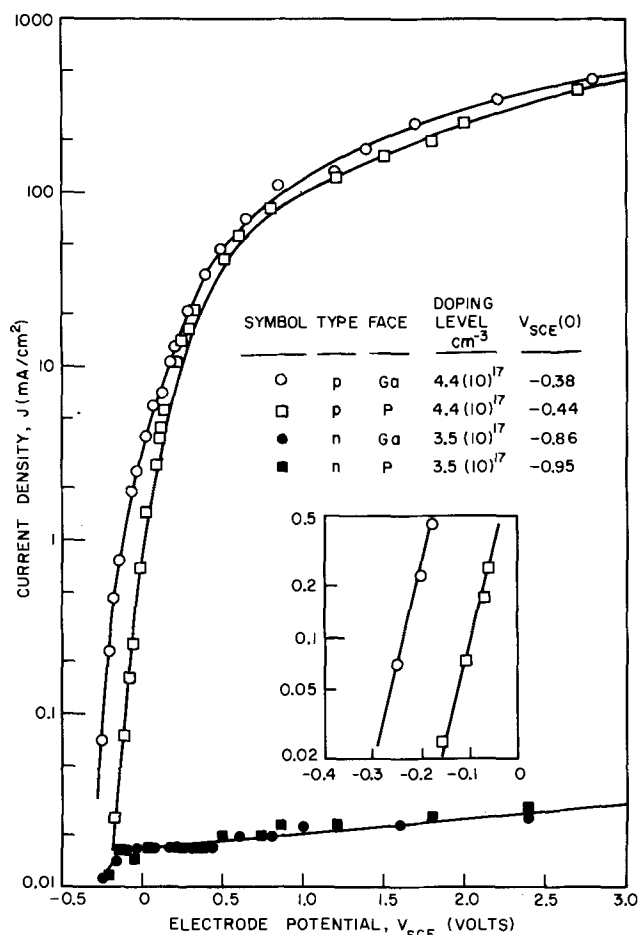


Fig. 2. Current density vs. electrode potential for n- and p-type gallium phosphide electrodes in 3N NaOH.

sity using rest potential as the arbitrary zero does not remove this difference but rather accentuates it. The rest potential is likely not the reversible potential, but rather a corrosion potential and is itself dependent on kinetic considerations.

The data plotted are for situations where no surface film growth is taking place. This is no problem on the P-surface where no film formation and consequent dropoff of current with time is observed. On the Ga face, however, above about 1 mA/cm² a film formation is observed and the current decreases by a factor

of two in a few tens of minutes unless the nitrogen bubbler is implemented as shown in Fig. 1. An intense stream of bubbles is directed onto the electrode so that the solution is vigorously agitated near the electrode. (For the P-face the current is completely independent of whether the bubbler is on or off.) These observations suggest that the reaction on the Ga face is mass transfer limited. It is known that sparingly soluble Ga(OH)₃, or perhaps hydrated Ga₂O₃, is one of the dissolution products (14) so it is expected that a film will form to such a thickness that electrochemical oxidation and dissolution of the oxidation product are balanced. Vigorous agitation reduces the mass transfer boundary layer thickness and allows dissolution of the film. The data presented are well into the range where more intense agitation produces no change in steady current density. It is not at present clear why no film tends to form on the P-face, but it is no doubt related to differences in the detailed reaction paths for the two surfaces. Straumanis *et al.* (9) have also observed that on GaAs a thicker film of Ga(OH)₃ is formed on the Ga face than on the As face.

There is also a difference in structure of the surfaces produced as shown in Fig. 3. The Ga surface has an "orange peel" texture while the P-face is smoothly polished. The features apparent on the P-face are similar to those observed after etching or polishing by other methods and are likely due to bulk crystal defects. The difference in surface roughness is probably sufficient to produce agreement between current density-voltage curves on the two faces at large current densities.

An effective dissolution valence, or electron number, may be defined as the number of electronic charges passing through the external circuit per dissolved atom. The data determined from integrated current and weight loss measurements are plotted in Fig. 4. It is seen that at least for current densities greater than 50 mA/cm² the effective valence is 3; that is, 6 charges per GaP molecule, which is consistent with the supposition that a Ga atom and a P atom dissolve as a unit as suggested by Gerischer (16) for GaAs. However, it is very difficult to explain the film formation on the Ga, but not the P-face in terms of such a model of dissolution.

Gerischer (10) has shown that GaAs is oxidized with the consumption of 6 holes to Ga³⁺ and As³⁺. Any contribution due to conduction band charge transfer is less than 0.1% of the total (11). Memming and Schwandt (14) conclude that, for GaP, dissolution is almost all (90+) per cent by holes. Here it will be assumed that only holes are involved.

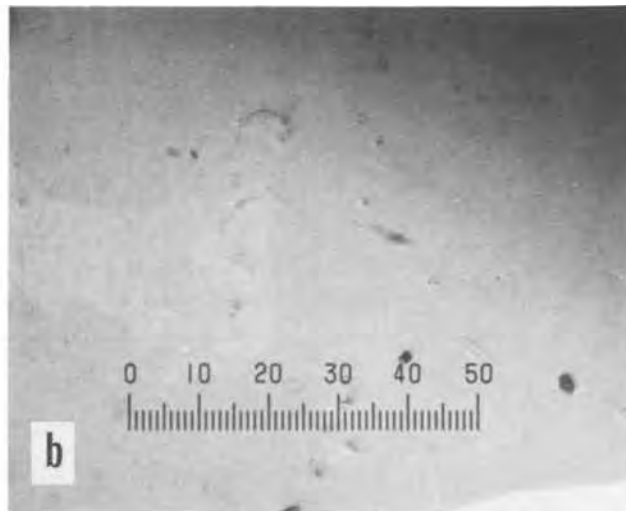
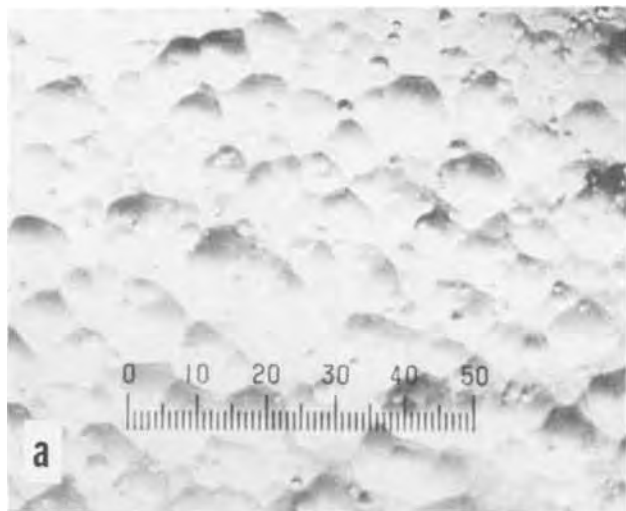


Fig. 3. Photomicrographs of electroetched surfaces after several minutes at $J \sim 200$ mA/cm²: a, gallium face; b, phosphorus face (10 = 100 μ).

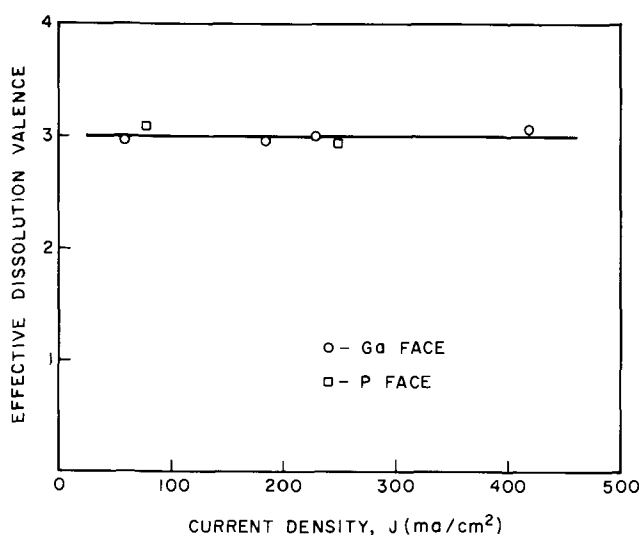
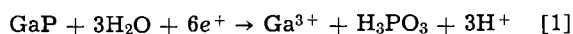


Fig. 4. Effective dissolution valence (or electron number) vs. current density. Symbol size is indicative of experimental uncertainty.

However, Memming and Schwandt (14) found that only 3 charges were transferred per GaP molecule in alkaline solution although 6 were involved in acid solution. Their measurements were based on colorimetric analysis of the solution and were for $J < 2$ mA/cm². They write the over-all reactions as (14)



in acid, and



in alkali. Presumably these are followed by reactions further oxidizing the phosphorus since the phosphorus is found as PO_4^- in either case. Ring-disk studies are in progress in an attempt to identify reaction products (see Appendix).

The fact that, in the present determinations, 6 rather than 3 charges are transferred per GaP molecule implies that some at present unknown reaction replaces Eq. [2]. The change from 3 to 6 cannot be explained on the basis of OH^- depletion at the electrode surface (and consequent reversion to Eq. [1]) since the limiting current for that to occur is expected to be several A cm⁻².

Selective Etching

It is seen from Fig. 2 that at potentials of two or three volts an etch rate ratio of $\sim 10^4$ exists between p- and n-type GaP doped to $\sim 4(10)^{17}$ cm⁻³. This presents the possibility of selectively removing p-material from p-n structures. The p-n configuration is satisfactory for GaP since the diffusion length for holes is short and injection of holes from p to n and

consequent dissolution of the n is unimportant. In silicon, where the diffusion length may be of the order of tenths of millimeters, this is a serious limitation (17) and it is in fact rather difficult to remove p from n without extensive etching of the n.

The samples used were liquid phase epitaxial ZnO doped p-type layers grown on the (111) P-face of n-type substrates. The doping levels were near those for the bulk samples used for J-V determinations. The samples were waxed down to a sapphire plate with p-side up, that is away from the plate, and an evaporated ohmic contact was provided near one edge of the slice. A constant potential source was used and the p-type layer selectively stripped off by lowering the wafer into solution using the same apparatus, which lowers the sample into the solution at a controllable rate, as has been used for similar silicon work described elsewhere [see Fig. 2 and 3 in Ref. (17)].

Junction delineation.—The selective removal of the p-type layer represents an effective means for revealing the p-n interface in a fashion previously unavailable in the study of GaP. Lowering the GaP wafer into solution generates a wedge of p-type GaP with a sharply defined leading edge at the p-n junction as shown in Fig. 5a. This photomicrograph clearly shows the sharp delineation of the p-n interface and also reveals the surface structure of the n-type layer upon which the p-type layer was grown. Vapor etching of the n-layer, or partial dissolution before regrowth, may account for the rough surface exposed.

In addition, Fig. 5a shows gross striations in the p-layer which run parallel to the p-n junction. Higher magnification of the p-n junction region (Fig. 5b) reveals a multitude of small defect structures within 1-3 μm of the actual junction; and we expect that this etching technique will be a valuable tool for defect study and identification.

The nature and cause of the striations and defects revealed by this etching are not understood at the present time. However, the presence of these defects may be expected to have a deleterious effect on device performance and reliability.

Mesa formation for light emitting diodes.—Fabrication of the quasi-planar beam-lead GaP diode requires the formation of isolated p-type mesas from the zinc and oxygen doped p-layer (18). Presently this involves careful control of the p-layer thickness and subsequent chemical etching for times calculated from known etch rates to achieve the desired mesas (19). The preparation of the p-layer is laborious and is necessitated by the limitations of the current GaP liquid-phase epitaxy growth technology which results in nonuniform layers. The use of selective removal of the p-layer by electrochemical etching is an attractive alternative method of mesa formation which, because of its self-limiting nature, should reduce the requirements on layer thickness uniformity.

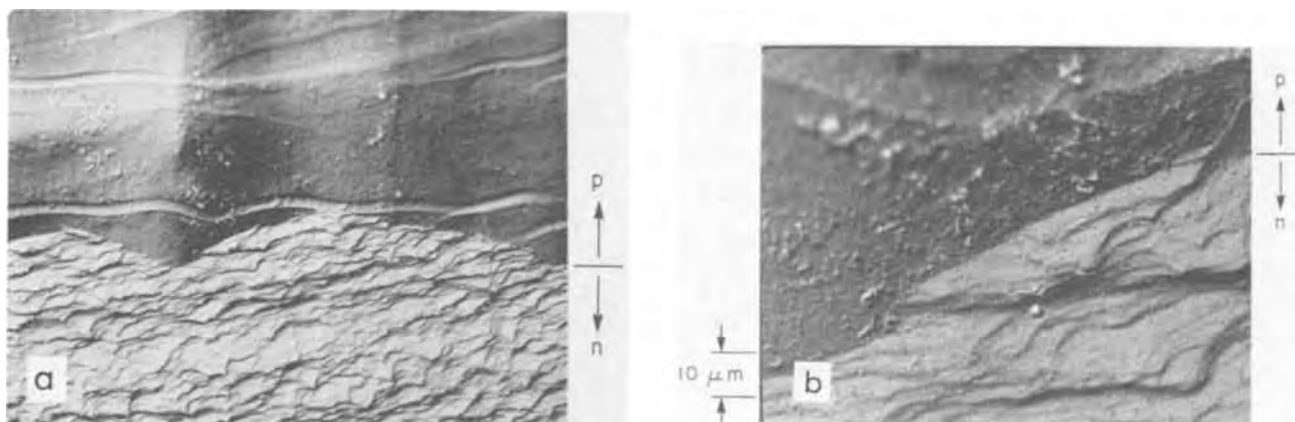


Fig. 5. Sample from which the p-epitaxial layer has been partially removed: a, 160X; b, 1000X.

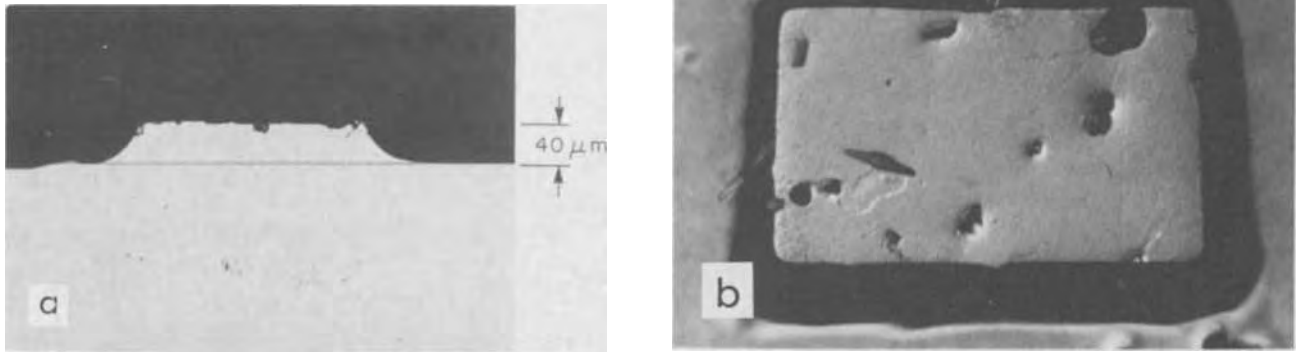


Fig. 6. Etched mesa structures for fabrication of gallium phosphide light emitting diodes: a, cross section view; b, top view

To demonstrate the feasibility of this technique a wafer of GaP with a p-layer $\sim 40 \mu\text{m}$ thick, and an ohmic contact near one edge, was coated with a layer of SiO_2 and a mesa pattern defined by standard photoresist technique. The wafer was subsequently etched as described above. A representative mesa formed by electrochemical etching is shown in Fig. 6a and 6b. The cross-section view indicates a smoothly contoured surface on the sides of the mesa. The p-n junction has been delineated on the cleavage face by etching in warm HNO_3 and clearly indicates the selective removal of the p-layer. The top view of a mesa in Fig. 6b shows that the mesa is quite uniform in size. The mesa is smaller than the original mask size. The undercutting of the mask, U is expected to be equal to the etch rate times the total time etched; that is

$$U = E L/R$$

where E is the etch rate, L is the length of the wedge

produced as the slice is lowered into solution (17), and R is the lowering rate. Since

$$R = LE/T$$

where T is the thickness of the layer removed (17)

$$U = T$$

That is, on the average, the mask is undercut by an amount equal to the layer thickness. That this is approximately true can be seen from Fig. 6. There is also a differential in the undercutting from one side of the mesa to the other since the slice is lowered into the solution. That is, there is a tendency to form a mesa with a trapezoidal rather than rectangular top. This differential is given by

$$\frac{\Delta U}{U} = \frac{WE}{RT}$$

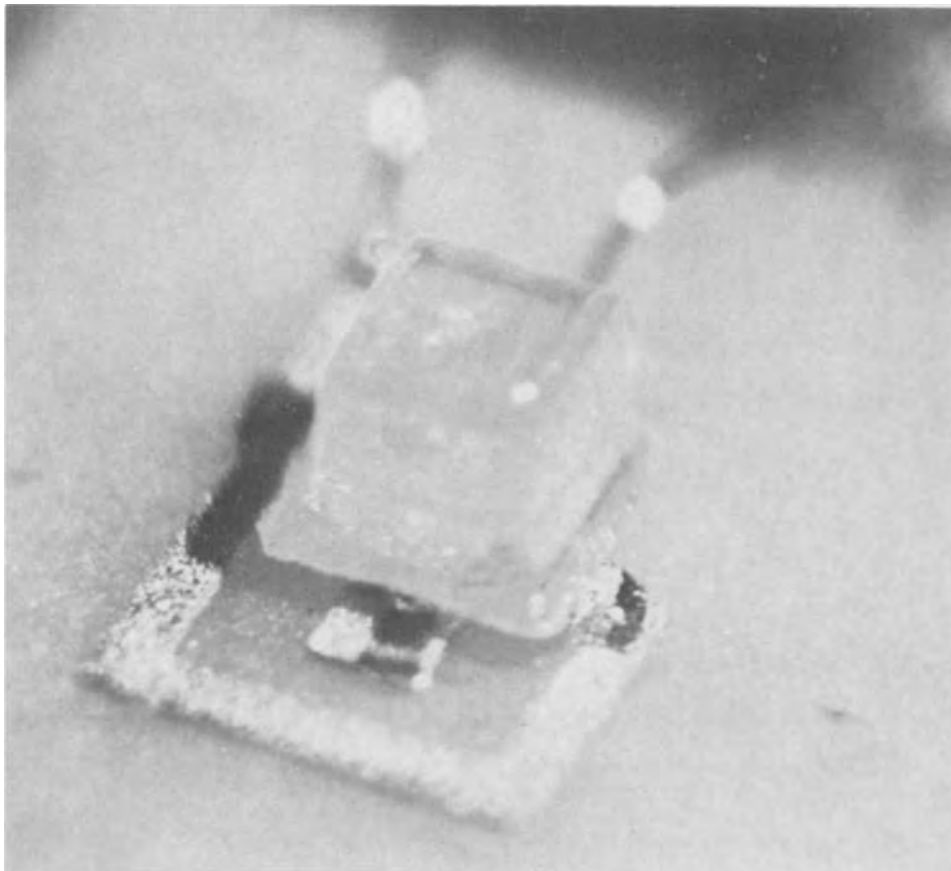


Fig. 7. Completed, quasi-planar beam lead diode.

where ΔU is the difference in undercutting from top to bottom and W is the mesa dimension in the lowering direction. Clearly, to minimize this, R should be large and E (or equivalently the potential) should be small. For $T = 25\mu$, typically $R = 3$ cm/hr and $V_{\text{cell}} = 4$ V. Of course V_{cell} must not be too small or R too large or else potential drops down the tapered slice become large and etch through nearest the contact, and consequent premature isolation occurs. It is important to note that, since the etching is electrochemical rather than chemical, the undercutting stops as soon as the p-layer between mesas is etched away; or, more precisely, any further etching is limited by the current drawn through a reverse biased p-n junction.

The defects and entrapped crystallites apparent in Fig. 6 were due to the nature of the material before etching and do not appear in device quality material. Figure 7 is a photomicrograph of a completed, quasi-planar LED (Light Emitting Diode) bonded to a ceramic chip. The device is roughly 250μ on a side, and typical device parameters are 10 mA at a forward voltage of 2V with an unencapsulated quantum efficiency of 2%.

Acknowledgments

We wish to thank M. Kuhn for his interest in and encouragement of this work; and P. J. Boddy and D. M. MacArthur for their interest in the electrochemical aspects.

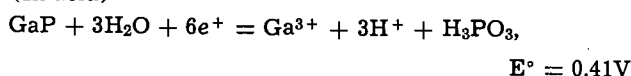
Manuscript submitted Nov. 22, 1971; revised manuscript received March 30, 1972. This was Paper 185 presented at the Cleveland, Ohio, Meeting of the Society, Oct. 3-7, 1971.

Any discussion of this paper will appear in a Discussion Section to be published in the June 1973 JOURNAL.

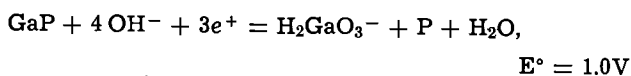
APPENDIX

Consideration of the inorganic chemistry of gallium and phosphorus [W. M. Latimer, "The Oxidation States of the Elements and Their Potentials in Aqueous Solutions," Prentice-Hall, Inc., Englewood Cliffs, N. J., (1952)] in light of the above discussion, and the fact that phosphine is observed to be liberated in all cases, suggests that:

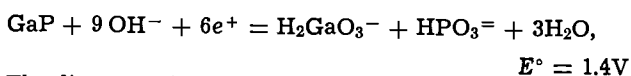
(In acid)



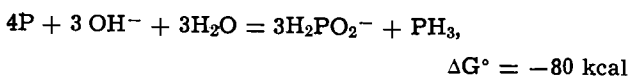
(In alkali, $J \lesssim 10$ mA cm⁻²)



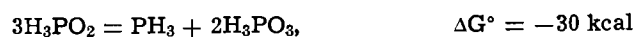
(In alkali, $J \gtrsim 10$ mA cm⁻²)



The disproportionation reactions



and

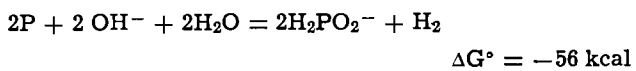


have rather large negative free energies and may partially account for the further oxidation of P at low current densities in basic solution.

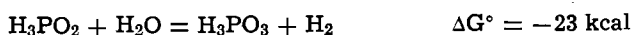
Since the phosphorus is finally found in the +5 oxidation state, and as phosphine, we presume that the reaction



which has a small positive free energy is pushed to right because of evolution of phosphine from the solution. Some hydrogen is expected to be evolved in basic solution through



and



competing with the disproportionation reaction. Ring-disk studies (D. M. MacArthur, private communication) indicate 1 to 10% of the phosphorus follows this reaction path. The fact that 6 charges are transferred at larger potentials, current densities, indicates that there, for reasons not particularly apparent but perhaps related to the PH_3 concentration, the phosphorus is more likely to enter into a reaction involving further charge transfer than into the disproportionation reactions.

REFERENCES

1. E. A. Efimov and I. G. Erusalimchik, "Electrochemistry of Germanium and Silicon," Chap. 9, Sigma Press, Washington (1963).
2. V. A. Myamlin and Yu. V. Pleskov, "Electrochemistry of Semiconductors," Chap. 5, Plenum Press, New York (1967).
3. J. I. Pankove, in "The Electrochemistry of Semiconductors," p. 290, P. J. Holmes, Editor, Academic Press, London (1962).
4. J. F. Dewald, *This Journal*, **104**, 244 (1957).
5. M. E. Straumanis and L. Hu, *ibid.*, **118**, 433 (1971).
6. H. C. Gatos and M. C. Lavine, *ibid.*, **107**, 427 (1960).
7. J. P. Krumme and M. E. Straumanis, *Trans. Met. Soc. AIME*, **239**, 395 (1967).
8. W. W. Harvey, *This Journal*, **114**, 472 (1967).
9. M. E. Straumanis, J. P. Krumme, and W. J. James, *ibid.*, **115**, 1050 (1968).
10. H. Gerischer, *Physik. Chem.*, **69**, 578 (1965).
11. H. Gerischer and J. Wallem-Mattes, *Z. Physik. Chem.*, **64**, 187 (1969).
12. L. N. Vozmilova, E. V. Buts, and G. B. Kaplum, *Sov. Electrochem.*, **4**, 629 (1968).
13. C. J. Nuese and J. J. Gannon, *This Journal*, **117**, 1094 (1970).
14. R. Memming and G. Schwandt, *Electrochim. Acta*, **13**, 1299 (1968).
15. K. H. Beckman and R. Memming, *This Journal*, **116**, 363 (1969).
16. H. Gerischer and J. Mattes, *Ber. Bunsenges.*, **69**, 578 (1965).
17. R. L. Meek, *This Journal*, **118**, 1240 (1971).
18. N. E. Schumaker, M. Kuhn, and R. A. Furnanage, *IEEE Trans.*, **ED 18**, 627 (1971).
19. L. A. Koszi, Private communication.

Organic Reactions in Gas Discharges Leading to Polymer Deposits

Arthur Bradley*

Surface Activation Corporation, Westbury, New York 11590

ABSTRACT

The ultimate products of static gas discharge in organic vapor are solid polymer deposits and inorganic gases. Analyses by gas chromatography of decomposition intermediates suggested common routes for many systems. Characteristic plasma reactions are decarbonylation and dehydrogenation, with solid resins arising via migration of ionized unsaturated species to the electrodes where they recombine as energetic neutral fragments. The last organic residue found in the vapor state after exhaustive discharge decomposition of any hydrocarbon is acetylene. Experimental evidence of the formation of the trifluoromethyl radical from perfluoroacetone is presented.

With very few exceptions, organic vapors subjected to excitation and ionization in an electrical discharge yield polymeric deposits on the electrodes. The process as a means for producing useful thin film coatings was patented in 1960 (1). The commercial possibilities which this new plasma technology suggested have provided the incentive for more than a decade of intensive applied research (2). There has been particular attention paid to fluorocarbon deposits, which may have utility as protective or water-repellent coatings, as dielectric layers, or release agents, but there are no substantial commercial applications at present.

Although the importance of normal chain propagation in gas discharge polymerization is doubtful, unsaturated "monomers" give the best adherent and coherent films. The deposits from aliphatic hydrocarbons and other simple organic compounds are brittle and of low utility. This paper attempts to explain these and related observations by considering the probable routes of decomposition and recombination of organic fragments in a plasma/electrode environment. There are no mechanisms presented but some apparently consistent and predictable reaction sequences are discussed.

Rates of conversion of organic vapor to solid polymer in terms of grams per kilowatt-hour have been determined for many compounds (3). Conventional monomers such as styrene and methyl methacrylate do not deposit films much faster than ethyl benzene or methyl acetate unless the electrodes are chilled to near the condensation point of the vapor. Direct-current discharges yield ten times as much polymer on the cathode as the anode. It seems likely that there is little or no polymerization in the vapor state and that molecules reach the electrode as positively charged fragments which are there converted to highly energetic neutral species.

We have speculated that polymerization results from random recombination of open bonds on the electrode surface, with no propagation in the ordinary sense (3). Nevertheless, the deposit from styrene shows many of the structural features of conventional polystyrene (e.g., similar IR spectra); that from tetrafluoroethylene is not unlike Teflon.

A static discharge (no exhaust or inflow of gas) in certain monomers results in a gradual decrease in pressure, indicating that severe fragmentation does not occur before species are ionized and drawn to the cathode. In general, these give the better quality films, and are discussed in some detail later in this report. On the other hand, aliphatic hydrocarbons, even unsaturated ones, as well as simple alcohols, ketones, car-

boxylic acids and esters, tend to decompose in the plasma. Polymer deposits obtained from methane, methanol, ethane, propane, isobutylene, hexane, acetone, ethylene, and acetylene were all similar in appearance, chemical composition (low H to C ratio), and physical properties. In each case, the polymer formed nonadherent brittle flakes or crumbled to powder. It is proposed that these solids all had a common antecedent: plasma decomposition intermediates such as ethylene and acetylene.

There is no general agreement in the extensive gas discharge literature on even the broadest aspects of polymer formation, much less on a mechanism (4, 5). Some authors visualize the organic monomers condensing on the electrode and there polymerizing after initiation by electron or ion bombardment (6-8). This might be appropriate for styrene but not for benzene, acetylene, or a host of saturated hydrocarbons. Others have, like us, found evidence of decomposition of the parent molecule in the plasma followed by recombination at the electrode surface (9-12).

Some of our more specific findings have been previously described. The similarity of deposits from styrene and ethyl benzene was reported by Brick and Knox (4). McTaggart (10) detected ethylene and ethane as by-products of the plasma polymerization of all paraffins from methane to decane and noted that the polymer obtained was not physically distinguishable from that deposited from acetone or methanol.

Vastola and Wightman (12) found that methane, ethane, and ethylene all deposited hydrocarbon films of similar composition in a microwave discharge. In each experiment, the by-product gas mixture was about 95% hydrogen plus a mixture of all three hydrocarbons and acetylene in approximately equal quantities (by mass spectroscopic analysis). Furthermore, the infrared spectra of the films from ethane and ethylene were found to be superimposable. Unfortunately, no spectral comparison with the acetylene deposit was reported. These authors suggest that the CH fragment might be a common intermediate in the deposition of solid polymer films from hydrocarbon gas discharges.

Williams and Hayes (8) found that no polymerization occurs on the anode of a d-c discharge and so dismissed the importance of electron bombardment. They recognized the advantage of condensation on a chilled electrode and concluded that glow discharge polymerization probably occurs exclusively at the electrode surface. However, since they confined their work to conventional monomers, they were inclined to overlook routes which involved neither initiation nor propagation. These authors proposed a classification of monomers by rate of reaction based on their likelihood to be adsorbed on electrode surfaces. The favored monomers on their list could also be described as the

* Electrochemical Society Active Member.

Key words: gas chromatography, plasma, thin films, acetylene, trifluoromethyl.

least likely to decompose in C₂ hydrocarbon intermediates.

Experimental Results

A large bell jar (18 in. diam) was used as the plasma reaction chamber. Pairs of clean tin-plated steel electrodes (0.006 × 4 × 6 in.) were mounted parallel and approximately 0.5 in. apart for each experiment. Gases were introduced via a feedthrough in the baseplate directly from commercial gas cylinders. Liquids were contained in a 250 ml round bottom flask attached by an O-ring seal "quick-coupling" to a fixture at the underside of the baseplate. A vapor pressure of at least 2 mm at room temperature was the only physical requirement of a "monomer." Alternating voltages of 3000-10,000 Hz were applied to the electrodes, approximately 300V being required (at 2 mm) to achieve a stable discharge covering the entire electrode surface. Discharge currents were maintained between 20 and 25 mA for the duration of experiments which lasted from 5 to 30 min.

Although a relatively small portion, much less than 1%, of the volume of gas contained in the bell jar was actually between the electrodes at any one instant, it appeared that circulation was excellent and that the body of gas was being acted upon uniformly. In many experiments, after 30 min there was only a trace of the original vapor left.

At the beginning of each experiment the bell jar was evacuated to below 0.05 mm with an oil pump. The gas or vapor from the liquid reservoir was admitted until the pressure reached 2 mm and then all valves were closed. Film depositions were carried out with no attempt made to maintain a constant pressure. It is characteristic of acrylonitrile and tetrafluoroethylene that the pressure decreases in such static discharges; with most materials there was a gradual pressure rise as hydrogen and other by-products accumulated.

Aliquots of the gas mixture were taken at intervals for analysis by an F & M Model 810 gas chromatograph. A sample of 25 cc at 2 mm was generally sufficient for identification of the major components on an activated charcoal column. The sampling chamber was opened to the column for 60 sec; 3 min later a programmed heating cycle began which raised the column from room temperature to 380°C in another 12 min. High-purity helium was employed as the carrier gas with a thermal conductivity detector registering each component as it emerged from the column. Most identifiable peaks were recorded on the chart by the time the heat cycle had reached its maximum temperature. It was kept hot for another 15 min to remove any residual components of the previous experiment before cooling to room temperature again for the next sampling.

Gases obtained for this investigation in standard cylinders from the Matheson Corporation included hydrogen, nitrogen, oxygen, carbon monoxide, carbon dioxide, methane, ethane, ethylene, acetylene, propane, isobutylene, tetrafluoromethane (Freon-14), fluorofrom (Genetron-23), hexafluoroethane (Freon-116), and perfluoropropane. Hexafluoroacetone was obtained from the General Chemical Division of Allied Chemical Corporation, Baton Rouge. Tetrafluoroethylene was supplied by the Thiokol Corporation, Moss Point, Mississippi.

Reagent grade acetone, methanol, and hexane were obtained from a commercial laboratory supply house. Acrylonitrile, methyl methacrylate, and allyl methacrylate were supplied by the Monomer Polymer Laboratories, Philadelphia.

In a typical experiment, hydrogen appeared as a sharp peak on the descending shoulder of the initial sampling response, barely 30 sec after the sampling chamber was closed (detected at the 1.5 min mark in Fig. 1, for example).

Oxygen and nitrogen were indistinguishable, the "air" peak coming at 2.5 min, followed by carbon

monoxide at 3, methane at 5, carbon dioxide at 8, and the family of C₂ hydrocarbons, usually acetylene > ethylene > ethane, between 10.5 and 13 min. Perfluorinated analogs appeared at almost the same intervals as the hydrocarbons. Fluoroform (trifluoromethane) was released from the column after tetrafluoromethane and before hexafluoroethane, as shown, for example, in Fig. 2.

Chromatograms under standard conditions were taken for each gas individually before they were identified as components of a mixture. Thus the peak for fluoroform alone was superimposable on the 8.5 min peak found in the hexafluoroacetone decomposition carried out with the electrodes wrapped with Mylar film.

Infrared absorption spectra for acrylonitrile film deposited on KBr pellets were recorded on the Perkin-Elmer Model 21 double-beam spectrophotometer. Peaks characteristic of primary, secondary, and tertiary amines with various hydrocarbon substituents were observed.

Powders and flakes of polymer removed from the electrodes (or gathered from where they had fallen) were submitted to the Schwarzkopf Analytical Laboratory, Woodside, Queens, New York. Some preparations were from a static gas phase and some had a continuous flow of fresh feed vapor and exhaust. Elemental analyses of C and H always totaled considerably less than 100% because of oxygen and some nitrogen absorbed by the polymer upon exposure to air. The oxygen take-up was not reduced by maintaining the bell jar vacuum for 6 hr after an experiment. Acrylonitrile polymer had lost about one-fifth of its nitrogen, indicating that perhaps 80% of the deposit was derived from intact monomer. The H/C ratio for acrylonitrile deposit suggests that many of the lost nitrogen atoms were fragmented as CN. Some typical analyses are given in Table I.

The absorption of oxygen by powdery organic polymers bristling with free radical sites was expected, but the trapping (or "fixation") of nitrogen by the same process was something of a surprise. Other workers who have detected nitrogen in glow discharge polymer have attributed it to air contamination of the hydrocarbon vapor (13).

The complete chromatogram records of this investigation would include some sixty readout charts. It is convenient to illustrate how these chromatograms were utilized with one chart for allyl methacrylate (Fig. 1) and two for hexafluoroacetone (Fig. 2). Features of the various chromatogram readouts applicable to other compounds are introduced where the specific plasma experiments are discussed in the following paragraphs.

Discussion

Since most organic compounds decompose when thermally excited to a small fraction of 1 eV, it is not surprising that even "cold plasma" energies (14) up to 15 eV tend to disrupt molecules extremely rapidly. Under the conditions described in this report, only acetylene and certain perfluorinated hydrocarbons survived the equivalent of 10 sec continuous plasma exposure, and that spread out over a 30 min period.

Any compound that can remain intact long enough for its ion to reach an electrode surface will be incorporated into a polymeric deposit forming thereon.

Table I. Typical analyses

Polymer from	%C	%H	%N	H/C ratio
Methane, static	78.4	7.02	0.85	1.07
continuous flow	69.8	6.3	—	1.08
Ethylene, static	72.1	6.8	—	1.13
Isobutylene, static	81.7	8.07	0.11	1.19
continuous flow	78.9	7.8	0	1.18
Hexane, static	81.6	8.0	—	1.18
Acrylonitrile	68.8	6.4	20.4	1.12
(Theory, C ₃ H _{3.5} N)	(67.9)	(5.7)	(26.4)	(1.00)

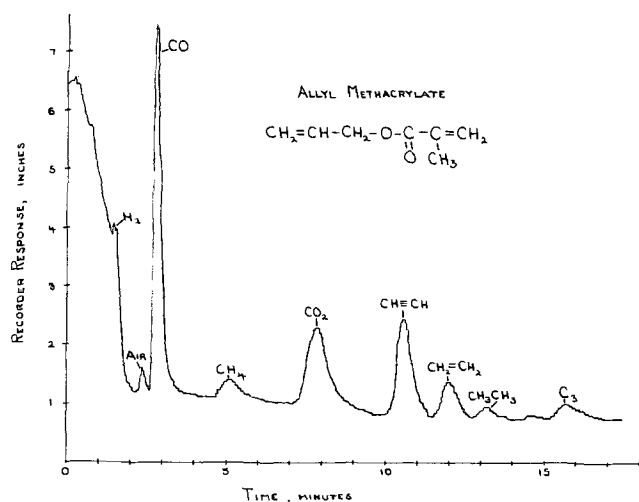


Fig. 1. Gas chromatogram of intermediate products from gas discharge in allyl methacrylate vapor (2 mm).

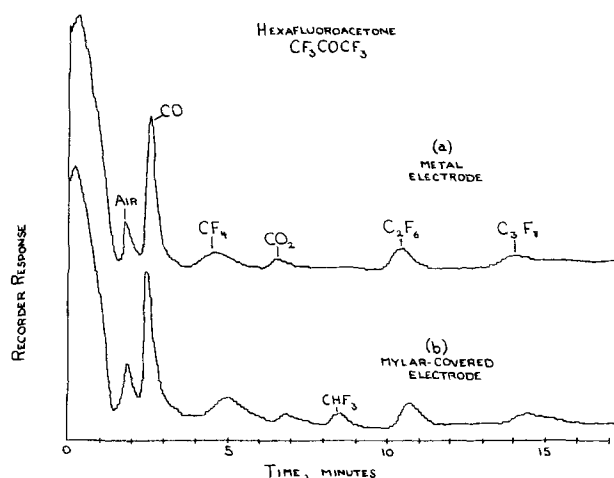


Fig. 2. Gas chromatogram of products from plasma decomposition of hexafluoroacetone vapor (3 mm) with (a) metal and (b) Mylar electrodes.

This type of molecule, even when unsaturated and presumably polymerizable, is rare. Thus isobutylene, C_4H_8 , yielded a polymer $C_4H_{4.8}$. Hexane gave a deposit of the same composition. The methane polymer was approximately $CH_{1.1}$. We must begin to suspect a common intermediate. By what route does this intermediate arise? Is it related to the well-known plasma synthesis of acetylene from methane (12, 15)? Clearly, there must be some pattern to these observations.

Plasma decomposition reactions.—Dehydrogenation is the most rapid single decomposition step, even for methane, where CH_2 is the "radical species present in important concentration" (15). Since the concentration of hydrogen builds up rapidly under plasma conditions, a certain amount of the reverse reaction (hydrogenation) also occurs in all systems. The result is that regardless of the starting composition, all hydrocarbon residues tend toward the same (gradually disappearing) mixture of ethane, ethylene, and acetylene. These three peaks are characteristically accompanied by hydrogen and methane, as illustrated in Fig. 1. Oxygen from organic compounds is often found both as carbon monoxide and carbon dioxide. The free element may also be observed as a decomposition product of carbon dioxide or water.

The actual equilibrium concentrations of C_2H_2 , C_2H_4 , and C_2H_6 in the presence of excess hydrogen in a discharge plasma are unknown, but they would certainly favor the triple bond compound. Acetylene is the last

surviving organic identifiable in the gas phase after exhaustive discharge of almost any compound containing carbon and hydrogen. Presumably it is consumed only by polymerization to C-H solid residues; elemental carbon was not observed as a product in this investigation, however long the plasma was sustained. It remains a possibility that ethylene or other unsaturated species could also yield polymer without breaking down to acetylene first, but H/C ratios in deposits from hydrocarbon plasmas consistently approach unity.

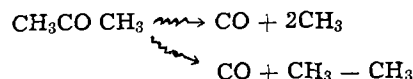
Ethane releases hydrogen faster than any other feed gas subjected to glow discharge. In one experiment, approximately 90% degraded in 15 min, at which time were observed 5% acetylene and lesser quantities of methane, ethylene, and a C_3 moiety. The hydrogen peak corresponded to 150% of the original volume of ethane.

Ethylene gives the same intermediate products during the course of its plasma degradation, although in different proportions. Methane and ethane peaks are barely more than traces. The yield of hydrogen from completely spent ethylene is half that obtained from similarly depleted ethane. The conversion to solid polymer is essentially quantitative in both cases. Unfortunately, the flaky, intractable solid bears no resemblance to polyethylene in any respect (unless the latter has been cross-linked and degraded by excessive radiation to a crumbly powder).

After dehydrogenation, the next most characteristic plasma reaction is decarbonylation. Carbon monoxide is one of the more stable species and one of the last survivors of exhaustive discharge treatment. The products observed in the early stages of glow discharge decomposition of acetone vapor indicate that the ketone decomposition quickly yields hydrocarbon fragments which then proceed via the ethane-ethylene-acetylene subsystem to polymeric deposits. Thus, after 10 min glow between metal plate electrodes, acetone yielded the products listed in Table II.

The high proportion of ethane suggests that there is a route from acetone to hydrocarbon that does not require free methyl radicals to be released, although some part of the C_2 concentration probably results from reactions of C_1 fragments. The consumption of methane certainly requires some such path. It is believed that once CO is released by the parent vapor it takes no significant part in the subsequent reaction scheme. Attempts to react CO with hydrocarbons in separate experiments have not been successful.

It is proposed that the initial decomposition of acetone follows both these routes



As the reactions continue on further discharge treatment, the proportions of C_2 fragments remain fairly constant and a C_3 peak appears. The parent ketone is completely depleted after 30 min and shortly thereafter all hydrocarbon peaks disappear, leaving solid deposit, hydrogen, carbon monoxide, some air from leakage, and traces of carbon dioxide. These are the same products, including the same quality polymer film, obtained from exhaustive plasma degradation of

Table II. Intermediate species identified in plasma degradation of acetone (% by volume)

Species	% by volume
Unreacted acetone	50
Hydrogen	About 30
Carbon monoxide	50
Methane	5
Ethane	9
Ethylene	3
Acetylene	7
Solid polymer (by weight)	About 25

ethane or ethylene, except for the carbon monoxide (which eventually begins to react with the hydrogen, see below).

It is of interest to review at this time the decomposition of the related perfluorinated ketone hexafluoroacetone. With this compound, decarbonylation is again the first degradation step. The reaction sequence is simpler, however, because C_2F_6 has little or no tendency to defluorinate. No significant amounts of C_2F_4 or C_2F_2 appear and only traces of solid can be found on the electrodes and these are probably due to impurities or leakage. This lends support to the hypothesis that the polymer in the hydrocarbon system is derived from unsaturated C_2 fragments.

The products observed after a 15-min discharge in hexafluoroacetone are CF_4 , C_2F_6 , and C_3F_8 . An experiment was carried out in which one electrode was covered with plastic film (one-mil Mylar polyester), serving as a source of hydrogen. This led to formation of fluoroform CHF_3 as an additional product and confirms that the perfluoromethyl radical CF_3 was an intermediate and probably participated in the reaction sequences leading to the various fluorocarbon products. Figure 2 reproduces the chromatograph record of the discharge products from hexafluoroacetone on metal (a) and organic (b) electrodes.

The type of experiment in which discharge products are allowed to react with substrates covering the electrodes can be extremely informative. The possibilities were by no means adequately explored in this investigation. However, one reaction, unrelated to the main subject matter of this paper, was examined, and the results are presented here as an aside of possibly general interest.

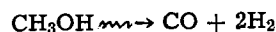
Reactions of polymer surfaces with oxygen plasma.—Oxygen was introduced at pressures of 2–4 mm into an electrode chamber in which the electrodes were variously wrapped with polyethylene, polypropylene, polyester film, and polyester fabric. In all cases CO_2 peaks appeared soon after discharge commenced and steadily grew in height as the condition was maintained. The area of the peaks corresponded to about one-third conversion of O_2 to CO_2 in 30 min with no sign of slowing down (Table III).

It has long been known that a polymer film exposed to an air discharge experiences changes in wetting angle and printability, and it has been shown that oxygen is incorporated onto the surface in the form of ether, carbonyl, carboxyl, hydroxy, and peroxy groups (16). It was not anticipated, however, that so much carbon would be removed from the substrate by the excited oxygen species. Cleavage of polymer chains must contribute heavily to the disruption of the surface and, in fact, must generally precede the formation of new oxidized groups. The accompanying lowering of the average chain length of polymer molecules gives real meaning to the term "oxidative degradation" as applied to the effects of corona discharges in air.

Conversion of methanol to polymer.—Before discussing methanol reactions it is first necessary to refer again to the reduction of carbon monoxide with hydrogen. The results of a plasma study of these gases were disclosed by Blaustein and Fu in 1967 (17). Although previous workers had found only methane as a product,

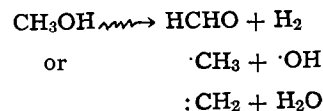
these workers identified the intermediates ethane and acetylene on the inevitable route to polymer, both in far greater quantity than could be accounted for by any specific reaction involving CO and H_2 . Oddly, ethylene was not found. Nevertheless, it appears that the methane-to-polymer route followed the familiar pattern outlined above involving a set of C_2 hydrocarbons.

It will be noted that no methanol was found as a product of a CO- H_2 plasma, although this reaction readily occurs at high pressure and is of commercial importance. However, the reverse reaction



predominated when methanol was used as feed gas in our discharge experiments. It is not surprising that within the first 10% decomposition of methanol, traces of methane and ethane were detected as gaseous by-products and the beginnings of polymer deposit observed. Longer treatment increased the peaks and added acetylene, and by the time the methanol was gone the usual organic residues had appeared in their typical proportions.

From what we know of the reactions in a CO- H_2 plasma (17), all of the products from methanol can be accounted for. There remain, however, possible minor contributions from alternate routes of decomposition, such as



These modes of degradation could lead to the same hydrocarbon intermediates. Neither formaldehyde nor water would have been detected by the analytical technique employed.

Polymerization of other monomers.—The foregoing has presented a possible common-denominator route for polymerization of a number of simple organic compounds in a gas discharge. The remainder of this paper surveys larger and more unsaturated molecules which show some evidence of conversion to solids by alternate routes. It particularly refers to the importance of temperature control of the electrodes. If the comments tend toward over-generalization the author can only plead that he has tried to assimilate the collected impressions of a generation of affiliated workers while maintaining one consistent over-all point of view.

Aromatic "monomers" such as benzene, toluene, naphthalene, pinene, thiophene, and pyrrole were not investigated by gas chromatography. Their film properties (3, 18) suggest that they are not converted to polymer solely via unsaturated C_2 hydrocarbons. This group, which might also include butadiene and cyclopentadiene, probably polymerize via larger ionized fragments containing multiple unsaturation. Their vapors deposit stable, adherent films from a discharge plasma, although it is well to restrict the thickness to 1 or 2μ . In thicker layers they crack and peel away from the substrate; they lack the flexibility, tenacity, and cohesion necessary to form a protective coating, nor do they conform well to an unusual shape.

It might be expected that genuine organic monomers (vinyl or allyl compounds with mildly polar functional group substituents) would deposit polymer from a gas discharge without producing a family of degradation products. In actual practice, no monomer fulfills this ideal behavior, but acrylonitrile probably comes as close as any.

The pressure in a chamber containing acrylonitrile begins to drop the moment a discharge is turned on. Only minor by-products appear: small peaks attributable to nitrogen and acetylene are observed after a few minutes. No detectable hydrogen, methane, ethane, or ethylene are produced as the conversion to solid continues.

Table III. CO_2 from O_2 discharge reactions with substrates

Peak heights, inches, from gas chromatograph

Electrode covering	CO_2 , 10 min	CO_2 , 30 min
None (control)	0.10	0.35
Polyethylene film (HD)	1.3	5.8
Polyethylene film (LD)	1.9	7.2
Polypropylene film	2.0	7.0
Polyester film (Mylar)	1.15	4.3
Scoured polyester fabric (Vycron)	2.3	7.6
Greige polyester fabric (Vycron)	2.4	8.4

Table IV. Organic "monomers" classified by polymerization route

Category	Description	Examples	Remarks
I	Polymerization is essentially via whole molecule	Acrylonitrile Perfluorinated olefins	Yield and quality of film not directly related to temperature of electrodes
II a	Molecule has tendency to degrade into large fragments with conjugated unsaturation which also polymerize	Styrene Vinyl pyrrolidine	Chilling electrode to near condensation point of monomer improves yield, and properties of film approach those of "conventional" polymer
II b	There is competition between whole-molecule polymerization and the slow route via C ₂ hydrocarbon intermediates	Allyl methacrylate Diallyl sulfide	Condensation conditions help in producing good quality films
III a	Principal route to polymer is via unsaturated fragments	Benzene Dicyclopentadiene	Control of electrode temperature probably has little or no effect
III b	Only route to polymer is via C ₂ hydrocarbons	Methane Acetone	No decent film obtained under any conditions

Analytical results suggest that only about 20% of the acrylonitrile polymer is derived from degradation products. However, it is believed that much of the direct polymerization involves the nitrile group. Amines of all description have been detected by infrared analysis, and the richly colored deposit absorbs oxygen readily, suggesting conjugate unsaturation. These observations are consistent with a nonpropagation model for polymerization, new bonds forming according to the random orientation of the various species immediately after being neutralized at the electrode. An acrylonitrile cation, formed in the plasma by electron bombardment, might carry most of its charge on the nitrile carbon, decreasing the probability of the nitrile function remaining intact in the macromolecular film deposit.

Yield alone does not give a clue to the degree of fragmentation, but rapid film deposition monomers like acrylonitrile, styrene, and acrylic acid will be sure to rank with the best in preserving monomer integrity into the solid. On the other hand, the perfluorinated olefins, lacking a defluorination mechanism analogous to dehydrogenation, are also polymerized fairly intact, although at a much slower rate. Polytetrafluoroethylene films prepared for capacitance use had essentially the same dielectric constant as bulk commercial Teflon, and came within one order of magnitude of its extremely low power factor (2).

A number of organic monomers roughly classifiable as unsaturated esters have been successfully used for producing colorless protective films over metal surfaces (2). It was somewhat surprising and disturbing therefore to find that they released the same family of related decomposition products as the simple oxygen-containing feed gases methanol and acetone. Thus, allyl methacrylate and methyl methacrylate gave carbon monoxide, carbon dioxide, acetylene, ethylene, and ethane, in the opening minutes of glow, in this decreasing order of importance. After 10 min, the CO peak had increased disproportionately, towering five times above those of CO₂ and acetylene, which in turn overshadowed ethylene, ethane, and the newly appeared methane and C₃ peaks (Fig. 1). Considerable hydrogen was also indicated at this time. Further discharge treatment (15 to 30 min) resulted in exhaustion of the hydrocarbon fragments, leaving traces of acetylene as the last survivor.

It must be concluded that one or more decarbonylation mechanisms compete with direct polymerization, and therefore, the solid product obtainable from these monomers (above condensation, at least) must contain a significant proportion of the C₂-hydrocarbon polymer previously characterized as undesirable in this report. This work suggests the importance of temperature control in custom deposition beyond that of yield or thickness. Gas phase reactions probably generate hydrocarbon fragments under all conditions, but a chilled substrate attracting a swarm of neutral monomer molecules converts some of these charged fragments to good use as initiators, and others may be harmlessly incorporated as copolymer.

It has long been suspected that condensate and near-condensate films show better adhesion to substrate, more flexibility, and improved appearance because

they represent a more conventional polymer, as if prepared under milder circumstances (8, 19). It is now somewhat clearer how this comes about, and why temperature control is so much more important in determining the properties of one polymer system and not another.

For example, acrylonitrile and perfluorinated monomers may be converted by glow discharge into polymer without undue concern about the substrate temperature. Styrene and allyl methacrylate, on the other hand, degrade significantly in the glow and should be deposited with careful attention to the role of condensation in excluding or diluting the undesirable decomposition fragments. The same considerations undoubtedly apply to most other useful monomers, possibly according to the categories suggested in Table IV. The brief descriptions of polymerization routes are presented as speculation, consistent with all observations in the laboratory but not yet rigorously proved.

By way of summary, it is our experience that useful films can be obtained from category I monomers as long as the electrodes are not allowed to overheat. Category II films benefit greatly from chilling the electrode to near the condensation temperature of the monomer. Category IIIa films are of generally inferior quality and IIIb films are not films in any real sense.

Manuscript submitted March 15, 1971; revised manuscript received April 27, 1972.

Any discussion of this paper will appear in a Discussion Section to be published in the June 1973 JOURNAL.

REFERENCES

1. J. Goodman, U.S. Pat. 2,932,591, April 12, 1960.
2. A. Bradley, *Ind. Eng. Chem. Prod. Res. Develop.*, **9**, 101 (1970).
3. A. Bradley and J. P. Hammes, *This Journal*, **110**, 15, 543 (1963).
4. R. M. Brick and J. R. Knox, *Modern Packaging* (Jan. 1965).
5. T. Williams, *J. Oil Colour Chemists' Assoc.*, **48**, 936 (1965).
6. R. L. Stewart, *Phys. Rev.*, **45**, 448 (1934).
7. J. A. Coffman and W. R. Browne, *Sci. Am.*, **212** (No. 6), 96 (June 1965).
8. T. Williams and M. W. Hayes, *Nature*, **209**, 769 (1966).
9. W. D. Harkins, *Trans. Faraday Soc.*, **30**, 221 (1934).
10. F. K. McTaggart, "Plasma Chemistry in Electrical Discharges," p. 197, Elsevier, New York (1967).
11. L. V. Gregor, *IBM J. Res. Dev.*, **12**, 145 (1968).
12. F. J. Vastola and J. P. Wightman, *J. Appl. Chem.*, **14**, 69 (1964).
13. Private communication, M. H. Wiley, Texas Woman's Univ., Denton, Texas.
14. A. Bradley and J. D. Fales, *Chem. Tech.*, **1**, 232 (1971).
15. H. Wiener and M. Burton, *J. Am. Chem. Soc.*, **75**, 5815 (1953).
16. D. T. Lohkamp, "Surface Reactions on Polyethylene Film Due to Corona Discharge Treatment," Thesis, Washington Univ. (St. Louis) 1964.
17. B. D. Blaustein and Y. C. Fu, in "Chemical Reactions in Electrical Discharges," p. 259, R. F. Gould, Editor, Am. Chem. Soc. Publications, Washington, D. C. (1969).
18. A. Bradley, *Trans. Faraday Soc.*, **61**, 773 (1965).
19. J. R. Knox and K. H. Teumer, U.S. Pat. 3,475,307, Oct. 28, 1969.

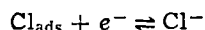
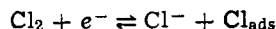
The Reduction of Chlorine on Carbon in $\text{AlCl}_3\text{-KCl-NaCl}$ Melts

Gerhard L. Holleck*

Tyco Laboratories, Inc., Bear Hill, Waltham, Massachusetts 02154

ABSTRACT

Using a rotating-vitreous, carbon disk electrode, the kinetic parameters for chlorine reduction in an $\text{AlCl}_3\text{-KCl-NaCl}$ (57.5-12.5-30 mole per cent [m/o]) melt were determined. It was found that the reduction of chlorine occurs according to the paths



with the first step being most probably rate determining. The apparent exchange currents were $(1 \pm 0.15)10^{-4}$ A/cm² at 130°C and $(2.1 \pm 0.3)10^{-4}$ A/cm² at 150.6°C.

The electrochemical reduction of chlorine in molten salts is of general interest to the development of high energy density batteries. One such proposed battery system is based on an aluminum anode and a chlorine cathode in a low melting aluminum chloride-alkali chloride eutectic (1). In a previous paper, we have dealt with the behavior of the aluminum electrode in $\text{AlCl}_3\text{-KCl-NaCl}$ melts (2). This work is concerned with the kinetics of chlorine reduction in such melts.

Despite the use of the chlorine electrode for a number of years as a reference electrode in fused salts (3), kinetic and mechanistic studies have been quite limited. Treadwell and Terebessi conducted emf studies of the cell $\text{Al/AlCl}_3\text{-KCl-NaCl/Cl}_2$ (4). Skundin *et al.* carried out studies of chlorine reduction in $\text{AlCl}_3\text{-KCl-NaCl}$ melts at 100°-150°C on Pt and Ir electrodes using linear sweep voltammetry (5). They estimated an exchange current of 10^{-4} A/cm² with no evidence of surface film formation. Drossbach and Piontelli both investigated the evolution of chlorine from chloride melts and found small polarizations (6, 7). The evolution of chlorine from LiCl-KCl melts in the temperature range of 425°-650°C was found to be resistance controlled primarily due to the gas film present on the electrode surface (8). Triaca *et al.* found that the dissolution of chlorine on graphite in molten LiCl was diffusion controlled at higher current densities which precluded mechanistic conclusions (9). Other studies of the reduction of chlorine on graphite electrodes in molten salts have been made by Ivanovskii *et al.* (10), Trusov and Borisova (11), and Swinkels (12).

In preliminary studies, we found that graphite-containing samples showed considerable swelling and disintegration in aluminum chloride-alkali chloride melts. Vitreous carbon, which did not show any attack, was chosen as a suitable electrode material for kinetic studies of chlorine reduction on carbon surfaces in $\text{AlCl}_3\text{-KCl-NaCl}$ melts using the rotating disk electrode technique.

Experimental

The rotating disk arrangement consisted of a sturdy stand on which a 1/15-hp Bodine motor and a precision ball bearing for the 0.25 in. rotating shaft were mounted. The motor speed was controlled by a Minarik speed control (SL-52). The coupling of the motor and the electrode shaft was accomplished by a nonslip belt. The rotation rate of the electrode was continuously monitored by the frequency modulation resulting from magnetic coupling of an electromagnet with an iron

gear mounted on the rotating shaft. This signal was amplified and displayed on a frequency counter. Electrical contact to the disk electrode was accomplished through a mercury pool in the top of the rotating shaft.

The electrochemical cell was made of a 50 mm Pyrex O-ring joint with a 30 mm-thick Teflon cover. The Teflon cover contained tapered holes to accommodate a liquid seal in the center with a 29/40 standard tapered joint surrounded by four 10/30 joints for the gas inlet and outlet as well as the counter and reference electrodes. A Teflon bell was fixed to the rotating shaft (Fig. 1). Silicone oil with a low vapor pressure was used as sealant liquid.

The rotating electrode consisted of a vitreous carbon rod (3 mm diameter, from Atomergic Chemicals Corporation) press fitted into hot Teflon. Details of the electrode construction are shown in Fig. 1. A vitreous carbon rod was used as counterelectrode and an Al electrode in the same melt, but in a separate compartment, served as reference electrode. The electrochemical cell was thermostated by a stirred silicone oil bath controlled to $\pm 0.2^\circ\text{C}$ by a Matheson Lab Stat

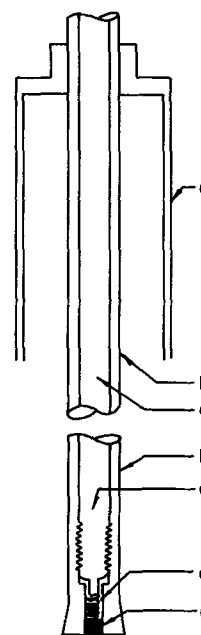


Fig. 1. Schematic diagram of rotating disk electrode: a) Teflon bell for liquid seal, b) Teflon, c) stainless steel shaft, d) contact spring, and e) vitreous carbon.

* Electrochemical Society Active Member.

Key words: aluminum chloride, molten salt, rotating disk, kinetic parameters.

proportional temperature control unit and a two-stage heating arrangement. The chlorine from a gas cylinder was passed through a trap filled with molecular sieves (Linde No. 5A) which had been dried at 375°C, under dry argon overnight, before entering the cell.

The experiments were conducted in the $\text{AlCl}_3\text{-KCl-NaCl}$ melt (57.5-12.5-30 m/o) at 130° and 150.6°C. The purification of AlCl_3 , and the preparation of the melts, has been described in detail elsewhere (2). Before introducing Cl_2 gas into the cell, cyclic voltamograms were taken at the carbon disk electrode (these showed no detectable faradic background current). Following this, the argon was replaced by Cl_2 , and a slow flow of Cl_2 was maintained above the melt surface. The progress of melt saturation was monitored by measuring the increase of the limiting current of the Cl_2 reduction with time at constant rotation speeds. Generally, the stirred melt was saturated with Cl_2 after 25 to 30 min.

Results

The open circuit potentials (measured vs. an aluminum reference electrode in a melt of the same composition and temperature) at 130° and 150°C were 2.10 and 2.06V, respectively. A typical current-voltage curve at 130°C, at a sweep rate of 200 mV/min, is shown in Fig. 2. A slight hysteresis was observed between the forward and the backward sweep. The hysteresis at low current densities was independent of rotation rate, whereas the differences between the forward and backward sweeps at, or close to, the limiting current region increased with increasing rotation rate. Figure 3 shows the change of current with time at constant potential at a rotation rate of 30 rps.

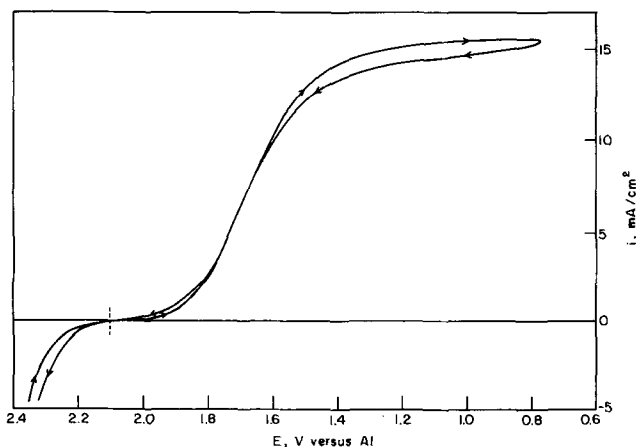


Fig. 2. Reduction of Cl_2 at rotating carbon disk electrode in $\text{AlCl}_3\text{-KCl-NaCl}$ (57.5-12.5-30 m/o) at 130°C, 20.8 rps, and 200 mV/min.

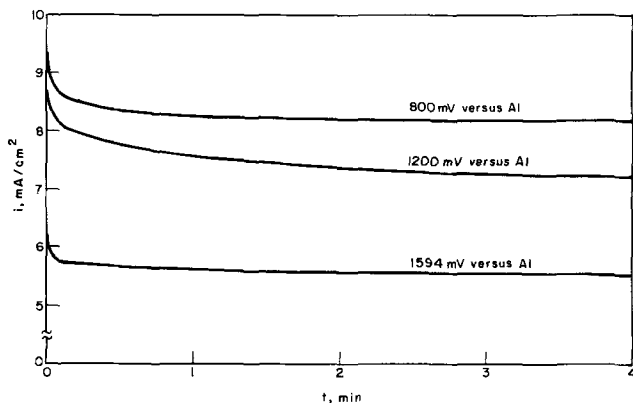


Fig. 3. Decay of Cl_2 reduction current with time upon potentiostatic steps to various potentials (vs. Al) at the rotating disk electrode in $\text{AlCl}_3\text{-KCl-NaCl}$ (57.5-12.5-30 m/o) at 130°C and 30 rps.

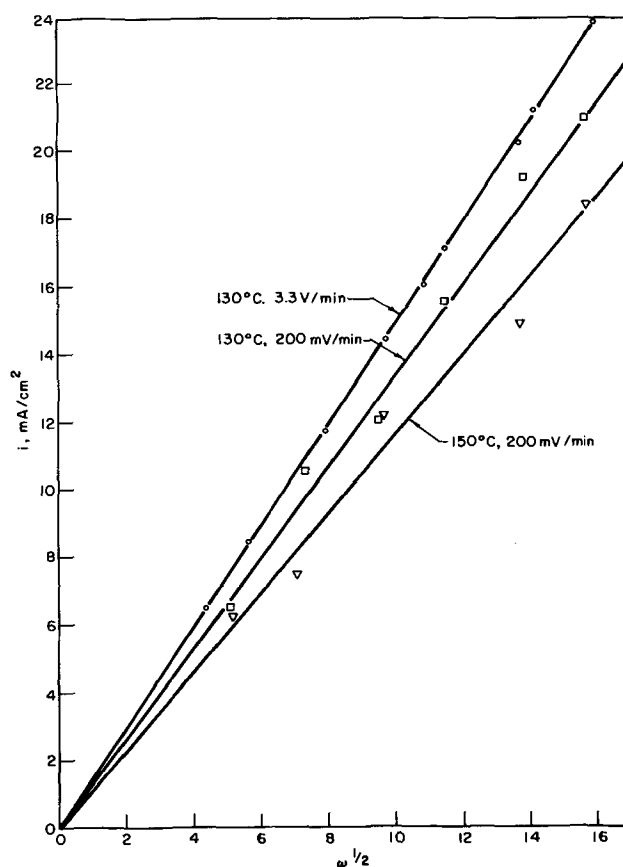


Fig. 4. Limiting currents for Cl_2 reduction vs. rotation rate at carbon electrode in $\text{AlCl}_3\text{-KCl-NaCl}$ (57.5-12.5-30 m/o).

Besides the buildup of the diffusion layer, we observed a relatively slow current decay which is clearly potential dependent. It is largest at 1.2V, in keeping with the current-voltage curves, and reaches a steady-state value after about 3 min. At 0.8 and 1.59V, steady-state values are more quickly established. This and the reproducibility of the current-voltage sweeps after returning to the open circuit potential suggest a potential dependent inhibition. The exact cause of this behavior is not yet known. However, it seems most likely that some melt impurity is involved.

Limiting currents of chlorine reduction as a function of rotation rate are shown in Fig. 4. The data show the linear relationship predicted for a mass transfer controlled reaction (13)

$$i_L = AnFD^{2/3}\nu^{-1/6}\omega^{1/2}C_0$$

where A = constant, D = diffusion coefficient, C_0 = bulk concentration of the electroactive species, ν = kinematic viscosity, $\omega = 2\pi N$ where N = rotation rate.

The limiting currents obtained from cyclic current-voltage sweeps at 3.3 V/min follow a straight line with a slope of 1.48 $\text{mA/cm}^2\omega^{1/2}$. The limiting current values from the slow current-voltage sweeps show larger scatter and a somewhat smaller slope (1.37 $\text{mA/cm}^2\omega^{1/2}$), reflecting the slow current decay mentioned above. At 150.6°C, a slightly smaller slope resulted, indicating that the increase in the factor $D^{2/3}\nu^{-1/6}C_0$ is overcompensated by a decrease of the Cl_2 solubility. The transport parameter ($D^{2/3}\nu^{-1/6}C_0$) is approximately 1.4×10^{-8} [$\text{mole cm}^{-2} \text{sec}^{-1/2}$] at 130°C from which the chlorine solubility can be estimated to about 5 mmole/liter.

Figure 5 shows the current potential data in a diffusion corrected Tafel plot of the form

$$\eta = \frac{2.3 RT}{\beta z F} \log i_0 - \frac{2.3 RT}{\beta z F} \log \frac{i}{1 - (i/i_L)} \quad [1]$$

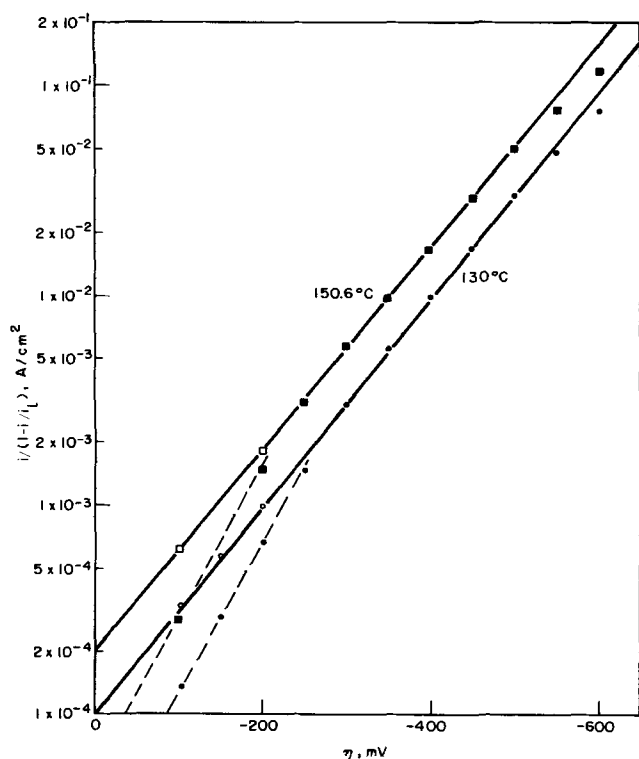


Fig. 5. Diffusion corrected Tafel plots for Cl_2 reduction, $\text{AlCl}_3\text{-KCl-NaCl}$ (57.5-12.5-30 m/o); (open symbols at low η represent returning sweep).

where the symbols have their usual meaning. The equation is obtained by substituting $C/C_0 = 1 - i/i_L$ in the expression for the cathodic current

$$i = -i_0 \frac{C}{C_0} \exp\left(\frac{-\beta z F \eta}{RT}\right)$$

It is applicable for a reaction with a simple rate determining step and of first order with respect to the diffusing species.

The experimental data in Fig. 5 show good Tafel behavior up to high overvoltages. The main Tafel slope was 200 mV at 130°C and 210 mV at 150.6°C. This suggests a one-electron transfer in the rate determining step with $\beta \approx 0.4$. At lower overvoltages (between $\eta = 50$ and 250 mV), the current of the cathodic going sweep follows a Tafel line with a decreased slope (130 mV/decade). On the returning potential sweep, no change in Tafel slope occurred. The exchange currents for chlorine reduction obtained from the main Tafel region were $(1.0 \pm 0.15) \cdot 10^{-4}$ A/cm² at 130°C, and $(2.1 \pm 0.3) \cdot 10^{-4}$ A/cm² at 150.6°C with an activation energy of 12 cal/mole.

The rotating disk electrode offers a particular advantage in determining the reaction order with respect to the reactants and products by studying the effect of rotation rate at a fixed potential as was illustrated by Frumkin and Aikazyan (14).

For the rate determining step, $qO + ze^- \rightarrow R$, we can write

$$\frac{i}{i^*} = \left(\frac{C_0^o}{C_0^\infty}\right)^q = \left(1 - \frac{i}{i_{L,c}}\right)^q \quad [2]$$

where i = measured current, i^* = activation controlled current, C_0^∞ and C_0^o are the concentration of species O in the bulk of the electrolyte, and at the electrode surface, respectively, and q = reaction order with respect to the diffusing species.

With $q = 1$, Eq. [2] converts to

$$\frac{l}{i} = \frac{l}{i^*} + \frac{l}{K\omega^{1/2}} \quad [3]$$

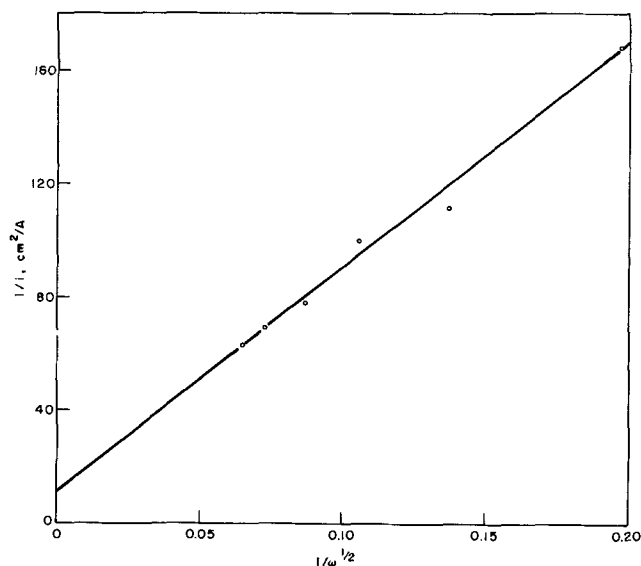


Fig. 6. Reduction of Cl_2 at constant potential (130°C, $E = 1.5V$ vs Al).

(K is the slope of the plot i_L vs. $\omega^{1/2}$) while $q = \frac{1}{2}$ (for instance) results in

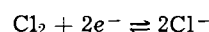
$$i^2 = (i^*)^2 - \frac{(i^*)^2}{K} \frac{i}{\omega^{1/2}} \quad [4]$$

A typical plot of l/i vs. $l/\omega^{1/2}$, according to Eq. [3], is shown in Fig. 6. The linear relationship of the experimental data suggests a reaction order of one. From the intercept at $l/i = 0$, $i^* = 80 \mu\text{A/cm}^2$ was calculated as found in the Tafel plots. The slope $l/K = 780 \text{ cm}^2\omega^{1/2}/\text{A}$ is in good agreement with K from Fig. 4.

From the initial slope of galvanostatic potential-time curves close to the open circuit potential, the double layer capacity was determined to $110 \pm 15 \mu\text{F/cm}^2$, which is larger than the 20 to 30 $\mu\text{F/cm}^2$ one would normally expect to find. The larger capacity values are most likely due to an increased roughness factor of the electrode and/or an adsorption capacitance.

Discussion

The over-all reaction



can occur according to two paths

- (a) $\text{Cl}_2 + e^- \rightleftharpoons \text{Cl}^- + \text{Cl}_{\text{ads}}$
- 1
- (b) $\text{Cl}_{\text{ads}} + e^- \rightleftharpoons \text{Cl}^-$
- (a) $\text{Cl}_2 \rightleftharpoons 2\text{Cl}_{\text{ads}}$
- 2
- (b) $\text{Cl}_{\text{ads}} + e^- \rightleftharpoons \text{Cl}^-$

The fact that the reaction for the chlorine reduction was found to be first order excludes the second path.

A calculation of the theoretical Tafel slopes of the first path, depending on whether step (a) or step (b) is rate determining, results in the following values.

Rate determining	Langmuir adsorption		Temkin adsorption	
	$\theta \rightarrow 0$	$\theta \rightarrow 1$	nonactivated	activated
1a	$-2RT/F$	$-2RT/3F$	$-2RT/F$ or	$-RT/F$
1b	$-2RT/3F$	$-2RT/F$	$-2RT/3F$	$-RT/F$

The experimentally determined main Tafel slope was $2.5 RT/F$. The above table shows that the value for the Tafel slope alone is not sufficient to distinguish between steps (a) and (b). The measured slope could reflect a rate-determining step according to 1a at low coverage of the electrode or according to 1b at large electrode coverage. Thus, additional information concerning the electrode coverage would be required.

Studies of the mechanism of chlorine evolution on graphite (9) in molten lithium chloride suggests, as the rate determining step, the combination of chlorine atoms on a surface with appreciable coverage. In fact, when scanning the rotating carbon electrode from the region of chlorine evolution to more cathodic potentials, one indeed observes, up to overvoltages of 250 mV, a lower Tafel slope which changes to $2RT/F$ at higher overvoltages probably indicating the change from an intermediate to low coverage. On the anodic going sweep, this low coverage is maintained until reaching anodic potentials.

Thus, we can conclude that the chlorine reduction on vitreous carbon in $AlCl_3$ -KCl-NaCl melts occurs according to path 1 with step 1a being most probably rate determining at higher polarizations with a low chlorine coverage on the electrode.

Acknowledgments

The author wishes to thank Dr. José Giner for many helpful discussions. This work was supported by the Electronics Research Center, National Aeronautics and Space Administration under Contract No. NAS-12-688.

Manuscript submitted Aug. 16, 1971; revised manuscript received Feb. 17, 1972.

Any discussion of this paper will appear in a Discussion Section to be published in the June 1973 JOURNAL.

REFERENCES

1. J. Giner and G. L. Holleck, Final Report by Tyco Laboratories, Inc. on Contract NAS-12-688, June 1970.
2. G. L. Holleck and J. Giner, *This Journal*, **119**, 1161 (1972).
3. A. F. Alabyshv, M. F. Lantratov, and A. G. Morachevskii, "Reference Electrodes for Fused Salts," The Sigma Press, Washington, D. C. (1965).
4. M. D. Treadwell and L. Terebessi, *Helv. Chim. Acta*, **18**, 103 (1935).
5. A. M. Skundin, V. Sh. Palanker, and V. S. Bagot-skii, *Elektrokhimiya*, **2**, 1453 (1966).
6. P. Drossbach, *Z. Elektrochem.*, **60**, 387 (1956).
7. R. Piontelli, G. Sternheim, and F. Fumgalli, *Ric. Sci.*, **28**, 160 (1958).
8. A. M. Shams El Din, *Electrochim. Acta*, **4**, 242 (1961).
9. W. E. Triaca, C. Solomons, and J. O'M. Bockris, *ibid.*, **13**, 1949 (1963).
10. L. I. Ivanovskii, G. K. Stepanov, M. T. Krasnovnikov, and O. S. Petenev, *Izv. Sibirsk. Otd. Akad. Nauk SSSR*, **4**, 48 (1961).
11. G. N. Trusov and S. I. Borisova, *Elektrokhimiya*, **1**, 709 (1965); (Eng. Transl., *Soviet Electrochem.*, **1**, 628 (1965)).
12. D. A. J. Swinkels, *This Journal*, **113**, 6 (1966).
13. V. G. Levich, "Physicochemical Hydrodynamics," Prentice-Hall, Inc., Englewood Cliffs, N. J. (1962). For a review of the rotating disk system, see A. C. Riddiford, in "Advances in Electrochemistry and Electrochemical Engineering," Vol. 4, P. Delahay, Editor, Interscience, New York (1966).
14. A. N. Frumkin and E. A. Aikazyan, *Dokl. Akad. Nauk SSSR*, **100**, 315 (1955), A. N. Frumkin and E. A. Aikazyan, *Izv. Akad. Nauk SSSR Otd. Khim. Nauk*, 202 (1959).

The Aluminum Electrode in $AlCl_3$ -Alkali-Halide Melts

Gerhard L. Holleck* and José Giner*

Tyco Laboratories, Inc., Bear Hill, Waltham, Massachusetts 02154

ABSTRACT

Passivation phenomena have been observed upon cathodic and anodic polarization of the Al electrode in $AlCl_3$ -KCl-NaCl melts between 100° and 160°C. They are caused by formation of a solid salt layer at the electrode surface resulting from concentration changes upon current flow. The anodic limiting currents increased with temperature and with decreasing $AlCl_3$ content of the melt. Current voltage curves obtained on a rotating aluminum disk showed a linear relationship between the anodic limiting current and $\omega^{-1/2}$. Upon cathodic polarization, dendrite formation occurs at the Al electrode. The activation overvoltage in $AlCl_3$ -KCl-NaCl (57.5-12.5-20 mole per cent [m/o]) was determined by galvanostatic current step methods. An apparent exchange current density of 270 mA/cm² at 130°C and a double layer capacity of $40 \pm 10 \mu F/cm^2$ were measured.

Molten salts have been investigated as electrolytes for high energy density batteries. The main disadvantage of the molten electrolyte batteries is the necessity for high temperature operation, which introduces many problems related to materials, construction, safety, etc. Furthermore, the insulation necessary in these high temperature batteries leads to a degradation of their energy density.

In this context, we have carried out studies of a high energy density battery based on an aluminum anode and a chlorine cathode with a molten $AlCl_3$ -electrolyte (1). Aluminum is a low cost, readily available material which is easy to handle and has a low equivalent weight. The use of low melting aluminum chloride-alkali-halide mixtures should overcome the problems associated with the high working temperatures of the present molten salt systems, while still retaining the

advantages of high energy density and relatively efficient electrode processes. The operating temperature of this system would be in the range of 120°-150°C, with a theoretical energy density of 650 Whr/lb. Furthermore, using an $AlCl_3$ -KCl-NaCl eutectic the battery can be started at 90°C and the addition of LiCl (2) could reduce the starting temperature to 61°C.

In this paper, we will discuss the processes occurring at the aluminum electrode in $AlCl_3$ -KCl-NaCl melts containing more than 50 m/o $AlCl_3$. The behavior of the chlorine electrode is discussed elsewhere (3).

Preparation and Purification of $AlCl_3$ -KCl-NaCl Melts

Thermal analysis of the $AlCl_3$ -KCl-NaCl system has been carried out by Fischer and Simon (4) and by Midorikawa (5). The $AlCl_3$ -rich region (>50% $AlCl_3$) constitutes the low temperature region of the phase diagram and is of specific interest for the investigations reported here. Different melting points and com-

* Electrochemical Society Active Member.

Key words: molten salts, aluminum-chlorine battery, passivation.

positions have been reported (4-8) for the ternary eutectic ranging from 70°C for $\text{AlCl}_3\text{-KCl-NaCl}$ (66-14-20 m/o) to 94°C for $\text{AlCl}_3\text{-KCl-NaCl}$ (62.13, 12.7-25.17 m/o). The most reliable value is probably 89°C for $\text{AlCl}_3\text{-KCl-NaCl}$ 63.5-16.5-20. Aside from the pseudobinary eutectics, $\text{NaAlCl}_4/\text{AlCl}_3$ (108°C), $\text{KAlCl}_4/\text{AlCl}_3$ (128°C), and $\text{NaAlCl}_4/\text{KAlCl}_4$ (125°C), very little is known about the actual phase diagram in this region and about the species present in the melt.

All experimental work was carried out in the argon atmosphere of a purge-type glove box. The melts were prepared with Baker "analyzed" KCl and NaCl. In exploratory experiments, $\text{AlCl}_3\text{-KCl-NaCl}$, 66-14-20 m/o melts were prepared using AlCl_3 from eight different manufacturers. Upon heating, grayish brown melts were readily formed. Other investigators (9) have also observed this coloration and attribute it to carbonaceous material and to the presence of FeCl_3 impurity in the AlCl_3 . By investigating the effect of intentional additions of FeCl_3 , it was confirmed that iron was the major impurity in all melts even where the AlCl_3 label stated "iron free" (10). AlCl_3 obtained from Fluka Chemicals (Switzerland) was found to contain the lowest impurity level, and was, thus, used as starting material for further purification.

After exploring several purification methods, we settled for the following procedure: a quartz rack containing three electrodes (an Al wire in the center, an Al sheet cylinder as counterelectrodes, and a Pt wire electrode) and a baffle were introduced into a heated 2 liter Pyrex resin reaction kettle containing a Teflon-coated, magnetic stirring bar. A 1500g batch of $\text{AlCl}_3\text{-KCl-NaCl}$ (67.5-13.38-19.12 weight per cent [w/o]) was introduced into the vessel and heated to 130°-140°C. At this temperature, the resulting melt had only a moderate AlCl_3 vapor pressure.

A high current (~10A) was passed between the Al electrodes with the wire as cathode for several minutes and aluminum dendrites were formed. These dendrites were partially separated from the wire electrode by reversing the current. Thus, clean high surface Al was produced *in situ*. (We found that, when using Al turnings, the effectiveness of this treatment varied from case to case probably due to the presence of an aluminum oxide layer.) The melt was kept under constant stirring at 140°C for 24 to 36 hr.

The progress of the exchange of Fe^{3+} for Al^{3+} was monitored by cyclic potential sweeps at the Pt wire electrode. A reduction in the ionic iron content by more than a factor of 25 was obtained. The temperature was then raised and the AlCl_3 evaporated into an air-cooled, 1 liter reaction kettle placed upside down on top of the reaction vessel. The material so treated was clear and produced virtually transparent eutectics without detectable residual current in the cyclic voltammetric curves obtained on Pt.

The Quasi-Steady-State Behavior of the Al Electrode

Experimental.—The investigations were carried out at three different $\text{AlCl}_3\text{-KCl-NaCl}$ compositions (melt I, 67-13.6-19.4 m/o; melt II, 59-17-24 m/o; and melt III, 57.5-12.5-30 m/o) and at three different temperatures (157°, 126°, and 105°C).

For the measurements on stationary wire electrodes, an electrochemical cell was constructed using two O-ring joints of 50-mm ID. The electrodes and the gas in and outlet tubes were connected with Teflon Swagelok fittings. The working electrode consisted of a pure Al wire of 1 mm diam covered with several layers of shrinkable Teflon tubing except for a length of 1.2 cm. The reference electrode, also an Al wire, was contained in a separate compartment with a narrow opening to protect it from changes in electrolyte concentration.¹ An Al wire spiral around the inside of the vessel served as counterelectrode. A platinum

¹ It had been established (11, 12) that an Al electrode is a stable reference in these melts, and all potentials are referred to this electrode in the particular melt investigated.

electrode sealed into glass was also included in the cell for measurements of the electrolyte background.

A pressure control, consisting of an electromagnetic valve and a mercury contact manometer, was used to maintain a constant argon pressure (normally, a positive pressure of 10 to 20 Torr was used). The cell was filled and assembled tightly in the glove box, then transferred into an air oven (temperature control $\pm 1^\circ\text{C}$), and connected to the argon line. No gas was passed through the cell to avoid concentration changes resulting from the appreciable vapor pressure of AlCl_3 over the melt. The appearance of the melt was clear, but it turned slightly grayish with time.

The rotating disk assembly and cell are described in detail elsewhere (3).

Results and discussion.—Melts I and II contained varying amounts of AlCl_3 at the KCl/NaCl ratio of the ternary eutectic. The KCl/NaCl ratio in melt III is the same as in the pseudobinary eutectic between NaAlCl_4 and KAlCl_4 . These melts promise to be more favorable for practical application than the composition of the ternary eutectic since they stay liquid over a wider concentration range at temperatures around 130°C.

Qualitatively the current voltage curves at an aluminum electrode are very similar in all melts. Typical examples are shown in Fig. 1-3. Figure 4 shows the

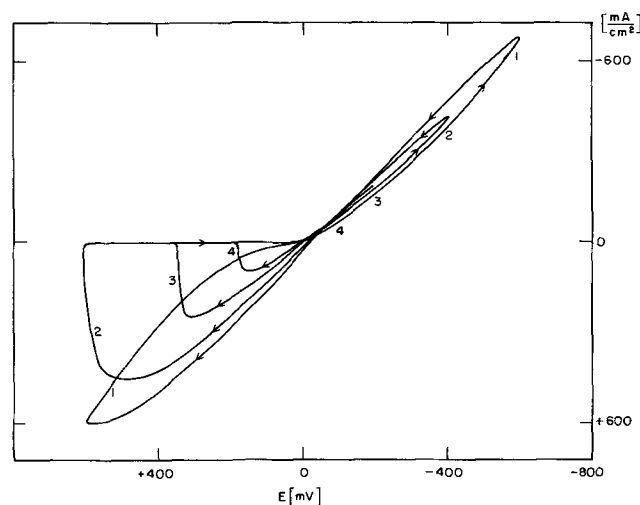


Fig. 1. Triangular potential scans at Al electrode, $\text{AlCl}_3\text{-KCl-NaCl}$ (67-13.6-19.4 m/o) 105°C, 400 mV/min (from 0.0 mV to E_{cath} to E_{anode} back to 0.0 mV, no IR correction).

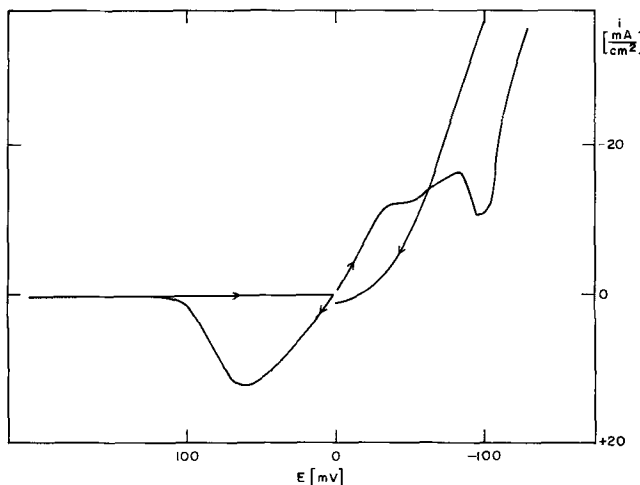


Fig. 2. Separate anodic and cathodic potential scans at an Al electrode. $\text{AlCl}_3\text{-KCl-NaCl}$ (59-17-24 m/o), 105°C, 20 mV/min (no IR correction).

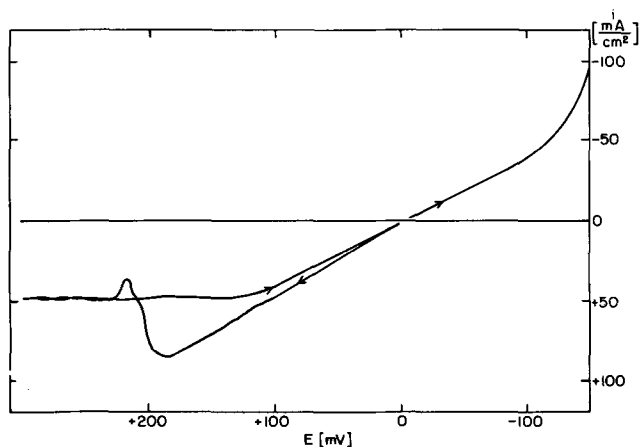


Fig. 3. Separate anodic and cathodic potential scans at an Al electrode. AlCl₃-KCl-NaCl (59-17-24 m/o) 157°C, 20 mV/min (no IR correction).

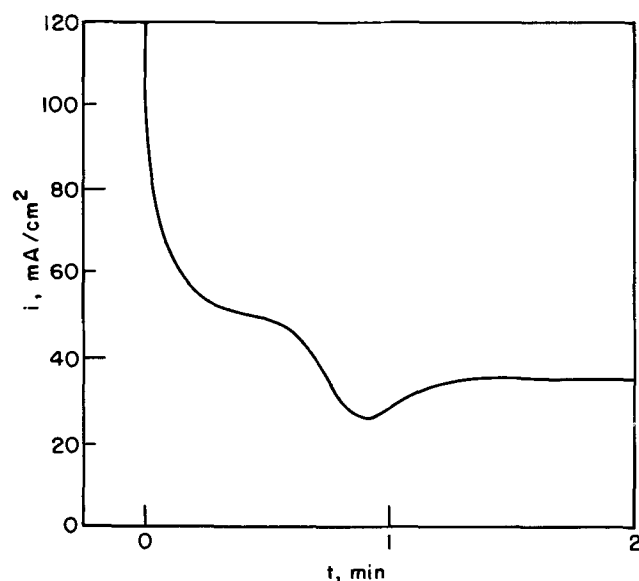


Fig. 4. Anodic current as a function of time upon potentiostatic polarization of Al electrode at 150 mV vs. Al in AlCl₃-KCl-NaCl (57.5-12.5-30 m/o) at 126°C (no IR correction).

anodic current as a function of time upon potentiostatic polarization of the Al electrode.

Anodic behavior.—The anodic potential sweeps in Fig. 1-3 show passivation phenomena. This anodic passivation of the Al electrode does not occur at a constant, defined potential. A closer examination reveals that the sudden current drop can be related to the charge passed (current and time) rather than to the potential. Figure 1 shows the correlation between anodic passivation and cathodic prepolarization for a low temperature with melt I. Comparison of the anodic and cathodic charges (represented by the area underneath the i - t curve) shows that they are nearly equal. This is even more obvious for cathodic and anodic current vs. time curves upon potentiostatic polarization for periods of varying length (not shown). This behavior seems to indicate that melt I (which is AlCl₃-rich) cannot tolerate much more anodic formation of AlCl₃ at this temperature without precipitating it in solid passivating form. On the other hand, if by cathodic pretreatment we form a diffusion layer close to the electrode which is poor in AlCl₃, then we are able to polarize the electrode anodically for a time necessary to replenish the initial AlCl₃ concentration until passivation occurs. Parallel to the current voltage

behavior of Fig. 1, it can be seen by microscopic *in situ* observation of the Al electrode (1) that it is shiny after cathodic polarization and becomes dull upon passivation. The fact that the anodic and cathodic charges are almost equal indicates a rather compact diffusion layer with practically no convection. As the cathodic prepolarization time is increased, the charge obtained prior to anodic passivation becomes smaller than the cathodic charge, as one would expect.

Cathodic behavior.—If the above explanation holds, we should expect a similar passivation effect at cathodic currents due to salt precipitation. In fact, current-voltage sweeps show indications of such behavior (for example, Fig. 2). In all cases, however, a subsequent current increase is found after indications of passivation. This is due to dendrite formation at the Al electrode. Long, shiny, Al dendrites can easily be seen growing into the electrolyte, thus enlarging the surface area.

The initiation of dendrite growth is a function of current and time. There seems to be a current value below which little dendrite formation is noticeable. This critical current value changes with conditions. Although more detailed information on the parameters governing dendrite formation is required, our results indicate a strong effect of concentration polarization and ionic conductivity on dendrite formation.

Effect of melt composition.—The most obvious difference between the potential scans of the different melts is a much higher, steady-state, anodic current after passivation in melts II and III compared to melt I. For example, at 156°C, the anodic limiting currents are approximately 2 mA/cm² for melt I, 50 mA/cm² for melt II, and 100 mA/cm² for melt III.

On the cathodic side, a deviation from the linear current-potential behavior appears at much larger current densities in melt I than in melt II. This again confirms our explanations of solid salt formation at the electrode. Melt II, which is less concentrated in AlCl₃, can support higher anodic current densities (that means it can accept more Al³⁺ without forming undissolved AlCl₃) than melt I. The latter, however, since it is more concentrated in AlCl₃, will be able to support higher cathodic currents before forming a passivating salt layer due to X-AlCl₄ precipitation (we disregard for the moment the additional complication of dendrite formation). The anodic current maxima (Fig. 3) are very likely due to supersaturation of the melt close to the electrode. After the first crystals have formed, the supersaturation breaks down. This is responsible for the following current dip.

The same effect can be seen in Fig. 4 which shows the anodic current as a function of time upon potentiostatic polarization. Thus, the limiting value of the steady-state current, besides depending on the usual transport properties, also depends on the capacity of the melt to accommodate concentration changes without surpassing the liquidus line of the phase diagram. This is clearly a function of melt composition.

Effect of temperature.—The effect of temperature on the current-voltage behavior of the Al electrode in the molten salt electrolyte, can be seen by comparing Fig. 2 and 3 obtained using the same melt. Although a considerable steady-state current can be obtained at 157°C (~50 mA/cm² in melt II), this steady-state current is practically zero at 105°C. Melt III shows limiting currents of approximately 100 mA/cm² at 157°C, and 34 mA/cm² at 126°C.

The temperature affects the results in several ways. First, there is the temperature dependence of the usual transport phenomena; for example, the viscosity decreases, and the diffusion coefficients increase with rising temperature. Much more important in our case, however, are considerations concerning the AlCl₃-KCl-NaCl phase diagram. We mentioned earlier the key role of solid salt formation. How large a concentration

change is necessary to surpass the liquidus line of the phase diagram is, to a large extent, a function of temperature (besides initial melt composition).

The temperature will surely have an effect on dendrite growth since this is controlled by diffusion and ohmic polarization. Further changes in conductivity, due to varying dissociation constants and changes in complex formation with temperature, are to be expected. These problems cannot, however, be discussed more closely on the basis of presently available data.

Effect of mass transport.—All results of our stationary polarization measurements at Al electrodes indicate that the anodic limiting currents are a function of the mass transport in the melt. We, therefore, expect the anodic limiting currents to depend on the diffusion layer thickness and, thus, on the rotation rate of a rotating Al disk electrode. The current which is controlled only by mass transfer is given by Levich (13)

$$i_L = A \cdot nFD^{2/3}v^{-1/6}\omega^{1/2}\Delta C$$

where A is a constant, D is the diffusion coefficient, ΔC is the concentration difference of the electroactive species in the bulk of the electrolyte, and at the electrode surface, v is the kinematic viscosity, and $\omega = 2\pi$ (rps), where rps = rotations per second. This equation implies a linear relationship between i_L and $\omega^{1/2}$ under diffusion controlled conditions.

As Fig. 5 shows, the experimental data can, indeed, be represented very well by a straight line in such a plot. The slight deviations from linearity and some variations in the individual current densities were to be expected. One must keep in mind that here we are actually dealing with the dissolution of a passivating solid salt layer at the rotating electrode, which is in many respects quite different from the idealized conditions for which the above equation is strictly valid. Further, at the high current densities observed, changes in the electrode itself cannot be avoided.

These results show clearly, however, the role of transport phenomena in removing reaction products

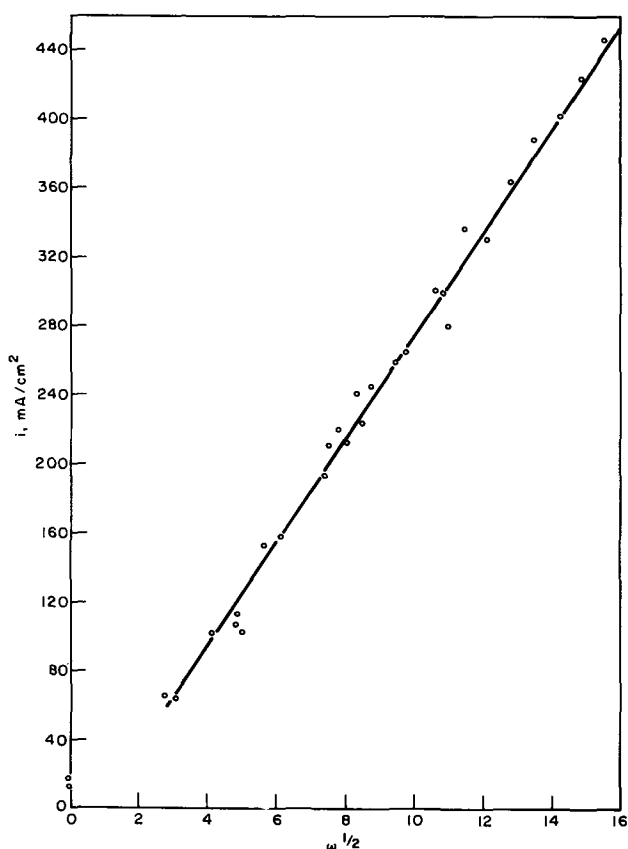


Fig. 5. Anodic limiting current at rotating Al disk electrode in $\text{AlCl}_3\text{-KCl-NaCl}$ (57.5-12.5-30 m/o) at 125°C .

from the electrode surface. They show further that high current densities can be obtained at Al electrodes at relatively low temperature if the transport limitations can be overcome.

The Transient Behavior of the Al Electrode

Previous measurements suggested that the charge-transfer processes at the Al electrode are quite fast. It is, therefore, necessary, in order to exclude the effect of concentration polarization, to use transient methods to investigate the electrode kinetics. We chose galvanostatic pulse measurements for this purpose.

Galvanostatic current step methods.—The galvanostatic technique, considering the double layer charging, was originally discussed by Berzins and Delahay (14) and, since then, has been used in several investigations. Following Graves, Hills, and Inman (15) we can write for small overvoltages ($\eta < 0.1 RT/nF$); and for sufficiently long times the potential transient as a function of a galvanostatic current pulse

$$\eta = \frac{-2RTit^{1/2}}{\pi^{1/2}n^2F^2C_0^0D^{1/2}} + \frac{RTi}{nF} \left[\frac{RTC_{dl}}{n^3F^3(C_0^0)^2D} - \frac{1}{i_0} \right] \quad [1]$$

Hence, a plot of $\eta/t^{1/2}$ should give a straight line of slope

$$\frac{d\eta}{d(t^{1/2})} = \frac{-2RTi}{\pi^{1/2}n^2F^2C_0^0D^{1/2}} \quad [2]$$

from which a value for $C_0^0D^{1/2}$ can be calculated.

When $t^{1/2} = 0$, then

$$\eta = \frac{RTi}{nF} \left[\frac{RTC_{dl}}{n^3F^3(C_0^0)^2D} - \frac{1}{i_0} \right] \quad [3]$$

and the intercept on the η axis, together with the value for $D(C_0^0)^2$ calculated above, will give a value for i_0 from Eq. [3].

An alternative method for calculating i_0 is the use of a special value of $t^{1/2}$ given by

$$t_0^{1/2} = \frac{\pi C_{dl}}{4i} \times \frac{d\eta}{d(t^{1/2})} \quad [4]$$

The corresponding overpotential, η_0 , can be found from the curve, and a value for i_0 calculated.

Both methods require the determination of the differential double layer capacity which can be obtained from the initial slope of the potential time trace at sufficiently short times (16).

Experimental.—In view of the facts mentioned above, it was necessary to use pulses with a short rise time and high current density. It was also necessary to be able to record small potential changes with time, which required a low noise level in the experimental setup and compensation of the ohmic drop in the solution. For the constant current pulses, the output of a Wavetek function generator (gated by a Tyco-built pulse generator to allow multiple pulse application) was used directly. The IR compensated, potential-time traces were obtained by feeding the potential of the two-electrode cell and the output of the IR compensation into the inputs of the differential amplifier of a Tektronic dual trace oscilloscope. The measurements were conducted at an Al disk electrode (0.385 cm^2). A sheet of pure Al (15 cm^2) served as the counterelectrode. The experimental setup, including the cell, showed a response time of about $1 \mu\text{sec}$. The melt $\text{AlCl}_3\text{-KCl-NaCl}$ (57.5-12.5-30 m/o) was thermostated by a temperature controlled silicone oil bath. Again, a slightly positive argon pressure was kept in the cell at all times.

Results and discussions.—From the initial slope of the potential-time traces at anodic and cathodic current pulses, a double layer capacity of $40 \pm 10 \mu\text{F/cm}^2$

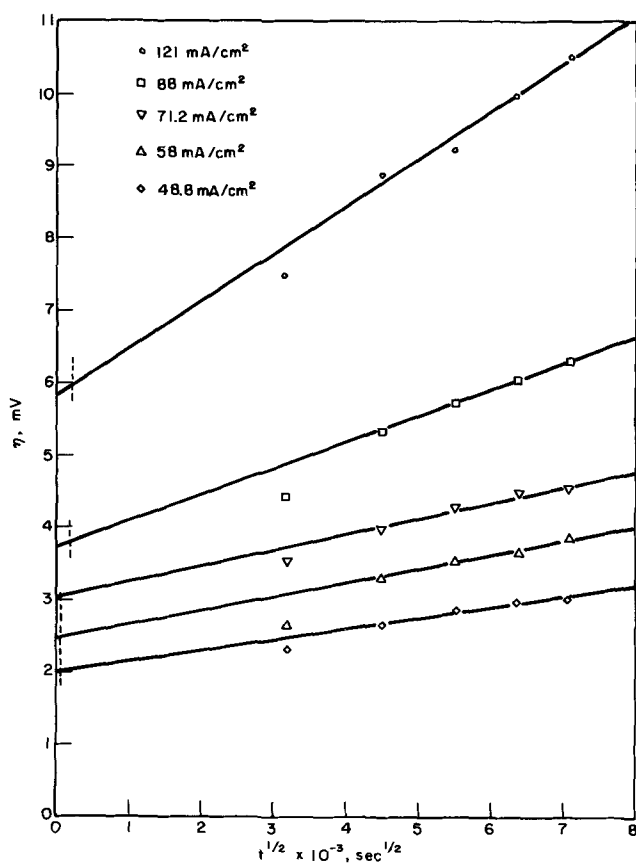


Fig. 6. Variation of overvoltage with time at Al electrode upon galvanostatic current step in AlCl₃-KCl-NaCl (57.5-12.5-30 m/o) at 130°C.

was determined. Considering the surface roughness, this suggests the absence of specific absorption effects.

Figure 6 shows a typical overvoltage vs. square root of time plot for various current densities. At times larger than 10 μ sec, the potential varies linearly with $t^{1/2}$. As expected, the slope of these lines increases with increasing current density. The times, $t_c^{1/2}$, according to Eq. [4] are also included in Fig. 6. Figure 7 shows a plot of i vs. activation overvoltage. At low overvoltages, one finds a linear relationship between current density and potential. With $n = 3$, the apparent exchange current at the Al electrode was determined as $i_0 = 268 \text{ mA/cm}^2$ at 130°C in the melt AlCl₃-KCl-NaCl (57.5-12.5-30 m/o).

Schulze and Hoff (17) recently investigated the transference of aluminum in a temperature gradient. From these measurements they deduced similar values for the exchange current at aluminum electrodes in AlCl₃-KCl-NaCl (66-14-20 m/o) between 160° and 230°C [i_0 (490°K) 0.86A, $Q = 9.7 \text{ kcal/mole}$]. They also assume that $n = 3$. Despite reports of multiple electron transfer in molten salts (18), a three-electron transfer as rate determining step for the aluminum electrode is not established. Thus, the available data are not sufficient to decide upon a detailed electrode mechanism. The aluminum electrode has been investigated also in molten AlCl₃-NaCl and AlCl₃ (LiCl-KCl) by Del Duca (19). The results are, however, too different in order to allow a meaningful comparison with the present investigation.

Finally, it is interesting to examine more closely the values obtained for the transport parameter, $C_0^0 D^{1/2}$. These values were found to be approximately 1.4×10^{-5} . Assuming a diffusion coefficient of $10^{-6} \text{ cm}^2/\text{sec}$ in the melt, one obtains for the concentration of the electroactive species $C_0^0 \approx 1.4 \times 10^{-5} \text{ mole/cm}^3$. This is about two orders of magnitude less than the excess AlCl₃ assuming 50 m/o AlCl₃ to be complexed as

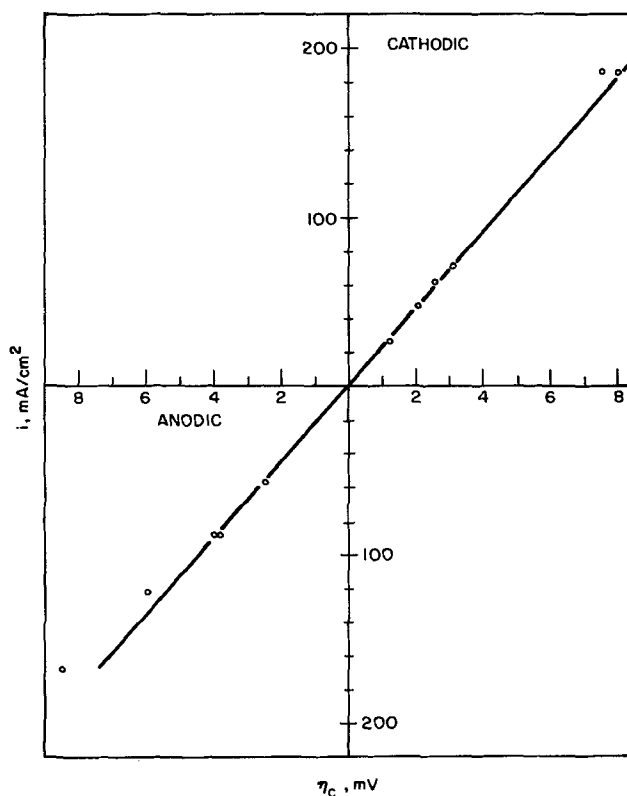


Fig. 7. Current density vs. activation overvoltage at Al electrode in AlCl₃-KCl-NaCl (57.5-12.5-30 m/o) at 130°C.

(AlCl₄)⁻. Unfortunately, practically nothing is known about the nature of the species present in the melt and about the complex formation in AlCl₃-rich melts.

Conclusions

The behavior discussed above in detail leads us to the following conclusions.

1. The passivation effect is due to the formation of a solid salt layer at the electrode surface caused by concentration changes during current flow.
2. The occurrence of passivation is not dependent on potential, but rather on current and time, i.e., on charge passed through the electrode. It also depends on the transport properties of the melt.
3. The occurrence of salt formation depends on the compositional stability of the melt towards concentration changes. It is strongly dependent on melt composition and on temperature.
4. At cathodic currents, dendrite formation occurs at the Al electrode.
5. The Al electrode itself is highly reversible and able to support large current densities at low activation overvoltage.
6. The polarization observed in the experiments is, to a large extent, ohmic in nature. It again depends on melt composition and temperature.

Acknowledgments

The authors wish to thank Dr. B. Burrows and Mr. M. Turchan for contributions to this investigation. This research was supported by the Electronics Research Center, U. S. National Aeronautics and Space Administration, under Contract No. NAS 12-688.

Manuscript submitted Aug. 16, 1971; revised manuscript received Feb. 17, 1972.

Any discussion of this paper will appear in a Discussion Section to be published in the June 1973 JOURNAL.

REFERENCES

1. J. Giner and G. L. Holleck, Final Report by Tyco Laboratories, Inc. on Contract No. NAS 12-688, June 1970.

2. W. E. Trout, Jr. and W. J. Triner, Jr. (University of Richmond) Report No. CCC-1024 TR 139, October 1955.
3. G. L. Holleck, *This Journal*, **119**, 1158 (1972).
4. W. Fischer and A. Simon, *Z. Anorg. Allgem. Chem.*, **306**, 1 (1960).
5. R. Midorikawa, *J. Electrochem. Soc. Japan*, **23**, 127 (1955).
6. H. Grothe, *Z. Elektrochem.*, **54**, 216 (1950).
7. R. Midorikawa, *J. Electrochem. Soc. Japan*, **23**, 352 (1955).
8. T. Chao, U. Microfilms, Ann Arbor, Michigan, 3704, 294, Dissertation Abstracts, **12**, 459 (1952).
9. T. C. F. Munday and J. D. Corbett, *Inorg. Chem.*, **5**, 1263 (1966).
10. J. Giner and G. L. Holleck, Report prepared under Contract No. NAS 12-688 for National Aeronautics and Space Administration (March 1970).
11. R. G. Verdick and L. F. Yntema, *J. Phys. Chem.*, **46**, 344 (1942).
12. V. A. Plotnikov, E. J. Kirichenko, and N. S. Fortunatov, *Zap. Inst. Khim. Akad. Nauk Ukr. R.S.R.*, **7**, 159 (1945).
13. V. G. Levich, "Physicochemical Hydrodynamics," Prentice Hall, Inc., Englewood Cliffs, N. J. (1962).
14. T. Berzins and P. Delahay, *J. Am. Chem. Soc.*, **77**, 6448 (1955); *Z. Elektrochem.*, **59**, 792 (1955).
15. A. D. Graves, G. J. Hills, and D. Inman in "Advances in Electrochemistry and Electrochemical Engineering," Vol. 4, P. Delahay, Editor, Interscience (1966).
16. D. Inman, J. O'M. Bockris, and E. Blomgren, *J. Electroanal. Chem.*, **2**, 506 (1961).
17. U. Schulze and H. Hoff, *Ber. Bunsenges. Physik. Chem.*, **74**, 687 (1970).
18. S. Senderoff and G. W. Mellors, *This Journal*, **113**, 66 (1966).
19. B. S. Del Duca, *ibid.*, **118**, 405 (1971).

Ring-Disk Electrode Study of the Reduction and Oxidation of Bismuth on Gold

S. H. Cadle and Stanley Bruckenstein*

Chemistry Department, State University of New York at Buffalo, Buffalo, New York 14214

ABSTRACT

The deposition and stripping of bismuth at a gold electrode was studied in 0.12M perchloric acid. Current-potential curves show four cathodic and four anodic processes at $E_D < +0.40V$ vs. SCE. Three of these processes correspond to the deposition and stripping of Bi(O) at underpotential. A maximum of one monolayer of Bi(O), corresponding to 590 $\mu\text{coulombs/cm}^2$ at $-0.05V$, was deposited on the electrode at underpotential. The fourth process was the deposition and stripping of bulk bismuth. The diffusion coefficient of Bi(III) was found to be 5.8×10^{-6} cm^2/sec . No Bi-Au alloy formation was observed. Bi(III) was found to adsorb on gold oxide. The quantity adsorbed is a function of the oxidation potential of the electrode and the concentration of Bi(III).

The deposition and stripping of bismuth on platinum electrodes was studied initially by Bowles (1) in perchloric acid media. In this study, he reported that bismuth deposits at underpotential on platinum. Recently we reinvestigated the deposition and stripping of bismuth on platinum using the rotating platinum ring-disk electrode (2). This work showed that the underpotential deposition of bismuth on platinum in 0.12M perchloric acid media was markedly irreversible in that underpotential bismuth oxidation occurred over the potential region 0.0 to +1.2V vs. SCE. We also found that bismuth (III) is adsorbed on platinum oxide. Because of the overlap in the potential regions of adsorption of bismuth (III) and underpotential deposition and stripping of bismuth (O), there is no electrode potential for which the surface of a platinum electrode is free of bismuth in one or another of its oxidation states. After deposition of multilayers of bismuth, oxidation resulted in the formation of five additional stripping peaks which were shown to be associated with four monolayers of bismuth and an alloy several monolayers deep.

Schmidt, Gyax, and Cramer (3) studied the deposition of bismuth on gold from hydrochloric acid media. They found that deposition at underpotential occurred in two potential regions, resulting in the plating of a single monolayer of bismuth. No alloy formation or adsorption was observed.

We felt that it would be valuable to study the plating and stripping of bismuth on gold from perchloric acid media using a rotating gold ring-disk electrode

(RGRDE) and contrast the behavior at gold with that observed at platinum.

It will be shown below that a monolayer of bismuth is deposited at underpotential on a gold electrode from perchloric acid media. A full monolayer of underpotential Bi(O) must be deposited before bulk deposition occurs. Also Bi(III) adsorbs on gold oxide but not on reduced gold.

Experimental

Solutions and equipment.—All solutions were prepared using triply distilled water. B and A reagent grade perchloric acid was used to prepare the 0.12M supporting electrolyte. Stock solutions of Bi(III) were prepared by dissolving Fisher reagent grade bismuth trioxide in perchloric acid solution. All solutions were deoxygenated by passing nitrogen through and over the solution. The nitrogen was passed through a hot column of finely divided copper dispersed on diatomaceous earth to remove any traces of oxygen from the gas.

The circuit for the ring-disk potentiostat (4) has been previously described, as has the electrochemical cell, the X-Y-Y' recorder and the rotator (4).

The projected area of the gold ring-disk electrode was 0.46 cm^2 . The electrode parameters, N , $B^{2/3}$, and S were 0.42, 1.22, and 0.66 respectively (4).

All potentials are reported vs. the saturated calomel electrode (SCE). Values of the number of $\mu\text{coulombs}$ passed per cm^2 are reported using the projected area of the electrode, uncorrected for roughness factor.

Electrode pretreatment.—The gold ring and disk electrodes were pretreated in the following manner:

* Electrochemical Society Active Member.
Key words: ring-disk electrode, adsorption, bismuth, gold, underpotential deposition.

(i) The electrode was polished with Buehler 0.05 μ gamma micropolish. (ii) Next it was oxidized at +1.6V for 5 min and reduced at -0.3V for 5 min. (iii) The electrode potential was then cycled repeatedly between +1.6 and -0.30V until a reproducible current-potential curve was obtained.

The electrode was reactivated periodically during the course of an experiment by oxidizing it at +1.6V, and then cycling its potential from +1.6 to -0.3V several times.

Results and Discussion

Bi(III) reduction.—The plating and stripping of bismuth on a gold ring-gold disk electrode was studied in 0.12M perchloric acid solution. Figure 1 shows the disk current-disk potential curve (I_D-E_D) and the corresponding ring current-disk potential (I_R-E_D) curve in a $2 \times 10^{-5}M$ Bi(III) solution for a ring potential, E_R , equal to -0.30V. The ring electrode potential chosen produces a convective-diffusion controlled-limiting wave for the reduction of Bi(III). Curves 1-3 correspond to increasing disk potential scan rates of 5, 20, and 50 mV/sec respectively.

Shielding of the ring electrode occurs for $E_D < +0.35V$, indicating the consumption of Bi(III) at the disk electrode. The shielding and the disk current are seen to be a function of the potential scan rate at $+0.35V \leq E_D \leq -0.23V$. In the disk electrode potential range $+0.35V \leq E_D \leq -0.05V$, I_D falls to zero if the potential scan is stopped indicating that only a finite quantity of bismuth can be deposited in this potential region. This bismuth is shown below to be underpotential deposited Bi(O). Figure 1, curve 1 demonstrates that the deposition of Bi(O) at underpotential occurs in three distinct potential regions labeled A-C, in contrast to the behavior observed by Schmidt *et al.* (3) in hydrochloric acid where only two underpotential deposition regions were observed. Peaks A-C disappear at higher scan rates because the deposition of Bi(O) becomes convective-diffusion controlled.

A steady-state Bi(III) reduction current is observed at the disk electrode $E_D = -0.05V$ (Fig. 1). A plot of the steady-state current at $-0.25V$ vs. $\omega^{1/2}$, the square root of the rotation velocity, is linear with a zero intercept proving that the limiting current is convective-diffusion controlled. The diffusion coefficient of Bi(III) was calculated using the Newman version (5) of the Levich equation to be 5.8×10^{-6} cm²/sec, the same as was found at the platinum disk electrode (2).

Bi(O) oxidation.—The oxidation of Bi(O) from a gold electrode exhibits current peaks at +0.30, +0.15,

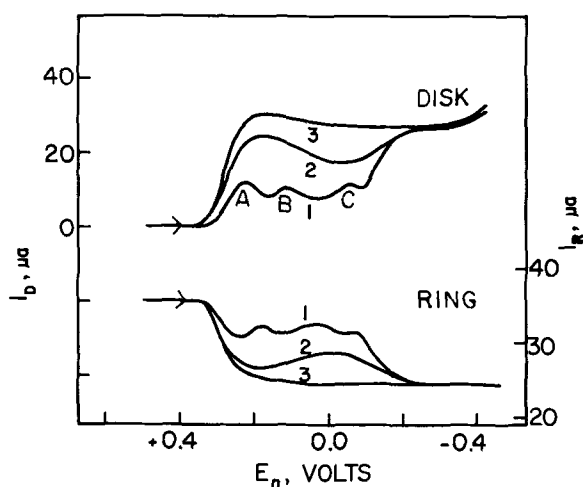


Fig. 1. Cathodic current-potential curve for a Bi(III) solution at a RGRDE. 0.12M HClO₄, $2 \times 10^{-5}M$ Bi(III), rotation speed 2500 rpm, ring potential -0.300V, potential scan rate curve (1), 5 mV/sec; curve (2), 20 mV/sec; curve (3), 50 mV/sec.

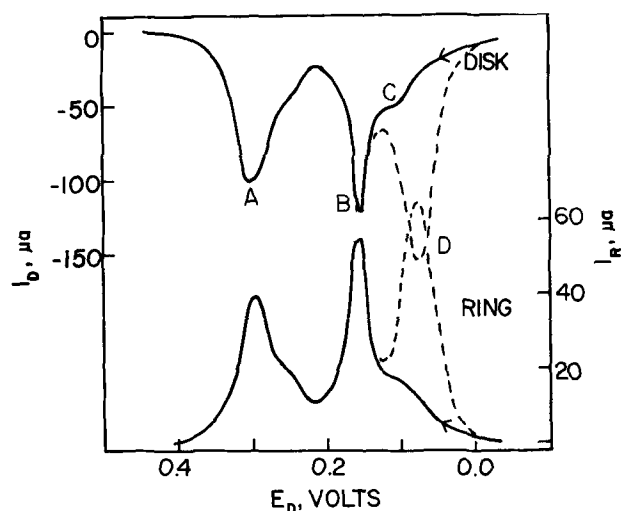


Fig. 2. Oxidation of Bi(III) from a gold electrode. 0.12M HClO₄, $2 \times 10^{-5}M$ Bi(III). — Disk electrode scanned anodic after a 15 min potential hold at -0.050V. --- Disk held at -0.100V for 40 sec, rotation speed 2500 rpm, ring potential -0.300V, potential scan rate 50 mV/sec.

+0.10, and +0.05V, peaks A-D in Fig. 2. The corresponding ring collection curves yielded the theoretical value of the collection efficiency for all four stripping peaks. The Bi(O) which strips at peaks A-C deposits before the Bi(O) which is oxidized at D. This fact was established by depositing various amounts of Bi(O), and oxidizing these films. Peak D is due to the oxidation of bulk deposits of Bi(O), while peaks A-C represent the stripping of underpotential Bi(O).

No Bi-Au alloy formation was observed electrochemically, in contradistinction to the situation for Pt-Bi(2). Also, no oxidizable species was detected by the ring electrode during the stripping process for ring potentials of +1.6 to -0.3V.

The quantity of Bi(O) deposited at underpotential on the disk electrode was determined as a function of potential from ring collection curves (Table I). The disk was potentiostated at various potentials in $2 \times 10^{-5}M$ Bi(III) solution for 15 min before scanning to anodic potentials in the range -0.05 to +0.4V to strip the Bi(O) deposited at underpotential. Potentiostating the electrode for longer periods of time did not increase the amount of Bi(III) collected. A maximum of 290 μ coulombs/cm² was oxidized at peak A. The maximum amount of Bi(O) plated at underpotential peaks A, B, and C ($E_D \cong -0.05V$) was 590 μ coulombs/cm².

Roughness factor.—The roughness factor of the gold disk electrode was estimated in three ways. Two of the methods have been reported previously, *i.e.*, the method of Brummer and Makrides (6), the method used by Woods (7), and the third is one we developed.

Brummer and Makrides suggest that a complete monolayer of oxygen is adsorbed on a gold electrode at +1.20V in 1M perchloric acid and corresponds to 400 μ coulombs/cm². One oxygen is adsorbed for each gold atom exposed on the surface. On our electrode we found that 596 μ coulombs/cm² of charge was required to reduce the electrode after oxidation at +1.20V, corresponding to a roughness factor of 1.49.

Table I. Underpotential deposition of bismuth on gold

Disk potential volts vs. SCE	Bismuth μ coulomb/cm ²	Surface coverage
-0.050	590	0.98
0.000	582	0.96
0.050	475	0.79
0.100	368	0.61
0.150	284	0.47
0.200	241	0.40
0.250	129	0.21
0.300	3.9	0.01

Woods estimated the true surface area of exposed gold in platinum-gold alloy electrodes by assuming that 300 $\mu\text{coulombs/cm}^2$ of charge is required to reduce a gold electrode when it is continuously cycled between -0.25 and $+1.25\text{V}$ at 40 mV/sec in 1M perchloric acid. Since the current-voltage curves for platinum-gold alloys are the sum of current-voltage curves for pure platinum and pure gold (7), Woods method for calculating the gold surface area of Pt/Au alloys should be as valid for calculating the roughness factor of gold electrodes as for gold-platinum alloys. We found that $402\ \mu\text{coulombs/cm}^2$ was required to reduce our electrode under Woods' conditions, yielding a roughness factor of 1.34.

In order to obtain a third estimate of the roughness factor of the gold disk electrode, Cu(O) was deposited at underpotential on the electrode from 0.12M perchloric acid solution. The deposition of Cu(O) on gold has been studied by Schmidt (8, 9). Assuming that copper deposits at underpotential on gold in the same manner that it deposits on platinum, i.e., in a single uniform monolayer where one copper atom is associated with one platinum atom (10), $400\ \mu\text{coulombs/cm}^2$ of the Cu(O) , should be deposited at underpotential on a gold electrode with a roughness factor of one. For our electrode $556\ \mu\text{coulombs/cm}^2$ of Cu(O) was deposited at underpotential, corresponding to a roughness factor of 1.39.

The average of the roughness factors determined by the three different techniques was 1.41 ± 0.10 , and all our results were obtained, either with an electrode having a roughness factor of 1.41, or the results were corrected to a roughness of 1.41, using the roughness factor determined from the deposition of copper at underpotential.

The last column in Table I gives the fractional surface coverage of Bi(O) on gold as a function of potential. These data were calculated from the second column of Table I assuming that $605\ \mu\text{coulombs/cm}^2$ Bi(O) constitute a single monolayer of close packed Bi atoms on a gold electrode with a roughness factor of 1.41.

Monolayer coverage charge.—The quantity of Bi(O) which constitutes monolayer coverage on a gold electrode was calculated assuming: (i) a 3 electron reduction of Bi(III) to Bi(O) , (ii) that a monolayer of oxygen adsorbed on gold, one oxygen atom per gold atom, is equal to $400\ \mu\text{coulombs/cm}^2$ for a roughness factor of 1.0 (5), and (iii) the atomic radii of gold and bismuth are 1.44 and 1.70\AA respectively. Since $400\ \mu\text{coulombs/cm}^2$ is the charge required for a 2 electron reduction to occur at every gold atom exposed at the surface of a gold electrode, $600\ \mu\text{coulombs/cm}^2$ would be required for the 3 electron reduction of Bi(III) to Bi(O) at every gold atom. However, since Bi(O) is larger than Au(O) it is necessary to multiply $600\ \mu\text{coulombs/cm}^2$ by the square of the ratio of the atomic radii of Au(O) to Bi(O) . Using this procedure, which has also been used by Bowles (11), we calculate that $430\ \mu\text{coulombs/cm}^2$ Bi(O) constitutes a monolayer on a gold electrode with a roughness factor of 1.

Adsorption of Bi(III) .—Figure 3 is an I_D - E_D curve in 0.12M perchloric acid in the presence and absence of $2 \times 10^{-5}\text{M}$ Bi(III) . The plating and stripping of underpotential bismuth is evident at $E_D = +0.40\text{V}$. The introduction of Bi(III) into the supporting electrolyte causes a small decrease in the quantity of surface gold which is oxidized during the anodic scan. During the cathodic scan, the presence of Bi(III) causes a marked shift in the cathodic direction, and a broadening of the gold oxide reduction peak.

The anodic I_D - E_D curve can be rationalized by assuming (i) that Bi(III) adsorbs on an oxidized gold electrode, and that (ii) this has an inhibiting effect on the oxidation of a small amount of remaining reduced gold, thus causing the decrease in the anodic current. The cathodic I_D - E_D curve demonstrates that

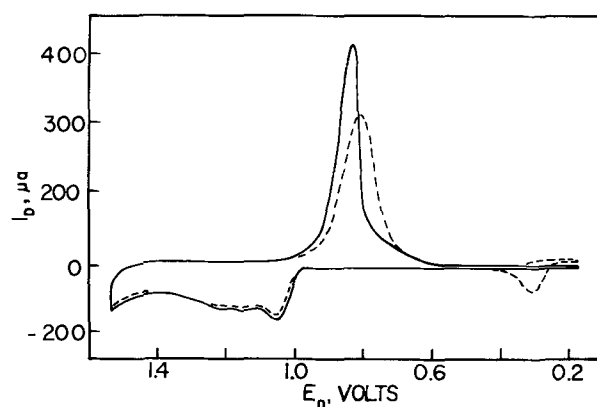


Fig. 3. Current-potential curve at a rotating gold disk electrode — 0.12M HClO_4 , - - - 0.12M $\text{HClO}_4 + 2 \times 10^{-5}\text{M}$ Bi(III) , rotation speed 2500 rpm , potential scan rate 100 mV/sec .

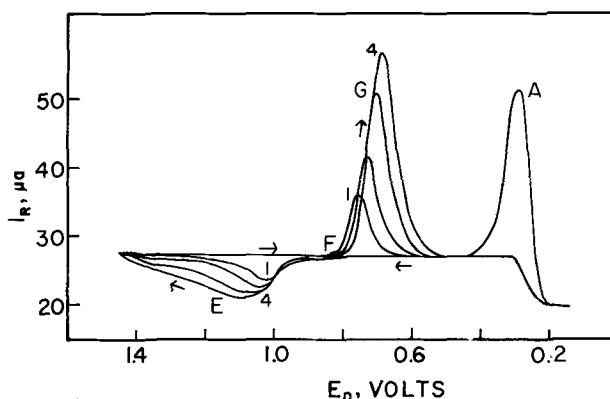


Fig. 4. Ring current-disk potential curves at a RGRDE 0.12M HClO_4 , $2 \times 10^{-5}\text{M}$ Bi(III) , rotation speed 2500 rpm , ring potential -0.300V . Potential scan rate curve (1), 25 mV/sec ; curve (2), 50 mV/sec ; curve (3), 100 mV/sec ; curve (4), 200 mV/sec .

the presence of adsorbed Bi(III) on the oxidized gold surface has a stabilizing effect on the oxidized gold causing the shift of the reduction peaks in the cathodic direction. The fact that the adsorbed Bi(III) has both an inhibiting effect and a stabilization effect on the oxidized gold appears to be inconsistent, unless we assume that the inhibition of the gold oxide formation is due to the physical blocking of the surface by the adsorbed Bi(III) .

Figure 4 presents a series of I_R - E_D curves obtained in a $2 \times 10^{-5}\text{M}$ Bi(III) solution at different potential scan rates. Curves 1-4 represent disk potential scan rates of 25 , 50 , 100 , and 200 mV/sec , respectively. In this discussion we are not particularly concerned with the behavior of the ring electrode at potential cathodic of $+0.4\text{V}$, since this has been previously discussed (see Fig. 1 and 2). We merely note that peak A in Fig. 4 corresponds to peak A in Fig. 2, and its independence of scan rate confirms the convective-diffusion controlled nature of the process leading to the deposition of underpotential bismuth (see Fig. 1).

During the anodic scan, at peak E, there is a decrease in the ring current for $E_D > 1.0\text{V}$, indicating the consumption of Bi(III) at the disk electrode. As the disk potential scan rate is increased to 200 mV/sec , the ring current becomes completely shielded. Since Bi(III) is not reduced in this potential region, the ring shielding can only be attributed to the adsorption of Bi(III) on gold oxide.

The adsorbed Bi(III) desorbs when the gold oxide is reduced and is collected at the ring giving a ring current peak at $+0.75\text{V}$ (peak G). The small peak F, at $+0.82\text{V}$ is due to the collection of a soluble gold

species which is also found to be collected in this supporting electrolyte solution (12). The charge involved in the shielding curve and the stripping peaks are equal, proving that all of the Bi(III) adsorbed on the anodic scan was desorbed during the cathodic sweep.

The shift in the ring collection peak potential in the cathodic direction with increasing disk potential scan rate is attributed to a slow kinetic step in the desorption process, since a corresponding shift in the gold oxide reduction peak at the disk was not observed.

The quantity of Bi(III) adsorbed at the disk electrode was determined as a function of disk potential by integration of ring collection curves. For this study the disk electrode was potentiostated, successively, at 0.10V intervals in the range 1.10-1.60V for 15 min in a $2 \times 10^{-5}M$ Bi(III) solution before scanning E_D in a cathodic direction. No adsorption experiments were conducted at potentials greater than +1.6V because surface roughening of the gold electrode occurs readily at these potentials (9).

The results of the adsorption experiments are given in Table II. A maximum of 0.28 monolayers of Bi(III) was adsorbed at +1.6V from a $2 \times 10^{-5}M$ Bi(III) solution.

Not unexpectedly, the adsorption of Bi(III) was also found to be concentration dependent. Table II lists the quantity of Bi(III) adsorbed at 1.4V as a function of concentration. An eightyfold increase in concentration resulted in a 2.3-fold increase in the quantity of Bi(III) adsorbed.

Table II. Adsorption of bismuth on gold

Disk potential volts vs. SCE	Bi(III) conc moles/l	Bi(III) adsorbed $\mu\text{coulomb}/\text{cm}^2$	Surface ^(a) coverage
1.100	2.0×10^{-5}	85	0.14
1.200	2.0×10^{-5}	124	0.20
1.300	2.0×10^{-5}	125	0.21
1.400	2.0×10^{-5}	149	0.25
1.500	2.0×10^{-5}	169	0.28
1.600	2.0×10^{-5}	170	0.28
1.400	2.0×10^{-6}	94	0.15
1.400	6.0×10^{-6}	123	0.22
1.400	1.6×10^{-5}	147	0.24
1.400	5.6×10^{-5}	186	0.31
1.400	1.6×10^{-4}	212	0.35

^(a) Based on our earlier calculation that 605 $\mu\text{coulombs}/\text{cm}^2$ is required for monolayer coverage on our gold electrode.

Conclusion

In marked contrast to the case of bismuth deposited on platinum, we find that there are potential regions at the gold disk electrode where the electrode surface is free of plated or adsorbed bismuth. Furthermore, again in marked contrast to the behavior of Bi(O) films on platinum, on gold no difficult-to-oxidize bulk alloy forms when bismuth deposits. With the use of gold electrodes the stripping of submonolayer and multimonomolayer films of bismuth can be recovered quantitatively after deposition.

Thus, gold should prove to be far superior to platinum as an electrode material for the anodic stripping analysis of Bi(III) solutions. For the latter purpose, in 0.12M HClO₄, deposition at -0.25V, and oxidation at +0.40V should prove satisfactory.

Acknowledgment

S.H.C. gratefully acknowledges the Electrochemical Society Summer Fellowship Award. In addition, this grant was partially supported by the AFOSR under Grant No. 70-1832.

Manuscript submitted Jan. 28, 1972; revised manuscript received May 8, 1972.

Any discussion of this paper will appear in a Discussion Section to be published in the June 1973 JOURNAL.

REFERENCES

1. B. J. Bowles, *Electrochim. Acta*, **15**, 737 (1970).
2. S. H. Cadle and S. Bruckenstein, *Anal. Chem.*, In press.
3. E. Schmidt, H. R. Gygax, and Y. Cramer, *Helv. Chim. Acta*, **53**, 649 (1970).
4. D. T. Napp, D. C. Johnson, and S. Bruckenstein, *Anal. Chem.*, **39**, 481, 1967).
5. J. Newman, *J. Phys. Chem.*, **70**, 1327 (1966).
6. S. B. Brummer and A. C. Makrides, *This Journal*, **111**, 1122 (1964).
7. B. Woods, *Electrochim. Acta*, **16**, 655 (1971).
8. E. Schmidt, P. Beutler, and W. J. Lorenz, *Ber. Bunsenges.*, **75**, 71 (1971).
9. W. J. Lorenz, I. Mourmtzis, and E. Schmidt, Jr., *Electroanal. Chem.*, **33**, 121 (1971).
10. S. H. Cadle and S. Bruckenstein, *Anal. Chem.*, **43**, 1858 (1971).
11. B. J. Bowles, *Nature*, **212**, 1456 (1966).
12. S. H. Cadle, Unpublished work.

Thermodynamic Properties of Manganous Chloride in Alkali Chloride Melts by Electromotive Force Measurements

A. S. Kucharski and S. N. Flengas*

Department of Metallurgy and Materials Science, University of Toronto, Toronto 181, Ontario, Canada

ABSTRACT

Electromotive force measurements on the $MnCl_2$ - ACl systems where $A = Li, Na, K,$ and Cs were made using cells of the type



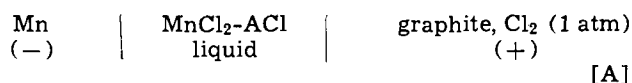
largely in the temperature range $600^\circ-900^\circ C$. The partial molar free energies, enthalpies, and entropies of mixing have been calculated from the emf results. The systems indicate negative deviations from ideality which are increasing from Li throughout to Cs . The concentration dependence of the partial molar enthalpies and entropies of mixing has been interpreted on the basis of the "complex ion" model previously developed which is applicable to reactive change asymmetrical fused salt mixtures. The entropy of mixing has been treated by postulating vibrational as well as a configurational contributions. The vibrational contributions have the largest negative values in the $MnCl_2$ - $CsCl$ system. The effect of the vibrational contribution on the partial molar properties is also discussed.

The thermodynamic properties of a number of transition metal chlorides dissolved in alkali chlorides have been determined recently by calorimetric and electrochemical methods.

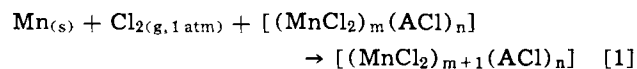
Papathodorou and Kleppa have measured the calorimetric heats of mixing in the binary systems $MnCl_2$ - ACl , $FeCl_2$ - ACl , $CoCl_2$ - ACl (1), and $NiCl_2$ - ACl (2), where, A represents the alkali metal cations $Li, Na, K, Rb,$ and Cs , here and throughout the paper. A common trend in these systems is that they have pronounced exothermic heats of mixing which increase as the size of the alkali metal cation in the binary mixtures becomes larger. Electrochemical measurements by Hamby *et al.* (3, 4) on the systems $NiCl_2$ - ACl and $CoCl_2$ - ACl , where A represents $Li, Na,$ and K , also indicate pronounced negative deviations from ideality and exothermic heat effects. The concentration dependence of the interaction parameters in the systems MCl_2 - ACl ($M = Mn, Fe, Co,$ and N) $\Delta H_M/X_1X_2$, determined from the calorimetric measurements by Papathodorou and Kleppa (1, 2), indicated a minimum at about 33 m/o (mole per cent) MCl_2 . The authors attributed this effect to the possible formation of a tetrahedrally coordinated MCl_4^{2-} species (1, 2). Thus, the heat of mixing was thought to originate from a heat of reaction and other heat effects resulting from the transformation of the covalently bonded pure salt to an ionic species, followed by changes in the coulombic and dispersion interactions during mixing.

The formation of tetrahedrally coordinated complexes in divalent metal chlorides was first suggested by Flood and Urnes (5) in their analysis of the phase diagrams of the systems $MgCl_2$ - ACl ($A = Na, K,$ and Rb), where the liquidus tie lines were predicted using activities calculated on the basis of the complete formation of the $MgCl_4^{2-}$ complex species. The calculations, however, were entirely based on configurational entropies and ignored the enthalpy contributions (6) which are now known to be quite significant.

In the present investigation the thermodynamic properties of the binary systems $MnCl_2$ - ACl where $A = Li, Na, K,$ and Cs , were studied by emf measurements using formation cells of the type



for which, the cell reaction is represented by



The results are interpreted in terms of the "complex ion model" presented previously (7) which is further extended to account for the unusual concentration dependence of the partial molar entropies of mixing.

There have been two previous electrochemical studies of the $MnCl_2$ - KCl , and the $MnCl_2$ - $NaCl$ systems by Bruneau *et al.* (8, 9). However, these authors have not measured the standard formation potential for pure $MnCl_2$, and in addition, only a few measured points are reported for the $MnCl_2$ - $NaCl$ system. The reported emf values indicate significant scatter and the uncertainties can be attributed to experimental difficulties associated with the use of graphite as an electrode in $MnCl_2$ melts, which are discussed in detail in the Experimental section.

Experimental

Anhydrous manganous chloride was prepared by a method similar to that employed by Corbett *et al.* (10). Reagent grade manganous chloride tetrahydrate was dehydrated in vacuum at $210^\circ C$ for 24 hr. To insure final dehydration, the pink solid was ground to a fine powder and slowly fused under a stream of anhydrous hydrogen chloride gas (Matheson Research Grade). In order to insure that no oxide would remain in the melt, anhydrous chlorine gas was also bubbled through the melt for 15 min followed by flushing with argon gas to remove the dissolved chlorine. After cooling under argon, the quartz glass container with the salt was transferred to a dry box. The glass was then broken under an inert gas atmosphere and the salt was stored in sealed containers until used. The chemical analysis of the purified manganous chloride indicated an average chlorine to manganese mole ratio of 2.005 ± 0.005 .

For all the alkali chlorides used in these experiments the dehydration procedure was essentially the same. The reagent grade alkali chlorides were purified initially by drying in vacuum for several days at $110^\circ C$,

* Electrochemical Society Active Member.

Key words: manganous chloride thermodynamic properties, complex ions; molten salts, manganous chloride emf measurements.

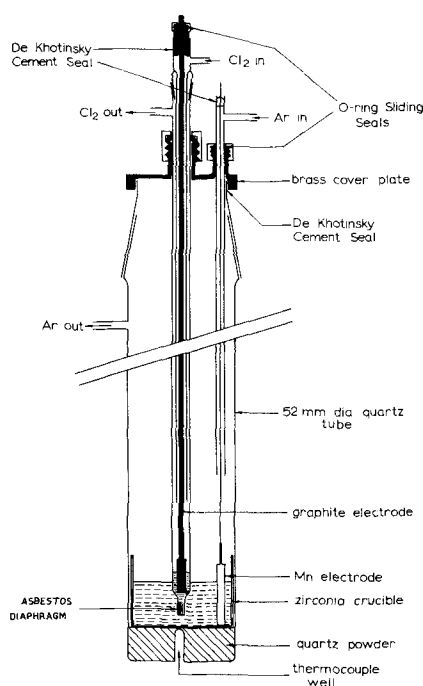


Fig. 1. EMF formation cell

followed by melting under a stream of anhydrous hydrogen chloride gas. When the salts were molten, the hydrogen chloride atmosphere was flushed out with argon. Chlorine gas was then bubbled through the melt for approximately 20 min, and finally, the melt was sparged with dry argon and allowed to solidify under an argon atmosphere. These purified salts were also stored in tightly sealed containers until used.

The design of the electrochemical cell used in these measurements is given in Fig. 1.

The cell consists of two half-cell compartments separated by an asbestos diaphragm. The purpose of the diaphragm was to hinder the diffusion of chlorine gas into the metal electrode compartment while allowing ionic transfer. The stability of the measured emf's in cells employing gaseous chlorine or sulfur vapor electrodes (11, 12) investigated previously in this laboratory has been attributed to the high resistance and the general chemical stability of these diaphragms.

The manganese metal electrode was prepared by melting electrolytic manganese (99.9%) in a closed-end alumina tube under an atmosphere of purified argon. A $\frac{1}{8}$ in. diam rod of tungsten, used for the electrical connections, was introduced into the molten metal and the liquid was allowed to solidify slowly. A flexible platinum wire was then welded to the tungsten rod and served as the final electrical lead to the potentiometer.

The chlorine electrode consisted of a graphite rod immersed in an atmosphere of pure chlorine gas (Matheson Research grade) as shown in Fig. 1. The graphite electrode was prepared in the standard manner (13). The electrodes were heated to 900°C and held at this temperature for 8 hr. Chlorine gas was then passed over the graphite for 12 hr and finally the system was evacuated for 8 hr. It was found that the electrolyte and particularly the manganous chloride-rich concentrations reacted with the graphite, since upon long immersion an electrode would become swollen and brittle.

An electron scanning photomicrograph was taken on such swollen graphite samples and indicated the presence of salt inclusions within the graphite matrix. The attack on graphite appears to be related to the chemical composition of the salt phase. For example, pure molten $MnCl_2$ caused more severe damage to the elec-

trode than the dilute solutions of $MnCl_2$ in alkali chlorides. Porous graphite was also more severely affected than the dense variety. It appears that upon long exposure to the melt manganese ions are capable of penetrating the bonded layer structure of graphite thus creating a volume increase accompanied by a loss of mechanical strength. This effect caused a serious deterioration in the electrochemical behavior of the chlorine electrode resulting in a drift of the potentials toward lower values.

Accordingly, to prevent the deterioration of the graphite electrode, the electrode was constructed from dense graphite, an experiment was always started at the lowest temperature, and the graphite electrode was connected to a vacuum sliding seal and could be withdrawn from the melt when not in use.

Graphite swelling due to chemical attack in $CdCl_2$ - $NaCl$ melts has also been reported by Dijkhuis (14). Graphite is also known to form electrically conducting lamellar compounds with gaseous Br_2 , Cl_2 , and a variety of halides (15).

It has been stated that a formation cell using a Mn electrode (13) cannot be used to determine the thermodynamic properties of $MnCl_2$ because manganese metal is soluble in the salt phase. Corbett *et al.* (10) have determined the solubility of Mn in $MnCl_2$ indirectly using the freezing point depression method. Because of the reactivity of manganese metal with Vycor, tantalum containers were used which also reacted to form a thin layer of $TaMn_2$. It was found that the solubility of manganese metal depresses the freezing point of $MnCl_2$ by $1.5^\circ \pm 1^\circ C$, corresponding to a Mn solubility of only 0.8 ± 0.5 m/o. Such small solubilities are not expected to affect the emf measurements as is demonstrated by the good agreement between the experimental and calculated standard potentials in the present work and by the reproducibility of the results upon heating and cooling.

At the beginning of a run, the cell was assembled, charged with the salts, and immediately evacuated. The system was heated slowly under vacuum to approximately 350°C to remove any trace of moisture present. At this point, the chlorine electrode and the manganese electrode compartments were flushed with chlorine and argon gas, respectively, and slowly heated to the fusion temperature of the salts.

Initial saturation of the molten solution with chlorine took about 1 hr during which the cell potential rose slowly. But once saturated with chlorine gas, the cell potential was stable and responded immediately to changes in temperature or chlorine gas pressure. The potentials obtained during heating over a period of 24 hr could be retraced on cooling indicating the reproducibility of the results. The reversibility of the measured emf's was also verified by polarization tests whereby a current from an external dry cell was passed through the cell. On disconnecting the applied potential the cell emf returned to its former equilibrium value to within ± 0.1 mV. The volatility of the salts did not have any significant effect on the results, since the cell potentials obtained during a heating cycle (to 850°C) could be reproduced on cooling, even at high manganous chloride concentrations. In order to compare the present results with values calculated from the available thermochemical data, the thermoelectric Pt-C junction potential was measured separately by short circuiting the ends of the carbon and platinum electrodes together at the hot junction. It was found that the carbon was positive with respect to the platinum and thus aided the electrochemical voltage. Therefore, this additional voltage was subtracted from the measured cell emf to give the true value.

The thermoelectric effect was fitted to a straight line given by the equation

$$E_{TE} \text{ (mV)} = -3.98 + 0.01289T \text{ (in Kelvins)} \quad [2]$$

with a standard deviation of 0.06 mV. This thermo-

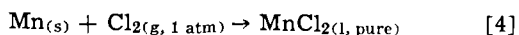
electric correction is only needed for the standard potential since it cancels when the data are used to calculate solution properties.

Results

Standard potential E° .—The free energy change for Reaction [1] is

$$\Delta \bar{G}_R = -ZFE \quad [3]$$

where E is the measured emf of a cell containing a solution as the electrolyte, and $\Delta \bar{G}_R$ is the free energy change for the reaction. If pure $MnCl_2$ is used as the electrolyte the cell potential, designated as E° , allows the direct calculation of the free energy of formation of pure $MnCl_2$ as given by Reaction [4]



through the relationship

$$\Delta G^\circ_R = -ZFE^\circ \quad [5]$$

From Eq. [3] and [5], and from the well-known expression for the activity, the equation relating the measured cell potential to the activity A_{MnCl_2} of $MnCl_2$ in solution is given as

$$E_{cell} = E^\circ - (RT/2F) \ln A_{MnCl_2} \quad [6]$$

The standard states for this calculation are, respectively, pure liquid $MnCl_2$ at all temperatures, pure solid Mn metal, and chlorine gas at 1 atm pressure. The experimentally measured E° values in the temperature range 660°–820°C corrected for the thermoelectric emf's are presented in Fig. 2.

These data may be compared with the standard potential calculated from free energy data tabulated by Kubaschewski *et al.* (16), Kellogg *et al.* (17), and Wicks and Block (18). It may be seen that good agreement to within ± 1 mV is obtained with the thermochemical calculation from the compilation of Wicks and Block (18).

At 990°K, α -Mn will transform to β -Mn with an endothermic heat effect of 535 cal. The free energy of the transformation and the heat capacities given by Wicks and Block (18) have been taken into account in the calculation of the standard cell potentials as a function of temperature using the Σ -function method. The experimental results are well represented by the following equations. For 990°K $> T > 923^\circ$ K

$$E^\circ = 2387.7 + 0.4043T \log T - 0.3729 \times 10^{-4} T^2 - 1.1138 \times 10^3 T^{-1} - 1.7179T \text{ (in mV)} \quad [7]$$

and for 1200°K $> T > 990^\circ$ K

$$E^\circ = 2372.6 + 0.2721T \log T - 0.78 \times 10^{-5} T^2 + 7.32 \times 10^2 T^{-1} - 1.3381T \text{ (in mV)} \quad [8]$$

Emf's obtained with a cell containing the $MnCl_2$ -ACl solutions represent Reaction [1]. The partial molar free

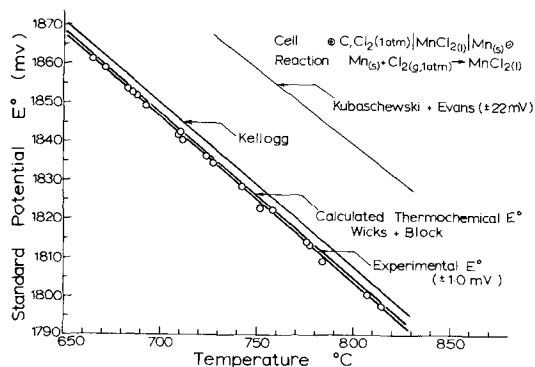


Fig. 2. Temperature dependence of the standard cell potential E° for $MnCl_2$ in mV. Curve labeled Experimental from the present investigation.

energy of mixing for $MnCl_2$, $\Delta \bar{G}_{MnCl_2}$, is given as

$$\Delta \bar{G}_{MnCl_2} = -ZF(E - E^\circ) \quad [9]$$

The partial molar free energies are related to the partial molar enthalpies and entropies of mixing by the Gibbs-Helmholtz relationship

$$\Delta \bar{G}_{MnCl_2} = \Delta \bar{H}_{MnCl_2} - T\Delta \bar{S}_{MnCl_2} \quad [10]$$

If the enthalpy and entropy of mixing are taken to be temperature independent the quantity $E - E^\circ$ can be expressed as a linear function of temperature over a narrow temperature range.

Partial molar enthalpies and entropies of mixing for $MnCl_2$ were obtained from the intercepts and slopes of the linear plots of $E - E^\circ$ vs. temperature for the four binary systems, as given in Fig. 3-6. The data are well represented by the least square lines shown. The maximum standard deviation in all four binary systems is 1.4 mV and the largest deviation of an individual experimental point is 2.6 mV. The equations of these lines are given in Table I, along with the standard and maximum deviations for each line. The partial molar excess free energies of mixing of $MnCl_2$, $\Delta \bar{G}^{XS}_{MnCl_2}$ at 800°C are also listed in Table I, along with the partial molar enthalpies and partial molar entropies of mixing for $MnCl_2$. These two properties are temperature independent within experimental errors as shown by the linearity of the plots.

Figure 7 shows the plot of E_{cell} vs. $\log X_{MnCl_2}$ for the four binary systems investigated.

The ideal line is drawn as a dashed line and corresponds to $A_{MnCl_2} = X_{MnCl_2}$. It is readily seen that the negative deviations increase as the size of the alkali metal cation becomes larger from Li through to Cs. The emf's reported by Bruneaux *et al.* (9) for the $MnCl_2$ -KCl system are also included as solid circles and indicate rather poor agreement with the present results. The activity isotherms at 800°C for $MnCl_2$ are shown in Fig. 8. The $MnCl_2$ -LiCl system shows the least negative deviation from ideality while the $MnCl_2$ -KCl and $MnCl_2$ -CsCl systems have the greatest negative

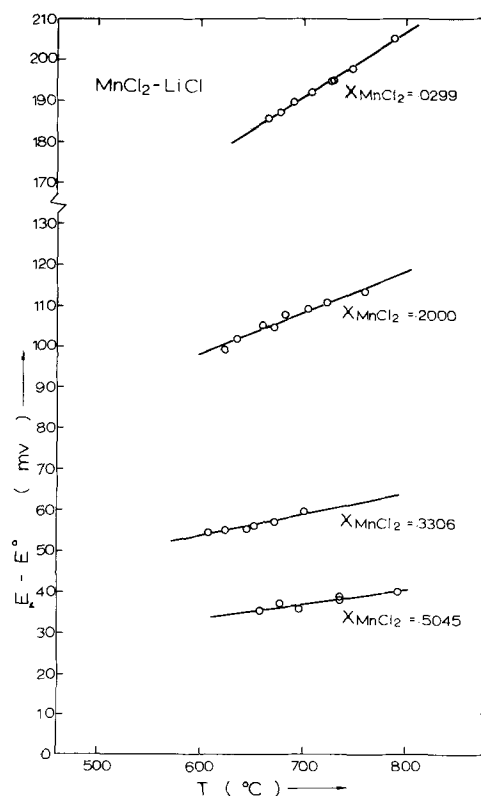


Fig. 3. Plots of $E - E^\circ$ vs. temperature for the $MnCl_2$ -LiCl system

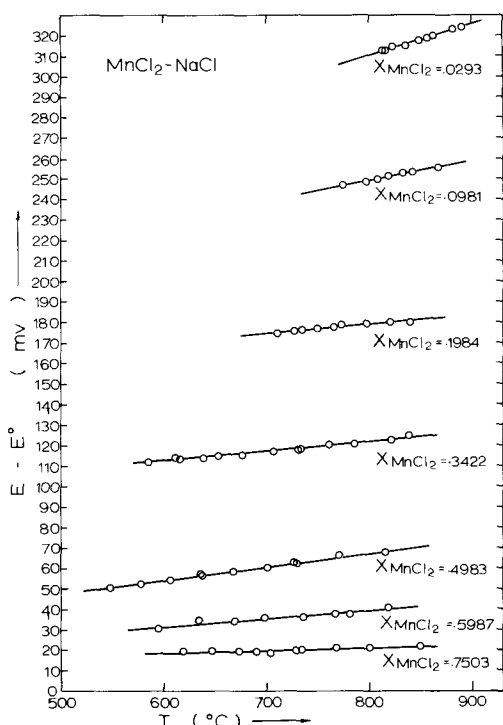


Fig. 4. Plots of $E - E^\circ$ vs. temperature for the $MnCl_2$ - $NaCl$ system.

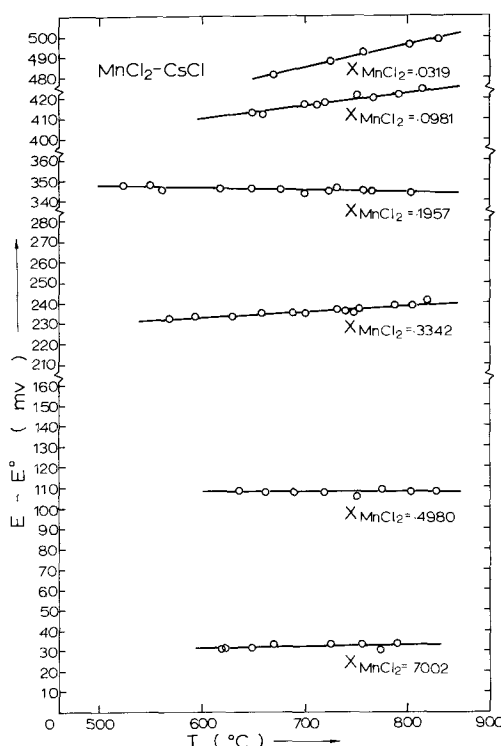


Fig. 6. Plots of $E - E^\circ$ vs. temperature for the $MnCl_2$ - $CsCl$ system

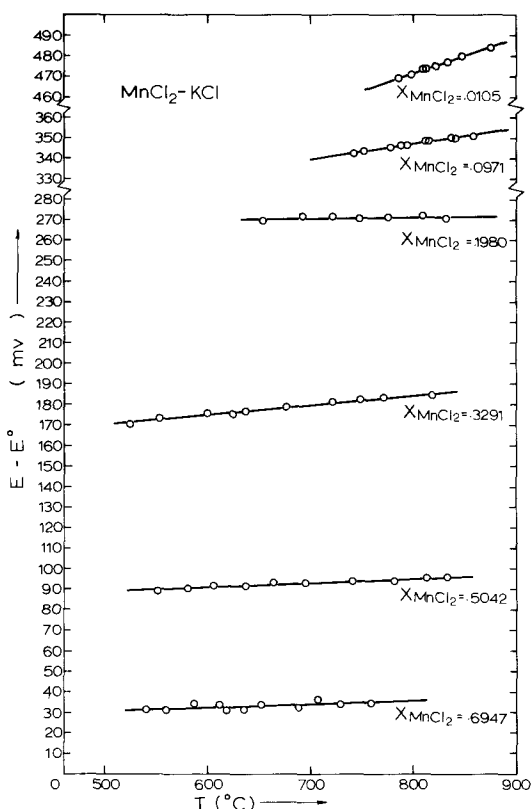


Fig. 5. Plots of $E - E^\circ$ vs. temperature for the $MnCl_2$ - KCl system

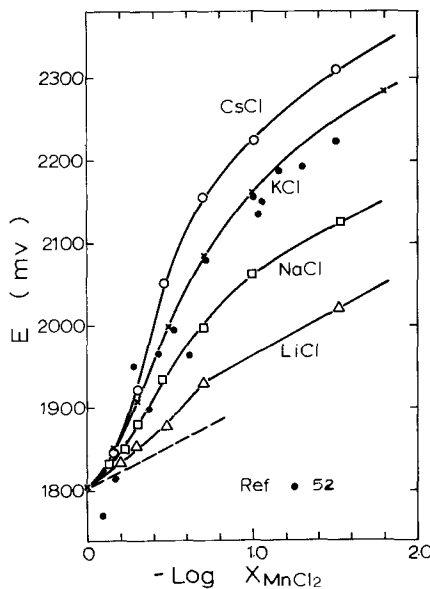


Fig. 7. Concentration dependence of the cell potentials for the binary ACl - $MnCl_2$ systems at $800^\circ C$.

deviations. The activities of the alkali chlorides shown in Fig. 9 were determined by the Gibbs-Duhem integration method from the corresponding partial molar excess free energies of $MnCl_2$.

Partial molar heats of mixing for the alkali chlorides in the four binary systems were calculated by the Gibbs-Duhem equation applicable to partial molar heats of mixing.

The results of these calculations are shown in Fig. 10-13 and in Table II. Partial molar heats of mixing

for $MnCl_2$ and the corresponding integral heats for each binary are also given.

From the standard deviations given in Table I the uncertainty in the calculated partial molar heats of mixing for $MnCl_2$ is estimated to be between 150 and 240 cal/mole. The uncertainty in the partial molar heats of mixing for ACl calculated by the graphical Gibbs-Duhem integration method cannot be given with any confidence because of the approximate nature of this method. However, if the partial molar heats of mixing for ACl are given uncertainties at least equal to those estimated for the $MnCl_2$ component, then the integral heats of mixing obtained from the well-known expression

$$\Delta H_M = X_1 \Delta \bar{H}_1 + X_2 \Delta \bar{H}_2 \quad [11]$$

should also have an uncertainty between 150 and 240 cal/mole of solution. For the $MnCl_2$ - $LiCl$ system this

Table I. Linear least squares fits for $E - E^\circ$ vs. temperature at several compositions in MnCl_2 -ACl system between 600° and 900°C

X_{MnCl_2}	$E - E^\circ$ (mV) = $A + BT$		Deviation		$\Delta\bar{G}_{\text{MnCl}_2}^{\text{xs}}$ 800°C (cal/mol)	$\Delta\bar{H}_{\text{MnCl}_2}$ 800°C (cal/mol)	$\Delta\bar{S}_{\text{MnCl}_2}$ 800°C (cal/°K·mol)
	A (mV)	B (mV/°K)	Standard (mV)	Maximum (mV)			
MnCl₂-LiCl							
0.0299	36.6	0.1584	0.4	0.6	-2,045	-1,688	7.30
0.2000	11.7	0.0993	0.9	1.4	-2,021	-541	4.58
0.3306	8.45	0.0517	0.5	0.6	-588	-390	2.38
0.5045	4.62	0.0332	0.9	1.3	-395	-213	1.50
MnCl₂-NaCl							
0.0293	149.8	0.1495	0.7	0.9	-6,787	-6,911	6.89
0.0981	148.8	0.0934	0.4	0.5	-6,539	-6,865	4.31
0.1984	135.0	0.0407	0.7	1.3	-4,792	-6,229	1.88
0.3422	72.7	0.0455	0.6	1.2	-3,320	-3,355	2.10
0.4983	-2.7	0.0649	0.4	0.8	-1,604	124	2.99
0.5987	-0.3	0.0368	1.0	1.4	-705	12	1.69
0.7503	7.6	0.0125	0.5	1.0	-356	-351	0.57
MnCl₂-KCl							
0.0105	288.3	0.1705	0.5	0.7	-12,021	-13,301	7.86
0.0971	267.6	0.0741	0.4	0.5	-11,039	-12,344	3.42
0.1980	265.5	0.0052	1.0	1.3	-9,049	-12,246	0.23
0.3291	133.2	0.0478	0.7	0.8	-6,144	-6,146	2.20
0.5042	73.1	0.0259	0.7	1.5	-2,930	-3,371	1.19
0.6947	18.6	0.0157	1.4	2.2	-859	-859	0.72
MnCl₂-CsCl							
0.0319	380.5	0.1075	0.6	0.8	-15,530	-17,553	+4.96
0.0981	356.4	0.0617	0.8	1.5	-14,547	-16,440	+2.84
0.1957	355.9	-0.0109	1.0	1.7	-12,393	-16,414	(-0.50)
0.3342	206.9	0.0293	1.1	2.2	-8,663	-9,546	+1.35
0.4980	109.2	-0.0015	1.2	2.6	-3,475	-5,036	(-0.07)
0.7002	27.2	0.0051	1.1	2.0	-746	-1,255	+0.23

$\Delta\bar{G}_{\text{MnCl}_2}^{\text{xs}} = \Delta\bar{G}_{\text{MnCl}_2} + RT \ln X_{\text{MnCl}_2}$ is the excess partial molar free energy of mixing.

uncertainty is significant but becomes less important in the more reactive systems MnCl_2 -CsCl.

The approximate integral heats of mixing obtained by this method are also given in Fig. 10-13 and are compared with the direct calorimetric measurements by Papatheodorou and Kleppa (1). It is apparent that the integral heats of mixing obtained by the emf method are at the most about 10% lower than the calorimetric results, with the exception of the MnCl_2 -LiCl system, for which, however, the disagreement appears to be within the uncertainty limits. It should be noted, however, that in the latter system the enthalpies of mixing are small and the errors which are inherent in the emf method become more significant. The agreement between the calorimetric and the electrochemical integral heats of mixing for the systems MnCl_2 -NaCl, MnCl_2 -KCl, and MnCl_2 -CsCl is within the

experimental error for the latter. The partial entropies of mixing for MnCl_2 were calculated from the temperature dependence of $E - E^\circ$ as stated earlier and are also given in Table I. From the uncertainties in the free energy and enthalpy data, the partial molar entropies of mixing reported herein are given with confidence to within ± 0.5 cal/°K. For the MnCl_2 -CsCl melts the slight negative entropies of mixing at $X_{\text{MnCl}_2} = 0.1957$ and $X_{\text{MnCl}_2} = 0.498$, appear to be inconsistent with the general trends.

Discussion

The thermodynamic properties of the MnCl_2 -ACl solutions and particularly the concentration dependence of the enthalpy and entropy of mixing may be understood through the application of the quasisemi-

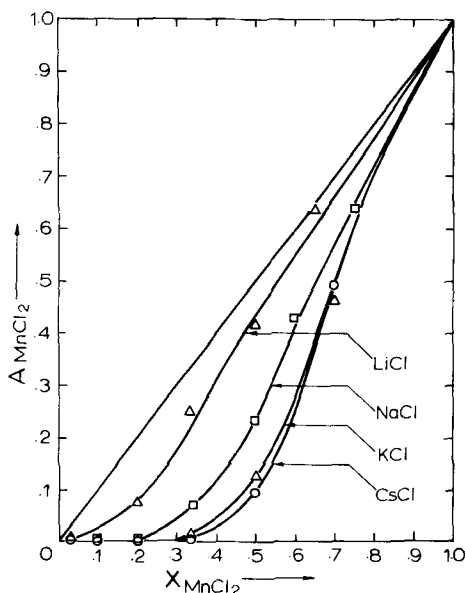


Fig. 8. Activities of MnCl_2 dissolved in alkali chlorides at 800°C

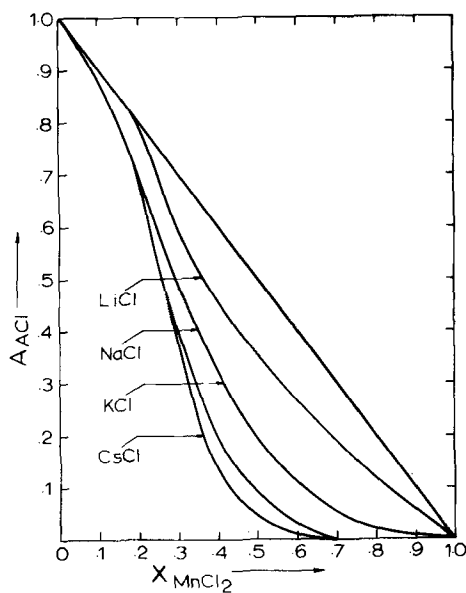


Fig. 9. Activities of ACl dissolved in MnCl_2 at 800°C

Table II. Partial molar and integral enthalpies of mixing

X_{MnCl_2}	$\bar{\Delta H}_{MnCl_2}$ cal/mol ⁻¹	$\bar{\Delta H}_{ACl}$ cal/mol ⁻¹	$\Delta H^{int,M}$ * This work cal/mol ⁻¹	$\Delta H^{int,M}$ (Papa- theodorou & Kleppa (1)) cal/mol ⁻¹ at 810°C
1—System: $MnCl_2$ -LiCl				
0.10	-930	-45	-130	-185
0.20	-560	-110	-200	-300
0.30	-390	-170	-230	-360
0.35	-335	-190	-240	—
0.40	-285	-220	-240	-390
0.50	-210	-280	-245	-370
0.60	-150	-355	-230	-310
0.70	-100	-450	-205	-250
0.80	-55	-590	-160	-160
0.90	-25	-875	-110	-70
2—System: $MnCl_2$ -NaCl				
0.10	-6,860	-5	-690	-635
0.20	-6,200	-120	-1340	-1180
0.30	-4,300	-780	-1830	-1600
0.35	-2,750	-1,530	-1880	-1690
0.40	-1,100	-2,520	-1950	-1840
0.50	-250	-3,080	-1670	-1760
0.60	-125	-3,240	-1370	-1560
0.70	-175	-3,340	-1050	-1300
0.80	-50	-3,415	-720	-920
0.90	-25	-3,580	-380	—
3—System: $MnCl_2$ -KCl				
0.10	-12,850	-16	-1290	-1310
0.18	—	—	—	-2230
0.20	-12,240	-112	-2540	—
0.30	-7,100	-1,770	-3370	—
0.33	—	—	—	-3540
0.35	-5,750	-2,100	-3375	-3650
0.40	-4,775	-3,000	-3710	-3785
0.49	—	—	—	-3600
0.50	-3,225	-4,190	-3710	—
0.60	-1,800	-5,970	-3470	-3160
0.64	—	—	—	-2870
0.70	-925	-7,645	-2840	—
0.80	-400	-9,080	-2140	—
0.90	-150	-10,520	-1190	-1105
4—System: $MnCl_2$ -CsCl				
0.1	-16,900	(-5)	-1690	-1880
0.18	—	—	—	-3380
0.2	-16,413	-108	-3370	—
0.3	-11,000	-1,942	-4650	—
0.35	-8,750	-3,030	-5030	—
0.40	—	—	—	-5240
0.48	—	—	—	-5370
0.50	-4,650	-6,038	-5340	-5260
0.60	-2,650	-8,500	-4990	—
0.63	—	—	—	—
0.70	-1,225	-11,150	-4200	-4500
0.78	—	—	—	-4020
0.80	-450	-13,514	-3060	-3272
0.90	-100	-15,400	-1630	—

* Average enthalpies in the temperature range 550°-850°C.

The partial molar enthalpies of mixing for $MnCl_2$ represents points taken from smooth curves drawn through the experimental results given in Table I. The partial molar properties for the ACl component were calculated by the Gibbs-Duhem integration method.

cal model for charge asymmetrical solutions presented in a previous publication (7).

The model is based on the concept that "complex ions" exist in molten salt solutions. However, the concept of complex ions in molten salts presented here is entirely different from that generally accepted in aqueous solutions. In dilute aqueous solutions because of the high dielectric constant of water, complex ionic species having a discrete structure may be considered to exist and the properties of the solutions may be interpreted by considering the behavior of point electrical charges in a dielectric medium.

In molten salts, the medium is totally ionic and because of the existence of strong short range electrostatic forces the requirement of local electrical neutrality is satisfied through the concept of interlocking anionic and cationic quasi lattices.

In this sense the liquid structure is continuous and the existence of discrete complex species is conceptually difficult. It is most likely that a "complex anion" in molten salts should be best represented by a configuration of a cation M^{n+} surrounded by anions X^- having a given coordination number within which the bond distances MX , and accordingly their energies, should be different from those expected to represent a noncomplexed dissociated ionic state. It is also con-

venient to take the noncomplexed state of the salt MX as that of the "pure MX ." Accordingly, the "complex" is expected to form only in the presence of a second salt AX which is considered to act as the ligand donor. Thus, the formation of the complex species is assumed to be the result of reactions of the type

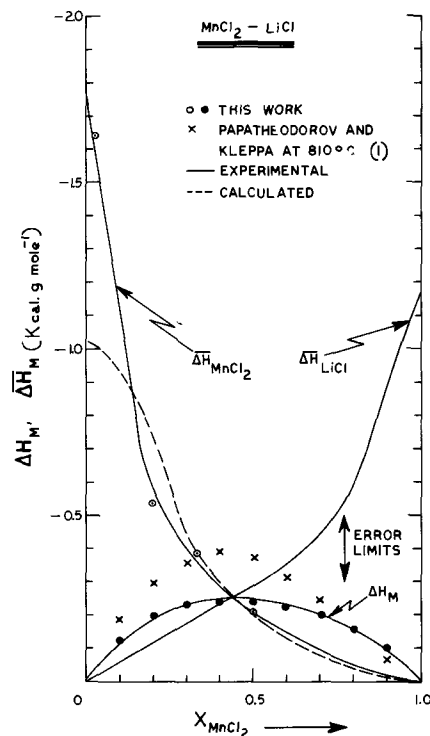
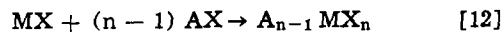


Fig. 10. Partial and integral enthalpies of mixing in the $MnCl_2$ -LiCl system. The graph includes the partial molar heats of mixing for $MnCl_2$ calculated from theory.

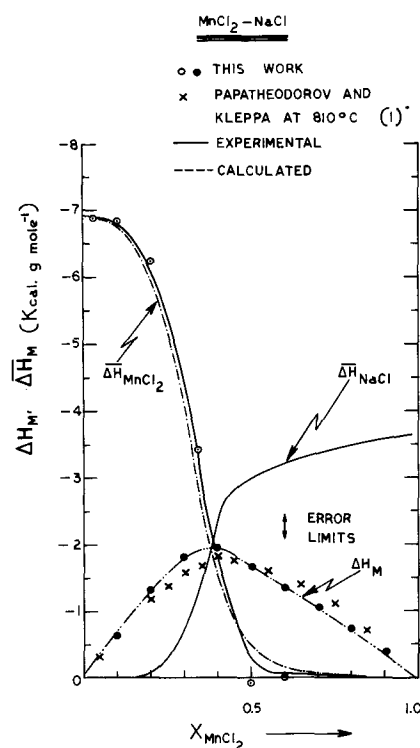


Fig. 11. Partial and integral enthalpies of mixing in the $MnCl_2$ -NaCl system. The graph includes the partial molar heats of mixing for $MnCl_2$ calculated from theory.

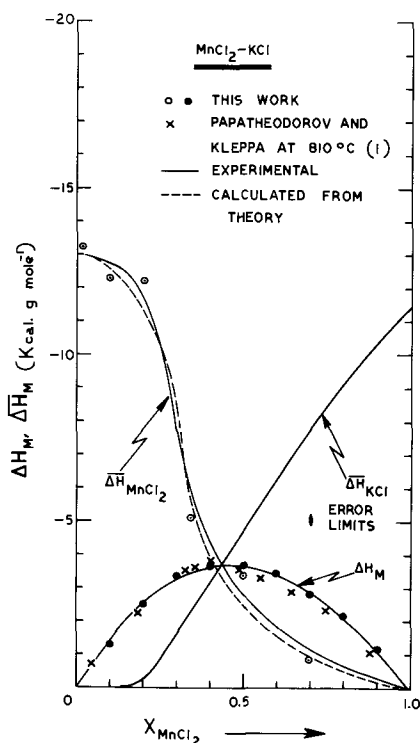


Fig. 12. Partial and integral enthalpies of mixing in the MnCl_2 -KCl system. The graph includes the partial molar heats of mixing for MnCl_2 calculated from theory.

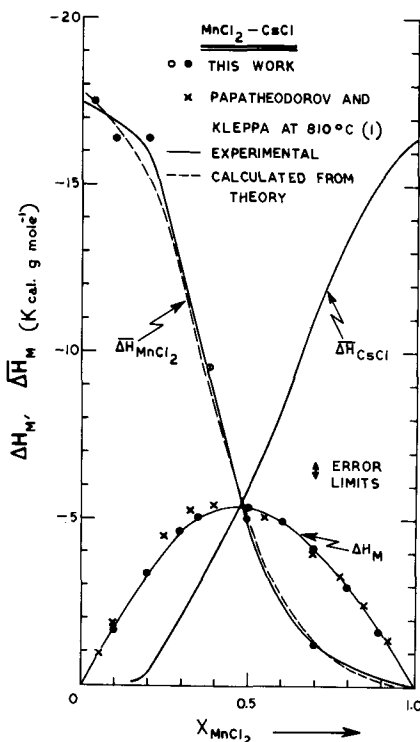


Fig. 13. Partial and integral enthalpies of mixing in the MnCl_2 -CsCl system. The graph includes the partial molar heats of mixing for MnCl_2 calculated from theory.

and the strength of the complex shall depend on the magnitude of the competing interactions of the A^+ and M^+ cations for the same ligand anions X^- .

In a melt containing both AX and MX , it is conceivable that two kinds of MX bonds could exist. M-X bonds having the bond distance describing the "complex" state, and M-X bonds describing the "free" MX species. The pure material is expected to have only bonds of the second type.

It is also evident that the continuity of the medium imposes the restriction that the "complex" anions are not discrete isolated species but are part of the ionic liquid structure and therefore their central M cations interact with other surrounding cations through bridging X^- anions. In a melt containing MX and AX components, it is meaningless to postulate a structure based on the MX_n anions occupying single anion lattice sites in addition to other free anions and cations. The structure should still be one represented by arrays of positive and negative ions in a continuous sequence in such a manner that positive ions are always surrounded by negative ones.

Since the only characteristic of a "complex" anion is the bond distance MX , its coordination configuration MX_n may be treated as a separate statistical entity. When MX is added to AX a "reaction" may be postulated according to the stoichiometry indicating the preferred coordination within the complex anion. For example, for a tetrahedrally coordinated complex between a divalent metal chloride and an alkali metal chloride, the reaction is represented by



Regarding the preferred coordination of complex ions in fused salts, the accumulated experimental evidence indicates that such coordinations are relatively simple. Thus, mixtures of monovalent cations appear to prefer the two-ligand configuration representing a linear or angular structure as in $\text{Ag}(\text{CN})_2^-$ (19). Mixtures of mono- with divalent cations appear to follow the tetrahedral coordination as in MgCl_4^{2-} . Finally, mixtures of mono- and tetravalent cations as in the systems, ZrCl_4 , TiCl_4 , HfCl_4 , with alkali chlorides (20) prefer to form octahedrally coordinated complexes of the type ZrCl_6^{2-} , TiCl_6^{2-} , and HfCl_6^{2-} . In these systems it has been shown that the thermodynamic properties of the solutions can be accounted for on the basis of the MCl_6^{2-} complex ion (21, 22).

From the previous discussion it follows that "complex" species in fused salts are not expected to dissociate in the same manner as their counterparts in aqueous solutions. The formation of the new type of M-Cl bond distances is initiated by the presence of the A^+ cations. Each added A^+ cation is expected to disturb one M-Cl bond and the "complex" should form "stoichiometrically."

Accordingly, the difference between the effects of various kinds of ACl ligand donors on the same MCl_2 salt shall be manifested as a heat effect, and the introduction of a dissociation constant into the treatment is not necessary for the mathematical treatment. In a solution containing various proportions of ACl to MCl_2 , the changes in the bond energies which may result from the replacement of one kind of neighboring ion by another, should result in changes in the over-all heat effect of mixing, and may be accounted for by assigning different values to the bond energies representing the various possible ionic combinations. Again the concept of a "dissociating complex" is not necessary.

However, if two or more "complex" coordinations are energetically favorable, then the concepts of equilibrium between "complex" species, and of dissociation, become significant.

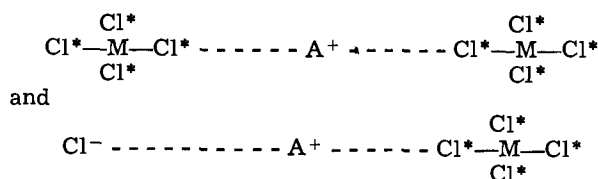
The present treatment is applicable to salt systems which appear to conform with the concept of a single complex configuration.

Theory of mixing of charge asymmetrical system forming complex anions.—Considering the binary mixture MCl_2 - ACl over the entire composition range, from pure MCl_2 to pure ACl , the complex A_2MCl_4 is expected to form quantitatively at a composition $X_{\text{MCl}_2} = 0.333$.

For compositions rich in ACl ; namely for $0.333 > X_{\text{MCl}_2} > 0$, the melt is taken to consist of unreacted ACl and the complex compound A_2MCl_4 . For com-

positions rich in MCl₂, namely for $1.00 > X_{MCl_2} > 0.333$, the melt may be taken to consist of unreacted MCl₂, and the complex compound A₂MCl₄.

The ionic compositions, assuming that the complex only dissociates into A⁺ cations and MCl₄²⁻ anions, may be calculated from the original mole fractions by a mass balance calculation and are given in Table III. For the common cation subsystem, ACI-A₂MCl₄, if the ability of the M²⁺ ions for interaction is considered as having been nearly satisfied through the formation of the "complex" anion MCl₄²⁻, it is reasonable to expect that the species present should be randomly distributed and that only next nearest neighbor type interactions should be significant. The solutions could then be treated as regular. Thus, the bond energies to be considered in the "pure" components ACI and A₂MCl₄ are characterized by the energies of the next nearest neighbor interactions, Cl⁻-A⁺-Cl⁻ and MCl₄²⁻-A⁺-MCl₄²⁻, respectively. The solution, in addition to the above interactions is also characterized by interactions of the type Cl⁻-A⁺-MCl₄²⁻. However, the concept of continuity in the structure of the ionic melt discussed earlier, requires that the MCl₄²⁻ species be nonexistent as an isolated entity. The A⁺ cations are expected to interact with the M²⁺ central cations in the "complex" species via bridging Cl⁻ anions. Thus, it is more realistic to describe the MCl₄²⁻ type interactions in pure A₂MCl₄ and the Cl⁻-A⁺-MCl₄²⁻ type interactions in the solution, as interactions between a central A⁺ cation and two chloride species representing ionic arrays of the type



where Cl⁻ and Cl* describe the states of chlorine in pure ACI and in the "complex" species, MCl₄²⁻, respectively.

It should be noted that although the number of MCl₄²⁻ configurations in the system is fixed by stoichiometry, the two types of chloride ions in the solution can readily exchange positions so that the probability of finding a chloride species of the Cl* type in any position is approximated by the fraction of the anionic positions occupied by the configuration MCl₄²⁻.

The "significant" interactions for the pure components and for their mixture are therefore best represented by the following energy terms. For pure ACI, the Cl⁻-A⁺-Cl⁻ type interaction is described by $E_{Cl-A-Cl}$; for pure A₂MCl₄, the Cl*⁻-A⁺-Cl* type interaction is described by $E_{Cl^*-A-Cl^*}$, and in the binary solution ACI-A₂MCl₄, the bond energies are the $E_{Cl-A-Cl}$, $E_{Cl-A-Cl^*}$, and $E_{Cl^*-A-Cl^*}$, where $E_{Cl^*-A-Cl^*}$ describes the new type of interaction discussed previously.

Since we are only concerned with the chloride ion coordination of the A⁺ cations the nearest neighbor coordination number for A⁺ should not be affected by mixing the charge asymmetrical system ACI-A₂MCl₄.

In this composition range, for a melt represented by the nominal mole fractions X_{ACI} and X_{MCl_2} , respectively, the "true" composition is given in Table III.

Within the subsystem ACI-A₂MCl₄ as the complex anions present in the mixture have originated from the total reaction of X_{MCl_2} gram-moles of MCl₂, the first part of the heat effect or the "reaction part" is simply proportional to the amount of complex formed, and is given by the equation

$$\Delta H_1 = X_{MCl_2} b_R \quad [14]$$

The constant b_R represents the heat of formation per gram-mole of complex according to

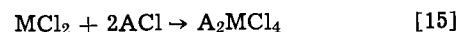
Table III. Mass balance for the MCl₂-ACI system

ACI	MCl ₂ ²⁻ Cl ⁻ , A ⁺	MCl ₄ ²⁻ A ⁺	M ²⁺ , Cl ⁻ , A ⁺ , MCl ₄ ²⁻	M ²⁺ Cl ⁻
0	0.333	0.333	0.333	1.0
ACI	A ₂ MCl ₄	A ₂ MCl ₄	A ₂ MCl ₄	MCl ₂
$X_{MCl_2} > 0.333$ $1.0 > X_{MCl_2} > 0.333$ $n_{MCl_2} = X_{MCl_2} - 0.5X_{ACI} = n_1, n_{ACI} = 0$ $n_{A_2MCl_4} = 0.5X_{ACI} = n_2$				
Ionic composition	Ionic fraction			
$n_{M^{2+}} = X_{MCl_2} - 0.5X_{ACI}$	$N_{M^{2+}} = \frac{2X_{MCl_2} - X_{ACI}}{1 + X_{MCl_2}}$			
$n_{A^+} = X_{ACI}$	$N_{A^+} = \frac{2X_{ACI}}{1 + X_{MCl_2}}$			
$n_{Cl^-} = 2X_{MCl_2} - X_{ACI}$	$N_{Cl^-} = \frac{4X_{MCl_2} - 2X_{ACI}}{4X_{MCl_2} - X_{ACI}}$			
$n_{MCl_4^{2-}} = 0.5X_{ACI}$	$N_{MCl_4^{2-}} = \frac{X_{ACI}}{4X_{MCl_2} - X_{ACI}}$			
$0.333 > X_{MCl_2} > 0$ $n_{MCl_2} = 0, n_{ACI} = X_{ACI} - 2X_{MCl_2} = n_1$ $n_{A_2MCl_4} = X_{MCl_2} = n_2$				
Ionic composition	Ionic fraction			
$n_{M^{2+}} = 0$	$N_{M^{2+}} = 0$			
$n_{A^+} = X_{ACI}$	$N_{A^+} = 1.0$			
$n_{Cl^-} = X_{ACI} - 2X_{MCl_2}$	$N_{Cl^-} = \frac{X_{ACI} - 2X_{MCl_2}}{X_{ACI} - X_{MCl_2}}$			
$n_{MCl_4^{2-}} = X_{MCl_2}$	$N_{MCl_4^{2-}} = \frac{X_{MCl_2}}{X_{ACI} - X_{MCl_2}}$			

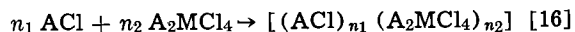
X indicates the original mole fractions in the solution which is prepared by mixing the components ACI and MCl₂.

n indicates the g-moles of a component.

N indicates ionic fractions after the complex forming reaction has taken place.



The second part or the "mixing part" of the total heat originates by the regular solution type mixing of the charge asymmetrical mixture containing n_1 g-moles of ACI and n_2 g-moles of A₂MCl₄ according to the reaction



This "mixing" part may be calculated by interpreting the energy of mixing as the difference between the internal energy of the solution from that of the pure components, where the previously described interactions are the only ones which are considered as being significant. Pair interactions of the same kind are taken to have the same energy in the pure components as in solution and cancel out.

The energy change in the mixing reaction is therefore

$$\Delta E_{mix}^{int} = E_{mix} - n_1 E_{ACI} - n_2 E_{A_2MCl_4} \quad [17]$$

The total number of next nearest neighbor interactions originating from a central A⁺ cation is given by $\frac{1}{2}NZ_1(n_1 + 2n_2)$ where N is the Avogadro number and Z₁ is the coordination number for ACI. In pure ACI and A₂MCl₄, the total numbers of such interactions are $\frac{1}{2}n_1 NZ_1$ and $n_2 NZ_1$, respectively. Hence, using the above relationships and taking the probability of finding a bonded Cl* as being the same as that of finding the entity MCl₄²⁻, the following expression has been derived (7) according to the method which is followed for regular solutions.

$$\Delta E_M = \frac{(X_{ACl} - 2X_{MCl_2})X_{MCl_2}}{X_{ACl} - X_{MCl_2}} \left[\frac{X_{ACl} - 2X_{MCl_2}}{X_{ACl} - X_{MCl_2}} b_1 + b_2 \right] \quad [18]$$

where

$$b_1 = \frac{1}{2}NZ_1 [E_{Cl^*-A-Cl^*} + E_{Cl-A-Cl} - 2E_{Cl^*-A-Cl}]$$

and

$$b_2 = \frac{1}{2}NZ_1 [4E_{Cl-A-Cl^*} - 3E_{Cl^*-A-Cl^*} - E_{Cl-A-Cl}]$$

are parameters to be determined from experimental results. By assuming that pressure-volume work is negligible, Eq. [18] can be used to represent the enthalpy of mixing ($\Delta E_M = \Delta H_M$). Thus, the total enthalpy will be given by the sum of Eq. [13] and [18], as shown below

$$\Delta H_M = X_{MCl_2}b_R + \frac{(X_{ACl} - 2X_{MCl_2})X_{MCl_2}}{X_{ACl} - X_{MCl_2}} \left[\frac{X_{ACl} - 2X_{MCl_2}}{X_{ACl} - X_{MCl_2}} b_1 + b_2 \right]$$

for

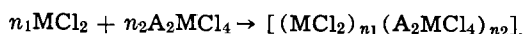
$$0.333 > X_{MCl_2} > 0 \quad [19]$$

It should be noted that the parameter b_2 is similar to that obtained from regular solution theory for a charge asymmetrical reciprocal salt mixture. The parameter b_1 is the result of charge asymmetry. Hence, the total integral heat of mixing in the reacting system is determined by the heat contribution due to the complex ion forming reaction, by a heat effect due to an exchange reaction between next nearest neighbor anions, and by asymmetry.

Considering the composition range in the subsystem $MCl_2 - A_2MCl_4$ from, $1.0 > X_{MCl_2} > 0.333$, the "true" composition of the solution is given in Table II. In this range the "reaction" part of the total mixing reaction is given by

$$\Delta H'_1 = 0.5X_{ACl}b_R \quad [20]$$

Once the complex has been formed the second part of the reaction involves mixing of the unreacted MCl_2 with A_2MCl_4 according to



Again, in this system the following different kinds of chloride ions should be considered: chloride ions which surround "free" M^{2+} or A^+ cations, and chloride ions bonded in the complex ionic configuration $[MCl_4^*]^{-2}$. Also, the cation M^{2+} in the complex $[MCl_4^*]^{-2}$ is bonded to the surrounding M^{2+} or A^+ "free" cations through bridging Cl^* ions. Accordingly, in a reciprocal salt mixture where the complex ion configuration is already present the significant interactions are the nearest neighbor cation to anion attractions. The various energy contributions are given as: E_{Cl-A} , E_{Cl^*-A} , E_{Cl-M} , E_{Cl^*-M} where the interactions E_{Cl-A} and E_{Cl-M} are also common in the pure components ACl and MCl_2 . It is also expected that if the nearest neighbor coordination number of the "free" M^{2+} cations is Z_1 , then the nearest neighbor coordination number of the A^+ cations should be $0.5Z_1$.

In a random system, the total number of bonds which emanate from the "free" A^+ and M^{2+} ions may be calculated from the average coordination number of the solution defined as

$$\begin{aligned} \bar{Z} &= \frac{n_1}{n_1 + 2n_2} Z_1 + \frac{2n_2}{n_1 + 2n_2} 0.5Z_1 \\ &= \frac{n_1 + n_2}{n_1 + 2n_2} Z_1 \end{aligned} \quad [21]$$

The total number of significant nearest neighbor type bonds in the solution is readily calculated as

$$\frac{1}{2}N(n_1 + 2n_2)\bar{Z} = \frac{1}{2}N(n_1 + n_2)Z_1$$

On the basis of the same assumptions as for the ACl rich solutions, the integral energy of mixing has been derived as (7)

$$\Delta E_M = \frac{(X_{MCl_2} - 0.5X_{ACl})0.5X_{ACl}}{(2X_{MCl_2} - 0.5X_{ACl})} \left[\frac{X_{MCl_2} - 0.5X_{ACl}}{X_{MCl_2} + 0.5X_{ACl}} b'_1 + b'_2 \right] \quad [22]$$

where

$$b'_1 = \frac{1}{2}NZ_1 [2E_{ACl} + 0.5E_{MCl^*} - 2E_{MCl} - 0.5E_{ACl^*}]$$

$$b'_2 = \frac{1}{2}NZ_1 [2E_{ACl} + 0.5E_{MCl^*} - E_{MCl} - 1.5E_{A-Cl^*}] \quad [23]$$

are interaction parameters.

The total integral heat of mixing is given as

$$\Delta H_M = 0.5X_{ACl}b_R + \frac{(X_{MCl_2} - 0.5X_{ACl})0.5X_{ACl}}{(2X_{MCl_2} - 0.5X_{ACl})} \left[\frac{X_{MCl_2} - 0.5X_{ACl}}{X_{MCl_2} + 0.5X_{ACl}} b'_1 + b'_2 \right]$$

for

$$1.0 > X_{MCl_2} > 0.333 \quad [24]$$

The second part of Eq. [25], is of the form

$$\Delta E_M = \frac{n_1n_2}{2n_1 + n_2} \left[\frac{n_1}{n_1 + 2n_2} b'_1 + b'_2 \right] \quad [25]$$

and accordingly, the parameter b'_2 describes the regular behavior of the solution when asymmetry effects are not accounted for. The effect of variable coordination number is represented by the asymmetric parameter b'_1 .

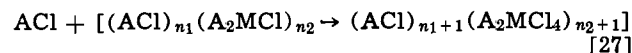
The above calculations indicate that the concentration dependence of the integral heat of mixing is a complex function of the concentration and that the entire heat of mixing curve may be accounted for by five parameters, b_R , b_1 , b_2 , b'_1 , and b'_2 . The application of this method to 27 reactive charge asymmetrical binary fused salt systems presented in the previous publication (7) shows that the interaction parameters are physically meaningful as they are related to the ionic radii of the ionic species in these melts.

Determination of energetic parameters.—The "reaction" parameter b_R may be obtained from an experimentally measured heat of mixing curve by substituting for $X_{MCl_2} = 0.333$ and solving either Eq. [19] or [24]. Thus

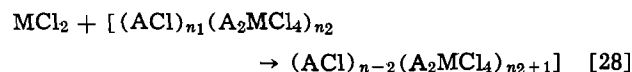
$$b_R = 3(\Delta H_M) \text{ at } X_{MCl_2} = 0.333 \quad [26]$$

The parameters b_1 and b'_2 may be determined from the partial molar heats of mixing.

In the $ACl - A_2MCl_4$ subsystem at $0.333 > X_{MCl_2} > 0$ the partial molar heats of mixing for ACl and MCl_2 may be represented by the following mixing reactions



and



The corresponding equations for the partial molar heats of mixing are derived by partial differentiation of Eq. [19] as

$$\begin{aligned} \Delta \bar{H}_{MCl_2} &= b_R \\ &+ \frac{(X_{ACl}^3 - 4X_{MCl_2}^3 - 7X_{MCl_2}X_{ACl}^2 + 12X_{ACl}X_{MCl_2}^2)}{(X_{ACl} - X_{MCl_2})^3} b_1 \\ &- \frac{2X_{MCl_2}^2 - (X_{ACl} - 2X_{MCl_2})^2}{(X_{ACl} - X_{MCl_2})^2} b_2 \end{aligned} \quad [29]$$

and

$$\Delta\bar{H}_{\text{ACl}} = \frac{X_{\text{MCl}_2}^2}{(X_{\text{ACl}} - X_{\text{MCl}_2})^2} \left[b_2 + \frac{2(X_{\text{ACl}} - 2X_{\text{MCl}_2})}{(X_{\text{ACl}} - X_{\text{MCl}_2})} b_1 \right] \quad [30]$$

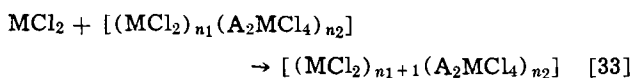
At $X_{\text{ACl}} = 2X_{\text{MCl}_2}$, or at the composition $X_{\text{MCl}_2} = 0.333$, Eq. [29] and [30] yield

$$b_2 = (\Delta\bar{H}_{\text{ACl}}) \quad [31]$$

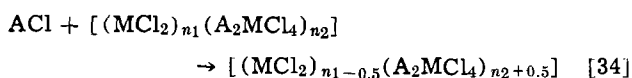
or

$$b_2 = \frac{b_{\text{R}} - (\Delta\bar{H}_{\text{MCl}_2})}{2} \quad [32]$$

In the $\text{MCl}_2 - \text{A}_2\text{MCl}_4$ subsystem, at $1.0 > X_{\text{MCl}_2} > 0.333$ the mixing reactions for ACl and MCl_2 are respectively



and



The partial molar heats of mixing for ACl and MCl_2 are obtained by partial differentiation of Eq. [24], and are, respectively

$$\Delta\bar{H}_{\text{MCl}_2} = \frac{0.0625X_{\text{ACl}}^4 + 1.25X_{\text{MCl}_2}^2X_{\text{ACl}}^2 - 0.75X_{\text{ACl}}^3X_{\text{MCl}_2}}{(2X_{\text{MCl}_2} - 0.5X_{\text{ACl}})(X_{\text{MCl}_2} + 0.5X_{\text{ACl}})^2} b'_1 + \frac{X_{\text{ACl}}^2}{4(2X_{\text{MCl}_2} - 0.5X_{\text{ACl}})^2} b'_2 \quad [35]$$

and

$$\Delta\bar{H}_{\text{ACl}} = 0.5b_{\text{R}} + \left[\frac{0.5^2X_{\text{MCl}_2} - X_{\text{MCl}_2}X_{\text{ACl}} + 0.375X_{\text{ACl}}^2}{(2X_{\text{MCl}_2} - 0.5X_{\text{ACl}})(X_{\text{MCl}_2} + 0.5X_{\text{ACl}})} - \frac{0.25X_{\text{ACl}}(X_{\text{MCl}_2} - 0.5X_{\text{ACl}})^2(X_{\text{MCl}_2} - X_{\text{ACl}})}{(2X_{\text{MCl}_2} - 0.5X_{\text{ACl}})^2(X_{\text{MCl}_2} + 0.5X_{\text{ACl}})^2} \right] b'_1 + \frac{(X_{\text{MCl}_2}^2 - X_{\text{ACl}}X_{\text{MCl}_2} - 0.125X_{\text{ACl}}^2)}{(2X_{\text{MCl}_2} - 0.5X_{\text{ACl}})^2} b'_2 \quad [36]$$

From Eq. [36] at a composition $X_{\text{MCl}_2} = 0.333$

$$(\Delta\bar{H}_{\text{ACl}}) = (b_{\text{R}} - b'_2)/2 \quad [37]$$

and from Eq. [35]

$$(\Delta\bar{H}_{\text{MCl}_2}) = b'_2 \quad [38]$$

From Eq. [31] and [37], it follows that

$$b_{\text{R}} = 2b_2 + b'_2 \quad [39]$$

Hence, the parameters b'_2 and b_2 may be determined directly from experimentally obtained partial molar heats of mixing of either ACl or MCl_2 at the stoichiometric composition of $\text{MCl}_2 = 0.333$.

The parameters b_1 and b'_1 may be determined from the equations for the integral heats of mixing [18] and [24] written in the following forms: For the composition range

$$0.333 > X_{\text{MCl}_2} > 0$$

$$\frac{(\Delta H_{\text{M}} - X_{\text{MCl}_2}b_{\text{R}})(X_{\text{ACl}} - X_{\text{MCl}_2})}{(X_{\text{ACl}} - 2X_{\text{MCl}_2})X_{\text{MCl}_2}} = \frac{X_{\text{ACl}} - 2X_{\text{MCl}_2}}{X_{\text{ACl}} - X_{\text{MCl}_2}} b_1 + b_2 \quad [40]$$

which is of the linear form

$$I = P b_1 + b_2$$

Similarly, from Eq. [24]

$$\frac{(\Delta H_{\text{M}} - 0.5X_{\text{ACl}}b_{\text{R}})(8X_{\text{MCl}_2} - 2X_{\text{ACl}})}{(2X_{\text{MCl}_2} - X_{\text{ACl}})X_{\text{ACl}}} = \frac{2X_{\text{MCl}_2} - X_{\text{ACl}}}{2X_{\text{MCl}_2} + X_{\text{ACl}}} b'_1 + b'_2 \quad [41]$$

which is of the linear form

$$I' = Q b'_1 + b'_2 \quad [42]$$

Because the calculations involve small difference between large numbers, it is best to obtain the parameters b_2 and b'_2 from the partial molar heats of mixing, and then use the linear plots predicted by Eq. [40] and [41] to evaluate the slopes b_1 and b'_1 . Alternatively, b_1 and b'_1 may be calculated by solving Eq. [19] and [24], for various points along the curve where b_{R} , b_2 , and b'_1 are known using the previously described methods.

Calculation of Entropies of Mixing

Following the same general method as previously, the entropy of mixing in a reactive binary salt mixture is calculated on the basis of the two main contributions. The "reaction" part which is simply proportional to the amount of the complex species formed in accordance with reaction [14], and a "random mixing" part which is calculated on the basis of ionic fractions.

The formation of a "complex" species is expected to be accompanied by changes in vibrational entropy while the mixing part should be entirely configurational.

In the compositional range, $1.0 > X_{\text{MCl}_2} > 0.333$ application of these concepts leads to the equation for the integral entropy of mixing which is of the form

$$\Delta S^{\text{int}}_{\text{M}} = 0.5X_{\text{ACl}}\epsilon - R[n_{\text{A}} + \ln N_{\text{A}} + n_{\text{Cl}} - N_{\text{Cl}} - n_{\text{MCl}_2} - \ln N_{\text{MCl}_2} - n_{\text{M}^2} + \ln N_{\text{M}^2}] \quad [43]$$

The expressions for the mole numbers n and for the ionic fractions N in terms of primary mole fractions are given in Table III. Similarly, in the composition range, $0.333 > X_{\text{MCl}_2} > 0$ the corresponding expression is

$$\Delta S^{\text{int}}_{\text{M}} = X_{\text{MCl}_2}\epsilon + R[n_{\text{Cl}} - \ln N_{\text{Cl}} - n_{\text{MCl}_2} - \ln N_{\text{MCl}_2}] \quad [44]$$

The parameter ϵ represents the change in vibrational entropy connected with Reaction [15].

The partial molar entropies of mixing for MCl_2 and ACl may be calculated from Eq. [43] and [44] by partial differentiation with respect to the corresponding mole fractions. In the concentration range $1.0 > X_{\text{MCl}_2} > 0.333$ the final equations expressed in terms of primary mole fractions are

$$\Delta\bar{S}_{\text{MCl}_2} = -R \ln \frac{4(2X_{\text{MCl}_2} - X_{\text{ACl}})^3}{(1 + X_{\text{MCl}_2}) \cdot (4X_{\text{MCl}_2} - X_{\text{ACl}})^2} \quad [45]$$

and

$$\Delta\bar{S}_{\text{ACl}} = 0.5\epsilon - \frac{R}{2} \left[\ln \frac{2(2X_{\text{MCl}_2} - X_{\text{ACl}})^3(1 + X_{\text{MCl}_2})}{X_{\text{ACl}}^3(4X_{\text{MCl}_2} - X_{\text{ACl}})} \right] \quad [46]$$

It is significant that the partial molar entropy of mixing for MCl_2 does not include any vibrational contributions. In this concentration range the solution process for a partial property of MCl_2 is represented by Reaction [33] and it is evident that the reaction does not include the formation of new complex species other than these already in existence. However, for the ACl component the solution process is given by Reaction

[34] and clearly involves the formation of one additional mole of complex species.

In the composition range $0.333 > X_{MnCl_2} > 0$, the partial molar entropies of mixing for ACl and $MnCl_2$ are given, respectively, as

$$\Delta \bar{S}_{MnCl_2} = \epsilon - R \ln \frac{X_{MnCl_2}(X_{ACl} - X_{MnCl_2})}{(X_{ACl} - 2X_{MnCl_2})^2} \quad [47]$$

and

$$\Delta \bar{S}_{ACl} = R \ln \frac{X_{ACl} - 2X_{MnCl_2}}{X_{ACl} - X_{MnCl_2}} \quad [48]$$

In this concentration range it is significant that the partial entropy of mixing for $MnCl_2$ includes vibrational contributions. The logarithmic term in Eq. [47] represents the configurational part to the total partial molar entropy of mixing. The partial molar entropy of mixing for ACl is entirely configurational because the addition of ACl to these ACl-rich solutions is not accompanied by the formation of additional moles of complex species.

The "configurational" part of the partial molar entropy of mixing from Eq. [45] and [47] was calculated and the results are presented in Fig. 14. Figure 14 also includes so-called "ideal" partial molar entropies of mixing given as $-R \ln X_{MnCl_2}$.

It is characteristic that the present calculation predicts the concentration dependence of the molar entropies of mixing which changes from positive to negative and then again to positive values. This behavior may be described as typical of complex ion fused salt systems.

Application of the complex ion model to the $MnCl_2$ -ACl systems.—From the integral heats of mixing for the binary systems $MnCl_2$ -LiCl, $MnCl_2$ -NaCl, $MnCl_2$ -KCl, and $MnCl_2$ -CsCl, the reaction parameters b_R , b_1 and b'_1 were obtained and are given in Table IV. Similarly, the interaction parameters b_2 , b'_2 were determined from the experimental partial molar heats of mixing of $MnCl_2$ and of the corresponding alkali chloride at $X_{MnCl_2} = 0.333$, and are also included in Table III. From Eq. [29] and [35] and the parameters in Table III the partial enthalpy of mixing of $MnCl_2$ was calculated over the entire concentration range and the results are compared with the experimental partial enthalpies of $MnCl_2$ in Fig. 10-13. The parameters b_R for the $MnCl_2$ -ACl systems are plotted in Fig. 15 vs. the radii of the alkali metal cations and the plot indicates a linear relationship. Good agreement is also ob-

Table IV. Enthalpy and entropy parameters for $MnCl_2$ -ACl system (cal/mol, cal/K·mol)

	CsCl	KCl	NaCl	LiCl
b_R	-14,700	-10,700	-5900	-720
b'_2	-9,500	-6,150	-3350	-350
b_2	-2,500	-2,200	-1250	-175
b'_1	-31,500	-20,750	+1875	-1770
b_1	-377	-501	+107	-415
ϵ	(-1.0)	(-0.2)	(+1.0)	-

tained with the b_R parameter determined from the calorimetric data of Papatheodorou and Kleppa (1, 7).

The entropy of mixing can also be used to test the model that has been proposed. The partial molar entropies of mixing obtained from the emf results are included in Fig. 14 for comparison with the calculated values.

It is evident that within the experimental uncertainty of ± 0.5 cal/°K the theoretical calculations are in fair agreement with the experimental results, particularly for the systems $MnCl_2$ -NaCl, $MnCl_2$ -KCl, and $MnCl_2$ -CsCl for compositions rich in alkali chloride. The $MnCl_2$ -LiCl system with the exception of one point appears to follow the "ideal" entropy curve and therefore its thermodynamic behavior should be described as "regular."

For solutions rich in ACl the difference between the experimental points and the configurational entropy curve may be attributed to vibrational contributions. Approximate values for ϵ in the various systems were calculated and are given in Table III. Similarly, for solutions rich in $MnCl_2$ where the partial molar entropies of mixing are entirely configurational the agreement is within experimental error, with the exception of two points at $X_{MnCl_2} = 0.5$ which correspond to the two systems $MnCl_2$ -KCl and $MnCl_2$ -CsCl.

It is evident that the model describes quite well the general trend in the concentration dependence of the excess partial molar entropies and enthalpies of mixing except for the LiCl system.

It is characteristic that the model predicts positive entropies in the $MnCl_2$ -rich compositions and entropies of mixing which change from positive to negative for the alkali chloride-rich compositions. In addition the transition from positive to negative values is occurring at about $X_{MnCl_2} = 0.333$, where the complex $MnCl_4^{2-}$ is expected to form stoichiometrically.

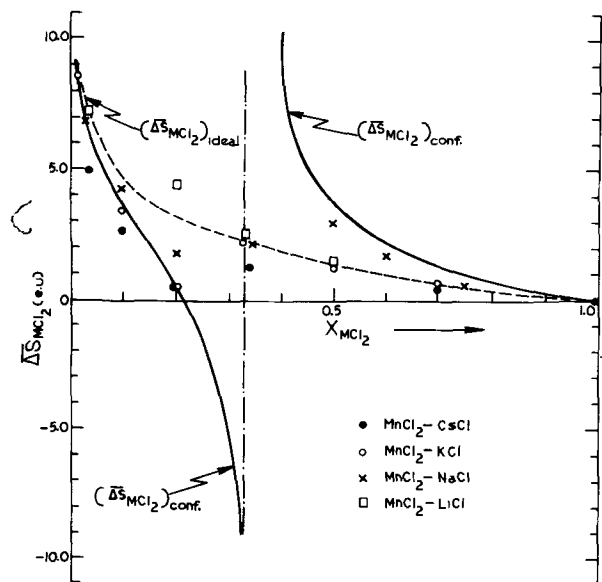


Fig. 14. Partial molar entropies of $MnCl_2$ in the alkali chloride systems. Comparison between theoretical and experimental values.

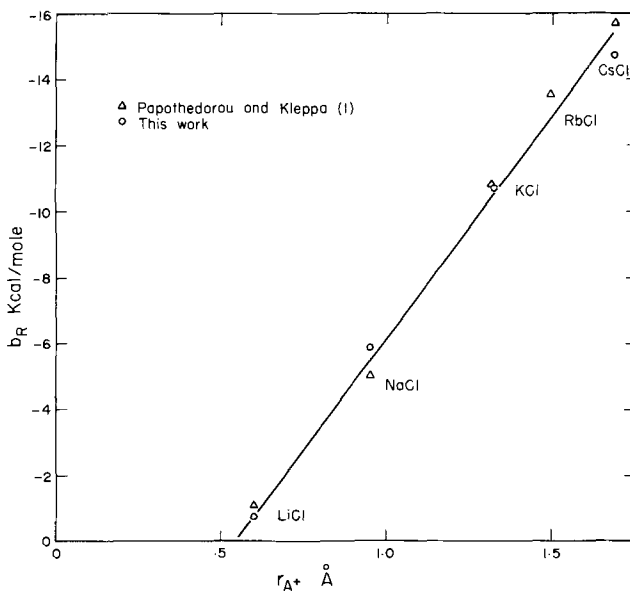


Fig. 15. Plot of b_R vs. the radii of alkali metal cations in the ACl- $MnCl_2$ binary systems.

The calculated values for the vibrational contributions ϵ given in Table III are consistent with the magnitude of the reaction parameters b_R . For example, the $MnCl_2$ - $CsCl$ system which has a large negative heat of formation b_R is also characterized by the most negative vibrational entropy. The $MnCl_2$ - $LiCl$ system which is characterized by a small enthalpy of formation b_R is best represented by configurational entropy only.

It is worthwhile to note that for dilute solutions at $X_{MnCl_2} \rightarrow 0$, the partial molar entropy of mixing given by Eq. [47] reduces to

$$\bar{\Delta S}_{MnCl_2} = \epsilon - R \ln X_{MnCl_2} \quad [49]$$

and accordingly, the excess partial molar entropies in this range may be identified with vibrational contributions.

SYMBOLS

N_i	ionic fraction of component i
X_i	mole fractions of component i
T	degrees Kelvin
R	ideal gas constant = $1.986 \text{ cal} \cdot \text{deg}^{-1}$.
F	Faraday's constant = $23,066 \text{ cal} \cdot \text{V}^{-1}$
E	emf in V or mV as cited
Z	electrochemical valency

Acknowledgment

The financial assistance to one of the authors (A.S.K.) by the National Research Council of Canada is gratefully acknowledged.

Manuscript submitted Dec. 16, 1971; revised manuscript received May 4, 1972.

Any discussion of this paper will appear in a Discussion Section to be published in the June 1973 JOURNAL.

REFERENCES

- G. N. Papatheodorou and O. J. Kleppa, *J. Inorg. Nucl. Chem.*, **33**, 1249 (1971).
- G. N. Papatheodorou and O. J. Kleppa, *ibid.*, **32**,

- 889 (1970).
- D. C. Hamby and A. B. Scott, *This Journal*, **115**, 704 (1968).
- D. C. Hamby and A. B. Scott, *ibid.*, **117**, 319 (1970).
- H. Flood and S. Urnes, *Z. Elektrochem.*, **59**, 834 (1955).
- F. G. McCarty and O. J. Kleppa, *J. Phys. Chem.*, **68**, 3846 (1964).
- S. N. Flengas and A. S. Kucharski, *Can. J. Chem.* (In press).
- M. Bruneaux, G. Darmois, and S. Ziolkiewicz, *Compt. Rend.*, **254**, 2967 (1962).
- M. Bruneaux, S. Ziolkiewicz, and G. Morand, *J. Chim. Phys.*, 1215 (1964).
- J. D. Corbett, R. T. Clark, and T. F. Munday, *J. Inorg. Nucl. Chem.*, **25**, 1287 (1963).
- A. D. Pelton and S. N. Flengas, *This Journal*, **117**, 1130 (1970).
- W. T. Thompson and S. N. Flengas, *Can. J. Chem.*, **46**, 1611 (1968).
- C. Dijkhuis, R. Dijkhuis, and G. J. Janz, *Chem. Rev.*, **68**, 253 (1959).
- C. Dijkhuis and J. Ketelaar, *Electrochim Acta*, **11**, 1622 (1966).
- F. A. Cotton and G. Wilkinson, "Advanced Inorganic Chemistry," p. 217, Interscience Publishers, Inc., New York (1964).
- O. Kubaschewski, E. Evans, and C. B. Alcock, "Metallurgical Thermochemistry," Pergamon Press, Toronto (1971).
- H. H. Kellogg, *J. Metals, Trans. AIME.*, **188**, 862 (1950).
- C. E. Wicks and F. E. Block, *U.S. Bur. Mines Bull.* **605** (1963).
- S. N. Flengas and Sir Eric Rideal, *Proc. Roy. Soc. A*, **233**, 443-454 (1956).
- R. L. Lister and S. N. Flengas, *Can. J. Chem.*, **43**, 2947 (1965).
- J. E. Dutrizac and S. N. Flengas, "Advances in Extractive Metallurgy-Symposium," Paper 24, The Institution of Mining and Metallurgy, London (1967).
- S. N. Flengas and P. Pint, *Can. Met. Quart.*, **8**, (2), 151 (1969).

Anodic Films in ECM Electrolytes: Onset of Passivation of Mild Steel in Nitrate Solution

Der-Tau Chin*

Electrochemistry Department, Research Laboratories, General Motors Corporation, Warren, Michigan 48090

ABSTRACT

A potentiostatic transient study was made of the passivation of mild steel in $NaNO_3$ solution. The current-time relation in the initial stage of the passivation process agreed with a model involving two-dimensional progressive nucleation and growth of a monolayer of oxide on the electrode surface. The rate of film formation was found to increase with the rate of electrode dissolution and with the nitrate concentration.

Since the discovery (1) that the quality of surface finish and dimensional control obtained in electrochemical machining (ECM) of steel is directly related to anodic film formation, a series of tests have been made in this laboratory to ascertain the nature of the film in various ECM electrolytes (2, 3). It has been found that in $NaCl$ and $NaClO_4$ solutions the passive film is initiated by the formation of a salt layer resulting from supersaturation of dissolution products in the immediate vicinity of the anode. Although such a film is capable of giving good surface finishes at high current densities, it lacks the ability to protect the metal surface located some distance from the

machining area facing the cathode. In $NaClO_3$ solution, a porous film resulting from anodic oxidation has been identified. This film not only gives excellent dimensional control, but also brings about mirror-like surface finishes on the machined area. In the present work, such testing has been extended to $NaNO_3$ solution.

Though numerous studies have been made on the passivation of iron or steel in nitrate solutions, most of them are confined to either acidic or alkaline conditions such as in HNO_3 or $NH_3-NH_4NO_3-H_2O$ systems. There are only a few studies reported in the literature concerning neutral nitrate solutions. Cowley, Robinson, and Kerrich (4) measured anodic polarization curves for mild steel in 10% NH_4NO_3 solution, and the effect

* Electrochemical Society Active Member.

Key words: rotating spherical electrode, potentiostatic transient.

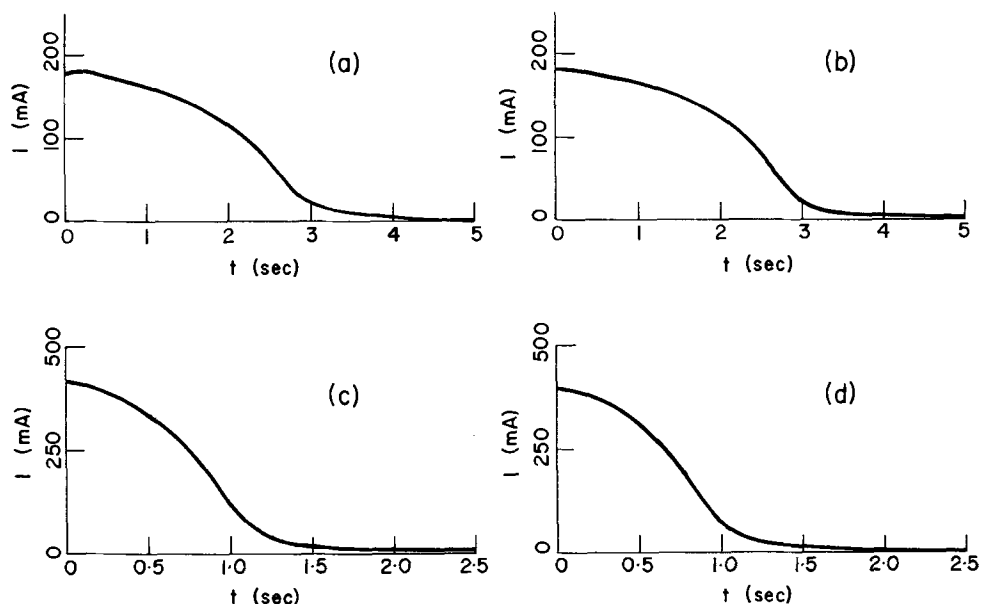


Fig. 1. Recorder traces of current transient in 2M NaNO_3 . The magnitude of applied potentiostatic pulses (vs. SCE) and the speed of anode revolution are: a, 0.2V, 0 rpm; b, 0.2V, 2500 rpm; c, 1.0V, 0 rpm; d, 1.0V, 2500 rpm.

of pH on the polarization curves was reported by Mieluch (5), who found that passivation occurred most easily at pH 7.5. In a later report, Mieluch (6) also described a study of the effect of crystallographic orientation on the passivation of Fe in concentrated NH_4NO_3 . The influence of fatty acids on the passivation of iron and steel in neutral nitrate solutions was investigated by Smialowski and Ostrowska (7).

This paper describes a potentiostatic transient study of a mild steel electrode in neutral NaNO_3 solutions. The mechanism of passivation is discussed with a two-dimensional nucleation and growth model for the formation of an oxide film on the electrode.

Experimental

A rotating hemispherical electrode was used for the study. The electrode consisted of a replaceable mild steel hemispherical head¹ mounted on one end of a cylindrical Teflon rod; the other end of the rod was attached to the spindle shaft of a high speed rotator. The mild steel head was 0.317 cm in radius and had a surface area of 0.628 cm^2 exposed to the electrolyte. Details of the experimental setup are given in previous reports (2, 3), and will not be repeated here.

Before the transient measurement, the surface of the mild steel electrode was degreased in isopropanol, cleaned in dilute HCl, and rinsed in distilled water. The clean electrode was then installed on the rotator and transferred into a cell filled with the test electrolyte. To remove any remaining trace of oxide on the surface, the electrode was further treated cathodically at -1.2V vs. SCE for one minute, and the system was permitted to rest for several minutes to allow the electrode potential to return to the steady-state value at open circuit. A constant anodic potential pulse was then applied to the electrode, and the current transient was recorded.

The electrolytes used were 1 to 4M NaNO_3 . The solutions were prepared by dissolving Baker analyzed-grade chemicals in distilled water; the pH of these solutions varied from 6.5 to 7.5 at room temperature. Before the start of each test the electrolyte was pre-saturated with nitrogen; and, during the run, a nitrogen atmosphere was maintained by passing the gas through the cell. All the experiments were performed at a constant room temperature of $24^\circ \pm 1^\circ\text{C}$.

Results

Figure 1 shows the recorder traces of current transients for two different passivity potentials in a 2M

NaNO_3 solution. For each potential pulse, the curves are given for two different rotational speeds: curves a and c at 0 rpm, and curves b and d at 2500 rpm. These curves are typical of the results obtained; so the raw data with other passivity potentials and other concentrations are not shown here.

It is seen for each curve, the current jumps to a large value at $t = 0$, and then drops smoothly to a small value. Stirring of the solution apparently has no effect on the current transient. It should be noted that, though the current drop between the initial value and the tail portion occurred within a few seconds, the time required to reach a steady-state value was very long. In this tail portion, the current continued to drop slowly, and often it took 30-60 min before a steady value was observed.

It has been found that during this initial current drop period, the logarithm of the current varied linearly with the cube of time. Figure 2 is a plot of I vs. t^3 on semilogarithmic scales for various potential pulses in 2M NaNO_3 solution. The effect of nitrate concentrations on the current transient is shown in Fig. 3, where the current obtained from a potential pulse of 1.0V vs. SCE is also plotted against the cube of time on semilogarithmic scales for three nitrate concentrations. It is seen that the rate of current drop increases with increase in both anodic potential and solution concentration.

The relationship between the initial current density and the steady-state polarization curve is shown in Fig. 4. The steady-state current densities for various nitrate concentrations and anode revolution rates are represented by the symbols, \circ , Δ , \square , etc. The dashed curves are the initial current densities obtained from the current transient curves. This figure demonstrates that the passive region lies between anode potentials from 0 to 1.2V vs. SCE. The current densities on the left of 0.0V vs. SCE represent the rate of active dissolution of iron into the electrolyte, and those on the right of 1.2V vs. SCE are the transpassive current densities. Variation in the nitrate concentration and stirring of the solution have no effect on the steady-state measurements. The initial current densities of the potentiostatic pulses appear to be smooth extensions of the steady-state current densities of the active dissolution states into the passive potentials.

Discussion

The behavior of current transients can be explained by a model of two-dimensional nucleation and growth for an anodic film on the electrode surface. The model involves the following assumptions: (i) the film nuclei

¹ Composition of the mild steel: Fe, 98.4%; Mn, 0.98% S, 0.29%; C, 0.1%; P, 0.06%; Si, 0.005%.

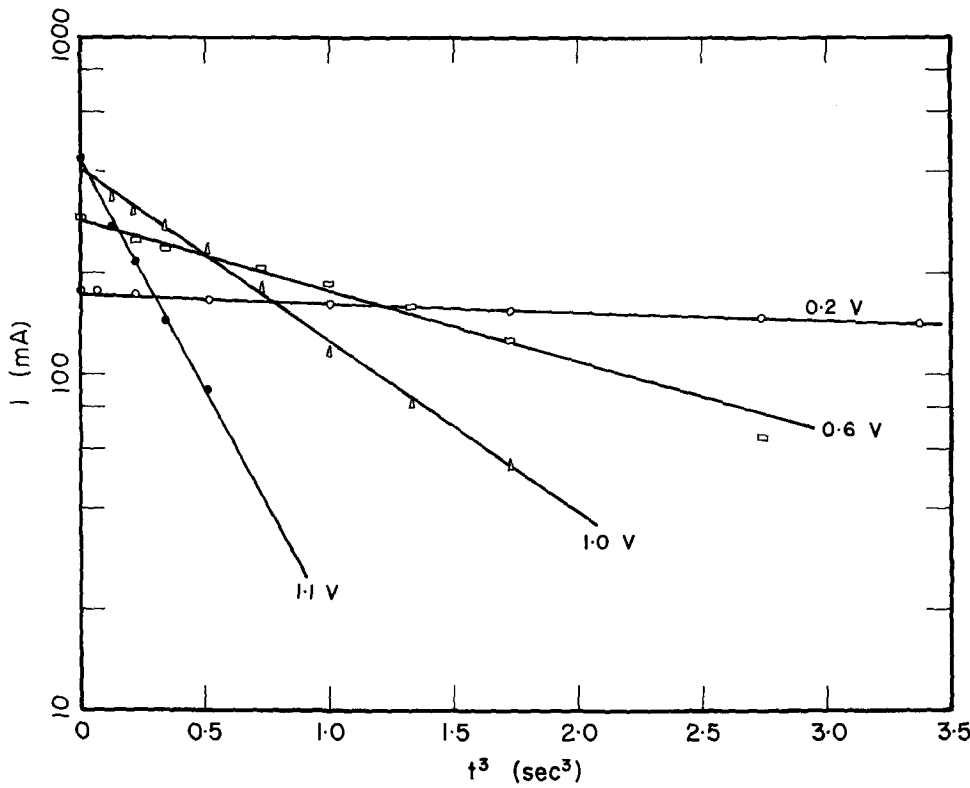


Fig. 2. i vs. t^3 for various potentiostatic pulses (vs. SCE) in 2M NaNO_3 .

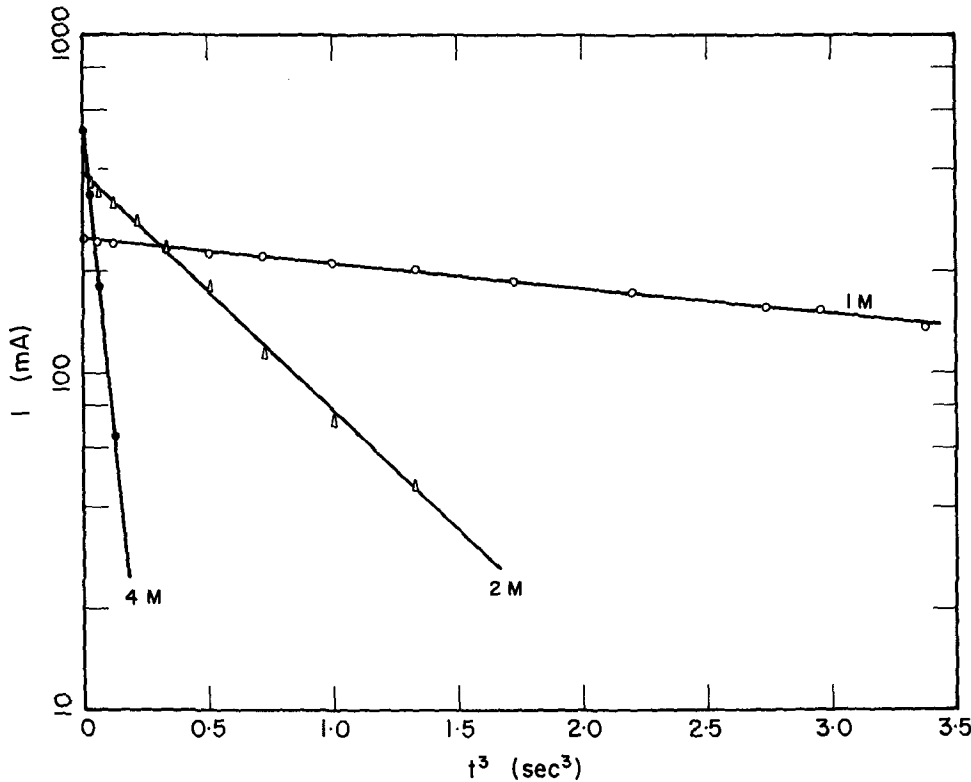


Fig. 3. i vs. t^3 for a potentiostatic pulse of 1.0V (vs. SCE) in three different concentrations of NaNO_3 solution.

occur randomly on the surface; (ii) only a monomolecular layer of the passive film is formed on the surface, and the growth of such a layer results in a decrease in the dissolution current; and (iii) the film is permeable to the metal ion, in other words, electrode dissolution can take place by diffusion of metal ions through the film. Under these circumstances, the current density/time relationships have been given by Armstrong, Porter, Bulman, and Thirsk (8, 9):

$$i_F = q_{\text{mon}} \nu^2 N t^2 \exp\left(-\frac{\pi}{3} \nu^2 N t^3\right) \quad [1]$$

(b) dissolution on the bare electrode surface

$$i_D = i_o \exp\left(-\frac{\pi}{3} \nu^2 N t^3\right) \quad [2]$$

(c) dissolution by diffusion through the film

$$i_D = i'_o \left\{ 1 - \exp\left(-\frac{\pi}{3} \nu^2 N t^3\right) \right\} \quad [3]$$

Here i_o and i'_o are the exchange current densities for the dissolution reactions occurring on the bare electrode surface and on the surface covered with the pas-

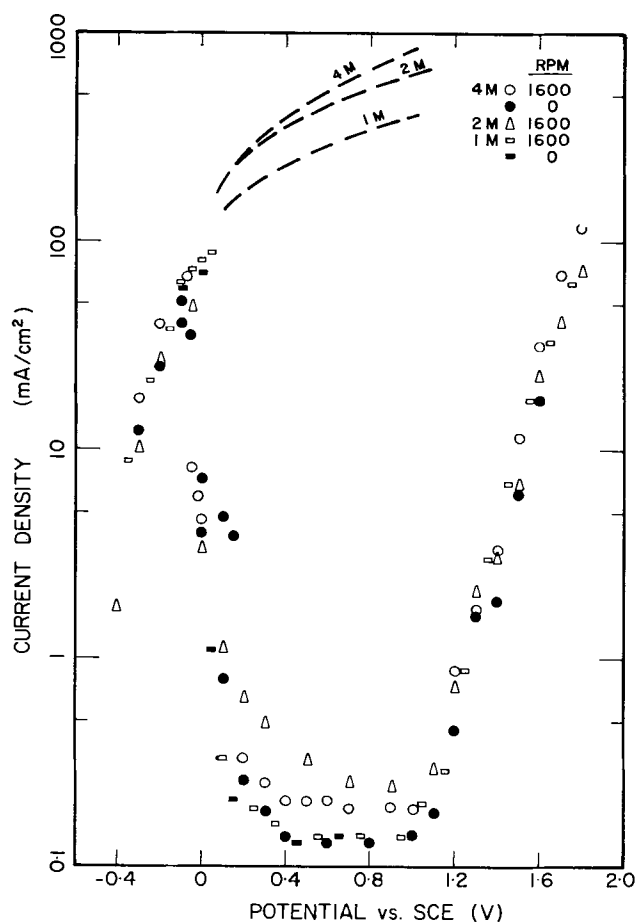


Fig. 4. Initial current density of the potentiostatic transient and the steady-state polarization curves for mild steel in NaNO_3 solution. The steady-state measurements are represented by the symbols, \circ , Δ , \square , etc. The dashed curves are the initial current densities obtained from the recorder output.

sive film, respectively; q_{mon} is the charge density for the formation of the monomolecular layer; N is the rate of nucleation of two dimensional centers; and v is the rate of film spreading from the nuclear centers.

The total current density is the sum of Eq. [1]-[3]. For the present study, one may assume that i_F and i_D are too small to be observed under the experimental conditions. Thus, the current measured is contributed mostly by the dissolution on the bare metal surface. Equation [2] suggests that a plot of the logarithm of the current against the cube of time would give a straight line. The results given in Fig. 2 and 3 demonstrate that the current transient for a mild steel electrode in sodium nitrate solutions agrees precisely with this model. Figure 4 further shows that the initial current density of the transient represents the rate of dissolution on the bare electrode surface and, thus, corresponds to i_0 in Eq. [2]. The cube root of the product, v^2N , can be regarded as an average rate of film formation on the electrode surface. Figure 5 is a semi-logarithmic plot of $\sqrt[3]{v^2N}$ vs. i_0 as calculated from the experimental data. It is seen that the film formation rate increases with the metal dissolution rate as well as with the nitrate concentration.

This film formation mechanism is further supported by Mieluch's (6) galvanostatic study of iron in concentrated ammonium nitrate solutions. His results give a charge density of 1.3 mcoulomb/cm² needed for the formation of an initial passive layer on the electrode surface. If one assumes that this initial layer is composed of Fe_3O_4 , as suggested in the literature (10), this amount of charge density would correspond to an oxide layer of monomolecular thickness on the electrode surface.

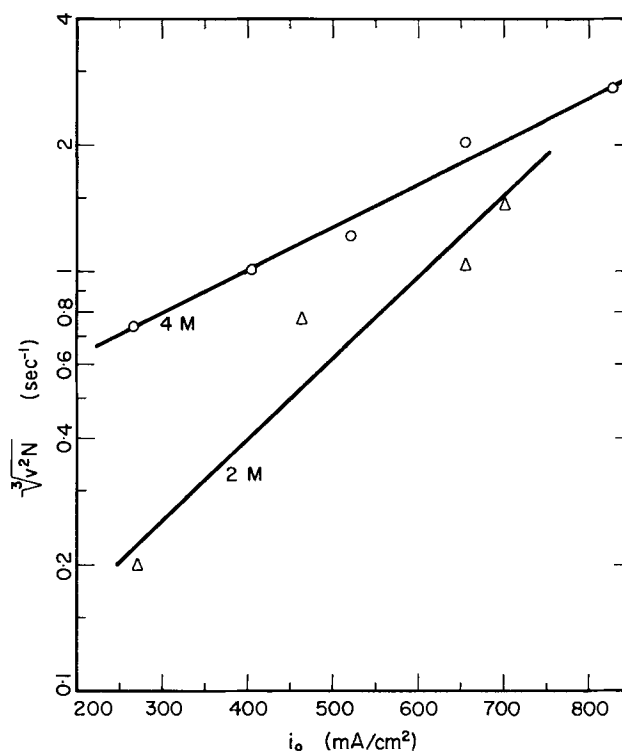


Fig. 5. Average rate of film formation vs. dissolution current density for two different NaNO_3 concentrations.

It should be noted that the transient data presented here represent only the initial stage of the passivation process. The present results do not account for thickening of the film, nor for possible transformation of phase layers in later stages of the passivation process. Further study is needed to resolve these problems.

Conclusions

The onset of passivity for mild steel in neutral nitrate solutions is characterized by formation of a monolayer of oxide on the electrode surface. The rate of formation increases with the rate of dissolution reaction as well as with nitrate concentration.

Manuscript submitted Jan. 18, 1972.

Any discussion of this paper will appear in a Discussion Section to be published in the June 1973 JOURNAL.

LIST OF SYMBOLS

i_0	exchange current density, A/cm ²
I	current, A
N	rate of nucleation of two dimensional centers, nuclei/cm ² sec
q	charge density, coulomb/cm ²
t	time, sec
v	rate of film spreading from the nuclear centers, cm/sec

Subscripts

D	dissolution of electrode
F	film formation process
mon	monomolecular layer

Superscripts

'	dissolution reaction occurring on the electrode surface covered with a layer of passive film
---	--

REFERENCES

- J. P. Hoare, M. A. LaBoda, M. L. McMillan, and A. J. Wallace, *This Journal*, **116**, 199 (1969).
- D. T. Chin, *ibid.*, **118**, 174 (1971); also in "Fundamentals of Electrochemical Machining," C. L. Faust, Editor, pp. 250-278, The Electrochemical Society Softbound Symposium Series, Princeton, N. J. (1971).
- D. T. Chin, *This Journal*, Accepted for publication.
- W. E. Cowley, F. P. A. Robinson, and J. E. Kerich, *Br. Corrosion J.*, **3**, 223 (1968).

5. J. Mieluch, *Bull. Acad. Polon. Sci., Ser. Sci. Chim.*, **13**, 33 (1965).
6. J. Mieluch, *ibid.*, **15**, 597 (1967).
7. M. Smialowski and T. Ostrowska, *Bull. Acad. Polon. Sci., Classe III*, **3**, 29 (1955).
8. R. D. Armstrong, D. F. Porter, and H. R. Thirsk, *J. Phys. Chem.*, **72**, 2300 (1968).
9. R. D. Armstrong, G. M. Bulman, and H. R. Thirsk, *J. Electroanal. Chem.*, **22**, 55 (1969).
10. M. Nagayama and M. Cohen, *This Journal*, **109**, 781 (1962).

Technical Notes



h-Pits Produced by Hydrating and Annealing Aluminum Foil

Cecil G. Dunn*¹

Research and Development Center, General Electric Company, Schenectady, New York 12301

and Donald R. Witter²

Electronic Capacitor and Battery Department, General Electric Company, Columbia, South Carolina 29202

This note reports some surface phenomena, including the formation of relatively large crystallographically oriented pits, on aluminum reacted with boiling water prior to heating in air. For identification purposes and to distinguish them from thermal pits or vacancy condensation pits (VC-pits) we call the present pits, h-pits. Although other studies have been reported of *in situ* dehydration of boehmite films (1), and high temperature reactions between boehmite films and the substrate aluminum (2), the present h-pit observations appear to be new.

The surface phenomena described in the following experiments were obtained using suitable hard (H19 temper) commercial grade 99.99% Al foil. The phenomena include: (i) crystallographically oriented pits, both within the aluminum grains and at the grain boundaries, that arise due to recrystallization and grain growth; (ii) networks of pits and occasionally gigantic grooves at grain boundaries; and (iii) partial networks of pits within grains.

Regarding pits within grains, samples of the hard foil were observed visually during relatively fast heating to about 600°C, since it was known that suitable foil, heated at a relatively high rate of temperature rise in the 200° to 300°C range (3-5) produced relatively large grains. Under oblique illumination, the grain structure was not visible in a sample given no pretreatment; but after a few minutes at about 600°C, grains ½ to 1 cm in size became visible in a sample given a pretreatment of 5 min in boiling water. The individual grains were visible prior to cooling. On the other hand, samples cooled to room temperature could be studied more thoroughly. Figure 1 shows the appearance of a sample held 30 min in air at 550°C after about a 1 min heating-up time. The large-grained structure was revealed by differences in reflected light intensity due to crystallographically oriented pits of about 5μ size and density near 10⁵ pits/cm². The uneven light reflections from some of the grains suggests the presence of a coarse subgrain structure. Incidentally, support for this view was obtained using the sink property that sub-boundaries (and boundaries) have for vacancies (6). Thus, samples of either the annealed foil or the hard foil were electropolished to provide

smoother surfaces, then held for 10 min in air at 600°C, and finally cooled at a suitable rate for VC-pit formation within the large subgrains.

From the above results one may conclude that the development of the h-pits is a consequence of the hydration treatment; and h-pits, since they can form at temperature, are unlike VC-pits, which form only after a drop in temperature.

Grain boundaries generally provided preferred sites for h-pits. This feature will be illustrated using a fine-grained structure developed in samples from the same lot of hard foil by holding them for 16 hr at 350°C after a low rate of temperature rise. At this point, some samples were given a 5 min hydration treatment at 100°C while others were given no treatment. Both kinds of samples were then held 30 min in air, at 550°C, as before. Again h-pits were abundantly present in samples given the hydration treatment and essentially absent



Fig. 1. Hard aluminum foil given a 5 min dip in boiling water prior to a 550°C anneal in air; oblique illumination. (X10).

* Electrochemical Society Active Member.

¹ Now retired.

² Present address: Research and Development Center, General Electric Company, Schenectady, New York.

Key words: oxidation, corrosion, recrystallization.



Fig. 2. Soft aluminum foil (after a 16-hr anneal at 350°C) given a 5 min dip in boiling water prior to a 550°C anneal in air. (X250).

in samples given no hydration treatment. Figure 2 is a typical micrograph showing a network structure due to a preferential formation of pits at grain boundaries. This feature is similar to results observed previously for hydrogen-doped aluminum involving no hydration treatments (7).

Another observation was that some grain growth occurred at 550°C including instances of relatively fast grain boundary migration. When this occurred after grain boundary pits had already formed, chains of pits and partial networks of pits were left within grains as might be expected. When pits along a grain boundary grew in size until they came together, "gigantic" grain boundary grooving occurred. Some instances of this phenomenon appear in Fig. 2. Careful inspection of the sample (and others using film lifting techniques) revealed the presence of a transparent oxide film over the entire surface. The h-pits, accordingly, are voids at the oxide-metal interface. Individual h-pit voids within a grain have a rather unique morphology and this is also evident to some degree in Fig. 2. Noting that {111} planes and {100} planes of the aluminum matrix are the preferred boundary planes for both hydrogen pores (8) and VC-pits (9), we suggest that the crystallographic orientations referred to earlier may involve the same {h k l} planes.

Using another lot of H19 commercial grade 99.99% Al, which had the property of recrystallizing to a fine-grained structure on heating rapidly (3-5), it was shown that the network pattern of grain boundary pits does not depend on the presence of a fine-grained structure at the time of hydrating the foil, which was the situation above. For example, the second lot of hard foil was given a 5 min hydration treatment at 100°C and the 30 min treatment in air, at 550°C, as

before. Results were similar to those illustrated in Fig. 2.

Mention may be made of some limited studies on the effect of holding temperature on samples given the hydration pretreatment. Holding 16 hr at 400°C, for example, produced h-pits. However, a similar treatment at 300°C produced no large pits, or pits that could be easily seen.

Other studies showed that the removal of the hydrate layer prior to annealing, by means of a boiling aqueous solution of CrO₃ and phosphoric acid (10, 11), essentially eliminated the formation of large h-pits. Thus, the presence of a hydrated film during the holding at 400°C and higher appears to be necessary for abundant h-pit formation.

For the most part, the above phenomena may be explained by the assumption that the h-pits actually are hydrogen pits (H-pits), with the hydrogen probably originating in an Al-hydrate film reaction (2). The literature is extensive on H-pores and surface blisters, the latter due to hydrogen precipitation within the aluminum but near the surface. Instances of hydrogen precipitation at a metal-oxide interface, undoubtedly, have been seen. In fact, based on proton injection results, Milacek *et al.* (12) conclude that "pitting is the result of accumulation of protons as hydrogen in voids which form at the oxide-metal interface." Also, previous work (7), involving superpurity aluminum with and without added hydrogen introduced during recasting, demonstrated the formation of H-pits in the hydrogen-doped samples annealed in air. A surface oxide film plays an important role in these instances because it prevents the escape of hydrogen, which, in turn, provides the driving force for the formation of voids at the oxide-metal interface.

Acknowledgments

D. W. Marsh obtained the photographs used in the illustrations, and A. W. Stirling made valuable comments during preparation of the manuscript. Reviewers' comments on the initial manuscript are gratefully acknowledged.

Manuscript submitted Dec. 27, 1971; revised manuscript received May 1, 1972.

Any discussion of this paper will appear in a Discussion Section to be published in the June 1973 JOURNAL.

REFERENCES

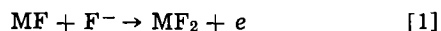
1. W. J. Bernard and J. J. Randall, Jr., *This Journal*, **107**, 483 (1960).
2. R. S. Alwitt, *ibid.*, **118**, 810 (1971).
3. D. Altenpohl, *Aluminium*, **33**, 306 (1957).
4. D. Altenpohl and W. Burgmann, Jr., *Z. Metallk.*, **59**, 364 (1968).
5. G. Ibe, *Metall*, **23**, 13, also 243 (1969).
6. P. E. Doherty and R. S. Davis, *Acta Met.*, **7**, 118 (1959).
7. C. G. Dunn and R. B. Bolon, Unpublished work.
8. G. Scharf, M. Schippers, W. Gruhl, G. Ibe, and H. Cordier, *Metall.*, **23**, 206 (1969).
9. D. Foss and O. H. Herbjornsen, *Phil. Mag.*, **13**, 945 (1966).
10. J. D. Edwards, *Proc. Am. Soc. Test Mat.*, **40**, 960 (1940).
11. D. Altenpohl, *Z. Metallk.*, **48**, 306 (1957).
12. L. H. Milacek, R. D. Daniels, and J. A. Cooley, *J. Appl. Phys.*, **39**, 2803 (1968).

An Interpretation of Anodic Dissolution and Corrosion of Some Film-Covered Electrodes

Ashok K. Vijh*

Hydro-Quebec Institute of Research, Varennes, P.Q., Canada

Consider anodic dissolution of metals in anhydrous hydrogen fluoride (AHF) proceeding via fluoride corrosion films (1, 2). Following Gerischer (3), anodic discharge of F^- ions of the AHF on the fluoride covered metal, MF, may occur either by participation of the conduction band of MF as



or, by involvement of the valence band as



The ratio of the two rate equations is given by (3)

$$\frac{v_2}{v_1} = \frac{p_s}{N_c} \exp - \left(\frac{\gamma Eg}{kT} \right) \quad [3]$$

where v_1 and v_2 are the rates for reactions [1] and [2], respectively; p_s is the hole concentration in the surface of MF at equilibrium; N_c is the effective density of states in the conduction band of MF; γ is a constant having value between 0.5 and 1, depending on the system; Eg is the band gap. Assuming value of $\gamma = 0.5$, and noting that $Eg \approx -2\Delta H_e$ where ΔH_e is the heat of formation per equivalent (4) of the MF, one has

$$v_2 \approx v_1 \frac{p_s}{N_c} \exp \left(\frac{\Delta H_e}{kT} \right) \quad [4]$$

For highly ionic fluoride films, Eg is large so that the dissolution proceeds almost entirely by a hole mechanism (3). One may, therefore, take v_1 as a negligible and relatively constant fraction of the over-all rate ($v_1 + v_2$). This would then give

$$\log v \propto K \left(\frac{\Delta H_e}{2.3 kT} \right) \quad [5]$$

* Electrochemical Society Active Member.
Key words: anodic dissolution, film-covered electrodes, hydrogen fluoride, fluoride films.

where v is the total rate of anodic dissolution and K is a constant. Application of Eq. [5] to the data (1, 2, 5) on anodic dissolution of metals in AHF shows its approximate validity (Fig. 1); i.e., as ΔH_e of MF becomes higher (more endothermic), $\log v$ increases. Similar considerations appear to be valid for anodic dissolution of metals in sulfamic acid-formamide solutions occurring via corrosion reaction films (6, 7).

Noting that, for electrode reactions \log rate is proportional to electrode potential V , and that, for some cases of open-circuit corrosion, one conjugate reaction determines almost exclusively the corrosion potential E_h (so that $V \approx E_h$) one gets

$$E_h \propto K \left(\frac{\Delta H_e}{2.3 kT} \right) \quad [6]$$

Examination of Eq. [6], in relation to the data given in Ref. (8) and (9), roughly supports its validity.

Manuscript submitted March 6, 1972.

Any discussion of this paper will appear in a Discussion Section to be published in the June 1973 JOURNAL.

REFERENCES

1. A. K. Vijh, *This Journal*, **115**, 1096 (1968).
2. A. K. Vijh, *Electrochim. Acta*, **6**, 441 (1971).
3. H. Gerischer, in "Physical Chemistry: An Advanced Treatise," Vol. IX A, H. Eyring, Editor, Academic Press, New York (1970).
4. A. K. Vijh, *J. Phys. Chem. Solids*, **29**, 2233 (1968); *This Journal*, **117**, 173 C (1970).
5. N. Hackerman, E. S. Snavely, Jr., and L. D. Fiel, *Corrosion Sci.*, **7**, 39 (1967).
6. I. A. Menzies, G. W. Marshall, and G. B. Griffin, *ibid.*, **9**, 287 (1969).
7. A. K. Vijh, *Electrochim. Acta*, **16**, 1427 (1971).
8. G. Butler, P. E. Francis, and A. S. McKie, *Corrosion Sci.*, **9**, 715 (1969).
9. "Corrosion," Vol. 1, pp. 2, 31, L. L. Shreir, Editor, John Wiley & Sons, Inc., New York (1963).

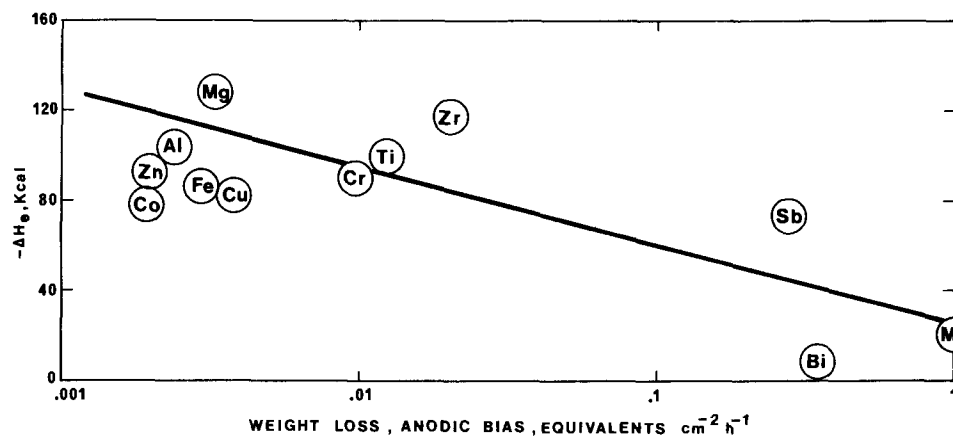


Fig. 1. A plot of anodic dissolution rate (2, 5) of the shown metals against heats of formation per equivalent of the most stable corresponding metal fluorides. The $-\Delta H_e$ value signifies half the band gap, Eg , for a given metal fluoride.

Electrochemical Preparation of Cadmium and Mercury Tellurides

M. H. Miles*

Department of Chemistry, Middle Tennessee State University, Murfreesboro, Tennessee 37130

and W. S. McEwan

Chemistry Division, Naval Weapons Center, China Lake, California 93555

Telluride compounds are of growing interest due to their properties as semiconductors and semimetals. The solid solution system $Cd_xHg_{1-x}Te$ is an outstanding infrared detector material (1). Cadmium telluride is useful for windows in infrared lasers and infrared modulators and also as a nuclear radiation detector (2). Although telluride compounds are often prepared by direct union of the elements at high temperatures, a convenient electrolytic method for preparing tellurides from aqueous solution at room temperature has been described (3). The application of electrochemical methods is investigated for the preparation of CdTe and HgTe.

Experimental

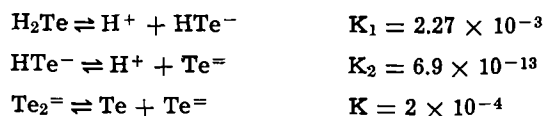
The tellurium electrodes used as the source of $Te^{=}$ ions were prepared by sealing a piece of this substance in glass tubing using Bipax epoxy (BA-2112) and making a mercury contact to a copper lead. The total resistance of this electrode was usually about 5-15 ohms. A cadmium rod was used as the source of Cd^{++} ions in the preparation of CdTe. Reagent mercury (II) acetate was used as the source of Hg^{++} ions in the preparation of HgTe. The quoted purities are 99.99% for the cadmium rod (Alfa Inorganics), and at least 99.5% for the tellurium stick (A. D. Mackay).

The ammonium acetate-acetic acid buffer solution used as the electrolyte was prepared from reagent chemicals by adding acetic acid to 1M NH_4OH to give a pH of 4.5. Electrochemical experiments were performed using the Beckman Electroscan 30 instrument and a one-compartment, beaker type, electrochemical cell containing the buffer solution and the appropriate electrodes. Nitrogen purified by bubbling through Fieser's solution was used to remove oxygen from the electrolyte solution (4). The closed electrochemical cell was placed in a plastic bag and kept under positive nitrogen pressure during electrolysis as an added precaution against oxygen.

The CdTe or HgTe precipitate formed during constant current electrolysis was washed, centrifuged, and dried under vacuum at 100°C for at least 12 hr. Atomic absorption spectroscopy, electrode weight losses, and precipitate weights were used to determine the composition of the material.

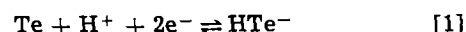
Results and Discussion

Knowledge of the products formed at the tellurium cathode is vital in this method. In aqueous solution we have the following equilibria (3, 5)



According to Panson (5), the major product of the tellurium cathode is $Te_2^{=}$ above pH 12, and $Te^{=}$ below pH 9. Figure 1 shows a cyclic voltamogram for the tellurium electrode in the pH 4.5 buffer solution. Reduction of tellurium occurs as the potential becomes more

negative than $-0.8V$ (vs. SCE). The telluride ions produced are readily oxidized during the anodic sweep as the potential increases beyond $-0.8V$. In slightly acidic solution the net reaction involved is likely



A brownish product was observed streaming from the electrode during the oxidation, probably due to Te particles formed. The ease of oxidation of the telluride ion reflects the concern for rigid precautions to exclude oxygen from the solution (3). Further electrochemical oxidation is observed as the potential sweeps beyond 0.2V; the oxidized substance formed is reduced during the following cathodic sweep at a peak potential of about $-0.45V$. The oxidation product is fairly insoluble as determined from the effects of stirring the solution and delaying the cathodic sweep. From the potential-pH equilibrium diagram for the tellurium-water system (6), these reactions probably involve the formation and corresponding reduction of TeO_2 . Uncompensated IR effects are present in the cyclic voltamograms, largely due to the 15 ohm resistance through the tellurium electrode. Slightly irregular behavior at the extreme potentials in Fig. 1 is due to the manual potential reversal switch of the Beckman instrument.

Cadmium telluride was produced by using a cadmium anode and a tellurium cathode in the pH 4.5

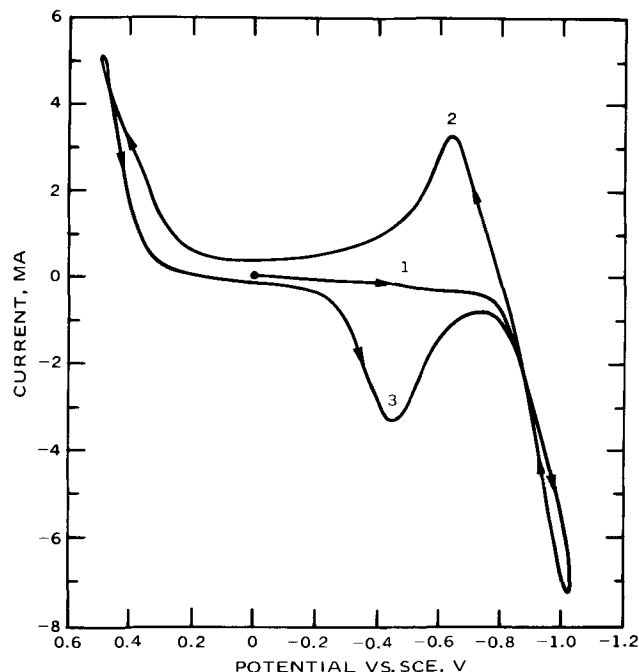


Fig. 1. Cyclic voltamogram for a tellurium electrode in a 1.0M $NH_4C_2H_3O_2 + HC_2H_3O_2$ buffer solution of pH 4.5. Order of potential sweeps: 1. Cathodic direction beginning at 0.0 V; 2. Following sweep in the anodic direction; 3. Following cathodic sweep. Potential sweep rate = 100 mV/sec; geometrical electrode area = 0.5 cm^2 ; $T = 27^\circ\text{C}$.

* Electrochemical Society Active Member.
Key words: atomic absorption, cadmium, mercury, oxygen, preparation, telluride.

Table I. Experimental and theoretical results for the formation of CdTe by the passage of 801 coulombs

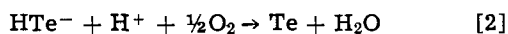
Electrode weight loss, g	Precipitate weight, g	Atomic absorption analysis	
		Lab A	Lab B
Experiment 1: 0.459 Cd	0.977	42.66% Cd	45.2% Cd
0.517 Te		55.84% Te	55.5% Te
Experiment 2: 0.480 Cd	0.992	44.79% Cd	42.5% Cd
0.514 Te		53.32% Te	58.5% Te
Experiment 3: 0.478 Cd	0.997	45.63% Cd	47.2% Cd
0.513 Te		46.58% Te	53.6% Te
Theoretical: 0.467 Cd		46.83% Cd	
0.530 Te		53.17% Te	

buffer solution stirred both by the bubbling N_2 and a magnetic stirrer. The Cd^{++} and $Te^=$ ions generated, combine to form a fine, dark precipitate of CdTe. The potential of the tellurium electrode with 0.5 cm^2 geometrical area, during constant reduction currents of 1, 10, and 100 mA, was $-0.86V$, $-1.05V$, and $-1.65V$ (vs. SCE), respectively, reflecting the uncompensated IR effects and the various types of overvoltage. The potential of the cadmium electrode, with 10 cm^2 geometrical area during constant anodic currents of 1, 10, and 100 mA, was $-0.77V$, $-0.72V$, and $-0.41V$, respectively.

Table I shows the results for three separate experiments, each involving the passage of 0.010A for 100 sec followed by 0.100A for 8000 sec between the cadmium anode and tellurium cathode to form the CdTe precipitate. Each product was analyzed by two independent laboratories using atomic absorption spectroscopy. Assuming that the lack of reproducibility is due to random errors in the analyses, the arithmetic means are $44.7 \pm 1.9\%$ for cadmium and $53.9 \pm 4.3\%$ for tellurium where the limits express the 95% confidence interval of the "Student t" statistical test (7). Identical samples tested by the same laboratory showed similar lack of reproducibility. The statistical test for the total (% Cd + % Te) gives $98.6 \pm 3.5\%$ at the 95% confidence interval. Slight oxidation of the precipitate due to exposure to air during washing and centrifuging may occur; however, this effect is not statistically significant at the 95% confidence level.

Significant deviations from the expected theoretical values, which indicate possible systematic error sources in the experiments, are found for the low cadmium composition of the product and for the low weight loss at the tellurium electrode.

The low analyses for cadmium are just significant at the 95% confidence level. A possible systematic error source is the reaction with oxygen

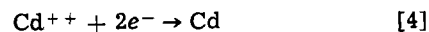
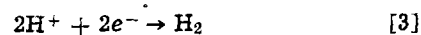


which would result in Te metal present in the precipitate and Cd^{++} ions left in solution without partners for precipitation. These Cd^{++} ions would, therefore, be lost during the washing and centrifuging operations. Apparently, the extreme precautions taken to exclude oxygen during electrolysis were not sufficient to completely eliminate the interfering reaction of the telluride ion with oxygen. In one experiment, where the solution was accidentally exposed to air during the electrolysis, the results of the analysis changed dramatically to 79.1% Te and 20.5% Cd indicating that the above reaction takes place very readily if any oxygen is available.

Any occurrence of reaction [2] would lead to high analyses for tellurium. Although many of the analyses for Te in Table I are higher than the theoretical value, the results are not statistically significant due to the large uncertainty in the atomic absorption results for this metal. Also, the questionable low value reported by Lab A for experiment 3 (Table I) tends to greatly reduce the arithmetic mean of these analyses.

The CdTe product is composed of black powder and lumps, very similar in appearance to particles of coal. Under the microscope, however, some fibrous material having a metallic luster is observed. Possibly such fibers consist of tellurium metal produced by reaction [2]. It is roughly estimated that these fibers represent less than 1% of the total product.

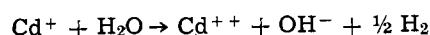
The low weight loss at the tellurium electrode is significant at the 99% confidence level indicating that systematic error sources are highly probable. Possible error sources include the reactions



occurring at the tellurium cathode in addition to the expected reaction [1]. Both of these reactions are thermodynamically possible in the potential region where tellurium reduction occurs.

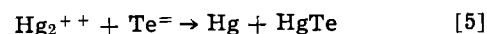
Reaction [3] would be expected to occur readily at the large negative potentials required for the electrochemical reduction of tellurium. Fortunately, however, the overvoltage for H_2 evolution on tellurium is high. Also, telluride ions tend to have a poisoning effect on the hydrogen evolution reaction (8). Any occurrence of reaction [3] will directly reduce the weight loss of the tellurium cathode but will have no effect on the composition of the precipitate since an equivalent amount of Cd^{++} ions will be left without $Te^=$ partners. Any occurrence of either reaction [2] or [3] would result in excess Cd^{++} ions left in solution, which may then be reduced and deposited at the tellurium cathode (reaction [4]) giving less than the expected weight loss for this electrode.

There is some controversy over the existence of the adsorbed monovalent cadmium ion, Cd^+ or Cd_2^{++} , as an intermediate in the cadmium electrode reaction (9, 10). One may speculate that such an intermediate might react chemically with other adsorbed species such as water



which would result in the electrode weight loss being larger than theoretical. Although the data in Table I is not statistically significant on this point, both experiments 2 and 3 gave larger than theoretical weight losses for the cadmium electrode. Further experiments established that this is due to slight chemical reaction of the cadmium during the experiment with the weakly acidic solution. Carefully designed experiments did not show any significant difference between the behavior of zinc and cadmium anodes. Both are electrochemically oxidized in the pH 4.5 buffer solutions by a two electron step to form the divalent ion.

Formation of the mercury double ion, Hg_2^{++} , prevents a satisfactory electrochemical preparation of HgTe. Use of a mercury anode and a tellurium cathode in the $NH_4C_2H_3O_2/H_2C_2O_4$ buffer solution results in a white column of precipitate forming above the electrode cup containing the mercury, while a black precipitate forms in solution. Apparently the mercury oxidizes to Hg_2^{++} which then precipitates upon the electrode as $Hg_2(C_2H_3O_2)_2$. Since mercury (I) acetate is sparingly soluble, the electrolytically produced $Te^=$ ions likely cause disproportionation of Hg_2^{++}



similar to the reaction with $S^=$ ion (11). Metallic films were observed in the electrochemical cell indicating contamination of the black HgTe formed with free mercury as suggested by reaction [5]. Atomic absorption analysis also showed excessive mercury in the product.

Preparation of HgTe is also possible by electrochemically generating $Te^=$ ions in solution by using a platinum anode with the tellurium cathode and then directly adding a soluble mercury (II) salt such as

mercury (II) acetate. Atomic absorption analyses of such a preparation by two separate laboratories gave 63.17%, 61.7% for mercury, and 35.78%, 38.9% for tellurium. This compares favorably with the theoretical values of 61.12% Hg and 38.88% Te for HgTe. However, it is experimentally difficult to prevent oxygen produced at the anode during electrolysis from mixing with the solution and oxidizing $\text{Te}^{=}$ ions. This particular problem could be avoided by using liquid ammonia solutions since N_2 is formed at the anode; however, in $\text{NH}_3\text{-NH}_4\text{NO}_3$ solutions (12), it was found from the electrode weight loss that the ditelluride ion, $\text{Te}_2^{=}$, is the major product at the cathode.

Conclusions

Cadmium telluride can be prepared by a simple electrochemical method. The purity of the CdTe is determined primarily by the extent of oxygen exclusion during electrolysis. Any oxygen present reacts with the electrochemically produced telluride ions resulting in contamination of the product with tellurium metal.

Formation of Hg_2^{++} at the anode complicates the electrochemical preparation of HgTe. However, addition of a mercury (II) salt to a solution of electrochemically generated telluride ions produces a precipitate of the desired product.

Acknowledgment

A summer position in 1971 as a visiting professor for M. H. M., at the Naval Weapons Center at China Lake, California, is gratefully acknowledged.

Manuscript submitted Dec. 7, 1971; revised manuscript received April 28, 1972.

Any discussion of this paper will appear in a Discussion Section to be published in the June 1973 JOURNAL.

REFERENCES

1. D. Long and J. L. Schmit, "Semiconductors and Semimetals," in "Infrared Detectors," Vol. 5, Chap. 5, R. K. Willardson and A. C. Beer, Editors, Academic Press, New York (1970).
2. R. O. Bell, N. Hemmat, and F. Wald, *IEEE Trans. Nucl. Sci.*, **17**, 241 (1970).
3. A. J. Panson, *Inorg. Chem.*, **3**, 940 (1964).
4. L. F. Fieser and M. Fieser, "Reagents for Organic Synthesis", p. 393, John Wiley & Sons, Inc., New York (1967).
5. A. J. Panson, *J. Phys. Chem.*, **68**, 1721 (1964).
6. M. Pourbaix, "Atlas of Electrochemical Equilibria in Aqueous Solutions", p. 567, Pergamon Press, New York (1966).
7. H. A. Laitinen, "Chemical Analysis," pp. 546-547, McGraw-Hill Book Co., Inc., New York (1960).
8. S. A. Awad, *J. Phys. Chem.*, **66**, 890 (1962).
9. K. E. Heusler and L. Gaiser, *This Journal*, **117**, 762 (1970).
10. T. Biegler, E. R. Gonzalez, and R. Parsons, *Collection Czech. Chem. Commun.*, **36**, 414 (1971).
11. F. A. Cotton and G. Wilkinson, "Advanced Inorganic Chemistry," pp. 481-483, Interscience Publishers, New York (1962).
12. M. H. Miles and P. M. Kellett, *This Journal*, **117**, 60 (1970).

Brief Communication



Characterization of Passivating Films on Fe-Cr Alloys by Soft X-Ray Spectroscopy

J. E. Holliday¹ and R. P. Frankenthal*

Edgar C. Bain Laboratory for Fundamental Research, United States Steel Corporation Research Center, Monroeville, Pennsylvania 15146

It is well known that chromium steels radically change their corrosion and electrochemical properties at about 12% chromium content (1). The low-Cr steels have properties similar to iron, while the stainless steels (Cr > 12%) behave similarly to chromium. It is probable that the composition, structure, and/or thickness of the passivating film on the stainless steels is different from that on the low-Cr steels. Few studies have been made of these properties of passivating films formed at room temperature on chromium steels, primarily because the films are thin (2-4 nm).² An electron diffraction study (2) of a series of iron-chromium alloys indicates that the film on alloys with Cr-content $\leq 12\%$ is an Fe-Cr spinel, the lattice parameter of which increases with increasing Cr-content; the film on alloys with Cr-content > 12% is amorphous in character. The passivating film on iron is $\gamma\text{-Fe}_2\text{O}_3$ and may include some Fe_3O_4 (3).

The applicability of soft x-ray spectroscopy to the characterization of relatively thick oxide films (> 10 nm) on transition metals has recently been reported (4). We wish to report a method of characterizing very thin films, e.g., passivating films, *in situ* on iron and iron-chromium alloys by soft x-ray spectroscopy. When a metal, alloy, or compound is bombarded with electrons of energy up to 3 kV, soft x-rays originating near the surface are emitted; the depth from which the x-rays come decreases with decreasing electron energy. The wavelength and intensity distribution of the x-ray band spectra are sensitive functions of the electronic structure of the emitter, i.e., ionization state. The effect of compound formation on the shape and wavelength of characteristic emission bands from the elements, as well as experimental techniques, has recently been reviewed by Holliday (5). In the present study the system was evacuated to 1×10^{-7} Torr and the target was cooled to reduce the probability of oxide growth.

For iron and chromium the L_{II} and L_{III} bands ($4s + 3d \rightarrow 2p$ transition) occur in the soft x-ray region. The L_{II} band is a ($4s + 3d \rightarrow 2p_{J_{1/2}}$) transition and

* Electrochemical Society Active Member.

¹ Present address: McDonnell Douglas Research Laboratory, St. Louis, Missouri 63166.

Key words: iron, iron-chromium alloys, oxide, passivating film, thin film.

² 1 nm = 10Å.

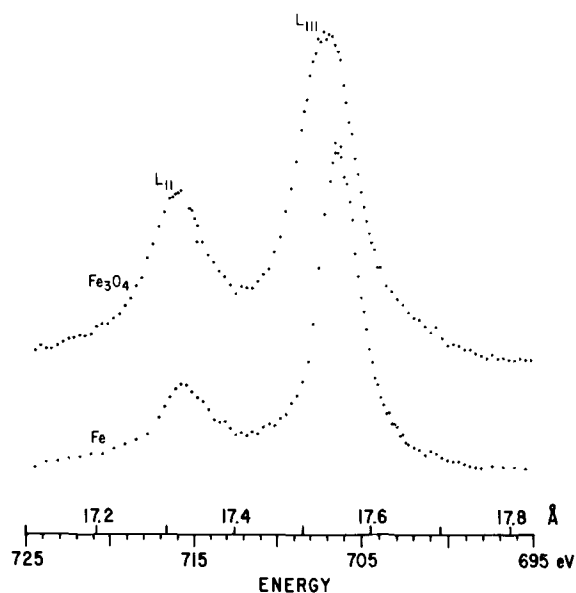


Fig. 1. $\text{FeL}_{\text{II,III}}$ bands from iron and from Fe_3O_4 measured at 2.5 kV. Spectrum of Fe_2O_3 is almost the same as that of Fe_3O_4 .

the L_{III} band is a $(4s + 3d \rightarrow 2p J_{3/2})$ transition. The spectrum consisting of both bands is usually designated $\text{FeL}_{\text{II,III}}$ for iron and $\text{CrL}_{\text{II,III}}$ for chromium. For this paper a superscript above the symbol of the element indicates the ionization state; the absence of a superscript indicates the band results from more than one ionization state.

A series of ferritic iron-chromium alloys from pure iron to Fe-24Cr has been examined. The specimens were passivated potentiostatically in 1N H_2SO_4 at 0.85V vs. SHE until a steady state was achieved. Frankenthal (6) has shown that this potential is sufficiently high so that the preferential-dissolution/-adsorption mechanism (7) is no longer important; instead passivity results from an oxide film. The $\text{FeL}_{\text{II,III}}$ and the $\text{CrL}_{\text{II,III}}$ band spectra of the passivated specimens were measured using a blazed grating analyzer of 3600 grooves/mm in a spectrometer with a 0.5m radius of curvature and a flow proportional counter as detector (8).³ To obtain accurate peak positions and intensity values, at least three runs were made for each spectrum.

The $\text{L}_{\text{II,III}}$ bands of the spectra of Fe, Fe_3O_4 , and Fe_2O_3 (Fig. 1) overlap to such an extent that their resolution is difficult. However, the ratio of the intensities of the Fe L_{II} and Fe L_{III} bands $\{\text{Fe}(\text{L}_{\text{II}}/\text{L}_{\text{III}})\}$ is greater for the oxides than for the metal (Fig. 1). Holliday (9) has shown that the change in the $\text{Fe}(\text{L}_{\text{II}}/\text{L}_{\text{III}})$ intensity ratio is a property of the surface oxide rather than self-absorption and that the ratio increases with increasing oxide thickness at constant accelerating voltage; for example, at 2.5 kV the ratio is 0.24 on oxide free iron and 0.45 on Fe_3O_4 and on Fe_2O_3 . For each alloy the $\text{Fe}(\text{L}_{\text{II}}/\text{L}_{\text{III}})$ ratio was determined from the spectra measured at 1.5 kV (Table I) and will be related to the thickness of the passivating film.

The $\text{CrL}_{\text{II,III}}$ band spectrum of each passivated alloy was measured at 3.0 kV; three spectra are shown in Fig. 2. It will be observed that there is a hump on the high energy side of the Cr L_{III} peak from the Fe-10Cr alloy. This hump could be due to self-absorption, electronic structure, or surface oxide. Self-absorption can be ruled out because chromium and iron are adjacent in the periodic table and iron has no emission or absorption edges in the vicinity of the Cr $\text{L}_{\text{II,III}}$ band. The fact that the energy separation of the hump and

³The Cr $\text{L}_{\text{II,III}}$ band spectra of the passivated 5Cr alloy was measured with a spectrometer with a 1m radius of curvature for greater resolution.

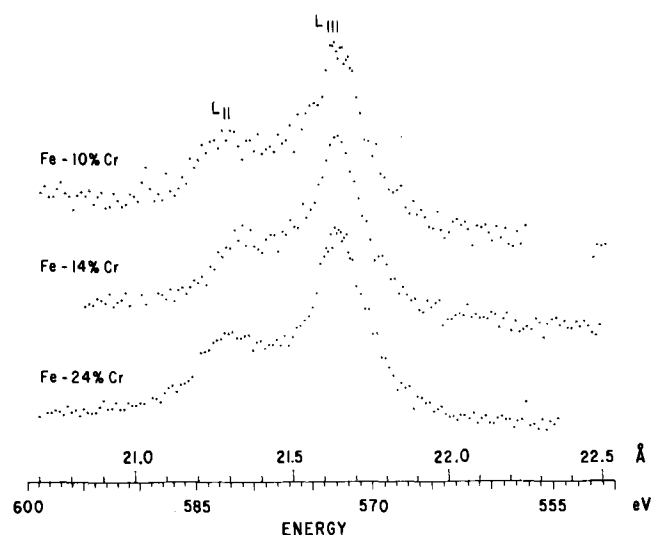


Fig. 2. $\text{CrL}_{\text{II,III}}$ bands from three passivated iron-chromium alloys measured at 3.0 kV.

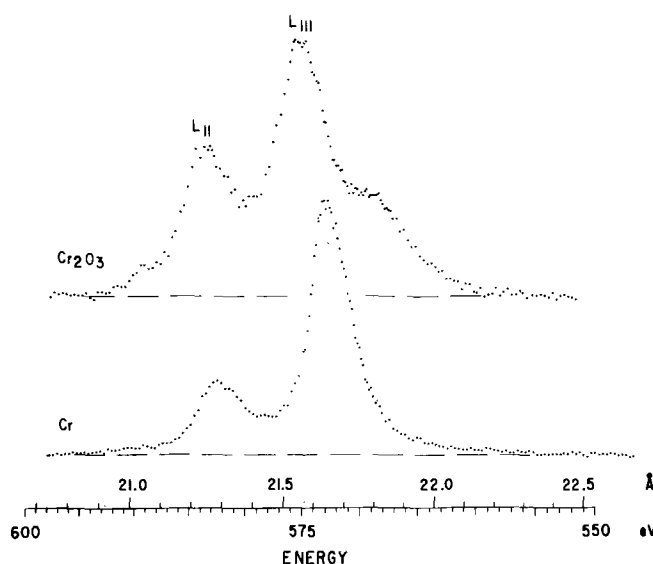


Fig. 3. $\text{CrL}_{\text{II,III}}$ bands from chromium and from Cr_2O_3 .

main peak (Fig. 2) is the same as that for the Cr $\text{L}_{\text{II,III}}$ bands from Cr_2O_3 and chromium metal (Fig. 3) indicates that the hump is due to Cr_2O_3 rather than a change in electronic structure. Further evidence that the hump is due to Cr_2O_3 rather than a change in electronic structure is obtained by measuring the Cr $\text{L}_{\text{II,III}}$ band from the Fe-10Cr alloy at 2 kV accelerating potential; the intensity of the hump relative to the main peak increased at 2 kV over that at 3 kV. This is expected if the hump is due to surface oxide since at lower accelerating voltages a greater portion of the x-rays come from nearer the surface. A more extensive treatment showing that the changes in Fig. 2 are due to surface oxide is given by Holliday (10).

From the above evidence it can be assumed that the Cr $\text{L}_{\text{II,III}}$ band spectra in Fig. 2 are composites from Cr_2O_3 and chromium metal. By knowing the relative heights, half-widths, and peak energy positions of the Cr $\text{L}_{\text{II,III}}$ bands from chromium and from Cr_2O_3 (Fig. 3), it was possible to resolve the Cr $\text{L}_{\text{II,III}}$ bands in Fig. 2 into the Cr $\text{L}_{\text{II,III}}$ bands from chromium metal and from Cr_2O_3 on a du Pont 310 Curve Resolver; two resolved spectra are shown in Fig. 4. They have been normalized to a constant $\text{Cr}^0\text{L}_{\text{III}}$ peak intensity. The peak intensity ratio $\text{Cr}^{3+}\text{L}_{\text{III}}/\text{Cr}^0\text{L}_{\text{III}}$, as calculated from the resolved spectra, is given in Table I for each

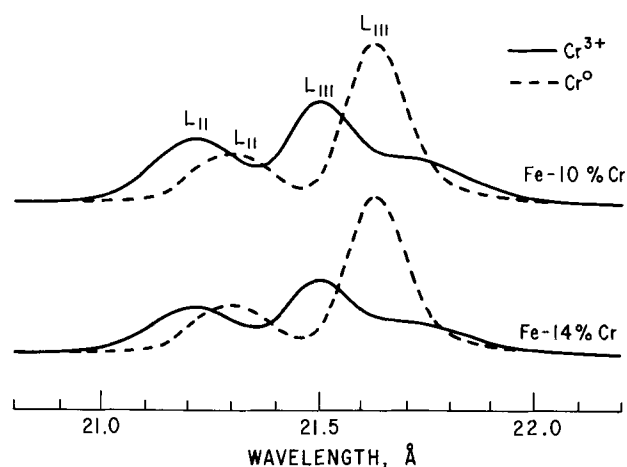


Fig. 4. Resolved $L_{II,III}$ bands of Cr^0 and Cr^{3+} from two iron-chromium alloys measured at 3 kV. Spectra have been normalized for constant Cr^0L_{III} intensity.

alloy. The precision of the ratios is limited by the precision with which the curves can be resolved.

To determine that the chromium oxide was not changed during electron bombardment, a 50Å film of chromium and Cr_2O_3 was electrodeposited onto an iron substrate. The thickness of the chromium oxide on the 50Å film, as determined by chemical analysis, was approximately 10Å. The relative intensities of the $Cr L_{III}$ bands from chromium and Cr_2O_3 were in agreement with chemical analysis data showing that electron bombardment in the present vacuum system does not change the film.

The changes in the $Fe(L_{II}/L_{III})$ and in the $Cr^{3+}L_{III}/Cr^0L_{III}$ intensity ratios (Table I) can be associated with major changes in oxide film thickness and composition over the alloy composition range from 10 to 14% chromium, the same range over which major changes occur in the electrochemical, corrosion (1), and crystallographic (2) properties of the alloys.

Assuming that the dilution of iron and its oxide by chromium and Cr^{3+} , respectively, does not appreciably effect the determination of the quantity of iron oxide from the $Fe(L_{II}/L_{III})$ intensity ratio, the change in this ratio between 10 and 14% chromium can be accounted for by a decrease in the oxide film thickness (9). Using this relationship and the fact that the oxide film on iron is 4 nm thick (11), the oxide on the high-Cr alloys is estimated to be about 2 nm thick. Although the above assumption may not be strictly valid, the results are qualitatively reasonable, inasmuch as the oxide film thickness on passivated chromium metal has been reported to be 1 nm (12).

Assuming the validity of the film thickness calculations and that changes in the $Cr^{3+}L_{III}/Cr^0L_{III}$ intensity

ratio should be determined primarily by changes in the quantity of Cr^{3+} in the oxide and/or Cr^0 in the alloy, the changes in this ratio with alloy composition (Table I) may be explained. The change in the ratio between the 5Cr and the 10Cr alloys is most likely due to the increase in Cr-content of the alloy with relatively small changes in oxide composition and/or thickness. The change in the ratio between 14Cr and the 24Cr alloys can best be accounted for by assuming an increase in the Cr^{3+} concentration of the oxide equal to the increase of chromium in the alloy, the oxide thickness remaining relatively constant. The change in the ratio between the 10Cr and the 14Cr alloys indicates that the Cr^{3+} concentration in the film is increasing approximately proportionately to the decrease in film thickness, i.e., the concentration doubles if the film thickness decreases from 4 to 2 nm. The changes in the Cr^{3+}/Fe^{3+} concentration ratio in the oxide with alloy composition will be even greater than the changes in Cr^{3+} concentration because each additional chromic ion in the oxide replaces a ferric ion, the densities of Cr_2O_3 , Fe_2O_3 , and Fe_3O_4 being equal.

The results of this initial study show that there are distinct differences in the spectra obtained from the different passivated alloys. While the interpretation of the present data is not unambiguous, it is consistent with significant changes in the oxide film thickness and composition in the alloy composition range from 10 to 14% chromium, in which range the major changes in the electrochemical and corrosion properties occur.

Acknowledgments

The authors wish to thank Dr. R. A. Oriani for helpful discussions and Mr. W. A. Hester for performing the soft x-ray measurements.

Manuscript submitted Nov. 8, 1971; revised manuscript received April 24, 1972. This was Paper 65 presented at the Cleveland, Ohio, Meeting of the Society, Oct. 3-7, 1971.

Any discussion of this paper will appear in a Discussion Section to be published in the June 1973 JOURNAL.

REFERENCES

- H. H. Uhlig, "The Corrosion Handbook," John Wiley & Sons, New York (1948).
- C. L. McBee and J. Kruger, Submitted to *Electrochim. Acta*.
- C. L. Foley, J. Kruger, and C. J. Bechtoldt, *This Journal*, **114**, 994 (1967).
- H. B. Krause, G. A. Savanick, and E. W. White, *ibid.*, **117**, 557 (1970).
- J. E. Holliday, in "Techniques of Metals Research," Vol. 3, Part I, Chap. 9, R. F. Bunshah, Editor, John Wiley & Sons, Inc., New York (1970).
- R. P. Frankenthal, *This Journal*, **116**, 1646 (1969).
- R. P. Frankenthal, *ibid.*, **116**, 580 (1969).
- J. E. Holliday, in "Soft X-Ray Band Spectra and Electronic Structure of Metals and Materials," D. J. Fabian, Editor, p. 101, Academic Press, London & New York (1968).
- J. E. Holliday, in "Advances in X-Ray Analysis," Vol 14, p. 243, C. S. Barrett, J. B. Newkirk, and C. Rudd, Editors, Plenum Press, New York (1971).
- J. E. Holliday, in "Band Structure Spectroscopy of Metals and Alloys," D. J. Fabian, Editor, Academic Press, London and New York, In press.
- K. G. Weil, *Z. Elektrochem.*, **59**, 711 (1955).
- T. Heumann and H. S. Panesar, *This Journal*, **110**, 628 (1963).

Table I. $Fe(L_{II}/L_{III})$ and $Cr^{3+}L_{III}/Cr^0L_{III}$ intensity ratios of Fe-Cr alloys

%C in alloy	$Fe(L_{II}/L_{III})$	$Cr^{3+}L_{III}/Cr^0L_{III}$
0	0.35 ± 0.005	—
5	0.34	1.1 ± 0.05
10	0.35	0.6
14	0.32	0.4
19	0.32	—
24	0.32	0.4



Successive Adsorptions of Hydrogen Bromide and Hydrogen Sulfide on Vapor-Deposited Lead Monoxide Layers

A. H. Boonstra and R. M. A. Sidler

Philips Research Laboratories, N.V. Philips' Gloeilampenfabrieken, Eindhoven, The Netherlands

ABSTRACT

The chemisorption of HBr on vapor-deposited PbO layers was investigated at different temperatures. At room temperature the reaction of HBr with the PbO surface molecules is followed by a fast reaction with the underlying molecules. At -160°C only the surface reaction was measured, resulting in an adsorption of HBr of 60% of a monolayer. Taking into account the decrease of the surface area caused by the adsorption of HBr, we conclude that a monolayer of HBr is chemisorbed. This means that as a result of this reaction the compound Pb_2OBr_2 is formed on the surface of the crystallites. Chemisorption of H_2S at room temperature on such a layer shows a coverage of H_2S of 40% of a monolayer. Optical measurements on these layers show an absorption edge of about 1.75 eV.

The photoconductive layer in the Plumbicon television pick-up tube consists mainly of polycrystalline PbO of the red modification.¹ These vapor-deposited layers have a specific surface area of about $50\text{ m}^2\text{g}^{-1}$ and are therefore particularly suitable for chemisorption experiments. It is known that after vapor-deposition of the PbO, the absorption edge of these layers can be shifted toward the red if the layer is treated with H_2S (1, 2). It is shown that by the adsorption of H_2S , at temperatures below -120°C , the oxygen atoms can be replaced, in stages, by sulfur atoms, resulting in the formation of surface compounds with bandgaps of 1.45, 1.05, and 0.80 eV corresponding to a chemisorption of H_2S to a surface coverage of about 0.25, 0.5, and 1 monolayer, respectively (3). The purpose of our investigations was to find out if this replacement of the oxygen atoms by steps is specific for sulfur atoms or whether it is also possible in the case of the reaction of HBr with PbO. Another possibility in this stepped process is a successive substitution by atoms of different elements.

Experimental Techniques

The primary PbO layers used in our investigations were prepared in the following way. An amount of about 0.5g PbO was evaporated from a platinum crucible. The PbO vapor passed through a gas atmosphere consisting of water vapor and oxygen, and condensed on a Pyrex substrate, maintained at a constant temperature. A detailed description of the evaporation technique is given elsewhere (3, 4).

After evaporation the tube was evacuated and transferred to an adsorption apparatus. In this apparatus the surface area of the PbO layer was measured by the BET method (5) at 78°K using krypton. The specific

area of these layers strongly depends on the temperature of the Pyrex substrate during the preparation. For example it is about $40\text{ m}^2\text{g}^{-1}$ at a substrate temperature of 120°C and about $60\text{ m}^2\text{g}^{-1}$ at a substrate temperature of 90°C . For our investigations we preferred to use PbO layers deposited at 90°C , in order to determine more accurately the changes of the surface area caused by chemisorption of gases. These layers have a typical thickness of $20\text{ }\mu\text{m}$ and consist of crystal plates (6) with dimensions of about $2 \times 0.5 \times 3.5 \cdot 10^{-3}\text{ }\mu\text{m}$, orientated perpendicularly to the substrate surface.

According to Dickens (7) the structure of red PbO can be described as a sandwich structure containing a plane of oxygen atoms flanked by two planes, each containing half the number of Pb atoms. The lone pairs of electrons of the lead atoms hold the sandwiches together by van der Waals forces. Therefore red PbO is expected to crystallize mainly in the form of plates parallel to the sandwich plane.

Assuming that this also occurs in our vapor-deposited PbO layers, the surface density of lead and of oxygen atoms is $1.25 \cdot 10^{15}\text{ cm}^{-2}$ (8, 9).

PbO layers prepared by our evaporation technique have a porosity of 50% and a mean space between the crystal plates of 5 nm. These properties of the layer make it possible for the gas molecules to penetrate readily into the spaces throughout the entire thickness of the layer. Therefore the depth of penetration of the gas molecules is only restricted by the reactivity of the gas with the surface of the solid.

A description of the chemisorption apparatus is given elsewhere (10). The chemisorption experiments were carried out as follows. A known amount of HBr was added to the PbO layer and the change of the HBr pressure was measured as a function of the adsorption time. The water vapor liberated during the reaction was frozen out of the gas mixture by cooling part of the system to -95°C using melting acetone.

Key words: chemisorption, photoconductivity, phosphors, adsorption, compound formation.

¹Plumbicon is a trade-mark of N. V. Philips' Gloeilampenfabrieken, Eindhoven.

1555

An interesting point is the adsorption of HBr at temperatures below room temperature, for example at about -160°C , at which in addition to chemisorption a physical adsorption of HBr also takes place. This temperature can be kept constant during the reaction, using melting 2-methylbutane. The change in the surface area of layers treated in this way was determined. The reactivity of these layers with H_2S was also investigated.

For the optical measurements, the windows with the PbO layers were removed from the tubes, after which the total (diffuse + specular) reflection spectra, R , and total transmission spectra, T , of the layer, illuminated with normal incident light, were measured on a Beckman DK 2A spectrophotometer with a special integrating sphere accessory. From these measurements the optical absorption spectra can be determined. As a result of the H_2S adsorption the color of the PbO layer was changed. After fracturing the layer the depth of penetration of H_2S into the PbO layer was examined under the microscope.

Adsorption Results

The chemisorption of HBr on a vapor-deposited PbO layer was measured as a function of the adsorption time at different temperatures. Some typical results are given in Fig. 1. We see that the adsorption velocity strongly depends on the temperature. At room temperature the pressure of the HBr decreased from 1 Torr to about 10^{-1} Torr as a result of the adsorption.

At -160°C the HBr pressure decreased to less than 10^{-4} Torr because in addition to a fast chemisorption there was also a physical adsorption. The latter amount could be readily desorbed from the PbO layer by cooling part of the apparatus with liquid N_2 . After desorption of this amount, the quantity of HBr which remains on the PbO layer was about 60% of a monolayer, independent of the adsorption time and the excess of HBr.

In this paper a monolayer adsorption means an adsorption of one gas molecule per PbO surface molecule. It is possible to chemisorb more HBr at -160°C if the layer is warmed up to room temperature after the first chemisorption, $\theta = 0.6$, and cooled down again to about -160°C . This chemisorption process can be repeated several times. The results of these processes are given in Fig. 2.

To get an impression of the value of θ_{HBr} as a function of the depth of penetration of HBr into the PbO layer, a number of PbO layers was covered with different quantities of HBr (Q_{HBr}) at -160°C . At room temperature, such a quantity of H_2S ($Q_{\text{H}_2\text{S}}$) was added to each of these layers so that the depth of penetration of H_2S ($D_{\text{H}_2\text{S}}$) into the PbO layer was larger than the

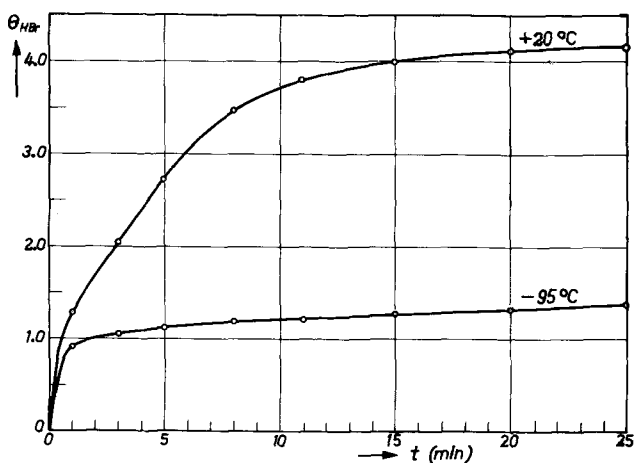


Fig. 1. Adsorption of HBr on the surface of a PbO layer at $+20^{\circ}\text{C}$ and -95°C , expressed in monolayers (θ_{HBr}), as a function of the adsorption time.

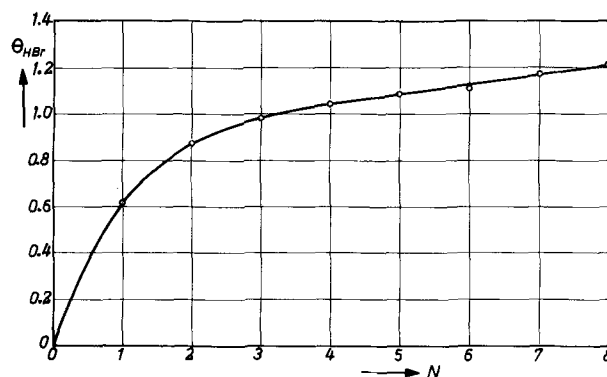


Fig. 2. Adsorption of HBr on the surface of a PbO layer at -160°C vs. the number of processes (N). Each process consists of cooling to -160°C , adsorbing HBr, and warming up the layer to room temperature.

depth of penetration of HBr (D_{HBr}). The water vapor liberated during this reaction was frozen out at -95°C with melting acetone. As a result of such a treatment, the part of the PbO layer covered with HBr and H_2S became deep red; that covered with H_2S only black; and the remaining part retained its original yellow-orange color.

After the adsorption measurements the layers were broken and the location of the boundaries of the colored parts measured under the microscope. A photograph of such a layer is given in Fig. 3.

Using these data and the known quantities of the adsorbed amounts of HBr the θ_{HBr} was calculated.

From previous experiments (3) we know that the $\theta_{\text{H}_2\text{S}}$ of a PbO layer is about 0.90. Therefore the coverage of H_2S of the part of the PbO layer covered with HBr ($\theta_{\text{HBrH}_2\text{S}}$) can also be calculated using the formula

$$\theta_{\text{HBrH}_2\text{S}} = \frac{Q_{\text{H}_2\text{S}} - (D_{\text{H}_2\text{S}} - D_{\text{HBr}})\theta_{\text{H}_2\text{S}}}{D_{\text{HBr}}} \quad [1]$$

The results are given in Table I. We see that the θ_{HBr} is about 0.60 and the $\theta_{\text{HBrH}_2\text{S}}$ about 0.40.

To gain insight into the significance of a $\theta_{\text{HBr}} = 0.60$, the influence of HBr adsorption on the surface area was determined. Therefore, the surface area of a number of PbO layers was measured, they were then treated at -160°C with an amount of HBr smaller than 60% of a monolayer, after which the surface area was again determined. The results are given in Fig. 4.

We see, that the surface area strongly diminishes as a result of the HBr adsorption. Assuming that the part of the layer on which HBr is adsorbed, is covered with a $\theta_{\text{HBr}} = 0.60$, and that the uncovered part of the layer

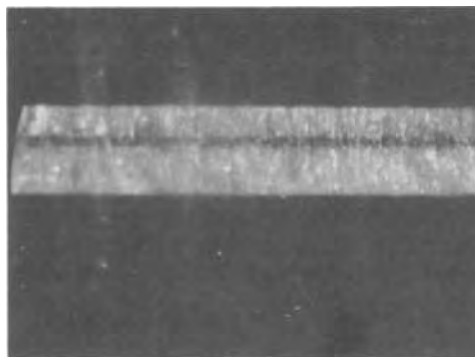


Fig. 3. Photograph of a PbO layer in which the small light-colored part is treated with 0.60 of a monolayer of HBr and 0.40 of a monolayer of H_2S , the dark-colored part being treated with a monolayer of H_2S only and the other light-colored part being the uncovered part of the layer.

Table I. Coverage of H₂S of part of PbO layer covered with HBr

Sample No.	Amount of HBr adsorbed at -160°C in % of a monolayer (Q_{HBr})	Amount of H ₂ S adsorbed at +20°C in % of a monolayer ($Q_{\text{H}_2\text{S}}$)	Depth of penetration of HBr (%) (D_{HBr})	θ_{HBr}	Depth of penetration of H ₂ S (%) ($D_{\text{H}_2\text{S}}$)	$\theta_{\text{HBr}, \text{H}_2\text{S}}$
1	9.9	25.1	16	0.63	36	0.43
2	20.1	24.5	35	0.58	47	0.40
3	28.0	30.5	45	0.62	57	0.44
4	30.1	35.2	50	0.61	64	0.44
5	30.4	28.5	50	0.61	57	0.44
6	46.5	39.7	81	0.57	90	0.39

Table II. Change of surface area of PbO layer on which HBr is adsorbed

Sample No.	Amount of HBr adsorbed at -160°C in % of a monolayer	Total surface area after HBr adsorption in % of the original surface area	A'/A (%)	θ'_{HBr}
1	58.0	57.7	58.0	1.03
2	55.7	59.5	56.5	1.08
3	54.5	57.5	53.0	1.13
4	53.4	62.7	54.0	1.11
5	45.5	65.8	54.5	1.10
6	38.0	72.4	57.0	1.08
7	30.1	78.5	57.5	1.05
8	22.1	84.0	56.5	1.06
9	12.1	90.8	54.5	1.10

does not undergo a change in surface area, we can calculate the change in surface area of the PbO layer on which HBr is adsorbed. In Table II the results of these calculations are given for a number of PbO layers. In the fourth column of this table the ratio is given between the surface area of the covered part of the layer and that of the same part of the layer before HBr has been adsorbed (A'/A). We see that as a result of the HBr adsorption the surface area of the covered part of the layer decreases to 55-60% of its original value. This decrease of the surface area occurs during chemisorption and not during the warming up of the tube to room temperature. This was determined by cooling some tubes to 78°K, directly after the chemisorption of HBr at -160°C, at which temperature the surface area was measured once again. This indicates that at -160°C, there is a surface recrystallization, made possible by the energy which is liberated as a result of the chemisorption of HBr. A calculation of the coverage of HBr based on the newly formed surface gives a θ_{HBr} of about one monolayer at all times, assuming the same density of Pb atoms per square centimeter. This means that half of the oxygen atoms of the PbO surface molecules are replaced by twice the number of bromine atoms.

To get an impression of the adsorption of H₂S on an HBr-covered PbO layer as a function of the depth of penetration, a number of PbO layers were covered at

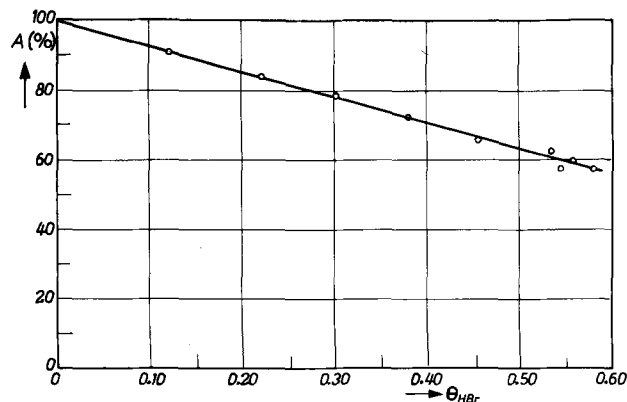


Fig. 4. Total surface area of PbO layers after the adsorption of HBr at -160°C, expressed in percentage of the total original surface area, vs. the amount of adsorbed HBr in monolayers.

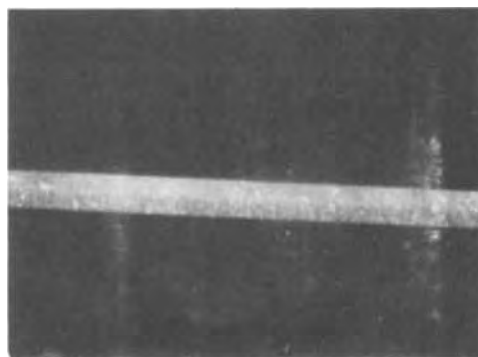


Fig. 5. Photograph of a PbO layer in which the dark-colored part is treated with HBr to a coverage of 0.60 and with H₂S to a coverage of 0.40. The rest of the layer is only treated with HBr to a coverage of 0.60.

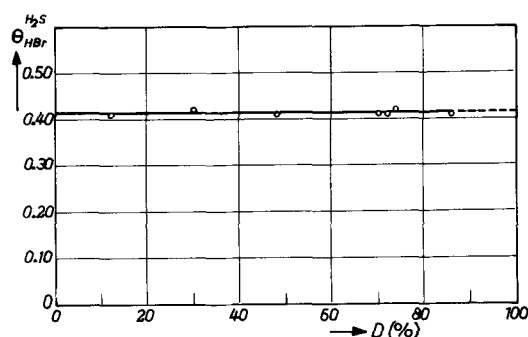


Fig. 6. H₂S adsorption at +20°C on a PbO layer previously treated with HBr at -160°C, vs. the depth of penetration (D) of H₂S into the PbO layer, expressed in percentages.

-160°C with an amount of HBr equivalent to about 60% of a monolayer. Different quantities of H₂S were added to these layers at room temperature. Determination of the surface area showed that the decrease of the area caused by the adsorption of H₂S was less than 10%. After fracturing the layers the depth of penetration of the H₂S in each of these layers was determined under a microscope. The determination of the boundary was possible because of the deep red color of the part of the PbO layer covered with HBr and H₂S, while the rest of the layer retained its yellow color. An example of such a layer is given in Fig. 5. The results of these measurements are given in Table III and Fig. 6. For each of the layers $\theta_{\text{HBr}, \text{H}_2\text{S}} = 0.40$ is found. This value of 0.40 is based on the original surface area. Taking into account the 40% decrease of the surface area caused by the chemisorption of HBr and the 10% decrease caused by the chemisorption of H₂S on such a layer, the coverage of H₂S, $\theta'_{\text{HBr}, \text{H}_2\text{S}}$, is then equal to 0.75.

This means that not only the oxygen of the surface layer of Pb₂OBr₂ is replaced by the sulfur of the H₂S but also a part of the oxygen of the second layer, because no desorption of a bromine compound was detected as a result of H₂S adsorption. When all the oxygen of the first monolayer is replaced by sulfur atoms

Table III. Depth of penetration of H₂S on HBr-covered PbO layer

Sample No.	Amount of HBr adsorbed at -160°C in % of a monolayer	Amount of H ₂ S adsorbed at +20°C in % of a monolayer	Depth of penetration of H ₂ S (%)	$\theta_{\text{HBr}, \text{H}_2\text{S}}$
1	53.2	4.8	12	0.41
2	55.9	10.6	25	0.42
3	50.6	19.8	48	0.41
4	52.3	28.4	70	0.41
5	54.3	29.5	72	0.41
6	52.1	31.0	74	0.42
7	54.0	35.6	86	0.41

then about a quarter of the oxygen of the second layer must also be replaced by sulfur atoms. This suggests the formation of two different sulfur compounds. More information about this can be obtained with the aid of optical measurements.

Optical Results

A property of the PbO layers covered successively with HBr at -160°C and H_2S at $+20^{\circ}\text{C}$ that interests us particularly is the wavelength at which the optical absorption of these layers becomes small and ultimately drops to zero.

In determining the absorption spectra one has to bear in mind that these vapor-deposited PbO layers scatter the incident light rather strongly. The form of the crystallites makes it impossible to handle the scattering rigorously. Therefore one has to fall back on the phenomenological reflection theory of Kubelka and Munk (11) on the basis of which Matzinger (12) shows, that the optical absorption (O) in the bandgap region can be approximated by

$$1 - R - T = O = \frac{\alpha D \left(1 + \frac{1}{2} \alpha D + \sigma D \right)}{1 + \left[\alpha + \sigma + \frac{1}{3} \alpha D (\alpha + 2\sigma) \right] D} \quad [2]$$

where D is the layer thickness, α is the absorption coefficient, and σ is the Kubelka-Munk scattering coefficient. Expression [2] is valid for $\alpha D (\alpha D + 2\sigma D)$ not exceeding one.

The product σD can be estimated from the reflection spectrum. For our layers this is generally somewhat smaller than one. Therefore, in the region of the bandgap ($\alpha D \ll 1$) the term $\alpha D (\alpha D + 2\sigma D)$ is also $\ll 1$. Hence expression [2] reduces to simply

$$O = \alpha D \frac{1 + \sigma D}{1 + \sigma D} = \alpha D \quad [3]$$

Our measurements showed that $O^{1/2}$ is linearly dependent on photon energy (Fig. 9), as is characteristic for indirect energy gap media. For very small values of O , deviations from the straight line show up. This absorption tail is always found in our vapor-deposited PbO layers and is probably caused by impurities. After subtraction of this absorption tail the energy bandgap is easily found.

Figure 7 shows the total reflection spectra, R , and the total transmission spectra, T , of a layer covered with 72% HBr at -160°C and one covered with 56% HBr at -160°C and 25% H_2S at $+20^{\circ}\text{C}$, while in Fig. 8 the superimposed spectra of these layers are shown.

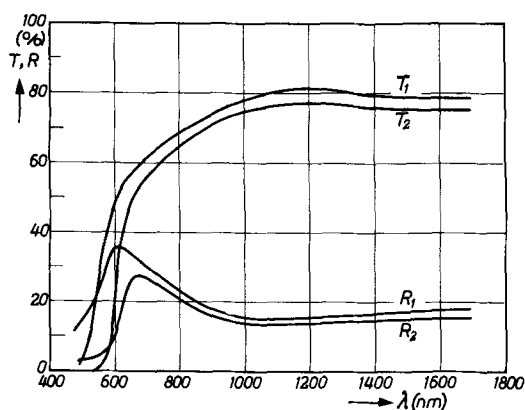


Fig. 7. Total reflection spectra (R) and total transmission spectra (T) as a function of the wavelength of the incident light, denoted by 1 for a PbO layer treated with HBr (sample 1 of Table IV) and by 2 for a PbO layer treated with HBr and H_2S (sample 4 of Table IV).

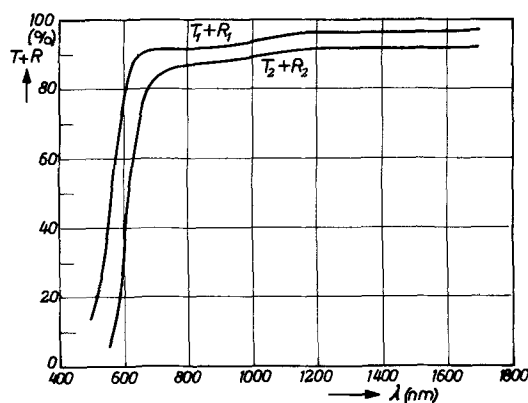


Fig. 8. Superposition of the total transmission and total reflection spectra ($T+R$) as a function of the wavelength of the incident light, 1 being used to denote sample 1 of Table IV, and 2 to denote sample 4 of Table IV.

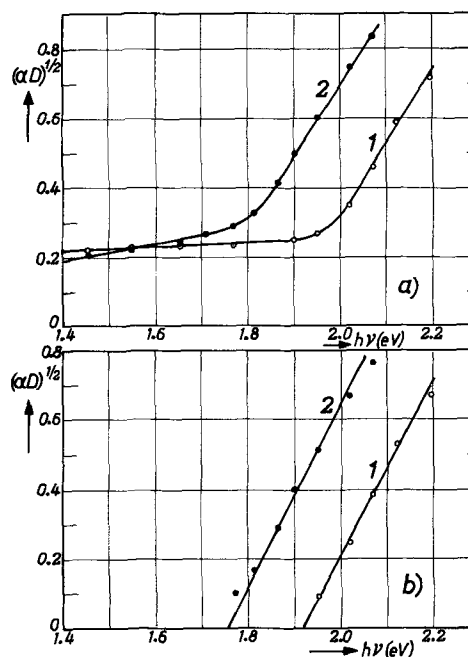


Fig. 9. (a) The absorption spectra of sample 1 (1) and sample 4 (2) of Table IV, vs $h\nu$. (b) The above absorption spectra after subtraction of an absorption tail found in our vapor-deposited PbO layers and probably caused by impurities.

The square root of the absorption curves of these layers, showing the bandgap energy, are given in Fig. 9. In Table IV the results of these measurements are given for a number of PbO layers treated in this way. Special care was taken to ensure that the depth of penetration of H_2S was less than that of HBr. For all the layers we found a value of the bandgap of about 1.75 eV. For some of the layers a bandgap of 1.55 eV was also found, but the intensity of the second branch was small.

Table IV. Bandgap energy of PbO layer

Sample No.	Amount of HBr adsorbed at -160°C in % of a monolayer	Amount of H_2S adsorbed at $+20^{\circ}\text{C}$ in % of a monolayer	E_{e_1} (eV)	E_{e_2} (eV)	E_{e_3} (eV)
1	72.2	—	1.92		
2	55.1	19.8		1.79	
3	51.0	20.0		1.77	
4	55.9	24.5		1.76	
5	55.8	25.5		1.77	1.56
6	54.3	29.5		1.74	
7	58.1	32.0		1.77	1.55
8	57.5	33.5		1.75	1.53

According to Matzinger (12) a good approximation of the value of the bandgap energy is also given by the wavelength at which the reflection curve shows its maximum value. In Fig. 7 we see that the values thus derived are 1.98 and 1.81 eV for a PbO layer covered with HBr and one covered with HBr and H₂S, respectively.

Conclusions

From the adsorption measurements of HBr on a PbO layer we may conclude that, at room temperature, the chemisorption of HBr is not restricted to the PbO of the surface layer but that HBr also reacts with the underlying PbO molecules. The reaction of the HBr with the bulk PbO molecules of the crystal plates can be suppressed by lowering the adsorption temperature. At -160°C only a surface reaction is measured, which results in a θ_{HBr} of 0.60.

As a result of this chemisorption the surface area of the layer is decreased. This reduction of the surface area can be understood when we remember that a PbO layer with a thickness of 20 μm is prepared in less than 5 min. Therefore besides large crystal plates a lot of plates with very small dimensions are also formed. By the energy liberated during chemisorption of HBr the large crystallites can grow at the cost of the small crystallites resulting in a decrease of the surface area of the layer.

Assuming that the surface area of the uncovered part of the layer does not alter, we see that the surface area of the part of the layer covered with a $\theta_{\text{HBr}} = 0.60$ diminishes to 60% of the original surface area. This suggests a surface recrystallization caused by the HBr adsorption. Assuming the same density of Pb atoms per square centimeter, we see a $\theta'_{\text{HBr}} = 1.0$ based on the newly formed surface. This means that half of the oxygen atoms of the surface molecules have been replaced by bromine atoms. In this process two bromine atoms are necessary to replace one oxygen surface atom. This is indicative of the formation of a new surface molecule having the formula of Pb₂OBr₂. A partial replacement of oxygen atoms of the PbO surface molecules by atoms of another element has already been found in the case of H₂S adsorption on a PbO layer, at a temperature of about -120°C (3).

It proves possible to replace the oxygen atom of the surface molecule Pb₂OBr₂ not only by bromine atoms but also by a sulfur atom. The adsorption of H₂S at +20°C results in a coverage of about 0.40 of a monolayer, calculated at the value of the original surface area, or in a coverage of H₂S of 0.75 calculated at the value of the surface area measured after the HBr and H₂S chemisorption.

This means that more oxygen atoms are replaced by sulfur atoms than are present in the Pb₂OBr₂ surface layer, so that a proportion of the oxygen atoms of the second layer must also be replaced by sulfur atoms.

For the replacement of the oxygen atoms of the first layer by sulfur atoms only an amount of H₂S of 0.50 of a monolayer is necessary. The rest of the H₂S will replace a quarter of the oxygen of the second layer. This suggests the formation of more than one sulfur compound.

However, from optical measurements we must conclude that only one new compound is formed because only one bandgap is found which has an energy of 1.75 eV. No bandgap energy of about 1.45 eV is measured which is expected if in the second layer the compound Pb₄O₃S was formed.

Therefore our hypothesis is that the first and the second monolayer interact to form a new surface layer consisting of a complex compound of lead, oxygen, sulfur, and bromine, which has the formula of Pb₈O₃S₃Br₄, instead of the formation of the compound Pb₂SBr₂ in the first layer and of the compound Pb₄O₃S in the second layer.

We hope that the existing techniques available for the study of surfaces will make it possible to confirm our conclusion concerning the structure of this surface compound.

Acknowledgments

We are indebted to Mr. B. H. Matzinger for many valuable discussions concerning the optical part of this work and to Mr. C. G. A. Kregting for his assistance with our experiments.

Manuscript received March 15, 1972.

Any discussion of this paper will appear in a Discussion Section to be published in the June 1973 JOURNAL.

REFERENCES

1. E. F. de Haan, F. H. Klaassen, and P. P. M. Schampers, *Philips Tech. Rev.*, **26**, 49 (1965).
2. U.S. Pat. 3,307,983.
3. A. Netten and A. H. Boonstra, *Surface Sci.*, **27**, 77 (1971).
4. L. Heijne, *Philips Res. Rept., Suppl. No. 4* (1961).
5. S. Brunauer, P. H. Emmet, and E. Teller, *J. Am. Chem. Soc.*, **60**, 309 (1938).
6. A. van der Drift, *Philips Res. Rept.*, **21**, 289 (1966).
7. B. Dickens, *J. Inorg. Nucl. Chem.*, **27**, 1503 (1965).
8. Structure Reports 11, p. 237 (1947-1948).
9. J. Leciejewicz, *Acta Cryst.*, **14**, 1304 (1961).
10. A. H. Boonstra, *Philips Res. Rept., Suppl. No. 3* (1968).
11. P. Kubelka and F. Munk, *Z. Tech. Physik.*, **12**, 593 (1931).
12. B. H. Matzinger, To be published.

Effects of Scale Porosity, Second-Phase Oxides, and Doping in the High-Temperature Oxidation of Cobalt and Dilute Cobalt-Chromium Alloys

Fred R. Billman

Alcoa Research Laboratories, Aluminum Company of America, Cleveland, Ohio 44105

ABSTRACT

The oxidation mechanisms of high-purity cobalt and dilute Co-Cr alloys have been investigated over a 950°-1350°C temperature range in oxygen atmospheres of 10-760 Torr. The 99.999% cobalt exhibited parabolic oxidation behavior for weight gains of up to 30 mg oxygen/cm² rectangular specimen surface. Parabolic kinetics were interrupted when fissures developed in the oxide scale as a result of mechanical stresses at the metal/scale interface or through anisotropic decomposition along CoO grain boundaries. Molecular oxygen then short-circuited to the porous inner scaling layer in accelerated attack of fresh Co surfaces. Diffusion of Co²⁺ through the CoO scale is considered to be the primary rate determining process during periods of steady-state oxidation. The effect of porosity at the metal/scale interface prior to perforation of the outer scaling layer is slight, but is believed to result in a small reduction of the oxidation rate due to a reduction in the CoO/Co contact surface through which cations enter the oxide. Co alloys containing 0.5, 3, 7, and 10 w/o (weight per cent) Cr also obey parabolic kinetics during formation of thinner scaling layers. Porosity and localized loss of scale adherence are aggravated by the presence of CoCr₂O₄ and Cr₂O₃ particles in the inner scaling layer to the extent that scale rupture mechanisms quickly obscure parabolic kinetics for chromium contents greater than 3 w/o at temperatures of 1150°C and above in 100 Torr oxygen. Under conditions where initial periods of steady-state parabolic oxidation were discernible on thermobalance curves, maximum reaction kinetics are associated with 1-2 w/o Cr additions (which approach the Cr³⁺ solubility limit in CoO) as rationalized by Wagner's semiconductor valence theories.

Previous oxidation studies of high-purity cobalt have been reported in the literature (1-8). Linear kinetics are observed during the growth of very thin oxide films, with a subsequent transition to parabolic growth kinetics for thicker oxide layers. At elevated temperatures CoO is a metal deficient, p-type semiconductor (9, 10) and the electrical conductivity of CoO at near atmospheric pressures, where singly charged cation vacancies supposedly predominate (9), is proportional to $P_{O_2}^{1/4}$ (9, 10). The self-diffusion of Co in CoO is reported to be proportional to $P_{O_2}^{1/n}$, where n varies from values of ~ 4 at 10^{-3} atm to ~ 3 at 1 atm oxygen over a 950°-1350°C temperature range (11). The parabolic rate constant for the high-temperature oxidation of cobalt has also been reported to obey a $P_{O_2}^{1/n}$ dependence where $4 > n > 3$ (1-4). Parabolic oxidation of cobalt is rationalized according to the Wagner theory (12). Cobalt cations diffuse from the metal/oxide interface via cation vacancies in the oxide lattice to combine with oxygen at the oxide/gas interface and cation diffusion through the oxide is considered to be the rate-controlling process.

Incremental additions of chromium have been reported to increase the Co-Cr alloy oxidation rate to a maximum value at approximately 10 w/o (weight per cent) chromium (6, 7). Further chromium additions decrease the alloy oxidation rate to a minimum value at approximately 20-30 w/o chromium, with increasing chromium concentrations above 30 w/o then increasing the oxidation rate up to that of unalloyed chromium (7, 13-16).

The rate-controlling process for oxidation of the dilute Co-Cr alloys (Cr < 10 w/o), like that for pure cobalt, is held to be diffusion of cations via cation vacancies in the CoO scale. Continuous increases in alloy oxidation rate with increasing chromium contents

of up to 10 w/o have been attributed to Cr³⁺ doping of the CoO scale according to the semiconductor valence approach proposed by Wagner (12). If the effect of doping is to be significant in the over-all oxidation rate of a dilute alloy, the solubility of the dopant in the matrix oxide must be greater than the native-defect concentration of that oxide at the ambient oxygen pressure.

The native-defect concentration of CoO is thought to be approximately 1% at 1200°C in oxygen at 1 atm (9). Although no data for Cr solubility in CoO are available, analogies with respect to a measured solubility of only 1-2% Cr in NiO (17) have been discussed (13) by Kofstad and Hed who argued that semiconductor valence effects would not be significant in explaining the differences in oxidation behavior between pure cobalt and the Co-10 w/o Cr alloy. They postulated that anisotropic CoO decomposition and rapid transport of gaseous oxygen across pores in the oxide serve to partially short-circuit the diffusion of cations through the scale.

Metallographic examinations of cross sections of partially oxidized dilute Co-Cr alloy specimens have revealed a duplex scale formation similar to that observed for dilute Ni-Cr alloys (18). A dense outer layer of CoO is separated from the metal by a porous inner layer of CoO containing dispersed particles of Cr₂O₃ and the spinel CoCr₂O₄. Internal oxide particles of Cr₂O₃ are also seen in a chromium-depleted region of the alloy, just beneath the metal/scale interface (7, 13). Kofstad and Hed have proposed that the presence of a sufficient volume fraction of dispersed spinel particles (Cr₂O₃ particles were not observed in the inner CoO layer in their investigation) can effectively reduce the cross-sectional area of the inner CoO scale available for cation diffusion, because diffusion of Co is several orders of magnitude slower in CoCr₂O₄ than in CoO (19, 20). This reduction in the diffusion path cross section would therefore explain the decreased

Key words: cobalt, Co-Cr alloys, alloy oxidation, high-temperature oxidation, parabolic oxidation, oxidation kinetics, oxide scale rupture, Cr³⁺ solubility rupture.

oxidation rate of a 10 w/o chromium alloy relative to an alloy of lesser chromium content.

In order to clarify some of these features, further study of the oxidation of pure cobalt and dilute cobalt-chromium alloys containing up to 7 w/o chromium was considered necessary. Comparison of results of these additional studies with the reported behavior of the Co-10 w/o Cr alloy permits a more thorough analysis of the processes by which the high-temperature oxidation of dilute Co-Cr alloys is enhanced relative to that of pure cobalt. Similar interpretations are thought applicable to dilute Ni-Cr alloys and other related systems in which the solubility of the aliovalent solute element in the oxide scale is small.

Experimental Procedure

Rectangular specimens of approximately 10 cm² surface area were cut from cold-rolled sheets of 99.999% cobalt and cobalt-chromium alloys prepared at Battelle Memorial Institute by vacuum-melting techniques. Chemical analyses of the material components are given in Table I. Specimens were polished through 600 metallographic paper, 0.5 μ diamond, ultrasonically cleaned, washed in water, and rinsed in trichloroethylene prior to each test.

The experimental apparatus has been described in detail in a previous report (13). As in previous studies reported by Kofstad and Hed (13), continuous kinetic weight measurements commenced with 1-2 min exposure of the specimen to furnace temperature, and after equilibration of the system to the desired oxygen pressure. Specimens did therefore experience an initial 1-2 min unrecorded oxidation interval during which specimen temperature and oxygen pressure were increasing to the regulated conditions at which kinetic measurements were taken. At completion of a test, specimens were lifted out of the hot zone, oxygen pressure was increased to 1 atm, and specimens were removed from the apparatus. Oxide scales on alloys containing less than 3 w/o chromium were comparatively adherent to the metal even after cooling in still air. However, the 3 and 7 w/o chromium alloy scales often separated from the remaining metal when cooled slowly from temperatures above 1050°C, necessitating quenching the oxidized coupon in a molten Pb-Bi alloy immediately after removal from the reaction chamber.

Oxidized specimens were mounted in epoxy and polished through 600 metallographic paper, 0.5 μ diamond, and Linde B alumina. A 1-5-min etch in 80 parts lactic acid, 5 parts HCl, 10 parts hydrogen peroxide, and 10 parts HNO₃ was utilized to accent the oxidized cross sections.

Results

Pure cobalt.—Figure 1 is a typical (weight-gain)² vs. time plot for the oxidation of 99.999% pure cobalt in 100 Torr oxygen over the 950°-1350°C temperature range (16).¹ Parabolic behavior is observed even within the first few minutes of exposure. Figure 2 summarizes the oxygen pressure dependence of the

¹This data for pure Co oxidation was previously published in Ref. (16).

Table I. Chemical analyses of materials

A. High-purity cobalt sheet for studies of elemental cobalt (supplied by Atomergic Chemicals), in ppm.										
Co	Ni	Si	Fe	Cu	Mg	Al	C	S		
99.999%	1	4	2	1	1	1	ND	ND		
B. Electrolytic cobalt used in preparation of all Co-Cr alloys (supplied by African Metals), in ppm.										
Co	S	C	Fe	Pb	Cu	Ni	Zn	Si	Mn	P
99.90%	0.00	0.008	0.008	0.0001	0.003	0.060	0.003	0.001	0.0003	0.003
C. Chromium used in preparation of all Co-Cr alloys (supplied by Delchrome), in ppm.										
Cr	C	O ₂	H ₂	N ₂	S	Si				
Bal.	80	130	1	10	60	70				

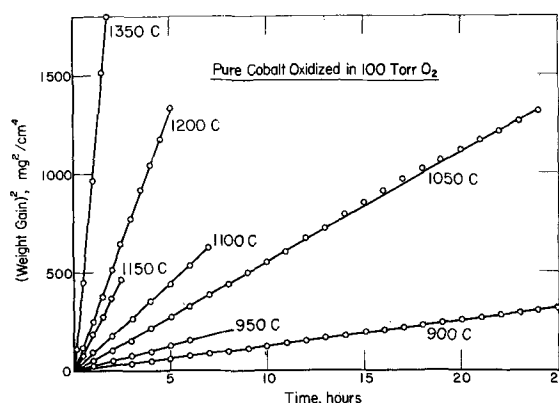


Fig. 1. Parabolic oxidation plot for pure cobalt in 100 Torr oxygen at 900°-1350°C.

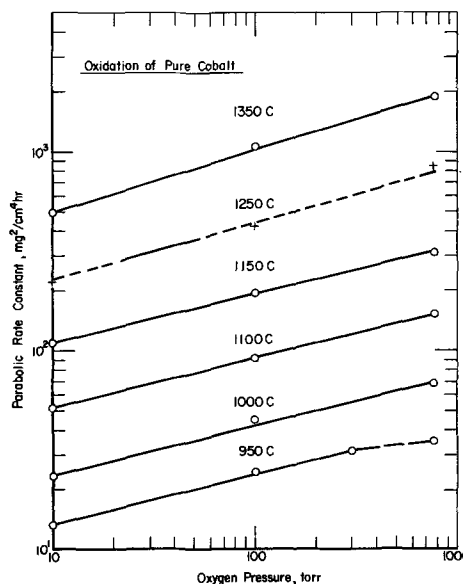


Fig. 2. Graph of oxygen pressure dependence of the parabolic scaling constant for pure cobalt over the 10-760 Torr P_{O_2} range.

parabolic rate constant over a P_{O_2} range of 10-760 Torr (16).¹ Values of the parabolic rate constant at 1250°C have been inferred from the observed temperature dependence. The negative deviation in slope at 950°C in 760 Torr oxygen is attributed to the formation of a surface layer of Co₃O₄. At all other temperatures and pressures investigated, CoO is the only stable oxide formed on pure cobalt. Within the accuracy of the data (k_p values were generally reproducible within $\pm 5\%$) a $k_p \propto P_{O_2}^{1/n}$ dependence was noted with $n = 3.3$.

Figure 3 is an Arrhenius plot of the parabolic rate constant for the oxidation of pure cobalt (16). A least squares analysis results in values of 36.0, 37.8, and 38.7 kcal/mole for the activation energy for oxidation in 10, 100, and 760 Torr oxygen, respectively.

Metallographic examination of cross sections through the oxidized cobalt specimens invariably revealed a region of porosity at the metal/oxide interface as shown in Fig. 4 for an oxidizing temperature of 1150°C. Co₃O₄, which precipitates during cooling of the oxidized specimen to room temperature, outlines grain boundaries in the outer CoO scale.

Previous investigators (2, 4) have reported the presence of porous inner layers on oxidized specimens of cobalt, which heretofore have been largely attributed to impurity effects or polishing artifacts. That such porosity does not result entirely from "metallographic pull-out" of the fine-grained oxide at the metal/oxide interface is verified by Fig. 5a and b. In this instance a crack developed in the external CoO oxide after 4 hr

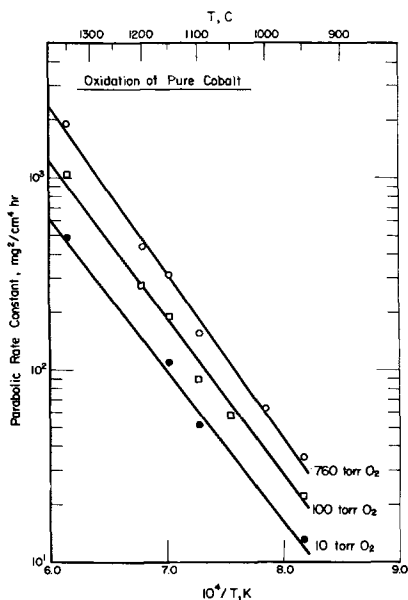


Fig. 3. Arrhenius plot of the parabolic rate constant for pure cobalt oxidation at temperatures of 950°-1350°C.

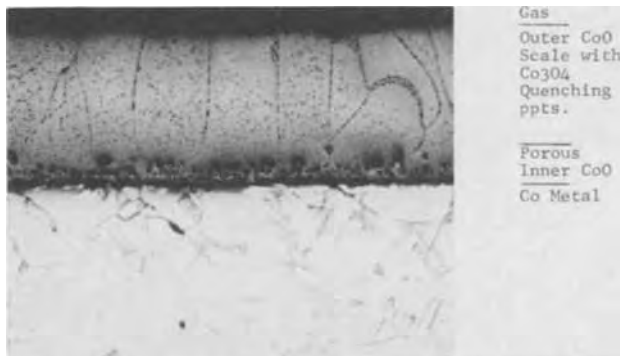


Fig. 4. Oxidized cross section of pure cobalt after 3.5 hr in 100 Torr oxygen at 1150°C. (X90).

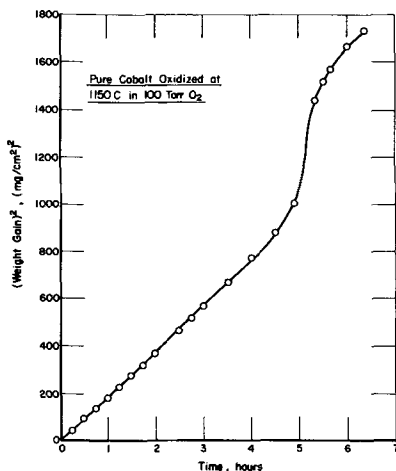


Fig. 5a. Parabolic oxidation plot for pure cobalt in 100 Torr oxygen at 1150°C depicting accelerated attack.

exposure in 100 Torr O₂ at 1150°C (as evidenced by the pronounced increase in the weight-gain data shown in Fig. 5a) and molecular oxygen penetrated the semi-continuous network of pores at the metal/oxide interface. Formation of a new and compact CoO layer occurred subsequently on the fresh metal surface. The position of the metal/oxide interface at the time of the scale rupture is delineated by a few remaining pores as shown in Fig. 5b.

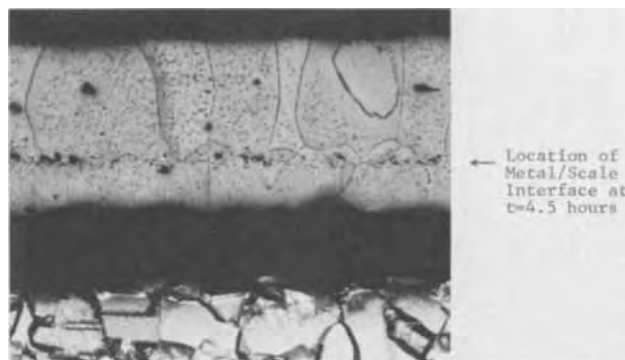


Fig. 5b. Cross section of specimen with oxidation kinetics given in Fig. 5a. (X80).

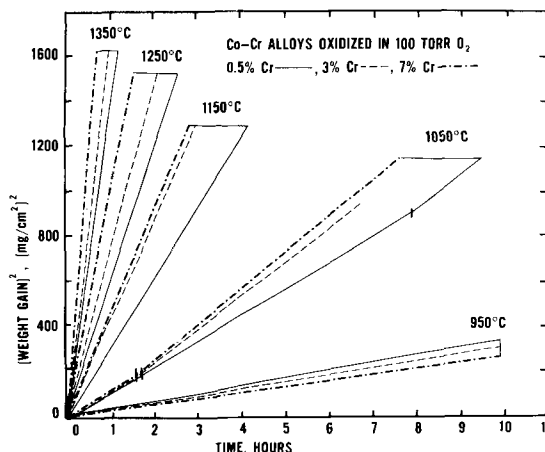


Fig. 6. Parabolic oxidation plot for Co-0.5%Cr, Co-3%Cr, and Co-7%Cr alloys oxidized in 100 Torr oxygen at 950°-1350°C.

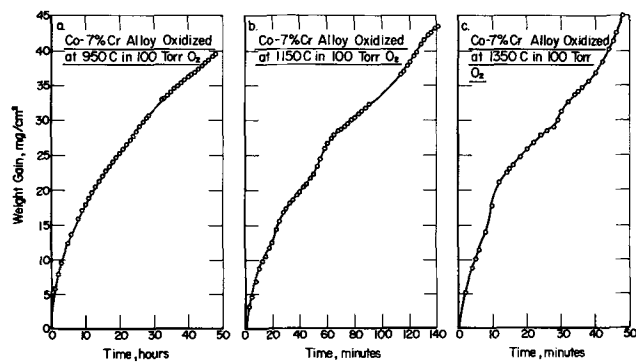


Fig. 7. Linear oxidation plot for Co-7%Cr alloy oxidized in 100 Torr oxygen, (a) at 950°C, (b) at 1150°C, and (c) at 1350°C.

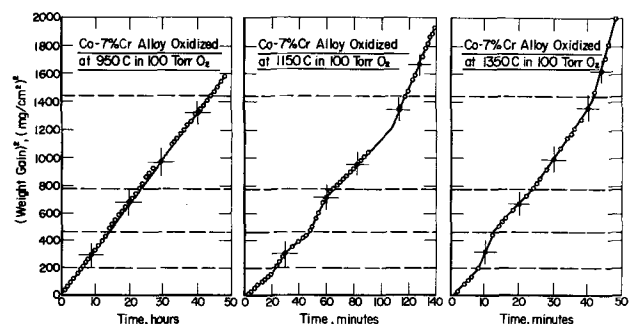


Fig. 8. Parabolic oxidation plot of data, (a) from Fig. 7a, (b) from Fig. 7b, and (c) from Fig. 7c.

Dilute cobalt-chromium alloys.—Figure 6 shows parabolic plots of the gravimetric data for the oxidation in 100 Torr oxygen of cobalt containing 0.5, 3, and 7 w/o chromium. The over-all oxidation behavior might be described as “approximately parabolic,” although oscillations in the parabolic kinetics are common as the reaction proceeds. These oscillations become slightly more pronounced at higher temperatures for a given composition and oxygen pressure as shown in Fig. 7a-c. Scale spallation upon cooling an oxidized specimen of a given alloy content was much more pronounced after oxidation at the higher temperatures. Scales for alloys containing $\geq 3\%$ chromium which cooled in still air generated cracks evenly around the perimeters of the rectangular specimens and nearly perfect sheets of oxide cleanly separated from the specimen faces.

The data from Fig. 7a-c in typical parabolic plots as shown in Fig. 8a-c reveal that the breaks in the kinetics occur at similar weight gain intervals (similar increments of scale thickness) at 1150° and 1350°C. Reproducibility of these oscillations was demonstrated for Co-10% Cr alloys in the previous report (13).

Irregularities in the oxidation rate can be correlated to the chromium content of a Co-Cr alloy. As demonstrated in Fig. 9, the scale thickness at which interruptions in the parabolic behavior occur decreases with increasing chromium contents. Oxidation of Co-Cr alloys with chromium concentrations of 3 w/o or greater, at temperatures of about 1150°C, produces interrupted kinetics within the first 10 mg of O₂ uptake/cm² specimen surface area. It therefore becomes very difficult to determine the initial parabolic oxidation rate, exclusive of any scale rupture effects, at the higher temperature.

Mechanisms by which oscillations in the parabolic behavior might occur during alloy oxidation may be rationalized through metallographic examination of the oxidized specimens. Figure 10a is a parabolic plot of the weight gain data for a Co-3% Cr alloy oxidized at 950°C in 760 Torr oxygen. Two distinct breaks in the parabolic kinetics are noted. At this temperature and pressure both Co₃O₄ and CoO are stable oxide phases, and the oxygen-rich Co₃O₄ phase will exist only in direct contact with oxygen at or near 1 atm pressure. In Fig. 10b, which is a photomicrograph of this same specimen, a white Co₃O₄ layer is visible at the gas/oxide interface directly above an adherent CoO layer. A region of porosity midway through the inner oxide is also outlined with Co₃O₄. The presence of continuous Co₃O₄ oxide layers, as distinguished from cooling precipitates, implies that the pores were in direct contact with the furnace environment after the interruption in kinetics. The absence of Co₃O₄ around

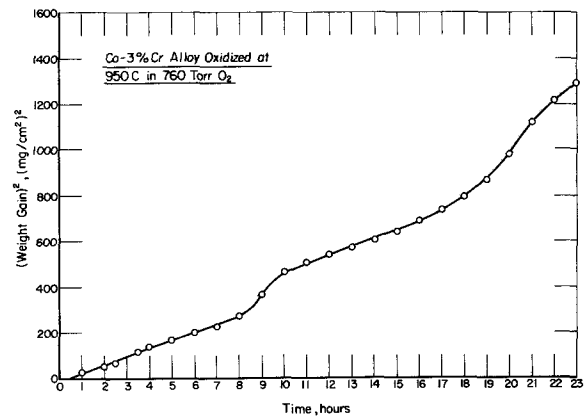


Fig. 10a. Parabolic oxidation plot of Co-3%Cr alloy oxidized in 760 Torr oxygen at 950°C depicting fluctuating kinetics.

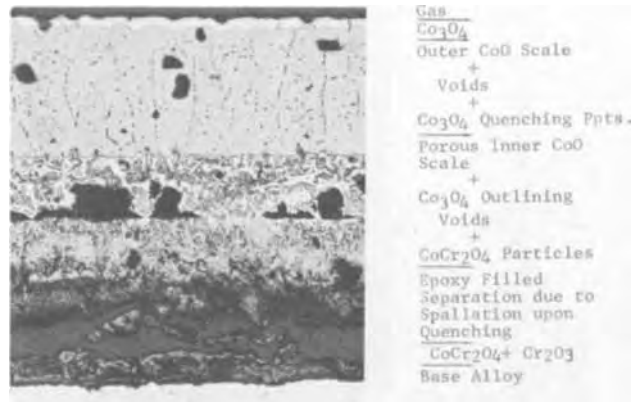


Fig. 10b. Oxidized cross section of Co-3%Cr alloy specimen from Fig. 10a. (X130).

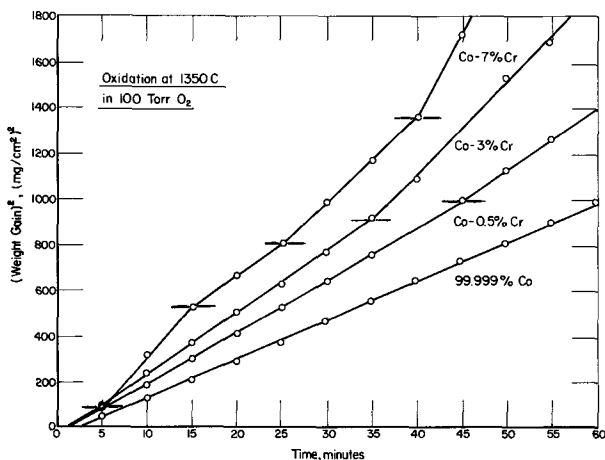


Fig. 9. Parabolic oxidation plots of 99.999% Co and Co containing 0.5-7%Cr oxidized in 100 Torr oxygen at 1350°C showing influence of chromium content on accelerated reaction.

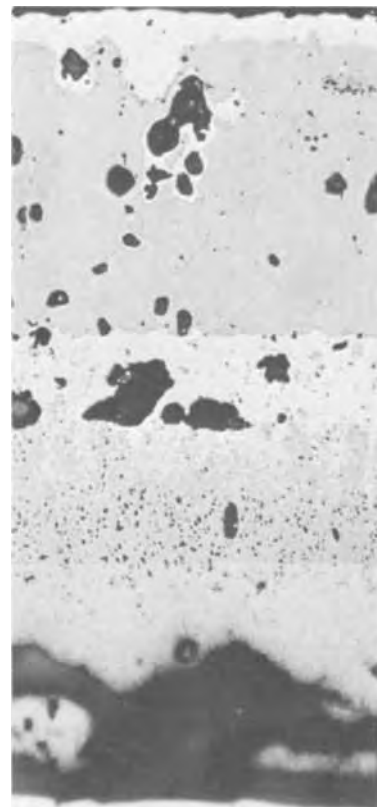


Fig. 10c. Oxidized cross section of same specimen as Fig. 10b showing path of molecular oxygen transport across outer CoO layer. (X340).

the vast majority of irregularly shaped pores in the outer CoO layer also verifies that molecular oxygen at ambient pressure is not easily transmitted through this layer. There was some evidence of molecular transport of oxygen from the furnace atmosphere to the porous inner layer via a few isolated grain boundaries or microcracks in the CoO oxide as shown in Fig. 10c.

Figure 11a is a parabolic plot of the weight gain data for the oxidation of a Co-7% alloy at 1150°C in 760 Torr oxygen and Fig. 11b is a photomicrograph of the same specimen. There is an apparent correlation between the number of line segments in the parabolic kinetics and the number of distinguishable layers in the porous inner oxide. Delineation of the separate inner layers results from the pronounced accumulation of spinel particles at the metal/scale interface until a loss of scale adherence occurs. In these experimental conditions, Co_3O_4 is not a stable oxide and only cooling precipitates of this more oxygen-enriched phase are seen. Frequently, the number of striations in the porous inner oxide is greater than the number of distinguishable portions of the weight gain vs. time curves, especially at specimen corners. Localized losses of scale adhesion do not significantly affect the over-all kinetics unless scale lifting is propagated across an appreciable portion of the specimen surface. Extensive metallographic examination of many different cross-sectional areas of a single oxidized coupon would therefore be necessary before a

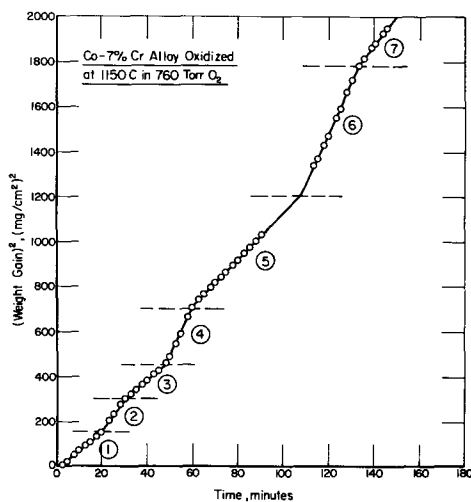


Fig. 11a. Parabolic oxidation plot of Co-7%Cr alloy oxidized in 760 Torr oxygen at 1150°C showing fluctuating reaction.

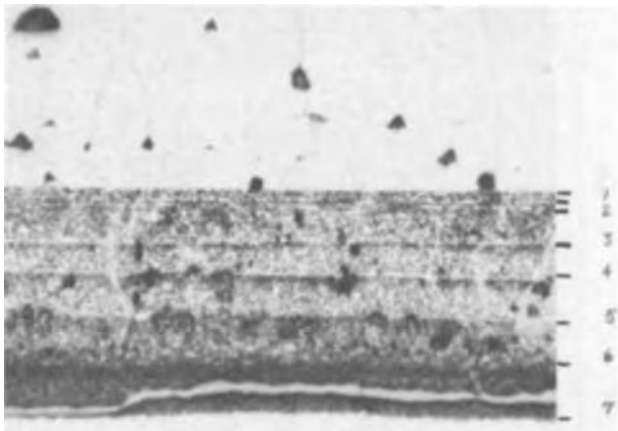


Fig. 11b. Oxidized cross section of Fig. 11a specimen showing multiple inner scaling layers. (X170).

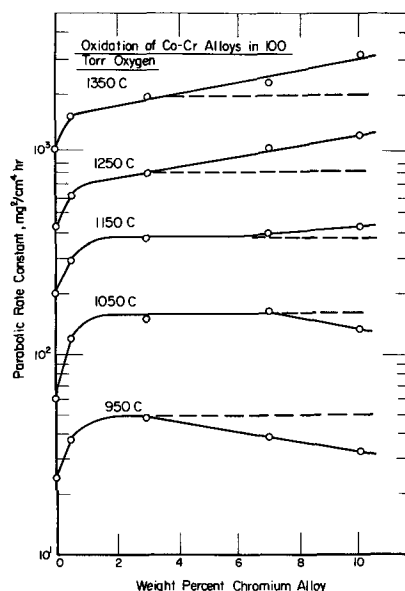


Fig. 12. Plot of parabolic oxidation rate constants in 100 Torr oxygen vs. chromium concentration over the 950°-1350°C temperature range.

definite correlation between a particular curve segment and a given inner oxide layer could be made.

Figure 12 summarizes the effect of dilute chromium additions on the parabolic oxidation rate constant over a 950°-1350°C temperature range in 100 Torr oxygen. Data points are intended to represent the initial parabolic rate constants as determined graphically prior to the onset of any distinguishable scale rupture effects.

Discussion

Pure cobalt.—These results are in very good agreement with the empirical relation determined by Snide, Myers, and Saxer (1) for the oxidation of pure cobalt cylinders at 950°-1250°C in oxygen atmospheres of 15-727 Torr. The pressure dependence obtained in this study was also reported by Mrowec, Walec, and Werber (2) for the oxidation of pure cobalt at 1000°C. Carter and Richardson obtained a $P_{\text{O}_2}^{0.29}$ dependence for pure cobalt oxidation at 1150°C (3) and $P_{\text{O}_2}^{0.28}$, $P_{\text{O}_2}^{0.30}$, and $P_{\text{O}_2}^{0.35}$ dependences for the diffusion of Co^{60} in CoO at 1000°, 1150°, and 1350°C, respectively (11).

The tracer diffusion data determined by Carter and Richardson (11) were corrected for the correlation factor (f) according to the equation $D_{\text{Co}^{60}} = f D_{\text{Co}}$ where $f = 0.78$ as suggested by Kofstad (10). Wagner's parabolic oxidation theory was then used to compare the calculated and experimental values of the parabolic rate constants for the oxidation of pure cobalt at 1000°, 1150°, and 1350°C. These data are given in Table II. Agreement between the calculated and experimental rate constants is similar with that of previous investigations at 1000°C (2, 3) and at 1150°C (1, 3) if the earlier data are also corrected with the corre-

Table II. Comparison of experimental vs. calculated k_p

Temperature, °C	Oxygen pressure, Torr	Wagner's rational rate constant, $Kr \times 10^9$ equiv/cm-sec	Parabolic rate constant, $\text{mg}^2/\text{cm}^2 \text{ hr}$		Deviation of experimental from calculated values, %
			Calculated	Experimental	
1000	760	1.28	130.0	63.0	-51.5
	100	0.63	63.7	45.0	-29.4
	10	0.28	28.2	23.0	-18.4
1150	760	5.15	521.0	312.0	-40.1
	100	2.80	283.0	193.0	-31.8
	10	1.40	141.0	110.0	-22.0
1350	760	31.3	3170.0	1880.0	-40.7
	100	17.8	1800.0	1054.0	-41.4
	10	9.31	940.0	545.0	-42.0

lation factor. Negative deviations from the calculated k_p values were noted in all four investigations, the magnitude of the deviation being slightly greater in this study. Note that the deviation increases with increasing oxygen pressure (i.e., increasing oxidation rate) at temperatures of 1000° and 1150°C, but is nearly independent of oxygen pressure at 1350°C.

Results of this investigation do not correlate the presence of a porous inner CoO layer on pure cobalt with an enhancement of the parabolic oxidation, in the exposure intervals prior to the development of cracks or fissures in the outer CoO scale. In fact, the slightly larger negative deviations of the experimental from the calculated k_p values [these data *vs.* results of other investigations (1, 2) in which no porosity was observed] suggest that porosity decreases the oxidation rate slightly by reducing the effective diffusion cross section of the scale, or by a reduction in the metal/scale contact surface through which cations leave the metal substrate. Further evidence for this interpretation is provided by a comparison of the density of oxide scales formed at 1150° and 1350°C.

Cross sections of several specimens oxidized at 1150° and 1350°C were examined metallographically. Some twenty separate scale thickness measurements were taken around the perimeter of each oxidized coupon, an average scale thickness was calculated, and the volume of oxide for each specimen was estimated using the original surface area of the sample and a geometrical correction for the additional volume of oxide formed at specimen corners. Relative oxide density approximations (average measured volume/measured weight-gain) revealed that after oxidizing pure cobalt at 1350°C in 100 Torr oxygen, the scale was approximately 20% less dense than when oxidized at 1150°C in 100 Torr oxygen. Original specimen size was identical in all cases, specimens had been exposed for approximately equal weight gains, and the external scale surfaces were found to be quite smooth and free of facets so that the measured scale thickness was very nearly equal around the entire perimeter of each oxidized coupon.

Although these density determinations are not sufficiently precise to offer conclusive proof that scale porosity increases as the reaction temperature increases, this is a distinct possibility which is intuitively satisfactory. The accumulation of vacancies at the metal/scale interface would be expected to increase (and the ability of the scale to undergo plastic deformation should decrease) as the flux of cation vacancies to the interface increases. However, the plasticity of the oxide might be expected to increase with increasing temperature and thereby counteract the effects of a more rapidly receding metal surface. This point has not been demonstrated in oxidation studies, and Van Den Broek and Meijering (21) argue that the ductility of high-melting-point oxides such as NiO (and CoO) does not increase very much with rising temperature in the vicinity of 950°C. An increasing rate of oxidation may therefore result in greater scale adhesion difficulties.

One additional feature was indicative of the presence of gross porosity in the inner CoO layer; comparison of the calculated oxide densities of different specimens oxidized under the same environmental conditions (1350°F in 100 Torr oxygen) revealed that scale was up to 15% more dense if an acceleration in the weight-gain kinetics had occurred. This increased scale density after a period of accelerated attack can be explained by a scale rupture mechanism. Porosity increases at the metal/oxide interface until a crack resulting from mechanical stresses occurs in the outer CoO layer, or until anisotropic dissociation along CoO grain boundaries perforates the scale thickness. In either case, molecular oxygen is suddenly transported from the ambient atmosphere through the semicontinuous network of pores along the metal/scale interface.

Oxidation of the freshly exposed Co surfaces occurs until the pores are at least partially closed and the supply of molecular oxygen from the atmosphere is terminated. Parabolic weight-gain kinetics are then restored and the cycle begins anew. There are many indications of such scale rupture effects in the literature (2, 4, 27, 21-30).

Dilute cobalt-chromium alloys.—At least three seemingly different modes of scaling behavior occur as a function of temperature, oxygen pressure, and chromium content over the 0-10 w/o Cr range. As shown in Fig. 12 the parabolic oxidation rate increases rapidly with increasing chromium concentrations up to 1-2 w/o Cr and then remains relatively constant with additional chromium concentration. This "parabolic rate plateau" is sensitive to temperature and oxygen pressure. If the oxidation reaction remains diffusion controlled, further chromium additions produce a decrease in k_p due to CoCr_2O_4 and/or Cr_2O_3 blocking of the Co^{2+} diffusing species. Such is the case at 950° and 1050°C at 100 Torr oxygen for chromium concentrations greater than 3 and 7 w/o, respectively. Analogous behavior has been found in the Ni-Cr system (31-33).

Local fractures or fissures in the scale and periods of accelerated attack become more frequent with increasing temperature and oxygen pressure in these dilute Co-Cr alloys due to the more rapid accumulation of mechanical stresses, porosity, and internal oxide particles at the metal/scale interface. At reaction temperatures above 1150°C in 100 Torr oxygen, alloys of greater than 3% Cr undergo these scale rupturing cycles even from the very early stages of oxidation. Positive deviations from the dashed "parabolic rate plateaus" at temperatures of 1150°C and above are thought to result from such scale rupture effects. At each temperature the plateau representing the maximum alloy oxidation rate (disregarding scale rupture effects) is very nearly equal to two times the oxidation rate of the cobalt base metal. The gross oxidation rate, which includes the combined effects of diffusion-controlled reaction and accelerated attack resulting from losses of scale adherence, increases with increasing chromium content to a maximum of approximately three times the oxidation rate of the cobalt base metal. The over-all enhancement factor of three was also found by Phalnikar *et al.* (7). The position of the maximum absolute oxidation rate as a function of chromium content is related to the temperature, the environment, degree of cold work, specimen geometry, and the proximity of the oxide composition to the equilibrium state as has also been found in the dilute Ni-Cr system (23).

In Fig. 8a-c a limited number of data points representing approximately equal increments of scale thickness have been denoted by a "+" symbol. It is significant to note that a straight line might reasonably fit these points and would, in fact, describe the gross oxidation kinetics; but, any mechanistic interpretation of a single rate constant calculated from this limited amount of data would be very misleading. Similar results are obtained if weight measurements are taken at equal time increments. The use of sensitive, continuous weight-gain measuring devices therefore seems imperative. Recent experimental techniques developed by Bruce and Hancock (28) indicate that scale rupture effects may be operative even when thermobalance charts show a smooth parabolic curve.

Oscillations in the weight-gain kinetics have been reported by Phalnikar, Evans, and Baldwin (7) for Co-Cr alloy oxidation, by Whittle and Wood (24) for Fe-Cr alloy oxidation, by Ali and Wood (27) for the oxidation of cold-worked Cu, Ni, and Fe, and by Van Den Broek and Meijering (21) for the oxidation of nickel and Ni-Cr alloys.

As discussed by Wood, Hodgkiss, and Whittle, (23) second-phase particles and Cr^{3+} ions in the host oxide

lattice affect the plasticity, strength, and adhesion of the scale and thereby tend to promote cracking, porosity, and a loss of scale adherence to the receding metal surface. Van Den Broek and Meijering (2) reported oscillations in the oxidation kinetics of dilute Ni-Cr alloys in which the wavelength of the oscillation always increased with increasing oxidation time. The increase in the oscillation period was attributed to the increasing relaxation possibilities when the absolute oxidation rate decreases. Although semiconductor valence effects in the CoO matrix do not solely determine the absolute alloy oxidation rate (accelerated attack resulting from loss of scale adherence dominates the over-all scaling rate for long-term exposures for alloys of greater than 3%Cr), they cannot be entirely discounted in rationalizing the sharp increases in the steady-state alloy oxidation rate with very small chromium additions.

Metallographic examination of the morphologies of the oxide scales on the 0.5-7 w/o chromium alloys indicated duplex scale formation of the same nature as those described in detail for the Co-10%Cr alloy. Spinel particles were not visible in the oxide scales on the 0.5%Cr alloy, except in a very narrow layer immediately at the metal/scale interface, whereas spinel particles were normally seen throughout the inner oxide layer for alloys of higher chromium content. This suggests a Cr solubility limit between 0.5 and 3% in CoO, over the 950°-1350°C temperature range. Alloys of this concentration fall within the zone of rapid, steady-state parabolic oxidation over exposure intervals equal to the periods of diffusion-controlled oxidation observed for pure cobalt.

The alloy oxidation enhancement factor (k_p , alloy/ k_p , cobalt) of two which was nearly constant for alloys of 3-10%Cr, where initial periods of steady-state parabolic oxidation were discernible, is probably the result of combined doping effects in the CoO lattice of Cr³⁺ and other impurity ions (such as Si, Mn, Fe, etc.) in the 99.90% cobalt base material.

Summary and Conclusions

The high-temperature oxidation of pure cobalt follows parabolic weight-gain kinetics until fissures in the oxide scale develop from mechanical stresses at the metal/scale interface and/or anisotropic decomposition along CoO grain boundaries after extended reaction times (i.e., after a weight gain of approximately 30 mg oxygen/cm² specimen surface under the conditions of this investigation). Molecular oxygen then flows through the porous inner scaling layer, formed by vacancy coalescence and loss of adhesion at the metal/scale interface, to attack fresh Co surfaces. The effect of porosity at the metal/scale interface prior to scale perforation is slight; but is believed to result in a small reduction in the oxidation rate due to a reduction in the CoO/Co contact surface through which cations enter the oxide. Diffusion of Co cations through the CoO scale is considered to be the primary rate determining process during periods of steady-state oxidation.

Oxidation of dilute Co-Cr alloys in the 950°-1350°C temperature range, like that of pure Co, is controlled primarily by the diffusion of Co²⁺ through the outer CoO scale as long as parabolic kinetics prevail. Porosity and localized loss of scale adherence are aggravated by the presence of CoCr₂O₄ and Cr₂O₃ particles in the inner scaling layer. As long as the outer CoO remains impervious to gaseous oxygen, porosity and the Cr₂O₃ and spinel oxide particles act as barriers to the transport of the Co cations. The presence of small amounts of trivalent cations in the CoO lattice (Cr³⁺ solubility ~ 1-2 w/o in CoO) does produce a factor of two increase in the parabolic oxidation of cobalt. These semiconductor valence effects become of lesser significance for Co-Cr alloys whose chromium content falls between 3 and 10 w/o, due to accelerated attack of the

metal substrate following rupture of the outer CoO scale and gaseous transport of oxygen through the porous inner layer.

As stated by Bruckman (22), the mechanism of scale growth of metals and alloys can be explained by Wagner oxidation theory provided that additional processes resulting from geometrical alterations of the metal/scale system are taken into account. In many instances these features are indistinguishable. The formation of blisters and microcracks in the oxide are not necessarily reflected in kinetic curves because of their very localized nature. Cracking which occurs so reproducibly and with such strong influence on thermobalance curves as found in this study affects extensive areas of the specimen surface. Vibrational frequency techniques for measuring oxidation rates (28) are reportedly much more sensitive to the formation of microcracks. In cases where duplex scales are formed, development of more sophisticated methods for separating mechanical effects from diffusion processes is necessary before more meaningful quantitative analyses of alloy oxidation mechanisms may be formulated.

Acknowledgment

This work was supported by NASA under Grant NGR 36-002-070 and was conducted during the period of February-November 1969 at Battelle Memorial Institute, Columbus, Ohio. The author wishes to express appreciation to Mr. R. O. Dodds for his help in the experimental work and to Drs. R. A. Rapp, A. Z. Hed, B. A. Wilcox, and G. R. Wallwork for their guidance.

Manuscript submitted Dec. 8, 1971; revised manuscript received April 14, 1972.

Any discussion of this paper will appear in a Discussion Section to be published in the June 1973 JOURNAL.

REFERENCES

1. J. A. Snide, J. R. Myers, and R. K. Saxer, *Cobalt*, **36**, 157 (1967).
2. S. Mrowec, T. Walec, and T. Werber, *Corrosion Sci.*, **115**, 812 (1968).
3. R. E. Carter and F. D. Richardson, *J. Metals*, **6**, 1244 (1954).
4. F. S. Pettit and J. B. Wagner, Jr., *Acta Met.*, **12**, 41 (1964).
5. G. C. Wood, J. M. Ferguson, B. Vaszko, and D. P. Whittle, *This Journal*, **114**, 535 (1967).
6. A. Preece and G. Lucas, *J. Metals*, **81**, 219 (1952).
7. C. A. Phalnikar, E. B. Evans, and W. M. Baldwin, Jr., *This Journal*, **103**, 429 (1956).
8. J. P. Foster and R. J. Reynik, *ibid.*, **115**, 812 (1968).
9. B. Fisher and D. S. Tannhauser, *J. Chem. Phys.*, **44**, 1663 (1966).
10. P. Kofstad, "High-Temperature Oxidation of Metals," John Wiley & Sons, Inc., New York (1966).
11. R. E. Carter and F. D. Richardson, *J. Metals*, **6**, 1244 (1954).
12. C. Wagner and K. E. Zimens, *Acta Chem. Scand.*, **1**, 547 (1947).
13. P. K. Kofstad and A. Z. Hed, *This Journal*, **116**, Parts I and II, 226 (1969).
14. P. K. Kofstad and A. Z. Hed, "Oxidation of Co-25 w/o Cr at High Temperatures," *ibid.*, **116**, 1542 (1969).
15. P. K. Kofstad and A. Z. Hed, "Oxidation of Co-35 w/o Cr at High Temperatures," *Werkstoffe Korrosion*, p. 894 (1970).
16. P. K. Kofstad and A. Z. Hed, "Mechanisms of Oxidation in the Co-Cr System," Proc. 4th Intern. Congr. Metallic Corrosion, Amsterdam (1969).
17. G. H. Meier, Ph.D. Dissertation, The Ohio State University (1968).
18. J. Moreau and J. Bernard, *J. Inst. Metals*, **83**, 87 (1954).
19. A. Morkel and H. Schmalzried, *Z. Phys. Chem. Neue Folge.*, **32**, 76 (1962).
20. R. Sun, *J. Chem. Phys.*, **28**, 290 (1958).
21. J. J. Van Den Broek and J. L. Meijering, *Acta Met.*, **16**, 375 (1968).
22. A. Bruckman, *Corrosion Sci.*, **7**, 51 (1967).
23. G. C. Wood, T. Hodgkiess, and D. P. Whittle, *ibid.*, **6**, 129 (1966).

24. D. P. Whittle and G. C. Wood, *This Journal*, **115**, 133 (1968).
 25. G. C. Wood and D. P. Whittle, *ibid.*, **115**, 126 (1968).
 26. J. E. Castle and G. C. Wood, Proc. Symposium on the Scanning Electron Microscope—The Instrument and Its Applications, III Research Institute, Chicago (1968).
 27. S. I. Ali and G. C. Wood, *J. Inst. Metals*, **97**, 6 (1969).
 28. D. Bruce and P. Hancock, *ibid.*, **97**, 140 (1969).
 29. N. Birks and H. Rickert, *ibid.*, **91**, 308 (1962).
 30. S. Mrowec, T. Werber, and M. Zastawnik, *Corrosion Sci.*, **6**, 47 (1966).
 31. G. S. Giggins and F. S. Pettit, Oxidation of Nickel-Chromium Alloys at Temperatures Between 800 and 1200°C, Pratt & Whitney, Advanced Materials R&D Lab. 68-024 (1968).
 32. G. C. Wood and T. Hodgkiss, *Nature*, **211**, 1358 (1966).
 33. G. E. Zima, *Trans. Am. Soc. Metals*, **49**, 924 (1957).

Effect of Cold Work on the Oxidation of Nickel at High Temperature

D. Caplan, M. J. Graham, and M. Cohen*

Division of Chemistry, National Research Council of Canada, Ottawa, Ontario, Canada K1A 0R9

ABSTRACT

The oxidation of cold-worked and annealed pure Ni in 1 atm O₂ was investigated from 700° to 1270°C in continuous weighing experiments for periods from 1 min to 20 hr and the oxidized specimens examined by diffraction, electron-optical techniques, and metallographic cross sections. Cold-worked Ni was found to oxidize faster than annealed Ni and form finer-grained oxide. Plots of the apparent parabolic rate constant, K_p , for cold-worked Ni show an initial high value that decreases rapidly as the oxide coarsens with time. For annealed Ni, K_p is lower, grain size larger, and both change little with time. Accordingly, a range of K_p values is obtained at each temperature and, on an Arrhenius plot of Ni oxidation, there is a corresponding variation in apparent activation energy, E_A . These results can be plausibly interpreted on the basis of oxide grain boundaries acting as easy diffusion paths for Ni through the NiO layer: for fine-grained oxide, K_p is higher and E_A lower. The oxide is thinnest (and the derived E_A highest) on Ni grains which form a single crystal overgrowth. A break in the Arrhenius plot around 1000°C is the result of transport below 1000° being largely by leakage paths while at higher temperatures volume transport is more important. The estimated activation energy for growth of the oxide layer is 54 ± 2 kcal/mol for transport by lattice diffusion and appreciably less for transport by grain boundary diffusion.

In previous studies of the oxidation of Fe(1, 2) it had been found that cold-worked Fe oxidized considerably faster than annealed Fe. The explanation proposed was that cold work suppressed the formation of diffusion cavities at the Fe₃O₄-Fe interface (cavities which otherwise would block cation transfer) and, in addition, that cation diffusion through Fe₃O₄ was faster through Fe₃O₄ formed on cold-worked Fe. At temperatures above 600°C, i.e., where a layer of FeO developed between the Fe₃O₄ and Fe, the effect disappeared: cold-worked and annealed Fe oxidized at the same rate with no diffusion cavities in either case.

The purpose of the present work was to obtain further information on the growth mechanism of oxide layers by studying the effect of cold work on the oxidation of Ni. Ni was chosen because only one oxide phase is formed, a factor expected to simplify inter-

pretation of the results. The NiO is similar in structure to FeO, thickens via cation vacancy diffusion as in FeO and Fe₃O₄, and can be investigated over a broad temperature range.

Experimental

Specimens 1 × 5 cm were cut from two grades of Ni strip, commercially pure (C.P.) Ni 0.035 cm thick and zone refined (Z.R.) Ni 0.025 cm thick. Table I shows the composition as determined by spark source mass spectroscopy on the as-received cold-rolled strip after electropolishing to remove surface contamination.

Specimens were prepared for oxidation by chemical polishing for 30 sec at 85°C in mixed concentrated acids (30 ml nitric, 10 ml sulfuric, 10 ml phosphoric, and 50 ml acetic), electropolishing for 30 sec at 17°C and 0.6 A/cm² in a 1:4 (by volume) solution of 71% perchloric acid in glacial acetic acid, annealing 1 hr at 1100°C in 30 Torr of purified Ar in a quartz tube, chemical and electropolishing as before, and etching

* Electrochemical Society Active Member.

Key words: kinetics, oxide grain structure, oxide growth mechanism.

Table I. Composition^(a) of Ni specimen materials, ppm by weight; balance Ni

	B	C	N	O	F	Na	Mg	Al	Si	P ^(d)	S	Cl	K	Ca	Ti	Cr	Mn	Fe	Co	Cu	W
C.P.Ni ^(b)	<0.01	2	4	12	<0.05	0.1	0.2	0.1	1	<0.2	1	0.3	0.1	1	0.04	0.4	0.05	17	<0.1	0.5	<0.2
Z.R.Ni ^(c)	0.06	30	0.2	2	<0.05	0.1	0.2	0.2	1	<0.2	<0.3	0.7	0.1	0.2	0.04	0.9	<0.01	8	<0.1	0.5	3

^(a) Semiquantitative analysis by spark source mass spectroscopy; accuracy estimated to be within a factor of two. H was not analyzed. Other elements from Li through U were not detected, indicating a content less than 0.1 ppmw. Analysis by Analytical Chemistry Section, N.R.C.C.

^(b) Commercially pure nickel, Ni-270 from International Nickel Company.

^(c) Zone refined pure nickel, Marz grade from Materials Research Corporation, prepared from Ni-270 by zone refining.

^(d) Analyzed colorimetrically.

Table II. Oxidation of zone refined and commercially pure Ni, annealed and cold worked

Run	Ni grade	Spec. prep.	Temp. (°C)	Total run time		$K_p^{(a)}$				$K_p^{(b)}$	Oxide layer ^(c)	
						0.1 hr	0.2 hr	1 hr	20 hr		Thick-ness (μ)	Grain size (μ)
1	Z.R.	Ann.	700	20		0.0024	0.0030	0.0036	0.002	0.00016	1.45	
2	Z.R.	Ann.	700	20		0.012	0.008	0.005	0.003		1.98	
3	Z.R.	C.W.	700	20		0.091	0.074	0.059	0.026		5.9	1.5
4	Z.R.	Ann.	900	20		0.053	0.048	0.033	0.037	0.019	5.92	
5	Z.R.	Ann.	900	30		0.039	0.039	—	—		0.98	
6	Z.R.	C.W.	900	20		1.00	0.85	0.61	0.32		19.8	3.3
7	Z.R.	Ann.	1100	20		1.00	0.865	0.740	0.650	0.61	25.4	
8	Z.R.	Ann.	1100	5		—	—	—	—		1.95	
9	Z.R.	C.W.	1100	20		5.78	4.62	2.91	1.10		39.9	9
10	Z.R.	C.W.	1100	10		5.66	—	—	—		7.0	2.4
11	Z.R.	Ann.	1270	20		6.00	5.97	5.75	5.21	4.98	72.0	300
12	Z.R.	Ann.	1270	20		6.76	6.51	6.18	5.35		72.7	
13	Z.R.	Ann.	1270	10		6.17	—	—	—		7.0	
14	Z.R.	Ann.	1270	3		—	—	—	—		4.1	
15	Z.R.	Ann.	1270	1		—	—	—	—		2.4	
16	Z.R.	C.W.	1270	20		15.7	13.4	9.05	5.30		78.1	22
17	Z.R.	C.W.	1270	10		12.9	—	—	—		11.1	5
18	C.P.	Ann.	700	20		0.009	0.006	0.005	0.0027	0.00020	1.77	
19	C.P.	C.W.	700	20		0.083	0.050	0.029	0.027		5.2	
20	C.P.	Ann.	900	20		0.074	0.065	0.063	0.067	0.020	7.7	
21	C.P.	C.W.	900	20		0.87	0.75	0.50	0.28		18.8	3.2
22	C.P.	Ann.	1100	20		2.0	1.88	1.64	1.09	0.61	34.9	20
23	C.P.	C.W.	1100	20		6.0	5.1	3.3	1.28		41.5	9
24 ^(d)	C.P.	C.W.	1100	20		4.70	4.1	2.9	1.37		41.6	
25 ^(e)	C.P.	—	1100	20		3.0	2.7	2.1	1.32		38.9	
26	C.P.	Ann.	1270	20		7.93	7.54	6.33	5.70	4.86	76.0	60
27	C.P.	Ann.	1270	20		6.73	6.51	6.33	6.15		76.6	
28	C.P.	C.W.	1270	20		14.5	12.3	8.48	5.90		79.2	22

^(a) Instantaneous values of the apparent parabolic rate constant calculated as $2w \, dw/dt$ from slope of oxidation curves at 0.1, 0.2, 1, and 20 hr. Units are ($\text{mg}^2 \text{cm}^{-4} \text{hr}^{-1}$); multiply by 2.78×10^{-10} to change to $\text{g}^2 \text{cm}^{-4} \text{sec}^{-1}$.

^(b) Local values of the apparent parabolic rate constant calculated as w^2/t from measurements of the thinnest oxide on metallographic cross sections.

^(c) Average oxide thickness calculated from wt. gain at end of run; diameter of average grain of outer oxide measured by Heyn intercept procedure.

^(d) Cold worked by shot peening with glass microspheres.

^(e) Cold rolled; standard procedure (chemical polish, electropolish, etch) except anneal omitted.

immediately in 0.8N nitric acid for 30 sec. The combination of chemical and electropolishing removed 13μ of Ni before annealing and 9μ after; etching removed 250Å. Average grain diameter after annealing was 0.1 mm for C.P. Ni and 0.6 mm for Z. R. Ni; the latter showed wide variations with some grains as large as 10 mm. Cold-worked (C.W.) specimens were prepared by the following additional treatment: abrasion for 7 min with 600-grit SiC paper lubricated with methanol, 3 min with 6μ diamond on nylon cloth lubricated with lapping oil, then ultrasonic cleaning in benzene, ether, and redistilled methanol. The abrasive treatment removed 4μ of Ni. An alternative cold-working procedure was shot-peening for 2 min with 50μ diam glass microspheres.

Oxidation runs at 700°–1270°C were carried out for times from 1 min to 20 hr in 1 atm of purified oxygen flowing up through a 3 cm ID vertical furnace tube at 100 ml/min. Runs were started 1 hr after specimen preparation by hanging the specimen on a sapphire hook, lowering into the hot zone of the mullite furnace tube, and connecting to an automatic balance of 0.1 mg sensitivity. Specimens reached temperature in 30 sec. Weight recording began at 20 sec but was judged reliable only after about 2 min when a steady state had been achieved. The hot weight at zero time was determined from before and after weighings at room temperature. Runs were ended by removing the specimens to cool in Ar. No oxide was lost during oxidation or cooling. Table II summarizes the experimental details; a number of variations from the procedure described are included.

Results

Oxidation curves.—Figures 1 and 2 show the 20 hr oxidation curves of cold-worked and annealed Z.R. Ni and C.P. Ni at 700°, 900°, 1100°, and 1270°C. Cold-worked metal oxidizes faster at each temperature for both materials. An intermediate degree of cold work yields an intermediate oxidation rate (curve 25 vs. 22 and 23, Fig. 2). Cold working by a different method (shot peening, curve 24) gives the same rapid rate as the standard abrasion procedure (curve 23). Reproducibility is good within each grade of Ni (e.g., curves

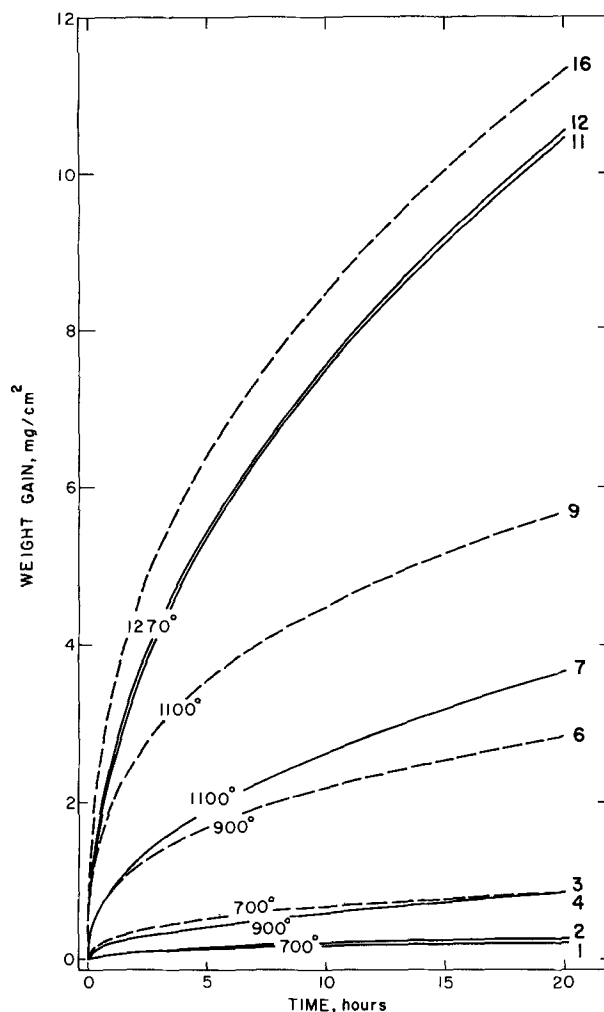


Fig. 1. Oxidation curves for Z.R. Ni from 700° to 1270°C. Oxidation is greater at each temperature for cold-worked Ni (broken lines) than annealed Ni (solid lines).

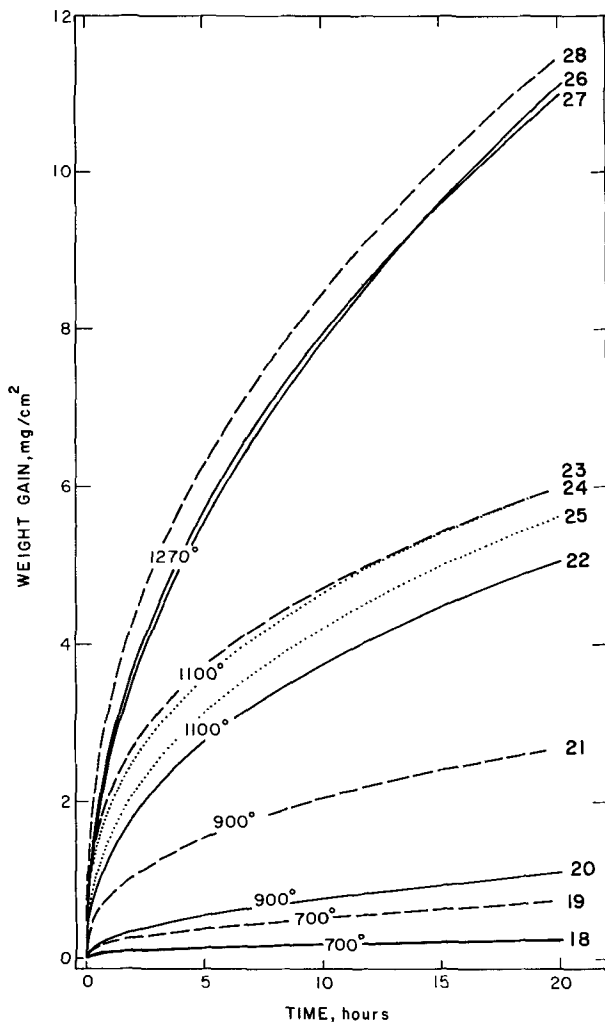


Fig. 2. Oxidation of C.P.Ni from 700° to 1270°C. Oxidation is greater for cold-worked Ni (broken lines) than annealed Ni (solid lines). Different methods of cold working give similar results (curve 24, shot-peened; curve 23, abraded). A lesser degree of cold work yields an intermediate oxidation rate—curve 25 (cold rolled) vs. curve 23 (abraded) and curve 22 (annealed).

1 and 2 or 11 and 12 for Z.R. Ni and 26 and 27 for C.P. Ni) but less so between grades: annealed C.P. Ni oxidizes faster than Z.R. Ni; in the cold-worked condition, however, the two grades oxidize at the same rate.

Rate constants.—Figures 3 and 4a show the instantaneous apparent parabolic rate constants, K_p , calculated from the oxidation data as $2w \, dw/dt$, plotted against time. (The data were processed by digitizing the weight gain strip charts from the recording balance and applying a computer program to yield plots of rate constants and oxidation curves directly.) For clarity, single representative runs are plotted; K_p values for all runs taken from the computer print-out at 0.1, 0.2, 1, and 20 hr are listed in Table II.

The K_p curves for cold-worked Ni differ in kind from those of annealed Ni: for the former, K_p is initially very high, decreases rapidly with time, and approaches a constant value at long times; for annealed Ni, K_p is comparatively constant throughout. The degree of convergence with time depends on temperature: after 20 hr at 700° and 900°, K_p remains appreciably higher for cold-worked than annealed Ni (Fig. 3), at 1100° it is slightly higher, but after 20 hr at 1270° K_p for cold-worked Ni has dropped to the value for annealed Ni (Fig. 4a). Figure 4b, c, d, and e are photomicrographs of the outer oxide surface (located on Fig. 4a by arrows) showing that the oxide

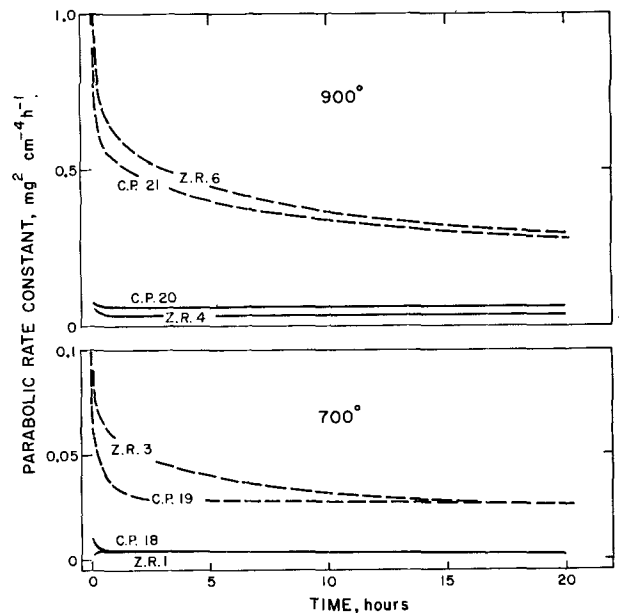


Fig. 3. Apparent parabolic rate constants, $2w \, dw/dt$, plotted against time for Z.R. and C.P.Ni at 700° and 900°. For cold-worked Ni (broken lines) K_p is high initially and decreases rapidly; for annealed Ni (solid lines) K_p is relatively constant. After 20 hr K_p still is appreciably higher for cold-worked than annealed Ni.

on cold-worked Ni is fine-grained initially, finer at lower temperature, and coarsens with time.

The variations in K_p are conveniently summarized on an Arrhenius plot, Fig. 5. The high values for cold-worked Ni at short times (0.1 hr) fall on a straight line over the full temperature range of 700°–1270° with a slope indicating a low apparent activation energy (E_A) of 28 kcal/mole. After 20 hr, E_A for cold-worked Ni at 700°–900°, despite the drop in K_p values, is still 28 kcal; at 1100°–1270° E_A for cold-worked Ni has increased from 28 to 41 kcal after 20 hr. The highest E_A is for annealed Ni from 1100° to 1270°—53 cal for Z.R. Ni and 49 kcal for C.P. Ni after 20 hr. K_p values for annealed Ni at 700° and 900° are high relative to the 1100°–1270° data for annealed Ni, giving rise to a break in the Arrhenius plot and a low apparent E_A (~34 kcal).

Oxide structure.—Figures 6–9 show the microstructure of the NiO layers formed at 700° and 900°. On cold-worked Ni an inner layer of small equiaxed NiO grains next to the metal (Fig. 6e, 7e, f, 8d, 9c, d) is overlaid with relatively coarse, columnar oxide. Grain size of the outer oxide after 20 hr is 0.0015 mm at 700° and 0.0033 at 900°C (Table II shows grain sizes at 700°–1270°). The layer is of uniform thickness, with small cavities distributed throughout, but in good contact with the metal (Fig. 7d, 8c).¹ The outer oxide surface is finely crystalline and at 700° shows a network of ridges that gives a cellular appearance (Fig. 6f, 10a).

Annealed Ni at 700° and 900° exhibits marked anisotropy of oxidation (Fig. 6–10). Over many metal grains the oxide is thin, smooth, and apparently monocrystalline (Fig. 6a,c, 8a,b, 9a,b); (111)Ni forms a thin, strongly epitaxed oxide layer with (111)NiO|| (111)Ni. Etching reveals no oxide grain boundaries (Fig. 8a) and single crystal patterns are obtained by x-ray and electron diffraction. On other substrate grains the oxide is thick and polycrystalline, approaching the fine-grained structure formed on cold-worked Ni. A ridge of thick polycrystalline oxide, and a corresponding trench in the metal, forms over Ni grain boundaries

¹ Various artifacts are created during etching of the metallographic sections, e.g., exaggeration of cavities in the oxide (Fig. 7e, 8d, 12c), a dark band between oxide and metal (Fig. 6a, d, 7a, 11c, 13c, 14c), pitting of the metal (Fig. 14a), and enhanced attack on fine oxide grains at the NiO–Ni interface (Fig. 8d, 9c).

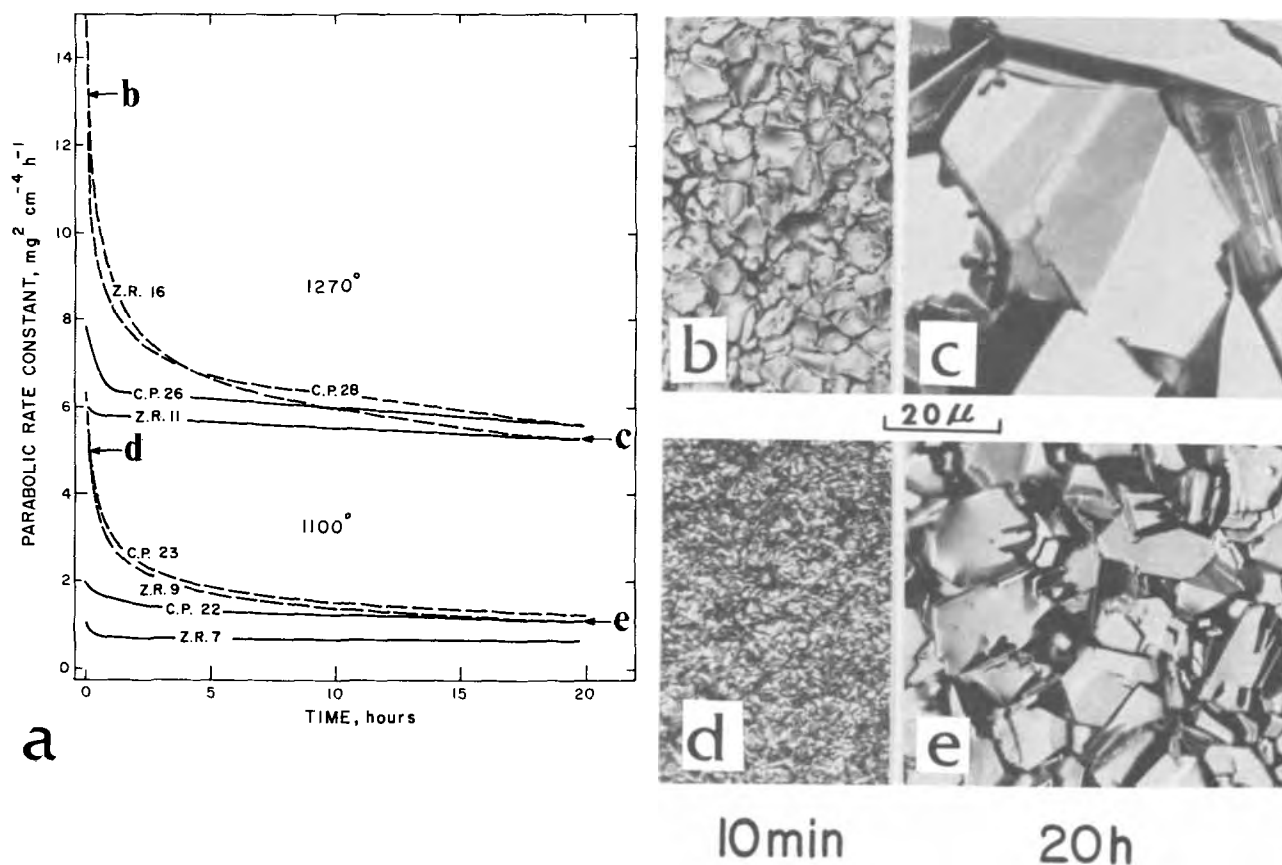


Fig. 4. (a) Apparent parabolic rate constants, $2w \frac{dw}{dt}$, for Z.R. and C.P. Ni at 1100° and 1270°. For cold-worked Ni (broken lines) K_p is high initially and decreases rapidly; for annealed Ni (solid lines) K_p is relatively constant. After 20 hr K_p becomes the same for cold-worked and annealed Ni at 1270°, but remains slightly higher at 1100°. (b), (c), (d), and (e) are photomicrographs at X750 of the outer oxide surface of cold-worked Z.R. Ni after 10 min and 20 hr at 1270° and 1100° [located on (a) by arrows; runs 17, 16, 10 and 9] showing the increase of oxide grain size on cold-worked Ni with time and temperature.

(Fig. 6-10). A similar ridge and trench develops, as expected, where a line of local cold work had been produced by lightly scratching the Ni surface before oxidation (Fig. 8b, 10d). The topography of the outer oxide surface at 700° and 900° is revealed more clearly by the SEM stereopairs in Fig. 10; details are given in the caption.

On annealed Ni at 700° and 900° cavities develop in the oxide on some areas and not on others. The oxide-metal interface is usually plane under thin oxide and rugged under thick oxide. When cavities occur in thick oxide, including oxide ridges, they are concentrated at the oxide-metal interface (Fig. 6a,b, 9a) suggesting cavity formation by condensation of cation vacancies. Since such cavities do not form on cold-worked Ni (Fig. 7d, 8c), where the oxide is as thick or thicker, presumably the cold-worked metal suppresses the nucleation of cavities by providing sinks for cation vacancies as was proposed for Fe (1).

Experiments in this program carried out at temperatures below 700° (650°, 400°, 375°, and 300°) displayed both the oxidation anisotropy of annealed Ni and the greater oxidation due to cold work, but specific results are not reported because the thermobalance was too insensitive to provide reliable kinetic data.

Figures 4 and 11 to 14 show the structure of the oxide formed at 1100° and 1270°C. On annealed Ni the layer is made up of columnar single grains with a plane outer surface parallel to the surface of the specimen. The thickness is uniform except that especially large oxide grains are somewhat thinner (Fig. 11a, 12b). The outer surface of each grain is concave or dish-shaped, i.e., thicker near the grain boundaries (Fig. 11b, 12a,b). Oxide grains are larger at 1270° than 1100° and larger on Z.R. Ni than C.P. Ni. (The metal grain size is also larger for Z.R. Ni than C.P. Ni; the average oxide

grain size is always less than that of the substrate metal but larger the coarser the metal.)

On cold-worked Ni the oxide at 1100° and 1270° is a uniform layer two or three grains thick made up of smaller, more equiaxed grains unrelated to the substrate grain structure (Fig. 11c, 12c, 13c, 14c). The outer oxide surface is randomly faceted rather than plane-parallel. (The latter is expected for a layer growing by a uniform diffusion-controlled process; randomly inclined facets indicate a nonuniform flux of reactant.) The oxide grain size is the same on C.P. Ni and Z.R. Ni, 0.009 mm at 1100° and 0.022 mm at 1270° after 20 hr. At short times the oxide grains are considerably smaller (Fig. 4b,d and Table II) whereas with annealed Ni little variation with time was found by microscopic examination of the short and long runs.

At 1100° and 1270° cavities develop in the Ni, both annealed and cold-worked, predominantly at the grain boundaries (Fig. 13a), and sometimes accompanied by internal oxidation (Fig. 12a). Isolated cavities are distributed throughout the oxide layer; good contact is maintained at the oxide-metal interface (Fig. 12a). The inner porous oxide layer observed in some other investigations (3, 4) is not evident. (The general subject of cavities in Ni oxidation will be part of a subsequent report.)

Discussion

The above experiments demonstrate that cold work affects both the grain size and growth rate of the oxide layer. Cold-worked Ni oxidizes faster than annealed Ni and forms finer-grained oxide which coarsens with time while the oxidation rate constant, K_p , decreases. On annealed Ni the oxide grain size and K_p change little with time. Noteworthy also is the anisotropy of oxidation below 1000° on annealed but not on cold-worked Ni, and the variation in the activation energy

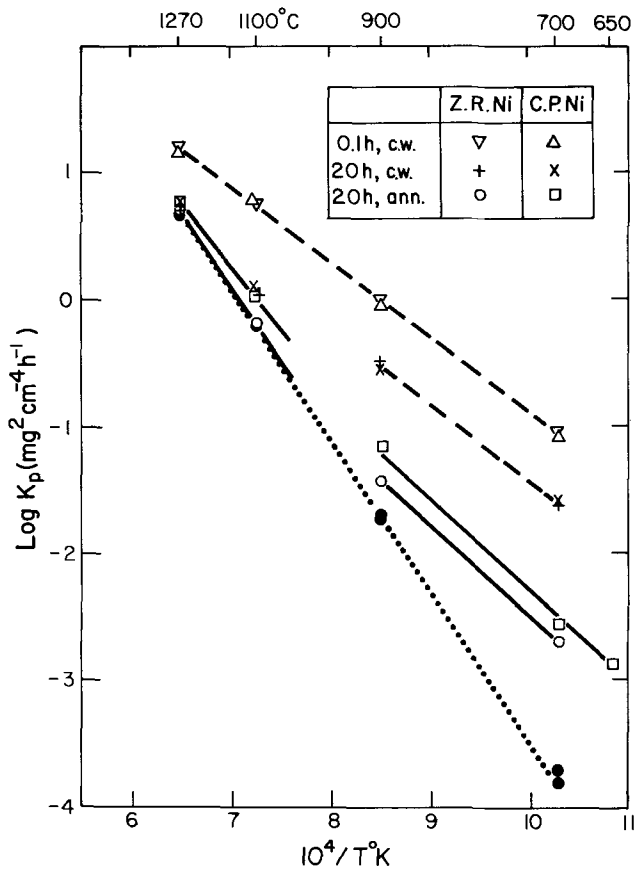


Fig. 5. Arrhenius plot of K_p calculated as $2w dw/dt$ for the oxidation of Z.R. and C.P. Ni, annealed (solid lines) and cold-worked (broken lines). Also shown are values of K_p calculated as w^2/t (filled circles—dotted line) from measurements of the thinnest oxide on annealed Ni at each temperature.

for oxidation E_A —high above 1000° , low below 1000° , and low at all temperatures for cold-worked Ni at short times. All these observations can be plausibly interpreted on the basis of oxide grain boundaries serving as easy diffusion paths for Ni through the NiO layer: with fine-grained oxide, K_p is higher and E_A lower.

The evidence for oxide grain boundaries acting as high-diffusivity paths is as follows: (i) Cold-worked Ni forms a finer-grained oxide layer than annealed Ni and oxidizes faster. (ii) K_p decreases with time for cold-worked Ni with an accompanying increase in oxide grain size. (iii) E_A is lower for fine-grained oxide as anticipated for a grain-boundary diffusion process. (iv) Oxidation anisotropy correlates with oxide grain size: the layer is thicker on substrate grains forming finer-grained oxide, and is especially thin for a single crystal oxide overgrowth.² (v) The oxide is thicker near oxide grain boundaries: at low temperature, ridges form where oxide grain boundaries emerge at the outer oxide surface; at high temperature, the leakage diffusion at the grain boundaries causes the outer surface of each oxide grain to be concave.

In a manner similar to Fe(2), cold-worked Ni, because of surface roughness, lattice mismatch, or polygonization during heating, develops a fine-grained oxide layer high in leakage paths and shows correspondingly high values of K_p . The coarse-grained oxide formed on annealed Ni provides few grain boundaries for leakage-enhanced diffusion and K_p values are consequently low. At high temperature the initially fine grains on cold-worked Ni coarsen rapidly causing K_p to decrease: after 20 hr K_p is the same for cold-worked and annealed Ni at 1270° and nearly the same at 1100° . Sufficient oxide grain growth has occurred to make the leakage path populations comparable. At 700° and 900° the initial fine-grained layer

² This has now been confirmed with some work here on oxidation of single crystals of various orientations.

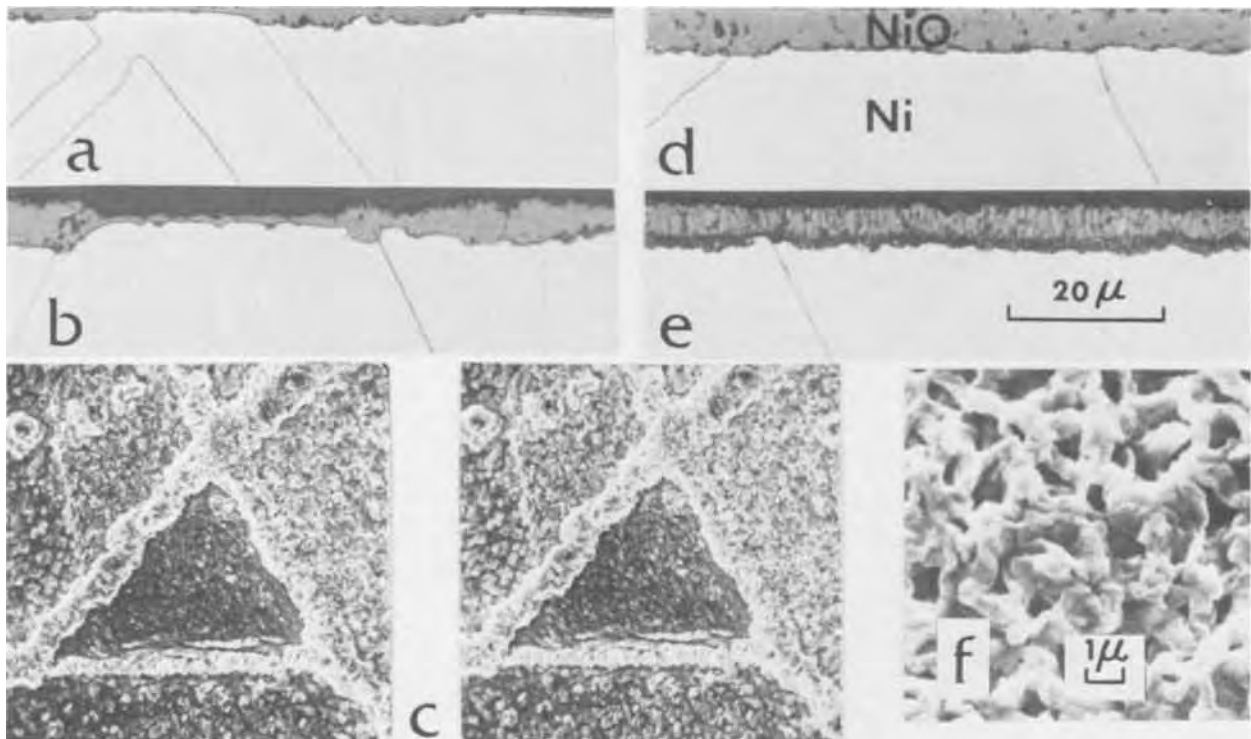


Fig. 6. Oxide structures formed on C.P. Ni in 20 hr at 700° . (a), (b), and (c) run 18, annealed. (d), (e), and (f) run 19, cold worked. In cross sections (at X1000) Ni etched in all and oxide etched in (e) to show inner fine-grained layer and outer columnar layer. (c) is SEM stereopair of oxide outer surface at X1000 showing oxidation anisotropy and oxide ridges over Ni grain boundaries. (f) is SEM photo at X5000 of outer surface of oxide showing ridged cellular structure on cold-worked Ni.

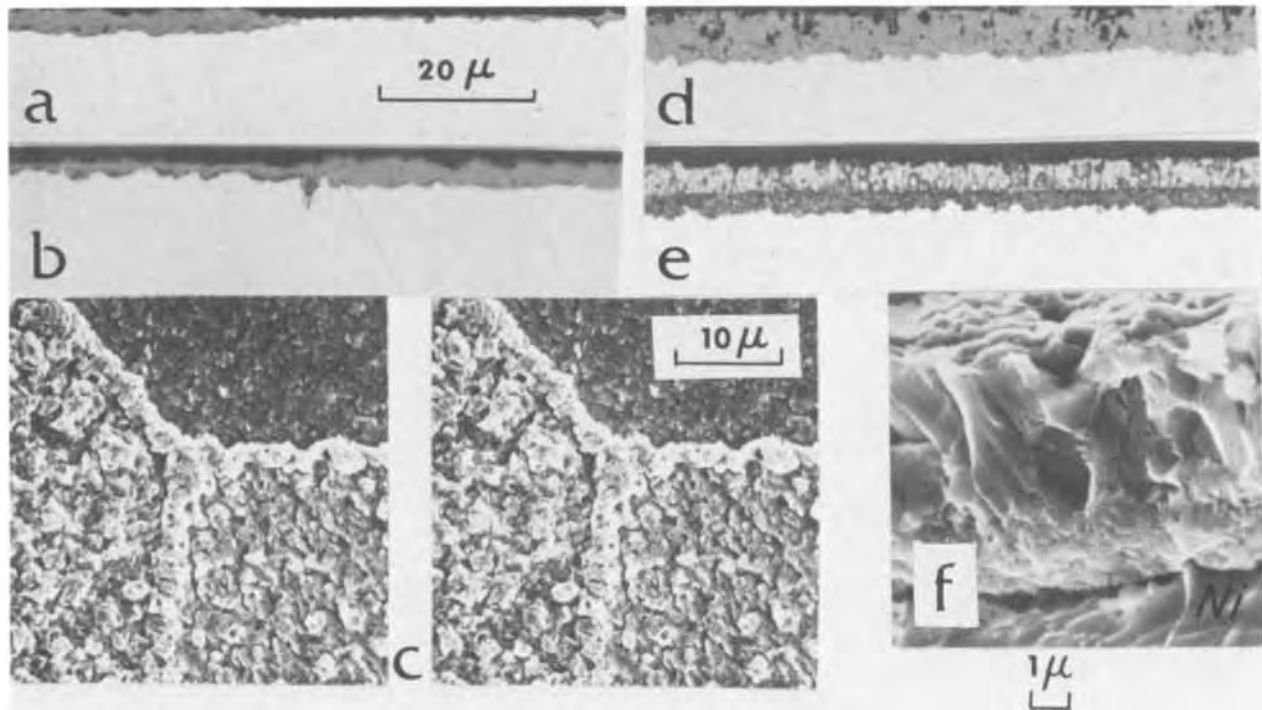


Fig. 7. Oxide structures formed on Z.R.Ni in 20 hr at 700°. (a), (b), and (c) run 1, annealed. (d), (e), and (f) run 3, cold worked. In polished sections (at X1000) (a) and (d) are unetched, (b) has metal etched, and (e) has oxide etched. (c) is SEM stereopair of oxide outer surface at X1400 showing oxidation anisotropy and oxide ridges over grain boundaries of annealed Ni. (f) is SEM photo at X5000 of fracture section showing as in (e) the inner fine-grained layer and outer coarser columnar layer on cold-worked Ni (metal deformed during fracture).

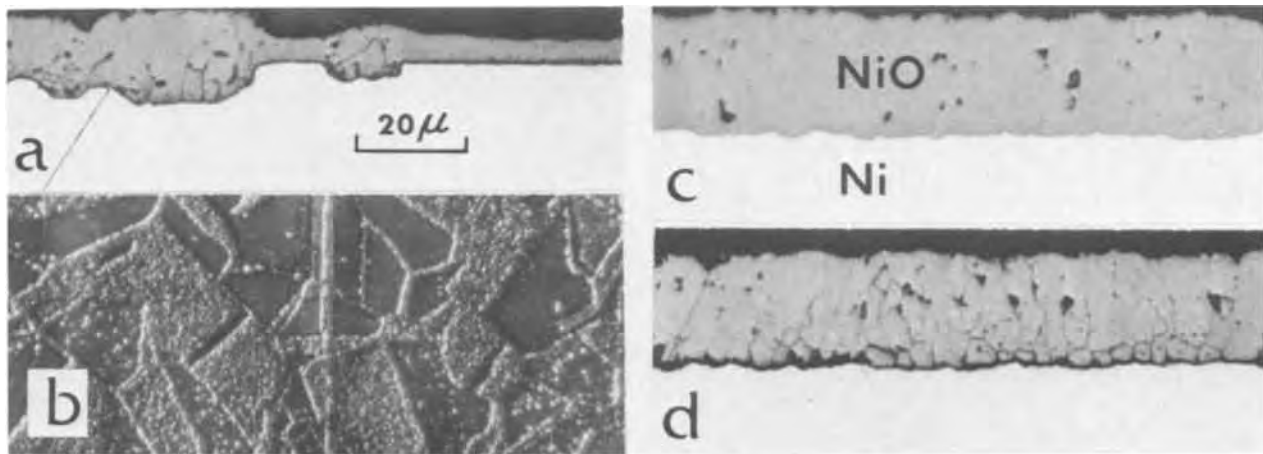


Fig. 8. Oxide structures formed on C.P.Ni in 20 hr at 900°. (a) and (b) run 20, annealed. (c) and (d) run 21, cold worked. In cross sections (at X750) Ni and NiO are etched in (a) and (d). (c) is unetched to illustrate good oxide-metal contact. Large cavities in fine-grained inner oxide in (d) are etching artifact. (b) is oxide outer surface at X60 showing oxidation anisotropy and ridging over Ni grain boundaries; central vertical bar is ridge of oxide formed over metal scratch.

persists and becomes overlaid with coarser columnar oxide. K_p decreases as the latter becomes a larger fraction of the total layer (and probably because of some grain growth in the inner layer, especially at 900°) and, though essentially constant after 20 hr, remains appreciably higher than the K_p for the coarse-grained layer on annealed Ni.

The anisotropy of oxidation on annealed Ni at 700° and 900° is related directly to the effect of substrate metal grains on the oxide grain size: thick oxide over Ni grains which develop fine polycrystalline oxide, intermediate when the polycrystalline oxide is coarser, and thin on Ni grains which form a single crystal overgrowth. Modification of the Ni surface by cold-working masks any effect of substrate orientation and yields a uniformly thick oxide unrelated to the structure of the underlying Ni.

Oxidation anisotropy is less evident at high temperature where grain coarsening eliminates the fine-grained oxide formed initially on some Ni orientations. The small early decrease in K_p with time of annealed Ni at 1270° and 1100° (Fig. 4a) results from this grain growth. Differences in thickness of the layer still remain after 20 hr. The thickness is least for the largest grains which presumably were a single crystal type of overgrowth from the start. That oxide grain boundaries are effective leakage paths even at 1100° and 1270° is demonstrated by the dished outer surface of the oxide grains that arises from the higher cation flux at the grain boundaries. This acts to maintain the thickness differential between different areas. For the largest grains surface mobility is inadequate to transport NiO far enough from the grain boundaries and thickening is solely by volume diffusion (which is al-

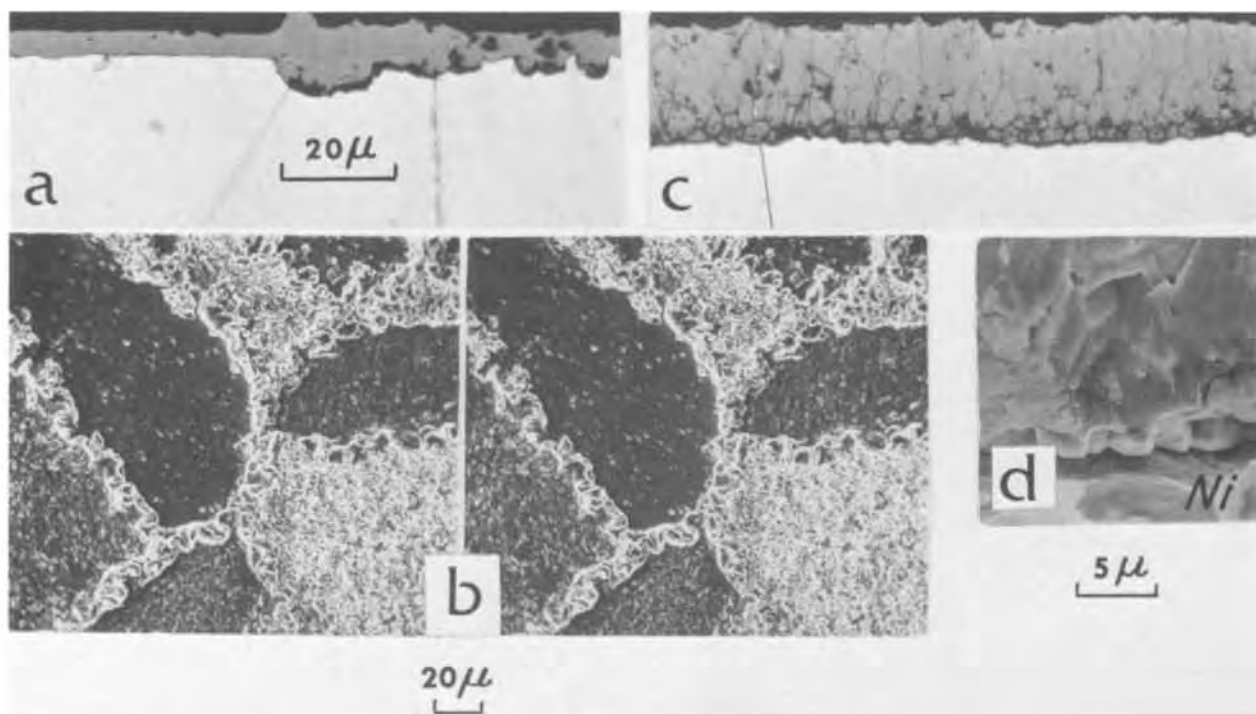


Fig. 9. Oxide structures formed on Z.R.Ni in 20 hr at 900°. (a) and (b) run 4, annealed. (c) and (d) run 6, cold worked. In polished sections (a) and (c) at X750, Ni is etched in (a) and Ni and NiO etched in (c). (b) is SEM stereopair of oxide outer surface at X300 showing oxidation anisotropy and ridging on annealed Ni. (d) is SEM photo of fracture section at X2000 showing small oxide grains near metal (bottom) seen in (c) as fine-grained inner layer (metal deformed during fracture).

ways occurring, irrespective of the presence or density of leakage paths). This mechanism for the dished outer oxide surface is consistent with the other observations and does not require the plastic deformation by compressive stresses in the oxide proposed by Rhines and Wolf (5).

Grain size can also explain the differences in K_p between annealed Z.R. and C.P. Ni. The oxide is finer-grained on C.P. Ni (as is the substrate metal), and K_p values are correspondingly higher. In the cold-worked condition the two materials, presumably because both are fine-grained, form oxide of the same grain size and no differences in K_p are found.

Activation energy.—The interrelationship between grain size and oxidation rate leads to a range of K_p values at each temperature and hence to the spread of apparent E_A values (Fig. 5) from 28 kcal/mol for cold-worked Ni at 0.1 hr to 53 kcal/mol for annealed Z.R. Ni after 20 hr at 1100° to 1270°. Ideally, two meaningful E_A values could be deduced, a high value for oxide growth via volume diffusion, and low for growth via leakage paths (6). In practice, uncertainty arises because transport is not exclusively by one or the other process and because of oxide layer variations that depend on time and temperature.

Although K_p values for cold-worked Ni at 0.1 hr lie on a straight line from 700° to 1270° (Fig. 5) representing an E_A of 28 kcal/mol, the true value is uncertain because the K_p values at the different temperatures should be for equal grain size, not equal times; as can be seen from Table II the grain size is larger at higher temperatures. Other perturbations are that the contribution from volume diffusion is greater at higher temperatures, and that at low temperature (700° and 900°) ridging at oxide grain boundaries means that the path length for leakage diffusion is longer than for the ideally uniform layer assumed in the calculation of K_p . In a subsequent publication (7) a treatment of the data to eliminate the contribution from lattice diffusion and decrease the influence of grain size yields a value of 38 kcal/mol, in agreement with values ob-

tained from work at 300°–700° (8, 9) where growth was almost exclusively by leakage diffusion.

At 1100° and 1270° the lowest K_p values are for annealed Z.R. Ni after 20 hr and, with the associated E_A of 53 kcal/mole, appear to best represent oxide layer growth by volume diffusion. However, from the local thickening at grain boundaries seen in the metallographic sections, it is evident that there still is some contribution from leakage path transport. Such a contribution is evident also in the higher K_p values, because of finer oxide grain size, of cold-worked Ni and annealed C.P. Ni after 20 hr at 1100° and 1270°; the lower apparent E_A of 49 kcal for annealed C.P. Ni indicates that, in contrast to Z.R. Ni, the oxide grain size is significantly finer at 1100° than 1270°.

Some guidance to the validity of 53 kcal/mol as representative of volume transport can be obtained by directing attention to the thinnest oxide formed on annealed Ni at each temperature, i.e., where the oxide layer is an extensive single crystal free of grain boundary leakage paths, and calculating local values of K_p as w^2/t by measuring the oxide thickness in cross section (1). Making the necessary but reasonable assumptions that a single growth process and good oxide-metal contact have existed from zero time, these minimum values of K_p (Table II) and the associated E_A best represent oxide growth by lattice diffusion only. (Note that Z.R. and C.P. Ni yield similar local K_p values; i.e., volume diffusion in the NiO does not depend on the specimen material used.) K_p values so obtained are plotted as filled circles in Fig. 5 (dotted line) and indicate an E_A value of 54 kcal/mol. The measurements are less reliable for the thinner oxides at 700° and 900°, but the data points lie adequately along the extrapolation from the 1270° and 1100° data. Values of K_p from single crystal experiments at 650° and 600° in a separate investigation (9) also lie satisfactorily along this extrapolation. A value of 54 ± 2 kcal/mol thus appears to be a realistic estimate of E_A for oxide growth by volume diffusion and applies over a temperature range from 600°–1270°, the corresponding oxide thicknesses being 100 to 10⁶ Å.

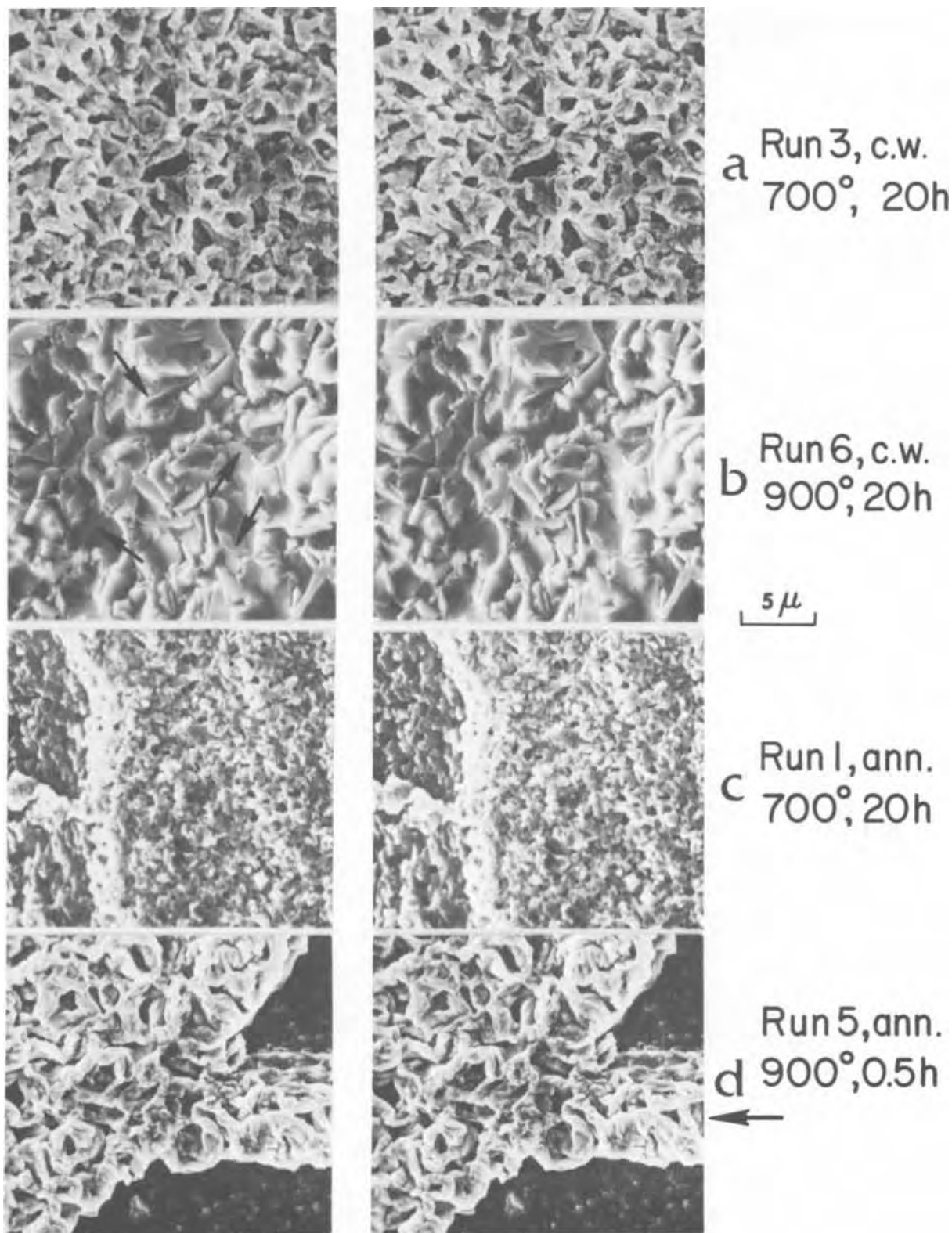


Fig. 10. Outer surface of oxide formed on Z.R.Ni at 700° and 900°. SEM stereopairs at X2500. (a) at 700°, honeycomb structure develops on cold-worked Ni from oxide ridges produced by preferential diffusion at oxide grain boundaries. (b) at 900°, oxide grain growth and greater surface mobility lead to replacement of ridges and honeycomb by finely-faceted, coarser-grained oxide; arrows indicate oxide grain boundaries [evident also on fracture section 9(d)]. (c) at 700°, annealed Ni also develops honeycomb structure at areas of thickest (polycrystalline) oxide. (d) Honeycomb structure forms at early stage on thick areas of annealed Ni at 900° also (but changes to structure of (b) at longer times); photo shows thick cellular oxide (left), thin oxide (right), and thick cellular oxide formed at metal scratch (arrow).

The intermediate values of K_p in Fig. 5 and the associated range of E_A values are of minor significance. They reflect the relative contributions of volume and leakage diffusion. The K_p values for cold-worked Ni after 20 hr at 700° and 900° are considerably lower

than at 0.1 hr but the E_A is the same, indicating merely that the concentration of leakage paths has decreased equally at the two temperatures and leakage transport still predominates. After 20 hr at 1100° and 1270° the decrease in K_p values and increased E_A for cold-

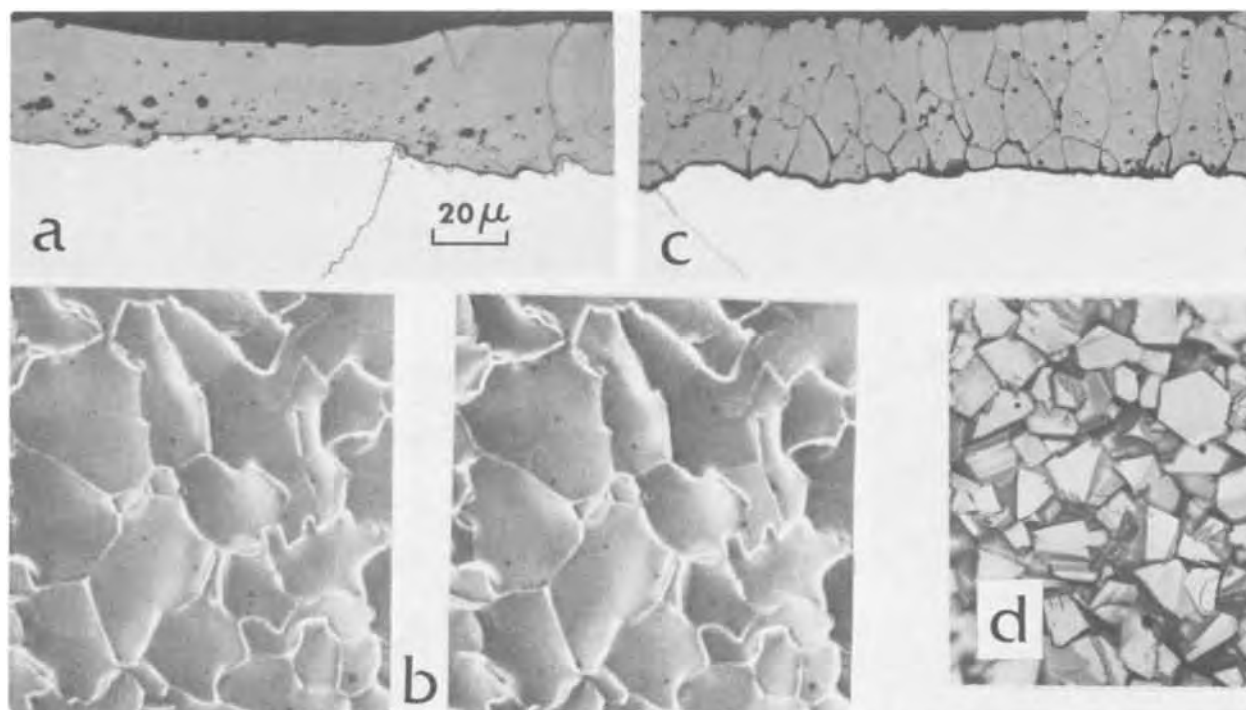


Fig. 11. Oxide structures formed on C.P. Ni in 20 hr at 1100°. (a) and (b) run 22, annealed. (c) and (d) run 23, cold worked. Ni and NiO etched in sections (a) and (c); spots on metal near oxide in (a) are etching artifact. (b) is SEM stereopair showing dishing of outer surface of oxide grains. (d) shows random facets on oxide outer surface on cold-worked Ni. X500.

worked Ni, compared to 0.1 hr, indicates that the progressive elimination of leakage paths by oxide grain growth has made volume diffusion a significant part of the transport process; the apparent E_A of 40 kcal/mol is an intermediate value reflecting the presence of fewer leakage paths at 1270° than 1100°. For annealed Ni at 700° and 900° the high K_p values, compared to an extrapolation of the 1270° and 1100° data, and lower E_A values (which causes a break in slope of the Arrhenius plot) again indicate transport mainly via leak-

age paths. Such breaks in Arrhenius plots have been reported previously for the oxidation of Ni (10-13) and other metals (14-18). It is reasonable that leakage-enhanced diffusion may explain anomalies in Arrhenius plots of metal oxidation generally, not just for Ni.

Implications

The rate constant for the oxidation of Ni is as much as 1000 times smaller when the NiO barrier layer is in the form of a single crystal, i.e., free of easy diffusion paths. The same phenomenon may apply as well to Co, Mn, Cu, and other metals. This has obvious potential practical importance for metals and alloys generally, provided that suitable oxidation procedures or surface treatments could be devised to form protective layers with few leakage paths.

A second point that arises from the observed major effect of leakage paths on oxidation resistance is that it may be necessary to reassess some prior work on the effect of alloying. If, as demonstrated here, two grades of pure Ni treated similarly can yield appreciably different oxidation rates because of differences in oxide grain size, the results of investigations into the effect of alloying additions, in which changes in oxidation rate have been ascribed to Wagner-Hauffe valency effects, could have been misinterpreted by unrecognized variations in oxide grain size produced by the alloying additives. Observations in the literature that the oxidation resistance of Ni increases with purity may similarly be an effect of oxide grain size, not impurities per se.

Conclusions

1. Cold-worked Ni oxidizes faster than annealed Ni because the oxide formed on cold-worked Ni is finer-grained and the oxide grain boundaries act as easy diffusion paths for Ni through the NiO barrier layer.
2. The apparent parabolic rate constant for cold-worked Ni is high initially but decreases rapidly as the oxide grain size increases with time. On annealed Ni the rate constant is lower, the oxide grain size larger, and both change little with time.
3. The activation energy for growth of the oxide layer is 54 ± 2 kcal/mol for transport by volume dif-

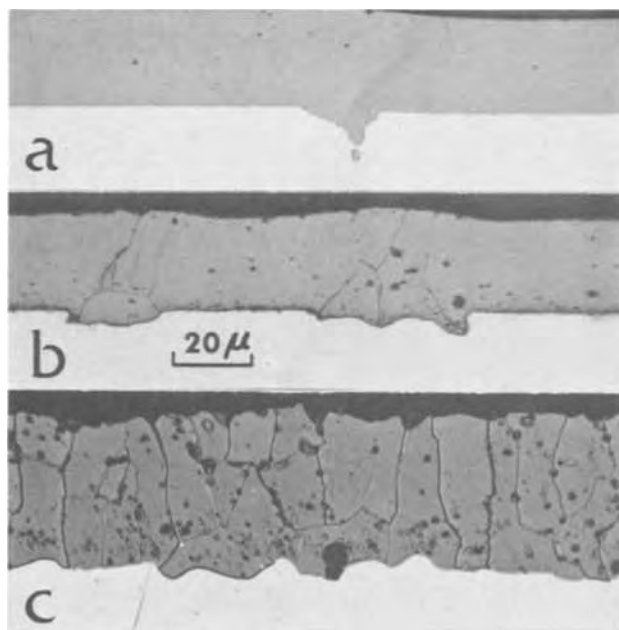


Fig. 12. Cross sections through oxide formed on Z.R. Ni in 20 hr at 1100°. (a) and (b) run 7, annealed; (a) is unetched to illustrate good oxide-metal contact; oxide etched in (b). (c) run 9, cold worked; pepper spots on oxide and metal are artifacts produced by sputter etching. X500.

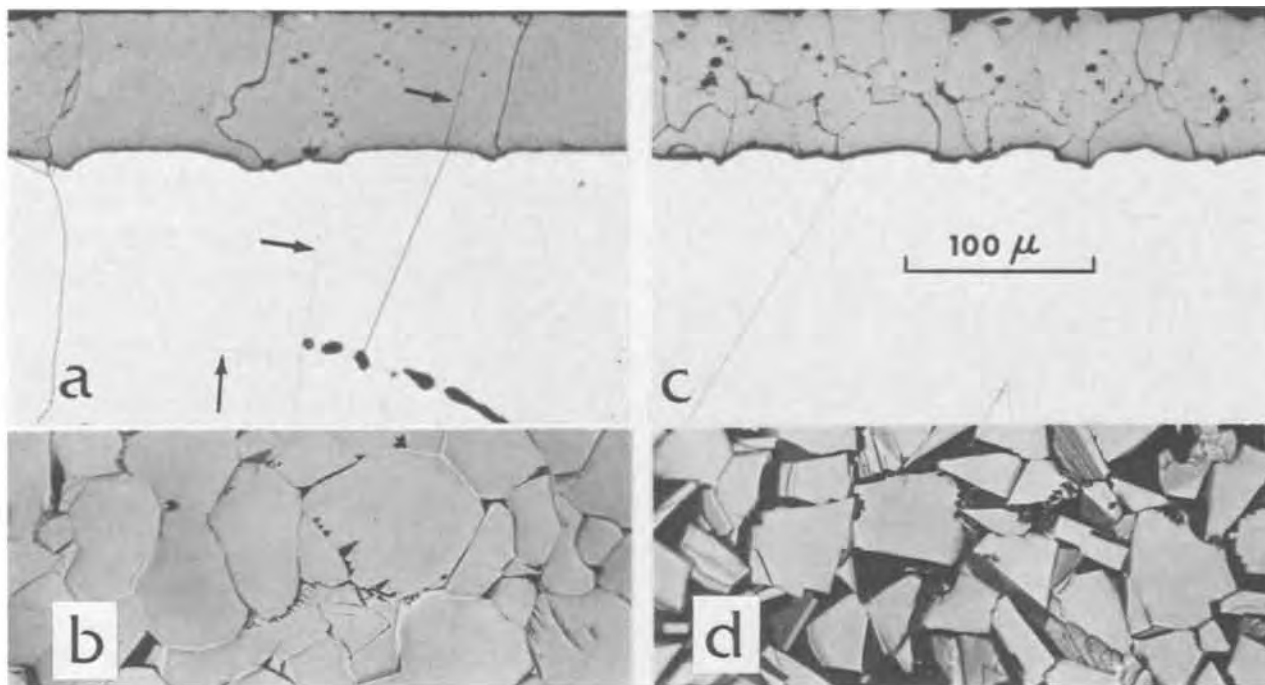


Fig. 13. Oxide formed on C.P. Ni in 20 hr at 1270°. (a) and (b) run 26, annealed. (c) and (d) run 28, cold worked. Ni and NiO etched in cross sections (a) and (c); lines in (a) marked by arrows are scratches, not grain boundaries. (b) and (d) show oxide outer surface. X250.

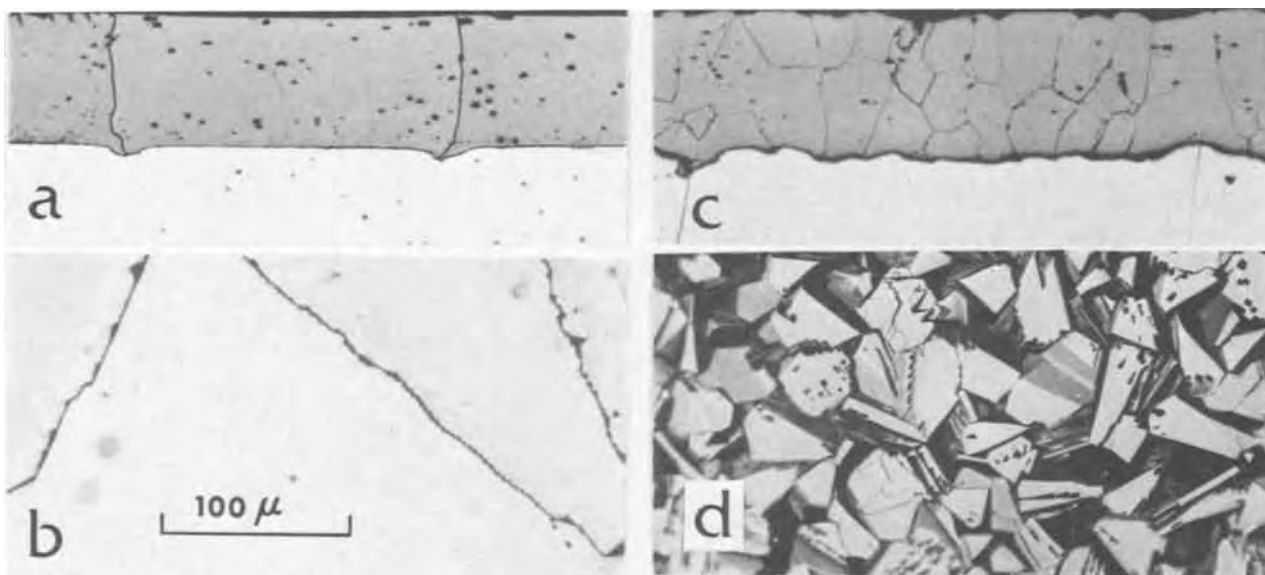


Fig. 14. Oxide formed on Z.R. Ni in 20 hr at 1270°. (a) and (b) run 11, annealed. (c) and (d) run 16, cold worked. Ni and NiO etched in cross sections (a) and (c); pepper spots on metal in (a) and dark band at Ni-NiO interface in (c) are etching artifacts. (b) and (d) show oxide outer surface. X250.

fusion and appreciably lower for transport via grain boundary leakage paths.

4. Marked anisotropy of oxidation occurs with annealed Ni below 1000°C because the substrate orientation affects the grain size and hence thickness of the oxide overgrowth. The oxide is thinnest on Ni grains which form a single crystal overgrowth.

5. The Arrhenius plot for Ni oxidation shows a break around 1000°C as a result of transport below 1000° being largely via leakage paths and because above 1000° there is extensive oxide grain growth and volume transport becomes more important.

6. An apparent difference in oxidation rate between zone-refined and commercially pure Ni is due to differences in grain size of the oxide layers. The oxidation

rates are the same for the two materials if the oxide grain size is the same.

Acknowledgment

The authors wish to thank Mr. G. I. Sproule and P. E. Beaubien for skillful assistance with the experimental work.

Manuscript submitted Feb. 15, 1972; revised manuscript received May 10, 1972.

Any discussion of this paper will appear in a Discussion Section to be published in the June 1973 JOURNAL.

REFERENCES

1. D. Caplan and M. Cohen, *Corrosion Sci.*, **6**, 321 (1966).

2. D. Caplan, G. I. Sproule, and R. J. Hussey, *ibid.*, **10**, 9 (1970).
3. J. A. Sartell and C. H. Li, *J. Inst. Metals*, **90**, 92 (1961).
4. D. L. Douglass, *Corrosion Sci.*, **8**, 665 (1968).
5. F. N. Rhines and J. S. Wolf, *Met. Trans.*, **1**, 1701 (1970).
6. J. M. Perrow, W. W. Smeltzer, and J. D. Embury, *Acta Met.*, **16**, 1209 (1968).
7. M. J. Graham, D. Caplan, and M. Cohen, *This Journal*, To be published.
8. M. J. Graham and M. Cohen, *ibid.*, **119**, 879 (1972).
9. M. J. Graham, G. I. Sproule, D. Caplan, and M. Cohen, *ibid.*, **119**, 883 (1972).
10. L. Berry and J. Paidassi, *Compt. Rend., Ser. C*, **262**, 1353 (1966).
11. L. Berry and J. Paidassi, *Mém. Sci. Rev. Mét.*, **65**, 651 (1968).
12. E. A. Gulbransen and K. F. Andrew, *This Journal*, **101**, 128 (1954).
13. E. A. Gulbransen and K. F. Andrew, *ibid.*, **104**, 451 (1957).
14. F. Morin and M. Rigaud, *Can. Met. Quart.*, **9**, 521 (1970).
15. C. A. Phalniker, E. B. Evans, and W. M. Baldwin, Jr., *This Journal*, **103**, 429 (1956).
16. J. Paidassi, M. G. Vallée, and P. Pépin, *Mém. Sci. Rev. Mét.*, **62**, 789 (1965).
17. J. Paidassi and A. Echeverria, *Acta Met.*, **7**, 293 (1959).
18. R. F. Tylecote, *J. Inst. Metals*, **78**, 259 (1950).

The Correlation Between Temperature Coefficient of Capacitance and Dielectric Loss in Tantalum and Tantalum-Aluminum Anodic Oxides

J. M. Schoen, R. C. Pitetti, and D. Jaffe

Bell Telephone Laboratories, Incorporated, Allentown, Pennsylvania 18103

ABSTRACT

A semi-empirical formula for temperature coefficient of capacitance (TCC) as a function of dielectric constant and loss ($\tan \delta$) is developed for isotropic oxides. Comparison is made between this formula and experimental values of TCC and $\tan \delta$ for the anodic oxides of sputtered tantalum and tantalum-aluminum alloy films. $\tan \delta$ was a function of alloy content and in addition was varied by heat treatments during interrupted anodization. Agreement between theory and experiment is considered adequate. It is concluded that the major contribution to TCC in Ta and Ta-Al anodic oxides comes from the dielectric loss, so that materials processing changes that reduce the loss should also reduce TCC.

Thin film capacitors based on anodic oxides of tantalum and tantalum-aluminum alloys are of interest for temperature compensating R-C network applications. An understanding of the factors contributing to the temperature coefficient of capacitance (TCC) of anodic oxides is necessary to insure proper control of the electrical properties of these components. Existing equations which attempt to relate TCC, dissipation factor ($\tan \delta$), and dielectric constant (κ) in various oxides do not predict these relationships satisfactorily for anodic oxides of tantalum and tantalum-aluminum alloys.

There is considerable literature devoted to the underlying processes governing the temperature coefficient of capacitance in bulk, solid dielectrics (1-7). Harrop and Campbell (8, 9) have made notable progress in applying these theories to thin films. In the present paper we refine Harrop and Campbell's work to the specific problem of TCC in thin oxide films with the dielectric constant in the range from 10 to 100. A semi-empirical formula for TCC as a function of κ and $\tan \delta$ is developed. Comparison is made between this formula and experimental measurements made on anodically formed oxides of tantalum and tantalum-aluminum [atomic per cent (a/o) Al \lesssim 52].

Theory

Harrop and Campbell (8, 9) have expressed the temperature coefficient of capacitance (TCC) of thin film capacitors in terms of the dielectric constant (κ), linear coefficient of thermal expansion (λ), dielectric loss

Key words: temperature coefficient of capacitance, dielectric loss, tantalum and tantalum-aluminum, anodic oxides.

($\tan \delta$), and electrical polarizability (α) of a macroscopic volume (V) of the dielectric. Their expression is

$$\text{TCC} = \frac{(\kappa - 1)(\kappa + 2)}{\kappa} [X + Y + Z] + \lambda + A \tan \delta \quad [1]$$

where

$$X = -\lambda = -\frac{1}{3V} \left(\frac{\partial V}{\partial T} \right)_P \quad [2]$$

$$Y = \frac{1}{3\alpha} \left(\frac{\partial \alpha}{\partial V} \right)_T \left(\frac{\partial V}{\partial T} \right)_P \quad [3]$$

$$Z = \frac{1}{3\alpha} \left(\frac{\partial \alpha}{\partial T} \right)_V \quad [4]$$

$$A = (5.0 \pm 1) \times 10^4 \text{ ppm}/^\circ\text{C} \quad [5]$$

Harrop and Campbell then define regions of κ and $\tan \delta$ in which one or two terms of Eq. [1] dominate. In these regions they obtain approximations to Eq. [1], plot TCC as a function of κ and/or $\tan \delta$, and compare the results with experiment. In most cases the agreement is quite good; however, a number of thin film dielectrics exist, notably the amorphous, anodic oxides of tantalum and tantalum-aluminum alloys for which the Harrop and Campbell approximations do not agree with experiment. In this paper it is demonstrated that this lack of agreement results from inappropriate approximations to Eq. [1], and not from a deficiency in the theory that leads to Eq. [1].

The approach taken in the present work is to start with Eq. [1] and, instead of defining regions in which

some terms dominate, to obtain a reasonable approximation to the entire equation. Attention is restricted specifically to amorphous, isotropic oxides. Bosman and Havinga (4) have made an extensive study of the variation of κ with temperature and pressure in cubic oxides and plot $X + Y$ and Z as a function of κ . In the range $10 \leq \kappa \leq 100$, these quantities closely follow the empirical formulas

$$X + Y = \{10 - 3 \log_{10} \kappa\} \text{ ppm}/^\circ\text{C} \quad [6]$$

$$Z = \{37 - 30 \log_{10} \kappa\} \text{ ppm}/^\circ\text{C} \quad [7]$$

Equations [6] and [7] should be representative of amorphous, isotropic oxides as well. Moreover, Her-spig (5) finds for oxides

$$\lambda \approx 7.5 \text{ ppm}/^\circ\text{C} \quad [8]$$

Substituting Eq. [5] to [8] into Eq. [1] yields

$$\text{TCC} \cong \left\{ \frac{(\kappa - 1)(\kappa + 2)}{\kappa} (47 - 33 \log_{10} \kappa) + 7.5 + 5.0 \times 10^4 \tan \delta \right\} \text{ ppm}/^\circ\text{C} \quad [9]$$

Equation [9] thus represents our approximation for TCC of amorphous isotropic oxides as a function of $\tan \delta$ and κ in the range $10 \leq \kappa \leq 100$. It is plotted in Fig. 1 as a function of κ ($10 \leq \kappa \leq 30$) with $\tan \delta$ as a parameter. To determine the theoretical TCC for a given κ and $\tan \delta$, it is only necessary to find the intersection of the TCC curve for the proper $\tan \delta$ with a vertical line extending from the abscissa at the proper value of κ . In the section on Comparison of Theory and Experiment, TCC values predicted by Eq. [9] are compared to experiment.

Experimental

4500Å β -Ta and Ta-Al films were obtained by d-c, diode sputtering in an argon atmosphere onto Corning 7059 glass slides with thermally oxidized Ta_2O_5 underlays. The cathode configurations used to obtain the various alloy films have been described previously (10, 11). The composition was determined using a spectrophotometric technique (12). Groups of films with average compositions of 52, 42, 36, and 25 a/o Al were processed into capacitors. X-ray determination of the alloy film structures showed that the 25 and 36 a/o Al films exhibited the β -Ta (13) phase, whereas the 42 and 52 a/o Al films were microcrystalline. No measurable amount of bcc phase was detected in any of the alloy films. β -Ta films were obtained from three different sources as indicated in Table I. X-ray diffrac-

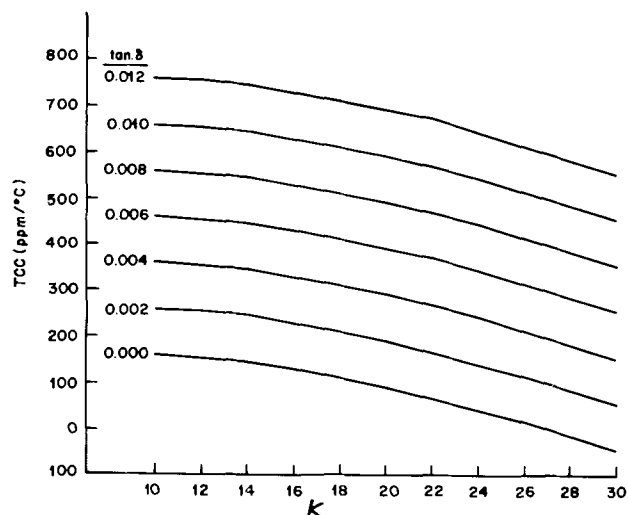


Fig. 1. TCC as a function of κ and $\tan \delta$ for amorphous, isotropic oxides.

Table I. Temperature coefficient of capacitance (TCC) and dielectric loss ($\tan \delta$) for β -Ta and Ta-Al capacitors with and without heat-treatment

Film	Heat-treatment,* (1 hr at $^\circ\text{C}$)	Meas. TCC (ppm/ $^\circ\text{C}$)	Meas. $\tan \delta$	TCC from Eq. [9]** (ppm/ $^\circ\text{C}$)	TCC from Eq. [10]** (ppm/ $^\circ\text{C}$)
β -Ta (source 1)	NHT	225	0.004	240	12
β -Ta (source 2)	NHT	220	0.004	240	12
β -Ta (source 3)	NHT	220	0.003	190	-38
β -Ta (source 1)	250	240	0.005	290	62
β -Ta (source 2)	250	300	0.006	340	112
β -Ta (source 3)	250	330	0.005	290	62
β -Ta (source 1)	350	600	0.012	640	412
β -Ta (source 2)	350	320	0.007	390	162
β -Ta (source 3)	350	650	0.013	690	462
75% Ta-25% Al	NHT	335	0.004	293	51
75% Ta-25% Al	350	715	0.012	693	451
64% Ta-36% Al	NHT	350	0.0048	335	91
64% Ta-36% Al	350	610	0.0092	555	311
58% Ta-42% Al	NHT	385	0.0048	340	98
58% Ta-42% Al	350	592	0.0083	510	268
48% Ta-52% Al	NHT	370	0.0060	406	161
48% Ta-52% Al	350	390	0.0061	411	166

* NHT = no heat-treatment.

** $\kappa = 25$ for β - Ta_2O_5 and as given in Table II for anodic Ta-Al oxides.

$\lambda = 7.5 \text{ ppm}/^\circ\text{C}$ for all oxides.

tion patterns indicated the films were predominantly β -Ta with estimated amounts of bcc of 30, 8 to 10, and 8 to 10% for source 1, 2, and 3, respectively.

The films were photolithographically etched into a 15 capacitor test pattern (14) (capacitor area = 0.1 cm^2) and then anodized to 200V. β -Ta films were anodized in 0.01% citric acid solution, while the alloy films were anodized in a 1:1 solution of ethylene glycol: oxalic acid. After reaching the prescribed voltage, the films were allowed to soak for 1 hr. However, some films were removed from the electrolyte after a half-hour soak, heat-treated for 1 hr at 250 $^\circ$ or 350 $^\circ\text{C}$, and then returned to the electrolyte to soak for an additional half hour. Capacitor fabrication was completed by evaporating 200Å NiCr-8000Å Au counterelectrodes through a mechanical mask.

Capacitance and $\tan \delta$ for capacitors situated in a Delta environmental chamber were measured at 1 kHz on a GR 1615-A capacitance bridge. Typical capacitance density was 0.065 $\mu\text{F}/\text{cm}^2$ for β -Ta capacitors measured between 60 $^\circ$ and 85 $^\circ\text{C}$. Capacitance densities of alloy capacitors measured between 25 $^\circ$ and 65 $^\circ\text{C}$ are given in Table II. Auxiliary measurements as a function of frequency indicated that there was no significant external series resistance contribution to $\tan \delta$ at 1 kHz.

Comparison of Theory and Experiment

In this section a comparison is made between the predictions of Eq. [9] and measurements of TCC and $\tan \delta$ for the anodic oxides of tantalum and tantalum-aluminum alloys. In addition, the experimental results are compared to Harrop and Campbell's expression for TCC in the appropriate range ($\kappa > 2$, $\tan \delta > 0.001$) (8, 9), which is

$$\text{TCC} = \{5.0 \times 10^4 \tan \delta - \lambda \kappa\} \text{ ppm}/^\circ\text{C} \quad [10]$$

Table II. Dielectric constant, capacitance density, theoretical intrinsic TCC, and anodization constant of tantalum and tantalum-aluminum alloy anodic oxides

Film	Capacitance density ($\mu\text{F}/\text{cm}^2$)	Alloy film anodization constant* (Å/V)	Forming voltage (V)	κ	Theoretical intrinsic TCC (Eq. [9]) (ppm/ $^\circ\text{C}$)
β -Ta	0.065	—	200	25.0	35
75% Ta-25% Al	0.058	15.2	200	19.9	93
64% Ta-36% Al	0.056	15.6	200	19.7	95
58% Ta-42% Al	0.053	15.9	200	19.0	100
48% Ta-52% Al	0.049	16.7	200	18.5	106

* Ref. (18).

It will be demonstrated that Eq. [9] leads to better agreement with experiment than does the Harrop and Campbell formula.

Equations [9] and [10] are two different approximations to the same theoretical expression, Eq. [1]. They differ only in their prediction of the intrinsic value of TCC. In Eq. [10] the intrinsic TCC is equal to $-\lambda\kappa$ and hence is always negative.

To check the validity of either Eq. [9] or [10] for a particular material, it is necessary to obtain measurements of TCC for different values of $\tan \delta$. Generally the range of $\tan \delta$ values for capacitors fabricated from the same material in the same fashion is quite limited. However, heat-treatments during anodization of β -Ta and Ta-Al films generally increased the $\tan \delta$ of the resulting oxide as is shown in Table I. The data obtained relative to the variation of TCC and $\tan \delta$ in β -Ta and Ta-Al films subjected to heat-treatments during anodization allowed the validity of Eq. [9] and [10] to be checked over a reasonable range of values.

A final parameter needed to make theoretical calculations of TCC is the dielectric constant of the material. For β -Ta₂O₅ this has been reported to range from 21.7 (15) to 27 (16, 17) and depends on whether mechanical or optical techniques are used to determine oxide film thickness. For the anodic oxides of Ta-Al, the capacitance density, forming voltage, and anodization constant (18) have been used to calculate κ . The results are given in Table II.

A TCC vs. $\tan \delta$ plot for β -Ta₂O₅ is illustrated in Fig. 2. The straight lines are plots of Eq. [9] for $\kappa = 22$ and 27. The experimental points are found to be distributed reasonably well between these lines.

In Fig. 3 TCC predicted by Eq. [9] for the anodic oxides of β -Ta (κ is taken at an intermediate value of 25) and Ta-Al is plotted against the experimental TCC. The straight line represents perfect correlation between theory and experiment. Note that the experimental points are generally, uniformly distributed about this line. In view of the uncertainties in the values of A in Eq. [1] and κ in Eq. [9], it is felt that the validity of the formula is adequately established. The results in Fig. 3 are additionally encouraging because Eq. [9] was derived without the use of data on either Al₂O₃ or Ta₂O₅. The values for TCC predicted by the Harrop and Campbell expression [Eq. (10)] are shown in Table I. Clearly the correlation between ex-

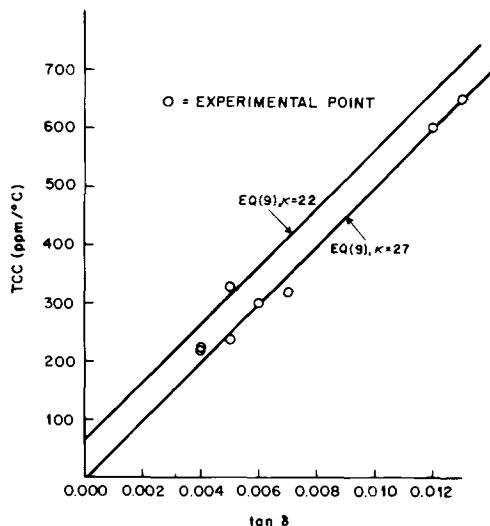


Fig. 2. TCC vs. $\tan \delta$ for β -Ta₂O₅

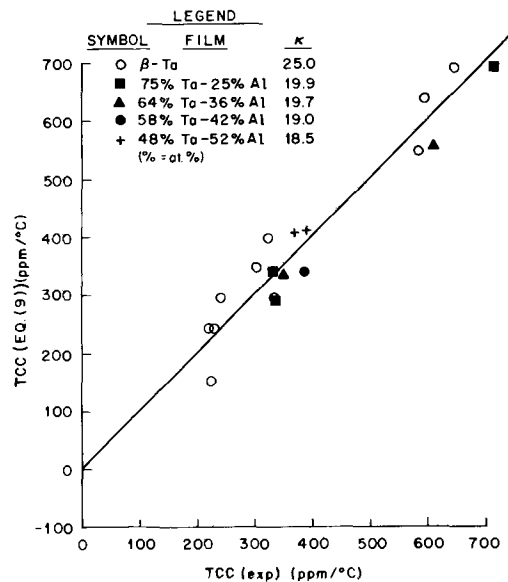


Fig. 3. TCC as calculated from Eq. [9] vs. TCC experimental

periment and Eq. [10] is not good. The points from Fig. 3 are also included in Table I.

The intrinsic ($\tan \delta = 0$) values of TCC predicted by Eq. [9] for the materials studies are all positive and are presented in Table II. Note that they never exceed 106 ppm/°C. On the other hand the experimental values of TCC never fall below 220 ppm/°C. This indicates that the $\tan \delta$ contribution to TCC is predominant for both β -Ta and Ta-Al anodic oxides and implies that changes in material processing steps which reduce $\tan \delta$ will reduce TCC as well.

Manuscript submitted Jan. 31, 1972; revised manuscript received April 14, 1972. This was Paper 98 presented at the Cleveland Meeting of the Society, Oct. 3-7, 1971.

Any discussion of this paper will appear in a Discussion Section to be published in the June 1973 JOURNAL.

REFERENCES

1. M. Gevers and F. K. du Pré, *Trans. Faraday Soc.*, **42**, 47 (1946).
2. M. Gevers, *Philips Res. Repts.*, **1**, 197, 279, and 298 (1946).
3. E. E. Havinga, *J. Phys. Chem. Solids*, **18**, 253 (1961).
4. A. J. Bosman and E. E. Havinga, *Phys. Rev.*, **129**, 1593 (1963).
5. A. Herspung, *Z. Angew. Phys.*, **20**, 369 (1966).
6. A. G. Cockbain and P. J. Harrop, *Brit. J. Appl. Phys. (J. Phys. D)*, **1**, 1109 (1968).
7. P. J. Harrop, *J. Mater. Sci.*, **4**, 370 (1969).
8. P. J. Harrop and D. S. Campbell, *Thin Solid Films*, **2**, 273 (1968).
9. P. J. Harrop and D. S. Campbell, "Handbook of Thin Film Technology," chap. 16, L. I. Maissel and R. Glang, Editors, McGraw-Hill Book Co., New York (1970).
10. C. A. Steidel and D. Gerstenberg, Proc. Electronic Components Conf., May 1969, p. 372.
11. F. Huber and D. Jaffe, Proc. Electronic Components Conf., May 1971, p. 198.
12. F. Huber and D. Jaffe, *J. Vacuum Sci. Techn.*, **8**, 480 (1971).
13. M. H. Read and C. Altman, *Appl. Phys. Letters*, **7**, 51 (1965).
14. D. A. McLean and F. E. Rostoczy, *Electrochem. Techn.*, **4**, 523 (1966).
15. D. Gerstenberg, *This Journal*, **113**, 542 (1966).
16. D. G. Muth, *J. Vacuum Sci. Techn.*, **6**, 749 (1969).
17. D. Gerstenberg, Ref. (9), chap. 19.
18. F. Huber, Current affiliation: Patent Office, Munich, Germany.

Crystal Growth from the Melt under Destabilizing Thermal Gradients

K. M. Kim, A. F. Witt,* and H. C. Gatos*

Department of Metallurgy and Materials Science,
Massachusetts Institute of Technology, Cambridge, Massachusetts 02139

ABSTRACT

Direct time correspondence between crystal growth behavior and the thermal characteristics of the melt under destabilizing gradients was established by means of "time markers" which were introduced into the growing crystals and simultaneously registered on the continuous recording of the thermal behavior of the melt. Employing Te-doped InSb, it was found that as solidification progressed, the melt exhibited successively turbulent convection, oscillatory thermal instabilities, and, finally, thermal stability. During turbulent convection, the crystals underwent pronounced transient back-melting and the average microscopic growth rate was found to be independent of, and about 20 times greater than, the average macroscopic growth rate; this microscopic growth rate was controlled by the convection characteristics of the melt and the thermal gradients in the solid. With the onset of oscillatory thermal instabilities, back-melting became less pronounced and then ceased. In this region the average microscopic and macroscopic growth rates were equal and the crystals exhibited fluctuations in dopant concentration with a periodicity identical to that of the thermal oscillations in the melt. Finally, under stabilized thermal conditions, the microscopic and macroscopic growth rates were identical and no localized fluctuations in dopant concentration could be detected. The Rayleigh numbers of the melt during a growth experiment ranged from 3×10^5 to 0. In view of the fact that the vertical thermal gradient changed only by a factor of about two during the entire growth, the wide range of Rayleigh numbers was the result of the changes in melt height. In the turbulent convection region, the Rayleigh numbers ranged from about 3×10^5 to about 4×10^3 , in the oscillatory region from 3×10^3 to 2×10^3 , and in the region of thermal stability from 10^3 to 0.

Single crystals grown from the melt under destabilizing gradients, as is the case of Czochralski-type arrangements, usually exhibit nonsteady-state growth characteristics (1) and inhomogeneous dopant segregation (2). This behavior has been attributed to temperature changes in the melt resulting from fluid dynamic effects associated with destabilizing thermal gradients (3). Most melt-grown single crystals exhibit in addition, other types of striations (dopant heterogeneities) which could be attributed to various origins, such as rotation in the presence of thermal asymmetry, to vibration, to deficient pulling mechanisms, and others. The nature of these heterogeneities has been extensively discussed in the literature (1). In this investigation the experimental conditions were such that none of the above-mentioned striations could occur and all dopant heterogeneities observed could be attributed to temperature variations in the melt. Theoretical models predict that, for a given fluid system, thermal instability may lead to either turbulent convection or thermal oscillations (4) depending on the acting forces and geometric and thermal configuration of the system. Both types of instabilities have been observed and their transient character has been studied primarily by varying the thermal gradients under fixed geometric conditions (5). A limited number of thermo-hydrodynamic studies in actual growth systems with horizontal and vertical arrangements have been carried out in the same way (6). Although impurity heterogeneities in crystals have been attributed to thermal fluctuations in the melt (7) (which lead to changes in the microscopic growth rate and thus to changes in the effective dopant segregation), their unambiguous cause and effect relationship has as yet not been established.

In view of the fact that the melt height changes continuously during crystal growth and in view of

the fourth power dependence of the Rayleigh number on the melt height (12), the present work was undertaken to study the thermal behavior of the melt as its height decreases continuously during actual crystal growth. Furthermore, the thermal behavior of the melt and its changes were directly correlated with growth characteristics including interface morphology, microscopic growth rate, and dopant segregation in the resulting crystal.

Experimental Apparatus and Procedure

The apparatus used in the present investigation is shown in Fig. 1. Polycrystalline InSb doped with Te ($1 \times 10^{18} \text{ cm}^{-3}$) was placed into the inner quartz tube, 1.33 cm ID and 10 cm long (referred to as the growth tube). This tube had a graphite insert at the bottom capable of accommodating the volume expansion during solidification and was mounted on a Lava pedestal. A 3 cm long InSb seed of (111) orientation was machined, etched to a diameter of 1.3 cm, and mounted to a water-cooled seed holder assembly which was then positioned in the apparatus and properly aligned. An outer quartz tube provided for a hydrogen ambient at about 1 mm Hg overpressure. A tube furnace 12 cm long, operated with proportional power control, was located coaxially around the outer tube. After flushing with hydrogen, the polycrystalline ingot was heated to above its melting point. Subsequently, the seed was lowered and after thermal equilibration brought in contact with the melt. The desired thermal gradient along the growth direction was established by adjusting the vertical position of the furnace and the flow of the coolant in the seed holder. Crystal growth was initiated and allowed to proceed at the desired rate by means of controlled power reduction. A linear decrease of the furnace temperature was obtained through a steadily increasing bucking voltage (motor-driven servosystem) in series with the output of the controlling thermocouple which was located in the

* Electrochemical Society Active Member.

Key words: melt growth, dopant heterogeneities, thermal, convection, thermal oscillations, time markers.

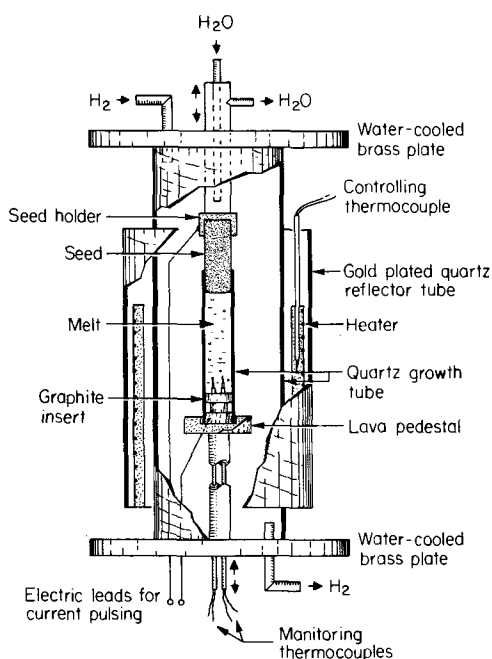


Fig. 1. Schematic diagram of the apparatus used for the study of crystal growth under destabilizing thermal gradients.

furnace. The experiments were carried out with a linear furnace temperature decrease of $0.27^{\circ}\text{C}/\text{min}$ resulting in an average macroscopic growth rate of $2\ \mu\text{m}/\text{sec}$. Temperature measurements in the melt were obtained with two Chromel-Alumel thermocouples (made of $75\ \mu\text{m}$ diameter wire) each mounted in a 1 mm ceramic tube and inserted through the bottom into the growth tube. The thermocouples were movable and the junctions could be positioned at any desired height in the melt during a growth experiment. The bare sensing junctions were protected with a thin insulating layer of "Insa-Lute" and showed high thermal response.

To permit the transmission of controlled current pulses across the crystal melt interface for introducing "time markers" and "rate striations" during growth, electrical contacts were made to the insulated seed holder and the graphite block in the bottom of the melt. Current pulses of the desired frequency and duration (ranging in the present experiments from 10 to 50 msec) were obtained from a function generator and programmable d-c power supply (8). During growth, each current pulse across the crystal-melt interface resulted in a readily detectable time marker in the crystal. Furthermore, each pulse was simultaneously registered by the temperature monitoring thermocouples in the melt and recorded as an instantaneous pen deflection on the temperature tracing. Thus, through the time markers any segment of the grown crystal could be correlated in time with the measured thermal fluctuations in the melt. A schematic diagram of the circuitry and the components used is shown in Fig. 2.

After each growth experiment, the crystal was cut along the $\langle 111 \rangle$ growth axis to expose a (211) plane. This plane was polished and appropriately etched (9) to reveal the growth and segregation characteristics. In most instances the crystals grown were single for a length of 10 to 15 mm and twinned for the remaining length. Since twinning does not interfere with the analysis of the growth characteristics, no attempt was made to eliminate it.

Experimental Results and Discussion

Thermal characterization of the melt.—In view of the dependence of the thermo-hydrodynamic behavior of fluids on thermal gradients (6), a series of experiments

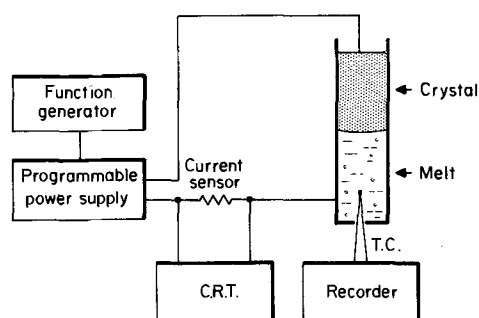


Fig. 2. Block diagram of the electronic arrangement for introducing time markers into the growing crystal and on the temperature recording.

was conducted in which the vertical thermal gradients in the melt were determined as a function of melt height. The measurements were performed under growth conditions by employing a thermocouple introduced into the melt through the bottom of the growth tube. This thermocouple could be moved vertically in the melt, as desired. In order to determine the vertical thermal gradients at various melt heights, crystal growth was arrested at predetermined intervals. At each arrest, the height of the melt level was determined and the temperature along the vertical growth direction up to the crystal-melt interface measured.

The results are shown in Fig. 3. It can be seen that the gradients were essentially constant for each given crystal-melt interface position (melt height). Their values decreased from $19^{\circ}\text{C}/\text{cm}$ at a melt height of 33 mm to $8^{\circ}\text{C}/\text{cm}$ at a melt height of 12 mm. Thermal fluctuations in the melt were most pronounced at the original growth interface position (33 mm melt height) and decreased discontinuously with decreasing melt height (see Fig. 4b).

No attempt was made to determine the prevailing lateral thermal gradients. Actually, in the presence of thermal fluctuations exceeding $\pm 10^{\circ}\text{C}$, at melt heights greater than 15 mm, such measurements would be of no particular significance; on the other hand, at melt heights ranging from 15 mm to zero, the growth interface was essentially horizontal (with only a slight curvature upward at the periphery), thus indicating that the prevailing lateral gradients were rather small.

It is of interest to point out that the thermal gradients and their changes with melt height observed under

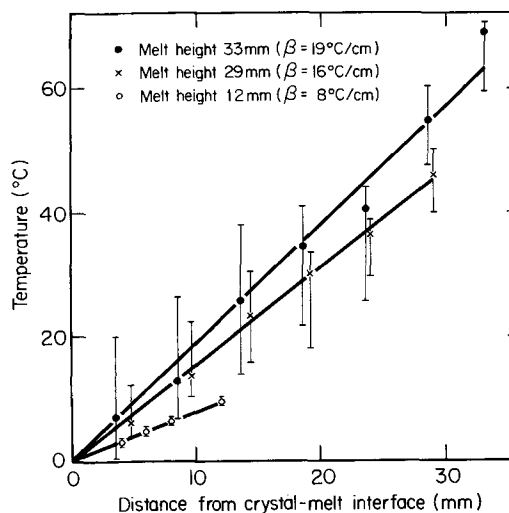


Fig. 3. Vertical temperature distribution in the melt for different crystal-melt interface positions (melt heights). The vertical bars represent the magnitude of the temperature fluctuations. The zero point in temperature corresponds to the melting point of InSb, 525°C .

the present conditions are of the same magnitude as those encountered in Czochralski-type systems.

Relationship between thermal characteristics in the melt and crystal growth on the macroscale.—The following experiment was designed to study the cause and effect relationship between the macroscopic growth behavior and the concurrent thermal conditions in the melt. An InSb crystal was grown at an average "macroscopic" growth rate of $2 \mu\text{m}/\text{sec}$. This growth rate was determined from the time required (at the indicated rate of furnace temperature decrease) to displace the crystal-melt interface by 30 mm (original melt height) in the downward direction. The thermal conditions prevailing during growth in the melt were continuously monitored by two stationary thermocouples (4 mm apart) located at the same height, 5 mm from the bottom of the melt. The thermocouple outputs were recorded at slow speed and with low sensitivity to permit comparison with the grown crystal on a macroscale. An etched section of the crystal cut along its growth axis and the corresponding thermal history of the melt are shown in Fig. 4. The temperature recordings (Fig. 4b) indicate three distinct regions with fundamentally different hydrodynamic behavior. On the top region, corresponding to melt heights ranging from 30 mm to about 15 mm, and with thermal gradi-

ents from $18^\circ\text{C}/\text{cm}$ to about $12^\circ\text{C}/\text{cm}$, pronounced random temperature fluctuations of about $\pm 10^\circ\text{C}$ were present. The mean temperature of these fluctuations is modulated with an average period of about 3 min and is phase shifted by about 180° in the two tracings. This thermal behavior is indicative of turbulent convection in the melt.

With continuing growth, the amplitude of the thermal fluctuations decreases sharply and minor perturbations of apparently constant frequency persist over a narrow region. In this region, (as is shown in detail below), the melt exhibits periodic thermal oscillations. The last portion of the temperature recordings shows only gradual temperature changes and no temperature fluctuations, indicating a high degree of thermal stability.

Thus, under the present conditions, solidification occurs first under the influence of turbulent convection, then under oscillatory thermal instability, and finally under thermal stability.

The growth and segregation behavior of the crystal, as revealed by high resolution etching, are shown in Fig. 4a. The effects of the changing thermal conditions in the melt are clearly visible; three distinctly different regions can readily be identified. On the top region, growth (to a crystal length of about 15 mm) is char-

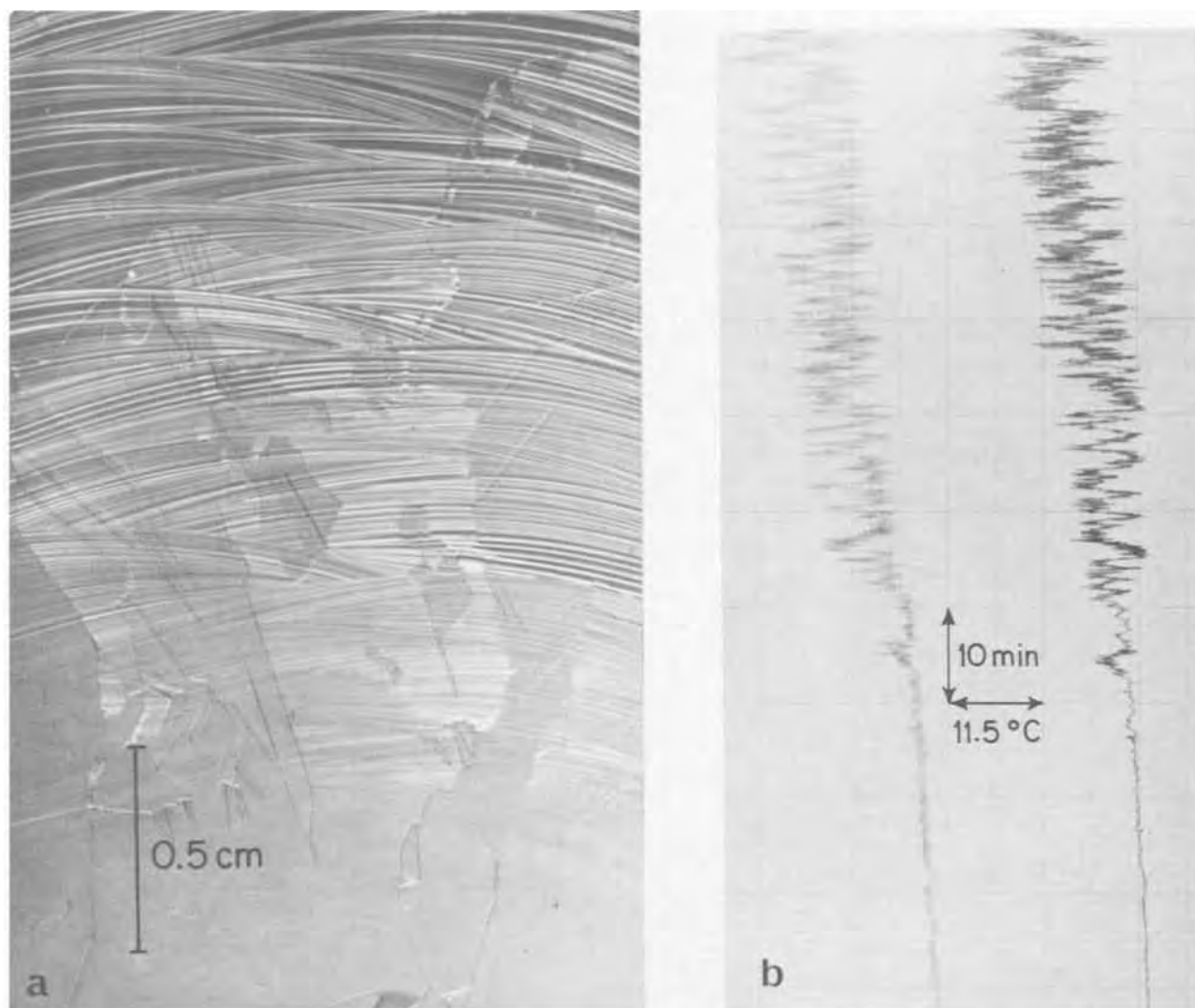


Fig. 4. (a) Photograph of etched crystal cut along the growth axis. The decreasing complexity of impurity striations from top to bottom reflects the thermo-hydrodynamic transition of the melt from turbulent convection to thermal stability. Note that the dopant striations are continuous across all twin boundaries indicating that twinning does not influence the over-all growth characteristics. (b) Recording of the temperature in the melt during the growth of the crystal depicted in Fig. 4(a). The two thermocouples were 4 mm apart and 5 mm from the bottom of the melt.

acterized by pronounced transient remelting (caused by turbulent convection in the melt). The clearly visible remelt lines indicate that the convective pattern is continuously changing with a frequency corresponding to that of the modulated mean temperature fluctuations (see below). The remelt lines further reflect complex changes in the growth interface morphology. With continuing growth, the intensity of dopant heterogeneities decreases abruptly and back-melting no longer takes place; the crystal exhibits a rather flat growth interface and only closely spaced dopant heterogeneities. The intensity of the dopant heterogeneities decreases continuously until in the bottom region (thermal stability region), homogeneous dopant segregation is encountered.

A detailed analysis of the three regions on a microscale is given below.

Direct time correspondence between crystal growth and the thermal characteristics of the melt on a microscale.—In order to study the relationship between the thermal melt-characteristics and crystal growth on a microscale, the melt behavior was monitored by two thermocouples, maintained (by periodic repositioning) at a distance of 3-6 mm from the advancing crystal-melt interface. The thermocouple signals were continuously recorded at high sensitivity (1 mV full scale) and at high speed (1 in./min).

Direct correspondence in time between the thermal behavior of the melt and crystal growth was obtained as indicated, by means of the time markers which were incorporated in the crystal during growth and simultaneously registered through the monitoring thermocouples. In this way, any point on a longitudinal section of the crystal could be directly related to the thermal behavior of the melt recorded at the time of growth.

The results of the growth behavior on a microscale are presented in three sections corresponding to the growth regions previously identified on a macroscale. These sections are presented in order of increasing complexity beginning with the region of thermal stability.

Growth under thermal stability in the melt.—Thermal stability in the melt during growth prevailed at melt heights ranging from about 10 mm to zero. A representative section of the grown crystal (about 6 mm from the end) together with the corresponding thermal recording is shown in Fig. 5. The photomicrograph of the etched specimen of Fig. 5a clearly shows the time markers introduced during growth by current pulses (15A) of 50 msec duration at intervals of 21.0 sec. To obtain a reference point for establishing an unambiguous direct time correspondence between the time markers in the crystal and on the temperature

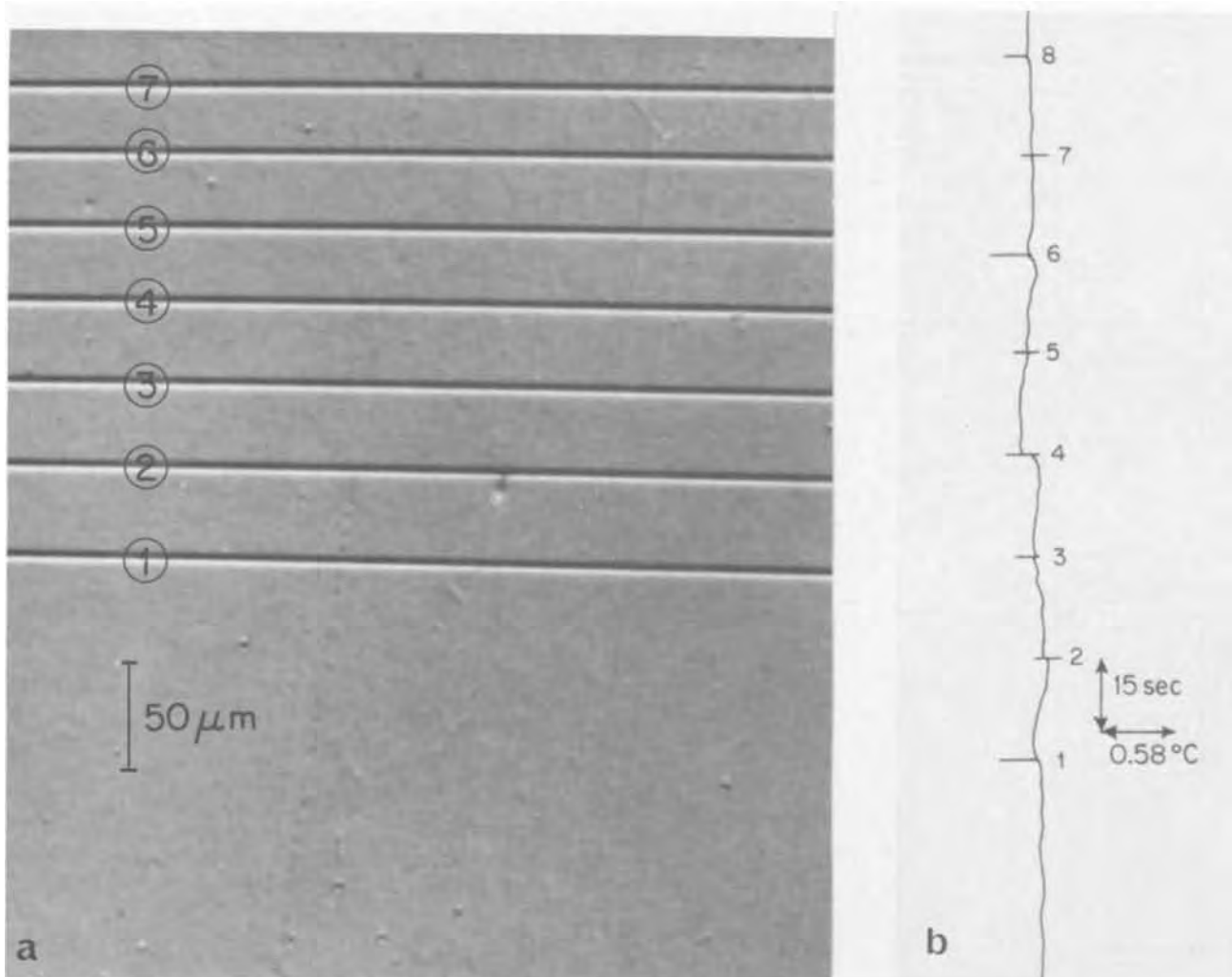


Fig. 5. (a) Section of crystal (cut along the growth axis) grown under thermal stability. No dopant heterogeneities can be seen. The horizontal lines (time markers) resulted from the current pulses applied at intervals of 21 sec. Line 1 corresponds to the last current pulse and serves as time reference. (b) Recording of the temperature in the melt during growth of the crystal segment depicted in Fig. 5(a). The thermocouple was located about 5 mm from the growth interface. The pen deflections are caused by the current pulses and allow establishing direct time correspondence with the grown crystal.

recording, the last current pulse was applied prior to the termination of growth. Thus, the last time marker in the crystal could be readily identified and was used as the absolute time reference.¹

The temperature recording containing the last pen deflection corresponding to the last current pulse, is shown in Fig. 5b. It is seen that no thermal perturbations were present and that the temperature was stable to within $\pm 0.1^\circ\text{C}$. The uniform appearance of the etched sample clearly indicates that the dopant distribution is homogeneous.

Each time marker was formed across the entire crystal-melt interface within the time duration of the current pulse (50 msec in the present case). Consequently, the time markers delineate the growth interface morphology at the time of their formation. The time markers in Fig. 5a show that the growth interface in the depicted section was essentially flat under conditions of thermal stability. The average microscopic growth rate calculated from the frequency and the spacing of the time markers is $1.8 \mu\text{m}/\text{sec}$ for the depicted region.

Growth under oscillatory thermal instability.—The condition of thermal stability encountered at small melt heights was preceded by oscillatory thermal in-

¹ It should be pointed out that current pulsing (introduction of time markers) in no way alters the over-all solidification characteristics.

stability at melt heights ranging from 15 to 10 mm. Figure 6 shows the last section of the crystal grown under temperature oscillations (at melt height of about 11 mm) together with the corresponding temperature recording. Direct time correspondence between the temperature recording and the depicted crystal was achieved by identifying the corresponding time markers.

It is seen in the photomicrograph of Fig. 6a that thermal oscillations result in faint lines (dopant heterogeneities) parallel to the time markers. The repetition rate of the dopant heterogeneities in the crystal (determined from the spacing of successive time markers which appear 21.0 sec apart) is 0.38/sec and, thus, identical to the frequency of the concurrent temperature oscillations (Fig. 6b).

It is of interest to note that the dopant heterogeneities caused by thermal oscillations are at all times continuous across the entire crystal and exactly parallel to the slightly curved time markers. Each time marker is formed across the growth interface with an interval of 50 msec which is significantly smaller than the period of the thermal oscillations (2.6 sec). Since each dopant striation is continuous and at a constant distance from the time markers across the entire crystal, the thermal perturbation must be "in phase" at all times across the crystal-melt interface.

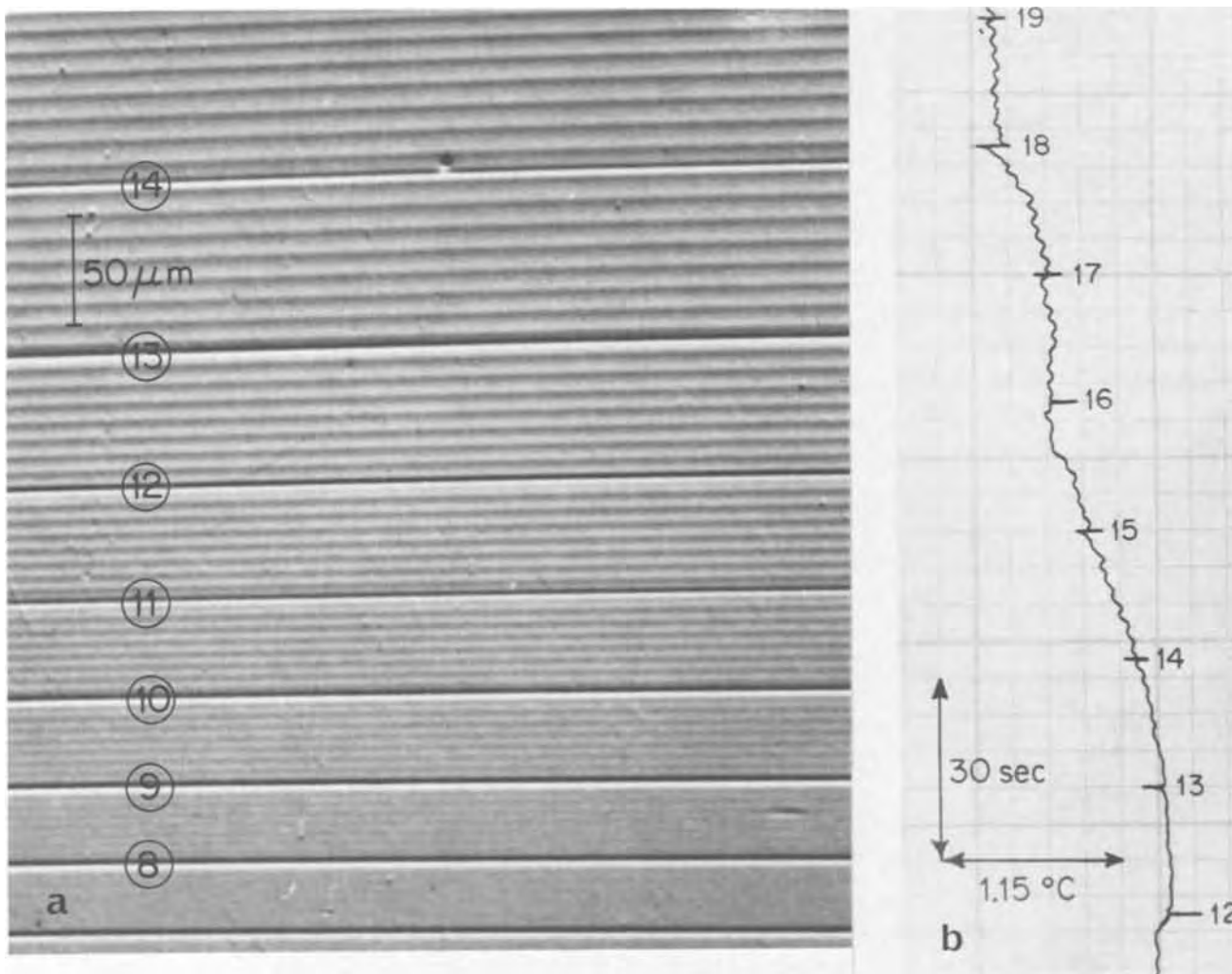


Fig. 6. (a) Section of crystal grown in the presence of thermal oscillations in the melt. The dopant heterogeneities caused by the thermal oscillations are clearly visible. Note that their spacing decreases from top to bottom. The time markers make it possible to establish that the frequency of the thermal perturbations is constant over the depicted region (the number of dopant heterogeneities between successive time markers is constant) and that the microscopic growth rate decreases from top to bottom (the spacing of successive time markers decreases). (b) Recording of the temperature in the melt during growth of the crystal segment depicted in Fig. 6(a).

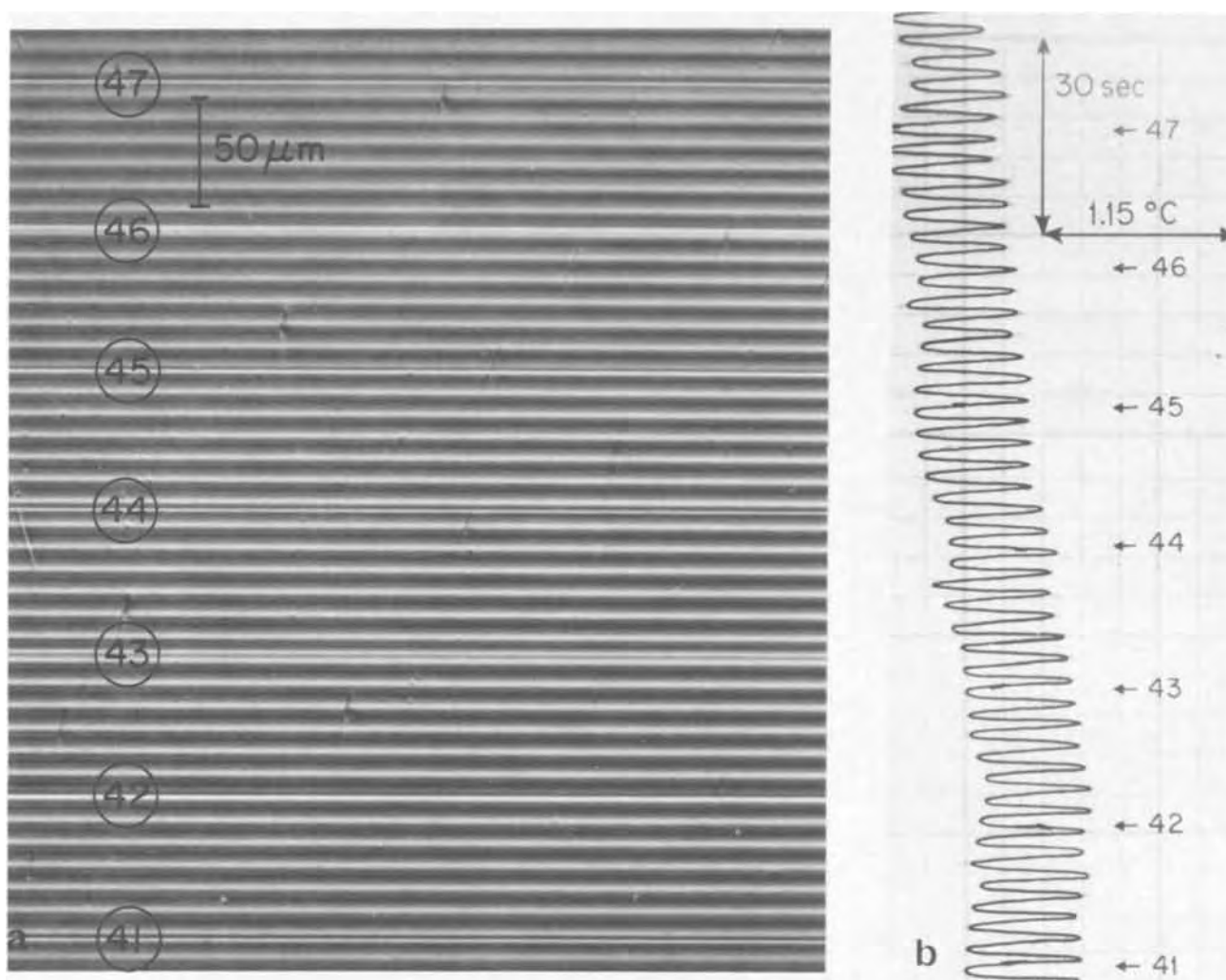


Fig. 7. (a) Section of crystal grown in the presence of thermal oscillations in the melt. Comparison with Fig. 6(a) shows that the dopant heterogeneities are here more pronounced, their frequency is decreased, and the microscopic growth rate is constant. Incipient remelting can be observed. (b) Recording of the temperature in the melt during growth of the crystal sement depicted in Fig. 7(a).

As seen in Fig. 6a, the frequency of the periodic dopant heterogeneities is constant over the depicted area. Their "intensity" decreases with decreasing melt height and can no longer be observed between the time markers 7 and 8. At the same time, the amplitude of the corresponding temperature oscillations decreases continuously (from its original value of $\pm 0.1^\circ\text{C}$) with decreasing melt height and becomes zero between the time markers 13 and 14. It appears that the striations between the time markers 14 and 8 are caused by temperature oscillations which lie below the detection limit of the temperature sensors ($\pm 0.01^\circ\text{C}$). Alternatively, it is possible that the temperature fluctuations are attenuated with distance from the growth interface, although other investigations (10) have found no evidence of attenuation in oscillatory thermal instabilities. In either case, these results demonstrate the extreme sensitivity of dopant segregation to small temperature fluctuations and the high resolving power of chemical etching for dopant heterogeneities.

At melt levels ranging from about 15 to 12 mm, the frequency of the thermal oscillations was found to be 0.29/sec and their amplitude higher but constant over a wide range. A representative photomicrograph and the corresponding temperature recording are shown in Fig. 7. Here also the frequency of the periodic dopant heterogeneities is identical with that of the thermal oscillations but their intensity indicates incipient remelting due to the higher amplitude of the thermal oscillations. The frequency change of the

thermal oscillations from 0.29/sec to 0.38/sec occurred abruptly within two time markers.

Growth under turbulent convection.—At melt heights ranging from 30 mm (start of growth) to about 20 mm, thermal instability appears in the form of random temperature fluctuations (Fig. 8b) with no discernable periodicity and widely varying amplitudes assuming peak values in excess of $\pm 5^\circ\text{C}$. These fluctuations of short duration are superimposed to pronounced variations ($\sim \pm 10^\circ\text{C}$) of the mean melt temperature which occur at relatively longer periods ranging from 2 to 4 min. The tracings of the two monitoring thermocouples (positioned symmetrically about the axis of the melt at equal height and 4 mm apart) indicate that the variations of the mean temperature are phase shifted by 180° ; i.e., while the one thermocouple registers a mean temperature "high" the other registers a mean temperature "low." There is however no apparent amplitude or phase relationship between the high frequency temperature fluctuations of the two temperature tracings.

The effects of this thermal behavior of the melt on the crystal growth characteristics and dopant segregation are shown in Fig. 8a. The pronounced segregation heterogeneities, identified as "remelt" striations, indicate a complex pattern of transient back-melting. The morphology of the intersecting remelt striations shows that growth occurred alternately on the left and right side of the crystal with a period of about 3 min,

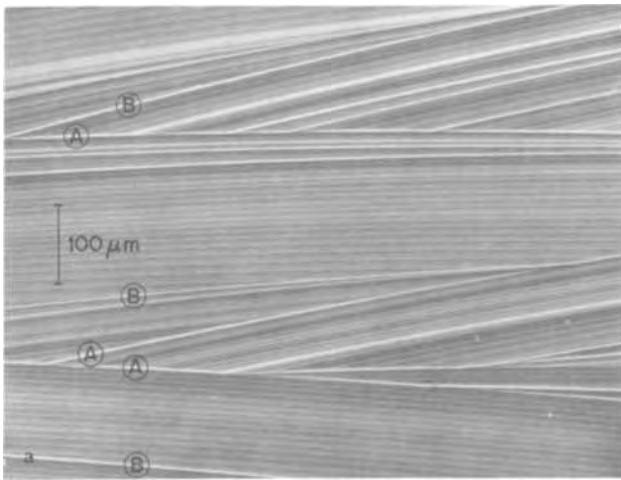


Fig. 8(a). Section of crystal grown in the presence of turbulent convection in the melt. Alternating regrowth and remelting on the left-hand side and the right-hand side are reflected in the morphology of the remelt striations (A). Brief remelting within the regrowth regions is evident from remelt striations (B). The faint lines throughout the depicted region are rate striations.

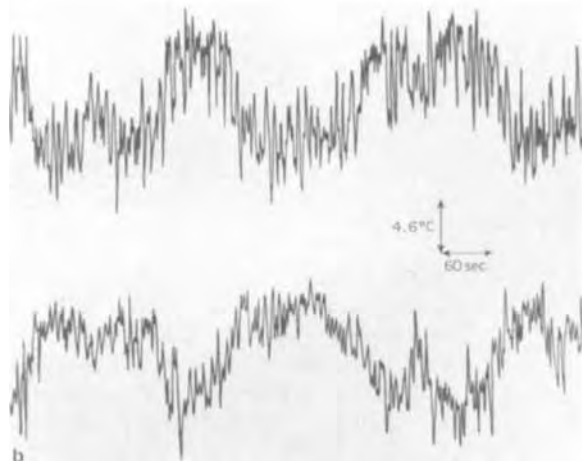


Fig. 8(b). Recording of the temperature in the melt during growth of the crystal segment depicted in Fig. 8(a). Note that the mean temperature variation of the melt, as recorded by two thermocouples positioned symmetrically about the axis of the melt, is phase shifted (see text).

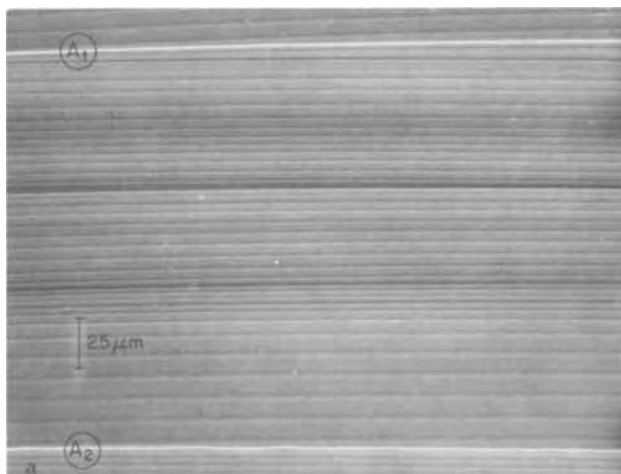


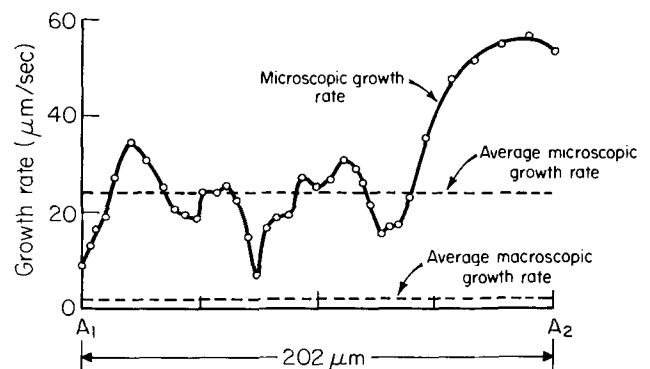
Fig. 9. (a) Photomicrograph of region regrown under turbulent convection in the melt. The rate striations introduced at a rate of 5/sec show pronounced variations of the microscopic growth rate within successive remelt lines. (b) Microscopic growth rates, as a function of time within remelt lines (A₁) and (A₂) of Fig. 9(a) as determined from the spacing and frequency of the rate striations.

corresponding to that of the mean temperature variations.

To permit the determination of the microscopic growth characteristics associated with this thermal behavior of the melt, rate striations with a frequency of 5/sec were introduced during growth (for a period of 5 min) at a melt height of approximately 25 mm, by applying current pulses (10A) of 20 msec duration. Representative microscopic growth behavior between two successive remelt striations is shown in the photomicrograph of Fig. 9a. The microscopic growth rates for this area were calculated from the known frequency and the measured spacing of the rate striations and are shown in Fig. 9b. It can be seen that the growth rate is irregular and reaches peak values in excess of 55 $\mu\text{m}/\text{sec}$. For the depicted region (between A₁ and A₂) the average microscopic growth rate is found to be about 28 $\mu\text{m}/\text{sec}$. Over a larger crystal region the average growth rate was found to be about 38 $\mu\text{m}/\text{sec}$ and thus about 20 times greater than the "average macroscopic growth rate." This striking discrepancy between microscopic and macroscopic rates was found throughout the crystal region grown under extensive transient back-melting.

The growth and segregation characteristics in this region can be explained from the morphology of the remelt striations, the microscopic growth rates, and the recorded thermal behavior of the melt. During each interval of increasing mean melt temperature (see Fig. 8b), extensive remelting takes place and the crystal-melt interface recesses. The terminal remelt growth interface, delineated by a remelt striation, is always concave and not normal to the growth direction. This morphology differs considerably from that expected under the prevailing vertical and horizontal thermal gradients. It clearly reflects the presence of pronounced convective melt flow; i.e., melt of higher temperature flows upward on one side of the growth tube while melt of lower temperature flows downward on the other side. This finding is consistent with the phase shift of the mean melt temperature variations registered by the monitoring thermocouples. Alternating remelting (and growth) on the left and right side of the crystal is attributed to a continuous rotational displacement of the convective flow about the vertical axis of the melt (11). Thus, upon a 360° rotation of the flow pattern ("shear flow"), the major portion of the region regrown during the period of decreasing mean melt temperature at this part of the interface is again remelted and only a small portion remains in the crystal.

The rate striations reveal clearly that, at the portion of the crystal-melt interface subjected to a decreasing



mean melt temperature, the crystal undergoes accelerated growth. Its rate is unrelated to the average macroscopic growth rate imposed by the power reduction. The microscopic growth rate is indeed controlled by the rate of the mean melt temperature decrease (associated with the low frequency temperature fluctuations, shown in Fig. 8b) and is modulated by the superimposed temperature fluctuations; in fact, for pronounced fluctuations, brief remelting takes place within the regrowth period.

With continuing growth, the peak values of the mean melt temperature variations decreased and appeared at longer intervals. At melt heights of less than about 18 mm, mean melt temperature variations are absent and the amplitude of the random temperature fluctuations is considerably decreased. Under these thermal conditions, random and intermittent back-melting of short duration is observed. With a further decrease in melt height the temperature fluctuations continue to exhibit a varying amplitude but assume distinct and constant periodicity (Fig. 10b). In this region, remelt striations are irregularly spaced indicating irregular growth rate modulations associated with the varying amplitude of the periodic thermal fluctuations (Fig. 10a). All dopant striations become continuous across the crystal, indicating that the thermal perturbations are "in phase" across the entire growth interface.

In this growth period, it is not possible to use time markers for establishing time correspondence between the recorded temperature oscillations and the dopant striations because some of the current pulses coincide

with remelting and do not form time markers in the crystal. However, since each recorded temperature fluctuation results in a continuous striation, it becomes possible to establish time correspondence by counting the striations and the temperature fluctuations starting with the first time marker after transient remelting ceases.

Thermo-hydrodynamic behavior of the melt.—The present results indicate that under destabilizing thermal gradients, the thermo-hydrodynamics of the melt control the growth and dopant segregation behavior. They further show that turbulent convection, oscillatory instability, and thermal stability are successively present during solidification. Since the vertical thermal gradients did not change significantly during the entire solidification and were virtually constant within each hydrodynamic transition region, it is suggested that the continuous decrease in melt height is responsible for the observed changes in thermo-hydrodynamic behavior of the melt.

The Rayleigh number (12), R , which is often used as a criterion for hydrodynamic behavior, exhibits linear dependence on the vertical thermal gradient, β , and fourth power dependence on the melt height, h

$$R = \frac{g\alpha\beta h^4}{\nu\kappa}$$

where g is the gravitational constant, α is the coefficient of volume expansion, ν the kinematic viscosity, and κ is the thermal diffusivity. Using the values $\alpha = 0.95 \times 10^{-4}/^\circ\text{C}$ (13), $\nu = 3.02 \times 10^{-3} \text{ cm}^2/\text{sec}$ (13),

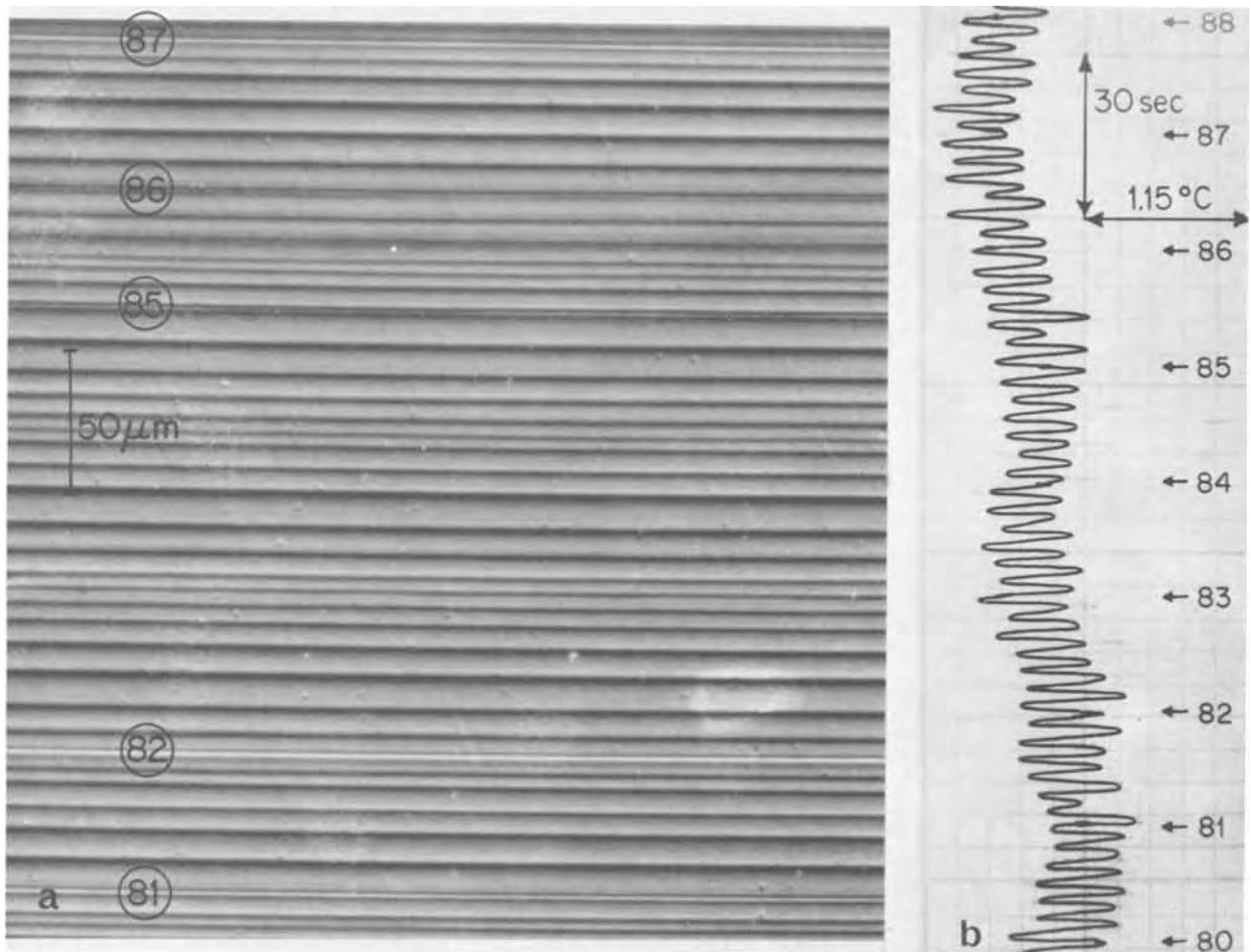


Fig. 10. (a) Photomicrograph of region grown after turbulent convection in the melt ceased and temperature fluctuations of varying amplitude but constant frequency prevailed. Intermittent remelting prevented the appearance of some of the time markers. (b) Recording of the temperature in the melt during growth of the crystal segment depicted in Fig. 10(a).

$\kappa = 0.2 \text{ cm}^2/\text{sec}$ (14), and the experimentally determined values of β and h , it is found that for the reported experiments, R ranges from about 3×10^5 , at the start of solidification, to zero at the end. The Rayleigh numbers characterizing the three regions of different thermo-hydrodynamic behavior, discussed above, are about 3×10^5 to about 4×10^3 for turbulent convection, 3×10^3 to 2×10^3 for oscillatory thermal instability, and 10^3 to 0 for thermal stability.

It is of interest to note that the transition from thermal instability to stability occurs at $R \cong 2 \times 10^3$ which is surprisingly close to the value of 1700 predicted for the onset of convective instability from theoretical considerations (15) where the assumed boundary conditions differ substantially from those in the present experiments. It is furthermore noteworthy that oscillatory thermal instability rather than a stationary pattern of convection in the form of Bénard cells (16) is observed upon the transition from thermal stability to thermal instability. Oscillatory thermal instability has been predicted (17) and has been found under destabilizing thermal gradients in the presence of transverse magnetic fields and/or rotation. More recently, temperature oscillations have also been observed in the absence of stabilizing forces and their origin has been attributed to horizontal thermal gradients (18). The present findings appear to be consistent with this point of view. Through the use of time markers it was shown that the temperature oscillations are "in phase" across the entire growth interface. This finding is of particular significance since the interface was detectably curved and appreciably deformed at twin boundaries. The present results gave no indication of a phase shift between the effects of the thermal perturbations at the steadily advancing growth interface and the thermal perturbations measured by the stationary thermocouple in the melt. Furthermore, it should be noted that no detectable phase shift was observed between the signals (oscillations) at the two monitoring thermocouples.

The presence of turbulent convection at large melt heights was confirmed through the growth and segregation behavior as well as through the recorded thermal behavior of the melt. Segregation effects in the grown crystal suggest further that, under the influence of horizontal gradients, the convective flow pattern undergoes a continuous rotational displacement along the axis of the melt. With decreasing melt height (decreasing Rayleigh number), convective flow gradually ceases and the random temperature fluctuations change first to periodic fluctuations of varying amplitude and ultimately to oscillations of constant frequency and amplitude. The present findings show clearly that time markers are not only valuable for investigating the microscopic growth behavior, but that they also constitute a powerful tool in establishing reference points in thermo-hydrodynamic studies.

The present study demonstrates the paramount importance of thermo-hydrodynamics in crystal growth, which has been widely recognized and has become the subject of numerous investigations in recent years. The approach used in this study relates directly the

hydrodynamic behavior of the melt to crystal growth and segregation characteristics. It is hoped that it will serve to bridge the existing gap between theoretical and experimental investigations.

Acknowledgments

The authors are grateful to the National Aeronautics and Space Administration for financial support. They are also indebted to Mr. M. Lichtensteiger for his valuable contributions to the design and implementation of the electronic arrangements and Mr. C. Herman for his skillful assistance with the experiments.

Manuscript submitted Dec. 8, 1971; revised manuscript received April 3, 1972.

Any discussion of this paper will appear in a Discussion Section to be published in the June 1973 JOURNAL.

REFERENCES

1. P. R. Camp, *J. Appl. Phys.*, **25**, 459 (1954); E. Billig, *Proc. Roy. Soc. (London)*, **A 229**, 346 (1955); H. Ueda, *J. Phys. Soc. Japan*, **16**, 61 (1961); W. R. Wilcox and C. D. Fullmer, *J. Appl. Phys.*, **36**, 2201 (1965); A. F. Witt and H. C. Gatos, *This Journal*, **115**, 70 (1968).
2. J. A. M. Dikhoff, *Solid State Electron.*, **1**, 202 (1960); M. G. Milvidskii and A. V. Berkova, *Soviet Phys. Solid State*, **5**, 517 (1963); J. R. Carruthers, *Can. Met. Quart.*, **5**, 55 (1966); A. F. Witt and H. C. Gatos, *This Journal*, **113**, 808 (1966); J. C. Brice and P. A. C. Whiffin, *Brit. J. Appl. Phys.*, **18**, 581 (1967).
3. A. Müller and M. Wilhelm, *Z. Naturforsch.*, **19a**, 254 (1964); G. S. Cole and W. C. Winegard, *J. Inst. Metals*, **93**, 153 (1964-1965); J. R. Carruthers, *J. Cryst. Growth*, **2**, 1 (1968).
4. R. Krishnamurti, *J. Fluid Mech.*, **42**, 295 (1970).
5. E. J. Harp and D. T. J. Hurle, *Phil. Mag.*, **17**, 1033 (1968); H. T. Rossby, *J. Fluid Mech.*, **36**, 309 (1969); P. A. C. Whiffin and J. C. Brice, *J. Cryst. Growth*, **10**, 91 (1971).
6. K. Morizane, A. F. Witt, and H. C. Gatos, *This Journal*, **113**, 51 (1966); D. T. J. Hurle, "Crystal Growth," H. S. Peiser, Editor, Pergamon Press (1967); B. Cockayne and M. P. Gates, *J. Mater. Sci.*, **2**, 118 (1967).
7. A. Müller and M. Wilhelm, *Z. Naturforsch.*, **19a**, 254 (1964); H. P. Utech and M. C. Flemings, *J. Appl. Phys.*, **37**, 2021 (1966).
8. M. Lichtensteiger, A. F. Witt, and H. C. Gatos, *This Journal*, **118**, 1013 (1971).
9. A. F. Witt, *ibid.*, **114**, 298 (1967).
10. E. J. Harp and D. T. J. Hurle, *Phil. Mag.*, **17**, 1033 (1968).
11. J. R. Carruthers, Private communication.
12. L. Rayleigh, *Phil. Mag., Series 6*, **32**, 529 (1916).
13. V. M. Glazov, S. N. Chizhevskaya, and N. N. Glagoleva, "Liquid Semiconductors," Plenum Press, New York (1969).
14. D. T. J. Hurle, E. Jakeman, and E. R. Pike, *J. Cryst. Growth*, **3**, 4, 633 (1968).
15. A. Pellew and R. V. Southwell, *Proc. Roy. Soc. (London)*, **A 176**, 312 (1940).
16. H. Bénard, *Ann. Chim. Phys.*, **23**, 62 (1901).
17. S. Chandrasekhar, *Phil. Mag., Series 7*, **43**, 501 (1952).
18. J. R. Carruthers and J. Pavilonis, *J. Appl. Phys.*, **39**, 5814 (1968).

Anodic Oxide Hydration Measured by Ion Probe Mass Spectrometry

G. A. Dorsey, Jr.

Kaiser Aluminum & Chemical Corporation, Center for Technology, Pleasanton, California 94566

ABSTRACT

The water content of barrier layer anodic alumina films was measured using the ion probe mass spectrometer: a method of sputtered ion mass analysis. Film thicknesses ranged from 100 to 2000 Å, with the oxides left intact on the basis metal during the analysis. The analytical procedure was first calibrated against standard samples of aluminum trihydroxides and monohydroxides. Then data were obtained for different thicknesses of boric-acid-anodized barrier layer oxides. The various aspects of the fragmentation patterns that were obtained are suggestive of a trihydroxide composition. Representative spectra are included, to illustrate the use of this method of surface analysis.

The ion probe mass spectrometer is a recent innovation for the inorganic analysis of thin films and other surface-related phenomena. It is also an equally useful instrument for the analysis of bulk inorganic materials, yielding a measure of compositional changes that take place as a function of the increased distance of beam penetration below the outer surface of the sample.

The sputter ion source technique was first developed by Herzog and Viehbock (1) but did not come into much use until 1966. Socha (2) recently reviewed the instrument and its related theory while Evens and Pemsler (3) have been among the many investigators to employ the technique; in this case, to the examination of tantalum films.

The unique feature of the ion probe is in its use of an energetic plasma beam of accelerated ions: positively charged argon ions, for example, at 5-15 keV. This primary beam is directed onto the surface of the sample, with the resultant sputtering of secondary ions from the sample. Neutral, negative, and positively charged secondary particles are formed, but only the positive ion yield is commonly analyzed via the detection system: mass spectrometry.

The sputtering process gives a geometrically uniform erosion pattern at low rates (~ 100 Å/min), for thin film analyses, or the erosion rate can be increased several hundred fold for bulk analyses, but at the sacrifice of erosion pattern uniformity. In either case, the advantage of the ion probe lies in its ability to provide a composition profile of sample components beginning at the outer surface of the specimen: at slow erosion rates, an almost monolayer-like sampling process.

Erosion rates and secondary ion yields are dependent on the species of bombarding ion and on the structural characteristics of the sample itself; this is aside from variations in instrumental parameters themselves. It therefore follows that, before a quantitative interpretation can be made from these data, a suitable experimental procedure must first be established, with standardized materials that are representative of the type of sample involved. Hydroxides present still another experimental complication, since the ion probe analysis is performed at a vacuum of 10^{-6} Torr. There is then the need to establish that a working equilibrium can indeed be attained, with respect to the water content of these samples, so that the experimental data can have significance in terms of the initial hydration of the sample. Unbound molecular water would be expected to be quickly lost during the initial stages of evacuation, prior to sample analysis. However,

Key words: anodic aluminas, sputter ion source mass spectrometry, hydration.

sorbed water and structural hydroxides might arrive at a working equilibrium with respect to the vacuum environment imposed by the analysis. Such a condition, if sufficiently reproducible, might then allow relevant data to be interpreted in terms of the initial water content of the oxide. This might partly resolve a discrepancy in data previously reported (4) for the degree of hydration of the anodic alumina barrier layer. Erdey *et al.* (5-7), Bogoyavlenskii (8) and Shreider (9) are also among those who found at least some degree of hydration in barrier layer aluminas formed in aqueous electrolytes. However many others, notably Burghers *et al.* (10), Vedder and Vermilyea (11), and Alwitt (12) present opposing data. While this lack of agreement can be partly attributed to differences in sample preparation and techniques of experimental measurement, there is still an obvious need for additional data to support either contention.

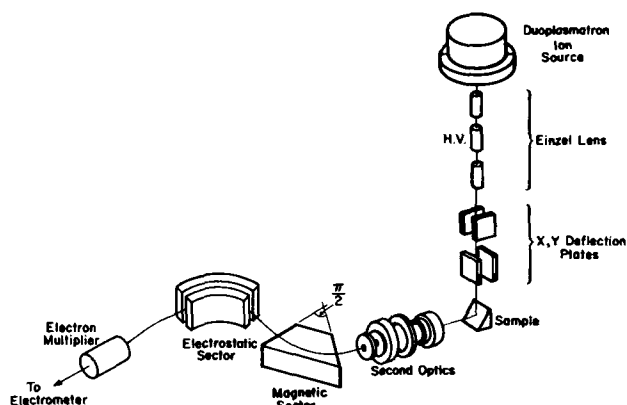
Experimental

Sample preparation.—Four reference samples of aluminum trihydroxides (2 of gibbsite and 2 of bayerite) and four reference samples of monohydroxide (all boehmites) were obtained through our Chemicals Division. These had been previously identified as suitable for use as standards, via x-ray diffraction and thermal analysis techniques. Approximately 0.5g of each alumina was compressed into a thin wafer, using 30 Ksi and a standard x-ray pelletizing die; no binder was employed, nor was any required. The result was a translucent wafer, with a hard and highly glazed surface. A dust-free section from a wafer was then mounted in a clean gold foil envelope, one side of which had a rectangular opening to expose the wafer surface during ion probe analysis; the gold foil allowed normal charge compensation procedures to be used.

Anodic oxides were prepared on clean alloy 1199 foil, using a 2M boric acid electrolyte at 60°C and 0.1 A/dm² current density. Forming voltages were varied from 6.7 to 101V. Total coating thicknesses, including both primary and secondary phases of the barrier layer oxide (4), ranged from 100 to 2000 Å; thicknesses were measured by coating impedance, infrared absorption, and electronoptical methods (4). After anodizing, the foils were thoroughly rinsed in flowing distilled water (cold) then air dried. Some were analyzed immediately, with the ion probe, while others (including remaining portions of earlier samples) were analyzed up to three weeks later; storage was under clean but ambient atmospheric conditions. Such delays, between sample preparation and analysis, did not alter the ion probe data in any detectable manner. However, the auxiliary methods of thickness measurement (impedance, ir) were performed immediately in each case.

The anodic oxides were left intact on the foil substrates, for ion probe analysis.

Ion probe mass spectrometer.—The commercial instrument employed (manufactured by GCA Technology Division, Bedford, Massachusetts) has been described in detail elsewhere (13) and is diagrammed in the following illustration, using a figure adapted from



Ref. (3). Research grade argon (Union Carbide—Linde Division) was used in the ion source, creating the primary ion beam (positively charged) which was directed toward the sample under a 10 keV potential. The beam diameter at the surface of the sample was 8 mm, the narrow diameter of the elliptical pattern produced by the beam. The instrument was adjusted to enhance the detection of molecular fragmentation patterns via an adjustment to the energy discriminating function governed by the target potential and the electrostatic analyzer of the instrument, a setting of 205V, to the "energy window" (13). Charge-up effects were eliminated through the use of a heated filament mounted close to the sample surface, ahead of the secondary extraction optics. Each analysis was begun at a vacuum of 10^{-6} Torr, including argon pressure, with both anodic oxides and compressed pellets of alumina standards.

With the glazed pellets of alumina standards, the pressure in the sample chamber immediately rose as the beam worked into the sample. An eightfold increase in pressure (to 8×10^{-6} Torr) was often observed, with approximately 2 hr required for the vacuum to be restored to its initially low value, either with or without the ion beam bombardment being continued. Perhaps this outgassing may partly have been due to the rupturing of the outer glazed surface of the compacted alumina pellet, exposing the entrained molecular water of the porous inner bulk to degassing. Spectra obtained during this degassing period showed, largely, molecular water ($^{18}\text{H}_2\text{O}^+$) indicating that the energy of the primary beam may have been partly dissipated by an outgassed layer of water vapor above the surface of the sample (Fig. 1). Coincident with the return to initial vacuum (10^{-6} Torr), the spectra stabilized and were then unchanging with respect to further erosion time. Erosion rate itself had no apparent effect on the time to equilibrium, nor did it alter the stability of the spectrum once equilibrium was obtained. It is thus possible to define experimental equilibrium, with respect to sample outgassing, by: (i) the return to initial vacuum level, (ii) the quantitative repeatability of spectral scans, and (iii) the quantitative stability of relevant peak intensities, in this case $^{16}\text{O}^+$ and $^{17}\text{OH}^+$, on a time scan basis. It follows naturally, however, that equilibrium conditions are most quickly met when sample quantity is kept to a minimum.

Owing to the comparatively small quantity of oxide involved, most anodized samples presented no measurable delay toward the establishment of experimental equilibrium, the exception being with those films whose

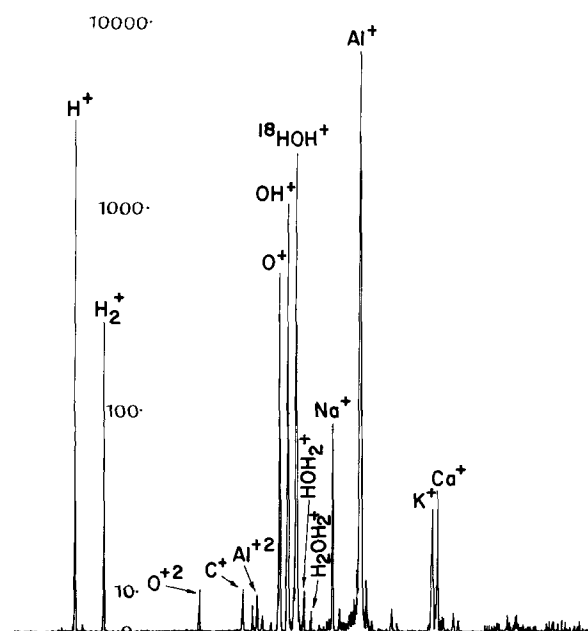


Fig. 1. Ion probe spectrum of gibbsite during initial stage of degassing, sample chamber pressure eightfold higher than initial value. Note intensity of $^{18}\text{HOH}^+$ species (5 decade intensity scale).

thickness was in excess of 1000Å. There, some amounts of residual surface (sorbed) water was found to a depth of ca. 150Å beneath the surface; afterward, these samples also met all criterion for experimental equilibrium.

Results and Discussion

Representative spectra of the various samples are included here, as an illustration of the type of data available with the instrument. In many cases, these spectra also contain data that are not part of the textual discussion, but which may interest those seeking additional detail.

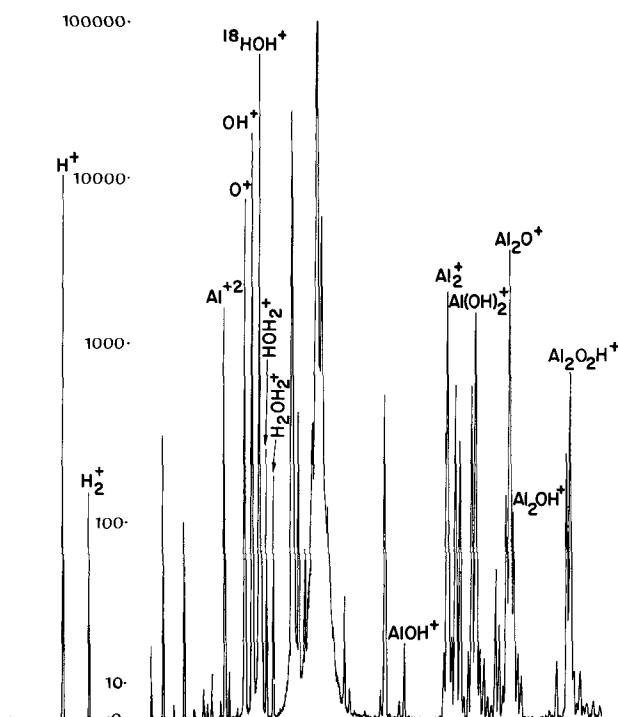


Fig. 2. Gibbsite prior to establishment of equilibrium. Note that more alumina fragmentation patterns are seen here, vs. Fig. 1, but $^{18}\text{HOH}^+$ intensity is still strong (5 decade intensity scale).

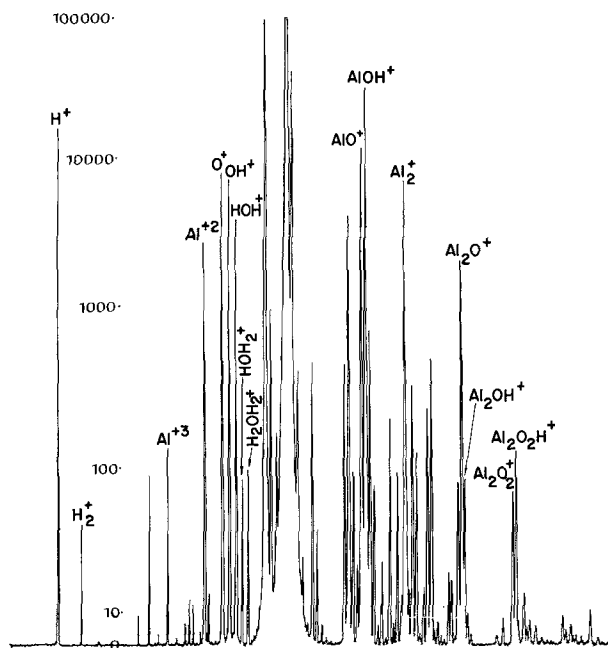


Fig. 3. Gibbsite approaching instrumental equilibrium, sample chamber pressure now fourfold higher than initial value. Note that the $^{18}\text{HOH}^+$ intensity is decreasing with respect to other species in the spectrum (5 decade intensity scale).

Figures 1-3 show the type of spectra encountered during the initial stages, prior to the establishment of experimental equilibrium, with compressed pellets of aluminum hydroxides. Initially, one of the strongest features in the spectrum is the peak of amu 18 due to $^{18}\text{HOH}^+$, as outgassing commences. Later (Fig. 2 and 3) aluminum-bearing fragmentation patterns become more pronounced, as outgassing decreases with a return toward initial vacuum in the sample chamber; these spectra are still obviously "wet," however, with such species as HOH_2^+ , H_2OH_2^+ , O_2H^+ , O_2H_2^+ , etc. All such peaks disappear from the spectrum of the same hydroxide when equilibrium conditions, as defined earlier, are established (Fig. 4).

Figure 5 shows the effect on the ratio of $^{17}\text{OH}^+$ to $^{16}\text{O}^+$, as equilibrium is attained: slowly for the comparatively large quantities of sample employed with the standard hydroxide pellets, and quickly with the considerably lesser quantities sampled in the case of the anodic oxides. This also illustrates the importance of obtaining data only in the equilibrium region of the sample. And though we have not done so, it would be reasonable to expect that an extreme delay in data collection, beyond the time-to-"equilibrium" for the particular sample, would result in the measurement of a lesser degree of apparent hydroxide in the sample.

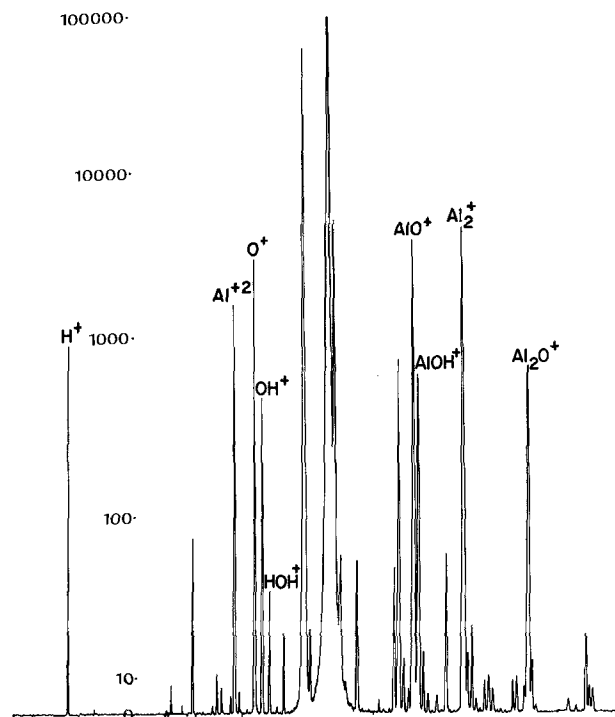


Fig. 4. Gibbsite at instrumental equilibrium. Note the absence of hydrous fragment species that characterized the spectra obtained prior to equilibrium (5 decade intensity scale).

It is reasonable to assume that the ratio of $^{17}\text{OH}^+$ to $^{16}\text{O}^+$ intensity would be a valid measure of the initial water content of the sample, exclusive of the unbound molecular water lost, to the vacuum, prior to analysis. But this assumption cannot be made until ion yields have been established with representative standards, in this case, aluminum trihydroxide (gibbsite and bayerite) and the monohydroxide/boehmite. Figure 6 shows the ion yield calibration, in this instance, for the $^{17}\text{OH}^+$ to $^{16}\text{O}^+$ ratio with these standards. At equilibrium, trihydroxides gave a ratio of 0.15 while the monohydroxide gave a ratio of 0.05. Figure 6 also shows companion data for anodic oxides, for comparison with these standards. The anodic oxides are represented by fourteen different thicknesses of anodic oxide barrier layer films. The average ratio of $^{17}\text{OH}^+$ to $^{16}\text{O}^+$, for the barrier layer, was also 0.15 ± 0.01 , with the more scattered data points belonging to oxide thicknesses less than 500\AA . It was experimentally difficult to measure the ratio accurately with the thinner films, especially those films with thicknesses less than 200\AA . Nevertheless, the apparent mole per cent water in these anodic oxide barrier layers was near 34%, basis the prior calibration against reference aluminas.

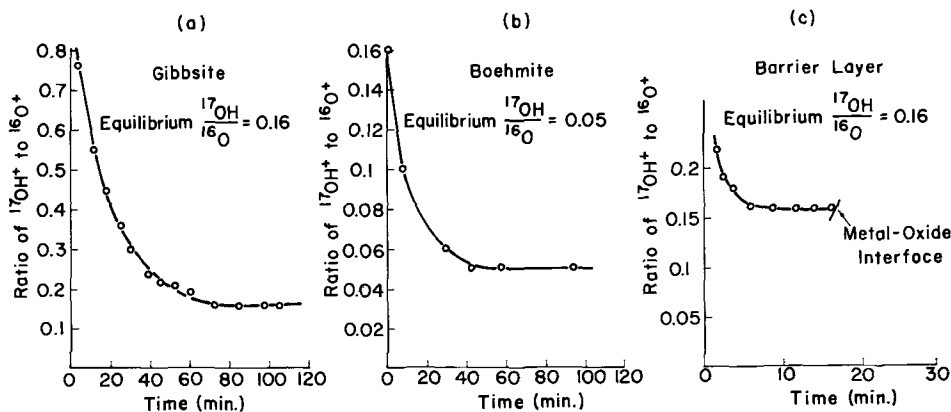


Fig. 5. Establishment of equilibrium conditions, as judged by the stability of the $^{17}\text{OH}^+$ to $^{16}\text{O}^+$ ratio, for (a) gibbsite, (b) boehmite, and (c) barrier layer anodic oxides. Thick barrier oxides require equilibrium conditioning but for a much shorter duration than with the massive quantities of alumina bulk standards. This time-to-equilibrium period was too brief to be measured with oxides thinner than 1000\AA .

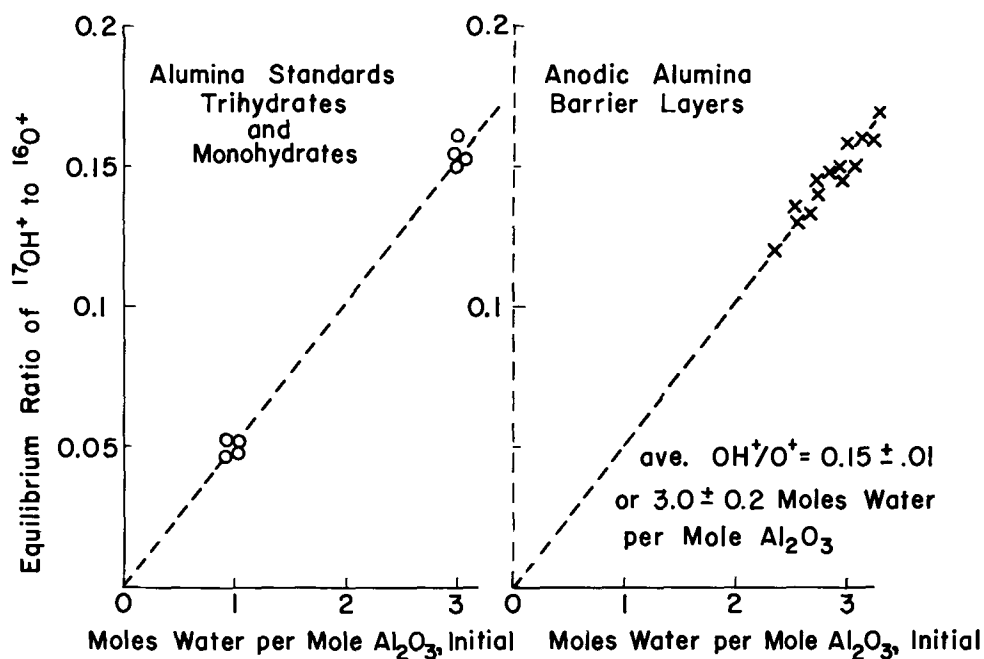


Fig. 6. Ion probe mass spectrometer determination of: (a) alumina standards, an ion yield calibration for $^{17}\text{OH}^+$ to $^{16}\text{O}^+$ ratio, and (b) anodic aluminas, 14 samples with film thicknesses ranging from 100 to 2000 Å, showing ratio of $^{17}\text{OH}^+$ to $^{16}\text{O}^+$.

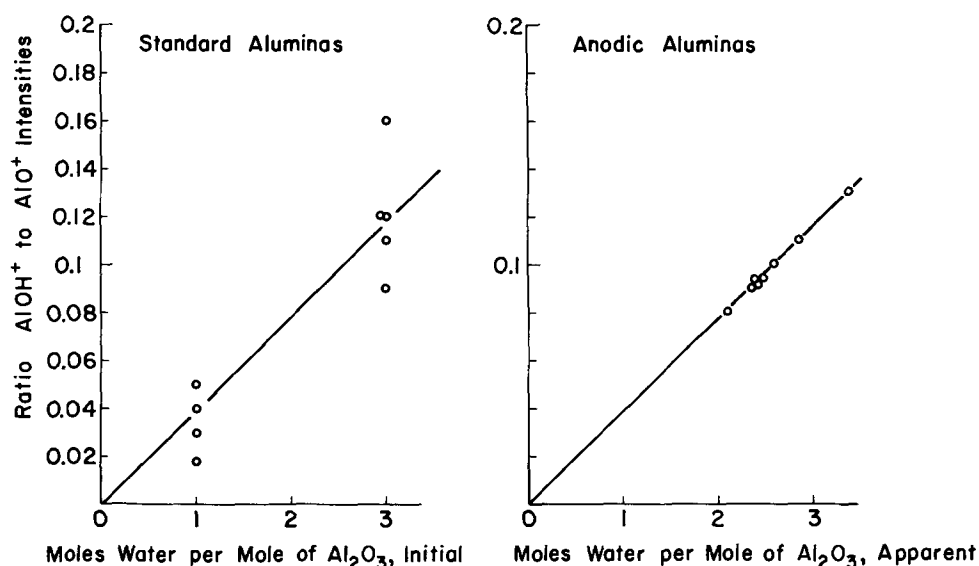


Fig. 7. Ion probe data for standard alumina hydroxides and barrier layer anodic oxides showing equilibrium ratios of $^{44}\text{AlOH}^+$ to $^{43}\text{AlO}^+$.

The ratio of $^{44}\text{AlOH}^+$ to $^{43}\text{AlO}^+$ also supports the measurement, as may be seen in Fig. 7; however, these results are experimentally less precise than the measurement of the ratio $^{17}\text{OH}^+$ to $^{16}\text{O}^+$. This difference in precision is largely due to the approximately tenfold lesser intensity of the $^{43}\text{AlO}^+$ species (*vs.* the $^{16}\text{O}^+$ species) which contributes quantitative error when employing the "fast scan" conditions (3 min, to amu 70) needed for a complete analysis of thin barrier layer anodic oxides. Then too, we might expect some degree of variation in molecular fragmentation pattern to be

characteristic of the structural differences (*i.e.*, crystallinity differences) between bayerite, gibbsite, and barrier layer anodic oxides. All this notwithstanding, the results shown in Fig. 7 are still consistent with the data obtained with the $^{17}\text{OH}^+$ to $^{16}\text{O}^+$ ratio (Fig. 6). Numerically, the $^{44}\text{AlOH}^+$ to $^{43}\text{AlO}^+$ ratio data gave the following average values: monohydroxides, 0.03 ± 0.01 ; trihydroxides, 0.12 ± 0.02 ; barrier layer oxides, 0.10 ± 0.02 .

Also in this regard, we can compare the ion yield data for these aluminas with the data adjusted with

Table I. Summary of adjusted ion yield data for standard alumina references and barrier layer anodic oxides

Sample	Adjusted ion ratios			
	$^{16}\text{O}^+/\text{Al}^{+3}$	$^{16}\text{O}^+/\text{Al}^{+2}$	$^{17}\text{OH}^+/\text{Al}^{+3}$	$^{17}\text{OH}^+/\text{Al}^{+2}$
Monohydrate reference (4 samples)	33.0 ± 4	1.7 ± 0.1	1.3 ± 0.3	0.07 ± 0.04
Trihydrate reference (5 samples)	34.0 ± 3	2.0 ± 0.1	5.0 ± 0.8	0.29 ± 0.03
Barrier layer oxides (10 samples)	39.0 ± 9	2.1 ± 0.3	5.7 ± 2.4	0.30 ± 0.09

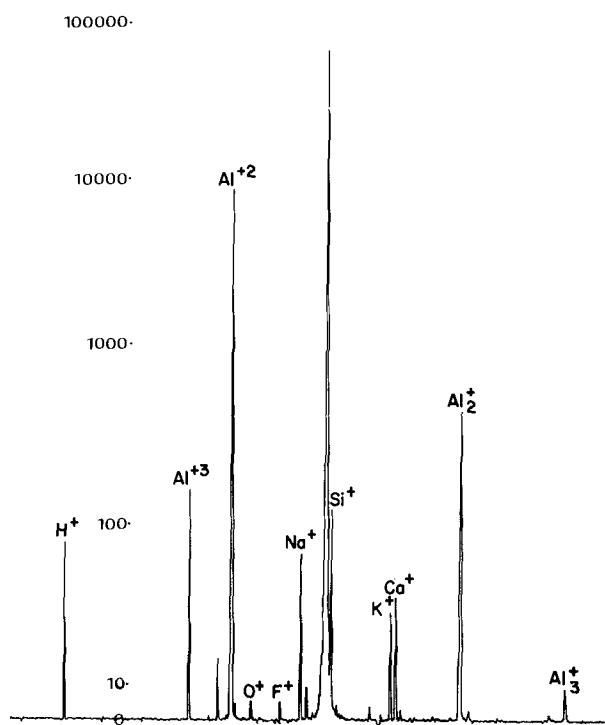


Fig. 8. Ion probe spectrum of basis alloy 1199 foil after beam-stripping of surface oxide (5 decade intensity scale).

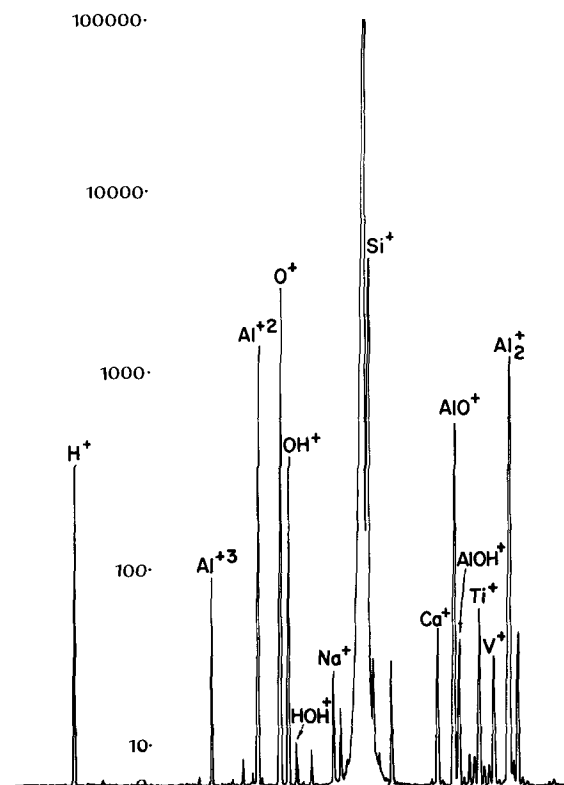


Fig. 10. Bayerite at instrumental equilibrium, with spectrum prepared using same "fast scan" conditions employed with anodic oxides (5 decade intensity scale).

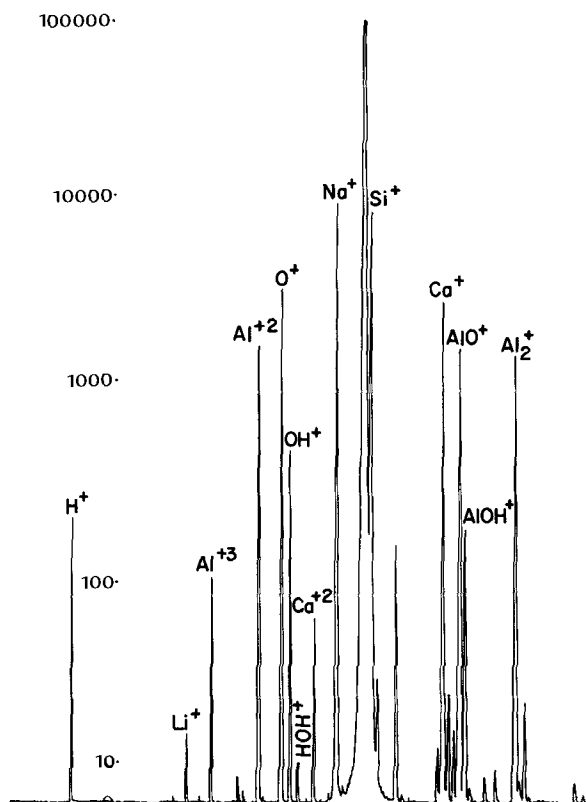


Fig. 9. Gibbsite at instrumental equilibrium, with spectrum prepared using same "fast scan" conditions employed with anodic oxides (5 decade intensity scale).

respect to the ion intensities of ${}^9\text{Al}^{+3}$ and ${}^{13.5}\text{Al}^{+2}$ species: "internal standards," to compensate for variations in instrumental operating parameters and differences in sample density. (The ${}^{27}\text{Al}^{+}$ species is the most intense in the spectrum of these oxides, and is always off-scale with the type of measurement sensitivity

employed here.) These adjusted data are best for the ${}^{13.5}\text{Al}^{+2}$ reference peak, which has approximately equal intensity with the ${}^{16}\text{O}^{+}$ and ${}^{17}\text{OH}^{+}$ peaks. It is also a measurement that is made within the same $\sim 100\text{\AA}$ increment of sample thickness that produced the measured ${}^{16}\text{O}^{+}$ and ${}^{17}\text{OH}^{+}$ peak intensities. The ${}^9\text{Al}^{+3}$ reference is of considerably lesser intensity, and is a measurement that is made $\sim 200\text{\AA}$ earlier in the film.

Table I shows these data, using ${}^9\text{Al}^{+3}$ and ${}^{13.5}\text{Al}^{+2}$ peak intensities as internal standard within the oxide. As would be expected, on a bulk-increment mole per cent basis, the oxygen-to-aluminum ratios are essentially the same for each alumina. Only the hydroxide-to-aluminum ratios are characteristic of the initial hydroxide composition of the samples.

Additional illustrations are seen in Fig. 8-12, Fig. 8 shows a spectrum of the substrate metal (alloy 1199 foil) essentially free of oxide in the area sampled by the ion beam erosion. This illustrates the negligible oxygen and hydroxide background in the instrument. Prepared in the same manner are representative spectra of gibbsite, bayerite, and barrier layer anodic oxides: Fig. 9-11, respectively. These illustrate the structural features, such as the ${}^{17}\text{OH}^{+}$ to ${}^{16}\text{O}^{+}$ ratio, already discussed. Figure 12 shows a time scan plot of ${}^{17}\text{OH}^{+}$ and ${}^{16}\text{O}^{+}$ intensities vs. erosion time (at $128\text{ \AA}/\text{min}$ erosion rate) into a barrier layer anodic oxide, to further illustrate the consistency of composition as a function of film thickness. As would be expected, the intensity of both species remains constant until the oxide-metal interface is encountered. Thereafter, the intensity of both species falls off sharply.

Acknowledgment

The writer wishes to thank the Kaiser Aluminum & Chemical Corporation for its support of this work and for its permission to publish these results.

Manuscript submitted Dec. 20, 1971; revised manuscript received April 17, 1972.

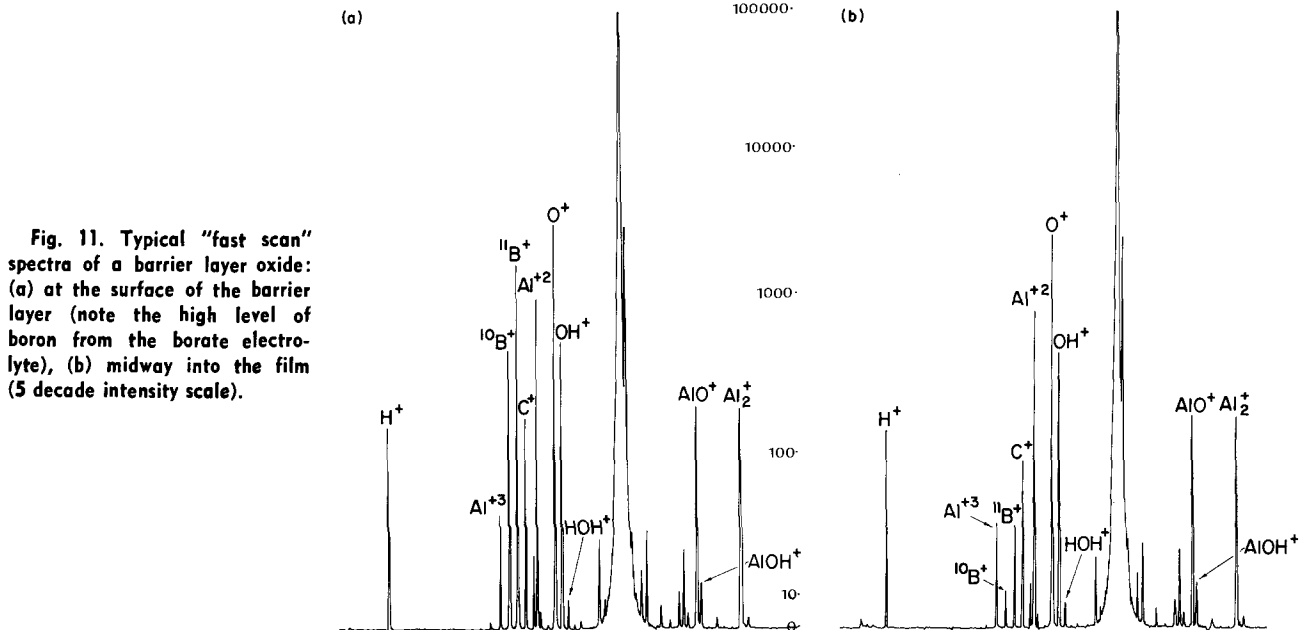


Fig. 11. Typical "fast scan" spectra of a barrier layer oxide: (a) at the surface of the barrier layer (note the high level of boron from the borate electrolyte), (b) midway into the film (5 decade intensity scale).

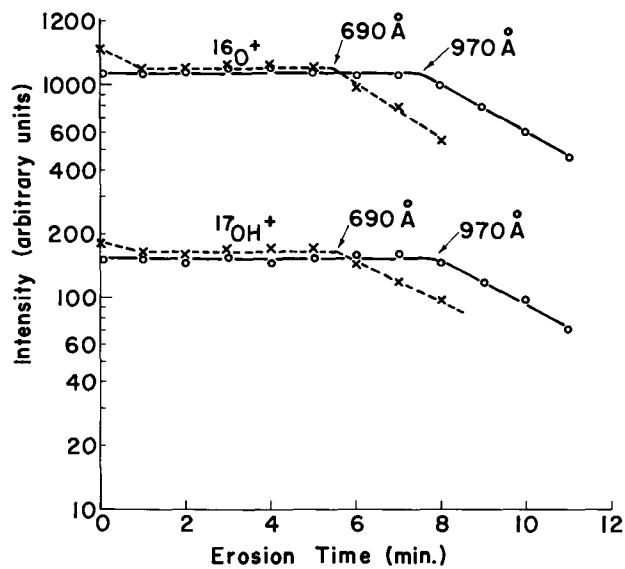


Fig. 12. Time scan of $^{17}\text{OH}^+$ and $^{16}\text{O}^+$ intensities vs. erosion time (at 128 Å/min) for typical barrier layer oxides; the intensity axis is logarithmic for ease in presentation.

Any discussion of this paper will appear in a Discussion Section to be published in the June 1973 JOURNAL.

REFERENCES

1. R. F. K. Herzog and F. P. Viehbock, *Phys. Rev.*, **76**, 855 (1949).
2. A. J. Socha, *Surface Sci.*, **25**, 147 (1971).
3. C. A. Evens, Jr. and J. P. Pemsler, *Anal. Chem.*, **42**, 1060 (1970).
4. G. A. Dorsey, Jr., *This Journal*, **116**, 466 (1969).
5. L. Erdey, T. Kormany, and S. Gal, *Z. Anal. Chem.*, **200**, 218 (1964).
6. L. Erdey, S. Gal, T. Kormany, and M. Mezey, *Proc. Conf. Appl. Phys. Chem. Met., Budapest*, **3**, 271 (1966).
7. L. Erdey, S. Gal, and M. Mezey, *Finomechanika*, **4**, 251 (1965).
8. A. F. Bogoyavlenskii, "Anodic Protection of Metals," paper presented at First Interuniversity Conference, Moscow, 1964.
9. A. V. Shreider, *J. Appl. Chem. USSR*, **39**, 2533 (1966).
10. W. G. Burghers, A. Claasen, and J. Zernike, *Z. Phys.*, **74**, 593 (1932).
11. W. Vedder and D. A. Vermilyea, *Trans. Faraday Soc.*, **65**, 561 (1969).
12. R. S. Alwitt, *This Journal*, **114**, 843 (1967).
13. R. F. K. Herzog, W. P. Poschenrieder, and F. G. Satkiewicz, NASA Contract No. NAS5-9254, GCA-TR-67-3-N (1967).

Dicing Induced Damage in GaP Electroluminescent Diodes

N. E. Schumaker and G. A. Rozgonyi*

Bell Telephone Laboratories, Incorporated, Murray Hill, New Jersey 07974

ABSTRACT

Batch processing of GaP electroluminescent (EL) diodes requires that the GaP wafer be separated into individual devices before lead bonding and final packaging. This paper describes an investigation of the effects of this mechanical dicing operation on the EL characteristics of GaP diodes. Chemical etching of the diced GaP diode after lead bonding has been found to be essential in achieving the maximum quantum efficiency of the completed device. The etchant used is a 3:1:1 solution of H_2SO_4 , 33% H_2O_2 , and H_2O at $60^\circ C$. The quantum efficiency is found to be dependent on the etching time with the efficiency reaching a maximum after approximately 5 min.

Efficiency and current-voltage measurements on unetched devices indicate the presence of surface leakage currents which decrease the external quantum efficiency of the completed device. Since it is believed that the presence of a damaged surface layer and its associated strain field can provide nonradiative leakage current paths, x-ray topography has been used to detect the existence of dicing-induced strain fields and to follow their removal as a function of etch time. X-ray topographs have also been obtained for samples initially cut with a wire saw and a diamond saw. Etching of the completed GaP diode effectively relieves the dicing-induced strain field and eliminates the surface leakage paths. This results in a device with maximum quantum efficiency and with reproducible current-voltage characteristics.

Batch processing of GaP wafers, essential for providing large quantities of GaP electroluminescent (EL) diodes, requires that the wafers be separated or diced into individual devices of uniform size and shape (1). This paper describes an investigation of the effects of this mechanical dicing operation on the EL characteristics of GaP diodes.

Empirically it had been observed that chemical etching improved the external EL efficiency of the completed GaP diode. This behavior suggested the presence of a damaged surface layer and an associated strain field which could provide nonradiative leakage current paths. This analysis has been confirmed by electrical measurements and by the use of x-ray topography to detect the existence of dicing-induced strain fields and to follow their removal as a function of etch time. The paper is divided into three sections. First, the dicing operation and the empirically observed effects of etching on the device will be described. Then the changes that occur in the device characteristics as a function of etch time are presented. Finally, the results of the x-ray topographs taken of step-etched GaP wafers cut by various techniques are analyzed and compared with the EL device data.

Dicing Operation and Device Etching

The procedure for batch processing GaP wafers is shown schematically in Fig. 1. The GaP wafer, after the growth of the two liquid phase epitaxial (LPE) layers, is lapped and polished to a uniform thickness of 0.25 mm. A distributed dot contact of 2% Si in Au is evaporated onto the n-type substrate, and 125 μm diameter dots of 1% Be in Au are evaporated onto the p-type LPE layer. After a high temperature alloy cycle to form ohmic contacts, the wafer is ready for separation into individual devices (0.4×0.4 mm) for bonding and inclusion in display packages. Although each step in the processing to obtain a completed GaP light emitting diode is being studied, only the dicing operation will be evaluated in this paper.

The external quantum efficiency of a completed GaP diode is dependent on the current density in the device. Similarly the radiation pattern of the device is strongly affected by the shape of the diode. For these two reasons it is important that the technique for separating or dicing the GaP wafer yield devices of

uniform size and shape. At the same time, the technique used should be rapid, reproducible, and reliable for application to large volume production.

Since the GaP wafers have {111} orientation and cleave in the $\langle 110 \rangle$ direction, conventional "scribe and cleave" techniques cannot be efficiently used to

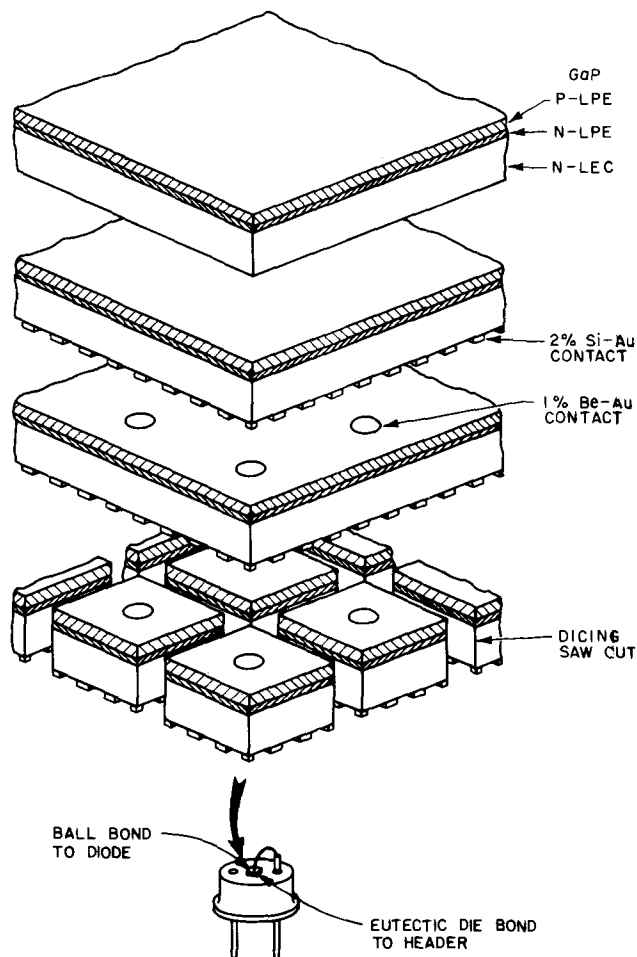


Fig. 1. Schematic drawing of batch process for GaP electroluminescent diodes.

* Electrochemical Society Active Member.

Key words: x-ray topography, strain, surface currents.

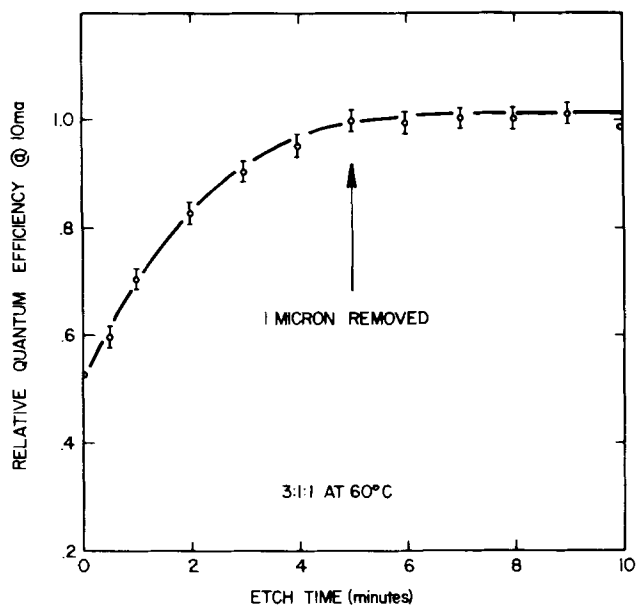


Fig. 2. Relative quantum efficiency at 10 mA as a function of the etch time for a sampling of slurry cut diodes.

provide the square shaped devices desired. Hence, mechanical dicing machines were considered as alternate means of obtaining discrete devices. A diamond saw, a wire saw, and a multiple blade slurry dicing machine¹ were examined in this study.

The dicing machine uses a mandrel consisting of numerous 50 μm thick stainless-steel blades separated by precision ground spacers which determine the size of the final device. The mandrel rotates at 10,000 rpm and is bathed in a water slurry containing 10-12 μm diameter silicon-carbide abrasive. The rotating mandrel directs the abrasive slurry against the GaP wafer. The thin stainless-steel blades do not contact the wafer at any time, and only the slurry abrades through the wafer. This cutting action results in a kerf loss of only 120 μm . The operation of the machine is fully automatic and a complete dicing cycle, requiring two cuts perpendicular to each other, is accomplished in 90 sec. The device dimensions across a wafer are maintained to within $\pm 3 \mu\text{m}$.

As mentioned in the introduction, devices fabricated using this dicing technique required chemical etching to achieve maximum EL efficiency. In particular, etching in a solution of H_2SO_4 , 33% H_2O_2 , and H_2O in a ratio of 3:1:1 at 60°C, improved the device properties significantly. The increase in EL efficiency at 10 mA forward current as a function of each etch time is shown in Fig. 2. This curve represents the behavior of a group of twenty devices from a single GaP wafer. The devices were etched for successively longer times and EL efficiency measured at the times indicated. In this group of devices a twofold increase in efficiency is found after etching for 5 min. Longer etch times do not significantly improve the efficiency, and excessive etching degrades device performance by undercutting contact areas.

Careful determination of the etch rate for the 3:1:1 solution at 60°C indicates that after 5 min about 1 μm of GaP would be removed. This has been subsequently confirmed by scanning electron microscope photographs of etched and unetched GaP diodes (2).

Electrical and Optical Measurements

The fact that such striking results were obtained by the removal of such a small amount of material from the GaP device, indicated the presence of a surface controlled effect. To demonstrate the magnitude of this effect, the quantum efficiency vs. current for a

¹ Taft-Pierce Manufacturing Company, Woonsocket, Rhode Island.

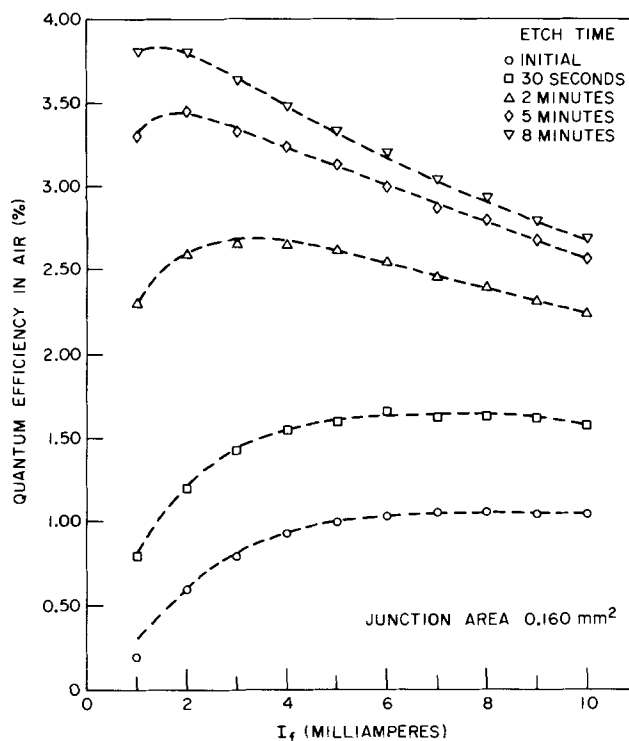


Fig. 3. Quantum efficiency in air as a function of forward current for various etch times for a slurry cut diode.

particular device after various etch times is shown in Fig. 3. This device was obtained from a different wafer of GaP than that used to generate the curve of Fig. 2 and indicates an even greater effect of etching. Note that the efficiency at 10 mA more than doubles when 1 μ is removed and the peak efficiency shifts to lower current density.

Since the presence of an absorbing surface film would require an absorption coefficient $\sim 10^3 \text{ cm}^{-1}$ to account for the magnitude of this effect, and, since one would expect no change in the shape of the efficiency vs. current curve due to an absorbing layer, a current leakage path in the diced GaP diode that was removed by etching was suspected. This was confirmed by the current-voltage data shown in Fig. 4 and 5.

In Fig. 4 the logarithm of the forward current vs. the forward voltage is shown for various etch times. One sees that for the unetched device the current-voltage dependence

$$I \propto I_0 e^{-\frac{qV_f}{nkT}}$$

at low bias gives an $n > 2$. However, as the diode is etched for successively longer periods of time, the value for n decreases and after 5 min $n \approx 2$. The current-voltage behavior of the unetched GaP diode with $n > 2$ is consistent with the presence of nonradiative recombination centers at the surface as discussed by Sah and others (3-5).

The reverse characteristics shown in Fig. 5 also change with etching. The unetched device is quite "leaky" and shows a soft reverse breakdown. Again, as the etching proceeds for longer times, the reverse leakage decreases to less than 1 nA at 10V and the diode exhibits a hard reverse breakdown.

Surface leakage currents can arise from a number of causes, principally surface contamination and surface damage. Since care was taken to avoid contamination on the device, the damage introduced during the dicing operation was expected to dominate the surface effect.

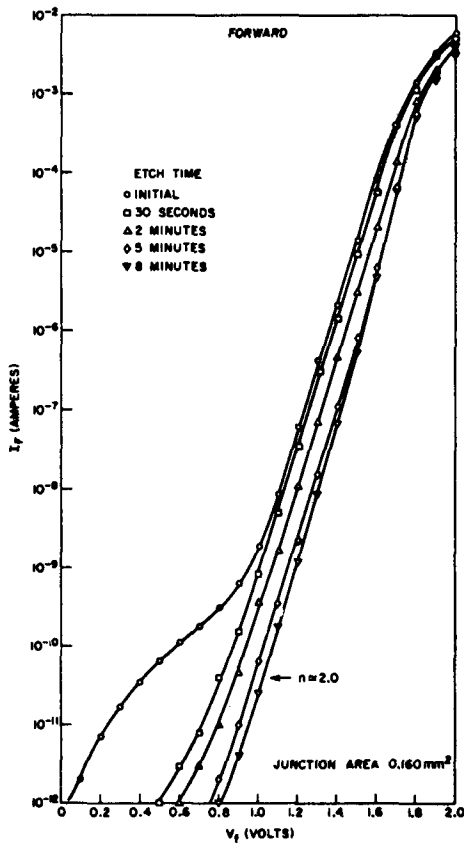


Fig. 4. Forward current-voltage characteristics for various etch times for a slurry cut diode.

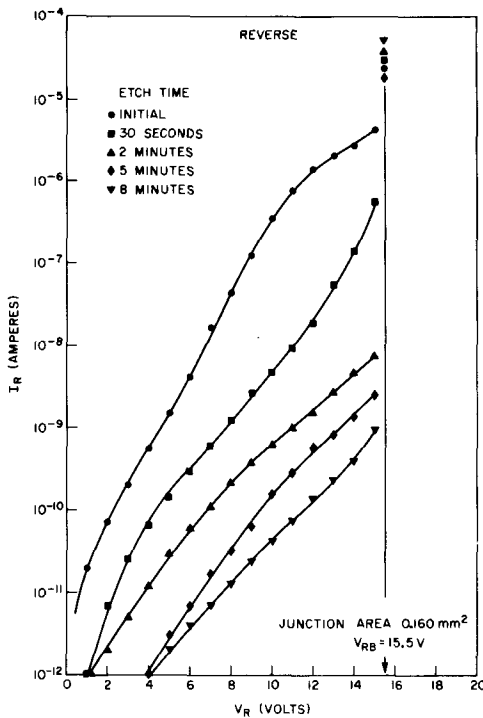


Fig. 5. Reverse current-voltage characteristics for various etch times for a slurry cut diode.

X-Ray Topographic Results

Since x-ray topography represents a sensitive technique for examining strain gradients in single crystals, it was used to evaluate the extent of the dicing-induced damage and its associated strain field. The samples which were evaluated by this method were prepared as shown schematically in Fig. 6. The {111} P-

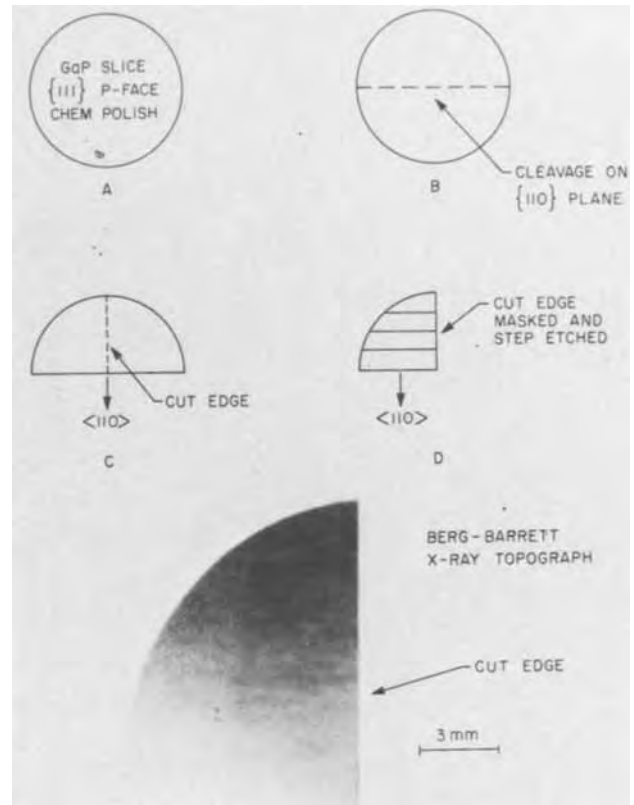


Fig. 6. Schematic showing procedure used to examine the effects of etching on cut and damaged wafer edges.

face of a substrate wafer cut from a GaP ingot grown by the liquid encapsulation Czochralski (LEC) technique was chemically polished using the polishing procedures described previously (6). The substrate wafer was then cleaved and a single cut was made in the <110> direction perpendicular to the cleavage plane. The cut edge and surface were then carefully masked with wax and successively etched to provide regions with different amounts of surface damage removal on the same sample. Berg-Barrett (reflection) topographs were then obtained using either {242} or {440} reflections; see Fig. 6e where the dark edge at the lower right edge represents the dicing-induced strain field.

The effectiveness of the etching procedure for a GaP substrate wafer, which was prepared in this fashion with etch periods sufficient to remove ~1 μm, 5 μm, and 15 μm of GaP from the slurry cut edge, is shown in the enlarged topograph of the cut edge in Fig. 7. The arrows point to various masked regions on the cut edge and the approximate amount of material removed is indicated. The lower right-hand edge of Fig. 7 clearly shows enhanced diffraction of the x-rays in the unetched region and indicates that the elastic strain field, due to dicing damage, extends for ~100 μm. The region directly above this in the figure has been etched for 5 min in 3:1:1 at 60°C to remove ~1 μm of GaP. Essentially, no enhanced diffraction is observed here indicating that the strain field has been relieved by the etching procedure. Note that the etch has been sufficiently light so that the rough chipped edge is still readily apparent. Further etching to remove ~5 μm and ~15 μm merely rounds and smooths the edge.

To correlate the removal of the damage and strain from the diced wafer with typical device measurements, e.g., those shown in Fig. 2, a second substrate of GaP was prepared and step-etched. In this case, etch periods of 30 sec, 1, 2, and 5 min were used and the resulting topograph is shown in Fig. 8. This figure confirms the rapid removal of the damage and strain in the GaP wafer and should be compared with the

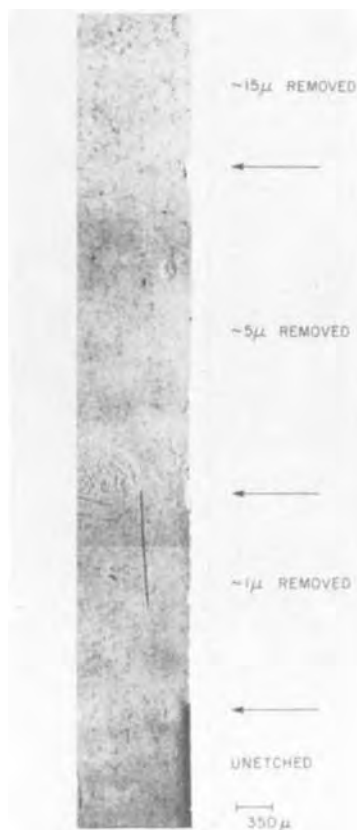


Fig. 7. X-ray topograph of a step-etched GaP wafer, slurry cut



Fig. 9. X-ray topograph of a step-etched GaP wafer, diamond saw cut.

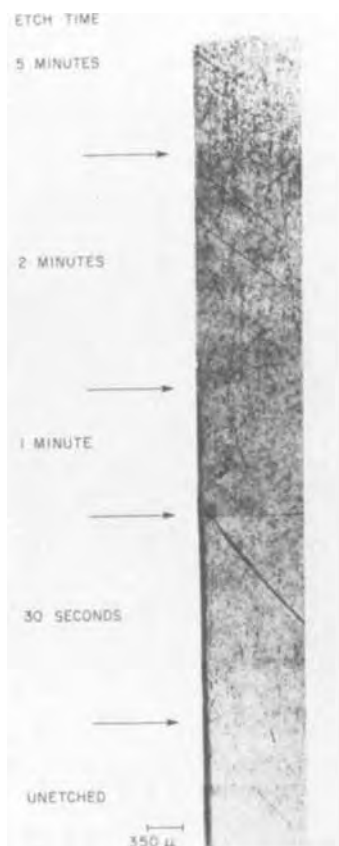


Fig. 8. X-ray topograph of a step-etched GaP wafer for short etch times, slurry cut.

efficiency *vs.* etch-time curve in Fig. 2. One sees that the extent of the dicing-induced strain fields is progressively reduced as the etch times are increased.

After 5 min of etching there is no apparent enhanced diffraction which is in qualitative agreement with the device results of Fig. 2.

Similar topographs were obtained for samples initially cut with a wire saw and a diamond saw. The results with a wire saw, using a silicon carbide abrasive, were essentially the same as those observed for the slurry dicing machine. However the topograph in Fig. 9, obtained on a step-etched GaP substrate wafer cut by a diamond saw, shows that enhanced diffraction is still present on the edge after the 1 μm deep etch has been used. In this case, after 5 μm of material is removed, there is no dicing-induced strain field remaining.

Conclusions

Using x-ray topography, mechanical dicing operations such as slurry cutting and diamond or wire sawing have been shown to introduce a shallow damaged layer on a GaP substrate wafer. The elastic strain field associated with this damage may extend as far as 100 μm into the wafer. Chemical etching to remove as little as 1 μm of material has been shown to relieve this elastic strain field. Efficiency and current-voltage measurements on devices prepared using slurry dicing indicate the presence of surface leakage currents which have a deleterious effect on the external quantum efficiency of the completed device. However, etching the diced device for 5 min in a solution of H_2SO_4 :33% H_2O_2 : H_2O a ratio of 3:1:1 at 60° removes $\sim 1 \mu\text{m}$ of material from the device which effectively relieves the strain field and eliminates the surface leakage paths. This results in a device with maximum quantum efficiency and with reproducible current-voltage characteristics.

Acknowledgments

The authors would like to thank M. Kuhn for useful discussions of the manuscript and L. A. Koszi for assistance in making the device measurements. The x-ray topographs were obtained by S. E. Haszko and F. A. Thiel.

Manuscript submitted Dec. 7, 1971; revised manuscript received May 10, 1972. This was Paper 88 presented at the Washington, D.C., Meeting of the Society, May 9-13, 1971.

Any discussion of this paper will appear in a Discussion Section to be published in the June 1973 JOURNAL.

Luminescence of Alkaline Earth Zirconium Silicates

W. L. Wanmaker,* J. W. ter Vrugt, and E. P. J. Meester

N.V. Philips' Gloeilampenfabrieken, Eindhoven, Netherlands

ABSTRACT

The luminescence of alkaline earth zirconium silicates has been investigated. The unactivated compounds show an ultraviolet emission band, which can be excited by cathode rays or by short-wavelength (190-210 nm) ultraviolet radiation. The excitation and emission can be ascribed to charge-transfer transitions between the oxygen and the zirconium ions. Activation of the alkaline earth zirconium silicates with various activators has been tried, lead giving the most efficient luminescence, e.g., in $\text{Ca}_2\text{ZrSi}_4\text{O}_{12}\text{-Pb}$ (λ_{max} of the emission at 355 nm) a quantum efficiency (with 254 nm excitation) of 52% was observed. Excitation and emission spectra, efficiencies, and temperature dependence of the lead-activated phosphors are presented.

In the $\text{MeO-ZrO}_2\text{-SiO}_2$ system (Me = Ca, Sr, Ba) various compounds have been described in the literature, viz., with Me = Ca the 2-1-4 and the 3-1-2 compounds (1, 2), with Me = Sr the 6-1-5 compound (3), and with Me = Ba the 1-1-3 and the 2-2-3 compounds (4).

The crystal structure of most of the alkaline earth zirconium silicates has not been determined up until now. The only exception is $\text{BaZrSi}_3\text{O}_9$ with a hexagonal unit cell ($a = 6.75\text{\AA}$ and $c = 10.00\text{\AA}$). In this compound Si_3O_9 -rings are present, with the Ba^{2+} and Zr^{4+} ions in trigonally distorted octahedra. $\text{BaZrSi}_3\text{O}_9$ is isomorphous with benitoite- $\text{BaTiSi}_3\text{O}_9$ (5). With the other alkaline earth zirconium silicates no isomorphous titanium silicates or zirconium titanates exist. Even the chemical composition of the compounds found in the three classes differs strongly, as follows from Table I (6-8).

Up until now only the luminescence of $\text{BaZrSi}_3\text{O}_9$ has been studied (5, 9, 10). For instance Blasse and Brill (5) found an efficient luminescence with Eu^{2+} - and with Ti^{4+} -activation. In the present investigation we tried to activate the alkaline earth zirconium silicates, mentioned above, with various activators, viz., Ce^{3+} , Eu^{2+} , Eu^{3+} , Tb^{3+} , Dy^{3+} , Sn^{2+} , Pb^{2+} , Ti^{4+} , Sb^{3+} , and Mn^{2+} .

Experimental

Powder samples were prepared by heating intimate mixtures of CaCO_3 , SrCO_3 , BaCO_3 , ZrO_2 , and SiO_2 at temperatures between 1100° and 1350°C. Two or more heatings lasting 2-4 hr were carried out. The activator elements were mostly added in an amount of 0.05-0.15 mole per mole of the host compound.

In many cases a two-step method was used to prepare the zirconium silicate phosphors. Tak and van Klinken (11) found this to be a useful procedure for the synthesis of $\text{BaZrSi}_3\text{O}_9\text{-Eu}^{2+}$, leading to a higher quantum efficiency of the phosphor as compared with the normal one-step preparation method. For instance, in the preparation of $\text{BaZrSi}_3\text{O}_9\text{-Pb}$ first $\text{BaSi}_2\text{O}_5\text{-Pb}$ is made at a temperature of 1100°C and the reaction product is refired twice at a temperature of 1350°C

- ### REFERENCES
1. N. E. Schumaker, B. H. Johnson, and R. A. Furnanage, Unpublished data.
 2. W. H. Hackett, Jr., Private communication.
 3. C. T. Sah, *IRE Trans. Electron Devices*-9, 94 (1962).
 4. D. J. Coppen and W. T. Matzen, *ibid.*, 9, 75 (1962).
 5. J. E. Iwersen, A. R. Bray, and J. J. Klaimack, *ibid.*, 9, 474 (1962).
 6. B. J. Gross, Private communication.

after the addition of 2 moles of ZrO_2 (i.e., 1 mole in excess) and 1 mole of SiO_2 per mole of $\text{BaSi}_2\text{O}_5\text{-Pb}$.

It pointed out that it is difficult to obtain the pure alkaline earth zirconium silicates, especially the strontium compound. Optical measurements as given in this paper were done, however, in the compounds corresponding to the formulas given. In these compounds no second phase could be detected by x-ray analysis.

X-ray powder diffraction patterns were taken on a Philips diffractometer using $\text{CuK}\alpha$ radiation.

Fluorescence, excitation, and reflection spectra were measured on a spectrofluorometer built in our laboratory. Two Jarrel-Ash $\frac{1}{4}$ meter monochromators with 600 grooves/mm gratings, blazed for 300 nm, are used as the excitation and as the fluorescence monochromator respectively. A 30W deuterium source with a suprasil window is used for the spectral range from 185 to about 400 nm, while a 55W halogen motorcar lamp covers the near-ultraviolet and visible regions. The source radiation is chopped with a frequency of 12 Hz and focused on the entrance slit of the excitation monochromator with the aid of a concave mirror.

The exit slit of the first monochromator is focused on the phosphor plaque, the reflected and the fluorescent radiation being concentrated on the entrance slit of the second monochromator. The intermonochromator optics consists of flat and concave mirrors to eliminate chromatic aberrations. The spectral bandwidth, both for excitation and fluorescence, was equal to or less than 6 nm.

The current from the photomultiplier (Philips XP 1003 with extended S-20 spectral response and with a quartz window) behind the exit slit of the fluores-

Table I. Compounds in the systems $\text{Me}^{\text{II}}\text{O-A}^{\text{IV}}\text{O}_2\text{-B}^{\text{IV}}\text{O}_2$

Me^{II}	(Me = Ca, Sr, Ba; A, B two from the elements Si, Ti, Zr)		
	$\text{A}^{\text{IV}} = \text{Ti}$, $\text{B}^{\text{IV}} = \text{Si}$	$\text{A}^{\text{IV}} = \text{Zr}$, $\text{B}^{\text{IV}} = \text{Si}$	$\text{A}^{\text{IV}} = \text{Zr}$, $\text{B}^{\text{IV}} = \text{Ti}$
Ca	CaTiSiO_5	$\text{Ca}_2\text{ZrSi}_4\text{O}_{12}$ $\text{Ca}_3\text{ZrSi}_5\text{O}_9$	$\text{CaZrTi}_2\text{O}_7$
Sr		$\text{Sr}_6\text{ZrSi}_5\text{O}_{18}$	
Ba	BaTiSiO_5 $\text{BaTiSi}_2\text{O}_7$ $\text{BaTiSi}_3\text{O}_9$ $\text{Ba}_2\text{TiSi}_2\text{O}_8$	$\text{BaZrSi}_3\text{O}_9$ $\text{Ba}_2\text{Zr}_2\text{Si}_5\text{O}_{12}$	

* Electrochemical Society Active Member.

Key words: luminescence, phosphors, alkaline earth, zirconium silicate, Pb^{2+} -activated.

cence monochromator, is amplified with a phase-sensitive 12 Hz amplifier and recorded. Reflection spectra may be recorded by scanning both monochromators synchronously.

Excitation spectra are corrected with the aid of the measured excitation spectra of sodium salicylate (12) (up to 350 nm), or in the near-ultraviolet and visible spectral range with that of 2,2'-dihydroxy-1,1'-naphthal-diazine (Lumogen LT-hellgelb from BASF) (13). Both phosphors show a constant quantum efficiency in a broad spectral region. The fluorescence spectra were calibrated with various NBS standard phosphors (14). As a reflection standard CaF_2 or BaSO_4 is appropriate.

Results and Discussion

Optical properties of the unactivated alkaline earth zirconium silicates.—On exciting $\text{BaZrSi}_3\text{O}_9$ with cathode rays, Blasse and Bril (5) found an ultraviolet emission band peaking at 285 nm. With ultraviolet excitation at wavelengths shorter than 220 nm a similar emission band could be detected. Excitation and emission of this compound were ascribed to charge-transfer transitions between the O^{2-} ions and the Zr^{4+} ions. Ultraviolet emission of the same type was found before in ZrP_2O_7 (15), and it might be expected in other Zr^{4+} -compounds as well (5).

Therefore we looked for a similar emission band in the other alkaline earth zirconium silicates prepared in the present investigation. As shown in Fig. 1 an ultraviolet emission band is present also in other alkaline earth zirconium silicates. Its maximum ranges from 285-340 nm when excited with cathode rays. With short-wavelength ultraviolet excitation (190-210 nm) this emission band is found at a slightly different wavelength, e.g., with the Ba compounds the emission maximum shifts from 285 to 330 nm, as may be seen from Fig. 2.

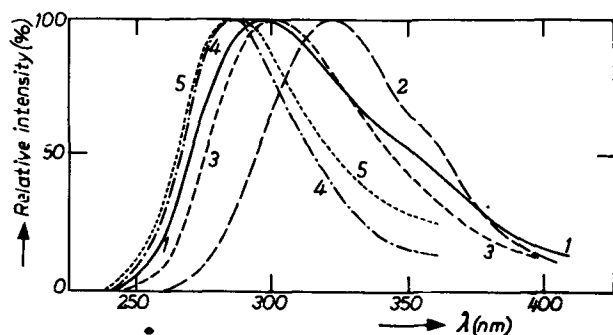


Fig. 1. Spectral energy distribution of the emission of alkaline earth zirconium silicates with cathode-ray excitation; curve 1, $\text{Ca}_2\text{ZrSi}_4\text{O}_{12}$; curve 2, $\text{Ca}_3\text{ZrSi}_2\text{O}_9$; curve 3, $\text{Sr}_6\text{ZrSi}_5\text{O}_{18}$; curve 4, $\text{BaZrSi}_3\text{O}_9$; curve 5, $\text{Ba}_2\text{Zr}_2\text{Si}_3\text{O}_{12}$.

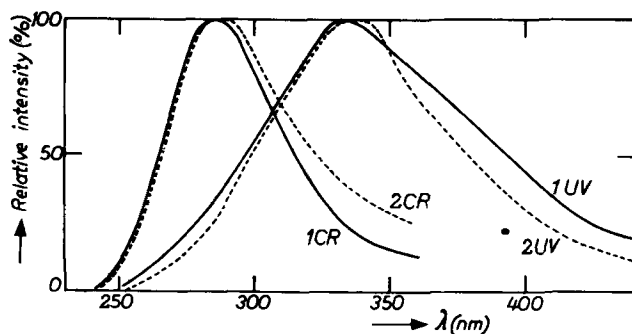


Fig. 2. Spectral energy distribution of the emission of barium zirconium silicates under cathode-ray and under 190 nm excitation respectively. Curve 1CR, $\text{BaZrSi}_3\text{O}_9$, cathode rays; curve 1UV, $\text{BaZrSi}_3\text{O}_9$, 190 nm; curve 2CR, $\text{Ba}_2\text{Zr}_2\text{Si}_3\text{O}_{12}$, cathode rays; curve 2UV, $\text{Ba}_2\text{Zr}_2\text{Si}_3\text{O}_{12}$, 190 nm.

The conclusion may be drawn that in both $\text{BaZrSi}_3\text{O}_9$ and $\text{Ba}_2\text{Zr}_2\text{Si}_3\text{O}_{12}$ the luminescence is connected with two kinds of transitions. This phenomenon could be similar to the occurrence of two emission bands in niobates and tantalates, e.g., $\text{Mg}_4\text{Nb}_2\text{O}_9$ and $\text{Mg}_4\text{Ta}_2\text{O}_9$ (16), depending on the wavelength of the exciting radiation and on the temperature. These two bands are ascribed to the appearance of singlet-singlet and triplet-singlet transitions (16). Just as in the above-mentioned niobates and tantalates the shift of the emission maxima in the zirconium silicates is about 5500 cm^{-1} .

Activated compounds.—In addition to the Eu^{2+} - and the Ti^{4+} -luminescence in $\text{BaZrSi}_3\text{O}_9$, as described before (5), in several of the host lattices investigated by us luminescence was observed with activator ions like Eu^{3+} , Eu^{2+} , Sn^{2+} , Ti^{4+} , Ce^{3+} , Tb^{3+} , Dy^{3+} , and Pb^{2+} . For instance with Ti^{4+} -activation in $\text{Ca}_2\text{ZrSi}_4\text{O}_{12}$ a broad emission band with a maximum at 480 nm and with a bandwidth at half-maximum intensity of 125 nm was observed and in $\text{Ba}_2\text{Zr}_2\text{Si}_3\text{O}_{12}$ - Eu^{2+} an emission band at 490 nm with a bandwidth of 80 nm. With Eu^{3+} -activation emission lines characteristic for transitions in the Eu^{3+} ion were observed, e.g., in $\text{Ca}_3\text{ZrSi}_2\text{O}_9$. In $\text{Ca}_2\text{ZrSi}_4\text{O}_{12}$ -Pb, Mn a Mn emission band ($\lambda_{\text{max}} = 610 \text{ nm}$) could be observed in addition to the Pb emission band at 355 nm.

The quantum efficiency (254 nm excitation) of most of these phosphors does not exceed a value of about 10%, with the exception of activation with lead, giving rise to values up to 50%. Therefore we will restrict ourselves in the following to Pb-activated phosphors.

Lead-activated compounds.—Spectral energy distribution curves (254 nm excitation) of the various lead-activated phosphors are given in Fig. 3. The maximum of the emission band shifts to longer wavelengths and broadens in the sequence Ca-Sr-Ba. With $\text{Ca}_3\text{ZrSi}_2\text{O}_9$ -Pb the emission band is nearly identical to that of the unactivated compound, but there exists a large difference between the excitation spectra. The unactivated compound can only be excited by radiation of wavelengths shorter than 210 nm, while the Pb-activated phosphor shows a strong narrow excitation band at 260 nm (Fig. 6), which is typical for that of the activator ion.

When measuring the emission spectra at 77K, the Ba compounds show a second narrow emission band at 330 nm, as is illustrated in Fig. 4. A second emission band does not occur in the other lead-activated alkaline earth zirconium silicates, the only effect observed with excitation at 77K being an increase in peak height of about 20-70% as compared with the value at room temperature.

The decay-time ($1/e$ -value) of the 400 nm emission band in both Pb-activated barium zirconium silicates is 6 μsec , while that of the 330 nm band showed to be 8.5 μsec (ultraviolet excitation at 77K). These values

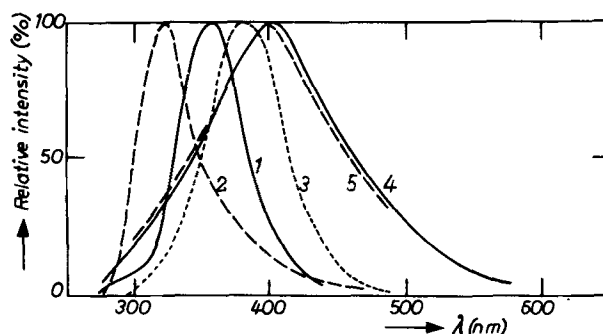


Fig. 3. Spectral energy distribution of the emission of $\text{Ca}_2\text{ZrSi}_4\text{O}_{12}$ -Pb (curve 1), $\text{Ca}_3\text{ZrSi}_2\text{O}_9$ -Pb (curve 2), $\text{Sr}_6\text{ZrSi}_5\text{O}_{18}$ -Pb (curve 3), $\text{BaZrSi}_3\text{O}_9$ -Pb (curve 4), and $\text{Ba}_2\text{Zr}_2\text{Si}_3\text{O}_{12}$ -Pb (curve 5). Mainly 254 nm excitation.

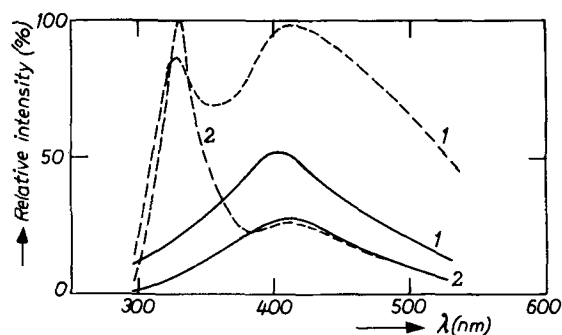


Fig. 4. Spectral energy distribution of the emission of $\text{Ba}_2\text{Zr}_2\text{Si}_3\text{O}_{12}\text{-Pb}$ and $\text{BaZrSi}_3\text{O}_9\text{-Pb}$ as measured at 77 and 293K respectively. Mainly 254 nm excitation. Curves 1, $\text{Ba}_2\text{Zr}_2\text{Si}_3\text{O}_{12}\text{-Pb}$. curves 2, $\text{BaZrSi}_3\text{O}_9\text{-Pb}$. Full curves, emission at 293K relative to that at 77K; dashed curves, emission at 77K.

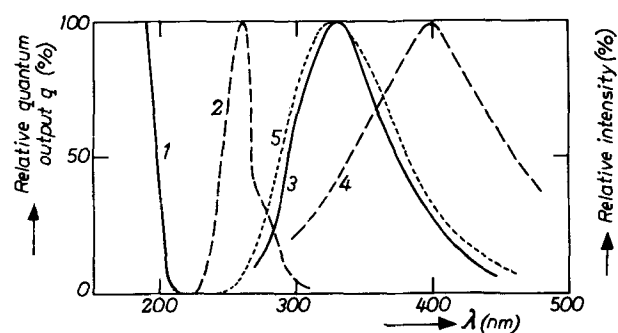


Fig. 5. Excitation spectra (relative quantum output) and spectral energy distribution of the emission of $\text{Ba}_2\text{Zr}_2\text{Si}_3\text{O}_{12}\text{-Pb}$, as measured at room temperature. Curve 1, excitation spectrum of the emission at 330 nm; curve 2, excitation spectrum of the emission at 400 nm; curve 3, emission spectrum under 190 nm excitation; curve 4, emission spectrum under 260 nm excitation; curve 5, emission spectrum under cathode-ray excitation.

are comparable to those found with other Pb-activated phosphors, indicating that both bands are due to transitions in the Pb ions.

One could assume, that the 330 nm emission band should have its origin in a host lattice transition, but the two following arguments support the explanation that a transition in a Pb-center is much more probable, viz.:

(i) The 330 nm emission band observed at 77K can be excited with 254 nm radiation; its excitation band coincides with that of the 400 nm emission band at room temperature. At 77K the excitation band of the 400 nm emission band, however, is very narrow and peaks at 245 nm. The host lattice emission of the alkaline earth zirconium silicates, on the contrary, can only be excited with radiation at wavelengths shorter than 210 nm (see Fig. 5).

(ii) When exciting $\text{Ba}_2\text{Zr}_2\text{Si}_3\text{O}_{12}\text{-Pb}$ with cathode rays or with 190-210 nm radiation (both giving rise to host lattice excitation, see above) a broad emission band at 330 nm occurs (see Fig. 5), differing in shape from the emission band excited by 254 nm radiation at 77K.

The occurrence of two lead-emission bands in $\text{BaZrSi}_3\text{O}_9\text{-Pb}$ and in $\text{Ba}_2\text{Zr}_2\text{Si}_3\text{O}_{12}\text{-Pb}$ might be due to transitions from different levels to the ground level (e.g., from $^3\text{P}_1$ or $^3\text{P}_0$ to the $^1\text{S}_0$ state) (17) in analogy to two excited levels in $\text{BaZrSi}_3\text{O}_9\text{-Ti}$ (5). The presence of lead in both Ba^{2+} - and Zr^{4+} -sites as Pb^{2+} , or as a combination of Pb^{2+} and Pb^{4+} , might be another explanation. The two emission bands might also be attributed to the existence of Pb-Pb pairs, as assumed by Schulman *et al.* in order to explain the occurrence of more emission bands in $\text{CaSiO}_3\text{-Pb}$ (18).

The luminescence intensity of the lead-activated alkaline earth zirconium silicates decreases rapidly (especially of the Ba-compounds) when heating the phosphors above room temperature. With the Ca- and Sr-compounds the luminescence has decreased to 50% of that at room temperature at 200°-250°C, while for the Ba-compounds this already occurs at 100°C.

The excitation and reflection spectra of the lead-activated alkaline earth zirconium silicates are presented in Fig. 6. All phosphors show a narrow excita-

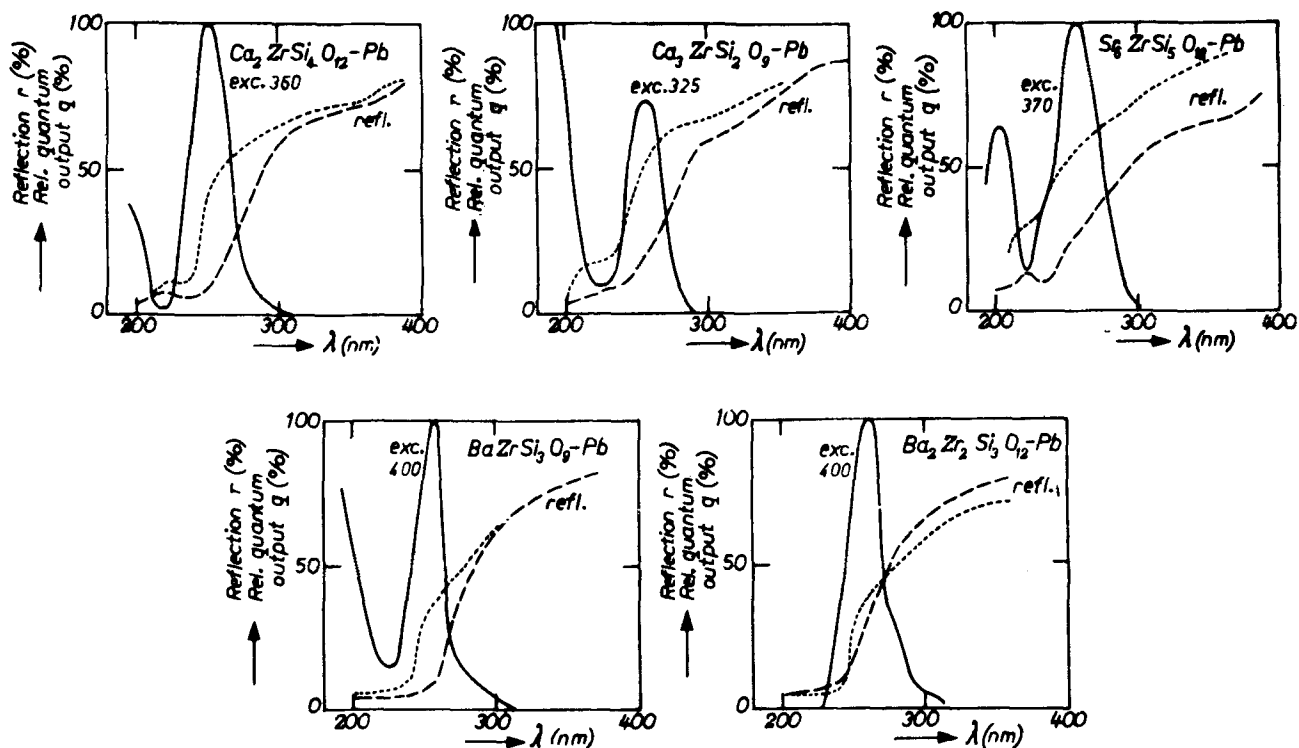


Fig. 6. Excitation spectra (relative quantum output q) (full curves) at the lead-emission band and diffuse reflection spectra (r) of the host compounds (dotted curves) and of the lead-activated phosphors (dashed curves). Numbers in the figure denote wavelength (nm) of measured emission.

Table II. Some properties of lead-activated alkaline earth zirconium silicates

Composition	Emission maximum (nm)	254 nm excitation		Cathode-ray excitation η (%)
		q (%)	Ref. (%)	
$\text{Ca}_2\text{ZrSi}_4\text{O}_{12}$	355	52	14	1.5
$\text{Ca}_3\text{ZrSi}_2\text{O}_9$	325	28	19	1
$\text{Sr}_6\text{ZrSi}_5\text{O}_{18}$	380	32	25	0.5
$\text{BaZrSi}_3\text{O}_9$	410	34	9	4
$\text{Ba}_2\text{Zr}_2\text{Si}_3\text{O}_{12}$	405	4	23	3

q = quantum efficiency for 254 nm excitation.

η = radiant efficiency for cathode-ray excitation (20 kV).

The lead concentration amounts to 0.1 mole per mole for the Ca and Sr compounds and to 0.15 mole per mole for the Ba compounds, as added to the firing mixture.

tion band; the band maxima show some change with composition from 250 to 265 nm. In most cases excitation occurs also at shorter wavelengths, viz., at about 200 nm, leading to the same emission spectrum as excitation with 250 nm. The shoulders observed in some excitation bands might be due to crystal field splitting of the 3P_1 level of the lead ions. Due to partial or total overlap of activator and host lattice emission, in some cases excitation at 200 nm (of the emission at the wavelengths labeled in the figure) must be partly attributed to the host lattice. The shape of the excitation bands in all relevant phosphors, viz., a sharp band at about 250 nm with a band width of 30-40 nm, is typical for lead-activated phosphors. Recently we found similar excitation bands with lead-activated alkaline earth germanates (19). A narrowing of the excitation bands and a slight shift to shorter wavelengths is found with some phosphors when measuring at 77K.

It follows from the excitation spectra, that in the region of a strong absorption of the host lattice (i.e., at wavelengths shorter than 230 nm) mostly a weak excitation of the lead-emission band only occurs. An exception to this is constituted by $\text{Ca}_3\text{ZrSi}_2\text{O}_9$ -Pb, for which compound host lattice and activator emission bands coincide. Therefore the conclusion may be drawn that in the relevant host lattices the energy transfer from the host lattice to the lead activator ions is negligible. This is confirmed by the measurements on $\text{Ba}_2\text{Zr}_2\text{Si}_3\text{O}_{12}$ -Pb given in Fig. 5, showing that with 190 nm and with cathode-ray excitation only host lattice emission was found; the lead-emission band appears when exciting at 254 nm, corresponding to a specific absorption in the activator ions.

In Fig. 6 the reflection spectra both of the host lattices and of the lead-activated phosphors are given. With $\text{Ba}_2\text{Zr}_2\text{Si}_3\text{O}_{12}$ -Pb we found only a very weak extra absorption band at 250 nm, when compared with the unactivated compound. The strong host lattice absorption of $\text{Ba}_2\text{Zr}_2\text{Si}_3\text{O}_{12}$, however, must be responsible for the low quantum efficiency of its lead emission (Table II). The poor energy transfer in the alkaline earth zirconium silicates may be ascribed to the small spectral overlap of the host-lattice emission band and the lead-activator absorption band. With $\text{BaZrSi}_3\text{O}_9$ -Ti, on the contrary, a very efficient energy transfer to the titanium center was found (5) due to the broad spectral overlap of the respective emission and absorption bands.

It follows from the excitation spectra, that most of the phosphors should be suitable for 254 nm excitation, as present in a low pressure mercury vapor discharge. Their quantum efficiency, however, is rather low (Table II), viz., a highest value of 52% was measured with $\text{Ca}_2\text{ZrSi}_4\text{O}_{12}$ -Pb. The latter phosphor, with a maximum emission wavelength at 355 nm, might be applied in lamps with a specific photochemical action, such as copying lamps.

Acknowledgments

The authors are indebted to Mr. J. G. Verlijsdonk for his assistance in preparing the phosphors, to Dr. A. Bril for the measurements with cathode rays, and to Mr. C. Bakker for measuring the reflection, excitation, and fluorescence spectra.

Manuscript submitted Jan. 31, 1972; revised manuscript received May 5, 1972. This was Paper 79 presented at the Houston, Texas Meeting, of the Society, May 7-11, 1972.

Any discussion of this paper will appear in a Discussion Section to be published in the June 1973 JOURNAL.

REFERENCES

- R. A. Kordyuk and N. V. Gul'ko, *Dokl. Akad. Nauk SSSR*, **142**, 639 (1962); *Chem. Techn. Section Transl.*, **6** (1962).
- P. G. Usov and E. P. Solomatina, *Izv. Tomsk. Politekhn. Inst.*, **185**, 135 (1970); *Chem. Abstracts*, **75**, Ref. 70887s (1971).
- Yu. M. Galkin and V. G. Chukhlantsev, *Izv. Akad. Nauk SSSR, Neorg. Mat.*, **1**, 2000 (1965); *Russ. J. Inorg. Mat.*, 1810 (1965).
- Yu. M. Galkin and V. G. Chukhlantsev, *Izv. Akad. Nauk SSSR, Neorg. Mat.*, **2**, 455 (1966).
- G. Blasse and A. Bril, *J. Solid State Chem.*, **2**, 105 (1970).
- R. C. de Vries, R. Roy, and E. F. Osborn, *J. Am. Ceram. Soc.*, **38**, 161 (1955).
- L. W. Coughanour, R. S. Roth, S. Marzullo, and F. E. Senneth, *J. Res. Nat. Bur. Std.*, **54**, 195 (1955).
- N. Köppen and A. Dietzel, *Naturwissenschaften*, **56**, 460 (1969).
- B. V. Shulgin, F. F. Gavrilov, V. K. Parskin, and V. G. Chukhlantsev, *Izv. Vysshikh Uchebn. Zavedenii Fiz.*, **10**, 122 (1967); *Chem. Abstracts*, **68**, Ref. 90905e (1968).
- B. V. Shulgin, F. F. Gavrilov, V. M. Stadukhin, V. G. Chukhlantsev, and A. L. Shalyapin, *Izv. Vysshikh Uchebn. Zavedenii Fiz.*, **11**, 17 (1968); *Chem. Abstracts*, **69**, Ref. 31804u (1968).
- M. G. A. Tak and O. J. van Klinken, Private communication.
- K. Watanabe and E. C. Y. Inn, *J. Opt. Soc. Am.*, **43**, 32 (1953).
- N. Kristianpoller and D. Dutton, *Appl. Opt.*, **3**, 287 (1964).
- A. Bril and W. Hoekstra, *Philips Res. Rept.*, **16**, 356 (1961).
- A. Bril and H. A. Klasens, *ibid.*, **7**, 421 (1952).
- G. Blasse and A. Bril, *J. Solid State Chem.*, **3**, 69 (1971).
- K. H. Butler, *J. Opt. Soc. Am.*, **37**, 365 (1947).
- J. H. Schulman, R. J. Ginther, and C. C. Klick, *ibid.*, **40**, 854 (1950).
- W. L. Wanmaker, J. G. Verriet, and J. W. ter Vrugt, *J. Solid State Chem.*, **3**, 69 (1971).

A New Method for Revealing Striations in High-Resistive Floating-Zone Silicon Crystals

A. J. R. de Kock and P. G. T. Boonen

Philips Research Laboratories, Eindhoven, Netherlands

ABSTRACT

Striations were revealed by preferential etching of preannealed longitudinal crystal slices taken from high-resistive floating-zone silicon crystals. The required preannealing treatment was carried out at a temperature between 1000° and 1200°C in a tubular furnace. A model for the mechanism of striation revealing is proposed. The influence of such striations on the performance of planar diodes is briefly discussed.

Several methods have been developed during the past decade for revealing impurity striations in silicon crystals. These striations, which reflect the shape of the solid-liquid interface present during crystal growth, can easily be made visible in heavily doped material by means of the pulsed copper-plating technique (1) or by preferential etching (2). For intermediate resistivities (1-100 ohm-cm) some special etching techniques with mixtures of HF-HNO₃ have been described (3, 4). Recently Kämper (5) has reported on a rather complicated method consisting of a series of successive etching treatments which can be applied to high-resistive floating-zone silicon.

In the present paper a new and simple method is described for revealing striations in high-resistive silicon crystals.

Experimental Procedure

The experimental procedure for revealing striations is as follows. Longitudinal slices, cut from the crystals to be investigated, are polished or chemically etched in order to remove any surface damage and subsequently annealed for a few hours in a tubular furnace at a temperature of between 1000° and 1200°C. After annealing a surface layer is removed from the slices by chemical etching or polishing. This is done in order to prevent the formation of a haze during the final step of the process, which consists of preferential etching for a few minutes with the CrO₃ etchant described by Sirtl and Adler (6). The preferential etching treatment reveals striations on the longitudinal sections, which are clearly visible under a normal optical microscope. No striations become visible if no annealing treatment is carried out prior to etching. The related spiral pattern formed on the surface of cross-sectional slices is less sharply defined, however. In those regions where the solid-liquid interface is nearly parallel to the cross-sectional surface no spiral pattern is formed during etching.

Results

The striations in a variety of floating-zone crystals have been examined. The electrical resistivity of the available crystals was in the range of 5-1500 ohm-cm, whether n-type or p-type. Crystals with high dislocation densities as well as dislocation-free crystals were used. The dislocation-free material contained either a striated distribution of vacancy clusters (7, 8) or was grown under such conditions that cluster formation was prevented (8). Independent of the level of doping, striations could be revealed in all those crystals. Some examples are shown in Fig. 1 and 2. Although clearly visible, the striation etch pattern in heavily dislocated crystals was less pronounced than in dislocation-free material. Furthermore, preferential etching also reveals dislocations. The dislocation etch pits formed

disturb the striation pattern in crystals containing high dislocation densities ($> 10^4 \text{ cm}^{-2}$).

The environment in which the annealing treatment can be carried out was found to be of minor importance. In most experiments nitrogen was used, but comparable results were obtained with argon or a mixture of nitrogen and water vapor, the latter causing oxidation of the samples. Good results were obtained with an annealing temperature of 1150°C. The minimum annealing time necessary for revealing of the striations was found to depend on the typical crystal, but not on the level of doping. However, a

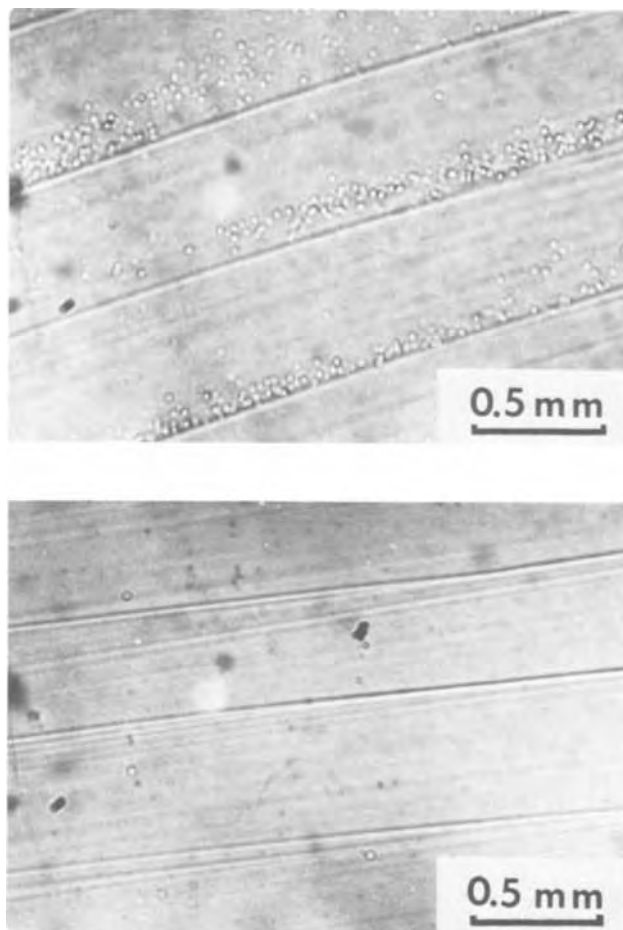


Fig. 1. Longitudinal sections of a dislocation-free floating-zone crystal grown in vacuum. Average distance grown per revolution: 0.5 mm. Resistivity: 100 ohm-cm, n-type. (a, upper) Annealed at 1000°C in nitrogen for 16 hr. Preferential etching (10 min) reveals striations and vacancy clusters. (b, lower) Annealed at 1150°C in nitrogen for 4 hr. Preferential etching (10 min) reveals striations only.

Key words: silicon, single crystals, impurity striations, planar devices.

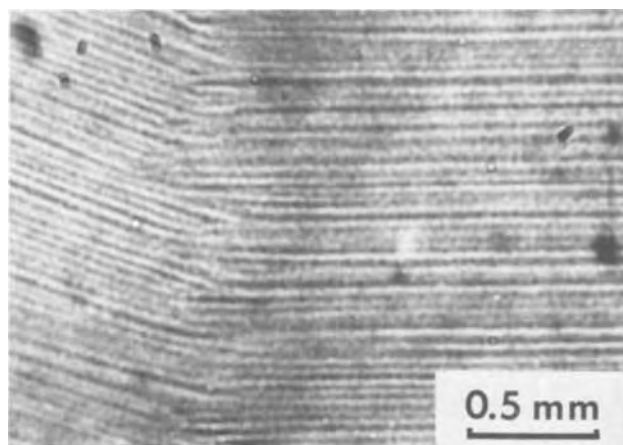


Fig. 2. Longitudinal section of a dislocation-free pedestal-pulled crystal grown in argon. Average distance grown per revolution: 0.03 mm. Resistivity: 208 ohm-cm, p-type. Anneal at 1150°C in nitrogen for 4 hr. Preferential etching (10 min). The solid-liquid interface exhibits a central (111) facet.

4-hr annealing treatment was found to be sufficient for all the crystals investigated. Although the cooling rate after annealing was not critical, the best results were obtained if the samples were cooled at a relatively slow rate (*e.g.*, from 1150° to 700°C in 15 min).

If the slices are coated with a layer of phosphorus glass prior to annealing, no striations are observed. It is well known (9) that such a glass layer prevents the penetration of metallic impurities, which are always present in a resistance-heated furnace, into the samples. If the annealing treatment is carried out in a rf-heated epitaxial reactor in an atmosphere of purified hydrogen, again no striations are revealed after subsequent preferential etching. In an epitaxial reactor contamination of the samples with metallic impurities is much less than in a resistance-heated furnace.

The method was also applied to a number of Czochralski-grown crystals with resistivities between 5 and 10 ohm-cm, whether n-type or p-type. In some of these crystals the striation pattern could be revealed easily, whereas this pattern was completely absent in some others.

Discussion

Neither the level of doping nor the type of dope used has any significant influence on the visibility of the striation etch pattern. It seems likely, therefore, that other impurities with distribution coefficients differing from unity, such as oxygen [$k \sim 0.5$ (10)] or carbon [$k \sim 0.1$ (11, 12)], play an essential part in the mechanism of striation revealing. Furthermore no striations were detectable if the samples were coated with phosphorus glass or if the annealing treatment was carried out under very clean conditions in a rf-heated epitaxial reactor. This indicates that metallic impurities are essential as well.

Accordingly the following explanation for the striation formation is proposed. During annealing at the temperatures indicated, point defects, in particular vacancies, are thermally generated. These point defects will associate with impurity atoms present in the as-grown material. As discussed previously (7, 8) association of vacancies and oxygen atoms may occur, resulting in the formation of vacancy-oxygen complexes. Such complexes can only be stable, at the anneal temperatures involved, if they contain more than three oxygen atoms (7, 8, 13). The oxygen concentration exhibits a periodic variation (striations) along the growth axis, caused by the periodic variation in growth rate usually occurring. Consequently the vacancy-oxygen complexes are formed in a similarly striated pattern, although the variation in complex

concentration is much more pronounced (7, 8). During cooling of the samples after annealing, the complexes partly remain unchanged, whereas some of them capture vacancies, giving rise to the formation of tiny vacancy clusters (7, 8).

It has been established that a strong interaction exists between vacancy clusters and metallic impurities such as copper (7, 8, 14) and lithium (15). Furthermore evidence has been obtained of an interaction between metallic impurities, for instance lithium, and small vacancy-oxygen complexes such as the A-center (15-17). It seems likely, therefore, that interaction takes place also between the vacancy-oxygen complexes, formed during annealing, and the metallic impurities introduced. Because of these interactions the metallic impurities are mainly concentrated in the direct neighborhood of the above-mentioned clusters and complexes. Consequently these impurities are distributed in a striated configuration similar to that of these microdefects. It is assumed that this striated distribution of metallic impurities is finally revealed by the preferential etching treatment. These striations again reflect the shape of the original solid-liquid interface which was present during crystal growth.

This model explains the absence of striations if insufficient amounts of metallic impurities are introduced during annealing. Furthermore during annealing in hydrogen this element rapidly diffuses into the silicon slices, resulting in a decreased rate of formation of vacancy-oxygen complexes (8). In heavily dislocated material a large amount of the metallic impurities are concentrated near the line defects, because of the strong interaction between dislocations and these impurities. This partly counteracts the formation of the striations. Differences in oxygen concentration in the various crystals as well as differences in the periodic variation of the oxygen concentration result in different rates of the diffusion-limited formation of the vacancy-oxygen complexes. This explains the material

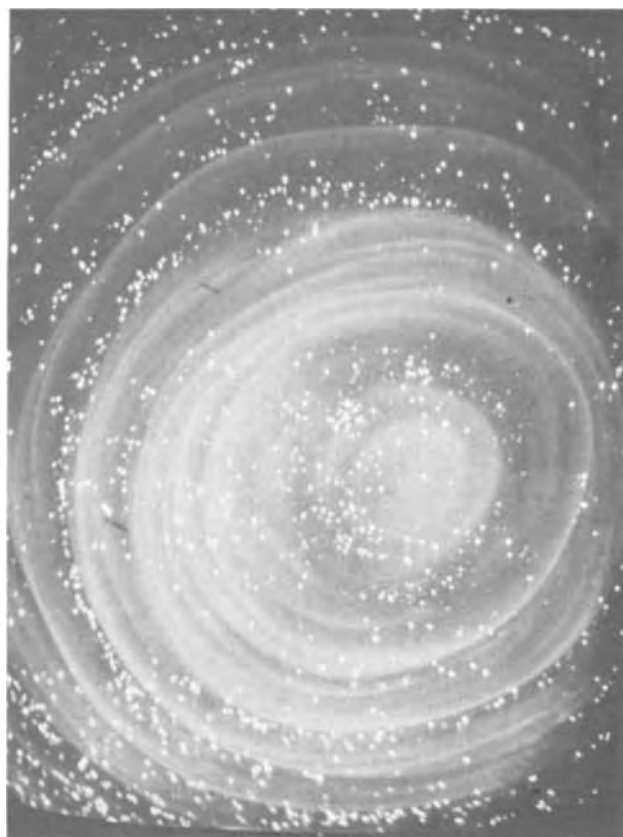


Fig. 3. TV picture obtained with a silicon vidicon containing a target of dislocation-free floating-zone silicon. Target not illuminated. Target voltage: 10V.

dependence of the minimum annealing time required for the formation of striations.

The irreproducible results obtained with crystals grown from the crucible are not well understood, but may be due to the high impurity content of these crystals. It is well known (18-20) that during high-temperature annealing precipitation of oxygen and carbon takes place in these crystals. This interferes with the vacancy-oxygen complex formation.

Influence of Striation Formation on the Performance of Planar Diodes

Planar devices are made by successive oxidation and diffusion processes. These processes are generally carried out in resistance-heated furnaces at temperatures similar to those at which the described metallic impurity striations are formed. Consequently such striations will form during the fabrication of the devices. Because the metallic impurities will partly be electrically active, these striations will particularly influence the performance of those devices made on silicon slices on which no epitaxial layer has been grown. An example of such a device is the silicon-vidicon.

Figure 3 shows the monitor picture obtained with such a silicon-vidicon TV pick-up tube. The target is made of a dislocation-free silicon slice containing vacancy clusters. As reported previously (7) the large white spots represent regions with leaky diodes caused by an interaction between metallic impurities and the grown-in vacancy clusters. However, at target voltages near the flatband voltage, slight variations in the diode leakage current occur, resulting in a clearly visible background spiral pattern. This pattern seems to be closely related to the described striated distribution of metallic impurities. It has been found (21) that an adequate getter diffusion greatly reduces the background pattern. This observation produces con-

clusive evidence that indeed metallic impurities are involved.

Manuscript received Jan. 31, 1972.

Any discussion of this paper will appear in a Discussion Section to be published in the June 1973 JOURNAL.

REFERENCES

1. J. A. M. Dikhoff, *Philips Tech. Rev.*, **25**, 195 (1963/1964).
2. F. Vieweg-Gutberlet, *Solid-State Electron.*, **12**, 731 (1969).
3. W. D. Edwards, *Can. J. Phys.*, **38**, 439 (1960).
4. T. F. Ciszek, "Semiconductor Silicon," p. 156, R. R. Haberecht and E. L. Kern, Editors, The Electrochemical Society Softbound Symposium Series, New York (1969).
5. M. Kämper, *This Journal*, **117**, 261 (1970).
6. E. Sirtl and A. Adler, *Z. Metallk.*, **52**, 529 (1961).
7. A. J. R. de Kock, *Appl. Phys. Letters*, **16**, 100 (1970).
8. A. J. R. de Kock, *This Journal*, **118**, 1851 (1971).
9. J. E. Lawrence, *Trans. AIME*, **242**, 484 (1968).
10. F. A. Trumbone, *Bell System Tech. J.*, **39**, 205 (1960).
11. E. Haas, W. Brandt, and J. Martin, *Solid-State Electron.*, **12**, 915 (1969).
12. T. N. Tucker, *This Journal*, **115**, 324C (1968).
13. J. W. Corbett, G. D. Watkins, and R. S. McDonald, *Phys. Rev.*, **135**, A1381 (1964).
14. T. S. Plaskett, *Trans. AIME*, **233**, 809 (1965).
15. A. J. R. de Kock, To be published.
16. J. W. Ferman and R. A. Swalin, in "Reactivity of Solids," p. 264, de Boer, Editor, Symposium, Amsterdam, 1962, Elseviers Publ. Co.
17. J. W. Ferman, *J. Appl. Phys.*, **39**, 3771 (1968).
18. W. Kaiser, *Phys. Rev.*, **105**, 1751 (1957).
19. I. L. Shul'pina, L. V. Lainer, M. G. Mil'vidskii, and E. P. Rashevskaya, *Soviet Physics-Solid State*, **9**, 1291 (1967).
20. V. V. Batavin, *Soviet Physics-Crystallography*, **15**, 100 (1970).
21. A. M. E. Hoeberechts, Private communication.

Ion Implantation and Annealing Effects in SiO₂ Layers on Silicon Studied by Optical Measurements

C. R. Fritzsche* and W. Rothmund

Institut für Angewandte Festkörperphysik, Freiburg i. Br., Germany

ABSTRACT

Phosphorus, arsenic, and argon ions were implanted into thermally grown SiO₂ layers with energies up to 115 keV. The effect of the implantations, its dependence upon dose, and the anneal behavior were studied by IR absorption and ellipsometric measurements. Observed effects are mainly due to radiation damage. A saturation of the damage is observed in the amorphous silica which up to now has only been observed in crystalline materials. Two annealing processes can be distinguished beginning near 100° and near 300°C. Results are compared with the annealing of SiO₂ produced by implantation. Models are proposed to describe the observed shift of absorption bands and the anneal behavior.

The effect of ion implantation on the properties of silicon dioxide layers is of interest in semiconductor device technology and studies of this topic may help to promote the basic research in amorphous materials. Some investigations have already been published reporting on ion migration, creation of traps and surface states, the improvement of the dielectric strength, and changes of the refractive index (1-4). Results show that radiation damage causes the observed effects in many cases.

* Electrochemical Society Active Member.

Key words: silicon dioxide, ion implantation, radiation damage, IR absorption.

Radiation damage in 40 keV xenon implanted amorphous SiO₂ has already been studied by Matzke (5) using electron diffraction and gas release techniques, but his work is more concerned with the behavior of damaged quartz. No information on changes in the atomic arrangements was provided by the electron diffraction measurements, and gas release studies are inherently difficult to combine with annealing.

We have therefore used optical methods, such as IR transmission spectroscopy and ellipsometry, to study how implantation and annealing alter the SiO₂ layers. This paper reports mainly on the behavior of ther-

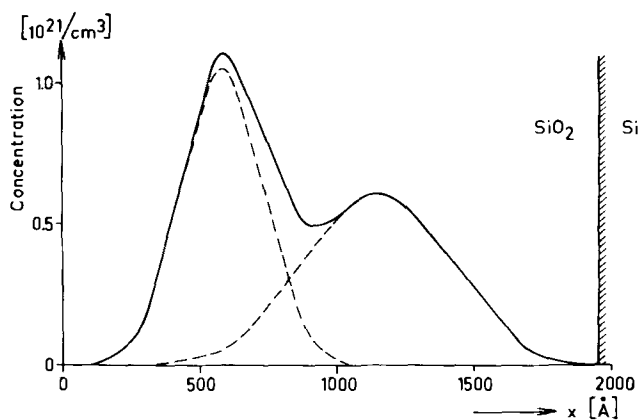


Fig. 1. Ion concentration profile after standard phosphorus implantation as calculated from LSS theory.

mally grown oxides after implantation of phosphorus. At first the dose dependence of damage production by 115 keV ions is studied. Then we describe annealing damage when 115 and 60 keV implants are made to yield an ion distribution like that shown in Fig. 1. Very high doses were chosen so that possibly formed compounds could be observed. Implantations with a lower dose or of other ions are reported also. In addition to the annealing studies we describe the formation of SiO_2 by implantation of oxygen into silicon.

While the behavior of the IR absorption after implantation can be fairly well explained, some of the annealing effects are not yet well understood.

Experimental

Silicon dioxide layers were grown thermally in dry oxygen at 1140°C on single crystal $10\ \text{ohm}\cdot\text{cm}$ p-type silicon wafers. The wafers were polished on both sides before oxidation, and both oxide layers were used for the optical absorption measurements. Layer thicknesses were chosen according to the penetration depth of the implanted ions as described below.

Implantations were made into both oxide layers of every sample, but half the area of the wafer was covered by an impermeable metal sheet so that a comparison of implanted and unimplanted material with otherwise identical properties was possible. The standard implantation used in most of the experiments was made in two steps with 115 and 60 keV, resulting in a profile as shown in Fig. 1 for phosphorus. This double implantation enlarges the range where the ion concentration is in the order of $10^{20}\ \text{cm}^{-3}$, and simultaneously keeps the concentration in the silicon low. The different heights of the two peaks resulting from the use of equal doses in both implantations is believed to be less important than the decay near the surface and the oxide silicon interface where the concentration is 2 to 3 orders of magnitude below the peak. Although no severe influence of the profiles on the results has been noticed, one should be aware that our results refer to two special profiles, the Gaussian and the one shown in Fig. 1. The optical properties were expected to depend primarily upon radiation damage. Normally the shape of the damage profile is similar to that of the ion concentration profile (6) but the peaks may be cut off by saturation.

Since the projected range R_p and the standard deviation ΔR_p , and hence the peak concentration at given energy and dose, depend upon the mass of the incident ion, it is, in principle, impossible to implant different ion species with completely identical parameters. We implanted phosphorus, arsenic, and argon and decided to keep the ion energy and the peak concentration C_R constant but to change the oxide thickness D and the implanted dose. Values were chosen so that calculated from LSS theory approximately

$$D = R_p + 3\Delta R_p \quad C_R = 6 \times 10^{20} [\text{cm}^{-3}]$$

for the 115 keV implantation. Thus the profiles for arsenic and argon can be taken from Fig. 1 by contraction in the abscissa direction proportional to R_p . In the experiments with variable dose the 60 keV implantation was omitted.

Dose was determined from the product of time and current at a beam control electrode taking into account the secondary emission of negative particles at the target as well as at the control electrode by multiplication with a correction factor. The correction was calculated from measurements with and without suppression of secondary emission before implantation. This procedure was tested by a variety of experiments with ion implanted semiconductors from which we conclude that 20% is the upper limit for discrepancies between calculated doses and real doses. The relative accuracy within a set of implantations is much better.

In all implantations with exception of the O^+ -implantation for the oxide production described later the flux was 9.3×10^{15} ions/ $\text{cm}^2 \cdot \text{sec}$ inside the beam and 1.7×10^{13} ions/ $\text{cm}^2 \cdot \text{sec}$ with respect to the implanted area. The exposure time of any point of the target during one sweep was about 5×10^{-5} sec.

No consideration was given to the charge built up in the insulating oxide. Its upper limit is given by the intrinsic breakdown voltage which is between 80 and 160V and will scarcely be reached because of the ionizing effect of the beam.

Infrared spectra were measured with a Beckman IR 9 spectrometer and the absorbance of the implanted and the unimplanted side of the sample was recorded alternately several times until the mean square deviation of the mean half width $\Delta\nu$ of the band near 9μ was close to $\pm 1\ \text{cm}^{-1}$. This was necessary because the magnitude of some effects was very close to the experimental error.

At the beginning of this work layer thicknesses were measured with an interference microscope after etching away part of the oxide and evaporation of aluminum over the etched step. Later, we used an ellipsometer and obtained in this way additional information on the refractive index. The difficulties in interpretation of both the interferometric as well as the ellipsometric measurements will be mentioned in the next section.

Results

A general demonstration of the effects of implantation and annealing is given in Fig. 2 and 3. The absorption bands normally found at 1083 and $459\ \text{cm}^{-1}$ are shifted to lower wave numbers and broadened by the implantation of phosphorus (figures) as well as arsenic and argon. The weak band at $810\ \text{cm}^{-1}$ is slightly shifted to higher wave numbers. Since this is important for interpretation and no further data are given in the figures, we present single and mean values for standard phosphorus and argon implantation in Table I.

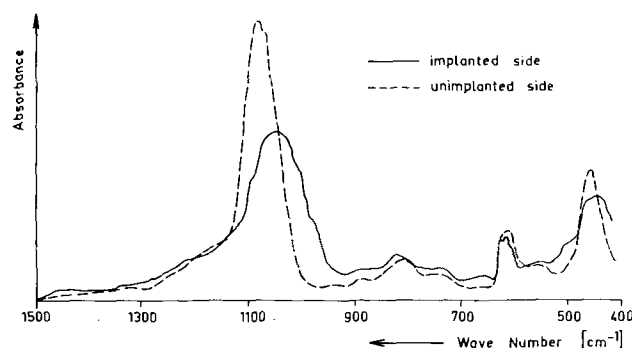


Fig. 2. Effect of phosphorus implantation on IR spectrum of SiO_2 . Room temperature implantation according to Fig. 1.

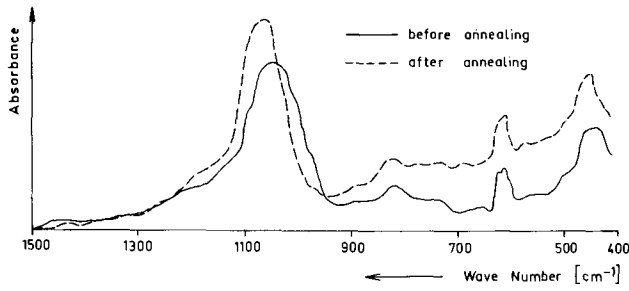


Fig. 3. Effect of 45 min 500°C annealing on IR spectrum of P⁺ implanted SiO₂. Same sample as in Fig. 2.

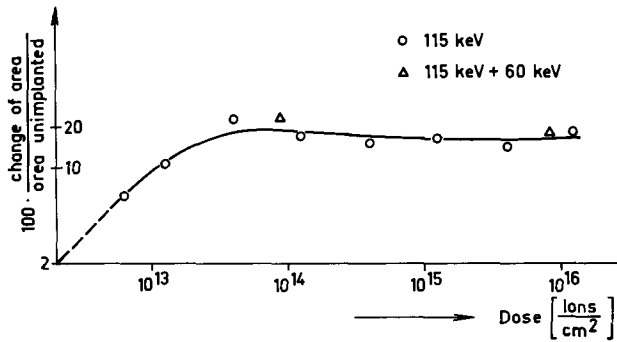


Fig. 4. Dose dependence of change in 1083 cm⁻¹ band area. P⁺ implantations.

Further effects of implantation are a decrease of the area of the 1083 cm⁻¹ band, an increase in layer thickness, and decrease of the refractive index. Annealing at several hundred degrees C alters the properties in the opposite direction as the implantation. The background absorption of the dashed curve in Fig. 3, which increases with decreasing wave number, will not be discussed in detail here. Until now it has only been observed after phosphorus implantations, and is caused by free-carrier absorption in the silicon substrate as can easily be checked after removal of the oxide. Formation of a phosphorus glass should result in an additional absorption band at 1335 cm⁻¹ (7). None of the investigated spectra showed this band even after annealing in air up to 700°C. We concentrate now on the strongest band near 1083 cm⁻¹ to which we refer as the 9μ band.

The influence of the phosphorus dose on the changes in area, peak location, and half width is shown in Fig. 4 and 5. All three curves show a saturation of the implantation effect near 10¹⁴ ions per square cm. The dashed line in Fig. 4 is purposely drawn according to proportionality of dose and loss of area. Measurements at a still lower dose would have been of little use because of the relatively high ratio of fluctuations to real change. The curve of the peak wavenumber ν_{max} resembles closely the dependence of dielectric breakdown upon dose, described elsewhere (3). The dose at which the peak appears is also in excellent agreement with reference (3).

The increase in peak wave number at very high doses is believed to be real, since it was well pronounced in a series of samples with small layer thick-

Table I. Shift of the 808 to 812 cm⁻¹ band by implantation

	Phosphorus		Argon	
	Unimplanted	Implanted	Unimplanted	Implanted
Single values	811 814	819 822 818	812 811	813 818 814
Mean value	812.5	819.7	811.5	815.0

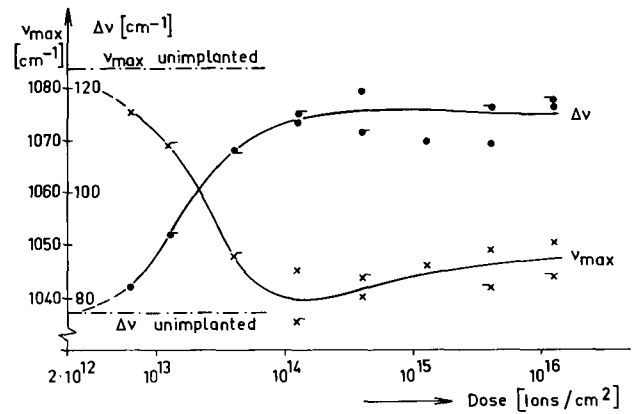


Fig. 5. Dose dependence of peak wave number ν_{max} and half width of the 9μ band. 115 keV P⁺ implantations.

nesses. Inaccuracies in layer thickness seem to cause the spreading of measurements in Fig. 5 because ΔR_p is only 268Å, and near the oxide silicon interface a path of 0.6 R_p is sufficient to change the concentration by a factor of 10 so that in the thicker layers a larger range of very low concentration exists than in the thinner ones. The little dashes at the measurement points in Fig. 5 indicate samples with thicknesses markedly different from $R_p + 3\Delta R_p$ (maximum difference 298Å). They are at the left of the points if the thickness was too high.

In the annealing experiments the double implantation illustrated in Fig. 1 was used. The dose was 4.1×10^{15} ions/cm² each for the two phosphorus implantations and thus beyond the saturation shown in Fig. 4 and 5. Possibly this is the reason, why the ν_{max} and $\Delta\nu$ values after implantation do not distinctly depend upon the profile as can be seen by comparison of the 4×10^{15} cm⁻² values in Fig. 5 (single implantation) and the initial values of Fig. 6 and 7 (double implantation). Figures 6 and 7 show isothermal annealing. After 45 min at 690°C in air the implantation effects have vanished to a high degree. Only the half width is still slightly increased. At 176°C and annealing times up to 140 min no changes in ν_{max} outside the experimental error can be observed. This was also true for arsenic and argon implantations. The half width, however, changes at this temperature. After phosphorus implantation it runs through a maximum at 176°C, while after argon and arsenic (similar to argon in Fig. 7) implantation $\Delta\nu$ decreases with increasing time even at 149°C. At a glance the result for phosphorus

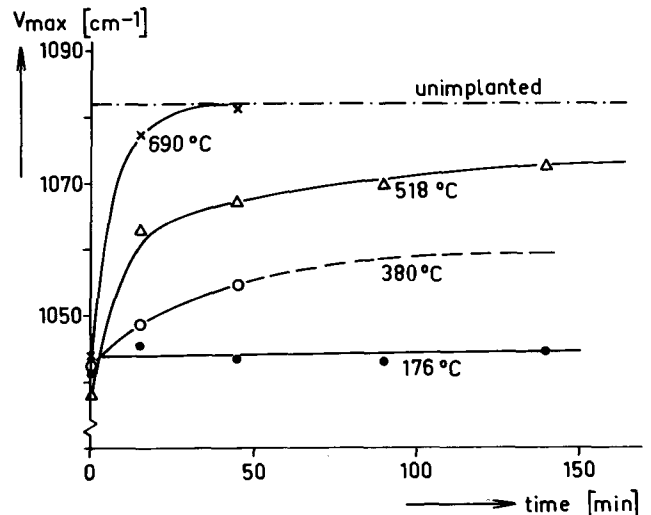


Fig. 6. Isothermal annealing after P⁺ implantation shown by the peak wave number of the 9μ band. Implantation according to Fig. 1.

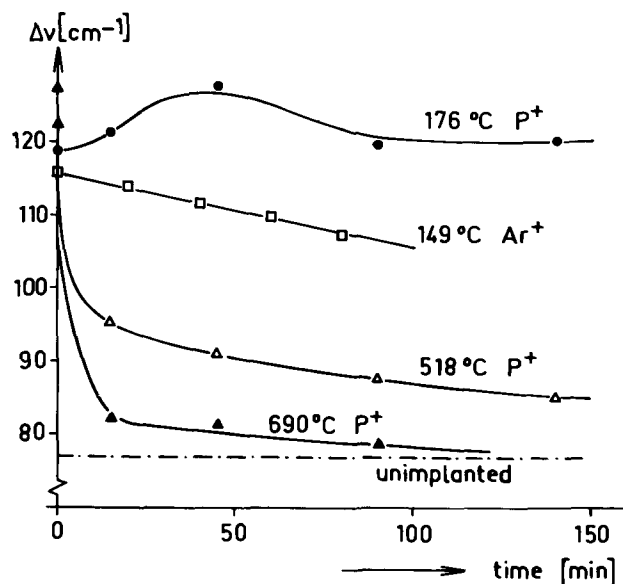


Fig. 7. Isothermal annealing after P^+ and Ar^+ implantation shown by the half width of the 9μ band. P^+ implantation according to Fig. 1. Argon dose 3×10^{15} each for the 115 and 60 keV implantation.

at $176^\circ C$ may appear somewhat dubious, particularly since an accidentally very low initial value could account for the shape of the curve. This, however, cannot happen in the case of isochronal annealing which is shown in Fig. 8. Here all points at different temperatures must be taken from different samples. We have plotted the remaining change in per cent of the initial change. For high dose phosphorus implantations all points (x and o) up to $541^\circ C$ lie above the 100% line with no exception. It is very unlikely that this had happened accidentally. The argon and arsenic implanted samples show the decrease mentioned above.

The low dose phosphorus implanted sample (\bullet) does not exceed the 100% line but lies between high dose phosphorus and argon. Some samples with single phosphorus implantation were also annealed, and part of the results has already been published (3). No significant difference between single and double implanted layers was noticed in the behavior of ν_{max} and $\Delta\nu$.

The anneal behavior of the band area is similar to that of the peak wave number shown in Fig. 6. At $700^\circ C$ the initial area is reached after 45 min. At $518^\circ C$ still 65% of the initial change are retained after 140 min. At $176^\circ C$ the area increases very slowly but, in contrast to ν_{max} , distinctly.

Interferometric measurements seem to indicate that the thickness increases with increasing dose up to 1.25×10^{14} ions/cm 2 . However, at the high doses a substantial amount of ions reach the silicon and this can

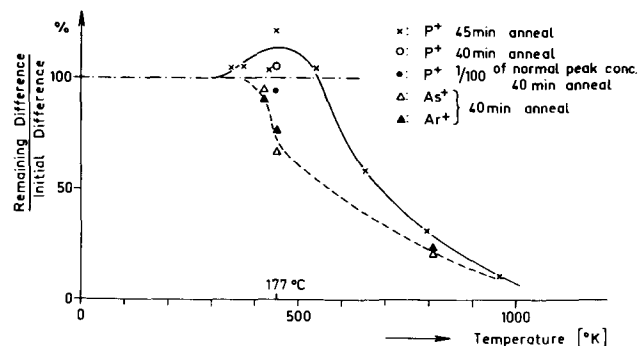


Fig. 8. Isochronal annealing shown by the half width of the 9μ band. Concentrations as in Fig. 1.

Table II. Thickness and refractive index at 5461\AA of argon implanted SiO_2 layer

Anneal time [min] at $176^\circ C$	Thickness [\AA]		Refractive index	
	Implanted	Unimplanted	Implanted	Unimplanted
0	1698	1596	1.382	1.434
20	1716	1594	1.378	1.437
40	1730	1587	1.375	1.439
60	1742	1599	1.372	1.437

Table III. Annealing of SiO_2 produced by ion implantation 30 min per step

Temperature, $^\circ C$	ν_{max} [cm^{-1}]	
	In air	In nitrogen
No anneal	1031	Not recorded
152	1030 (only 20 min)	1026
169	1030	Not performed
268	1037	Not performed
380	1041	1033
500	1047	1048
700	1074	1063

lead to considerable errors. The implanted silicon was found to be attacked by the hydrofluoric acid used for the step etching described above at least if the calculated surface concentration reaches $6 \cdot 10^{18} cm^{-3}$ and then the step to be measured is higher than the layer thickness. If the refractive index of the silicon surface changes, the ellipsometric measurements will be wrong also. We restrict ourselves therefore to the presentation of data obtained at low dose or with layer thicknesses of at least $R_p + 3.2 \Delta R_p$. Interference measurements on such samples implanted with 115 keV phosphorus showed an increase in thickness of 1.8 and 3.6% at 6.25×10^{12} and 1.25×10^{14} ions/cm 2 respectively.

Results of ellipsometric measurements after standard argon implantation are shown in Table II. The implantation has increased the thickness. Annealing at $176^\circ C$ results in a further increase. Thus interferometric as well as ellipsometric measurements show that implantation increases the thickness markedly. The refractive index is diminished on the implanted side and decreases during annealing.

As a supplement we have investigated the annealing of SiO_2 layers produced by ion implantation. O^+ ions were implanted with 70; 40; 20 keV and 1.3×10^{18} ; 8.5×10^{17} ; 5.0×10^{17} ions/cm 2 respectively into n-type silicon substrates. A low current density of $7.2 \mu A/cm^2$ at maximum was chosen because a high density may possibly result in effects similar to annealing. The peak wave number of the 9μ band after implantation as well as after annealing is given in Table III. Two samples were annealed one in air and one in nitrogen for 30 min at different temperatures. The spectra of the original and the $700^\circ C$ air annealed sample are shown in Fig. 9. The shift of the 9μ peak towards higher wave numbers begins at $268^\circ C$ which is about the same temperature at which the annealing anomalies of P^+ implanted layers disappear (Fig. 8).

Discussion

The effect of implantation on the optical properties of thermally grown SiO_2 films can partially be under-

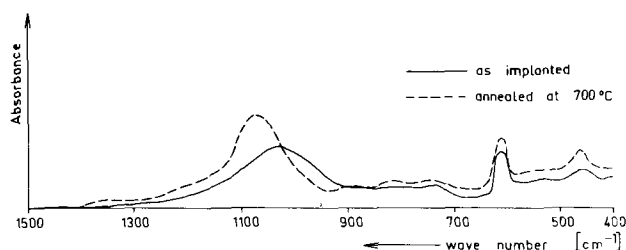


Fig. 9. IR spectra of implantation produced SiO_2 . Annealing in steps of 30 min according to Table III (air).

stood as a consequence of a decrease in density. The increase in thickness indicated in the first line of Table II is about 6%. The total implanted dose was 6×10^{15} ions/cm² into a layer containing about 10^{18} silicon and oxygen atoms/cm². Hence the increase in thickness is one order of magnitude above the increase in number of atoms/cm² and indicates a decrease in density. Pliskin and Lehman (8) investigated the optical properties of thermally grown as well as of pyrolytically deposited and heat-treated oxide layers with densities between 2.09 and 2.23 g/cm³ and found that the less dense oxides have a lower refractive index and show the 9μ band at lower wave numbers in agreement with our observations. Besides the density broken bonds may immediately contribute to the band shift as discussed below. Pliskin and Lehman describe the relationship between density ρ and refractive index n by

$$\rho = -4.784 + 4.785 n \quad [1]$$

If the volume changes only by the thickness D and the mass is constant, Eq. [1] means that in very good approximation one should find

$$(n - 1)D = C \quad [2]$$

where C is a constant. From the first and the third column of Table II we find that in the annealing experiments at 176°C our data fulfill Eq. [2] excellently with deviations in C of less than one tenth of a per cent. This shows that during 176°C annealing n is simply controlled by the density.

Primak *et al.* (9) have reported that after exposure within a nuclear reactor the density and refractive index of vitreous silica are increased in contrast to our results after ion implantation into thermally grown layers. This discrepancy may be caused by differences in the structure of the materials rather than by the different masses of the irradiated particles since Bayly and Townsed (4) found an increased refractive index independent of the ion species implanted into silica glass. On the other hand Primak *et al.* (9) report a decrease of density and refractive index in quartz after irradiation in contrast to their own results with vitreous silica. That means that even qualitatively the radiation effects depend strongly upon the structure of the solid. The loss in band area after implantation can be interpreted as a loss of absorbing oscillators because the area is proportional to the integral

$$\int \alpha_\nu d\nu = N \cdot \frac{\pi e^2 (n^2 + 2)^2}{3\mu c \cdot 9n} \quad [3]$$

where α_ν is the absorption coefficient at wave number ν , N the number of oscillators, μ the reduced mass, e the net electronic charge, and n the refractive index (11). From Table II and Eq. [3] we find, that even at the high concentrations reached by the standard implantation the change of n would change the integral by 4% while according to Fig. 4 the area changes by 19% at a dose of 6×10^{13} cm⁻². Hence most of the change can be attributed to N . Since the area increases during annealing the loss of oscillators is not due to sputtering of the oxide and may be understood as a consequence of broken bonds.

By the concept of broken bonds we get an interpretation of the opposite shift of the 1083 and 810 cm⁻¹ bands. Matossi (12) has shown that connected SiO₄ groups give two active frequencies which can be derived from a frequency of a single group by changing the mass m of the connecting atom to $m/2$ or to $m = \infty$ and that the 810 cm⁻¹ band may be derived with $m = \infty$ from the 900 cm⁻¹ due to single SiO₄ systems, while 1083 cm⁻¹ corresponds to $m/2$. Thus, if connecting oxygen atoms are thrown to interstitial sites during implantation both bands should move towards an intermediate frequency in agreement with our observations. Displacement of silicon may also contribute to the shift. Arsenic as well as argon implantations

show qualitatively the same effect as phosphorus implantations but no indication was seen that the spectra depend upon the implanted species. Therefore the curves in Fig. 4 and 5 mean that with increasing dose an increasing number of displacements is produced until at about 10^{14} incident ions per square cm, the damage saturates. Such a saturation is well known from crystalline materials but there it is accompanied by a loss of long range order and this condition was defined as "amorphous" [see Mayer *et al.* (6), pp. 98 and 99]. Our layers are amorphous already before implantation but in another sense. Their structure is glassy and can still be damaged. Nevertheless, our investigations indicate that the saturation can be caused by the impossibility of breaking all bonds or of keeping them broken and is not necessarily related to the loss of long range order. It is commonly assumed that in amorphous silica the SiO₄ tetrahedrons form rings and the number of sides of the resulting polygons is close to 5 (13). From the maximum loss of about 20% shown in Fig. 4 and from Eq. [3] one may guess that saturation is reached when approximately every ring contains one damaged tetrahedron. From the specific weight of 2.2 g/cm³ and the layer thickness of 1950 Å a number of about $4 \cdot 10^{17}$ SiO₂ groups per cm² results. Thus, below saturation the number of displacements per incident 115 keV phosphorus ion is in the order of 10^3 which is the value to be expected (6).

The annealing experiments show at least two different processes. Figures 7 and 8, Table II, and the measurements of band area show that slightly above 100°C the atoms begin to change their places while Fig. 6 shows no indication that the network reorders to its initial structure. Possibly it is a recombination of interstitials and vacancies which is going on at these low temperatures. An annealing process in the same temperature range was also observed by Fahrner and Goetzberger (2) who found that surface states produced by 30 keV implantation of 10^{13} cm⁻² N⁺ ions into MOS structures begin to anneal at about 130°C and disappear at 300°C within 2 hr. We hesitate to interpret the increase in $\Delta\nu$ observed in phosphorus implanted samples since the determination of $\Delta\nu$ needs the assumption of a zero level which may be influenced by the overlap of bands and the free carrier absorption shown in Fig. 3. But, whatever the reason for the broadening may be, it is a special feature of the phosphorus implantation. Possibly the phosphorus is transiently incorporated into the silicon oxygen network while arsenic and argon are not.

In all annealing experiments above 268°C, all the investigated properties of the oxide alter in direction to their initial values. The behavior suggests that in amorphous silica the SiO₄ tetrahedrons tend to an arrangement which is not completely at random. The partial order may break down with increasing damage in a certain analogy to the formation of an amorphous layer in implanted crystals. The order is probably not yet present in implantation produced or in anodically grown oxides. The latter show a spectrum similar to that of damaged thermal SiO₂ and are not much influenced by implantation (3). The temperature at which the rearrangement begins is surprisingly low and demonstrates the necessity of using low beam currents if one wants to study the process of oxide formation by the ion beam itself separately from the effect of heat. From other work (2) where our implantation machine was used and distinct annealing effects were observed between 100° and 150°C we estimate that 130°C is an upper limit for the wafer temperature reached during our implantations. Freeman *et al.* (10) have used 1 mA/cm² and reached a wafer temperature of 600°C. They find the 9μ band at about 1059 cm⁻¹ in good agreement with our data in Table III.

As to the formation of phosphorus glass by implantation three reasons for the nondetection of the $P = 0$ band at wave number 1335 cm⁻¹ are taken into con-

sideration. Either the range where the phosphorus concentration is sufficiently high was too small, the anneal temperatures were too low, or additional oxygen is necessary. We do not believe that the non-detection is caused by the choice of transmission instead of reflectance measurements because this choice was made in accordance with the work of Fraenz *et al.* (7) who found the band very pronounced in transmission.

Results

The interdependence of density, refractive index and IR absorption of thermally grown SiO₂ layers on silicon after ion implantation or subsequent annealing above 300°C resemble the results of Pliskin and Lehmann (8) in the sense that implantation decreases, and high temperature annealing increases the density. The opposite shift of the bands at 1083 cm⁻¹ and 810 cm⁻¹ supports the Matossi model (12) for the vibration of linked groups of atoms. The number of bonds which remain broken after implantation is restricted. In the damaged material single atoms can move at temperatures near 100°C. Rearrangement of the initial structure begins slowly near 300°C, and at 700°C most of the change is finished within 45 min. High dose phosphorus implantations do not result in the formation of a phosphorus glass but at slightly elevated temperature transient reactions of the phosphorus with the damaged oxygen-silicon network seem to take place.

Acknowledgments

Thanks are expressed to H. Seelewind and G. Sixt for their assistance and aid in the optical measurements, to A. Axmann and J. Schaub who carried out the implantations, K. Eisele who took care of the

oxidations and to W. Haydl for his suggestions concerning the manuscript.

Manuscript submitted Oct. 7, 1971; revised manuscript received May 10, 1972.

Any discussion of this paper will appear in a Discussion Section to be published in the June 1973 JOURNAL.

REFERENCES

1. C. R. Fritzsche, A. Goetzberger, A. Axmann, W. Rothemund, and G. Sixt, *Radiation Effects*, **7**, 87 (1971).
2. W. Fahrner and A. Goetzberger, 2nd Internat. Conf. Ion Implantation, Garmisch-Partenkirchen (1971).
3. C. R. Fritzsche, A. Axmann, and H. Seelewind, "Proc. Europ. Conf. Ion Implantation, Reading 1970," p. 123, Peregrinus Ltd., Stevenage, England.
4. A. R. Bayly and P. D. Townsed, "Proc. Europ. Conf. Ion Implantation, Reading 1970," p. 120, Peregrinus Ltd., Stevenage, England.
5. H. J. Matzke, *Phys. Status Solidi*, **18**, 285 (1966).
6. J. W. Mayer, L. Erikson, and J. A. Davies, "Ion Implantation in Semiconductors," Academic Press (1970).
7. I. Fraenz, W. Langheinrich, and K.-H. Loecherer, *Telefunken-Zeitung*, **37**, 194 (1964).
8. W. A. Pliskin and H. S. Lehman, *This Journal*, **112**, 113 (1965).
9. W. Primak, L. H. Fuchs, and P. Day, *Phys. Rev.*, **92**, 1064 (1953).
10. J. H. Freeman, G. A. Gard, J. H. Stephen, and F. B. Whiting, "Proc. Europ. Conf. Ion Implantation, Reading 1970," p. 74, Peregrinus Ltd., Stevenage, England.
11. W. Kaiser, P. H. Keck, and C. F. Lange, *Phys. Rev.*, **101**, 1264 (1956).
12. F. Matossi, *J. Chem. Phys.*, **17**, 679 (1949).
13. H. A. Robinson, *J. Phys. Chem. Solids*, **26**, 209 (1965).

Properties of Ammonia-Free Nitrogen-Si₃N₄ Films Produced at Low Temperatures

R. Gereth and W. Scherber

AEG-Telefunken, Semiconductor Division, Heilbronn, Germany

ABSTRACT

Thin Si₃N₄ films are deposited on silicon substrates by the reaction of SiH₄ and N₂ in an rf glow discharge at substrate temperatures between 25° and 500°C. These films are hereafter referred to as "nitrogen-Si₃N₄ films." At optimum growth conditions an index of refraction of 2, a breakdown field strength of 10⁷ V/cm, a flatband surface charge of 1.5 × 10¹² cm⁻², and a very high stability against bias temperature stress is obtained. With changing SiH₄ concentration the stoichiometry of the nitride films can be varied between highly nitrogen-rich and silicon-rich films resulting in a corresponding wide variation of physical and electrical film properties. Hysteresis-free and highly stable MNS varactors can be accomplished by an *in situ* glow discharge exposure in H₂ and N₂ atmosphere, respectively.

During the past years many publications (1-8) have been concerned with the outstanding properties of Si₃N₄ films for semiconductor applications. Most Si₃N₄ films investigated thus far have been fabricated from ammonia and silane or another appropriate Si-compound. It is surprising that nobody tried to produce Si₃N₄ films by simply starting from N₂ and SiH₄, since handling and purification of ammonia is very difficult. The gases N₂ and SiH₄ are easily available in an extremely pure grade. Therefore, they should represent

the ideal starting materials for the fabrication of ultra-clean Si₃N₄ films.

After completion of the present investigation it was learned that Kuwano (9) mentioned in 1968 that Si₃N₄ could possibly be formed out of SiH₄ and N₂. Off hand, the reaction looks rather simple but it does not take place under normal conditions. To overcome this difficulty the reaction was allowed to proceed in the presence of an rf glow discharge. This way, very good Si₃N₄ films could be fabricated at temperatures below 400°C starting from SiH₄ and N₂.

It is the purpose of the present paper to describe the new low-temperature Si₃N₄ films which for the sake of

Key words: silicon nitride films, semiconductor technology, low-temperature device passivation, glow discharge, chemical vapor deposition.

simplicity are referred to as "nitrogen-Si₃N₄ films." Using the equivalent terminology the standard pyrolytic Si₃N₄ films made out of SiH₄ and NH₃ are referred to as "ammonia-Si₃N₄ films."

The first part of the paper deals with the experimental results. Both the physical and the electrical properties of the nitrogen-Si₃N₄ films and their dependence on deposition parameters are described. The second part discusses the experimental film data. A comparison between ammonia- and nitrogen-Si₃N₄ films is made. A summary of the most interesting features of the new nitrogen-Si₃N₄ films concludes the paper. A preliminary brief report about the present work has been published (10).

Experimental Results

Deposition apparatus.—The standard pyrolytic deposition of Si₃N₄ films requires relatively high reaction temperatures in the range from 600° to 900°C and the use of ammonia, which cannot easily be purified from water residues and alkali contaminants. The new Si₃N₄ deposition method employs only SiH₄ and N₂ as reaction partners. The nitrogen-Si₃N₄ films are deposited in an rf glow discharge at temperatures below 500°C.

Figure 1 illustrates the nitrogen-Si₃N₄ deposition reactor. It is a high vacuum-tight apparatus because the affinity of SiH₄ to O₂ is many orders of magnitude greater than the affinity of SiH₄ to N₂, meaning that small amounts of O₂ in the apparatus are completely deposited in the nitride layer. The entire gas flow system is made of welded stainless steel pipes with high vacuum connections. A diffusion pump is used to check the tightness of the system at any time. The system can be pumped down to an ultimate pressure of 10⁻⁶ Torr.

The gases SiH₄, N₂, and H₂ contain less than 1.5 ppm H₂O or O₂. SiH₄ was used in two different dilutions, namely 1.5% SiH₄ in He and 2% SiH₄ in N₂. These two gas mixtures are characterized by the following notations: SiH₄ (He) and SiH₄ (N₂), respectively. The volume ratio SiH₄/N₂ in the reaction chamber can be varied from 10⁻⁴ to 0.15 by mixing the SiH₄ gas with a separate N₂ stream. The working pressure during nitride deposition is controlled by the inlet valves while the rotary pump is running at constant pumping rate.

The reaction chamber consists of a horizontal quartz tube, 90 cm long with a diameter of 7 cm. The wafer carrier also is made of quartz. It is resistance heated and covers an area of 4 × 11 cm. The glow discharge inside the reaction chamber is excited by an rf coil or two capacitor plates located outside the quartz tube. The rf generator is operating at a frequency of 500 kHz. The heating filament of the wafer carrier is arranged perpendicular to the direction of the electric field in both modes avoiding variation of substrate temperature with the rf field strength.

The nitride films are deposited on polished p-type silicon wafers cut parallel to the (111) plane and hav-

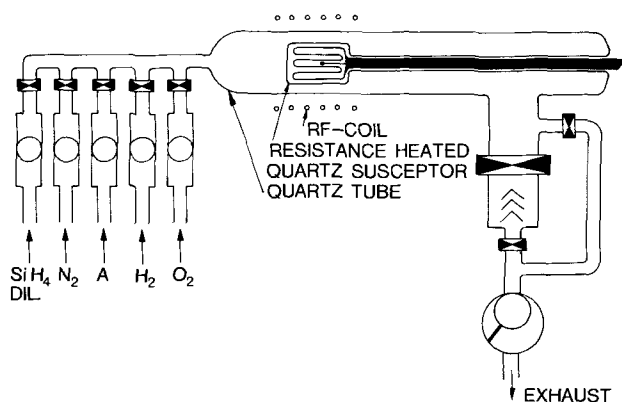


Fig. 1. Silicon nitride deposition apparatus

ing a resistivity of 500 ohm-cm. The wafers are pre-cleaned in HF and hot HNO₃ with intermediate rinses in deionized water.

Measuring techniques.—Nitride thickness and index of refraction are measured by means of an ellipsometer. Nearly all experiments are conducted with 600-1000Å thick films. Samples for electrical evaluation are supplied with evaporated aluminum dots having a diameter of 0.4 mm on the nitride side. Capacitance measurements are made using a 100 kHz bridge with 10 Hz bias sweep. The C-V plots are automatically displayed on a cathode-ray tube.

Growth rate.—The growth rate of the nitrogen-Si₃N₄ films is a linear function of the rf power. Between 100 and 700W the growth rate increases from zero to 400 Å/min. For the present investigations an rf power slightly above 100W is used. Substrate temperature and total pressure have no remarkable influence on the growth rate.

Figure 2 shows the rate of film deposition vs. SiH₄/N₂ ratio at constant rf power for the SiH₄(N₂) (results denoted by solid circles) and the SiH₄(He) system (results denoted by open circles). If SiH₄ is diluted in He an increase of the SiH₄/N₂ ratio means a dilution of both reaction partners. Therefore, the growth rate remains nearly constant.

The growth rate can be enhanced substantially by an addition of a small amount of hydrogen to the gas mixture. The effect is not yet completely understood but it is very useful to get sufficient growth rate at extreme low power setting. No variation of film properties with presence of hydrogen could be observed.

The uniformity of film thickness across the wafers is excellent if the glow discharge is induced by two parallel field plates. Variation of film thickness across a 1 in. wafer is typically ±5%. Using the cylindrical rf coil rather good uniformity can be achieved only by an optimum combination of rf power and gas pressure.

Pinhole density.—Pinholes in the nitride films are detected by a special etchant consisting of 17 ml ethylenediamine, 3g pyrocatechol, and 8 ml water. The etchant penetrates the nitride films through smallest pinholes and attacks the silicon substrate. The pinhole density is extremely sensitive to the preceding cleaning procedures. *In situ* glow discharge treatments in N₂, Ar, H₂, or O₂ are most effective. Furthermore the pinhole density can be reduced with decreasing rf power. The extreme increase of deposition time at low power setting can be compensated by the addition of hydrogen mentioned above.

The nitrogen-Si₃N₄ films deposited at minimum power exhibit less than 10 pinholes per mm². This value depends strongly on the preceding fabrication steps like polishing, cleaning, and rinsing procedures.

Substrate temperature, silane concentration, dilution, pressure, and film thickness do not affect the pinhole density.

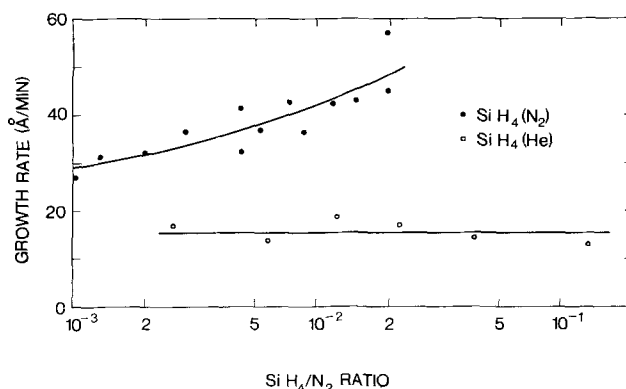


Fig. 2. Growth rate as a function of SiH₄/N₂ ratio for the SiH₄(N₂) and the SiH₄(He) system.

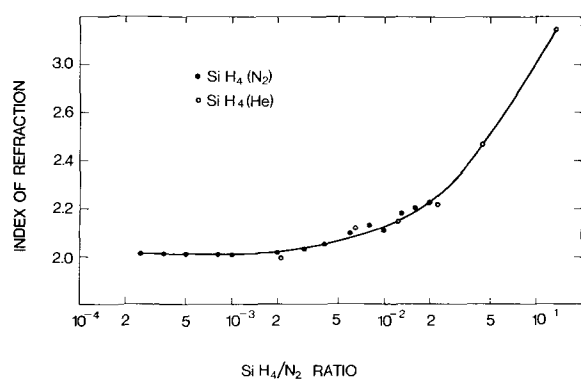


Fig. 3. Index of refraction as a function of SiH₄/N₂ ratio for the SiH₄(N₂) and the SiH₄(He) system.

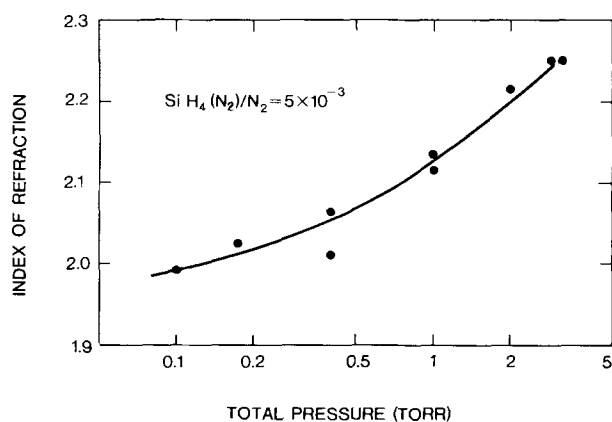


Fig. 4. Index of refraction as a function of total pressure

Optical properties.—The index of refraction of the nitrogen-Si₃N₄ films has been measured as a function of the SiH₄/N₂-ratio (Fig. 3), total pressure in the reaction chamber (Fig. 4), and substrate temperature (Fig. 5). The rising index of refraction for SiH₄/N₂ ratios above 2×10^{-3} is thought to be caused by the increasing Si content as is discussed later. Because of the strong dependence of the index of refraction on the total gas pressure, most of the films employed in the present experiments have been produced at a constant pressure of 1 Torr. Figure 5 suggests that nitrogen-Si₃N₄ films produced at substrate temperatures between 350° and 500°C have the same index of refraction. Unless otherwise noted constant substrate temperature of 350°C has been chosen.

The infrared transmission spectrum between 2.5 and 20 μ is shown in Fig. 6. A broad absorption peak lies between 9.5 and 14 μ with a maximum at 12 μ. This is very similar to the IR absorption peak of pyrolytic

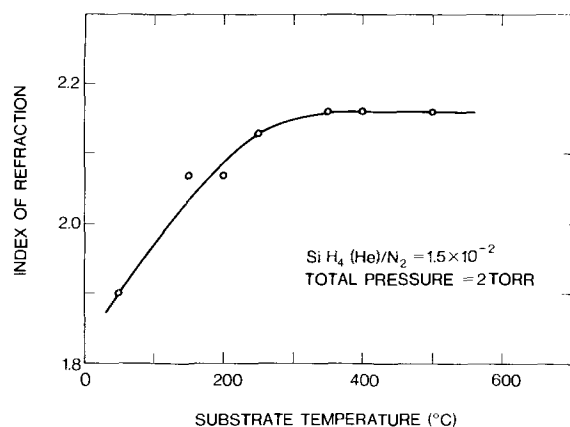


Fig. 5. Index of refraction as a function of substrate temperature

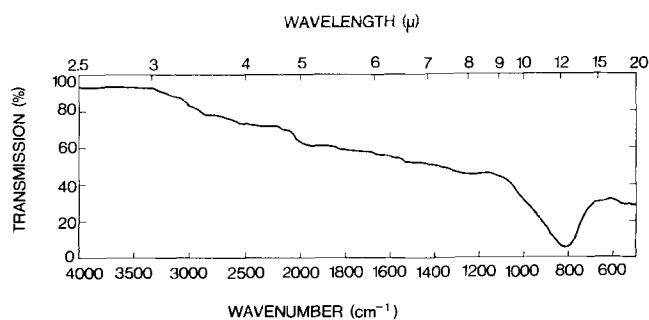


Fig. 6. Typical infrared transmission spectrum

nitride films deposited from SiH₄ and NH₃ at 700°C. Ammonia-free nitride films seem to be very pure. No SiO₂ component at 9.4 μ could be detected on any sample, unless the reactor was leaky. Other possible compounds like Si ≡ N at 4.7 μ, Si-H at 4.7 μ, N-H at 3.0 and 6.4 μ, and Si-NH-Si at 8.6 μ cannot be detected by IR in the nitrogen-Si₃N₄ film. This simplicity in structure is not usual in films starting from ammonia or in sputtered silicon nitride films.

A shift of the maximum absorption peak to shorter wavelengths is observed with increasing substrate temperature and decreasing SiH₄/N₂ ratio. Our data on this subject are fully comparable to those given by Kuwano (12).

Etch rate.—Similar to ammonia-Si₃N₄ films the etch rate of nitrogen-Si₃N₄ films produced in the glow discharge is strongly dependent on the highest temperature the films are subjected to. The etch rates in buffered and diluted HF are shown in Fig. 7 as a function of substrate temperature. The strong apparent densification effect can be usefully employed in device fabrication: deposition temperatures up to 300°C guarantee easy etching of the nitride film and post-annealing steps at temperatures as high as 1000°C produce adequate chemical resistance. The variation of etch rate with the SiH₄/N₂ ratio is shown in Fig. 8 by the open circles. Maximum values are obtained at 1.5×10^{-3} SiH₄(N₂)/N₂. The solid line in Fig. 8 gives the ratio of nitrogen to silicon atoms in the films as determined from back-scattering experiments (11). The higher the silane concentration in the reaction chamber, the higher is the Si concentration in the deposited nitride film. A SiH₄/N₂ ratio of 1.5×10^{-3} results in films with a N/Si value of 1.33 as calculated for Si₃N₄. It is interesting to note that a decrease in etch rate was observed for both silicon-rich and nitrogen-rich nitride films.

Dielectric breakdown.—The breakdown field strength of the nitrogen-Si₃N₄ films prepared at 350°C has a value of 10⁷ V/cm (Fig. 9). It is constant over a wide variation of gas composition. Above 2×10^{-2} SiH₄(He)/N₂ it deteriorates due to the Si enrichment

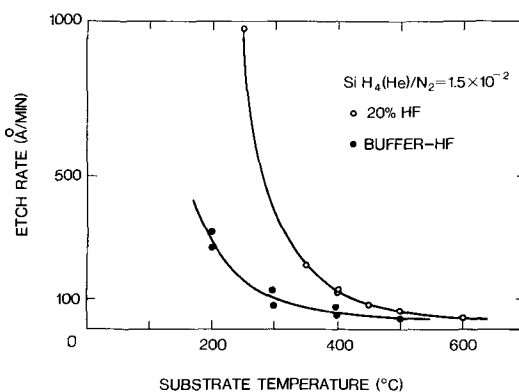


Fig. 7. Etch rate in buffered HF and in 20% HF as a function of substrate temperature.

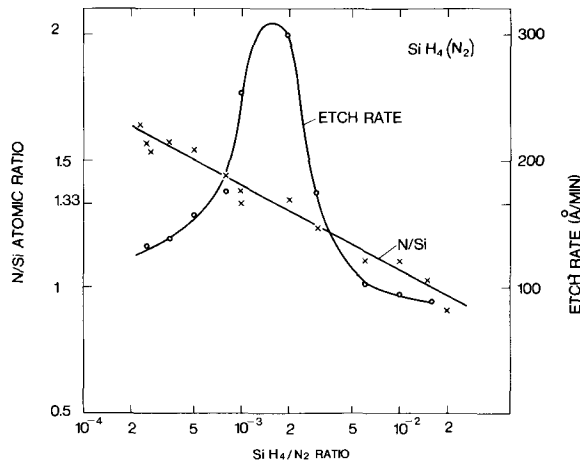


Fig. 8. Etch rate in 20% HF and N/Si atomic ratio as a function of SiH₄/N₂ ratio.

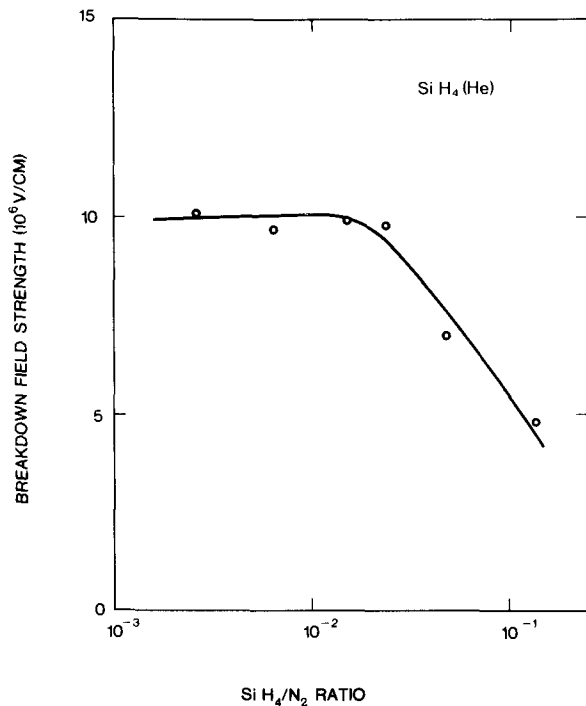


Fig. 9. Breakdown field strength as a function of SiH₄/N₂ ratio

in the film. An increase in substrate temperature from room temperature to 400°C drastically improves the breakdown field strength (Fig. 10).

C-V measurements.—The capacitance of metal-nitride-silicon (MNS) structures monitored as a function of applied bias yields the well-known C-V curves illustrated in Fig. 11. The flatband voltage is a measure of the electrical charge contained in the entire system. One talks about a hysteresis effect if the C-V curve is split during the sweeping cycle. During the present experiments the bias was automatically varied 10 times per second between minus and plus 50V. The hysteresis effect is normally related in the literature (13) to the existence of a thin natural oxide layer between Si₃N₄ and Si. Traps are located at the interface between oxide and nitride. These traps are charged and discharged during the C-V measurement causing the hysteresis of the C-V curve. The charge transport through such thin oxide layers occurs by tunneling (14).

C-V measurements have been employed to explore the influence of an *in situ* glow discharge precleaning step on the properties of the nitrogen-Si₃N₄ films.

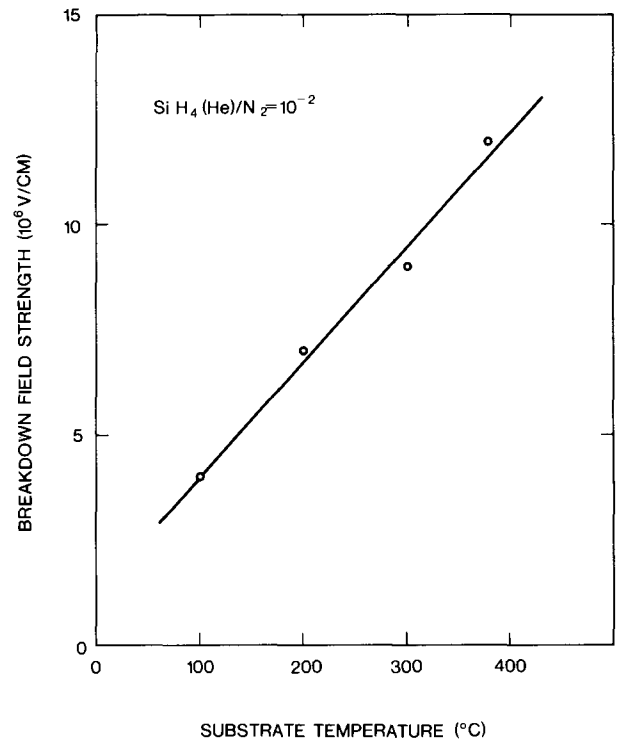


Fig. 10. Breakdown field strength as a function of substrate temperature.

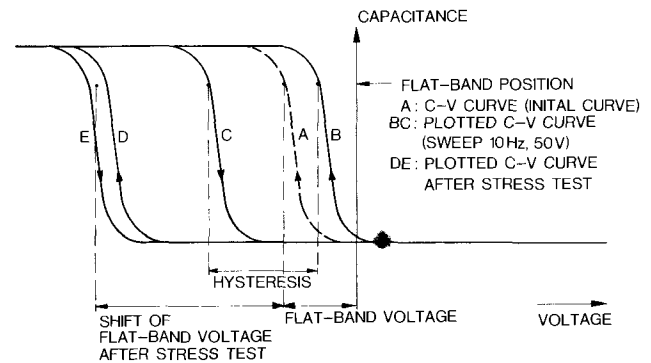


Fig. 11. MIS capacitance measurements. Definition of parameters

Prior to the actual deposition cycle the wafers are exposed to a glow discharge treatment of 30 min at temperatures of 350°C. Interesting results are obtained by this treatment. Figure 12 lists some of them. The empty rectangles illustrate the flatband voltages measured on samples pretreated in N₂, A, H₂, O₂, and those without pretreatment. There is no major effect visible. Only an O₂ glow discharge pretreatment reduces the flatband voltage to values corresponding to a flatband charge below 10¹² cm⁻².

The picture is different for the hysteresis effect. No hysteresis can be observed on samples whose surface has been treated in a H₂ glow discharge just prior to the nitride deposition. The O₂ glow discharge produces a rather pronounced hysteresis of opposite sign. The resulting C-V curve resembles that one shown in Fig. 11 if the directions of starting and returning curve are interchanged.

Figure 12 also contains the results of a bias stress test. The shift of the flatband voltage was registered after a potential of -30V has been applied for 1 min to the metal contact of the MNS structures. Essentially no shift of the flatband voltage was observed on N₂ treated samples. Again after an O₂ treatment the behavior of the test sample is inverted, the shift of the flatband voltage being in the opposite direction.

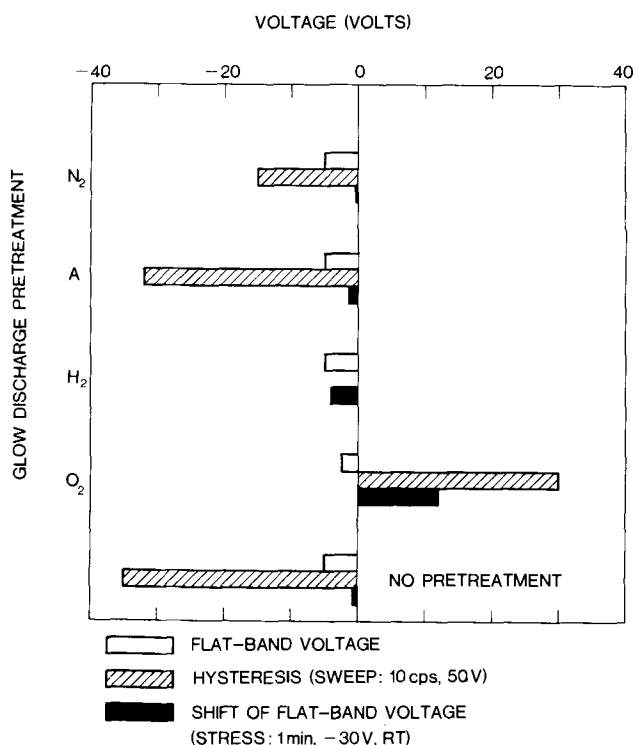


Fig. 12. Effect of glow discharge pretreatment on flatband voltage, hysteresis, and stability of different discharge atmospheres.

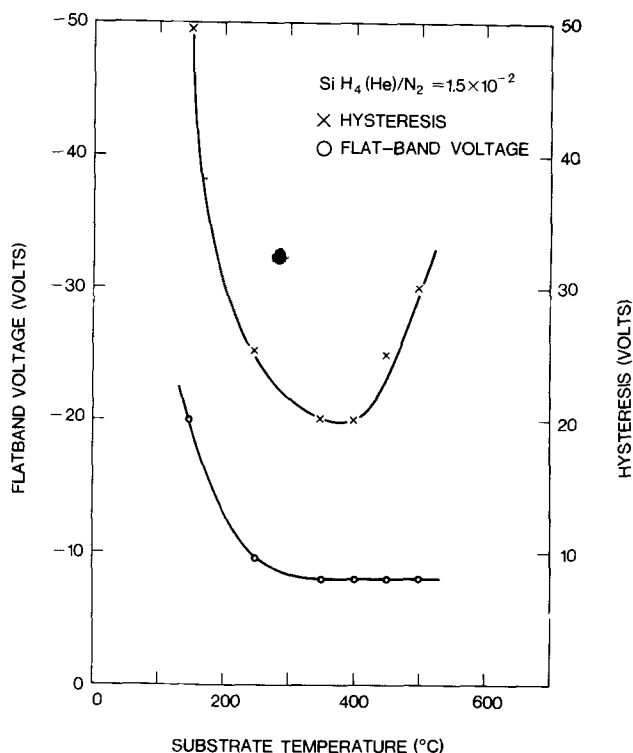


Fig. 13. Flatband voltage and hysteresis as a function of substrate temperature.

Figure 13 reveals the relationship between flatband voltage, hysteresis, and substrate temperature during film production. Temperatures of 350° to 400°C are necessary to bring hysteresis and flatband voltage to their minimum values. A variation of the SiH_4/N_2 ratio has no influence on the flatband voltage. The hysteresis, however, exhibits a maximum value in the range between 10^{-3} and $5 \cdot 10^{-3}$ SiH_4 content (see Fig. 14). In Fig. 15 results of bias temperature stress tests on

MNS samples fabricated with different SiH_4/N_2 ratios are shown. The shift of flatband voltage was measured after a negative field of 2×10^6 V/cm has been applied to the metal contact for 10 min at 200°C. Again the SiH_4/N_2 ratios between 10^{-3} and 4×10^{-3} yield optimum results in analogy to the above described measurements of physical properties.

Discussion

The various experimental results are widely consistent among each other and allow a clear picture to be drawn of the investigated nitrogen- Si_3N_4 films. The most striking fact is the strong dependence of nearly every film property on the gas composition. Therefore, controlling of gas flow and pressure must be done very carefully and reliably to achieve constant film deposition. In the pure $\text{SiH}_4(\text{N}_2)$ system, SiH_4/N_2 ratios of 10^{-3} to 3×10^{-3} yield N/Si ratios in the film of 1.25 to 1.4 and maximum etch rates (Fig. 8) both revealing good Si_3N_4 stoichiometry. The measurements of index of refraction, infrared absorption, electrical stability, and C-V hysteresis confirm this result. In comparison, the pyrolytic deposition of Si_3N_4 out of SiH_4 and NH_3 is less sensitive to gas composition: the silane concentration can be increased up to nearly 10% without changing the film qualities (5, 8). The required greater excess of N_2 in the ammonia-free deposition method results from the higher activation energy of N_2 compared to NH_3 .

In the $\text{SiH}_4(\text{He})$ system, both the SiH_4 and the N_2 partial pressures are reduced, which decreases the nitride growth rate as can be seen in Fig. 2. Both curves of growth rate in Fig. 2 cannot be extrapolated to the origin. For the $\text{SiH}_4(\text{N}_2)$ system this behavior can only be interpreted as follows. Already at the lowest silane concentration the reaction is limited by the nitrogen concentration or, strictly speaking, by the concentration of activated nitrogen atoms.

Substrate temperature is an important deposition parameter. The minimum temperature necessary to grow good quality films lies around 350°C. This conclusion can best be derived from the measurements of the index of refraction (Fig. 5). At higher substrate temperatures the films become denser. The etch rate reduces and the infrared absorption peak shifts to shorter wavelengths. The hysteresis, however, increases (Fig. 13). This latter effect is not yet fully understood. Kuwano (12) also observed an increased hysteresis effect while using a substrate temperature of 500°C instead of 300°C. He suggested that ionized Si atoms might be responsible for the increased hysteresis effect. In light of the present new results which show that the index of refraction remains constant above 350°C (Fig. 5) and the hysteresis drops at higher silane concentrations (Fig. 14) the above explanation must be reconsidered.

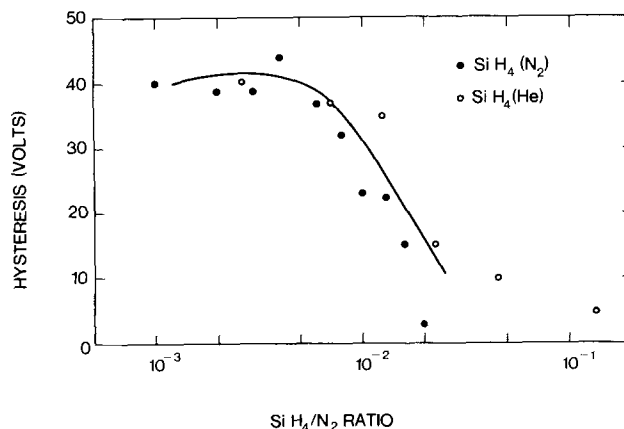


Fig. 14. Hysteresis as a function of SiH_4/N_2 ratio for the $\text{SiH}_4(\text{N}_2)$ and the $\text{SiH}_4(\text{He})$ system.

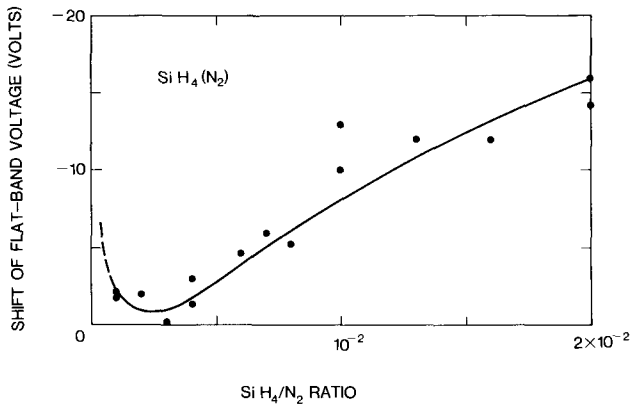


Fig. 15. MNS stability as a function of SiH₄/N₂ ratio. BT stress conditions: 10 min, 20V, 200°C.

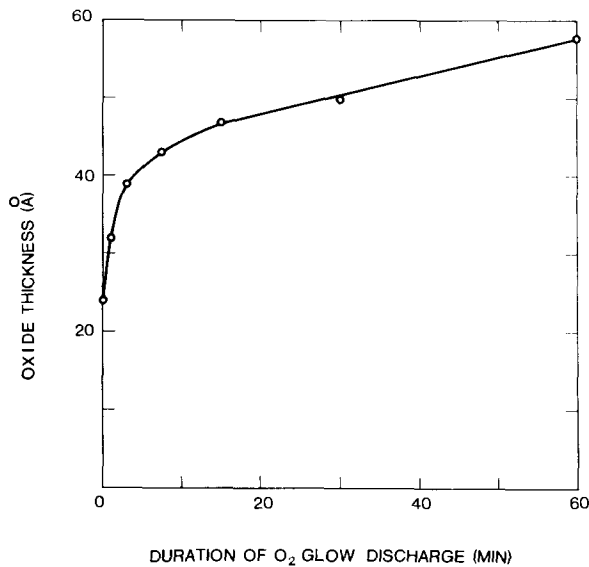


Fig. 16. Oxide growth as a function of duration of O₂ glow discharge.

The complete absence of hysteresis on H₂-treated silicon surfaces means that the natural oxide layer is removed. The nitride layer directly borders the silicon. In this structure no field-induced charge transport is possible within one sweeping cycle of the C-V curve. However, great instability occurs under long time stress even at room temperature.

The N₂ treatment lowers the hysteresis and improves the stability in contrast to an A treatment: the number of traps is reduced if N₂ can act on the surface. Perhaps the N₂ glow discharge allows a very slow but perfect growing of the first nitride molecules. The threshold voltage above which hysteresis occurs does not change either by the N₂ or by the A treatment, meaning that the oxide thickness remains unaffected. This is different after the O₂ treatment where the threshold voltage rises from approximately 10V up to 20V which could be explained by an increase of oxide thickness. Ellipsometric measurements (Fig. 16) demonstrate that an O₂ glow discharge of 30 min indeed produces an oxide thickness of 50Å, twice its original thickness.

The effect that the sign of the hysteresis and of the instability are inverted after O₂ treatment (Fig. 12) is not easy to explain. One might speculate that the plasma-grown oxide layer polarizes easily when an electric field is applied.

Summary and Conclusions

Nitrogen-Si₃N₄ films have been deposited on p-type silicon wafers by initiating the reaction between SiH₄

and N₂ with the help of a glow discharge. The film properties are in general comparable to those of pyrolytic nitride films deposited from SiH₄ and NH₃. They offer, however, additional advantages. The absence of ammonia makes it easier to deposit oxide- and sodium-free nitride films. Deposition is possible at temperatures well below 400°C. The substrate surface can be cleaned *in situ* by a suitable gas discharge treatment to achieve better stability or to tailor special properties of the films. The nitride properties can be widely varied by the deposition parameters, especially by the silane concentration in the plasma. Nitrogen-rich, silicon-rich, or even pure silicon films can be produced deliberately.

The properties of ammonia-free nitrogen-Si₃N₄ films can be summarized as follows:

(a) Predicted nitride stoichiometry is obtained at a substrate temperature of 350°C and a SiH₄/N₂ ratio of 1.5×10^{-3} related to a total gas pressure of 1 Torr during deposition.

(b) At substrate temperatures below 350°C the nitride films become less dense showing higher etch rate, larger flatband voltage, increased hysteresis, smaller index of refraction, reduced breakdown field strength, and an infrared absorption peak occurring at lower frequencies.

(c) At substrate temperatures above 350°C, hysteresis increases again, but no silicon enrichment can be detected in the film.

(d) The SiH₄/N₂ ratio directly determines the stoichiometry of the nitride films. Between 10^{-4} and 2×10^{-2} SiH₄ content the atomic ratio N/Si in the film varies from 1.7 to 0.9.

(e) The index of refraction increases with the silicon content of the film. Nitrogen-rich films have constant index of refraction with a value slightly above 2.

(f) Nitride films with theoretical Si₃N₄ stoichiometry exhibit maximum HF etch rate and maximum C-V hysteresis. Both effects are useful to optimize deposition parameters.

(g) The hysteresis can be avoided entirely by exposing the silicon surface to an H₂ glow discharge just prior to nitride deposition. Stability of MNS varactors can be improved by a N₂ glow discharge treatment.

(h) Shallow oxide layers on silicon surfaces from 20 to 60Å can be obtained reproducibly and at low temperatures by a glow discharge treatment in an oxygen atmosphere.

(i) The nitride deposition rate can be increased by a factor of two or more by adding some per cent hydrogen to the reactive gas mixture.

The optimum deposition temperature for the nitrogen-Si₃N₄ films lies nearly 500°C below that for ammonia-Si₃N₄ films. Even at room temperature, nitride films with reasonable quality can be produced which are suitable for the passivation of temperature-sensitive device structures.

The absence of ammonia is an obvious bonus. Working with ammonia means higher risk of getting water and alkali contaminants which are the cause of deleterious instabilities in SiO₂ films. Nitrogen-Si₃N₄ films are, therefore, perfectly tailored for the low-temperature passivation of clean oxide layers in connection with MOS and planar devices. Further applications are the hermetic sealing of metalized devices and the Ge and GaAs technology. The nitrogen-Si₃N₄ films are an excellent diffusion barrier against Zn and Ga. For example, a nitrogen Si₃N₄-film of 400Å thickness masks against a 5 hr Zn diffusion step carried out at 860°C.

Acknowledgment

The authors are grateful to H. Holzer who designed the glow discharge apparatus and assisted in performing the experiments.

Manuscript submitted Dec. 16, 1971; revised manuscript received Feb. 4, 1972. This was Paper 114 presented at the Los Angeles Meeting of the Society, May 10-15, 1970.

Any discussion of this paper will appear in a Discussion Section to be published in the June 1973 JOURNAL.

REFERENCES

1. H. F. Sterling and R. C. G. Swann, *Solid State Electron.*, **8**, 653 (1965).
2. V. Y. Doo, D. R. Nichols, and G. A. Silvey, *This Journal*, **113**, 1279 (1966).
3. R. C. G. Swann, R. R. Mehta, and T. P. Cauge, *ibid.*, **114**, 713 (1967).
4. T. L. Chu, C. H. Lee, and G. A. Gruber, *ibid.*, **114**, 717 (1967).
5. K. E. Bean, P. S. Gleim, R. L. Yeakley, and W. R. Runyan, *ibid.*, **114**, 733 (1967).
6. S. M. Hu and L. V. Gregor, *ibid.*, **114**, 826 (1967).
7. T. Sugano, K. Hirai, K. Kuroiwa, and K. Hoh, *Jap. J. Appl. Phys.*, **7**, 122 (1968).
8. G. A. Brown, W. C. Robinette, Jr., and H. G. Carlson, *This Journal*, **115**, 948 (1968).
9. Y. Kuwano, *Jap. J. Appl. Phys.*, **7**, 88 (1968).
10. R. Gereth, H. Holzer, and W. Scherber, Paper 144 presented at the Los Angeles Meeting of the Society, May 10-15, 1970.
11. O. Meyer and W. Scherber, *J. Phys. Chem. Solids*, **32**, 1909 (1971).
12. Y. Kuwano, *Jap. J. Appl. Phys.*, **8**, 876 (1969).
13. M. Zerbst, IEEE European Meeting, Invited paper, Munich, March 1969.
14. D. Frohman-Bentchkowsky and M. Lenzlinger, *J. Appl. Phys.*, **40**, 3307 (1969).

Voltage-Controlled Multicolor CRT Phosphors: Preparation and Characteristics

J. S. Prener* and J. D. Kingsley*

General Electric Corporate Research and Development, Schenectady, New York 12301

ABSTRACT

Since the range of electrons in a solid is a function of their initial energy it is possible to construct high-resolution multicolor cathode-ray phosphor screens in which the color is determined by the accelerating potential. A nonluminescent layer of controlled thickness is formed upon the surface of each grain of a green or cyan phosphor. This coating is prepared either by the diffusion of a killer impurity such as cobalt from the surface into the bulk or by the homogeneous precipitation of undoped ZnS upon each phosphor grain. The coated phosphor is then intimately mixed with any efficient standard red emitting phosphor such as $\text{YVO}_4:\text{Eu}$ or $\text{Gd}_2\text{O}_3:\text{Eu}$. A screen consisting of an intimate mixture of two component phosphors is then deposited by the same method used to prepare monochrome screens. Four distinct colors, useful for information display, can be observed in the red-green system. Quite acceptable two-primary-color television pictures have been demonstrated in the red-cyan phosphor system.

A beam of electrons impinging upon a phosphor excites each particle from the surface to some maximum depth. The distance in the solid at which the beam energy is reduced essentially to zero is called the ultimate or maximum range of electrons. The range of an electron is a function of its initial energy (1). Many different types of multicolor cathode ray tube (CRT) screens have been constructed based on the control of the penetration of the electrons into the phosphor. These screens emit radiation of different colors at different accelerating potentials.

In one early version (2) of such a screen, two or more phosphors, each emitting a different color under cathode-ray excitation, were laid down in successive thin layers upon the glass substrate. This geometry requires that the phosphor layers have thicknesses less than one micrometer if the CRT is to operate at convenient accelerating potentials (less than 30 kV). If particulate phosphors are used, the layers must consist of particles having diameters of a few tenths of a micrometer. These layers are very difficult to form and the small phosphor particles tend to be inefficient. The use of thin layers of transparent phosphor films has also been proposed (3), but such films are noteworthy for their low luminescence efficiency. These thin film screens are also substantially more difficult, and consequently more expensive, to produce than conventional screens. The required film thickness depends on the angle of incidence of the electron beam, thus on the distance from the center of the screen.

Another geometry has been proposed by Messineo *et al.* (4). They proposed coating one or more layers

of submicrometer size phosphor particles upon the surface of a larger phosphor particle emitting light of a different color, using a gelatin absorption process described by Kell (5). Thus a multilayered structure occurs within each phosphor grain rather than over the area of the screen. The requirement that the coating phosphor particles be submicrometer in size limits the usefulness of this type of screen since such small particles are difficult to obtain and, as previously indicated, generally exhibit a low luminescence efficiency.

The various difficulties discussed can be avoided by using normal size phosphor particles and preparing a mixed two-component phosphor screen by the same method used for monochrome television picture tubes. One of the phosphors (*e.g.*, a green or cyan one) is prepared with a nonluminescent surface layer of a given thickness upon each grain. The other component (*e.g.*, a red or orange one) may be any efficient phosphor. A CRT having a two-component screen of this type emits red or orange light for all values of the accelerating potential. The green or cyan phosphor contributes to the tube emission only if the accelerating potential exceeds a threshold value which is determined by the energy required for the ultimate range to exceed the "dead" layer thickness. Since the electron beam encompasses a large number of phosphor grains, any inhomogeneities within a grain or differences among grains are averaged over the area of the beam. In order to be useful and economical the nonluminescent or dead layers must be produced in a controlled, reproducible and preferably simple manner.

We have produced nonluminescent surface coatings upon individual (ZnCd)S phosphor grains by two different methods and measured the dependence of the

* Electrochemical Society Active Member.

Key words: phosphors, luminescence, cathode-rays, color.

luminescence intensity under cathode ray excitation on accelerating voltage for changes in process variables. These methods are:

(i) A nonluminescent layer of undoped ZnS or CdS of a specified thickness is deposited on the surface of each phosphor grain by homogeneous precipitation.

(ii) A luminescence "killer" impurity, Co, is diffused in from the surface of each grain to a specified depth.

These processes and the properties of the multicolor CRT displays achieved using these phosphors are the subjects of this paper.

Messineo *et al.* (4) described the use of Co for producing a nonluminescent barrier layer between a phosphor grain emitting one color and very small phosphor particles of another emission color absorbed on the surface of the larger particle. They gave little information, however, on the luminescent properties of the Co-diffused phosphor. We found that the Co diffusion into a thin surface layer completely quenched the afterglow of the entire particle. Presumably a small fraction of the Co diffused into the entire phosphor grain in amounts sufficient to quench the normally long afterglow without decreasing the luminescence efficiency to any large extent (6). The first method above for producing nonluminescent surface layers permitted us to make a multicolor display screen with a long afterglow. The luminescence intensity of these ZnS-coated phosphors as a function of the accelerating voltage has been analyzed and shown to be consistent

with the power loss of an electron beam in traversing a solid (7).

ZnS-Coated ZnS:Cu

Experimental

Coatings of undoped ZnS on ZnS:Cu phosphor grains were produced by homogeneous precipitation (8). The coating thickness could be controlled by varying the ratio of phosphor to zinc ions in solution, since all the zinc was precipitated after a sufficient time. After the precipitation of ZnS was complete, the phosphor was filtered, washed, and dried. The large number of ZnS:Cu crystallites provided efficient nucleating sites so that precipitation of ZnS occurred primarily on these rather than upon the container walls or on other nucleating particles present. Microscopic examination showed the presence of only the original ZnS:Cu grains and less than 1% of the precipitation took place upon the container walls. Furthermore, upon the precipitation of CdS coatings, microscopic examination showed that the normally colorless, transparent ZnS grains were still transparent but orange in color. The coating thicknesses, ranging from 0.051 to 0.51 μm , were calculated from the quantity of ZnS precipitated and the particle size distribution of the uncoated ZnS:Cu phosphors as measured with a Coulter Counter [see Ref. (7)]. The coated phosphor samples were settled on Ag plates using dilute barium acetate and potassium silicate as a binder. Four Ag plates were

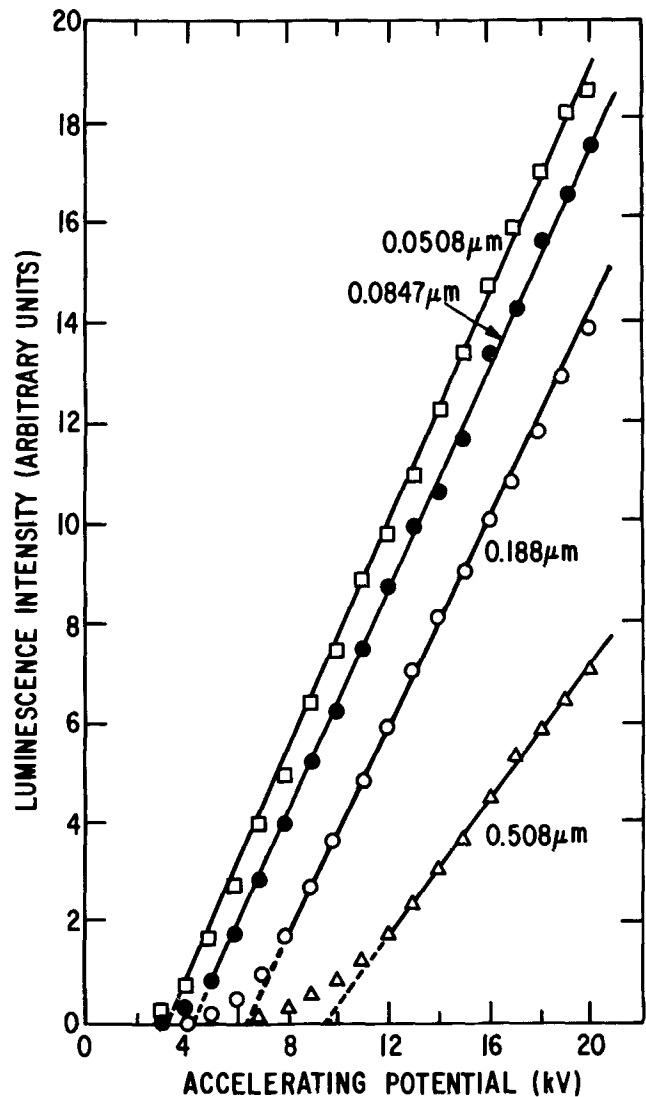
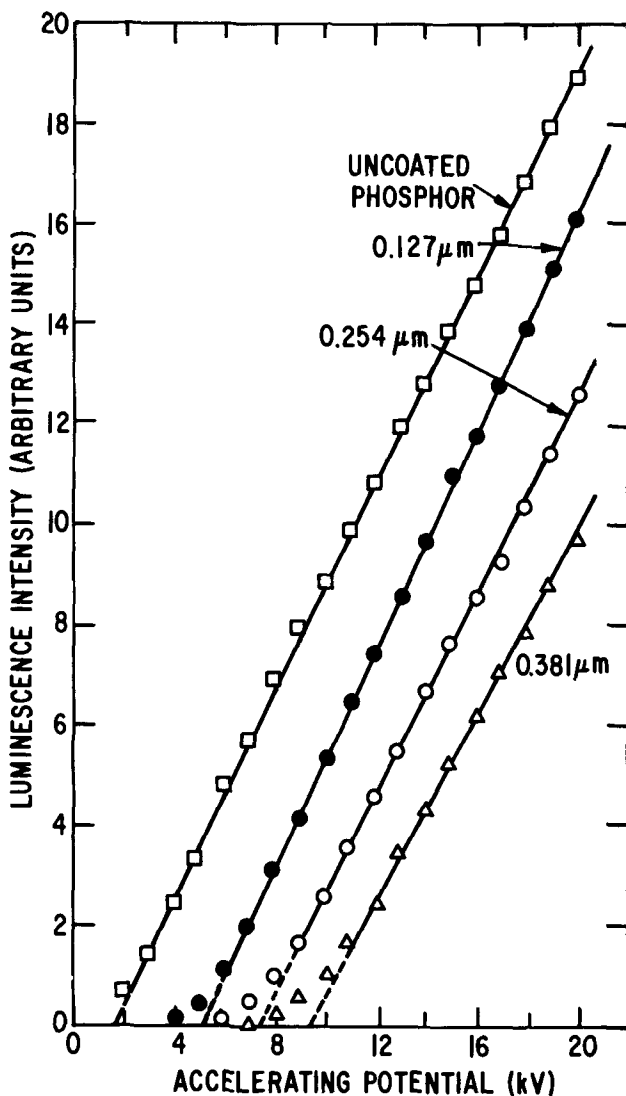


Fig. 1a (left), b (right). Luminescence intensity as a function of accelerating potential for ZnS-coated ZnS:Cu phosphors. The coating thicknesses in μm are marked on the curves.

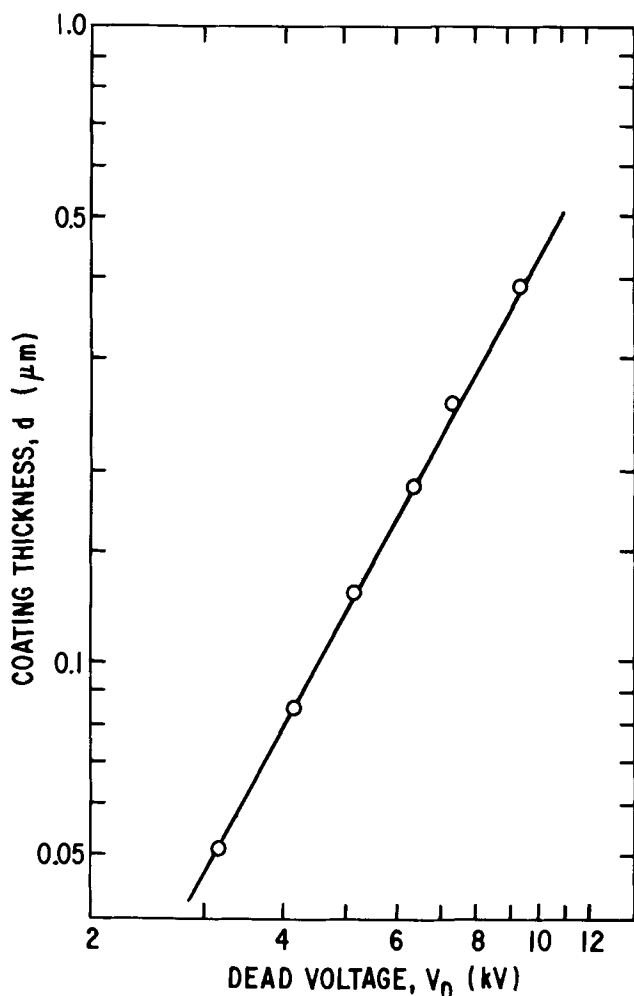


Fig. 2. Variation of dead voltage with ZnS coating thickness on ZnS:Cu phosphors.

mounted on a rotating head of a demountable CRT and the luminescence intensity was measured at constant beam current with varying accelerating potential (9). The intensity of the emitted light was measured with a monochromator and photomultiplier.

Results

Plots of the luminescence intensity as a function of accelerating potential are shown in Fig. 1a and 1b. With the coating thickness varying from 0.051 to 0.51 μm the "dead voltages" obtained by extrapolating the straight portion of each curve to zero intensity varied from 3.0 to 9.5 kV; the dead voltage of the uncoated phosphor was 1.5 kV. A log-log plot of coating thickness against dead voltage in Fig. 2 indicates that the thickness is related to the dead voltage by

$$d = 7.3 \times 10^{-7} V_0^{1.77} \quad [1]$$

when d is measured in cm and V_0 in kV. Measurements on many samples showed the process to be quite reproducible and the duration of the long green afterglow was not affected by the ZnS coatings. Some coated samples were fired in a flowing H_2S atmosphere for one hour at 500°C. There was a slight reduction in the dead voltage values after firing.

Screens having two phosphor components were made up by mixing the ZnS-coated ZnS:Cu with a red emitting phosphor and settling the mixture on a Ag substrate. The color variation with accelerating potential of a screen made by mixing ZnS:Cu having a coating thickness of 0.25 μm with $\text{YVO}_4:\text{Eu}$ in a weight ratio of 3:1 was studied. The emitted light was red at 5 kV, red-orange at 8 kV, orange at 11 kV, yellow at 13 kV, and green at 17 kV.

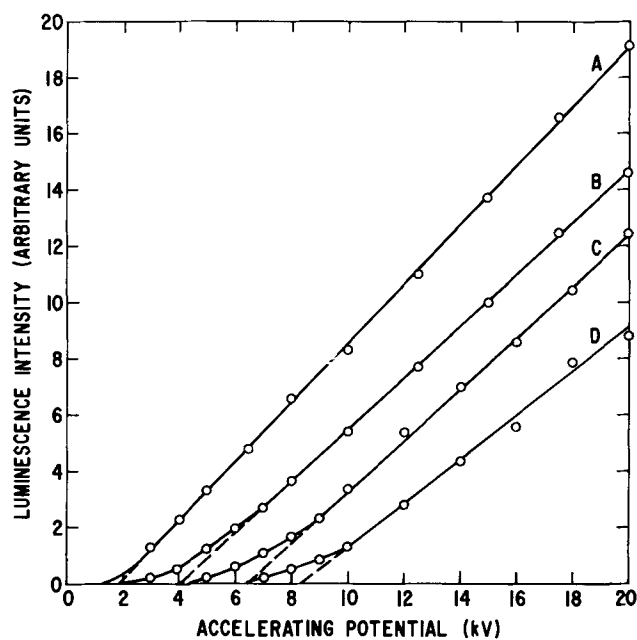


Fig. 3. Luminescence intensity as a function of accelerating potential at constant beam current for some typical Co-diffused (ZnCd)S:Ag phosphors; A. unfired phosphor; B. 650°C for 10 min; C. 650°C for 2 hr, D. 700°C for 2 hr.

Cobalt-Diffused (ZnCd)S:Ag

Experimental

Two phosphors were used: (i) a $(\text{Zn}_{0.69}\text{Cd}_{0.31})\text{S}:\text{Ag}$ phosphor of the type used as the green component (color coordinates $x = 0.29$, $y = 0.61$) of the P22 phosphor commonly used in the aperture mask color television CRT's and (ii) a $(\text{Zn}_{0.82}\text{Cd}_{0.18})\text{S}:\text{Ag}$ cyan phosphor with color coordinates $x = 0.16$, $y = 0.39$. The former was used for constructing multicolor information display CRT's and the latter for building a two-primary-color television picture tube.

The phosphor was agitated in a water suspension and cobalt sulfide was precipitated on the particles in a manner similar to that described by Messineo *et al.* (4). The phosphor was then filtered, washed, and dried.

Small batches were fired in a neutral argon or nitrogen atmosphere at temperatures ranging from 550° to 800°C for either 10 min or 2 hr at temperature. The furnace was regulated to $\pm 2^\circ\text{C}$ and the temperature was determined by a thermocouple located very close to the sample. Samples of the Co-diffused phosphor were sieved through a 200 mesh nylon screen, settled on Ag plates, and measured as described above.

Results

Some typical intensity-voltage curves are shown in Fig. 3. The dead voltage is a function of the thickness of the "killed" region of the phosphor grain due to Co diffusion. It depends on both the annealing time and temperature.¹ The dead voltages are shown in Fig. 4 and vary linearly with temperature over the range studied. Firing for 10 min at a given temperature yields the same result as firing for 2 hr at a temperature 75°C lower.

The diffusion coefficient of Co in $\text{Zn}_x\text{Cd}_{1-x}\text{S}$ fired in argon can be estimated from the dead voltage values. It is assumed that the thickness of the nonluminescent region, d , is given by $d = \sqrt{Dt}$ where D is the diffusion coefficient, $D_0 \exp(-E/kT)$, at temperature T and t is the diffusion anneal time. From the results discussed above (Fig. 2), the relationship between the thickness of the dead layer and the dead voltage V_0

¹ A (ZnCd)S phosphor was also measured without a binder by pressing it into a shallow depression in an Al block. The measured dead voltage was identical to that found using a binder.

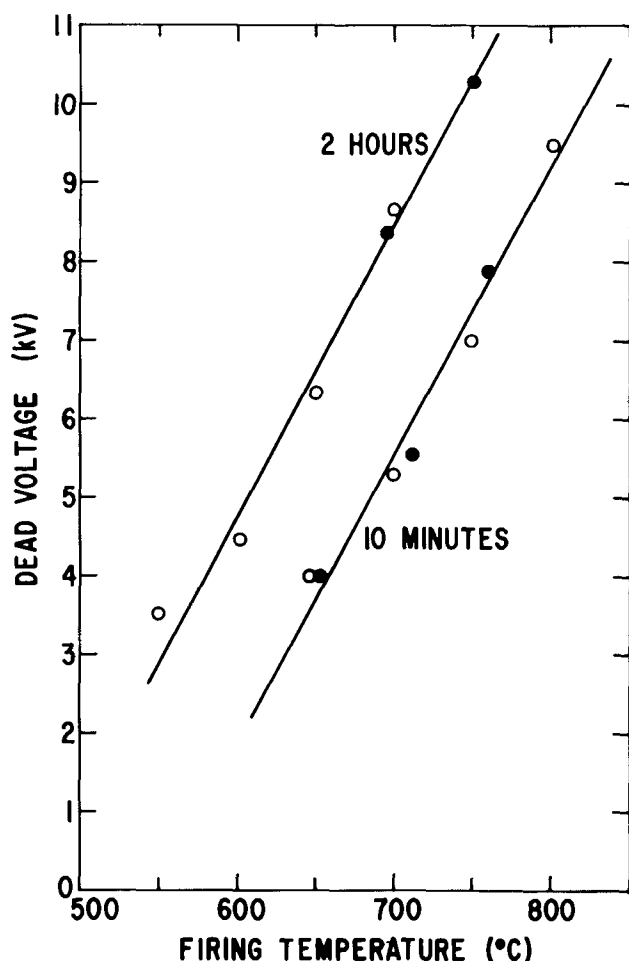


Fig. 4. Dead voltage of Co-diffused (ZnCd)S:Ag phosphors as a function of the firing temperature for a 10 min and a 2 hr anneal: $Zn_{0.69}Cd_{0.31}S:Ag$ green phosphor (●); $Zn_{0.82}Cd_{0.18}S:Ag$ cyan phosphor (○).

for ZnS is given by Eq. [1]. Assuming that the relationship is the same for (ZnCd)S, the diffusion coefficient is given by

$$D = 53 \times 10^{-14} V_0^{3.54} / t \quad [2]$$

where D is in cm^2/sec , V_0 in kV, and t in seconds.

In determining D from Eq. [2], we have used the V_0 data of Fig. 4 from the 2 hr anneals. The true anneal time is uncertain for the runs in which the samples were kept 10 min at temperature. Since the sample and fused quartz firing tube were cold when placed in the hot furnace, the time required for the sample temperature to rise to the furnace temperature was itself of the order of 10 min. For the 10 min data, therefore we would, in Eq. [2], have to use some value of t greater than 600 sec. In Fig. 5, $\log D$ is plotted against $10^3/T$. A least squares fit gives the activation energy $E = 1.54$ eV and $D_0 = 1.30 \times 10^{-5}$ cm^2/sec . The values of d as determined from Eq. [1] ranged from 0.07 μm for the 2 hr anneal at 554°C to 0.48 μm for the 2 hr anneal at 750°C.

We observed that Co is a much better "killer" impurity than either Fe or Ni for obtaining controlled thicknesses of nonluminescent layers. Both Fe and Ni gave products of very low efficiency even for low temperature anneals. The findings of Weakliem (10), that substantial amounts (0.1%) of Ni can be introduced into ZnS and CdS at 800°C in a few hours whereas several days were required to introduce an equivalent amount of Co, might very well explain the difference in behavior observed with Ni and Co. Even a 10 min anneal may be sufficient to introduce Ni concentrations sufficiently high to markedly decrease

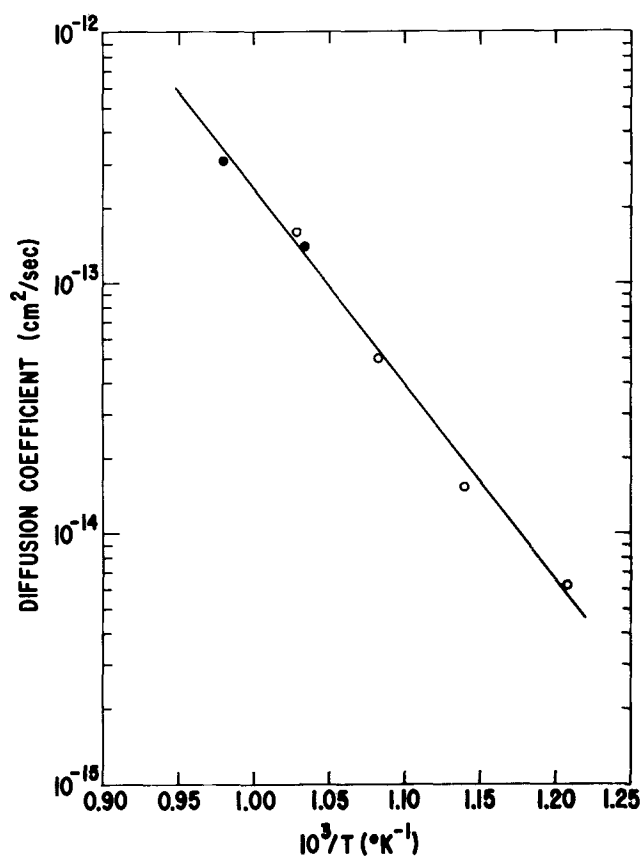


Fig. 5. The computed values of the diffusion coefficients of Co in $Zn_xCd_{1-x}S$ plotted against $10^3/T$. $Zn_{0.69}Cd_{0.31}S:Ag$ green phosphor (●); $Zn_{0.82}Cd_{0.18}S:Ag$ cyan phosphor (○).

the luminescence efficiency throughout the bulk of the phosphor grains rather than just in a surface layer. There appear to be no data on the diffusion of Fe in ZnS or CdS.

Information Display Screens

The Co-diffused phosphor was mixed by tumbling with a red emitting phosphor ($Gd_2O_3:Eu$ or $YVO_4:Eu$), and the two-component phosphor was settled on Ag plates as before. The dependence of the color coordinates of the emitted light on accelerating potential was determined from the emission spectra corrected for spectral sensitivity of the detector. In Fig. 6, this dependence is shown on a C.I.E. plot for a mixture of one part by weight of $YVO_4:Eu$ and four parts of $Zn_{0.69}Cd_{0.31}S:Ag$ into which Co had been diffused at 710°C for 10 min. The $YVO_4:Eu$ and four-to-one ratio were chosen so that four distinct colors could be displayed with a total accelerating potential variation of two to one. Clearly distinguishable shades of red, orange, yellow, and green were obtained at 4, 5, 6, and 8 kV. The brightness was adequate, even at the lowest operating potential, to display computer-generated graphics and alphanumeric.

If fewer than four distinguishable colors are desired one can reduce the required accelerating voltage change or alternatively enhance the brightness at the lower operating potentials either by increasing the fraction of the red component or by using a phosphor whose emission color is more orange.

Two-Primary-Color Television Screens

The basic requirements on a two-primary-color TV system are first that it be capable of showing pictures in black and white and second that fleshtones be accurately reproduced, since we are most aware of any lack of color fidelity in the appearance of human skin. If one requires that the screen can display "pure" white, (i.e., Illuminant C) and fleshtones, then the

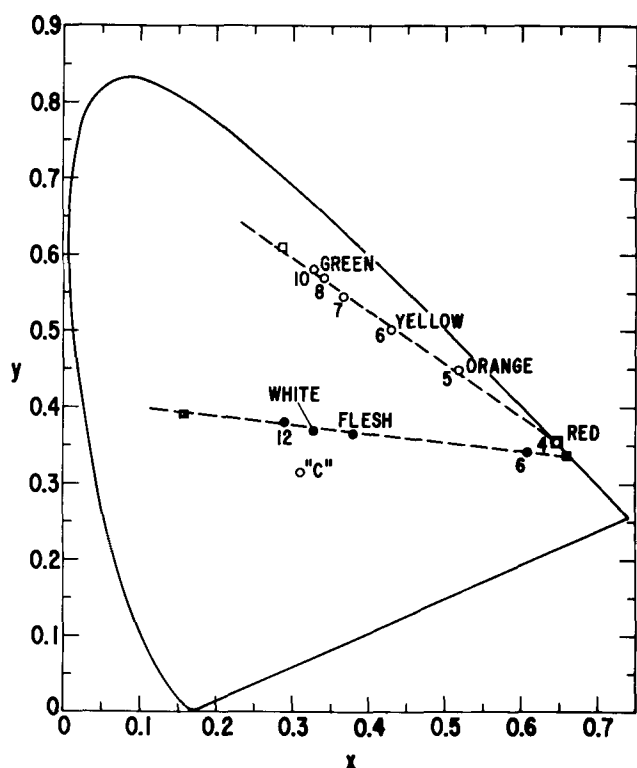


Fig. 6. Color coordinates of two-component phosphor screens operated at various accelerating potentials indicated by the numbers. The color coordinates of the component phosphors are shown by (■) and (□) and the color coordinates of Standard Illuminant C are given by point "C". One part by weight of $\text{YVO}_4\text{:Eu}$ and four parts by weight of $\text{Zn}_{0.69}\text{Cd}_{0.31}\text{S:Ag}$ into which Co was diffused for 10 min at 710°C (○). One part by weight of $\text{Gd}_2\text{O}_3\text{:Eu}$ and four parts by weight of $\text{Zn}_{0.82}\text{Cd}_{0.18}\text{S:Ag}$ into which Co was diffused at 700°C for 2 hr (●).

primary colors must be orange and a bluish cyan. It was determined experimentally that a more pleasing display resulted from using the red $\text{Gd}_2\text{O}_3\text{:Eu}$ phosphor as one primary color and a greenish cyan for the second primary color. The cyan phosphor, $\text{Zn}_{0.82}\text{Cd}_{0.18}\text{S:Ag}$ with color coordinates $x = 0.16$ and $y = 0.39$, was

chosen to maintain the capability of displaying flesh-tones while compromising the white purity.

Since a moderately high average brightness of 50 ft-L was desired, the saturation of the high voltage primary color was also compromised. The two primary colors are indicated on Fig. 6 by their respective operating potentials of 6 and 12 kV. With a 12 in. diagonal, single-gun CRT, an average beam current of 0.5 mA, a 100% faceplate transmission, and a 50% duty cycle for each operating potential, we obtained a brightness of 49 ft-L for white ($x = 0.33$, $y = 0.37$), 43 ft-L for cyan ($x = 0.29$, $y = 0.38$), and 6 ft-L for red ($x = 0.61$, $y = 0.34$). Even though the high voltage primary is quite desaturated one obtained the impression of an essentially "full-color" picture although there were obviously no brilliant blues or greens.

Acknowledgments

The authors gratefully acknowledge the help of A. LaTorre, A. W. Clock, and S. J. Lubowski in preparing the phosphor samples and in measuring the luminescence intensity-voltage characteristics.

Manuscript submitted Jan. 31, 1972; revised manuscript received May 5, 1972. This was Paper 160 presented at the Cleveland, Ohio, Meeting of the Society, Oct. 3-7, 1971.

Any discussion of this paper will appear in a Discussion Section to be published in the June 1973 JOURNAL.

REFERENCES

- G. F. J. Garlick, in "Luminescence in Inorganic Solids," P. Goldberg, Editor, Academic Press (1966).
- L. R. Koller and F. E. Williams, U.S. Pat. 2,590,018, (1950).
- D. A. Cusano and P. T. Studer, U.S. Pat. 2,958,002, (1954).
- P. J. Messineo, Skillman, and S. M. Thomsen, U.S. Pat. 3,294,459 (1966).
- R. D. Kell, U.S. Pat. 3,275,466 (1966).
- P. D. Johnson, Natl. Electron. Conf. Proc., **XI**, 1, (1955).
- J. D. Kingsley and J. S. Prener, *J. Appl. Phys.*, To be published.
- L. Gordon, M. L. Salutsky, and H. H. Willard, "Precipitation from Homogeneous Solution," Chapt. 6, John Wiley and Sons, New York (1959).
- For details of the equipment used for the cathode ray excitation, see G. W. Ludwig and J. D. Kingsley, *This Journal*, **117**, 348 (1970).
- H. A. Weakliem, *J. Chem. Phys.*, **36**, 2117 (1962).

GaAs_{1-x}P_x Electroluminescent Diodes Made by Zn Diffusion in an Open-Tube System

K. K. Shih* and J. M. Blum*

IBM Thomas J. Watson Research Center, Yorktown Heights, New York 10598

ABSTRACT

An open-tube process has been used for Zn diffusion in $\text{GaAs}_{1-x}\text{P}_x$ coated with SiO_2 films to form p-n junctions. Electroluminescent diodes made by this method have a brightness of 600 ft-L at 5 A/cm^2 with no etching of the surface required. The effects of temperature, time, and SiO_2 thickness on junction depth, efficiency, and brightness of the diodes are described.

Zn diffusion into III-V compounds such as GaAs , $\text{GaAs}_{1-x}\text{P}_x$ has commonly been carried out in sealed quartz tubes (1). The quality of the vacuum in the

ampoule and the arsenic pressure in the system are critical factors in the control of junction depth and surface concentration, and therefore make reproducibility difficult. In addition, it was found that Zn and As vapors attack the window openings when the process is used on an oxide masked wafer. This makes

* Electrochemical Society Active Member.

Key words: $\text{GaAs}_{1-x}\text{P}_x$, electroluminescent diode, Zn diffusion, III-V alloy.

subsequent processes difficult to control. It was found that by depositing a thin additional layer of SiO₂ on the surface of the wafer, the surface erosion can be avoided. Shorts *et al.* (2) and Becke *et al.* (3) have studied Zn diffusion in GaAs coated with SiO₂ in a closed-tube system. They found that SiO₂ proved effective in lowering surface concentrations and preventing surface deterioration during diffusion. Since a thin protecting film of SiO₂ is necessary to protect the surface from erosion, the open-tube process was used instead of the conventional closed-tube system. We will describe here the effects of the Zn source temperature, the diffusion temperature, the oxide thickness, and the diffusion time using the open-tube diffusion of Zn into GaAs_{1-x}As_xP on light emitting diode characteristics.

Experimental

Tellurium-doped GaAs_{1-x}P_x wafers obtained from Monsanto Company were used in this work. Most of the wafers, according to the vendors specifications, were within the following specifications: x , in the formula GaAs_{1-x}P_x was 0.39 ± 0.01 ; $n \cong 2 \pm 1 \times 10^{17}$, and the total thickness of the vapor-grown epitaxial layer on GaAs was about 80 μm with approximately the first 36 μm graded in composition with the remaining portion having constant composition. These wafers were selected on the basis that they all had similar epitaxial layer characteristics so that the effects of various diffusion parameters could be evaluated. It should be noted that more efficient diodes have been made here from other material.

The SiO₂ layers which were used to protect the semiconductor surface from erosion were deposited by a pyrolytic decomposition process. Before deposition, the wafers were cleaned in toluene, acetone, and alcohol. The deposition occurs at 500°C as a result of the decomposition of tetraethylorthosilicate (TEOS) in an oxygen atmosphere. SiO₂ films with a thickness of 500-4000Å have been produced with a deposition rate of about 60 Å/min.

The diffusion apparatus is shown in Fig. 1 and consists of a two-zone furnace so that the temperature of the source and wafers can be adjusted independently. A flow of N₂ was maintained through the system between diffusion runs. Zn pellets of 6-9's purity were loaded in a boat at the entrance of the source end of the tube and wafers were loaded in a flat plate at the other end. The nitrogen gas was turned off and forming gas was then turned on to flow at a rate of about 400 cc/min for 30 min to flush the system. After that, the Zn boat was first pushed into the source region zone 1 and after 10 min the wafers were pushed into the diffusion region zone 2 of the furnace. The diffusion of Zn into GaAs_{1-x}P_x was investigated with the wafer temperature (T_w) maintained at the same temperature as the source (T_{Zn}). Temperatures of 700°, 750°, 800°, and 850°C were used with diffusion times ranging from 30 min to 4 hr. Diffusions at a fixed wafer temperature (T_w) of 800°C but with different source temperatures (T_{Zn}) of 700°, 750°, and 800°C for 1 hr have also been carried out.

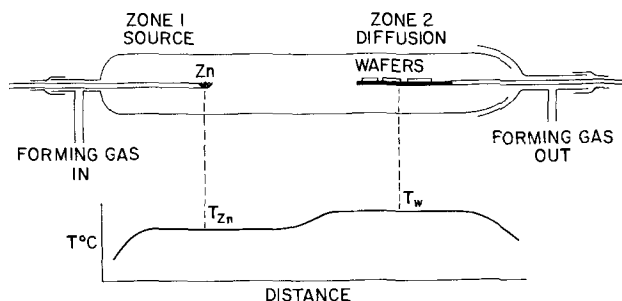


Fig. 1. Furnace system and temperature profile for diffusions

After diffusion, the wafers were removed from the diffusion zone. The forming gas was then turned off and the nitrogen turned on prior to removing the wafers from the furnace. The SiO₂ films were removed after the diffusion. The junction depth was measured by developing the junction interface with a HF:H₂O₂:3H₂O etch in a cleavage plane normal to the junction. Diodes were made by electroplating Au-Sn on the substrate side of the wafer after the substrate is thinned to reduce series resistance. Small cleaved sections with an area of about 10⁻³ cm² were mounted on a header and an aluminum wire was ultrasonically bonded directly to the top p surface. The external quantum efficiencies and brightnesses of these diodes were then measured. The external quantum efficiencies were measured with an integrating sphere type of apparatus using Si photodiodes as detectors. The brightness was measured with a Spectra Brightness Spot Meter viewing an 8 mil diameter area.

Results and Discussion

Initially, the effects of oxide thickness on the diffusion were studied. It was found that with oxide thicknesses less than 500Å, a nonuniform junction depth often resulted. On the other hand, if the oxide thickness was about 4000Å the oxide sometimes cracked and gave erratic junction depths. Hence, most of our data were from wafers deposited with 1000 and 2000Å SiO₂ films. Examination of these wafers after diffusion indicated smooth clean surfaces with junction depth uniformity within $\pm 5\%$.

The junction depth X_j for various Zn diffusions with the same source and wafer temperatures between 700° and 850°C and for 1000 and 2000Å thick SiO₂ films was found to vary almost linearly with the square root of the diffusion time while the diffusion times ranged from 30 min to 4 hr. This relationship indicates that open-tube Zn diffusion into GaAs_{1-x}P_x obeys Fick's law (4). In the case where the wafer temperature is kept constant at 800°C for 1 hr, the junction depth can be decreased by a factor or two by reducing the source temperature from 800° to 700°C.

Figure 2 shows the junction depth X_j vs. the SiO₂ thickness for temperatures between 700° and 850°C when $T_{Zn} = T_w$ for a 1-hr Zn diffusion. This figure indicates that at the lowest temperature (700°C) the junction depth is almost independent of oxide thickness, while at a higher temperature (850°C), the junction depth decreases drastically with increasing

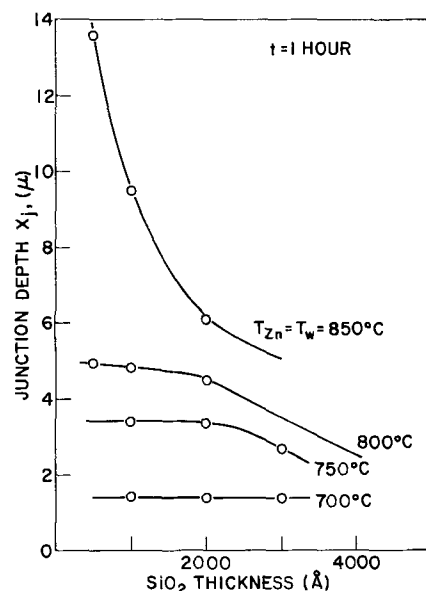


Fig. 2. Junction depth as a function of SiO₂ thickness for a 1-hr diffusion when $T_{Zn} = T_w$.

oxide thickness. The reason for the anomalous results in Fig. 2 is not understood and we cannot conjecture any theory without additional experimental data.

The junction depth also decreases with increasing donor concentration and increasing phosphorous concentration in the wafers. Because of the limited number of experiments done in this area, no quantitative results are reported here.

The sheet resistance of the diffused layers has been measured by the four point probe method. It was found that at a given junction depth, the sheet resistance of the layers diffused in the open-tube system is at least an order of magnitude higher than that using a ZnAs₂ source in a closed-tube system. This suggests that the Zn concentration in the oxide-coated GaAs_{1-x}P_x layers diffused by the open-tube method must be lower than in layers diffused by the conventional ZnAs₂-source closed-tube method (5).

These results are confirmed by surface concentration (C_0) measurements made on the same wafers using the plasma resonance method (6). For the wafers diffused at $T_{Zn} = T_w = 800^\circ\text{C}$ with a 2000Å thick SiO₂ film on the surface, C_0 is approximately equal to $3.5 \times 10^{19} \text{ cm}^{-3}$. The lowest C_0 measured is about $1.4 \times 10^{19} \text{ cm}^{-3}$ when $T_{Zn} = T_w = 700^\circ\text{C}$ with a 1000Å thick SiO₂ film on the surface during diffusion. C_0 is approximately equal to $1.1 \times 10^{20} \text{ cm}^{-3}$ if ZnAs₂ source is used in a closed ampoule diffused at 800°C .

The external quantum efficiency and wavelength of the diffused GaAs_{1-x}P_x diodes have been measured. It was found that the efficiency did not vary very much in our diffusion studies even though the temperatures of the source and wafers were changed between 700° and 850°C . The results show that the efficiency of diodes made with an SiO₂ thickness of 2000Å is about 20% better than that of 1000Å. The average efficiency was about 10^{-3} at 6600Å for uncoated diodes. The highest value obtained so far was about 2.4×10^{-3} at 6650Å for an uncoated diode.

Brightness measurements were made on hundreds of diodes whose areas varied from about $0.8 \times 10^{-3} \text{ cm}^2$ to $1.2 \times 10^{-3} \text{ cm}^2$. Figure 3 demonstrates the effects of diffusion time on brightness when the wafer temperature and source temperature are equal. Each point on the curves represents the average of several diodes. The brightness at current density = 10 A/cm^2 is plotted for comparison. When the temperature was increased from 700° to 800°C , the brightness also increased. A maximum value is obtained at 800°C for 1-hr diffusion. When the temperature increases further to 850°C , an adverse result was obtained which could have been caused by an increase in nonradiative recombination centers formed at the higher temperature. When the wafer temperature was kept constant at 800°C , some improvement in brightness can be obtained at a lower source temperature because the junction depth decreases with decreasing source temperature and this results in less light absorption at the surface.

The effect of junction depth on the brightness of the diodes was studied and the results are shown in Table I. At about the same shallow junction depths (under $\sim 2.5 \mu\text{m}$, runs A, A' and B, B' in Table I), the brightness of the diodes can be off by a factor of 3-4 depend-

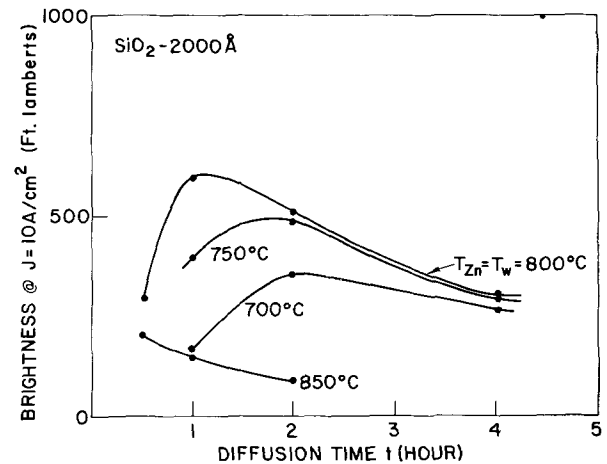


Fig. 3. Luminance of GaAs_{1-x}P_x diodes at 300°K at current density = 10 A/cm^2 as a function of diffusion time at different temperatures when $T_{Zn} = T_w$.

ing on the diffusion conditions. When the junction depth is about $4\text{-}5 \mu\text{m}$ deep (see C and C' in Table I), the difference in brightness can still be large depending on diffusion conditions. However, when the junction depths are deeper as in runs D, E, and F the brightness drops substantially. This shows that for junction depths of less than $\sim 5 \mu\text{m}$ the specific diffusion conditions (i.e., time and temperature) play a significant role in determining the luminance characteristics. However, as the diffusion depth increases, the particular diffusion conditions have less influence. The luminance of these devices has been improved by removing part of the diffused region by etching the surface.

We have performed a closed-tube diffusion on the same wafer used in the above studies using a ZnAs₂ source and a diffusion at 800°C for 45 min [i.e., the same method described by Herzog *et al.* (5)]. The junction depth was about $5 \mu\text{m}$. Without etching the surface the brightness of the diodes measured at 10 A/cm^2 was about 200 ft-L. This low brightness is probably due to the higher Zn concentration in the diodes made by closed-tube diffusion without an SiO₂ film. Besides, it is possible that a thin surface film could form during the diffusion process which has high absorption coefficient for red emission. Surface etching is required on diodes made from that type of diffusion in order to achieve maximum brightness.

Run B in Table I corresponds to a 1-hr diffusion at $T_{Zn} = T_w = 800^\circ\text{C}$ with a 4000Å SiO₂ deposited on the surface, and run A corresponds to a 1-hr diffusion at $T_{Zn} = 700^\circ\text{C}$ and $T_w = 800^\circ\text{C}$ with a 2000Å SiO₂ film on the surface. These two diffusions gave comparable brightness and junction depth results. Since a 4000Å SiO₂ film usually cracks during the diffusion process the diffusion conditions corresponding to run A are preferred. The shallow junction may cause high sheet resistance which is not desirable for some applications. If lower sheet resistance is required, the diffusion condition corresponding to run C which has a deeper junction depth ($\sim 4.5 \mu\text{m}$) and higher surface

Table I. Table of luminance characteristics for various diffusion conditions and junction depths

Run No.	Source temp, T_{Zn} ($^\circ\text{C}$)	Wafer temp, T_w ($^\circ\text{C}$)	Diffusion time, t (hr)	SiO ₂ thickness, d (Å)	Junction depth, X_j	Brightness at current density = 10 A/cm^2 , B (ft-L)
A	700	800	1	2000	1.5	700
A'	700	700	1	2000	1.4	150
B	800	800	1	4000	2.5	650
B'	800	800	0.5	2000	2.1	220
C	800	800	1	2000	4.5	600
C'	850	850	0.5	2000	4.8	200
D	750	750	4	2000	6.1	250
E	800	800	4	2000	8.8	250
F	850	850	2	2000	12	75

Zn concentration can be used. The diffusion conditions for both runs A and C are the same except the source temperature. Hence it appears that the best diffusion conditions for attaining high brightness are to deposit 2000Å thick SiO₂ films on GaAs_{1-x}P_x wafers and to diffuse for 1 hr at 800°C while keeping the Zn source temperature between 700° and 800°C.

From measurements made on many diodes from many different wafers other than those particular ones used in this work it is evident that in addition to diffusion conditions wafer quality plays a very important role in the resulting ultimate diode characteristics. Superior luminance characteristics were achieved using the optimum open-tube diffusion conditions found in this work from wafers not used in this series of experiments. Typically the results from better quality wafers at 10 A/cm² were between 700 and 900 ft-L. The best wafer measured produced 55, 600, and 1050 ft-L at current densities of 1, 5, and 10 A/cm², respectively. All of these results were achieved without any surface etching.

In conclusion, it has been shown that SiO₂ films on the surface during diffusion offers surface protection allowing the retention of smooth surfaces. With this protection, open-tube diffusions can be used. The surface zinc concentration is lowered by the SiO₂ film. High brightness results are achieved in these diodes with no etching of the surface required. These results produce a true planar process. In addition, the open-tube approach enables many diffusions to be carried out in quick succession avoiding the complications associ-

ated with encapsulation under vacuum which is necessary in the closed-tube system. While only work on GaAs_{1-x}P_x is reported here, the process has been successfully applied to other III-V semiconductor materials such as Al_xGa_{1-x}As, GaP, and GaAs.

Acknowledgments

The authors gratefully acknowledge the technical assistance of C. B. Burstell, J. F. DeGelormo, and V. Garrison and helpful discussions with M. R. Lorenz. We thank H. P. Pogge for making available some of the Monsanto wafers and J. Philbrick for measuring the surface concentrations.

Manuscript submitted Feb. 1, 1972; revised manuscript received April 21, 1972.

Any discussion of this paper will appear in a Discussion Section to be published in the June 1973 JOURNAL.

REFERENCES

1. D. L. Kendall in, "Semiconductor and Semi-metals," Vol. 4, p. 163, Willardson and Beer, Editors, Academic Press, New York (1968).
2. S. R. Shorts, J. A. Kanz, and E. C. Wurst, Jr., *Trans. Met. Soc. AIME*, **230**, 300 (1964).
3. M. Becke, D. Flatley, W. Kern, and D. Stolnitz, *ibid.*, **230**, 307 (1964).
4. P. G. Shewmon in "Diffusion in Solids," McGraw-Hill Publishing Co., Inc., New York (1963).
5. A. H. Herzog, W. O. Graves, and M. G. Craford, *J. Appl. Phys.*, **40**, 1830 (1969).
6. J. W. Philbrick, C. A. Dillus, and C. P. Schneider, To be published.

Determination of the Component Activities in the System In-Ga Using a Solid Oxide Electrolyte Technique

K. A. Klinedinst, M. V. Rao, and D. A. Stevenson*

Department of Materials Science and Engineering, Stanford University, Stanford, California 94305

ABSTRACT

An electrolytic technique utilizing the cell, Pt|W|Ga, β -Ga₂O₃|calcia stabilized zirconia|Ga-In, β -Ga₂O₃|W|Pt, has been used to measure activities of Ga in liquid In-Ga alloys in the temperature range 800°-950°C. The Ga activities and the In activities, calculated from the Gibbs-Duhem equation, show modest positive deviation from Raoult's law. The activities are compared with previously measured and computed values. The parameter α_{GaIn} (defined by $\ln \gamma_{\text{Ga}}/[1 - N_{\text{Ga}}]^2$) is seen to have a very small composition dependence in the temperature range studied. The partial molar excess entropies of solution of Ga, calculated using the measured free energies and previously measured values for the heats of mixing, are demonstrated to be negative and small.

There is both practical and fundamental interest in the thermochemistry of the Ga-In system. The system comprises one binary of a number of ternary systems of practical interest. For example, the compounds Ga_xIn_{1-x}As and Ga_xIn_{1-x}P are of current interest because of their potential applications as infrared and visible light emitting diodes, respectively. In the growth of ternary mixed crystals in the systems using liquid phase epitaxial growth techniques, knowledge of the ternary phase diagrams is essential. Because sufficient information of this type is unavailable, investigators have endeavored to estimate portions of the ternary phase diagrams using thermochemical data for the respective binaries, together with some information on the pseudobinaries (1). A recent study has employed an interpolative technique, using a limited amount of experimental information about the ternary (2).

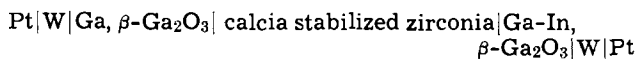
A recent review of the Ga-In system (3) has described a number of inconsistencies in the present information in the literature concerning the phase diagram, the calorimetric measurement of the heats of mixing in the liquid (4-6), and the Gibbs free energy of mixing in the liquid, determined from activity measurements (7). It was proposed that the free energies were in error (3). Other information in the current literature also suggests that the previously measured activities may be incompatible with the other thermochemical information, and in particular, may be a bit high. An analysis of the available heat of mixing and the phase diagram information using a linear programming optimization technique (8) resulted in α_{InGa} values (with α defined as $\ln \gamma_{\text{In}}/[1 - N_{\text{In}}]^2$) that were considerably smaller than those obtained from the existing activity data (7). Furthermore, several investigators have successfully applied a quasichemical model to the In-Ga-As, In-Ga-Sb, and In-Ga-P systems using a value of α which was fortuitously taken

* Electrochemical Society Active Member.

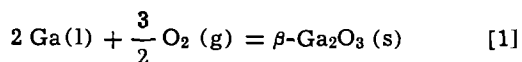
Key words: solution thermodynamics, liquid alloys, free energy.

to be smaller by a factor of 2.303 than the reported experimental value (owing to a misinterpretation of the data) (9-13).

In light of the present uncertainty about the thermochemistry of this system, particularly concerning the free energies of mixing, a direct measurement of activities appeared desirable. The activities of Ga in liquid Ga-In solutions were measured using an electrochemical cell employing a solid oxide electrolyte. The electrochemical cell can be represented as



The equilibrium reactions at each electrode may be written as



$$K = \frac{a_{\text{Ga}_2\text{O}_3}}{a_{\text{Ga}}^2 P_{\text{O}_2}^{3/2}} \quad [2]$$

with K being a constant for a given temperature. Assuming unit activities for Ga_2O_3 and pure Ga

$$a_{\text{Ga}}^{-4/3} = \frac{P_{\text{O}_2}(\text{Ga-In}, \text{Ga}_2\text{O}_3)}{P_{\text{O}_2}(\text{Ga}, \text{Ga}_2\text{O}_3)} \quad [3]$$

where a_{Ga} is the activity of Ga in the Ga-In alloy. The partial pressures of O_2 are related to the cell emf by the relation

$$E = \frac{RT}{4F} \ln \frac{P_{\text{O}_2}(\text{Ga-In}, \text{Ga}_2\text{O}_3)}{P_{\text{O}_2}(\text{Ga}, \text{Ga}_2\text{O}_3)} \quad [4]$$

Thus one obtains

$$\ln a_{\text{Ga}} = - \frac{3EF}{RT} \quad [5]$$

where E is the cell emf and F is the Faraday constant.

Experimental

A schematic diagram of the cell is given in Fig. 1. The Ga, $\beta\text{-Ga}_2\text{O}_3$ reference electrode was contained in the bottom of a calcia-stabilized zirconia (CSZ) vacuum-tight tube, $\frac{1}{4}$ in. in diameter and 18 in. long. Small pieces of solid gallium were placed in the bottom

of the tube and melted with a heat gun. $\beta\text{-Ga}_2\text{O}_3$ powder was placed on top of the pool of liquid gallium. The Ga-In, $\beta\text{-Ga}_2\text{O}_3$ electrode was contained in the bottom of an alumina tube, $\frac{1}{8}$ in. in diameter and 14 in. long. A layer of $\beta\text{-Ga}_2\text{O}_3$ powder was placed in the bottom of the tube, and weighed pieces of gallium and indium were placed on top of the $\beta\text{-Ga}_2\text{O}_3$ powder.

Pure argon gas was used to blanket both electrodes. It was purified by passing through activated Linde 4-A molecular sieve and titanium metal sponge (heated to 850°C). The argon line was constructed of stainless steel tubing with stainless steel Swagelok connectors. The argon was transported to the reference electrode via a $\frac{1}{8}$ in. diameter alumina tube. The lead wires to the electrodes were 0.010 in. platinum wire, with short pieces of tungsten wire spot welded to them just above the surfaces of the two electrodes. The tungsten thus provided the contact between the liquid metals and the platinum wires, and was found not to dissolve in the liquid gallium or gallium-indium alloys. The lead wire from the alloy electrode was grounded.

The cell was assembled with Viton O-ring connectors and was positioned so that the electrodes were in the constant temperature zone of a resistance-heated Marshall furnace. The temperature profile of the furnace was adjusted so that it was uniform to within $\pm 1^\circ\text{C}$ from the bottom of the alumina tube to a point well above the platinum-tungsten junctions in the electrode lead wires. The cell temperature was measured with a Pt-13% Rh thermocouple in thermal contact with the outside of the alumina tube containing the alloy electrode. The cell temperature was controlled with a Barber-Colman Model 357A Digiset null balance controller. The cell potential and the Pt-13% Rh thermocouple potential were measured with a L&N K-3 potentiometer and a L&N 9834 null detector.

At the start of each experiment, the cell was heated and alternately evacuated and flushed with the purified argon gas. When the cell temperature exceeded 200°C , the cell was filled with the argon, and a slow flow was maintained over both electrodes throughout the duration of the experiment. The CSZ tube was positioned so as to dip below the surface of the alloy electrodes.

The cell was heated slowly to 900°C and maintained at this temperature for several hours for the equilibration of the alloy components and for the saturation of the electrodes with oxygen by the dissolution of the $\beta\text{-Ga}_2\text{O}_3$ powder in the liquid metals. The temperature was then raised to 950°C and the cell was again allowed to equilibrate until the cell emf was constant with time (about 2 hr). The emf was then recorded and the temperature was lowered in increments of 50° to 800°C . At each temperature, the cell was allowed to equilibrate before the emf value was recorded. In some cases, in order to test the reversibility of the electrode reactions, readings were taken during both ascending and descending temperature cycles. The equilibrium cell voltages at a given temperature always agreed to within ± 0.5 mV.

To be certain that the alternating current in the furnace windings was not inducing stray voltages in the cell circuit, the power supply to the furnace was occasionally turned off just before the cell emf was recorded. No indication of such interference was ever observed. Further, no significant differences in cell voltages were observed to result from using different CSZ tubes or different reference electrode samples. Similarly, the emf values for identical samples at corresponding temperatures agreed to within ± 0.5 mV.

The gallium used was 7-9's purity, manufactured by Eagle-Picher Industries, Inc. The indium, also 7-9's purity, was produced by Cominco American, Inc., while the $\beta\text{-Ga}_2\text{O}_3$ was 4-9's purity from Research Organic/Inorganic Chemical Company. The vacuum-tight CSZ tubes contained 7.0 w/o (weight per cent) calcia and were manufactured by the Zirconium Corporation of America.

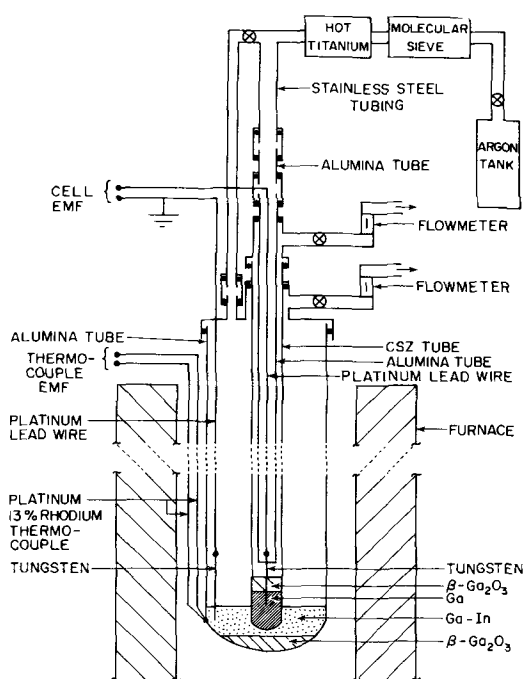


Fig. 1. Schematic diagram of the experimental apparatus

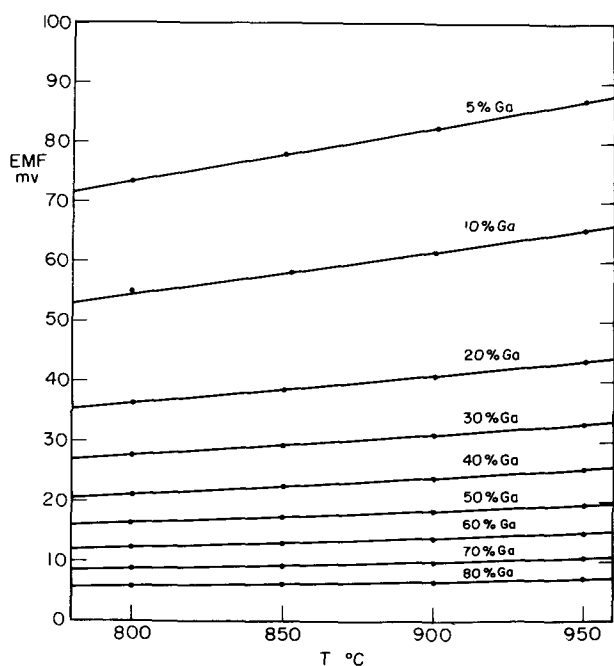


Fig. 2. Experimental emf values vs. temperature

Results and Discussion

The emf vs. temperature plots are shown in Fig. 2 for each of the compositions studied. In every case, the three higher temperature points follow linear relationships very closely.

Activities of Ga were calculated using Eq. [5]. The indium activities were calculated using the Gibbs-Duhem equation

$$N_{\text{Ga}} d \ln \gamma_{\text{Ga}} + N_{\text{In}} d \ln \gamma_{\text{In}} = 0 \quad [6]$$

Both sets of values are listed in Table I, together with the cell voltages. The activities are substantially smaller than those reported by Macur, Edwards, and Wahlbeck (7). They estimated α'_{InGa} (defined by

Table I. Experimental emf's and activities of Ga

N_{Ga}	Temperature, °K	EMF, mV	a_{Ga}	a_{In}^*
0.0502	1223.0	86.97	0.0836	0.9512
	1174.0	82.43	0.0864	0.9512
	1123.0	77.87	0.088	0.9513
0.0988	1072.0	73.64	0.0911	0.9513
	1223.0	65.45	0.154	0.9045
	1174.0	61.80	0.159	0.9048
0.2002	1125.0	58.40	0.1636	0.9050
	1073.0	55.10	0.1668	0.9051
	1223.0	43.43	0.289	0.816
0.2997	1172.5	41.08	0.294	0.817
	1122.5	38.72	0.300	0.818
	1073.0	36.35	0.307	0.819
0.4018	1223.0	32.89	0.391	0.733
	1173.0	31.19	0.396	0.735
	1124.0	29.57	0.400	0.737
0.4999	1073.0	27.79	0.406	0.738
	1223.0	25.44	0.484	0.653
	1173.0	24.07	0.489	0.656
0.6006	1123.0	22.58	0.496	0.659
	1073.0	21.35	0.500	0.660
	1223.5	19.26	0.578	0.572
0.6972	1173.0	18.32	0.580	0.572
	1125.0	17.34	0.584	0.576
	1073.0	16.35	0.588	0.580
0.7976	1223.0	14.75	0.588	0.582
	1173.0	13.95	0.657	0.487
	1123.0	13.15	0.661	0.492
0.8233	1073.0	12.51	0.665	0.497
	1223.0	10.47	0.669	0.500
	1173.0	9.86	0.742	0.393
0.8233	1123.0	9.41	0.7457	0.400
	1073.0	8.89	0.7465	0.404
	1223.0	8.21	0.749	0.409
0.8233	1173.0	7.21	0.814	0.286
	1123.0	6.72	0.819	0.293
	1073.0	5.98	0.823	0.297

* Calculated using Gibbs-Duhem equation.

$\log_{10} \gamma_{\text{In}} / [1 - N_{\text{In}}]^2$ at three temperatures and selected compositions, using a Knudsen effusion technique. The disparity between our data and theirs is not unexpected, since discrepancies between their results and those of previous studies have already been noted (3, 8). Some measure of the inconsistency in the Macur *et al.* data is indicated by the fact that the heats of mixing calculated by them using their measured activities give a value of 2200 cal/mole at $N_{\text{In}} = 0.5$, which compares unfavorably with the Bros *et al.* value of 265 cal/mole (5).

Rao and Tiller (8) conducted an analysis, using a linear programming optimization technique, in which the liquidus (6, 14) and heat of mixing data (4) were simultaneously analyzed. Using an iterative technique, they obtained a consistent set of α 's (in the solid and liquid solutions) and phase equilibrium lines. The experimental activities in this work at all the temperatures are in good agreement with those computed using the Rao and Tiller α -parameters. By way of example, the comparison is shown graphically in Fig. 3 for the 950°C points. The figure also includes our calculated indium activities and all of the experimental values for the activity of In at 950°C reported by Macur *et al.* (7).

Several thermochemical quantities were computed using the experimental information. The parameter α_{GaIn} can, in general, be expected to have the form (15)

$$\alpha_{\text{GaIn}} = l + a N_{\text{In}} + b/T + c N_{\text{In}}/T \quad [7]$$

where l , a , b , and c are constant with temperature and composition. This is consistent with the assumption that the heats and excess entropies of mixing are independent of temperature. This is usually a good assumption in metallic systems and has been validated for the heats by Bros (4) and Bros *et al.* (5) for the system In-Ga. They further showed that the heats are symmetrical about the $N_{\text{Ga}} = 0.5$ composition point, thus indicating (15) that the parameter c in the equation above is essentially zero. The calculated values of α_{GaIn} are given in Fig. 4 as functions of composition and show only a slight composition dependence of α_{GaIn} at all the temperatures. The fact that the slopes are independent of temperature is consistent with the above deduction that $c \approx 0$. The α -function is very sensitive to changes in activity, particularly at high Ga concentrations. Therefore, the consistency displayed in Fig. 4 shows the inherent accuracy of the technique. The nature of the scatter is systematic, i.e., the deviation for each composition from the best fit line is essentially the same for each of the temperatures. The extreme sensitivity of the α -function at compositions approaching pure Ga makes the calculation of α at $N_{\text{Ga}} = 0.80$ unreliable and, although the points have been plotted, the degree of correspondence with the other points is scarcely significant.

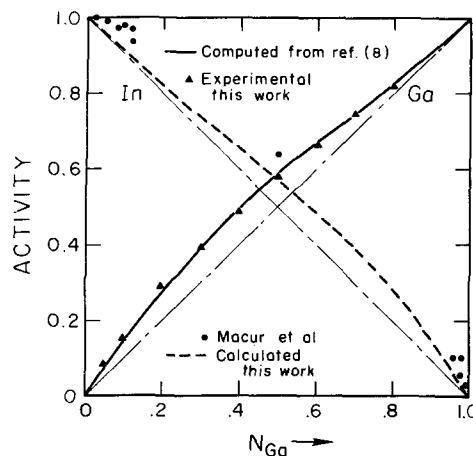


Fig. 3. Activities of Ga and In at 1223°K

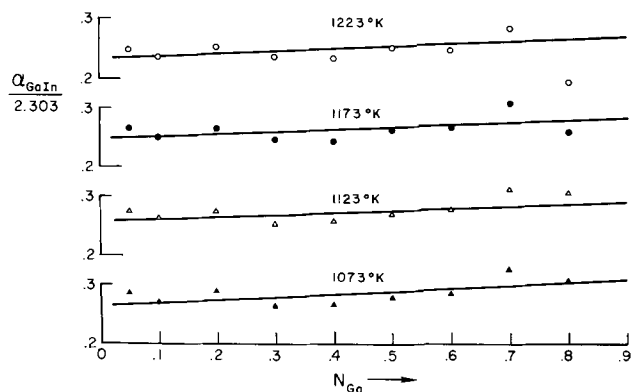


Fig. 4. Dependence of α_{GaIn} on N_{Ga}

This method cannot be expected to give accurate heats and entropies of mixing because of the inherent uncertainties, in general, in the deduction of entropies and enthalpies indirectly from the free energy measurements. Nevertheless, these quantities were calculated in order to show the general consistency in the measurements. The partial molar heats and excess entropies of solution of Ga can be calculated from the slopes and intercepts of the emf vs. temperature lines, since

$$\Delta \bar{F}_{\text{Ga}} = -nEF = \Delta \bar{H}_{\text{Ga}} - T\Delta \bar{S}_{\text{Ga}} \quad [8]$$

Figure 5 shows $\Delta \bar{H}_{\text{Ga}}$ and ΔH^{M} , the partial molar heat of solution of Ga and the integral heat of mixing, respectively. The latter was calculated assuming that the ΔH^{M} was symmetrical about the $N_{\text{Ga}} = 0.50$ composition point. Considering the associated uncertainties, the comparison with the points of Bros *et al.* (5) and Predel and Stein (6) is reasonable. The maximum difference in the ΔH^{M} occurred with the data of Bros *et al.* at 50% Ga and is of the order of 70 cal. The $\Delta \bar{S}_{\text{Ga}}$ values calculated from the slopes were scattered on a trajectory slightly more positive than that for an ideal solution. A more meaningful calculation is that of the excess entropies using the free energies measured in this work and the heats of mixing of Bros *et al.* (5), which appear to be very accurate. $\Delta \bar{S}^{\text{xs}}_{\text{Ga}}$ has been

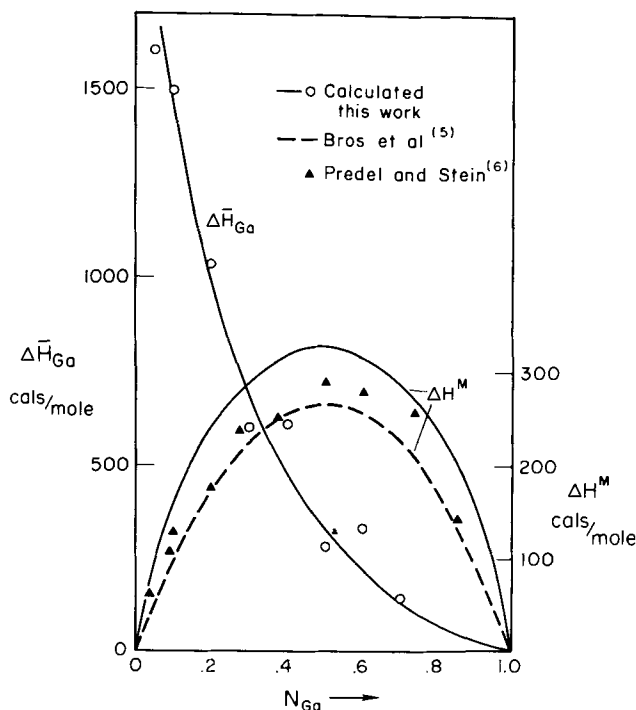


Fig. 5. Heats of mixing in liquid In-Ga alloys

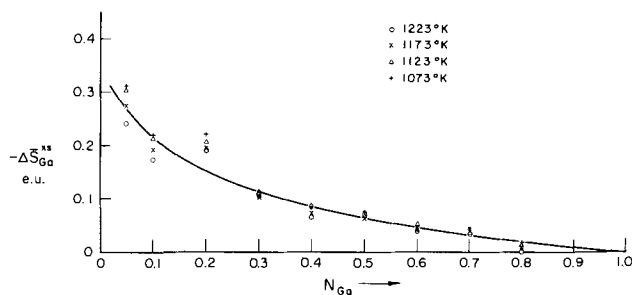


Fig. 6. Dependence of calculated values of $\Delta \bar{S}^{\text{xs}}_{\text{Ga}}$ on N_{Ga} in In-Ga alloys.

calculated in this fashion at all the four temperatures, and the results plotted in Fig. 6. Considering the sensitivity of the scale upon which the plot is made, the resulting set of points shows good consistency. Table II lists thermochemical quantities of 1223°K obtained using this excess entropy curve and the Bros *et al.* (5) heats of mixing.

Certain aspects of the experimental technique merit discussion. An important consideration is the solubility of oxygen in the In-Ga alloy and the extent of ternary interaction, since the system is in reality the ternary In-Ga-O and is merely being approximated to be the binary In-Ga. The effect, however, is expected to be small in the present system due to low oxygen solubility. The solubility of O in liquid Ga is of the order of 10^{-3} a/o (atomic per cent) at 800°C (16). The component activities are not expected to be influenced by the small oxygen concentration. Another source of error, loss of the constituents by evaporation, is also unimportant in this system since the vapor pressures of Ga and In are of the order of 10^{-5} - 10^{-6} atm at 950°C.

Another consideration is the relative stability of the various oxides in the system. The free energy of formation of $\beta\text{-Ga}_2\text{O}_3$ is very much more negative than those of Ga_2O , In_2O , and In_2O_3 . Therefore, the stable oxide present at all times can be expected to be $\beta\text{-Ga}_2\text{O}_3$. Separate electrode chambers and argon streams prevented communication between the two electrodes via the gas phase, thus eliminating another possible source of error.

The error limits set on the activity values at each of the temperatures can be ascribed to the ± 0.5 mV reproducibility discussed previously, and other sources such as any electronic conductivity present in the calcia-stabilized zirconia. The consistency of the results appears to indicate a very small contribution, if any, from this last source.

The partial pressures of oxygen in equilibrium with Ga and $\beta\text{-Ga}_2\text{O}_3$ may be calculated from the free energy of formation data for $\beta\text{-Ga}_2\text{O}_3$, as obtained by Pankratz and Kelley (17). Several investigators (18, 19) have determined the values of oxygen partial pressure corresponding to an ionic transference number, t_i , equal to 0.99 for the calcia-stabilized zirconia electrolyte. The oxygen partial pressures in equilibrium

Table II. Thermochemical quantities at 1223°K calculated using Fig. 6 and Bros *et al.* (5) data

N_{Ga}	$\Delta \bar{H}_{\text{Ga}}^*$	$\Delta \bar{S}^{\text{xs}}_{\text{Ga}}$	$\Delta \bar{F}^{\text{xs}}_{\text{Ga}}$	a_{Ga}
0.1	859	-0.215	1122.0	0.158
0.2	678	-0.150	870.0	0.286
0.3	520	-0.113	658.0	0.393
0.4	382	-0.086	487.0	0.489
0.5	265	-0.064	343.0	0.576
0.6	170	-0.047	228.0	0.659
0.7	95.5	-0.032	134.7	0.740
0.8	42.4	-0.018	64.5	0.822
0.9	10.6	-0.009	21.6	0.908

* From heats of mixing of Bros *et al.* (5).

with Ga and β -Ga₂O₃ are larger than those reported to correspond to $t_i = 0.99$. Since the oxygen partial pressures in equilibrium with the Ga-In alloys and β -Ga₂O₃ are uniformly larger than those in equilibrium with mixtures of Ga and β -Ga₂O₃, we are justified in expecting that the electrolyte exhibits practically pure ionic conductivity for the range of temperature and oxygen partial pressure encountered in this work.

Conclusions

The galvanic cell technique, utilizing CSZ as the solid electrolyte, was used to measure the activities of Ga in liquid Ga-In alloys. The measured activities are significantly smaller than those reported previously and are in good agreement with activities calculated from heats of mixing and liquidus determinations. The partial molar excess entropies of solution were determined to be negative and small.

Similar measurements on other systems relevant to the III-V binary and ternary semiconducting compounds are desirable in order to provide a sound basis for the processing of these materials. The present technique appears appropriate for determining isothermal activities in systems containing Ga or In as the least noble constituent.

Acknowledgments

The indium used in this study was kindly provided by the Materials Research Department of the Hewlett Packard Laboratory. This research was supported by the Advanced Research Projects Agency through the Center for Materials Research at Stanford University.

Manuscript submitted Jan. 17, 1972; revised manuscript received April 27, 1972.

Any discussion of this paper will appear in a Discussion Section to be published in the June 1973 JOURNAL.

REFERENCES

1. M. Ilegems and G. L. Pearson, in "Proceedings 1968 Symposium on GaAs," p. 3, Inst. of Physics and Physical Soc., London (1969).
2. T. Y. Wu and G. L. Pearson, *J. Phys. Chem. Solids*, **33**, 409 (1972).
3. F. H. Hayes and O. Kubaschewski, *J. Inst. Metals*, **97**, 381 (1969).
4. J. P. Bros, *Compt. Rend.*, **263**, 977 (1966).
5. J. P. Bros, R. Castanet, and M. Laffitte, *ibid.*, **264**, 1804 (1967).
6. B. Predel and D. W. Stein, *J. Less-Common Metals*, **18**, 49 (1969).
7. G. J. Macur, R. K. Edwards, and P. G. Wahlbeck, *J. Phys. Chem.*, **72**, 1047 (1968).
8. M. V. Rao and W. A. Tiller, *J. Mater. Sci.*, **7**, 14 (1972).
9. G. Stringfellow and P. E. Greene, *J. Phys. Chem. Solids*, **30**, 1779 (1969).
10. G. A. Antypas, *This Journal*, **117**, 1393 (1970).
11. A. W. Mabbitt, *J. Mater. Sci.*, **5**, 1043 (1970).
12. G. M. Blom and T. S. Plaskett, *This Journal*, **118**, 1831 (1971).
13. G. M. Blom, *This Journal*, **118**, 1834 (1971).
14. W. J. Swirbely and S. M. Selis, *J. Phys. Chem.*, **58**, 33 (1954).
15. M. V. Rao and W. A. Tiller, *J. Phys. Chem. Solids*, **31**, 191 (1970).
16. L. M. Foster and J. Scardefield, *This Journal*, **116**, 494 (1969).
17. L. B. Pankratz and K. K. Kelley, *U. S. Bur. Mines, Rept. Invest.* **6198** (1963).
18. J. W. Patterson, E. C. Bogren, and R. A. Rapp, *This Journal*, **114**, 752 (1967).
19. J. D. Tretyakov, *Neorg. Materials (USSR)*, **2**, 501 (1966).

Technical Notes



Growth Via Leakage Paths of Nickel Oxide on Nickel at High Temperatures

M. J. Graham, D. Caplan, and M. Cohen*

Division of Chemistry, National Research Council of Canada, Ottawa, Ontario, Canada K1A 0R9

In the high temperature oxidation of nickel, parabolic kinetics are expected since growth of the oxide layer proceeds by a diffusion process, the outward movement of cations. In experiments with annealed and cold-worked nickel (1) in which cold-worked nickel developed finer-grained oxide and oxidized more rapidly, it was concluded that the faster oxidation resulted from the large number of high-diffusivity paths provided by the fine-grained oxide. The apparent instantaneous parabolic rate constant, $2W \cdot dW/dt$,¹ decreased with oxidation time because the preferred paths for diffusion are progressively eliminated by a combination of annealing and grain growth.

It follows that this apparent parabolic rate constant is made up of two components: the normal lattice diffusion, plus a contribution from so-called leakage

paths (1-12). For cold-worked nickel the contribution from leakage paths is greatest at short times and low temperatures; that from lattice diffusion is small at low temperatures, < 700°C, but becomes appreciable as the temperature is increased. By correcting oxidation rates on cold-worked nickel for lattice diffusion, and by taking into account leakage path density changes during growth, it is possible to calculate parabolic rate constants and an activation energy for growth via leakage paths only. The paper outlines the evaluation of the rate constants and the activation energy.

Treatment of Data

The contribution from lattice diffusion may be determined from oxidation data on annealed nickel. The thinnest oxides formed on annealed nickel, from 700° to 1270°C, are monocrystalline and are considered to grow exclusively by lattice diffusion. Parabolic rate constants (as W^2/t) were determined by Caplan *et al.* (1) from thickness measurements of the thinnest oxides

* Electrochemical Society Active Member.

Key words: kinetics, leakage-path diffusion.

¹ K_p , as $2W \cdot dW/dt$, is obtained as the product of the measured slope of the weight gain curve at any time and twice the weight gain at that time. Units used are $\text{mg}^2 \text{cm}^{-2} \text{hr}^{-1}$.

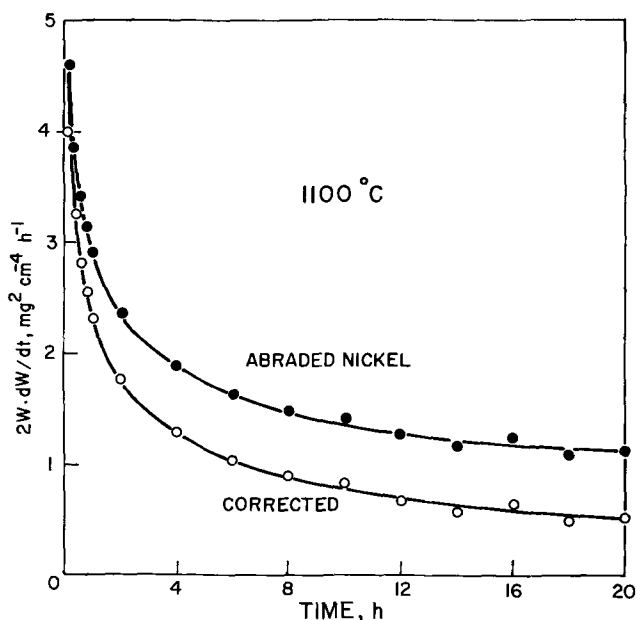


Fig. 1. Values of $2W \cdot dW/dt$ from oxidation at 1100°C of Ni cold-worked by abrasion with 600-grit SiC (1) (filled circles); and values corrected for the contribution from lattice diffusion ($K_p = 0.60 \text{ mg}^2\text{cm}^{-4}\text{hr}^{-1}$) to give values of $2W \cdot dW/dt$ for growth via leakage paths (open circles).

and an activation energy of $54 \text{ kcal mole}^{-1}$ was found for growth by lattice diffusion (see Fig. 3). Values of W and $2W \cdot dW/dt$ for growth via leakage paths only, are thus obtained by subtracting from data on abraded nickel the weight gain and rate given by the parabolic rate constants for lattice growth. Figure 1 shows the corrected $2W \cdot dW/dt$ values at 1100°C .

The rate of oxygen uptake, dW/dt , is proportional to N , the number of easy diffusion paths per unit area. The rate of uptake also decreases as the oxide thickens, because transport is by diffusion. Thus, for growth via leakage paths

$$\frac{dW}{dt} = K_1 \frac{N}{W} \quad \text{or} \quad 2W \cdot \frac{dW}{dt} = 2K_1N \quad [1]$$

Since $2W \cdot dW/dt$, the instantaneous parabolic rate constant, diminishes with time as the density of low resistance paths decreases (Fig. 1), the data at different temperatures can best be compared by extrapolating values of $2W \cdot dW/dt$ to zero time. It is necessary to assume that the density of paths at zero time, N_0 , does not vary significantly with temperature. Over a limited temperature range this is a reasonable assumption for a given surface preparation, oxidation pressure, etc. As it is not feasible to compare values of $2W \cdot dW/dt$ at the same grain size for different temperatures, the assumption of an invariant N_0 with temperature is considered to be the least objectionable compromise. It is difficult to determine values of $2W \cdot dW/dt$ at $t = 0$ by extrapolation because of the very rapid initial decrease (Fig. 1); Eq. [1] will, therefore, be modified to yield these values more readily.

The decrease in the density of easy diffusion paths could be by a first order reaction or by a grain growth process. A first order rate expression was used by Evans *et al.* in a mechanism based on mutual pore blocking (2, 3) and later applied by Smeltzer *et al.* to the oxidation of titanium, zirconium, and hafnium (6). The treatment assumes that the rate of decrease of paths is dependent upon the number of paths remaining, i.e.

$$-dN = K_2N \, dW$$

or

$$N = N_0 e^{-K_2W} \quad [2]$$

Substituting for N in Eq. [1] we have

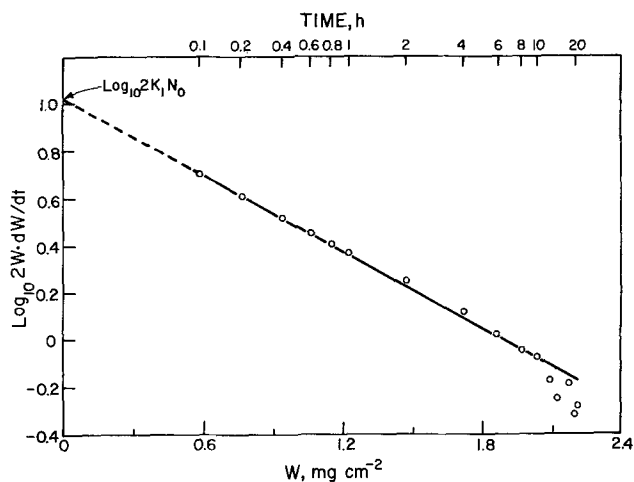


Fig. 2. Plot of $\log_{10} 2W \cdot dW/dt$ against W for data on abraded Ni at 1100°C corrected for the contribution from lattice diffusion (corresponding oxidation times are also indicated); $\log_{10} 2K_1N_0$ is the initial value of $\log_{10} K_p$ used in determining the activation energy for growth via leakage paths.

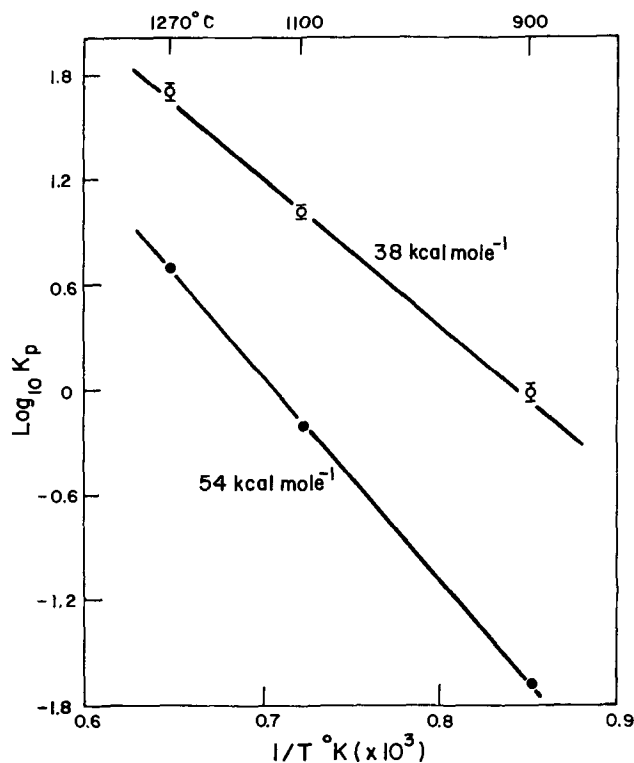


Fig. 3. Arrhenius plot for Ni oxidation from 900° to 1270°C ; the activation energies are $38 \pm 2 \text{ kcal mole}^{-1}$ for growth by leakage path diffusion (this study) and $54 \text{ kcal mole}^{-1}$ for growth by lattice diffusion [Ref. (1)] (the error bars indicate the uncertainty in evaluating the intercept, $\log_{10} 2K_1N_0$).

$$2W \cdot \frac{dW}{dt} = 2K_1N_0 e^{-K_2W} \quad [3]^2$$

or

$$\log_{10} 2W \cdot \frac{dW}{dt} = \log_{10} 2K_1N_0 - \frac{K_2W}{2.303} \quad [4]$$

$2K_1N_0$ is the initial value of the instantaneous parabolic rate constant (at $W = 0$, $t = 0$) to be used in determining the activation energy for growth via leak-

² Integrating Eq [3] results in the rate expression

$$\frac{e^{K_2W}}{K_2} \left[W - \frac{1}{K_2} \right] + \frac{1}{K_2^2} = K_1N_0t$$

age paths. From Eq. [4] values may be obtained from the intercept of a plot of $\log_{10} 2W \cdot dW/dt$ against W . Data on abraded nickel, corrected for lattice diffusion, did yield a straight line when plotted in this form and the intercept value of $\log_{10} 2K_1N_0$ was readily determined. The plot for data at 1100°C is shown in Fig. 2. At long times, where the number of leakage paths is approaching a minimum, W tends to a constant value as $2W \cdot dW/dt$ approaches zero.

Although the data comply reasonably well with a first order reduction in leakage paths, other rate expressions are not precluded. An alternative one based on a decrease in leakage paths by a grain growth process (8) did not, however, fit the data as well, nor could good measures of $2K_1N_0$ be obtained. As our primary concern in this treatment is to obtain values of K_p at zero time, in order to provide the activation energy for leakage path growth, the precise manner in which the density of low resistance paths decreases with time is of secondary importance. Hence, values of $2K_1N_0$ readily obtained from plots, as in Fig. 2, have been adopted in determining the activation energy. Figure 3 shows K_p as $2K_1N_0$ plotted in Arrhenius form and the activation energy for growth via leakage paths of NiO on Ni from 900° to 1270°C is found to be 38 ± 2 kcal mole⁻¹. This is in agreement with values of 41 and 37 kcal mole⁻¹ determined by Graham *et al.* in nickel oxidation studies from 300° to 700°C where growth was almost exclusively by transport, presumably of cations, via high-diffusivity paths (11, 12). These values are significantly less than 54 kcal mole⁻¹ representing growth by lattice diffusion.

Acknowledgment

The authors thank Dr. R. J. Hussey for helpful discussions.

Manuscript submitted Feb. 15, 1972; revised manuscript received May 10, 1972.

Any discussion of this paper will appear in a Discussion Section to be published in the June 1973 JOURNAL.

REFERENCES

1. D. Caplan, M. J. Graham, and M. Cohen, *This Journal*, **119**, 1205 (1972).
2. D. E. Davies, U. R. Evans, and J. N. Agar, *Proc. Roy. Soc. (London)*, **A225**, 443 (1954).
3. U. R. Evans, "The Corrosion and Oxidation of Metals." Edward Arnold, London (1960).
4. E. A. Gulbransen and K. F. Andrew, *This Journal*, **101**, 128 (1954).
5. K. R. Lawless and A. T. Gwathmey, *Acta Met.*, **4**, 153 (1956).
6. W. W. Smeltzer, R. R. Haering, and J. S. Kirkaldy, *ibid.*, **9**, 880 (1961).
7. J. M. Perrow, W. W. Smeltzer, and R. K. Ham, *ibid.*, **15**, 577 (1967).
8. J. M. Perrow, W. W. Smeltzer, and J. D. Embury, *ibid.*, **16**, 1209 (1968).
9. G. B. Gibbs, *Corrosion Sci.*, **7**, 165 (1967).
10. J. V. Cathcart, G. F. Petersen, and C. J. Sparks, Jr., *This Journal*, **116**, 664 (1969).
11. M. J. Graham and M. Cohen, *ibid.*, **119**, 879 (1972).
12. M. J. Graham, G. I. Sproule, D. Caplan, and M. Cohen, *ibid.*, **119**, 883 (1972).

The High Temperature Sulfidation Properties of Nickel-Chromium Alloys

G. Romeo*

Research and Development Center, General Electric Company, Schenectady, New York 12301

and W. W. Smeltzer*

Department of Metallurgy and Materials Science, McMaster University, Hamilton, Ontario, Canada

The reaction between sulfur vapor and nickel-chromium alloys has been the subject of a comprehensive study by Mrowec, Werber, and Zastawnik (1). The sulfidation kinetics and the morphologies of the corrosion products were investigated for the whole range of binary alloy compositions at temperatures from 600° to 900°C and at 1 atm sulfur pressure. With the help of marker studies, a sulfidation model was proposed that accounted for the parabolic growth of the scales as a result of diffusion processes. At very low, as well as at very high alloy chromium contents, homogeneous sulfide scales were found consisting respectively of a solid solution of chromium sulfide in nickel sulfide or *vice-versa*. In the intermediate alloy composition range a duplex scale was reported, the outer layer of which was homogeneous and consisted of nickel sulfide ($Ni_{1-x}S$), while the inner layer was heterogeneous and its morphology varied with the amount of chromium in the alloy. In particular, the inner layer on alloys containing more than 20 weight per cent (w/o) Cr consisted of chromium sulfide (Cr_2S_3) as a dispersing phase for islands and needle-shaped crystals of nickel sulfide. These findings were exemplified by micrographs and x-ray images of the

cross section of a Ni-32.6 w/o Cr alloy sulfidized at 900°C. Since the nickel sulfide stringers lay across the inner chromium sulfide layer, linking the metal with the outer nickel sulfide layer, the hypothesis was advanced that these stringers could provide preferential paths for the outward diffusion of nickel ions.

More recently, Romeo, Smeltzer, and Kirkaldy (2) have reported a study of the sulfidation of a Ni-20 w/o Cr alloy at 700°C in hydrogen-hydrogen sulfide atmospheres, the composition of which varied in the range 5-100 volume per cent (v/o) H_2S . The kinetics also conformed, in this case, to the parabolic law and duplex scales were obtained as corrosion products. However, examination with the optical and the scanning electron microscope did not show any evidence of heterogeneity in the inner chromium sulfide layer. Electron microprobe counting indicated nickel solubility in the inner layer of about 2-3 atomic per cent (a/o). They concluded that outward diffusion of nickel ions could take place through the inner chromium sulfide layer, its whole cross section providing a bridge for nickel transport towards the gas phase. Occupation of chromium sites by nickel ions has indeed been suggested (1) to explain the slower sulfidation rate of low nickel content Ni-Cr alloys with respect to pure chromium.

* Electrochemical Society Active Member.

Key words: sulfidation, nickel-chromium alloys, sulfide morphologies, nickel-nickel sulfide eutectic.

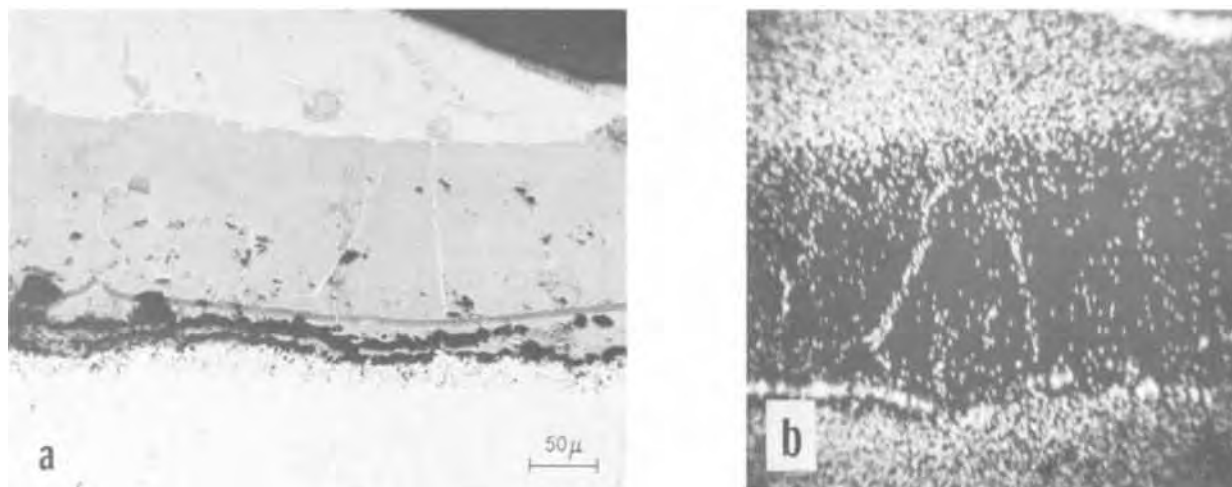


Fig. 1a. Duplex sulfide scale formed on a Ni-35 weight per cent (w/o) Cr alloy in a H_2 -10% H_2S atm at $850^\circ C$; nickel sulfide stringers can be seen in the inner chromium sulfide layer; the outer nickel sulfide layer was molten at reaction temperature. Fig. 1b. X-ray $Ni_{K\alpha}$ image of the specimen cross section.

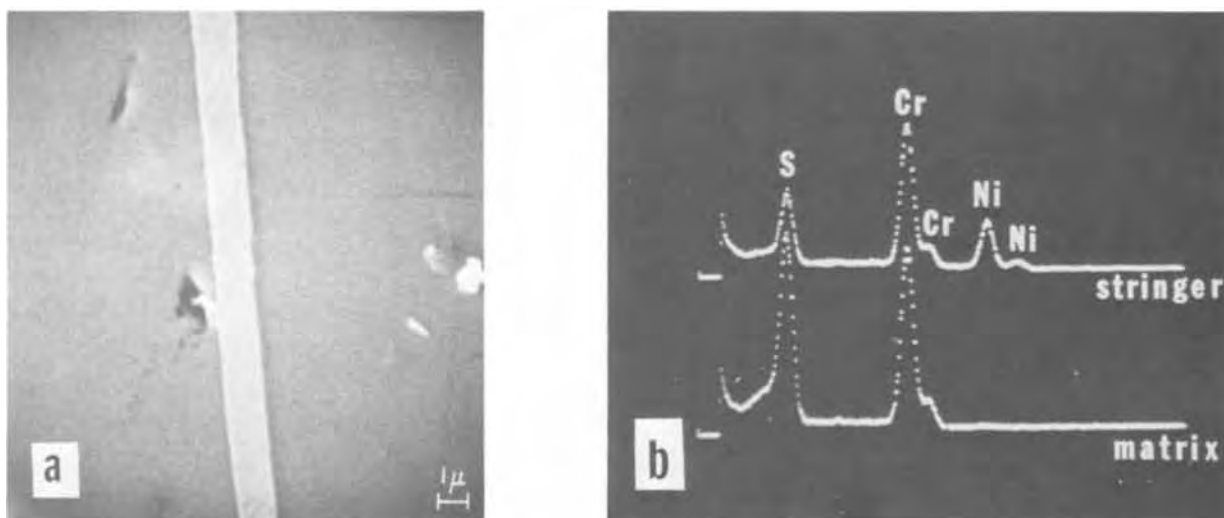


Fig. 2a. Scanning electron microscope image of a nickel sulfide matrix; Fig. 2b, x-ray characteristic peaks of the elements present in the stringer and the matrix.

In the course of the above study (2), the tendency was noticed for the Ni-Cr alloy to form a liquid sulfide phase at relatively low temperature. It is well known that the eutectic, Ni-Ni₃S₂, exhibits a melting point of $645^\circ C$. Consequently, sulfidation of Ni-Cr alloys could possibly lead to gas-liquid-solid reactions at temperatures above $800^\circ C$. The striking difference in the morphology of scales formed in H_2 - H_2S atmospheres on a Ni-20 w/o Cr alloy at 700° and $900^\circ C$ was reported a decade ago by Hancock (3). While at the lower temperature a duplex uniform sulfide scale was formed, at the higher temperature spheroidal chromium sulfide particles were imbedded in a nickel-nickel sulfide matrix which was liquid at reaction temperature.

We consider, accordingly, the possibility that liquid nickel sulfide formation may cause the needle-shaped heterogeneities in the inner layer reported by other authors (1). For example, Fig. 1a shows the cross-section of a Ni-35 w/o Cr alloy sulfidized at $850^\circ C$ in a H_2 -10% H_2S atm, and the corresponding x-ray $Ni_{K\alpha}$ image as shown in Fig. 1b. A sudden rapid weight gain of the specimen attached to a thermogravimetric balance indicated the formation of liquid nickel sulfide. The presence of nickel sulfide stringers running across the inner chromium sulfide layer is evident in the

micrographs. Most probably the liquid has wet the chromium sulfide solid layer, dissolving it preferentially at grain boundaries.

This point of view is supported by analyses run with a solid-state x-ray detector mounted on a scanning electron microscope. This device can detect the presence of elements with atomic number equal or greater than 9 (4). Figure 2a shows a highly magnified micrograph of a nickel sulfide stringer, taken with the scanning electron microscope. The electron beam was then focused on the stringer and on the adjacent chromium sulfide matrix. The resulting x-ray spectra are shown in Fig. 2b. The matrix spectrum shows the K_α and K_β peaks for chromium and the K_α peak for sulfur, while the stringer spectrum shows additional K_α and K_β peaks for nickel. This accounts for some solubility of chromium sulfide in the liquid nickel sulfide.

In conclusion, sulfidation of Ni-Cr alloys at sufficiently low temperature takes place entirely as a gas-solid reaction which may lead to formation of a duplex sulfide scale consisting of homogeneous layers of chromium and nickel sulfides. A likely cause of heterogeneity in the inner layer at higher temperatures is the formation of a liquid nickel sulfide phase which occurs as stringers in the solid chromium sulfide layer.

This occurrence is actually recognized as a feature of accelerated corrosion of Ni-base alloys exposed to sulfur bearing atmospheres.

Acknowledgment

The authors are indebted to M. F. Ciccarelli for the electron microprobe and S.E.M. analyses. The work by one author (W. W. Smeltzer) was carried out under the auspices of Falconbridge Nickel Mines Limited.

Manuscript submitted March 17, 1972; revised manuscript received May 10, 1972.

Ohmic Contacts to Zinc Telluride

W. D. Baker¹ and A. G. Milnes*

Electrical Engineering Department, Carnegie-Mellon University, Pittsburgh, Pennsylvania 15213

Zinc telluride is a wide-gap (2.25 eV), p-type, II-VI semiconducting compound. One of the important problems in the fabrication of devices from ZnTe is the preparation of suitable ohmic contacts. We report here the results of some quantitative measurements on ohmic contacts to this semiconductor.

Experimental

The ZnTe samples were bars with a 1 mm by 1 mm cross section and a 3 mm length. They had a carrier concentration in the low 10^{16} cm⁻³ range. The bars were first solvent cleaned and chemically etched, and then contacts were made to the ends of the bars by alloying, evaporation, or plating. After the contacts were masked with wax, the bars were given a final light etching. Various etches were investigated and three were used. These etches are: etch in hot, 50% NaOH for a few seconds followed by a rinse in warm, dilute NaOH and then warm water rinses (1); etch in a solution of 40 ml H₂O, 5 ml H₂SO₄, 1g K₂Cr₂O₇ at 60°C for about a minute followed by warm water rinses (2); or etch in a 1-5% solution of Br in methanol for 1-2 min followed by methanol rinses. Different etches caused no detectable difference in the ohmic contact quality.

Many of the contacts considered were immediately rejected after a curve-tracer examination because of very high resistance or extreme nonlinearity of the volt-ampere characteristic. Table I summarizes the unsatisfactory contacts. All of these contacts were subjected to various heat cycles without significant improvements in their behavior.

Some successful contacts were found from previous literature, and from our experiments, and four types of contact were studied for linearity and contact resistance quantitatively at 300°K, and qualitatively at 196°K and 77°K. The contacts examined were tin + 1%

* Electrochemical Society Active Member.

¹ Present address: Electrical Engineering Department, West Virginia University, Morgantown, West Virginia 26506.

Key words: semiconductor, zinc telluride, ohmic contacts.

Table I. Unsatisfactory ohmic contacts to ZnTe

Alloyed		Evaporated	Plated
Bi	In + Sn	Ag	Cu
In	Pb + Ag	Au	Ni
Pb	Pb + Sb		
Sn	Sn + Ag		
Te	Sn + Au		
Tl	Sn + Sb		
	Wetalloy 232*		

* Trademark for a proprietary alloy of Hg, Ga, and Tl manufactured by Victor King Laboratories, Los Altos, Calif.

Any discussion of this paper will appear in a Discussion Section to be published in the June 1973 JOURNAL.

REFERENCES

1. S. Mrowec, T. Werber and M. Zastawnik, *Corrosion Sci.*, **6**, 47 (1966).
2. G. Romeo, W. W. Smeltzer, and J. S. Kirkaldy, *This Journal*, **118**, 740 (1971); *ibid.*, **118**, 1336 (1971).
3. P. Hancock, "First International Congress on Metallic Corrosion, London, 1961," p. 193, Butterworths (1962).
4. E. Lifshin, in "Energy Dispersion X-ray Analysis; X-ray and Electron Probe Analysis," ASTM Special Technical Publication 485, p. 140 (1971).

arsenic alloy, electroless gold, lithium-diffused, and silver-diffused contacts. The tin-arsenic contacts were alloyed at 400°C for 1 min in a hydrogen atmosphere with 1% HCl gas present as a flux. The electroless gold was plated from a water solution of HAuCl₄. The lithium diffused contacts were formed using the technique of Aven and Garwacki (1) in which the contact area is coated with a LiNO₃ solution and then heated to 350°C for about 1 min in a hydrogen atmosphere. The silver diffused contacts were made by coating the contact area with an AgNO₃ solution which was dried and then heated to 400°C for about 1 min in a hydrogen atmosphere. Both the lithium- and silver-diffused contacts were covered with electroless gold.

Contact resistance measurements were made by passing a current through the bar and then probing the potential along the bar. The resulting plot of voltage vs. distance was extrapolated to the ends of the bar to infer the contact drop. The contact drop divided by

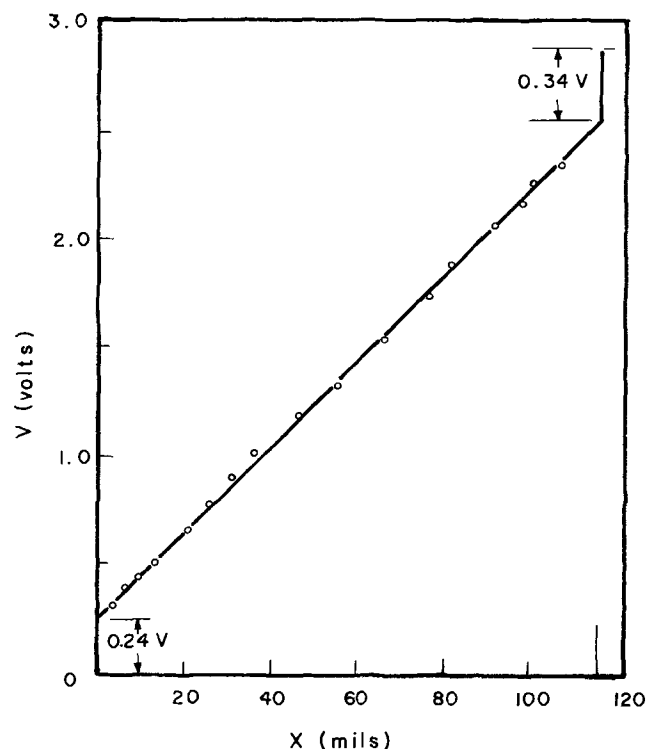


Fig. 1. Voltage vs. distance along a ZnTe bar with two lithium-doped contacts at $T = 300^\circ\text{K}$ and current density $= 0.7$ A/cm².

Table II. Contact measurements on ZnTe ($1 \times 10^{16} \text{cm}^{-3}$ free holes)

Contact	Average specific resistance (300°K) (ohm-cm ²)	Maximum useful current density (300°K) (A/cm ²)	Useful at 77°K
Electroless Au	3.0×10^{-1}	<0.2	No
Sn + 1% As alloy	8.6×10^{-1}	>2	No
Li diffused	2.8×10^{-1}	>2	Yes
Ag diffused	4.0×10^{-2}	>2	Yes

the current density is the specific contact resistance. The potential probe was a tinned phosphor-bronze wire finely pointed. It was necessary to form the probe contact by a capacitor discharge in order to form a reliable contact to the ZnTe surface (3).

Results

A typical plot of voltage vs. distance is shown in Fig. 1 for a lithium diffused contact at room temperature with a current density of 0.7 A/cm². The resulting specific contact resistances for the two contacts are 0.34 ohm-cm² and 0.49 ohm-cm². Reversal of the current direction did not change the measured contact resistance. Similar curves were obtained for the other

contact materials (4). For the silver-diffused contacts, the voltage vs. distance curves tend to flatten out near the ends of the bar, suggesting that the contacts actually penetrate a few mils into the bar. This behavior has been seen previously with silver layers on ZnTe, and the penetration has been attributed to electromigration, which can be observed as filament-like projections of silver into the ZnTe (5).

The results of the contact measurements are given in Table II, from which it can be seen that the lithium-of silver-diffused contacts have the lowest resistance.

Manuscript submitted Feb. 10, 1972; revised manuscript received May 3, 1972.

Any discussion of this paper will appear in a Discussion Section to be published in the June 1973 JOURNAL.

REFERENCES

1. M. Aven and W. Garwacki, *This Journal*, **114**, 1063 (1967).
2. R. D. Widmer *et al.*, *J. Cryst. Growth*, **6**, 237 (1970).
3. H. Frank and S. Azim, *Solid-State Electron.*, **10**, 727 (1967).
4. W. D. Baker, Ph.D. Thesis, Carnegie-Mellon University, Pittsburgh, Pa. (1971).
5. A. G. Fischer, Westinghouse Research Laboratory, Pittsburgh, Pa., Private communication.

Brief Communication



Identification of Chemical Constituents of Defects in Silicon

Jacques M. Assour

RCA Laboratories, Princeton, New Jersey 08540

Selective chemical etching with Sirtl or Dash etches is commonly used to determine the presence of defects caused by chemical impurities in silicon bulk wafers, epitaxial layers, and diffused regions. Defects in the shape of cones, platelets, protrusions, and various dendritic structures usually appear after etching. In practice, we have found the impurity concentrations in these defects to be below the detection level presently achieved by mass spectrometry and electron-probe microanalysis in agreement with Yanagawa (1) and Green (2). In this note we report new results on the chemical constituents of a number of chemical defects observed in processed silicon devices. The chemical constituents were identified with a secondary ion emission mass spectrometer (3). The sensitivity limit of this spectrometer ranges between 1 ppm to 1 ppb, thus providing a powerful tool to identify the impurity concentrations of the defects. Because of the fine spatial resolution of this instrument (1 to 2 μm), we have been able to identify uniquely several defects and, in some cases, trace their origins.

The samples were first etched to reveal the defects and then thoroughly cleaned to remove surface contamination. The presence of the chemical constituents at a defect was confirmed by analyzing reference silicon areas in the samples which are free of defects. In other words, the impurities reported here were detected only at the defect sites.

Key words: chemical constituents of defects, silicon, identification.

Protrusions from Epitaxial Surfaces

Fast growing protrusions from epitaxial semiconductor surfaces were seen on silicon by Yanagawa (1) and their characteristics were described by Green (2). Typical protrusions observed here on 100 μm thick epitaxial layers, deposited on <111> silicon n-type substrates, are shown in Fig. 1 a and b. Their height is 3-5 times the thickness of the deposited epitaxial layer and their diameter varies from 40-100 μm . The detected chemical constituents of these defects are CO₂, SiO, SiN, hydrides and hydroxyl groups. All of the impurities are present in the protrusions but with varying concentrations. Since the sources of these impurities are many, and critically depend on the conditions of the epitaxial deposition system, no attempt has been made yet to isolate uniquely the source of these contaminants. It has been noted (4), however, that the density of these defects is a strong function of the graphite rf susceptor which supports the wafers during epitaxial deposition; a newly applied SiC coating results in a high density of these protrusions, whereas a coat of pure silicon results in a decreased density.

Impurity Precipitates in Boron Diffused Layers

The properties of boron nitride (BN) wafers as planar diffusion sources for boron have been described by Goldsmith *et al.* (5) and Rupprecht and Stack (6).

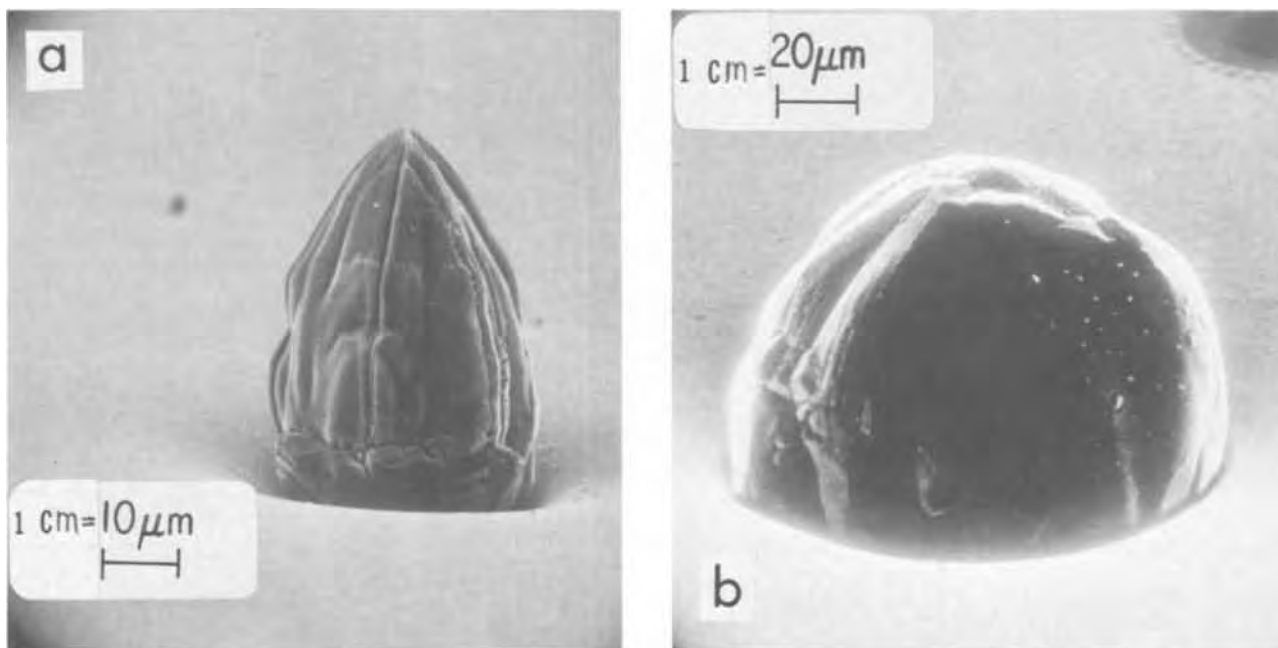


Fig. 1 a and b. Fast growing protrusions from epitaxial silicon surface.

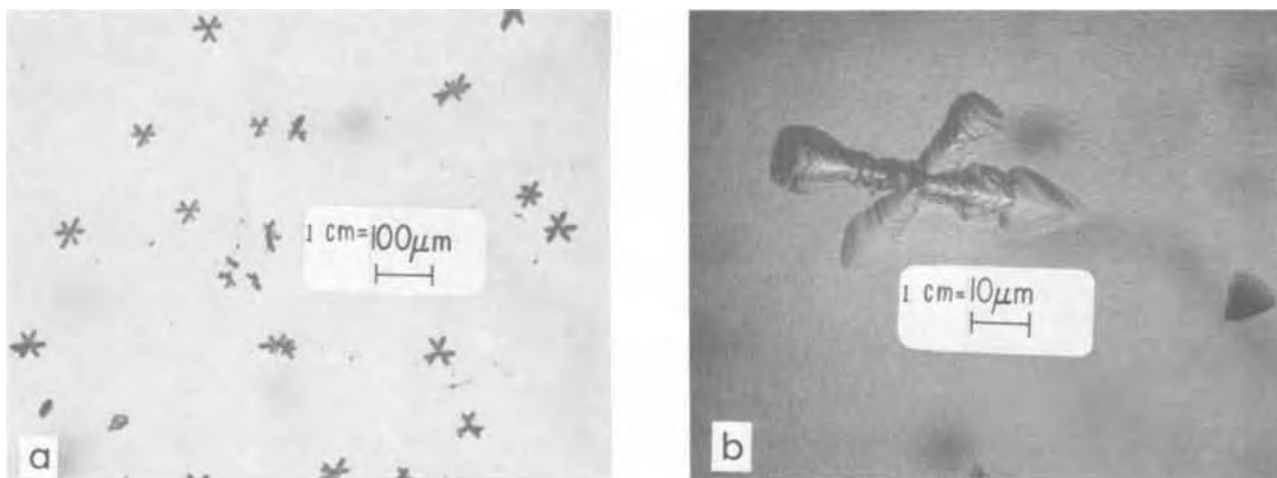


Fig. 2 a and b. Boron and oxygen precipitates after boron diffusion deposited from a grade M, BN diffusion source.

Two grades of BN diffusion sources are available:¹ grade A and grade M. Grade M consists of boron nitride in a silica matrix. The impurity precipitates observed in p-type diffused layers from the above sources are shown in Fig. 2a and b and Fig. 3. The dendritic structure in Fig. 2 is obtained after diffusion from an overly used grade M boron nitride source. The chemical constituents of these defects were boron and oxygen. Based on our observations below, the source of these impurities has been traced to the poor oxidation condition of the BN wafer. Analysis of control wafers, heat-treated in the same furnace but without exposing them to the BN source, has confirmed the clean condition of our gases and furnace. The defects were not present prior to the boron diffusion but were detected after exposure to the BN source. Moreover, the density of these defects markedly decreased with successive chemical etching of the boron-diffused layer and finally disappeared at the n-type substrate. After proper cleaning (5, 6) and reoxidation of the BN wafer, p-type diffused layers deposited from this BN source had no defects.

The defects with a trapezoid geometry, as shown in Fig. 3, were detected in a p-type diffused layer de-

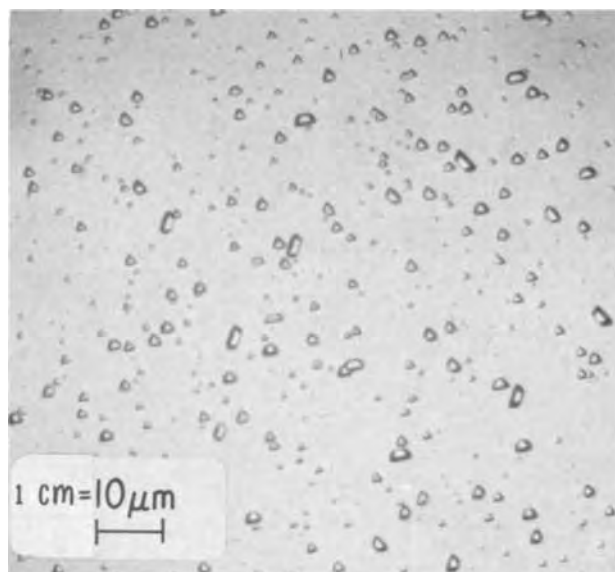


Fig. 3. Aluminum precipitates after boron diffusion deposited from a grade A, BN diffusion source.

¹ The Carborundum Company, Niagara Falls, New York.

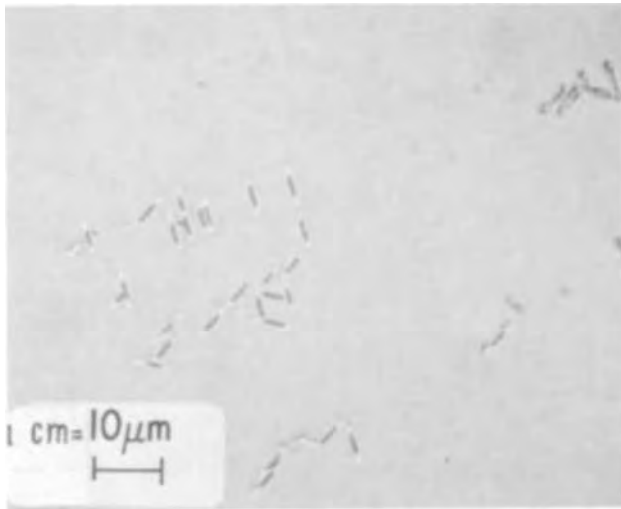


Fig. 4. Copper and silver precipitates in epitaxial silicon after thermal oxidation.

posited from a grade A boron nitride source. Analysis by secondary ion-emission mass spectrometry has revealed that these defects are predominantly Al precipitates, although traces of Na, K, Ca, Mg, Cu, and O₂ were also detected in the sample. We believe that all these impurities originate from the BN diffusion source for the following reasons. The defects are observed only after exposure to the BN source. As mentioned above, the density of these defects decreases with successive etching of the p-type diffused layer and disappear at the n-type substrate. Proper reoxidation of the BN wafer eliminates these defects. Moreover, emission spectrographic analysis of grade A boron nitride wafers¹ has revealed the following metallic impurities in ppm: Al = 600-6000, Cu = 3-30,

Ti = 3-30, Ca = 1500-15,000, Ni = 100-1000, Fe = 30-300, Si = 500-5000, Cr = 100-1000, Mn = 10-100, Mg = 150-1500. Analysis by mass spark-source spectrometry of other commercially available BN wafers has also revealed (7) the above metallic impurities.

Metallic Precipitates in Silicon after Thermal Oxidation

This sample consisted of an n-type epitaxial layer, 8 μm thick, grown on a <111> n⁺ substrate. The silicon wafer was then thermally oxidized in the presence of H₂O vapor. After Sirtl etching, defects in the shape of elongated cigars, as shown in Fig. 4, were found randomly distributed in the epitaxial layer. The impurity constituents of these defects are Cu and Ag. The source of these metallic impurities has been tentatively identified as contamination introduced with the H₂O vapor during thermal oxidation.

In summary, we have demonstrated that secondary ion emission mass spectrometry is a powerful tool to identify impurity concentrations of defects in silicon. It is hoped that further analysis will uniquely isolate the source of contaminants during processing of semiconductor devices.

Manuscript submitted April 13, 1972; revised manuscript received May 15, 1972.

Any discussion of this paper will appear in a Discussion Section to be published in the June 1973 JOURNAL.

REFERENCES

1. T. Yanagawa, *Proc. IEEE*, **57**, 1621 (1969).
2. J. M. Green, *Metallurgical Transactions*, **1**, 647 (1970).
3. A. J. Socha, *Surface Sci.*, **25**, 147 (1971).
4. N. Goldsmith and P. Robinson, Private communication.
5. N. Goldsmith, J. Olmstead, and J. Scott, Jr., *RCA Rev.*, **28**, 344 (1967).
6. D. Rupprecht and J. Stach, Abs. 176, p. 453, *Electrochem. Soc. Extended Abstracts*, Fall Meeting, Cleveland, Ohio, Oct. 3-7, 1971.
7. A. I. Stoller, Private communication.



Sulfur Trioxide, Oxygen, Platinum Electrode in a Fused Sulfate

F. J. Salzano* and L. Newman

Brookhaven National Laboratory, Upton, New York 11973

ABSTRACT

The behavior of the $O_2, SO_3, Pt / (Na, Li, K)_2SO_4$ electrode was studied at SO_3 concentrations in the parts per million range. The cell studied consists of two similar electrodes isolated from each other by a solid cation permeable membrane. One electrode is a reference electrode through which passes an air or oxygen stream containing a fixed and known concentration of SO_2 . Through the other electrode is passed a similar gas stream containing a variable concentration of SO_2 . The SO_2 passes into each electrode through a platinum inlet tube which converts a fraction of the SO_2 in the gas stream to SO_3 . The emf *vs.* concentration behavior of this cell was studied and shown to exhibit Nernstian behavior. This work shows that the cell has possible applications in continuous monitoring of ambient air for both SO_2 and SO_3 , *i.e.*, sulfuric acid aerosols.

A number of gas-metal-fused salt electrodes have been described in the literature. These include: halogen-carbon-halide melts, carbon dioxide-oxygen-platinum-carbonate melts, oxygen-platinum solid oxide, oxygen-platinum-oxide melts, and others (1). These electrodes are widely used in basic electrochemistry studies and in measurements of thermodynamic properties. However, these gas electrodes and others not as well developed can also be the basis for practical monitoring devices useful for measuring the activities of gaseous species. Recently, Boxall and Johnson (2) have described a hitherto undeveloped sulfur trioxide-oxygen-platinum ($Li, Na, K)_2SO_4$ electrode. They studied the emf of this electrode *vs.* a silver, silver ion reference electrode at $550^\circ C$ when the SO_3 and oxygen concentrations at the electrode were varied from 0.390 to 0.842 atm and 0.036 to 0.577 atm, respectively. This investigation showed that at high concentrations of SO_3 the emf is a linear function of $\log P(SO_3) P^{1/2}(O_2)$, where $P(SO_3)$ is the partial pressure of SO_3 and $P^{1/2}(O_2)$ is the square root of the partial pressure of oxygen. From the slope of their line we calculate that there are two electrons involved in the electrode reaction.

Flood and Boye (3) have utilized the SO_2, O_2 electrode to obtain thermodynamic information on the systems



They suggest that the electrode reaction involves the oxidation of SO_2 by oxide ion to SO_3 and that two electrons are involved per mole of SO_2 . However, they are careful to point out that the details of the electrode reaction are unknown and the effects they observe may also be attributed to the oxygen electrode. In any case, the performance of the SO_2, O_2 platinum

electrode is intimately related to the SO_3, O_2 platinum electrode in a sulfate melt because of the equilibrium reaction between SO_2, O_2 , and SO_3 .

In this paper we describe work with the SO_3, O_2 platinum electrode in a $(Li, Na, K)_2SO_4$ melt in which we studied the variation in emf *vs.* oxygen and air containing parts per million concentrations of SO_2 in contact with the electrode. In these cells a quartz glass membrane was used to completely isolate each gas electrode. Quartz glass is an effective barrier for SO_3 but is permeable to the cations in the melt (4, 5). Control of the SO_2 concentration at the low levels required in this work was accomplished with sulfur dioxide permeation tubes (6, 7). In addition to showing that the results obtained are consistent with the idea that the SO_3, O_2 platinum electrode is basically an oxygen electrode the results obtained suggest that this cell has potential application as a practical monitoring device for SO_2 or SO_3 , *i.e.*, $H_2SO_4 \cdot xH_2O$ aerosols, in ambient air.

Theory

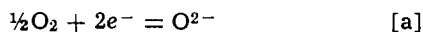
The emf *vs.* concentration relation for the cell

O_2, Pt	Cation permeable glass $Na_2SO_4, K_2SO_4, Li_2SO_4$	Pt, O_2	[I]
+		+	
SO_3 (unknown conc)		SO_3 (known conc)	
+		+	
Na_2SO_4		Na_2SO_4	
K_2SO_4	Cation permeable glass $Na_2SO_4, K_2SO_4, Li_2SO_4$	K_2SO_4	[II]
Li_2SO_4		Li_2SO_4	

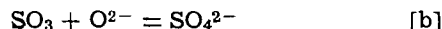
can be derived based on the simple assumption that the system behaves as an oxygen electrode. It will be seen that the experimental results obtained in this work and the work of Boxall and Johnson (2) and Flood and Boye (3) are consistent with these assumptions. Cell I consists of two similar $SO_3, O_2, Pt / SO_4^{2-}$

* Electrochemical Society Active Member.
 Key words: sulfur trioxide, sulfate melt; SO_3, SO_2, O_2 platinum electrodes; quartz membranes; monitoring SO_3, SO_2 in air.

electrodes. Oxygen gas containing a low, but fixed concentration of SO_3 , i.e., 1% or less, is passed through one of the electrodes, designated as the reference electrode (r). The other electrode is called the working electrode (w) and through it is passed oxygen containing a variable or unknown concentration of SO_3 . We assume that at each electrode the following equilibria exist



and



We can combine [a] and [b] and write as the over-all reaction



Thus, we assume that the basic electron transfer step is equilibrium [a]. If these are the only reactions to consider then it can be easily shown that the emf of the cell is given by the relation

$$\text{emf} = -\frac{RT}{2F} \ln \frac{P_r(\text{SO}_3)}{P_w(\text{SO}_3)} - \frac{RT}{4F} \ln \frac{P_r(\text{O}_2)}{P_w(\text{O}_2)} \quad [1]$$

where $P_r(\text{SO}_3)$, $P_w(\text{SO}_3)$ and $P_r(\text{O}_2)$, $P_w(\text{O}_2)$ are the partial pressures of SO_3 and O_2 at the reference (r) and working (w) electrode, respectively. Thus, the emf of the cell depends on two terms, the first involves the partial pressures of SO_3 and the second involves the partial pressure of oxygen at the respective electrodes. If we consider that the concentrations of SO_3 and O_2 at the reference electrode are fixed then we can write

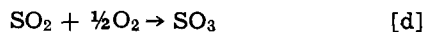
$$\text{emf} = E_0(T) - \frac{RT}{2F} \ln P_w(\text{SO}_3) P_w(\text{O}_2)^{1/2} \quad [2]$$

When the partial pressure of oxygen in each electrode gas stream in cell I is the same we can simplify Eq. [1] to

$$\text{emf} = -\frac{RT}{2F} \ln \frac{P_r(\text{SO}_3)}{P_w(\text{SO}_3)} \quad [3]$$

Boxall and Johnson studied the behavior of the SO_3/O_2 platinum/ SO_4^{2-} electrode at 550°C , at very high concentrations of SO_3 . From their plot of emf vs. $\log P(\text{SO}_3) P(\text{O}_2)^{1/2}$ we calculate a value of $RT/2F$ equal to 84 mV. This compares to the theoretical value of 82 mV which shows that their data are consistent with this simple model.

The response of cell I when SO_2 is injected into the oxygen stream rather than SO_3 can be considered by including the effect of the reaction



The free energy change for reaction [d] is well known (8). High temperatures favor the formation of lower partial pressures of SO_3 . When the concentration of SO_2 injected into the oxygen is low we expect the rate of conversion to SO_3 to be first order with respect to the inlet concentration of SO_2 , i.e., for a small degree of conversion. This reaction is slow and in the commercial manufacture of SO_3 a platinum or metal oxide catalyst is employed to increase the rate of reaction. Thus, at a high fixed flow rate the fraction of SO_2 converted is expected to be small and approximately independent of the inlet concentration. Thus, we expect at the reference electrode

$$P_r(\text{SO}_3) = X_r P_r(\text{SO}_2)$$

and at the working electrode

$$P_w(\text{SO}_3) = X_w P_w(\text{SO}_2)$$

where X is the fraction of SO_2 converted to SO_3 and $P_r(\text{SO}_2)$ and $P_w(\text{SO}_2)$ are the inlet partial pressures of SO_2 at the respective electrodes. If the electrodes and flow rates are matched then

$$X_r \approx X_w \quad [4]$$

and we expect the relation

$$\text{emf} \approx -\frac{RT}{2F} \ln \frac{P_r(\text{SO}_2)}{P_w(\text{SO}_2)} \quad [5]$$

to hold to a fair approximation. In this paper we will show that Eq. [5] holds at SO_2 concentrations at the 1 ppm level by volume. Thus, it follows that Eq. [2] and [3] are valid at SO_3 concentration just below the parts per million range in air and oxygen gas at temperatures in the range of $650^\circ\text{--}750^\circ\text{C}$.

Experimental

Cell and experimental apparatus.—The electrochemical cell studied consisted of two similar but independent electrodes each enclosed in a gas-tight cation permeable quartz membrane. A schematic diagram of the cell assembly is shown in Fig. 1. Each electrode consisted of a 12 mm OD quartz tube having a wall thickness of approximately 1 mm. Each had a closed hemispheric end and was filled with a eutectic mixture of Na_2SO_4 , K_2SO_4 , and Li_2SO_4 to a level of 12 mm. A 40 mil platinum electrode wire was immersed approximately 5 mm into the salt melt. The platinum wire was threaded through a quartz inlet tube of approximately 3 mm OD. The tube terminated approximately 1 or 2 mm above the salt. We found it was not practical or necessary to bubble the gas directly into the salt melt. In some cases the inlet tube was $\frac{1}{8}$ in. OD platinum which had a 5 mm extension immersed in the salt. Both electrodes were immersed in a common salt bath contained in a gold crucible. The gas space over the salt was purged with helium. Dry oxygen is also suitable. The whole cell is contained in a quartz enclosure which is further enclosed in a stainless steel electrical shield. The purpose of the shield is to eliminate inductive pick-up by the wire leads in the cell. The shield is grounded and the working electrode is connected to the shield. The emf developed by the cell was measured with a Keithley Model No. 602 electrometer and measured against a General Resistance digital bucking voltage source Model No. DAV-45D. The output of the electrometer and the temperature were continuously recorded on a two-pen recorder, Honeywell Electronik 19.

Each electrode had an independent gas supply. The gas supply to the reference electrode was commercial oxygen or breathing air. The gas supply to the working electrode was similar but in some experiments room air was pulled through the electrode by means of a vacuum pump and the flow controlled with a throttle valve at the outlet of the cell. The flows through each

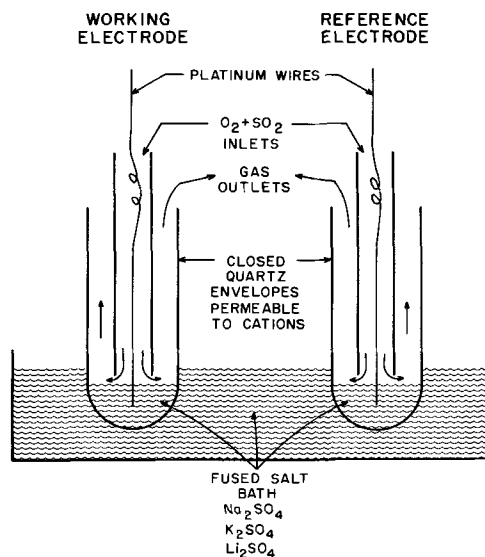


Fig. 1. Schematic diagram of the experimental cell used to study the behavior of the SO_3 , O_2 , $\text{Pt}/\text{SO}_4^{2-}$ electrode.

of the electrodes were measured independently with floating ball flowmeters which were continuously checked against the rate of movement of a soap bubble film through a standard volume. In general, the flow rate could be varied from 30 to 300 cm³/min.

The sulfur dioxide used in these experiments was injected into the respective gas streams in one of two ways. At concentrations in the range of 1% the SO₂ was taken from a cylinder of anhydrous sulfur dioxide (Matheson Company). It was metered into the oxygen stream by means of a small flowmeter. Under these conditions the size of SO₂ flow rate could be held constant, but was not known very accurately. The flow of SO₂ was varied over the range of 0.5-2 cm³/min.

In the more refined measurements at the parts per million level we employed sulfur dioxide permeation tubes (6, 7) as a source. These are Teflon tubes ¼ in. in diameter which range in length from 3 to 30 cm. These tubes contain liquid sulfur dioxide and are sealed at each end. The tubes leak sulfur dioxide by diffusion at a fixed rate at a given temperature. The concentration of SO₂ was varied by passing the gas stream over different length tubes. Calibration of the SO₂ permeation tubes was accomplished by the standard technique of measuring the loss in weight with time. The smallest tube (SST) the intermediate tube (IST), and the largest tube (LST) lost SO₂ in the ratio of 1:5:8. The initial rate of the SST was 0.7 µg/min at 27°C. This value was not constant during the course of these experiments and decreased to 0.5 µg/min. The IST was obtained from the National Bureau of Standards and used exclusively in the reference electrode gas stream. The other tubes were obtained from Analytic Instrument Development, Inc.

Preparation of the salt.—Standard reagent grade Li₂SO₄, Na₂SO₄, and K₂SO₄ were obtained from the Baker Chemical Company. The reagents were weighed out in the mole proportions 78:13.5:8.5, respectively, thoroughly mixed, and dried at 250°C. The powder was placed in a 2 in. OD × 4 in. high gold crucible and slowly heated while a stream of oxygen containing approximately 1% SO₂ was passed through the apparatus. The salt was heated to 650°C and held overnight. The apparatus was then evacuated at 650°C with a mechanical roughing pump and cooled. The melting point was in the range of 540°-546°C compared to the expected value of 512°C. Small portions of this salt were removed from the crucible and used in the electrode assemblies. The rest of the salt was used in the common salt bath in which the electrodes were immersed. The salt is initially treated with SO₂ in order to overcome its tendency to etch the glass.

Procedure using permeation tubes.—The two electrodes were loaded with the sulfate salt which was melted with a hand torch under a stream of dry oxygen and the platinum wires were positioned in the melt in each electrode. The electrodes were then positioned in the cell in the furnace. Oxygen or air containing from 1 to 10 ppm SO₂ was passed through both electrodes while the cell was brought to temperature. At 650°C the electrodes were positioned in the bath and the cell heated to 700°C and held overnight. The flow in the reference electrode was adjusted to the desired level in general from 100 to 300 cm³/min. This reference gas was continuously passed over the (IST) National Bureau of Standard's SO₂ permeation tube. After one day, the source of SO₂ in the working electrode gas stream was removed and pure oxygen or air was allowed to pass into this electrode. In general, it took several hours to clear all the SO₂ from the electrode, i.e., for the emf to reach a stable value. In general, the concentration of SO₂ at a given flow rate was changed by putting different size permeation tubes, i.e., SST or LST, in the gas stream of the working electrode.

Results

The emf of the cell at 700°C vs. the flow rate of oxygen was measured when SO₂ was injected at a fixed rate into the oxygen stream passing through the working electrode. In these initial experiments pure oxygen was used as the reference electrode gas. In this series of experiments the inlet tube of the reference electrode and working electrode were quartz glass. Results were obtained at oxygen flow rates in the range of 30-300 cm³/min and SO₂ injection rates of 0.5-2 cm³/min. When the flow rate or equivalent concentration is plotted on a log scale vs. the emf for a fixed rate of SO₂ injection, we obtained a straight line with a slope very close to the expected value of 97 mV/decade of concentration as predicted from Eq. [5]. A typical plot of oxygen flow rate and concentration vs. the emf in millivolts is shown in Fig. 2. The concentration range covered is from 0.3 to 2% SO₂. The scatter in the data is due to the difficulty of holding the rate of SO₂ injection at a precisely fixed value.

In another series of experiments the variation in emf of the cell was studied when the concentration of SO₂ passing through the working electrode was varied at a fixed flow rate of oxygen. The sources of SO₂ in these experiments were two Teflon permeation (6, 7) tubes with leak rates in the ratio of 1:8. The concentration range studied was from 1 to 8 ppm with a flow rate in the working electrode equal to 275 cm³/min. The emf vs. SO₂ concentration was studied using commercial oxygen and air stored in steel cylinders. The concentration of SO₂ in the reference electrode was 15 ppm. In all the experiments performed at parts per million levels of SO₂, the inlet tube in each electrode was ⅛ in. platinum. The results obtained in one experiment are shown in Fig. 3, which is a plot of the SO₂ concentration on a log scale vs. the emf in millivolts. The results obtained using air and oxygen in both electrodes are similar when the reference electrode concentration is held at a fixed level. Both sets of data points fall very close to the approximate expected line based on Eq. [5]. The slope as predicted is 97 mV/decade. This is based on the assumption that two electrons per mole of SO₂ are involved in the electrode reaction. The highest emf observed was 220 mV ob-

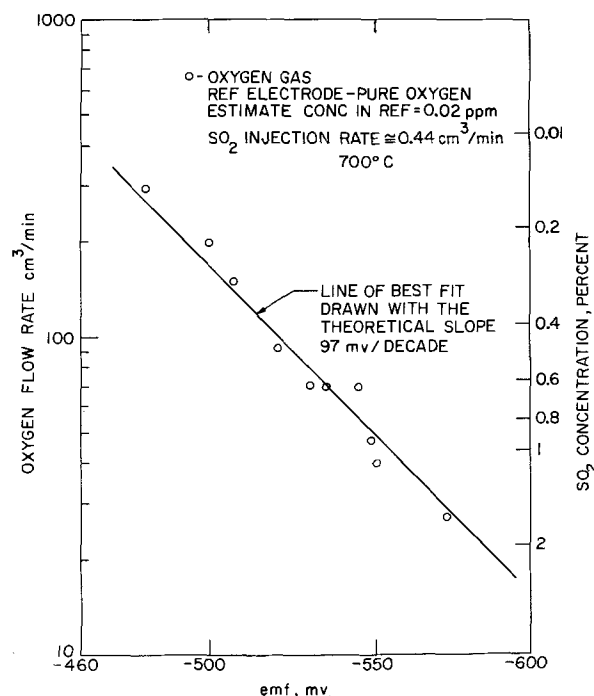


Fig. 2. Effect of SO₂ concentration at the 1% level on the emf of the cell determined by fixing the rate of SO₂ injection and varying the flow rate through a quartz inlet tube.

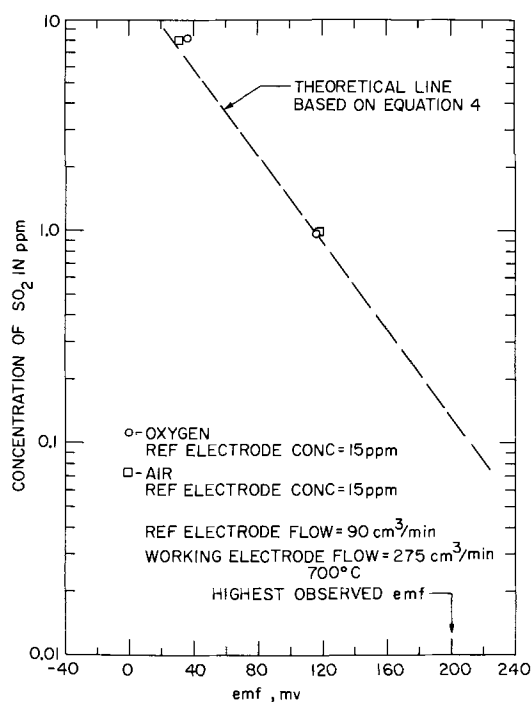


Fig. 3. Variation in emf of the cell as a function of the SO₂ concentration at the parts per million level showing no difference in behavior between air and oxygen.

tained when pure bottle air is passed through the reference electrode. This corresponds to 0.08 ppm SO₂, which is high and probably results from residual system contamination introduced into the oxygen stream. Similar results were obtained at oxygen flow rates of 100 cm³/min which correspond to a factor of three increase in SO₂ concentration.

When gases containing different oxygen activities are passed through each electrode, *e.g.*, air and oxygen, the cell emf responds to changes in the oxygen activity. In fact, the response to changes in oxygen activity was used as a standard test for evaluating the responsiveness of every new cell prior to experiments involving SO₂ injection. When the working electrode gas is changed from air to oxygen (0.2-1.0 atm) in the absence of SO₂, the emf change is within a millivolt of the expected value, *i.e.*, 33.7 mV at 700°C. This is true in the absence or presence of SO₂ in the gas streams and at flow rates in the range of 300-30 cm³/min. Increasing the oxygen or SO₂ partial pressure causes the emf to change in the same direction as predicted from Eq. [2]. Thus, nitrogen does not affect the performance of the cell even at very low concentrations of SO₂.

In one set of experiments an effort was made to sample and analyze the SO₂ concentration in the working and reference electrode gas streams. The reference electrode concentration was estimated to be 5 ppm and chemical analysis gave a number close to this value. The concentration of SO₂ in the working electrode stream was calculated to be 8 ppm whereas a value of 11 ppm was obtained by chemical analysis. The corresponding emf values at these two levels showed good agreement with the estimated expected value based on Eq. [5]. In some experiments a sample of room air was passed through the working electrode while bottled air containing 5.9 ppm SO₂ was passed through the reference electrode. Typical results are shown in Fig. 4. The data points show good agreement with expected slope but are displaced 28 mV in the direction of higher emf values relative to bottled air. This can be interpreted to mean a lower SO₂ concentration in the working electrode gas stream when room air is used (see Discussion).

An attempt was made to produce SO₃ in the oxygen stream by reacting SO₂ with a platinum filament built

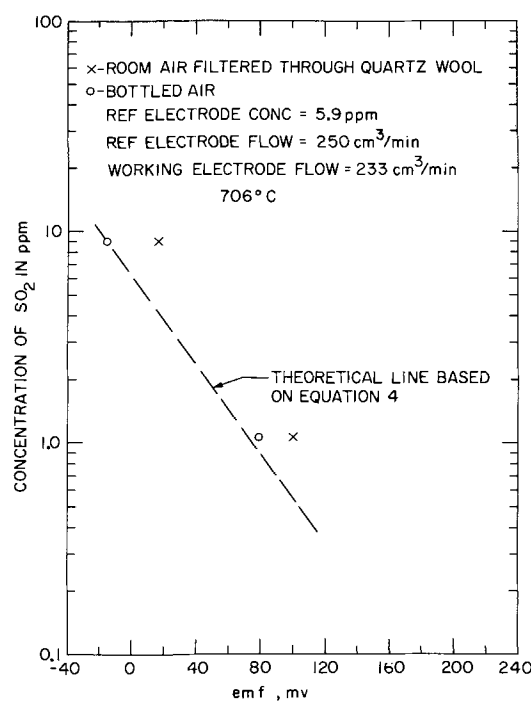


Fig. 4. Calibration of the cell using ambient air as the working electrode gas.

into the gas feed line leading to the cell. At a filament temperature of $\approx 500^\circ\text{C}$ a significant amount of SO₃ was produced which reacted with available moisture to form H₂SO₄ which collected on a cold wall $\frac{1}{2}$ in. from the filament. A significant degree of conversion of SO₂ to SO₃ was also evident from the emf of the cell which increased when the filament was turned on suggesting a decrease in the concentration of SO₂ in the gas stream.

Although it was not practical to make a direct addition of SO₃ to the gas stream we did demonstrate in an indirect way that the cell responded to SO₃. This was accomplished by studying the variation in the emf of the cell at different flow velocities through the platinum inlet tube. In this case the concentration of SO₂ in the gas stream was held constant by passing air at a fixed flow rate (≈ 300 cm³/min) over one of the permeation tubes. The flow rate through the cell was varied by allowing part of the flow over the permeation tube to bypass the cell, while the rest of the flow was passed into the cell through the $\frac{1}{8}$ in. platinum inlet tube which carried the gas into the hot zone and over the surface of the molten salt. Some typical data are shown in Fig. 5 which is a plot of the flow rate through the cell on a log scale, *vs.* the emf in millivolts on a linear scale. In this experiment the oxygen flow through the cell was varied from 30 to 300 cm³/min at SO₂ concentration of 0.7 and 5 ppm at 710° and 610°C. We observed that the emf changed by ~ 55 mV when the flow is varied over this range. We interpret this dependence of emf on the flow rate to be due to a greater degree of conversion of SO₂ to SO₃ at the lower flow rates. This effect was very reproducible and the response kinetics of the cell were measured in minutes when the flow rate was changed from one level to either a higher or lower level.

Furthermore, this effect was independent of concentration in the range studied and gave the same slope of 55 mV/decade at 610°, 710°, and 750°C. When no SO₂ was injected into the working electrode gas stream the emf was independent of flow rate in the range studied.

Discussion

The behavior of the SO₂, O₂, platinum/SO₄⁻² electrode has been studied in the range of SO₂ concentra-

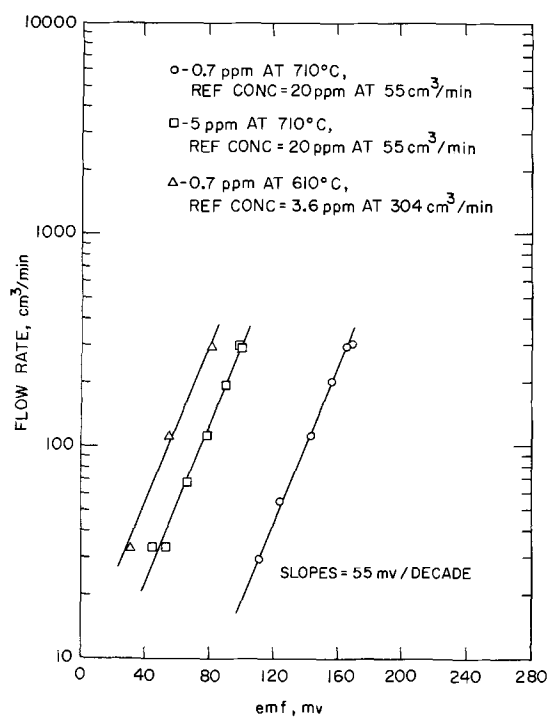
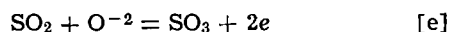


Fig. 5. Effect of flow rate on the emf of the cell when the concentration of SO₂ is held constant at the parts per million level.

tions from 1% to 1 ppm. This electrode is in reality similar to the SO₃, O₂, platinum/SO₄⁻² electrode studied by Boxall and Johnson (2). Considering their work and the present results, the behavior of this electrode has now been examined in the concentration range of 80% SO₃ to below 1 ppm and it is found to exhibit Nernstian behavior over this range. The performance of this electrode is consistent with equilibria [a] and [b], and Eq. [1], [2], and [3]. This electrochemical system can be regarded as an oxygen electrode which coupled with equilibrium [b] is responsive to SO₃ according to equilibrium [c]. However, if we combine equilibria [a] and [d] we obtain for the overall electrode reaction



which is the reaction suggested by Flood and Boye (3). Thus, the mechanism of this electrode can be regarded from different points of view, but it is our contention that it is basically an oxygen electrode according to equilibrium [a]. As such, impurities present in the salt which affect equilibrium [b] will affect the SO₃ (SO₂) response of the cell, but may not have any effect on the oxygen response of the cell. Accordingly, we have observed, in one cell, poor response to SO₂, but this cell gave the expected response to changes in oxygen activity.

The agreement of the emf vs. SO₂ concentration results obtained from this cell with that expected from Eq. [5] at parts per million concentrations of SO₂ is somewhat fortuitous since Eq. [5] is an approximation. We would expect to get agreement only when the electrodes are perfectly matched, i.e., when they convert the exact same fraction of SO₂ to SO₃. Such good agreement however, was not observed in all cells, but the correct slope of Eq. [5] is always obtained. This type of situation is demonstrated in Fig. 4 where the results are displaced 28 mV higher than the expected line, whereas this cell gave the expected results with bottled air. It is known that the rate of SO₂ emission from the permeation tubes is decreased at humidity levels above 10%. We believe that the higher humidity of the ambient air can account for the unexpected shift of these results from the expected line.

The expected equilibrium ratio of SO₂/SO₃ at 700°C in air is approximately unity. However, the degree of

conversion of SO₂ to SO₃ at flow rates around 300 cm³/min was small. This is indicated by the results of chemical analysis of the outlet gas and arises because of the short residence time of the gas in the inlet tube. A more basic question is whether the conversion of SO₂ to SO₃ took place in the inlet line (1/8 in. platinum tube) or at the gas-salt interface in the electrode in the experiments at parts per million levels of SO₂. In one cell in which the surface area of the salt was reduced from 12 to 3 mm and the salt volume reduced to 1/20 the normal value we observed the predicted magnitude of response to changes in the concentration of SO₂ at the parts per million level. Also, the variation in emf with changes in velocity at a fixed concentration of SO₂ at the parts per million level was always 55 mV/decade of flow rate in all the cells studied independent of the surface area or volume of the salt melt in the electrode.

The value of 55 mV/decade of flow rate is interpreted to mean that the SO₃ concentration changes by a factor of 3.7 (Eq. [3]) when the flow rate is varied by a factor of 10. These results indicate that the partial pressure of SO₃ in the gas passing over the salt is approximately proportional to the inverse square root of the flow rate. The exact value observed is 0.57 which is obtained by dividing the slope of Fig. 5, i.e., 55 mV/decade by the value of 97 mV/decade obtained from Eq. [3]. This inverse proportionality between the partial pressure of SO₃ and the square root of the flow rate is expected under laminar flow conditions where the rate of conversion is controlled by diffusion through a gas film at the platinum surface. This result suggests a technique of obtaining controlled or proportioned concentration of SO₃ at low levels for experimental applications connected with atmospheric pollution monitoring.

The results reported in this study demonstrate the performance of the SO₃, O₂, platinum/SO₄⁻² electrode at sub ppm levels of SO₃ and show that this cell has promise as a practical device for detecting SO₃, SO₂, H₂SO₄, and perhaps decomposable sulfate salts in air. This possibility warrants some brief further discussion. It appears that the basic response of the cell is to SO₃; however, it is clear from this work that the cell can be used to quantitatively measure the concentration of SO₂ in an air stream. Measurement of SO₂ concentrations in air can be accomplished under the following conditions:

1. The air passed through the working electrode initially contains no SO₃.
2. The reference electrode contains a fixed and known concentration of SO₂ at approximately the level being measured in the working electrode.
3. The working and reference electrodes are matched, i.e., the fraction of SO₂ converted to SO₃ in the two electrodes is the same and small. Under these conditions the cell emf is a direct quantitative measure of the concentration of SO₂ in the air stream. These conditions appear to have been achieved in the experimental cells studied. Further, we have showed that when platinum is inserted into a quartz inlet line of a cell (hot zone) the potential changes to a level which indicates approximately an order of magnitude increase in the concentration of SO₃. The emf returns to the original value when the platinum is removed. Similarly, these cells show a velocity dependence at a fixed concentration of SO₂. This is due to the higher degree of conversion of SO₂ to SO₃ at the lower flow rates. Thus, the gas stream passing through the cell is not at equilibrium with respect to the ratio of SO₂/SO₃ at the flow rates studied. At the operating temperature of the cell (700°C) the equilibrium SO₂/SO₃ ratio calculated from thermodynamic data is approximately unity (8).

Where some uncertainty lies is in adopting this method to quantitatively measure the concentration of SO₃ in an air stream, especially when the stream con-

tains comparable levels of SO₂ and SO₃. However, even in this case, where a significant amount of SO₂ is present, it appears possible to design a cell to limit or minimize the degree of conversion of SO₂ to SO₃. Very preliminary work suggests that the interference ratio of SO₂/SO₃ could be reduced to perhaps 100:1, i.e., a unit amount of SO₂ gives a signal equivalent to 1/100 times the same concentration of SO₃. Assuming this is accomplished one still must solve the problem of supplying the reference electrode with a fixed and known concentration of SO₃. One could resort to calibration of the working electrode vs. some standard reference electrode. However, all these questions deal with the development of a practical device for detecting SO₂ or SO₃. We do recognize that this electrochemical system is basically an oxygen electrode which also responds to oxidizing or reducing impurities if they are present at appreciable concentration levels in an air stream. Further, this cell has been tested only under laboratory conditions and all the possible problem areas relating to the development of monitoring devices have not been defined. However, the cell has some very attractive features, foremost being its simplicity and the fact that it can have its own built-in standard, i.e., a reference electrode containing a known level of SO₃.

Acknowledgment

This is to acknowledge the significant contribution of Andrew M. Davis to this work. Mr. Davis did the initial exploratory experimental work which led eventually to the development of the final cell arrange-

ment and gas supply system. Also, our thanks to Dr. H. S. Isaacs for the many useful discussions and suggestions made in the course of this work. This work was performed under the auspices of the United States Atomic Energy Commission.

Manuscript submitted Jan. 14, 1972; revised manuscript received May 26, 1972.

Any discussion of this paper will appear in a Discussion Section to be published in the June 1973 JOURNAL.

REFERENCES

1. A. F. Alabyshev, M. F. Lantratov, and A. G. Morachevskii, "Reference Electrodes for Fused Salts," Translation by Adam Peiperl, The Sigma Press Publishers, Washington, D. C.
2. L. G. Boxall and K. E. Johnson, *This Journal*, **118**, 887 (1971). See also the Ph.D. Thesis by L. G. Boxall, "Electrode Potentials in Fused Alkali Metal Salts," submitted to the University of Saskatchewan, Regina Campus, Regina, Saskatchewan, March 1970.
3. H. Flood and N. Chr. Boye, *Z. Electrochem.*, **66**, 184 (1962).
4. Kurt H. Stern, *J. Phys. Chem.*, **74**, 1323 (1970).
5. Kurt H. Stern, *ibid.*, **74**, 1329 (1970).
6. A. E. O'Keefe and G. C. Ortman, *Anal. Chem.*, **38**, 760 (1966).
7. Permeation tubes are available from the National Bureau of Standards as Standard Reference Material No. 1625, No. 1626, and No. 1627 and from Analytical Instrument Development, Inc., Westchester, Pa.
8. K. H. Stern and E. L. Weise, Nat. Bur. Stand. Reference Data Series NSRDS-NBS-7, Oct. 1, 1966.

Corrosion Fatigue of Copper and Alpha-Brass

Stuart S. Birley and Desmond Tromans

Metallurgy Department, The University of British Columbia, Vancouver, 8, British Columbia, Canada

ABSTRACT

Corrosion fatigue of copper and alpha-brass of nominal composition Cu:29Zn has been investigated in near neutral aqueous electrolytes using a rotating bend test fatigue machine. The electrolytes employed were pre-oxygenated solutions of ammoniacal copper sulfate for both copper and alpha-brass specimens, and pre-oxygenated solutions of sodium chloride and copper sulfate for copper specimens. All electrolytes reduced the fatigue life relative to a reference environment of preoxygenated double distilled water, and electron diffraction studies of undisturbed fatigue fracture surfaces revealed the presence of cuprous oxide. Accordingly, the mechanism of corrosion fatigue was believed to be generally consistent with a model based on enhanced localized electrochemical dissolution at the tip of the fatigue crack due to the formation and rupture of cuprous oxide films in a manner similar to that proposed for tarnish rupture theories of stress-corrosion cracking. The oxide was considered to form by a deposition process and supplementary studies on concentration cells arising from turbulence effects, differences in oxygen concentration, and differences in pH allowed discussion of the possible anodic and cathodic reactions.

It is well known from the review articles by Gough (1), Gilbert (2), and Evans (3) that the failure lifetime of both pure metals and alloys tested under cyclic loading conditions of fatigue is affected markedly by the environment. Even a test conducted under such apparently innocuous conditions as exposure to the normal atmosphere yields a shorter lifetime than tests conducted under vacuum (4, 5); for example, Wadsworth (6) has shown that an air pressure of 10^{-5} mm Hg may increase the fatigue life of copper by a factor of 20. Furthermore, the fact that both pure metals and alloys are noticeably prone to premature failure under corrosion fatigue conditions in a variety of environ-

ments is in marked contrast to the static tensile loading situation of stress-corrosion cracking (SCC) where pure metals are not normally susceptible and environments are usually specific (3, 7). The only reasonably documented situation in which SCC of a pure metal has been reported is contained in the work of Pugh and his colleagues (8, 9) on the SCC of copper in concentrated ammonia solutions containing dissolved copper.

In spite of the considerable published work on corrosion fatigue, most studies have been phenomenological in nature and no well established mechanism incorporating the effect of environment has emerged. It is believed that electrochemistry plays a role during fatigue crack propagation in aqueous environments

Key words: electron diffraction, fatigue, corrosion, tarnish, copper, brass.

because cathodic protection and corrosion inhibitors often reduce damage (3, 10). Furthermore, the damaging species in atmospheric environments appears to be oxygen (1, 2). The oxidation characteristics of the metal appear to have an important bearing on the matter because Wadsworth (6) has shown that oxygen affected the corrosion fatigue life of aluminum, iron and copper but not gold. Also, water was as effective as oxygen on aluminum but without effect on copper. However, when considering the conjoint presence of water and oxygen Gough and Sopwith (11) found they exerted a catalytic effect on fatigue cracking of copper and its alloys. In view of these observations, speculation on the mechanism of corrosion-fatigue cracking has included proposals that failure in atmospheric environments may involve adsorption of oxygen and/or water molecules on the surface of the fatigue crack which may lower the surface energy (10) and/or prevent rewelding of crack surfaces on successive portions of the fatigue cycle (5, 10, 12). Avery and Backofen (13) have proposed a "slip ratchet" mechanism for crack formation based on oxide formation at freshly exposed slip steps preventing slip reversal on the same slip plane. Other proposals, which relate to aqueous environments, include enhanced electrochemical dissolution at the crack tip because of (i) "disarrayed metal" at the bare crack tip (3), and (ii) as a result of oxygen concentration cells set up at the crack (2,10)—particularly in neutral or near neutral electrolytes (2).

The purpose of the present study was to conduct corrosion fatigue tests on alpha-brass (Cu:29.38Zn) and copper of 99.99% purity in near neutral aqueous ammoniacal environments known to produce SCC in alpha-brass, but not copper, and then to compare corrosion fatigue of the copper in near neutral nonammoniacal environments. In this manner, it was hoped to determine whether or not there are any possible mechanistic similarities between corrosion fatigue and SCC of alpha-brass and then to determine if any such similarities are applicable to corrosion fatigue of copper, bearing in mind that SCC of copper has not been reported in the environments studied.

Experimental Procedure

Materials.—The alpha-brass and copper were received in the form of hard drawn bar of 0.375 in. diameter. The brass was from the same batch as that used in a previous study (14) and chemical analysis established the composition in terms of weight percentages as 70.47% Cu, 29.38% Zn, with total impurities <0.15%. The copper was obtained from Koch Light with a reported purity of 99.99%.

The ammoniacal solutions employed for the experimental studies were of the general type used by Mattsson (15). However, whereas Mattsson's solutions contained 0.05M Cu and a total of 1M NH₃, the present solutions were of the composition used by Johnson and Leja (16) containing 0.04M Cu and 3M NH₃. The preparation procedures of Johnson and Leja were rigidly followed in order to eliminate the aging and precipitation phenomena observed by Mattsson (15). All solutions were made from double distilled water which was subsequently boiled to remove CO₂ and then oxygenated immediately prior to preparation of the solutions. Required Cu and NH₃ values were obtained by preparing solutions containing 0.04M CuSO₄ and 1.5M (NH₄)₂SO₄. Near neutral pH values were investigated ranging from pH 4.4 to pH 8.0 for Cu and pH 5.5 to pH 8.0 for the brass. The pH values were adjusted by additions of 2N NH₄OH and measured to an accuracy of ±0.05 pH units with a Corning Model 10 pH meter.

Nonammoniacal solutions employed were 0.04M CuSO₄ (pH = 4.7) and 2M NaCl (pH = 5.0) prepared from double distilled and pre-oxygenated water. The reference environment was double distilled and pre-oxygenated water.

Specimens and testing.—The fatigue specimens were of cylindrical form machined with a reduced, but curved, gauge section as shown in Fig. 1a. The curved gauge section eliminated notch effects and ensured a maximum bending fatigue stress at the midpoint of the gauge section corresponding to a minimum diameter of 0.25 in. The specimens were polycrystalline with a grain size of ~0.001 in. and were tested in the annealed condition (550°C for 1 hr). The surfaces were cleaned in 40% aqueous HNO₃ following the heat-treatment. Fatigue testing was conducted on a rotating beam fatigue machine operating at 1700 rpm. The aqueous environment was contained in a tygon tubing cell surrounding the specimen and was introduced into the cell through a hypodermic needle placed between the specimen and tubing so as to completely fill the cell with liquid and eliminate air. The cell is shown schematically in Fig. 1b. All tests were conducted at 20°C utilizing a maximum bend stress of 30,000 psi for the alpha-brass and 21,000 psi for the copper.

The fatigue life was defined as the number of fatigue cycles to complete fracture and all values reported in the text are based on the mean average of three identical tests for the alpha-brass, and two identical tests for the copper.

Concentration cells.—Supplementary concentration cell experiments were conducted with pairs of copper and pairs of alpha-brass electrodes immersed in the various aqueous environments. Each electrode in a pair was immersed in the environment in one compartment of a two-compartment cell, the compartments being separated by a porous partition similar to the cells described by Evans (3). Potential differences between the two electrodes were measured with a Heathkit potentiometric recorder.

Three types of concentration cell were employed: (i) Turbulence-type concentration cell produced simply by bubbling inert nitrogen through one compartment only. The turbulence transported reactant species to, or, product species from the electrode thereby generating a possible moto-electric effect (3). (ii) Oxygen concentration cell produced by bubbling oxygen through one compartment while bubbling nitrogen through the second compartment. Equalized conjoint flow rates of oxygen and nitrogen were maintained in order to minimize interference from moto-electric effects. (iii) pH concentration cell produced by creating a pH difference between the two compartments.

Electron diffraction studies.—Corrosion products present on actual undisturbed fatigue-fracture surfaces were identified by electron diffraction studies conducted at 100 kV. The studies were performed in the high

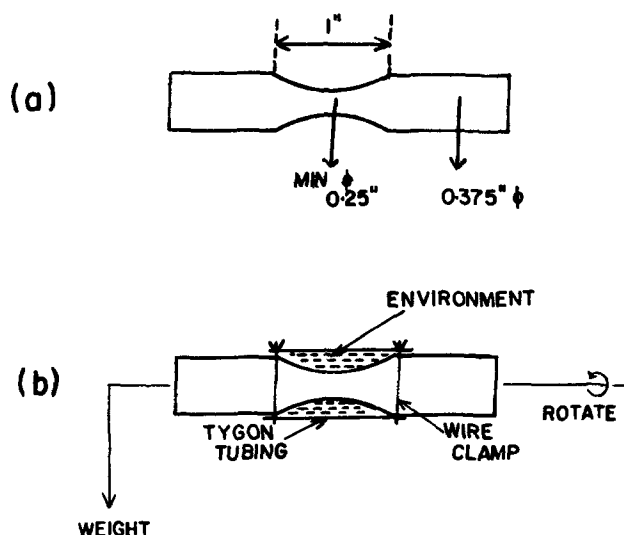


Fig. 1 (a). Dimensions of copper and alpha-brass fatigue specimens. (b). Schematic diagram of corrosion fatigue cell.

resolution diffraction accessory of a Hitachi HU11A electron microscope in which the macroscopic plane of the surface of interest was placed parallel to the incident electron beam and electron diffraction ring patterns obtained by transmission through protuberances on the surface. It was possible to locate the position of the electron beam on the surface of interest by observing the specimen through a port in the diffraction chamber. Whenever the beam was incident upon a protuberance an electron induced light emission effect was visible, the phenomenon being known as cathodoluminescence (17-19). Consequently, it was possible to ensure that diffraction patterns from the fatigue portion of the fracture surface, and not the final overload fracture portion, were studied.

The diameter of the electron beam was maintained at ~ 0.01 in., which was ten times larger than the grain size of the polycrystalline specimens. This enabled polycrystalline ring patterns to be produced from the copper matrix and alpha-brass matrix adjacent to fracture surfaces when either no corrosion products, or, only traces of corrosion products were present on the fatigue-fracture surfaces.

Phases present on actual surfaces were determined by comparing the observed interplanar spacings with those reported in the literature (20), and by comparing visual estimates of the intensities of electron diffraction rings with theoretical estimates of the integrated intensities (14). The procedural details of the technique have been discussed elsewhere (14).

Fractography.—Conventional two-stage replica electron microscopy was used to observe fractographic detail of fatigue fracture surfaces. It was hoped to quantitatively relate the spacing of fatigue striations on the fracture surface with the effect of environment on fatigue life. Unfortunately, although such striations were observed in all environments and appeared to increase in spacing with decreasing fatigue life, quantitative measurements were obscured by slip lines on the striations due to the magnitude of the fatigue amplitude employed (21).

Observations and Discussion

Fatigue life.—The alpha-brass exhibited a reduced fatigue life in the range of ammoniacal solutions employed as compared to the life in water. The actual relationship between life and pH of ammoniacal environment gave a U-shaped curve whereby the fatigue life was reduced by a maximum factor of ~ 7.5 at pH 6.8, and by a factor of ~ 2 at pH values 5.5 and 8.0, as evidenced in Fig. 2. Such a U-shaped type of re-

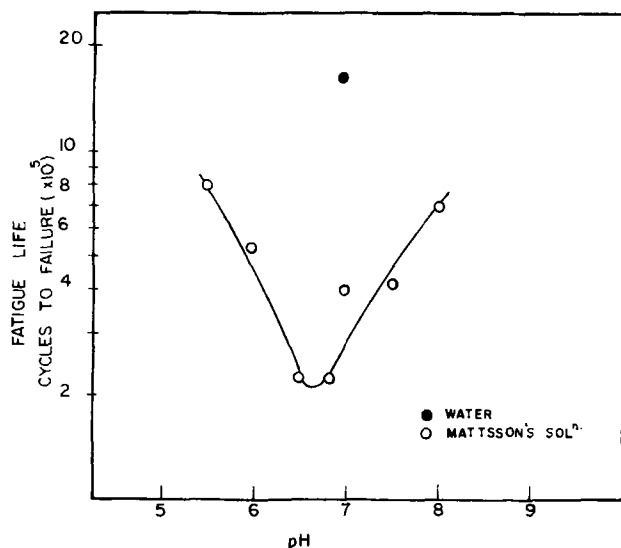


Fig. 2. Fatigue life of alpha-brass in Mattsson's type ammoniacal copper sulfate solution $[0.04M \text{CuSO}_4 + 1.5M (\text{NH}_4)_2 \text{SO}_4]$ as a function of pH. Fatigue life plotted on log scale.

lationship is commonly observed for SCC lifetimes (i.e., time to fracture) in these types of solutions within the same pH range (15, 16, 22) and, furthermore, the minimum SCC life occurs at the same general value of pH ~ 6.8 as that for minimum fatigue life.

The copper also exhibited a reduced fatigue life in all of the ammoniacal environments employed, as compared to water, and exhibited a very slight tendency toward minimum lifetimes in the pH range 5.5-6.8, as shown in Fig. 3. However, the dependence of life upon pH was not as pronounced as that of alpha-brass, being reduced by a maximum factor of only ~ 2.5 within the pH region 5.5-6.8, and by a factor of ~ 2 in pH regions of 4.4 and 8.0. Furthermore, it appeared that ammoniacal complexes were not specifically necessary for the reduced fatigue life of copper because near neutral solutions of $0.04M \text{CuSO}_4$ (pH 4.7) and $2M \text{NaCl}$ (pH 5.0) gave lifetimes more or less identical to ammoniacal solutions of similar pH, as depicted in Fig. 4.

Fatigue crack path.—Optical studies of fatigue tested and sectioned specimens revealed that the fatigue-crack path was similar in both copper and alpha-brass in all environments employed. There was no specific

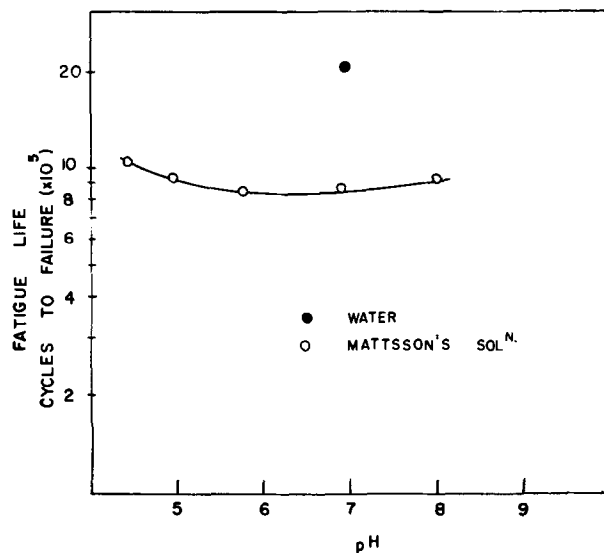


Fig. 3. Fatigue life of copper in Mattsson's type ammoniacal copper sulfate solution $[0.04M \text{CuSO}_4 + 1.5M (\text{NH}_4)_2 \text{SO}_4]$ as a function of pH. Fatigue life plotted on log scale.

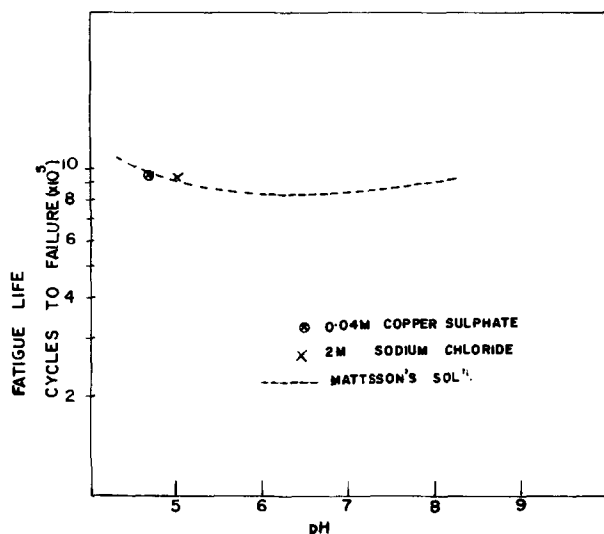


Fig. 4. Comparison of fatigue life of copper in $0.04M \text{CuSO}_4$ and $2M \text{NaCl}$ solutions relative to life of copper in Mattsson's type ammoniacal copper sulfate solution $[0.04M \text{CuSO}_4 + 1.5M (\text{NH}_4)_2 \text{SO}_4]$. Fatigue life plotted on log scale.

dependence of crack path upon environment. The crack followed a mixed transgranular and intergranular path approximately normal to the tensile stress components. These observations were important insofar as they precluded the possibility of the marked reduction in fatigue life of alpha-brass in the ammoniacal solution of pH 6.8 being associated with preferential intergranular corrosion. Such preferential corrosion has been reported by some workers on unstressed alpha-brass specimens exposed to near neutral ammoniacal environments of different composition from the present studies (8, 23). (It may also be noted that prolonged immersion of annealed and unstressed alpha-brass in the ammoniacal environment of pH 6.8 used in the present study failed to reveal any preferential penetration.)

Diffraction studies of fatigue fractures.—In view of the similar dependence of both fatigue life and SCC life of alpha-brass upon the pH of the ammoniacal environment it appeared that electron diffraction experiments might reveal other similarities regarding corrosion films on fracture surfaces. Previous electron diffraction work (14) on alpha-brass obtained from the same batch as that used in the present studies has shown that Cu_2O is present on SCC fracture surfaces produced in identical ammoniacal copper sulfate solutions of similar pH range (5.9-8.0) to those employed in the present work. Consequently, electron diffraction studies were conducted on fatigue-fracture surfaces of alpha-brass and revealed reflections consistent with the presence of Cu_2O in the pH range investigated (5.5-8.0). The details for the specific case of pH 6.8, where fatigue cracking is most rapid, are shown in Table I. [N.B. At this point it is pertinent to note that Mattsson (15) also observed corrosion films on the original surfaces of alpha-brass specimens subjected to SCC in ammoniacal copper sulfate solutions. However, it is not possible to completely correlate his corrosion films with those observed on fracture surfaces in the present studies due to four basic reasons: (i) The majority of his corrosion film analyses were based on visual observations, e.g., "interference colors" in the pH range 5.5-5.7 and "a thin grey deposit" at pH 7.7, and it is known that the color of Cu_2O is dependent on a number of conditions (14, 24); (ii) Mattsson employed an unspecified "microscopic examination" to detect the presence of Cu_2O in the "black coatings" formed in the pH range 6.3-7.3; (iii) Mattsson's observations were not conducted on the actual fracture surfaces and the environment inside a SCC or fatigue crack may be different from that in the bulk solution; (iv) Mattsson's alpha-brass and ammoniacal copper sulfate solutions were of different composition to those employed

in the present study and his solutions were subject to aging and precipitation phenomena.]

The electron diffraction techniques were applied to the copper specimens fatigued in the ammoniacal environments and revealed that all fatigue fracture surfaces contained Cu_2O . The details for the specific situation of pH 5.5 in the region of minimum fatigue life are given in Table I. Furthermore, electron diffraction studies of fatigue fracture surfaces of copper obtained in 2M NaCl and 0.04M CuSO_4 environment were also consistent with the presence of Cu_2O as shown in Table I. In addition, the presence of Cu_2O on fracture surfaces in the copper sulfate environment is reasonably consistent with the observations of Miller and Lawless (25) who used electron diffraction techniques to confirm the formation of Cu_2O films on the surfaces of unstressed copper single crystals immersed in a stronger solution of pre-oxygenated copper sulfate (0.2M CuSO_4 , pH 3.8).

Electron diffraction studies were also conducted on the fatigue-fracture surfaces of copper and alpha-brass produced in the reference environment of pre-oxygenated double distilled water. Comparison of the interplanar spacings of the rings and their visual intensities with data for Cu_2O , copper, and alpha-brass (14, 20, 26) revealed a predominance of the copper matrix and alpha-brass matrix at the fracture surfaces, as shown in Table II. The presence of Cu_2O could be detected only in trace amounts, as evidenced by the weak oxide reflections in Table II.

Thus, two important observations arose from the electron diffraction studies. First, all environments except the reference environment produced well-formed films of Cu_2O on the fatigue-fracture surfaces, whereas the more slowly fatigue-cracking situation in the reference environment produced only traces of Cu_2O on the fracture surface. Second, the studies confirmed a further similarity between SCC of alpha-brass and corrosion fatigue of copper and alpha-brass in that all fracture surfaces contained Cu_2O .

Formation of Cu_2O and electrode reactions.—The detection of Cu_2O on the corrosion-fatigue fracture surfaces necessitated a consideration of its mechanism of formation because of the possible influence of the oxide on the corrosion fatigue behavior. For example, if corrosion fatigue involved electrochemical dissolution of the metal the formation of Cu_2O on the fracture surface would serve three purposes: (i) prevent further dissolution of the sides of the crack, (ii) localize dissolution to the crack tip which is the only point at which the Cu_2O product is readily parted by the deformation processes to expose fresh metal, and (iii) the Cu_2O film is an electronic semiconductor (27, 28) and

Table I. Identification of phases on corrosion-fatigue fracture surfaces

Electron diffraction observations										
α -brass in 0.04M CuSO_4 1.5M $(\text{NH}_4)_2\text{SO}_4$ pH 6.8		Copper in 2M NaCl sol. pH 5.0		Copper in 0.04M CuSO_4 sol. pH 4.7		Copper in 0.04M CuSO_4 1.5M $(\text{NH}_4)_2\text{SO}_4$ pH 5.5		Data for Cu_2O ^(14, 20)		
d(A)	I_v	d(A)	I_v	d(A)	I_v	d(A)	I_v	hkl	d(A)	I_e (%)
2.98	w	2.98	vw	2.96	vw	2.98	vw	110	3.02	12
2.50	vs	2.46	w	2.52	vs	2.50	vs	111	2.465	100
2.09	m	2.10	m	2.10	m	2.10	m	200	2.135	28
1.80*	s			1.75	vw	1.74	vw	211	1.743	4
1.50	m	1.49	w	1.51	m	1.50	m	220	1.510	36
								310	1.350	1
								311	1.287	27
								222	1.233	5
								321	1.141	1
								400	1.067	4
				1.04	w			330, 411	1.007	0.5
0.99	w							331	0.9795	9
						0.95	vw	420	0.9548	5

* Corresponds to (200) reflection from underlying brass.

Note: hkl = Miller indices of Bragg-reflecting crystal planes.

d(A) = Interplanar spacing of crystal planes in angstrom units.

I_e (%) = Relative theoretical integrated intensity of electron beam reflections expressed as a percentage of the strongest reflection.

I_v = Relative visual intensity of observed reflections: vs = very strong; s = strong; m = medium; w = weak; vw = very weak.

Table II. Identification of phases on corrosion-fatigue fracture surfaces

Electron diffraction observations		Copper in pre-oxygenated water		Data for α -brass ^(14,20)			Data for copper ^(14,20)			Data for Cu_2O ^(14,20)		
α -brass in pre-oxygenated water		d(A)	I_v	hkl	d(A)	I_o (%)	hkl	d(A)	I_o (%)	hkl	d(A)	I_o (%)
		2.98	ew							110	3.02	12
2.46	w	2.48	vw							111	2.465	100
2.12	s	2.11	s	111	2.124	100	111	2.088	100	200	2.135	28
1.81	ms	1.81	m	200	1.84	43	200	1.808	44			
										211	1.743	4
1.51	vw	1.51	w							220	1.510	36
										310	1.35	1
1.28	m	1.28	m	220	1.301	23	220	1.278	23	311	1.287	27
										222	1.233	5
1.09	m	1.09	m	311	1.108	24	311	1.09	25	321	1.141	1
1.06	w	1.04	w	222	1.062	7	222	1.0436	7			
										400	1.067	4
										330, 411	1.007	0.5
										331	0.9785	9

Note: hkl = Miller indices of Bragg-reflecting crystal planes.

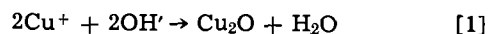
d(A) = Interplanar spacing of crystal planes in angstrom units.

I_o (%) = Relative theoretical integrated intensity of electron beam reflections expressed as a percentage of the strongest reflection in the given crystal.

I_v = Relative visual intensity of observed reflections: s = strong, ms = medium strong, m = medium, w = weak, vw = very weak, ew = extremely weak.

would not eliminate the electrochemical dissolution process by electronically insulating the Cu_2O covered cathodic surface. In its general terms, such a role for Cu_2O would be similar to the tarnish rupture models for SCC of alpha-brass in ammoniacal solutions first proposed by Forty and Humble (29) and developed later by McEvily and Bond (30) and the present authors (14).

It is generally believed that formation of Cu_2O in aqueous environments has its origins in electrochemical behavior. However, at the present time the specific reactions involved have not been established, as evidenced by the reviews of Pugh (8, 31). Recent studies by Green *et al.* (32) and the present authors (33) suggest that the oxide is formed by a precipitation process. Consequently, it is probable that Cu_2O precipitation involves a local increase in cuprous ion species and/or hydroxyl ions such that the solubility product of Cu_2O is exceeded. The reaction may be expressed in the general form



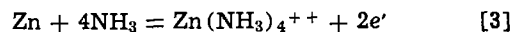
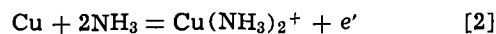
where Cu^+ may represent a complex ion containing ligands. Such a general reaction has been considered in the literature by previous workers (14, 31, 34).

The local concentration of cuprous ions may be controlled by anodic dissolution of copper atoms to yield cuprous ion species and/or the cathodic reduction of cupric ion species. The hydroxyl ion concentration will be controlled by pH and the cathodic reduction of dissolved oxygen. Furthermore, the actual precipitation reaction may occur directly on the electrode surfaces via the interaction of hydroxyl ions with adsorbed cuprous ion species, as suggested by Pugh (31). The concentration cell studies were designed to provide further information on the possible electrode reactions.

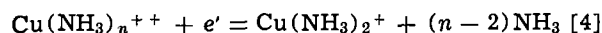
Turbulence-type concentration cell.—In all environments turbulence arising from the bubbling of inert nitrogen through one compartment of the two compartment cell, or by stirring the environment in one compartment, always caused the copper or alpha-brass electrode in the turbulent environment to be anodic with respect to the corresponding copper or alpha-brass electrode in the static environment. Potential differences of 5–15 mV were recorded on open circuit. These observations indicated that the electrochemical reactions were under anodic control and governed by removal of product species from the anode (*e.g.*, corrosion films) or diffusion of reactant species to the anode.

The observations were interesting because Bertocci (35) developed an electrochemical model for dissolu-

tion of brass in ammoniacal solutions which was under cathodic polarization concentration control. According to this model the anodic process involves dissolution of copper and zinc to form complex ionic species, *e.g.*



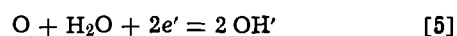
The diffusion controlled cathodic process was considered to be the reduction of cupric ion complexes. The general form of the reaction may be written



where n = number of NH_3 ligands.

Bertocci's model was developed for dissolution in the absence of corrosion film formation and recent work by Pugh and Green (36) supports the model under these conditions. However, the present electron diffraction studies have shown that Cu_2O films were formed in the specific environments currently employed. Consequently, the availability of anodic sites for dissolution will be governed by the availability of film-free surface whereas the cathodic reaction (Eq. [4]) is able to occur on film-free or Cu_2O -covered surfaces because Cu_2O has electronic conducting properties (27, 28) and may be an effective cathodic surface (37). In addition, the Cu_2O film is believed to be porous (14, 29, 32) and the anodic reaction may be further affected by the necessity for reactant species (*e.g.*, NH_3) to diffuse through the pores in order to interact with the film-free surface. Hence, under conditions where Cu_2O films are formed, it is reasonable to anticipate that cathodic polarization concentration may not be the controlling process even though the anodic and cathodic reactions are the same as in Bertocci's model.

Oxygen concentration cell.—The conjoint equalized flow of nitrogen and oxygen through separate compartments of the two-compartment cell showed that in both the distilled water environment and 2M NaCl solution (pH = 5.0) the electrode in the oxygen-rich solution was always cathodic with respect to the electrode in the oxygen-poor solution. The observations held for pairs of copper electrodes and pairs of alpha-brass electrodes, the open-circuit potential differences being 20–30 mV. Thus, in these environments the principal cathodic reaction appeared to be the reduction of dissolved oxygen, *e.g.*



Such a reaction is consistent with the observations that natural corrosion of copper is promoted by differ-

ential aeration cells (10) and that the main cathodic reaction on most metals in near neutral electrolytes containing dissolved oxygen is the oxygen reduction reaction (2, 3).

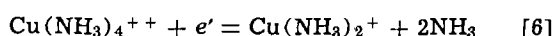
Closed-circuiting of the electrodes in the 2M NaCl solution yielded a current of ~ 0.5 mA with a consequent increase in pH of the cathodic compartment after a few hours. The pH change was readily observed visually by adding phenolphthalein indicator to the solution which caused the oxygen-rich electrolyte in the cathodic compartment to turn red as the hydroxyl ion concentration increased.

Closed circuiting of the electrodes in the double distilled water environment yielded a negligible current consistent with the very low electrical conductivity of such water.

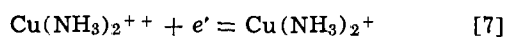
Similar oxygen concentration cell experiments in the 0.04M CuSO_4 solution (pH 4.7) and the ammoniacal copper sulfate solutions in the pH range 5.5-7.5 for alpha-brass and 4.4-7.5 for the copper showed the electrode in the oxygen-rich solution to be only slightly cathodic. Open-circuit potential differences were ~ 5 mV suggesting that the reduction of oxygen was not an important cathodic reaction in these solutions. Hence, it is probable that the reduction of cupric ion species is the principal cathodic corrosion reaction in these environments.

Raising the pH of the ammoniacal copper sulfate solutions to 8.0 produced marked cathodic behavior of the copper and brass electrodes in the oxygen-rich compartments. Open-circuit potentials of ~ 70 mV were recorded. Such behavior is consistent with the studies of Johnson and Leja (16) who observed that SCC of alpha-brass in these solutions was influenced by dissolved oxygen only at pH values > 8.0 . Thus, oxygen reduction (Eq. [5]) may be a major cathodic reaction in this particular solution.

The preference for oxygen reduction over the cathodic reduction of cupric complexes (Eq. [4]) in copper ammoniacal solutions of pH ~ 8.0 may be related to the average number of ammonia ligands, n , attached to the cupric complex ion, $\text{Cu}(\text{NH}_3)_n^{++}$. Johnson and Leja (16) have shown that in these solutions $n = 1$ at pH ≈ 5.6 , $n = 2$ at pH ≈ 6.3 , $n = 3$ at pH ≈ 7.0 , and $n = 4$ at pH ≈ 8.0 . Thus, at pH 8.0 where $n = 4$, the rate of reduction of $\text{Cu}(\text{NH}_3)_4^{++}$ may be slow due to the steric effects of four NH_3 ligands at the cathode. For example, the following reduction reaction for $n = 4$



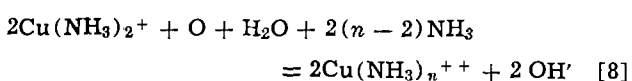
involves a change in the number of NH_3 ligands between cupric and cuprous species. However, when $n = 2$ at pH ≈ 6.3 the following reduction reaction



does not involve a change in number of NH_3 ligands and may be a favored reaction (16).

The $\text{Cu}(\text{NH}_3)_2^+$ complex with two NH_3 ligands was chosen as the product of the reduction reaction because it appears to be the equilibrium complex of dissolved cuprous species in the general pH range studied, as evidenced by published pH-potential diagrams for the homogeneous system with dissolved copper (15, 38).

Alternatively, dissolved oxygen may not be directly involved in the cathodic reduction reaction at pH 8.0 in the ammoniacal copper sulfate solution. Instead, it may act indirectly by oxidizing cuprous species to the cupric state thereby increasing the concentration of cupric ions available for reduction at the cathode. Such a role for oxygen has been considered by Bertocci (35), and Pugh and Green (31,36) and may be represented in a general form by Eq. [8]

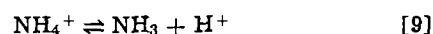


In this situation, the effect of pH would appear to

lie in creating sufficient NH_3 to allow favorable conditions for formation of the tetrammine cupric complex, $\text{Cu}(\text{NH}_3)_4^{++}$, because oxygen concentration effects only became markedly noticeable at pH 8.0 where the number of NH_3 ligands, n , approached 4 (16). The importance of $n = 4$ and the relative rapidity with which the reaction depicted by Eq. [8] is expected to proceed is undoubtedly related to the fact that cupric ions form four strongly bonded unidentate ligands in aqueous solutions (39,40). In the present solutions these ligands may be H_2O and/or NH_3 groups, although in practice the number of H_2O ligands is usually omitted in equations. However, the NH_3 ligand is more strongly bonded than the H_2O ligand (39,40) and if the pH is high enough, sufficient NH_3 will be available to allow formation of four very strong NH_3 ligands. Thus, it is postulated that the reaction depicted by Eq. [8] proceeds rapidly only when the number of NH_3 ligands on the cupric ion is increased to $n = 4$.

pH cells.—Studies on pH cells were confined to the ammoniacal copper sulfate solutions in the pH range 5.5-8.0. It was observed that the compartment containing high pH solution was anodic with respect to the electrode in the compartment containing low pH solution. The results are summarized in Table III where open-circuit potentials in excess of 100 mV were observed.

Increasing the pH (i.e., lowering $[\text{H}^+]$ concentration) displaces the ammonium dissociation reaction



to the right and increases the concentration of $[\text{NH}_3]$ species. Thus, if the anodic process involves dissolution of metal via the formation of complex ion species with ammonia ligands (e.g., Eq. [2] and [3]), the availability of ammonia molecules may dictate the dissolution rate and render the process under anodic control. Under these conditions, the high pH environment will be anodic with respect to the low pH environment, as observed.

Proposed events within the corrosion-fatigue crack.—The fatigue cycle itself is capable of generating a crack in ductile metals purely by plastic deformation processes (5,41), each cycle leading to an increment of crack advance during the propagation stage. Thus, in principle, any environment which is able to promote dissolution of the metal should, if given sufficient time depending upon frequency of fatigue cycle (4), contribute an increment of crack advance via dissolution during each cycle and reduce the fatigue life. It is not necessary for the environment to produce a crack under static load conditions (i.e., SCC). Naturally, if factors are present which localize dissolution to the tip of the crack, and not the sides of the crack, the environment will be more effective in reducing the fatigue life. Consequently, the present studies suggest that the basic effect of the aqueous solutions employed for corrosion fatigue of both copper and alpha-brass is to provide an electronically conducting film of Cu_2O which localizes anodic dissolution processes to the tip of the fatigue crack, this being the only point at which the film is readily parted by the localized deformation processes. Such a Cu_2O film was detected by the electron diffraction studies, and its presence also appears to be in reasonable agreement with published thermo-

Table III. pH Concentration cell potentials in aqueous 0.04M CuSO_4 + 1.5M $(\text{NH}_4)_2\text{SO}_4$ solutions

pH of solution		Open-circuit potential difference (mV)	
Anode	Cathode	Alpha-brass electrodes	Copper electrodes
6.8	5.5	37	12
8.0	6.8	150	125
8.0	5.5	185	135

dynamic considerations (15, 38, 42, 43). Thus, the model for corrosion fatigue contains the elements of the tarnish rupture and parting models developed for SCC of alpha-brass (14, 29, 30).

The anodic reaction on copper sites appears to be the dissolution of copper atoms to form dissolved cuprous ionic species. The principal cathodic reaction in the solutions containing dissolved cupric ion species (i.e., Mattsson-type solution and 0.04M CuSO_4) appears to be the reduction of cupric species to cuprous species. In the absence of dissolved cupric species (i.e., 2M NaCl and double-distilled water), the cathodic reaction is the reduction of dissolved oxygen. The cuprous oxide forms by deposition when the concentration of cuprous species and hydroxyl ions is such that the solubility product of Cu_2O is exceeded (Eq. [1]). Deposition of Cu_2O is expected to be governed by the availability and mobility of cuprous species because hydroxyl ions have a high mobility due to proton jumps (44) and are readily available from the dissociation of water.

The actual rate of anodic dissolution of fresh exposed metal atoms at breaks in the Cu_2O film at the tip of the fatigue crack is strongly affected by the environment. Thus, in the double-distilled water environment, where the cathodic reaction is reduction of oxygen, the high ohmic resistance of the electrolyte severely restricts the length of crack over which oxygen concentration cells will be effective and this environment should yield the longest lifetimes, as observed in Fig. 2 and 3.

Regarding copper in the ammoniacal copper sulfate solutions, the anodic dissolution of copper to form cuprous species is enhanced by the presence of NH_3 groups which form a cuprous complex with two strongly bonded unidentate NH_3 ligands (40) ($\text{Cu}(\text{NH}_3)_2^+$). Hence, with reference to Fig. 3, increasing the pH from 4.4 to 6.8 increases the concentration of $[\text{NH}_3]$ (Eq. [9]) and should produce a tendency for enhanced anodic dissolution of copper and a reduction in fatigue lifetime, as observed. Further increases in pH to 8.0 should continue to yield enhanced anodic dissolution of copper. However, if the physical nature of the Cu_2O film in this pH range is such that it is not fully protective and contains breaks at points other than the tip of the fatigue crack, the enhanced dissolution will not be confined to the tip of the crack and will not fully contribute to a further reduction in fatigue life. If the breaks are sufficiently numerous the fatigue life may actually increase, as observed.

The same general considerations discussed for copper are also expected to apply to corrosion fatigue of the alpha-brass in ammoniacal copper sulfate solutions (Fig. 2). However, the effect of pH may be more dramatic because of the presence of zinc atoms. For example, below pH ~ 6.8 the zinc enters the solutions as Zn^{++} ions with no ammonia ligands (38, 42). Hence, with reference to Fig. 2, increasing the pH from 5.5 to 6.8 increases the concentration of $[\text{NH}_3]$ available to enhance the anodic dissolution of copper atoms and, because the alloy contains only $\sim 70\%$ copper, there is effectively more $[\text{NH}_3]$ available to assist dissolution than for pure copper at the same pH. This, together with the influence of the high thermodynamic activity of zinc on the dissolution kinetics suggested by Green *et al.* (32) could account for the marked reduction in fatigue life at pH ~ 6.8 .

Other factors which undoubtedly complicate the quantitative aspects of the corrosion fatigue lifetimes are variations in environment and alloy composition which affect the semiconducting properties of the Cu_2O film and modify its ability to function as an effective cathode and localize the anodic reaction. It is well known (27, 45) that the conductivity of cuprous oxide depends upon deviations from stoichiometry which affect the cuprous ion, cupric ion, and oxygen ion concentrations in the semiconductor. The effect of oxygen partial pressure on the stoichiometry of Cu_2O has been

much studied (27, 45), but apparently there is no information in the literature regarding the effect of aqueous environment variables (e.g., pH) on conductivity of precipitated Cu_2O . Furthermore, there appears to be no published studies on the effect of trace quantities of divalent zinc ions, Zn^{++} , in the Cu_2O lattice on the conductivity of Cu_2O (28). Some preliminary studies on the effect of trace additions of divalent Be^{++} on the conductivity of Cu_2O have been reported (46), but they do not illuminate the present work.

Conclusions

Studies on the corrosion fatigue of copper and alpha-brass in near neutral aqueous solutions of pre-oxygenated ammoniacal copper sulfate (0.04M CuSO_4 + 1.5M $(\text{NH}_4)_2\text{SO}_4$), and of copper in pre-oxygenated aqueous solutions of both sodium chloride (2M NaCl) and copper sulfate (0.04M CuSO_4), were consistent with the following conclusions:

1. All environments yielded a reduced fatigue lifetime relative to a reference environment of pre-oxygenated double-distilled water.

2. All fatigue fracture surfaces contained a cuprous oxide corrosion film.

3. The cuprous oxide film localized the anodic dissolution of metal atoms to the tip of the fatigue crack where the film was readily parted by deformation processes. Thus, the general elements of tarnish formation and rupture models developed to explain SCC of alpha-brass were applicable to corrosion fatigue of both copper and alpha-brass.

4. The major cathodic reduction reaction was the reduction of cupric ion species in the environments containing dissolved copper, and reduction of oxygen in the absence of dissolved copper.

Acknowledgments

The authors wish to thank the Canadian Defence Research Board for financial assistance under Grant No. DRB 9535-50. Also, the assistance of Mr. J. E. Northcott in the early stages of the work and stimulating discussions with Dr. E. Peters of the University of British Columbia are gratefully acknowledged.

Manuscript submitted May 17, 1971; revised manuscript received May 8, 1972.

Any discussion of this paper will appear in a Discussion Section to be published in the June 1973 JOURNAL.

REFERENCES

1. H. J. Gough, *J. Inst. Metals*, **49**, 17 (1932).
2. P. T. Gilbert, *Met. Rev.*, **1**, 379 (1956).
3. U. R. Evans, "The Corrosion and Oxidation of Metals," E. Arnold Ltd., London, (1961).
4. A. J. Kennedy, "Processes of Creep and Fatigue in Metals," p. 316, Oliver and Boyd, Edinburgh, (1962).
5. W. J. Plumbridge and D. A. Ryder, *Met. Rev.*, **136**, 119 (1969).
6. N. J. Wadsworth, in "Internal Stresses and Fatigue in Metals," Rassweiler and Grube, Editors, p. 382, Elsevier, Co., Amsterdam, (1959).
7. H. H. Uhlig, in "Proceedings of Conference on Fundamental Aspects of Stress Corrosion Cracking," Staehle, Forty, and van Rooyen, Editors, p. 86, N.A.C.E. (1969).
8. E. N. Pugh, J. V. Craig, and A. J. Sedriks, in "Proceedings of Conference on Fundamental Aspects of Stress Corrosion Cracking, Staehle, Forty, and van Rooyen, Editors, pp. 118, 151, N.A.C.E. (1969).
9. E. N. Pugh, W. G. Montague, and A.R.C. Westwood, *Corrosion Sci.*, **6**, 345 (1966).
10. H. H. Uhlig, "Corrosion and Corrosion Control," John Wiley and Sons, New York, p. 124 (1963).
11. H. J. Gough and D. G. Sopwith, *J. Inst. Metals*, **56**, 55 (1935).
12. F. E. Fujita, "Fracture of Solids," Drucker and Gilman, Editors, p. 657, Interscience, New York (1963).
13. D. H. Avery and W. A. Backofen, "Fracture of Solids," Drucker and Gilman, Editors, p. 339, Interscience, New York (1963).

14. S. S. Birley and D. Tromans, *Corrosion*, **27**, 297 (1971).
15. E. Mattsson, *Electrochim. Acta*, **3**, 279 (1961).
16. H. E. Johnson and J. Leja, *Corrosion*, **22**, 178 (1966).
17. G. Remond, S. Kimoto, and H. Okuzumi, Paper presented at 3rd. Annual Scanning Electron Microscopy Symposium, I.I.T. Res. Inst., Chicago, April 1970.
18. M. D. Muir, P. R. Grant, G. Hubbard, and J. Mundell, Proceedings of 4th Annual Scanning Electron Microscopy Symposium I.I.T. Res. Inst., Chicago, April 1971.
19. P. M. Williams and A. D. Yoffe, *Phil. Mag.*, **18**, 555 (1968); *Radiation Effects*, **1**, 61 (1969).
20. A.S.T.M. X-ray Card Index File.
21. D. A. Meyn, *Trans. Am. Soc. Metals*, **61**, 42 (1968).
22. D. Tromans, N. A. Dowds, and J. Leja, in Proceedings of Conference on Fundamental Aspects of Stress Corrosion Cracking, Staehle, Forty, and van Rooyen, Editors, p. 154, N.A.C.E. (1969).
23. D. H. Thompson and A. W. Tracy, *Trans. A.I.M.E.*, **185**, 100 (1949).
24. R. G. Dakers and J. Halpern, *Canad. J. Chem.*, **32**, 969 (1954).
25. G. T. Miller, Jr. and K. R. Lawless, *This Journal*, **106**, 854 (1959).
26. W. B. Pearson, "Handbook of Lattice Spacings and Structure of Metals," Vol. 2, p. 892, Pergamon Press, New York (1967).
27. N. F. Mott and R. W. Gurney, "Electronic Processes in Ionic Crystals," Dover Publications, Inc., New York (1964).
28. F. A. Kröger, "The Chemistry of Imperfect Crystals," North-Holland Pub. Co., Amsterdam (1964).
29. A. J. Forty and P. Humble, *Phil. Mag.*, **8**, 247 (1963).
30. A. J. McEvily and A. P. Bond, *This Journal*, **112**, 131 (1965).
31. E. N. Pugh, Proceedings of N.A.T.O. Advanced Study Institute on Stress Corrosion, Portugal, March 29-April 2, 1971. J. C. Scully, Editor, In press.
32. J. A. S. Green, H. D. Mendelberg, and H. T. Yolken, *This Journal*, **117**, 433 (1970).
33. S. S. Birley and D. Tromans, *ibid.*, **118**, 636 (1971).
34. H. W. Pickering and P. R. Swann, *Corrosion*, **19**, 373 (1963).
35. U. Bertocci, *Electrochim. Metallorum*, **3**, 275 (1968).
36. E. N. Pugh and J.A.S. Green, *Met. Trans.*, **2**, 3129 (1971).
37. L. Graf and H. R. Lacour, *Z. Metallk.*, **51**, 162 (1960).
38. H. E. Johnson and J. Leja, *This Journal*, **112**, 638 (1965).
39. F. Basolo and R. G. Pearson, "Mechanisms of Inorganic Reactions: Study of Metal Complexes in Solution," John Wiley and Sons, New York (1958).
40. L. E. Orgel, "An Introduction to Transition-Metal Chemistry: Ligand-Field Theory," Methuen and Co., London (1960).
41. C. Laird and G. C. Smith, *Phil. Mag.*, **7**, 847 (1962).
42. F. Letowski and J. Niemic, *This Journal*, **113**, 629 (1966).
43. M. Pourbaix, "Atlas of Electrochemical Equilibria in Aqueous Solutions," Pergamon Press, New York (1966).
44. R. W. Gurney, "Ionic Processes in Solution," McGraw-Hill Book Co., New York (1953).
45. N. N. Greenwood, "Ionic Crystals Lattice Defects and Non-stoichiometry," Butterworths, London (1968).
46. M. O'Keeffe and W. J. Moore, *J. Chem. Phys.*, **35**, 1324 (1961).

Hydrogen Evolution Reaction at Sodium Tungsten Bronzes in Acid Solutions

D. B. Šepa, D. S. Ovcin, and M. V. Vojnović

Institute for Chemistry, Technology and Metallurgy, 11000 Belgrade, Yugoslavia

ABSTRACT

Hydrogen evolution reaction in acid solutions ($-0.7 < \text{pH} < 2.0$) at sodium tungsten bronze electrodes of various compositions ($0.45 < x < 0.83$) have been investigated using the galvanostatic steady-state method. The mechanism of the hydrogen evolution reaction has been proposed. A weak electrocatalytic effect dependent on the bronze composition has been found.

Only a few data concerning the hydrogen evolution reaction (HER) in acid solutions at sodium tungsten bronzes, Na_xWO_3 , are available in the literature (1-4). The hydrogen dissolution reaction has been studied at some transition metal tungsten bronzes (5), at hydrogen tungsten bronzes (6, 7), and at sodium tungsten bronzes (the term bronze is used to refer to the latter for brevity) (8). The available information, however, is insufficient to present a full picture of the kinetics of the HER in this system.

It is the purpose of this paper to make a contribution to better understanding of the HER at the bronzes in acid solutions.

Experimental

Ten large crystals of the bronzes (approximately $15 \times 15 \times 15$ mm) of compositions $0.45 < x < 0.83$ were grown on gold wire by the electrolytic reduction of a molten mixture of reagent grade sodium tungstate and tungsten trioxide in an alumina crucible (9). Plates about 1 mm thick were cut from these crystals, polished on the finest emery paper, and then washed in

1N NaOH solution and hot distilled water. Finally, the plates were mounted in an appropriate Teflon holder.

An all-glass three-compartment cell was used. The HER was studied in sulfuric acid solutions of various pH values ($-0.7 < \text{pH} < 2.0$), while purified hydrogen was bubbled through the solution. Measurements of cathodic Tafel lines were carried out using the galvanostatic steady-state method. Potentials were measured against the hydrogen electrode in the same solution.

Results

It was found that the reversible potential of the HER is not established at the bronze electrodes in acid solutions saturated with hydrogen. Rest potentials within the range 0.2-0.5V, and usually about 0.3V, were established.¹

If a bronze electrode is cathodically polarized and care is taken that steady-state conditions of measurements are strictly applied, a complex V -log i relationship is obtained, as presented in Fig. 1 (Down and

¹ Potentials throughout the paper are referred to the scale of the hydrogen electrode in the same solution, unless otherwise stated.

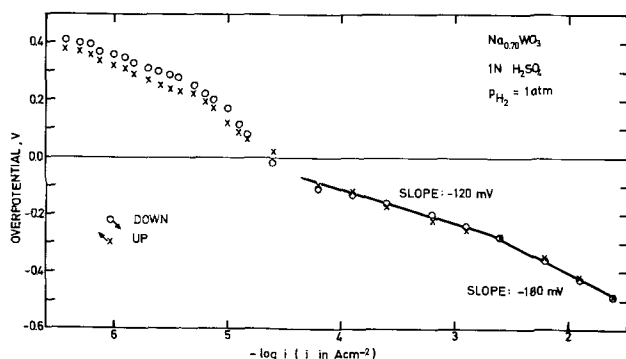


Fig. 1. Typical steady-state cathodic V - $\log i$ relationship

up measurements of this line require about 10 hr.) The following features concerning this V - $\log i$ relationship should be noted:

(i) In the range of overpotentials between 0.4 and 0.2V some electrode process occurs, which has been noted also by Vondrak and Balej (3, 4) and by Armstrong *et al.* (8), when they studied the behavior of the bronzes in acid solutions by potential sweep method. It is interesting that Glemser and Neumann (10), who studied hydrogen tungsten bronzes, and Broyde (5), who studied a number of tungsten bronzes of transition metals, also observed an electrode process at overpotentials of about 0.3V.

(ii) At lower overpotentials a limiting current, not determined by mass transport from the solution, of approximately $(2-5) \times 10^{-5} \text{ A-cm}^{-2}$ was observed. The composition of the bronze and the pH of the solution showed no effect on the value of this limiting current.

(iii) At overpotentials higher than about -0.1V the HER is the predominant electrode process. Two Tafel lines of slopes close to -120 and -180 mV were obtained. At current densities higher than approximately $10^{-3} \text{ A-cm}^{-2}$ intensive evolution of hydrogen at the surface of electrodes was observed.

It is interesting to note that quite a different shape of V - $\log i$ relationship is obtained if steady-state measurements are not strictly applied. A typical quasi-steady-state V - $\log i$ relationship, obtained by faster measurements, is presented in Fig. 2. (A line needed about an hour to be measured.) The first down-measured line is rather complex and any linear part cannot be clearly traced. After several repeated up and down measurements in the current density region above approximately $(2-5) \times 10^{-5} \text{ A-cm}^{-2}$ two linear parts with slopes close to -120 and -180 mV are clearly distinguished, overlapping the line obtained in the steady-state measurements. In the region of lower current densities, however, a qualitatively new picture is obtained. It is possible to get straight lines of slopes varying from -40 to -120 mV, which are usu-

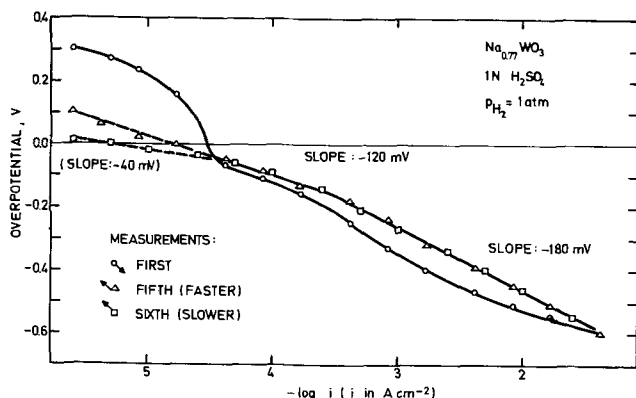


Fig. 2. Various shapes of quasi-steady-state cathodic V - $\log i$ relationships.

ally stretched to more positive potentials than the reversible hydrogen potential. The changes of potential in this region of current densities are very slow. Depending on the speed of recording the potentials, different slopes can be obtained. The quasi-steady-state performance of the electrode in this region of current densities was shown in the following way: after a longer period of time (order of an hour), the potential of an electrode tends to get more positive, approaching slowly the corresponding steady-state value.

The dependence of the kinetics of the HER on the pH value of the solution is given in Fig. 3 and 4. Both linear parts of the Tafel lines, with slopes of -120 and -180 mV have the same value of the parameter $\partial V / \partial \text{pH}$ close to -120 mV per pH unit (measured on the pH independent scale).

When the Tafel line with the slope of -120 mV is extrapolated to the hydrogen reversible potential, the exchange current density of the HER is obtained. It was found that the rate of the HER, taken as the logarithm of the exchange current density, is slightly dependent on the composition of the bronze electrodes with a maximum value of about $3 \times 10^{-5} \text{ A-cm}^{-2}$ in the vicinity of $x = 0.65$, as shown in Fig. 5.

Discussion

A model of the surface of the bronzes in acid solutions has been reported (11, 12) and an explanation of the electrochemical behavior of the surface has been proposed. This model is based on the existence of a nonstoichiometric, hydrated tungsten oxide-like layer at the surface. The rest potential, established at the bronzes in acid solutions, according to this model corresponds to an oxide potential of a metal electrode. Hence, the part of cathodic line in Fig. 1 between the

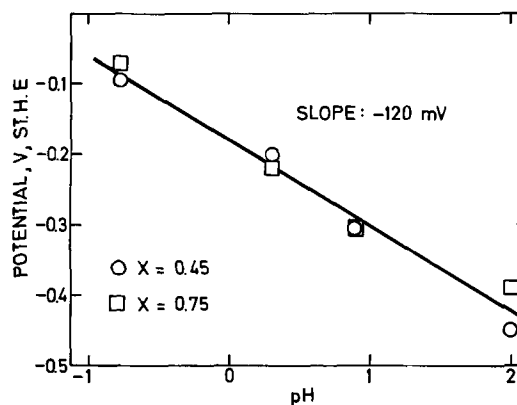


Fig. 3. The pH dependence of the HER at Na_2WO_3 in acid solutions. Part of the Tafel line with the slope of -120 mV. Potentials taken at constant current density of $1.5 \times 10^{-4} \text{ A-cm}^{-2}$.

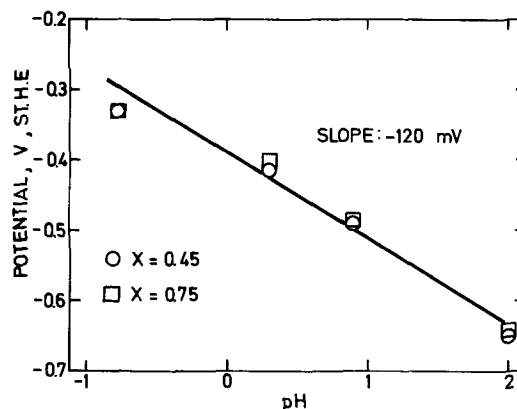


Fig. 4. The pH dependence of the HER at Na_xWO_3 in acid solutions. Part of the Tafel line with the slope of -180 mV. Potentials taken at constant current density of $3 \times 10^{-3} \text{ A-cm}^{-2}$.

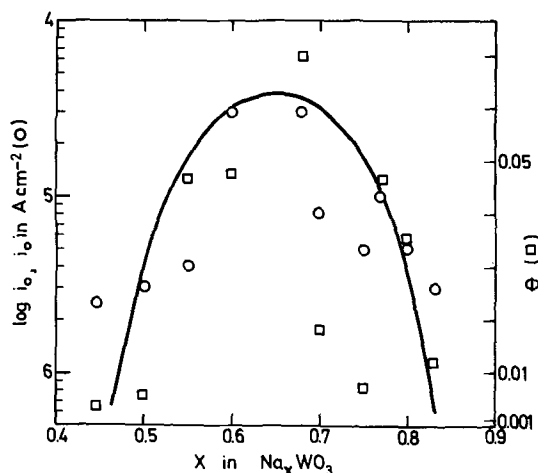


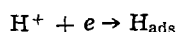
Fig. 5. Electrocatalytic effect for the HER at the bronzes. Solution of 1N H₂SO₄ saturated with hydrogen.

rest potential and the reversible hydrogen potential represents the process of reduction of the hydrated oxide layer of the bronze.

When hydrogen is evolved at the bronze electrode in acid solutions, the oxide layer at the surface is reduced, and a surface with properties close to the bulk-metallic phase is finally obtained. Hence, any kinetic information obtained in the region of current densities lower than about $(2-5) \times 10^{-5}$ A-cm⁻² does not refer to the HER, but to slow changes in the character of the surface layer of the bronze. Therefore, interpretation of slopes of Tafel lines obtained in this range of current densities attributed by some authors (3, 4) to the HER, is responsible for the considerable discrepancies among data on the kinetics of the HER, as presented in Table I.

Finally, it should be stated that the data concerning the hydrogen evolution and dissolution reactions refer to two substantially different states of the surface of the bronze electrode, and cannot be used together in mechanistic considerations of the reaction kinetics.

The set of kinetic parameters obtained in this paper fits the mechanism of coupled discharge and catalytic steps already theoretically discussed by Thomas (13).



Theoretical and experimental kinetic parameters are compared in Table II. The agreement is satisfactory.

In this mechanism the change of the slope of the cathodic Tafel line from -120 to -180 mV is due to the change in the coverage of the atomic hydrogen

Table I. Kinetic parameters of the HER at the sodium tungsten bronze electrodes in acid solutions

Electrolyte	x in Na _x WO ₃	$-\partial V / \partial \log i$	$\partial V / \partial \text{pH}$	Electrode pretreatment	Reference
1N H ₂ SO ₄	0.5	180		Cathodic polarization 2-20 min at -0.3V	1
	0.65	140*			
	0.8	200*			
(10 ⁻¹ -10 ⁻²)N H ₂ SO ₄	0.65	120	-120	Cathodic polarization 5 min at -0.5V	2
1N H ₂ SO ₄	0.74	120**		Cathodic polarization 15 sec at -0.8V	3
1N H ₂ SO ₄	0.71	120**	-65**	—	4

* At these electrodes lower slopes close to -75 and -130 mV, respectively, have been observed in the region of current densities lower than about 1×10^{-4} A cm⁻².

** Authors reported the change of slope to the value of -40 mV at lower overpotentials (below -0.2V). The pH dependence for this part of Tafel line is reported to be -35 mV.

Table II. Comparison of theoretical and experimental kinetic parameters for the mechanism proposed

	Kinetic parameter	Theoretical	Experimental
Low overpotentials	$dV/d \log i$	$-2.303 2RT/F$	-120
	$dV/d \text{pH}$	$-2.303 2RT/F$	-120
	$d \log i_0/d \text{pH}$	-1/2	-0.51
High overpotentials	$dV/d \log i$	$-2.303 3RT/F$	-180
	$dV/d \text{pH}$	$-2.303 2RT/F$	-120
	$d \log i_0/d \text{pH}$	-1/3	-0.35

Table III. Experimental values of the potential where the change of the slope of the cathodic Tafel line occurred (1N H₂SO₄)

x in Na _x WO ₃	0.45	0.50	0.55	0.60	0.68
Overpotential, V	430	380	150	140	110
x in Na _x WO ₃	0.70	0.75	0.77	0.80	0.83
Overpotential, V	250	340	150	180	300

from Langmuir to Temkin conditions of adsorption (13). When this mechanism is theoretically treated it is possible to calculate the potential dependence of the coverage with atomic hydrogen along the part of Tafel line with the slope of -120 mV. It has been found that $\partial V / \partial \ln \theta = -4RT/F$. Assuming that the change of the slope always occurred when the threshold of the Temkin region was reached, i.e., when $\theta = 0.2$, and if experimentally found values of potentials of the change of the slope from -120 to -180 mV are taken into account (cf. Table III), it is possible to calculate the coverage of the atomic hydrogen the bronzes would have at the reversible hydrogen potential. The values of coverages of atomic hydrogen at the reversible potential calculated in this way appeared to be dependent on the composition of the bronze with a maximum in the vicinity of $x = 0.65$, as presented in Fig. 5. The electrocatalytic effect on the HER at the bronzes is self-explanatory if Fig. 5 is considered, since maxima for both dependencies practically overlap.² It is interesting to note that the value of the maximum coverage of atomic hydrogen at the reversible potential, obtained in this way, is about 6%. This value is close to the 3% calculated by Jones and Loebl (15, 16) for adsorption of hydrogen at the bronzes from the gas phase.

Acknowledgment

This paper was presented at the 22nd I.S.E. Meeting in Dubrovnik, 1971.

Manuscript submitted Feb. 24, 1972; revised manuscript received June 12, 1972.

Any discussion of this paper will appear in a Discussion Section to be published in the June 1973 JOURNAL.

² Bockris et al. (14) reported a minimum in the vicinity of $x = 0.6$, but from measurements at only three electrodes of different composition (1). Vondrak and Balej (3, 4), however, claimed the linear dependence of $\log i_0$ vs. x , i.e., the rate of the reaction proportional to the free electron concentration in the bronze.

REFERENCES

- R. J. Mannan, Ph.D. Thesis, University of Pennsylvania, Philadelphia, 1967.
- M. V. Vojnović and D. B. Šepa, *Bull. Chem. Soc. Beograd*, **30**, 16 (1968).
- J. Vondrak and J. Balej, XXI C.I.T.C.E. Meeting, Prague, 1970, Extended Abstracts, p. 361.
- J. Vondrak and J. Balej, XXII I.S.E. Meeting, Dubrovnik, 1971, Extended Abstracts, p. 170.
- B. Broyde, *J. Catalysis*, **10**, 13 (1968).
- B. S. Hobbs and A. C. C. Tseung, *Nature*, **222**, 556 (1969).
- A. C. C. Tseung and B. S. Hobbs, *Platinum Met. Rev.*, **13**, 146 (1969).
- R. D. Armstrong, A. F. Douglas, and D. E. Williams, *Energy Conversion*, **11**, 7 (1971).
- A. Damjanović, D. Šepa, and J. O'M. Bockris, *J. Res. Inst. Catalysis, Hokkaido Univ.*, **16**, 1 (1968).

10. O. Glemser and C. Neumann, *Z. anorg. Chem.*, **265**, 288 (1951).
11. M. V. Vojnović and D. B. Šepa, XXII I.S.E. Meeting, Dubrovnik, 1971, Extended Abstracts, p. 167.
12. M. V. Vojnović, D. B. Šepa, and D. S. Ovcin, *Croatica Chim. Acta.*, **44**, 89 (1972).
13. J. G. N. Thomas, *Trans. Faraday Soc.*, **57**, 1603 (1961).
14. J. O'M. Bockris, A. Damjanovic, and R. J. Mannan, *J. Electroanal. Chem.*, **18**, 349 (1968).
15. F. T. Jones, Ph.D. Thesis, Polytechnic Institute of Brooklyn, Brooklyn, 1960.
16. F.T. Jones and E. M. Loebl, *J. Phys. Chem.*, **73**, 894 (1969).

The Corrosion of Zinc Anodes in Aqueous Alkaline Electrolytes

D. P. Gregory,¹ P. C. Jones,² and D. P. Redfearn

Research Department, Energy Conversion Limited, Basingstoke, Hampshire, England

ABSTRACT

Rates of self-discharge of porous zinc electrodes in alkaline electrolytes have been measured under a variety of conditions by monitoring the rate of hydrogen evolution. The rate was found to decrease with the addition of lead or mercury to the zinc, the presence of zincate in the electrolyte, and increasing electrolyte concentration up to 5M KOH. Above 5M KOH the rate increased with increasing KOH concentration.

Batteries which provide the highest ratio of power and energy to volume or weight employ negative electrode materials, e.g., zinc or magnesium, which are thermodynamically unstable in most aqueous electrolytes.

For the case of zinc in aqueous alkali, anodic dissolution of the active material and cathodic evolution of hydrogen occur simultaneously, the former resulting in oxide or hydroxide precipitation on the zinc surface and formation of soluble complex anions. Self-discharge of the zinc anode is prejudicial to the battery not only because of the loss of dischargeable capacity with time but, in addition, the need to incorporate a hydrogen venting system makes the battery more prone to deterioration through evaporation of the electrolyte.

The realization that the rate of deterioration of batteries utilizing a zinc electrode is closely related to the rate of hydrogen evolution has led to investigations directed toward the measurement of hydrogen evolved from zinc anodes immersed in battery-type electrolytes. It has long been realized that the rate of hydrogen evolution is minimized by the addition of inhibitors which increase the hydrogen over-potential, e.g., mercury or lead.

Recently, Snyder and Lander (1) have studied the corrosion reaction on commercial, amalgamated zinc anodes complete with separator paper. They found that the rate of hydrogen evolution decreased with increasing electrolyte concentration from 5 w/o (weight per cent) (1M) to 40 w/o (10M) KOH and was also reduced by decreasing the temperature and increasing the mercury content up to 4 w/o HgO. Amalgamation of the silver grid material had little or no effect on the rate of hydrogen evolution. These authors also concluded that the presence of zincate ion in the electrolyte increased the rate at which hydrogen was evolved.

Rüetschi (2) studied the corrosion rate of amalgamated zinc and found, in contrast to Snyder and Lander, that the hydrogen evolution rate increased with KOH concentration above 1M. It was also observed that the rate decreased with the presence of zincate

ions above 2M KOH. However, data on the physical properties of the powdered materials used in these experiments were not reported.

Dirkse and Timmer (3) measured the corrosion rate of amalgamated and nonamalgamated zinc wire in KOH electrolytes under a variety of conditions and confirmed Rüetschi's observation that the presence of zincate ions lowers the rate of corrosion for amalgamated zinc. In contrast to Rüetschi, they found that, for amalgamated zinc, increasing the electrolyte concentration above 30-35 w/o (7-8.5M) KOH decreased the corrosion rate.

The present work was undertaken because of these conflicting results and to establish information on the effects of the following variables: choice of inhibitor (lead or mercury), choice of electrolyte (KOH or NaOH), choice of grid material (silver or copper), pretreatment of grid material, presence of zincate, and temperature on the corrosion rate of porous zinc electrodes.

Experimental

Procedure.—Zinc samples were sealed in borosilicate glass cells of ~250 cm³ capacity as shown in Fig. 1. The cells were filled with electrolyte under

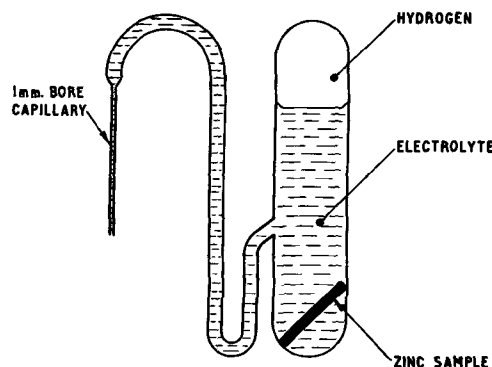


Fig. 1. Electrolytic cell

¹ Present address: Institute of Gas Technology, Chicago, Illinois 60600.

² Present address: International Nickel Ltd., Thames House, London S.W.1, England.

Key words: hydrogen evolution, inhibition, self-discharge, porous electrodes.

vacuum and, except for the capillary outlet, were immersed in thermostatically controlled water baths ($\pm 1^\circ\text{C}$). Twenty-four hours were allowed for equilibration before readings were commenced.

Hydrogen, evolved from the reaction of zinc with alkali, accumulated in the cylindrical portion of the cells and displaced an equal volume of electrolyte through the capillary side arm. The volume of hydrogen was measured by the daily titration of the electrolyte displaced from the cell. Average titers were of the order of 25 cm^3 to minimize error and were determined to an accuracy of $\pm 0.1\text{ cm}^3$. All results were corrected to room temperature. Errors arising from evaporation and carbonation of the displaced electrolyte had no adverse effect because the analysis involved the titration for total alkali (hydroxide ion plus carbonate ion).

All experiments were carried out in triplicate and the duration of the experiments was between twenty and sixty days depending on temperature.

Materials.—All reagents were Analar grade and distilled water was used throughout.

Two types of zinc sample were used. For the initial parts of the investigation zinc battery anodes were prepared by the reduction of zinc oxide compacts, in some cases mixed with lead monoxide or mercuric oxide, on silver mesh grids. All anodes were analyzed for zinc, lead, or mercury and zinc oxide, the content of the latter being $\sim 2\text{ w/o}$. These were then sectioned to give samples of cross-sectional area $\sim 3\text{ cm}^2$, thickness $\sim 0.3\text{ cm}$, and weight $\sim 2.5\text{ g}$. Zinc anodes prepared in this manner had a high surface area ($\sim 0.8\text{ m}^2\text{g}^{-1}$) and a porosity of $\sim 72\%$.

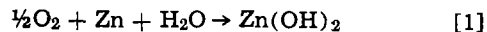
For the examination of grid materials and their pretreatment, electrolytic zinc powder, prepared by electrodeposition from a zincate bath, was pressed on to the grid substrate at pressures up to 5 ton/in.^2 , giving zinc anode samples of similar dimensions to those above with a surface area of $>1.5\text{ m}^2\text{g}^{-1}$ and a porosity of $\sim 70\%$.

The grid substrates were either silver mesh or expanded high conductivity copper, supplied by Expanded Metal Company. Grids were amalgamated by immersion in acidified mercuric acetate solution (0.2M) for 2 min after degreasing in trichloroethylene and etching in hydrochloric acid (1M).

Zincate saturated electrolytes were analyzed and found to contain $102\text{ g}\cdot\text{l}^{-1}$ zinc oxide in 10M KOH.

Results and Discussion

The method used by the present investigators was first employed by Craig (4). Modified apparatus have since been used by other investigators (1-3). A sealed system has been used to minimize the possibility of zinc undergoing self-discharge by the reduction of oxygen on the surface of the zinc according to reaction [1]



Previous experiments (5) have shown that self-discharge by oxygen reduction proceeds at a faster rate than self-discharge by hydrogen evolution. Consequently, it has been suggested (6) that the measure of hydrogen evolution under these circumstances may not represent the behavior of batteries on storage. In the present experiments the back diffusion of oxygen or carbon dioxide was minimized by the use of a fine bore capillary tube (0.1 mm) and the authenticity of the method was confirmed by monitoring the rate of hydrogen evolution from zinc-air batteries sealed in 1 in. thick perspex containers under a nitrogen atmosphere, using a mercury manometer. Excellent agreement was observed between the two rates of hydrogen evolution as shown in Fig. 2 and, as a further check, the remaining dischargeable capacity of the batteries after prolonged storage in these containers agreed with that predicted on the basis of the hydrogen evolution data.

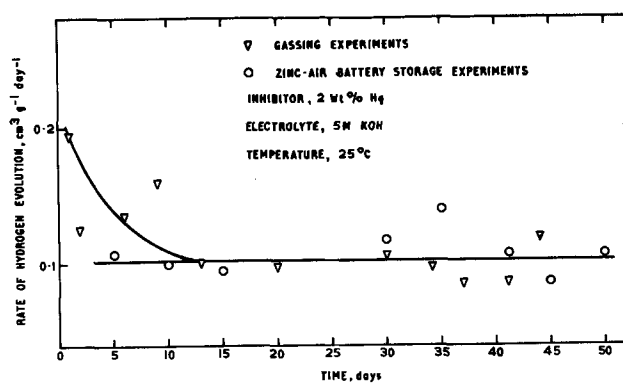
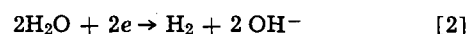


Fig. 2. Comparison between rates of hydrogen evolution from gassing experiments and zinc-air battery storage experiments.

Figure 3 illustrates typical dependences of the rate of hydrogen evolution with time. The measurements were taken over a period of days rather than hours because, first, the time required to achieve saturation of the electrolyte with hydrogen is approximately 24 hr for an evolution rate of $0.1\text{ cm}^3\text{g}^{-1}\text{day}^{-1}$ (7), and, second, the initial rate of hydrogen evolution is high and steady-state conditions are only maintained after 2-10 days depending on temperature. During this period a surface coating of zinc oxide or hydroxide is formed on the highly active zinc.

Zinc electrodes containing no inhibitor.—The dependence of the rate of hydrogen evolution on KOH concentration for anodes containing no inhibitor is shown in Fig. 4. The rate exhibits a minimum at $\sim 2\text{M}$ KOH. These results are in conflict with those reported by Snyder and Lander (1) and Dirkse and Timmer (3), who both found that the rate of hydrogen evolution decreased with increasing KOH concentration over the range 1-12M.

Rüetschi (2) and Dirkse and Timmer (3), on the basis of the dependence of the rate on activity of water, postulated that the hydrogen evolution reaction [2] is rate controlling, while the dissolution of the zinc proceeds simultaneously



The dependence of the rate of hydrogen evolution on electrolyte concentration, over the range 0.1-2M, also suggests that the hydrogen evolution reaction is rate controlling.

However, above 2M KOH the direct dependence of the rate on hydroxyl ion concentration suggests a

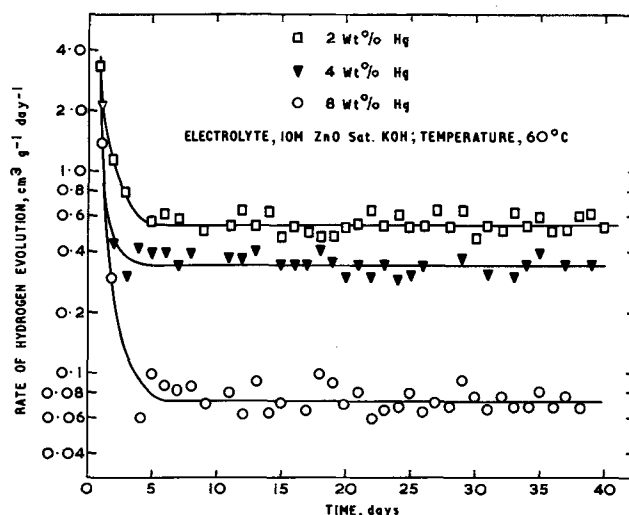


Fig. 3. Time dependence of the rate of hydrogen evolution for zinc anodes containing mercury inhibitor.

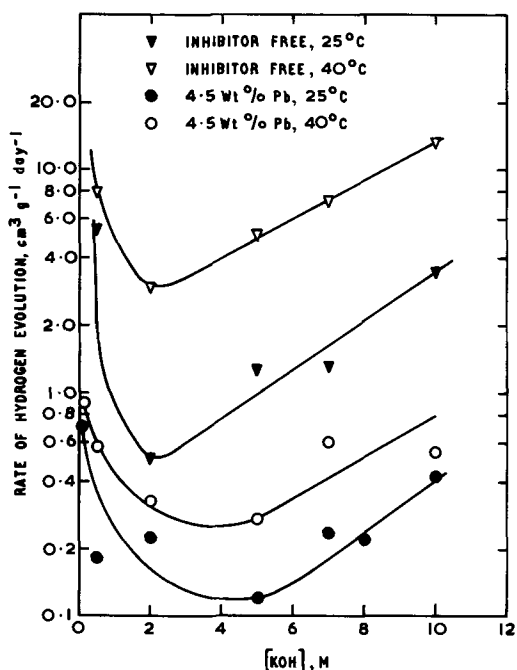
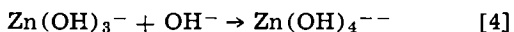
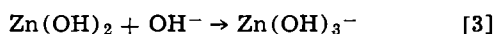


Fig. 4. Dependence of the rate of hydrogen evolution on KOH concentration for inhibitor-free and lead-containing zinc anodes.

change in the rate-controlling reaction from [2] to a reaction involving the anodic oxidation of the zinc. This may be explained if the anodic dissolution of the zinc proceeds via a different mechanism at high KOH concentration. The slope $d \log_{10}(\text{rate})/d \log_{10}C_{\text{OH}^-}$ approximates to one, suggesting that one hydroxyl ion is involved in the rate-determining process, assuming the OH^- concentration at the interphase approximates to that in the bulk. The rate-determining process may be represented by either Reaction [3] or [4]



The species $\text{Zn}(\text{OH})_3^-$ has been postulated by both Dirkse (8) and Gerischer (9).

An alternative explanation to a change in reaction mechanism is that the rate of dissolution of the charge transfer product, ZnO or $\text{Zn}(\text{OH})_2$, becomes limiting. McBreen (10) and Dirkse (11) have found that the diffusion coefficient for zincate ion decreases with increasing KOH concentration. The anodic process is unlikely to be solely controlled by diffusion; convection, particularly within a porous structure, also plays an important role and may explain why the results are at variance with those reported by Dirkse and Timmer for nonporous electrodes.

Zinc electrodes containing lead inhibitor.—The addition of lead to zinc electrodes reduces the rate of hydrogen evolution which is in agreement with the observations of Mansfeld and Gilman (12) and Borchers and Krug (13).

Figure 5 shows that the rate of hydrogen evolution is more or less independent of lead content from 1 to 9 w/o over the temperature range investigated.

The dependence of the rate of hydrogen evolution on KOH concentration for zinc electrodes containing lead inhibitor (Fig. 4) is similar to that exhibited by inhibitor-free electrodes but the minimum occurs at a higher KOH concentration, $\sim 5\text{M}$. Below 5M KOH the rate-controlling reaction is likely to be hydrogen evolution. The change in gradient once again suggests a change in the rate-controlling reaction to one of the steps in the anodic oxidation of zinc. The rate in electrolytes of concentration $>5\text{M}$ is lower than that reported for inhibitor-free anodes and this can be explained if the dissolution process is retarded by the

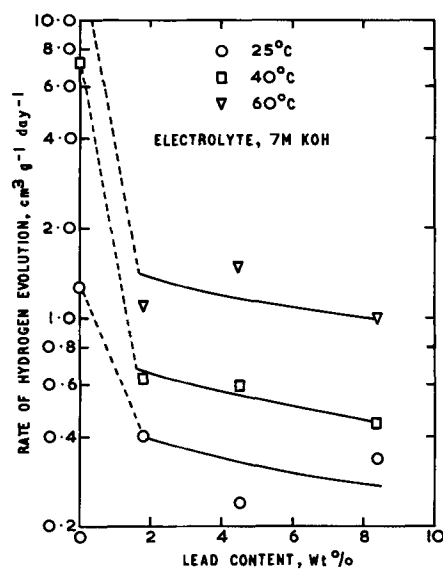


Fig. 5. Dependence of the rate of hydrogen evolution on lead content.

presence of lead at the active sites of the zinc surface which act as a barrier to the passage of zinc species from the electrode as suggested by Mansfeld and Gilman (14).

Zinc electrodes containing mercury inhibitor.—**Mercury content.**—Figure 6 shows the rate dependence as a function of mercury content at various temperatures. Increasing mercury content decreases the rate of hydrogen evolution which is in line with the prediction that the presence of mercury increases the hydrogen over-potential and agrees with the findings of Snyder *et al.* (1) and Yardney (15). The mercury content required to reduce the rate of hydrogen evolution to an acceptable level increases with increasing temperature and corresponds to 2-3 w/o Hg at 25°C, 3-4 w/o at 40°C, and 6-8 w/o at 60°C.

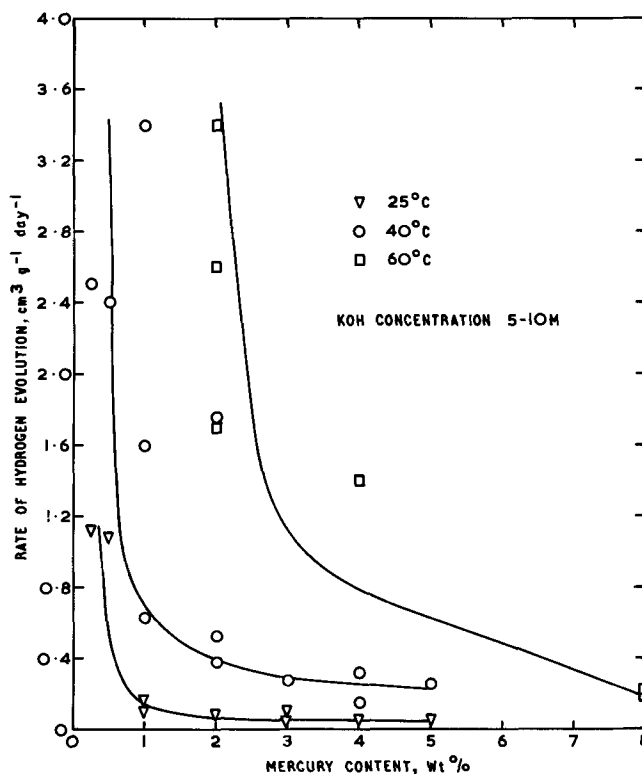


Fig. 6. Dependence of the rate of hydrogen evolution on mercury content.

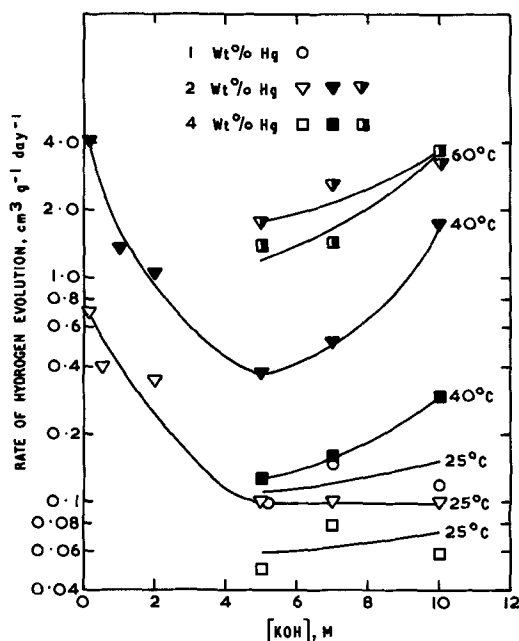


Fig. 7. Dependence of the rate of hydrogen evolution on KOH concentration for zinc anodes containing mercury inhibitor.

KOH electrolyte.—The effect of KOH concentration on the rate of hydrogen evolution for constant mercury content at 25°, 40°, and 60°C is shown in Fig. 7. A minimum in the rate curve is observed at ~5M KOH. Rüetschi (2) found that the rate increased with increasing temperature. In addition, this worker observed that, in the case of zincate-containing electrolytes, the rate decreased initially then increased with a minimum occurring at ~5M KOH. Snyder *et al.* (1) observed a linear relationship for the plot of log (rate) vs. [KOH] whereas Dirkse *et al.* (3) observed an irregular dependence of the rate on KOH concentration at 25°C but found an increase in the rate from ~5 to 8.5M KOH, followed by a rapid decrease to ~12M KOH.

Zincate-saturated electrolytes.—The presence of zincate significantly reduces the rate of self-discharge (see Table I). This observation is in agreement with the results reported by Dirkse *et al.* (3) and Rüetschi (2) but is at variance with those reported by Snyder *et al.* (1).

NaOH electrolyte.—The use of NaOH electrolyte results in a lower rate of hydrogen evolution than that observed for KOH (Table II). This may be a result of the lower activity of water in NaOH compared with KOH electrolyte, or a change in the nature of the solution species involved in the reaction. The rate of hydro-

Table III. Enthalpies of activation (kcal mole⁻¹) for hydrogen evolution from zinc anodes with different inhibitor contents

	5M KOH	7M KOH	10M KOH	10M ZnO sat. KOH
Inhibitor free	18.4	22.0	17.5	—
Lead inhibitor 4.5 w/o	9.4	9.1	11.2	—
Mercury inhibitor				
1 w/o	—	17.4	—	—
2 w/o	15.4	19.0	24.0	8.2
4 w/o	17.6	15.0	22.5	16.2

Table IV. Rate of hydrogen evolution (cm³ g⁻¹ day⁻¹) from zinc anodes containing different grid materials in 10M KOH electrolyte

Grid material	25°C	40°C	50°C	60°C
Copper	0.23 ± 0.05	0.75 ± 0.06	2.3 ± 0.2	3.0 ± 0.4
Amalgamated copper	0.19 ± 0.04	0.57 ± 0.05	1.6 ± 0.2	3.8 ± 0.4
Silver	0.30 ± 0.04	0.63 ± 0.05	1.6 ± 0.1	3.0 ± 0.5
Amalgamated silver	0.31 ± 0.03	—	—	4.3 ± 0.5

gen evolution as a function of the NaOH concentration was not investigated and consequently it is not possible to differentiate between these alternatives.

Temperature dependence of the rate of hydrogen evolution.—The apparent enthalpies of activation for different electrolyte concentrations and inhibitor contents are summarized in Table III. The average enthalpies of activation for the hydrogen evolution reaction are 19.3 kcal mole⁻¹ for inhibitor-free, 9.9 kcal mole⁻¹ for lead, and 17.3 kcal mole⁻¹ for mercury-containing anodes. These are in broad agreement with enthalpy values reported in the literature (16).

Grid materials.—Table IV shows the rate of hydrogen evolution for anodes fabricated using copper, amalgamated copper, silver, and amalgamated silver current collector screens in 10M KOH at different temperatures. Copper and silver current collectors give similar rates and amalgamation of the silver screen has little effect on the rate of self-discharge. Amalgamation of the copper screen, however, gives a reduction in the rate of hydrogen evolution at temperatures <50°C.

Examination of the mercury-coated grid materials by optical microscopy has shown that whereas the copper grid has a surface deposit of mercury, the silver has not. The brittle nature of the latter suggests that amalgamation has occurred and has resulted in alloy formation. However, conflicting evidence is found in the phase diagrams (17) for Ag-Hg and Cu-Hg which show equally steep liquidi, indicating that the rate of solubility of mercury is similar in both substrates.

Table I. Effect of zinc oxide saturated electrolyte on the rate of hydrogen evolution (cm³ g⁻¹ day⁻¹)

Mercury content, w/o	10M KOH			10M ZnO sat. KOH		
	25°C	40°C	60°C	25°C	40°C	60°C
0.25	1.13 ± 0.05	2.5 ± 0.4	—	0.80 ± 0.05	—	—
0.5	1.08 ± 0.05	2.4 ± 0.4	—	0.70 ± 0.05	—	—
1	—	3.4 ± 0.2	—	—	1.3 ± 0.1	—
2	0.10 ± 0.01	1.76 ± 0.05	3.4 ± 0.5	0.12 ± 0.02	0.24 ± 0.02	0.52 ± 0.05
4	0.06 ± 0.01	0.32 ± 0.01	3.8 ± 0.2	0.020 ± 0.005	0.060 ± 0.005	0.33 ± 0.05
8	—	—	0.20 ± 0.02	—	—	0.070 ± 0.005

Table II. Comparison of the rates of hydrogen evolution (cm³ g⁻¹ day⁻¹) from zinc anodes in KOH and NaOH electrolytes at 40°C

Electrolyte	1 w/o Hg	2 w/o Hg	4 w/o Hg	5 w/o Hg
10M KOH	3.4 ± 0.2	1.76 ± 0.05	0.32 ± 0.01	—
10M ZnO sat. KOH	1.3 ± 0.1	0.24 ± 0.02	0.060 ± 0.005	—
10M NaOH	—	0.87 ± 0.05	0.17 ± 0.02	0.17 ± 0.02
10M ZnO sat. NaOH	0.160 ± 0.005	0.64 ± 0.01	—	0.100 ± 0.005

Conclusions

Self-discharge of the zinc anode is inhibited by the addition of lead or mercury to the zinc. The rate is independent of lead content over the range 1.8-8.4 w/o, whereas increasing the mercury content is found to decrease the rate in agreement with the results of Snyder and Lander (1) and Rüetschi (2).

The dependence of the rate on KOH concentration shows a minimum between 2 and 5M KOH. Similar behavior was observed for inhibitor-free, lead and mercury containing anodes. These results agree, over part of the concentration range, with those reported by Rüetschi (2) and Dirkse and Timmer (3). The discrepancies between the results obtained by the latter authors and those reported may be attributed to the different type of zinc anode used in the experiments.

The self-discharge rate in NaOH is lower than in KOH. The effect of saturating the electrolyte with zincate is to reduce the rate of self-discharge, agreeing with the observations of Rüetschi and Dirkse *et al.* but differing from the results reported by Snyder *et al.*

Amalgamation of the silver grid material has little or no effect on the rate of self-discharge agreeing with the findings of Snyder *et al.* (1). The use of an amalgamated copper grid, however, significantly reduces the rate of self-discharge.

Acknowledgment

The authors wish to thank Miss S. L. Coombs for carrying out the experimental work for this investigation and Energy Conversion Limited for permission to publish this paper.

Manuscript submitted Aug. 17, 1971; revised manuscript received May 14, 1972.

Any discussion of this paper will appear in a Discussion Section to be published in the June 1973 JOURNAL.

REFERENCES

1. R. N. Snyder and J. J. Lander, *Electrochem. Technol.*, **3**, 161 (1965).
2. P. Rüetschi, *This Journal*, **114**, 301 (1967).
3. T. P. Dirkse and R. Timmer, *ibid.*, **116**, 162 (1969).
4. D. N. Craig, see G. W. Vinal, "Primary Batteries," p. 96, John Wiley & Sons, Inc., New York (1951).
5. D. P. Gregory, P. C. Jones, and D. P. Redfearn, Unpublished data.
6. E. M. Otto and W. G. Eicke, Jr., *This Journal*, **104**, 199 (1957).
7. P. Rüetschi and R. F. Amlie, *J. Phys. Chem.*, **70**, 718 (1966).
8. T. P. Dirkse, *This Journal*, **101**, 328 (1954).
9. H. Gerischer, *Z. Physik. Chem.*, **202**, 302 (1953).
10. J. McBreen, Study to Improve the Zinc Electrode for Spacecraft Electrochemical Cells, 2nd Quarterly Report on Contract NAS 5-10231, Yardley Electric Corp., New York (1967).
11. T. P. Dirkse, Paper presented at 7th Power Sources Convention, Brighton, 1970.
12. F. Mansfeld and S. Gilman, *This Journal*, **117**, 1328 (1970).
13. Von H. Borchers and H. Krug, *Werkstoffe Korrosion*, **22**, 125 (1971).
14. F. Mansfeld and S. Gilman, *This Journal*, **117**, 588 (1970).
15. M. N. Yardney, U.S. Pat. 2,983,777 (1956).
16. B. E. Conway, "Electrochemical Data," pp. 337-350, Elsevier Publishing Co., Houston (1952).
17. M. Hansen, "Constitution of Binary Alloys," pp. 829 and 845, McGraw Hill Publishing Co., New York (1958).

Radiotracer Studies of Metal-Metal Ion Exchange Inhibition Using Organic Inhibitors

Sally Shinew Twining and David S. Newman*

Department of Chemistry, Bowling Green State University, Bowling Green, Ohio 43403

ABSTRACT

The metal-metal ion exchange rate in silver and cadmium systems has been studied using radiotracers in solutions containing organic inhibitors. The inhibitors were *endo-cis*-2,3-dimethylolbornane(I) and *endo-cis*-5,6-dimethylol-2-norbornene(II). In the silver system, inhibitor(I) showed an inhibition efficiency of 53% and inhibitor(II) showed an inhibition efficiency of 56%. In the cadmium system, inhibitor(I) showed <3% inhibition and inhibitor(II) showed 16% inhibition. These data and the arguments given suggest the inhibitor molecules in the silver system are being adsorbed through the unpaired electrons of the oxygen while in the cadmium system the inhibitor molecules are being adsorbed through the unpaired electrons of the oxygen and the double bond electrons of inhibitor(II). A model for the metal-solution interface is given.

In a previous metal-metal ion exchange study (1) it was shown that a judiciously chosen series of organic molecules could be employed to yield information about the structure of the metal-solution interfacial region and the electrochemical processes taking place therein. The molecular "probes" used were butane-1,4-diol, *cis*-2-butene-1,4-diol, and 2-butyne-1,4-diol. In the present investigation the molecules *endo-cis*-2,3-dimethylolbornane, (I), and *endo-cis*-5,6-dimethylol-2-norbornene, (II), were used to further probe the interfacial region in the Cd-Cd⁺⁺ and Ag-Ag⁺ systems. The structures of these two organic molecules are shown in Fig. 1.

It is easily seen that compounds (I) and (II) are similar to the straight chain diols but with a bulky cyclopentyl group attached to the middle of the chain. All five inhibitors are, in fact, 1,4 diols. However, the

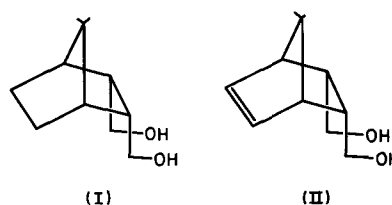


Fig. 1. Inhibitor(I), *endo-cis*-2,3-dimethylolbornane and inhibitor(II), *endo-cis*-5,6-dimethylol-2-norbornene

* Electrochemical Society Active Member.

Key words: corrosion inhibition, adsorption, metal-metal ion exchange.

bulky cyclopentyl group is hydrophobic and should therefore cause an increase in the "structuring" of the water in its immediate vicinity. This structuring should increase the water's surface tension and tend to push the norbornane compounds from the metal surface. As a result the inhibition efficiencies, given by the equation

$$I = [(R_0 - R_i)/R_0] 100 \quad [1]$$

where R_0 is the rate of exchange with no inhibitor and R_i is the rate with inhibitors, should be lower in the norbornane systems than in the butane diol systems.

The interpretation of any differences in the mode of interaction between metal and norbornane molecules should be easier than with the butane diols because the two norbornane molecules have, but for the double bond, nearly the same structures. Moreover, the entropy of adsorption of (I) and (II) should be less than the entropy of adsorption of the butane diols. The microscopic imperfections in the surface layer of the metal crystal are relatively insignificant because re-exchange is taking place at a rapid rate. Therefore after a very short time, probably less than a few seconds, the original outermost layer of metal has been completely replaced. This means that the surface does not have to be absolutely clean for results to be significant. In addition, the increase in radioactivity of the disk as a function of time is determined by the slow self-diffusion process which further reduces transient errors introduced by minor surface imperfections.

Experimental Details

General.—The experimental apparatus and techniques used in this study are similar to those used in previous studies (1, 2).

The radioactivity was measured with a Beckman liquid scintillation counter (Model LS 133) using a standard PPO-POPOP-Toluene scintillation cocktail. All experiments were performed at 25°C. The solutions were deoxygenated and stirred with nitrogen. The inhibitor concentration was 0.001M and the metal ion concentration was 0.1M. All crystal surfaces were polished to a mirror finish. Reagent grade salts were used in each case. The edges of the Cd disks and the edges and one face of the silver disks were coated with paraffin. The exposed faces were then cleaned with chloroform to remove excess paraffin and other organic material present.

Preparation of (I) and (II).—Inhibitor (II) was synthesized by a method first described by Alder and Roth (3). This compound was then hydrogenated using Birch's technique (4) to obtain (I). After each ex-

change experiment the inhibitor was isolated and identified by means of its IR spectrum to assure that no structural change had occurred.

Cadmium-cadmium ion exchange.—The disks were handled the same as in the previous study (1) except that they were annealed for 12 hr at 175°C. The dimensions of each disk were approximately 1.90 cm in diameter and 2.3 mm thick. The surface of the single crystal was parallel to the 10 $\bar{1}0$ plane of the crystal. The disks were electropolished to a shiny flat surface by a technique described by King and McKinney (5). Cd^{115m} was used as the radiotracer. Each disk was immersed in solution for 7½ hr.

Silver-silver ion exchange.—Single-crystal silver disks approximately 3 mm thick were cut from a single-crystal rod approximately 2 cm in diameter. The surface of the disk was parallel to the 210 plane. The disks were chemically polished by the method of Levinstein and Robinson (6) to give a flat shiny surface free from strain and pits. The disks were annealed for 18 hr at 850°C to remove the strains and distortions acquired during the polishing process. Ag^{110m} was used as the radiotracer.

The glass cells were covered with dark fabric bags to prevent light from entering. The disks were immersed in the solutions for periods of time ranging from four to sixteen days, removed from solution, washed by various techniques, and counted. In one series of experiments the disks were washed under a stream of water for 15 min per side. In another series they were washed for 30 min per side. A third set of disks was gently rocked in a water bath for 5 min. The washed disks were put back in solution so that the effect of the washing technique on the exchange rate could be studied.

Results

The results of the cadmium-cadmium ion exchange study using inhibitors I and II are shown in Table I. The results of the four-day immersion experiments in the silver-silver ion system are given in Table II. In both tables the efficiencies of the butane diol series are given for reference. Figures 2 and 3 and Table III show the results of the experiments with silver using different washing techniques.

From the information provided by the standards, the total activity, a_t , of the experimental disks, in terms of counts per minute, was converted to gram atoms per square centimeter.

The exchange process is controlled by self-diffusion into the single crystal. This process is analogous to

Table I. Cadmium metal-cadmium-ion exchange

Measurement	System						
	Inhibitor I	Inhibitor II	Uninhibited	Butane (1) 1,4 diol	cis-2 Butene diol	2 Butyne 1,4 diol	Uninhibited
R , g-atoms/cm ² sec × 10 ¹¹	1.73	1.51	1.79	1.91	1.15	1.07	2.42
I , %	3.3	16.2	—	21.1	51.8	55.4	—
$(C_0^{2/3}$ atoms/cm ²) × 10 ⁻¹⁴	7.83	7.14	8.02	10.0	7.95	7.50	11.9
S_1 , %	2.4	11.0	—	16.0	34.0	36.8	—
Average area of molecule, A^{22}	57.2	62.4	—	55.7	44.4	69.6	—
$X_{in}^{(ads)}$	0.006	0.026	—	0.06	0.212	0.127	—
ΔG^\ddagger , kcal/mole	1.0	-0.591	—	-1.08	-1.96	-1.58	—

Table II. Silver metal-silver ion exchange

Measurement	System						
	Inhibitor I	Inhibitor II	Uninhibited	Butane (1) 1,4 diol	cis-2-Butene diol	2 Butyne 1,4 diol	Uninhibited
R , g-atoms/cm ² sec × 10 ¹⁴	2.53	2.39	5.37	4.6	2.7	3.7	21.0
I , %	52.8	55.5	—	68	74	70	—
$(C_0^{2/3}$ atoms/cm ²) × 10 ⁻¹⁶	3.42	3.29	5.62	5.4	3.8	4.6	14.9
$(C_0^{2/3}$ atoms/cm ²) × 10 ⁻¹⁶	0.53	0.54	0.88	0.56	0.38	0.45	1.5
S_1 , %	39.2	41.4	—	64	75	68	—
Average area of molecule, A^{22}	145	145	—	30.4	27.4	28.6	—
$X_{in}^{(ads)}$	0.053	0.055	—	0.70	0.90	0.76	—
ΔG^\ddagger , kcal/mole	-0.79	-0.97	—	-5.7	-11.2	-6.9	—

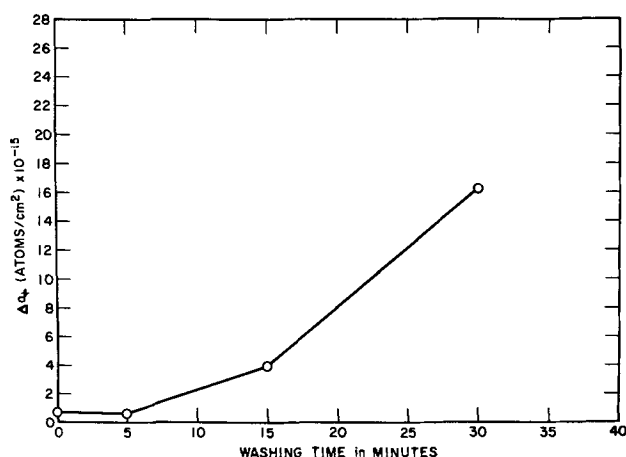


Fig. 2. Activity increase in a four-day immersion period using various washing times of the silver disks.

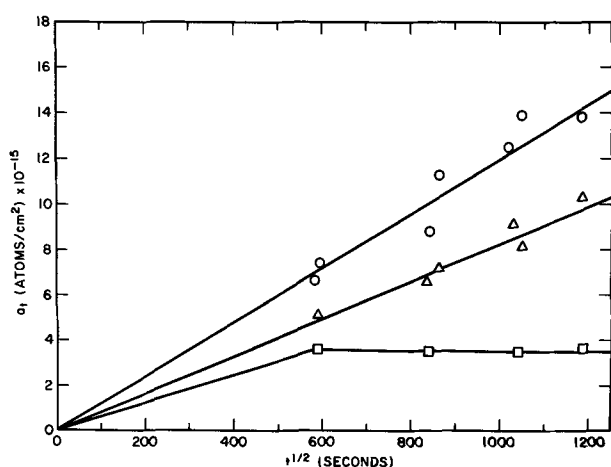


Fig. 3. Activity of silver disks washed for 15 min under a stream of water every four days and then reimmersed in solution.

heat conduction (7). The equation for self-diffusion is Fick's second law

$$\frac{\partial C}{\partial t} = \frac{D \partial^2 C}{\partial x^2} \quad [2]$$

where D , the diffusion coefficient is independent of concentration. In this equation C is the concentration, t is time, and $\partial C / \partial x$ is the concentration gradient. This equation with the appropriate boundary conditions (1) becomes

$$\frac{da_t}{dt} = C_0 D^{1/2} (\pi t)^{-1/2} \quad [3]$$

where a_t is the total activity, C_0 the surface concentration of cadmium, and D the diffusion coefficient. On integration Eq. 3 gives

$$a_t = 2C_0 \pi^{-1/2} (Dt)^{1/2} \quad [4]$$

From Eq. [4] the surface concentration was calculated. The diffusion coefficient used for cadmium was $3.6 \times 10^{-15} \text{ cm}^2/\text{sec}$. This value was used by King and

Table III. Inhibitor efficiencies using different washing methods in the Ag-Ag⁺

Washing method	I (%), Inhibitor (I)	I (%), Inhibitor (II)
Initial	52.8	55.5
Water bath	41.3	55.6
15 min stream of water	42.4	54.6
30 min stream of water	43.6	53.5

McKinney (5) for single-crystal cadmium at 25°C. The diffusion coefficient used for silver was $1.6 \times 10^{-21} \text{ cm}^2/\text{sec}$. This value was calculated for the 210 plane based on the values determined by Tingley (8) for the 110 and 111 planes.

The values for R were obtained by dividing the total activity in gram atoms per square centimeter by the time of immersion.

The percentage of the disk covered by inhibitor, S_i , was calculated from the equation

$$S_i = 100 [1 - (C_{oi}/C_{ou})^{2/3}] \quad [5]$$

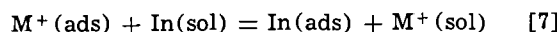
where C_{oi} and C_{ou} are the inhibited and uninhibited surface concentrations, respectively.

The surface area covered by each inhibitor molecule was estimated, using Dreiding Molecular Models, from the possible orientations of the inhibitors on the metal surface for the proposed mode of adsorption. Since Dreiding models give bond lengths and bond angles only, the appropriate atomic radius was added to the outermost hydrogen atoms.

The free energy of adsorption was calculated from the equation (1)

$$\Delta G^\circ = -RT \ln \left[\frac{[X_{In}(\text{ads})][X_{M^{++}}(\text{sol})]}{[X_{M^{++}}(\text{ads})][X_{In}(\text{sol})]} \right] \quad [6]$$

where the X_i 's are the mole fractions of the various species in the two dimensional cross-sectional area. This equation assumes the chemical reaction for metal-metal ion exchange in the presence of inhibitors is



In calculating the surface concentrations a roughness factor of 1.1 was assumed because this roughness factor gives a C_0 very close to the best value for the bulk density of cadmium. The measured geometric area was multiplied by this factor to give a "corrected surface concentration," C_0' . The surface concentration of inhibitor was obtained by multiplying the percentage of the disk covered by inhibitor, S_i , by the correction factor for the area of this disk, 1.1, and then dividing by the surface area of the molecule. The surface concentration of the adsorbed metal ion was obtained from $C_0'^{2/3}$. In the cadmium system C_0 was calculated from Eq. [4] and found to be equal to the bulk concentration of cadmium metal. In the silver system values calculated from $C_0'^{2/3}$ were about six times the average bulk concentration at the silver surface. For this reason the values for C_0 used for silver were the number of atoms for the 210 surface. This was multiplied by 1.1, the roughness factor, to obtain the corrected surface concentration C_0' . This assumption is plausible because the holes in the silver surface are too small to seriously affect the inhibitor concentration at the surface but large enough to cause an increase in the rate of Ag-Ag⁺ exchange.

Discussion

In the cadmium system, (I) showed an inhibition efficiency of about 3% while (II) showed an inhibition efficiency of 16% (Table I). Based on the results in the cadmium system using the butane diol series (1) and the structure of the inhibitors used in this study, these results are reasonable. The difference in the inhibitor efficiencies between (I) and (II) suggests that the norbornene molecule is lying flat on the cadmium surface and bonding through its π -electrons and the hydroxyl groups. The attraction for the metal surface by the hydroxyl groups is nearly balanced by the hydrophobic effect of the large cyclopentyl group as can be seen by the $I_{(I)}$ value of $\sim 3\%$. This conjecture is further borne out when the 21% I value for butane 1,4 diol (1) is compared with the 3% value found for $I_{(I)}$. The increase in inhibitor efficiency with the addition of the double bond is less in the norbornane diol series than in the butane diol series. This is true even though the π -character of the double bond in (II) is greater

due to the ring strain of the molecule. The difference in efficiency can be explained by the hydrophobic nature of the cyclopentyl group and by the fact that the cyclopentyl group cannot lie flat on the metal surface.

Inhibitors (I) and (II) are more efficient in the silver system than in the cadmium system. As shown in Table II, (I) has an average efficiency of 53% while (II) has an average efficiency of 56%. This should be compared with the inhibition efficiencies of butane 1,4 diol, *cis*-2-butene 1,4 diol, and 2-butyne 1,4 diol which are also alike.

There is virtually no chance that the adsorbed inhibitors change the basic mode of self-diffusion within a crystal. To do so, the adsorbed molecule would have to change the migration energy and the energy of vacancy formation or dislocation pipe formation as well as the fluctuation probability. In the absence of any information to the contrary, this sort of change must be considered highly unlikely. The comparison in efficiency between the two series of alcohols in the silver system is valid despite the nearly 30% difference in D_{Ag} for the two crystals used because I reflects the relative difference in exchange rate, rather than the absolute difference. This can be easily proven mathematically. Let

$$R_o = k_o D^{\alpha}_{Ag} \quad [8]$$

and

$$R_i = k_i D^{\alpha}_{Ag} \quad [9]$$

where k_i and k_o are constants of proportionality and α is any power. Substituting these expressions into Eq. [1], it is easily seen that the D 's cancel. Therefore, when one I is compared with another, the difference in the value for D does not exert a direct influence since the self-diffusion coefficients cancel.

Because each of the norbornane systems exhibits nearly the same inhibition efficiency, it is unlikely that the π -electrons of (II) are contributing to the bonding. This implies that the inhibitors are either perpendicular to the metal surface; adsorption occurring through the unpaired electrons on the oxygen or else they are sticking to the surface for a time that is very long in comparison to the time a silver ion is adsorbed onto the surface. This latter possibility is highly unlikely so we are left with two plausible modes of adsorption. One mode would be with an oxygen bonded to the surface while the second oxygen would be hydrogen bonded to the water. The other mode is with both hydroxyl groups directed toward the metal surface.

The decrease in inhibitor efficiency in the norbornane diol series relative to the butane diol series is again probably due to the hydrophobic cyclopentyl group.

The free energies of adsorption for (I) and (II) (Tables I and II) are lower than in the butane diol series (I). This is to be expected because (I) and (II) cannot bond as strongly to the metal surface. Because of the rigid cage of the cyclopentyl groups, (I) and (II) should have a lower entropy of adsorption than the butane diol series even though (I) and (II) are larger molecules.

In order to further interpret the inhibition efficiencies, the self-diffusion mechanism must be considered. Dislocations in single-crystal silver were shown to exist at room temperature by Levinstein and Robinson (6). These authors used both an etch pit technique and the Lambot x-ray method (9) and found a dislocation density ranging from 1×10^7 to 5×10^7 dislocation pipes per square centimeter.

Models for dislocation pipe diffusion in silver have been postulated by several authors (10-12). Vardiman and Achter (13) demonstrated the plausibility of these models by obtaining excellent agreement between their diffusion data and predictions from the dislocation pipe models over the temperature range 250°-450°C. Moreover, extrapolation of high-temperature diffusion data

to low temperatures gave a self-diffusion coefficient that was some twelve orders of magnitude lower than the measured self-diffusion coefficient (14). In other words, dislocations were found by two different experimental techniques. Models based on these dislocation pipes were constructed and predictions on the basis of these models were shown to be in excellent agreement with experimental data. Extrapolation of D vs. $1/T$ from high-temperature data based on a vacancy diffusion mechanism gave absurd results.

We therefore assume that self-diffusion in Ag occurs via a diffusion pipe mechanism even though in the previous study this mechanism was suggested only as a possibility. Self-diffusion in cadmium however, occurs via a vacancy mechanism so that the difference in mode of diffusion should greatly affect the measured inhibition efficiencies. In the silver system, when an inhibitor molecule blocks a dislocation pipe there is virtually no other way for a silver atom to enter the crystal. In the cadmium system this is not the case. If it is assumed that the bond strength between oxygen and silver and between oxygen and cadmium are not too different, then a choice between the modes of adsorption of the norbornane diol series can be made. The mode of adsorption which places both hydroxyl groups on the metal surface is the favored orientation.

Because one hydrophobic cyclopentyl group reduces the inhibition efficiency more than 30%, in the cadmium system [comparing the butene diol with (II)] then it would be expected that the same two molecules would differ by roughly 30% in the silver system. However, in the silver system the inhibition efficiency is reduced less than 20%. This implies that butene diol bonds to the surface only through one hydroxyl group while (II) bonds to the surface through both hydroxyl groups; the extra 10% efficiency arising from the additional O...M bond.

It is worthwhile pursuing the idea of dislocation pipes further. In this study the rate of increase in activity of a given silver disk was affected by the method of washing. If the disks were slowly rocked in a water bath for 5 min per side the increase in activity was nearly the same as the increase in the activity if the disk was not removed and washed. However, if the disk was washed under a vigorous stream of water an increase in activity occurred roughly proportional to the time of washing.

Using a value of 6.6×10^6 dynes/cm² (15) as the pressure necessary to introduce a dislocation into a crystal of silver and assuming the velocity of the water at the surface of the disk to be $V = \sqrt{2gh}$, a value of about 350 cm/sec is obtained for a 60 cm high column of water. The volume of a stream of water with a 1 cm² cross section hitting the surface in unit time is $Q = AV = 350$ cm³/sec. For a 30-min washing this gives a pressure of 6.2×10^8 dynes/cm² which means 100 dislocations can be introduced if a constant hydrostatic pressure over a perfectly smooth surface is assumed. One hundred dislocations/square centimeter is an absolute minimum and the actual number introduced will certainly be higher because a turbulent stream is striking an imperfect surface and local pressures will be much higher than 6.2×10^8 dynes/cm². Therefore, the force of the stream of water probably introduced more dislocation pipes into the metal surface but whether or not any other factors are involved cannot be determined with any certainty.

It should be pointed out that Tingley (7) found very little increase in activity of single-crystal silver in 0.1M AgNO₃ solutions after a four day initial exchange period, even though the silver crystals were taken from the solution, washed, and then put back into solution. The exact washing procedure used is not known.

In the presence of inhibitors, vigorous washing also increased the activity, but the efficiencies remained nearly the same as is shown in Table III. Since it is

hard to duplicate washing conditions, the data are not very precise. These data, however, also tend to confirm the hypothesis that the inhibitors are blocking dislocation pipes. Therefore, we propose the following scheme for evaluating the effect of a dislocation pipe on the apparent inhibition efficiency and for classifying inhibitor efficiencies generally. We define ΔI as representing a unit of efficiency equivalent to a 10% decrease in the exchange rate. An uninhibited system would have a ΔI equal to 0 and a completely inhibited system would have a ΔI equal to 10. Based on the data for cadmium in Table I and the inhibitor efficiencies of the straight chained diols we assigned the values for ΔI shown in Table IV to the various functional groups. The way in which these values were obtained can be shown by using the cyclopentyl group as an example. Comparing $I_{\text{butene diol}}$ with $I_{(\text{C})}$, it can be seen that the former can be taken as 50% or $5\Delta I$ and the latter as 20% or $2\Delta I$. Therefore, the cyclopentyl group must be contributing $-3\Delta I$. $I_{(\text{C})}$ is assumed to be zero. Differences in adsorption of the organic molecules due to differences in exposed crystal face may exist (16) but should exert a second-order effect. The organic compound is competing with water for adsorption sites so that the exposed crystal face affects the difference in the ability of water and the ability of the inhibitor to adsorb. The difference in exposed surface can only manifest itself as a "difference in this difference" and is taken into consideration when the efficiencies are rounded off. Therefore, comparison between adsorption onto the 111 crystal face and the 210 crystal face can be made.

Using the values for I in Table IV, we now calculate the contribution of a hole in the silver system using the equations

$$\Delta I + X = 7\Delta I \text{ (straight chain diols)} \quad [10]$$

$$2\Delta I + X - 3\Delta I = 5\Delta I \text{ (norbornane diols)} \quad [11]$$

In both equations X is $6\Delta I$. It should be noted that in Eq. [11], $2\Delta I$ is used because 2 OH groups are assumed to be bonded to the silver.

We next propose a simple model for the surface of the metal at the metal solution interface based on our data. This model has little real basis but can explain the qualitative differences in behavior of the five inhibitor molecules and does allow predictions to be made for future experiments. We first assume that the metal surface consists of positive holes and negative electrons. To neglect the possible effects of aggregates, we next assume the electron density and the positive hole density are the same.

The configuration of positive holes and negative electrons is shown schematically for both Ag and Cd in Fig. 4. In this figure the 2 butyne, 1,4-diol is shown adsorbed onto the surface in the most appropriate orientation. It is clear from this picture that this diol would lie flat in cadmium but perpendicular in silver.

We further postulate that in the silver system the dislocation pipes are extensions of the positive holes with a diameter approximately that of a silver atom (14). Since there are probably some eight orders of magnitude fewer dislocation pipes than silver atoms (6), even though the norbornane group has two OH groups bonding to the metal surface, the chance of the molecule blocking two dislocation pipes is nearly zero. Moreover, the bulky cyclopentyl group prevents both OH groups from going into a given dislocation pipe, whereas, the straight chained diols can penetrate the pipes quite deeply.

Table IV. Efficiency units

Functional group	Value ΔI
OH	+1
C—C	0
C=C	+3
C≡C	+4
Cyclopentyl group	-3

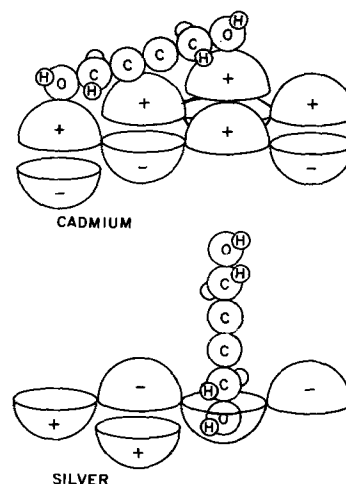


Fig. 4. Model surfaces for cadmium and silver with 2-butyne-1,4-diol adsorbed on the surfaces.

It is also easily seen how this model accounts for the qualitative differences in the two metal systems as well as the relative I values at the concentrations involved. In the cadmium system the molecules are expected to lie flat while in the silver system they should be perpendicular because the oxygen of the hydroxyl group is sticking down into a positive region.

In addition to arising naturally from our data this model is consistent with the work of other authors. The different distribution of charges in the two metals is reasonable because of the different signs of the Hall effect (17). This model is consistent with Bell and Levine's (18) double layer model when applied to a metal surface rather than a colloidal wall.

Discussion of Errors

The inhibitor efficiencies in both the $\text{Ag}^+ - \text{Ag}$ and the $\text{Cd}^{++} - \text{Cd}$ systems are probably accurate to $\pm 5\%$ while the thermodynamic data are probably only accurate to $\pm 15\%$. This is because of the uncertainty in the areas of the inhibitors determined by Dreiding models. In the silver system the error is probably slightly greater than these estimates due to the dislocation pipes and the ambiguity in the proper value of the diffusion coefficient. In the cadmium system the error is probably less due to the greater accuracy of the measurement of the surface area.

The data for the silver system in this study is more accurate than in the previous study (1) because the C_0 value for silver was only about six times rather than ten times (1) the bulk concentration of silver at the surface which means that the surfaces are probably more uniform.

SYMBOLS

I	inhibition efficiency, %
ΔI	efficiency unit equal to 10% I
R	rate of exchange
a_t	total activity acquired by the disk
C_0	surface concentration, atoms/cm ³
D	self-diffusion coefficient
S_i	percentage of surface covered by inhibitor
ΔG°	standard free energy of adsorption

Acknowledgment

The authors wish to thank the faculty research committee of Bowling Green State University for its generous support.

Manuscript submitted Nov. 24, 1971; revised manuscript received May 12, 1972.

Any discussion of this paper will appear in a Discussion Section to be published in the June 1973 JOURNAL.

REFERENCES

1. D. S. Newman, J. McCarthy, and M. Heckaman, *This Journal*, **118**, 541 (1971).

2. D. S. Newman, *J. Chem. Educ.*, **42**, 424 (1965).
3. Kurt Alder and Wolfgang Roth, *Chem. Ber.*, **83**, 161 (1954).
4. Hunter Birch, *J. Org. Chem.*, **21**, 970 (1956).
5. C. V. King and N. E. McKinney, *Can. J. Chem.*, **37**, 205 (1959).
6. H. J. Levinstein and W. H. Robinson, *J. Appl. Phys.*, **33**, 3149 (1962).
7. John Crank, "The Mathematics of Diffusion," Clarendon Press, Oxford, England (1960).
8. I. E. Tingley, *This Journal*, **112**, 60 (1965).
9. J. Auleytner, "X-Ray Methods in the Study of Defects in Single Crystals," p. 83, Pergamon Press, Oxford, England (1967).
10. G. R. Love, *Acta Met.*, **12**, 731 (1964).
11. Lars Luther, *J. Chem. Phys. Rev.*, **43**, 2213 (1965).
12. E. W. Hart, *Acta Met.*, **5**, 597 (1957).
13. R. G. Vardiman and M. R. Acter, *Trans. Met. Soc. AIME*, **245**, 178 (1969).
14. J. C. Fisher, *J. Appl. Phys.*, **22**, 74 (1951).
15. Charles Kittel, "Introduction to Solid State Physics," John Wiley & Sons, Inc., New York (1971).
16. K. J. Bachmann and K. J. Vetter, *Z. Phys. Chem. (N.F.)*, **51**, 98 (1966).
17. J. M. Ziman, "Electrons and Phonons," p. 488, Oxford University Press, London (1963).
18. G. M. Bell and S. Levine, "A Modified Poisson-Boltzmann Equation in Electric Double Layer Theory," Chapt. 19 of the "Chemical Physics of Ionic Solutions," B. E. Conway and R. G. Barradas, Editors, John Wiley & Sons, Inc., New York (1964).

On the Mechanism of Localized Corrosion of Iron and Stainless Steel

I. Electrochemical Studies

H. W. Pickering^{*.1} and R. P. Frankenthal^{*.2}

Edgar C. Bain Laboratory for Fundamental Research, United States Steel Corporation, Research Center, Monroeville, Pennsylvania 15146

ABSTRACT

During pitting of iron and stainless steels the potential drop across the interface of the dissolving surface within the pit is in the region of active metal dissolution, even when the potential of the specimen surface is controlled at potentials as high as +1.4 (SHE), as well as during natural corrosion. This conclusion is supported by measurements of the potential of the electrolyte within pits and by the observation that hydrogen gas is produced within the pits. From calculations of the concentration and potential gradients within the electrolyte in a pit it is further concluded that existing models of pit growth are inconsistent with these data. A modified model of pit growth is presented which involves growth by active dissolution and includes a high resistance path resulting from a constriction caused by a hydrogen bubble. This model of pit growth is also believed to apply to the propagation of crevices and, in some instances, of intergranular attack.

The concentration of the various ionic species and the potential ϕ of the electrolyte within a pit are different from the values in the bulk electrolyte (1-10). The signs of these gradients are usually known for simple pitting situations, e.g., when the current within the pit is maintained by a single electrochemical reaction. Quantitative descriptions of the concentration and potential gradients, however, are lacking even for simple cases of pitting. Beck and Grens (11) have obtained quantitative results for a complex stress corrosion cracking system, and Vermilyea and Tedmon (12) have obtained results using a simplified approach for crevice attack. Composition changes within growing pits have been most recently emphasized in the experimental investigations of Pourbaix (8), of Brown and co-workers (13, 14), and of Troiano and co-workers (15, 16). Potential variations within pits in iron were measured over a decade ago by Herbsleb and Engell (7) and more recently within crevices in stainless steels and Ti alloy by others (17-19). Variations of one volt or more were measured between the bulk electrolyte and the electrolyte at the bottom of pits and crevices in these investigations. This result is surprising since, as will be shown for pitting and has been shown for other types of localized corrosion (11, 12), only a small

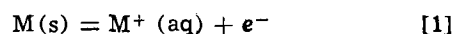
fraction of this potential can be accounted for by an IR-drop through an unobstructed column of electrolyte within the pit or crevice. Stolica (20) has observed sharp oscillations of the potential during early stages of pitting on Fe-Cr alloys in 1N H₂SO₄ containing small amounts of Cl⁻; their frequency and magnitude depended on the Cl⁻ concentration.

Only a few investigators have reported the egress of gas bubbles from pits. For ferrous materials Forchhammer and Engell (21) observed the evolution of bubbles from pits during elevated-temperature exposure to neutral chloride solutions. They assumed the gas to be H₂. Masing and Altenpohl (22) and Kaesche (23) observed the egress of bubbles from pits in aluminum.

The purpose of the present paper is to determine the potential $E(x)$ across the interface at the bottom of a dissolving pit, the potential $E(x)$ at any distance x into the pit, the potential $\phi(x)$ in the electrolyte within the pit, and to compare these results with theoretical values.

Theoretical

The concentration of the various ionic species and the potential ϕ in the electrolyte are calculated as a function of distance x into the pit (Fig. 1) for a steady-state current density i_M and the following conditions. A single charge-transfer reaction of the type



^{*} Electrochemical Society Active Member.

¹ Present address: Department of Materials Sciences, The Pennsylvania State University, University Park, Pennsylvania 16802.

² Present address: Bell Telephone Laboratories, Murray Hill, New Jersey 07974.

Key words: active dissolution, crevice corrosion, pitting, potential gradients.

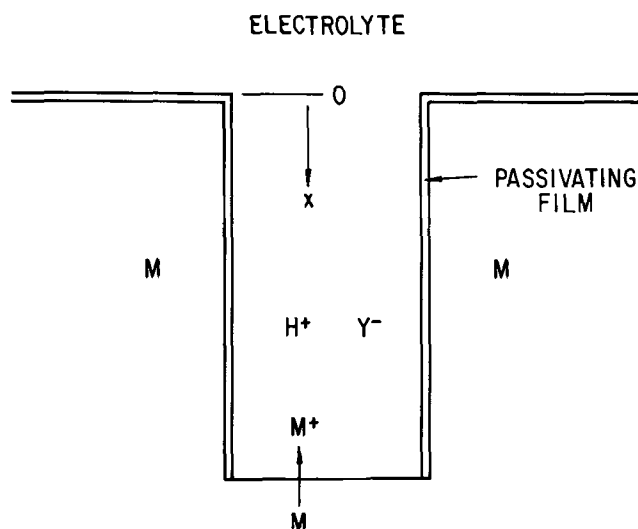


Fig. 1. Schematic of pit in which dissolution occurs only at bottom.

occurs in a moderately concentrated, completely dissociated acid HY ; Y^- is a noncomplexing monovalent ion. During growth of a pit, metal dissolution occurs only at the bottom; recession of the metal surface is disregarded.

As an approximation the transport equations for dilute solutions without regard to ionic interaction are used. Then the Nernst-Einstein equation interrelating diffusivity and electrochemical mobility holds. One has for the fluxes j of the various ionic species for (quasi) steady-state conditions

$$j_{\text{H}^+} = -D_{\text{H}^+} \left(\frac{dc_{\text{H}^+}}{dx} + c_{\text{H}^+} \frac{F}{RT} \frac{d\phi}{dx} \right) = 0 \quad [2]$$

$$j_{\text{Y}^-} = -D_{\text{Y}^-} \left(\frac{dc_{\text{Y}^-}}{dx} - c_{\text{Y}^-} \frac{F}{RT} \frac{d\phi}{dx} \right) = 0 \quad [3]$$

$$j_{\text{M}^+} = -D_{\text{M}^+} \left(\frac{dc_{\text{M}^+}}{dx} + c_{\text{M}^+} \frac{F}{RT} \frac{d\phi}{dx} \right) = -\frac{i_{\text{M}}}{F} \quad [4]$$

in which D is the diffusion coefficient, c the concentration of the indicated species, T the absolute temperature, F the Faraday constant, and R the gas constant. The fluxes H^+ and Y^- vanish (Eq. [2] and [3]) at steady state since these ions are neither formed nor consumed by the electrode reaction. The right member of Eq. [4] has a negative sign since metal ions move in the negative direction of the x coordinate ($x = 0$ at opening and $x = X$ at bottom of pit).

The boundary conditions are assumed to be

$$c_{\text{H}^+} = c^0 \text{ at } x = 0 \quad [5]$$

$$c_{\text{Y}^-} = c^0 \text{ at } x = 0 \quad [6]$$

$$c_{\text{M}^+} = 0 \text{ at } x = 0 \quad [7]$$

in which c^0 is the bulk concentration of HY .

In addition, the electrical potential ϕ at $x = 0$ is defined as zero

$$\phi = 0 \text{ at } x = 0 \quad [8]$$

and since the concentrations of the ionic species must conform to the law of electrical neutrality, one has

$$c_{\text{H}^+} + c_{\text{M}^+} = c_{\text{Y}^-} \quad [9]$$

Equations [2] through [9] are sufficient to calculate c_{H^+} , c_{Y^-} , c_{M^+} , and ϕ as functions of distance x .

Dividing through Eq. [2] and [4] by D_{H^+} and D_{M^+} , respectively, adding corresponding sides and rearranging, and substituting Eq. [9] gives

$$-\frac{dc_{\text{Y}^-}}{dx} - c_{\text{Y}^-} \frac{F}{RT} \frac{d\phi}{dx} = -\frac{i_{\text{M}}}{D_{\text{M}^+} + F} \quad [10]$$

From Eq [3] and [10] it follows that

$$\frac{dc_{\text{Y}^-}}{dx} = \frac{i_{\text{M}}}{2D_{\text{M}^+} + F} \quad [11]$$

$$\frac{F}{RT} \frac{d\phi}{dx} = \frac{i_{\text{M}}}{2c_{\text{Y}^-} - D_{\text{M}^+} + F} \quad [12]$$

Integrating Eq. [11] and using the boundary condition in Eq. [6] one obtains

$$c_{\text{Y}^-} = c^0 + \frac{i_{\text{M}}x}{2D_{\text{M}^+} + F} \quad [13]$$

Substituting Eq. [13] in Eq. [12], integrating, using the boundary condition in Eq. [8] and introducing the symbol $\psi = F\phi/RT$, one obtains

$$\psi = \frac{F\phi}{RT} = \ln \left(1 + \frac{i_{\text{M}}x}{2D_{\text{M}^+} + Fc^0} \right) \quad [14]$$

Integrating Eq. [2] and [4] and using the boundary conditions in Eq. [5] and [7] respectively, one obtains

$$c_{\text{H}^+} = c^0 e^{-\psi(x)} \quad [15]$$

$$c_{\text{M}^+} = \frac{i_{\text{M}}}{FD_{\text{M}^+}} e^{-\psi(x)} \int_0^x e^{\psi(x)} dx \quad [16]$$

in which $\psi = F\phi/RT$ is given by Eq. [14] as a function of x . Substituting Eq. [14] in Eq. [15] and [16] and integrating Eq. [16] yields

$$c_{\text{H}^+} = \frac{2D_{\text{M}^+} + Fc^0}{2D_{\text{M}^+} + Fc^0 + i_{\text{M}}x} \quad [17]$$

$$c_{\text{M}^+} = \frac{4D_{\text{M}^+} + Fc^0 i_{\text{M}}x + (i_{\text{M}}x)^2}{2D_{\text{M}^+} + F(2D_{\text{M}^+} + Fc^0 + i_{\text{M}}x)} \quad [18]$$

The results from Eq. [13], [14], [17], and [18] for $D_{\text{M}^+} = 10^{-5} \text{ cm}^2\text{-sec}^{-1}$ and $c^0 = 1 \text{ mol-liter}^{-1}$ are plotted in Fig. 2, in which the concentrations of the ionic species and the potential ϕ are given in terms of the product of the depth x into the pit and of the current density i_{M} . The concentration of metal ions, c_{M^+} , increases with increasing x or i_{M} as expected in as much as metal ions are formed at the bottom of the pit, $x = X$. The concentration of anions (Y^-) increases and that of hydrogen ions (H^+) decreases from the bulk value, c^0 , with increasing x or i_{M} . This is in accord

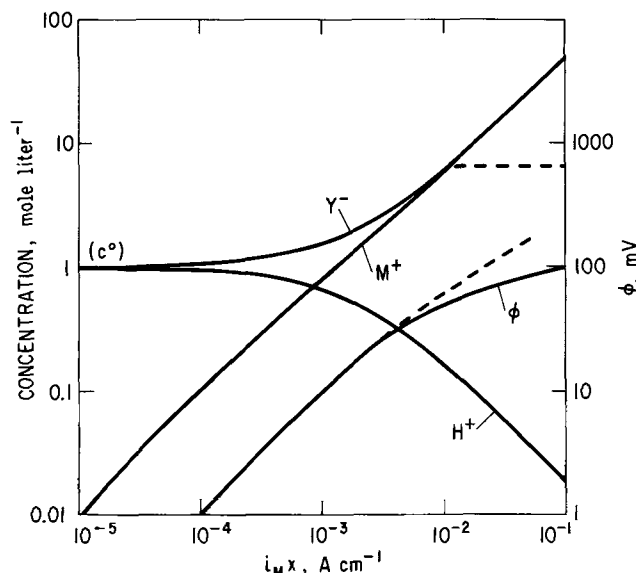


Fig. 2. Concentrations of Y^- , H^+ , and M^+ and ϕ as a function of the product of the depth x and the current density i_{M} calculated from Eq. [13], [17], [18], and [14], respectively. c^0 is the bulk concentration of acid HY .

with the tendency for anions to move toward the bottom of the pit and cations to move away from the anode for the prevailing potential gradient, ϕ , increasing toward the anode. At $t > 0$ the total concentration of ionic species within the pit is greater than the bulk concentration.

Departures from the calculated curves, occurring as a result of precipitation of salts and ionic interactions, are schematically indicated by the dashed lines in Fig. 2. The present theory, therefore, applies in an approximate manner to i_{Mx} products less than about 10^{-2} A-cm $^{-1}$ with variations from system to system depending mainly on the solubility product of the metal salt.

The above calculations may be extended to other pit geometries, e.g., hemispherical ones, and to other anodic reactions including those in which complexing, hydrolysis, or other interactions must be considered; the calculations become more complex. Changing geometries do not change the results qualitatively. If other anodic reactions are considered, the concentration gradients of the ionic species will change and may even be of opposite sign, but the magnitude of the potential ϕ is relatively unaffected.

Experimental Procedure

Most of the experiments were performed on Ferro-vac E iron; additional experiments were done on three stainless steels: Fe-20Cr (ferritic), Fe-18Cr-8Ni (austenitic), and Type 304 stainless steel. The composition of the iron and the alloys and their thermal treatments are shown in Tables I and II, respectively. The various electrolyte solutions (Table III) were prepared from reagent grade chemicals and doubly distilled water.

A sample was prepared by mounting the specimen, including a lead for electrical connection, in epoxy and polishing it with an aqueous suspension of 1 μ m particles of alumina prior to insertion in the cell. The exposed area was 0.42 cm 2 .

For some "single-pit" experiments a Lucite plate 0.14 cm thick containing a small hole 0.07 cm in diameter was bonded to the specimen surface with ethylene chloride. This arrangement gave a small, exposed metal area (0.005 cm 2), so that reasonably accurate pitting current densities can be obtained from the measured current. Regular samples were used in the experiments unless indicated otherwise.

A two compartment, three electrode cell was used. The main compartment contained the specimen and a platinum counterelectrode; a saturated calomel reference electrode was connected to the main compartment by a Luggin capillary. The three electrodes were connected to a Wenking potentiostat in the usual manner.

To measure potential variations inside a pit a microprobe reference electrode was used. It consists of a fine glass capillary (0.005 cm outside diameter) connected by means of a salt bridge to a mercury-mercurous sulfate reference electrode. The microprobe is attached to a three-directional micromanipulator with a resolution of 2.5 μ m. The specimen and microprobe can be viewed continuously through a stereomicroscope (7-30X).

The microprobe at any depth x into the pit measures the potential across the metal/electrolyte interface plus any potential drops that exist between that

Table II. Thermal history of iron and stainless steels

Iron	{ Annealed at 1000°K in vacuum and air cooled Annealed at 1150°K and air cooled Annealed at 1150°K and quenched in brine Annealed at 1400°K and quenched in brine Cold-rolled sheet
Fe-20Cr	
Fe-18Cr-8Ni	
304 Stainless	

Table III. Summary of systems studied

Metal	Solution composition
Fe	(a) 0.5M H ₂ SO ₄ , 3 mM NaCl (pH 0.3)
	(b) 0.05M H ₂ SO ₄ , 0.45M K ₂ SO ₄ , 3 mM NaCl (pH 1.85)
	(c) 0.5 mM H ₂ SO ₄ , 0.5M Na ₂ SO ₄ , 3 mM NaCl (pH 3.9)
	(d) 1M HClO ₄ , 3 mM NaCl (pH 0.1)
	(e) 0.05M KHP, 0.023M KOH, 10 mM KCl, 0.5M K ₂ SO ₄ (pH 4.5)*
Stainless steels	(f) 0.05M KHP, 0.023M KOH, 10 mM KCl (pH 4.5)*
	(g) 0.05M H ₂ SO ₄ , 0.5M NaCl (pH 1.1)
	(h) 0.1M Fe ₂ (SO ₄) ₃ , 0.05M H ₂ SO ₄ , 0.5M NaCl (pH 1.0)
	(i) Solution (h) plus H ₂ O ₂
	(j) 0.4M FeCl ₃ , HCl (pH 0.9)
	(k) 0.5M NaCl (pH 6)

* Solution of Vetter and Strehblow (10).

interface and the probe tip. The potential difference $\{E(x=0) - E(x)\}$ is $\phi(x)$. For the single-pit experiments $x=0$ is defined as the external surface of the Lucite plate.

The procedure for each experiment was as follows: the specimen was introduced into the empty cell, was properly aligned with respect to the microscope and microprobe, electrical connections were made, the potentiostat was set for a potential in the passive region, and the electrolyte solution was introduced. When a pit became sufficiently large, i.e., its diameter was 5-10 times that of the microprobe, the microprobe was introduced into the pit and the potential measured as a function of distance into the pit and as a function of time. The potentials were measured with an Orion Model 801 pH meter and recorded on a Honeywell Elektronik 19 recorder. The net anodic current supplied by the potentiostat was also measured on a recorder or oscilloscope.

All experiments, unless otherwise noted, were conducted in air-saturated solutions at room temperature, 296°K. All potentials are reported with respect to the standard hydrogen electrode (SHE).

Results

The most extensive data were obtained for iron in the sulfate solutions. The potential of the specimens was controlled at 0.85, 1.00, or 1.20V. Initially the current density is greater than 1 A-cm $^{-2}$, but rapidly decreases to its passive value (between 10^{-5} and 10^{-4} A-cm $^{-2}$ for the different electrolytes). Within minutes the current begins to rise, and sometime later the pits are observed as black specks by *in situ* microscopic examination. As the pits grow, they first appear dull, but then, as if going through a transition,¹ become bright and shiny and one could easily recognize the "polished," hemispherical appearance described in the literature (6, 25).

The behavior of iron in 1M HClO₄ is somewhat more complex. At low Cl $^{-}$ concentrations ($< 10^{-2}$ M) pits usually are not observed until after long times (hours),

¹ In Part II (24) the various stages of pit growth are documented by scanning electron microscopy.

Table I. Composition* of iron and stainless steels

Metal	C	Mn	P	S	Si	Cu	Ni	Cr
Iron	0.004	0.001	0.002	0.006	0.0003	0.014	0.002	0.004
Fe-20Cr	0.014	0.068	0.003	0.005	0.014	<0.01	<0.03	20.2
Fe-18Cr-8Ni	0.001	0.052	0.002	0.005	<0.03	<0.01	9.00	17.7
304 Stainless	0.056	1.93	0.033	0.008	0.46	0.21	9.11	18.6

* Weight per cent.

although anodic current bursts (to be described below) begin much earlier. At higher Cl^- concentrations the specimens frequently do not passivate and either rapid pitting or over-all surface dissolution occurs. The pits go through several stages of growth and eventually attain a well-defined polyhedral shape (24).

For all systems studied (Table III) gas bubbles were found within the pits and crevices, under conditions of applied potential and under natural corrosion (open-circuit) conditions. The formation of gas within the pits is thought to be important to the general mechanism of pitting and crevice corrosion; this is described in detail later.

Transient current behavior.—During pitting of iron in the sulfate solutions [(a), (b), and (c) in Table III] the current exhibits a marked transient behavior (Fig. 3). Although observed for both the regular and the single-pit specimens, the transients are more easily resolved in the latter because the area of nonpit surface and, hence, the base current are very small. The magnitude of the base current and of the bursts increases with increasing Cl^- concentration.

In the HClO_4 solution (d) the current bursts frequently begin before passivation is complete and well before any pits can be observed. After each burst the current immediately declines to the base value, as repassivation of the activated area occurs. The magnitude of the bursts increases with time and eventually rises as high as several milliamperes. If a particular current burst is associated with a pit nucleus, the local current density must be orders of magnitude higher than that calculated for the total sample area.

The average rate of pit growth, determined on the assumption that the largest pit grew from the time of the departure of the current from the passive value until termination of the test, is 0.2-0.3 $\text{A}\cdot\text{cm}^{-2}$ for iron in the sulfuric acid solution (a) in good agreement with literature values (7). Somewhat higher growth rates were obtained for iron in the HClO_4 and Na_2SO_4 (pH 3.9) solutions.

In view of the transient behavior it is clear, though, that the average growth rate is comprised of widely differing momentary rates. This was evident in data obtained for single-pit samples; e.g., in Fig. 3 the peak current density at the highest Cl^- ion concentration is $> 0.3 \text{ A}\cdot\text{cm}^{-2}$ whereas the current density between bursts is only about $0.04 \text{ A}\cdot\text{cm}^{-2}$. With other specimens current densities as high as $0.7 \text{ A}\cdot\text{cm}^{-2}$ were obtained.²

Potential microprobe measurements.—Potential microprobe measurements were made for regular and for

² If the response time of the recorder (0.5 sec full scale) is slow relative to the rise time of the current or if the area of pitting has been overestimated, the true current densities may be considerably higher than reported here.

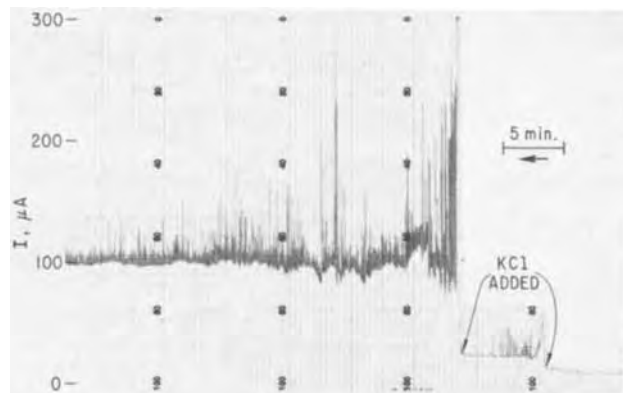


Fig. 3. Segment of the current record for a single-pit iron specimen in solution (c) illustrating transient behavior and the effect of Cl^- on the magnitude of the base current and of the current bursts. Time increases from right to left.

single-pit iron samples in the sulfate solutions. Results were the same with both specimen arrangements. The measured potential E with the microprobe placed near the opening of the pit was the same as that set by the potentiostat. As the microprobe was moved into the pit, the measured potential shifted in the less noble (negative) direction. Typical data for a single-pit iron specimen in the H_2SO_4 solution (c) are shown in Fig. 4. For this solution with its low Cl^- ion concentration strong current bursts are not normally observed. Insertion of the probe to within about 0.02 cm of the pit bottom, however, stimulates pit growth; one observes strong current and matching potential bursts (Fig. 5).

In this region of transient behavior, i.e., $x > 0.13 \text{ cm}$

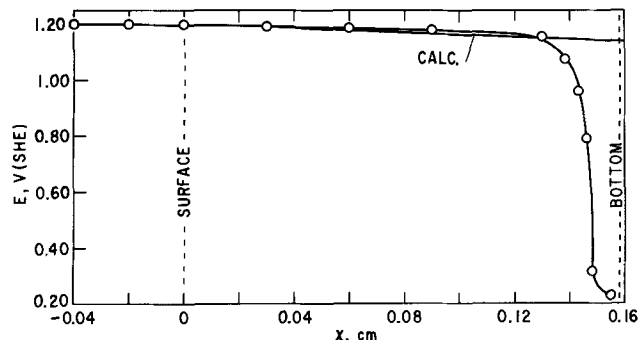


Fig. 4. Plot of measured potential as a function of depth x into the pit for a single-pit iron specimen in solution (c). For $x > 0.13 \text{ cm}$ transient behavior is observed; plotted potentials are the least noble ones. Potentials calculated from Eq. [14] and the relation $E(x) = E(x=0) - \phi(x)$ are given for comparison; i_M is the measured current divided by the area of the hole in the Lucite.

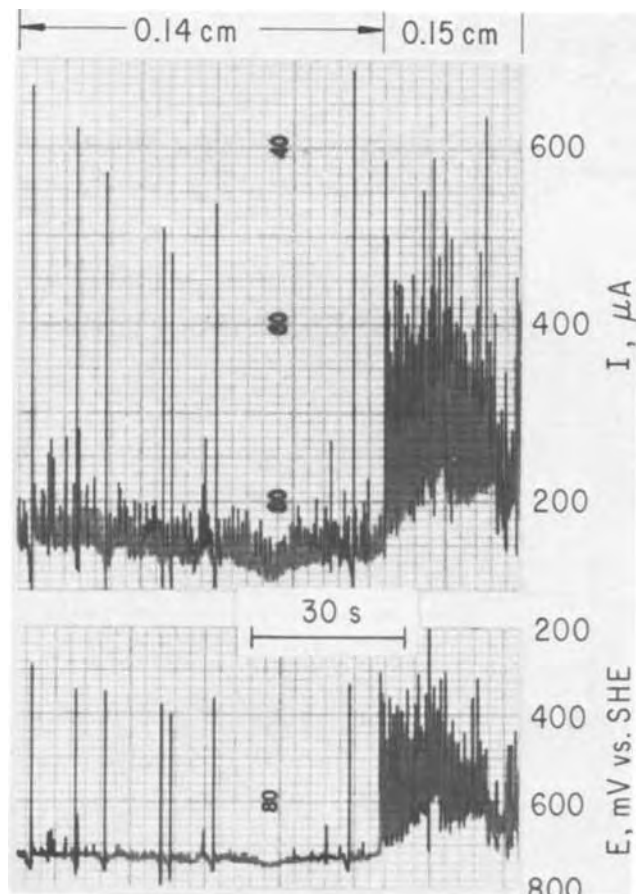


Fig. 5. Segments of the current and potential record for a single-pit iron specimen in solution (c) illustrating that the current and potential transients are in phase.

(Fig. 4), changes in the potential E were observed as great as 0.97V in the less noble direction relative to the potential of the external surface; this corresponds to $\phi = 0.97V$.

In other runs even larger departures of the measured potential from the surface value were observed. The least noble potential measured was $E(x \cong X) = -0.21V$ with the surface held at $E(x = 0) = 0.84V$ in solution (c); this corresponds to $\phi = 1.05V$. Potential variations of this magnitude also were observed with the surface held at 1.20V for the regular and for the single-pit samples in solutions (a) and (c).

Formation of gas bubbles in the pits.—*In situ* examination with the optical microscope revealed that for every system studied (Table III) and for both potentiostatic and open-circuit (corrosion) control, gas bubbles formed within the growing pits and crevices (at various interfaces including grain boundaries). For the low pH solutions in which visibility was not obscured by corrosion products the bubbles were observed to be in a constant state of rapid motion. For iron in the acidic solutions gas bubbles freely emanated from the pits; this occurred also for the system, Fe20Cr in solution (g), which exhibits grain boundary attack. For the other systems the bubbles were observed when the contents of the pit or crevice were disturbed with a glass fiber.

The frequency at which bubbles freely emanated from pits was lower than that of the current and potential bursts (Fig. 5) by about one order of magnitude. The size of an emitted bubble is generally the same as that of the pit from which it comes. In the less acidic solutions corrosion product is sometimes attached to the bubbles as they rise through the electrolyte. This material is left as a residue when the bubbles disappear at the electrolyte surface.

The egress of bubbles occurs over a wide range of applied potential. In one experiment using an Fe20Cr sample in solution (g) (pH 1.1) the potential E at the external surface was step-changed (with the potentiostat) to less noble values after pitting, grain boundary attack and bubble egress were well established at the initial value of 1.4V. The sample was held at each new potential for a time which was long compared to that of the transient response after switching. The potentials in sequence were 1.4, 0.24, 0.00, -0.10 , and $-0.20V$. At each potential, pit growth and the egress of bubbles were observed. The current and the number of pits from which bubbles emanated decreased as the potential was lowered, indicating that some pits were becoming inactive. However, even at the relatively active potential of $-0.20V$ at least one pit remained active; the current at this potential was 20 μA compared to 3 mA at 0.24V.

A movie of the egress of bubbles from pits was made. A few frames are shown in Fig. 6. Each cluster of white specks (light reflections) represents a pit. In (b) a bubble is just emerging from the (circled) pit. In (c) and (d) it is rising within the electrolyte and is easily recognized by the two, large diffuse spots, one of which is a reflection.

With an iron specimen held at 1.0V in solution (a) the emanating gas was collected by placing the flanged end of a Pyrex tube in the electrolyte and over the specimen surface. The gas and some solution were sucked into an evacuated bulb, after which the gas was extracted from the electrolyte and analyzed in a mass spectrometer. A blank (gas extracted from electrolyte which had not been subjected to the corrosion test) was analyzed in an identical manner. The results are given in Table IV. The H_2 content of the test sample greatly exceeds that in the blank. Nitrogen gas is present in essentially the same amount in both samples as it should be for air-saturated solutions. The low O_2 content of the test sample indicates that oxygen is reduced at the specimen surface during the corrosion experiment.

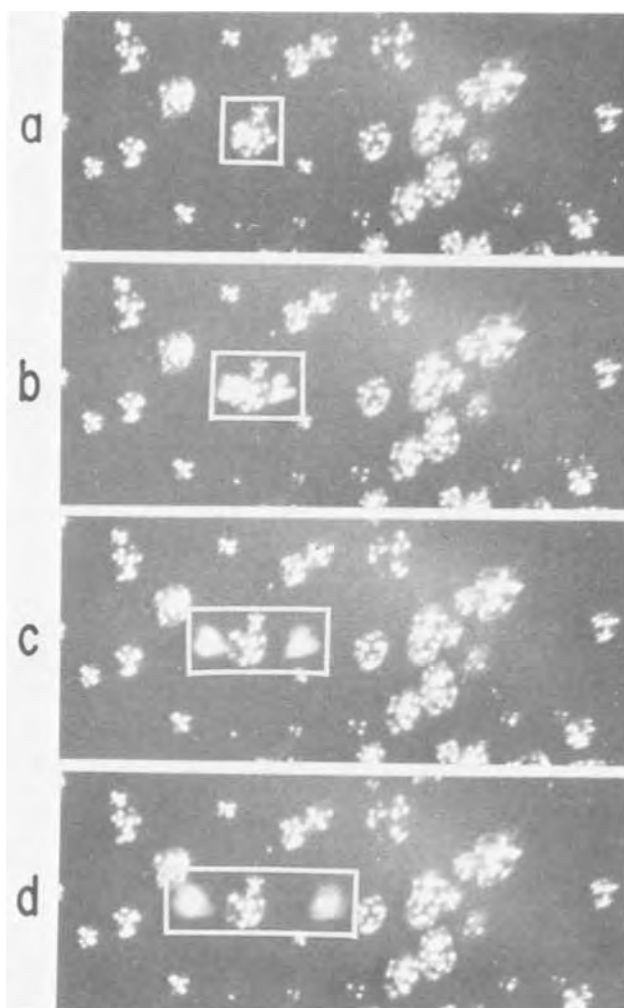


Fig. 6. Four consecutive frames of a movie showing the egress of bubbles from pits in iron in solution (a). A bubble (large diffuse spot) and its reflection are shown in rectangular area.

Discussion

In the present experiments, as well as those of Herb-
sleb and Engell (7), the product $i_M x$ was usually less than $10^{-2} A\text{-cm}^{-1}$. Under these conditions and in the absence of a solid corrosion product, the variation of the potential ϕ with distance x should be approximately given by Eq. [14] or an analog equation for the particular system under consideration,³ as depicted in Fig. 2; the maximum ϕ to be expected is of the order of 0.1V, in agreement with other calculations (11, 12). With the single-pit specimens a test of the theory is possible, since the average current density is known. Up to certain values of x the agreement between the measured potential variations and the theory is good, Fig. 4. At pit depths for which the sharp potential bursts were observed, the data do not agree with the theory.

An explanation of the lack of agreement between theory and experiment in the deeper portions of the pit

³ For semiquantitative purposes Eq. [14] adequately describes the electrical potential behavior for all systems and was used for all calculations in the present paper.

Table IV. Mass spectrometric analysis of gas collected from electrolyte during pitting of Fe, and from fresh (blank) electrolyte (arbitrary units)

	Test	Blank
H_2	110	3.5
N_2	1520	1570
O_2	16	450

seemingly lies in an increased resistance of the electrolyte path, since by the nature of the microprobe experiment the 1V variation in ϕ occurs completely in the electrolyte phase. The resistance, R , of the electrolyte path as a function of distance x may be obtained from experimental data, such as in Fig. 5, using Ohm's law, and is given in Fig. 7 for a single-pit iron specimen in solution (c). The resistance in the region $0 < x < 0.14$ cm is at all times in good agreement with calculated values using ϕ from Eq. [14]; the electrolyte resistivity calculated for this region is 8 ohm-cm, whereas that of the bulk solution is 5 ohm-cm. At depths of $x \cong 0.14$ cm the solution resistance increases sharply. The break in the curve corresponds to the depth at which strong transient behavior began. Over

any short period of time, $\sim 10^2$ sec, for which the depth X of the pit does not change appreciably $R(x)$ may be obtained from either the peak or the base values of the i and E data; that obtained from the base value is always less than that from the peak value (though still much greater than that extrapolated from $x < 0.14$ cm); the significance of this result is described later. The resistances at $x > 0.14$ cm in Fig. 7 were obtained from the peak values. The source of these high ohmic drops is discussed later.

Active dissolution in pit growth.—The microprobe potential measurements indicate that the potential $E(X)$ at (or near) the bottom of the pit may be as negative as $-0.2V$, which is in the region of active metal dissolution. The least noble potential possible is the reversible potential of the local metal-electrolyte system plus the overpotential for pit growth by active dissolution. The measurement, however, is complicated by the formation of hydrogen gas, the presence of which leads to possible constriction effects between the pit surface and the gas bubble, and between the bubble and the probe.⁴ Since the presence of the bubble prevents insertion of the probe into regions of close approach of the bubble with the pit surface, the least noble electrode potential within the pit may be more negative than the least noble measured value.

The evolution of hydrogen gas from the pits, crevices, and grain boundaries under conditions of applied potential and under natural corrosion conditions indicates that the potential at the bottom of these local cells must be more negative than the reversible hydrogen potential, which is $< 0.0V$ since the pH is > 0.0 for

⁴ The constriction between the bubble and the probe cannot be the source of the large measured ϕ since negligible current flows in this region.

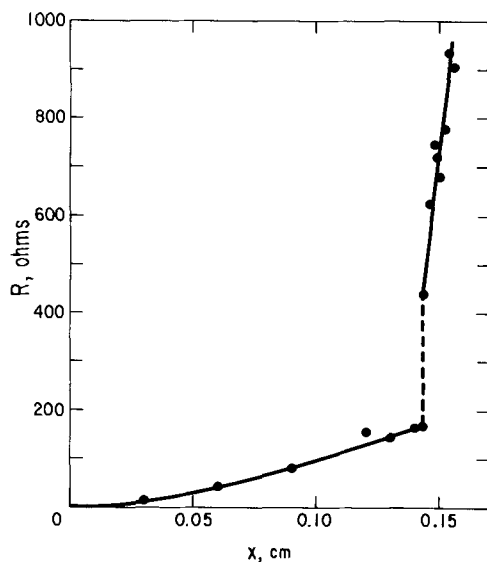


Fig. 7. Plot of the resistance of the electrolyte obtained from the measured current and potential as a function of depth x for a single-pit iron specimen in solution (c).

all systems. This is further evidence that the potential of the dissolving surface is in the region of active metal dissolution for all types of local cell corrosion studied. In Part II (24) an analysis of scanning electron micrographs also indicates that localized corrosion processes occur by active dissolution.

Role of hydrogen gas in pit and crevice growth.—Although the data strongly support the conclusion that pit and crevice growth occur by active metal dissolution, it remains to be explained how a potential as low as $\sim -0.2V$ is attained at the bottom of the pit or crevice when the potential across the interface at $x = 0$ may be as noble as $+1.4V$; i.e., the cause of IR drops as large as $1.6V$. The simple pitting model shown in Fig. 1, as well as any of different geometry or any involving other electrochemical reactions such as hydrolysis of the cations, are inadequate to account for this result. Existing models of pit and crevice growth are also inconsistent with the break in the plot of measured potential and resistance as a function of distance x (Fig. 4 and 7). This includes the pitting model in which a large potential drop across a surface film has been postulated by Franck (6); in the present experiments the measured potential variation is totally within the electrolyte phase, as demonstrated in the data of Fig. 4 and 7, in which the break in the plots occurs well above the bottom of the pit.

The presence of a gas bubble at the bottom of the pit (or crevice) provides an explanation for the large measured ohmic drop. A constriction most likely exists between the bubble and the pit surface, Fig. 8. Since this constriction is a path of current flow, a large IR (ϕ) is obtained by virtue of the high current density in this region. In this way a high ϕ is obtained within the electrolyte phase without a significant increase either in the resistivity of the electrolyte or in the local rate of metal dissolution. For somewhat smaller potential variations ($< 0.35V$) during pitting on aluminum, Masing and Altenpohl (22) proposed that gas bubbles at the mouth of the pit produced a high resistance path. In the present study the high resistance path must clearly be at the bottom of the pit.

The sharp potential fluctuations may be related to the observed continual motion of the bubbles within the pits. Movement of a bubble results in (momentary) relief of the constriction at any particular site which in turn results in a shift of the local electrode potential to more positive values. "Relaxation" of the bubble to its former position restores the constriction allowing again for a more negative potential at this site, followed by relief of the constriction, etc. The lower resistance calculated from the base than from the peak values of the current and potential data is in agreement with a variable constriction effect. Repassivation at a particular site within the pit is unlikely, since the time between occupancies by the bubble is much less than the 10^3 - 10^4 sec (26, 27) required for complete passivation. Bubble motion may be related to ionic transport in and out of the constricted region, to local

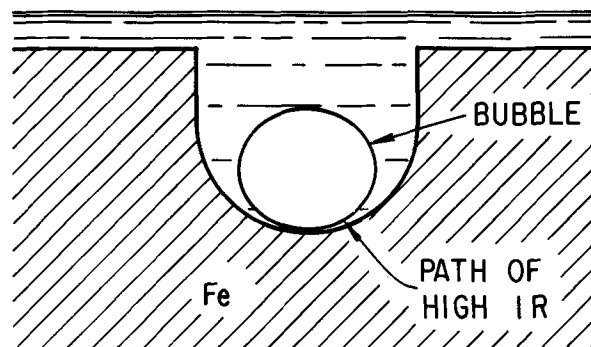


Fig. 8. Schematic of a pit illustrating a high-resistance electrolyte path caused by a bubble.

heating of the electrolyte solution, or to discontinuous growth of the bubble. Discontinuous growth of bubbles has been reported during hydrogen discharge on platinum by Ludwig and Yeager (28).

The formation of a second bubble after egress of the first was always observed to occur with a rather regular frequency and for the duration of the applied potential. This may be an indication that a "tail" of the emitted bubble functions as the nucleus of the next bubble. Such a process has been observed by Green (29) using high-speed photography for the largely different conditions of very high rates of hydrogen discharge on palladium.

The gas has been identified as hydrogen for the pitting of iron. No attempt at identification has been made for the stainless steels since there is no reason to expect a different gas at the measured potentials.

The fact that the gas is hydrogen may be important because its formation causes a decrease in the local H^+ concentration which tends to balance a momentary surge in cation concentration. Hence the maintenance of electroneutrality within the pit is aided by the formation of hydrogen gas. The tendency for the concentration of hydrogen ions within the pit in general to decrease is shown in Eq. [17].

We deduce from the above considerations that pit growth occurs by active dissolution of the metal, and that the electrode potential of the pit surface is controlled by a constriction within the pits which, in the general case, is hydrogen gas. Inclusion of a constriction as a basic element in the pit-growth process is appealing since a high ϕ value can be obtained at relatively low currents.

Other forms of constriction.—It does not necessarily follow, though, that hydrogen bubbles are always the source of the constriction or that a constriction is always necessary. For example, at less noble surface potentials, at which lower ϕ (IR) values are required to shift the potential into the region of active dissolution, pores of a solid reaction product are a potential form of constriction.

For still smaller differences between the potential at the external surface and that at the bottom of the local cell the need for a constriction vanishes. This happens when the resistance of an unobstructed column of electrolyte within a pit or crevice is sufficient (for the given current density) to shift the electrode potential into the active region. Then the concentration and potential profiles given by Eq. [13], [14], [17], and [18] (or their analogs for the particular system under consideration) should approximately apply for not too large $i_M x$ values at all distances x into the pit.

Pit initiation.—The model in Fig. 8 and the above discussion pertain only to propagation of a pit, *i.e.*, the necessary conditions, including the presence of a gas bubble at the bottom of the pit, are presumed to have been established by "nucleation" events. Such events include the "breakdown" of the passivating film, the subsequent surge of current which quickly subsides as a result of polarization effects and the simultaneous or subsequent nucleation of a hydrogen bubble. Bubble nucleation requires that a potential in the region of hydrogen evolution is established at least momentarily by means other than the bubble-constriction effect. One possibility is that the initial (transient) current density at the site of film breakdown is much higher than those measured during pit growth.

The data indicate that very high momentary currents do occur in the form of (a) initial current densities of at least 2 A-cm^{-2} and (b) the occurrence of isolated current bursts (ranging up to more than 1 mA) at the initial stage of pitting when the general surface is completely passivated. The peak currents in (b) seemingly yield very high current densities since the area associated with film breakdown must surely be very small. In addition Franck (30) has measured transient current densities between 10 and 20 A-cm^{-2}

for iron in $1N \text{ H}_2\text{SO}_4$. In view of these considerations there appears to be no need at the present time to postulate some other form of constriction for nucleation of a hydrogen bubble within a pit embryo.

Conclusions

By direct measurement with a microprobe of the potential changes within the electrolyte and by the observation of gas, identified as hydrogen, within the pits and crevices, it is established that the potential across the interface of the dissolving surface within pits in Fe is in the active region of iron dissolution. The same is concluded for ferritic and austenitic stainless steels since gas bubbles were also regularly observed within pits and crevices (at various interfaces including grain boundaries) in these steels. Hence for iron and austenitic and ferritic stainless steels in numerous electrolyte solutions ranging in pH from 0.1 to 6 and under conditions of applied potentials as high as $+1.4$ and as low as $-0.2V$ and under open-circuit (natural corrosion) conditions, pit and crevice growth is believed to occur by active metal dissolution.

The potential, ϕ , in the electrolyte phase within the pit accounts for the difference in measured potential between the pit bottom and the external (passive) surface. The magnitude of ϕ increases to $\phi > 1V$ when the applied potential is about $1V$ (SHE) or higher; ϕ , however, is not steady at this magnitude but peaks in a rather regular fashion. The pitting current or rate of pit growth peaks in phase with ϕ . As a result, the instantaneous rate of pit growth varies over a wide range.

The presence of hydrogen gas, the large increase in potential in the electrolyte, and the transient behavior are features which are not adequately accounted for in any previously existing model of pit or crevice growth. A model of local cell corrosion is presented which includes a high resistance path to current flow; in many cases this path may be the constricted region between a gas bubble and the pit or crevice surface. The large ϕ can be accounted for by high local current densities in the constricted region. Motion of the gas bubble can account for the transient behavior.

Acknowledgments

We gratefully acknowledge the contributions of P. J. Byrne who prepared the specimens and assisted in other aspects of the work, the gas analysis by F. N. Davis and H. H. Podgurski, and discussions with R. A. Oriani, S. Barnartt, and L. S. Darken, all of this laboratory, and critical comments on the theoretical section by C. Wagner of the Max-Planck Institut für biophysikalische Chemie.

Manuscript submitted Jan. 28, 1972; revised manuscript received May 20, 1972.

Any discussion of this paper will appear in a Discussion Section to be published in the June 1973 JOURNAL.

REFERENCES

1. J. R. Baylis, *Chem. Met. Eng.*, **32**, 874 (1925); *Ind. Eng. Chem.*, **18**, 370 (1926).
2. H. H. Uhlig, *Trans. AIME*, **140**, 411 (1940).
3. Y. M. Kolotyrkin, *Corrosion*, **19**, 261t (1963).
4. T. P. Hoar, *Discussions Faraday Soc.*, **1**, 299 (1947); *Trans. Faraday Soc.*, **45**, 683 (1949).
5. N. D. Greene and M. G. Fontana, *Corrosion*, **15**, 25t, 32t (1959).
6. U. F. Franck, *Werkstoffe Korrosion*, **11**, 401 (1960).
7. G. Herbsleb and H. J. Engell, *Z. Elektrochem.*, **65**, 881 (1961); *Werkstoffe Korrosion*, **17**, 365 (1966).
8. M. Pourbaix, *Corrosion*, **26**, 431 (1970).
9. T. P. Hoar, D. C. Mears, and G. P. Rothwell, *Corrosion Sci.*, **5**, 279 (1965).
10. K. J. Vetter and H. H. Strehblow, *Ber. Bunsenges. Physik. Chem.*, **74**, 1024 (1970).
11. T. R. Beck and E. A. Grens, II, *This Journal*, **116**, 177 (1969).
12. D. A. Vermilyea and C. S. Tedmon, Jr., *ibid.*, **117**, 437 (1970).

13. B. F. Brown, C. T. Fujii, and E. P. Dahlberg, *ibid.*, **116**, 218 (1969).
14. J. A. Smith, M. H. Peterson, and B. F. Brown, *Corrosion*, **26**, 539 (1970).
15. J. H. Shively, R. F. Hehemann, and A. R. Troiano, *ibid.*, **23**, 215 (1967); *ibid.*, **22**, 253 (1966).
16. C. F. Barth, E. A. Steigerwald, and A. R. Troiano, *ibid.*, **25**, 353 (1969).
17. N. D. Greene, W. D. France, Jr., and B. E. Wilde, *ibid.*, **21**, 275 (1965).
18. W. D. France, Jr. and N. D. Greene, Jr., *ibid.*, **24**, 247 (1968).
19. C. M. Chen, F. H. Beck, and M. G. Fontana, *ibid.*, **27**, 234 (1971).
20. N. Stolica, *Corrosion Sci.*, **9**, 205 (1969).
21. P. Forchhammer and H. J. Engell, *Werkstoffe Korrosion*, **20**, 1 (1969).
22. G. Masing and D. Altenpohl, *Z. Metallk.*, **43**, 433 (1952).
23. H. Kaesche, *Z. Physik. Chem., N.F.*, **26**, 138 (1960); **34**, 87 (1962).
24. R. P. Frankenthal and H. W. Pickering, *This Journal*, **119**, 1304 (1972).
25. T. P. Hoar, *Corrosion Sci.*, **7**, 341 (1967).
26. R. P. Frankenthal, *This Journal*, **116**, 1646 (1969).
27. R. P. Frankenthal, *Electrochim. Acta*, **16**, 1845 (1971).
28. F. Ludwig and E. Yeager, "Hydrogen Overpotential on Platinum," (Feb. 1968), AD-672360.
29. J. A. S. Green, Ph.D. Thesis, Queens University of Belfast (1965).
30. U. F. Franck, *Z. Naturforsch.*, **4a**, 378 (1949).

On the Mechanism of Localized Corrosion of Iron and Stainless Steel

II. Morphological Studies

R. P. Frankenthal*¹ and H. W. Pickering*²

Edgar C. Bain Laboratory For Fundamental Research, United States Steel Corporation Research Center, Monroeville, Pennsylvania 15146

ABSTRACT

The initiation and growth of pits on iron and of crevices and pits on stainless steels in numerous electrolyte solutions, both under potentiostatic and under natural corrosion conditions, have been studied by scanning electron microscopy. The pit morphology on iron is controlled primarily by solution composition: in sulfate-containing solutions the pits are initially crystallographic, but then become polished; in nonsulfate-containing solutions they always remain crystallographic. On stainless steels the pit morphology is determined by solution composition and by the nature of the initiation site; it depends only secondarily on alloy composition. In stainless steels, both austenitic and ferritic, crevice corrosion is the prevalent corrosion form; pitting is initiated only at significantly higher potentials. The results are in agreement with an electrochemical study that showed that the potential across the interface in all local corrosion cells is in the active part of the anodic polarization curve of the metal and that pits and crevices propagate by the same mechanism.

In another paper (1) we discuss the mechanism of pit and crevice propagation on iron and stainless steel as deduced from potential measurements within pits and from the presence of H₂ bubbles in pits and crevices. It is shown that the potential across the interface of the dissolving surface is in the active region of the anodic polarization curve of the metal even when the passivated surface is at a potential more than 1V more positive (noble). The potential difference between the dissolving surface of the local cell and the passive surface of the metal is deduced to be an IR-drop resulting from a high-resistance constriction between the H₂-bubble and the pit bottom. It is concluded that pits and crevices propagate by the same mechanism in all systems studied.

In this paper pits and crevices are examined by scanning electron microscopy (SEM). Observations on their initiation and growth on iron and stainless steels in a variety of electrolyte solutions are related to the mechanistic conclusions in Part I (1). The conditions for pitting and crevice corrosion are discussed for potentiostatically controlled and for natural (open-circuit) corrosion.

Few studies have been conducted on the morphology of corrosion pits and on how the morphology changes

with time and corrosion conditions. The subject has been briefly reviewed by Schwenk (2), Hoar (3), and Szklarska-Smialowska (4). Additional studies include those by Ashworth *et al.* (5) on the pitting of mild steel in chloride-containing basic solutions, by Vetter and Strehblow (6) on the pitting of iron in potassium acid phthalate (KHP) buffers containing chloride and a combination of chloride and sulfate, by Bianchi *et al.* (7) on pitting of stainless steel under potentiostatic and under chemically controlled conditions, and by Janik-Czachor (8) on the pitting of iron in a borate buffer containing chloride.

Many studies have been made to determine the nature of sites at which pits are initiated. The subject has been reviewed by Szklarska-Smialowski (4). It appears that the sites are very much a function of the metal (its structure and composition), the composition and distribution of inclusions and other phases, and the corrosion conditions; no generalizations can be made.

Experimental

The systems studied (Table I) are the same as those described in Part I (1), in which the specimen composition, heat-treatment, preparation, experimental arrangement, and procedures are also given.

The specimens were held by means of a potentiostat at a potential which in the absence of Cl⁻ would be in the passive range. However, all the solutions, with the exception of the 10% FeCl₃ and the 3% NaCl, were

* Electrochemical Society Active Member.

¹ Present address: Bell Telephone Laboratories, Murray Hill, New Jersey 07974.

² Present address: Department of Material Sciences, The Pennsylvania State University, University Park, Pennsylvania 16802.

Key words: crevice corrosion, morphology pitting, propagation.

Table I. Summary of systems studied and nature of the local corrosion cell

Metal	Solution composition	Corrosion condition	Local cell
Fe	(a) 0.5M H ₂ SO ₄ , 3 mM NaCl (pH 0.3)	Potentiostatic	Pits
	(b) 0.05M H ₂ SO ₄ , 0.45M K ₂ SO ₄ , 3 mM NaCl (pH 1.85)	Potentiostatic	Pits
	(c) 0.5 mM H ₂ SO ₄ , 0.5M Na ₂ SO ₄ , 3 mM NaCl (pH 3.9)	Potentiostatic	Pits
	(d) 1M HClO ₄ , 3 mM NaCl (pH 0.1)	Potentiostatic	Pits
	(e) 0.05M KHP, 0.023M KOH, 10 mM KCl, 0.5M K ₂ SO ₄ (pH 4.5)*	Potentiostatic	Pits
	(f) 0.05M KHP, 0.023M KOH, 10 mM KCl (pH 4.5)*	Potentiostatic	Pits
Type 304 stainless steel	(g) 0.05M H ₂ SO ₄ , 0.5M NaCl (pH 1.1)	Potentiostatic	Pits, crevices
	(h) 0.1M Fe ₂ (SO ₄) ₃ , 0.05M H ₂ SO ₄ , 0.5M NaCl (pH 1.0)	Natural corrosion	Crevices
	(i) Solution (h) + H ₂ O ₂	Natural corrosion	Pits, crevices
	(j) 0.4M FeCl ₃ acidified with HCl to pH 0.9	Natural corrosion	Pits, crevices
	(j) 0.4M FeCl ₃ acidified with HCl to pH 0.9	Potentiostatic	Pits, crevices
	(k) 0.5M NaCl (pH 6)	Natural corrosion	Crevices
	(k) 0.5M NaCl (pH 6)	Potentiostatic	Pits, crevices
	(g) 0.05M H ₂ SO ₄ , 0.5M NaCl (pH 1.1)	Potentiostatic	Pits, crevices
Fe-20Cr (ferritic)	(g) 0.05M H ₂ SO ₄ , 0.5M NaCl (pH 1.1)	Potentiostatic	Pits, crevices
Fe-18Cr-8Ni	(g) 0.05M H ₂ SO ₄ , 0.5M NaCl (pH 1.1)	Potentiostatic	Pits, crevices

* Solution of Vetter and Strehblow (6); KHP—potassium acid phthalate.

sufficiently dilute in Cl⁻ so that the specimens passivate at least partially before the onset of pitting; even in the FeCl₃ and NaCl solutions localized corrosion is observed. The experiments were conducted in air-saturated solutions at room temperature. All potentials are reported relative to the standard hydrogen electrode (SHE).

The natural corrosion experiments were conducted under identical conditions, except that no potential was applied.

The scanning electron micrographs were taken in stereo with a Cambridge Stereoscan microscope. It is essential to examine the micrographs in stereo to understand fully the processes that occur; a monocular examination misses many important factors. An x-ray spectrometer attached to the microscope permits elemental analysis of selected areas of the specimen being viewed, e.g., reaction-product films or inclusions.

Results and Discussion

Two types of localized corrosion (pitting and crevice corrosion) have been studied (Table I). On iron, pitting is the prevalent corrosion form. In the stainless steels crevice and pitting corrosion are observed; the extent of each depends on the potential regardless of how it is applied, i.e., potentiostatically or by a chemical redox couple under natural corrosion conditions.

We will first treat potentiostatically controlled localized corrosion for both iron and the stainless steels and then discuss natural localized corrosion for the stainless steels.

Potentiostatic control.—For iron in all of the solutions pitting only is observed, except when poor contact between the metal and the metallographic mount causes crevice corrosion.¹ On the other hand, for the stainless steels crevice corrosion is the prevalent corrosion form; for example, for Type 304 stainless steel in 0.05M H₂SO₄ + 0.5M NaCl, crevices are observed at potentials below 0.2V, whereas pits are seen only above 0.8V. It is evident that crevice corrosion is easier to initiate and/or propagate than pitting. As may be seen below, the same is true under natural corrosion conditions.

The appearance and the morphology of the pits and crevices depend in a complex manner on the composition of the electrolyte, the presence of inclusions and other phases in the metal, and its composition. We will first discuss pit formation and growth in iron and then in the stainless steels.

Iron.—Pit initiation appears to be random; no attempt has been made to determine pit density as a function of crystallographic orientation.

Initially in all systems (Table I) simple crystallographic pits are formed; i.e., pits bounded by crystallographic planes (Fig. 1). Their growth thereafter is a

¹ In this study the metal/metallographic-mount interface formed a natural crevice.

function of solution composition. In sulfate solutions the pits become hemispherical with the walls of the pits honeycombed by crystallographic planes (Fig. 2); the transition from the initial stage to this one is not understood. As the pits continue to grow, polishing begins at the bottom of each pit and progressively moves up the walls until they are smoother than le derriere d'enfant (Fig. 3). SEM studies of the surfaces of these pits show no visible structure at 10,000X magnification, indicating that any steps must be less than 20 nm (200Å) in height. It is these smooth, bright, hemispherical pits that are generally described in the literature, e.g., Ref. (3 and 9). The reasons for the transition from the faceted structured to the polished one is discussed below.

In perchloric acid solution two different growth paths have been observed (Fig. 4-7); in both paths the pit walls maintain their faceted structure and polishing is never observed. In the first path (Fig. 4 and 5) the simple crystallographic pit continues to grow with the same planes developing continuously; the pit crosses grain boundaries, but maintains its relatively simple structure. The other path (Fig. 6 and 7) results in a spongy, porous structure, the growth of which requires further investigation. In this path, growth also proceeds by the dissolution of crystallographic planes; even the spongy, porous structure is bounded by facets.

In the KHP solution containing no sulfate, pit growth proceeds in a manner similar to the first path

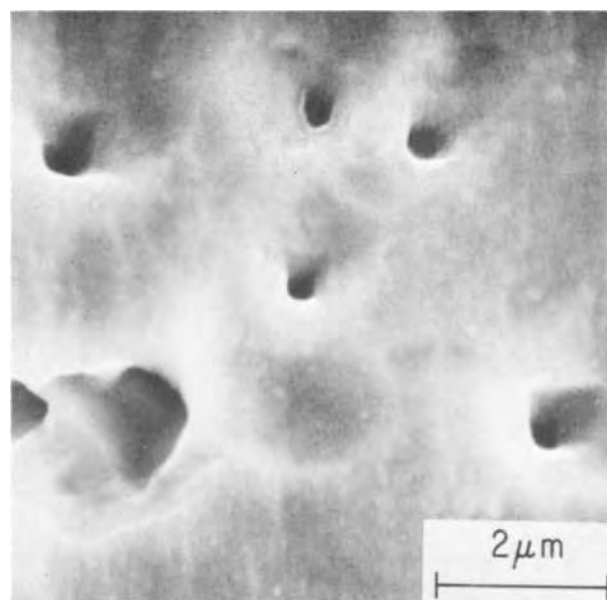
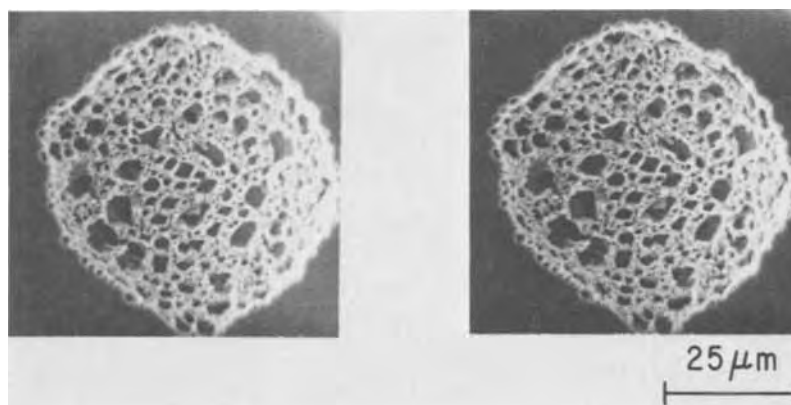


Fig. 1. Crystallographic pits that are typical of initial stage of pitting of iron in all solutions.

Fig. 2. Stereo pair. Intermediate stage of pitting on iron in sulfate solutions, showing nearly hemispherical pit with honeycomb cells; honeycomb cells are bounded by crystallographic planes. Solution (a); potential held at 0.85V.



in perchloric acid solution. In the KHP solution containing sulfate, the initial, faceted structure vanishes as rounding and some polishing occurs, similar to that described for the sulfate solutions. Vetter and Strehlow (6) have also studied this system and reported similar observations.

It has frequently been stated, *e.g.*, Ref. (3), that pits in iron, stainless steel, and other metals are not crystallographic, but hemispherical and polished. These data show this not to be so. Rather, the shape and morphology depend on the composition of the electrolyte solution.

Crystallographic morphologies are observed at all stages of pitting in sulfate-free solutions (Fig. 4-7) and during the early stages in sulfate-containing solutions (Fig. 1 and 2). This is expected (10, 11) when anodic dissolution of a metal surface occurs under film-free conditions in the active potential range of the anodic polarization curve, *i.e.*, when Tafel behavior is observed. Indeed, faceting occurs under these conditions during the dissolution of Fe in H_2SO_4 and in $HClO_4$ solutions (Fig. 8); similar results are observed in HCl solution. Microprobe potential measurements (1) show that the potential across the interface of the dissolving surface of a pit is in the active region, even when the potential of the specimen surface is maintained in the passive region. Thus crystallographic

pits are expected to form if film-free conditions are maintained.

Smoothing and brightening of the surface, as observed for pits at later stages of growth in sulfate solutions (Fig. 3), is not characteristic of Tafel behavior, but is indicative of a mass-transport controlled reaction, *e.g.*, diffusion in the electrolyte (12). Diffusion-limited anodic dissolution of iron in H_2SO_4 is observed in the potential range from -0.1 to $+0.5V$, the current density being about $0.2 A/cm^2$ (13-15); the diffusion-limited current density results from the formation of a ferrous sulfate film (14). Our measurements (1) indicate that the potential and current density within pits on iron correspond closely to these values; the polishing of the pits agrees with these facts. The pits initially form with a crystallographic morphology presumably because time is required to form the ferrous sulfate polishing film. The transition from the crystallographic morphology to the polished one begins at the bottom of the pit and moves upward to the rim (Fig. 3), inasmuch as the solution is most concentrated in ferrous and sulfate ions at the bottom (1), and hence film formation is initiated there.

The crystallographic morphology is maintained in the other solutions indicating that a polishing film does not form. This is consistent with the anodic polarization curves for iron in the different solutions and

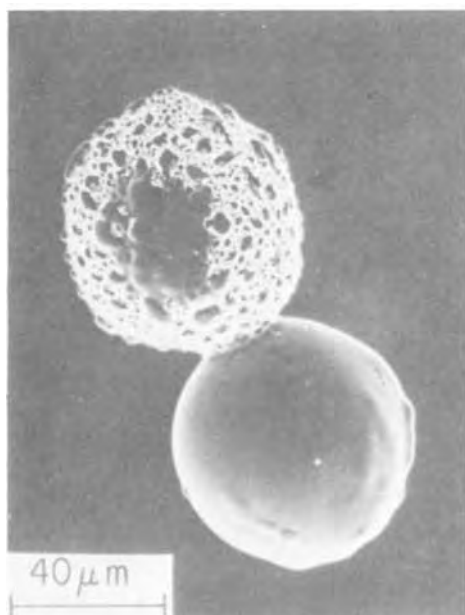


Fig. 3. Transition from intermediate to advanced stage of pitting on iron in sulfate solutions, showing start of polishing at bottom of pit and a completely polished pit. Solution (a); potential held at 0.85V.

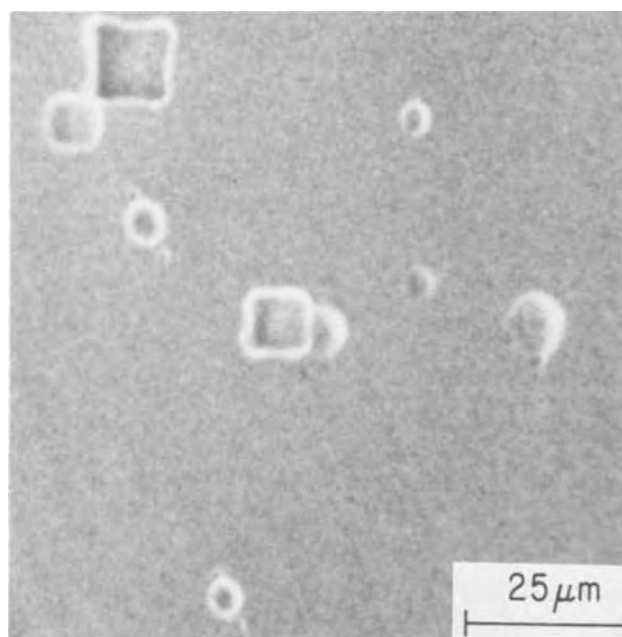


Fig. 4. Intermediate stage of pitting on iron in $HClO_4$ solution (path 1, see text), showing simple crystallographic pits. Solution (d); potential held at 1.00V.

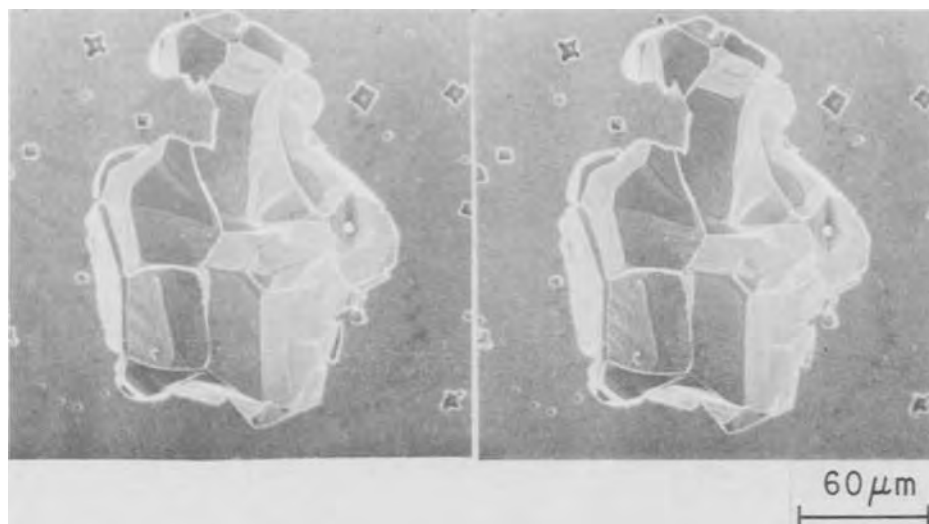


Fig. 5. Stereo pair. Advanced stage of pitting on iron in HClO_4 solution (path 1, see text), showing faceted walls of pit and grain boundaries within the pit. Intermediate stage of pitting is also visible. Solution (d); potential held at 1.00V.

with the solubility products of the various salts. Although a diffusion-limited current is observed in the active region for iron in H_2SO_4 (9, 14) none is found for iron in the other solutions, e.g., Fig. 9;² the solubility products of the various ferrous salts (Table II) indicate that hydrated ferrous sulfate is the least soluble.

Stainless steels.—Within the confines of this study, the various stainless steels behave similarly; hence they are considered as a group. Also the results in the different solutions are essentially the same, unless indicated otherwise. As stated above crevices are the prevalent corrosion form. They start at the interface between the steel and the metallographic mount, propagate under the surface of the steel, and eventually penetrate the surface from underneath (Fig. 10). It is reasonable to conclude that crevices propagate by the same mechanism as pits, since the potential across the interface of a dissolving surface in a crevice is also in

² At low current densities (see insert, Fig. 9) the Tafel relationship is obeyed. At high current densities ohmic control exists, as evidenced by the linear $E-i$ relationship. Passivation occurs at 0.55V, the same potential at which it occurs in H_2SO_4 .

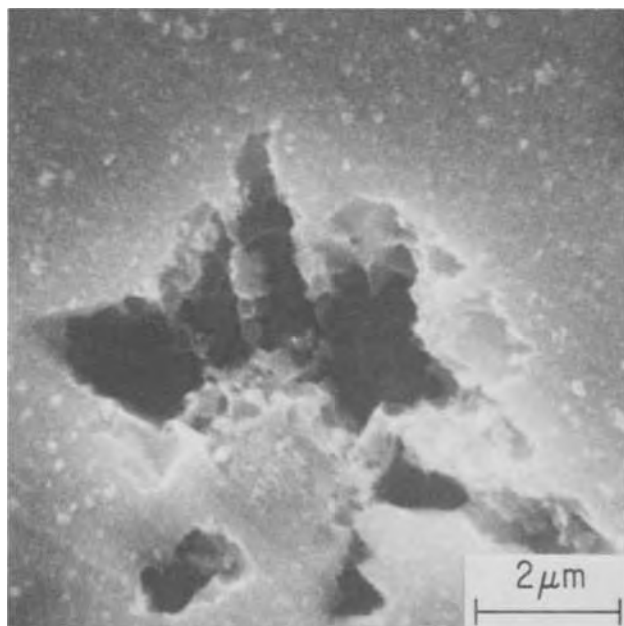


Fig. 6. Intermediate stage of pitting on iron in HClO_4 solution (path 2, see text), showing highly complex growth pattern. However, walls of pit are faceted. Solution (d); potential held at 0.84V.

the active part of the anodic polarization curve of the metal (1).

Pits are usually not initiated at potentials below 0.7V;³ most of the pitting studies were conducted at

³ This is an approximate value, the potential varying with solution composition. No effort was made to determine whether a critical pitting potential exists and, if so, what it is.

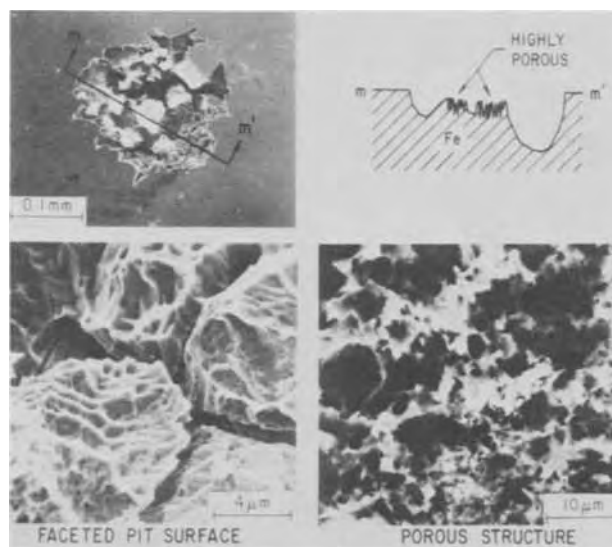


Fig. 7. Intermediate and advanced stage of pitting on iron in HClO_4 solution (path 2, see text). Upper left, entire pit; upper right, schematic of cross section m-m', lower left, faceted pit walls; lower right, spongy, porous structure bounded by crystallographic planes. Solution (d); potential held at 1.22V.

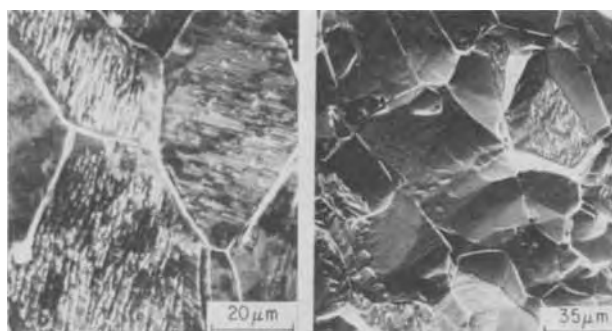


Fig. 8. Surface of iron etched in active potential region of anodic polarization curve in (a, left) 1N HClO_4 at -0.16V and in (b, right) 1N H_2SO_4 at -0.15V , showing faceted surfaces.

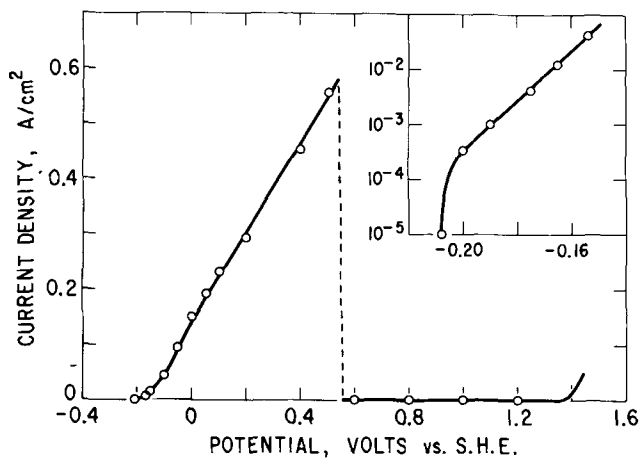


Fig. 9. Measured anodic polarization curve of iron in 1N HClO_4 . At low potentials (see insert) Tafel behavior is observed. Between 0.0V and the passivation potential, 0.55V, the system is under ohmic control. No diffusion-limited current region is observed. Plot in insert has been corrected for IR drop.

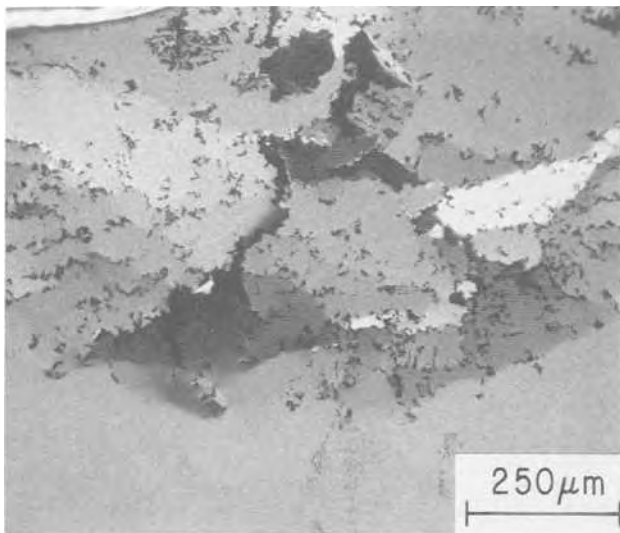


Fig. 10. Crevice corrosion in Type 304 stainless steel, solution (g); potential held at 0.40V. Part of the interface between the specimen and the metallographic mount is seen at upper left. Corrosion proceeded from interface under surface, finally penetrating surface at many sites.

potentials between 1.0 and 1.4V, in which range two types of pits are observed: pits of the first type (Fig. 11), which never appear to grow larger than 20 or 30

Fig. 11. Examples of pits not associated with inclusions found on stainless steel. (a, left) Crystallographic pit that is typical of initial stage of pitting in all solutions. Solution (j); potential held at 1.0V. (b, right) More advanced stage in sulfate-containing solutions, showing disappearance of some of the crystallographic structure. Solution (g); potential held at 1.0V.

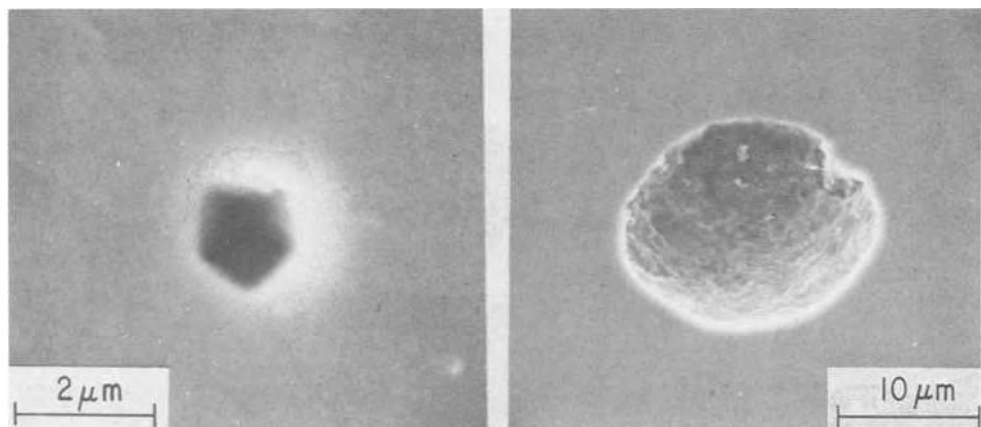


Table II. Apparent* solubility products, calculated from data in Ref. (16)

Compound	T, °C	K_{sp}
$\text{FeSO}_4 \cdot 7\text{H}_2\text{O}$	25	3
$\text{Fe}(\text{ClO}_4)_2 \cdot 6\text{H}_2\text{O}$	20	70
$\text{FeCl}_2 \cdot 4\text{H}_2\text{O}$	20	90

* Based on concentrations.

μm in diameter, are similar to those observed on Fe. These pits are not associated with inclusions. The small ones are crystallographic (Fig. 11a) and are observed to form in each solution. The larger ones (Fig. 11b) are observed only in solutions containing sulfate. It appears that, though rounded, these do not undergo polishing, presumably because the $\text{Cl}^-:\text{SO}_4^{2-}$ ratio of 10:1 is too great to permit supersaturation of the solution with ferrous sulfate.

The second type of pit, the most common one and that normally observed in the optical microscope, is initiated at inclusions in the matrix (Fig. 12a)⁴ and is not observed to be crystallographic. From the study of stereomicrographs of many pits, it is believed that each pit grows radially under the metal surface away from the inclusion; further surface penetration comes from underneath, giving rise to the lace-like structure that spreads away from the inclusion (Fig. 12b, 13). Stereo examination of these micrographs indicates that the external surface of the lace-like cover is smooth except for the small holes, and that the underside is rough, indicating that this structure is the result of dissolution from within the pit. As the pit grows the cover eventually is completely dissolved, leaving a large open pit, the bottom of which is normally rough with occasional evidence of faceting. Similar observations have been made by Streicher (17) and by Rosenfeld and Danilow (18), but they did not associate the initiation of these pits with inclusions.

The pits associated with inclusions and crevices appear to propagate in a similar manner and presumably by the same mechanism (1); they grow to almost any size, while those pits not associated with inclusions become repassivated early in their history. One explanation of this difference is that enhanced diffusion and convection in the more open, inclusion-free pits prevent the solution from becoming sufficiently concentrated in Cl^- and/or H^+ to sustain pitting; thus repassivation occurs. Conversely repassivation is less likely to occur in the covered pits and crevices. In addition, their highly concentrated solutions could be responsible for the absence of crystallographic structure because a viscous layer or a precipitate that limits the rate of dissolution may form.

⁴ X-ray microanalysis indicates that the inclusion seen in Fig. 12a contains Mn, Cr, Ti, and Al.

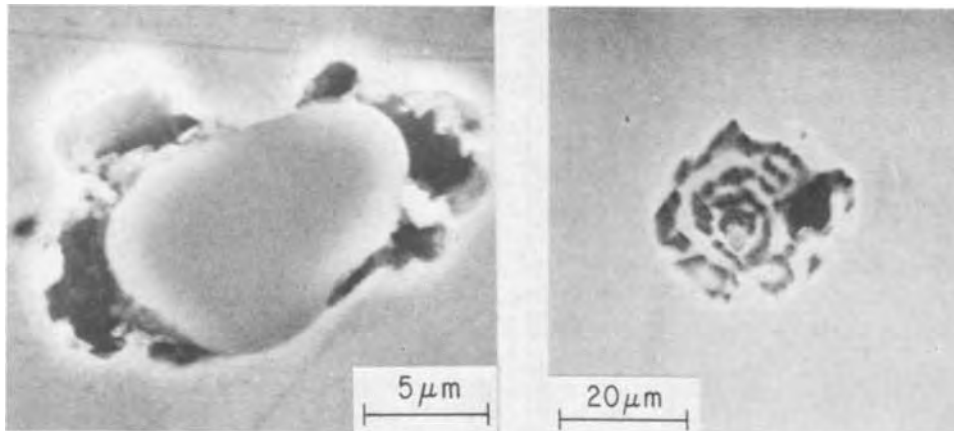


Fig. 12. Pitting in stainless steel at inclusions (a, left) initial stage. Solution (g); potential held at 1.0V. (b, right) Intermediate stage, showing that pit has grown under the surface and finally penetrated from underneath, producing lace-like cover over pit. Solution (i); natural corrosion.

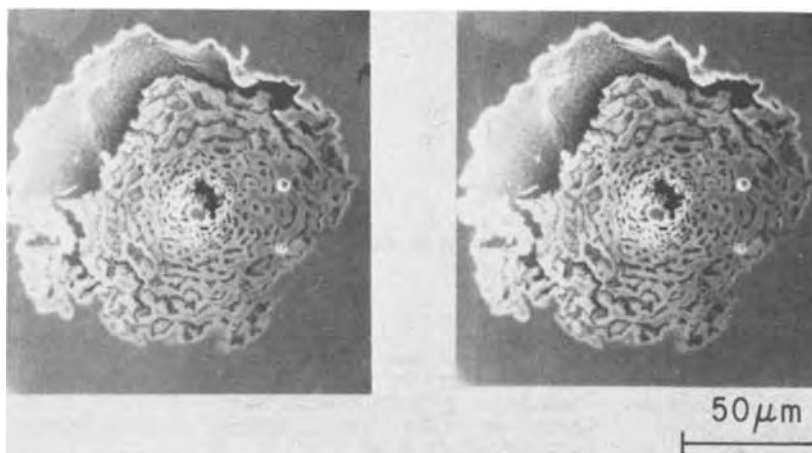


Fig. 13. Stereo pair. More advanced stage of pitting in stainless steel initiated at an inclusion, showing how pit has propagated under and penetrated through the surface from underneath; during last stage of growth lace-like cover dissolves exposing entire pit. Solution (g); potential held at 1.0V.

Natural corrosion.—Iron becomes active when immersed in a solution of $\text{Fe}_2(\text{SO}_4)_3$ containing a trace of Cl^- , even though this solution has a redox potential of 0.9V (as measured on an inert electrode) which is in the passive region of iron; the reason is that Fe^{+++} reacts with the iron to form Fe^{++} , thereby polarizing the iron to a potential in the active region. Stainless steels, on the other hand, do not activate under these conditions. Thus our studies were confined to the stainless steels, with most experiments conducted on Type 304.

The results indicate that the corrosion potential is the main factor controlling the type of local cell that is initiated, similar to the observations for potentiostatically controlled corrosion. In those solutions in which the corrosion potential is low, only crevice corrosion occurs. For example, when the steel is immersed in a solution of $\text{Fe}_2(\text{SO}_4)_3$ containing some Cl^- (pH 1; redox potential, 0.9V) the initial⁵ corrosion potential is 0.6V and rapidly falls to 0.3V or less; only crevice corrosion is observed. However, when H_2O_2 is added, the corrosion potential jumps to 0.7V and pits develop (Fig. 12b). In a NaCl solution in which the steel exhibits a low corrosion potential, only crevice corrosion is observed. But in acidified FeCl_3 solution in which the corrosion potential is initially above 0.7V, both pitting and crevice corrosion occur; the pits generally are bounded by crystallographic facets and remain small, similar to those discussed above and shown in in Fig. 11a. The pits at inclusions were not observed in the FeCl_3 solution, the reason for which is not clear. Crevices that form under natural corrosion conditions have the same appearance as those that form under potentiostatic conditions. Thus the propagation mechanism is most likely the same.

⁵ Measured about 2 sec after immersion.

Conclusions

The pitting of iron and the pitting and crevice corrosion of stainless steels have been studied under potentiostatically controlled and under natural corrosion conditions. The morphological studies on iron are consistent with the previous conclusion (1) that the potential across the interface of the dissolving surface inside the pit is in the active part of the anodic polarization curve of the metal, even when the potential across the interface of the passivated surface is more than 1V more positive. The surface morphology of the pit is controlled by the composition of the electrolyte solution. If a rate-limiting film can form within the pit, *e.g.*, in sulfate solutions, a pit initially bounded by crystallographic planes will become hemispherical and polished. However, if a film does not form, *e.g.*, in perchlorate solution, the pit will remain bounded by facets, similar to those observed during active anodic dissolution of bulk specimens.

For the stainless steels it has been shown that crevice corrosion is the prevalent form of corrosion and that pitting can be initiated only at relatively high potentials. The results are the same for ferritic and for austenitic alloys, for the numerous electrolyte solutions used, and for potentiostatic and for natural corrosion conditions. The propagation of most pits and crevices appears to be controlled by the same factors. Most pits in stainless steels, but not all, are initiated at inclusions. They grow under the surface away from the inclusion and eventually penetrate the surface from underneath. Pits not associated with inclusions do not grow to an appreciable size, presumably because the entire pit cavity is exposed to the bulk solution and mixing of the solutions facilitates repassivation.

Acknowledgments

We gratefully acknowledge the contributions of Mr. C. E. Brickner and Mr. W. Gundaker who performed the scanning electron microscopy, Mrs. P. J. Byrne who prepared the specimens and assisted with other aspects of the work, and discussions with Dr. J. L. Bomback, all of this laboratory.

Manuscript submitted Jan. 28, 1972; revised manuscript received May 20, 1972.

Any discussion of this paper will appear in a Discussion Section to be published in the June 1973 JOURNAL.

REFERENCES

1. H. W. Pickering and R. P. Frankenthal, *This Journal*, **119**, 1297 (1972).
2. W. Schwenk, *Corrosion*, **20**, 129t (1964).
3. T. P. Hoar, *Corrosion Sci.*, **7**, 341 (1967).
4. Z. Szklarska-Smialowska, *Corrosion*, **27**, 223 (1971).
5. V. Ashworth, P. J. Boden, J. S. Ll. Leach, and A. Y. Nehru, *Corrosion Sci.*, **10**, 481 (1970).
6. K. J. Vetter and H. H. Strehblow, *Ber. Bunsenges. Physik. Chem.*, **74**, 1024 (1970).

7. G. Bianchi, A. Cerquetti, F. Mazza, and S. Torchio, *Corrosion Sci.*, **10**, 19 (1970).
8. M. Janik-Czachor, *Brit. Corrosion J.*, **6**, 57 (1971).
9. U. F. Franck, *Werkstoffe Korrosion*, **11**, 401 (1960).
10. F. C. Frank, "Growth and Perfection of Crystals," p. 411, R. H. Doremus, B. W. Roberts, and D. Turnbull, Editors, John Wiley & Sons, Inc., New York (1958).
11. D. A. Vermilyea, "Advances in Electrochemistry and Electrochemical Engineering," Vol. 3, p. 211, P. Delahay, Editor, Interscience Publishers, New York (1963).
12. C. Wagner, *This Journal*, **101**, 225 (1954).
13. K. F. Bonhoeffer, *Z. Metallk.*, **44**, 77 (1953).
14. H. Kaesche, "Die Korrosion der Metalle," pp. 179-197, Springer-Verlag, Berlin (1966).
15. G. Herbsleb and H. J. Engell, *Z. Elektrochem.*, **65**, 881 (1961).
16. W. F. Linke, "Solubilities of Inorganic and Metal-Organic Compounds," Fourth Edition, Vol. I, Am. Chem. Soc., Washington, D. C. (1958).
17. M. A. Streicher, *This Journal*, **103**, 375 (1956).
18. I. L. Rosenfeld and I. S. Danilow, *Z. Physik. Chem.*, **226**, 257 (1964).

Optical Properties of Chromium-Plated Steel

R. F. Hoekelman*

United States Steel Corporation, Research Laboratory, Monroeville, Pennsylvania 15146

ABSTRACT

The color and the reflectivity of the chromium-plated steel product now being used in the manufacture of containers were examined. A 45-degree Gardner glossmeter was used to determine specular reflectivity and a General Electric Spectrophotometer was used to determine diffuse reflectivity and color in terms of tristimulus numbers and corresponding chromaticity values. Chromium-plated steel with a low level of surface oxides has a blue hue and greater specular and diffuse reflectivity than the unplated steel base. As the chromium oxide level increases, the blue hue decreases and the surface acquires a golden-tan hue. The specular reflectivity decreases with an increase in chromium oxide level and varies with the angle of illumination with respect to the steel rolling direction. The diffuse reflectivity likewise decreases with an increase in the chromium oxide level. There is a linear relationship between the oxide level and the sum of x and y chromaticity values. When chromium-plated steel was coated with a translucent lacquer, the hue of the product still varied in accordance with the hue of the original steel. Heating the chromium-plated steel in air increased the oxide level and the $(x + y)$ chromaticity value. From the data obtained in this study it would appear that the rate of surface oxidation of the chromium metal upon being heated in air at 260°C is 11 mg Cr/m² hr (1.0 mg Cr/ft² hr).

Chromium-coated steel is being used as an alternative to tin-plate for making cans for beer, beverages, and some foods. Light-gauge steel (0.006 to 0.011 in. or 0.152 to 0.279 mm thick) is electroplated with chromium to a thickness of about 7.6 nm (5 mg Cr/ft²) and has a surface oxide about 7 to 20 nm thick containing 0.4 to 1.4 mg Cr⁺³/ft². To minimize scratching and to facilitate handling, a light oil film about 5.1 nm thick (0.25g per base box) is applied to the material. This product, known in the industry as tin-free steel chromium-type (TFS-CT), cannot be soldered; but new methods (welding or cementing) of side-seam construction in manufacturing have made the use of chromium-plated steel for containers practical.

A bright, uniform metallic appearance is a desirable feature of chromium-plated steel. The lustrous metal beneath the semitransparent lacquers often used on beer and beverage cans lends eye appeal and enhances product recognition. However, examination of various lots of material shows that chromium-plated steel has a range of color, texture, and luster. Thus, to provide

information as to the possible cause of these variations, the reflectance and the color of various TFS materials were determined and the results compared with other properties of the material. When TFS-CT is heated and lacquered, as in the usual can-making operations, the optical properties change; thus, the degree of color change with heating and lacquering was likewise determined.

Materials and Experimental Work

Chromium-plated steel was obtained from various sources: commercial product, experimental material produced on pilot-line equipment, and individual specimens prepared as stationary cathodes in bench-scale plating baths. Some specimens of chromium-plated steel were made by a one-step process; that is, the chromium metal and the surface coating of oxide were deposited simultaneously in one electroplating operation. Other specimens were prepared in two steps; the metallic chromium was deposited in one operation and the chromium oxide in a second operation. For the heating and lacquering experiments, chromium-plated specimens were prepared on bench equipment

* Electrochemical Society Active Member.

Key words: color, tin-free steel, chromium oxide, spectrophotometry.

with the same steel base to ensure uniformity of the steel surface.

To determine the optical properties of the steel base, the specimens were treated to remove the oxide films normally present. The steel surface was cleaned by degreasing, pickling in 10% sulfuric acid solution at room temperature for one minute, rinsing in water, pickling in 5% citric acid at room temperature for one minute, rinsing with an organic solvent such as acetone or methanol, and drying in a hot air stream. For certain measurements, the chromium oxide coating on the TFS-CT was removed by immersion in a 10N solution of sodium hydroxide at 195°F (89°C) for 10 min followed by cold-water rinsing and drying in a stream of hot air.

In the experiments concerning the effect of heating on the optical properties of TFS-CT, a laboratory oven was used for room-atmosphere tests, and a tube furnace was used for tests with nitrogen and nitrogen-hydrogen atmospheres. No attempt was made to further purify the bottled gas obtained from a commercial supplier.

The optical properties of lacquered TFS-CT were also determined. The type of lacquer used, the coating weights, and the curing conditions are shown in Table I.

The optical measurements were made with a Gardner Laboratory 45-degree portable glossmeter GG-9020 (P-45), and a General Electric Spectrophotometer, Catalog No. 7015E30G, was used to measure the color of TFS-CT specimens by reflected light in the visible region of the spectrum. The color of the diffuse reflected light was determined after the specular reflection was adsorbed on a black surface. The spectrophotometer gave two outputs, a graph of per cent reflectance vs. wavelength of light from 380 to 700 nm, and a computation of the tristimulus values X, Y, and Z. These tristimulus numbers are based on a system chosen by the International Commission on Illumination so that all the spectral colors could be matched by positive amounts of three theoretical primaries (1). The light source used in the spectrophotometer was the standard CIE Source C as described in the ASTM Designation, E308-66 (2).

Results and Discussion

Several factors influence the appearance of chromium-plated steel. Variations in surface roughness can cause changes in the distinctness of image and the ratio of the coefficients of specular to diffuse reflectivity. If the surface becomes covered with oxide, oil, or foreign matter, the over-all luster will be affected. For example, specular gloss of sheet steel varies with the angle of illumination to the rolling direction, and with chromium oxide weight, as shown in Fig. 1. Chromium-coated steel with an oxide coating containing less than 0.16 mg Cr³⁺/dm² (1.5 mg Cr³⁺/ft²) is more reflective than the cleaned steel surface; but as oxide coating weight increases, the specular reflectivity decreases.

The diffuse reflectivity of TFS-CT, represented by the Y tristimulus value measured by the spectrophotometer, is shown in Fig. 2. The diffuse reflectivity also decreases with an increase in oxide coating weight. The specimens tested for diffuse reflectivity, Fig. 2,

Table I. Lacquer used on TFS-CT

Type of lacquer	Color	Weight of coating,* mg/8 in. ² (mg/0.0052m ²)	Curing time, min- utes	Curing temperature, °F (°C)
Epoxy amine	Colorless	17.9	8	375° (190°)
Polybutadiene	Gold	37.0	10	400° (205°)
Epoxy	Gold	18.4	10	400° (205°)

* All panels were dip-coated.

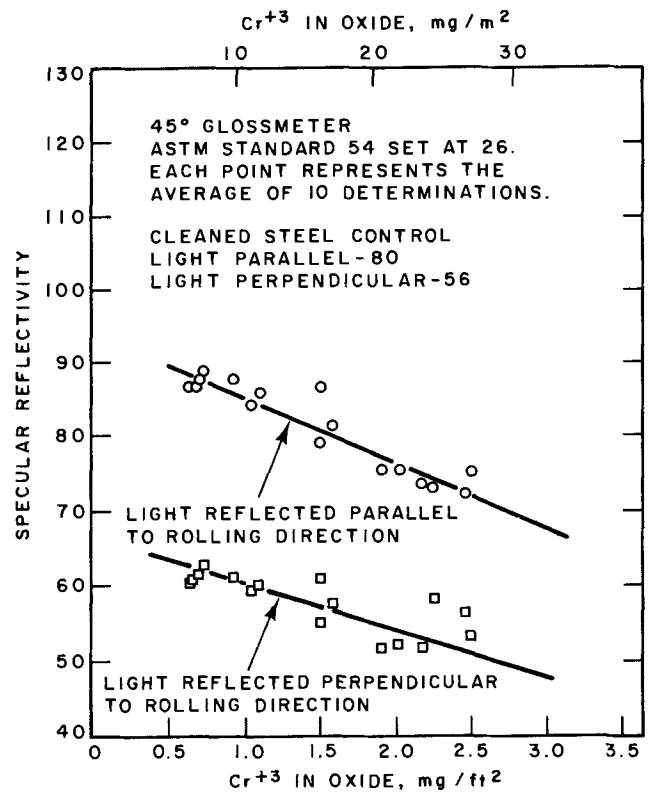


Fig. 1. Specular reflectivity of TFS-CT of varying oxide coating weights.

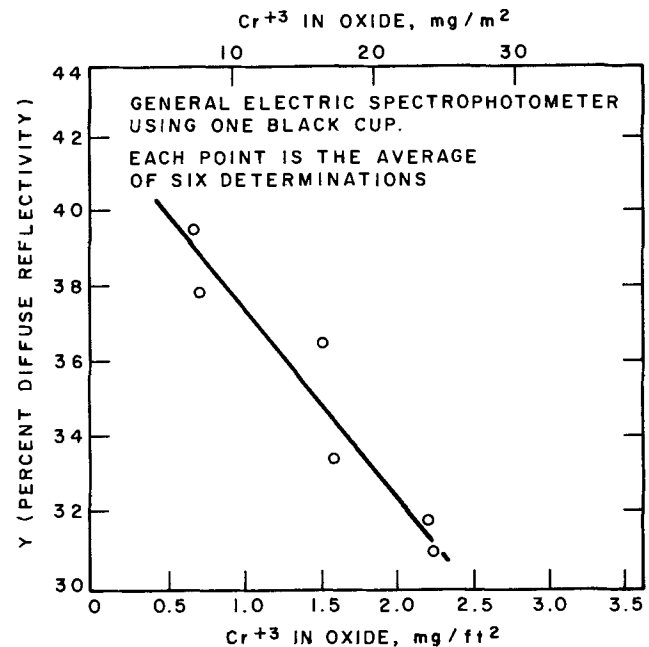


Fig. 2. Diffuse reflectivity of TFS-CT of varying oxide coating weights.

are portions of the same samples tested for specular reflectivity and shown in Fig. 1. These samples were prepared by using a single sheet of steel, and measurements of the optical properties of only one surface are shown. Measurements of reflectivity of the obverse surface show quite different results because the surface roughness differs.

Color of TFS-CT and correlation with oxide coating weight.—The diffuse reflectivity varies with the wavelength of visible light, as shown in Fig. 3. The standard white ceramic Vitrolite reflects much more light than the metal surfaces, and, consequently, the metals ap-

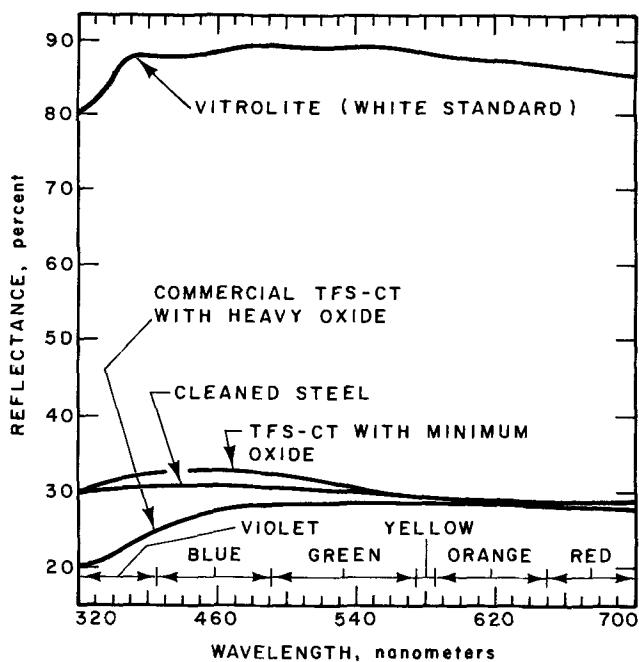


Fig. 3. Diffuse reflectance as a function of wavelength

pear gray rather than white. Steel reflects about the same amount of light at all wavelengths and has the neutral gray color. Metallic chromium has peak reflectivity in the blue region of the spectrum, whereas chromium covered with a heavy oxide coating has depressed reflectivity in the blue region. Metallic chromium, therefore, has a bluish tint, and TFS-CT with heavy oxide on the surface appears golden tan. Gardam (3) has reported on the colors of metals and alloys and has found chromium to be one of the bluest of metals.

The values of the reflectivities can be integrated over the visible spectrum to give the tristimulus numbers as described by Clydesdale and Francis (4). These numbers specify quantities of red, green, and blue primary colors making up the color of the specimen. The tristimulus numbers can be converted into chromaticity values as follows

$$x = \frac{X}{X + Y + Z} \quad y = \frac{Y}{X + Y + Z}$$

where X , Y , and Z are tristimulus numbers and x and y are chromaticity values. A chromaticity diagram, Fig. 4, shows the locus of chromaticity values for the various TFS-CT samples clustered about the illuminant point, an indication of low intensity of color. Figures 5 and 6 show chromaticity diagrams of TFS-CT with various oxide coating weights on four different steel sheets. (Note that only a portion of the chromaticity diagram is shown and the x and y coordinates have been greatly expanded.) Although different plating solutions were used, the locus of chromaticity coordinates for TFS-CT lies along a single line on the chromaticity diagram.

The color of TFS-CT ranges from the blue hue (475 nm) of metallic chromium through neutral or gray and into the yellow region of the spectrum having a dominant wavelength of about 578 nm. Because the blue color is absorbed by the oxide coating, it is reasonable to expect that the oxide coating weight would be related to the seldom-used z chromaticity value. However, to obtain a positive slope on a graph of coating weight vs. chromaticity value, coating weight could be plotted against $(1 - z)$ or against $(x + y)$ since $x + y + z = 1$. In Fig. 7 and 8, the Cr^{+3} in the oxide determined analytically is directly proportional to the $(x + y)$ chromaticity. Although there is some spread in the data, as shown by extrapolation to zero oxide coating weight, giving a value of $(x + y)$

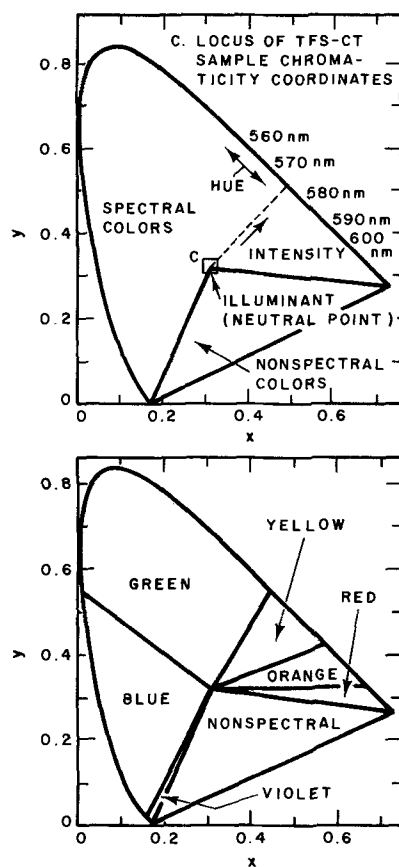


Fig. 4. Chromaticity diagram showing positions of the colors

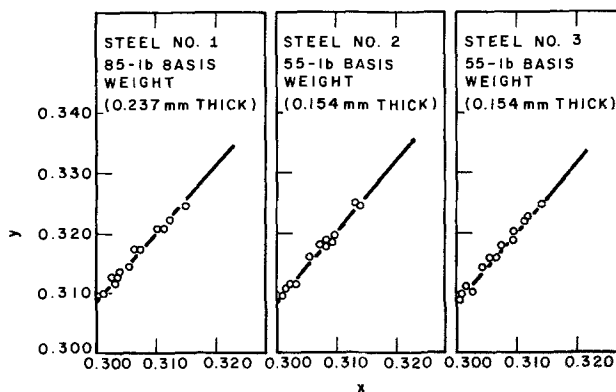


Fig. 5. Chromaticity diagram for TFS-CT with variable oxide coating weights on three different steel substrates.

chromaticity of 0.6064 ± 0.003 , an equation can be written to represent the data fairly well. The oxide coating weight, W , expressed as $\text{mg Cr}^{+3}/\text{ft}^2$ is related to $(x + y)$ chromaticity as

$$W = 83.41(x - y) - 50.58$$

where x and y are chromaticity values determined from tristimulus numbers as described previously. W may be converted to $\text{mg Cr}^{+3}/\text{m}^2$ by multiplying by 10.7.

Accuracy of data.—To determine the value of the $(x + y)$ chromaticity at zero oxide coating, the oxide coatings were stripped from 28 samples of TFS-CT according to the method prescribed by Shuto (5). Chromaticity was determined and the $(x + y)$ values had a spread of ± 0.0012 . The average value, 0.6084, was 0.0020 higher than the average of the extrapolated values discussed previously. This positive deviation seems reasonable because chromium metal in contact with air will always have some oxide on its surface.

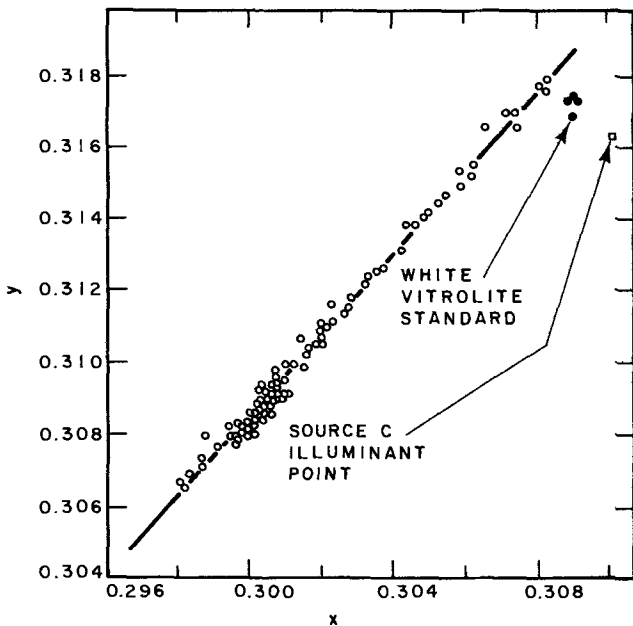


Fig. 6. Chromaticity diagram for a programmed experiment to produce TFS-CT with different oxide coating weights on a single steel substrate.

In another test, the same samples were placed in the sample holder of the spectrophotometer with the rolling direction vertical rather than horizontal. The spread in chromaticity was ± 0.0012 , but the average value of $(x + y)$ was 0.003 higher than with the same samples held in a horizontal position. The degree of change in color with a change in surface texture was not determined, but some of the point spread in the curves shown in Fig. 7 and 8 may be due to surface irregularity.

The x-ray fluorescence method of chemical analysis for chromium is also sensitive to surface texture, but blank (unplated) panels are used to adjust the zero point and improve the accuracy. The analysis of the chromium in both metallic and oxide coatings is expected to be accurate to $\pm 0.3 \text{ mg Cr}^1/\text{ft}^2$ ($\pm 3.2 \text{ mg Cr}^1/\text{m}^2$). More than 95% of the data fall within the limits of the experimental errors just outlined.

Effect of lacquer coatings on the color of TFS-CT.—Since most TFS-CT is lacquered before being used for beverage or food containers, how is the color of the TFS-CT affected by the lacquer? To answer this question, three lacquers were applied to TFS-CT and the

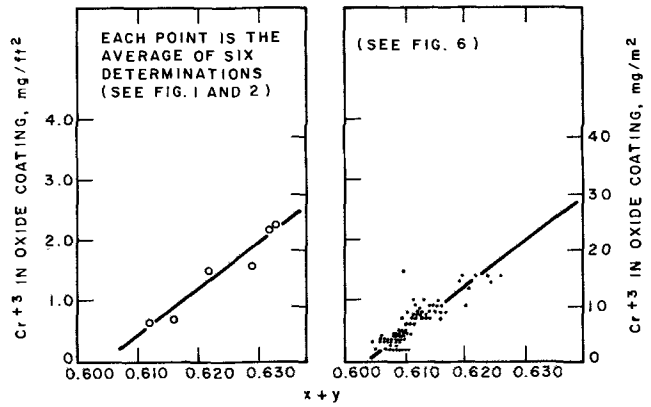


Fig. 8. Oxide coating weight vs. $(x + y)$ chromaticity

colors of the products were measured and compared with the original colors of the TFS-CT. In Fig. 9, 10, and 11, the chromaticity values of both lacquered and unlacquered panels are shown. The color of the TFS-CT affects the color of the lacquered panel. The spread in chromaticity values for the lacquered panels is less than that for the unlacquered panels in all three cases. The difference in color of TFS-CT is made somewhat less apparent by lacquering.

Effect of heating on the color of TFS-CT.—When TFS-CT is used for beer or beverage containers, it is first lacquered and the lacquered material cured. Sometimes the TFS-CT is processed one side at a time so that one side is unlacquered during the first heating cycle. If heating is moderate and the heating cycle is short, relatively little change occurs in the TFS-CT. However, as the temperature increases or the heating cycle lengthens, the oxide coating undergoes chemical and physical changes (6). Briefly, when the temperature is raised above 300°F (149°C), and the baking time goes beyond 30 min, water is driven out and the oxide becomes more crystalline and much less soluble in alkaline solution. Analytical data with respect to Cr^{+3} are questionable for heated TFS-CT, and no accurate determination of the rate of oxidation has been made.

There are unanswered questions about the optical properties of heated TFS-CT. Consider, for example, how does the oxide coating thickness vary with heating when the water is driven off and the coating is becoming more crystalline? Does this chemical change alter the basic color, transparency, or refractive index of the oxide? These questions cannot be answered directly, but tristimulus data can be examined for TFS-

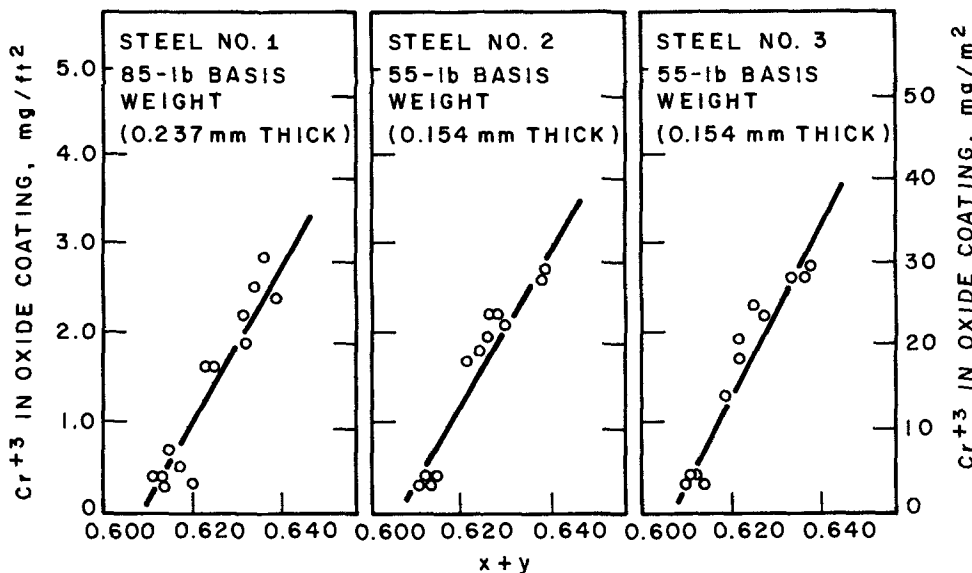


Fig. 7. Cr^3 in oxide vs. $(x + y)$ chromaticity for three steel substrates.

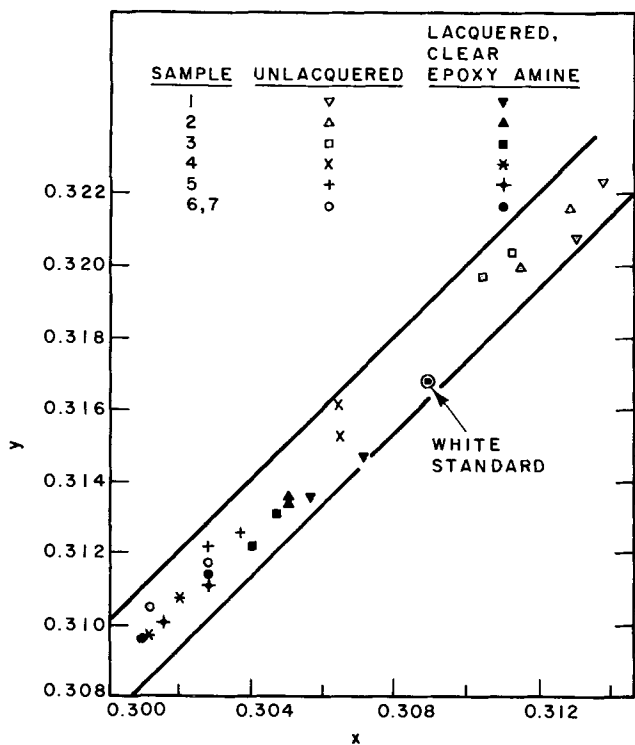


Fig. 9. Chromaticity of lacquered and unlacquered TFS-CT

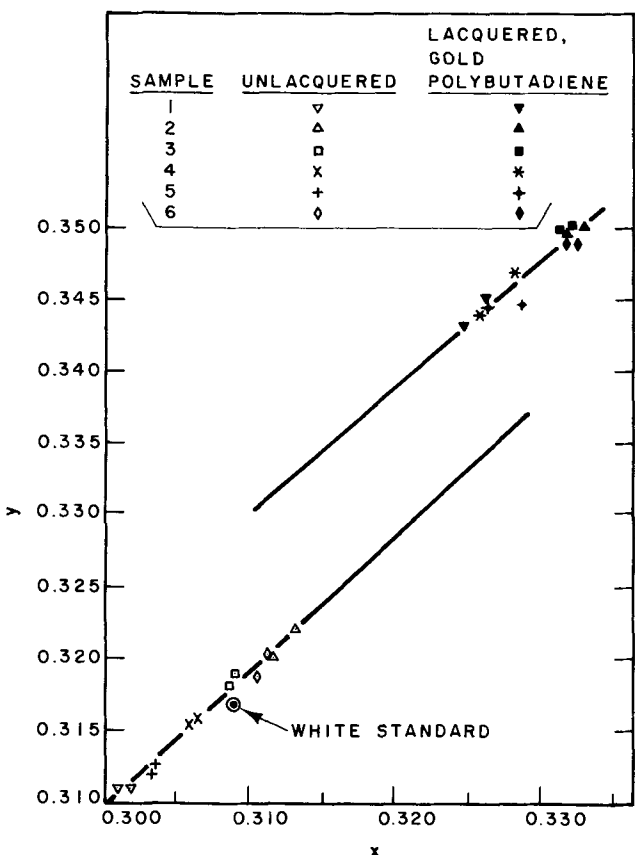


Fig. 10. Chromaticity of lacquered and unlacquered TFS-CT

CT before and after heating. The chromaticity diagram of Fig. 12 shows that heating TFS-CT in air for 30 min at 500°F (260°C) moves the chromaticity numbers to the top right of the figure as though each specimen (except one) had been oxidized. TFS-CT heated in an inert atmosphere shows little change in chromaticity numbers, Fig. 13, and thus leads to the conclusion that the optical properties do not change significantly when

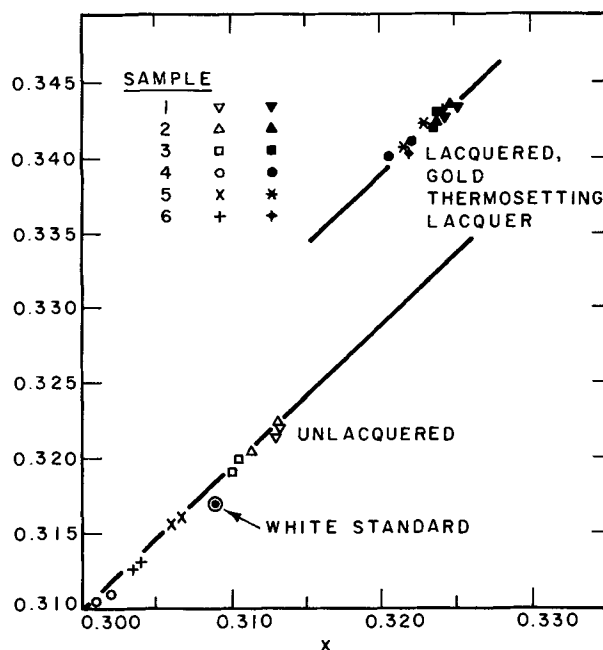


Fig. 11. Chromaticity of lacquered and unlacquered TFS-CT

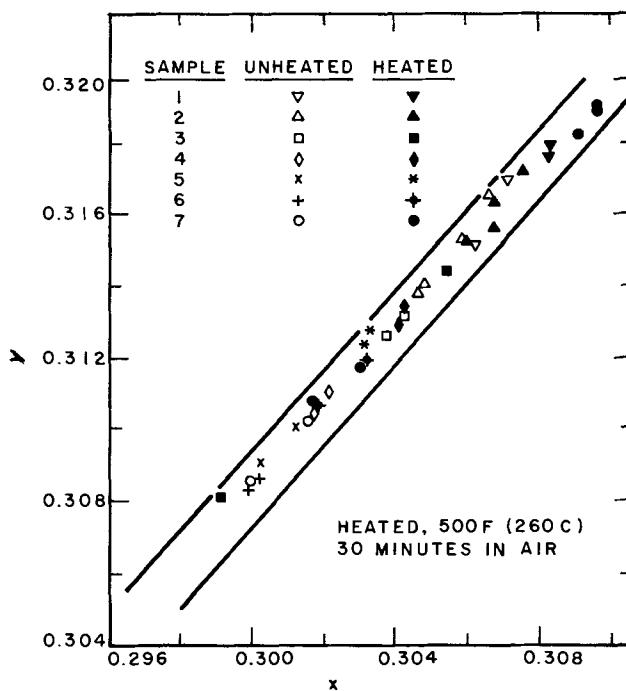


Fig. 12. Chromaticity diagram for TFS-CT before and after heating.

TFS-CT is heated in an inert atmosphere to 500°F (260°C) for 30 min.

When TFS-CT is heated in air, the increase in the amount of oxide, indicated by the change in chromaticity in Fig. 12, can be calculated for each specimen by using the chromaticity numbers ($x + y$) and the equation relating ($x + y$) to oxide coating weight. The calculated increase in coating weight is plotted as a function of the average coating weight in Fig. 14. The scatter in the data is remarkably small and there is some indication that increased oxide coating weight reduces the rate of oxidation, as might be expected intuitively. From Fig. 14 it is apparent that the rate of oxidation of bare electroplated chromium metal in air is about 1.0 mg Cr/ft² hr at 500°F (11 mg Cr/m² hr at 260°C).

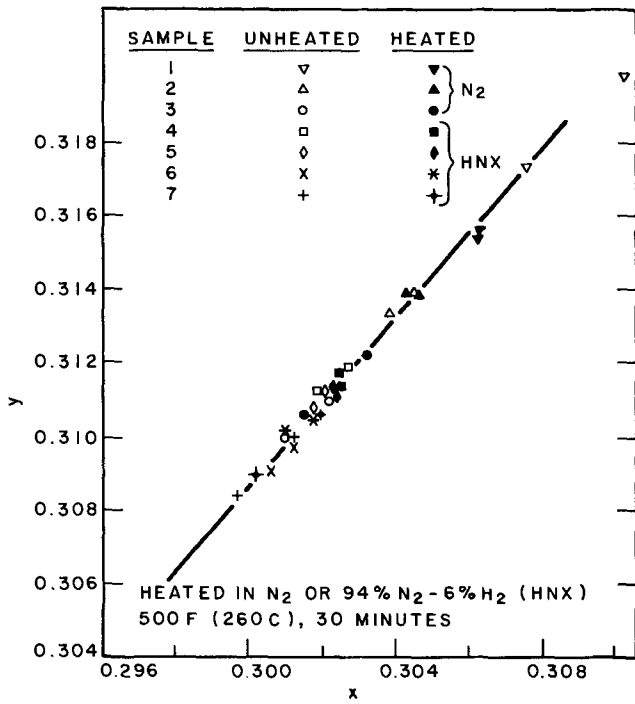


Fig. 13. Chromaticity diagram for TFS-CT before and after heating.

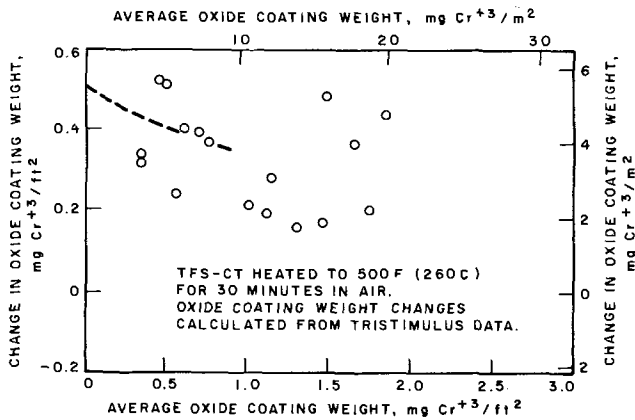


Fig. 14. Apparent increase in oxide coating weight during heating

Summary

TFS-CT has a brighter appearance than steel, and the brightness is related to the amount of chromium oxide present on the TFS-CT surface and the texture

of the surface. TFS-CT surfaces with little or no oxide have the brightest appearance. The specular reflectivity of TFS-CT measured with a 45-degree glossmeter was a function of the coating weight of chromium oxide when the same steel base was used to prepare all samples. Likewise, the diffuse reflectivity as measured by a spectrophotometer gave a similar result. When different steel surfaces were involved, however, the amount of light reflected was strongly dependent on surface roughness and the angle of incident light with respect to the rolling direction.

The surface roughness had only a minor effect on the color of TFS-CT. The color of chromium is slightly blue but as the oxide coating on TFS-CT builds up, the blue is absorbed in proportion to the thickness of the oxide. In this way the oxide coating weight (in mg/Cr³⁺/ft²) has been correlated with the chromaticity values *x* and *y* to give the equation $W = 83.41(x + y) - 50.58$.

The effect of oxide coating weight on the colors of lacquered TFS-CT has been observed for both colorless and gold lacquers. The effect of changes in oxide coating weight on changes in the color of TFS-CT is greatest for the bare product and somewhat less for the lacquered product depending on the type of lacquer used.

Heating TFS-CT in air causes physical, chemical, and color changes in the oxide coating, but the color of that coating remains remarkably stable when TFS-CT is heated in an inert atmosphere. Electrodeposited chromium oxidizes at 500°F (260°C) in air at the rate of 1.0 mg Cr/ft² hr (11 mg Cr/m² hr).

Manuscript submitted April 13, 1972; revised manuscript received May 26, 1972.

Any discussion of this paper will appear in a Discussion Section to be published in the June 1973 JOURNAL.

REFERENCES

1. F. M. Clydesdale and F. J. Francis, *Food Product Development*, **2**, 50 (1969).
2. ASTM Designation: E308-66, "Recommended Practice for Spectrophotometry and Description of Color in CIE 1931 System," Revision and Consolidation of Methods D791 and D306, adopted 1966.
3. G. E. Gardam, *Trans. Inst. Metal Finishing*, **44**, 186 (1966).
4. F. M. Clydesdale and F. J. Francis, *Food Product Development*, **2**, 62 (1969).
5. E. Shuto and Y. Kondo, "Study on Cathode Film on Steel Treated in Dilute Chromic Acid Solution," Interfinish '68, 7th International Metal Finishing Conference, Hanover, May 5-8, 1968.
6. O. Yanabu, T. Saito, K. Doi, T. Enari, K. Miyakawa, and H. Kawasaki, "Latest Technical Development of Chromium Plated Steel Strip," Interfinish '68, 7th International Metal Finishing Conference, Hanover, May 5-8, 1968.

Some Aspects of Electrode Erosion in Arc Heaters

K. Mosley,¹ A. E. Guile, and D. Dring

Department of Electrical and Electronic Engineering,
University of Leeds, Leeds LS2 9JT, Yorkshire, England

ABSTRACT

Very little information has been published on the erosion of electrodes occurring when the cathode and anode spots of arcs move over their surfaces for long periods. The results of measurements made during a study of an arc heater are reported herein. Operating an arc at 180A d.c. in argon at pressures between 2 and 73 atm has shown that the cathode erosion rate can vary by at least two orders of magnitude for relatively small changes in arc velocity. Phenomenological observation of electrode surfaces indicates that gas in the electrode material plays a very important role in electrode erosion.

In a number of applications in chemical engineering, aeronautics, and other fields, electric arcs are commonly used to heat gases at atmospheric pressure and above. Particularly where the processes involve operation for very long times, the erosion of the electrodes must be minimized in order to avoid costly shutdown of plant to replace electrodes. It is also frequently necessary to reduce the contamination of the heated gas by electrode material. In attempting to reach these objectives the arc terminations may be moved or rotated by transverse magnetic fields or by gas flow. For example, a recent paper (1) has shown that for a 200A arc in air at atmospheric pressure between water-cooled copper electrodes, a 2:1 reduction in the erosion rate occurred following a 3:1 increase in the strength of the applied transverse magnetic field. Most of the existing data on the erosion of electrode materials comes from the switchgear field, where short-duration arcs are drawn following metal-bridging processes. These arcs, which are in a quasi-stationary condition, may either occur at atmospheric or higher pressures, or may be vapor arcs in an enclosure initially under high vacuum.

The observations reported herein, made during a study (2) of the conditions of energy balance for d-c arcs rotated for several hours in argon at pressures between 2 and 73 atm, suggest that relatively large changes in cathode erosion can be associated with changes in arc velocity.

Experimental Procedure

The equipment used has been described more fully elsewhere (3). Figure 1 shows the basic arrangement in which a high-pressure gas pump circulated gas upward through the annular gap G between the concentric outer anode A and the inner cathode C. After heating by the arc, which was rotated by the axial field of F₁ and F₂, the gas passed into the heat exchanger on its return to the pump. To stabilize the arc at high gas mass flow rates it was necessary to pass a current of up to 1.5 kA through the central conductor M so that the field produced interacted with the arc to give a force in opposition to the aerodynamic force exerted by the gas flow.

Preliminary experiments in argon established that there was no noticeable erosion of the water-cooled copper anode, hence a single anode could be used in all the tests.

Prior to each test a new cathode was weighed to 0.01g and inserted in the arc chamber which was then evacuated to an initial air pressure between 1 and 6×10^{-3} Torr, before filling with argon of 99.995% purity. Experiments (see Table I) with brass cathodes were carried out under steady-state temperature conditions, at several gas flow rates for a given gas, gas pressure,

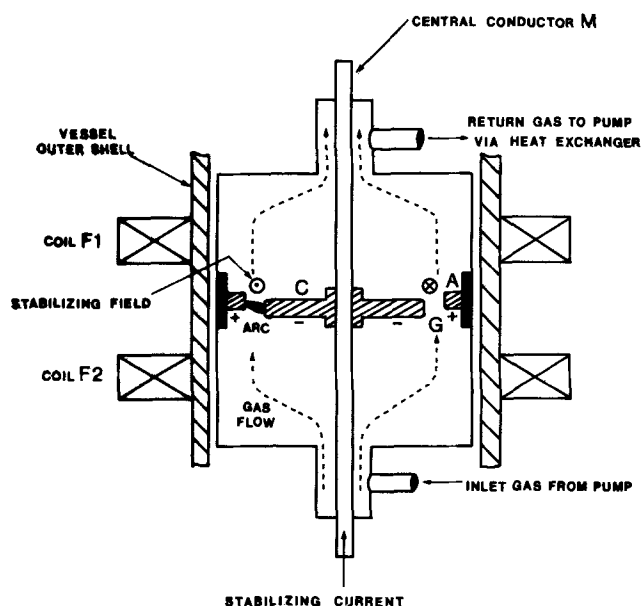


Fig. 1. Simplified diagram of electrode arrangement

and radial electrode gap in an axial magnetic field of 0.071 Tesla (Wb/m^2). This procedure was repeated over the whole range of gas pressures for different electrode gaps. Due to erosion, six cathodes had to be used in these experiments; mainly because with the small radial gaps used, the arc voltage, and hence the energy input to the arc, was very sensitive to even a relatively small increase in the gap.

Cathodes were of brass to specification BS 249, the analysis of which is given in Table I, or of phosphorous-

Table I. Cathode and test environment details for tests in argon at 180A using brass (BS 249)* (Range of gas flow rate 0.5 to 6.5 m/sec)

Test or cathode number	Increase in electrode gap due to cathode erosion (cm)	Residual air pressure (Torr)	Estimated max oxygen conc in argon (ppm by weight)	Range of pressures for which results were obtained (atm)
A1	None (initial gap 0.254 cm)	0.012	5†	2.56-9.15
A2	0.254-0.319	0.006	5†	2.56-73.0
A3	0.254-0.319	0.011	5†	2.56-73.0
A4	0.259-0.323	0.7	60	2.56-73.0
B1	0.516-0.531	0.7	60	2.56-51.3
C1	0.762-0.838	0.015	5†	2.56-9.15
C2	0.762-0.825	1.0	26	2.56-29.6

† 55-60% Cu, 2-3.5% Pb, and remainder Zn apart from 0.75% impurities.

* Oxygen concentration governed by a level existing in gas bottles. Quoted by British Oxygen Company as 5 ppm maximum. Water vapor content also 5 ppm (maximum) in bottles.

¹ Present address: Morganite Ceramic Fibres Ltd.
Key words: arc cathode, anode erosion, vaporization.

deoxidized nonarsenical copper to BS 1172 (minimum copper content 99.85%, 0.015-0.08% P).

Experimental Results

In preliminary experiments in argon with the arc chamber initially evacuated to 10^{-2} Torr, the erosion results shown in Table II were obtained for brass and copper cathodes. After the arc had run for 33 min on the brass cathode there was only a fine adherent gray deposit of zinc on the anode surface directly opposite the arcing surface of the cathode, while in the arcing chamber a very fine blue-black powder, identified as cupric oxide, was found. When the copper cathode was used, copper particles were found to be loosely attached to the anode surface opposite the cathode, and particles up to 1 mm long were found in the arc chamber. With the copper cathode the arc was much less stable than with the brass cathode, and this relatively greater stability has also been observed for low-pressure arcs (4). The arc luminosity obtained with the copper cathode was insufficient to make the optical probe record a velocity signal, but from previous experiments (5) using the same electrode material and the same gas it was established that the arc velocity was most probably about 36 m/sec, although a stable low-speed mode at a velocity as low as 20 m/sec was a possibility. The erosion rate for copper given in Table II is plotted against the mid-point of this velocity range in Fig. 2 and a dotted line is drawn joining this point *f* to the curve *c* plotted from the data of Harry (1), the justification for which will be discussed later.

It was not practicable to fit a new cathode after arcing under each condition of gas flow rate and gas pressure, because (i) the main purpose of the work was not concerned with erosion measurement, (ii) a very large number of other measurements were required in a limited time, and (iii) replacement of an electrode involved two days work. The erosion results given in Table I, therefore, cover a range of arcing conditions at various argon flow rates and pressures for each cathode.

For each cathode listed in Table I which was tested at a current I ($= 180\text{A}$) for all gas pressures and flow rates, the total weight loss W in grams may be written as

$$W = I \sum_{a=1}^m e_a t_a \quad [1]$$

where m is the total number of different gas pressures for which the particular cathode was tested, t_a is the arcing time for any particular pressure, and e_a is the unknown erosion rate for the average arc velocity over the range of gas flow rates explored at the same pressure. (For the highest pressures where maximum erosion occurred, the reduction in arc velocity when the gas flow rate was increased to its greatest value was less than 5%.) Equation [1] assumes that erosion may be expressed in gram/coulomb for these rotating arcs. This assumption is often made for static and for moving arcs although it has been shown (6) for arcs between copper surfaces of contactors in air up to 300A that $dW/dt = KI^{1.6}$. Thus the possibility of an

Table II. Cathode erosion at 2.56 atm with an argon flow of 1.12 to 1.15 m/sec

Measurement	Cathode material	
	Brass (BSS 249)	Copper (BSS 1172)
Initial weight (g)	2328.34	2412.47
Loss in weight (g)	0.32	11.53
Time of test (min)	33.0	13.0
Arc current (A)	176	156
Erosion rate (g/coulomb)	9.2×10^{-7}	9.5×10^{-6}
Arc speed (m/sec)	30	20 to 32 (estimated)

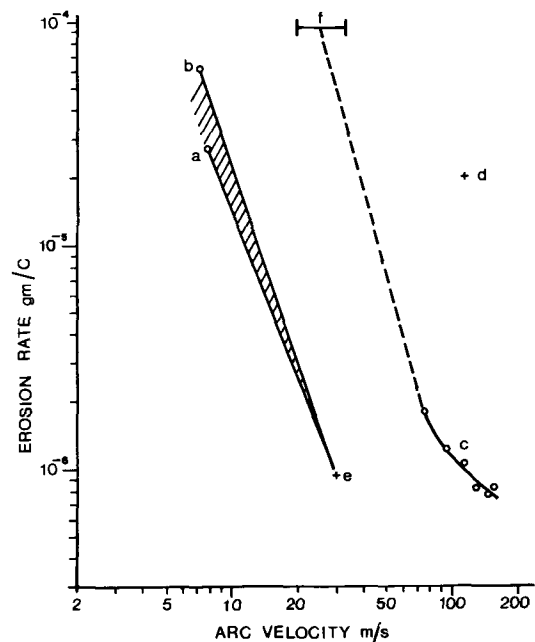


Fig. 2. Estimated cathode erosion characteristics. Curve *c*, copper in air [Ref. (1)]; point *d*, brass in air [Ref. (1)]; point *f*, copper in argon; shaded region between lines *ae* and *be*, brass in argon.

exponent greater than unity for the current cannot be ruled out. However, since the current was kept constant for all the present tests this difficulty was not encountered.

Equation [1] further assumes that the erosion rate depends on the arc velocity rather than on argon flow rate or pressure, and that where increased erosion has been reported for a magnetically driven arc with increase in gas pressure (7), the increase could be attributed to the reduction in arc velocity at a constant magnetic field. Support for the suggestion that erosion is relatively insensitive to gas pressure variation may be found from tests (8) on copper contacts in air which gave similar erosion rates at pressures between 11 and 23 atm. Also the results were in good agreement with others obtained at atmospheric pressure (6).

Because of the scatter which occurs in erosion rates when similar experiments are repeated (1), Eq. [1] was solved separately for each of the cathodes instead of assuming that e_a is always identical for a given pressure p_a and hence arc velocity. From a number of observations made during the course of this work, such as the large amount of vapor condensed on the molybdenum radiation shields of thermocouples, it was clear that the erosion occurred mainly at the highest pressures. It was found that the results for the erosion of brass in argon could be described by a straight line on Fig. 2, radiating from a point *e* which represents the measured brass erosion in the preliminary tests (Table II). The line *ae* gave the exact value of total loss W for cathode B1; line *be* gave only a discrepancy of 0.5% for cathodes A2 and A4 and 1.8% for C2. The area between lines *ae* and *be* is therefore considered to describe the erosion of the brass cathodes used for arc speeds between 7.3 and 31 m/sec running stably in argon over the pressure range 2.5-73 atm. It is interesting to note that the slopes for lines *ae* and *be* are almost the same as that of the line *fc* joining the two points for copper cathodes in air or argon.

Discussion of Results

Figure 2 shows that for a cathode root speed of 30 m/sec, the erosion of the copper cathode was 100 times larger than that of the brass cathode. When the latter was used, the anode surface was covered with a fine deposit of zinc while fine cupric oxide powder was found within the arcing chamber. If the cathode spot

temperature is limited by evaporative processes, then reduction in the zinc content of the brass at the emitting sites may occur since its boiling point (at atmospheric pressure) is less than half that of copper or lead. Experimental evidence of such zinc depletion at the surface of an arc track has been found (9) by means of an electron probe analyzer for arcs moving retrograde in argon at pressures below 1 atm. The fact that zinc was found on the anode suggests that it was carried across the gap by cathode jets, the velocities of which may be 10^3 or 10^2 m/sec when there is little electrode vaporization (10), and which therefore exceed considerably the axial argon velocities of 0.5–6.5 m/sec.

When a copper cathode was used, irregularly shaped pieces of bright copper up to 1 mm long were found in the arcing chamber, together with relatively large globules of copper on the lower parts of the anode, while the downstream parts of the anode surface were covered with a weakly adherent layer of cupric oxide. The copper particles on the anode surface showed evidence of having been molten while traveling in the high-temperature regions of the arc, whereas the irregular particles found in the arcing chamber had clearly not been molten as a consequence of having been ejected clear of the high-temperature regions.

The copper to specification BS 1172 used for the cathode can contain oxygen in solid solution, in pockets, or as copper oxides within the bulk metal, despite the phosphorous used as a deoxidizing agent, whereas the brass is virtually free of oxygen (11). Under the intense heating effects of the cathode root, oxygen present just below the surface may dissociate from oxides or come out of solution to create a void containing high-pressure gas. When the surface adjacent to this highly pressurized void becomes sufficiently weak due to root heating, the gas can escape "explosively," taking with it a relatively large amount of the surface metal. Similarly, microscopic regions of high-pressure gas can be produced by phosphorous which boils at 282°C. Furthermore, oxygen linking with phosphorous to form phosphorous pentoxide may result in zone weakening of the material especially at grain boundaries. It has been observed (12) that a higher erosion rate occurred for a continuously rotating arc on a copper cathode with 0.045% phosphorous than for copper having a 0.034% content. The lack of large eroded particles from a brass cathode may therefore be attributed to the insignificant amounts of oxygen or phosphorous.

Scanning electron microscope photographs (13) of cathode tracks on copper provide further evidence that gas eruptions just below the surface can occur and blast away surface metal. Photomicrographs such as Fig. 3 revealed irregular depressions containing approximately circular holes within which were smaller holes which in turn contained even smaller cavities. Photographs of brass cathodes under similar conditions of arcing did not show such cavities.

In the search for the most suitable materials for vacuum switches, evolution of gas was encountered from ordinary and O.F.H.C. copper and even from the best grade of vacuum-melted copper which was then available (14). Furthermore, whenever electrode material collected on shields was of a coarse globular nature it was accompanied by large bursts of gas from the electrodes. Heating to fusion followed by ejection of material by evolution of occluded gas has sometimes been assumed (15). The presence of fused material on an anode was observed to coincide with a sudden pressure rise caused by gas evolution or vaporization of high vapor pressure materials (16).

At atmospheric pressure or above, this process does not seem to have been discussed previously in connection with cathode erosion, but, in a 4 kA discharge of 10^{-8} sec duration, "flares" photographed coming from a copper anode were tentatively identified as a directed

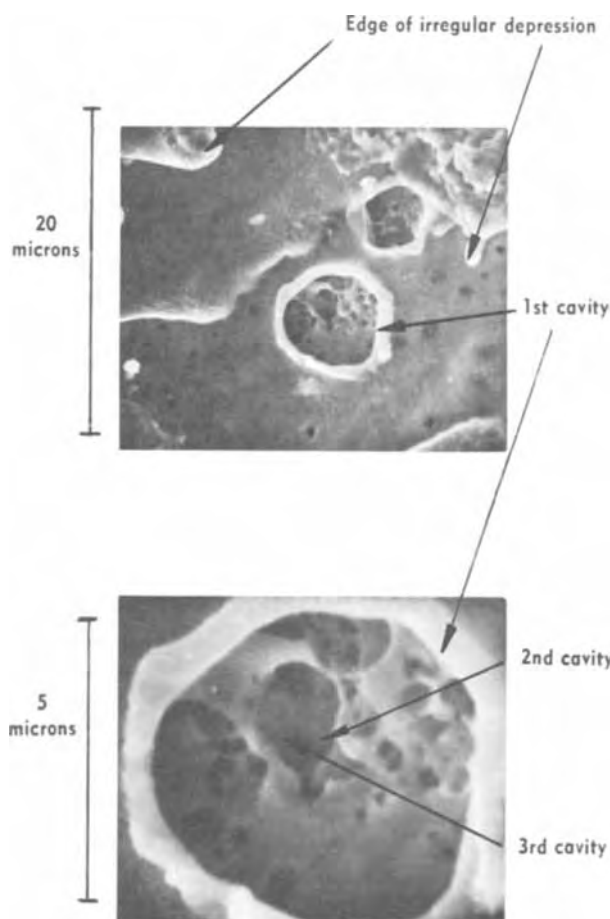


Fig. 3. Stereoscan microphotographs of cavities on copper cathode

"explosive type" of erosion (17). It was implied that a difference in conductivity between the molten surface and base metal was more likely to be responsible than gas in the electrode. No explosive-type erosion of large particles was observed with the copper anode used throughout the present tests, which suggests that the anode current densities being several orders of magnitude below those on the cathode, and the magnetic movement combined to prevent local temperatures at anode roots reaching a level at which sufficient gas pressure developed to tear out metal. Wilson (18) tentatively suggested that a secondary mechanism of the combined cathode and anode erosion of a pair of contacts at atmospheric pressure was vaporizing electrode material blasting out liquid droplets.

It seems likely that the explosive process proposed in this paper explains the reason for recommendations (19) that electrodes used for arc heating in the production of metal oxides should be of essentially void-free material and that they should be tested ultrasonically for number and size of voids. The term essentially void-free is applied to an electrode having less than one part per million by volume of voids in the part liable to consumption by the arc, and with each void being less than 450μ in any dimension.

For a copper cathode, the possibility of almost continuous variation of erosion between Harry's results in air and the results herein for argon, as represented by the dotted line joining c to f, may be due to the

gradual changeover from evaporative erosion of surface layers at low erosion levels, to a larger-scale explosive-type erosion at f . The latter would be much less dependent on the ambient gas in which arcing occurs.

Comparison of points d and e in Fig. 2 appears to indicate that a brass cathode can be eroded far more rapidly in air than in argon. The speed of arc rotation on circular electrodes affects the amount of reoxidation and this, together with the destruction of oxide layers at emitting sites, which depends on the type of gas (4), affects the distribution of these sites relative to their positions at earlier revolutions. When emission consistently recurs at or very near the old sites, the local temperatures and the erosion are likely to be greater than when the search for favorable emission sites causes them to be spread over a large area. There is certainly evidence (4) that in air, arc cathode roots tend to rotate over the same narrow track where evaporation destroys the oxide layers. However, during the time the roots take to complete one revolution, these very hot surfaces form thicker oxide and chemisorbed gas layers on which emission can be established more easily than on surrounding areas. This is supported by localized grooving of a brass cathode in air (1) and of a stainless steel cathode when run in air during the present experiments.

When running an arc on brass cathodes in argon, it was found necessary for arc stability to have a certain minimum amount of air in the system as is well known (20), so that some reoxidation could occur. For a given residual air content in the apparatus on evacuation, the maximum possible gas flow rate at a given pressure which could be attained without arc extinction was found to decrease as the electrode gap was increased, but this maximum flow rate could be increased by allowing more air to remain in the system before arc ignition. For a given flow rate and pressure the instability increased with arc running time, possibly because oxygen in the flowing gas became insufficient to reoxidize to full emission the points on the cathode nearest to the anode root, and the cathode root was forced to wander to more remote points where emission was easier. Table I shows that a few parts per million of oxygen were sufficient for stable operation but the maximum variation in oxygen content was insufficient to have a significant effect on erosion. It should be noted, however, that at least for silver contacts in mixtures of nitrogen and oxygen, it has been found (21) that above or below a certain oxygen content the erosion can rise steeply, and may be related to humidity. The erosion of copper cathodes in a plasma torch at currents up to 600A, was greater in pure oxygen than in air (22). Measurements for copper contacts in air (23) suggest an erosion range between about 7×10^{-6} g/coulomb at 8A and 1.3×10^{-4} g/coulomb at 180A. Earlier results of copper cathodic erosion given by Holm (24) which are about double these values, have been erroneously interpreted (25) as ranging from 1.3×10^{-9} g/coulomb at a current per spot (I/n where there are n spots) of 1A to about 10^{-7} g/coulomb at currents per spot of 10 kA and upward. In fact these currents up to 10 kA for which Holm gave erosion results were total arc currents (I). The currents at individual emitting sites at the cathode surface in air appear from experiments in this laboratory to be of the order of 10A.

The cathode erosion rates measured in the present work are far below those reported for copper contacts in air (23), and Fig. 2 suggests that an increase in velocity may reduce the erosion rate still further. Some results (26, 27) have shown, however, that for homogeneous contact materials operating in air at 1 atm, too great an increase in magnetic field can lead to greater erosion for currents from 100A to 10 kA, and this was attributed to increased spatter of volatile

material. At currents below 100A and fields below 0.1 Tesla this spatter did not occur.

Since an arc rotating around a circular track makes a number of revolutions before attaining a steady velocity (5, 28), erosion data (even when obtained from moving arcs) may not necessarily be applicable to continuously rotating arcs. In general the velocity of an arc traveling over linear electrodes is not the same as that of a continuously rotating arc (29), and the method used by Dethlefsen (7) of driving a 6 kA arc over a linear surface in about 1 msec, although yielding data on a wide range of metals, does not necessarily apply directly to continuously operating devices. Furthermore, it does not distinguish between cathode and anode erosion, and introduces transitions between single and double arc which may cause discontinuities in the erosion process which could be very significant in such a short test.

The effect of grain size on erosion has so far been little explored and both increase and decrease in contactor electrode wear has been found to occur as grain size was increased (30, 31).

Porous tungsten electrodes impregnated with barium-calcium-aluminate suffered less erosion than thoriated tungsten, but linear electrode tests showed them to have an erosion rate in air at least an order of magnitude higher than copper (32).

It would appear, therefore, that insufficient information exists to enable an optimum choice of electrode materials and arc parameters that will minimize erosion in equipment using high-power continuously rotating arcs. It seems clear that such data cannot be provided by calculations of the transient temperature distribution at electrode surfaces (1, 33), but only by a systematic investigation attempting to provide data with the widest possible validity over the wide range of arc conditions and environments employed in gas heaters and other continuously operating devices.

Acknowledgments

This work was supported by a Ministry of Technology Contract and the authors gratefully acknowledge this support. They also thank Dr. J. Sikorski for making the scanning electron microscope facilities available.

Manuscript submitted Sept. 1, 1971; revised manuscript received ca. March 1, 1972.

Any discussion of this paper will appear in a Discussion Section to be published in the June 1973 JOURNAL.

REFERENCES

1. J. E. Harry, *J. Appl. Phys.*, **40**, No. 1, 265 (1969).
2. K. Mosley, University of Leeds, Ph.D. Thesis (1969).
3. K. Mosley, *The Engineer*, 687 (1967).
4. T. J. Lewis and P. E. Secker, *J. Appl. Phys.*, **32**, No. 1, 54 (1961).
5. K. A. Naylor and A. E. Guile, *Brit. J. Appl. Phys.*, **18**, 1295 (1967).
6. C. Turner, H. W. Turner, and F. Frey, E.R.A. Report No. 5119 (1966).
7. R. Dethlefsen, A.R.L. Report No. 68-0112 (1968).
8. L. Gosland and H. W. Baldrey, E.R.A. Report G/T190 (1946).
9. D. W. Wright, University College of North Wales, Thesis (1968).
10. R. Wienecke, *Z. Physik*, **143**, 128 (1955).
11. A. C. Galton, Private communication (1967).
12. J. E. Harry, University of Aston in Birmingham, Ph.D. Thesis (1968).
13. D. J. Hamilton, Unpublished.
14. J. D. Cobine and T. A. Vanderslice, *IEEE Trans. Comm. and Electron.*, **82**, 240 (1963).
15. D. L. Clingman and T. L. Rosebrock, U.S.A.F. Office of Aerospace Research, Engineering Dept., Report No. 3283 (1963).
16. H. C. Ross, *IEEE Trans. Component Parts*, **CP-10**, 155 (1963).
17. H. Fischer and C. C. Gallagher, U.S.A.F. Office of Aerospace Research, Optical Physics Laboratory Report No. AFCRL-67-0446 (1967).

18. W. R. Wilson, *Trans. A.I.E.E., Power and Systems*, **74**, 657 (1955).
19. British Patent Specification No. 1,129,833 (1968), U.S. Patent Application No. 400,644 (1964).
20. G. E. Doan and J. L. Myer, *Phys. Rev.*, **40**, 36 (1932).
21. M. R. Swinehart, "Proceedings of the International Research Symposium on Electric Contact Phenomena," University of Maine, pp. 301-316 (1961).
22. M. H. Weatherly and J. E. Anderson, *Electrochem. Technol.*, **3**, 80 (1965).
23. R. Holm, "Electric contacts—theory and application," 4th ed., Springer-Verlag, Berlin, Heidelberg, New York (1967).
24. R. Holm, *J. Appl. Phys.*, **20**, 715 (1949).
25. M. F. Hoyaux, "Arc Physics," Springer-Verlag, Berlin, Heidelberg, New York (1968).
26. G. Unger, *Elektrotech. Z. (E.T.Z.)*, **A88**, 33 (1967).
27. K. H. Schroder, *Elektrotech. Z. (E.T.Z.)*, **A90**, No. 16, 393 (1969).
28. G. Burkhard, *Elektrie*, **6**, 229 (1966).
29. A. E. Guile, E. D. Blix, and H. C. Spink, "Proceedings VIIth International Conference on Phenomena in Ionized Gases," **1**, 745 (1966).
30. H. W. Turner and C. Turner, *Electrical Times*, **153**, No. 1, 3 (1968).
31. W. Kuczowski, *Przegląd Elektrotechniczny*, **44**, No. 12, 533 (1968).
32. U.S. Air Force Report ASD-TDR-62-729, Part II, Vol. 2 (1962).
33. R. L. Phillips, "Proceedings of a specialists meeting on arc heaters and MHD accelerators for aerodynamic purposes, Belgium," AGARDograph 84, Part II, 797 (1964).

Electrochemical Behavior of Nitric Oxide in 4M H₂SO₄ on Platinum

Dilip Dutta* and D. Landolt*

*Energy and Kinetics Department, School of Engineering and Applied Science,
University of California, Los Angeles, California 90024*

ABSTRACT

The electrochemical reactivity of different nitrogen oxides or their absorption products in sulfuric acid was investigated by potential scan measurements. Experiments were carried out at 23°C with platinum electrodes. Among the substances studied only HNO₂ and NO exhibited well-defined oxidation and reduction currents. The electrochemical reactions of NO in 4M H₂SO₄ were studied in detail by using a rotating disk electrode. Mass transport limited currents were observed for both oxidation and reduction. From the variation of the limiting current with rotation rate the diffusion coefficient of NO was determined to be 0.9×10^{-5} cm²/sec.

Little work has been reported so far in the literature which deals with the characterization of electrochemical reactions of nitrogen oxides. This is surprising in view of the proposed application of electrochemical current measurements for continuous monitoring of nitrogen oxide air pollutants (1, 2). Electrochemical techniques might also provide useful tools for the investigation of the complicated chemical reaction sequences that take place on absorption of nitrogen oxides in aqueous solutions (3, 4). Furthermore, the mechanism of nitric acid reduction is of interest in corrosion research since HNO₃ is frequently used as a pickling or a polishing agent for metals. Considerable controversy exists at present over whether the charge transfer step involved in HNO₃ reduction involves the reacting species NO₂ or NO (5-11). In the absence of oxygen, NO can be absorbed in aqueous solution without undergoing disproportionation reactions contrary to the behavior of NO₂ (3, 4). The study of its electrochemistry is therefore relatively simple. The thermodynamics of the NO/HNO₂ electrode have been investigated by Schmid and Neumann (12), but no data are available at present about reaction kinetics.

The purpose of this study was twofold. On one hand, because of the absence of such data in the literature, the relative reactivity of different nitrogen oxides or their absorption products was to be characterized by potential scan measurements. Rotating disk experiments were then to be used to study in more detail the electrochemical behavior of NO. The data of this

study were to be a first step toward providing a rational basis for a possible development of new electrochemical monitoring methods for nitrogen oxides.

Experimental

Apparatus.—The rotating disk electrode assembly consisted of a variable speed motor (Bodine 1/8 hp d-c motor) driving a rotating shaft by means of pulleys. Constant rotation speeds between 100 and 15,000 rpm could be obtained which were measured by means of a stroboscope. The rotating electrode assembly included a commercial quill (Dumore Company) and a removable disk electrode. Contact to the electrode shaft was made by means of slip rings. A 1.5 liter glass cell was bolted to a fixed PVC cell cover. An "O" ring, placed between the cell and PVC cover, and a water seal arrangement at the shaft prevented any contact of the electrolyte solution with air. Standard Teflon fittings were used to insert thermometer, Luggin capillary, and two glass frits for gas bubbling into the cell. One of the frits used for deaeration prior to experiments was placed into the electrolyte solution. The other frit was located above the solution and served for passing gas during experimental runs. A saturated calomel electrode served as reference. A platinum foil counterelectrode was separated from the working electrode compartment by a glass frit located in the center at the bottom of the cell. The working electrode was a platinum disk 0.79 cm in diameter, silver soldered onto a stainless steel shaft and press fitted into a Teflon insulation.

Initial potential scan experiments with different nitrogen oxides were performed in a conventional sealed-glass cell with a platinum wire electrode. An

* Electrochemical Society Active Member.

Key words: nitrogen oxides, rotating disk electrode, nitric acid, monitoring of air pollutants.

Anotrol 4700 M potentiostat in connection with a function generator (Exact, Type 255) or a multipurpose electrochemistry unit (Princeton Applied Research, Model PAR170) were used as power supply. Potentials were measured by means of a Keithley Electrometer (Model 602) and current voltage curves were recorded on a x-y recorder.

Preparation of solutions.—Solutions were prepared with analytical grade chemicals and doubly distilled water. HNO_2 solutions were prepared by slowly adding required quantities of a 0.1M NaNO_2 stock solution from a pipette to a stirred solution of the supporting electrolyte cooled in an ice salt bath. Saturated NO solutions were prepared by first deaerating the system for at least 8 hr with prepurified nitrogen. Then 99.9% pure NO (Air Products Corporation) was bubbled through the solution for approximately 3 hr. Rotating disk measurements indicated that this time was ample to reach saturation of the sulfuric acid solutions with NO. To remove possible NO_2 impurities the NO, prior to bubbling it through the cell, was passed through two wash bottles containing NaOH. Data obtained with the rotating disk electrode (see below) showed that HNO_2 contamination during the experiments, resulting from the possible presence of traces of oxygen during gas saturation, was less than 10% of the NO concentration. When necessary, experimental data were corrected for the presence of this contamination.

Electrode pretreatment.—Pretreatment of the platinum working electrode is critical for insuring reproducible results. The following procedure was adopted. Prior to immersion into the electrolyte solution, the electrode was cleaned with soap and doubly distilled water and dried. It was further cleaned by refluxing benzene for about 1 min. Electrolytic pretreatment in 0.5M H_2SO_4 was then given as follows: cathodic pretreatment at 50 mA/cm² for 2 min, anodic treatment at 50 mA/cm² for 1 min, and further cathodic pretreatment at the same current density for 2 min.

The electrode was then immersed in the solution. After deaeration, but prior to the experimental run, the electrode was again cathodically polarized and hydrogen was evolved for 2 min. This was followed by anodic polarization of the electrode for 1 min near to the oxygen evolution potential (but not evolving oxygen). Finally, the electrode was once again cathodically treated for 2 min.

For each of the individual solutions and reactants studied, the first experiment carried out was a cathodic scan starting from the open-circuit potential. Prior to this, the electrode had been subjected to a short anodic pretreatment for 15 sec at 300 mV positive of the open-circuit potential. The cathodic experiments were followed by anodic scans between the open-circuit potential and potentials just below the oxygen evolution region. Prior to anodic runs, the electrode had been subjected to a cathodic polarization for 15 sec at 300 mV negative of the open-circuit potential. In some cases a complete scan between the hydrogen and oxygen evolution potentials was also measured. Several experimental runs were always conducted to check for reproducibility.

Determination of NO solubility.—For the quantitative interpretation of limiting current measurements, the saturation concentration of NO in 4M H_2SO_4 had to be known. Because literature values were not available, an experimental titration procedure was developed based on data given by Kolthoff and Elving (13). The airtight apparatus used consisted of a calibrated burette and a titration vessel (Fig. 1). Sulfuric acid solution contained in the 250 ml burette was deaerated with purified nitrogen for approximately 8 hr. Pre-purified NO was then bubbled through the solution for 2 hr to reach saturation. Care was taken to exclude any traces of oxygen. A 200 ml flask containing 100 ml of 0.001M KMnO_4 was connected to the burette.

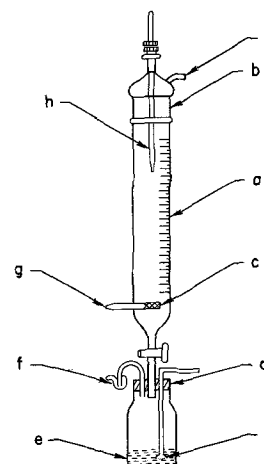


Fig. 1. Apparatus for determining NO concentration in H_2SO_4 . a, 250 ml graduated burette containing sulfuric acid; b, ground glass stopper; c, glass frit for gas bubbling; d, rubber stopper; e, potassium permanganate solution; f, gas bubbler; g, gas inlet; h, thermometer; i, gas outlet to wash bottle.

The KMnO_4 solution was deaerated with nitrogen for 3 hr. Then 100 ml of the NO-saturated sulfuric acid solution was slowly added to the KMnO_4 which oxidizes NO to NO_3^- (13). After completion of the reaction the flask containing the KMnO_4 was removed and the excess KMnO_4 was titrated with a freshly prepared 0.1M acidified FeSO_4 solution. The end point was observed potentiometrically by measuring the potential of a platinum wire electrode vs. a saturated calomel electrode with a Keithley electrometer. Two blank experiments carried out in the absence of NO showed the titration procedure to give results to an accuracy of better than 1.4%. In the presence of NO the following data were obtained. Experiment A: $T = 22.4^\circ\text{C}$, volume titrated 102.5 ml, FeSO_4 used in back titration 0.88 ml, NO concentration 1.34×10^{-3} mole/liter. Experiment B: $T = 23.0^\circ\text{C}$, volume titrated 106.5 ml, FeSO_4 used in back titration 1.02 ml, NO concentration 1.24×10^{-3} mole/liter. This yields an average value of $1.29 \pm 0.05 \times 10^{-3}$ moles/liter for the saturation concentration of NO in 4M H_2SO_4 at $22.7^\circ \pm 0.3^\circ\text{C}$.

Results

Qualitative information on the cathodic reactivity of different nitrogen oxides is contained in Fig. 2, which gives potential scan measurements on a stationary wire electrode. Deaerated 4M H_2SO_4 was used as an electrolyte to which different nitrogen oxides were added. Before each scan experiment the electrode was subjected to a potential 300 mV anodic to the open-circuit potential for 15 sec. Then repetitive scanning at 1 V/min was initiated starting from the open-circuit potential. The traces shown in Fig. 2 represent the second cycle. The initial cathodic scans frequently differed slightly from those shown but subsequent scans were usually identical. The scan in pure 4M H_2SO_4 (Fig. 2a) showed the usual hydrogen adsorption and desorption peaks on platinum. Addition of 0.01 mole/liter NaNO_3 to the sulfuric acid did not measurably affect the behavior, indicating that nitrate ion was not reduced. Addition of approximately 0.01 mole/liter NaNO_2 to the sulfuric acid solution led to three well-defined reduction steps (Fig. 2c), in agreement with data reported by Schmid and Lobeck (10). According to these authors, the first two steps of HNO_2 reduction each involve the over-all transfer of one electron per molecule of reactant while the third step involves the over-all transfer of two electrons. The relative magnitude of the observed HNO_2 reduction steps in Fig. 2c is consistent with this view. The cathodic scan measured in NO saturated 4M H_2SO_4 (Fig. 2d) exhibited two well-defined reduction steps at potentials correspond-

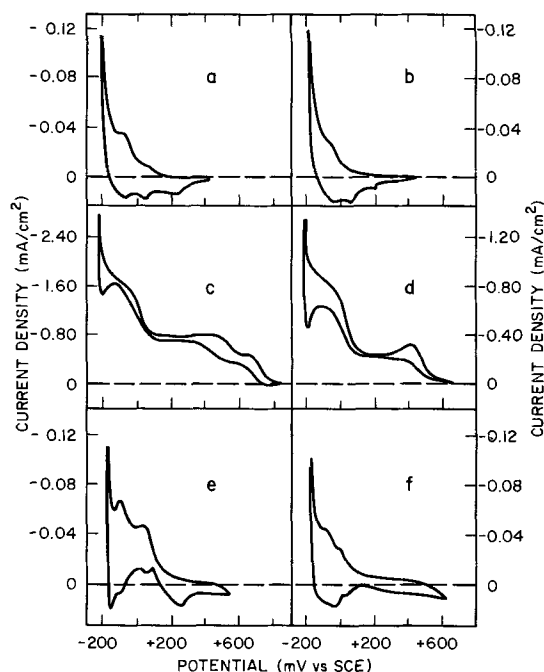


Fig. 2. Cathodic potential scans on stationary Pt wire electrode. Scan rate 1 V/min, $T = 23^\circ\text{C}$. (a) 4M H_2SO_4 , (b) 4M $\text{H}_2\text{SO}_4 + 0.01\text{M NaNO}_3$, (c) 4M $\text{H}_2\text{SO}_4 + \text{approx. } 0.01\text{M NaNO}_2$, (d) 4M H_2SO_4 saturated with NO, (e) 4M H_2SO_4 saturated with N_2O , (f) 4M $\text{H}_2\text{SO}_4 + 0.01\text{M } (\text{NH}_2\text{OH})_2\text{H}_2\text{SO}_4$.

ing to the second and third HNO_2 reduction steps. The N_2O voltage scan shown in Fig. 2e was obtained after saturating a 4M H_2SO_4 with 99.99% pure N_2O (Liquid Carbonic Corporation), the literature value of the saturation concentration being 0.018 mole/liter. In spite of this high N_2O concentration in the solution, cathodic currents in the potential region between +200 and -180 mV vs. SCE were extremely small, indicating that N_2O reduction on platinum is strongly inhibited. The potential scan of Fig. 2f was obtained in a 4M H_2SO_4 solution to which 0.01M hydroxylamine sulfate had been added. The observed trace was identical to that of the pure H_2SO_4 , i.e., hydroxylamine is not reduced cathodically in the potential region between +200 and -180 mV vs. SCE. Anodic potential scan measurements performed with the same electrode in 4M H_2SO_4 are given in Fig. 3. After prepolarization at 300 mV negative to the open-circuit potential, several repetitive potential scans were performed. For the experiments in pure H_2SO_4 , results for repetitive scans were identical. Platinum oxidation was observed at approximately 800 mV and oxygen evolution set in above 1600 mV. The platinum oxides reduced at potentials between 700 and 200 mV. This behavior of platinum is well known. Addition of 0.01M sodium nitrate did not affect the current trace (Fig. 3b). On the other hand, addition of approximately 0.01M sodium nitrite to the sulfuric acid solution (Fig. 3c), lead to a well-pronounced oxidation current which had already been observed by Schmid and Lobeck (10). According to these authors it corresponds to the oxidation of nitrous acid to nitric acid. Repeating the anodic cycle without intermediate cathodic pretreatment leads to a substantial decrease in the oxidation currents. This fact together with the observed sharpness of the oxidation peaks indicates that the platinum oxidation state affects HNO_2 oxidation kinetics. The same holds true for the oxidation of NO (Fig. 3d). Two peaks were observed here, the second of which corresponded to the oxidation peak of HNO_2 . Upon repeating the cycle without intermediate platinum oxide reduction the first NO oxidation peak disappeared while the height of the second peak was strongly reduced.

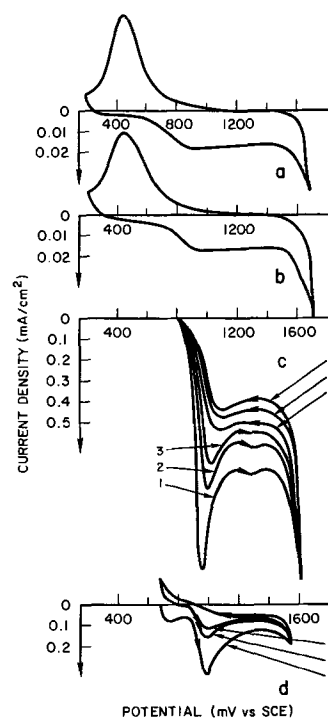


Fig. 3. Anodic potential scans on stationary Pt wire electrode. Scan rate 1 V/min, $T = 23^\circ\text{C}$, (a) 4M H_2SO_4 , (b) 4M $\text{H}_2\text{SO}_4 + 0.01\text{M NaNO}_3$, (c) 4M $\text{H}_2\text{SO}_4 + \text{approx. } 0.01\text{M NaNO}_2$, (d) 4M H_2SO_4 saturated with NO.

The cathodic reduction of NO was further investigated by means of the rotating disk electrode. Limiting current plateaus, the height of which increased with rotation rate (Fig. 4), indicated that the first reduction step is diffusion controlled. A plot of limiting current vs. the square root of rotation rate yielded a straight line with a slope of $6.7 \times 10^{-5} \text{ A sec}^{1/2}/\text{cm}^2 \text{ rad}^{1/2}$ (Fig. 5). The points in Fig. 5 represent two independent experiments with fresh solution. To compute the limiting current for NO reduction (Fig. 5) a correction had to be made for the unavoidable presence of a small amount of HNO_2 impurity which is evidenced in Fig. 4 by the finite current value in the potential region between 600 and 450 mV. Because HNO_2 is reduced in two steps, twice the value of the residual limiting current was subtracted from the measured limiting current value of Fig. 4.

Figure 6 shows NO oxidation currents measured on a rotating disk electrode. Each current-potential curve was measured after a brief cathodic pretreatment had been given to the electrode. A strong effect of rotation

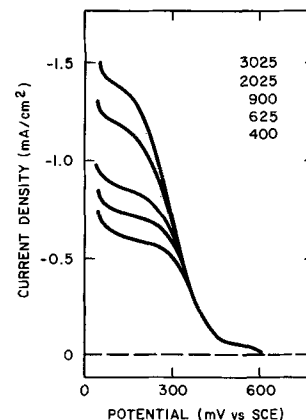


Fig. 4. Cathodic polarization curves measured in 4M H_2SO_4 saturated with NO on rotating disk electrode. Scan rate = 0.5 V/min, $T = 23^\circ\text{C}$; numbers indicate rpm.

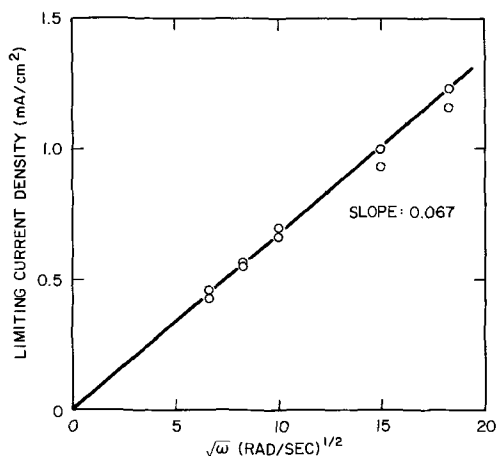


Fig. 5. Limiting current values for NO reduction as a function of rotation rate.

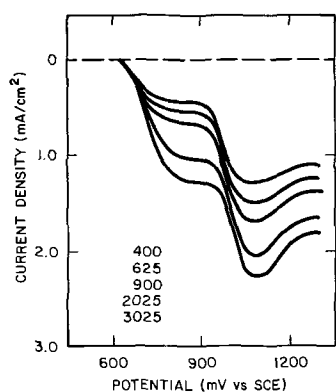


Fig. 6. Anodic polarization curves measured in 4M H₂SO₄ saturated with NO on rotating disk electrode. Scan rate = 0.5 V/min, T = 23°C, numbers indicate rpm.

rate on step height is observed. The second step exhibits a peak rather than a current plateau. In view of the slow scan rates employed, it is concluded that this peak is not due to a nonsteady-state mass transfer situation but to the development of an oxide layer on the platinum anode which slows down the oxidation reaction at higher potentials. The limiting current of the first step and the peak current for the second step are plotted for two independent experiments performed with new solutions in Fig. 7. The straight line obtained when the limiting current is plotted vs. the square root of rotation rate indicates that the first step is diffusion controlled. The slope of 6.7×10^{-2} mA sec^{1/2}/cm² rad^{1/2} is identical to that derived from the cathodic reduction data (Fig. 5). The peak height of the second wave does not yield a straight line when plotted vs. $\sqrt{\omega}$. At high rotation rates kinetic limitations apparently become important. This is also evidenced by the much poorer reproducibility of these currents compared to those of the first step. Poor reproducibility is typical for reactions which are surface controlled. At low rotation rate the peak currents representing the second NO oxidation step approach a tangent having a slope three times that of the straight line representing the limiting currents of the first oxidation step.

Kinetic parameters of the surface reaction corresponding to the first oxidation step can be determined by a technique described by Jahn and Vielstich (14) employing the rotating disk electrode. For irreversible first-order charge transfer reactions partly controlled by mass transfer, one may set

$$\frac{1}{i} = \frac{1}{i_s} + \frac{B}{\sqrt{\omega}} \quad [1]$$

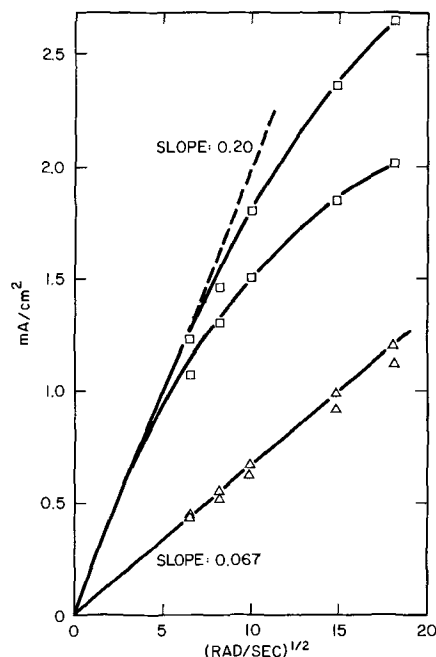


Fig. 7. Limiting current values for NO oxidation as a function of rotation rate; Δ first oxidation step, \square peak current of second oxidation step.

where i_s is the charge transfer current corrected for mass transfer effects, B is a constant, and ω is the rotation rate. Figure 8 shows a plot of $1/i$ vs. $1/\sqrt{\omega}$ derived from the current voltage curves for NO oxidation on the RDE. According to Eq. [1] the intercepts of the straight line with the $1/i$ axis represent the reciprocal of the charge transfer current i_s at infinite rotation rate. The logarithm of i_s is plotted as a function of potential in Fig. 9. Tafel behavior with a slope of 110 ± 10 mV is exhibited. The data of Fig. 9 represent two independent experiments with new solutions and different disk electrodes.

Potential scan experiments at different scan rates were performed in 4M H₂SO₄ solutions saturated with NO at a stationary disk electrode. Peak currents for both oxidation as well as reduction were found to be a linear function of the square root of scan rate. Peak potentials for both oxidation and reduction waves are plotted vs. the logarithm of scan rate in Fig. 10. The

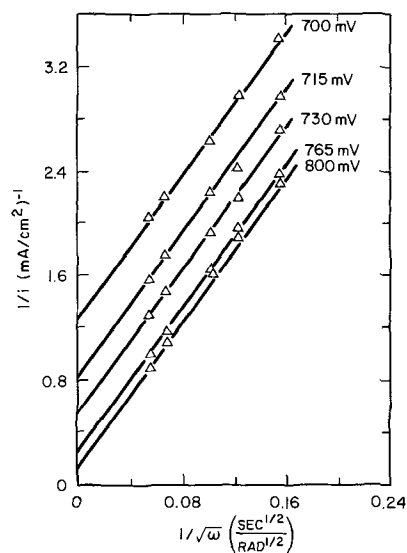


Fig. 8. Reciprocal current density as a function of the square root of reciprocal rotation rate for NO oxidation on rotating disk electrode.

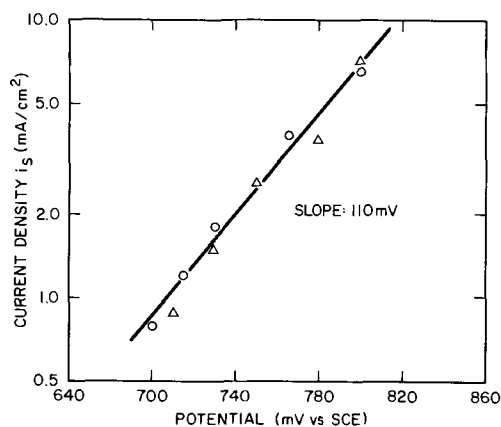


Fig. 9. Tafel plot for NO oxidation on Pt in 4M H₂SO₄ derived from rotating disk electrode data; ○, △ two independent experiments with fresh solution.

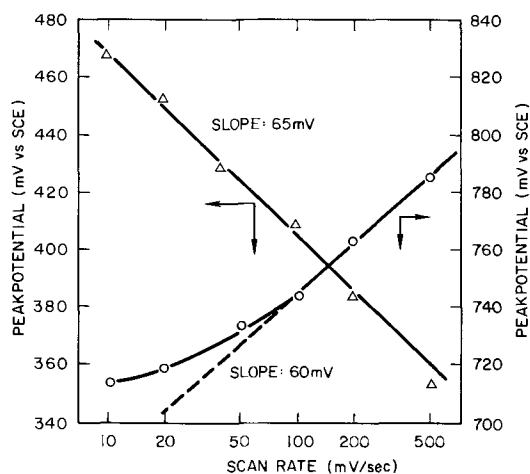


Fig. 10. Peak potentials as a function of scan rate measured on stationary platinum disk in 4M H₂SO₄ saturated with NO; △ reduction of NO, ○ oxidation of NO.

cathodic curve exhibits a straight line of slope 65 mV. The anodic curve is flat at low scan rates but approaches a slope of 60 mV at high scan rates.

Discussion

Oxidation as well as reduction of NO proceeds stepwise. The first oxidation and the first reduction steps involve the same number of electrons transferred because the slopes of Fig. 5 and 7 are the same. Both limiting currents are mass transfer controlled and one electron is transferred per reactant molecule. The latter is concluded from the following observations: (i) the Tafel slope for NO oxidation (first step) is 110 ± 10 mV (Fig. 9), corresponding to a charge transfer coefficient of $\alpha = 0.54$ and an electron transfer number, $n = 1$. (ii) The variation of peak potential with scanning rate (Fig. 10) for NO reduction approaches 60 mV/decade consistent with an irreversible one-electron charge transfer process (16). Oxidation of NO at low scan rates proceeds reversibly, but at high scan rates the variation of E_p with $\log \lambda$ also approaches the 60 mV characteristic for an irreversible one-electron charge transfer process. (iii) Schmid and Lobeck (10) showed that reduction of the primary reaction intermediate of HNO₂ reduction involves the transfer of one electron per reactant molecule. The data of Fig. 2 confirm that NO is indeed the primary reaction intermediate of HNO₂ reduction, and therefore the observed NO reduction step represents an over-all one-electron transfer process.

Once the number of electrons is established, the limiting current measurements on a rotating disk elec-

trode can be used for determining the diffusion coefficient of NO in 4M H₂SO₄. The limiting current is related to the bulk NO concentration c_b , diffusion coefficient D , kinematic viscosity ν , and rotation rate ω by the Levich equation (15)

$$i_l = 0.62 n F c_b D^{2/3} \nu^{-1/6} \omega^{1/2} \quad [2]$$

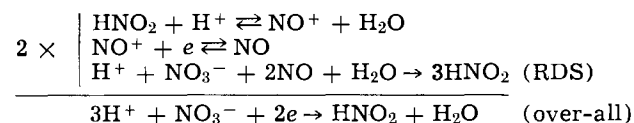
The kinematic viscosity of 4M H₂SO₄ is 1.53×10^{-2} cm²/sec at 25°C (10). With the measured saturation concentration of NO of 1.29×10^{-3} moles/liter and the measured slopes of Fig. 5 and 7 one obtains for the diffusion coefficient $D = 0.90 \times 10^{-5}$ cm²/sec.

It is of interest to take a look into the possible reaction sequences involved in the stepwise oxidation and reduction processes encountered. It is likely that the reduction of NO on platinum proceeds to hydroxylamine as the final product (Fig. 2), the behavior being analogous to that of HNO₂ (10). It may be noted, however, that N₂O does not appear to be a reaction intermediate in spite of the fact that its oxidation state is consistent with that resulting from a one-electron reduction process of NO. This is concluded because Fig. 2 shows that the reaction product generated during the initial NO reduction step (involving the transfer of one electron per reactant molecule) is much more reactive in the potential range between +100 and -180 mV than N₂O is. It is likely that substances of identical oxidation state as N₂O, such as HNO or NO⁻ are the reaction intermediates in NO reduction.

Oxidation of NO yields HNO₂ which at more anodic potentials is further oxidized to HNO₃. This view is consistent with the relative magnitude of the slopes of Fig. 7 representing the first and second NO oxidation steps. It may be noted that the heterogeneous reaction rates of both reactions strongly decrease with increasing oxidation state of the platinum surface (Fig. 3). Therefore the kinetic data for NO oxidation given in Fig. 9 holds for a cathodically pretreated anode only. The rate of HNO₂ oxidation is maximum in the potential region of beginning oxygen coverage but decreases at higher potentials. It is very possible, therefore, that the HNO₂ oxidation mechanism involves interactions with chemisorbed oxygen on the platinum surface in a similar way as, for example, found during oxidation of methanol (17).

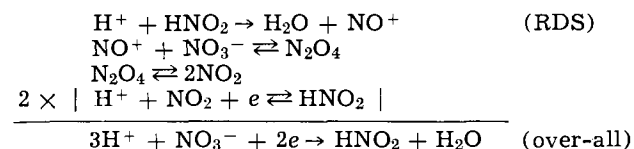
The observed two-step oxidation of NO has implications with respect to proposed reaction sequences for HNO₃ reduction on platinum. According to Schmid (7-10), HNO₃ reduction involves the reaction sequence

Scheme I



On the other hand, Vetter (5,6) proposed the sequence

Scheme II



Both sequences involve a number of chemical and electrochemical steps, but they exhibit significant differences with respect to the charge transfer reaction involved. Scheme I contains only one charge transfer reaction, namely the reduction of NO⁺ to NO. If one applies this reaction scheme in reverse order to the present NO oxidation experiments, one expects to find only a single oxidation step the height of which depends on the rate of the slow chemical reaction (RDS). On the other hand, when scheme II is applied to the oxidation of NO, two different charge transfer proc-

esses are required, one involving the oxidation of NO to HNO₂, the other the oxidation of HNO₂ to NO₂. The present experiments clearly exhibit two different NO oxidation steps and therefore they are more consistent with scheme II than with scheme I. Additional kinetic experiments will have to be carried out with NO and HNO₂ solutions before detailed oxidation mechanisms can be established. Particular attention will have to be given to the observed influence of the oxygen coverage of the platinum surface on the reaction kinetics. This has not been included in any of the above reaction schemes.

Conclusions

Nitric oxide absorbed in sulfuric acid solution exhibits well-defined oxidation and reduction reactions on a platinum electrode.

Nitric oxide reduction proceeds in two steps. The first step exhibits a mass transfer controlled limiting current, the magnitude of which corresponds to a charge transfer reaction involving one electron per NO molecule.

Nitric oxide oxidation also proceeds in two steps. The first step leading to HNO₂ exhibits a mass transfer limited current plateau. The second step corresponding to the oxidation of HNO₂ to HNO₃ is only partly governed by mass transfer. Oxidation of the platinum electrode inhibits the reaction.

Rotating disk experiments in 4M H₂SO₄ at 23°C yield a diffusion coefficient of nitric oxide, $D_{NO} = 0.9 \times 10^{-5}$ cm²/sec.

Acknowledgment

This work was supported by Air Pollution Research Funds of the University of California, Los Angeles.

Manuscript submitted March 22, 1972; revised manuscript received May 24, 1972.

Any discussion of this paper will appear in a Discussion Section to be published in the June 1973 JOURNAL.

REFERENCES

1. R. Chand and P. R. Cunningham, *IEE Trans.*, **GE8**, 158 (1970).
2. R. Chand and R. V. Marcote, *Am. Inst. Chem. Engrs. 8th Annual Meeting*, Feb. 1971, Houston.
3. W. L. Jolly, "The Inorganic Chemistry of Nitrogen," W. A. Benjamin, New York (1964).
4. F. A. Cotton and G. W. Wilkinson, "Advanced Inorganic Chemistry," 2nd Edition, Interscience (1966).
5. K. Vetter, *Z. Phys. Chem.*, **194**, 199, 284 (1950).
6. K. Vetter, "Electrochemical Kinetics," p. 490, Academic Press (1967).
7. G. Schmid, *Ber. Bunsenges.*, **63**, 1184 (1959).
8. G. Schmid, *ibid.*, **65**, 531 (1961).
9. G. Schmid and G. Krichel, *ibid.*, **68**, 677 (1964).
10. G. Schmid and M. A. Lobeck, *ibid.*, **73**, 189 (1969).
11. G. Schmid and H. N. Heckner, *Electrochim. Acta*, **16**, 131 (1971).
12. G. Schmid and U. Neumann, *Z. Phys. Chem. N. F.*, **54**, 150 (1967).
13. I. M. Kolthoff and P. J. Elving, "Volumetric Analysis," *Part III*, Vol. 5, p. 239 (1961).
14. W. Vielstich and D. Jahn, *Ber. Bunsenges.*, **64**, 43 (1960).
15. V. G. Levich, "Physicochemical Hydrodynamics," Prentice Hall (1962).
16. R. S. Nicholson and I. Shain, *Anal. Chem.*, **36**, 706 (1964).
17. W. Vielstich, "Brennstoff Elemente," p. 73, Springer Verlag (1965).

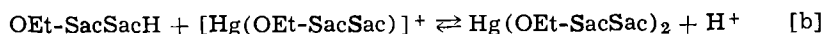
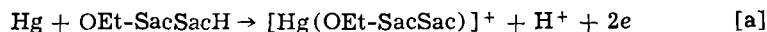
Polarographic and Coulometric Studies of O-Ethylthioacetothioacetate and O-Ethylthioacetate

A. M. Bond,* A. R. Hendrickson, and R. L. Martin

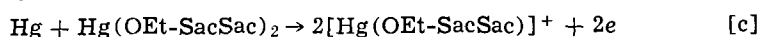
Department of Inorganic Chemistry, University of Melbourne, Parkville, Victoria, Australia

ABSTRACT

The polarographic and coulometric behavior of O-ethylthioacetothioacetate (OEt-SacSacH) has been characterized in acetone/0.1M Et₄NClO₄ at the DME. Electrolysis of OEt-SacSacH in acetone at a potential of +0.45V relative to Ag|AgCl involves oxidation of the mercury electrode via the consecutive reactions



On the polarographic time-scale Reaction [b] is slow and the electrode process at the DME is represented by Eq. [a]. The $E_{1/2}$ value is concentration dependent having the value $E_{1/2} = +0.226\text{V}$ at infinite dilution. The neutral mercury(II) complex formed under electrolysis conditions enhances oxidation at the mercury electrode ($E_{1/2} = +0.145\text{V}$).



The oxidation electrode process is strongly influenced by adsorption phenomena leading to an additional wave at high concentrations. The characteristics of the adsorption can be followed closely by electrocapillary curves, a-c desorption waves, and d-c current-time curves. An irreversible reduction wave is observed at $E_{1/2} = -1.43\text{V}$ for OEt-SacSacH. Comparative studies with the related compound O-ethylthioacetate are reported briefly.

Early speculation on the electrochemical properties of dithioacetylacetonato complexes on the basis of its odd numbered chelate ring suggested these compounds

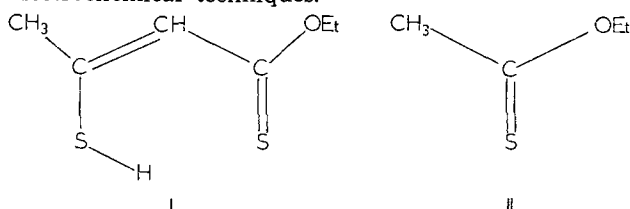
would not undergo reversible electron addition and subtraction reactions (1). However, following the successful synthesis of dithioacetylacetonato (SacSac) complexes of all the Group VIII metals (2-6) it has been shown that most of these compounds are reduced reversibly at the DME in acetone (7-8).

* Electrochemical Society Active Member.

Key words: polarography, coulometry, O-ethylthioacetothioacetate, O-ethylthioacetate.

Unfortunately, with the dithioacetylacetonato series, the parent ligand SacSacH, can only be isolated in the form of a nonco-ordinating adamantane-type dimer ($C_5H_8S_2$)₂. However, the spectral characterization of the closely related O-ethylthioacetothioacetate I (OEt-SacSacH) and its Zn(II), Cd(II), and Hg(II) chelates has been recently reported (9). As part of continuing electrochemical studies of these and related 1,3-dithio ligands and complexes, we report here the polarographic properties of this sulfur-based ligand at the DME. The results of this study have shown that interaction between the compound and the mercury surface is exceedingly complex, although this behavior is not unprecedented for sulfides or sulfur-containing compounds in solvents other than acetone.

The polarographic behavior (oxidation and reduction) of O-ethylthioacetate II as well as that of OEt-SacSacH has been examined in acetone at the DME. The oxidative, reductive, and adsorption behavior of OEt-SacSacH has been examined by alternating and direct current polarography, coulometry, and related electrochemical techniques.



Experimental

Polarography.—Conventional d-c polarography was carried out in May and Baker Analytical Reagent acetone with tetraethylammonium perchlorate (0.1 mole liter⁻¹) as supporting electrolyte. A three-electrode, iR compensated system as described in Ref. (7) was employed, the reference electrodes being Metrohm Ag|AgCl EA425 electrodes (0.1 mole liter⁻¹ LiCl) in acetone. The glass capillary dropping mercury electrode had the following characteristics in acetone (0.1M Et₄NClO₄) at open circuit and with a mercury column height of 40 cm: flow rate of Hg, $m = 1.48$ mg sec⁻¹; drop time, $t = 4.70$ sec; $m^{2/3}t^{1/6} = 1.68$ mg^{2/3} sec.^{-1/2}. Short controlled drop times were achieved with a Metrohm Polarographie stand E354. The a-c polarographic studies utilized a PAR Model 170 Electrochemistry System (Princeton Applied Research Corporation). The major portion of the ohmic iR drop across the solution was compensated for with the three-electrode potentiostat although no positive feedback compensation for the ohmic potential drop of the DME was used in either the a-c or d-c work.

The test solutions, thermostated in a water-jacketed cell at 20°C, were degassed with argon for 20 min before use unless otherwise specified. A slow stream of argon was passed over the test solution while measurements were being taken. Both electrodes (reference and auxiliary) behaved identically although they yielded an $E_{1/2}$ value for Rh(SacSac)₃ of -1.09 V to be compared with the published result of -1.05 V (7). As reported (7), the potential of the electrodes was stable (± 2 mV) over a period of three months. The discrepancy of 40 mV for the Rh(SacSac)₃ reduction may be attributable to the use of acetone of a different origin from that employed in the previous work. In the present work, the use of May and Baker acetone has allowed the polarographically usable potential range to be extended to -2.2 V vs. Ag|AgCl. The addition of traces of water lowered this to -2.0 V vs. Ag|AgCl, the limit previously reported with BDH AnalaR acetone (7). The decrease in the negative potential limit by addition of water to the acetone system has been commented on by Coetzee and Siao (10).

Coulometry.—The number of electrons involved in the oxidation steps (n) has been determined by coulometry. Electrochemical oxidation of a 0.1M Et₄NClO₄/

acetone solution of the ligand ($\sim 10^{-3}$ mole liter⁻¹) was achieved with 3.00 ml of solution on a mercury pool electrode having an area of approximately 2 cm². The mercury pool replaced the DME in the usual polarographic arrangement, with a Pt wire as the auxiliary electrode thereby reducing the bulk and ohmic resistance of the electrode system and enabling the employment of small volumes for electrolysis. The DME was also positioned in the solution enabling the concentration of unoxidized ligand and other electroactive species to be conveniently monitored.

The solution was thoroughly stirred by magnetic stirrer and concentrations of compounds determined at 5-min intervals. Current (~ 0.3 mA)-time curves were plotted by the recorder and manually integrated. After 30-min electrolysis n was calculated from plots of "charge consumed" vs. concentration of the relevant species. As the oxidation potential of the compound is considerably more positive than the reduction potential of oxygen, degassing was not required. To minimize evaporation the electrolysis vessel was surrounded by a moat of acetone and the apparatus sealed. Blank runs, where no electrolysis occurred showed a slight decrease ($< 1\%$) in the concentration of the ligand over 1 hr, presumably due to acetone from the moat "distilling" into the 0.1M Et₄NClO₄ solution.

Materials.—Tetraethyl ammonium perchlorate was prepared by neutralization of a 25% solution of Et₄NOH with 20% HClO₄. The precipitated product was recrystallized twice from EtOH (95%) and finally from MeOH (AR). Preparation of Et₄NClO₄ by this method obviates the need for many careful recrystallizations to remove the last traces of the electroactive halide ion, always present in samples of Et₄NClO₄ prepared by the metathesis of tetraethyl ammonium iodide (7) or bromide (10) and NaClO₄. Pure Et₄NClO₄ was dried and stored under vacuum over silica gel.

O-Ethylthioacetate and O-ethylthioacetothioacetate were prepared and purified as described previously (9). May and Baker "Pronalys" acetone was used throughout.

Results and Discussion

The polarographic behavior of OEt-SacSacH, being the parent ligand of a series of metal complexes also studied by polarography, is of particular interest and has been examined in detail. Although the electrochemistry of the sulfur-based ligand at a mercury surface is very complex, the present data have enabled the nature of the electrode process and ensuing reaction to be unraveled. The ligand exhibits one reduction and one oxidation wave at the DME (Fig. 1). The oxidation and associated adsorption phenomena are discussed in detail in the first instance.

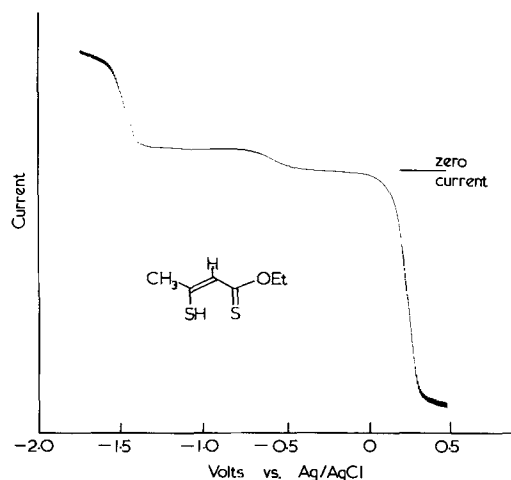


Fig. 1. Complete d-c polarogram of OEt-SacSacH (natural drop time).

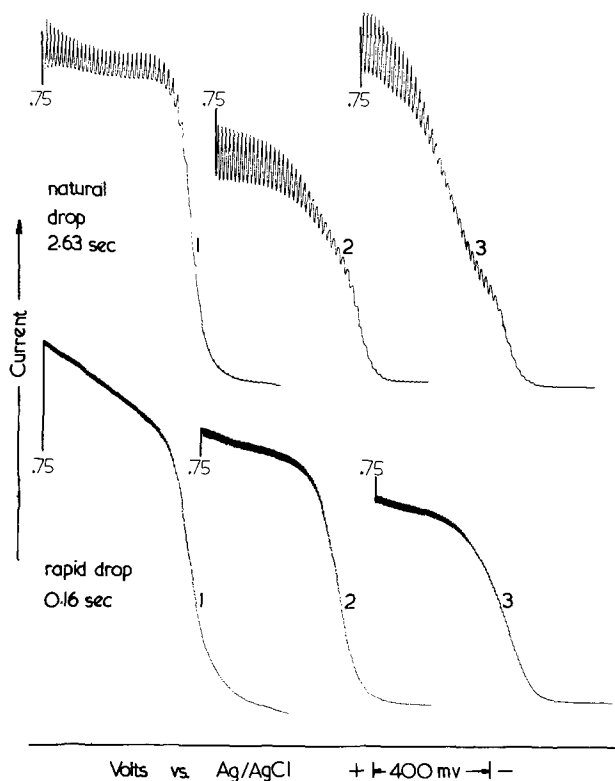


Fig. 2. Natural and rapid polarograms of oxidation process with OEt-SacSacH at approximate concentrations of 1, 5×10^{-4} M; 2, 2×10^{-3} M; and 3, 2.5×10^{-3} M. Current scale has been adjusted for each solution and drop time.

Oxidation.—Both the nature and $E_{1/2}$ value of the oxidation step are concentration dependent. The $E_{1/2}$ values measured over the concentration range 1×10^{-4} to 1×10^{-3} M extrapolate at infinite dilution to the $E_{1/2}$ value of $+0.226 \pm 0.004$ V vs. Ag/AgCl.

At concentrations greater than 10^{-3} M it becomes apparent that adsorption and related inhibition of the electrode process are operative at the mercury surface. In this higher concentration region, the oxidation wave splits into two (Fig. 2). However, the total limiting current for the two waves (i_d total) increases linearly with both concentration (Fig. 6), and \sqrt{h} (h = column height of mercury), confirming that the overall limiting current is diffusion controlled. As NMR studies on OEt-SacSacH in CDCl_3 have established that the compound exists in a thio-enol form in this solvent (9) the complex anodic behavior of the compound is not due to a mixture of thio-enol and thione forms.

The electrolysis of OEt-SacSacH solutions at a mercury pool electrode is complicated by the increase in concentration of a species exhibiting an oxidation wave with an $E_{1/2}$ value less positive than that exhibited with OEt-SacSacH (Fig. 3). At the completion of the electrolysis in the presence of the ligand, the polaro-

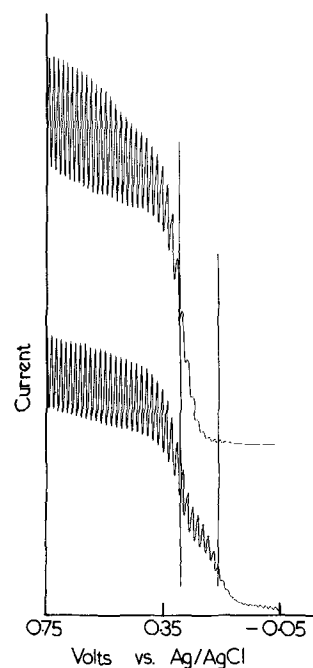
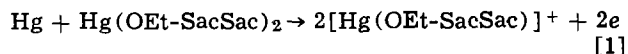


Fig. 3. Oxidation region of solutions of OEt-SacSacH before (upper wave) and after (lower wave) partial electrolysis at a mercury pool electrode, illustrating growth of oxidation wave of $\text{Hg}(\text{OEt-SacSac})_2$ at more negative potentials.

gram of the remaining species is identical with a polarogram of $\text{Hg}(\text{OEt-SacSac})_2$, even down to the pre-wave on the reduction step (11). These data have been taken as evidence that the product from the over-all reaction of the oxidation process at a mercury surface is $\text{Hg}(\text{OEt-SacSac})_2$. This is one of the few examples where the mercury complex is both known and soluble, and studies are considerably facilitated because of this.

The coulometric experiments of OEt-SacSacH were carried out at $+0.45$ V vs. Ag|AgCl and as can be seen from Table I this potential is sufficiently positive to oxidize mercury in the presence of both OEt-SacSacH and $\text{Hg}(\text{OEt-SacSac})_2$; i.e., the oxidation waves observed are actually due to the oxidation of $\text{Hg}(0)$ to $\text{Hg}(II)$ in both cases.

The relatively stable $[\text{Hg}(\text{OEt-SacSac})]^+$ moiety is not oxidized at this potential as evidenced by the fact that solutions of $\text{Hg}(\text{OEt-SacSac})_2$ exhibit only a single two-electron oxidation step in the potential range 0.00 to $+0.75$ V vs. Ag|AgCl with $[\text{Hg}(\text{OEt-SacSac})]^+$ as the product [1] (11).



Returning to the oxidation of mercury in the presence of the free ligand: the coulometric measurement of n has been determined by monitoring the concentration of free OEt-SacSacH from the oxidation wave.

Table I. Some polarographic parameters of O-ethylthioacetate, OEt-SacSacH, and $\text{Hg}(\text{OEt-SacSac})_2$

Compound	$\text{CH}_3\text{C}(\text{S})\text{OEt}$		OEt-SacSacH		$\text{Hg}(\text{OEt-SacSac})_2$	
	Oxidation	Reduction	Oxidation	Reduction	Oxidation	Reduction
$E_{1/2}$ volt vs. Ag AgCl	+0.7*	-2.08	+0.226**	-1.428	+0.145†	-0.41‡
$E_{1/4}-E_{3/4}$ (mV)	—	54	60	68	50	62
Nature of wave	Oxidation	Reduction	Oxidation	Reduction	Oxidation	Reduction
Drop time (sec)	1.67	0.67	1.78	1.85	6.00	1.95
Potential at which drop time measured (volt)	+0.5	-2.2	+0.5	-1.6	+0.2	-0.6

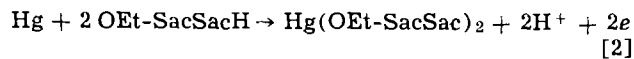
* See text.

** Extrapolated to infinite dilution.

† Markedly drop time dependent.

‡ Reduction step also exhibits a prewave at ~ 0.20 V.

The oxidation waves due to OEt-SacSacH and Hg(OEt-SacSac)₂ are sufficiently well separated to afford reasonably accurate estimates of their respective concentrations from their diffusion currents. The coulometric value of $n = 1.1 \pm 0.1$ electrons/mole of OEt-SacSacH and the identification of Hg(OEt-SacSac)₂ as the product of electrolysis defines the over-all electrode process as



The prior isolation of Hg(OEt-SacSac)₂ (9) has enabled the increase in absolute concentration of the mercury (II) complex, present at all stages of the electrolysis to be accurately monitored. Figure 4 graphically illustrates the course of the electrolysis. When all free OEt-SacSacH has been consumed, further electrolysis causes the concentration of Hg(OEt-SacSac)₂ to decay by Eq. [1]; exactly the same behavior as observed for the electrolysis of solutions of pure Hg(OEt-SacSac)₂.

Although the coulometry logically sets the n value at one electron for the over-all oxidation process it can be shown that the actual electron transfer step involves two electrons.

Comparison of the diffusion-controlled limiting current for the oxidation of mercury in the presence of OEt-SacSacH has been made with that of sodium diethyldithiocarbamate. The results were obtained under identical conditions in acetone/0.1M Et₄NClO₄ on 1.00 $\times 10^{-3}$ M solutions of these compounds at a controlled drop time of 0.32 sec. At this concentration, solutions of diethyldithiocarbamate exhibit a one-electron oxidation wave at a DME in acetone (12) in an analogous manner to its behavior in aqueous media (13, 14). The diffusion current for the oxidation of OEt-SacSacH is 2.04 times that for the one-electron process of dithiocarbamate at equal concentrations. Assuming approximately equal diffusion coefficients for these two ligands the electron transfer step with OEt-SacSacH is defined as a two-electron process. To our knowledge, diethyldithiocarbamate is the only ligand with a sufficiently well-characterized electrode process in acetone for this type of comparison.

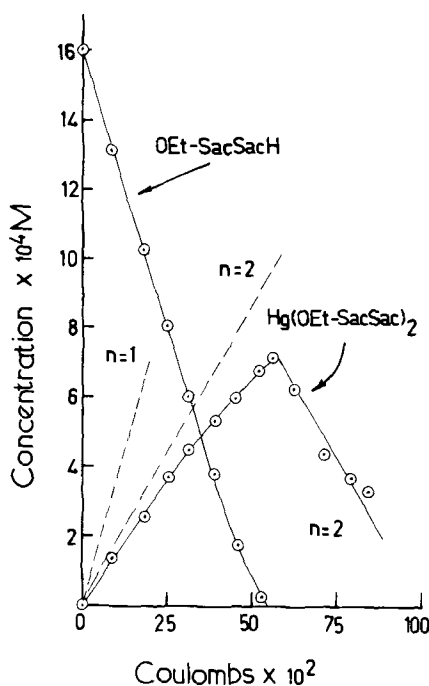
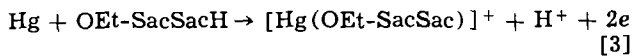


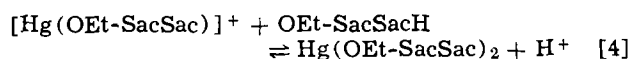
Fig. 4. Complete electrolysis of OEt-SacSacH at a mercury pool electrode. Dashed lines, labeled $n = 1$ and $n = 2$ are calculated lines per mole of compound. Circles represent experimentally determined concentrations of OEt-SacSacH and Hg(OEt-SacSac)₂.

It must be remembered that the coulometric value of $n = 1$ is obtained for the over-all process of electron transfer and coupled chemical reaction, i.e., Eq. [2]. Furthermore the gradient of the straight line plot of $\log [(i_d - i)/i]$ vs. $E_{d.e.}$ (63 mV) at a concentration $< 10^{-3}$ M and the known polarographic behavior is consistent with an irreversible $2e$ oxidation step.

In view of the two-electron transfer at the electrode, the electrolysis of solutions of OEt-SacSacH presents a very unusual set of reactions. The initial two-electron transfer (Eq. [3])



produces a cationic product which undergoes a slow reaction with the excess ligand to yield the well-characterized complex Hg(OEt-SacSac)₂ (Eq. [4]).



Obviously Reaction [4] must be slow on the polarographic time scale but is readily observed in the coulometric experiment.

As an examination of the respective $E_{1/2}$ values in Table I indicates, this newly formed, neutral complex enables mercury to be more easily oxidized than does the starting material, OEt-SacSacH. The oxidation via Hg(OEt-SacSac)₂ probably accounts for the greater proportion of current flowing toward the completion of the electrolysis. However, as this latter oxidation consumes one mole of electrons per mole of OEt-SacSacH on the coulometric time scale and is regenerative with respect to Hg(OEt-SacSac)₂ in the presence of excess ligand, this consecutive process does not perturb the coulometric results.

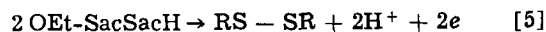
Burnett *et al.* (13) have obtained a coulometric n value of 0.83 ± 0.03 for the oxidation of mercury in the presence of [acac]⁻ and have attributed the low value to the formation of [Hg(acac)₃]⁻. Addition of OEt-SacSacH to solutions of Hg(OEt-SacSac)₂ does not appreciably alter the oxidation potential of the complex, suggesting that this system is not complicated by increased co-ordination of the Hg(II) ion to give [Hg(OEt-SacSac)₃]⁻.

The deviation of the coulometric results from $n = 1$ for the consumption of OEt-SacSacH and $n = 2$ for Hg(OEt-SacSac)₂ could be rationalized if Eq. [4] is represented as an equilibrium with an equilibrium constant

$$K_e = \frac{[\text{Hg(OEt-SacSac)}_2][\text{H}^+]}{[\text{OEt-SacSacH}][\text{Hg(OEt-SacSac)}^+]}$$

If this postulated equilibrium step is correct, it follows that the continuing generation of final products and the irreversible electrolytic depletion of starting materials would lead to a slight curvature of the electrolysis plots.

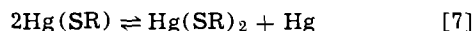
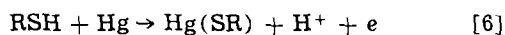
There is no evidence to suggest that any significant quantity of the ligand is oxidized to a disulfide dimer (Eq. [5])



Indeed, in the early stages of the coulometric oxidation, the increase in concentration of Hg(OEt-SacSac)₂ is almost that expected from the decrease in ligand concentration, providing positive evidence against the formation of the dimer. The coulometry is adequately rationalized by the consecutive and concurrent reactions described by Eq. [1], [3], and [4] assuming a slight acid dissociation of Hg(OEt-SacSac)₂.

Although the anodic dissolution of mercury is facilitated by the following compounds in the order: Hg(OEt-SacSac)₂ > OEt-SacSacH >> acetone, the irreversibility of the electrode process for the first two at least, makes it impossible to draw any conclusions of thermodynamic significance from this fact.

The oxidation process for dithiocarbamate solutions at the DME is summarized as (13, 14)



This process differs from that for OEt-SacSacH as the initial transfer step involves only one electron. The electron transfer is followed by a rapid disproportionation with the over-all process being reversible. This oxidation process appears to be operative for a range of thio complexes (16-19). Although Eq. [6] and [7] give the same over-all electrode reactions as OEt-SacSacH, the stability of $[\text{Hg}(\text{OEt-SacSac})]^+$ and the two-electron transfer as elucidated by the diffusion current ratios and electrode characteristics safely dismisses this alternative process in the present work.

Electrocapillary curves.—The electrocapillary curve (drop time vs. potential) has been redetermined (20) for the acetone/0.1M Et_4NClO_4 system (Fig. 5). Due to the sensitive nature of these measurements and the high volatility of the solvent, solutions were not deoxygenated. The well-defined curve exhibits an electrocapillary maximum at about 0 volt vs. Ag|AgCl. The addition of ($1.84 \times 10^{-2}\text{M}$) the surface active compound, OEt-SacSacH markedly decreases the surface tension, with a substantial reduction in drop time at potentials more positive than -0.5V . The point where this curve joins the curve for acetone/ Et_4NClO_4 containing no surface active compound ($\sim -0.6\text{V}$), represents the negative adsorption-desorption potential of the ligand. The large shift in the electrocapillary maximum is not unusual for thio compounds, e.g., $\text{NaClO}_4/\text{S}^{2-}$, -0.37V (21); $\text{CH}_3\text{COONH}_4$, KNO_3 /diethyldithiocarbamate, -0.3V , estimated from data in Ref. (13).

Not unexpectedly, the positive branch of the curve exhibits complications over the potential region defined by the oxidation process (Fig. 5). Glutathione (22) and diethyldithiocarbamate (13) exhibit similar behavior. The present effect can be attributed to many causes, e.g., a lowering of the concentration of OEt-SacSacH at the electrode surface due to the oxidation process or a different surface activity of the product of oxidation. Unfortunately, the data is insufficiently informative to provide a completely definitive explanation.

Parallel experiments with OEt-SacSacH and $\text{Zn}(\text{NO}_3)_2 \cdot 6\text{H}_2\text{O}$ in acetone/0.1M Et_4NClO_4 (11) indi-

cate that the nitrate anion acts as a proton acceptor with the subsequent formation of $\text{Zn}(\text{OEt-SacSac})_2$. With $\text{Zn}(\text{ClO}_4)_2 \cdot 6\text{H}_2\text{O}$ however, neither the perchlorate anion nor the acetone accepts the proton, and polarographic studies show the ligand does not chelate to Zn(II) ions in this medium. From this evidence it seems unlikely that the ligand loses its proton on adsorption to the DME unless the adsorbed anionic form of the ligand confers an unexpectedly large stabilization over the adsorbed neutral ligand.

A-C polarography and desorption wave.—Preliminary a-c studies on OEt-SacSacH in acetone at concentrations $< 10^{-3}\text{M}$ show three peaks corresponding to the oxidation process ($E_s = 0.29\text{V}$), reduction (-1.28V), and a presumed tensammetric or desorption wave (-0.54V). On increasing concentration of OEt-SacSacH, the a-c oxidation peak becomes quite complex as expected from the adsorption and related inhibition phenomena to be discussed in further detail below.

Extended deoxygenation of solutions of OEt-SacSacH indicates that the small wave present in the d-c polarograph at -0.59V is not due to dissolved oxygen. The wave persists in separate preparations of OEt-SacSacH and is not believed to be an impurity, but is assumed to be the result of the desorption of the ligand on proceeding to more negative potentials. The kink reflects the difference in capacity of the double layer at potentials where the mercury surface is covered by the surface-active ligand and at those where the normal electrical double layer exists (23). The potential of the kink is in agreement with the negative adsorption-desorption potential obtained from the electrocapillary (-0.6V) and a-c (-0.5V) studies.

Further aspects of adsorption.—As well as the adsorption phenomena exhibited by the protonated ligand (or less likely its deprotonated form) a further concentration dependent adsorption is operative at the DME on oxidation of the mercury in the presence of the ligand.

At low concentrations ($< 1 \times 10^{-3}\text{M}$) the anodic wave exists as a well-defined, although irreversible, single wave at a drop time of 2.00 sec. The $E_{1/2}$ value of the wave shifts cathodically on decreasing concentration of OEt-SacSacH to yield an extrapolated $E_{1/2}$ value of $+0.226\text{V}$ vs. Ag/AgCl at infinite dilution. On increasing the concentration of OEt-SacSacH the diffusion current increases monotonically up to a concentration of $\sim 1 \times 10^{-3}\text{M}$. On further increasing the concentration the limiting current of this first wave (i_{d1}) remains approximately constant. A second wave with an $E_{1/2}$ slightly more anodic than that of the first wave is generated at concentrations $> 1 \times 10^{-3}\text{M}$.

The $E_{1/2}$ of this second wave also moves anodically on increasing the concentration of OEt-SacSacH. Unfortunately, superposition of the mercury oxidation wave on this second wave renders evaluation of its limiting current (i_{d2}) unreliable at concentrations $> 3 \times 10^{-3}\text{M}$. The limiting current for the first oxidation wave is easily monitored to high concentrations and remains relatively constant, cf., $11 \mu\text{A}$ at $1.3 \times 10^{-2}\text{M}$. Similar behavior has been observed from the sulfide anion in aqueous media (24-29) and diethyldithiocarbamate (13, 14).

It has been suggested that the oxidative behavior of the sulfide anion may be due to the presence of both S^{2-} and SH^- in solution (24), although an alternative explanation involving adsorption of oxidation product (HgS) at the DME in the form of a monolayer and 3-D crystals on increasing concentration of S^{2-} leading to inhibition of further oxidation accounts for the three waves reported (25-29). The recent observations of a fourth wave for the sulfide system (30) may require both theories for complete understanding.

For OEt-SacSacH, the constancy of the limiting current for the first wave at concentrations $> 10^{-3}\text{M}$

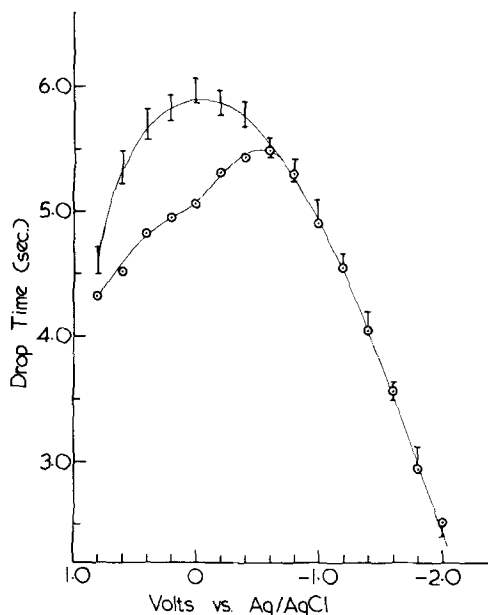


Fig. 5. Electrocapillary curves of (□) acetone/0.1M Et_4NClO_4 and (○) acetone/0.1M $\text{Et}_4\text{NClO}_4 + 1.84 \times 10^{-2}\text{M}$ OEt-SacSacH.

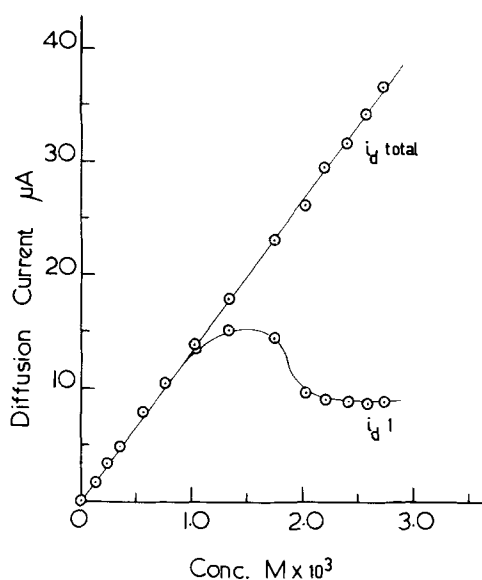


Fig. 6. Concentration dependence of limiting currents for the oxidation wave of Hg in the presence of OEt-SacSacH (drop time 2.00 sec).

(Fig. 6, drop time of 2.00 sec) suggests that the electrode surface is probably covered by adsorbed compound at all concentrations greater than this. It is apparent from the same figure that up to a concentration of $10^{-3}M$ the limiting current described by the first wave is diffusion controlled. At concentrations $> 10^{-3}M$ the sum of i_{d1} and i_{d2} , i.e., $i_{d \text{ total}}$, indicates the total limiting current is diffusion controlled (Fig. 6) although the shift in potential of the second wave indicates that the oxidation is more difficult to accomplish at the covered electrode. Julien and Bernard (29) have attributed the corresponding shift of $E_{1/2}$ to more positive potentials with increasing concentration in the S= example to the ohmic resistance of the adsorbed film, an explanation which is not inconsistent with the present findings for OEt-SacSacH.

Although this inhibition phenomena has not been reported for the thio compounds; β -mercaptopropionic acid (18), ethylthioglycolate (19), methoxyethylthioglycolate (16), thiolactic acid (17), or glutathione (22), it seems possible to the present authors that this phenomenon may be evident with these compounds at greater concentrations than those reported.

Current-time curves (Fig. 7) on ~ 8 sec drops have been drawn out with the Metrohm recorder at selected potentials across the oxidation waves exhibited by solutions of OEt-SacSacH. Unfortunately limited recorder response has not enabled the point of zero current and zero time to be drawn out. This has resulted in some curves (0.50-0.65V) appearing to present negative currents. The curves dramatically illus-

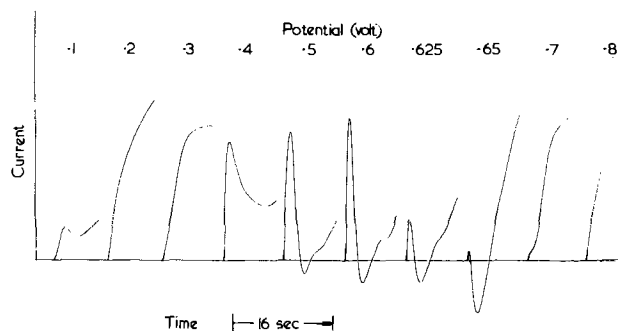


Fig. 7. Current-drop time curves shown at various potentials across the oxidation wave (OEt-SacSacH). Current scale not the same at all potentials.

trate the adsorption at the DME with the classical initial rise of current at all potentials and the subsequent fall at potentials where adsorption inhibits further oxidation, i.e., 0.40-0.65V. These curves have parallels in the sulfide examples (29).

From these curves it would appear that at shorter drop times (induced by premature mechanical disengagement of slow growing drops) the abbreviated current-time curves should be less influenced by adsorption phenomena and as expected, the resulting over-all polarographic wave shows less perturbation from adsorption (cf., Fig. 2 and 8). However, other considerations are also important here as the limiting current of the first wave (i_{d1}) actually increases slightly with decreasing drop time.

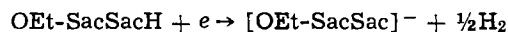
At concentrations $> 10^{-3}M$ the oxidation wave has a marked dependence on drop time; for example, the wave showing clearly 50% contributions from i_{d1} and i_{d2} at a natural drop time of 2.57 sec becomes a slightly distorted single wave at a rapid drop time of 0.16 sec (Fig. 2). The effect of the rapid drop technique on the recording of the oxidation waves at increasing concentration of OEt-SacSacH is illustrated in Fig. 2.

Undoubtedly the electrode process is less complicated at short drop times and the value of the rapid polarographic techniques in studying electrode processes complicated by adsorption phenomena is clearly illustrated.

Reduction.—The reduction wave ($E_{1/2} = -1.43V$) for the ligand conforms to a linear \sqrt{h} vs. i_d plot indicating that the limiting current is diffusion controlled. From the electrocapillary and current-drop time curves it is apparent that the reduction occurs with the ligand in a nonadsorbed state.

The $E_{1/4} - E_{3/4}$ value of 68 mV and the a-c polarography indicates the electrode process exhibits kinetic complications. Unlike the product of the oxidation process, the product of reduction has not been isolated or characterized. However, the following observations have enabled constructive suggestions to be made on this process.

As the oxidation step involves a two-electron transfer, the ratio of diffusion currents for the oxidation and reduction waves (2.2:1) at a controlled drop time (0.32 sec) defines the reduction as a one-electron step. This dismisses the possibility of radical dimerization (31, 32) as observed with dibenzoylmethane (33) ($n = 0.5$) and suggests reduction involving the evolution of hydrogen



This is the operative process with acetylacetonate (acacH) (34). The complicating keto-enol conversion observed for the reduction of acacH is not relevant for OEt-SacSacH as this compound exists entirely in

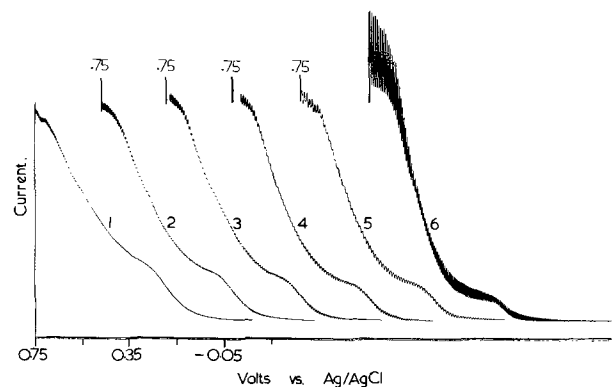


Fig. 8. Drop time dependence of oxidation wave (OEt-SacSacH $\sim 10^{-2}M$). Drop time: 1, 0.16 sec; 2, 0.20 sec; 3, 0.24 sec; 4, 0.28 sec; 5, 0.32 sec; 6, 0.95 sec. All curves run $+0.75$ to $-0.05V$ vs. Ag|AgCl.

the reactive thio-enol form. Addition of small quantities of 40% tetrabutylammonium hydroxide deprotonates OEt-SacSacH to [OEt-SacSac]⁻, and as expected from the suggested reduction mechanism, the reduction wave vanishes completely.

The reduction of free H⁺ ions in acetone/Et₄NClO₄ has been examined by addition of small quantities of 60% HClO₄. The E_{1/2} value of the well-defined reduction wave is very dependent on water content, moving to more negative potentials on increasing concentrations of water. Hence the least negative E_{1/2} obtained, -0.88V can only be regarded as a lower limit for this reduction potential. Molecules containing an X-H unit which can be reduced to X⁻ and H₂, fall at more negative potentials, e.g., H₂O and acacH are reduced toward the potential limit of the solvent, -2.2V. Although E_{1/2} values for these nonreversible reductions may be misleading, it is pleasing to note that the proposed reduction of the S-H unit falls at a more negative potential than that of free H⁺ ions.

O-Ethylthioacetate.—Finally it is of interest to compare the polarographic behavior, in acetone, of OEt-SacSacH (I) with that of O-ethylthioacetate (II) (Table I). The latter compound exhibits both oxidative and reductive activity toward the potential limits of the solvent. The oxidation wave, superimposed on the foot of the mercury oxidation wave, appears to have an E_{1/2} of approximately +0.7V although it is not feasible to accurately evaluate polarographic parameters. The reduction step at E_{1/2} = -2.08V vs. Ag|AgCl has an (E_{1/4}-E_{3/4}) value of 54 mV. A solution of the compound slowly coats the mercury pool with a dark decomposition or reaction product. Although the nature of the reduction product is not completely understood for either compound it is readily apparent that the thiol function of OEt-SacSacH is more amenable to reduction. It is presumed that the resonance stabilized mercury complex formation affords an easier oxidation of the mercury in solutions of OEt-SacSacH than O-ethylthioacetate where the product of oxidation cannot achieve such stabilization.

Acknowledgment

One of us (A. R. H.) gratefully thanks the C.S.I.R.O. for a Postgraduate Studentship.

Manuscript submitted Feb. 25, 1972; revised manuscript received May 15, 1972.

Any discussion of this paper will appear in a Discussion Section to be published in the June 1973 JOURNAL.

REFERENCES

- G. N. Schrauzer, *Accounts Chem. Res.*, **2**, 72 (1969).
- R. L. Martin and I. M. Stewart, *Nature*, **510**, 522 (1966).
- C. G. Barraclough, R. L. Martin, and I. M. Stewart, *Australian J. Chem.*, **22**, 891 (1969).
- G. A. Heath and R. L. Martin, *Chem. Comm.*, 951 (1969).
- G. A. Heath and R. L. Martin, *Australian J. Chem.*, **23**, 1721 (1970).
- G. A. Heath and R. L. Martin, *ibid.*, **24**, 2061 (1971).
- A. M. Bond, G. A. Heath, and R. L. Martin, *This Journal*, **117**, 1362 (1970).
- A. M. Bond, G. A. Heath, and R. L. Martin, *Inorg. Chem.*, **10**, 2026 (1971).
- A. R. Hendrickson and R. L. Martin, *Australian J. Chem.*, **5**, 257 (1972).
- J. R. Coetzee and W. S. Siao, *Inorg. Chem.*, **2**, 14 (1963).
- A. M. Bond, A. R. Hendrickson, and R. L. Martin, To be published.
- A. M. Bond, A. T. Casey, and J. R. Thackeray, Unpublished results, University of Melbourne.
- W. Stricks and S. K. Chakravarti, *Anal. Chem.*, **34**, 508 (1962).
- D. J. Halls, A. Townshend, and P. Zuman, *Anal. Chim. Acta*, **41**, 51 (1968).
- J. N. Burnett, L. K. Hiller, Jr., and R. W. Murray, *This Journal*, **117**, 1028 (1970).
- R. S. Saxena and R. Singh, *Ind. J. Chem.*, **8**, 448 (1970).
- R. S. Saxena, P. Singh, and M. L. Mittal, *ibid.*, **7**, 1149 (1969).
- R. S. Saxena and K. C. Gupta, *J. Ind. Chem. Soc.*, **47**, 101 (1970).
- R. S. Saxena and U. S. Chaturvedi, *Ind. J. Chem.*, **9**, 453 (1971).
- A. M. Bond, *This Journal*, **118**, 1588 (1971).
- A. Frumkin, *Ergels. exkat. Naturw.*, **7**, 254 (1928).
- W. Stricks and I. M. Kolthoff, *J. Am. Chem. Soc.*, **74**, 4646 (1952).
- B. Breyer and H. H. Bauer, "Chemical Analysis," Vol. 13 "Alternating Current Polarography and Tensammetry," p. 273, Interscience Publishers, (1963).
- S. Zdanov and B. Kiselev in, "Polarography, 1964," Vol. 1, p. 473, G. J. Hills, Editor, London (1966).
- J. Revenda, *Collection Czech. Chem. Commun.*, **6**, 453 (1934).
- I. M. Kolthoff and C. S. Miller, *J. Am. Chem. Soc.*, **63**, 1405 (1941).
- G. Duyckaerts, *Bull. Soc. Roy. Sci., Liège*, **17**, 313 (1948).
- A. Trifonov, *Izv. him. inst. Bulg. A.N.*, **4**, 21 (1956).
- L. Julien and M. L. Bernard, *Rev. Chim. Miner.*, **5**, 521 (1968).
- A. M. Bond and D. R. Canterford, Unpublished results, University of Melbourne (1971).
- R. Pasternak, *Helv. Chim. Acta*, **31**, 753 (1948).
- G. Semerano and A. Chisini, *Gazz. Chim. Ital.*, **66**, 504 (1936).
- R. C. Buchta and D. H. Evans, *Anal. Chem.*, **40**, 2181 (1968).
- T. E. Neal and R. W. Murray, *ibid.*, **42**, 1654 (1970).

Protonation of the Anion Radicals of 2,5-Substituted Oxazoles and Oxadiazoles with Hydroquinone in *N,N*-Dimethylformamide

S. L. Smith, L. D. Cook, and J. W. Rogers

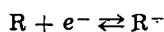
Department of Chemistry, Midwestern University, Wichita Falls, Texas 76308

ABSTRACT

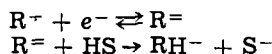
The influence of the proton donor hydroquinone on the polarographic reduction of a series of phenyl and naphthyl-substituted oxazoles and oxadiazoles in DMF has been studied. Cyclic voltammetric data taken at potentials of the first of two polarographic waves at a hanging mercury drop electrode suggest that the oxadiazoles and 2-naphthyl-substituted oxazoles are reduced via a two-electron ECE process at large proton donor to compound ratios. Phenyl-substituted oxazoles are reduced in only one polarographic wave with an n apparent of 4.0 at high proton donor to compound ratios.

The electrode reduction mechanisms of representative 2,5-aromatic-substituted oxazoles and oxadiazoles in *N,N*-dimethylformamide (DMF) were recently presented (1, 2). The compounds 2,5-diphenyloxazole and 2-(1-naphthyl)-5-phenyloxazole are reduced in *N,N*-dimethylformamide in two polarographic steps according to the mechanism

First wave:



Second wave:

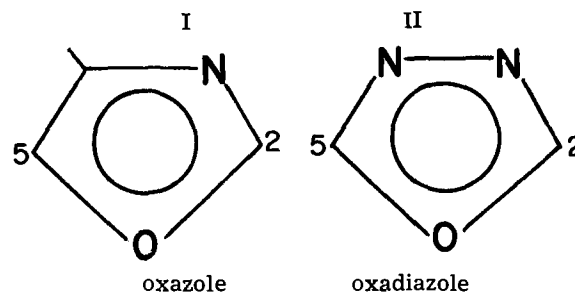


where HS is solvent or other weak proton donor. The anion radical, R^- , and protonated dianion, RH^- , are long-lived in the absence of efficient proton donors. Similarly substituted oxadiazoles are reduced accordingly with an additional electrochemical step at potentials near the solvent-supporting electrolyte potential limit (2).

The effects of proton donors on the reduction processes were studied to confirm the postulated mechanisms in DMF (1, 2). The polarographic current plateaus of the 2-phenyl-substituted oxazoles appeared to vary with added proton donors in a manner similar to the polarographic processes of most aromatic hydrocarbons with both plateaus coalescing to one at high proton donor to compound ratios (1, 3, 4). The influence of added proton donors on the polarographic reduction of oxadiazoles is in general uniform, but different from the oxazole behavior and previously reported results of studies on the electrochemical reduction of aromatic hydrocarbons in aprotic media containing controlled quantities of proton donors (2-5). The polarographic data previously presented suggested that the oxadiazole π -radical produced by a reversible one-electron process is either, not readily protonated in the presence of water and hydroquinone (HQ), or protonated but not reduced further at potentials near the first $E_{1/2}$ of the parent compound (2, 3). These observations are not consistent with theory and suggested the need for a more systematic and thorough investigation of the reactions of electrochemically produced intermediates of oxazole and oxadiazole heterocyclics with proton donors in aprotic media. The importance of the role of proton donor species on the electroreduction mechanism of aromatic hydrocarbons has been discussed in detail by Mark and others (6, 7). The controlled protonation of heterocyclic anions has not been treated in detail.

Key words: anion, heterocyclic, protonation.

We wish now to report studies in which polarographic and cyclic voltammetric techniques were employed to investigate the production and protonation of the anion radicals of 2,5-diphenyloxazole, 2-(1-naphthyl)-5-phenyloxazole, 2-(4-fluorophenyl)-5-phenyloxazole, 2-(3-methoxyphenyl)-5-phenyloxazole, 2-(4-methoxyphenyl)-5-(1-naphthyl) oxadiazole, 2-(4-methoxyphenyl)-5-(2-naphthyl) oxadiazole, 2,5-diphenyloxadiazole, 2-(4-fluorophenyl)-5-phenyloxadiazole and 2-(4-fluorophenyl)-5-(2-naphthyl) oxadiazole (note structures I & II) in DMF containing controlled quantities of hydroquinone (HQ). A small portion of the data presented is repetitious, but its inclusion with new data clarifies salient points. The test compounds were chosen to illustrate the influence of 2,5-substituent variations on the reactivity of the anion produced at the first polarographic plateau of each compound.



The complete study included electrochemical measurements in DMF and acetonitrile, both containing controlled quantities of water and HQ. Both substances functioned most effectively as proton donors in acetonitrile. Water functioned as a very weak donor in DMF. These results and the fact that HQ is an effective donor and electroinactive in DMF have been noted previously (5, 6). Although the influence of a set amount of proton donor varied with solvent-donor combinations the general electrochemical behavior (number and type of reactions) of the test materials was not altered. Consequently, we have chosen to report data only from studies in DMF-HQ media.

Polarographic Data

The compound 2,5-diphenyloxazole exhibits two diffusion-controlled, one-electron polarographic waves in dry DMF solvent (Table I, Fig. 1). The currents of both plateaus are enhanced equally by a factor of 40% when the test solution is made 1.75 mM in HQ. The current increase continues with additionally added HQ until at 5.25 mM HQ the first wave exhibits an n

apparent¹ of 2.0 and is kinetically controlled.² The second plateau also exhibits an n apparent of 2.0 but is diffusion controlled. The current changes are accompanied by a +20 mV shift in the $E_{1/2}$ of the first wave and a +60 mV shift of the second. Further additions of HQ causes the first wave to grow at the expense of the second with the total current of both waves remaining constant (Fig. 1). Addition of enough HQ to bring the test solution to 50 mM effects limiting behavior with only one diffusion-controlled polarographic wave observed at $-2.10V$ vs. SCE with an n apparent of 4.0, (Fig. 1 and 2).

The n apparent of the first wave of 2,5-diphenyloxazole, given as a function of added HQ in Fig. 2, summarizes the electroactivity of the compound in the presence of various amounts of HQ. The behavior is similar to that of alternant aromatic hydrocarbons (3, 5, 6).

Addition of inductively releasing or withdrawing substituents to the phenyl ring at the oxazole 2-position shift $E_{1/2}$ values but effect no significant changes in the electrochemical behavior of the heterocyclic in pure DMF or DMF-HQ mixtures (Table I). Polarographic data given in Fig. 2 show that the n apparent of the first polarographic wave of 2-(3-methoxyphenyl)-5-phenyloxazole and 2-(4-fluorophenyl)-5-phenyloxazole varies with added HQ in the same manner as 2,5-diphenyloxazole. The second polarographic wave of 2-(4-fluorophenyl)-5-phenyloxazole exhibits a diffusion current corresponding to an n apparent of 2.0 in dry DMF. The controlled addition of HQ enhances the diffusion currents of both plateaus. At concentrations of HQ greater than 5.25 mM the first wave grows at the expense of the second with increasing amounts of HQ. One wave corresponding to a 4-electron diffusion-controlled process and observed at -2.06 vs. SCE represents limiting behavior. Further additions of HQ do not alter this limiting behavior. As with 2,5-diphenyloxazole and 2-(3-methoxyphenyl)-5-phenyloxazole, addition of HQ influences the extent of reduction at each plateau with the end product of both waves (n apparent of 4.0) not altered by the addition of any quantity of HQ greater than 5.25 mM.

Substitution of a naphthyl group at the heterocyclic 2-position does not significantly alter the electrochemical behavior of the oxazole ring in dry DMF (Fig. 3, Table I). The anodic shift in the $E_{1/2}$ of both plateaus of 2-(1-naphthyl)-5-phenyloxazole relative to those of 2,5-diphenyloxazole in dry DMF is expected (8). The compound does however exhibit a polarographic behavior in the presence of HQ significantly different from that of the other test oxazoles (Fig. 3). The first polarographic wave of the compound does not demonstrate the same reactivity to small quantities of added proton donor as that of the previously discussed oxa-

¹ n apparent = i/i_d where i is the polarographic limiting current in the DMF-HQ system, and i_d is the diffusion current of the first wave of the compound in dry DMF.

² The plateau current is independent of the corrected mercury head height above the dme.

Table I. Polarographic half wave potentials in DMF

Compound	$-E_{1/2}(1)$	$-E_{1/2}(2)$	$-E_{1/2}(3)$
2,5-diphenyloxazole	2.16	2.52	—
2-(3-methoxyphenyl)-5-phenyloxazole	2.06	2.37	—
2-(4-fluorophenyl)-5-phenyloxazole	2.13	2.48	—
2-(1-naphthyl)-5-phenyloxazole	1.86	2.24	—
2,5-diphenyloxadiazole	1.95	2.34	2.63
2-(4-fluorophenyl)-5-phenyloxadiazole	1.96	2.36	2.64
2-(4-fluorophenyl)-5-(2-naphthyl)oxadiazole	1.81	2.16	2.48
2-(4-methoxyphenyl)-5-(2-naphthyl)oxadiazole	1.78	2.22	— ^(a)
2-(4-methoxyphenyl)-5-(2-naphthyl)oxadiazole	1.75	2.18	— ^(a)

^(a) Third wave visible near solvent-supporting electrolyte background.

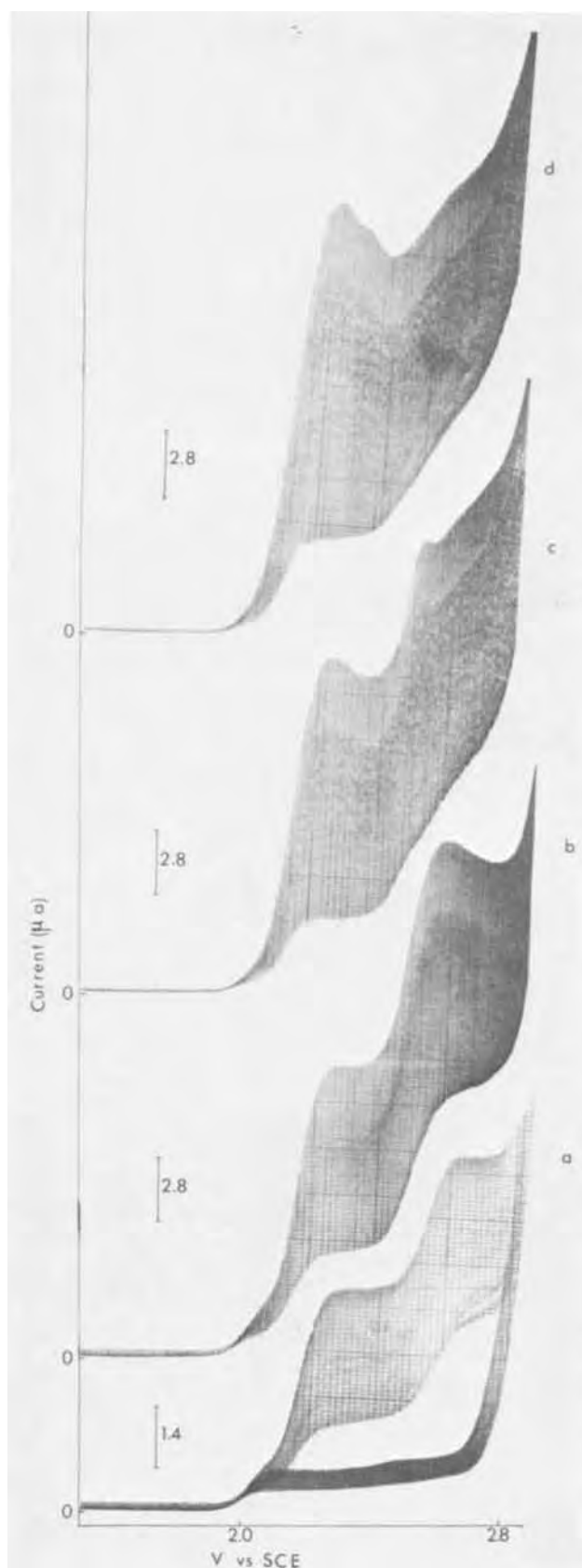


Fig. 1. Polarograms of 2,5-diphenyloxazole in DMF containing (a) no HQ, lower curve is supporting electrolyte polarogram run at current sensitivity 10 times that of polarograms of 2,5-diphenyloxazole; (b) 1.75 mM HQ; (c) 17.5 mM HQ; and (d) 52.5 mM HQ.

zoles (Fig. 2). The current of this plateau exhibits kinetic complications and is enhanced slightly by 5.25 mM HQ (Fig. 3). It reaches a limiting value corresponding to a 2-electron diffusion-controlled process at

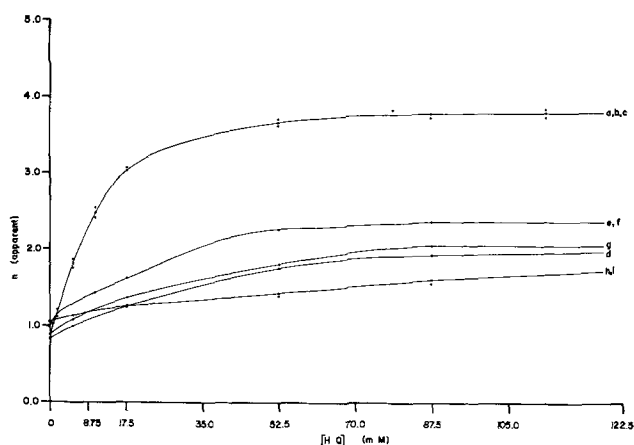


Fig. 2. The polarographic n apparent in DMF vs. the millimolar concentration of added HQ for (a) 2,5-diphenyloxazole, (b) 2-(4-fluorophenyl)-5-phenyloxazole, (c) 2-(3-methoxyphenyl)-5-phenyloxazole, (d) 2-(1-naphthyl)-5-phenyloxazole, (e) 2,5-diphenyloxadiazole (f) 2-(4-fluorophenyl)-5-phenyloxadiazole, (g) 2-(4-fluorophenyl)-5-(2-naphthyl) oxadiazole, (h) 2-(4-methoxyphenyl)-5-(2-naphthyl) oxadiazole, and (i) 2-(4-methoxyphenyl)-5-(1-naphthyl) oxadiazole.

HQ concentrations greater than 50.0 mM. The wave does not coalesce with those more cathodic at any proton donor to oxazole ratios investigated (Fig. 3). The current of the second wave is enhanced to a greater extent than that of the first by the addition of small quantities of HQ (Fig. 3). At HQ concentrations as low as 1.75 mM a third wave, kinetically controlled, is observed with an $E_{1/2}$ of $-2.47V$ vs. SCE (Fig. 3). The second diffusion plateau along with the kinetic current are greatly enhanced with further additions of HQ (Fig. 3). A significant anodic shift of the kinetic-controlled wave accompanies the current growth with added HQ (Fig. 3). At HQ concentrations near 17.5 mM the second current plateau and the kinetic current coalesce into one diffusion controlled polarographic wave with current corresponding to an n apparent of 4.0 (Fig. 3). The reduction of the naphthyl-substituted oxazole at high proton donor concentrations requires a total of 6 electrons per molecule.

All 2,5-aromatic substituted oxadiazoles exhibited three polarographic waves in dry DMF (Table I, Fig. 4). A reversible electron transfer followed by a rapid protonation of the dianion is the process responsible for the second wave. The most cathodic of the three waves results from a multielectron ring opening reaction (2). The two most cathodic waves are quite sensitive to small quantities of added HQ and in general coalesce to one diffusion-controlled multielectron step at HQ concentrations greater than 5.25 mM (Fig. 4).

An interesting feature of the polarography of the oxadiazoles is the relative insensitivity of the first polarographic wave to added HQ (Fig. 2 and 4). This wave, representing the reversible production of an anion π -radical of each compound in dry DMF, exhibits kinetic complications at HQ concentrations as low as 5.25 mM. However, a maximum n apparent of approximately 2.0 and diffusion-controlled behavior is only approached in experiments conducted in DMF with large concentrations of HQ (Fig. 2). The rate of approach to the limiting behavior, as a function of added HQ, is dependent upon the structure of the 2,5-substituents (Fig. 2). The first wave of the compound 2,5-diphenyloxadiazole exhibits the greatest sensitivity to added HQ, showing kinetic complications at 5.25 mM HQ and approaching a limiting n apparent of 2.1 at HQ concentrations ten times greater (Fig. 2). Substitution of fluorine on the 2-phenyl substituent did not influence the electroactivity of the compounds (Fig. 2). Replacement of the 5-phenyl with a naphthyl function

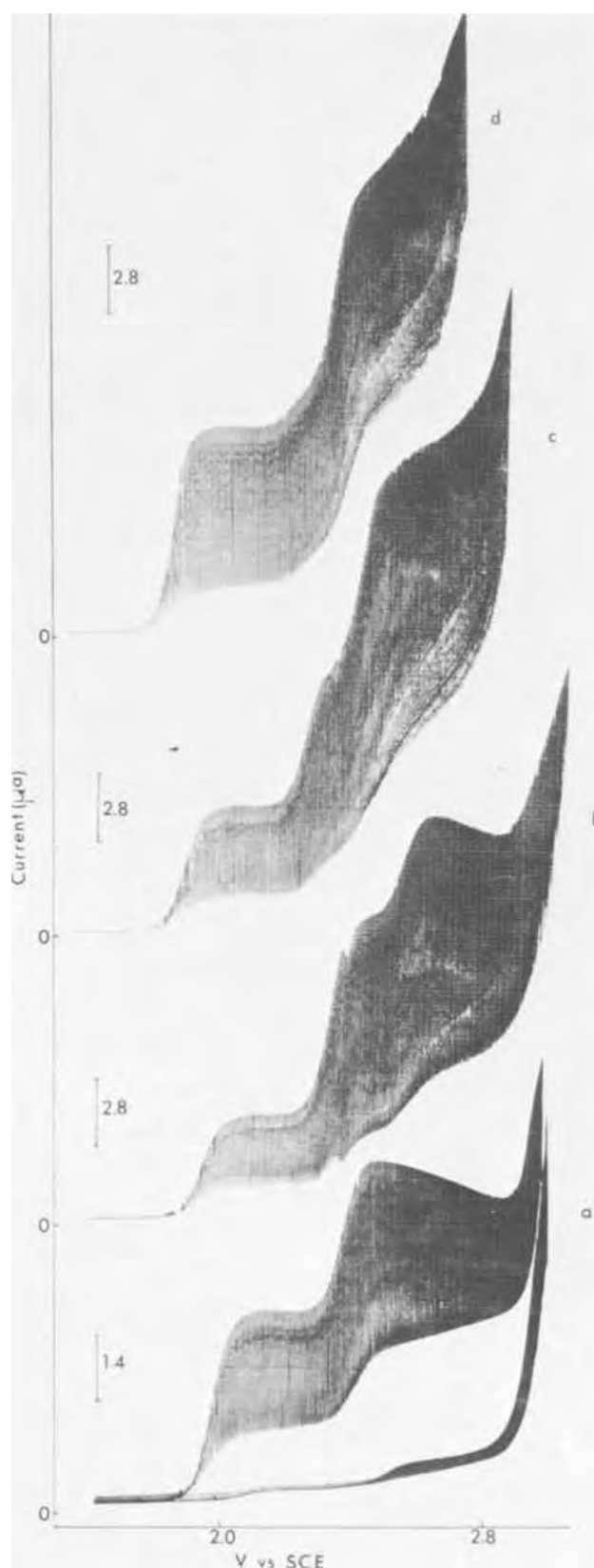


Fig. 3. Polarograms of 2-(1-naphthyl)-5-phenyloxazole in DMF containing (a) no HQ, lower curve is supporting electrolyte polarogram run at current sensitivity 10 times that of polarograms of 2-(1-naphthyl)-5-phenyloxazole; (b) 5.25 mM HQ; (c) 17.5 mM HQ; and (d) 87.5 mM HQ.

(α or β) diminished the sensitivity of the first wave to added proton donor (Fig. 2). The change in behavior is not as dramatic as that resulting from the same substitution at the oxazole 2-position (Fig. 2). The

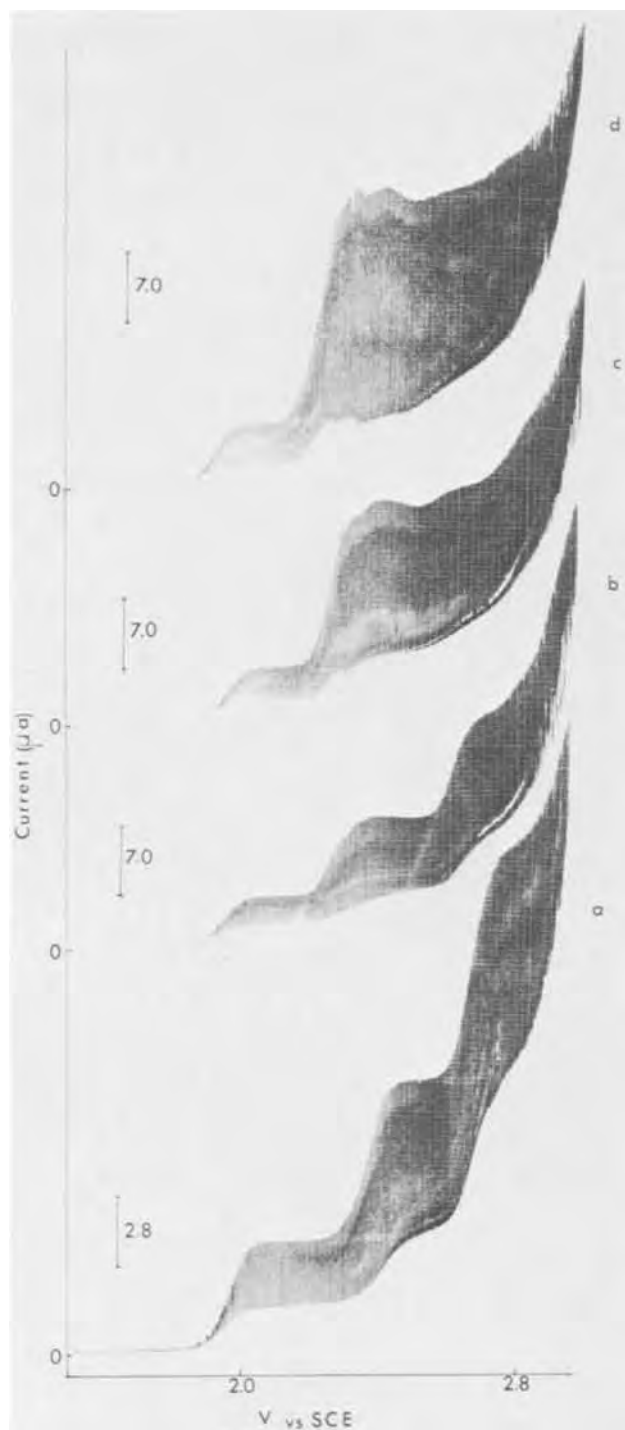


Fig. 4. Polarograms of 2,5-diphenyloxadiazole in DMF containing (a) no HQ, (b) 1.75 mM HQ, (c) 5.25 mM HQ, and (d) 52.5 mM HQ.

first polarographic wave of the compound 2-(4-methoxyphenyl)-5-(2-naphthyl) oxadiazole exhibits the least sensitivity of all compounds to added HQ, approaching a limiting n apparent of 2.0 only at concentrations of HQ near 120 mM (Fig. 2).

Cyclic Voltammetric Data

Cyclic voltammetry provides an excellent means by which the homogenous reactions of radical intermediates may be qualitatively studied and compared. To investigate the nature of the processes responsible for the behavior of the most anodic polarographic wave of each compound, cyclic voltammograms of compounds representative of four of the curves shown in Fig. 2 were recorded at a hanging mercury drop electrode (HMDE). The experiments were conducted at

several n apparent values of the first polarographic wave of each compound. Complete cyclic voltammetric data for the first wave of 2,5-diphenyloxazole, 2,5-diphenyloxadiazole, 2-(1-naphthyl)-5-phenyloxazole and 2-(4-methoxyphenyl)-5-(2-naphthyl) oxadiazole are given in Table II as a function of amount of added proton donor.

Cyclic voltammetric data confirm that each of the compounds studied are reversibly reduced to a stable anion radical at potentials cathodic of the first polarographic wave in DMF with no added HQ (Table II). The first cyclic wave of 2,5-diphenyloxazole recorded at 3.5 mM HQ reflects kinetic complications (Fig. 5 and 6). The wave broadens and the ratio of anodic to cathodic current, $(i_p)_a/(i_p)_c$, diminishes with decreas-

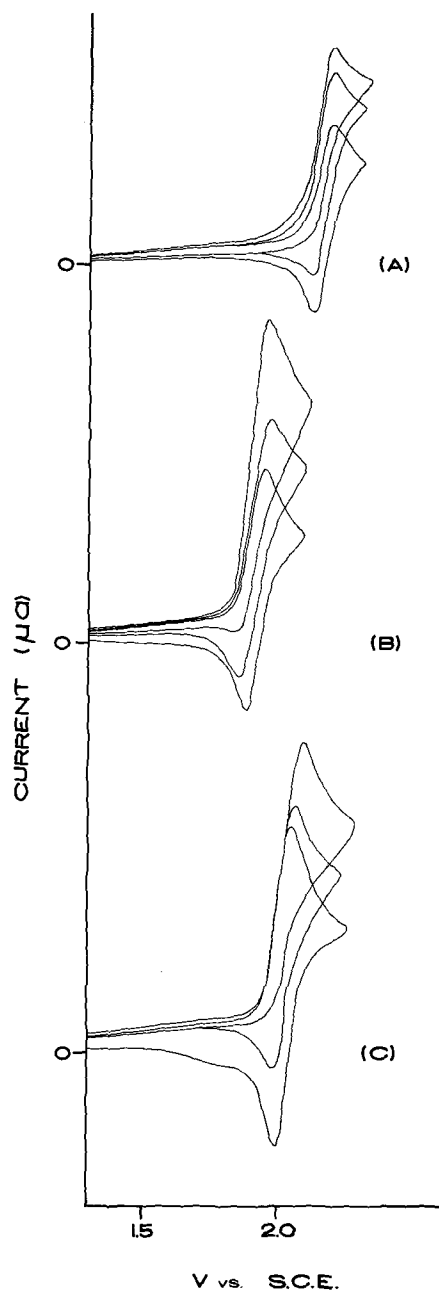


Fig. 5. (a) Cyclic voltammograms of 2,5-diphenyloxazole recorded at 10.56 V/min at a HMDE in DMF containing 0.0, 3.5, and 6.0 mM HQ. (b) Cyclic voltammograms of 2-(1-naphthyl)-5-phenyloxazole recorded at 10.00 V/min at a HMDE in DMF containing 0.0, 32.5, and 105 mM HQ. (c) Cyclic voltammograms of 2,5-diphenyloxadiazole recorded at 10.80 V/min at a HMDE in DMF containing 0.0, 21.5, and 105 mM HQ. The switching potential E_s is 200 mV past E_p and the drop size uniform for all voltammograms.

ing potential sweep rate (v) (Table II, Fig. 6). The current function, $(i_p)_c/v^{1/2}$, varies slightly at larger sweep rates and greater at the lower rates, increasing with decreasing v (Table II). A 10 mV anodic shift of the cathodic peak potential is observed for a tenfold increase in the potential sweep rate (Table II, Fig. 6). No anodic current is observed on the reverse going segment of cyclic experiments conducted in 6.0

Table II. Cyclic voltammetric data

2,5-diphenyloxazole						
HQ (mM)	$n^{(a)}$	v (V/min)	$-(E_p)_c$ (V)	$(E_p)_c - (E_p)_a$ (mV)	$(i_p)_a / (i_p)_c^{(b)}$	$(i_p)_c / V^{1/2}$ ($\mu A \text{ volt}^{-1/2} \text{ min}^{-1/2}$)
0.00	1.00	10.56	2.19	60	1.00	3.21
		7.91	2.19	60	1.00	3.18
		5.27	2.19	60	1.00	3.18
		2.64	2.19	60	1.00	3.24
		1.06	2.19	60	1.00	3.15
3.50	1.50	10.56	2.19	70	0.88	4.80
		7.91	2.19	80	0.85	4.90
		5.27	2.19	90	0.50	5.05
		2.64	2.20	110	0.25	5.80
		1.06	2.20	— ^(c)	— ^(c)	7.25
6.00	2.00	10.56	2.19	— ^(c)	— ^(c)	5.45
		7.91	2.19	— ^(c)	— ^(c)	5.70
		5.27	2.19	— ^(c)	— ^(c)	6.15
		2.64	2.20	— ^(c)	— ^(c)	7.90
		1.06	2.20	— ^(c)	— ^(c)	10.04
105.00	4.00 ^(d)	10.56	2.18	— ^(c)	— ^(c)	9.90
		7.91	2.18	— ^(c)	— ^(c)	10.01
		5.27	2.17	— ^(c)	— ^(c)	11.00
		2.64	2.16	— ^(c)	— ^(c)	13.40
		1.06	2.15	— ^(c)	— ^(c)	14.10
2-(1-naphthyl)-5-phenyloxazole						
0.00	1.00	10.00	1.93	60	1.00	4.24
		7.50	1.93	60	1.00	4.18
		5.00	1.93	60	1.00	4.15
		2.50	1.93	60	1.00	4.40
		1.00	1.93	60	1.00	4.18
17.50	1.25	10.00	1.94	100	1.00	4.12
		7.50	1.94	90	1.00	5.30
		5.00	1.92	90	0.95	5.55
		2.50	1.92	87	0.90	6.30
		1.00	1.92	87	0.85	6.80
30.00	1.50	10.00	1.93	110	0.89	5.61
		7.50	1.93	110	0.87	5.65
		5.00	1.93	110	0.81	6.15
		2.50	1.93	110	0.69	7.10
		1.00	1.92	—	0.45	8.25
50.00	1.75	10.00	1.94	120	— ^(c)	6.30
		7.50	1.94	120	— ^(c)	6.55
		5.00	1.93	120	— ^(c)	7.20
		2.50	1.92	— ^(c)	— ^(c)	8.60
		1.00	1.92	— ^(c)	— ^(c)	9.80
105.00	2.00	10.00	1.94	— ^(c)	— ^(c)	8.60
		7.50	1.92	— ^(c)	— ^(c)	9.00
		5.00	1.91	— ^(c)	— ^(c)	9.70
		2.50	1.91	— ^(c)	— ^(c)	11.40
		1.00	1.90	— ^(c)	— ^(c)	12.40
2,5-diphenyloxadiazole						
0.0	1.00	10.80	2.03	60	1.00	5.40
		8.10	2.03	60	1.00	5.20
		5.40	2.03	60	1.00	5.40
		2.70	2.03	60	1.00	5.30
		1.08	2.03	60	1.00	5.10
12.0	1.50	10.80	2.03	65	1.00	5.10
		8.10	2.03	65	1.00	5.00
		5.40	2.03	65	1.00	5.10
		2.70	2.03	65	0.90	5.60
		1.08	2.03	65	0.90	5.70
22.0	1.75	10.80	2.03	80	0.85	5.75
		8.10	2.03	80	0.80	5.86
		5.40	2.03	80	0.70	6.50
		2.70	2.03	80	0.50	7.20
		1.08	2.03	80	— ^(c)	8.15
30.0	2.00	10.80	2.04	90	0.70	5.95
		8.10	2.04	90	0.50	6.00
		5.40	2.03	95	0.40	6.35
		2.70	2.03	— ^(c)	— ^(c)	7.45
		1.08	2.03	— ^(c)	— ^(c)	8.90
105.0	2.10	10.80	2.06	— ^(c)	— ^(c)	7.34
		8.10	2.05	— ^(c)	— ^(c)	7.35
		5.40	2.05	— ^(c)	— ^(c)	7.70
		2.70	2.03	— ^(c)	— ^(c)	8.60
		1.08	2.02	— ^(c)	— ^(c)	8.75

Table II. (Cont.)

2-(4-methoxyphenyl)-5-(2-naphthyl) oxadiazole						
HQ (mM)	$n^{(a)}$	v (V/min)	$-(E_p)_c$ (V)	$(E_p)_c - (E_p)_a$ (mV)	$(i_p)_a / (i_p)_c^{(b)}$	$(i_p)_c / V^{1/2}$ ($\mu A \text{ volt}^{-1/2} \text{ min}^{-1/2}$)
0.0	1.00	9.60	1.86	60	1.0	3.20
		7.20	1.86	60	1.0	3.40
		4.80	1.86	60	1.0	3.40
		2.40	1.86	60	1.0	3.50
		0.96	1.86	60	1.0	3.40
65.0	1.50	9.60	1.88	85	0.9	3.92
		7.20	1.88	85	0.8	4.00
		4.80	1.88	85	0.6	4.15
		2.40	1.88	85	0.5	4.93
		0.96	1.88	85	— ^(c)	5.62
122.5	1.75	9.60	1.88	110	0.6	3.82
		7.20	1.88	110	0.5	4.15
		4.80	1.88	100	0.3	4.25
		2.40	1.88	— ^(c)	— ^(c)	5.05
		0.96	1.87	— ^(c)	— ^(c)	6.24
175.0	2.00	9.60	1.88	— ^(c)	— ^(c)	4.37
		7.20	1.88	— ^(c)	— ^(c)	5.05
		4.80	1.88	— ^(c)	— ^(c)	5.15
		2.40	1.87	— ^(c)	— ^(c)	6.20
		0.96	1.86	— ^(c)	— ^(c)	7.45

(a) n apparent from polarographic data.

(b) $E\lambda$ (switching potential) = 120 mV.

(c) No anodic peak.

(d) Limiting value of n apparent.

(e) Base line for small anodic current could not be determined.

mM HQ (Table II, Fig. 5). The cathodic current peak sharpens and the potential continues to shift anodically with an increase in v at this HQ concentration (Table II). This particular behavior is contrary to that for a concerted electrochemical step in which a chemical reaction or reactions is coupled to heterogenous electron transfers (9). It is found, however, that the peak potential and current function of voltammograms conducted at HQ concentrations effecting a limiting n apparent of 4.0 behave in a manner consistent with a single, complex electrochemical step (Table II).

The cyclic voltammograms of 2-(1-naphthyl)-5-phenyloxazole recorded at potentials of the first polarographic wave begin to exhibit definite kinetic effects at HQ concentrations near 17.5 mM (Table II). The effects become much more pronounced at slightly higher HQ concentrations (Table II, Fig. 5 and 6). At concentrations of 50 mM or greater no anodic current is observed at sweep rates up to 10 V/min (Fig. 5, Table II). All parameters of cyclic voltammograms of this compound at all HQ concentrations are consistent with a process in which a chemical reaction is coupled between two reversible electron transfer steps (ECE process) with the product of the reaction more reducible than the parent compound (9). The rate of the coupled reaction is proportional to the ratio of proton donor to parent compound; Fig. 5 and 6 illustrate this assertion (9).

The compound 2,5-diphenyloxadiazole behaves in a manner quite similar to that of 2-(1-naphthyl)-5-phenyloxazole (Table II, Fig. 5 and 6). The kinetic complications become apparent at slightly lower HQ concentrations. The voltammogram parameters of the compound 2-(4-methoxyphenyl)-5-(2-naphthyl) oxadiazole are consistent with an ECE process with kinetic complications and limiting behavior observed at considerably higher HQ concentrations than the other compounds (Table II).

Discussion

A study of the influence of HQ on the reduction of oxazoles and oxadiazoles places the compounds into two basic categories. One category includes compounds exhibiting a limiting behavior of one diffusion-controlled polarographic wave with an n apparent of 4.0 and the other includes compounds exhibiting, as limiting behavior, two diffusion waves with the first approaching an n apparent of 2.0 at high HQ concentrations. The first includes the 2,5-phenyl-substituted

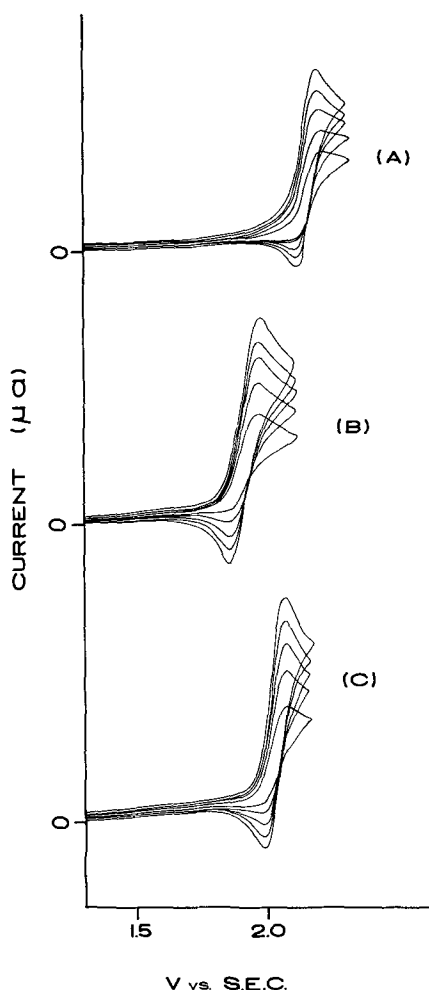
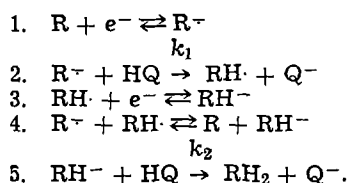


Fig. 6. (a) Cyclic voltammograms of 2,5-diphenyloxazole recorded in DMF containing 3.5 mM HQ at a HMDE at 10.56, 7.91, 5.27, 2.54, and 1.06 V/min. (b) Cyclic voltammograms of 2-(1-naphthyl)-5-phenyloxazole recorded in DMF containing 32.5 mM HQ at a HMDE at 10.00, 7.50, 5.00, 2.50, and 1.00 V/min. (c) Cyclic voltammograms of 2,5-diphenyloxadiazole recorded in DMF containing 21.5 mM HQ at a HMDE at 10.80, 8.10, 5.40, 2.70, and 1.08 V/min. The switching potential E_s is 120 mV past E_p and the drop size uniform for all voltammograms.

oxazoles and the second the oxadiazoles and 2-(1-naphthyl)-5-phenyloxazole.

Cyclic voltammetric data suggest that the oxadiazoles and 2-(1-naphthyl)-5-phenyloxazole are reduced via a two-electron ECE process to a dihydro species at the first polarographic wave in the presence of HQ. The complete mechanism probably may be represented by the sequence of steps (10)



Step 5 has been shown to be very fast in the presence of small quantities of proton donor (10). Also, the sensitivity of the second polarographic wave to small quantities of HQ relative to the first wave of each compound confirms that the step is very rapid with respect to step 2. The type equilibrium expressed in step 4 has been shown to lie almost completely to the right for aromatic hydrocarbons. The similar voltammetric behavior of oxazole and oxadiazoles with that of certain aromatic hydrocarbons suggests that this equilibrium also exists to the right for the compounds

under study. These facts are consistent with the observed ECE type behavior.

The difference in rate of approach to limiting behavior exhibited by the oxadiazoles and 2-(1-naphthyl)-5-phenyloxazole in Fig. 2 is a result of differences in k_1 of each compound. Mark has pointed out that for an ECE type mechanism the rate of protonation (step 2) relative to the rate of diffusion of R^- away from the electrode surface is an important factor in determining polarographic and voltammetric wave characteristics (6). If the proton donor concentration is high and/or the constant k_1 is large, then step 2 occurs near the electrode surface and behavior as described herein is expected.

Values of the rate constant, k_1 , for the reaction of the oxadiazoles and 2-(1-naphthyl)-5-phenyloxazole with HQ were estimated from a plot of the polarographic n apparent vs. the product of the pseudo first order rate constant, $k_1[HQ]$, and the drop time, t , after the method of Nicholson *et al.* (11). The values of k_1 appear to be of the same order of magnitude as similar constants for protonation of aromatic hydrocarbon radicals in DMF and acetonitrile (4, 12). The rate constants range from 0.1 liters $mM^{-1} sec^{-1}$ for 2,5-diphenyloxadiazole and 2-(4-fluorophenyl)-5-phenyloxadiazole to 0.05 for 2-(1-naphthyl)-5-phenyloxazole and 2-(4-fluorophenyl)-5-(2-naphthyl) oxadiazole and 0.04 for 2-(4-methoxyphenyl)-5-(2-naphthyl) oxadiazole.

It should be noted that these rate constants obtained assuming pure ECE behavior are possibly in error due to the previously recognized ECE contribution to the total reduction process. However, this possible error is appreciable only at high n apparent values and the rate constants given were measured at an n apparent near 1.4.

Comparison of the k_1 values relative to the curves in Fig. 2 shows that the increased conjugation due to naphthyl for phenyl substitution at the 2 or 5-position carbon has a significant slowing influence upon the rate of protonation of the anion radicals of the oxadiazoles. Electronic effects of substituents on the 2 or 5-position phenyl slightly alter the rate of protonation of the naphthyl substituted oxadiazoles.

Naphthyl substitution at the oxazole 2-position completely alters the electrochemical reduction mechanism of the oxazole ring in the presence of proton donors. At large proton donor to oxazole ratios 2-(1-naphthyl)-5-phenyloxazole is reduced in two polarographic steps with the first appearing to be a two-electron ECE process resulting in a dihydro species (1). The k_1 of this process is comparable to that of the oxadiazoles. At large proton donor to oxazole ratios the phenyl-substituted oxazoles are all reduced in one polarographic step exhibiting an n apparent of 4.0. The unusual cyclic voltammetric data taken of these compounds in DMF in the presence of HQ may be explained in terms of two electrochemical processes occurring at very similar voltages. The first leads to the dihydro compound, RH_2 , and the second to saturated-ring or ring-opened products (1, 2). At intermediate HQ concentrations the second step is cathodic enough of the first to cause cathodic current peak broadening and a cathodic shift at the slower sweep rates (Fig. 5). At large proton donor concentrations the two processes coalesce to one concerted step due to an anodic shift of the second process. The resulting voltammetric wave exhibits properties consistent with a complex, but concerted reduction process (Table II).

Bezuglyi *et al.* have studied the polarographic reduction of oxazoles and oxadiazoles in aqueous methanol at various pH values (13). This work and that presented herein provide a description of the electrochemistry of these heterocyclics in all media ranging from the protic to the closely aprotic. Bezuglyi found that 2-(1-naphthyl)-5-phenyloxazole exhibited a single two-electron wave in aqueous methanol at pH

values ranging from 3.8 to 12.2 (13). The $E_{1/2}$ of this process corresponds to the most anodic of the two waves of this compound observed in solutions containing large concentrations of HQ (Fig. 3). The multi-electron process occurring at more cathodic potentials and probably resulting in ring-opened products is not observed in aqueous methanol solutions (13). The limiting behavior of the oxadiazoles in DMF containing HQ corresponds to the behavior of the compounds in aqueous methanol (13).

A major difference is observed in the electrochemical behavior of the phenyl-substituted oxazoles in DMF containing large quantities of HQ and in aqueous methanol (13). These substances are reduced via a single, six-electron wave in aqueous methanol but in a four-electron process in DMF-HQ, suggesting ring-saturation without ring-opening in DMF-HQ.

Experimental

Apparatus.—The electrodes and accessories for electrochemical measurements have been described previously (1). All solutions were 1 mM in electroactive compound unless otherwise stated. The reference electrode, saturated calomel, made contact with the solution through an agar plug behind a Pyrex frit. Water leakage through this tip was found to be negligible in experiments of short time duration. The cyclic voltammetric data were recorded on a Bolt-Barnak-Newman X-Y plotter using a Wenking potentiostat and Exact wave form source for potential control. The polarograms were recorded with a Beckman Electroscan 30 electroanalytical system.

Chemicals.—Spectroquality DMF containing approximately 0.03% water was obtained from Eastman Organic Chemicals. The solvent was vacuum distilled from anhydrous CuSO_4 before use. Hydroquinone was obtained from J. T. Baker Chemical Company and was recrystallized from a 50% water ethyl-ether solution. All compounds were purchased from Alfred

Bader Chemical Company and were recrystallized from pure methanol before use. The preparation and purification of tetra-N-propylammonium perchlorate has been described previously (1).

Acknowledgment

The authors gratefully acknowledge the financial support of the Robert A. Welch Foundation (Grant No. AO-337).

Manuscript submitted April 5, 1972; revised manuscript received June 2, 1972.

Any discussion of this paper will appear in a Discussion Section to be published in the June 1973 JOURNAL.

REFERENCES

1. W. N. Greig and J. W. Rogers, *This Journal*, **117**, 1141 (1970).
2. G. L. Smith and J. W. Rogers, *ibid.*, **118**, 1089 (1971).
3. P. H. Given and M. E. Peover, *J. Chem. Soc.*, **1960**, 385.
4. J. Janata, J. Gendell, R. C. Lawton, and H. B. Mark, Jr., *J. Am. Chem. Soc.*, **87**, 4529 (1965).
5. K. S. V. Santhanam and A. J. Bard, *ibid.*, **88**, 2669 (1966).
6. J. R. Jezorek and H. B. Mark, Jr., *J. Phys. Chem.*, **74**, 1627 (1970).
7. N. H. Velthorst and G. J. Hoijsink, *J. Am. Chem. Soc.*, **87**, 4529 (1965).
8. A. Streitwieser, "Molecular Orbital Theory for Organic Chemists," John Wiley & Sons, Inc., New York (1962).
9. R. S. Nicholson and I. Shain, *Anal. Chem.*, **37**, 179 (1965).
10. S. Hayano and M. Fujihira, *Bull. Chem. Soc. Japan*, **44**, 1496 (1971).
11. R. S. Nicholson, J. M. Wilson, and M. L. Olmstead, *Anal. Chem.*, **38**, 542 (1966).
12. J. Janata and H. B. Mark, Jr., *J. Phys. Chem.*, **72**, 3616 (1968).
13. V. D. Bezuglyi, N. P. Shimanskaya, and E. M. Peresleni, *Zh. Obshch. Khim.*, **34**, 3540 (1964).

Mass Transfer to Point Electrodes on the Surface of a Rotating Disk

Der-Tau Chin*¹ and Mitchell Litt

School of Chemical Engineering, University of Pennsylvania, Philadelphia, Pennsylvania 19104

ABSTRACT

A zeroth order perturbation solution is presented for the rate of laminar mass transfer to three types of point electrodes embedded in the surface of an insulating rotating disk—those sensitive to radial, tangential, and local velocity components. It is shown that the diffusion current density on the point electrode increases with decreasing geometrical parameter defined as the ratio of the electrode size to the radial location of the electrode on the disk surface. With a properly chosen geometrical parameter, it is possible to obtain a current density ten times greater than that on the disk electrode at a given rotational speed. From the electroanalytical point of view, this offers experimental advantages in the study of fast surface reactions.

An experimental setup for studying the transfer characteristics of such electrodes is described. A diffusion-controlled redox reaction is used for the measurement. The results indicate that the "local" and the "tangential" electrodes give reasonable agreement with the theory prediction. However, data from the "radial" electrode scatter randomly around the predicted values. This failure of the radial electrode to behave properly appears to be consistent with thin-ring experiments reported in the literature.

Study of point electrodes mounted flush on the surface of a rotating disk is of interest to both electrochemists and engineers. Such an electrode, because

of its small surface area and high-rate convective transport, offers practical advantages in the study of high rate electrode reactions (1). To the engineers, the electrode may be used to investigate the nature of flow near the disk surface (2-4). While the theory of laminar flow and mass transfer on the rotating disk

* Electrochemical Society Active Member.

¹ Present address: Electrochemistry Department, Research Laboratories, General Motors Corporation, Warren, Michigan 48090.

Key words: convective diffusion, limiting current.

has been well developed, this is true only for a disk whose surface is completely active, that is, where there is a nonzero axial gradient at every point of the disk surface. Since the point electrode introduces active areas only at small selected points on the disk surface, the previous solutions for mass transfer are inapplicable, and a suitable theory, even for laminar flow, does not exist.

Though there have been a number of studies of heat and mass transfer to partially active rotating disks, these have primarily been disks with some part of the surface, usually the center, blocked off. Gregory and Riddiford (5) found that no significant change occurred in the mean mass transfer coefficient until the central area blocked off exceeded about 10% of the total disk area. This effect presumably occurs because of the radial gradients introduced by the blocked-off area, for in a completely active disk, there are no radial gradients and the surface is "equally accessible" to mass transfer. Levich (6) has obtained a theory for a disk with active rings; however, preliminary measurements by Avdeyeva on thin rings gave results some 20-30% lower than those predicted. Schnurr (7) studied heat transfer with a stepwise discontinuous surface temperature. Albery *et al.* (8) have published extensively on the study of reactions using ring-disk electrodes.

In this work, we are attempting to study the transfer characteristics of the point electrodes on the surface of an insulating rotating disk. A preliminary measurement of the rate of mass transfer on a circular point electrode was made by Serafi (9) in a diffusion-controlled redox system. The present authors have extended such measurements to the transition and the turbulent regions with both circular and rectangular point electrodes. A theory has also been derived to correlate data in the laminar region. This paper describes: (i) details of the theoretical analysis, and (ii) the experimental setup as well as the results of time-averaged measurements in a ferricyanide/ferrocyanide redox system. In the transition and the turbulent regions, the rate of mass transfer is found to be oscillating due to flow fluctuations near the disk surface. The results of these fluctuation measurements and their implications to flow instability has been presented elsewhere (10-11).

Theoretical

The theory of heat and mass transfer to point sources in pipe flow and flat plate has been developed by Mitchell and Hanratty (2), and Ling (12). Here we present an analysis for the point electrodes mounted on the surface of an insulating rotating disk. Three types of the electrodes are considered: (i) the "tangential electrode," which is a long, narrow mass sink mounted parallel to the radial direction, so that it responds only to convective transfer due to the tangential velocity component; (ii) the "radial electrode," which is also a long, narrow mass sink mounted parallel to the tangential direction, so that it responds only to the radial velocity component; (iii) the "local electrode," which is a small circular mass sink, and responds to the local velocity relative to the disk surface (3). Since the development for each of these electrodes is similar, we shall give details of the analysis only for the tangential electrode, and list only results for the other two.

Let us consider a mass sink having an average distance of $r = oo'$ from the disk center (Fig. 1). The sink is rectangular in shape, and its small dimension is on the order of the thickness of the momentum boundary layer. Its area is so small compared with the disk surface that a separate Cartesian coordinate system may be taken for the space concerned. We choose such a system with its origin at point o' . Since the disk is rotating with a constant speed, ω , about its axis, the coordinates fixed on the disk surface are traveling with a constant velocity, $r\omega$. The coordinate z is normal to the disk surface, and y is along the radial direction. The coordinate x is parallel to the circumferential direction of the disk, and points towards the opposite direction of rotation. This assumption leads to $V_z = 0$ in accordance with the equation of continuity for fluid flow. Also, for the case of the tangential electrode, we have $L \ll W$; thus, the equation of convective diffusion may be reduced to

$$V_x^* \frac{\partial \Phi}{\partial x^*} = \frac{1}{R Sc} \frac{\partial^2 \Phi}{\partial x^{*2}} + \frac{\epsilon}{Sc} \frac{\partial^2 \Phi}{\partial z^{*2}} \quad [1]$$

where $x^* = x/L$; $z^* = z\sqrt{\omega/\nu}$; $\Phi = (C - C_x)/(C_0 - C_x)$; $V_x^* = V_x/r\omega$; $\epsilon = L/r$; $R = Lr\omega/\nu$; $Sc = \nu/D$.

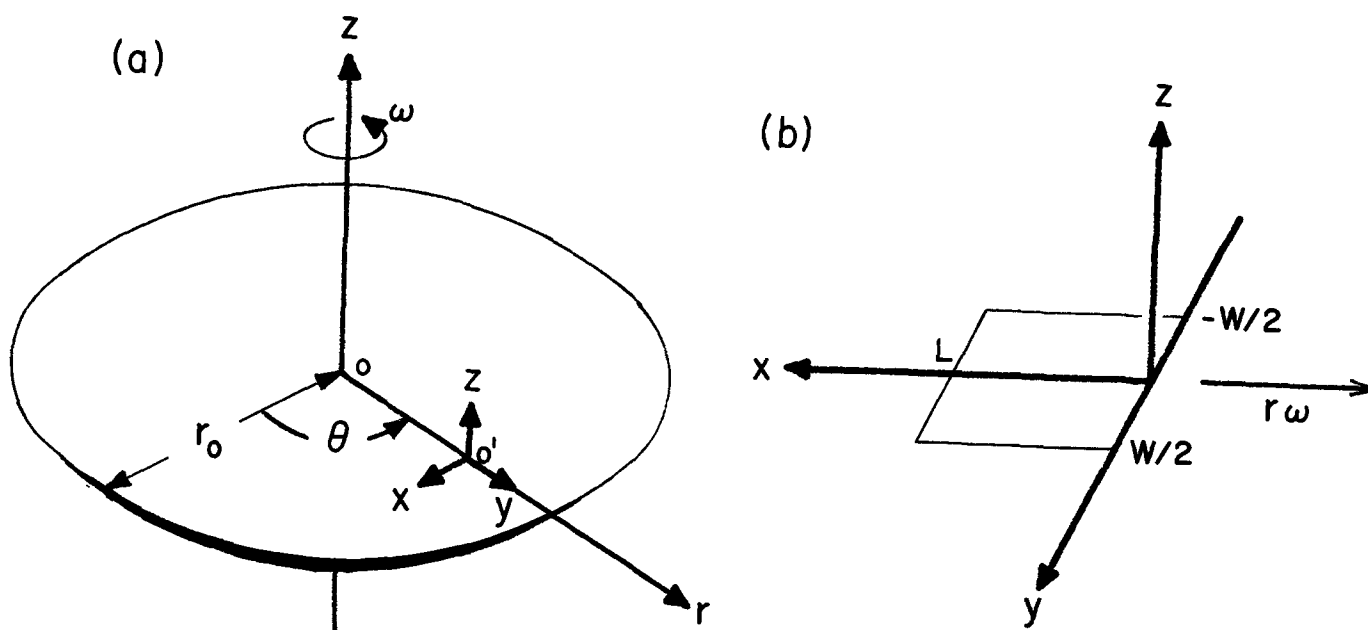


Fig. 1. Cartesian coordinate system for point electrodes on the surface of a rotating disk. (a), Location of the electrode; (b), close view of the electrode surface.

The boundary conditions are

$$\left. \begin{aligned} \phi &= 1 && \text{at the electrode surface;} \\ \partial\phi/\partial z^* &= 0 && \text{at the surface of the insulating} \\ &&& \text{rotating disk;} \\ \phi &= 0 && \text{at } x^* \rightarrow \pm \infty \text{ and } z^* \rightarrow \infty \end{aligned} \right\} [2]$$

Mathematically this is a multi-singularity problem resulting from the nonuniformity of the boundary conditions around the electrode surface. The singular regions can be classified into: (i) the leading edge, $x^* \rightarrow 0, z^* \rightarrow 0$; (ii) the trailing edge, $x^* \rightarrow 1, z^* \rightarrow 0$; (iii) the main region over the electrode surface, $0 < x^* < 1, z^* \rightarrow 0$; and (iv) the wake region, $x^* > 1, z^* \rightarrow 0$. Only the main region solution is of principal interest to practical applications. It has been shown by Chin (13) that the contribution of mass flux at the electrode surface from the other regions is negligibly small for $Sc > 100$, and $R > 10$. Thus we shall only present the method of solution for the main region. The development of equations for the other singular regions is given in Chin (13), and will not be repeated here.

Following the standard procedure of a singular perturbation method, we introduce a stretched coordinate

$$Z = Sc^{1/3} z^* [3]$$

for the coordinate z^* in the main region, and assume that the dimensionless concentration, ϕ , can be expanded in an asymptotic series of Sc

$$\phi = \phi_0(x^*, Z) + Sc^{-2/3} \phi_1(x^*, Z) + \dots [4]$$

To solve Eq. [1], one also requires an expression for the velocity component V_x^* . For the rotating coordinates considered here, the velocity V_x^* is related to the tangential velocity component, V_θ , of the rotating disk by

$$V_x^* = 1 - V_\theta/\tau\omega [5]$$

Using Cochran's series solution (14) in the vicinity of the disk surface, we have

$$V_x^* = -G_1 z^* - (F_1/3)z^{*3} + \dots [5a]$$

For laminar flow, the dimensionless gradients, F_1 and G_1 , are constant (0.510 and -0.616 , respectively). Substituting Eq. [3]-[5a] into Eq. [1] and equating the terms having the same order in Sc lead to the following zeroth order perturbation equation

$$-G_1 Z \frac{\partial \phi_0}{\partial x^*} = \epsilon \frac{\partial^2 \phi_0}{\partial Z^2} [6]$$

with the boundary conditions

$$\left. \begin{aligned} \phi_0 &= 1 && \text{at } Z = 0 \text{ for } 0 < x^* < 1 \\ \phi_0 &= 0 && \text{at } Z \rightarrow \infty \end{aligned} \right\} [7]$$

The above equation and boundary conditions are seen to be identical to the Leveque problem (15) of heat transfer in the entrance region of pipe flow. The same result was also obtained by Hanratty (2) and Ling (12) for their geometries. In those instances, this results from a prior assumption of a linear velocity profile near the surface. In this instance, the zeroth order solution becomes equivalent to such an assumption; however, this method of formulating the problem is more general and provides the basis for correcting

the approximate solution by numerical integration of the first order equation.

If we define a mass transfer coefficient K as

$$N_z|_{z=0} = K(C_o - C_s) = -\frac{D}{WL} \int_{-W/2}^{W/2} dy \int_0^L dx \left(\frac{\partial C}{\partial z} \right)_{z=0} [8]$$

then, using the results of the Leveque solution, it can be shown that the Sh for the main region becomes

$$Sh = (KL/D) = -0.807 G_1^{1/3} \epsilon^{1/6} R^{1/2} Sc^{1/3} [1 + 0(Sc^{-2/3})] [9]$$

For laminar flow, $G_1 = -0.616$, so that

$$Sh = 0.687 \epsilon^{1/6} R^{1/2} Sc^{1/3} [1 + 0(Sc^{-2/3})] [9a]$$

In the presence of an excess supporting electrolyte, the average diffusion current density on the electrode surface is related to K by

$$i = nFK(C_s - C_o) [10]$$

and Eq. [9a] can be rearranged in dimensional form as

$$i = 0.687 nF(C_s - C_o) (\tau/L)^{1/3} D^{2/3} \nu^{-1/6} \omega^{1/2} [11]$$

Note that this equation differs from the Levich solution of the rotating disk electrode (6) by only a numerical factor and a geometrical ratio, $\tau/L = \epsilon^{-1}$; thus, dividing Eq. [11] by the Levich solution, we have

$$i/i_D = K/K_D = 1.11 \epsilon^{-1/3} [12]$$

Here the subscript, D , denotes the process occurring at the disk electrode whose entire surface is subject to mass transfer. Equation [12] implies that the diffusion current density on the point electrode increases with decreasing geometrical parameter, ϵ . For a typical value of $\epsilon = 0.001$ used in this study, the current density on the point electrode would be 10 times greater than that on the disk electrode. In electrochemical studies, the upper limit that the rotating disk electrode can be used to determine the first-order surface rate constant, is 0.1 cm/sec (1). The point electrode technique is therefore capable of extending this limit to 1.0 cm/sec without difficulty.

Like most electrode geometries, however, the point electrode suffers from a nonuniform current distribution across the surface; the limiting current density near the leading edge tends to be greater than in the main region. This may introduce some errors for the study of irreversible reactions. For reversible electrochemical systems, lack of uniform accessibility does not present a serious problem, for it does not change the current-potential relations obtained from the Nernst diffusion layer concept (8).

Results for the radial and the local electrode are given in Table I. It should be noted that the radial electrode has dimensions, $W \ll L$, and the definition of ϵ and R has been changed to

$$\epsilon = W/\tau, \quad R = W\tau\omega/\nu \quad (\text{for radial electrode})$$

Also in deriving the equations for the local electrode, the circular sink has been approximated as a square mass sink having the same surface area as the circular

Table I. Summary of theoretical results

Type of electrode	Zeroth order correlation for laminar flow	Comparison with disk electrode	Estimated fractional error for K
Local	$\sqrt{\pi} Kd/2D = 0.749 \epsilon^{1/6} R^{1/2} Sc^{1/3}$	$K/K_D = 1.21 \epsilon^{-1/3}$	$Sc^{-1/3}$
Radial	$KW/D = 0.645 \epsilon^{1/6} R^{1/2} Sc^{1/3}$	$K/K_D = 1.04 \epsilon^{-1/3}$	$Sc^{-1/3}$
Tangential	$KL/D = 0.687 \epsilon^{1/6} R^{1/2} Sc^{1/3}$	$K/K_D = 1.11 \epsilon^{-1/3}$	$Sc^{-1/3}$

d is the diameter of the local electrode, L and W are the width (short dimension) of the tangential and the radial electrodes, respectively. K_D is the mass transfer coefficient of a rotating disk electrode whose entire surface is subject to mass transfer.

one. Thus to use the results for the local electrode, ϵ and R should be

$$\epsilon = (\sqrt{\pi}/2) d/r, \quad R = (\sqrt{\pi}/2) dr\omega/\nu$$

(for local electrode)

where d is the diameter of the local electrode. Mass transfer to a ring electrode has been treated by Levich (6), and our result for the radial electrode agrees with his result for a narrow ring on the disk surface.

Experimental

The diffusion controlled reaction used is the oxidation-reduction of potassium ferricyanide and ferrocyanide in aqueous solution. Details of the reaction and its application to mass transfer studies can be found elsewhere (2, 9, 13, 16-17). In the present study, a solution containing 0.01M potassium ferricyanide, 0.01M potassium ferrocyanide, and 1.0M potassium chloride is used for the experiments. Small platinum electrodes mounted flush with the surface of a Lucite rotating disk are used as cathodes. The anode is a platinum foil with a very large surface area, so that the cell current is controlled by the cathode reaction.

The complete system consists of a cell tank containing the anode, a Lucite spinning disk, and a drive assembly equipped with slip-ring contacts. The cell container is a cylindrical Lucite tank, 53 cm ID and 32 cm deep. Six Lucite baffles are evenly spaced along the container wall. The anode is located on the cell bottom; it is a sheet of platinum foil, 0.3 mm thick, 15 cm diameter, cemented to a Lucite plate and has a surface area of 176 cm² exposed to the electrolyte.

The Lucite spinning disk is composed of three separate sections. Figure 2 illustrates the details of construction. The upper section is made from a 10 cm Lucite rod. The upper end of this section is threaded to fit a glass-epoxy shaft of the slip-ring contact; the other end, with an Amphenol 12-contact polarized receptacle on its center, is designed to accommodate either a 10 cm diameter disk, or an adapter for fitting on a 15 cm disk. The 15 cm disk is made from a 0.6 cm Lucite sheet, and is machined to fit the adapter to form a bell-shaped rotating disk. A Lucite nose cemented on the center of the inner face of the disk serves as a base for an Amphenol 12-contact polarized plug. The plug matches with the Amphenol receptacle of the upper section when the disk is fastened to the adapter.

Two 15 cm Lucite disks having flush-mounted surface electrodes have been constructed. The types and location of platinum electrodes on each disk are as follows:

(i) The first disk has 12 circular platinum local electrodes on the outer surface. The electrodes are made from platinum wires, 0.0127-0.0381 cm in diameter. The radial location of the electrodes ranges from 4 to 6 cm. Holes to accommodate these electrodes are drilled first, and the platinum wires are inserted through the holes. The space between the hole walls and the platinum is filled with epoxy cement, and

the outer face is then smoothed and polished. The platinum leads on the inner face are connected electrically to the Amphenol plug.

(ii) The second disk contains 12 radial and 12 tangential electrodes made from a platinum foil. The dimensions of these surface mounted electrodes are 0.03 mm wide by 0.254 cm long. They are evenly located on the disk surface with radial positions varying from 2.5 to 6.2 cm (13).

The slip-ring contacts, the drive assembly, an electric motor, and a tachometer generator combine to make an integral drive unit. The slip-ring assembly is the same as reported by Serad (9) and will not be discussed further. The lower end of the slip-ring shaft screws into the upper section of the rotating disk; the upper end of the shaft is attached to a coupling connecting with the drive assembly. A Reliance 1 hp d-c motor is used to drive the rotating assembly. A Minarik SH 293 motor control is used in conjunction with the motor. The motor is mounted with a 48XL timing pulley which gives a pulley ratio of 2:1 and allows a speed range of 250-2000 rpm for the rotating disk.

A 6V battery is used as the power supply to the electrochemical cell. The applied potential drop across the anode and the cathodes is controlled by a 350 ohm potentiometer. The cell current is determined by passing the current through a 1000 ohm standard resistor. Since the current fluctuates when flow becomes turbulent, a 10,000 MF capacitor in conjunction with a microvoltmeter (Keithley 151) is used to measure the time-averaged component of the current. For each electrode, the current/potential curves are first measured to determine the limiting current plateau. A proper potential setting is then chosen for the potentiometer, and the limiting currents are measured at various rotational speeds. To avoid interference from the nearby electrodes, this measurement is made for only one electrode at a time, while all the other electrodes on the disk surface are at open circuit.

Results and Discussion

In a diffusion-limited electrode reaction, the mass transfer coefficient, K , is related to the measured current density by Eq. [10]. At the limiting current density, the surface concentration of the diffusing ion goes to zero, giving

$$K = i_{lim}/nFC_x \quad [13]$$

For the ferricyanide/ferrocyanide reaction, $n = 1$, and all the other quantities are known or measured, so that K may be calculated. For turbulent flow, the mass transfer coefficient will have a time-averaged and a fluctuating component. In this paper we shall present results only of the time-averaged component measurement. Results of the fluctuating component measurement have been reported elsewhere (10-11).

Figure 3 is a plot of the time-averaged mass transfer coefficient vs. rotational speed for a 0.0381 cm diameter local electrode located at various positions on the disk surface. These curves are typical of the data obtained, so the raw data with the other electrodes and other positions are not shown. The measurements with smaller size local electrodes gave very poor reproducibility because of small area and very low currents being measured, and these data will not be reported. The main features of the curves are: (i) a linear region with a slope of $\frac{1}{2}$ for low rotational speeds, which presumably represents the laminar region; (ii) a break-point signifying the beginning of flow instability which occurs at different speeds for different radial positions; (iii) a second break-point, again at different speeds, presumably signifying transition to fully developed turbulence. In this final region, the curves again are linear with a slope slightly greater than $\frac{1}{2}$. As would be expected, the break-point speed

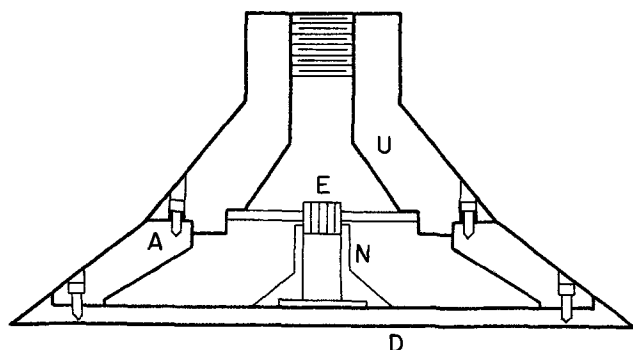


Fig. 2. Rotating disk. A, adapter; D, 15 cm Lucite disk; E, electric connector; N, Lucite nose; U, upper section.

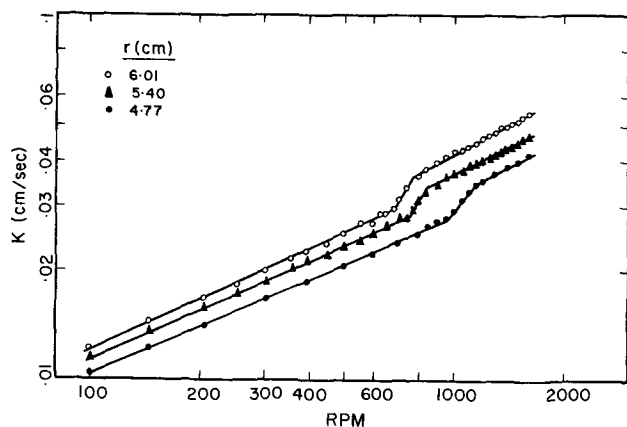


Fig. 3. Time-averaged mass transfer coefficient vs. rotational speed for a 0.0381 cm diameter local electrode. The measurement is carried out at a room temperature of 22°C.

for an electrode located at a smaller radius, is higher than that for an electrode located at a larger radius. This demonstrates that on a given disk, the laminar, transition, and turbulent regimes exist simultaneously at different radii.

As seen from the results shown in Table I, one would expect that a log-log plot of $Sh/\epsilon^{1/6}Sc^{1/3}$ vs. R would be linear with a slope of $1/2$ for laminar flow. Figures 4-6 show the results for the local, the radial, and the tangential electrodes.

There is considerable variation in the degree with which the theory appears to correlate the experimental results. From Fig. 4, we see that all the data for the 0.0381 cm diameter local electrode seem to be well correlated. Not only is the slope of the line predicted, but the theoretical coefficient seems to agree well except at the very end of small R , where edge effects may start to become important. Figure 6 indicates that while the data points for different radii are not brought together as well, the theory still gives relatively good agreement for the tangential electrode. Again, there seems to be deviation at the lower Reynolds numbers based upon the electrode width.

Figure 5 shows that agreement between the theory and the data is not quite satisfactory for the radial electrode. While each of the individual electrodes seems to follow a line of proper slope, it is apparent that the theory does not take the ϵ factor into account properly. The failure of the radial electrode to behave properly is consistent with Avdeyeva's (6) mass transfer measurement on thin-ring electrodes. His

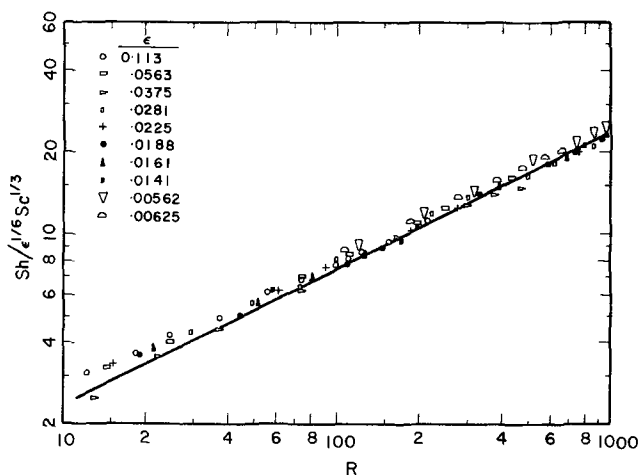


Fig. 4. Laminar mass flux to a 0.0381 cm diameter local electrode. The measurement is carried out over the range of Re from 108 to 167,000, and Sc between 1030 and 1470. The solid line is the theoretical prediction. Some of the data are taken from Ref. (9).

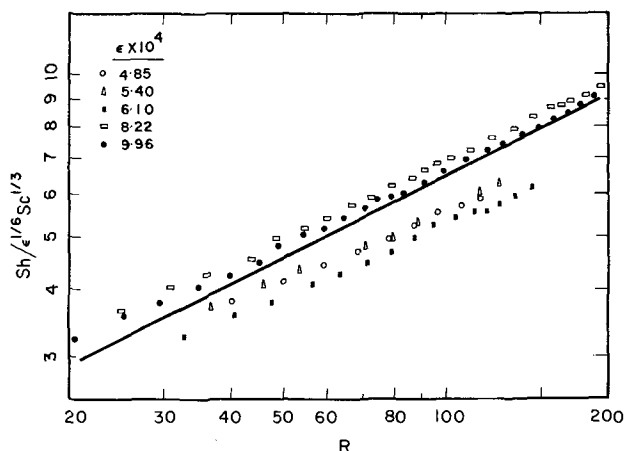


Fig. 5. Laminar mass flux to the radial electrode. The measurement is carried out over the range of Re from 20,500 to 240,000, and Sc between 1300 and 1420. The solid line is the theoretical prediction.

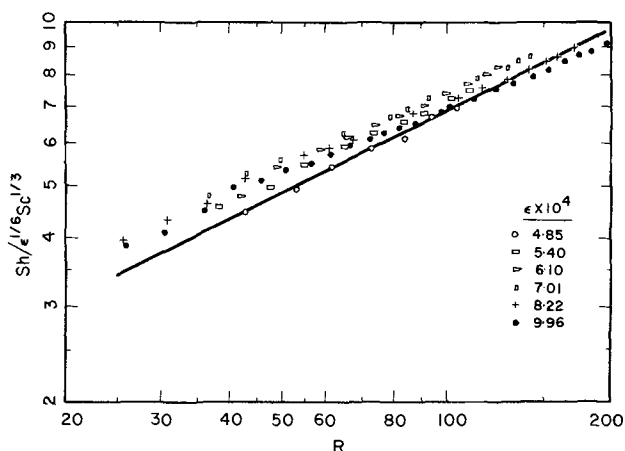


Fig. 6. Laminar mass flux to the tangential electrode. The data cover the range of Re from 21,400 to 204,000, and Sc between 1200 and 1270. The solid line is the theoretical prediction.

results gave 20-30% lower than those predicted from Levich's ring theory. At present there is no reasonable explanation for the discrepancy. However, we may conclude that for any given radial electrode, the theory correctly predicts variation with the Reynolds number.

In order to determine the Schmidt number variation, experiments were made using a 0.3% carboxymethylcellulose (CMC) solution, which has Schmidt numbers on the order of 4000. The results indicate that while some greater scatter is produced because of the slightly non-newtonian character (the shear stress is proportional to the shear rate raised to a power of 0.9) of the solution, in general the $1/3$ power Schmidt number dependency is confirmed (Fig. 7).

One additional result which is easily obtained from the curves shown in Fig. 3 is information on the transition Reynolds numbers for the rotating disk flow. The break-points at different radii can be brought together, if one replots Fig. 3 in the form of K vs. $Re = r^2\omega/\nu$. Based upon these data, we have found that the initial instability begins at $Re = 2.3 \times 10^5$, and the transition to turbulence takes place at $Re = 3.0 \times 10^5$. These values compare favorably with Gregory and Walker's result of 1.9×10^5 and 2.9×10^5 obtained with a china clay method (18). The transitional Reynolds number also agrees with the results of a recent study of turbulent mass transfer to the disk electrode (19). More detailed pictures concerning the transition of flow near the rotating disk are discussed in Ref. (11).

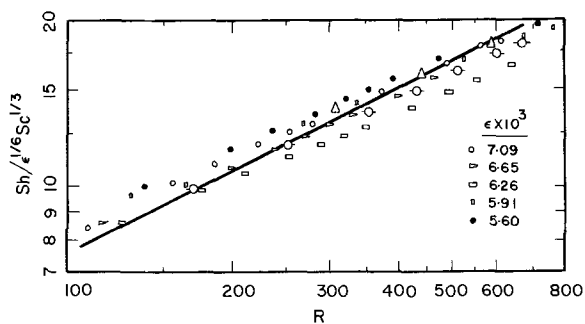


Fig. 7. Laminar mass flux to the local electrode in a solution containing 0.3% CMC7LP. The Schmidt number of the system is 3930. For comparison, some of the data obtained at $Sc \sim 1000$ are also plotted as Δ and $-\circ-$. Again, the solid line is the theory prediction.

Conclusions

Based upon the above discussions, we may conclude that the theoretical results listed in Table I appear to give a reasonable correlation with the experimental data in laminar flow, particularly for the local and the tangential electrodes. For a given rotational speed, the diffusion current density on the point electrode can be made 10 times greater than that on the disk electrode; this offers experimental advantages in the study of fast surface reactions.

Acknowledgment

The authors would like to thank Professor Ira Cohen for his help in formulating and solving this problem. This work was supported in part by National Science Foundation Grant GK 452.

Manuscript submitted Jan. 6, 1972; revised manuscript received May 19, 1972.

Any discussion of this paper will appear in a Discussion Section to be published in the June 1973 JOURNAL.

LIST OF SYMBOLS

C	concentration of the diffusing ion, g-mole/cm ³
C_0	concentration at the electrode surface, g-mole/cm ³
C_∞	bulk concentration, g-mole/cm ³
D	diffusivity of the diffusing ion, cm ² /sec
d	diameter of local electrodes, cm
F	Faraday constant, 96,500 coul/g-equiv
F_1	dimensionless radial velocity gradient, $d(V_r/r\omega)/dz^*$, at the disk surface
G_1	dimensionless tangential velocity gradient, $d(V_\theta/r\omega)/dz^*$, at the disk surface
i	diffusion current density, A/cm ²
i_D	diffusion current density on the rotating disk electrode, A/cm ²
i_{lim}	limiting current density, A/cm ²
K	mass transfer coefficient defined in Eq. [8], cm/sec
K_D	mass transfer coefficient of the rotating disk electrode, cm/sec
L	width of tangential electrodes (short dimension), cm
N_z	average mass flux per unit area normal to the disk surface, g-mole/cm ² sec
n	number of electrons transferred in electrode reactions, g-equiv/g-mole
o	center of the disk
o'	the origin of the moving coordinate system (x, y, z), or the location of point electrodes on the disk surface

r	radial coordinate, or the location of point electrodes, cm
R	Reynolds number based upon the width of point electrodes, (electrode width) $r\omega/\nu$, dimensionless
Re	Reynolds number based upon the radial position on the disk surface, $r^2\omega/\nu$, dimensionless
Sc	Schmidt number, ν/D , dimensionless
Sh	Sherwood number defined as (electrode width) K/D , dimensionless
V_r	radial velocity component of the rotating disk flow, cm/sec
V_θ	tangential velocity component of the rotating disk flow, cm/sec
V_x	velocity component along the x -direction, cm/sec
V_x^*	dimensionless velocity defined as $V_x/r\omega$
\bar{W}	width of radial electrodes (short dimension), cm
x	moving coordinate parallel to the circumferential direction of the rotating disk, but opposite to the direction of rotation, cm
x^*	dimensionless distance in the x -direction, x/L
y	moving coordinate along the radial direction of the rotating disk, cm
z	axial coordinate, cm
z^*	dimensionless axial distance, $z\sqrt{\omega/\nu}$
Z	stretched axial distance defined as $Sc^{1/3}z^*$, dimensionless
ϵ	geometrical parameter defined as (electrode width) $/r$, dimensionless
ν	kinematic viscosity, cm ² /sec
Φ	dimensionless concentration, $(C - C_\infty)/(C_0 - C_\infty)$
Φ_0	dimensionless zeroth order concentration, see Eq. [4]
Φ_1	dimensionless first order concentration, see Eq. [4]
ω	angular velocity of the rotating disk, rad/sec

REFERENCES

1. A. C. Riddiford, in "Advances in Electrochemistry and Electrochemical Engineering," P. Delahay, Editor, pp. 47-116, Interscience, New York (1966).
2. J. E. Mitchell and T. J. Hanratty, *J. Fluid Mech.*, **26**, 199 (1966).
3. L. P. Reiss and T. J. Hanratty, *AIChE J.*, **9**, 154 (1963).
4. L. P. Reiss and T. J. Hanratty, *ibid.*, **8**, 245 (1962).
5. D. P. Gregory and A. C. Riddiford, *J. Chem. Soc.*, **731**, 3756 (1956).
6. V. G. Levich, "Physicochemical Hydrodynamics," Prentice-Hall, Englewood Cliffs, N. J. (1962).
7. N. M. Schnurr, *J. Heat Transfer*, **86C**, 467 (1964).
8. W. J. Albery and M. L. Hitchman, "Ring-Disc Electrodes," Oxford University Press, London (1971).
9. G. Serad, Ph.D. Dissertation, University of Pennsylvania, Philadelphia, Pennsylvania (1964).
10. M. Litt and D. T. Chin, Preprint 30 G Presented at the 61st Annual Meeting of the American Institute of Chemical Engineers, Los Angeles, California (1968).
11. D. T. Chin and M. Litt, *J. Fluid Mech.*, To be published.
12. S. C. Ling, *J. Heat Transfer*, **85C**, 230 (1963).
13. D. T. Chin, Ph.D. Dissertation, University of Pennsylvania, Philadelphia, Pennsylvania (1969).
14. W. G. Cochran, *Proc. Cambridge Phil. Soc.*, **30**, 365 (1934).
15. M. A. Leveque, *Ann. Mines*, **13**, 283 (1928).
16. D. T. Chin, *This Journal*, **118**, 1764 (1971).
17. L. Gordon, J. S. Newman, and C. W. Tobias, *Berichte der Bunsengesellschaft*, **70**, 414 (1966).
18. N. Gregory, J. T. Stuart, and W. S. Walker, *Phil. Trans. Royal Soc. London*, **248A**, 155 (1955).
19. B. T. Ellison and I. Cornet, *This Journal*, **118**, 68 (1971).



An Electrochemical Technique for Microsectioning Copper

Nghi Q. Lam, Steven J. Rothman, and L. J. Nowicki

Materials Science Division, Argonne National Laboratory, Argonne, Illinois 60439

In recent years, various techniques for removing thin uniform sections from a metallic sample have been investigated. These techniques have important applications in measuring depth distributions of implanted ions and radiation damage, and are also useful in determining the diffusion coefficient in solids. These techniques include electrochemical (1-7), vibratory polishing (8), ordinary chemical dissolution (9-10), formation and dissolution of films other than oxides (11), bombardment-induced dissolution of surface layers (12-13), and low-energy sputtering (14-16).

The electrochemical technique consists of forming an anodic oxide layer that can be either mechanically stripped or chemically dissolved without attacking the metal substrate. Although this method has proved reliable for microsectioning metallic samples, it has not been applied to copper. To date, the technique used to section copper has been based on the formation and dissolution of corrosion films of copper iodide (11). In this communication, we report the development of an electrochemical technique for the removal of thin sections of copper to determine small diffusion coefficients.

Experimental Methods and Results

Surface preparation.—Monocrystalline copper rods 0.97 cm in diameter were grown from copper (99.999% pure) by the Bridgman method and spark-cut into disks a few millimeters thick. After polishing through 0.3μ Al_2O_3 , the samples were chemically polished with a solution composed of 15 ml of saturated chromic acid and 6 ml of 10% HCl. The chemical polishing was performed by swabbing the copper surface with a wet cotton-tipped applicator saturated with the solution. Chemical polishing in this manner for 20 min removed a layer $\sim 150\mu$ thick, which was far greater than the depth of the region deformed in mechanical polishing. At the end of this polishing step, the sample was washed with a solution of 1% HCl in ethanol, then with alcohol, and dried in warm air. The entire surface obtained was optically flat and free of pits.

Sectioning.—Most of the anodizing experiments were made on a copper single crystal of random orientation that had been irradiated for 25 min in a flux of 10^{12} thermal neutrons/cm²-sec. Counts/min were converted to micrograms of copper using the specific activity of the crystal (⁶⁴Cu), which was 6.30×10^3 cpm/ μg .

A copper wire was fastened to the back of the specimen with silver paint for the electrical connection. The sample was masked with Tygon protective paint so that only the polished surface was exposed to the electrolyte, which consisted of 0.1g Na_2SO_4 per liter of water. The cathode was a thin strip of platinum. A counting bottle was used as an anodizing cell so that after each sectioning the electrolyte and the cathode could be counted for ⁶⁴Cu activity. This was important because the copper oxide formed was strongly dissolved during anodizing. After anodizing, the remaining copper oxide films, which, if thick enough, showed

uniform interference colors, were dissolved in a solution of 0.1% HCl in ethanol.

To determine whether this solvent attacks the copper, oxide layers of different thicknesses were formed on the irradiated copper crystal by anodizing with current densities of 0.5 and 1.0 mA/cm² for 30 sec. The sample was then immersed in the 0.1% HCl-ethanol solution, and the activity of the solution was counted as a function of time. As shown in Fig. 1, the 0.1% HCl-ethanol solution dissolved the oxide quickly and attacked the copper to a negligible extent. About 10 sec were sufficient to dissolve an oxide layer $\sim 500\text{\AA}$ thick.

The thickness of copper removed is plotted as a function of anodizing time in Fig. 2 for various current densities. The lines do not go through zero because of the formation of natural oxide before anodizing, a phenomenon also observed on Al (1), Mo (6), Si (3), and W (2). The thickness removed in each anodizing-dissolution step was determined by counting both the anodizing cell and the solvent for ⁶⁴Cu content and by using the corrected-for-decay value of specific activity to convert to micrograms of copper.

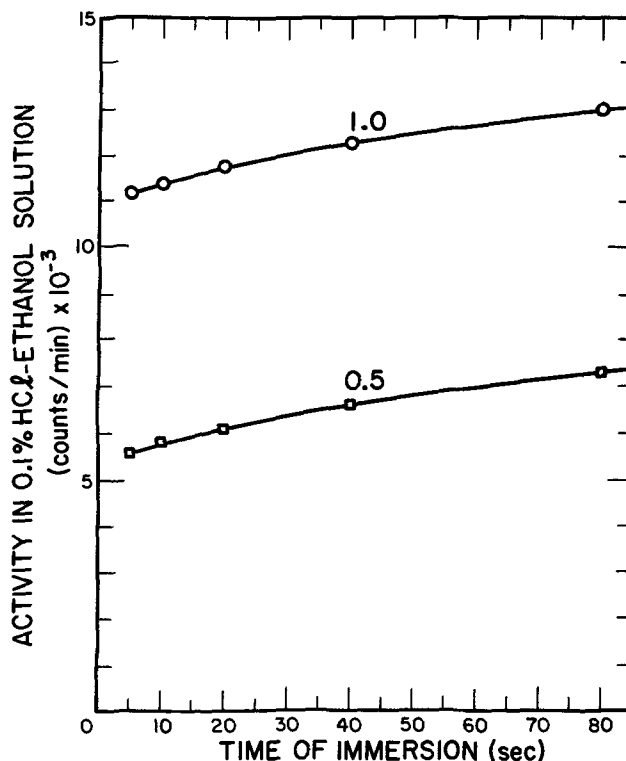


Fig. 1. Plot of ⁶⁴Cu activity of 0.1% HCl-ethanol solution after immersion of an anodized copper sample in solvent for various times. The different thicknesses of copper oxide were formed by anodizing for 30 sec with current densities of (□) 0.5 and (○) 1.0 mA/cm².

Key words: copper, anodization, sectioning, thin films.

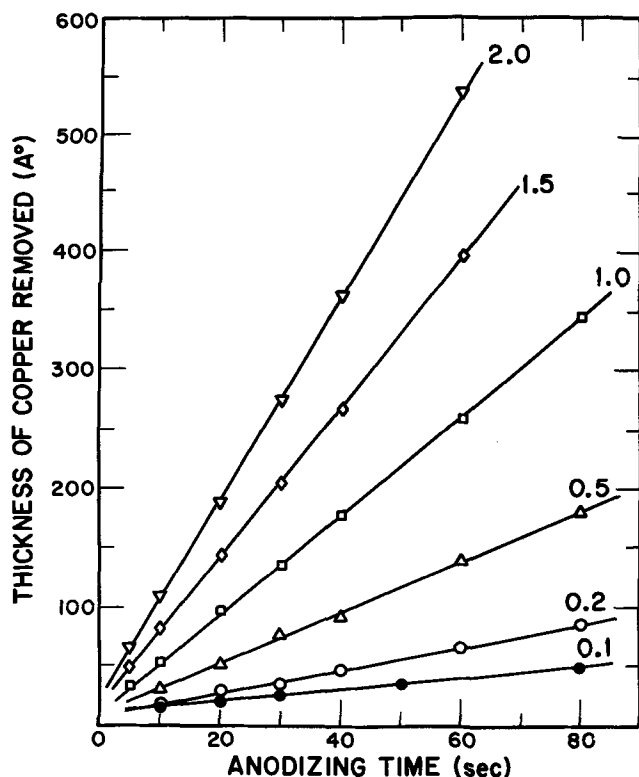


Fig. 2. Calibration of anodizing of monocrystalline copper in aqueous electrolyte that contained 0.01% Na_2SO_4 . The numbers on the curves indicate the anodic current densities in units of mA/cm^2 .

The relative amounts of activity in the electrolyte and stripping solution depended on the current density and anodizing time. The amount of material removed per anodizing step under identical conditions was reproducible to $\pm 3\%$. The sample was also weighed on a microbalance before and after removal of 20 sections. The difference between amounts of material removed, as measured by the two techniques was less than 9%, which is within experimental error. The step height on a nonradioactive copper crystal, part of which was masked by a spot of Tygon paint, was measured on an interference microscope after anodizing and removing 45 sections under the same current-density and time conditions. The step height agreed, within experimental error, with the thickness removed from the radioactive sample. Interference microscopy showed that the copper surface remained clean and flat after sectioning.

The thickness of copper that was anodically oxidized in 1 sec, deduced from the slopes of the curves in Fig. 2, is plotted in Fig. 3 as a function of current density. The anodizing rate x' in $\text{Å}/\text{sec}$ is related to the current density i in mA/cm^2 by the equation $x' = 4.2i$.

The same anodizing treatments on a (100) face of a copper single crystal yielded the same anodic film thickness, which indicated that the anodizing rate is orientation independent. The same observation was made in anodizing gold (4) and silver (7).

Summary

The anodic oxidation technique can be used to remove thin uniform sections from copper. An aqueous

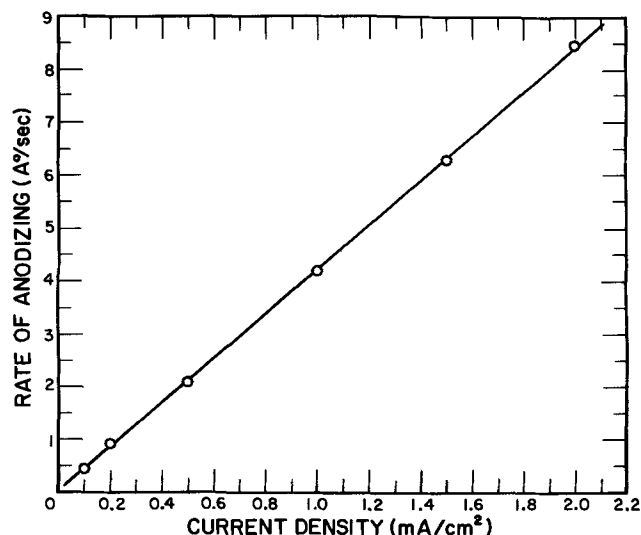


Fig. 3. Relationship between rate of anodizing and anodic current density.

solution of 0.01% Na_2SO_4 was used as the electrolyte. A solution of 0.1% HCl in ethanol appears to be the best solvent for removing the copper oxide. The rate of anodizing increases linearly with the current density, according to the relation $x' = 4.2i$.

Acknowledgment

Work performed under the auspices of the U.S. Atomic Energy Commission.

Manuscript received June 5, 1972; revised manuscript received June 29, 1972.

Any discussion of this paper will appear in a Discussion Section to be published in the June 1973 JOURNAL.

REFERENCES

1. J. A. Davies, J. Friesen, and J. D. McIntyre, *Can. J. Chem.*, **38**, 1526 (1960).
2. M. McCargo, J. A. Davies, and F. Brown, *Can. J. Phys.*, **41**, 1231 (1963).
3. J. A. Davies, G. C. Ball, F. Brown, and B. Domeij, *ibid.*, **42**, 1070 (1964).
4. J. L. Whitton and J. A. Davies, *This Journal*, **111**, 1347 (1964).
5. R. E. Pawel, *Rev. Sci. Instr.*, **35**, 1066 (1964).
6. M. R. Arora and R. Kelly, *This Journal*, **119**, 270 (1972).
7. Nghi Q. Lam, S. J. Rothman, and L. J. Nowicki, *ibid.*, **119**, 715 (1972).
8. J. L. Whitton, *J. Appl. Phys.*, **36**, 3917 (1965).
9. B. Perović and T. Jokić, VI^e Conf. Intern. sur les Phénomènes d'Ionisation dans les Gas, Paris, Vol. II, p. 15 (1963).
10. R. Kelly, *J. Appl. Phys.*, **39**, 5298 (1968).
11. T. Andersen and G. Sørensen, *Rad. Effects*, **2**, 111 (1969).
12. C. Jech, *Phys. Status Solidi*, **27**, 573 (1968).
13. Nghi Q. Lam and R. Kelly, submitted to *Can. J. Phys.*
14. H. Lutz and R. Sizmann, *Z. Naturforsch.*, **19a**, 1079 (1964).
15. R. Kelly, *Can. J. Phys.*, **46**, 473 (1968).
16. D. Gupta and R. T. C. Tsui, *Appl. Phys. Letters*, **17**, 294 (1970).

Multinuclear Growth of Dislocation-Free Planes in Electrocrystallization

V. Bostanov, R. Roussinova, and E. Budevski

Division of Electrochemical Power Sources, Bulgarian Academy of Sciences, Sofia, Bulgaria

The importance of two-dimensional nucleation for the electrodeposition of metals was recognized as early as 1931 by Volmer and Erdey-Gruz (1). This mechanism was confirmed experimentally in recent years only using dislocation-free crystal planes (2). The kinetics of the process were closely investigated and a number of kinetic parameters were also obtained. A short account of some of the latest results attained with dislocation-free planes of silver single crystals will be given in this paper. The preparation technique and the experimental conditions are the same as described in Ref. (2) and more detailed in Ref. (3).

The growth of dislocation-free planes is governed by two-dimensional nucleation. At low current densities the overpotential oscillates around a value which is the critical value where the rate of two-dimensional nucleation becomes noticeable. This wavering of the potential (Fig. 1) is evidently connected with the reiterating nucleation process. In the initial stage the plane is completely intact and does not expose sites of growth. When the current is switched on, the overpotential rises rapidly, thus increasing the probability for the nucleation process. A nucleus can be formed only after the critical value of the overvoltage is exceeded. Once a nucleus is formed, the electrode begins to offer an increasing number of growth sites proportional to the periphery of the growing monolayer, the deposition of the metal becomes easier, and the overvoltage drops. Propagating over the surface, the step surrounding the new layer reaches the bounds of the plane and begins to dissolve. With this, the number of growth sites diminishes and the overvoltage rises again, making possible the nucleation of a second layer. The period of this reiterating process is determined by the electric charge required for the formation of a monolayer and is inversely proportional to current density.

Using a potentiostatic pulse technique, the kinetics of nucleus formation were investigated and Volmer's equation

$$I = k_1 \exp(-k_2'/\eta) \quad [1]$$

was verified. Here I denotes the nucleation rate ($\text{sec}^{-1} \text{cm}^{-2}$), η is the overpotential (V), and k_2' contains the specific edge energy, ϵ , of a monatomic layer. For the cubic plane of silver in 6N silver nitrate solution a value of $2.1 \cdot 10^{-6} \text{ erg} \cdot \text{cm}^{-1}$ was found for ϵ .

It should be stressed again that the growth process at low current densities is a periodic one and a steady state cannot be reached. This is due to the fact that, once a nucleus is formed, the overpotential drops rapidly below the critical nucleation value according to the increasing periphery of the spreading monolayer. A new nucleus can be formed only after the completion of the previous monolayer.

In contrast, at high current densities, a wavering of the potential is observed only in the initial stage. The initial oscillations are very similar to those obtained at low current densities but they die away gradually and a steady state is reached (Fig. 2). The picture is very characteristic for the case and highly reproducible. The period of the oscillations is inversely proportional to the current density; and the product of these two quantities gives an amount of electricity equivalent to the deposition of one monatomic layer of silver. The number of oscillations in the transition period is

Key words: crystal growth, electrocrystallization, silver single crystals, two-dimensional nucleation.

nearly constant and slightly decreases with increasing current density. The microscopic observation of the crystal plane in the steady-state condition reveals a slightly visible surface profile.

The explanation of the described effect is obviously connected with a multinuclear type of growth. At high current densities the overpotential remains for a relatively longer period at a high value, and more than one nucleus can be formed. When this period becomes longer, the probability for nucleus formation on the already formed first layer of nuclei increases; and a multilayer structure is obtained. The process is wavering only in the initial stage, but the multilayer surface structure determines a dying away of the initial oscillations and a steady state is reached.

The first theoretical approach to the problem of multinuclear growth at constant supersaturation (corresponding to constant overvoltage) was made by Hillig (4), who derived an expression for the rate of growth in terms of the two-dimensional nucleation rate and the rate of propagation of monatomic steps. A more precise calculation was made later by Borovinskii and Zindergosen (5) and by Armstrong and Harrison (6). Using mathematical simulation the same problem was treated also by Bertocci (7). Nonsteady-

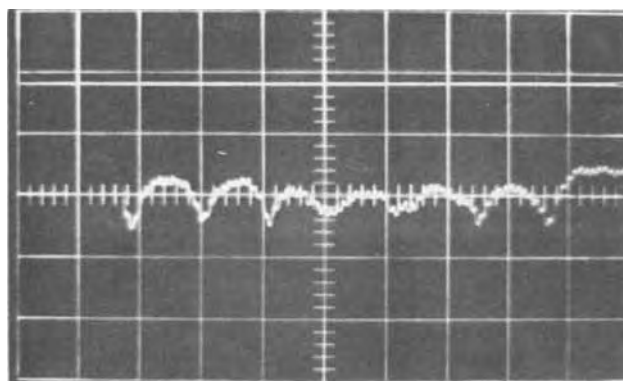


Fig. 1. Fluctuations of the overpotential at constant current growth of a dislocation-free cubic plane: current density, $5.8 \cdot 10^{-4} \text{ A} \cdot \text{cm}^{-2}$; vertical sensitivity, 5.2 mV/cm, time base 0.2 sec/cm.

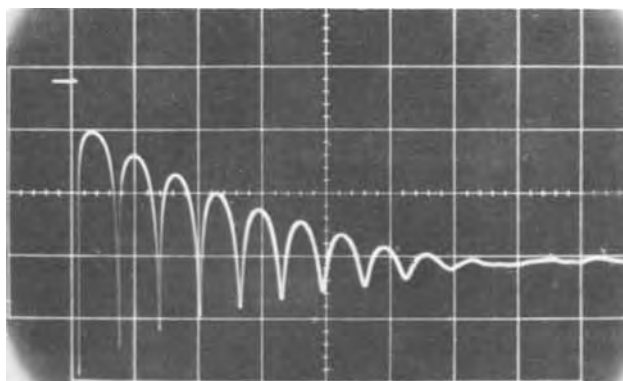


Fig. 2. Damped oscillations at high current densities: current density $2.5 \cdot 10^{-2} \text{ A} \cdot \text{cm}^{-2}$; vertical sensitivity, 5 mV/cm, time base 10 msec/cm.

state corrections of the nucleation process were introduced recently by Stoyanov (8). The first to adapt the problem to the case of electrodeposition were Armstrong and Harrison. They used Kolmogorov's equation (9), adapted to the case of electrolytic growth by Fleischman and Thirsk (10), and arrived at an expression of the form in Eq. [2] given below. They showed, in addition, that, in the initial stage, oscillation of the current should be observed which must die away when a steady-state multilayer structure of the surface is attained.

The theory obviously describes, very well, the experimentally obtained facts. Moreover, according to Borovinskii and Zindergosen the number of monolayers for which a steady state is reached should be about eight, which seems to be experimentally verified (Fig. 2). In all treatments for the steady-state current density an expression of the form

$$i = q_{\text{mon}} \alpha I^{1/3} v^{2/3} \quad [2]$$

is obtained, where I is the rate of nucleation ($\text{sec}^{-1} \text{cm}^{-2}$), v the propagation rate ($\text{cm} \cdot \text{sec}^{-1}$) of monatomic steps, and q_{mon} the amount of electricity required for the formation of a monatomic layer ($\text{coulombs} \cdot \text{cm}^{-2}$). The constant, α , varies in narrow limits from theory to theory.

It was already shown that the two-dimensional nucleation rate can be expressed by Volmer's Eq. [1] and is dependent on the overvoltage. For the second term in Eq. [2], the rate of propagation of monosteps v , we can assume a linear dependence on overvoltage (small values of the overvoltage are understood)

$$v = k\eta \quad [3]$$

This relation was found to be consistent with experiment (11) in the explanation of the current-square overvoltage law found on planes with screw dislocations following Frank's spiral growth theory. It was recently confirmed by Bostanov and Roussinova (12) in a very close investigation of the propagation rate of monatomic steps on dislocation-free crystal planes.

Having in mind Eq. [1] and [3], Eq. [2] can be transformed to

$$\log i \eta^{-2/3} = \log q_{\text{mon}} \alpha k_1^{1/3} k_2^{2/3} - k_2/3\eta$$

Plotting $\log i/\eta^{2/3}$ vs. $1/\eta$, an easy verification of the theory can be obtained (Fig. 3). The slope of the curve contains the specific edge energy ϵ [see for instance Ref. (2)], for which a value of $2.2 \cdot 10^{-6} \text{ erg} \cdot \text{cm}^{-1}$ was found. This value is in excellent agreement with the value obtained from the experiments with single nuclei described above (2).

A discrepancy of more than four to six orders of magnitude of the frequency factor k_1 obtained from both experiments was found. This discrepancy can hardly be ascribed to defects of the theories. So, for instance, the consideration of nonstationary effects as made by Stoyanov (8) cannot explain this large deviation of k_1 in both cases. Remembering that the only difference in the process of nucleation is the fact that nucleation at high current densities proceeds on a

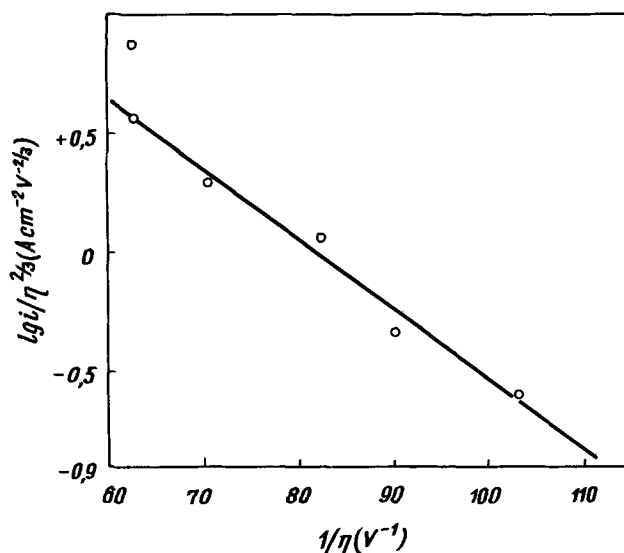


Fig. 3. Experimental plot of $\log i \cdot \eta^{-2/3}$ vs. η^{-1} (the overvoltage, η , is corrected for the ohmic potential drop in the electrolyte).

fresh surface, adsorption effect could also be taken into account. The larger value of k_1 found in this case seems to be consistent with this idea.

Manuscript submitted Feb. 18, 1972; revised manuscript received May 15, 1972. This was Paper 140 presented at the Cleveland, Ohio, Meeting of the Society, Oct. 3-7, 1971.

Any discussion of this paper will appear in a Discussion Section to be published in the June 1973 JOURNAL.

REFERENCES

1. T. Erdey-Gruz and M. Volmer, *Z Physik. Chem.*, **157**, 165 (1931).
2. E. Budevski, V. Bostanov, T. Vitanov, Z. Stoyanov, A. Kotzeva, and R. Kaishev, *Phys. Status Solidi*, **13**, 577 (1966); *Electrochim. Acta*, **11**, 1697 (1966).
3. V. Bostanov, A. Kotzeva, and E. Budevski, *Bull. Inst. Chim. Phys., Akad. Bulgare Sci.*, **6**, 33 (1967).
4. W. B. Hillig, *Acta Met.*, **14**, 1868 (1966).
5. L. A. Borovinskii and A. N. Zindergosen, *Dokl. Akad. Nauk SSSR*, **183**, 1308 (1968).
6. R. Armstrong and J. Harrison, *This Journal*, **116**, 328 (1969).
7. U. Bertocci, *Surface Sci.*, **15**, 286 (1969).
8. S. Stoyanov, *Comm. Dep. Chem., Bulgare Acad. Sci.*, **3**, 491 (1970).
9. A. N. Kolmogorov, *Izv. Akad. Nauk Uz. SSR, Ser. Fiz. Mat.*, **3**, 356 (1937).
10. M. Fleischmann and H. R. Thirsk in "Advances in Electrochemistry and Electrochemical Engineering" Vol. 3, p. 123, P. Delahay, Editor, John Wiley & Sons, Inc., New York (1963).
11. V. Bostanov, R. Roussinova, and E. Budevski, *Comm. Dept. Chem., Bulgare Acad. Sci.*, **2**, 885 (1969); also c.f. R. Kaishev and E. Budevski, *Contemp. Phys.*, **8**, 489 (1967).
12. V. Bostanov and R. Roussinova, To be published.

Chemical Analysis of Electrodeposited Ni-Ni Bonds by Auger Electron Spectroscopy

H. L. Marcus, J. R. Waldrop, F. T. Schuler, and E. F. C. Cain

North American Rockwell Science Center and North American Rockwell Rocketdyne Division,
Thousand Oaks, California 91360

Successfully obtaining a mechanically strong, reliable metal-metal bond in an electrodeposition process is not always a straightforward, well-understood procedure. Thin electrodeposits, for example, will exhibit poor peel resistance unless plating bath conditions are carefully optimized, traditionally through experience, trial, and, perhaps, luck. It is not surprising, then, that diagnosis and correction of poor results is often difficult, especially if the problem is due to contamination on the surface where electrodeposition is to occur. However, as Harris (1) has suggested, Auger electron spectroscopy (AES) is a method of surface chemical analysis particularly well suited for determining electrodeposition surface contaminants. Even so, not much work has been done in this application of AES.

The principal strengths of AES lie in an ability to detect elements in the first few atomic layers of a surface (typically $\sim 10\text{\AA}$) and a sensitivity to elements throughout the periodic table (2). Briefly, in AES a sample is excited by a beam of kilovolt electrons (the primary beam) and the resulting secondary electrons are energy analyzed with an electron spectrometer. In the energy range between 0-1000 eV especially, the secondary electron spectrum contains peaks arising from the emission of Auger electrons by elements at the sample surface (hence, Auger electron spectrum), the position of a given peak in energy is characteristic of a particular element. For a fuller description of AES and further references see the recent reviews by Chang (3), and Sickafus and Bonzel (4).

In this paper we report experiments using AES to determine the chemical composition at electrodeposited Ni-Ni interfaces so as to diagnose and solve a vexing fabrication problem in a relatively direct manner. Specifically, thick nickel laminates were formed from a series of individual electrodeposits, each finished piece of material thereby having several metal-metal bonds. The resulting bulk material showed in tensile testing no degradation of mechanical properties (yield or ultimate strength) over pure Ni. On the other hand, samples of the material sometimes showed minimal resistance to crack formation and propagation along a bond surface. By using AES techniques the chemical effects causing the Ni-Ni bond embrittlement were determined.

Experimental Procedure

The nickel laminate used in these experiments was electrodeposited from a nickel-sulfamate bath. After a thickness of about 0.2 in. was deposited, the material was removed from the deposition bath and the surface smoothed mechanically. The electrodeposit was then chemically polished followed by cathodic activation in a sulfuric acid bath. Next it was placed back into the sulfamate bath for continued nickel deposition. This was continued for several cycles until a deposit about 1 in. thick was formed. Samples $0.10 \times 0.14 \times 1.0$ in. were cut from the deposit, the 1.0 in. direction being parallel to the growth direction. The samples were evaluated for tensile properties along the growth direction and resistance to impact loading transverse to the growth direction. Samples from material with low-impact strength were used for the AES studies.

Two kinds of AES experiments were performed, each in a different type system. The apparatus for the first

type of experiment was an ultrahigh vacuum (10^{-10} Torr) bakable system equipped with a sensitive cylindrical mirror electron spectrometer (5) and an electron gun producing a primary electron beam ~ 0.4 mm in diameter for sample excitation. With this system, the experimental procedure is to first bake the system at 200°C to reduce active gases, then to fracture a nickel laminate *in situ* for immediate AES chemical analysis. The resulting spectra are recorded as $dN(E)/dE$ vs. E curves, where $N(E)$ is the relative number of electrons at energy E . After the initial AES analysis, the chamber is backfilled with high-purity argon and the sample argon ion sputtered in the manner of Marcus and Palmberg (6, 7). This technique allows the determination of a chemical profile into the fracture surface, with the underlying assumption that the 400 eV argon ions used have unity-sputtering efficiency.

The second AES experiments involved AES performed in a scanning electron microscope (SEM) (8). This technique offers high spatial resolution ($\sim 0.3\mu$) point-by-point surface chemical analysis, albeit with a loss in sensitivity compared to the apparatus described above. For our experiments the newly developed MacDonald and Waldrop (9) method of Auger electron images was employed to determine the spatial homogeneity of any bond surface impurity found. An Auger electron image for a particular element is a two-dimensional array of points, with each image point denoting the presence or absence of the element at a corresponding sample surface point. If a conventional SEM micrograph is obtained of the same area over which an Auger image is taken, a direct two-dimensional comparison of surface topography and surface elemental distribution is made.

Results and Discussion

Figure 1a shows the Auger electron spectrum from a nickel-nickel laminate that fractured in vacuum at room temperature along the bond surface. The spectrum is dominated by the presence of peaks characteristic of silver. In addition, copper, which normally will coplate with nickel, is present in abundant amounts. To determine the extent of high silver concentration, the surface was sputtered with argon ions. Figure 1b is an Auger electron spectrum with approximately 20\AA of surface removed. It is immediately apparent that the silver is virtually absent and that the spectrum is basically that of nickel. Copper is still present at a level significantly higher than that shown in a spectrum taken away from the bond line, indicating excess copper electrodeposition close to the bond surface.

The source of the silver at the bond line was determined by analyzing the bond surface immediately after the various stages of the electrodeposition process. During the cathodic activation process, thin layers of silver appeared that were as thick as 50\AA , depending upon the activation parameters used. Metallic silver used at an earlier processing stage dissolved into the activation solution; this was the source of the silver in solution. No quantitative measurement of the silver concentration was made.

To determine the homogeneity of the silver over the bond surface, samples of the nickel-nickel laminate were fractured in an SEM equipped for AES. The SEM micrograph of the surface is shown in Fig. 2a. The

Key words: surface chemistry, fracture, transient deposition.

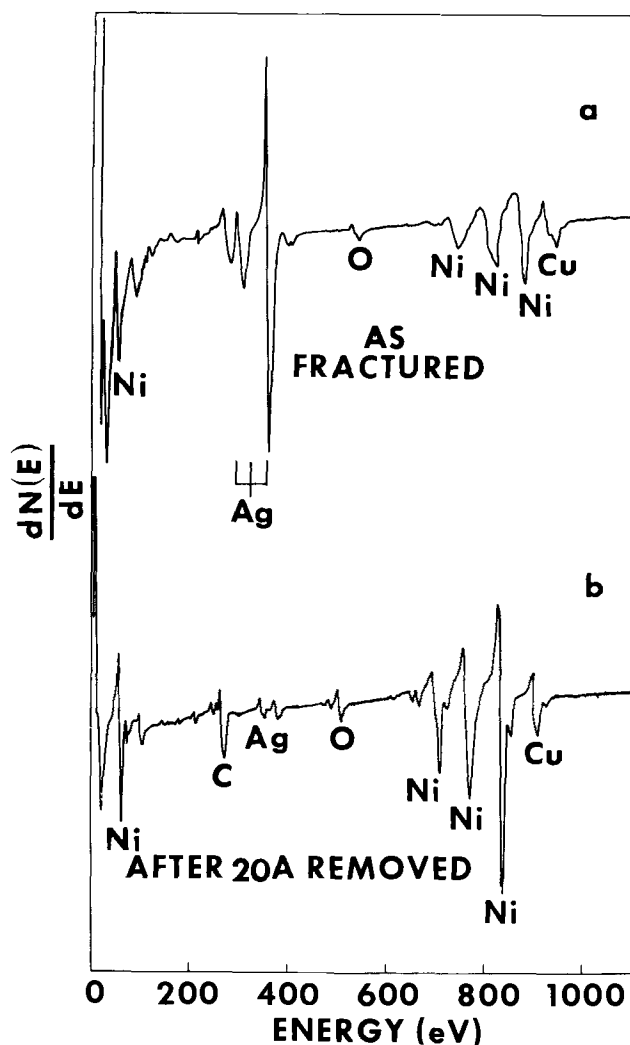


Fig. 1. Auger electron spectra from bond surface. (a) Initial, as fractured, (b) after 20Å removed from surface.

flat surface of the bond surface dominates, but small regions that apparently plastically deformed during fracture are also observed. Figure 2b shows the two-dimensional Auger electron image of silver over the fracture surface. An image point is white if a silver peak is present with a height greater than a predetermined minimum value. It is immediately apparent that the surface is totally covered except where some plastic tearing had apparently taken place. This is consistent with the minimal thickness of the silver described previously.

When the small amounts of silver present were removed from the activation baths the metal-metal bonds were no longer fracture sensitive. The fact that the silver alone was the primary cause of the embrittlement while the copper was not is consistent with the formation of brittle nickel-silver intermetallic interfaces. Since the copper-nickel system does not contain any intermetallics, it is not surprising that it does not behave as an interface embrittler.

The main emphasis in this paper has been on the determination of fracture surface chemistry of electrodeposited material using AES. It is clear that AES serves as a means of determining the chemistry associated with the interface layer in plating, electroforming, or any other deposition process where transient behavior can be expected.

Conclusions

1. Auger electron spectroscopy was used to identify the chemical composition of brittle electrodeposited nickel-nickel interfaces. Both silver and copper were found to be present at higher than the bulk concentration.

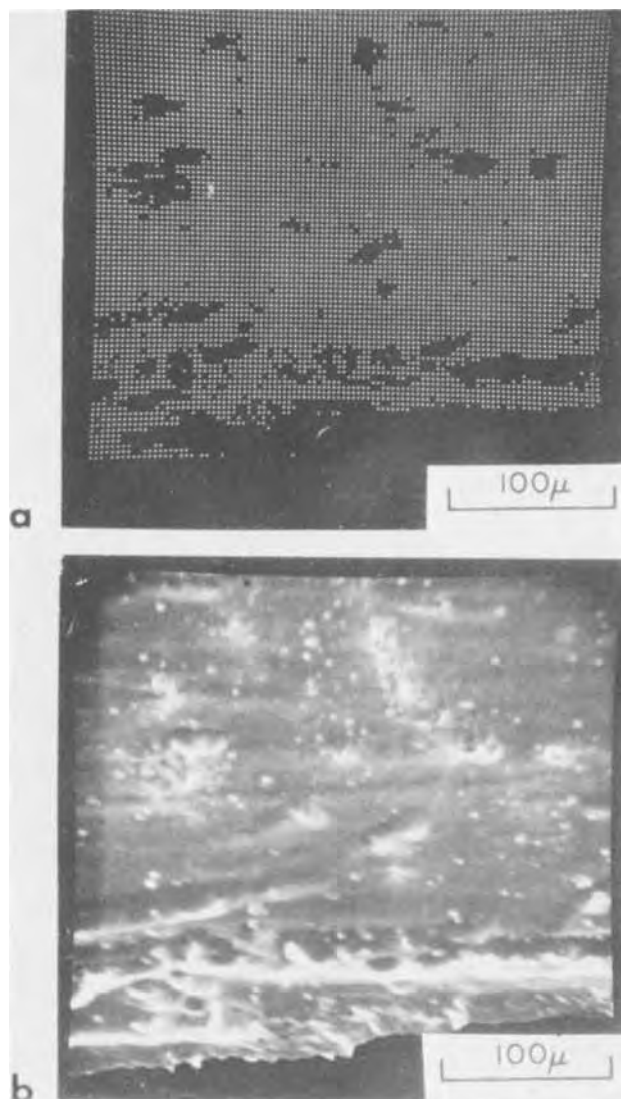


Fig. 2. (a) Auger electron image for Ag over bond surface. (b) SEM secondary electron micrograph of bond surface.

2. Using argon ion sputtering profiles, the extent of the excess silver was determined to be less than 20Å but the copper was present after removal of about 100Å.

3. AES in the SEM of the fractured nickel-nickel shows a uniform profile distribution of silver, except where limited amount of plastic deformation took place.

4. Removal of the silver from the electrochemical activation baths stops the embrittlement.

Manuscript submitted April 27, 1972; revised manuscript received May 22, 1972.

Any discussion of this paper will appear in a Discussion Section to be published in the June 1973 JOURNAL.

REFERENCES

1. L. A. Harris, *J. Appl. Phys.*, **39**, 1428 (1968).
2. L. A. Harris, *ibid.*, **39**, 1419 (1968).
3. C. C. Chang, *Surface Sci.*, **25**, 53 (1971).
4. E. N. Sickafus and H. P. Bonzel, *Progress in Surface and Membrane Science*, **4**, 115 (1971).
5. P. W. Palmberg, G. K. Bohn, and J. C. Tracy, *Appl. Phys. Letters*, **15**, 15 (1969).
6. H. L. Marcus and P. W. Palmberg, *Trans. Met. Soc. AIME*, **245**, 1664 (1969).
7. P. W. Palmberg and H. L. Marcus, *Trans. ASM*, **62**, 1016 (1969).
8. N. C. MacDonald, Proc. of the Fourth Annual SEM Symposium, O. Johari, Editor, ITTRI, 89 (1971).
9. N. C. MacDonald and J. R. Waldrop, *Appl. Phys. Letters*, **19**, 315 (1971).

Electrolytic Preparation of Azobenzenes

S. Wawzonek* and T. W. McIntyre

Department of Chemistry, University of Iowa, Iowa City, Iowa 52240

The macroscale electrolytic oxidation of aromatic amines to azobenzenes in acetonitrile is complicated in some examples by the formation of azophenines (1). The objective of the present work was to determine whether such side reactions could be minimized by using aqueous media for the oxidation. The electrode reactions were assumed to be similar to those in acetonitrile since anodic waves are reported for aromatic amines in aqueous media (2).

Experimental

Electrochemical oxidations were carried out in a 600 ml dye beaker using a Coor's porous cup (7.5 cm × 2.6 cm) for the cathode compartment. The cathode was a coil of No. 16 copper wire and the anode was a rotating platinum screen cylinder. The cell was cooled with ice water during the electrolysis. In the oxidation of dispersions or solutions of aniline, the anolyte was steam distilled and the distillate was extracted with pentane. The pentane solution was washed with dilute hydrochloric acid and upon removal of the solvent gave azobenzene. The hydrochloric acid solution upon neutralization gave aniline. A portion of the residue from the steam distillation was dissolved in acetonitrile and examined polarographically for nitrobenzene.

In the oxidation of substituted anilines the anolyte was evaporated to dryness and the residue was washed with water, dried and extracted with either ethyl acetate or chloroform, and the solution was chromatographed on alumina. Identification of products was made by infrared spectra and comparison with authentic samples.

Electrolytic oxidation of *p*-anisidine.—*p*-Anisidine (1.0g) was oxidized in an aqueous dimethylformamide (1:4) solution (90 ml) containing 0.5M sodium nitrate and pyridine (10 ml) at 10V under nitrogen. The initial current of 0.1A dropped to 0.02A after 9 hr. The anolyte was added to ice (100g) and the resulting solution was extracted with ether. Removal of the ether gave a solid which was dissolved in benzene and chromatographed on alumina. The first fraction obtained was 4,4'-dimethoxyazobenzene (0.033g); mp 162°-163°. The second fraction was an oil which upon crystallization from ethanol gave a dark red powder which was rechromatographed on alumina using benzene. The first fraction was tetra-*p*-methoxyazophenine (0.157g); mp 236°-237°. The second fraction

* Electrochemical Society Active Member.

Key words: electrolytic oxidation, aromatic amines, aqueous media.

gave 2-amino-5-(*p*-methoxyanilino)-*p*-benzoquinone-bis-(*p*-methoxyanil) (0.056g); mp 161°-163° [Ref. (3) 164°]. The acetyl derivative melted at 213° [Ref. (3) 213°]. Heating the 161°-163° compound with *p*-anisidine and concentrated hydrochloric acid gave tetra-*p*-methoxyazophenine (3).

Results and Discussion

The results obtained in the electrolytic oxidation of aromatic amines are summarized in Table I and indicate that the best yields of azobenzene were obtained from the oxidation of aniline dispersions. Passing air through the solution during the electrolysis did not affect the yields of azo compound and did not convert the intermediate radicals into nitrobenzene. The main by-product was aniline black.

Use of dispersions of substituted anilines in a mixture of acetonitrile and water did not increase the yield materially over that from solutions using mixtures of dimethylformamide and water.

The oxidation of *p*-anisidine in a mixture of dimethylformamide and water differed from the behavior observed in acetonitrile (1); 2-amino-5-*p*-methoxyanilino-*p*-benzoquinone-bis(*p*-methoxyanil) was isolated in addition to the azo compound and azophenine. The isolation of these products indicates that the presence of water does not materially affect the course of the oxidation of aromatic amines. The yield of azophenine was greater (15.7%) however than that obtained in acetonitrile (1) (8.6%).

Acknowledgment

The authors wish to acknowledge the support of the U.S. Army Research Office under Contract DA-31-124-ARO-D-406 and Grant No. DA-ARO(D)-31-124-G351.

This work was abstracted in part from the Ph.D. thesis of T. W. McIntyre, February 1967.

Manuscript submitted April 18, 1972; revised manuscript received June 22, 1972.

Any discussion of this paper will appear in a Discussion Section to be published in the June 1973 JOURNAL.

REFERENCES

1. S. Wawzonek and T. W. McIntyre, *This Journal*, **114**, 1025 (1967).
2. V. D. Bezuglyi and Yu. I. Beilis, *Zh. Analit. Khim.*, **20**, 1000 (1965).
3. D. G. H. Daniels and B. C. Saunders, *J. Chem. Soc.*, 2112 (1951).

Table I. Electrolytic oxidation of aromatic amines in aqueous media

Compound	Solvent	Electrolyte	Applied voltage	Amp	Duration	Products
Aniline ^(a) (10g) + air	H ₂ O (160 ml)	1M KOH	8	1	4 hr	Azobenzene (21%) Aniline (5%)
Aniline ^(a) (10g) + N ₂	H ₂ O (160 ml)	1M KOH	8	1	4 hr	Azobenzene (18%)
Aniline ^(b) (8g) + N ₂	(1:2) H ₂ O-CH ₃ CN (150 ml)	0.5M KOH	15	0.4	10 hr	Azobenzene (4.2%)
Aniline ^(b) (8g) + air	(1:2) H ₂ O-CH ₃ CN (180 ml)	0.5M KOH	15	0.4	10 hr	Azobenzene (8.8%) Aniline (9%)
<i>p</i> -Nitroaniline ^(a) (2.0g) + N ₂	(3:5) H ₂ O-CH ₃ CN (100 ml)	0.5M NaOAc	15	0.5-0.1	3 hr	4,4'-Dinitroazobenzene (2.8%)
2,4-Dinitroaniline ^(a) (2.0g) + N ₂	(3:5) H ₂ O-CH ₃ CN (160 ml)	0.5M NaOAc	15	0.5-0.1	3 hr	2,2',4,4'-Tetranitroazobenzene (38%) 2,4-Dinitroaniline (41.5%)
2,4-Dinitroaniline ^(b) (1g) + N ₂	(1:3) H ₂ O-DMF (100 ml)	0.5M NaNO ₃	10	0.1-0.01	6 hr	2,2',4,4'-Tetranitroazobenzene (31%) 2,4-Dinitroaniline (63%)
2,4-Dichloroaniline ^(b) (2.0g) + N ₂	(2:1) H ₂ O-DMF (100 ml)	1M NaNO ₃	10	0.1	7 hr	2,2',4,4'-Tetrachloroazobenzene (38%) ^(c) 2,4-Dichloroaniline (22%)
2,4,6-Trichloroaniline (1.0g) + N ₂	pyridine (10 ml) DMF (100 ml) pyridine (10 ml)	0.5M NaNO ₃	10	0.05	6 hr	2,2',4,4',6,6'-Hexachloroazobenzene (47.5%) 2,4,6-Trichloroaniline (20%)

^(a) Dispersion.

^(b) Solution.

^(c) The yield obtained of this compound in acetonitrile (1) was 30.1%.

Periodic Phenomena During the Anodic Dissolution of Iron in Sodium Chloride Solutions

J. Postlethwaite¹ and A. Kell

University of Manchester, Institute of Science and Technology, Manchester 1, England

Periodic phenomena related to unstable surface films have been previously observed for a wide variety of metal electrode systems. These films may be the pre-passive salt films formed prior to true passivation by an oxide film (1) or may be the thicker films present during electropolishing (2) or other high-rate dissolution processes similar to those encountered in electrochemical machining (3). This note describes the periodic potential oscillations that have been observed during the galvanostatic anodic dissolution of iron in 20 weight per cent (w/o) NaCl solution. This work was part of a study aimed at a better understanding of the factors controlling the electrode processes associated with "wild-cutting," which occurs in NaCl solutions during electrochemical machining at the low CD region at the edge of the machining zone.

The iron electrodes, nominal composition, Si trace, Sn 0.007, P 0.016, Ni 0.020, Cd 0.03, Cd 0.06, Mn 0.36 w/o, were at the bottom of a 3.8 cm square flow duct (Fig. 1), which was preceded by an entry length of 30 equivalent diameters. The anode was stopped off with lacquer to give a working surface 0.5×2 cm long; excessive undercutting and major changes in the electrode geometry were found with smaller working surfaces. The anode potentials were measured with respect to an Ag/AgCl reference electrode with a probe terminating 2 mm above the downstream end of the anode. An interrupter technique which has been described previously (4, 5) was used to determine the ohmic contribution to the overpotentials. The total anode overpotential was measured after 5 min at each current setting following which the IR drop was determined. Separate experiments were done with the electrolyte stagnant and flowing with Reynolds numbers in the range 4000 to 30,000.

Tafel behavior was observed (Fig. 2) up to around 200 mA/cm^2 following which there was an increase in the resistance to the dissolution process shown by the increased slope of the electrolysis curves. These curves are corrected for ohmic overpotential as described later. The latter part of the electrolysis curves corresponds to the start of the ECM regime and especially to the low CD "wild-cutting" processes, and it was in this region of the electrolysis curves that the potential

oscillations were observed. A typical potential-time trace is shown in Fig. 3a. Following the initial rapid rise in the potential there was a slow secondary rise followed by a steady potential region and then after 17 sec the potential started to oscillate with an approximately constant amplitude. The individual fluctuations are discerned in Fig. 3b, where the frequency is seen to be around 50 Hz. The oscillations which occurred in both the stagnant and flowing solutions had a maximum amplitude at intermediate CD's; decreasing in amplitude and increasing in frequency at the higher CD's.

The interrupter measurements showed the fluctuations to be largely ohmic in nature. The ohmic overpotentials were determined from the blank section on the waveform on an oscilloscope screen when a continuous series of constant current pulses, with equal on and off times, was applied to the cell. As discussed elsewhere (5) the maximum potential attained during each pulse, after some number of pulses has been passed, corresponds to the steady-state potential for the appropriate CD. At the higher CD's, the oscillograms initially took the characteristic shape (Fig. 4a) observed at $\text{CD} < 200 \text{ mA/cm}^2$; but after some time had elapsed both the amplitude and shape of the transients started to change, as shown in Fig. 4b, and the waveform started to cycle between the two forms as shown in Fig. 4c. During this behavior a secondary potential growth occurred and the resulting higher overpotential was seen to be mainly ohmic in nature. The maximum value of these oscillations were the same as those obtained during the "steady-state" experiments described above, and it seems that these former oscillations were in fact due to factors which changed the ohmic resistance but had little effect on the activation overpotential.

The electrolysis curves shown in Fig. 2, were constructed on the basis of the minimum value of the overpotential, after the onset of the potential oscillations. The IR drop in this condition was taken as the value given when the waveform had the form shown in Fig. 4a.

¹ Present address: Faculty of Engineering, University of Saskatchewan, Regina Campus, Regina, Saskatchewan, Canada.

Key words: periodic, electrochemical-machining, iron, interrupter, overpotential.

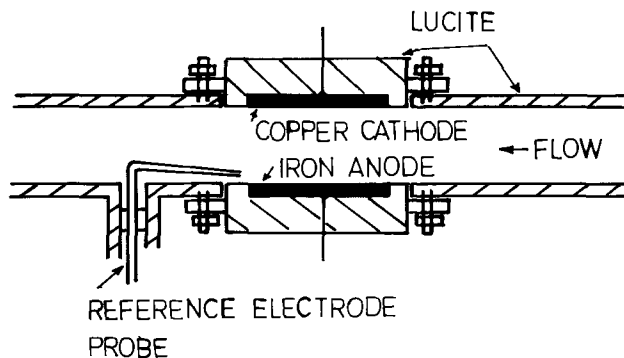


Fig. 1. The electrochemical flow cell. The flow duct was 3.8 cm square, with the working surface of the anode 0.5×2 cm longitudinal to the direction of the flow.

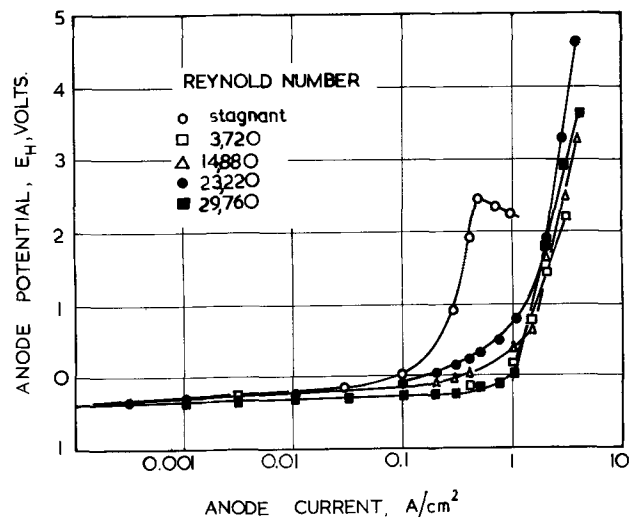


Fig. 2. Electrolysis curves, corrected for ohmic overpotential, for anodic dissolution of iron in 20 w/o NaCl solution at 25°C.

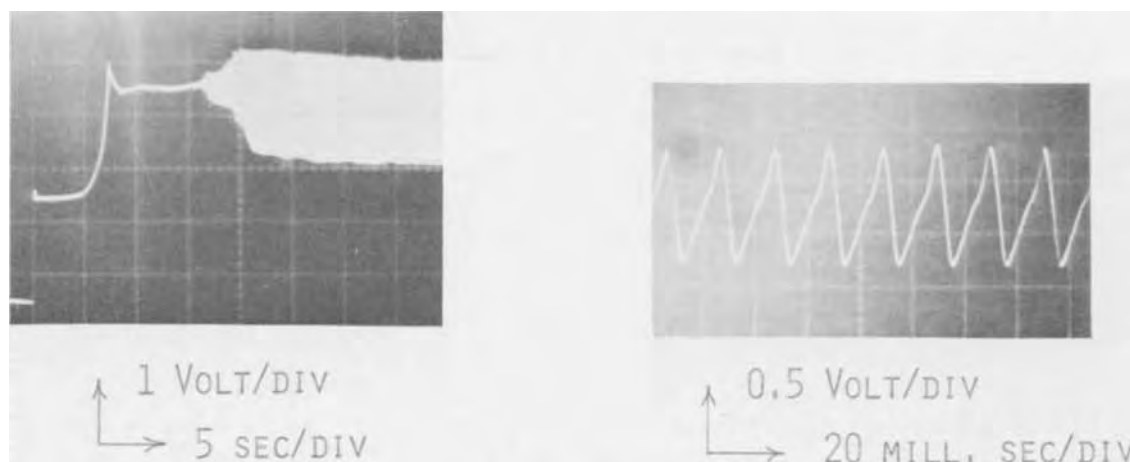


Fig. 3. Periodic fluctuations of the potential during the "steady-state" galvanostatic analysis of the anodic dissolution of iron at 2 A/cm², 20 w/o NaCl solution, Reynolds number, 4000.

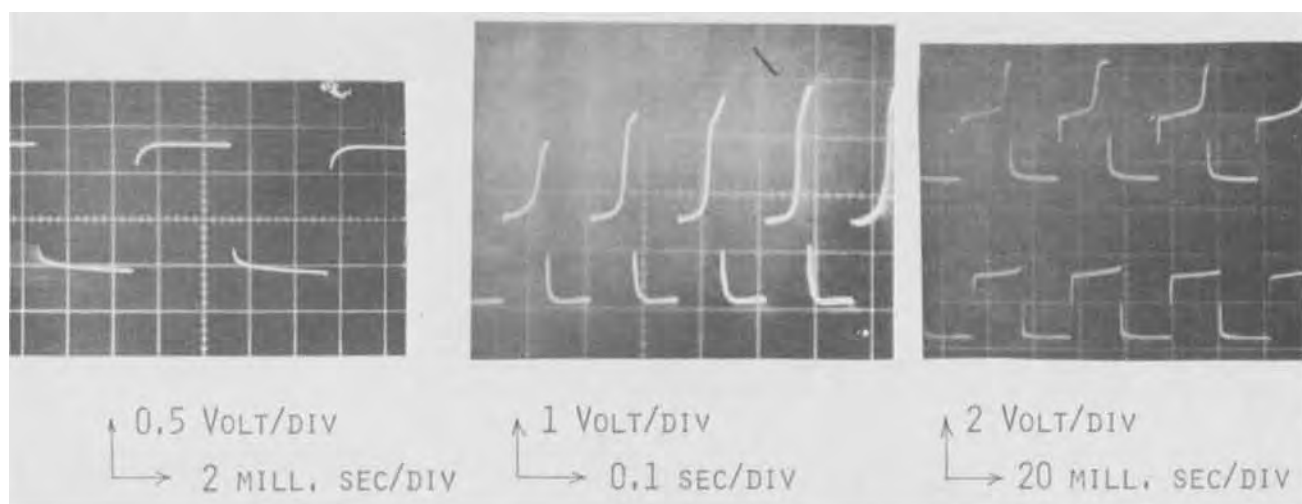


Fig. 4. Potential-time behavior during pulsed current analysis of iron in 20 w/o NaCl solution; (a), 2 A/cm², oscillogram in absence of secondary growth; (b), 2 A/cm², secondary potential growth with increased IR drop; (c) 4 A/cm² the two extreme forms of the waveform in the presence of the cyclic secondary growth. Reynolds number, 4000.

The most likely reason for the potential oscillations is the presence of an unstable porous nonprotective film. Hoare (6) and Chin (7) have reported the presence of nonprotective films on Fe in NaCl solutions and other workers (3) have used motion photography to demonstrate the relation between potential oscillations and the formation and disruption of such films during the high-rate dissolution of copper.

The electron microprobe analysis of a film formed at 2 A/cm² during this work showed the film to contain 70% Fe. The sample was prepared in a beaker cell and withdrawn with the current still switched on. Line analysis gave many spots of 100% Fe, which indicates an extremely porous film, although the film may have been disturbed after the electrolysis. However, whatever the nature of this film, it seems that such films and the related periodic phenomena may play an important part in the "wild-cutting" processes and require further investigation.

REFERENCES

1. U. R. Evans, "The Corrosion and Oxidation of Metals," p. 230, E. Arnold, London (1960).
2. H. T. Francis and W. H. Colner, *This Journal*, **97**, 237 (1950).
3. J. Cooper, R. H. Muller, and C. W. Tobias, in "Fundamentals of Electrochemical Machining," Charles L. Faust, Editor, p. 300, The Electrochemical Society Softbound Symposium Series, Princeton, N. J. (1971).
4. J. Postlethwaite and D. M. Sharp, *Electrochim. Acta*, **13**, 571 (1968).
5. J. Postlethwaite and D. M. Sharp, *Trans Inst. Chem. Engrs.*, **47**, T198, (1969).
6. J. P. Hoare, *This Journal*, **117**, 142 (1970).
7. D. T. Chin, in "Fundamentals of Electrochemical Machining," Charles L. Faust, Editor, The Electrochemical Society Softbound Symposium Series, Princeton, N. J. (1971).

Electrolytic Reduction of Titanium Chlorides in Fused Alkali-Chloride Eutectics

F. Quemper, D. Deroo,* and M. Rigaud*

Department of Metallurgical Engineering, Ecole Polytechnique de Montréal, Montreal, P. Q., Canada

There is great interest today in the problem of an electrolytic method for producing titanium metal. One of the procedures involves the reduction of titanium halides in the fused LiCl-KCl eutectic.

Many authors (1-10) have studied the reduction mechanism of titanium chlorides. Bockris and co-workers (3) have concluded from polarographic measurements that the deposition of titanium in fused alkali-chlorides occurs by a secondary electrode process. This mechanism, which is also proposed by Dean (4) involves the primary reduction of an alkali-metal ion.

The secondary process has been contested by Reid (9) and later by Baboian *et al.* (10). These authors propose a direct mechanism for reduction of Ti(III) and Ti(II).

In this paper data are presented for the reduction of titanium tetra-, tri- and dichloride in fused LiCl-KCl and LiCl-NaCl eutectics. The influence of impurities in commercial titanium tetrachloride has also been investigated.

Experimental

The LiCl-KCl and LiCl-KCl-NaCl eutectic mixtures were prepared from Fisher Scientific chemical products, first dried and kept in a vacuum oven. Just before introducing titanium halides, the eutectics were electrolyzed with graphite electrodes at 1.5V for 24-48 hr.

Electrochemical measurements were carried out in a cylindrical furnace with a constant temperature zone 8 in. high. Temperature was controlled to $\pm 0.5^\circ\text{C}$ by a Chromel-Alumel thermocouple, which was enclosed in an alumina sheath in the melt, and controlled by a Lindberg Hevi-Duty furnace regulator.

Current potential curves were plotted by use of a potentiostat Tacussel PRT 20-10 Z coupled with a triangular wave generator GSTP-2 Tacussel and a Hewlett Packard XY recorder.

The electrochemical cell was a graphite crucible in a Pyrex glass cylinder. Anode and cathode were graphite cylinders (1/4 in. diameter). The anodic compartment was isolated by a sintered glass diaphragm. The reference electrode was described by Littlewood and was used in the Ag/Ag(I) system (11).

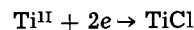
Titanium tetrachloride (Fisher Scientific) was a commercial product containing impurities. Pure titanium trichloride and dichloride were prepared by reaction of TiCl₄ vapor on Ti chips at high temperature (12).

Results and Discussion

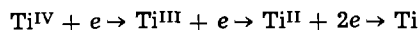
The current-potential curves for TiCl₄, TiCl₃, TiCl₂ reduction at 450°C in LiCl-KCl eutectic are shown in Fig. 1. We obtained the same results in LiCl-KCl-NaCl eutectic at the same temperature. The range of concentration is limited by the solubility of titanium tetrachloride at this temperature.

* Electrochemical Society Active Member.
Key words: electrolytic reduction, titanium, titanium chlorides, alkali-chloride eutectics.

In the case of TiCl₄, we observed four waves. The last wave, which appears just before alkali-metal ion discharge, corresponds exactly with the wave obtained by reduction of TiCl₂. By comparison with the results of Baboian and the equilibrium potentials given in the literature, it is possible to attribute to this wave the reaction



The same argument used for respectively the first and the second wave leads to the total mechanism.



The third wave is the most significant. It was first observed by Russian workers (13) and does not appear with pure TiCl₃. The Ti(Cl₂)³⁻ complex identified in the melt by some authors (14, 15), will give a wave in the case of TiCl₄ but also with pure TiCl₃. So, the hypothesis of kinetic wave of complex reduction is not applicable.

The impurity discharge is more probable. The most important impurities in titanium tetrachloride are: vanadium chloride, stannous chloride, and titanium oxychloride produced by hydrolysis.

Although the discharge potential of VII corresponds exactly with this wave (Fig. 2), the limiting current is too large for the amount of vanadium chloride in the melt. The concentration of stannous chloride is also negligible and may be neglected. Hence it is thought oxychloride reduction is responsible for the additional wave.

In conclusion, the primary mechanism of titanium halides reduction was confirmed. It is noted that pure titanium production from these melts will be in delicate balance due to hydrolysis of TiCl₄ and probable

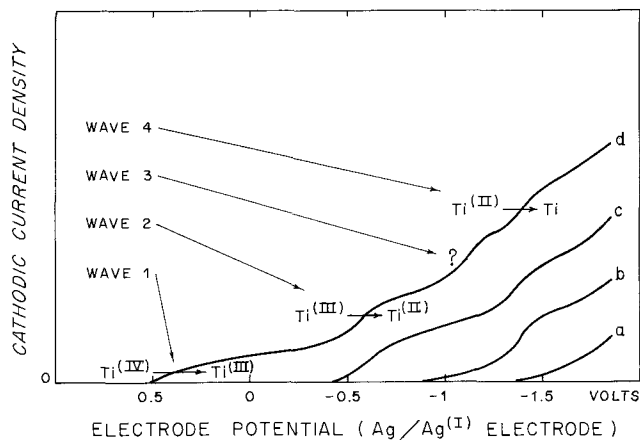


Fig. 1. Typical cathodic potential sweep on graphite electrode in LiCl-KCl eutectic, 450°C, 66 mV min⁻¹. a, solvent; b, solvent + TiCl₂; c, solvent + TiCl₃; d, solvent + TiCl₄.

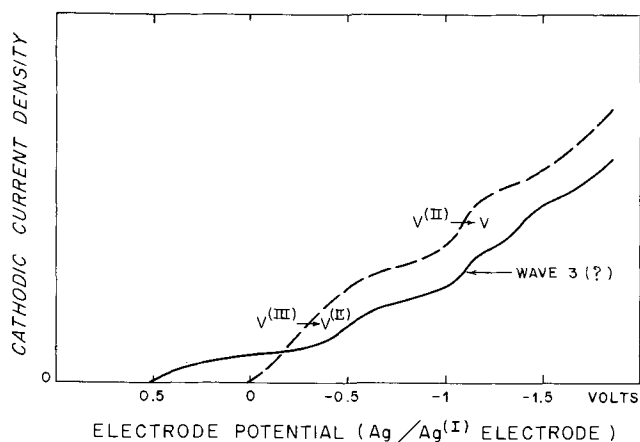


Fig. 2. Comparison between third wave of TiCl_4 reduction and V^{III} reduction wave (LiCl-KCl , 450°C , 66 mV mn^{-1}).

co-discharge of alkali metal ion (the last wave appears 100 mV before the solvent wall).

Acknowledgments

This work, conducted in the Metallurgical Engineering Department of the École Polytechnique, Montreal

was supported by the National Research Council of Canada under contract A-6536, and by CRP 254-71.

Manuscript submitted Nov. 5, 1971.

Any discussion of this paper will appear in a Discussion Section to be published in the June 1973 JOURNAL.

REFERENCES

1. B. J. Fortin, L. Gravel, J. G. Wurm, and R. J. A. Potvin, *This Journal*, **106**, 428 (1959).
2. A. Brenner and S. Senderoff, *ibid.*, **99**, 223C (1952).
3. J. O'M. Bockris, G. J. Hills, I. A. Menzies, and L. Young, *Nature*, **178**, 654 (1956).
4. R. S. Dean, *Metal. Ind. (London)*, **90**, 143 (1957).
5. H. K. Worner, G. M. Willis, and H. W. Worner, *This Journal*, **100**, 18C (1953).
6. M. J. Rand and L. J. Reimert, *ibid.*, **111**, 429 (1954).
7. M. A. Steinberg, S. S. Carlton, M. E. Sibert, and E. Wainer, *ibid.*, **102**, 332 (1955).
8. M. V. Smirnov and N. A. Loginov, *Izv. Sibirsk Otd. Akad. Nauk SSSR*, **64** (1962).
9. W. E. Reid, Jr., *This Journal*, **108**, 393 (1957).
10. R. Baboian, D. L. Hill, and R. A. Bailey, *Can. J. Chem.*, **43**, 197 (1965).
11. R. Littlewood, *Electrochim. Acta*, **3**, 270 (1961).
12. P. Ehrlich, H. J. Hein, and H. Kuhn, *Z. Anorg. Chemie*, **292**, 139 (1957).
13. R. V. Chernov, Private communication (1971).
14. M. V. Smirnov and N. Krasnov, *Trans. Elec. Urals Akad. Sci.*, **1**, 22 (1960).
15. A. Krohm and C. W. Bohn, *Plating*, **58**, 237 (1971).



Ion Implantation Effects of Nitrogen, Boron, and Aluminum in Hexagonal Silicon Carbide

Arrigo Addamiano,* Gordon Wood Anderson, James Comas,
Harold L. Hughes, and William Lucke

Naval Research Laboratory, Washington, D. C. 20390

ABSTRACT

The effects of the implantation of $^{14}\text{N}^+$, $^{11}\text{B}^+$, and $^{27}\text{Al}^+$ ions in hexagonal 6H SiC crystals were studied through optical and microanalytical methods. The optical data taken for 60 keV $^{14}\text{N}^+$ implants indicate that little damage occurs up to a fluence of 10^{14} cm^{-2} . For fluences between 10^{14} cm^{-2} and $1.3 \times 10^{15} \text{ cm}^{-2}$, there is a rapid increase of the optical absorption below $\sim 3 \text{ eV}$ with a broad absorption tail extending into the near infrared. For larger fluences, the optical absorption close to the band edge actually decreases. The band edge shifts to lower energies with increasing fluence. The radiation damage begins to anneal at low temperatures but is not completely removed until annealing at 1400°C . Boron and aluminum behave similarly to nitrogen as far as the general behavior of the damage in the implanted regions is concerned. Boron implanted crystals with peak concentrations in the 10^{20} cm^{-3} range show weak yellow "boron" luminescence in the implanted areas after annealing. Qualitative thermoelectric power measurements indicate that boron implants up to this level do not result in conversion of n-type layers to p-type layers. For the aluminum implants conversion from n-type to p-type was observed for the highest fluence used, $5 \times 10^{15} \text{ cm}^{-2}$. The impurity profiles measured before and after annealing for crystals irradiated with different fluences show that the distribution of the impurities is broader than predicted by the LSS theory and changes with fluence. Upon annealing the impurities migrate toward the surface.

Silicon carbide lies between silicon and diamond in its physical and chemical properties. Like silicon and diamond it is chemically very stable. Its dissociation temperature (1), 2830°C , compares favorably to the melting point of silicon, 1412°C , and to the graphitization temperature of diamond (*ca.* 1100°C). In common with silicon and at variance with diamond, silicon carbide can be routinely doped p- and n-type. An additional interesting feature of silicon carbide is the fact that it exists in a large number, over 150, of closely related polymorphic modifications, usually referred to as polytypes. The bandgaps of some of the common polytypes are known to range from 2.3 to 3.3 eV (2-7). Thus, silicon carbide has an enormous potential for device fabrication. Unfortunately, techniques for growing and doping silicon carbide crystals have been restricted to high temperature, vapor phase, or silicon solvent methods (8). Recently ion implantation techniques have been added to the possible approaches for semiconductor doping, and new work on silicon carbide has been reported (9-11). Ion implantation looks very attractive *a priori* because it permits room temperature control of both impurity levels and impurity profiles. Usually removal of the radiation damage calls for annealing at moderately high temperatures, too low for ordinary diffusion of the impurities to occur. With this in mind, we decided to investigate the effects of the implantation of nitrogen, boron, and aluminum into

hexagonal 6H SiC crystals. We report in this paper some of the results of our investigation.

Experimental

The apparatus used for the boron and nitrogen implantations is similar to other low energy (100 keV or less) accelerators already described in the literature (12) and is capable of producing resolved beams from 5 to 60 keV. The beams are produced by extracting ions from a radio frequency excited source into which a gas containing the desired species is leaked. The extracted beam is accelerated and focused by a series of lenses before entering an analyzing magnet. The beam passes through an in-line liquid nitrogen trap before entering the target chamber. Resolved beams in the 100 nA range for $^{11}\text{B}^+$ at 60 keV are routinely obtained.

The aluminum implantations were done at the Langley Research Center of NASA and at the Hughes Research Laboratories, Malibu, California. The implanted 6H SiC crystals were sublimation-grown platelets of hexagonal contour. Colorless "undoped" crystals, and green, n-type, nitrogen-doped crystals with net donor concentrations in the $1 \times 10^{18} - 5 \times 10^{18}/\text{cm}^3$ range were used. The undoped crystals were usually high resistivity p-type plates. For the implantations the crystals were mounted with their c-axes approximately parallel to the ion beams except the Al implanted crystals which were offset by 12° and 7° . In some experiments selected areas of the crystals were shielded from the incident beam. By so doing the effect

* Electrochemical Society Active Member.
 Key words: ion implantation, silicon carbide impurity profiles, optical absorption, nitrogen, boron, aluminum doping.

1972

of the ion bombardment and of the annealing treatments could be more conveniently observed.

For the removal of the radiation damage the implanted crystals were annealed in silicon carbide crucibles in neutral atmospheres at temperatures of 400°-1400°C.

The analyses of the impurity profiles in the crystals, before and after annealing, were made at the Battelle Memorial Institute, Columbus, Ohio, using a Cameca Ion Analyzer IMS 300. In this instrument the composition of a microvolume of a sample is obtained by ion etching the sample surface and performing a mass analysis of the ions sputtered from the surface (31). In our work a 10 keV $^{16}\text{O}^-$ beam was used to ion etch the surface of the SiC crystals, and the etching rate in the implanted region was measured using an interference microscope. The analysis was repeated several times for each sample focusing the sputtering beam on different regions of the implanted area. Good reproducibility was observed in all cases.

The optical transmission measurements were performed with a Cary 14 spectrophotometer on samples at room temperature.

Nitrogen Implantations

A green body color and absorption at about 0.62 and 0.42 μm are typically observed at room temperature in 6H SiC crystals containing nitrogen impurities at carbon lattice sites (13, 14). Optical measurements on colorless plates irradiated with 60 keV $^{14}\text{N}^+$ ions thus seemed particularly suitable to study the effects of this donor type impurity. The implantation schedule for a colorless, high resistivity p-type crystal, SiC No. 15, is shown in Table I.

Following each $^{14}\text{N}^+$ implantation, transmission measurements were made from 0.35 to 2.6 μm . Figure 1 shows some of the optical density variations as the fluence is increased from zero to $2.5 \times 10^{17} \text{ cm}^{-2}$. Originally the spectrum is flat through the near infrared and the visible to the band edge. A broad, structureless tail extending from the absorption edge to 8000 cm^{-1} , analogous to that observed in some amorphous semiconductors (16-18), develops as the fluence is increased to about $1.2 \times 10^{16} \text{ cm}^{-2}$. A shoulder is observed at about 10,000 cm^{-1} with a further increase in fluence. A small shift of the band edge to lower energies is also noticeable.

Figure 2 shows the variation of optical density with fluence at 4300, 5000, and 10,000 Å. It is seen that a very rapid increase of the optical density occurs near the band edge for fluences of 10^{14} to $1.3 \times 10^{15} \text{ cm}^{-2}$. For very high fluences the optical density actually decreases with increasing fluence. At these fluence levels, however, the absorption shoulder at 10,000 Å increases markedly with increasing fluences.

Annealing experiments.—After the implantation run No. 10 (cf. Table I), the sample SiC No. 15 was annealed according to the schedule presented in Table II. After each annealing period, the optical spectra of the heavily ($2.5 \times 10^{17} \text{ cm}^{-2}$) and lightly ($6.6 \times 10^{14} \text{ cm}^{-2}$)

Table I. 60 keV $^{14}\text{N}^+$ implantations in SiC No. 15^a

Run	Fluence (cm^{-2})	Peak conc ^(b) (cm^{-3})
1	7.5×10^{12}	9.8×10^{17}
2	4.5×10^{13}	5.8×10^{18}
3	7.5×10^{13}	9.8×10^{18}
4	3.9×10^{14}	5.1×10^{19}
5	6.6×10^{14} (a)	8.6×10^{19} (a)
6	1.3×10^{15}	1.7×10^{20}
7	4.0×10^{15}	5.2×10^{20}
8	1.2×10^{16}	1.5×10^{21}
9	6.9×10^{16}	9.0×10^{21}
10	2.5×10^{17}	3.3×10^{22}

(a) Only part of the crystal was implanted above $6.6 \times 10^{14} \text{ cm}^{-2}$. We refer to the lower implant region as SiC No. 15l and to the higher implant region as SiC No. 15h.

(b) Peak concentrations calculated from the data of Lindhard et al. (15).

irradiated zones of crystal SiC No. 15 were measured and compared. Selected data are shown in Fig. 3 and 4. After annealing at 550°C, much of the radiation damage is removed from the lightly implanted region, SiC No. 15l. Practically no radiation damage can be detected in SiC No. 15l after annealing above 1000°C. The heavily implanted region, SiC No. 15h, still exhibits damage effects after annealing at 1400°C. Neither the implantation alone nor the annealing treatments introduced

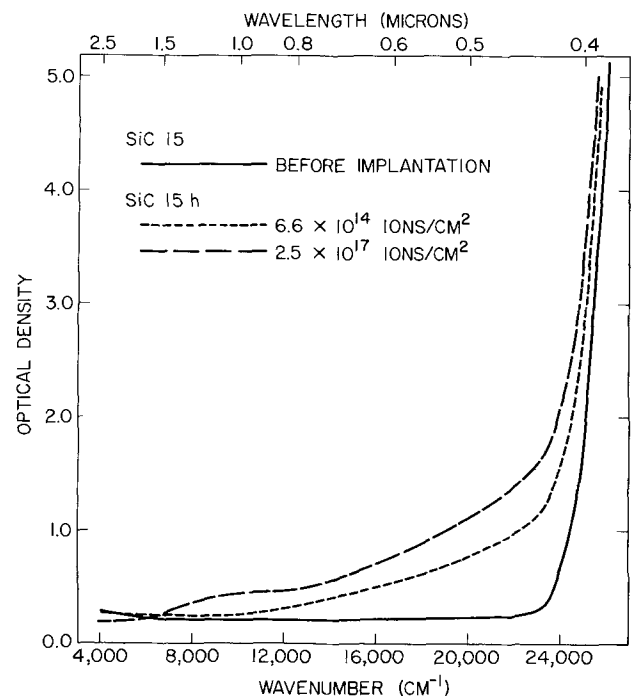


Fig. 1. Typical room temperature optical absorption spectra of hexagonal SiC, sample SiC No. 15, with increasing ion implanted nitrogen dose (fluence). At a dose of $6.6 \times 10^{14} \text{ cm}^{-2}$ half the sample, called SiC No. 15l, was masked to prevent further implantation. The other half of the sample, SiC No. 15h, was subjected to further increases in dose.

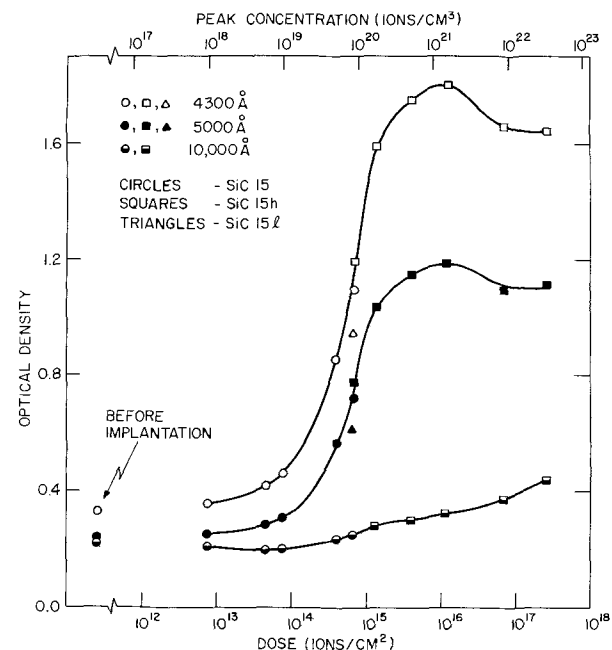


Fig. 2. Room temperature optical density as a function of implanted nitrogen dose (fluence) for sample SiC No. 15 at 4300, 5000, and 10,000 Å. At a dose of $6.6 \times 10^{14} \text{ cm}^{-2}$ half the sample, called SiC No. 15l, was masked to prevent further implantation. The other half, SiC No. 15h, was subjected to further increases in dose.

Table II. Annealing schedule for SiC No. 15

°C	Time (hr)	Atmosphere
450	24	Nitrogen
550	40	Nitrogen
680	26	Nitrogen
810	24	Nitrogen
930	24	Nitrogen
1040	24	Nitrogen
1250	0.5	Argon
1400	0.25	Argon

the absorption typical of nitrogen at carbon sites. The crystal was visibly brown for $^{14}\text{N}^+$ fluences in excess of 10^{14} cm^{-2} . After 1400°C annealing, SiC No. 15l had recovered the original color, and SiC No. 15h showed light brown islands, separated by transparent areas. Figures 5 and 6, which are low magnification photographs of the area of SiC No. 15 where SiC No. 15h and SiC No. 15l meet, show the effect of annealing at different temperatures.

Thermoprobe measurements indicate that after annealing at 1040°C the irradiated crystal surface changed from high resistivity p-type to weakly n-type. After annealing at 1400°C the thermoprobe response for SiC No. 15h was markedly n-type.

Nitrogen profiles.—Because of the interference of the N^+ and CO^{++} ions, the nitrogen analyses were made using $(^{14}\text{N}^{16}\text{O})^-$ and $(^{28}\text{Si}^{14}\text{N})^-$ ions as the measured ion species. Figure 7 shows the measured unannealed and annealed profiles of a 60 keV $^{14}\text{N}^+$ implant (SiC No. 34) at a fluence of $6.6 \times 10^{16} \text{ cm}^{-2}$ and the theoretical profile as derived from the LSS theory (15). The ^{14}N data are plotted as detector current ratio, I/I_0 , where I_0 is the main peak current in the distribution, vs. depth in Å. The $(^{28}\text{Si}^{14}\text{N})^-$ ion current was measured for these analyses, and a $(^{29}\text{Si}^{12}\text{C})^-$ signal was monitored during each run for signal normalization.

Since the nitrogen profile for very high doses might be significantly affected by sputtering during implantation, we have tried to measure the step height, if any, between implanted and adjacent nonimplanted areas of the crystals. A Zeiss interferometer was used for the measurements. No sputtering step was detected for any of the high dose 60 keV ^{14}N implanted samples. Estimated from the resolution of the inter-

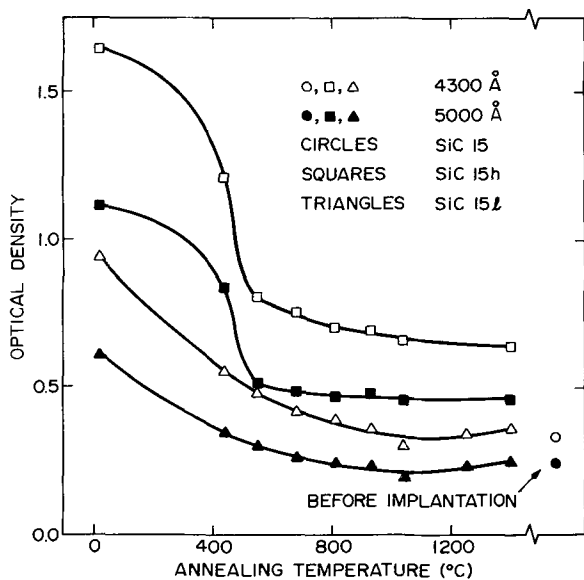


Fig. 3. Room temperature optical density as a function of annealing temperature for sample SiC No. 15 at 4300 and 5000Å. One half of the sample, SiC No. 15h, was subjected to a maximum nitrogen fluence of $2.5 \times 10^{17} \text{ cm}^{-2}$ and the other half, SiC No. 15l, to a maximum fluence of $6.6 \times 10^{14} \text{ cm}^{-2}$. The data before implantation were measured on the full sample SiC No. 15.

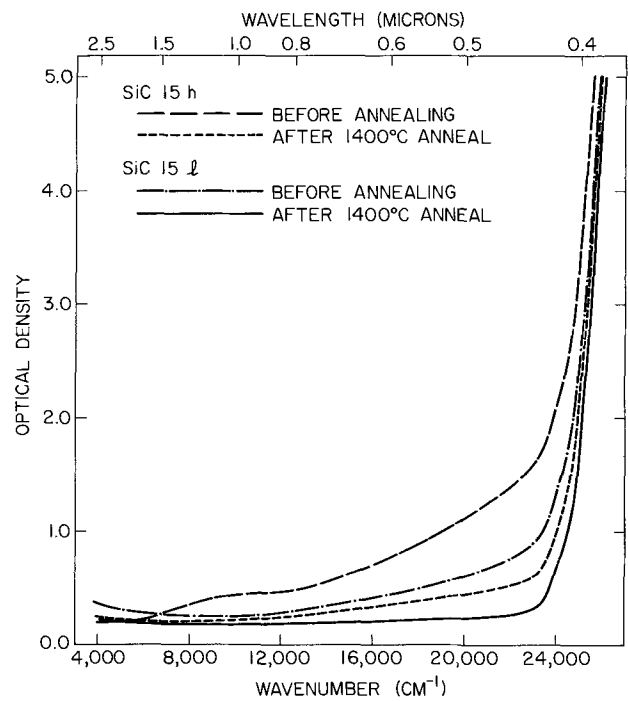


Fig. 4. Room temperature optical absorption spectra of sample SiC No. 15 before annealing and after the final anneal at 1400°C . One half of the sample, SiC No. 15h, was subjected to a maximum nitrogen fluence of $2.5 \times 10^{17} \text{ cm}^{-2}$ and the other half, SiC No. 15l, to a maximum nitrogen fluence of $6.6 \times 10^{14} \text{ cm}^{-2}$.



Fig. 5. SiC No. 15 showing the heavily implanted area (SiC No. 15h; dark area) and the lightly implanted area (SiC No. 15l) after annealing 24 hr at 450°C in nitrogen. Note that the lightly implanted area has already recovered substantially from the damage. The heavily implanted area is no longer optically homogeneous. The region between SiC No. 15h and SiC No. 15l is the transition in fluence between the areas. Magnification $20\times$.

ferometer we find that for our implantation conditions the sputtering yield is less than ~ 0.1 .

We have no explanation at present for the relatively high surface concentration which falls to a minimum

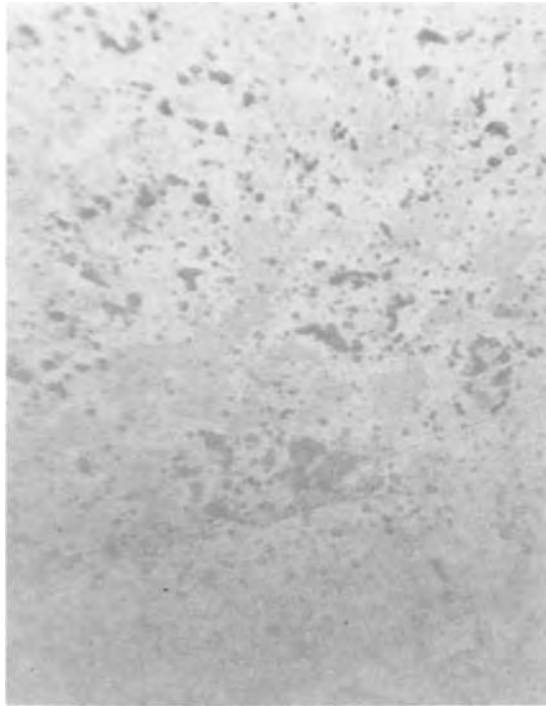


Fig. 6. SiC No. 15h after 24 hr annealing at 1040°C in nitrogen. Brownish amorphous islands alternate with regions of greater transparency. Magnification 200X.

at about 300 and 200Å for the unannealed and for the annealed profiles, respectively, but do not believe that it has a significant effect on the remainder of the profiles. Comparison of the unannealed profile with the theoretical curve shows that the predicted peak depth is about 15% less than that measured for the unannealed sample, while the predicted straggling is about 28% less. As can be seen the effect of the annealing is to shift the main peak towards the surface by approximately 250Å from the unannealed profile.

The effect of increasing the fluence five-fold plus the thermal treatments listed in Table II is shown in Fig. 8, which shows the $(^{14}\text{N}^{16}\text{O})^-$ ion current for crystal SiC No. 15h. Comparison with the theoretical profile clearly shows that the combined effect of the increase of fluence and of the thermal treatments on the profile is to shift the peak significantly towards the surface and to increase the full width at half maximum (FWHM) by 20%.

Boron Implantations

Since 6H SiC crystals containing boron and nitrogen have a yellow room temperature fluorescence (19) when excited by 3650Å radiation, the boron implantations were made preferentially in nitrogen doped crystals. Such crystals do not have any room temperature fluorescence, but show a strong blue luminescence when cooled to 77°K (14). Different crystals were implanted with 30 and 60 keV $^{11}\text{B}^+$ ions to get peak concentrations from 1.0×10^{17} to $4.8 \times 10^{20} \text{ cm}^{-3}$. For a fluence of 10^{14} cm^{-2} , corresponding to peak concentrations of $\sim 10^{19} \text{ cm}^{-3}$, or more, a brownish surface layer developed as a consequence of the implantations.

A gradual clearing of the damaged surfaces occurred after annealing the crystals at 100°C intervals from 550° to 1050°C. After annealing at 1050°C, by visual inspection the crystals appeared to have completely recovered from the damage. The implanted surfaces, however, did not show the yellow "boron" luminescence at room temperature or the original blue luminescence at 77°K. Further annealing in silicon carbide crucibles in argon at 1250° and 1400°C resulted in the reappearance of the blue low temperature lumines-

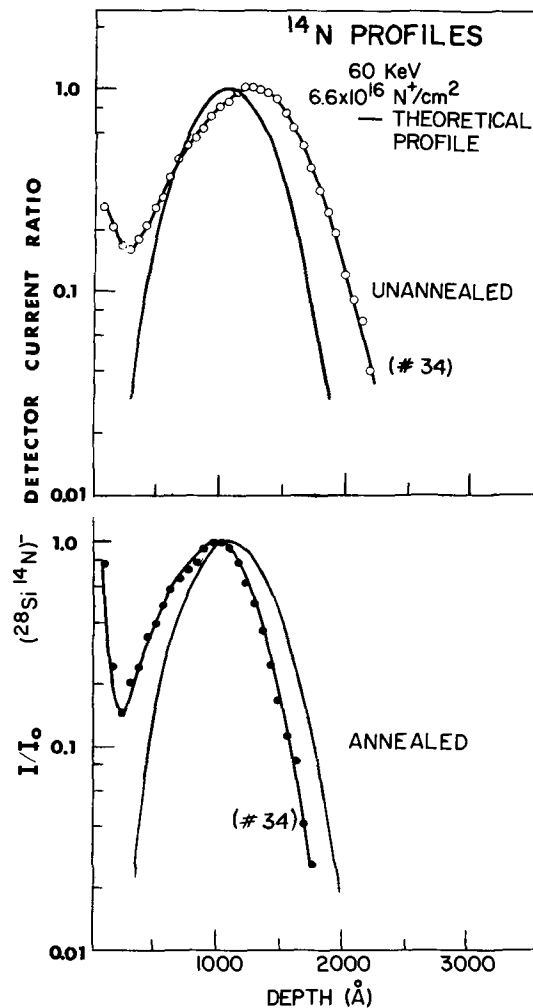


Fig. 7. Unannealed and annealed profiles from crystal No. 34 implanted with 60 keV $^{14}\text{N}^+$ ions to a fluence of $6.6 \times 10^{16} \text{ ions/cm}^2$. The crystal was annealed in argon at 1400°C for 15 min in a silicon carbide crucible. The data are plotted as $(^{28}\text{Si}^{14}\text{N})^-$ detector current ratio, I/I_0 , where I_0 is the peak current in the distribution, vs. depth in Å. A $(^{29}\text{Si}^{12}\text{C})^-$ signal was monitored during each profile run for $(^{28}\text{Si}^{14}\text{N})^-$ signal normalization. A 60 keV ^{14}N theoretical distribution is plotted on the graph in atomic per cent vs. depth.

cence. Moreover, a weak room temperature "boron" luminescence appeared in the irradiated areas of some of the nitrogen doped, green colored crystals irradiated to boron peak concentrations in the range of 10^{20} cm^{-3} . Thermoprobe measurements indicate that even for this implantation level, the yellow fluorescing layers retained n-type conductivity. Colorless crystals or crystals implanted to low boron fluence did not show any room temperature fluorescence after annealing at 1400°C. Coating of the implanted crystals with a 2000Å thick layer of sputtered SiO_2 before annealing did not lead to different results.

Boron profiles.—Figure 9 shows the measured unannealed profiles of crystals irradiated with 30 and 60 keV $^{11}\text{B}^+$ ions. The data are plotted as $^{11}\text{B}^+$ detector current ratio, I/I_0 , where I_0 is the peak current in the distribution, vs. depth in Å. A $^{12}\text{C}^+$ signal was monitored during each profile run for signal normalization. The agreement with the profiles predicted by the LSS theory (15) is only qualitative. The theoretical peak depths are about 20% less than those measured, and the straggling, as measured by the FWHM, is about 40% less. Some of these differences may be due to the large relative atomic number and mass differences of the constituent atoms (^{28}Si and ^{12}C). The tails extending on the deep side of the peaks are typical of implants

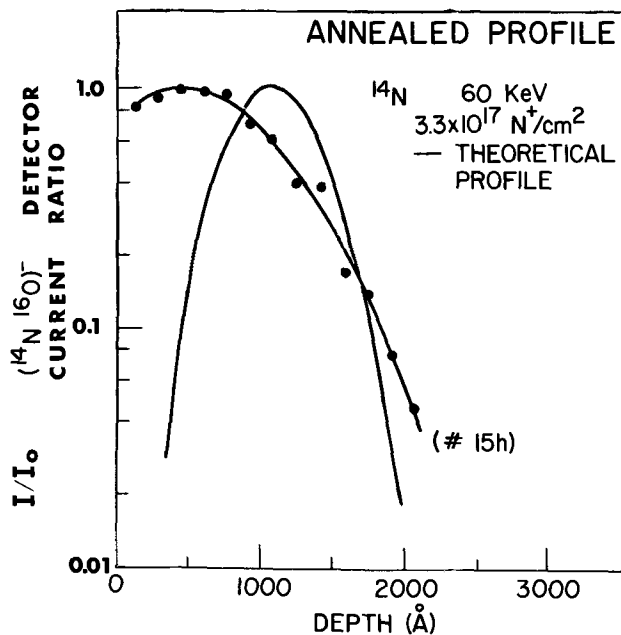


Fig. 8. Profile of ^{14}N distribution in sample No. 15h after annealing in argon at 1400°C for 15 min in a silicon carbide crucible. The crystal was implanted with 60 keV $^{14}\text{N}^+$ ions to a fluence of 3.3×10^{17} ions/cm 2 , which is a fivefold increase in fluence of the annealed sample (No. 34) shown in Fig. 7. The data are plotted as $(^{14}\text{N}^{16}\text{O})^-$ detector current ratio, I/I_0 , where I_0 is the peak current in the distribution, vs. depth in \AA . A $(^{29}\text{Si}^{12}\text{C})^-$ signal was monitored during the run for $(^{14}\text{N}^{16}\text{O})^-$ signal normalization. A 60 keV ^{14}N theoretical distribution is plotted on the graph in atomic per cent vs. depth.

where, as in this case, no attempts were made to suppress channeling. They also may be due, in part, to a radiation enhanced diffusion mechanism, similar to that observed in silicon (20, 12).

After annealing at 1400°C , no boron was detected by the microanalyzer in crystals implanted with 30 and 60 keV $^{11}\text{B}^+$ to peak concentrations $\lesssim 10^{19}$ cm $^{-3}$. A weak yellow boron luminescence was seen, however, when the crystals were excited by 3650 \AA uv. It is estimated that after annealing there is less than 1×10^{11} boron atoms cm $^{-2}$ in the implanted areas of these crystals.

Aluminum Implantations

Four n-type plates were implanted to fluences of 2×10^{11} cm $^{-2}$, 4×10^{11} cm $^{-2}$, 4×10^{12} cm $^{-2}$, and 4×10^{13} cm $^{-2}$, respectively, with 60 keV $^{27}\text{Al}^+$ ions impinging at an angle of 12° to the c-axis direction. Three additional crystals (No. 30, 31, and 32) were implanted to fluences of 5×10^{13} cm $^{-2}$, 5×10^{14} cm $^{-2}$, and 5×10^{15} cm $^{-2}$, respectively, with $^{27}\text{Al}^+$ ions impinging at a 7° angle to the c-axis direction. For a fluence of 5×10^{13} cm $^{-2}$ or more, the implanted areas acquired a dark brown discoloration similar to that of boron and nitrogen implanted crystals. The discoloration disappeared after annealing for 15 min in argon at 1400°C . Thermoprobe measurements indicated that for a fluence of 5×10^{15} cm $^{-2}$ (crystal SiC No. 32) the implanted crystal surface converted from n-type to p-type. For the 5×10^{14} cm $^{-2}$ (SiC No. 31) and the 5×10^{13} cm $^{-2}$ (SiC No. 30) implants a marked decrease of the original n-type signal resulted as a consequence of the implants.

Aluminum profiles.—Figure 10 shows the profiles for the unannealed crystals No. 30, 31, and 32. The data are plotted as $^{27}\text{Al}^+$ detector current ratio I/I_0 , where I_0 is the peak current in the distribution, vs. depth in \AA . A $^{24}\text{C}_2^+$ signal was monitored during each profile determination for signal normalization. Crystal No. 30 had a nonuniform aluminum background and

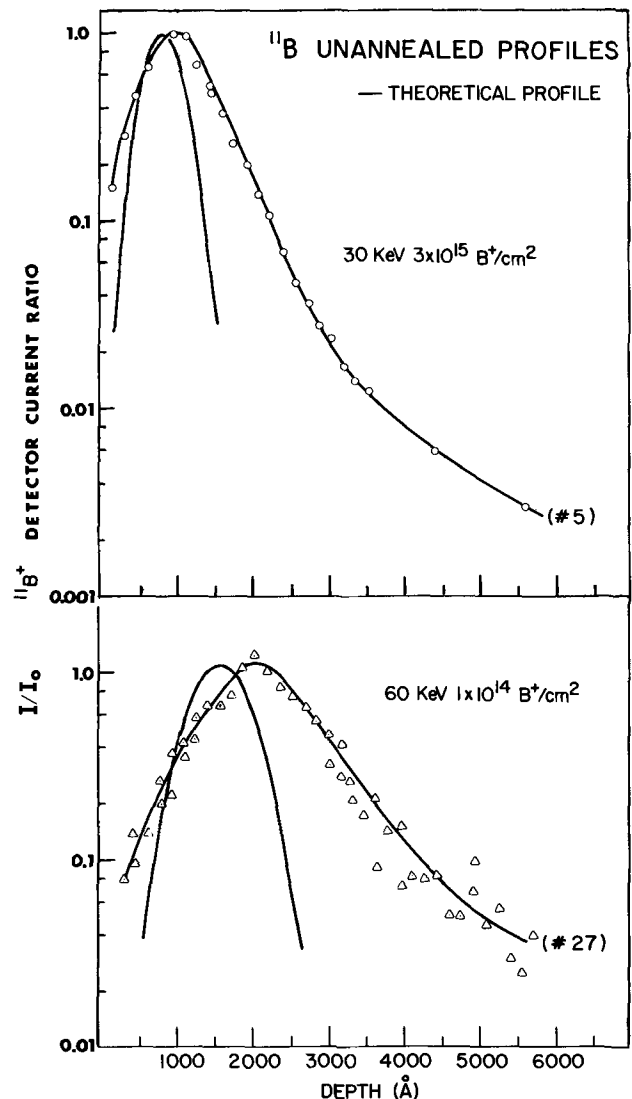


Fig. 9. Unannealed profiles from crystals No. 15 and No. 27 implanted with 30 and 60 keV $^{11}\text{B}^+$ ions to a fluence of 3×10^{15} and 1×10^{14} ions/cm 2 , respectively. A $^{12}\text{C}^+$ signal was monitored during each profile run for $^{11}\text{B}^+$ signal normalization. Theoretical 30 and 60 keV ^{11}B profiles are plotted on the same graph in atomic per cent vs. depth.

the implant concentration lies near the aluminum detectability limit of the ion analyzer. Therefore, only the region near the surface is presented. The aluminum profile calculated from the LSS theory (15) is also shown.

The agreement with the theory is only qualitative. For example, the predicted peak for the 5×10^{14} implant is about 35% less deep than the measured one, and the predicted straggling is about 57% less. Moreover, these differences increase for the heavier implant to 51% and 71%, respectively. At the moment we can only suggest the presence of a radiation-enhanced diffusion mechanism. An analogous effect has been observed in MgO implanted with 3.0 MeV Ne^+ ions (21). The MgO damage profile curves obtained by monitoring the damage as the bombarded surface is chemically removed show that as the fluence increases the FWHM increases and the damage peak increases in depth.

Figure 11 shows the profiles after annealing at 1400°C for 15 min. For SiC No. 30 the distribution shows a sharp gradient up to the surface. For SiC No. 31 and SiC No. 32 two regions are now present: a sharp gradient peaking at the surface and a broad distribution extending deeper into the crystal with relatively flat maxima at about 1300 \AA . The considerable increase in

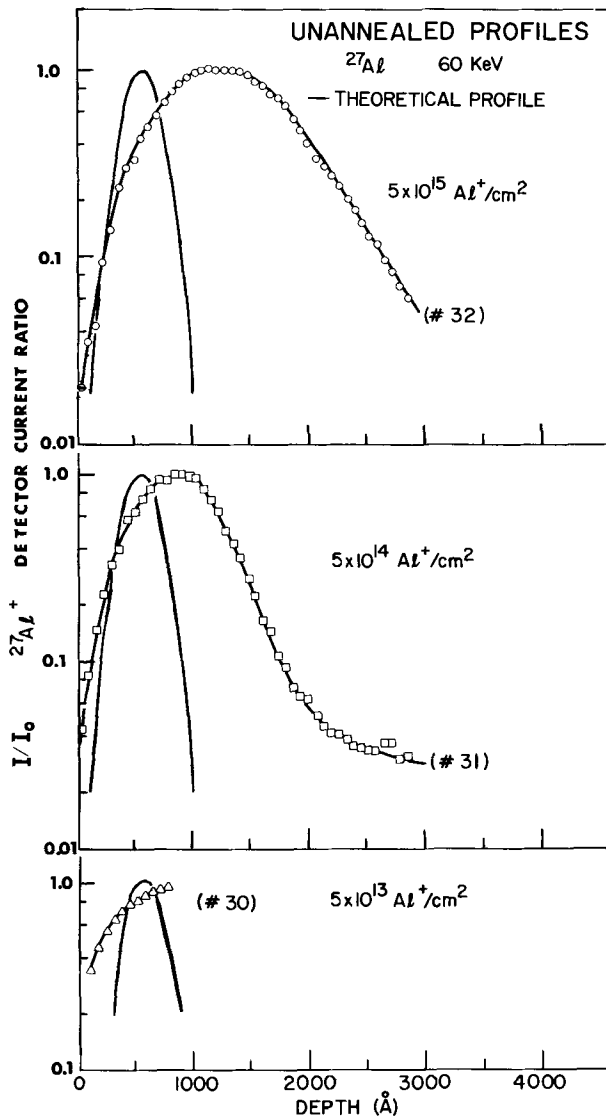


Fig. 10. Profiles from crystals No. 30, 31, and 32 implanted with 60 keV $^{27}\text{Al}^+$ ions to a fluence of 5×10^{13} , 5×10^{14} , and 5×10^{15} ions/cm 2 , respectively. The data are plotted as ^{27}Al detector current ratio, I/I_0 , where I_0 is the peak current in the distribution, vs. depth in \AA . A $^{24}\text{C}_2^+$ signal was monitored during each profile run for $^{27}\text{Al}^+$ signal normalization. Crystal No. 30 had a nonuniform Al background and the Al concentration was near the Al^+ detectability limit of the ion microprobe; therefore only the surface region is presented. A 60 keV Al theoretical profile is plotted on the same graph in atomic per cent vs. depth.

the concentration of the surface aluminum is probably responsible for the appearance of p-type conductivity in SiC No. 32 and the related effects in SiC No. 31 and SiC No. 30.

Discussion

In all cases the primary effect of the ion implantation was the formation of a brownish disordered surface layer. Except for cases of extreme fluences, (for example, SiC No. 15h), annealing at 1400°C eliminated the radiation damage and restored the original 77°K luminescence of the crystals. Moreover, in crystals containing a suitable amount of nitrogen donors, the typical boron room temperature luminescence in the yellow region appeared after implantation to high boron levels and annealing at 1400°C. Obviously, annealing regenerated the original crystal structure, and conversion to polytypes stable at low temperatures, such as the 2H and the 3C polytypes, did not occur. This observation is important because, in the event of a change in crystal structure, only heterojunctions could, in general, be prepared by ion implantation in SiC.

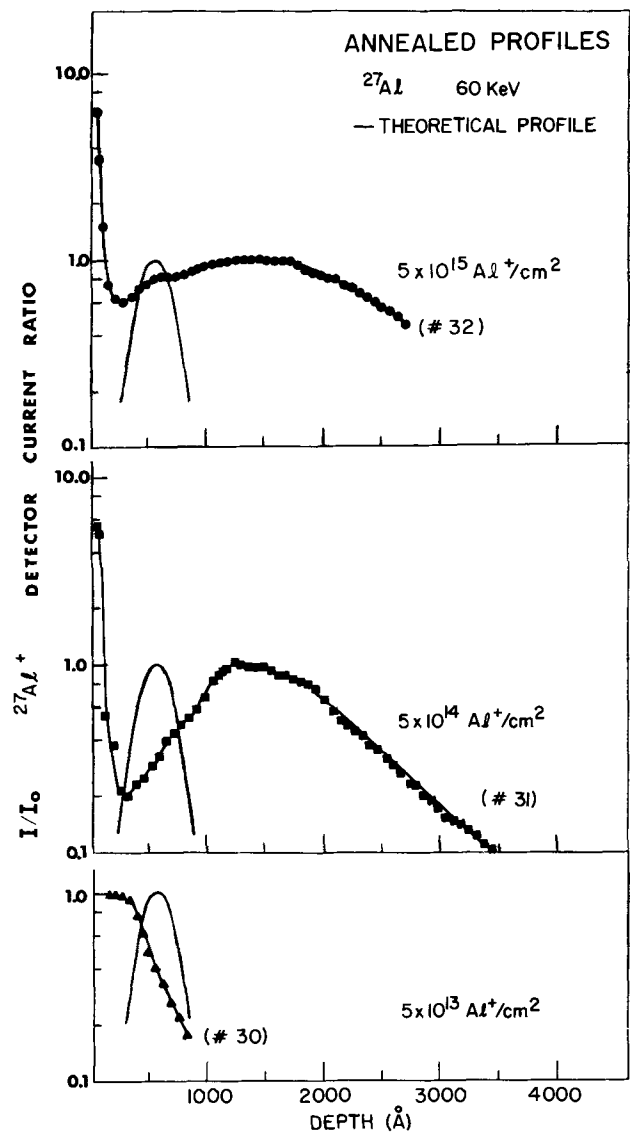


Fig. 11. Al profiles from crystals No. 30, 31, and 32 after annealing in argon at 1400°C for 15 min in silicon carbide crucibles. The data are plotted as $^{27}\text{Al}^+$ detector current ratio, I/I_0 , where I_0 is the peak current in the distribution, vs. depth in \AA . A $^{24}\text{C}_2^+$ signal was monitored during each run for $^{27}\text{Al}^+$ signal normalization. A 60 keV Al theoretical profile is plotted in atomic per cent vs. depth.

Homojunctions would be restricted to one or two polytypes.

Nitrogen implantation and annealing produced n-type conductivity in the implanted areas of originally p-type crystals. This behavior has been attributed by Dunlop and Marsh (11) to the existence of a substantial fraction, $\sim 1/3$, of nitrogen atoms at donor sites in the SiC lattice after annealing. It must be remembered, however, that n-type conductivity in 6H SiC was observed also after bombardment with alpha particles, neutrons, and electrons (22-24). Thus donor type defects may contribute to the observed conductivity.

Reflection electron diffraction observations indicate that an amorphous layer is formed as a result of the ion implantation at high fluences. Localized electronic states may occur in the electronic bandgap due to the disorder (16-18) of this amorphous semiconductor layer. The absorption tail extending from the band edge to lower energies thus may be due to electronic excitations at these localized states.

With increasing fluence the shoulder at $10,000 \text{ cm}^{-1}$ in SiC No. 15h (Fig. 1 and 4) increases markedly after

the band tail absorption near the fundamental edge begins to decrease (Fig. 2). Subsequently, this shoulder anneals out completely (Fig. 4). It is thought that the shoulder may result from the development of aggregate defect centers at high fluences. Thus localized electronic states of lower energy may occur at the aggregate centers, and the absorption at $10,000\text{ cm}^{-1}$ may be due to electronic excitations at these aggregates. The optical data indicate that a small reversible shift of the band edge of SiC occurs as a result of $^{14}\text{N}^+$ implantation (Fig. 1 and 3). This behavior is quite different from that of GaAs and GaP, where large reversible shifts of the optical absorption edge were observed after implantation with argon ions and neutrons (25-27), and is in line with the well-known ability of SiC to withstand radiation damage better than silicon and germanium.

The profiles of the implanted impurities, before annealing, show that qualitative agreement exists with the LSS theory (15), but the impurity distributions are characterized by the presence of a tail extending deeply into the crystals. Similar observations have been reported for silicon (28) and for other materials (12). Apparently channeling and/or enhanced diffusion effects cannot be neglected. Moreover, for aluminum, as shown by the profiles in Fig. 10, the peak position and FWHM change with the fluence.

The profiles of the annealed samples are difficult to interpret in detail. In all cases the impurities diffuse to the surface during annealing. The rate of diffusion may depend on the impurity, on the depth below the surface, on the fluence level, and on the associated damage. If diffusion is particularly fast for the layers immediately below the surface, the impurities in that region migrate to the surface rapidly and, if trapped there, create the surface maxima observed in some of the nitrogen and aluminum implants (crystals No. 31, 32, and 34, Fig. 11 and 7). Outdiffusion during the implantation might be invoked to explain the ^{24}N profile observed for crystal No. 34 before annealing (Fig. 7).

The presence of large Al peaks at the surface of the ^{27}Al implanted crystals after annealing and the conversion from n- to p-type conductivity in the case of SiC No. 32, is particularly interesting. Marsh *et al.* (9, 10) have reported the possible presence of a p-type layer in n-type β SiC as a consequence of low energy aluminum implantations. Significantly, none of the other impurities implanted by them at room temperature (Be, B, Ga, In, Te, N, P, As, Sb) resulted in p-type conversion. Thus, Al may be in a special position compared to other Group III dopants. It is known that aluminum substitutes for silicon in the SiC lattice (29), as might be expected upon consideration of the similarity of the tetrahedral covalent radii of aluminum (1.26Å) and silicon (1.17Å) (30). At the annealing temperature of 1400°C , silicon slowly evaporates from the surface of the SiC crystals, and leaves behind a carbon rich layer. Under these conditions it is possible that the aluminum atoms close to the surface migrate and replace, fully or in part, the missing silicon atoms with consequent formation of a steep gradient in the concentration of the surface aluminum.

We may conclude this discussion by stating that ion implantation looks very promising as a means to make SiC devices. In particular, the appearance of room temperature boron luminescence and the presence of surface aluminum and nitrogen after annealing clearly indicate that the possibility of preparing doped layers by room temperature ion implantation in silicon carbide does exist. Additional work is in progress to learn how to prepare active devices by this technique.

Acknowledgments

We wish to thank R. M. Potter, General Electric Company, Cleveland, Ohio, for some of the crystals used in this research. We are obliged to Herbert

Hendrickson's ion implantation group at NASA, Langley, Virginia, and to the Hughes Research Laboratories, Malibu, California, for some of the aluminum implantations. We wish to thank R. Baxter and B. Phillips, Battelle Memorial Institute, Columbus, Ohio, for their cooperation in getting the microanalytical data. We are obliged to J. E. Davey for electron diffraction patterns and to K. R. Gleason for preparing SiO_2 coated crystals. Also, we wish to thank and gratefully acknowledge R. D. Kirk for making available to us the high-temperature furnace used for annealing the crystals.

Manuscript submitted Jan. 31, 1972; revised manuscript received June 9, 1972. This was Paper 196RNP presented at the Cleveland, Ohio, Meeting of the Society, Oct. 3-7, 1972.

Any discussion of this paper will appear in a Discussion Section to be published in the June 1973 JOURNAL.

REFERENCES

1. R. I. Scace and G. A. Slack, "Silicon Carbide—A High Temperature Semiconductor," J. R. O'Connor and J. Smiltens, Editors, pp. 24-28, Pergamon Press, New York (1960).
2. W. J. Choyke and L. Patrick, *Phys. Rev.*, **127**, 1868 (1962); *ibid.*, **172**, 769 (1968).
3. W. J. Choyke, D. R. Hamilton, and L. Patrick, *ibid.*, **133**, A1163 (1964); *ibid.*, **139**, A1262 (1965).
4. D. R. Hamilton, L. Patrick, and W. J. Choyke, *ibid.*, **138**, A1472 (1965).
5. L. Patrick, W. J. Choyke, and D. R. Hamilton, *ibid.*, **137**, A1515 (1965); *ibid.*, **132**, 2023 (1963).
6. L. Patrick, D. R. Hamilton, and W. J. Choyke, *ibid.*, **143**, 526 (1966).
7. G. Zanmarchi, *Philips Res. Rept.*, **20**, 253 (1965); 7th International Congress Physics of Semiconductors, Paris 1964 (Academic Press-Dunod) paper B-6 p. 57.
8. See, for instance, the papers presented at the First [1959; cf. Ref. (1)] and Second International Conference on SiC [1968; cf. *Mat. Res. Bull.*, **4**, 1-372 (1969) (Pergamon Press)].
9. O. J. Marsh and H. L. Dunlap, *Radiation Effects*, **6**, 301 (1970).
10. R. R. Hart, H. L. Dunlap, and O. J. Marsh, *ibid.*, **9**, 261 (1971).
11. H. L. Dunlap and O. J. Marsh, *Appl. Phys. Letters*, **15**, 311 (1969).
12. See, for instance, J. W. Mayer, L. Eriksson, and J. A. Davies, "Ion Implantation in Semiconductors," Academic Press, New York (1970).
13. J. A. Lely, *Ber. Deutsch. Keram. Ges.*, **32**, 229 (1955).
14. J. A. Lely and F. A. Kröger, "Semiconductors and Phosphors," M. Schön and H. Welker, Editors, p. 514, Interscience, New York (1958).
15. J. Lindhard, M. Scharff, and H. E. Schiott, *Kgl. Danske Videnskab. Selskab, Mat. Fys. Medd.*, **33**, No. 14 (1963).
16. N. F. Mott, *Advan. Phys.*, **16**, 49 (1967).
17. M. H. Cohen, H. Fritzsche, and S. R. Ovshinsky, *Phys. Rev. Letters*, **22**, 1065 (1969).
18. G. W. Anderson and W. D. Compton, *J. Chem. Phys.*, **52**, 6166 (1970).
19. A. Addamiano, *This Journal*, **111**, 1294 (1964); *ibid.*, **113**, 134 (1966).
20. D. Meyer and J. W. Mayer, *Physics Letters*, **31A**, 387 (1970).
21. B. D. Evans, J. Comas, and P. R. Malmberg, *Bull. Am. Phys. Soc.*, **16**, 1393 (1971).
22. P. Nagels and M. Denayer, "Radiation Damage in Semiconductors," p. 225, Paris-Royumont, (1964); Academic Press, New York.
23. E. W. J. Mitchell and M. J. Moore, *ibid.*, p. 235.
24. M. A. Il'in, M. G. Kosaganova, V. N. Solomatin, Yu. V. Barinov, and Yu. V. Bulgakov, *Soviet Physics-Semiconductors*, **5**, 443 (1971).
25. J. E. Davey, T. Pankey, P. R. Malmberg, and W. H. Lucke, *Appl. Phys. Letters*, **17**, 323 (1970).
26. T. Pankey, Jr., and J. E. Davey, *J. Appl. Phys.*, **41**, 697 (1970).
27. J. E. Davey and T. Pankey, *ibid.*, **40**, 212 (1969).
28. V. M. Pistryak, A. K. Gnap, V. F. Kozlov, R. I.

Garber, A. I. Fedorenko, and Ya. M. Fogel', *Soviet Phys.-Solid State*, **12**, 1005 (1970).
 29. A. Addamiano, *This Journal*, **115**, 196C (1968).
 30. L. Pauling, "The Nature of the Chemical Bond,"

2nd ed., p. 179, Cornell Univ. Press, Ithaca, N. Y. (1945).
 31. C. A. Anderson, *J. Mass Spectrometry and Ion Physics*, **2**, 61 (1969).

Oxygen and Metal Activities of the Iron-Nickel-Oxygen System at 1000°C

Haydn Davies* and W. W. Smeltzer*

Department of Metallurgy and Materials Science, McMaster University, Hamilton, Ontario, Canada

ABSTRACT

The equilibrium oxygen pressures for Fe-Ni alloys coexisting with their oxides have been determined at 1000°C using an electrochemical cell with a calcia-zirconia electrolyte. These pressures were related to compositional determinations of the solid phases and the Fe-Ni-O isotherm at 1000°C. Oxygen pressure over the wustite-alloy phase field increases from 1.32×10^{-15} atm for Fe-FeO equilibrium to 5.5×10^{-14} atm for the invariant three-phase field of wustite containing 0.51 a/o (atom per cent) Ni, spinel containing 0.6 a/o Ni, and an alloy containing 79.6 a/o Ni. The oxygen pressure subsequently increased through the spinel-alloy phase field to 2.5×10^{-11} atm, that of the invariant phase field composed of spinel containing a calculated composition of 11.4 a/o Ni, nickel oxide containing 42.5 a/o Ni, and an alloy containing 99.6 a/o Ni. Iron behaved ideally up to the alloy content of 40 a/o Ni, but then exhibited small negative deviations, whereas nickel deviated negatively at alloy compositions greater than 10 a/o Fe. The spinel-alloy equilibria have been described by a Gibbs-Duhem calculation and by a structural model for the spinel based on a lattice point defect model.

The thermodynamics of the Fe-Ni-O system containing solid phases at high temperatures has been investigated by several workers (1-12). Measurements based on gas equilibration and electromotive force techniques have been chiefly utilized to determine partial and integral thermodynamic properties of the alloys. In several investigations (6, 9, 11, 12), measurements of oxygen activities have been combined with determinations of compositions and structures of the solids to define the fields within the ternary phase diagram, the results for the isotherm at 1000°C being most extensive (11). The purpose of this work, accordingly, was to obtain additional information concerning the dissociation pressures of wustite and spinel equilibrated with the alloys and to collate the information from the various sources into a complete description of the ternary system at 1000°C.

Experimental

A solid-state electrochemical technique using calcia-stabilized zirconia as the electrolyte was used to determine the dissociation pressures of the oxides. The cell, which was similar to that of Charette and Flengas (13), is illustrated in Fig. 1. The inner reference electrode compartment consisted of a 12 in. long tube of calcia-stabilized zirconia (B grade) supplied by the Zirconium Corporation of America. The outer electrode compartment consisted of the exterior Mullite tube containing an alumina crucible. The arrangement of the electrodes and platinum leads, with respect to the electrolyte, was that shown by Roeder and Smeltzer (6). These components were placed inside a grounded Nionel tube to shield the platinum electrode leads from any inductive field produced by the furnace windings. The cell temperature was determined by a Chromel-Alumel thermocouple calibrated *in situ*, and all emf's were measured with a high impedance potentiometer. Temperatures were controlled to $\pm 1^\circ\text{C}$ and cell voltages measured to 10^{-4}V .

There are several references to the need for "closed cell design" involving two hermetically sealed half-cell compartments to prevent oxygen transfer, via the gas phase, between the electrode compartments. Initially, both compartments were sealed under vacuum, but later experiments used a common vacuum of 10^{-6} Torr. No difference in results was obtained. The present design involving electrodes of metal/oxide compacts together with protective amounts of metal-metal oxide powders was satisfactory for both of the above conditions, and maintained equilibrium cell potentials. Fe/FeO was used as the reference electrode for all experiments.

The electrode materials were fabricated as tablets 0.25 in. diameter by 0.10 in. thick by compressing, at

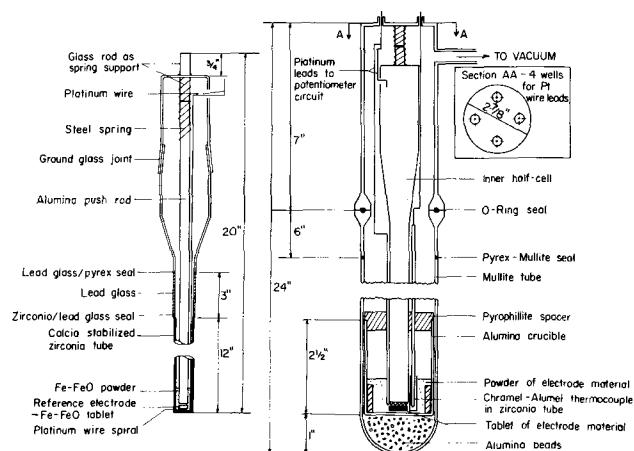
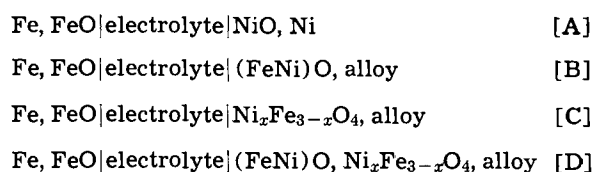


Fig. 1. Electrochemical cell assembly containing a solid calcia-stabilized zirconia electrolyte tube.

* Electrochemical Society Active Member.
 Key words: thermodynamics, Fe-Ni-O system, metal and oxygen activities.

15,000 psi, powders of iron and nickel [99.99 w/o (weight per cent) pure] in predetermined proportions with one, or more, of the oxides (99.6 w/o pure) consisting of nickel oxide, magnetite, and nickel ferrite. The tablets were sealed in quartz tubes containing argon (oxygen content less than 2 ppm) and then annealed at 1000°C for 28 days. They were subsequently cooled to room temperature within 1 min by quenching. Both these tablets and those subjected to emf measurements exhibited identical compositional and structural properties. Techniques for metallographic preparation of the specimens and their chemical analyses using a Cameca electron-probe microanalyzer have been described (11). Fe-Ni alloys, FeO, Fe₃O₄, and NiFe₂O₄ were used as standards for preparing compositional calibration curves for this instrument.

Electromotive force measurements were made for the following cells.



Since the reaction is transfer of oxygen from the cathode to anode compartment, the emf is (14)

$$E = \frac{RT}{4F} \ln P_{O_2''}/P_{O_2'} \quad [1]$$

Here $P_{O_2''}$ and $P_{O_2'}$ are the dissociation pressures of the oxides in the cathode and anode compartments, respectively. For reversible potentials, the compositions of the solid phases must remain unchanged. The factors which affect the accuracy and reliability of this technique have been described by Steele and Alcock (15, 16) and Sellars and Maak (17). In this investigation, the cell was alternately evacuated and flushed with purified argon, which had been freed of O₂, CO, and H₂ by passage over activated copper and unreduced copper oxide catalysts held at 150°C, and then freed of H₂O and CO₂ by passage through Ascarite and a liquid nitrogen trap. The cell was then evacuated to 10⁻⁶ Torr and continually pumped throughout the equilibration period at 1000°C and the subsequent measurement period at temperatures over the range 800°-1060°C. For cells A and B, the equilibrium time was initially 20 days but subsequent work showed that two days were sufficient. The equilibration time for cell C was 20 days but the cell emf remained unchanged after 10 days at temperature. Cell D was equilibrated for 26 days, but the emf did not change after 20 days.

The method of Diaz and Richardson (18) was used to measure the emf. At any supposed equilibrium state, the cell was disturbed by passing a small current equivalent to 0.01-0.1 coulombs and the emf value subsequently determined from the plateau in the cell emf vs. time curves. The most extensive measurements were made on the cells operating at 1000°C. Measurements were also made at temperatures within the range 800°-1100°C by cycling the temperature to values below and above 1000°C and allowing the cell to stabilize for a period of 1 hr.

Cells B and C correspond to the fields containing a metal phase in the Fe-Ni-O phase diagram. Cell D corresponds to the invariant equilibrium between alloy, nickel oxide containing iron in solid solution, and an iron-nickel spinel. Attempts were also made to prepare electrodes describing the invariant equilibrium between alloy, wustite-containing nickel in solid solution, and an iron-nickel spinel. However, we were unsuccessful because this latter three-phase field is of very narrow compositional extent (11) and the compositions of the fabricated tablets adjusted to two-phase regions during the annealing periods.

Table I. Least squares analyses of emf

Sample	E (mV) = A + BT(°K)		Standard deviation (mV)
	A (mV)	B (mV/°K)	
WA1	8.38	0.038	0.9
WA2	4.90	0.048	0.9
WA3	-13.96	0.073	0.4
WA4	12.54	0.058	0.6
WA5	14.38	0.059	0.5
SA1	-68.06	0.135	0.4
SA2	23.31	0.096	0.9
SA3	-44.76	0.153	0.7
SA4	-18.01	0.141	0.7
SA5	45.26	0.108	0.8
SA6	45.61	0.133	0.6

Results

Cell A.—Emf values over the range 600°-1050°C could be correlated by the linear equation

$$E(\text{mV}) = 157.1 + 0.101T(^\circ\text{K}) (\pm 0.9 \text{ mV}) \quad [2]$$

These values were in good agreement with published values and the least square representation of these results (16)

$$E(\text{mV}) = 157.6 + 0.10T(^\circ\text{K}) (\pm 0.9 \text{ mV}) \quad [3]$$

Cell B.—The emf values at temperatures in the range 800°-1060°C and the linear relationships for the cell temperature coefficients obtained by the method of least squares are given in Fig. 2 and Table I, respectively. The alloys investigated contained up to 75.9 a/o Ni.

Cell C.—The results are also represented in Fig. 2 and Table I. In this case, the alloy compositions ranged from 91.6 to 98.7 a/o Ni.

Cell D.—The emf was determined only at 1000°C. Its value was 270 ± 1 mV.

The compositions determined by the electron microprobe technique for the coexisting oxide and alloy phases at 1000°C are recorded in Table II. The mass concentrations obtained experimentally have been converted to atomic concentrations which are also given.

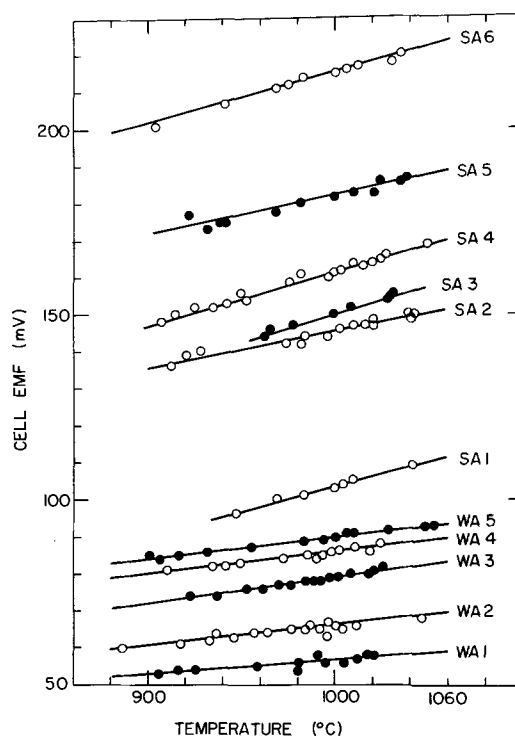


Fig. 2. Electrical potentials vs. temperature for cells B and C. The composition designations for the plots correspond to those in Table II.

Table II. Electron microprobe analyses of coexisting alloy and oxide phases at 1000°C

Sample	Alloy composition				Oxide phase identification	Oxide composition				Oxide formula
	w/o Ni	w/o Fe	a/o Ni	a/o Fe		w/o Ni	w/o Fe	a/o Ni	a/o Fe	
WA1	60.8 (±0.4)	39.4 (±0.5)	59.5	40.5	Wustite	*	76.1 (±0.3)	—	47.8	Fe _{0.917} Ni _{0.083} O
WA2	66.6 (±0.4)	33.0 (±0.5)	65.5	34.5	Wustite	*	75.9 (±0.3)	—	47.6	Fe _{0.912} Ni _{0.088} O
WA3	71.8 (±0.4)	28.5 (±0.5)	70.6	29.4	Wustite	*	75.5 (±0.3)	—	47.3	Fe _{0.902} Ni _{0.098} O
WA4	74.7 (±0.4)	25.7 (±0.5)	73.5	26.5	Wustite	*	75.4 (±0.3)	—	47.1	Fe _{0.897} Ni _{0.103} O
WA5	76.5 (±0.4)	23.4 (±0.5)	75.7	24.3	Wustite	*	75.3 (±0.3)	—	47.1	Fe _{0.892} Ni _{0.108} O
SA1	82.6 (±0.4)	17.2 (±0.4)	81.8	18.2	Spinel	*	70.9 (±0.6)	0.9	41.9	Ni _{0.06} Fe _{2.94} O ₄
SA2	92.0 (±0.4)	8.7 (±0.4)	91.6	8.4	Spinel	*	70.1 (±0.8)	1.3	41.6	Ni _{0.06} Fe _{2.94} O ₄
SA3	93.4 (±0.4)	7.4 (±0.4)	93.1	6.9	Spinel	7.6 (±0.5)	64.6 (±1.0)	4.4	38.5	Ni _{0.31} Fe _{2.69} O ₄
SA4	95.5 (±0.4)	3.9 (±0.3)	95.2	4.8	Spinel	9.7 (±0.5)	63.1 (±1.0)	5.3	37.5	Ni _{0.37} Fe _{2.63} O ₄
SA5	97.8 (±0.4)	4.3 (±0.3)	97.5	2.5	Spinel	12.9 (±0.8)	59.4 (±1.3)	8.0	35.4	Ni _{0.52} Fe _{2.48} O ₄
SA6	98.8 (±0.4)	1.4 (±0.3)	98.7	1.3	Spinel	14.8 (±0.8)	57.5 (±1.5)	8.6	34.2	Ni _{0.60} Fe _{2.40} O ₄
Spinel-alloy-oxide	99.7 (±0.3)	0.4 (±0.2)	99.6	0.4	Spinel	22.6 (±1.0)	49.6 (±1.5)	13.1	29.7	Ni _{0.82} Fe _{2.06} O ₄
					Nickel oxide	67.3 (±0.2)	10.7 (±0.4)	42.5	7.5	Ni _{0.85} Fe _{0.15} O

* For samples WA1-SA2, the nickel contents of the oxide phases were calculated from the measured iron compositions assuming that the metal to oxygen ratio was that of pure wustite at the same oxygen pressure.

Discussion

The Fe/FeO electrode was used as reference in the galvanic cells. Steele (16) has assessed the available calorimetric and high-temperature equilibrium values and described the dissociation pressure of wustite by

$$\log(P_{O_2} \text{ atm})_w = \frac{-27643.7}{T} + 6.833 \left(\pm \frac{54.64}{T(^{\circ}\text{K})} \right), [873^{\circ}\text{-}1600^{\circ}\text{K}] \quad [4]$$

The dissociation pressures of the investigated oxides were calculated by means of Eq. [1] and [4]. These values could be used with the corresponding compositional determinations of the coexisting oxide and alloy phases to describe the variation of the oxygen activity over the Fe-Ni-O isotherm at 1000°C. Further thermodynamic information concerning the various phase equilibria can also be calculated for particular approximations and assumptions. This is outlined as each phase field is discussed in detail.

Variation of equilibrium oxygen pressure with alloy composition.—Figure 3 shows the values of oxygen

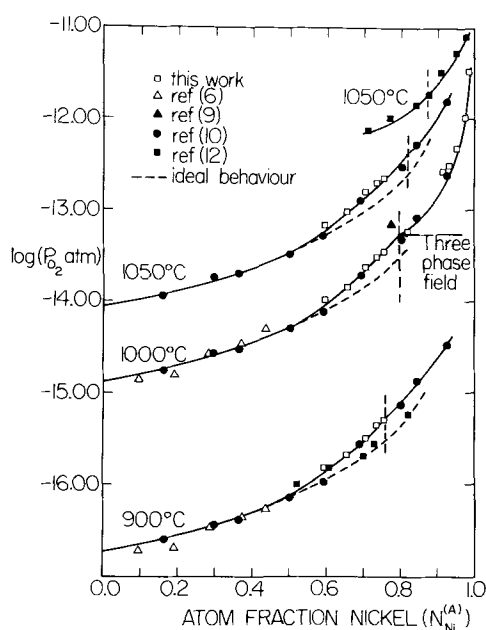


Fig. 3. Dissociation pressures of the oxides coexisting with Fe-Ni alloys at 900°, 1000°, and 1050°C. The dashed curves represent the ideal pressures for wustite-alloy equilibria assuming ideal behavior of iron in the alloy.

pressures calculated from the emf determinations as a function of atom fraction nickel in alloy, N_{Ni}^A , at 900°, 1000°, and 1050°C. Results from this and other investigations (6, 9, 10-12) are included. The results of this investigation are in good agreement with reported values except for those of Ono *et al.* (12) at 1050°C. The invariant oxygen pressure and alloy composition reported by Kushko *et al.* (9) for the wustite-spinel-alloy equilibrium is also included. The ideal curve shown for wustite-alloy equilibria was computed assuming ideal behavior of iron in the alloy. At 1000°C, the terminal composition of the alloy for wustite stability has been reported as 0.803 (8), 0.775 (9), 0.796 (11), and this study has used the latter value consistent with the corresponding compositions of wustite and spinel phases. The only reported terminal alloy composition at 900°C is 0.76 (8). At 1050°C, there are two reported values: 0.82 (8) and 0.88 (12). All of these terminal compositions are shown as vertical lines in Fig. 3.

Wustite-alloy phase field.—Dalvi and Smeltzer (11) have described the Fe-Ni-O isotherm at 1000°C and reported that wustite can coexist with alloys containing up to 79.6 a/o Ni. The corresponding terminal composition of wustite was 0.51 a/o Ni. The equilibrium oxygen pressure over this phase field increases, with increasing values of N_{Ni}^A , from that corresponding to the iron-wustite equilibrium to the invariant oxygen pressure associated with the three-phase field, wustite-spinel-alloy. Accordingly, the experimental curve of P_{O_2} vs. N_{Ni}^A in Fig. 3 was extrapolated to the above limiting alloy composition to obtain an invariant pressure of $5.5 (\pm 0.2) \times 10^{-14}$ atm. These values are to be compared to limiting values of $N_{Ni}^A = 0.775$ and an oxygen pressure of 7.1×10^{-14} atm determined by Kushko *et al.* (9) using a gas equilibration method.

Wustite composition as a function of oxygen pressure.—The effect of nickel content in wustite on its dissociation pressure is shown in Fig. 4. The parameter representing the nickel content is the metal atom fraction based on the total metallic content of the wustite phase. Note that the invariant oxygen pressure for wustite-spinel-alloy equilibrium is less than the magnetite-wustite dissociation pressure. Therefore the nickel metal atom fraction in the spinel must be greater than that in the wustite.

Thermodynamic properties of alloy.—The dissociation pressure of wustite equilibrated with the alloy is given by the relationship

$$P_{O_2} = \frac{(a_{FeO}^w)^2}{(a_{Fe}^A)^2} \cdot P_{O_2}^w \quad [5]$$

where $P_{O_2}^w$ is the dissociation pressure of wustite equilibrated with pure iron. For $a_{FeO} \sim 1$ and $a_{Fe}^A = N_{Fe}^A$, this reduces to the ideal relationship which produced the ideal behavior curves in Fig. 3. The experimental

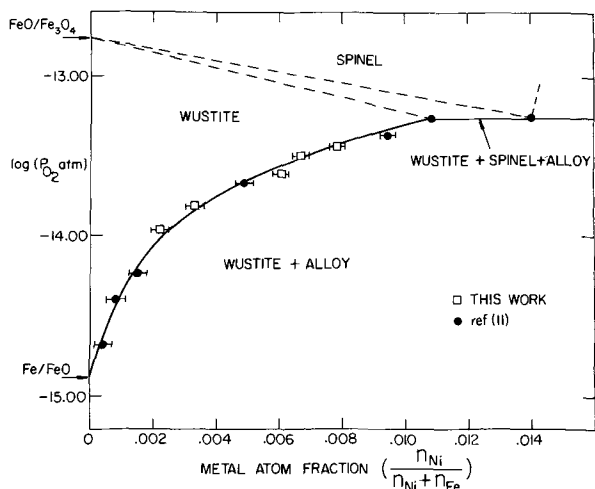
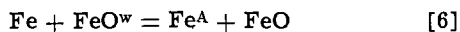


Fig. 4. Dissociation pressure of wustite equilibrated with Fe-Ni alloys at 1000°C vs. the nickel atom metal fraction in the oxide.

values of oxygen pressure, however, become greater than the calculated values, with increasing N_{Ni}^A , due to negative deviations of iron from ideality.

Activities of iron in the alloys may be obtained by considering the virtual reaction for cell B, assuming pseudobinary behavior. The virtual cell reaction is



where FeO^w represents wustite equilibrated with an alloy. From the Nernst equation

$$E = \frac{RT}{2F} \ln a_{FeO^w} / a_{Fe^A} \quad [7]$$

The wustite phase contained small amounts of nickel, less than 0.5 a/o, but its effect on the wustite activity is unknown. The data of Swaroop and Wagner (19) provided values for wustite activity at each measured oxygen pressure assuming that negligible error is introduced by neglecting the effect of nickel. The values of the iron activities were then calculated over the compositional range of wustite stability using Eq. [7]. The values of nickel activities were then obtained by numerically integrating the Gibbs-Duhem relationship, following the method of Darken and Gurry (20). Activity data reported by Kushko *et al.* (9) and Gattellier *et al.* (10) were used for the composition range $0.8 \leq N_{Ni}^A < 1$. The variations of the iron and nickel activities are shown in Fig. 5. Values of activities previously determined by the electrochemical (6, 10) and gas equilibration (2, 9) methods are included. The results illustrate that iron behaves ideally up to approximately 40 a/o Ni and shows negative deviations at larger nickel concentrations. Nickel, on the other hand, behaves ideally only up to an alloy iron content of 10 a/o. The nickel activity coefficient over its range of Henrian behavior, 0-40 a/o Ni, was calculated to be 0.82.

The deviations from ideality nevertheless are relatively small. This behavior is illustrated in more detail by the plots in Fig. 6 showing the ideal and actual free energy of mixing curves. Since the activities have been determined, the excess free energy of mixing may be expressed as

$$\Delta G(\text{excess}) = RT(N_{Fe^A} \ln \gamma_{Fe} + N_{Ni^A} \ln \gamma_{Ni}) \quad [8]$$

where γ represents an alloy activity coefficient. The maximum excess, which occurs at an alloy nickel atom fraction of 0.53, is only -240 cal/g-atom. This small degree of nonideality corresponds to previous findings (1, 2).

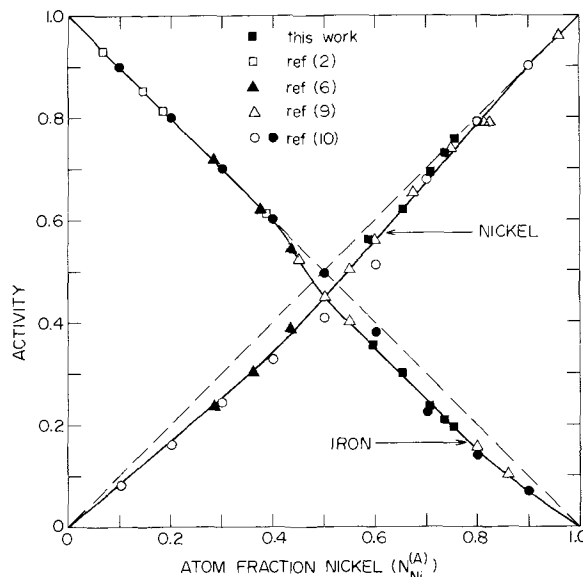


Fig. 5. Activities of iron and nickel in Fe-Ni alloys at 1000°C

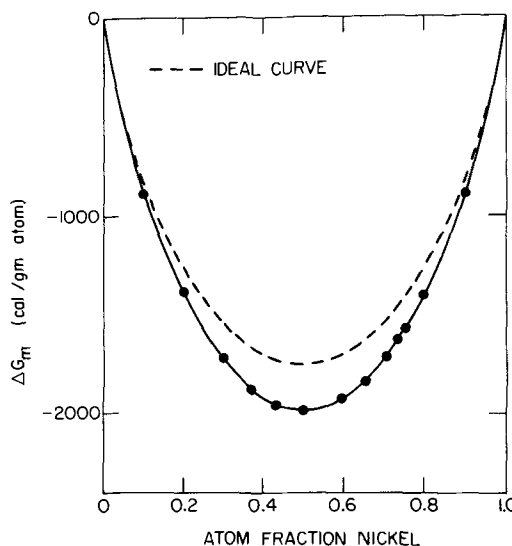


Fig. 6. Ideal and actual free energy of mixing curves for the Fe-Ni alloy system at 1000°C.

Spinel-alloy phase field.—It has been shown previously (11), and confirmed in this investigation, that a spinel, represented by the formula $Ni_xFe_{3-x}O_4$ where $0.04 \leq x < 1$, can coexist with alloys ranging in composition from 79.6 to 99.6 a/o Ni. The equilibrium oxygen pressures over this phase field are shown in Fig. 7. This plot consists of oxygen pressures determined directly by the electrochemical cell technique and of pressures calculated by applying the Gibbs-Duhem relationship to the experimentally determined values of the equilibrium compositions of the coexisting spinel and alloy phases.

The isothermal, isobaric Gibbs-Duhem relationship applied to the alloy and spinel phases gives

$$N_O^A d \ln a_O^A + N_{Ni^A} d \ln a_{Ni^A} + N_{Fe^A} d \ln a_{Fe^A} = 0 \quad [9]$$

$$N_O^S d \ln a_O^S + N_{Ni^S} d \ln a_{Ni^S} + N_{Fe^S} d \ln a_{Fe^S} = 0 \quad [10]$$

where N_i is the atom fraction and a_i is the activity of a species i in the alloy (A) and spinel (S) phase. The variation of oxygen activity with respect to nickel activity will then be

$$\frac{d \ln a_O}{d \ln a_{Ni}} = \frac{N_{Ni^S} N_{Fe^A} - N_{Ni^A} N_{Fe^S}}{N_O^A N_{Fe^S} - N_{Fe^A} N_O^S} \quad [11]$$

Since the oxygen solubility in the alloy is very small, < 0.015 w/o (21), the term $N_O^A N_{Fe^S} \approx 0$. The spinel

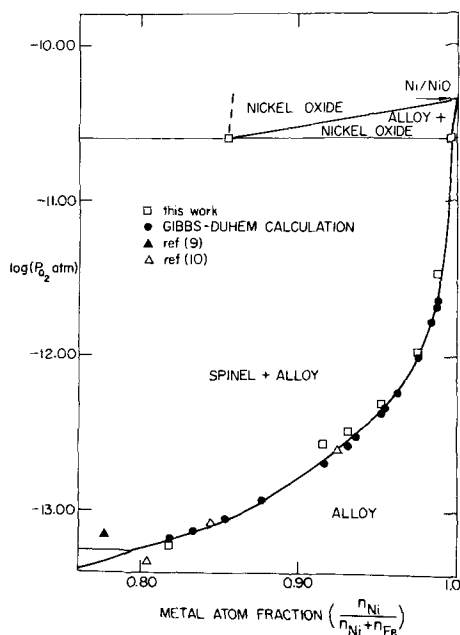


Fig. 7. Dissociation pressure of spinel equilibrated with Fe-Ni alloys at 1000°C vs. the nickel atom fraction in the alloy.

may be written as $Ni_xFe_{3-x}O_4$ assuming stoichiometry of the oxygen sublattice. Accordingly

$$N_{Ni^S} = \frac{x}{7}; N_{Fe^S} = \frac{3-x}{7}; N_{O^S} = \frac{4}{7} \quad [12]$$

Therefore

$$\frac{d \ln a_O}{d \ln a_{Ni}} = \frac{3N_{Ni^A} - x}{4(1 - N_{Ni^S})} \quad [13]$$

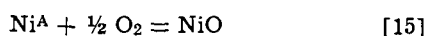
For $N_{Ni^A} > 0.796$, $0.98 < \gamma_{Ni^A} \leq 1.0$ (9, 10), and with $a_O = (P_{O_2})^{1/2}$, Eq. [13] becomes

$$\log \frac{P_{O_2}}{P_{O_2}^*} = 1.50 \log \frac{1 - N_{Ni^A}^*}{1 - N_{Ni^A}} - 0.217 \int_{N_{Ni^A}^*}^{N_{Ni^A}} \frac{x}{N_{Ni^A}(1 - N_{Ni^A})} dN_{Ni^A} \quad [14]$$

In this equation, $N_{Ni^A}^* = 0.796$ and $P_{O_2}^* = 5.5 \times 10^{-14}$ atm are the alloy composition and the invariant oxygen pressure for the wustite-spinel-alloy phase field. Thus the oxygen pressure across the spinel-alloy phase field can be computed for each of the alloy compositions given in this investigation and for those reported previously (11).

Figure 7 shows that the oxygen pressure increases very rapidly for $N_{Ni^A} > 0.985$ terminating at the horizontal line representing the pressure for the spinel-nickel oxide-alloy phase field. This invariant oxygen pressure was determined from cell D to be $2.5(\pm 0.1) \times 10^{-11}$ atm which should be compared with a value of 1×10^{-11} atm determined by a gas equilibration method (9).

The spinel-nickel oxide-alloy phase field is the lower bound, with respect to oxygen pressure, of the nickel oxide-alloy phase field, which can be described by the pseudobinary reaction



At 1000°C, the dissociation pressure of pure nickel oxide is 4.4×10^{-11} atm (16). Since the measured value of the equilibrium oxygen pressure was 2.5×10^{-11} atm over the alloy with nickel activity equal to 0.996, the calculated value of the activity for nickel oxide was 0.75. A value of 0.73 has been reported for this activity at 1050°C (12). However, the measured value for the mole fraction of nickel oxide in this investigation was 0.85 which is larger than the previously reported value of 0.74 at 1050°C.

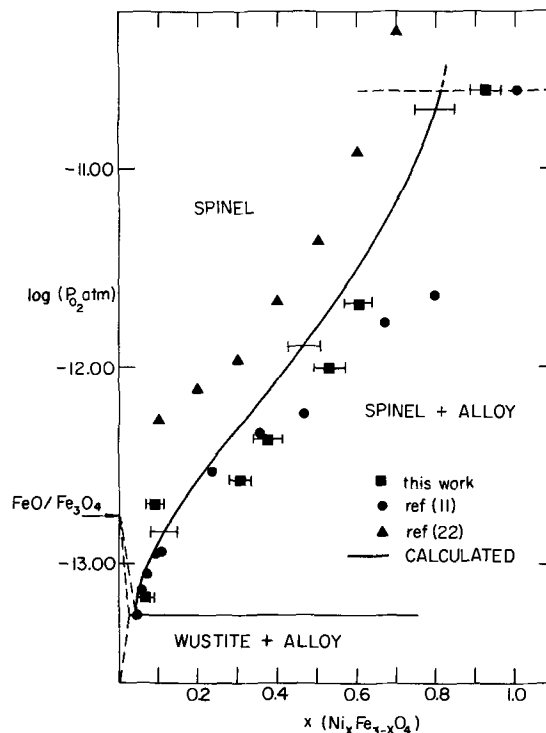


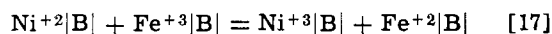
Fig. 8. Dissociation pressure of spinel equilibrated with Fe-Ni alloys at 1000°C vs. the nickel metal atom fraction in the oxide.

Spinel composition as a function of oxygen pressure.—Figure 8 illustrates the increasing equilibrium oxygen pressure of the spinel as its nickel content is increased. Three sets of values are given: those based on the oxygen pressure and composition determinations of this investigation, experimental values reported by Tretjakow and Schmalzried (22), and pressures calculated from the Gibbs-Duhem relationship, Eq. [14], using reported compositional determinations of the spinel and alloy phases (11).

A curve may be calculated to represent these results from a lattice defect model for this spinel proposed by Schmalzried (23). Consider the spinel phase as $Ni_xFe_{3-x}O_4$ and denote the tetrahedral cation sites as the A sublattice and the octahedral sites as the B sublattice. Assume, as with Schmalzried, that the concentration of ferric ions on tetrahedral sites in this inverse spinel is unaffected by nickel substitution into octahedral sites, i.e., $Fe^{3+}|A| = 1$. Since the anionic sublattice is stoichiometric, the divalent and trivalent cations on B sites may be expressed as

$$Ni^{3+}|B| = z; Ni^{2+}|B| = x - z; Fe^{3+}|B| = 1 - z; Fe^{2+}|B| = 1 - x + z \quad [16]$$

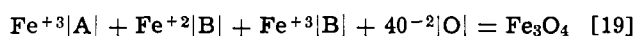
The following reactions may be considered. The oxidation and reduction of cations on octahedral sites may be represented as



and

$$K_1 = \frac{z(1 - x + z)}{(x - z)(1 - z)} \quad [18]$$

where ideal behavior of the ions has been assumed. The transfer of oxygen to form stoichiometric spinel may be represented by

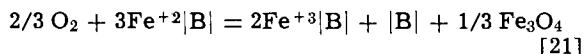


Therefore

$$(1 - z)(1 - x + z) = a_{Fe_3O_4} \quad [20]$$

To obtain Eq. [20], it has been implicitly assumed that the magnetite constituent of the spinel behaves ideally, and that the spinel may be considered as a solid solu-

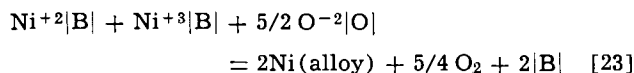
tion of the terminal compounds, i.e., x moles of NiFe_2O_4 with $(1 - x)$ moles of Fe_3O_4 . Uptake of oxygen by the spinel leads to formation of uncharged vacancies in the octahedral sublattice by the following reaction



Accordingly

$$K_2 = \frac{(1 - z)^2(|\text{B}|)(a_{\text{Fe}_3\text{O}_4})^{1/3}}{(P_{\text{O}_2})^{2/3}(1 - x + z)^3} \quad [22]$$

Finally, a defect equation may be used to represent equilibrium of the alloy with spinel



yielding

$$K_3 = \frac{(a_{\text{Ni}})^2(P_{\text{O}_2})^{5/4}(|\text{B}|)^2}{(x - z)z} \quad [24]$$

Equations [18], [20], [22], and [24] may be combined to give

$$\log x - 3.1667 \log(1 - x) = \log a_{\text{Ni}} + 1.292 \log P_{\text{O}_2} - \log K \quad [25]$$

where $K = (K_1^2/K_2K_3)^{1/2}$ under the restriction that $z \ll x$ (the ionization energy of divalent to trivalent nickel is about 6 eV). The constant K can be calculated from the experimental determinations associated with the wustite-spinel-alloy which serves as the lower bound, with respect to oxygen pressure, for the spinel-alloy phase field. The value of $\log K$ is $-15.92 (\pm 0.13)$, the uncertainty arising from the uncertainties attributed to the parameters of the three-phase field, i.e., $x = 0.042 (\pm 0.008)$, $a_{\text{Ni}} = 0.78 (\pm 0.01)$, $\log P_{\text{O}_2} = -13.26 (\pm 0.05)$. Values of oxygen pressures vs. atom fractions of nickel were obtained from Fig. 7 and Eq. [25] solved for the corresponding values of nickel contents in the spinel. This predicted variation of spinel composition with oxygen pressure is shown by the curve in Fig. 8. The error bars on the curve denote uncertainties arising from the computation using uncertainties in the values of a_{Ni} and $\log K$, and are not a measure of the accuracy of the assumptions in the model.

The computed curve, despite the arbitrary assumption of ideality for the ionic species in the spinel, is close to a best-fit curve through the experimental results. The compositions of the spinel based on electron microprobe determinations of nickel contents lie on the nickel-rich side of the computed curve. The error bars on the experimental results are from standard deviations of the counts from spinel phases. The two major problems in analyzing spinel phases by the electron-microprobe technique were the polishing

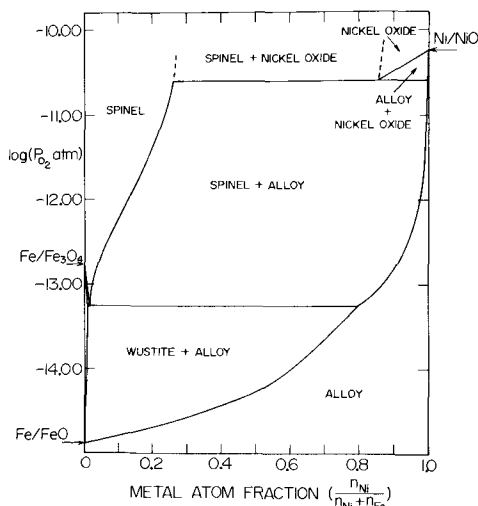


Fig. 9. Oxygen pressure as a function of the nickel atom metal fraction for each solid phase in the Fe-Ni-O isotherm at 1000°C.

of these phases, and the standards required. In this work, Fe_3O_4 and NiFe_2O_4 were used as standards, and intermediate compositions were obtained by a linear interpolation between these two compositions. The discrepancies between the sets of experimental results for the spinel compositions cannot be explained.

Oxygen pressure variation over the Fe-Ni-O isotherm at 1000°C.—Figure 9 shows the oxygen pressure as a function of the nickel content of each phase over the portion of the isotherm for which a metal phase exists. It has been compiled from Fig. 3, 4, 7, and 8 and the curves represent the best fit to available results.

Over the wustite-alloy phase field, the oxygen pressure increases, with increasing nickel content, from 1.32×10^{-15} atm corresponding to iron-wustite equilibrium, to 5.5×10^{-14} atm which is the invariant oxygen pressure associated with the wustite-spinel-alloy phase field. The nickel contents of the phases in this field are 0.5 a/o for wustite, 0.6 a/o for spinel, and 79.6 a/o for the alloy. Over the spinel-alloy phase field, the oxygen pressure increases to the invariant value of 2.5×10^{-11} atm for spinel-nickel oxide-alloy equilibrium. The spinel and nickel oxide are represented as $\text{Ni}_{0.8}\text{Fe}_{2.2}\text{O}_4$ and $\text{Ni}_{0.85}\text{Fe}_{0.15}\text{O}$, respectively, but the compositional determinations of spinel vary from $\text{Ni}_{0.65}\text{Fe}_{2.35}\text{O}_4$ to NiFe_2O_4 (11, 12, 22) and of nickel oxide from $\text{Ni}_{0.74}\text{Fe}_{0.26}\text{O}$ to $\text{Ni}_{0.87}\text{Fe}_{0.13}\text{O}$ (11, 12). The alloy contains 99.6 a/o Ni. Nickel oxide subsequently exists in equilibrium with metal up to the dissociation pressure of pure nickel oxide, 4.4×10^{-11} atm.

Acknowledgments

This work was carried out by H. Davies in partial fulfillment of the requirements for award of the Ph.D. degree at McMaster University. He wishes to acknowledge the award of a Pier Fellowship, National Research Council of Canada. This research was carried out under auspices of the National Research Council of Canada. The authors are indebted to A. D. Dalvi for helpful discussions.

Manuscript submitted Feb. 9, 1972; revised manuscript received May 22, 1972.

Any discussion of this paper will appear in a Discussion Section to be published in the June 1973 JOURNAL.

REFERENCES

- O. Kubaschewski and O. von Goldbeck, *Trans. Faraday Soc.*, **45**, 959 (1949).
- R. A. Oriani, *Acta Met.*, **1**, 448 (1953).
- M. J. Brabers and C. E. Birchenall, *Corrosion*, **14**, 179 (1958).
- A. E. Paladino, Jr., *J. Am. Ceram. Soc.*, **42**, 168 (1959).
- W. A. Dench, *Trans. Faraday Soc.*, **59**, 1279 (1963).
- G. A. Roeder and W. W. Smeltzer, *This Journal*, **111**, 1074 (1964).
- G. S. Viktorovich and D. I. Lisovskii, *Tsvetnyye Metall. (English Transl.)*, **7** (11), 49 (1966).
- G. S. Viktorovich, V. A. Gutin, and D. I. Lisovskii, *ibid.*, **7** (12), 54 (1966).
- M. T. Kushko, V. F. Balakirev, R. Y. Dobrovinskii, G. M. Popov, A. N. Men, and G. I. Chufarov, *Russ. J. Phys. Chem.*, **43**, 1739 (1969).
- C. Gatellier, D. Henriot, and M. Olette, *C. R. Acad. Sci. Paris, Serial C*, **271**, 453 (1970).
- A. D. Dalvi and W. W. Smeltzer, *This Journal*, **117**, 1431 (1970).
- K. Ono, K. Yokogawa, A. Yamaguchi, and J. Moriyama, *J. Japan Inst. Metals*, **35**, 750 (1971).
- G. G. Charette and S. J. Flengas, *This Journal*, **115**, 796 (1968).
- K. Kiukkola and C. Wagner, *ibid.*, **104**, 379 (1957).
- B. C. H. Steele and C. B. Alcock, *Trans. AIME.*, **233**, 1359 (1965).
- B. C. H. Steele, "Electromotive Force Measurements in High Temperature Systems," p. 3, C. B. Alcock, Editor, American Elsevier Publishing Co. (1968).
- C. M. Sellars and F. Maak, *Trans. AIME.*, **236**, 457 (1966).

18. C. M. Diaz and F. D. Richardson, Ref. (16), p. 43.
 19. B. Swaroop and J. B. Wagner, Jr., *Trans. AIME.*, **239**, 1215 (1967).
 20. L. S. Darken and R. W. Gurry, "Physical Chemistry of Metals," McGraw Hill Book Co. Inc. (1953).
 21. M. Hansen, "Constitution of Binary Alloys," p. 1024, McGraw Hill Book Co. Inc. (1958).
 22. J. D. Tretjakow and H. Schmalzried, *Ber. Bunsengesellschaft*, **70**, 180 (1966).
 23. H. Schmalzried, *Prog. Solid State Chem.*, **1**, 265 (1965).

Highly Conductive, Transparent Films of Sputtered $\text{In}_{2-x}\text{Sn}_x\text{O}_{3-y}$

D. B. Fraser and H. D. Cook

Bell Telephone Laboratories, Incorporated, Murray Hill, New Jersey 07974

ABSTRACT

Highly conductive, transparent films of $\text{In}_{2-x}\text{Sn}_x\text{O}_{3-y}$ have been deposited by d-c diode sputtering with Ar, O_2 , N_2 , Xe, and O_2 -Ar mixtures. Sputtering targets with different $\text{In}_2\text{O}_3/\text{SnO}_2$ ratios were utilized and the best results were obtained with pure Ar or Xe gas and targets containing 9-13 mole per cent (m/o) SnO_2 . The lowest film resistivity achieved was 1.77×10^{-4} ohm-cm, but routine films had resistivity values of about 3×10^{-4} ohm-cm. The use of a very low sputtering gas throughput (10^{-2} - 10^{-1} Torr liter/sec) was found to be necessary to develop films with a slight oxygen deficiency. Targets differing in density (porosity) differ in their susceptibility to reduction so that sputtering conditions depend on target density. The films have excellent adherence and will tolerate cleaning, heating, polishing, and bonding without failure. They may be etched in heated acids with standard photoresist techniques used to define electrode geometry. Exposure of the films to temperatures of 500°C in air will cause an approximate factor of 3 increase in resistance at room temperature. Sputtered films with sheet resistance of 1.6 ohms/square, 73% light transmission, and 14% reflection at 500 nm have been obtained. Suitable antireflection coated films of 5-7 ohms/square possessing over 97% light transmission appear feasible.

We wish to describe deposition techniques for and film properties of $\text{In}_{2-x}\text{Sn}_x\text{O}_{3-y}$ (ITO), a substitutional alloy oxide system with oxygen vacancies. Because of their low visible light attenuation, high electrical conductivity, stability, and good adherence sputter deposited films of ITO are expected to find wide application in electrooptic device technology.

Transparent, conductive films have generally been obtained by vapor deposition of thin metal films or by use of vapor reacted films of Sb-doped SnO_2 (1). Recently, characteristics of films of In_2O_3 (2, 3), Sn incorporated in In_2O_3 (4, 5), SnO_2 (3, 6), and Sb incorporated in SnO_2 (7), deposited by sputtering have been described.

In the sputtered pure oxides the reported resistivity at room temperature is approximately 10^{-2} ohm-cm after vacuum or other reducing, annealing treatment. Unless severe reduction has taken place, the oxide films display a high light transmission in the visible. Incorporation of donors such as Sb in SnO_2 and Sn in In_2O_3 yields higher conductivity without the optical absorption caused by excessive reduction. Vossen (5) has recently reported the deposition of films of ITO by rf sputtering using targets of 20 m/o $\text{SnO}_2:\text{In}_2\text{O}_3$. Resistivity values of 6.25×10^{-4} ohm-cm and optical properties similar to those reported here were obtained.

The films described here have been utilized in display devices such as ferroelectric ceramic light valves (8), liquid crystal light valves (9), and electrooptic polarization switches (10).

Sputtering Procedure

Some attempts were made to deposit In_2O_3 films by d-c diode, reactive sputtering of In and In-Sn alloys with mixtures of Ar- O_2 . However, these films were deposited at very low rates with excessive substrate

heating and the films had to be reduced by subsequent heat-treatment in nitrogen. Much more satisfactory films were achieved directly by d-c sputtering from In_2O_3 and In_2O_3 - SnO_2 , hot-pressed ceramic targets.¹ Three target sizes were utilized, 4.45 cm, 12.7 cm, and 22.8 cm diameters with most of the films described here sputtered from the 12.7 cm targets. A potential difference of 4-5 kV was used with an approximate current density of 1 mA/cm² for the small targets and 0.5 mA/cm² for the large targets. The target-to-substrate spacing varied from 5 to 7.5 cm. A thermocouple gauge was used to indicate chamber pressure and 20×10^{-3} Torr was the average pressure indicated during film deposition. Both the target and substrate holder were water-cooled. The substrates were borosilicate glass slides, Corning 7059 glass slides or vitreous silica slides. No attempt was made to thermally lock the substrates to the water-cooled holder.

The best films of ITO are obtained with a controlled throughput of gas. A 4 in. oil diffusion pump equipped with a liquid nitrogen trap was used to pump on the chamber, an 18 in. glass cylinder of either 20 or 50 liter volume. Most of the films to be discussed here were deposited without liquid N_2 in the trap since early in the investigation film properties did not appear to be dependent on cooling the trap. The chamber was equipped with an aluminum shutter that was placed between the target and substrate during pump-down and predeposition sputtering. Initially, the chamber was pumped to 10^{-6} Torr and then the pumping system was throttled to maintain the admitted sputtering gas at approximately 20×10^{-3} Torr. This usually corresponded to a very low gas throughput

¹ Targets were obtained from two sources: (i) Haselden Company, San Jose, California (this company supplied the In_2O_3 target and the high density 9 m/o $\text{SnO}_2:\text{In}_2\text{O}_3$ targets), and (ii) Materials Research Corporation, Orangeburg, New York (this company supplied all other targets).

Key words: transparent electrode indium-tin oxide, sputtered sheet conductors.

rate of $\sim 10^{-2}$ Torr liter/sec but many films were deposited at throughput rates of $\sim 10^{-1}$ Torr liter/sec.

The sputtering gases used were O_2 , N_2 , Ar, Xe, and gas mixtures such as Ar- O_2 , and O_2 - N_2 . No purification of the gases was attempted. Generally, the best film properties were obtained with pure Ar or pure Xe, however, the cost of using Xe may outweigh its advantage of higher deposition rate than Ar. Details of the influence of the sputtering gas will be considered in the discussion of film properties.

Initially in the investigation only porous targets were used and a target conditioning procedure was followed when pure inert gases were to be used to deposit test films. The procedure consisted of sputtering with a gas mixture of 80% O_2 and 20% Ar for as long as 1.5 hr, subsequently, sputtering could be carried out using Ar or Xe. After such an oxidizing treatment the porous target could be operated for more than 6 hr of accumulated sputtering time with pure Ar at low throughput rates with no apparent film deterioration. Prolonged sputtering in a pure inert gas resulted in films with a dark appearance showing that excessive reduction had occurred. With Ar or Xe the porous target would slowly acquire a dark appearance which was ascribed to a reduction of the surface. The darkening disappeared after sputtering with the O_2 -Ar mixture.

Later in the investigation deposition procedures were modified so that porous targets could be used, without the O_2 -Ar preoxidation. The procedure consisted of sputtering with Ar only and to begin film deposition on the substrates after only 4-10 min of sputtering with the shutter between target and substrate. Without the O_2 -Ar oxidation apparently sufficient O_2 was adsorbed from the laboratory atmosphere when the system was open, to permit film deposition for 30 min.

The dense targets were used in a similar manner with pure Ar except that predeposition sputtering with the shutter in place was of 3-5 min duration and actual single deposition times could exceed 2 hr duration.

Deposition rates of $\sim 1 \mu\text{m/hr}$ were routinely obtained with Ar. The highest rates ($2.5 \mu\text{m/hr}$) were obtained with Xe and the lowest rates ($\sim 0.5 \mu\text{m/hr}$) with O_2 and the O_2 - N_2 mixtures.

Physical Properties of the Films

Film structure.—The structure of bulk In_2O_3 is bcc (11). X-ray diffraction by the ITO films deposited during this investigation revealed a similar structure. A strong fiber texture was also detected with the [111] direction normal to the substrate. This preferred alignment of the [111] direction has been reported for pure In_2O_3 films (3) deposited by sputtering. However,

Vossen (5) has reported a [100] direction normal to the substrate for ITO. The different orientation may be due to differences in deposition parameters such as substrate temperature.

The preferred orientation of these films may be better appreciated by studying the scanning electron micrographs made of two representative samples. In Fig. 1, a film approximately $2 \mu\text{m}$ thick deposited by sputtering with an Ar- O_2 mixture is shown at two magnifications, the apparent viewing angle is 45° . The lower magnification shows a uniform crystallite size for the sputtered layer but considerable surface roughness. At higher magnification, the projections appear as high as $0.5 \mu\text{m}$ and are about $0.3 \mu\text{m}$ wide. It should be noted that a film such as described here will scatter light and can supply enough friction that the film side of the substrate plate can be discerned by light rubbing with a finger.

A film approximately $1.3 \mu\text{m}$ thick deposited by sputtering with Ar is shown in Fig. 2 at the same magnifications as in Fig. 1. In the micrograph obtained at the lower magnification a uniform crystallite size is also observed for this film. At higher magnification, however, the crystallites of this film appeared to project only as high as $0.25 \mu\text{m}$ and are about $0.15 \mu\text{m}$ wide. The two films depicted in Fig. 1 and 2 also differed strongly in their light scattering properties with the film of Fig. 1 scattering more. In the visible region of the spectrum these films behave as dielectrics, and the increased light scattering is related to crystallite size and the height of projection.

Where necessary, adequate polishing has been effected by the use of either 0.05 or $0.3 \mu\text{m}$ grain size alumina and a soft cloth. To remove all scratches produced by the alumina grit the films have then been polished with a combination chemical-mechanical polish.² Films polished with this two-step process have appeared smooth when viewed in a scanning electron microscope.

One general observation should be noted: smaller crystallites with lower projections are obtained if higher power is used in the plasma (e.g., 0.7 mA or greater per cm^2 of target at 5 kV). The ITO films described here have been deposited on thermally stable substrates which tolerate high plasma powers. However, more delicate substrates such as single-crystal, single-domain BaTiO_3 and thin ferroelectric ceramic plates have also been used. Slower deposition on these substrates results in slightly larger ITO crystallites with some increase in light scattering evident, especially when porous targets are used.

² Syton HT-30, Monsanto Company, St. Louis, Missouri.

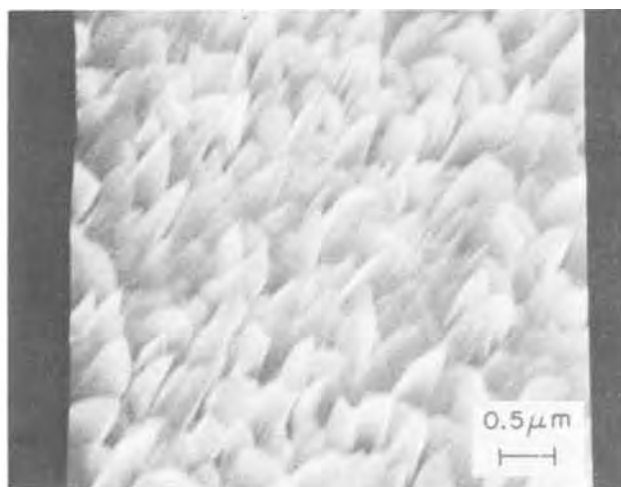
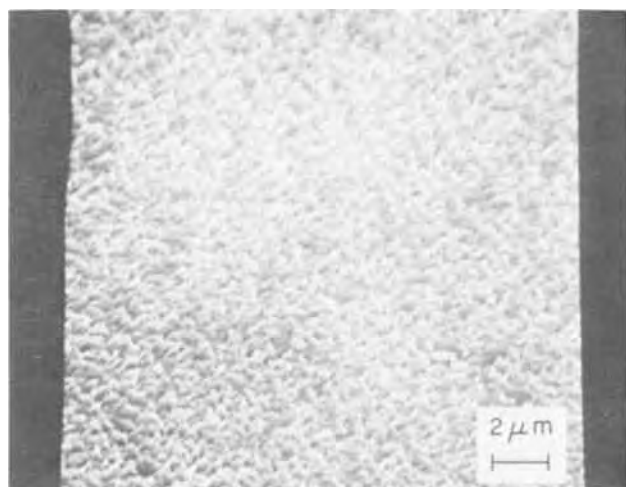


Fig. 1. Scanning electron micrographs of an $\text{In}_{2-x}\text{Sn}_x\text{O}_{3-y}$ film sputtered from an In_2O_3 -9 m/o SnO_2 target with an Ar- O_2 gas mixture. The apparent viewing angle is 45° .

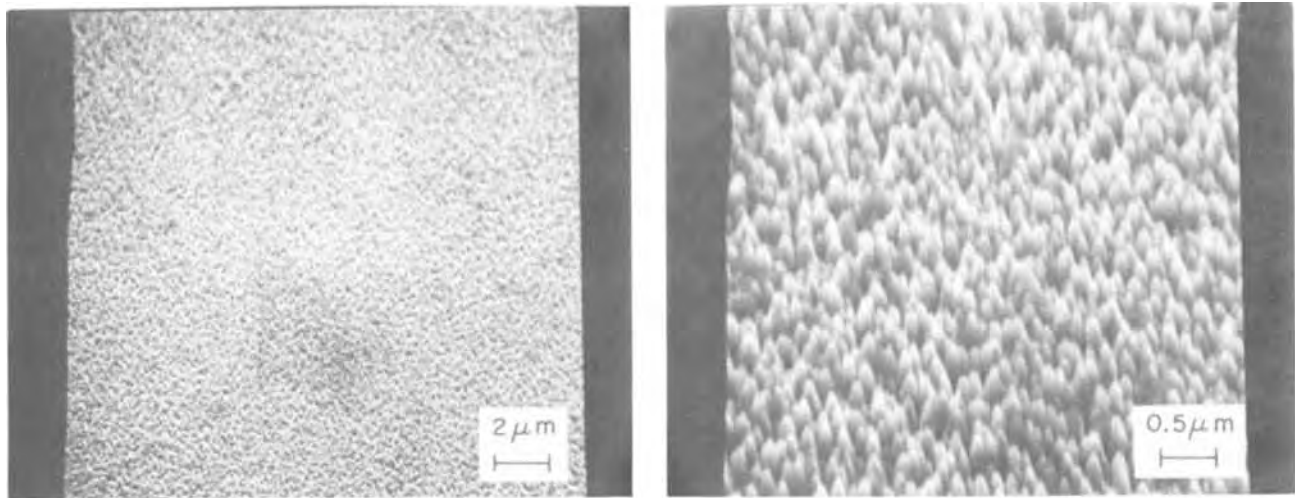


Fig. 2. Scanning electron micrographs of an $\text{In}_{2-x}\text{Sn}_x\text{O}_{3-y}$ film sputtered with Ar only from an In_2O_3 -9 m/o SnO_2 target.

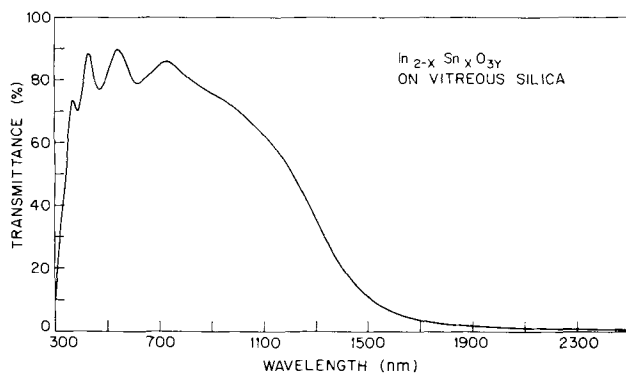


Fig. 3. Transmission characteristics from 300 to 2500 nm of an $\text{In}_{2-x}\text{Sn}_x\text{O}_{3-y}$ film on vitreous silica sputtered from an In_2O_3 -9 m/o SnO_2 target.

Optical properties.—Films of ITO sputtered with Ar are highly transparent in the visible as may be seen in the plot of per cent transmission vs. wavelength shown in Fig. 3. The data plotted in Fig. 3 were obtained from a $0.5 \mu\text{m}$ thick film sputtered with Ar from an In_2O_3 -9 m/o SnO_2 target. A vitreous silica substrate 0.5 mm thick was used. The structure of this film is similar to that depicted in Fig. 2. The reflection data for this film obtained at an angle of incidence of 14° , are shown for a similar spectral range in Fig. 4. Both the transmission and reflection data are accurate to within 1% and show channel spectrum fringes. Assuming negligible light absorption the reflectance maxima occurring near 480 and 620 nm yield refractive index values of 2.03 and 1.95, respectively, which are in good agreement with the index values measured by Müller (2) for pure In_2O_3 films. Transmission fringes have been used to obtain the values of film thickness, d , shown in Table

I. Fringes near 500 nm in wavelength have been used with a refractive index of 2.0. From the data presented in Fig. 3 and 4, it is evident that the light absorbed or scattered by the ITO film is about 2% of the incident near 500 nm and that the major cause of transmission loss is reflection. It is clear that suitable antireflection coatings and substrates would permit in excess of 97% of the light to be transmitted within a given spectral region near 500 nm wavelength for such ITO films. The film described here has a sheet resistance of approximately 7 ohms/square. Films with similar optical characteristics have been deposited with even lower sheet resistances (approximately 5 ohms/square).

The achievement of the lowest possible resistivity is of practical significance in that it provides some freedom in selecting the film thickness while still maintaining satisfactorily low sheet resistance. For example, thin films have very broad interference transmission maxima and the use of low resistivity films permits useful sheet resistance to be obtained with maximum transmission ($\sim 90\%$) over a band of wavelengths.

A potentially useful characteristic of these sputtered films is their high reflectivity in the infrared. Transmission data obtained through film and substrate and reflection data are shown out to $15 \mu\text{m}$ in Fig. 5. The sample used for these measurements was the same as that used for obtaining the data of Fig. 3 and 4. For comparison the reflection data obtained for the vitreous silica substrate are also included in Fig. 5. The transmission is essentially zero over the entire infrared spectrum scanned. The infrared mirror properties are evident in the reflection data from the film surface since none of the characteristics of underlying vitreous silica reflection was detected.

Carrier concentration can be related by a simple theory to the wavelength corresponding to minimum reflectivity which occurs before the onset of constant high reflectivity at longer wavelengths (12). Calcula-

Table I.

Nominal target composition	Sputtering gas, conditions	R (ohm/square)	d (μm)	% T (at 500 nm)	ρ (10^{-4} ohm-cm)	Figure of merit (% T/R)
In_2O_3	Ar	26.8	0.500	77	13.4	2.87
$\text{In}_2\text{O}_3 + 9 \text{ m/o } \text{SnO}_2$	O_2	285.0	0.262	81	74.5	0.284
$\text{In}_2\text{O}_3 + 9 \text{ m/o } \text{SnO}_2$	O_2	8.14	0.755	87	6.15	10.7
	(then reduced in N_2 at 300°C)					
$\text{In}_2\text{O}_3 + 9 \text{ m/o } \text{SnO}_2$	O_2/Ar (10/90)	12.2	1.02	83	12.5	6.80
$\text{In}_2\text{O}_3 + 9 \text{ m/o } \text{SnO}_2$	N_2	69.4	0.223	86	15.5	1.24
$\text{In}_2\text{O}_3 + 9 \text{ m/o } \text{SnO}_2$	Ar	3.23	0.840	70	2.72	21.7
$\text{In}_2\text{O}_3 + 9 \text{ m/o } \text{SnO}_2$	Xe	3.21	0.770	79	2.47	24.6
$\text{In}_2\text{O}_3 + 9 \text{ m/o } \text{SnO}_2$	Ar	3.10	0.573	83	1.77	26.8
	(T > 500°C substrate)					
SnO_2	Ar	9×10^4	0.335	78	$3.02 \times 10^{+4}$	8.68×10^{-4}
$\text{SnO}_2 + 7 \text{ m/o } \text{Sb}_2\text{O}_3$	Ar	550.0	0.990	64	540.0	0.116

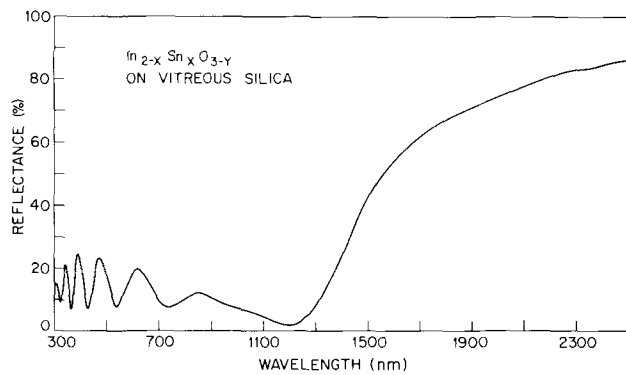


Fig. 4. Reflection characteristics from 300 to 2500 nm of an ITO film on vitreous silica sputtered from an In_2O_3 -9 m/o SnO_2 target. The angle of incidence is 14° .

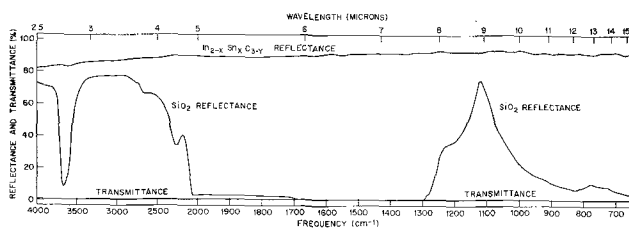


Fig. 5. Transmission and reflection for wavelengths from 2.5 to $15 \mu\text{m}$ of an ITO film on vitreous silica sputtered from an In_2O_3 -9 m/o SnO_2 target. For comparison, a trace of the vitreous silica reflectance is also shown. The reflectance data were obtained at an angle of incidence of 14° .

tions based on the wavelength for this minimum reflectivity of an ITO film have yielded a carrier concentration that agreed well with a value based on Hall measurements. Since not all the ITO films of this investigation have been measured for both reflectance and transmittance, the transmission at $1.5 \mu\text{m}$ was chosen arbitrarily as a rough indication of carrier concentration. For empirical purposes of film evaluation, a roughly linear relation over a limited range of film resistivity and transmission at $\lambda = 1.5 \mu\text{m}$ was found; 10% transmission for $\rho = 3.5 \times 10^{-4}$ ohm-cm and 77% transmission for $\rho = 13 \times 10^{-4}$ ohm-cm. The ITO films compared were sputter deposited from a single 9 m/o SnO_2 : In_2O_3 target.

It was found that films deposited using gas mixtures, such as O_2 - N_2 , O_2 -Ar, or O_2 - N_2 -Ar, scattered light much more than films deposited using a single gas. This scattering could be observed even in films less than $1 \mu\text{m}$ thick by placing the coated substrate plate edge-on in an intense light beam. The path of the light beam was clearly revealed by scattering. The scattering is related to the larger more protrudent crystallites formed more readily at the lower film deposition rates obtained with the gas mixtures.

Electrical properties.—The properties of a number of representative films are listed in Table I. The resistivity values were obtained from bridge measurements of sheet resistance and thickness values obtained from transmission channel spectra. These results are representative of resistivity values obtained directly from the sputtering process and involve no post-deposition annealing except where specifically indicated. A film approximately $1.5 \mu\text{m}$ thick deposited by sputtering with Ar and a 9 m/o SnO_2 : In_2O_3 target was measured by the van der Pauw technique (13) and the parameters obtained were: resistivity, $\rho = 3 \times 10^{-4}$ ohm-cm; carrier density, $n = 8.6 \times 10^{20}$ cm^{-3} ; Hall mobility, $\mu_H = 24$ $\text{cm}^2/\text{V}\text{-sec}$.

Since the goal is to obtain stable films with the lowest sheet resistance and highest optical transparency, a figure of merit for the films has been obtained by

dividing per cent light transmitted at 500 nm (obtained from an average transmission curve drawn through the fringes over the range 450-550 nm) by the sheet resistance of the film. The figure of merit has units of [(per cent transmission) \cdot (square/ohm)]. For brevity, these units will be dropped and the figure of merit will be cited as a number.

Factors Determining Film Characteristics

Target composition.—Incorporation of substitutional Sn into the In_2O_3 crystal structure yields donor centers; consequently, the Sn content of the target influences the resistivity of the sputtered films. Targets were obtained which ranged in composition from In_2O_3 to SnO_2 with a series of the mixed oxides varying from 2 to 23 m/o SnO_2 in In_2O_3 .

In order to evaluate the influence of target composition on film properties, a standard procedure was developed for putting a target into service. The target to be tested was first oxidized in Ar- O_2 by sputtering for 30 min. Three distinct sputter depositions were then made using Ar only and resistivity values were obtained from the third deposition. Argon throughout was maintained at approximately 0.01 Torr liter/sec and all other parameters were maintained constant during the series of depositions.

Comparison of the film resistivities on the basis of nominal target composition yielded a discrepancy for films deposited using a target containing 7 m/o SnO_2 . As a result, a count ratio of Sn/In obtained from x-ray fluorescence of the actual films was used for a relative Sn content value. Since all films were about $0.4 \mu\text{m}$ thick it was assumed that this analysis would be valid for a relative comparison. Some of the targets had a speckled appearance and some segregation of the oxides during the target fabrication could have occurred which would cause a discrepancy between the nominal target composition and actual film composition. Incorporation of impurities such as Sb, Pb, Ti, or Bi in a target could also increase the film resistivity (5) and cause some of the scatter in Fig. 6.

A plot of sputter deposited film resistivity vs. the x-ray measured Sn/In ratio is shown in Fig. 6 for targets containing from 0 to 23 m/o SnO_2 . Small variations in oxygen vacancy content could account for the scatter of the points. Lowest resistivity films occur for Sn/In ratios from 0.18 to 0.28. These low resistivity films were deposited using targets containing 9, 11, and 13 m/o SnO_2 . Vossen (5) obtained minimum resistivity from targets containing 20 m/o SnO_2 while the present investigation yielded minimum resistivity in films obtained from targets containing about 10 m/o SnO_2 . The discrepancy in optimal target composition may be ascribed to differences in film deposition conditions.

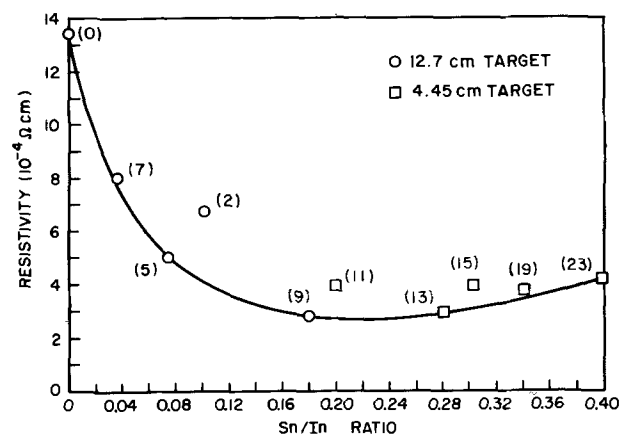


Fig. 6. Resistivity of In_2O_3 films containing varying amounts of SnO_2 plotted as a function of the Sn/In ratio measured by x-ray fluorescence. The numbers in parentheses indicate nominal SnO_2 m/o content of the targets used.

For the films, no significant light absorption was measured and only the reflection loss limited transmission. Not shown in Fig. 6 is the resistivity representative of the SnO_2 target. Under similar sputtering conditions, the SnO_2 target yielded films with ρ values of 0.1 ohm-cm to more than 10 ohm-cm.

One point concerning the data in Fig. 6 should also be made. Note that the effect of adding even an optimal amount of Sn to the In_2O_3 film is only to decrease the resistivity by an approximate factor of 4 from that obtained from a target containing only In_2O_3 . The data shown in Table I and Fig. 6 indicate that film resistivity is more sensitive to the oxygen vacancy content than it is to the Sn content. For example, the ITO film deposited by sputtering with O_2 gas and a 9 m/o SnO_2 : In_2O_3 target yielded a resistivity more than a factor of 5 greater than that of the film obtained by sputtering Ar and the In_2O_3 target. Further, sputtering with O_2 gas and a 9 m/o SnO_2 : In_2O_3 target and then reducing the film in N_2 at 300°C yielded a resistivity only a factor of 2 greater than that obtained for films deposited from the same target using Ar. These results indicate that the same target may yield vastly different resistivities depending on the extent to which oxygen vacancies are incorporated into the deposited films.

For comparison, in addition to the films of SnO_{2-y} , films of $\text{Sn}_{1-x}\text{Sb}_x\text{O}_{2-y}$ were also deposited using the same sputtering parameters as this series of ITO films. The results for two representative films are included in Table I. The Sn-based films show higher resistivity and lower light transmission when deposited by the same methods as the ITO films. As in the case of ITO films, the resistivity of the Sn-based films was primarily dependent on oxygen deficiency. Further oxygen deficiency would have to be incorporated to lower the Sn-based film resistivity to values comparable to those for the In-based films.

Target density.—Most of the sputter deposition of ITO was carried but using targets with 70-80% of solid density. However, two targets with over 90% solid density were acquired and the films deposited with these targets differed from those obtained from the less dense targets. All the targets used in a comparison of films from porous and dense sources were nominal 9 m/o SnO_2 : In_2O_3 . Generally, less light scattering was observed in ITO films obtained from the dense targets. Also, single long duration sputter depositions resulted in dark (more reduced) films when porous targets were used and much lighter films when dense targets were used.

Porous targets.—A series of films was deposited using a 12.5 cm diameter target. Prior to each deposition the target was conditioned by sputtering with an Ar- O_2 mixture for 10 min. The duration of the film deposition for each test film was 30 min. Only Ar gas was admitted during each deposition period. Power was kept at 275W and spacing fixed at approximately 7 cm. The variable for the deposition series was Ar throughput.

The results of varying the Ar throughput and sputtering from a porous target are shown in Fig. 7-10. In Fig. 7, sheet resistance is plotted vs. throughput, and it may be seen that sheet resistance varied by more than a factor of 6 over the series. Film thickness varied by more than a factor of 6 over the series. Film thickness varied by more than a factor of 2 (Fig. 8) with higher rates of deposition occurring at greater throughput of Ar. Resistivity vs. throughput is shown in Fig. 9 where an approximate factor of 4 decrease is shown over the range of throughput. From Fig. 9, it may be seen that increasing the throughput of the Ar should yield lower film resistivity. For the sputtering conditions used in this series of depositions such increases of Ar throughput would also yield more light absorption. A figure of merit was calculated for each film but because transmission was limited only by reflection for this series of films, the figure of merit was simply the inverse of the sheet resistance values of Fig. 7.

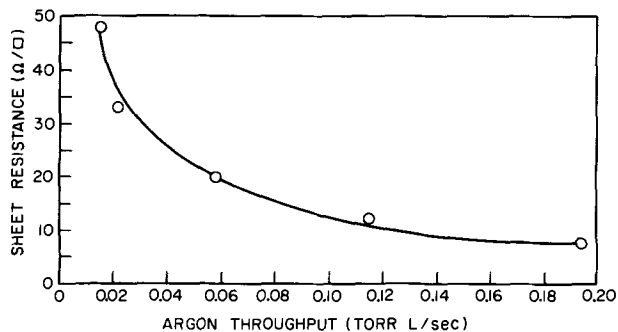


Fig. 7. Sheet resistance obtained after 30 min of sputtering vs. Ar throughput.

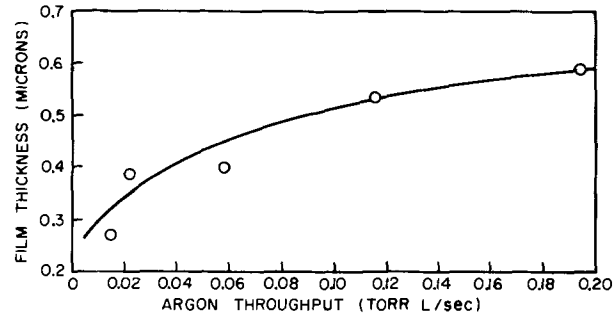


Fig. 8. Film thickness for a 30 min deposition vs. Ar throughput

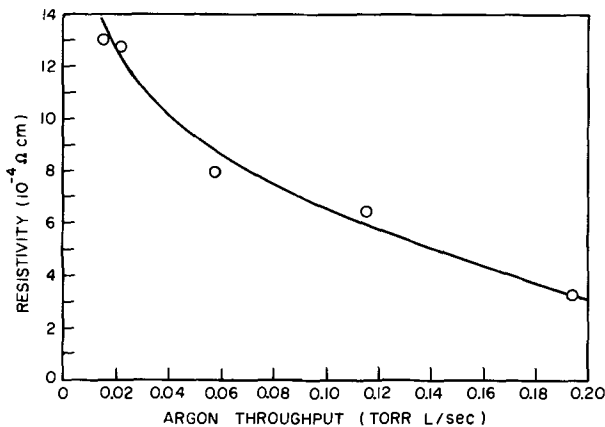


Fig. 9. Film resistivity obtained for a 30 min deposition as a function of Ar throughput.

The results obtained with a porous target and Ar throughput variation can be interpreted in terms of oxygen removal by an increasing flow of Ar through the sputtering chamber. At high throughput, the increased Ar flow may scatter more O_2 from the region between the target and substrate, thus contributing to lower resistivity in the deposited film. Similarly, with more Ar present between the target and substrate, the sputtering is more efficient and the rate of deposition will be increased. In the case of porous targets additional oxygen loss is attributed to poor heat transfer through the target which causes the surface of the porous target to operate at a higher effective temperature than a dense target. Some of these hypotheses have been investigated in experiments with porous and dense targets.

A 7059 slide with Au-Cr electrodes defining a clear square in the center of the slide was used to show that continual reduction occurs during deposition. Leads were attached to the metal electrodes and sheet resistance was measured at intervals during the deposition. A 22.5 cm diameter target was used and the throughput of Ar was 0.01 Torr liter/sec. The target was not conditioned by sputtering with Ar- O_2 . Pre-deposition sputtering against a shutter was performed

for 10 min. Resistance was measured after approximately 8 min of sputtering. From previous results the deposition rate of the film was assumed to be approximately constant. Resistance of the square film area was measured directly and the product of resistance times elapsed deposition time (Rt) was assumed to be proportional to the bulk resistivity of the film. A plot of Rt vs. t is shown in Fig. 10 where a decrease of over 75% in the value of the product occurs for the total deposition period. This is interpreted in terms of continuous outgassing of the target and an increase in the state of reduction of the film as sputtering proceeds. A break in the curve is due to reabsorption of air when the system was vented to the atmosphere and operated for 30 sec with the shutter masking the substrate. The film layer deposited after the brief exposure to the atmosphere shows a different rate of change of resistivity as the target outgasses. For sputter depositions of 1 hr with this particular target the films were strongly reduced and darker in appearance than films deposited for the same total time with a brief interruption to introduce oxygen after 20 min of sputtering.

Dense targets.—Two dense targets 12.5 cm in diameter were acquired and similar ITO films were obtained from them.

A series of films was deposited using one of the dense targets. Argon throughput was approximately 0.1 Torr liter/sec and power in the discharge was 275W. Pre-deposition sputtering was performed for 10 min with the shutter in place, and Ar- O_2 sputtering was not used to condition the target. The films were deposited by continuous sputtering without interruption for re-admission of air. From the linear relation of film thickness and deposition time (Fig. 11) the deposition rate appears to be constant. Sheet resistance vs. time is plotted in Fig. 12 and figure of merit vs. time in Fig. 13. From a plot of $\ln I/I_0$ vs. thickness, a value for the absorption constant at 500 nm was obtained, $\alpha \sim 10^3 \text{ cm}^{-1}$ ($0.4 \text{ dB}/\mu\text{m}$).

The resistivity of these films varied from 4.3×10^{-4} to 2.9×10^{-4} ohm-cm for the shortest and longest sputtering times respectively. This change in resistivity

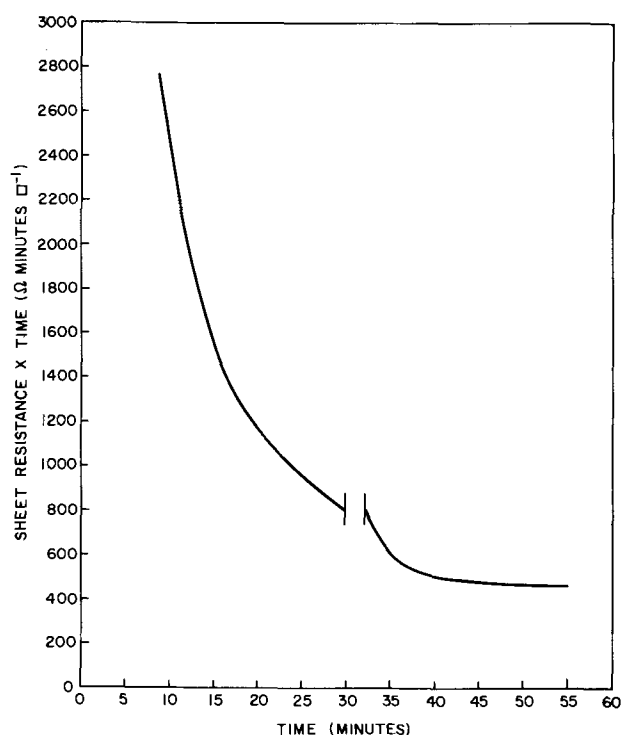


Fig. 10. Product of film sheet resistance times elapsed time vs. elapsed time. The break in the curve shows where sputtering was stopped, system vented, and 30 sec was spent sputtering against the shutter.

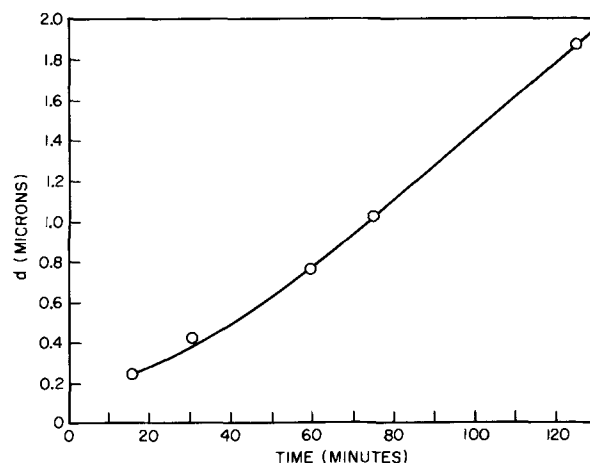


Fig. 11. Film thickness vs. sputtering time

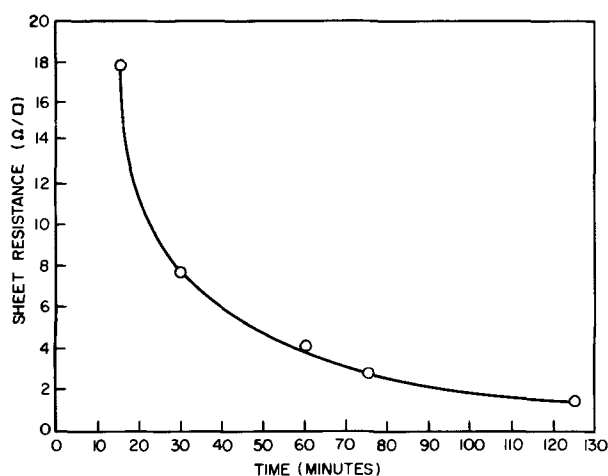


Fig. 12. Film sheet resistance vs. sputtering time

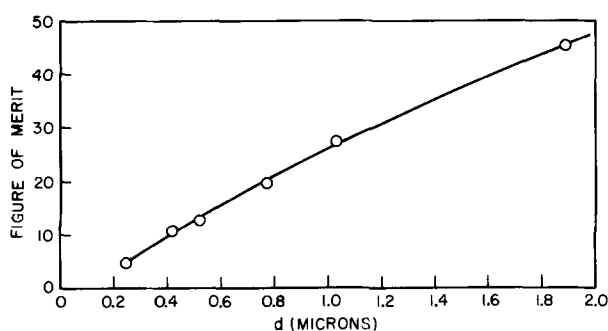


Fig. 13. Figure of merit of films vs. sputtering time

is considerably less than the change in Rt (Fig. 10) displayed by the film obtained from a porous target and is attributed to a lower rate of oxygen loss by the dense target. From the assumption of constant resistivity of 3×10^{-4} ohm-cm and optical absorption of 10^3 cm^{-1} , a maximum figure of merit of 84 should be obtained in a film $7 \mu\text{m}$ thick from the dense target.

In summary, the differences that are observed between ITO films obtained by sputtering with Ar from dense or porous targets are: (i) Dense targets yield a smaller gradient in the state of reduction through the film thickness and hence a smaller gradient in resistivity. (ii) Dense targets do not appear to be as sensitive to Ar throughput. (iii) Single depositions resulting in thick ITO films without excessive light absorption are more easily performed with dense targets. (iv) ITO films obtained from porous targets tend to scatter light more than films obtained from dense targets.

The gradient in resistivity through the film thickness may be minimized by increasing the predeposition sputtering with a shutter in place. However, the characteristics of a given target may require that different sputtering procedures be followed than those described for the porous and dense targets of this investigation.

Thermal effects (target and substrate).—Thermal effects are evident at both the substrate and the target. Preliminary results have shown that bonding a substrate to the water-cooled holder increases the film resistivity by more than a factor of 10^2 . This higher resistance is attributed to a lower concentration of oxygen vacancies. Generally, the higher the substrate temperature, the lower the film resistivity. An example of a film deposited on a substrate above 500°C is given in Table I. A film resistivity of 1.77×10^{-4} ohm-cm was obtained. Normal substrate temperature was about 420°C during film deposition.

Target surface temperature effects have been varied by operating a porous target at the same power continuously and intermittently with a 50% duty cycle and an on time of 30 sec. The modulation was accomplished by on-off switching the d-c potential applied to the target. For the same total elapsed sputtering times the films deposited continuously had approximately half the resistivity of films deposited with the intermittent plasma. Both target and substrate temperatures are lower in intermittent operation of the plasma, and more oxygen will be retained by the target surface and more will be accepted by the growing film.

Applications

Films of ITO deposited by sputtering from 9 m/o $\text{SnO}_2:\text{In}_2\text{O}_3$ targets have been used for a variety of applications. The majority of films deposited on 7059 slides have been used as conductive substrates for sputter-deposited CdS films (14), allowing the CdS films to be tested through the ITO layer which acts as an ohmic contact. The ITO-CdS interface has exhibited excellent adherence and CdS films over $20 \mu\text{m}$ have been deposited without adherence failure. Many films have been deposited on light valve devices, such as the strain-biased ferroelectric ceramic (ferpic) (8), and the ITO has not suffered adherence failure even though strained to more than 10^{-3} in tension. In the same device, a layer of photoconductive CdS is coated with ITO and adherence failures at this surface have occurred only when the surface of the CdS has been contaminated with diffusion pump vapor. Some films have also been utilized in liquid crystal light valve devices. A variety of heater requirements have been satisfied, such as a hot stage for a microscope and a substrate heater for CdS film deposition. The substrate heaters have operated at temperatures as high as 350°C in a sputtering chamber with less than 5% change in the room temperature resistance. Substrate heaters of 3 ohm/square sheet resistance have operated at 250°C for over 300 hr in a sputtering chamber without change or failure. At room temperature, no measurable changes in sheet resistance have occurred in specimens exposed to the laboratory ambient for 2 years.

The ITO films described here would appear to be ideally suited to longitudinal electrooptic devices such as optical polarization switches used in digital light deflector systems. Low optical loss and a low resistivity for high switching speeds and minimal thermally induced refractive index gradients are obvious advantages.

For electrooptic device applications where transparent electrodes of a specific geometry are required, the difficulties associated with sputter-deposition through a mask may be avoided by etching. Various heated acids such as sulfuric, chromic, phosphoric, or

mixtures of hydrochloric and acetic acids have been used. A most satisfactory etchant has been oxalic acid in 0.1 molar concentration, which at 50°C , etched ITO films through photoresist defined patterns (15). Pattern definition below $10 \mu\text{m}$ has been achieved.

Conclusions

Directly usable, highly conductive transparent films of ITO have been deposited by a d-c diode sputtering process. Use of pure Ar or Xe as the sputtering gas yields low resistivity material, but the use of only inert gas requires low throughput rates to avoid excessive reduction of the film and target. Lowest resistivity films have been obtained for In_2O_3 targets containing from 9 to 13 m/o of SnO_2 . Target density is important in that more reduced films are obtained from a porous target under a given set of sputtering conditions and conditions must be optimized for an individual target. Generally, high density targets are superior. With suitable antireflection coatings, it is feasible to obtain films with sheet resistances of only a few ohms per square and optical transmission in excess of 95% in regions of the visible spectrum. Due to the excellent adherence and to the desirable optical and electrical properties of the ITO films, application has been found in the strain-biased ferpic, liquid crystal light valves, and as substrates for testing photoconductive films.

Acknowledgments

The authors wish to thank F. Ermanis for the Hall effect measurements, G. Kammlott for the scanning electron micrographs, Miss B. Prescott for the optical measurements, J. Kessler for the x-ray fluorescence analysis. Mrs. M. H. Read for analysis of the x-ray diffraction patterns and Miss E. W. Sweeney for etching the films.

Manuscript submitted Oct. 14, 1971; revised manuscript received Feb. 9, 1972. This was Paper 29 presented at the Washington, D.C., Meeting of the Society, May 9-13, 1971.

Any discussion of this paper will appear in a Discussion Section to be published in the June 1973 JOURNAL.

REFERENCES

1. R. E. Aitchison, *Australian J. Appl. Sci.*, **5**, 10 (1954).
2. H. K. Müller, *Phys. Status Solidi*, **27**, 723 (1968).
3. L. I. Burbulyavichus *et al.*, *Izv. Akad. Nauk. SSSR Neorgan. Mat.*, **5**, 551 (1969).
4. (a) V. A. Williams, *This Journal*, **113**, 234 (1966). (b) Y. T. Sihvonen and D. R. Boyd, *Rev. Sci. Instr.*, **31**, 992 (1960). (c) V. M. Vainshtein *et al.*, *Izv. Akad. Nauk. SSSR Neorgan. Mat.*, **4**, 357 (1968). (d) J. M. Pankratz, Paper 28, AIME, 1971 Conference, San Francisco, California.
5. J. L. Vossen, *RCA Rev.*, **32**, 289 (1971).
6. S. Yamanaka and T. Oohashi, *Jap. J. Appl. Phys.*, **8**, 1058 (1969).
7. J. L. Vossen, Third Symposium on Deposition of Thin Films by Sputtering, University of Rochester, September 9, 1969.
8. J. R. Maldonado and A. H. Meitzler, *Proc. IEEE*, **59**, 368 (1971).
9. D. L. White and M. Feldman, *Electron. Letters*, **6**, 837 (1970).
10. A. H. Meitzler, J. R. Maldonado, and M. R. Portnoff, Paper 18.7, 1971 IEEE/OEA, CLEA Mtg., Washington, D. C.
11. H. E. Swanson *et al.*, *Nat. Bur. St. (U.S.) No. 539*, 5, 26 (1955).
12. V. M. Vainshtein and V. I. Fistul, *Sov. Phys. Semicond.*, **4**, 1278 (1971) and T. S. Moss, "Optical Properties of Semiconductors," Academic Press, Inc., New York (1959).
13. L. J. van der Pauw, *Philips Res. Rept.*, **13**, 1 (1958).
14. D. B. Fraser and H. Melchior, Submitted to *J. Appl. Phys.*
15. KTRF Eastman Kodak, Rochester, New York.

Rectification by Anodic Oxide Films on Zirconium

N. Ramasubramanian* and T. Trottier

Chalk River Nuclear Laboratories, Atomic Energy of Canada Limited, Chalk River, Ontario, Canada

ABSTRACT

The electrical conduction characteristics of anodic oxide films on zirconium were studied using evaporated metal and aqueous electrolyte contacts. All the films tested showed electrolytic rectification. In the dry systems rectification was not observed, but asymmetry in conduction was pronounced in the case of films grown in the nitric acid solution. Capacitance measurements under an applied d-c bias provided no positive evidence for the presence of a p-n junction either in the bulk oxide or at the oxide-electrolyte boundary. The conduction characteristics were influenced by the anodizing electrolyte used: (i) the relatively flaw-free films grown in KOH gave nonohmic but nearly symmetrical I - V curves; (ii) a porous and hydrated oxide film, essentially monoclinic zirconia, grown in HNO_3 resulted in asymmetric conduction; and (iii) phosphate ion incorporation in oxides grown in a solution containing phosphoric acid led to space charge limited current flow characteristics.

Rectification of the electric current by anodic oxide films on zirconium is known to occur when contacted by aqueous electrolyte solutions (1). In the dry system the only reported case of rectification is by films grown in nitric acid and carrying evaporated aluminum electrodes (2). The oxide films grown in nitric acid have been shown to be unique, however. Unlike the oxides grown in a number of other electrolytes, the nitrate grown films are porous and consist of small crystallites, mostly of monoclinic ZrO_2 (3, 4). Electrical conductivity measurements using evaporated metal contacts have been reported by a number of workers. In the case of anodic oxide films grown in KOH on Van Arkel zirconium, Harrop and Wanklyn reported p-type conductivity from thermo emf measurements; whereas Dawson and Creamer assumed n-type conductivity (5, 6). Thus, electrolytic and dry rectification by anodic zirconia films remains unexplained. Moreover, the effect of impurities already present in the starting material and defects introduced during growth on the conduction characteristics has been disregarded. In the present study we have chosen three different anodizing solutions known to result in relatively flaw-free, anion incorporated and porous oxide films and used electrolyte and evaporated metal contacts to investigate whether rectification is a bulk property of anodic zirconia films. A study of the electrical conduction in zirconia films is a part of our research program on understanding the oxide growth and corrosion of zirconium and its alloys.

Experimental

Crystal bar zirconium, supplied by Wah Chang Corporation was mechanically polished, pickled in a HF-HNO_3 mixture, washed, and anodized by the fixed voltage method to various voltages from 10 to 100V in each of the following solutions: 0.1% KOH, 1% HNO_3 , and a complex organic solution containing phosphoric acid (7). Diode structures were formed by evaporating counterelectrodes, 3 and 6 mm in diameter, of Al, Au, and Pd or by contacting with a saturated solution of NH_4NO_3 . In the latter case the contact area was defined by the opening in a rubber gasket pressed down on to the oxide surface. Each specimen ($2 \times 2 \times 0.1$ cm) carried 6 diode units of a counterelectrode material and a total of ~ 300 diodes were tested. The sample tube was evacuated to 10^{-5} Torr and filled with helium to atmospheric pressure. The I - V curves were recorded at a sweep rate of 1 V/min using conventional electronic equipment; a 10^4 ohm series resistance and a Keithley differential voltmeter 662 were used to measure the currents. In some cases the curves were

traced at different polarization rates; occasionally the diode was left in the biased condition for a fixed period of time at the end of a polarization step. An a-c impedance bridge (GR-1650A) was used for capacitance measurements at 1 kHz under an applied d-c bias.

Results

Shorting to the base zirconium was a common occurrence in thin films (10-25V) carrying evaporated metal contacts; most of these diodes were found in the shorted state immediately after the evaporation step and a few of them became highly conducting during testing, with applied potentials of only a few volts. A majority of the I - V data was therefore collected for films formed from 40 to 100V when evaporated metal contacts were used. Gold and palladium electrodes were often associated with a switching to a high-conductivity state during the measurements. All the I - V tracings showed some hysteresis effects; this was more pronounced in the case of nitric acid grown films. The results are presented under the headings of the counterelectrode material concerned.

Heating the diode to temperatures $> 298^\circ\text{K}$ (the forming temperature) always resulted in irreversible changes in the conduction characteristics. The measurements were therefore made first at room temperature and then at lower and higher temperatures, respectively and the room temperature characteristics were checked subsequent to each temperature change. The oxide films grown in the KOH and organic solution showed surface features similar to those of the original pickled surfaces when examined on the scanning electron microscope. The HNO_3 grown films were different in this respect. A few areas where the cracking of the oxide film extended to $10 \mu\text{m}$ or more were present (Fig. 1a); a number of areas of localized cracking (the density of such spots averaging to about $10^4/\text{cm}^2$) similar to that in Fig. 1(b) were evident.

Aluminum contacts.—The asymmetric conduction was observed mainly with the films grown in the nitric acid solution. In Fig. 2 the results obtained when testing a 40V film grown in that solution are shown in the $\log I$ vs. V plots. The anodic direction was not effectively blocking in the sense of rectification; currents comparable to those in the cathodic direction began to flow at 4 to 5V of applied potential. The effect of varying the temperature was also seen to be distinctly different for the anodic and cathodic portions. In the temperature range of $273^\circ\text{--}333^\circ\text{K}$, the slope of the cathodic portions increased by nearly four times, whereas the anodic portion of the curves remained very nearly parallel to each other. Similar results were obtained with films grown up to 75V in the solution.

* Electrochemical Society Active Member.

Key words: zirconium, anodic oxide, electrolytic rectification, dry conduction.

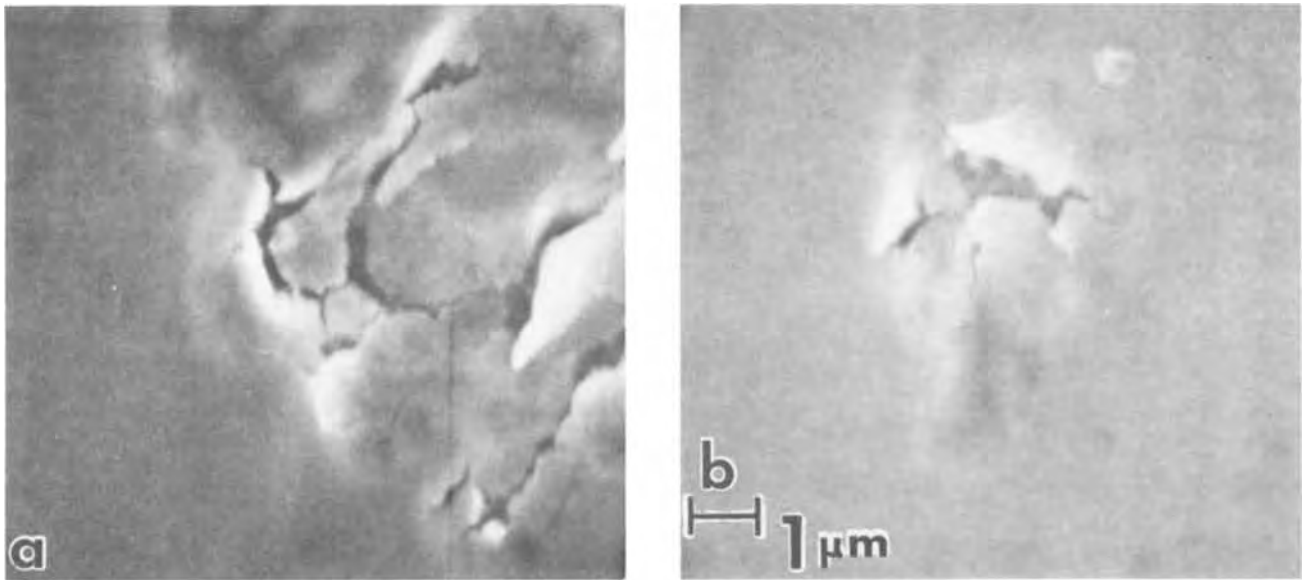


Fig. 1. Scanning electron micrographs of a 62V anodic oxide film grown in 1% HNO₃ solution

An important observation was that varying the forming voltage did not result in any systematic changes in the *I-V* characteristics. They were more or less the same for the various film thicknesses studied. A set of curves showing the anodic and cathodic current flow at room temperature in these films is given in Fig. 3. The data obtained in the case of a 20V film, which became highly conducting during the measurements, is also included for the sake of comparison. The hysteresis effects are described later in the palladium section.

The films grown in 0.1% KOH passed currents under anodic and cathodic bias with much less asymmetry than the HNO₃ grown films. The difference in the applied voltage required for a minimum measurable current flow was about 1V higher when the zirconium was anodic than when cathodic. A set of curves showing the effect of temperature on the current flow through a 40V film grown in the KOH solution is plotted in Fig. 4. The anodic current flow did not fit the exponential voltage dependence relation. Attempts to fit the data to other commonly observed relations such as Schottky emission and SCLC (space charge limited current) were equally unsuccessful; however the data up to ~6V gave reasonable linear fits when

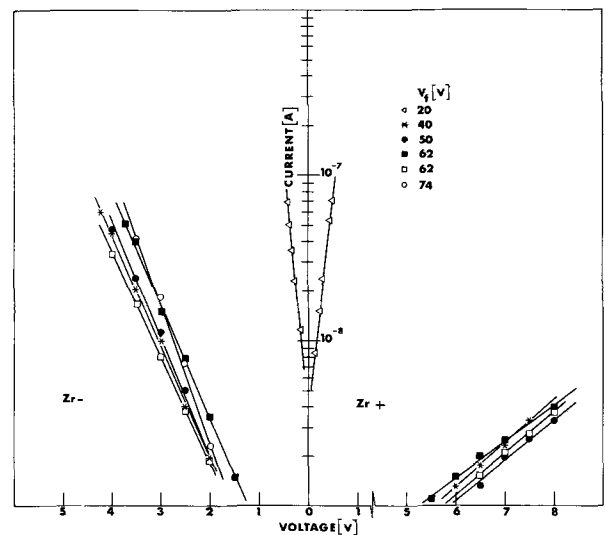


Fig. 3. Influence of forming voltage on the current flow at room temperature through zirconia films grown in nitric acid solution; aluminum counterelectrode area 0.0675 cm².

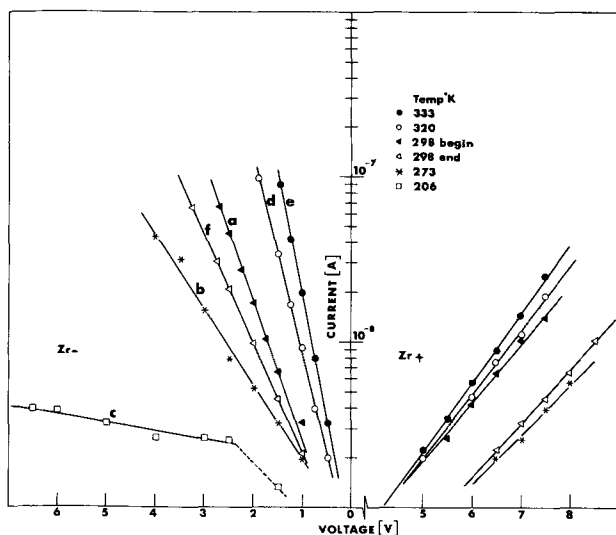


Fig. 2. Current-voltage characteristics at different temperatures of a 40V anodic oxide film grown in 1% HNO₃; area of the aluminum counterelectrode 0.27 cm².

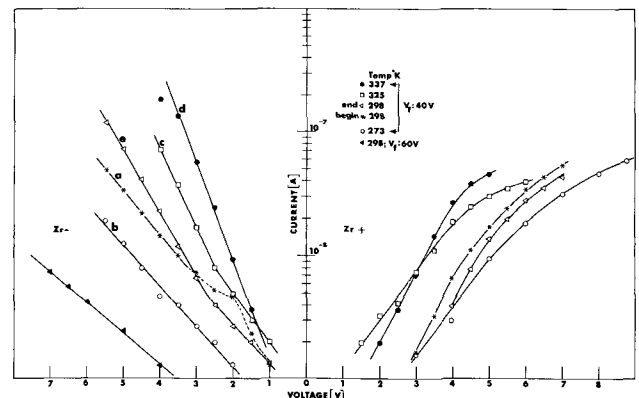


Fig. 4. Zirconium-anodic oxide grown in 0.1% KOH solution—aluminum 0.27 cm²; effect of temperature on the conduction characteristics for a 40V film and comparison at room temperature with a 60V film.

plotted as $\log I$ vs. $V^{1/2}$ or $\log V$. With increase in the forming voltage the KOH grown films became more resistive; under comparable temperature and applied voltage conditions the current flow and the slope of the $\log I$ vs. V plots decreased with increase in film thickness.

When the current flow through the films grown in the three solutions was compared the films grown in the complex organic solution were found to be the most resistive. It is known that phosphate ion is incorporated in the oxide during growth in the organic solution and as a result the growth constant (oxide thickness/forming voltage) is lower than for KOH grown films (7). However, with films grown to the same forming voltage and under comparable testing conditions, the diodes carrying the oxide grown in the organic solution passed currents an order of magnitude less than those carrying the KOH grown films. Unlike the HNO_3 and KOH grown films the oxide grown in the organic solution showed large variations in the current density when different areas of a specimen were tested and often exhibited self-healing type current bursts (rapid rise and fall in current) during the I - V measurements. When such current transients were absent the data obtained fitted an $I \propto V^n$ relation. A set of such plots for a 100V film is shown in Fig. 5. The linearity of the plots and their 'n' values strongly suggest a space charge limited current flow. The asymmetry between the cathodic and anodic portions was similar to that observed with the KOH grown films but less distinct than that found in the case of HNO_3 grown films.

Gold contacts.—The films grown in the three solutions had one common characteristic. A majority of the diodes switched to a high conductivity state at room temperature under an applied bias of $\sim \pm 6\text{V}$. When such bistable switching did not occur the I - V characteristics were similar to those described for the Al counterelectrode, except that the currents passed were slightly lower. The oxide grown in the organic solution was the most resistive and the data for these diodes gave linear plots on $\log I$ vs. $\log V$ scales.

Palladium contacts.—The results were essentially similar to those described for the gold counterelectrodes. The influence of the polarization rate and a holding time at the end of polarization on the I - V

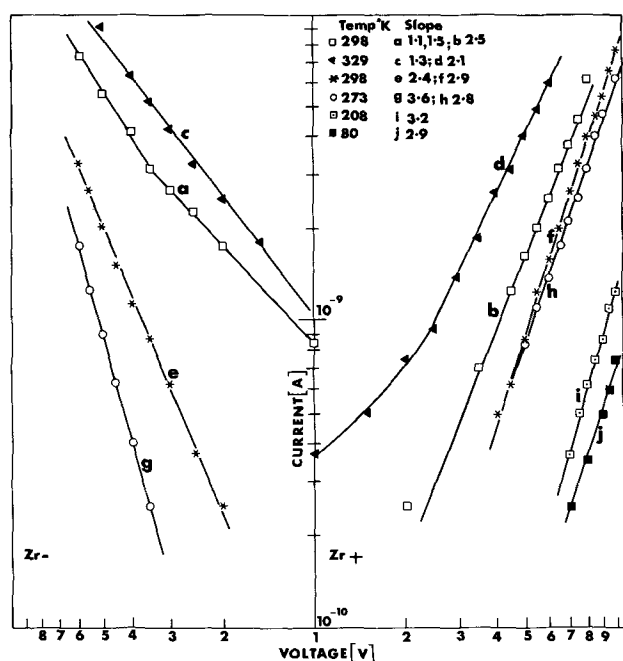


Fig. 5. Current-voltage characteristics of a 100V anodic oxide film on zirconium grown in the complex organic solution; area of aluminum counterelectrode 0.27 cm^2 (a-d) and 0.0675 cm^2 (e-j).

characteristics is shown in Fig. 6 for a diode carrying a 62V film grown in the nitric acid solution. At sweep rates $> 1 \text{ V/min}$ much hysteresis was observed in the tracings. However, no systematic change was observed in the successive I - V tracings due to varying the holding time at the end of each cathodic polarization step. In tracing these curves the diode was polarized in the usual manner to 3.5V and held at that potential for a time Δt . Then the applied voltage was reduced to zero and a set of such curves traced for various Δt values. In another set of experiments a negative potential of 4V was applied to anodized zirconium at room temperature and while under the applied bias the temperature was lowered to 205°K . The I - V tracings then obtained at this lower temperature were identical to those traced at this temperature in the normal manner.

NH_4NO_3 solution contacts.—All the oxide films, grown to various voltages from 10 to 100V in the three solutions rectified the current. In the cathodic direction gas bubbles could be seen on the oxide surface when the bias exceeded $\sim 2\text{V}$. The blocking in the anodic direction improved with increasing oxide thickness in general; the films grown in nitric acid were poorer in this respect. In Fig. 7 a typical set of curves is shown for films of various thicknesses grown in the KOH solution; data for the other two types of films are also plotted for the sake of comparison.

Impedance Measurements under an Applied D-C Bias

In Fig. 8 the change in capacitance against applied d-c bias is plotted for a few diodes. With the NH_4NO_3 solution contacts, for films grown in all three solutions to the various forming voltages, the capacitance showed a gradual increase with bias in the cathodic direction. At 3-4V the readings were unsteady and increased to large values rather suddenly; gas bubbles collected on

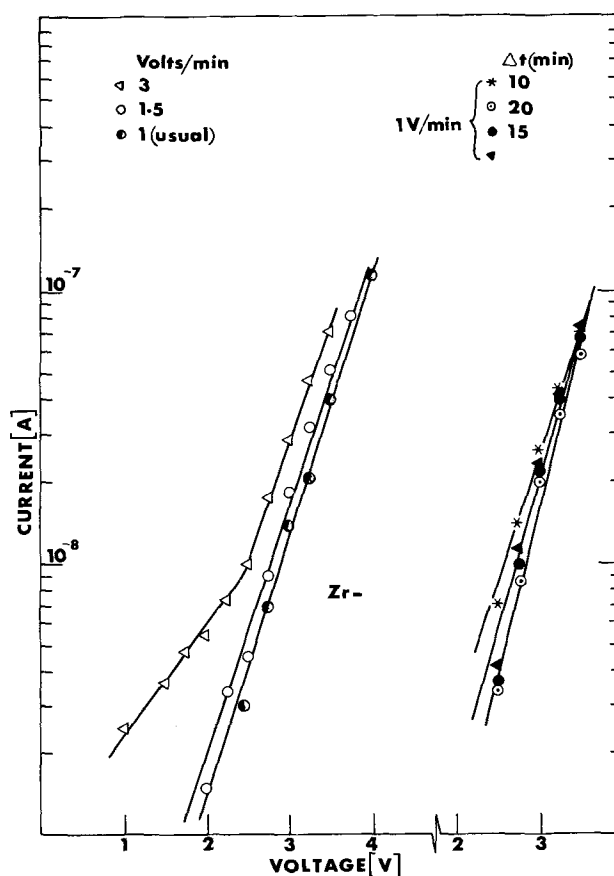


Fig. 6. Influence of the polarization rate and a holding time at the end of polarization on the current-voltage characteristics at room temperature of a diode; zirconium-60V anodic film grown in 1% HNO_3 solution—palladium 0.27 cm^2 in area.

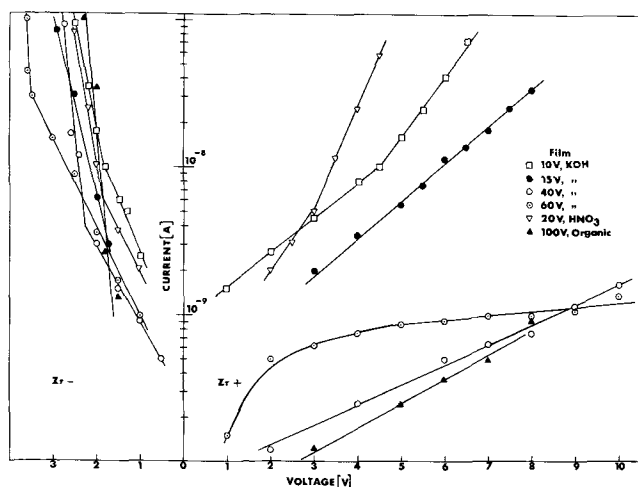


Fig. 7. Current-voltage characteristics obtained on anodic zirconia films when using saturated ammonium nitrate solution contacts; electrolyte contact area is 0.15 cm^2 .

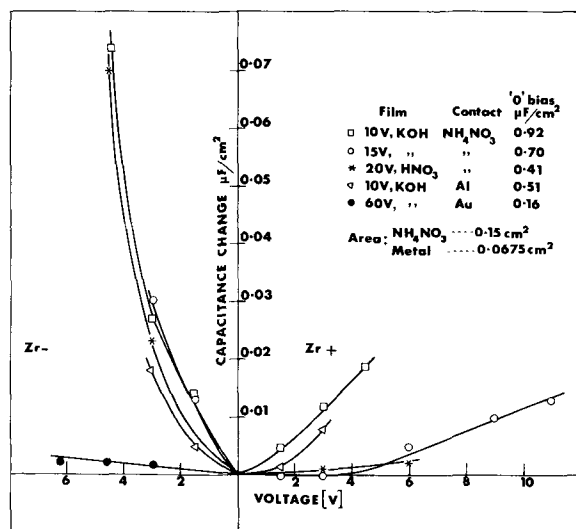


Fig. 8. Change in capacitance vs. applied d-c voltage at room temperature.

the oxide surface. Under anodic bias conditions the capacitance readings either were steady or increased much less rapidly than during cathodic bias. None of the specimens tested showed a decrease in capacitance. Only a few diodes carrying thin anodic oxide films and evaporated metal contacts were tested because of the inherent shorting problem; in all such cases the capacitance increased with the bias voltage in both the directions. When thick films carrying metal contacts were tested the capacitance increased rapidly at a bias of 1.5-3V in the anodic direction; under cathodic bias the curves were similar to that shown in Fig. 8.

Impurities in Zirconium

The purity of the crystal bar material used in the present investigation is comparable to that used by a number of other workers. The major metallic impurities were Fe (82 ppm) and Hf (72 ppm); other elements such as Al, Cr, Cu, Ni, and Ti were present in quantities ≤ 20 ppm. After the mechanical and chemical polishing steps microscopic examination of the surface showed no singularities. The scanning electron micrograph (SEM) of such a surface is shown in Fig. 9(a). A variety of aqueous electrolyte solutions was tried for anodizing; when a dilute (0.001N) KMnO_4 solution was used some peculiarities were noticed. In the KMnO_4 solution zirconium could be anodized, as in other electrolytes, up to $\sim 100\text{V}$. At the end of the first anodizing step, generally around 5-10V, examina-

tion of the surface showed a thick porous oxide growth at selected areas and this surface structure persisted throughout the rest of the anodizing steps. In Fig. 9(d) is shown the electron micrograph (EM) of a two-stage replica of such an anodized sample. When a zirconium sample was made cathodic to $\sim 5\text{V}$ in the same solution, preferential reduction of MnO_4^- at selected spots was noticed. The SEM and EM of the replica of this deposit are shown in Fig. 9(b) and (c). By carrying out the reduction step first, washing off the deposit in a solution of oxalic acid and then anodizing, it can be shown that the areas where preferential reduction and thick porous oxide growth occur are the same. Thus it would seem that the impurities are present in areas of extremely minute size whose presence can be revealed by their specificity towards reagents such as KMnO_4 .

Discussion

From the data published in the literature the information relevant to the present study regarding anodic oxide growth on zirconium can be summarized as follows: (i) oxide films grown in nitric acid solution are porous (3), (ii) phosphate ion is incorporated during growth in the complex organic solution (7), (iii) KOH grown films are free of occluded ions and less porous (3, 7), and (iv) transmission electron optical studies of the stripped films have shown them to consist of microcrystallites distributed in a matrix that is probably amorphous; the nitrate grown films are unique in being essentially all monoclinic ZrO_2 , whereas films grown in most other electrolytes have $\cong 75\%$ of cubic ZrO_2 (3, 4).

The presence of a p-n or p-i-n junction, resulting from nonstoichiometry induced by the oxide growth process, is often proposed in explaining mechanisms of thermal oxidation and rectification. The decrease in capacitance to be expected with applied d-c bias in the anodic (reverse) direction is a means of checking for the existence of such junctions in the oxide or at the oxide-counter-electrode boundary (8, 9). It is also believed that transition from homogeneous conduction by bulk oxide to the heterogeneous or local response at flaws occurs with increase in oxide thickness (10). In the present study, on thin zirconia films the capacitance showed an increase with anodic bias for both metal and electrolyte solution contacts. Of the three types of films tested, the ones grown in KOH should be relatively flaw free; if a homogeneous conduction process was responsible for rectification then one would expect these films to rectify. But the asymmetry in conduction (dry conditions) was pronounced in the nitric acid grown films which showed extensive cracking of the oxide and the work function of the electrode material was without influence on the $I-V$ characteristics. These observations inevitably lead to the conclusion that if a junction is grown in during anodization or formed by the contacting electrode then it is not the dominant factor in determining the electrical conduction under the testing conditions employed here.

The conduction characteristics of the oxide grown in KOH might be expected to represent those of the pure oxide (7). It is evident from the results presented here, that contrary to the assumptions made by Dawson and Creamer (6), the conduction in these films is not ohmic. The current flow under negative bias is more of a field-activated type transport (reference to Charlesby's work in this respect is made later) whereas that under positive bias is more complicated involving probably more than one type of process.

The films grown in the organic solution were the most resistive and their $I-V$ data are seen to fit a SCLC relation. This finding is in agreement with Banter's observation and would support his model of a stationary negative space charge, created by the immobile phosphate ions in the outer oxide layers, controlling the anodic growth and the electrical conductivity (7). Because of the bistable switching and large

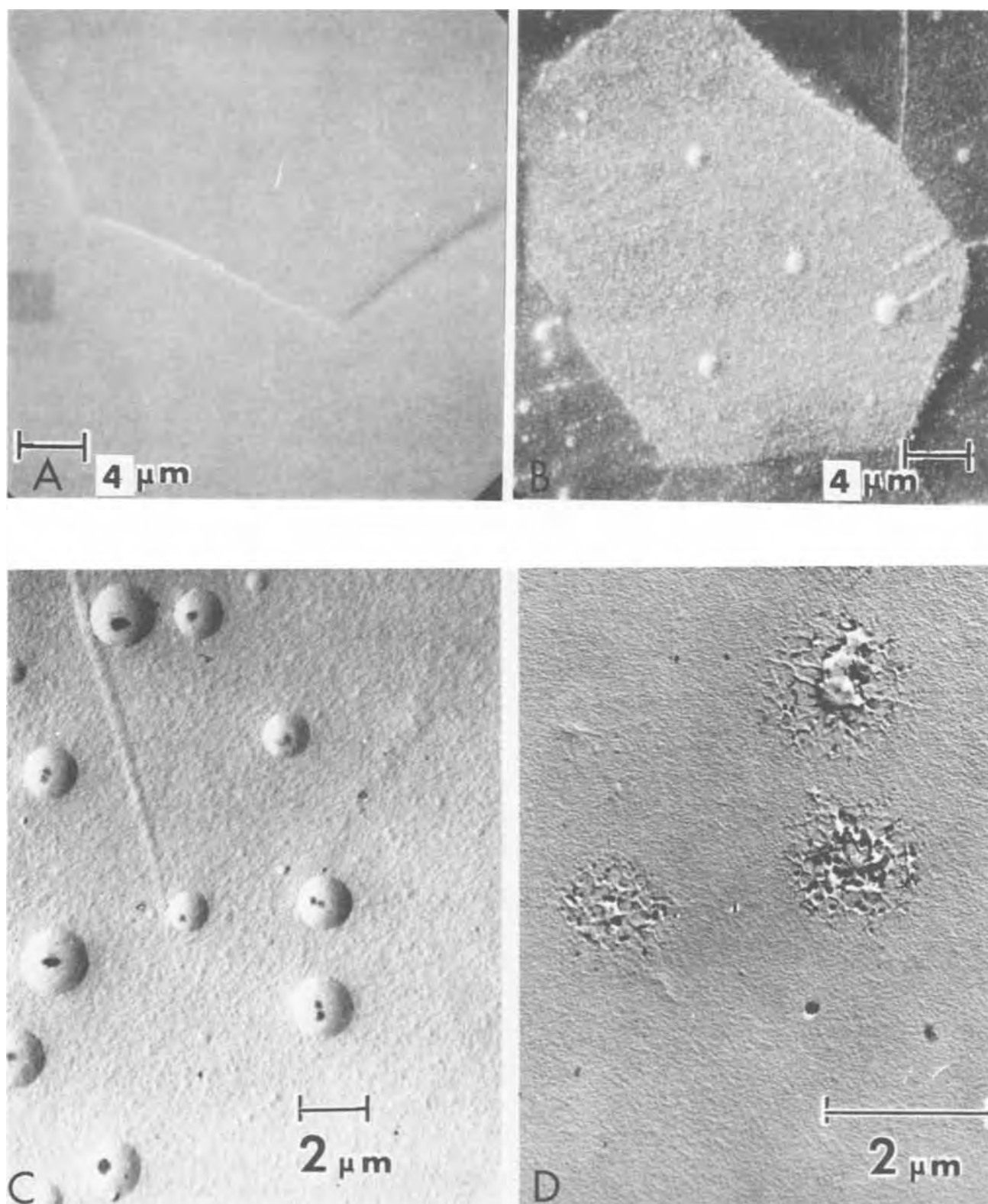


Fig. 9. Scanning electron micrographs: (a) pickled zirconium surface and (b) cathodic reduction of MnO_4^- on zirconium. Electron micrographs of two-stage replicas: (c) cathodic reduction of MnO_4^- and (d) another specimen anodized in KMnO_4 solution to 25V.

variations in current density over different areas of a specimen the thickness dependence of the current could not be checked.

Asymmetry in conduction, pronounced hysteresis effects and independence of the current flow on the forming voltage (40-75V) were observed only with the nitric acid grown films and must therefore be the properties of a porous film of monoclinic zirconia. Ac-

cording to Banter the nitrate grown films are hydrated as well (7); the porosity of these films would imply that much of this hydration water is that locked inside the pores. Based on these facts and the observation that the polarization rate had a marked influence on the current flow and no systematic changes resulted in the I - V characteristics when the diodes were left in the biased state (repeatedly) for long periods of

time, it is suggested that protonic migration (from the bound water) along the cracks and pores leads to a high field region in the oxide and results in an easy forward electronic current having characteristics similar to that observed in the case of KOH grown films. Information on the permeability to protons of monoclinic and cubic zirconia would be helpful in this connection.

The electrical conduction of anodic zirconia films when using dry contacts is thus seen to be influenced by the anodizing electrolyte used and could be correlated with the anion incorporation, hydration, and porosity. It might therefore be inferred that in the case of oxide films grown in the three solutions employed here the current flow is mainly through the oxide. However, the possibility exists that the properties of the oxide grown on and around the impurities are also influenced by the anodizing electrolyte and might be the areas of major electronic conduction in these anodic films. These impurity centers have been shown to be the preferred sites of electron flow and reaction in the reduction of cuprous iodide to copper (11). Though the presence of the impurity centers was not detected on microscopic examination of the surface, stress-corrosion cracking experiments in methanol/iodine solutions have revealed the presence of small lenticular second phase precipitates (probably a Zr-Fe phase) in the grain boundaries of crystal bar zirconium (12). Therefore contributions to the conduction by the impurities present in the material cannot be ignored and as is evident from Fig. 9 a contact area $\leq 1.2 \times 10^{-7} \text{ cm}^2$ would be required to eliminate such contributions.

Charlesby interpreted the anodic leakage current through zirconia films in terms of a field assisted (in surmounting an energy barrier) transport because the I - V data fitted a "sinh law" (13). This proposal was rejected by Vermilyea (14), and Young has commented on both these suggestions and pointed out that the conduction is likely to be through cracks in the oxide (15). The cathodic current flow through KOH and HNO_3 grown films when evaporated metal contacts were used is seen to fit a $\log I \propto V$ relation (high field approximation of the "sinh law") in the present study. However, the slope of such plots showed an increase with temperature; whereas a decrease is expected if the current flow was of the field assisted type obeying the "sinh law." The physical significance of the observed $\log I \propto V$ relation is thus not clear.

Electrolytic rectification was observed on all the films tested the common source of which could be traced to one or more of the following: microfissures (impenetrable by evaporated metal contacts) present in anodic films in general, existing impurities, or the property of the ZrO_2 /electrolyte interface.

Conclusions

Rectification by anodic oxide films on zirconium was not observed when evaporated metal counterelectrodes

were used. Electrolytic rectification was observed. Capacitance-voltage measurements gave no positive evidence for the presence of a p-n or p-i-n junction in the diodes. The conduction characteristics were influenced by the anodizing electrolyte used; the asymmetry in conduction observed in the case of nitric acid grown films is ascribed to the porous and hydrated oxide grown in these solutions; the incorporation of phosphate ions during growth is related to the space-charge limited current flow in films grown in a complex organic solution containing phosphoric acid. The electrical conduction in anodic oxide films on crystal-bar zirconium (the material generally accepted as being of high purity) is not simple as has been assumed previously; the impurities present are likely to be the main contributing factors and work on pure zirconium single crystals might elucidate the situation.

Acknowledgments

The authors wish to thank Drs. B. Cox and T. A. Eastwood who read the manuscript and suggested improvements.

Manuscript submitted Feb. 9, 1972; revised manuscript received May 22, 1972.

Any discussion of this paper will appear in a Discussion Section to be published in the June 1973 JOURNAL.

REFERENCES

1. J. N. Wanklyn and R. Aldred, *This Journal*, **106**, 529 (1959); B. Cox and D. L. Speirs, Atomic Energy of Canada Ltd., Report No. AECL-2690, March 1967.
2. J. Mochniak, *Acta Physica Polon.*, **xxx**, 559 (1966).
3. B. Cox, *This Journal*, **117**, 654 (1970).
4. R. A. Ploc, "Septieme Congrès International De Microscopie Electronique," Grenoble, Vol. II, p. 371 (1970).
5. P. J. Harrop and J. N. Wanklyn, *Brit. J. Appl. Phys.*, **16**, 155 (1965).
6. D. K. Dawson and R. H. Creamer, *ibid.*, **16**, 1643 (1965).
7. J. C. Banter, *This Journal*, **114**, 508 (1967).
8. Y. Sasaki, *J. Phys. Chem. Solids*, **13**, 177 (1960).
9. F. Huber, in "Electrolytic Rectification and Conduction Mechanisms in Anodic Oxide Films," P. F. Schmidt and D. M. Smyth, Editors, p. 162, The Electrochemical Society Softbound Symposium Series, New York (1967).
10. D. A. Vermilyea, *J. Appl. Phys.*, **36**, 3663 (1965); *This Journal*, **115**, 177 (1968).
11. N. Ramasubramanian, *This Journal*, **116**, 1237 (1969).
12. B. Cox, Atomic Energy of Canada Ltd., Report No. AECL-3551, January 1970.
13. A. Charlesby, *Acta Met.*, **1**, 348 (1953).
14. D. A. Vermilyea, *ibid.*, **2**, 346 (1954).
15. L. Young, "Anodic Oxide Films," p. 141, Academic Press, New York (1961).

Epitaxial Substrate Carrier Concentration Measurement by the Infrared Interference Envelope (IRIE) Technique

Alvin H. Tong,* Paul A. Schumann, Jr.,* and William A. Keenan*

IBM Components Division, East Fishkill Facility, Hopewell Junction, New York 12533

ABSTRACT

Infrared interference measurement of epitaxial thickness requires knowledge of the substrate carrier concentration to correct for the phase shift at the epitaxial layer-substrate interface. A nondestructive technique which measures the epitaxial substrate carrier concentration is described. It uses the information contained in the infrared interference envelope (IRIE) which is the same reflection spectrum used in the epitaxial thickness measurement. A model and experimental results are presented for silicon with a substrate carrier concentration ranging from $1 \times 10^{19} \text{ cm}^{-3}$ to $1 \times 10^{21} \text{ cm}^{-3}$.

Optical measurement techniques are becoming increasingly important and popular because they offer the advantages of being nondestructive and contactless. One of the most important optical measurement techniques in the semiconductor industry is the infrared interference technique for the measurement of epitaxial layer thickness introduced by Spitzer and Tananbaum (1) in 1961. At the suggestion of W. Pliskin, extended work was carried out by Schumann *et al.* (2) which showed that the phase shift on reflection at the epitaxial layer-substrate interface was a function of the wavelength and the substrate carrier concentration, and therefore must be accounted for in calculating the thickness. Since then, the substrate carrier concentration was assumed from prior knowledge, measured before deposition of the epitaxial layer, or obtained by a subsequent independent measurement such as the spreading resistance profile with correction factors (3). However, the substrate carrier concentration changes during deposition of the epitaxial layer due to out-diffusion of substrate dopant, thus making the prior measurement inaccurate. Unfortunately, the spreading resistance profile technique is destructive.

This paper discusses a nondestructive and contactless technique to measure the epitaxial substrate carrier concentration. It uses the information contained in the infrared interference envelope (IRIE) which is the same reflection spectrum used for the epitaxial thickness measurement.

Theory

For normal incidence, the reflection coefficient for a homogeneous sample can be expressed in terms of the refractive indexes of the sample and of the medium adjacent to its reflecting surface

$$R = \left| \frac{n_0 - \bar{n}_1}{n_0 + \bar{n}_1} \right|^2 \quad [1]$$

For an air to semiconductor interface where $n_0 = 1$, Eq. [1] becomes

$$R = \left| \frac{1 - \bar{n}_1}{1 + \bar{n}_1} \right|^2 \quad [2]$$

or

$$R = \frac{(1 - n_1)^2 + k_1^2}{(1 + n_1)^2 + k_1^2} \quad [3]$$

where $\bar{n}_1 = n_1 - ik_1$, the complex refractive index, n_1 is the real part of the index of refraction, and k_1 is the extinction coefficient.

When the reflection coefficient is measured as a function of wavelength in the infrared, a minimum occurs

near the plasma resonance frequency. The wavelength at which this minimum occurs, λ_{min} , is a function of the carrier concentration of the sample through the optical constants as expressed in Eq. [3]. This technique for measuring the carrier concentration is called plasma resonance (4). This technique uses a set of calibration curves, λ_{min} vs. N (free carrier concentration), as shown in Fig. 1 for silicon. Plasma resonance provides a nondestructive and contactless measurement of the surface carrier concentration of a semiconductor sample.

The optical constants (n_1, k_1) have been measured (5) for n- and p-type silicon in the infrared from 2.5 to 50 μm with carrier concentrations ranging from 10^{15} cm^{-3} to 10^{19} cm^{-3} . The results show $n_1 \geq 2.5$ and $k_1 \leq 0.1$ throughout the range. For higher carrier concentrations ($> 10^{20} \text{ cm}^{-3}$), k_1 has been reported to be ~ 0.4 (6). Thus, throughout the range of carrier concentration 10^{15} cm^{-3} to 10^{20} cm^{-3} , $k_1^2 \ll 1$. From these results, the condition $(n_1 + 1)^2 > (n_1 - 1)^2 \gg k_1^2$ is satisfied throughout the range of interest and Eq. [3] can be simplified to

$$R = \left(\frac{1 - n_1}{1 + n_1} \right)^2 \quad [4]$$

In the case of an epitaxial layer with thickness d_1 over a substrate as shown in Fig. 2, the reflection coefficient for normal incidence (7) can be expressed as

$$R = \frac{r_1^2 + 2r_1r_2 \cos(2\delta_1 - \phi) + r_2^2}{1 + 2r_1r_2 \cos(2\delta_1 - \phi) + r_1^2r_2^2} \quad [5]$$

where

$$r_1 = \left| \frac{n_0 - \bar{n}_1}{n_0 + \bar{n}_1} \right| \quad [6]$$

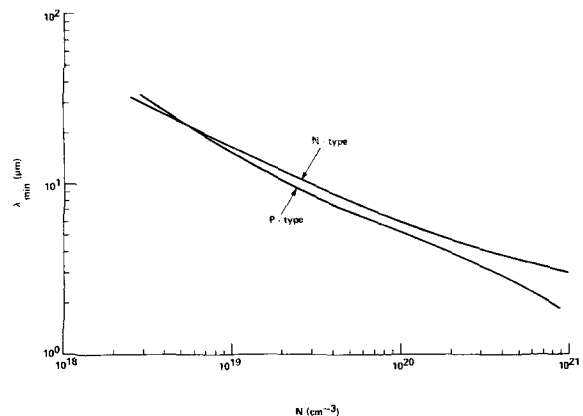


Fig. 1. Plasma resonance calibration curves of carrier concentrations vs. wavelength for both N- and P-type silicon.

* Electrochemical Society Active Member.
Key words: infrared interference, silicon, plasma resonance, epitaxial layer thickness, carrier concentration.

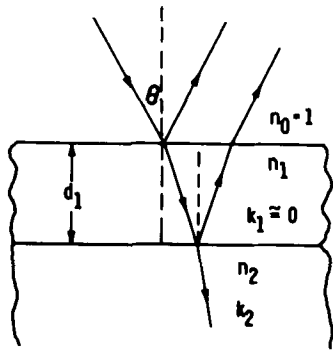


Fig. 2. Light incident at angle θ on sample with epitaxial layer

is the magnitude of the Fresnel coefficient at the air-layer interface

$$r_1 = \left| \frac{\bar{n}_1 - \bar{n}_0}{\bar{n}_1 + \bar{n}_0} \right| \quad [7]$$

is the magnitude of the Fresnel coefficient at the layer-substrate interface

$$\delta = \frac{2\pi}{\lambda} n_1 d_1 \quad [8]$$

is the change in phase of the beam on traversing the epitaxial layer (where λ is the vacuum wavelength of the incident light)

$$\bar{n}_1 = n_1 - ik_1$$

is the complex refractive index of the epitaxial layer

$$\bar{n}_2 = n_2 - ik_2$$

is the complex refractive index of the substrate, and

$$\phi = \tan^{-1} \left(\frac{2n_1 k_2}{n_1^2 - n_2^2 - k_2^2} \right) \quad [9]$$

is the phase shift at the layer-substrate interface.

In the high resistivity epitaxial layer, the extinction coefficient k_1 is usually assumed to be zero.

From Eq. [5], it can be shown that minima of the reflectance curve occur at values of $n_1 d_1$ given by

$$n_1 d_1 = \frac{\lambda}{4} \left[(2m + 1) + \frac{\phi}{\pi} \right] \quad [10]$$

where $m = 0, 1, 2, 3, \dots$. Once the phase shift at the interface is accounted for, the thickness of the epitaxial layer d_1 can be determined, since n_1 is known, λ is observed, and m can be determined from two successive minima. The values of the reflectance at these points are

$$(R)_{\min.} = \left(\frac{r_1 - r_2}{1 - r_1 r_2} \right)^2 \quad [11]$$

Using $n_0 = 1$ for air, and $n_1 = 3.42$, and $k_1 \sim 0$ for the epitaxial layer, the magnitudes of the Fresnel coefficients become

$$r_1 = \frac{n_1 - n_0}{n_1 + n_0} = \frac{3.42 - 1}{3.42 + 1}$$

and

$$r_2 = \left(\frac{(n_2 - n_1)^2 + k_2^2}{(n_2 + n_1)^2 + k_2^2} \right)^{1/2}$$

For the exceptional case where $n_2 = n_1 = 3.42$ at very short wavelength

$$r_2 = \frac{k_2}{\sqrt{(n_2 + n_1)^2 + k_2^2}} \ll r_1 < 1$$

and Eq. [11] becomes

$$(R)_{\min.} = r_1^2 = \left(\frac{n_1 - 1}{n_1 + 1} \right)^2$$

In most situations, however, $(n_2 - n_1)^2 \gg k_2^2$, so

$$r_2 = \frac{n_2 - n_1}{n_2 + n_1}$$

Equation [11] then becomes

$$(R)_{\min.} = \left(\frac{n_1^2 - n_0 n_2}{n_1^2 + n_0 n_2} \right)^2 = \left(\frac{11.7 - n_2}{11.7 + n_2} \right)^2 \quad [12]$$

for

$$n_0 = 1, \quad n_1 = 3.42$$

Equations [12] and [4] are identical in form, the only difference being the numerical constants. Equation [12] thus demonstrates that, similar to the plasma resonance technique, a minimum of the $(R)_{\min.}$'s occurs, and it is a function of the substrate carrier concentration through the optical constant n_2 . A comparison between the IRIE and the plasma resonance technique in Fig. 3 shows the reflectivity vs. wavelength for the two techniques. The IRIE technique relates the wavelength at which the envelope of the minima or valleys exhibits a minimum to the substrate carrier concentration. Plasma resonance can be considered the limit of this IRIE reflectance curve as the epitaxial thickness goes to zero.

Calibration Curves

A step junction was assumed at the layer-substrate interface and the reflectance was calculated both for N on N⁺ and P on P⁺ silicon epitaxial layers for the wavelength range 2.5 to 150 μm .

Figure 4 is a typical plot of the $(R)_{\min.}$'s vs. wavelength (i.e., the lower envelope of the reflectance curve) for N-type Si. Note that the minimum is very sharp and its magnitude is close if not equal to zero. The data points show the various thicknesses of the epitaxial layer. The resulting smooth curve indicates that the IRIE minimum is independent of the epitaxial layer thickness.

The theoretical calibration curves of λ (envelope)_{min.} vs. the substrate carrier concentration are shown in Fig. 5 for N- and P-type silicon.

Experimental Results

A typical infrared interference reflectance curve is shown in Fig. 6 for an N⁺ on N epitaxial layer. From this trace, the lower envelope is drawn and the minimum of this envelope is located. Then the substrate carrier concentration is determined from the calibration curves in Fig. 5. Results shown in Fig. 7 are compared to those obtained from the spreading resistance profile with correction factors and the plasma resonance technique. Plasma resonance was performed on the substrate after the epitaxial layer had been removed. The correlation coefficient of 0.95 attests to the validity of this technique. The discrepancy between the values of substrate concentration determined by IRIE and the other techniques is due to the fact that the calibration curve was constructed from theo-

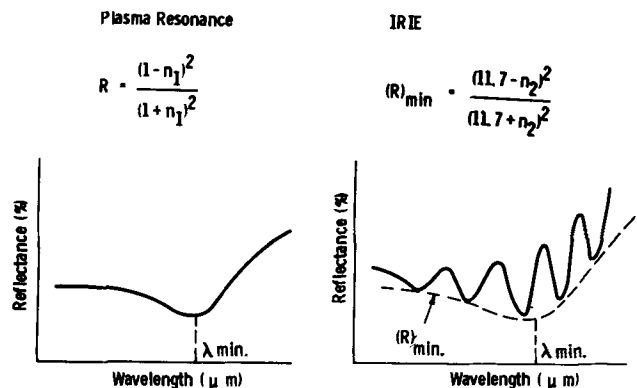


Fig. 3. Plasma resonance and IRIE reflectance curves compared

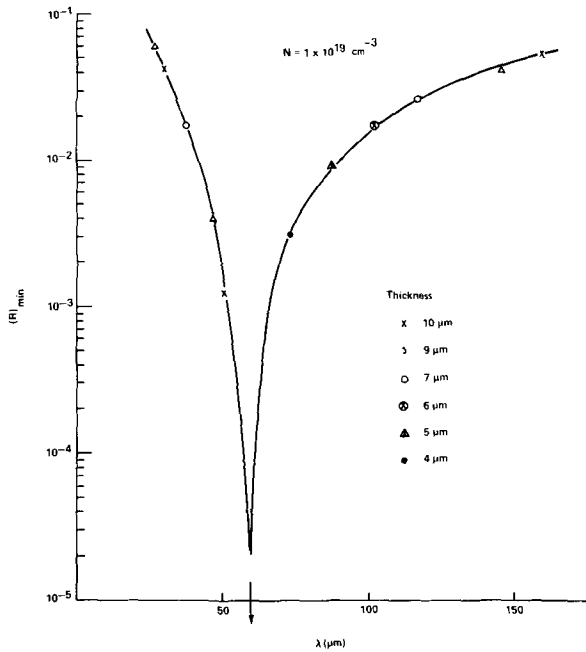


Fig. 4. $(R)_{\min}$. vs. wavelength (the lower envelope of the reflectance curve) for N on N^+ silicon, with $N^+ = 10^{19} \text{ cm}^{-3}$, for epitaxial layers of different thicknesses.

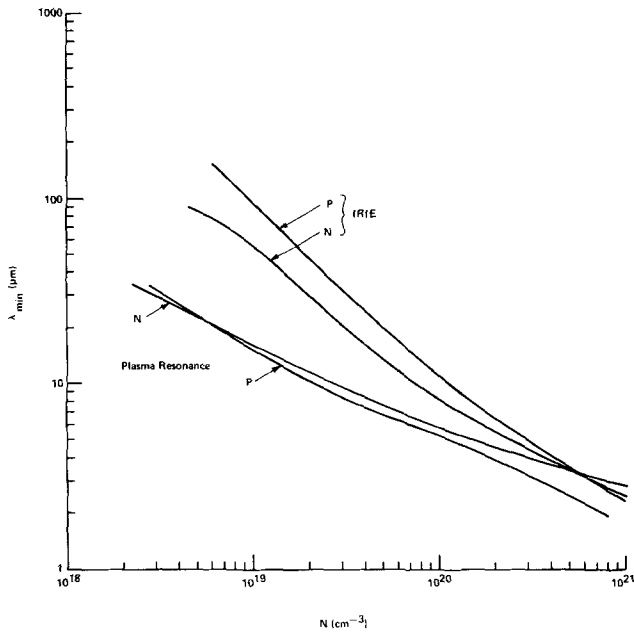


Fig. 5. Calibration curves of λ (envelope) $_{\min}$. vs. substrate carrier concentration.

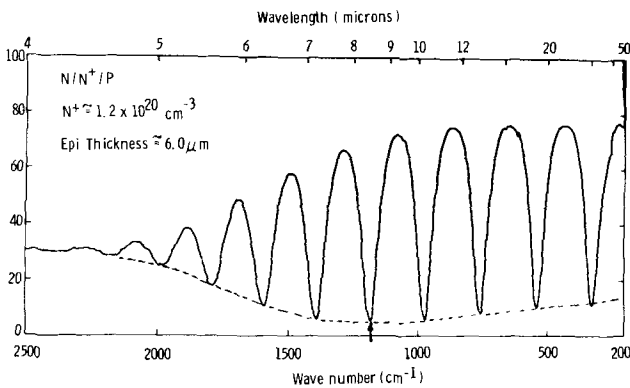


Fig. 6. Typical infrared interference reflectance curve

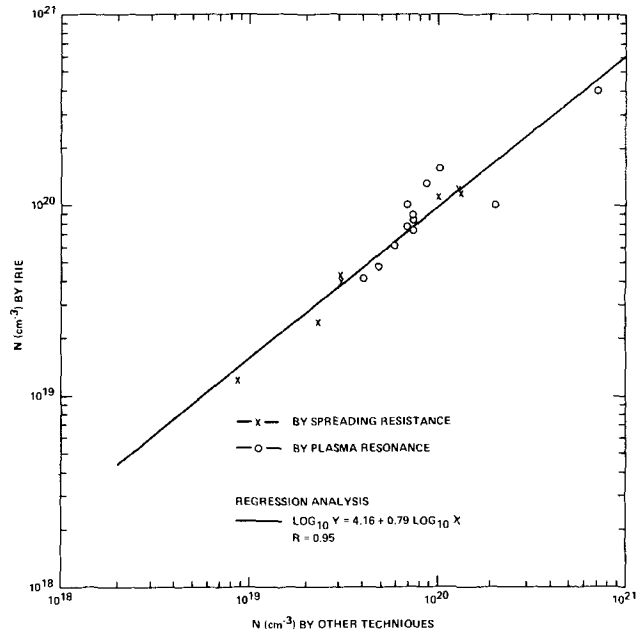


Fig. 7. Comparison of the IRIE technique with other methods for determining substrate carrier concentration.

retical calculations. In actual practice the calibration curve would be calculated from measured results.

Discussion

Schumann and Schneider (8) have reported a technique which gives the epitaxial layer thickness as well as the substrate carrier concentration. It requires the magnitude of the reflectance extremum (maximum or minimum) to be measured as well as the wavelength at which the extremum occurs. Therefore, the spectrophotometer must be calibrated to give an accurate measurement of the magnitude of the absolute reflectivity.

However, the IRIE technique does not require an "absolute" magnitude measurement but instead requires locating the minimum of the interference envelope. To locate this minimum accurately, it is desirable to have as many interference fringes as possible. Therefore, a thick epitaxial layer, for instance 5 μm , gives good results. When the epitaxial layer thickness is less than 3 μm , the number of interference minima is not adequate to locate accurately the minimum of the envelope and this thickness represents the lower limit for this technique. The carrier concentration range of application is also limited by the spectrophotometer available. For a spectrophotometer having a 2.5-50 μm range in wavelength, the range of application for silicon is approximately $1 \times 10^{19} \text{ cm}^{-3}$ to $1 \times 10^{21} \text{ cm}^{-3}$.

Acknowledgment

The authors wish to thank Mr. C. P. Schneider and Miss L. Pietrogallo for their respective contributions in the measurements of the infrared reflectance and spreading resistance profile.

Manuscript submitted Oct. 7, 1971; revised manuscript received March 31, 1972.

Any discussion of this paper will appear in a Discussion Section to be published in the June 1973 JOURNAL.

REFERENCES

1. W. G. Spitzer and M. Tannebaum, *J. Appl. Phys.*, **32**, 744 (1961).
2. P. A. Schumann, Jr., R. P. Phillips, and P. J. Olsheski, *This Journal*, **113**, 368 (1966).
3. T. H. Yeh and K. H. Khokhani, *ibid.*, **116**, 1461 (1969).

4. E. E. Gardner, W. Kappallo, and C. R. Gordon, *Appl. Phys. Letters*, **9**, 432 (1966).
5. P. A. Schumann, Jr., W. A. Keenan, A. H. Tong, H. H. Gegenwarth, and C. P. Schneider, *This Journal*, **118**, 145 (1971).
6. W. G. Spitzer, G. W. Gobelli, and E. A. Trumbore, *J. Appl. Phys.*, **35**, 206 (1964).
7. M. Born and E. Wolf, "Principles of Optics," 3rd revised ed., Pergamon Press Ltd., Oxford (1965).
8. P. A. Schumann, Jr. and C. P. Schneider, To be published in *J. Appl. Phys.*

Capacitance-Voltage Measurements with a Mercury-Silicon Diode

P. J. Severin and G. J. Poedt

Philips Research Laboratories, Eindhoven, Netherlands

ABSTRACT

The capacitance of a Schottky barrier diode measured as a function of reverse voltage yields the dope concentration and eventually the thickness of an epitaxially grown silicon layer. It is shown that mercury can be used as the metal contact to the silicon. This allows for a rapid and nondestructive C-V measurement, particularly when combined with an automated instrument. The results obtained with different surface treatments are discussed. For reliable and reproducible results N-type silicon should be covered with a thin oxide layer about 50Å thick, which can easily be made wet chemically. The precision which can be attained with this system in actual practice amounts to $\pm 2\%$ or better and the accuracy depends on the definition of thickness used. This technique with the mercury contacting accessory works equally well on GaAs and GaP.

In many semiconductor applications the impurity density N as a function of depth x below the surface is an important parameter.

The most appropriate method to date to measure this function is to form a Schottky barrier diode and to use the well-known relationships between the capacitance C of the diode, the applied reverse voltage V , and the depletion layer boundary depth x . For a metal-semiconductor diode the equations

$$C = \frac{dQ}{dV} = \left[\frac{\epsilon \epsilon_0 O^2 N}{2(V + V_d)} \right]^{1/2} \quad [1a]$$

and

$$C = \frac{\epsilon O}{x} \quad [1b]$$

yield

$$N = \frac{2}{\epsilon \epsilon_0 O^2} \left[\frac{dC^{-2}}{dV} \right]^{-1} \quad [1c]$$

where $O = \pi A^2$ is the diode surface area, V_d is the diffusion potential, and ϵ and e have their usual meaning. Hence, on measuring C as a function of V , $N(x)$ is found.

Hilibrand and Gold (1) showed experimental results with the C-V method and Thomas, Kahng, and Manz (2) demonstrated the validity by experiments on epitaxially grown silicon layers.

Usually with the C-V method the change in capacitance C per small increment in reverse voltage V is measured on a capacitance bridge. This technique is rather time consuming and the profile is found after some tedious calculations. Amron (3) produced a simple slide rule facilitating this procedure. Recently, a number of proposals (4-14) have been made to overcome this difficulty electronically and some instruments have become commercially available. They are all based on clever use of the nonlinear circuit properties incorporated in Eq. [1a] to [1c], as discussed originally by Meyer and Gulbrandsen (15). The authors also use an automated instrument designed and built some years ago by Rusche (16). It operates at a 2 MHz carrier wave modulated with a 2 kHz signal modulation using a constant current unit like Copeland's instrument (4, 5).

Key words: epitaxial layer thickness, diode capacitance, mercury, silicon.

All these instruments have in common that they greatly facilitate the capacitance-voltage measurement, but the speed-determining step remains the production of a diode either by evaporation of a metal dot which is eventually alloyed in, or by shallow diffusion of an opposite type impurity. At the very earliest stage of silicon device processing a metal probe is required which can be used locally and instantaneously to non-destructively form a diode. This paper deals with a mercury probe-silicon diode which satisfies these requirements and which can be used for reliable C-V measurements. The difficulties encountered are not specific to the Rusche instrument and are equally valid when the mercury probe is coupled to another automated instrument or to an ordinary C-V bridge.

Mercury Probe

From the very beginning of the study of MOS structures mercury, in particular as a drop, has been used as an electrode for ease in measuring the oxide and silicon capacitance as a function of d-c voltages (17, 18). Hammer (19) positioned the sample on a rubber O-ring in which the mercury is pressed from below. He obtained in this way a precision of contact surface area of 5% and with a Teflon probe instead of an O-ring he claims even an order better. As far as the authors are aware, no description has been given in the literature of mercury as a contact material to silicon for the purpose discussed in this paper.

The experiments described in this paper were performed with a mercury probe in an accessory as shown in Fig. 1. In a perspex block (1) a channel (2), 2 mm across is bored which at one end is connected to an air pressure valve and at the top end is narrowed to a diameter of about 0.5 mm over a length of 13 mm and closed by the slice (3) under investigation. The channel is partially filled with mercury. The silicon slice is pressed onto the perspex by two steel pins (4 and 5) connected to a lever (6), with a spring as schematically presented in Fig. 1. After letting into the channel (2) air with an excess pressure amounting to about 0.3 atm the mercury contacts the silicon and forms a diode. The electrical contact to the mercury is made with screw (7) which penetrates into the channel and to the silicon with the probes (4) and (5), which can be used separately as current and voltage probes. The

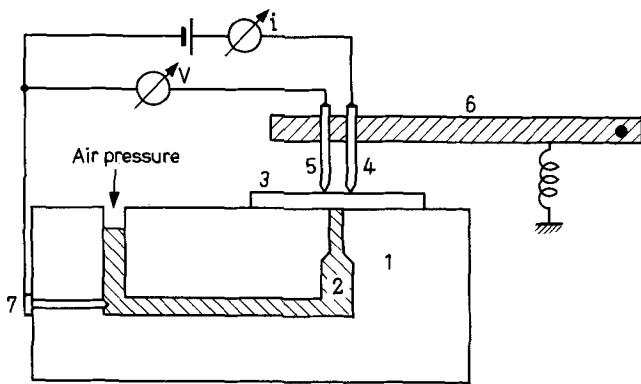


Fig. 1. Schematic drawing of the mercury-silicon contacting accessory: perspex block (1), mercury column (2), silicon slice (3), contact probes (4,5), lever (6), contact to mercury (7). The d-c circuit is also shown, in case there is no back side contact barrier, probes 4 and 5 can be connected.

perspex mercury-silicon contact accessory is shielded in an earthed metal box.

Mercury-Silicon Capacitance Compensation Procedures

Assuming now that the contact of the mercury probe to the silicon has been made, in principle a C-V curve could be measured.

However, it is clear that parasitic capacitances in parallel may invalidate any pertinent conclusions on the impurity density if they are not properly compensated for. The parasitic capacitance can be divided formally into an edge, a stray, and an encapsulation capacitance; they are indistinguishable in actual practice. The edge capacitance C_V is due to the nonhorizontal boundary of the depleted region, which Goodman (20) estimated $C_V = \pi^2 \epsilon A$ and Copeland (21) computed to be remarkably smaller, viz. $C_V = 1.5\pi \epsilon A$. The effect of the edge on the measured capacitance can be evaluated by doing the same experiment with various contact diameters. It is important to note that both in the elementary estimate and in the more detailed calculations it is found that C_V is independent of x and N . By the stray capacitance, C_s , is meant the capacitance between the mercury column and the slice. By the encapsulation capacitance, C_e , is meant the capacitance between the mercury column and the enclosure including the slice.

A second impediment to the sufficiently reliable use of the C-V technique is due to a reverse current which may be too high for the instrument. A phase sensitive detector should therefore be incorporated.

Finally, because the squared diode surface area figures in Eq. [1], the diameter $2A$ should be reproducible and accurately known: it has been found from microscopic inspection of the contact made against a microscope slide that $A = 249 \pm 1 \mu\text{m}$.

The mercury-silicon capacitance cannot be adequately discussed without a brief description of the method by which the difficulties arising from parasitic capacitance can be overcome. Two ordinary capacitors C_1 and C_2 are measured and the instrument produces formally depth readings x_1 and x_2 . The slope $(C_1 - C_2)/(x_1^{-1} - x_2^{-1})$ corresponding to a value of the parameter ϵ_0 generally does not agree with the value found microscopically. The instrument is then calibrated for the appropriate area so that these values coincide to yield $Cd = 20 \text{ pF} \cdot \mu\text{m}$. The intercept in the C vs. x^{-1} plot is reduced to zero by compensating with a built-in opposite-phase current. Then the mercury contact to a silicon slice with plated reverse side is connected to the instrument and assuming that the impurity density N is uniform, the undesired capacitances are eliminated by measuring the dope profile over a certain depth, say from 3 to 4 μm , and adjust-

ing the compensating facilities such that N is a constant over that range. A more refined technique which needs a shorter range of virtually constant N , uses the formal identity between the fundamental equation

$$N = \frac{2e}{e} \frac{V}{x^2} \quad [1d]$$

and the equation on which the instrument is based and which is merely a property of the electronic circuitry

$$N = 10^{14} \frac{V_2}{x^2} \quad [1e]$$

where N is expressed in cm^{-3} , x in μm , and V_2 is the 2 kHz output voltage in mV. The instrument is properly calibrated when V_2 and V reduced by the appropriate constants are read equal. After correct adjustment and calibration the impurity density can be measured.

In general, parasitic capacitances are quite unaccessible, but in order to get a feel for their effects the following experiments have been done. First the equipment is properly compensated with the mercury column at some distance from the slice and subsequently in the measurement situation, making N constant, as described above. The difference between the two readings turns out to be independent of slice resistivity and of depth: with a 3 and 18 ohm-cm N-type slice between 1 and 10 μm the compensation capacitance amounts to about 0.80 pF. In a second experiment the equipment is again properly compensated with the mercury column at some distance from the slice and subsequently with a thin sheet of Polythene, of thickness $\delta = 30 \mu\text{m}$, between the mercury and the slice. The difference between the two readings amounts to about 0.70 pF. In both experiments part of the compensation capacitance is due to a change ΔC_e in encapsulation capacitance. Assuming these to be equal the compensation capacitance in the first experiment equals $\Delta C_e + C_V$ and in the second experiment $\Delta C_e + C_p$, where C_p is the capacitance due to the Polythene sheet with $\epsilon = \epsilon_p \epsilon_0$.

A more precise measurement is done when the equipment is properly compensated in the measurement situation and subsequently with the Polythene sheet of thickness δ between the mercury and the slice. The difference between the two readings is 0.10 pF. When the experiment is repeated with thickness 2δ , the difference is 0.175 pF. From the equations $C_V - C_p = 0.10 \text{ pF}$ and $C_V - C_p/2 = 0.175 \text{ pF}$ it follows that $C_p = 0.15 \text{ pF}$ and $C_V = 0.25 \text{ pF}$. This value of C_p suggests that $\epsilon = 3.8 \epsilon_0$ which has been found to hold by varying the thickness. The stray capacitance associated with C_p can be neglected. In the experimental arrangement with $A = 249 \mu\text{m}$ and $\epsilon = 11.8 \epsilon_0$ Goodman's formula yields $C_V = 0.29 \text{ pF}$, which shows better agreement than Copeland's formula.

Similar effects were reported by Copeland (4) who found with a given diode diameter $C_V = 0.15 \text{ pF}$ whereas $C_V = 0.09 \text{ pF}$ was expected. His suggestion that the additional capacitance is probably due to a slight change in probe stray capacitance as the probe is moved into position can be in agreement with the observation reported above, though it may refer to part of the effect.

Mercury-Silicon Capacitance Measurement

In actual practice, the Rusche instrument with the mercury probe is used continuously to evaluate N-type Si layers epitaxially grown on an N^+ substrate. The range of applicability is limited at the lowly doped side by the very small capacitance at high voltage and at the highly doped side by the relatively high voltage necessary to reach a given depth, whereas the maximum voltage is increasingly limited by breakdown. In Fig. 2, V is plotted vs. N with d as a parameter from Eq. [1d] and the N -scale is shown converted to the

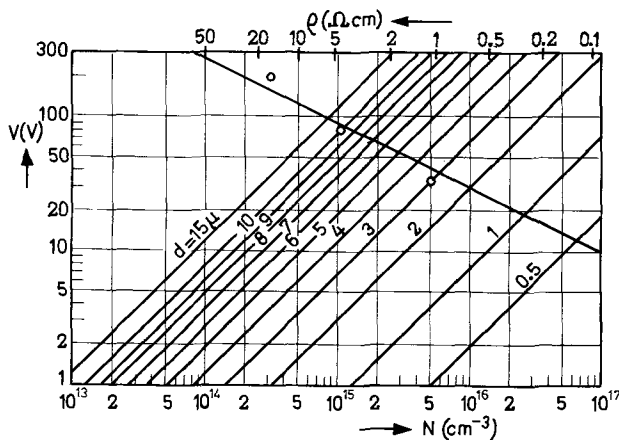


Fig. 2. Range of applicability of the C-V method for measuring a layer of thickness d and charge carrier density N or resistivity ρ is limited by breakdown. The parallel straight lines are obtained from Eq. [1] with $\epsilon = 11.8$, ϵ_0 and $O = 196.10^{-9}$ m² and the breakdown characteristic is drawn with slope 0.5 through some measured points.

resistivity ρ from Sze and Irvin's (22) curves. The breakdown voltage as a function of N is drawn with slope 0.5 through some experimental points, roughly according to Schumann's (23) theory.

When the depletion layer reaches the epitaxial layer-substrate interface this is very clearly manifested on the instrument. In this way not only can the resistivity ρ be determined but also, with some established criterion, the thickness d of an epitaxial layer. This is particularly important for layers which are too thin to be accurately measured with the conventional infrared multiple interference (IMI) technique, say for, $d \leq 3$ μm . The thickness d_i as measured by the IMI technique is uniquely determined and is further operationally defined by the formalism used for the interpretation (24). However, the definition of thickness as measured with the C-V method should be agreed on before the measurement: in general terms d_α , where $N(d_\alpha) = \alpha N_{\text{epi}}$. In fact mainly the thickness definition d_x where $N(d_x) = N_{\text{substr}} = \infty$, is used. Because the thickness is not uniquely defined, Mantena and Barrera's (25) suggestion to use the IMI measured thickness value d_i and compensate at punch-through where C is known to be $\epsilon A^2/d_i$, does not eliminate the ignorance of parasitic capacitances to the extent required, especially in the case of thick layers. For thin layers, where the parasitic capacitance is relatively unimportant, this method could work, but the IMI technique cannot be used then. In fact, the C-V method is the only method available to date for direct thickness measurement of thin layers.

The precision obtainable depends on the instrument used: taking into account all sources of error the precision should amount to $\pm 10\%$, but in actual practice the reproducibility is found to be $\pm 2\%$. The accuracy of the method is tentatively demonstrated in Table I. The four-point probe (fpp) measured resistivity is compared to the C-V measured dope concentration N converted to ρ with Sze and Irvin's (22) curves and satisfactory agreement is found. It should be realized in interpreting these results that a slice is essentially nonuniform in resistivity, as convincingly demonstrated with the spreading resistance technique (26). The four-point probe method itself is capable of mea-

suring with a precision of about 0.5% but because the result represents a weighted average over several square millimeters it is subjected to larger errors (27). The nonuniformity also affects the capacitance-voltage measurement results. The same mercury contacting accessory has also been used successfully on bulk GaAs and GaP where the reverse sides should be properly contacted and on epitaxially grown N on N⁺ GaAs layers (28) where this difficulty does not arise to such extent.

Mercury-Silicon Diode

In the preceding section the instrument has been described as far as relevant and its application to the precise, accurate, nondestructive and rapid determination of thickness and resistivity of epitaxially grown layers has been explained. The much more complicated question as to why the mercury probe works so well is semiquantitatively discussed in this section.

It has been found experimentally that the slice should be polished and that before mercury contact to the silicon is actually made, the slice should be thoroughly cleaned and chemically oxidized by boiling it for about 1 min in HNO₃ or H₂O₂ + H₂SO₄. This preparation process produces an oxide layer between 20 and 50 Å thick, as do all room-temperature wet oxidizing agents (29-32). It has been found that without such thin oxide interfacial layer no reliable C-V measurements can be made on N-type silicon.

Experiments on mercury-silicon surface barriers have, as far as the authors are aware, only been reported by Donald (33).

Neither the very thin nor the thick oxide layer theories are applicable to the type of mercury contact which this paper deals with. With the intermediate insulating layer thickness, between 10 and 100 Å, quantum-mechanical tunneling is the dominant mechanism (34-38). Because the voltage drop is entirely across the oxide layer, the applied bias sweeps the Fermi level in the metal along the different semiconductor levels. Between coincidence with the top of the valence band and the bottom of the conduction band, conductance in this system is very low and this conductance well is typically from 1 to 2V wide. This depends on the energy gap and interface state density. At the edges the d-c current rises steeply and the I-V plot is fairly symmetric. If the doping level of the semiconductor is low or the oxide film is very thin, most of the voltage drop occurs across the semiconductor, which then forms a depletion region, and the metal Fermi level is not free to move, but is pinned to the semiconductor Fermi level. Dahlke and Sze (35) published two I-V characteristics, which under these conditions show a roughly exponential rise in the forward direction and a slowly varying current in the reverse direction. Strong dependence on the ambient temperature proved that emission exceeded tunneling as the current controlling process.

Similar I-V characteristics have been measured with the mercury-thin oxide-covered silicon diode. An example is shown in Fig. 3. The conductance well typical of tunneling is not observed because the voltage drop is mainly across the depletion layer in this lowly doped material and the conventional diode equations are not satisfied because of the presence of the oxide interface.

The influence of the oxide layer and the silicon-doping type and level is more clearly illustrated in Fig. 4. Both low- and high-conductivity N-type silicon, mercury contacted just after HF-etching (labeled INe and hNe, respectively) show low-resistance ohmic

Table I. Some measurement data obtained with the four-point probe and C-V methods on five N-type and three P-type Si slices

	N					P		
fpp ρ (ohm-cm)	0.27	0.64	1.16	4.3	7.1	1.23	4.3	10.8
C-V ρ (ohm-cm)	0.29	0.62	1.19	4.2	7.3	1.30	4.5	11.0
$\rho_{\text{ev}} - \rho_{\text{fpp}}$	+7.4	-3.1	+2.5	-2.3	+2.8	+5.7	+4.6	+1.9
ρ_{fpp}	100%							

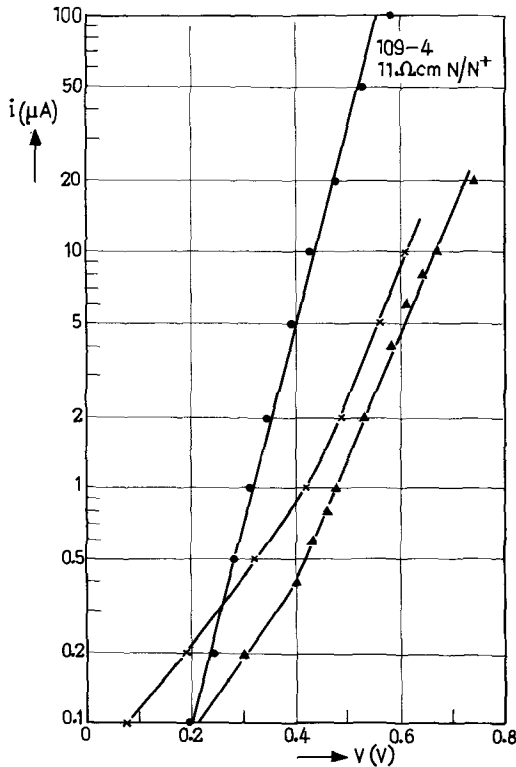


Fig. 3a. Some I-V characteristics of thin oxide-covered, N-type Si slices in the forward direction.

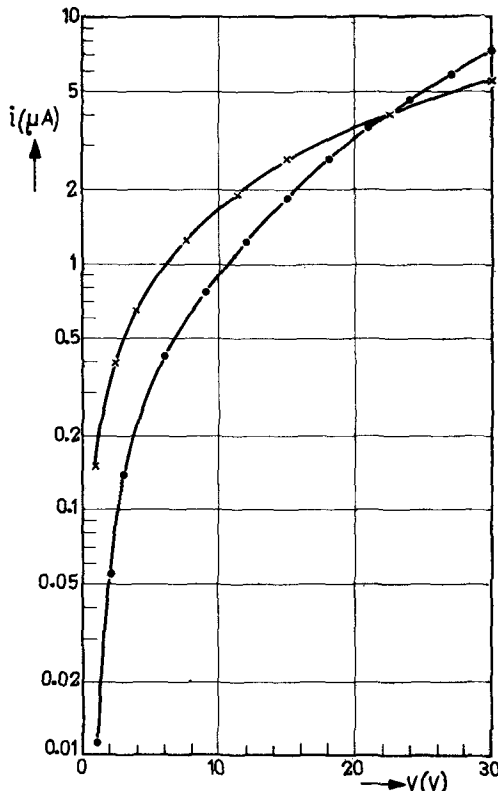


Fig. 3b. Some I-V characteristics of thin-oxide covered, N-type Si slices in the reverse direction.

characteristics. When oxidized before the mercury contact is applied, the highly doped material (labeled hNo) shows the conductance well discussed above, whereas under reverse bias the lowly doped material (labeled lNo) develops a depletion layer, which presents the dominant barrier to current flow. The forward biased parts of the lNo and hNo materials are

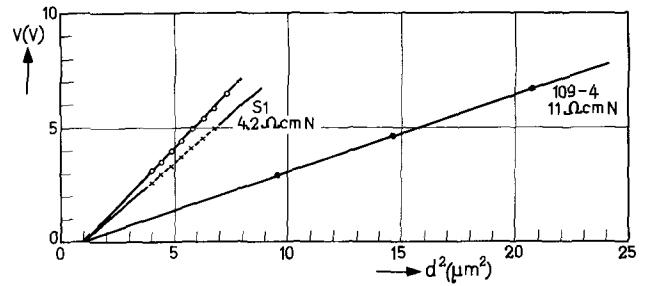


Fig. 3c. Some C-V curves of thin-oxide covered, N-type Si slices

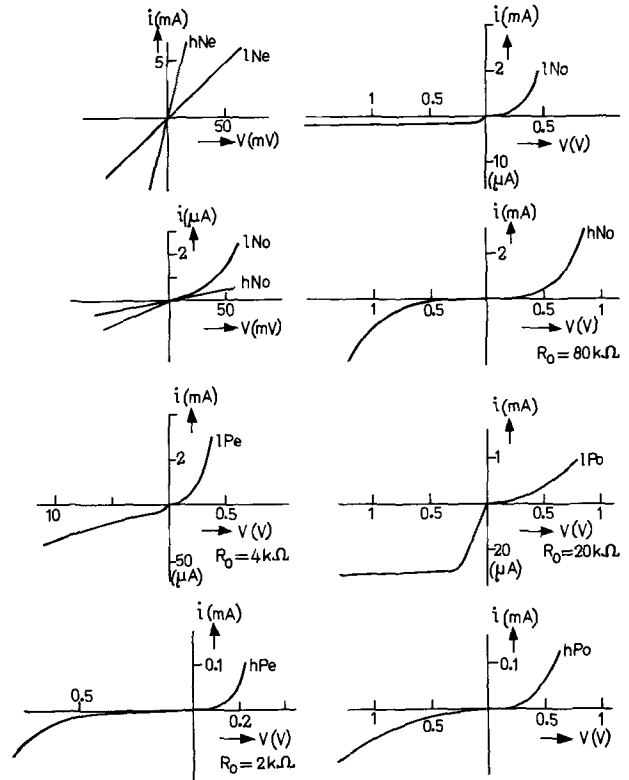


Fig. 4. I-V characteristics of eight essentially different diodes on silicon: highly and lowly doped (h and l), N and P-type (N and P), thin oxide layer-covered or etched (o or e). Note that the forward and reverse currents have different scales. The following materials are used: 1 ohm-cm, 10 μm thick, N-type epitaxial layer on 10⁻² ohm-cm N⁺-type substrate (lN), 0.008 ohm-cm N-type (hN), 2.8 ohm-cm, 9 μm thick P-type epitaxial layer on 10⁻² ohm-cm P⁺-type substrate (lP) and 10⁻² ohm-cm P-type (hP).

about equal, in both charge transport is controlled by the tunneling process because the main voltage drop is across the oxide. The ratio of forward to reverse current in lNo material is about 10⁴ and in hNo material the conductance well is centered at about 0.2V reverse bias. From the low-voltage I-V characteristic the zero-bias barrier resistance R₀ is found for both lNo and hNo material to be equal to about 10⁵ ohms and apparently the leakage current density J_s is determined by the oxide layer.

The considerations and evidence discussed above can be summarized by stating that in lowly doped material the oxide layer is thick enough to present a barrier to current flow and thin enough to allow the reverse bias voltage drop to exist across the semiconductor depletion layer. This enables a capacitance voltage measurement to be made. The thin oxide series capacitance is completely negligible with respect to the depletion layer capacitance and conductance via small holes in the oxide layer must be excluded because of the ensuing high spreading resistance which is not measured.

To P-type material, HF-etched before mercury is applied, no ohmic contact can be made. This is to be expected because for a particular metal the barrier heights to N- and P-type material add to about the semiconductor energy gap (39, 40). Therefore, hPe material produces about the same I - V characteristic as hPo material and lPo material does not produce a more pronounced diode characteristic than lPe material.

Summarizing it can be said that lowly doped P-type material can be C-V measured with the mercury probe equally well with or without oxide layer.

Some examples of plots of V vs. $d^2 \sim 1/C^2$ are given in Fig. 3c. The presentation is not typical, because with the automated instrument reading the d-c reverse voltage is not needed; it is merely shown in order to exemplify the validity of the method. The diffusion voltage as read from the intercept is typically between 0.5 and 1.5V. It cannot be used simply to characterize the material probably because surface charge and the interfacial layer are important for the actual value. Such effects have been discussed by Cowley (41) and Sze (42) for Si, GaAs, and GaP.

Discussion of Epitaxial Layer Measurements

In the procedure outlined above it is assumed that over a small depth the impurity density is uniform. Epitaxially grown layers satisfy this requirement and home-grown N on N⁺ layers with resistivities between 0.1 and 20 ohm-cm are currently measured with the mercury probe and automated equipment as far as the impurity density and thickness ranges plotted in Fig. 2 allow. The breakdown voltage boundary should not be considered as accurate and sharp because it depends to some extent on surface damage and preparation and cleanliness of the epitaxial layer surface. It is evident that for an N on N⁺ layer in the thickness range which can be measured with IMI this C-V method obviates the N on P check slice procedure and for very thin N on N⁺ layers it presents a new, rapid and non-destructive technique. In Fig. 5 the results of evaluation of a batch of rather thin epitaxially grown N on N⁺ layers are shown. It would have been very difficult to obtain these results in any other way, and they cannot be checked easily. Similar results on a batch of thicker layers are presented in Fig. 6 and the thickness is compared to the data obtained with IMI. It is clear that a discrepancy must exist between the two sets of results due to the incompatibility of the definitions used.¹ Because a fairly constant difference between both sets exists it is reasonable to assume that the precision obtained with the C-V method is well within the limit indicated above, $\pm 5\%$. A typical epitaxial layer measurement is shown in Fig. 7.

Acknowledgment

The authors wish to express their thanks to Dr. Hagen and Dr. van Opdorp for discussions on the nature of the mercury-silicon diode.

¹ The same argument can be put forward against introducing the IMI measured thickness for spreading resistance data interpretation.

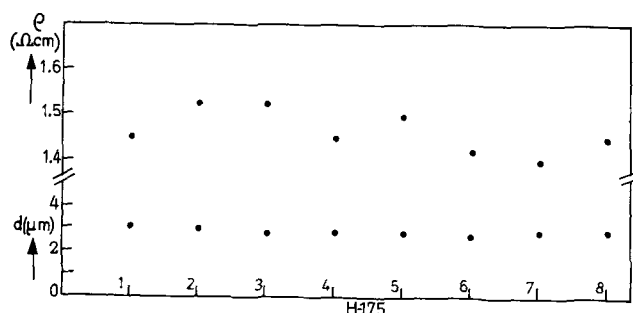


Fig. 5. Resistivity ρ and the thickness d , C-V measured with d_x criterion on a batch of eight epitaxially grown N on N⁺ layers (H175). The numbers correspond to the centers of the eight slices, positioned in a row on the susceptor.

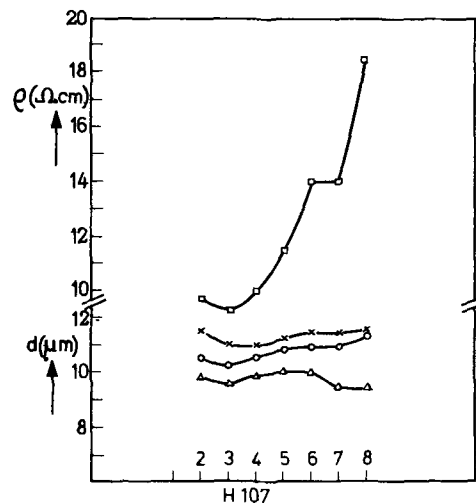


Fig. 6. Resistivity ρ , and the thickness d , C-V measured with the $d_{1,1}$ criterion (Δ), the d_x criterion (\circ), and IMI measured (\times) on a batch of eight epitaxially grown N on N⁺ layers (H107). No gas dope was added to the silane, and the resistivity increases along the susceptor probably due to autodoping. The numbers correspond to the centers of the eight slices, positioned in a row on the susceptor.

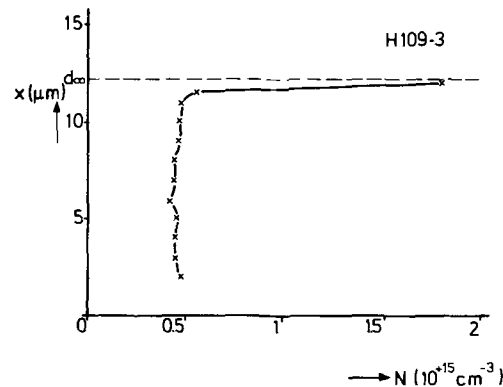


Fig. 7. Dope concentration as a function of depth in an epitaxially grown N on N⁺ layer (H109-3). The uncorrected (24) IMI measured thickness $d_i = 12.9 \mu\text{m}$, whereas $d_x = 12.25 \mu\text{m}$.

Manuscript submitted Nov. 29, 1971; revised manuscript received March 29, 1972.

Any discussion of this paper will appear in a Discussion Section to be published in the June 1973 JOURNAL.

REFERENCES

1. J. Hilibrand and R. D. Gold, *RCA Rev.*, **21**, 245 (1960).
2. C. O. Thomas, D. Kahng, and R. C. Manz, *This Journal*, **109**, 1055 (1962).
3. I. Amron, *Electrochem. Technol.*, **2**, 327 (1964).
4. J. A. Cope and, *IEEE Trans. Electron. Devices*, **ED-16**, 445 (1969).
5. R. R. Spiwak, *IEEE Trans. Inst. Measurement*, **IM-18**, 197 (1969).
6. P. J. Baxandall, *Electronics*, **42**, No. 7, 179 (1969); No. 11, 7 (1969).
7. P. J. Baxandall, D. J. Colliver, and A. F. Fray, *J. Phys. E*, **4**, 213 (1971); **4**, 472 (1971).
8. D. Leenov and R. G. Steward, *Proc. IEEE*, **56**, 2095 (1968).
9. W. Tantraporn, *J. Appl. Phys.*, **40**, 4665 (1969).
10. A. Ambrozy, *Solid State Electron.*, **13**, 347 (1970).
11. B. J. Gordon, H. L. Stover, and R. S. Harp, "Silicon Device Processing," Nat. Bur. Stds. Special Publication 337, p. 273 (1970).
12. F. P. Califano and A. Luciano, *Rev. Sci. Instr.*, **41**, 865 (1970).
13. C. A. T. Salama and F. Holmes, *Solid State Electron.*, **14**, 178 (1971).
14. H. Ahlers, *Nachrichtentechnik*, **19**, 92 (1969).
15. N. I. Meyer and T. Gulbrandsen, *Proc. IRE*, **51**, 1631 (1963).

16. G. Rusche, Valvo, Hamburg, Private communication.
17. K. H. Zainiger, *RCA Rev.*, **27**, 341 (1966).
18. G. Abowitz and E. Arnold, *Rev. Sci. Instr.*, **38**, 564 (1967).
19. R. Hammer, *ibid.*, **40**, 292 (1969).
20. A. M. Goodman, *J. Appl. Phys.*, **34**, 329 (1963).
21. J. A. Copeland, *IEEE Trans. Electron. Devices*, **ED17**, 404 (1970).
22. S. M. Sze and J. C. Irvin, *Solid State Electron.*, **11**, 599 (1968).
23. P. A. Schumann, *This Journal*, **115**, 1197 (1968).
24. P. J. Severin, *Appl. Optics*, **9**, 2381 (1970); **11**, 691 (1972).
25. N. R. Mantena and J. S. Barrera, *Solid State Electron.*, **12**, 1000 (1969).
26. P. J. Severin, *ibid.*, **14**, 247 (1971); "Silicon Device Processing," Nat. Bur. Stds. Special Publication 337, p. 224 (1970).
27. P. J. Severin, *Philips Res. Rept.*, **26**, 279 (1971); **26**, 359 (1971).
28. F. D. Hughes, R. F. Headon, and M. Wilson, *J. Phys. E*, **5**, 241 (1972).
29. M. J. Turner and E. H. Rhoderick, *Solid State Electron.*, **11**, 291 (1968).
30. R. J. Archer, *This Journal*, **104**, 619 (1957).
31. A. Mayer and D. A. Puotinen, "Silicon Device Processing," Nat. Bur. Stds. Special Publication 337, p. 431 (1970).
32. E. H. Rhoderick, *J. Physics D*, **3**, 1153 (1970).
33. D. K. Donald, *J. Appl. Phys.*, **34**, 1758 (1963).
34. P. V. Gray, *Phys. Rev.*, **140A**, 179 (1965).
35. W. E. Dahlke and S. M. Sze, *Solid State Electron.*, **10**, 865 (1967).
36. J. Shewchun, A. Waxman, and G. Warfield, *ibid.*, **10**, 1165 (1967).
37. A. Waxman, J. Shewchun, and G. Warfield, *ibid.*, **10**, 1187 (1967).
38. L. B. Freeman and W. E. Dahlke, *ibid.*, **13**, 1483 (1970).
39. M. Hirose, N. Altaf, and T. Arizumi, *Japan. J. Appl. Phys.*, **9**, 260 (1970).
40. B. L. Smith and E. H. Rhoderick, *Solid State Electron.*, **14**, 71 (1971).
41. A. M. Cowley, *J. Appl. Phys.*, **37**, 3024 (1966).
42. A. M. Cowley, and S. M. Sze, *ibid.*, **36**, 3212 (1965).

High Concentration Arsenic Diffusion in Silicon from a Doped Oxide Source

Richard B. Fair

Bell Telephone Laboratories, Incorporated, Reading, Pennsylvania 19603

ABSTRACT

The properties of As-doped SiO_2 and As-doped Ge/ SiO_2 diffusion sources as a function of the O_2 concentration in a horizontal, open-tube deposition chamber are examined. The effect of the Ge doping in the oxide is to enhance the etch rate and to reduce As_2O_3 incorporated during the oxidation of AsH_3 . The elemental As thus formed diffuses more rapidly than As_2O_3 in the oxide, thus enhancing the transport of As across the Si-oxide interface. A prediffusion H_2 anneal of the oxide is shown to produce a similar effect. Control of the source doping by varying the O_2 concentration in the deposition chamber, C_{O_2} , is shown to result in diffusions where the sheet resistance, R_S , varies as $(\text{C}_{\text{O}_2})^{-1}$. In terms of the molecular fraction of As in the oxide, $\text{C}_{\text{As}}^{\text{SiO}_2}$, $R_S \propto (\text{C}_{\text{As}}^{\text{SiO}_2})^{-2}$. R_S is shown to decrease with time as $t^{-1/2}$ for $t \gtrsim 40$ min. For shorter times the diffusion of As is complicated by the changing surface concentration of the electrically active fraction of As. Singly diffused As profiles in Si are shown to be described by the solutions to the diffusion equation with a concentration-dependent diffusion coefficient. However, the preanneal in H_2 is shown to cause the subsequently diffused As to have an anomalous electrical profile.

The use of arsenic-doped oxides has been reported for several years (1-6). Recently, these oxides have shown much promise as emitter diffusion sources in planar transistor processing (7). In general, the advantages of using doped oxide diffusion sources have been well reviewed (8, 9). However, little is known about the relationships that exist between the properties of arsenic-doped oxides and the characteristics of diffusions from them. It is the purpose of this paper to present the results of a study of shallow, high concentration arsenic diffusions in silicon from doped oxides whose chemical compositions have been experimentally determined. Two general types of doped oxides were deposited in a horizontal, open-tube reactor: As-doped SiO_2 and As-doped Ge/ SiO_2 . These films were deposited on silicon substrates by the oxidation reactions of AsH_3 , SiH_4 , and GeH_4 or GeCl_4 with O_2 . The following sections describe the dependence of As doping in the oxides on the O_2 concentration in the reaction chamber. As a diffusion source, the effects of oxide composition and prediffusion annealing are discussed.

Key words: arsenic, diffusion, doped oxides.

Experimental

The horizontal open-tube deposition furnace that was used in this study is shown schematically in Fig. 1. This unit has the capability of depositing doped and undoped SiO_2 films from the oxidations of silane

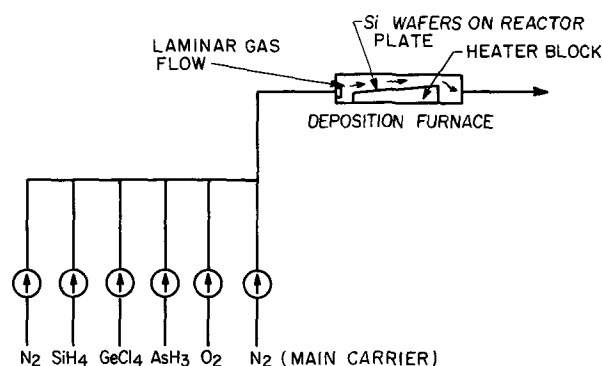


Fig. 1. Schematic diagram of the arsenic-doped germano silicate oxide deposition system.

(SiH₄), and the gaseous compounds of the doping species. Doping gases were controlled by mass flowmeters. The reactor plate was heated by a 4 kW resistive-type heater block. For a typical deposition, wafers were placed on a vitreous carbon reactor plate. The reactor plate was placed on the heater block, and then the gases were introduced into the chamber (rectangular cross section, volume ≈ 300 in.³). Using a N₂ carrier gas flow rate of 92 l/min, the 5% SiH₄, 10% AsH₃, and O₂ flow rates were typically 0.7, 0.08, and 5 l/min, respectively. Deposition occurred in excess AsH₃ at ≈ 500 Å/min for a heater temperature of 470°C. For a total oxide thickness of 3000Å, slice-to-slice uniformity was ± 200 Å over ten, 1½ in. wafers.

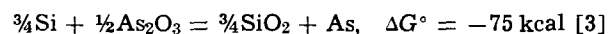
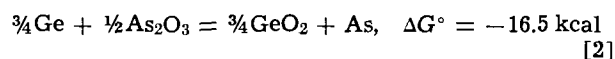
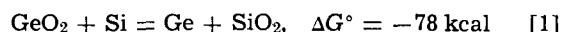
All diffusions were performed in <100>, 1 ohm-cm p-type Si wafers, 1½ in. in diameter. These wafers were cut from Czochralski-grown crystals. They were then chemically lapped, Syton polished, and cleaned. Prior to oxide deposition the wafers were rinsed in a buffered HF solution.

Properties of the Source Oxide

The dependence of As doping in the deposited oxide upon O₂ concentration in the reaction chamber was investigated by varying the O₂ flow rate with all other gas flows held constant. Room temperature infrared spectra were obtained of as-deposited oxides so that the As₂O₃ content could be determined, and neutron activation measurements were made in order to determine the total As doping in the oxides. The infrared spectra of As-doped SiO₂ and As-doped Ge/SiO₂ films deposited with C_{O₂} = 0.073 (mole fraction of O₂ computed with respect to the total gas mixture) are compared in Fig. 2. These kinds of spectra have been thoroughly analyzed by Arai and Terunuma (10) and by Abe *et al.* (7). From the 10.7μ absorption lines [due to symmetric stretching vibrations of As₂O₃ (11)] it was estimated that the amount of As₂O₃ incorporated into the As-doped SiO₂ films increases superlinearly with C_{O₂} over the range 0.045 \leq C_{O₂} \leq 0.073. However, over the same range the As₂O₃ density increases as C_{O₂}^{1/2} for the Ge/SiO₂ system. Also for the case C_{O₂} = 0.073 the As₂O₃ density in the SiO₂ film is approximately 40% larger than the As₂O₃ density in the Ge/SiO₂ film. At C_{O₂} = 0.053 the As₂O₃ concentration in the SiO₂ film is larger by 13%. In order to determine if the increased As₂O₃ doping in the SiO₂ films is due to a difference in the oxidation kinetics of the AsH₃-SiH₄ system as compared with the AsH₃-SiH₄-GeCl₄ system, neutron activation of these same oxides was per-

formed in order to determine total arsenic concentrations. The results of some of these measurements are summarized in Table I for 3000Å thick films. The total As concentration, [As], increases approximately as C_{O₂}^{1/2} for both the As-SiO₂ and the As-Ge/SiO₂ systems, which agrees with the independent observations of Weber (12). However, the [As] in the As-doped SiO₂ films is larger for a given O₂ concentration than in the As-doped Ge/SiO₂ films. A possible explanation for this is that the GeCl₄ or GeH₄ molecules in the gas phase "tie-up" O₂ molecules for oxidation, leaving a lower concentration of O₂ available for the oxidation of AsH₃ and SiH₄.

In order to try to understand the effect that the addition of Ge has on the incorporation of As₂O₃ into the deposited oxides, it is necessary to study the kinetics of the various reactions. However, some insight can be obtained if the following thermodynamically favorable reactions are considered at 470°C (13, 14)



where ΔG° is the standard free energy of the reaction. Regarding reaction [1] the presence of GeO₂ in the Ge/SiO₂ films can be seen from the spectra of Fig. 2. At 11.5μ the weak GeO₂ absorption band is visible when the As-Ge/SiO₂ spectrum is subtracted from the As-SiO₂ spectrum. However etch rate measurements indicate that the total Ge doping density in these films is 1.5-2 $\times 10^{21}$ atoms/cm³ (4, 12) [approximately 8 a/o (atom per cent) in SiO₂]. If all of this 8 a/o of Ge were in the form of GeO₂, it is expected that a more pronounced absorption band would have been detected (4). The presence of other Ge compounds could not be detected in full-spectrum measurements. Consequently, it is probable that elemental Ge dominates in the As-doped Ge/SiO₂ oxides. The Si in Reactions [1] and [3] is the Si wafers and that Si which is formed by the pyrolysis of SiH₄. Consequently, the presence of Ge appears to enhance the [As] over the [As₂O₃] directly through Reaction [2], although Reaction [3] may contribute significantly to the [As]:[As₂O₃] ratio.

Diffusion Studies

In this section the characteristics of As-doped oxide diffusion sources are discussed in light of the information presented above.

Prediffusion annealing.—In order to investigate the effects of prediffusion annealing on the doped oxide characteristics, six silicon samples were simultaneously deposited with 1500Å of As-doped SiO₂. These films were then capped with 1500Å of SiO₂. Three slices were annealed in H₂ and three in O₂, all at 900°C for 20 min. Film quality of the H₂ and O₂ annealed slices was excellent. All six slices were then placed in a 1000°C, O₂ furnace for 30 min. The average sheet resistances, R_S, the R_S ranges, and the diffused layer junction depths in the silicon were as follows

$$R_{S\text{H}_2} = 34.4 \pm 2.5\% \text{ ohms/square}, \quad x_J = 0.18\mu$$

$$R_{S\text{O}_2} = 38.3 \pm 1.5\% \text{ ohms/square}, \quad x_J = 0.22\mu$$

Table I. Oxide* arsenic doping as a function of O₂ concentration

Oxide composition	C _{O₂}	As ₂ O ₃ doping (area of absorption) curve	Total As doping, [As] (atoms/cm ²)
As-SiO ₂	0.073	70	8.35 $\times 10^{18}$ } C _{O₂} ^{1/2}
	0.053	45	
As-Ge/SiO ₂	0.073	51	7.45 $\times 10^{18}$ } C _{O₂} ^{1/2}
	0.053	40	

* All oxide films were 3000Å thick.

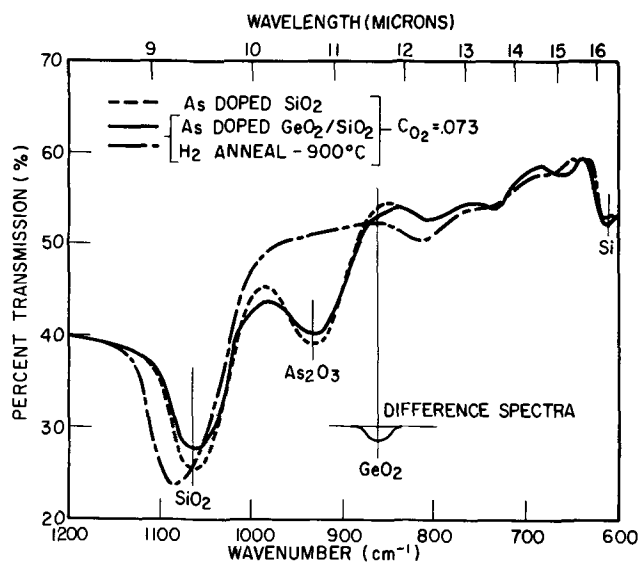


Fig. 2. Infrared spectra of as-deposited As-SiO₂ and As-Ge/SiO₂ oxides for the O₂ concentration of 0.073. The spectrum of an H₂ annealed film is shown for comparison (900°C for 20 min).

The room temperature infrared spectrum of the H₂ annealed doped oxide is shown in Fig. 2. It can be seen that the H₂ anneal has completely reduced the As₂O₃ in the film. Diffusions that were performed at 1000°C for 30 min in H₂ yielded diffused layers of R_S ≈ 300 ohms/square. These observations are in agreement with the results of Arai and Terunuma (10). It can, therefore, be concluded that diffusion in O₂ is important for the efficient transport of As from the oxide to the Si. Such transport may depend on the presence of As₂O₃ according to Reaction [3]. The effect of the H₂ anneal appears to be similar to the effect of incorporating Ge into the source oxide, i.e., to form elemental As which apparently can diffuse through SiO₂ more rapidly than As₂O₃. The increased diffusivity of "As" in Ge/SiO₂ was verified at 1270°C where D_{As, Ge/SiO₂}/D_{As, SiO₂} ≈ 1.5 was measured. Enhanced As diffusivity in GeSiO₂ also was suggested by Abe *et al.* (7) as the cause of enhanced As doping in Si.

Effect of O₂ concentration on the diffusion of As in Si.

—The dependence of sheet resistance and junction depth on the As concentration in the oxide source was investigated. Arsenic diffusions into silicon were performed from doped oxides that were deposited with O₂ concentrations between 0.025 and 0.073 mole fraction. The AsH₃ and SiH₄ concentrations were held constant at 0.00008 and 0.00043, respectively. The deposition temperature was 470°C measured in the heater block. After each deposition the individual wafers were scribed, and groups of four pieces were then diffused for 15, 25, 30, 40, and 60 min, respectively. Sheet resistances and junction depths (angle-lap and HNO₃-HF stain) were measured on each piece, and the results for each diffusion time were averaged. The experiments were repeated with Ge doping in the oxides (mole fraction of GeH₄ = 0.00003).

The results of these measurements for 1000°C, 30-min diffusions in O₂ are shown in Fig. 3. The sheet resistance is seen to vary approximately as (C_{O₂})⁻¹. Resistivity profiles of these diffusions were then obtained by a differential four-point probe technique, and Irvin's (15) curves were used to obtain the resulting electrically active As-doping profiles. Integration over these profiles yielded the total number of electrically active As atoms/cm², Q. In Fig. 4 Q is shown plotted against the molecular fraction of As in the source oxide. For two diffusions, the Q of the As in the Si was determined by neutron activation analysis as well as by resistivity measurements. These data are indicated in Fig. 4 by a superscript, n.

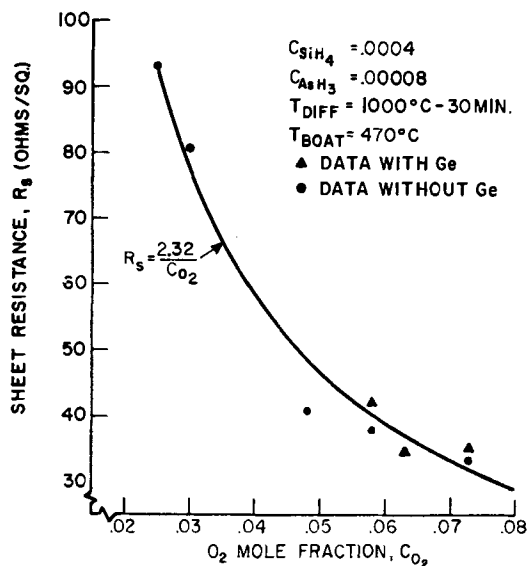


Fig. 3. Variation of the sheet resistance of diffused As layers in Si with O₂ concentration in the deposition chamber.

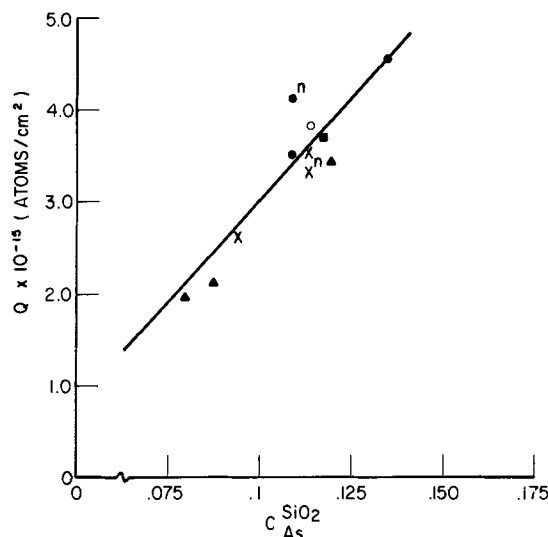


Fig. 4. Total arsenic concentration in silicon vs. molecular fraction of arsenic in the doped oxide source following 1000°C diffusion in O₂. As-SiO₂ source: ▲ 30 min; ● 60 min. As-Ge/SiO₂ source: ◻ 20 min; × 60 min. H₂-As-Ge/SiO₂ source: ■ 30 min. n: neutron activation data.

In order to determine the dependence of R_S on C_{As}^{SiO₂}, the molecular fraction of As in SiO₂, the empirical equations

$$R_S = \frac{2.32}{C_{O_2}} \quad [4]$$

$$C_{As^{SiO_2}} = 0.45 C_{O_2}^{1/2} \quad [5]$$

can be combined to give

$$R_S = \frac{0.47}{(C_{As^{SiO_2}})^2} \quad [6]$$

This result is plotted in Fig. 5 along with experimental data (from 1000°C, 30-min diffusions only).

The variation of the sheet resistance with diffusion time is shown in Fig. 6. It can be seen that there is approximately a 13% dip in the curves at t = 30 min. For times greater than 40 min, the sheet resistance decreases as (t)^{-1/2}. From t = 25 min to t = 30 min, R_S decreases approximately as t⁻¹. The theoretical dependence of R_S on t can be approximated if it is assumed that the electron mobility of the As-doped Si remains constant for concentrations ≥ 10¹⁹ atoms/cm³. It has been shown that for a constant C_S diffusion (16)

$$R_S = \frac{1.56 \times 10^{17}}{x_j C_S} \quad [7]$$

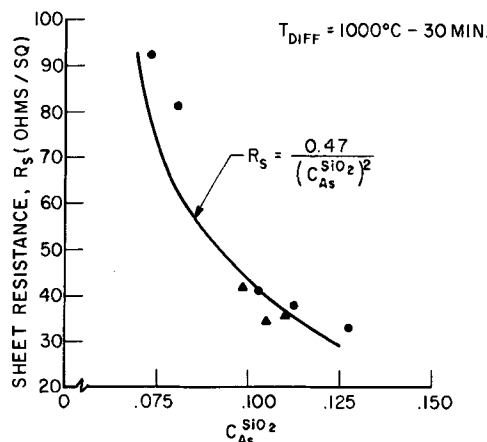


Fig. 5. Variation of the sheet resistance with molecular fraction of As in the source oxide.

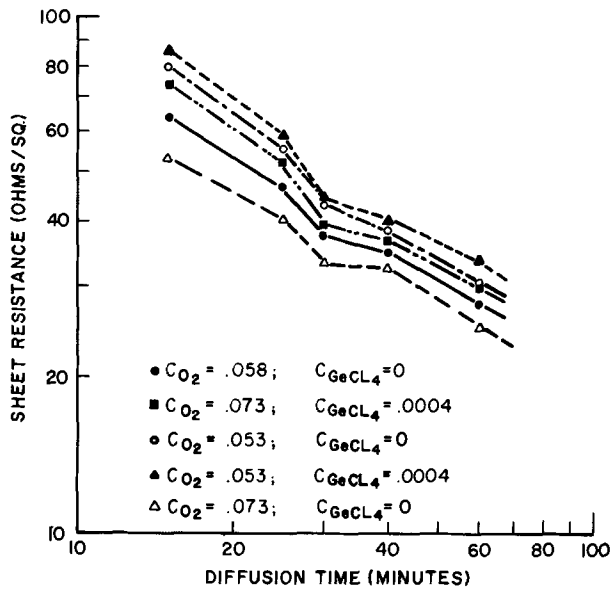


Fig. 6. Variation of sheet resistance with diffusion time

where C_s is the electrically active surface concentration (atoms/cm³). The validity of Eq. [7] is not dependent on the type of As diffusion source. From Fig. 7, x_j can be seen to increase approximately as $t^{1/2}$ for As diffusions into 1 ohm-cm p-Si at 1000°C. Under such conditions, x_j can be written as (16)

$$x_j = 2.3 \sqrt{\frac{C_s D_1 t}{n_i}} \quad [8]$$

where D_1 is the intrinsic diffusivity of As, and n_i is the intrinsic electron density. Substitution of Eq. [8] into Eq. [7] yields

$$R_s = \frac{6.8 \times 10^{16}}{C_s^{3/2}} \sqrt{\frac{n_i}{D_1 t}} \quad [9]$$

It can be seen that R_s is a sensitive function of surface doping concentration, C_s . If C_s is constant, then R_s decreases as $t^{-1/2}$. However, the C_s vs. t data collected from As diffusions performed with the same source oxides ($C_{O_2} = 0.058$, $GeCl_4 = 0$) are shown in Fig. 8. It can be seen that C_s becomes approximately constant for $t \geq 35$ min, near the beginning of the $t^{-1/2}$ decrease of R_s . For $t < 35$ min it is felt that the dominant

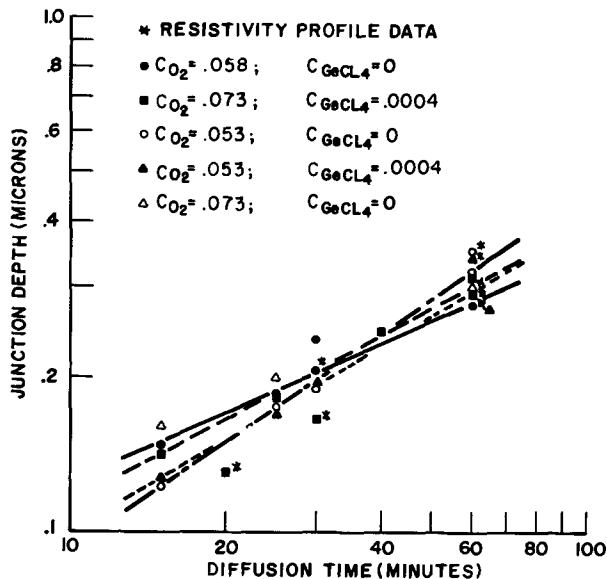


Fig. 7. Variation of As-diffused layer junction depths in Si with diffusion time (1000°C in O₂).

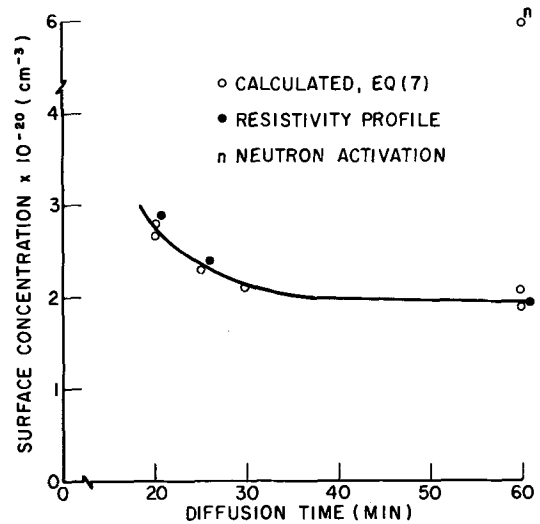


Fig. 8. Variation of surface concentration with diffusion time (diffusion from an As-doped SiO₂ source, $C_{O_2} = 0.073$, $T = 1000^\circ\text{C}$).

effect on C_s is the establishment of equilibrium between monatomic As⁺ ions and inactive As complexes. According to the annealing studies of Schwenker *et al.* (17), considerable time is required for equilibrium to obtain (15-30 min at 1000°C). Also, the fact that the doped oxide source is finite will cause an eventual decrease in C_s .

Diffusion profiles.—Shallow arsenic diffusion profiles in silicon were obtained experimentally by a step anodization process in which the sheet resistance was measured as a function of depth. Irvin's curves were then used to deduce the concentration profiles. These profiles are shown in Fig. 9, 10, and 11. The sources for these diffusions were As-doped SiO₂, As-doped Ge/SiO₂, and H₂-annealed As-doped Ge/SiO₂, respectively. The theoretical profiles were obtained by numerically solving the diffusion equation

$$\frac{\partial C}{\partial t} = \frac{\partial}{\partial x} \left(D_{Si} \frac{\partial C}{\partial x} \right) \quad [10]$$

where D_{Si} is given by the expression (18)

$$D_{Si} = \frac{D_1 C}{n_i}$$

It can be seen that C_s is higher for the profile shown in Fig. 10 than for the profile shown in Fig. 9 (an addi-

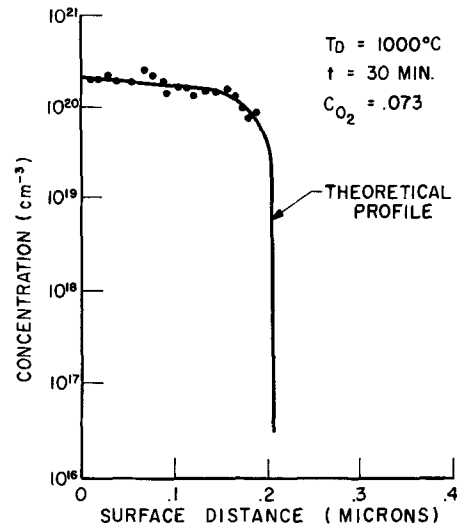


Fig. 9. Singly diffused As profile in Si. The diffusion source oxide was the As-SiO₂ system (1000°C for 30 min).

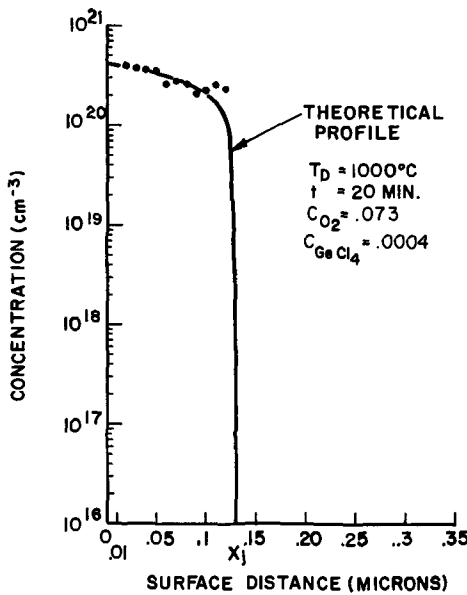


Fig. 10. Singly diffused As profile in Si. The diffusion source oxide was the As-Ge/SiO₂ system (1000°C for 20 min).

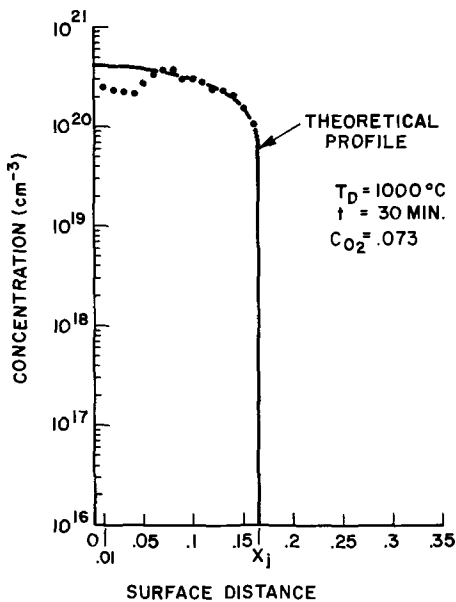


Fig. 11. Singly diffused As profile in Si. The diffusion source oxide was the H₂ annealed (900°C for 20 min), As-Ge/SiO₂ system (1000°C for 30 min).

tional 10-min diffusion would bring C_s shown in Fig. 10 down by only 15%). Thus, the effect of Ge doping in the oxide has been to increase C_s, in agreement with previous results (7). The H₂ prediffusion anneal has been shown to lower the sheet resistance of the subsequently diffused As layer. However, it can be seen in Fig. 11 that the expected increase in C_s does not occur. The experimental profile deviates from the theoretical profile in the first 600Å of the Si. The reason for this is not clear at this time, nor is it certain that this effect is real. If there exists a large concentration of nonelectrically active As (clusters, complexes, etc.) in the surface region, the electron mobility could be significantly lowered. The lower mobility would yield lower inferred values of As doping from Irvin's curve.

The transistor profile that resulted when As was diffused into Si with an initially predeposited B layer (no oxidation) is shown in Fig. 12. A comparison is indicated between the total As doping profile (obtained by neutron activation analysis) and the profile obtained by conductivity measurements and Irvin's curves. The total doping in the surface is consistently

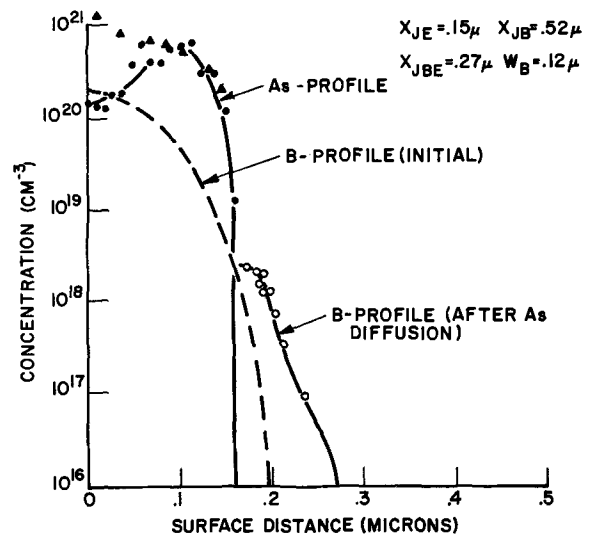


Fig. 12. Sequentially diffused B-As transistor profile. Boron diffusion: 870°C, 30 min; BN predeposited. Arsenic diffusion: 1000°C, 30 min from As-SiO₂ source deposited at C_{O₂} = 0.058. ▲ Activation analysis. ● Resistivity measurements.

three to five times greater than the measured electrical doping (for As diffusion into initially p-type Si). This may be due to vacancy undersaturation in the crystal as a result of the very high concentrations of As. Thus, in order for equilibrium conditions to exist, As atoms would jump into interstitial sites and then condense into clusters or vacancy-As complexes (19, 20). Near the emitter-base junction it can be seen that the inferred electrically active As exceeds the measured total As. This might be due to the enhanced carrier mobility as a result of ion pairing (21). The collector-base junction was retarded by 65% during the As diffusion. Similar results were obtained when the As was diffused from an As-doped Ge/SiO₂ source except that the electrical surface concentration was only 8 × 10¹⁹ cm⁻³.

Microwave transistors that have been fabricated with the doped oxide emitter diffusion have exhibited low leakage currents (I_{CEO} < 2 nA), low noise figure (3.5 db at 1.3 GHz) and high cutoff frequency (f_T = 7.5 GHz). Direct-current gains have been in the range of 50 to 100.

Summary and Conclusions

The properties of As-doped oxides that were deposited in a horizontal open-tube reactor have been investigated. Neutron activation measurements indicate that the total As density is greater in the As-SiO₂ oxides than in the As-Ge/SiO₂ oxides when the deposition conditions are similar. However, the total As doping was observed to increase as C_{O₂}^{1/2} for both types of oxides.

In the deposition chamber, GeO₂ is formed by the oxidation of GeH₄ (or GeCl₄). The Si substrate and the Si which is formed by the pyrolysis of SiH₄ appear to reduce most of the GeO₂ to Ge. The existence of unpaired Ge probably contributes to the enhanced etching of the doped oxides (5:1 differential etch rate over thermally grown SiO₂). Elemental Ge also acts to reduce As₂O₃ that is formed during the oxidation of AsH₃. The elemental As thus formed in the doped film probably diffuses more rapidly than As₂O₃. However, the presence of As₂O₃ is necessary for the efficient transport of As across the Si-oxide interface. These effects can account for, (i) the higher As surface concentrations in Si after diffusions in O₂ from Ge-doped oxides, and (ii) the lower As surface concentrations in Si after diffusions in an H₂ ambient.

For 1000°C, 30-min diffusions in Si from As-doped oxide sources, the sheet resistance, R_s, decreases approximately as (C_{O₂})⁻¹. In terms of the molecular

fraction of As in SiO_2 , $R_S \propto (C_{\text{As}}^{\text{SiO}_2})^{-2}$. As a function of time, R_S decreases as $t^{-1/2}$ for $t > 40$ min at 1000°C . For shorter times the diffusion of As is complicated by the changing surface concentration of the electrically active fraction of As.

A decrease in the concentration of electrically active As in the surface is observed for diffusions performed in O_2 with a preanneal in H_2 . An increase in the concentration of electrically active As is observed when As diffuses into highly doped p-type Si. These variations can probably be explained by the influences of complexes and ion pairing or carrier mobility. Such effects were not included in the establishment of Irvin's curve.

Manuscript submitted Nov. 1, 1971; revised manuscript received April 21, 1972. This was Paper 43 presented at the Houston Meeting of the Society, May 7-11, 1972.

Any discussion of this paper will appear in a Discussion Section to be published in the June 1973 JOURNAL.

REFERENCES

1. D. B. Lee, *Solid State Electron.*, **10**, 623 (1967).
2. A. Cuccia, G. Shrank, and G. Queirolo, Paper 305 presented at the New York Meeting of the Society, May 4-9, 1969.
3. T. B. Swanson and R. Hull, Paper 87 presented at the Detroit Meeting of the Society, Oct. 5-9, 1969.
4. H. Teshima, Y. Tarui, and O. Takeda, *Bull. Electrochem. Lab. Japan*, **33**, 631 (1969).
5. J. Wong and M. Ghezzi, *This Journal*, **168**, 1540 (1971).
6. P. C. Parekh, D. R. Goldstein, and T. C. Chan, *Solid State Electron.*, **14**, 281 (1971).
7. T. Abe, K. Sato, M. Konaka, and A. Niyazaki, *Proc. 1st Conf. Solid State Devices*, Tokyo, 1969, Suppl. to *J. of Japan Soc. Appl. Phys.*, **39**, 88 (1970).
8. M. L. Barry and P. Olofsen, *This Journal*, **116**, 854 (1969).
9. D. M. Brown and P. R. Kennicott, *ibid.*, **118**, 293 (1971).
10. E. Arai and Y. Terunuma, *Jap. J. Appl. Phys.*, **9**, 691 (1970).
11. R. V. Adams, *Phys. Chem. Glasses*, **2**, 101 (1961).
12. G. R. Weber, To be published.
13. J. F. Elliot and M. Gleiser, "Thermochemistry for Steelmaking," Addison-Wesley Publishing Co., Reading, Mass. (1960).
14. F. D. Richardson and J. H. E. Jeffes, *J. Iron Steel Inst.*, **160**, 261 (1948).
15. J. C. Irvin, *Bell System Tech. J.*, **41**, 387 (1962).
16. R. B. Fair, *J. Appl. Phys.*, **43**, 1278 (1972).
17. R. O. Schwenker, E. S. Pan, and R. F. Lever, *ibid.*, **42**, 3195 (1971).
18. S. M. Hu and S. Schmidt, *ibid.*, **39**, 4272 (1968).
19. V. I. Fistul, "Heavily Doped Semiconductors," Plenum Press, New York (1969).
20. S. Dash and M. L. Joshi, *IBM J. Res. Develop.*, **14**, 453 (1970).
21. H. Reiss, C. S. Fuller, and F. J. Morin, *Bell System Tech. J.*, **35**, 535 (1956).

Liquid Phase Epitaxial Growth of Silicon in Selected Areas

H. J. Kim

Bayside Research Center, GTE Laboratories Incorporated, Bayside, New York 11360

ABSTRACT

A liquid phase epitaxial technique has been used for growing thin Si-contact pedestals selectively on planar diffused diodes. Best results were obtained using a solution of 80 w/o (weight per cent) Sn and 20 w/o Pb with additions of 0.46 w/o Si and 0.1 w/o Ga and cooling at a rate of $0.8^\circ\text{C}/\text{min}$ from 750° to 700°C . The amount of Si added was determined from a calculation based on the regular solution method. The various growth parameters used and their effect on morphology, doping level, nucleation, and growth, and the electrical characteristics of the contact pedestals are discussed.

The growth of various III-V compound-semiconductors by liquid-phase epitaxial techniques has been widely practiced (1-4). Recently, this technique was used also to grow low-defect-density silicon layers on {111} and {100} substrates (5). One of the advantages of the liquid phase epitaxial growth technique over the vapor phase epitaxial technique is that the growth can occur at a much lower temperature, making it possible to be below the polymorphic or plastic transformation temperature.

In this paper a liquid phase epitaxial technique is described for selectively growing highly doped epitaxial silicon pedestals for use as ohmic contacts on planar diffused diodes. The Si contact is believed superior to conventional metallic contacts, particularly for severe thermal environments where the temperature may fluctuate considerably creating openings in these whiskerless diodes. This selective growth technique could also be extended to produce elevated electrodes for a silicon photodiode array.

Key words: epitaxial, silicon, diode, ohmic contact, thermodynamics, phase diagram, gallium, tin, lead.

The basic mechanism of the LPE growth, and various parameters which affect the growth morphology, doping level, nucleation, and growth, are discussed. Also, thermodynamic calculations of Si-solubility limits for Sn-Pb alloys are given. Growth conditions found most suitable for the formation of silicon diode contact pedestals are described.

Experimental

A vertical solution-growth system similar to systems used for the growth of GaAs (6,7) was adopted for this study. A horizontal growth-system (1) was also tried with less successful results. The system was operated using an H_2 atmosphere to prevent oxidation of the melt. However, there was always a thin layer of slag on the surface of the melt which attached to the substrate during dipping, resulting in nonuniform nucleation. To avoid such a slag-contact during dipping, a special substrate holder was devised. The specimen holder, shown in Fig. 1, facilitated isolating slag in one compartment created by the holder and allowed

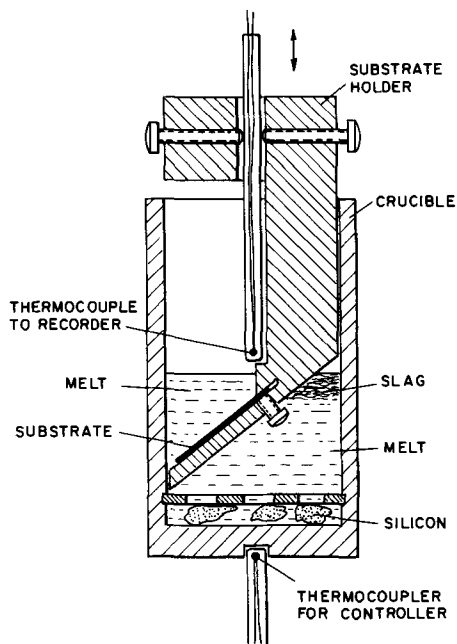


Fig. 1. Crucible and substrate holder

fresh melt to wet the substrate. The holder and the crucible were made of either quartz or graphite.

A silicon planar diode slice having $127\ \mu\text{m}$ (5 mil) diameter diffusion windows was chemically cleaned to remove thin oxide films in the diode windows. The cleaned surfaces were protected by immediately depositing a thin layer of Ni (or Au) nonelectrolytically. This wafer was then placed in the cold zone of the furnace, and after a hydrogen flow was established, the wafer was introduced into the melt. The Sn-Pb-Si melt composition used was determined from thermodynamic calculations based on the data from respective binaries as shown below. The amount of Ga added to the melt as a dopant was determined from several experimental runs. In general, the melt was maintained at an equilibration temperature about 200°C higher than the dipping temperature for several hours to homogenize the melt. The temperature was then reduced prior to insertion of the substrate.

After introducing the substrate into the melt, it was necessary to raise the melt temperature about 5°C above the initial dipping temperature to solution-etch the diode surface for improved wetting. A slow cooling rate of $0.8^\circ\text{C}/\text{min}$ was initiated to permit uniform growth of silicon inside the windows. After the growth of epitaxial Si layers, the substrate was gradually withdrawn from the melt to the cold zone of the furnace to minimize thermal stress in the wafer.

Calculation of Si Solubility in Sn-Pb Melts

The solubilities of Si in Sn-Pb alloy melts can be calculated with emphasis on Sn-rich alloys using a regular solution approach originally used for the In-Sb-Ge system by Lehovc and Slobodskoy (8). Although a quasi-chemical approach has been used for similar systems (In-Ga-As, In-As-Sb, Ge-Si-Sn, and Ge-Si-Pb) by others (9), the assumption of a regular solution for the present system can be justified. This is based on the fact that all three elements are in the same column in the Periodic Table, indicating the least chemical interaction.

The activity coefficient of Si in Si-Sn-Pb ternary melts can be written as

$$\gamma_1 = \exp \left\{ \frac{[(1 - X_1)^2/RT] \cdot [A_{12} + A_{13}r - A_{23}r/(1+r) - T(B_{12} + B_{13}r)]}{1+r} \right\}$$

where X is the mole fraction, r the ratio of the mole fraction of Sn to that of Pb, and A and B are the inter-

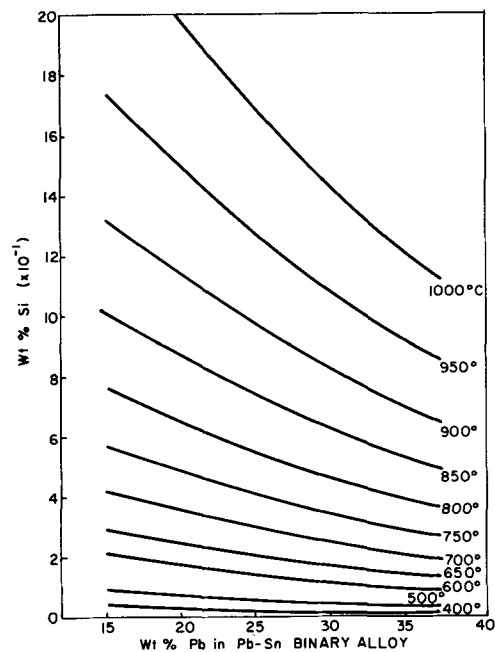


Fig. 2. Solubility of Si in Sn-Pb melts

action parameters. The numbers 1, 2, and 3 designate Si, Sn, and Pb, respectively. The plots of Si solubility in various Sn-Pb melts at various temperatures are shown in Fig. 2. The interaction parameters for Sn-Si and Pb-Si were obtained from Thurmond and Kowalchik (10). The interaction parameter A_{23} for Sn-Pb alloy was obtained by plotting T vs. X_{Sn} taken from the phase diagram since

$$A_{23} - B_{23}T = \frac{T \Delta S_{\text{Sn}}^f - \Delta H_{\text{Sn}}^f - RT \ln X_{\text{Sn}}}{(1 - X_{\text{Sn}})^2}$$

The following are values of the constants used:

$$\begin{aligned} A_{12} &= 8,145 \text{ cal/mol} & B_{12} &= 1.5 \text{ cal/mol} \\ A_{13} &= 19,830 \text{ cal/mol} & B_{13} &= 4.58 \text{ cal/mol} \\ \Delta S_{\text{Sn}}^f &= 3.3 \text{ cal/mol deg.} & \Delta H_{\text{Sn}}^f &= 1,665 \text{ cal/mol} \\ A_{23} &= 1,790 \text{ cal/mol} & B_{23} &= 0 \end{aligned}$$

Results and Discussion

Growth of undoped silicon pedestals.—The regular solution approach provided a guide to determine the amount of Si required to saturate an 80-20 Sn-Pb melt, and a relatively wide temperature range was studied for silicon LPE growth using these melts. The best results were obtained when the growth was initiated at a temperature of 750°C . According to the calculation, 0.46 w/o (weight per cent) Si is the solubility limit in an 80-20 Sn-Pb melt at 750°C .

Figure 3 shows the growth of Si pedestals having hexagonal morphology on (111) substrate. Figure 4 is a similar growth on (100) silicon substrate. The facet formation, terminating at the apex of the pedestal, is a most pronounced feature. The criteria used to judge the quality of undoped silicon pedestals were uniformity in height and size, restricted lateral growth, flatness of the top of the growth, and cleanliness of the slice surface after growth.

There was one major difficulty in choosing an optimum melt composition and growth temperature. As shown in the hypothetical ternary phase diagram (Fig. 5) which was deduced from the three binaries, there

exists an immiscible two-liquid zone. The extent of this zone has not been determined. If the two-liquid

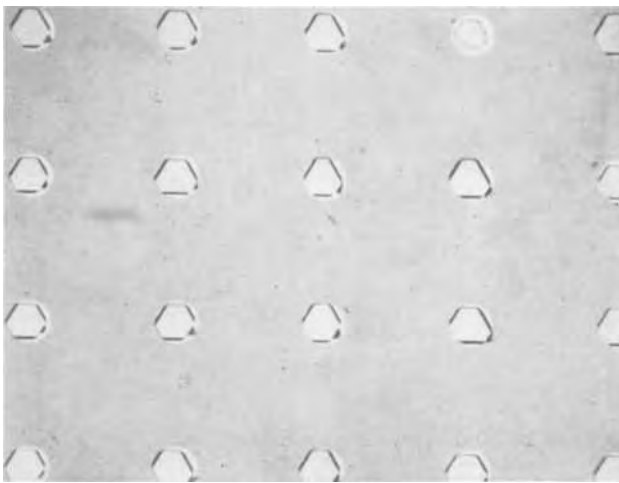


Fig. 3. Growth temperature 750°-700°C. Undoped silicon growth on (111) substrate.



Fig. 4. Growth of undoped silicon pedestals in oxide windows on (110) substrate.

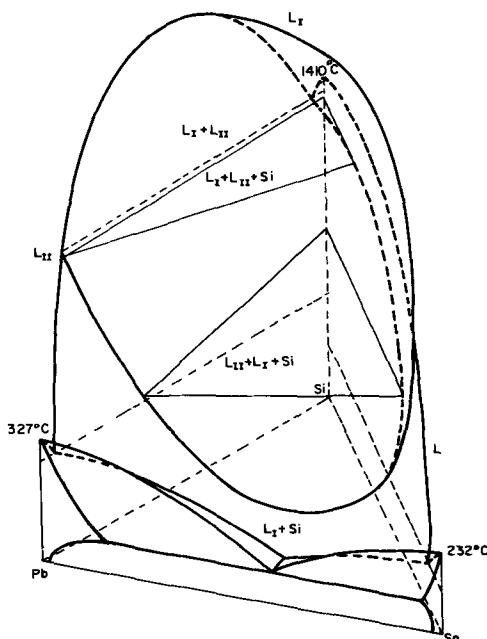


Fig. 5. Hypothetical ternary diagram of Sn-Pb-Si showing an immiscible two-liquid zone.

zone extends down to the growth temperatures used (750°-700°C), the epitaxial growth must occur by the monotectic reaction where only Liquid I is responsible

for the formation of solid silicon and the heavier Liquid II remains at the bottom of the crucible. In a few cases, it was observed that the lower part of the substrate did not have any growth but was solution-etched. It is not possible to determine whether such results indicate the passage through the two-liquid zone during cooling or the existence of nonequilibrium Liquid II which occurred at the higher homogenization temperature (900°C) employed before the growth.

The optimum cooling rate for the growth should be dictated by the speed with which silicon atoms diffuse to the growth interface since the total amount of silicon dissolved in the solution is small. Because the present LPE growth process occurs under a transient condition without ever reaching a steady-state condition, and the thickness of the growth is small, it is highly unlikely that constitutional supercooling will occur during growth. According to Tiller *et al.* (11), there must be an incubation distance for the occurrence of the constitutional supercooling and the distance is of the order of 1 mm for a typical experimental case. The observed flat growth interface further verifies the absence of such supercooling. Thus, the energetics associated with impurity and Si incorporation at the growth interface are more important aspects to be considered.

Doped Silicon Growth

Several solutions (Al, Ga, Pb, Sn, and Pb + Sn) containing silicon were used in attempts to grow highly doped p-type Si-contact pedestals on diodes. The main problem associated with incorporating a p-type doping impurity in the growth was the resulting change of nucleation and growth energetics. This change appears to be delicately balanced with respect to the dopant concentration, the cooling rate, and the growth temperature. For example, various Ga additions ranging from 0.001 to 1.0 w/o in Sn solutions were tried to grow p⁺ pedestals at 850°C. There was, for a given cooling rate, a critical dopant concentration, below which no appreciable growth was observed. Such a critical concentration was also affected by the type of protective metal film used (either Ni or Au). Apparently, the combined effect of Ni or Au and Ga atoms alters the surface energy state of the substrate.

The best results were obtained using the same growth temperature (750°-700°C) and the same Pb-Sn melt composition (20-80 w/o) as used in the undoped Si growth plus ~0.1 w/o Ga. A cooling rate of 0.8°C/min was also the optimum value for high yield and uniform growth as seen in Fig. 6a. This growth condition produced well-defined silicon contacts as shown in the cross-sectional view of the growth (Fig. 6b). Little change was produced in electrical characteristics of the junctions, as illustrated in Fig. 7.

Neither Ni nor Au protecting films affected the growth for Pb-Sn melts. However, both higher dopant concentration (0.2 w/o) and faster cooling rate (1.6°C/min) produced a poor yield and nonuniformity in growth. Although slower cooling rates or lower dopant concentrations yielded a good morphological result, the amount of dopant incorporated in the growth was not high enough for good forward characteristics of diodes. Lower doping concentrations confirm the theoretical prediction as shown in the following equations (12, 13).

$$C_s = k_0 C_0 (1 - g)^{k_0 - 1}$$

and

$$k_0 = \frac{k_0}{k_0 + (1 - k_0) \exp\left(\frac{-Rd}{D}\right)}$$

where C_s is the concentration of dopant in the epitaxial growth, C_0 the average concentration of dopant in the liquid, k_0 the ratio of concentrations of the dopant in the solid and the liquid in equilibrium with it, g the fraction of the liquid that has solidified in the system, and d the thickness of the boundary layer through

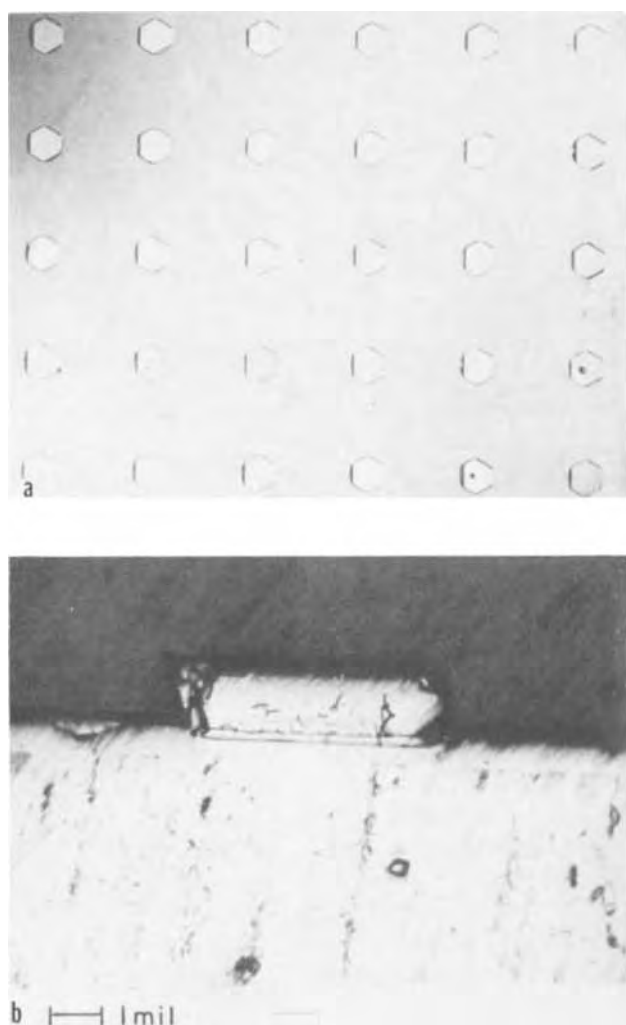


Fig. 6. Growth of Ga-doped Si contact pedestals on (111) substrate. (a) Top view; (b) cross-sectional view. Vertical lines may be dislocation loops.

which the solute must diffuse (10^{-1} - 10^{-3} cm). The effective distribution coefficient k_e , which is defined as the ratio of the concentrations of solute in the solid that is formed to the average value for the liquid, approaches the maximum value of one as the growth rate (R) increases and $k_e = k_0 < 1$ at very low growth rates. Also, in view of the above equation, no stirring or agitation was employed in the present experiment. This permits the incorporation of as much dopant as possible, since the mixing of the liquid decreases d and effectively increases the diffusion coefficient D of the dopant.

In addition to the effect of dopant concentration and cooling rate on nucleation of Si layers, impurity atoms and solvent atoms are known to greatly influence the growth morphology. In growing pure Si from a Si melt, (111) planes are the slowest growing and most stable faces. The epitaxial growth of Si on a (111) substrate can be treated as the growth of a twin having the substrate plane as a twin plane. According to Wagner (14), in the twin plate having a hexagonal morphology bounded by (111) planes, the re-entrant twin edge is a nucleation site for new layers on the edges of the plate, and growth occurs in a $\langle 112 \rangle$ direction. However, impurity or dopant atoms and solvent atoms can alter the surface energy of the substrate stabilizing other crystallographic planes, and this change in turn affects the size-to-thickness ratio of the growth pedestals. Faust et al. (15) examined platelets of Si grown from several metal solutions and ranked them in order of increasing size to thickness ratio as follows

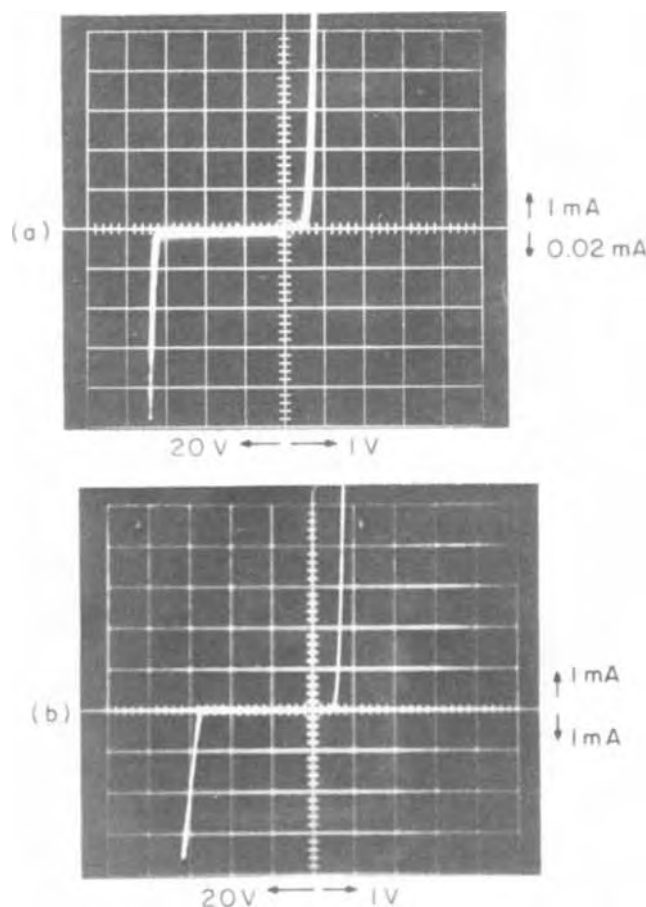


Fig. 7. Forward and reverse bias characteristics of silicon diodes. (a) Through Si-contact pedestal, (b) without the pedestal.

$\text{Au} \approx \text{Au} + \text{Sb} \approx \text{Au} + \text{Ga} < \text{Sn} \approx \text{Ga} < \text{Zn} < \text{Ag} < \text{Al}$

It was impossible to deduce from the above findings how the combination of Ni (or Au used for substrate protection), Sn, Pb, and Ga would affect the growth morphology. Only an empirical determination of the optimum concentration of the various elements plus the optimum cooling rate and growth temperature was possible in obtaining a desirable size-to-thickness ratio of the growth.

Summary

The liquid-phase epitaxial technique for growing thin Si-contact pedestals on $127 \mu\text{m}$ (5 mil) diameter diodes was demonstrated. This process was found to be very sensitive to melt composition, cooling rate, and growth temperature. The critical parameters which give an optimum growth with respect to yield, size, and substrate cleanliness were obtained. A solution of 80 w/o Sn and 20 w/o Pb with 0.46 w/o Si and 0.1 w/o Ga additions produced the most favorable growth. The optimum cooling rate and growth temperature range were $0.8^\circ\text{C}/\text{min}$ and 750°C - 700°C , respectively. The solubility limits of Si in Sn-Pb solutions were calculated assuming regular solutions and used as a guide to prepare a saturated solution at a given growth temperature. The Au or Ni film used as a protective coating prior to growth did not affect the growth of Si from Sn-Pb melts. For the maximum incorporation of Ga into the pedestal, it was necessary to keep the solution from being agitated during growth.

Acknowledgment

The author wishes to acknowledge the technical assistance of Mrs. Eugenia Kelley. The author also would like to thank Dr. P. Wang for initiating and supervising this program, Dr. R. Yee for participating in the early stage of the work, and F. J. Reid for critically reviewing this paper.

Manuscript submitted Oct. 15, 1971; revised manuscript received June 2, 1972. This was Paper 179 presented at the Atlantic City Meeting of the Society, Oct. 4-8, 1970.

Any discussion of this paper will appear in a Discussion Section to be published in the June 1973 JOURNAL.

REFERENCES

1. H. Nelson, *RCA Rev.*, **24**, 603 (1963).
2. M. R. Lorenz and M. Pilkuhn, *J. Appl. Phys.*, **37**, 4094 (1966).
3. H. Rupprecht, J. M. Woodall, and G. D. Pettit, *Appl. Phys. Letters*, **11**, 81 (1967).
4. J. M. Woodall, H. Rupprecht, and W. Reuter, *This Journal*, **116**, 899 (1969).
5. L. A. D'Asaro, R. W. Landorf, and R. A. Furnanage, "Semiconductor Silicon," p. 233, The Electrochemical Society, New York (1969).
6. H. Rupprecht, "Proceedings of International Symposium on GaAs," p. 57, Institute of Physics and the Physical Society, London (1966).
7. E. W. Williams and D. M. Blacknall, *Trans. AIME*, **239**, 387 (1967).
8. K. Lehovc and A. Slobodskoy, *This Journal*, **111**, 65 (1964).
9. G. B. Stringfellow and P. E. Greene, *J. Phys. Chem. Solids*, **30**, 1779 (1969), and talk given at the Electrochemical Soc. Meeting, Detroit, 1969.
10. C. D. Thurmond and M. Kowalchik, *Bell System Tech. J.*, 169 (1960).
11. W. A. Tiller, K. A. Jackson, J. W. Rutter, and B. Chalmers, *Acta Met.*, **1**, 428 (1953).
12. W. G. Pfann, "Zone Melting," John Wiley & Sons, Inc., New York (1958).
13. J. A. Burton, R. C. Primm, and W. P. Slichter, *J. Chem. Phys.*, **21**, 1987 (1953).
14. R. S. Wagner, *Acta Met.*, **8**, 57 (1960).
15. J. W. Faust, H. F. John, and C. Pritchard, *J. Crystal Growth*, **3**, 321 (1968).

Chlorine Adsorption at a Titanium Surface

Segregation from the Bulk Crystal

Interaction with Chlorine Gas

Tennyson Smith

Science Center, North American Rockwell, Thousand Oaks, California 91360

ABSTRACT

Experiments have been conducted with a single crystal of Ti [exposing the (0001) face] in an ultrahigh vacuum system ($\sim 10^{-10}$ Torr) using Auger spectroscopy, ellipsometry, and surface potential difference measurements to monitor adsorbed chlorine on the surface. It was discovered that although the impurity level of chlorine and sulfur in the bulk crystal are < 1 ppm, these elements segregate from the bulk to the crystal surface at elevated temperatures with a segregation coefficient $\sim 10^5$ to 10^6 . Above 600°C sulfur displaces the chlorine from the surface. Segregation coefficients and diffusion coefficients are measured for chlorine as a function of temperature. Adsorption of chlorine gas on a clean Ti surface occurs as a nonactivated process with a sticking coefficient ~ 0.05 . The adsorption isotherms are consistent with dissociation of molecular chlorine to atomic chlorine. The change in work function of the Ti surface with a monolayer of Cl with respect to a clean surface is $+1.2\text{V}$. The index of refraction of the film is about 2.4 and the thickness of a monolayer is approximately 4.5\AA . Ellipsometer data show that more than a monolayer of chlorine will form at room temperature and a chlorine pressure of $\sim 10^{-7}$ Torr. It is concluded that at room temperature the diffusion coefficient and segregation coefficient are much too low to allow chlorine to segregate to the surface at a crack tip during stress corrosion cracking unless the stress and increased local temperature are sufficient to lower the diffusion activation energy.

The stress corrosion cracking (SCC) of Ti alloys in aqueous solutions has been related to the chloride ion concentration in solution (1-3). However, as the chloride ion concentration is decreased the rate of crack propagation asymptotically approaches a limiting value.

The question arises as to the possibility that chlorine impurity within the Ti metal may segregate from the bulk to the crack tip surface, thus providing the chlorine atoms. It has been shown (4, 5) and is shown in this paper that indeed chlorine atoms of very small concentration in the Ti bulk (~ 0.2 ppm) segregate to the Ti surface with a very large segregation coefficient (~ 1 Cl atom per 3 Ti atoms) if the temperature is high enough. However, it is concluded that the rate of segregation is much too slow and the segregation coefficient too small to account for an appreciable Cl segregation at a crack surface at room temperature. The possibility that the stress in the crack tip region lowers

the activation energy for diffusion sufficiently to allow rapid diffusion to the crack tip region at room temperature needs further investigation.

Experimental

The ultrahigh vacuum system was a Varian low energy electron diffraction unit (Model 981) with special windows in side flanges for ellipsometry.

Ellipsometry.—A good description of ellipsometry can be found in Ref. (6). In brief, when plane polarized light is reflected from a surface the light becomes elliptically polarized. That is, the surface renders a phase shift (Δ) in the normal and parallel components of the polarized light as well as a change in the ratio of the amplitudes ($\tan \psi$) of these components. The experimental parameters measured with the ellipsometer are the polarizer angle p and the analyzer angle a , which are directly related to Δ and ψ ; $\Delta = 2p + \pi/2$ and $\psi = a$ (in zone 1). There are four quadrants (zones) related to the polarizer, analyzer, and compensator angles. It has been shown (6) that averaging

* Electrochemical Society Active Member.

Key words: ellipsometry, Auger spectroscopy, surface potential measurements.

the readings in all four zones minimizes the alignment errors. Unless otherwise stated, the ellipsometric results were obtained by averaging the data in the four zones. A compensator (quarter wave plate) is used to compensate for the ellipticity such that the reflected beam is plane polarized and thus can be nulled with the analyzer.

If the surface is clean, Δ and ψ are directly related to its complex index of refraction $\hat{n}_s (\equiv n_s(1 - i\kappa_s))$. The subscripts of the real part n_s and imaginary part κ_s , refer to the substrate the subscript f will refer to the film. κ_s is sometimes referred to as the attenuation index or extinction coefficient. If the surface has a film of different index ($\hat{n}_f \neq \hat{n}_s$), Δ and ψ (and therefore p and a) are directly related to \hat{n}_s , \hat{n}_f , and the film thickness.

Components of a Rudolph ellipsometer (sensitivity 0.01°) were mounted such that the beam from a mercury arc passed through a filter (removed 99% of the light except in the range 5100–5650Å) to isolate the 5461Å spectral line. The polarizer and compensator were placed before the reflecting surface, with the analyzer and detector after the reflecting surface.

Angle of incidence.—To obtain a very accurate value for the angle of incidence, a quartz prism was mounted directly above the sample. The prism was designed (7) such that, when the beam which was reflected from its base surface and the beam which was reflected from the internal prism surfaces were in coincidence, the base surface was aligned with an angle of incidence 79.81° . The sample could then be aligned to within 0.01° of this angle.

Windows.—It is imperative to minimize the birefringence of windows in order to obtain accurate values for the optical constants by ellipsometry. Fused silica windows, selected for very low birefringence were obtained¹ and sealed on to quartz to Pyrex to stainless steel ($\frac{1}{8}$ in. OD) tubes. These window assemblies were then welded to Conflat flanges to match the UHV system. To test the windows, two of the steel tubes were connected to a rubber hose with a tee connection for attaching to a vacuum pump. The windows were then placed in the ellipsometer in the straight through configuration. The windows were rotated with and without vacuum while observing the photometer indicator in its most sensitive mode. Movement of the photometer needle of less than the smallest division, when the windows were placed in the beam, indicated the birefringence of the windows was negligible ($\sim 0.01^\circ$) with or without vacuum. After welding the steel tubes to the flanges, ellipsometric readings were made on the polished Ti sample in the UHV system. Changes of the p and a values were $\sim 0.01^\circ$. It was concluded that window effects are negligible.

Auger electron spectroscopy.—The Auger electron spectrometer was constructed as a four grid system according to Palmberg and Rhodin (8). The grid system was made of 1 mil 100×100 , Type 304 stainless steel wire mesh ($\sim 81\%$ transparent) that was formed with the technique described by Todd (9). The electron gun was a Model SE-3K 15μ obtained from Superior Electronics,² modified with a 1×5 mil W ribbon filament and operated at 3 kV. The electron beam had an angle of incidence of 80° with respect to the sample. The Auger measurement yields the derivative of the energy distribution function ($dN(E)/dE$) vs. the voltage applied to the retarding grid (E).

Work function measurements.—The surface potential difference (SPD) between the sample and a W reference electrode was measured by the Kelvin vibrating capacitor technique and was automatically recorded by the servo-mechanism of Palevsky (10). The W refer-

ence electrode was mounted on a flange with a bellows such that it could be vibrated from outside the vacuum system and positioned adjacent to the sample as desired. The reference electrode could be cleaned by resistive heating.

Sample manipulation.—The sample was mounted on a Varian multipurpose feed-through (954-5031) and could be rotated into position for simultaneous SPD and ellipsometer measurements or rotated 180° from this position for Auger measurements. The sample holder was made of Mo. Immediately behind the sample was a W filament heating element. Two thermocouples touched the sample surface at different points. The temperature could be maintained constant to $\pm 3^\circ\text{C}$ by a temperature controller connected to a third thermocouple.

Ion guns.—A Cs ion gun was constructed by melting a few milligrams of Cs impregnated zeolite on a platinum ribbon. The ribbon was connected to W leads that were electrically insulated from the stainless steel cylinder surrounding the ribbon. The ribbon could be heated to drive off Cs^+ which was accelerated to the crystal by giving the ribbon a positive potential with respect to ground. A grid a few millimeters in front of the ribbon could be given a negative potential with respect to the ribbon in case the ion current became limited by saturation of the ion vapor at the ribbon surface. The ion current was monitored by placing a high impedance electrometer between the sample and ground. The ion current, I , only indicates the flux of Cs^+ that is adsorbed and neutralized by an electron in the crystal or receives an electron from the crystal and desorbs as an atom. If ions are reflected from the crystal surface as ions and become neutralized at the walls of the UHV system they are not monitored by the electrometer. The advantages of the Cs ion gun are: (i) it can be operated in the system with ultrahigh vacuum; (ii) it can be used to sputter clean and etch at high voltage or for Cs adsorption at low voltage; and (iii) currents up to $50 \mu\text{A}$ can be obtained, depending on the crystal substrate. For example, good conducting surfaces (metals) give high currents, poor conducting surfaces such as $\text{Si}_3\text{N}_4/\text{Si}$ charge up and currents of the order of $1 \mu\text{A}$ or less are obtained. With titanium specimens the Cs^+ gun is undesirable because both Cs and Ti have an Auger peak at about 47 eV, which is the most indicative of the Ti surface cleanliness. However, if no peaks were observed at 560 and 580 eV for Cs, the 47 eV peak was interpreted to be due to Ti.

The Ar ion gun was a Varian Model 922-0013. Argon bombardment is advantageous with titanium specimens since the Auger peaks do not coincide. However, Ar must be let into the system and only low currents can be obtained in the pressure range necessary to keep the Vac Ion pumps working ($< 10^{-5}$ Torr).

Samples.—The Ti sample was $1 \times 11/32 \times 1/16$ in. single crystal cut to expose the (0001) basal plane. The surface was polished to a mirror finish with 600 silicon carbide paper and etched to remove surface damage. The final chemical polish consisted of 1μ alumina in a solution, 1 part ammonium hydroxide, 1 part distilled water, and 1 part 30% hydrogen peroxide. The hydrogen peroxide was added last and was fresh. A Microlon "D" pad was mounted on the chemical lap and the sample was held down with heavy pressure for approximately 5 min. The surface was specular but not optically flat. The sample and manipulator were ultrasonically cleaned in acetone before placing in the UHV system.

Chlorine pressure.—A Varian dual range ionization gauge (Model No. 971-0014) was used to measure the gas pressure. A table of ionization probability values was supplied with the ionization gauge, for various gases. These values are used to calculate the correct pressure from the meter reading with the meter calibrated for N_2 . No ionization probability for Cl_2 was

¹ Dynasil Corporation, Berlin, New Jersey.

² 208 Peagent Ave., Clifton, New Jersey 07015.

available. A fairly smooth correlation exists between the ionization probabilities (compared to N_2) and the mass spectroscopic sensitivities compared to N_2 , for various gases (see Table I). From the mass spectroscopic sensitivity of 2 for Cl_2 (as compared to N_2) the ionization probability was estimated to be 2. The meter readings were therefore multiplied by 2 to obtain the Cl_2 pressure.

Results

Chlorine and Sulfur Segregation

Auger spectrograms.—For comparison with the Auger spectrograms reported here, Table II gives the electron energy values for which Auger peaks have been observed for various elements. Figure 1 shows the Auger spectrogram for the Ti sample immediately after placing it in the UHV system. The major peak at 272V indicates heavy carbon contamination which remained after cleaning the sample in acetone. Aside from the Ti peaks and the C peak, small peaks are observed for O, S, and Cl. Figure 2 is the Auger spectrogram for the Ti sample after heating to 600°C for about 2 min. The instrument sensitivity was 2.5 times greater for Fig. 2 than for Fig. 1, therefore, for comparison with Fig. 2, the peak heights in Fig. 1 should be multiplied by 2.5. Heating the sample has removed much of the carbon contamination but has caused Cl and S to segregate from inside the Ti crystal to the surface. The possibility that Cl and S are degassed from the adjacent sample holder and heater does not seem likely because these contaminants did not appear on heating freshly deposited Al films on Al samples in the same holder. Study (11) of the interaction of chlorine gas with Al films showed that stable chloride films are formed at room temperature and Cl_2 pressure $\sim 10^{-7}$ Torr. No Cl or S was detected on the Ti sample after heating the adjacent W reference electrode to 1200°C.

The Auger peak to peak heights, defined as the distance between the top and bottom of a peak (see the arrows in Fig. 2), will be designated APPH. The units of $dN(E)/dE$ and APPH are arbitrary, so that, only the relative magnitudes have significance.

Figure 3 shows, as a function of the time of heating, the Auger peak to peak heights for Cl and S, and the 47 eV peak (interpreted as Ti, since no peaks at 560 and

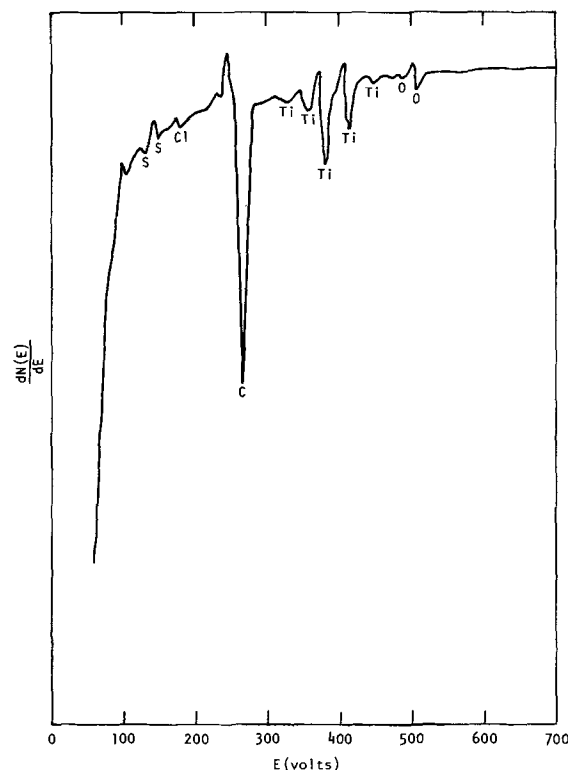


Fig. 1. Auger spectrogram for the Ti single crystal before heating or cleaning by ion bombardment.

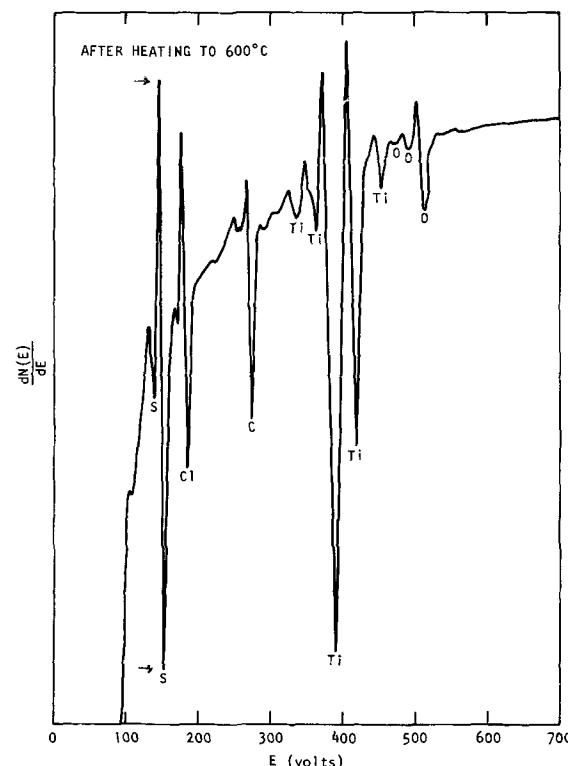


Fig. 2. Auger spectrogram for the Ti crystal after heating to 600°C.

Table I. Comparison of ionization probabilities with mass spectroscopic sensitivity (both with respect to N_2)

Gas	Mass spec. sensitivity	Ionization probability
N_2	1	1
Ar	0.69	0.85
CO_2	0.83	0.95
O_2	1.21	1.22
H_2	2.46	2.00
Ne	3.76	4.22
He	4.9	6.22
Cl_2	2.0	(2.0)*

* Estimate.

Table II. Energies at which Auger peaks are observed*

The most intense peak values are in italics

Element	Electron energies
W	24, 40, 50, 82, 108, 135, 160, 172, 198, 210, 265, 340
Ti	28, 47, 327, 350, 360, 372, 380, 417, 452
Si	61, 75, 88, 1510, 1550, 1600
Mo	20, 28, 40, 80, 87, 120, 140, 150, 162, 190, 212
C	272
O	477, 495, 515
N	382
Cs	46, 60, 400, 415, 470, 480, 560, 580
Cl	180
S	140, 150
Ar	213, 218

* Varian Chart of Auger Electron Energies, Varian Vacuum Division.

580 were observed for Cs). At 500°C for the first 90 min the Cl APPH increased rapidly then leveled off at about 130. Since the 47 eV electrons for Ti relate primarily to the outermost layer of Ti, the Ti (47) APPH is complimentary to the Cl APPH and decreases from 195 to 28. At 90 min the surface was bombarded with Cs^+ at 500V, 5 μA , 500°C for 5 min. The Cs^+ sputtering removed Cl (lowered Cl APPH from 130 to 25) and increased the Ti (47) APPH. Further heating of the sam-

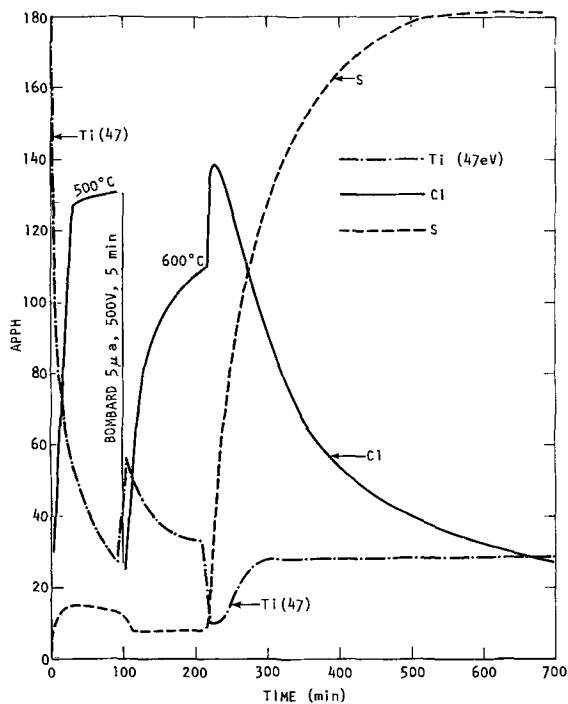


Fig. 3. Auger peak to peak heights (APPH) for Ti (47 eV), Ti (380 eV), Cl, S, C, and O as a function of time and temperature.

ple at 500°C caused the Cl to segregate again but at a slower rate. The S APPH increased from about 2 to 15 during the first 90 min and decreased to 8 by the Cs⁺ bombardment. Although the C APPH only changed slightly (APPH ~ 22), the O APPH decreased from ~15 to zero in 20 min, then increased to 2 during the first 200 min. At 210 min the temperature was increased to 600°C. The C and O peaks were not observed on the spectrogram after about 10 min at 600°C. The S APPH increased rapidly and leveled off at about 180 at 700 min. The Cl APPH increased sharply during the first 10-15 min at 600°C, then decreased as the Cl was displaced by S. The high energy 380 eV Ti peak (APPH ~ 35) was only slightly affected during the entire treatment, indicating that the heat-treatment has little effect on Ti two or three atom layers beneath the surface.

Cs⁺ bombardment.—In Fig. 4 a plot is given of the ratio of the APPH of Ti (47 eV peak) Cl and S to that

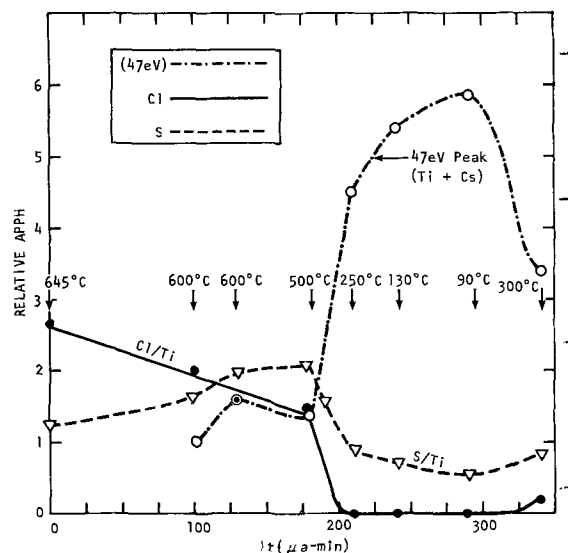


Fig. 4. APPH for Cl, S, and the 47 eV peak (Ti or Cs) as a function of Cs⁺ bombardment at 500V. The temperature was changed, during the bombardment, to those indicated across the plot.

of Ti (380 eV) as a function of ion bombardment exposure at various temperatures. Since the APPH for Ti (380 eV) is only slightly affected by adsorption at the surface for low coverage, the ratio of the APPH values to that for Ti (380 eV) at low coverage is used in order to avoid the necessity of calibrating the Auger spectrometer for each measurement. In the temperature range from 645° to 500°C, and integrated ion current ($I t = 0$ to 180 $\mu A \cdot min$), the Cl peak decreased and the S and Ti (47 eV) peaks increased. Lowering the temperature to 250°C caused the Cl peak to rapidly approach zero and the S peak to decrease. The peak at 47 eV is drastically increased (due to the Cs and Ti 47 eV peaks) on removal of Cl and S from the surface. Increasing the temperature from 90° to 300°C caused a reappearance of the Cl peak and corresponding decrease in the Ti (47 eV) peak. The Ti surface can be cleaned of Cl and S if the temperature is low enough that the rate of segregation is slower than the sputter cleaning process. However, one cannot be sure that the surface is not contaminated with Cs. Other experiments have shown that bombardment with Ar ions also cleans the surface of Cl and S but leaves Ar if the temperature is too low. The cleanest Ti surface (very small Ar, Cl, and S peaks) was obtained by bombarding with Ar ions at about 550°C.

Figure 5 shows Auger results for the APPH of chlorine relative to the Ti 380 eV peak (designated Cl/Ti), as a function of time, temperature, and Cs⁺ bombardment. From Fig. 5 an estimate of the diffusion coefficient and concentration of chlorine on the surface and in the bulk can be made.

Diffusion coefficient.—The diffusion equations are developed in the Appendix for the following model. It is assumed that the process controlling the rate of Cl segregation at the Ti surface (as in Fig. 5) is diffusion of Cl in the bulk crystal to the interface. Thus, each time the crystal is annealed the surface concentration ($C_s(t)$) approaches equilibrium with respect to the bulk concentration ($C(l,t)$) and each time the surface is cleaned a concentration gradient forms within the crystal, causing the Cl to diffuse to the surface. It is assumed that the process of atom transfer from within the crystal (adjacent to the surface) is rapid with respect to diffusion to the interface so that equilibrium is maintained between the bulk and the surface at the interface. This boundary condition is expressed

$$C_s(t) = K C(l,t) \quad [1]$$

where K is the equilibrium constant. K has the same dimensions as the crystal thickness l (i.e., centimeters) since $C(l,t)$ has the dimension atoms/cubic centimeter and $C_s(t)$ has the dimension atoms/square centimeter.

Plots of $C_s(\infty) - C_s(t)$ vs. t are given on semilog paper in Fig. 6, which corresponds to the data between $t = 0$ and $t = 100$ min (524°C), and $t = 107$ to 120 min (670°C) in Fig. 5. From analysis of the theoretical equation

$$\frac{\partial C(x,t)}{\partial t} = D \frac{\partial^2 C(x,t)}{\partial x^2} \quad [2]$$

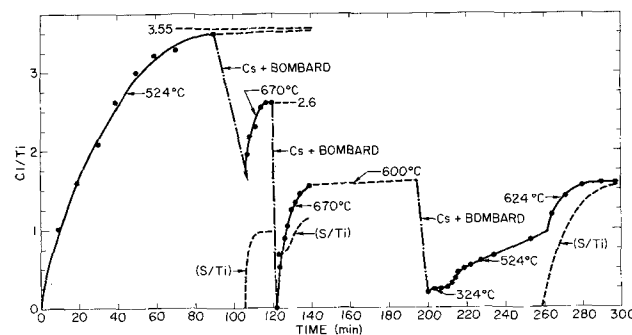


Fig. 5. Plot of chlorine segregation vs. time at various temperatures. The dashed line marked S/Ti represents sulfur segregation.

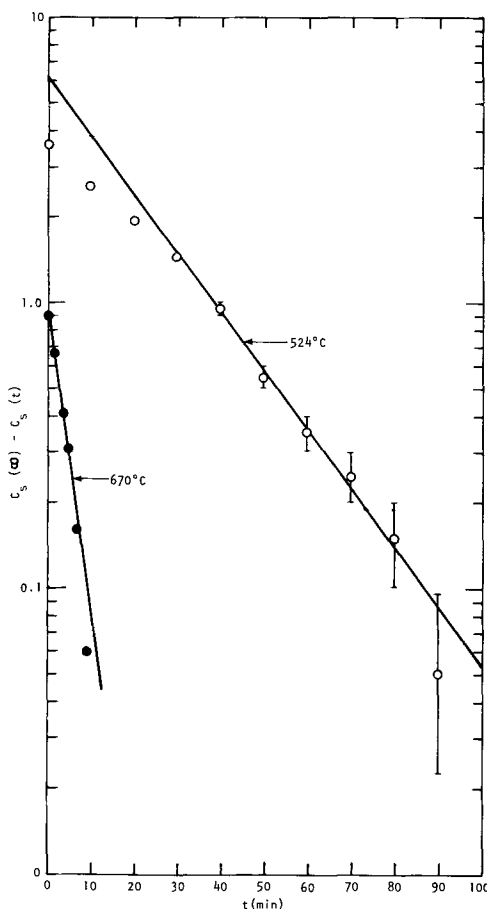


Fig. 6. Plot of $C_s(\infty) - C_s(t)$ vs. time

(see the Appendix), the plots in Fig. 6 should be linear at large t , as observed. As $C_s(t) \rightarrow C_s(\infty)$ at 100 and 120 min, the relative experimental error becomes very large. Extrapolation of the upper line of Fig. 6 (524°C data) to $t = 0$ gives an intercept of 6.2. As shown in the Appendix, this intercept is equal to

$$2l^2KC_0/[l(l+K) + K^2\kappa_1^2] \approx 6.2 \quad [3]$$

where $C_0 = C(x,0)$ is the homogeneous concentration after an anneal and κ_1 is the first root of the transcendental equation. At $t \rightarrow \infty$

$$lKC_0/(l+K) \sim 3.55 \quad [4]$$

where 3.55 is estimated to be the equilibrium value in Fig. 5. One of the roots of the transcendental equation (Appendix, Eq. [A-12]) is

$$\kappa_1 K/l = -\tan \kappa_1 \quad [5]$$

Solving Eq. [3], [4], and [5] yields

$$\kappa_1 = 2.87 \quad [6]$$

$$K/l = -0.097 \quad [7]$$

$$K = 0.0154 \quad [8]$$

since the thickness of the crystal was $l = 0.159$ cm. The slope of the line (524°C) in Fig. 6 (see Eq. [A-15], [A-16], and [A-17], Appendix) yields

$$\tau_1 = l^2/\kappa_1^2 D \approx 1250 \text{ sec} \quad [9]$$

where τ_1 is a time constant and D is the diffusion coefficient. The diffusion coefficient for Cl in Ti at 524°C proves to be

$$D \approx 2.4 \times 10^{-6} \text{ cm}^2/\text{sec} \quad [10]$$

Similar calculations for the 670°C line yields

$$\kappa_1 = 2.0 \quad [11]$$

$$K/l = 1.1 \quad [12]$$

$$K = 0.175 \quad [13]$$

$$D = 2.6 \times 10^{-5} \text{ cm}^2/\text{sec} \quad [14]$$

From values of D at the two temperatures the following equation for the diffusion of chlorine in Ti is obtained

$$D \approx 9 \exp(-24,100/RT) \text{ cm}^2/\text{sec} \quad [15]$$

and

$$K \approx 10^5 \exp(-25,000/RT) \text{ cm} \quad [16]$$

Chlorine concentrations.—As will be shown, adsorption of a monolayer of chlorine from the gas phase yields a value of $(\text{Cl}/\text{Ti}) \approx 9.1$. Based on the ionic and atomic diameters (i.e., Cl^- 3.6Å, Ti 2.6Å), Anderson and Gani (12) show that for a regular array of Cl^- on a Ti (0001) face, $C_s \sim 4.5 \times 10^{14}$ ions/cm² and for a random array $C_s \sim 3 \times 10^{14}$ ions/cm². The average, $C_{s,\text{avg}} \approx 3.7 \times 10^{14}$ ions/cm², is in close agreement with the measured (10) value ($C_s \approx 3.6 \times 10^{14}$ ions/cm²). Therefore the surface concentration can be calculated from the Auger values of (Cl/Ti) as

$$C_s(t) \approx [(\text{Cl}/\text{Ti})/9.1] \times 3.6 \times 10^{14} \text{ atoms/cm}^2 \quad [17]$$

The value of the bulk concentration, $C_{o,0}$, at $t = 0$ in Fig. 5, can be obtained from the kinetic data (Eq. [4] and [8]); if the value $C_s(\infty) \approx 3.55$ is multiplied by $3.6 \times 10^{14}/9.1$ (Eq. [17]) to obtain units of atoms/square centimeter, i.e.

$$C_{o,0} \approx 10 \times 10^{15} \text{ atoms/cm}^3 \quad [18]$$

A similar calculation for $C_{o,100}$ from $C_s(\infty) \approx 2.6$ at 120 min yields

$$C_{o,100} \approx 1.2 \times 10^{15} \text{ atoms/cm}^3 \quad [19]$$

A check on the values from the kinetic data can be made with the equilibrium data as follows: since at equilibrium the concentration in the bulk will be directly proportional to that on the surface, $C_{o,100}/C_{o,120} \approx 3.55/2.6 = 1.36$. Also a mass balance gives $(C_{o,100} - C_{o,120}) = 0.9 \times 3.6 \times 10^{14}/9.1 = 3.6 \times 10^{13}$ atoms/cm², where 3.6×10^{13} corresponds to the amount of Cl transferred from the bulk to the surface between $t = 107$ and 120 min (Fig. 5). Solving for $C_{o,100}$ and $C_{o,120}$ yields

$$C_{o,100} \approx 0.8 \times 10^{15} \text{ atoms/cm}^3 \quad [20]$$

$$C_{o,120} \approx 0.6 \times 10^{15} \text{ atoms/cm}^3 \quad [21]$$

The correlation between the kinetic result in Eq. [19] and the equilibrium result in Eq. [20] for $C_{o,100}$ is considered to be good, lending support to the proposed segregation model.

Prior to the experiment represented in Fig. 5, about 5×10^{14} atoms/cm² had been removed by ion bombardment. Therefore the initial impurity concentration in the Ti crystal was $\sim 1.3 \times 10^{16}$ atoms/cm³, or 0.2 ppm, since there are $\sim 5.68 \times 10^{22}$ atoms Ti/cm³. If the concentration on the surface is expressed in volume units rather than surface units, using 4.5Å as the thickness of a chlorine monolayer, a segregation coefficient can be defined as (see Eq. [2])

$$K_s = K/4.5 \times 10^{-8} = 2.2 \times 10^7 K \quad [22]$$

From Eq. [8] and [22], at 524°C

$$K_s \approx 3.4 \times 10^5 \quad [23]$$

and at room temperature (using Eq. [16])

$$K_s \approx 1.3 \times 10^{-6} \quad [24]$$

Chlorine Adsorption From the Gas Phase

Ellipsometric and SPD results.—Ellipsometric values for p and a were measured before and after exposure to chlorine gas. From these values of p and a the refractive index of Cl adsorbed on Ti was calculated to be approximately 2.4 (if it is assumed that the film is

transparent to 5461Å light). Plots of the calculated change in film thickness as a function of time (for $P_{Cl} \approx 2 \times 10^{-7}$ and $P_{Cl} \approx 10^{-7}$ Torr, and room temperature) are given in Fig. 7(a). The experimental values of the change in Δ (i.e., $-\delta\Delta$) are given on the right ordinate in Fig. 7(a). The change in film thickness per degree change in $-\Delta$ proves to be $\sim 4.25\text{\AA}$. The change in film thickness per degree change in ψ is $\sim 14.7\text{\AA}$.

The SPD results, which correspond to the ellipsometer results, are given in Fig. 7(b), with an additional curve for $P_{Cl} \approx 2 \times 10^{-8}$ Torr. ΔV is the surface potential difference between the Ti surface and the polycrystalline W reference electrode. $\delta(\Delta V)$ is the change in ΔV from the value for the clean Ti surface. Values of $\delta(\Delta V)$ are positive and level to approximately constant values with time. This indicates that the chlorine concentration on the surface approaches its equilibrium value at a particular chlorine pressure (P_{Cl}) and temperature (24°C). However, the ellipsometric results show that the Cl film thickness does not level off in the time of the experiment. This indicates that a second layer is forming. Apparently the SPD and Auger measurements are only sensitive to the outer layer, whereas the ellipsometer detects further film growth at room temperature. For comparison with our SPD measurements note that Anderson and Gani (10) observed $\delta(\Delta V) \approx 2.1\text{V}$ for a film, 5 atom layers of Cl on Ti (presumably at $P_{Cl} \sim 10^{-3}$ Torr). They found that exposing the Ti sample to $P_{Cl} = 10^{-3}$ Torr at 600°K for 10 min, followed by pumping then cooling to room temperature removed some Cl and reduced $\delta(\Delta V)$ from 2.1 to 1.1. The value of 1.1V corresponds with the result in Fig. 7(b) for $P_{Cl} \sim 10^{-7}$ Torr, with about 1.5 atom layers of chlorine.

There is a slight change in slope of the thickness and $\delta(\Delta V)$ vs. t curves ($P_{Cl} \approx 2 \times 10^{-7}$ Torr) at about 600 sec (Fig. 7). This effect has been observed (9) for Cs adsorption on Ti and W, and is interpreted to indicate the beginning of a second layer. If this is the case [from Fig. 7(a)] the thickness of the first monolayer of Cl on Ti is about 4.5\AA . This corresponds with the average of the Cl^- diameter (3.6\AA) and the TiCl diameter (5.4\AA).

Auger results.—Figure 8 shows the ratio of the APPH for chlorine to that for Ti (380 eV), referred to as (Cl/Ti) , as a function of time and chlorine pressure. The curve at 2×10^{-8} Torr and chlorine pressure (Fig. 8) increases with time but levels to a constant

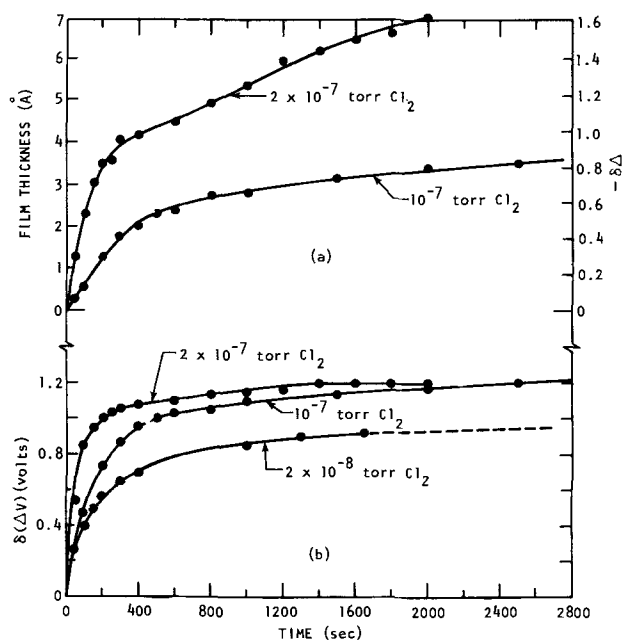


Fig. 7. Plot of calculated film thickness, $-\delta\Delta$, and $\delta(\Delta V)$ vs. time for chlorine adsorption from the gas phase at 24°C .

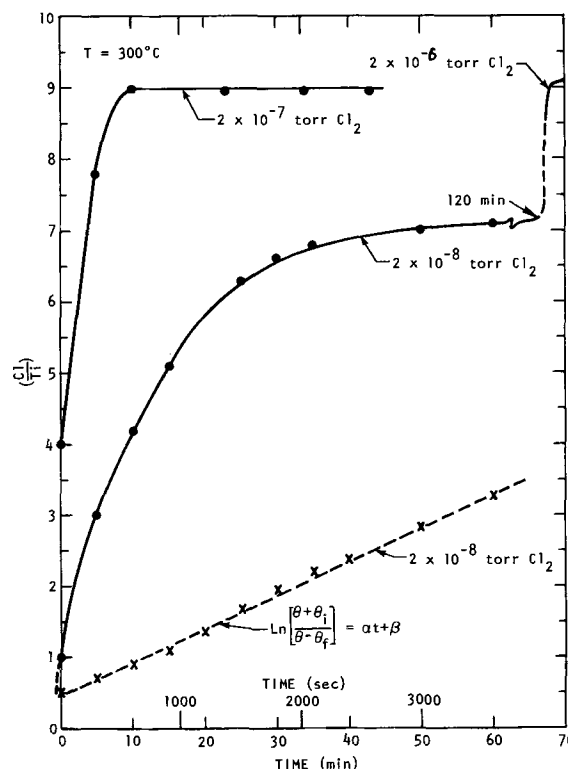
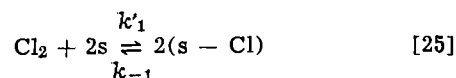


Fig. 8. Plot of chlorine adsorption (with Auger spectroscopy) as a function of time and chlorine pressure with the Ti sample at 300°C . The dashed straight line is the average of the values of $\text{Ln}[(\theta + \theta_i)/(\theta - \theta_f)]$ calculated from the curve at 2×10^{-8} Torr Cl_2 .

value (7.4) between 60 and 120 min. At 120 min the chlorine pressure was increased to 2×10^{-6} Torr; the (Cl/Ti) value increased and leveled off at 9.1. After removing the chlorine from the surface (to $(\text{Cl}/\text{Ti}) = 4$) by Cs^+ bombardment ($P_{\text{Cl}_2} \sim 5 \times 10^{-10}$ Torr) the chlorine pressure was increased to 2×10^{-7} Torr, yielding the curve labeled as such in Fig. 8. At the higher pressure, chlorine adsorption was much more rapid and leveled off at $(\text{Cl}/\text{Ti}) = 9$. It was concluded that the saturation value for Cl on Ti corresponds to a value of $(\text{Cl}/\text{Ti}) \approx 9.1$ so that θ can be obtained from $\theta \approx (\text{Cl}/\text{Ti})/9.1$.

Kinetic equations.—If chlorine gas adsorbs on Ti with dissociation, the reaction can be represented



where s represents a surface site and $s - \text{Cl}$ represents a chlorine atom adsorbed on a site. The forward rate constant is k'_1 and the reverse (desorption) rate constant is k_{-1} . Let N_s be the number of sites available and n_{Cl} the number occupied, so that the fraction occupied is $\theta = n_{\text{Cl}}/N_s$. The rate of adsorption can be expressed

$$d\theta/dt = k'_1 P_{\text{Cl}} (1 - \theta)^2 - k_{-1} \theta^2 \quad [26]$$

At equilibrium $d\theta/dt = 0$, yielding

$$\theta_f = (1 - \sqrt{k_{-1}/k'_1}) / (1 - k_{-1}/k'_1) \quad [27]$$

where $k_1 = k'_1 P_{\text{Cl}}$. Integration of Eq. [26] yields the relation between θ and t

$$\text{Ln}[(\theta + \theta_i)/(\theta - \theta_f)] = \alpha t + \beta \quad [28]$$

where

$$\theta_i = -[(1 + \sqrt{k_{-1}/k'_1}) / (1 - k_{-1}/k'_1)] \quad [29]$$

$$\alpha = 2\sqrt{k_{-1}k'_1} \equiv 2k_1(1 - \theta_f)/\theta_f \quad [30]$$

$$\beta = \text{Ln}[(\theta_0 + \theta_i)/(\theta_0 - \theta_f)] \quad [31]$$

$$\theta_0 = \theta \text{ at } t = 0 \quad [32]$$

For the curve at $P_{Cl} \approx 2 \times 10^{-8}$ Torr, $\theta_f \approx 7.4/9.1 = 0.81$ and from Eq. [27], $k_{-1}/k_1 \approx 0.055$, yielding $\theta_i \approx -1.30$ from Eq. [29]. Values of (Cl/Ti) from Fig. 8 were used to calculate θ vs. t . The X's in Fig. 8 are the calculated values of $\ln[(\theta + \theta_i)/(\theta - \theta_f)]$ vs. t , using the experimental values 0.81, -1.30, and 0.11 for θ_f , θ_i , and θ_0 , respectively. The linearity of the curve between 0 and 60 min is very sensitive to θ_f ; for example, the curve becomes concave to the time axis for $\theta_f > 0.81$ and convex to the time axis for $\theta_f < 0.81$. The slope of the dashed line in Fig. 8 yields the approximate value $\alpha \approx 0.047$ and from Eq. [30], $k_1 \approx 0.1$ (min^{-1}) and $k_{-1} \approx 0.0055$ (min^{-1}).

A check on the value of k_1 (and therefore the adsorption model), obtained from the dashed curve in Fig. 8 (i.e., from α), was made by measuring the initial rate of chlorine adsorption as a function of P_{Cl} and temperature with Auger spectroscopy. The initial rates $d(Cl/Ti)/dt$ are shown in Fig. 9. The pressure values along the abscissa in Fig. 9 are ion gauge readings. These readings must be multiplied by 2 to make the ionization probability correction for chlorine as mentioned in the experimental section. Although the scatter of the experimental data in Fig. 9 is rather large, they can be used to estimate the relationship between the initial rates and Cl_2 pressure. From the line drawn through the data

$$d(Cl/Ti)/dt|_{\theta \rightarrow 0} \approx 0.6 \times 10^6 P \text{ sec}^{-1} \quad [33]$$

yielding

$$d\theta/dt|_{\theta \rightarrow 0} \approx 0.7 \times 10^5 P \text{ sec}^{-1} \quad [34]$$

At $P_{Cl} = 2 \times 10^{-8}$ Torr (as for the dashed curve in Fig. 8), $k_1 \approx 0.09 \text{ min}^{-1}$; within experimental error of the value from Fig. 8 (i.e., $k_1 \approx 0.1 \text{ min}^{-1}$). Calculation of the initial rate at $P_{Cl} = 2 \times 10^{-8}$ Torr with the value of $k_1 = 0.1 \text{ min}^{-1}$ is indicated by the symbol \otimes in Fig. 9. A second check on k_1 is obtained by calculating values of $d\theta/dt|_{\theta \rightarrow 0}$ and therefore $d(Cl/Ti)/dt|_{\theta \rightarrow 0}$, from the SPD measurements in Fig. 7(b). The values of $d(Cl/Ti)/dt|_{\theta \rightarrow 0}$ from Fig. 7(b) are represented by the symbol Δ in Fig. 9 and are within experimental scatter of the other values.

It is observed from Fig. 9 that, within experimental error, the initial rate of chlorine adsorption is inde-

pendent of the sample temperature, indicating the reaction to be a nonactivated process.

Sticking coefficient.—It is of interest to calculate the probability (sticking coefficient) that a chlorine molecule will stick once it has struck the Ti surface. The forward rate constant can be expressed in terms of the sticking coefficient (designated S), the rate of gas impingement ν , and the pressure P_{Cl} by

$$k'_1 = 2S\nu/N_s P_{Cl} \quad [35]$$

since $dn_{Cl}/dt|_{\theta \rightarrow 0} = 2S\nu \equiv N_s(d\theta/dt)|_{\theta \rightarrow 0}$. The rate of chlorine gas impingement per unit area at P_{Cl} and at gas temperature T , is

$$\nu = P_{Cl}/\sqrt{2\pi m_{Cl}kT} \quad [36]$$

where m_{Cl} is the mass of a chlorine molecule and k is the Boltzmann constant. The equation for the sticking coefficient becomes

$$S = (k'_1 N_s \sqrt{2\pi m_{Cl}kT})/2 \quad [37]$$

The slope of the line in Fig. 9 is 0.6×10^6 , yielding $d\theta/dt|_{\theta \rightarrow 0} \approx 0.7 \times 10^5 P \text{ sec}^{-1}$ and

$$k'_1 \approx 0.7 \times 10^5 (\text{Torr-sec})^{-1}$$

However, in order to calculate S , k'_1 must be in units of square centimeter/dyne-second, so that

$$k'_1 \approx 0.7 \times 10^5 / 1.31 \times 10^3 \approx 50 (\text{cm}^2/\text{dyne-sec})$$

From Eq. [37]

$$S \sim 0.05$$

for chlorine on Ti.

Other possibilities exist. For example, chlorine may adsorb in a precursor state as a molecule, which then dissociates. If equilibrium is rapid with respect to the precursor state, the concentration of molecular chlorine on the surface can be expressed by a Langmuir isotherm

$$\theta_p = K_p P / (1 + K_p P)$$

where θ_p is the fraction of the surface covered with molecular chlorine and K_p is the equilibrium constant. For very small values of P ($K_p P \ll 1$), $\theta_p \approx K_p P$. The equilibrium constant can be expressed in terms of the rate of adsorption into the precursor state, $S\nu_1$, and the rate of desorption, ν_{-1} , by

$$K_p = S\nu_1/\nu_{-1}$$

where $\nu_1 = \nu/P$. If chlorine does equilibrate in a precursor state, the experimental value 0.6×10^6 in Eq. [33] relates to $k'_1 K_p$ rather than k'_1 and S cannot be determined until K_p and ν_{-1} are known. In this case the experimental slope taken as k'_1 is $k'_1 K_p$ and the rest of the analysis remains unchanged.

Summary and Conclusions

Although elements such as hydrogen and oxygen dissolve in Ti at high temperature, it has been demonstrated that chlorine and sulfur segregate from within the Ti crystal to the surface if the temperature is high enough. The fact that the Ti (380 eV) Auger peak is only slightly affected by the segregation process while the APPH for Ti (47 eV) is complementary to the APPH for Cl, indicates that only the outer layer has the high concentration of Cl. The segregation coefficient (ratio of Cl concentration at the surface to that in the bulk) is of the order of 10^5 at 525°C, but is reduced to $\sim 10^{-6}$ at room temperature due to the large positive enthalpy change (~ 25 kcal/mole) for the segregation process. Although it appears that these facts contradict the mechanism for SCC mentioned in the introduction, these tests were not conducted with the sample under stress. The large stresses and local heating that exist in the crack tip region may lower the diffusion activation energy and the segregation enthalpy,

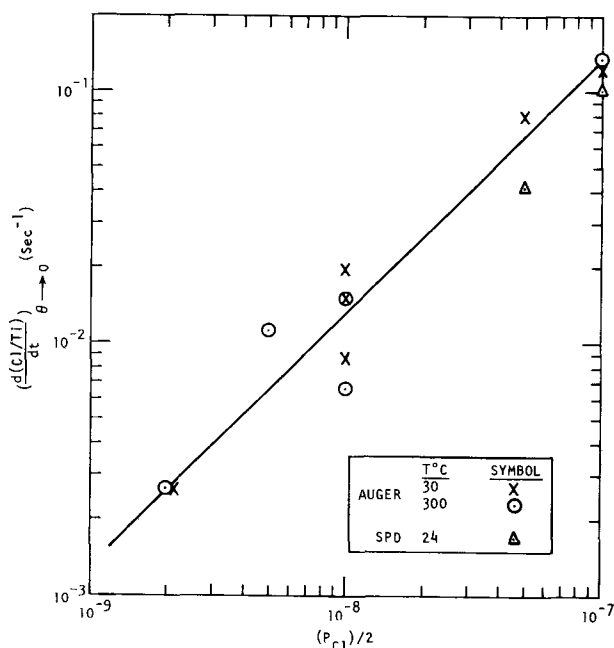


Fig. 9. Log-log plot of initial Cl adsorption rates as a function of chlorine pressure.

in which case it is conceivable that segregation could occur rapidly enough at room temperature. If the SCC requires ~ 1 Cl atom per 3 Ti atoms at the surface, and the bulk concentration is ~ 0.1 ppm, the stress zone at the crack tip must extend at least 10^6 atom layers deep in order to supply sufficient Cl to the surface. Further experiments are needed to investigate the effect of stress on the segregation process.

It has been demonstrated that chlorine segregates at a lower temperature and a faster rate than sulfur. At higher temperatures sulfur displaces chlorine at the surface.

Adsorption of chlorine from the gas phase is postulated to be a nonactivated process, the rate of initial adsorption being independent of the temperature of the sample. The adsorption rate on a bare Ti surface is directly proportional to the gas pressure, with a sticking coefficient of ~ 0.05 .

Ellipsometric data indicate that more than a monolayer of chloride will form on Ti at room temperature and at a chlorine pressure in the 10^{-7} Torr range. However, the SPD and Auger measurements seem to be sensitive to the outermost layer only. The index of refraction of the chloride layer is ~ 2.4 and the effective thickness of the layer at monolayer coverage proves to be about the average between a chlorine ion (3.6\AA) and the sum of the Ti^{+2} and Cl^- diameters (5.4\AA), i.e., $\sim 4.5\text{\AA}$. Table III gives a summary of the fundamental constants that have been determined for the segregation process for the Cl-Ti system.

Acknowledgment

I would like to thank Dr. E. R. Cohen for the derivation of the equations in the Appendix and Dr. E. Parry for his careful review of the paper.

Manuscript submitted July 26, 1971; revised manuscript received April 24, 1972.

Any discussion of this paper will appear in a Discussion Section to be published in the June 1973 JOURNAL.

APPENDIX

Solution of the Diffusion Equations

Assume that the physical system can be represented by the following mathematical model

1. The diffusion equation is

$$\frac{\partial C(x,t)}{\partial t} = D \frac{\partial^2 C(x,t)}{\partial x^2} \quad [\text{A-1}]$$

2. Initial concentration constant throughout a region $0 < x < l$, surface concentration initially zero

$$C(x,0) = C_0, \quad C_s(0) = 0 \quad [\text{A-2}]$$

3. Impermeable boundary at $x = 0$

$$\frac{\partial C}{\partial x}(0,t) = 0 \quad [\text{A-3}]$$

4. Fixed segregation constant between impurity concentration in the medium and on the surface

$$C_s(t) = KC(l,t) \quad [\text{A-4}]$$

so that K is the equivalent thickness of the boundary

layer required to contain the same amount of impurity, at the concentration level in the medium, as is present in the surface layer.

5. Conservation of matter: impurities which diffuse from the medium must be accounted for at the surface

$$\int_0^l [C_0 - C(x,t)] dx = \int_0^t -D \frac{\partial C}{\partial x}(l,t') dt' = C_s(t) \quad [\text{A-5}]$$

To solve the set of equations [A-1]-[A-5] the most convenient procedure is to use the method of Laplace transforms; let $f(x,s)$ be the transform of $C(x,t)$. Then

$$sf(x,s) = C_0 + D \frac{d^2 f}{dx^2}(x,s) \quad [\text{A-6}]$$

$$\frac{df}{dx}(0,s) = 0 \quad [\text{A-7}]$$

$$\int_0^l \left[\frac{C_0}{s} - f(x,s) \right] dx = -\frac{D}{s} \frac{df}{dx}(l,s) = kf(l,s) \quad [\text{A-8}]$$

The solution of the differential equation, [A-6], including the boundary condition, [A-7], is immediately

$$f(x,s) = \frac{C_0}{s} + A(s) \cosh \sqrt{\frac{s}{D}} x \quad [\text{A-9}]$$

and when this is introduced into Eq. [A-8] one obtains

$$-A(s) \sqrt{\frac{D}{s}} \sinh \sqrt{\frac{s}{D}} l = \frac{KC_0}{s} + KA(s) \cosh \sqrt{\frac{s}{D}} l$$

or

$$A(s) = -\frac{KC_0}{\sqrt{Ds} \sinh \sqrt{\frac{s}{D}} l + Ks \cosh \frac{s}{D} l} \quad [\text{A-10}]$$

The transform is therefore

$$f(x,s) = \frac{C_0}{s} - \frac{KC_0 \cosh \sqrt{\frac{s}{D}} x}{\sqrt{Ds} \sinh \sqrt{\frac{s}{D}} l + Ks \cosh \sqrt{\frac{s}{D}} l} \quad [\text{A-11}]$$

This function has a simple pole at $s = 0$ with a residue $lC_0/(l + K)$ as well as poles given by the roots of the transcendental equation

$$\frac{\tan \kappa_n}{\kappa_n} = -\frac{K}{l}, \quad s_n = -D\kappa_n^2/l^2 \quad [\text{A-12}]$$

For large n the roots are approximately

$$\kappa_n \approx \left(n - \frac{1}{2} \right) \pi + \frac{l}{\left(n - \frac{1}{2} \right) \pi K} + \dots \quad [\text{A-13}]$$

The residue at $s = s_n$ is

Table III. Some fundamental constants for the segregation process, of chlorine-titanium system

	Temperature, °C			Equation
	Room	524	670	
Sticking coefficient	0.05			
Segregation coefficient	$\sim 10^{-8}$	3×10^5	4×10^6	$K_s \approx 2.2 \times 10^{13} \exp(-25,000/RT)$
Diffusion coefficient	$\sim 10^{-17}$	2.4×10^{-6}	2.6×10^{-5}	$D \approx 9 \exp(-24,100/RT)$

$$\frac{2KC_0 \cosh \sqrt{\frac{s_n}{D}} x}{\sqrt{\frac{D}{s_n}} \sinh \sqrt{\frac{s_n}{D}} l + l \cosh \sqrt{\frac{s_n}{D}} l + 2K \cosh \sqrt{\frac{s_n}{D}} l + Kl \sqrt{\frac{s_n}{D}} \sinh \sqrt{\frac{s_n}{D}} l}$$

$$= \frac{2KlC_0 \cos(\kappa_n x/l)}{[(k+l)l + K^2 \kappa_n^2] \cos \kappa_n}$$

and the complete solution becomes

$$\frac{C(x,t)}{C_0} = \frac{l}{l+K} \left[1 - 2 \sum_{n=1}^{\infty} \frac{\cos(\kappa_n x/l) \exp(-\kappa_n^2 Dt/l^2)}{\left[1 + \frac{K^2 \kappa_n^2}{l(l+K)} \right] \cos \kappa_n} \right] \quad [\text{A-14}]$$

For $t > 4l^2/\pi^2 D$, the concentration reaches its equilibrium value, $C(x, \infty) = lC_0/(l+K)$, asymptotically with an exponential relaxation; for very small values of t ($t \ll 4l^2/\pi^2 D$) the series is slowly convergent but the successive terms alternate in sign.

Then

$$C_s(t) = KC(l,t) = (lC_0/l+K) \left[1 - 2 \sum_{n=1}^{\infty} \frac{e^{-\kappa_n^2 Dt/l^2}}{(1 + K^2 \kappa_n^2/l(l+K))} \right] \quad [\text{A-15}]$$

Let

$$\tau_1 = l^2/\kappa_1^2 D$$

$$C_s(\infty) = lC_0/(l+K)$$

$$C_s(\infty) - C_s(t) = 2lC_0/(l+K)$$

$$\{ [e^{-t/\tau_1} (1 + K^2 \kappa_1^2 l(l+K))] - \dots \} \quad [16]$$

$$= C_0 2l^2 K e^{-t/\tau_1} / [l(l+K) + K^2 \kappa_1^2] - \dots \quad [17]$$

REFERENCES

1. T. R. Beck, *This Journal*, **114**, 551 (1967).
2. T. R. Beck, *ibid.*, **115**, 890 (1968).
3. T. R. Beck and E. A. Grens, II, *ibid.*, **116**, 177 (1969).
4. T. W. Haas, J. T. Grant, and G. J. Dooley III, *J. Vacuum Sci. Technol.*, **7**, 43 (1970).
5. H. E. Bishop, J. C. Rivière, and J. P. Coad, *Surface Sci.*, **24**, 1 (1971).
6. F. L. McCrackin *et al.*, *J. Res. Nat. Bur. Std.*, **67A**, 363 (1963).
7. L. B. Emmons and M. P. Givens, *Appl. Opt.*, **7**, 2127 (1968).
8. P. W. Palmberg and T. N. Rhodin, *J. Appl. Phys.*, **39**, 2425 (1968).
9. C. J. Todd, *J. Sci. Instr.*, **42**, 755 (1965).
10. H. Palevsky *et al.*, *Rev. Sci. Instr.*, **18**, 288 (1947).
11. T. Smith, To be published in *Surface Science*.
12. J. R. Anderson and M. S. J. Gani, *J. Phys. Chem. Solids*, **23**, 1087 (1962).

Gas Flow Pattern and Mass Transfer Analysis in a Horizontal Flow Reactor for Chemical Vapor Deposition

R. Takahashi and Y. Koga

Central Research Laboratory, Hitachi Ltd., Kokubunji, Tokyo, Japan

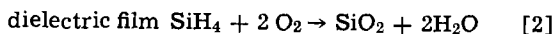
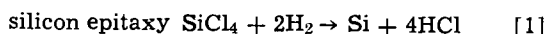
and K. Sugawara*

Semiconductor and Integrated Circuit Division, Hitachi Ltd., Kodaira, Tokyo, Japan

ABSTRACT

To study mass transfer characteristics in a vapor deposition reactor, gas flow patterns in a horizontal tube were investigated. Combined free and forced convection spiral flow and pure forced convection laminar flow were observed depending on experimental conditions of various flow rates and pressures. Further, local deposition rates under two flow behaviors were numerically obtained by solving a three-dimensional mass conservation equation. It was estimated on the basis of calculated results that forced convection laminar flow in a rectangular reactor produced better uniformity on the deposition rate distribution across the width than did combined convection spiral flow.

The chemical vapor deposition process has been widely used in the field of crystal growth and dielectric film formation. For instance, the following deposition reactions can be cited as examples



(in N_2 carrier gas)

Since the deposited layer must be of uniform thickness, it is necessary to study the distribution of deposi-

tion rates in a flow reactor. It is well known that the deposition rate is frequently controlled by mass transfer of reactant in the gas phase (1). In such a case, the gas flow pattern is an important factor affecting thickness distribution of the deposited layer.

When the susceptor in a deposition reactor tube is locally heated by usual high-frequency induction, a temperature difference appears between the susceptor and the tube wall. Under such circumstances, the flow in the reactor is subject to the influence of free convection induced by the buoyancy force. The flow in which free convection modulates on forced convection is called the combined flow or mixed flow.

* Electrochemical Society Active Member.
Key words: combined convection, low pressure operation, concentration profile, layer thickness distribution.

In the case of horizontal tubes, free convection acts perpendicularly to the direction of forced convection flow. In situations where the forces of free and forced convection are nearly equal to one another, the gas flow pattern becomes the spiral form (2, 3).

However, it can be predicted that the combined flow converts to a pure forced flow under an operating condition such as a large Reynolds number, Re , or a small Grashof number, Gr , where Re is the controlling parameter for forced convection flow and Gr is the controlling parameter for free convection flow.

This work was conducted to ascertain the transition region between pure forced flow and combined flow by observing gas flow patterns, and to theoretically study the relationship between the two flow behaviors and corresponding deposition characteristics.

Experimental

Figure 1 shows the schematic diagram of the experimental apparatus for observing the gas flow patterns. Four kinds of reactors were used: namely, two circular quartz tubes (60 and 113 mm ID) and two rectangular quartz tubes (40 × 70 mm and 70 × 118 mm), all four tubes 1200 mm long. Silicon carbide heaters were placed at the bottom of each tube, on which a flat iron plate was set in order to obtain a uniform temperature distribution by sandwiching a quartz insulator plate in between. The flow gases used were nitrogen and helium. The fluid characteristics of helium gas resemble those of hydrogen gas which is commonly used in vapor deposition. Titanium tetrachloride ($TiCl_4$) vapor was mixed through the capillary with the flowing gas in the tube. $TiCl_4$ was converted into titanium dioxide by reaction with the water moisture contained in the flow gas. The fine particles of TiO_2 formed were utilized to trace the gas flow. Velocity disturbance by the $TiCl_4$ vapor was negligible compared with main flow velocity because of a small quantity of titanium tetrachloride vapor.

A movie camera was used to photograph the gas flow patterns from the side as well as from the end of the tube. Sectional photography of the gas flow pattern was made by focusing on the specified section illuminated by spotlights.

Gas flow rates were from 0 to 60 liters/min, and pressure varied from 160 to 760 Torr. The temperature of the flat plate and the reactor wall were measured by a Pt-Pt · Rh thermocouple. In measuring temperature of a gas phase, radiation from a heated plate may cause an error. Consequently, three thermocouples with 0.2, 0.5, and 1.0 mm diameters were used. When the temperature is plotted graphically against the diameter, the point extrapolated to the zero diameter should give the true gas temperature (4).

Experimental Results

Gas flow patterns in horizontal tubes were photographed by a 16 mm movie camera under conditions producing various flow rates and pressures. In this paper, the patterns shown by photographs were selected from the 16 mm movie films.

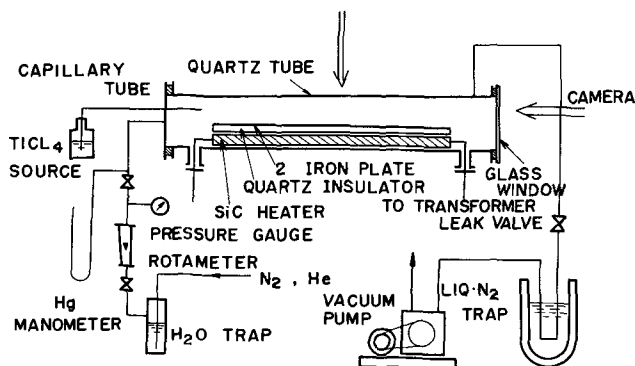


Fig. 1. Schematic diagram of experimental apparatus

It is known that fluid in an enclosed region heated from below forms a two-dimensional vortex pattern by free convection (5-7). In the case of combined flow, fluid motion is three-dimensional. However, we can observe a sectional pattern similar to the free convection pattern by projecting a three-dimensional streamline at a cross section of a tube. Figure 2 shows the flow pattern in a cross section at a very small flow rate. Although dynamical flow behavior is not visible in the photograph, the heated gas moved upward, starting from the center portion of the iron plate, then downward along the tube wall. This motion is designated as positive motion and its reverse motion as negative. Generally, motion by free convection starts from the point where viscosity is lowest (8). In most of this experiment, two vortex patterns with positive motion were observed independently from tube geometries, which implies that the temperature distribution across the tube width had the highest point at the center of the plate due to heat loss toward the tube wall.

Since the vortices by free convection were modulated by forced convection directed to the outlet, the flow streamline actually became a spiral pattern. In the situation where two vortices exist in a cross section of the tube, two spiral flow patterns were generated in the tube.

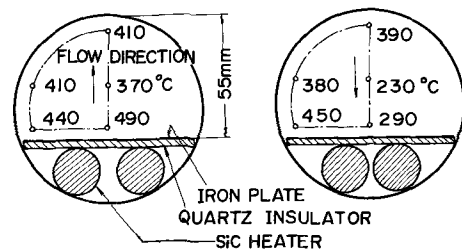
With an increase of the flow rate, pitch of the spiral streamline was gradually extended in the axial direction of the tube; however, on the sectional pattern, the following behaviors were observed.

In the nitrogen flow system, the positive vortex motion observed at a low flow rate converted to a negative one. To examine this behavior, temperature distribution in the cross section was measured corresponding to the vortex pattern, as shown in Fig. 3; that is, horizontal temperature distribution near the heated plate over the width had the lowest point at the width center when the flow rate was high. It appears that this difference between temperature distribution is related to whether or not the thermal boundary layer was fully developed.

Under a fully developed state, temperature of the gas stream did not vary in the flow direction, and horizontal temperature distribution over the width



Fig. 2. Vortex patterns produced in a rectangular tube



(a) N_2 10 l/min

(b) N_2 40 l/min

Fig. 3. Temperature profiles varying with flow rates



Fig. 4. Vortex patterns varying with flow rates: (a, left) He 1 liter/min; (b, center) He 5 liters/min; (c, right) He 10 liters/min

was governed by heat loss as stated previously. In the region where the thermal boundary layer was not fully developed, on the other hand, horizontal temperature distribution depended on the velocity distribution of forced convection over the width, so that temperature of the gas stream in the center part of the tube became lower than that in the outer part, and consequently, the vortex motion was negative.

Length of the thermal entrance region for laminar flow is well known by the relation

$$L/De = 0.05 \text{ Re} \cdot \text{Pr} \quad [3]$$

where L is thermal entrance length and De is hydraulic diameter of a tube. Although the entrance length for combined flow somewhat differs from that for laminar flow, from the above relation it is still estimated that the position of observing the flow pattern, when it is 150 mm apart from the inlet edge of the heated plate, lies in the thermal entrance region when the reverse of the vortex motion is observed.

In the helium flow system, vortex patterns were shifted to the corners of the cross section with increasing flow rates, as shown in Fig. 4. According to the above estimation thermal boundary layers were fully developed in all experiments. If the vortex was induced locally at a position where forced convection velocity is small, pattern variation occurred under circumstances that the small velocity zone was reduced to the corner with increasing flow rates. However, detailed analysis remains to be conducted on the hydrodynamic problem.

Under further increased flow rates, the forced convection became predominant, although there was complex behavior induced by expansion of both the thermal and hydrodynamic entrance regions.

A decrease in the Grashof number, which consists of factors such as temperature difference and gas density, imparts to the flow pattern the same effect as an increase in flow rate. McComas and Eckert (9) have conducted operations at low pressure in order to ob-

tain negligible free convection heat transfer data. In the present study, pressure dependence on a fully developed spiral flow was examined. Figure 5 shows the effect of pressure at a constant flow rate. At low pressure the pure forced convection streamline was observed in contrast with the vortex motion at atmospheric pressure. The low-pressure operation was effective in producing laminar flow in a CVD reactor.

Summary of Observation Results

As described previously, two modes of flow can exist in a horizontal CVD reactor. The problem is to determine the transition region between the two flow patterns.

Sparrow (10) has studied combined convection heat transfer on a vertical surface, in which he theoretically classified the flow criteria by using a parameter, Gr/Re^2 , introduced from the momentum conservation equation as follows

$$\text{Gr}/\text{Re}^2 > 16 \quad \text{free convection flow} \quad [4]$$

$$16 > \text{Gr}/\text{Re}^2 > 0.3 \quad \text{combined flow} \quad [5]$$

$$0.3 > \text{Gr}/\text{Re}^2 \quad \text{forced convection flow} \quad [6]$$

Additionally, from the heat transfer data, Metais and Eckert (11) have reported regimes for flow through vertical and horizontal circular tubes. These criteria are defined by deviation between the actual heat flux and the heat flux caused by pure convection. The transition region for a semicircular or rectangular tube may differ from the above criteria.

Conditions for the transition region obtained from observation results in the present experiment are described in Table I. Values in the table are for the flow parameters at which vortex motion disappears in the tube cross section.

Regarding combined flow on a horizontal flat plate, a parameter of $\text{Gr}/\text{Re}^{2.5}$ has been theoretically derived by Mori (12). For simplicity, however, a parameter of

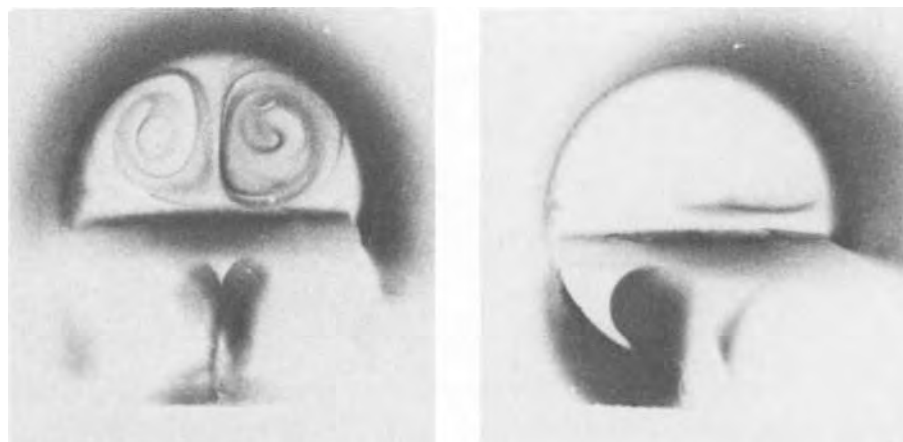


Fig. 5. Effect of pressures on flow patterns: (a, left) 760 Torr 1 liter/min; (b, right) 160 Torr 1 liter/min.

Table I. Fluid parameters representing the disappearance of vortices

Tube type	Maximum distance between hot plate tube wall (mm)	Equivalent diameter D_e (mm)	Flow rate (l/min)	Re	Gr	Gr/Re ²
Nitrogen gas						
64 mm circular	55	43	5	45	8,200	4.1
113 mm circular	45	55	60	228	23,000	0.4
70 × 40 rectangular	19	26	5	35	1,600	1.4
70 × 118 rectangular	57	62	20	140	46,000	2.3
118 × 70 rectangular	49	82	20	100	30,000	3.0
118 × 70 rectangular	39	66	20	80	9,800	3.0
118 × 70 rectangular	29	52	20	80	4,800	1.5
Helium gas						
64 mm circular	55	43	14	14	153	0.8
64 mm (160 Torr)	55	43	1	1.3	4	2.2
70 × 40 rectangular	19	26	5	4.3	22	1.2
70 × 40 rectangular	9	18	No vortex	—	—	—
118 × 70 rectangular	39	66	20	13	600	3.5
118 × 70 rectangular	29	52	10	5	90	3.5

Gr/Re² was employed because Gr^{1/2}/Re corresponds to a dimensionless velocity ratio of free convection velocity to forced convection velocity.

As shown in the table, the disappearance of vortex occurred under the transition condition of Gr/Re² = 0.4 to 4.1, although it is difficult to give precise values since transitions are gradual in observing flow patterns.

Moreover, note that vortex by free convection was observed at small Grashof numbers in the helium flow system. In general, free convection vortex in the horizontal space bounded by two plane surfaces appears under the conditions of Gr · Pr > 1700 (8). Although the limiting condition for producing free convection depends on reactor geometry (13, 14), the values described in the table are very small. This may be due to heat loss, effects based on the entrance regions, the gravity force of titanium dioxide particles, and so forth; however, such details will be left to advance study.

Theoretical Consideration on the Relation between Flow Behaviors and Deposition Characteristics

Deposition under forced convection laminar flow.—Thickness distribution of the deposited layer makes a difference between pure forced convection laminar flow and combined convection spiral flow. The problem can be examined theoretically by solving a mass conservation equation of the diffusing species, of which the general form is

$$\nabla v \cdot c = D_m \nabla^2 c \quad [7]$$

where ∇ denotes the operator, $\partial/\partial x + \partial/\partial y + \partial/\partial z$, ∇^2 is the Laplace operator, v the velocity vector of the gas flow, c the concentration of the reactant, and D_m the effective diffusion coefficient.

Solutions of this equation under different boundary conditions have been obtained from the analogous relation between mass and heat transfer. For example, the mass transfer correlation in isothermal laminar flow over a flat plate is given by

$$\text{Sh} = 0.332 \text{Re}^{1/2} \text{Sc}^{1/3} \quad [8]$$

where Sh represents the local Sherwood number defined by kz/D_m with k the mass transfer coefficient, z the distance along the gas flow; Re is defined by wz/ν with w the flow velocity, ν the kinematic viscosity; and Sc represents the Schmidt number defined ν/D_m . In detail, the above is a solution obtained from the following equation under a situation of the variable hydrodynamic boundary layer thickness

$$w \partial c/\partial z + v \partial c/\partial y = D_m \partial^2 c/\partial y^2 \quad [9]$$

where w is a gas velocity component in the flow direction, z , and v is a y -direction velocity component perpendicular to z .

If the hydrodynamic boundary layer is fully developed, the term (including the velocity component, v) can be neglected. Regarding a special condition of the linear velocity profile, $w = \alpha y$, there is Leveque's solution on heat transfer (8). The equivalent mass transfer

rate equation can be written as

$$N = D_m (\partial c/\partial y)_{y=0} = \frac{c_0 D_m}{0.893} \left(\frac{\alpha}{9 D_m z} \right)^{1/3} \quad [10]$$

On the other hand, a solution to the parabolic velocity profile has been solved by Pigford (15). Further, Rundle (16) has reported an analytical solution of the following two-dimensional diffusion equation in the same velocity field

$$w(y) \partial c/\partial z = D_m (\partial^2 c/\partial z^2 + \partial^2 c/\partial y^2) \quad [11]$$

In an actual reactor, moreover, velocity is also distributed over the width. Fully developed velocity profiles in a rectangular and a semicircular section, used frequently for chemical vapor deposition, have been calculated by Andrew (17), who suggested important information that deposition in a rectangular reactor gave better thickness distribution than that in a semicircular reactor.

In this study, deposited layer thickness distributions in a rectangular reactor in which velocity is distributed on both the axial and the width direction were examined in a three-dimensional diffusion system as follows

$$w(x,y) \partial c/\partial z = D_m (\partial^2 c/\partial x^2 + \partial^2 c/\partial y^2 + \partial^2 c/\partial z^2) \quad [12]$$

Consideration was given, in particular, to the dependence of diffusion along the width on thickness distributions. Also, the axial diffusion effect was considered in the equation since vapor deposition is usually conducted at small Reynolds numbers, although it may be neglected in the ranges of Re · Sc > 10 (18).

Generally, the velocity profile under laminar flow fully developing in a rectangular reactor is expressed by the complex formula (17, 19); however, a convenient simple expression (19) is given by

$$w/w_{\max} = (1 - |\xi|^m)(1 - |\zeta|^2) \quad [13]$$

where $\xi = 1 - (2x/B)$, $\zeta = 1 - (2y/H)$, B and H are the respective width and height of the reactor, and m is a constant which is determined by the aspect ratio of the reactor section.

By using dimensionless variables, the mass conservation equation can be written as

$$W \partial C/\partial Z = \frac{1}{\text{Sc}} (\partial^2 C/\partial X^2 + \partial^2 C/\partial Y^2 + \partial^2 C/\partial Z^2) \quad [14]$$

where $C = c/c_0$, $X = x/H$, $Y = y/H$, $Z = z/H$, and $W = wH/\nu$.

Boundary conditions are $C = 0$ at $Y = 0$ when the reaction rate is very large at the deposition surface; consequently, the deposition rate is controlled by diffusion, $C = 1$ at $Z = 0$, $\partial C/\partial Z = 0$ at $Z = L/H$ ($L =$ reactor length), $\partial C/\partial X = 0$ at $X = 0$ and B/H , and $\partial C/\partial Y = 0$ at $Y = 1$.

Concentrations distributed three-dimensionally in a reactor were numerically calculated by using a finite

difference approximation method. The finite difference representation can be expressed by approximated concentrations on six grid points around a selected point as follows

$$W(i,j) \frac{C(i,j,k+1) - C(i,j,k-1)}{2\Delta Z} = \frac{1}{Sc} \left[\frac{C(i+1,j,k) - 2C(i,j,k) + C(i-1,j,k)}{\Delta X^2} + \frac{C(i,j+1,k) - 2C(i,j,k) + C(i,j-1,k)}{\Delta Y^2} + \frac{C(i,j,k+1) - 2C(i,j,k) + C(i,j,k-1)}{\Delta Z^2} \right] \quad [15]$$

where i , j , and k are grid numbers spacing in the X , Y , and Z direction, respectively. Calculation was effected with a digital computer, HITAC 5020F.

From the concentration gradient at the deposition surface, the mass transfer rate N is

$$N(x,z) = D_m(\partial c/\partial y) = \frac{c_0 D_m}{H} (\partial C/\partial Y) = k_m \Delta c \quad [16]$$

If the diffusion boundary layer consists of the original concentration c_0 , that is $\Delta c = c_0$, and if there is a successive concentration gradient, the dimensionless concentration gradient is equivalent to the Sherwood number as

$$R = (\partial C/\partial Y)_{Y=0} = k_m H/D_m = Sh \quad [17]$$

The deposition rate is

$$G = \frac{m}{M_p} \left(\frac{\partial C}{\partial Y} \right)_{Y=0} \quad [18]$$

For the values of $D_m = 5 \text{ cm}^2/\text{sec}$, $c = 0.005 \text{ mol}$, and $H = 3 \text{ cm}$, a unit dimensionless concentration gradient $R = 1$, corresponds to a deposition rate of $G = 0.5 \text{ } \mu/\text{min}$. Therefore, $(\partial C/\partial Y)_{Y=0}$ implies a dimensionless deposition rate.

Figure 6 shows calculated rate distributions across the width of a rectangular reactor of the aspect ratio $B/H = 1$. Distributions in a case where diffusion along the width is not considered in the mass conservation equation are also given for reference by the hyphenated lines. It is obvious that the diffusion effect along the width cannot be neglected.

However, this consideration is still insufficient. At the shallow position of a reactor the deposition rate may be controlled by the chemical reaction rate because of the thin diffusion boundary layer thickness. In addition, existence of a hydrodynamic and thermal entrance region will effect a complex rate distribution

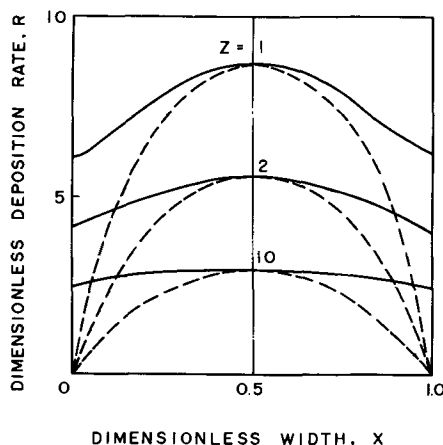


Fig. 6. Theoretical deposition characteristics for forced convection laminar flow inside a rectangular tube.

such as the deposition characteristics reported by Sutton (20). These behaviors will be analyzed by more detailed study, considering the above mechanisms.

Deposition under combined free and forced convection spiral flow.—The problems of combined flow have been studied by a number of investigators in the field of heat transfer. On the other hand, regarding studies of combined convection mass transfer, for instance, investigations are found such as mass transfer from gas phase to horizontal cylinder during chemical vapor deposition (21, 22) or diffusion in a semipermeable plate associated with free convection (23).

In a flow system in which free convection acts perpendicular to forced convection, the flow is three-dimensional; thus, the theoretical expression on fluid dynamics is complex. Recently, combined flow with a spiraling character in a circular tube was studied by Newell *et al.* (24), and also the behavior of vortexes under combined flow was reported by Uchida and Mori (25).

In this work, mass transfer under combined convection spiral flow is studied to evaluate the deposited layer thickness distribution in a vapor deposition reactor. Consideration is given to the rectangular reactor to make a comparison with the deposition characteristics under forced convection laminar flow.

We now assume an incompressible and Newtonian fluid with constant physical properties, except for a fluid density in the buoyancy term. When combined flow is fully developed

$$\partial u/\partial z = 0, \quad \partial v/\partial z = 0, \quad \text{and} \quad \partial w/\partial z = 0 \quad [19]$$

dimensionless conservation equations can be stated as follows:

Momentum

$$U \frac{\partial U}{\partial X} + V \frac{\partial U}{\partial Y} = -\frac{\partial P}{\partial X} + \frac{\partial^2 U}{\partial X^2} + \frac{\partial^2 U}{\partial Y^2} \quad [20]$$

$$U \frac{\partial V}{\partial X} + V \frac{\partial V}{\partial Y} = -\frac{\partial P}{\partial Y} + \frac{\partial^2 V}{\partial X^2} + \frac{\partial^2 V}{\partial Y^2} + Gr' \cdot T \quad [21]$$

$$U \frac{\partial W}{\partial X} + V \frac{\partial W}{\partial Y} = -\frac{\partial P}{\partial Z} + \frac{\partial^2 W}{\partial X^2} + \frac{\partial^2 W}{\partial Y^2} \quad [22]$$

Continuity

$$\frac{\partial U}{\partial X} + \frac{\partial V}{\partial Y} = 0, \quad \frac{\partial W}{\partial Z} = 0 \quad [23]$$

Energy

$$U \frac{\partial T}{\partial X} + V \frac{\partial T}{\partial Y} = \frac{1}{Pr} \left(\frac{\partial^2 T}{\partial X^2} + \frac{\partial^2 T}{\partial Y^2} \right) \quad [24]$$

Diffusion

$$U \frac{\partial C}{\partial X} + V \frac{\partial C}{\partial Y} + W \frac{\partial C}{\partial Z} = \frac{1}{Sc} \left(\frac{\partial^2 C}{\partial X^2} + \frac{\partial^2 C}{\partial Y^2} + \frac{\partial^2 C}{\partial Z^2} \right) \quad [25]$$

where $U = uH/\nu$, $V = vH/\nu$, $W = wH/\nu$, and $T = 2(\theta - \theta_0)/(\theta_h - \theta_l)$ in which θ_h is the upper surface temperature, θ_l the lower surface temperature, and θ_0 the average temperatures $(\theta_h - \theta_l)/2$.

The boundary conditions given for this system are

$$\begin{aligned} U = V = W = 0 & \text{ at all surfaces} \\ T = 1 & \text{ at } Y = 0, \quad T = -1 \text{ at } Y = 1 \\ \partial T/\partial X = 0 & \text{ at } X = 0 \text{ and } X = B/H \\ C = 1 & \text{ at } Z = 0, \quad C = 0 \text{ at } Y = 0, \quad \partial C/\partial Y = 0 \text{ at } \\ & Y = 1 \\ \partial C/\partial X = 0 & \text{ at } X = 0 \text{ and } X = B/H, \quad \partial C/\partial Z = 0 \text{ at } \\ & Z = L/H \end{aligned}$$

The derived equation by combining Eq. [20] and [21] is known as the vorticity equation, that is

$$U \frac{\partial Q}{\partial X} + V \frac{\partial Q}{\partial Y} = Gr' \frac{\partial T}{\partial X} + \frac{\partial^2 Q}{\partial X^2} + \frac{\partial^2 Q}{\partial Y^2} \quad [26]$$

where $Q = (\partial V/\partial X) - (\partial U/\partial Y) = -\nabla^2\phi$ and ϕ is the stream function defined by $U = \partial\phi/\partial Y$ and $V = \partial\phi/\partial X$. This equation has been solved numerically by Fromm (5), Samuels and Churchill (6), and others (7, 26-28) on the problem of two-dimensional free convection.

The present calculation for three-dimensional combined flow was conducted by utilizing the numerical solution of unsteady-state free convection using a central finite difference approximation, the details described in Ref. (6, 29, 30). When free convection velocity is obtained from the vorticity and energy equations, a momentum equation with respect to the axial velocity can be solved by the successive approximation method. The axial velocities in laminar flow, expressed according to Eq. [13], were used as initially approximated values. Also, this equation was solved under a constant condition of pressure drop. From the determined velocity components, the mass conservation equation was solved and the mass transfer rate was finally evaluated. Computation required about 1 to 5 min for values of certain Gr, Pr, Re, and Sc on the digital computer, HITAC 5020F.

Figure 7 shows the vortex streamlines of a combined flow projected on the cross section of a rectangular reactor. The calculation result refers to a rectangular reactor with an aspect ratio of $B/H = 2$, which theoretically produces two vortex motions (5), because two vortices were frequently found in the present observation of flow patterns. The referenced streamlines represent positive vortex motion; if the stream functions have opposite signs, vortex motion becomes negative.

Under the same reactor geometry, axial velocity distributions over the width are shown in Fig. 8. It is evident from the figure that axial velocity is largest at the center of each projected vortex pattern on the cross section of a reactor (hyphenated lines indicate laminar flow).

Figure 9 reveals contour maps of computed isoconcentration profiles. By the positive motion of free convection vortices, gas of the dilute concentration moves upward at the width center so that the mass transfer

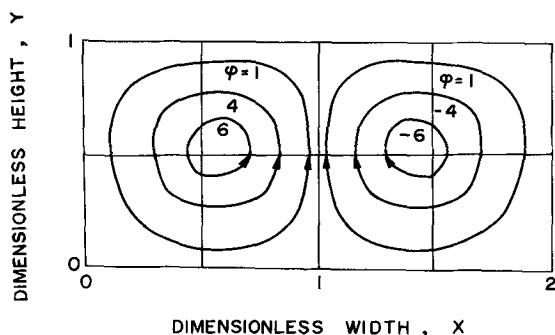


Fig. 7. Streamlines of combined flow projected on a cross section ($Gr' = 3000$, $Pr = 1$, and $B/H = 2$).

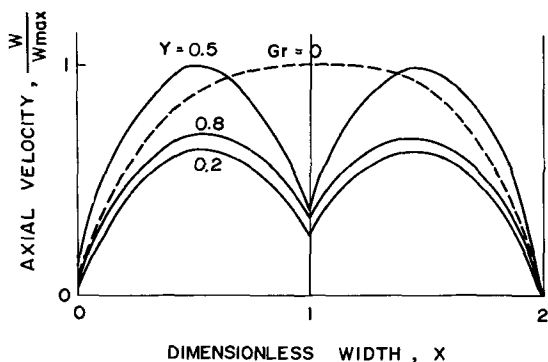


Fig. 8. Axial velocity profiles across the width ($Gr' = 3000$, $Pr = 1$, and $B/H = 2$).

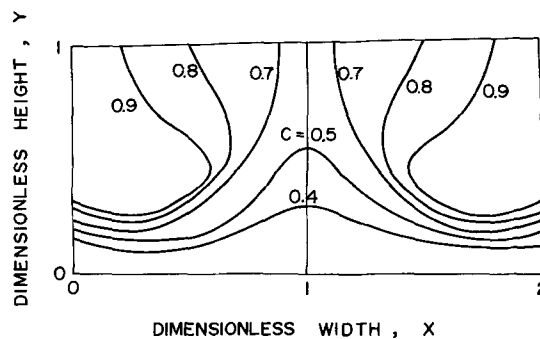


Fig. 9. Concentration contour lines in a cross section for $Gr' = 3000$, $Pr = 1$, $Re = 200$, $Sc = 1$, $Z = 5$, and $B/H = 2$.

rate at this position becomes minimum at the width center.

For three types of gas flow (forced convection laminar flow, and combined convection spiral flows with positive and negative vortex motions) the deposition characteristics represented by the dimensionless mass transfer rate are shown in Fig. 10.

Deposition characteristics under combined flow are generally wavy compared with those under forced convection laminar flow. Although a uniform rate distribution exists under the properly selected Grashof number, predictable from deposition characteristics between forced convection laminar flow and combined convection spiral flow with positive vortex motion, control to attain an optimum operating condition may be difficult. In the case of forced convection laminar flow, deposition characteristics can be further improved by using a rectangular reactor with large aspect ratios because of flatness velocity distribution over the width. The formation of forced convection laminar flow in a chemical vapor deposition reactor can be effectively realized by low-pressure operation.

Conclusions

1. In horizontal tubes simulating a vapor deposition reactor, two modes of flow (combined free and forced convection spiral flow, and pure forced convection laminar flow) were observed, depending on experimental conditions of various flow rates and pressures. In particular, straight streamlines were found at low pressure.
2. With increasing flow rates, reverse vortex motion and eccentricity of the vortex center were observed.
3. Transition between the two flow modes occurred in the range of $Gr/Re^2 = 0.4$ to 4.1.
4. The three-dimensional diffusion equation was solved numerically under two conditions. Concentration and deposition rate distributions across and along the tube were calculated on the basis of a rectangular reactor.
5. It was estimated from calculation results that forced laminar flow in the rectangular reactor revealed

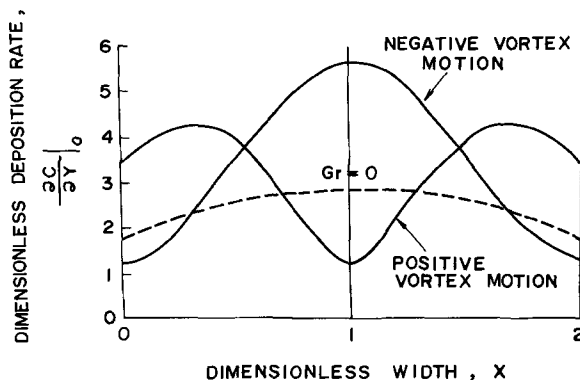


Fig. 10. Deposition characteristics corresponding to flow behaviors

an excellent uniformity of deposition rate across the width in contrast to combined flow.

Acknowledgments

The authors wish to thank Dr. Eiichi Hori, Chief Researcher of the Hitachi Mechanical Laboratory for his encouragement and constructive criticisms during the course of the work. Acknowledgments are also made to Professor Hiroshi Kubota, Tokyo Institute of Technology, and Assistant Professor Yutaka Uchida, University of Electrocommunications, for their various suggestions and enlightening discussions.

This paper is based on a talk presented under the title "Convective Mass Transfer Analysis of Silicon Epitaxial Deposition. Part I," at the Second International Conference on Chemical Vapor Deposition, Los Angeles, California, May 1970.

SYMBOLS

B	width of a rectangular reactor, cm
c	gas phase concentration of the species of interest, g/cc
Δc	concentration difference, g/cc
c_0	initial concentration, g/cc
C	dimensionless concentration, c/c_0
c_p	specific heat of fluid, cal/g \cdot $^{\circ}$ C
D_e	hydraulic diameter, cm
D_m	effective diffusion coefficient of the species of interest, cm ² /sec
G	growth rate, cm/sec
Gr	Grashof number, $g\beta H^3 \Delta\theta / \nu^2$, dimensionless
Gr'	Grashof number based on $1/2$ temperature difference
H	height of rectangular reactor, cm
i	i 'th grid point
j	j 'th grid point
k	k 'th grid point
k_m	mass transfer coefficient, cm/sec
L	length of a deposition zone to the axial direction, cm
m	constant
M	molecular weight of the species of interest
M	molecular weight of the deposition film
N	mass transfer rate, g/cm ² sec
P	dimensionless pressure, $pH^2/\rho'\nu^2$ (p -fluid pressure, ρ' -mass density of fluid)
Pr	Prandtl number, $c_p\mu/\lambda$, dimensionless
Q	dimensionless vorticity
R	dimensionless concentration gradient
Re	Reynolds number, $De\bar{w}/\nu$
Sc	Schmidt number, ν/D_m
Sh	Sherwood number, $k_m z/D_m$
T	dimensionless temperature, $2(\theta - \theta_0)/(\theta_h - \theta_1)$
u	velocity in x -direction
U	dimensionless velocity in x -direction, uH/ν
v	velocity in y -direction
V	dimensionless velocity in y -direction, vH/ν
w	velocity in z -direction
\bar{w}	mean velocity of fluid
W	dimensionless velocity in z -direction, wH/ν
x	coordinate in the width direction of reactor
X	dimensionless width in x -direction, x/H
y	coordinate in the height direction of reactor
Y	dimensionless height in y -direction, y/H
z	coordinate in the axial direction of reactor
Z	dimensionless length in z -direction, z/H
α	constant
β	coefficient of thermal expansion
θ	temperature, $^{\circ}$ C
λ	thermal conductivity of fluid, cal/cm sec $^{\circ}$ C

ξ	$1 - (2x/B)$
ζ	$1 - (2y/H)$
ν	kinematic viscosity, cm ² /sec
ρ	density of the deposited material
φ	dimensionless stream function

Manuscript submitted March 10, 1971; revised manuscript received May 15, 1972.

Any discussion of this paper will appear in a Discussion Section to be published in the June 1973 JOURNAL.

REFERENCES

1. S. E. Bradshaw, *Int. J. Electron.*, **121**, 205 (1966).
2. A. S. Grove, *Ind. Eng. Chem.*, **58**, 48 (1966).
3. T. Hanzawa and U. Ito, *Chem. Eng. Japan*, **34**, 1333 (1970).
4. M. Hirata, Preprint presented at the Symposium on Combustion of Heat Transfer Society of Japan, Tokyo (1968).
5. J. E. Fromm, *Phys. Fluids*, **8**, 1757 (1965).
6. M. R. Samuels and S. W. Churchill, *Am. Inst. Chem. Engrs. J.*, **13**, 77 (1967).
7. Y. Mori and Y. Uchida, *Trans. Japan Soc. Mech. Engrs.*, **31**, 1511 (1965).
8. S. T. Hsu, "Engineering Heat Transfer," D. van Nostrand Co., Inc., New York (1963).
9. S. T. McComas and E. R. G. Eckert, *J. Heat Transfer*, **88**, 147 (1966).
10. E. M. Sparrow, R. Eichhorn, and J. L. Gregg, *Phys. Fluids*, **2**, 319 (1959).
11. B. Metais and E. R. G. Eckert, *J. Heat Transfer*, **86**, 295 (1964).
12. Y. Mori, *ibid.*, **83**, 479 (1961).
13. Y. Mori, W. Nakayama, and Y. Uchida, *J. Japan Soc. Mech. Engrs.*, **70**, 66 (1967).
14. I. Catton, *J. Heat Transfer*, **92**, 186 (1970).
15. R. B. Bird, W. E. Stewart, and E. Lightfoot, "Transport Phenomena," John Wiley & Sons, Inc., New York (1960).
16. P. C. Rundle, *Int. J. Electron.*, **24**, 405 (1968).
17. R. W. Andrew, D. M. Rynne, and E. G. Wright, *Solid State Technol.*, **12**, 61 (1969).
18. T. Vermeulen, *Ind. Eng. Chem.*, **44**, 636 (1952).
19. D. B. Holmes and J. R. Vermeulen, *Chem. Eng. Sci.*, **123**, 717 (1968).
20. R. P. Sutton, Preprint presented at the 1st International Symposium on Silicon Material Science and Technology of Electrochem. Soc., New York (1969).
21. H. E. Carlton and J. H. Oxley, *Am. Inst. Chem. Engrs. J.*, **13**, 571 (1967).
22. H. E. Carlton and J. H. Oxley, "Proceeding of the Conference on Chemical Vapor Deposition," Electrochem. Soc., Inc. New York (1967).
23. K. R. Ramanadhan and W. N. Gill, *Am. Inst. Chem. Engrs. J.*, **15**, 872 (1969).
24. P. H. Newell and A. E. Bergles, *J. Heat Transfer*, **92**, 83 (1970).
25. Y. Uchida and Y. Mori, Preprint presented at the 7th Symposium of Heat Transfer Society of Japan (1970).
26. G. de Vahl Davis, *Int. J. Heat Mass Transfer*, **11**, 1765 (1968).
27. R. K. MacGregor and A. F. Emery, *J. Heat Transfer*, **91**, 391 (1969).
28. G. N. Faris and R. Viskanta, *Int. J. Heat Mass Transfer*, **12**, 1295 (1969).
29. P. L. T. Brian, *Am. Inst. Chem. Engrs. J.*, **7**, 367 (1961).
30. M. E. Newell and F. W. Schmidt, *J. Heat Transfer*, **92**, 159 (1970).

Arsenic Diffusion in Silicon Using Low As_2O_3 -Content Binary Arsenosilicate Glass Sources

J. Wong and M. Ghezzi*

General Electric Corporate Research and Development, Schenectady, New York 12301

ABSTRACT

Arsenic diffusion from a low- As_2O_3 content arsenosilicate glass film into silicon has been measured in the range 1000°-1200°C. The activation energy is found to be 4.1 ± 0.1 eV in good agreement with previous work. Concentration dependence of the diffusion coefficient of arsenic in silicon has been evaluated from the diffusion profiles using the Boltzmann-Matano analysis. In addition, the masking ability of SiO_2 toward arsenic diffusion and some diffusion parameters of arsenic in SiO_2 have been estimated.

Most of the diffusion studies performed on arsenic in silicon have been based on a gas-to-solid diffusion technique (1-8). The use of doped oxides such as binary arsenosilicate glasses in the process of solid-to-solid state diffusion of arsenic into silicon has only been recently realized since the work of Lee (9). Subsequent investigations by various authors (10-13) showed that glasses prepared from the reaction system suggested by Lee suffer severe "glass damage" when heated to 1000°C and up.

A more recent study (14, 15) shows that CVD arsenosilicate films on silicon in the range 2-20 m/o (mol per cent) As_2O_3 exhibit film detachment upon heat-treatments at 800°C and up. Thermal stresses generated in the film, arising from a mismatch of expansion coefficient with the silicon substrate are largely responsible for the observed film detachment from the substrate. However, when the amount of As_2O_3 in the film is reduced to 1.0 m/o As_2O_3 and below, film detachment and consequent glass damage can be eliminated altogether even at temperatures as high as 1100°C.

In this paper, the diffusion characteristics of arsenic in silicon from these low As_2O_3 -content arsenosilicate glass films are reported. The advantages of using doped oxides in the technique of solid-to-solid state diffusion for device fabrication are well known (16-19). In the case of arsenic diffusion, one distinct advantage of using arsenosilicate glass sources is that the quantity of total arsenic involved is very small (0.1 mg or less) compared with a source of the order of grams, which must be vaporized in the technique of gas-to-solid diffusion using either open or sealed tubes. Thus, health hazards due to arsenic poisoning may be reduced considerably. The junction depths and sheet resistivities of diffused layers have been measured systematically as a function of time and temperature of diffusion. Effects of source concentration and diffusion ambient on these two parameters were also studied wherever possible. Moreover, in view of the current recognition of concentration dependence of impurity diffusion in silicon at high impurity concentration (from 10^{19} cm^{-3} and up), diffusion profiles in silicon at various temperatures have been determined experimentally so as to enable a more meaningful evaluation of arsenic diffusivities and surface concentrations in silicon.

Finally, by diffusing arsenic through a barrier layer of SiO_2 into silicon, the masking ability of SiO_2 toward arsenic diffusion has been studied as a function of SiO_2 thickness, temperature, and As_2O_3 concentration in the glass. In addition, some useful diffusion parameters of arsenic in SiO_2 can be estimated using a simple model.

Experimental

Glass deposition.—The silicon substrates used for glass deposition and subsequent diffusion of arsenic

were 1 ohm-cm p-type (100)-surface oriented wafers 2.5 cm in diameter and 0.05 cm thick. These were heavily etched in a conc HNO_3 -conc HF solution (3:1 by volume) and rinsed thoroughly in distilled water prior to deposition. Arsenosilicate films were deposited by a CVD technique using argon-diluted reaction mixtures of SiH_4 , AsCl_3 , and O_2 . The materials and deposition apparatus have been described elsewhere (14, 15). All films were deposited at 450°C. Compositions of the as-deposited films were determined nondestructively by infrared absorption spectroscopy using a published calibration for the IR absorbance ratio *vs.* mol per cent As_2O_3 obtained by chemical analysis (14). All arsenosilicate films had a thickness of about 7000Å, which is greater than the largest diffusion length of arsenic in the glass in these experiments.

In order to study the masking effect of a barrier layer of SiO_2 on arsenic diffusion into silicon, a layer of SiO_2 was grown thermally on the bare silicon at 1000°C. The thickness of this thermal SiO_2 was determined ellipsometrically prior to arsenosilicate deposition and arsenic diffusion.

Diffusion.—A conventional horizontal diffusion furnace consisting of an electrically heated fused quartz tube having a projecting side arm for sample loading was used. The temperature of the constant temperature zone (1½ in. long) was controlled to within 2°C at 1100°C. Diffusions were performed in either argon or oxygen.

Sample preparation.—Two modes of sample preparations were used prior to the diffusion experiments. For initial determinations of junction depth x_j and electrical resistivity V/I of diffused layers as a function of temperature and time of diffusion, and thickness of the sandwiched thermal SiO_2 layer, the wafer was divided into four quarters after glass deposition. Each of these quartered wafers was then diffused individually at the preset conditions. For profile determinations, after the glass source had been deposited the wafer was halved, each piece was then diffused at the desired conditions.

After diffusion in Ar and glass removal, a thin grayish brown film was found to remain on the silicon substrate. This film, which is insoluble in the buffered HF etching solution, renders the silicon surface hydrophilic and can be removed simply by mechanical wiping. When the diffusion is performed in O_2 , however, the resultant silicon surface is hydrophobic. Formation of this so-called "brown skin" has recently been reported (13) but its chemical nature is still uncertain.

Junction depth and sheet resistivity.—The junction depth and sheet resistivity of diffused layers were determined by the standard methods of angle lapping and staining, and the four-point probe technique, respectively. The former was calculated from the width of the white band in the micrograph of the

* Electrochemical Society Active Member.

Key words: arsenic diffusion in silicon, η -type glass source.

junction after staining using the appropriate magnification factor and beveling ratio. An accuracy of $\pm 0.035\mu$ has been estimated with the present procedure. By switching the probe orientation on the wafer three times and reverting the current polarity, six V/I measurements were made on each sample. The arithmetic average of these V/I values was then converted to sheet resistivity using Smits' table (20).

Profile determination.—Arsenic-diffusion profiles were determined using the technique of anodization-sectioning in conjunction with the four-point probe differential sheet resistivity measurements (1, 21). The theory underlying this technique has recently been reviewed by Donovan and Evans (22). The procedure of profiling consisted of successively measuring the sheet resistivity of the diffused layer followed by removal of a silicon layer of controlled thickness, and was repeated until a sheet resistivity of ~ 2000 ohm/square was reached.

All anodizations were performed in a diluted aqueous HNO_3 solution at a constant voltage of 25V for 30 min. Under these conditions it was found that the thickness of the resultant anodized layer decreases with increase in sheet resistivity of the diffused layer due to a lower impurity surface concentration and/or junction depth. Ten reference anodized oxides of thickness varying in the range 200–1200Å were prepared and their thickness measured by ellipsometry. The thickness of each individual anodized layer on the diffused samples was then determined to within 50Å by comparing with the color of the reference samples. From the refractive index of the anodized SiO_2 (1.415–1.420 at $\lambda = 5460\text{Å}$) the thickness of silicon removed at each anodization was estimated to correspond to 0.40 times the thickness of the anodized oxide. The oxide was subsequently removed by etching in a buffered HF solution. The depth at any point is then the sum of the silicon increments already removed.

Results

Junction depth and sheet resistivity of diffused layers.—Two experimental parameters are of importance in the characterization of diffused layers in semiconductor technology. These are the junction depth x_j and sheet resistivity ρ_s of the diffused layer. In the present investigation these parameters were studied systematically as a function of temperature and time of diffusion and thickness of a sandwiched SiO_2 layer. Variation in As_2O_3 concentration in the diffusion source was somewhat limited due to the occurrence of glass damage on bare silicon when films containing more than 1 m/o As_2O_3 are heat-treated at 1000°C and up (15).

In Fig. 1, the junction depth x_j and sheet conductivity ρ_s^{-1} of the diffused layers are plotted as a function of the square root of diffusion time, \sqrt{t} . Diffusions were performed in an Ar ambient using a 0.8 m/o As_2O_3 arsenosilicate glass, 7000Å thick in each case. Linearity is obtained in the x_j vs. \sqrt{t} plots while a monotonic increase in ρ_s^{-1} with \sqrt{t} is observed at all temperatures. The diffusion is enhanced in the presence of O_2 as shown by the higher junction depths and higher sheet conductivities at 1100°C.

The junction depth and sheet resistivity of diffused layers have also been studied as a function of thickness of the sandwiched SiO_2 layer for a constant diffusion time of 4 hr at 1100° and 1150°C in Ar. The results are plotted in Fig. 2 and 3 for a 0.8 m/o As_2O_3 source and a 2.5 m/o As_2O_3 source, respectively. It can be seen that x_j decreases and ρ_s increases monotonically with thickness of the SiO_2 layer, demonstrating a positive masking effect of the thermal oxide toward arsenic diffusion. The masking ability of a given SiO_2 layer decreases with increase in As_2O_3 content in the diffusion source.

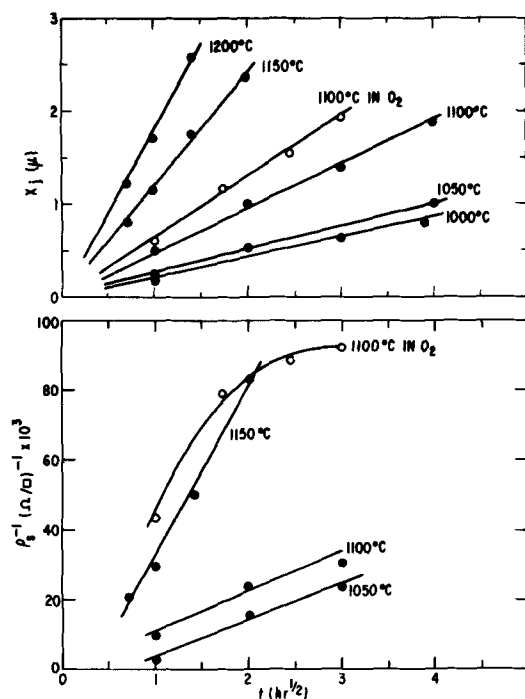


Fig. 1. Plots of (a, top) x_j and (b, bottom) ρ_s^{-1} of arsenic diffused layers in silicon vs. square root of diffusion time at various temperatures of diffusion in Ar (closed circles) and in O_2 (open circles). The diffusion source in each case was a film of 7000Å arsenosilicate glass containing 0.8 m/o As_2O_3 .

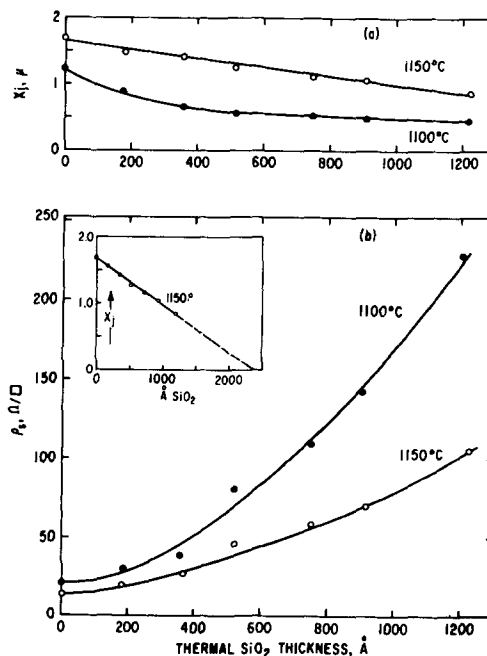


Fig. 2. Plots of (a) x_j and (b) ρ_s of arsenic-diffused layers in silicon vs. thickness of barrier SiO_2 at 1100° and 1150°C. All diffusions were performed in Ar for 4 hr using glass sources containing 0.8 m/o As_2O_3 . Inset in Fig. 2(b) is an extrapolation to the masking thickness of SiO_2 .

An attempt to evaluate the dependence of x_j and ρ_s at higher As_2O_3 concentration in the glass source proved to be unsuccessful due to the onset of severe glass damage from 5 m/o As_2O_3 and up. Nevertheless, the x_j and ρ_s data obtained by diffusing As from various As_2O_3 -content glasses up to 16 m/o As_2O_3 through a 519Å SiO_2 layer at 1100° and 1150°C for 4 hr in Ar are given in Fig. 4. Monotonicity is lost in the composition region of glass damage.

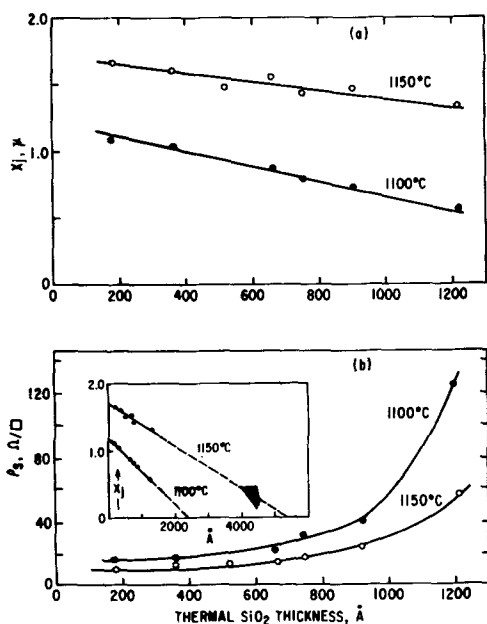


Fig. 3. Plots of (a) x_j and (b) ρ_s vs. thickness of barrier SiO_2 . Diffusion conditions were identical to those shown in Fig. 2, except a 2.4 m/o As_2O_3 arsenosilicate source was used. Inset in Fig. 3(b) shows extrapolation to the masking thickness of SiO_2 .

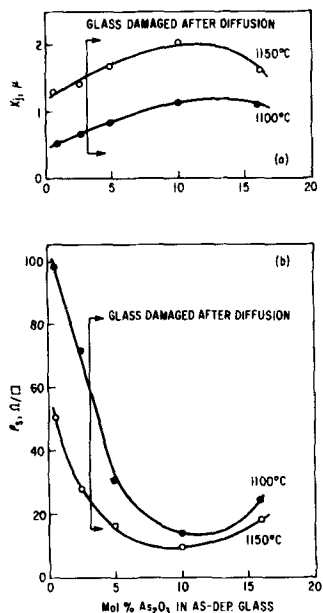


Fig. 4. Plots of (a) x_j and (b) ρ_s vs. glass composition at 1100° and 1150°C. All diffusions were performed through a 520Å barrier SiO_2 in Ar. Note glass damage beyond 2.5 m/o As_2O_3 .

Arsenic-diffusion profiles.—In Fig. 5, the sheet conductivity is plotted as a function of depth into the diffusion layer at various temperatures of diffusion in Ar for 4 hr from a 0.8 m/o As_2O_3 glass source on bare silicon. The data for a similar diffusion in an oxygen atmosphere are also given in Fig. 5. The conductivity data were then statistically regressed and the differential conductivity as well as the differential carrier concentration at each point were obtained with a computer routine. The latter quantity is calculated using the effective mobility values compiled by Irvin (23). The profiles are given in Fig. 6 and represent the ionized arsenic distributions at various diffusion temperatures. It is of interest to note that the flat regions in the initial portion of the concentration profiles at 1000°, 1050°, and 1100°C are merely a manifestation of the linearity in the initial portions of the

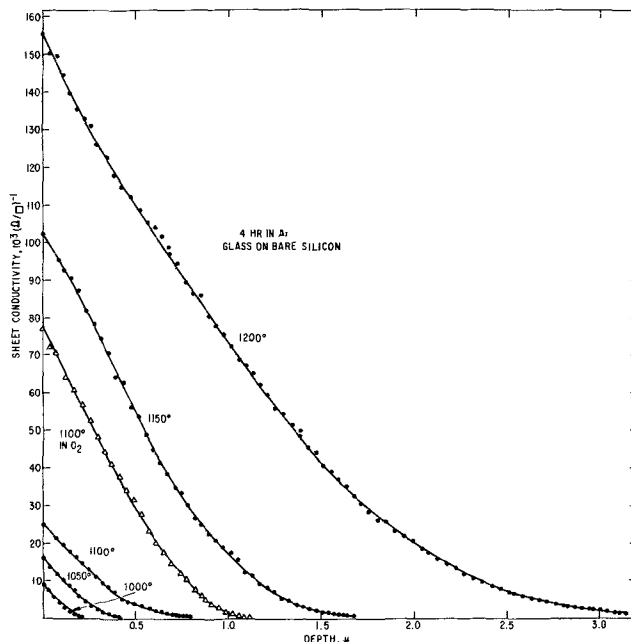


Fig. 5. Sheet conductivity profiles of diffused layers at various temperatures. The diffusion source in each case consisted of a 0.7 m/o As_2O_3 arsenosilicate film, 7000Å thick. Note the open triangles for diffusion in O_2 .

respective sheet conductivity profiles (see Fig. 5). Similarly, the upward convexity and concavity in the initial portions of the conductivity profiles at 1150° and 1200°C in Fig. 5 are accordingly reflected in the respective concentration profiles in Fig. 6.

The carrier concentration profiles resulted from a 4-hr diffusion of arsenic from various As_2O_3 -content arsenosilicate glasses through a layer of thermal SiO_2 of various thickness have also been studied at 1150°C. The sheet conductivity profiles in these diffused layers are given in Fig. 7, from which the carrier concentrations were determined and are shown in Fig. 8. The masking effect of the sandwiched SiO_2 layer in reducing both the carrier concentration in silicon at a given depth and the over-all junction depth can easily be seen from the profiles. For example, in going from a diffusion through bare silicon (Fig. 8 curve a) to a diffusion through a 519Å SiO_2 (Fig. 8 curve d) the carrier concentration at the surface drops from 6×10^{19} to $2.4 \times 10^{19} \text{ cm}^{-3}$. Furthermore, increasing the thickness of the SiO_2 layer will lower the surface carrier concentration as well as the junction depth (cf. Fig. 8 curve c and e). Enhanced diffusion in the presence of O_2 was again observed (cf. curves b and c in Fig. 8).

Discussion

Junction depth and sheet resistivity.—It can be seen from Fig. 1 that the junction depth, x_j , of the diffused layer varies linearly with the square root of diffusion time, \sqrt{t} , in either an argon or oxygen ambient at all the temperatures investigated. This linear relationship holds if the arsenic concentration $N(x, t)$ in the neighborhood of the background concentration, N_B , is given by

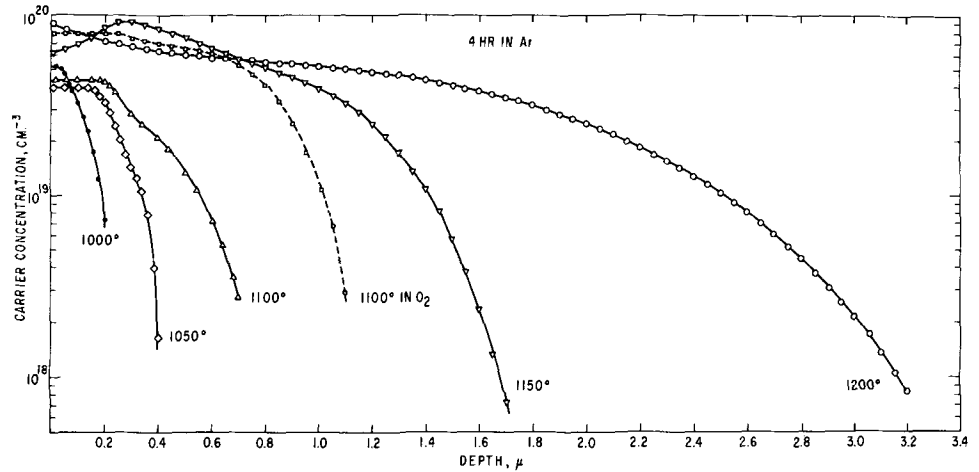
$$N(x, t) = F(x/\sqrt{t}) \quad [1]$$

where x is the distance from the silicon surface, t is the diffusion time, and F is a function of diffusion temperature, impurity concentration in the glass, and impurity diffusivity in silicon. When x is equal to the junction depth, x_j , Eq. [1] becomes

$$N_B = F(x_j/\sqrt{t}) \quad [2]$$

As all the experiments were conducted on silicon wafers of equal resistivity with doped glasses of the

Fig. 6. Carrier concentration profiles in silicon calculated from the corresponding conductivity profiles shown in Fig. 5. The points are computer generated at regular depth intervals.



same composition, Eq. [2] is equivalent to

$$x_j = [F^{-1}(N_B)] \sqrt{t} \quad [3]$$

where F^{-1} is the inverse of F and $F^{-1}(N_B)$ is a constant at a given temperature.

Furthermore, if the concentration profile can be described by Eq. [1], then the surface concentration, N_s , in silicon is invariant with time and equal to $F(0)$. This is the case when the glass layer is thick enough to be regarded as semi-infinite (17). Thus, a new normalized function, $f(x/\sqrt{t})$, can be introduced by the relationship

$$f(x/\sqrt{t}) = F(x/\sqrt{t})/N_s \quad [4]$$

with

$$f(0) = 1 \quad [5]$$

$$f(\infty) = 0$$

The second boundary condition is justified by the physical requirement that impurities diffuse into silicon with a finite rate. At low impurity concentrations where the diffusion coefficient D of As in Si is concentration independent a simple erfc distribution results, and

$$f(x/\sqrt{t}) = \text{erfc}(x/2\sqrt{Dt}) \quad [6]$$

which satisfies the boundary conditions of Eq. [5].

The sheet resistivity, ρ_s , of the diffused layer is related to the carrier concentration $n(x)$ by

$$\rho_s^{-1} = \int_0^{x_j} q \mu(n) n(x) dx \quad [7]$$

where q is the electron charge and μ the carrier mobility which is a function of the total impurity concentration. At high arsenic concentrations, the number of carriers is only a fraction ϕ of the total arsenic impurity concentration N (24, 25). Furthermore, this fraction is a function of N (26), so that Eq. [7] becomes

$$\rho_s^{-1} = q \int_0^{x_j} \mu(N) \phi(N) N(x) dx \quad [8]$$

Using Eq. [1] and [4] to substitute for N , we have

$$\rho_s^{-1} = qN_s \int_0^{x_j} \mu\left(\frac{x}{\sqrt{t}}\right) \phi\left(\frac{x}{\sqrt{t}}\right) f\left(\frac{x}{\sqrt{t}}\right) dx \quad [9]$$

Introducing a new variable $\eta = \frac{x}{\sqrt{t}}$, Eq. [9] becomes

$$\rho_s^{-1} = q N_s \sqrt{t} \int_0^{x_j/\sqrt{t}} \mu(\eta) \phi(\eta) f(\eta) d\eta \quad [10]$$

The integral in Eq. [10] is not a function of time, as x_j/\sqrt{t} is constant and equal to $F^{-1}(N_B)$ (from Eq.

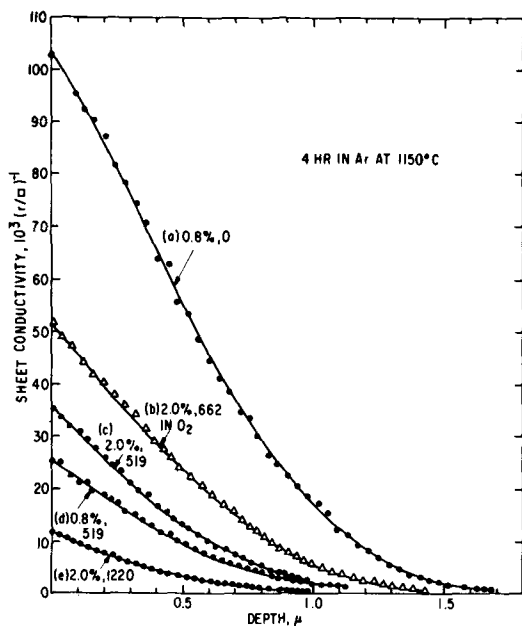


Fig. 7. Sheet conductivity profiles of diffused layers at 1150°C as a function mol per cent As₂O₃ in the diffusion source and barrier SiO₂ thickness. Note the open triangles for diffusion in O₂.

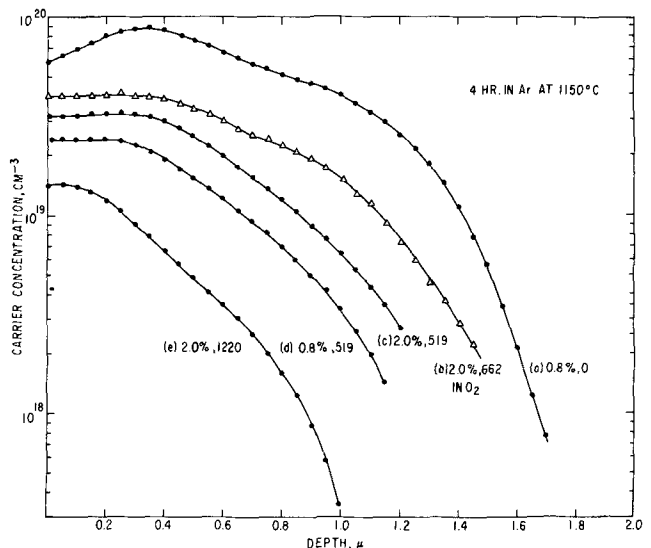


Fig. 8. Carrier concentration profiles in silicon calculated from the corresponding conductivity profiles shown in Fig. 7. The points are computer generated at regular depth intervals.

[3]). This implies that the sheet conductivity varies as the square root of time, as can be seen from the isothermal plots of ρ_s^{-1} vs. \sqrt{t} shown in Fig. 1(b).

It must be noted however that any deviation of the concentration profile in the vicinity of the silicon surface from that given by Eq. [1] and [4] would modify the \sqrt{t} dependence of the sheet conductivity. This is because close to the surface, the concentration is highest and provides the largest contribution to the integral in Eq. [10]. On the contrary, the time dependence of x_j is related to the evolution in time of the profile tail and linear plots of x_j vs. \sqrt{t} are obtained when $N(x, t)$ can be expressed by Eq. [1] for large values of x . Thus, the linearity of x_j vs. \sqrt{t} can be attained independently from the linearity of ρ_s^{-1} vs. \sqrt{t} , and vice versa.

In the presence of an oxygen ambient, deeper junction depths and higher sheet conductivities are obtained when compared with those of identical wafers diffused in an inert atmosphere of argon under the same conditions (see Fig. 1). This enhancement of arsenic diffusion in silicon is further manifested by the higher surface carrier concentrations observed in the profiles at 1100° and 1150°C as shown respectively in Fig. 6 and 8. Similar enhancements have recently been noted for boron and phosphorus diffusion in silicon in an oxidizing ambient (27).

It has been established that oxygen diffuses as an ionic species in silica in the process of thermal oxidation of silicon (28). If a similar ionic species is present in binary borosilicate, phosphosilicate and arsenosilicate glasses, diffusion of the impurity in the glass in the vicinity of the glass-silicon interface can be field-aided. Thus, it is conceivable that an enhanced impurity flux can be obtained at this interface to give rise to higher surface concentrations in the presence of O₂. Furthermore, a higher surface concentration can also result in higher concentrations of impurity along the profile (compare with those obtained in Ar). This in turn would increase the diffusivity of the impurity and give rise to a deeper junction.

Profiles and arsenic diffusivity in silicon.—The diffusion profiles shown in Fig. 6 and 8 can generally be described by a region of almost constant concentration near the silicon surface, followed by a region where the carrier concentration decays rapidly. Preliminary examination suggests that they do not at all appear to conform to simple complementary error functions which postulate an approximate exponential decrease in concentration in going into the junction. In Fig. 9, a direct comparison is made of the measured profiles at 1000° and 1100°C (from Fig. 6) with the corresponding erfc profiles calculated from the measured junction depths and sheet resistivity of the diffused layers based on Irvin's curves (23). It is clear from Fig. 9 that the erfc predicts a higher than actual concentration at the surface and a lower than actual concentration gradient in the vicinity of the junction. A similar "non-erfc" profile at a higher surface carrier concentration of 1.7×10^{20} cm⁻³ has also been reported (7) for the diffusion of arsenic into silicon at 1200°C using a Si(As) powdered source in an evacuated closed quartz capsule.

Indeed, it is well established experimentally that the actual diffusion profiles of Group III and V impurities in silicon at high doping concentration and deep diffusion cannot be correctly described by a simple erfc function (5, 7, 12, 21, 29-43). The assumed erfc profile bears essentially no relevant relationship with the actual profile except at low concentrations ($\leq 10^{19}$ cm⁻³), where the diffusivity becomes a constant. In the semiconductor industry and literature, a "fictive diffusivity" is often employed, which is so defined as to make the measured junction depth and sheet resistivity, the two arbitrarily chosen parameters for the

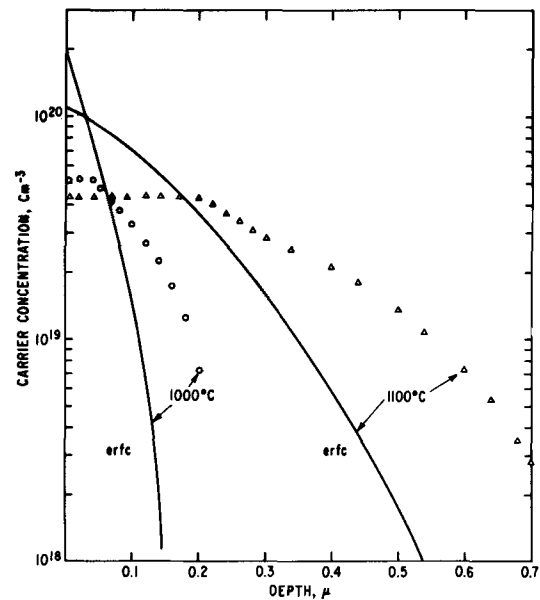


Fig. 9. Comparison of erfc distribution with actual profiles at 1000° and 1100°C from Fig. 6.

characterization of a diffused layer, coincide with a presumed erfc profile. The fictive diffusivity is also made to vary with surface concentration and background concentration (1, 7, 44). Basic inconsistencies such as those illustrated in Fig. 9 often arise as a result of the difference between the nature of an erfc and an actual profile. To avoid these discrepancies, Hu and Schmidt (5) have pointed out that it is necessary to abandon the concept of a constant diffusivity and to consider interaction of first-order importance in the treatment of the diffusion process.

One probable reason for a deviation from the erfc distribution of the carrier concentration profiles resulted in the present diffusion of arsenic from an arsenosilicate glass source into silicon is that the diffusion coefficient of arsenic is not a constant. Using the Boltzmann-Matano method (45, 46) an effective diffusion coefficient \bar{D} of arsenic in silicon as a function of carrier concentration can be calculated. If \bar{D} is only a function of carrier concentration which in turn will change only with x/\sqrt{t} but not with x and t separately, where x is the depth into the junction and t is the diffusion time, then

$$\bar{D}_{cx} = -\frac{1}{2t} \left(\frac{dx}{dc} \right)_{cx} \int_0^{c_x} x dc \quad [11]$$

From the profiles shown in Fig. 6 and using Eq. [11], the value of \bar{D} as a function of carrier concentration is calculated by means of a computer routine. The results are given in Fig. 10 for various diffusion temperatures. At carrier concentration $\geq 10^{19}$ cm⁻³, \bar{D}_{As} rises sharply with increase in carrier concentrations at all temperatures. Furthermore, at diffusion temperatures of 1100°C and higher, distinct maxima in the \bar{D}_{As} vs. carrier concentration plots are evident, which interestingly enough are quite analogous to those calculated recently by the IBM group (47, 48). A somewhat similar maximum in the diffusion coefficient of boron in silicon at 1050°C from a borosilicate glass source has also been reported by Brown and Kennicott (44) who plotted D as a function of surface concentration calculated by assuming erfc distributions.

It must be emphasized, however, that the diffusion coefficient of arsenic calculated from the carrier concentration profiles is valid only (a) if the carrier concentration profiles obtained for various diffusion times coincide with one another when plotted against the

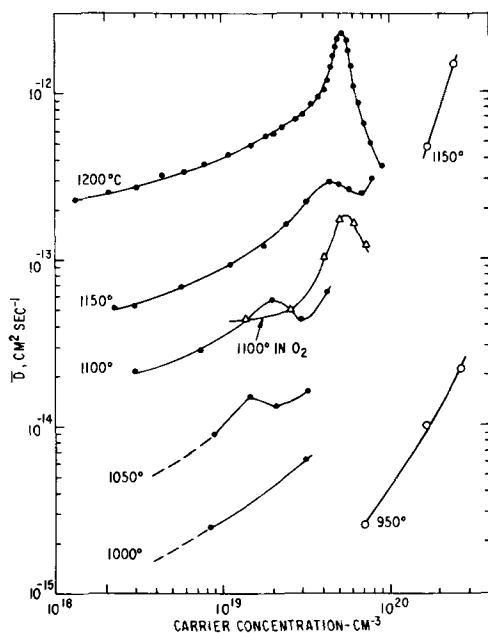


Fig. 10. Plots of \bar{D}_{As} obtained from the Boltzmann-Matano analysis of the profiles shown in Fig. 6 vs. carrier concentration at various temperatures. Open circles are the data of Masters and Fairfield's (6) at 950° and 1150°C.

normalized distance x/\sqrt{t} , and (b) if the ratio of the concentration of electrically active arsenic to that of the total arsenic is invariant with depth into silicon. In Fig. 11, the carrier concentration profiles of two identical samples diffused under the same conditions for two different times are plotted against x/\sqrt{t} . No exact coincidence of the profiles is obtained. Therefore, the effective diffusion coefficient obtained from the Boltzmann-Matano transformation is only approximate and the results shown in Fig. 10 are at best to be regarded as formal.

Strong concentration dependence of arsenic diffusivity in silicon has recently been observed by Masters and Fairfield (6) in their isoconcentration diffusion experiments at various background doping levels using a neutron activated Si(As) source powder in evacuated quartz capsules. Their isoconcentration results at 950° and 1150°C are also plotted in Fig. 10 for comparison.

The temperature dependence of \bar{D}_{As} can be obtained from Fig. 10 by plotting $\log_{10} \bar{D}_{As}$ as a function of the reciprocal absolute temperature of diffusion at constant carrier concentration. In Fig. 12 the lines (a), (b), and (c) represent the least squares fits of the corresponding data at carrier concentrations of $4 \times$

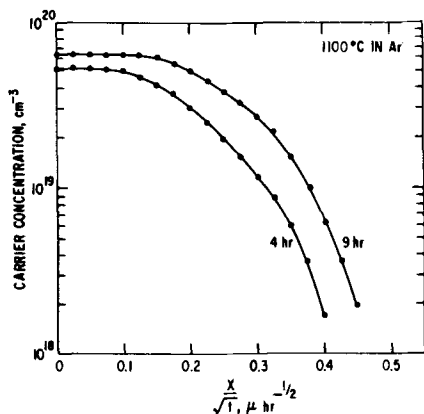


Fig. 11. Carrier concentration in two identical samples vs. normalized distance.

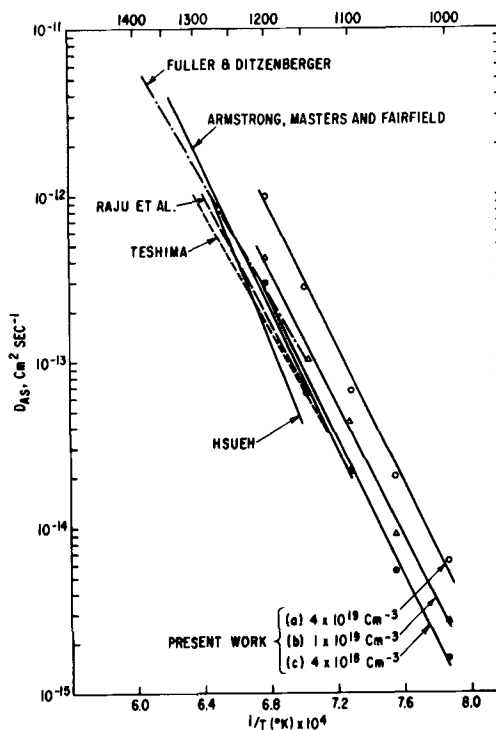


Fig. 12. Temperature dependence of arsenic diffusivity in silicon

10^{19} cm^{-3} , $1 \times 10^{19} \text{ cm}^{-3}$, and $4 \times 10^{18} \text{ cm}^{-3}$, respectively, using an Arrhenius-type expression of the form

$$\log_{10} D = \log_{10} D_0 - \frac{Q}{2.303kT} \quad [12]$$

where D_0 is the pre-exponential term in $D = D_0 \exp(-Q/kT)$, Q is the activation energy of diffusion, and $k = 0.86 \times 10^{-4} \text{ eV deg}^{-1}$, the Boltzmann constant. With a standard deviation of 8% in the corresponding $\log_{10} D$ vs. $1/T$ plots, the diffusivity data may be represented by (a) $D = 110 \exp(-4.1 \text{ eV}/kT)$, (b) $D = 25 \exp(-4.0 \text{ eV}/kT)$, and (c) $D = 44 \exp(-4.2 \text{ eV}/kT)$, giving an activation energy of $4.1 \pm 0.1 \text{ eV}$ for the diffusion of arsenic in silicon. This value appears to be constant in the concentration range¹ of 4×10^{18} – $4 \times 10^{19} \text{ cm}^{-3}$ and compares well with an "accepted" value of $3.9 \pm 0.3 \text{ eV}$ cited by Millea (49). Data on the temperature dependence of arsenic diffusivity in silicon by other workers (1, 3, 6, 8, 50) are also plotted in Fig. 12. Direct comparison is difficult in light of the fact that the previous calculations of D_{As} were based on assumed erf distribution profiles with surface concentration as the concentration variable. However, the combined results of Armstrong (3) and Masters and Fairfield (6) on intrinsic silicon agree quite well with the present data at carrier concentration of $4 \times 10^{18} \text{ cm}^{-3}$. The results of Hsueh (8) obtained from gas-solid diffusions using an AsH_3 source give $D_0 = 8.3 \times 10^4 \text{ cm}^2 \text{ sec}^{-1}$ and $Q = 5.2 \text{ eV}$, and appear unreliable.

Diffusion through a barrier SiO_2 layer.—In a recent systematic study (15) it has been shown that vapor-deposited binary arsenosilicate films on bare silicon exhibit glass detachment and consequent glass damage when glasses containing more than 1 m/o As_2O_3 are heat-treated at 1000°C and up. When glass damage occurs, undesirable characteristics such as irregular diffusion fronts and appearance of deep spikes are introduced into the resultant diffused layers (14). The

¹ Note that only \bar{D}_{As} values in the carrier concentration range of 4×10^{19} to $4 \times 10^{18} \text{ cm}^{-3}$ (i.e., those below the maximum value in Fig. 10) are considered in the temperature dependence plots (Fig. 12). This is because of the fact that a maximum in the D vs. concentration plot results simply from a change in curvature of the corresponding concentration profile, which may or may not be significant experimentally in the present work.

diffusion of arsenic from these binary arsenosilicate glasses on bare silicon is therefore limited to the use of low As_2O_3 -content sources (< 1 m/o As_2O_3). However, by inserting a barrier layer of pure SiO_2 between the silicon substrate and arsenosilicate glass, the concentration of As_2O_3 in the source can be increased to 2.5 m/o As_2O_3 without introducing glass damage when heat-treated to 1150°C . Thus, by diffusing arsenic through a barrier layer of SiO_2 it is possible to obtain an estimate of the effects of source concentration on the diffusion of arsenic in silicon. Furthermore, diffusion parameters of arsenic in SiO_2 and the masking ability of the latter may also be measured.

From the results shown in Fig. 2(a) and 3(a), the junction depth of diffusion layer in silicon decreases linearly with increasing thickness of the barrier SiO_2 layer. The masking thickness of the barrier layer at the given diffusion conditions is obtained by extrapolating to $x_j = 0$ (51) [see insets in Fig. 2(b) and 3(b)]. Thus, diffusing from a 0.8 m/o As_2O_3 glass source at 1150°C for 4 hr, a 2400Å thickness SiO_2 layer is required for complete masking, whereas diffusing from a 2.5 m/o As_2O_3 source at 1100° and 1150°C for 4 hr, masking thicknesses of 2400 and 5300Å are required, respectively. Under the same conditions of temperature and time of diffusion, therefore, a higher As_2O_3 content source requires a thicker SiO_2 layer for complete masking. Alternatively, for a given masking thickness of barrier SiO_2 , a lower diffusion temperature is required for diffusion from a higher As_2O_3 -content source at constant time.

Of interest too is the lack of upward convexity in all the x_j vs. SiO_2 thickness plots shown in Fig. 2(a) and 3(a). This suggests that the segregation coefficient of arsenic in silicon and SiO_2 is equal to or greater than 1 in accordance with the impurity-redistribution model of Grove *et al.* (51, 52).

Furthermore, with increasing thickness of barrier SiO_2 layer the sheet resistivity of the diffused layer increases [see Fig. 2(b) and 3(b)]. This simply implies that there is a progressive reduction of the total amount of arsenic entering the silicon substrate. From the carrier concentration profile shown in Fig. 8, it can be seen with clarity that not only the total amount of arsenic diffusing into silicon was reduced but also its concentration at the surface was substantially lowered.

Arsenic diffusion parameters in SiO_2 .—The ratio of the diffusion coefficient of arsenic in SiO_2 , D_1 , to that in Si, D_2 can be calculated from the x_j vs. SiO_2 thickness data shown in Fig. 2(a) and 3(a) by using the relation

$$\sqrt{\frac{D_1}{D_2}} = \frac{x_B}{(x_j)_N - (x_j)_B} \quad [13]$$

where x_B is the thickness of the barrier SiO_2 layer, and $(x_j)_N$ and $(x_j)_B$ are the measured junction depths obtained by diffusing without and with the barrier layer, respectively. This relation has been developed by Barry and Olofsen (17) for diffusion of a dopant from a glass source through a barrier layer of pure SiO_2 into a semiconductor substrate. The results are summarized in Table I.

Table I. Calculated D_1/D_2 ratios as a function diffusion temperature at two source concentrations

As_2O_3 in glass, m/o	D_1/D_2^*	
	1100°C	1150°C
0.8	0.012	0.018
2.5	0.037	0.102

* Each D_1/D_2 ratio tabulated is the arithmetic average of the set of values calculated from the respective data points in Fig. 2(a) or Fig. 3(a).

It can be seen from Table I that the diffusion coefficient of arsenic in SiO_2 is lower than that in silicon by approximately 2 to 1 order of magnitude depending on source concentration and diffusion temperature. Of more interest is the increase of the D_1/D_2 ratio with both increase in temperature and source concentration. A positive temperature coefficient of this ratio implies a negative slope in the plot of $\ln D_1/D_2$ vs. $1/T$, as is evident from the following

$$\ln \left(\frac{D_1}{D_2} \right) = \ln \left(\frac{D_1^0}{D_2^0} \right) - \frac{Q_1 - Q_2}{kT} \quad [14]$$

where D_i^0 are the pre-exponential terms in the Arrhenius expression: $D = D^0 \exp \left(\frac{-Q}{kT} \right)$, and Q_1 and

Q_2 are the activation energies of diffusion for arsenic in SiO_2 and silicon, respectively. This in turn implies that $Q_1 - Q_2$ is positive and that the activation energy of diffusion of arsenic in SiO_2 is greater than that in silicon. Using the combined data of Horiuchi and Yamaguchi (53), Brown and Kennicott (44) on boron diffusivity in SiO_2 , and Millea's compilation (49) on boron diffusivity in silicon, a similar trend is found for the activation energies of diffusion for boron in SiO_2 (3.78 eV) and in silicon (3.71-3.69 eV). In the case of phosphorus, however, Sah *et al.* (54) found that the ratio D_1/D_2 is relatively insensitive to temperature, at least in the range 1100° - 1150°C . The present data show that $Q_1 - Q_2$ for arsenic is of the order 1 ± 0.5 eV.

The 3- to 5-fold increase in the D_1/D_2 ratio with increase in As_2O_3 concentration in the source is worth noting. In the model of Barry and Olofsen (17), it was assumed that (i) the diffusion coefficient D_1 of dopant is the same in both the glass source and pure SiO_2 and (ii) D_2 is concentration independent. The fact that D_1/D_2 changes with source concentration implies that the diffusivity of arsenic in the arsenosilicate source varies with concentration and the validity of the first assumption above is therefore questionable. A strong dependence on the phosphorus concentration has also been noted by Thurston *et al.* (55) in studying P-diffusion in SiO_2 with radiotracers. Furthermore, it has been shown in the discussion earlier that the diffusivity of arsenic in silicon is concentration dependent in the range presently studied.

It must be remarked, therefore, that the above diffusion parameters calculated for arsenic in SiO_2 are best to be regarded as qualitative estimates. Further refinements of the model and more experimental data are needed to substantiate quantitative evaluation of these parameters.

Summary and Conclusion

Diffusion of arsenic in silicon from low As_2O_3 -content arsenosilicate glass sources was investigated. The glass films were prepared by chemical vapor deposition using argon-diluted mixtures of SiH_4 , AsCl_3 , and O_2 at 450°C . When diffusion experiments were carried out with glass in direct contact with silicon, the film composition was held below 1 m/o As_2O_3 to avoid glass detachment at 1000°C and higher (14, 15). However, with a barrier layer of thermal SiO_2 sandwiched between the glass and silicon, the As_2O_3 content in the glass could be increased to 2.5 m/o As_2O_3 without introducing detachment at diffusion temperatures.

The resultant arsenic-diffused layers in silicon were evaluated (a) by measuring the junction depth x_j and sheet conductivity ρ_s^{-1} as a function of time and temperature of diffusion in both argon and oxygen ambients (see Fig. 1); (b) by measuring x_j and ρ_s as a function of thickness of the barrier SiO_2 layer at two temperatures and two source concentrations (see Fig. 2-4); and (c) by determining the carrier concentration profiles as a function of diffusion temperature (Fig. 6),

and barrier SiO₂ thickness and source concentrations (Fig. 8).

The above experimental data show that:

1. The slopes of Arrhenius plots of $\log \bar{D}_{As}$ vs. $1/T$ (Fig. 12) at various carrier concentrations in the range 4×10^{18} to 4×10^{19} cm⁻³ correspond to an activation energy of 4.1 ± 0.1 eV in good agreement with an "accepted" value for arsenic in silicon (49).

2. The diffusion of arsenic in silicon is enhanced in the presence of O₂ to yield deeper junctions and higher surface concentrations than those in Ar at constant glass composition.

3. The diffusion profiles of arsenic in silicon are different from those of an erfc distribution.

4. The ratio of the diffusion coefficient of arsenic in SiO₂ to that in silicon increases with increase in temperature. $Q_1 - Q_2$ is estimated to be 1.0 ± 0.5 eV.

Acknowledgments

We are much indebted to L. F. Cordes for his comments and assistance in the profiling technique, and his generous loan of the computer routines for analyzing the diffusion data. We are grateful to D. M. Brown for the use of his equipment and facilities. We thank E. A. Taft and R. J. Connery for the ellipsometric measurements of film thickness and preparation of thermal oxide, respectively. Suggestions and encouragement given by M. Garfinkel in the course of this work are gratefully acknowledged. Helpful discussions with J. W. Mitchell, R. N. Hall, and P. V. Gray are also appreciated.

Manuscript submitted Jan. 14, 1972; revised manuscript received May 23, 1972.

Any discussion of this paper will appear in a Discussion Section to be published in the June 1973 JOURNAL.

REFERENCES

- C. S. Fuller and J. A. Ditzenberger, *J. Appl. Phys.*, **27**, 544 (1956).
- C. J. Frosch and L. Derick, *This Journal*, **104**, 547 (1957).
- W. J. Armstrong, *ibid.*, **109**, 1065 (1962).
- W. J. Armstrong and M. C. Duffy, *Electrochem. Technol.*, **4**, 475 (1966).
- S. M. Hu and S. Schmidt, *J. Appl. Phys.*, **39**, 4272 (1968).
- B. J. Masters and J. M. Fairfield, *ibid.*, **40**, 2390 (1969).
- S. Dash and M. L. Joshi, *IBM J. Res. Develop.*, **14**, 453 (1970).
- Y. W. Hsueh, *Electrochem. Technol.*, **6**, 361 (1968).
- D. B. Lee, *Solid State Electron.*, **10**, 623 (1967).
- H. Teshima, Y. Tarui, and O. Takeda, *Bull. Electro-chem. Lab. Jap.*, **33**, 631 (1969).
- A. Cuccia, G. Shrank, and G. Queirolo in "Semiconductor Silicon," Rolf R. Haberecht, Editor, p. 506, The Electrochemical Society Softbound Symposium Series, New York (1969).
- E. Arai and Y. Terunuma, *Japan. J. Appl. Phys.*, **9**, 691 (1970).
- P. C. Parekh, D. R. Goldstein, and T. C. Chan, *Solid State Electron.*, **14**, 281 (1971).
- J. Wong and M. Ghezzi, *This Journal*, **118**, 1540 (1971).
- J. Wong, *ibid.*, **119**, 1071 (1972); **119**, 1080 (1972).
- M. L. Barry and P. Olofsen, *Solid State Technol.*, **11**, 39 (1968).
- M. L. Barry and P. Olofsen, *This Journal*, **116**, 854 (1969).
- C. F. Gibbon in "Silicon Device Processing," p. 21, Nat. Bur. Std. (1970).
- M. L. Barry in "Silicon Device Processing," p. 175, Nat. Bur. Std. (1970).
- F. M. Smits, *Bell System Tech. J.*, **37**, 711 (1958).
- E. Tannenbaum, *Solid State Electron.*, **2**, 123 (1961).
- R. P. Donovan and R. A. Evans, in "Silicon Device Processing," p. 123, Nat. Bur. Std. (1970).
- J. C. Irvin, *Bell System Tech. J.*, **41**, 387 (1962).
- S. Chou, L. A. Davidson, and J. F. Gibbons, *Appl. Phys. Letters*, **17**, 23 (1970). b. R. O. Schwenker, E. S. Pan, and R. F. Lever, *J. Appl. Phys.*, **42**, 3195 (1971).
- T. L. Chiu and H. N. Ghosh, *IBM J. Res. Develop.*, **15**, 477 (1971).
- C. Kittel, "Introduction to Solid State Physics," 3rd edition, p. 312, John Wiley & Sons, Inc., New York (1967).
- H. Higuchi, M. Maki, and Y. Takano, Paper 78 presented at Los Angeles Meeting of the Society, May 10-15, 1970.
- P. J. Jorgensen, *J. Chem. Phys.*, **37**, 874 (1962).
- B. McDonald and F. C. Collins, *Bull. Am. Phys. Soc.*, **6**, 106 (1961).
- I. M. Mackintosh, *This Journal*, **109**, 392 (1962).
- P. A. Iles and B. Leibenhaut, *Solid State Electron.*, **5**, 331 (1962).
- J. J. Chang, *IEEE Trans.*, **ED-10**, 357 (1963).
- M. L. Joshi and F. Wilhelm, *This Journal*, **112**, 185 (1965).
- R. A. McDonald, G. E. Ehlenberger, and T. R. Huffman, *Solid State Electron.*, **9**, 807 (1966).
- K. H. Nicholas, *ibid.*, **9**, 35 (1966).
- M. C. Duffy, F. Barson, J. M. Fairfield, and G. H. Schwuttke, *This Journal*, **115**, 84 (1968).
- J. C. C. Tsai, *Proc. IEEE*, **9**, 1499 (1969).
- S. Dash and M. L. Joshi in "Silicon Device Processing," p. 202, Nat. Bur. Std. (1970).
- H. Rupprecht, *Bull. Am. Phys. Soc.*, **8**, 228 (1963).
- S. Maekawa and T. Oshida, *J. Phys. Soc. Japan*, **19**, 233 (1964).
- G. L. Vick and K. M. Whittle, *This Journal*, **116**, 1142 (1969).
- Y. Nakajima, S. Ohkawa, and Y. Fukukawa, *Japan. J. Appl. Phys.*, **10**, 162 (1971).
- Non-erfc diffusion profiles of arsenic, phosphorus, and boron in silicon are reported in Ref. 5, 7, 12, and 39; 21, and 29-35; and 36-38, respectively.
- D. M. Brown and P. R. Kennicott, *This Journal*, **118**, 293 (1971).
- P. G. Shewmon, "Diffusion in Solids," p. 29, McGraw Hill Book Co., New York (1963).
- B. I. Boltaks, "Diffusion in Semiconductors," p. 113, Academic Press (1963).
- D. P. Kennedy and P. C. Murley, *Proc. IEEE*, **59**, 335 (1971).
- T. L. Chiu and H. N. Ghosh, *IBM J. Res. Develop.*, **15**, 472 (1971).
- M. F. Millea in "Silicon Device Processing," p. 156, Nat. Bur. Std. (1970).
- P. S. Raju, N. R. K. Rao, and E. V. K. Rao, *Indian J. Pure Appl. Phys.*, **2**, 353 (1964).
- A. S. Grove, "Physics and Technology of Semiconductor Devices," p. 77, John Wiley & Sons, Inc., New York (1967).
- A. S. Grove, O. Leistiko, and C. T. Sah, *J. Appl. Phys.*, **35**, 2695 (1964).
- S. Horiuchi and J. Yamaguchi, *Japan. J. Appl. Phys.*, **1**, 314 (1962).
- C. T. Sah, H. Sello, and D. A. Tremere, *J. Phys. Chem. Solids*, **11**, 2 (1959).
- M. D. Thurston, F. E. Battocletti, and G. M. Rogers, "Impurity Profile in the Oxide Region," Final Report by Ohio State University, Research Foundation on Contract DA-36-039-SC-87426 (1964).



Effects of Hydrogen Annealing on High Power RF Sputtered Al_2O_3 Films on Silicon

P. K. Ajmera, M. A. Littlejohn, and J. R. Hauser

North Carolina State University, Raleigh, North Carolina 27607

A study of radio-frequency (rf) sputtered Al_2O_3 films has indicated that the density, dielectric constant, and index of refraction of these films increase while the P-etch rate decreases with increasing target-power density (1). In spite of these superior physical properties, Al_2O_3 films obtained by high-power rf sputtering have a serious drawback in that the surface-charge density located at the Al_2O_3 -Si interface also increases with increasing power density (1). This high density of positive surface-charge results in large negative values of the flat-band voltages (V_{FB}) of metal- Al_2O_3 -Si (MAS) devices fabricated from high-power sputtered films. This makes high-power sputtered Al_2O_3 films unsuitable as insulating layers for field effect metal-insulator semiconductor devices.

In this paper the results of a post-deposition annealing treatment which reduces the value of the effective surface-charge density in MAS devices are described. Metal- Al_2O_3 - SiO_2 -Si (MAOS) devices are also investigated, and the effects of the annealing treatment on some of the electrical properties of the MAOS devices are reported. The improved properties of high-power rf sputtered Al_2O_3 films offers the possibility for improved performance of MAOS memory elements (2).

Sample Preparation

Al_2O_3 films were deposited on both p- and n-type silicon substrates. The substrates were polished single-crystal Czochralski silicon slices of (111) orientation. The resistivity of the substrates was between 5-10 ohm-cm.

The rf sputtering system used was similar to the one described elsewhere (1) except for the fact that no provision was made for applying a magnetic field in the sputtering chamber. The rf sputtering power density was 500W which corresponded to a power density of 3.95 W/cm² at the target. A value of target-power density greater than 2.5 W/cm² has been found to yield an effective value of the positive surface-charge density located at the Al_2O_3 -Si interface greater than 10^{13} e/cm². This value can not be significantly reduced by annealing in nitrogen gas at 300°C (1). For an effective surface charge density of 2×10^{13} e/cm² located at the Al_2O_3 -Si interface, the magnitude V_{FB} of a MAS device is greater than 40V for a 1000Å sputtered Al_2O_3 film.

Two sets of sputtering runs were made. The first set of runs were made at a pressure of 5×10^{-3} Torr and a target-to-substrate distance of 1.8 in. In this set of runs either only argon or 20% oxygen along with argon was present in the plasma during the film deposition. High-purity argon and oxygen carrier gases were used. For convenience, films obtained from this set of runs will be identified as those obtained by "method 1". The second set of sputtering runs were made at a pressure of 7.5×10^{-3} Torr with a target-to-substrate distance of 1.7 in. The plasma, for all the runs made in this

set, contained 20% oxygen-80% argon. For convenience, this second set is referred to as "method 2." For both methods, the target voltage was 3.53 kV (peak value), the plate current was about 0.5A, and the substrate holder was grounded and water-cooled. The target was a 99.98% (or better) pure disk of Al_2O_3 . Films were deposited on both p- and n-type substrates simultaneously during each run. The deposition rate of the Al_2O_3 films was 90 Å/min for method 1 when only argon was present in the plasma and was 70 Å/min with 20% oxygen. The rates, along with other physical properties such as dielectric constant and breakdown strength compared favorably with values reported by Salama (1).

MAS devices were fabricated from Al_2O_3 films of thicknesses varying from about 500 to 4400Å and obtained by method 1. In the case of MAOS devices, prior to Al_2O_3 deposition, approximately 200Å of SiO_2 was thermally grown in dry oxygen at 900°C. The MAOS devices were fabricated from Al_2O_3 films of thicknesses varying from about 500 to 3140Å obtained by method 2. Aluminum dots (10 mil diameter) were evaporated on the oxide layers to form the metal contacts for MAS and MAOS structures. Aluminum was also evaporated on the back of the Si substrates. Annealing of the oxide layers was always carried out prior to the metal evaporation. A standard probe was used to test MAS and MAOS devices on which no long-time bias stresses were applied. MAOS devices, on which long-time bias stresses were applied, were mounted on TO-5 headers, bonded, and sealed in an argon atmosphere prior to testing.

Experiment and Results

Standard C-V techniques were used to study the electrical properties of MAS and MAOS structures. A "slow" and a "fast" C-V system was used. The "slow" C-V system required 22-23 sec while the "fast" C-V system, which is described in detail elsewhere (3), required 55 msec for the complete bias sweep. Slow C-V measurements were made on both MAS and MAOS devices while fast C-V measurements were made on MAOS devices.

Slow C-V measurement results on MAS devices.— Slow C-V measurements on MAS devices fabricated from unannealed Al_2O_3 films obtained by method 1 and in argon plasma showed no variation of capacitance with d-c bias voltage between ± 40 V, or up to the breakdown value. The fact that the capacitances of MAS devices fabricated from films deposited in argon plasma on p-type Si substrates increased on applying external illumination while the capacitances of devices on the corresponding n-type substrates were insensitive to external illumination suggested the presence of a large negative value of the flat-band voltage. This corresponds to the presence of a large density of positive charges either in the oxide or at the Al_2O_3 -Si interface, or both. This is in agreement with the results

Key words: aluminum oxide, sputtering, H₂-annealing, films, MIS.

of Salama (1). Also, no changes in capacitance with bias were observed on MAS devices fabricated from films obtained by method 1 or method 2 and deposited in argon and oxygen plasma for d-c bias sweep voltages between $\pm 40V$ or the breakdown value. This indicated the presence of a high density of charges in the bulk of the Al_2O_3 and/or at the Al_2O_3 -Si interface for films sputtered with 20% oxygen in the plasma as well.

Portions of a 950Å, Al_2O_3 film obtained by method 1 in an argon plasma were annealed in either: (i) nitrogen gas at 720°C for 20 min; or in (ii) oxygen gas at 730°C for 20 min; or in (iii) forming gas (95% N_2 , 5% H_2) at 425°C for 75 min. The slow C-V curves of the MAS devices fabricated from the above differently annealed portions of the same Al_2O_3 film were similar to the unannealed case in that none of them showed any change in the capacitance value with the applied d-c bias voltage sweeps up to $\pm 40V$ or the breakdown value. In Salama's studies of rf sputtered Al_2O_3 MAS devices (1), annealing in N_2 at 300°C had little or no effect on the oxide charge for power densities above 2.5 W/cm².

In one further attempt to reduce the oxide charge the Al_2O_3 films fabricated in either argon plasma or in argon and oxygen plasma by method 1 were annealed in H_2 gas at 710°C for about 10 min. Slow C-V curves were observed on MAS devices fabricated from the above hydrogen annealed films. The presence of surface states and/or a change in flat-band voltage during the bias sweep time may account for the gradual change in the value of capacitance with the applied d-c bias sweep observed on these H_2 -annealed devices. Both positive and negative values of flat-band voltages were observed; however, most of the devices made from films sputtered in argon plasma had large negative flat-band voltages. The devices made from films sputtered with both argon and oxygen in the plasma had smaller negative, zero, or positive flat-band voltages. For this reason MAOS devices reported in this paper were fabricated from films sputtered with both argon and oxygen plasma.

Hysteresis was observed on the slow C-V curves of the hydrogen-annealed MAS devices. This hysteresis was, in general, found to be negligibly small for devices having a positive value of the flat-band voltage. The devices with negative values of flat-band voltages, and especially those with large negative values, showed considerably larger hysteresis. The magnitude and the direction of the hysteresis loop were found to be dependent on the applied bias voltage sweep. At low values of applied bias sweep, the direction of the hysteresis loop corresponded to that observed for ion-migration in the oxide, while at higher values of the applied bias sweep, it corresponded to the direction observed for charge injection occurring at the oxide-semiconductor interface. An instability due to charge injection has also been observed on MAS devices fabricated from low power (<2.5 W/cm²) sputtered films (1). Ion migration at lower applied electric fields and charge injection at higher applied electric fields were found to be the dominant type of instabilities observed in these MAS devices. A high density of surface states and a probable presence of change in flat-band voltage during the bias sweep time make the high-power sputtered Al_2O_3 films deposited over Si and reported on in this paper unsuitable for solid-state field effect device technology.

Slow C-V measurement results on MAOS devices.—To avoid the undesirable Al_2O_3 -Si interface, the properties of MAOS structures were studied. This structure has been reported on by several other authors (4-6). MAOS devices were fabricated from (i) unannealed films, (ii) films annealed in hydrogen at 710°C for 10 min, and (iii) films annealed in nitrogen at 720°C for 10 min following the hydrogen-gas annealing as in step (ii) above.

Slow C-V shifts were observed on all MAOS devices including the ones made from unannealed films. The shapes of the C-V curves of MAOS devices indicated a significant reduction of surface states, with unannealed devices having effective surface-charge densities of approximately 5×10^{11} e/cm². However, the MAOS devices fabricated from H_2 - and N_2 -annealed films showed a larger number of surface states than the MAOS devices fabricated from unannealed films or films annealed in hydrogen alone. Nitrogen-gas annealing following the hydrogen-gas annealing seemed to distort the shapes of the C-V curves of the MAOS devices, especially at the higher bias sweep voltages. The flat-band voltages of the MAOS devices made from unannealed films were either slightly positive, zero, or slightly negative (between -0.5 - $0.5V$) while those of devices made from hydrogen-annealed films or hydrogen- and nitrogen-annealed films were always negative (less than $-0.5V$) indicating the introduction of a net positive charge in the oxide upon annealing.

Ion migration was found to be the dominant type of instability observed on the MAOS devices for small values of applied fields. Charge injection occurring at the SiO_2 -Si interface was found to be the dominant type of instability at higher applied bias voltages. Charge injection at the SiO_2 -Si interface was observed on annealed MAOS devices for both polarities of the applied bias voltages. Charge injection was observed at smaller magnitudes of applied negative bias voltages as compared to applied positive bias voltages. The positive bias voltages were at least twice the magnitude of the negative bias voltages required to observe charge injection. However, most devices began to conduct excessively before charge injection could be observed for positive bias voltages. Charge injection at the SiO_2 -Si interface was observed on unannealed MAOS devices on the application of high-negative bias voltages only. The magnitudes of negative fields necessary to observe the effects of charge injection in unannealed devices were higher than the magnitudes of the negative fields necessary to observe the effects of charge injection in the corresponding annealed devices. No charge injection was observed on MAOS devices made from unannealed films for positive bias voltages as large as the breakdown values.

Fast C-V measurement results on MAOS devices.—The stability of MAOS devices under applied bias stresses was investigated in detail since Al_2O_3 - SiO_2 double-layer structures showed a greater promise for practical applications. The fast C-V measurement technique was used to obtain changes in V_{FB} with applied bias time at 40°C. A fast C-V system is not only more accurate, as the error due to changes in V_{FB} during the bias sweep time is reduced, but also makes observation of changes in V_{FB} possible for a small duration of bias time.

Data on MAOS devices fabricated from unannealed, hydrogen-annealed, and hydrogen- and nitrogen-annealed portions of a 930Å sputtered Al_2O_3 film obtained by method 2 are presented. Figures 1 and 2 show changes (ΔV_{FB}) in V_{FB} from the initial value just prior to application of bias plotted against bias-time for two separate bias voltages. A positive value of ΔV_{FB} denotes change in V_{FB} which corresponds to ion migration in the oxides while a negative value of ΔV_{FB} denotes change in V_{FB} due to charge injection at the oxide-semiconductor interface, regardless of the polarity of the applied bias voltage.

Under applied positive bias voltages of magnitudes up to 10V, the hydrogen-annealed devices, in general, were found to have the largest values for ΔV_{FB} while the unannealed devices were found to have the smallest values for ΔV_{FB} for a given bias time (Fig. 1). Under applied negative gate voltages charge injection at the oxide-silicon interface was, in general, found to occur in the hydrogen- and nitrogen-annealed devices for the shortest duration of bias time (Fig. 2).

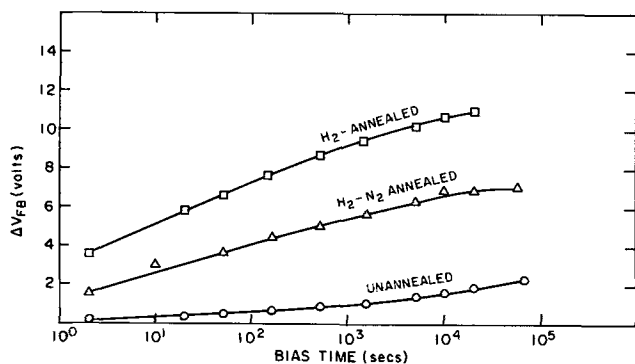


Fig. 1. ΔV_{FB} vs. time for +10V applied bias (930Å Al_2O_3 and 200Å SiO_2 on a n-type Si substrate).

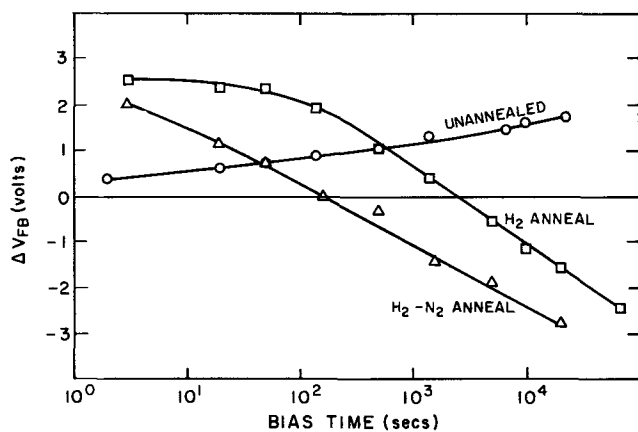


Fig. 2. ΔV_{FB} vs. time for -20V applied bias (930Å Al_2O_3 and 200Å SiO_2 on a n-type Si substrate).

The unannealed devices were again found to be the most stable with no observable charge injection occurring at the SiO_2 -Si interface for bias-times in the range of 10^4 - 10^5 sec for applied negative bias of up to -20V. The values of ΔV_{FB} were considerably greater for positive values of applied bias voltages for all devices considered as compared to the applied negative bias voltages of the same magnitudes as long as the effects due to charge injection were not significant. This is evident from Fig. 3 which shows ΔV_{FB} with bias time for an unannealed device for various values of applied positive and negative biases.

The flat-band voltage of each device was allowed to recover to its initial value by shorting its leads for at least 6 hr after the completion of each bias cycle. The change in V_{FB} of the device from the initial value of V_{FB} before the application of a bias cycle was noted after each recovery period. Significant changes in V_{FB}

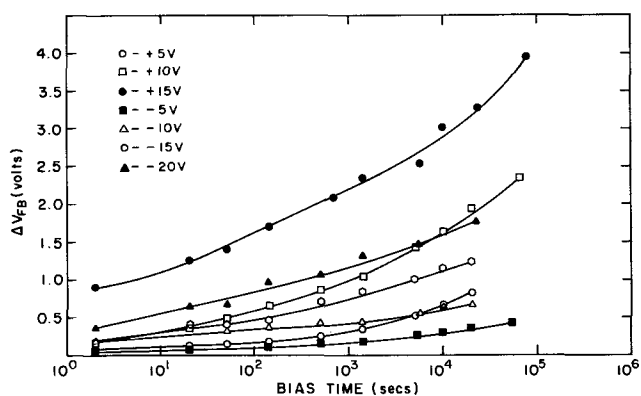


Fig. 3. ΔV_{FB} vs. time for various bias voltages for an unannealed MAOS device (930Å Al_2O_3 and 200Å SiO_2 on a n-type Si substrate).

were obtained after the recovery period for annealed devices. It should be remembered here that the values of ΔV_{FB} were also correspondingly high for the annealed devices. The most significant changes in V_{FB} after the recovery period for annealed devices occurred after the application of a -20V bias cycle. For this value of applied bias the effects of charge injection across the SiO_2 -Si interface were also simultaneously significant. Even after shorting the device for 48 hr the initial value of V_{FB} could not be recovered after a -20V bias cycle. This indicated the presence of deep trapping centers in the sputtered film. No significant changes in the values of V_{FB} were obtained for unannealed devices after each recovery period following the completion of the applied-bias cycles. Simultaneously, no significant charge injection was observed on unannealed devices. The values of V_{FB} and consequently the values of ΔV_{FB} for annealed devices were hence found to depend upon the previous bias history.

Discussion of instabilities associated with MAOS devices.—Ion migration was the dominant type of instability observed in MAOS devices at low values of applied electric fields. The hydrogen-annealed MAOS devices showed the largest positive values of ΔV_{FB} corresponding to the largest amount of ion migration in the bulk of oxide layers. Nitrogen annealing following the hydrogen annealing seemed to reduce this ion density somewhat to yield smaller amounts of ion migration in hydrogen- and nitrogen-annealed MAOS devices. Unannealed devices were the most stable, having the least amount of ion migration.

Charge injection across the SiO_2 -Si interface was observed in MAOS devices at high values of applied electric fields. Charge injection was also found to be strongly dependent on the applied field. Schottky emission at 40°C is not the likely cause for the observed charge injection as the energy barrier present at the Si- SiO_2 interface is fairly large (7). The SiO_2 thickness of 200Å is small enough to suggest the presence of Fowler-Nordheim tunneling through the reduced barrier width of SiO_2 at fairly high applied fields. A possible mechanism for charge injection under an applied negative field can be Fowler-Nordheim tunneling of holes from the Si into the traps located at the Al_2O_3 - SiO_2 interface through the reduced effective barrier width of the SiO_2 layer. An equivalent mechanism can also be injection of electrons from the Al_2O_3 into the Si.

Conclusions

MAS devices fabricated from high-power sputtered films in argon plasma or in argon and oxygen plasma had large values of effective surface-charge densities. High temperature H_2 -gas annealing reduced the value of this effective surface-charge density. Ion migration at low values of applied electric field and charge injection at the SiO_2 -Si interface at higher applied electric fields were the dominant type of instabilities in MAS and MAOS devices. However, MAOS devices showed fewer surface states than MAS devices. Significant changes in the flat-band voltages were observed with applied bias stresses for both the hydrogen-annealed and hydrogen-nitrogen annealed MAOS devices. Unannealed MAOS devices were found to be the most stable devices under prolonged applied bias stresses. The double-layer Al_2O_3 - SiO_2 structure over Si shows a greater promise than the MAS structure for possible use of high-power sputtered Al_2O_3 films in device technology.

Manuscript submitted Dec. 3, 1971; revised manuscript received June 12, 1972.

Any discussion of this paper will appear in a Discussion Section to be published in the June 1973 JOURNAL.

REFERENCES

1. C. A. T. Salama, *This Journal*, **117**, 913 (1970).
2. C. A. T. Salama, *ibid.*, **118**, 1993 (1971).

3. J. R. Bridges, Unpublished Ph.D. thesis, Department of Electrical Engineering, North Carolina State University at Raleigh. University Microfilms, Ann Arbor, Michigan.
4. M. T. Duffy and A. G. Revsez, *This Journal*, **117**, 372 (1970).
5. R. A. Abbott and T. I. Kamins, *Solid-State Electron.*, **13**, 565 (1970).
6. H. E. Nigh, J. Stach, and R. M. Jacobs, *IEEE Trans. Electron Devices*, **ED-14**, 631 (1967).
7. R. Williams, *Phys. Rev.*, **140**, A569 (1965).

An Effect of Organic Electron Donors and Acceptors on a Real Silicon Surface

J. A. Jackson, J. R. Szedon, and T. A. Temofonte

Westinghouse Research Laboratories, Pittsburgh, Pennsylvania 15235

Semiconductor surface-state effects have received considerable attention in the past. From a practical point of view, electrical effects of such states can strongly influence and often limit the performance of semiconductor devices, e.g., by the formation of conducting-surface channels, by the limitation of junction-blocking voltage capability due to surface breakdown, by the addition of a surface-generation component to a junction-reverse current, and by other effects. Before the development of silicon-device technology and the use of thermally grown silicon dioxide for device passivation, a great deal of work was done on electrical-surface effects of various chemical species. In general, this work was empirical, establishing the electrical effects of, for example, water vapor on germanium (1), acetone vapor on silicon (2), and etchants and metallic impurities on germanium (3). Some attempts have been made to provide detailed models for the interaction of chemical species with semiconductor surfaces, e.g., water on silicon (4) and amines on germanium (5).

Basic work on treating chemical effects on silicon-surface properties has diminished significantly with the development of silicon dioxide passivation technology. This was probably due to the great difficulty in controlling and modelling surface-defect effects for the case of silicon surfaces coated with thick amorphous dielectric films. However, from a practical point of view, the effect of organic materials used in packaging unpassivated semiconductor devices is of considerable interest. Impurities arising from poorly matched stoichiometry affect the elevated temperature performance of microdiodes (6) and recent work has attempted to characterize the relative effect of different types of impurities (7).

For the present work we return to the case of an unpassivated, real silicon surface, i.e., a silicon surface covered by a thin (~ 10 – 40\AA) layer of residual oxide. Our aim is to demonstrate that both positive and negative charge can be induced at a silicon surface by the *a priori* selection of an organic material on the basis of its known ability to donate or attract electronic charge.

Work on the adsorption of amines on germanium transistors (5) suggested that the relative effect of this group of compounds is associated with the ease of electron donation to the semiconductor surface. Amines have an unshared pair of electrons which they can donate to suitable molecules which exhibit electron-accepting ability. The ease with which an amine, $\text{NR}_1\text{R}_2\text{R}_3$, can lose an electron is determined by the nature of the group R. If R is electron repelling, then ease of electron donation is increased. One of the strongest electron donors (8) is N,N,N, N-tetramethyl-p-phenylene-diamine (TMPD). In this paper, we have compared the effects of TMPD with a strong electron attractor on the surface conduction behavior of a field-

effect transistor. The cyano group has a known electron-withdrawing effect; tetracyanoethylene (TCNE) is one of the strongest electron acceptors (8) known and for this reason was chosen for investigation of this effect. For a comparison of the effects of these two compounds, both were purified¹ then dissolved (approximately 20% by weight) in electronic-grade benzene.

Charge effects of the organic materials on real silicon surfaces were evaluated by noting the change in conductance of surface-controlled field-effect transistors (9) prepared without gate electrodes. Since the chemical species were chosen to produce strong electron donating and extracting effects, transistors were fabricated on both n-type (20 ohm-cm) and p-type (30 ohm-cm) silicon. Shallow diffusions (2–4 μm) of boron and phosphorus, respectively, were made into these materials to provide the source and drain contacts. The silicon surfaces were passivated with thermally grown silicon dioxide (5400 \AA) except for the channel areas (25 \times 350 μm) in which the organic materials were expected to have their effect.

Consider first a structure of the type $n^+/p/n^+$ which is capable of detecting mobile electrons induced in the silicon channel window area. Prior to immersion in the benzene solvent, the drain-source current was less than 10 μA at 4V. After immersion of the device in the undoped solvent, and with application of a 4V peak, full-wave rectified voltage to the device,² the conductance had increased as shown by the lower curve of Fig. 1. This current could be reduced to zero

¹ Recrystallized from ethanol/water, washed twice with ethanol and dried at 24°C under vacuum for 16 hr. Melting points: TMPD 50.0°C, TCNE 197.5°C.

² A Tektronix Type 575 Curve Tracer was used.

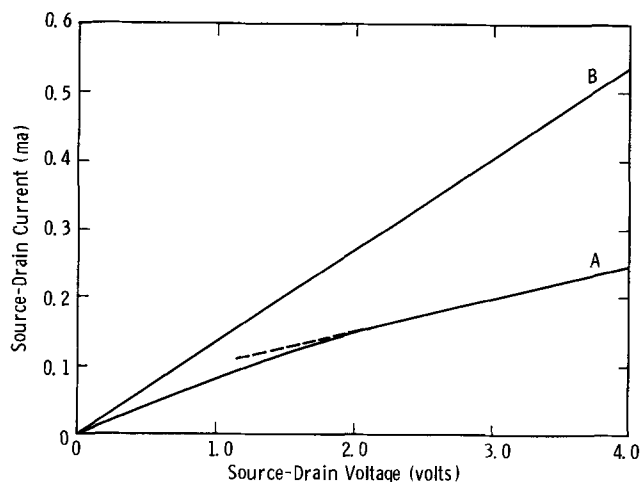


Fig. 1. Current-voltage behavior of n-channel gateless field-effect transistor showing effect of an organic electron donor. A, benzene solvent only; B, compound II in benzene.

3. J. R. Bridges, Unpublished Ph.D. thesis, Department of Electrical Engineering, North Carolina State University at Raleigh. University Microfilms, Ann Arbor, Michigan.
4. M. T. Duffy and A. G. Revsez, *This Journal*, **117**, 372 (1970).
5. R. A. Abbott and T. I. Kamins, *Solid-State Electron.*, **13**, 565 (1970).
6. H. E. Nigh, J. Stach, and R. M. Jacobs, *IEEE Trans. Electron Devices*, **ED-14**, 631 (1967).
7. R. Williams, *Phys. Rev.*, **140**, A569 (1965).

An Effect of Organic Electron Donors and Acceptors on a Real Silicon Surface

J. A. Jackson, J. R. Szedon, and T. A. Temofonte

Westinghouse Research Laboratories, Pittsburgh, Pennsylvania 15235

Semiconductor surface-state effects have received considerable attention in the past. From a practical point of view, electrical effects of such states can strongly influence and often limit the performance of semiconductor devices, e.g., by the formation of conducting-surface channels, by the limitation of junction-blocking voltage capability due to surface breakdown, by the addition of a surface-generation component to a junction-reverse current, and by other effects. Before the development of silicon-device technology and the use of thermally grown silicon dioxide for device passivation, a great deal of work was done on electrical-surface effects of various chemical species. In general, this work was empirical, establishing the electrical effects of, for example, water vapor on germanium (1), acetone vapor on silicon (2), and etchants and metallic impurities on germanium (3). Some attempts have been made to provide detailed models for the interaction of chemical species with semiconductor surfaces, e.g., water on silicon (4) and amines on germanium (5).

Basic work on treating chemical effects on silicon-surface properties has diminished significantly with the development of silicon dioxide passivation technology. This was probably due to the great difficulty in controlling and modelling surface-defect effects for the case of silicon surfaces coated with thick amorphous dielectric films. However, from a practical point of view, the effect of organic materials used in packaging unpassivated semiconductor devices is of considerable interest. Impurities arising from poorly matched stoichiometry affect the elevated temperature performance of microdiodes (6) and recent work has attempted to characterize the relative effect of different types of impurities (7).

For the present work we return to the case of an unpassivated, real silicon surface, i.e., a silicon surface covered by a thin (~ 10 – 40\AA) layer of residual oxide. Our aim is to demonstrate that both positive and negative charge can be induced at a silicon surface by the *a priori* selection of an organic material on the basis of its known ability to donate or attract electronic charge.

Work on the adsorption of amines on germanium transistors (5) suggested that the relative effect of this group of compounds is associated with the ease of electron donation to the semiconductor surface. Amines have an unshared pair of electrons which they can donate to suitable molecules which exhibit electron-accepting ability. The ease with which an amine, $\text{NR}_1\text{R}_2\text{R}_3$, can lose an electron is determined by the nature of the group R. If R is electron repelling, then ease of electron donation is increased. One of the strongest electron donors (8) is N,N,N, N-tetramethyl-p-phenylene-diamine (TMPD). In this paper, we have compared the effects of TMPD with a strong electron attractor on the surface conduction behavior of a field-

effect transistor. The cyano group has a known electron-withdrawing effect; tetracyanoethylene (TCNE) is one of the strongest electron acceptors (8) known and for this reason was chosen for investigation of this effect. For a comparison of the effects of these two compounds, both were purified¹ then dissolved (approximately 20% by weight) in electronic-grade benzene.

Charge effects of the organic materials on real silicon surfaces were evaluated by noting the change in conductance of surface-controlled field-effect transistors (9) prepared without gate electrodes. Since the chemical species were chosen to produce strong electron donating and extracting effects, transistors were fabricated on both n-type (20 ohm-cm) and p-type (30 ohm-cm) silicon. Shallow diffusions (2–4 μm) of boron and phosphorus, respectively, were made into these materials to provide the source and drain contacts. The silicon surfaces were passivated with thermally grown silicon dioxide (5400 \AA) except for the channel areas (25 \times 350 μm) in which the organic materials were expected to have their effect.

Consider first a structure of the type $n^+/p/n^+$ which is capable of detecting mobile electrons induced in the silicon channel window area. Prior to immersion in the benzene solvent, the drain-source current was less than 10 μA at 4V. After immersion of the device in the undoped solvent, and with application of a 4V peak, full-wave rectified voltage to the device,² the conductance had increased as shown by the lower curve of Fig. 1. This current could be reduced to zero

¹ Recrystallized from ethanol/water, washed twice with ethanol and dried at 24°C under vacuum for 16 hr. Melting points: TMPD 50.0°C, TCNE 197.5°C.

² A Tektronix Type 575 Curve Tracer was used.

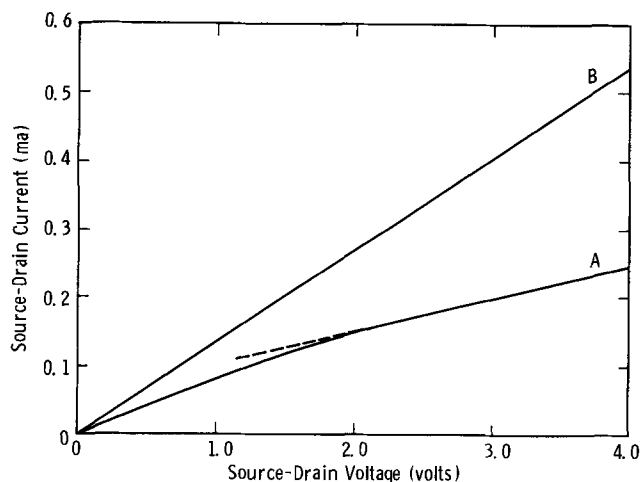


Fig. 1. Current-voltage behavior of n-channel gateless field-effect transistor showing effect of an organic electron donor. A, benzene solvent only; B, compound II in benzene.

by reverse biasing the substrate with respect to both the source and the drain. Such a result indicated that the conduction was occurring within the silicon near its outer surface and not in the solvent or at the solvent-silicon interface.³ A similar conduction effect was observed on immersion of the complementary $p^+/n/p^+$ transistor structure into undoped benzene. Since enhanced conduction was noted on both types of structures, we ascribe the effect to creation of a conducting channel within the silicon by electrostatic induction due to potential propagated from the drain electrode. The conductivity value for benzene ($\sim 10^{-7}$ mho cm^{-1}) is large enough to support the propagation of drain potential over the silicon surface, but is too low to be observed directly in terms of source-drain leakage. Such propagation, supported by low conductivity of a solid organic dielectric material at elevated temperatures, is well established (10). This model is also consistent with the observed increase of conduction with drain bias (with a time lag of 1–2 sec).

Addition of TMPD to the benzene solvent increased the electronic channel current in the $n^+/p/n^+$ transistor as shown in Fig. 1. The increase in conductance in the 2–4V range of source-drain voltage was 7×10^{-5} mhos, corresponding to a density of 4×10^{10} sites/ cm^2 if an electron surface mobility value of 600 $\text{cm}^2/\text{V sec}$ is assumed (11). The level of conduction induced by the dopant was not sensitive to drain bias in the range indicated in the figure. For this reason, we attribute the additional conduction to induction of mobile electrons at the silicon surface by the electron-donating action of the organic dopant. To rule out the possibility of enhanced drain-potential propagation by the action of the dopant in benzene, we immersed a complementary ($p^+/n/p^+$) device in benzene with the same dopant and saw no increased channel conduction in that case. When removed from the doped solution and introduced into undoped benzene, the $n^+/p/n^+$ device still exhibited strong channel conduction which did not decay significantly over the period of the test (~ 5 min). This suggests that the electron donor becomes strongly associated with the silicon surface.

Complementary observations were made when a $p^+/n/p^+$ transistor was immersed in benzene doped with TCNE. Hole conduction increased by 3×10^{-5} mhos above the level for the undoped solvent, corresponding to approximately the same charge site density, $4 \times 10^{10} \text{ cm}^{-2}$, as in the case of TMPD, when the lower surface mobility of holes is taken into account (11). A cross-effect experiment, introduction of a structure of the $n^+/p/n^+$ type into benzene doped with TCNE, resulted in no enhanced conduction. This indicated, as in the case of TMPD, that the dopant does not cause enhanced conduction in the solution, which could allow the drain potential to affect the silicon to a greater degree than in the case of the undoped benzene.

We interpret the increased hole conduction for the $p^+/n/p^+$ device immersed in the solution doped with TCNE as being due to the ability of the dopant to accept negative charge. The following is proposed to explain the effect. A molecule of TCNE on the real silicon surface is initially neutral. The electron-deficient region associated with the π bond could provide empty electronic states into which electrons from the silicon surface might tunnel, even with the thin oxide present. The radical anion derived from the TCNE would then represent a static negative charge requiring compensating positive charge within the silicon supplied by ionized donors and mobile holes. We do not exclude the possibility of electron transfer back to the silicon by tunneling, but in our case the effect is not dominant. The observed effect is one of net electron extraction to form a region of negative-charge exterior

³ This feature of distinguishing between solvent and semiconductor mechanisms makes the ungated FET structure an extremely powerful tool for "wet" surface studies.

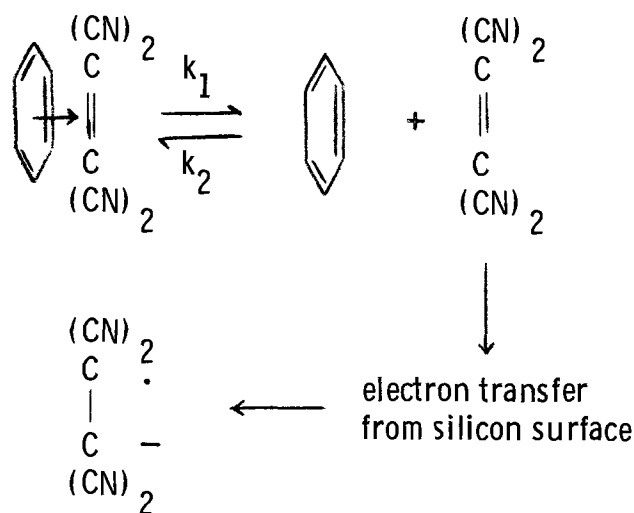


Fig. 2. Formation of cationic intermediate from charge-transfer complex.

to the silicon. The donor effect of TMPD can be explained in a similar manner, if we invoke the formation of a radical anion (or dianion), which gives rise to a sheet of positive charge adsorbed on the surface.

In experiments involving TCNE, ultrasonic agitation resulted in conduction enhancement, about 2.5 times above that observed in the studies with TMPD. The data reported above for both p and n devices were obtained with ultrasonic agitation. We speculate that a concentration gradient of the electron donor or acceptor exists near the silicon surface which limits the rate of formation of the reactive intermediate. Agitation may be viewed as destroying this concentration gradient and hence allowing for higher concentrations of the additives at the surface. The observed effect of agitation suggests that the rate-determining step (for TCNE, k_1 in Fig. 2) is dissociation of the TMPD-benzene or TCNE-benzene complexes, with the relative effect reflecting the difference in their stabilities.

More detailed studies of the electronic interactions are needed to determine if the organic compounds affect the generation-recombination behavior of the real surface or if they result in carrier mobility behavior at the silicon surface significantly different from that inferred from studies on passivated surfaces.

Manuscript submitted Nov. 4, 1971; revised manuscript received March 20, 1972.

Any discussion of this paper will appear in a Discussion Section to be published in the June 1973 JOURNAL.

REFERENCES

1. K. H. Kingston, *Phys. Rev.*, **98**, 1966 (1955).
2. H. Statz and G. A. de Mars, *ibid.*, **111**, 169 (1958).
3. S. R. Morrison, Proceedings of the Second Semiconductor Surfaces Conference, **14**, 214, Pergamon Press (1960).
4. O. Jantsch, *Surface Sci.*, **3**, 155 (1965).
5. G. A. Kataev, V. A. Presnov, E. N. Batueva, Yu. G. Kataev, and L. A. Lyuze, from a compilation of translation of Russian papers entitled "Surface Properties of Semiconductors," p. 151, A. N. Frumkin, Editor, Consultants Bureau (1964).
6. J. Licari and G. V. Browning, *Electronics*, **40**, 101 (1967).
7. R. C. Olberg, *This Journal*, **118**, 129 (1971).
8. L. J. Andrews and R. M. Keefer, "Molecular Complexes in Organic Chemistry," Holden-Day, San Francisco, Calif. (1964).
9. F. P. Heiman and S. R. Hofstein, *Electronics*, **37**, 50 (1964).
10. T. A. Temofonte and J. R. Szedon, Ninth Annual Proceedings, Reliability Physics, 107 (1971).
11. S. M. Sze, "Physics of Semiconductor Devices," 514, John Wiley & Sons, New York (1969).

The Solidus Boundary in the GaAs-GaP Pseudobinary Phase Diagram

L. M. Foster,* J. E. Scardefield, and J. F. Woods

IBM Thomas J. Watson Research Center, Yorktown Heights, New York 10598

In previous articles of this series (1-5), phase boundaries of the pseudobinary phase diagrams of a number of III-V compound semiconductor systems were reported and, in cases where the data were sufficiently complete, thermodynamic analyses were carried out. The objective of this continuing investigation is to arrive at a model which will contribute towards a better understanding of the nature of these interesting solids.

In order for similarities and differences between various systems to be apparent, quite precise data for the phase diagrams are required. Although it is now known that, with a few recognized exceptions (4), there is complete miscibility in the solids of the III-V alloy systems, in many cases the phase boundaries are only approximately known. Osamura and Murakami (6) reported data for the solidus of the GaAs-GaP system, but the points are badly scattered, have wide error limits and, in fact, fall on either side of the ideal boundary so that even an approximate calculation of the departure from ideality cannot be made. In the present note, we will report new data for the solidus boundary of this system.

Points on the solidus boundary were obtained by a technique that was developed by two of the authors for determining the boundary of the InP-GaP system (1). In this method, a pellet pressed from intimately mixed powders of the two components (GaAs and GaP) is encapsulated in fused silica and held at a constant temperature within the two-phase region of the phase diagram for sufficient time for equilibration of the liquid and solid phases to be achieved (typically, a few days). The sample is then quenched and the composition of the solid-solution phase is determined by electron-microprobe analysis. This composition corresponds to a point on the solidus boundary at the equilibration temperature.

Seven solidus points were determined for the GaAs-GaP system. These are listed in Table I and are shown in Fig. 1. The crystal lattice parameter of the primary solid-solution phase in each sample was also determined. This phase can readily be distinguished from the quenched liquid in the x-ray powder pattern, since it is present in the largest amount and has a smaller a -parameter than any other composition in the sample. That Vegard's law is strictly followed in this system throughout the entire composition range is seen in Fig. 2.

The excess free energy of mixing in a binary system can be calculated if both solidus and liquidus curves are known (2). There are no liquidus data for the GaAs-GaP system; however, an estimate of this quantity can be made if the liquid is assumed to be ideal. Justification for this assumption lies in the fact that in

the systems studied to date, nonideality in the solid solutions has always been substantially greater than in the liquids (1-5), and quite strongly dependent on the difference in lattice parameter between the two components of the alloy. The parameter difference in GaAs-GaP (3.7%) is about midway between that of GaAs-AlAs (0.16%) and InSb-GaSb (6.1%), both of which had essentially ideal liquids.

Following the procedure described in Ref. (2) to determine the excess free energy of mixing, $B^s x(1-x)$, gives $B^s/RT = 0.2 - 0.12x$, where x is the mole fraction of GaP. The solid curves in Fig. 1 show the resulting fit to the solidus data, and the calculated liquidus curve, assuming $B^l = 0$. The significance of the excess free energy in the GaAs-GaP system, and the relation of this system to the other III-V alloy systems will be presented elsewhere (7).

Acknowledgment

The authors wish to thank Mr. J. D. Kuptsis for performing the electron microprobe analyses, and Mr. J. N. Karasinski for the x-ray examination.

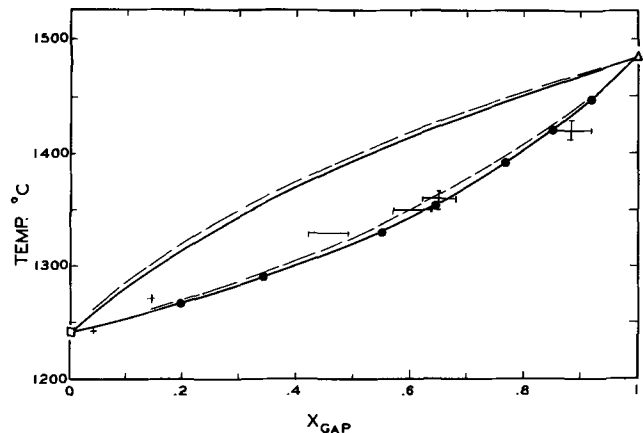


Fig. 1. GaAs-GaP phase diagram. ● This work; + Ref. (6); Δ R. J. Chicotka, IBM (unpublished results); □ B. D. Lichter and P. Sommelet, *Trans. AIME*, 245, 1021 (1969); --- Calculated ideal; — Calculated with ideal liquid ($B = 0$) and $B^s = RT(0.2 - 0.12x)$.

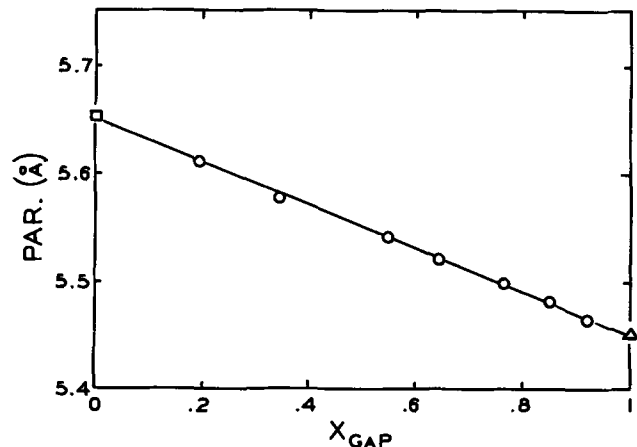


Fig. 2. Crystal-lattice parameter for GaAs-GaP solid-solution alloys. ○ This work; □ $a_{\text{GaAs}} = 5.653\text{Å}$; Δ $a_{\text{GaP}} = 5.451\text{Å}$, G. Giesecke and H. Pfister, *Acta Cryst.*, 11, 369 (1958).

Table I. Solidus data and lattice parameters in the $\text{GaAs}_{(1-x)}\text{P}_x$ system.

T°C	x	a(Å)
1267	0.194	5.612
1290	0.341	5.577
1329	0.548	5.542
1354	0.644	5.521
1392	0.766	5.499
1420	0.850	5.482
1448	0.920	5.465

* Electrochemical Society Active Member.
Key words: phase diagrams, compound semiconductors, solution theory.

Manuscript submitted May 18, 1972.

Any discussion of this paper will appear in a Discussion Section to be published in the June 1973 JOURNAL.

REFERENCES

1. L. M. Foster and J. E. Scardefield, *This Journal*, **117**, 534 (1970).
2. L. M. Foster and J. F. Woods, *ibid.*, **118**, 1175 (1971).
3. L. M. Foster and J. E. Scardefield, *ibid.*, **118**, 495 (1971).
4. L. M. Foster and J. F. Woods, *ibid.*, **119**, 504 (1972).
5. L. M. Foster, J. E. Scardefield, and J. F. Woods, *ibid.*, **119**, 6 (1972).
6. K. Osamura and Y. Murakami, *Japan J. Appl. Phys.*, **8**, 967 (1969).
7. L. M. Foster and J. F. Woods, To be published.

Growth of Silver Crystals in the Meniscus Region

Richard J. Roethlein*¹

Research & Development Laboratories, Sprague Electric Company, North Adams, Massachusetts 01247

Recently, it has been observed that at the junction of the three-phase interface of a partially immersed silver foil in an acid solution containing silver ions, there is a tendency for silver crystals to grow under certain conditions. Tests conducted on both polished and etched silver foils indicate that this phenomenon is due to a slight temperature differential between the liquid electrolyte and the vapor immediately above the electrolyte level. A series of tests was run in which the electrolyte and surrounding atmosphere were completely saturated with nitrogen in order to rule out any effects due to differential aeration. The electrolyte used was 20N phosphoric acid containing a silver ion concentration ranging from 0.1 to 1.0N Ag⁺ ions. Tests were conducted in a sealed Pyrex cell containing a partially immersed silver or gold foil. When the cell was placed in an oil bath, so that a slightly lower temperature occurred in the vapor immediately above the electrolyte, silver crystals were observed to grow in the region of the interface on both the gold and silver substrate (Fig. 1). This was observed to take place for electrolyte temperatures above 40°C and became more accentuated with increasing temperature. Temperature measurements immediately above the electrolyte level showed that a 1° or less temperature differential existed. In the absence of any silver ions in solution, no crystal growth or corrosion of the substrate was observed to occur at any temperature up to 85°C.

Visual inspection of the silver foil while immersed in the electrolyte indicated that the region where crystal growth occurred closely coincided with the area of meniscus formation. Measurements of the vertical length of the crystal deposition zone are approximately

0.28 cm, which corresponds to the meniscus height measured previously in phosphoric acid on partially immersed platinum electrodes (1). Above the region of crystal growth the silver foil surface showed evidence of severe corrosion attack. In this region, there is a thin film of electrolyte on the surface of the foil having a thickness of less than 1μ (1). The application of small cathodic currents (5-100 μA/cm²) under these conditions only accelerated the rate of crystal growth and corrosion. The accelerated rate of corrosion during current flow is probably due to concentration changes caused by the rapid depletion of silver ions in the upper meniscus thin-film region. Tests conducted on partially immersed gold foils produced similar results in that a silver crystal build-up occurred only in the region of meniscus formation. In the case of a gold substrate, no corrosion was evident in the region of film formation.

The test cell apparatus was then placed in an oven where the whole unit could be kept at a uniform temperature. Tests were conducted on both partially immersed silver and gold foils at various temperatures up to 85°C. In no case did silver crystal growth or corrosion occur either on the submerged portion or in the meniscus region. After one week in an air saturated system at 85°C, no growth occurred; however, when the cell was placed back in an oil bath where a temperature differential occurred, crystal growth was evident after a few hours. In the absence of a thermal gradient, the application of a cathodic current to the partially immersed electrode produced a uniform deposit of silver on the submerged portion of the electrode, which gradually tapered off in the meniscus region.

This investigation indicates that the silver deposition-dissolution reactions occurring in the region of the gas/liquid interface on a substrate are due to a slight temperature differential. The effect of differential aeration for the case under consideration has been shown to be of negligible consequence. With the formation of a temperature gradient at an electrode-electrolyte interface, there is a corresponding potential gradient also formed. The potential gradient is approximately 0.2 mV for each degree-temperature differential. In the case of simple metal-metal ion reaction



which has a high exchange current, such as silver, a very small potential gradient can cause a considerable amount of dissolution and deposition to occur. Current-potential curves for this system exhibit a large variation in current for slight changes in potential (2). Other metals having lower exchange currents would exhibit a proportionally lower tendency to be affected by this type of phenomenon. Factors such as differen-

* Electrochemical Society Active Member.
¹ Present address: Olin Corporation, New Haven, Connecticut 06504.

Key words: electrodeposition, corrosion, thermal gradient, crystal growth.

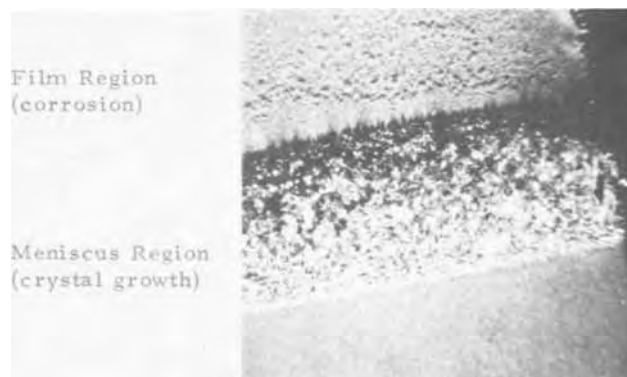


Fig. 1. Ag foil partially immersed, 24 hr 70°C (20X)

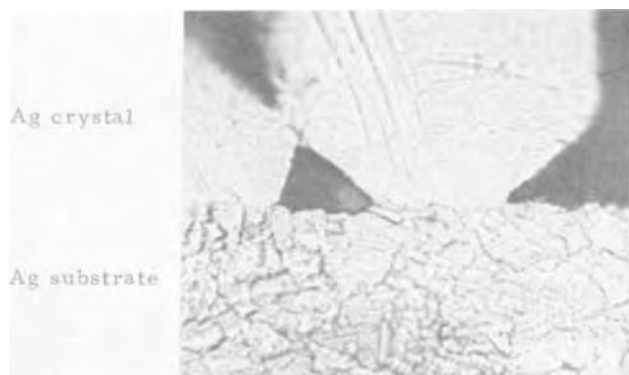


Fig. 2. Cross section Ag crystal (700X)

tial aeration could then become a predominant corrosion mechanism.

Figure 2 is a cross section of a silver foil which had been partially immersed and upon which crystal

growth had occurred. After polishing and etching with a 1:1 ammonia hydroxide-hydrogen peroxide solution, the presence of twin planes was revealed in the crystal growth structure. The growth of twins has previously been shown to be important in the dendritic growth of face-centered cubic metal crystals (3-5), where the reentrant groove between two facets at the twin plane provides a low-energy site for mobile silver adions to deposit into lattice positions.

Manuscript submitted July 8, 1971; revised manuscript received Sept. 15, 1971.

Any discussion of this paper will appear in a Discussion Section to be published in the June 1973 JOURNAL.

REFERENCES

1. R. Roethlein and H. Maget, *This Journal*, **113**, 581 (1966).
2. R. Roethlein, To be published.
3. J. Faust and H. John, *This Journal*, **108**, 855 (1961).
4. J. Faust, *ibid.*, **114**, 1311 (1967).
5. T. Reddy, *ibid.*, **113**, 117 (1966).

Chemical Vapor Deposition of Phosphosilicate Glasses from Mixtures of SiH_4 , O_2 , and POCl_3

M. Ghezzi*

General Electric Corporate Research and Development, Schenectady, New York 12301

In the fabrication of n-channel MOS transistors with the refractory metal gate technology (1), the drain and source regions are obtained by diffusion through a thin thermal oxide from a phosphosilicate layer in an inert ambient. The use of phosphosilicate glass prepared from oxidation of silane and phosphine resulted in a soft reverse breakdown characteristic of the diodes formed by the substrate and the diffused regions. As this high-leakage current was due to heavy-metals contamination in the silicon substrate, it was thought that the gettering action of the phosphosilicate glass was not sufficient and could be enhanced by the substitution of phosphine with phosphorus oxychloride, due to the gettering efficiency of chlorine compounds (2). This led to an experimental investigation of the feasibility of phosphosilicate glass preparation from a mixture of silane, oxygen, and phosphorus oxychloride at low substrate temperature.

1 ohm-cm p-type silicon wafers with a (100) surface orientation sliced from Czochralski-grown crystals were used as substrates. The wafers were lapped and chemically polished on both sides before depositing the glass.

The reactor and gas flow system was similar to that previously described by Wong and Ghezzi (3). The flow rates of the gases in the reactive mixture were: argon, used as a carrier gas, 3200 cc/min; 1% silane in argon, 240 cc/min; oxygen, 20 cc/min; and argon bubbling through phosphorus oxychloride from 10 to 20 cc/min. The deposition temperature varied between 300° and 500°C, while the temperature of the phosphorus oxychloride was 24°C, corresponding to a vapor pressure of 34 mm Hg (4).

The deposition time was adjusted to the deposition rate in order to obtain films of constant thickness (6000Å) as determined by interference colors assuming for the PSG the refractive index of pyrolytic SiO_2

(5). Transmission infrared spectra were taken on the glasses as deposited and from them the molar fraction of P_2O_5 in the glass was determined using a calibration curve, which will be published (6). A summary of the deposition parameters is presented in Table I, which shows that both the film deposition rate and the molar fraction of P_2O_5 in the glass increase with the substrate temperature and the molar fraction of POCl_3 in the reactive mixture.

Diffusion experiments were carried out at 1050° and 1100°C in argon for different periods of time. After diffusion, the glass layers appeared damaged in various degrees, due to the presence of Newton interference rings as shown in Fig. 1. From the number of fringes it was estimated that the height of these defects was often several times larger than the film thickness suggesting the possibility of a film detachment from the substrate for relieving compressive stresses. Furthermore it was observed that the damage increased with the heat-treatment temperature and the molar fraction of P_2O_5 in the glass. A comparison between PSG layers of equal composition and exposed to the same heat-treatment, but prepared with phosphine rather than phosphorus oxychloride showed that the phosphine deposition system yielded glasses more resistant to damage, capable of maintaining structural integrity after 1 hr at 1100°C in argon and up to 12 mole per cent (m/o) P_2O_5 . The glass structure or its

Table I. Deposition parameters

Substrate temperature (°C)	Argon flow rate bubbling through POCl_3 (cc/min)	Deposition rate (Å/min)	Mole per cent POCl_3 + SiH_4 mixture	Mole per cent P_2O_5 in the glass
300	10	550	15.7	3.5
400	10	800	15.7	4.2
500	10	950	15.7	4.2
300	20	700	27.3	7.8

* Electrochemical Society Active Member.

Key words: phosphosilicate glasses, phosphorus oxychloride, silicon diffusion, glass damage.

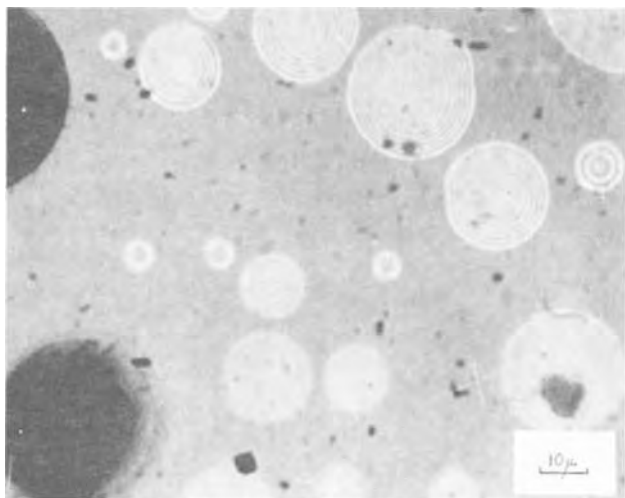


Fig. 1. Micrograph of a silicon wafer coated with a thin layer (~6000Å) of phosphosilicate glass (4.2 m/o P₂O₅) after heat-treatment in argon at 1050°C for 1 hr. Circular interference fringes and large dark areas correspond to glass damage.

adhesion characteristics to the substrate might be responsible for this interesting result.

After diffusion, sheet resistivity and junction depth were measured using a four-point probe and by angle lapping and staining. The beveling ratio was 20:1. Figure 2 shows a picture of a beveled sample after staining.¹ The accuracy of the junction depth determination was estimated to be ± 0.1μ. The diffusion data are plotted in Fig. 3, which shows the time dependence

¹The composition of the staining solution was: 49% HF: 70% NH₄OH: 100% CH₃COOH = 1:2:12 by volume. This solution was chosen for its property of not stripping the glass during staining, which allows for a more accurate determination of the junction depth, due to the better definition of the glass-silicon interface.

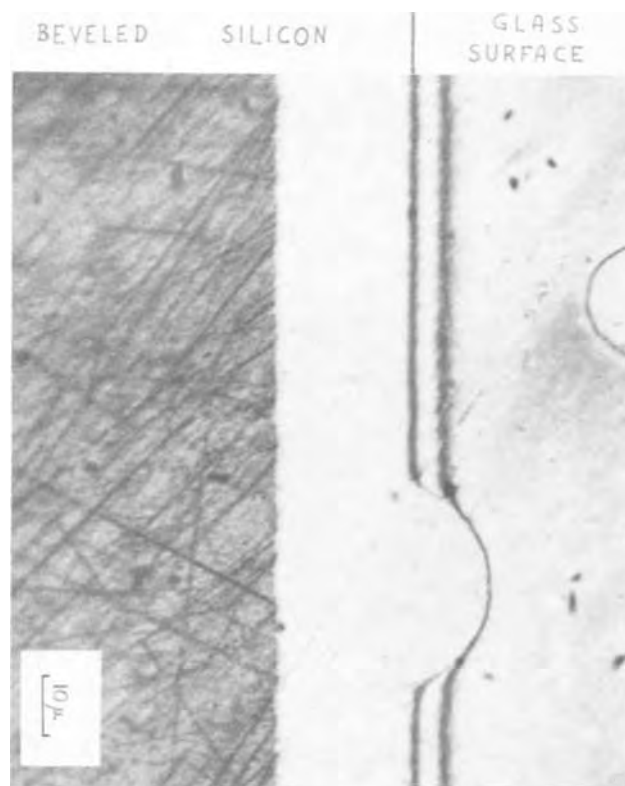


Fig. 2. Micrograph of an angle-lapped section of a p-type (100) surface oriented 1 ohm-cm Si wafer coated with phosphosilicate glass (4.2 m/o P₂O₅) and diffused in argon at 1100°C for 1 hr. Beveling ratio is 20:1. The junction depth is 1.1μ.

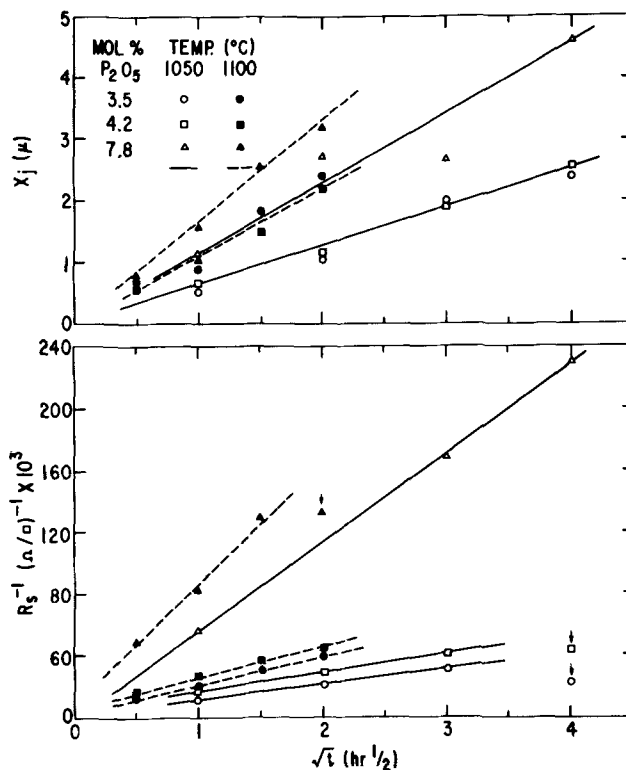


Fig. 3. Plots of junction depth and sheet conductivity of the diffused layers as a function of the square root of diffusion time at two diffusion temperatures (1050°C and 1100°C) and for three phosphosilicate glass compositions (3.5, 4.2, and 7.8 m/o P₂O₅). Points marked with arrows in the bottom plot correspond to badly damaged glass and irregular diffusion front.

of the junction depth and the sheet conductivity for two diffusion temperatures (1050° and 1100°C) and for glasses of different composition (3.5, 4.2, and 7.8 m/o P₂O₅).

Assuming a complementary error function diffusion profile and making use of Irvin curves (7), the surface concentration, C_s, and the diffusion coefficients of P in Si, D, were computed from each set of junction-depth and sheet-resistivity measurements, and the results averaged over different diffusion times before their presentation in Table II. As expected, both C_s and D increased with the molar fraction of P₂O₅ and with the temperature of diffusion, providing a further proof of the concentration dependence of D at high-impurity levels. Moreover the small increase of C_s with temperature was attributed to the temperature dependence of the ratio between the diffusion coefficients of P in Si and SiO₂, due to the difference in the corresponding activation energies [3.7 eV in SiO₂ vs. 4.2 eV in Si, as computed from Barry's data (8)].

As the purpose of this investigation was to use phosphorus oxychloride for the deposition of a PSG with enhanced gettering action, this property was tested in the fabrication of planar diodes using a patterned molybdenum layer mask (1) and diffusing through a thin thermal oxide layer. No significant im-

Table II. Diffusion coefficients of phosphorus in silicon, D, and surface concentrations, C_s, as a function of diffusion temperature and composition of the phosphosilicate glass

Mole per cent P ₂ O ₅ in the glass	1050°C		1100°C	
	D (cm ² /sec)	C _s (cm ⁻³)	D (cm ² /sec)	C _s (cm ⁻³)
3.5	4.2 × 10 ⁻¹⁴	4.9 × 10 ¹⁹	1.2 × 10 ⁻¹³	6.1 × 10 ¹⁹
4.2	4.2 × 10 ⁻¹⁴	7.3 × 10 ¹⁹	1.2 × 10 ⁻¹³	8.2 × 10 ¹⁹
7.8	1.1 × 10 ⁻¹³	2.3 × 10 ²⁰	2.3 × 10 ⁻¹³	2.7 × 10 ²⁰

provement was observed in the leakage current and the reverse current-voltage characteristics of these diodes still presented a soft breakdown. For obtaining an avalanche breakdown, it was found that the PSG had to be in contact with the silicon substrate, and this result was independent from the phosphorus compound used in the preparation of the PSG.

Summary

Chemical vapor deposition of phosphosilicate glass layers on silicon from an argon diluted mixture of silane, oxygen, and phosphorus oxychloride was investigated in an effort to enhance the gettering action of the PSG for heavy metals during diffusion. Properties of these glasses as diffusion sources of P in Si were studied in terms of glass composition and diffusion temperatures. In parallel experiments with glasses prepared from oxidation of phosphine and silane at low temperature, it was found that the phosphorus oxychloride glasses are more susceptible to glass damage than the phosphine ones. Furthermore the gettering action of the PSG appears unrelated to the deposition system, but strongly dependent on the use or not

of a thin thermal-oxide film between the PSG and the Si substrate.

Acknowledgments

The author wishes to thank Dr. D. M. Brown and Dr. M. Garfinkel for reviewing the manuscript and suggesting many interesting ideas.

Manuscript submitted Aug. 20, 1971; revised manuscript received May 11, 1972.

Any discussion of this paper will appear in a Discussion Section to be published in the June 1973 JOURNAL.

REFERENCES

1. D. M. Brown *et al.*, *Solid-State Electron.*, **11**, 1105 (1968).
2. P. H. Robinson and F. P. Heiman, *This Journal*, **118**, 141 (1971).
3. J. Wong and M. Ghezzi, *ibid.*, **118**, 1540 (1971).
4. D. R. Stull, *Ind. Eng. Chem.*, **39**, 540 (1947).
5. R. J. Archer, *J. Opt. Soc. Am.*, **52**, 970 (1962).
6. A. S. Tenney and M. Ghezzi, To be published.
7. J. C. Irvin, *Bell System Tech. J.*, **41**, 387 (1962).
8. M. L. Barry, *This Journal*, **117**, 1405 (1970).

Brief Communication



Selective Growth of Heteroepitaxial GaP on Si Substrates

Osamu Igarashi

Electrotechnical Laboratory, Tanashi, Tokyo, Japan

Selective homoepitaxial depositions of Si and GaAs have long been realized. The method consists of the deposition of an epitaxial layer on selected areas of the substrate which are exposed by windows in a protective film. Using the same technique, we succeeded in depositing heteroepitaxial GaP selectively on Si substrates.

It has been reported that GaP layers deposited on Si substrates have serious cracks (1, 2). The GaP layer is separated into small regions of random sizes by the cracks. This phenomenon is undesirable from the practical viewpoint of device fabrications. By the use of selective-growth technique, this unfavorable cracking can be overcome. In this case, however, a selectively grown GaP layer without the cracks is relatively small in size (less than 0.02 mm²).

The selective growth of the heteroepitaxial GaP layer was carried out on the (111), (110), (100), and 5° off (111) faces of Si substrates. The Si substrate surfaces were thermally oxidized in wet oxygen to produce an oxide layer of about 10,000Å thickness. Windows or slits were formed in the SiO₂ film by the use of photolithographic techniques and appropriate etchants.

A growth system reported previously by the present author (1) was employed to prepare the heteroepitaxial layer. The growth method is essentially the same as a close-spaced technique described by Nicoll (3). In our system, the GaP source and Si substrate wafers were spaced by about 1 mm in an atmosphere of purified hydrogen gas, and were surrounded by graphite

blocks and an alumina ring. These materials were heated to the desired temperatures by the graphite blocks coupled to an external rf coil. During growth periods, the source to substrate temperature difference was about 20°C. The source temperature was up to 1160°C. Prior to deposition process, the Si substrate was slightly gas-etched in an atmosphere of dried 1 HCl/50 H₂ mixture at about 1200°C. After deposition, a number of Ga droplets was observed on the GaP source wafer surface.

In our growth apparatus, any transport agent was not intentionally introduced. We thought that the transport of the GaP source occurs by evaporation of the source material because of the significantly high vapor pressure of Ga metal dissociated from GaP. The equilibrium vapor pressure of Ga is 2×10^{-2} mm Hg at 1100°C (4). However, another possible transport mechanism is the water-vapor transport reaction due to the presence of small amounts of water vapor in the hydrogen ambient. Robinson has deposited GaAs with growth rates of 1-3 mils/hr using a close-spaced technique without intentionally introducing a transport agent. It has been concluded that the transport agent in the growth system is residual water vapor in the system which reacts with the GaAs source to form the volatile species Ga₂O (5). Moreover, it may be pointed out that the transport of GaP in our system takes place by the reaction with residual HCl gas remaining in the reaction chamber after the gas etching. However, it should be added that the GaP source can be transported to the substrate even in a deposition chamber in which any trace of HCl is not used.

Key words: selective growth, heteroepitaxial GaP, Si substrate, SiO₂.

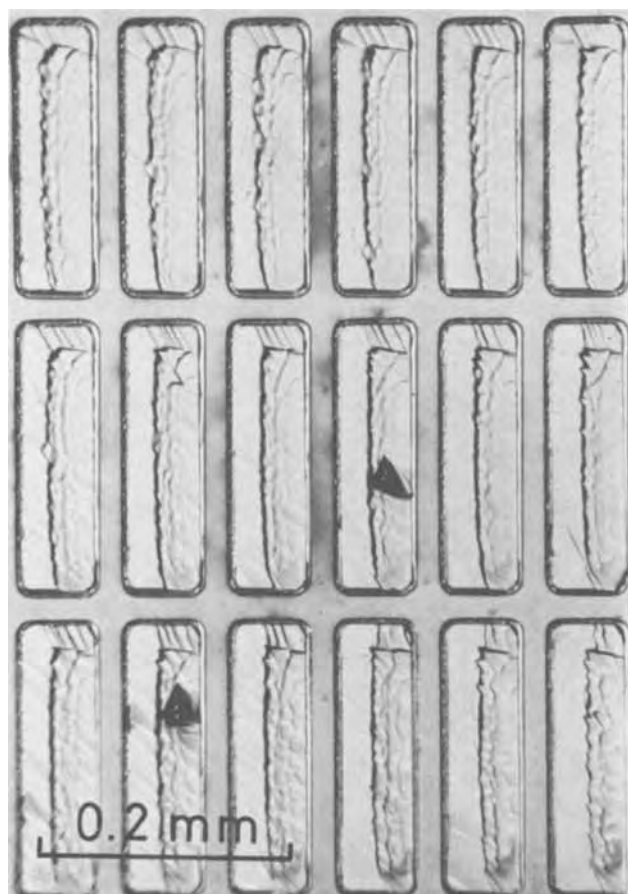


Fig. 1. Photomicrograph of selectively grown GaP (about 5μ thickness) in windows etched through SiO_2 film on 5° off (111) face of a Si substrate.

Figure 1 shows an optical photomicrograph of a GaP layer deposited on 5° off (111) face of a Si substrate at 1100°C . The growth rate of the GaP islands in Fig. 1 was about $1\mu/\text{min}$. As can be seen from the micrograph, the masked regions are free from GaP deposits. The best surface appearance of deposited GaP heteroepitaxial layers was obtained when 5° off (111) face of the Si substrate was employed. Figure 2 shows an x-ray back-reflection micro-Laue pattern originating from a GaP island in Fig. 1. Cu radiation was used. The diameter of the x-ray beam incident on the sample was between 60 and 80μ . In Fig. 2, a pair of Laue spots is recognized. One set of these Laue spots disappears when the x-ray beam is incident on a region where GaP is not deposited. Thus, one set of the spots is due to the Si substrate and the other due to the GaP deposit. It should be noted that the separation

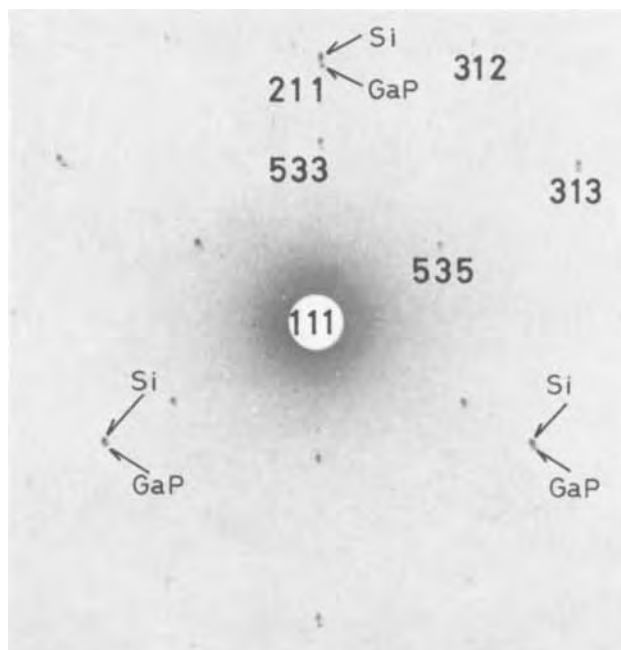


Fig. 2. X-ray back-reflection micro-Laue pattern originated from a GaP island in Fig. 1. A pair of Laue spots is observed. One set of the spots is due to the GaP deposit and the other due to the Si substrate.

of the Laue spots originating from the GaP deposit and the Si substrate indicates the presence of a tilt misorientation between the [111] axes of these two crystals. The angle of the misorientation is probably less than 30° .

Acknowledgment

The author wishes to thank Shin-Etsu Handotai Company, Ltd. and the Silicon Division of Chisso Corporation for providing thermally oxidized Si crystals used in this work. The author is also indebted to T. Iizuka for comments on the manuscript.

Manuscript submitted Jan. 4, 1972; revised manuscript received June 14, 1972.

Any discussion of this paper will appear in a Discussion Section to be published in the June 1973 JOURNAL.

REFERENCES

1. O. Igarashi, *J. Appl. Phys.*, **41**, 3190 (1970).
2. J. Noack and W. Möhling, *Phys. Status Solidi*, (a) **3**, K229 (1970).
3. F. H. Nicoll, *This Journal*, **110**, 1165 (1963).
4. C. D. Thurmond, *J. Phys. Chem. Solids*, **26**, 785 (1965).
5. P. H. Robinson, *RCA Rev.*, **24**, 574 (1963).



Electrical Evaluation of Doped and Undoped Cobalt Chromite as the Interconnection Material for High-Temperature, Zirconia-Electrolyte, Fuel-Cell Batteries

C. C. Sun, E. W. Hawk, and E. F. Sverdrup

Westinghouse Electric Corporation, Research and Development Center, Pittsburgh, Pennsylvania 15235

ABSTRACT

Cobalt chromite is an electronically conductive oxide stable in both air and mixtures of H_2-H_2O and $CO-CO_2$ having oxygen partial pressures greater than 10^{-15} atmospheres at $1000^\circ C$. It is potentially useful as a material to interconnect cells of a high-temperature, zirconia-electrolyte, fuel-cell battery. The $1000^\circ C$ resistivities and conductivity-types of cobalt chromite doped with manganese and vanadium were measured over the range of oxygen partial pressures of interest for fuel cell operation. Vanadium-doped cobalt chromite increased in resistivity on exposure to air. Two mole per cent manganese doping resulted in stable $1000^\circ C$ resistivities of 6 ohm-cm in air and 50 ohm-cm in H_2-H_2O mixtures having an oxygen partial pressure of 10^{-15} atm. These resistivities are sufficiently low to make manganese-doped cobalt chromite useful for the fuel-cell battery application.

The individual cells of a thin-film, high-temperature, fuel-cell battery using zirconia electrolytes are connected in series by a film of an electrically conductive oxide which joins the air and fuel electrodes of adjacent cells, as shown in Fig. 1. Previous work (1) established that cobalt chromite was a possible interconnection material for fuel cells operating at $1000^\circ C$. Electrical characteristics were studied by Copp *et al.* (2), Bradburn and Rigby (3), and Schmalzried (4). Resistivity at $1000^\circ C$ in air varied by two orders of magnitude—2, 70, and 200 ohm-cm were reported respectively by these authors.

Measurements of a 80μ thick film of undoped cobalt chromite separating the air and fuel atmospheres in the fuel-cell battery configuration gave an "effective double-atmosphere resistivity" of approximately 200 ohm-cm. This is four times higher than desired for practical fuel-cell batteries.

In choosing dopants to enhance the electrical conductivity of cobalt chromite, the observation of Bradburn and Rigby (3), that the B cations in the normal spinel structure AB_2O_4 play an important role in determining the conductivity, was considered. Cobalt aluminate displays resistivities several orders of magnitude higher than both cobalt chromite and nickel chromite. Inspection of a model of spinel reveals possible conducting paths by way of 3d electron interchange between adjacent B ions because of their collinearity and small B-B separation. Both manganese, which has a +3 ionic radius of 0.62\AA and four 3d orbital electrons, and vanadium, having a +3 ionic radius of 0.66\AA and two 3d orbital electrons, should be able to occupy chromium sites as the Cr^{+3} ionic radius is 0.64\AA and has three 3d orbital electrons. Either vanadium or manganese might be expected to introduce defects in the normal 3d electronic structure of cobalt chromite and hence enhance the conductivity. Based on these considerations, it was decided to em-

ploy manganese sesquioxide and vanadium sesquioxide as dopants to lower the resistivity of cobalt chromite. As discussed later, there is experimental evidence that some manganese actually substituted for cobalt.

This study investigated the feasibility of lowering the resistivity of cobalt chromite by doping with vanadium or manganese. Both resistivity and conductivity-type were measured. Measurements were made in the range of oxygen partial pressures between 0.2 and 10^{-15} atm using air, nitrogen, and nitrogen-hydrogen-water vapor mixtures. The temperature range studied extended from 600° to $1200^\circ C$.

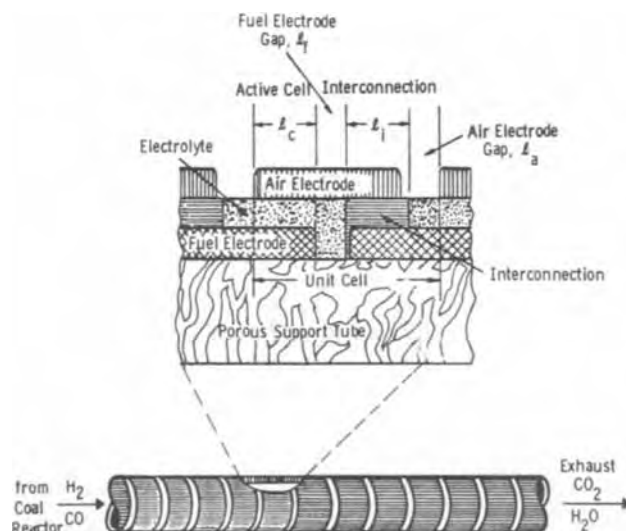


Fig. 1. Cross section through the wall of a thin-film fuel cell battery.

Experimental

Starting Materials

Cobalt chromite.—Three types of cobalt chromite varying in stoichiometry and particle size were used to prepare the test specimens. Their properties are summarized below.

Cobalt chromite, Poly Research, -325 mesh.—Cobalt chromite supplied by Poly Research Corporation is slightly rich in its chromium content with chromium/cobalt ratio of 2.29. X-ray diffraction identifies the presence of trace amounts of chromium oxide. The Poly Research cobalt chromite was sieved to obtain -325 mesh powder for preparation of specimens.

Cobalt chromite, Poly Research, air-milled.—The Poly Research cobalt chromite was air-milled by Northern Chemical Company to achieve particles of submicron size. Average particle diameter estimated from an electron micrograph of the air-milled cobalt chromite powder was 0.3μ .

Cobalt chromite, Pfizer.—Cobalt chromite supplied by Chas. Pfizer and Company, Inc. is slightly excess in cobalt. The chromium/cobalt ratio is 1.92 as compared with $\text{Cr/Co} = 2$ for perfect stoichiometry and $\text{Cr/Co} = 2.29$ for the chromium-rich cobalt chromite from Poly Research. The Pfizer cobalt chromite is of submicron particle size, similar to that of the air-milled, Poly Research material.

Vanadium oxide.—Reagent grade of V_2O_5 from Fischer was used. It was kept under nitrogen during handling.

Manganese oxide.—Reagent grade, fine-particle Mn_2O_3 was supplied by Poly Research Corporation.

Preparation of Test Bars

Undoped cobalt chromite bars.—Undoped bars were prepared using the three different types of starting materials in the following manner.

Cobalt chromite of -325 mesh size range, obtained by sieving the Poly Research material, was first cold-pressed at 10 ksi to form bars of approximate dimensions $1\text{ cm} \times 1\text{ cm} \times 3\text{ cm}$. The bars were then sintered in air for 48 hr at 1500°C .

Both the air-milled, Poly Research material and the Pfizer cobalt chromite were prepared by first cold-pressing at 10 ksi. The bars were sintered at 1500°C in air for 24 hr, followed by equilibrating the bars in a hydrogen-water mixture at oxygen partial pressure of 10^{-9} atm for an additional 24 hr at 1500°C . This atmosphere was achieved by saturating a nitrogen-5% hydrogen forming gas with water vapor at 58°C . Figure 2 is a scanning electron micrograph of the fractured surface of an undoped bar after sintering.

Vanadium-doped cobalt chromite bars.—Doping was achieved by dry-milling appropriate amounts of vanadium sesquioxide and Poly Research cobalt chromite, cold-pressing and sintering at 1530°C for 48 hr in a hydrogen-water mixture of oxygen partial pressure of 10^{-9} atm. Electron microprobe traces (of 5μ resolution) showed a continuous vanadium distribution throughout the cobalt chromite sample. X-ray diffraction identified the doped bar as having spinel structure. Electron and x-ray scanning microscopy did not detect a second phase. Figure 3 shows typical electron micrograph of the 2 m/o¹ (mole per cent) vanadium-doped cobalt chromite bar.

Manganese-doped cobalt chromite bars.—In the case of manganese-doped samples, doping was achieved by ball-milling appropriate amounts of manganese sesquioxide and Pfizer cobalt chromite, cold-pressing, and

¹ Throughout this paper $X^{\text{m/o}}$ of vanadium- or manganese-doped cobalt chromite symbolizes X moles of V_2O_5 (or Mn_2O_3) in $(100 - X)$ moles of CoCr_2O_4 , i.e., molar per cent of manganese = $\frac{X}{X + [100 - X]}$

$\frac{X}{X + [100 - X]}$

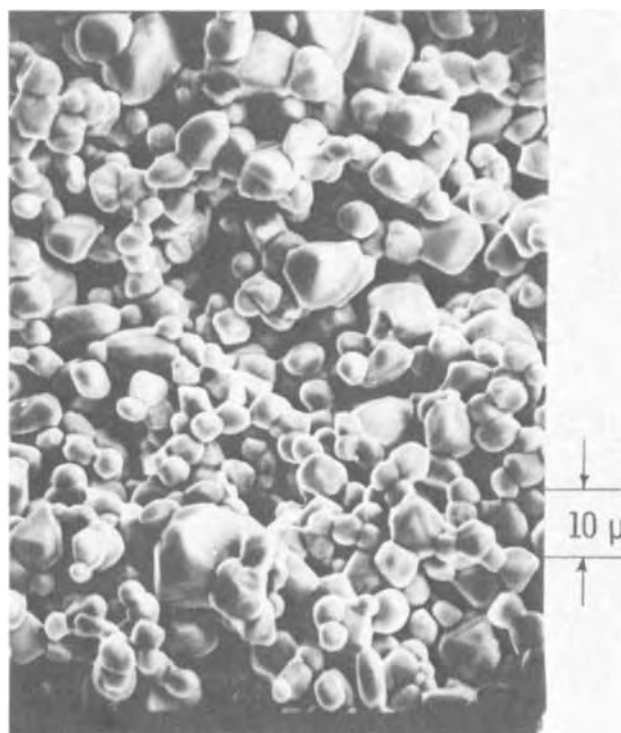


Fig. 2. Electron micrograph of an undoped Co-rich CoCr_2O_4 sintered bar (fractured surface).

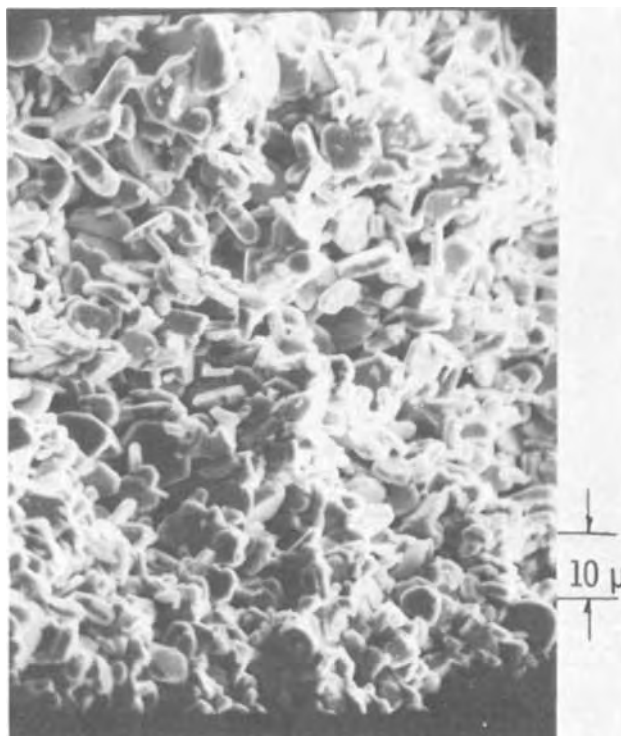


Fig. 3. Electron micrograph of a 2 m/o V-doped CoCr_2O_4 sintered bar (fractured surface).

sintering. Special effort was taken to disperse the fine particles of the mixture to increase the probability of successful doping during sintering. Sintering was carried out in two steps. First, the pressed bars were sintered at 1500°C in air for 24 hr. Under these sintering conditions, Mn_2O_3 is expected to be oxidized to Mn_3O_4 , which is a normal spinel (5). Formation of a solid solution between the two normal spinels, Mn_3O_4 and CoCr_2O_4 , was expected at this stage. During the second step of sintering, the bars were equilibrated

with a hydrogen-water mixture at an oxygen partial pressure of 10^{-9} atm at 1500°C for an additional 24 hr.

In all the manganese-doped cobalt chromite bars, the electron and x-ray scanning microscopic analysis revealed the presence of a small percentage of a spherical-shaped second phase which was rich in cobalt. Figure 4 is a typical scanning electron micrograph of the 2 m/o manganese-doped cobalt chromite bars. An x-ray diffraction pattern of the 9 m/o manganese-doped cobalt chromite indicated the presence of traces of metallic cobalt. Since the lower limit of sensitivity was 5%, the absence of cobalt lines on x-ray powder diagrams of the 2 and 4 m/o manganese-doped samples did not exclude the possibility of cobalt presence in these samples.

Lattice parameters of the undoped and manganese-doped cobalt chromite were determined from the x-ray diffraction patterns and they were

a_0 (undoped CoCr_2O_4)	= 8.320 Å
a_0 (2 m/o Mn-doped CoCr_2O_4)	= 8.341 Å
a_0 (4 m/o Mn-doped CoCr_2O_4)	= 8.344 Å
a_0 (9 m/o Mn-doped CoCr_2O_4)	= 8.360 Å

It can be noticed that the lattice parameter increases as a function of manganese doping. As Mn^{+3} cation is smaller than Cr^{+3} (0.62 Å for Mn^{+3} vs. 0.64 Å for Cr^{+3}), a decrease in lattice parameter would be expected had Mn^{+3} substituted in the Cr^{+3} sites of the cobalt chromite lattice. This is the opposite to what we observed.

Comparison of ionic sizes and electronic configuration of Mn^{+2} and Co^{+2} (0.80 Å for Mn^{+2} and 0.72 Å for Co^{+2}) shows the possibility of Mn^{+2} substituting in Co^{+2} sites in the cobalt chromite lattice. As Mn^{+2} is larger than Co^{+2} , substitution of Co^{+2} by Mn^{+2} would be expected to result in expansion of the lattice parameter of the cobalt chromite spinel. If this had been the doping mechanism, the Co^{+2} , which was freed by Mn^{+2} from the cobalt chromite lattice, would have been reduced to cobalt metal during the second step of the sintering under oxygen partial pressure of 10^{-9}

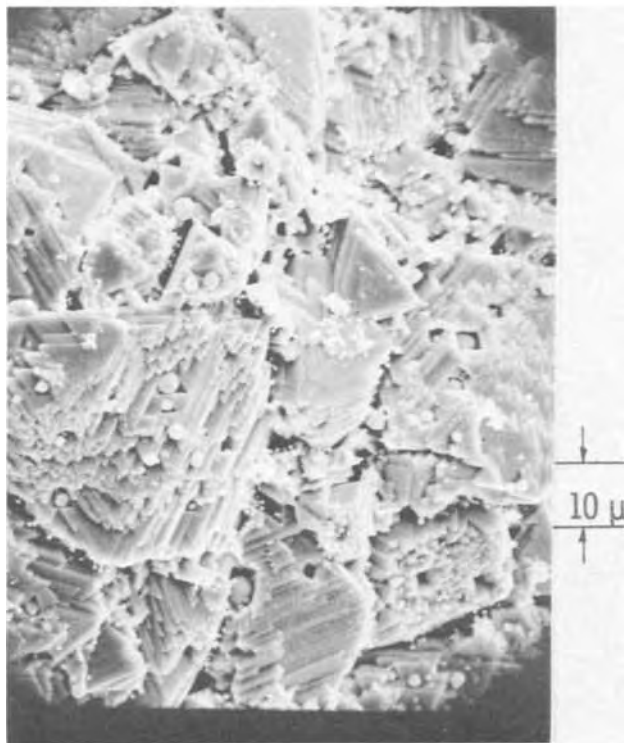


Fig. 4. Electron micrograph of a 2 m/o Mn-doped CoCr_2O_4 sintered bar (fractured surface).

atm at 1500°C . Indeed, x-ray diffraction detected the presence of traces of cobalt metal in the 9 m/o manganese-doped sample.

The undoped specimens sintered to 48-55% of theoretical density, the vanadium-doped specimens reached 64-70% of theoretical density, while the manganese-doped specimens achieved 75-90% of the theoretical density of cobalt chromite. Comparison reveals that vanadium oxide and manganese oxide at low doping levels, especially 2 m/o and 4 m/o of manganese oxide, serve as densification aids to cobalt chromite sintering. These results compare with the results reported by Bron and Diesperova (6), who found that additives, whose cations could replace Cr^{+3} (e.g., Ti^{+4} , Fe^{+2} , Fe^{+3} , Zr^{+4} , Mn^{+2} , Mn^{+3}), considerably accelerated the rate of formation and sintering of magnesium chromite spinel. The fact that the oxide dopants not only improve conductivity but also promote densification of cobalt chromite is worth special notice, because the interconnection of the high-temperature thin-film fuel-cell batteries must be both highly conductive and gas-impermeable.

Electrical Measurements

Two bars of each composition were tested. One bar was located in the hot zone of the tester furnace for resistance measurement using the d-c, four-probe technique and the other bar placed toward one end of the same furnace where a thermal gradient existed for thermoelectric studies. From the gauge lengths and the dimensions of the specimen bars, the resistance measurements are accurate to $\pm 20\%$.

Resistivity and Seebeck effect were measured as functions of temperature, in the range of 600°C - 1200°C , and oxygen partial pressure, in the range $P_{\text{O}_2} = 0.2$ to 10^{-15} atm using air, nitrogen, and nitrogen-hydrogen-water mixtures. The oxygen partial pressures were measured using a stabilized zirconia oxygen gauge operating at 1000°C with air as the reference.

Results

Undoped cobalt chromite.—Figure 5 shows the temperature dependence of resistivity of undoped chromium-excess cobalt bars in air and nitrogen. The thermoelectric measurements indicated that the chromium-rich cobalt chromite displayed p-type conductivity throughout the oxygen partial pressure range of 0.21 to 10^{-15} atm. Figure 6 presents the Seebeck coefficients determined by our experiments as a function of oxygen partial pressure. Schmalzried's results are shown for comparison.

Figure 7 shows the oxygen partial pressure dependence of resistivity at 1000°C of the two types of un-

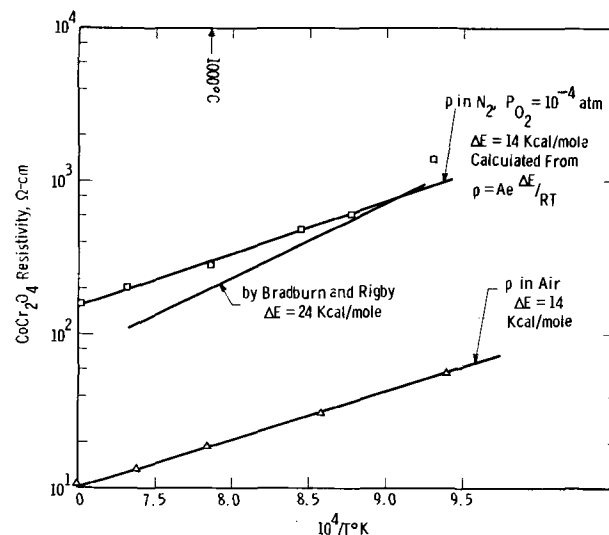


Fig. 5. Measured resistivity of undoped Cr-excess CoCr_2O_4 in air and N_2 as a function of the reciprocal of absolute temperature.

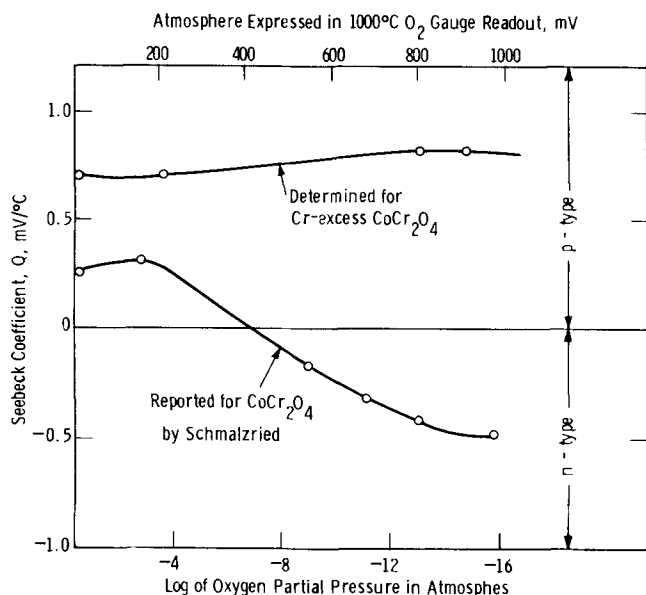


Fig. 6. Seebeck coefficient determined for the Cr-excess cobalt chromite as a function of oxygen partial pressure.

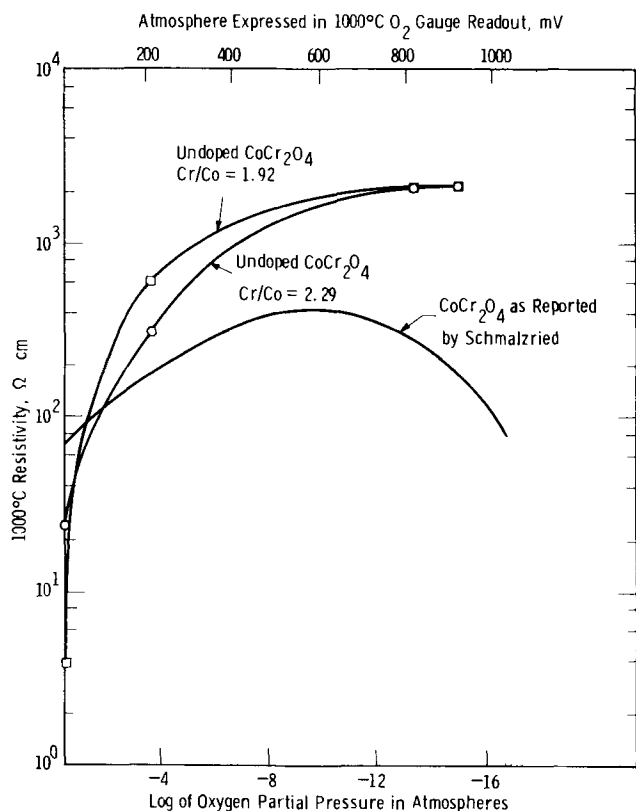


Fig. 7. Comparison of resistivity of two types of cobalt chromite

doped cobalt chromite specimens. They are compared to Schmalzried's data. It can be concluded that both types of cobalt chromite display a 1000°C resistivity of less than 25 ohm-cm in air and a 1000°C resistivity of about 2×10^3 ohm-cm in fuel atmospheres despite the difference in chromium/cobalt ratios.

Vanadium-doped cobalt chromite.—The chromium-rich cobalt chromite with 1 and 2 m/o of vanadium sesquioxide doping were sintered in reducing atmosphere ($P_{O_2} = 10^{-9}$ atm at 1530°C) to preserve vanadium cations in the +3 valence state. Electrical measurements were first performed in the same atmosphere to speed the atmosphere equilibration process and the results are shown in Fig. 8-10. Figures 8 and 9 demon-

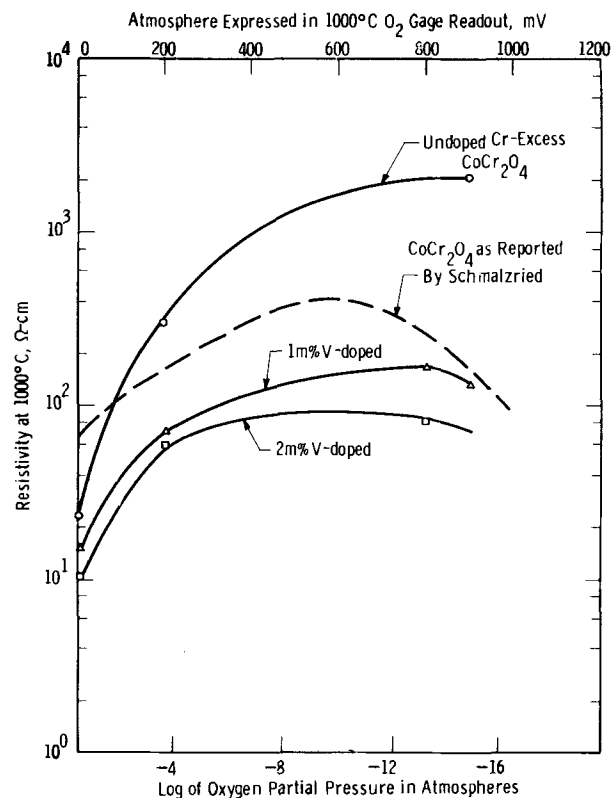


Fig. 8. Effects of V-doping on $CoCr_2O_4$ resistivities as a function of oxygen partial pressure.

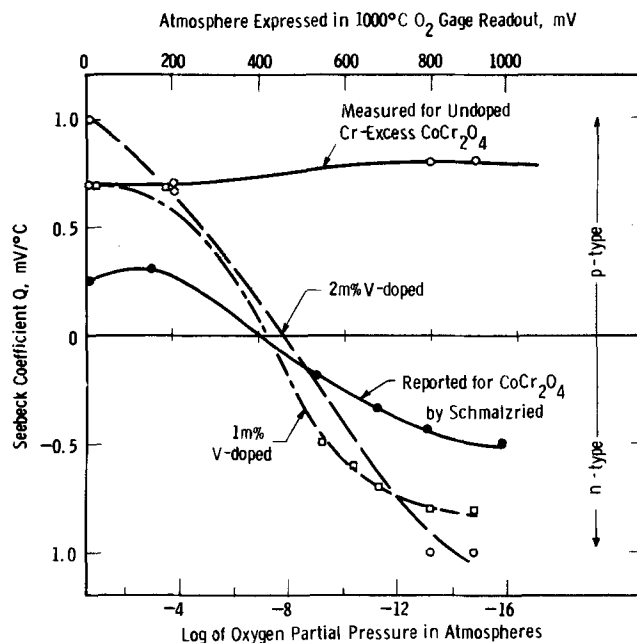


Fig. 9. Effects of V-doping on Seebeck coefficients as a function of oxygen partial pressure.

strate respectively the variations of resistivity and Seebeck coefficient with oxygen partial pressure. Figure 10 shows the temperature dependence of the resistivities. From Fig. 8-10, it can be observed that vanadium doping of cobalt chromite enhances n-type conductivity at low oxygen partial pressures. Resistivity is reduced initially by a factor of 15 with 1 m/o and a factor of 25 with 2 m/o of vanadium doping at an oxygen partial pressure of 10^{-14} atm. Vanadium doping reduced the 1000°C resistivity in air from 22 ohm-cm to 15 ohm-cm by 1 m/o vanadium doping and from 22 ohm-cm to 10 ohm-cm by 2 m/o doping. The improvement of bar density, from 48% theoretical density of

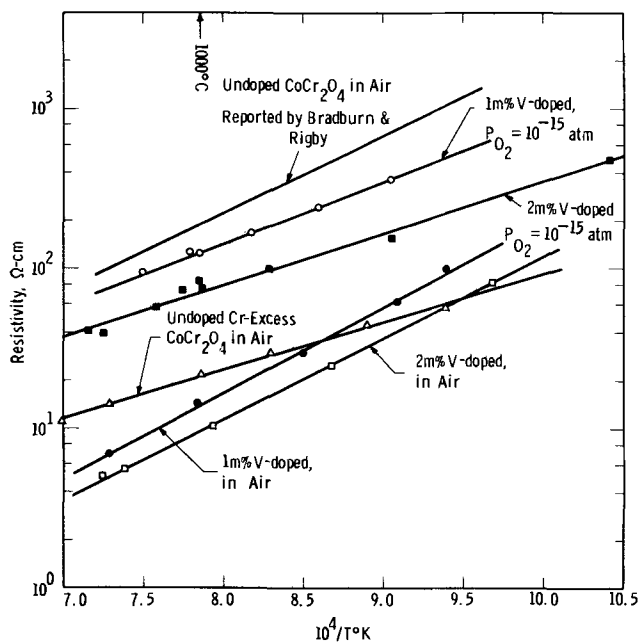


Fig. 10. Effects of V-doping on CoCr_2O_4 resistivities in air and fuel atmospheres as functions of $1/T$.

the undoped bars to 64% for 1 m/o and 70% for 2 m/o vanadium-doped bars, must be considered in interpreting the resistivity results.

As the oxygen partial pressure was increased over 10^{-10} atm, gradual loss of vanadium dopant by oxidation and vaporization occurred. This was verified by chemical analysis of the bar before and after electrical tests in the oxidizing atmosphere and by spectrographic analysis of a dark deposit on the upstream portion of the testing apparatus. The loss of vanadium was accompanied by an $n \rightarrow p$ transition in conductivity type and an irreversible increase in resistivity at low oxygen partial pressures. Figure 11 shows the change in resistivity at low oxygen partial pressures of the vanadium-doped cobalt chromite vs. time of sample exposure to air. The resistivity of the vanadium-doped cobalt chromite in air remained nearly unchanged apparently being insensitive to vanadium loss to the 30% vanadium losses measured.

Manganese-doped cobalt chromite.—Figure 12 shows a plot of resistivity in air and in fuel atmospheres as a function of molar per cent of manganese doping at 1000°C . Doping with 2 to 4 m/o of manganese oxide reduces the resistivity by almost two orders of magnitude under low oxygen partial pressures. The resistivity of the 2 m/o manganese-doped cobalt chromite in

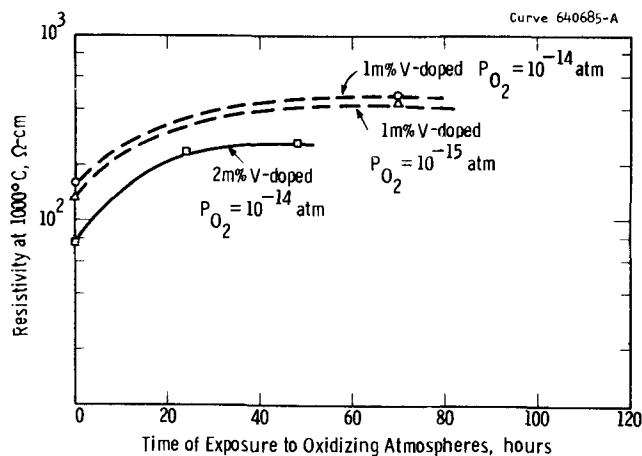


Fig. 11. Increase of V-doped CoCr_2O_4 resistivity in fuel atmosphere as a function of exposure time to oxidizing atmosphere.

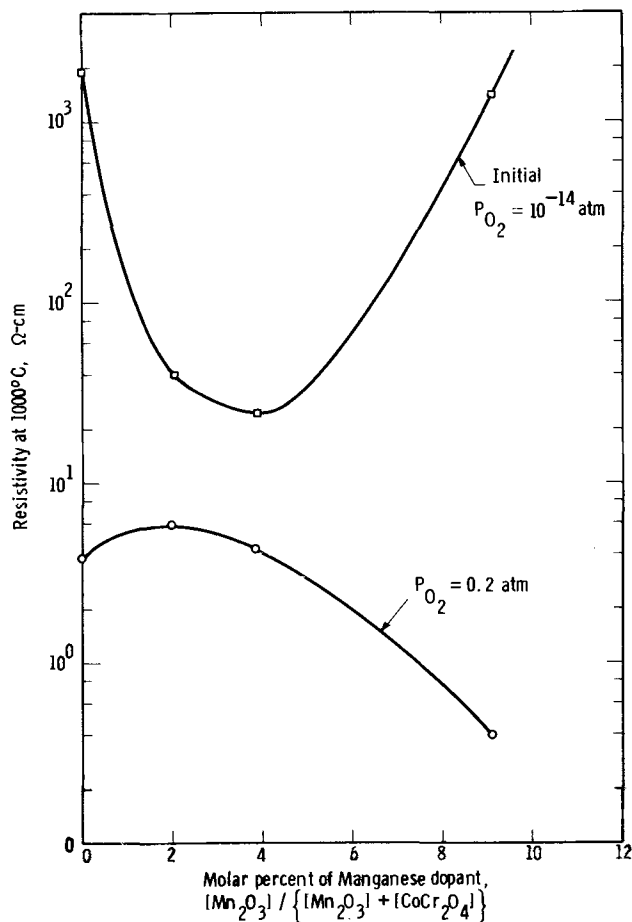


Fig. 12. Effect of manganese doping on CoCr_2O_4 resistivities in air and fuel atmospheres.

fuel atmosphere is stable over the 26 days of total testing time and is independent of sample cycling to an oxidizing atmosphere. Its resistivity in air also appears to be stable (Fig. 13). The resistivity of 4 m/o manganese-doped cobalt chromite increases steadily on exposure to the fuel atmosphere. It decreases slightly with time in air. The resistivity of 9 m/o manganese-doped cobalt chromite is also unstable. It can be concluded from these tests that the 2 m/o manganese-doped cobalt chromite is close to the optimum doping level. Its resistivity is least sensitive to oxygen partial

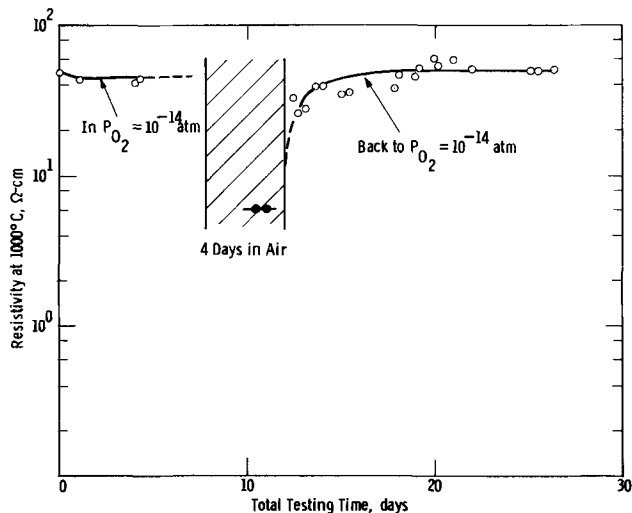


Fig. 13. Resistivity of 2 m/o Mn-doped CoCr_2O_4 as a function of testing time.

pressure change and most stable with respect to testing time and atmosphere cycling.

Conclusions

Undoped-cobalt chromite.—Commercially supplied, undoped-cobalt chromite had a resistivity in air at 1000°C of 20 ohm-cm. At 1000°C in hydrogen-nitrogen-water vapor mixtures, having an oxygen partial pressure of 10^{-14} atm, the resistivity was 2000 ohm-cm. The order of magnitude of the resistivity and the conductivity type was not sensitive to deviations of cobalt and chromium content from the ideal stoichiometric ratio of two parts chromium to one part cobalt between Cr/Co ratio of 1.9 to 2.3. Resistivity in air of undoped cobalt chromite is low enough for the fuel cell application. Resistivity in low oxygen-partial-pressure fuel gas atmospheres is two orders of magnitude too high.

Measurements of thermoelectric power showed that the sample having a chromium to cobalt ratio of 2.3 displayed "p"-type conductivity over the oxygen partial pressure range 10^{-15} to 0.2 atm and at temperatures between 600° and 1200°C.

Vanadium-doped cobalt chromite.—The resistivity of cobalt chromite at low oxygen partial pressure can be reduced by vanadium doping. Two mole per cent of V_2O_3 doping lowered the resistivity of cobalt chromite at 1000°C from 2000 to 80 ohm-cm at an oxygen partial pressure of 10^{-14} atm.

The resistivity of the vanadium-doped cobalt chromite was not stable after the samples were exposed to atmospheres having oxygen partial pressures higher than 10^{-10} atm. The increase in resistivity was associated with a loss of vanadium from the samples when in oxidizing atmospheres. The resistivity in air was not affected by the addition or the loss of the vanadium dopant. Vanadium-doped cobalt chromite was an "n"-type conductor at low oxygen partial pressures and a "p"-type conductor in air. As vanadium was lost, the magnitude of the thermoelectric power in the low oxygen partial pressure atmosphere decreased, changed sign, and approached the values typical of the "p"-type conductivity observed with the undoped material. Only one strategy was used to incorporate the vanadium doping in the spinel and these results are specific to that diffusion-sintering schedule.

Manganese-doped cobalt chromite.—Three levels of manganese doping were tested: 2, 4, and 9 m/o Mn_2O_3 . Cobalt chromite containing 2 m/o Mn_2O_3 displayed

stable resistivities. Resistivity at an oxygen partial pressure of 10^{-14} atm was lowered from 2000 to 50 ohm-cm at 1000°C. Resistivity in air was 6 ohm-cm. Resistivity at 1000°C was stable over a testing period of 26 days in the low oxygen partial pressure atmosphere. It was not affected by cycling to air.

The resistivity of the 4 and 9 m/o manganese sesquioxide-doped cobalt chromite varied with time.

Manganese-doped cobalt chromite also displayed "p"-type conductivity.

Manganese-doped cobalt chromite is sufficiently conductive to be a satisfactory cell interconnection for zirconia electrolyte fuel cells operating at temperatures near 1000°C. At this temperature level, coal gasification rates are high enough that a practical coal reacting fuel-cell power system can be engineered.

Acknowledgments

The Westinghouse Electric Corporation and the Office of Coal Research—U. S. Department of the Interior jointly sponsored this work directed toward a practical fuel cell power system capable of utilizing coal as a fuel. The authors would like to express their appreciation of the support of Mr. Neal P. Cochran, Chief of Utilization, Office of Coal Research and Mr. Paul Towson, Division of Utilization. The efforts of Mr. Robert L. Eback in preparing chromite dispersions were also appreciated.

Manuscript submitted March 8, 1972; revised manuscript received May 8, 1972. This was Paper 16 presented at the Cleveland, Ohio, Meeting of the Society, Oct. 3-7, 1971.

Any discussion of this paper will appear in a Discussion Section to be published in the June 1973 JOURNAL.

REFERENCES

1. E. F. Sverdrup *et al.*, 1970 Final Report, Project Fuel Cell, OCR R&D Report No. 57, Government Printing Office Catalog No. I63.10:57.
2. A. N. Copp, M. Nakahira, and G. W. Brindley, *This Journal*, **113**, 237 (1966).
3. T. E. Bradburn and G. R. Rigby, *Trans. Brit. Ceram. Soc.*, **52**, 417 (1952).
4. H. Schmalzried, *Berichte der Bunsengesellschaft*, **67** (1), 93 (1963).
5. E. M. Levin, C. R. Robbins, and H. F. McMurdie, "Phase Diagrams for Ceramists," The American Ceramic Society, Columbus, Ohio (1964).
6. V. A. Bron and M. I. Diesperova, *Silikaty i Okisly v Khim. Vysokikh Temperatur*, Moscow, Sb. 134-145 (1963).

Equilibrium Phases in the Lithium-Sulfur System

Ram A. Sharma*

Electrochemistry Department, Research Laboratories, General Motors Corporation, Warren, Michigan 48090

ABSTRACT

Equilibrium phases in the lithium-sulfur system on the sulfur side of Li_2S (the only compound observed in this system) were determined using an unusual vapor transport technique. In this method, equilibrium compositions of the melts at various temperatures can be obtained by utilizing the transport of sulfur vapor from one melt to a second one. The lithium-sulfur phase diagram exhibits a large miscibility gap which extends from the monotectic composition, 65.5 mole per cent (m/o) sulfur, to almost pure sulfur (0.035 m/o lithium) at the monotectic temperature, $362^\circ \pm 3^\circ\text{C}$. The melting point of lithium sulfide was found to be $1365^\circ \pm 10^\circ\text{C}$. The results are also presented as the lithium sulfide-sulfur phase diagram, in which the miscibility gap extends from the monotectic composition, 73.7 m/o sulfur, to nearly pure sulfur (0.0175 m/o lithium sulfide). A comparison of the liquidus at the Li_2S -liquid region of the Li_2S -S system with those constructed using Temkin's model indicates the probable existence in these melts of sulfide species such as S_2^{2-} , S_3^{2-} , and S_4^{2-} , in addition to S^{2-} .

Among the systems considered in the development of a high-temperature molten-salt battery for vehicular propulsion, sodium-sulfur and lithium-sulfur appear to be promising, practical, and economical (1). Basic thermodynamic data, which are essential in the development of these batteries, are available to some extent for the sodium-sulfur system (2, 3), but to still lesser extent for the lithium-sulfur system (4-6). This investigation was conducted to determine the equilibrium phase diagram of the lithium-sulfur system. These data were also used to gain some insight into the nature of the lithium-sulfur melts.

The normal techniques used in the determination of phase diagrams cannot be applied to the lithium-sulfur system. Lithium and sulfur are very corrosive and consequently the choice of container materials is limited. The container which cannot be made of metal because of sulfur or sulfide reaction, has to be sealed to avoid the loss of sulfur by vaporization. The phases involved appear to have similar densities and are very fluid; therefore, the quenching technique cannot be used indiscriminately because of the difficulty in obtaining satisfactory phase separation. Differential thermal analysis (DTA) and thermal analysis can only be used in limited regions because the melts undercool, coupled with the fact that the phase boundaries rise very steeply with change in composition.

Therefore, an unusual vapor transport technique was developed in which equilibrium compositions of the melts were obtained through transfer of sulfur vapor from one melt to a second one. This simple and inexpensive technique can also be used to determine the phase diagrams of other systems involving one or more volatile components.

Experimental

Materials.—Sulfur of 99.999% purity was used. Lithium sulfide was used in the form of a white powder; its lithium content was found by chemical analysis to be 29.8 weight per cent (w/o) (30.26 w/o theoretical). Its x-ray powder diffraction pattern data are given in Table I. The stronger diffraction lines agree with those calculated from the data reported by Zintl *et al.* (7). The present pattern also shows more and weaker lines for which these authors might not have bothered to report the data.

* Electrochemical Society Active Member.

Key words: lithium, sulfur, lithium sulfide, equilibrium phases.

Apparatus.—A Kanthal-wound tubular furnace, capable of being rocked through an angle of approximately 90° , was used to heat the mixtures. The furnace, suitable for use up to 1000°C , had external terminals from its heating element every 2.0 in. By manipulating the power supply to two different segments of the furnace element, a constant-temperature zone about 6 in. long was obtained. Two concentric stainless-steel containers (2 in. diam \times 6 in. long and 1 in. diam \times 6 in. long) were placed inside the uniform temperature zone to provide further uniformity of temperature (Fig. 1). Auxiliary apparatus used with the furnace included a furnace controller and a temperature recorder. Calibrated Chromel-Alumel thermocouples were used for measuring temperatures. A Leeds and Northrup potentiometer was also used to confirm the melt temperatures recorded.

Sealed containers, made of silica (Vycor), were used for lithium-sulfur melts of low lithium content and at lower temperatures. These containers, shown in Fig. 2, were fabricated in uncommon shapes in an effort to obtain clear separation of the phases on quenching. Dense-graphite containers were used for melts of high lithium content and at higher temperatures. The

Table I. X-ray diffraction data of powdered Li_2S taken with $\text{CuK}\alpha$ -radiation, using nickel filter by 114.6 mm camera

2θ	I	d (Å)	2θ	I	d (Å)
15.9	VVW	5.57	56.3	M	1.631
20.4	VVW	4.35	58.2	VVW	1.583
23.3	W	3.82	59.0	VVW	1.563
24.7	W	3.60	60.3	VVW	1.532
27.3	VVS	3.26	65.9	MS	1.415
29.2	VW	3.06	72.1	S	1.299
30.6	VVW	2.92	74.9	MS	1.267
31.6	S	2.83	83.5	S	1.156
32.7	VW	2.74	89.8	S	1.091
35.4	VW	2.53	100.3	MS	1.003
36.4	VVW	2.47	106.7	S	0.960
37.6	VVW	2.39	108.9	MS	0.947
38.7	VVW	2.32	118.0	S	0.899
40.8	VW	2.21	125.2	S	0.868
45.3	VS	1.999	127.7	M	0.858
48.2	VW	1.886	139.2	M	0.822
50.5	VVW	1.805	149.5	S	0.798
53.6	S	1.708	154.3	MS	0.790

VVW = Very, very weak
W = Weak
S = Strong
M = Medium
MS = Medium to strong

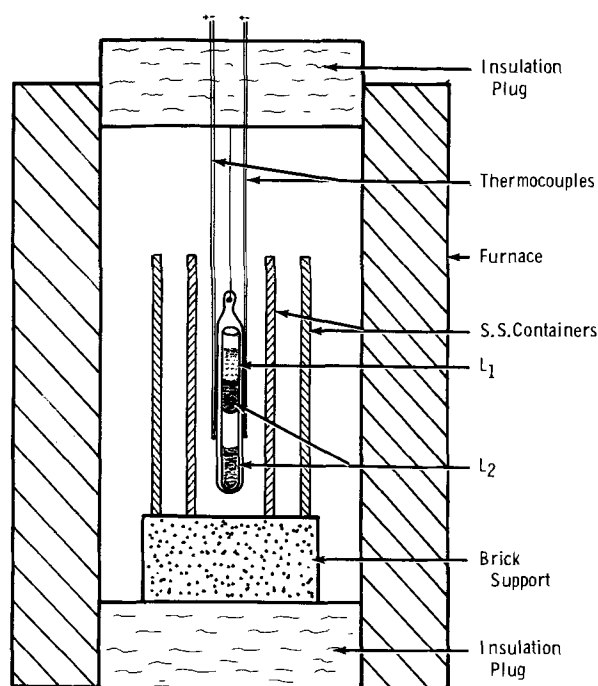


Fig. 1. The equilibrium apparatus

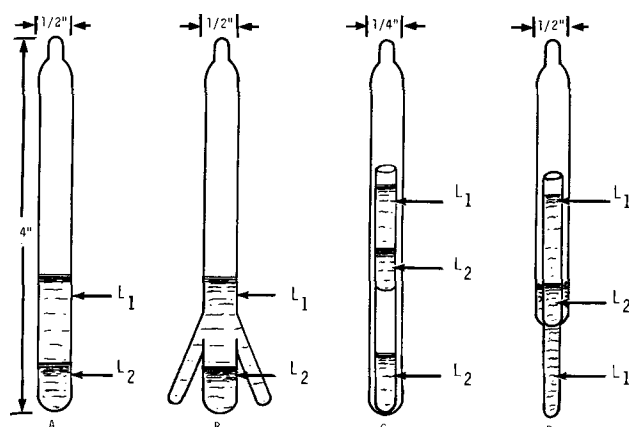


Fig. 2. The melt containers

graphite containers were sealed in silica (Vycor) capsules to avoid sulfur loss by vaporization.

Procedure.—Lithium sulfide and sulfur were used in preparing the lithium-sulfur melt compositions because lithium and sulfur react violently.

Quenching methods.—In the preliminary experiments, the desired amounts of lithium sulfide and sulfur were mixed thoroughly and about 5g of this mixture were placed in a silica capsule (Fig. 2A) inside a helium-atmosphere dry box. The silica capsule was then sealed under vacuum and placed in the uniform temperature zone of the rocking furnace. The furnace, while rocking, was slowly heated to the desired temperature. The silica capsules were kept at this temperature for 24-72 hr for equilibration. After the equilibration period, which was normally about 24 hr, the silica capsule was quenched in 10% LiCl solution at -10°C . On solidifying, two layers were formed. The bottom layer was dark red in color. The top layer was yellow in color and had a lower concentration of lithium than did the bottom layer.

Chemical analyses of samples from the two solidified layers were used to determine the compositions of the respective liquids at the equilibrium temperature. The general pattern of the equilibrium phase diagram, consisting of a miscibility gap and a solid-liquid region on the sulfur side of the lithium-sulfur system, could be

obtained from these preliminary experiments. It was also observed from these experiments that the rocking was not necessary for equilibration of melts above 500°C , and that the lighter yellow liquid undercooled and appeared to separate into two layers before solidifying.

To circumvent the undercooling of the lighter yellow liquid, silica capsules with side arms (Fig. 2B) were used in subsequent experiments. In these experiments, sulfur was solidified in the side arms of the capsule, and a lithium-sulfur solidified melt (approximately 37 m/o lithium) prepared separately, was placed in the bottom of the capsule. Additional sulfur was then solidified in the capsule over the lithium-sulfur mixture and in the region extending above the side arms. The capsule was sealed under vacuum. The procedure was then the same as that for capsules without side arms. After equilibration and quenching, chemical analyses of the solidified contents of the side arms were used to determine the composition of the lighter yellow liquid, and analyses of the lower portion for determining the composition of the dark red liquid. The compositions of the equilibrium liquids could be determined by this technique only up to about 600°C . Above this temperature, the silica capsule was observed to react with the lithium-sulfur melt and occasionally to explode. The silica capsule might possibly react with a certain amount of lithium of the melt shifting its composition to a higher concentration of sulfur.

Vapor transport technique.—For determination of the compositions of the liquids in the two-liquid region at higher temperatures ($>600^{\circ}\text{C}$), and to check the compositions at lower temperatures, an unusual, simple technique was developed—the vapor transport technique. In this method, two graphite crucibles were used (Fig. 2C), one containing a lithium-sulfur melt with a composition slightly different than the expected equilibrium composition, and the other containing a melt composition from within the two-liquid region. The second crucible was placed above the first one in a silica capsule. The capsule was sealed under vacuum and placed in the uniform temperature zone of the furnace. The furnace was slowly heated, without rocking, to the desired temperature and kept at this temperature for 24-72 hr. The contents of the two graphite crucibles were thus equilibrated by transfer of sulfur through the vapor phase. After equilibration, which normally required no more than 24 hr, the capsule was cooled to room temperature in a jet of air. The composition of the melt at the equilibrium temperature was determined from the chemical analyses of the total contents of the bottom graphite crucible. At lower temperatures, and for compositions with higher sulfur concentrations, a slightly modified arrangement was used (Fig. 2D). In this arrangement, the liquid with concentration of lithium less than equilibrium was placed in the bottom extension of the silica capsule, and the two-liquid mixture was contained in a silica tube located in the upper part of the capsule. The silica capsule was sealed under vacuum and quenched in 10% LiCl solution at -10°C . The composition of the melt at the equilibrium temperature was determined from the chemical analysis of the total content of the extension of the silica capsule. The results obtained using this procedure were the same as were obtained from the two-graphite-crucible quenched-in-air method.

The technique of using two graphite crucibles for the container was also used to determine the liquid composition in the solid-liquid region of the phase diagram. In this case, solid lithium sulfide, instead of the two-liquid composition, was contained in one graphite capsule.

The melting points of lithium sulfide and of sulfur, and the monotectic temperature at 6.0, 7.1, 16.3, 21.2, 31.0, and 41.0 m/o Li_2S were determined using both the heating and cooling curves from differential

thermal analyses performed with Mettler Thermo-analyzer. The specially designed sample holders of dense graphite were used to determine the melting point of lithium sulfide, while graphite as well as silica sample holders were used to determine the monotectic temperature. Alumina was mostly used as a reference material.

Chemical analysis.—The melts containing lithium sulfide-sulfur were leached from the weighed graphite crucibles with boiling water. The process was repeated several times. After that, the crucible was dried and then soaked in carbon disulfide for 10 min or so, and then the crucible was again dried and weighed. The crucible was examined with a stereo microscope before melt dissolution and at the end to be sure that all the material was removed. The difference in weights of the graphite crucible with and without the melt was taken as sample weight.

The carbon disulfide solution was evaporated to dryness, and the residue was treated with water. This solution and the water extract were combined in a 100 ml volumetric flask and diluted to the volume. An appropriately measured aliquot of this solution was transferred to a beaker, nitric acid was added, and the solution was evaporated to dryness to remove the sulfide ions. A solution of potassium chloride was added to a water solution of the dried residue in a volumetric flask, the solution diluted to volume, and lithium was determined by flame photometry *vs.* standard solution containing the same concentration of potassium chloride. The analysis method was checked for accuracy by determining lithium in pure lithium sulfide, and sulfur and lithium sulfide mixtures. The analysis was found to be accurate within $\pm 1\%$ of the amount present.

Results and Discussion

The phase equilibrium results obtained by the various techniques are summarized in Table II. The equilibrium phase diagram of the lithium-sulfur system based on these measurements is shown in Fig. 3; sulfur-rich compositions are shown enlarged in the insert in this figure. The measurements represented by the open circles in Fig. 3 were deliberately not in-

Table II. Equilibrium compositions at various temperatures in the lithium-sulfur system

Temp, °C	Mole per cent lithium		Experimental technique	
	Li-rich liquid, L_2	Sulfur-rich liquid, L_1		
Two-liquid region				
374	34.12	0.035	Quenching the equilibrated melts	
415	34.61	0.031		
456	32.90	0.070		
532	32.90	0.150		
537	31.50	0.350		
588	30.80	0.220		
682	30.50	0.330		
522	—	0.055		Vapor transport technique
620	—	0.322		
728	29.45	—		
776	22.74	—		
787	—	0.597		
809	24.40	—		
815	21.29	—		
843	18.60	—		
834	—	0.642		
838	—	4.536		
860	9.16	9.160		
Solid-liquid region				
376	34.70	—	Vapor transport technique	
442	37.93	—		
472	38.87	—		
484	36.39	—		
497	38.83	—		
550	37.47	—		
632	39.93	—		
698	44.08	—		
791	44.67	—		
854	50.13	—		
867	46.95	—		
893	50.93	—		
983	50.73	—		
1365	66.66	—		DTA

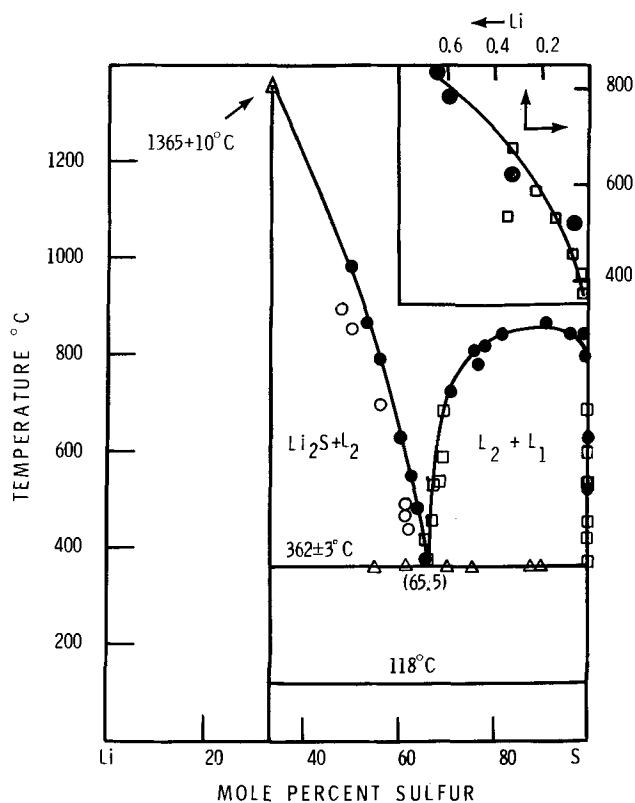


Fig. 3. The equilibrium phase diagram of the lithium-sulfur system. ● and ○, vapor transport techniques; □, quenching technique; Δ, differential thermal analysis technique.

cluded in delineating the liquidus. The measurements indicate slightly high percentages of lithium as a result of incomplete dissolution of the sample in the early developmental stages of the chemical analysis. The liquidus was drawn through the points obtained after the difficulty of dissolving the sample was removed.

The melting point of lithium sulfide was determined to be $1365 \pm 10^\circ\text{C}$, in good agreement with the recently reported value of 1372°C (4). The literature value (5) of 975°C is in considerable disagreement with both of these results. The melting point of sulfur was determined to be 118°C , in good agreement with the literature value (8) of 119°C .

In the range of compositions investigated, only one solid compound, Li_2S [and not the other two, Li_2S_2 and Li_2S_4 reported by Pearson and Robinson (6)], was observed (x-ray analysis of the solidified samples) in the lithium-sulfur system. A monotectic was observed at 34.5 m/o lithium and $362^\circ \pm 3^\circ\text{C}$. The monotectic temperature is in good agreement with the value of 365 determined elsewhere (4). The monotectic composition found in the present work is slightly lower than 37.0 m/o determined by the latter workers. In the present investigation, the monotectic composition was determined by arriving at an equilibrium between lithium sulfide and a Li-S melt on one side, and between a lithium-sulfur melt and a two-liquid-phase melt on the other side. Therefore, the monotectic composition reported here, 34.5 m/o lithium, should not be in error by more than the error involved in the chemical analysis, and is considered to be accurate to ± 1 m/o. The solubility of lithium in the sulfur-rich liquid, 0.035 m/o lithium at the monotectic temperature, is also in disagreement with the 0.3 m/o lithium reported by these workers (4). Although it could not be measured precisely by the vapor transport technique, the consolute temperature, or critical solution temperature appears to lie between 838° and 860°C . The data reported by Pearson and Robinson (6) such as the compounds Li_2S_2 and Li_2S_4 , a liquidus and melting point of

Li_2S , 900°-975°C for lithium-sulfur system have no agreement with the present data.

The results have also been presented in Fig. 4 as the lithium sulfide-sulfur phase diagram, in which form they may be treated elegantly in terms of Temkin's model of molten salt mixtures (9). The Li_2S -S system has a miscibility gap extending from the monotectic composition, 26.3 m/o Li_2S , to nearly pure sulfur (0.0175 m/o Li_2S), at the monotectic temperature of $362 \pm 3^\circ\text{C}$.

From the equilibrium phase diagram of the lithium sulfide-sulfur system, almost pure liquid sulfur (0.017-0.15 m/o Li_2S) is observed to be in equilibrium with a melt of approximately constant composition (26-22 m/o Li_2S) in the temperature range of 362°-700°C. This small variation with temperature of the sulfur concentration in the lithium-sulfur melt indicates that the heat of solution of sulfur in these melts is nearly zero. This means that the bonding energy of sulfur in the nearly pure sulfur is not much different than the bonding energy of sulfur in the lithium-sulfur melt containing about 24 m/o Li_2S . This also indicates the degree of ease with which sulfur can transfer from one liquid to another.

Temkin's model for molten salt mixtures (9) appears to be appropriate to apply to melts of the lithium sulfide-sulfur system. In this model, the activity, $a_{Y_{1y}Z_{1z}}$, of a given component, $Y_{1y}Z_{1z}$, of a molten salt mixture is given by the product of the ionic fractions of the cations and anions in the mixture

$$a_{Y_{1y}Z_{1z}} = (X_{Y_1})^y \cdot (X_{Z_1})^z \quad [1]$$

The cationic fraction is given by

$$X_{Y_1} = \frac{n_{Y_1}}{\sum_{i=1}^s n_{Y_i}} \quad [2]$$

where n_{Y_i} is the number of moles of cations, Y_i , in the

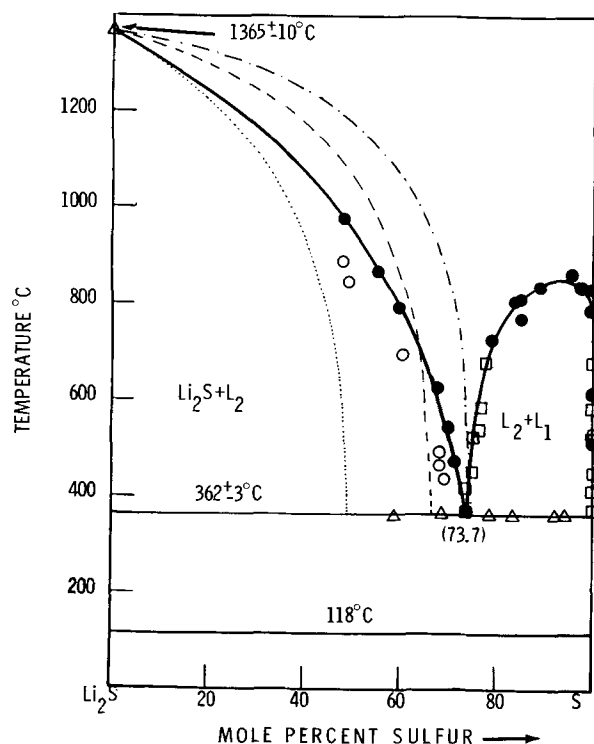


Fig. 4. The equilibrium phase diagram of the lithium sulfide-sulfur system. ● and ○, vapor transport technique; □, quenching technique; △, differential thermal analysis technique ——— through experimental points ·····, - - - - -, and - · - · - lines on assuming Temkin's model and reactions [3], [4] and [5], respectively.

molten salt mixture, assuming that the salts are completely ionized. An analogous definition applies for the anionic fraction. The term, s , is the number of constituent salts. The Temkin model assumes that the cations (anions) are randomly distributed on sites equal in number to the total number of cations (anions).

Pure molten Li_2S is assumed to ionize completely to Li^+ and S^{2-} . The solution of additional sulfur in the Li_2S -sulfur melt is assumed to proceed by any of the reactions



These reactions do not appear unreasonable in view of the ease with which sulfur can transfer from one liquid melt to another, as pointed out before. The mole fraction of Li_2S in these Li_2S -S melts would then be

$$\frac{2n_{\text{Li}_2\text{S}} - 100}{n_{\text{Li}_2\text{S}}}, \frac{3n_{\text{Li}_2\text{S}} - 100}{2n_{\text{Li}_2\text{S}}}, \text{ and } \frac{4n_{\text{Li}_2\text{S}} - 100}{3n_{\text{Li}_2\text{S}}}$$

for reactions [3], [4], and [5], respectively. The mole fraction of Li_2S is equal to the product of the ionic fractions because of the presence in the melts of lithium as the only cation, consequently, the mole fraction of Li_2S is equal to the activity of Li_2S if the melt obeys Temkin's model.

The activity of lithium sulfide in melts of the Li_2S -S system may be related to the liquidus temperature, T , by the simplified equation

$$\ln a_{\text{Li}_2\text{S}} = -\frac{\Delta H_m}{RT} \left(1 - \frac{T}{T_m} \right) \quad [6]$$

where ΔH_m is the heat of fusion and T_m is the melting point of lithium sulfide. In this relation, the difference between the heat capacities of liquid and solid lithium sulfide is assumed to be zero. The melting point of lithium sulfide, 1365°C, was determined in this investigation. ΔH_m , which is not available in the literature, has been calculated to be 10.5 kcal/mole by assuming reaction [3] and applying Temkin's model to the lithium sulfide-sulfur melts at very low concentrations of sulfur using the phase diagram data of this investigation.

Using the activities of Li_2S calculated from Eq. [6], and assuming the Li_2S -S melts obey Temkin's model, the liquiduses corresponding to reactions [3], [4], and [5] have been constructed and are presented in Fig. 4. The constructed liquiduses have shapes similar to those determined experimentally. At higher temperatures and lower sulfur concentrations, the liquidus based on reaction [3] has best agreement with the experimentally determined one, implying that the sulfur exists preponderantly as S_2^{2-} . This may be expected since the most likely species to form on the initial addition of sulfur to Li_2S would be the next higher sulfide polymer, S_2^{2-} . At lower temperatures and higher sulfur concentrations, the liquidus based on reaction [4] has the best agreement with the experimental curve. This also is to be expected since species like S_3^{2-} are likely to form with an increase of sulfur concentration in a Li_2S -S melt, and since the tendency is for higher sulfide polymers to exist at lower temperatures. General agreement with the liquidus determined curve indicates the possibility that the species S_4^{2-} may form with a further increase in the sulfur concentration.

In the situation where sulfur can transfer without much difficulty from nearly pure sulfur to the Li_2S -S melt, and when a general agreement is observed between the liquiduses constructed on the basis of reactions [3], [4], and [5] and that determined experimentally, a distribution of the different species rather than one particular species is more likely to occur. The

concentration of species such as S_2^{2-} may be predominant at lower concentrations of sulfur, and species such as S_4^{2-} at higher concentrations of sulfur.

In addition to the above, an approximation of the partial pressure of sulfur over Li_2S -S melts can be obtained from these results. For example, at $500^\circ C$, sulfur containing 0.1 m/o lithium is in equilibrium with lithium-sulfur containing 32 m/o lithium, so the partial pressure of sulfur over these two melts is the same. At the same temperature, another melt containing 37 m/o lithium is in equilibrium with Li_2S , so the partial pressure of sulfur over this melt is the same as that over Li_2S . The partial pressure of sulfur over Li_2S at $500^\circ C$ can be approximated as 10^{-2} atm by treating lithium-sulfur melts similar to sodium-sulfur melts (3). If we assume that the partial pressure of sulfur over the 32 m/o lithium melt is approximately the same as that over the 37 m/o lithium melt, then the partial pressure of sulfur over the melt of sulfur containing 0.1 m/o lithium is approximately 10^{-2} atm. This means that the addition of 0.1 m/o lithium has lowered the vapor pressure of sulfur from about 2.0 atm (10) to about 10^{-2} atm. This can also be inferred from experiments where two liquids, one containing higher and the other lower concentrations of sulfur, were sealed in a silica capsule and heated to about $850^\circ C$. The fact that the silica capsule did not rupture indicates that the vapor pressure of sulfur is definitely far lower than that of pure sulfur, which is about 60 atm under these conditions (10).

This lowering of the sulfur vapor pressure may not be unexpected if the addition of lithium helps to increase the chain length of sulfur as a result of lithium and sulfur being metallic and nonmetallic in nature, and the lithium ions presumably being located at the ends of these chains. Then the situation becomes similar to that of an ionic melt, where a sulfur chain

behaves like a large anion, and the sulfur vapor pressure is comparable to that over any ionic sulfide melt.

Acknowledgments

The author wishes to thank J. L. Johnson, A. H. Jones, and Miss F. A. Forster, Chemistry Department, for chemical analyses, and x-ray analysis. He also wishes to thank J. F. Rhodes, Metallurgy Department, and R. A. Murie, Electrochemistry Department for the differential thermal analysis.

Manuscript submitted March 2, 1972; revised manuscript received July 14, 1972.

Any discussion of this paper will appear in a Discussion Section to be published in the June 1973 JOURNAL.

REFERENCES

1. E. H. Hietbrink and S. B. Tricklebank, ASME Publication-70-WA/Ener-7, New York, Dec. 1970; E. J. Cairns and H. Shimotake, *Science*, **164**, 1347 (1969).
2. T. G. Pearson and P. L. Robinson, *J. Chem. Soc.*, 1473 (1930); N. K. Gupta and R. P. Tischer, *Abstracts*, pp. 769-772, Electrochem. Soc. Extended Abstracts, Spring Meeting, Los Angeles, May 10-15, 1970.
3. A. Tedar and J. Tiberg, *Acta Chem. Scand.*, **24**, 991 (1970).
4. E. J. Cairns, J. P. Ackerman, P. D. Hunt, and B. S. Tani, *Abstracts*, pp. 118-120, Electrochem. Soc. Extended Abstracts, Fall Meeting, Cleveland, Ohio, Oct. 3-7, 1971.
5. R. P. Elliott, "Constitution of Binary Alloys," McGraw-Hill Book Company, New York (1965).
6. T. G. Pearson and P. L. Robinson, *J. Chem. Soc.*, 413 (1931) and 1983 (1931).
7. Von E. Zintl *et al.*, *Z. Electrochem.*, **40**, 588 (1934).
8. B. Meyer, "Elemental Sulphur," Interscience Publishers, Inc., New York (1965).
9. M. Temkin, *Acta Physiocochem. URSS*, **20**, 411 (1945).
10. E. H. Baker, *Trans. Min. and Met.*, Pt. C93 (1971).

A Computer-Operated Facility for Research Testing of Secondary Batteries

R. F. Scarr* and F. W. Meszaros

Union Carbide Corporation, Consumer Products Division, Research Laboratory, Cleveland, Ohio 44101

ABSTRACT

A working computer-operated system for the cyclic testing of up to 192 secondary batteries is described. The computer, operating on-line in a time-sharing mode, may conduct as many as 12 independent tests simultaneously. This approach has several advantages over other automated methods including: greater flexibility in test formatting, real-time updating of characteristic quantities for each battery, real-time data reduction, systematic information filing, and a logical capability which facilitates the handling of contingencies. System technique, configuration, and capabilities are discussed as an approach to battery testing.

The testing of experimental cells is an important function in the research and development of battery systems. Until recently, it had been difficult to combine the attributes of quality and quantity into one installation because, for any particular testing device, capacity and complexity appeared to be mutually exclusive properties. With the advent of computer systems, however, it seemed reasonable to apply such technology to the problem of comprehensive testing of large numbers of batteries.

In view of the effort required to develop a computer-operated battery test system, it would be instructive to describe a particular installation as an example of one solution to the problem of battery testing. A computer-operated facility for the cyclic testing of secondary batteries has been in operation at Parma Technical Center since May, 1970. While the nature of any individual battery test system is oriented toward the specific needs of its users, a general description of this system may aid in the planning and design of other installations. It is the purpose of this paper to describe various considerations in conceiving this battery test system, the techniques used, and the results achieved.

* Electrochemical Society Active Member.

Key words: battery:tester, tester:computer-operated, computer-operated battery tester.

The Parma Technical Center system, in its present configuration, has evolved from an earlier version which was first developed about eight years ago (1). Its general function is to cycle batteries continuously through a repeated step-wise sequence of constant current, constant resistance, or open-circuit modes, while test data are continually sensed and stored. Its intended use as a tool in battery research and development, however, called for special flexibilities to be built into the system to satisfy the many potential users.

Maximum freedom was required in such capabilities as the available current range, the resolution of time and voltage, the number of data points per position, and the sequencing of the various test modes. In addition it was necessary to protect the well-being of the test samples; hence the system had to be capable of detecting malfunctions during the progress of the test.

While these functions could have been performed adequately by an electromechanical system, the justification for computer operation was based on four additional capabilities which could be achieved in no other way. With one exception these features are related to the efficiency of the data handling process. First, voltage and current integrals can be computed in real time, that is, at the instant the data are obtained. Second, data reduction can be performed in real time, thus minimizing the storage requirements necessary to describe adequately the battery behavior. Third, data are stored in an organized fashion making the information retrieval problem less cumbersome. Fourth, the computer brings into the system a logical capacity which permits interpretation of contingency situations and the ability to act on them.

Most computer-operated battery test systems, such as those of the Martin-Marietta Corporation (2), Western Electric Company (3), San Francisco Bay Naval Shipyard (4), and Electric Storage Battery Research Center (5), as well as our original version, have utilized computers which are totally dedicated to the test facility. This approach has the advantage of minimizing problems of data transmission over appreciable distances and eliminating logical interference from background (or nonprocess) jobs.

In the present case, however, there were several advantages to be gained with remote operation utilizing the central laboratory computer on a time-shared basis. The larger central computer affords more powerful computing capability, less expensive and more regular maintenance, more complete software support, greater economy and flexibility in equipment options, etc. As a result, it has been possible to exploit more fully than the smaller systems the potentialities of computer operation, particularly with regard to information retrieval and contingency situations.

System Capabilities and Techniques

This battery test system is capable of testing up to 192 secondary batteries in 12 groups (or banks) of 16 positions each. Environmental chambers are available in which tests may be conducted at constant temperatures between -40° and 100°C . Each bank may be operated independently of the others in accordance with a predetermined but variable pattern of unit operations called steps. Each repetition of the pattern is designated one cycle. A cycle may consist of up to six steps selected from a choice of four modes:

1. Constant current charge
2. Constant current discharge
3. Constant resistance discharge
4. Open-circuit rest

Constant current in the range of $50\ \mu\text{A}$ to 5A is generated by a separate power supply for each bank. Up to six different current levels in any mode may be established. The computer does not control the current, but it can select the designated setting and monitor the level. If the current has deviated from the desired level by more than a specified amount, the batteries are placed on standby and an error message is sent.

Battery voltages are checked 100 times an hour at regular intervals. Each battery position also has provision for an auxiliary data point which may be used for a reference electrode voltage, temperature, pressure, or any other input as desired.

At the moment each reading is obtained, certain computational operations are performed which if accomplished at any other stage in the data handling process would be less efficient. First, the voltage of each battery is used to update the accumulated voltage from which the average voltage is later to be calculated. Next, it is determined if the battery voltage has changed significantly from the voltage most recently stored in memory. If so, the new value and the time at which it was measured is added to the file. The incremental voltage which is used to decide whether or not to store the newly acquired data is a variable, subject to user specification. This technique, which has been used in other installations, results in concentrating the most voltage-time data points in the regions of greatest change. The data required to characterize the charge/discharge curves to the desired accuracy are thereby minimized. The final step in the scanning sequence is to determine if the battery voltage remains within a pre-established limit. If not, the battery is temporarily removed from test until the beginning of the next step.

The format of a hypothetical test showing some of the variables and their corresponding accuracy which the user can specify is given in Table I. It will be noted that operation at multiple current levels may be achieved. Step-wise constant current, if properly adjusted, can be used to approximate constant voltage operation. The voltage logging increment is chosen to produce the desired number of data points for each step. If the battery should reach the cutoff voltage before the time limit, it is temporarily placed on open-circuit until the beginning of the next step. Actual current control is much better than the current tolerance would indicate. This specification represents only the maximum deviation which the user will accept before the test is suspended. At the completion of step five, the sequence repeats beginning at step one. The first cycle may be initiated at any step desired.

The test data are stored temporarily in an organized format on a half-million word disk. Once each day, at a designated time, the data accumulated on disk for the previous 24 hr are transferred to magnetic tape. At the earliest opportunity, this tape is used to produce a printed report of the day's results. Thus, the turnaround time for the primary record of the test is nominally 24 hr or less.

The structure of the data file on magnetic tape, shown in Table II, is organized to expedite data proc-

Table I. Battery test format example

Step No.	Mode	Load	Current tolerance	Voltage limit (V)	Voltage logging increment (mV)	Duration (hr)
1.	Const. curr. chg.	750 mA	$\pm 25\ \text{mA}$	1.550	20	0.25
2.	Const. curr. chg.	100 mA	$\pm 10\ \text{mA}$	1.550	15	4.00
3.	Open circ. rest					0.50
4.	Const. resist. dischg.	2.50 ohm		1.000	10	1.00
5.	Const. curr. dischg.	-200 mA	$\pm 20\ \text{mA}$	0.900	10	1.50
6.	Not used					

Table II. Magnetic tape data format

- I. Day number
- II. Voltage-time data points, up to 38,400 sets
 - A. Position number
 - B. Combined cycle and step number
 - C. Elapsed time in step
 - D. Battery terminal voltage
 - E. Auxiliary data point
- III. Step summary information
 - A. First bank on test
 - 1. General information
 - a. Alpha-numeric report heading
 - b. Test position occupancy indicator
 - c. Data handling specifications
 - d. Test control specifications
 - 2. Raw sums data: current and voltage integrals, time to cutoff
 - a. First step completed
 - i. First battery position
 - ii. Second battery position
 - iii. Etc., up to 16 positions
 - b. Second step completed
 - c. Etc., up to 38 steps
 - B. Etc., up to 12 banks
 - C. Second bank on test

essing. Each daily tape begins with the day number for identification and thereafter is divided into two main sections. The first contains the voltage-time data for all batteries on test in chronological order, that is, without regard to bank or cycle. Since, in practice, voltage-time profiles are required only infrequently by the user, this file is actually sorted only when necessary. The next section contains the step summaries and other information arranged by bank. Sequential arrangement of test data in this fashion facilitates efficient retrieval of results. Each daily tape output contains all the data necessary to reconstruct the test in prescribed detail. Further data processing, including recall of earlier results, may be performed on the raw data as needed.

Primary record reports may be obtained in either abbreviated or complete forms. The abbreviated type, which is most frequently used, presents a summary of characteristic quantities for each test unit in the bank. Summary data consists of the following descriptive quantities evaluated for each complete step:

1. Time to cutoff
2. Charge added or removed
3. Average voltage, or in the case of open-circuit steps, the final voltage
4. Energy content
5. Electrical efficiency

The complete format lists, in addition to the summary data, all the voltages and corresponding elapsed times obtained during cycling, one test position to a page. If a reference electrode is provided in the battery, the anode- and cathode-to-reference voltages will be given as well.

An example of this format is given in Fig. 1 for an actual test performed on so-called "zinc limited cells." These were specially fabricated 0.5 A-hr rechargeable alkaline cells which were being used to study how anode-limited capacity affects cycle life. The cells contained a Cd/Cd(OH)₂ reference electrode to permit characterization of single electrode behavior. The cyclic test specified by the investigator consisted of a three-step tapered charge period to bring the cell to a maximum state of charge (with voltage cutoff protection), followed by constant current discharge at a fairly substantial rate to discharge the cell to a preselected limit. The final step was a momentary open-circuit period to record the voltage of a discharged cell at rest. The test format is illustrated in the lower half of Fig. 2. The accuracy with which the system followed the test may be seen in the voltage-time profile of Fig. 2. It will be noted that the cell reached its specified voltage limit in the discharge step as well as two of the charge steps, whereupon it was automatically placed on temporary stand-by.

Occasionally, interruptions in the normal progress of a test may occur from either intentional or acci-

UNION CARBIDE CONSUMER PRODUCTS COMPANY
PARMA TECHNICAL CENTER
BATTERY TEST FACILITY

BANK NUMBER 11 DAY NUMBER 212

ZINC LIMIT CELL

POSITION NUMBER 1 CYCLE NUMBER 11

	TIME TO CUTOFF	AMPERE HOURS	AVG. OR FINAL D/C VOLTAGE	WATT HOURS	EFFCY
STEP 1	0.30	0.179	1.501	0.268	
STEP 2	1.03	0.308	1.633	0.503	
STEP 3	0.67	0.067	1.637	0.110	
STEP 4	0.74	-0.550	1.157	-0.637	0.992
STEP 5	0.01	0.000	1.297		

STEP NO.	ELAPSED TIME (HOURS)	BATTERY VOLTAGE (VOLTS)	CATH-REF VOLTAGE (VOLTS)	ANODE-REF VOLTAGE (VOLTS)
1	0.01	1.385	0.491	-0.894
1	0.09	1.468	0.554	-0.914
1	0.23	1.549	0.620	-0.929
1	0.30	1.583	0.660	-0.923
2	0.50	1.625	0.790	-0.835
2	0.69	1.667	0.888	-0.779
2	0.87	1.709	0.968	-0.741
2	1.03	1.752	1.061	-0.691
2	3.00	1.540	0.998	-0.542
3	0.07	1.573	1.024	-0.549
3	0.22	1.604	1.051	-0.553
3	0.37	1.636	1.080	-0.556
3	0.49	1.671	1.111	-0.559
3	0.58	1.705	1.142	-0.563
3	0.65	1.739	1.169	-0.570
3	0.67	1.753	1.180	-0.573
3	3.60	1.558	1.017	-0.541
4	0.01	1.455	0.946	-0.509
4	0.03	1.412	0.915	-0.497
4	0.05	1.380	0.888	-0.491

Fig. 1. Complete daily report on test data

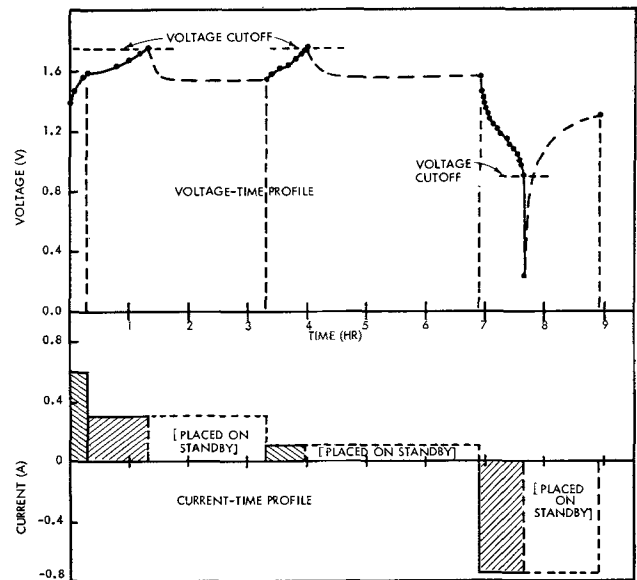


Fig. 2. Reconstruction of voltage-time profile for test format given.

dental causes. The system is capable of automatically detecting, characterizing, and denoting such interruptions on all pertinent reports.

System Configuration and Operation

The configuration of the battery test system hardware is given in Fig. 3. All of the equipment to the left of the dashed line is situated in the computer center, located 400 ft from the battery test room which is shown to the right of the dashed line. The two installations are connected by cable.

The heart of the system is an IBM 1800 Process Control Computer with 24K words of core memory. This computer constitutes the regular data processing facility for an institution of over 500 employees. In addition to operating the battery test facility 24 hr a day,

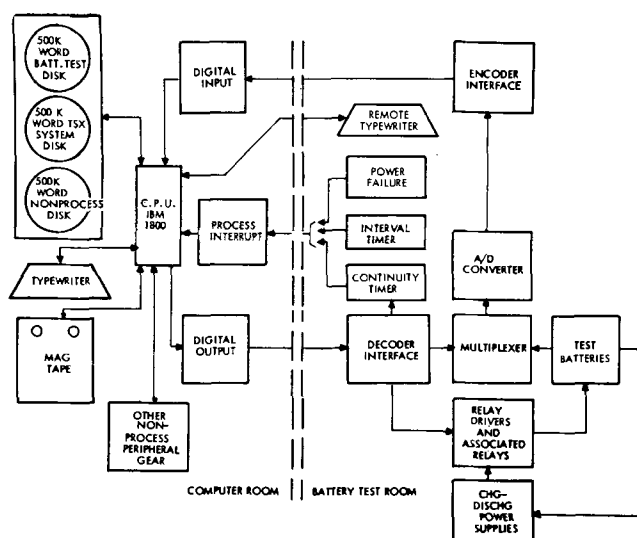


Fig. 3. Block diagram of battery test system

it also runs another data acquisition system and supports a full load of scientific and business programming on a time-shared basis. Of the three 500K word disks installed in the system, one is dedicated to the battery test facility for data and program storage. A magnetic tape unit is used only once a day to record data dumped from the disk. One 16-bit word of digital input is used to receive information from the battery test facility. Instructions to the battery test facility are transmitted through the 16-bit digital output. Other peripheral gear includes those devices not normally used by the battery test facility, such as a printer, typewriter, card reader/punch, and incremental plotter.

The system operates on an interrupt basis through the process interrupt which is a set of inputs used to signal the computer of some event in the battery test room. Thus, the interval timer interrupts the computer from its time-sharing operation once every 36 sec to begin the scan of the battery test positions. The computer determines sequentially which test position is to be read and sends the appropriate instruction to the decoder. The multiplexer, a reed relay scanner, selects

the designated data point. The corresponding voltage is then digitized by the A/D converter. After a specified delay, namely 10 msec, the computer picks up the result through the encoder. During this delay, as well as at the conclusion of the scan period, the computer temporarily returns to time-sharing.

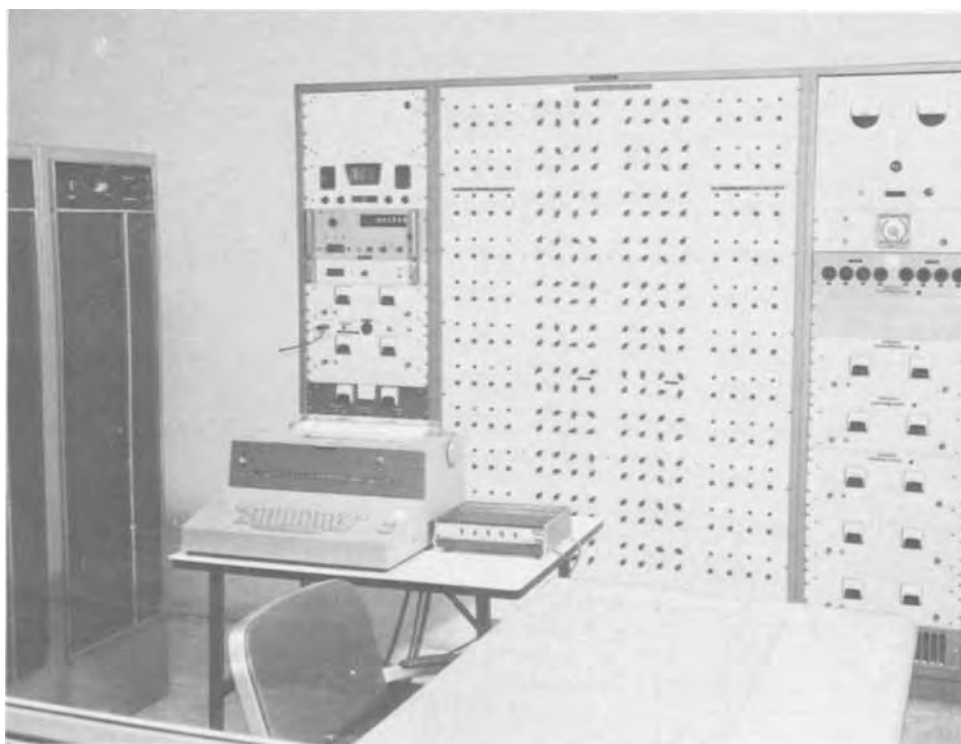
The status of each battery and power supply is controlled by relays and their associated drivers. If, due to an error, there should be a loss of communication between computer and battery test facility, the continuity timer will switch the entire system to standby in order to protect the test batteries. The remote typewriter fulfills many functions: it may be used to interrogate the computer memory on the status of a test, to receive error messages, to transmit instructions modifying a test once it is in progress, and to exercise manual control over the system hardware. That portion of the equipment located in the battery test room is shown in Fig. 4 and 5.

It is estimated that over-all the battery test job actually uses the central processing unit (CPU) of the computer only 5% of the time. There is, therefore, little interference with other simultaneous processing the computer may be doing. In cases where the non-process job is largely input/output there is no observable effect, while with jobs that are confined to the CPU, running time is slowed by a maximum of 30%.

One of the most useful features of the system to which the computer is particularly adaptable is the ability to modify a test once it is in progress. This may be accomplished in two ways. If the change may be anticipated, it may be programmed to occur automatically at a predetermined point. Using this capability, batteries may be preconditioned in one sequence and tested in another. If, on the other hand, a program change is required immediately, the typewriter is used in a conversational mode to alter specifications contained in computer memory. Certain logical safeguards are incorporated into the typewriter routine to prevent inadvertent program modification.

The main part of the computer program for the battery test facility, written in assembler language, occupies 1056 words of core memory. It contains the basic scan routine and other programs which are used every time a clock interrupt is received. Battery test also uses about 2000 words of "Inskel/Common" a

Fig. 4. Battery test room equipment and control panel. In the foreground is the remote typewriter. The equipment bay at the left contains the interface. The control panel at the rear, from the top down, contains: (left)—multiplexer, A/D converter, low-level analog amplifier, and several bank power supplies; (center)—level controls for presettable current channels; (right)—relay power supply, interval timer, and the remaining bank power supplies.



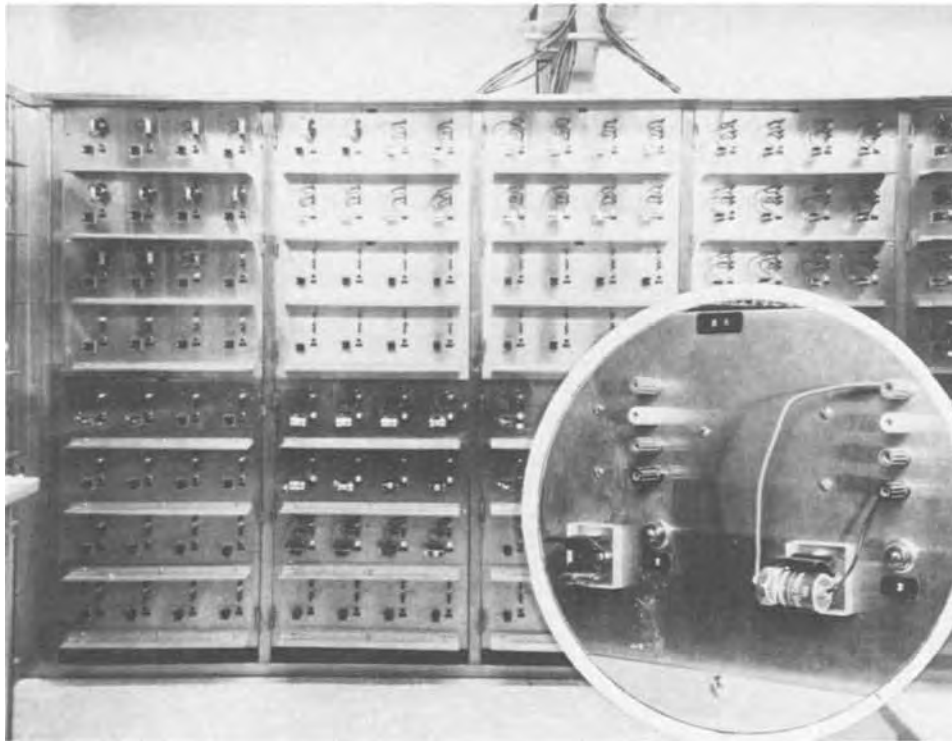


Fig. 5. Battery test stand. Test batteries are mounted on stainless steel panel. Individual test position is pictured in inset showing data point terminals and signal light.

region of core which is reserved only for data storage. This region contains instantaneous test data, test specifications, and other information continually used by the system. Thus, the total core space assigned permanently and specifically to the battery test operation is only just over 3000 words.

The rest of the battery test program consists of auxiliary subprograms which are used less frequently than the main program. They are called from disk only when needed, swapping temporarily with whatever program resides in core at the moment. Subprograms to start a bank, or to change its operating mode, or to dump the disk to tape are in this category. These programs are written largely in Fortran. Furthermore, because they are not an integral part of the operating system but are utilized on a "job" basis, it is not necessary to interrupt battery testing in order to modify these programs when required.

Development of the original programs sufficient to get the system into production required about 2 man-years of effort. Since then, the computer approach to this operation has permitted program modification and improvement to be an on-going process.

System Evaluation and Summary

The reliability of this battery test system has been good. Although it runs 24 hr a day, it is attended by a single operator only during daytime working hours. System interruptions, when they occur, stem from one of three causes with about equal frequency: line power flicker or failure, malfunction of a peripheral device in the computer room which binds up the central processor unit, or logical program errors in a non-process (background) job. As a result of such causes, the system is down less than 4 hr a month.

Preventive maintenance on the computer and peripherals is performed biweekly. Normally this does not require the suspension of battery testing. About once every 2 months, it is necessary to suspend testing for a few hours. At such times shutdown is accomplished under programmed control so as not to influence unduly the test results.

Operating cost for this system varies somewhat with the utilization level. At 100% occupancy of test positions, the daily operating cost exclusive of personnel

is about 42 cents per cell. This figure includes equipment rental, allocated computer operating costs, and the cost of final data processing.

In summary, this computer-operated battery test facility has provided a reliable, accurate means of testing a large number of batteries of all types for a varied group of users. Time-sharing of the computer has worked to our advantage. All the data necessary to reconstruct the test are contained on magnetic tape in easily stored and retrievable format. Further data processing, in addition to that normally furnished, is thereby facilitated. Modification of the basic system, when desired, is accommodated by the modular nature of both the hardware and software.

Acknowledgments

The authors are deeply grateful to the following individuals for their contributions to this project: to Mr. T. P. LaFramboise for the original design of the interface; to Mr. A. F. Deckert, Jr., for his part in installing the system; and to Mr. D. L. Wright who has made many important modifications to the hardware and who, at present, is the system operator.

Manuscript submitted April 5, 1972; revised manuscript received July 12, 1972. This was Paper 25 presented at the Cleveland, Ohio, Meeting of the Society, Oct. 3-7, 1971.

Any discussion of this paper will appear in a Discussion Section to be published in the June 1973 JOURNAL.

REFERENCES

1. R. J. Brodd, "Computer Controlled Battery Test Facility," NASA Battery Workshop, Washington, D.C., Oct. 1966, pp. 197-203.
2. Martin Marietta Corp., "Nickel-Cadmium Battery Test Project: Relationship Between Operation, Life and Failure Mechanism," Vol. 1, Contract No. NAS 5-3027, Final Rept., Feb. 1, 1963 through July 31, 1966.
3. J. J. Schumann and Solomon Zlotnick, *Western Electric Engineer*, 12, 15 (1968).
4. D. O. Newton, in "Power Sources 2," D. H. Collins, Editor, pp. 213-230, Pergamon Press, New York (1970).
5. D. L. Beals, R. B. Roe, and A. M. Anton, Paper 173 presented at Electrochem. Soc. Meeting, Washington, D.C., May 9-13, 1971.

Phase Equilibria in Lithium-Chalcogen Systems

II. Lithium-Sulfur

P. T. Cunningham, S. A. Johnson, and E. J. Cairns*

Argonne National Laboratory, Chemical Engineering Division, Argonne, Illinois 60439

ABSTRACT

The equilibrium phase diagram of the lithium-sulfur system has been investigated. A miscibility gap extends from 0.2 to 37.0 atom per cent (a/o) lithium above a monotectic temperature of 364.8°C; the critical temperature is greater than 600°C. The only intermediate phase found is Li_2S , which melts at 1372°C.

Recent research and development work on high-specific-power, high-specific-energy secondary cells based on alkali metal/chalcogen couples (1) has focused attention on the need for more complete phase equilibrium data for these systems. The work reported here was undertaken as part of a broad program to determine the lithium-chalcogen phase diagrams. Results for lithium-selenium have been published (2).

Previous work on the lithium-sulfur system has not been extensive.¹ Bergstrom (3) reported the preparation of lithium sulfide and polysulfides in liquid ammonia. Pearson and Robinson (4) have reported their preparation in aqueous and alcoholic solution and by direct combination of the elements under boiling naphthalene. Pearson and Robinson also reported a portion of the Li-S phase diagram between Li_2S and Li_2S_2 , indicating that Li_2S was stable up to its observed melting point (900°-975°C) and that Li_2S_2 was slightly decomposed at its reported melting point of 369.5°C. The compound Li_2S prepared in liquid ammonia has been reported to have an antifluorite structure (5) with a lattice parameter of 5.708Å.

Experimental

Materials.—The sulfur used was a special high-purity (99.999+%) grade obtained from American Smelting and Refining Company, South Plainfield, New Jersey. The lithium, a high-purity reactor grade (99.98%), and lithium sulfide (97+%) were obtained from the Foote Mineral Company, Philadelphia, Pennsylvania. These materials were used without further purification. Li_2S was mixed with the appropriate terminal phase in a purified-helium-atmosphere glove box (6) to obtain the desired composition for the various experiments. The samples were contained in borosilicate glass, quartz, aluminum, vitreous graphite, or niobium depending on the temperature range covered and the sample composition.

Apparatus and procedures.—The experimental techniques used included thermal analysis (heating and cooling curves), differential thermal analysis (DTA), high-temperature centrifugation, chemical analysis, and x-ray diffraction.

Heating and cooling curves were obtained on samples weighing from 10 to 20g using a furnace-well attached to the floor of the helium-atmosphere glove box (7). Sulfur-rich samples for thermal analysis were contained in borosilicate glass, quartz, or aluminum vessels, which were usually sealed to prevent rapid sulfur loss. The necessity of sealing the sample container made cooling curves almost useless because of extreme undercooling of samples that were not vigorously stirred. Some samples were run in open containers with stirring but the compositions of these

samples are uncertain. Temperatures were measured with platinum *vs.* platinum-10% rhodium thermocouples fabricated from wire which had been calibrated against NBS pure tin (mp 231.88°C), zinc (mp 419.58°C), and aluminum (mp 660.0°C).

DTA samples, which weighed about 80 mg, were contained in aluminum or niobium capsules with press-fit caps. Data were obtained with a du Pont Model 900 Differential Thermal Analyzer using a 5°C/min rate of temperature change with a powdered alumina reference material and a dynamic helium atmosphere. The thermocouples used were described above and the over-all accuracy of the apparatus was determined to be $\pm 1^\circ\text{C}$ using NBS standard quartz and KNO_3 .²

The melting point of Li_2S was determined using a molybdenum-wound resistance furnace. The samples were placed in niobium or vitreous graphite crucibles and heated in an argon atmosphere. Temperature was measured with a calibrated optical pyrometer and the occurrence of fusion was visually determined.

Chemical analysis was used to determine the compositions of materials taken from samples in which phase separation occurred. Phase separation under normal gravity was usually slow, and in many cases a high-temperature centrifuge was used to increase the rate of phase separation. A mixture of Li_2S and sulfur having the over-all composition of interest was placed in a quartz ampoule, which was evacuated and sealed. The ampoules were placed in a rocking furnace and mixed for several hours (in some cases several days) at a temperature about 25°C above the planned centrifugation temperature prior to placing them in the centrifuge. After centrifugation for several hours at speeds corresponding to centrifugal forces about 250 times normal gravity, the ampoules were quenched in liquid nitrogen and placed in a helium-atmosphere glove box where they were broken open and the zones of the samples were carefully separated mechanically. The same quenching and separation procedure was used for samples in which phase separation was achieved at normal gravity after 7 to 10 days at temperature. Chemical analysis was carried out on the separated materials using flame photometry to analyze for lithium. The sulfur content was calculated by difference. The accuracy of this procedure ($\pm 5\%$ of the lithium weight) was confirmed by analyzing several samples for sulfur as well, using standard gravimetric techniques.

X-ray diffraction powder patterns were obtained for a large number of samples having a wide variety of compositions and thermal histories, using a 114.6 mm Debye-Scherrer camera with $\text{CuK}\alpha$ radiation.

Results and Discussion

All of the experimental results are summarized in Fig. 1. The thermal analysis and DTA results, which

* Electrochemical Society Active Member.

Key words: lithium, chalcogen, sulfur, sulfide.

¹ During the preparation of this paper, it came to our attention that R. Sharma had also studied this system concurrently and had also prepared a manuscript.

² The quartz and KNO_3 are SRM 755 and SRM 756, respectively, available from the Office of Standard Reference Materials, National Bureau of Standards, Washington, D.C. 20234.

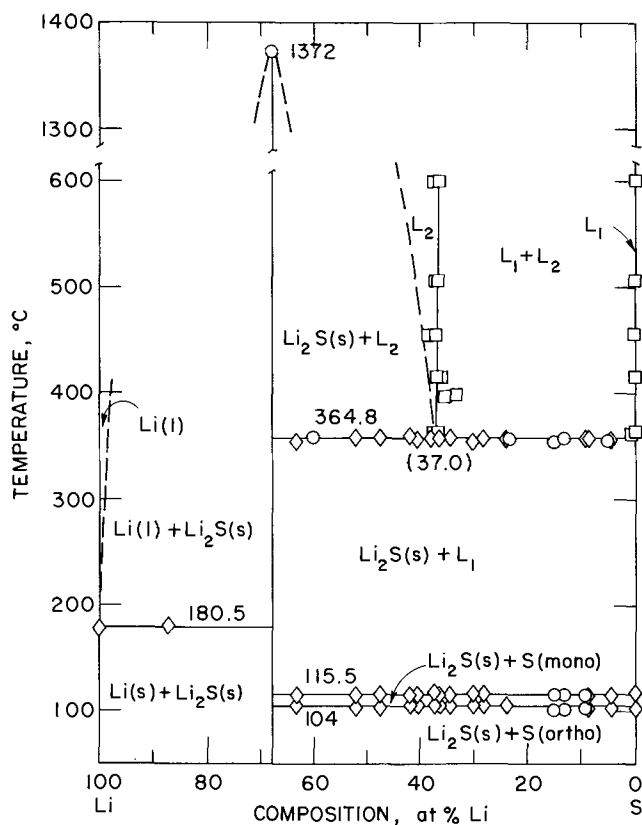


Fig. 1. Partial phase diagram of the lithium-sulfur system. ○, Thermal analysis; ◇, DTA; □, chemical analysis.

are presented in Table I, show that five thermal effects were observed. The few measurements made on the lithium-rich side of Li_2S indicate that Li_2S does not affect the melting point of pure lithium (180.5°C) within the accuracy of these measurements ($\pm 1^\circ\text{C}$) and that there are no other thermal invariants present in this composition range below 860°C . The melting point of Li_2S was observed to be $1372^\circ \pm 10^\circ\text{C}$ in the resistance furnace for samples contained in both niobium and vitreous graphite crucibles. This value is considerably higher than that reported by Pearson and

Robinson (4), who indicated that their experiments were vitiated by rapid reaction of the samples with their glass and porcelain containers, a problem which we also encountered.

On the sulfur-rich side of Li_2S , thermal effects were observed at $104.0^\circ \pm 3.7^\circ\text{C}$, $115.5^\circ \pm 1.0^\circ\text{C}$, and $364.8^\circ \pm 4.0^\circ\text{C}$. These temperatures are weighted averages where the weighting is admittedly somewhat subjective. The indicated uncertainties show the variance of the data. The effects observed at 104° and 115.5°C are associated with the transformation from α (orthorhombic) sulfur to β (monoclinic) sulfur and the melting of β sulfur, respectively. The accepted value for the $\alpha \rightarrow \beta$ transition is 95.5°C (8) but in none of our experiments, even with pure sulfur, was the effect observed at this temperature. The fact that the α - β transition is observed about 10° above the equilibrium temperature is typical and in good agreement with the temperature for the appearance of the β form in thin films of α sulfur (9). Pure sulfur was observed to melt at 118.0°C in our experiments, in fair agreement with the accepted value of 118.9°C (8). With lithium present, this transition was observed at 115.5°C , which is significantly lower than 118.9°C and is presumably the temperature of a eutectic reaction [$L_1 \rightarrow \text{Li}_2\text{S}(s) + \beta$ sulfur].

The thermal effect at 364.8°C is attributed to a monotectic reaction [$L_2 \rightarrow \text{Li}_2\text{S}(s) + L_1$]. The extent of the miscibility gap (see Fig. 1) was determined by chemical analysis of material taken from two easily distinguishable zones, which were observed in samples quenched from temperatures above 375°C , and of overall composition from 15 to 30 a/o lithium. The upper zone was very similar to pure sulfur which had the same thermal history, whereas the lower zone was a red, glassy-appearing material which appeared to be homogeneous but which gave a room-temperature x-ray powder pattern clearly showing Li_2S and α sulfur. These zones are associated with the separated liquid phases L_1 and L_2 , respectively (see Fig. 1). Separation of the liquid phases under normal gravity was slow; about 6 days were required to achieve clear separation. With centrifugation at 250g, separation was achieved in 6 hr. Chemical analyses, the results of which are shown in Table II, were performed on material that was mechanically separated. Considerable care was taken to insure that the samples were homogeneous and cross-contamination, which would lead to an apparent narrowing of the miscibility gap, was

Table I. Summary of thermal data on the lithium-sulfur system

Over-all composition (a/o Li in S)	Method ^(a)	Container material	Maximum temperature (°C)	Temperature of thermal effects observed (°C) ^(a)				
100 (Li)	DTA	Nb	475	180.3				
87.1	DTA	Nb	860	180.7				
66.7 (Li_2S)	DTA	Al	400	No effect observed				
66.7 (Li_2S)	TA	Quartz	1080	No effect observed				
66.7 (Li_2S)	Visual	Nb	1425					
66.7 (Li_2S)	Visual	Vitreous graphite	1400	1372				
63.3	DTA	Al	400	109.3	114.6	359.1	1372	
60.0	TA	Al	395	—	—	367.0		
52.2	DTA	Al	400	102.6	114.5	365.0		
47.5	DTA	Al	410	102.9	115.5	366.8		
41.9	DTA	Nb	405	106.3	116.4	369.2		
40.5	DTA	Nb	405	105.6	116.4	364.1		
37.3	DTA	Al	420	105.6	118.1	366.0		
36.4	DTA	Al	405	105.0	116.4	365.5		
34.3	DTA	Al	405	104.9	115.4	367.1		
30.0	DTA	Al	400	105.0	116.3	360.7		
28.2	DTA	Al	405	105.2	115.6	367.1		
23.7	DTA	Al	405	105.0	—	364.1		
23.1	TA	Al	390	—	—	365.9		
14.8	TA	Glass	400	101.9	114.7	359.5		
13.0	TA	Glass	410	101.0	115.0	365.0		
9.3	TA	Glass	500	102.7	114.6	366.0		
9.0	DTA	Al	400	102.6	114.5	363.4		
8.6	DTA	Al	390	102.6	114.9	365.0		
5.0	TA	Glass	400	—	—	361.0		
4.7	DTA	Al	400	102.6	114.9	363.0		
0.0 (S)	DTA	Al	395	102.6	118.0	—		
			Weight average values	104.0	115.5	180.5	364.8	1372

^(a) Methods used were heating and cooling curves (TA) where the reported temperatures are those of thermal arrests, and differential thermal analyses (DTA) where reported temperatures are those of the intersection.

Table II. Summary of chemical analysis

Temperature prior to quenching (°C)	Component analyzed (see Fig. 1)					
	L ₁			L ₂		
	Sample weight (g)	Lithium weight (mg)	Atom per cent lithium	Sample weight (g)	Lithium weight (mg)	Atom per cent lithium
602	0.0995	0.054	0.25	0.0961	10.9	37.3
602	0.1340	0.084	0.29	0.1573	17.2	36.2
508	0.4032	0.15	0.17	0.2248	25.4	37.1
508	0.3087	0.099	0.15	0.1923	21.4	36.7
456	0.1771	0.082	0.21	0.1615	19.3	38.5
456	0.3421	0.15	0.20	0.1143	12.8	36.8
417	0.1735	0.012	0.032	0.1319	14.8	36.8
417	0.1448	0.0097	0.031	0.1910	20.7	36.0
396	—	—	—	0.4123	43.4	35.2
396	—	—	—	0.1717	16.8	33.4
377	0.3580	0.26	0.34	0.1684	19.0	37.0
375	0.1558	0.21	0.62	0.1523	17.0	36.7
375	0.2777	0.48	0.79	0.1981	22.0	36.6

avoided. Scatter in the data for the lithium-rich side of the miscibility gap is generally within the experimental uncertainty of the analysis ($\pm 5\%$ of the lithium weight present), but there is greater scatter on the sulfur-rich side. Based on these results, the region of immiscibility is taken to be from about 0.2 to 37.0 a/o lithium at the monotectic temperature.

Thermal effects associated with liquidus crossings were not observed. Attempts to establish the location of the upper liquidus by determination of the equilibrium sulfur vapor pressure as a function of temperature for compositions greater than 37 a/o lithium gave very scattered results. The time necessary for equilibration between the vapor and the condensed phase was at least several days. It is significant that the vapor pressure of samples with less than 34 a/o lithium was not significantly different from that for pure sulfur within the experimental uncertainty ($\pm 10\%$).

X-ray powder patterns were taken on a large number of samples of various compositions and thermal histories. In all cases, the observed lines were accounted for by the appropriate terminal phase and Li₂S.

The phase diagram which we have found for the lithium-sulfur system is very much like that for the lithium-selenium system, and previous comments (2) regarding that system and the implications of the phase equilibria in terms of the performance and design of electrochemical cells will not be repeated. Additional investigation of the lithium-sulfur system is needed in the region between Li₂S and lithium and at temperatures greater than 600°C.

Acknowledgments

The authors are indebted to Argonne's Analytical Support Group for assistance in x-ray and chemical analyses and to Dr. R. C. Vogel and Dr. A. D. Tevebaugh for their encouragement and support. This work was performed under the auspices of the United States Atomic Energy Commission.

Manuscript submitted April 13, 1972.

Any discussion of this paper will appear in a Discussion Section to be published in the June 1973 JOURNAL.

REFERENCES

1. E. J. Cairns and H. Shimotake, *Science*, **164**, 1347 (1969); E. J. Cairns, R. K. Steunenberg, and H. Shimotake in "Encyclopedia of Chemical Technology" Supplement Volume, 2nd ed, p. 120, John Wiley and Sons, Inc., New York (1971). These articles review work on lithium chalcogen cells, as well as other high temperature systems and contain additional references.
2. P. T. Cunningham, S. A. Johnson, and E. J. Cairns, *This Journal*, **118**, 1941 (1971).
3. F. W. Bergstrom, *J. Am. Chem. Soc.*, **48**, 146 (1926).
4. T. G. Pearson and P. L. Robinson, *J. Chem. Soc.*, **1930**, 413.
5. E. Zintl, A. Harder, and B. Dauth, *Z. Elektrochem.*, **40**, 588 (1934).
6. C. E. Johnson, M. S. Foster, and M. L. Kyle, *Nucl. Applications*, **3**, 563 (1967).
7. C. E. Johnson, S. E. Wood, and C. E. Crouthamel, *J. Inorg. Chem.*, **3**, 1487 (1964).
8. "Handbook of Chemistry and Physics", 52nd ed., The Chemical Rubber Co., Cleveland, Ohio (1971).
9. "Elemental Sulfur," B. Meyer, Editor, Interscience, New York (1965).

Electrochemical Behavior of Titanium

Effect of Ti(III) and Ti(IV)

N. T. Thomas* and Ken Nobe*

School of Engineering and Applied Science, University of California, Los Angeles, California 90024

ABSTRACT

Anodic polarization of titanium in 1N H₂SO₄ containing Ti(IV) showed that Ti(IV) inhibited dissolution and facilitated passivation. Polarization of titanium in 1N H₂SO₄ containing both Ti(III) and Ti(IV) indicated that Ti(III) accelerated the anodic dissolution of titanium in both the active and passive region. An empirical expression for anodic dissolution of titanium in 1N H₂SO₄ was obtained

$$i_a = k_a [H^+]^{0.53} \exp(0.43 F\phi/RT)$$

A dissolution mechanism based on the barrier layer model and Temkin adsorption of an adsorbed intermediate is shown to be consistent with the experimental data. A similar mechanism is used to interpret the accelerated dissolution of titanium with Ti(III).

Not many investigations on the effect of trivalent and tetravalent titanium on the polarization of titanium electrodes have been reported. Andreeva and Kazarin (1) and Weiman (2) reported that tetravalent titanium had an inhibiting effect on the corrosion of titanium in

sulfuric acid and in boiling 5% HCl, respectively. Tsvetnova *et al.* (3) found that the presence of trivalent titanium had a depassivation effect on passive titanium. In this study, the effect of tetravalent and trivalent titanium on the electrochemical behavior of titanium is examined.

* Electrochemical Society Active Member.

Key words: anodic dissolution, polarization, corrosion.

Experimental

Details of the experimental apparatus are given elsewhere (4). Tetravalent titanium in sulfuric acid was prepared by a method given by Codell (5) with a slight modification. A solution of 1g of tetravalent titanium in one liter of 1N H₂SO₄ was prepared as follows. Two grams of purified titanium (Fisher Scientific Company) was placed in a beaker and 200 ml of distilled water were added followed by 55.6 ml of concentrated sulfuric acid. The mixture was warmed gently on a hot plate until all the titanium dissolved to give a violet-colored solution. Then, quantities of 30% H₂O₂ were added until an orange-colored solution was obtained. The solution was heated until it was colorless. The solution was then cooled and transferred to a 2 liter volumetric flask and diluted to 2 liters. The pH of this solution was 0.25. It should be noted that in the method described by Codell (5) small amounts of HF were used to facilitate the dissolution of titanium. In the present case, HF was not added. The solutions of lower concentrations of tetravalent titanium were prepared by diluting the appropriate quantity of the stock solution with 1N H₂SO₄.

Ti(III) was obtained as a stock solution of titanous sulfate (Lamotte Chemical Company, titanous sulfate, 20% standardized solution). The analysis of the stock solution showed that the solution contained 1.35M Ti(III) and, in addition, 0.3M of Ti(IV). Hence, for this study, tetravalent titanium was always present in solutions of trivalent titanium.

When a steady-state corrosion potential of titanium was attained in 1N H₂SO₄, the appropriate quantity of tetravalent or the trivalent and tetravalent titanium solution were added. After a steady-state corrosion potential was attained, cathodic and anodic polarization of titanium were performed.

Results and Discussion

Effect of Ti(IV).—The presence of the tetravalent ion increased the corrosion potential of titanium in the noble direction. The corrosion potential of titanium at different concentrations of Ti(IV) is shown in Table I. At a concentration above 5 mM Ti(IV) the electrode self-passivated.

The cathodic polarization of titanium in the presence of Ti(IV) is shown in Fig. 1 and indicates that a reduction reaction, in addition to the hydrogen evolution, occurs between the corrosion potential and -950 mV vs. SCE. The reduction of Ti(IV) can be obtained by subtracting the rate of hydrogen evolution from the total cathodic current. The reduction currents of Ti(IV) which is shown in Fig. 2 exhibit limiting currents. The limiting current values obtained are given in Table I. According to Latimer (6) the oxidation-reduction potential of the Ti(III)/Ti(IV) couple is -142 mV vs. SCE. Therefore, it is assumed that the limiting diffusion current observed is due to the reduction of Ti(IV) to Ti(III).

Figure 3 shows the anodic polarization of titanium in the presence and the absence of Ti(IV). As shown in this figure, the presence of Ti(IV) decreased the anodic current in the active region. Although there was no change in the primary passivation potential, the

Table I. Electrochemical parameter for titanium in 1N H₂SO₄ containing Ti(III) and Ti(IV)

Ti(III) mM	Ti(IV) mM	ϕ_{corr} mV vs. SCE	i_{corr} μ A/cm ²	ϕ_{pp} mV vs. SCE	i_{cc} μ A/cm ²	i_p μ A/cm ²	t_L μ A/cm ²
11.6	2.6	-630	7	-520	18	5	60
17.8	4.0	-615	10	-520	16	10	140
24.5	5.5	-600	13	-520	15	16	190
35.0	7.8	-280	—	—	—	17	—
0	0	-680	9	-520	24	0.5	—
0	1.0	-645	9	-520	21	0.5	40
0	2.0	-625	8	-520	18	0.5	100
0	4.2	-580	6	-520	12	0.4	140

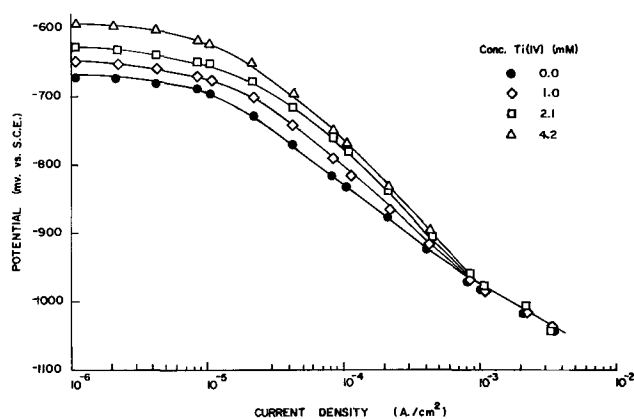


Fig. 1. Cathodic polarization of titanium in 1N H₂SO₄ containing Ti(IV).

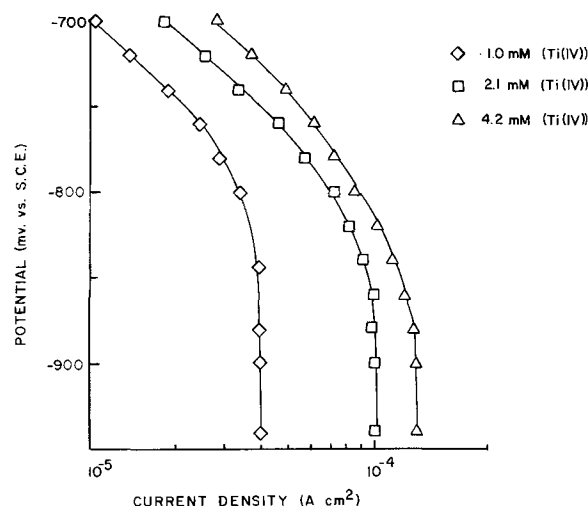


Fig. 2. Electrochemical reduction of Ti(IV)

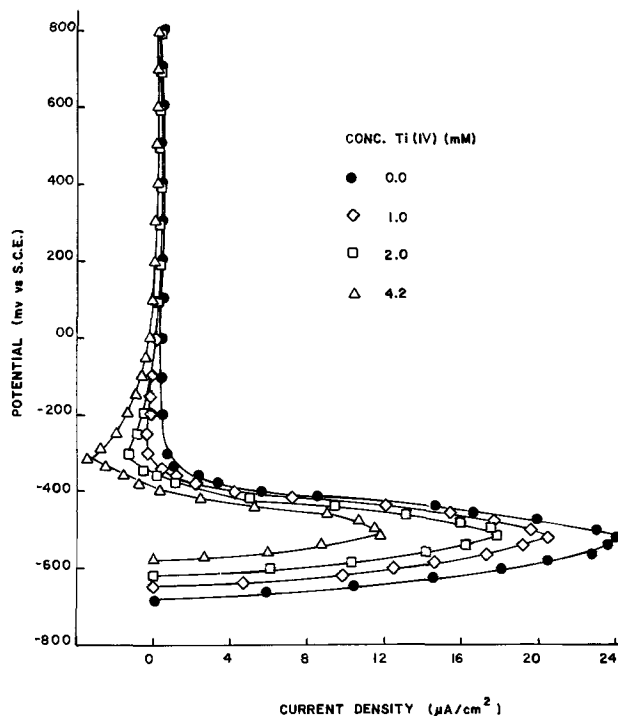


Fig. 3. Anodic potentiostatic polarization of titanium in 1N H₂SO₄ containing Ti(IV).

presence of Ti(IV) decreased the critical current. During the anodic polarization of titanium in Ti(IV) solutions, a small cathodic current was observed in the

initial part of the passive region between -400 to 200 mV vs. SCE, indicating a net reduction reaction in this potential region. The presence of Ti(IV) has apparently no effect on the passive current at more positive potentials.

Figure 4 shows the anodic dissolution current at -580 mV vs. SCE and the critical current for titanium corrected for both the h.e.r. and the reduction of Ti(IV). As seen in the Fig. 4, the presence of Ti(IV) decreased the anodic dissolution of titanium and also the critical current. This decrease in anodic dissolution and critical current was found to be proportional to the concentration of Ti(IV). Thus, it is apparent that Ti(IV) inhibits the anodic dissolution of titanium. After anodic polarization, the titanium electrode remained passive.

Effect of Ti(III).—Figure 5 shows the cathodic polarization of titanium in the presence and the absence of the mixture of Ti(III) and Ti(IV). Between the corrosion potential and -950 mV vs. SCE a second reduction process in addition to hydrogen evolution was observed. The rate of the second reduction process can be obtained by subtracting the rate of the h.e.r. from the net cathodic current. This reduction current is plotted vs. the potential in Fig. 6 and a limiting current was observed. These limiting reduction currents

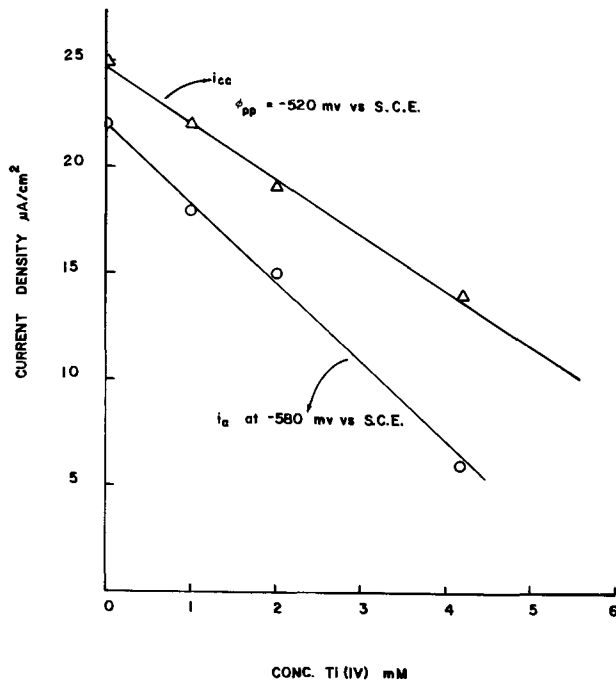


Fig. 4. Anodic current and critical current density of titanium vs. Ti(IV) concentration.

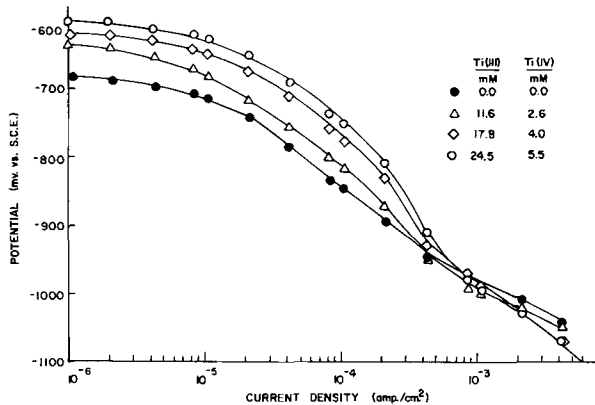


Fig. 5. Cathodic polarization of titanium in 1N H₂SO₄ containing Ti(III) and Ti(IV).

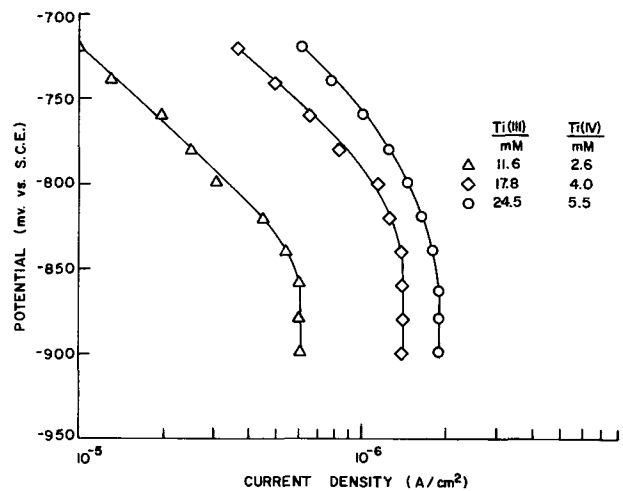


Fig. 6. Electrochemical reduction of Ti(IV) in the presence of Ti(III).

which increased with an increase in concentration of Ti(III) and Ti(IV) is presented in Table I. According to Latimer (6) the redox potential of the Ti(III)/Ti(II) couple is -0.610 V vs. SCE. On the other hand, the theoretical work of George and McClure (7) indicates that the redox potential of Ti(III)/Ti(II) is -2.54 V vs. SCE. The experimental data of Oliver and Ross (8) supports the calculations of George and McClure (7) indicating that the reduction process observed during the cathodic polarization of titanium in the presence of Ti(III) and Ti(IV) is the reduction of Ti(IV) to Ti(III) and not Ti(III) to Ti(II).

Figure 7 shows a plot of limiting reduction current vs. concentration of Ti(IV). The square symbols represent the limiting current obtained without Ti(III) in the solutions. The circle symbols represent the limiting current obtained for solutions containing both Ti(III) and Ti(IV). As seen in Fig. 7, the two sets of limiting currents are consistent. Therefore, by both thermodynamic considerations and comparison of the two sets of reduction currents, it seems reasonable to assume that the second reduction current on titanium in solution containing both Ti(III) and Ti(IV) is due solely to the reduction of Ti(IV).

Figure 8 shows the results of the anodic polarization of titanium in 1N H₂SO₄ in the presence and the absence of the mixture of Ti(III) and Ti(IV). At a concentration of 35 mM Ti(III) and 7.8 mM Ti(IV), titanium was passive. For solutions containing only Ti(IV), as stated above, titanium passivated at concentrations of 5 mM Ti(IV) and above. The passivation of titanium in solution containing 35 mM of Ti(III)

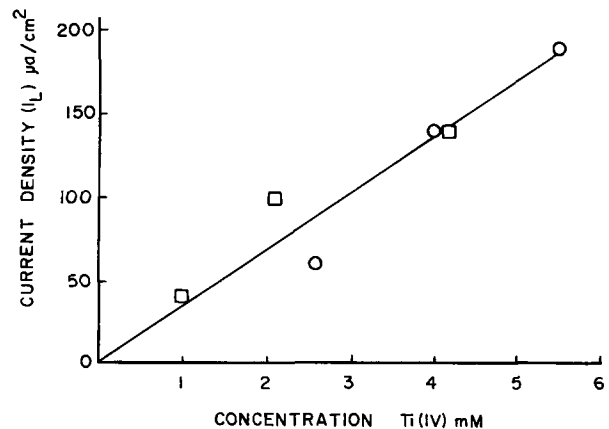


Fig. 7. Limiting diffusion currents of Ti(IV) reduction. Square points represent data for Ti(IV) solutions. Circle points represent data for solutions containing Ti(IV) and Ti(III).

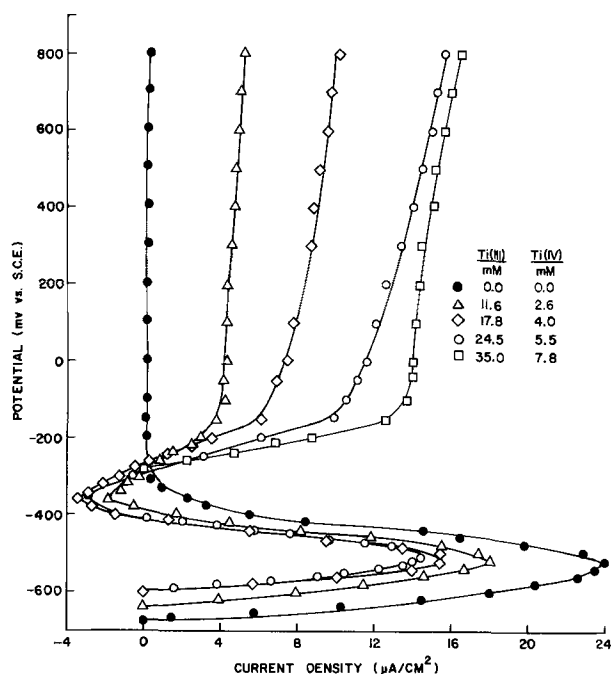


Fig. 8. Anodic potentiostatic polarization of titanium in 1N H₂SO₄ containing Ti(III) and Ti(IV).

and 7.8 mM of Ti(IV) can be attributed to the presence of Ti(IV). The passive corrosion potentials observed with the mixture of Ti(IV) and Ti(III) were considerably lower than those of the passive corrosion potential observed with only Ti(IV) indicating a marked activation of titanium in the passive region due to Ti(III).

As seen in Fig. 8, the presence of both Ti(III) and Ti(IV) decreased the anodic current and the critical current density. However, no change in the primary passivation potential of titanium in the mixture of Ti(III) and Ti(IV), -520 mV vs. SCE, was observed. At the corrosion potential of titanium in solutions containing both Ti(III) and Ti(IV), the corrosion current of titanium can be calculated by summing the rate of the h.e.r. and the rate of Ti(IV) reduction. These calculated corrosion currents are given in Table I. In the above calculations, the Ti(IV) reduction current was obtained by extrapolating the cathodic curve in Fig. 6 to the corrosion potential of titanium in solution containing both Ti(III) and Ti(IV); the rate of the h.e.r. was obtained by extrapolating the h.e.r. Tafel line to the same potential.

If the anodic dissolution of titanium is independent of Ti(III), the corrosion current of titanium in solutions containing both Ti(III) and Ti(IV) should have been smaller than the values obtained. Comparison of the corrosion current of titanium in solutions containing 17.8 mM Ti(III) and 4.0 mM Ti(IV) with the corrosion current of titanium in 4.2 mM Ti(IV) solution indicates that Ti(III) has an accelerating effect on the dissolution of titanium.

The rates of anodic dissolution of titanium in solutions containing Ti(III) and Ti(IV) at -580 mV vs. SCE after correction for the h.e.r. and Ti(IV) reduction are given in Table II. Table II gives some anodic dissolution rates of titanium in the presence of Ti(IV) and Fig. 4 shows that the decrease in anodic current was proportional to the concentration of Ti(IV). As seen in Table II, the anodic current of titanium in the presence of both Ti(III) and Ti(IV) is larger than the value expected when Ti(IV) only was present. Table II also gives the anodic current of titanium in the absence of Ti(IV) and Ti(III) at -580 mV vs. SCE. From the above results the anodic current of titanium in the presence of only Ti(III) is estimated and presented in Table II. In the potential range of active

Table II. Calculated electrochemical parameters for titanium in 1N H₂SO₄ containing only Ti(III)

Ti(III) mM	Ti(IV) mM	Anodic dissolution current* for titanium at -580 mV vs. SCE μA/cm ²				Critical current μA/cm ²			
		<i>i_a</i> (O)	<i>i_a</i> (α)	<i>i_a</i> (β)	<i>i_a</i> (γ)	<i>i_{cc}</i> (O)	<i>i_{cc}</i> (α)	<i>i_{cc}</i> (β)	<i>i_{cc}</i> (γ)
11.6	2.6	—	14	12	24	—	19	18	26
17.8	4.0	—	12	7	27	—	19	14	30
24.5	5.5	—	12	1	33	—	19	10	34
0	0	22	—	—	—	25	—	—	—

* Corrected for the h. e. r. and Ti(IV) reduction.
(O) 1N H₂SO₄ (0 mM Ti(III), 0 mM Ti(IV)).
(α) For solutions containing Ti(III) and Ti(IV).
(β) For solutions containing only Ti(IV).
(γ) Calculated values for solutions containing only Ti(III)
 $i(\gamma) = i(O) + i(\alpha) - i(\beta)$.

titanium dissolution, the oxidation of Ti(III) to Ti(IV) is not possible thermodynamically. Hence, it seems reasonable to assume that Ti(III) accelerated anodic dissolution of titanium in the active region. It should be noted that the calculated anodic dissolution of titanium in the presence of Ti(III), *i_a*(γ), was based on the assumption that the inhibiting effect of Ti(IV) is independent of Ti(III). A log-log plot of *i_a*(γ) vs. concentration of Ti(III) in Fig. 9 shows that

$$\frac{\partial \log i_a(\gamma)}{\partial \log [\text{Ti(III)}]} = 0.5 \quad [1]$$

The critical currents of titanium in the presence of both Ti(III) and Ti(IV), only Ti(IV) and in the absence of Ti(III) and Ti(IV) after considering h.e.r. and Ti(IV) reduction are given in Table II. The critical current in solutions containing only Ti(III) have been estimated from the above results and are given in Table II. These results show that Ti(III) increased the critical current of titanium.

During potentiostatic anodic polarization of titanium in solutions containing both Ti(IV) and Ti(III), a small cathodic current between -400 and -275 mV vs. SCE was observed. This observed net cathodic current is probably due to the reduction of Ti(IV) to Ti(III).

As seen in Fig. 8, Ti(III) increased the apparent passive current. The passive currents were independent of the rotation speed of the electrode indicating the absence of mass transfer effects. The passive current of titanium in solutions containing both Ti(III) and Ti(IV) at +800 mV vs. SCE is presented in Table I.

After anodic polarization the electrode remained passive at all concentrations of Ti(III) and Ti(IV) studied and the passive corrosion potential was -270 ± 15 vs. SCE. This passive corrosion potential was much lower than the passive corrosion potential of titanium in 1N H₂SO₄ in the presence and absence of Ti(IV).

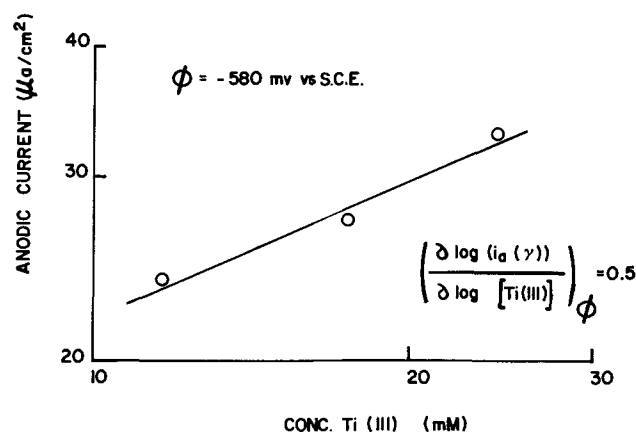


Fig. 9. Anodic current, *i_a*(γ), vs. Ti(III) concentration

The observed depassivation of titanium with Ti(III) is in accord with the results of Tsvetnova (3) who reported that Ti(III) depassivated titanium in 1N H₂SO₄ solution containing 4.2 mM Ti(III) at 65°C. According to Tsvetnova the passive current increased by approximately a factor of 20. The present study also showed that the presence of Ti(III) appreciably increased the passive current of titanium in 1N H₂SO₄ at 25°C. For example, at a concentration of 24.5 mM Ti(III), the passive current increased by approximately a factor of 40.

Anodic dissolution in the absence of Ti(III) and Ti(IV).—Studies on the mechanism of titanium dissolution in H₂SO₄ have been difficult due to the small active region observed. It has been reported (4) that the anodic polarization of titanium in sulfuric acid at different pH showed that anodic dissolution increased with increase in the concentration of hydrogen ions. The increase in anodic dissolution of titanium with acid concentration has also been shown by others (9, 10).

Since the corrosion potential of titanium did not change with rotation of the electrode, the active corrosion potential observed for titanium is due to activation-controlled anodic dissolution of titanium and hydrogen evolution. In the vicinity of the active corrosion potential the net current can be written

$$i = k_a [H^+]^{Z_a} e^{\frac{\alpha_a F}{RT} \phi} - k_H [H^+]^{Z_H} e^{-\frac{\alpha_c F}{RT} \phi} \quad [2]$$

where k_a and k_H are rate constants for anodic dissolution of titanium and hydrogen evolution, respectively. Z_a and Z_H are reaction orders with respect to hydrogen ions for anodic dissolution of titanium and the h.e.r., and α_a and α_c are the over-all transfer coefficients for the anodic and cathodic reactions, respectively.

Equation [2] can be written

$$i = i_{\text{corr}} \left(e^{\frac{\alpha_a F}{RT} \Delta\phi} - e^{-\frac{\alpha_c F}{RT} \Delta\phi} \right) \quad [3]$$

where $\Delta\phi = \phi - \phi_{\text{corr}}$

For very small $\Delta\phi$ values, Eq. [3] can be written

$$i = i_{\text{corr}} (\alpha_a + \alpha_c) \frac{F}{RT} \Delta\phi \quad [4]$$

and

$$R_p = \left(\frac{\partial \Delta\phi}{\partial i} \right)_{\Delta\phi \rightarrow 0} = \frac{RT}{i_{\text{corr}} (\alpha_a + \alpha_c) F} \quad [5]$$

Figure 10 shows a linear plot of $\Delta\phi$ vs. current for potentiostatic anodic and cathodic polarization of titanium at different pH. [A similar plot of galvanostatic experiments are given in Fig. 6 of Ref. (11)]. The slope of each curve is the polarization resistance, R_p . From the polarization resistances determined and the corrosion current and the h.e.r. Tafel slope values reported in Ref. (11), Eq. [5] gives the average calculated value of α_a as 0.43. Since the expression for anodic Tafel slope is

$$b_a = \left(\frac{\partial \phi}{\partial \log i_a} \right) = 2.3 \frac{RT}{\alpha_a F} \quad [6]$$

b_a is 140 mV.

$$i_{\text{corr}} = k_a [H^+]^{Z_a} e^{\frac{\alpha_a F}{RT} \phi_{\text{corr}}} - k_H [H^+]^{Z_H} e^{-\frac{\alpha_c F}{RT} \phi_{\text{corr}}} \quad [7]$$

Thus

$$\phi_{\text{corr}} = \frac{RT}{(\alpha_a + \alpha_c)} \{ \ln k_H - \ln k_a + \ln [H^+] (Z_H - Z_a) \} \quad [8]$$

$$\left(\frac{\partial \phi_{\text{corr}}}{\partial \text{pH}} \right) = -2.3 \frac{RT [Z_H - Z_a]}{(\alpha_a + \alpha_c) F} \quad [9]$$

It has been reported (11) that the corresponding potential of titanium was independent of pH in the pH

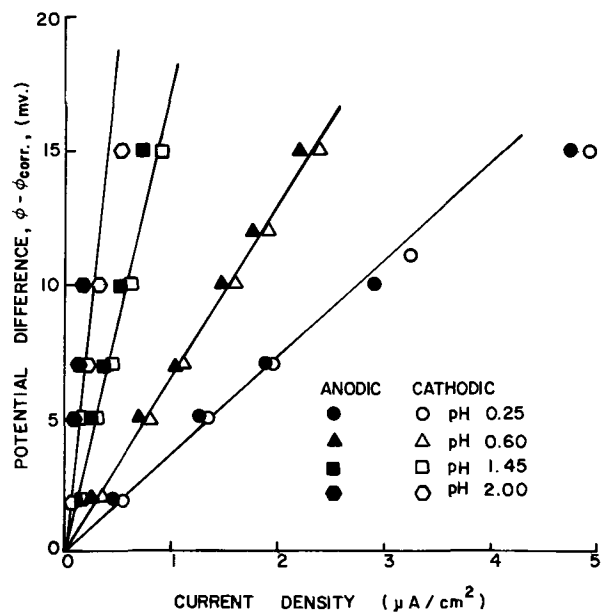


Fig. 10. $(\phi - \phi_{\text{corr}})$ vs. current density

range studied. Similar independence of corrosion potential with acid concentration was observed by others (9, 12). Thus, Eq. [9] shows that the anodic reaction order with respect to hydrogen ions is equal to the cathodic reaction order with respect to hydrogen ion concentration. In studies of the h.e.r. on titanium (11) it was found that the hydrogen evolution reaction order was 0.6 with respect to hydrogen ions. Thus, the anodic reaction order with respect to hydrogen should be about 0.6.

Anodic polarization Tafel lines for titanium dissolution can be constructed from the corrosion potentials, corrosion currents, and the anodic Tafel slope. From such a plot, the anodic reaction order with respect to hydrogen ion can be determined by plotting $\log i_a$ vs. pH at constant potential. This latter plot is shown in Fig. 11 which shows that

$$\left(\frac{\partial \log i_a}{\partial \text{pH}} \right)_{\phi} = -0.53 \quad [10]$$

Hence, the reaction order for anodic dissolution of titanium with respect to hydrogen ions is shown to be about 0.53.

In the active region, the current due to anodic dissolution of titanium can be obtained at the applied

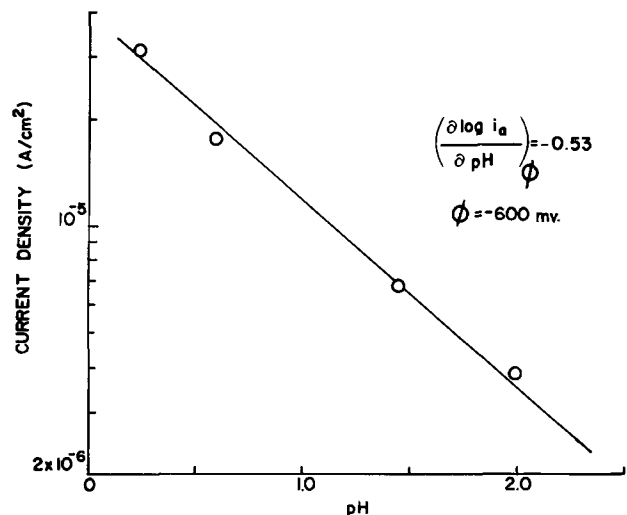


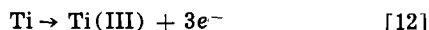
Fig. 11. Anodic dissolution of titanium vs. pH

potential by adding the hydrogen evolution current (obtained by extrapolating the Tafel line for h.e.r. to the applied potential) with the measured anodic current. Figure 12 shows these results during potentiostatic polarization in the vicinity of corrosion potential. From Fig. 12 the anodic Tafel slopes obtained were 135 mV, and the reaction order for anodic dissolution of titanium with respect to hydrogen ions was 0.57. The above results of the anodic Tafel slope and reaction order are in agreement with the results obtained from an analysis of the polarization resistances, corrosion currents, and cathodic Tafel slope.

In this study it has been shown that in the vicinity of corrosion potential, the anodic dissolution rate of titanium in H_2SO_4 can be expressed by the rate expression

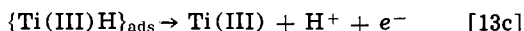
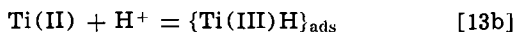
$$i_a = k_a [H^+]^{0.53} e^{\frac{0.43 F}{RT} \phi} \quad [11]$$

A mechanism for the dissolution of titanium must be consistent with the pH dependence and the presence of an oxide film on the surface (13, 14). When titanium dissolves in acid solution, the over-all process is (15, 16)



This process does not take place in a single step, but rather in a series of individual reaction steps [e.g., see Ref. (17)].

As discussed earlier, the titanium surface is covered with an oxide film at the active corrosion potential. During anodic dissolution, titanium is assumed to pass through this film. The following scheme for titanium dissolution is proposed



In the above sequence, it is assumed that step a takes place at the metal-oxide interface and steps b and c occur at the oxide-solution interface. The reaction rate of step a depends on the potential at the metal-oxide interface, ϕ_f , and the rates of step b and c depend on the potential at the oxide-solution interface, ϕ_s . It can be shown that Eq. [11] for anodic dissolution of titanium can be derived by assuming step c is rate controlling with Temkin behavior of the adsorbed $\{Ti(III)H\}_{ads}$ species. It is also assumed that the film reaction (step a) and step b are both at equilibrium.

The total potential, ϕ , observed can be written as $\phi = \phi_f + \phi_s$ where ϕ_f and ϕ_s are the potential across the metal oxide film and metal-oxide solution interface, respectively. Since step a is the film reaction and is assumed to be in equilibrium, Eq. [14] can be applied to the metal-oxide interface (18)

$$\phi_f = \phi_f^0 + \frac{RT}{2F} \ln [Ti(II)] \quad [14]$$

With Temkin adsorption behavior of the adsorbed

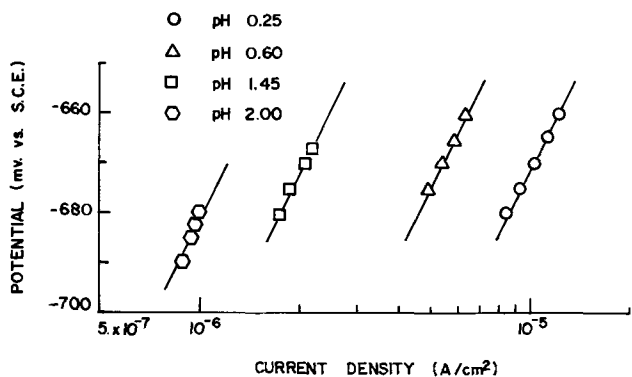


Fig. 12. Anodic dissolution of titanium vs. potential

$\{Ti(III)H\}_{ads}$ species, the rate expression for step b and c can be written as

$$r_2 = k_2 [H^+] e^{-\beta f \theta} - k_{-2} e^{(1-\beta) f \theta} \quad [15]$$

$$r_3 = k_3 e^{(1-\gamma) f \theta} e^{\frac{\alpha F \phi_s}{RT}} \quad [16]$$

where β , γ , and α are symmetry factors and $f\theta$ is the function which accounts for the change of free energy of activation with coverage of $\{Ti(III)H\}_{ads}$. When step b is in equilibrium, the value of $f\theta = \ln k_2 - \ln k_{-2} + \ln [H^+]$. By substituting the value of $f\theta$ in Eq. [16]

$$r_3 = k_3 \left(\frac{k_2}{k_{-2}} \right)^{(1-\gamma)} [H^+]^{(1-\gamma)} e^{\frac{\alpha F \phi_s}{RT}} \quad [17]$$

Since $\phi = \phi_s + \phi_f$ and ϕ_f is given by Eq. [14], Eq. [17] can be transformed to Eq. [18]

$$i_a = k [Ti(II)]^{-\alpha/2} [H^+]^{(1-\gamma)} e^{\frac{\alpha F \phi}{RT}} \quad [18]$$

where k is a rate constant. For constant concentration of $Ti(II)$ in the film, the equation for the anodic current can be written

$$i_a = k [H^+]^{(1-\gamma)} e^{\frac{\alpha F \phi}{RT}} \quad [19]$$

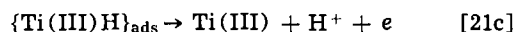
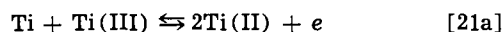
With the usual value of the symmetry factor of 0.5, the anodic dissolution rate for titanium can be expressed as

$$i_a = k [H^+]^{0.5} e^{\frac{F \phi}{2RT}} \quad [20]$$

which is comparable to the experimental rate expression (Eq. [11]).

By comparing Eq. [19] and [11], the symmetry factors obtained in this investigation for the adsorption of $\{Ti(III)H\}_{ads}$ and the charge transfer reaction at the oxide-solution interface are 0.47 and 0.43, respectively.

Anodic dissolution in the presence of Ti(III).—In the study of anodic dissolution of titanium in the presence of $Ti(III)$, the reaction order for anodic dissolution with respect to $Ti(III)$ was found to be 0.5. To account for the effect of $Ti(III)$ on the anodic dissolution of titanium, the following mechanism for titanium dissolution in the presence of $Ti(III)$ is proposed



In the above sequence, it is assumed that step a occurs at the metal-oxide interface and steps b and c occur at the oxide-solution interface. The reaction rate of step a depends upon the potential at the metal-oxide interface, ϕ_f , and the reaction rate of step c depends upon the potential at the oxide-solution interface, ϕ_s . It will be shown below that a rate expression can be derived giving fractional orders with respect to $Ti(III)$ and hydrogen ions for the anodic dissolution of titanium by assuming step c is rate controlling, Temkin behavior of the adsorbed $\{Ti(III)H\}_{ads}$, and step a and b are in quasi-equilibrium.

The total potential, ϕ , is

$$\phi = \phi_f + \phi_s \quad [22]$$

Since step a, the film reaction, is assumed to be in quasi-equilibrium

$$\phi_f = \phi_f^0 + \frac{RT}{F} \ln \frac{[Ti(II)]^2}{[Ti(III)]} \quad [23]$$

By utilizing the Temkin adsorption isotherm for the adsorbed species, the rate expressions for step b and c, respectively, are

$$r_2 = k'_2 [H^+] e^{-\beta' f \theta} - k'_{-2} e^{(1-\beta') f \theta} \quad [24]$$

$$r_3 = k'_3 e^{(1-\gamma')f\theta} e^{\frac{\alpha'F\phi_s}{RT}} \quad [25]$$

Since step b is in quasi-equilibrium, $f\theta = \ln k'_2 - \ln k'_{-2} + \ln [H^+]$. By substituting this value of $f\theta$ in Eq. [25]

$$r_3 = k'_3 \left(\frac{k'_2}{k'_{-2}} \right)^{(1-\gamma')} [H^+]^{(1-\gamma')} e^{\frac{\alpha'F\phi_s}{RT}} \quad [26]$$

Equations [26], [22], and [23] give the anodic dissolution current

$$i_a = k' \frac{[Ti(III)]^{\alpha'}}{[Ti(II)]^{2\alpha'}} [H^+]^{(1-\gamma')} e^{\frac{\alpha'F\phi}{RT}} \quad [27]$$

For constant concentration of Ti(II) in the film, Eq. [27] becomes

$$i_a = k' [Ti(III)]^{\alpha'} [H^+]^{(1-\gamma')} e^{\frac{\alpha'F\phi}{RT}} \quad [28]$$

For $\alpha' = \gamma' = 0.5$, the anodic dissolution rate for titanium can be expressed as

$$i_a = k' [Ti(III)]^{0.5} [H^+]^{0.5} e^{\frac{F\phi}{2RT}} \quad [29]$$

Equation [29] predicts a Tafel slope of 120 mV for anodic dissolution of titanium in sulfuric acid and reaction orders of 0.5 with respect to both hydrogen ions and Ti(III). Experiments have shown that for the anodic dissolution of titanium, the reaction order with respect to Ti(III) is 0.5 which agrees with the predicted value. It was shown above that the anodic dissolution of titanium in the absence of Ti(III) was 0.5 order with respect to hydrogen ions. Thus, the proposed mechanism seems to provide a consistent interpretation for the observed acceleration of titanium dissolution by Ti(III).

Conclusions

The electrochemical behavior of titanium in 1N H₂SO₄ indicates that Ti(IV) is readily reduced electrochemically, but Ti(III) is not reduced, at least in the potential range investigated. Above a concentration of 5 mM Ti(IV), titanium self-passivates. At lower concentrations, Ti(IV) is shown to inhibit active anodic dissolution. In contrast, both Ti(III) and hydrogen ions are shown to accelerate anodic dissolution. The apparent electrochemical reaction orders for anodic dissolution are one-half with respect to both Ti(III) and H⁺. By postulating an adsorbed intermediate, {Ti(III)H}_{ads}, and Temkin adsorption behavior, mechanisms for the anodic dissolution of titanium in 1N H₂SO₄ in the presence and absence of Ti(III) consistent with the electrochemical data have been devised.

Acknowledgment

This work is part of the University of California research program on sea water desalination.

Manuscript submitted March 1, 1972; revised manuscript received July 3, 1972.

Any discussion of this paper will appear in a Discussion Section to be published in the June 1973 JOURNAL.

LIST OF SYMBOLS

b_a	anodic Tafel slope
F	Faraday constant
f	Temkin parameter
i	current density, A/cm ²

i_a	anodic dissolution current density, A/cm ²
$i_a(\gamma)$	anodic dissolution current density of titanium in the presence of Ti(III), A/cm ²
i_{cc}	critical current density, A/cm ²
i_{corr}	corrosion current density, A/cm ²
i_L	limiting current density for Ti(IV) reduction, A/cm ²
i_p	passive current density, A/cm ²
k_a	anodic rate constant for titanium dissolution
k_H	cathodic rate constant for hydrogen evolution reaction
k_2, k_{-2}	rate constants in Eq. [15]
k_3, k_{-3}	rate constants in Eq. [16]
k'_2, k'_{-2}	rate constants in Eq. [24]
k'_3	rate constant in Eq. [25]
k_c	rate constant in Eq. [18]
k'_c	rate constant in Eq. [27]
R	gas constant
R_p	polarization resistance, ohm · cm ²
T	absolute temperature, °K
Z_a	reaction order for titanium dissolution with respect to hydrogen ions
Z_H	reaction order for the hydrogen evolution reaction with respect to hydrogen ions
α	symmetry factors in Eq. [16]
α'	symmetry factors in Eq. [25]
α_a	over-all anodic charge transfer coefficient
α_c	over-all cathodic charge transfer coefficient
β	symmetry factors in Eq. [15]
β'	symmetry factors in Eq. [24]
γ	symmetry factors in Eq. [16]
γ'	symmetry factors in Eq. [25]
ϕ	electrode potential, V
ϕ_{corr}	corrosion potential, V
$\Delta\phi$	$\phi - \phi_{corr}$
ϕ_f	potential across the metal oxide film, V
ϕ_f^0	standard potential for the film reaction, V
ϕ_{pp}	primary passivation potential, V
ϕ_s	potential across the oxide-solution interface, V
θ	surface coverage

REFERENCES

- V. V. Andreeva and V. I. Kazarin, *Proc. Acad. U.S.S.R., Phys. Chem. Sec.*, **123**, 877 (1958).
- S. H. Weiman, *Corrosion*, **22**, 98 (1966).
- R. V. Tsvetnova and A. I. Krasilschikov, *Russ. J. Phys. Chem.*, **39**, 109 (1965).
- N. T. Thomas and K. Nobe, *This Journal*, **116**, 1748 (1969).
- M. Codell, "Analytical Chemistry of Titanium Metal and Alloys," p. 25, Interscience Publishers, Inc., New York (1959).
- W. M. Latimer, "Oxidation Potentials," Prentice Hall, Inc., Englewood Cliffs, N. J. (1952).
- P. George and D. S. McClure, "Progress in Inorganic Chemistry 1," Interscience Publishers, Inc., New York (1959).
- J. W. Oliver and J. W. Ross, Jr., *J. Am. Chem. Soc.*, **85**, 2565 (1963).
- J. M. Peters and J. R. Myers, *Corrosion*, **23**, 326 (1967).
- R. D. Armstrong, J. A. Harrison, H. R. Thirsk, and R. Whitfield, *This Journal*, **117**, 1003 (1970).
- N. T. Thomas and K. Nobe, *ibid.*, **117**, 622 (1970).
- D. Schlain *et al.*, *ibid.*, **102**, 102 (1955).
- N. D. Tomashov, R. M. Al'tovskii, and A. G. Arakelov, *Proc. Acad. Sci. U.S.S.R., Phys. Chem. Sec.*, **121**, 593 (1958).
- T. R. Beck, *This Journal*, **115**, 890 (1968).
- M. E. Straumanis and P. C. Chen, *Corrosion*, **7**, 229 (1951).
- T. C. Franklin and H. V. Siklemian, *J. Inorg. Nucl. Chem.*, **12**, 181 (1959).
- J. O'M. Bockris, D. Drazic, and A. R. Despic, *Electrochim. Acta.*, **4**, 329 (1961).
- R. E. Meyer, *This Journal*, **107**, 847 (1960).

Electrodissolution Kinetics of Iron in Chloride Solutions

III. Acidic Solutions

Robert J. Chin* and Ken Nobe*

School of Engineering and Applied Science, University of California, Los Angeles, California 90024

ABSTRACT

The dissolution kinetics of iron in acidic chloride media has been investigated by potentiostatic polarization. An anodic Tafel slope of approximately 70 mV/decade was obtained. An increase in the chloride ion concentration, at a constant pH, increased the dissolution rate of iron. The following empirical rate expressions for iron dissolution and hydrogen evolution have been determined from the experimental data

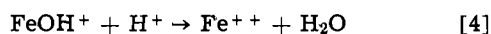
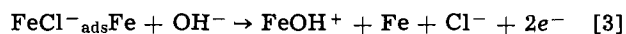
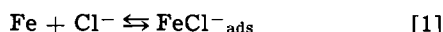
$$i_a = k_a [\text{Cl}^-]^{0.5} [\text{OH}^-]^{0.6} \exp(0.85 F\phi/RT)$$

$$i_c = k_c [\text{H}^+] \exp(-F\phi/2RT)$$

The rate expression for iron dissolution can be developed theoretically by a mechanism which includes the direct participation of chloride ions in the dissolution of iron.

Mechanistic studies on metallic dissolution in aqueous media have been mainly focused on the effect of pH at constant anion concentration. However, there has been some work considering the direct participation of anions in metallic dissolution. The effect of anions on the kinetics of metallic dissolution has been reviewed by Kolotykin (1). Foley (2) has reviewed the specific case of the effect of chloride ions on the dissolution of iron.

Lorenz (3) studied the dissolution of iron in 0.5N H₂SO₄ in the absence and presence of KCl. He found that below 0.1N, chloride ions did not affect the anodic polarization behavior of iron. An anodic Tafel slope of 30 mV was obtained. For concentrations greater than 0.1N, increasing the chloride ion concentration decreased the rate of iron dissolution and changed the anodic Tafel slope to 60 mV. At zero or low chloride ion concentrations, Lorenz (3) interpreted his results for iron dissolution in terms of the Heusler mechanism (4). At high chloride ion concentrations the direct participation of the chloride ions in the dissolution process was surmised and Lorenz proposed the following mechanism to explain the experimental data



By assuming step [3] as rate determining with the surface coverage of FeCl⁻_{ads} approaching unity, the above mechanism predicts a Tafel slope of 60 mV and a reaction order with respect to chloride ion concentration of -1.

Heusler and Cartledge (5) studied the adsorption of iodide ions on iron and its effect on the dissolution rate of iron in 1N H₂SO₄. At a given potential, increasing the iodide concentration increased the adsorption of iodide and decreased the dissolution rate of iron. It was concluded that the iodide ion participated in the dissolution of iron by providing a second dissolution path for iron and occurred in parallel with the Heusler mechanism.

Kolotykin and co-workers (6, 7) investigated the dissolution of iron in H₂SO₄-Na₂SO₄ and HCl-NaCl solutions. In both types of solutions an increase in the anion concentration increased the dissolution rate of iron. This increase in the rate of dissolution could not be attributed solely to a change in the solu-

tion pH. It was concluded that both the sulfate and chloride ions participate in the dissolution of iron, and both have an accelerating effect. By addition of KCl to 0.1N H₂SO₄, the dissolution rate of iron was found to decrease with increasing KCl concentration up to 0.1N, similar to the observations of Lorenz (3) and Heusler and Cartledge (5). However, further increase in KCl concentration increased the dissolution rate. Kolotykin's interpretation of these results were based on the competitive adsorption of chloride and sulfate ions on the iron surface. The retarding effect observed when chloride ions were added to H₂SO₄ was attributed to the displacement of sulfate ions by chloride ions on the iron surface.

In a subsequent study by Lorenz and co-workers (8), it was concluded that the SO₄⁼ ions did not participate directly in the dissolution of iron. Experiments were performed in the absence of chloride ions, but the ionic strength of the electrolyte varied with the sulfate ion concentration.

The competitive adsorption of sulfate and chloride ions on iron was studied by Hackerman and Stephens (9) using radiotracer techniques. Their results indicated that small quantities of chloride ions in a sulfate solution increased sulfate ion adsorption. On the other hand, large chloride ion concentrations decreased sulfate ion adsorption. The inverse effect was shown with chromium by Maksimchuk and Rosenfeld (10). Additions of sulfate to chloride solutions lowered the amount of adsorbed chloride ion.

As shown above, it is evident that the effect of chloride ions on the dissolution of iron is complicated by the presence of sulfate ions. Although the sulfate ion may not participate directly in the dissolution mechanism, as suggested by Lorenz *et al.* (8), its effect on the adsorption of chloride ions must be considered. Thus, it is difficult to interpret the data obtained for a SO₄⁼/Cl⁻ system because of the indirect participation of SO₄⁼ ions.

In this study the effect of chloride ions, at constant pH, on the kinetics of iron dissolution is investigated using steady-state polarization techniques. The pH effect is also examined by using an inert supporting electrolyte to maintain a high and constant ionic strength. The perchlorate ion was chosen because it is not believed to adsorb strongly on iron (11) nor has it very strong tendencies to serve as ligands in complex formations (12).

Experimental

Cylindrical electrodes (1.24 cm in diameter and 0.95 cm in length) were made from Ferrovac E iron rods.

* Electrochemical Society Active Member.
Key words: corrosion, mechanism, polarization.

The test electrodes were used in the form of rotating disks with exposed cross-sectional surface areas of 1.2 cm². The exposed surface was polished with increasingly finer grades of aluminum oxide paper, followed by degreasing with boiling benzene in a Soxhlet column for 3 hr. After degreasing, the electrodes were annealed at 700°C for 1 hr in a vacuum. The electrodes were mounted in a Teflon assembly which allowed only the prepared cross-sectional surface to be exposed to the electrolyte.

A three-electrode cell of Teflon and Pyrex glass was used in the experiment. The Teflon top has entry ports for the test electrode, a Luggin probe, a thermometer, and a bubbler for the saturating gas. The Luggin probe connected the reference electrode (saturated calomel electrode) compartment to the test cell, while the auxiliary electrode (platinized platinum) compartment was separated from the test cell by a fritted glass disk. More details of the experimental apparatus can be found elsewhere (13).

Solutions were prepared from reagent grade chemicals and doubly distilled water. Two type of solutions were employed: (i) 0.1N HClO₄ + x N NaCl + y N NaClO₄ (x + y = 1.9); (ii) m N NaCl + n N HCl (m + n = 1.0). In the first set of solutions the chloride ion concentration was varied while maintaining both the total ionic strength and the pH constant. In the second set of solutions the pH was varied while both the total ionic strength and the chloride ion concentration were held constant. The pH of the test solutions were measured with a Beckman pH meter.

Before immersion of the test electrode, the test electrolyte was deoxygenated for several hours with pre-purified nitrogen. Potentiostatic polarization was performed using a Wenking potentiostat. The electrode potential was measured with a Keithley 621 R electrometer and the current was measured with a Simpson 269 ammeter.

Results

Anodic polarization curves for iron in deoxygenated type 1 solutions are shown in Fig. 1. The Cl⁻ concentration was varied between 0.01 and 1.9N. Increasing the Cl⁻ concentration shifted the polarization curves in the more active direction. This means that the rate of the anodic reaction is increased by the Cl⁻. For all the Cl⁻ concentrations a Tafel slope of approximately 70 mV was obtained in the vicinity of the corrosion potential. Deviation from this Tafel region is observed for low Cl⁻ concentrations at more noble potentials. The deviation takes the form of a sharp increase in current density with potential, starting at approximately -350 mV vs. SCE.

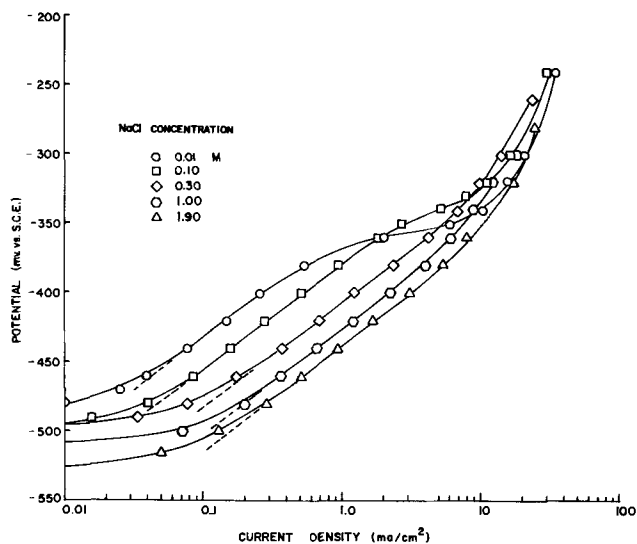


Fig. 1. Anodic polarization of iron in deoxygenated 0.1N HClO₄. Effect of Cl⁻ concentration.

An increase in the pH shifted the anodic polarization curves of iron towards the more active direction as shown in Fig. 2. Again a Tafel slope of approximately 70 mV was obtained. Atomic Absorption (A.A.) analysis of the electrolyte during polarization for dissolved iron was converted to current density-potential data by using Faraday's law. A comparison of the polarization data and the A.A. data for iron in 1N HCl is also shown in Fig. 2. Good agreement is observed between the two methods showing that the polarization curve corresponds to iron dissolution.

Cathodic polarization of iron is shown in Fig. 2 at different pH values. Increasing the pH decreased the rate of hydrogen evolution at a given potential. A cathodic Tafel slope of approximately 115 mV was obtained.

The corrosion potential was a function of both the pH and the Cl⁻ concentration as shown in Fig. 3. Increasing the pH and Cl⁻ concentrations shifted the corrosion potential in the active direction. The corrosion current density was determined by the intersection of the corrosion potential and the extrapolation of the anodic Tafel lines. The effect of pH and Cl⁻ concentration on the corrosion current density is shown in Fig. 4. The corrosion current increased with increase in the chloride ion concentration and hydrogen ion concentration.

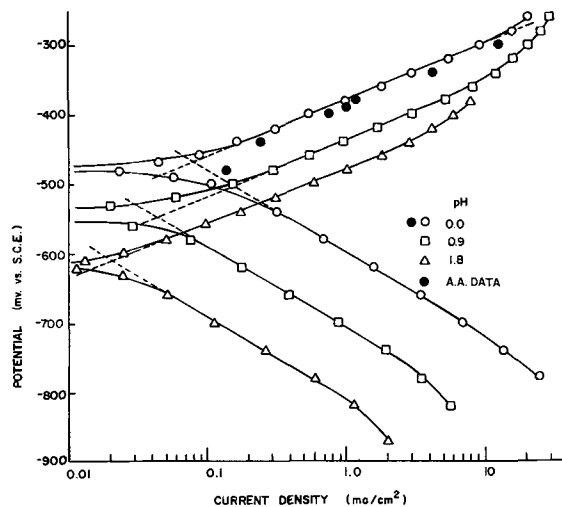


Fig. 2. Anodic and cathodic polarization of iron in deoxygenated 1N Cl⁻ solution. Effect of pH.

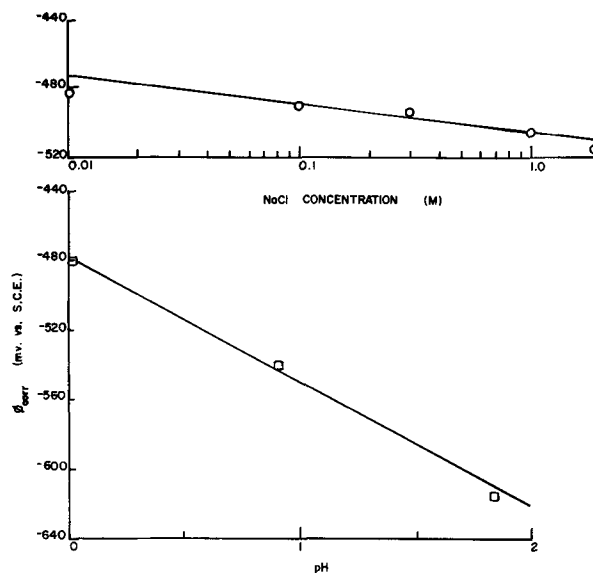


Fig. 3. Effect of Cl⁻ concentration and pH on the corrosion potential of iron.

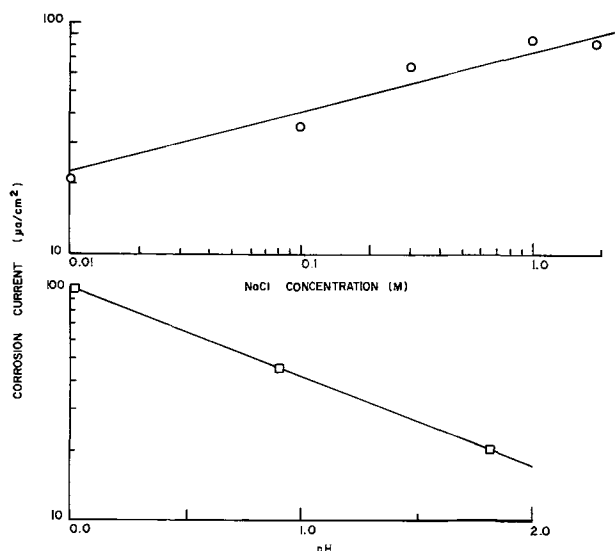


Fig. 4. Effect of Cl⁻ concentration and pH on the corrosion current density of iron.

Discussion

The electrode potential measured vs. the saturated calomel electrode can be divided into four components: the potential drop across the double layer; the zeta potential; the IR potential drop; a liquid junction potential between the solution and the reference. For electrode kinetic studies, the latter three must be subtracted from the measured potential. The zeta potential is not appreciable for high ionic strength electrolytes and the IR drop is negligible for highly conductive solutions. By use of Henderson's equation (14), the liquid junction potential was estimated and found to be only significant for the 1N HCl system. In the latter electrolyte, it was determined as 15 mV.

The reaction order with respect to the hydroxyl ion concentration for iron dissolution can be determined from the corrected polarization curves by a plot of log current vs. pH, at a constant potential, in the Tafel region. This plot is shown in Fig. 5 and shows that

$$\left(\frac{\partial \log i_a}{\partial \text{pH}} \right)_{[\text{Cl}^-], \phi_a} = 0.6 \quad [5]$$

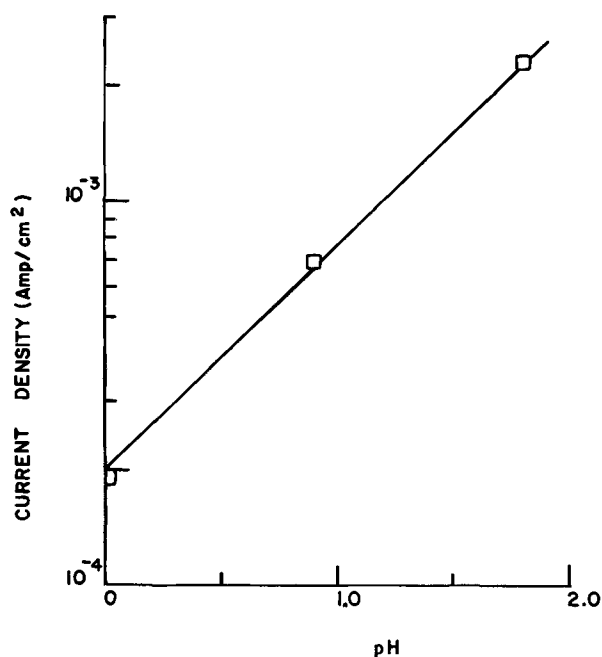


Fig. 5. Reaction order plot with respect to pH for iron dissolution. $\phi_a = -450$ mV.

Without correction of the polarization curves, the data would yield a reaction order with respect to the hydroxyl ion concentration of 0.8, which is close to the values reported by other workers for the same system (15, 16).

The reaction order with respect to chloride ion concentrations for iron dissolution can be obtained in a similar manner. The log current vs. log chloride ion concentration plot is shown in Fig. 6 and shows that

$$\left(\frac{\partial \log i_a}{\partial \log [\text{Cl}^-]} \right)_{\text{pH}, \phi_a} = 0.5 \quad [6]$$

Similarly, the reaction order with respect to the hydrogen ions for hydrogen evolution is determined from a plot of log i_c vs. pH at constant potential in the cathodic Tafel region. Figure 7 shows that

$$\left(\frac{\partial \log i_c}{\partial \text{pH}} \right)_{\phi_c} = -1.0 \quad [7]$$

The experimental results can be summarized by the following expressions

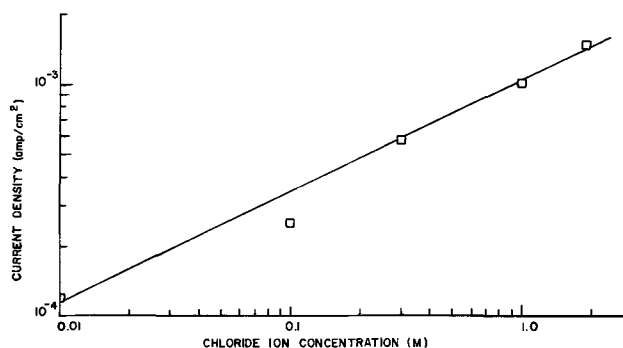


Fig. 6. Reaction order plot with respect to chloride ions for iron dissolution. $\phi_a = -425$ mV.

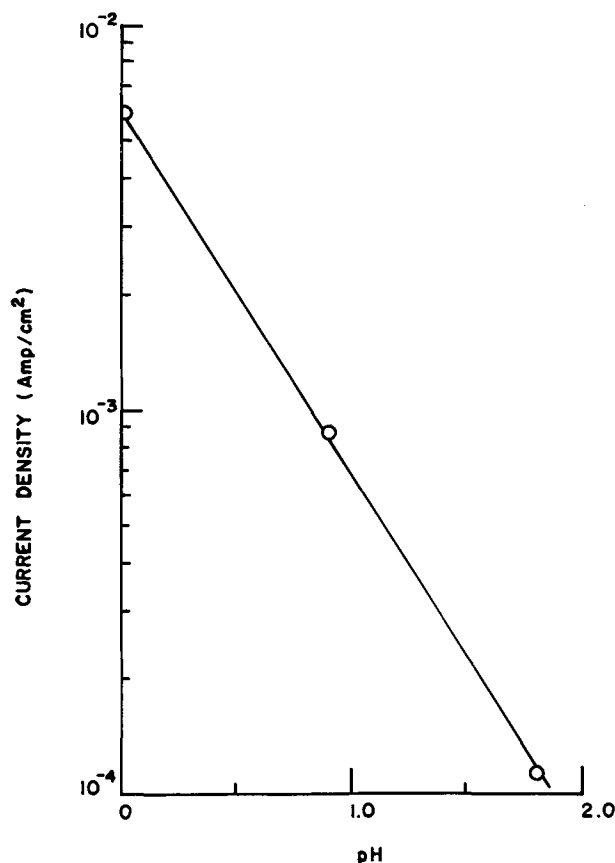


Fig. 7. Reaction order plot with respect to pH for the hydrogen evolution reaction. $\phi_c = -700$ mV.

$$i_a = k_a [\text{OH}^-]^{0.6} [\text{Cl}^-]^{0.5} \exp [0.85 \mathbf{F}\phi/RT] \quad [8]$$

$$i_c = k_c [\text{H}^+] \exp - [\mathbf{F}\phi/2RT] \quad [9]$$

$$\left(\frac{\partial \phi_{\text{corr}}}{\partial \text{pH}} \right)_{[\text{Cl}^-]} = -70 \text{ mV/pH} \quad [10]$$

$$\left(\frac{\partial \phi_{\text{corr}}}{\partial \log [\text{Cl}^-]} \right)_{\text{pH}} = -20 \text{ mV/decade} \quad [11]$$

$$\left(\frac{\partial \log i_{\text{corr}}}{\partial \text{pH}} \right)_{[\text{Cl}^-]} = -0.4 \quad [12]$$

$$\left(\frac{\partial \log i_{\text{corr}}}{\partial \log [\text{Cl}^-]} \right)_{\text{pH}} = 0.3 \quad [13]$$

The rate expression for the hydrogen evolution reaction (Eq. [9]) is in accord with the work of Bockris (17) and Kelly (18) and is consistent with a mechanism in which the discharge step is rate controlling.

The anodic Tafel slope of 70 mV/decade obtained in this study is comparable to the values reported by Foroulis (19), Stern and Roth (20), and Smialowska and Dus (21) for iron in acidic chloride solutions. On the other hand, Hurlen (22) reported 30 mV/decade for iron in 1N HCl, Podesta and Arvia (23) obtained values ranging from 37 to 61 mV/decade for iron in 2N NaCl (pH 1.78-2.73) and Felloni (15) reported values ranging from 44 to 70 mV/decade for iron in 1N (HCl + NaCl). Foroulis (19) has attributed the difference in anodic Tafel slopes obtained by various workers to the differences in chloride ion concentrations and the experimental techniques used.

The corrosion potential behavior of iron in deoxygenated HCl-NaCl systems in this study are fairly consistent with data in the literature. For deoxygenated 1N HCl, Foroulis (19) reported -460 mV, Felloni (15) -466, and Cammarota *et al.* (24) -494 mV. In this study, a corrosion potential of -475 mV was observed for iron in 1N HCl.

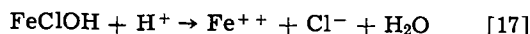
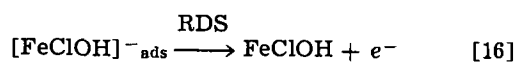
Felloni (15) reported a -51 mV change in corrosion potential with each unit change in pH. Kelly (18) found -60 mV/pH for iron in H₂SO₄ and Podesta and Arvia (23) found -62 mV/pH in both perchlorate and chloride solutions. The change in corrosion potential with pH observed in this study was -70 mV/pH.

A corrosion current density of 100 μA/cm² was obtained for iron in 1N HCl and is lower than the 400 μA/cm² reported by Hurlen (22) but higher than the 45 μA/cm² obtained by Felloni (15). For iron in 4% NaCl (pH 1.5) Stern and Roth (20) reported a corrosion current of 260 μA/cm². Podesta and Arvia (23) found that the corrosion current density was pH dependent in acidic halide media within the pH range of 0-5. They observed that

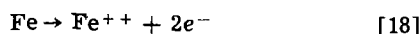
$$\left(\frac{\partial \log i_{\text{corr}}}{\partial \text{pH}} \right) = -0.5 \pm 0.1 \quad [14]$$

Bockris and co-workers (17) report approximately the same value for iron corrosion in sulfate media. The value observed by Felloni (15) for iron in acidic chloride media was -0.06. In this study $\left(\frac{\partial \log i_{\text{corr}}}{\partial \text{pH}} \right) = -0.4$.

The following mechanism is proposed for iron dissolution in deoxygenated chloride media



where the over-all reaction is



The kinetic parameters predicted by this mechanism are dependent on the adsorption behavior of the intermediate, $[\text{FeClOH}]^-_{\text{ads}}$. If the adsorbed intermediate follows Temkin adsorption behavior, the rate equations for the reaction in Eq. [15] can be written as (25)

$$r_1 = k_1 (1 - \theta) [\text{Cl}^-] \exp (\beta \mathbf{F}\phi/RT) \exp (-\gamma f\theta) \quad [19a]$$

$$r_{-1} = k_{-1} \theta [\text{H}^+] \exp [-(1 - \beta) \mathbf{F}\phi/RT] \exp [(1 - \gamma) f\theta] \quad [19b]$$

where r_1 and r_{-1} are the rates of the forward and backward reactions, respectively; θ is the surface coverage of the adsorbed intermediate; $[\text{H}^+][\text{Cl}^-]$ are the bulk concentrations of hydrogen and chloride ions; γ, β are the symmetry factors; f is the Temkin parameter; and k_1 and k_{-1} are the rate constants for the forward and backward reaction, respectively.

For Temkin adsorption, $0.2 < \theta < 0.8$. Therefore, in comparison with the exponential terms in θ (Eq. [19a] and [19b]), the variations in the $(1 - \theta)$ and θ pre-exponential terms are negligible and can be combined with the constants k_1 and k_{-1} , respectively (26). Equations [19a] and [19b] become

$$r_1 = k'_1 [\text{Cl}^-] \exp (\beta \mathbf{F}\phi/RT) \exp (-\gamma f\theta) \quad [20a]$$

and

$$r_{-1} = k'_{-1} [\text{H}^+] \exp [-(1 - \beta) \mathbf{F}\phi/RT] \exp [(1 - \gamma) f\theta] \quad [20b]$$

Within the reaction in Eq. [15] in quasi-equilibrium

$$r_1 = r_{-1} \quad [21]$$

and

$$f\theta = \ln \left\{ \frac{k'_1}{k'_{-1}} \frac{[\text{Cl}^-]}{[\text{H}^+]} \exp (\mathbf{F}\phi/RT) \right\} \quad [22]$$

The rate of the reaction in Eq. [16] can be written as

$$r_2 = k_2 \theta \exp (\alpha \mathbf{F}\phi/RT) \exp (\epsilon f\theta) \quad [23]$$

Since the pre-exponential term in θ is negligible in comparison to the exponential term (26), the rate equation can be written as

$$r_2 = k'_2 \exp (\alpha \mathbf{F}\phi/RT) \exp (\epsilon f\theta) \quad [24]$$

where α and ϵ are symmetry factors. Substituting Eq. [22] for $f\theta$ in Eq. [24] yields

$$r_2 = k'_2 \left(\frac{[\text{Cl}^-]}{[\text{H}^+]} \right)^\epsilon \exp \left[(\epsilon + \alpha) \frac{\mathbf{F}\phi}{RT} \right] \quad [25]$$

By assuming values of 1/2 for the symmetry factors, Eq. [25] can be expressed as

$$i_2 = k''_2 [\text{Cl}^-]^{0.5} [\text{OH}^-]^{0.5} \exp [\mathbf{F}\phi/RT] \quad [26]$$

Thus, the proposed mechanism predicts values of 60 mV, 0.5, and 0.5 for the anodic Tafel slope, the reaction order with respect to the chloride ion concentration, and the reaction order with respect to the hydroxyl ion concentration, respectively. These calculated values are in good agreement with the experimental data.

By setting $\phi = \phi_{\text{corr}}$ and $i_a = i_c = i_{\text{corr}}$ in the theoretical expressions for iron dissolution and hydrogen evolution the following expressions are obtained

$$\left(\frac{\partial \phi_{\text{corr}}}{\partial \text{pH}} \right)_{[\text{Cl}^-]} = -60 \text{ mV/pH}$$

$$\left(\frac{\partial \phi_{\text{corr}}}{\partial \log [\text{Cl}^-]} \right)_{\text{pH}} = -20 \text{ mV/decade}$$

$$\left(\frac{\partial \log i_{\text{corr}}}{\partial \text{pH}} \right)_{[\text{Cl}^-]} = -0.5$$

$$\left(\frac{\partial \log i_{\text{corr}}}{\partial \log [\text{Cl}^-]} \right)_{\text{pH}} = 0.2$$

These relationships agree reasonably well with the experimental results (Eq. [10] to [13]).

As shown in Fig. 1, the abrupt change in the polarization of iron in low concentrations of chloride ions at the higher potentials suggest a change in the dissolution mechanism. It should be noted that at these higher potentials the dissolution rates are sufficiently large that the measured potential must be corrected for the IR potential drop. It is surmised that two dissolution mechanisms occur simultaneously. One involves the direct participation of the chloride ions in the dissolution of iron, and the second is independent of chloride ions. At low polarization the former mechanism is dominant, but at higher polarization a dissolution mechanism such as the one proposed by Bockris (17) may be dominant.

Acknowledgment

This work was supported by a grant from the Office of Saline Water, U.S. Department of the Interior.

Manuscript submitted Jan. 6, 1972; revised manuscript received July 5, 1972.

Any discussion of this paper will appear in a Discussion Section to be published in the June 1973 JOURNAL.

REFERENCES

1. Ya. M. Kolotyrkin, *Russ. Chem. Rev.*, **31**, 160 (1962).
2. R. T. Foley, *Corrosion*, **26**, 58 (1970).
3. W. J. Lorenz, *Corrosion Sci.*, **5**, 121 (1965).
4. K. E. Heusler, *Z. Elektrochem.*, **62**, 582 (1958).
5. K. E. Heusler and G. H. Cartledge, *This Journal*, **108**, 732 (1961).
6. G. V. Golovina, G. M. Florianovich, and Ya. M. Kolotyrkin, *Zashchita Metallov*, **2**, 41 (1966).
7. G. M. Florianovich, L. A. Sokolova, and Ya. M. Kolotyrkin, *Electrochim. Acta.*, **12**, 879 (1967).
8. W. J. Lorenz, G. Eichkorn, and C. Meyer, *Corrosion Sci.*, **7**, 359 (1967).
9. N. Hackerman and S. J. Stephens, *J. Phys. Chem.*, **58**, 904 (1954).
10. V. P. Maksimchuk and I. L. Rosenfeld, *Doklady Akad. Nauk SSSR*, **131**, 354 (1960).
11. T. Murakawa, T. Kato, S. Nagaura, and N. Hackerman, *Corrosion Sci.*, **7**, 657 (1967).
12. F. A. Cotton and G. Wilkinson, "Advanced Inorganic Chemistry," 2nd ed., Interscience, New York (1967).
13. R. J. Chin, Ph.D. Dissertation, UCLA, September, 1971.
14. D. A. MacInnes, "The Principles of Electrochemistry," Dover Publications, New York (1961).
15. L. Felloni, *Corrosion Sci.*, **8**, 133 (1968).
16. H. Lorenz, H. Yamaoka, and H. Fischer, *Ber Bunsenges, Phys. Chem.*, **67**, 932 (1963).
17. J. O'M. Bockris, D. Drazic, and R. Despic, *Electrochim. Acta*, **4**, 325 (1961).
18. E. J. Kelly, *This Journal*, **112**, 124 (1965).
19. Z. Foroulis, *ibid.*, **113**, 532 (1966).
20. M. Stern and R. M. Roth, *ibid.*, **104**, 390 (1957).
21. A. Szaklarska-Smialowska and B. Dus, *Corrosion*, **23**, 130 (1967).
22. T. Hurlen, *Acta Chem. Scand.*, **14**, 1533 (1960).
23. J. J. Podesta and A. J. Arvia, *Electrochim. Acta*, **10**, 171 (1965).
24. C. P. Cammarota, L. Felloni, G. Palmgarini, and S. Sostero, *Corrosion*, **26**, 129 (1970).
25. E. Gileadi and B. E. Conway, "Modern Aspects of Electrochemistry," Vol. 3, J. O'M. Bockris and B. E. Conway, Editors, Butterworths, London (1964).
26. R. Parsons, *Trans. Faraday Soc.*, **54**, 1053 (1957).

The Morphological Changes of Low Index Planes of Copper Single-Crystal Electrodes near Equilibrium

V. Markovac*

Scientific Research Staff, Ford Motor Company, Dearborn, Michigan 48121

ABSTRACT

The behavior of low index planes of copper single-crystal electrodes, simultaneously exposed to deaerated and pre-equilibrated acidic copper sulfate solution, has been studied. The surface topographies indicated that a small net dissolution reaction occurred, due to traces of oxygen present in the experimental system, in spite of all the purification steps applied. Potential differences between electrodes were within 1 mV. A low rate dissolution reaction occurred everywhere on the exposed surfaces of all specimens, but the extent of dissolution varied over the surface of the same specimen, indicating considerable heterogeneity of the metal crystal surfaces. The surface features formed during dissolution on all electrodes, like grooves, pyramidal pits, macro ledges, hillocks, etc., are consistently bounded by the {210}, {111}, and {100} planes. The application of Batterman's stability conditions indicates that these planes are slow dissolving and stable, under present experimental conditions. The crystallographic characteristics of these planes, in relation to the process of dissolution, are discussed. Mechanisms of formation of these surface features are proposed utilizing the terrace-ledge-kink model for metal crystal dissolution, and considering the effects of crystallographic structure, surface imperfections, and adsorbed inhibiting species on the step motion over the surface, for the given rate of dissolution.

The work of Jenkins and Bertocci showed that under conditions of "true equilibrium," in acidic copper sulfate solution, no copper single crystal orientation spontaneously changed with time (1). Also, no differences in equilibrium potentials could be measured between different orientations, within their limits of

experimental accuracy of less than 1 mV (2). When air was permitted to leak into the system, the existing equilibrium was destroyed and dissolution of copper occurred (3). This resulted in potential differences arising between differently oriented copper single-crystal electrodes and produced morphological changes on the electrode surfaces.

Under the experimental conditions employed in this work, true equilibrium was not attained. Very prob-

* Electrochemical Society Active Member.
Key words: dissolution, crystallographic planes, motion of steps, adsorption, inhibiting species.

ably due to some last trace of oxygen, net dissolution currents of about $1 \mu\text{A}/\text{cm}^2$ or less were present. Since the exchange current densities for copper single crystals in the corresponding solution are of the order of magnitude of mA/cm^2 (4), it seems reasonable to conclude that the electrodes were very near to the equilibrium state.

In this work it has been demonstrated that a low rate dissolution of copper occurred everywhere on the exposed surfaces of all three low index planes of copper single-crystal electrodes, even though the system was only slightly displaced from equilibrium, exhibiting potential differences of less than 1 mV between low index orientations. The very interesting morphological changes on the surfaces of all three electrodes, developed during dissolution, will be discussed. It has been recognized that a study of morphological changes can be very helpful in the understanding of mechanisms of metal crystal dissolution. The experimental results show that the {210}, {111}, and {100} planes limit the surface features formed during dissolution on the low index copper single-crystal electrodes. The application of the Batterman-Irving stability conditions (5, 6) indicates that these planes are slow dissolving and stable. The mechanisms of formation of these surface features can be explained using the terrace-ledge-kink model for a crystal surface of Kossel (7) and Stranski (8) in which the nearest-neighbor atomic interaction is assumed. The effects of crystallographic structure, surface imperfections, and adsorbed inhibiting species on the motion of dissolution steps are also considered.

Experimental

Materials.—The high purity MARZ grade¹ single-crystal electrodes, used in these studies, were disk shaped, diameter 20 mm and thickness 10 mm, and cut parallel to the (111), (100), and (110) planes. The crystals were first mechanically polished with emery papers through to 600, and then with 0.3 and 0.05μ alumina. Finally, the crystals were electropolished in a copper-containing phosphoric acid electrolyte [60 weight per cent (w/o) H_3PO_4]. Electropolishing was carried out at a constant voltage of 1.75V, and a high-purity copper sheet served as the cathode. After ~ 60 min, the upper layer of the specimen surface, damaged by mechanical polishing, was removed and a smooth, very bright finish was obtained. In order to remove traces of phosphate film, immediately after electropolishing the crystal was rinsed with distilled water, immersed in 10% solution of phosphoric acid, washed in a stream of distilled water, rinsed successively in ethyl alcohol, and dried with a jet of pure oxygen (9, 10). The general orientation of the electropolished copper single-crystal electrodes was determined by Laue back-reflection x-ray diffraction. The misorientation was determined with a Picker Diffractometer, and the average deviation was found to be $\pm 0.5^\circ$ from the exact low index planes. The average dislocation density, in the crystals prepared in this manner, was $\sim 5 \times 10^6 \text{ cm}^{-2}$. The dislocation density of copper single crystals was determined by etching in Livingston's etchant (11).

The acidic 0.25M CuSO_4 solution, used in these studies, was prepared by dissolving the twice-recrystallized copper sulfate in triply distilled water, and the analytical reagent grade sulfuric acid was added in order to obtain a 0.1M solution with respect to H_2SO_4 . The solution was pre-equilibrated in the storage vessel by immersion of MARZ grade spectrographically pure copper wire, and deaerated by passing

¹ The MARZ grade, 99.999%, copper single crystals were obtained from the Materials Research Corporation, Orangeburg, New York. Typical mass spectrographic analysis for this material shows the following main impurities: Zn = 5, Al = 2, O = 1.3, S = 1, Mo < 5, K < 1, Ni < 1, P < 1, Pd < 1, Sn < 1, V < 1, H < 0.6, Ca < 0.7, Fe < 0.7, Mg < 0.5, Mn < 0.5, Na < 0.5, Ta < 0.5, Rare Earths < 1 ppm by weight.

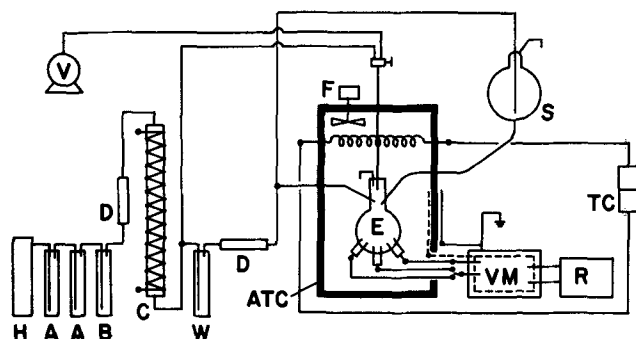


Fig. 1. Schematic diagram of apparatus: H, hydrogen tank; A, washing bottle with Fieser's solution; B, washing bottle with H_2SO_4 ; D, drop collector; C, column with active copper; W, washing bottle with H_2O ; ATC, air thermostat and Faraday cage; F, fan; TC, thermostatic circulator; E, electrochemical cell; S, storage vessel; V, vacuum system; VM, voltmeter; R, chart recorder.

ultra high purity hydrogen through it for at least 1 month (12).

Apparatus.—The experimental apparatus, shown in Fig. 1, consisted of an electrochemical cell with storage vessel, hydrogen purification unit, and electrical equipment.

The modified² tripod-type electrochemical cell was similar to the one used by Jenkins and Bertocci (1). The cell was placed in an air thermostat, supplied with an outside thermostatic circulator, surrounded by a Faraday cage, and maintained at $23^\circ \pm 0.1^\circ\text{C}$. The electropolished copper single-crystal electrodes were mounted in the "legs" of the tripod cell, so that in each leg only one low index surface of disk-shaped electrode was exposed to the solution. The legs of the tripod cell were symmetrically positioned. The storage vessel of 5 liters capacity was connected with the cell via a glass tube provided with 2 three-way solution lubricated stopcocks. The system was made of Pyrex glass. All taper joints and stopcocks were precision high vacuum grade, and those which were not in contact with solution, were greased with Apiezon N vacuum stopcock grease. The system was provided with a vacuum pump for the evacuation of the cell.

The solutions in the cell and the storage vessel were kept under a stream of moist highly purified hydrogen. The UHP tank hydrogen, with an oxygen content of less than 1 ppm, was further purified by passing through two washing bottles filled with Fieser's solution (13) and a column filled with active copper spread on infusorial earth maintained at 205°C (14).

The potential differences between electrodes were measured by a high input impedance differential voltmeter, Hewlett-Packard Model 740B, and recorded by the Cleveite Brush Mark 250 chart recorder. The accuracy of voltage measurements was $\pm 5 \mu\text{V}$.

Procedure.—The three freshly electropolished low index copper single-crystal electrodes were mounted in the cell, and the assembly was connected to the lines of solution, hydrogen, and vacuum as shown in Fig. 1. Before the introduction of solution, the cell was repeatedly evacuated and flushed with dry hydrogen at least 20 times. The first amount of solution (~ 200 ml), which was passed through the connecting tube between the storage vessel and the cell, was discarded via the three-way stopcock on the cell. After that, the solution was admitted into the cell, and the potential differences between the electrodes were continuously measured during 500 hr, which was the duration of a typical experimental run.

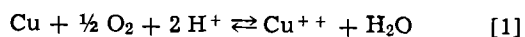
After the experiment, the surfaces of all specimens were investigated microscopically. In all cases where

² In order to reduce the number of possible leaks (faulty seals), the glass electrode and the side port with the sealed platinum wire (1) were omitted from this cell.

surface features were large enough, the surface morphology was studied by optical microscopy. Orientations of revealed surface facets were determined with the Unitron two-circle microgoniometer Model GM-5. Details of these surface features were studied by electron microscopy using parlodion replicas and a carbon film substrate shadowed with platinum at an angle of 45° to the plane of the surface. In some instances, where additional information about the inclination of fine facets was desired, the replicas were platinum shadowed at angles of 10°, 15°, 20°, and 30°. Occasionally, inclinations were also calculated from the variations in emulsion density of the shadowed replica micrograph plates. Densitometry was performed by a double-beam recording microdensitometer Model MK IIC, Joyce, Loebel and Company, Limited. The ledge heights were determined by measurement of the shadowed replicas, using the shadows cast by polystyrene spheres of 0.250μ as reference. The dissolution rates were calculated on the basis of all material removed from the electrode surfaces.

Results

After the experiment, the surfaces of all specimens were slightly etched, indicating that the small net dissolution of copper occurred, and suggesting that the true equilibrium was not attained. The potential differences between low index copper single-crystal electrodes, measured in these studies, were within 1 mV. The potential of the (100) electrode was always positive or anodic in relation to those of the (110) and (111) electrodes, and this is in agreement with the observations of other authors, for nonequilibrium conditions (1). The slight dissolution of copper was attributed to traces of oxygen present in the experimental system (1), in spite of all purification steps applied and efforts made to isolate the system from the air. The dissolution of copper can be described by a general corrosion reaction (3)



The rate of dissolution depends on the diffusion of oxidizing species, through the solution to the metal surface (3, 12). Therefore, the rate of dissolution on all electrodes should be the same (15). Although dissolution of copper occurred everywhere on the exposed surfaces of all electrodes, the extent of dissolution was different on different areas of the same electrode, indicating considerable heterogeneity of the metal crystal surfaces. However, different surface features characteristic for the particular crystal planes were formed during dissolution, indicating that the process of dissolution is also crystallographically affected. Obviously, measured potential differences are indicative of dissolution processes taking place on the low index planes of copper single-crystal electrodes.

The possible sources of oxygen present in these experiments are considered to be: the bulk copper crystal, copper sulfate solution, hydrogen gas, adsorption on the walls of the cell, and leakage of air into the system. Since it was not possible to avoid this problem by improved experimental conditions, it seems that the oxygen adsorbed on the walls of the cell is the most probable cause of dissolution (system was not bakeable). However, small contributions from the other possible sources cannot be entirely excluded.

The effect of adsorbed contaminants on the formation of pits on the (111) plane.—Under the corrosion conditions at the highest rate encountered, calculated to be about $1 \mu\text{A}/\text{cm}^2$, randomly distributed macro pits were observed on the (111) specimen surface. The shape of the pits was an inverse triangular pyramid with the edges of the base parallel to the $\langle 112 \rangle$ directions (Fig. 2a). The pit density was $\sim 10^2 \text{ cm}^{-2}$, about four orders of magnitude less than the measured dislocation density for this specimen, indicating that

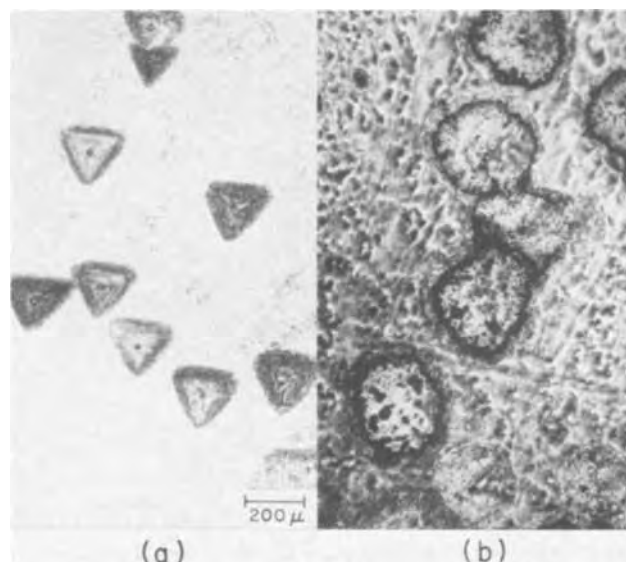


Fig. 2. Effect of surface adsorbed contaminants on pit formation on the (111) plane: (a) decreased amount of surface adsorbed contaminants; (b) increased surface contamination.

only a fraction of the existing dislocations were revealed during dissolution under these experimental conditions (16-18). In this experiment a liquid nitrogen trap was used in order to prevent appreciable back-streaming of oil vapor from the vacuum pump to the cell, during repeated evacuation and hydrogen flushing, before the introduction of solution into the cell.

To demonstrate the effect of surface adsorbed contaminants, another experiment was performed on the freshly prepared surface of the same crystal. The same experimental conditions were employed, but without the liquid nitrogen trap, allowing the hydrocarbon molecules, from the back-streaming oil vapor, to enter the cell and adsorb on the specimen surface (19). As a vacuum source a Welch pump Model 1400 with a Duo-Seal pump oil, supplied by the Welch Scientific Company, Skokie, Illinois, was used.

After the experiment, only rounded pits were observed, as shown in Fig. 2b. The formation of triangular pits, under the conditions of decreased amount of surface adsorbed contaminants, and rounded pits with increased surface contamination, indicate that in the presence of a greater amount of contaminants the anisotropic motion of dissolution steps become isotropic (20-22). The rounding of pyramidal pits, at increased inhibitor concentration, was studied extensively by Ives *et al.* (21, 23) in the system lithium fluoride-aqueous solution of ferric chloride. After giving up the diffusion-control hypothesis, Ives postulated that increased concentration of adsorbed inhibitors stabilizes the large number of monatomic steps (23). Based on the works of Burton *et al.* (24) and Keller (23), Ives concluded that for monatomic steps the stable configuration is rounded. Hence, pyramidal pits become rounded and finally attain conical shape. To the author's knowledge, the mechanism of rounding of triangular pits on copper single crystals has not been discussed hitherto. Although Ives' explanation for lithium fluoride seems suitable, it is believed that more experimental evidence for copper single crystals would be desirable.

In these experiments a large number of hillocks were observed on the specimen surface (Fig. 2). The surface between pits and hillocks was generally smooth and covered with a large number of more or less resolvable steps (ledges). Under the conditions of decreased surface contamination, both hillocks and ledges appear to be more crystallographic than in the

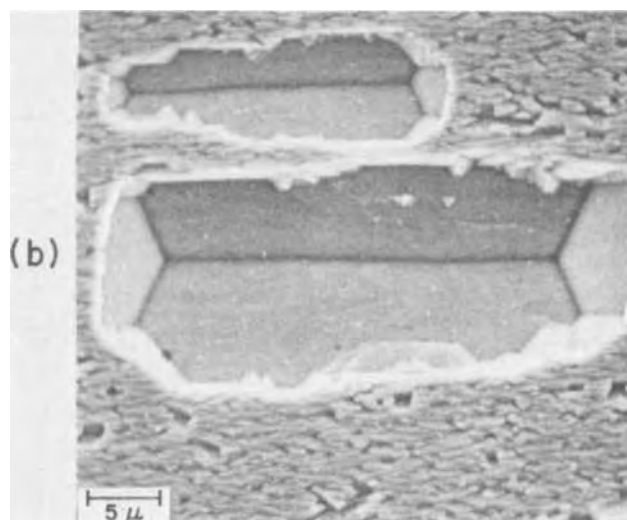
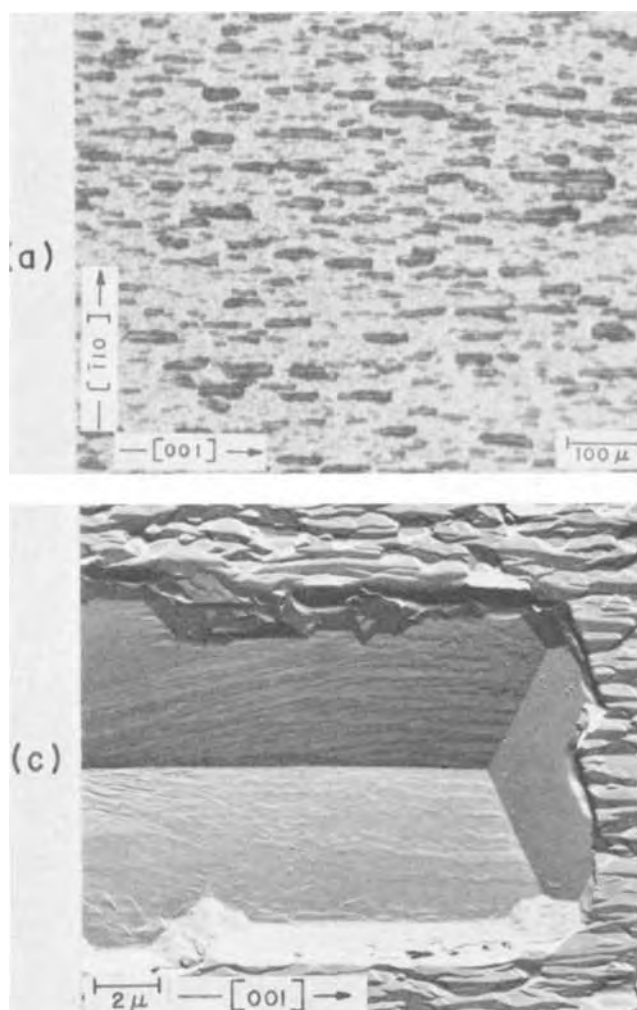


Fig. 3. (a) Photomicrograph of grooves formed during dissolution on the (110) plane; (b) scanning electron micrograph of a groove showing two side faces and two "closing" facets; (c) electron micrograph showing the details of the groove facets and the "ridge and valley" structure on the rest of the surface.

case of greater contamination (19). The characteristics of these surface features will be discussed later.

In all subsequent experiments the oil pump was replaced by other vacuum sources, not containing oil (e.g., water aspirator). Nevertheless, experimental results still indicate the presence of some surface adsorbed species, although in much smaller quantities, suggesting other possible sources of inhibiting particles, like the copper sulfate solution, and the bulk crystals.

The formation of grooves on the (110) electrode.—In all subsequent experiments the three low index copper single-crystal electrodes were simultaneously exposed to the solution, at corrosion rates calculated to be $\sim 0.5 \mu\text{A}/\text{cm}^2$ or less. After the experiment, the surface of the (110) electrode was partially covered by big grooves which were all aligned parallel to the $\langle 100 \rangle$ direction (Fig. 3a). The grooves were bounded by two large side faces parallel to the same $\langle 100 \rangle$ direction (Fig. 3b). On the groove side faces arrays of fine ledges parallel approximately to the $\langle 100 \rangle$ direction were always observed (Fig. 3c). In contrast, the groove's closing facets were always ledge free and very smooth. Between the big grooves a large number of smaller, less well-developed grooves or a "ridge and valley" structure were observed, which were also aligned parallel to the $\langle 100 \rangle$ direction.

Since some of the grooves were reasonably regular, the crystallographic information on side faces and facets could be obtained utilizing simple geometric analysis (Fig. 4). The side faces of 24 measured grooves show a mean slope of 18.1° , toward the original (110) plane, and a mean deviation of -0.3° from the theoretical (210) plane, which is at an angle of 18.4° . The width of the grooves was in the range of $8\text{--}26 \mu$. Although the side faces of experimentally obtained

grooves are slightly terraced, it may be concluded that their mean slopes still indicate that they correspond to the $\{210\}$ planes (26). The measured mean inclination of the smooth facets at the ends of grooves was 35.1° , with a deviation of only -0.2° from the theoretical (111) plane, which should be at 35.3° . Hence, it seems reasonable to assume that the smooth "closing" facets of grooves correspond to the low index $\{111\}$ planes.

The "ridge and valley" structure between big grooves (Fig. 3c) appears to be composed of facets similar to those of the big grooves, but they do not attain sufficient size very probably due to lack of a constant dissolution source (27).

The formation of pyramidal pits on the (100) electrode.—Under the same conditions, under which the

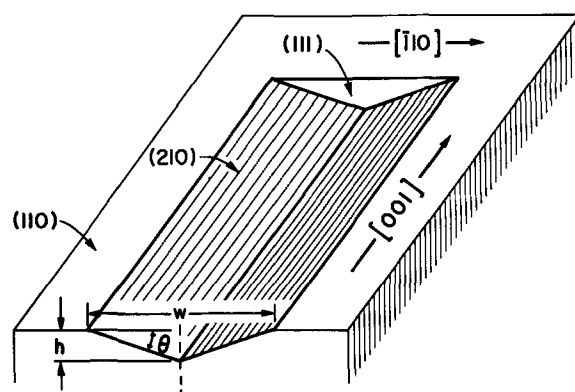


Fig. 4. Schematic presentation of profile and perspective view of a groove developed on the (110) plane.

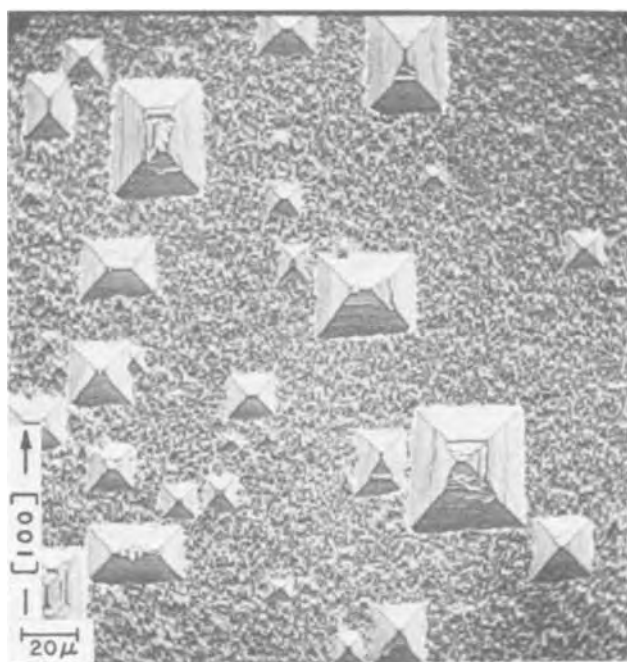


Fig. 5. Scanning electron micrograph of pits developed on the (100) plane.

big grooves were formed on the (110) electrode, on the surface of the (100) electrode randomly distributed, crystallographically well-defined etch pits were observed. The pits have the shape of an inverse rectangular pyramid with the base edges always parallel to one of the $\langle 100 \rangle$ directions (Fig. 5). The density of

pyramidal pits was $\sim 10^3 \text{ cm}^{-2}$, i.e., about 3-4 orders of magnitude less than the average dislocation density for these crystals. Besides regular square pyramids, pits with the shape of truncated and extended pyramids were also observed. Details of these pyramidal pits are shown in Fig. 6. On the side faces of these pyramidal pits, arrays of fine ledges parallel approximately to the $\langle 100 \rangle$ direction were always observed. Truncated pyramidal pits observed in these studies are sometimes very shallow, with large flat bottoms; but sometimes they are almost complete pyramids, lacking only the apex. The rest of the surface, between pyramidal pits, is covered with tiny facets (Fig. 6), which look similar to those of the pyramidal pits; but they do not attain macro size, again probably due to the lack of constant dissolution source. At the bottom of these facets, a horizontal plane parallel to the original $\{100\}$ surface is frequently revealed.

A schematic presentation of pyramidal pits developed on the (100) electrode during dissolution is shown in Fig. 7. The regular shape of these pits offers crystallographic information about the pit side faces. The measurement of 75 experimentally obtained pyramidal pits (regular, truncated, and extended) shows the mean inclination of their side faces to be 27.4° . The range of widths of these pits was $8\text{-}28\mu$. Since the theoretical (210) plane forms an angle of 26.6° with the original (100) plane, it may be concluded that the sides of pyramidal pits correspond to the $\{210\}$ planes. Accordingly, they are the same planes which were noted after dissolution of the (110) electrode (Fig. 4). The ball model of a square-based pyramidal pit developed on the (100) plane is shown in Fig. 8.

The formation of macro steps and hillocks on the (111) electrode.—Although all three electrodes, the (110), (100), and (111), were simultaneously exposed

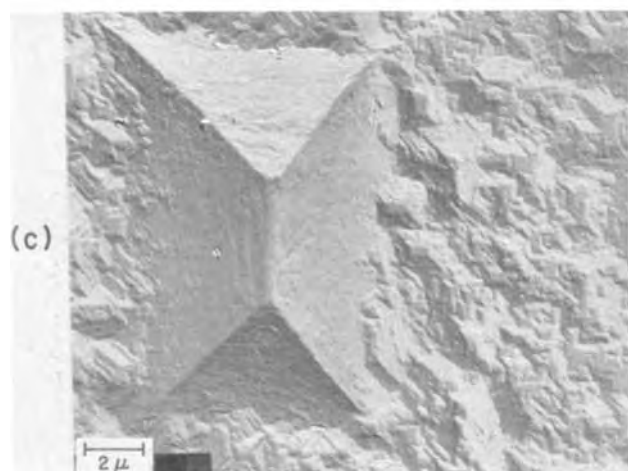
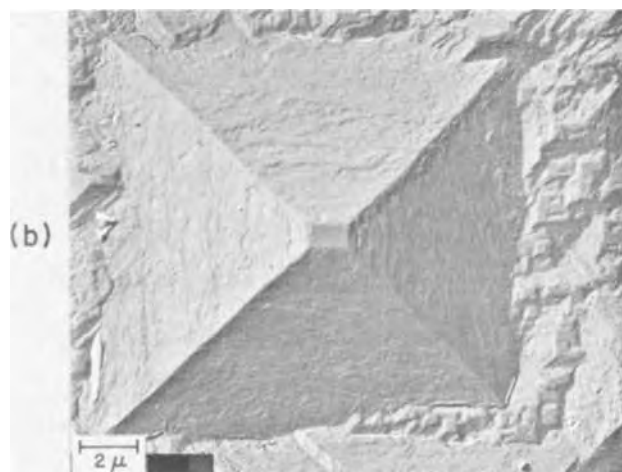
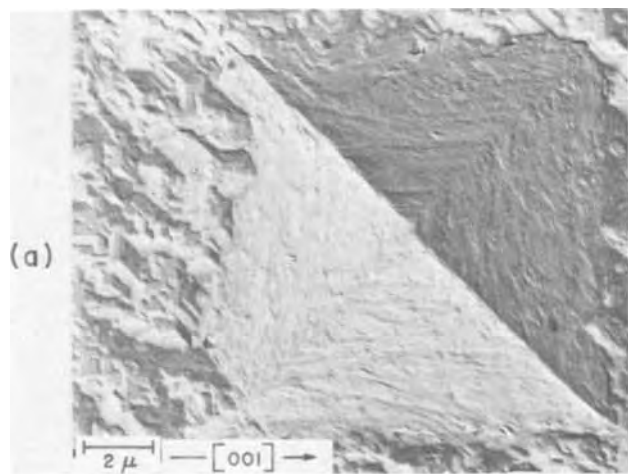


Fig. 6. Electron micrographs of pyramidal pits formed during dissolution on the (100) plane: (a) simple pyramidal pit; (b) truncated pyramidal pit; (c) extended pyramidal pit. Arrow indicates the crystallographic direction for all three micrographs.

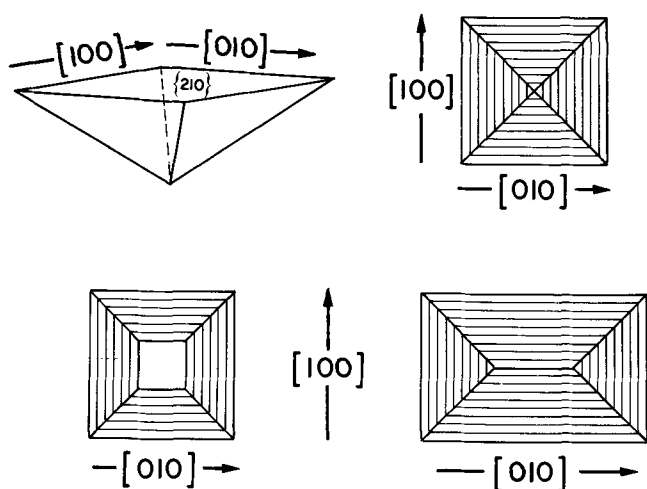


Fig. 7. Schematic presentation of pyramidal pits formed during dissolution on the (100) plane.

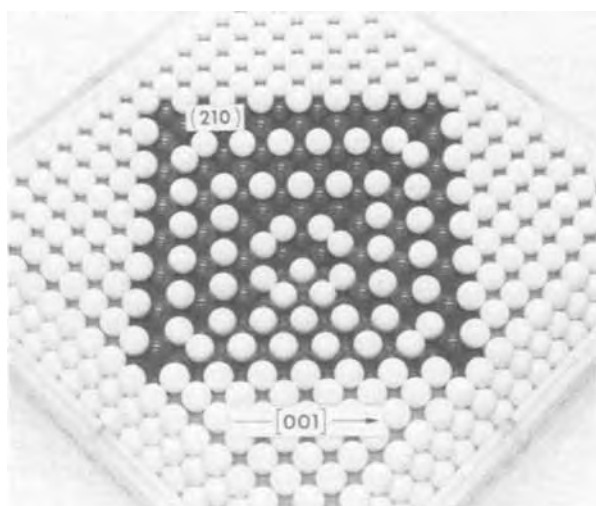


Fig. 8. Ball model of a square-based pyramidal pit developed on the (100) plane. The light balls in the {210} planes represent kink atoms.

to solution, no grooves or pits were observed on the (111) electrode; only macro steps (ledges) and hillocks were found on this surface. The dissolution steps visible on the electron micrograph, shown in Fig. 9a, have the fronts rather irregularly shaped with the height ranging from 200Å up. Frequently, the hillock concentration is larger in the vicinity of the step fronts than on the terraces. The size of hillocks is in the range from several hundred angstroms up to a few microns. A detailed picture of hillocks is shown in Fig. 9b. Very often, hillocks have the shape of hexagonal pyramids, but some of them clearly resemble their triangular origin and look like triangular pyramids with three small additional facets developed on the corners at the pyramid base (Fig. 9b). The edges at the base of pyramidal hillocks are parallel to one of the $\langle 112 \rangle$ directions which lie in the (111) plane. A few hillocks have the shape of extended pyramids (Fig. 9b) which consist of two half pyramids with their apexes connected by a line parallel to one of the $\langle 112 \rangle$ directions. Between hillocks and large macro steps (Fig. 9b and c), a smooth ledge-free surface, parallel to the original surface, and corresponding to the low index (111) plane, is revealed during dissolution.

On some parts of the specimen surface the steps were very large, up to several microns (Fig. 9b and c). These steps look quite crystallographic and clearly

present threefold symmetry. The fronts of macro steps or macro ledges look like high index planes having fine ledges similar to those already observed at the sides of grooves and pyramidal pits on the (110) and (100) electrodes, respectively. The mean inclination of 10 experimentally obtained macro ledges was 39.0° , which is in good agreement with the theoretical (210) plane, which should be at 39.2° . The straight edges at the base of macro ledges were nearly parallel to the $\langle 112 \rangle$ directions, and the measured angles between them were in the range of 115° - 125° . On the ground of these experimental results, it was possible to construct the model which may correspond to the planes revealed during dissolution. On the ball model shown in Fig. 10, the (210) and (120) planes are presented as a possible set of planes developed during dissolution. The angle between edges at the base is 120° , in agreement with the values found experimentally. The base is, of course, the low index (111) plane. The appearance of the {210} planes as limiting planes of surface features formed during dissolution of copper single-crystal electrodes is in agreement with Jenkins' observation of "extensive faceting with near {012} orientations," under similar experimental conditions (3).

Discussion

The stability of planes revealed by dissolution.—The stabilization of planes revealed during dissolution can be demonstrated utilizing the conditions for the occurrence and stability of etch hillocks and pits developed by Batterman (5) and extended by Irving (6). Detailed atomic dissolution mechanisms are not considered in this approach, and the dissolution rate is regarded as a vector property of a macroscopic surface. In general, the Batterman stability conditions show that, upon dissolution, convex surfaces are limited by fast dissolving planes, while concave surfaces are limited by slow dissolving planes.

The application of these conditions to the grooves, pyramidal pits, and macro ledges observed on the (110), (100), and (111) electrodes respectively (Fig. 3c, 6a, 9c) shows that all orientations between limiting {210} planes are faster dissolving planes. The same applies for the range of orientations between the low index {111} planes and the groove side faces (Fig. 3c and 4), and between macro ledges and revealed basic {111} planes (Fig. 9c and 10). All these planes should be the faster dissolving ones. Accordingly, the {210} and {111} planes are slowly dissolving planes.

For the application of the stability conditions on the pyramidal pits formed on the (100) electrode (Fig. 5 and 6), it has to be emphasized that the formation of pyramidal pits has been related to active sites³ on the electrode surface. These active sites are characterized by an increase in the local dissolution rate. At the apex of a pit a high dissolution rate is predicted, and this is the direction of the enhanced dissolution rate, say, due to a dislocation. If, for any reason, pyramidal pits lose their dislocations (28) or the other causes of enhancement of dissolution rate (29), they will become truncated, revealing the {100} plane (Fig. 6b). The tendency of newly revealed bottoms of truncated pyramidal pits toward widening, and the appearance of the {100} flats on the faceted rest of the surface (Fig. 6) suggest that the actual dissolution rate of the {100} plane is probably slower than the rate for contiguous facets.

The extended pyramidal pits observed on the (100) electrode (Fig. 6c) consist of two half pyramids with their apexes connected by a line which is always parallel to the one of the $\langle 100 \rangle$ directions. The stable square-based pyramidal pit should have the same dissolution rate on all faces. The appearance of extended pyramidal pits suggests a slight difference in

³ In order to form observable macro pits, the active sites should have some continuity into the bulk crystal, e.g., dislocations or rod-shaped impurity zones (26).

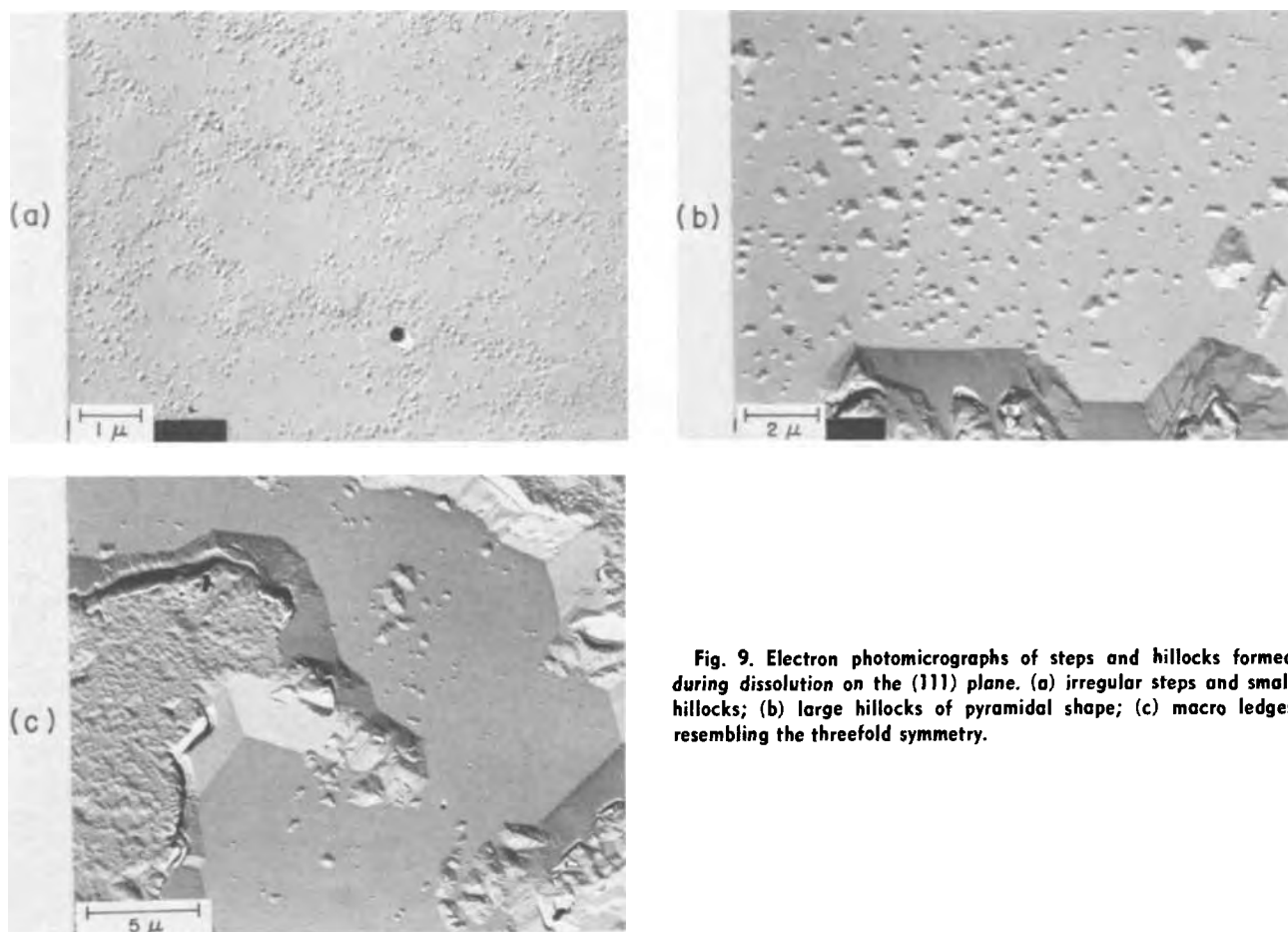


Fig. 9. Electron photomicrographs of steps and hillocks formed during dissolution on the (111) plane. (a) irregular steps and small hillocks; (b) large hillocks of pyramidal shape; (c) macro ledges resembling the threefold symmetry.

dissolution rate between two pairs of side faces on the same pit, exhibiting the extension line between the faster dissolving planes. The mechanism by which one pair of planes dissolves faster than the other, crystallographically equivalent pair of planes is not yet understood.

The application of the stability conditions to the hillocks formed on the (111) electrode indicates that all orientations between the hillock's faces and the basic (111) plane are faster dissolving ones (Fig. 9b). At the same time the orientations between neighboring hillock faces should be the slowly dissolving planes. The trend toward widening and revealing of large areas of smooth, close-packed, low index (111) planes (Fig. 9b and 9c) suggests that these planes dissolve slower than the bounding macro ledges and hillock faces. This observation looks contradictory, because the Batterman stability conditions predict that the hillock planes should dissolve slower than the sur-

rounding crystal surface. In order to explain this phenomenon, one may assume that on the original electropolished surface of the (111) electrode there are a large number of active sites (see later), where locally enhanced dissolution takes place, very probably in a step-wise manner. This process shall continue until the real (111) flats are revealed, and the macro ledges are formed (Fig. 9b and 9c). At this stage, it seems likely that most of the dissolution reaction takes place at the macro ledges (38) which may "grow together," forming the hillocks, as a transient form in the process of dissolution. These ideas are supported by the fact that hillocks are observed only on the (111) electrode, they cover a wide range of sizes, their side faces look the same or similar to macro ledges, and their apexes are fairly sharp. The occurrence of extended hillocks indicates that a pair of slightly faster dissolving planes exist, forming a ridge between them (6).

The experimental results presented here show that the {210}, {111}, and {100} planes consistently limit the surface features formed during dissolution on the low index copper single-crystal electrodes. The application of Batterman's stability conditions to these surface features indicates that the {111}, {100}, and {210} planes are slowly dissolving and stable planes, under present experimental conditions.

The atomistic characteristics of planes revealed by dissolution.—In the previous paragraph, the dissolution rate of a crystal surface was regarded as a function of orientation. Here, an attempt is made to elucidate the characteristics of revealed planes, utilizing the well-known terrace-ledge-kink model for a crystal surface of Kossel (7) and Stranski (8), in which the nearest-neighbor atomic interaction is assumed.

It was experimentally established that surface features like grooves and pyramidal pits formed during dissolution on the surfaces of the (110) and (100)

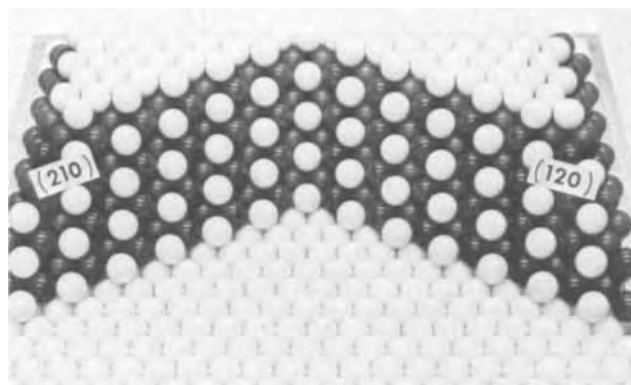


Fig. 10. Ball model of a set of two {210} planes formed on the (111) plane. The light balls in the {210} planes represent kink atoms.

electrodes, respectively, have the edges parallel to the $\langle 100 \rangle$ directions (Fig. 3 and 5). Due to the fact that the steps parallel to the $\langle 100 \rangle$ directions, in fcc crystals, are not parallel to the close-packed directions, they necessarily must be kinked. Actually, the $\langle 100 \rangle$ oriented steps are so heavily kinked that every second atom in the step is a kink atom, as can be seen in Fig. 8 and 11. The same applies for the macro ledges, parallel to the $\langle 112 \rangle$ directions, formed on the surface of the (111) electrode (Fig. 9c and 10). Here, the kink motion as a concept is not applicable (there is no length of step between kinks, along which they can move), and the only process for dissolution is the "step motion" by the successive removal of atoms at the salient corners of the kinked step (30). The $\{210\}$ plane consists of a large number of kinked steps with a small step spacing, i.e., it necessarily contains a high concentration of kinks, and therefore is a highly roughened orientation (31).

The appearance of the $\{210\}$ planes as relatively stable planes observed on the surfaces of all three low index copper single-crystal electrodes suggests a preferential adsorption of inhibiting species,⁴ from the solution, on the surfaces of this orientation (26). The preferential adsorption may be attributed to some special structural attraction between the $\{210\}$ planes and adsorbed species, e.g., the "hole" arrangement between kink atoms (32), which can be seen on ball models in Fig. 8, 10, 11. In addition, the occurrence and stabilization of the kinked edges parallel to the $\langle 100 \rangle$ direction⁵ was explained by Keller (25), postulating that the velocity of a step is given by a balance between the number of atoms removed from the step and the number of atoms "trapped" into it. It was assumed that the trapping processes take place preferentially at the kinked $\langle 100 \rangle$ -step with its "re-entrant corners" rather than at the close-packed $\langle 110 \rangle$ -step. In this way, the motion of the $\langle 100 \rangle$ -step should be slowed down more than that of the close-packed $\langle 110 \rangle$ -step, and the edges parallel to the $\langle 100 \rangle$ direction could appear.

The sides of experimentally obtained grooves, pyramidal pits, and macro ledges on the (110), (100), and (111) electrodes, respectively, were covered with arrays of fine ledges (Fig. 3c, 6, and 9c); and the measured inclinations of these faces, corresponding to the $\{210\}$ planes, are considered the average values. Although the real surfaces of these features are not identical to those of the ideal ball model, it is likely that, on the average, they represent kink stepped arrangements similar to those on the ball models, seen

⁴ Inhibiting species adsorbed on the electrode surface can be impurities and/or components from the solution.

⁵ K. W. Keller (25) studied the evaporation of ionic crystals of sodium chloride, where the $\langle 100 \rangle$ direction is the close-packed direction, and the $\langle 110 \rangle$ is the kinked one. In metallic fcc crystals the situation is reversed.

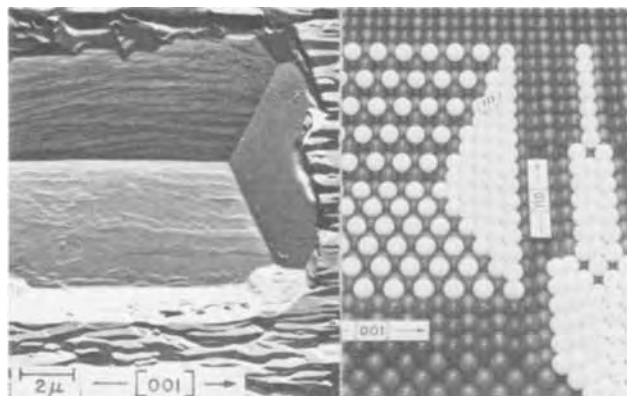


Fig. 11. Left: Electron micrograph of part of a groove formed on the (110) plane. Right: The same feature is presented on a ball model.

in Fig. 8, 10, and 11. The formation of arrays of ledges or terracing has been related to the kinetics of monatomic step motion which under certain conditions, like adsorption of inhibiting species and/or impurities, may lead to step bunching and formation of visible surface ledges (26, 33-35). This experimental fact also supports the idea of adsorption of inhibiting species on the electrode surface.

It is interesting to note that the (111) planes revealed during dissolution on the (110) and (111) electrodes (Fig. 3c, 4, 9), as well as the (100) planes at the bottom of truncated pyramidal pits and the faceted rest of the surface, revealed on the (100) electrode (Fig. 6), were always ledge free and smooth. This experimental fact suggests that on the really low index surfaces the bunching of steps, due to the adsorption of inhibiting species, is less effective than on the $\{210\}$ planes. It is likely that the dissolution process at these low index planes proceeds via monatomic steps and/or bunched steps, but of such diminished height that they are unresolvable by electron microscopy. This is in agreement with the Cabrera and Vermilyea postulation, that the morphological changes are a result of changes in the step motion on different crystal faces, due to differences in the amount of impurities adsorbed on different faces (36).

The mechanism of the formation of surface features revealed by dissolution.—An attempt has been made to describe a possible mechanism for the formation of grooves on the surface of the (110) electrode, as shown in Fig. 11. On the left side an electron micrograph of part of a groove is shown, and on the right side the same feature is represented by a ball model with the (110) plane as the base plane. Let us assume that dissolution starts at some active sites, and on the basis of the pair-wise interaction model it is expected that it will continue along the rows of close-packed atoms, parallel to the $\langle 110 \rangle$ direction, as shown on the right side of Fig. 11. It is likely that dissolution will continue in this direction until the propagation is slowed down and eventually blocked by the accumulated contaminants or other inhibiting species at the front of dissolution steps (20, 36). This depends, of course, on the rate of dissolution for the given degree of surface contamination. In order to sustain a given dissolution rate, the process should continue in the areas of lowest adsorption density; and that is, according to Frank (33) the area where the previous step passed, "sweeping" the adsorbed impurities. Accordingly, dissolution may proceed deeper into the substrate and laterally (parallel to the $\{111\}$ plane, and also parallel to the $\langle 100 \rangle$ direction) forming the grooves and revealing the $\{111\}$ planes at their ends.

The step-wise model of metal crystal dissolution takes into consideration two aspects of formation of visible surface features (e.g., pits, etc.), outlined by Gilman *et al.* (28), Cabrera (37), and Ives *et al.* (26): first, nucleation of monatomic steps at a source; and second, the step motion away from this source. Sources of dissolution steps are mainly surface defects (e.g., dislocations) and misorientations of the actual surfaces from the low index planes. Measured dislocation densities for copper single-crystal electrodes, used in these studies, were of the order of magnitude of $\sim 10^6$ cm^{-2} . In addition, it can be shown that for a misorientation of 0.5° from the low index planes, about 10^5 monatomic steps per the length of 1 cm result on a copper crystal surface (38, 39). Also, it is very probable that the electropolishing used in this work introduces a moderate undulation of the surface, which results in an increased number of monatomic steps on the specimen surface. Consequently, it is very likely that the total number of steps, or potential dissolution sites, existing on all electrodes is large enough to sustain the low dissolution rates used in this work, and the nucleation of new steps does not

appear necessary (15). Accordingly, it seems reasonable to assume that the motion of dissolution steps (monatomic and bunched) away from their origin, rather than the step origins themselves, affect the formation of different surface features, during the dissolution of low index copper single-crystal electrodes.

The large smooth areas, corresponding to the (111) plane, revealed during dissolution on the (111) electrodes (Fig. 9) are indicative of a step-wise ledge mechanism of dissolution and suggest that the step motion across the (111) plane was able to remove material required by the given rate of dissolution. In contrast, the appearance of etch pits and fine facets on the (100) electrode (Fig. 6) suggests that the motion of steps over the (100) plane was more impeded and was not able to sustain the given dissolution rate; and therefore dissolution proceeded around more active sites (dislocations) forming the pits.

The idea of a very slow or impeded motion of dissolution steps across the surface of the (100) electrode is supported by the behavior of potential differences measured between different low index copper single-crystal electrodes, during dissolution. A typical set of potential differences between the (111) electrode and the other two low index electrodes as a function of time are presented in Fig. 12. In this case, the (111) electrode may be considered as a reference electrode. Although the absolute value of the equilibrium electrode potential was not obtained, the relations between these potential differences indicate the relations between corresponding overpotentials. Accordingly, the dissolution, or more precisely the motion of dissolution steps, on the (100) electrode proceeds at higher, more anodic, overpotentials than on the other electrodes,⁶ indicating an impeded and very slow step motion. The same pattern of higher overpotentials and "very slow and difficult" step motion, for the (100) surface was found by others, at anodic dissolution of copper single crystals in various electrolytes: chloride solution, Bertocci (40); perchlorate solution, Jenkins (38); and sulfate solution, Jenkins and Durham (39).

In the last part of the experiment an overpotential decay to a lower value was observed for the (100) electrode (Fig. 12). It seems possible that during dissolution the electrode surface and/or the adsorption on the surface change to the extent that the effect of the original structure of the (100) electrode on the process of dissolution disappears. This explanation is in accordance with the conclusion made by Jenkins (38) that once facets are developed on the surface, little reaction takes place on the areas covered by low index facets, and the surface no longer acts in a uniform manner.

⁶ It is presumed that possible differences in the active surface areas on different electrodes do not cause these differences in the measured overpotentials.

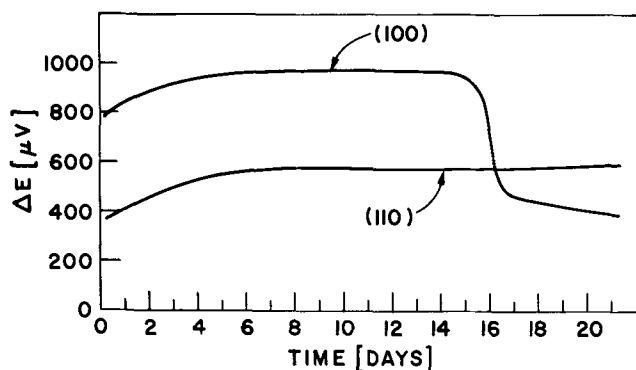


Fig. 12. Typical set of potential differences between the (111) electrode and the other two low index copper single-crystal electrodes, measured during dissolution in acidic copper sulfate solution.

The formation of pits on the (100) electrode and macro ledges on the (111) surface, when both electrodes are simultaneously exposed to dissolution, may be explained by the interaction of surface adsorbed species on the structures of the respective planes. In Fig. 13 the ball models of the monatomic dissolution steps are presented in both the (100) and the (111) planes. In both cases, the inhibiting species or contaminants of different sizes are randomly distributed. Following the very simple "nearest-neighbor" approximation, it is obvious that each species on the (100) plane is bound to 4 nearest neighbors, and on the (111) plane, to 3 nearest neighbors. Based on this, one may assume that the adsorption is stronger on the (100) plane than on the (111) surface. When a dissolution step starts at some active site and moves across the surface "sweeping" (41) and "pushing" the contaminants ahead of its front (20, 36) it is likely that it will be impeded and slowed down more on the (100) plane than on the (111). In order to sustain a given dissolution rate, the removal of material on the (100) plane continues in the areas of high activity and lowest adsorption density; and those are, according to Frank (33), the areas where the previous steps have just passed, forming the pits around active sites, forming dislocation pits. On the (111) surface the retardation of dissolution steps (monatomic and bunched) is less severe, and the step motion may remove the material required by the given rate of dissolution. Under these conditions, of course, there are no reasons for the formation of classical types of pyramidal pits on the (111) plane.

It seems likely that the dissolution step motion across crystallographically different surfaces, and the corresponding overpotentials, are affected by the adsorption of inhibiting species on these surfaces. This idea is in general agreement with the findings of Jenkins *et al.* (38, 39) that the measured overpotentials show pronounced orientation effects, but no influence of step density. According to proposed interpretations, for the given experimental conditions, it does not seem decisive for the process of dissolution how many steps are present on the surface, but rather how they are "pinned" by the adsorbed species. The observation that overpotentials for the (100) plane are higher than for other orientations, as found in various solutions (38-40), also supports this interpretation. However, the complexity of the time-dependent adsorption and its effect on dissolution processes permit, at the present time, only a qualitative treatment of these phenomena.

Conclusions

1. Under present experimental conditions the true equilibrium for copper single-crystal electrodes was not attained; instead a slight net dissolution reaction occurred, caused very probably by traces of oxygen present in the system.
2. Dissolution reaction occurred everywhere on the exposed surfaces of all specimens. The extent of dis-

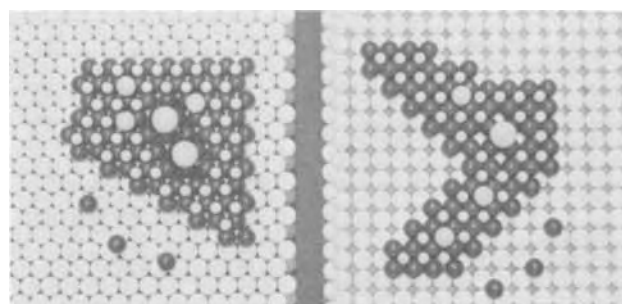


Fig. 13. Ball models of monatomic dissolution steps (dark balls) presented on the (111) plane (left), and on the (100) plane (right). Light balls on the upper layers represent adsorbed inhibiting species.

solution was different on different areas of the same specimen, indicating clearly considerable heterogeneity of the metal crystal surfaces.

3. The {210}, {111}, and {100} planes consistently limit the surface features, like grooves, pyramidal pits, macro ledges, etc., formed during dissolution on the low index planes of copper single-crystal electrodes. According to Batterman's stability conditions, these are slowly dissolving and stable planes, under present experimental conditions.

4. The mechanisms of formation of these surface features can be explained utilizing the step-wise ledge model for metal crystal dissolution, and considering the effects of crystallographic structure, surface imperfections, and adsorbed inhibiting species on the step motion across the surface, for the given rate of dissolution.

Acknowledgment

The author wishes to express his gratitude to Dr. J. V. Petrocelli, Dr. W. L. Winterbottom, and Dr. R. P. Tischer for valuable suggestions and critical review of the manuscript. He would also like to thank Dr. N. A. Gjostein and Dr. E. N. Sickafus for helpful discussions. The technical assistance of Mrs. C. Kelly in x-ray measurements, and Messrs. J. W. Sprys and G. M. Greene in electron metallography, are gratefully acknowledged.

Manuscript submitted March 23, 1972; revised manuscript received June 6, 1972. This was Paper 131 presented at the Atlantic City Meeting of the Society, Oct. 4-8, 1970.

Any discussion of this paper will appear in a Discussion Section to be published in the June 1973 *JOURNAL*.

REFERENCES

- L. H. Jenkins and U. Bertocci, *This Journal*, **112**, 517 (1965).
- U. Bertocci, L. D. Hulett, Jr., L. H. Jenkins, and F. W. Young, Jr., in "Reactivity of Solids," J. W. Mitchell *et al.*, Editors, p. 325, John Wiley & Sons, Inc., New York (1969).
- L. H. Jenkins, *This Journal*, **113**, 75 (1966).
- A. Damjanović, T. H. V. Setty, and J. O'M. Bockris, *ibid.*, **113**, 429 (1966).
- B. W. Batterman, *J. Appl. Phys.*, **28**, 1236 (1957).
- B. A. Irving, *ibid.*, **31**, 109 (1960).
- W. Kossel, *Nachr. Ges. Wiss. Göttingen*, **135**, (1927).
- I. N. Stranski, *Z. Physik. Chemie*, **136**, 259 (1928), and **B11**, 421 (1931).
- F. W. Young, Jr., J. V. Cathcart, and A. T. Gwathmey, *Acta Met.*, **4**, 145 (1956).
- E. C. Williams and M. A. Barrett, *This Journal*, **103**, 363 (1956).
- J. D. Livingston, *J. Appl. Phys.*, **31**, 1071 (1960).
- L. H. Jenkins and J. O. Stiegler, *This Journal*, **109**, 467 (1962).
- L. F. Fieser, *J. Am. Chem. Soc.*, **46**, 2639 (1924).
- A. Fricke and J. Kubach, *Z. Elektrochem.*, **53**, 76 (1949).
- F. W. Young, Jr., and L. D. Hulett, in "Metal Surfaces," W. Robertson *et al.*, Editors, p. 375, Am. Soc. for Metals, Metals Park, Ohio (1963).
- P. C. Cammorata, G. Palombarini, and M. Servidori, *Electrochim. Metal.*, **4**, 300 (1969).
- I. Garz, H. Worch, and W. Schatt, *Corrosion Sci.*, **9**, 1 (1969).
- N. Cabrera, in "Semiconductor Surface Physics," R. H. Kingston, Editor, p. 327, University of Penn. Press, Philadelphia (1957).
- W. L. Winterbottom and J. P. Hirth, in "Condensation and Evaporation of Solids," E. Rutner *et al.*, Editors, p. 347, Gordon and Breach, New York (1964).
- R. Kaischew and E. Budevski, *Contemp. Phys.*, **8**, 489 (1967).
- M. B. Ives and M. S. Baskin, *J. Appl. Phys.*, **36**, 2057 (1965).
- J. J. Gilman, in "The Surface Chemistry of Metals and Semiconductors," H. C. Gatos, Editor, p. 136, John Wiley & Sons, Inc., New York (1960).
- M. B. Ives and R. O. McElroy, Technical Report No. 10 to the U.S. Office of Naval Research, Contract No. 3925(00), (1967).
- W. K. Burton, N. Cabrera, and F. C. Frank, *Phil. Trans. Roy. Soc. London*, **A243**, 299 (1951).
- K. W. Keller, in "Crystal Growth," H. S. Peiser, Editor, p. 629, Pergamon Press Ltd. (1967).
- M. B. Ives and D. D. McAusland, *Surface Sci.*, **12**, 189 (1968).
- M. B. Ives, *Ind. Eng. Chem.*, **57**, 34 (1965).
- J. J. Gilman, W. G. Johnston, and G. W. Sears, *J. Appl. Phys.*, **29**, 747 (1958).
- A. R. C. Westwood, H. Oppenhausser, Jr., and D. J. Goldheim, *Phil. Mag.*, **6**, 1475 (1961).
- M. B. Ives, *J. Phys. Chem. Solids*, **24**, 275 (1963).
- W. L. Winterbottom, in "Surfaces and Interfaces, I. Chemical and Physical Characteristics," Burke, Reed, Weiss, Editors, p. 133, Syracuse University Press, Syracuse, New York (1967).
- N. A. Gjostein, A. Metallurgical View of Surfaces, EM 68-515, Copyright Am. Soc. of Tool and Manuf. Engrs. (1968), and Private Communication (1970).
- F. C. Frank, in "Growth and Perfection of Crystals," Doremus *et al.*, Editors, p. 411, John Wiley & Sons, Inc., New York (1958).
- L. D. Hulett, Jr., and F. W. Young, Jr., *This Journal*, **113**, 410 (1966).
- T. R. Ramachandran and M. B. Ives, *J. Appl. Phys.*, **38**, 3675 (1967).
- N. Cabrera and D. A. Vermilyea, in "Growth and Perfection of Crystals," Doremus *et al.*, Editors, p. 393, John Wiley & Sons, Inc., New York (1958).
- N. Cabrera, in "The Surface Chemistry of Metals and Semiconductors," H. C. Gatos, Editor, p. 71, John Wiley & Sons, Inc., New York (1960).
- L. H. Jenkins, *This Journal*, **117**, 630 (1970).
- L. H. Jenkins and R. B. Durham, *ibid.*, **117**, 1506 (1970).
- U. Bertocci, *ibid.*, **113**, 604 (1966).
- W. L. Winterbottom, *J. Appl. Phys.*, **40**, 3810 (1969).

Insoluble Polybromides of Quaternary Ammonium Salts and Their Phase-Transitions in the Presence of Aqueous Bromine-Bromide Solution

Francesco Rallo and Paolo Silvestroni

Istituto di Chimica della Facoltà di Ingegneria, Rome, Italy

ABSTRACT

By progressive addition of bromine to aqueous 1.0*F* NaBr solutions containing quaternary ammonium bromides, the precipitation and phase transitions of tetramethylammonium-, tetrabutylammonium-, and phenyltrimethylammonium polybromides have been potentiometrically detected at constant temperature. The results show existence of solid $\text{TMABr}_{3,9}$, $\text{TBABr}_{3,7,8,9,11}$, and $\text{PhTMABr}_{3,5,7}$. Addition of bromine to a saturated TMAClO_4 solution leads to the precipitation of only TMABr_9 .

Polyhalide salts of inorganic and organic cations have been well known for a long time, and have recently been reviewed by Popov (1, 2); the most common examples of polyhalide anions are univalent groups formed by an odd number of the same or mixed halogen atoms. Among the organic polyhalides, quaternary ammonium salts are the most representative class: many of these are quite stable, probably because the large size of such cations adapts well to the dimensions of polyhalide anions. This geometrical stability seems to be of importance also in inorganic polyhalides (2).

Since the publication of the first extensive synthesis report (3), most of the experimental work on quaternary ammonium polyhalides has been done with polyiodides or mixed iodide-halide compounds. Polybromides have been rather neglected, chiefly because their large bromine vapor pressure prevents studies on crystalline compounds at room temperature. To our knowledge, only tetramethylammonium bromide-bromine (4) and tetrabutylammonium bromide-bromine (5) phase diagrams have been reported. It has been shown that tetramethylammonium bromide (TMABr) is able to form the tribromide TMABr_3 and the enneabromide TMABr_9 , both solid at room temperature, and probably also another adduct containing 16 bromine molecules, with an incongruent melting point at 5.2°C. For the tetrabutylammonium bromide (TBABr)-bromine system the phase diagram shows the existence of the tribromide TBABr_3 and the heptabromide TBABr_7 . The stability constant of TBABr_3 in organic solvents has also been evaluated (6).

Our work on organic polybromides is connected with their potential practical use in improving the performances of zinc-bromine secondary cells. Several patents (7) claim that quaternary ammonium salts are suitable for retaining a large amount of bromine, as polybromides, in the pores of the positive electrode. This reduces the diffusion of bromine toward the negative zinc electrode, raising the self-discharge time and the electrical capacity of the cell in comparison with simple zinc-bromine cell (8), in which the elemental bromine is adsorbed on the active carbon paste of the anode.

For the practical use of a quaternary ammonium salt in zinc-bromine secondary cells, three major requirements must be fulfilled:

(i) The polybromide formation must be reversible. Oxidative bromination of the salt would, of course, drastically reduce the number of charge-discharge cycles. The formation of a polybromide with low bro-

mine vapor pressure would give an emf too low for practical purposes.

(ii) The salt should give polybromides containing a large number of bromine molecules per mole of salt, otherwise the increase in weight over the simple zinc-bromine cell could not be compensated for by the increased electrical capacity of the cell.

(iii) The polybromides should be solid in order to prevent liquid bromine-rich compounds from percolating from the positive electrode.

On the basis of these considerations, we studied the formation of insoluble polybromides by progressive additions of elemental bromine to a NaBr solution containing quaternary ammonium salts. The precipitation of polybromides and their phase-transitions in bromine-richer solid or liquid compounds has been followed potentiometrically, at constant temperature, by measuring after each bromine addition, the emf between a saturated calomel electrode and a Pt electrode immersed in the solutions. Following this procedure in experiments with TMABr and TBABr , we obtained quite quickly results agreeing with conventional phase diagrams, and we extended our research to other quaternary ammonium salts. In this paper we report the results related to tetramethylammonium, tetrabutylammonium, phenyltrimethylammonium bromides and perchlorates; other measurements relating to the behavior of penta-, hexa- and decamethylen-bis-trimethylammonium bromides ("methonium" salts, containing a two-valent cation) are being carried out at present in our laboratory.

Experimental

Bromine (Carlo Erba RP), NaBr (BDH Lab. Reag.), NaClO_4 (BDH Analar) were used as received. TMABr (Fluka), TBABr (Fluka or Carlo Erba RP), and phenyltrimethylammonium bromide (PhTMABr , Fluka) were crystallized twice from ethanol or water-ethanol mixtures, and kept in a desiccator over P_2O_5 . The respective perchlorates were prepared by precipitation from aqueous concentrated solutions of bromides and NaClO_4 , crystallized twice from water and dried at room temperature over P_2O_5 .

The reaction cell was a cylindrical Pyrex vessel, about 200 cc capacity, thermostated by a water jacket, and fitted with a ground glass cover with four holes; two of these were used for the introduction of the two electrodes (a Pt wire electrode and a saturated calomel electrode, with a procelain plug). One of the other two holes was used for the introduction of a microburette with a Teflon-glass stopcock for bromine delivery. Using the fourth hole, a small glass-spoon electrically heated, was introduced inside the cell just below the

Key words: polybromides, potentiometry, zinc-bromine secondary cells.

burette tip (about 3 cm above the solution level). Additions of the progressive aliquots of bromine to the solution were made by dropping a known amount of liquid bromine from the microburette to the glass- spoon inside the cell, then heating the spoon until all the bromine had evaporated, leaving the vapors to be absorbed by the solution which was kept constantly and rapidly stirred. In this way the polybromides separate in the form of fine particles, and their subsequent phase transitions are reasonably rapid. If the bromine is added to the solution directly as liquid drops, the formation of some mixed polybromide-bromine lumps is unavoidable, and this requires a much longer time for reaching the solution-precipitate equilibrium.

The emf between platinum and calomel electrodes was measured by a Leeds & Northrup Model 8687 potentiometer; the cell temperature was controlled within $\pm 0.05^\circ\text{C}$.

As an example of a typical experiment, 10.0 mmoles of TMABr were dissolved in 50.0 ml of 1.0F NaBr solution in the reaction cell. Then bromine was gradually added to the solution, usually in 0.1 ml aliquots. After each addition, a time of 5-20 min was required for the equilibrium, and the emf was recorded. The bromine was added until the solution was saturated with liquid bromine. The plot emf vs. amount of added bromine shows several steps, indicating the initial precipitation of TMABr_3 and its subsequent transformation into TMABr_9 .

A part of the added bromine is of course bound to the insoluble polybromides and the rest remains in solution as Br_3^- , Br_5^- etc. To allow for this amount of bromine which does not enter into the insoluble polybromides composition, a blank potentiometric curve was previously recorded by adding successive amounts of bromine to 50.0 ml of 1.0F NaBr solution. The total amount of bromine in the solution for each emf value, is determined by this curve. In the experiments with ammonium salts, the amount of bromine fixed as insoluble polybromides (indicated as "bromine uptake" in the curves reported in this paper) has been calculated, for each emf value, as the difference between the amount of the added bromine and the amount of bromine in solution (from the blank curve).

After this correction, the resulting plot emf vs. bromine uptake has the same meaning as a plot made by measuring the bromine vapor pressure during the addition of bromine to pure TMABr. In fact, the measured emf is a function of the activity ratio $a_{\text{Br}_2}/a_{\text{Br}^-}^2$ but after the precipitation of the tribromide, which is quite insoluble, the a_{Br^-} in the solution is practically equal both in the polybromide and blank solution. For all the subsequent phase transformations the blank curve corrections are operative.

Results and Discussion

In Fig. 1, curve 1 shows the compositions and the physical states of the insoluble polybromides formed during the bromine uptake by TMABr dissolved in 1.0F NaBr solution at $t = 25^\circ\text{C}$. At point f the solution becomes saturated with liquid bromine, which gradually dissolves the enneabromide previously formed. No other solid adducts appear on subsequent bromine additions.

This behavior agrees with the phase diagram of the TMABr- Br_2 system (4) which shows the existence of a eutectic between TMABr_3 and TMABr_9 of composition $\text{TMABr}_{4.65}$ and a melting temperature of 15.8°C . At $t = 25^\circ\text{C}$, according to the phase diagram, polybromides are completely liquid in the composition range $\text{TMABr}_{4.4}$ - $\text{TMABr}_{4.95}$. In our experiments the corresponding composition range (c-d tract) was larger, very likely due to the presence of a small amount of water in the nonaqueous phase. A similar enlargement of the liquidity range in presence of aqueous solution has already been noted also by Bloch *et al.* (4).

In experiments at a temperature lower than eutectic, no liquid adducts are formed in the range TMABr - TMABr_9 as shown in Fig. 1, curve 2.

After the end of the experiment, by bubbling N_2 in the solution for 12 hr, all the bromine fixed by TMABr is eliminated. A subsequent curve of bromine uptake is superimposable on the previous one. We repeated the experiment three times on the same TMABr solution, always obtaining the same results, and thus demonstrating in our experimental conditions, the absence of irreversible appreciable brominations between TMABr and bromine.

Fig. 1. EMF values for bromine uptake by: Curve (1) (circles), $10.0 \cdot 10^{-3}$ mole of TMABr in 50.0 ml of 1.0F NaBr solution; $t = 25^\circ\text{C}$. Curve (2) (squares), as in curve (1); $t = 0^\circ\text{C}$. Curve (3) (triangles), $10.0 \cdot 10^{-3}$ moles of TMAClO_4 in 50.0 ml of 1.0F NaBr and 1.0F NaClO_4 solution; $t = 25^\circ\text{C}$.

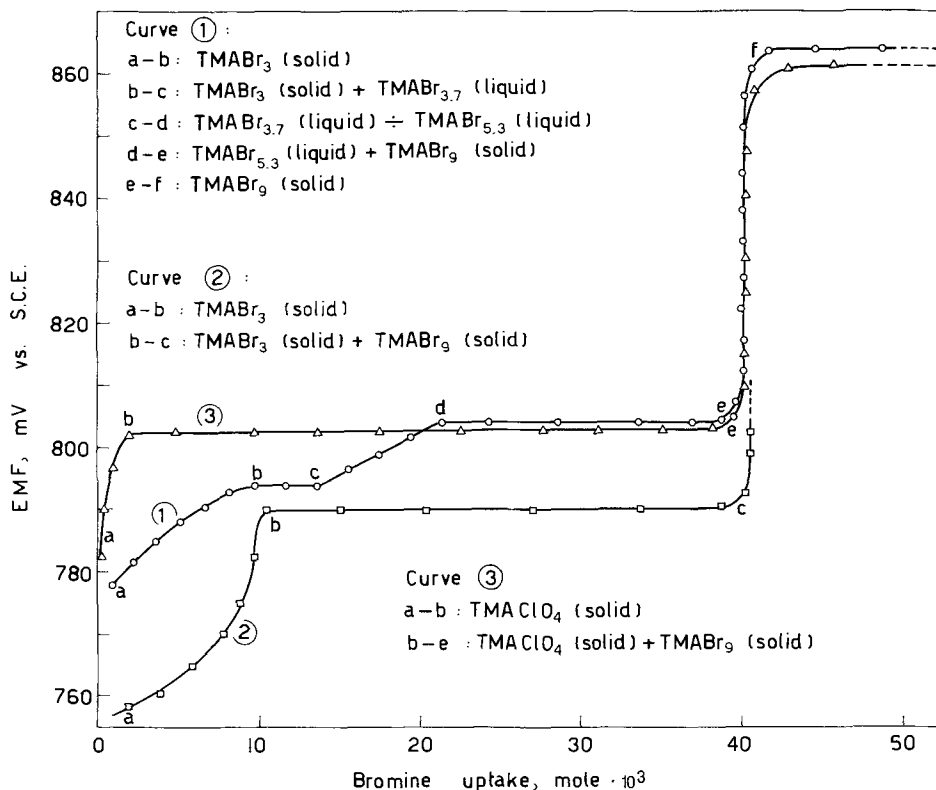
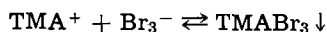


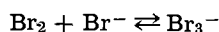
Figure 1, curve 3 shows the emf variations during the bromine uptake by TMAClO_4 which is only slightly soluble in water. Our measurements at $t = 25^\circ\text{C}$ made by comparing the conductivity of the saturated solution diluted twenty times and the conductivities of TMAClO_4 solutions of known concentrations, gave, for the saturation concentration, the value $(7.50 \pm 0.05) \cdot 10^{-2}\text{F}$, agreeing with previous findings (9). In the experiment related to curve 3 in Fig. 1, the solubility is made even lower by the presence of NaClO_4 in the solution, and at the beginning of the experiment the 10.0 mmoles of TMAClO_4 are almost completely insoluble.

The value of emf measured in the invariant tract b-e of Fig. 1, curve 3 (802 mV) is very near to that measured during the d-e tract of Fig. 1, curve 1 (804 mV). Moreover, in experiments made with TMABr in 1.0F NaBr and 1.0F NaNO_3 solution, at a similar ionic strength of the solution used for TMAClO_4 experiments, emf value of d-e tract of Fig. 1, curve 1 is practically coincident with that of b-e tract of Fig. 1, curve 3. It is therefore evident that for the addition of bromine to a saturated TMAClO_4 , 1.0F NaBr and 1.0F NaClO_4 solution at $t = 25^\circ\text{C}$, the only insoluble polybromide formed is the enneabromide TMABr_9 , without any formation of tribromide and liquid mixtures $\text{TMABr}-\text{Br}_2$ of various composition. This indicates that if the TMA^+ concentration in the solution is rather low, on adding bromine the TMABr_9 precipitates earlier than the activity product $a_{\text{TMA}^+} \cdot a_{\text{Br}_3^-}$ reaches the value corresponding to the tribromide precipitation.

For the equilibrium



it is possible to calculate the activity product because the value of the equilibrium constant for the reaction



is known (10), but for the enneabromide precipitation equilibrium the analogous calculation is not feasible because the value of the Br_9^- ion formation constant is not known, even should this ion exist in solution.

Therefore, a numerical quantitative verification of our opinion about the relative solubilities of tribromide and enneabromide does not seem possible at the present time.

Nevertheless our observation of the precipitation of enneabromide starting from the sparingly soluble TMAClO_4 is in agreement with the results of Bloch *et al.* (4), who also observed separation of enneabromide only, by adding bromine to dilute solutions (less than 0.115F) of TMABr .

Figure 2, curve 1 shows the compositions of the insoluble polybromides formed during the bromine uptake by TBABr dissolved in 1.0F NaBr solution at $t = 15^\circ\text{C}$. This temperature was chosen to avoid the formation of liquid polybromides since the existence of a eutectic between TBABr_3 and TBABr_7 with melting temperature at $t = 28^\circ\text{C}$ is known (5). In fact, at $t = 15^\circ\text{C}$, all the polybromides formed until the salt fixed 5 moles of bromine per mole are solid. The solution becomes saturated by liquid bromine at point 1.

The phase diagram (5) does not show the existence of TBABr_8 , TBABr_9 , and TBABr_{11} compounds. They are probably compounds with an incongruent melting point, undetectable with the technique used by the authors of the above-mentioned paper in the determination of the phase diagram.

The low emf value measured during the precipitation of TBABr_3 indicates a very low solubility in water of this polybromide. Unlike the behavior of TMAClO_4 , the tribromide TBABr_3 precipitates even by addition of bromine to a saturated TBAClO_4 , 1.0F NaBr and 1.0F NaClO_4 solution.

Also for the polybromides formed by TBABr , we found no oxidations and good reversibility of the bromine uptake by repeated bromine additions and eliminations with N_2 bubbling.

The compositions of the insoluble polybromides formed during the bromine uptake by PhTMABr in 1.0F NaBr solution at $t = 25^\circ\text{C}$ are shown in Fig. 2, curve 2. The solution becomes saturated by liquid bromine at point f. The curve is practically identical

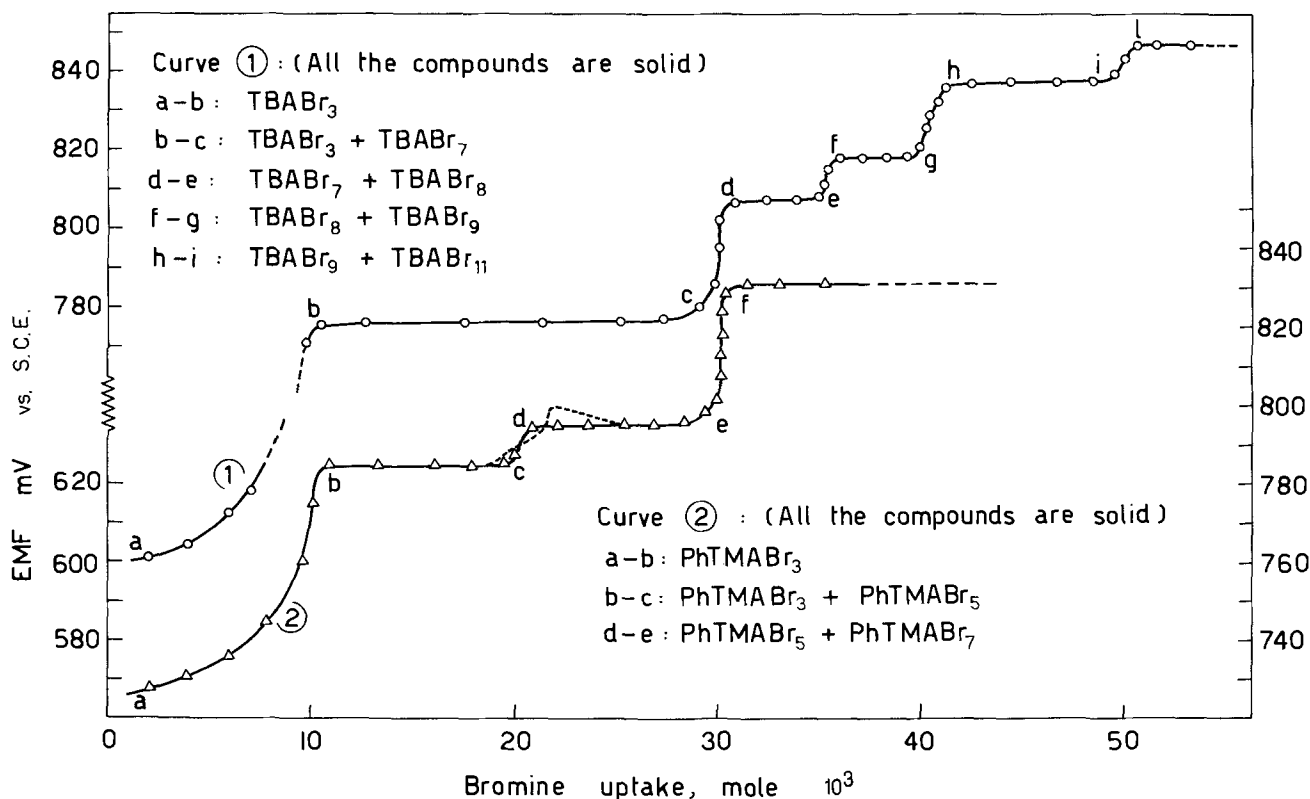


Fig. 2. EMF values for bromine uptake by: Curve (1) (circles), 10.0×10^{-3} moles of TBABr in 50.0 ml of 1.0F NaBr solution; $t = 15^\circ\text{C}$. Curve (2) (triangles), 10.0×10^{-3} moles of PhTMABr in 50.0 ml of 1.0F NaBr solution; $t = 25^\circ\text{C}$.

for 10.0 mmoles of solid PhTMAClO₄ in the presence of 50.0 ml of 1.0F NaBr and 1.0F NaClO₄ solution. Therefore in this case, as with TBAClO₄, the presence of the perchlorate does not prevent the tribromide precipitation.

The PhTMABr₅-PhTMABr₇ transition is particularly slow. Only with very slow additions of bromine vapors and rapid stirring, is it possible to avoid supersaturation phenomena, indicated with a dotted line near the c-d tract in Fig. 2, curve 2.

The existence of PhTMABr₃ is known. (This compound is commercially available and is used for organic brominations in nonaqueous solvents.) The compounds PhTMABr₅ and PhTMABr₇ have not been reported to date.

Conclusions

The potentiometric titrations we made represent a convenient screening method for detecting the formation of quaternary ammonium polybromides in a condensed phase. The results obtained with TMABr at *t* = 25°C and at *t* = 0°C confirmed the existence of the solid compounds TMABr₃ and TMABr₉, and the possibility of a eutectic between them. With TBABr we confirmed, at *t* = 15°C, the existence of the solid tribromide and heptabromide, and we obtained experimental evidence about the formation of solid TBABr₈, TBABr₉, and TBABr₁₁. PhTMABr, at 25°C, is able to form the solid PhTMABr₃, PhTMABr₅, and PhTMABr₇. All the polybromides we studied release all the added fixed bromine by N₂ sweeping at room temperature.

We consider of interest the results obtained with TMAClO₄; its direct transformation in solid TMABr₉ at 25°C makes this salt particularly suitable for practical use in zinc-bromine secondary cells because it

avoids the formation of liquid polybromides (obtained, on the contrary, with TMABr) and because the four bromine molecules are fixed at the same emf value.

Acknowledgment

We would like to thank Mr. M. Lecci for his valuable help during the longest bromine uptake experiments.

Manuscript submitted Nov. 24, 1971; revised manuscript received May 24, 1972.

Any discussion of this paper will appear in a Discussion Section to be published in the June 1973 JOURNAL.

REFERENCES

1. A. I. Popov and R. E. Buckles, "Inorganic Syntheses," Vol. 5, p. 167, McGraw-Hill Book Co., New York (1957).
2. A. I. Popov, "Halogen Chemistry," Vol. 1, p. 225, Academic Press, London (1967).
3. F. D. Chattaway and G. Hoyle, *J. Chem. Soc.*, 654 (1923).
4. R. Bloch, L. Farkas, J. Schnerb, and F. Winogron, *J. Phys. Chem.*, **53**, 1117 (1949).
5. P. L. Mercier and C. A. Kraus, *Proc. Nat. Acad. Sci. U.S.*, **42**, 65 (1956).
6. R. E. Buckles, A. I. Popov, W. F. Zelezny, and R. J. Smith, *J. Am. Chem. Soc.*, **73**, 4525 (1951).
7. R. Bloch, U.S. Pat. No. 2,566,114 (1951); J. S. Dereska, U.S. Pat. No. 3,057,760 (1962); M. De Rossi, Ital. Pat. No. 860,943 (1970).
8. S. Barnartt and D. A. Forejt, *This Journal*, **111**, 1201 (1964).
9. C. L. De Ligny, D. Bax, M. Alfenaar, and M. G. L. Elferink, *Rec. Trav. Chim.*, **88**, 1183 (1969).
10. D. B. Scaife and H. J. V. Tyrrel, *J. Chem. Soc.*, 386 (1958); J. Dubois and F. Garnier, *Bull. Soc. Chim. France*, 1715 (1965).

Cathodic Synthesis of Tetraalkyltin Compounds

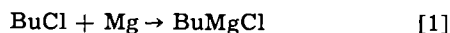
Harris E. Ulery

Organic Chemicals Department, E. I. du Pont de Nemours & Company, Wilmington, Delaware 19899

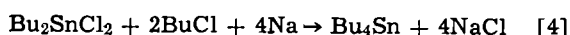
ABSTRACT

Methyl bromide and allyl bromide are efficiently reduced at a tin electrode to form tetramethyl and tetraallyl tin. A variety of other bromides with appreciably more negative reduction potentials also produce tetra-substituted tin compounds but the yields are lower. At higher potentials, cathode disintegration is a consequence of the competitive reduction of the carrier electrolyte (Et₄N⁺Br⁻).

The present manufacture (1) of organotin compounds (chiefly dibutyl derivatives) uses the following Grignard process



Of lesser importance is the Wurtz-Fittig synthesis which employs finely dispersed sodium



↑
Recycle

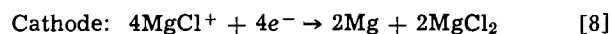


A sodium-tin alloy process is also known analogous to that used in tetraethyl lead (TEL) manufacture



Key words: tin cathode, tetraalkyl tin, tetramethyl tin, tetraallyl tin, electrolysis, cathode disintegration, alkyl bromides, reduction.

In recent years a number of related anodic syntheses of organometallics have been devised (2). Typical of these are Ziegler's electrolytic aluminum alkyl process (2b) and the Grignard process (2c). While these are currently applied to the manufacture of lead tetraalkyls (e.g. Eq. [7] and [8]) (3) they represent potential routes to tin compounds if the tendency of this metal toward anodic passivation can be overcome (4).



Formally these electrochemical syntheses are analogous to the chemical methods described above where the anode may be viewed as providing the required oxidized form of the recipient metal. Fundamentally, each of these schemes depends on a reactive metal (Na, Mg, etc.) to provide the substantial energy required to initially reduce a carbon-halogen bond to a carbanion-oid species



The principal variations in these anodic schemes relate to how the fate of R^- is controlled.

Each of these processes has been criticized (1a) because the use of the reactive metals, which are not in all cases reclaimed, lead to inflated raw material costs. Also, the methods are hazardous to operate. A procedure for the direct addition of alkyl groups to tin, therefore, would be a matter of considerable technical merit.

One obvious solution is to circumvent the use of a reactive metal by supplying all the energy for alkyl halide reduction electrochemically. In 1963 Silversmith and Sloan (5) reported that a number of soft metals could be sacrificed cathodically by an alkyl halide with the consequent formation of the polyalkyl metal. This work was both a refinement and generalization of the earlier finding by Calingaert (6) that Et_4Pb was formed during the electrolysis of an EtI solution between lead electrodes. Our purpose at this time is to report on some initial studies of the application of this reaction to the synthesis of organotins.

Experimental

Apparatus.—Electrolyses were conducted in a 100 cm^2 discoid cell operated at 10A. Cathode and anode were separated by an Amfion® C-310 ion exchange membrane. Catholyte and anolyte were independently circulated through external reservoirs and heat exchangers, and vented through wet test flowmeters. The cathode was fabricated from $\frac{1}{4}$ in. cast tin plate which analyzed at 99.85%. The anode was constructed from oil impregnated electrolytic grade graphite.

Procedure.—For the batch electrolyses the anolyte consisted of 570g of an acetonitrile solution containing 35 weight per cent (w/o) tetraethylammonium bromide (TEAB) and 10 w/o water. The TEAB was present in ca. 27% excess over the amount needed to form the tribromide. The concentration of MeBr was set initially at 1 molar: the total amount of catholyte, therefore, varied as indicated in Table II. Both catholyte and anolyte were circulated at 500 ml/min. The temperature stabilized near 50°C. The total current passed was 0.5 Faraday.

The continuous electrolyses utilized additional feed reservoirs. Electrolysis was allowed to proceed with recirculation only for the first 10 min, at which time the soluble tin concentration was about 2.5%. A feed/bleed rate of about 7 g/min was then established to maintain an approximately constant concentration of tin in the circulating stream. The temperature was maintained at 35°C.

The amount of tetramethyl tin found was determined by vapor phase chromatography. The total soluble tin was obtained by polarographic analysis.

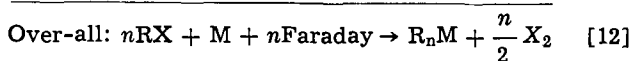
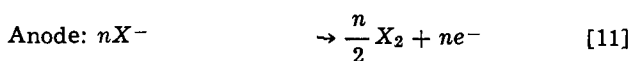
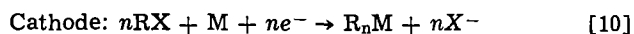
Electrolyte densities.—Densities of the three component systems $R_4N^+Br^- \cdot H_2O \cdot MeCN$ were obtained to allow the conversion between weight per cent compositions and fundamental concentration units. These data were fitted to the following regression equation

$$d_4^{25} = 0.7768 + 0.002202P_w + \alpha P_s + \beta P_w P_s$$

where P_w and P_s are the true weight per cent of water and tetraalkyl ammonium bromide. The regression coefficients and standard errors of estimate are given in Table I.

Results and Discussion

The general reaction under study is



The case where $RX =$ an alkyl bromide and $M = Pb$

Table I. Regression coefficients and standard errors of estimates for densities of the three-component system $R_4N^+Br^- \cdot H_2O \cdot MeCN$

R=	$\alpha \times 10^2$	$\beta \times 10^4$	σ
Me— ^(a)	0.7747	-0.6222	0.015
Et—	0.4007	-0.6085	0.002
n-Pr	0.2631	-0.0224	0.006
n-Bu	0.2264	+0.3134	0.009

^(a) $Me_4N^+Br^-$ forms two liquid phases at some compositions. These data refer to the monophasic liquid compositions only.

has been studied previously (7, 8). It was found that with methyl bromide the reaction is exceedingly efficient and essentially quantitative yields of tetramethyl lead based on both electricity and lead consumed are possible. With ethyl bromide, n is between 3 and 4 and lower yields of both Et_4Pb and Et_6Pb_2 are formed.

General scope of the reaction.—The versatility of the sacrificial tin cathode is suggested by the data in Table II. The yields assume the stoichiometry of Eq. [12] with $n = 4$; they are based on the conversion of cathode material to a soluble organic form and are referred to the consumption of current (% el) and of tin (% Sn). Electrical yield losses were found to be due largely to three competing processes: (i) reduction of RX to RH , (ii) dimerization of RX to $R-R$, and (iii) reduction of the tetraethylammonium bromide (TEAB) electrolyte to triethylamine. Tin yield losses were due primarily to cathode sloughing and to a lesser extent the formation of insoluble organic and inorganic tin salts. The tetra-substituted tin product was identified in several cases by using known standards with gas chromatography and/or mass spectrometry.

Since the results indicate that the electrolyses of methyl and allyl bromide are both qualitatively and quantitatively superior to the other examples, these were examined in some detail.

$(CH_3)_4Sn$ yield vs. catholyte compositions.—Previous work with lead cathodes (7, 8) had shown that the reduction process was sensitive to catholyte composition. The results of Table II, therefore, do not correspond necessarily to optimum values. The results of a systematic variation in the concentrations of H_2O , TEAB, and MeBr are shown in Table III for a series of batch electrolyses. The minimum values for the water and MeBr concentrations were set to avoid excessive sloughing of Sn. The TEAB concentration is constrained by its solubility and by the power requirements of the cell. In order that the MeBr and tin concentration changes be about the same for each run, the total amount of catholyte was different for each level of MeBr. The reproducibility of the data was limited by minute membrane damage and lack of temperature control; high temperatures developed during reduction led to outgassing of MeBr.

A series of continuous electrolyses provided better control of composition variables and temperature

Table II. Reduction of organic bromides (RBr) at a tin cathode

R	Yields ^(a)		R_4Sn identified
	% el	% Sn	
1. Me—	80-100	up to 100%	Yes
2. Et—	10-15	50-80	Yes
3. n-Pr	25	66	Yes
4. i-Pr	5-15	25-75	No
5. n-Bu	10-30	15-45	Yes
6. i-Bu	13	90	(b)
7. Br— $(-CH_2)_3-$	1	70	(b)
8. $CH_2=CH_2-CH_2-$	75 ^(a)	75 ^(a)	Yes
9. Ph—	20	84	Yes
10. $PhCH_2-$	1	50	(b)
11. $PhCH_2=CH_2-CH_2-$	2	60	(b)

^(a) The remaining 25% current passed and Sn consumed were accounted for by the formation of $(R_3SnBr)_x \cdot R_3SnOH$.

^(b) Identification of product not attempted.

^(c) Catholyte = 20% TEAB, 2.5% H_2O .

Table III. TMT—Batch electrolyses

Initial catholyte composition			Total of catholyte	% Sn ^(a) loss	% Gas ^(b) formed	Cell volt.	Electrons/g-atom Sn
% H ₂ O	% MeBr	% TEAB					
1.5	10	5	950	88.9	42	8.5	4.42
1.5	10	5	950	98.8	46	9.0	4.09
1.5	20	5	475	92.2	71	7.5	4.35
3.5	10	18	950	95.4	60	7.0	4.23
3.5	20	18	475	97.0	75	6.5	4.14
5.5	15	12.5	633	82.1	65	6.7	4.87
5.5	15	12.5	633	92.2	68	6.7	4.35
10.5	10	5	950	61.2	114	7.1	6.56
10.5	20	5	475	69.7	111	7.0	5.75
10.5	10	20	950	80.7	82	6.5	4.95
10.5	20	20	475	71.4	120	6.7	5.60

(a) Electrical basis assuming a 4-electron process.

(b) Electrical basis assuming a 2-electron process. Figures include entrained MeBr and, therefore, may exceed 100%.

(Table IV). The concentration of tin in the catholyte reached 1.5-2.5 w/o. Water permeation from the anolyte increased the average level in catholyte by 0.8-1.8% over the initial value. Under the conditions of these experiments all the consumed tin present in the product catholyte was as a soluble material. Furthermore, gas chromatographic analysis indicated that TMT is indeed the major reaction product initially.¹ Consequently cathode weight loss in the absence of sloughing may be taken as a crude measure of TMT formation. All the data at present indicate that current efficiencies must be based on a 4-electron process (Eq. [10]).

Product yields.—Regression analysis of the results in Table III indicates that most of the variations in yields based on cathode weight loss is accommodated simply by the differences in water and TEAB content; changes in the initial concentration of MeBr did not significantly influence tin consumption. That decreased water concentrations promote higher yields of the organometallic product is to be expected on the basis of competition, and is a familiar fact in the cathodic synthesis of tetramethyl lead (8). By comparison, the influence of water is about 3 times larger in the case of TMT than for TML. This agrees favorably with the factor of 5-6 predicted solely on the basis of polarographic studies of the hydrogen overvoltage on tin and lead cathodes in related electrolytes.

Increasing the carrier electrolyte increases the consumption of tin. While regression analysis attributes a much smaller role to TEAB than to water, it is by no means insignificant. Discussion of this point will be deferred to a later section, but it should be pointed out that when the TEAB concentration is set above about 5% in relatively dry systems, sloughing of tin is observed; the current efficiency with respect to solu-

¹ The catholytes are unstable and some alkyl tin bromides and insoluble tin compounds form due to the presence of air and traces of Br₂ and HBr. The cathodic formation of lower alkyltin products will be discussed in a later paper.

Table IV. TMT—Continuous electrolyses

Initial catholyte composition			% loss	% Sn ^(a) sludge	% Gas ^(b) evolved	% Sn ^(c) found	Electrons/g-atom Sn
% H ₂ O	% MeBr	% TEAB					
1	10	3	88	0	21	74	4.62
1	10	12	80	37	24	84	3.68
1	10	12	85	24	14	— ^(d)	3.94
1	12	10	77	30	25	— ^(d)	5.18
1	15	8	95	0	21	80	4.25
1	20	3	94	0	28	82	4.29
1	20	12	85	20	25	— ^(d)	3.53
3	10	3	93	0	25	90	4.29
3	10	12	91	0	31	91	4.43
3	20	3	91	0	32	(107)	4.41
3	20	12	95	0	29	94	4.23

(a) Electrical basis, assuming 4-electron process.

(b) Electrical basis, assuming 2-electron process.

(c) Total soluble tin as per cent of total tin loss.

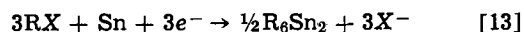
(d) Membrane leak prevented determination.

bilized tin is not as high. Increasing the water content raises the level of TEAB required to cause sloughing.

Gassing.—The evolution of gas is a 2-electron process. It appears to be the major side reaction under optimal conditions. Accordingly, gas production and tin consumption are inversely related and display opposite dependencies on water and TEAB concentrations. This was not true with alkyl bromides with much higher reduction potentials than MeBr. In these cases some triethyl amine is obtained from the reduction of tetraethyl ammonium ion.

Tetraallyltin.—The reduction of allyl bromide under conditions similar to those used with MeBr results in an efficient sacrifice of the tin cathode. The results parallel those obtained by a strictly chemical method (9), for the preparation of tetraallyl tin. About 75% of the tin consumed appears in a soluble form, which at least initially seems to be mostly tetraallyl tin (g.c. analysis). The remaining 25% is accounted for as an amorphous, MeCN insoluble product containing 37-46% Sn corresponding to the probable composition (R₃SnOH)_x · (R₃SnBr). When water is replaced by MeOH and allyl chloride is used, no solid complex was formed.

Less than 4 electrons/atom of consumed tin were required on the average in spite of a nominal loss of electrical efficiency as a consequence of the formation of gas.² It is quite probable that a 3-electron process is competing with the "normal" 4-electron reaction



The formation of hexaallylditin would be consonant with the earlier observation (7) that hexaalkyldilead compounds are favored when the alkyl groups are so large as to inhibit the formation of four carbon bonds to one central metal atom. Table V shows that under similar conditions the reaction at a lead electrode (which also produces some insoluble complex) is comparatively less efficient. With neither metal was sloughing of the cathode material itself observed. This is reasonable, since the reduction potential of allyl bromide is similar to that of MeBr.

Sludge formation.—At low water concentrations, the extent of sludging increases very rapidly with catholyte TEAB content. The sludge is composed primarily of metal fines together with some salts. An interesting trend can be discerned: sludge rates increase rapidly as the catholyte approaches saturation with respect to TEAB. Table VI shows that the per cent of saturation is rather constant for a given level of sludge

² Propene was identified among the off-gases.

Table V. Batch electrolysis of allyl bromide

% H ₂ O	% TEAB	% C ₃ H ₅ Br	Metal, M	Cathode loss (g-atom)	Electrons/g-atom M
3	18	20	Sn	0.129	3.85
3	18	10	Sn	0.116	4.27
3	5	20	Sn	0.133	3.73
3	5	10	Sn	0.127	3.91
1 (MeOH)	3 (TEAC)	30 C ₃ H ₅ Cl	Sn	0.115	43.0
3	5	10	Pb	0.017	12.9
3	5	20	Pb	0.033	11.3
1	2	30	Pb	0.029	6.5

Table VI. Sludge formation as a function of catholyte composition

H ₂ O (w/o)	TEAB solubility (w/o)	% of max TEAB present when sludge yield is		
		0%	10%	20%
0	13	8	23	39
1	20	10	20	31
2	24	8	17	30
3	28	11	21	32
4	31	6	23	41

Avg. 9 ± 3% 21 ± 4% 37 ± 7%

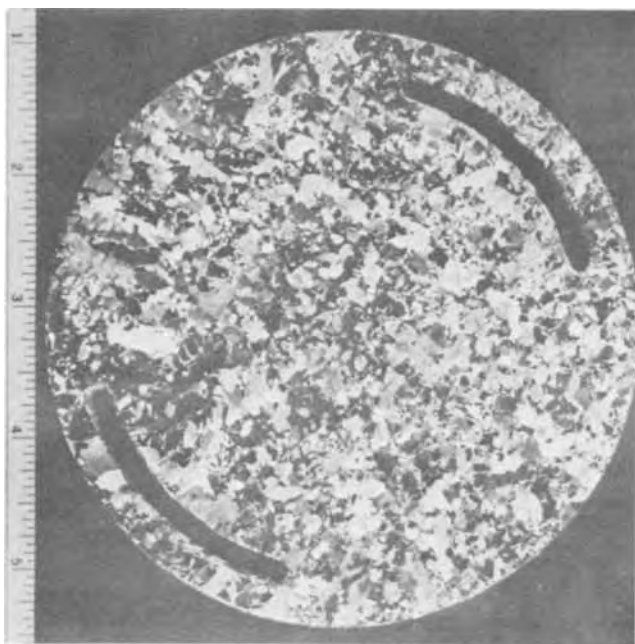


Fig. 1. Tin cathode after electrolysis of MeBr/TEAB/MeCN, no sludging.

formation during MeBr reduction in spite of the overall change in solution composition.

Other data also implicate the carrier electrolyte as a responsible factor in the formation of sludge: (i) Poorer solvents for TEAB (eq. propionitrile, benzonitrile) produce more sludge for a given concentration of electrolyte. (ii) Co-solvents with reduction potentials lower than TEAB in particular hydroxylic solvents, inhibit sludging; by contrast, relatively non-polar unreactive solvents such as benzene, diglyme, and tetramethyl tin increase sludge rates. A lead cathode behaves in much the same way (8). (iii) Qualitatively, less cathode sloughing is observed with tetrapropyl ammonium and tetrabutyl ammonium salts than with the corresponding tetraethyl ammonium salts. (iv) High current densities and poor catholyte circulation both promote sludge formation suggesting that high local potentials are responsible for non-faradaic metal removal (see below).

In the absence of extensive cathode disintegration the reduction of MeBr at a tin or lead electrode is unique. This is the only alkyl bromide that yields a specularly etched cathode in which the crystalline

detail of the metal is preserved down to the submicron level (Fig. 1 and 2). All other depolarizers studied have decidedly more negative reduction potentials (7) and these remove metal in an apparently random fashion such that no microscopic evidence of cathode crystallinity is preserved (Fig. 3 and 4). When trace metal fines are produced with MeBr, cratering is observed along microcrystalline edges and corners (Fig. 2b), but not on faces—in other words, pitting appears where the local potential is the highest (10).

It is suggested that reduction of the tetraethyl ammonium cation and subsequent implantation of the product (Et_4N^+) is responsible for the formation of cathode sludges. Implantation of alkali metals is frequently observed at soft metal cathodes (11) including Pb and Sn. Often it results in cathode disintegration. Seebeck's remarkable and still curious ammonium amalgam (12) is an analogous phenomenon. In fact, both Me_4N^+ and Et_4N^+ yield amalgams (13), although that of the latter is appreciably less stable owing to the greater ease of fragmentation expected when the ethyl group is present.

While the details of the implantation process *per se* remain obscure, it is clear that the first step—reduction of the cation—readily explains many of our observations. The relatively high potential required to reduce Et_4N^+ is not accessible as long as other reducibles are present. It is not surprising, then, that the following order for sludge inhibition is observed for a given weight per cent of additive: $\text{H}_2\text{O} > \text{MeOH} > \text{glycerol} > \text{polyethylene glycol}$. The reverse might be expected if adsorption of the inhibitor was responsible instead of the hydroxyl group activity. Finally, we note that when a 0.5% $\text{H}_2\text{O}/10\%$ TEAB/acetonitrile solution is subjected to electrolysis at (0.1 A/cm²), the electronmicrographs of the surface (Fig. 5) resembled those obtained from cathodes sacrificed to higher alkyl bromides (cf. Fig. 4). The principal off-gas was ethane, while triethylamine was a major product in solution. That reduction proceeds through the intermediate Et_4N^+ is reasonable, since the cathode fines were found to possess a residual reactivity toward water.

Acknowledgments

I am indebted to M. R. Kegelman who designed the electrolytic cell used in this work and who shared with me much of his experience in the electrolytic synthesis of tetramethyl lead. The electronmicrographs were obtained by W. S. Kay. Chromatographic, mass spectrographic, and elemental analyses were conducted by the staff of Jackson Laboratory's Analytical Division. Finally, I wish to mention particularly T. Tessmer, whose manipulative skills and general laboratory as-

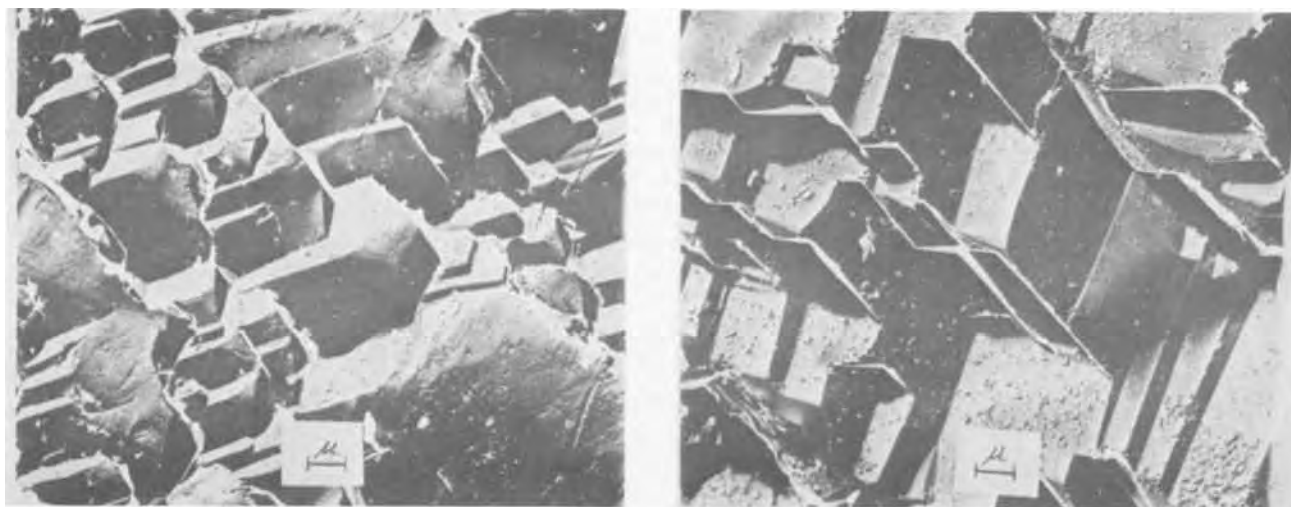


Fig. 2. Detail of tin cathode after electrolysis of MeBr/TEAB/MeCN. (a, left) No sludging; (b, right) trace sludging.

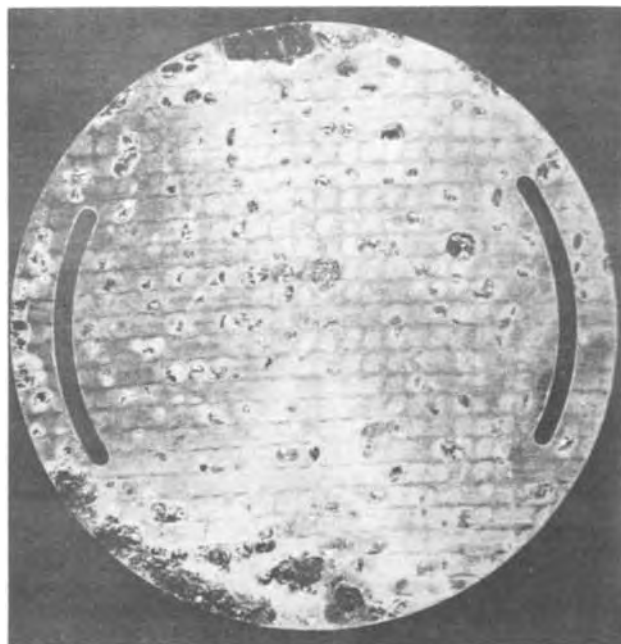


Fig. 3. Tin cathode after electrolysis of EtBr/TEAB/MeCN, heavy sludging. Pattern due to membrane supporting screen.



Fig. 5. Detail of tin cathode after electrolysis of TEAB/MeCN, very heavy sludging.

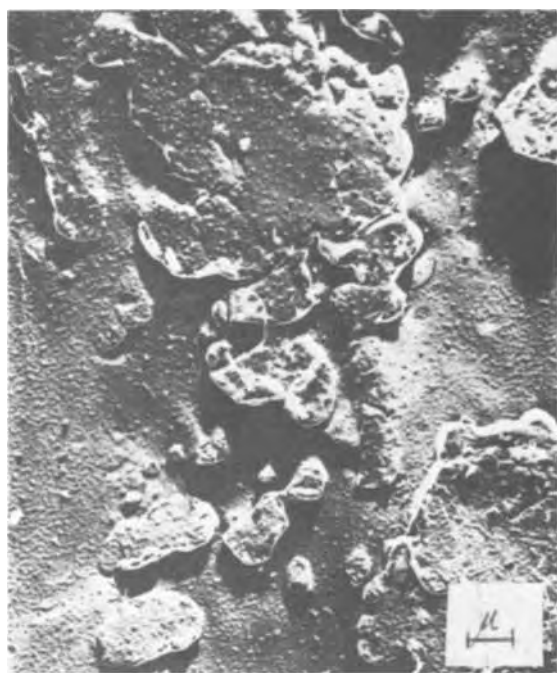


Fig. 4. Detail of tin cathode after electrolysis of EtBr/TEAB/MeCN, heavy sludging.

sistance were an invaluable contribution throughout this study.

Manuscript submitted Nov. 15, 1971.

Any discussion of this paper will appear in a Discussion Section to be published in the June 1973 JOURNAL.

REFERENCES

- (a) H. V. Smith, "The Development of Organotin Stabilizers," Tin Research Institute Publication No. 302 (1959);
- (b) C. R. Cramer, *Tin and Its Uses*, No. 46, 1 (1959).
- (a) E. M. Marlett, *Ann. N.Y. Acad. Sci.*, **125**, 14 (1965).
- (b) K. Ziegler, German Pat. No. 931,107 (1955).
- (c) D. G. Braithwaite, U.S. Pat. No. 3,007,857 and 3,007,858 (1961).
- See for example: Anon., *Chem. Eng. News*, **42**, 52 (1964).
- (a) K. Ziegler and H. Lehmkuhl, German Pat. No. 1,127,900 (1962).
- (b) P. Kobetz and R. C. Pinkerton, U.S. Pat. No. 3,028,320 (1962).
- (c) K. Ziegler and O. W. Steudel, *Ann. Chem.*, **652**, 1 (1962).
- (d) H. E. French and M. Drane, *J. Am. Chem. Soc.*, **52**, 4904 (1930).
- E. F. Silversmith and W. J. Sloan, U.S. Pat. No. 3,197,392 (1965).
- (a) G. H. F. Calingaert, U.S. Pat. No. 1,539,297 (1925).
- (b) B. Mead, Brit. Pat. No. 1,567,159 (1925).
- (c) cf. J. Tafel, *Ber.*, **44**, 327 (1911).
- (d) see also: R. E. Plump and L. B. Hammett, *Trans. Electrochem. Soc.*, **73**, 523 (1938).
- H. E. Ulery, *This Journal*, **116**, 1201 (1969).
- K. C. Smeltz, U.S. Pat. No. 3,392,093 (1968).
- K. V. Vijayaraghavan, *J. Indian Chem. Soc.*, **22**, 135 (1945).
- C. Kasper, *Trans. Electrochem. Soc.*, **77**, 353, 365 (1940).
- B. N. Kabanov, I. I. Astakov, and I. G. Kiseleva, *Russ. Chem. Revs. (English Transl.)*, **34**, 775 (1965).
- A. Seebeck, *Ann. Chim.*, **66**, 191 (1808).
- H. N. McCoy and W. C. Moore, *J. Am. Chem. Soc.*, **33**, 273 (1911).

Electron Microscope Study of Breakdown and Repair of Anodic Films on Aluminum

J. Zahavi* and M. Metzger*

Department of Metallurgy and Mining Engineering and Materials Research Laboratory,
University of Illinois at Urbana-Champaign, Urbana, Illinois 61801

ABSTRACT

In films forming in 2.4M H₂SO₄ at 5 mA/cm², many breakdown events including pit initiation were found to occur continually but to be followed by almost immediate repair, so that the stability of film growth was due not to the absence of breakdown but to the efficacy of repair. A relation between the sites of breakdown and substrate structure was not indicated. Film growth was interpreted as occurring through a compact film at pore bases, as in the classical mechanism, and also through breakdown—extension of a pore near to the metal interface—and repair by reanodization to form a hemisphere of compact film extending into the substrate. An interpretation of the geometrical structure of the film is proposed.

Considerable investigation of the stability of surface films in electrolytes has been done through the macroscopic electrochemistry of anodic behavior in passivation and pitting, electrolytic polishing and formation of protective or dielectric films by anodizing. Since film breakdown is usually localized in cases of interest, insight into the mechanisms of failure may be sought through direct observations of the microtopography of the initial failure events by electron microscopy. For application to corrosion of aluminum, the initial work was based on films formed in sulfuric acid, so that the extensive anodizing literature [the subject of a recent review (1)] could be used as partial guide and reference, but at a low current density yielding thinner slowly growing films.

In constant-current anodizing of aluminum in sulfuric acid (typically 15% or 1.5M at C.D. between 10 and 100 mA/cm²), the cell voltage (referred to a Pt cathode) first rises rapidly with growth of a film and then, usually after passing through a maximum, levels off at a steady-state value (2, 3). At least by the early part of the voltage plateau, pores are initiated by preferential film dissolution along channels from the external surface and the film then develops the classical more or less hexagonal array of pores with a scalloped barrier layer at the base (4) and maintains this structure during thickening by growth through the barrier layer and dissolution of film at pore bases (3, 4). The rate of purely chemical dissolution as measured by several methods is only $\lesssim 1$ Å/min (5-7) and is respon-

sible only for some tapering of the pore walls toward their mouths and some external film surface dissolution, and the rapid pore-base dissolution which keeps pace with the imposed C.D. is attributed to a field-assisted process (8), the details of which are not known. A discussion of classical pore growth has been given recently by O'Sullivan and Wood in connection with studies in phosphoric acid, where steady-state voltage was high (~ 100 V) and where films many microns thick could be studied in section as well as on their surfaces and the relations between forming voltage and the dimensions of the pore structure determined (9). For sulfuric acid anodizing, the relation found for pore diameter was 9-10 Å/V and for cell diameter 25-28 Å/V (3); the value for barrier layer thickness was not determined [this was 10 Å/V in phosphoric acid (9)]. The details of the pore initiation process are not established. A useful relation has been derived from constant-voltage anodizing studies in which pore

formation in various electrolytes was found to accompany protracted current decay (10-13) and thus could be associated with the condition, according to high-field film growth theory, that the forming field had fallen to a sufficiently low value (11). The concept that film dissolution is inhibited at high fields has also received support from constant C.D. studies in sulfuric acid (2).

This paper is sometimes concerned with deviations from the classical pore structure, and it is helpful to refer in general to the conducting columns of electrolyte in the film as "channels" and reserve the term "pores" for those approximating the classical model in character and dimensions. The term "breakdown" is used here not in the electrochemical sense of a fall in film resistance but only in a broad geometrical sense of creation of a film-free zone or highly conductive path (e.g., by dissolution or cracking) which extends to or almost to the film-substrate interface. Since this may be merely creation of an advance channel through the barrier-layer film at the base of an existing channel or pore, porous film growth and breakdown are likely to be related phenomena. The initial breakdown event within a thin film would not normally be observable directly but its incidence and character would be inferred from the microtopography of the resulting pit in the substrate or zone of repaired film. The present observations necessarily lead to geometrical models and do not deal directly with questions discussed elsewhere concerning the chemical structure of the film and the state of hydration at various levels (14).

Experimental

99.999% aluminum sheet containing in ppm wt. 2.4 Fe, 1.5 Si, 1.0 Cu, and 0.6 Mg as major impurities (Lot III-A) was milled into blanks 20x10x1 mm with a narrow tab and these were annealed in air 24 hr at 650°C and cooled in an air stream. They were etched in 10% HF and electropolished in 20 volume per cent (v/o) 70% perchloric acid in ethanol at -10° to -15° C for 10 min at 100 mA/cm², then rinsed in a jet of ethanol and dried. The intention was to standardize the procedure and the initial state of the surface while holding close to the conditions found previously (15) to yield surfaces without grain boundary grooves or level differences between grains; longer polishing times are normally required to yield a featureless surface. Anodic films were formed in a stirred bath of 2.4M H₂SO₄ at $25.0^\circ \pm 0.2^\circ$ C at 5 mA/cm² from a constant-current source with a 50 cm² platinum cathode for times up to 30 min. The acid concentration (and the

* Electrochemical Society Active Member.

Key words: film-breakdown, film-repair, pitting, aluminum.

batch itself) was the same as used previously to study the structure-related free corrosion behavior of Lot III-A (16).

Surfaces were examined by optical microscopy and by scanning electron microscopy after applying a thin carbon layer to prevent charging in the beam. Films stripped in mercuric chloride solution were examined in transmission [flakes of MoO_3 smoke (17) being used for focusing], and carbon replicas preshadowed at 35° with platinum were taken of outer and inner film surfaces, the film being removed in 10% HF without attack of the platinum. Film thickness estimated from the transparency to 100 kV electrons showed the formation efficiency was low; the 30 min film, opaque to the beam, was checked by an interferometric method and found to be near $\frac{1}{2} \mu\text{m}$ thick.

Results and Discussion

Kinetics.—Galvanostatic anodizing at C.D. of 25–100 mA/cm^2 gave cell voltage-time curves, as for 50 mA/cm^2 in Fig. 1a, similar to those reported previously for slightly lower acid concentrations (2, 3). At lower C.D. the maximum was broader and the plateau lower and 5 mA/cm^2 (Fig. 1b) was chosen as yielding suitable conditions for this work. The curve displayed on a millivolt recorder was smooth with only weak voltage fluctuations in the region of the maximum; recording the curve on an oscilloscope with much higher frequency response did not reveal substantially larger fluctuations. Instead of the initial linear rise of voltage seen at higher C.D., the 5 mA/cm^2 curves showed a change in slope near $\frac{1}{2}\text{V}$. If before anodizing the specimen were either etched 2 min in 10% HF or treated with the hot chromic-phosphoric acid film stripping solution to remove the residual electropolishing film (about 200Å) and leave only the much thinner film remaining after a water rinse, the curve was altered somewhat below 1V, but the remainder of the curve was unchanged.

Optical and scanning microscopy.—Examination of anodized surfaces by bright-field optical microscopy or by scanning electron microscopy revealed small repaired pits of micron size with densities of $\sim 10^2$ per cm^2 . Many of these pits formed early in the anodizing process but they soon ceased to grow. Figure 2a shows the secondary-electron image of the surface of the film over a pit after 25 sec anodizing; the anodic film over the pit had been lifted and cracked. The specimen-current image gives a "radiograph" reflecting the thickness of film overlying the substrate and so could be used to give some information in depth. This image (Fig. 2b) was everywhere darker over the pit, i.e., the total film thickness was greater there indicating that a repair film had already formed. It was deduced

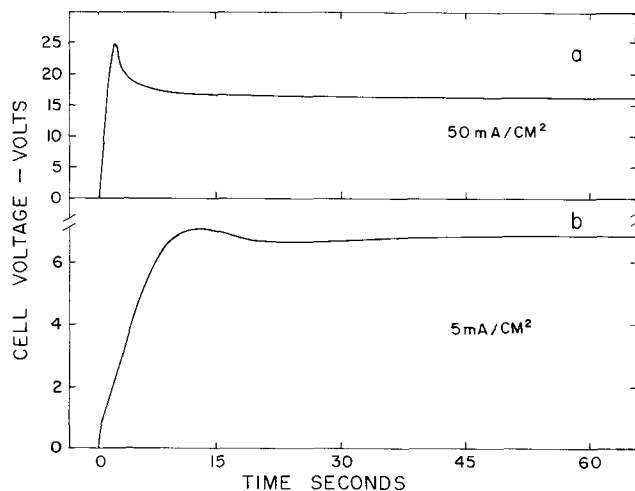


Fig. 1. Cell voltage-time in 2.4M H_2SO_4

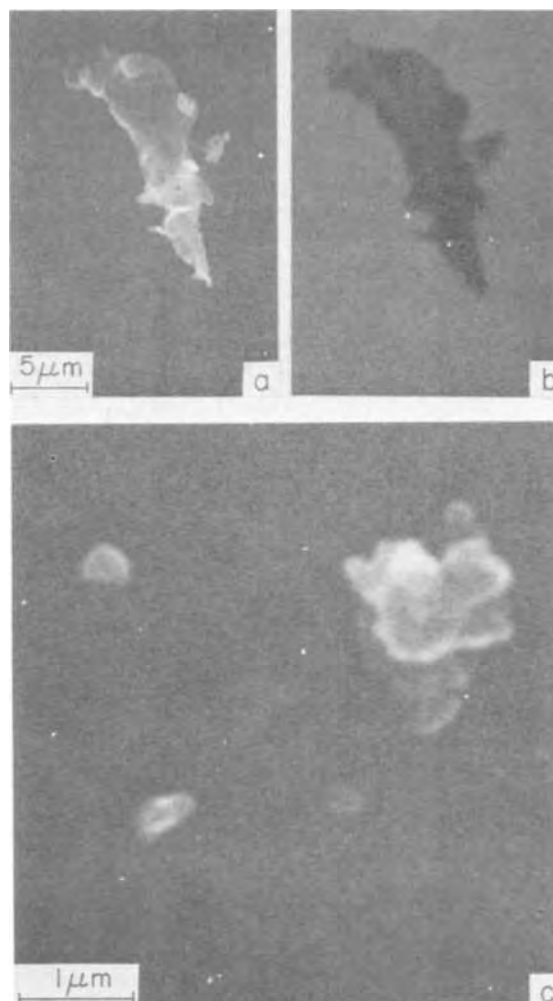


Fig. 2. Scanning electron micrographs at small pits in anodized specimens. (a) after 25 sec, secondary-electron image; (b) same field, specimen-current image; (c) after 15 min, cluster of pits of typical size, secondary-electron image.

that pitting began by undermining the original film (3) and the repair process was a rapid reanodization of the exposed metal at high local C.D. This repair was effective; in specimens examined after longer anodizing times, pits such as those in Fig. 2a were no larger and most of the scattered pits present were smaller and associated with very little perturbation of the external surface of the film, as illustrated by the group shown at higher magnification in Fig. 2c. Wood and O'Sullivan had found that at 10 mA/cm^2 pits formed in sulfate solutions only above pH 1.1 (3). In the present experiments, the absence of distinct pitting was due not to the absence of a tendency for pit formation but to the capacity for rapid repair.

A more sensitive method for detecting the presence of geometrical features beneath the film is dark-field optical microscopy, which is sensitive to minor irregularities in the metal surface. In the original electropolished surface, this revealed some bright spots (Fig. 3a) attributed to shallow depressions remaining from pits produced in the course of electropolishing and now almost removed by the subsequent electropolishing. In specimens anodized 84 sec or more, there were many more spots ($\sim 10^5$ per cm^2) in the dark-field view (Fig. 3b) (many of these were too faint to survive reproduction). Only a small fraction of these could be identified by optical or scanning microscopy and most are thought to have represented some of the many small depressions in the metal-film interface revealed in the replica studies described in the following section.

The spots in anodized specimens showed no apparent preference for grain boundaries nor was the appearance of individual boundaries altered greatly from that observed in the electropolished state where grain boundary grooves were usually visible as faint lines (arrows in Fig. 3a), their appearance varying somewhat with the short polishing times employed. The distribution of spots within the grains of anodized specimens was not strongly associated with subgrain boundaries, as determined in specimens for which the substructure had been previously established by etching. It was conceivable that the spots might be associated with segregations of iron or other impurities, which under free corrosion conditions at much lower C.D. ($\sim 10^{-2}$ mA/cm²) lead to the formation of small pits in sulfuric and other acids (16). This was checked by subjecting zone-refined aluminum containing only about 0.1 ppm Fe and Cu to the same treatment, and the dark-field micrographs (Fig. 3c) were found to be essentially the same. The events giving rise to the bright spots were thus not strongly structure- or impurity-sensitive.

Transmission and replica studies.—Transmission studies, made on the plateau of the cell voltage-time curve, were limited mainly to anodizing times up to 150 sec because of the fogged background and obscuring of detail in thicker films. These studies (Fig. 4) revealed structures which were nonclassical in several respects. For one, instead of the classical pore structure appearing as rounded 60-70Å light spots on a uniform darker ground, the channels observed were usually elongated or streaked and there was considerable detail in the background. Also, the film showed numerous dark zones indicative of breakdown and repair events, these being prominent at low magnifications (Fig. 4f).

With regard to the dark zones, it was determined by varying the focus that these represented locally greater mass thickness. The presence of the zones was reflected in the external surface replicas (Fig. 5a and b) only in minor ways. It was on the film underside (Fig. 6) that the events were manifest. The larger ones appear in Fig. 6c and d as rounded projections extending out from the film and thus representing the locally thicker regions of film giving rise to the dark zones in the transmission image. For shorter anodizing times, the zones were smaller and less prominently reflected in the film underside topography (Fig. 6a and b). In general, it appeared that in the course of anodizing breakdown-repair events occurred continually in one

form or another at the base of the film and the underside replicas revealed those that had taken place shortly before the time of observation before the projections were obscured by continuous uniform film growth.

Extensive selected-area diffraction of these zones revealed no evidence of the crystallinity shown by Zahavi and Yahalom to be associated with breakdown zones at higher C.D. and higher plateau voltages (18, 19). This could be checked even for the 900 sec film by using a defocused (phase contrast) image to locate the zones.

The events visible on the film underside replicas corresponded to depressions in the substrate-film interface which could serve as light scattering centers in dark-field optical microscopy. Most of the events observed were too small to provide sufficient intensity for detection in the present optical studies. However, the events covered a wide size range and the underside replicas did reveal a number of breakdown-repair events or repaired pits larger than those shown in Fig. 6c and d, and it was deduced that the weak light spots in the dark-field optical micrographs originated at these ($> 0.1 \mu\text{m}$ across). The electron-microscope studies indicated that the breakdown could occur at any point on the surface and thus supported the conclusion of the optical studies that these events were not limited to boundaries or impurity segregations in the substrate.

A case of local growth of repair film in to the substrate had been described by Renshaw (20) who studied the anodizing of aluminum (in chromic acid) through a substantial pre-existing compact film and found large hemispheres of porous film growing from the base of the compact film. This was a different situation, its point of interest being not an anomaly in the character of the porous film itself but the fact that it started to grow only from discrete locations where the compact layer had been penetrated.

Consideration is now given to the nonclassical aspects of the pore structure. In transmission, the structure that developed (Fig. 4d) appeared to consist of major channels or pores of somewhat irregular shape and between them some finer ones usually of lower contrast and sometimes running in strings. The appearance of the channels changed somewhat on tilting in a manner which suggested many were inclined to the normal or jogged [they were not sloped uniformly in one grain as has been reported (21)] and their apparent shapes were related to this. The diameters and spacings of the

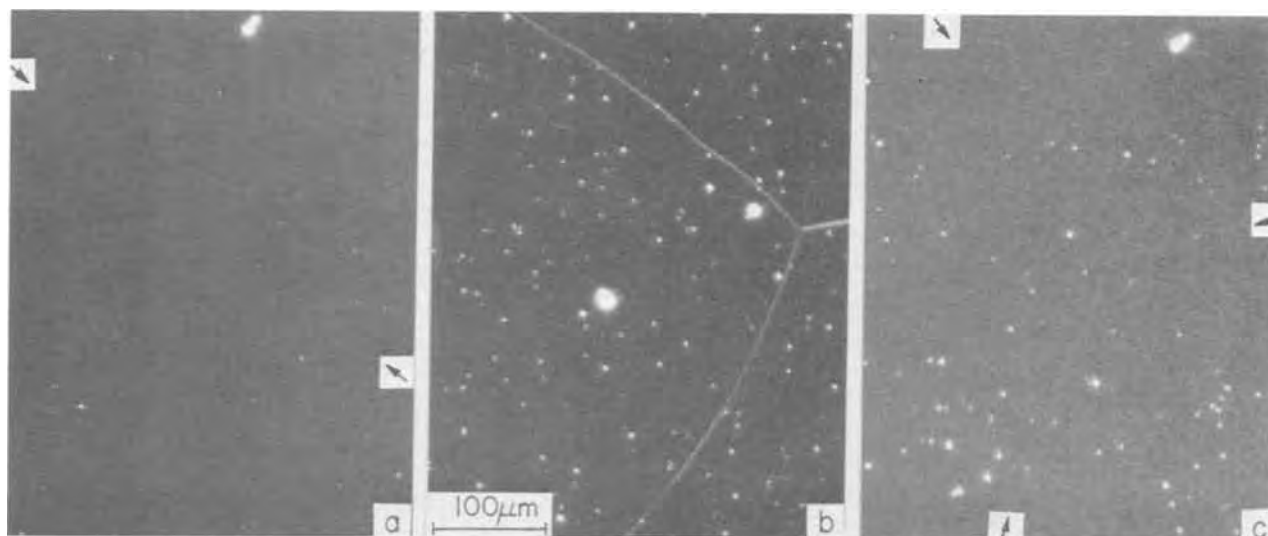


Fig. 3. Dark field optical micrographs of specimens: (a) as electropolished, (b) after anodizing 30 min, (c) zone-refined aluminum after anodizing 84 sec. Arrows indicate positions of faintly visible grain boundaries.

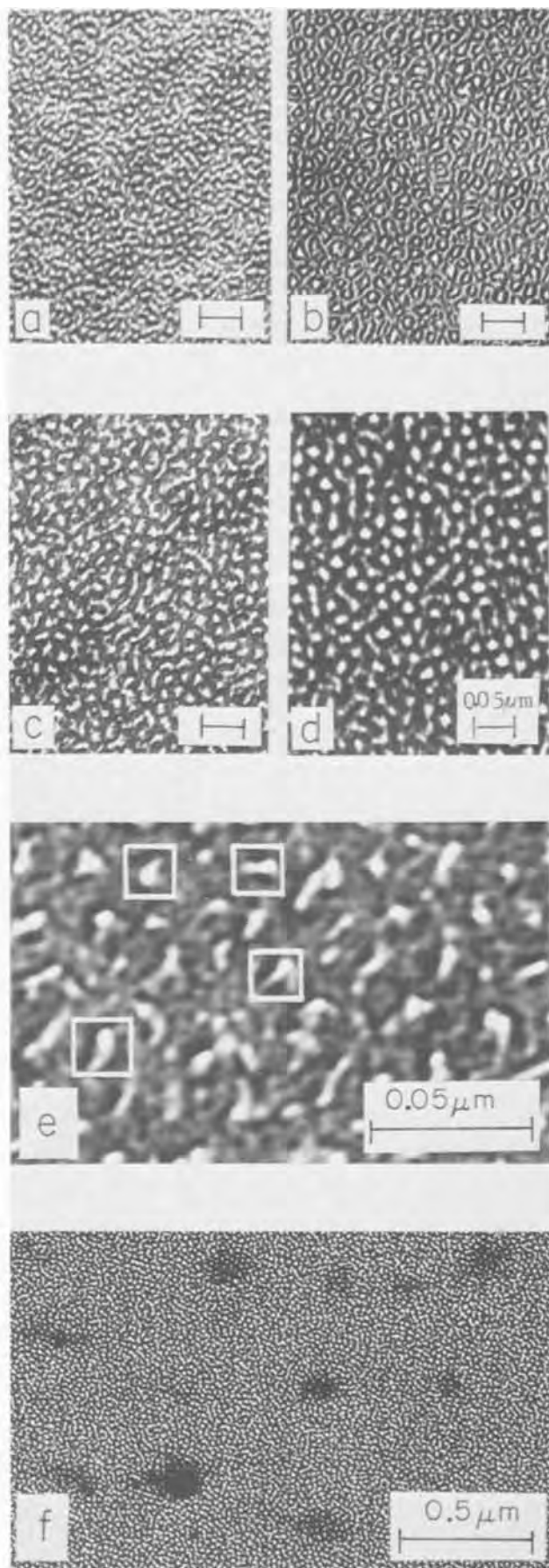


Fig. 4. Transmission electron micrographs at 100 kV of films formed for various times. (a) 15 sec, (b) 25 sec, (c) 84 sec, (d) 150 sec, (e) 25 sec at higher magnification showing the details of the channels in the film, (f) 84 sec at lower magnification showing breakdown-repair events.

major channels after 150 sec were approximately those expected from Wood and O'Sullivan's figures (3, 9) for the classical pore structure at the present cell voltage. The channel density was about half the value observed at 15 sec (just after reaching the voltage plateau) (Fig. 4a). The density at 15 sec was approximately $7 \times 10^{11} \text{ cm}^{-2}$ both in transmission (Fig. 4a) and in the channel mouths visible on the external surface replica (Fig. 6a); this density was retained at the external surface, as seen in the 900 sec film (Fig. 6b) where the only substantial change from Fig. 6a was that a few of the channel mouths were enlarged. These observations indicated that the origin of the change in channel density seen in transmission was that certain channels ceased to grow and thus yielded insufficient contrast to be visible after the film thickened. The density of active channels could not be determined from the dimensions of the pattern in the film-underside replicas (Fig. 6c and d) because it was not possible to make a clear distinction between the bases of active cells and residual breakdown-repair events.

The over-all view given by these observations is that film structure evolved toward the classical model but was perturbed and modified as a result of the breakdown-repair events. It appeared that in the early part of the cell voltage plateau ($t < 25$ sec) many small events were occurring more or less simultaneously all over the film but later (84-1800 sec) the events were multiple or clustered and occurred intermittently at various locations.

Elementary breakdown-repair process.—The interpretation of the basic processes occurring in the present work makes use of the ideas derived from previous porous-film studies cited in the introduction. It is supposed that a system of channels (not necessarily straight) is present and the film is growing continuously through a 10 A/V barrier layer at the bases of these, as in "normal" growth of a porous film. In breakdown, certain channels become extended near to the metal interface (Fig. 7a) (usually at some angle to the normal), and this breakdown is followed by rapid repair in one of the ways indicated in Fig. 7b. In event 1, the repair current is supposed limited by channel resistance. In event 2, there is no such limitation and hemisphere growth proceeds as rapid formation of a barrier layer film at constant voltage to a limiting thickness h_c of 13-14 A/V determined by the instantaneous cell voltage. The hemisphere as formed, before protracted current decay, is tentatively viewed as compact. If the passage of the high local repair-current density initiates a subsequent breakdown, the result will be a multiple event consisting of overlapping hemispheres. Figure 7b, event 3, shows a double event. The topography of the larger ($\sim 0.1 \mu\text{m}$) events in the film underside, as in Fig. 6c and d, is consistent with the interpretation that they are clusters of smaller units.

If the cell voltage remains constant as on the plateau of Fig. 1, the film at hemispheres 2 and 3 can suffer no immediate further growth but must await decay of the current at their channels and extension of these by some field-assisted dissolution process to reduce barrier-layer thickness to 10 A/V. During this short period before normal film growth at the repair hemispheres resumes there is normal continuous film growth at the bases of the other channels, as in Fig. 7c. There is thus a leveling effect on the film underside profile tending to keep film growth relatively uniform.

A special mechanism for the breakdown event depicted in Fig. 7a is not required. This event may be viewed as a condition where the film-dissolution rate at the channel base has jumped ahead of the film-growth rate instead of keeping pace with it as in continuous film growth, *i.e.*, the film thickness at the channel base has undergone a large fluctuation from

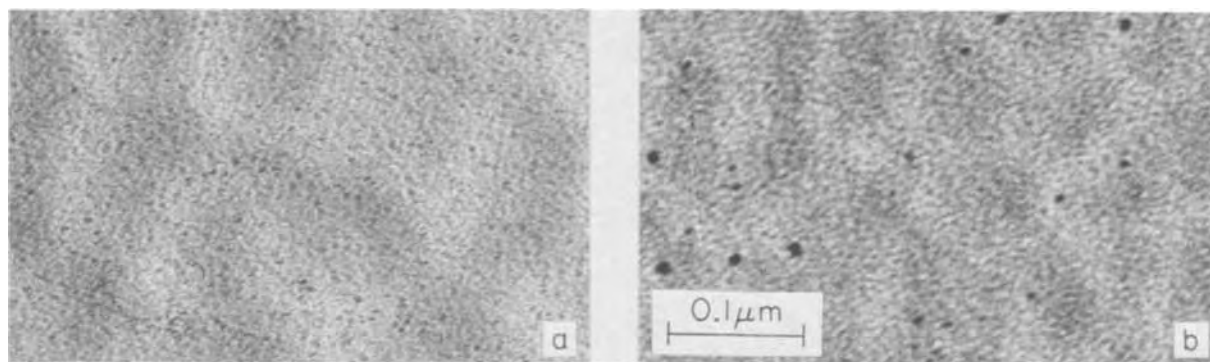


Fig. 5. Single-stage Pt-shadowed carbon replicas of external film surface after (a) 25 sec and (b) 15 min anodizing.

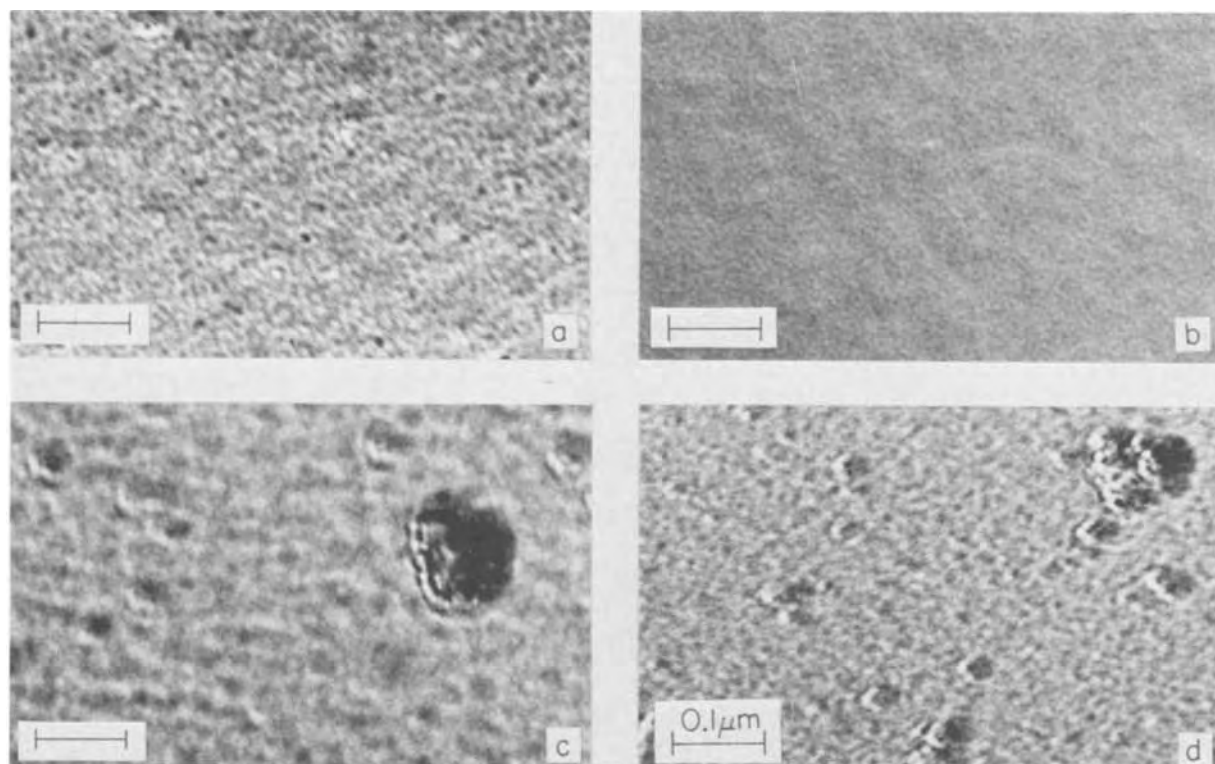


Fig. 6. Replicas of film at metal interface after (a) 15 sec, (b) 25 sec, (c) 300 sec, and (d) 900 sec.

the normally self-regulated value h_p , so that breakdown is not seen as representing a basically new or different process. The breakdown event itself was not observed directly in this work, but micrographs of such a process (the formation of channels extending from the base of a large pore) have been shown by O'Sullivan and Wood in sections of a film formed at 115V in phosphoric acid when the voltage was reduced to 85V (9). Since channel-base dissolution is viewed as field-assisted or associated with the passage of current, the schematic of breakdown in Fig. 7a assumes a small ion current in the film.

The nature of the breakdown process which initiated the observed pits is not clear. It is to be noted that in addition to the relatively few repaired pits detected by scanning microscopy the presence of an undetermined number of much smaller size was indicated in the replicas. This was deduced from the distinctly angular outlines of some of the repair events (several are visible in Fig. 6d). The angularity could have arisen if there had been a brief period of metal dissolution beneath the film yielding a small geometric pit which was then repaired, as indicated schematically in Fig. 8. Some nonangular repair events may also have involved pitting before repair. In experiments in

progress in which Cl^- is added to the acid, a breakdown-pitting-repair process is readily identified and the film formation efficiency is found to be lower, as required if part of the impressed current is used for metal dissolution. Even for the sulfuric acid without additions, metal dissolution is thought to have consumed a significant fraction of the impressed current. Recent studies by the oxygen nuclear microanalysis technique have indicated that in sulfuric acid anodizing there is a substantial direct dissolution current (22).

Breakdown and film structure.—A schematic view of how breakdown is related to the appearance of pores and channels in transmission is given in Fig. 9. The occurrence of individual breakdown-repair events at pores B, D, C is represented by the segments running at an angle to the normal, the straight segments at the bases of these pores representing the resumption of continuous growth. The breakdown at C had caused it to advance ahead of B which then became inactive. As viewed in transmission normal to the film (e.g., Fig. 4d), A and E would appear as rounded pores and C and D as elongated ones and B would be elongated with somewhat lower contrast. The nonuniform spacing of these is implied in Fig. 9. The channels F-K which

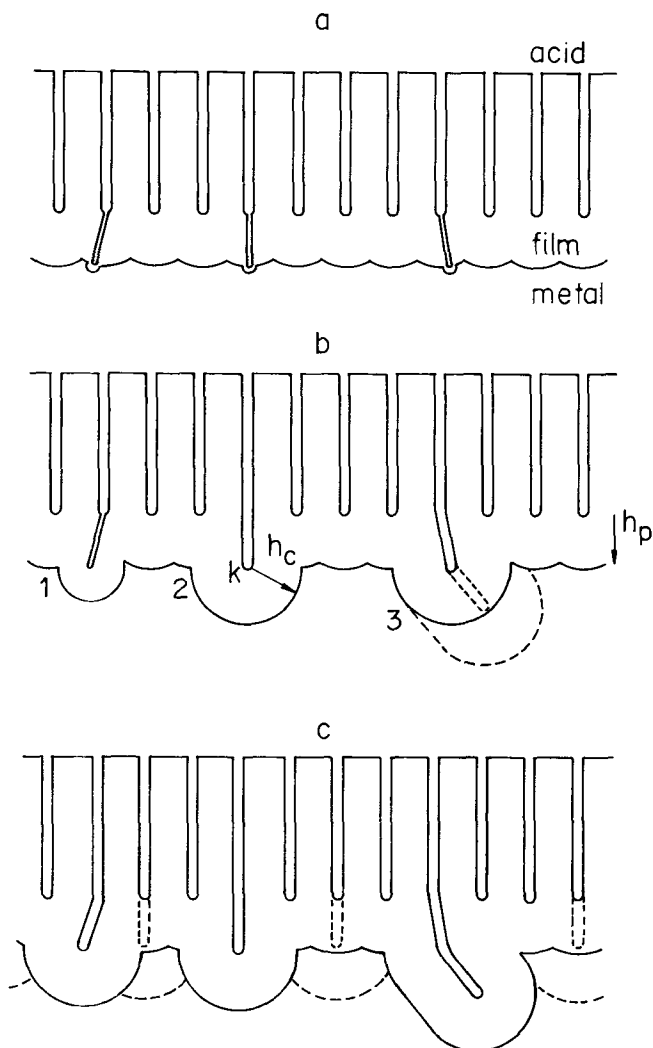


Fig. 7. Schematic of breakdown-repair. (a) Breakdown at three channels. (b) Three forms of repair event (the volume change associated with hemisphere formation is not represented). (c) Normal film growth continuing at the bases of some of the other channels; the repair hemispheres, having reached limiting thickness, h_c , have temporarily stopped growing.

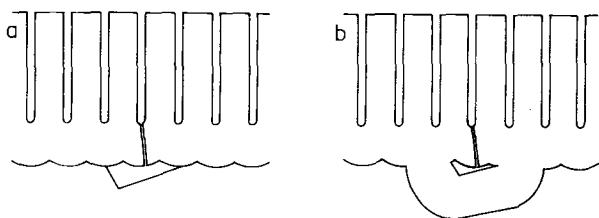


Fig. 8. Schematic of pitting-repair. (a) Small geometric pit growing beneath the film. (b) Film just after reanodization of the surface of the pit.

became inactive at an earlier stage would appear as small spots of low contrast if visible above the background. The distribution of pores and channels in the transmission image for anodizing times ≥ 84 sec was apparently often related to the processes occurring in multiple not individual breakdown repair events and is not interpreted in Fig. 9. The microscopic evidence for jogging or sloping of pores indicative of the individual breakdown-repair processes visualized is best seen in the 25 sec film, a high magnification transmission view of which is given in Fig. 4e. In this, a number of pores (boxed) can be seen with rounded central regions plus lower contrast tails (sometimes termi-

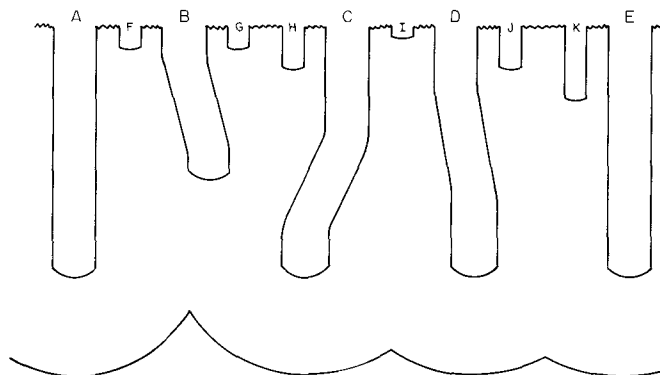


Fig. 9. Schematic of the structure at the base of the film illustrating the interpretation of the appearance of the pores in the transmission micrographs.

nating in a small low contrast satellite spot) as expected for a pore consisting of a long straight section and a short inclined one. The tails are usually associated with a distinct dark border indicative of the extra thickness provided by the repair hemisphere.

Remarks on mechanisms.—The high incidence of breakdown was not unique to the surface preparation used here as shown by observations, to be described subsequently, of films formed after preparing the surface by several different methods. In view of this and of the result that breakdown sites were not necessarily associated with defects in the substrate, the incidence of breakdown is regarded as the consequence of a tendency inherent in the film growth process itself. Given the present limited knowledge of the mechanisms of film dissolution, only rather general notions and plausibility arguments can be dealt with.

It seems useful to view breakdown as related to the phenomenon of pore initiation (i.e., channel formation) in a compact film on aluminum when the forming field falls to a sufficiently low value, as in constant voltage anodizing with protracted current decay (11). The breakdown process in a film containing channels, as represented in Fig. 7a, may be viewed as initiation of "pores" in the compact film at the channel bases. Now in constant current anodizing, use of a low forming C.D. yields a lower average forming field throughout the anodizing and thus is according to the view presented more favorable for film dissolution. It is necessary to postulate that the tendency to form and extend channels is always present from the start of anodizing in sulfuric acid and that it is strong enough at the lower C.D. used here to produce breakdown of the type shown in Fig. 7a. One factor conceivably significant at low plateau voltages where channels are narrow is the formation of constrictions in certain channels by mechanical readjustments to volume changes associated with the formation of new film at the base of the old; this could cause channel resistance, normally negligible, to rise and the forming field at the base to fall.

In considering any effects produced by the repair event, it appears that despite the possibly high local C.D. associated with it local heating was not a major factor in this work. In forming at higher C.D. and higher cell voltages, it is known that there is significant bulk heating, recently measured for compact films on aluminum (23,24), and that breakdown-repair can be accompanied by local heat input rapid enough to produce local crystallization of the amorphous film, which requires a temperature $>600^\circ\text{C}$ (24). The nature of the heat flow problem, pointed out by Young (25), is that the heat flow path to the substrate is so short that there is rapid heat transfer and little temperature difference across the film and normally

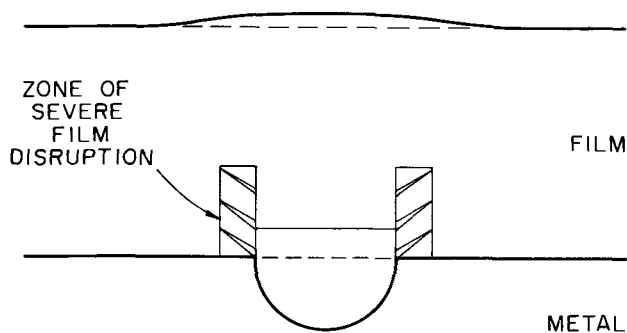


Fig. 10. Schematic of film disruption produced by punching action of repair hemisphere.

film and substrate heat up together, as recently verified by detailed calculations for tantalum (26). The creation of a hot spot requires unusually fast local heat input. For a rough estimate of local temperature rise in the present work, heat input was considered localized at point K in Fig. 7b and the Joule heating idealized in terms of a continuous point source (in an infinite medium) (27) operating long enough to form the repair hemisphere. The hemisphere is so small that even with the choice of a high rate of charge input and a short pulse, e.g., 1 msec, the local temperature rise estimated was negligible.

If local heating is eliminated, any perturbation of the film by the repair event is to be sought in a mechanical process. This is likely to originate in the volume change involved in converting the hemisphere of Al to Al_2O_3 , which is 50-60% depending on the value used for oxide density. This volume change must be taken up by forming a thickness of oxide greater than that of the metal from which it formed. The repair hemisphere at the base of a pre-existing film thus tends to force the overlying film outward. To the extent the hemisphere can be idealized as a punch acting on the overlying cylinder of film, it will disrupt the film along the boundary of this cylinder, as represented schematically in Fig. 10. The film above the hemisphere is a low-density solid containing channels and the nature of its response under these circumstances is not clear. However, one can visualize not only consolidation processes (closing of channels) occurring but also something like formation of a conical crack within the film near its base or of short oblique cracks in the shear zone. It is assumed a crack would not persist as such but be converted into a string of discrete channels by chemical and mechanical processes in the course of film growth. A mechanical disturbance of the film could account for (i) the tendency of the repair event to trigger additional breakdowns at its periphery and so produce the multiple events observed; (ii) the initiation of a pit. The scheme of Fig. 7a does not predict breakdown extending to the metal-film interface and initiating a pit, but these would be accomplished by the formation of a crack, as in Fig. 10, which intersects an existing channel and creates a continuous path of electrolyte extending to the metal. Note that the mechanical effect is seen not as the cause of the original breakdown but as a product of its repair. Recent studies on silicon crystals have made use of x-ray topography to show that tensile stress gradients were not the cause but the result of film "breakdown" (28).

In addition to calling attention to the role breakdown-repair can play in the evolution of film structure

and to certain features worthy of close study, the thrust of the present work is that breakdown of an anodic film (including pit initiation) may occur continually at lower C.D. even when there are no gross manifestations of film failure or pitting, and film stability depends on the efficacy of repair. This notion is likely to be applicable to other anodic processes.

Acknowledgments

This work was sponsored by the U.S. Army Research Office-Durham. In the use of the electron-microscope facilities of the Materials Research Laboratory, which are supervised by R. J. Anderson (who provided Fig. 4e) and J. Woodhouse, it also received support from the U.S. Atomic Energy Commission and the Advanced Research Projects Agency. One of the authors (J. Z.) acknowledges with thanks a grant from the Yad Avi Ha-Yishuv Foundation.

Manuscript submitted Aug. 12, 1971; revised manuscript received June 28, 1972.

Any discussion of this paper will appear in a Discussion Section to be published in the June 1973 JOURNAL.

REFERENCES

1. J. W. Diggle, T. C. Downie, and C. W. Goulding, *Chem. Rev.*, **69**, 365 (1969).
2. J. Yahalom and T. P. Hoar, *Electrochim. Acta*, **15**, 877 (1970).
3. G. C. Wood and J. P. O'Sullivan, *ibid.*, **15**, 1865 (1970).
4. F. Keller, M. S. Hunter, and D. L. Robinson, *This Journal*, **100**, 411 (1953).
5. M. S. Hunter and P. Fowle, *ibid.*, **101**, 514 (1954).
6. M. Nagayama and K. Tamura, *Electrochim. Acta*, **12**, 1097 (1967).
7. J. W. Diggle, T. C. Downie, and C. W. Goulding, *ibid.*, **15**, 1079 (1970).
8. T. P. Hoar and N. F. Mott, *J. Phys. Chem. Solids*, **9**, 97 (1959).
9. J. P. O'Sullivan and G. C. Wood, *Proc. Roy. Soc. London*, **A317**, 511 (1970).
10. M. S. Hunter and P. F. Towner, *This Journal*, **108**, 139 (1961).
11. T. P. Hoar and J. Yahalom, *ibid.*, **110**, 614 (1963).
12. A. J. Brock and G. C. Wood, *Electrochim. Acta*, **12**, 395 (1967).
13. J. S. L. Leach and P. Neufeld, *Corrosion Sci.*, **9**, 413 (1969).
14. J. F. Murphy and C. E. Michelson, *Proc. Conf. on Anodising Aluminium*, The Aluminium Development Association, London, 1962, p. 83.
15. O. P. Arora and M. Metzger, *Trans. Met. Soc. AIME*, **236**, 1205 (1966).
16. J. A. Isasi and M. Metzger, *Corrosion Sci.*, **11**, 631 (1971).
17. R. L. Patterson and C. M. Wayman, *Rev. Sci. Instr.*, **11**, 1213 (1963).
18. J. Zahavi, D.Sc. Thesis, Technion, Israel Institute of Technology (1970).
19. J. Yahalom and J. Zahavi, *Electrochim. Acta*, **15**, 1429 (1970).
20. T. A. Renshaw, *This Journal*, **108**, 185 (1961).
21. R. W. Franklin and D. J. Stirland, *ibid.*, **110**, 262 (1963).
22. C. Cherki and J. Siejka, submitted to *This Journal*.
23. F. R. Applewhite, J. S. L. Leach, and P. Neufeld, *Corrosion Sci.*, **9**, 305 (1969).
24. J. Yahalom and J. Zahavi, *Electrochim. Acta*, **16**, 603 (1971).
25. L. Young, *Trans. Faraday Soc.*, **53**, 229 (1957).
26. J. Zahavi and J. Yahalom, *Electrochim. Acta*, **16**, 89 (1971).
27. H. S. Carslaw and J. C. Jaeger, "Conduction of Heat in Solids," 2nd ed., Oxford, (1959).
28. J. Zahavi, I. A. Blech, and J. Yahalom, *This Journal*, **118**, 1809 (1971).

Some Aspects of the Chemistry of Tin Sensitizing Solutions

N. Feldstein,* J. A. Weiner, and G. L. Schnable*

RCA Corporation, David Sarnoff Research Center, Princeton, New Jersey 08540

ABSTRACT

In the electroless plating of dielectric substrates, sensitization and activation pretreatments are used to provide catalytic sites. The presence of the catalytic sites provides a path for the initiation of the electroless plating process. Based upon findings in this laboratory, a new sensitizing composition containing tin(II) and tin(IV) compounds was developed. This sensitizer was found to be particularly useful in the case of hydrophobic surfaces, and has resulted in good uniformity of metallic coverage on hydrophobic surfaces. In preparing the final sensitizer composition, the use of aged stannic chloride solution was responsible for the improved performance. The present investigation reveals the various chemical changes taking place during the aging of stannic chloride solution. Based upon the current findings, it is believed that during the aging process, a slow formation of a β -stannic acid takes place. This material is a polymeric form, which causes a light scattering effect to take place. It is the presence of β -stannic acid and its interaction with tin(II) that accounts for the improvement in sensitizer performance.

It has been demonstrated (1-3) that contact angle measurements can be an effective technique by which sensitizer solutions may be evaluated. It was also demonstrated (1, 2) that the addition of stannic compounds to tin-type sensitizers can have a major influence on the effectiveness of such solutions, especially when hydrophobic substrates are employed. The results obtained (1, 2) employed sensitizers prepared by aging the stannic chloride stock solution prior to mixing with SnCl_2 solution. Specially prepared and aged (4-6) stannic chloride solutions are most effective when added in low concentrations to solutions for the sensitization of dielectric substrates. By contrast, the stannic chloride normally present in typical stannous chloride does not result in improved wetting in spite of the fact that it is present in the same approximate concentration range as the added aged stannic chloride concentrations.

However, according to Cohen *et al.* (7, 8) the presence of stannic ions in conventional sensitizers (SnCl_2/HCl) constitutes the basis for a proposed mechanism of sensitization. Employing the Mossbauer spectroscopy of tin, a model based upon colloidal stannic hydroxide (hydrated oxide) with bound stannous ions on the colloid surface was proposed. This colloid is present in bulk solution as well as on the sensitized surface. Sard (9), using electron diffraction had shown that sensitized films derived from conventional SnCl_2 sensitizers are adsorbed clumps of material several hundred angstroms in diameter. Luce *et al.* (10) and Drotar *et al.* (11) also described sensitizers in which excess stannic chloride was added to conventional sensitizer media (SnCl_2/HCl). However, in all cases, no attempt was made to precondition the stannic solution while in the present work, the stannic halide solutions are first prepared, allowed to age, and then mixed with the stannous chloride solution. Bernhardt (12) described a sensitizer in which stannic chloride was incorporated into a sensitizer media, and the final solution was permitted to age for about 2 weeks before use. While this procedure provided improvement in performance, the approach was reported to be limited to solutions in which the acidity content is relatively low. More recently, Kenney *et al.* (13) have indicated that colloidal suspensions of tin oxides or iron oxides can wet hydrophobic surfaces; however, details related to solution preparation are not at present available. In this

paper, the aging phenomenon of the stannic chloride solution has been examined in greater depth as related to the sensitization process. Based upon these findings, a model accounting for the effect(s) of stannic ions (1, 2) in tin sensitizers is proposed.

Experimental Procedures

Chemicals and solutions.—Most of the common chemicals used throughout this investigation were Baker reagent grade. The less common chemicals were c.p. grade. The acids used were Mallinckrodt electronic grade. The water used was deionized and then distilled.

Contact angle measurements and substrate preparation.—The procedure adopted was to measure the contact angle following the sensitization step. Details for the preparation of substrates, and for substrate treatment have been described in detail previously (2).

Spectral absorbance.—The spectral absorbance measurements in the visible range were made using a Beckman DB-G spectrophotometer. In all cases, air was the reference.

Conductance measurements.—Conductance measurements were made using a Beckman Type RC 16B2 conductivity bridge. The conductivity cell used had a cell constant of 1.0 cm^{-1} , and all measurements were taken at $23^\circ \pm 1^\circ \text{C}$.

pH measurements.—These measurements were made using a Corning pH/Controller, Model 10-C.

Nephelometric measurements.—Nephelometric measurements were made using a Coleman Model 9 Nephelometer. The reference standard used was Coleman Nephelos Standard 21. A 25-mm diameter immersion well and 19-mm diameter cells were used. The null reading method for total nephelos was employed, as suggested in Coleman Manual D-202D.

Results and Discussion

In the course of this investigation, it became apparent that the aging of stannic chloride solutions plays a major role in the sensitization process. Although the chemistry of aging stannic solutions was a subject of research at the beginning of the 20th century (14), some of the available references are vague. In the following section, certain aspects of the aging process and of the interaction of stannic-stannous components are reviewed as an introduction to the model proposed.

* Electrochemical Society Active Member.
Key words: sensitizer, aging of stannic solutions, electroless plating.

On the Aging of Stannic Chloride Solution

It was previously demonstrated (1, 2) that the extent of lowering of the contact angle after sensitization (for solutions having stannic and stannous together) is greater than either of the corresponding values resulting from immersion of hydrophobic substrates in stannic or stannous solutions, respectively. This observation suggests that some interaction may exist between the stannic and the stannous components. To test whether this interaction is unique to the tin(II)/tin(IV) system, the results of Tables I and II are submitted. In Table I, the contact angle was examined upon replacement of the stannous ion by an equivalent concentration of other divalent ions while holding the concentrations of aged stannic chloride, sodium chloride, and hydrochloric acid at fixed values. As seen from Table I, in all cases except for the incorporation of stannous chloride, the resulting contact angle is either the same as the control solution ($7.5 \times 10^{-3}M$ $SnCl_4$, $2M$ $NaCl$, and $4.7 \times 10^{-1}M$ conc. HCl) or greater. In view of these results, it appears that the interaction between the stannous and stannic ions is of specific chemical nature rather than a coulombic type interaction between the stannic ions and the divalent ions added. Further examination of these results shows that the divalent salts added may be divided into two categories. In the first category ($MnCl_2$, $NiCl_2$, $Co(NO_3)_2$, and $CuCl_2$) the resulting contact angle is either the same or slightly greater than that of the control stannic solution, while in the second category ($MgCl_2$, $ZnCl_2$, and $PdCl_2$) the resulting contact angle values are considerably greater than the control value (48 degrees). Poor wetting has resulted when employing these solutions. The reasons for this behavior are not apparent. However, a combination of stannous chloride and zinc chloride with added aged stannic component provided good wetting and good plating uniformity of subsequently applied electroless deposits. It would thus seem that the interaction of stannous/stannic is very strong in comparison to the zinc/stannic interaction.

In Table II the resulting contact angle is shown as varying with the addition of tetravalent ionic salts to a fixed conventional-type sensitizer solution ($SnCl_2/HCl$). As seen from Table II, there is a significant lowering of the contact angle (55° vs. 67° for the control solution) only in the case of $SnCl_4$. These results fur-

Table I. Contact angle^(a) variations vs. divalent salts used

Salt	Contact angle (degrees)
None	48
$MnCl_2$	50
$NiCl_2$	53
$Co(NO_3)_2$	55
$CuCl_2$	49
$MgCl_2$	62
$ZnCl_2$	72
$PdCl_2$	71
$SnCl_2$	27

^(a) All solutions composed of: $7.5 \times 10^{-3}M$ $SnCl_4$, $2M$ $NaCl$, and $4.7 \times 10^{-1}M$ HCl to which $1.3 \times 10^{-1}M$ of divalent salts were added. Measurements were made on AZ-1350 resist.

Table II. Contact angle^(a) vs. tetravalent salt^(b) in sensitizer^(c)

Salt	Contact angle (degrees)
None	67
ZrF_4	68
$Th(NO_3)_4$	66
$Ce(NH_4)_2(NO_3)_6$	69
$SnCl_4$	55

^(a) Measurements were made on AZ-1350 photoresist.

^(b) Solutions of $10^{-2}M$ Zr , Th , and Ce were aged 24 hr. The $SnCl_4$ solution ($0.5M$) was aged about 1 week.

^(c) Final composition used composed of $1.3 \times 10^{-1}M$ $SnCl_2$, $4.7 \times 10^{-1}M$ HCl , and $1.0 \times 10^{-2}M$ of tetravalent salt.

ther support the previous conclusion that a unique chemical interaction between the stannic and stannous ions probably accounts for the improved effectiveness of the tin sensitizer solutions.

From the initial discovery of the improved sensitizer composition, it has been apparent that aging of the stannic chloride solution is an essential factor responsible for the improvement. In order to gain a better insight into the aging phenomenon and its role in the sensitization process, the data of Fig. 1-3 and Table III are submitted.

Figure 1 shows the variations in contact angle as aging (at room temperature) of the stannic chloride stock solutions takes place. In all cases, it is apparent that the contact angle decreases as the stannic chloride stock solution is allowed to age. Moreover, decreasing the concentration of the stannic chloride stock solution provides a more rapid and effective aging process.

In Fig. 2 the absorbance spectra of the tin solutions in the near ultraviolet range are shown. As seen, the

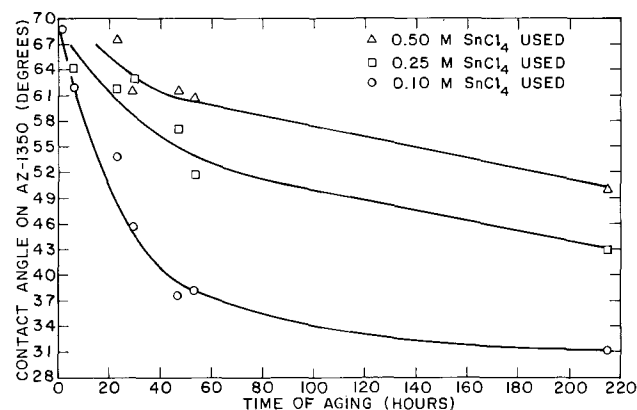


Fig. 1. Contact angle variations vs. aging time on AZ-1350 resist. Solutions prepared composed of $0.47M$ HCl , $0.13M$ $SnCl_2$, and $7/5 \times 10^{-3}M$ $SnCl_4$.

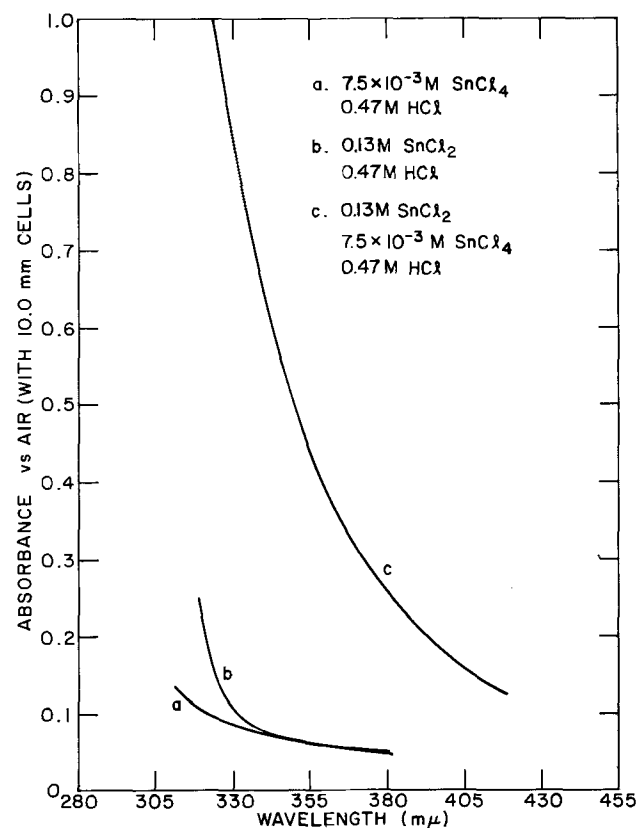


Fig. 2. Absorbance vs. wavelength for stannous, stannic, and mixed tin solutions.

resulting absorbance values of the combined solution of stannous and stannic components is nonadditive in comparison to the absorbance curves for the two components individually. This behavior is consistent with the previous observation by Browne *et al.* (15) on the optical interaction of stannous and stannic ions.

Craig *et al.* (16) suggested that the intense nonadditive adsorption of light by systems containing an element in two different oxidation states may be regarded as being due to the vibration of electrons between the atoms in the two different oxidation states. Other systems reported (17, 18) to exhibit this effect are: Fe(II)/Fe(III), Cu(I)/Cu(II), Ti(III)/Ti(IV), Tl(I)/Tl(III), Sb(III)/Sb(IV), and others. More recently, an extensive review related to this broad phenomenon was made by Allen and Hush (18). Hush designated the above systems as "homonuclear intervalence-transfer systems." It should be noted that the optical interaction (Fig. 2, curve C) takes place only under specific conditions. The mixed complex which forms may be completely dissociated upon the addition of complexing agents for either the stannous or stannic ions. A typical complexing agent is the chloride ion. Complementary to the results of Fig. 1, Fig. 3 is provided in which the absorbance of sensitizer solutions was monitored as the continuous aging of the stannic chloride stock solutions was taking place. As the aging process for the stannic solution proceeds, the absorbance of the sensitizer solutions is increased, but eventually levels off. The results of Fig. 3 further support the advantages of using aged dilute stannic chloride stock solutions, as this provides a more rapid aging, and a more effective sensitizer solution. From the results of Fig. 1 and 3, it is believed that a colloidal specie(s) (whose predecessor is stannic chloride) is formed during the aging process. The presence of such specie(s) can provide the improvement in the wetting process, and also in the formation of a colored stannous-stannic complex. The formation of such complex may be inhibited in bulk solution if excess sodium chloride is added (17); however, the improvement in the sensitization process is retained. Further examination of the results of Fig. 1 and 3 suggests that a reciprocal relation exists between the measured contact angle and solution absorbance (for the conditions examined without excess sodium chloride) during the different stages of the aging process. Specifically, as the contact angle values decreased, the solution absorbance values increased. The existence of this correlation (in the absence of excess chloride) justified further investigation in which only spectral absorbance measurements were taken. From the reciprocal relationship, the trend in spectral absorbance may be used in estimating the contact angle and hence the effectiveness of the sensitizer solution(s). Figure 4 shows the spectral absorbance of sensitizer solutions made from stock stannic

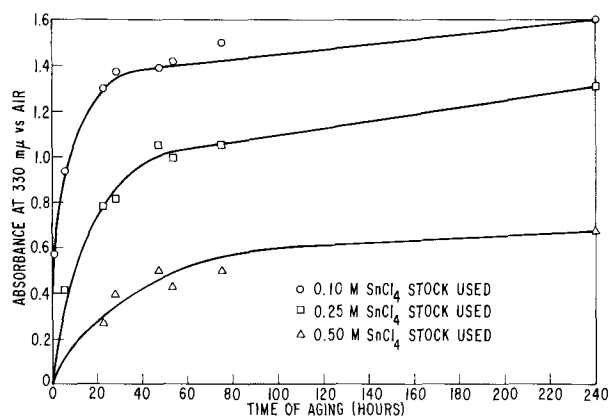


Fig. 3. Absorbance vs. aging of stannic solutions. Solutions prepared composed of 0.47M HCl, 0.13M SnCl₂, and 7.5×10^{-3} M SnCl₄. Cell length = 10 mm.

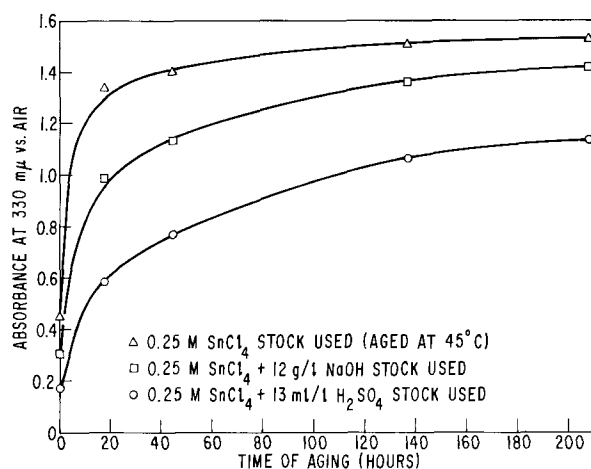


Fig. 4. Absorbance vs. aging condition of stannic solutions. Solutions prepared composed of 0.47M HCl, 0.13M SnCl₂, and 7.5×10^{-3} M SnCl₄. Cell length = 10mm.

chloride which has been aged under varied conditions. As seen, aging of stock solution (0.25M SnCl₄) at 45°C provides an improvement in comparison to aging the same solution with added alkali or acids, or to aging at room temperature (see Fig. 3). Furthermore, the addition of alkali provides a slight accelerating effect of the aging in comparison to the case in which acid was added. Attempts to age the stannic chloride (0.25M) in aqueous media having a higher acid content (e.g., 10N HCl, H₂SO₄, or HNO₃) showed that the aging process is totally inhibited. Sensitizer solutions made by this approach did not provide the improved wetting characteristics.

In Table III, the effectiveness of aging condition and concentrations is demonstrated. In order to determine the effectiveness of the aging condition, the concentration of aged stannic chloride necessary to give a fixed absorbance value (0.72 absorbance) was determined.

From these results, it is apparent that more effective aging is carried out at higher temperatures and at lower stannic concentrations. Under such optimized conditions, less of the aged stannic chloride solution is required in order to yield a given absorbance level or a specific wetting characteristic. This observation seems to be consistent with prior reports on the hydrolysis of stannic solutions. Collins *et al.* (19, 20) have demonstrated that the extent of hydrolysis for stannic chloride solutions is decreased as the concentration of the tin is increased. Specifically, the authors (20) reported 94 and 72% hydrolysis for 0.197N and 0.396N stannic solution which were allowed to age at 25°C. Mellor (14) reported that heating of stannic solution does accelerate the hydrolysis. However, caution should be exercised as prolonged heating of such solution(s) produces a heavy precipitation which is probably due to the formation of stannic hydroxide (hydrated stannic oxide). This same precipitation was also found during the aging (at room temperature) of stock solutions having a stannic chloride content below about 0.1M.

Table III. Effect of temperature and concentration on rate of aging of stannic chloride solutions

Molar concentration of SnCl ₄	Aging temperature, °C	Concentration used, ^(a) molar
0.50	80	6.0×10^{-3}
0.50	45	25×10^{-3}
0.25	80	2.8×10^{-3}
0.25	45	5.2×10^{-3}
0.10	45	3.6×10^{-3}

^(a) Concentration required to give absorbance of 0.72 ± 0.01 vs. air at 330 mμ. In all cases [Sn⁺²] = 0.13M and [HCl] = 0.47M. Cell length = 10.0 mm.

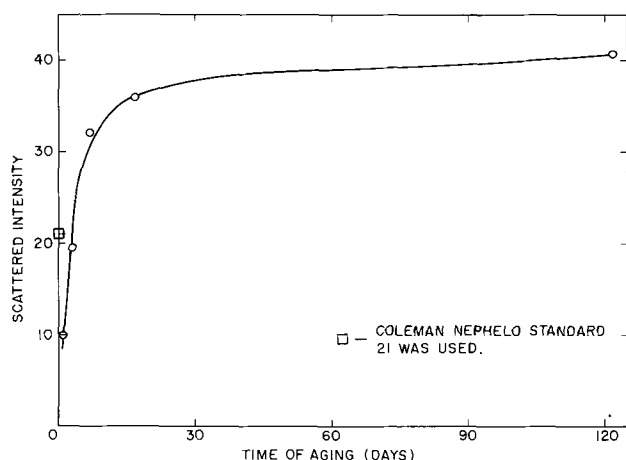


Fig. 5. Scattered intensity vs. aging time of 0.50M SnCl_4 solution.

In Fig. 5, the variation in turbidity taking place during the aging process for a stannic chloride stock solution is shown. The results of Fig. 5 closely resemble the general characteristics of Fig. 3 and 4. With the increased turbidity taking place during the aging process, there must be an increase in the number and/or size of colloidal particles which cause the Tyndall effect. The colloidal particles are a polymerized specie(s) containing tin(IV). In a recent publication, Cohen *et al.* (7, 8) proposed a model for the mechanism of conventional sensitizers. In their proposed model, the presence of stannic hydroxide (or hydrated stannic oxide) colloids in bulk solution was invoked as being primarily responsible for the sensitization process. The stannous ions were reported bound onto these colloids in a compositional ratio of 1-tin(II) to 2-tin(IV).

Although the current report and the published work of Cohen (7, 8) both describe the presence of colloidal particles containing tin(IV), it should be apparent that these are different colloids. These two colloids, although their formulas are not known, result in different chemical and physical characteristics of the final sensitizer solutions. Moreover, the colloidal particles [polymerized specie(s) containing tin(IV)] present in the current system may be physically included with conventional sensitizer solution or be used prior to the immersion in the conventional sensitizers (2). In both cases good plating uniformity has resulted on hydrophobic surfaces. By contrast, the colloids present in conventional sensitizers proposed by Cohen *et al.* (7, 8) are not effective when used with hydrophobic substrates, and they are an integral part of the sensitizing media and cannot be separated from the stannous component.

In order to ascertain the nature of ionic reaction(s) taking place during the aging process, conductance measurements were made. Figure 6 shows the manner by which solution conductance varies with aging time. In all cases, independent of aging condition, solution conductance is increased in a manner which resembles the characteristics results of Fig. 3. In Table IV, the pH changes during the aging process are summarized for typical stannic chloride stock solutions. In all cases, there is an actual decrease in solution pH. The trend is in good agreement with the results of Gueron (21). Based upon the increase in hydrogen ion concentration taking place (Table IV), an estimate of change in solution conductance was made. Specifically, for a 0.25M SnCl_4 aged at room temperature, a 0.11 mho increase in conductance was anticipated. The experimentally found value (Fig. 6) was a change of approximately 0.09 mho. The difference between the experimental and anticipated values is probably due to the net effect of the hydrolysis reaction and the polymerization of the stannic ions. The latter effect decreased solution conductance. Furthermore, based upon the

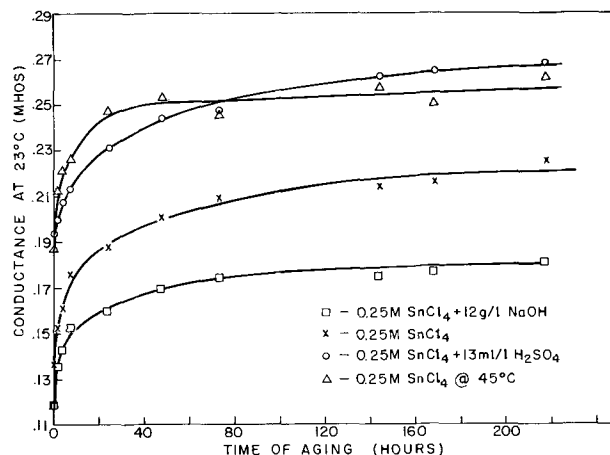


Fig. 6. Conductance variations vs. aging of stannic chloride solutions.

results of Table IV, it would appear that the number of hydrogen ions liberated, relative to the initial stannic ion concentration, is increased as the concentration of stannic ion is decreased. This observation further supports the optimized condition for aging stannic solutions. This relative ratio (last column of Table IV) is probably an average value, with individual aged stannic species having a greater or lower ratio than the average value.

The Proposed Mechanism of Sensitization

Before proposing a physical model that accounts for the improvements associated with the stannous-stannic sensitizer solution, a brief review of pertinent literature references and findings from this laboratory will be made.

1. As has been demonstrated in Fig. 2 and 3 of this paper, and in the reports by Browne (15), Craig (16), and Paul (17), there is an apparent chemical interaction between the stannous and aged stannic components resulting in a mixed complex. The mixed complex formed has been reported to have a fixed stoichiometric ratio of stannous to stannic ions. Specifically, Paul *et al.* (17) reported a 1:4 Sn(II)-Sn(IV) complex while Browne *et al.* (15) reported a 1:1 Sn(II)-Sn(IV) complex.

2. In a previous publication (2), it has been demonstrated that the aged stannic chloride may be either incorporated along with conventional type sensitizers (SnCl_2/HCl), or may be used as a separate immersion step prior to the immersion in conventional sensitizers. In both cases, equivalent results were obtained following the plating step.

3. As the concentration of aged stannic component (β -stannic acid) is increased to or above the approximate level of the stannous concentration, the uniformity of metal deposition is decreased. Although this type of composition is not used, it does reflect an interesting aspect of the mechanism of the sensitization process.

Based upon the findings of this investigation and previous reports on the subject of stannic chloride hydrolysis, the following key steps are proposed to ac-

Table IV. Effect of aging on the pH^(a) of stannic solutions

[SnCl_4]	pH as prepared	Final pH	$\Delta[\text{H}^+]/\text{Sn}^{++}$
0.10	0.94	0.52 ^(b)	2.0
0.25	0.50	0.19 ^(b)	1.3
0.50	0.38	0.06 ^(c)	0.9
2.00	-0.05	-0.12 ^(c)	0.08

(a) Buffer 1.00 as reference.

(b) Aged for 30 days.

(c) Aged for 10 days.

count for the mechanism taking place during the sensitization process.

Case A: Immersion in aged stannic solution prior to immersion in stannous solution.—(i) Upon immersion in aged stannic solution, a retention, by adsorption or other mechanism, of the aged stannic component takes place on the dielectric surface. This adsorption step is an equilibrium reaction with some specie(s) existing in bulk solution. The active specie(s) is probably a β -stannic acid which is slowly formed during the aging process.

(ii) Upon immersion in stannous solution, the stannous ion is adsorbed at the interface. In fact, it is the presence of the β -stannic component at the interface that provides new boundary conditions which result in a new kinetic path for the adsorption of the stannous component on the surface. This path is probably the same chemical reaction which leads to the formation of the mixed tin(II)/tin(IV) complex. This reaction probably provides the driving force for the formation of a final stabilized surface layer consisting of both stannic and stannous components. In the formation of such a layer, the stannous component may have also replaced a fraction of sites previously occupied by the stannic component and/or be adsorbed in sites which were vacant at the conclusion of step (i).

Case B: Immersion in sensitizer solution composed of stannous and aged stannic components.—Under this condition, it is possible that the mechanism described in Case A takes place. It is also possible to postulate that the existing mixed complex tin(II)/tin(IV) is directly adsorbed onto the surface. This alternative, however, is unlikely in view of the fact that if the concentration of aged stannic component is made larger than the stannous component (approximately $1.5\times$), there is a deterioration in the uniformity of plating. This behavior is due to the fact that most of the stannous ions are tightly held in the mixed complex present in the solution phase and are not available for adsorption at the interface. This condition can be rectified by the addition of sodium chloride which causes a dissociation of the mixed complex, hence liberating "free" stannous capable of adsorbing at the interface. Alternatively, using the stannic component prior to the stannous immersion step also rectifies this trend. In subsequent studies (22), the results of surface characterization of sensitized layers using radiochemical tin-113 have been found to support the proposed mechanism. The results of the surface characterization also further distinguish between the current colloid and that proposed by Cohen (7, 8).

Conclusions

Aged stannic chloride solution has been shown to have a significant role in improving the performance of conventional sensitizer solutions. The aging process in the stannic halide solution is believed to be a slow transformation of an α -stannic acid to a β -stannic acid form (14, 19, 21). Such transformation is probably due to a water elimination reaction resulting in a general structure of the type (21)



where n may have values of 1, 2, 3, etc. reflecting the extent of polymerization. In the above structure some further water condensation may take place. The increasing β -stannic acid character of such solutions results in a Tyndall effect, probably due to the colloidal nature of the β -stannic acid. Furthermore, as the concentration of β -stannic component is increased, im-

provements in the sensitizer solution's wetting performance have resulted.

Conditions which optimize the formation of the β -stannic acid were found to be consistent with earlier reports on this subject. Specifically, acceleration in the aging process was found with increased temperature and/or decreased stannic concentrations. High acid content as well as high concentrations of sodium chloride were found to inhibit the α to β transformation. The transformation of the α -stannic acid to the β -stannic acid is generally irreversible under normal conditions. However, under those conditions in which the aging process is inhibited, some degree of reversibility of the β -stannic to α -stannic does take place.

Although the current work was focused upon the improvement of sensitizers on hydrophobic surfaces, it should be apparent that the current finding may be used for other processes in which it is necessary to convert hydrophobic surfaces to hydrophilic type. Hydrophobic surfaces immersed in aged stannic solution only were converted to hydrophilic type and this property was retained for at least several days.

Acknowledgments

The authors wish to thank J. A. Amick and P. Rappaport for their encouragement and support in this investigation.

Manuscript submitted March 13, 1972; revised manuscript received May 18, 1972. This was Paper 215 presented at the Miami Beach Meeting of the Society, Oct. 8-13, 1972.

Any discussion of this paper will appear in a Discussion Section to be published in the June 1973 JOURNAL.

REFERENCES

1. N. Feldstein and J. A. Weiner, *Plating*, **59**, 140 (1972).
2. N. Feldstein and J. A. Weiner, *This Journal*, **119**, 668 (1972).
3. N. Feldstein and J. A. Weiner, Paper No. 215, presented at Electrochem. Soc. Meeting, Miami Beach, Florida, Oct. 8-13, 1972.
4. Staff Editor, *Chemical and Engineering News*, **50**, February 21, p. 17, (1972).
5. Staff Editor, *Electronic Packaging and Production*, **12**, p. 15, April (1972).
6. Staff Editor, *Industrial Finishing*, **48**, p. 112, May (1972).
7. R. L. Cohen, J. F. D'Amico, and K. W. West, *This Journal*, **118**, 2042 (1971).
8. R. L. Cohen and K. W. West, *ibid.*, **119**, 433 (1972).
9. R. Sard, *ibid.*, **117**, 864 (1970).
10. D. M. Luce and B. L. Berdan, and M. L. Selker, U.S. Pat. 3,245,862 (1966).
11. J. S. Drotar, A. A. Parker, and K. A. Snyder, U.S. Pat. 3,573,973 (1971).
12. G. Bernhardt, U.S. Pat. 3,616,296 (1971).
13. J. T. Kenney, W. P. Townsend, and J. A. Emerson, Am. Chem. Soc., 162nd National Meeting, Colloid Division, Abstract No. 90 (1971).
14. J. W. Mellor, "Comprehensive Treatise on Inorganic and Theoretical Chemistry," Vol. VII, p. 404, Longmans Green and Co., New York (1927).
15. C. I. Browne, R. P. Craig, and N. Davidson, *J. Am. Chem. Soc.*, **73**, 1946 (1951).
16. R. P. Craig and N. Davidson, *ibid.*, **73**, 1951 (1951).
17. A. D. Paul, K. T. Robbins, and C. V. Overfield, *Proc. West Va. Acad. Sci.*, **38**, 237 (1966).
18. G. C. Allen and N. S. Hush in "Progress in Inorganic Chemistry," F. A. Cotton, Editor, Vol. 8, p. 357, Interscience Publishers, New York (1967).
19. G. E. Collins and J. K. Wood, *J. Chem. Soc. (London)*, **121**, 441 (1922).
20. G. E. Collins and J. K. Wood, *ibid.*, **123**, 452 (1923).
21. J. Gueron, *Ann. Chim.*, **11**, 225 (1935).
22. N. Feldstein, *This Journal*, Submitted for publication.

The Use of Organic Additives to Stabilize and Enhance the Deposition Rate of Electroless Copper Plating

Leonard N. Schoenberg*

Bell Laboratories, Murray Hill, New Jersey 07974

ABSTRACT

A persistent problem in the use of electroless copper baths has been their tendency to decompose spontaneously. Materials previously proposed as stabilizers have, in general, the undesirable effect of decreasing the plating rate of the bath. It has been found in the present work that the organic additive 8-hydroxy-7-iodo-5-quinoline sulfonic acid (HIQSA) not only stabilizes electroless copper baths but also enhances the plating rate by as much as 50%. The additive 2-iodo-3-pyridinol stabilizes the solutions but has little effect on the plating rates. An explanation for this behavior is set forth and is supported by the stabilizing effect, if any, of other organic additives with structures similar to HIQSA.

Interest in electroless copper plating has increased recently because of its use in the manufacture of printed circuits and its potential application to many other processes. A persistent problem in the use of these baths has been their tendency to decompose spontaneously. Many materials have been proposed to serve as stabilizers (1) but in general these have the undesirable effect of decreasing the plating rate of the bath. Okinaka and Blom (2) found that a large amount of methanol could stabilize electroless copper baths with only a minimal decrease in the plating rate. Another approach involves stabilizing a copper bath by the incorporation of less frequently used complexing agents (3). This paper discusses organic additives which stabilize electroless copper solutions not only without adversely affecting the plating rate but in some cases actually enhancing it. The use of thiourea and other compounds both to stabilize and increase the plating rate of electroless nickel baths has been reported by deMinjer and Brenner (4).

The organic additives chosen for study are shown in Fig. 1. All were obtained from Aldrich Chemical Company, Inc. and used without further purification. Most of the experimental work was carried out with 8-hydroxy-7-iodo-5-quinoline sulfonic acid (HIQSA). The other additives shown were surveyed because of their partial resemblance to HIQSA and their potential to support the proposed mechanism of stabilization-acceleration discussed in a subsequent section.

Determination of Bath Stability

Electroless baths often spontaneously decompose (*i.e.*, deposit metal) after a certain time whether or not

* Electrochemical Society Active Member.
Key words: electroless plating, copper plating.

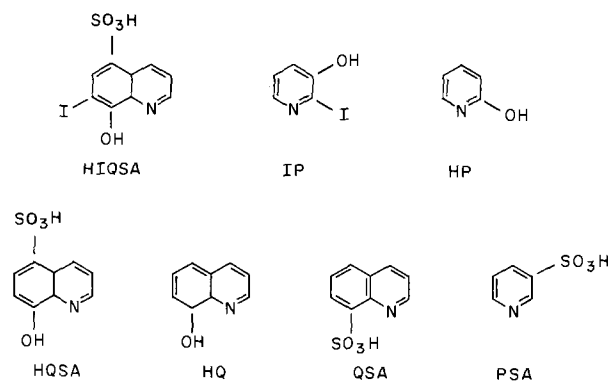


Fig. 1. Structural formulas of the organic additives surveyed in the present work.

they are in active use. Small metallic nuclei may form and initiate plating or decomposition may be started by random variables such as dust particles or other impurities. Thus decomposition time is variable and solutions prepared in identical fashion may have non-identical lifetimes. It was decided that the best way to achieve consistent behavior and to determine the effect, if any, of an additive was to run stability tests at an elevated temperature with the addition of controlled amounts of impurities.

The composition of the electroless copper bath selected for study was 0.02M cupric sulfate pentahydrate ($\text{CuSO}_4 \cdot 5\text{H}_2\text{O}$), 0.1M disodium ethylenediaminetetraacetate dihydrate ($\text{Na}_2\text{EDTA} \cdot 2\text{H}_2\text{O}$), 0.4M formaldehyde (added as paraformaldehyde), and sufficient sodium hydroxide to obtain a pH value of 12.8. Forty-five milliliter aliquots of the solution were placed in a 75°C constant temperature water bath.

To evaluate stabilizing additives, bath decomposition was accelerated by the following method. [A similar means of inducing decomposition of electroless nickel baths was used by Ramirez (5).] After a 5-min interval to allow the solutions to reach 75°, three small drops of an activating solution containing palladium were added. The activating solution is used in metalizing nonconductors. It is made by dissolving 1g of palladium chloride in 10 ml of concentrated hydrochloric acid and diluting to one liter. (Palladium activator can be carried over into an electroless copper bath during actual printed circuit processing.) At 75°C, an additive free bath decomposes instantaneously. However, with the addition of various organic additives bath life can be extended significantly as shown in Table I. The time to decomposition reported in Table I may vary depending on the time between bath preparation and testing, the exact bath composition (which fluctuates due to normal experimental error), and random variables such as dust particles, etc. The importance of Table I is to show that certain organic

Table I. Decomposition times (minutes) of an electroless copper bath (0.02M $\text{CuSO}_4 \cdot 5\text{H}_2\text{O}$, 0.1M $\text{Na}_2\text{EDTA} \cdot 2\text{H}_2\text{O}$, 0.4M HCHO, pH 12.8) with different amounts of organic additives

Additive	Amount (mg/l)					
	0	1	11	33	110	220
8-hydroxy-7-iodo-5-quinoline sulfonic acid (HIQSA)	0	0.6	8.5	19	>150	>150
2-iodo-3-pyridinol (IP)	0	3	20	75	—	—
2-hydroxy pyridine (HP)	0	0	5	7.5	—	—
8-hydroxy-5-quinoline sulfonic acid (HQSA)	0	0	2	4	—	—
8-hydroxy quinoline (HQ)	0	Forms precipitate		—	—	—
8-quinoline sulfonic acid (QSA)	0	0	0.5	1	—	—
3-pyridine sulfonic acid (PSA)	0	0	0	0	—	—
Potassium iodide (KI)	0	2	2.5	2.5	—	—

additives markedly improve bath stability under accelerated decomposition conditions and therefore would be expected to improve stability under normal operating conditions as well.

It can be seen that two additives are highly effective in stabilizing the bath, namely, HIQSA and 2-iodo-3-pyridinol (IP). These were selected for further study. It can also be noted that iodide ion alone, in equivalent quantities, while it has some stabilizing influence cannot be considered an effective bath stabilizer.

Plating Rate Studies

Plating rate measurements were carried out on 0.002 in. thick copper rectangles of approximate dimension $1 \times \frac{1}{2}$ in. The substrates were etched for 15 sec in 20% nitric acid, rinsed, activated for 1 min in the 0.1% palladium chloride solution, and rinsed again. This resulted in a reproducible metallic palladium surface for plating rather than a possibly variable surface of cuprous oxide. The substrates were held in a vertical position by Teflon holders. Plating was usually done from 90 ml aliquots of the various electroless copper solutions at room temperature. Plating times varied from 1 to 7 hr. The 7-hr plating experiments were done from 180 ml of solution to ensure a large excess of copper ions. The thicknesses of the copper deposits were determined by weight gain measurements making the usual assumptions that the deposit thickness is uniform over the entire surface and that the deposit density is that of bulk copper. The appearance of the copper is the same as that deposited from an additive free bath. No measurements of ductility or other physical properties were made.

The results with various amounts of HIQSA are shown in Fig. 2. The plating rates are plotted as the differences (in $\mu\text{M/hr}$) between an additive free bath and a bath containing a given amount of HIQSA. This is done to eliminate effects due to random variables such as the solution composition and age, exact room temperature, etc. Each point on the curve is an average of at least two determinations. The plating rate of an additive free bath is in the vicinity of $1 \mu\text{M/hr}$ so that the maximum of the curve represents an increase in plating rate of about 50%.

Less extensive data of the same sort for additions of IP are presented in Fig. 3. It can be seen that IP has much less accelerative effect on the bath.

Discussion of Results

To understand the action of HIQSA on an electroless copper bath, the effects of stabilization and acceleration must be discussed separately.

For an additive to be an effective bath stabilizer it must interact with at least two different kinds of impurities. The first type is ionic impurities such as Pd^{2+} which if reduced by formaldehyde to the metallic state

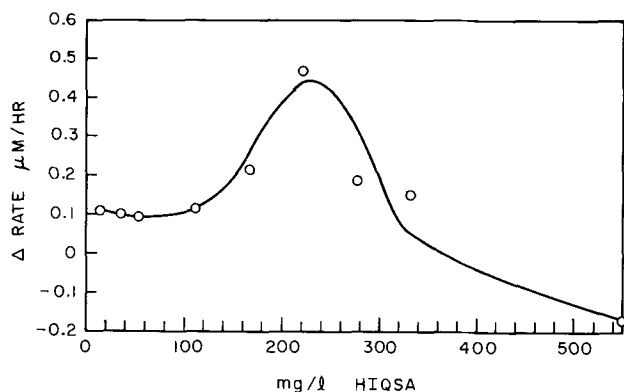


Fig. 2. Change in plating rate of an electroless copper solution (0.02M $\text{CuSO}_4 \cdot 5\text{H}_2\text{O}$, 0.1M $\text{Na}_2\text{EDTA} \cdot 2\text{H}_2\text{O}$, 0.4M HCHO , pH 12.8) with varying amounts of HIQSA.

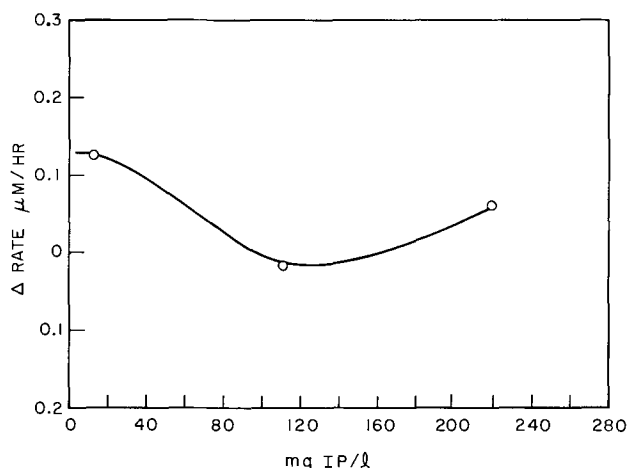


Fig. 3. Change in plating rate of an electroless copper solution (0.02M $\text{CuSO}_4 \cdot 5\text{H}_2\text{O}$, 0.1M $\text{Na}_2\text{EDTA} \cdot 2\text{H}_2\text{O}$, 0.4M HCHO , pH 12.8) as a function of added IP.

could initiate electroless plating in the bulk of the solution. The second type is small metallic nuclei or cuprous oxide particles which may be formed in the solution as electroless plating proceeds.

HIQSA may inhibit decomposition by the first type of impurity by using its nitrogen and hydroxide functions to form a chelate. This chelate contains the same type of linkage as those formed by metal ions and 8-hydroxy quinoline (HQ), a well-known sequestering agent and the parent compound of HIQSA (Fig. 4). The sulfonic acid group of HIQSA is responsible for HIQSA complexes being more water soluble than HQ complexes.

HIQSA may prevent decomposition of the bath by metal nuclei or cuprous oxide particles by being adsorbed through the iodide portion of the molecule (Fig. 5). We have previously shown that iodide ions in sufficient quantity can poison electroless copper baths (7). These strongly adsorbed species are thought to inhibit the kinetics of the electroless deposition.

Plating is not completely inhibited by adding the proper amount of HIQSA because it is not present in large enough quantities to poison the surface on which it is desired that plating occur, although larger amounts of additive do decrease the rate as expected. This is in agreement with the observations of Gutzeit (8), who in a discussion of electroless nickel plating states that the adsorption density of stabilizing ions is a direct function of the radius of curvature of the catalytic body so that small particles are more rapidly and com-

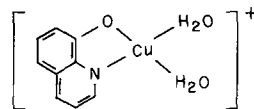


Fig. 4. Structural formula of diaquo 8-hydroxy quinoline (4)

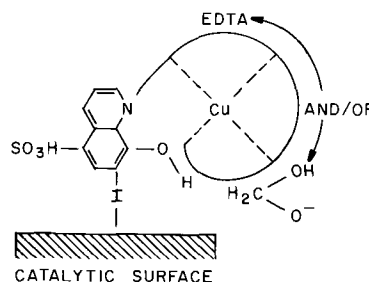


Fig. 5. Speculative schematic representation of the adsorption of HIQSA on a catalytic surface and subsequent bond formation to a chelated copper ion in the solution. The copper ion in solution is bonded to EDTA and/or methylene glycolate.

pletely poisoned. This observation is not elucidated further by Gutzeit. It is clear, however, that after plating has begun, the behavior cannot be explained by an area effect alone since if a large surface and a small particle are present in the same solution at the same time, they will be covered with the same number of adsorbed particles per unit area. The difference in poisoning of small and large surfaces must be due in some way therefore to the difference in their surface to volume ratios which can be expressed in terms of radius of curvature. Their surface energies or electrical potentials may be different, for example.

The accelerative effect of HIQSA in proper quantity may be explained by visualizing it adsorbed through the iodide atom on portions of the catalytic surface. The complexing part of the molecule is then extending into the bulk of the solution where it is able to form a bond to nearby chelated copper ions (Fig. 5). This would tend to accelerate plating by making it easier for the Cu^{2+} -ligand bond to be broken. When HIQSA is present in large quantities, however, it is able to poison the entire catalytic surface and electroless plating is slowed and finally stopped. (In practice, the addition of very large quantities of HIQSA results in the formation of a precipitate, presumably containing copper and HIQSA.)

The hypothesis discussed above is supported by the results with additives other than HIQSA. The additives that do not contain an iodide atom have not nearly as much stabilizing effect. The most striking example of this difference is HQSA, a molecule identical to HIQSA except for the absence of the iodine atom in the former.

The other molecule which has a large stabilizing effect is IP. This molecule, however, has much less accelerative effect (Fig. 3). This is consistent with the proposed explanation for acceleration since IP contains no adjacent nitrogen and hydroxide functions to enable it to chelate with a copper ion.

A more definitive explanation of the unique behavior of HIQSA could be obtained by a study of its effect on the current-voltage curves of the two half reactions. Information of this nature for an additive-free electroless copper solution of this type has already been obtained by Okinaka (9). The effect of various additives on the electrochemical potential of nickel and cobalt baths has been discussed by Feldstein and Lancsek (10).

Faster Plating Bath

Although electroless copper plating baths which plate at 1.0-1.5 $\mu\text{M}/\text{hr}$ are fast enough for most applications which involve a subsequent electrolytic metalization, there are certain advantages to be gained in using a bath with a faster plating rate. Consequently some baths with higher copper concentrations than those described previously were investigated.

The most promising formulation consisted of 0.06M $\text{CuSO}_4 \cdot 5\text{H}_2\text{O}$, 0.3M $\text{Na}_2\text{EDTA} \cdot 2\text{H}_2\text{O}$, 0.4M HCHO, and NaOH sufficient to obtain a pH of 12.8. The change in plating rate of this bath as a function of HIQSA added is depicted in Fig. 6. It can be seen that the curve is of the same general shape as that of the less concentrated bath (Fig. 2). The maximum is at about 170 mg/liter of HIQSA and represents a plating rate of about 3.1

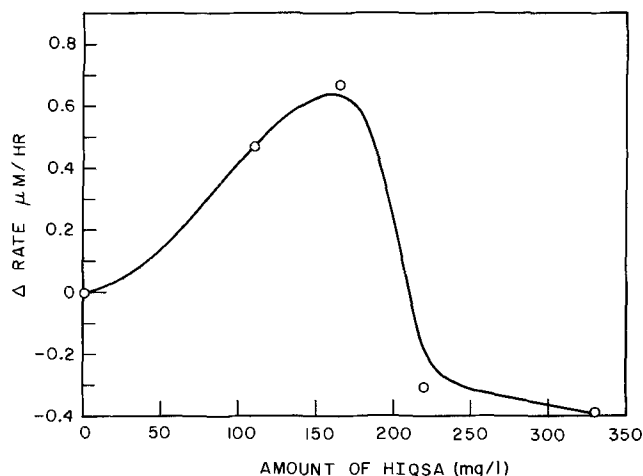


Fig. 6. Change in plating rate of a more concentrated electroless copper solution (0.06M $\text{CuSO}_4 \cdot 5\text{H}_2\text{O}$, 0.3M $\text{Na}_2\text{EDTA} \cdot 2\text{H}_2\text{O}$, 0.4M HCHO, pH 12.8) as a function of added HIQSA.

$\mu\text{M}/\text{hr}$. This bath was able to withstand 45 sec at 75° after the addition of PdCl_2 . While not a long time, this is still better than the performance of a comparable additive-free bath. It is apparent that an electroless copper solution containing HIQSA could be tailored for speed or stability depending on the application for which it would be used.

Acknowledgment

It is a pleasure to acknowledge helpful discussions with P. J. Boddy and D. R. Turner.

Manuscript submitted April 14, 1972; revised manuscript received June 21, 1972.

Any discussion of this paper will appear in a Discussion Section to be published in the June 1973 JOURNAL.

REFERENCES

- a. F. Pearlstein, U.S. Pat. 3,222,195.
- b. S. Hodoley and J. F. McCormack, U.S. Pat. 3,515,563.
- c. R. J. Zeblicky, F. W. Schneble, and J. F. McCormack, U.S. Pat. 3,485,643.
- d. W. Clauss, U.S. Pat. 3,492,135.
- e. K. Heymann, G. Woldt, and H. Grundel, U.S. Pat. 3,454,416.
- f. C. R. Shipley, Jr. and M. Gulla, U.S. Pat. 3,457,089.
- g. R. Merker and S. Lucca, U.S. Pat. 3,453,123.
- h. E. Torigai, G. Okuno, and H. Malkawa, U.S. Pat. 3,377,174.
- Y. Okinaka and A. M. Blom, Unpublished work.
- D. G. Foulke, U.S. Pat. 3,318,711.
- C. H. deMinjer and A. Brenner, U.S. Pat. 2,929,742.
- E. R. Ramirez, U.S. Pat. 2,884,344.
- D. P. Mellor in "Chelating Agents and Metal Chelates," F. P. Dwyer and D. P. Mellor, Editors, Academic Press, New York (1964).
- L. N. Schoenberg, Unpublished work.
- G. Gutzeit, Symposium on Electroless Nickel Plating, ASTM Special Technical Publication No. 265 (1959).
- Y. Okinaka, Unpublished work.
- N. Feldstein and T. S. Lancsek, *This Journal*, **118**, 869 (1971).

The Electroreduction of Beta-Aminoethyl Mercurials

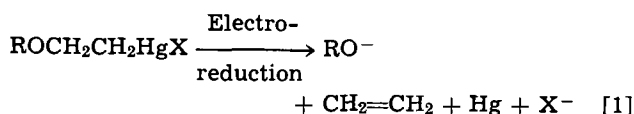
John H. Wagenknecht*

Central Research Department, Monsanto Company, St. Louis, Missouri 63166

ABSTRACT

2-(Piperidino)-ethylmercuric chloride (I) and 2-(diethylamino)ethylmercuric chloride (II) are each reduced by two separate one-electron reductions in DMF or 50% ethanol. The products formed are the corresponding bis-2-aminoethylmercury compound and/or the secondary amine (piperidine or diethylamine) depending on the solvent and reduction potential. Only traces of tertiary amine were detected. Bis[2-(piperidino)-ethyl] mercury (III) is reduced to piperidine in 50% ethanol, but no reduction occurs in DMF.

Studies of the electroreduction of mercuric salt-olefin addition products have been reported by several groups (1, 2). Alkoxy- and hydroxymercuration products show electroreduction behavior similar to simple alkylmercuric halides (3) except that reduction leads to regeneration of olefin (reaction [1])



under acidic conditions (2). The alkoxy- and hydroxymercuration products undergo two separate one-electron reductions just as the simple alkylmercuric halides. Aminomercuration products ($>\text{N}-\text{CH}_2\text{CH}_2\text{HgX}$), however, are reported to undergo only a single two-electron reduction (2). The products of that reduction were not reported.

Studies at this laboratory have shown that 2-(piperidino)-ethylmercuric chloride (I) and 2-(diethylamino)-ethylmercuric chloride (II) in fact do exhibit two one-electron polarographic reduction waves in aqueous alcohol, and the reduction products are similar to those obtained from oxymercuration products. The basic electroanalytical data and the results of macroelectrolyses of I, II, and bis[2-(piperidino)-ethyl] mercury (III) are reported in this paper.

Experimental

Literature preparations were used for the synthesis of 2-(piperidino)-ethylmercuric chloride (4), 2-(diethylamino)ethylmercuric chloride (4), and 1,4-dipiperidinobutane (5). Piperidine, diethylamine, ethylene, mercuric chloride, and N-ethylpiperidine were obtained commercially and used as received. Tetraethylammonium tetrafluoroborate was prepared from aqueous tetraethylammonium hydroxide and aqueous tetrafluoroboric acid. The water was stripped from the salt and it was then recrystallized from methanol. EtOH-water mixtures were made up from 200-proof EtOH and distilled water. The DMF (dimethylformamide, Fisher D-119) was distilled at reduced pressure from anhydrous CuSO_4 and then passed through a column of Linde 3A molecular sieves.

Polarograms were obtained with a Sargent Model XXI polarograph. A simple H-shaped two-electrode cell was used with the secondary electrode (and reference) being a saturated calomel electrode. The capillary constants were $M = 1.19$ mg/sec and $t = 9.0$ sec (open circuit, distilled water), and the mercury column height was 50 cm. Depolarizer concentrations were 1.0 mM with 0.1M $\text{Et}_4\text{N}^+\text{BF}_4^-$ as the supporting electrolyte.

Cyclic voltammetry was obtained at a hanging mercury drop electrode with a SCE reference electrode and platinum wire secondary electrode. The instru-

ments used were a Wenking Model 66TS10 potentiostat, an Exact Electronics Inc. Model 505 function generator, and a Tektronix Type 502 oscilloscope.

Coulometry was carried out in a fine-glass frit divided three-compartment cell with a Pt foil anode, mercury pool cathode, and SCE reference electrode. The substrate concentration was 10 mM with 0.1M $\text{Et}_4\text{N}^+\text{BF}_4^-$ as the supporting electrolyte. A Wenking Model 66TA1 potentiostat was used to carry out the coulometry.

Macroelectrolyses were performed in a medium glass frit divided H cell with Hg pool cathode (7 cm diam) and Pt foil anode. The cell was cooled in a tap water bath at approximately 20°C. The cathode potential was controlled vs. a SCE reference electrode which contacted the cathode via a Luggin capillary. The cathode compartment volume was 200 ml and the anode compartment volume was 50 ml. The supporting electrolyte was a 1M $\text{Et}_4\text{N}^+\text{BF}_4^-$. The catholyte was stirred with a magnetic stirrer or overhead mechanical stirrer. Electrolyses were carried out with either a Chemical Electronics Corporation (1.6A model) or a Wenking (Model 60HU1/90) potentiostat.

The nmr spectra were obtained using a Varian T-60 nmr spectrometer and the gas chromatography was carried out with a F&M Model 720 gas chromatograph with a Model 1609 flame-ionization attachment.

Electrolysis of I in DMF.—Ten grams of I were added to the cathode compartment and the electrolysis was carried out at -0.9V vs. SCE. After 20 hr, the current was less than 10 mA and the electrolysis was stopped. A total of 0.0304 Faraday of electricity had been passed or 1.055 Faradays per mole of I. No N-ethylpiperidine or 1,4-dipiperidinobutane and only a trace of piperidine were detected in the catholyte by g.c. analysis. The DMF was distilled from the catholyte at reduced pressure and the residue was extracted with ether. The ether was stripped from the ether extract and the residue was stirred at reduced pressure (0.001 mm) to remove residual DMF. The residue was 5.0g (82%) of crude (nmr analysis) bis[2-(piperidino)-ethyl] mercury (III). This oil was distilled at reduced pressure (0.04 mm) boiling at 123°C with a slight amount of decomposition at the beginning of the distillation.

Anal. Calcd. for $\text{C}_{14}\text{H}_{28}\text{N}_2\text{Hg}$: C, 39.56; H, 6.64; N, 6.59. Found: C, 39.83; H, 6.89; N, 6.66.

The nmr spectrum (Fig. 4) consists of multiplets centered at $\delta = 1.15$ (4H, $-\text{CH}_2-\text{Hg}$), 1.45 (12H, methylenes not adjacent to N in the piperidine ring), 2.35 (8H, methylenes adjacent to N in the piperidine ring) and 2.75 (4H, $>\text{N}-\text{CH}_2-\text{CH}_2-\text{Hg}$). The satellites formed by splitting due to Hg^{199} are faintly visible in the spectrum.

A similar electrolysis in DMF carried out at -2.5V vs. SCE gave identical results with 1.04 Faradays of electricity passed per mole of I and a 91% crude yield

* Electrochemical Society Active Member.

Key words: β -aminoethyl mercurials, polarography, coulometry, cyclic voltammetry, macroelectrolyses.

of III. Again, only a trace of piperidine¹ was detected by g.c. analysis and no N-ethylpiperidine or 1,4-dipiperidinobutane were detected.

Electrolysis of I in 50% EtOH.—Five grams of I were added to the catholyte and the electrolysis was carried out at $-0.5V$ vs. SCE. After 0.0144 Faraday of current (1.01 Faradays/mole of I) had passed, the current was negligible. Gas chromatographic analysis showed the presence of 0.14g of piperidine. The solvent was stripped from the catholyte and the residue was extracted with ether. Evaporation of the ether left a residue of 1.8g (59%) of crude III (nmr analysis).

A similar electrolysis was carried out at $-0.5V$ vs. SCE for 1.02 Faradays/mole of I and then the potential was increased to $-1.8V$ vs. SCE and an additional 1.08 Faradays/mole of I was passed. Analysis as above showed 0.55g (78%) of piperidine and no III.

An electrolysis of I in 50% EtOH was carried out as above except the potential was set at $-1.3V$ vs. SCE and 5 ml concentrated HCl was added to the catholyte. Then 1.25 Faradays/mole of I was passed and analysis as above showed 0.241g (20%) of piperidine and 2.07g (67%) of III.

Electrolysis of II.—The reduction of 8g of II was carried out in DMF containing 0.1M $Et_4N^+BF_4^-$. The potential was set at $-0.8V$ vs. SCE and a total of 1.05 Faradays of electricity/mole of II was passed. The DMF was stripped from the catholyte at reduced pressure and the residue was extracted with ether. Evaporation of the ether left a dark oily mixture. This was treated with petroleum ether and decolorizing carbon. The solution was filtered and the filtrate was stripped of solvent to give a clear oil which was distilled in a short-path distillation apparatus at reduced pressure (0.05 mm). The product distilled as a relatively unstable clear liquid boiling at approximately 130° . The nmr spectrum ($DCCl_3$) was consistent with bis(2-diethylaminoethyl) mercury having overlapping signals at $\delta = 1.08$ (16H, CH_3^- , and $-CH_2-Hg$), a multiplet at $\delta = 2.87$ (4H, $N-CH_2-CH_2-Hg$)² and a quartet at $\delta = 2.51$ (8H, $CH_3CH_2-N<$).

Anal. Calcd. for $C_{12}H_{28}N_2Hg$: C, 35.93; H, 7.04; N, 6.99. Found: C, 37.23; H, 6.97; N, 6.65.

Results

The results of polarography, coulometry, and macroelectrolyses of I, II, and III are shown in Table I. The polarographic waves in 50% EtOH were normally shaped and only the waves indicated were present. Polarograms obtained with I or II that had been stored

¹ It is important to note that pyrolysis of III leads to formation of piperidine requiring that a correction be made for g.c. analysis of any solution containing III since piperidine was always formed by pyrolysis of III in the injection port. The piperidine peak area was related to III concentration in known samples so that a fairly accurate correction could be made.

² These sharp peaks are spaced like the ones in Fig. 4 at a comparable chemical shift.

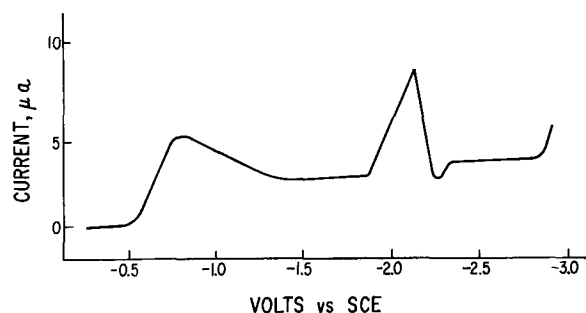


Fig. 1. Polarogram of I in DMF containing 0.1M $Et_4N^+BF_4^-$

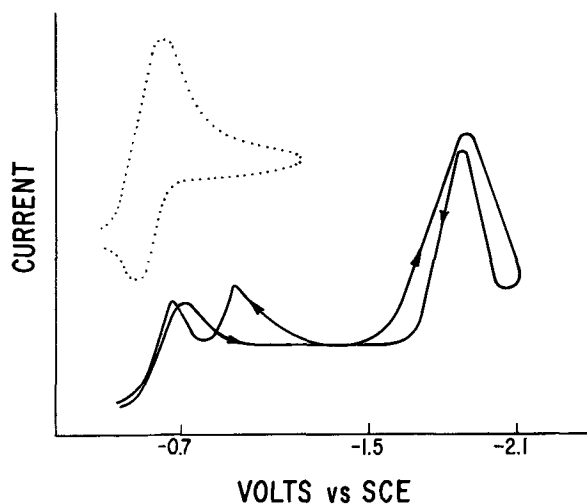


Fig. 2. Cyclic voltammograms of I in DMF containing 0.1M $Et_4N^+BF_4^-$. Solid line represents 0.1 V/sec sweep rate and dashed line shows 1.0 V/sec sweep rate.

for a few days and had apparently partially decomposed showed maxima on the second waves. Polarograms of I and II obtained in DMF were abnormally shaped, and that for I is shown in Fig. 1. Note that the maximum at around $-2.2V$ precedes a wave with the diffusion current less than twice the first wave value. The polarogram for II in DMF is similarly shaped. Compound III is not reduced in DMF.

Cyclic voltammetry of I and II at a hanging Hg drop in DMF were unusual and scans of I at different sweep rates are shown in Fig. 2. Compound II gave similar cyclic voltammograms. Compound I in 50% EtOH shows two irreversible broad peaks at -0.82 and $-1.65V$ vs. SCE (Fig. 3). Compound II shows two irreversible broad peaks at -0.69 and $-1.50V$ vs. SCE. The reverse trace showed a negative current peak (i.e., the same direction as the forward trace) similar to those in Fig. 2 at slow sweeps. The macroelectrolyses

Table I. Electrochemical reduction data

Compound	Solvent	$E_{1/2}^a$	I_d	n^b	Products ^c (yield)
$\text{NCH}_2\text{CH}_2\text{HgCl}$ (I)	50% ethanol	-0.375 -0.70	1.04 0.91	0.92 1.96	III (59%) + piperidine (11%) III (67%) + piperidine (20%) ^d
	DMF	-0.72 -2.05^f	1.99 ^e 1.08	0.98 —	III (82%) III (91%)
$(C_2H_5)_2NCH_2CH_2HgCl$ (II)	50% ethanol	-0.35 -0.62	1.01 1.09	0.88 —	—
	DMF	-0.70 -2.0^f	1.97 ^e 0.87	— —	$[(C_2H_5)_2NCH_2CH_2]_2Hg$
$(\text{NCH}_2\text{CH}_2)_2Hg$ (III)	50% ethanol	-1.5^f	—	2.12	Piperidine

^a Volts vs. SCE.

^b Faradays of electricity/mole of substrate determined coulometrically at a potential just past the crest of the corresponding polarographic wave.

^c From macroelectrolyses at a potential just beyond the crest of the corresponding polarographic wave.

^d Electrolysis carried out in the presence of HCl.

^e Minimum value between the first and second maximum. See Fig. 1.

^f Beginning of the maximum.

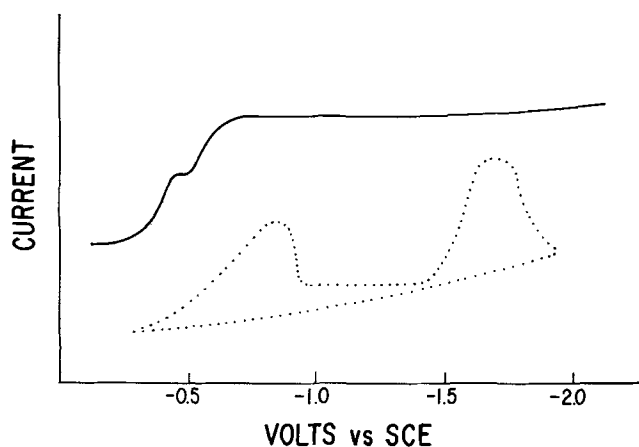


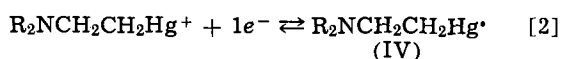
Fig. 3. Polarogram (solid line) and cyclic voltammogram (dashed line 2 v/sec) of I in 50% ethanol containing 0.1M $\text{Et}_4\text{N}^+\text{BF}_4^-$

were generally carried out with approximately 0.1M substrate. Since all of the electroanalytical results were similar, the only macroelectrolysis for II was carried out to obtain a sample of $(\text{Et}_2\text{NCH}_2\text{CH}_2)_2\text{Hg}$. No 1,4-dipiperidinobutane was detected in any of the electrolysis products. Only traces of N-ethylpiperidine were ever detected in the electrolysis products.

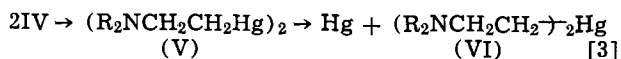
In addition to the coulometric data in Table I, it was found that for I in 50% ethanol after complete electrolysis at -0.5V vs. SCE approximately 1 Faraday of current/mole of I was passed and no extra current would pass at -1.2V , but at -1.8V an additional 1 Faraday of current/mole of I was passed. II behaved similarly. A macroelectrolysis of I carried out similarly yielded 0.14g (20%) of piperidine on complete reduction at -0.5V (1.02 Faradays/mole I). The potential was then increased to -1.8V vs. SCE , an additional 1.08 Faradays of electricity per mole of I was passed and the yield of piperidine increased to 0.55g (78%).

Discussion

The results of coulometry and cyclic voltammetry of I and II indicate an initial reversible one-electron reduction (reaction [2]), contrary to the previous report (2). It is also evident that the intermediate IV is consumed by

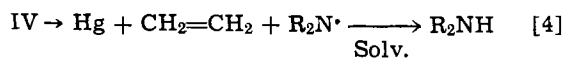


some fairly fast reactions since no reverse is obtained with slow-sweep cyclic voltammetry. Apparently, two reaction pathways are required to explain the two products observed in macroelectrolyses. Reaction [3] is shown as simple



dimerization of the radical IV to form an intermediate (V) which would be likely to disproportionate to free mercury and VI at room temperature, as has been observed in the reduction of simple alkylmercuric salts (6).

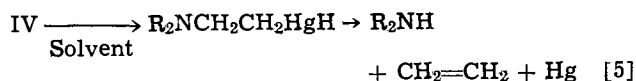
An additional reaction route for IV must occur, however, to account for the formation of piperidine at the first wave. The simplest reaction to write is reaction [4]



It is not apparent from reaction [4] why one might get different rates³ in different solvents (as we observe in DMF and 50% ethanol). The addition of amino radicals to olefins is a well-known reaction (7) and

³ One of the referees suggested the different rates in reaction [4] may be due to the equilibrium in reaction [2].

the opposite of the first part of reaction [4]. Reaction [5] allows for a solvent effect and bypasses the step of elimination

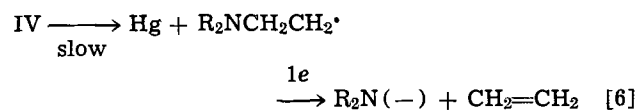


of an aminoradical from ethylene. One can envisage a concerted reaction of the hydride involving a 5-member cyclic intermediate. There is evidence, however, that a simple alkylmercuric hydride decomposes to form the alkyl-free radical (8).

The absence of the intermediate $\text{R}_2\text{NCH}_2\text{CH}_2^\bullet$ (expected in reaction [4]) is further indicated by the absence of 1,4-dipiperidinobutane in the electrolysis products.

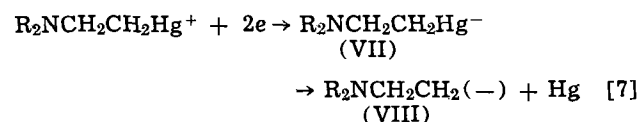
The cyclic voltammograms obtained in DMF are interesting in that at fast sweeps a reversible $1e^-$ reduction is indicated (Fig. 2), as has been reported for the reduction of mercuric salts by others (9). However, at slow sweeps an inverse peak occurs on the reverse sweep, indicating a radical intermediate presumably reacting with the mercury drop (10). In this case, the addition of mercury to the surface (reaction [3]) may be responsible for the unusual behavior. The first and second reductions were indistinguishable in the cyclic voltammograms in 50% ethanol (Fig. 3). However, a second peak occurred at a potential at which no polarographic reduction wave appears. This second peak was found to correspond to that for the reduction of III in 50% ethanol. The III is formed at the first reduction by reactions [3], [10], or [11] (see below) and remains at the drop surface long enough to be reduced when its reduction potential is reached. During polarographic reduction a two-electron reduction not leading to III (see below) is already occurring when the potential of the reduction of III is reached and, therefore, no wave is obtained. The III formed at the first polarographic wave is, of course, dissipated because of the fresh drops being formed every few seconds.

The I_d values shown in Table I for the first waves of I and II in DMF seem too high for a one-electron reduction. Rapid-scan cyclic voltammetry indicates a $1e^-$ reduction, coulometry and macroelectrolysis at higher concentration indicate a one-electron reduction, and polarography in 50% ethanol indicates a one-electron reduction. Therefore, to obtain a greater than one-electron reduction in DMF requires a relatively slow solvent dependent reaction of the one-electron reduction product leading to a reducible product. A possible pathway is shown in reaction [6]. A simple alkyl radical would probably not be reduced (11-12) or reduced only very slowly (13)



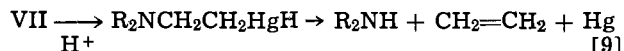
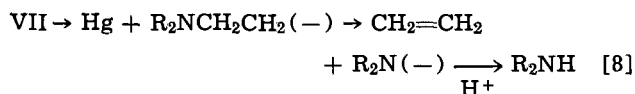
at this potential, but the beta-amino group may allow the reduction to occur rapidly. At higher concentrations (coulometry and macroelectrolysis) reaction [3] predominates. In 50% ethanol the rate of reaction [5] may be faster than that of reaction [6]. Reaction [5] does not form a reducible species and, therefore, only a one-electron reduction occurs.

The total I_d value beyond the second polarographic wave corresponds to a two-electron reduction (reaction [7])



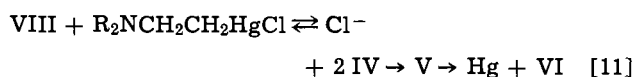
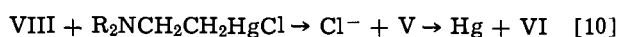
Under dilute conditions (polarography) the intermediate VII undergoes reactions like [8] or [9]. The second

wave



shows a large (1.3V) potential shift between DMF and 50% ethanol. This same effect is observed in the reduction of III for, whereas the reduction begins at -1.5V in 50% ethanol, no polarographic wave occurs in DMF. Addition of 1.3V to the value in 50% ethanol gives -2.8V or reduction in the region of electrolyte discharge. Reduction of dialkylmercurials has been reported to occur in this region (14); however, we were unable to reproduce those results.

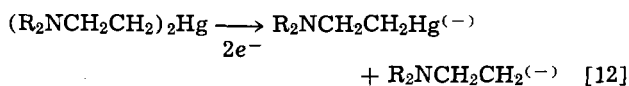
Under macroelectrolysis conditions at the potential of the second wave the products appear to be those of a one-electron reduction. However, routes to the bismercurial (VI) are straightforward via two-electron reduction products (reactions [10] and [11])



Reaction [10] is a nucleophilic-displacement reaction, similar to a variety of known replacement reactions at mercury (15). Reaction [11] is an electron-transfer disproportionation reaction, common in cases in which 1- and 2-electron reduction products are formed (16). Both are second-order resulting in the same product and, thus, are indistinguishable.

These reactions do not explain the other products obtained or the apparent two-electron reduction in 50% ethanol by coulometry and polarography. Reactions [8] and [9] are possible routes to the observed product, piperidine. Reaction [8] does not seem likely, however, in view of the fact that only traces of N-ethylpiperidine were detected, even when the reduction was carried out in the presence of hydrochloric acid. Under conditions of polarography and coulometry in 50% ethanol, reaction [9] appears to occur more rapidly than [10] or [11]. However, under macroelectrolysis conditions the concentration of $\text{R}_2\text{NCH}_2\text{CH}_2\text{HgCl}$ is much higher and the region near the cathode is probably quite basic (17) even though the bulk solution is acidic, thus, allowing reactions [10] or [11] to compete favorably with [9].

The reduction of III (initially formed by reduction of I) in 50% ethanol leads only to piperidine and no N-ethylpiperidine. It would seem that the reduction would proceed as in reaction [12]



The intermediate $\text{R}_2\text{NCH}_2\text{CH}_2^{(-)}$ would be expected to lead to at least some N-ethylpiperidine. It may be possible that the reduction is a concerted process with $\text{R}_2\text{N}^{(-)}$ and ethylene leaving as the first electron is added so that there is never any free $\text{R}_2\text{NCH}_2\text{CH}_2^{(-)}$ formed.

Although electroreduction of I apparently does not lead to N-ethylpiperidine, the chemical reduction of I to N-ethylpiperidine may be accomplished with sodium amalgam and various metal hydrides (18). Reduction of I with sodium borohydride is reported to yield some III in addition to N-ethylpiperidine; however, their product is reported as a solid (mp 128°), whereas the product (III) obtained here is a distillable colorless

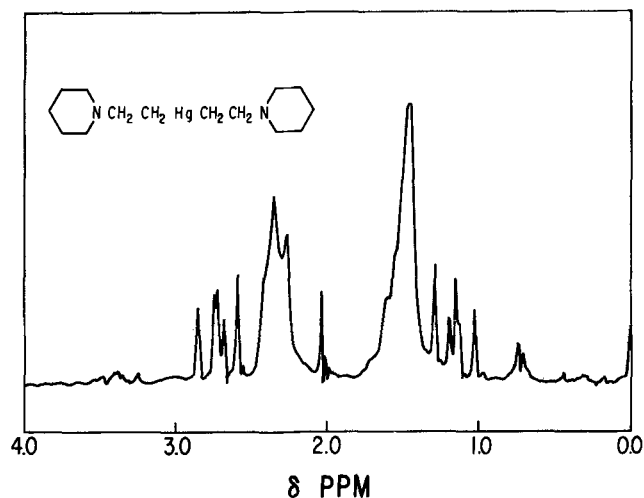


Fig. 4. Proton nmr spectrum of bis [2-(piperidino)-ethyl] mercury

liquid. The nmr spectrum of III is included (Fig. 4) as further evidence for the structure.

Acknowledgment

The author wishes to thank Dr. M. M. Baizer for helpful discussions and Mr. W. O. Jackson for technical assistance.

Manuscript submitted March 3, 1972; revised manuscript received June 23, 1972.

Any discussion of this paper will appear in a Discussion Section to be published in the June 1973 JOURNAL.

REFERENCES

- B. Fleet and R. D. Jee, *Talanta*, **16**, 1561 (1969), and references therein.
- I. A. Esikova, O. N. Temkin, A. P. Tomilov, R. M. Flid, and G. P. Pavlikova, *Soviet Electrochem.*, **7**, 133 (1971), and references therein.
- D. J. Pietrzyk, *Anal. Chem.*, **42**, 145R (1970), and previous reviews in that series by D. J. Pietrzyk and/or S. Wawzonek.
- A. N. Nesmeyanov and K. A. Kocheshkov, "Methods of Elemento-organic Chemistry," Vol. 4, p. 163, North-Holland Publishing Co., Amsterdam (1967).
- C. D. Lundsford, R. S. Murphey, and E. K. Rose, *J. Org. Chem.*, **22**, 1225 (1957).
- C. A. Kraus, *J. Am. Chem. Soc.*, **35**, 1732 (1913).
- F. Minisci and R. Galli, *Tetrahedron Letters*, **1964**, 167.
- D. J. Pasto and J. A. Gontarz, *J. Am. Chem. Soc.*, **91**, 719 (1969).
- C. Degrand and E. Laviron, *Bull. Soc. Chim. France*, **1968**, 2228, 2233.
- D. A. Tyssee, *J. Electroanal. Chem.*, **30**, 14 (1971).
- J. H. Wagenknecht and M. M. Baizer, *This Journal*, **114**, 1095 (1967).
- C. K. Mann and K. K. Barnes, "Electrochemical Reactions in Nonaqueous Systems," p. 204, Marcel Dekker, Inc., New York (1970).
- J. L. Webb, C. K. Mann, and H. M. Walborsky, *J. Am. Chem. Soc.*, **92**, 2042 (1970).
- K. P. Butin, I. P. Beletskaya, A. N. Kashin, and O. A. Reutov, *J. Organometal. Chem.*, **10**, 197 (1967).
- F. G. A. Stone and R. West, "Advances in Organometallic Chemistry," Vol. 2, pp. 204-207, Academic Press, New York (1964).
- N. L. Holy and J. D. Marcum, *Angew. Chem. Int. Ed.*, **10**, 115 (1971).
- M. R. Ort and M. M. Baizer, *J. Org. Chem.*, **31**, 1647 (1966).
- J. J. Perie and A. Lattes, *Bull. Soc. Chim. France*, **1971**, 1378.

Electrode Reactions on Demetalized Surfaces

Ashok K. Vijh*

Hydro-Quebec Institute of Research, Varennes, P. Q., Canada

ABSTRACT

Many electrode reactions occurring nominally on metals proceed in fact on a demetalized surface produced by formation of a semiconducting surface reaction film on the electrode. A viewpoint is presented that in these cases of electrode reactions, the electrode kinetic behavior should be interpreted in terms of solid-state surface properties (especially the bandgap and thence semiconductivity and solid-state cohesion) of the surface film rather than the electronic properties of the underlying metal. Equations are formulated to take this into account and the considerations developed provide a basis to interpret a large amount of literature data on the following subjects: oxygen reduction reaction; oxygen evolution reaction; anodic dissolution of metals in anhydrous hydrogen fluoride and in sulfamic acid-formamide solutions; $\text{Fe}(\text{CN})_6^{4-}/\text{Fe}(\text{CN})_6^{3-}$ reaction on platinum, oxide films, and oxides; and possibly the open-circuit corrosion potentials of some common metals.

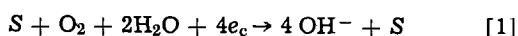
A vast majority of common electrode reactions occurring on metals proceed, in fact, on surfaces that have been demetalized to some extent, by formation of either a chemisorbed layer or a thicker film approaching a phase compound. This is particularly true of anodic reactions, although several cathodic reactions (e.g., hydrogen evolution, oxygen reduction, some electroorganic reductions, etc.) also involve reaction intermediates which can impart a demetalized character to the electrode surface.

In some cases of anodic reactions in which the metallic electrode is clearly covered by a multilayer ($\gg 10\text{\AA}$) surface film, one would expect the properties of the latter to affect the rate of the electrode reaction. The film properties of interest in this connection are such as the estimated semiconductivity, solid-state cohesion (i.e., lattice energies, bond energies, heats of formation, melting points, boiling points, etc), and the defect structure.

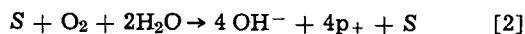
The object of the present paper is to attempt an interpretation of some electrode reactions involving surface films in terms of semiconductivity and related properties of the latter.

Theory

To formulate the argument, consider reduction of oxygen on an oxide-covered metal surface denoted by S . In acidic solutions, the over-all reaction may proceed either by participation of electrons of the conduction band, e_c , of S as



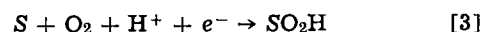
or by involvement of holes of the valence band as



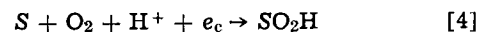
Here it is assumed that the oxygen reduction occurs by the four-electron process. Parenthetically, the following argument will not be affected even when one assumes a two-electron reduction. It also is assumed that the oxide substrate, S , on the metal is sufficiently thick ($\gg 10\text{\AA}$) and hence may be treated as a bulk semiconducting surface. For the oxide reduction reaction, which proceeds at high anodic potentials (with respect to the hydrogen electrode), this assumption clearly would be fulfilled for metals such as Cu, Cr, Pd, Cd, Ni, Fe, Co, Zn, Mg, and even Ag and Au on which anodization can result in quite thick oxides. For the case of Pt and other "noble" metals, however, this assumption perhaps is fulfilled only marginally since phase oxide growth generally is not observed, although three to four layers (ca. 10\AA) can be formed

easily even on platinum. In any case there is direct evidence (1) to support that the oxide on platinum, although relatively thin, sustains a potential drop of about 0.7V (at $100\ \mu\text{A}\cdot\text{cm}^{-2}$) across it under conditions of anodization; hence it may be treated approximately as a semiconducting surface.

A possible rate-determining step (rds) for oxygen reduction (on oxide-covered platinum) in acidic solutions may be as (2)



which may be written in two alternative forms involving either e_c or p_v as



or



The rates of these two alternative mechanisms may be represented as (3)

$$i_4 = ZF k_4 [\text{O}_2] [\text{H}^+] \exp(-E^*_4/RT) \quad [6]$$

and

$$i_5 = ZF k_5 [\text{O}_2] [\text{H}^+] \exp(-E^*_5/RT) \quad [7]$$

where i_4 and i_5 are the rates (current densities); Z is the number of electrons (or holes) transferred in the rds (one in the present example); k_4 and k_5 are constants; F is the Faraday constant; $[\text{O}_2]$ and $[\text{H}^+]$ are the concentration of oxygen and protons (hydrated of course) on the surface S ; E^*_4 and E^*_5 are the effective activation energies for the steps [4] and [5], respectively, under conditions of a given applied potential. Concentrated solutions have been assumed so that there is virtually no potential drop in the diffuse double layer of the solution. In any case, for the wide bandgap semiconductors, potential drops across the Helmholtz and the diffuse double layers may be neglected.

Following Gerischer (3), we note that the presence of a hole, used in reaction [5], in the valence band signifies that an electron has been excited from a bonding state in the valence band to an antibonding state in the conduction band. The energy difference between the initial states for reactions [4] and [5] would thus be equal to the bandgap value, E_g . Since the transition states for reactions [4] and [5] are relatively closer to their final states, as argued by Gerischer (3), the difference in the activation energies for the two steps, namely, $(E^*_4 - E^*_5)$ will be close to the E_g ; i.e., one has

$$E^*_4 - E^*_5 = \gamma E_g; \quad 0.5 < \gamma < 1 \quad [8]$$

By adding rate equations [6] and [7], one gets the total rate of oxygen reduction, i_t as

* Electrochemical Society Active Member.
Key words: oxygen reaction, anodic dissolution, corrosion films, electrode reactions, semiconductor electrochemistry.

$$i_t = k' \exp(-E^*_4/RT) + k'' \exp(-E^*_5/RT) \quad [9]$$

where

$$k' = ZF k_4 [O_2] [H^+]$$

and

$$k'' = ZF k_5 [O_2] [H^+]$$

Dividing Eq. [9] by $k'' \exp(-E^*_5/RT)$, one obtains

$$\frac{i_t}{k'' \exp(-E^*_5/RT)} = \frac{k' \exp(-E^*_4/RT)}{k'' \exp(-E^*_5/RT)} + 1 \quad [10]$$

or

$$i_t = K \left\{ K' \exp\left(-\frac{E^*_4 - E^*_5}{RT}\right) + 1 \right\} \quad [11]$$

where

$$K = k'' \exp(-E^*_5/RT)$$

and

$$K' = \frac{k'}{k''}$$

Combination of Eq [8] and [11] gives

$$i_t = K \left\{ K' \exp\left(-\frac{\gamma E_g}{RT}\right) + 1 \right\} \quad [12]$$

In Eq. [12], for a given oxide substrate, S , all the quantities in the right-hand side are constant provided that one works at a constant temperature T . If now one assumes that for a number of oxide substrates, S , constants K , K' , and γ change in a relatively minor way as compared to the bandgap value, E_g , one would expect a rough correlation between i_t and E_g values. That the effect of E_g in Eq. [12], for a large number of oxide substrates, is indeed paramount as compared to any possible variations of K , K' , and γ , as assumed, appears to be borne out by some experimental evidence presented below where the overpotential (at constant i_t) increases with increasing E_g values for a number of oxide substrates; this, of course, is the same thing as the increasing i_t with decreasing E_g values at a given overpotential (i.e., Eq. [12]). It may be added that although Eq. [12] has been formulated for the reduction of oxygen on an oxide-covered electrode, the considerations developed should apply to any electrode reaction proceeding on a film-covered metal by means of reactions such as [1] and [2] in which an exchange of electrons or holes is involved.

Electrocatalysis of the Oxygen Reaction on Oxide-Covered Metals

In Fig. 1, results of Kozawa *et al.* (4) for the reduction of oxygen on metals (presumably covered by oxide films) are plotted against the corresponding E_g values of the oxides. At a given current density, higher electrode potentials, E , are associated with higher bandgap values, as predicted above. In order to extend this plot to some more metals for which the E_g values are not available, one may examine the graph of $-\Delta H_e$, the heat of formation per equivalent for the highest valent oxide, against the E values since (5)

$$E_g \approx 2(-\Delta H_e) \quad [13]$$

This has been done in Fig. 2 where increasing $-\Delta H_e$ ($\approx \frac{1}{2} E_g$) values are associated with higher electrode potentials for oxygen reduction at a given current density as reported by Kozawa *et al.* (4); Fig. 2 thus extends to some other metals the conclusions drawn from Fig. 1.

In order to make sure that these correlations are not merely fortuitous because of the particular set of oxygen reduction data chosen, it is necessary to examine them in relation to data reported by other workers. Figure 3 gives the E (at a given i_t) vs. E_g plot for several oxide-covered metals on which oxygen reduction data have been reported by Khumotov (6), after Tomashov (7). These E values are plotted against the

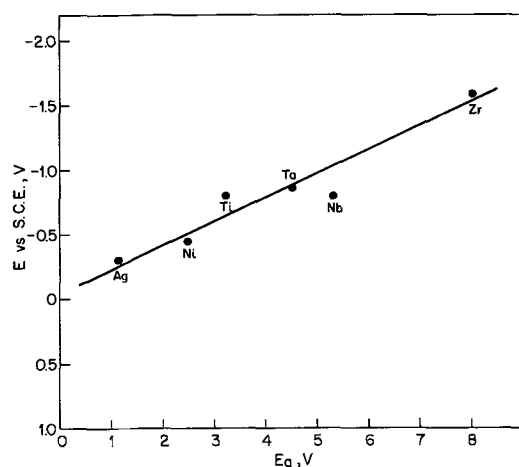


Fig. 1. Plot of electrode potential E (vs. SHE) for oxygen reduction at $20 \mu\text{A}\cdot\text{cm}^{-2}$ in 0.15M NaCl solution (phosphate buffer, pH 7.22) on the (oxide-covered) shown metals vs. the bandgap, E_g , values for the corresponding oxides. E and E_g values are from Ref. (4) and (18), respectively.

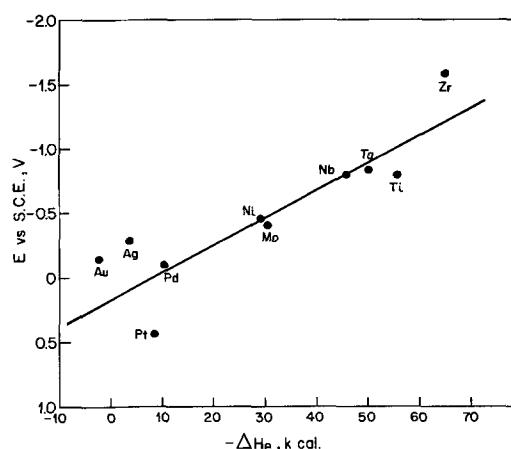


Fig. 2. E values for oxygen reduction (same data as in Fig. 1) now plotted against $-\Delta H_e$ ($\approx \frac{1}{2} E_g$) values of the oxides of the shown metals. The $-\Delta H_e$ values are taken from Ref. (18) and (21) and the references cited therein.

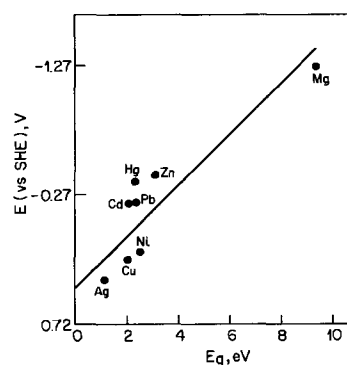


Fig. 3. Plot of electrode potential E (vs. SHE, in $0.5\text{M NaCl} + 0.005\text{M Na}_2\text{CO}_3 + 0.005\text{M NaHCO}_3$, at $1 \text{ mA}\cdot\text{cm}^{-2}$) for oxygen reduction (6, 7) on the (oxide-covered) shown metals vs. the E_g values (21, 22) for the corresponding oxides.

corresponding $-\Delta H_e$ ($= \frac{1}{2} E_g$) values in Fig. 4. It is clear that the data of Kozawa *et al.* (4) and Tomashov (7) sustain the theoretical prediction, i.e., at a given rate, higher electrode potentials are observed on oxide-covered metals whose oxides have high E_g values (Fig. 1-4).

The $-\Delta H_e$ values not only signify half the bandgaps (5), but they are also related to the enthalpy (in its

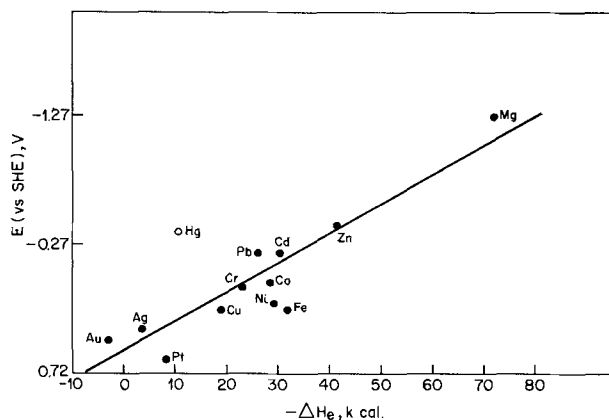
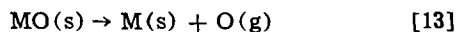


Fig. 4. Plot of E for oxygen reduction (same data as in Fig. 3) vs. the $-\Delta H_e (= \frac{1}{2} E_g)$ values (18, 21) of the highest valent oxides of the shown metals.

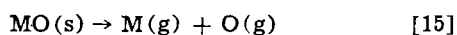
normalized form, i.e., as per equivalent (8) of the reaction



where s and g denote solid and gas, respectively; MO is the metal oxide, i.e., the substrate S in the kinetic equations above. The enthalpy change in reaction [13], $(\Delta H)_{13}$, is

$$(\Delta H)_{13} = -\Delta H_e + \frac{1}{4}\Delta H_D \quad [14]$$

where $\frac{1}{4}\Delta H_D$ is the heat of dissociation, per equivalent, of the oxygen molecule (note: ΔH_D is heat of dissociation per mole, $\frac{1}{2}\Delta H_D$ per atom, and $\frac{1}{4}\Delta H_D$ per equivalent). For all the oxides, $\frac{1}{4}\Delta H_D$ is of course the same so that the bond rupture in Eq. [13], i.e., the enthalpy per equivalent of reaction [14], may be represented by the heat of formation per equivalent, ΔH_e . It may be added that usually the bond energy (9) is represented by the heat of atomization per equivalent, i.e., the enthalpy of the bond rupture



For our considerations, however, the bond energy of Eq. [15] is not relevant since bond breaking or formation involved in various electrochemical steps never converts the metal to its gaseous form. Since the metal in the MO bond always stays as a solid, the bond energy corresponding to the rupture in Eq. [14] is appropriate. One thus concludes that $-\Delta H_e$ values not only represent $\frac{1}{2}E_g$ but are also an index of the average energy of a bond likely to be involved in an electrochemical step on the oxide-covered electrodes.

With the preceding comments in mind, we proceed to examine a third set of data, due to Appleby (2), on oxygen reduction. The correlation between electroactivity and the $-\Delta H_e$ values for the metals examined by Appleby does not follow the predictions made in the section on theory here. Instead, one obtains a volcano plot. This probably would emphasize that for these metals, the semiconductivity (and thence E_g or $-2\Delta H_e$) is perhaps not the paramount factor (cf. Eq. [11]) and that the overriding consideration is probably the energy of the MO bonds as represented by $-\Delta H_e$. This is not at all unexpected for these "noble" metals (Fig. 5) on which the E_g values are small and the effect of oxide mainly shows up in terms of the strength of the MO bonds involved as predicted in the theories, e.g., of Parsons (10) and Gerischer (11). A similar volcanic relation also results for the oxygen evolution reaction (oer) when the data taken from Reuttschi and Delahay (12), supplemented by the data given by Hoare (13), are plotted against the $-\Delta H_e$ value (Fig. 6). The significance and interpretation of Fig. 6 is, of course, quite similar to that of Fig. 5.

It may be mentioned that any attempts to estimate bond energy values from the Pauling-type equations

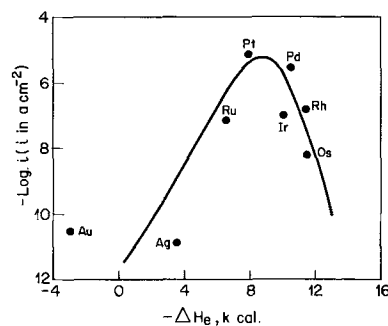


Fig. 5. Oxygen reduction rate at 800 mV (SHE) in 85% orthophosphoric acid (2) on the shown (oxide-covered) metals plotted against the $-\Delta H_e$ values (18, 21) of the corresponding oxides.

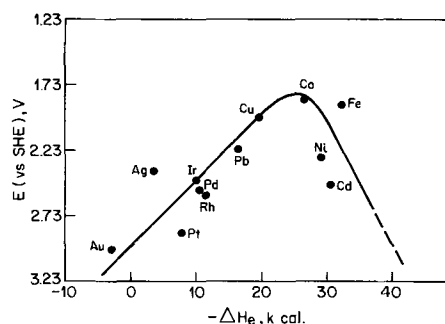


Fig. 6. Electrode potential E (vs. SHE), V, for the oxygen evolution reaction, at $1 \text{ A}\cdot\text{cm}^{-2}$ in 1 M KOH solution, as given in Ref. (12) plotted against the $-\Delta H_e$ values (18, 21) of the oxides of the shown metals. The oxygen evolution data for Rh and Ir taken from Hoare (13); although the data on Ir is for acidic solutions, it may be used in the present plot (by adjusting the potential scales to the alkaline solutions) since the mechanism of oxygen evolution on Ir is the same both in acidic and alkaline solutions.

(12) are not relevant for the present case since these equations give estimates of isolated MO molecules in the gas phase. Similar comments also apply to the spectroscopic values of the MO bond strengths.

Anodic Dissolution of Film-Covered Metals

It was shown previously (14, 15), on the basis of data of Hackerman *et al.* (16) that in the anodic dissolution of a large number of metals in anhydrous hydrogen fluoride (AHF), the dissolution proceeds via relatively thick fluoride corrosion films. Further, it was noted that the solid-state properties of the fluoride films determine the anodic dissolution rates of the underlying metals. Since the dissolution of the semiconducting surface film must proceed by reactions involving electron-hole exchange between the fluoride film and the electrolyte (similar to reactions [1] and [2]), the data (16) may now be examined in terms of Eq. [12]. In Fig. 7, the normalized anodic dissolution rates of metals are plotted against the corresponding $-\Delta H_e (= \frac{1}{2} E_g)$ values. The log dissolution rate roughly increases with decreasing $-\Delta H_e$ values as required by Eq. [12].

The theoretical ideas developed here may also be applied to the case of anodic dissolution of metals in sulfamic acid-formamide solutions (17, 18). The anodic dissolution in this case proceeds via electrode films bound to the metal by M-S bonds. It is of interest, therefore, to plot the $-\Delta H_e (= \frac{1}{2} E_g)$ values of metal sulfides against the anodic dissolution rates of metals (Fig. 8). Log (anodic dissolution rate) increases with decreasing bandgap values in agreement with Eq. [12].

Redox Reactions

One may now examine the behavior of redox reactions such as $\text{Fe}(\text{CN})_6^{4-}/\text{Fe}(\text{CN})_6^{3-}$ in relation to the

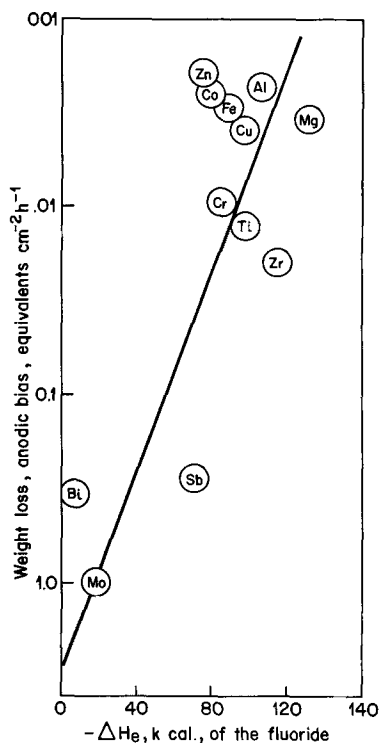


Fig. 7. Plot of normalized (i.e. equivalents cm⁻² hr⁻¹) anodic dissolution rates (16) of the shown (fluoride-covered) metals vs. the $-\Delta H_e (= \frac{1}{2} E_g)$ values (14, 15) of the corresponding highest valent fluorides. The anodic dissolution data on Cd is not included since the fluoride film on Cd is nonadherent and nonprotective, a case not relevant to the theory of film-covered electrodes developed here. It may be mentioned that, perhaps for the foregoing reason, the anodic dissolution data on Cd does not follow the rough trend shown in Fig. 7.

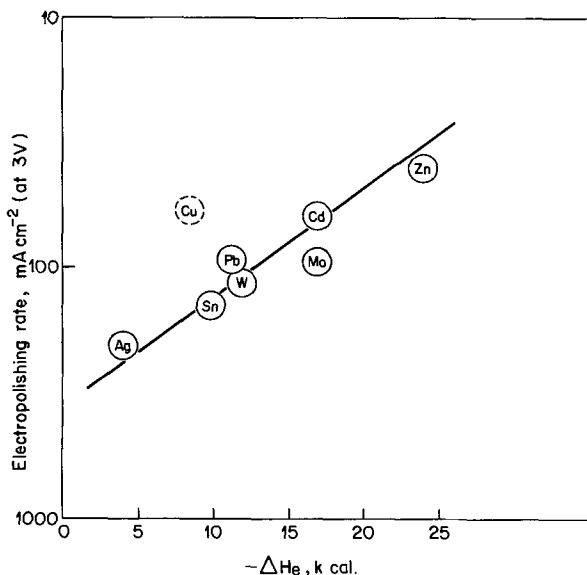


Fig. 8. Electropolishing (i.e., the anodic dissolution) rates at a typical (3V vs. Cd/CdCl₂ in KCl-saturated formamide) anodic potential of the shown (film-covered) metals, in sulfamic acid-formamide solutions (17, 18), vs. the $-\Delta H_e (= \frac{1}{2} E_g)$ values of the corresponding highest valent metal sulfides (18).

viewpoint developed here. Moshtev (19) has recently reported standard exchange current densities of this reaction on oxide-free platinum (hence $E_g = 0$), some oxide films (SnO, γ -Fe₂O₃, TiO₂) and some bulk oxides (NiO, ZnO). Since primary electrocatalytic effects of the substrate on redox reactions are zero, it is valid to use the exchange current density on Pt as the refer-

ence point ($E_g = 0$), for the electron exchange involved in the reaction. A plot of exchange current densities vs. the E_g values again shows that higher rates in general are associated with low E_g values (Fig. 9), which is qualitatively consistent with Eq. [12].

Open-Circuit Corrosion Potentials

For open-circuit potentials of common metals under certain experimental conditions, it is possible to show that the estimated semiconductivity of the corrosion reaction films is related to the mixed corrosion potentials. The arguments involved are substantially different from those formulated here, although the crucial role of the semiconductivity of reaction films on the demetalized electrodes is again indicated. The treatment has been presented previously (20) and need not be elaborated here.

Comments on the Scope and Limitations of the Theory

An assumption in the present theoretical treatment is that the thickness of the solid semiconducting films is greater than the Debye length L_D , which may be taken as the effective width of the space charge region. This assumption would appear to be contestable at first sight since the L_D is usually regarded as in the region ca. 10³-10⁴Å (23) which would be greater than the thickness of electrodic films observed in some of the cases discussed. The Debye length is given by the formula (24)

$$L_D = \left(\frac{\epsilon k T}{4\pi n e^2} \right)^{1/2} \quad [16]$$

where ϵ is the dielectric constant of the film, k is the Boltzmann constant, T is the absolute temperature, n is the density of the electronic charge carriers, and e is the electronic charge. It is observed that for high density of charge carriers (ca. $\geq 10^{18}$ -10²⁰ carriers cm⁻³) and reasonable values of dielectric constant (ca. 50), one can, in fact, observe values of L_D substantially less than 10Å and even approaching the width of the Helmholtz layer. Although application of the semiconductor space charge theory to such cases would appear debatable, considerable success has been achieved in fitting the experimental data to theory for several cases of this kind; e.g., electrode reactions on bulk graphite (25), NiO (26), PbO₂ (27), and sodium-tungsten bronzes (28). On the basis of this evidence, it is concluded that the theory developed here is applicable even to quite thin films, provided that the n values are quite high, an assumption likely to be valid for the electrodic films by virtue of their nonstoichiometry and "doping" resulting from their intrinsically composite nature. It should be mentioned, however, that for thin films there exists the very real possibility of tunneling from the metal Fermi level to the reactants in the Helmholtz double layer. This latter situation would not be easy to reconcile with the theory and the correlations presented here. If the tunneling barrier is assumed to lie within the film, however, as

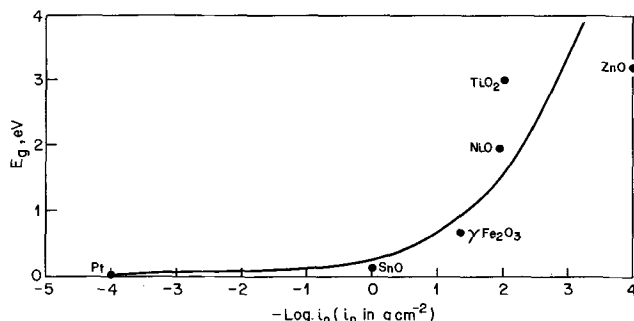


Fig. 9. Plot of exchange current densities of the Fe(CN)₆⁴⁻/Fe(CN)₆³⁻ reaction on Pt, SnO, γ -Fe₂O₃, NiO, TiO₂, and ZnO (19) against the corresponding E_g values (E_g for Pt = 0).

previously considered (29, 30), the bandgap of the film would again be the crucial factor in the rate equations since it would determine the width of the tunnel barrier.

A point that merits some further comment here is the definition of terms in the rate equations [6] and [7]. In these equations, the activation energies E^{**}_4 and E^{**}_5 have been written as under conditions of a given applied overpotential. One may in fact separate the "chemical" free energy of activation (corresponding to the overpotential, η , approaching zero) and its potential-dependence in these equations and write

$$i_4 = ZF k_4 [O_2] [H^+] \exp(-E^{**}_4/RT) \exp^{-\eta F/RT} \quad [6a]$$

and

$$i_5 = ZF k_5 [O_2] [H^+] \exp(-E^{**}_5/RT) \quad [7a]$$

where E^{**}_4 and E^{**}_5 refer to the activation energies at equilibrium (no overpotential) for the steps 4 and 5, respectively; η would, of course, operate almost entirely in the space charge region of the semiconducting film. In other words, one is now writing Eq. [6] and [7] as Eq. [6a] and [7a] in order to show explicitly the potential-dependence of rate. It should be noted that these equations have been written for a cathodic reaction (oxygen reduction) in which the potential-dependence of rate is $\exp^{-\eta F/RT}$ for the electron current and unity for the hole current assuming a wide gap semiconductor; for an anodic reaction, of course, the reverse situation holds true. By combining Eq. [6a] and [7a] one gets

$$i_t = \text{const} \exp^{-\eta F/RT} \quad [9a]$$

The Tafel slope then would be ca. 60 mV/decade at room temperature. The experimental slope for the oxygen reduction reaction and oxygen evolution reaction (at low current densities) on platinum in alkaline solutions is indeed about 60 mV (31). In most of the other cases of electrode reactions on film-covered electrodes Tafel slopes equal to 120 mV or, frequently, higher than 200 mV are observed. These values of slopes, although not easily reconciled with the treatment presented here, can be interpreted in different ways, all of which assume a part of the potential drop as operating across the semiconducting film (32, 33). When the high Tafel slopes indicate that only a fraction of the potential drop operates across the film with the rest available across the Helmholtz double layer, one is led to conclude the possible influence of surface states, arising from adsorption of reactants, intermediates, or products, on the reaction kinetics. Although the present theory does not take into account the surface states explicitly, an obvious extension on these lines may be mentioned. Let us suppose that a radical reaction intermediate gets chemisorbed on the film and creates a surface state with the energy term of its unpaired electron as E_R and lying, of course, within the bandgap. In this case, the E_g of Eq. [12] would be replaced by the energy difference between the energy term E_R and the energy at the bottom of the conduction band, E_C . Now if, $(E_C - E_R/E_g)$ is roughly constant for a given electrodic film (e.g., oxide) on a series of metals, the present theory would stay valid. Alternatively, if E_R is close to the valence band edge for every metal, the theory would remain unchanged, notwithstanding the surface states. However, if the ratio $(E_C - E_R/E_g)$ is not constant, not even roughly, for a series of metals, the theory would be inapplicable in its present form and would need some very complicated modifications, the nature of which is not completely clear at this time.

One should probably mention that factors k_4 and k_5 in the rate equations are frequency factors and would be expected to be of similar magnitude; one could thus have used only one symbol for both of them except that the present notation helps point out their different origins in different rate equations.

Conclusions

A case is presented that for electrode processes proceeding via formation of solid electrode films, attention should primarily be focused on the role of these films in the electrode reactions. A possible way of taking into account the semiconductivity of these films is outlined and the ideas stated appear to provide interpretation of literature data on: oxygen evolution and reduction reactions; anodic dissolution of metals in some systems; redox reactions; and open-circuit potentials of metals.

Acknowledgments

Thanks are due to Dr. J. P. Randin and Dr. P. Lenfant for numerous discussions in which the possibilities of the interpretations given in this paper were developed.

Manuscript submitted April 27, 1972; revised manuscript received June 26, 1972.

Any discussion of this paper will appear in a Discussion Section to be published in the June 1973 JOURNAL.

REFERENCES

1. K. J. Vetter and J. W. Schultze, *J. Electroanal. Chem.*, **34**, 141 (1972).
2. A. J. Appleby, *Cat. Rev.*, **4**, 221 (1970).
3. H. Gerischer in "Physical Chemistry: An Advanced Treatise," Vol. IX A, H. Eyring, Editor, Academic Press (1970).
4. A. Kozawa, V. E. Zilionis, and R. J. Brodd, *This Journal*, **117**, 1474 (1970).
5. A. K. Vijh, *J. Phys. Chem. Solids*, **29**, 2233 (1968), *This Journal*, **117**, 173C (1970).
6. N. E. Khumotov, *Russ. J. Phys. Chem. (English Transl.) Consultants Bureau*, **37**, 270 (1963).
7. N. D. Tomashov, As quoted by N. E. Khumotov in Ref. (6).
8. A. K. Vijh and P. Lenfant, *Can. J. Chem.*, **49**, 809 (1971).
9. R. Howald, *J. Chem. Ed.*, **45**, 163 (1968).
10. R. Parsons, *Trans. Faraday Soc.*, **54**, 1053 (1958).
11. H. Gerischer, *Bull. Soc. Chim. Belges*, **67**, 506 (1958).
12. P. Reutschi and P. Delahay, *J. Chem. Phys.*, **23**, 195 (1955).
13. J. P. Hoare, "Electrochemistry of Oxygen," Interscience Publishers (1968).
14. A. K. Vijh, *This Journal*, **115**, 1096 (1968).
15. A. K. Vijh, *Electrochim. Acta*, **16**, 441 (1971).
16. N. Hackerman, E. S. Snively, Jr., and L. D. Fiel, *Corrosion Sci.*, **1**, 39 (1967).
17. I. A. Menzies, G. W. Marshall, and G. B. Griffin, *ibid.*, **9**, 287 (1969).
18. A. K. Vijh, *Electrochim. Acta*, **16**, 1427 (1971).
19. R. V. Moshtev, *ibid.*, **16**, 2039 (1971).
20. A. K. Vijh, *Corrosion Sci.*, **12**, 105 (1972).
21. A. K. Vijh, *Electrochim. Acta*, **17**, 91 (1972).
22. P. J. Harrop and D. S. Campbell, *Thin Solid Films*, **2**, 273 (1968).
23. V. G. Levich in, "Advances in Electrochemistry and Electrochemical Engineering," Vol. 4, P. Delahay, Editor, Interscience Publishers (1966).
24. W. Mehl in, "Reactions of Molecules at Electrodes," N. S. Hush, Editor, John Wiley & Sons, Inc., and Interscience Publishers (1971).
25. J. P. Randin and E. Yeager, *J. Electroanal. Chem.*, **36**, 257 (1972).
26. D. M. Tench and E. Yeager, Tech Report No. 28, Project NR 359-451, Office of Naval Research (1970).
27. W. Mindt, *This Journal*, **116**, 1076 (1969).
28. J. McHardy, Ph.D. Thesis, University of Pennsylvania (1972).
29. P. J. Boddy, D. Kahng, and Y. S. Chen, *Electrochim. Acta*, **13**, 1311 (1968).
30. A. K. Vijh, *Corrosion Sci.*, **11**, 411 (1971).
31. A. Damjanovic in, "Modern Aspects of Electrochemistry," Vol. 5, J.O'M. Bockris and B. E. Conway, Editors, Plenum Press (1969).
32. R. E. Meyer, *This Journal*, **107**, 847 (1960); A. K. Vijh and B. E. Conway, *Chem. Rev.*, **67**, 623 (1967).
33. A. K. Vijh, "Electrochemistry of Solid Materials," Marcel Dekker, Inc., New York (1973).

Speculation on Some Effects of Complexation and Anion-Induced Adsorption on the Polarography of Indium in Acidic Halide and Thiocyanate Media

A. M. Bond*

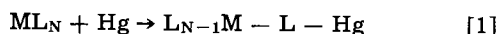
Department of Inorganic Chemistry, University of Melbourne, Parkville, Victoria, 3052, Australia

ABSTRACT

Some phenomena found in the polarographic reduction of indium(III) in acidic halide and thiocyanate media have been studied by a-c polarography. Speculation on the role of complex formation and anion-induced adsorption on the polarographic reduction at potentials near the half-wave potential are given. At low ligand concentrations the a-c peak potential is believed to be influenced by anion-induced adsorption while at high ligand concentrations the value is the thermodynamic value predicted from bulk complexation equilibria. The unusual d-c minimum found at more negative potentials and the above phenomena are discussed in terms of the coupled occurrence of electroinactive $[\text{In}(\text{H}_2\text{O})_x]^{3+}$ ions at potentials where the complexed ion is electroactive and anion-induced adsorption. The reduction mechanism at the half-wave potential and at more negative potentials are concluded to be similar. The irreversible reduction of the uncomplexed indium ion is attributed to the slow rate of exchange of co-ordinated water, in agreement with other workers.

A number of recent publications have dealt with the adsorption of metal complexes on mercury electrodes from solutions containing anions that also adsorb on mercury (1-12). Several different experimental techniques have been used in these studies including such methods as chronocoulometry and chronopotentiometry. From these studies, two mechanisms have been proposed to account for the experimental findings.

The first mechanism, suggested by O'Dom and Murray (4), assumed that one particular complex species present in the solution, ML_N , adsorbed on the mercury surface to produce an adsorbed species with the same chemical composition



An alternative proposal by Anson and Barclay (5) differs from the above in that interaction with anions already adsorbed on the mercury occurs according to scheme [2]



Data supporting the second scheme as being the predominant one have been obtained for a number of metals and cations (11), although in several studies (9, 10), authors have been unable to choose between reactions [1] and [2]. The bulk of evidence therefore indicates at least that the second scheme is the more usual one.

The influence of anion-induced adsorption in some areas of polarography has previously been considered. In particular, Barker and Bolzan (13) looked at the influence on maxima in d-c polarography and other areas of a-c, rf, square wave, and pulse polarography. Other workers (14-17) have also examined the analytical implications of anion-induced adsorption on a wide variety of polarographic techniques.

From these studies on anion-induced adsorption it is apparent that complexation of metal ions both in the bulk of the solution and at the electrode surface can be extremely important in determining the nature of the observed electrode reaction. Reduction of the metal ion complex could occur in the adsorbed state. The adsorbed complex can be quite different from the complex existing in the bulk solution and this could

profoundly influence the observed electrode process, compared with that based on calculations of bulk equilibria. Speculation on the polarographic reduction of indium(III) in halide and thiocyanate media is now considered in terms of complexation and anion-induced adsorption. In particular possible influences of anion-induced adsorption at the half-wave potential are considered and then these ideas extended to more negative potential regions where a minimum is frequently observed in the d-c polarography of indium.

Experimental

An indium stock solution was prepared by dissolving indium(III) perchlorate in concentrated perchloric acid. Appropriate aliquots of this stock solution were taken to give solutions for polarography, $4.6 \times 10^{-4}\text{M}$ in indium and 0.8M in perchloric acid.

The thiocyanate solution was prepared from laboratory grade NaSCN, analyzed by titration against standard silver nitrate (the Volhard method). The halides fluoride, chloride, bromide, and iodide were added as the sodium salt.

The ionic strength of 3.0 was maintained by addition of sodium perchlorate. The concentrations of chloride, bromide, iodide, and thiocyanate used are shown in the tables.

All solutions were degassed with oxygen-free nitrogen.

The temperature was maintained at $30^\circ \pm 0.1^\circ\text{C}$.

All potentials measured in this work are relative to an Ag|AgCl reference electrode (5M NaCl), separated from the indium solutions with a salt bridge containing 5M NaClO₄.

Polarograms were obtained using a Metrohm Polarecord E261. The a-c polarography was carried out using the Metrohm AC Modulator E 393 with an a-c voltage of 10 mV, rms at 50 Hz.

To minimize cell impedance, a-c polarography was carried out with a three-electrode system, tungsten being used as the auxiliary electrode. Rapid polarographic techniques with controlled drop times of 0.16 sec were achieved with the Metrohm Polarographic Stand E 354.

Results and Discussion

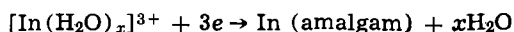
Indium(III) electrode process at the DME.—In non-complexing acid media, such as perchloric or nitric acid, one drawn out irreversible indium(III) wave is

* Electrochemical Society Active Member.

Key words: anion-induced adsorption, polarography, indium complexes.

observed (18). The addition of a low concentration of certain ligands can accelerate the normally slow and irreversible polarographic reduction of the aquated ion $\text{In}(\text{H}_2\text{O})_x^{3+}$ and in several aqueous electrolyte solutions such as the halides (18, 23-25) and the pseudo-halide, thiocyanate (26-28), a reversible three-electron reduction wave is observed. However at potentials considerably more negative than the half-wave potential, a curious minimum appears on the d-c polarogram. On the a-c polarogram a negative admittance is observed over the potential region where the minimum appears on the d-c polarogram (27). The nature of the three-electron reduction wave and the minimum have been the subject of a large number of papers [see Ref. (25-32) for instance].

The nonreversible reduction of indium in perchloric acid was confirmed in this work with no polarographic wave being observed prior to reduction of the hydrogen ion. In 0.8M HClO_4 available evidence (33) shows that hydrolysis of indium is suppressed and $[\text{In}(\text{H}_2\text{O})_x]^{3+}$ is the major species present. Data by Eigen (34) shows that the characteristic half-life for H_2O substitution in the inner co-ordination sphere is of the order of 10^{-3} sec. This is a relatively slow rate of exchange of water and an irreversible electrode process for reduction to the metal could be expected, as the solvated water molecules have to be eliminated (35)



This conclusion is essentially in agreement with that reached by Aikens and co-workers (23, 36).

In accordance with previous studies on bismuth (37), it is suggested that if a covalently bonded ligand displaces the co-ordinated water and this ligand has a fast and close to diffusion-controlled rate of exchange, then the rate of the electrode process can be accelerated to the reversible value. Whether the complex is formed in the bulk solution or at the electrode surface via anion-induced adsorption as in Eq. [2] should be irrelevant.

In high concentrations of chloride, bromide, iodide, and thiocyanate plots of E_{de} vs. $\log i/(i_d - i)$ were linear, with slopes very close to the theoretically expected value of 20 mV for a reversible three-electron reduction. $E_{1/2}$ was independent of indium(III) concentration and drop time.

The a-c polarograms were highly symmetrical with half-widths of 34 ± 2 mV. Theoretically, the half-widths for a reversible electrode reaction should be approximately $90/n$ mV (at 25°C and for an applied a-c voltage of $\leq 8/n$ mV). The value of 34 mV (uncompensated for iR drop) obtained with an applied a-c voltage of 10 mV and at 30°C is thus in satisfactory agreement with the theoretically expected value. Good agreement was obtained between $E_{1/2}$ from d-c polarography and the summit potential E_s from the a-c polarograms. E_s was independent of indium(III) concentration and drop time.

With high halide or thiocyanate concentrations, d-c and a-c polarograms are well defined and easily interpreted, and the parameters $E_{1/2}$, E_s , i_d , or I_s are easily evaluated, where $E_{1/2}$ = d-c half-wave potential, E_s = a-c summit potential, i_d = d-c limiting current, and I_s = a-c summit current.

At low halide or thiocyanate concentrations d-c polarograms are somewhat difficult to analyze. The heights of the waves are very much lower than for high halide concentrations and the limiting height (i_l or i_d) of the wave is ill-defined because of the minimum. Thus the value of i_d to be used in plots of E_{de} vs. $\log i/(i_d - i)$ is difficult to ascertain and the reversibility of the electrode reaction is uncertain. The a-c polarograms at low concentrations (Fig. 1) are still easily evaluated for E_s , from the potential of the wave at maximum alternating current. $E_{1/2}$ values, however, require a knowledge of the limiting current, which in the presence of the minimum is not readily known,

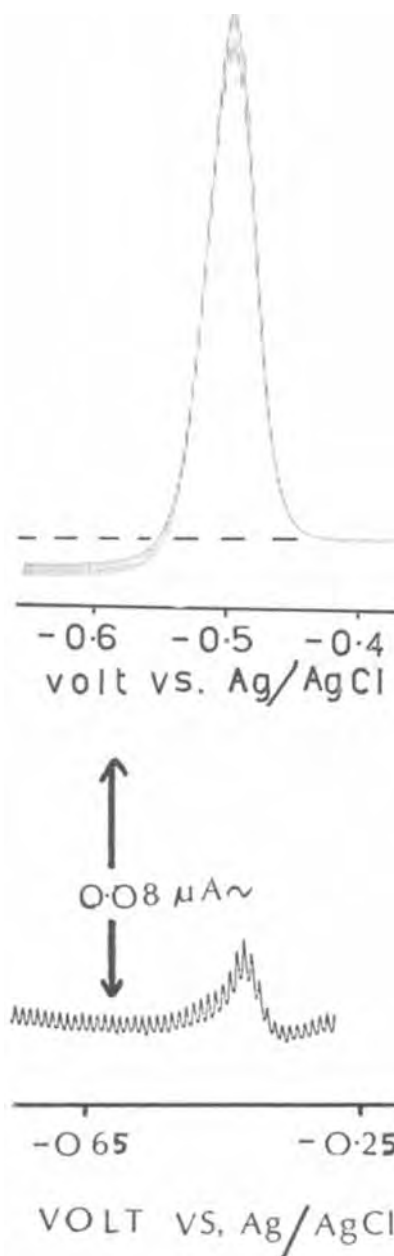
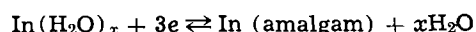


Fig. 1. Typical rapid a-c polarograms of $\text{In}(\text{III})$ at low halide or thiocyanate concentrations for which the minimum occurs $[\text{NaCl}]$. (a, upper) 6×10^{-2} M, (b, lower) 10^{-3} M.

so that accurate $E_{1/2}$ values at low halide levels cannot be determined.

It was observed that E_s values become more positive with decreasing halide concentration. For the four systems, chloride, bromide, iodide, and thiocyanate, an extrapolation of E_s vs. ligand concentration to zero ligand concentration, gave a value of -0.44 V vs. Ag/AgCl (Fig. 2). This value of E_s could represent the thermodynamic value for the uncomplexed ion, i.e., for the electrode process



but this point is considered further at a later stage as complications introduced by adsorption could effect this value.

For the lower concentrations of halide reported in the tables, the height of the a-c and d-c waves are functions of ligand concentration.

The a-c electrode process, despite the decrease in height with decreasing halide concentration, does not appear to alter from being highly reversible from the point of view of both shape and peak potential at least

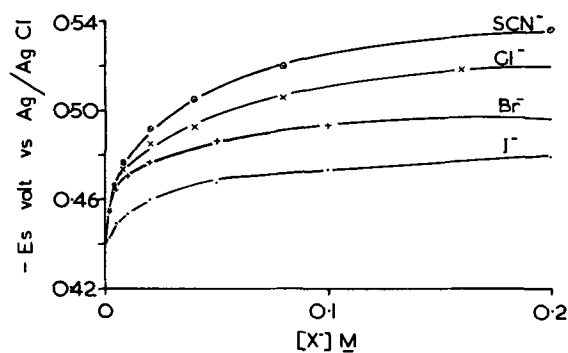


Fig. 2. Extrapolation of E_s to zero ligand concentration to obtain an apparent (E_s)_f.

down to 10^{-3} M in ligand concentration. With decreasing ligand concentration the E_s value always becomes more positive as stated above. This is consistent with the electrode reaction being reversible, the changes in E_s being predominantly thermodynamic ones due to complex formation. If the charge transfer had become less reversible, say quasi reversible, then it would be expected that considerable broadening of the a-c wave would occur and that the E_s values would eventually become more negative, rather than positive, with decreasing halide concentration, because of increasing kinetic control.

Although many other systems undergo anion-induced adsorption, and presumably with increased co-ordination, the peculiarities of the indium(III) electrode process appear to be manifestations of the $\text{In}^{3+}(\text{aq})$ species being electroinactive at d-c potentials where $[\text{InX}_n]^{(3-n)x}$ complexes are electroactive.

The height of the reversible wave would appear to be dependent on the concentration of In(III) -ligand complex present, which in turn appears to be influenced by adsorption phenomena and kinetics of adsorption at the DME.

Thus it can be postulated that the over-all electrode process at potentials near the half-wave potential is as follows:

Indium(III) species in the bulk of the solution are transferred toward the electrode by diffusion. Any uncomplexed In^{3+} is irreversibly reduced, and complexed In(III) reversibly reduced at the DME. The indium(III) complex species are in rapid equilibrium with each other and near or at the DME, interaction can occur with adsorbed ligand, prior to reduction of indium(III) to indium (amalgam).

The height of the resultant a-c or d-c polarographic waves therefore reflects the concentration of indium(III) complex present near the electrode, rather than in the bulk of the solution: that is, a form of the mechanism Pospisil and De Levie derived for low concentrations of thiocyanate [at potentials where the minimum is observed (32)] is believed to be operative at all d-c potentials. More generally, it is concluded that scheme [2] is operative and at low halide concentrations this step is rate determining and is followed by reversible charge transfer: that is, despite the fact that at low ligand concentrations the bulk solution consists almost entirely of uncomplexed In^{3+} , anion induced adsorption permits reduction of indium(III) complexes to occur in the adsorbed state.

Chloride, which forms a strong indium(III) complex, but is not strongly adsorbed (relative to other ligands) is influenced mainly by complex formation in the bulk of the solution. The electrode reaction therefore remains diffusion controlled and the height of the reversible wave increases with increasing chloride concentration because of the increase in concentration of indium complex.

Iodide, which is strongly adsorbed at the DME and forms only a weak complex, is much more influenced

by complex formation of indium near the electrode surface with adsorbed iodide.

The adsorption \rightleftharpoons desorption equilibrium of halide must also be taken into account (12) and probably explains in part the presence of the minimum. Around the potential of the indium complex wave, which is near the electrocapillary maximum, the adsorbed ligand concentration would be expected to change substantially with potential as desorption occurs. The concentration of the adsorbed ligand at potentials beyond the electrocapillary maximum would decrease especially sharply at more negative potentials. The concentration of indium complexes formed near or at the electrode would thus also decrease as the potential becomes more negative and if this was a significant source of complexation then the height of the d-c wave beyond $E_{1/2}$ value, in the normally diffusion-controlled potential range, would also decrease. The decrease in the adsorbed ligand at the electrode surface can in this way give rise to the minima.

Limiting current at very high chloride concentrations.—If the increase in direct or alternating current for indium(III) arises from the combined effects of electroinactive In(aq)^{3+} and anion-induced adsorption, it follows that under conditions where all the In(III) is complexed, that the limiting current should be almost independent of ligand concentration. For bromide, iodide, and thiocyanate it has been suggested that much of the complexation occurs in the double layer via anion-induced adsorption. However, for chloride considerable complexation probably exists in the bulk solution. Calculations of the percentage of each In(III) species present in the bulk solution can be made quite readily by appropriate computational techniques (38), using reported stability constants from the literature. Results for chloride are given in Table I. As stability constant data are notoriously variable, calculations based on three sets of data which cover the range of answers present in the literature, are

Table I. Percentage distribution of the various indium(III) species in the indium(III)-chloride system as a function of chloride concentration

% In^{3+}			% InCl^{2+}			% InCl_2^+			% InCl_3			-log[Cl ⁻]
A*	B**	C†	A*	B**	C†	A*	B**	C†	A*	B**	C†	
0	0	0	0	0	0	1	2	3	99	97	97	-0.5
0	0	0	0	0	0	2	3	4	98	97	96	-0.4
0	0	0	0	0	0	2	4	5	98	96	95	-0.3
0	0	0	0	0	1	2	5	6	97	95	93	-0.2
0	0	0	0	0	1	3	6	7	97	94	92	-0.1
0	0	0	0	1	1	4	7	9	96	92	90	0.0
0	0	0	0	1	2	5	9	11	95	90	87	0.1
0	0	0	1	1	3	6	11	13	94	88	83	0.2
0	0	0	1	2	5	7	13	16	92	84	79	0.3
0	0	1	1	3	7	9	16	18	90	81	73	0.4
0	0	1	2	5	11	11	19	21	87	76	67	0.5
0	0	2	3	7	15	13	22	24	83	71	59	0.6
0	0	4	5	10	20	16	26	25	79	64	51	0.7
0	0	7	7	14	26	19	28	26	74	57	41	0.8
0	1	10	11	19	32	21	31	26	68	49	32	0.9
1	1	15	15	26	38	24	32	24	60	41	24	1.0
1	2	21	21	33	42	26	33	21	52	33	17	1.1
2	3	28	27	40	44	27	32	17	43	25	11	1.2
3	5	35	35	47	44	28	30	14	35	19	7	1.3
4	7	43	42	53	43	27	27	11	27	13	4	1.4
6	9	50	49	58	40	25	23	8	20	9	3	1.5
9	12	57	55	62	36	22	20	6	14	6	1	1.6
12	16	63	60	64	32	19	16	4	9	4	1	1.7
16	20	69	62	64	28	16	13	3	6	3	0	1.8
20	25	74	63	63	24	13	10	2	4	2	0	1.0
25	31	79	63	61	20	10	8	1	2	1	0	2.0
30	36	83	61	57	16	8	6	1	2	1	0	2.1
36	42	86	57	53	14	6	4	1	1	0	0	2.2
42	48	88	53	48	11	4	3	0	1	0	0	2.3
48	54	91	48	43	9	3	2	0	0	0	0	2.4
54	60	93	43	38	7	2	2	0	0	0	0	2.5
60	66	94	38	33	6	2	1	0	0	0	0	2.6
66	71	95	33	28	5	1	1	0	0	0	0	2.7
71	76	96	28	24	4	1	0	0	0	0	0	2.8
76	80	97	24	20	3	0	0	0	0	0	0	2.9
80	83	98	20	17	2	0	0	0	0	0	0	3.0

* Column A was calculated assuming $\text{Log } \beta_1 = 2.4$, $\text{Log } \beta_2 = 3.6$, $\text{Log } \beta_3 = 5$.

** Column B was calculated assuming $\text{Log } \beta_1 = 2.3$, $\text{Log } \beta_2 = 3.4$, $\text{Log } \beta_3 = 4$.

† Column C was calculated from data given in Ref. (52), i.e., $\text{Log } \beta_1 = 1.4$, $\text{Log } \beta_2 = 2.2$, $\text{Log } \beta_3 = 3.2$.

All percentages are calculated as mole percentages.

given. From the three sets of data it can be seen that the percentage of $\text{In}(\text{aq})^{3+}$ becomes less than 1 when $\log [\text{Cl}^-]$ lies in the range -0.9 to -0.3 , i.e., for chloride concentrations between about 0.1 and 0.5M. From Table II it can be seen that for chloride, I_s ceases to become strongly dependent on chloride concentration over this same concentration range. Similarly, the d-c i_d value is almost independent of chloride concentration above about 0.1M, and the minimum for indium(III) reduction disappears at this high chloride concentration.

With the other systems, similar calculations on the percentage distribution of each species as a function of ligand concentration can be made and it is most evident that the limiting, direct, or alternating currents, which are essentially independent of ligand concentration, are obtained long before all of the $\text{In}(\text{III})$ has been complexed in the bulk solution, in accordance with the theories put forward in this work.

Influence of fluoride.—In previous work, the other common halide, fluoride, has not been considered. Fluoride, being very small and virtually nonpolarizable, is one of the least adsorbable ligands available (39) and its behavior might therefore be different from the other halides and thiocyanate. With fluoride being nonadsorbable, but forming quite strong complexes, it would, in fact, be expected that complexation should occur only in the bulk solution, and that complexation via anion-induced adsorption should not be possible. In view of this difference expected for fluoride it would obviously be advantageous to study the influence of fluoride on the polarographic behavior of indium(III). However, to study fluoride, several difficulties are encountered, and it is not surprising that the influence of fluoride is unknown to date. First, fluoride exists in acid media as hydrofluoric acid, which rapidly etches the glass dropping mercury electrode capillary, thus prohibiting measurements with conventional polarographic apparatus. Second, hydrofluoric acid is a weak acid, and under the acid conditions used to study indium(III) reduction, it cannot be assumed that the analytical and free fluoride concentrations are identical. In fact, there will be very little free fluoride available. Third, the insolubility of $\text{Na}_3[\text{InF}_6]$ could lead to problems (40, 41).

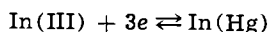
Elsewhere it has been reported that rapid polarographic measurements can be used to overcome problems of etching the glass capillary (42, 43) under the conditions of this work. The other two difficulties do, however, limit the amount of work that can be done with fluoride, to the following:

(i) With the same conditions used for the other halides no reversible polarographic wave was observed around -0.4V vs. $\text{Ag}|\text{AgCl}$ on addition of fluoride.

(ii) Addition of weighed quantities of fluoride to solutions containing $4.6 \times 10^{-4}\text{M}$ indium and about 10^{-2}M chloride, bromide, iodide, or thiocyanate did not cause any alteration to the reversible indium(III) wave outside of those changes attributable to changes in ionic environment.

While the conclusions that can be made from the work on fluoride are limited, it has at least been shown that traces of fluoride do not give rise to phenomena consistent with anion-induced adsorption and this is in accord with ideas presented in this paper.

A-C summit potential.—Importantly, the reversibility of the electrode process for high ligand concentrations has been established in the above discussion in at least one sense. Work by Moussa *et al.* (44), who measured standard rate constants, k_s , for the exchange



by faradaic impedance methods however, is probably even more convincing.

In 1M NaCl they calculated k_s to be 3.4×10^{-2} cm-sec $^{-1}$ and in 1M NaBr, k_s was 6.5×10^{-1} cm-sec $^{-1}$.

These rate constants are certainly sufficiently fast, particularly in bromide media, to define the d-c electrode process as being reversible. Furthermore, in the a-c sense, they are fast enough, so that provided low frequency a-c polarography is used, as in this work, E_s should equal the reversible half-wave potential $E_{1/2}^f$ (45, 46) if normal conditions are operative: that is, provided anion-induced adsorption of some other phenomenon does not alter the E_s value substantially (47).

If the a-c summit potential is equivalent to the "normal" thermodynamic half-wave potential, then the use of this value as a function of ligand concentration in standard polarographic equations could be expected to lead to stability constants in excellent agreement with those obtained by potentiometry, ion exchange, solvent extraction, etc.

In a-c polarography the a-c summit potential, E_s , is used instead of the d-c $E_{1/2}$ value and the equation to be solved is a modified form of the DeFord-Hume relationship (48)

$$F_0(X) = \text{antilog} \left\{ 0.4343 \frac{nF}{RT} [E_s]_f - (E_s)_c \right. \\ \left. + \log \frac{(I_f)}{(I_c)} \right\} = \sum_{j=0}^j \beta_j C_x^j$$

where $F_0(X)$ is introduced for convenience to represent the experimentally measurable quantity on the left-hand side of the equation. β_j is the formation constant of the j th complex, C_x the concentration of the complex-forming substance, and the subscripts f and c refer to the free ion and complex ion, respectively. Other symbols are those conventionally used in polarography.

The DeFord-Hume equation can be solved for the various β_j values by a considerable number of computational procedures. In this work the graphical method described in detail in the original paper was used with the appropriate $F_j(X)$ functions, where for example

$$F_1(X) = \frac{F_0(X) - 1}{[C_x]}, \quad F_2(X) = \frac{F_1(X) - \beta_1}{[C_x]}, \quad \text{etc.}$$

The reduction wave for indium(III) in the absence of halide is irreversible so that the $(E_s)_f$ value cannot be determined directly. Thus the value of E_s extrapolated to zero ligand concentration or described previously was used in the first instance.

The term $\log(I_f)/(I_c)$ in the DeFord-Hume equation, which is normally measured by d-c polarography as $\log(i_d)_f/(i_d)_c$ cannot be calculated for indium(III) because of the nature of the electrode process. The term therefore had to be neglected. The ratio would be expected to be small in any case so that this approximation should be a good one.

Results, assuming the DeFord-Hume (48) or the simpler Lingane (49) equations to apply, are given below.

DeFord-Hume method.—Indium(III)-chloride system.—Figures 3, 4, and 5 and Table II show the graphical method of calculation of the indium(III)-chloride system. Three complexes were observed with $\beta_1 = 3 \times 10^3$ (InCl^{2+}), $\beta_2 = 1.5 \times 10^5$ (InCl_2^+), and $\beta_3 = 1.3 \times 10^6$ (InCl_3).

Indium(III)-bromide system.—Table III and Fig. 3, 4, and 6 show the graphical method of calculation of the indium(III)-bromide system. Three complexes were observed with $\beta_1 = 2.5 \times 10^4$ (InBr^{2+}), $\beta_2 = 2.0 \times 10^4$ (InBr_2^+), and $\beta_3 = 7.7 \times 10^4$ (InBr_3).

Indium(III)-iodide system.—Table IV and Fig. 3 and 7 show the graphical method of calculation of the indium(III)-iodide system. One iodide complex was observed with $\beta_1 = 3.5 \times 10^2$ (InI^{2+}).

Indium(III)-thiocyanate system.—Table V and Fig. 3, 4, and 8 show the graphical method of calculation of

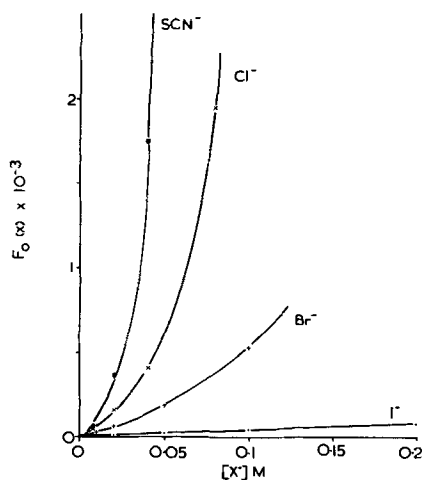


Fig. 3. Graphical analysis of the $F_0(X)$ functions for the various complex systems as shown.

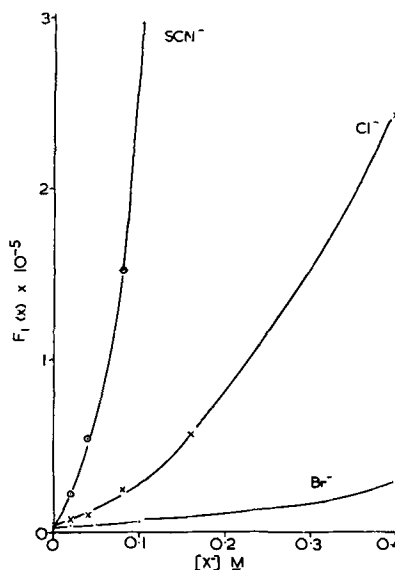


Fig. 4. Graphical analysis of the $F_1(X)$ functions for the various complex systems as shown.

the indium(III)-thiocyanate system. Three complexes of thiocyanate were observed with $\beta_1 = 3 \times 10^3$ ($\text{In}(\text{SCN})^{2+}$), $\beta_2 = 9 \times 10^5$ ($\text{In}(\text{SCN})_2^+$), $\beta_3 = 3.3 \times 10^6$ ($\text{In}(\text{SCN})_3$).

Lingane method.—Figure 9 shows the Lingane (49) method of evaluation of complex ion systems. Plots of $E_s (=E_{1/2})$ vs. log concentration of halide or thiocyanate are given. This clearly shows, as do the β_n values, that the order of stability is $\text{SCN}^- > \text{Cl}^- > \text{Br}^- > \text{I}^-$. These plots also show the existence of three complexes of thiocyanate, chloride, and bromide. The plots may conveniently be described by three straight lines of slopes 20, 40, and 60 mV, respectively, corresponding to the complexes InX^{2+} , InX_2^+ , and InX_3 . For the iodide, however, only InI^{2+} is indicated over most of the concentration range studied. The last two points on the graph at very high iodide concentration depart from the straight line and provide evidence for a second weak complex.

Comparison with other data.—Table VI shows a comparison of results obtained in this work with some other studies at similar ionic strength and temperatures. The order of stability established in this work of $\text{SCN}^- > \text{Cl}^- > \text{Br}^- > \text{I}^-$ appears to be consistent with most other results.

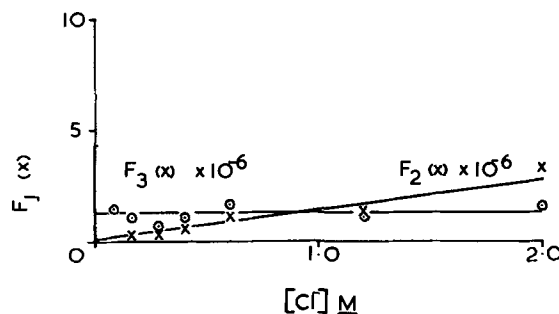


Fig. 5. Graphical analysis of the $F_2(X)$ and $F_3(X)$ functions for the chloride system.

It can be seen in Table VI that the polarographic results obtained in the present work and in other studies are in general significantly higher than those reported by other techniques, especially in the case of iodide. However, the nature and number of complexes formed are acceptable.

Table II. Analysis of $F_j(X)$ functions for the chloride system

Conc Cl ⁻ , M	-E _s (V vs. Ag/AgCl)	I _s , μA~	F ₀ (X)	F ₁ (X)	F ₂ (X)	F ₃ (X)
0.000	0.4400	—	1.000	—	—	—
0.004	0.4650	0.11	17.66	4165	—	—
0.008	0.4733	0.26	45.81	5601	—	—
0.020	0.4844	0.68	164.0	8150	2.575 × 10 ³	—
0.040	0.4923	1.13	406.5	1.014 × 10 ⁴	1.785 × 10 ³	—
0.080	0.5060	2.07	1959	2.448 × 10 ⁴	2.685 × 10 ³	1.5 × 10 ³
0.160	0.5192	2.58	8923	5.576 × 10 ⁴	3.298 × 10 ³	1.1 × 10 ³
0.280	0.5290	2.88	2.748 × 10 ⁴	9.814 × 10 ⁴	3.400 × 10 ³	0.7 × 10 ³
0.400	0.5400	3.05	9.727 × 10 ⁴	2.432 × 10 ⁵	6.005 × 10 ³	1.1 × 10 ³
0.600	0.5525	3.16	4.088 × 10 ⁵	6.813 × 10 ⁵	1.131 × 10 ⁴	1.7 × 10 ³
1.200	0.5665	3.26	2.041 × 10 ⁶	1.701 × 10 ⁶	1.418 × 10 ⁴	1.1 × 10 ³
2.000	0.5828	3.46	1.327 × 10 ⁷	6.635 × 10 ⁶	3.318 × 10 ⁴	1.6 × 10 ³

Table III. Analysis of $F_j(X)$ functions for the bromide system

Conc Br ⁻ , M	-E _s (V vs. Ag/AgCl)	I _s , μA~	F ₀ (X)	F ₁ (X)	F ₂ (X)	F ₃ (X)
0.000	0.4400	—	1.000	—	—	—
0.002	0.4547	0.67	5.41	2.205 × 10 ³	—	—
0.005	0.4632	1.04	14.36	2.672 × 10 ³	—	—
0.010	0.4704	1.70	32.84	3.184 × 10 ³	—	—
0.020	0.4765	2.20	66.16	3.258 × 10 ³	—	—
0.050	0.4855	2.53	186.0	3.700 × 10 ³	2.40 × 10 ⁴	8.0 × 10 ⁴
0.100	0.4944	2.63	5.269 × 10 ³	5.258 × 10 ³	2.76 × 10 ⁴	7.6 × 10 ⁴
0.500	0.5245	2.78	1.640 × 10 ⁴	3.280 × 10 ⁴	6.06 × 10 ⁴	8.1 × 10 ⁴
1.000	0.5400	2.82	9.727 × 10 ⁴	9.727 × 10 ⁴	9.48 × 10 ⁴	7.5 × 10 ⁴
1.500	0.5502	2.81	3.139 × 10 ⁵	2.093 × 10 ⁵	1.38 × 10 ⁵	7.9 × 10 ⁴
2.000	0.5570	2.83	6.855 × 10 ⁵	3.428 × 10 ⁵	1.70 × 10 ⁵	7.5 × 10 ⁴

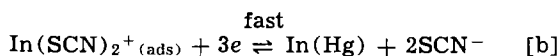
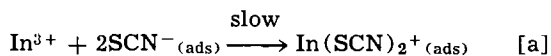
Table IV. Analysis of $F_j(X)$ functions for the iodide system

Conc I ⁻ , M	$-E_s$ (V vs. Ag/AgCl)	$I_s, \mu A \sim$	$F_0(X)$	$F_1(X)$
0.000	0.4400	—	1.000	—
0.002	0.4446	1.50	1.696	348
0.005	0.4485	2.09	2.655	331
0.010	0.4531	2.31	4.500	350
0.020	0.4580	2.39	7.903	345
0.050	0.4660	2.20	19.83	376
0.100	0.4715	2.06	37.26	363
0.200	0.4775	1.89	74.22	371
0.500	0.4860	1.89	197.0	392
1.000	0.4945	1.75	523.0	522

That the polarographically obtained stability constants are higher than "accepted" values is extremely interesting. The experimental errors involved in the present study are considerable. A recent paper by Momoki and Ogawa (59) discusses this aspect of indium(III) systems in detail. $(E_s)_f$ is an extrapolated value and the major contributions to the $F_0(X)$ function $[(E_s)_f - (E_{1/2})_c]$, could be in error by several millivolts. However, despite considerable uncertainty in the $F_0(X)$ functions the values of β_j calculated by polarographic procedures still do not appear to be in agreement with other data.

This apparent anomaly needs an explanation. The net conclusion one could draw from these data is that the summit potential is not in agreement with the thermodynamic standard potential, E° , at least at some ligand concentrations. The number and nature of the complexes in the Lingane plot given in Fig. 9 is basically derived from data at high ligand concentrations. These are essentially correct so it would appear that E_s values at high ligand concentrations are in agreement with those calculated from complexation existing in the bulk solution. The magnitude of the β_n values however strongly depends on the $(E_s)_f$ value used. This value is an extrapolated one and is derived essentially from the data obtained at low ligand concentrations.

At low ligand concentrations, the major species present in the bulk solution is electroinactive $In(aq)^{3+}$, and the electrode process is assumed to occur through mechanism [2] via anion-induced adsorption. For the particular example of low thiocyanate concentration, Pospisil and De Levie (32) have shown that the electrode process is consistent with

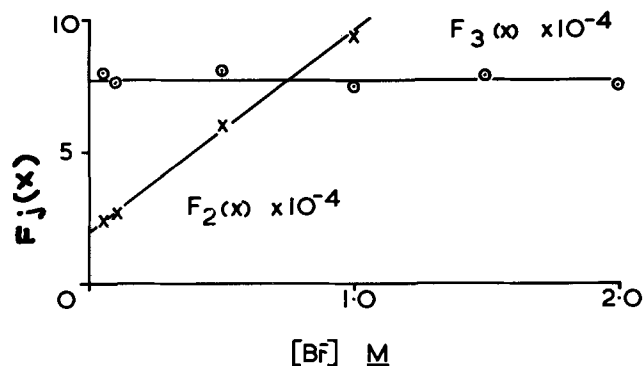
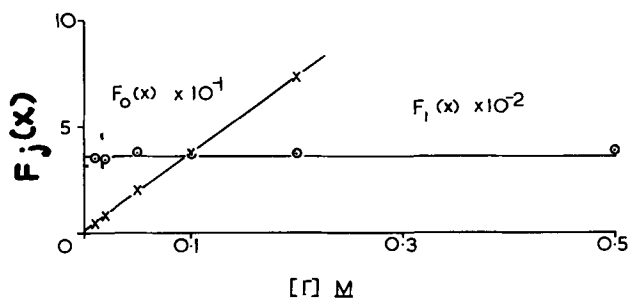
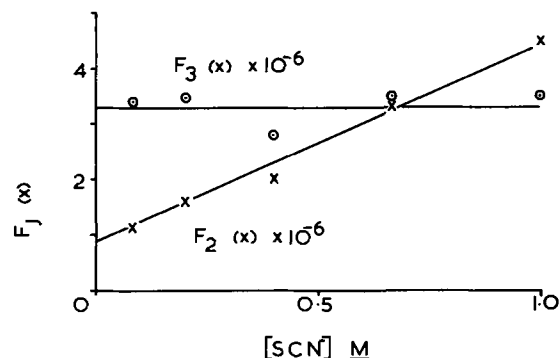


where the adsorption step is much slower than charge transfer and presumably is rate determining near $E_{1/2}$.

Measurements in this work are consistent with rapid and reversible charge transfer because the shape of both a-c and d-c waves is close to Nernstian. However below the $10^{-2}M$ ligand concentration range the electrode process is kinetically controlled to varying degrees by the anion-induced adsorption step occurring prior to reduction of the complex as in scheme [2] or step [a] reported for the thiocyanate system (32). This could influence the E_s value so that it no longer reflects the thermodynamic value expected from bulk complexation existing in bulk solution.

Table V. Analysis of $F_j(X)$ functions for the thiocyanate system

Conc SCN ⁻ , M	$-E_s$ (V vs. Ag/AgCl)	$I_s, \mu A \sim$	$F_0(X)$	$F_1(X)$	$F_2(X)$	$F_3(X)$
0.000	0.4400	—	1.000	—	—	—
0.004	0.4670	2.09	22.23	5.308×10^3	—	—
0.008	0.4766	2.46	67.00	8.250×10^3	—	—
0.020	0.4914	2.62	366.4	1.827×10^4	7.635×10^5	—
0.040	0.5050	2.55	1746	4.363×10^4	1.0157×10^6	—
0.080	0.5180	2.45	7773	9.115×10^4	1.177×10^6	2.89×10^6
0.200	0.5365	2.42	6.506 $\times 10^1$	3.253×10^5	1.612×10^6	3.46×10^6
0.400	0.5551	2.33	3.248×10^5	8.120×10^5	2.023×10^6	3.57×10^6
0.667	0.5636	2.10	1.462×10^6	2.192×10^6	3.283×10^6	2.81×10^6
1.000	0.5733	2.02	4.456×10^6	4.456×10^6	4.453×10^6	3.55×10^6

Fig. 6. Graphical analysis of the $F_2(X)$ and $F_3(X)$ functions for the bromide system.Fig. 7. Graphical analysis of the $F_0(X)$ and $F_1(X)$ functions for the iodide system.Fig. 8. Graphical analysis of the $F_2(X)$ and $F_3(X)$ functions for the thiocyanate system.

Calculations based on data presented in Ref. (36) suggest that the E_s value extrapolated to zero ligand concentration [similar to Cozzi and Vivarelli's d-c $E_{1/2}$ value (23, 24)] is more positive than the correct $(E_s)_f$ value and hence stability constant determinations using this value give rise to large β_n values: that is, when the influence of the anion-induced adsorption step becomes rate determining and is likened to a prior chemical reaction, the E_s value becomes more positive than the reversible half-wave potential.

However, if the extrapolation of $E_{1/2}$ to zero ligand concentration is limited to concentrations above $2 \times$

Table VI. Comparison of values obtained for halide and thiocyanate complexes of indium(III) in various studies

	Log β_1	Log β_2	Log β_3	Method	Reference
Chloride	3.5	5.2	6.1	Polarographic	This work
	4.3	6.1	—	Polarographic	23 and 24
	2.4	3.6	4.0	Cation exchange	50
	2.3	2.5	3.6	Polarographic & potentiometric	51
Bromide	1.4	2.2	3.2	Cation exchange	52
	2.6	4.1	—	Solvent extraction	53
	3.4	4.3	4.9	Polarographic	This work
	3.8	4.8	—	Polarographic	23 and 24
Iodide	1.4	2.9	—	Polarographic & potentiometric	51
	2.1	3.4	4.0	Spectrophotometric ^(a)	54
	2.0	3.1	3.3	Cation exchange	50
	2.4	3.3	3.2	Solvent extraction ^(b)	53
Thiocyanate	2.5	—	—	Polarographic	This work
	3.1	3.8	—	Polarographic	23 and 24
	1.0	2.3	—	Potentiometric	55
	1.6	2.6	2.5	Cation exchange	50
Thiocyanate	2.0	—	—	Glass electrode	56
	2.0	2.2	2.2	Solvent extraction	53
	3.5	5.9	6.5	Polarographic	This work
	2.6	3.6	4.6	Potentiometric	55
	2.6	4.0	4.7	Potentiometric ^(c)	57
	2.1	3.2	4.2	Polarographic ^(d)	58
	2.4	4.1	5.1	Solvent extraction ^(e)	53

^(a) Log $\beta_4 = 4.8$ [InBr₄⁻].

^(b) Log $\beta_4 = 2.2$ [InBr₄⁻].

^(c) Log $\beta_4 = 4.8$ [In(SCN)₄⁻].

^(d) Log $\beta_4 = 4.2$ [In(SCN)₄⁻]; log $\beta_5 = 4.8$ [In(SCN)₅²⁻]; log $\beta_6 = 4.8$ [In(SCN)₆³⁻].

^(e) Log $\beta_4 = 4.6$ [In(SCN)₄⁻]; log $\beta_5 = 5.5$ [In(SCN)₅²⁻].

10⁻²M when kinetic considerations of the electrode process will not be as important [as was done by Momoki and Ogawa (59)] then in agreement with ideas presented in this paper it would appear that the correct $(E_{1/2})_f$ value is obtained for use in standard polarographic equations for determining stability constants. This work therefore clarifies some apparently anomalous results concerning stability constant determination by polarographic methods and shows how discrepancies have arisen.

In conclusion it can therefore be said that although some aspects need a more detailed explanation, the basic findings in this work appear to be consistent with the results and discussion given by other workers (20, 25-32). All studies show the importance of adsorption and complex formation on the polarography of indium (III).

Acknowledgment

The author wishes to express his appreciation to Mr. A. B. Waugh for assistance in obtaining some of the results reported in this paper.

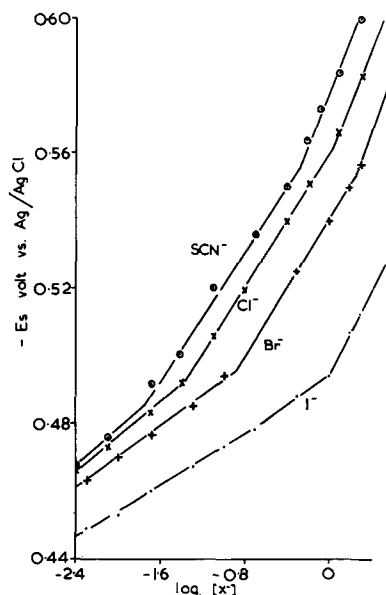


Fig. 9. Lingane's method of graphical analysis of the In(III) complexes.

Manuscript submitted Aug. 16, 1971; revised manuscript received June 12, 1972.

Any discussion of this paper will appear in a Discussion Section to be published in the June 1973 JOURNAL.

REFERENCES

- R. W. Murray and D. J. Gross, *Anal. Chem.*, **38**, 392 (1966).
- F. C. Anson, J. H. Christie, and R. A. Osteryoung, *J. Electroanal. Chem.*, **13**, 343 (1967).
- G. W. O'Dom and R. W. Murray, *Anal. Chem.*, **39**, 51 (1967).
- G. W. O'Dom and R. W. Murray, *J. Electroanal. Chem.*, **16**, 327 (1968).
- F. C. Anson and D. J. Barclay, *Anal. Chem.*, **40**, 1791 (1968).
- B. Timmer, M. Sluyters-Rehbach, and J. H. Sluyters, *J. Electroanal. Chem.*, **18**, 93 (1968).
- D. J. Barclay and F. C. Anson, *This Journal*, **116**, 438 (1969).
- E. Kowalski and F. C. Anson, *ibid.*, **116**, 1208 (1969).
- G. Lauer and R. A. Osteryoung, *Anal. Chem.*, **41**, 1882 (1969).
- M. Caselli and P. Popoff, *J. Electroanal. Chem.*, **23**, 41 (1969).
- D. J. Barclay and F. C. Anson, *ibid.*, **28**, 71 (1970).
- M. Caselli, L. Lampugnani, and P. Papoff, *ibid.*, **34**, 367 (1972).
- G. C. Barker and J. A. Bolzan, *Z. Analyt. Chem.*, **216**, 215 (1966).
- R. Kalvoda, W. Astine, and M. Heyrovsky, *Anal. Chim. Acta*, **50**, 93 (1970).
- R. Kalvoda and J. Ai-Chua, *J. Electroanal. Chem.*, **8**, 378 (1964).
- G. Donoso N., M. A. Santa Ana V., and I. Chadwick, *Anal. Chim. Acta*, **42**, 109 (1968).
- H. Sohr and L. Liebestrau, *Z. Analyt. Chem.*, **219**, 409 (1966).
- I. M. Kolthoff and J. J. Lingane, "Polarography," 2nd Edition, Vol. 2, pp. 519-520, Interscience, New York/London (1952).
- E. D. Moorhead and W. M. MacNevin, *Anal. Chem.*, **34**, 269 (1962).
- J. J. Lingane, *J. Am. Chem. Soc.*, **61**, 2099 (1939).
- A. J. Engel, J. Lawson, and D. A. Aikens, *Anal. Chem.*, **37**, 203 (1965).
- J. A. Schuffe, M. F. Stubbs, and R. E. Witman, *J. Am. Chem. Soc.*, **73**, 1013 (1951).
- D. Cozzi and S. Vivarelli, *Z. Elektrochem.*, **57**, 408 (1953).
- D. Cozzi and S. Vivarelli, *ibid.*, **58**, 907 (1954).
- M. Bu'ova, *Coll. Czech. Chem. Commun.*, **19**, 1013 (1951).
- H. Shirai, *J. Chem. Soc. Japan, Pure Chem. Sect.*, (*Nippon Kagaku Zasshi*), **81**, 1248 (1960).
- T. Takahashi and H. Shirai, *Rev. Polarog. (Kyoto)*, **11**, 155 (1963).
- A. G. Stromberg and K. Z. Brainina, *Zh. Fiz. Khim.*, **35**, 2016 (1961).
- N. Tanaka, T. Takeuchi, and R. Tamamushi, *Bull. Chem. Soc. Japan*, **37**, 1435 (1964).
- R. DeLevie and A. A. Husovsky, *J. Electroanal. Chem.*, **22**, 29 (1969).
- R. DeLevie and L. Pospisil, *ibid.*, **22**, 277 (1969).
- L. Pospisil and R. DeLevie, *ibid.*, **25**, 245 (1970).
- D. D. Perrin, *Pure Appl. Chem.*, **20**, (1969).
- M. Eigen, *ibid.*, **6**, 97 (1963).
- A. M. Bond, *J. Phys. Chem.*, **75**, 2640 (1971).
- J. G. Lawson and D. A. Aikens, *J. Electroanal. Chem.*, **15**, 193 (1967).
- A. M. Bond, *Electrochim. Acta*, **17**, 769 (1972).
- A. M. Bond, *Coord. Chem. Rev.*, **6**, 377 (1971).
- J. Heyrovsky and J. Kuta, "Principles of Polarography," p. 20, Academic Press, New York (1966).
- T. Rhyll, *Acta Chem. Scand.*, **23**, 2667 (1969).
- T. Flatmark and O. Vesterborg, *ibid.*, **20**, 1497 (1966).
- A. M. Bond and T. A. O'Donnell, *Anal. Chem.*, **41**, 1801 (1969).
- A. M. Bond, *J. Electroanal. Chem.*, **23**, 269 (1969).
- A. A. Moussa, M. M. Romia, and F. E. Hoakal, *Electrochim. Acta*, **15**, 1391 (1970).
- D. E. Smith, "Electroanalytical Chemistry," Vol. 1, Chap. 1, A. J. Bard, Editor, Marcel Dekker Inc., New York (1966).
- A. M. Bond, *This Journal*, **117**, 1145 (1970).
- A. M. Bond and G. Hefter, *J. Electroanal. Chem.*, **31**, 477 (1971).

48. D. D. DeFord and D. N. Hume, *J. Am. Chem. Soc.*, **73**, 5321 (1951).
 49. J. J. Lingane, *Chem. Rev.*, **29**, 1 (1941).
 50. B. G. F. Carleson and H. Irving, *J. Chem. Soc.*, **1954**, 4390.
 51. Ya. D. Fridman, R. I. Sorochan, and N. V. Dolgashova, *Russ. J. Inorg. Chem.*, **7**, 1110 (1962).
 52. J. A. Schuffe and H. M. Eiland, *J. Am. Chem. Soc.*, **76**, 960 (1954).
 53. Y. Hasegawa, *Bull. Chem. Soc. Japan*, **43**, 2665 (1970).
 54. E. A. Burns and D. N. Hume, *J. Am. Chem. Soc.*, **79**, 2704 (1957).
 55. N. Sunden, *Svensk. Kem. Tidskr.*, **66**, 50 (1954).
 56. T. Moeller, *J. Am. Chem. Soc.*, **64**, 953 (1942).
 57. A. M. Golub and V. M. Samoilenko, *Ukrain. Khim. Zhur.*, **29**, 472 (1963).
 58. T. P. Radhakrishnan and A. K. Sundaram, *J. Electroanal. Chem.*, **5**, 124 (1963).
 59. K. Momoki and H. Ogawa, *Anal. Chem.*, **43**, 1664 (1971).

Rotating Ring-Disk Electrode Studies of Corrosion Rates and Partial Currents: Cu and Cu₃₀Zn in Oxygenated Chloride Solutions

Barry Miller* and Maria I. Bellavance

Bell Telephone Laboratories, Incorporated, Murray Hill, New Jersey 07974

ABSTRACT

The corrosion of copper and Cu₃₀Zn in oxygenated 0.1M HCl-1M NaCl has been studied by ring-disk electrode methods. The corrosion rates at open circuit as a function of rotation speed and temperature have been measured on an instantaneous basis through ring currents for the oxidation of the copper(I) product. Results have been confirmed against solution analyses. Automatically recorded partial current curves have been obtained as a function of copper and alloy potential by scanning currents both anodic and cathodic to the open-circuit condition. The Tafel plots from the anodic partial currents of copper and alloy disks under immersion corrosion at several temperatures have been derived and compared to the predictions of a simultaneous dissolution model.

Aqueous corrosion processes at homogeneous metal surfaces with simultaneously applied external currents, i , may ideally be interpreted in terms of the additivity of all the coupled anodic, i_a , and cathodic, i_c , partial currents and their dependence on electrode potential (1). The dissolution rate of metal or alloy, $i_a = i - i_c$, and the (mixed) corrosion potential at open circuit can be determined from the summed partial current-potential curves. The necessary engineering information is chiefly the dependence of i_a at $i = 0$ on solution, temperature, surface, and mass transport parameters.

To these ends electrochemical techniques involving only the test specimen generally depend on passing external currents and relating the measured potentials, as by linear polarization (2), to the corrosion rate through Tafel parameters. More extensive perturbation of the electrode allows extrapolation of Tafel lines to the corrosion potential at the expense of altering the surface and conceding instant response. The corrosion current to a known oxidation state can, of course, be determined from the weight loss of metal or the equivalent analysis of the contacting solution. Limitations of these averaging procedures and others have been discussed by Stern and Weisert (3). A methodology for measuring instantaneous corrosion rates by soluble oxidants at an open circuited specimen is obviously of advantage and is an established experimental capability of the rotating ring-disk electrode (RRDE) system (4-6). This use simply involves special cases exploiting the general properties of the electrode pair which have been developed since the initial stimulus of Frumkin and Levich (7-9).

The $\omega^{1/2}$ dependence of results gained from rotating disk electrode (RDE) experiments alone has been

used in corrosion studies to discriminate between mass transport and kinetic control, as shown particularly by Zembura and co-workers (10, 11, and *loc. cit.*) and by Heitz (12). Earlier work has been reviewed by Riddiford (13). In these investigations, however, chemical analysis of the solution was required to determine the equivalent disk dissolution current for comparison to the Levich equation for mass transport control (a linear $\omega^{1/2}$ dependence of the limiting current). Coupling the well-defined transport parameters of the disk and the geometrically determined collection properties of the ring allows a real-time monitoring of the disk processes which assists considerably in the interpretation of the corrosion system.

In this work we describe the acquisition of resolved partial current-potential curves and corrosion rate data for copper and Cu₃₀Zn disks in oxygenated acidic chloride media by means of amperometry at ring electrodes. These corrosion rates have been compared to those obtained by atomic absorption spectroscopy on simultaneously sampled contacting solutions. The total applied current, the partial anodic component, and their logarithmic values have been automatically recorded on both sides of the corrosion potential. Data have been obtained over a range of temperatures and rotation speeds to interpret the results kinetically.

In the Cu-Zn binary alloy, significant work was done with the RRDE by Feller (14) and Pickering and Wagner (15) on the question of selective dissolution in sulfate media during the anodization of disks. De-zincification effects begin as β and higher zinc content phases appear. Confirmation of nonselective anodic dissolution for the α -alloy in ammoniacal solution was also obtained in this laboratory (6). In this latter work, a split ring-disk electrode capable of monitoring both copper and zinc dissolution at the same time was applied along with the conventional technique.

* Electrochemical Society Active Member.

Key words: anodic dissolution, alloy corrosion, brass, solid solutions.

For all these experiments, disk dissolution currents were above the critical $10^{-6} \mu\text{A}/\text{cm}^2$ level below which Pickering and Byrne (16) found zinc preferentially dissolved from the α -brasses by colorimetric analysis of the solutions. In nonring studies, Marshakov and Bogdanov (17) found no dissolution selectivity from rotated α -phase alloy specimens in 0.5M NaCl or HCl, comparing anodic dissolution currents with polarographic analyses of the resulting solutions. Skorchelletti *et al.* (18) concluded from the hysteresis shifts in repetitive E - i traces of α -brasses more than 25% in zinc in NaCl solution that selective dissolution occurred. These effects, however, were superimposed on film formation in nonstirred solutions. The corrosion rates which could be reasonably measured with the ring electrode in the present work are all above those critical values (16) at which selectivity apparently ceases, and the alloy surface is thus expected to be removed uniformly unless there is specific interaction with the corrodent, products, or medium.

The anodic dissolution of binary homogeneous alloys considered as atomically dispersed heterogeneous alloys has been discussed with similar results by both Mueller (19) and Steigerwald and Greene (20). In situations where surface enrichment does not occur even though the component standard potentials are widely separated (for α -brass, when $i_a > 10^{-6} \text{ A}/\text{cm}^2$), they predict a limiting case in which the current-potential curves are dominated by the more noble component. Data relative to this conclusion where the currents are due both to soluble oxidants and anodic dissolution have been obtained in this work.

Experimental

Reagents.—The solution used in all experiments was 0.1M HCl-1M NaCl, prepared from reagent grade chemicals and triply distilled water.

Ring-disk electrodes and control circuitry.—Two ring-disk electrodes were employed, both with gold split rings. One was equipped with a pure copper disk, the second with a 70.1 atomic per cent (a/o) Cu-29.9 a/o Zn (α -brass) disk. The electrodes were normally operated in a shorted split-ring configuration equivalent to the conventional ring-disk electrode. Electrode construction and control circuitry are all described in detail elsewhere (6).

The geometric parameters of the two electrodes were as follows: Cu disk, $r_1 = 0.238 \text{ cm}$, $r_2 = 0.263 \text{ cm}$, $r_3 = 0.322 \text{ cm}$, $A = 0.178 \text{ cm}^2$, $N = 0.336$; α -brass disk, $r_1 = 0.236 \text{ cm}$, $r_2 = 0.263 \text{ cm}$, $r_3 = 0.319 \text{ cm}$, $A = 0.176 \text{ cm}^2$, $N = 0.323$. The inactive areas of the ring divisions were accounted for in determining N .

A third electrode containing a gold disk was amalgamated for use as a mercury surface ($r_1 = 0.238 \text{ cm}$, $A = 0.178 \text{ cm}^2$). The solid metal surfaces (including the amalgam prior to applying a drop of mercury) were polished down to a 0.3μ Linde A finish. Excess mercury on the amalgam electrode was spun off at 10,000 rpm.

In addition to the basic control circuitry, two logarithmic operators (Philbrick/Nexus 4350) were used to record $\log i$ and $\log i_a$ from their respective current follower sources at 5 V/decade. The electrode speed control scheme has been described elsewhere (21). The temperature of the solution was controlled by means of a jacketed cell and external thermostated bath. A central Luggin capillary underneath the disk surface led to a saturated calomel electrode at ambient temperature (effects on potential due to the Luggin tip-SCE temperature gradient have been ignored in this work). A Beckman RC-19 bridge was used to measure the conductivity of the electrolyte for correction of IR losses from the capillary position beneath the disk and the Newman theory (22).

Procedure and preliminary measurements.—An initial solution volume of 125 to 150 ml was used for

each of the runs in which concurrent analyses were to be done. In such cases, 5 ml samples were withdrawn at known time intervals, typically every 30 min. The determinations of copper and zinc at the approximately 1 mg/liter levels involved were carried out by direct atomic absorption spectroscopy of the samples, using standards prepared by dilution in the pure cell electrolyte. Analytical accuracy at 1 ppm was estimated to be $\pm 5\%$, improving above that level. All the runs made for purposes of comparison to solution analyses were carried out under open-circuit conditions at the disk, using a zero current galvanostatic configuration. The ring current at an appropriate controlled potential was simultaneously monitored on a strip chart recorder.

In the chloride solutions, the dissolution of copper is to Cu(I), thus allowing monitoring of the partial anodic current of copper from the disk through the oxidation of Cu(I) to Cu(II) at the ring. For a pure copper disk and one-electron reactions at both ring

and disk, $i_a = \frac{i_r}{NA}$. It was independently established

that the loss of Cu(I) by reaction with oxygen during transit from disk to ring was negligible and that no intermediates in oxygen reduction at the disk were reoxidized at the applied ring monitoring potentials. The first was done with split ring measurements showing the equality of Cu(I) oxidation and reduction at the half rings when Cu(I) was generated at the disk with an applied current in the presence of oxygen, using a coulometric technique (23). The second was inferred from the identity of the anodic current potential curves observed at the gold ring during both applied disk current under nitrogen and open-circuit corrosion in the presence of oxygen. Only Cu(I) \rightarrow Cu(II) waves were observed at the monitoring potentials of +0.40-0.45V vs. SCE. These conclusions are further substantiated by the comparison of solution analyses to electrochemical prediction, as reported below. It was further established that the gold rings are not anodically responsive to hydrogen generated by impressed cathodic currents in the experiments involving disk current scan.

In brass dissolution, the product Zn(II) does not interfere with the anodic reaction of Cu(I) at the ring, but since mercury-coated rings were not used with the brass disk as in an earlier study (6) and also because oxygen was present, the rate of zinc dissolution could not be directly measured. The collection efficiency for copper from the alloy, N_{Cu} , is, however, given by the ring current i_r for the Cu(I) \rightarrow Cu(II) + e reaction divided by i_a , and for nonselective dissolution, N_{Cu} may be calculated from the geometric N , the atomic fractions f_{Cu} and f_{Zn} , and the number of electrons involved in the individual anodic dissolution reactions ($n_{\text{Cu}} = 1$, $n_{\text{Zn}} = 2$) as

$$N_{\text{Cu}} = N \left[\frac{f_{\text{Cu}} n_{\text{Cu}}}{f_{\text{Cu}} n_{\text{Cu}} + f_{\text{Zn}} n_{\text{Zn}}} \right] = (0.323) (0.540) = 0.174.$$

Experimental agreement with this value indicates nonselective dissolution and, in such circumstances, the zinc dissolution can be calculated by difference. From the above, the partial anodic current of zinc from the disk as determined from the Cu(I) oxidation ring current is $\left(\frac{i_r}{0.174} \right) (1 - 0.540)$. For comparison

to the chemical analyses, the ring current-time integral was recorded on the strip chart with a Disc Chart integrator if necessary, but usually the current traces were either nearly constant or quite linearly changing with time and an average current was easy to determine. For both copper and alloy disks, the residual ring currents were estimated by cathodically protecting the disk with sufficient current to suppress any anodic reaction and measuring the resulting i_r , which was

then independent of any further increase in the cathodic protection current. The solution levels of copper ions were always kept low enough that Cu(II) etching of metal did not make a significant contribution to the corrosion rates.

For determining the current-potential curves, the applied disk current was scanned between anodic and cathodic limits which corresponded respectively to the end of the linear i_r vs. i traces and to the point where i_r reached a constant (residual) value. The linear trace

extends to $i \approx i_a$, where oxygen reduction becomes negligible. The value of i_r at $i = 0$ read from these curves compared very well to the i_r obtained at a constant open-circuit condition when the surface changes due to corrosion or anodization had stabilized. Disk potentials were recorded with i and i_r on a two-pen 'YYY' recorder, and when a logarithmic display of the current outputs was made, the residual ring current was subtracted from the total ring current before the log operator. The potential of the disk was corrected for IR drop before display by analog subtraction of the appropriate fraction of the voltage from the disk current follower from the measured potential between the SCE and disk electrode.

Results and Discussion

A current-potential curve for the reduction of oxygen saturated 0.1M HCl-1M NaCl at a rotating copper disk is given in Fig. 1 along with curves of nitrogen, air, and oxygen at an amalgamated disk. The mixed potential corrosion reaction for copper under oxygen is evident from the steep rise in the copper curve as it approaches the zero current axis. The limiting current for the well-defined oxygen step at mercury corresponds to a two-electron reduction, as is known from polarography. Satisfactory limiting currents on copper were not obtained in this acidic electrolyte, and therefore the corrosion current densities later obtained were compared to the oxygen-limiting current densities at the mercury disk for identical rotation speeds and temperatures.

In studying the open circuited copper disk under O₂, it was first necessary to establish that the limiting current for Cu(I) oxidation at the ring was related to the anodic partial current density by the expression

$$i_a = \frac{i_r}{NA}$$

The electrochemical evidence for this has

already been given. The comparison between currents and dissolved metal was then done with the $i_r - t$ integrals and the solution sample analyses. The collection efficiency N obtained under O₂ and N₂, as discussed earlier, was consistent with the geometrically calcu-

lated 0.336 for numerous combinations of rotation speed and temperature. An experimental value was obtained in each run and used in the $\frac{\int i_r dt}{NA}$ calculation.

The results of the comparison are given in Tables I and II for two runs at different temperatures, showing total ppm Cu in the solution phase.

These experiments were carried out for totals of 2 and 3 hr, respectively, so as to get several increments of copper sufficient for analysis by atomic absorption into solution. The quoted values of i_r are the averages during the sampling periods. The agreement between electrochemical and analytical results is generally within the experimental error. On this basis, we quote all other i_a results from ring data alone, except for some corresponding analytical comparisons for α -brass.

The increase in average corrosion rate during successive sampling periods, as indicated by the i_r values in Tables I and II, is typical of these experiments. A spread approaching a factor of 2 from the starting rate to a stabilized value was normal. Initial rates could usually be raised by pre-etching the polished surface with CuCl₂ solution on twill cloth before immersion. Data for the same temperature and rotation speed, but from different runs, will be seen to be subject to this drift in corrosion rate to varying degrees. However, where systematic changes in a variable were to be analyzed, the surfaces were allowed to stabilize before measurements were begun. Thus similar trends rather than exact reproducibility are to be expected depending on the exact surface condition.

The rotation speed dependence of i_a , calculated from ring currents, is given in Fig. 2 at several temperatures along with the 2 electron limiting current for O₂ reduction at amalgamated gold under the same conditions. The reduction at the limiting current at mercury shows the expected linear $\omega^{1/2}$, oxygen transport governed behavior. The corrosion current at the copper disk at open circuit, however, increases weakly and nonlinearly with $\omega^{1/2}$, indicating that control by a surface kinetic process is more important than control by transport.

The current due to oxygen transport to the mercury disk changes very little with temperature increase because of the near compensation of higher diffusion coefficient of oxygen and reduced concentration (solubility) in the Levich equation

$$i = 0.62 nF \nu^{-1/6} \omega^{1/2} D^{2/3} (C^b - C^s) \quad [1]$$

The net corrosion rate at copper, however, is strongly

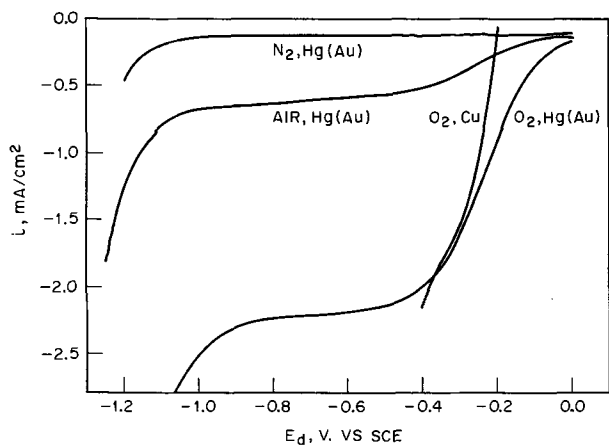


Fig. 1. Controlled potential cathodic sweeps in 0.1M HCl-1M NaCl for an amalgamated gold disk under N₂, air, or O₂ saturation (scan rate 10 mV/sec) and for a copper disk under O₂ saturation (scan rate 5 mV/sec). Rotation speed 1600 rpm, all scans.

Table I. Ring current prediction and solution analysis, 50°C, 0.1M HCl-1M NaCl, copper disk open circuit, gold ring at +0.4V vs. SCE, 1600 rpm, oxygen saturation

Cell volume, ml	Net average i_r , μA	Time, min	Increment Cu from i_r , mg/liter	Total Cu in solution, mg/liter i_r	Total Cu in solution, mg/liter Analysis
150	33.9	30	0.81	0.81	0.83
145	38.1	30	0.94	1.75	1.74
140	43.0	30	1.10	2.85	2.79
135	45.1	30	1.20	4.05	3.94

Table II. Ring current prediction and solution analysis, 30°C, 0.1M HCl-1M NaCl, copper disk open circuit, gold ring at +0.45V vs. SCE, 1600 rpm, oxygen saturation

Cell volume, ml	Net average i_r , μA	Time, min	Increment Cu from i_r , mg/liter	Total Cu in solution, mg/liter i_r	Total Cu in solution, mg/liter Analysis
150	14.0	30	0.35	0.35	0.47
145	14.5	30	0.37	0.72	0.81
140	20.0	30	0.53	1.25	1.32
135	24.0	30	0.66	1.91	1.86
130	24.0	30	0.63	2.59	2.51
125	24.2	30	0.72	3.31	3.19

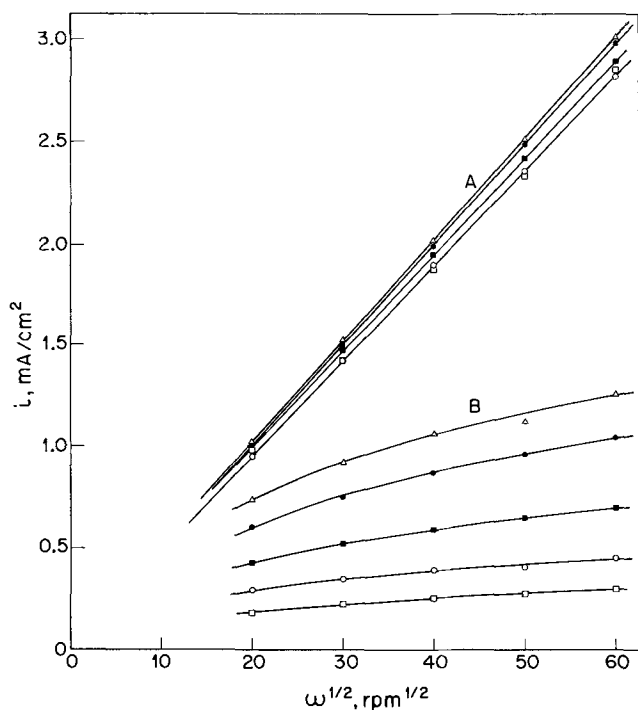


Fig. 2. Disk current densities vs. $\omega^{1/2}$ as a function of temperature in 0.1M HCl, 1M NaCl, O_2 saturated. A, amalgamated gold disk electrode, two electron limiting current for oxygen reduction at -0.60 to $-0.75V$ vs. SCE. B, copper disk-gold ring electrode, partial anodic current at disk calculated from ring current at $E_r = 0.40V$ vs. SCE. \square $20^\circ C$, \circ $30^\circ C$, \blacksquare $40^\circ C$, \bullet $50^\circ C$, \triangle $60^\circ C$.

influenced by temperature, increasing by a factor of 4 or more at all speeds for a 20° - $60^\circ C$ change. At constant speed, these data give reasonably linear logarithmic plots vs. $\frac{1}{T}$, as shown in Fig. 3 for 1600 rpm. The

magnitude of the resulting activation energy, 6.6 kcal/mole, represents the summation of effects of the several temperature dependent thermodynamic, kinetic, and diffusive processes which influence the corrosion rate.

At $60^\circ C$ the percentage of the $2e$ limiting oxygen current represented by i_a is 72 at $20 \text{ rpm}^{1/2}$ and this decreases to 42 at $60 \text{ rpm}^{1/2}$. The net surface concentration of unreacted oxygen increases with rotation speed

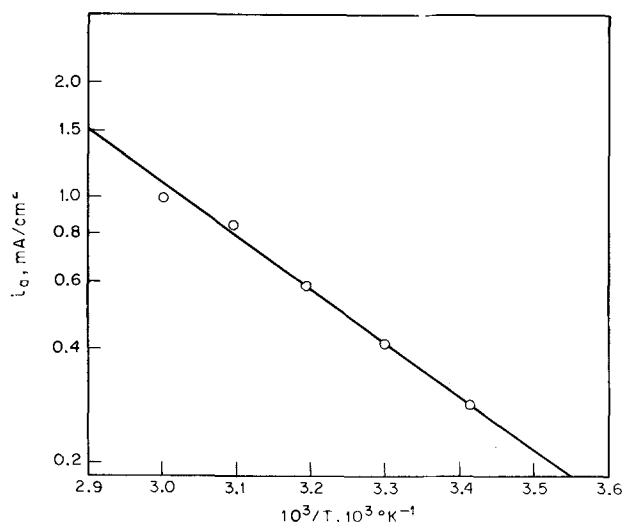


Fig. 3. Partial anodic current density at open-circuit copper disk under O_2 saturation vs. $10^3/T$; currents from ring current. Rotation speed 1600 rpm, 0.1M HCl-1M NaCl. T range 20° - $60^\circ C$.

and anodic partial current, primarily because the activation overpotential of the oxygen reduction reaction more than compensates for the decrease in the cathodic concentration overpotential. The situation at lower temperatures is even more dominated by the kinetics of the cathodic reaction.

The anodic half-reaction may be studied independently under a nitrogen atmosphere, and dissolution curves for the copper disk are shown in Fig. 4 with both linear and log recording of the current over a range beyond both limits of the corrosion data in Fig. 2. The log slope at $30^\circ C$ is 69 mV/decade of current. The theoretical shift due only to concentration overpotential at constant rotation speed is 60.1 mV, indicating that the $Cu/CuCl_2^-$ reaction has a sufficiently high exchange current that it contributes only a small activation overpotential at these current densities.

After establishing the behavior of the copper disk under nitrogen, comparable curves under oxygen were obtained using controlled current scans crossing zero applied current. At the same time, both the corresponding $Cu(I) \rightarrow Cu(II)$ limiting ring current and disk potential were recorded to derive plots of i_a vs. E_d at fixed speeds for the 20° - $60^\circ C$ range, and the results are shown in Fig. 5. The corrosion currents at open circuit are indicated and are within 10% of the range of rates expressed as ring currents in the longer term experiments of Tables I and II.

A more complete picture is given by a plot of i and i_a against E_d , as in Fig. 6. These curves are plotted from individual points taken from recorded traces and i_c calculated by difference. It is experimentally convenient to do the original recording with i and i_r on different

axes so that the residual current region ($\text{true } i_a \approx 0$) and the $i_a \propto i$ region ($i_c \approx 0$) are immediately apparent. It should be emphasized that the corrosion current measurement depends only on knowing the oxidation state changes at the ring and the disk and the collection efficiency, and the same is true for the partial current curves. If the disk films over, as by corrosion product precipitation or a similar passivating mechanism, the steady-state ring current still measures the net corrosion rate. Complications are, of course, introduced by ring deactivation or reactions in transit.

Logarithmic recording provides an alternative presentation of these results, giving plots of $\log i$ and $\log i_a$ vs. E_d . An example at $40^\circ C$ under oxygen is

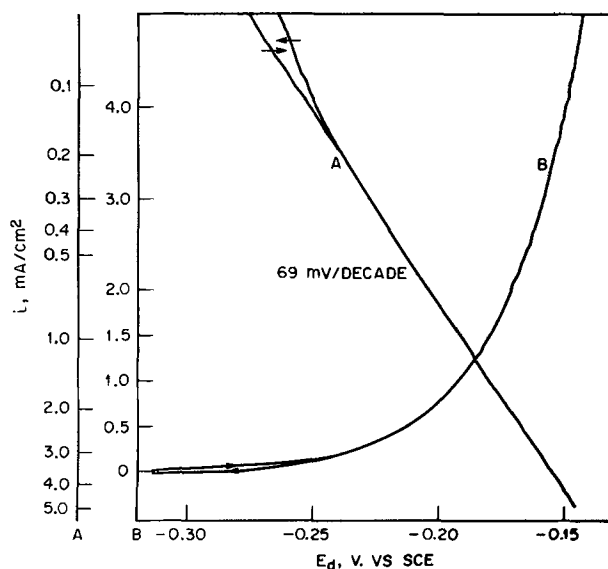


Fig. 4. Direct (B) and log (A) recording of current density vs. E_d for anodization of a copper disk under N_2 from zero to maximum current and reverse. Rotation speed 1600 rpm, temperature $30^\circ C$, 0.1M HCl-1M NaCl. $di/dt = 1 \mu A/sec$.

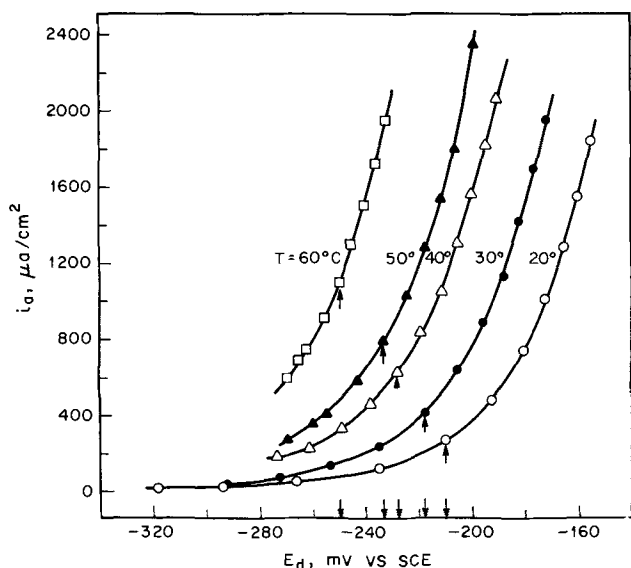


Fig. 5. Controlled current copper disk scans in cathodic direction from anodic start, displaying partial anodic current density (from ring current) vs. E_d as a function of temperature. $di/dt = 1 \mu A/sec$. \circ 20°C, \bullet 30°C, \triangle 40°C, \blacktriangle 50°C, \square 60°C. 0.1M HCl-1M NaCl. Corrosion currents and potentials at $i = 0$ points indicated on figure. $di/dt = 1 \mu A/sec$.

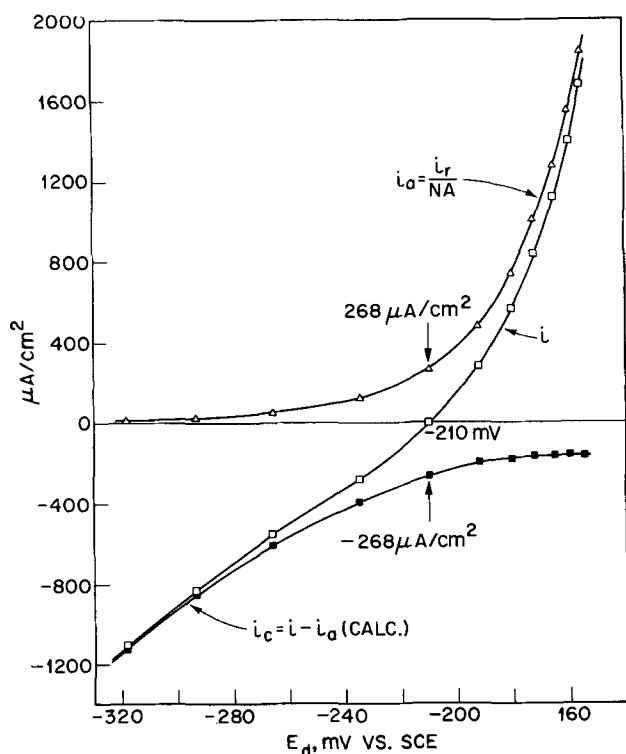


Fig. 6. Applied and partial anodic and cathodic current densities for a copper disk under O_2 saturation. i_a from i_r , i_c calculated from $i - i_a$. Rotation speed 1600 rpm, temperature 20°C, 0.1M HCl-1M NaCl. Corrosion current and potential indicated on figure. $di/dt = 1 \mu A/sec$.

shown in Fig. 7. The slope of the $\log i_a$ tracing is 69 mV/decade $\left(\frac{2.303 RT}{F} = 62.1 \text{ mV} \right)$, consonant with

the purely anodic and largely transport-controlled dissolution under N_2 at 30°C of Fig. 4.

The measurements in Fig. 7 have been carried 80 mV negative of the corrosion potential. The net ring current at this point was only about 3 μA , but with careful correction for residual current, linear $\log i_a - E_d$ behavior is typically found down to this level. Such data

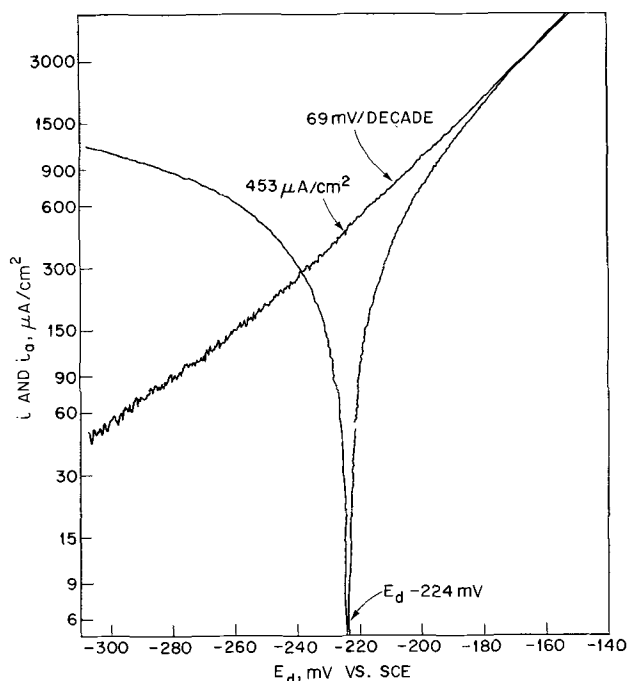


Fig. 7. $\log i$ and $\log i_a$ for Cu disk under O_2 saturation and controlled current scan from anodic to cathodic limits. i_a from i_r at $E_r = +0.45V$ vs. SCE. $di/dt = 0.9 \mu A/sec$, rotation speed 1600 rpm, temperature 40°C. Ring current corrected for residual measured when disk is cathodically protected. E_d corrected for ohmic resistance of 6.5 ohms. 0.1M HCl-1M NaCl. Tafel slope, corrosion current, and corrosion potential indicated on figure.

are collected in a single sweep of a few minutes, and the corrosion potential and current are directly measured along with the anodic Tafel parameters. If desired, i_c or $\log i_c$ could be computed by an analog $i - i_a$ subtraction as well.

Tafel plots for the partial anodic currents accumulated from $i_a - E_d$ data as shown above are presented in Fig. 8 for the 20°-60°C range. For this set of data the slopes run from 70 (20°C) to 75 (60°C) mV/decade $\left(\frac{2.303 RT}{F} \right)$. A separate run

at 40°C (Fig. 7) gave 69 compared to the 73 mV/decade in Fig. 8. A reproducibility within a 5 mV/decade span of the slope at each temperature was typical for all times of exposure and for log or linear recording in spite of the slow changes of corrosion rate in the initial period of exposure of the originally polished surface. It was, however, contingent upon keeping the scan rate $\frac{di}{dt}$ low enough to be a minimal factor in

determining the slope; excessive rates produced high slopes. The nearly reversible slope (concentration overpotential) for the anodic reaction at all temperatures combined with the transport and current level dependent rates of Fig. 2 further substantiates cathodic activation overpotential as the dominant controlling factor in the corrosion rate.

Similar approaches may be taken with an alloy once it is established that dissolution is nonselective and that one component's product may be monitored to determine the over-all rate. Collection efficiencies for pure anodic dissolution in proportion to atomic composition have been confirmed for copper-zinc alloys similar to the present example in sulfate, chloride, and ammoniacal media (6, 14, 15, 24). Under open-circuit oxygen corrosion, where a collection efficiency cannot be measured in the usual electrochemical way $\left(\frac{i_r}{i} \right)$,

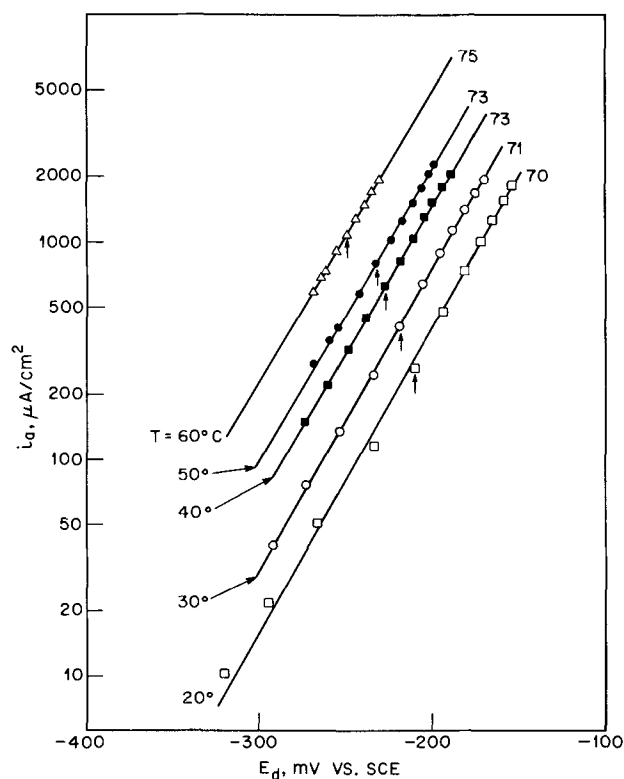


Fig. 8. Plots of partial anodic current density vs. potential for Cu disk under O₂ saturation as a function of indicated temperature. *i_a* from *i_r*. Tafel slopes in mV/decade *i_a* indicated on figure. Open-circuit condition indicated by arrows. Rotation speed 1600 rpm, 0.1M HCl-1M NaCl.

the absence of preferential dissolution effects can only be assured by independent analysis. Although it was earlier shown that with this alloy (6) the copper/zinc dissolution ratio can be measured directly with a split ring-disk electrode under nitrogen, such measurements in general would have to take into account the possible interfering reactions at the ring of the reduction of the oxidant (here oxygen) or the reoxidation of its product.

The results of ring current measurements for copper, of calculations for zinc on the basis of nonselective dissolution, and of atomic absorption analyses for both metals are shown for two runs in Tables III and IV. The agreement between the electrochemical and analytical results at the concentration levels involved is satisfactory. Considering especially the time spans involved in each run (170 and 375 min), the results confirm that no significant degree of preferential dissolution occurs at *i_a* values attributable to oxygen corrosion in these oxygen saturated solutions.

We thus calculate the total dissolution rates (as currents) for the Cu30Zn disk for other experiments solely on the basis of ring currents detecting copper. Measurements under nitrogen with anodic dissolution

Table III. Ring current prediction and solution analysis, 40°C, 0.1M HCl-1M NaCl, Cu30Zn disk open circuit, gold ring +0.45V vs. SCE, 1600 rpm, oxygen saturation

Cell volume, ml	Net average <i>i_r</i> , μA	Time, min	Increments from <i>i_r</i> , mg/liter		Total from <i>i_r</i> , mg/liter		Analysis, mg/liter	
			Cu	Zn*	Cu	Zn*	Cu	Zn*
125	8.0	30	0.23	0.10	0.24	0.10	0.35	0.13
120	24.8	70	1.77	0.78	2.00	0.88	2.00	0.84
115	40.8	70	3.04	1.33	5.04	2.21	4.90	2.10

$$* \text{Mg/liter Zn} = (\text{mg/liter Cu}) \left(\frac{29.9}{70.1} \right) \left(\frac{65.37}{63.54} \right).$$

Table IV. Ring current prediction and solution analysis, 30°C, 0.1M HCl-1M NaCl, Cu30Zn disk open circuit, gold ring at +0.45V vs. SCE, 1600 rpm, oxygen saturation

Cell volume, ml	Net average <i>i_r</i> , μA	Time, min	Increments from <i>i_r</i> , mg/liter		Total from <i>i_r</i> , mg/liter		Analysis, mg/liter	
			Cu	Zn*	Cu	Zn*	Cu	Zn*
130	3.4	20	0.06 ₄	0.03	0.06 ₄	0.03	0.15	0.03 ₇
125	5.3	90	0.47	0.20	0.53	0.23	0.63	0.23
120	7.5	90	0.69	0.30	1.22	0.53	1.26	0.50
115	9.2	80	0.78	0.35	2.00	0.88	2.00	0.80
110	10.2	75	0.85	0.37	2.85	1.25	2.79	1.13

$$* \text{Mg/liter Zn} = (\text{mg/liter Cu}) \left(\frac{29.9}{70.1} \right) \left(\frac{65.37}{63.54} \right).$$

gave an average copper collection efficiency of 0.171, as against the theoretical 0.176 for nonselective dissolution, in agreement with the corrosion results under oxygen at open circuit.

From simultaneously recorded disk and ring currents, the total anodic (*i_{a,Cu}* + *i_{a,Zn}*) partial current, the applied current, and the cathodic component (by subtraction) were obtained as a function of α-brass disk potential as shown in Fig. 9 for a 60°C run. When the current scan data are plotted in logarithmic form, the set of Tafel lines for the 20°-60°C range in Fig. 10 is obtained. These data may be compared to those in the equivalent plots for pure copper in Fig. 8. From the analytical data in Tables I-IV and from the anodic currents at the corrosion potential in the two groups of Tafel plots (Fig. 8 and 10), it is apparent that the brass disk electrodes corrode at slower rates than the copper, in spite of the negative shift of the corrosion potential relative to pure copper at each temperature and the consequent increase in activation overpotential for the cathodic process. This suggests that the exchange current for oxygen reduction at the 70/30 α-brass disk is lower than that at the high-purity

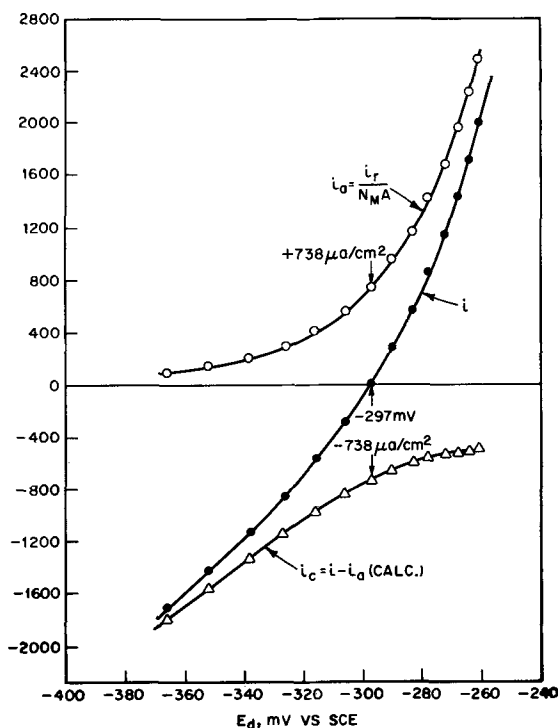


Fig. 9. Applied and partial anodic current density (*i_{a,Cu}* + *i_{a,Zn}*) for Cu30Zn under O₂ saturation. *E_r* = +0.45V vs. SCE, *i_{a,Cu}* obtained from *i_r*, (*i_{a,Cu}* + *i_{a,Zn}*) calculated for nonselective dissolution. Rotation speed 1600 rpm, temperature 60°C. 0.1M HCl-1M NaCl. Corrosion current and potential indicated. *di/dt* = 1 μA/sec.

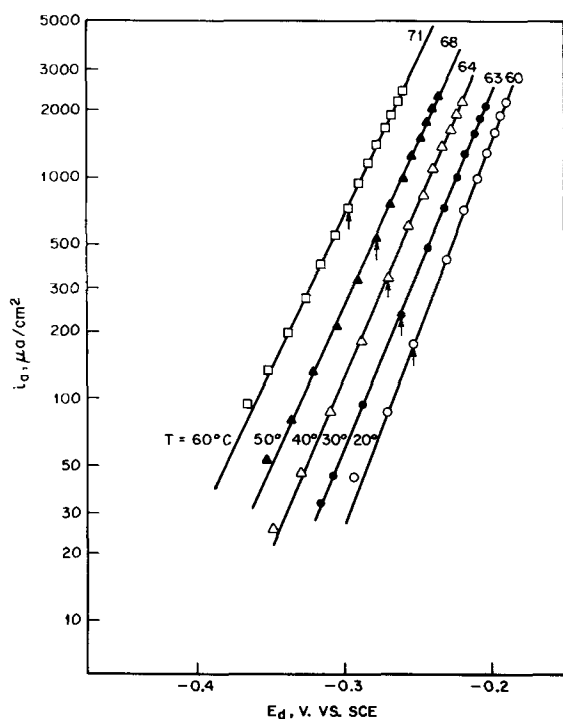


Fig. 10. Plots of partial anodic current density ($i_{a,Cu} + i_{a,Zn}$) for $Cu_{30}Zn$ under O_2 saturation as a function of indicated temperature. $E_r = +0.45V$ vs. SCE, currents obtained as in Fig. 9. Tafel slopes in mV/decade total i_a as indicated on figure. Rotation speed 1600 rpm, 0.1M HCl-1M NaCl.

copper disk by more than enough to compensate for the more negative potential.

The slopes of the Tafel lines in Fig. 10 are only slightly lower than those of Fig. 8, show the same trend with temperature, and are each essentially equal to $\frac{2.303 RT}{F}$. Similar and distinctly copper-like

behavior of the α -phase alloys has been observed in a systematic study of the polarization curves of a spectrum of Cu-Zn compositions in sulfate solutions by Feller (14) as well as in chloride solutions (17, 18). In Feller's study all the α -brass electrode curves crossed the zero current axis within 50 mV of pure copper, and only the zinc rich ϵ -phases had zinc-like i - E curves which fell more than 800 mV negative of those of copper.

For single phase solid solutions dissolving at potentials so much more positive than the standard potential of the more electroactive component (zinc), the partial anodic behavior is dominated by the co-dissolving base metal (copper), but the corrosion rate itself is controlled by the exchange current of the alloy surface for the cathodic reaction, oxygen reduction. Tomashov (25) claims that, at comparable current densities, the oxygen overpotential at zinc is about 0.7V higher than that at copper. An effect in this direction would be consistent with the present results.

The constraint of nonselective dissolution

$$\frac{i_{Cu}}{i_{Zn}} = \frac{f_{Cu}n_{Cu}}{f_{Zn}n_{Zn}} \quad [2]$$

has been verified here by both ring-disk electrode and solution analysis results. If the total dissolution current at a given potential were written as that of a heterogeneous alloy, with the respective surface areas and appropriate partial current densities of the pure components, then (26)

$$Ai_a = a_{Cu}i_{Cu}^0 + a_{Zn}i_{Zn}^0 \quad [3]$$

It would be expected from the widely divergent standard potentials of copper and zinc that $i_{Zn}^0 \gg$

i_{Cu}^0 and thus $i_a \approx a_{Zn}i_{Zn}^0$, so there would be dezincification rather than uniform dissolution. Such "heterogeneous behavior" is found experimentally for the very low currents and the limited periods sustainable by solid-state transport mechanisms (15, 16).

However, it is apparent in the present experiments that both Eq. [2] and [3] have to hold simultaneously for the substitutional solid solution dissolving at the values of i_a observed here. Combining Eq. [2] and [3] with the relations $\sum a_i = A$ and $\sum f_i = 1$ (20), it is readily shown that

$$i_a = \frac{i_{Zn}^0 i_{Cu}^0 (f_{Cu}n_{Cu} + f_{Zn}n_{Zn})}{i_{Zn}^0 f_{Cu}n_{Cu} + i_{Cu}^0 f_{Zn}n_{Zn}} \quad [4]$$

Ignoring any interactions between copper and zinc, then the tendency of i_{Zn}^0 to be much greater than i_{Cu}^0 simplifies Eq. [4] to

$$i_a \approx i_{Cu}^0 \frac{(f_{Cu}n_{Cu} + f_{Zn}n_{Zn})}{f_{Cu}n_{Cu}} = 1.85 i_{Cu}^0 \quad [5]$$

Thus the same supposition that leads to surface enrichment at low currents requires that the alloy appear distinctly copper-like, but somewhat more active, when it is dissolved uniformly. Stated otherwise, when the alloy is forced to dissolve at the current levels caused by oxygen saturated, nonfilming acidic chloride media, the solid solution cannot act as a heterogeneous system and dezincify.

This simple approach suggests that the brass Tafel lines (Fig. 10) should lie negative to the copper lines (Fig. 8) at the same total anodic current and temperature by some $\frac{2.303RT}{F} \log 1.85$ mV or by 16-18 mV

over the temperature range studied. The values of the average separations for three current densities (200, 500, and 2000 $\mu A/cm^2$) are 34, 30, 28, 34, and 35 mV at 20°, 30°, 40°, 50°, and 60°C, respectively. The respective brass corrosion potentials are 43, 43, 42, 45, and 47 mV more negative than those of copper, while the ratios of corrosion currents at these temperatures are 1.51, 1.73, 1.79, 1.49, and 1.49, averaging about 1.6. This would give an additional separation of some $\frac{2.303RT}{F}$

$\log 1.6$ or 12-13 mV, accounting well for the 42-47 mV separation of the corrosion potentials as compared with the 28-35 mV separation at equal total anodic currents.

The predictions by the naive model of a 16-18 mV separation and of identical Tafel behavior are thus qualitatively in line with the measurements at the several temperatures, especially when one considers that the standard potentials of copper and zinc in chloride solution are separated by $\sim 1V$ and the reversible Nernst factors differ by a ratio of two. The relatively close correspondence is very likely largely dependent on well-controlled mass transport which has not been typical of most previous attempts at such correlations.

Summary and Conclusions

In the copper (disk)-gold (ring)-chloride-oxygen system, measurements of instantaneous corrosion rates at the disk have been made and demonstrated by independent solution analysis to be equivalent to mass or volume loss rates. With the geometric properties of the system, the ring measurements provide continuous monitoring of the partial anodic current at the disk. Instantaneous corrosion rates may be determined without the prior assumptions as to the shape of the partial curves in the vicinity of the corrosion potential that are characteristic of the usual electro-

chemical approaches and with considerably increased accuracy.

Such solution analyses were also carried out on an actively corroding alloy, Cu₃₀Zn, where the corrosion reaction was determined to be nonselective toward the alloy components. The over-all corrosion rate could then be monitored by the oxidation at the ring of the copper product, Cu(I). For other metals or alloys, ring reaction schemes appropriate to the given case must necessarily be selected. For example, if the products are not electroactive in the potential range normally accessible to ring materials (as with Al or Mg disks), the decrease in flux of corrodent to the reacting disk or a corrodent product (such as H₂O₂ or H₂) might be measured. Thus i_c might be the directly monitored quantity and i_a calculated, instead of the reverse as applied in this study.

A major feature of the ring technique is the instantaneous feedback on corrosion rate. It is commonplace that corrosion rates of metallic samples often change with exposure time, even if the solution conditions are held constant, because of surface alterations. Ring measurements instantly respond to such behavior or any other system changes, such as inhibiting additives, as long as the monitoring ring reaction is not interfered with. Data reported in this paper show these surface effects when corrosion rate measurements under the same external conditions are repeated in different runs. Standard pretreatments, such as pre-etching the samples briefly after polishing, accelerate the achievement of the higher corrosion rates characteristic of longer exposures. For other physical examination studies, the advantage of measuring corrosion without externally perturbing the surface is desirable. The ring current gives a direct measure of the activity of the surface without the averaging necessary in integral techniques which might obscure the effects. The cathodic behavior of copper and copper-zinc alloys toward oxygen is an example of correlating partial current measurements with potential so as to understand surface controlled relative reaction rates toward a common oxidant.

Simple models of the dissolution behavior of a solid solution (19, 20) appear to give good correlation between the i - E curves of the more noble component and the alloy. Ring-disk electrode approaches to such problems offer the necessary control of concentration overpotential and detection of dissolution ratios that are required to obtain valid experimental data in this area.

Acknowledgment

The authors are grateful to T. Y. Kometani for the atomic absorption spectroscopy analyses.

LIST OF SYMBOLS

A	disk area, cm ²
a_M	area of metal M in alloy surface, cm ²
C^b	bulk concentration, moles/liter
C^s	surface concentration, moles/liter
D	diffusion coefficient, cm ² /sec
E_d	disk potential, V
E_r	ring potential, V
F	Faraday's constant, coulombs/equivalent
f_M	atomic fraction of metal M in alloy
i	applied current density at the disk, A/cm ²
i_a	partial anodic current density at the disk, A/cm ² (in the alloy the sum of the partial anodic current densities of the components)

i_c	partial cathodic current density at the disk, A/cm ²
i_M	partial anodic current density of metal M from alloy disk, A/cm ²
i_M^0	partial anodic current density for pure metal M, A/cm ²
i_r	ring current, A
IR	ohmic drop in solution, disk to probe, V
N	geometric collection efficiency
N_M	collection efficiency for metal M, N_M/i_a
n, n_M	number of electrons transferred per mole of reaction (of M)
R	universal gas constant, joule/mole-°K
r_1	disk radius, cm
r_2	inner ring radius, cm
r_3	outer ring radius, cm
SCE	saturated calomel electrode
t	time, sec
T	temperature, absolute °K (°C where so labeled)
ν	kinematic viscosity, cm ² /sec
ω	rotation speed, rpm

Manuscript submitted Feb. 25, 1972; revised manuscript received May 30, 1972. This was Paper 44 presented at the Miami Beach, Florida, Meeting of the Society, Oct. 8-13, 1972.

Any discussion of this paper will appear in a Discussion Section to be published in the June 1973 JOURNAL.

REFERENCES

- C. Wagner and W. Traud, *Z. Elektrochem.*, **44**, 391 (1938).
- M. Stern and A. Geary, *This Journal*, **104**, 56 (1957).
- M. Stern and E. Weisert, *Proc. Amer. Soc. Test. Mat.*, **59**, 1280 (1959).
- G. W. Tindall and S. Bruckenstein, *Anal. Chem.*, **40**, 1402 (1968).
- D. Jones and N. Hackerman, *Corrosion Sci.*, **8**, 565 (1968).
- B. Miller, *This Journal*, **116**, 1117 (1969).
- A. N. Frumkin and L. N. Nekrasov, *Doklady Akad. Nauk. SSSR*, **126**, 115 (1959).
- A. N. Frumkin, L. N. Nekrasov, V. Levich, and Yu. Ivanov, *J. Electroanal. Chem.*, **1**, 84 (1959).
- W. J. Albery and M. L. Hitchman, "Ring-Disc Electrodes," Oxford University Press, London (1971).
- Z. Zembura, *Corrosion Sci.*, **8**, 703 (1968).
- Z. Zembura, *Electrochim. Acta*, **10**, 859 (1965).
- E. Heitz, *Werkstoffe Korrosion*, **15**, 63 (1964).
- A. C. Riddiford, in "Advances in Electrochemistry and Electrochemical Engineering," Vol. 4, p. 47, P. Delahay, Editor, Interscience Publishers, Inc., New York (1966).
- H. G. Feller, *Corrosion Sci.*, **8**, 259 (1968); Habilitationarbeit, Technische Universität Berlin (1965).
- H. W. Pickering and C. Wagner, *This Journal*, **114**, 698 (1967).
- H. W. Pickering and P. J. Byrne, *ibid.*, **116**, 1492 (1969).
- I. V. Marshakov and V. P. Bogdanov, *Russ. J. Phys. Chem.*, **38**, 1041 and 1044 (1964).
- V. V. Skorcheletti, I. A. Stepanov, and E. P. Kuksenko, *J. App. Chem. USSR*, **31**, 1813 (1958).
- W. A. Mueller, *Corrosion*, **18**, 73 (1962).
- R. F. Steigerwald and N. D. Greene, *This Journal*, **109**, 1026 (1962).
- B. Miller and S. Bruckenstein, *ibid.*, **117**, 1032 (1970).
- John Newman, *ibid.*, **113**, 501 (1966).
- B. Miller, To be published.
- A. M. Taylor, *This Journal*, **118**, 854 (1971).
- N. D. Tomashov, "Theory of Corrosion and Protection of Metals," p. 178 *et seq.*, Macmillan, New York (1966).
- M. Stern, *Corrosion*, **14**, 329 (1958).



Electrochemistry of Sulfur in LiCl-KCl Eutectic

John H. Kennedy* and Frank Adamo*

Department of Chemistry, University of California, Santa Barbara, California 93106

The blue solution of sulfur is a well documented phenomenon. An intense blue solution is observed in fused KSCN upon decomposition of KSCN or after the introduction of sulfur or various sulfides (1, 2). A polarographic study of fused KSCN or KSCN-NaSCN eutectic has illustrated that SCN^- is reduced to S^{2-} and CN^- (3). The authors cited references to the blue color of sulfur, however their discussion did not reveal the development of the blue color during their study. It has been recently suggested (4) that impurities of sulfur and sulfide may cause the blue color in molten KSCN. The blue solution of sulfur has been observed many times in the LiCl-KCl eutectic. Greenberg, Sundheim, and Gruen (5) gave evidence that the blue solution in fused LiCl-KCl is caused by diatomic sulfur molecules in the triplet state. Delarue (6-9), in his electrochemical investigation of sulfur and sulfide salts in LiCl-KCl melt, observed an intense blue color when sulfur was added to the melt or when sulfide salts were oxidized by various metal ions. Although the blue color was not directly investigated, Delarue assumed that the blue solution was dissolved sulfur. Recently, Bodewig and Plambeck (4) reported the electrochemical behavior of sulfur and sulfide in the LiCl-KCl eutectic. They observed that a blue color was generated when sulfur, initially a colorless solution, was coulometrically reduced to sulfide. Further investigation showed that the blue color disappeared when chlorine was generated at the electrode, or when the potential was held at a constant value which was 0.3V more positive than the decomposition potential of sulfur, or when a vacuum was applied. The blue color reappeared upon addition of sulfur. It was ascertained that both sulfide and sulfur must be present to form the blue color. Bodewig and Plambeck subsequently concluded that the blue solution was a polysulfide formed from sulfur and sulfide, *i.e.*, $\text{S}_x^{2-} + \text{S}_x \rightleftharpoons \text{S}_{x+1}^{2-}$. Further investigation using uv spectroscopy (10) seemed to confirm the authors' suggestion that the blue solution was a polysulfide. It was definitely shown that neither sulfur nor sulfide alone produced a blue solution.

Although many reasons for the formation of the blue solution of sulfur have been suggested, until recently no detailed investigation of the nature of the blue solution of sulfur had been reported. However, Giggenbach (11) recently gave evidence that the sulfur species producing the blue coloration in DMF and other aprotic polar organic solvents is the anion radical, S_2^- . UV spectroscopy of tetrasulfide, in 25% DMF-water mixture, showed two bands in the visible and near-uv region near $23.10 \times 10^3 \text{ cm}^{-1}$ and $36.2 \times 10^3 \text{ cm}^{-1}$. A third absorption at $16.2 \times 10^3 \text{ cm}^{-1}$ developed and increased when more DMF was added. Subsequently, it was shown that the tetrasulfide was in equilibrium with S_2^- , and that the equilibrium favored the anion radical as the DMF content of the solvent mixture increased. More recently, Merritt and Sawyer (12) re-

ported the electrochemistry of sulfur, S_8 , in DMSO. Cyclic voltammetry and controlled potential electrolysis revealed that sulfur is reduced to S_8^{2-} in two reversible one-electron steps. The product of the first reduction step is S_8^- , a stable anion radical. Although the products of the reduction steps are easily oxidized, reoxidation of S_8^{2-} was shown not to be a simple two-step oxidation. Chronopotentiometry and uv spectroscopy established that S_8^- dimerizes, the formation constant of the dimer being $5 \times 10^3 \text{ M}^{-1}$. That is, S_8^- is electrochemically oxidized to S_8 , and the S_8^- radical dimerizes to $(\text{S}_8)_2^-$. The dimer then is electrochemically oxidized to 2S_8^0 . Interestingly enough, although Merritt and Sawyer did not report the observance of a blue solution, S_8^- was found to absorb at $16.2 \times 10^3 \text{ cm}^{-1}$, the same frequency Giggenbach (11) reported for the absorption of S_2^- . The similarity of these two studies seems to indicate that the blue solution of sulfur is caused by an anion radical of sulfur, but the number of molecules associated with the radical is uncertain or varies. Recent ESR investigations of sulfur in various media (13) support this supposition.

This paper presents additional electrochemical evidence for sulfur species in fused LiCl-KCl.

Experimental

Apparatus.—A Beckman Electroscan 30 was used for all electrochemical operations. The temperature of the melt was controlled by a Barber-Colman temperature controller, while a Glas-Col heating mantle for a 250 ml Griffin-type beaker was used to heat the melt.

As illustrated in Fig. 1, a 400 ml tall-form, lipless, Berzelius beaker was used as the electrolysis cell. The cell was covered by a 1 in. thick asbestos stopper in which appropriate standard tapered holes were drilled to accommodate the glassware. A 6 mm glass tubing encased the Chromel-Alumel thermocouple, while an asbestos-wick isolation compartment and a coil of platinum foil, 0.003 in. by 0.5 in. by 2.0 in. served as the reference electrode. A carbon rod $\frac{1}{8}$ in. in diameter, enclosed in a 10 mm sealing tube with a medium porosity fritted disk, was used as the auxiliary electrode. When controlled potential electrolysis of sulfur was carried out, a 10 mm sealing tube with a medium porosity fritted disk, sealed to a straight vacuum adapter, served to isolate the sulfur and the working electrode, a gold foil 0.005 in. by 1 in. by 1 in., heat sealed to a gold wire. A stirring assembly was attached to the top of the vacuum adapter. A length of 12 mm glass tubing was substituted for the working electrode compartment, illustrated in Fig. 1, during cyclic voltammetry studies.

All experiments were carried out under a nitrogen atmosphere which was provided by way of a straight vacuum adapter with $\frac{1}{4}$ 14/20 ground glass joints and an extended inner tube. A two-way stopcock was used to regulate the passage of nitrogen over or through the melt. A small air hole was blown in reference and auxiliary electrode compartments about 2 in. above

* Electrochemical Society Active Member.
Key words: cyclic voltammetry, controlled potential electrolysis, molten salts, sulfur, lithium chloride-potassium chloride eutectic.

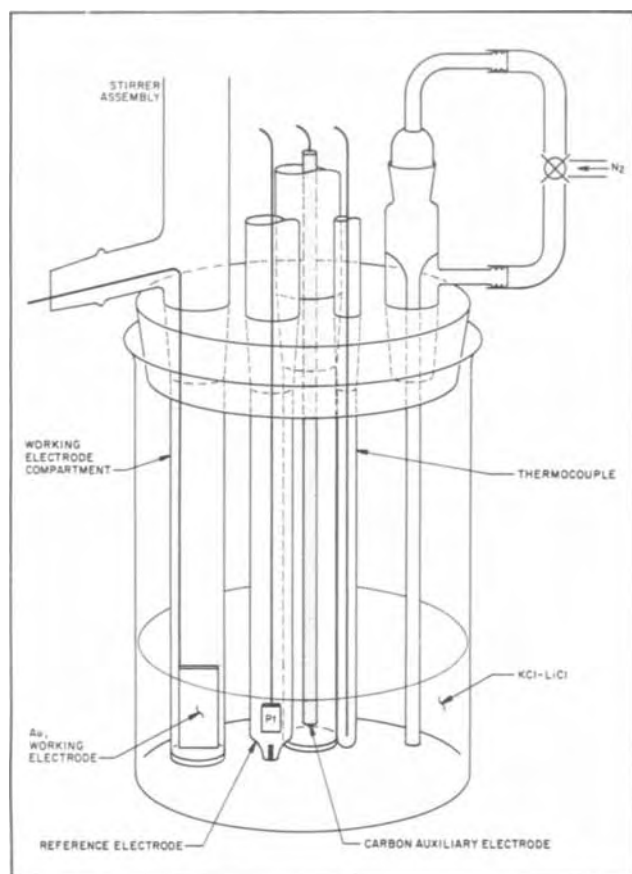


Fig. 1. Diagram of cell used for cyclic voltammetry

the level of the melt to accommodate a nitrogen atmosphere.

Reagents.—Reagent grade lithium chloride and potassium chloride were used. Small quantities of sulfur were heated in test tubes at 120°C overnight. Before using, a test tube was broken, and the lump of sulfur was used directly. Nitrogen was dried by passage through a column of Silica Gel.

Solvent.—The LiCl-KCl eutectic salt mixture was prepared by combining 400g of lithium chloride and 488g of potassium chloride in a large jar and tumbling the mixture overnight until homogeneous. About 600g of the mixture was then purified as described by Bodewig and Plambeck (4). Four Berzelius beakers were dried at 120°C for 2-3 hr and were placed in a vacuum desiccator. After quickly transferring 100-125 ml of the molten eutectic to each of the beakers, the desiccator was flushed with dry nitrogen. Upon cooling, the beakers were quickly sealed with Parafilm.

Procedure.—For each experiment, the glassware was cleaned with chromic acid cleaning solution, and the electrodes were appropriately assembled. The cell assembly was placed in an empty beaker and oven dried at 120°C for two or more hours. After the LiCl-KCl eutectic was allowed to become molten under a nitrogen atmosphere, the cell assembly was quickly transferred to the cell. The isolation compartments were then allowed to fill over a period of 2-6 hr. A Pt(II)/Pt reference electrode was coulometrically generated using a Sargent Coulometric Current Source. A current density of 7.5 mA/cm² was employed anodically, giving rise to a concentration of 0.01-0.02M in platinum (II). All measured potential values were converted to the 1.0M Pt(II)/Pt standard molar platinum electrode (SMPE). The temperature was adjusted to 420°C, and after purging the melt for a few minutes, a cyclic voltammogram of the blank solution was recorded.

Cyclic voltammetry of sulfur was begun after about 0.1g of a lump of sulfur was dropped through the isolation compartment. For controlled potential electrolysis of sulfur, the working electrode was previously fitted closely against the inner wall of the isolation compartment. The gold wire was extended out through the sidearm of the vacuum adapter. A constant potential was applied at a value more negative than the corresponding peak potentials of interest. Using a constant speed stirrer connected to a Variac to adjust the speed of rotation, the blank was electrolyzed until a constant residual current was obtained. A small lump of sulfur, about 0.015g, was added to the melt through the sidearm of the vacuum adapter and the sulfur was electrolyzed at an appropriate controlled potential. The *n*-value for the electrolysis was evaluated from the recorded current vs. time curve. On subsequent runs, the electrolysis was stopped and a cyclic voltammogram of the partially electrolyzed solution was recorded. Cyclic voltammetry of the completely electrolyzed solution was also carried out.

After each experiment, the reference electrode isolation compartment was removed and placed in a desiccator. After cooling to room temperature, the isolation tube was gently broken and the solid salt mixture analyzed according to procedures described by Bodewig and Plambeck (4).

Results

Cyclic voltammetry.—The cyclic voltammogram of sulfur in LiCl-KCl eutectic is shown in Fig. 2. The initial scan showed a sharp rise in current at -0.9V vs. SMPE, however, rather than the formation of a peak, a limiting current was observed. As the scan was continued, a peak at -1.37V vs. SMPE developed. Two anodic peaks, at -1.10 and -0.83V vs. SMPE, were observed when the scan was reversed. On the second and succeeding cycles, a peak at -1.13V vs. SMPE appeared where the initial rise in current was observed, as illustrated in Fig. 2. Coincidental with the initial rise in current, a blue color developed at the working electrode. As the cyclic voltammetry was continued, the blue color intensified until the entire solution was opaque. Cyclic voltammetry using a large gold foil electrode showed that the initial formation of the blue color occurred only at the electrode interface. The blue solutions were decolorized by standing for several hours, or more quickly by putting the melt under vacuum. This phenomenon indicates that the blue species or its decomposition product has a measurable vapor pressure at 420°C.

The curves in Fig. 2 show that two steps are involved in the electrochemical reduction of sulfur. At a scan rate of 200 mV/sec, the products of the reduction are easily reoxidized. However, the reactions are not strictly reversible, i.e., the difference between the cathodic peak potential and anodic peak potential at 420°C was not equal to 132 mV/*n* where *n* is the num-

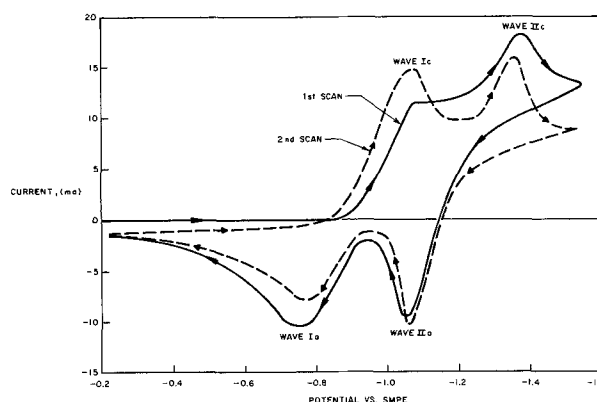


Fig. 2. Cyclic voltammetry of sulfur in 100 ml LiCl-KCl eutectic at 420°C. 0.3g S; sweep rate 200 mV/sec.

ber of electrons transferred. The separation between the peak potentials of the first wave did not vary with scan rate from 200 to 40 mV/sec. In contrast, the separation of the peak potential of wave II decreased as the scan rate was varied from 200 to 40 mV/sec. In fact, the separation of the peak potentials was 130 mV when the scan rate was set at 40 mV/sec; consequently, the second reduction step may be approaching electrochemical reversibility at slow scan rates, assuming that only one electron is involved in the reduction step. If the potential scan was reversed at -1.2V the anodic peak at -0.83V was identical to the peak observed after scanning to -1.6V . Thus, the anodic peak at -0.83V is directly associated with the cathodic peak at -1.13V .

When the solution was cathodically scanned to -1.8V vs. SMPE and held at that potential, the current increased. After holding the potential at -1.8V for 3-5 min, the solution was anodically scanned. The peak of wave II decreased slightly; while wave I increased severalfold. Also, the peak potential of Wave I was shifted approximately $+0.05\text{V}$. Reversing the scan showed only the normal development of the cathodic peaks.

Controlled potential electrolysis.—A weighed amount of sulfur was electrolyzed at a potential of -1.1V vs. SMPE . The current vs. time was recorded and then integrated (by counting squares) after the current reached the previously determined residual current value. The area above the residual current value was considered to be sulfur reduction and computed as Faradays/g-atom of sulfur or $e^-/\text{S atom}$. Since the sulfur was trapped in the electrode compartment, loss as vapor was minimized. The values reported are the largest obtained from several runs since the only major source of error was leakage of sulfur vapor from the electrolysis cell.

The current vs. time curve showed that the sulfur was not being reduced in the normal manner, i.e., the current vs. time curve did not follow the normal exponential decay. The current remained constant for 2-3 min and then gradually dropped to a lower constant value. After another minute or so, the current again dropped to a lower constant value. This sequence continued throughout the electrolysis. Controlled potential electrolysis of the first reduction step, which took about 8 hr to complete, revealed that $0.265 e^-/\text{S atom}$ was involved in the first cathodic step. Controlled potential electrolysis of the second reduction step at -1.4V , which took about 1 hr, behaved in the normal manner, i.e., the current decayed exponentially with time. The n -value was determined to be an additional $0.72 e^-/\text{S atom}$. Anodic oxidations of the product of the reduction at controlled potential were rapid. Controlled potential electrolysis at -1.0V vs. SMPE gave an n -value of $0.833 e^-/\text{S atom}$; while further oxidation at -0.7V vs. SMPE gave an n -value of $0.201 e^-/\text{S atom}$.

A very intense blue solution was formed immediately after the initiation of the controlled potential electrolysis of the first reduction step. The cyclic voltammogram of the blue solution midway through the electrolysis is shown in Fig. 3. The initial rise in current did not develop into a peak, rather, a limiting current was observed. A peak, at -1.51V vs. SMPE developed as the scan was continued. The anodic scan revealed two peaks at -1.10V vs. SMPE and -0.85V vs. SMPE . Although the cyclic voltammogram is similar to the cyclic voltammogram of the elemental sulfur, the initial cathodic rise and the cathodic peak were shifted to more negative values. The blue color became less intense as the electrolysis at the first cathodic wave neared completion. When controlled potential electrolysis at the second cathodic wave was carried out, the blue color disappeared. The solution turned blue when oxidation at controlled potential was carried out, although the color was not intense. Sulfur

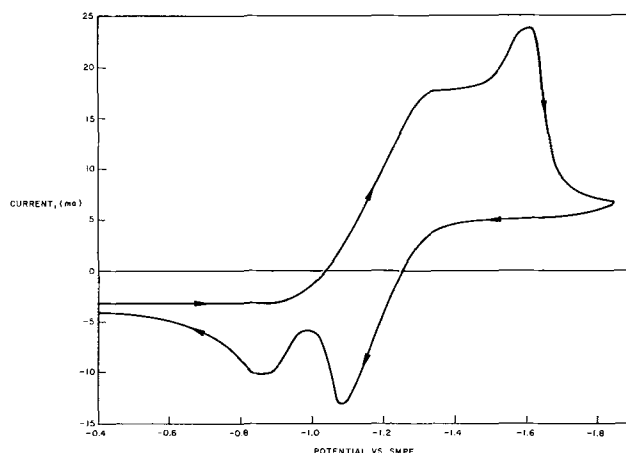
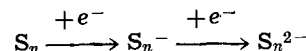


Fig. 3. Cyclic voltammetry of sulfur during controlled potential electrolysis at -1.15V vs. SMPE . 0.612g S ; sweep rate 200 mV/sec . Electrolysis was about 50% completed when scan taken.

vapors collected on the wall of the isolation tube above the level of the melt, when controlled potential electrolysis of the second anodic wave was carried out.

Discussion

The electrochemical reduction of sulfur proceeds through two steps. The curves in Fig. 2 indicate that the same number of electrons are involved in each step. Initial scans were somewhat different than succeeding scans because of undissolved sulfur present initially. After the sulfur dissolved, the cyclic voltammograms were reproducible. Based on the similarity of the results in LiCl-KCl to the results in DMSO (12), the two reduction steps can be described as follows



where $n \geq 2$.

Controlled potential electrolysis showed that $1e^-/\text{S}$ was involved during reduction or subsequent oxidation and, thus, the final reduction product can be described as S_m^{m-} . However, it cannot be concluded that $n = m$ since additional reactions could occur during the long-term controlled potential electrolysis which were not observed during cyclic voltammetry. In fact, the results of controlled potential electrolysis carried out at the first reduction step of -1.1V vs. SMPE indicate that n may be 3 or 4. Both cyclic voltammetry and controlled potential electrolysis have shown that the product of the first reduction step is the sulfur species producing the blue solution.

Acknowledgment

The authors wish to thank the donors of the Petroleum Research Fund, administered by the American Chemical Society, for financial support of this work.

Manuscript submitted May 28, 1971; revised manuscript received May 30, 1972.

Any discussion of this paper will appear in a Discussion Section to be published in the June 1973 JOURNAL.

REFERENCES

1. E. Paterno and A. Mazzuchelli, *Gazz. Chim. Ital.*, **38**, 137 (1908).
2. H. Lux and H. Anslinger, *Chem. Ber.*, **94**, 1161 (1961).
3. R. E. Panzer and M. J. Schaer, *This Journal*, **112**, 1136 (1965).
4. F. G. Bodewig and J. A. Plambeck, *ibid.*, **116**, 607 (1969).
5. J. Greenberg, B. R. Sundheim, and D. M. Gruen, *J. Chem. Phys.*, **29**, 461 (1958).
6. G. Delarue, *Bull. Soc. Chim. France*, 906 (1960).
7. G. Delarue, *ibid.*, 1654 (1960).
8. G. Delarue, *Silicates Ind.*, **27**, 69 (1961).
9. G. Delarue, *Chimie Analytique*, **44**, 91 (1962).

10. F. G. Bodewig and J. A. Plambeck, *This Journal*, **117**, 904 (1970).
11. W. Giggenbach, *J. Inorg. Nucl. Chem.*, **30**, 3189 (1968).
12. M. V. Merritt and D. T. Sawyer, *Inorg. Chem.*, **9**, 211 (1970).
13. S. D. McLaughlan and D. J. Marshall, *J. Phys. Chem.*, **74**, 1359 (1970).

Lead Anode Deterioration as a Function of Depth of Operation

R. P. Hollandsworth and E. L. Littauer*¹

Electrochemistry Department, Lockheed Aircraft Service Company, Ontario, California 91761

In recent years, considerable attention has been devoted to the development of impressed current cathodic protection (ICCP) systems for ships and offshore structures. Significant economies accrue from the use of permanent anodes in such installations because of the cost and inconvenience of drydocking ships outside of normal maintenance schedules, and with offshore structures, the need to employ divers for servicing. In the latter case, such servicing can be extremely difficult with structures in deep water.

ICCP systems are generally self-regulating with the permanent anodes connected to the positive side of a power supply comprising a step down transformer from a 220 or 440V line, a rectifier, and with control frequently accomplished with a saturable-core reactor in conjunction with a silver-silver chloride reference electrode. The negative of the power supply is connected to the structure. In principle, the system is analogous to a potentiostat. Protective potential of steel in sea water is in the range -800 to -850 mV vs. Ag/AgCl, and this range is set on the controller.

Systems are designed in modular form with outputs ranging from 50-3500A. The protective current required is determined from data of water conductivity, flow by rate, bare area of steel, and anode position. Anodes range in size from 1-2 ft long to 16 ft and are mounted on a dielectric shield to assist in distribution of current to all areas of the structure. Anodes may be mounted on the structure or mounted remotely; the latter method assists current distribution but may introduce complications such as stray current effects.

The most often used permanent anode in ICCP systems of ocean structures has been Pb based, e.g., Pb alloys such as Pb, 6% Sb, 1% Ag, and Pb-Pt bielectrodes. The latter are less expensive because the cost of Pt for microelectrodes is less than that of Ag in the alloy anode. Also the Pb-Pt bielectrode is capable of operating at somewhat higher current densities (C.D.) which leads to a smaller anode for the same duty.

With Pb based anodes the active surface becomes a layer of PbO₂ which forms over the original Pb surface upon anodic polarization in sea and fresh water. The mechanisms and conditions of formation of the chemically passivating PbO₂ have been extensively dealt with in the literature (1-3). Under normal conditions there is little further involvement of the underlying metal once a limiting thickness of PbO₂ has formed. The predominant electrode process becomes evolution of Cl₂ and/or O₂, depending on the C.D. and salinity of the electrolyte. Initial formation of PbO₂ follows a path similar to that manifested by Pb in SO₄²⁻ containing electrolytes, where an initial layer of essentially nonconducting crystallites of PbSO₄ are converted to PbO₂. This happens within interstices in the crystallite layer at points at the metal solution interface where the potential exceeds that of the Pb_{aq}²⁺ → PbO₂ reaction.

In fresh water the initial nonconducting layer is a lower oxide; in saline water this precursor to chemical passivation is PbCl₂. In both cases the layer is eventually converted to PbO₂ through a heterogeneous reaction (3).

Recent service experience with Pb-based anodes, operating at depths greater than 25m, has revealed a deterioration rate far greater than that observed in surface operation. Anode failures have been indicated by a gradual (or sudden) increase in resistance, and inspections of failed anodes have shown: (i) separation of the PbO₂ from the Pb, with a thick, intervening layer of PbCl₂ intermixed with lower oxides, and (ii) the thickness of PbO₂ growth is far greater than observed on anodes operating at modest depths for an equal length of time. No explanation for these deteriorating effects is to be found in prior literature which has considered the influence of alloy composition (4), effect of microelectrodes (1), temperature (5), and water velocity (6). Accordingly, the present study was undertaken to examine the problem in detail under controlled laboratory conditions, with the intention of discovering the mechanism of the depth effect as well as defining the pressure conditions under which Pb anodes can be expected to operate without deterioration.

Experimental

To simulate deep-ocean conditions in the laboratory, the experiments were performed in pressurized (316) stainless steel test vessels (Fig. 1) equipped with flanged top, anode receptacle, automatic pressure regulating valve, and pressure gauge. Prepressurization was accomplished with argon, which is inert towards the electrode processes and is relatively insoluble in sea water.

The production of hydrogen and chlorine was limited to less than 10% of the ullage volume by changing solutions regularly and by automatic pressure relief valves which maintained the pressure within 2 psi of the desired value. One liter of artificial sea water (ASTM D-1141-52) was contained in the vessel, the ullage volume being about 0.5l.

Tantalum, which forms an insulating anodic oxide in sea water, was chosen as the anode support thus avoiding interferences in the electrode chemistry. Anodes were cast into cylinders 1.75 cm × 1 cm diameter. The Pb-Pt bielectrodes were made using 99.5% Pb, 0.5% Sb alloy (Bunker Hill Company). A piece of 0.76 mm (30 mil) diameter, 10% Ir/Pt wire, 0.4 cm long was inserted into an undersized hole in one end so that 0.15 cm protruded; into the other end a hole was tapped to accommodate the 0.125 cm diameter threaded tantalum rod. The Pb, 6% Sb, 1% Ag anodes were prepared from analytical grade Pb, Sb, and Ag. The ingredients were weighed, melted, and mixed in a porcelain crucible and cast. Analysis showed the composition to be 92.8% Pb, 6.2% Sb, and 1.0% Ag which conformed to MIL-A-23871 for lead silver anodes. Anodes were preformed for 7 days in artificial sea water at C.D. 5 mA/cm² above those to be used in their

* Electrochemical Society Active Member.

¹ Present address: Electrochemistry Department, Lockheed Palo Alto Research Laboratory, Palo Alto, California 94304.

Key words: anode dissolution, pressure hydrostatic, lead anode, cathodic protection.

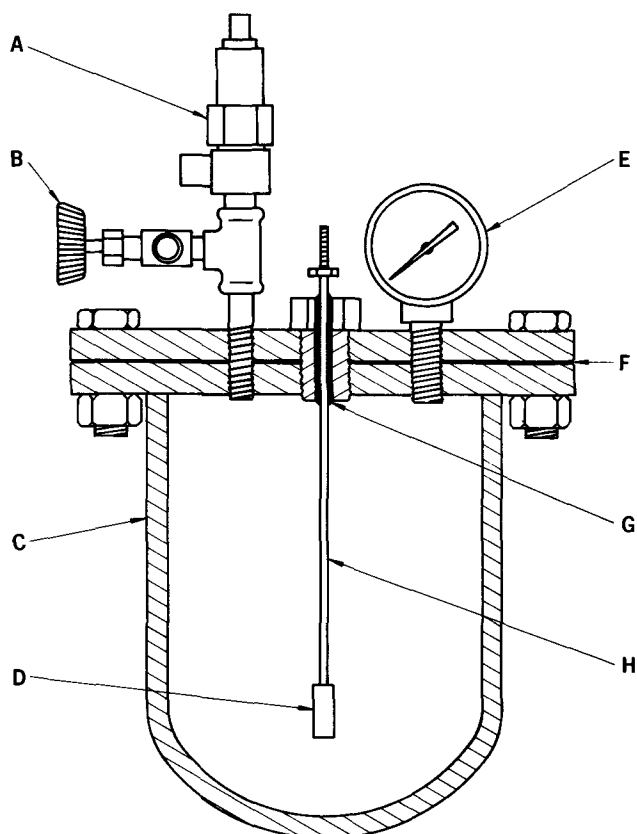


Fig. 1. Pressure test vessel. A: pressure control relief and valve; B: pressurization valve; C: pressure vessel; D: lead anode; E: pressure gauge; F: Teflon gasket; G: epoxy insulation; H: tantalum connecting rod.

respective long-term tests. This preforming period was arbitrarily chosen since measurements revealed very little change in the PbO_2 layer after 2 or 3 days.

During the pressure tests, the solution was changed at such intervals that the variation in Cl^- concentration was always less than 0.1N. A previous study (3) showed little difference in electrode behavior in the range 0.5N to 0.1N on preformed anodes, and it is thus believed that the variation occurring in the present experiments would not be a significant affector of the electrode processes of interest. It was also calculated that the hydrogen and chlorine evolved never occupied more than 10% of the ullage volume. The electrolyte became saturated with chlorine during the runs; however, earlier work (7) showed that dissolved chlorine has no significant influence on the anodic behavior.

The C.D.'s were chosen on the basis of the upper operating limits of the anodes, *i.e.*, 30 mA/cm^2 for the lead silver alloy (6) and 40 mA/cm^2 for bielectrodes (8). These limits have been established by laboratory and field experience over a number of years.

Constant d.c. (<0.1% a.c.) was supplied by an Electronic Measurements No. C614 instrument to a bank of the test vessels connected in series. Tests were run for 17, 30, 60, and 90 days at which time the thickness of the PbO_2 layers on the anodes were measured by slicing off cross sections and observing with a graticule equipped microscope.

Information on the actual weight of Pb converted to PbO_2 was obtained by physical removal of the dioxide followed by dissolution in an aqueous solution containing 2% KI, 10% CH_3COOH , and 5% CH_3COONa . Pb is not dissolved by this solution within the time required to dissolve the PbO_2 . The PbO_2 quantity was determined by either titration against standard $\text{Na}_2\text{S}_2\text{O}_3$, or by atomic absorption spectrophotometry.

Results

Photographs 1-6 in Fig. 2 are characteristic of the series. Photographs 1-3 represent the Pb-Pt bielectrode at 40 mA/cm^2 and photographs 4-6 show the Pb, 6% Sb, 1% Ag anode at 30 mA/cm^2 ; observations from all the experiments typically illustrated by the photographs are:

(i) Cracking and striations in the PbO_2 layer increase with depth.

(ii) Extent of blister formation and subsequent blister rupture and spalling of PbO_2 increases with depth. Blister formation is frequently associated with gassing but with Pb anodes in chloride solutions, blister formation is a way of relieving stresses at the Pb- PbO_2 interface. The PbO_2 formed in this system is quite porous and has a bulk volume about double that of the substrate.

(iii) Rate of growth, *i.e.*, continuing thickening of PbO_2 increases with increasing depth. This is further illustrated in Fig. 3 which was obtained by measurement of cross sections, accuracy being about 25%.

(iv) Failure of the lead silver anode, as shown in photograph 6 (Fig. 2) occurred after only about 0.3 to 0.6 cm of PbO_2 growth because the dioxide separated from the underlying Pb. This failure is depicted in the curve of applied voltage *vs.* time at constant C.D., Fig. 4, and is representative of failures observed in ICCP operations; *i.e.*, anode malfunction due to the onset of a large resistance increase.

From Fig. 4 it may be noted that the electrode shown in photograph 6 functioned normally at steady voltage for 7 days, but the voltage requirement increased at that time. With the high-voltage capability of the

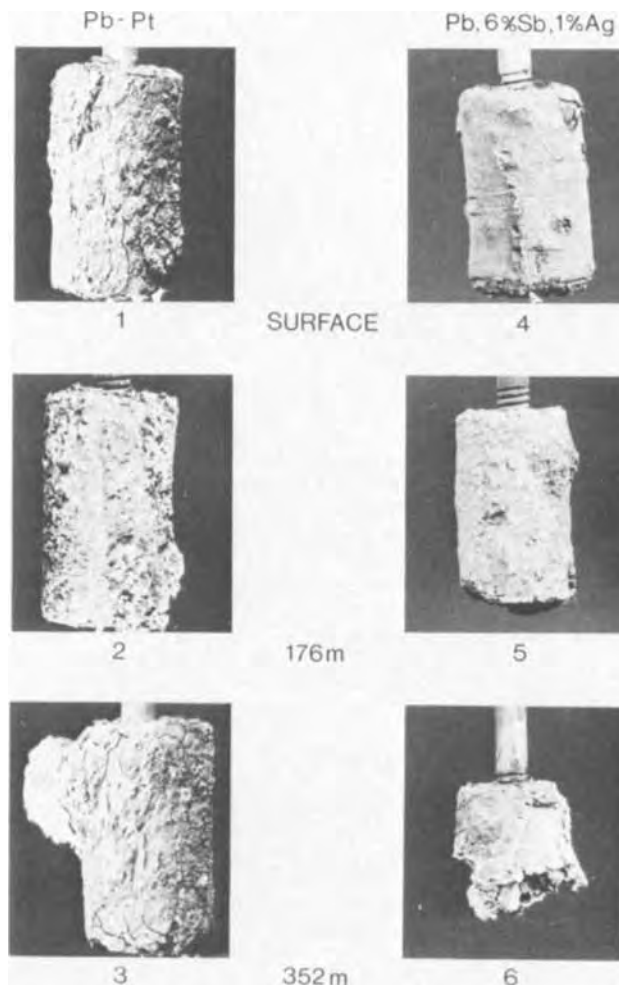


Fig. 2. Anode degradation (Photos 1, 2, 4, and 5 taken after 60 days, photo 3 after 30 days, and photo 6 after 17 days of test).

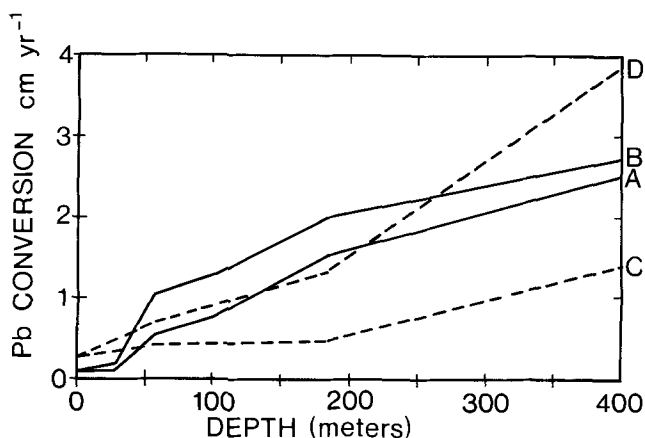


Fig. 3. Conversion of Pb \rightarrow PbO₂ after 60 days of test. A: Pb-Pt bielectrode at 20 mA/cm²; B: Pb-Pt bielectrode at 40 mA/cm²; C: Pb, 6% Sb, 1% Ag at 15 mA/cm²; D: Pb, 6% Sb, 1% Ag at 30 mA/cm².

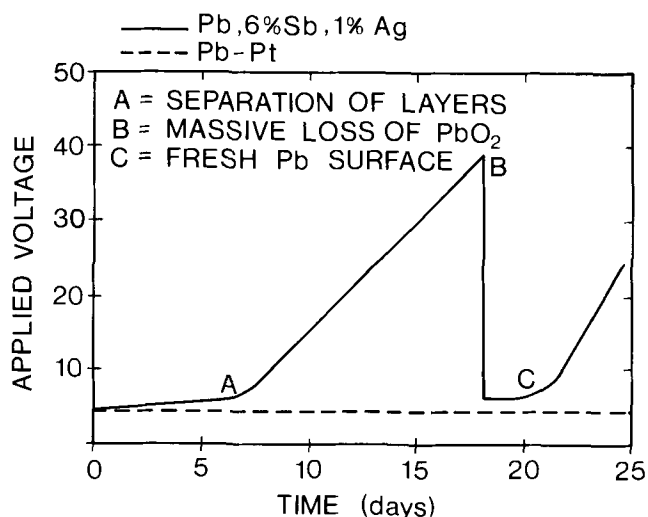


Fig. 4. Failure sequence of Pb, 6% Sb, 1% Ag alloy anode

power supply used in this study, it was found that a maximum was reached after about 17 days, and this maximum was associated with the total surface deperitization shown. The voltage rise from day 7 onward reflected the gradually increasing separation of the PbO₂ from the underlying Pb, accompanied by the high resistance of the cavity formed between the two electrically conducting interfaces. The PbO₂ finally spalled off completely at 17 days exposing a fresh Pb surface. Then once a fresh adherent thin layer of PbO₂ had reformed, the anode reverted back to normal low-voltage behavior for a few days. This sequence of failure events was observed with the Pb alloy anode at depths greater than 30m regardless of the C.D., the anode functioning normally for a longer time as the C.D. was decreased.

The Pb-Pt bielectrode did not suffer from this type of failure even though the rate of PbO₂ growth was somewhat greater, but separation of the dioxide from the Pb also occurred at depths greater than about 30m. However, the Pt microelectrodes effectively provided a current path between the Pb and PbO₂ across the nonconducting cavity and permitted normal operation for long periods.

Discussion

In the first part of this discussion, the practical significance of the experimental data is considered. In the second part an hypothesis is presented which explains why depth of operation is an affector of anode deterioration independent of mechanical pressure forces.

Figure 3, obtained from the experimental data, shows the influence of depth on the rate of the conversion reaction Pb \rightarrow PbO₂. Pb anodes will apparently function with an acceptably low-deterioration rate at depth to about 20m but at greater depths the conversion rate increases significantly. However, before operational limits can be established, it is necessary to calculate anode life as a function of depth. These data, obtained assuming a conventional Pb anode 1.3 cm (0.5 in.) thick, are shown in Fig. 5. The points were calculated by referring to the thickness of PbO₂ on controls run at atmospheric pressure alongside the pressure test specimens. Since a Pb-based anode operating at normal depths manifests very little conversion once a limiting thickness has formed, the additional growth at high pressures may be obtained by subtraction. To predict the life of Pb-Pt bielectrodes, we selected 75% conversion as representing a totally depleted anode since field experience has shown that these anodes will operate normally up to this level of conversion. On the other hand, with the Pb alloy, the criterion of useful anode life has to be determined differently. This is because at depths \geq 30m the anode ceased to operate after about 30% conversion, (0.3 to 0.6 cm) of PbO₂, because the dioxide layer separated from the underlying metal, leaving a high-resistance cavity. This separation, due to abnormal stresses on the thick layers at depth, has been confirmed by field experience. Thus we selected the onset of high resistance as the criterion of lifetime for the alloy anodes in Fig. 5.

A phenomenological view of the problem may be obtained by considering the difference in electrochemical behavior of an anode at the surface and at the depth. Calculations based on data obtained with a fully formed bielectrode at 40 mA/cm² and at atmospheric pressure showed that 6×10^{-5} % of the current is used for oxidation of Pb \rightarrow PbO₂ and that the remainder is involved in decomposition of the electrolyte. However, at a depth of 180m, 2×10^{-3} % of the current is used for Pb oxidation ($30 \times$ increase), which is reflected by the greatly reduced useful anode life. An explanation is not readily apparent from the literature since published data are sparse on the influence of pressure on heterogeneous inorganic electrochemical processes. Initially, when Pb or Pb alloys are made anodic in Cl⁻ containing electrolytes, the Pb corrodes as Pb_{aq}²⁺. If the C.D. is sufficient, the plumbous ions react with Cl⁻ at or in close proximity to the corroding electrode and a mechanically passivating film of PbCl₂ develops. When passivation is complete or nearing completion, the current path is restricted to interstices and pores in the crystalline layer and the potential increases at constant current to a level sufficient that lead aquocations derived either from the metal surface or from dissolving PbCl₂ crystallites, may be oxidized through inter-

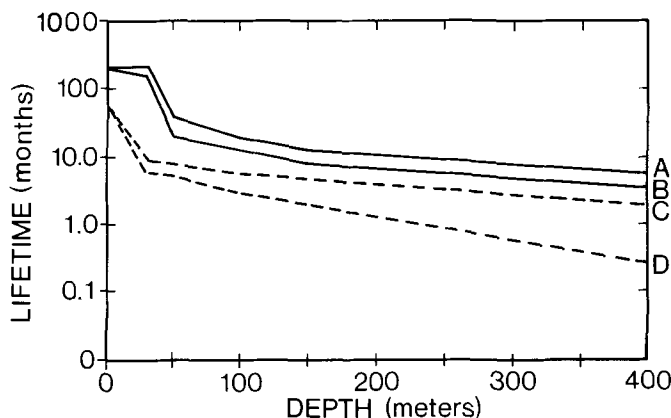
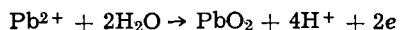


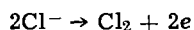
Fig. 5. Calculated anode lifetime. A: Pb-Pt bielectrode at 20 mA/cm²; B: Pb-Pt bielectrode at 40 mA/cm²; C: Pb, 6% Sb, 1% Ag alloy at 15 mA/cm²; D: Pb, 6% Sb, 1% Ag alloy at 30 mA/cm².

action with water dipoles or hydroxyl ions at the metal solution interface to PbO_2



$$E = 1.455 - 0.1182 \text{ pH} - 0.0295 \log a_{\text{Pb}^{2+}} \quad [1]$$

The PbO_2 then grows within and over the PbCl_2 . The exact mechanism is different for Pb alloys and bielectrodes, but so long as there is electrical continuity between the two conducting species (Pb and PbO_2), the surface becomes totally covered with the dioxide and eventually any underlying PbCl_2 is converted. Once PbO_2 has formed, oxidation of Cl^- to Cl_2 , and to a smaller extent H_2O to O_2 , is observed to occur on the chemically passivated PbO_2 surface. Actually, O_2 evolution is energetically favored over chlorine, but it is highly irreversible on PbO_2 , and may be disregarded except at high C.D.'s or in low salinities. Thus, the alternate reaction to Pb oxidation is



$$E = 1.359 + 0.0295 \log p_{\text{Cl}_2} - 0.059 \log a_{\text{Cl}^-} \quad [2]$$

By inserting values for $a_{\text{Pb}^{2+}}$ and pH into Eq. [1], one may show that the reversible potential is 1.04V. [The $a_{\text{Pb}^{2+}}$ and pH at the Pb/solution interface were previously determined in 0.5M NaCl to be 1.07×10^{-4} and 4.5, respectively (9)]. Also, the reversible potential for the Cl^-/Cl_2 reaction at a similar anode was calculated to be 1.33V (9). Thus, from reversible thermodynamic considerations, continued oxidation of Pb is to be expected, but this heterogeneous reaction is kinetically much slower and more irreversible than Cl_2 evolution which, therefore predominates. It will also be observed that there is no pressure sensitive term in Eq. [1], and that a pressure of 100 atm only increases the reversible potential of [2] by 59 mV. Thus, it becomes apparent that a reversible thermodynamic treatment is inadequate to explain the pressure responsiveness of the system, but it may be predicted from le Chatelier's principle that reaction [2] will be hindered with increasing pressure. A study of chemical reaction kinetics under pressure has been given by Hamann (10) who considered collision theory and transition state (or activated complex) theory and showed that hydrostatic pressure effects are best explained by transition state theory. However, to obtain specific quantitative data, it is necessary to have knowledge of the elementary intermediate reactions in oxidations [1] and [2], and such information is not yet available. Experiments to determine the kinetics of the reactions of interest will be the subject of a future

paper. But, at the present time we believe that as depth increases, the $\text{Pb} \rightarrow \text{PbO}_2$ reaction remains essentially constant, while the $\text{Cl}^- \rightarrow \text{Cl}_2$ reaction decreases, and this causes more coulombs to be available for the Pb conversion reaction.

Conclusions

Pb-based anodes have been shown to operate with normal low conversion of $\text{Pb} \rightarrow \text{PbO}_2$ only to depths of about 30m. Below this depth, serious deterioration occurs, and such anodes cannot be recommended for deep-water use. Pb-Pt bielectrodes and Pb, 6% Sb, 1% Ag alloy also show a dramatic increase in conversion in comparison to surface operation. For example, with Pb-Pt bielectrode at 40 mA/cm² conversion increase rates at 176 and 352m were 30 and 41 ×, respectively.

The thick, chemically passive, PbO_2 layers developed cracks and fissures and separated from the underlying Pb but, with the bielectrode, electrical conductivity was shown to be maintained through the microelectrode, thus delaying failure. The mechanical forces causing the separation of Pb from PbO_2 probably also increase with depth and thus amplify the problem. The increasing conversion rate of $\text{Pb} \rightarrow \text{PbO}_2$ with increasing depth is postulated to be due, at constant current, to the coulombs not used for the $\text{Cl}^- \rightarrow \text{Cl}_2$ reaction. These coulombs become available because the rate of the Cl_2 evolution reaction is believed to decrease under pressure while the Pb oxidation rate remains essentially constant.

Manuscript submitted Jan. 6, 1972; revised manuscript received July 10, 1972.

Any discussion of this paper will appear in a Discussion Section to be published in the June 1973 JOURNAL.

REFERENCES

1. E. L. Littauer and L. L. Shreir, Proceedings First International Corrosion Congress, London (1961).
2. L. L. Shreir, *Corrosion*, **17**, 188 (1961).
3. H. Helber and E. L. Littauer, *Corrosion Sci.*, **10**, 411 (1970).
4. D. B. Peplow and L. L. Shreir, *Corrosion Technol.*, **4**, 16, (1964).
5. E. Sato, M. Kashiwabara, and S. Yoshida, *Anti-Corros. Methods Mater.*, **1**, 27 (1965).
6. I. Geld, *J. Buships*, **14**, (4), 5 (1965).
7. E. L. Littauer, Ph.D. Thesis, University of London (1961).
8. LAS Marine Services Division, Private communication.
9. E. L. Littauer and L. L. Shreir, *Electrochim. Acta*, **12**, 465 (1967).
10. S. D. Hamann, "Physio-Chemical Effects of Pressure," Academic Press, New York (1957).

Thermodynamic Activity of $\text{Na}_2\text{O}-\text{B}_2\text{O}_3$ Melt

Use of Stabilized Zirconia as an Electrode Constituent

Seichi Sato, Toshio Yokokawa, Hideaki Kita, and Kichizo Niwa

Department of Chemistry and The Research Institute for Catalysis, Hokkaido University, Sapporo 060, Japan

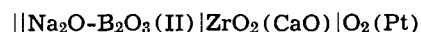
In the thermodynamic studies of the oxide melts such as borates, silicates, and phosphates, the electromotive force technique has been applied on various occasions. However, difficulties in the construction of the reference electrode and especially the selection of the electrode materials, which specifies the well-defined electrode reaction, have retarded a wide use of this method, aside from the problem of the liquid junction potential.

Meanwhile, CaO stabilized ZrO_2 has proven to be an excellent solid electrolyte (1), which can be used

to measure oxygen pressure in gaseous atmosphere, oxygen content in liquid metals and so on (2). The present authors have shown this material to be very satisfactory for the measurement of the thermodynamic activity of Na_2O in $\text{Na}_2\text{O}-\text{B}_2\text{O}_3$ melt. The unique characteristics of this electrode are discussed.

Experimental

The concentration cell is the type



Key words: O_2/O^- reference electrode, acid-base of oxide melt, $\text{Na}_2\text{O}-\text{B}_2\text{O}_3$.

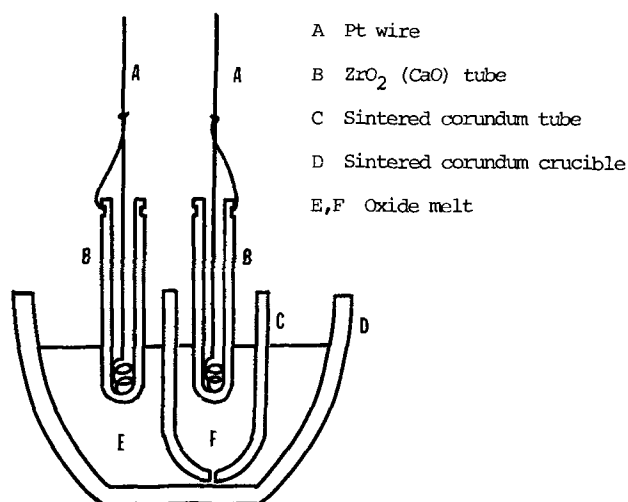
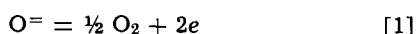


Fig. 1. Cell assembly

and its construction is shown in Fig. 1. The electrode reaction is given by



which proceeds in the forward direction at the left electrode and backward at the right electrode when a current of 2 Faradays passes from left to right in the cell. The potential gap across the ZrO₂-oxide melt interface is assumed to be set up so as to equalize the electrochemical potential of O[⊖] in both phases. Further, if it is assumed as usual that Na⁺ is the sole carrier of the virtual electric current through the liquid junction, the liquid junction potential is given by

$$E_{lj} = - (1/F) (\mu_{\text{Na}^+ \text{(I)}} - \mu_{\text{Na}^+ \text{(II)}}) \quad [2]$$

where μ_{Na^+} is the chemical part of the electrochemical potential of Na⁺ in the melt. Accordingly, the net electromotive force is represented as

$$\begin{aligned} E &= \frac{1}{2F} (\mu_{\text{O}^{\ominus} \text{(I)}} - \mu_{\text{O}^{\ominus} \text{(II)}}) + \frac{1}{F} (\mu_{\text{Na}^+ \text{(I)}} - \mu_{\text{Na}^+ \text{(II)}}) \\ &= \frac{RT}{2F} \ln \frac{a_{\text{Na}_2\text{O} \text{(I)}}}{a_{\text{Na}_2\text{O} \text{(II)}}} \end{aligned} \quad [3]$$

where $a_{\text{Na}_2\text{O}}$ is the thermodynamic activity of Na₂O. In Fig. 1, platinum wire (A) is in electric contact with the inside bottom of the zirconia tube, the latter being grooved for suspension. The corundum tube (C) which separates the two melts is furnished with a hole of 0.3 mm diameter at the bottom. The assembly in a reaction tube was heated in a resistance furnace in air atmosphere. A stainless tube was introduced between the furnace tube and the reaction tube and was grounded. The voltage was measured both by an ordinary potentiometer and by a vibrating reed electrometer (Takeda Riken TR-84M type). It took about 4 hr for the emf to approach close to constant value. Usually the measurement was carried out in 12 hr after the charge. It remained constant for several days. The sample melt was prepared from H₃BO₃ and Na₂CO₃ of the guaranteed reagent grade.

Results and Discussion

The measurement was carried out for the Na₂O-B₂O₃ melt over the composition range 0.65-0.95 mole per cent (m/o) B₂O₃, the melt of 0.95 being used as a reference. The results are shown in Fig. 2. The data obtained from the measurement with the bare platinum wire without the zirconia tube are also plotted. Only small but systematic deviation is found in the two sets. Stegmaier and Dietzel (3) have measured the activities of Na₂O, K₂O, and Li₂O in the binary borates with a cell in which platinum wire electrodes were dipped into the

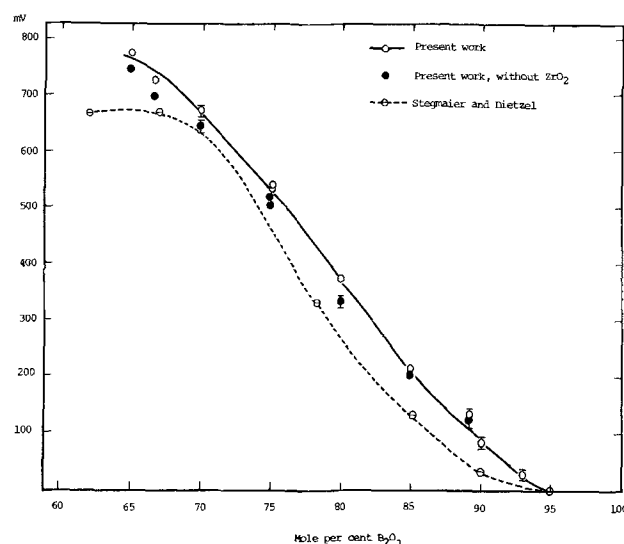


Fig. 2. Emf value as functions of composition at 850°C

melt. The data are reproduced in Fig. 2 where the emf value is shifted for easy comparison, although they measured it referred to 0.5-0.7 m/o alkali oxides. The order of magnitude and gradations of emf value are in fair agreement among the three sets of data. This suggests two facts. First, either the oxygen pressure in the melt at the platinum electrode without the ZrO₂ tube is in equilibrium with gaseous atmosphere or the electrode potential is determined practically at the gas-metal-oxide coexisting surface on the platinum wire. Second, the assumption that the electrochemical potential of O[⊖] is at the same level across the ZrO₂-melt interface is correct. In passing, one must note that the magnitude of emf corresponds to 10⁷ of the activity ratio at 0.65 to 0.95 m/o B₂O₃ (Eq. [3]). This drastic change reminds one of the hydrogen ion concentration in an aqueous solution. This behavior is not observed in typical binary melts and will be understood better in terms of the acid-base character of the melt. Thus, while O[⊖] from Na₂O neutralizes B₂O₃ to various degrees depending upon the strengths of basicity and acidity of Na₂O and B₂O₃ respectively and upon their compositions, while Na⁺ ion remains free.

The features of this electrode are the following. (i) The oxygen pressure is well defined. Although platinum or graphite rod electrodes have been used in the investigations of this kind, the pressure of O₂ or CO has not been specified except in a few cases (4). (ii) Since there is no electronic conduction through the ZrO₂ phase, the molecular oxygen dissolved in the melt cannot take part in the electrode reaction. This gives an advantage that the fugacity of molecular oxygen in the melt can be handled freely, being independent of the basic oxide content. A procedure of this sort becomes important, for example, when one wishes to measure the concentration ratio of Fe²⁺/Fe³⁺ as functions of oxygen pressure and the basicity of an iron-containing melt separately. Parenthetically, the fugacity of molecular oxygen in the melt can be measured by the ordinary technique with ZrO₂ (2). (iii) The possible contamination due to ZrO₂-melt reaction is a shortcoming, as this might give rise to interference in reversibility of the emf with respect to O[⊖]. In the present system zirconia showed a much higher resistance against contamination than sintered corundum.

The present method will widen the applicability of the emf technique to systems for which otherwise reversible electrode cannot be constructed. This electrode will function well as the reference electrode when one might want to measure a single electrode potential of an anode or a cathode in electrolysis of an oxide melt. There is no need of bubbling of O₂ gas

on the surface of the electrode (4). This electrode is in principle analogous to the glass electrode in a pH meter in which a thin glass layer functions reversibly only to hydrogen ion.

Manuscript submitted April 14, 1972; revised manuscript received June 8, 1972.

Any discussion of this paper will appear in a Discussion Section to be published in the June 1973 JOURNAL.

REFERENCES

1. H. Schmalzried, *Z. Phys. Chem.*, **38**, 87 (1963).
2. See for example W. A. Fischer, and W. Ackermann, *Arch. Eisenhüttenw.*, **37**, 43 (1966).
3. W. Stegmaier and W. Dietzel, *Glastechn. Ber.*, **18**, 353 (1940).
4. A. Ghosh and T. B. King, *Trans. AIME.*, **245**, 145 (1969).



Oxidation Properties of a Zirconium-2.7 w/o Niobium Alloy in the Temperature Range 650°-1000°C

V. F. Urbanic and W. W. Smeltzer*

Department of Metallurgy and Materials Science, McMaster University, Hamilton, Ontario, Canada

ABSTRACT

The reaction kinetics and structures of the alloy/oxide composite system were determined for a Zr-2.7 weight per cent Nb alloy exposed at temperatures over the range 650°-1000°C in oxygen at 1 atm pressure. These kinetics may be represented by a parabolic-linear relationship. The zirconia scales contained small amounts of the intramolecular oxide, $6\text{ZrO}_2 \cdot \text{Nb}_2\text{O}_5$. An investigation was carried out on the morphological development of the columnar scale and the underlying layer of oxygen stabilized α -Zr plates in the β -Zr alloy during parabolic oxidation. The sequence of the reaction product layers was consistent with predictions from the Zr-Nb-O phase diagram.

Investigations on the oxidation properties of Zr-Nb alloys containing 2-3 w/o (weight per cent) Nb at elevated temperatures have been only carried out to a limited extent (1-5). The reaction kinetics over the temperature range 300°-1000°C are characterized initially by continuously decreasing rates followed by transitions to more rapid approximately constant rates. At temperatures less than the $\alpha + \beta$ eutectoid point at 610°C, a martensitic alloy oxidizes more rapidly than the Widmanstätten-structured alloy (2, 3). The zirconia scales may contain small amounts of the intramolecular oxide, $6\text{ZrO}_2 \cdot \text{Nb}_2\text{O}_5$ (2-5). At temperatures higher than 900°C, parabolic oxidation of a β -structured alloy gives rise to the formation of an oxygen stabilized columnar zone of α -Zr plates beneath the scale (4, 5). The objectives of this investigation, accordingly, were to determine the temperature dependence of the oxidation kinetics for the alloy in the $\alpha + \beta$ and β -Zr structures and to examine the morphological development of the scale and α -Zr columnar layer in the β -Zr alloy.

Experimental

A thermogravimetric technique was employed to measure the oxidation rates of alloy plates and spheres. The assembly which has been described contained an Ainsworth, Type AU-1, balance for continuously recording weight gains up to 400 mg to a sensitivity of 0.02 mg (6). Test temperatures were controlled to $\pm 2^\circ\text{C}$. A specimen was lowered into the reaction zone and held for 15 min to ensure temperature equilibration after the assembly had been flushed with argon purified of oxygen and water vapor. The assembly was subsequently pumped down to less than 10^{-4} Torr and oxygen, 99.99% pure, then admitted to a pressure of 760 Torr. At the termination of a run, the specimen was quenched by rapidly raising it into the air-cooled portion of the assembly.

The material was a Zr-2.7 w/o Nb alloy received as a 2 mm thick sheet and as a bar. Analyses for impuri-

ties have been presented, the residual oxygen content in the alloy being 1100 ppm (2). Plates prepared from the sheet, $2 \times 1 \times 0.2$ cm, were wet abraded on 220 to 600-grit silicon carbide papers, polished on 6 and 1μ diamond laps lubricated with kerosene followed by acetone washing and drying. Spherical specimens were prepared from the bar by machining pieces to a diameter of approximately 1 cm. They were then hand-abraded as above and lap-polished using a jig which permitted specimen rotation and polishing of the entire surface. The specimens, which were sealed in evacuated quartz capsules and annealed at 1000°C for 1 hr and furnace cooled, exhibited a typical β -cooled structure of coarse acicular α -grains.

Oxidized specimens were mounted in araldite self-setting epoxy resin. Abrasion was carried out to 600-grit silicon carbide with kerosene as lubricant. Final polishing at the 6 and $\frac{1}{4}\mu$ stages was completed on nylon cloths impregnated with diamond paste. Specimens used for metallographic examinations were etched in an aqueous solution containing 30 v/o (volume per cent) H_2SO_4 , 30 v/o HNO_3 , and 10 v/o HF. Oxides were identified by x-rays using the powder method and reflection diffraction with nickel filtered $\text{CuK}\alpha$ radiation. X-ray diffraction measurements of the oxide in the underside of a scale could be made by dissolving away metal in the etching solution held at approximately 70°C. A Cambridge scanning electron microscope was useful for distinguishing various phases in the scale and underlying metal. Variations of niobium concentration in the alloy and oxide phases were qualitatively determined using a Cameca electron probe microanalyzer.

Results

The results are classified into those obtained at temperatures in the range 650°-991°C using plate specimens and those obtained at 1000°C using the spherical specimens. It is evident from the Zr-Nb phase diagram (7) that these temperatures lie within the $\alpha + \beta$ phase field extending from 610° to 840°C or the high temperature β -Zr phase field.

* Electrochemical Society Active Member.

Key words: zirconium-niobium alloys, oxidation kinetics, oxide scale, alloy microstructures.

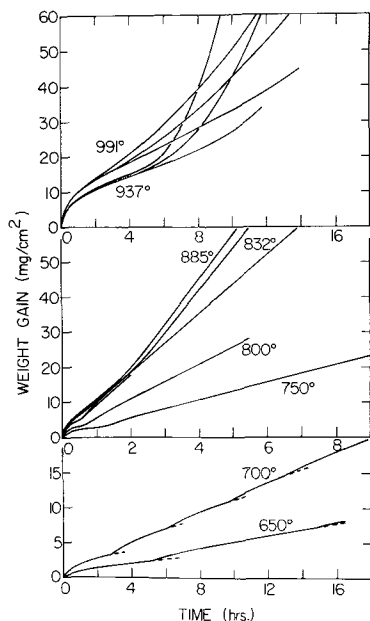


Fig. 1. Oxidation curves for the Zr-2.7 w/o Nb alloy plate specimens at temperatures over the range 650°-1000°C in oxygen at 1 atm pressure.

Oxidation curves for the plates are shown in Fig. 1. A continuously decreasing oxidation rate was observed during early exposure stages up to a transition to more rapid kinetics after approximately 5 hr at 650°C and within 2 hr at 885°C. The curves exhibited periodic discontinuities at 650° and 700°C which occurred more frequently at the latter temperature. At temperatures from 750° to 885°C, the transition led directly to linear kinetics. Specimens exposed at 937° and 991°C showed transitions within 4 hr to more rapid continuously increasing kinetics during the subsequent exposures examined.

A scale after the termination of a run at temperatures within the range 650°-885°C was colored white and extensively cracked. Specimens exposed at 937° and 991°C were covered predominantly by gray compact oxide and characterized by white cracked oxide at edges and corners. The powder x-ray patterns of the white and gray oxide were identical and similar to the pattern for monoclinic zirconia with the exception of one reflection at 2.97Å which corresponded to a spacing for the tetragonal oxide, $6\text{ZrO}_2 \cdot \text{Nb}_2\text{O}_5$. The alloy was composed of $\alpha + \beta$ phases at temperatures to 885°C. At 937° and 991°C, the alloy microstructure was characterized by a layer of α -Zr plates extending into the β -Zr substrate at areas covered by a gray compact scale. This columnar alloy structure was not present at regions where oxide cracking had caused enhanced localized scale growth. These latter observations correspond to those previously reported for alloys oxidized within the range 870°-990°C (4).

Continuous oxidation of the β -Zr alloy was extended to longer periods by employing the spherical specimens. As illustrated in Fig. 2, the shape of the oxidation curve at 1000°C is similar to that obtained upon oxidizing a plate specimen. The region of continuously decreasing oxidation rate, however, was extended beyond 16 hr. The adherent compact scales on the spheres, as shown in Fig. 3, were of lighter gray color with increasing exposure. White oxide was only observed at localized regions of cracked scale after the transition to more rapid oxidation.

A unique columnar structure of oxygen stabilized α -Zr plates existed under the compact scale formed on the β -Zr alloy. This structure is illustrated in Fig. 4. The martensitic matrix is a consequence of the transformation which occurs when a specimen is quenched. An interesting feature of the α -Zr layer,

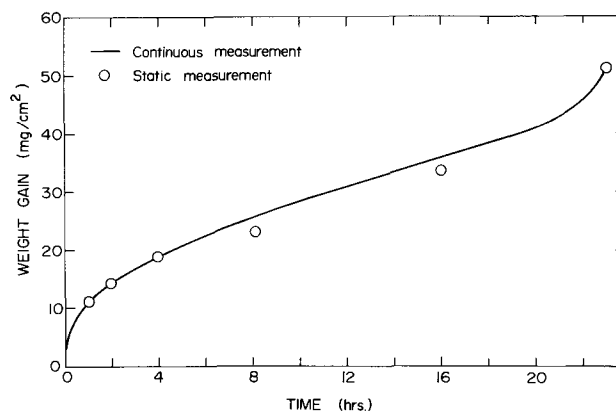


Fig. 2. Oxidation curve for the Zr-2.7 w/o Nb alloy spherical specimens at 1000°C in oxygen at 1 atm pressure obtained by the continuous gravimetric technique and by static tests involving specimen weighings before and after exposures.

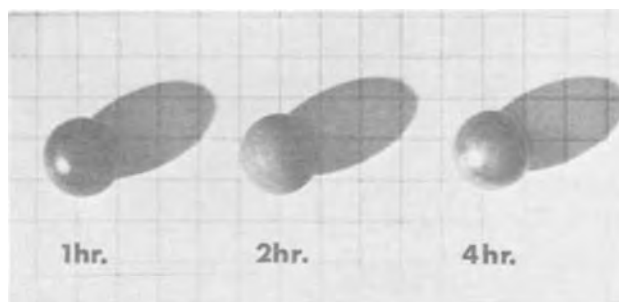


Fig. 3. Spherical specimens oxidized at 1000°C

which is evident in Fig. 4 and readily apparent at higher magnifications as shown in Fig. 5, is the occurrence of a finer columnar structure near the metal/oxide interface. The coarse and fine structures differed from one another since they exhibited different etching properties. The intercolumnar regions of the coarse structure was simply transformed β -Zr whereas the material between the columnar plates of the fine structure was an oxide. Note that these oxide stringers extend inward right from the metal/oxide interface.

The external compact scale, α -Zr + oxide, and $\alpha + \beta$ layers formed in the alloy spheres grew at rates which continuously decreased with increasing exposure. As illustrated by the parabolic plots in Fig. 6, growth of these reaction product layers was determined by a diffusional mechanism involving inward oxygen migration.

Metallographic examination using the oil immersion technique of the oxide formed over the α -Zr plates demonstrated that the scale also exhibited a columnar structure not unlike that of the underlying alloy. This feature is illustrated in Fig. 7. An intercolumnar region generally appears to contain a lighter phase with the exception of a dark phase near the metal/oxide interface. The scale at the metal/oxide interface subjected to reflection x-ray diffraction only revealed monoclinic zirconia. Powder samples of the scales, nevertheless, exhibited a reflection corresponding to $6\text{ZrO}_2 \cdot \text{Nb}_2\text{O}_5$ which possibly arises from the lighter appearing discontinuous phase. Attempts were made using the electron-microprobe to determine the variations in niobium concentration across the columnar regions in the alloy and scale. It was only possible to conclude from lateral scans parallel to the alloy interface, however, that these regions were enriched in niobium since limitations were imposed on the validity of the results due to their small physical dimensions.

Discussion

The kinetics obeyed a parabolic relationship in the early stages of the reaction. This characteristic is

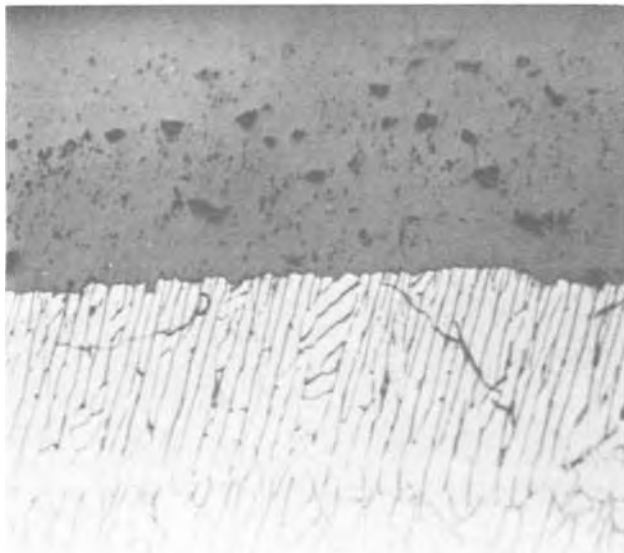
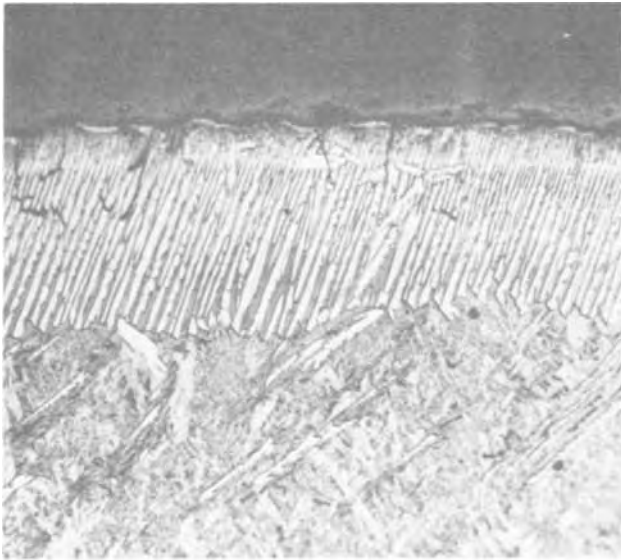


Fig. 4. Cross sections of spheres oxidized at 1000°C for 1 hr (upper) and 23 hr (lower) micrographs (140X). The micrographs illustrate the scales and the columnar zones beneath the scales in the β -Zr alloy.

illustrated by the plots in Fig. 8 for oxidation of the plates at several temperatures and for the spheres at 1000°C. Scale growth, accordingly, was determined initially by a diffusional mechanism for inward migration of oxygen since zirconia is an oxygen-conducting oxide (8).

Arrhenius plots of the parabolic and linear oxidation constants are shown in Fig. 9. Values of the linear rate constants were determined from linear sections of the curves or from limiting tangents after the transitions from parabolic kinetics. The $\alpha + \beta$ alloy apparently oxidizes by a common mechanism over the temperature range 650°-885°C. The activation energies for parabolic and linear oxidation over this temperature range are 38 and 31 kcal/g-atom, respectively. Linear oxidation was associated with scale breakdown by cracking but the role of the scale as a barrier to oxidation remains undefined. Parabolic oxidation above 937°C nevertheless, proceeded at a lower rate than predicted from extrapolation of the Arrhenius relation. Oxygen dissolved in the alloy is known to cause an upward shift of the $\beta/\alpha + \beta$ phase boundary temperature (9). In particular an oxygen content of 1400 ppm in a 2½ w/o Nb alloy, which is approximately the

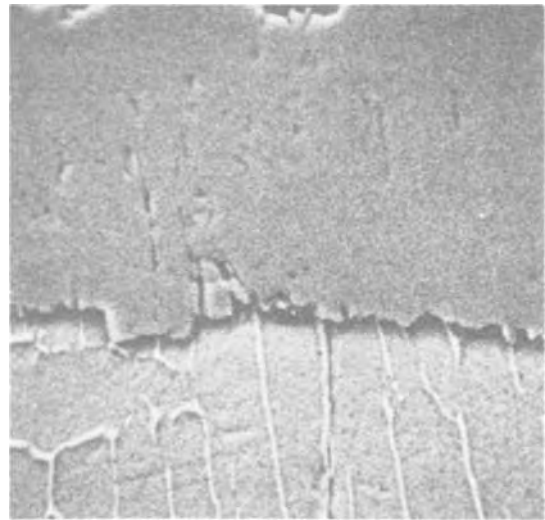


Fig. 5. Scanning electron micrograph of the scale and the α -Zr columnar alloy region formed at 1000°C exhibiting oxide stringers in the intercolumnar regions of the alloy (1000X). The metallographically polished specimen was chemically etched.

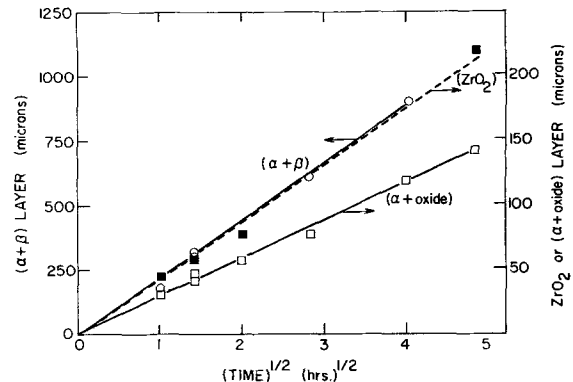


Fig. 6. Parabolic plots for the growth of the scale, α -Zr + oxide stringer layer, and $\alpha + \beta$ columnar layer in the alloy at 1000°C.

impurity content of the alloy, raises this temperature to 925°C. Thus the transition in the kinetics to a lower value above 885°C was associated with a distinctly different morphological development involving concurrent formation of a scale and an unique columnar layer of α -Zr plates in the β -structured alloy.

A description of the oxidation properties of the β -Zr alloy at 1000°C may be formulated from the results for the spheres. Cross sections were characterized by a compact scale, a region of internal oxidation comprised of α -Zr plates and oxide stringers, and a layer of α -Zr as coarse columnar plates in the β -alloy matrix. Since growth of these reaction product layers followed parabolic relationships determined by a diffusional mechanism involving inward oxygen migration, the alloy-oxygen system may be considered as a diffusional couple.

The ternary isotherm available for 1500°C (10) is used to discuss the formation of the solid phases since the binary representations on the ternary diagram coincide with phase boundaries of the respective binary diagrams at 1000°C. A schematic representation for the compositions and microstructures of the oxidized alloy is shown in Fig. 10 by superimposing a path on the ternary phase diagram to correspond to the sequence of observed reaction product layers. This path which emerges into the β -phase at 2.7 w/o Nb defines the interior alloy matrix. On its emergence into the $\alpha + \beta$ phase field, the crossing of tie-lines represents precipitation of α -Zr and growth of the $\alpha + \beta$ coarse columnar

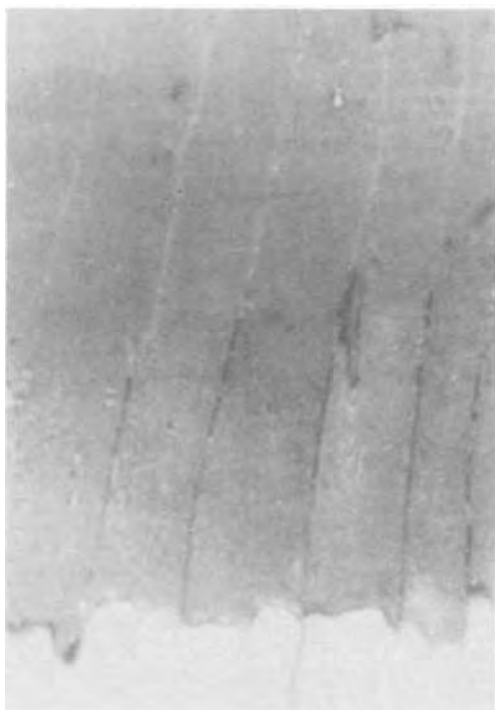


Fig. 7. Micrograph of the cross section of the scale formed on the Zr-2.7 w/o Nb alloy at 1000°C illustrating its columnar structure (2460X).

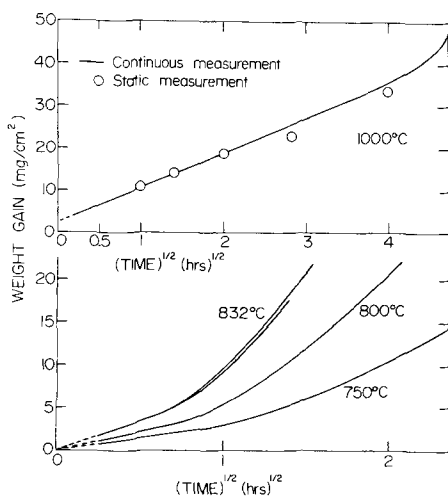


Fig. 8. Parabolic oxidation plots for the uptake of oxygen by the alloy plates at 700°, 750°, and 832°C and the spheres at 1000°C.

layer. Crossing of the $\alpha + \beta + \text{ZrO}_2$ phase field defines the interface between the $\alpha + \beta$ and $\alpha + \text{ZrO}_2$ layers. Formation of zirconia stringers as an internal oxide signified that the composition path must cut tie-lines in the $\alpha + \text{ZrO}_2$ field. This columnar layer was readily distinguishable in the cross sections due to its fine structure in comparison to that of the $\alpha + \beta$ layer. Since oxygen solubility in β -Zr decreases with increasing niobium concentration, niobium was segregated into the intercolumnar β -Zr regions as the primary α -Zr plates grew. Consequently, oxygen supersaturation created in the β -Zr was relieved by nucleation and growth of the finer secondary α -Zr plates. Niobium enrichment also led to formation of the observed dark niobium-enriched zirconia stringers extending up to the alloy/scale interface and into the adjacent scale. It was only feasible, however, to detect this niobium enrichment by the electron probe technique due to the small width of the intercolumnar regions. Subsequent emergence of the diffusion path from the zirconia

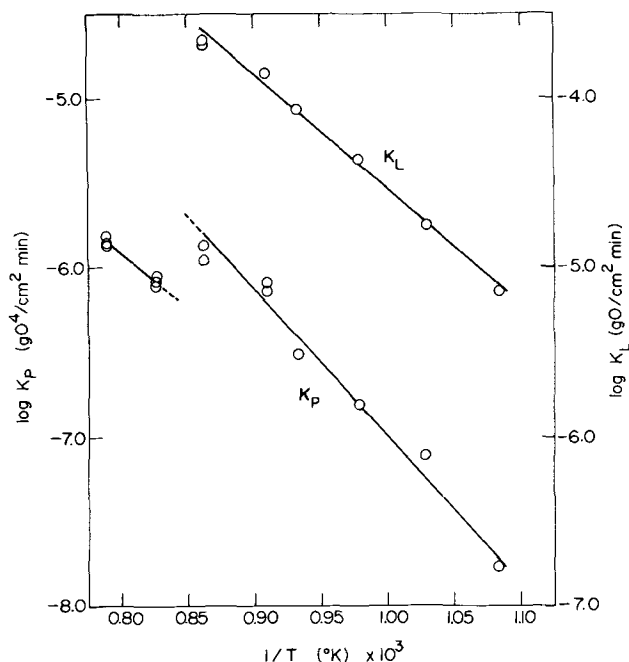


Fig. 9. Arrhenius plots for the parabolic and linear oxidation constants of the Zr-2.7 w/o Nb alloy over the temperature range 650°-885°C.

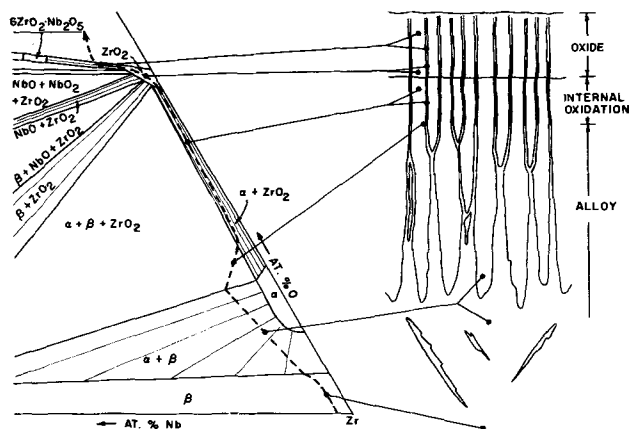


Fig. 10. A schematic representation of the reaction product layers formed on oxidizing the Zr-2.7 w/o Nb alloy at 1000°C and the sequence of these layers plotted as a compositional path on the Zr-Nb-O phase diagram.

field into the $\text{ZrO}_2 + 6\text{ZrO}_2 \cdot \text{Nb}_2\text{O}_5$ field at an angle incident to tie-lines is consistent with the x-ray and metallographic results for the presence of the intramolecular oxide within the scale.

Conclusions

A Zr-2.7 w/o Nb alloy exposed to oxygen at 1 atm pressure at temperatures in the range 650°-1000°C exhibits parabolic kinetics during early exposure stages followed by a transition to more rapid kinetics. The scale became extensively cracked in the post-transition interval. Small amounts of the intramolecular oxide, $6\text{ZrO}_2 \cdot \text{Nb}_2\text{O}_5$, were contained within the zirconia scales. The temperature coefficient of the parabolic oxidation constants changed to a lower value in the range 885°-937°C which was associated with the formation of a columnar zone of α -Zr plates in the β -structured alloy by inward diffusion of oxygen. The scale which formed over the α -Zr plates exhibited a similar columnar structure and zirconia stringers extended inward along the alloy intercolumnar boundaries. Diffusional growth of the reaction product layers was

consistent with predictions from the Zr-Nb-O phase diagram.

Acknowledgments

This research was carried out under auspices of the Defence Research Board of Canada. This paper is based on the thesis submitted by V. F. Urbanic to McMaster University in partial fulfilment of the requirements for the M.Sc. degree.

Manuscript submitted March 15, 1972; revised manuscript received June 6, 1972.

Any discussion of this paper will appear in a Discussion Section to be published in the June 1973 JOURNAL.

REFERENCES

1. S. Nomura and C. Akutsu, *Electrochem. Technol.*, **4**, 93 (1966).
2. M. G. Cowgill and W. W. Smeltzer, *This Journal*, **114**, 1089 (1967).
3. M. G. Cowgill and W. W. Smeltzer, *ibid.*, **115**, 471 (1968).
4. M. G. Cowgill, S. H. Wong, and W. W. Smeltzer, *ibid.*, **115**, 927 (1968).
5. J. P. Guerlet and P. Lehr, *J. Nucl. Mater.*, **28**, 165 (1968).
6. R. Logani and W. W. Smeltzer, *J. Oxidation Metals*, **1**, 3 (1969).
7. H. Richter, P. Wincierz, K. Anderko, and U. Zeicker, *J. Less Common Metals*, **4**, 252 (1962).
8. A. Madeyski, D. J. Poulton, and W. W. Smeltzer, *Acta Met.*, **17**, 579 (1969).
9. J. Wintron and R. A. Margatroyd, *Electrochem. Technol.*, **4**, 358 (1966).
10. C. T. Simms, W. D. Klopp, and R. I. Jaffee, *Trans. Am. Soc. Metals*, **51**, 256 (1959).

Electron Injection into Anodic Valve Metal Oxides

II. Further Experimental Results for Ta₂O₅, Nb₂O₅ and Al₂O₃

N. I. Jaeger,* G. P. Klein,* and B. Myrvaagnes

*P. R. Mallory & Company, Inc., Laboratory for Physical Science,
Northwest Industrial Park, Burlington, Massachusetts 01803*

ABSTRACT

Electron injecting contacts can be formed at valve metal oxide/semiconducting metal oxide interfaces with applied fields of the order of some 10⁶ V/cm. Electronic current injection as a function of time and applied field (activation) has been measured for Ta/Ta₂O₅, Nb/Nb₂O₅, and Al/Al₂O₃ electrodes in contact with Fe₂O₃ as the semiconducting transition metal oxide. The activation process is explained on the basis of interacting ionic and electronic processes with the ionic charge transport following the empirical field law for anodic oxide growth $i = A \exp(BF)$. The explicit dependence of the electronic process on parameters of the ionic conduction process has been confirmed by determining the ionic conduction parameters from the field and temperature dependence of the activation process. Quantitative agreement with values reported from measurements of the kinetics of anodic oxide growth has been obtained. The electronic current resulting from activation of Nb/Nb₂O₅/Fe₂O₃ and Ta/Ta₂O₅/Fe₂O₃ electrodes in contact with electrolytes showed a field dependence typical for thermionic emission. Linear $\log i$ vs. $F^{1/2}$ characteristics could be obtained extending over 4-5 decades with slopes in agreement with thermionic emission following a Poole-Frenkel mechanism. It appears that valve metal/valve metal oxide/semiconducting oxide electrodes with two oxides in intimate but initially blocking contact provide model systems for the generation of coulombic centers from which thermally activated electron emission with Poole-Frenkel characteristic can take place. The barrier height for the thermionic emission process and its change with progressing activation has been determined from measurements of the temperature dependence of the electronic current with applied field and state of activation as parameters. The barrier heights were found to be of the order of 1 eV.

In a recent publication (1) it has been shown that homogeneous electronic currents of the order of 10 mA/cm² could be injected into anodic tantalum oxide under high field conditions after inserting a thin layer of semiconducting transition metal oxide between the valve metal oxide and the electrolyte. The transition metal oxide layer restricted ionic migration while providing electronic equilibrium between the electrolyte and the surface of the valve metal oxide.

Figure 1 shows a schematic of the experimental system. A thin layer of iron or manganese oxide was deposited on the valve metal oxide. Upon application of a constant voltage between metal substrate and counterelectrode equivalent to a field required for ionic migration, the level of electronic current injection was found to rise with time over several decades. A typical injecting Ta/Ta₂O₅/Fe₂O₃ electrode would con-

sist of Ta substrate, anodic Ta₂O₅, and reactively-sputtered Fe₂O₃. In response to the applied field of the order of 5 × 10⁶ V/cm an ionic current started to flow

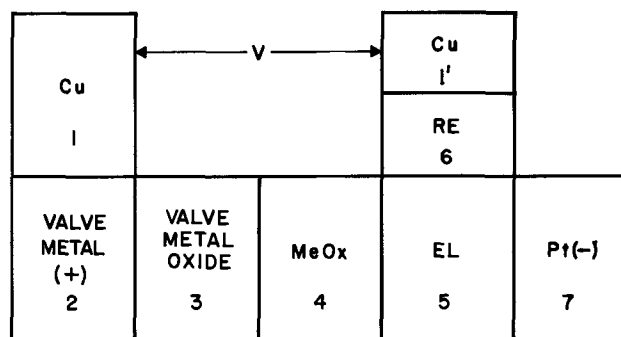


Fig. 1. Schematic of experimental system: V, applied voltage; El, electrolyte; RE, reference electrode; Pt, counterelectrode.

* Electrochemical Society Active Member.

Key words: electron injection, Poole-Frenkel mechanism, thin film conduction, ionic interface polarization, anodic aluminum oxide, niobium oxide, tantalum oxide.

in the anodic oxide. Migration of oxygen ions away from and metal ions towards the Ta₂O₅/Fe₂O₃ interface resulted in the accumulation of positive charge in the Ta₂O₅ near this interface due to the limited availability of oxygen ions from the electrolyte. This corresponds to a polarization of the interface in an electrochemical sense which causes increased electron injection from the contact. The semiconducting oxide with dominating electronic conductivity does not totally block the supply of oxygen ions from the electrolyte. In conjunction with the electrolyte the semiconducting oxide provides an electrical contact that is not plagued by destructive breakdowns as is common with metal counterelectrodes at the high applied fields.

In the case of Ta/Ta₂O₅/Fe₂O₃ electrodes the time-dependent increase of the electronic conductivity with constant applied field, the field dependence of this activation process, and the field dependence of the electronic current have been interpreted as Poole-Frenkel thermionic emission at the anodic oxide/iron oxide interface coupled with the high field ionic conduction mechanism of the anodic oxide.

The electronic current was found to follow a thermionic emission characteristic

$$i_{el} = i_{0,el} \exp(e\beta F^{1/2} - \phi)/kT \quad [1]$$

with e , charge of an electron; β , field-lowering coefficient in agreement with Poole-Frenkel emission; F , applied field, ϕ , energy barrier at zero field; k , Boltzmann constant; T , absolute temperature. The process of activation was interpreted in terms of a reduction of the energy barrier ϕ as a function of the ionic current resulting in a time-dependent increase of the electronic current at constant applied field

$$\phi = \phi_0 - \text{const } t i_{ion} = \phi_0 - \text{const } t A \exp(BF) \quad [2]$$

with ϕ_0 , energy barrier at zero field prior to activation; t , time. The empirical relationship

$$i_{ion} = A \exp(BF) \quad [3]$$

with $A = i_0 \exp(-W/kT)$, B , field constant of the ionic conductivity, was used to describe the field dependence of the ionic current for the high field case (2). As an approximation, the lowering of the emission barrier in Eq. [2] was assumed to be proportional to the polarization of the interface. Combination of Eq. [1] and [2] led to an expression for the increase of the electronic current with time (activation)

$$\log_{10} i_{el} = \text{const} - \text{const } t A \exp(BF) \quad [4]$$

with a slope of

$$s = \text{const } A \exp(BF) \quad [5]$$

In this paper additional experimental results obtained for the activation process of Al/Al₂O₃/Fe₂O₃ and Nb/Nb₂O₅/Fe₂O₃ electrodes, the electronic current-field characteristic of Nb/Nb₂O₅/Fe₂O₃ electrodes, as well as measurements of the temperature dependence of the activation process and the electronic conductivity of Ta/Ta₂O₅/Fe₂O₃ electrodes will be presented. The results support our model for homogeneous electronic current injection into anodic tantalum oxide and its applicability to valve metal oxides other than Ta₂O₅.

Experimental

Valve metal electrodes were prepared by anodic formation of the oxide following standard procedures. Capacitor grade Ta and Nb foil was degreased and chemically polished in a hot mixture of H₂SO₄ (98%): HNO₃ (70%): HF (49%)-5:2:2 followed by rinsing in HF (49%) and distilled water. The metals were vacuum annealed at 2000°C (Nb) and 2100°C (Ta) for 2 hr. The vacuum treatment was found to considerably reduce the number of electronically active impurity sites in the anodic oxides to be formed subsequently and became a prerequisite for the reliable measure-

ment of controlled electronic current injection. Anodization at 1 mA/cm² was carried out in 0.1M H₃PO₄ or 0.1M H₂SO₄ at room temperature. The oxide films were aged for 30 min at voltage, back-etched in HF for up to 10 sec, reformed and again aged for 30 min. The procedure resulted in a significant decrease in the number of sites where localized electronic current injection into the anodic oxides in contact with the semiconducting oxides could be observed already at low voltages. The improvement is probably due to the removal of impurities accumulated in the surface of the anodic films during formation (3).

Aluminum foil (99.999%) was degreased, etched in 1M KOH for 30 min, rinsed in distilled water and formed at 0.3 mA/cm² to 100V in 0.1M potassium phosphate solutions (pH = 7).

Thin layers of semiconducting iron oxide (FeO_x with $x \leq 1.5$) were deposited by reactive sputtering in a rf sputtering system (Materials Research Corporation—Model SEM-8620) with water cooled target and substrate holders. Target to substrate distance was 9 cm. The target material consisted of 99.9% iron. Reactive sputtering was carried out in argon/oxygen mixtures containing between 1 and 20% oxygen. Typical sputtering conditions were: 100W power input and 6×10^{-3} Torr total gas pressure yielding deposition rates of 7-10 Å/min. Electron bombardment of Nb₂O₅ and Ta₂O₅ substrates during sputtering was found to cause irreversible changes in the anodic oxides effecting the reproducibility of subsequent measurements. This effect could be suppressed by a tantalum shield having the dimensions of the substrate (2.5 cm × 10 cm, for example) that was placed between target and substrate about 4 cm above the substrate. The deposition rate was lowered by about one third. Deviations in the thickness of the iron oxide film deposited in the shadow of the shield were only about 10% across a 2.5 cm wide substrate which indicated diffusion-controlled deposition of the sputtered material. Al/Al₂O₃ anodes were sputtered without shield.

Following the deposition of the iron oxide layer the specimens were returned to the electrolytic cell. To insure the insolubility of the iron oxide, measurements were carried out in 0.5M standard acetate buffer solutions. High resolution anodic printing (4) was used to determine the homogeneity of the electronic conductivity on a microscale during the activation process. Only Nb/Nb₂O₅/Fe₂O₃ and Ta/Ta₂O₅/Fe₂O₃ specimens which did not exhibit any appreciable electronic conductivity at point defects during a voltage scan from zero to the activation voltage were used in the experiments. The electrodes were masked with Mylar tape (Mystic No. 7003) and a series of experiments carried out with one area (0.07-0.3 cm²) exposed at a time. In the case of Al/Al₂O₃/Fe₂O₃ electrodes the contribution of defect conduction to the homogeneous electronic conductivity established by activation could not be estimated from voltage scan anodic printing experiments. The anodes broke down in contact with the KI/starch printing gel electrolyte with about one half of the formation voltage applied. However, prints indicating homogeneous electronic current distribution similar to Ta and Nb-electrodes could be obtained from specimens following their activation in phosphate electrolytes.

The field dependence of the activation process of Ta/Ta₂O₅/Fe₂O₃ electrodes was measured at temperatures between 0° and 65°C.

The temperature dependence of the electronic current with constant applied field was measured in the temperature range from 5° to 75°C for various stages of the activation process. Activation was carried out at the highest temperature to be used in the temperature measurements. This was found to be necessary in order to avoid erroneous results due to continued activation during the temperature cycle. The temperature dependence was measured after terminating

the activation process at a desired electronic current level and decreasing the applied field sufficiently to stabilize the current. It was observed that the electronic current decreased somewhat with time and reached a constant value within minutes after the applied field had been lowered. This indicated a partial reversion of the activation process. The temperature was varied continuously at rates between 4°C/min and 12°C/min starting and ending at 75°C.

Measurements for different stages of the activation process were carried out either by activating different areas on the specimen to different levels or by continuing activation of the same area following one temperature cycle at the preceding level. Comparing Ta and Nb, the Ta system proved to be the more stable and reproducible of the two with respect to the temperature measurements.

Results and Discussion

Anodic activation.—Field and temperature dependence of the activation process.—The time dependent increase of the electronic current is shown in Fig. 2 for three different electrodes at 20°C: Ta/(1960Å)Ta₂O₅/Fe₂O₃, Nb/(1960Å)Nb₂O₅/Fe₂O₃, and Al/(1630Å)Al₂O₃/Fe₂O₃. A 200Å film of Fe₂O₃ was deposited by reactive sputtering using identical deposition conditions for all specimens (80% Ar + 20% O₂, 6 × 10⁻³ Torr, 100W). This was important in order to permit comparison of the results for different anodic oxides, since it had been found that the rate of activation and the detailed structure of the activation curve depended on the properties of the sputtered oxide which are sensitive to the deposition conditions.

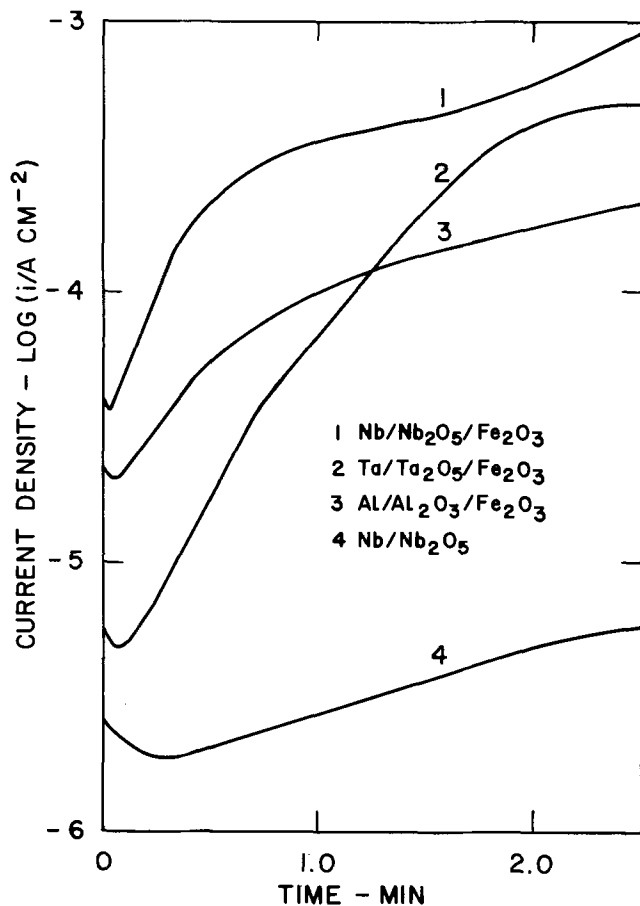


Fig. 2. Current-time characteristic of the activation process for: 1, Nb/1960Å Nb₂O₅/200Å Fe₂O₃ electrode, activation field $F' = 3.5$ mV/cm; 2, Ta/1960Å Ta₂O₅/200Å Fe₂O₃ electrode, activation field $F' = 5.2$ mV/cm; 3, Al/1630Å Al₂O₃/200Å Fe₂O₃ electrode, activation field $F' = 6.2$ mV/cm; 4, reanodization curve of Nb/1960Å Nb₂O₅ anode following activation (curve 1) and subsequent dissolution of the Fe₂O₃ layer. $F' = 3.5$ mV/cm.

All measurements of the activation process refer to linear sections of the $i-t$ curves, mostly the initial linear increase. The effect of the electronic properties of the sputtered transition metal oxide in conjunction with the redox electrolyte on the activation process will be discussed in a subsequent paper.

The activation curves have, approximately, the same initial slope indicating the same rate of ionic interface polarization, i.e., an approximately equal ionic current flowing in all three anodic oxides. To obtain similar slopes the applied field had to be increased from 3.5 mV/cm for Nb₂O₅ to 5.2 mV/cm for Ta₂O₅, and 6.2 mV/cm for Al₂O₃, which corresponds to the decrease of the ionic conductivities of the anodic oxides given in the literature (5). Microscopic inspection of anodic Ta and Nb oxide and reanodization experiments following the dissolution of the Fe₂O₃ layer subsequent to activation had shown the activation process to be a surface effect that caused no apparent changes in the properties of the bulk of the oxide.

Curve 4 (Fig. 2) is the reanodization curve for the Nb/Nb₂O₅ anode measured after the dissolution of the iron oxide layer subsequent to activation (curve 1) with the same field applied. It also represents the normal reanodization curve at constant voltage following the anodic formation of oxide. The ionic current is likely to be smaller than the total reanodization current because of some residual electronic contribution. From the level of the current of the reanodization curve, it was concluded that the contribution of ionic current to the measured activation current (curves 1-3) was negligible even for early stages of the activation process. The rate of increase of the electronic current with time was found to be very sensitive to the applied field. Applied voltage was converted to field neglecting any voltage drop across Fe₂O₃ and polarization at the Fe₂O₃/electrolyte interface. This appears justified for the low current densities involved and at least for the linear regime of the activation curve, which is interpreted as current injection limited by coulombic centers at the valve metal oxide/Fe₂O₃ interface. Galvani potential differences between the various phases were estimated as described previously (1) and were taken into account when calculating the true field in Fig. 5, 6, and 8.

Figure 3 shows the field dependence of the activation process for a Nb/(1960Å)Nb₂O₅/(200Å)Fe₂O₃ electrode in the applied voltage range from 69 to 73.1V at 20°C. Figure 4 depicts a similar set of curves for a Ta/(1740Å)Ta₂O₅/(200Å)Fe₂O₃ electrode in the applied voltage range from 80 to 86V at the higher temperature of 41.5°C.

According to Eq. [5] $\log s \sim BF$ (s , slope of activation curve $\log i_{e1}$ vs. t) which means that the field constant B of the ionic conductivity of the anodic oxide can be obtained from the slope of a plot of $\log s$ vs. the applied field. The initial linear slope s of the activation curves (Fig. 3 and 4) was used in these plots, but it was found that other linear parts of the activation curves could have been used as well.

The result obtained from the set of activation curves shown in Fig. 3 for a Nb/Nb₂O₅/Fe₂O₃ electrode is presented in Fig. 5. The plot of $\log s$ vs. the applied field is a straight line. From its slope the field constant B was calculated. The results for Nb₂O₅, Al₂O₃, and Ta₂O₅ (1) obtained at 20°C have been listed in Table I. Comparison with values reported in the literature (5) from direct measurements of the field dependence of the ionic conductivity of the respective anodic oxides indicates good agreement with our measurements.

The temperature dependence of the field constant B was determined for Ta₂O₅ by measuring the field dependence of the activation process at four temperatures between 0° and 65°C for Ta/(1740Å)Ta₂O₅/(200Å)Fe₂O₃ electrodes. Plots of $\log s$ vs. the applied field as observed for one electrode at four temperatures are shown in Fig. 6. The results of four independent mea-

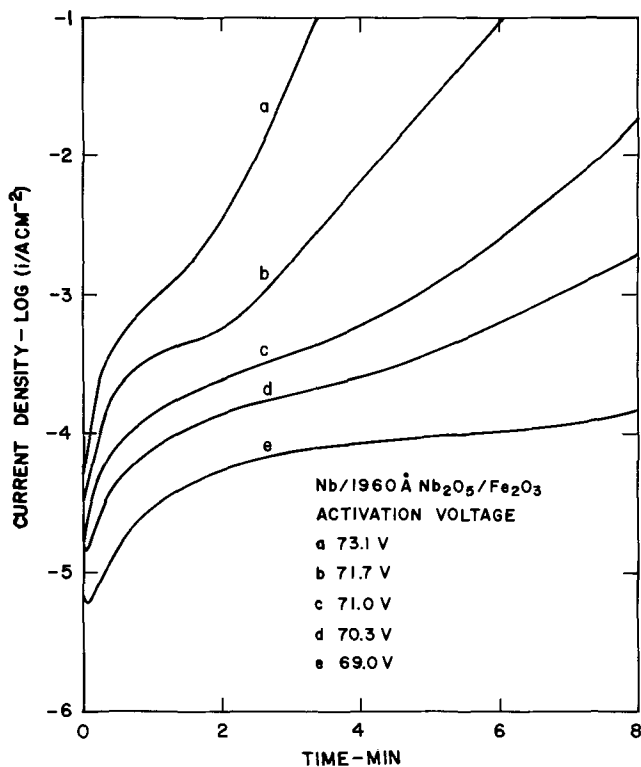


Fig. 3. Rate of activation as a function of the applied field $F' = V/d$ for Nb/1960 Å Nb₂O₅/200 Å Fe₂O₃ electrodes at 20°C; field range: 3.52-3.73 mV/cm.

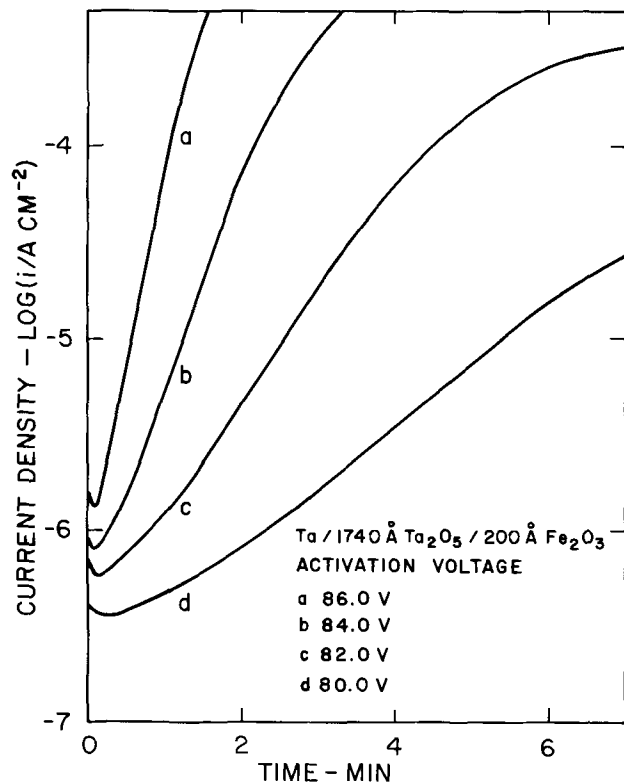


Fig. 4. Rate of activation as a function of the applied field $F' = V/d$ for Ta/1740 Å Ta₂O₅/200 Å Fe₂O₃ electrodes at 41.5°C; field range: 4.60-4.94 mV/cm.

measurements at each temperature have been listed in Table II. They show B to be independent of temperature in the observed range. This is in agreement with results by Vermilyea (2) and Young (6) from studies of the temperature dependence of the Tafel slope for the anodic formation of tantalum oxide.

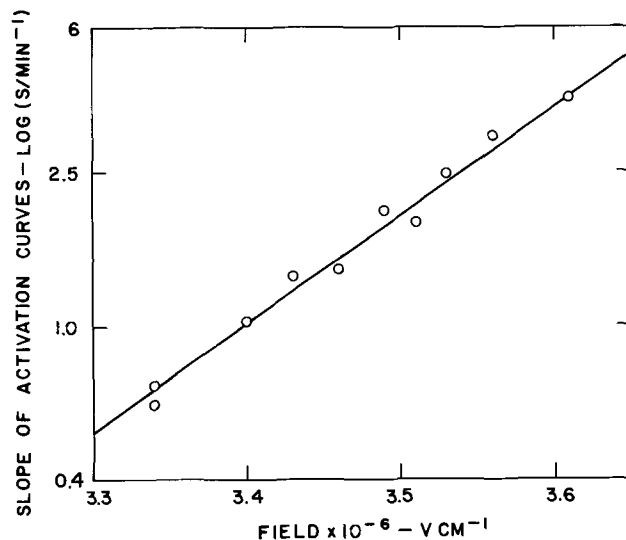


Fig. 5. Slope of activation curves (from Fig. 3) vs. the true field $F = \Delta V/d$ in Nb₂O₅. $\Delta V =$ applied voltage, V corrected for Galvani potential differences (1).

At constant applied field the rate of activation increased rapidly with temperature. Since B was found to be temperature independent, this result meant that the pre-exponential factor (Eq. [3]) was responsible for the temperature dependence. From our measurements, the activation energy W (Eq. [6]) for ionic conduction at zero field could be determined.

$$A = i_{o,ion} \exp\left(-\frac{W}{kT}\right) \quad [6]$$

Log s vs. $1/T$ was plotted in Fig. 7 for constant field $F = 4.81$ mV/cm in Ta₂O₅ using the data from Fig. 6. The rate of activation s was directly measured at 21° and 41°C, while values for 3.5° and 64°C were extrapolated from the respective log s vs. field plots, since at the given field the activation was either too slow or too fast to allow a correct determination of the rate of activation s to be made. A value of $W = 0.75$ eV was calculated from the slope of the log s vs. $1/T$ plot in Fig. 7 in close agreement with a value reported by Vermilyea (2) from measurements of the temperature dependence of the ionic conductivity ($W = 0.71$ eV). The results of the temperature measurements are subject to the same interpretations put forward in the literature and discussed by Young (5) to explain a lack of temperature dependence of the Tafel slope for the anodic formation of tantalum oxide.

Table I. Field constant B of the ionic conductivity from measurements of the field dependence of the activation process (B_{exp}) in comparison with values from measurements of the kinetics of anodic oxide growth (B_{ion})

	$B_{exp} \times 10^6$ (cm V ⁻¹)	$B_{ion} \times 10^6$ (cm V ⁻¹)
Ta ₂ O ₅	4.95 ± 0.2	5.2
Nb ₂ O ₅	6.6 ± 0.7	6.4
Al ₂ O ₃	4.4 ± 0.5	4.9 ± 0.5

Table II. Field constant B of the ionic conductivity of Ta₂O₅ from measurements of the field dependence of the activation process in the temperature range 3°-60°C

°C	$B \times 10^6$ (cm V ⁻¹)
3	4.9 ± 0.2
20	5.0 ± 0.2
40	5.2 ± 0.2
60	5.2 ± 0.2

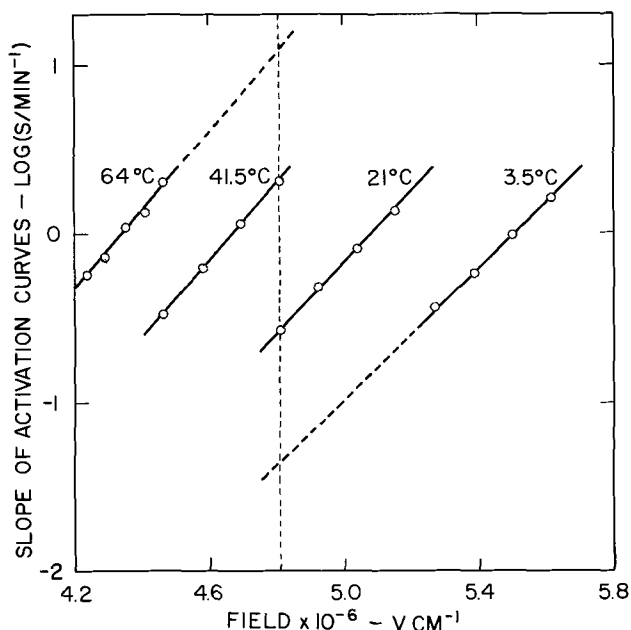


Fig. 6. Slope of activation curves (from Fig. 4 for 41.5°C) vs. the true field $F = \Delta V/d$ in Ta_2O_5 . $\Delta V =$ applied voltage V corrected for Galvani potential differences (1).

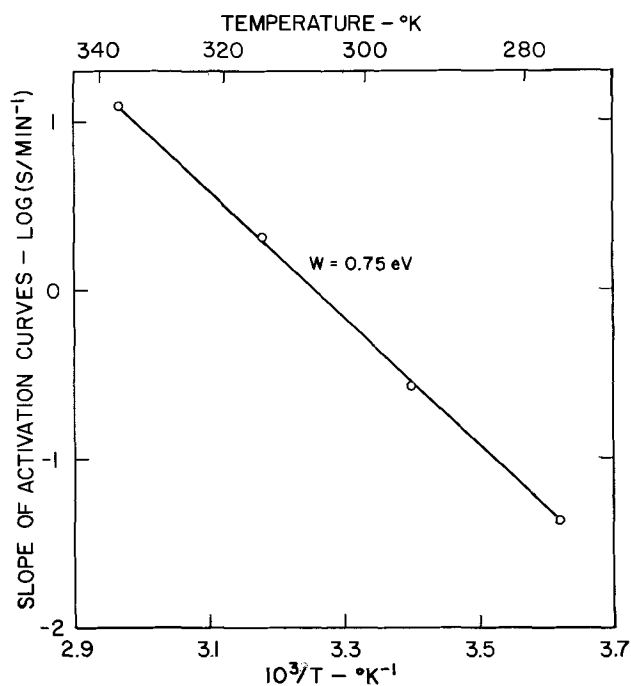


Fig. 7. Slope of activation curves at constant applied field ($F = 4.81$ mV/cm) vs. $1/T$ for $Ta/1740\text{\AA} Ta_2O_5/200\text{\AA} Fe_2O_3$ electrode. Temperature range 3.5°-64°C.

A direct coupling of ionic and electronic processes has been postulated to explain the observed behavior of the electronic current during activation experiments. From our measurements the characteristic parameters of the ionic processes were obtained in quantitative agreement with values from measurements of the kinetics of anodic film growth. In particular, the field and temperature dependence of the ionic processes were deduced correctly from the characteristics of the electronic process for three different oxides. This is considered conclusive evidence of the basic correctness of the assumptions underlying our model of the activation process.

Current-field characteristic of the electronic conduction process resulting from activation.—Current-field

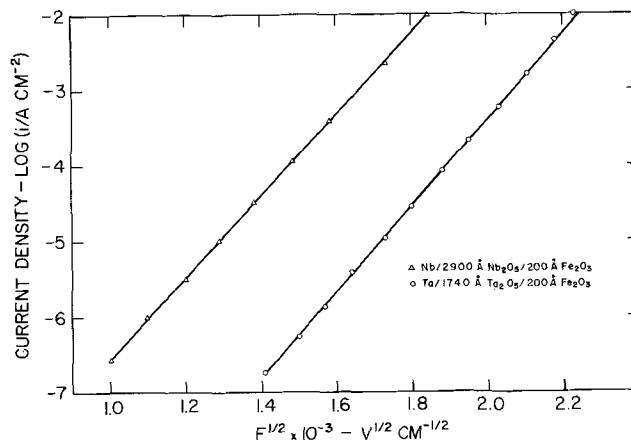


Fig. 8. Current-field characteristics of $Ta/1740\text{\AA} Ta_2O_5/200\text{\AA} Fe_2O_3$ electrode (\circ) and of $Nb/2900\text{\AA} Nb_2O_5/200\text{\AA} Fe_2O_3$ electrode (Δ) following activation to 10 mA/cm², 20°C. Field corrected for contribution of Galvani potential differences to applied voltage (1).

characteristics were measured after activation to different electronic current levels. The measurements were made at decreasing and increasing fields. Typical results are shown in Fig. 8 for two anodic oxide films: (2900Å)Nb₂O₅ and (1740Å)Ta₂O₅, both sputtered with 200Å films of Fe₂O₃. The dependence of the logarithm of the homogeneous electronic current density on the square root of the applied field was found to be a linear one over as many as 5 decades of current for any given state of activation.

The linear $\log i$ vs. $F^{1/2}$ dependence (Fig. 8) is characteristic for thermionic emission over a field-lowered barrier (Eq. [1]). Previous results showed agreement with the concept of electron emission from coulombic centers generated in the process of activation. This mechanism can be described by the simple Poole-Frenkel theory (7-10) which will be used here. The field lowering coefficient β (Eq. [1]) is given by

$$\beta = \left(\frac{e}{\pi\epsilon_0\epsilon} \right)^{1/2}$$

with e , electronic charge; ϵ_0 , permittivity of vacuum; and ϵ , relative dielectric constant.

The slope of the $\log i$ vs. $F^{1/2}$ plots can be used to calculate the field lowering coefficient β . The dielectric constant is the only uncertain value in the formula for β . Some authors (7, 8) on the subject favor the use of the high frequency dielectric constant ($\epsilon_\infty = n^2$; n , refractive index). Recently, Hill (10) proposed to use a value of the form $\bar{\epsilon} = (\epsilon_1^{-1} - \epsilon_2^{-1})^{-1}$ with ϵ_1 and ϵ_2 the high and low frequency dielectric constants of the bulk material, respectively. Table III gives the values for the dielectric constants ϵ_{exp} as calculated from the slopes of $\log i$ vs. $F^{1/2}$ curves assuming Poole-Frenkel emission. For both Ta₂O₅ and Nb₂O₅ the high frequency dielectric constants computed from the respective refractive indices are in excellent agreement with experimental values obtained from the slopes of $\log i - F^{1/2}$ curves when the Poole-Frenkel formula is used. $\bar{\epsilon} = (\epsilon_1^{-1} - \epsilon_2^{-1})^{-1}$ values were calculated using for the low frequency dielectric constants the values ϵ_2 , (Ta₂O₅) = 27.6 and ϵ_2 , (Nb₂O₅) = 41.4 (5). The

Table III. Dielectric constants ϵ_{exp} from $\log i$ vs. $F^{1/2}$ plots in comparison with ϵ_∞ and $\bar{\epsilon}$. ϵ_∞ was calculated from the indices of refraction (5). $\bar{\epsilon}$ was calculated according to Hill (10)

	ϵ_{exp}	$\epsilon_\infty = n^2$	$\bar{\epsilon}$
Ta ₂ O ₅ ¹	4.7	5.1	6.2
Nb ₂ O ₅	6.0	6.0	7.0

agreement of ϵ_{exp} with $\bar{\epsilon}$ is less satisfactory and there appears no need to introduce an intermediate dielectric constant into the theory describing the experimental system. Within the limits of the simple Poole-Frenkel theory describing the field assisted emission of electrons from coulombic centers (traps), the results presented in this paper provide quantitative verification of that theory over a wide range of current densities (5 decades) and for two different materials.

Temperature dependence of the electronic conduction process.—Thermionic current emission according to Eq. [1] is characterized by an expression for the activation energy

$$\Delta E = e\beta F^{1/2} - \phi \quad [7]$$

which consists of the zero field barrier modified by the applied field. The mechanism of electronic activation, i.e., the time-dependent increase of the electronic current with the applied field as parameter rests on the assumption that ionic interface polarization leads to a time dependent decrease of the activation energy. Consecutive states of activation should, therefore, be characterized by thermionic emission barriers ϕ reduced in the same sequence. Measurements of the temperature dependence of the electronic current at constant applied field should yield the barrier height as a function of the pre-established state of activation

$$\log_{10} i_{\text{el}} = \text{const} + \frac{e\beta F^{1/2} - \phi}{kT} \quad [8]$$

Such measurements are shown in Fig. 9 for a Ta/(1740Å)Ta₂O₅/(200Å)Fe₂O₃ electrode and three consecutive states of activation (electronic current levels). In Fig. 10 similar measurements for four consecutive states of activation of a Nb/(1590Å)Nb₂O₅/(200Å)Fe₂O₃ electrode are shown. In all cases, linear

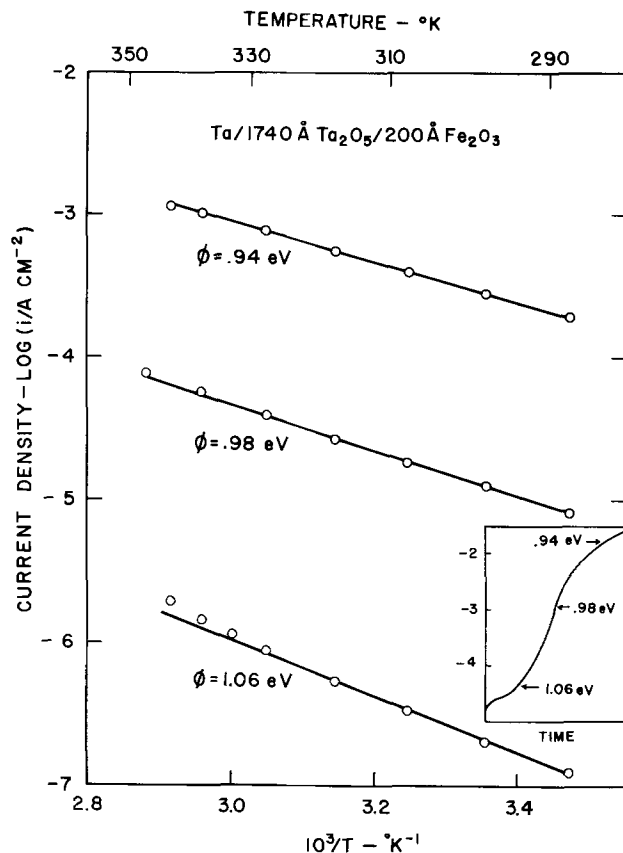


Fig. 9. Temperature dependence of electronic activation current for three consecutive states of activation at constant applied voltage (65V) in the temperature range 5°-75°C. Ta/1740Å Ta₂O₅/200Å Fe₂O₃ electrode was activated at 80V, 75°C. The activation curve is shown in insert.

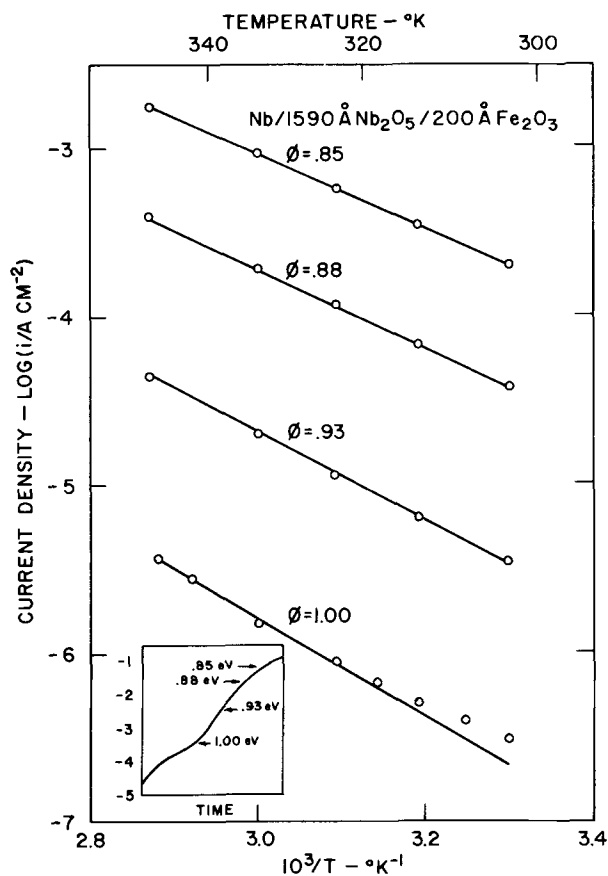


Fig. 10. Temperature dependence of electronic activation current for four consecutive states of activation at constant applied voltage (30V) of Nb/1590Å Nb₂O₅/200Å Fe₂O₃ electrode following activation at 50V, 75°C. Temperature range 20°-75°C. The activation curve is shown in insert.

$\log i_{\text{el}}$ vs. $1/T$ plots were obtained in a temperature range from 5° through 75°C.

The corresponding activation curves for Ta₂O₅ and Nb₂O₅ have been inserted in Fig. 9 and Fig. 10, respectively. Their particular structure is related to the specific electronic properties of the iron oxide deposited in these cases. The interface polarization process was found to proceed independently of the particular type of iron oxide which means that the lowering of the emission barrier could be considered a function of ionic charge transfer alone. Thermionic Poole-Frenkel characteristics were obtained at any point of the activation curves independent of the particular structure of the activation curve.

From the slopes of $\log i - 1/T$ lines in Fig. 9 (Ta/Ta₂O₅/Fe₂O₃) the activation energies for three consecutive states of activation were found to be in eV 1.06, 0.98, and 0.94 ± 0.02 from the lowest to the highest states of activation corresponding to 4.7×10^{-5} , 1.3×10^{-3} , and 1.8×10^{-2} A/cm², respectively, for activation at 80V, 74°C. For an increase of the electronic current level by three decades a decrease in the barrier height ϕ by 0.12 eV was measured. By extrapolating the barrier height linearly to zero activation, an initial barrier of 1.1 eV was found for the Ta/Ta₂O₅/Fe₂O₃ electrode (Fig. 11).

From Fig. 10 the activation energies for four consecutive states of activation of a Nb/Nb₂O₅/Fe₂O₃ electrode were found to be in eV 1.00, 0.93, 0.88, and 0.85 from the lowest to the highest state of activation corresponding to 3.8×10^{-4} , 3.8×10^{-3} , 2.2×10^{-2} , and 6.8×10^{-2} A/cm², respectively, for activation at 50V, 75°C. Linear extrapolation of the barrier height to zero activation is shown in Fig. 11 along with results obtained for another Nb/(1590Å)Nb₂O₅/FeO_x electrode activated under the same conditions. While the rate of

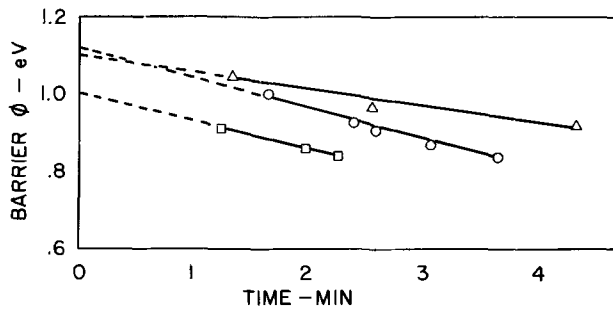


Fig. 11. Linear extrapolation of the barrier height ϕ to zero activation (Δ), Ta/1740Å Ta₂O₅/200Å Fe₂O₃ electrode; (\circ), Nb/1590Å Nb₂O₅/200Å Fe₂O₃ electrode; (\square), Nb/1590Å Nb₂O₅/200Å FeO_x electrode ($x < 1.5$).

barrier lowering was the same for both electrodes, the initial barrier heights (1.1 eV and 1.0 eV, respectively) were found to depend on the properties of the sputtered iron oxide, mainly its degree of oxidation. The lower initial barrier would correspond to the iron oxide with the lower oxidation state.

A further check of the thermionic $\log i_{el} - F^{1/2}$ characteristic attributed to a Poole-Frenkel mechanism of electronic current injection follows from Eq. [7]. The activation energy ΔE would be expected to show a square root dependence on the applied field (11). In this case, the activation energy was obtained from $\log i_{el} - 1/T$ plots with the applied field as parameter. Measurements were carried out after a fixed state of activation had been established at 1.8×10^{-2} A/cm², 80V, 75°C. The results given in Fig. 12 show the expected linear dependence of ΔE on $F^{1/2}$.

Conclusions

Anodic oxides on valve metals such as Ta, Nb, and Al in contact with electrolytes behave as insulators because the rate of electron injection remains low even at field strengths sufficient for ionic migration. The normal reaction of valve metal/valve metal oxide electrodes in aqueous solutions and at fields of the order of some 10^6 V/cm is additional oxide formation with negligible electronic current. Several monolayers of semiconducting transition metal oxides like FeO_x, MnO_x, and others, deposited on top of the valve metal oxide sufficiently suppress the transfer of ions to the valve metal oxide/semiconducting oxide interface to cause the formation of an electron injecting contact. The results presented in this paper have demonstrated

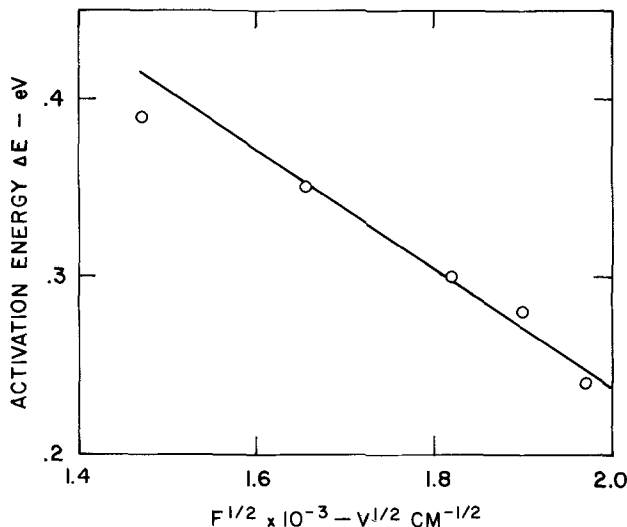


Fig. 12. Activation energy $\Delta E = e \beta F^{1/2} - \phi$ vs. $F^{1/2}$ for Ta/1740Å Ta₂O₅/200Å Fe₂O₃ electrode following activation at 80V, 75°C to 1.8×10^{-2} A/cm².

that this mechanism is common to at least three valve metal/valve metal oxide electrodes.

Electronic current injection as a function of time and applied field (activation) was measured for the Ta/Ta₂O₅, Nb/Nb₂O₅, and Al/Al₂O₃ electrodes with Fe₂O₃ as the semiconducting transition metal oxide:

Mechanism of activation.—The assumption of interacting ionic and electronic processes formed the basis of a model for the activation process of Ta/Ta₂O₅/Fe₂O₃ electrodes published earlier. By assuming that the underlying ionic charge transport followed the empirical current field law for anodic oxide growth ($i = A \exp BF$), a relationship for the time dependence of the activation process could be derived with explicit dependence of the electronic process on the parameters of the ionic conduction process. The validity of this model was confirmed by determining the parameters of the ionic process from measurements of the field and temperature dependence of the electronic activation for three valve metal oxides. Quantitative agreement was found for B values obtained from the field dependence of the rate of activation and values from measurements of the kinetics of film growth for Ta/Ta₂O₅, Nb/Nb₂O₅, and Al/Al₂O₃ electrodes. In addition, the temperature dependence of the activation process at constant applied field was found to follow from the temperature dependence of the ionic process with B independent of temperature, the temperature dependence arising from the pre-exponential factor A . From the temperature dependence of A the activation energy of ionic migration could be determined. It was found to agree well with data from kinetic measurements of the ionic process.

The data presented in this paper fully confirm earlier measurements and provide quantitative evidence of the coupling of ionic migration and electron injection in electrodes of the general type valve metal/valve metal oxide/semiconducting oxide.

Ionic polarization in the contact between solids, of which oxide/oxide contacts of the type investigated here are a characteristic example, can lead to conditions favorable to electron injection into the "insulating" oxide thus changing a blocking into an injecting contact. This general mechanism can lead to homogeneous electron injection, as was found to be the case in the systems studied, or to localized electron injection caused by impurities. Thermal effects or carrier multiplication may eventually lead to destructive breakdown of the dielectric in either case. The deposition of a homogeneous semiconducting oxide layer provided for an experimentally controllable system. The use of an electrolytic contact in our experiments is believed to contribute to the electrical stability of the valve metal/valve metal oxide/semiconducting oxide electrodes. The semiconducting oxide/electrolyte contact gives evidence of limiting the injection current at the higher activation levels in a way that prevents catastrophic breakdown and destruction of the specimen. The same is not true for semiconducting oxide/metal contacts. While indications of an initially similar activation mechanism were present in the latter case as well, catastrophic breakdowns destroyed the specimens before any detailed measurements could be made.

Mechanism of electron injection.—The electronic current resulting from activation of Nb/Nb₂O₅ and Ta/Ta₂O₅ electrodes with thin layers of Fe₂O₃ showed a field dependence typical for thermionic emission. $\log i_{el}$ vs. $F^{1/2}$ characteristics could be measured extending over 4-5 decades of current density. The slopes of these current-field characteristics agreed closely with those predicted for thermionic conduction following a Poole-Frenkel mechanism. For both the Ta and Nb electrodes the dielectric constants determined from the slopes of $\log i$ vs. $F^{1/2}$ curves agreed well with the high frequency constants of the respective anodic oxides. The measurements presented in this paper are,

thus, in excellent agreement with the basic Poole-Frenkel theory.

Experimental systems of this kind with two oxides in intimate but initially blocking contact provide nearly perfect model systems for the generation of coulombic centers in the boundary region between the two oxides which become the source of thermally activated electron emission with Poole-Frenkel characteristic.

It should be noted that the usual distinction between interface and bulk mechanisms (e.g., Schottky vs. Poole-Frenkel characteristic) cannot be applied to the experimental system valve metal oxide/semiconducting oxide. Even though the sources of electron emission into the valve metal oxide are being generated in the interface region between the two oxides, the physical reality would appear to match as close as possible the model situation of the Poole-Frenkel theory (10). In our case, this model situation can be described as the field assisted emission of electrons from coulombic centers, e.g., oxygen vacancies as a result of local non-stoichiometry, into the conduction band of the valve metal oxide. It is the activation process which leads to the generation of such coulombic centers in a manner controlled by the ionic charge separation across the valve metal oxide/semiconducting oxide interface. Agreement of the measured value of the dielectric constant with the high frequency dielectric constant of the valve metal oxide demonstrated that the valve metal oxide provided the dielectric environment of the coulombic centers in conformity with the model situation of emission from centers located in the bulk of the oxide.

Measurements of the temperature dependence of the electronic current with the applied field and state of activation as parameters yielded activation energies of the Poole-Frenkel thermionic emission process. Both the original barrier height and its change with progressing activation could be determined. Typically, the barrier height prior to activation was close to 1 eV decreasing by several tenths of an electron volt with increasing polarization of the valve metal oxide/semiconducting oxide interface.

Manuscript submitted March 20, 1972; revised manuscript received June 9, 1972.

Any discussion of this paper will appear in a Discussion Section to be published in the June 1973 JOURNAL.

REFERENCES

1. G. P. Klein and N. I. Jaeger, *This Journal*, **117**, 1483 (1970).
2. D. A. Vermilyea, *Acta Met.*, **1**, 282 (1953).
3. G. P. Klein, *This Journal*, **113**, 348 (1966).
4. G. P. Klein, *ibid.*, **117**, 1581 (1970).
5. L. Young, "Anodic Oxide Films," Academic Press Inc., New York (1961).
6. L. Young, *Trans. Faraday Soc.*, **50**, 153 (1954).
7. W. S. Goruk, L. Young, and F. G. R. Zobel, in "Modern Aspects of Electrochemistry," Vol. 4, p. 176 ff, J. O'M Bockris, Editor, Plenum Press, New York (1966).
8. A. K. Jonscher, *Thin Solid Films*, **1**, 213 (1967).
9. J. G. Simmons, *Phys. Rev.*, **166**, 166 (1968).
10. R. M. Hill, *Phil. Mag.*, **23**, 59 (1971).
11. R. M. Hill, *Thin Solid Films*, **1**, 39 (1967).

Devitrification of Steam-Grown Silicon Dioxide Films

R. L. Meek* and R. H. Braun

Bell Laboratories, Murray Hill, New Jersey 07974

ABSTRACT

Devitrification of steam-grown SiO₂ films has been studied as a function of time and temperature, with special attention to impurity effects, by monitoring the refractive index of the film and by examining the time, temperature, and impurity dependent degradation of the dielectric strength. Monitoring of the refractive index showed that partial devitrification may occur in a time scale of weeks at room temperature if the oxide was significantly [$\sim 2(10)^{15}$ cm⁻²] sodium contaminated and had, in addition, a high-temperature ($\sim 1000^\circ\text{C}$) anneal while contaminated. As-grown slices, for which the sodium contamination level is $<10^{11}$ cm⁻², showed no evidence of devitrification. Electron diffraction observations confirmed the interpretation of the refractive index changes. Dielectric breakdown behavior indicated that the function of the high-temperature anneal was to modify the manner in which the sodium was incorporated into the silica film although nucleation phenomena may also be important. The activation energy for dielectric strength degradation is ~ 0.1 eV which is much less than the activation energy for devitrification of pure bulk fused silica (2.2 eV).

Silicon dioxide films thermally grown on silicon form a cornerstone of the planar device technology and steam-grown oxides have found wide usage partly because the growth rate is much larger than is the case for films grown in dry oxygen, and because lower oxidation temperatures are possible. Here we report observations on the devitrification of initially amorphous, steam-grown silicon dioxide films.

It has, in fact, been known for a long time that silica films grown in sodium contaminated, by sodium or a num-

ber of other things, are apt to contain crystallites (1-5) and that such films possess inferior electrical properties. Sugano *et al.* (6) have carried out an electron diffraction study in which they found that the incidence of crystallinity in grown oxide films was increased by the incorporation of water (steam-grown) or boron and suppressed by the incorporation of P or Sb. They did not, however, consider changes with time explicitly.

Pavlov and Shitova (7) and Nagasima (8a) have also performed oxide structure analyses, using electron diffraction and infrared absorption, of films grown on silicon in clean, dry or wet ambients. The atomic

* Electrochemical Society Active Member.

Key words: devitrification, silicon dioxide, sodium contamination, ellipsometry, dielectric breakdown.

arrangement as determined from the electron diffraction spacings and the infrared absorption spectrum is very similar to that of bulk fused silica. The structure was found to be independent of film thickness and whether the oxide was grown wet or dry. No crystallized regions were observed, although changes with time were again not dealt with. The apparent discrepancy between these results and those of Sugano *et al.* (6) for the case of wet oxides may be related to undetected differences in the level of other impurities, especially Na.

There is also a large literature [see Ref. (8b), for example] on devitrification of bulk glass which shows the devitrification rate to be dramatically increased by the addition of impurities (8b-13), especially water (12, 13) and sodium (11). Although fused silica is thermodynamically unstable relative to the crystalline phases, rearrangement is immeasurably slow at low temperatures; usually measurable devitrification does not take place below about 1000°C (10). [The activation energy for crystallization of pure SiO₂ glass is 51.2 kcal/mole (14) (2.2 eV) so that the rate at room temperature may be expected to be infinitesimally small compared to the rate at 1000°C, all other things being equal.]

The bulk glass devitrification product is cristobalite (10), as might be expected, even though quartz is the room temperature stable form, since the local arrangement of atoms in the SiO₄ tetrahedra in glass corresponds very closely to the arrangement in cristobalite (7, 8b, 15, 16). Impurities can, however, lead to other devitrification products (8b, 10) notably tridymite, but apparently only when present in concentrations greater than 0.5% (10, 11, 17). Sugano *et al.* (6) found a high incidence of tridymite, as is to be expected since their films contained large amounts of impurities. Balyagin (18) has reported that when fused silica was heated for 5 min in hydrogen at 1000°C, isolated microcrystallization took place. Steam-grown oxides are expected to contain significant amounts of hydrogen as OH or H₂O.

It might be supposed that grown silica films on silicon behave considerably differently with respect to reconstruction than does bulk glass. However, most previous studies have not revealed rapid crystallization of grown films even when contaminated. Revesz (19) found that films aged for 15 hr in dry N₂ at 1200°C remained noncrystalline. Stickler and Faust (4) observed some changes in intensity distribution in the electron diffraction patterns from samples held at 450°C in vacuum for 90 hr but they had not devitrified, since no sharp rings were seen, while Knopp and Stickler (20) found crystallized portions in films held at 1235°C in vacuum for several hours. Brodsky and Cubicciotti (21) found that the vitreous oxide formed on their samples exhibited x-ray diffraction lines corresponding to α -cristobalite and quartz after it had been heated overnight at 1200°C. Their oxide was doubtless very impure as the silicon used was only 98%. These results are consistent with the data on bulk glass. On the other hand, a recent electron diffraction study in this laboratory (22) showed that initially amorphous steam-grown oxides sometimes devitrified at room temperature within a few weeks after fabrication.

Experimental

Refractive index.—In order to monitor the occurrence of any devitrification or other structural or density changes in the films, the refractive index in the visible region has been measured as a function of time. This method has the advantage of simplicity and it is obvious that the measurement process cannot induce devitrification.

The refractive index was measured using a Gaertner Model L119 ellipsometer. Measurements were made in the first and third zones and the usual precision techniques were used (23). The refractive index and thick-

ness were determined from the psi and delta derived from measured angles by comparison to computer calculated values.

Both structural changes and density changes may of course contribute to changes in the refractive index. In order to identify a refractive index change with devitrification, it is necessary to have other substantiating evidence; in this work, electron diffraction and optical microscopy. However, we expect that devitrification of fused silica, for which $n = 1.46$ at the mercury green line (5461Å) and room temperature, to either cristobalite, for which $n = 1.485$, or tridymite, for which $n = 1.47$, will result in an increased refractive index. In fact, if it is assumed that devitrification is the only change, we can compute the expected refractive index change from the relation between polarizability, index of refraction and density (24). In this way we estimate that an increase equal to the reproducibility of the measurements corresponds to about 1% devitrification. Of course, other changes, notably water content and density changes of the glass itself can also produce significant refractive index changes.

The oxides for refractive index measurements were grown at 1050°C in atmospheric pressure steam to thicknesses of either 1250 or 3700Å in order to utilize the maximum sensitivity for measurement of n . The substrates were <111>, 0.5 ohm-cm, p-type. Initial measurements of the refractive index and thickness were made at several points on the wafer. When variations over a wafer were greater than the reproducibility at a given point, the slice was discarded. The reproducibility of the settings at a given point corresponded to a precision in n of ± 0.0003 and in the thickness of $\pm 15\text{Å}$.¹ The slices were then kept in various atmospheres at various temperatures and the refractive index and thickness were monitored for times beyond a month (700 hr).

Dielectric breakdown strength.—It is known (3, 5) that the presence of crystallites in silica films causes a degradation in dielectric properties. In particular, breakdown strengths fall around two principal values; about $2(10)^6$ V/cm (secondary breakdown) and about $8(10)^6$ V/cm (primary breakdown). [There are also sometimes a few tertiary breakdowns at $\sim (10)^6$ V/cm

which correlate with gross visible defects and pinholes.] Only the primary breakdown voltage is found for clean grown oxides and the secondary breakdown voltage is thought to correlate with areas of the film which contain very small crystallites not detectable by optical microscopy. It might be expected then that the behavior of the distribution of breakdown voltages could be used to determine the extent of devitrification of the film. It can be shown (25) by some simple arguments that the number of defects per unit area, σ , is related to the fraction of secondary (and tertiary) breakdowns, f , by

$$\sigma = \frac{1}{A} \left(\frac{f}{1-f} \right) \quad [1]$$

where A is the electrode area. Clearly σ is some function of the extent of devitrification of the film. It has previously been demonstrated (3, 5) that for a given oxide (constant σ) the appropriate relationship between f and A is obtained.²

Steam oxide films for these measurements, 1100 \pm 100Å thick, were grown on <100> boron-doped p-type

¹By reproducibility at a given point, we mean the difference in values obtained when the slice is removed from the instrument, replaced, and remeasured on nominally the same area of the wafer. If left in place, the reproducibility in simply resetting angles corresponds to a precision in n of $3(10)^{-4}$ and in thickness of 1Å. Since it was not possible to age and heat-treat the wafers *in situ*, the former error values are the significant ones; and we unfortunately lose the, potentially very interesting, data on changes in thickness (or density).

²Chou and Eldridge (3) and Fritzsche (5) in fact use $\sigma = (1/A) \ln(1/(1-f))$ which, as Price (25) points out, is incorrect since the defects are indistinguishable and must be counted as such, i.e., Bose-Einstein rather than Boltzmann statistics must be used. For small f , the calculated σ is, of course, essentially the same, for large f it is much different.

silicon having a resistivity of 10 ohm-cm. The electrode was a mercury probe (26) and the electrode area was 0.5 mm². A ramp voltage was applied in a sense so that the semiconductor surface was in accumulation, at a rate of 1 V/sec. [Chou and Eldridge (3) found the breakdown voltage distribution to be independent of ramp rate at least in the range 10⁻² to 1 mV/cm-sec.] Breakdown is defined as the point of occurrence of the first current spike ($\sim 10^{-6}$ A-cm⁻²). The breakdown voltage is determined at about 100 points on each slice and the data plotted vs. per cent less than the value. [Bar graphs may also be prepared as was done by Chou and Eldridge (3) and are in some respects more informative, especially when there are large fractions of secondary and tertiary breakdowns.]

Results

Refractive index changes.—A first set of experiments was carried out in a dry, nonoxidizing ambient (dry N₂). The results are given in Fig. 1 where the change in refractive index is plotted vs. the time since oxidation. n_0 is the initial refractive index, and a positive Δn would likely correspond to devitrification. At room temperature (25°C), no significant refractive index changes were observed in a month's time. At 875°C the refractive index began to decrease at about 100 hr, dropping to a lower, nearly constant value at about 300 hr. This is not devitrification (Δn has the wrong sign) but is probably stabilization of the glass film. The stabilization time for bulk glass at this temperature is of the order of hundreds of hours (27) and the observed change is consistent with the fact that for bulk silica glass the refractive index increases with increasing fictive temperature below 1600°C (28). The thickness of the oxide in all experiments remained constant ($\pm 15\text{\AA}$) and is not discussed further.

A second set of experiments, the results of which appear as Fig. 2, was performed in room air where the water vapor partial pressure was about 10 Torr. Again at room temperature (25°C), the refractive index at

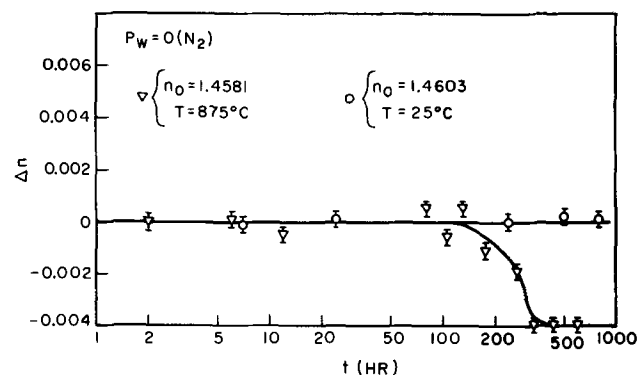


Fig. 1. Change in refractive index vs. time for samples aged in dry nitrogen, P_w is the water vapor partial pressure in the aging ambient.

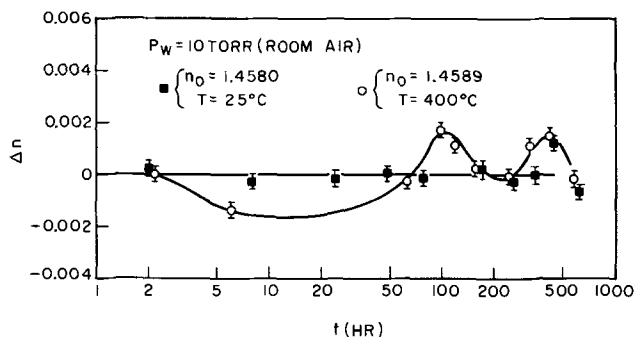


Fig. 2. Change in refractive index vs. time for samples aged in room air.

first decreased to a minimum at about 15 hr, then increased to a maximum at 100 hr, followed by another minimum and maximum at 250 and 400 hr, respectively. The detailed origin of this behavior is not clear. It probably involves structural rearrangement of Si-O-H groups, absorption of water, and the aforementioned stabilization. [Incorporation of water probably reduces the refractive index as the index for opal, SiO₂ × H₂O, is less than that of fused silica. Hetherington and Jack (29) have also shown that the refractive index of commercial fused silicas decreases with increasing "water" content. Typically, the refractive index of an oxide film grown in dry oxygen is greater than that of a film grown in wet oxygen or steam (30). Although the refractive index of high-pressure steam oxides is still greater; their structure is doubtless much different, as evidenced by their higher density (30). It should also be noted that the refractive indices of the complex sodium/alumina/boro/silicate glasses, as well as that for crystalline quartz, are greater than for cristobalite.] We must also expect a few monolayers of adsorbed water on the SiO₂ surface at room temperature and partial pressures greater than a few Torr (31). However, all films were exposed to the normal humid atmosphere during measurement so that this was a constant factor, since relative humidity and temperature were constant. Figure 3 presents some additional data taken for samples kept in nitrogen ambients with controlled water vapor partial pressures. The general behavior was similar to the samples of Fig. 2. There is, in summary, no evidence of devitrification.

The oxide has also been stripped in several hundred angstrom thick layers from slices kept at room temperature for many weeks and the refractive index measured as removal of the oxide progressed. The refractive index was found to be uniform within the precision of the measurements which, of course, varies with thickness. Also, these and other slices having had various treatments were partially etched and/or angle lapped, and then examined microscopically under polarized light in order to detect the incidence of any metastable internal crystallites as described by Wagstaff (16). None were found. A slice which had been kept at room temperature in room ambient for 2000 hr was examined by electron diffraction (32). The pattern obtained was characteristic of vitreous silica and no evidence of crystallization was seen, that is no diffraction rings were seen.

Finally, sodium contamination was considered as a cause of devitrification. Slices were boiled in a 0.25N NaCl solution for an hour and rinsed thoroughly in D. I. water upon removal. The sodium was diffused in by annealing the slice in dry N₂ at 600°C for about 20 hr. The refractive index change of a slice treated in this manner corresponds qualitatively to that of a slice which had not been sodium contaminated. The effect of the NaCl solution boil is to cause the refractive index to be very near 1.458 irrespective of its

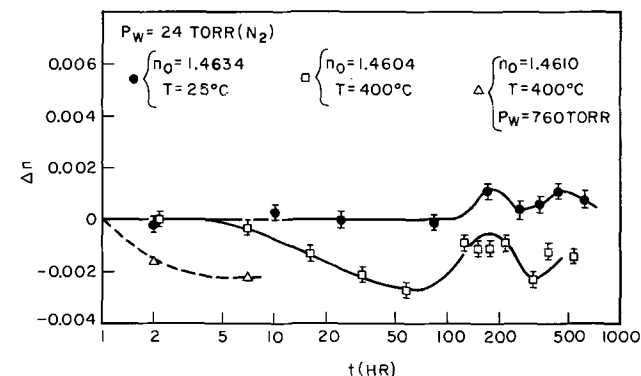


Fig. 3. Change in refractive index vs. time for samples aged in wet nitrogen.

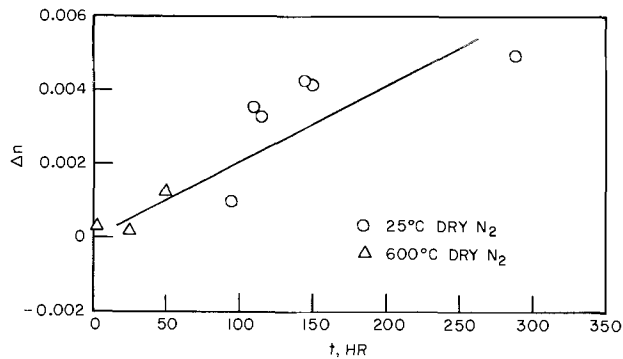


Fig. 4. Change in refractive index vs. time for sodium-contaminated samples aged in dry nitrogen.

initial value. After the 600°C treatment it returns to very near (± 0.001) its initial value. A sodium contaminated slice was also examined by electron diffraction (32) after being aged at room temperature in room ambient for about 1000 hr. Some slight banding but no sharp lines were observed in the diffraction pattern. No crystallized regions could be detected by optical microscopy.

However, if the slice is annealed for 5 min at 1000°C in dry nitrogen after the 600°C drive-in, the behavior is markedly different. (The 5-min treatment is chosen as the longest time at 1000°C which causes no measurable refractive index change.) Refractive index vs. time data for two samples treated in this way are plotted in Fig. 4. At room temperature there was now a steady increase in refractive index, to $\Delta n = +0.005$ at 290 hr. A slice aged about 500 hr at room temperature was again examined by electron diffraction (32). Many very sharp rings were observed. Photomicrographs of samples aged for a longer time (about 2000 hr) show optically active, presumably crystallized areas, Fig. 5. If the drive-in step is omitted, but the slice is annealed

for 5 min at 1000°C, larger features, Fig. 5c and d, are observed which are confined to the first 500Å or so of oxide. The smaller crystallites of Fig. 5a and b are apparent throughout the film.

Degradation of dielectric-breakdown strength.—In Fig. 6 are plotted measured breakdown voltage distributions. First, it may be noted that the distribution of primary breakdowns is decidedly not normal but is rather fairly represented by a straight line (to about 10%) on log-probability coordinates. That is, the distribution is skewed toward lower breakdown voltages. This is only to be expected as there should be a reasonably well-defined maximum breakdown voltage (the true dielectric strength) with some potential of breakdown at any smaller voltage corresponding to various structural imperfections.

Second, it can be seen that for an as-grown oxide there are essentially no secondary breakdowns and that sodium contamination (after growth) plus drive-in, does not materially affect the distribution. There is also no change with aging at least for up to 50 hr at temperature up to 500°C or for many days at room temperature. This is in agreement with the absence of crystallization indicated by the refractive index measurements.

However, after a 5-min anneal at 1000°C the mean breakdown strength is reduced by about 35% although there are still effectively no secondary breakdowns (curve 4, Fig. 6). This would seem to imply that the high-temperature treatment changes the manner in which the sodium is incorporated into the oxide so that, in fact, a somewhat different dielectric structure having a different dielectric strength is produced. Five minutes at 1000°C does not change the distribution for an uncontaminated oxide (Fig. 6, curve 5). Curves 1, 2, 3, and 5 agree, within slice to slice variations. It may be noted that a structure change producing such a large change in dielectric strength might also be expected to produce a refractive index change which is, of course, not observed. However, it may simply be

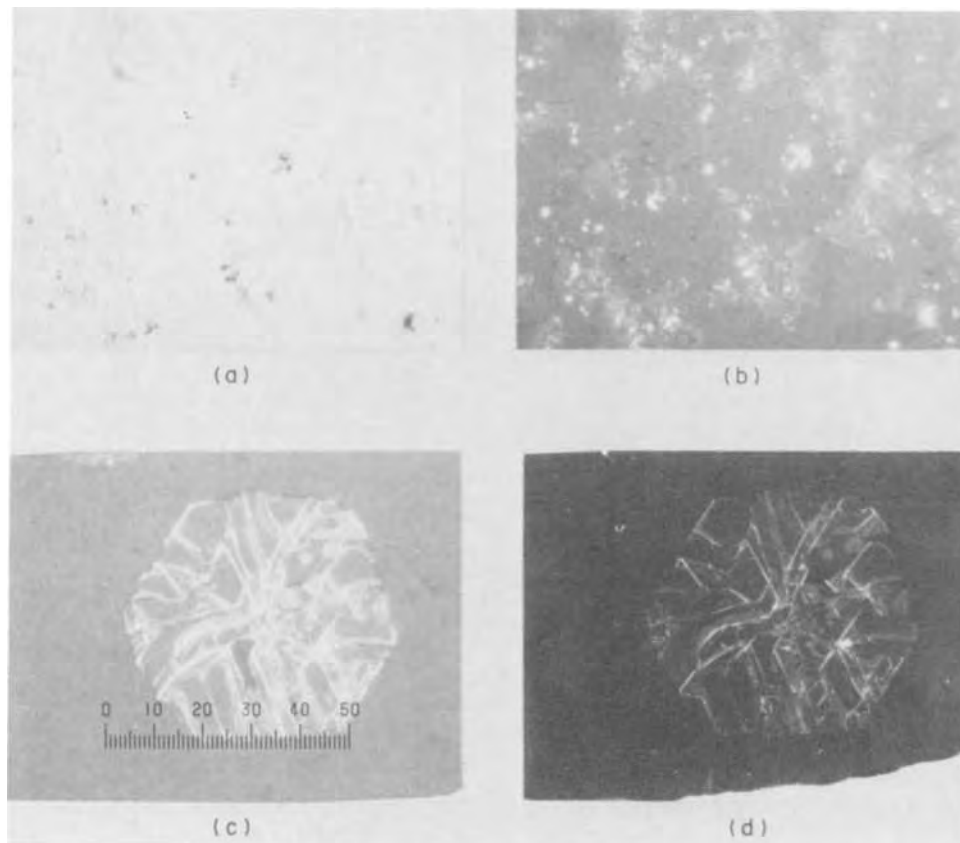


Fig. 5. Photomicrographs of sodium-contaminated sample surfaces aged about 2000 hr in room ambient. (a) and (c) are for parallel and (b) and (d) for crossed polarizers. (c) and (d) had the sodium drive-in step omitted. $10 = 25\mu$.

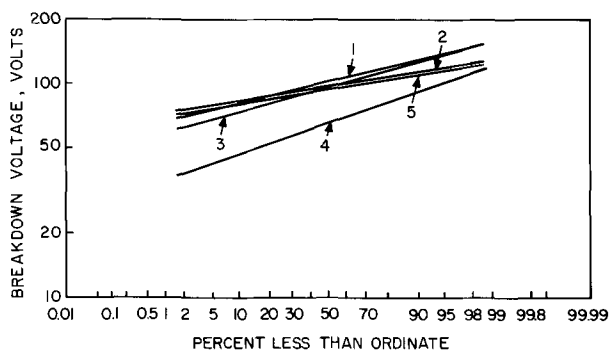


Fig. 6. Distribution of oxide breakdown voltages. Curve 1, as grown; curve 2, after Na contamination; curve 3, after Na drive-in; curve 4, after 5 min at 1000°C; and curve 5, uncontaminated, after 5 min at 1000°C.

that compensating changes in refractive index due to two or more mechanisms have taken place.

In Fig. 7, breakdown voltage distributions of sodium-contaminated and 1000°C annealed oxides are plotted for various elapsed times at room temperature. The fraction of secondary breakdowns increased with time and at longer times tertiary breakdowns began to appear. Figures 8 and 9 present similar data for temperatures of 300° and 600°C.

Discussion

Refractive index changes.—It is seen that changes in refractive index attributable to devitrification occurred only if slices were sodium contaminated and then subjected briefly (5 min) to a high temperature (1000°C). As grown, the sodium contamination level is known to be $<10^{11}$ cm $^{-2}$ from neutron activation analysis (33). The total sodium contamination introduced has been measured (34) using the flame photometry method (35) and found to be $\sim 2(10)^{15}$ cm $^{-2}$. The 600° or 1000°C treatments do not change this contamination level. After contamination by boiling in NaCl

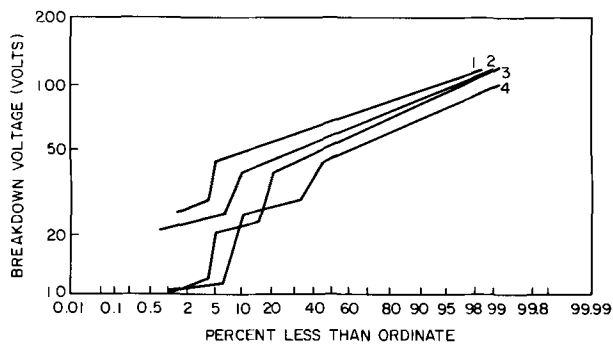


Fig. 7. Distribution of breakdown voltages for Na contaminated oxides aged at 25°C. Curve 1, 24 hr; curve 2, 48 hr; curve 3, 110 hr; and curve 4, 450 hr.

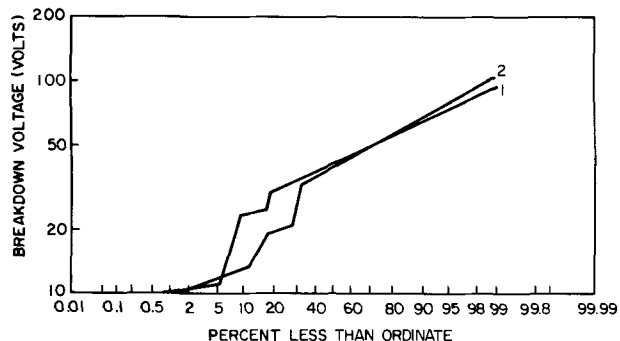


Fig. 8. Distribution of breakdown voltages for Na contaminated oxides aged at 300°C. Curve 1, 19 hr; and curve 2, 42 hr.

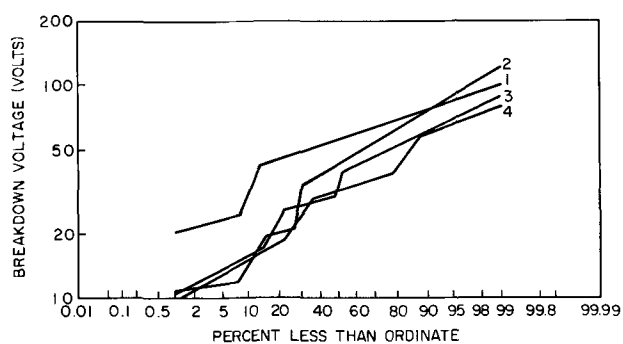


Fig. 9. Distribution of breakdown voltages for Na contaminated oxides aged at 600°C. Curve 1, 5 hr; curve 2, 22 hr; curve 3, 42 hr; and curve 4, 69 hr.

solution, the sodium has been driven into the oxide by diffusing at 600°C for about 24 hr in order to simulate a naturally occurring, grown-in sodium distribution. (Buck *et al.* (36) found in their tracer experiments that evaporating radioactive sodium on the oxide surface and then diffusing at 600°C for 22 hr produced Na profiles similar to those found in grown contaminated films.)

The need for a high-temperature step is consistent with the observations of previous investigators. Mathews *et al.* (37) found when oxides were contaminated with sodium and heated above 600°C that a visible change took place which was interpreted as devitrification and alkali glass formation. Below 600°C no visible reaction occurred. Chou and Eldridge (3) found that degraded dielectric breakdown behavior correlated with the existence of crystallized regions in the oxide and that it was more severe with a higher sodium content. However, they also observed, when $\sim 5(10)^{12}$ extra (mobile) sodiums per square centimeter were added to the oxide, by boiling in NaCl solution after growth, that very little additional devitrification and degradation of dielectric properties were observed, at least for heating up to 50 min at 500°C. Nagasima and Enari (38) observed visible crystallites of cristobalite when about a monolayer of Na atoms was deposited on a silicon surface before oxidation in the neighborhood of 1100°C.

The conclusion is, then, that sodium contamination can cause partial devitrification of grown oxide films to occur at room temperature in a few hundred hours. However, it is apparently necessary that the slices have had a high temperature treatment after being sodium contaminated. The sodium contamination may reduce the activation energy for devitrification. Some data for a sodium-contaminated and activated slice kept at 600°C are given in Fig. 4. It is not advantageous to monitor refractive index at elevated temperature beyond about 100 hr since the total refractive index change includes changes due to processes other than devitrification (compare Fig. 1 and 4). However, if it is assumed that Δn is due to devitrification, for the temperatures and times of Fig. 4, which seems reasonable since uncontaminated oxides showed no change in n (Fig. 1), we can estimate an upper limit for the activation energy. If $n \propto t$ is assumed, $E < 0.04$ eV and if $E \propto t^2$ is assumed, $E < 0.09$ eV. While sodium contamination may enhance the devitrification, the necessity of a brief high-temperature treatment suggests that either nuclei must first be present for any significant devitrification to take place at room temperature or that the high-temperature treatment changes the manner in which the sodium is incorporated into the oxide structure. This is likely related to the distinction between bound and unbound sodium in SiO $_2$ (39-41). It may also be expected that the enhanced devitrification will be more serious for wet oxides since it is well

known that water enhances sodium incorporation (42, 43).

Dielectric breakdown strength.—In Fig. 10 is plotted the equivalent surface defect density computed from the fraction of primary breakdowns according to Eq. [1]. The data may be represented for the range of times and temperatures covered by

$$\sigma = (a_0 e^{-E/kT}) t \quad [2]$$

where t is the time, with $a_0 \approx 10 \text{ hr}^{-1}$ and $E \approx 0.1 \text{ eV}$. Since we cannot propose a model relating the observed linear (in time) increase of σ to the microscopic details of the devitrification process, it is not clear that this activation energy is that for devitrification. A more direct quantitative determination of the devitrification is needed. A possibility might be a light scattering experiment where measurement of the scattering coefficient should give a direct measure of the extent of devitrification.

It would also be desirable to investigate the effect of the level of sodium contamination. For $<10^{11} \text{ Na atoms cm}^{-2}$ devitrification does not occur while for $\sim 10^{15} \text{ Na atoms cm}^{-2}$ room-temperature devitrification does occur. Such measurements could also be valuable in deciding the importance of nucleation since, if that is the important step, the kinetics should go as the sodium concentration to some power, n , where n is the number of sodium atoms incorporated into a nucleus. It should be emphasized that the present experiments only show sufficient, although not perhaps necessary, conditions for room temperature devitrification to take place.

Conclusions

Monitoring of the refractive index of steam-grown silicon dioxide films on silicon indicates that, in agreement with prior electron diffraction studies (22), partial devitrification may occur in a time scale of weeks at room temperature; but the present study indicates this occurs only if the oxide is significantly sodium contaminated and, in addition, has had a high-temperature treatment while contaminated. Dielectric breakdown behavior indicates that the function of the high-temperature anneal is to modify the manner in which the sodium is incorporated into the silica film, although nucleation phenomena may also be important. The activation energy for dielectric strength degradation is $\sim 0.1 \text{ eV}$.

However, since devitrification of bulk silica glass even when grossly sodium contaminated, does not

proceed at measurable rates at room temperature (8b) it must also be concluded that there may exist subtle structural and/or stoichiometric differences between bulk silica glass and amorphous-grown silica films. There is no real reason to believe that a grown amorphous film must have precisely the same structure as fused silica having a fictive temperature equal to the film-growth temperature since the grown film has never gone through a molten phase and therefore may not be able to relax to the same structure as the true glass. Stabilization studies on grown films would seem to be in order. Stoichiometrically, there are, of course, small gradients in oxygen and perhaps silicon concentration remaining from the growth process. Also, it may be noted that the oxide is under compressive stress as grown (44). Since cristobalite is more dense (2.3 g/cm^3 opposed to 2.2 g/cm^3) than fused silica this may be expected to enhance the devitrification of grown films compared to bulk glasses.

Acknowledgments

The authors are indebted to A. C. Adams and R. H. Kaiser for use of their ellipsometric apparatus, to W. R. Knolle for Na contamination measurements, and to J. Drobek for electron diffraction measurements and several useful discussions. Further thanks are due to P. J. Boddy, R. K. Curran, and especially J. R. Brews for useful comments on the manuscript.

Manuscript submitted March 13, 1972; revised manuscript received June 6, 1972.

Any discussion of this paper will appear in a Discussion Section to be published in the June 1973 JOURNAL.

REFERENCES

1. L. A. D'Asaro, *Solid-State Electron.*, **1**, 3 (1960).
2. S. W. Ing *et al.*, *This Journal*, **109**, 221 (1962).
3. N. J. Chou and J. M. Eldridge, *ibid.*, **117**, 1287 (1970).
4. R. Stickler and J. W. Faust, *Electrochem. Technol.*, **4**, 277 (1966).
5. C. Fritzsche, *Z. Angew-Phys.*, **24**, 48 (1967).
6. T. Sugano *et al.*, *Jap. J. Appl. Phys.*, **7**, 715 (1968).
7. P. V. Pavlov and E. V. Shitova, *Sov. Phys.—Cryst.*, **12**, 95 (1967).
- 8a. N. Nagasima, *Japan. J. Appl. Phys.*, **9**, 879 (1970).
- 8b. H. Rawson, "Inorganic Glass-Forming Systems," Academic Press, London (1967).
9. V. Gottardi and B. Locardi, *Phys. Chem. Glass.*, **5**, 137 (1964).
10. J. D. Fleming, "Fused Silica Manual," Georgia Institute of Technology, Atlanta (1965).
11. M. Coquerelle, *Silicates Ind.*, **26**, 505 (1961).
12. O. W. Florke, *Ber. Deut. Keram. Ges.*, **38**, 89 (1961).
13. F. E. Wagstaff, Doctoral Dissertation, University of Utah, Salt Lake City (1962).
14. L. Vaskova and J. Hlavac, *Silikaty*, **13**, 211 (1969).
15. J. D. MacKenzie and J. L. White, *J. Am. Ceram. Soc.*, **43**, 170 (1960).
16. F. E. Wagstaff, *Phys. Chem. Glass.*, **10**, 50 (1969).
17. G. D. Rieck, *Chem. Weekblad.*, **48**, 712 (1952).
18. I. E. Balyagin, *Sov. Phys.—Cryst.*, **7**, 746 (1963).
19. A. G. Revesz, *Phys. Status Solidi*, **24**, 115 (1967).
20. A. N. Knopp and R. Stickler, *Electrochem. Technol.*, **5**, 37 (1967).
21. M. B. Brodsky and D. Cubicciotti, *J. Am. Chem. Soc.*, **73**, 3497 (1951).
22. J. Drobek, Unpublished.
23. R. J. Archer, "Ellipsometry," Gaertner Sci. Corp., Chicago (1968).
24. E. U. Condon and H. Odishaw, Editors, "Handbook of Physics," p. 6-109, McGraw-Hill Book Co., New York (1958).
25. J. E. Price, *Proc. IEEE*, **58**, 1290 (1970).
26. R. Hammer, *Rev. Sci. Instr.*, **41**, 292 (1970).
27. R. W. Douglas and J. O. Isard, *J. Soc. Glass Technol.*, **35**, 206 (1951).
28. R. Brückner, *J. Non-Cryst. Solids*, **5**, 123 (1970).
29. G. Hetherington and K. H. Jack, *Phys. Chem. Glass.*, **3**, 129 (1962).
30. R. M. Burger and R. P. Donovan, Editors, "Fundamentals of Silicon Integrated Device Technol-

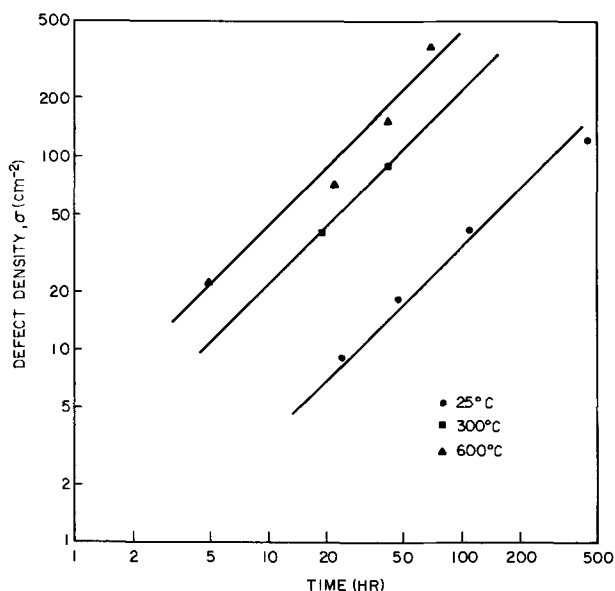


Fig. 10. Apparent surface defect density vs. aging time for Na contaminated oxides annealed at various temperatures.

- ogy," Vol. I, Prentice Hall, Englewood Cliffs, N. J. (1967).
31. L. Holland, "The Properties of Glass Surfaces," Chap. 4, Chapman and Hall, London (1964).
 32. J. Drobek, Private communication.
 33. R. Schmidt, Private communication.
 34. W. R. Knolle, Private communication.
 35. J. E. Barry *et al.*, *This Journal*, **116**, 257 (1969).
 36. T. M. Buck *et al.*, *ibid.*, **114**, 862 (1967).
 37. J. R. Mathews *et al.*, *ibid.*, **112**, 899 (1965).
 38. N. Nagasima and H. Enari, *Japan. J. Appl. Phys.*, **10**, 441 (1971).
 39. A. G. Revesz and K. H. Zaininger, *R C A Rev.*, **29**, 33 (1968).
 40. F. M. Fowkes and T. E. Burgess, *Surface Sci.*, **13**, 184 (1969).
 41. S. R. Hofstein, *Solid State Electron.*, **10**, 657 (1967).
 42. T. E. Burgess *et al.*, *This Journal*, **116**, 1005 (1969).
 43. G. L. Holmberg *et al.*, *ibid.*, **117**, 677 (1970).
 44. R. J. Jaccodine and W. A. Schlegel, *J. Appl. Phys.*, **37**, 2429 (1966).

High Resistance Anodic Film Formation on Bismuth with or without Appearance of Induction Period

S. Ikonopisov and Ts. Nikolov

Department of Physical Chemistry, Higher Institute of Chemical Technology, Sofia 56 (Darvenitsa), Bulgaria

ABSTRACT

The galvanostatic oxidation of bismuth in aqueous oxalic acid solutions has been studied at various anodic current densities, J , electrolyte concentrations, N , and temperatures, T . An induction period was found to appear always when J is lower than a critical value, specific for given N and T . Relations considering the duration of the induction period as a function of J , N , and T , and the dependence of the linear potential rise on time in absence of induction period or after its expiration have been established. These relations are explained on the basis of a model considering the precipitation of crystals of a slightly soluble bismuth compound which isolates a part of electrode surface. When the current density on the rest (uncovered) surface reaches the critical value, an anodic film begins to grow on it, causing corresponding increase in the anodic potential.

The formation of anodic oxide films on bismuth has been studied until recently in neutral and alkaline media only (1-6). Masing and Young (3) have found that the steady-state kinetics of anodizing Bi in dilute NaOH solution are analogous to those of the typical valve metals, and the potential-transient behavior is somewhat different. De Smet and Hopper (6) reported that the usual relation between the current density and the change in overpotential with respect to charge passed (which may be considered to be proportional to the field) is not valid for the galvanostatic anodization of bismuth in Na_2CO_3 solution, while the open-circuit transient is similar to that of tantalum.

The anodic oxidation of Bi in H_2SO_4 solutions has been reported quite recently by Ammar and Khalil (7). They have shown that in dilute H_2SO_4 solutions bismuth could be anodized to voltages over 100V. It has been observed in our laboratory that high-resistance anodic films could be formed in a number of aqueous and nonaqueous solutions of acids. The kinetics of growth and the properties of the films appeared to be strongly affected by the composition and concentration of the electrolyte. The present investigation was undertaken to obtain quantitative data on the appearance of an induction period during the anodization of bismuth in aqueous oxalic acid solutions.

Experimental

The anodization was carried out under constant current conditions (using an electronic galvanostat), thermostatic regulation, and stirring of the electrolyte. A conventional one-compartment electrolytic cell without deaeration was employed. The specimens with a surface area of about 12 cm^2 were cut out in the form

of plates from a block of high-purity bismuth (5 ppm). Electrical contact was made by soldering a wire to the specimen and insulating the wire with a glass tube. The tube penetrated into the metal and its edge was additionally insulated with epoxy resin. The electrodes were mechanically and electrochemically polished, brightened, and washed prior to anodization as described by Masing and Young (3). At the end of selected intervals of anodizing time the anodization was interrupted. The anodes were washed in conductivity water and dried and photomicrographs were taken by automatic microscope (Neophot 2, C. Z., Jena).

De Smet and Hopper (6) have found that visible light causes large changes in the overpotential of the bismuth electrode while undergoing galvanostatic anodization with low current densities. Our experiments have shown that the illumination with visible light did not noticeably influence the appearance and duration of the induction period or the rate of subsequent potential rise. Actually, the photoeffect was found by De Smet and Hopper to decrease with increasing applied current density and to disappear for current densities above 10^{-4} A/cm^2 . Consequently, the lack of photoeffect in our experiments is probably due to the higher values of the current densities used. Therefore, a shadowed instead of a darkened room has been used. Each of the present data is an average value of many experiments.

Results

Formation of anodic films without induction period.— Under certain conditions (low temperatures and low concentration of the electrolyte and high current densities) the kinetics of the anodization of Bi in aqueous solutions of $(\text{COOH})_2$ are similar to those in alkaline solutions (Fig. 1, curve A). Under galvano-

Key words: anodic, anodization, bismuth, oxide, film, induction period.

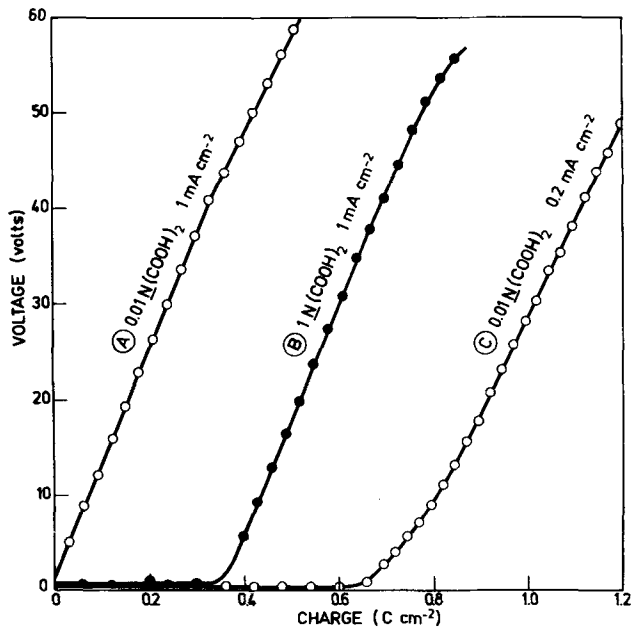


Fig. 1. Potential vs. charge at various concentrations and current densities. Temperature 293.2°K.

static conditions the potential drop, U_f , across the film increases linearly with time, thus with Q , the total charge density passed. The range of this linear potential rise depends on the anodizing current density, J , and temperature, T , and vary from 40 to 70 (V) for $J < 10 \text{ mA cm}^{-2}$ and $274 < T < 333 \text{ (}^\circ\text{K)}$.

A linear relationship was found between the rate of potential rise ($\partial U_f / \partial Q$) and the logarithm of current density J for the limited ranges of J in which the potential rise starts without any induction period. The results for three temperatures are shown in Fig. 2. Such a relationship

$$J = A_1 \exp \left[B_1 \left(\frac{\partial U_f}{\partial Q} \right)_{Q_{\text{ind}}=0} \right] \quad [1]$$

is typical for anodic formation of nonporous films. Nevertheless, the constants $\log A_1$ and B_1 are not linear functions of $1/T$

$$\log A_1 = 26.28 - \frac{1.23 \times 10^4}{T} + \frac{8.9 \times 10^6}{T^2}, \quad \log (\text{A/cm}^2)$$

$$B_1 = -0.302 + \frac{1.37 \times 10^2}{T} - \frac{9.95 \times 10^3}{T^2}, \quad \text{C cm}^{-2} \text{ V}^{-1}$$

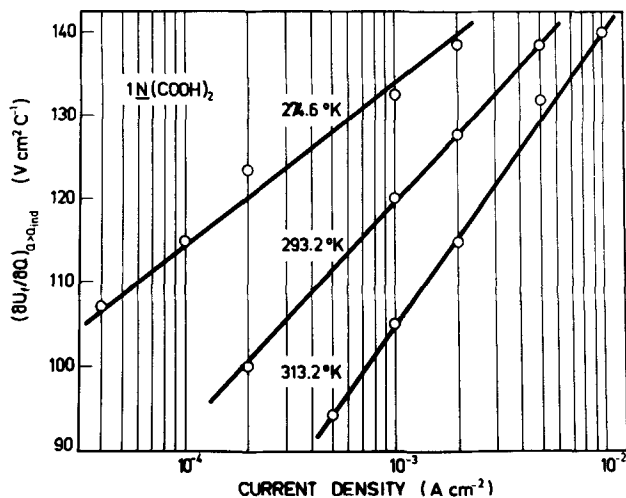


Fig. 2. Rate of change of potential as a function of the current density at different temperatures.

in contrast to the relationships usually found in the case of not very wide ranges of J and T .

Appearance and duration of the induction period.— Under suitable change of the conditions, e.g., a reduction of the current density and (or) an increase of the electrolyte concentration, the type of $U_f(Q)$ -relationship changes radically. After switching on the anodic polarization no increase in U_f is observed for a time defined as “induction period” (Fig. 1, curves B and C). The duration of this induction period can be conveniently represented under various conditions by the density of the “unproductive charge,” Q_{ind} , that has passed during the induction period. After this period, U_f begins to increase rapidly and linearly up to high values (Fig. 1).

The appearance and duration of the induction period were found to depend mainly on three parameters: electrolyte concentration N , current density J , and temperature T . As can be seen from Fig. 3, the induction period does not appear when the solution of $(\text{COOH})_2$ is sufficiently diluted. It appears at a certain concentration and increases rapidly with the increase of the concentration and simultaneously a wide scattering of the experimental results for Q_{ind} is observed. Above a certain electrolyte concentration the unproductive charge reaches a constant and reproducible value. All present results are obtained in that range of concentration that provides good reproducibility.

The duration of the induction period increases with the increase of temperature. Figure 4 illustrates the temperature dependence, under suitable conditions, of the induction period.

The increase of the current density shortens the induction period. It turns out that a linear dependence exists between $Q_{\text{ind}}^{2/3}$ and $\log J$ (Fig. 5), described by the expression

$$J = A_2 \exp - (B_2 Q_{\text{ind}}^{2/3}) \quad [2]$$

where the constants A_2 and B_2 are temperature functions

$$\log A_2 = -17.8$$

$$+ \frac{1.1 \times 10^4}{T} - \frac{1.87 \times 10^6}{T^2}, \quad \log (\text{A cm}^{-2})$$

$$B_2 = 100 - \frac{6.68 \times 10^4}{T} + \frac{1.13 \times 10^7}{T^2}, \quad (\text{C cm}^{-2})^{-2/3}$$

After the induction period the anode potential begins to increase in a linear fashion with time, and thus

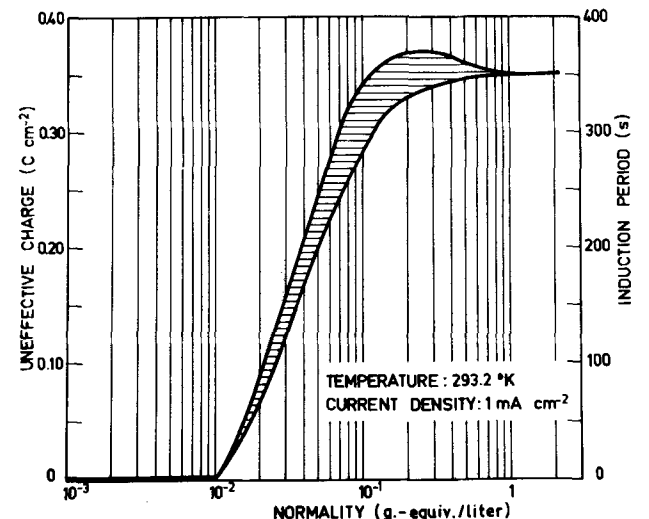


Fig. 3. Dependence of unproductive charge on the electrolyte concentration. The shaded area limits the dispersion of experimental results.

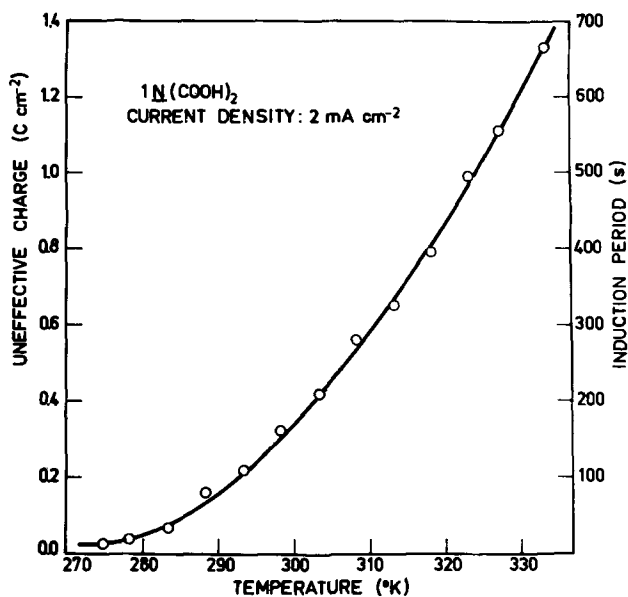
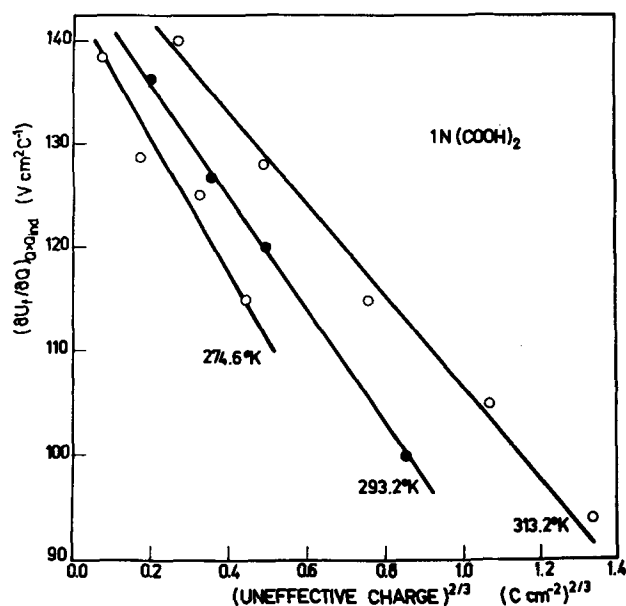
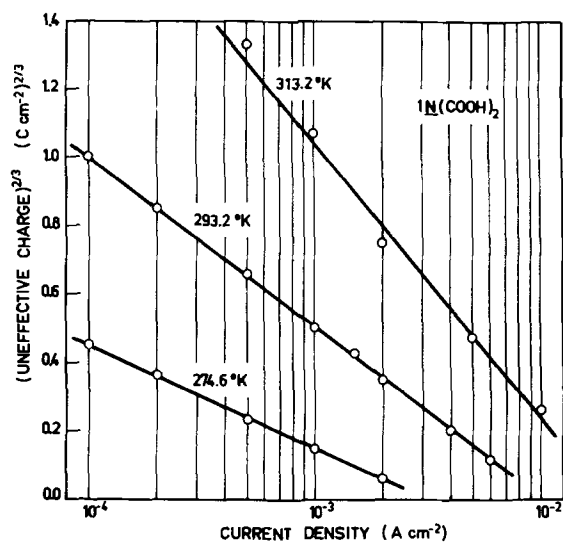


Fig. 4. Temperature dependence of induction period

Fig. 6. Dependence between the rate of potential rise after the induction period and $Q^{2/3}$ at different temperatures.Fig. 5. Plot of $Q_{ind}^{2/3}$ vs. $\log J$ at different temperatures

with the electric charge Q , until film breakdown commenced (plots B and C of Fig. 1). Experimental results indicate that a linear relation exists between the slope of $U_f(Q)$ -curves after the induction period and the quantity $Q_{ind}^{2/3}$. This relation is represented in Fig. 6 and is expressible in the form

$$\left(\frac{\partial U_f}{\partial Q}\right)_{Q>Q_{ind}} = A_3 - B_3 Q_{ind}^{2/3} \quad [3]$$

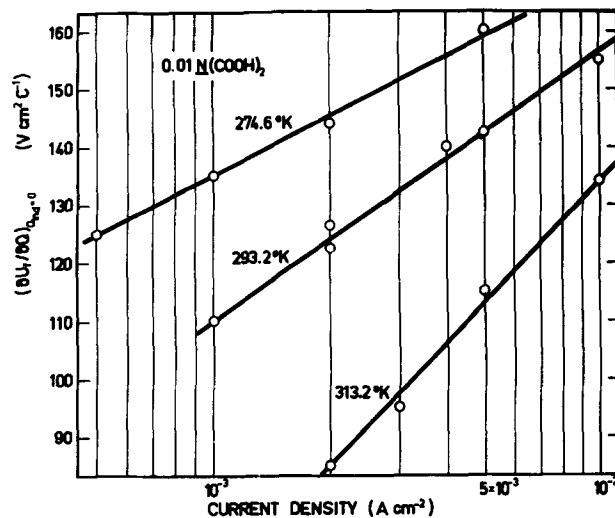
where

$$A_3 = 330 - \frac{9.02 \times 10^4}{T} + \frac{1.07 \times 10^7}{T^2}, \quad \text{V cm}^2 \text{ C}^{-1}$$

$$B_3 = -468 + \frac{2.58 \times 10^5}{T} - \frac{3.07 \times 10^7}{T^2}, \quad (\text{C cm}^{-2})^{-2/3}$$

Equations [2] and [3] suggest an exponential relation between J and the rate of linear potential increase (50-70V) after the induction period, $(\partial U_f/\partial Q)_{Q>Q_{ind}}$, analogous to the corresponding relationship when the potential rise commences without induction period (Eq. [1]). The experimental data are given in Fig. 7 and can be described by the expression

$$J = A_4 \exp [B_4 (\partial U_f/\partial Q)_{Q>Q_{ind}}] \quad [4]$$

Fig. 7. Slope of $U_f(Q)$ -curves after the induction period vs. current density at different temperatures.

however, the values of the constants A_4 and B_4 differ considerably from those in Eq. [1], viz.

$$\log A_4 = -101.3 + \frac{6.37 \times 10^4}{T} - \frac{1.06 \times 10^7}{T^2}, \quad \log (\text{A cm}^{-2})$$

$$B_4 = 1.36 - \frac{8.64 \times 10^2}{T} + \frac{1.43 \times 10^5}{T^2}, \quad \text{CV}^{-1} \text{ cm}^{-2}$$

Direct observations of the electrode surface.—During the anodization without an induction period the overall anode surface remains flat and bright interference colors appear with the growth of the film. Small crystals appear and grow only at isolated surface sites. On the contrary, when the process begins with a prolonged induction period, the crystals occupy a considerable part of the surface. When the process was carried out at high temperatures (e.g., 60°C) the crystals were well shaped with a clearly expressed hexagonal symmetry. At low temperatures the crystals grow as acicular druses.

In the beginning of the induction period, under conditions of high temperature and low current densities

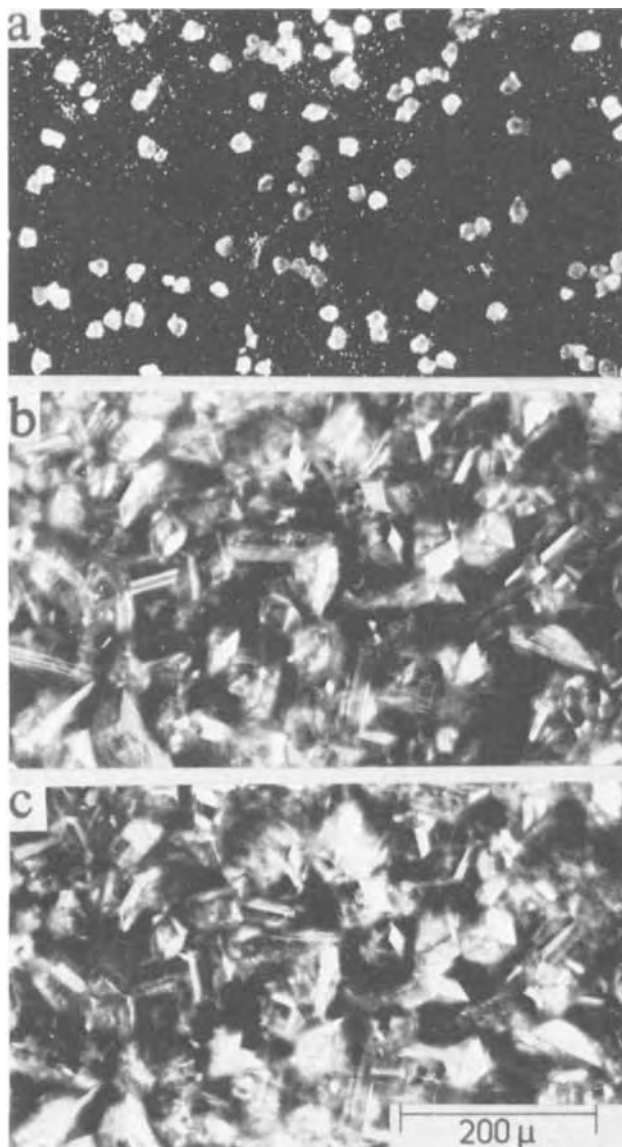


Fig. 8. Dark field photomicrograph of one and the same part of the surface of the electrode anodized in $1N$ $(COOH)_2$ with 1 mA/cm 2 at $60^\circ C$. a, In the beginning of the induction period (about $0.05 Q_{ind}$); b, at the end of the induction period; and c, when the electrode potential has reached the value of $30V$.

(providing high values for Q_{ind}), some crystals are formed (Fig. 8a), grow bigger and at last cover almost the total metal surface (Fig. 8b). The increase of U_f after the induction period does not change the surface picture (Fig. 8c).

Under conditions of a short induction period the crystals cover only a small part of the electrode surface (Fig. 9a). After completion of the induction period, the crystal size and number increased (Fig. 9b), together with the increase of the electrode potential.

It is worthwhile to mention that the electrodes were cut out of large-sized crystals of polycrystalline bismuth. It was observed that the number, size, and spatial orientation of the crystals grown during the induction period were different on the different substrate crystal faces; this effect was not investigated in detail.

Nature and structure of the films.—X-ray diffraction patterns of the crystal films mechanically removed from the electrode surfaces, and reflective electronograms of the anodized electrode surfaces, were taken. X-rayograms and electronograms showed the lack of lines typical for α - and β - Bi_2O_3 . It turned out that the

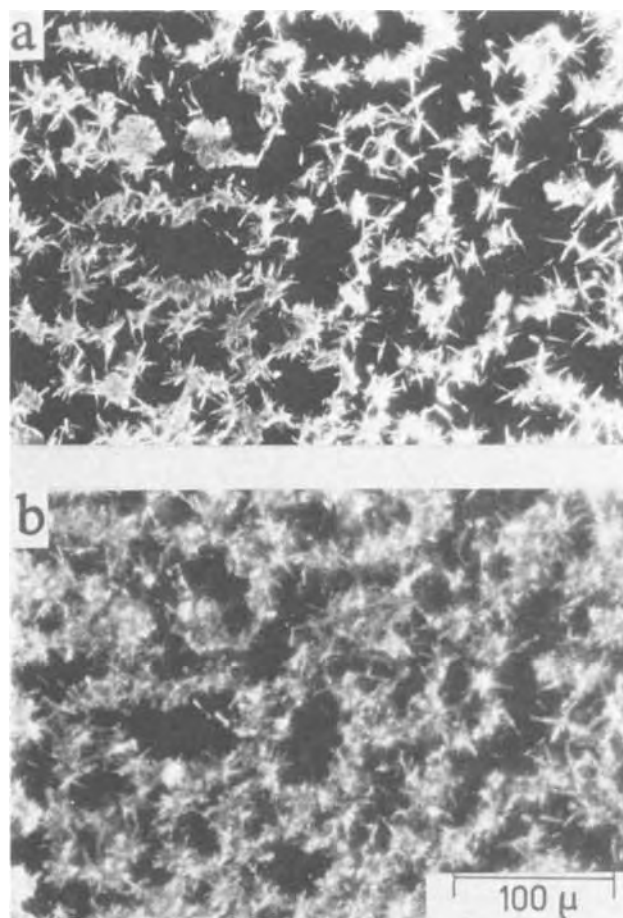


Fig. 9. Electrode surface anodized in $1N$ $(COOH)_2$ with 2 mA/cm 2 at $1.5^\circ C$. a, At the end of the induction period; and b, when the electrode potential has reached $30V$.

films were composed from $Bi(OH)_3$ or $Bi_2O_3 \cdot CO_2 \cdot H_2O$, but it is difficult to distinguish these compounds by means of the electronographic and x-rayographic analysis because of the very close values of the interplanar distances.

Discussion

The appearance of induction time during anodic passivation of some metals [e.g., Cd, Pb, Zn (8), Fe (9), Cr (10), Sn (11), Hg (12), and Ni (13)] is well known, the mechanism of the phenomenon being under discussion (14-18). The passive state in all these cases is related with the formation of a very thin film bearing 1-2V only. Something of the sort of an induction period (a transition from a low to a higher rate of potential increase) have been observed in galvanostatic anodization to high voltages of bismuth (19) and of vanadium (20). A vividly outlined induction period followed by a linear potential rise to high voltages does not seem to be a specific phenomenon for bismuth only. Preliminary investigations have shown the appearance in some cases of a fairly well-expressed induction period during anodization of antimony (21) and molybdenum (22) to high voltages. An attempt for a semiquantitative interpretation of this phenomenon by considering the elementary processes is given below.

Elementary processes.—The possible elementary processes at the electrode surface both when the anodic polarization causes the growth of a continuous anodic film and when dissolution of the metal takes place, are schematically shown in Fig. 10.

Three simultaneous processes seem to occur when the electrode is completely covered with anodic film: (I) Formation of anodic film as a result of the flowing of ionic component J_{gr} , of the current. It is usually

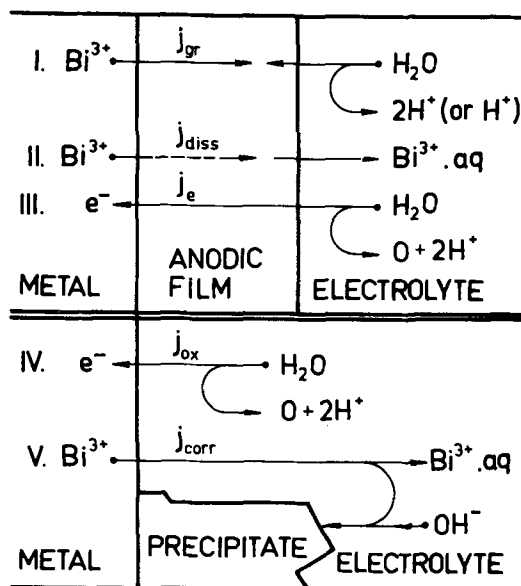


Fig. 10. Schematic representation of the possible processes during anodic polarization of Bi in solutions of $(\text{COOH})_2$.

assumed that the metal ions move through the film, but the results would not be changed if the anion mobility is commensurable or higher. (II) The dissolution of the anodic film with a rate expressed by the ionic current J_{diss} . (III) Electronic conduction of the anodic film. This electronic component of the current, J_e , is connected with the oxygen evolution at the anode and does not influence the anodic film thickness.

There appear to be two processes of interest in the absence of continuous anodic film: (IV) Oxygen gas liberation at the metal (current density J_{ox}), and (V) Anodic dissolution of the metal with an ionic current density J_{corr} . A part of the bismuth ions formed deposit on the cathode, while the rest precipitate as crystals of a slightly soluble compound [$\text{Bi}(\text{OH})_3$ or $\text{Bi}_2\text{O}_3 \cdot \text{CO}_2 \cdot \text{H}_2\text{O}$] on the anode surface.

The appearance and duration of the induction period are considered to result from variations in the relative rates of these elementary processes.

Anodic film formation without induction period.—This situation corresponds to the growth of anodic film which covers the electrode surface completely from the beginning of the process (a thin primary oxide film is supposed to exist before the anodic polarization). The continued growth of the anodic film requires satisfying the condition $J_{\text{gr}} > J_{\text{diss}}$.

The total current density, J , can be expressed as a sum of the three current components, $J = J_{\text{gr}} + J_{\text{diss}} + J_e$. Thus the efficiency Λ of anodic film formation is

$$\Lambda = \frac{J_{\text{gr}}}{J} = \frac{J_{\text{gr}}}{J_{\text{gr}} + J_{\text{diss}} + J_e} \quad [5]$$

The current components J_{diss} and J_e are probably functions of N and T , hence Λ will also depend on N and T . The film thickness D can be obtained using Faraday's law

$$D = \frac{M_f}{6F\rho_f} Q\Lambda \quad [6]$$

where ρ_f is the density of the film, M_f is its molecular weight, F is Faraday's number, and Q is the charge density. Using Eq. [6], the potential drop U_f across the anodic film can be determined

$$U_f = DE = \frac{M_f E}{6F\rho_f} Q\Lambda \quad [7]$$

where E is the electric field strength. It is seen that the linear increase of U_f with Q , found in galvanostatic

anodization at given N and T , and in the absence of an induction period, i.e.

$$\left(\frac{\partial U_f}{\partial Q} \right)_{J,T,N} = \text{const} \quad [8]$$

requires both

$$(\Lambda)_{J,T,N} = \text{const} \text{ and } (E)_{J,T,N} = \text{const} \quad [9]$$

or

$$J_{\text{gr}} \gg J_{\text{diss}} + J_e \quad [10]$$

As will be shown, condition [10] contradicts the non-linear dependence of the constants in Eq. [1] on $1/T$. For this reason it may be concluded that in the absence of the induction period the efficiency Λ and the field strength E are not functions of the film thickness (conditions [9] are satisfied).

The dependence $J_{\text{gr}}(E, T)$ is represented by the well-known equation

$$J_{\text{gr}} = A \exp - \left(\frac{B - \alpha E}{kT} \right) \quad [11]$$

which is theoretically a first approximation for not very wide E and T ranges, and is usually observed in formation of insulating anodic films (e.g., [23]). A , B , and α are positive constants. From Eq. [5], [7], and [11] the total current density is obtained as

$$J = \frac{J_{\text{gr}}}{\Lambda} = \frac{A}{\Lambda} \exp - \left(\frac{B}{kT} \right) \exp \left[\frac{6F\rho_f \alpha}{M_f k T \Lambda} \left(\frac{\partial U_f}{\partial Q} \right) \right] \quad [12]$$

This equation is identical with the experimentally established Eq. [1]. Furthermore, expression [12] shows that the constants in Eq. [1]

$$A_1 = \frac{A}{\Lambda(N,T)} \exp - \left(\frac{B}{kT} \right) \quad \text{and} \quad B_1 = \frac{6F\rho_f \alpha}{M_f k T \Lambda(N,T)} \quad [13]$$

must depend on T not only directly, but also through the function $\Lambda(N,T)$, i.e., $\log A_1$ and B_1 should be non-linear functions of $1/T$, as was found experimentally. Moreover, this fact shows that $\Lambda < 1$ and the sum of the current components $J_{\text{diss}} + J_e$ is of the order of J_{gr} , i.e., condition [10] is not satisfied and Λ and E are independent of D (condition [9] is valid).

Appearance of induction period.—During the induction period the electrode surface is not covered with continuous anodic film. In this case it is necessary for the rate of film dissolution to be higher than the rate of its growth

$$J_{\text{diss}} \geq J_{\text{gr}} \quad [14]$$

The result is a dissolution of the primary oxide film in the beginning of the process and subsequently metal dissolution and an oxygen evolution commence.

A quantitative description of the processes yielding Eq. [14] is difficult. Only a qualitative description based on the general properties of J_{gr} and J_{diss} are given. While the ionic conductivity J_{gr} of the film is a function of E and T , the dissolution rate J_{diss} is also dependent on the electrolyte concentration N , being greater for higher N . The absence of induction period ($Q_{\text{ind}} = 0$) at given J and T and low N become comprehensible, because at sufficiently low N the condition $J_{\text{diss}} < J_{\text{gr}}$ is satisfied. The current density J_{diss} increases with the increase of N and can reach the value of J_{gr} ($J_{\text{diss}} \approx J_{\text{gr}}$) under certain concentrations. In that range of concentrations small changes in the conditions may lead to partial or total dissolution or rebuilding of the anodic film, thus explaining the observed wide dispersion of the data for Q_{ind} . A further increase of N would make condition [14] valid, i.e.,

$J_{diss} > J_{gr}$, which leads to a reproducible induction period.

The current components J_{gr} and J_{diss} depend also on the total current density, J . A decrease of J causes the appearance of an induction period. Using this one may assume that J_{diss} decreases less rapidly with the decrease of J than does J_{gr} . Hence, the value of J must be lower than some boundary value J^* at given T and N in order to satisfy condition [14] and have an induction period appear.

Duration of the induction period.— The duration of the induction period (the uneffective charge Q_{ind}) may also be determined on the basis of the assumption for a minimum current density, J^* , necessary for a continuous growth of anodic film. If $J < J^*$ (for given T and N) an anodic film is not formed and $J = J_{ox} + J_{corr}$. The current component J_{corr} increases the concentration of bismuth ions around the anode and leads to a precipitation insoluble compound on the metal surface. The crystals of this compound isolate some part S_{is} of each square centimeter of the anode surface. Hence, the real current density J_{real} over the free surface $(1 - S_{is})$ increases. This process takes place until S_{is} becomes large enough, S_{is}^* , for J_{real} to become $J_{real} = J^*$, determining the end of the induction period and the magnitude of Q_{ind} .

Using this model, Q_{ind} may be determined as a function of J at given T and N . An increase in S_{is} of dS_{is} results in a change of J_{real} by dJ_{real} , which is proportional to the instantaneous value of J_{real} and to dS_{is}

$$dJ_{real} = C_{is}J_{real}dS_{is}$$

where C_{is} is a coefficient. Integration from the beginning of the process ($S_{is} = 0$ and $J_{real} = J$) to the end of the induction period ($S_{is} = S_{is}^*$ and $J_{real} = J^*$) yields

$$J = J^* \exp - (C_{is}S_{is}^*) \quad [15]$$

where

$$(J^*)_{T,N} = \text{const}$$

The area covered with the crystals, S_{is} , depends on their volume V_{is} . If the anodic surface is large enough for the growth of a great number of precipitated crystals, which is the case in our experiments, and taking into account the chaotic orientation of the crystals, it is not difficult to show that the coated surface S_{is} at any moment and at the end of the induction period is, respectively

$$S_{is} = V_{is}^{2/3} \text{ and } S_{is}^* = V_{is}^*{}^{2/3} \quad [16]$$

On the other hand, we could assume that at given T and N the volume of the precipitated crystals is proportional to the charge Q that had been passed

$$V_{is} = K_{is}(T,N)Q \text{ i.e., } V_{is}^* = K_{is}(T,N)Q_{ind} \quad [17]$$

where the constant K_{is} is a function of T and N . Substituting Eq. [16] and [17] into [15] yields

$$J = J^*(T,N) \exp - [C_{is}K_{is}(T,N)Q_{ind}^{2/3}] \quad [18]$$

which is identical with the empirical relation [2] provided that

$$A_2 = J^*(T,N)$$

and

$$B_2 = C_{is}K_{is}(T,N)$$

It is difficult to determine how these constants (A_2 and B_2) depend on the temperature, because the change of T changes the rate of metal corrosion and the diffusion coefficient, consequently the relation between the metal deposits on the cathode and the precipitated crystals of bismuth compound on the anode. Even the crystal shape may be changed (the relative number of the acicular crystals increases with the decrease of the temperature). In general, the diffusion of the bismuth ions and their deposition on

the cathode, the oxygen evolution on the anode, the solubility of the precipitated crystals, etc., increase with the increase of temperature at given J and N . Hence, a smaller amount of the precipitated crystals will correspond to unit charge at higher temperature, i.e., the constant K_{is} in Eq. [17] will be lower. Correspondingly, a larger charge will be required in order to reach a current density $J_{real} \cong J^*$ and to start the anodic film growth. Moreover, the value of J^* will also be higher at higher temperature, because of the reduction of the anodization efficiency with the increase of the temperature (see Eq. [6]). All this explains qualitatively the increase of Q_{ind} with T found in the experiments (Fig. 4).

Growth of anodic film after the induction period.— After the expiration of the induction period the electrode potential begins to increase linearly with the charge density Q that had passed (Fig. 1). This linear relation (condition [8]) proves that after the induction period, as it was in the case of the absence of the induction period, the film growth efficiency Λ and the field strength E are independent of the film thickness, i.e., condition [9] is also satisfied. The fact that the slope $(\partial U_f / \partial Q)_{N,T,Q > Q_{ind}}$ is a function of the total current density or of the duration of induction period (Fig. 6 and 7, Eq. [3] and [4]), however, cannot be explained directly with the model proposed for interpretation of the duration of the induction period. According to this model at the end of the induction period the current J_{real} passing through the surface not covered with precipitated crystals $(1 - S_{is}^*)$ must reach a certain critical value J^* , independent of the total current density. Then the growth of anodic film on the free surface, leading to the increase of the electrode potential, will be realized always by the same current density, and from Eq. [12]

$$J = J^* = \frac{A}{\Lambda} \exp - \left(\frac{B}{kT} \right) \exp \frac{6F\rho_f\alpha}{M_f kT\Lambda} \left(\frac{\partial U_f}{\partial Q} \right)_{Q=Q_{ind}} = \text{const} \quad [19]$$

it follows that

$$\left(\frac{\partial U_f}{\partial Q} \right)_{Q=Q_{ind}} = \text{const}$$

Hence, if the surface covered with the precipitated crystals does not increase further after the expiration of the induction period, the slope $(\partial U_f / \partial Q)_{Q > Q_{ind}}$ should be independent of the total current density and Q_{ind} which is in contradiction to the experimental data.

The empirical data (Eq. [3] and [4]) require an assumption of an additional increase of the surface insulated by the precipitated crystals, causing an increase of the slope $(\partial U_f / \partial Q)$ proportional to the free surface $(1 - S_{is}^*)$ at the end of the induction period

$$\left(\frac{\partial U_f}{\partial Q} \right)_{Q > Q_{ind}} = \left(\frac{\partial U_f}{\partial Q} \right)_{Q=Q_{ind}} + b(1 - S_{is}^*) \quad [20]$$

where b is a constant at given T and N .

Substituting [16] and [17] into [20] one may obtain an expression identical with the empirical equation [3]

$$\left(\frac{\partial U_f}{\partial Q} \right)_{Q > Q_{ind}} = \left(\frac{\partial U_f}{\partial Q} \right)_{Q=Q_{ind}} + b - bK_{is}^{2/3}Q_{ind}^{2/3} \quad [21]$$

where the constants

$$A_3 = \left(\frac{\partial U_f}{\partial Q} \right)_{Q=Q_{ind}} + b \text{ and } B_3 = bK_{is}^{2/3}$$

should be functions of the temperature as it was found experimentally.

The dependence between the total current density, J , and the slope $(\partial U_f/\partial Q)_{Q>Q_{ind}}$ could be obtained from Eq. [21] and [18]

$$J = J^* \exp - \left\{ \frac{C_{is}K_{is}^{1/3} [(\partial U_f/\partial Q)_{Q=Q_{ind}} + b]}{b} \right\} \exp \frac{C_{is}K_{is}^{1/3}}{b} \left(\frac{\partial U_f}{\partial Q} \right)_{Q>Q_{ind}} \quad [22]$$

This Eq. [22] is identical with the empirical relation [4], where the quantities

$$A_4 = J^* \exp - \left\{ \frac{C_{is}K_{is}^{1/3} [(\partial U_f/\partial Q)_{Q=Q_{ind}} + b]}{b} \right\}$$

and

$$B_4 = \frac{C_{is}K_{is}^{1/3}}{b}$$

must have constant values at given T and N , which was confirmed by the experiment.

Conclusion

The established anodic behavior of bismuth in aqueous oxalic acid solutions can be explained by a model taking into account the existence of a critical current density determining the appearance of the induction period at each temperature and electrolyte concentration. An induction period does not appear if the anodic current density exceeds some critical value. A continuous anodic film grows from the beginning of the process causing a linear increase of the anode potential with time.

If the current density is lower than the critical one, the film growth is retarded. The current is used for metal dissolution and oxygen evolution. Crystals of a slightly soluble compound precipitate on the anode surface during this induction period. These crystals isolate some part of the surface and cause an increase of the current density on the free surface. When the current density reaches the critical value the induction period terminates and an anodic film begins to grow on the free surface, causing an increase of the anodic potential. In the beginning of this process, the surface insulated by precipitated crystals increases additionally and proportionally to the free surface in the end of the induction period, and after that a steady-state anodization is achieved.

The linear increase of the anodic potential with time in the absence of induction period or after its expiration suggests that the film growth efficiency and field strength across the anodic film are independent of the film thickness.

The found empirical dependences of this somehow unusual kinetics of anodization would be valuable

even if the proposed explanations are not quite correct.

Acknowledgment

The authors are indebted to Dr. R. Raichev for helpful discussions.

Manuscript submitted Feb. 18, 1972; revised manuscript received May 8, 1972.

Any discussion of this paper will appear in a Discussion Section to be published in the June 1973 JOURNAL.

REFERENCES

1. A. Güntherschulze and H. Betz, *Z. Physik*, **71**, 106 (1931).
2. V. Cupr and E. Dvorakova, *Chemické Listy*, **50**, 1492 (1956); *Collection Czech. Chem. Commun.*, **22**, 305 (1957).
3. L. Masing and L. Young, *Can. J. Chem.*, **40**, 903 (1962).
4. W. McNeill and L. Gruss, *This Journal*, **110**, 853 (1963).
5. A. M. Borshchevskiy and V. V. Skorchelletti, *Zashchita metal.*, **1**, 624 (1965).
6. D. J. De Smet and M. A. Hopper, *This Journal*, **116**, 1184 (1969).
7. I. A. Ammar and M. W. Khalil, *Electrochim. Acta*, **16**, 1379 (1971).
8. P. E. Lake and E. J. Casey, *This Journal*, **105**, 52 (1958); J. P. G. Farr and N. A. Hampson, *Electrochem. Technol.*, **6**, 10 (1968); M. A. V. Devanathan and S. Lakshmanan, *Electrochim. Acta*, **13**, 667 (1968).
9. U. F. Frank and K. G. Weil, *Z. Elektrochem.*, **56**, 814 (1952).
10. Th. Heumann and F. W. Diekötter, *ibid.*, **62**, 745 (1958).
11. N. A. Hampson and N. E. Spencer, *Brit. Corros. J.*, **3**, 1 (1968).
12. J. O'M. Bockris, M. A. V. Devanathan, and A. K. N. Reddy, *Proc. Roy. Soc.*, **279A**, 327 (1964).
13. J. O'M. Bockris, A. K. N. Reddy, and M. G. B. Rao, *This Journal*, **112**, 1133 (1966).
14. A. K. N. Reddy and B. Rao, *Can. J. Chem.*, **47**, 2687, 2693 (1969).
15. R. D. Armstrong, M. Fleischmann, and H. R. Thirsk, *Trans. Faraday Soc.*, **61**, 2238 (1965).
16. J. A. Harrison, S. K. Rangarajan, and H. R. Thirsk, *This Journal*, **113**, 1120 (1966).
17. A. K. N. Reddy, *J. Electroanal. Chem.*, **28**, 217 (1970).
18. R. D. Armstrong, *ibid.*, **28**, 221 (1970).
19. S. Ikonopisov and Ts. Nikolov, *Compt. Rend. Acad. Bulgare Sci.*, **24**, 55 (1971).
20. R. G. Keil and R. E. Salomon, *This Journal*, **115**, 628 (1968).
21. S. Ikonopisov, A. A. Girginov, and V. K. Tsochev, *Compt. Rend. Acad. Bulgare Sci.*, **25**, 653 (1972).
22. S. Ikonopisov, *J. Electroanal. Chem.*, **35**, Appl., 1 (1972).
23. S. G. Christov and S. Ikonopisov, *This Journal*, **116**, 56 (1969).

Oxidation State of Anodic Tantalum Oxide after Heat-Treatment

I. Galvanostatic Method as Applied after Heating in Vacuum

Gerhart P. Klein*

P. R. Mallory & Company Inc., Laboratory for Physical Science, Burlington, Massachusetts 01803

ABSTRACT

During heat-treatment of anodic Ta₂O₅ in vacuum (10⁻⁵ Torr) at temperatures in the range from 200° to 700°C oxygen exchange between the anodic oxide, the Ta substrate, and the atmosphere was observed. Galvanostatic reanodization experiments resulted in potential-time (charge) curves which could be used to determine the oxidation state of heat-treated TaO_n as a function of the distance from the electrolyte/oxide interface into the oxide. Profiles of the oxidation state across the oxide were measured for tantalum oxide anodized in 0.1M H₃PO₄ and 0.1M H₂SO₄ after heat-treatment at 10⁻⁵ Torr and 500°C. Of several experimental variables, the time of heat-treatment and the oxide thickness were chosen to illustrate the method of determining oxidation state profiles for the case of heat-treatment in vacuum. In all cases treated in this paper the reduction was carried out to the extent that the oxide as a whole exhibited high electronic conductivity.

Anodic tantalum oxide is amorphous as formed on its substrate (1). If stripped it can be recrystallized at temperatures above about 600°C (2, 3). Below this temperature no change in its structure was observed. Crystalline forms of tantalum oxide are formed during the thermal oxidation of tantalum in oxygen containing atmosphere in this lower temperature range. Also, special anodization conditions can lead to crystalline tantalum oxide [field crystallization (4)]. In the experiments presented in this paper only tantalum oxide in its amorphous form was involved.

Vermilyea (4, 5) had found an effect of heat-treatment on the dissolution rate of Ta₂O₅ and, at the same time, significant changes in the film capacitance upon heating in air, and more so in vacuum or hydrogen atmosphere. Later, Smyth *et al.* (6-10) studied in detail the effect of heat-treatment in air on the dielectric properties of Ta₂O₅. These authors interpreted their results in terms of interactions of the amorphous oxide both with the underlying Ta substrate and the surrounding gas phase.

The incorporation of anions from the electrolyte into the anodically grown oxide was demonstrated by Randall *et al.* (11) for electrolytes containing phosphate and sulfate ions. Incorporation of phosphorous and sulfur was limited to about the outer half of the oxide, indicating that the transport numbers were close to 0.5 for both tantalum and oxygen ions. Similar results were obtained from reanodization curves after heat-treatment of such films in vacuum (12).

This paper reports the results of experiments in which Ta/Ta₂O₅ specimens anodically formed in electrolytes containing phosphate and sulfate ions were heat-treated in vacuum followed by reanodization under constant current conditions. From potential-charge curves (reanodization curves, RAC) the charge required to restore partially reduced TaO_n to its original oxidation state (Ta₂O₅) was obtained while potential was used to measure distance into the oxide from the electrolyte/oxide interface. Thus, profiles of the oxidation state of TaO_n across the oxide film could be measured by electrochemical means.

Experimental

Specimen preparation and anodization.—Specimens used in this study were prepared in the usual way: capacitor grade Ta sheet (Berylco-Kawecki Company) was chemically polished in a mixture of 5 parts H₂SO₄, 2 parts HNO₃, and 1.5 parts HF (all reagent grade,

* Electrochemical Society Active Member.

Key words: anodic tantalum oxide, vacuum heat-treatment, reanodization, galvanostatic potential-charge curves, oxidation state profile.

concentrated), followed by dipping in HF for about 10 sec, rinsing in distilled water, and vacuum annealing at 2100°C for 1 to 3 hr at 10⁻⁵-10⁻⁶ Torr. Anodization was done in Pyrex glass cells with Ta counter-electrodes. Solutions were prepared from A.R. reagents and distilled water. To standardize anodization rates independent of any electronic leakage currents or area variations anodization was done at programmed linearly increasing voltage corresponding to constant current anodization. Stabilization at the anodization voltage was avoided since the incorporation of anions from the electrolyte during anodization had been found to be current dependent (11). Stabilization at constant voltage would have led to a gradient in the foreign ion concentration near the oxide/electrolyte interface.

Heat-treatment.—Vacuum heat-treatment was carried out in a furnace inside a bell jar vacuum system. Constant pressure was maintained by means of an automatic pressure regulator (Granville Phillips). A furnace (Centorr Associates) with cylindrical resistance heated zone (2.5 in. diam × 5 in. high, Hoskins alloy heating element, Inconel heat shields) was mounted on an 18 in. diam vacuum feedthrough collar. The specimens were heated inside vertical quartz tubes which rested on the bottom heat shields. They could be lowered into the hot zone and raised out of it by means of wires operated by a rotary feedthrough. Temperature distribution was found to be within 5°C of the control thermocouple for a specimen 7.5 cm long × 1.25 cm wide.

Galvanostatic reanodization.—The loss of oxygen during heat-treatment was determined quantitatively from potential-charge (reanodization) curves (RAC's). After annealing the specimens were reanodized at constant current density and the voltage was recorded as a function of time. The schematic experimental electronic circuit is shown in Fig. 1A. It consisted of constant current supply (Electronic Measurements Model C633), electrometer (Keithley Model 610A), and strip chart recorder (Hewlett-Packard Model 7101). To make efficient use of the specimens after heat-treatment circular areas (0.3 cm²) were masked off with pressure sensitive tape with silicone adhesive (Mystic Company No. 7305). A specimen with several test areas masked off in this way was mounted on a support plate. The end was clamped against a copper block to provide electrical contact to the substrate. A drop of electrolyte (e.g., 0.1M H₂SO₄) was placed on a test area and a platinum wire mesh, serving as counter-electrode, was brought in contact with the electrolyte (Fig. 1B). This experimental arrangement proved

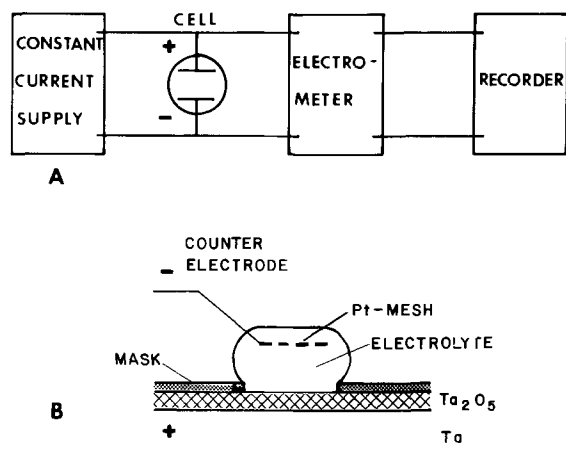


Fig. 1. A. Schematic of electronic circuit used to measure reanodization curves. B. Masked off test area on Ta/TaO_n specimen.

highly advantageous as it permitted several tests to be performed on a given specimen. The test areas were sharply defined by the tape. No edge effect or electrolyte undercutting was observed.

Potential was measured against the platinum counterelectrode, *i.e.*, the potential of the hydrogen electrode in the same solution, approximately. No corrections for ohmic potential drop in the electrolyte and "pre-existing" oxide were applied since only thick oxides (typically 160V anodization voltage) and low current densities (typically 0.2 mA/cm²) were used. Any error from these sources was within the general experimental inaccuracy.

Sectioning of tantalum oxide.—In some cases RAC's were measured after partial removal of tantalum oxide in 48% HF which was saturated with NH₄F at room temperature (13). The addition of NH₄F reduced the rate of attack and more uniform dissolution of the film resulted. The amount of oxide removed was measured by comparison with a color gauge. The difference in thickness could also be obtained from the difference in reanodization voltage, as is shown later.

Capacitance measurements.—Capacitance measurements were performed in an experimental setup similar to the one used for reanodization experiments. The electrolyte used was 5M H₂SO₄ and the counterelectrode was a platinized Pt grid. Capacitance was measured with a digital capacitance bridge (Micro Instruments Model 5300) at a frequency of 120 Hz.

Results and Discussion

Anodization and reanodization (RAC) curves.—Under the condition of negligible electronic charge transfer across the oxide/electrolyte interface the anodization of Ta at constant current density is characterized by a linear increase of voltage and oxide thickness with time. With suitably pretreated high-purity Ta the ratio $i_{ion}/i = 1 - i_{el}/i \approx 1$ (i_{ion} = ionic, i_{el} = electronic, i = total current), which means that under galvanostatic anodization conditions nearly all charge is used to form anodic oxide (1). Since the field is constant during constant current anodization, the thickness of the oxide is proportional to the anodization voltage.

Figure 2 shows characteristic reanodization curves C-F after heat-treatment in comparison with an original anodization curve A and the reanodization and continued anodization curve B of a specimen without heat-treatment. The linear rise of potential with charge in curve A for the anodization of Ta at 0.2 mA/cm² indicates that the rate of oxide growth is constant. The Ta/Ta₂O₅ specimen previously anodized to 160V showed a behavior as in curve B when subjected to further anodization at 0.2 mA/cm². The potential rose

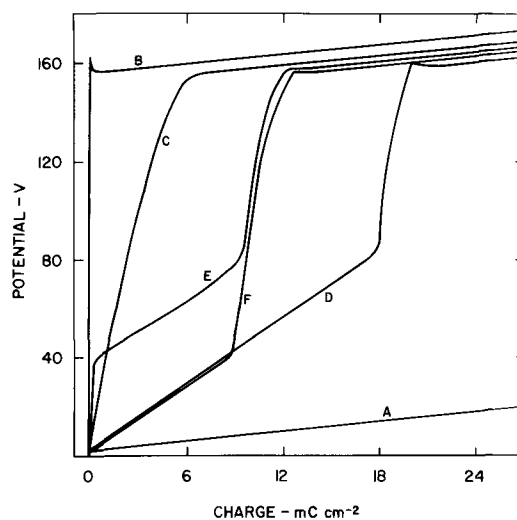


Fig. 2. Anodization (A) and reanodization (B-F) curves of anodic tantalum oxide. All curves were measured at 0.2 mA/cm². With the exception of A, all anodizations were done at 0.3 mA/cm² in the electrolytes given below. Heat-treatment of specimens C-F was carried out at 500°C, 10⁻⁵ Torr, for 120 min.

Curve	Electrolyte	Voltage, V (Anodization of Ta)
A	0.1M H ₃ PO ₄	0-160
B	0.1M H ₃ PO ₄	0-160
C	0.1M H ₂ SO ₄	0-160
D	0.1M H ₃ PO ₄	0-160
E	0.1M H ₃ PO ₄	0-80
	0.1M H ₂ SO ₄	80-160
F	0.1M H ₂ SO ₄	0-80
	0.1M H ₃ PO ₄	80-160

steeply exceeding the original formation voltage (V_A) in an overshoot, followed by a decay of the overshoot and a linear rise of potential, characteristic of the rate of further oxide formation. The slope of this section of curve B was identical to curve A.

When Ta/TaO_n specimens which had previously been anodized to 160V followed by heat-treatment at 10⁻⁵ Torr, 500°C were subjected to the same anodization conditions, the potential-charge curves C-F were obtained. Their slopes in the potential range to V_A fell between those of curves A and B indicating that substantial amounts of charge were required to reach the original anodization voltage. Beyond V_A the slope was again found to be identical to that of curve A. Curve C was obtained with a specimen which had been anodized in 0.1M H₂SO₄ to 160V followed by heat-treatment at 500°C, 10⁻⁵ Torr, for 120 min. A smooth rise of potential with charge without abrupt changes in slope (except near V_A) was found. Curve D shows the reanodization behavior of a specimen which had been anodized in 0.1M H₃PO₄ to 160V followed by heat-treatment under the same conditions as above. In this case the potential-charge curve to V_A showed two sections with different slopes: to about $V_A/2$ the slope was nearly linear and much shallower than that of curve C. Beyond $V_A/2$ the slope became steeper approaching that of the upper part of curve C. The remaining curves E and F were obtained with specimens that had been anodized, consecutively, in 0.1M H₃PO₄ and 0.1M H₂SO₄ followed by heat-treatment under the same conditions as before. In the case of curve E, anodization in 0.1M H₃PO₄ to 80V was followed by anodization in 0.1M H₂SO₄ from 80 to 160V. In the case of curve F, the sequence of anodizations in H₃PO₄ and H₂SO₄ was reversed. Curve E exhibited three distinctly different slopes before reaching V_A : to about $V_A/4$ the slope was steep and similar to curve C (anodization in 0.1M H₂SO₄), between $V_A/4$ and $V_A/2$ the shallower slope of curve D (anodization in 0.1M H₃PO₄) was evident, and above $V_A/2$ the slope was

again steep and similar to the upper parts of curves C and D. In curve F only two slopes were in evidence: to $V_A/4$ the slope was shallow and approached that of curve D (anodization in 0.1M H_3PO_4) while above $V_A/4$ curve F was nearly identical with the corresponding part of curve C.

The general shape of reanodization curves (RAC's) was found to be a function of variables relating to the anodization of the original oxide (type and concentration of electrolyte, rate of anodization, anodization voltage V_A , among others) and the conditions of heat-treatment (pressure, temperature, time). Depending on the conditions of heat-treatment, the reanodization charge expressed as a fraction of the anodization charge could vary between 0 and nearly 100%. At the given pressure the limiting temperatures for these conditions to be established were, approximately, 300° and 700°C.

The specific examples given in Fig. 2 illustrate the differences in RAC's arising from differences in the electrolyte used during anodization. The RAC's shown in Fig. 2 do not represent steady-state conditions in the oxide, however, at 500°C, 10^{-5} Torr, and 160V anodization the further change of their shape with time would be a slow one beyond times of the order of 120 min. For this reason, they can be considered to reflect quasi steady-state conditions. In the context of this paper no attempt is being made to systematically present results of the dependence of RAC's on the variables of anodization and heat-treatment. Instead, typical RAC's are used to illustrate the method of galvanostatic reanodization and its application to the measurement of profiles of the oxidation state across heat-treated TaO_n .

The RAC's C-F of Fig. 2 have in common that substantial quantities of charge, amounting to as much as 10% of the charge stored in oxide anodized to the same voltage V_A , were consumed during the process of reanodizing heat-treated oxide to the original anodization voltage, V_A . This charge consumed during reanodization could, in principle, be either ionic or electronic charge. It will be necessary to account for the charge consumed during reanodization and to establish the type of charge transfer in the oxide and across the oxide/electrolyte interface before an interpretation of the changes occurring during heat-treatment in vacuum can be attempted.

Initial potential drop.—A further common characteristic of curves C-F is the absence of a steep initial rise of potential immediately following the switching on of constant current. Any appreciable resistance in the experimental system would lead to a corresponding potential drop which would appear with a rate of increase determined by the rate of capacitor charging. An extreme case of this kind is illustrated by curve B which showed a potential drop equivalent of the ionic resistance of the original oxide. In this case, the presence also of an initial overshoot of potential beyond V_A indicated initial excess resistance to ionic migration as compared to the steady-state resistance. The absence of an initial potential drop showed that the anodic oxide film as a result of heat-treatment had lost its insulating properties. Whether this was due to changes at the oxide/electrolyte interface facilitating electron injection, or changes in the oxide itself increasing its electronic conductivity will have to be established.

Anodization electrolyte.—A comparison of RAC's C-F reveals the influence of the anodization electrolyte on the behavior of Ta_2O_5 during heat-treatment in vacuum and subsequent reanodization to V_A . From radiotracer experiments by Randall *et al.* (11), quantitative information is available concerning the incorporation of ions from the anodization electrolyte into an outer layer, extending to about the mid-point of the oxide. The outer layer is formed by tantalum ion migration and oxide formation at the electrolyte/

oxide interface which explains the possibility of ionic inclusions during oxide growth. The inner half of the oxide remains unaffected by the electrolyte since it is the result of oxygen ion migration and oxide growth at the oxide/metal interface. According to Randall (11), the amount of phosphorous incorporated into anodic Ta_2O_5 from dilute H_3PO_4 was substantially greater than the amount of sulfur that was incorporated from dilute H_2SO_4 , concentrations of the two acids being equal.

Curve C was obtained with Ta_2O_5 anodized in 0.1M H_2SO_4 , while curve D was the result of anodization in 0.1M H_3PO_4 . The presence of phosphorous in the latter case must have been responsible for the difference in reanodization curves, which showed a shallow slope to about $V_A/2$ for phosphorous-containing oxide. In separate experiments, it was established that this slope was dependent on the concentration of phosphorous in the anodic oxide showing a decrease with increasing concentration. By contrast, the slope of RAC's of oxide anodized in dilute H_2SO_4 , as well as a large number of other electrolytes (*e.g.*, oxalic, nitric, hydrochloric acid, and their salts) was found to be independent of the concentration of the anodization electrolyte. For this reason, it seems justified to assume that curve C (H_2SO_4) was representative of anodic Ta_2O_5 which was not affected by inclusions from the electrolyte. The results shown in curves E and F for consecutive anodizations in 0.1M H_3PO_4 and 0.1M H_2SO_4 correspond directly to the additional duplex structure of the outer half of the oxide. With anodization in H_3PO_4 followed by H_2SO_4 , the layer containing phosphorous was buried underneath a layer containing sulfur. Reversing the sequence of anodizations reversed the sequence of the layers. The inner half of the oxide again was not affected by incorporation of ions.

The fact that phosphorous incorporation was limited to the outer half of the oxide established by tracer experiments (10) together with the observation that the reduced slope of curve D (caused by anodization in H_3PO_4) was traversed first during reanodization lead to an important qualitative conclusion: in RAC's of the type shown in Fig. 2 the potential scale from zero to V_A can be related in the process of reanodization to a traversing of the oxide from the oxide/electrolyte interface to the oxide/metal interface. The results of curves E and F with consecutive anodizations confirm this conclusion in that the sequence of characteristic slopes in the RAC's corresponded directly to the sequence of layers in the oxide.

The close correspondence of those parts of the RAC's extending from $V_A/2$ to V_A for all anodization electrolytes indicates that this part of the oxide is unaffected by ionic inclusions from the electrolyte, in agreement with the results by Randall *et al.* (10). The continuity in the slope of curve C between the outer and inner parts of the oxide is further confirmation for the previous conclusion that oxide anodized in dilute H_2SO_4 is unaffected by ionic inclusions as regards its behavior during heat-treatment in vacuum under the given conditions.

Nature of charge consumed during reanodization.—For the correct interpretation of the RAC's of heat-treated tantalum oxide it is essential to determine the charge-consuming reactions during reanodization to V_A . In particular, the distribution of the total charge between electronic and ionic reactions must be established. Any electronic charge transferred across the oxide/electrolyte interface would be consumed in redox reactions, *i.e.*, under the given experimental conditions the evolution of oxygen. However, this was not observed during reanodization even though the total measured charge, if electronic, should have led to visible gas evolution. For this reason, the major part of the charge could not have been electronic.

To determine the extent of any minor electronic contribution to the total charge and to establish the

ionic current efficiency of reanodization, the more sensitive redox print-out method (14) for detecting electronic current (e.c.) was used. Several such experiments were performed with heat-treated Ta/TaO_n specimens. With high purity Ta used in this study the results were negative. No uniformly and negligible nonuniformly distributed electron transfer across the oxide/electrolyte interface was detectable during reanodization.

When less pure Ta specimens were used increased nonuniformly distributed impurity conduction was found. Figure 3 illustrates a case where the effect of e.c. on the reanodization curve could not be neglected. A print-out of the e.c. distribution was obtained by reanodizing a specimen with KI/starch gel as the electrolyte. The specimen had been anodized to 160V in 0.1M H₃PO₄ followed by heat-treatment at 500°C, 10⁻⁵ Torr for 120 min. The gel was supported by Millipore paper and lifted off the specimen after constant current reanodization in steps of 10V. Fresh electrolyte was used in every voltage interval. The RAC shown in Fig. 3A was obtained during the print-out experiment. The anodic prints obtained in the indicated intervals are shown next to the corresponding segments of the RAC. There was no indication of any uniformly distributed e.c., however, random patterns of e.c. indicating the presence of impurities were observed. As was shown previously (14, 15), heat-treatment of Ta or Ta/Ta₂O₅ specimens may cause electronically active impurities to appear at the surface of the anodic oxide. No e.c. had been detected in the specimen of Fig. 3 prior to heat-treatment.

That surface impurities were the cause for e.c. in this case could be demonstrated by the following experiment which revealed, at the same time, the strong influence of the electrolyte on surface impurities and resulting e.c. It was noticed that areas on the same specimen adjacent to the one for which the prints of Fig. 3A were obtained gave the dashed reanodization curve when reanodized in 0.1M H₂SO₄. In a separate experiment adjacent areas were reanodized as indicated in Fig. 3B and C. One masked-off area was first anodized to 10V in 0.1 H₂SO₄ followed by print-out anodization in KI for which a clear print was obtained (Fig. 3B). Another area was first anodized in KI resulting in the intensely colored print and little rise in potential (Fig. 3C). This was followed by anodization to 10V in 0.1M

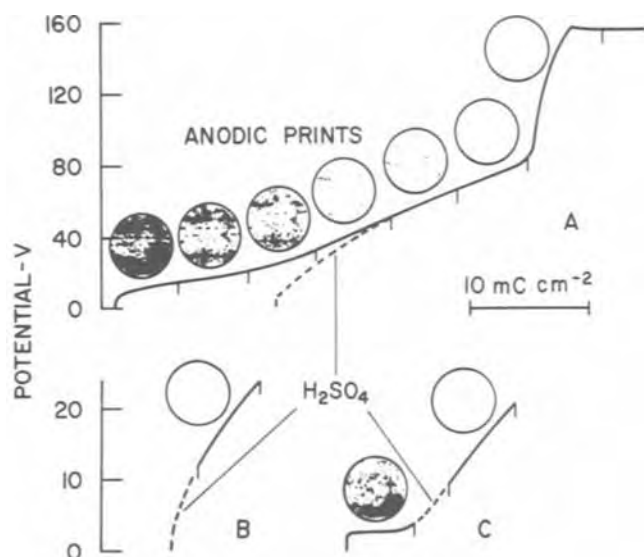


Fig. 3. Reanodization of heat-treated tantalum oxide combined with anodic print-out of electronic conductivity. Anodic prints were obtained by reanodizing in KI/starch printing electrolyte during 1 min intervals before exchange of printing medium. Diameter of original print 0.5 cm. Dashed RAC's indicate reanodization in 0.1M H₂SO₄. For further details, see text.

H₂SO₄ and a further print-out anodization. The second print was clear. Whatever impurities had been present after heat-treatment they were deactivated during reanodization in H₂SO₄, while KI/starch gel required much longer time to accomplish the same. Figure 3A showed that KI reanodization was seriously affected by e.c. to about 50V with slight impurity related non-uniform e.c. even above this level. Dissolution of impurities by an electrochemical mechanism tied to the passage of current was the most likely course of deactivation.

These results show that RAC's can be severely distorted in the presence of impurities and the resulting electronic charge transfer. These problems can be minimized by the use of high-purity materials and reanodization in dilute acid (e.g., 0.1M H₂SO₄) which, as was shown, eliminated the effect of any remaining impurities. Anodic prints were used to detect any residual e.c. Comparison of the print-out intensity with a set of test patterns made it possible to estimate the fraction of electronic charge and thus current efficiency of reanodization. Specimens were rejected if the electronic charge exceeded a few per cent of the total charge.

These experiments demonstrated conclusively that the charge consumed during reanodization was ionic charge and that the ionic processes responsible for the reanodization behavior of heat-treated TaO_n proceeded with an ionic current efficiency approaching 1.0.

Restoration of heat-treated tantalum oxide.—The ionic charge consumed during reanodization to V_A must be related directly to the changes that took place in anodic tantalum oxide during heat-treatment. It is postulated that reanodization means restoration of partially reduced oxide TaO_n to its original oxidation state Ta₂O₅. This interpretation is suggested by the fact that the slopes of the reanodization curves C-F in Fig. 2 fall between those of the anodization of bare Ta (curve A) and the reanodization of 160V Ta₂O₅ without heat-treatment (curve B). With this assumption, the charge consumed during reanodization to V_A would measure the amount of oxygen lost during heat-treatment. If at the same time the potential scale can be related to position in the oxide, then it will be possible to determine the oxidation state of tantalum oxide after heat-treatment as a function of the distance from either the oxide/electrolyte or oxide/metal interface.

From previous experiments, the following conclusions pertain to this assumption:

1. The absence of an initial potential drop during reanodization at constant current showed that the oxide, after heat-treatment under the given experimental conditions, had become electronically conductive throughout.
2. Electron transfer across the oxide/electrolyte interface was found to be inhibited. This means that only ions could be transferred across this interface and that reanodization had to begin at the oxide/electrolyte interface and proceed inward toward the metal.

The following experiments are intended to provide additional evidence in support of the above assumptions.

Step-reanodization curves.—The relationship of charge required to reach a particular potential on the RAC with position in the oxide could be established experimentally by measuring reanodization curves after partial stripping of oxide. In Fig. 4 a series of RAC's is shown that were measured from different steps in the oxide. The step pattern dissolved into the oxide is illustrated schematically at the bottom of Fig. 4. The specimen used in this experiment was of the type shown in Fig. 2, curve D. It had been anodized in 0.1M H₃PO₄ to 160V and heat-treated at 10⁻⁵ Torr, 500°C for 120 min. The top curve (solid line, marked step 0) represents the RAC of the oxide as a whole. The subsequent curves (marked steps 1-5) were measured at progressively deeper steps in the oxide. Their origins were shifted to the right to make the first tran-

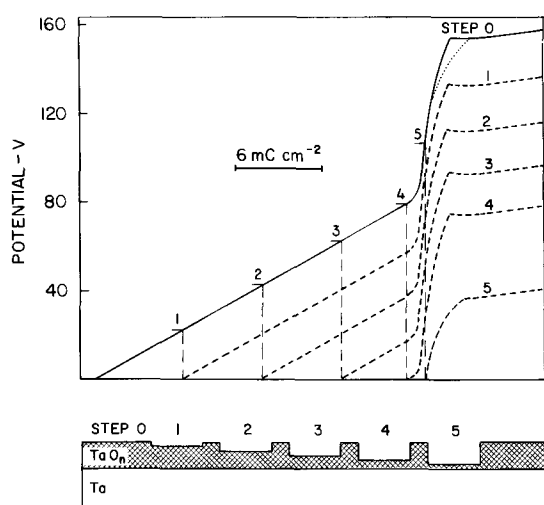


Fig. 4. Reanodization curves of heat-treated tantalum oxide from steps of different height dissolved into the oxide (see schematic at bottom). The origins of curves 1-5 were shifted to the right such that the steep sections of each curve coincided, on the abscissa, with that of the original RAC ("step 0"). By upward shifting curves 1-5 could be superimposed on the original RAC. The only deviation occurred near V_A and was indicated by the dotted line. Anodization: 0.1M H_3PO_4 , 0.3 mA/cm², 160V. Heat-treatment: 500°C, 10^{-5} Torr, 120 min.

sition points (from the shallow to the steep slope) coincide on the abscissa relative to the "step 0" curve. With progressing penetration into the oxide, progressive removal of the shallow linear part of the RAC left of the transition point to the steeper slope was observed. Then the removal of the transition point itself and the subsequent steep curve segment followed. At their top end all curves showed a sharp transition to the shallow slope associated with further anodization, corresponding to the original V_A .

As the oxide was stripped increasing portions of the original RAC were cut off. The remaining curve segments were identical to corresponding sections of the original curve. By shifting curves 1-5 upward they could be superimposed on the original curve. They matched closely except at the top end where the slope of the last step RAC (step 5) deviated somewhat from the previous curves. This effect is believed to be related to the potential overshoot which was much more pronounced in Fig. 2, curve B, but still affected reanodization curves of the type shown in Fig. 4 in some small degree.

The magnitude of the potential overshoot and its effect on the shape of the transition region from the steep reanodization slope to the shallow anodization slope depends on the extent of reduction of the anodic oxide. The further the reduction goes, the smaller its effect. In the context of this paper the specimens used had been subjected to heat-treatment conditions sufficiently severe to minimize the overshoot and reduce its influence on the results to within the over-all experimental error.

The results of this experiment provided evidence for the previously stated assumption that reanodization of heat-treated tantalum oxide began at the electrolyte/oxide interface and continued toward the metal. At the same time it showed that the reanodization potential could be considered a direct measure of distance into the oxide from the oxide/electrolyte interface. In the following it will be shown that reanodization potential and distance into the oxide were linearly related.

It is assumed that in the process of reanodization partially reduced oxide is restored to its original oxidation state with properties similar to those of originally formed anodic oxide. The field required to move ions through restored oxide can then be expected to be of

comparable magnitude as the field required for anodization. In addition, during anodization the field at constant current density is known to remain constant independent of anodization voltage, making voltage a linearly related measure of oxide thickness. It appears reasonable, therefore, to assume that the same holds true for the field in oxide restored to the maximum oxidation state after reanodization.

Field differences between anodization and reanodization could arise due to differences in the structure of as-anodized and heat-treated oxide and variations of the dielectric constant with inclusions of ions from the electrolyte. However, the available evidence suggests that these are minor effects which may affect the accuracy of the distance scale without changing either the qualitative picture or the charge-related quantitative aspect, i.e., the determination of the oxidation state.

Comparison of thickness measurements from interference color and reanodization voltage.—During heat-treatment in vacuum with moderate partial reduction of tantalum oxide the interference color of the oxide did not change noticeably, a fact which had been noted by Vermilyea (4). Only when the reduction reached low oxidation states of TaO_n ($n < 1.5$) did the oxide interference color change to a metallic appearance. Interference color can, therefore, be used as a measure of thickness as long as the reduction has not been carried too far.

Reanodization experiments can also be used to measure oxide thickness. In Fig. 4 the voltage equivalent of the height of the steps dissolved into the oxide could be obtained from the vertical displacement of the step reanodization curves 1-5 with respect to the original RAC at a point beyond the steep section of the curves. Beyond the points on the RAC's corresponding to V_A reanodization had been completed and the difference in voltage was caused by the removal of the oxide over the corresponding step.

Figure 5, curve A shows a comparison of thickness measurements on a specimen similar to the one illustrated in Fig. 4, as determined by comparison with a color gauge and by reanodization. The color gauge was calibrated in terms of anodization voltage. The voltage equivalent of thickness was plotted against the duration of oxide dissolution in HF/NH_4F for a particular

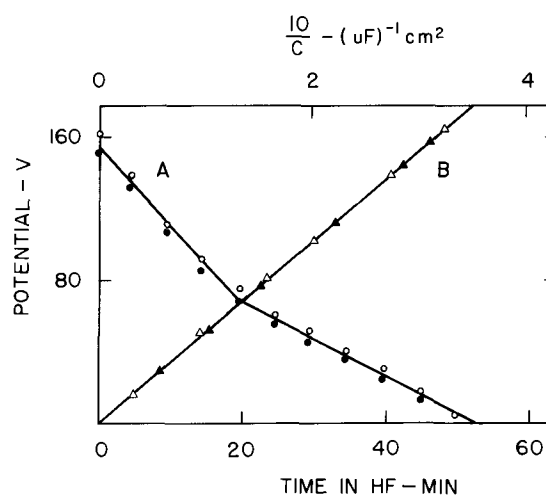


Fig. 5 A. Comparison of oxide thickness remaining after stepwise dissolution in HF/NH_4F . \circ Thickness (in volts) measured by reanodization (0.1 mA/cm²); \bullet thickness by comparison with color gauge. B. Reciprocal capacitance vs. thickness (in volts). \triangle Ta specimen after anodization to given voltages (0.1 mA/cm²); \blacktriangle tantalum oxide heat-treated, dissolved in steps and reanodized to same point on original RAC (corresponding to anodization voltage V_A). Anodization: 0.1M H_3PO_4 , 0.3 mA/cm², 160V. Heat-treatment: 500°C, 120 min, 10^{-5} Torr.

step. The rates of oxide dissolution of the outer and inner parts of the oxide were noticeably different which gave rise to a change in slope at about the midpoint of the oxide. However, for both sections color chart and reanodization yielded closely corresponding values for the thickness. The generally lower voltage readings from the color chart may have been caused in part by the lack of standardization between the two methods. Significantly, the displacement, within experimental error, was constant over the full range indicating that a linear relationship existed between the potential differences as obtained from reanodization curves after dissolution of steps into the oxide, and the corresponding changes in interference color.

Comparison of thickness measurements from capacitance measurements and reanodization voltage.—Capacitance measurements provide an alternative method for determining oxide thickness. Since substantially reduced oxide exhibited high electronic conductivity capacitance measurements could only be applied to reanodized oxide. Again, a step pattern was dissolved into heat-treated oxide of the same kind used in the previous experiment. The remaining oxide on each step was reanodized to a point on the step RAC equivalent to V_A on the original RAC (transition point between steep part of RAC and shallow slope of continued anodization). In Fig. 5, curve B the reciprocal of capacitance (top scale) was plotted vs. the thickness of oxide as measured by reanodization. For comparison, $1/C$ vs. anodization voltage was also measured for a Ta specimen anodized to various voltages. Both types of measurements fell on the same straight line indicating that $C \times V = \text{const}$, consequently $\epsilon \times F = \text{const}$ (V , voltage equivalent of oxide thickness; ϵ , relative dielectric constant; F , field), a result generally found for anodic oxides of the same chemical nature (11).

The linear relationship between $1/C$ and reanodization potential on the one hand, and thickness determined via interference colors and reanodization potential on the other substantiate the earlier conjecture about a linear relationship between reanodization potential and distance into the oxide measured from the electrolyte/oxide interface.

Dependence of RAC's on current density.—The amount of charge required to restore partially reduced tantalum oxide to its maximum oxidation state should be independent of the current density used in the galvanostatic experiment. It is assumed that electronic leakage currents can be neglected. Since potential is used as a measure of distance into the oxide, it is an additional requirement that the linear relationship between reanodization potential and distance be maintained independent of the current density used. In cases where initial potential drop and/or potential overshoot are observed, this condition may not be fulfilled. The observed potential has to be corrected before it can be used as a linear measure of distance into the oxide. While the corrections can be carried out, they were not necessary in the cases discussed in this paper.

In order to establish experimentally whether the above assumptions were justified, a group of RAC's were measured with current densities varying from 0.05 to 1.0 mA/cm². The specimen was of the type illustrated in Fig. 2, curve D (0.1M H₃PO₄, 160V, 10⁻⁵ Torr, 500°C, 120 min) and exhibited three sections with the characteristic slopes related to the outer, phosphorous-containing oxide, the inner phosphorous-free oxide, and continued anodization. The transition between different slopes occurred, on the potential scale, at points V_m and V_A with V_m indicating the boundary of the P-containing oxide and V_A the boundary of the previously formed anodic oxide. The charges required to reach these points were q_m and q_A , respectively. The experimental results have been summarized in Table I. The ratio V_m/V_A measuring the fraction of P-containing oxide was found to be close to 0.5 for all current

Table I. Characteristic voltage transition points and reanodization charge as a function of current density

C.D., mA/cm ²	V_m/V_A	q_m , mC/cm ²	q_A , mC/cm ²	q_m/q_A
0.05	0.50	11	12.7	0.86
0.1	0.50	11.3	13	0.87
0.2	0.50	10.8	12.2	0.88
0.5	0.505	10.3	12	0.86
1.0	0.505	10.1	11.8	0.86

densities. The charge required to reach V_m was $q_m = (10.7 \pm 0.44)$ mC/cm² and the charge to reach V_A was $q_A = (12.3 \pm 0.45)$ mC/cm². For five current densities varying by a factor of 20 (0.05-1 mA/cm²), the charges q_m and q_A measured to V_m and V_A , respectively, were independent of current density within a standard deviation of less than $\pm 5\%$ of the average charge.

The constancy of the ratio of the charges q_m/q_A together with the constancy of the corresponding voltage ratio demonstrated that any current density dependent effects during reanodization acted equally on the outer and the inner oxide. The inclusion of phosphorous in the outer layer and its higher degree of reduction compared to the inner oxide had no effect on the measurement of position in the oxide by means of potential, as long as it was expressed as a fraction of V_A . Absolute distance measurements require a calibration of the potential scale by optical measurements, for example, since the determination of V_A from RAC's is dependent on current density.

Repeatability of the effect of heat-treatment.—It was shown that the incorporation of phosphorous into an outer part of the oxide film was responsible for a greater loss of oxygen during vacuum heat-treatment than would occur under similar conditions in the presence of sulfur, or the absence of any foreign ions. The increased loss of oxygen could not be accounted for by assuming that P was incorporated in the form of P₂O₅ and that it was the source of lost oxygen. The P content of Ta₂O₅ was found to be of the order of a few atom per cent (10) when anodization was done in dilute H₃PO₄, while the oxygen loss could amount to a much larger fraction of the total oxygen content of the oxide depending on the conditions of heat-treatment. In whatever form P was incorporated into the oxide during anodization causing increased oxygen loss during heat-treatment in vacuum, the effect should not repeat itself after the first heat-treatment and reanodization if P had been lost during the first vacuum treatment. Figure 6 shows the results of repeated cycles of heat-treatment and reanodization in 0.1M H₃PO₄ for 80 and 160V Ta₂O₅. The partial reduction of the oxide in the outer part of the film clearly repeated itself, even though differences were observed in the degree of reduction. For 160V Ta₂O₅ the trend was for the first heat-treatment to result in a slightly greater loss of oxygen than for subsequent cycles, while the opposite was found for 80V (and lower) oxides. The significance of these trends is not clear; however, the differences are significantly larger than the experimental uncertainty. The result of these experiments was that phosphorous which caused the increased loss of oxygen was not removed during repeated heat-treatments in vacuum.

Effect of heat-treatment on the structure of tantalum oxide.—Anodic tantalum oxide is amorphous and its structure has been described as glasslike (3). Electron and x-ray diffraction patterns show only very diffused rings from which an upper limit of about 10Å has been estimated as the size of microcrystals, if indeed there are any. Nothing is known about their structure and whether they can be considered as nuclei of any of the known crystalline modifications of Ta₂O₅. In the context of this study structural changes during heat-

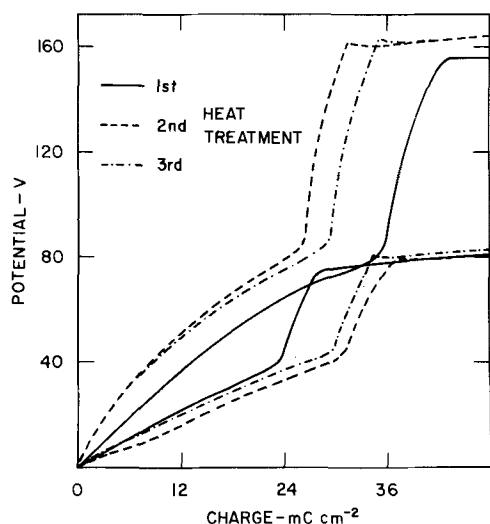


Fig. 6. RAC's for three cycles of heat-treatment and reanodization. Anodization: 0.1M H_3PO_4 , 0.3 mA/cm 2 , 80 and 160V, respectively. Heat-treatment: 500°C, 90 min, 10^{-5} Torr. Reanodization: 0.1M H_3PO_4 , 0.2 mA/cm, 80 and 160V, respectively.

treatment had to be considered since the ionic charge consumed during reanodization could have been related to changes in the structure of the oxide. For example, if microcrystals were in fact present and could act as nuclei for the growth of crystalline oxide, then heat-treatment might lead to increased crystallinity of the oxide. The ionic charge might then be required to fill gaps between crystalline areas. If microcrystals were absent or could not act as nuclei, then nucleation would have to occur before any recrystallization could take place. In this case, there would be little reason for ionic charge consumption unless crystallization occurred during reanodization itself. Light and electron microscopy, as well as electron reflection diffraction, were applied to oxide films after heat-treatment at 10^{-5} Torr in the temperature range of 650°C for several hours. No changes in oxide topography or any significant sharpening of electron diffraction patterns could be observed which would indicate recrystallization of existing amorphous oxide. It was, therefore, concluded that no significant structural changes had taken place during heat-treatment in vacuum and that ionic charge could not have been consumed in any structure related phenomenon.

Mechanism of reanodization.—The formation of tantalum oxide is a high-field process and involves the migration of both oxygen and tantalum ions through the existing oxide (2, 16). The migration of the latter leads to oxide formation at the oxide/electrolyte interface and results in the incorporation of ions from the electrolyte into oxide growing at this interface (11). Oxygen migration leads to oxide formation at the oxide/metal interface. At constant current, the voltage increases linearly with thickness and the electric field is constant. After heat-treatment in vacuum and some loss of oxygen the anodic oxide as a whole becomes electronically conductive, as evidenced by reanodization curves starting from very low voltage. Reanodization starts at the electrolyte/oxide interface and proceeds inward toward the metal. Ionic migration can only occur in such parts of the oxide which have been restored or the required high field could not be established. The absence of homogeneous electron injection from the electrolyte shows that the properties of the electrolyte/oxide interface of restored and original oxide are the same.

It is proposed that the mechanism of reanodization may be similar to that of anodization with the difference that no tantalum ions enter the oxide from the tantalum substrate until the existing reduced oxide has

been restored in its entirety. It can be assumed that both tantalum and oxygen ions migrate during reanodization. In this case Fig. 7 shows, schematically, the partially restored oxide. Distance is expressed as a fraction of the total oxide thickness, which extends from $x = 0$ (electrolyte/oxide interface) to $x = 1$ (oxide/metal interface).

After partial reanodization to a depth x_2 , the restored oxide consists of three layers: the outermost layer from $x = 0$ to x_1 resulting from the migration of tantalum ions from the reduced oxide to the electrolyte/oxide interface (reaction I). These ions represent part of the metal excess in the reduced oxide over the stoichiometric composition of Ta_2O_5 . The formation of "fresh" tantalum oxide at the electrolyte/oxide interface can be expected to proceed under further incorporation of ions from the electrolyte. The second layer consisting of restored stoichiometric oxide extending from x_1 to x_2 results from the migration of oxygen ions from the electrolyte/oxide interface inward (reaction II) and, at the same time, the migration of tantalum ions outward (reaction I). In reaction II oxygen ions combine with excess tantalum at the boundary x_2 between restored and reduced oxide. In the third layer consisting of reduced oxide and extending from x_2 to $x = 1$, the current is carried by electrons. The migration of oxygen does not lead to the formation of "fresh" oxide as does the migration of tantalum ions since it replaces oxygen in the existing oxide. For this reason no additional oxide free of inclusions is formed.

In the process of reanodization, the total oxide thickness remains constant until the restoration reaches the oxide/metal interface. At this point, additional oxide is formed and tantalum ions are added from the substrate. For these reasons, fresh oxide formed by tantalum ion migration during reanodization is oxide formed from metal excess in the reduced oxide by a change of place of metal ions between reduced oxide and the oxide/electrolyte interface. The charge that is measured as a function of potential is the result of the sum of the partial ionic current densities.

The measured voltage across the restored oxide is the sum of voltage drops across the fresh and the restored oxide. It appears reasonable to assume that the field in the two kinds of oxide is of comparable magnitude. In addition, it can be assumed that the transport number for cation migration during reanodization is similar to that during anodization ($n_{\text{Ta}} \approx 0.5$). This means that about half of the metal excess existing after heat-treatment would be converted into fresh oxide. Since the integral reanodization charge was, typically, of the order of one tenth or less of the corresponding anodization charge to the same voltage (see Fig. 2, curve D) one estimates the voltage equivalent

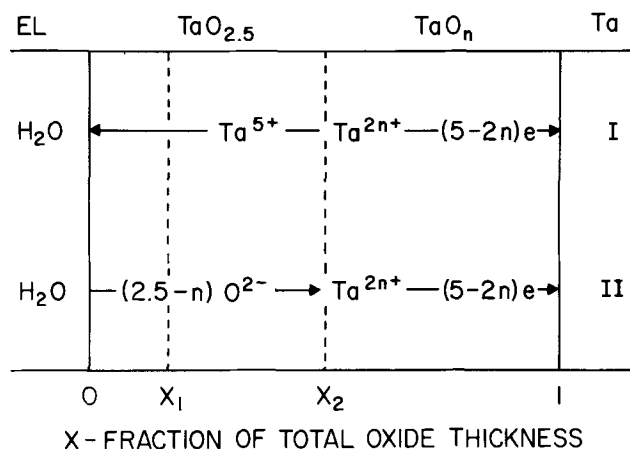


Fig. 7. Schematic diagram of reactions occurring during reanodization after heat-treatment in vacuum.

lent of the thickness of fresh oxide to about one twentieth or less of the total anodization voltage. This means that any differences in the potential scale arising from fresh oxide are completely negligible within the experimental error.

Oxidation state of tantalum oxide.—Reanodization curves of the type shown in Fig. 2, curves C-F can be used to establish the profile of the oxidation state n of heat-treated TaO_n . This is possible since the position in the oxide is related directly to the reanodization voltage while the measured charge represents the amount of oxygen lost during heat-treatment. It should be noted that corrections are required in the presence of initial potential drop and potential overshoot. However, this problem does arise in cases of strong reduction in vacuum which is the case for all examples presented in this paper.

The procedure for deriving the profile of the oxidation state of TaO_n as a function of distance from the outer interface into the oxide is straightforward once a correct potential-charge curve has been obtained. It is based on a point by point comparison of the slope y of a particular RAC with the slope y_0 of the anodization curve. The rate of continued anodization after complete reanodization of the heat-treated oxide is identical with the rate of anodization of tantalum. (It is important to measure y_0 sufficiently far from V_A to exclude any influence of oxygen dissolved in the substrate during heat-treatment.) The slope $y(V_i)$ of the reanodization curve at potential V_i was obtained by numerical differentiation of the reanodization curve. With V_A as a measure of total oxide thickness, the distance into the oxide was expressed as a fraction of the total oxide thickness $x = V/V_A$. The oxidation state was calculated from Eq. [1]

$$n(x) = 2.5(1 - y_0/y(x)) \quad [1]$$

where y_0 = rate of anodization ($Ta \rightarrow Ta_2O_5$) ($V \text{ mC}^{-1} \text{ cm}^2$), y = rate of reanodization ($TaO_n \rightarrow Ta_2O_5$) ($V \text{ mC}^{-1} \text{ cm}^2$), V_A = anodization voltage, and x = fraction of total oxide thickness (from el/ox interface) measured in terms of reanodization voltage.

Accuracy of oxidation state profiles.—The limitations on the accuracy of the electrochemical determination of reanodization potential and charge have already been discussed. Once potential-charge curves have been obtained the derivation of the oxidation state profile becomes a mathematical operation which can be done with the desired accuracy. For experimental reasons, the determination of the oxidation state becomes the more accurate the higher the oxidation state of TaO_n after heat-treatment is. [A reanodization slope which is double the anodization slope means that n has reached an oxidation state ($n = 1.25$) which is already half the maximum ($n = 2.5$). Compare this to the change in n from 2.25 to 2.47 for a change in the reanodization slope from 10 to 100 times the anodization slope.]

For constant current density, y and y_0 are measured with about the same absolute error Δy , causing the greater uncertainty with low values of y . For this reason, relative changes at high oxidation states can be determined with high accuracy since y_0 can then be considered constant, in spite of the relatively large error.

Somewhat greater uncertainty may exist at the outer and inner limits of the profile. Near the outer interface of the oxide, electronic current would be most noticeable which would result in an apparent decrease of oxidation state (Fig. 3). The absence of this condition has been confirmed by print-out tests for all profiles given in this paper. Near the inner interface, the accuracy may be affected by the presence of some residual effect of the potential overshoot even in cases of substantial reduction as defined earlier. This may increase the error in V_A slightly and, at the

same time, make the gradient to appear somewhat steeper than it was in reality. It is estimated that because of the combined sources of error $x = V/V_A$ was accurate to within about 5% only and the profile became difficult to derive within about the same percentage of the oxide/metal interface.

Profiles of the Oxidation State of TaO_n after Heat-Treatment

Anodization in 0.1M H_3PO_4 .— Ta/Ta_2O_5 specimens were prepared by anodization to 160V in 0.1M H_3PO_4 . Heat-treatment was carried out at 500°C, 10^{-5} Torr, for 15, 90, 180, and 360 min. The profiles of the oxidation state shown in Fig. 8 were obtained from reanodization curves (e.g., Fig. 2 curve D) measured at a current density of 0.2 mA/cm².

The sequence of four profiles illustrates the increasing loss of oxygen as a function of the time of heat-treatment. As was shown before, the presence of phosphorous in the outer half of the oxide caused the rate of loss of oxygen to increase over that observed in the inner oxide. For this reason, an abrupt change in oxidation state was observed near the center of the oxide and the segments of the oxidation state profiles of the two layers showed characteristic differences with time of heat-treatment. In the inner oxide a gradient of $n(x)$ toward the metal was observed which changed only slowly with time. The direction of the gradient indicated that oxygen was lost to the metal substrate.

In the outer oxide a steeper gradient toward the inside was found after 15 min of heat-treatment. The direction of the gradient again indicated loss of oxygen to the metal. The oxidation state at the electrolyte (atmosphere) oxide interface remained at its maximum, $n(x = 0) = 2.5$. The oxidation state of the outer oxide was reduced in large part below that of the inner oxide because of the presence of phosphorous in the former. However, oxygen seemed to have diffused mainly to the substrate. The profile measured after 90 min of heat-treatment showed a further reduction of the oxidation state of the outer oxide. A gradient toward the inside remained while $n(x = 0)$ dropped to a lower value than previously observed. After 180 min a gradient toward the atmosphere/oxide interface appeared in addition to the gradient toward the metal. At the same time part of the profile of the outer oxide became nearly horizontal, indicating constant $n(x)$. After 360 min $n(x)$ had become constant throughout the outer oxide with an oxidation state approaching TaO_2 . It should be noted that this was not an equilibrium composition. Further changes in the profile and the oxidation state of both the outer and inner oxide occurred with continued heat-treatment. However, these further changes occurred much more slowly which gives reason to consider the profile

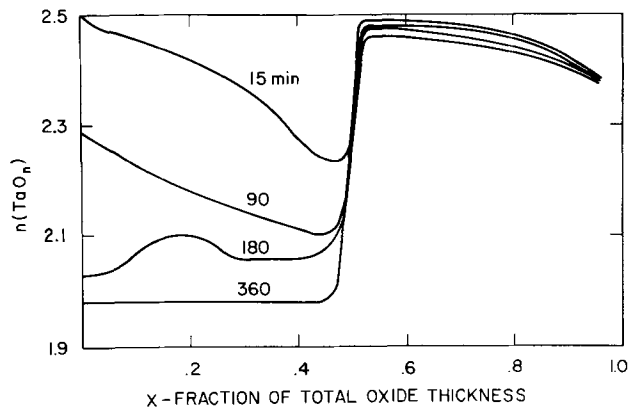


Fig. 8. Profiles of the oxidation state of TaO_n after heat-treatment in vacuum. Anodization: 0.1M H_3PO_4 , 0.3 mA/cm², 160V. Heat-treatment: 500°C, 10^{-5} Torr, for times given in graph.

reached after 360 min as a quasi-stationary state. The time sequence of oxidation state profiles for anodic Ta_2O_5 anodized in 0.1M H_3PO_4 can serve as a basis for the elucidation of the kinetics of the reduction of tantalum oxide, a task which goes beyond the scope of this paper.

Anodization in 0.1M H_2SO_4 .— Ta/Ta_2O_5 specimens were prepared by anodization in 0.1M H_2SO_4 to three different thicknesses: 40, 80, and 160V. The experimental conditions of heat-treatment were 500°C, 10^{-5} Torr, and 120 min. RAC's were measured as in the previous case and oxidation state profiles shown in Fig. 9 were computed from the potential-charge curves.

A major difference between the profiles of Fig. 8 and 9 is the absence of a duplex layer structure in the case of anodization in H_2SO_4 . Even though some sulfur may be incorporated into the oxide, it appeared not to have any effect on the rate of oxygen loss during heat-treatment. For this reason, no discontinuity in the $n(x)$ profiles was observed near the center of the oxide.

The profiles shown in Fig. 9 for different oxide thickness after the same time at temperature are, in a way, comparable to profiles of one thickness after different times, such as shown in Fig. 8.

Since changes in the oxidation state result from the exchange of oxygen with the adjoining metal and gas phases, it can be expected that thicker oxides containing larger quantities of oxygen will require longer times than thinner ones to reach a similar profile of the oxidation state. For this reason, the loss of oxygen will have progressed farthest in the thinnest oxide for the same duration of heat-treatment.

The profile of the 160V oxide exhibited a shallow gradient of the oxidation state from the oxide/atmosphere to within a short distance of the oxide/metal interphase. At the former interphase, the oxidation state remained close to its maximum value $n(x=O) \approx 2.5$. Near the metal a steep gradient was observed as expected if oxygen was lost to the metal.

Both of the thinner oxides (80 and 40V) revealed a nearly symmetric profile with gradients of the oxidation state both to the metal and the atmosphere. At both interphases the oxidation state dropped to values below $TaO_{1.5}$. Loss of oxygen to both metal and atmosphere was indicated.

Consecutive anodizations in 0.1M H_3PO_4 and 0.1M H_2SO_4 .—The set of three profiles shown in Fig. 10 was obtained from Ta/Ta_2O_5 specimens that had been anodized first in 0.1M H_3PO_4 to $V_A/2$ (20, 40, 80V, respectively), followed by anodization from $V_A/2$ to V_A in 0.1M H_2SO_4 (20 to 40, 40 to 80, and 80 to 160V, respectively). The conditions of heat-treatment were the same as in the previous case. It had been shown previously (11) that anodization of this kind resulted in multilayered structures with the inner half of the oxide free from inclusions while the outer half was made up of clearly separated layers with P and S incorporation in the sequence of anodization, i.e., in

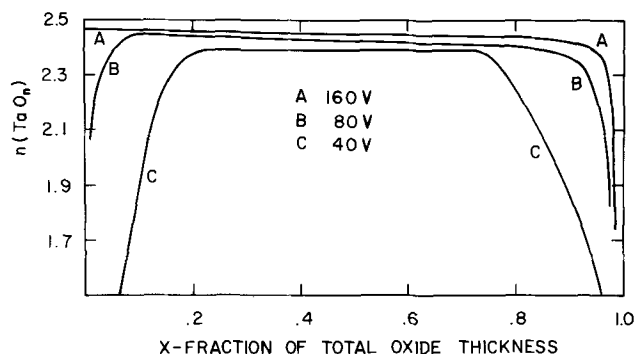


Fig. 9. Profiles of the oxidation state of TaO_n after heat-treatment in vacuum. Anodization: 0.1M H_2SO_4 , 0.3 mA/cm², voltages as given in graph. Heat-treatment: 500°C, 10^{-5} Torr, 120 min.

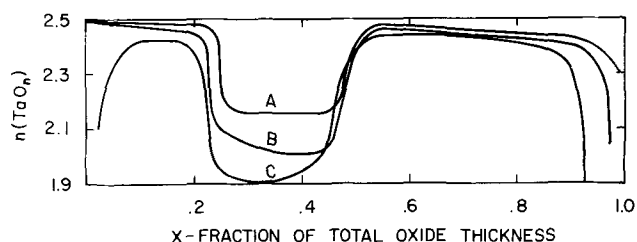


Fig. 10. Profiles of the oxidation state of TaO_n after heat-treatment in vacuum. Anodization (0.3 mA/cm²): A 0-80V in 0.1M H_3PO_4 ; 80-160V in 0.1M H_2SO_4 ; B 0-40V in 0.1M H_3PO_4 ; 40-80V in 0.1M H_2SO_4 ; C 0-20V in 0.1M H_3PO_4 ; 20-40V in 0.1M H_2SO_4 . Heat-treatment: 500°C, 10^{-5} Torr, 120 min.

this case P-containing oxide buried under S-containing oxide. The profiles of Fig. 10 correspond directly to this oxide structure.

The outermost quarter of the oxide showed the behavior typical of anodization in H_2SO_4 , while the following quarter showed a behavior typical of anodization in H_3PO_4 . Abrupt changes in the oxidation state were found between the P-containing oxide and both neighboring types of oxide. The inner oxide showed a gradient of the oxidation state toward the metal similar to the corresponding parts in both previous examples (Fig. 8 and 9). The 80-S/80-P oxide revealed a gradient of the oxidation state in the S-containing and inclusion-free oxide toward the metal indicating loss of oxygen to the metal. At the oxide/atmosphere interphase the oxidation state remained at its maximum $n(x=O) = 2.5$. The P-containing oxide sandwiched between these two layers again showed increased loss of oxygen, with constant $n(x)$. The 40-S/40-P oxide lead to a similar profile, with the oxidation state generally lower than in the previous case. In the 20-S/20-P oxide the same trend continued with the exception of a gradient of the oxidation state toward the atmosphere/oxide interphase. This trend paralleled that observed in Fig. 9 for both the 80 and 40V oxides. In the present case, the development of the gradient toward the atmosphere/oxide interphase was delayed and appeared only in the thinnest of the three oxides.

Mechanism of oxide reduction.—The examples of oxidation state profiles given in this paper are intended to illustrate the method of deriving such profiles from galvanostatic reanodization curves. The reaction of anodic tantalum oxide with the adjoining metal and gas phases is a dynamic process which precludes the establishment of true equilibrium conditions, except after very long times which would be impractical experimentally. For this reason none of the profiles given represent equilibrium conditions, at most they can be considered as quasi stationary after the initial more rapid changes.

The profiles given in this paper, for the most part, appear to be determined by the kinetic limitations of the decomposition of anodic tantalum oxide. They depended, in addition to the time of heat-treatment and the thickness of the oxide, on numerous other experimental variables, such as pressure and temperature of heat-treatment and the anodization conditions in cases where effects of incorporated ions were observed. The results of the study of these variables will be published in the future.

At this time, some qualitative conclusions can be drawn concerning the mechanism of oxide decomposition. The inner oxide, which can be considered free of inclusions from the anodization electrolyte, tended to lose oxygen to the metal substrate with the rate determined by diffusion. From the initial gradients of the oxidation state in the outer oxide it can also be concluded that oxygen was lost to the substrate from oxide further removed from the substrate. In the

case of P-inclusions substantial amounts of oxygen originating in the outer oxide had to be transported to the metal by diffusion. However, the profile of the oxidation state revealed that the profile was not determined by the gradient of the oxygen partial pressure in the oxide alone but depended also on the composition of the oxide, especially the presence or absence of phosphorous. This does not mean that different equilibrium oxidation states exist for oxide with phosphorous and without. Available evidence indicates that phosphorous affects only the rate of oxide decomposition, i.e., its kinetics through a catalytic effect and that after sufficiently long times similar quasi-stationary states are reached in all cases.

For the oxide/atmosphere interphase the profiles presented in this paper lead to a surprising conclusion. In those profiles that were measured after short heat-treatment (Fig. 8, 15 min) in the case of anodization in H_3PO_4 , or for thick oxides (Fig. 9 and 10: 160V) the oxidation state remained high at the interphase itself while a gradient toward the metal was in evidence. After longer time of heat-treatment, and with thinner oxides, the profiles revealed a pronounced gradient of the oxidation state toward the oxide/atmosphere interphase. These observations can only mean that anodic tantalum oxide can lose oxygen to the atmosphere at the temperature and pressure used during heat-treatment. The initially high oxidation state at the phase boundary itself suggests a rate-limiting phase boundary reaction. After a sufficient degree of reduction diffusion appeared to become rate limiting. In the case of P-containing oxide further complications seem to arise from the stability of transitory intermediate oxidation states as revealed by constant segments of the oxidation state profiles.

The observation of a loss of oxygen in anodic tantalum oxide at oxygen pressures of the order of 10^{-5} Torr and at $500^\circ C$ shows that a significant difference exists between this oxide and any crystalline modifications of Ta_2O_5 (17). The results given here show that anodic tantalum oxide can under these conditions be reduced to lower oxides with an oxidation state n below 1.5. For β - Ta_2O_5 the deviation from stoichiometry was immeasurably small below 700° - $800^\circ C$ and still estimated to as low as $x = 10^{-9}$ for Ta_2O_{5-x} at about $1200^\circ C$ and 10^{-11} Torr oxygen pressure (17).

Conclusions

1. Constant current reanodization of anodic tantalum oxide which had been subjected to heat-treatment in vacuum (e.g., 10^{-5} Torr O_2 , $500^\circ C$) lead to potential-charge curves which indicated that substantial amounts of charge were required to reach the original anodization potential of the oxide. It could be shown that this charge was ionic charge consumed in the restoration of partially reduced tantalum oxide (TaO_n) to its original oxidation state (Ta_2O_5).

2. The restoration of the oxide was proceeding with ionic current efficiencies $i_{ion}/i \approx 1.0$, similar to the anodization of high-purity tantalum. Uniform or non-uniform electronic charge transfer could be shown to be negligible within the sensitivity of the KI-starch print-out method.

3. The rate of loss of oxygen during heat-treatment was found to be strongly dependent on ions which were incorporated into an outer half of the anodic oxide during anodization. Phosphorous incorporation led to increased rate of loss, in the outer part of the oxide, compared to oxide free of ions from the electrolyte (inner part). Oxide anodized in dilute H_2SO_4 showed a behavior similar to oxide free of ions. Oxide anodized, consecutively, in dilute H_3PO_4 and H_2SO_4 resulted in reanodization curves after heat-treatment which corresponded directly to the multilayered structure established by radiotracer experiments (11).

4. From reanodization curves at constant current charge as a function of reanodization potential could

be determined. It was shown that reanodization potential was linearly related to distance into the oxide from the electrolyte/oxide interface. Thus, charge required to restore partially reduced tantalum oxide could be measured as a function of distance in the oxide. From such measurements the profile of the oxidation state of heat-treated tantalum oxide across its thickness could be derived.

5. The oxidation state n of partially reduced tantalum oxide was arrived at by comparing the slope of its reanodization curve with that obtained for the anodization of tantalum at the same current density. Several profiles of the oxidation state $n(x)$ (where $x = V/V_A$, distance from the electrolyte/oxide interface) of tantalum oxide anodized in dilute H_3PO_4 and H_2SO_4 were presented in this paper. Additional experimental variables were time of heat-treatment and oxide thickness.

None of the profiles given represented equilibrium conditions. Under certain conditions quasi-stationary states were reached. They represent typical examples of transitory oxidation state profiles after substantial reduction in vacuum.

6. During heat-treatment in vacuum (typically $500^\circ C$, 10^{-5} Torr, 120 min) the anodic oxide lost oxygen to the metal substrate, as well as to the atmosphere. This conclusion was based on the direction of the gradients of oxygen deficiency in the oxidation state profiles.

7. The observed deviations from stoichiometry in amorphous anodic tantalum oxide resulting from heat-treatment at temperatures between 300° and $700^\circ C$ and at pressures of the order of 10^{-5} Torr are far larger than expected for tantalum oxide in the crystalline state (17). Little if any tendency for recrystallization was found for anodic oxide under the given experimental conditions. Both observations indicate that amorphous oxide may be more fundamentally different from crystalline oxide than was assumed in the past. It is expected that further investigations of its behavior during heat-treatment, especially the kinetics of reduction and oxidation, will help to further clarify some of these differences.

Acknowledgment

The author thanks Mr. P. Orthmann for his skillful assistance with the experiments and Dr. N. I. Jaeger for valuable comments on this paper.

Manuscript submitted May 8, 1972; revised manuscript received May 12, 1972.

Any discussion of this paper will appear in a Discussion Section to be published in the June 1973 JOURNAL.

REFERENCES

1. L. Young, "Anodic Oxide Films," Academic Press, New York (1961).
2. C. J. Dell'Oca, D. L. Pulfrey, and L. Young, "Physics of Thin Films," Vol. 6, Academic Press, New York (1971).
3. D. A. Vermilyea, *This Journal*, **104**, 485 (1957).
4. D. A. Vermilyea, *ibid.*, **102**, 207 (1955).
5. D. A. Vermilyea, *Acta Met.*, **5**, 113 (1957).
6. D. M. Smyth, G. A. Shirn, and T. B. Tripp, *This Journal*, **110**, 1264 (1963).
7. D. M. Smyth and T. B. Tripp, *ibid.*, **111**, 1271 (1963).
8. D. M. Smyth, G. A. Shirn, and T. B. Tripp, *ibid.*, **111**, 1331 (1964).
9. D. M. Smyth, G. A. Shirn, and T. B. Tripp, *ibid.*, **113**, 100 (1966).
10. D. M. Smyth, *ibid.*, **115**, 186 (1968).
11. J. J. Randall Jr., W. J. Bernard, and R. R. Wilkinson, *Electrochim. Acta*, **10**, 183 (1965).
12. G. P. Klein, Paper 38 presented at the Dallas Meeting of the Electrochemical Society, May 7-12, 1967.
13. J. P. S. Pringle, *This Journal*, **119**, 482 (1972).
14. G. P. Klein, *ibid.*, **117**, 1581 (1970).
15. G. P. Klein, *ibid.*, **113**, 348 (1966).
16. J. A. Davies, J. P. S. Pringle, R. L. Graham, and F. Brown, *ibid.*, **109**, 999 (1962).
17. P. Kofstad, *ibid.*, **109**, 776 (1962).

NaLnF₄:Yb³⁺,Er³⁺ (Ln:Y,Gd,La): Efficient Green-Emitting Infrared-Excited Phosphors

Tsuyoshi Kano, Hajime Yamamoto, and Yoshiro Otomo

Central Research Laboratory of Hitachi Ltd., Kokubunji, Tokyo, Japan

ABSTRACT

Hexagonal NaLnF₄:Yb³⁺,Er³⁺ (Ln:Y,La,Gd) was found to be an efficient green-emitting phosphor with infrared excitation. It was prepared by firing a mixture of Na₂SiF₆ and coprecipitated Ln_{1-y-z}Yb_yEr_zF₃ at 630°C in an argon atmosphere. The optimum firing condition of NaYF₄:Yb³⁺,Er³⁺ was revealed to lie in the region where (a) the decomposition reaction Na₂SiF₆ → 2NaF + SiF₄ is complete, (b) liquid NaF-NaY_{1-y-z}Yb_yEr_zF₄ and hexagonal NaY_{1-y-z}Yb_yEr_zF₄ are coexistent, and (c) the phase transition of NaY_{1-y-z}Yb_yEr_zF₄ from hexagonal to cubic does not occur. When pumped by a Si-doped GaAs diode, properly prepared NaY_{0.57}Yb_{0.39}Er_{0.04}F₄ is 4 ~ 5 times as bright as the commercially available LaF₃:Yb³⁺,Er³⁺.

Many visible-emitting, infrared-excited phosphors have been reported as candidates for up-conversion devices. Typical examples are LaF₃:Yb³⁺,Er³⁺ (1-3), YF₃:Yb³⁺,Er³⁺ (1, 2, 4), BaYF₃:Yb³⁺,Er³⁺ (5) as green-light emitting and YOC1:Yb³⁺,Er³⁺ (6), Y₂O₃:Yb³⁺,Er³⁺ (7) as red-light emitting phosphors. In Y₃OCl₇:Yb³⁺,Er³⁺ (6), red and yellow visual response have been reported at high and low Yb concentrations, respectively.

Among IR-to-visible converting phosphors, rare earth fluorides containing Yb³⁺ and Er³⁺ were the first efficient series studied and the improvement of efficiencies has been reported on BaF₂-YF₃ systems containing Yb³⁺ and Er³⁺. A series of experiments in search of more efficient host materials on the binary fluorides doped with Yb³⁺ and Er³⁺ is a natural consequence in the course of the development of IR-to-visible converting phosphors. As constituent ions to be substituted by Yb³⁺ and Er³⁺, Y³⁺, Gd³⁺, and La³⁺, abbreviated as Ln, are admittedly the first candidates.

In selecting another constituent element besides Ln in binary fluorides, it is of experimental convenience to choose the elements of which fluorides are stable solids having melting points not too low to be used as starting materials or intermediate products for firing. The elements having higher valency than 3 are thus excluded in the first stage because the fluorides of these elements are mostly gases, liquids, or low melting solids at ordinary conditions. This aspect restricts the elements under consideration to monovalent, divalent, and trivalent ones. Of the binary fluorides of these ions and Ln, alkali metal-rare earth fluorides are the systems where few studies have been made on the IR-to-visible conversion using Yb³⁺ and Er³⁺.¹ They have been reported as diluents to YbOC1 and related compounds to have tunable emission of green to red depending on excitation intensities (8). IR-to-visible conversion in LiYF₄ has been reported using Yb³⁺ and Ho³⁺. The measured efficiency, however, was an order of magnitude smaller than for YF₃:Yb³⁺,Er³⁺ (9). It is not clear whether the lack of efficient phosphors reported in this system is simply due to incomplete investigations or has some physical basis. One possible reason is that the alkali metal-rare earth fluoride systems generally have complex phase diagrams (10) which make it difficult to obtain well-crystallized single-phase materials. As is shown in the detailed phase diagram of NaF-YF₃ in Fig. 1 (11), for example, the transition in NaYF₄ between hexagonal and cubic

phases occurs at 691°C. If one wants to fire phosphors at temperatures lower than the transition temperature in order to have purely single-phase materials, an elaborate technique will be required to obtain well-crystallized homogeneous products because of the low firing temperatures. This requirement is met by the use of the decomposition reaction of Na₂SiF₆ and the selection of correct firing temperature and mixing ratio as described in this paper.

The new synthetic method makes it possible to obtain fluoride phosphors at comparatively low firing temperature without using hydrofluoric acid gas. This firing condition contributes much to the ease of preparing fluoride phosphors, because conventional quartz tubes can be used. The characteristic firing condition of the method in this work is compared with the

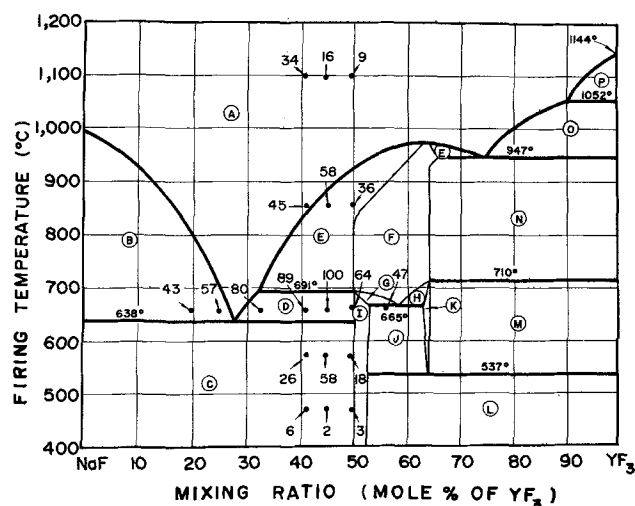


Fig. 1. Phase diagram of NaF-YF₃ (11) showing relative luminescence intensities of the fired mixtures of Na₂SiF₆ and Y_{0.80}Yb_{0.19}Er_{0.01}F₃ with IR excitation.

A Liquid, B NaF + liquid, C NaF + hexagonal NaF·YF₃, D hexagonal NaF·YF₃ + liquid, E fluorite cubic NaF·YF₃ - 5NaF·9YF₃ solid solution + liquid, F fluorite cubic NaF·YF₃ - 5NaF·9YF₃ solid solution, G hexagonal NaF·YF₃ ss + cubic NaF·YF₃ - 5NaF·9YF₃ ss, H cubic NaF·YF₃ - 5NaF·YF₃ ss + ordered 5NaF·9YF₃ ss, I hexagonal NaF·YF₃ ss, J hexagonal NaF·YF₃ ss + ordered 5NaF·9YF₃ ss, K ordered 5NaF·9YF₃ ss, L hexagonal NaF·YF₃ ss + orthorhombic YF₃, M ordered 5NaF·9YF₃ + orthorhombic YF₃, N cubic 5NaF·9YF₃ + orthorhombic YF₃, O orthorhombic YF₃ + liquid, P high-temperature YF₃ + liquid.

Key words: fluorides, luminescence, phosphors, infrared.

¹ During the revision of this manuscript, we noted the paper (14) describing the emission of NaY_{0.7}Yb_{0.29}Er_{0.03}F₄. In the paper, a private communication (15) was cited which indicated the strong luminescence of the phosphor under IR radiation. A related patent application has been disclosed recently (16).

Table I. Methods of preparing IR-to-green converting phosphors activated with Yb^{3+} and Er^{3+} ions

La_2O_3	$\xrightarrow{900^\circ\text{--}1100^\circ\text{C, in HF}}$	LaF_3	[Ref. (2)]
$\text{YF}_3, \text{BaF}_2$	$\xrightarrow{950^\circ\text{--}1000^\circ\text{C, in HF}}$	BaYF_3	[Ref. (5)]
$\text{YF}_3, \text{BeF}_2, \text{NH}_4\text{F}$	$\xrightarrow{1100^\circ\text{C, in N}_2}$	$\text{YF}_3(\text{BeF}_2)^*$	[Ref. (4)]
$\text{YF}_3, \text{Na}_2\text{SiF}_6$	$\xrightarrow{630^\circ\text{C, in Ar}}$	$\text{NaYF}_4(\text{NaF})^*$	[This work]

*Materials in parentheses act as flux.

reported methods of preparing typical IR-to-green converting phosphors in Table I.

Experimental

Powder samples were prepared by firing the mixtures of Na_2SiF_6 (Morita Chemical Industry Company, Ltd.) and $\text{Ln}_{1-y-z}\text{Yb}_y\text{Er}_z\text{F}_3$. The latter was coprecipitated from an aqueous nitrate or chloride solution of the proper composition by hydrofluoric acid and dried in air at 120°C for a day. The raw materials were fired in covered platinum crucibles contained in a quartz tube in a purified argon atmosphere. The purified argon was obtained by using a rare gas purifier (Japan Pure Hydrogen Company, Inc.). The gaseous SiF_4 evolved during the firing was trapped by aqueous NaOH solution. The aqueous Ln (containing Yb, Er) nitrate and chloride solutions were obtained by dissolving 99.999% pure oxides (Shin-Etsu Chemical Industry Company, Ltd.) in nitric acid and hydrochloric acid, respectively.

The relative luminescence intensities of the powder samples were measured under infrared excitation using a 1 kW tungsten-iodine lamp with a Toshiba IR-D1B filter as an exciting light source and RCA-1P22 photomultiplier as a detector. An interference filter with a window around 546 nm ($\Delta\lambda_{1/2} < 11$ nm) in front of the detector selected the green luminescence. For the comparison of luminescence intensities, thick powder layers (ca. 150 mg/cm²) were prepared on metal patches with a butyl acetate binder and were mounted at an identical position. The spectral energy distribution of the luminescence was measured with a Spex 1400 II grating monochromator using a RCA-7265 photomultiplier as a detector.

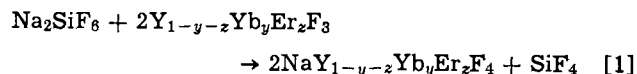
Differential thermal analysis was carried out by using the apparatus (M8006) made by Rigaku Denki Company, Ltd.

The power conversion efficiency of the phosphor-coated light-emitting diode was obtained relative to GaAsP light-emitting diode whose efficiency had been determined elsewhere in this laboratory. The ratio of visible light output of these two different types of light-emitting diodes was obtained by comparing the spectral energy distribution of the emission of diodes set in an integrating sphere.

The brightness of the phosphor-coated diodes was measured by using a Pritchard photometer (Photo Research Company).

Results and Discussion

We obtained $\text{NaY}_{1-y-z}\text{Yb}_y\text{Er}_z\text{F}_4$ by reacting Na_2SiF_6 with coprecipitated $\text{Y}_{1-y-z}\text{Yb}_y\text{Er}_z\text{F}_3$ in an argon atmosphere for 1 hr at various temperatures according to the reaction



With y and z arbitrarily chosen to be 0.19 and 0.01, respectively, the mixing ratio of Na_2SiF_6 and $\text{Y}_{0.80}\text{Yb}_{0.19}\text{Er}_{0.01}\text{F}_3$ and the firing temperature were varied to determine the optimum conditions. The relative green luminescence intensities of the fired mixtures upon IR excitation are shown on the $\text{NaF}\text{-YF}_3$

phase diagram (Fig. 1).² The cubic phase in the high-temperature regions was found, by x-ray analysis, not to be retained at room temperature with the cooling rate of about 50°C/hr that we employed. As is evident from Fig. 1, the most efficient phosphors can be prepared in region D where hexagonal NaYF_4 and the liquid are coexistent. Thermal characteristics related to phosphor preparation in the temperature region concerned are shown in Fig. 2. In this figure, the thermal decomposition curve of Na_2SiF_6 (a) and the differential thermal analysis of the fired product (c) are compared with the dependence of the luminescence intensity of the fired products (optimum mixing ratio) on the firing temperature (b). The data shown in Fig. 2 (b) and (c) are on the phosphor samples having the optimum concentration of Yb^{3+} and Er^{3+} (see Fig. 3 and 4). As is shown in Fig. 2(a), the decomposition of Na_2SiF_6 begins around 500°C and is complete around

² It is to be pointed out that the temperature scale of Fig. 1 is shifted upward relative to the scale appropriate to the actual system studied. As the phase diagrams of the sodium fluoride rare earth trifluoride systems (10) show that the phase transition temperatures decrease with the decrease of the ionic radii of the rare earth elements, the phase transition temperatures of $\text{NaF}\text{-YF}_3$ systems are expected to decrease by the partial substitution of Yb and Er for Y. The actual location of the optimum point in the phase diagram was confirmed by the thermal measurement (Fig. 2).

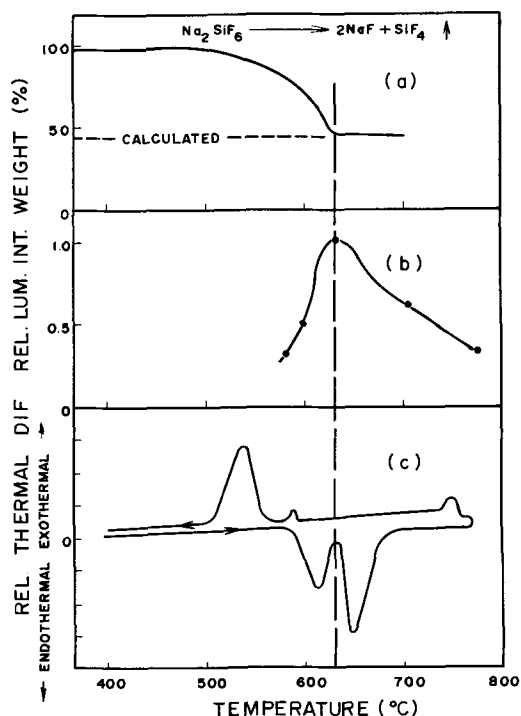


Fig. 2. Thermal characteristics related to phosphor preparation. (a) Thermogravimetry of Na_2SiF_6 in N_2 . Rate of temperature increase: 10°C/min . (b) Relative luminescence intensity of $\text{NaY}_{0.57}\text{Yb}_{0.39}\text{Er}_{0.04}\text{F}_4$ under IR excitation vs. firing temperature at the optimum mixing ratio. (c) Differential thermal analysis of $\text{NaY}_{0.57}\text{Yb}_{0.39}\text{Er}_{0.04}\text{F}_4 + 0.2\text{NaF}$ (10°C/min).

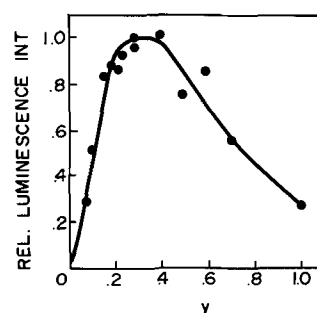


Fig. 3. Relative green luminescence intensities of $\text{NaY}_{(0.99-y)}\text{Yb}_y\text{Er}_{0.01}\text{F}_4$ with IR excitation.

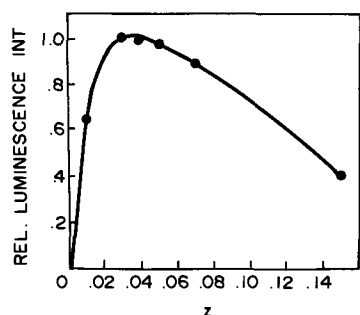
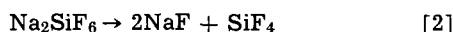


Fig. 4. Relative green luminescence intensities of $\text{NaY}_{0.61-z}\text{Yb}_{0.39}\text{Er}_z\text{F}_4$ with IR excitation.

650°C when the temperature is increased at the rate of 10°C/min. The observed weight loss closely corresponds to the calculated weight of SiF_4 gas evolved according to reaction [2]



The endothermic peak around 610°C in Fig. 2(c) corresponds to the formation of eutectic liquid phase of NaYF_4 and NaF at 638°C. This correspondence was confirmed by the DTA experiment. When the same sample was etched by dilute HCl to remove NaF, the endothermic peak around 610°C was completely removed. The endothermic peak around 650°C corresponds to the transition from hexagonal $\text{NaY}_{1-y-z}\text{Yb}_y\text{Er}_z\text{F}_4$ to cubic $\text{NaY}_{1-y-z}\text{Yb}_y\text{Er}_z\text{F}_4$. Upon cooling, the inverse transition occurs around 540°C as is shown by the exothermic peak.³ The observed exothermic transition (cubic-hexagonal) is consistent with the result of x-ray analysis described previously. In the case of NaYF_4 , an endothermic peak at 690°C due to the phase transition from hexagonal to cubic has been reported (12). The comparison of the transition temperatures observed on $\text{NaY}_{0.57}\text{Yb}_{0.39}\text{Er}_{0.04}\text{F}_4$ -NaF system with those reported on NaYF_4 -NaF system shows that the transition temperatures are lower in the former than in the latter.

From the above discussions, it is concluded that the optimum firing temperature at 630°C lies in the temperature region where (i) the decomposition of Na_2SiF_6 is just complete, (ii) a liquid phase is formed, and (iii) a cubic phase is not formed.

These conditions may favor the formation of good luminescent crystals of the hexagonal phase because (i) the SiF_4 gas evolved is expected to remove oxygen impurities which are known to be strong quenchers of IR-excited green luminescence, (ii) the intermediate NaF would readily react with $\text{Y}_{1-y-z}\text{Yb}_y\text{Er}_z\text{F}_3$ as is usual for freshly formed products of decomposition reactions, (iii) the liquid phase would behave as a flux to help crystal growth, and (iv) the product is free from inhomogeneity arising from quenching of the high-temperature cubic phase and from imperfections produced by the phase transition in the cooling process. An experimental support of (i) is provided by the fact that efficient phosphors are obtained by firing mixtures of Na_2SiF_6 and $\text{Y}_{0.57}\text{Yb}_{0.39}\text{Er}_{0.04}\text{F}_3$ in platinum crucibles having extra Na_2SiF_6 at the bottom. The extra Na_2SiF_6 charged at the bottom of the crucible significantly contributes to the reproducible formation of efficient phosphors, although the decomposition product NaF at the bottom does not contact and react with $\text{Y}_{1-y-z}\text{Yb}_y\text{Er}_z\text{F}_3$.

In addition to the use of Na_2SiF_6 as a starting material, another essential point is to use coprecipitated $\text{Y}_{1-y-z}\text{Yb}_y\text{Er}_z\text{F}_3$. If one uses mixtures of separately precipitated YF_3 , YbF_3 , and ErF_3 , one can obtain only gray-colored samples whose luminescence intensities

³ The small exothermic peak observed around 590°C is probably due to the local solidification of the liquid because it is removed by etching the sample.

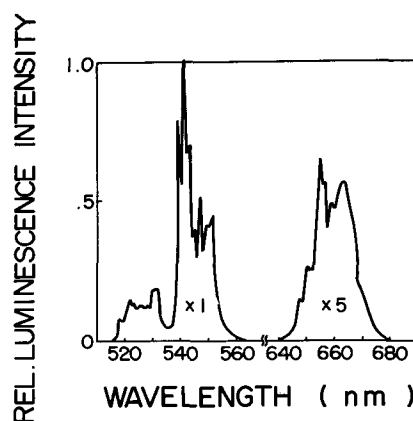


Fig. 5. Spectral energy distribution of the luminescence of $\text{NaY}_{0.57}\text{Yb}_{0.39}\text{Er}_{0.04}\text{F}_4$ with IR excitation at room temperature.

are smaller by a factor of five than those of samples prepared from coprecipitated fluorides.

As is shown in Fig. 1, the most efficient phosphors can be prepared not from stoichiometric mixtures but from those having some excess Na_2SiF_6 . The resulting excess NaF contributes to the formation of a liquid phase that helps crystal growth. The fired samples contain a small amount of NaF and its removal by solution in water or acids did not change the luminescence intensities significantly.

The efficiency of the fired products was found to be sensitive to the firing program which controls the decomposition rate of reaction [2]. A typical firing program is as follows: the starting mixtures ($1.2 \text{ Na}_2\text{SiF}_6 + 2\text{Y}_{0.57}\text{Yb}_{0.39}\text{Er}_{0.04}\text{F}_3$) put in platinum crucibles having $0.3 \text{ Na}_2\text{SiF}_6$ at the bottom) are heated to 630°C in about 1 hr, kept at that temperature for 3 hr, and cooled to room temperature in about 10 hr.

The efficient phosphors obtained were found by x-ray analysis to have the hexagonal gagarinite structure in accord with the phase diagram of NaYF_4 . A spectroscopic analysis of the phosphor revealed ca. 0.1 w/o (weight per cent) of Si as a major impurity.

The dependences of luminescence intensities of $\text{NaYF}_4:\text{Yb}^{3+}$, Er^{3+} on the concentration of Yb^{3+} and Er^{3+} are shown in Fig. 3 and Fig. 4. The optimum concentrations of Yb^{3+} and Er^{3+} are 30 ~ 40 m/o (mole per cent) and 3 ~ 4 m/o, respectively.

The spectral energy distribution of the luminescence of $\text{NaY}_{0.57}\text{Yb}_{0.39}\text{Er}_{0.04}\text{F}_4$ upon IR excitation is shown in Fig. 5. The ratio of the intensity of green luminescence to that of red luminescence decreases with the increase of exciting IR intensity. The data shown in Fig. 5 were measured on the phosphor coated on a domed Si-doped GaAs diode (10% eff.) operated with 50 mA current. The green and red emission originate from the electronic transitions, $^2\text{H}_{11/2}$, $^4\text{S}_{3/2} \rightarrow ^4\text{I}_{15/2}$ and $^4\text{F}_{9/2} \rightarrow ^4\text{I}_{15/2}$ of Er^{3+} , respectively. The emission around 540 nm due to the transition $^4\text{S}_{3/2} \rightarrow ^4\text{I}_{15/2}$ is dominant and the resulting emission appears pure green. The lifetime of the green emission ($\tau_{1/e}$) was observed to be 1.2 msec under IR excitation with a Si-doped GaAs diode.

Table II. Relative luminescence intensities of NaLnF_4 (Ln:Y,Gd,La,Yb,Er,Ho) with IR excitation

Composition	Rel. lum. int.
$\text{NaY}_{0.57}\text{Yb}_{0.39}\text{Er}_{0.04}\text{F}_4$	400-540
$\text{NaY}_{0.80}\text{Yb}_{0.19}\text{Er}_{0.01}\text{F}_4$	170
$\text{NaLa}_{0.80}\text{Yb}_{0.19}\text{Er}_{0.01}\text{F}_4$	155
$\text{NaGd}_{0.80}\text{Yb}_{0.19}\text{Er}_{0.01}\text{F}_4$	135
$\text{NaY}_{0.40}\text{Gd}_{0.40}\text{Yb}_{0.19}\text{Er}_{0.01}\text{F}_4$	140
$\text{NaY}_{0.32}\text{Gd}_{0.24}\text{La}_{0.24}\text{Yb}_{0.19}\text{Er}_{0.01}\text{F}_4$	145
$\text{NaY}_{0.80}\text{Yb}_{0.19}\text{Ho}_{0.01}\text{F}_4$	23
$\text{LaF}_3:\text{Yb, Er}^*$	100

* The typical IR-to-visible conversion phosphor used on the commercially available green-emitting diode of the IR-to-visible conversion type (GE-SSL-3).

Table III. Variations of conversion efficiencies of phosphors kept in various conditions

Composition	Condition	Period	Luminescence intensity relative to the phosphor just fired (%)
NaY _{0.80} Yb _{0.19} Er _{0.01} F ₄	Kept in desiccator with silicagel	118 days	100
	Kept in closed vessel with water	118 days	100
NaY _{0.57} Yb _{0.39} Er _{0.04} F ₄	Kept at 100°C in air	4 days	97
	Boiled with water then kept at 100°C in air	20 min	88
		1 day	
	Treated with dil. HCl sol.	5 hr	98
	Coated with polystyrene binder on GaAs:Si diode operated with 50 mA current	4414 hr	86*
	Coated with epoxy resin on GaAs:Si diode operated with 100 mA current	3477 hr	91*

* These values include deterioration of GaAs:Si diodes and binders.

Relative luminescence intensities of NaLnF₄:Yb³⁺, Er³⁺ or Ho³⁺ (Ln = Y,Gd,La) prepared by the method described for NaYF₄:Yb³⁺, Er³⁺ are summarized in Table II. The phosphor having the composition of NaY_{0.57}Yb_{0.39}Er_{0.04}F₄ was found to be 4-5 times brighter than commercial LaF₃:Yb³⁺, Er³⁺ on a Si-doped GaAs diode by comparing the green light output of the two phosphors coated on identical diodes. The resultant over-all power conversion efficiency of the green-emitting diode reaches 0.01% with 60 mW (1.2V, 50 mA) d-c power, when the phosphor is coated with polystyrene binder on a 0.6 × 0.6 mm Si-doped GaAs diode⁴ having 3% conversion efficiency. When the phosphor is settled from aqueous suspension on a GaAs diode and covered with epoxy resin, the over-all power efficiency of the green-emitting diode increases to 0.02%. The brightness of the phosphor-coated diodes was measured to be 250-350 ft-L⁵ at the brightest spot with 100 mA current. In comparing the values of brightness with those of direct light-emitting diodes, it should be taken into consideration that the emitting area of phosphor layers is an order of magnitude larger than that of Si-doped GaAs. The brightness is expected to increase 4-11 times by using 6-10% eff. Si-doped GaAs diodes (13) because the dependence of the green luminescence intensity on the exciting infrared light intensity is quadratic. By coating the phosphor on a 10% GaAs:Si domed diode with glycerin binder, we have obtained a green-emitting diode having over-all power efficiency of 0.2% with 470 mW input d-c power, which is the highest value so far reported on the green-emitting diode of the IR-to-visible conversion type.

The conversion efficiency of the phosphor-coated light-emitting diode decreases to ½ when the temperature increases from 25° to 65°C.

The results of test experiments on the stability of NaY_{0.57}Yb_{0.39}Er_{0.04}F₄ to heat-treatment in air are

⁴ Emission peak: 957 nm.

⁵ These values were obtained after thermal equilibrium was attained with the power supply on. The initial brightness was 2.6 times higher than that at thermal equilibrium. The efficiency of the GaAs diode decreased to 2% at thermal equilibrium with 100 mA current.

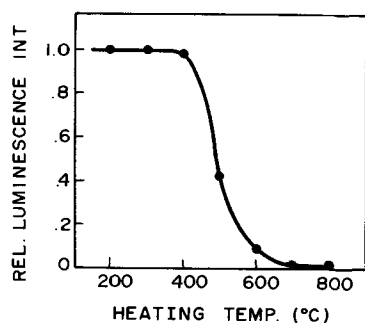


Fig. 6. Relative green luminescence intensities of NaY_{0.57}Yb_{0.39}Er_{0.04}F₄ after heating for 2 hr in air.

shown in Fig. 6. As shown in the figure, the efficiency of the phosphor is not affected by the heat-treatment lower than 400°C in air. Other results of stability tests of NaYF₄:Yb³⁺, Er³⁺ are summarized in Table III. They show that there is no significant degradation of the phosphor under the conditions investigated.

In conclusion, we have succeeded in preparing a new class of efficient and stable infrared-excited phosphors using decomposition reactions. The decomposition reactions evolve nonoxidizing gases and provide intermediate products which are very useful for the formation of efficient fluoride phosphors.

Acknowledgments

The authors are greatly indebted to A. Suzuki for most of the evaluation experiment, to T. Suzuki for coating phosphors on diodes and evaluating them, and to M. Nakano for preparation of many samples of the phosphors.

Manuscript submitted March 21, 1972; revised manuscript received June 5, 1972. This was Paper 82 presented at the Houston Meeting of the Society, May 7-12, 1972.

Any discussion of this paper will appear in a Discussion Section to be published in the June 1973 JOURNAL.

REFERENCES

- R. A. Hewes and J. F. Sarver, *Bull. Am. Phys. Soc., Ser. II*, **13**, 687 (1968).
- R. A. Hewes and J. F. Sarver, *Phys. Rev.*, **182**, 427 (1969).
- S. V. Galginaitis and G. E. Fenner, International Conference on Gallium Arsenide, Dallas, Texas, October 1968.
- L. G. Van Uitert, L. Pietroski, and W. H. Grodkiewicz, *Mater. Res. Bull.*, **4**, 777 (1969).
- H. J. Guggenheim and L. F. Johnson, *Appl. Phys. Letters*, **15**, No. 2, 51 (1969).
- L. G. Van Uitert, S. Singh, H. J. Levinstein, L. F. Johnson, W. H. Grodkiewicz, and J. E. Geusic, *ibid.*, **15**, No. 2, 53 (1969).
- I. Ladany, P. N. Yocom, and J. P. Wittke, *Electrochem. Soc. Extended Abstracts*, Washington, D. C., Meeting, May 9-13, 1971, No. 52.
- L. G. Van Uitert, H. J. Levinstein, and W. H. Grodkiewicz, *Mater. Res. Bull.*, **4**, 381 (1969).
- R. K. Watts and W. C. Holton, *Solid State Commun.*, **9**, 137 (1971).
- R. E. Thoma, "The Rare Earth Halides," *Progress in the Science and Technology of the Rare Earths*, Vol. 2, p. 90, L. Eyring, Editor, Pergamon Press (1966).
- R. E. Thoma, G. M. Hebert, H. Insley, and C. F. Weaver, *Inorg. Chem.*, **2**, 1005 (1963).
- B. P. Sobolev, D. A. Mineev, and V. P. Pashutin, *Soviet Physics-Doklady*, **8**, 545 (1963).
- I. Ladany, *J. Appl. Phys.*, **42**, 654 (1971).
- J. L. Sommerdijk, *J. Luminescence*, **4**, 441 (1971).
- G. Blasse and A. Brill, Private communication on NaYF₄:Yb³⁺, Er³⁺ to Ref. (14).
- Japanese Patent Application Public Disclosure No. 5909 (1972).

Chemical Vapor Deposited Polycrystalline Silicon

M. E. Cowher and T. O. Sedgwick*

IBM Thomas J. Watson Research Center, Yorktown Heights, New York 10598

ABSTRACT

Mirror smooth thin films of polycrystalline silicon suitable for FET device processing have been chemically vapor deposited from silane at 650°C on different insulating materials. Hall mobilities of p-type and n-type films have been measured for carrier concentrations between $10^{14}/\text{cc}$ and $10^{20}/\text{cc}$. Unusually high mobilities, within a factor of two of bulk silicon, were obtained in the $10^{14}/\text{cc}$ to $10^{17}/\text{cc}$ carrier concentration range. *In situ* vapor doping control was irreproducible for carrier concentrations below $5 \times 10^{18}/\text{cc}$. Evidence from radiochemical analysis, electron microscopy, and x-ray analysis indicates that there is a large concentration of electrically inactive dopant which is postulated to be in the grain boundaries. Undoped polysilicon films could be deposited with resistivities greater than 10^6 ohm-cm.

Polycrystalline Si (poly Si) films are beginning to have a wide spread impact on semiconductor device technology. Bean *et al.* (1) first described the thermal conductivity of thick poly Si films which were to be used for a dielectric isolation scheme for single-crystal Si devices. More recently, poly Si has been used as the gate in a self-aligned gate process in field effect transistor (FET) fabrication (2). A direct antecedent of this paper was the report of the fabrication of a reasonably good FET in a poly Si film by Fa and Jew (3) which brought poly Si into the realm of active device materials. In all probability, poly Si devices will never compete with single-crystal Si devices in applications requiring high speed and high packing density. However, poly Si devices may fill a need in other applications requiring devices to be fabricated over large areas and where single-crystal substrates are not available.

There seems to be general agreement that the smoothest polycrystalline deposits are composed of extremely fine, randomly oriented grains (4-7). Such fine grain deposits have been made most successfully via the pyrolysis of silane at temperatures between 500° and 700°C. Ford *et al.* (6) reported that smaller grains were obtained on Si_3N_4 - than on SiO_2 -covered substrates in a H_2 atmosphere, but uniformly fine grains were found on both SiO_2 and Si_3N_4 using a He deposition ambient atmosphere. Most workers report an increasing degree of preferred grain orientation and crystallite size as the temperature is increased above 700°C, independent of the chemical deposition system.

There are little data in the literature on the variation of Hall mobility with carrier concentration, especially at low carrier concentration levels. The most extensive data are those of Kamins (8) who reported that in layers grown at 1035°C from silane, the mobility reached a maximum of $40 \text{ cm}^2/\text{V-sec}$ in p-type samples doped with boron to the $10^{18}/\text{cc}$ level and decreased for both higher and lower doping levels. The mobility peaked similarly in arsenic-doped samples but the maximum mobility was only $30 \text{ cm}^2/\text{V-sec}$. With the exception of the diffused samples of Kamins, where a mobility approximately $\frac{1}{2}$ that of bulk is obtained for samples above $10^{19}/\text{cc}$, reported mobility values have been scarce, irreproducible, and usually a factor of 10 to 100 times below bulk values (1, 6, 9, 10).

Most workers (6, 8, 9, 10) have reported that doping control during growth was very difficult, and in some cases significant amounts of dopant were incorporated into the crystal in an inactive state.

The present study was undertaken to find first, a poly Si deposition process which would produce a very smooth film suitable for standard photoresist device processing, and thus avoid the thick film growth and

polish-back technique used by Fa and Jew. Second, the potential for doping during growth and the Hall mobilities of the resulting doped films are evaluated. A model is proposed to account for the unusually high Hall mobilities and irreproducible doping levels found for our samples doped below $2 \times 10^{17}/\text{cc}$.

Experimental Procedure

Poly Si films were deposited from SiH_4 - H_2 mixtures at temperatures between 600° and 750°C or from SiBr_4 - H_2 mixtures at 750°-900°C in conventional vertical induction-heated reactors. For a summary of system conditions, see Table I. The set of conditions for each system termed "operating conditions" were employed to deposit all poly Si films for electrical, chemical, and crystallographical analysis. Layers typically 1-3 μm thick were grown on three different substrates; 1.3 μm thermal SiO_2 on Si, fused quartz, and sapphire. All the quantitative data reported in this study were taken on layers $2.0 \pm 0.1 \mu\text{m}$ thick. The films were either undoped or were doped during growth with B_2H_6 (p-type) or with PH_3 (n-type) in the range 10^{14} - 10^{20} atoms/cc. The surface quality of the deposited films depended markedly both on substrate preparation procedures and on deposition conditions. The crucial step in the preparation of all substrates was found to be an "aqueous oxidation" (11) in a solution of 3 parts 30% stabilized H_2O_2 to 97 parts H_2O at 90°C for about 20 min just prior to deposition. Since the crystallite size decreased with decreasing temperature, giving rise to smoother surfaces, most depositions were made at the lowest possible temperature. The smoothest films, comparable to good epitaxial Si, were deposited at 650°C in the SiH_4 system on SiO_2 . In the SiBr_4 - H_2 system, the best films (matte surface) were grown at 840°C; depositions below 840°C were avoided because of the tendency of submicron films to be discontinuous. There is a slight degradation of surface quality of the films deposited from SiH_4 - H_2 with increasing dopant concentration at 650°C. However, there was no problem obtaining continuous submicron films in this system. Undoped poly Si films deposited from both systems exhibited a measured resistivity of $\cong 10^6$ ohm-cm and

Table I. System conditions for deposition of poly Si films from SiH_4 - H_2 and SiBr_4 - H_2 mixtures

Conditions	SiH_4	SiBr_4
Temperature, °C	600-750 (650)	750-900 (840)
Si/H_2	3×10^{-3} - 4×10^{-4} (3.7×10^{-3})	1×10^{-2} - 5×10^{-4} (9×10^{-3})
Growth rate, Å/min	30-600 (600)	200-3000 (2500)
Surface morphology	Shiny to matter (shiny)*	Matte to rough (rough)*

* Electrochemical Society Active Member.

Key words: mobility, doping, grain structure, low temperature.

* Operating conditions.

several high-concentration diffusions were made on these undoped samples.

Tallysurf measurements were made across an etched step to determine film thickness. To make electrical measurements on doped samples, six, terminal Hall bars were cut ultrasonically from the wafers, so that the current flow was parallel to the sample surface. Standard d-c Hall measurements were made to determine resistivity, mobility, and carrier concentration. A modified four-point-probe technique was used to measure the resistivity of the undoped samples. A selected number of n-type (phosphorus-doped) samples were analyzed for total phosphorus content using radiochemical analysis. Several p-type (boron-doped) samples were studied for crystallite size, boron precipitation, and preferred orientation using carbon surface replicas, glancing angle x-ray analysis, scanning electron microscopy (SEM), and high-voltage electron microscopy (HVEM).¹ The samples were either cleaved (for SEM) or the substrates were removed by chemical etching and ion milling for (HVEM).

Results

Film morphology and grain structure.—The most important factors in obtaining smooth poly Si films in the SiH₄ system were the use of careful cleaning procedures, especially the peroxide cleaning steps, and the use of low film-deposition temperature. The best deposits were obtained on thermal SiO₂. Of somewhat poorer quality were deposits on fused SiO₂, and the few deposits made on sapphire were distinctly less uniform. The surface quality of deposits on thermal

¹ The HVEM pictures were taken by R. M. Fischer and A. Szirmai at the U.S. Steel Fundamental Research Laboratory in Monroeville, Pennsylvania.

SiO₂ was quite reproducible but any relaxation in the cleaning procedure or inadvertent contamination led to seriously degraded, nonuniform surfaces. Electron micrographs of two poly Si samples grown at 650°C on thermal SiO₂ and doped with boron, one lightly (10¹⁴/cc) and another heavily (10¹⁹/cc), are shown in Fig. 1. The electron micrographs of carbon surface replicas (A) show the extremely fine-grain texture of the lightly doped sample. This appears as a very highly reflecting surface to the naked eye comparable to good epitaxial Si layers. This photograph was taken in a slightly defected area to show the few large Si grains protruding above the surface which were occasionally seen and which represent the only obvious defects in the surface. A water mark on a wafer or an unclean wafer will give rise to a very high density of such grains. The heavily doped sample shows an over-all rough surface texture due to large grains. Electron diffraction patterns (B) and high-voltage electron transmission micrographs (C) show that the lightly doped sample consists of fairly uniform random grains 250-350Å in size and the heavily doped samples of slightly preferred <110> oriented grains 2000-3000Å in size. The scanning electron micrographs of a fractured edge of the poly Si films show essentially no texture in the lightly doped sample. However, columnar growth does appear in the heavily doped samples. No evidence of a boron-rich phase was observed in any sample using HVEM. These results are summarized in Table II along with data obtained on an intermediate doped sample which exhibited properties intermediate between those found above.

Phosphorus-doped samples deposited at 650°C appeared visually identical to the boron-doped samples

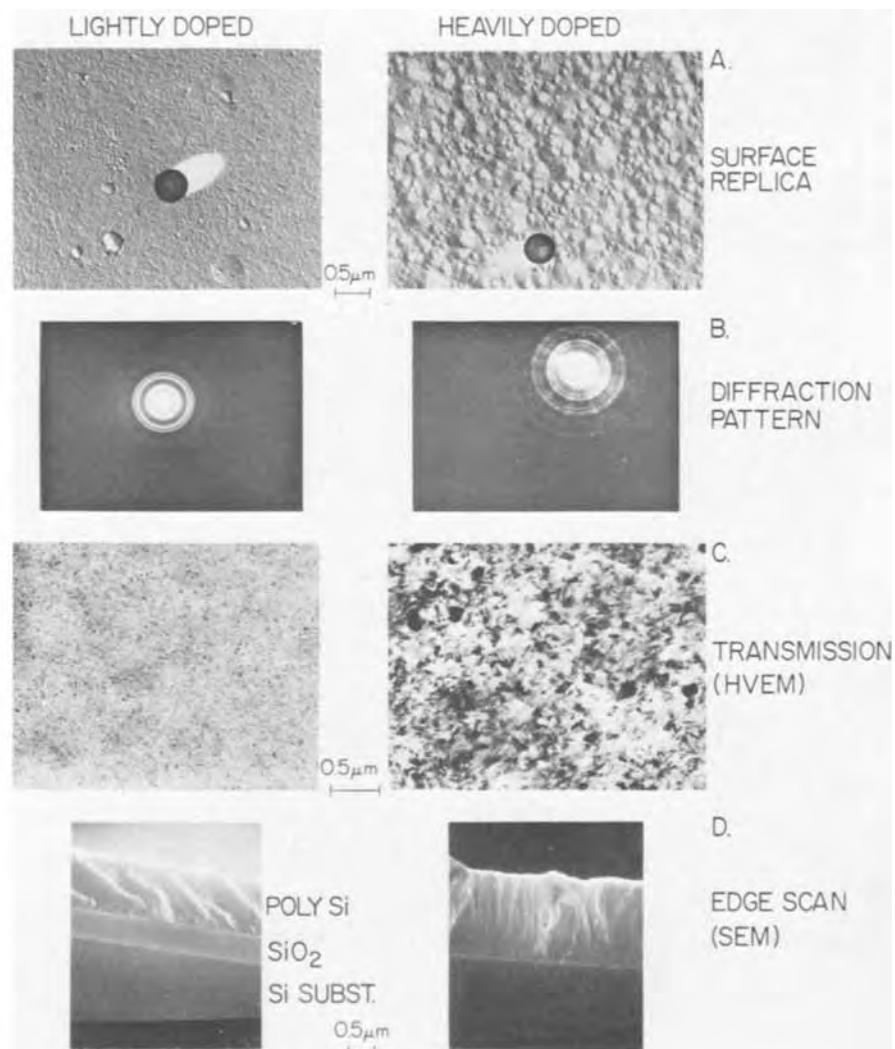


Fig. 1. Film morphology and grain structure of lightly (10¹⁴/cc) and heavily (10¹⁹/cc) boron-doped polycrystalline silicon grown at 650°C on thermal SiO₂.

Table II. Characteristics of boron-doped poly Si deposited on thermal SiO₂

Surface morphology	Mirror smooth	Slightly dull	Slightly matte
Carrier conc, N_A , cm ⁻³	10 ¹⁴	10 ¹⁷	10 ¹⁹
Grain size, Å	250-350	900-1100	2000-3000
Grain orientation	Random	Mostly random	Preferred <110>

as a function of doping level. Although no detailed electron microscope examination of the phosphorus samples was made, the visual similarity and similar results from glancing x-ray diffraction patterns of both phosphorus- and boron-doped samples lead us to believe that the grain structure is similar. The somewhat rougher surface of the phosphorus samples grown at 840°C is presumably associated with larger grain size. The grain structure of the diffused samples was not studied.

Doping during growth.—Most samples were doped during growth with either PH₃ or B₂H₆. Figure 2 shows the electrically active boron dopant or carrier concentration, N_A , of films deposited on both thermal SiO₂ and fused quartz substrates as a function of boron-to-silicon ratio, B/Si, in the vapor. (To avoid confusion in the following, the composition of the vapor is always referred to as a ratio, B/Si or P/Si, and is a pure number, e.g., 10⁻⁵. The concentration of carriers or electrically active dopant, N_A or N_D , in the crystal is always referred to on a concentration basis, e.g., 10²⁰/cc.) The N_A values were obtained from Hall measurements. For high doping levels, 5×10^{18} /cc to 2×10^{19} /cc, N_A was proportional to the B/Si ratio as is usually the case and as is shown for boron-doped single-crystal Si grown at high temperature, as indicated by two different curves (Fig. 2, curves A and B) from the literature (11, 12). The highest doping concentration obtained, 4×10^{19} /cc, is close to the solubility limit (13) of boron in Si extrapolated to 650°C. The extremely rapid decrease in N_A below a B/Si atom ratio of $\sim 5 \times 10^{-5}$ is unprecedented as far as we know in a SiH₄ system. In this range it was not possible to predict or control the value of N_A within the range of values from 10¹⁴/cc to 5×10^{18} /cc by setting the B/Si vapor phase ratio. The samples grown on fused quartz seem

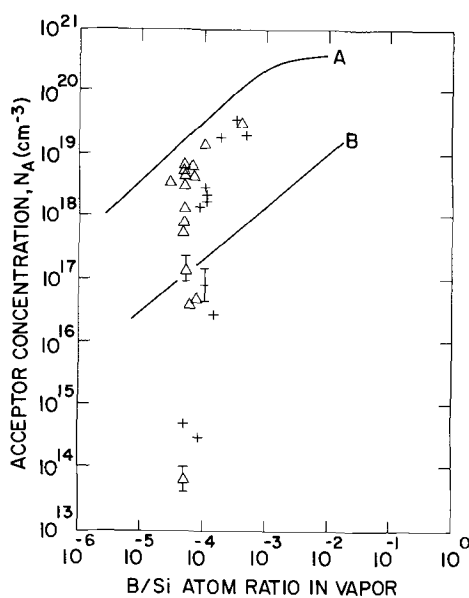


Fig. 2. Acceptor concentration, N_A , vs. B/Si atom ratio in vapor for poly Si samples deposited from SiH₄ at 650°C. Δ , Thermal SiO₂ substrates; +, fused quartz substrates. Single-crystal doping: -, boron doping of Si from B₂H₆ and SiCl₄-H₂ at 1500°K, A (11); B (12).

to show the same precipitous decrease of N_A with decreasing B/Si ratio but at a slightly higher B/Si value.

Figure 3 shows the variations of electrically active phosphorous dopant or carrier concentrations, N_D , deposited at 650° and 840°C as a function of the phosphorous to silicon ratio, P/Si, in the vapor. In a manner similar to the boron results, N_D , between 5×10^{18} /cc and 3×10^{19} /cc, is roughly proportional to P/Si. Above 3×10^{19} /cc, N_D is no longer proportional to P/Si but it does depend on P/Si in a manner closely parallel to single-crystal doping curves (Fig. 3, curves A and B) obtained at high temperature (12, 14). The values of N_D drop precipitously when the P/Si atom ratio is decreased below $\sim 5 \times 10^{-5}$. Therefore it was not possible to control doping levels below 5×10^{18} /cc by varying P/Si. There seems to be no essential difference between the data points obtained from deposits made at 840°C in the SiBr₄-H₂ system and those obtained at 650°C in the SiH₄-H₂ system. The maximum value of N_D observed agrees well with the solubility limit (15) of phosphorus in Si extrapolated to the two deposition temperatures.

Figure 4 shows the electrically active dopant concentration, N_D , and the total phosphorous dopant concentration, N_D^T , from neutron activation analysis of some samples as a function of P/Si. Some of the samples had N_D values too low to measure. The N_D and N_D^T points joined by dotted lines are for individual samples on which it was possible to make both measurements. N_D^T is found to be proportional to P/Si over the whole range and the data are fit by Eq. [1]

$$N_D^T = \text{P/Si} \cdot 35 \times 10^{22} \quad [1]$$

which is drawn as the solid line in Fig. 4. The dramatic drop off in N_D as N_D^T decreases linearly with P/Si is discussed later and a model is postulated (see dashed curve) to describe this phenomenon. The difference between N_D^T and N_D which is N_{GB} is referred to as the electrically "inactive" dopant concentration and is discussed in detail in the section on Doping during growth.

$$N_{GB} = N_D^T - N_D \quad [2]$$

Hall mobility of poly Si doped during growth.—The Hall mobility, μ_H , was obtained from the ratio of the Hall signal and the resistivity as measured at room temperature and is shown for p- and n-type samples respectively in Fig. 5 and 6.

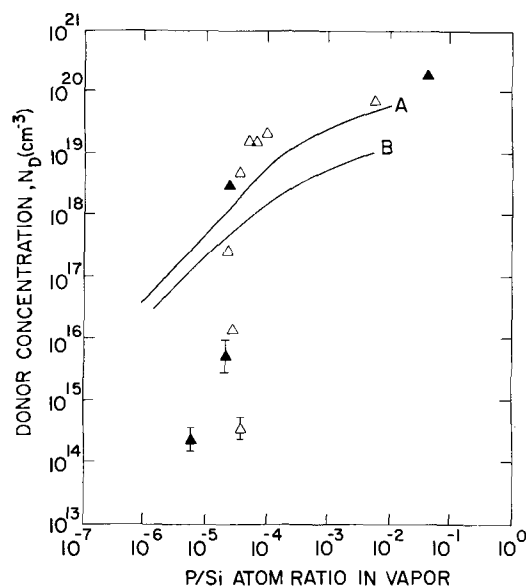


Fig. 3. Donor concentration, N_D , vs. P/Si atom ratio in vapor for poly Si samples deposited on thermal SiO₂ substrates. Δ Deposited at 650°C from SiH₄, \blacktriangle deposited at 840°C from SiBr₄-H₂. Phosphorous-doped single-crystal silicon, A (14); B (12).

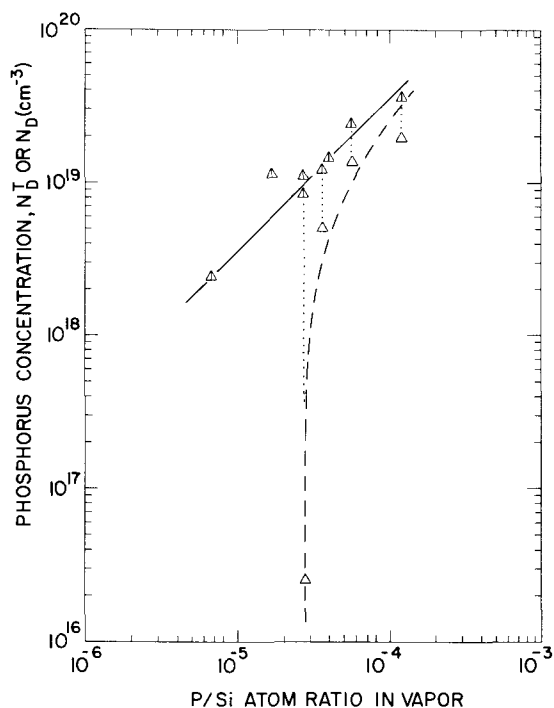


Fig. 4. Total phosphorous concentration, N_D^T , and donor concentration, N_D , vs. P/Si atom ratio in vapor for poly Si deposited from SiH_4 at 650°C . Δ Total phosphorous concentration, \triangle donor concentrations, — see Eq. [1] in text, - - - calculated from Eq. [4] in text.

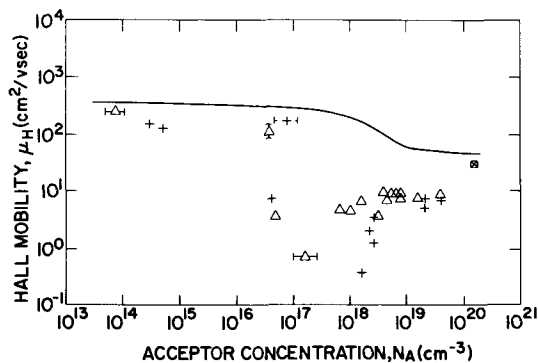


Fig. 5. Hall mobility, μ_H , vs. acceptor concentration, N_A , for poly Si samples doped with boron and deposited from SiH_4 at 650°C . — Single crystal mobility (16), \triangle thermal SiO_2 substrates, + fused quartz substrates, \boxtimes sample diffused using BBr_3 at 1000° for 5 min.

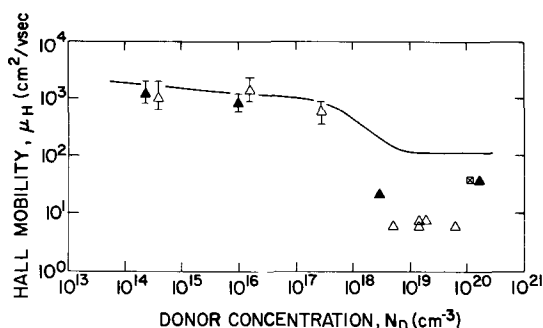


Fig. 6. Hall mobility, μ_H , vs. donor concentration, N_D , for poly Si samples doped with phosphorous and deposited on thermal SiO_2 . — Single crystal mobility (16), \triangle deposited at 650°C from SiH_4 , \blacktriangle deposited from $\text{SiBr}_4\text{-H}_2$ at 840°C , \boxtimes sample diffused using POCl_3 at 825°C for an 8-min cycle.

The variations of μ_H with carrier concentration, N_A , N_D , is quite similar for both p- and n-type samples. For carrier concentrations above $5 \times 10^{18}/\text{cc}$, the Hall

mobility of poly Si grown at 650°C is 1/10 (p-type) to 1/30 (n-type) of bulk values (16). On the other hand, the two diffused samples and the one n-type sample, doped to $2 \times 10^{20}/\text{cc}$ carrier concentration and grown at 840°C , exhibit values of μ_H $\frac{1}{2}$ to $\frac{1}{4}$ of that of bulk. With decreasing carrier density from $5 \times 10^{18}/\text{cc}$ down to about $2 \times 10^{17}/\text{cc}$, the mobility of p-type samples decreases and becomes more variable. Somewhat surprisingly, in the further decrease of doping below $10^{17}/\text{cc}$, the Hall mobility of both n- and p-type samples rises and is 1/2 to 1/3 that of bulk samples down to $10^{14}/\text{cc}$ carrier density. At the lower doping levels, the Hall measurements become more difficult and are less reproducible. Data were included in Fig. 5 or 6 only if the Hall signal was greater than 60% of the current-voltage drop in the sample and only if all three Hall voltages were of correct sign and if the data were consistent in every other way. Even when employing these criteria, most of the data were included (8 out of 13 samples).

Undoped samples always had a resistivity $> 10^6$ ohm-cm, as measured by a modified four-point-probe method, but the Hall signals were too low to be measured by our apparatus.

Discussion

Structure.—With regard to surface smoothness of undoped samples, our results appear comparable to those of Ford *et al.* (6) and Deluca (4) who also grew poly Si at low temperatures. Our poly Si grains, like theirs, are around 300\AA in diameter and are randomly oriented. Unlike Ford, who grew from SiH_4 in He, we find small grain size and highly uniform surfaces deposited from SiH_4 in a hydrogen ambient. This may be due to the peroxide cleaning step we employed which is so important in preparing substrates. The increase in particle size up to 3000\AA as the doping increases up to $10^{19}/\text{cc}$ has not been reported previously. The simultaneous appearance of a slightly preferred $\langle 110 \rangle$ orientation with the larger grain size is curious because it has been observed that an increase in deposition temperature produces exactly the same two associated effects. The smooth and shiny films obtained on thermal SiO_2 show that it is the most uniform substrate of those used and that poly Si is extremely sensitive to variations in nucleating conditions.

Doping during growth.—Figure 4 shows that the sharp decrease in N_D for low P/Si values occurs even though the total phosphorous content of the samples remains proportional to P/Si. Thus, some of the phosphorous is present in the crystal in a form which does not contribute significantly to electrical conductivity.

Similarly, Kamins (8) has reported that in vapor-doped poly Si grown at 1035°C , N_D , the electrically active arsenic concentration, is less than the total As concentration below $10^{18}/\text{cc}$. He has also inferred from an indirect method that boron-doped samples behave similarly. Although we have no data on total boron content of our boron-doped samples, we presume for the remainder of the discussion that they behave in the same manner as the one doped with phosphorous.

As regards the location of these electrically "inactive" atoms, we have considered several models: (i) preferential deposition in grain boundaries which we feel is most likely, (ii) distributed deposition in grain boundaries and in the bulk, and (iii) formation of interstitials or clusters in the bulk of the grains. We first present the most likely model (i) and finally make a few comments about why (ii) and (iii) are unsatisfactory. We feel the inactive atoms are deposited in the grain boundaries because the assumption that deposition occurs in the bulk of the grains leads to a contradiction as follows: from Fig. 4 it may be seen that the effective bulk concentration of inactive dopant atoms, N_{GB} , is high $\sim 10^{19}/\text{cc}$. If these atoms were in the bulk they would be ionized, although the carriers must be trapped somewhere to explain their inactivity. The

$10^{19}/\text{cc}$ density of ionized impurities would necessarily limit the maximum mobility that could be measured to values of about $100 \text{ cm}^2/\text{V}\cdot\text{sec}$ (from bulk curve Fig. 6), which is an order of magnitude smaller than actually observed because of ionized impurity scattering. Therefore we conclude that the inactive atoms are in the grain boundaries. A distinct, separate, three-dimensional phase, e.g., SiB_6 or SiP , was not observed in the HVEM examination of samples, and it probably was not formed because we are still more than an order of magnitude below the solubility limit for either boron or phosphorous in Si.

In order to account for the very rapid change of, say, N_D with P/Si ratio, it is necessary to postulate that no dopant atoms are deposited in the bulk of the crystallites until the grain boundaries are completely saturated. After the boundaries are saturated, any further increase in P/Si will result in dopant atoms being incorporated into the bulk of the crystallites. Quantitatively this model may be described as follows: the electrically inactive dopant concentration, N_{GB} , given by Eq. [2], is now defined to be the equivalent bulk density, (atoms/ cm^3) of dopant atoms but which are located in the grain boundaries! For a simple grain geometry such as a cube

$$N_{GB} = \frac{3 \times A \times D_s \times S}{V} \quad [3]$$

where A is the area of one cubic grain face, V the volume, D_s the surface atom density of Si (1.35×10^{15}), S the fraction of surface atoms covered or associated with an electrically inactive dopant atom, and the factor 3 is the equivalent number of cube faces ($\frac{1}{2}$ the total) associated solely with this grain.

Combining [2] and [3] and assuming an average grain size of 1000\AA , (or $A = 10^6 \text{ \AA}^2$, $V = 10^9 \text{ \AA}^3$) we have

$$N_D = N_D^T - 4.05 \times 10^{20} S \quad [4]$$

where N_D^T is given by Eq. [1] for the data in Fig. 4. We have fit Eq. [4] to the data of Fig. 4 using S as an adjustable parameter. The best fit (dashed curve) describes the N_D data very satisfactorily, with S equal to 0.024, and exhibits the rapid change of N_D with P/Si. From Eq. [3] then, N_{GB} equals $9.7 \times 10^{18}/\text{cc}$.

Let us now point out that the alternative model which postulates that dopant atoms are distributed in equilibrium concentrations between the grain boundaries and the bulk of the grains cannot explain the present result. Such a model would give a doping curve with N_D proportional to P/Si but with a lower intercept on the N_D axis. It would not predict the observed sharp decrease of N_D with decreasing P/Si below the value of 5×10^{-5} .

We also believe that the inactive dopant atoms are not present as interstitials or clusters in the bulk of the grains for the following two reasons: first, both interstitials and clusters would be expected to increase in concentration slowly with increasing total dopant concentration, which is not observed. Second, the concentration of such clusters would probably vary with temperature, which is not observed in Fig. 3 data.

Mobility.—The Hall mobility, μ_H , of poly Si samples in Fig. 5 and 6 is always observed to be less than that of the bulk. This is consistent with the expectation that grain boundaries will necessarily lower μ_H . Let us now consider various portions of the doping range separately.

At doping levels above $2 \times 10^{18}/\text{cc}$, we note that our results and those of Kamins, Ford, and Mai indicate that high-temperature processing either during growth or during diffusion is necessary to achieve high mobility. From $2 \times 10^{18}/\text{cc}$ to $2 \times 10^{17}/\text{cc}$, no one reports very high mobilities but the trend of the mobility change with decreasing doping is different for different investigations. We do not have a satisfactory ex-

planation for mobility in either of the above ranges and will not speculate further here on its cause.

We have developed, however, a basic explanation to account for the unusually high mobility² of most of our samples doped from $2 \times 10^{17}/\text{cc}$ down to $10^{13}/\text{cc}$. Historically, it is in this doping range where μ_H , measured in many different polycrystalline materials, has been found to be much lower than in bulk single crystals. The mobility lowering has usually been attributed to the presence of potential barriers at grain boundaries which have an increasingly detrimental effect on the mobility as the carrier concentration is decreased.

Now, because of the extremely small dimensions (200-1000 \AA) of the poly Si grains in this doping range, the usual band model of a potential barrier is inappropriate. For instance, at a doping level of $10^{16}/\text{cc}$, the space charge width is much larger than the average diameter of the grains, which is about 1000 \AA . However, even if a potential barrier picture is inappropriate, trapped charges at surface states in the grain boundaries would still lower mobility, and trapped charges at grain boundaries are likely to be present in any case due to structural defects which are inevitably present due to random orientation of neighboring grains.

However, since we do not observe low mobility, it seems reasonable to suspect that such barriers or charge scattering centers are effectively removed or compensated in our films.

At this point we would like to speculate on two alternative mechanisms by which the trapped charge centers might be eliminated or compensated:

1. The hydrogen present at our low growth temperature eliminates surface states in the grain boundaries.

In support of this model we note that low-temperature, 300°-500°C, but not high-temperature hydrogen annealing has been very effective in removing fast surface states at Si-SiO₂ interfaces (18).

2. The presence of the large, $\sim 10^{19}/\text{cc}$, concentration of the previously described electrically inactive boron and phosphorous atoms compensates surface states in the grain boundaries.

With regard to this model, we note first that Dumin (19) has obtained significant evidence, in layers of single crystal Si grown on sapphire near 1200°C, for the presence of a high density of acceptors in the middle of the upper half of the bandgap and donors in the middle of the lower half of the bandgap. These centers increase in concentration near the Si-sapphire interface and may be due either to an impurity or a structural defect or both. Kamins postulated that similar defects are present in poly Si films.

Specifically, we postulate that the electrically inactive boron and phosphorous atoms may be pairing with and therefore compensating defects to produce either neutral pairs or localized dipoles in the grain boundaries. These pairs would be relatively ineffective in lowering mobility. The low temperature of our depositions would favor pair formation which would be less likely at higher deposition temperatures. In the same way, if the free energy of formation of such pairs were very high compared to the free energy of dissolving boron or phosphorous in Si, this would explain why the grain boundaries apparently become completely saturated with dopant before any dopant appears in the bulk of the crystallites, as already discussed. If there is a one-to-one pairing of inactive dopant atoms with defects, then the surface defect density is in the 10^{13} defects/ cm^2 range. It is important to note that the relatively shallow acceptors and donors (boron and phosphorous) would be able to compensate any defect charge center of the opposite type

² The high mobility found here cannot be explained by the inhomogeneity effects discussed by Wolfe *et al.* (17). In his model, anomalously high mobilities are observed only when the total amount of dopant greatly exceeds that which is present in our samples.

as long as the defect has the deeper electronic energy level.

Summary

It has been shown that thin polycrystalline silicon films having mirror smooth surfaces suitable for photoresist processing can be deposited at low deposition temperatures over large areas on thermal SiO₂. These films exhibit mobility values approximately 50% of bulk values in the concentration range between 10¹⁴/cc to 10¹⁷/cc and above 10¹⁹/cc. This implies that fabrication of FET's in the 10¹⁶/cc doping range and the use of heavily doped Si for gate material looks quite promising.

It is suggested that the irreproducible doping during growth and the unexpected high mobility of lightly doped samples are associated and caused by the selective deposition of dopant atoms in grain boundaries which compensate local structural defects. The resultant pairs are electrically neutral and therefore do not adversely affect the mobility. (Alternatively, hydrogen may compensate or eliminate the structural defects.)

Above 10¹⁹/cc, diffusion processes yield samples with higher mobility and doping levels than does doping during growth.

The feasibility of fabricating FET's in poly Si is supported by the Hall mobility in the 10¹⁶-10¹⁷/cc carrier concentration range, reported in the present work, on the premise that some other doping process be employed other than doping during growth.

Acknowledgments

We would like to express our appreciation to the many members of the staff who have contributed to this work. We would especially like to acknowledge the assistance of H. Keller and J. F. Woods in measuring and interpreting the Hall measurements, and of J. E. Lewis in carrying out the neutron activation analyses. In addition we would like to thank T. B. Light, V. J. Silvestri, C. J. Kircher, and S. Lahiri for many helpful discussions.

Manuscript submitted April 25, 1972; revised manuscript received June 21, 1972.

Any discussion of this paper will appear in a Discussion Section to be published in the June 1973 JOURNAL.

REFERENCES

1. K. E. Bean, H. P. Hentzschel, and D. Colman, *J. Appl. Phys.*, **40**, 2358(C) (1969); Paper 326 presented at Electrochem. Soc. Meeting, New York City, May 5-9, 1969.
2. L. L. Vadasz, A. S. Grove, T. A. Rowe, and G. E. Moore, *IEEE Spectrum*, **6**, 28 (1969).
3. C. H. Fa and T. T. Jew, *IEEE Trans. Electron Devices*, **ED-13**, 290 (1966).
4. R. D. DeLuca, Paper 283 presented at Electrochem. Soc. Meeting, New York City, May 5-9 (1969).
5. M. E. Cowher and T. O. Sedgwick, Paper 58 presented at Electrochem. Soc. Meeting, Washington, D. C., May 9-13, 1971.
6. K. D. Ford, R. Thomas, and S. J. Laverty, Paper 172 presented at Electrochem. Soc. Meeting, Cleveland, Oct. 3-7, 1971.
7. A. L. Fripp and R. L. Stermer, *This Journal*, **117**, 1569 (1970).
8. T. K. Kamins, *J. Appl. Phys.*, **42**, 4357 (1971).
9. C. C. Mai, T. S. Whitehouse, R. L. Thomas, and D. R. Goldstein, *This Journal*, **118**, 331 (1971).
10. E. Sirtl and H. Seiter, *ibid.*, **113**, 506 (1966).
11. P. Rai-Choudhury and E. I. Salkowitz, *J. Crystal Growth*, **7**, 361 (1970).
12. R. M. Warner, Jr., Editor, "Integrated Circuits," pp. 284, 285, McGraw-Hill, New York (1965).
13. G. L. Vick and K. M. Whittle, *This Journal*, **116**, 1142 (1969).
14. E. Sirtl, "Festkorper Probleme VI," p. 27, O. Madelung, Editor, Vieweg: Braunschweig, Germany (1967).
15. F. A. Trumbore, *Bell System Tech. J.*, **39**, 210 (1960).
16. M. Neuberger and S. J. Wells, "Silicon Electronic Properties," pp. 84-86, Information Center, Hughes Aircraft Co., Culver City, Calif. (1969).
17. C. M. Wolfe, G. E. Stillman, and J. A. Rossi, *This Journal*, **119**, 250 (1972).
18. D. M. Brown and P. V. Gray, *ibid.*, **115**, 760 (1968).
19. D. J. Dumin, *Solid State Electron.*, **13**, 415 (1970).

Diffusion of Boron from Shallow Ion Implants in Silicon

Sigurd Wagner

Bell Telephone Laboratories, Incorporated, Murray Hill, New Jersey 07974

ABSTRACT

The use of shallow ion implants as diffusion sources was studied on bare (111) silicon wafers implanted at room temperature with 30 keV, 3·10¹⁴ cm⁻² boron. Samples were annealed in purified argon at 900°, 1000°, and 1100°C. The diffusion profiles of boron are determined by in-diffusion into the silicon and by dissolution, to equilibrium, in the thin oxide layer on the surface. The amount of boron retained in silicon decreases during the initial period of an anneal and then remains constant. More boron is retained the higher the temperature and the lower the oxygen content in the ambient gas. With ~10 ppm O₂ in argon, losses range from 15 to 35% of the implanted dose. Experimental results are reasonably well represented by the mathematical formalism developed. The experimental data indicate that the values listed in the literature for sheet conductivity mobilities of holes are too low.

The anneal of boron implanted at room temperature into silicon can be thought to proceed in two steps. The electrical activity of the dopant is developed during a brief heat-treatment at a relatively low temperature, typically (1, 2) 30 min at 850°C. Under these conditions the diffusion length, $2\sqrt{Dt}$, in undamaged silicon is

Key words: ion implantation, diffusion, silicon.

small as compared to the standard deviation in the Gaussian distribution of the implanted boron. The concentration profile of the dopant can be expected to remain essentially that of the original implant, even if some damage-enhanced diffusion occurs initially.

Anneals at higher temperatures and for longer periods of time alter the concentration profile of the

implanted boron in addition to developing its electrical activity. This paper reports the characterization of such "diffusion anneals." (111) silicon was implanted at room temperature with a dose of $3 \cdot 10^{14}$ cm $^{-2}$ boron ions of 30 keV energy in a random direction. The wafers were annealed in a purified argon atmosphere.

Analysis

The as-implanted distribution, after a 30-min anneal at 850°C, is well approximated by a Gaussian distribution with its maximum in the surface of the wafer (Fig. 1)

$$C(x, t = 0) = C(x = 0, t = 0) \cdot e^{-x^2/4\alpha}$$

$$= \frac{Q}{\sqrt{\pi\alpha}} \cdot e^{-x^2/4\alpha} \quad [1]$$

(A list of symbols is provided at the end of the paper.) This distribution represents the source for subsequent diffusion into the silicon and into the very thin oxide layer which grows on the silicon surface even in purified argon. As the experimental results will indicate, this SiO $_2$ layer is in equilibrium with the boron on the silicon side of the SiO $_2$ /Si interface, and the loss of boron to the ambient gas is negligible (see Discussion section). Therefore, all "out-diffusion" can be accounted for by an infinitely thin sink, of growing capacity, and located at the SiO $_2$ /Si interface. The movement of this interface relative to the bulk of the silicon can be neglected because the oxides grown are only up to a few hundred angstrom units thick.

An analytical expression for the rate by which the capacity of the boron sink increases is obtained from a characterization of the oxide growth. After ion implantation and cleaning a 10-30Å layer of oxide covers the silicon. During the anneal rapid initial oxidation occurs up to an oxide thickness of the order of 100Å. Then the growth begins to proceed according to the linear rate law (3)

$$u = A_1 + A_2 t \quad [2]$$

Recent experimental data (4) indicate that the onset of parabolic (after linear) growth occurs at thicknesses as low as 200Å. In any case no single existing theoretical expression fits the oxide growth from virgin oxide to a few hundred angstrom units. It is proposed to represent this region by a phenomenological parabolic law

$$u = \sqrt{Bt} \quad [3]$$

which neglects the oxide existing at $t = 0$, but takes the initial rapid growth and the subsequent slowdown into account.

The diffusion equation can now be derived in a manner similar to that of diffusion from a predeposited source into a thick oxide growing on the silicon, with negligible diffusivity in the oxide. This case was analyzed by Huang and Welliver (5).

Diffusion into the silicon from the ion implanted source, without net flux across the interface, is described by

$$C_+(x, t) = C_+(0, t) \cdot e^{-\frac{x^2}{4(\alpha + Dt)}}$$

$$= \frac{Q}{\sqrt{\pi(\alpha + Dt)}} \cdot e^{-\frac{x^2}{4(\alpha + Dt)}} \quad [4]$$

However, the actual boundary condition at the interface results from diffusion into the growing oxide while equilibrium is maintained at the interface and within the oxide (for the oxide, boron implanted and boron incorporated by growth is neglected)

$$D \frac{\partial C}{\partial X} \Big|_{x=0, t} = -k \cdot \left\{ C(0, t) \cdot \frac{\partial}{\partial t} u(t) + u(t) \cdot \frac{\partial}{\partial t} C(0, t) \right\} \quad [5]$$

The second term on the right-hand side of Eq. [5] is smaller than the first until $\partial \ln C(0, t) / \partial \ln t = -1/2$, when the net flux across the interface becomes zero, and the first term becomes small as compared to its initial value. Therefore the equation for out-diffusion from the silicon can be solved (6) approximately, by neglecting the second term, to give

$$C_-(x, t) = A(t) \operatorname{erfc} \left(\frac{x}{2\sqrt{Dt}} \right) \quad [6]$$

$A(t)$ is found by combining the derivative of Eq. [6] with Eq. [5]

$$C_-(x, t) = -C(0, t) \cdot \frac{\sqrt{\pi}}{2} \cdot k \cdot \sqrt{\frac{B}{D}} \cdot \operatorname{erfc} \left(\frac{x}{2\sqrt{Dt}} \right) \quad [7]$$

The diffusion equation and the boundary conditions are linear. Therefore the actual impurity profile can be obtained by adding $C_-(x, t)$, Eq. [7], to $C_+(x, t)$, Eq. [4], and by solving for $C(0, t)$ at $x = 0$

$$C(x, t) = C_+(x, t) + C_-(x, t)$$

$$= \frac{Q}{\sqrt{\pi(\alpha + Dt)}} \left\{ e^{-\frac{x^2}{4(\alpha + Dt)}} - \frac{1}{1 + \frac{2}{\sqrt{\pi}} \cdot \frac{1}{k} \cdot \sqrt{\frac{D}{B}}} \cdot \operatorname{erfc} \left(\frac{x}{2\sqrt{Dt}} \right) \right\} \quad [8]$$

The amount of boron retained in the silicon is

$$Q(t) = Q + \Delta Q(t) = \int_{x=0}^{\infty} C(x, t) dx$$

$$= Q \left\{ 1 - \frac{1}{1 + \frac{2}{\sqrt{\pi}} \cdot \frac{1}{k} \cdot \sqrt{\frac{D}{B}}} \cdot \frac{2\sqrt{Dt}}{\pi\sqrt{\alpha + Dt}} \right\} \quad [9]$$

The latter equation has several important consequences. First, boron is lost only during an initial period; the amount of boron retained in the silicon remains virtually constant as soon as $Dt \gg \alpha$. Second, the loss $\Delta Q(t)$ increases with decreasing $1/k \cdot \sqrt{D/B}$, that is, the larger $1/k \cdot \sqrt{D/B}$, the more boron is retained. $1/k \cdot \sqrt{D/B}$ can be made large by keeping the concentration of oxidant as low as possible, and by annealing at as high a temperature as possible: the enthalpy of activation for the oxidation (3), ~ 2 eV \cdot mole $^{-1}$, is much smaller than that for diffusion which is ~ 3.5 eV \cdot mole $^{-1}$. k appears to be independent of temperature. Therefore

$$\frac{\partial}{\partial T} \left(\frac{1}{k} \cdot \sqrt{\frac{D}{B}} \right) > 1 \quad [10]$$

In spite of the superposition of an erfc-profile on the Gaussian distribution, accurate coefficients of diffusion can be obtained when $x \gg \sqrt{Dt}$ and $Dt \gg \alpha$. Then D is calculated from the slope of a plot of $\ln C$ vs. x^2

$$\frac{\partial \ln C(x,t)}{\partial (x^2)} \cong -\frac{1}{4(\alpha + Dt)} + \frac{1}{\left(1 + \frac{2}{\sqrt{\pi}} \cdot \frac{1}{k} \cdot \sqrt{\frac{D}{B}}\right) \sqrt{\pi}} \frac{\sqrt{Dt}}{x^3} \cong -\frac{1}{4(\alpha + Dt)} \quad [11]$$

Experimental

7-14 ohm-cm As-doped silicon wafers (3.2 cm diam, ~0.025 cm thickness) with polished (111) surfaces were implanted with 30 keV boron ions in a random direction, ~7° off the {111} axis, at a dose of $3 \cdot 10^{14}$ cm⁻². Whole wafers, or chips, were cleaned consecutively in organic solvents, conc HF, conc HNO₃, conc HF, and water. Slices were annealed on a quartz boat in the quartz liner of a resistance-heated furnace. Purified argon (99.996%, nominally less than (in ppm) 7 O₂, 2 H₂, 30 N₂, 2 CH₄, 2 CO₂, dew point -95°C \pm 0.037 ppm H₂O) served as a protective gas; it was run through an acetone-dry ice trap to keep the maximum actual dew point at -78°C. The argon flux was 0.5 cm · sec⁻¹ (STP) except during and for 3 min after insertion of a sample, when a flux of 5 cm · sec⁻¹ (STP) was maintained.

Concentration profiles were determined mainly by anodization profiling and sheet conductivity measurements. Chips were anodized in a potassium nitrite-tetrahydrofurfural solution (7) (2.8g KNO₂ in 100 ml THFol) while being irradiated with light from a tungsten-halogen lamp. A constant current-constant voltage automatic crossover power supply was set to deliver 15 mA cm⁻² and voltages between 196V (\cong 500Å Si) and 294V (\cong 750Å Si). The anodization was stopped when the current had decayed to virtually zero. The thickness of anodic oxides was measured by visual comparison with an oxide chart calibrated by ellipsometry.

A square array four-point probe (point spacing 0.064 cm, 0.0025 cm tip radius, 50g load per point) was used for the sheet conductivity measurements. Linearity of signal voltage with applied current was frequently checked. The signal voltage ranged from ~1 to ~100 mV (8). A few sheet conductivities were also measured on a Van der Pauw configuration (9) with In-Sn soldered contacts. Agreement was to within 3%.

All samples were profiled to beyond the pn junction. When the junctions were deeper than 1 μm, x_j , calculated from the sum of the thickness of the anodic oxides were within 10% of x_j from angle lapping, staining, and interferometry.

$(\Delta\kappa_s/\Delta x)_n$ was calculated for each profiling step n , and, except for the first step $n = 1$, smoothed by arithmetically averaging over $n - 1, n, n + 1$. Then C was obtained from the equation

$$\left(\frac{\Delta\kappa_s}{\Delta x}\right)_x \cong \left(\frac{\partial\kappa_s}{\partial x}\right)_x = -C \cdot q \cdot \mu_h(C) \quad [12]$$

The hole mobility μ_h and its dependence on C are discussed in the Appendix.

Carrier concentrations were also obtained from Hall effect measurements on Van der Pauw patterns. Concentrations were measured on as-annealed chips, and on several specimens profiled by the copper-displacement technique ($2\text{Cu}^{2+} + \text{Si} = 2\text{Cu} + \text{Si}^{4+}$) with intermittent anodizations to smooth the silicon surface.

Thickness and refractive index of surface oxides were determined by ellipsometry.

Results

The concentration profiles of two implants annealed for 30 min at 850°C are plotted as log C vs. x^2 in Fig. 1. The experimental data are reasonably well approxi-

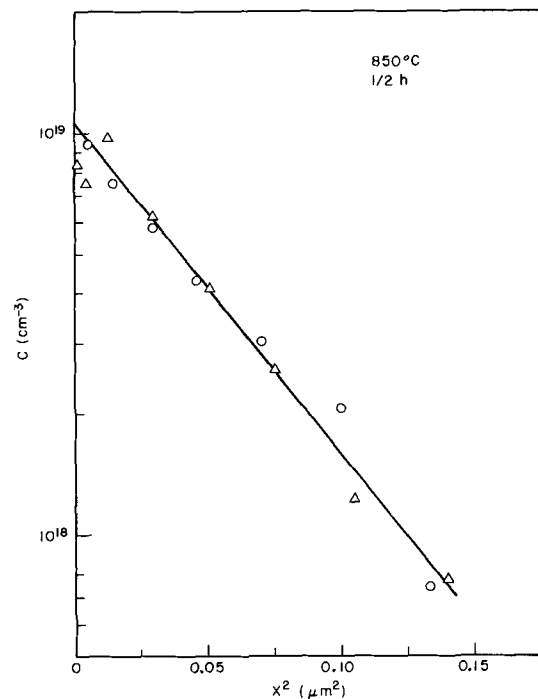


Fig. 1. Profile of implant after 30 min anneal at 850°C

ated by a straight line (Gaussian distribution) corresponding to

$$C(x,t=0) = 1.05 \cdot 10^{19} \cdot e^{-\frac{x^2}{4 \cdot 1.36 \cdot 10^{-10}}} \quad [13]$$

The amount of active dopant

$$\int_0^{\infty} C(x,t=0) dx = C(x=0,t=0) \cdot \sqrt{\pi\alpha} = 2.12 \cdot 10^{14} \text{ cm}^{-2} \quad [14]$$

indicates that not all of the implanted boron had yet developed its electrical activity. This activity develops most slowly in the high-concentration portion of an implant (10), thus in a narrow region near $x = 0$ in the present case. Consequently a further anneal to $3 \cdot 10^{14}$ carriers per square centimeter would not have had a significant effect on the slope of the implanted profile and on α .

Experimental profiles for the 900°, 1000°, and 1100°C anneals are presented in Fig. 2, 3, and 4, respectively. The diffusion coefficient at 1100°C (from the 4-, 9-, and 16-hr profiles) is $1.7 \cdot 10^{-13}$ cm² sec⁻¹, at 1000°C (from the 12- and 48-hr profiles) $1.7 \cdot 10^{-14}$ cm² sec⁻¹. The 900°C profiles are very steep at high x due to partial penetration of the probe points through the junction. Here D was derived from the difference in slope of the 42- and 168-hr profile at intermediate x^2

$$D_{2-1} = -\frac{1}{9.212(t_2 - t_1)} \left[\frac{\Delta(x^2)}{\Delta(\log C_2)} - \frac{\Delta(x^2)}{\Delta(\log C_1)} \right] \quad [15]$$

and was found to be $1.5 \cdot 10^{-15}$ cm² sec⁻¹. The diffusion coefficients are in very good agreement with those of Ref. (11) for diffusion from a doped oxide source, and with those of Ref. (12) for diffusion from a B₂O₃-saturated N₂ atmosphere.

The amount of boron retained in the silicon, $Q(t)$, was arrived at by integration of the C vs. x curves, and in part also by (uncorrected) Hall measurements. These data are shown in Fig. 5. The mobilities leading to two different sets for the sheet conductivity data are discussed in the Appendix.

In Fig. 6 the oxide growth at 1100°C is shown to proceed approximately by a parabolic law with $B = 8.9 \cdot 10^{-17}$ cm² sec⁻¹. At 900° and 1000°C the oxide growth was irregular, probably because of variations

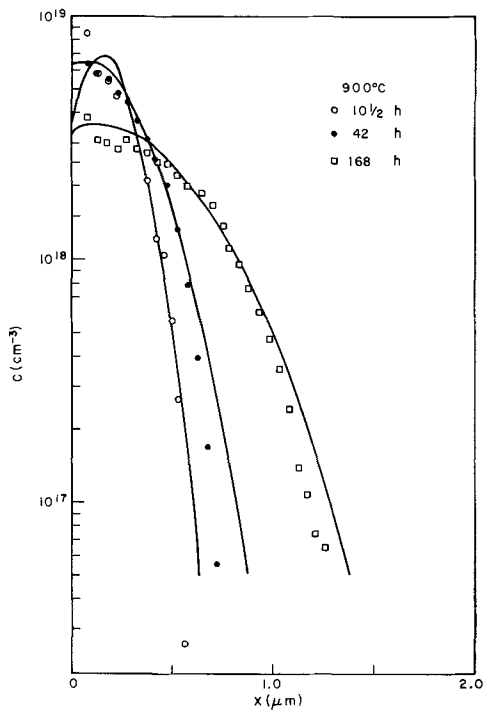


Fig. 2. 900°C diffusions; experimental points and calculated profiles.

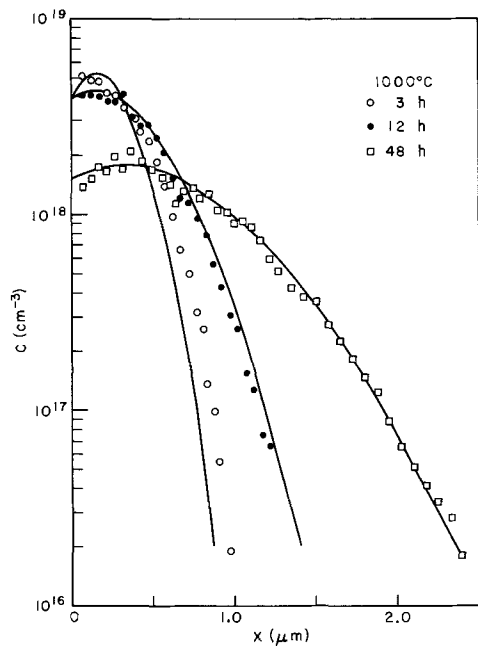


Fig. 3. 1000°C diffusions; experimental points and calculated profiles.

in the oxygen and water content (dew point) of the ambient gas during the long annealing times involved. For these cases B was calculated separately for each sample as $B = u^2/t$.

The distribution coefficient of boron between the oxide and the silicon, k , was derived from the amount of boron lost from the silicon, $\Delta Q(t)$, the thickness of the oxide, u , and the concentration of boron in silicon at the interface, $C(x = 0, t)$

$$k = \frac{\Delta Q(t)}{u \cdot C(0, t)} \quad [16]$$

Because of the scatter brought in with $\Delta Q(t)$, $C(0, t)$, and u , considerable scatter can be expected for k . The average value (from all but the shortest anneal at each

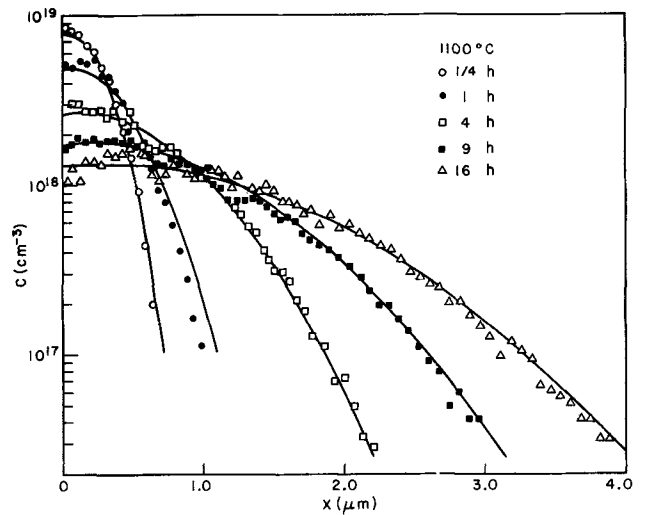


Fig. 4. 1100°C diffusions; experimental points and calculated profiles.

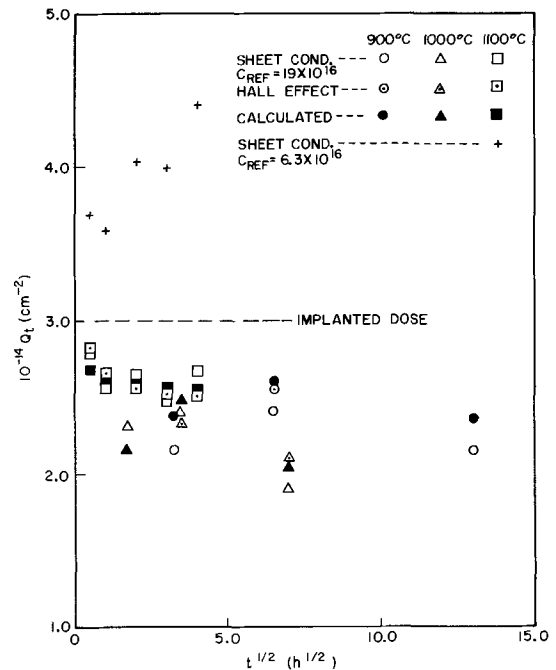


Fig. 5. Amount of boron retained in silicon

temperature) is $k = 16 \pm 5$. k is low for short anneals because the boron has not yet attained equilibrium within the oxide.

A summary of data is presented in Table I. The diffusion profiles calculated using Eq. [8] and the B and k values just discussed are shown as solid lines in Fig. 2, 3, and 4; the calculated retained doses, $Q(t)$, are given in Fig. 5.

Discussion

The experimental results were used as a basis for assumptions made for the analysis of the boron diffusion. The initial profile is well approximated by a Gaussian distribution with its maximum at $x = 0$ (Fig. 1). The growth of the oxide can be expressed in terms of a parabolic rate law (Fig. 6). A constant coefficient of distribution of boron between oxide and silicon, and equilibration within the oxide, is supported by the data of Table I, although with a considerable margin of error. However, the values for k are satisfactory in view of the possible errors in u , $C(0, t)$, and especially in the "lost" portion of boron, $\Delta Q(t)$, which is found as difference of two larger quantities, Q (implanted) and $Q(t)$. The complexity of the processes occurring in

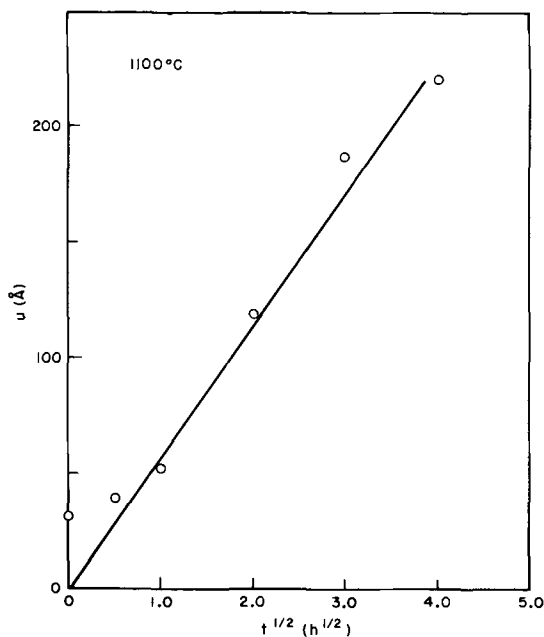


Fig. 6. Thickness of oxides, 1100°C anneals

the oxide must also be kept in mind: fresh oxide grows at the SiO_2/Si interface and displaces previously grown SiO_2 which has a higher content in boron. Boron will therefore diffuse toward the interface not only from the bulk silicon, but also from outer layers of the oxide. At 900°C, the growth rate B and the diffusion coefficient of boron in SiO_2 (13) are of comparable magnitude and nonuniformity of the boron concentration in SiO_2 might result. Of course, there is always the question whether such very thin oxide layers can be treated as bulk phases. Altogether the value of $k = 16 \pm 5$ compares favorably to values given in the literature for the case of thick oxides grown on bulk-doped silicon (14), $k = 3$, silicon with boron predeposits (5, 15), $k = 9$ and $k = 10$, and for the transfer of boron from a $\text{SiO}_2 + \text{B}_2\text{O}_3$ layer to silicon (11), $k \approx 50$.

The calculated profiles (Fig. 2, 3, and 4) and retained doses (Fig. 5) agree well with the experimental results and support the physical concept put forward. No significant losses of boron to the ambient gas did occur since the entire implanted dose is accounted for by the boron retained in the silicon plus that dissolved in the oxide.

One simplifying assumption for the present study was that the diffusion length of B in SiO_2 is at least comparable to the thickness of the SiO_2 -layer. The capacity of the oxide for boron is then proportional to its thickness, and the key quantity determining the retained dose is $1/k \cdot \sqrt{D/B}$. There is another case of practical interest which can be approached in a similar manner: implantation through a thick layer of oxide, into the silicon and subsequent anneal without further growth of oxide. The oxide layer must be thick in comparison to the diffusion length of boron in the oxide. Let the maximum concentration of the implant be in the SiO_2/Si interface. During a brief anneal the boron

will equilibrate across the interface and two essentially Gaussian profiles will be set up, one in SiO_2 , the other in Si . If all secondary effects are neglected, the amounts of boron in Si , $Q(\text{Si})$, and in SiO_2 , $Q(\text{SiO}_2)$, are then related to the respective concentrations at the interface, $C(\text{Si})$ and $C(\text{SiO}_2)$, by

$$Q(\text{Si}) = C(\text{Si}) \cdot \sqrt{\pi \cdot D(\text{Si}) \cdot t} \quad [17]$$

and

$$Q(\text{SiO}_2) = C(\text{SiO}_2) \cdot \sqrt{\pi \cdot D(\text{SiO}_2) \cdot t} \quad [18]$$

The maximum of both profiles will be in the interface, where

$$C(\text{SiO}_2) = k \cdot C(\text{Si}) \quad [19]$$

Combining Eq. [17], [18], and [19], one obtains

$$\frac{Q(\text{Si})}{Q(\text{SiO}_2)} = \frac{1}{k} \cdot \sqrt{\frac{D(\text{Si})}{D(\text{SiO}_2)}} \quad [20]$$

If $\sqrt{D(\text{Si})} > k\sqrt{D(\text{SiO}_2)}$, the boron tends to remain in the silicon. If $\sqrt{D(\text{Si})} < k\sqrt{D(\text{SiO}_2)}$, much of it will diffuse into the oxide. At 1100°C, with $D(\text{Si}) = 1.7 \cdot 10^{-13} \text{ cm}^2 \text{ sec}^{-1}$ and $k = 16$ from the present investigation, and $D(\text{SiO}_2) = 3.5 \cdot 10^{-17} \text{ cm}^2 \text{ sec}^{-1}$ from Ref. (13)

$$\frac{1}{k} \cdot \sqrt{\frac{D(\text{Si})}{D(\text{SiO}_2)}} \approx 4 \quad [21]$$

Thus it appears feasible to retain a major portion of the boron implanted through an oxide layer if the diffusion anneal is performed without any concurrent oxidation. The enthalpy of activation, ΔH^\ddagger , for diffusion in Si , $3.5 \text{ eV} \cdot \text{mole}^{-1}$, is slightly smaller than that for diffusion in SiO_2 , $3.8 \text{ eV} \cdot \text{mole}^{-1}$ (13). As a result the tendency for diffusion into the oxide increases with increasing temperature. However, the difference in ΔH^\ddagger is small and diffusion at an elevated temperature is advisable for expediency.

Acknowledgments

The author thanks R. A. Moline and R. W. Treible for their active support in supplying the implants, and R. H. Kaiser for the ellipsometric measurements. He is indebted to C. F. Gibbon, J. C. C. Tsai, and T. E. Seidel for discussions, to E. I. Povilonis for much experimental advice, and to P. F. Schmidt for information about the anodizing equipment.

Manuscript submitted Feb. 14, 1972; revised manuscript received July 21, 1972.

Any discussion of this paper will appear in a Discussion Section to be published in the June 1973 JOURNAL.

APPENDIX

Hole Mobility $\mu_h(C)$

The amount of dopant retained in the silicon, $Q(t)$, was obtained by integration of the concentration profiles as described in the experimental section. Initially hole mobilities, μ_h , were taken from Ref. (16); they agree with the values used in Ref. (17). The mobility vs. concentration relationship has been shown to fit an empirical Fermi-distribution curve (18)

Table I. Summary of experimental data

T [°C]	900	900	900	1000	1000	1000	1100	1100	1100	1100	1100
t [hr]	$10^{1/2}$	42	168	3	12	48	$1/4$	1	4	9	16
D [$\text{cm}^2 \text{ sec}^{-1}$]	—	$1.5 \cdot 10^{-15}$	—	—	$1.7 \cdot 10^{-14}$	—	—	—	$1.7 \cdot 10^{-13}$	—	—
$10^{-18} \cdot C(0, t)$ [cm^{-3}]	8.6	6.9	3.6	5.4	4.3	1.3	8.6	5.6	3.0	1.7	1.0
$10^{-14} \cdot Q_t$ [cm^{-2}]	{ Sheet cond. Hall Calculated	2.16	2.41	2.16	2.31	2.40	1.90	2.78	2.55	2.63	2.47
		—	2.56	—	—	2.48	2.10	2.80	2.65	2.55	2.50
		2.28	2.60	2.36	2.15	2.33	2.06	2.67	2.59	2.56	2.55
x_j [μm]	{ Angle lap Profile	0.4	0.7	1.4	0.9	1.2	2.5	0.6	1.0	2.4	3.3
		0.6	0.75	1.5	1.0	1.3	2.7	0.65	1.15	2.35	3.3
$10^8 \cdot u$ [cm]	120	40	120	136	120	390	39	52	119	187	220
B [$\text{cm}^2 \text{ sec}^{-1}$]	$3.8 \cdot 10^{-17}$	$1.1 \cdot 10^{-16}$	$2.4 \cdot 10^{-16}$	$1.7 \cdot 10^{-16}$	$3.3 \cdot 10^{-17}$	$8.8 \cdot 10^{-17}$	—	—	$8.9 \cdot 10^{-17}$	—	—
k	8.1	21.3	19.6	9.6	11.8	22.2	6.7	15.4	10.4	17.0	15.4

$$\mu_h(C) = \frac{\mu_{\max} - \mu_{\min}}{1 + (C/C_{\text{ref}})^\beta} + \mu_{\min} \quad [22]$$

with $\mu_{\max} = 495 \text{ cm}^2 \text{ sec}^{-1} \text{ V}^{-1}$, $\mu_{\min} = 47.7 \text{ cm}^2 \text{ sec}^{-1} \text{ V}^{-1}$, $\beta = 0.76$, and $C_{\text{ref}} = 6.3 \cdot 10^{16} \text{ cm}^{-3}$.

Use of this equation with the constants given above resulted in integrated doses, $Q(t)$, considerably larger than the total implanted dose of $3 \cdot 10^{14} \text{ cm}^{-2}$ which is considered to be accurate to $\pm 3\%$. $Q(t)$ for the 1100°C anneals is shown in the upper portion of Fig. 5. A similar observation has been made by Tsai (19) for a 100 keV boron implant with a dose of $1 \cdot 10^{15} \text{ cm}^{-2}$. (The wafer was capped, after implantation, with SiO_2 deposited from ethyl orthosilicate, and annealed in argon for 1 hr at 1050°C . The total dose found by integration of the concentration profile was $1.3 \cdot 10^{15} \text{ cm}^{-2}$.)

Errors in $(\Delta\kappa_s/\Delta x)$ can be ruled out as cause for this discrepancy because of the agreement of κ_s measured with the four-point probe with κ_s on a Van der Pauw pattern with soldered contacts, and because of the agreement of the junction depths, x_j , from anodization with those from angle lapping. In-diffusion of p-type impurities from the furnace can also be excluded: in case of in-diffusion no concentration maxima could appear at $x > 0$.

It was therefore concluded that the hole mobilities taken from the literature were too low in the concentration range of interest ($10^{17} < C < 10^{19} \text{ cm}^{-3}$). Extrapolation of $Q(t)$ of the 1100°C samples to $3 \cdot 10^{14} \text{ cm}^{-2}$ at $t = 0$ was taken as criterion for correct mobilities. The assumption was made that the values for μ_{\max} and μ_{\min} , which are independent of C , are correct as well as the shape of the μ_h vs. C curve, which is determined by β . Thus a new μ_h - C relationship was established by merely shifting the existing curve parallel to the C -axis to a higher value of $C_{\text{ref}} = 19 \cdot 10^{16}$. μ_h and κ are plotted vs. C in Fig. 7 and 8, respectively.

Carrier concentrations from uncorrected Hall measurements now agree well with $Q(t)$ from sheet conductivity measurements (Fig. 5). A plot of the total amount of dopant under a given depth x

$$\int_x^{x_j} C dx$$

as calculated from (uncorrected) Hall measurements,

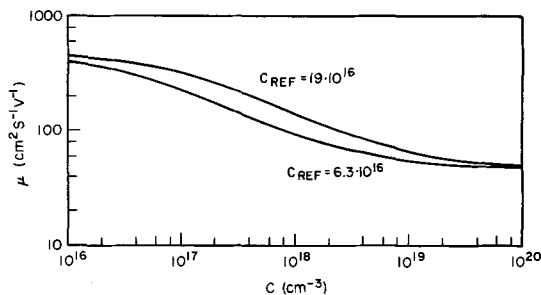


Fig. 7. Hole mobility vs. total boron concentration. $C_{\text{REF}} = 6.3 \cdot 10^{16}$ literature; $C_{\text{REF}} = 19 \cdot 10^{16}$ this study (25°C).

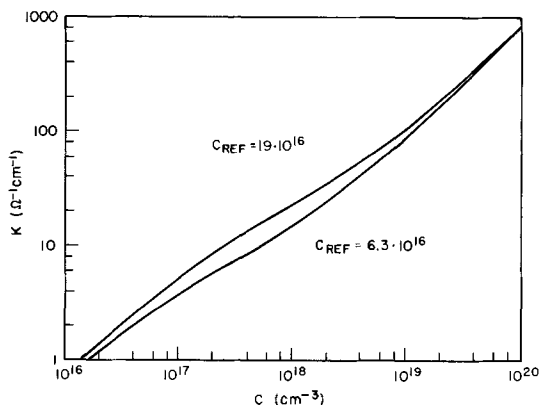


Fig. 8. Conductivity vs. total boron concentration. $C_{\text{REF}} = 6.3 \cdot 10^{16}$ literature; $C_{\text{REF}} = 19 \cdot 10^{16}$ this study (25°C).

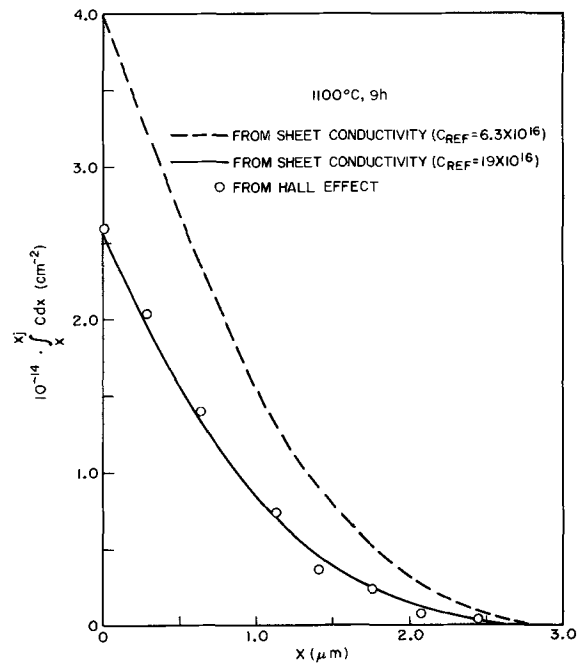


Fig. 9. $\int_x^{x_j} C dx$ for 9 hr anneal at 1100°C

and from sheet conductivity measurements with both $C_{\text{ref}} = 6.3 \cdot 10^{16}$ and $C_{\text{ref}} = 19 \cdot 10^{16} \text{ cm}^{-3}$ is shown in Fig. 9 for the 9-hr anneal at 1100°C .

SYMBOLS

- A_1, A_2 oxidation constants
- α one half of the variance of the as-implanted Gaussian distribution [cm^2]
- B parabolic rate constant [$\text{cm}^2 \text{ sec}^{-1}$]
- β exponent determining the shape of the hole mobility curve
- C total concentration of boron in silicon [cm^{-3}]
- C_+ conc of boron from Gaussian diffusion [cm^{-3}]
- C_- formal concentration of boron due to out-diffusion into oxide [cm^{-3}]
- D diffusion coefficient of boron in silicon [$\text{cm}^2 \text{ sec}^{-1}$]
- ΔH^\ddagger enthalpy of activation [eV mole^{-1}]
- k distribution coefficient of boron between SiO_2 and Si
- κ_s sheet conductivity [$(\text{ohm/square})^{-1}$]
- κ bulk conductivity ($\text{ohm}^{-1} \text{ cm}^{-1}$)
- $\mu_h(C)$ mobility of holes as a function of total dopant concentration [$\text{cm}^2 \text{ sec}^{-1} \text{ V}^{-1}$]
- μ_{\max} upper limit of mobility of holes in silicon
- μ_{\min} lower limit of mobility of holes in silicon
- Q total implanted dose [cm^{-2}]
- $Q(t)$ dose of boron retained in silicon at time t [cm^{-2}]
- $\Delta Q(t)$ loss of boron up to time t [cm^{-2}]
- q electronic charge [C]
- t time elapsed since beginning of anneal [sec]
- u thickness of oxide [cm]
- x distance from SiO_2/Si interface [cm]

REFERENCES

1. T. E. Seidel and A. U. MacRae, *Radiation Effects*, **7**, 1 (1971).
2. T. E. Seidel in, "Ion Implantation in Semiconductors," pp. 47-57, J. Graul and I. Ruge, Editors, Springer Verlag, New York (1971).
3. B. E. Deal and A. S. Grove, *J. Appl. Phys.*, **36**, 3770 (1965).
4. Y. T. Van der Meulen, Paper 80 presented at Electrochem. Soc. Meeting, Washington, D.C., May 9-13, 1971.
5. J. S. T. Huang and L. C. Welliver, *This Journal*, **117**, 1577 (1970).
6. H. S. Carslaw and J. C. Jaeger, "Conduction of Heat in Solids," Clarendon Press, Oxford (1959).
7. P. F. Schmidt, T. W. O'Keeffe, J. Oroshnik, and A. E. Owen, *This Journal*, **112**, 800 (1965).

8. A. H. Tong and A. Dupnock, *ibid.*, **118**, 390 (1971).
9. R. R. Hart and O. J. Marsh, "Ion Implantation Doping Technique," AFAL-TR-69-399, Dec. 1969, 72 pages.
10. J. M. Fairfield and B. L. Crowder, *Trans. Met. Soc. AIME*, **245**, 469 (1969).
11. M. L. Barry and P. Olofsen, *This Journal*, **116**, 854 (1969).
12. A. D. Kurtz and R. Yee, *J. Appl. Phys.*, **31**, 303 (1960).
13. D. M. Brown and P. R. Kennicott, *This Journal*, **118**, 293 (1971).
14. A. S. Grove, O. Leistiko, and C. T. Sah, *J. Appl. Phys.*, **35**, 2695 (1964).
15. T. Kato and Y. Nishi, *Japan. J. Appl. Phys.*, **3**, 377 (1964).
16. E. M. Conwell, *Proc. IRE*, **46**, 1281 (1958).
17. J. C. Irvin, *Bell System Tech. J.*, **41**, 387 (1962).
18. D. M. Caughey and R. E. Thomas, *Proc. IEEE*, **55**, 2192 (1967).
19. J. C. C. Tsai, Private communication.

P-Type Dopants for GaP Green Light Emitting Diodes

O. G. Lorimor and M. E. Weiner*

Bell Telephone Laboratories, Murray Hill, New Jersey 07974

ABSTRACT

In an effort to reduce the red Zn-O emission in GaP green LED's, acceptors other than Zn were considered. Crystals were grown and green LED's fabricated from C- and Mg-doped material. In the C-doped crystals a half-power dependence of $N_a - N_d$ as a function of CH_4 partial pressure up to a maximum attainable $N_a - N_d$ of $\sim 1.5 \times 10^{17} \text{ cm}^{-3}$ at 900°C was found. Mg-doped crystals were grown with $N_a - N_d$ up to 10^{19} cm^{-3} . In double LPE green LED's fabricated from a C,N-doped layer grown on a Te,N-doped layer, the external electroluminescent quantum efficiency, η , was as high as 0.1% at 200 A/cm^2 . For single liquid phase epitaxy (LPE) diodes with a Mg,N-doped p-layer, $\eta = 0.006\%$. For the acceptors Be and Mg (and also for Si and Al) thermodynamic calculations are presented which consider the formation of the nitride of the dopant through the interaction with the NH_3 used to simultaneously dope the crystals with N. These calculations show that at typical LPE growth temperatures and under conditions where the Ga is saturated with N, the order of increasing solubility is $\text{Be} < \text{Al} < \text{Si} < \text{Mg}$. The low solubility of Al precludes the growth of heavily N-doped $\text{Ga}_x\text{Al}_{1-x}\text{P}$ from Ga-rich melts. These calculations also predict the low $N_d - N_a$ which results with simultaneous Si and N doping. No such reaction involving the formation of a nitride limits the solubility of C during the LPE growth process.

One of the present problems in the growth of material for the fabrication of GaP green LED's is the elimination of the red Zn-O pair bound exciton emission which accompanies the green. Presently both n- and p-type LPE layers (1) grown by an open-flow dipping technique contain unintentionally added oxygen. All diodes in which the p-layer is Zn-doped emit some red light which indicates the presence of Zn-O pairs in the p-layer (2). In addition, the room temperature electroluminescent (EL) spectrum usually shows the $\sim 1.35 \text{ eV}$ infrared emission band which has been identified as the bound-to-free transition at an isolated substitutional O atom (3). Diodes fabricated from Te,N-doped material where the junction is made by Zn diffusion (4) behave similarly (5).

The most obvious way to eliminate the red emission is to eliminate the O from the crystal. The possible sources of O include the Ga, the polycrystalline GaP used to saturate the melt, the fused quartz furnace tube and crucible, the H_2 gas stream and the NH_3 mixture used for N doping. The difficulty in determining the relative importance of such possible O sources and eliminating them is compounded by the lack of a simple, accurate method of measuring the O content of the LPE layers. Consequently, in addition to seeking methods of reducing or eliminating the O contamination, it is also attractive to seek other means of eliminating the red emission, in particular, the replacement of Zn by another acceptor. However, in doing so one must consider the interaction of the dopant with the NH_3

which is used as the source of N to obtain the green emission. For example, if one considers a dopant having a very stable oxide, (thus reducing O solubility in Ga) one must also consider whether that element also has a stable nitride.

The acceptors Be, C, and Mg, will be considered in detail. Because of the fast diffusivity of Be (6), only C and Mg have been used experimentally as dopants in this study. C does not form a stable nitride and thus its solubility is not expected to be significantly influenced by the simultaneous doping with N. Consequently only the interaction of NH_3 with Be and Mg will be considered in the calculations. Although not acceptors, the interaction of NH_3 with Al and Si will also be considered.

Experimental

C,N- and Mg,N-doped layers have been grown for use as the p-layers in LED's. The C-doped LPE layers were grown in an open-flow dipping system from 900°C (1). The layers were grown on $\{111\}\text{B}$ oriented liquid encapsulated Czochralski grown (LEC) substrates or on a Te- or Te,N-doped n-type LPE layer which had previously been grown at 1000°C . C-doped layers, ranging in thickness from $\sim \frac{1}{2}$ to 1 mil, were grown by cooling the melt 11°C at a rate of 6°C/hr . Three of the C-doped layers were also doped with N to $\sim 1 \times 10^{19} \text{ cm}^{-3}$ by the addition of NH_3 to the gas stream (1, 7).

Matheson ultra-high purity (99.97%) CH_4 gas was used as the source of C and introduced directly into the flowing gas stream. In order to give the melt time to saturate with C, growth of the crystal was not started until ~ 40 min after the CH_4 was turned on.

* Electrochemical Society Active Member.

Key words: gallium phosphide, light-emitting diodes, liquid phase epitaxial growth.

At a CH₄ partial pressure $p_{CH_4} < 0.50$ atm, no blackening of the furnace tube due to decomposition of the CH₄ was noticed. At an unknown p_{CH_4} but larger than $p_{CH_4} = 0.7$ atm, the furnace tube was heavily coated with C due to CH₄ decomposition. Consequently, the study was restricted to $p_{CH_4} \leq 0.50$ atm.

The Mg-doped LPE layers were grown in an open-tube modified version of the slider system described by Panish *et al.* (8). The slider assembly was graphite while the furnace tube was quartz. Elemental Mg of 99.99% purity cleaned by etching in dilute HCl was used as a source of Mg. It was found that when the melt was not capped with a graphite lid, the quartz tube above the melt was severely attacked by the Mg vapor. Even with the lid covering the melt a white substance, assumed to be MgO, formed on the melt surface.

The Mg-doped layers were grown from 950°C by cooling 20°C at a rate of 20°C/hr. The surfaces of the layers appeared to be of high quality. They had small "terraces," but were smoother than layers grown in the dipping system. However, they were nonuniform in thickness. Frequently little or no growth was found over part of the substrate while ~1 mil was found in other areas. This large thickness nonuniformity was not observed when undoped or Te doped layers were grown in the same system.

The net acceptor concentrations, $N_a - N_d$ were determined by surface barrier capacitance measurements using a Copeland profiler (9). The measurements were primarily made on the surface of the layers. An in-depth profile of one of the C-doped layers showed no decrease in $N_a - N_d$ with increasing depth from the surface verifying that sufficient time was given for the melt to come into equilibrium with the CH₄.

Results

Figure 1 shows the net acceptor concentration as a function of the CH₄ partial pressure in the gas stream for the C-doped LPE layers. Although very few data points were taken, they fall reasonably well on a straight line with a slope of 1/2. In all cases the background $N_d - N_a \approx 6 \times 10^{15}$ n-type is considerably exceeded. Figure 2 shows $N_a - N_d$ as a function of Mg concentration in the Ga + GaP melt. Because some of the Mg added to the melt was removed as MgO, the Mg dissolved in the melt for a crystal growth run was actually less than that added and shown as the abscissa in Fig. 2. Consequently, for any given Mg concentration the value of $N_a - N_d$ shown is only a lower limit on what one would measure if no MgO formed. However, this data does show that one can easily Mg-dope GaP to 1×10^{19} cm⁻³ and gives a lower bound of 0.02 for the distribution coefficient at 950°C. Consequently, Mg can be used to give the needed $N_a - N_d$ for green LED's.

Two of the C-doped layers were grown on n-type LPE layers previously grown at 1000°C (1). Diodes were fabricated from both of these LPE structures. The characteristics of these diodes are shown as samples 1 and 2 in Table I.

The n-layers in samples 1 and 2 are comparable both in $N_d - N_a$ and minority carrier lifetime

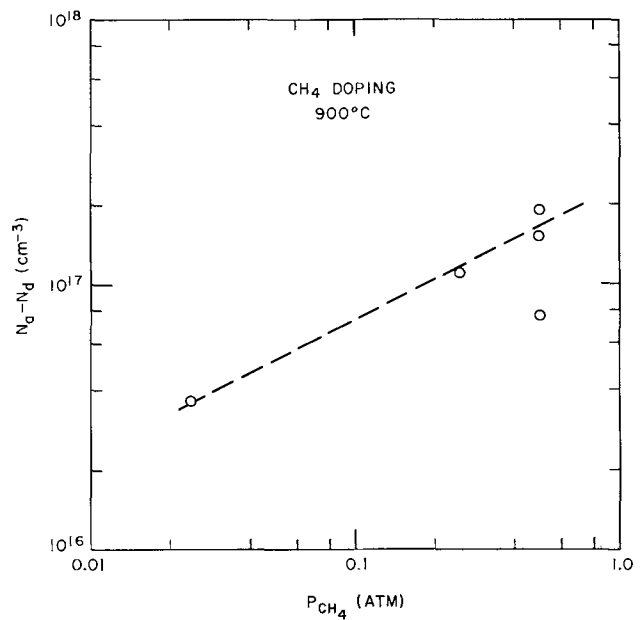


Fig. 1. Net acceptor concentration as a function of CH₄ partial pressure for GaP LPE layers grown near 900°C.

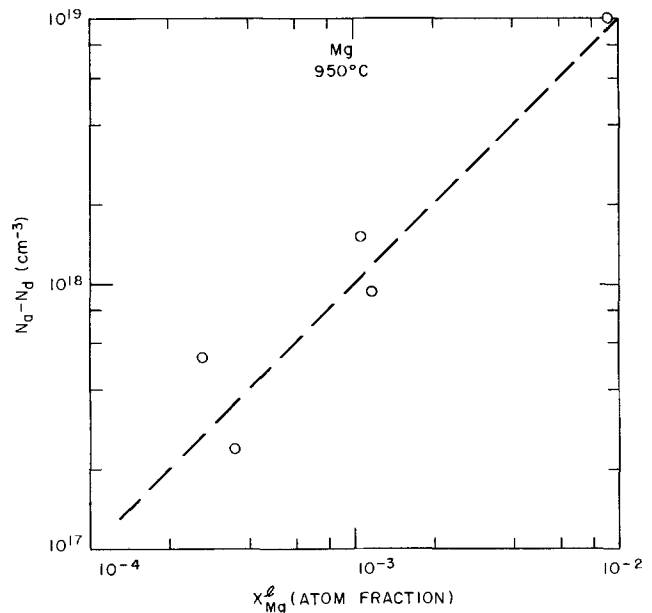


Fig. 2. Net acceptor concentration as a function of Mg concentration in the liquid for GaP LPE layers grown near 950°C.

to those which have produced diodes of $\eta > 0.1\%$ with Zn,N-doped p-layers. The minority carrier lifetime of the p-layer in sample 1 is comparable to that found in Zn-doped layers. However, the $N_a - N_d$ of both p-layers is lower than that usually needed ($\sim 5 \times 10^{17}$ cm⁻³) to produce efficient diodes.

Table I

Diode number	N-Layer			P-Layer			η_{BL}	Diode type
	Dopant	$N_d - N_a$ (cm ⁻³)	τ_{mc} (ns)	Dopants	$N_a - N_d$ (cm ⁻³)	τ_{mc} (ns)		
1	Te	3.5×10^{17}	54	C, N	1.5×10^{17}	39	0.019, 50 mA AC (100 A/cm ²)	mesa
2	Te, N	7.5×10^{16}	86	C, N	7.5×10^{16}	—	0.1, 100 mA AC (75 A/cm ²)	die
3	Sn	3×10^{17}	LEC substrate	Mg, N	1.5×10^{18}	12	0.006, 50 mA AC (100 A/cm ²)	mesa

Properties of layers composing the diodes discussed in this study. τ_{mc} is the minority carrier lifetime as measured by the green PL decay time.

Thus, considering that the n-layer in sample 1 contains no intentionally added N, the encapsulated quantum efficiencies of these samples are quite good. The value of 0.10% at 100 mA (75 A/cm²) pulsed for sample 2 is larger than that measured for many Zn,N/Te,N-doped diodes. Consequently, C itself appears to be an acceptable acceptor from a luminescent point of view. Its actual usefulness is limited because of its low solubility in Ga at 900°C.

Sample 3 is a diode fabricated from a Mg,N doped layer grown directly onto an n-type LEC substrate. The efficiency, although low, is comparable to that observed by Logan *et al.* (7) for single LPE structures on LEC substrates. In addition, in the slider system the lid, and possibly the MgO layer, over the melt probably inhibited the NH₃ from saturating the melt with N.

Figure 3 shows the EL spectrum of diode 1 at 100 mA (200 A/cm²). The energy positions of the nitrogen bound exciton and its phonon replicas are indicated by the arrows (10). The arrow at 1.78 eV indicates the position of the red Zn-O emission if it were present (2). The low energy rise in emission is due to the free-to-bound transition involving oxygen which peaks near 1.35 eV (3). The broad, weak peak near 1.75 eV is presently unidentified but has been observed previously (11-13). The spectrum from diode 3 was found to be very similar to that of diode 1.

At current densities of 50 to 100 A/cm⁻², green-to-red ratios of 30:1 to 100:1 were obtained for all three samples. Thus, the use of C or Mg as a p-type dopant is a satisfactory way of obtaining large green-to-red ratios.

Interaction of Dopants with NH₃

The elements, Be, Mg, Al, and Si form stable nitrides. Thus, when simultaneously doping with one of these elements and N, the nitride of the element may form reducing the concentration of the element in the melt. The following calculations consider these reactions in such simultaneous doping.

The only nitrogen source considered in these calculations is NH₃. It is the purpose of this analysis to find what combinations of ammonia partial pressure, p_{NH_3} , and concentration of dopant in the liquid, X^{dopant} , are permissible. Thus the following reactions must be considered

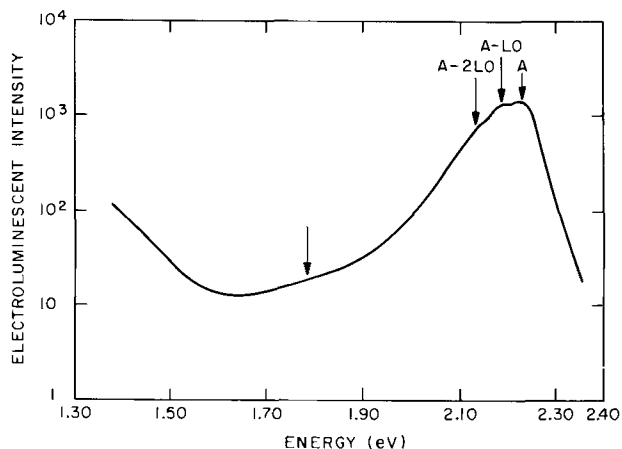
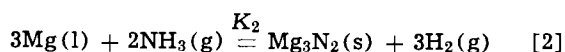
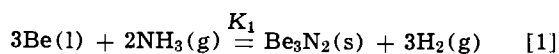
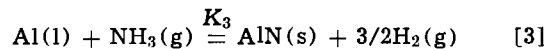


Fig. 3. Room temperature electroluminescent intensity as a function of photon energy for C,N/Te-doped, diode 1. The energy positions of the N bound exciton A-line and its phonon replicas as determined from optical absorption are noted. The arrow near 1.78 eV denotes where the peak energy position of the Zn-O red emission would fall if it were present.



It is assumed that $p_{\text{H}_2} = 1$ atm and that solutions containing Mg and Al are ideal, *i.e.*, the activity coefficients γ_{Mg} and γ_{Al} are unity. Activity coefficients for Be and Si are attainable from the Be-Ga and Si-Ga binary phase diagrams (14), if it is assumed that phosphorus and nitrogen do not influence these coefficients. These activity coefficients are listed in Table II. Thus

$$X^{\text{Be}}{}^{3/2} p_{\text{NH}_3} = \frac{1}{K_1^{1/2} \gamma_{\text{Be}}^{3/2}} \quad [5]$$

$$X^{\text{Mg}}{}^{3/2} p_{\text{NH}_3} = \frac{1}{\sqrt{K_2}} \quad [6]$$

$$X^{\text{Al}} p_{\text{NH}_3} = \frac{1}{K_3} \quad [7]$$

$$X^{\text{Si}}{}^{3/4} p_{\text{NH}_3} = \frac{1}{K_4^{1/4} \gamma_{\text{Si}}^{3/4}} \quad [8]$$

Note that it is assumed that the solid nitride exists only at unit activity. This may not be valid for Al since $\text{Ga}_{1-x}\text{Al}_x\text{N}$ could form. In this case, the allowed concentration of Al in the solution is less than the value calculated. The equilibrium constants K_1 , K_2 , K_3 , and K_4 were calculated from data in the JANAF tables (15) and are listed in Table III.

In addition to interacting with certain dopants, NH₃ also reacts with Ga to form GaN. The minimum pressure of NH₃ at which GaN forms is the maximum equilibrium pressure of NH₃ in the system. If the activity coefficient of nitrogen in Ga is independent of concentration, the presence of dopants, and if no nitrides form, the concentration of nitrogen in the solution is proportional to the NH₃ pressure.

In Fig. 4, the maximum dopant concentrations for which the nitrides of Be, Mg, Si, and Al do not form are plotted *vs.* the NH₃ partial pressure. In addition, the value of p_{NH_3} at which GaN forms is shown (16).

The permissible dopant concentrations and NH₃ pressures lie in the area to the left of the dopant curve and below the GaN line. In the region above the dopant curve and below the GaN line, the dopant will be removed from the solution as a nitride until the dopant curve is reached. Thus, from Fig. 4, it may be seen that only very small amounts of Al can exist in solution at a reasonable NH₃ pressure. Clearly, one will not be able to produce heavily N-doped $\text{Ga}_x\text{Al}_{1-x}\text{P}$ by growth from Ga rich melts.

Table II

T (°C)	γ_{Be}	γ_{Si}
800	43	2.5
900	26	2.0
950	20	1.8
1000	16	1.5
1050	14	1.4

Activity coefficients for Be and Si dissolved in liquid Ga determined from the Be-Ga and Si-Ga phase diagrams from Ref. (14).

Table III

T (°C)	K_1	K_2	K_3	K_4
800	1.71×10^{27}	4.11×10^{18}	2.30×10^{13}	8.04×10^{34}
900	1.33×10^{25}	1.14×10^{17}	1.72×10^{12}	1.31×10^{32}
950	1.59×10^{24}	2.37×10^{16}	5.52×10^{11}	7.96×10^{30}
1000	2.25×10^{23}	5.55×10^{15}	1.94×10^{11}	6.07×10^{29}
1050	3.71×10^{22}	1.29×10^{15}	7.39×10^{10}	5.75×10^{28}

Equilibrium constants for reactions [1]-[4] determined from free energy data in the JANAF tables [Ref. (15)].

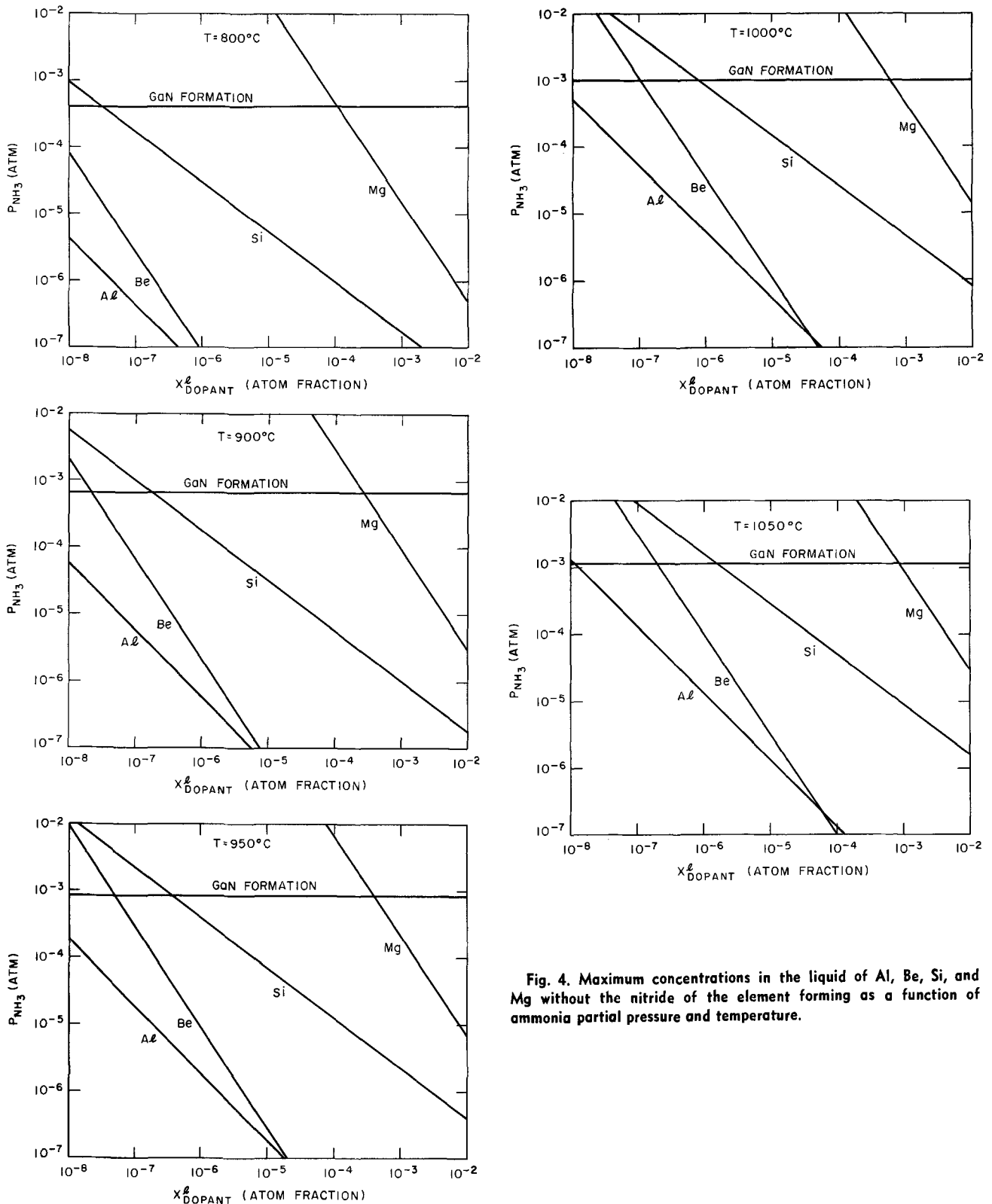


Fig. 4. Maximum concentrations in the liquid of Al, Be, Si, and Mg without the nitride of the element forming as a function of ammonia partial pressure and temperature.

Silicon has been used as an n-type dopant. In a typical experiment an LPE layer was grown at 1000°C with zero NH_3 partial pressure and X_{Si}^{L} (added to melt) $\approx 2.5 \times 10^{-5}$. From surface barrier capacitance measurements $N_d - N_a = 1.4 \times 10^{17} \text{ cm}^{-3}$ in this layer. In another layer, grown under the same conditions except for the ammonia partial pressure being held constant at $p_{\text{NH}_3} = 7 \times 10^{-4} \text{ atm}$, $N_d - N_a = 3 \times 10^{16} \text{ cm}^{-3}$. This result is consistent with the data in Fig. 4. The Si added to the melt would be expected to react with the NH_3 forming Si_3N_4 until an actual Si concentration in the liquid of $X_{\text{Si}}^{\text{L}} = 1.3 \times 10^{-6}$ is reached. If it is assumed that the $N_d - N_a = 3 \times 10^{16} \text{ cm}^{-3}$ is the

total Si concentration in the solid, a value for the distribution coefficient of 0.5 is obtained. This value compares favorably with a value of ~ 0.7 estimated from the low Si concentration end of the calculated curve for the Si solubility for 1040°C from Trumbore *et al.* (17).

Magnesium appears to be a suitable dopant from the viewpoint of its reaction with NH_3 . Only at very high doping levels should problems with the NH_3 interaction occur.

Conclusions

LPE layers have been grown using C and Mg as p-type dopants. The spectra of diodes fabricated from material where the p-layer was doped with one or the

other showed green-to-red ratios $>30:1$ at 100 mA. This ratio is considerably larger than $\sim 10:1$ ratio that has been found in many diodes where the p-type dopant is Zn (7).

At 900°C the maximum $N_a - N_d$ in the C-doped crystals that could be achieved was $< 2 \times 10^{17} \text{ cm}^{-3}$.

In one case a Te,N-C,N diode with a quantum efficiency of 0.10% at 100 mA pulsed was measured. This efficiency is quite good in view of the low p-type doping attainable with C compared to the doping level of $\sim 5 \times 10^{17} \text{ cm}^{-3}$ in high-efficiency green LED's where Zn is the p-type dopant. Consequently, although C appears to be a satisfactory acceptor from a luminescence point of view, it is presently not felt to be a suitable dopant when LPE growth is at 900°C for use in these diodes because of its low solubility. However, at higher growth temperatures it is possible that the solubility of C would increase.

Mg, on the other hand, is amply soluble in GaP to provide the optimum doping level. However, its strong affinity for O makes this dopant difficult to use during crystal growth. Consequently, further studies using Mg as a dopant are dependent upon developing more nearly O free systems.

Thermodynamic calculations show that when one simultaneously dopes with NH_3 and an element having a stable nitride, the nitride of the element may form and reduce the concentration of the doping element in the melt. This process can be particularly important at the $(10^{-4} < p_{\text{NH}_3} < 10^{-3} \text{ atmospheres})$ pressures of

NH_3 needed to heavily N-dope the LPE layers. Such a reaction precludes the simultaneous heavy doping of GaP with N and Al or Be. While such a reaction is expected for Mg, it is not likely at the doping levels of interest. No such reaction may occur for C. Experimental results for LPE layers where heavy Si and N doping were attempted are consistent with the thermodynamic calculations.

Acknowledgments

We wish to thank D. D. Roccasecca for his assistance in the materials growth, R. Z. Bachrach for the spectra and diode efficiencies, and J. Mann and R. Furnage for the diode fabrication. The assistance of G. Forsyth for the $|N_d - N_a|$ measurements, and F. A. Trumbore for helpful discussions is much appreciated.

Manuscript submitted Feb. 18, 1972; revised manuscript received July 31, 1972.

Any discussion of this paper will appear in a Discussion Section to be published in the June 1973 JOURNAL.

REFERENCES

- O. G. Lorimor, L. R. Dawson, R. Z. Bachrach, D. D. Roccasecca, and R. G. Sobers, To be published.
- T. N. Morgan, B. Welber, and R. N. Bhargava, *Phys. Rev.*, **166**, 751 (1968).
- J. M. Dishman, *ibid.*, **3B**, 2588 (1971).
- L. C. Luther, H. C. Casey, Jr., S. E. Haszko, A. S. Jordan, O. G. Lorimor, and G. A. Rozgonyi, *J. Electronic Materials*, **1**, 54 (1972).
- D. A. Harrison, MM 71-2313-10.
- M. Ilegems and W. C. O'Mara, *J. Appl. Phys.*, **43**, 1190 (1972).
- R. A. Logan, H. G. White, and W. Weigman, *Solid-State Electron.*, **14**, 55 (1971).
- M. B. Panish, S. Sumski, and I. Hayashi, *Metalurgical Trans.*, **2**, 795 (1971).
- J. A. Copeland, *IEEE Trans. Electron Devices*, **ED-16**, 445 (1969).
- P. J. Dean, M. Gershenzon, and G. Kaminsky, *J. Appl. Phys.*, **38**, 5332 (1967).
- M. Gershenzon, R. A. Logan, and D. F. Nelson, *Phys. Rev.*, **149**, 580 (1966).
- D. F. Nelson, *ibid.*, **149**, 574 (1966).
- P. J. Dean, *Bull. Am. Soc.*, **16**, 328 (1971).
- M. Hansen and K. Anderko, "Constitution of Binary Alloys," McGraw-Hill Book Co., New York (1958).
- JANAF Thermochemical Tables, published by the U.S. Department of Commerce (1965).
- C. D. Thurmond, Private communication.
- F. A. Trumbore, H. G. White, M. Kowalchik, and D. L. Nash, *This Journal*, **112**, 1208 (1965).

Lifetimes and Diode Characteristics in Epitaxial Silicon

P. Rai-Choudhury* and D. K. Schroder

Westinghouse Research Laboratories, Pittsburgh, Pennsylvania 15235

ABSTRACT

The lifetime in epitaxially grown silicon p- and n-layers and the reverse I-V characteristics of diodes fabricated in such layers, were measured as a function of various growth temperatures and substrates of different dopants and doping concentrations. The epitaxial layers were grown by the hydrogen reduction of silicon tetrachloride. It was found that layers grown at 1100°C had significantly higher lifetimes (up to 200 μsec) and higher breakdown voltages than those grown at higher temperatures. Furthermore, layers grown on heavily phosphorus-doped substrates had much better characteristics than those grown on antimony- or lightly phosphorus-doped substrates. Chelating of the substrates prior to epitaxial growth had the effect of reducing the scatter as well as increasing the value of the lifetime. Gettering with P_2O_5 had a lesser effect on the diode characteristics than it did on the lifetime.

Recent comparisons of microinhomogeneities in epitaxial silicon with those in melt grown silicon indicate that conventional epitaxial silicon from the $\text{SiCl}_4\text{-H}_2$ system is comparable to the best melt grown materials(1). In terms of oxygen content, epitaxial silicon is comparable to float-zoned silicon. However,

devices fabricated in vapor grown silicon often have poor junction characteristics (2). The substrate surface is frequently contaminated with metallic impurities before epitaxial layers can be grown. Unless these contaminants are more soluble in the substrate (such as Au in P-doped n^+ Si) or pinned strongly by the substrate, these metals will diffuse into the growing layer reducing the minority carrier lifetime. Recent

* Electrochemical Society Active Member.

Key words: temperature, substrates, gettering, phosphorus.

work by Kern and Puotinen (3) on the effectiveness of peroxide cleaning in reducing organic, ionic, and metallic impurities, and the work of Robinson *et al.* (4) on HCl gettering to increase the minority carrier lifetime, give some indication of the effects of surface contamination. Chang (5) has observed by the Leed-Auger method that heat-treatments above 1000°C were accompanied by the appearance of metallic impurities at the surface, which sometimes totaled over 1×10^{14} atoms/cm² for a 5 min heat-treatment at 1250°C. Thus, metallic impurities that are usually present as surface contaminants and as rejected solutes from the bulk during heat-treatment, often decide the fate of the device. It is generally found that p-n junctions involving epitaxial silicon, such as epitaxial-substrate junctions, epitaxial-epitaxial junctions, or diffused junctions into epitaxial silicon, give either high-reverse leakage current or considerably lower junction breakdown voltage than diffused junctions in melt grown silicon. The epitaxial junction is located either near the substrate-epitaxial interface, where the substrate surface has been extensively treated, or in the epitaxial material grown on such a treated surface. In either case, there is the possibility that significant contamination of the junction or of the entire epitaxial layer exists. Thus the importance of cleaning the substrates effectively before epitaxial growth cannot be over-emphasized.

Epitaxial structures are more susceptible to post-growth contamination than diffused structures. The dislocations generated in the epitaxial reactor are thermally induced (6), relatively clean, extend over larger thicknesses, and are widely separated. Any post-heat-treatment operation, such as base or emitter diffusion of transistors, could decorate these dislocations with heavy metals, which might develop shorted or extremely leaky junctions. The dislocations generated in a diffusion furnace are impurity induced, already decorated (being located in the heavily doped diffused region), and are usually more dense. Both types of dislocations are essentially edge in character and slip on the system (111)[110]. While the mobility of the diffusion induced dislocations may be different from those induced thermally (7), the latter type may be more harmful.

The reason for the inferior performance of devices fabricated in epitaxial silicon, in spite of their high structural perfection, is not clear. The present investigation was undertaken with the hope of gaining a better understanding of this problem and improving the epitaxial silicon. In this study the carrier lifetime and diode characteristics in the epitaxial silicon are measured under various processing conditions. Some of the important variables considered are cleaning procedure, growth temperature, and substrate material.

Experimental Procedure

The silicon substrates used were n-type, 2° off the (111) orientation, float zoned as well as Czochralski grown. The dopants in the heavily doped substrates were deliberately chosen as phosphorus (1×10^{20} atoms/cm³) which causes lattice contraction, and antimony (5×10^{18} atoms/cm³) which may slightly dilate the silicon lattice. The substrates were either chemically polished or chem-mechanically polished by the silicon dioxide polishing technique (8) and were free of any mechanical damage. Three methods of substrate cleaning were followed. The first consisted of degreasing in acetone and trichloroethylene followed by boiling in H₂SO₄:HNO₃:3:1. Each step was followed by extensive rinsing in Super Q water, i.e., continuously recycled deionized water. This method will be designated for convenience as DSN. The second method consisted of an additional final step of treating the wafers with ammoniummethylenediaminetetracetate (EDTA), a complexing agent for metals, followed by repeated rinsing in Super Q water. This second method

is designated as DSNE. In the third method, the EDTA was replaced by an H₂O-H₂O₂-NH₄OH treatment to remove organic contaminants and by an H₂O-H₂O₂-HCl treatment to remove metallic impurities. This method is designated as DSNP and is described in detail by Kern *et al.* (3).

The epitaxial layers of silicon were grown on these substrates following an *in situ* HCl etch. Epitaxial growth was carried out in a conventional horizontal rf heated system, having a silicon-coated graphite susceptor. The SiCl₄ partial pressure was typically 8×10^{-3} atm, the gas velocity was 41 cm/sec, and the reactor was of rectangular cross section 8 cm × 5 cm. Six wafers were normally used for each run, and to eliminate any run-to-run or day-to-day variability in the data, a given run always included two wafers of each of three substrates, rendering the results more meaningful. Silicon was deposited from the H₂-SiCl₄ system and doped with B₂H₆ and AsH₃ as desired. Hydrogen was Pd-purified and all materials were of ultrapure grade. Epitaxial layers were grown at three temperatures 1100°, 1150°, and 1250°C.

The carrier concentration profiles and thicknesses of the grown layers were determined by the spreading resistance technique (9). They were typically 20-30μ thick. To measure the lifetime it is undesirable to use techniques that require a p-n junction, since the formation of a junction can alter the very properties we want to measure. Methods that rely on the decay of excess carriers are also not suitable since they involve the minority carrier diffusion length. This can be much longer than the epi-layer thickness and the measured lifetime in that case is an epi-layer/substrate combination.

For these reasons we chose the pulsed MOS capacitor technique (10) in which the generation lifetime (11) is determined. Here, the generation of carriers in the space-charge region is measured. Hence, small volumes are sampled and the sample volume can be easily controlled through the appropriate choice of gate diameter and gate voltage step. The gate diameter was 12 mil and the depleting voltage step was between 50 and 100V creating a silicon space-charge region width of about 10μ for a 2500Å thick oxide.

The MOS capacitors were formed by chemical vapor deposition of SiO₂ at 750°C using the silane-oxygen process. Aluminum dots were evaporated through a metal mask. The effect of the Si-SiO₂ interface on the pulsed MOS-C response is made negligible by hydrogen annealing (12) and a proper analysis of the data (13).

Diode measurements were made on p-n junctions which were of three types, (i) shallow diffused junctions into the epitaxial layers (boron diffusion into n-epitaxial layers); (ii) substrate-epitaxial junctions (only used for boron-doped epitaxial layers on n-type substrates); (iii) epitaxial-epitaxial junctions formed by growing a layer of opposite conductivity on the first epitaxial layer. Mesa diodes were fabricated which were subsequently passivated by the 750°C deposited oxide and hydrogen annealed. Some diodes were gettered in a two-zone P₂O₅ furnace with the source at 250°C and the silicon wafers at 950°C for 45 min in an argon ambient to see if the lifetime could be improved.

We found that the p-n junctions were more difficult to analyze than the lifetimes, since they involve not only the epitaxial layer, but also a second region of opposite conductivity, plus the added complexity of the junction itself. Therefore, the interpretation of the I-V measurements is more complicated.

Results

Lifetimes.—N-epitaxial layers.—The lifetime data for n-epitaxial layers are presented first. These layers were grown on three types of substrates: (i) 0.0009 ohm-cm phosphorus-doped, (ii) 10 ohm-cm phos-

phorus-doped, and (iii) 0.008 ohm-cm antimony-doped; at three temperatures: 1100°, 1150°, and 1250°C. In addition, a comparison was made between the DSN cleaning procedure and cleaning using a chelating agent.

The effect of the cleaning procedure is seen in Fig. 1 by comparing the lifetime values at 1150°C for the three substrates. It is quite obvious that the chelated wafers had significantly higher lifetimes than those cleaned in the same manner, but not chelated. This points out the heavy metal complexing property of the chelating agent. Although it is not obvious from the data points in that figure—each point is the average of 10 measurements—the scatter in the data for wafers treated with the EDTA chelating agent is considerably less than that for wafers not chelated. For example when the substrate was not chelated, the lifetime in the layer grown on heavily phosphorus doped substrate at 1150°C varied from 1.6 to 28 μsec ; using chelated substrates the lifetimes improved to 91 to 120 μsec . A comparison of these two sets of data points at 1150°C, which were the first to be done in these experiments, prompted us to use a chelating agent for all other runs.

The second, very important observation to be made on Fig. 1 is that the lifetime increases for lower growth temperatures. Although the lifetime values do not all change by the same amount, the trend of higher lifetimes for lower temperatures is certainly obvious.

The third observation is that consistently higher lifetimes were obtained on layers grown on degenerately phosphorus-doped substrates. We have found this to be the case for all layers grown during this investigation—n and p-type.

In an attempt to improve the lifetime of those layers grown on the lightly phosphorus-doped or degenerately antimony-doped substrates, they were gettered, using the conditions described earlier. This treatment had essentially no effect on the lifetime, indicating that the impurities responsible for the lifetime degradation cannot be easily removed by this gettering procedure.

p-epitaxial layers.—The lifetime data for p-epitaxial layers are shown in Fig. 2. Having found on n-layers that chelating had a significant effect on the lifetime, all substrates were chelated prior to p-epitaxial growth. The substrates were identical to those used for the n-layers.

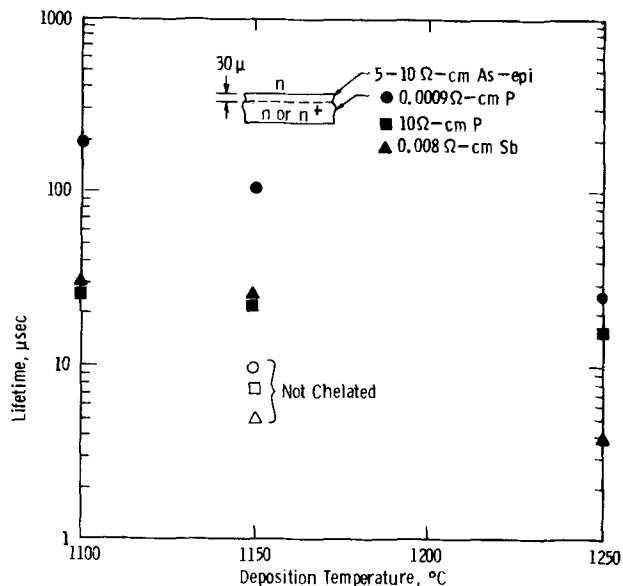


Fig. 1. Lifetimes in n-epitaxial layers as a function of deposition temperature. For 1150°C lifetimes with and without chelating are shown. All others are chelated.

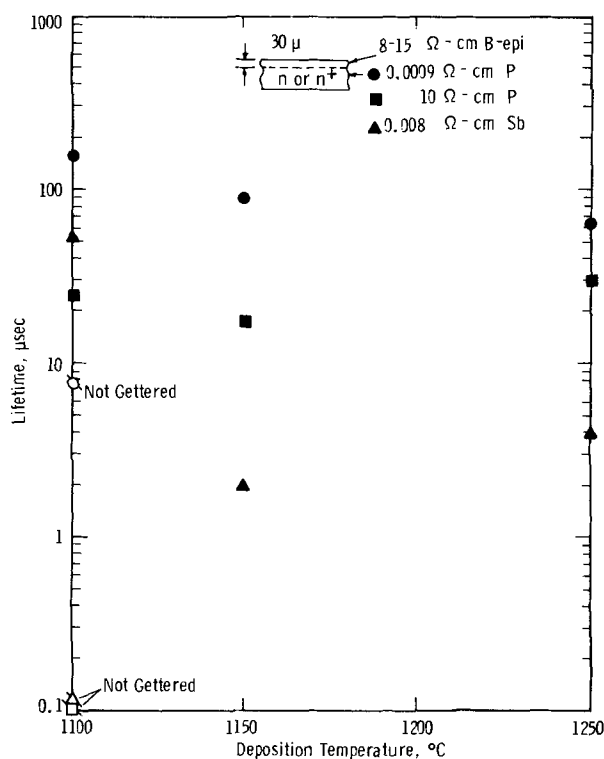


Fig. 2. Lifetimes in p-epitaxial layers as a function of deposition temperature. For 1100°C lifetimes before and after gettering are shown. All others are gettered.

However, in contrast to the results of Fig. 1, where P_2O_5 gettering had little effect on the lifetimes, very significant lifetime improvements were observed on the p-layers following the P_2O_5 gettering cycle. For example, for the 1100°C deposition temperature, values before and after gettering are shown and lifetime increases by a factor of over 100 were observed. Similar effects were measured at the other deposition temperatures, but for these temperatures only the lifetimes after gettering are shown. During the gettering cycle, both surfaces of the wafers were exposed to the phosphorus ambient and the thin n^+ skin on the p-epitaxial layer was etched off prior to the low temperature oxide deposition.

Similar to the observations on n-layers, the p-layers also showed an increase in lifetime values for lower epitaxial growth temperatures, and the layers grown on the heavily phosphorus-doped substrates again yielded the highest lifetime.

I-V characteristics.—The lifetime results showed the following definitive trends: the lower the deposition temperature, the higher the lifetime; layers grown on heavily phosphorus-doped substrates gave consistently better lifetimes. It is known that impurities that influence the lifetime, e.g., heavy metals, can also have a pronounced effect on the I-V behavior of reverse-biased diodes (14). They can cause microplasmas which result in excessive leakage currents or low breakdown voltage. To correlate our lifetime data with junction behavior, we measured the breakdown voltage of p-n junctions formed in the epitaxial layers.

n-epitaxial layers.—A typical impurity concentration profile of an n-layer on a heavily phosphorus-doped substrate is shown in Fig. 3 indicating absence of any doping nonuniformity arising either from poor system control or contamination. The layer thickness was around 30μ and the doping varied between 5×10^{14} and $2 \times 10^{15} \text{ cm}^{-3}$ insuring bulk and not punch-through breakdown for all but the lowest dopant concentrations.

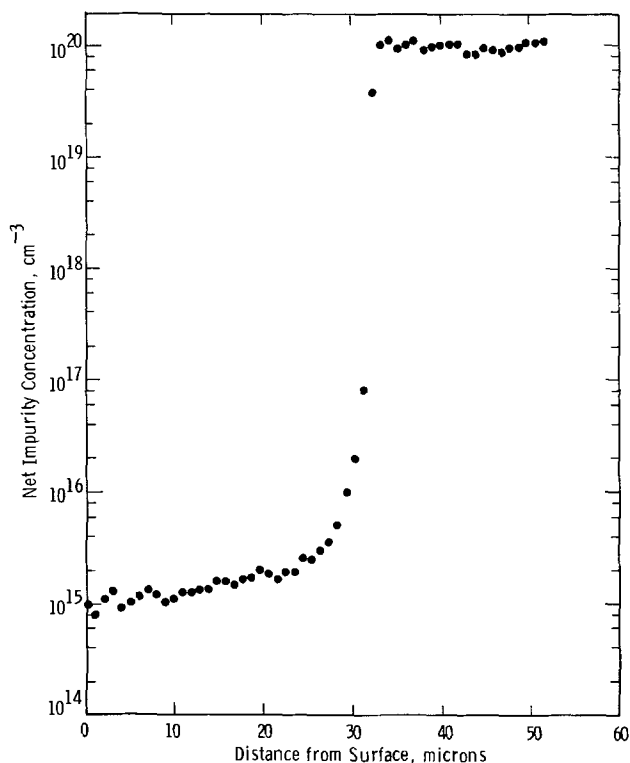


Fig. 3. Typical impurity concentration profile of an n-epitaxial layer on a heavily phosphorus-doped substrate.

The diodes were formed by either a shallow boron diffusion into the layer or growing a p⁺ epitaxial layer on top of the n-layer. 40 mil diameter mesa diodes were then etched which were subsequently passivated by an oxide deposition as shown in the insert of Fig. 4. The results of voltage breakdown measurements are shown in Fig. 4 and Tables I and II. The ratio of measured breakdown to the theoretical

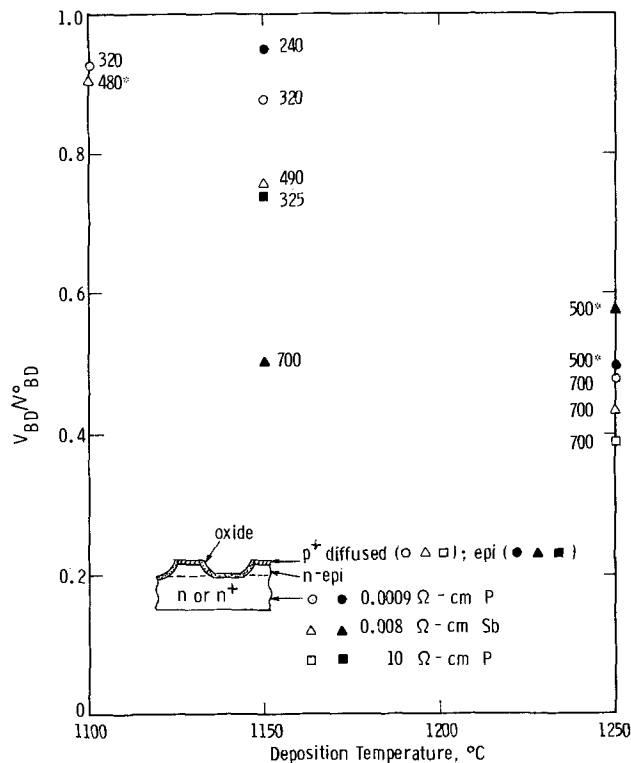


Fig. 4. Ratio of measured to theoretical breakdown voltage of diodes in n-epitaxial layers as a function of deposition temperature. The open points are for diffused and the solid points for epitaxial diodes. The numbers beside the points are the theoretical breakdown voltages, where the starred numbers indicate breakdown under punch-through conditions.

Table I. Characteristics of diffused diodes on n-epitaxial layers^(a)

Substrate	Clean- ing	Growth temp.	Layer doping	Rev. voltage at current <20 μA 5 mA		V ^o _{BD}
P 0.0009 ohm-cm	DSN	1150	1 × 10 ¹⁵	250	320	320
	DSNE	1100	1 × 10 ¹⁵	265	300	320
	DSNE	1150	1 × 10 ¹⁵	220	280	320
	DSNE	1250	4 × 10 ¹⁴	260	335	700
	DSNP	1150	1 × 10 ¹⁵	255	310	320
Sb 0.008 ohm-cm	DSN	1150	6 × 10 ¹⁴	250	400	490
	DSNE	1100	1 × 10 ¹⁵	265	440	480 ^(b)
	DSNE	1150	6 × 10 ¹⁴	250	370	490
	DSNE	1250	4 × 10 ¹⁴	235	300	700
	DSNP	1150	5 × 10 ¹⁴	240	470	580
P 10 ohm-cm	DSNE	1250	4 × 10 ¹⁴	200	275	700

^(a) All wafers were chelated using DSNE procedure before diffusion.
^(b) Indicates theoretical punch-through breakdown voltage.

Table II. Characteristics of epitaxial-epitaxial diodes on n-epitaxial layers

Substrate	Clean- ing	Growth temp.	Layer doping	Rev. voltage at breakdown	V ^o _{BD}
P 0.0009 ohm-cm	DSNE	1150	1.5 × 10 ¹⁵	235 @ <10 μA	240
	DSNE	1250	2 × 10 ¹⁴	245 @ <10 μA	500 ^(a)
Sb 0.008 ohm-cm	DSNE	1150	4 × 10 ¹⁴	350 @ 200 μA	700
	DSNE	1250	2 × 10 ¹⁴	290 @ 20 μA	500 ^(a)
P 50 ohm-cm	DSNE	1150	1 × 10 ¹⁵	240 @ 20 μA	325

^(a) Indicates theoretical punch-through breakdown voltage.

values, corresponding to the layer doping, is plotted as a function of the deposition temperature. The open points refer to diffused diodes and the solid ones to epitaxial-epitaxial diodes. The numbers beside the points are the theoretical breakdown voltages, with the starred quantities indicating that the breakdown is determined by punch-through of the space-charge region to the n⁺ substrate.

The processing and growth conditions as well as doping concentrations of the layers are given in Table I. The reverse voltage values are given for two values of current, less than 20 μA and 5 mA, where the 5 mA value was used as the breakdown voltage measure. Also shown are the theoretical breakdown voltages (15). Similar data for the epitaxial-epitaxial diodes are shown in Table II.

The general trend of these measurements is in accord with the lifetime data, i.e., lower growth temperatures yielded devices with breakdown voltages closer to the theoretical values. Also, diodes fabricated on heavily phosphorus-doped substrates had higher breakdown values than the other two substrates. These diodes also exhibited harder I-V characteristics, while the others frequently had a very soft breakdown. The very low V_{BD} of the lightly doped layers (2-4 × 10¹⁴ cm⁻³, with their correspondingly high V^o_{BD}) may be partly due to surface effects.

Contrary to the lifetime data, the cleaning procedure had little influence on the breakdown characteristics, as evidenced by the data in Table I. The chelating and H₂O₂ cleaning of the substrates did not give significantly different results than those of the substrates not so cleaned.

The epitaxial-epitaxial diodes behaved very much like the diffused ones. This indicates that such junctions are not inherently poor, but that the junction characteristics are much more dependent on the quality of the layer with the lower doping.

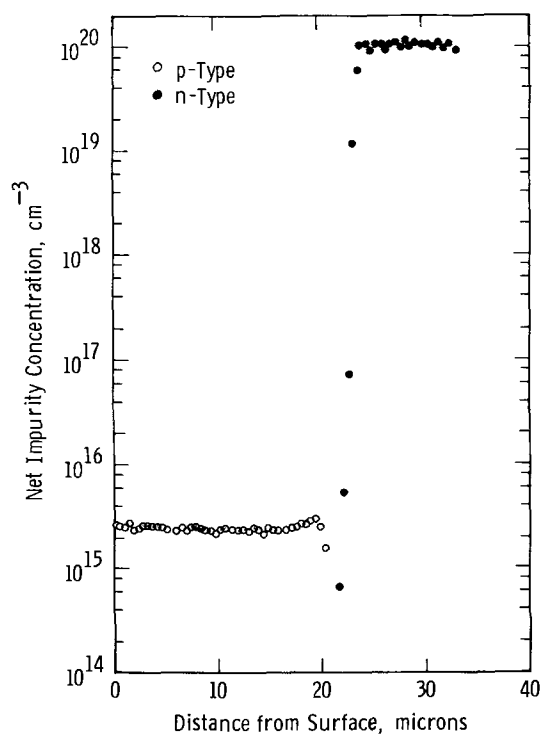


Fig. 5. Typical impurity concentration profile of a p-epitaxial layer on a heavily phosphorus-doped substrate.

P-epitaxial layers.—An impurity concentration profile of a p-layer on a heavily phosphorus-doped substrate is shown in Fig. 5. This is typical of the p-epitaxial layers showing the doping uniformity and a well-defined step junction. Since a natural junction is formed when a p-layer is grown on an n-type substrate, only the substrate-epitaxial junctions were evaluated for these layers. The results for 1100°C growth temperature and DSNE chelating are shown in Table III. The diodes fabricated on phosphorus-doped substrates had higher breakdown voltages than those on antimony-doped substrates, as measured on n-layers. However, there was no notable difference between the lightly and heavily phosphorus-doped substrates. We tried to improve the reverse characteristics by phosphorus gettering, the process which had a noticeable effect on the lifetime of p-layers. But, as is evident in Table III, gettering had little effect on the breakdown voltage.

Similar to n-layers, higher growth temperatures yielded junctions with poorer reverse characteristics. Those measurements, however, were not as conclusive as the n-layer results, and are not shown in Table III.

Discussion

From Fig. 1 and 2 it is obvious that the highest lifetimes were obtained on both n- and p-type layers grown on heavily phosphorus-doped substrates. These substrates were characterized by the presence of considerable inhomogeneities, such as, impurity striations, phosphorus-induced precipitates, and dis-

locations. However, an examination in transmission electron microscopy indicated that the epitaxial layers grown on these substrates were of good quality, and comparable to layers grown on dislocation-free, high perfection, high resistivity substrates. Sirtl etching (16) of the layers grown on these substrates revealed only a few dislocations, the number of which decreased with decreasing growth temperature. However, x-ray topographs of the epitaxial layers with and without the substrates indicated the apparent presence of strain which Sirtl etch failed to reveal. Although the origin of these apparent strain effects is not known, their presence in layers grown on degenerate phosphorus-doped substrates at all temperatures, reduces their importance as lifetime controlling factors, since the lifetime in these layers was very high. Thus, with the exception of a slight variation in the dislocation density at a very low level, the layers on all substrates were free from any precipitates and stacking faults. Hence, an explanation of the lifetime results should primarily come from point defect considerations. Point defects, such as, vacancies, carbon, oxygen, heavy metals, and various complexes can form numerous deep energy levels (17), reducing the carrier lifetime.

The high values of the lifetime in the n-type layers can be taken as an indication that the deposition system was free of lifetime-killing impurities. The fact that the lifetime in the p-type layers before gettering was low is probably connected with the B_2H_6 doping system. Although gettering improved the lifetime in the p-layers near the top surface, the p-n junction, i.e., the epitaxial layer-substrate interface region was not effectively cleaned.

The reason for such high lifetimes in the epitaxial layers grown on heavily phosphorus-doped substrates is not clearly understood. We offer the following conjecture as a possible explanation. The type and location of the impurity-pinning centers in epitaxial silicon (e.g., thermally induced dislocations extending the entire thickness of the wafer) are such, that the impurities cannot be gettered as effectively as in diffused junctions in bulk material. The diffusion induced dislocations on the other hand are formed in the heavily doped side of the junction, with a maximum dislocation density located away from the junction plane (18, 19) and are decorated with the diffusing dopant. Thus the epitaxial silicon is generally more susceptible to contamination, and once contaminated, affects the device behavior adversely. The diode characteristics and the lifetime results together with the observed effects of chelating indicate that the lifetime-killing impurities originate primarily from the substrate surface, rather than from the epitaxial growth system. High phosphorus concentration contracts the silicon lattice and increases the affinity and solubility of heavy metals, such as Cu, Ag, and Au. Any heavy metal contamination introduced during substrate preparation may be held more effectively by degenerate phosphorus-doped substrates than by antimony or lightly phosphorus-doped substrates during subsequent epitaxial growth. If the growth temperature is sufficiently high so as to render these adsorbed impurities mobile then the grown layer becomes contaminated causing a decrease in the measured lifetime. The metallic impurities probably constitute the primary mode of layer contamination, either as individual point defects or as complexes with other point defects, such as vacancies. Decoration of dislocations with metallic is most likely only a secondary mode of contamination.

Summary

Epitaxial n- (arsenic-doped) and p-layers (boron-doped) were grown on phosphorus and antimony-doped substrates at temperatures from 1100°-1250°C. The generation lifetime was measured in these layers

Table III. Characteristics of substrate-epitaxial diodes on p-epitaxial layers grown at 1100°C

Substrate	Gettering	Layer doping	Rev. voltage at current		V_{BD}
			<20 μ A	5 mA	
P 0.0009 ohm-cm	None	1×10^{15}	210	255	320
	P ₂ O ₅	1×10^{15}	250	280	320
Sb 0.008 ohm-cm	None	1×10^{15}	50	60	320
	P ₂ O ₅	1×10^{15}	45	60	320
P 10 ohm-cm	None	1×10^{15}	250	265	320
	P ₂ O ₅	1×10^{15}	280	315	320

by the pulsed MOS-C technique and the reverse junction characteristics were obtained on diodes formed in these layers.

The lifetimes in both types of layers were comparable. They improved when the substrates were cleaned using a heavy metal complexing chelating solution. Lifetimes of several hundred microseconds were measured on layers grown at 1100°C, but higher growth temperatures caused the lifetimes to decrease. The layers grown on heavily phosphorus-doped substrates had higher lifetimes than those grown on lightly phosphorus-doped or heavily antimony-doped substrates. Phosphorus pentoxide gettering had little effect on the lifetimes in the n-layers but resulted in a significant increase for the p-layers. This is probably due to lifetime killing impurities of the B₂H₆ doping system.

The trend of the lifetime results was generally also observed when the breakdown voltage of the diodes was measured. The layers grown at the lower temperature (1100°C) had breakdown voltages closer to theoretical values than those grown at higher temperatures. The diodes formed in layers grown on heavily phosphorus-doped substrates had better characteristics than those grown on the other two substrates. Gettering had a lesser effect on the diode characteristics than it did on the lifetimes.

There was no significant difference between diodes formed by boron diffusion into the n-layers and those fabricated by growing a p-layer on the n-layer. This shows that epitaxial-epitaxial junctions can be as good as diffused-epitaxial junctions. For the epitaxial p-layers on the n-substrates, the epitaxial-substrate junctions showed some good behavior but on the whole gave poorer results than those above.

Acknowledgment

We wish to thank G. A. Gruber, P. D. Blais, W. Cifone, and R. F. Yut for technical assistance.

Manuscript submitted Feb. 9, 1972; revised manuscript received May 25, 1972.

Any discussion of this paper will appear in a Discussion Section to be published in the June 1972 JOURNAL.

REFERENCES

1. P. Rai-Choudhury, *J. Crystal Growth*, **10**, 291 (1971).
2. Y. C. Kao and G. A. Gruber, Paper 94 presented at Electrochem. Soc. Meeting, Los Angeles, May 10-15, 1970.
3. W. Kern and D. A. Puotinen, *RCA Rev.*, **31**, 187 (1970).
4. P. H. Robinson and F. P. Heiman, *This Journal*, **118**, 141 (1971).
5. C. C. Chang, *Surface Sci.*, **23**, 283 (1970).
6. P. Rai-Choudhury and W. J. Takei, *J. Appl. Phys.*, **40**, 4980 (1969).
7. A. D. Paddock and S. H. Carpenter, *Trans. AIME*, **1**, 651 (1970).
8. R. J. Walsh and A. Herzog, Monsanto Co., U.S. Pat. 3,170,283 (1965); E. Mendel, *SCP and Solid State Technology*, **10**, 27 (1967).
9. R. G. Mazur and D. H. Dickey, *This Journal*, **113**, 255 (1966).
10. F. P. Heiman, *IEEE Trans. Electron Devices*, **ED-14**, 781 (1967).
11. D. K. Schroder and J. Guldborg, *Solid-State Electron.*, **14**, 1285 (1971).
12. P. Balk, Paper 109 presented at Electrochem. Soc. Meeting, San Francisco, May 9-13, 1965.
13. D. K. Schroder and H. C. Nathanson, *Solid-State Electron.*, **13**, 577 (1970).
14. A. Goetzberger and W. Shockley, *J. Appl. Phys.*, **31**, 1821 (1960); S. W. Ing, R. E. Morrison, L. L. Alt, and R. W. Aldrich, *This Journal*, **110**, 533 (1963).
15. S. M. Sze, "Physics of Semiconductor Devices," John Wiley & Sons, New York (1969).
16. E. Sirtl and A. Adler, *Z. Metallk.*, **52**, 529 (1961).
17. A. R. Bean, R. C. Newman and R. S. Smith, *J. Phys. Chem. Solids*, **31**, 739 (1970); S. M. Sze and J. C. Irvin, *Solid-State Electron.*, **11**, 599 (1968).
18. S. Prussin, *J. Appl. Phys.*, **32**, 1876 (1961); B. G. Cohen, *Solid-State Electron.*, **10**, 33 (1967).
19. J. E. Mann and N. P. Sandler, *Phys. Failure Electron.*, **2**, 145 (1964).

Zn(PO₃)₂ Glass as a Doping Source for GaP(Zn,O)

A. S. Jordan, L. Derick, R. Caruso, and M. Kowalchik

Bell Telephone Laboratories, Incorporated, Murray Hill, New Jersey 07974

ABSTRACT

As an alternative to elemental Zn and Ga₂O₃ powder, Zn(PO₃)₂ glass has been utilized as a convenient simultaneous source of Zn and O to dope GaP. The synthesis of Zn(PO₃)₂ from ZnO and (NH₄)₂HPO₄ is described together with some of its advantageous properties (low melting point, compactness, small surface area for adsorption). Zn(PO₃)₂ was employed in the preparation of GaP liquid-phase epitaxial layers (on vapor grown substrates) and of solution-grown (SG) platelets, for which red electroluminescence and photoluminescence efficiency maximization curves were determined, respectively. The results are comparable to those obtained previously by using Zn and Ga₂O₃. Analysis of the photoluminescence measurements, absorption spectra, and below-gap excitation spectra on SG platelets indicates that the incorporation chemistry of Zn and O from Zn(PO₃)₂ is in accord with previous findings using Zn and Ga₂O₃. Since the nonradiative shunt path component of the minority carrier lifetime in SG platelets is hole concentration dependent for growth solutions containing Zn(PO₃)₂ as well as for those containing Zn and Ga₂O₃, it seems unlikely that the "killer center" associated with the shunt path is related to the background impurities introduced by these dopants.

The early work of Starkiewicz and Allen (1) on GaP red light-emitting diodes (LED's) demonstrated the key role of Zn and O in the generation of the red light, which is now known to arise from the decay of excitons bound to Zn-O nearest neighbor pairs (2, 3). The

Key words: light-emitting diodes, crystal growth, compound semiconductors, photoluminescence.

usual sources of Zn and O are Zn pellets and Ga₂O₃ powder, although ZnO (4, 5), Zn₃(PO₄)₂ (5), and GaPO₄ (5) have also been used or considered. In this paper we report on the use of Zn(PO₃)₂ glass as a promising dopant with certain advantages over these sources, and we consider the luminescent properties

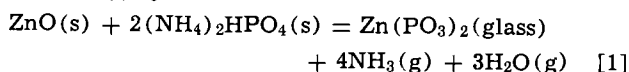
of Zn₂O-doped GaP crystals grown from solutions containing Zn(PO₃)₂.

Our search for an alternative approach was motivated by several considerations. First, the use of a glass should be advantageous due to the reduced adsorption of impurities from the atmosphere as compared with Ga₂O₃ powder, which has a large surface area.¹ Second, a single compact dopant was sought to eliminate the cumbersome handling of Zn pellets and Ga₂O₃ powder. Third, a source was desired with a melting point below the typical growth temperature (~1040°C) (7) of GaP by liquid-phase epitaxy (LPE), in order to achieve rapid mixing and dissolution of the dopants in the solution during the warmup cycle. Zn(PO₃)₂ glass, which melts at ~870°C (8), seemed to satisfy these requirements. Finally, in order to determine whether impurities contaminating Ga₂O₃ powder introduce nonradiative "shunt path" (9, 10) centers, Zn(PO₃)₂ was chosen because it can be synthesized without using Ga or Ga₂O₃.

It was shown earlier that the incorporation of Zn in GaP pulled by the liquid encapsulation Czochralski (LEC) technique from melts containing Zn(PO₃)₂ follows the calculated solid solubility for Zn at 1465°C (11). Recently, the photoluminescent properties of GaP pulled by LEC from stoichiometric melts and non-stoichiometric solutions with Zn(PO₃)₂ additions have been given (12). Electroluminescence efficiencies as high as 2.7% have been reported on annealed and encapsulated diodes prepared by double LPE on n-type LEC substrates, where the p-type LPE layer was grown from a solution containing Zn(PO₃)₂ (13). The major objective of this paper is to describe our experiments concerning the utilization of Zn(PO₃)₂ for doping GaP grown either by LPE on vapor-grown (VG) substrates (Work done prior to the availability of LEC substrates.) or by slow cooling of unseeded solutions of Ga saturated with GaP.

Experimental Procedure

Synthesis of Zn(PO₃)₂.—Zn(PO₃)₂ was synthesized from ZnO and (NH₄)₂HPO₄, both with 99.999% nominal purity, by the reaction



In a typical run stoichiometric proportions of the powdered ingredients were mixed thoroughly and loaded into a shallow Pt dish.² The mixture was placed in a box-type furnace, slowly heated to ~1000°C, and held there for at least 1 hr. Reaction [1] proceeded to completion, yielding only Zn(PO₃)₂ glass and gaseous H₂O and NH₃ which were exhausted via an inverted quartz casserole (covering the Pt dish) that served as a chimney. Finally, the liquid glass was poured onto a clean quartz plate to solidify, crushed into convenient size pieces, and stored in a N₂ dry box to prevent hydration.

GaP crystal growth.—The feasibility of using Zn(PO₃)₂ was first demonstrated by the sealed-tube single LPE growth of Zn₂O-doped GaP layers on S-doped n-type VG GaP substrates with a net donor concentration of ~6 × 10¹⁷ cm⁻³. The substrates were deposited by the wet hydrogen vapor transport method (14) on GaAs seeds, removed from the seeds, and mechanically polished on the {111} P-face to a thickness of ~0.3 mm. A modification of the sealed-tube tipping technique (15) was used to grow a series of LPE layers from GaP-saturated Ga solutions containing between ~0.02 and 0.25 mole per cent (m/o) Zn(PO₃)₂. The VG substrate, sometimes as large as 12 mm by 20 mm, was pinned by a quartz rod to a quartz pedestal before the evacuation and sealing of the fused

quartz capsule. The pin permitted the termination of LPE growth at will by a 180° rotation of the capsule along its horizontal axis. Usually ~40 μm thick films were deposited by cooling from 1050° to 600°C at 10°C/min.

In addition, Zn₂O-doped GaP platelets were grown by cooling saturated solutions of GaP in Ga (SG). Typically, unseeded solutions containing 6.9 m/o GaP and between ~10⁻³ and ~2 × 10⁻¹ m/o Zn(PO₃)₂ in a BN crucible were placed in a fused quartz tube which was then evacuated and sealed. The ampoule was heated to ~1160°C, held for 2 hr, and cooled to 900°C at 5°C/hr.

Experimental Results and Discussion

Point contact electroluminescence measurements were performed at 2 and 10 mA on several 250 μm mesa diodes fabricated from each p-type LPE, n-type VG structure. The variation of η_{EL} at 10 mA as a function of the nominal Zn(PO₃)₂ concentration in the LPE solution is presented in Fig. 1. The maximum value of η_{EL} is achieved between ~0.1 and ~0.15 m/o Zn(PO₃)₂. By bonding and encapsulating in epoxy, the η_{EL} of the "best" diode was increased from its point contact values of 0.60% at 2 mA and 0.52 at 10 mA³ to 1.20 and 1.05%, respectively.

Trumbore *et al.* (16) reported point contact η_{EL} for similar unannealed diodes prepared by depositing a Zn₂O-doped p-type layer from a Zn, Ga₂O₃-containing tipping solution onto VG substrates. Their η_{EL} values were 0.11% and 0.23% for S- and Te-doped substrates,⁴ respectively (N_D - N_A = ~4 × 10¹⁷ cm⁻³). With respect to Zn, their solution composition of 0.15 m/o Zn is the same as the composition leading to our maximum η_{EL}. These workers added only 0.05 m/o Ga₂O₃ to their solution whereas we provided an amount equivalent to 0.3 m/o Ga₂O₃ (0.15 m/o Zn(PO₃)₂). However, additions in excess of 0.008 m/o Ga₂O₃ at ~1040°C lead

³ The η_{EL} at 2 mA of annealed and encapsulated diodes prepared identically but replacing Zn(PO₃)₂ with Zn and Ga₂O₃ in our LPE system is 1.3%. All the values of η_{EL} in Fig. 1 are for unannealed LPE layers. Although no detailed study of annealing was undertaken here, the diodes with the maximum efficiency showed no improvement with annealing, in agreement with previous findings at similar Zn concentrations in the tipping solution (7).

⁴ It should be noted, however, that in the work of Trumbore *et al.* (16) η_{EL} of 0.5% was reported for a presumably Si-contaminated n-type VG substrate.

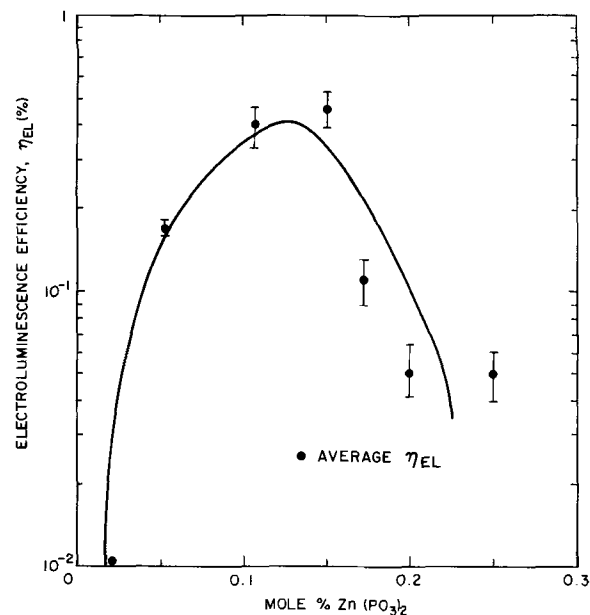


Fig. 1. Point contact electroluminescence efficiency, η_{EL}, of GaP mesa diodes at 10 mA as a function of Zn(PO₃)₂ concentration in the LPE solution. The net donor concentration of the S-doped VG substrates is ~6 × 10¹⁷ cm⁻³. The top and bottom of each error bar represent the highest and lowest efficiency mesa diodes fabricated from the same slice.

¹ Recently S, a shallow donor impurity, was found to be introduced with Ga₂O₃ additions in some GaP crystals (6).

² Although these powdered ingredients may contain adsorbed impurities, most of these are expected to be removed by volatilization during the high temperature synthesis.

to the saturation of the Ga-GaP-Ga₂O₃ ternary solution (13), and it seems likely that both results were obtained on GaP layers of comparable oxygen concentration.

We also studied the photoluminescence properties of the Zn(PO₃)₂-doped SG unannealed platelets. To prepare planar, parallel specular surfaces the platelets were polished on the {111} Ga and P faces on a tin lap with a 0.1 μm diamond polish. For two runs, although the platelets were polished, their small size precluded the preparation of parallel surfaces. For every crystal the red (7000Å) internal photoluminescence quantum efficiency (9), η_{PL}, was measured at 25°C under excitation with the 4880Å line of an argon laser. The dependence of η_{PL} on Zn(PO₃)₂ concentrations in the solution is shown in Fig. 2.

Recent experimental and theoretical results concerning the optical properties of Zn₂O-doped GaP (9, 12, 17-19) provide a model for a self-consistent estimation of the total substitutional oxygen concentration, N_{O,t}, the total zinc concentration, N_{Zn,t}, and the nonradiative shunt path component, τ_n, of the total minority carrier lifetime. For the platelets with planar and parallel surfaces we obtained absorption spectra and below-bandgap excited photoluminescence spectra, the latter with the 5682Å line of a krypton laser. These measurements, in connection with η_{PL}, led to the determination of the minority carrier lifetimes, τ_m (17). Then, from a previously established correlation (18) of the absorption coefficient at 0.8 eV with hole concentration, we estimated the hole concentration and N_A - N_D. A knowledge of N_A - N_D and η_{PL} permits the calculation of the branching ratio, s (9, 18).

Appropriate combinations of s and τ_m yield τ_n (9, 12) and the concentration of Zn-O complexes, N_{ZnO}

$$1/\tau_n = (1 - s)/\tau_m \quad [2]$$

and

$$N_{ZnO} = s/v\sigma_{nt}\tau_m \quad [3]$$

where v is the thermal velocity of the electrons and σ_{nt} is the cross section for the capture of minority carrier electrons by the Zn-O center. In addition, the relative concentration of unpaired substitutional oxy-

gen can be estimated by a combination of N_{ZnO}, η_{PL}, s, and the ratio of the infrared (1.32 eV) to red (1.77 eV) signal strengths, obtained from the below-gap photoluminescence spectra (18). This relative value in comparison with the optical properties of a previously characterized standard SG crystal (9) yields an absolute value for the concentration of unpaired substitutional oxygen, N_{O+}.

If Zn and O are the only electrically active impurities in these SG platelets, then a knowledge of N_A - N_D, N_{O+}, and N_{ZnO} permits the calculation of N_{O,t} and N_{Zn,t} (18). In Fig. 2 we present N_{O,t} and N_{Zn,t} as a function of Zn(PO₃)₂ concentration in the solution. The calculated Zn solid solubility isotherm in GaP (11) and the estimated O solubility in liquid Ga saturated with Ga₂O₃ and GaP (13), both for 1100°C, are also shown. It can be seen that the experimental N_{Zn,t} values for SG crystals grown between 1160° and 900°C can be reasonably well represented by the theoretical 1100°C solubility isotherm. N_{Zn,t} for the platelet with maximum efficiency (η_{PL} = 4%) is comparable with the net acceptor concentration reported by Saul *et al.* (7) for high efficiency p-n junctions.

It has been previously mentioned that the Zn solubility in GaP pulled by LEC from Zn(PO₃)₂-containing melts also follows the theoretical 1465°C curve. For these crystals the experimental and calculated distribution coefficients derived from Ref. (11) are 0.16 and 0.19, respectively, which should be compared with the distribution coefficient of 0.096 reported for GaP pulled by LEC from melts containing metallic Zn (20). Evidently, in contrast to Zn, when Zn(PO₃)₂ is used in this open system, the loss of Zn from the LEC charge during heating to the melting point of GaP is almost negligible.

According to Fig. 2, in agreement with thermodynamic considerations (13) and recent results on LPE growth (21), N_{O,t} remains constant above the ternary solubility limit (13) in the solution. Very recent measurements using prompt α-particle nuclear microanalysis to directly determine N_{O,t} in LPE layers grown at ~1100°C (22) and electrical data on SG crystals (23) are in accord with the indicated lower limits (7 × 10¹⁶ cm⁻³) of the estimated values shown in Fig. 2 along the plateau.

In Fig. 3, we show the variation of 1/τ_n (obtained by using Eq. [2]) with hole concentration. The data strongly support a linear dependence of 1/τ_n on hole concentration, as has been suggested elsewhere (9, 24). According to Dishman *et al.* (9), this relationship is consistent with the presence of a killer center in SG GaP which is a deep acceptor impurity with a concentration independent of the Zn doping level. Because the capture of electrons by this center proceeds via an Auger process by moving a free hole deep into the valence band, a linear relationship between 1/τ_n and hole concentration results. Since our growth solutions were doped with Zn(PO₃)₂ whereas those of Dishman *et al.* (9) were doped with Zn and Ga₂O₃, it seems unlikely that the killer center is related to the chemical contaminants present in either doping source.

In previous work a correlation has been established between 1/τ_n and relative Ga-vacancy concentration for Zn₂O-doped GaP pulled by LEC from stoichiometric and nonstoichiometric solutions (12). In stoichiometric LEC samples, 1/τ_n appeared to be independent of hole concentration (18). As all the SG crystals in the present study were grown in the same temperature range, their Ga-vacancy concentration is expected to be reasonably constant. Thus, we may speculate that an additional killer center is present in SG crystals, such as a Ga-vacancy-O complex (25), which may be responsible for SG crystals not having a higher η_{PL}.

Some qualitative considerations are in order concerning the shape and position of the η_{PL} curve in Fig. 2. Initially, η_{PL} increases from 2.1 to 4.0% with increas-

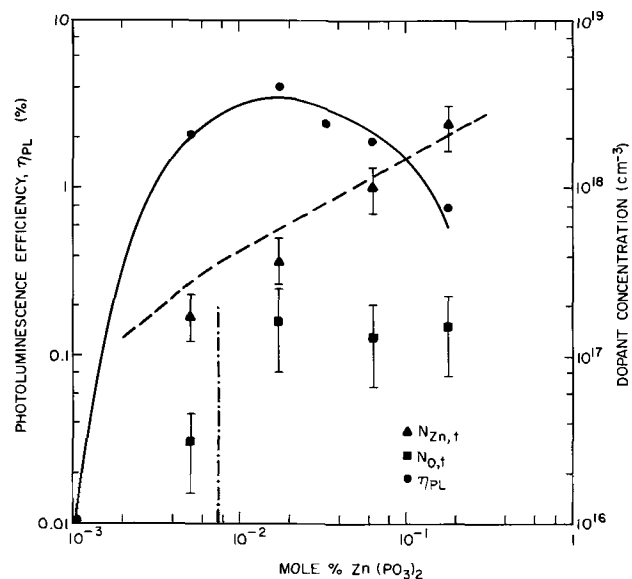


Fig. 2. Photoluminescence quantum efficiency, η_{PL}, of SG platelets as a function of Zn(PO₃)₂ concentration in the growth solution. The estimated total dopant concentrations N_{O,t} and N_{Zn,t} are also shown. The dashed line is the calculated Zn solubility isotherm for GaP at 1100°C (11). The vertical line represents the estimated O solubility in the solution of the Ga-GaP-Ga₂O₃ system at 1100°C, converted to m/o Zn(PO₃)₂ (13). The error bars for N_{O,t} and N_{Zn,t} are consistent with Ref. (9) and (18), respectively. The η_{PL} of 0.01% for 10⁻³ m/o Zn(PO₃)₂ is an upper limit.

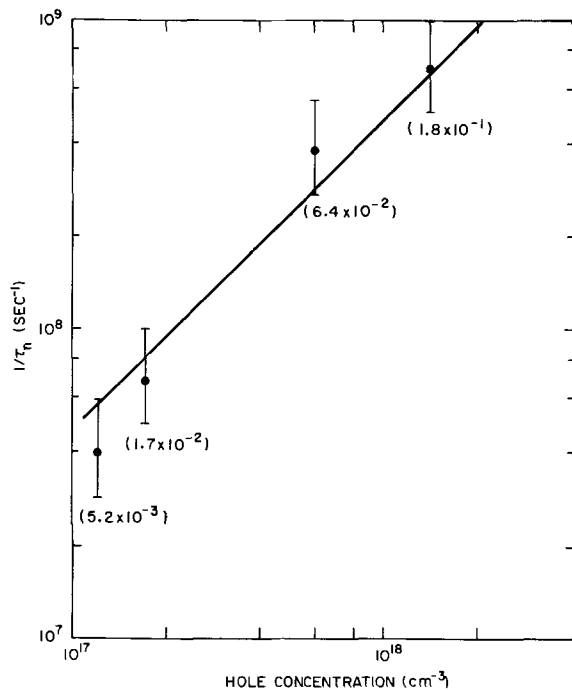


Fig. 3. Reciprocal of nonradiative shunt path component of electron lifetime, $1/\tau_n$, vs. hole concentration for the SG platelets shown in Fig. 2. The error bars for $1/\tau_n$ are based on Ref. (17). The $\text{Zn}(\text{PO}_3)_2$ concentration in the growth solution corresponding to each platelet is given in parenthesis in m/o.

ing $\text{Zn}(\text{PO}_3)_2$ concentration. This is largely due to a rise of N_{ZnO} from $\sim 6 \times 10^{15}$ to $1.6 \times 10^{16} \text{ cm}^{-3}$, which is only partially counteracted by the decrease of τ_n . On the other hand, since the decrease of η_{PL} from 1.9 to 0.76% [with greater $\text{Zn}(\text{PO}_3)_2$ additions] is accompanied by a slight increase of N_{ZnO} from 3.2×10^{16} to $3.6 \times 10^{16} \text{ cm}^{-3}$, this decrease is mainly due to the drop in τ_n . A similar η_{PL} curve has recently been presented by Dishman *et al.* (9) for unannealed SG crystals grown in the same temperature range as ours from solutions doped with Zn and Ga_2O_3 . Somewhat similar η_{PL} curves have also been obtained by Gershenson *et al.* (26) for SG platelets prepared from solutions containing various amounts of Zn and Ga_2O_3 . However, Gershenson *et al.* (26) achieved their peak efficiency at 0.1 a/o Zn, whereas we find a maximum at 0.02 m/o $\text{Zn}(\text{PO}_3)_2$. Since their SG platelets were grown by cooling from 1050°C, the composition shift is in accord with the known solid solubility behavior of Zn in GaP (11). To incorporate equal amounts of Zn in GaP, less Zn is required in the solution for the higher temperature growth than for the lower temperature one. This explanation also applies to the composition shift between the η_{EL} curve of Fig. 1 and the η_{PL} curve of Fig. 2.

In conclusion, the present study demonstrates that $\text{Zn}(\text{PO}_3)_2$ glass is a convenient alternative to Zn and Ga_2O_3 as a source of Zn,O-doping in GaP. The luminescence efficiencies of GaP LED's and SG platelets grown from solutions containing $\text{Zn}(\text{PO}_3)_2$ are comparable to those of samples grown from solutions doped with Zn and Ga_2O_3 . An analysis of the optical measurements for SG crystals suggests that the incorporation chemistry of Zn and O from a $\text{Zn}(\text{PO}_3)_2$ source is in accord

with previous results using Zn and Ga_2O_3 , and that the killer center is not related to the background impurities introduced by either of these dopants. Further systematic work on the preparation of annealed single and double LPE structures on LEC substrates is required to determine whether the use of $\text{Zn}(\text{PO}_3)_2$ can lead to a significant improvement in doping control and device performance.

Acknowledgments

We acknowledge the assistance of E. A. Sigety in the initial preparation of $\text{Zn}(\text{PO}_3)_2$. We are grateful to F. A. Trumbore for his continuing interest in this work and for many helpful discussions. Beneficial comments by J. M. Dishman and J. S. Jayson are also acknowledged.

Manuscript submitted Jan. 24, 1972; revised manuscript received ca. June 23, 1972. This was Paper 49 presented at the Houston, Texas, Meeting of the Society, May 7-11, 1972.

Any discussion of this paper will appear in a Discussion Section to be published in the June 1973 JOURNAL.

REFERENCES

1. J. Starkiewicz and J. W. Allen, *J. Phys. Chem. Solids*, **23**, 881 (1962).
2. T. N. Morgan, B. Welber, and R. N. Bhargava, *Phys. Rev.*, **166**, 751 (1968); C. H. Henry, P. J. Dean, and J. D. Cuthbert, *ibid.*, **166**, 754 (1968).
3. J. D. Cuthbert, C. H. Henry, and P. J. Dean, *ibid.*, **170**, 739 (1968); M. DiDomenico, Jr., J. M. Dishman, and K. P. Sinha, *ibid.*, **B4**, 1270 (1971).
4. H. G. Grimmeiss and H. Koelmans, *Philips Res. Rept.*, **15**, 290 (1960).
5. H. G. Grimmeiss, W. Kischio, and H. Scholz, *Philips Tech. Rev.*, **26**, 136 (1965).
6. R. H. Saul, *J. Electronic Materials*, **1**, 16 (1972).
7. R. H. Saul, J. Armstrong, and W. H. Hackett, Jr., *Appl. Phys. Letters*, **15**, 229 (1969).
8. F. L. Katnack and F. A. Hummel, *This Journal*, **105**, 125 (1958).
9. J. M. Dishman, M. DiDomenico, Jr., and R. Caruso, *Phys. Rev.*, **B2**, 1988 (1970).
10. W. Rosenzweig, W. H. Hackett, Jr., and J. S. Jayson, *J. Appl. Phys.*, **40**, 4477 (1969).
11. A. S. Jordan, *This Journal*, **118**, 781 (1971).
12. A. S. Jordan, A. R. Von Neida, R. Caruso, and M. DiDomenico, Jr., *Appl. Phys. Letters*, **19**, 394 (1971).
13. M. Kowalchik, A. S. Jordan, and M. H. Read, *This Journal*, **119**, 756 (1972).
14. C. J. Frosch, *ibid.*, **111**, 180 (1964).
15. R. H. Saul and W. H. Hackett, Jr., *ibid.*, **117**, 921 (1970).
16. F. A. Trumbore, M. Kowalchik, and H. G. White, *J. Appl. Phys.*, **38**, 1987 (1967).
17. R. Caruso, *ibid.*, **42**, 5055 (1971).
18. R. Caruso, M. DiDomenico, Jr., H. W. Verleur, and A. R. Von Neida, *J. Phys. Chem. Solids*, **33**, 689 (1972).
19. J. M. Dishman, *Phys. Rev.*, **B3**, 2588 (1971).
20. S. F. Nygren, C. M. Ringel, and H. W. Verleur, *This Journal*, **118**, 306 (1971).
21. R. H. Saul and W. H. Hackett, Jr., *ibid.*, **119**, 542 (1972).
22. E. C. Lightowers, J. C. North, A. S. Jordan, L. Derick, and J. L. Merz, Unpublished work.
23. L. M. Foster and J. Scardefield, *This Journal*, **116**, 495 (1969).
24. J. M. Dishman, *Phys. Rev.*, **B5**, 2258 (1972).
25. P. J. Dean, *ibid.*, **B4**, 2596 (1971).
26. M. Gershenson, F. A. Trumbore, R. M. Mikulyak, and M. Kowalchik, *J. Appl. Phys.*, **36**, 1528 (1965).

Nonuniform Lateral Ionic Impurity Distributions at Si-SiO₂ Interfaces

D. J. Silversmith

Bell Telephone Laboratories, Incorporated, Murray Hill, New Jersey 07974

ABSTRACT

The transport of mobile sodium ions to the Si-SiO₂ interface in a metal-oxide-semiconductor capacitor causes gross distortions of the capacitance-voltage characteristics. While these changes might be interpreted as increased surface-state densities, this paper shows experimentally that the surface-state densities are unchanged by mobile ion concentrations in the 10¹²/cm² range. By comparison of high- and low-frequency capacitance vs. voltage measurements and conductance vs. voltage measurements, it is shown that the distortion of C-V curves can be explained by fluctuations imposed on the surface potential by a nonuniform pileup of sodium ions at the Si-SiO₂ interface. This argument is further supported by a theoretical reproduction of the experimental C-V curves obtained by a statistical summation of ideal curves.

Although the theoretical nature of the voltage dependence of capacitance in metal-oxide-silicon (MOS) structures is well-understood, experimental measurements generally show significant deviations from the ideal curves. In addition to flatband voltage shifts caused by fixed charge in the oxide and metal contact potentials, deviations from the ideal capacitance structure in the depletion domain have been ascribed to surface states, N_{ss} , at the Si-SiO₂ interface (1). We have observed a change of structure in the capacitance-voltage (C-V) structure when sodium impurities, introduced during device fabrication, are driven to the Si-SiO₂ interface. Related measurements, however, indicate no change in the surface-state density with changes in location of ionized impurities in the oxide. These changes in the capacitance structure are reversible and appear to be caused by potential variations due to a nonuniform distribution of sodium at the Si-SiO₂ interface.

This physical hypothesis was studied by comparing quasi-static and high frequency surface-state measurements with conductance measurements. These comparisons have allowed us to distinguish between distortion caused by charge inhomogeneities introduced by sodium ions near the interface and distortions caused by carrier trapping sites (fast surface states) which might have been introduced by drifted sodium.

C-V Measurements

The experimental data in Fig. 1 is typical of the MOS C-V data. The pair of curves on the right are the quasi-static ramp and 1 mHz high-frequency curves with sodium ions accumulated under the field plate. The two curves on the left are the quasi-static and high-frequency curves with ions at the silicon interface, with all measurements taken at room temperature. The high- and low-frequency curves were aligned by matching zero capacitance at high frequency with zero displacement current (quasi-static) and setting the oxide capacitance to coincide with the quasi-static displacement current in accumulation. This test device consisted of a nominal 2000Å SiO₂ grown in a dry thermal O₂ ambient at 1100°C on a 10 ohm-cm N-type substrate. After oxidation, wafers were given a 15 min nitrogen *in situ* anneal at 1100°C and then removed from the furnace. Field plates were 20 mil diameter dots of 200Å Cr and 2000Å Au. The pair of curves with flatband voltages (V_{FB}) near -0.5V correspond to the sodium ions quenched at the metal-SiO₂ interface, while the pair of curves with V_{FB} at -1.5V had the ions quenched at the Si-SiO₂ interface. "Quenching" is

Key words: MOS devices, sodium contamination, interface charge distribution, apparent surface states.

accomplished by a $\pm 10V$ bias stress at 250°-300°C for 3 min and a rapid quench to room temperature under bias. The bias stress procedure is compatible with an ion-surface density measurement by the high-temperature quasi-static method (2). In addition to a ΔV_{FB} corresponding to 1.1×10^{11} ions/cm², the pair of curves corresponding to ions at the Si-SiO₂ interface show an extension along the voltage axis near flatbands.

Surface-state density (N_{ss}) was determined for both sets of C-V measurements using a method based on the uniform MOS device model which compares the high- and low-frequency curves (3), and is given in Fig. 2. The voltage dependence of the surface potential is found from the quasi-static curve, and the dispersion between this curve and the high-frequency curve from accumulation through depletion gives the surface-state density as a function of energy from the band edge appropriate to the Si doping type. The surface-state densities for this MOS device with sodium at either side of the oxide is the same (within experimental accuracy) and has a minimum value of 7.5×10^{10} cm⁻²/eV at 0.3 eV below the conduction band edge. Since the N_{ss} appears to be unchanged by sodium position, the change in capacitance structure appears to be caused by ion pileup at the Si-SiO₂ interface.

Conductance Measurements

Nicollian and Goetzberger (4) have performed definitive measurements of surface states by the con-

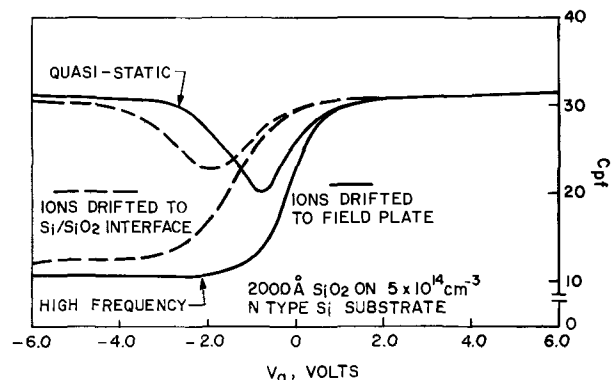


Fig. 1. High frequency and quasi-static C-V characteristics from an MOS device with ions frozen in at one, and then the other, of both oxide interfaces. For sufficiently negative bias, both quasi-static curves correspond to the same value of C_{ox} as in accumulation. At -10V, both high-frequency curves have the same value of C_{min} in inversion.

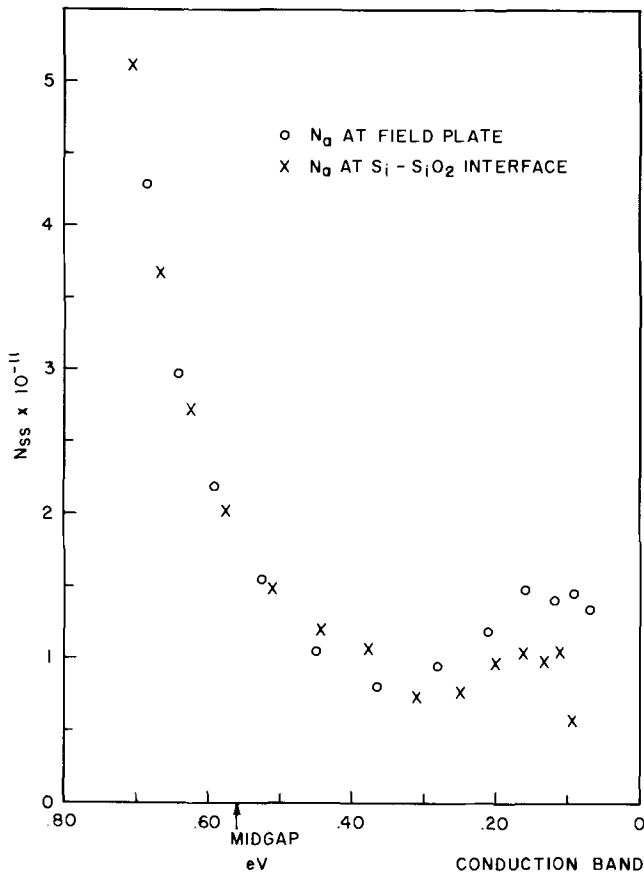


Fig. 2. Si-SiO₂ surface-state density as a function of energy from the Si conduction band edge determined from data of Fig. 1. The field plate consisted of a 20 mil diameter Cr-Au dot.

ductance technique and have shown that the measured equivalent parallel conductance is dominated by surface states. The magnitude of the conductance peak is related to N_{ss} since the loss mechanism is controlled by majority carrier capture and emission at surface states. Figure 3 illustrates simultaneous high-frequency

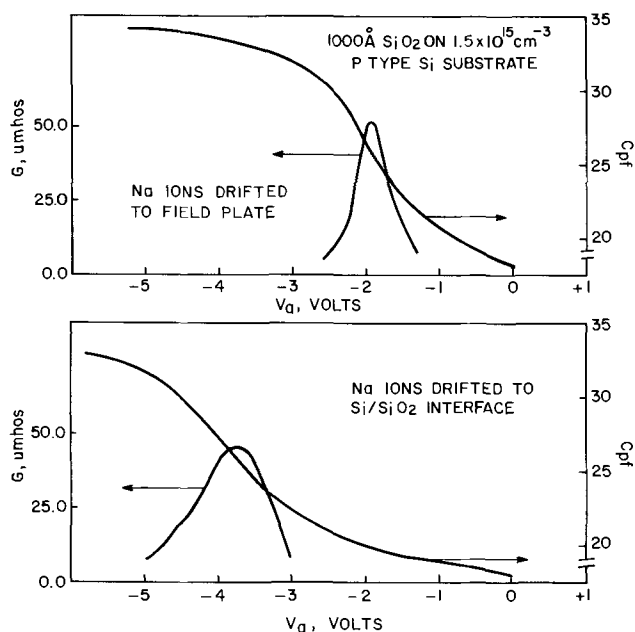


Fig. 3. Simultaneous measurements of high-frequency capacitance and conductance for an MOS device with ions frozen in at both oxide interfaces.

capacitance and conductance measurements for a device with ions quenched at both interfaces in the MOS structure. The device was 1000 Å SiO₂ grown in a dry thermal furnace at 1100°C on a substrate of 1 ohm · cm P-type Si, and given a 15 min *in situ* nitrogen anneal at 1100°C. To avoid problems due to sodium drift under bias, measurements were taken using the pulse method (5). Pulse length was 3 msec with a 6% duty cycle, and the measurement frequency was 10 kHz. The measurements in Fig. 3 were taken at room temperature, but related curves have been taken down to 160°K. Because of the use of the pulse method, the capacitance near zero volts corresponds to deep depletion, not inversion. With ions at the Si-SiO₂ interface the depletion domain appears to extend an additional volt on the capacitance curve. The flatband shift is equivalent to 3.5×10^{11} ions/cm². The decrease in conductance peak with sodium at the Si-SiO₂ interface as seen in Fig. 3 may indicate, in fact, a slight decrease in N_{ss} , but this decrease is not significant as it is more probably due to statistical broadening caused by the non-uniform sodium surface distribution.

If $G_{p, MAX}$, the magnitude of the conductance peak with ions at the Si-SiO₂ interface were significantly greater than $G_{p, MAX}$ without ions at this interface, we would have proven that N_{ss} increases with ions at the Si-SiO₂ interface. Our experiment, on the contrary, indicates that within experimental accuracy N_{ss} remains the same—with or without Na ions at the Si-SiO₂ interface. We would expect a large increase in N_{ss} if structural changes in the C-V curves were due to sodium-induced surface states; consequently the spreading of the C-V curve along the voltage axis is attributable to statistical fluctuations in the local surface potential caused by lateral nonuniformities in the surface distribution of sodium ions. The effect of the nonuniform distribution of ions near the Si-SiO₂ interface increases as they are drifted to this interface because of straight-forward electrostatic considerations. The observed C-V and G-V curves are attributable to a summation of ideal MOS curves, with their effective flatband voltages distributed about the mean, according to the statistical variations in local charge density. This model is developed in the rest of this paper for low surface sodium densities ($<10^{12}/\text{cm}^2$).

Theoretical Models

Nicollian and Goetzberger (4) have discussed effects of small local variations in surface potential caused by a random distribution of fixed oxide charges under conditions of negligible sodium contamination. The C-V characteristic was calculated for the two dimensional case where the potential in the Si varies both in a direction perpendicular to the semiconductor surface as well as along the surface. In this model the oxide charges influence the capacitance by introducing ripples in the surface potential. The crux of this model is the subdivision of each MOS device into a parallel network of smaller devices, each with a characteristic area α . Within each area the capacitance is independent of the distribution of charge, and the surface potential is uniform. The problem is then transformed from a distribution of charge to one of a distribution of surface potential values over an ensemble of devices connected in parallel. This point of view has been corroborated by the work of DiStefano (6). DiStefano has observed the formation of inhomogeneities in the Si-SiO₂ barrier contact potential as sodium ions are drifted to this interface.

For the case of sodium ions, which may introduce large variations, the mathematics of this model must be modified by appeal to a number of experimental observations. Because the density of charged interface states is small compared to the image charge induced by ions at the Si-SiO₂ interface, there is no need to be specifically concerned with changes in surface potential fluctuations due to interface states. Within the oxide

it is assumed that all transportable sodium is ionized, and in the vicinity of the Si-SiO₂ interface the ions appear as a fixed charge distribution (7). A uniform fixed charge distribution manifests itself as a voltage shift on the C-V characteristic. The amount of shift is linear with fixed charge density and is inversely proportional to distance from the Si-SiO₂ interface as expected from effective charge arguments. Snow *et al.* (7) have shown that the distribution of ions perpendicular to the interface is very narrow when ions have been driven to the silicon interface. When ions are quenched at the Si-SiO₂ interface, the distribution does not extend deeply into the bulk and a lateral distribution of sodium ions is sufficient to describe the distribution of flatband voltages. This is a less detailed approach than in Ref. (4).

Castangne and Vapaille have discussed the fluctuations in capacitance structure in terms of a fluctuation of the effective charge (8). Their point of view is different from ours as they consider fluctuations in the surface potentials at the Si-SiO₂ interface rather than local flatband voltage shifts caused by fluctuations in the local ion density. The formalism with respect to variance as a statistical fitting parameter is, however, virtually the same and good agreement with experiment is obtained. Although conductance measurements confirm that little change in N_{ss} takes place—within the sensitivity of the measurement—on drifting ions to the Si-SiO₂ interface, visual comparison of the structural changes in the depletion region for high frequency and quasi-static curves indicate a change in the dispersion in many cases. Because the Gaussian distribution, as used by Castangne and Vapaille, is symmetrical about the mean, the apparent dispersion cannot be reproduced in this model. Castangne and Vapaille, in fact, are unable to reproduce any dispersion in their calculation although it is quite obvious in their experimental data.

Gamma Distribution Statistics

We have attempted to reproduce the observed distortion by a statistical summation of ideal MOS C-V curves. The model assumes that a one-dimensional parallel capacitor array represents a MOS device with a slowly varying distribution of ions along the Si-SiO₂ interface. Consider subdividing the area of a hypothetical Si-SiO₂ interface under the field plate into an array of N equal areas. Suppose that we could determine the number of ions in each of the N areas. From this information we could plot a histogram with the number of ions per unit area on the abscissa and the number of such areas on the ordinate. This histogram represents the distribution of ions along the surface of a MOS capacitor.

Figure 4 shows continuous variable distributions we have found applicable in this work to sodium ions along the Si-SiO₂ interface. This is a Gamma distribution of the form

$$f_{\Gamma}(x) = \frac{x}{\beta^2} e^{-x/\beta}$$

where β is the fitting parameter. x corresponds to the number of ions per unit area. The mean μ and variance σ^2 are related by $\sigma^2 = \mu^2/2 = 2\beta^2$. As seen in Fig. 4, the distribution cuts off abruptly at $x = 0$ with first

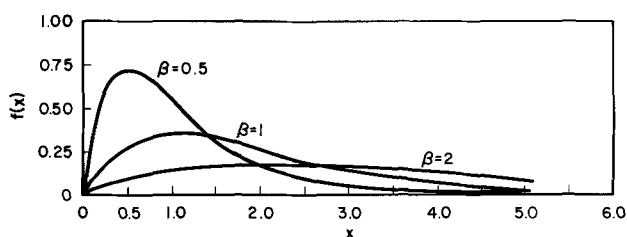


Fig. 4. Gamma distributions with different values of β

derivative $f'_{\Gamma}(0) = 1/\beta^2$, peaks at $x = \beta$, and the integral from $x = 0$ to 6.65β is 0.99. The distribution is skewed toward values of $x > \beta$ with a point of inflection at $x = 2\beta$. The sharp cutoff at $x = 0$ is equivalent to having no negative charges. The skewed behavior is what would be expected for low level ionic contamination. Even with 10^{12} ions/cm² there would be only one sodium ion for every 1000 silica molecules.

The Gamma distribution as used in our calculation has had values skewed to the left, that is $x \rightarrow -x$, because the free variable in this distribution model is the relative flatband shift. Boulin (9) has shown that the transformation from distributed surface charge to relative flatband shift is linear, but with an inversion of the horizontal axis. Since the free variable in this distribution calculation is the relative flatband shift, β is in units of volts. The sharp cutoff of the Gamma distribution with a proper choice of β insures that we have no positive ΔV_{FB} contributions to the statistics; such contributions would be inconsistent with positive sodium ions.

Results from Model Calculations

Calculations for typical N- and P-type materials are described in a pictorial algorithm in Fig. 5. The calculations proceed from computer-generated theoretical high- and low-frequency curves. For purposes of illustration, the ideal quasi-static curve is shown in Fig. 5. For a value on the voltage axis mesh, say V_0 , the zero of the Gamma distribution—skewed toward negative voltage values—is aligned with ideal curve. The entire high- and low-frequency curves are multiplied point by point with the aligned Gamma distribution, and the product is integrated from $V = -6.65\beta$ to $V = 0$. The resulting value

$$C_0 = \int_{-6.65\beta}^0 C(V) f_{\Gamma,\beta}(V - V_0) dV$$

is the averaged capacitance for the point V_0 , which is

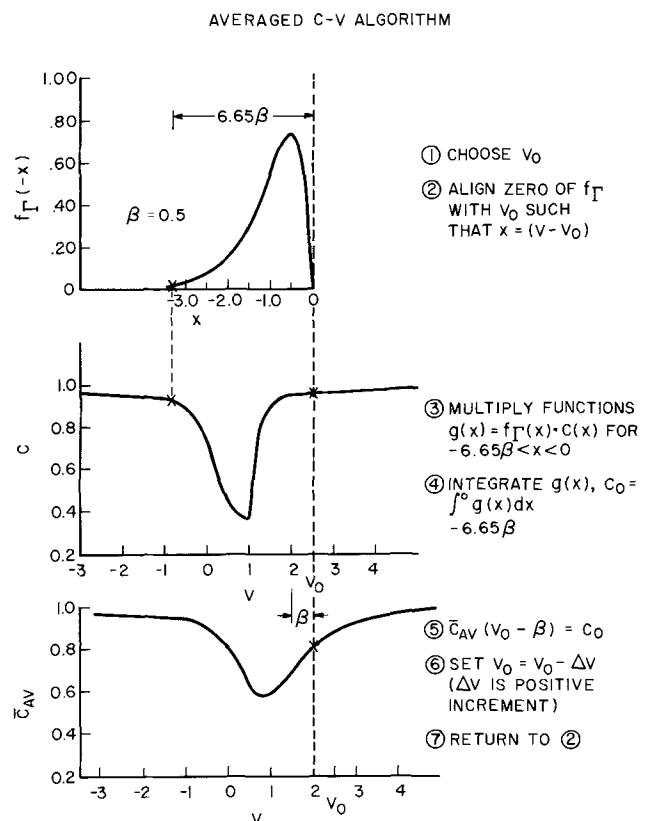


Fig. 5. Illustrated algorithm for obtaining "averaged" C-V curve from the convolution of the ideal curve with the Gamma distribution.

a point on the statistical C-V characteristic corresponding to the starting voltage. For purposes of comparison, values of C_o , as in the lowest curve of Fig. 5, are arbitrarily plotted at $V_o - \beta$ because the maximum of the Gamma distribution is at β . For clarity, the linear shift in the voltage due to the over-all flatband shift has not been included. The calculation gives only the relative structural changes due to lateral variations; the linear voltage shift along the V axis has to be determined separately from

$$\Delta V_{FB} = \frac{1}{C_{ox}d} \int_0^d Z\rho(z) dz$$

as in Ref. (6).

Figure 6 shows a comparison between the ideal C-V characteristics, dashed line, and the statistically summed calculations, solid line, for both low and high frequencies for a typical P-type device. The distortion caused by fluctuations superimposed on the surface potential is clearly evident and resembles the experimentally observed reversible distortion. A more suitable fitting procedure for experimental data would be to commence the mapping from the measured C-V characteristic with ions at the metal-oxide interface, instead of from the ideal C-V curve. In this way one can conveniently account for the effect of N_{ss} initially present. An initial calculation of this type (9), also with $\beta = 0.5$, indicates excellent agreement, and is given in Fig. 7. $\beta = 0.5$ corresponds, roughly, to a $\pm 50\%$ local deviation in the ion density. For example, one could consider an average ion density of 10^{11} ions/cm²

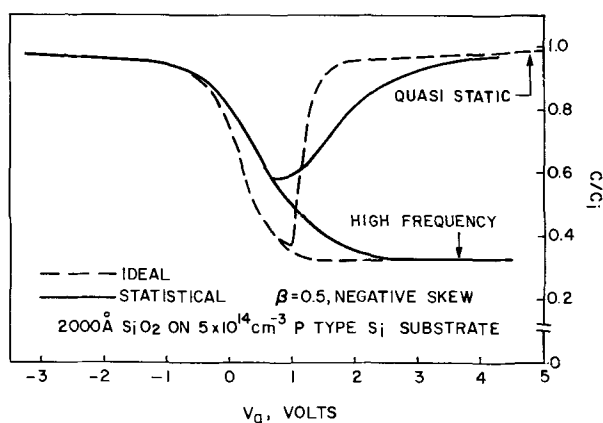


Fig. 6. Model calculation for statistical fluctuations on typical P-type substrate MOS devices.

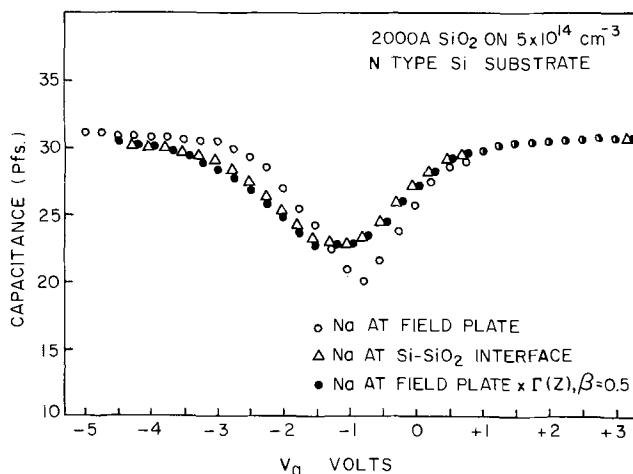


Fig. 7. Quasi-static data of Fig. 1. showing a comparison between the C-V curve with sodium ions at the Si-SiO₂ interface and the corresponding "averaged" C-V curve using the C-V curve (for the same device) with ions at the field plate as "ideal" data.

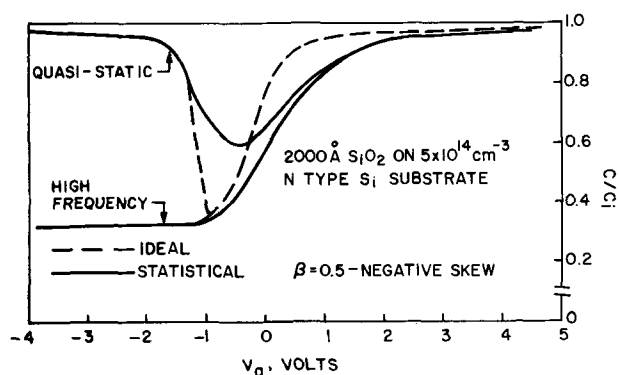


Fig. 8. Model calculation for statistical fluctuations on typical N-type substrate MOS devices.

cm² as measured by the over-all flatband shift, but with a local deviation of about 5×10^{10} /cm².

Figure 8 shows similar comparative results for a typical N-type device. In addition to the distortion noted for the P-type substrate in the previous figure, there is a dispersion evident about flatbands. The apparent surface-state density as indicated by the dispersion would amount to about 10^{11} cm⁻²/eV if it were real. But this dispersion is an artifact of the algorithm we have used. This artifact is related to the use of a skewed distribution for the local relative flatband voltage shifts. It would be difficult to determine if this artifact exists in real data because the actual surface-state densities are also on the order of at least 10^{11} cm⁻²/eV. This effect may have been noted in the literature (10-12) and may account for the recurring concern about interaction between surface states and low-level inherent ionic contaminants.

The success of this statistical model in describing the effect of sodium drift on the C-V characteristic substantiates the applicability of the parallel capacitor array model. Since this simple model would be invalid if the surface charge were, in fact, randomly distributed, the need for further study of the appropriateness of the random distribution approach is indicated.

Conclusions

For sodium impurity levels of less than 10^{12} cm⁻², the transport of ions from one oxide interface to the other in an MOS device results in a marked change in the measured C-V and G-V characteristics, in addition to the flatband voltage shift. Measurements of surface-state density, N_{ss} , indicate no changes with ion location. The structural changes in capacitance and conductance are ascribed to statistical fluctuations in the surface density of sodium ions at the Si-SiO₂ interface. In the absence of a sufficiently simple and straightforward *a priori* calculation of the ion surface distribution, a model is devised which maps an ideal C-V characteristic into a distribution of flatband voltages and results in the "averaged" C-V characteristic. Although a special form of the Gamma distribution has been used in the model because it appeared to be particularly applicable, other similarly skewed distributions may be applicable. While this model applies specifically to long range nonuniformities, it is sufficient to demonstrate that a nonuniform distribution of ions can cause an apparent distortion of the C-V structure.

Acknowledgments

During the course of this work, I have had a number of helpful conversations with R. J. Strain and E. H. Nicollian. D. McE. Boulin contributed his programming expertise. R. C. Beirsto spent many tedious hours taking data, and I appreciate his patience.

Manuscript submitted March 13, 1972; revised manuscript received July 5, 1972.

Any discussion of this paper will appear in a Discussion Section to be published in the June 1973 JOURNAL.

REFERENCES

1. P. V. Gray, *Proc. IEEE*, **57**, 1543 (1969); I. M. Terman, *Solid-State Electron.*, **5**, 285 (1962).
2. M. Kuhn and D. J. Silversmith, *This Journal*, **118**, 966 (1971).
3. M. Kuhn, *Solid-State Electron.*, **13**, 873 (1970).
4. E. H. Nicollian and A. Goetzberger, *Bell System Tech. J.*, **46**, 1055 (1967).
5. A. Goetzberger and E. H. Nicollian, *J. Appl. Phys.*, **38**, 4852 (1967).
6. T. H. DiStefano, *Appl. Phys. Letters*, **19**, 280 (1971).
7. E. H. Snow *et al.*, *J. Appl. Phys.*, **36**, 1664 (1965).
8. R. Castangne and A. Vapaille, *Compt. Rend. Acad. Sci., Paris*, **B-270**, 1347 (1970); R. Castangne and A. Vapaille, *Electron. Letters*, **6**, 691 (1970).
9. D. McE. Boulton, To be published.
10. B. E. Deal *et al.*, *This Journal*, **114**, 266 (1967).
11. P. L. Castro and B. E. Deal, *ibid.*, **118**, 280 (1971).
12. E. Kooi, *Philips Res. Rept.*, **21**, 477 (1966).

The Thermal Decomposition of Germane

Lou H. Hall*

Texas Instruments, Incorporated, Dallas, Texas 75222

ABSTRACT

The kinetics of the thermal decomposition of germane were studied in a dynamic system. The effect of substrate temperature on growth rate in the range of 300°-450°C was investigated. The effect of germane concentration on the growth rate of germanium was also studied. The mole fraction of germane was varied from 3 to 30 ($\times 10^{-3}$). The carrier and diluent were nitrogen. Both zero and first order reactions were observed. Activation energies were found to be 0.75 eV (17 kcal) and 1.20 eV (28 kcal) for the zero and first order reactions, respectively. The zero order is ascribed to a heterogeneous reaction while the first order is ascribed to a homogeneous reaction. Comparisons with results obtained from other studies are made.

The use of chemical vapor deposition (CVD) techniques to grow films for use as coatings is well known. Recently, we employed this technique to grow germanium films for use as anti-reflection coatings for application in aviation optical systems.

Germane, GeH_4 , is a gas which thermally decomposes irreversibly on any surface heated above about 280°C to yield a germanium deposit (1-3). Hogness and Johnson (2), and Tamaru *et al.* (3) have reported studies on the kinetics of the thermal decomposition of germane by a static method. This method consists of using an isothermal vessel which is evacuated to less than 10^{-4} mm Hg. This vessel is attached to a mercury manometer and enables the decomposition of germane to be followed by measuring the initial pressure of germane as well as the final pressure (unreacted germane and hydrogen). Hogness and Johnson found the rate to be proportional to the one-third power of germane pressure at the higher temperatures (275°-375°C) with an inhibition by hydrogen in a lower temperature range (2). However, Tamaru *et al.* found zero and first order reactions (3). The zero and first order reactions were ascribed to heterogeneous and homogeneous decomposition processes, respectively.

Dumin (4), and Papazian and Reisman (5) have reported the epitaxial growth of germanium from the decomposition of germane on spinel and gallium arsenide substrates, respectively. Our germanium films were to be used as coatings on infrared glasses for application in the 8-14 μm region. These glasses have low softening temperatures, below 400°C, so it was necessary to have a low-temperature film growth. Single-crystal materials are obviously desirable; however, amorphous or small polycrystalline material can also have low loss due to surface or grain boundary scattering. If large-grain polycrystalline material is used the surface is rough and scattering is large.

This paper presents data on the kinetics of the thermal decomposition of germane in a dynamic system in a temperature range of 300°-450°C.

Experimental

The decomposition of germane was studied by measuring the rate of deposition of germanium as a function of substrate temperature and concentration of germane. The substrates used were single-crystal silicon wafers ($\langle 111 \rangle$ oriented; mechanically polished) and silicon wafers which had a 1000Å oxide coating. The substrates were cleaned prior to use by Caro's acid (mixture of 280 ml H_2SO_4 and 120 ml H_2O_2) and then rinsed thoroughly with deionized water. The wafers were left in deionized water until ready for loading into the reactor. The wafers were removed one at a time and blown dry with high-pressure nitrogen. The procedure is similar to that reported by Berkenblit *et al.* for the low temperature disproportionation of GeI_2 (6).

The thicknesses of the germanium films were obtained by partial masking of the film and removing the unmasked portion by use of a 35% solution of hydrogen peroxide at 50°C. The thicknesses were mechanically measured by use of the Talystep I. In general, the film thicknesses ranged from 2000 to over 20,000Å with the majority being between 10,000 and 20,000Å.

The reactor used was a horizontal quartz tube with an ID of 2 in. and approximately 12 in. in length. The system was rf heated by loading into a 5½ in. \times 1¾ in. \times ¾ in. carbide-coated graphite susceptor. The substrate temperatures were measured by use of an infrared radiation thermometer. Emissivity and absorption corrections were made for the silicon substrates and quartz tube (7, 8). Substrate temperatures ranged from 300° to 450°C. Uncertainty in temperature was less than $\pm 5^\circ\text{C}$. Nitrogen was used as the carrier and diluent gas and was kept at a flow of 1 liter/min for most of the studies. Pure germane (99.999%) was obtained from Matheson and was used without additional purification. The mole fraction was varied from approximately 3×10^{-3} to 30×10^{-3} , 3 to 30 cc/min.

Results and Discussion

At low temperatures (300°C) there was a difference in the growth rate on the oxidized and nonoxidized

* Electrochemical Society Active Member.
Key words: chemical vapor deposition, thin films, germanium, kinetics.

silicon substrates. The growth rates are 70 and 50 Å/min, respectively. The films were approximately 1000 Å thick. This may be due to a difference in nucleation on the two surfaces. However, at higher temperatures and concentrations (and much thicker films) there was no significant difference in growth rate on the two surfaces.

Figure 1 shows the effect of germane concentration on the growth rate at four different temperatures (300°, 350°, 375°, and 400°C). The log C vs. log R graph (concentration vs. growth rate) shows both zero and first order zones. Each data point represents at least two depositions. The deviation from the average growth rate was typically $\pm 5\%$ or less. At 300°C the slope is zero even at the highest concentration used; however, the higher the substrate temperature the lower the germane concentration need to obtain a zero slope. Growth rates varied from 70 Å/min at a low temperature and concentration to over 2600 Å/min at the highest temperature and concentration. At the higher temperatures and concentrations the decomposition becomes uncontrollable and "cracking or fallout" occurs. For depositions at 450°C and 1.6% germane concentration, the germane had decomposed on the walls of the reactor prior to reaching the monitor slice. This premature decomposition is ascribed as the reason for the bending of the first order curves towards zero slope at higher temperatures and concentrations. The data suggest that two kinds of reactions are taking place, zero and first order, with the former predominate at low temperature and/or low concentration and the latter predominate at high temperature and high concentration.

Figure 2 shows the effect of temperature on the deposition rate. The log R vs. $1/T$ plot provides an activation energy for both the zero and first order reactions. Applying the Arrhenius equation, activation energies of 0.75 ± 0.02 and 1.20 ± 0.02 eV (17 and 28 kcal) were obtained for the zero and first order reactions, respectively.

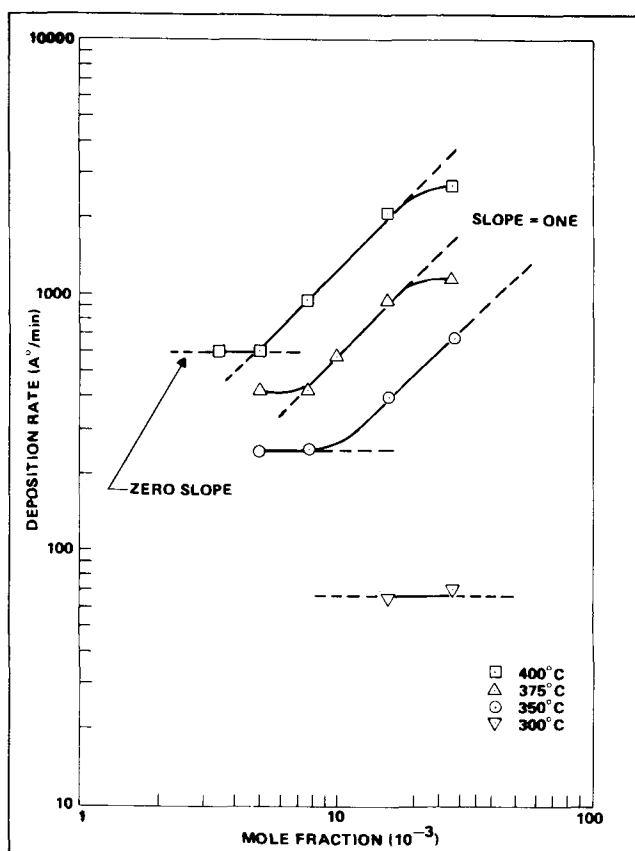


Fig. 1. Effect of germane concentration on deposition rate

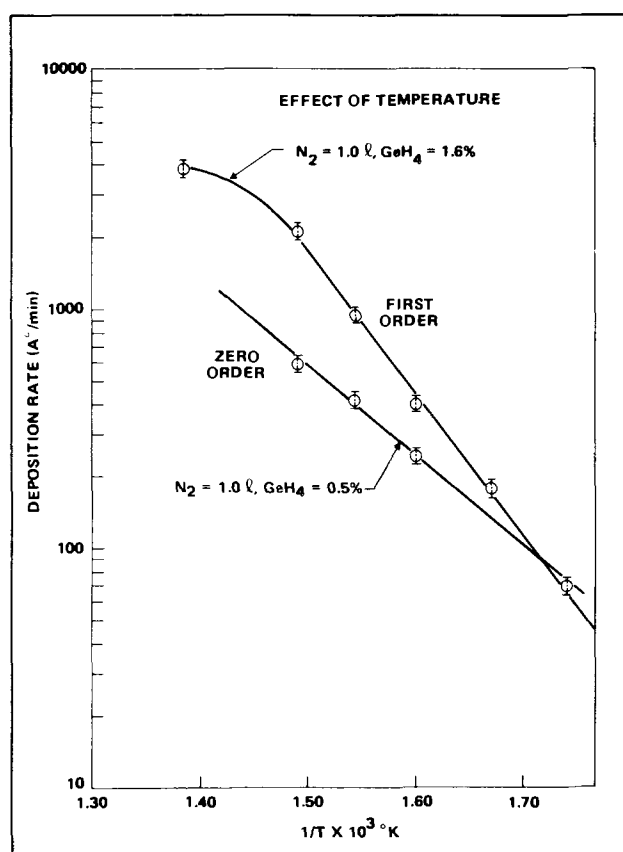


Fig. 2. Effect of substrate temperature on deposition rate

Tamaru *et al.* (3) suggested that in the static system the zero and first order reactions are taking place simultaneously and showed that the zero order reaction was heterogeneous decomposition at the substrate surface and the first order reaction was homogeneous decomposition in the gas stream (3). These conclusions appear to be valid for the dynamic system also. Figure 3a shows the surface smoothness of a film whose growth is predominately controlled by the zero order reaction. In Fig. 3b droplets are seen on the surface of a film whose growth is predominately controlled by the first order reaction; however, films with smooth surfaces could also be obtained from depositions which were predominately controlled by the first order (homogeneous) reaction.

This behavior may be understood by the following considerations. The following diagram (Fig. 4) shows a substrate with a heterogeneous and homogeneous reaction zone.

As long as the substrate surface is properly prepared (cleaned, etc.), a heterogeneous-controlled reaction will provide films with smooth surfaces. It is interesting that films obtained from conditions which indicate a homogeneous reaction have very smooth surfaces. If gas phase decomposition occurs sufficiently close to the surface then the decomposed germanium atoms can diffuse to the surface before large clusters are formed or "fallout" occurs. The quality of films obtained from this homogeneous reaction depends on the germane concentration and total flow rate.

The heterogeneous reaction is zero order. In addition, an increase in linear gas stream velocity has no effect on growth rate. The latter is in accordance with a surface controlled reaction as described by Reisman and Berkenblit (9). The fact that the homogeneous and heterogeneous reactions are proceeding simultaneously makes it difficult to determine the rate controlling process for the homogeneous reaction. If an isothermal reactor is used to study the homogeneous decomposition of germane, it is expected that the amount of

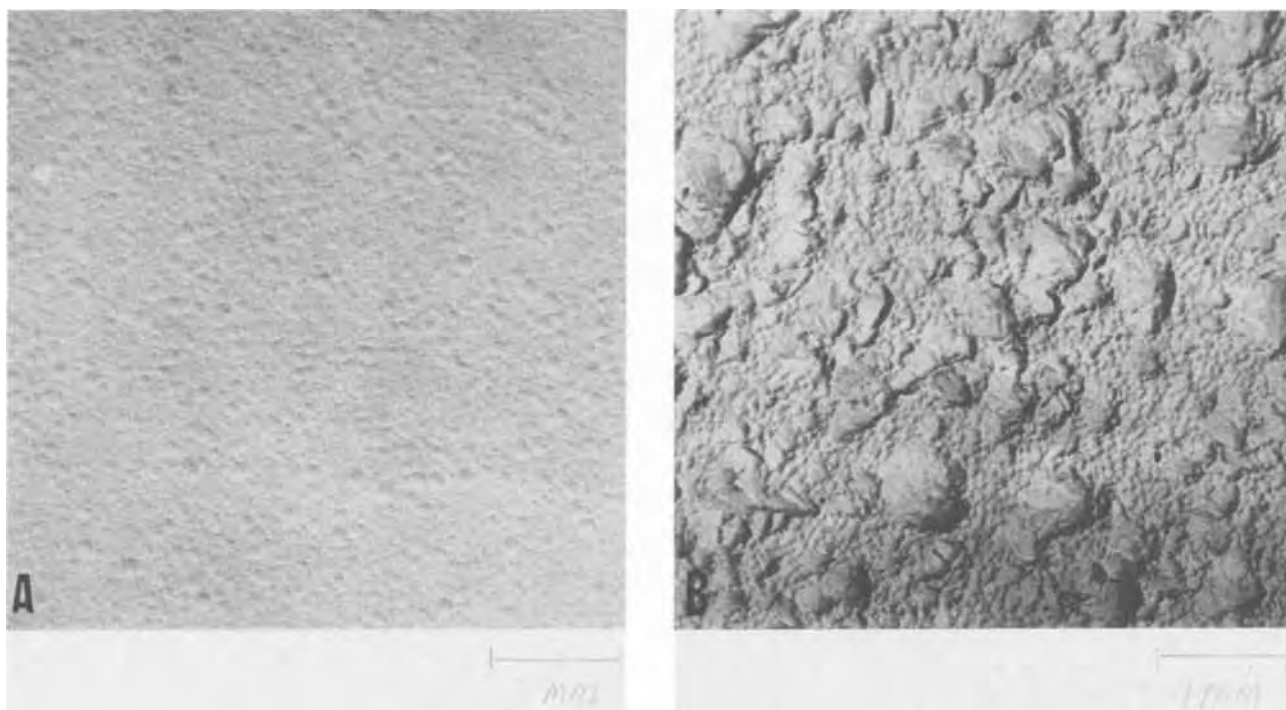


Fig. 3. Electron micrographs showing the surface of germanium films deposited on single crystal silicon substrates. Replica techniques were used. A, 300°C substrate temperature, 1.6% Ge, 7500Å; B, 375°C substrate temperature, 1.6% Ge, 7500Å.

germane decomposed would be a function of both the temperature and germane concentration. However, in the present study there is a temperature gradient from the susceptor to the walls of the reactor, T_s (substrate temperature) and T_w' (a temperature d distance away from the substrate) (see Fig. 4). Decomposition begins for any gas which passes through this zone (for the homogeneous case). The greater the flux of germane into this zone the faster the decomposition. Several factors can lead to an increase in decomposition rate of germane in the homogeneous zone. These are: (i) an increase in total flow, keeping the germane concentration constant, (ii) an increase in germane concentration, keeping the total flow constant, and (iii) an increase in the zone dimensions, *i.e.*, d in Fig. 4. However, the total flow can also affect the size and shape of the homogeneous zone, *e.g.*, through cooling. Depending upon several factors, *e.g.*, total flow rate and geometry of homogeneous zone, the decomposed germanium may not reach the substrate. The germanium could be deposited either upstream or downstream of the monitor wafer. Experimentally we have observed both an increase and decrease in growth rate with increase in total flow.

As long as the homogeneous zone has a small d , decomposed germanium atoms apparently can diffuse to the surface and become part of the deposited film before large clusters are formed or "fallout" occurs.

A large difference was noted in activation energies reported here and by Tamaru *et al.* for the static studies (3). The differences between activation energies [$(E_a^1 - E_a^0)_{\text{static}} = (E_a^1 - E_a^0)_{\text{dynamic}}$] for the zero and first order reactions are the same for both the static and dynamic system, but there is a significant difference between activation energies ($E_{a^1}^{\text{static}} = 51$ kcal/mole, $E_{a^1}^{\text{dynamic}} = 28$ kcal/mole). Dumin

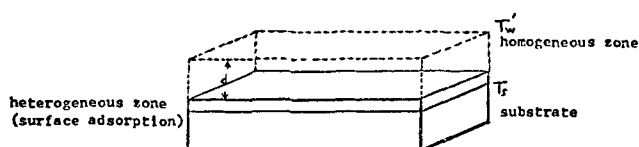


Fig. 4. Heterogeneous and homogeneous reaction zones

has studied the decomposition of germane in hydrogen in a temperature region of 575°-750°C and reported an activation energy of 47.5 kcal/mole (4).

The decomposition of germane, GeH_4 , has the products of solid germanium and hydrogen gas. Both the static decomposition of germane and the epitaxial growth of germanium from germane and hydrogen are similar in that hydrogen might be expected to act in a similar fashion. A flowing nitrogen ambient may condition the surface differently than H_2 , and in addition sweep the hydrogen by-products away from the surface. Also, nitrogen gas occupies the major portion of the gases in the reaction zones in this study and certain normal or activated properties of N_2 may have a definite effect on the activation energy. We have observed an increase in growth rate of approximately 30% for silicon dioxide films when grown in nitrogen as compared to growth in argon (10).

The data presented supports an effect of nitrogen, impurity less than 5 ppm combined H_2O and O_2 , on either the mechanism of decomposition, or through an activated species, the activation energy.

Still, the effect of impurities, or the possibility that the homogeneous (or heterogeneous) process may not be kinetically controlled and mass transport is occurring cannot be completely eliminated as factors in the lowering of the activation energies relative to previous work.

Conclusion

The growth of germanium films from the thermal decomposition of germane in nitrogen was studied and the decomposition was found to proceed by two different reactions, a zero and first order reaction. These were ascribed to heterogeneous and homogeneous processes. Activation energies were calculated and found to be 0.75 eV and 1.2 eV, respectively, for the zero and first order reactions. The decomposition obtained by a static method (3) was compared to that obtained in the dynamic system, and the results are similar.

Acknowledgments

The author wishes to thank Don Shaw for helpful discussions of the results and Imogene Killen for technical assistance.

This work has been partially supported by the Air Force Aeronautical Systems, Wright Patterson AFB under Contract F33615-71-C-1891.

Manuscript submitted March 16, 1972; revised manuscript received June 5, 1972.

Any discussion of this paper will appear in a Discussion Section to be published in the June 1973 JOURNAL.

REFERENCES

1. R. B. Corey, A. W. Laubengayer, and L. M. Dennis, *J. Am. Chem. Soc.*, **47**, 112 (1925).

2. T. R. Hogness and W. C. Johnson, *ibid.*, **54**, 3583 (1933).
3. K. Tamaru, M. Boudart, and H. Taylor, *J. Phys. Chem.*, **59**, 801 (1955).
4. D. J. Dumin, *This Journal*, **114**, 749 (1967).
5. S. A. Papazin and A. Reisman, *ibid.*, **115**, 961 (1968).
6. M. Berkinblit, A. Reisman, and T. B. Light, *ibid.*, **115**, 966 (1968).
7. F. G. Allen, *J. Appl. Phys.*, **28**, 1510 (1957).
8. F. Jona and H. R. Wendt, *ibid.*, **37**, 3637 (1966).
9. A. Reisman and M. Berkenblit, *This Journal*, **113**, 146 (1966).
10. L. H. Hall, Unpublished results.

Nitride Layer Growths on Liquid Thorium and on Solid Thorium Carbon Alloys

R. Benz

Los Alamos Scientific Laboratory, University of California, Los Alamos, New Mexico 87544

ABSTRACT

Nitride layers were formed on thorium-carbon alloys by reaction with nitrogen (1-1600 Torr) at temperatures between 1400° and 2400°C. Values of scale thicknesses of face-centered cubic (fcc) ThN on liquid thorium and of Th(C,N) on solid alloys with C/Th = 0.10, 0.20, and 0.30 were found to be proportional to the square-root of time of reaction indicating growth rates are controlled by diffusion. Calculated composition-average values of concentration-gradient type interdiffusion coefficients in pure ThN at 1900°, 2100°, and 2400°C can be represented by the equation $D = 254 \exp(-99.4 \pm 30 \text{ kcal/mole})/RT$. Diffusion coefficients in the Th(C,N) layers are approximated by the same method: cross effects due to presence of carbon are neglected. The results show that the nitrogen diffusion rate in Th(C,N) increases with carbon content and with decreasing nitrogen pressure. Nitrogen-rich Th(C,N) layers formed on alloys with C/Th ratio $\cong 0.4$ are preceded by a carbon-rich front containing ThC₂ precipitate. This observation together with the assumption of negligible mobility of thorium atoms leads to the conclusion that carbon diffuses "uphill" against a concentration gradient. The phenomena also occurs in the analogous U(C,N) phase during reaction under similar conditions. With increasing carbon content, nitrogen diffusion is suggested to change from a vacancy mechanism in pure ThN to a substitution mechanism in carbon-rich Th(C,N).

In a recent investigation of the Th-C-N system (1), equilibration of thorium-carbon alloys with nitrogen was observed to be extremely slow under certain conditions. The usual solution to an equilibration problem of increasing the anneal time proved unsuccessful. For example, increasing the holding time of 1-mm chips of ThC in 1 atm N₂ at 1800°C from 6 to 600 hr did not give products perceptibly closer to equilibrium. Explanation of this difficulty, as may be seen in the results of this investigation, is that atomic fluxes during the reaction are coupled causing an "uphill" diffusion of carbon (diffusion up a concentration gradient) and consequently to segregation of carbon and thorium. Darken first reported having observed "uphill" diffusion in austenitic steels (2). It also occurs in uranium-carbon alloys reacting with nitrogen. The phenomena, which can occur in systems with three or more components, may be more prevalent than has been previously supposed.

In what follows, nitride layers are described which form on thorium-carbon alloys by reaction with nitrogen. At nitrogen pressures below the decomposition pressure of Th₃N₄, the reaction rate is controlled by diffusion and no evidence for outward migration of thorium is observed. Under this condition, the growing nitride layer may be either single-phase face-centered cubic, fcc, Th-ThC-ThN solid solution, denoted

Th(C,N), two distinct Th(C,N) phases, or a mixture of Th(C,N) and monoclinic ThC₂ and/or ThCN. Important for interpretation of diffusion processes occurring in the growing layer is a knowledge of the thorium-carbon-nitrogen phase diagram (1) and the composition at the outer surface of the growing layer. The latter information was obtained from results of equilibration experiments which are described first.

Experimental

Materials.—Alloys were prepared with crystal-bar thorium metal (Metal Hydrides, Division of Ventron Corporation, Beverly, Massachusetts), spectroscopic graphite (National Carbon Company, Union Carbide Corporation, Fostoria, Ohio), and prepurified nitrogen (Big Three Industrial Gas and Equipment Company, Houston). Thorium metal specimens and thorium-carbon alloys were arc melted by P. L. Stone as previously described (3). Powder ThN was obtained by vacuum decomposition of Th₃N₄ (4).

Apparatus and procedure.—Specimens were placed in a tungsten crucible which was heated by induction in a vacuum chamber. Equilibration experiments were thus made with finely divided powders of the appropriate thorium-carbon alloy. The powder was equilibrated with nitrogen at selected pressures and quenched in a stream of helium. Compositions of the fcc Th(C,N) phase coexisting with ThC₂ and with ThCN were determined from unit cell dimensions with the assump-

Key words: diffusion in ThN, diffusion in ThN-ThC solid solutions, uphill diffusion, decomposition pressure of Th₃N₄, decomposition pressure of ThCN.

tion of a linear variation from the value of 5.159 Å in pure ThN to 5.346 Å in pure ThC. Nitrogen decomposition pressures of Th_3N_4 , carbon-rich Th_3N_4 , and ThCN were determined with powder ThN, $\text{ThC}_{0.20}$, and $\text{ThC}_{1.00}$, respectively. The experiments were carried out at a series of different nitrogen pressures for a given temperature and the decomposition pressure was deduced from x-ray diffraction pattern determinations of the presence or absence of the respective phases in samples of the products. Layer growths of ThN on liquid thorium were made with the thorium spheroids supported on a bed of ThN powder. They were reacted in nitrogen at selected temperatures and quenched in a stream of helium. Ternary nitride layer growths were made with alloy chips having dimensions of $3 \times 3 \times 4$ mm. Each specimen was heated for a selected period of time in nitrogen at a fixed pressure and quenched in the same way. Layer thicknesses were measured with a microscope disk calibrated with a vernier.

Results

Equilibration experiments.—Room temperature unit cell dimensions, a_0 , of powders which had been equilibrated with various nitrogen pressures and at various temperatures are listed in column 3 of Table I. Values of x in the formula $\text{ThC}_{1-x}\text{N}_x$ were calculated with the assumption of a linear dependence on a_0 and are shown in column 4. As seen in the phase diagrams illustrated in Fig. 1 and 2, the extent of solution of nitrogen in ThC_2 is less than 1% and the amount of carbon that can precipitate (as ThC_2) from the nonmetal saturated $\text{Th}(\text{C},\text{N})$ on cooling is comparatively small too. Thus the $\text{Th}(\text{C},\text{N})$ phase at temperature can also be represented to a good approximation by the formula $\text{ThC}_{1-x}\text{N}_x$ with the same room temperature values of x .

The nitrogen decomposition pressure at a given temperature was taken as the lowest nitrogen pressure at which the nitrogen-rich phase was identified in quenched products. The thus determined decomposition pressures of pure Th_3N_4 , of Th_3N_4 [$+$ ThCN + $\text{Th}(\text{C},\text{N})$], i.e., Th_3N_4 coexisting with ThCN + $\text{Th}(\text{C},\text{N})$, and of ThCN [$+$ ThC_2 + $\text{Th}(\text{C},\text{N})$], i.e.,

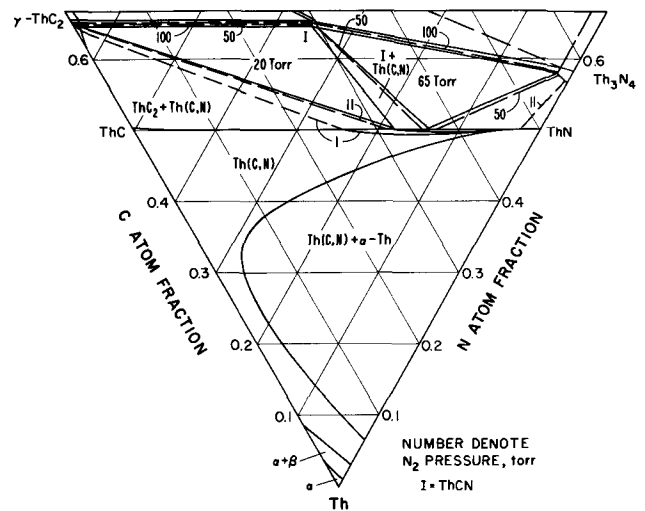


Fig. 1. Thorium-carbon-nitrogen 1600°C phase diagram and pressure isotherms.

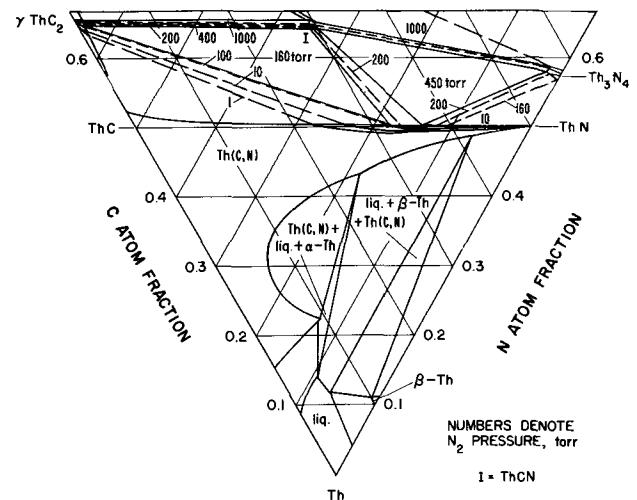


Fig. 2. Thorium-carbon-nitrogen 1800°C phase diagram and pressure isotherms.

Table I. Room-temperature fcc lattice parameters and x values of nonmetal-saturated $\text{Th}(\text{C},\text{N})$, $\text{ThC}_{1-x}\text{N}_x$, after equilibration with nitrogen at various pressures and temperatures

Temperature, °C	p_{N_2} , Torr	$a_0 \pm 1 \text{ mÅ}^*$	x
2200	1000	5.218	0.683
	100	5.251	0.485
	10	5.293	0.283
	1	5.328	0.096
2000	1400	5.224	0.651
	1000	5.224	0.651
	100	5.241	0.560
	10	5.265	0.432
1900	440	5.222	0.661
	100	5.224	0.651
	10	5.262	0.448
	1	5.274	0.384
1800	180	5.224	0.651
	100	5.225	0.645
	10	5.246	0.533
	1	5.260	0.459
1700	59	5.220	0.672
	10	5.237	0.581
	1	5.280	0.352
	1600	18	5.224
10		5.227	0.635
1		5.248	0.523
1500		5	5.227
	1	5.230	0.619

* These are values extrapolated to $\theta = 90^\circ$ by the Nelson-Riley function with the computer program of Vogel and Kemper (13).

ThCN coexisting with ThC_2 + $\text{Th}(\text{C},\text{N})$, are plotted in Fig. 3. Based on the results listed in Table I and Fig. 3, pressure isotherms at 1600° and 1800°C were deduced. These are shown schematically in Fig. 1 and 2 respectively.

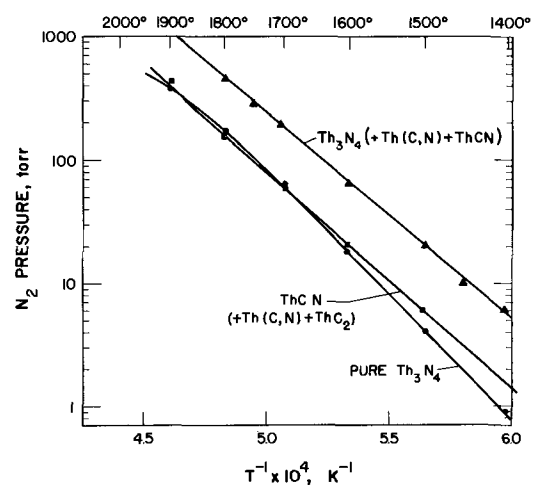


Fig. 3. Nitrogen decomposition pressures of pure Th_3N_4 , Th_3N_4 coexisting with ThCN + $\text{Th}(\text{C},\text{N})$, and ThCN coexisting with $\text{Th}(\text{C},\text{N})$ + ThC_2 as a function of temperature.



Fig. 4. Photomicrograph of a typical ThN scale growth that was formed on liquid thorium in 1520 Torr nitrogen at 2100°C (X100).

ThN scales formed on liquid thorium.—At first attempts were made to form diffusion-controlled scale growths of ThN on solid thorium. ThN scales which were formed on thorium at temperatures of 1400°–1700°C were found, however, always to be porous indicating that ThN scales do not grow by diffusion.

Next, experiments were made to produce diffusion-controlled ThN scale growths on liquid thorium analogous to those previously described to produce diffusion-controlled UN layer growths on liquid uranium metal (5). The resulting ThN scales were dense. A typical scale growth is illustrated in Fig. 4. Layer thicknesses, x_s , corrected for a small thermal contraction as calculated with high-temperature x-ray diffraction data (6) are listed in column 4 of Table II. The nitrogen pressures and times at temperature, t , are listed in columns 2 and 3, respectively.

Th(C,N) scales formed on solid alloys with C/Th = 0.10, 0.20, and 0.30.—Based on high-temperature x-ray diffraction results (6) and the thorium-carbon-nitrogen phase diagram (1), volume difference between Th(C,N) and coexisting α -thorium is expected to diminish with increasing carbon content. The difference, of course, becomes zero at a critical composition where the two phases merge into a single phase, e.g., where the carbon atom fraction reaches the value of about 0.3 at 1800°C as seen in Fig. 1. Simultaneously, lattice strains induced by volume change when thorium-carbon alloys react with nitrogen may be expected to diminish with increasing C/Th ratio and eventually yield scales free of voids.

Table II. ThN reaction-layer data and composition-average chemical interdiffusion coefficients

Temperature, °C	Nitrogen pressure, atm	Time, hr	x_s , μm	u	\bar{D} , cm^2/sec
1900	0.4	0.33	9.5	0.0872	2.5×10^{-8}
		1.00	15.0		
		4.00	33.0		
2100	2.00	0.25	22.0	0.0923	16.0
		1.00	44.0		
		4.00	101.0		
	0.20	0.25	22.0	16.0	
		1.00	48.0		
		4.40	101.0		
2400	2.00	0.125	52.0	0.0939	170.0
		0.500	111.0		
		0.750	133.0		

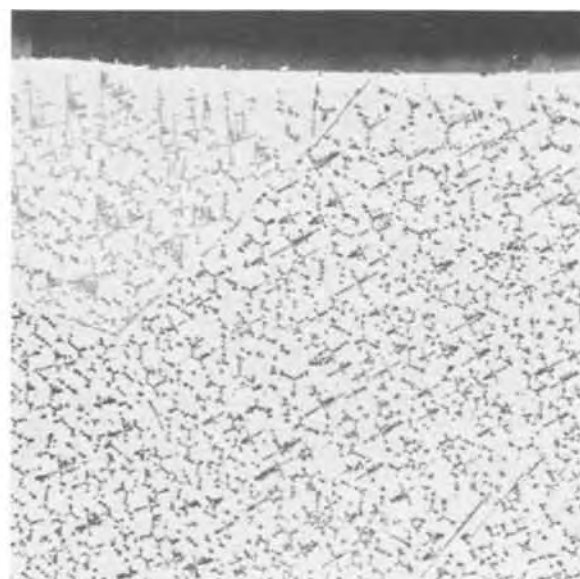


Fig. 5. Photomicrograph of a scale growth on a thorium-carbon alloy with C/Th = 0.1 after annealing in 90 Torr nitrogen at 1750°C. No porosities are seen in the faintly visible surface fcc Th(C,N) phase (top). Precipitate particles of Th(C,N) are seen in the central thorium-rich phase (bottom area) (X100).

Experiments were made to form nitride scales on rectangular-shaped thorium-carbon alloys with the dimensions $3 \times 3 \times 4$ mm. The scales formed on alloys with C/Th = 0.05 were found to be porous but the porosity was less than that formed on carbon-free solid thorium metal. No porosity was at all perceptible in scales grown on alloys with C/Th = 0.10 to 0.40 providing the nitrogen pressure during reaction did not exceed the decomposition pressure of $\text{Th}_3\text{N}_4 + \text{ThCN} + \text{Th(C,N)}$. Microstructure of a typical scale is seen in Fig. 5. Th(C,N) scales were grown on alloys with C/Th = 0.10, 0.20, 0.30 by reaction with nitrogen at the $\text{ThCN} + \text{ThC}_2 + \text{Th(C,N)}$ decomposition pressure and the temperatures of 1400°, 1500°, 1600°, 1700°, 1750°, and 1800°C. The anneal times and resulting layer thicknesses are listed in columns 4 and 5 of Table III. In addition, one measurement was made with the lower pressure of 2 mm at 1600°C and the results are listed in row 15 of Table III. The scale thicknesses grown in 19 Torr N_2 at 1600°C are proportional to the square root of time at temperature. Other conditions being the same, the thicknesses are greater in alloys with higher C/Th ratios. This effect results, in part, from

Table III. Th(C,N) reaction-layer data and composition average interdiffusion coefficients

Temperature, °C	p_{N_2} , Torr	Alloy C/Th	Time, hr	x_s , μm	u	\bar{D} , cm^2/sec
1800	150	0.20	0.5	32	0.45	66×10^{-10}
1800	150	0.30	0.5	37	0.517	
1750	100	0.20	0.5	30	0.17	44
1750	100	0.30	0.5	66	0.36	53
1700	50	0.10	0.5	5.5	0.13	25
1700	50	0.20	0.5	7	0.15	32
1600	19	0.10	16	11	0.11	4.2
1600	19	0.20	0.1	1	0.12	4.8
1600	19	0.20	4.2	7	0.12	5.4
1600	19	0.20	16.1	12	0.12	4.4
1600	19	0.30	0.1	2	0.18	8.0
1600	19	0.30	1.0	6	0.18	7.7
1600	19	0.30	4.2	12	0.18	7.7
1600	19	0.30	16.1	26	0.18	8.7
1600	2	0.10	16	16	0.11	9
1500	5	0.10	12.6	5	0.15	1.02
1400	0.8	0.10	2	1.3	0.12	0.50
1400	0.8	0.20	2	1.6	0.18	0.63

decreasing width of the thorium Th(C,N), two-phase region and, in part, from subsequently described increasing rate of diffusion with increasing C/Th ratios.

Information on the direction of nitrogen diffusion was obtained by comparison of x-ray diffraction powder patterns of samples taken from the outer surfaces with those taken from the centers of reacted specimens. The results revealed no evidence for carbon to redistribute during the reaction. The direction of nitrogen flux in Th(C,N) scales is concluded to coincide with directions of nearly constant C/Th ratio. The directions are presumably parallel to isochemical potential curves of carbon. Representative nitrogen paths are illustrated in Fig. 6 on the 1600°C isotherm. The diffusion paths in alloys with C/Th ratio up to 0.40 begin on the nitrogen-rich boundary of Th(C,N). The diffusion paths in Fig. 6 cross the Th(C,N) phase in a skewed path deviating slightly from paths of the constant C/Th ratio as previously inferred from lattice parameter data. The slight skewing is suggested on the basis of the course of the $\text{ThCN} + \text{ThC}_2 + \text{Th(C,N)}$ decomposition pressure isotherm according to which the most stable and equilibrium composition of Th(C,N) assumed to prevail at the outer surface of the reaction layer is $\text{ThC}_{0.35}\text{N}_{0.65}$. The diffusion paths in Fig. 6 terminate in the nitrogen-rich boundary of α -thorium in accord with the observation that composition gradients level rapidly in the latter phase.

Reaction layers formed on alloys with C/Th > 0.4.—

Observations with alloys in this composition region are mostly qualitative but cover a wide range of composition in the ternary phase diagram and form an important basis for an interpretation of the diffusion mechanism in Th(C,N). Reaction layers very often consisted of complex mixtures of phases. Unless stated otherwise, only reactions in nitrogen at the $\text{ThCN} + \text{ThC}_2 + \text{Th(C,N)}$ decomposition pressure are described. Reaction with alloys having C/Th = 0.4 to 1.0 produce a surface layer of nitrogen-rich Th(C,N) having a nitrogen content only slightly lower than that which was found on the previously described alloys with lower carbon content. Microstructures of the reaction layers differ from the previously described ones in having ThC₂ precipitate present in the Th(C,N) forming a continuous series of solid solutions between the outer surface and the central alloy composition. Reaction in nitrogen at lower pressures yielded surface Th(C,N) with lower nitrogen content and the ThC₂ precipitate was distributed over a broader region. Based on these observations representative nitrogen diffusion paths were drawn as illustrated in Fig. 6. In specimens with the lower C/Th ratios of 0.4 to 0.8

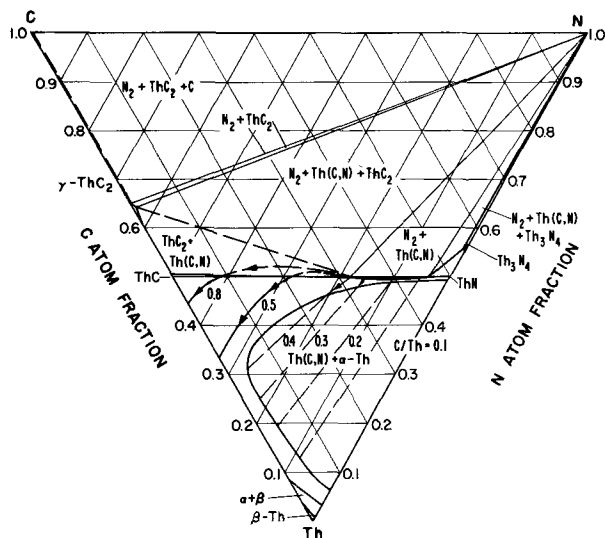


Fig. 6. Typical nitrogen diffusion paths in 19 Torr nitrogen on the thorium-carbon-nitrogen 1600°C isotherm.

nitrogen penetration depths were greater and the ThC₂ precipitate appeared as small particles in relatively minor proportions as illustrated in Fig. 7. In alloys with the higher carbon contents of C/Th = 0.9 and 1.0 the ThC₂ precipitate appeared as a continuous layer such as seen in Fig. 8.

Net nitrogen uptake by ThC_{1.00} in 1 and in 100 Torr nitrogen was determined. The specimens experienced weight gains of 5.0 and 4.2 mg nitrogen, respectively, in ½ hr at 1800°C. Microscopic examination of the products revealed a small amount of ThC₂ at the Th(C,N) grain boundaries.

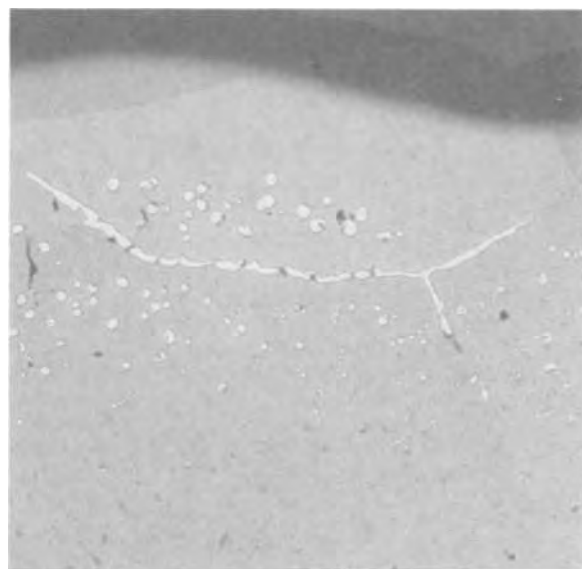


Fig. 7. Photomicrograph of an alloy with C/Th = 0.40 after annealing in 150 Torr nitrogen at 1800°C and quenching. The nitrogen is near the ThCN + Th(C,N) + ThC₂, three-phase, equilibrium pressure. Precipitate particles of ThC₂ (light area) are seen embedded in Th(C,N). The ThC₂ particles formed at temperature showing that carbon was displaced inward by flux of nitrogen in the Th(C,N) phase (X100).

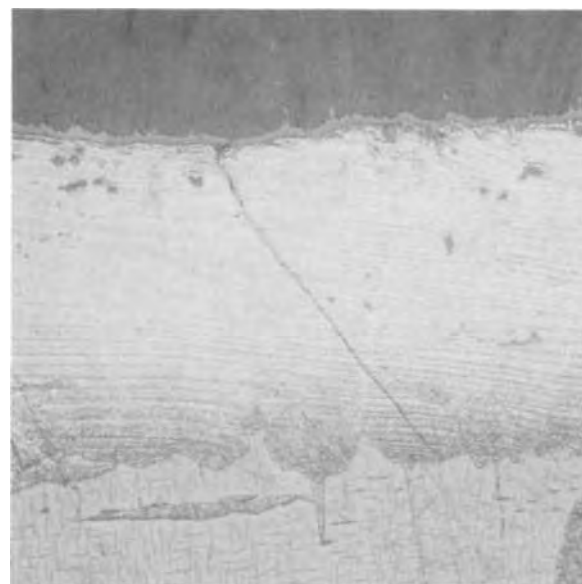


Fig. 8. Photomicrograph of an alloy with C/Th = 1.00 after annealing for 9 hr in 1520 Torr nitrogen at 1500°C and quenching. The nitrogen pressure exceeds the ThCN + ThC₂ + Th(C,N) and the Th₃N₄ + Th(C,N) + ThCN equilibrium pressures. The sequence of phase layers beginning with the outer layer at top (dark area) is Th₃N₄ + ThCN → Th(C,N) → ThC₂ (+ small amount of ThCN) → ThC (X300).

Discussion

Diffusion coefficients in the binary ThN phase.—Concentration-gradient type interdiffusion coefficients were calculated with the equation

$$\bar{D} = x_s^2/4tu^2 \quad [1]$$

as previously described (5) [see also Jost (7a)]. Values of the parameter u , as listed in column 5 of Table II, were calculated from the equation

$$(X_{N''} - X_{N'}) / (X_{N''} - X_{N^0}) = \pi u \exp u^2 \operatorname{erf} u \quad [2]$$

in which the value of the nitrogen atom fraction in ThN at the gas-scale interface was taken as $X_{N''} = 0.500$, that in ThN at the scale-liquid interface was taken as $X_{N'} = 0.494$ corresponding to N/Th = 0.975 (4), and values of the nitrogen atom fraction in the liquid thorium-nitrogen alloys, X_{N^0} , were calculated from published liquidus data (4). According to Wagner (8), the symbol \bar{D} represents an average value

$$\bar{D} = \frac{1}{X_{N''} - X_{N'}} \int_{X_{N'}}^{X_{N''}} \tilde{D} dX_N \quad [3]$$

of the local interdiffusion coefficient \tilde{D} . The calculated \bar{D} values as listed in column 6 of Table II can be represented by the equation

$$\bar{D} (\text{cm}^2/\text{sec}) = 254 \exp(-99.4 \pm 30 \text{ kcal/mole})/RT \quad [4]$$

where T denotes temperature in degrees Kelvin, indicating an effective activation energy for diffusion of 99.4 kcal/mole. The latter value may be compared with 120 ± 25 kcal/mole reported for the analogous UN phase (5).

The \bar{D} values for ThN at 2100°C are seen in Table II to be essentially the same for 0.20 as for 2.00 atm nitrogen, a ten-fold difference in nitrogen pressure (p_{N_2}). Values of \bar{D} for the analogous UN phase at elevated temperatures have also been reported to be insensitive to changes in p_{N_2} in the same pressure range (5). This is consistent with our observations that the composition of neither ThN nor UN changes appreciably with equilibrium p_{N_2} in the stated pressure range. It is also compatible with a vacancy mechanism for nitrogen diffusion as proposed for UN (5) and as suggested for the ThN phase, if one assumes in accord with observations, that the N/metal ratio does not exceed the stoichiometric value of one in 2 atm nitrogen. Flux rate of nitrogen in a binary phase can be written

$$j_N = -\frac{D_N^S C_N}{RT} \frac{d}{dx} \mu_N \quad [5]$$

where D_N^S denotes nitrogen self-diffusion coefficient and C_N is the nitrogen concentration (gram-atoms/cubic centimeter). Other things being equal, a ten-fold increase in p_{N_2} corresponding to an increase in μ_N by some 5 kcal/mole might be expected to appreciably increase the observed j_N value, whereas j_N is in fact insensitive to changes in p_{N_2} from 0.20 to 2.00 atm. Qualitatively, this comes about because, according to the vacancy theory of diffusion, D_N^S is proportional to the concentration of nitrogen vacancies (N_v) and an increase in p_{N_2} decreases N_v and, therefore, decreases D_N^S so as to compensate for the increase in the effective $d/dx \mu_N$. Reported composition average values of D_N^S [denoted $\bar{D}_{s,ON}$ in Ref. (5)] as deduced with the aid of Eq. [5] for UN are lower in value for $p_{N_2} = 2.00$ than for $p_{N_2} = 0.20$ atm by a factor of about 5 (5).

Diffusion coefficients in the ternary Th(C,N) solid.—The Onsager equations describing one-dimensional isothermal fluxes (gram-atom/square centimeter-second) of carbon and nitrogen relative to thorium are, respectively

$$j_C = -k_{C,C} \frac{\partial}{\partial x} \mu_C - k_{C,N} \frac{\partial}{\partial x} \mu_N \quad [6]$$

$$j_N = -k_{N,C} \frac{\partial}{\partial x} \mu_C - k_{N,N} \frac{\partial}{\partial x} \mu_N \quad [7]$$

at each point in the isotropic solid. The instantaneous chemical potential gradient of the general component i representing either carbon or nitrogen in the direction of flow is $\partial/\partial x \mu_i$ and the coefficients k_{ij} are generally functions of composition, pressure, and temperature. Transformations to other reference coordinate systems, as is well known, do not change the form of the flux equations, but do generally change the k_{ij} values.

Acquisition of data to integrate the flux equations is a formidable task and, as usual, simplifying assumptions are made to describe behavior under limiting conditions. With assumptions of negligible drift velocity of thorium and of negligible volume change,¹ flux of thorium relative to an ordinary coordinate system such as one fixed to the outer surface of the solid can be written

$$J_{Th} = -K_{Th,C} \frac{\partial}{\partial x} \mu_C - K_{Th,N} \frac{\partial}{\partial x} \mu_N = 0 \quad [8]$$

It follows that measurements of j_C and j_N , defined relative to thorium, are identical to those measured relative to the surface coordinate system of reference. Thus, $k_{ij} = K_{ij}$ and fluxes referred to the coordinate system fixed at the system's surface can be written

$$j_C = -K_{C,C} \frac{\partial}{\partial x} \mu_C - K_{C,N} \frac{\partial}{\partial x} \mu_N \quad [9]$$

$$j_N = -K_{N,C} \frac{\partial}{\partial x} \mu_C - K_{N,N} \frac{\partial}{\partial x} \mu_N \quad [10]$$

Only Eq. [10] is used in the subsequent analysis. It simplifies in the two limiting cases that nitrogen diffuses in directions parallel to the thorium or to the carbon isochemical potential curves. When nitrogen diffuses at all points in directions of constant μ_{Th} , Eq. [10] becomes

$$j_N = -D' \frac{\partial}{\partial x} X_N \quad [11]$$

where $D' = [K_{N,N} - K_{N,C} X_N/X_C] \partial/\partial X_N \mu_N$, X_C and X_N are the carbon and nitrogen atom fractions, and μ_N is a function of the single composition variable X_N in view of the pseudobinary character of the system. In the second case, nitrogen diffuses in a direction sufficiently close to curves of constant μ_C and Eq. [10] can be written

$$j_N = -D \frac{\partial}{\partial x} X_N \quad [12]$$

where $D = K_{N,N} \partial/\partial X_N \mu_N$.

Along the diffusion paths in nitrogen-rich Th(C,N) the fcc unit cell dimensions change only very little so that volume changes can be neglected. Equation [12] with D a constant is assumed to describe the diffusion of nitrogen in the nitrogen-rich Th(C,N) scales. Solution to the diffusion problem is analogous to that previously described for nitrogen diffusion in pure ThN. Value of \bar{D} were calculated from observed scale thicknesses with Eq. [1] and u values were calculated with Eq. [2]. The nitrogen atom fractions in Th(C,N) at the Th(C,N)-gas interface was obtained with the formula $X_{N''} = \frac{1}{2}(1 - [C/Th])$, where C/Th denotes the carbon-to-metal ratio of the initial alloy. The nitrogen atom fraction in Th(C,N) at the alloy-scale interface,

¹ The discussion has to be qualified because volume changes in Th(C,N) can be finite. Extreme fractional change in volume that can occur on the ThC-ThN tie line is given by the fractional volume difference between pure ThC and ThN: $\frac{V_{ThC} - V_{ThN}}{V_{ThN}} = 0.11$

X_N' , and that in the central alloy, X_N^0 , were calculated for the initial C/Th ratios and published phase diagrams (1). \bar{D} values thus deduced for alloys having various initial C/Th ratios are listed in column 7 of Table III and are plotted in Fig. 9 where results obtained with pure ThN are also shown. The \bar{D} values for the alloys have a greater uncertainty than those for pure ThN because of greater uncertainty in the X_N values. Precision of the results, however, shows that the \bar{D} tend to higher values in alloys with higher C/Th ratios. The results in rows 7 and 15 of Table III show that the effect of lowering the nitrogen pressure at 1600°C is to increase the \bar{D} value from 4.2×10^{-10} cm²/sec (row 7) in 19 Torr to 9×10^{-10} cm²/sec (row 15) in 2 Torr nitrogen. Increase of \bar{D} with decreasing nitrogen pressures is in accord with the postulated vacancy diffusion mechanism because an increase in nonmetal vacancy concentration occurs in the Th(C,N) phase in nitrogen at lower pressures and this can increase rate of transport. The vacancy mechanism explains the very high rates of diffusion in the extreme metal-rich alloys.

Reaction of an alloy with C/Th = 0.4 at the same low nitrogen pressure of 2 Torr at 1600°C produced a distinct enrichment of carbon in the outer part of the Th(C,N) scale. Based on lattice parameter values obtained with samples, the C/Th ratios are roughly estimated as 0.55 in the surface and 0.25 in the center of the specimen. Redistribution of carbon was not observed in scales formed on alloys with C/Th = 0.1 and 0.2 that had been reacted under otherwise the same conditions. Based on an extension of the analysis of Wagner (9) and reported free energy of mixing ThC and ThN (10) valid at more elevated temperatures, the redistribution of carbon in the Th(C,N) scale leads to the conclusion that $D_{S_C}^S > D_{S_N}^S$. This result has to be regarded as tentative, however, because the composition of Th(C,N) scales produced under the described conditions deviates considerably from that of a dilute solution of thorium in the monocompound $\text{ThC}_{1-x}\text{N}_x$.

Rates of diffusion of nitrogen in nonmetal-rich Th(C,N) can be calculated from the nitrogen uptake data at 1800°C. Nitrogen diffusion in nonmetal-sat-

urated Th(C,N) is tentatively assumed to be described by Eq. [11] with D' constant. The assumption of constant μ_{Th} leading to Eq. [11] may not be strictly correct. In justification, one can argue on physical grounds that variation of μ_{Th} is probably not large. As may be seen in the final results, D' is not constant but varies with composition. The values to be determined, therefore, are composition averages and are denoted by \bar{D}' . As previously noted the composition of Th(C,N) coexisting with ThC_2 is close to the ThC-ThN tie line. Thus, the surface composition in the diffusion specimens can be described to a good approximation as a ThC-ThN solid solution and, based on Table I, consists of 54.1 and 35.5 m/o (mole per cent) ThC in 1 and 100 Torr N_2 , respectively. Values of \bar{D}' were calculated on the assumption of semi-infinite diffusion with the equation $\bar{D}' = \pi/t (q/2aC^s)^2$ (7b), where q is the gram atoms of nitrogen absorbed in time t and C^s is the surface concentration of nitrogen (gram-atom/cubic centimeter). The \bar{D}' values thus obtained are 5.3×10^{-8} cm²/sec in 1 Torr and 1.0×10^{-8} cm²/sec in 100 Torr nitrogen. These values are somewhat low due to the growth of reaction produced ThC_2 precipitate that reduces the effective area, a . This effect, however, influences both values by approximately the same factor because q and, hence, the quantity of ThC_2 precipitate are about the same in both experiments. The \bar{D}' value is higher for the Th(C,N) phase with 54.1 m/o ThC than that with 35.5 m/o ThC. This trend can be expected to continue with increasing carbon contents approaching pure ThC.

jc - j_N coupling.—The ThC_2 precipitate always appears in layer growths at a position displaced appreciably inward from the specimen outer surface. This observation cannot be attributed to migration of the precipitated ThC_2 particles *per se* because unreasonable assumptions would be required. The displacement of carbon is concluded to be caused by diffusion of carbon, during reaction, "uphill" against a carbon concentration gradient in Th(C,N).

We have observed that similar phenomena occur when the analogous UC phase is reacted with low-pressure CO and/or nitrogen. Evidently, carbon diffuses "uphill" in U(C,N) too. Carbon-rich fronts thus formed can be seen in published photomicrographs of products of reaction of UC with CO as reported by Erwin (11) and of UC with nitrogen as reported by Leitnaker, Lindemer, and Fitzpatrick (12). The solid solutions, $\text{ThC}_{1-x}\text{N}_x$, have been reported to be regular with respect to the components ThC and ThN at temperatures above 2500°C (10). It is reasonable to assume that stoichiometric $\text{ThC}_{1-x}\text{N}_x$ is a regular solution at the temperatures under discussion too. One may not conclude, however, that nonmetal-saturated Th(C,N) with very slightly greater nonmetal content is a regular solution. Component chemical potentials generally show a strong variation with composition having inflections near stoichiometric compositions. Thus, μ_{ThC} and μ_{ThN} can be expected to change considerably in magnitude with small deviations from the stoichiometric regular-solution monocompound $\text{ThC}_{1-x}\text{N}_x$, i.e., with a small increase in (C + N)/Th ratio above unity. The "uphill" diffusion must, therefore, be ascribed to a change in sign of $\partial/\partial x_{\text{ThC}} \mu_C$ from negative in the regular solution $\text{ThC}_{1-x}\text{N}_x$ to positive in the nonmetal saturated Th(C,N) at a (C + N)/Th ratio only slightly greater than unity, e.g., between 1.00 and 1.03 at 1800°C. Evidence for this can be seen by examination of phase relations in Fig. 2 where the composition of Th(C,N) coexisting with $\text{ThC}_2 + \text{ThCN}$ is $\text{ThC}_{0.35}\text{N}_{0.65}$. At this composition μ_C must have a value approaching μ_C^0 , the value in pure graphite, and μ_C must decrease in the ThC_2 -saturated Th(C,N) phase boundary in the direction of ThC. Based on well-established phase relations in the U-C-N system, and the fact that $\mu_C = \mu_C^0$ in nitrogen-rich U(C,N) where it coexists with

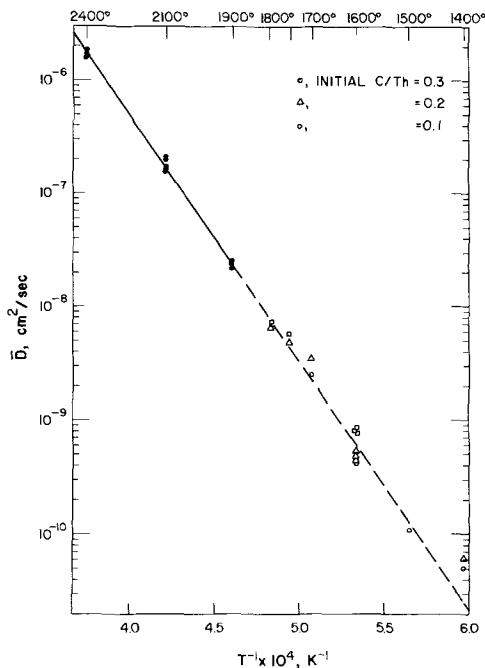


Fig. 9. Composition average chemical interdiffusion coefficients in pure ThN and in Th(C,N) as calculated from layer growth rates. For comparison, a line drawn through the results for pure ThN is extrapolated to lower temperatures as a broken line.

graphite one can show analogously that $\partial/\partial x \mu_C$ and $\partial/\partial x X_C$ have opposite signs in the greater part of the nonmetal-saturated U(C,N) phase boundary too (1200°-1800°C and 5-1000 Torr N₂). Thus, observed phase relations are qualitatively in accord with first principles in showing that carbon "uphill" diffusion is accompanied by a decrease in μ_C in both the Th(C,N) and the analogous U(C,N) phase.

Interpretation of the diffusion data.—Migration of nitrogen atoms through the intact thorium sublattice in the ThN layer growths requires a vacancy mechanism whence flux of nitrogen atoms is accompanied by an equal and opposite flux of vacancies on the nonmetal sublattice. In accordance with this mechanism, \bar{D} values in nitrogen-rich ternary Th(C,N) are observed to increase with decreasing nitrogen pressure. Values of \bar{D} increase with increasing carbon content (and with increasing unit cell dimensions) in the ternary monocompound phase ThC_{1-x}N_x, i.e., near the ThN-ThC tie line. With increasing C/Th ratio above about 0.35 ($x < 0.65$), coupling between j_C and j_N becomes appreciable resulting in carbon "uphill" diffusion. A mechanism leading to such a coupling is obtained with the reasonable assumption that carbon atoms have to move off lattice sites in order to make room for oncoming nitrogen atoms. A carbon atom does not have to wait for a sublattice vacancy to come along, however, because at these compositions it is energetically possible for it to join a neighboring carbon to form a C₂ group. Excess carbon thus built up in front of the nitride layer eventually precipitates as ThC₂. At compositions intermediate to that of pure ThN and ThC_{1-x}N_x with $x < 0.65$, a transition between the two diffusion mechanisms evidently occurs.

Summary

The following measurements were made: (a) compositions of ThC_{1-x}N_x coexisting with ThC₂ and with ThCN in nitrogen at various pressures and at various temperatures; (b) nitrogen decomposition pressures of Th₃N₄, Th₃(N,C)₄, and of ThCN; and (c) nitrogen diffusion coefficients in the binary ThN phase and in

the ternary Th(C,N) solid solutions at compositions near the monocompound.

Evidence is presented for "uphill" diffusion of carbon in the ternary solid solution Th(C,N) and some thermodynamic implications are discussed. The observations explain the observed tendency for carbon and thorium to segregate in the course of reaction of thorium-carbon alloys with nitrogen at moderate pressures.

Acknowledgment

The author thanks C. Wagner for a written discussion, and J. D. Farr for a discussion, and M. G. Bowman and R. D. Baker for support of the work. This work was done under the auspices of the United States Atomic Energy Commission.

Manuscript submitted May 19, 1971; revised manuscript received May 23, 1972. This was Paper 120 presented at the Atlantic City Meeting of the Society, Oct. 4-8, 1970.

Any discussion of this paper will appear in a Discussion Section to be published in the June 1973 JOURNAL.

REFERENCES

1. R. Benz and J. E. Troxel, *High Temp. Sci.*, **3**, 422 (1971).
2. L. S. Darken, *Trans. AIME*, **180**, 430 (1949).
3. R. Benz and P. L. Stone, *High Temp. Sci.*, **1**, 114 (1969).
4. R. Benz, C. G. Hoffman, and G. N. Rupert, *J. Am. Chem. Soc.*, **89**, 191 (1967).
5. R. Benz and W. B. Hutchinson, *J. Nucl. Mater.*, **36**, 135 (1970).
6. R. Benz and G. Balog, *High Temp. Sci.*, **3**, 511 (1971).
7. W. Jost, "Diffusion in Solids, Liquids, Gases," Academic Press (1960); (a) p. 69, (b) p. 22.
8. C. Wagner, *Acta Met.*, **17**, 99 (1969).
9. C. Wagner, *Corrosion Sci.*, **9**, 91 (1969).
10. R. Benz, *J. Nucl. Mater.*, **31**, 93 (1969).
11. Guy Ervin, Jr., in "High Temperature Technology," p. 409, 3rd Intern. Symp. on High Temperature Technology, Stanford Res. Inst., Butterworths, London.
12. J. M. Leitnaker, T. B. Lindemer, and C. M. Fitzpatrick, *J. Am. Ceram. Soc.*, **53**, 479 (1970).

Technical Note



Dislocation Etchants for β' -Gd₂(MoO₄)₃

A. S. Bhalla¹

National Physical Laboratory of India, Delhi, India

Gadolinium molybdate Gd₂(MoO₄)₃, an important rare-earth molybdate, exhibits both the ferroelectric and ferroelastic properties (1-3). The ferroelectric phase below 159°C has an orthorhombic structure with mm2 point group (4, 5) symmetry. Recent interest in its potentialities as an acoustooptic and as ferroelectric laser host call for studies on the imperfection in the crystal and their role in its properties. So far no dislocation etching studies have been reported on the single crystal of Gd₂(MoO₄)₃. In this note some chemical etchants are reported which could be useful for revealing the dislocation sites and to study the

interaction of the dislocations with the domain walls and their movement.

Samples were cut in the shape of a rectangular plate with edges parallel to the crystallographic *a*, *b*, *c* axes. The *c*-face was polished with 0.3 and 0.1 μ Al₂O₃ powders in succession. Samples were then etched at room temperature, using various alkalis, acids, and salts. Hydrochloric and nitric acids were found to be the best etchants to reveal the dislocation sites in the crystal with the etching times 10 sec and 45 sec, respectively. Different concentrations of these acids were tried and practically all dilutions produced the pits equally well on the faces of the crystals (Fig. 1). The pits are considered to be dislocation etch pits on the following grounds:

¹ Present address: Materials Research Laboratory, The Pennsylvania State University, University Park, Pennsylvania 16802.
Key words: chemical etching, crystal defects, ferroelectric materials.



Fig. 1. Dislocation etch pits produced on the (001) face by dilute HNO₃ (40%), $\times 400$.

- (i) The prominent etch pits were point-bottomed and continued etching did not alter this feature but only made the pits deeper and larger.
- (ii) If HNO₃ was first used to produce the pits on the sample, subsequent etching with HCl just made the pits bigger and deeper.
- (iii) When the samples were polished after etching and re-etched, the pits reappeared at the same locations.
- (iv) Grain boundaries were revealed by the etchants (Fig. 2).

The above observations justify the conclusion that the pits were at the dislocation sites and these acids can be used to detect and study the dislocation in (001) face of the β' -Gd₂(MoO₄)₃.

Further investigations in the mobility of the dislocations and the influence of the electric field in it are in progress and the detailed results will be reported elsewhere.



Fig. 2. Low-angle grain boundary and the pile up of dislocations against it, were revealed by HNO₃:H₂O (1:3), $\times 350$.

Acknowledgments

The author is grateful to Prof. Ajit Ram Verma, Director of NPL, for the encouragement during this work and Prof. K. Vedam of MRL for his valuable suggestions. Thanks are also due to Prof. L. E. Cross of MRL for providing the crystals of Gd₂(MoO₄)₃.

Manuscript submitted June 6, 1972.

Any discussion of this paper will appear in a Discussion Section to be published in the June 1973 JOURNAL.

REFERENCES

1. H. J. Borchardt and P. E. Bierstedt, *Appl. Phys. Letters*, **8**, 50 (1966).
2. L. E. Cross, A. Fouskova, and S. E. Cummins, *ibid.*, **21**, 812 (1968).
3. S. E. Cummins, Paper 440 presented at Electrochem. Soc. Meeting, Montreal, Quebec, Canada, Oct. 6-11, 1968.
4. E. T. Keve, S. C. Abraham, and J. L. Bernstein, *J. Appl. Phys.*, **54**, 3185 (1971).
5. W. Jeitchko, *Acta Cryst.*, **B28**, 60 (1972).



The Low-Temperature Polarization of Platinum-Catalyzed Air Cathodes in Alkaline Electrolyte

K. F. Blurton*

Energetics Science Inc., New York, New York 10470

ABSTRACT

Polarization curves have been determined for oxygen reduction on Teflon-bonded platinum black diffusion electrodes in 30% KOH solution in the temperature range of 25° to -40°C. From this data the exchange current densities as a function of temperature and the activation energy at zero overpotential for oxygen reduction on platinum-catalyzed electrodes have been calculated and it was shown that the cathode potential at any current *vs.* a standard hydrogen electrode increased (became more anodic) with decreasing temperature.

Recent observations (1, 2) have indicated that the performance of zinc/air batteries decreases markedly at temperatures below 0°C. The purpose of this study, therefore, was to determine the influence of temperature on the polarization of the air cathodes.

Polarization curves were determined for oxygen reduction on Teflon-bonded platinum black diffusion electrodes in 30% KOH solution at temperatures from 25° to -40°C in the current density range of zero to 200 mA/cm². From this data the exchange current densities as a function of temperature and the activation energy at zero overpotential for oxygen reduction on Pt electrodes have been calculated. In addition it has been shown that, although the cathode polarization increased with decreasing temperature, the cathode potential at any current *vs.* a temperature-independent standard hydrogen electrode increased (became more anodic) with decreasing temperature.

Experimental

Steady-state polarization curves for oxygen reduction on Teflon-bonded platinum black electrodes were determined galvanostatically in oxygen-saturated and in air-saturated 30% KOH solution at temperatures of 25°, 5°, -10°, and -40°C.

The electrodes were tested in a floating electrode cell (3). The working electrode (geometric area 1 cm²) was supported in a gold spring and it was floated on the surface of the electrolyte. Current collection from the gold spring to the external circuit was made via a platinum wire. The counterelectrode was a platinum gauze on which platinum was electro-deposited. The reference electrode was a mercury/mercuric oxide electrode which was placed in a Luggin capillary and immersed in the test electrolyte. The IR drop between the floating electrode and the tip of the Luggin capillary was determined using an interrupter technique and all potentials given in this paper have been corrected for IR drop.

It is essential when determining the kinetic parameters for oxygen reduction that Teflon-bonded electrodes are made so that a change in the catalyst load-

ing does not change the electrode structure. We were able to prepare reproducible platinum electrodes by the same procedure as that of Vogel and Lundquist (4). These electrodes were prepared with Pt (Engelhard Industries) loadings of 2.9, 4.7, 6.8, and 10.0 mg/cm², 30 w/o (weight per cent) of Teflon 30 (E.I. du Pont de Nemours) and gold-plated tantalum as the current collector. The current due to oxygen reduction on the current collector and electrode holder was negligible (less than 1 mA/cm²) at all potentials.

The 30% KOH solution was prepared from Baker Analyzed Reagent grade chemical and triply distilled water. Oxygen, which was obtained from cylinders, and laboratory air were used without purification. The cell temperature was maintained at 25°C with a water bath, at 5°C with ice and water, at -10°C with ice and salt water, and at -40°C with dry ice and acetone.

The polarization curves were determined both by increasing the current density stepwise from open circuit to 200 mA/cm² and by decreasing the current density stepwise from this current density to open circuit. There was no significant difference in the potentials at a given current when either increasing or decreasing the applied current and this indicates that the steady-state potential was attained. At each applied current, the cathode potential was steady within 2-3 min at all temperatures.

The platinum area of the Teflon-bonded diffusion electrodes was measured by determining the charge due to the oxidation of adsorbed hydrogen using the periodic triangular voltage sweep technique on submerged electrodes (5). This technique gave a value of 24 m²/g for the Pt surface area.

Results

The potential of the mercury/mercuric oxide electrode is temperature dependent (6) and therefore, the polarization data is recorded *vs.* the overpotential for oxygen reduction and *vs.* the cathode potential with respect to the standard hydrogen electrode (SHE).

The cathode overpotential was calculated from the experimental cathode potentials *vs.* Hg/HgO electrode and the reversible oxygen electrode potential *vs.* Hg/HgO. The cathode potential with respect to SHE was

* Electrochemical Society Active Member.

Key words: oxygen electrode, electrocatalysis, metal/air batteries.

Table I. Calculated electrode potentials as a function of temperature

Temperature (°C)	Oxygen electrode potential (V)	
	vs. Hg/HgO	vs. SHE
25	0.303	0.316
5	0.315	0.355
-10	0.323	0.385
-40	0.339	0.450

calculated from the overpotential and the reversible oxygen electrode potential *vs.* SHE. The calculated values of the reversible oxygen electrode potential *vs.* Hg/HgO and *vs.* SHE are given in Table I.

The reversible oxygen electrode potential *vs.* Hg/HgO is independent of the KOH concentration and therefore, these potentials at each temperature (Table I) were calculated from the standard potentials and temperature coefficients of the oxygen and mercury/mercuric oxide electrodes (6).

The reversible oxygen electrode potential *vs.* SHE was calculated from the Nernst relationship

$$e = e^{\circ} + RT/4F \ln a^2_{H_2O}/a^4_{OH^-} \quad [1]$$

The values of e° at each temperature were calculated from the standard potential at 25°C and the temperature coefficient of the oxygen electrode, and the water activity was calculated from the ratio of the vapor pressure of the KOH solution (7) to the saturated water vapor pressure (8). The activity of the hydroxyl ion was calculated from the KOH concentration and the activity coefficient at 25°C (9), since the activity of KOH solutions is essentially independent of temperature over the range 25° to -40°C (7).

Semilogarithmic plots of current per unit weight of platinum (milliamperes per milligram of Pt) *vs.* overpotential and *vs.* cathode potential with respect to SHE are shown in Fig. 1-4 for oxygen reduction on Teflon-

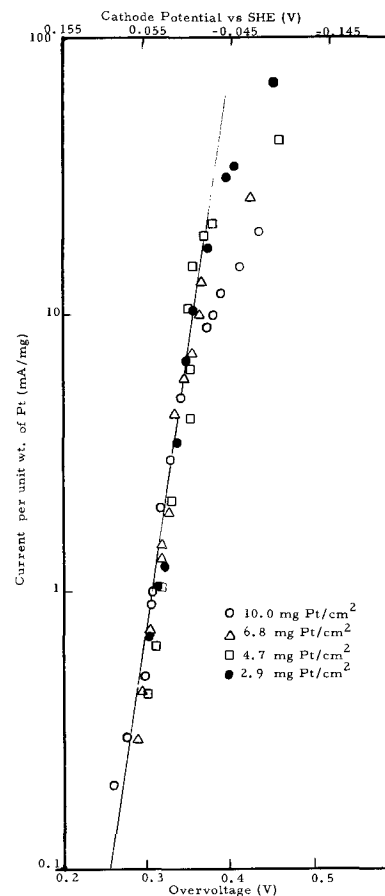


Fig. 2. Polarization curve for oxygen, 30% KOH solution at 5°C

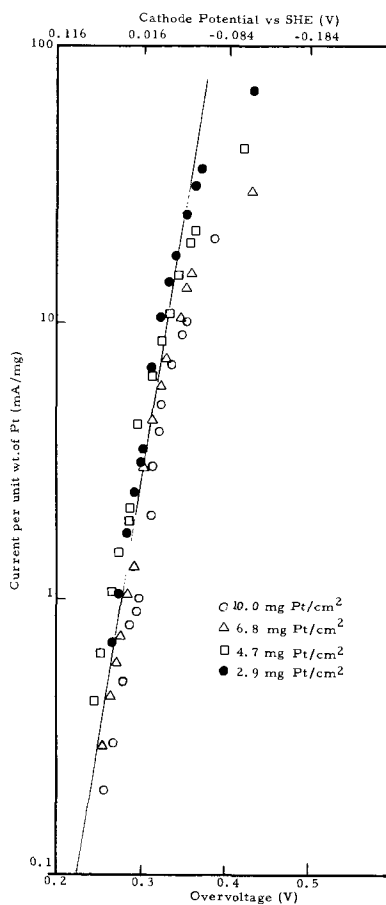


Fig. 1. Polarization curve for oxygen, 30% KOH solution at 25°C

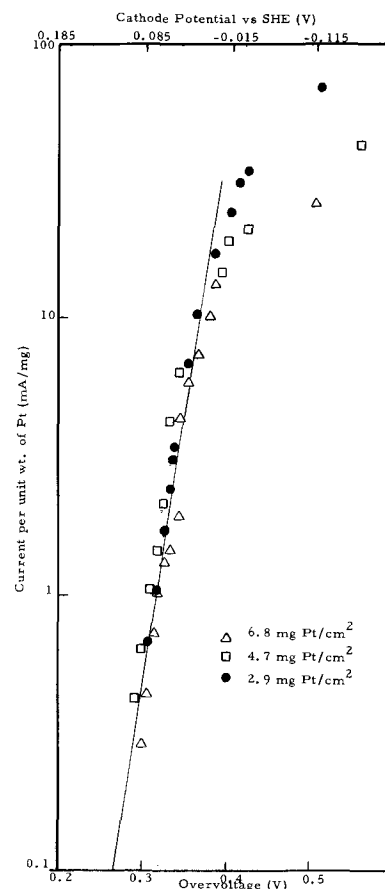


Fig. 3. Polarization curve for oxygen, 30% KOH solution at -10°C.

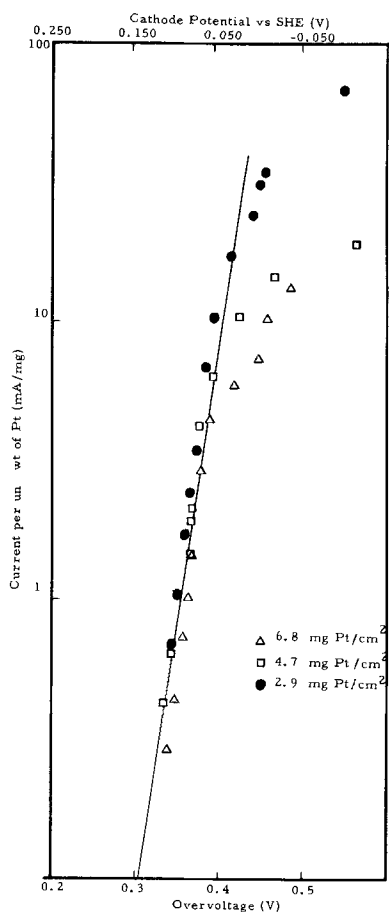


Fig. 4. Polarization curve for oxygen, 30% KOH solution at -40°C .

bonded platinum black electrodes in oxygen-saturated 30% KOH solution at 25° , 5° , -10° , and -40°C , respectively. These plots refer to polarization data obtained with several Pt electrodes and the applied current density can be obtained from the values of milliamperes per milligram of Pt and the electrode loadings. The Tafel plots were linear over approximately two decades of current, and the current per unit weight of Pt in the Tafel region was independent of the Pt loading (Fig. 1-4). The value of the current per unit weight of Pt at which the semilogarithmic plots deviated from linearity decreased with increasing Pt loading and with decreasing temperature.

The linearity of the Tafel plots, and the independence of the current per unit weight of platinum in the Tafel region on the platinum loading, indicate (4, 10, 11) that gas concentration polarization is absent, that the internal ohmic polarization across the electrode is negligible, and that the electrode structure did not change when the electrode loading was varied. Thus, the exchange current densities can be calculated as a function of temperature from these polarization curves (Fig. 1-4).

The values of the exchange current per unit weight of Pt (amperes per milligram), the exchange current density based on the real Pt area (amperes per square centimeter), the Tafel slope ($\partial V/\partial \log i$), and the vapor pressure (7) of 30% KOH solution (p) are given in Table II. The exchange currents per unit weight of Pt were calculated by extrapolating the semilogarithmic plots to the reversible oxygen potential at each temperature, while those based on the real Pt area were calculated from the exchange current per unit weight of Pt and the experimentally determined value of the Pt surface area of $24\text{ m}^2/\text{g}$.

These values of the exchange currents are for an oxygen partial pressure of $(1-p)$ atm. However the values of p are so small (Table II) that the exchange

Table II. Kinetic data for oxygen reduction

Temperature ($^{\circ}\text{C}$)	Exchange current A/mg	Exchange current A/cm^2 *	$\partial V/\partial \log i$ (mV/decade)	$2.303 RT/F$ (mV)	VP of KOH solution† (mm Hg)
25	1.0×10^{-8}	4.2×10^{-11}	55	59	13.4
5	2.5×10^{-9}	1.0×10^{-11}	54	55	3.5
-10	9.6×10^{-10}	4.0×10^{-12}	52	52	0.9
-40	5.2×10^{-11}	2.2×10^{-13}	49	46	0.1

* Calculated using platinum surface area of $24\text{ m}^2/\text{g}$.

† From Ref. (7).

currents are essentially those for O_2 at 1 atm pressure. The value of the exchange current density at 25°C on Pt black electrodes in 30% KOH solution (Table II) was comparable with that determined for oxygen reduction on Pt foil electrodes at 25°C in 0.1N KOH solution ($5 \times 10^{-11}\text{ A}/\text{cm}^2$) (12), but differed by an order of magnitude from those determined in 0.1N NaOH solution ($1 \times 10^{-10}\text{ A}/\text{cm}^2$) (13) or in 1N KOH solution ($3 \times 10^{-12}\text{ A}/\text{cm}^2$) (14). This difference may be due to the lower effect of electrolyte impurities on high area Pt black than on low area Pt foil electrodes or to differences in the oxidation states of the platinum surfaces (15).

The expected variation of the Tafel slope with temperature was found (Table II) and the value of the Tafel slope was equal to RT/F . Similar values of the Tafel slope at 25°C were also found for oxygen reduction on Pt foil electrodes in dilute alkaline solutions (12-14).

Figure 5 shows the semilogarithmic plot of current density vs. overvoltage and vs. cathode potential with respect to SHE for oxygen reduction on a Pt electrode (loading $4.7\text{ mg of Pt}/\text{cm}^2$) in oxygen- and in air-saturated KOH solution at -10°C . The overvoltage for

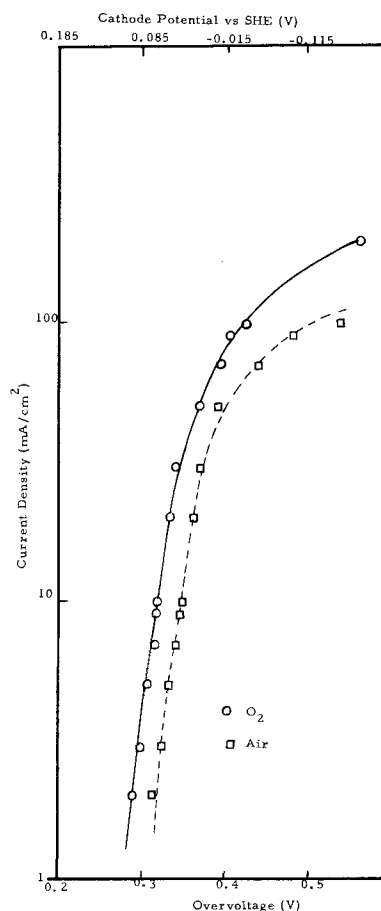


Fig. 5. Polarization curve for air, 30% KOH solution at -10°C , electrode loading $4.7\text{ mg of Pt}/\text{cm}^2$.

oxygen reduction in the Tafel region increased by approximately 28 mV on switching from oxygen at 1 atm to air at 1 atm (Fig. 5).

The polarization increase ($\Delta\eta$) at a constant current density in the Tafel region on changing from oxygen to air at the same total pressure is given by (10)

$$\Delta\eta = \frac{\partial V}{\partial \log i} \log \frac{P_{\text{air}}}{P_{\text{O}_2}} \quad [2]$$

where P_{air} and P_{O_2} are the oxygen partial pressures in air and oxygen, respectively.

At -10°C the calculated value (Eq. [2]) of $\Delta\eta$ is 36 mV and this is in satisfactory agreement with the experimental value of 28 mV. There was good agreement between the calculated and experimental values of $\Delta\eta$ with other electrodes and at the other temperatures.

At applied current densities greater than 100 mA/cm², droplets of electrolyte were observed on the gas side of the electrode (i.e., electrode "weeping" occurred). Electrode weeping was not observed at current densities in the activation polarization region. The amount of electrolyte exuded by the electrode increased with increasing current density and the gas side of the electrode dried very quickly on decreasing the applied current density below 100 mA/cm². The electrodes could not be observed at low temperatures and, therefore, it is not known whether the current density at which weeping occurs is temperature dependent.

Electrode weeping in alkaline electrolyte has been observed by other workers (4, 16). This behavior indicates that the electrolyte is under a current dependent force which is sufficiently large to overcome the surface tension within the electrode pores, and it has been claimed (16) that this force is due to the mutual diffusion of water and electrolyte in the electrode pores. It is eliminated in metal/air batteries by coating the gas side of the cathode with a hydrophobic barrier.

Discussion

Comparison of the polarization data at each temperature (Fig. 1-4) shows that the overvoltage for oxygen reduction increases with decreasing temperature.

However the variation in the reversible oxygen electrode potential with temperature is included in these measurements of overvoltage. In order to analyze the low-temperature behavior of metal/air cells, the cathode potential with respect to a temperature-independent electrode must be known. It was for this reason that the cathode potential at each applied current density was calculated with respect to SHE, since this potential is, by definition, zero at all temperatures (17).

The comparison of the semilogarithmic plots of current per unit weight of Pt at each temperature (Fig. 1-4) shows that the cathode potential with respect to SHE at each current density increased (became more anodic) with decreasing temperature. Thus this variation of cathode potential with temperature acts to increase the voltage of metal/air cells with decreasing temperature.

The difference between the cathode potentials with respect to SHE at two temperatures was greater at current densities in the Tafel region (activation control) than at higher current densities [activation and gas diffusion control (11)]. For example with a Pt loading of 2.9 mg/cm², the cathode potential at 10 mA/cm² was 65 mV more anodic at -40°C than at 25°C , whereas at 200 mA/cm² it was 22 mV more anodic at -40°C than at 25°C . This change is due to the influence of the mass transport parameters (oxygen solubility and diffusion coefficient) on the electrode polarization at the higher current densities.

The present results in the Tafel region can be used to analyze metal/air battery performance curves since

the polarization is independent of electrode structure and the current at any potential is proportional to the Pt loading. However the results at higher current densities (activation and gas diffusion control) only indicate the general trend in the variation of cathode potential with temperature and this data is not directly comparable with other Pt loading electrodes since the current at a given potential is not proportional to Pt loading. Furthermore the cathode polarization at higher current densities was complicated by electrode weeping and this results in an increase in electrode polarization since gas diffusion to the electrode/electrolyte interface then occurs through an electrolyte film on the gas side of the electrode.

Figure 6 shows the Arrhenius plot of the logarithm of the exchange current density vs. the reciprocal of temperature. The value of the activation energy at zero overpotential for the oxygen electrode calculated from this plot was 11.3 kcal/mole. No correction was made for changes in the oxygen solubility with temperature but this correction would be small.

The present value for the energy of activation is significantly lower than those determined with Pt foil electrodes in 1N KOH solution (22.5 kcal/mole) (18) and in 0.1N NaOH solution (15.4 kcal/mole) (19). The variation in these values is probably due to the different conditions under which the measurements were made. Thus the present values were obtained from cathode polarization data on oxide-free Pt electrodes, whereas the previous values (18, 19) were calculated from oxygen evolution data on oxide-covered Pt surfaces.

Thus in alkaline electrolyte the energy of activation for the oxygen electrode is less on oxide-free Pt electrodes than on oxide-covered Pt electrodes whereas in acid electrolyte the energy of activation is greater on oxide-free Pt electrodes (20, 21). This difference in the energy of activation on oxide-free and oxide-covered Pt surfaces in alkaline and acid electrolyte may be associated with the higher coulombic efficiency for hydrogen peroxide formation in alkaline electrolyte compared with that in acid electrolyte (12, 22-24).

Acknowledgments

The author thanks Mr. C. Oswin and Mr. D. Rutt for technical assistance.

Manuscript submitted Feb. 15, 1972; revised manuscript received July 5, 1972.

Any discussion of this paper will appear in a Discussion Section to be published in the June 1973 JOURNAL.

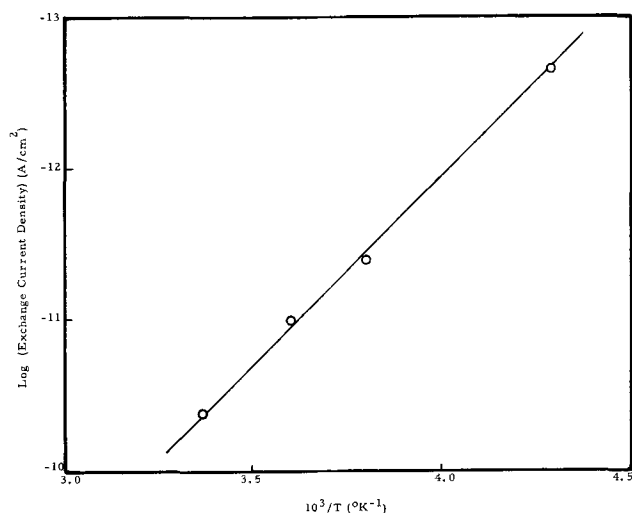


Fig. 6. Arrhenius plot of log exchange current density vs. $1/T$

REFERENCES

1. D. T. Ferrell and A. J. Salkind, Power Systems for Electric Vehicles Symposium, Sponsored by U.S. Dept. HEW, April 1967, p. 61.
2. J. F. Henry and E. G. Katsoulis, Paper 30 presented at the Electrochemical Soc. Meeting, Cleveland, Oct. 3-8, 1971.
3. J. Giner and S. Smith, *Electrochem. Technol.*, **5**, 61 (1967).
4. W. M. Vogel and J. T. Lundquist, *This Journal*, **117**, 1512 (1970).
5. K. F. Blurton, P. Greenberg, H. G. Oswin, and D. Rutt, *ibid.*, **119**, 559 (1972).
6. A. J. deBethune and N. A. Swedeman Loud, "Standard Aqueous Electrode Potentials and Temperature Coefficients," C. A. Hampel (1964).
7. P. Bro and H. Y. Kang, *This Journal*, **118**, 1430 (1971).
8. "Handbook of Chemistry and Physics," 43rd edition, The Chemical Rubber Publishing Co. (1961).
9. R. A. Robinson and R. H. Stokes, *Trans. Faraday Soc.*, **45**, 612 (1949).
10. J. T. Kosinski, Paper 32 presented at the Electrochemical Soc. Meeting, Detroit, Oct. 5-9, 1969.
11. J. A. S. Bett, E. Washington, and K. Routis, Paper 285 presented at the Electrochemical Soc. Meeting, Los Angeles, May 10-15, 1970.
12. A. Damjanovic, M. A. Genshaw, and J. O'M. Bockris, *This Journal*, **114**, 1107 (1967).
13. D. S. Gnanamuthu and J. V. Petrocelli, *ibid.*, **14**, 1036 (1967).
14. A. Damjanovic, A. Dey, and J. O'M. Bockris, *ibid.*, **113**, 739 (1966).
15. A. J. Appleby and A. Boruka, *ibid.*, **116**, 1212 (1969).
16. J. G. Bannochie, "Power Sources 3," p. 417, D. H. Collins, Editor, Oriel Press (1971).
17. D. A. MacInnes, "The Principles of Electrochemistry," Dover (1961).
18. A. Damjanovic, A. Dey, and J. O'M. Bockris, *Electrochim. Acta*, **11**, 791 (1966).
19. H. P. Stout, *Discussions Faraday Soc.*, **1**, 246 (1947).
20. A. J. Appleby, *This Journal*, **117**, 328 (1970).
21. A. J. Appleby, *J. Electroanal. Chem.*, **24**, 97 (1970).
22. K. F. Blurton and E. McMullin, *This Journal*, **116**, 1476 (1969).
23. K. F. Blurton and E. McMullin, *Energy Conversion*, **9**, 141 (1969).
24. A. Kozawa, *J. Electroanal. Chem.*, **8**, 20, (1964).

Conductivity of Beta-Alumina and Its Dependence on Sodium and Magnesium Content

John H. Kennedy* and Anthony F. Sammells*

Department of Chemistry, University of California, Santa Barbara, California 93106

ABSTRACT

The relationship between conductivity and sodium content has been investigated for sintered beta-alumina containing MgO. Conductivities of 3.5×10^{-3} , 8.0×10^{-3} , and 4.4×10^{-3} ohm⁻¹-cm⁻¹ were found for material containing 1, 2, and 4% MgO, respectively, with optimum sodium content. Experimental conductivities for 1 and 2% MgO agree well with calculated values assuming one additional sodium ion for each magnesium ion present. Resistance measurements were made in the frequency range 0.75-10 kHz, and conductivities were calculated from resistances extrapolated to infinite frequency. Electrode contact was made using thin films of silver and gold following glow discharge cleaning techniques.

Beta alumina has been known for a considerable time and was originally thought to be a crystallographic variation of alumina (1). It was soon established that sodium oxide was essential to the synthesis of beta-alumina from aluminum oxide and that it is in fact an alkali aluminate of ideal stoichiometry Na₂O · 11Al₂O₃ (2). The x-ray analysis (3, 4) has proven conclusively that beta-alumina consists of a hexagonal layer-type structure of spinel-type blocks containing four layers of cubic close-packed oxygen atoms with aluminum ions occupying all of the sites normally occupied by the aluminum and magnesium ions in MgAl₂O₄ spinel. The sodium-containing layers are separated from the spinel blocks by Al-O-Al bonds. More recently, single crystals of beta-alumina were shown to exhibit rapid sodium ion diffusion in the plane perpendicular to the c-axis (5) and that the sodium could be almost completely exchanged in suitable molten salts for Ag, K, Li, Rb, and, to a lesser extent, Cs ions. Sodium ions have exhibited the largest diffusion coefficient, and the mechanism of diffusion has been shown conclusively to be interstitialcy (5, 6). Beta-alumina normally is found with an excess of sodium when compared to the ideal stoichiometry, and it has been suggested (7) that this excess can be

stabilized by the presence of Al³⁺ vacancies in the spinel.

For beta-alumina to be of utility as an electrolyte in a battery system, practical ceramic-type shapes must be formed from the single crystals. This necessitates the sintering of pressed material under strictly controlled conditions so that the sintered product will have a final density close to that of the single crystal. Sintered compacts of beta-alumina for use as an electrolyte have been reported previously (8-10) and have been used in the experimental sodium-sulfur battery. This battery operates in excess of 300°C so as to keep the reactants molten, and at such temperatures, beta-alumina has a very high conductivity of approximately 0.2 (ohm-cm)⁻¹. The conductivities reported at room temperature by various workers have not only been relatively low, but erratic and dependent on the type of electrode contact used as well as on the sintering conditions.

Sintering conditions reported (8-11) have varied between 1600° and 1900°C with times ranging between 15 min and several hours. It has always been found necessary to use coarse beta-alumina packing so as to provide an alkaline atmosphere to reduce sodium loss.

It has been shown (5, 7) that the interstitialcy mechanism of migration of ions through beta-alumina depends on an excess of sodium present and that the incorporation of MgO into the sintered material in-

* Electrochemical Society Active Member.
Key words: beta-alumina, ionic conductivity, magnesium oxide, thin films.

creases the ionic conductivity of the sintered material (9, 12). This suggests that there might be some relation between the amount of MgO present in the sintered material and sodium content required for optimum conductivity. Before any comparison can be made however, a method for achieving reproducible satisfactory electrode contacts must be established.

Several approaches have been made to achieve good electrode contacts to both single crystals and sintered compacts of beta-alumina. The reported ionic resistivities in most cases have been made at high frequency so as to minimize the faradaic impedance at the electrode-electrolyte interface. Yao and Kummer (5) while working with single crystals of beta-alumina and indium electrodes reported resistivity values at room temperature of 30 ohm-cm at 500 kHz and 46 ohm-cm at 50 kHz, and the resistivity value was found to be frequency independent between 0.5 and 1.5 mHz. Whittingham and Huggins (7) used a silver resinate solution on single crystals of silver beta-alumina in conjunction with mechanically pressed silver electrodes to achieve a resistivity of 150 ohm-cm at room temperature and a frequency independent range of 0.1-100 kHz. Using sintered beta-alumina containing 2% MgO, Wynn Jones and Miles (9) reported ionic resistivities between 400 and 600 ohm-cm with a 4-probe d-c technique using silver metal in contact with the ceramic via solid sodium hydroxide. Recently, Armstrong *et al.* (10) illustrated the necessity for determining frequency dependence when resistivities were measured on sintered material and worked with a variety of electrodes and, in particular, reported resistivities at room temperature of the order of 550 ohm-cm at a frequency of 1.592 kHz when using sodium electrodes.

It is quite evident from the literature that electrode contact to single crystals of beta-alumina is easier to achieve than to sintered compacts. This is because there is a greater roughness factor in the sintered material, and therefore it is more difficult to make good contact with the entire surface. In single crystals, contact can be made by initial mechanical contact followed by high-temperature annealing so as to bond the electrode to the crystal. Whittingham and Huggins (6) also reported achieving good contact to single crystals by the novel use of tungsten bronze electrodes. Such techniques have not been satisfactory with sintered material. Satisfactory electrode contacts can be made to sintered pellets using thin-film techniques only if the substrate is perfectly clean before evaporation. One method for cleaning sintered pellets *in situ* which we used in this study was glow discharge. Such cleaning techniques minimize any possible contact resistance that might result so that the final extrapolated resistivity should closely represent the true bulk resistivity of the electrolyte.

The frequency dependence of the faradaic impedance has been known for some time (13, 14). It is also well known that such impedance is proportional to the reciprocal of the square root of frequency

$$\Delta R = k\omega^{-1/2}$$

where ΔR is the faradaic impedance, ω is the frequency, and k is a proportionality constant. The measured resistance, R_m , consists of both bulk resistance, R , and the faradaic impedance at the interface

$$R_m = R + \Delta R = R + k\omega^{-1/2}$$

A linear extrapolation of resistances measured at different frequencies to infinite frequency by plotting R_m against $\omega^{-1/2}$ will eliminate or at least minimize the error due to faradaic impedance. Resistance measurements were made in the frequency range 0.75-10 kHz in this study. The use of higher frequencies can lead to additional complications in the interpretation of results (15). The dependence of the infinite frequency resistivity on sodium content was determined using

sintered pellets of beta-alumina with fixed percentages of MgO and thin-film electrodes of gold or silver. The sintering conditions were strictly controlled so as to produce final sintered densities in a narrow range so that a valid comparison could be made from one pellet to another in each run.

As has been observed by others, the final sodium content of beta-alumina after sintering was always less than the initial content, and in order to correlate the measured resistivity with sodium content, a sodium analysis on each pellet after sintering was necessary. The sodium content was determined by ion-exchanging sodium by silver with silver nitrate and subsequent analysis for sodium in the silver nitrate by atomic absorption.

Experimental

Preparation of samples prior to sintering.—Alcoa beta-alumina (325 mesh) (11) was ground to particle size 0.5-1 μ in a grinding mill using alumina balls. Ethylene glycol was used as a grinding aid, and the final particle size was determined with a Unitron U11 microscope. The MgO and Na₂CO₃ of similar particle size were mixed with the ground beta-alumina in a Fisher mechanical mortar and pestle (alumina). To this powder was then added a binder (2% carbowax 1000 as a 10% aqueous solution) and the material allowed to dry at 110°C over a 24-hr period. Pellets were made in a KBr-type press at 16,000 psi, and the binder was removed by slowly heating to 400°C and leaving 24 hr.

Sintering conditions.—Pellets were sintered in an Astro ultra-high temperature graphite resistance furnace Model No. 1000A-2560 under oxidizing conditions with the use of a muffle tube assembly. The graphite heating elements surrounding the alumina muffle tube were protected by a nitrogen atmosphere. Pellets were kept covered with a coarse 325 mesh beta-alumina during the sintering process so as to maintain an alkaline atmosphere and hence reduce the loss of sodium. The pellets, together with the beta-alumina packing, were kept in a covered alumina crucible during the sintering. Slow heating rates of 250°C/hr were maintained so as to prolong the muffle tube life. Temperatures of 1700°-1800°C were achieved over extended periods of time. Temperature control was maintained by a boron-graphite thermocouple connected to a L&N 6261 Electromax C.A.T. controller. Recorded temperatures were measured directly by use of a Micro Optical pyrometer (Pyrometer Instrument Company) through a viewing port in the side of the furnace.

Application of thin-film electrodes.—Evaporations of silver and gold were performed in a Veeco 776 automatic high vacuum evaporator. Electrode contact was improved with the use of glow discharge cleaning of the substrate with oxygen at 10⁻³ Torr using low potentials. If too high a potential was used in the glow discharge process the first electrode became oxidized during cleaning of the second face of the pellet. This oxidation was eliminated by the use of nitrogen in the second cleaning process. Nitrogen was not as effective in cleaning the substrate as oxygen, but the pellet was thoroughly cleaned on the first cleaning so that nitrogen was satisfactory for the second cleaning.

Resistivity measurements.—Measurements of pellet resistance were made with a General Radio 1650A impedance bridge at frequencies between 10⁺⁴ and 500 Hz by the use of a Wavetek Model 111 voltage-controlled generator. Resistivity values were calculated from resistance measurements extrapolated to infinite frequency and the pellet dimensions.

Atomic absorption spectrophotometry.—Sodium analysis was accomplished by first ion-exchanging the sodium for silver by heating pellets at 220°C for 24 hr with AgNO₃. The exchange process was carried out twice to ensure complete exchange of sodium. A third exchange did not indicate any more exchangeable

sodium in the sintered pellets. Sodium in the silver nitrate was then analyzed on a Jarrell-Ash 82-270 Atomsorb atomic absorption spectrophotometer by comparing with an appropriate calibration curve.

X-ray diffraction.—Surface x-ray diffraction of sintered beta-alumina pellets was accomplished with a Philips x-ray diffraction instrument with $\text{CuK}\alpha$ radiation, a Philips Type 52572 scintillation counter, and a chart recorder.

Results

It was found that particle size and homogeneity were critical in preparing beta-alumina containing MgO. A particle size of $0.5\text{-}1\mu$ gave a suitable final density. Variation in the sodium content was achieved by thoroughly mixing sodium carbonate of similar particle size to the starting material prior to pellet formation. Pellets were made at pressures of 16,000 psi giving a "green" density of 1.91. When pressures greater than this were used, laminations occurred in the green pellet and it readily fell apart. The binder was removed slowly in a conventional tube furnace by heating slowly to 400°C and leaving at this temperature for 24 hr. Attempts to remove the binder more rapidly than this in the sintering furnace gave noticeably lower final densities. Although it is unlikely that any sodium loss would occur at such low temperatures the pellets were covered with coarse beta-alumina during the binder removal. The pellets were covered to a depth of $\frac{1}{2}$ in. in coarse 325 mesh beta-alumina in the alumina crucible prior to sintering, and a thin layer of packing was also placed between individual pellets since without such separation there was a tendency for the pellets to sinter together. The sintering furnace was heated up at a rate of 250°C/hr (the recommended rate for the alumina muffle tube). The sintering temperatures and times varied significantly between pure beta-alumina and that containing MgO. With pure beta-alumina, final densities close to theoretical could be achieved with temperatures of 1720°C for 2 hr, but when 1 or 2% MgO was added, the required sintering conditions were 1750°C for 7 hr. With 4% MgO, the best sintering conditions were 1830°C for 6 hr but were not completely satisfactory in achieving maximum density. It has been noted before that the rate of sintering of ceramic material, alumina in particular, is reduced when MgO is added (16) due to its effect on the grain boundary mobility. However, other authors (9) report that lower temperatures were sufficient for beta-alumina doped with 2% MgO, but this has not been our experience.

Two other crystalline forms of beta-alumina containing MgO have been reported and designated β'' - (17) and β''' -alumina (18). However, there was no indication of β'' -, or β''' -, or α -alumina in our sintered pellets from x-ray analysis. There was an indication of a small amount of a second phase of sodium aluminate (possibly microdispersed) in many samples. No preferred orientation was observed in the sintered pellets.

Several types of electrodes were investigated including silver paint, sodium amalgam, and metal thin films. A large frequency dependence for the silver paint indicated poor electrode contact to the beta-alumina, and in the case of sodium amalgam, difficulty was found in even achieving contact. Most satisfactory results were obtained with thin films of silver and gold, and only the results obtained with these electrodes are reported here. Silver was found to make a better electrode contact to the beta-alumina than did gold. This was determined by the larger frequency dependence of the measured resistance on samples containing gold electrodes when compared to those samples having silver electrodes as shown on Fig. 1 and 2. Electrode contact was also improved by the use of glow discharge cleaning prior to electrode deposition, and samples treated in this manner exhibited a lower frequency dependence of the measured resistance than those not treated by this cleaning process.

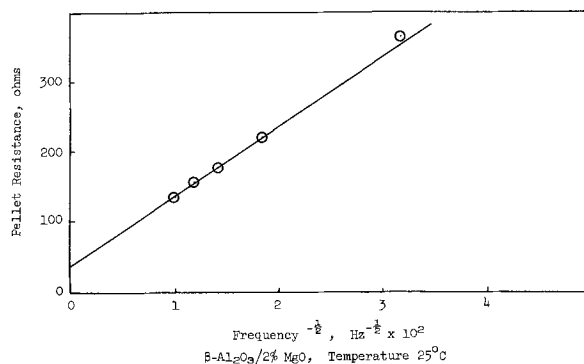


Fig. 1. Frequency dependence for $\beta\text{-Al}_2\text{O}_3$ pellets with evaporated gold thin-film electrodes.

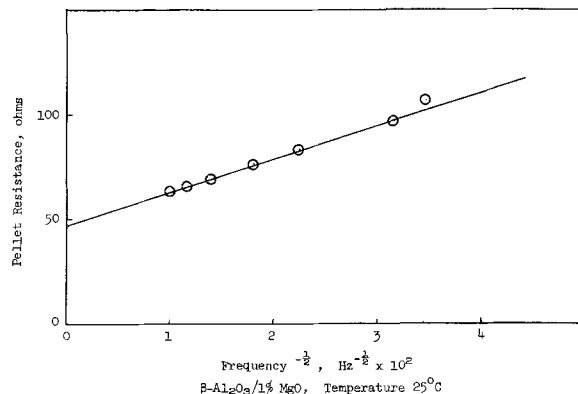


Fig. 2. Frequency dependence for $\beta\text{-Al}_2\text{O}_3$ pellets with evaporated silver thin-film electrodes.

The final densities of 1 and 2% MgO samples ranged between 3.0 and 3.1 with the majority in the range 3.0 and 3.05. The density of 4% MgO material was only 2.9, and attempts to obtain greater density than this with longer sintering times or higher temperatures did not succeed. In this case, smaller particle sizes might provide greater green densities prior to sintering. However, since the main purpose of this investigation was to determine the optimum stoichiometry of sodium for maximum conductivity, the lower density pellets were satisfactory.

Resistivity measurements were made *vs.* frequency using a pellet holder with gold contacts, and no change in the resistance values was observed with change in pressure. Typical measurements are shown in Fig. 1 for silver electrodes and Fig. 2 for gold electrodes. The resistivity was measured from the pellet thickness and area occupied by the electrode. The electrode contact was not found to deteriorate with time in a vacuum system but when exposed to the atmosphere some deterioration with time was observed as shown in Fig. 3. This deterioration with time was attributed to the slow oxidation of the silver electrode thus increasing the contact resistance between electrode and electrolyte. Sintered pellets kept in a reasonably dry atmosphere for several months before applying electrodes exhibited essentially the same conductivity as fresh pellets. All resistance measurements on the pellets reported here were made immediately after electrode deposition.

The correlation between extrapolated resistivity and sodium content for a fixed percentage of MgO is shown in Fig. 4, 5, and 6. The minimum resistivity values were: 288 ohm-cm for 1% MgO at 6.8% Na_2O , 125 ohm-cm for 2% MgO at 7.4% Na_2O , and 227 ohm-cm for 4% MgO at 9.5% Na_2O . Conductivity values, calculated from resistivities, were 3.5×10^{-3} (ohm-cm) $^{-1}$ for 1% MgO at 6.8% Na_2O , 8.0×10^{-3} (ohm-cm) $^{-1}$ for 2% MgO at 7.4% Na_2O , and 4.4×10^{-3} (ohm-cm) $^{-1}$ for 4% MgO at 9.5% Na_2O .

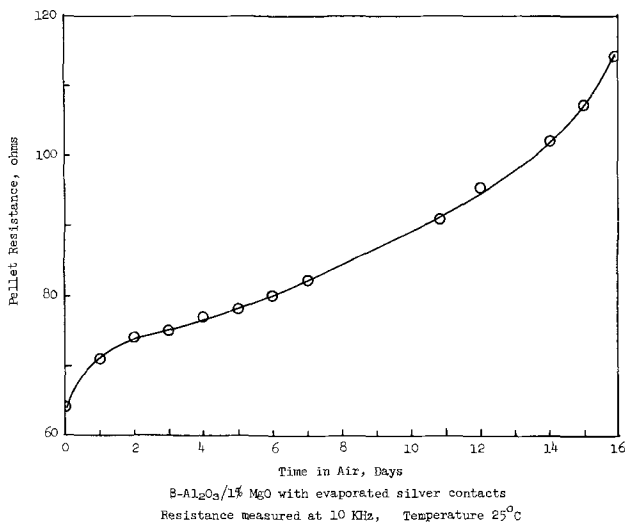


Fig. 3. Increase of pellet resistance with time exposed to the atmosphere.

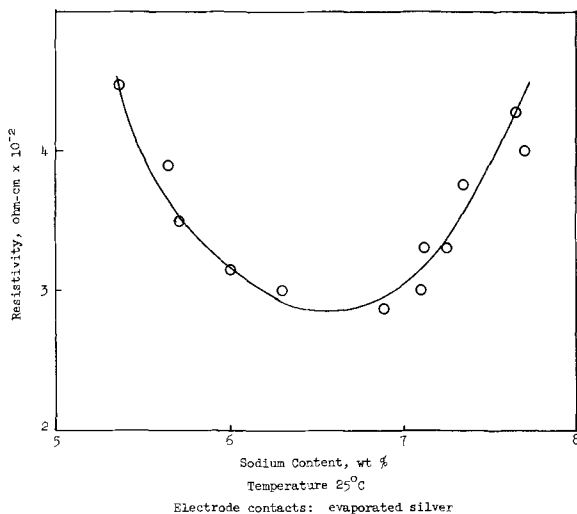


Fig. 4. Resistivity as a function of sodium content for β - Al_2O_3 /1% MgO pellets.

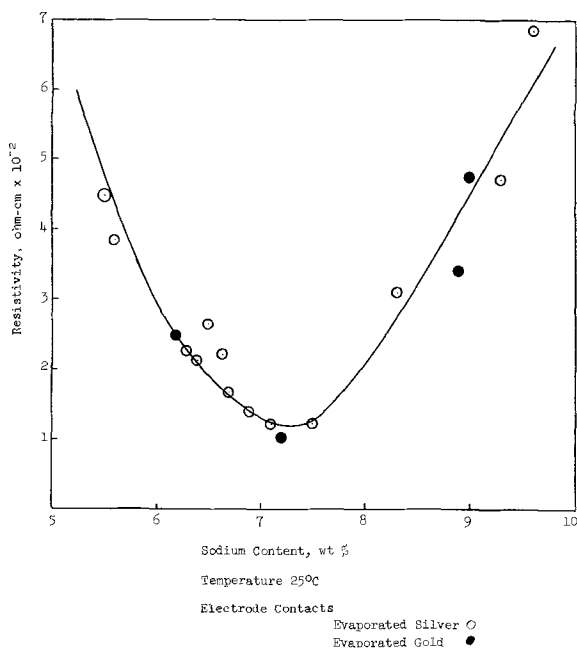


Fig. 5. Resistivity as a function of sodium content for β - Al_2O_3 /2% MgO pellets.

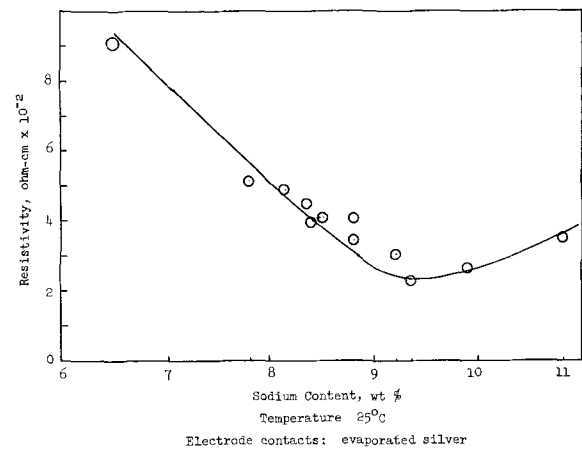


Fig. 6. Resistivity as a function of sodium content for β - Al_2O_3 /4% MgO pellets.

Discussion

From consideration of charge neutrality it can be hypothesized that magnesium which becomes incorporated into the beta-alumina structure on Al^{3+} sites will increase the number of interstitial sodium ions that can be stabilized. This hypothesis is reasonable when one recalls that the spinel-type blocks of beta-alumina have the same structure as the spinel MgAl_2O_4 . From this possible correlation between magnesium substitution and sodium ion interstitials, an optimum sodium content and maximum conductivity for any given MgO content can be calculated.

The theoretical Na_2O content for pure beta-alumina is 5.24%, but our studies and those of other investigators (3-5) have shown that "pure" beta-alumina contains excess sodium. Our beta-alumina was found to contain an average sodium content of 6.1% and had a conductivity of 6.7×10^{-4} (ohm-cm) $^{-1}$ at 25°C. This represents a 16% excess Na_2O content which may be stabilized by Al^{3+} vacancies or other defects present in the "pure" material. The addition of 2 w/o (weight per cent) MgO to the beta-alumina is equivalent to 0.59 mole of Mg^{2+} per mole of beta-alumina and should stabilize an additional 0.59 mole of interstitial sodium ions. This would amount to an additional 1.5 w/o Na_2O giving an expected optimum sodium content of $6.1 + 1.5 = 7.6$ w/o Na_2O . There is no requirement that when 2% MgO is incorporated the material will still contain the same number of other defects, but Fig. 5 shows that a maximum conductivity was found at 7.4% MgO, quite close to the calculated value.

Similar calculations for material containing 1 and 4% MgO give expected Na_2O contents of 6.85 and 9.1 w/o. Again, Fig. 4 and 6 show that maximum conductivity was achieved at a Na_2O content of 6.8 w/o for the material containing 1% MgO and 9.5 w/o for material containing 4% MgO, both values being close to the values calculated above.

Conductivity values for undoped β - Al_2O_3 sintered to a density similar to the doped materials were in the range 5.3 - 7.1×10^{-4} ohm $^{-1}$ -cm $^{-1}$. If the median value of 6.6×10^{-4} ohm $^{-1}$ -cm $^{-1}$ is used as a base reference value, then any increase in conductivity resulting from the additional interstitial sodium ions can be calculated assuming additivity with this base reference value

$$\sigma_{\text{tot}} = \sigma_0 + \sigma_{\text{MgO}}$$

where σ_{tot} = total conductivity, σ_0 = base reference conductivity contribution, and σ_{MgO} = conductivity contribution from addition of MgO stabilizing higher concentrations of interstitial sodium ions.

If we assume for the moment that the additional sodium ions will have a mobility equal to that measured for pure beta-alumina (1.56×10^{-5} cm 2 /sec-V at 25°C) the σ_{MgO} contribution can be calculated using

the equation

$$\sigma_{\text{MgO}} = N_{\text{MgO}} \mu q$$

where N_{MgO} is the concentration of magnesium atoms (which equals the additional concentration of sodium ions incorporated into the $\beta\text{-Al}_2\text{O}_3$), μ is the mobility of the additional sodium ions in $\beta\text{-Al}_2\text{O}_3$, and q is the unit of charge. The number of conductive sodium ion interstitials will equal the number of magnesium ions introduced, and for 2% MgO this is

$$N_{\text{MgO}} (\text{ions/cm}^3) = \frac{3.0 \text{ g } \beta\text{-Al}_2\text{O}_3 \times 0.02 \text{ g MgO/g } \beta\text{-Al}_2\text{O}_3 \times 6.02 \times 10^{23}}{\text{cm}^3 40 \text{ g MgO/mole}} = 9 \times 10^{20}$$

Therefore

$$\sigma_{\text{MgO}} = 9 \times 10^{20} \times 1.56 \times 10^{-5} \times 1.6 \times 10^{-16} = 2.25 \times 10^{-3} (\text{ohm-cm})^{-1}$$

for 2% MgO at 25°C. Consideration of tortuosity in the polycrystalline material would suggest that the measured conductivity based on pellet geometry should be smaller than the calculated value. The true tortuosity factor is unknown, but Wynn Jones and Miles (9) concluded it might be as high as 3-5.

Another possible difference between conductivity in single crystals and observed conductivity in polycrystalline materials is the contribution of grain boundaries. Some solid electrolytes such as silver bromide exhibit enhanced conductivity from grain boundary conduction and a lower activation energy (19). However, Wynn Jones and Miles suggest a grain boundary contact resistance with a higher activation energy which may impede conductivity (9). We have observed various values of activation energy from conductivity measurements over the temperature range -50° to $+70^\circ\text{C}$ of 3-5 kcal/mole compared to the single crystal value of 3.8 kcal/mole (5). This would seem to indicate that possibly some contact resistance was present in some of our sintered pellets, but its contribution was small. Therefore, it is reasonable to compare our conductivity measurements with those on single crystals keeping in mind these differences.

On the other hand, this calculated value of conductivity based on tracer diffusion coefficient (from which the mobility was calculated) must be increased by the correlation factor for the interstitialcy type mechanism accepted for beta-alumina (5). There is still some debate as to the correct correlation factor to use for the polycrystalline material, but recent evidence (20) suggests that 3 is an appropriate value at room temperature. In fact, with higher sodium contents found in β'' , correlation factors as high as 7-8 have been observed at room temperature. Neglecting the unknown tortuosity factor and possible increased correlation factor above 3, we expect a contribution to conductivity from the interstitial sodium stabilized by the 2% MgO of $6.75 \times 10^{-3} (\text{ohm-cm})^{-1}$. The total conductivity would then be

$$\sigma_{\text{tot}} = 6.6 \times 10^{-4} + 6.75 \times 10^{-3} = 7.41 \times 10^{-3} (\text{ohm-cm})^{-1}$$

which compares well with the observed value of $8.0 \times 10^{-3} (\text{ohm-cm})^{-1}$ at 7.4 w/o Na_2O . This agreement may be somewhat fortuitous because of the uncertainties in tortuosity, correlation factor, and mobility of the additional sodium ions. The additional sodium ions in magnesium-containing $\beta\text{-Al}_2\text{O}_3$ may actually be more mobile by occupying alternate sites and/or exhibit higher correlation factors which would counteract the tortuosity effect expected for polycrystalline materials. Aside from these uncertainties, the measured

values are consistent with the proposed model for magnesium doping of $\beta\text{-Al}_2\text{O}_3$.

The calculated value for 1% MgO is $4.1 \times 10^{-3} (\text{ohm-cm})^{-1}$ compared to the observed value of $3.5 \times 10^{-3} (\text{ohm-cm})^{-1}$. The observed conductivity of beta-alumina containing 4% MgO was considerably lower than the predicted value of $14.2 \times 10^{-3} (\text{ohm-cm})^{-1}$ and is attributed to the low density of these pellets. There appears to be a limit to the amount of MgO that can be incorporated into the beta-alumina structure and lies between 2 and 4% MgO.

Pellets containing larger amounts of sodium than the optimum value showed a decreased conductivity. This, we believe, was caused by the excess sodium leading to increased amounts of sodium aluminate since the beta-alumina structure cannot accommodate the additional sodium ions. A quantitative correlation between sodium aluminate content and conductivity could not be made because the amount in all samples was extremely small, and x-ray analysis could not conveniently be performed on pellets used for conductivity studies.

In conclusion, it has been shown that magnesium oxide will stabilize additional sodium ions in beta-alumina leading to increased conductivity, and the increase in conductivity is proportional to MgO content up to at least 2 w/o.

Acknowledgment

The authors acknowledge financial support from PHS Research Grant, No. 1 R01 APO 1527-01, Office of Air Programs of EPA. The authors also wish to thank Mr. Neil Nighman for assistance in setting up glow discharge and thin-film procedures.

Manuscript submitted March 13, 1972; revised manuscript received June 21, 1972.

Any discussion of this paper will appear in a Discussion Section to be published in the June 1973 JOURNAL.

REFERENCES

1. G. A. Rankin and H. E. Merwin, *J. Am. Chem. Soc.*, **38**, 568 (1916).
2. R. R. Ridgeway, A. A. Klein, and W. O'Leary, *Trans. & J. Electrochem. Soc.*, **70**, 71 (1936).
3. W. L. Bragg and J. West, *Z. Krist.*, **77**, 255 (1931).
4. C. A. Beavers and M. A. S. Ross, *ibid.*, **97**, 59 (1937).
5. Y. Y. Yao and J. T. Kummer, *J. Inorg. Nucl. Chem.*, **29**, 2453 (1967).
6. M. S. Whittingham and R. A. Huggins, *J. Chem. Phys.*, **54**, 414 (1971).
7. M. S. Whittingham and R. A. Huggins, *This Journal*, **118**, 1 (1971).
8. J. T. Kummer and N. Weber, U.S. Pat. 3,404,035, Oct. 1, 1968.
9. I. Wynn Jones and L. J. Miles, *Proc. Brit. Ceram. Soc.*, **19**, 161 (1971).
10. R. D. Armstrong, T. Dickinson, and J. Turner, *This Journal*, **118**, 1135 (1971).
11. T. L. Francis, F. E. Phelps, and G. MacZura, *Am. Ceram. Soc. Bull.*, **50**, 615 (1971).
12. A. Imai and M. Harata, Paper 277 presented at the Electrochem. Soc. Meeting, Los Angeles, May 10-15, 1970.
13. E. Warburg, *Ann. Phys.*, **6**, 125 (1901).
14. G. Jones and S. M. Christian, *J. Am. Chem. Soc.*, **57**, 272 (1935).
15. J. Braunstein and G. D. Robbins, *J. Chem. Ed.*, **48**, 52 (1971).
16. P. J. Jorgenson, *J. Am. Ceram. Soc.*, **48**, 207 (1965).
17. M. Bettman and C. R. Peters, *J. Phys. Chem.*, **73**, 1774 (1969).
18. M. Bettman and L. L. Turner, *Inorg. Chem.*, **10**, 1442 (1971).
19. I. Shapiro and I. M. Kolthoff, *J. Chem. Phys.*, **15**, 41 (1947).
20. L. J. Miles, I. Wynn Jones, A. D. Le Claire, and A. H. Rowe, Paper 166 presented at the Electrochem. Soc. Meeting, Houston, May 7-11, 1972.

Electron Microscope Study of the Nucleation and Growth of Electroless Cobalt and Nickel

S. L. Chow, N. E. Hedgecock, and M. Schlesinger

Department of Physics, University of Windsor, Windsor, Ontario, Canada

and J. Rezek

Department of Engineering Materials, University of Windsor, Windsor, Ontario, Canada

ABSTRACT

High-resolution electron micrographs and diffraction patterns of thin discontinuous cobalt and nickel films deposited electrolessly under various conditions are presented. It is concluded that nickel, when deposited from strongly alkaline solutions assumes a fcc structure. Evidence is presented that the structure of cobalt deposits can be either fcc or hcp depending on the chemistry of the metalizing solution. Mixed cobalt-nickel films appear to form a fcc structure like nickel.

Chemically (electrolessly) deposited nickel films can be considered as a binary system of nickel and phosphorus. Some previous studies (1) have suggested that the initial structure of as-deposited Ni-P film is metastable. Heat-treatment, it was found, will transform it to a more stable state of a two-phase system consisting of fcc nickel and tetragonal Ni₃P. In the as-deposited state we are dealing with a "liquid like" material (2). By this one means a solid solution of phosphorus in a very fine polycrystalline nickel system. The average size of the crystallites was recently estimated (3) to be about 10-20Å. It should be remembered that the catalytic sites on which the film growth is initiated were stated (2) to be of about the same dimensions. This state of affairs is quite well established for nickel deposited from acidic metalizing solutions. Films deposited from alkaline solutions, in the as-deposited state, exhibit a degree of crystallinity depending on their phosphorus content. It is the aim of the present communication to study this crystallinity in some detail. It will become evident that a comparison between Ni-P, Ni-Co-P, and Co-P, all grown chemically, yields important information concerning this crystalline state.

Experimental

The films in this investigation were grown on microscope slide glasses coated with Formvar (4g polyvinyl-formal in one liter of ethylene dichloride). They were floated off the glass substrate in distilled water.

The detailed compositions of the sensitizing, activating, and acidic metalizing solutions for the deposition of nickel were given in Ref. (2).

The compositions of the alkaline metalizing solution for the deposition of electroless nickel is given in Table I, along with the compositions of the solutions used for mixed Co-Ni-P films (with a 65% nickel content) and for Co-P films. The technique of transmission electron microscopy was used throughout the present work. Our instrument is a Hitachi HU-12 electron microscope operated at 100 kV.

All chemicals used in the present work were supplied by Fisher or Canlab and were used without further purification.

Experimental Results

In Fig. 1 we present the electron micrographs of electrolessly deposited nickel from different alkaline

solutions (see Table I). The pH values of the different solutions corresponding to the figure are (a) pH = 7, (b) pH = 8, (c) pH = 9, (d) pH = 10, and (e) pH = 11.

In Fig. 2 we present the corresponding electron diffraction patterns of these films. The deposition times had to be varied (see figure captions) as change of the pH does affect the deposition rate, and our aim here was to compare films of similar thicknesses. The effect of increased pH is best seen by comparing the corresponding diffraction patterns. In order to ensure that these effects were due to change in pH (and hence phosphorus content) and not merely an effect of the different deposition rates, the following was done. We prepared some films using a hot (85°C) metalizing bath. At an elevated temperature the deposition rate is markedly enhanced. We found that for a given pH, raising the temperature from 20° to 85°C had about the same effect on the rate as increasing the pH at room temperature by 1. The diffraction pattern, however, is not affected by temperature, and is thus determined by the pH (and phosphorus content).

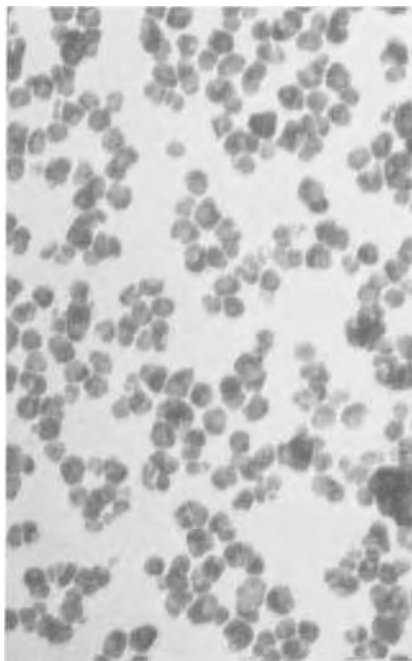
Next we investigated the mixed Ni-Co-P films (see Table I). Here too, the pH of the metalizing solutions was varied. In Fig. 3 we present the micrographs for films grown from solutions with (a) pH = 7.5, (b) pH = 8.5, and (c) pH = 10.5. Figure 4 depicts the corresponding electron diffraction patterns. Here again

Table I. Composition of metalizing solution for deposition of electroless nickel and for mixed Co-Ni-P and Co-P films

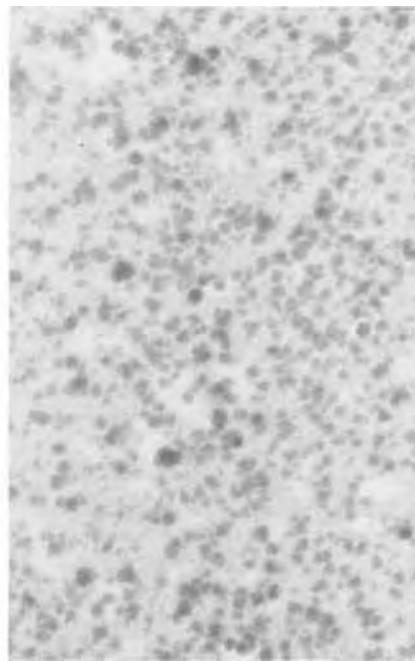
	Ni-P,* g/l	Ni-Co-P* (65% Ni), g/l	Co-P,* g/l
Nickel sulfate, NiSO ₄ ·6H ₂ O	30	30	—
Cobalt sulfate, CoSO ₄ ·7H ₂ O	—	30	35
Sodium hypophosphite, NaH ₂ PO ₂ ·H ₂ O	10.6	20	5-40
Sodium citrate, Na ₃ C ₆ H ₅ O ₇ ·2H ₂ O	100	—	35
Rochelle salt, NaKC ₄ H ₄ O ₆ ·4H ₂ O	—	200	—
Ammonium chloride, NH ₄ Cl	53.6	—	—
Ammonium sulfate, (NH ₄) ₂ SO ₄	—	50	70

* pH adjusted with NaOH.

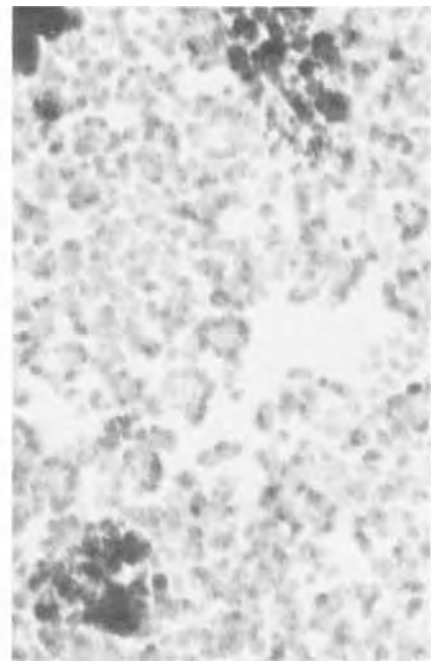
Key words: films, nucleation, crystallization, electroless.



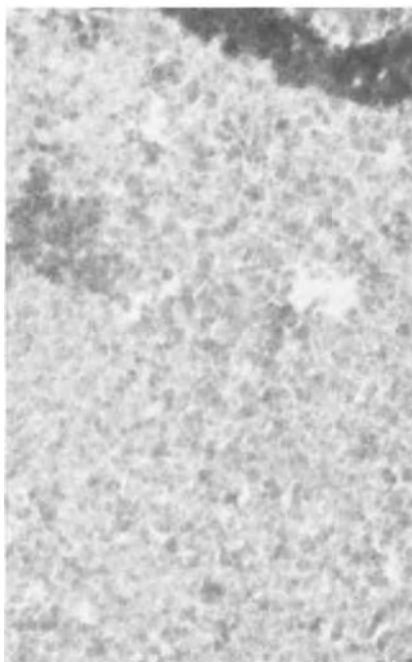
(a) pH = 7, deposition time 9 min



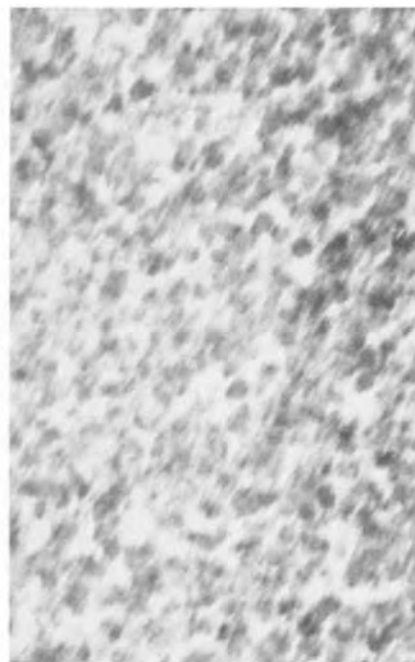
(b) pH = 8, deposition time 8 min



(c) pH = 9, deposition time 2½ min



(d) pH = 10, deposition time 2½ min



(e) pH = 11, deposition time 1½ min

Fig. 1. Transmission electron micrographs of electrolessly deposited nickel from different alkaline solutions.

1000Å

the pH affects the deposition rate, so different deposition times were employed as given in the figure captions.

Finally we took up the study of Co-P films. Here again, initially the effect of the pH of the metalizing solution was investigated. It must be noted, however, that in the case of Co-P one can, essentially, change the pH and the phosphorus content independently. The latter is done by simply varying the concentration of the sodium hypophosphite.

In Fig. 5 we present the effect of these variables on the nucleation and growth of thin electroless Co-P

films. Specifically, Fig. 5(a)I is the electron micrograph of a Co-P film grown from a metalizing solution with pH = 7 and a hypophosphite concentration of 40 g/liter. Figure 5(b) is the same except with pH = 10 and Fig. 5(c) with pH = 12. In order to show the effects of hypophosphite concentration, Fig. 5(a)II corresponds to 5g of hypophosphite/liter, with pH = 7. The corresponding electron diffraction patterns are shown in Fig. 6(a)I to 6(c), and 6(a)II. It will be noted that essentially no changes can be observed in comparing the patterns in Fig. 6. The hexagonal shaped

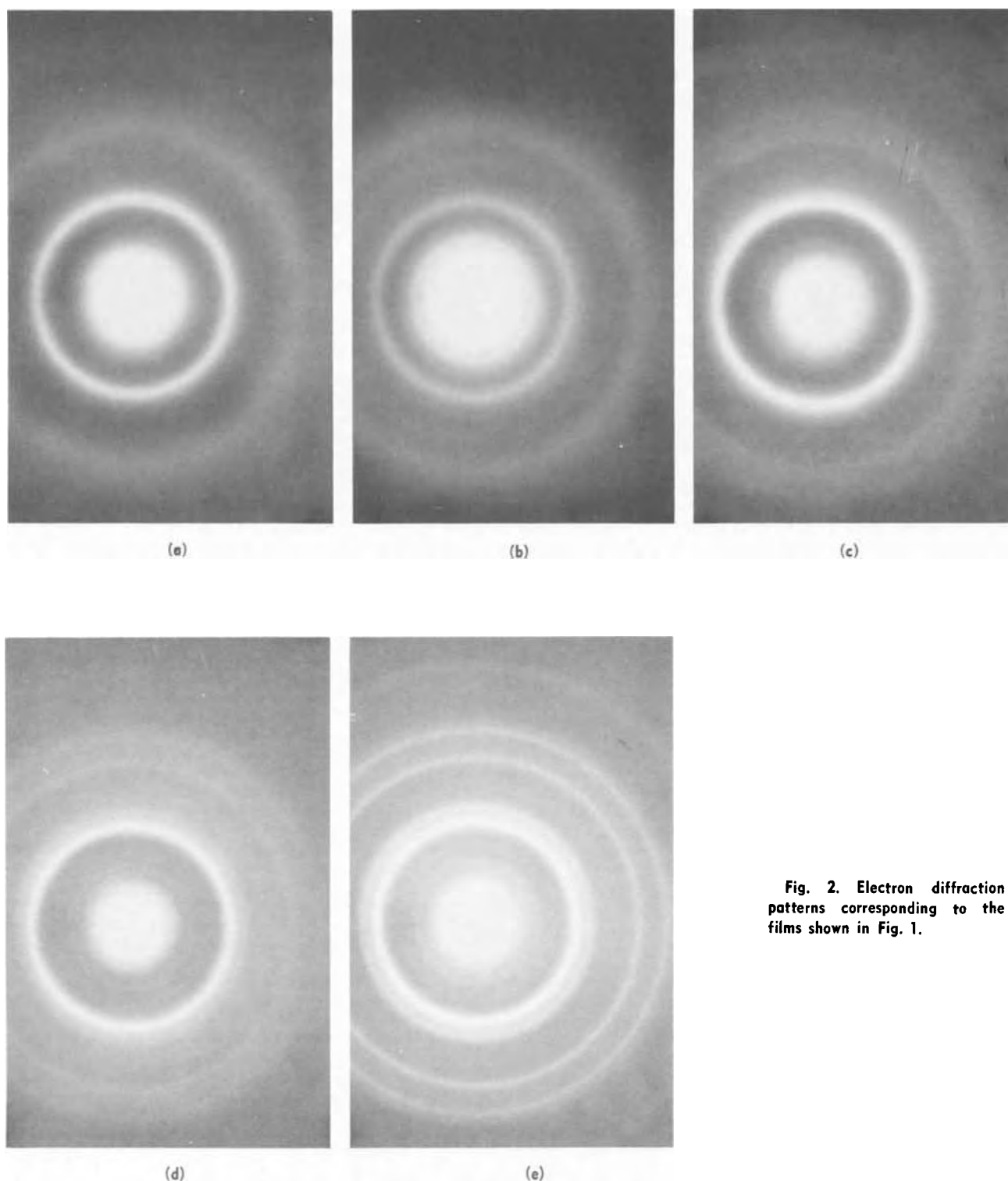


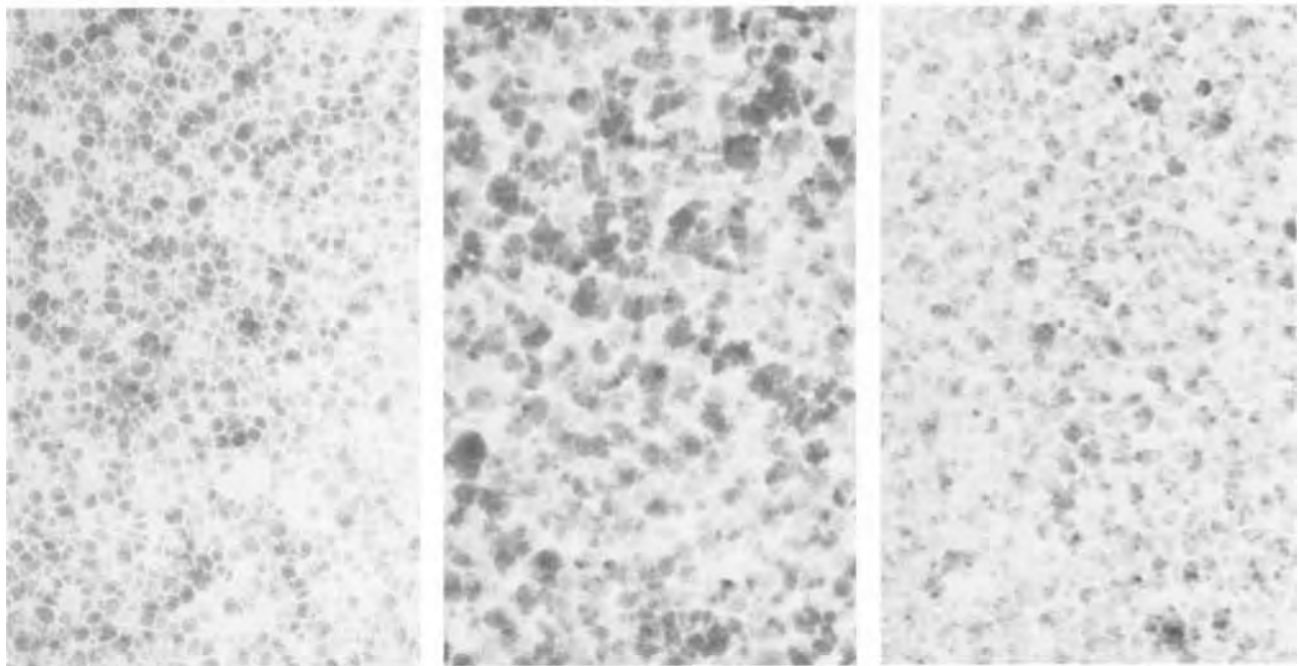
Fig. 2. Electron diffraction patterns corresponding to the films shown in Fig. 1.

islands in Fig. 5(a)I are perhaps indicative of the hcp structure of as-deposited Co-P. The time of deposition varied and is given in the corresponding captions.

Discussion

Effects of the amounts of phosphorus on the magnetization of nickel were studied by Albert *et al.* (4). They too controlled the level of phosphorus by changing the pH of the metalizing bath. This they did since the amount of phosphorus incorporated into the films increases as the pH of the bath decreases.

Consequently in our case on "passing" from Fig. 1(a) to 1(e) the amount of phosphorus in the films decreases. Assuming the as-deposited films to be (see above) a solid solution of phosphorus in a very fine polycrystalline system, it is not unreasonable to expect that decreasing the phosphorus content should result in an increase in the average size of crystallites. This is not immediately observable by comparing the micrographs in Fig. 1. The electron diffraction patterns shown in Fig. 2, however, demonstrate this point very clearly.



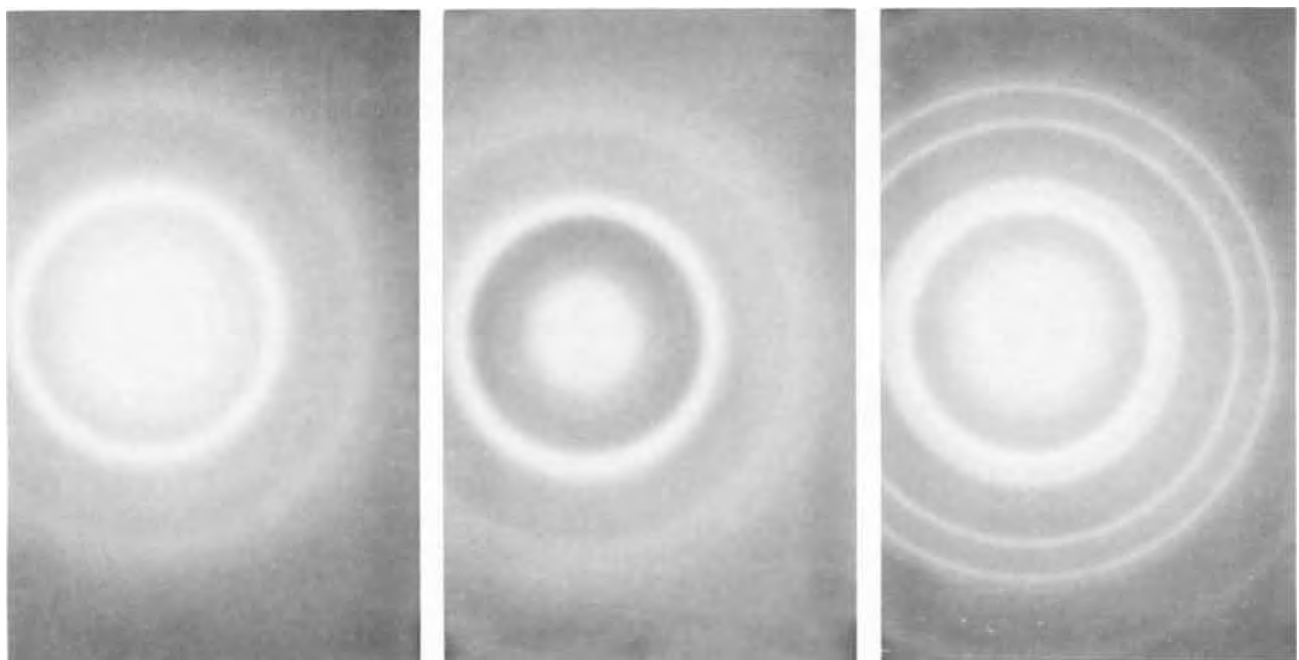
(a) pH = 7.5, deposition time 8 min

(b) pH = 8.5, deposition time 4 min

(c) pH = 10.5, deposition time 2½ min

Fig. 3. Transmission electron micrographs of electrolessly deposited mixed nickel-cobalt (65% nickel) films.

┌──────────┐
1000Å



(a)

(b)

(c)

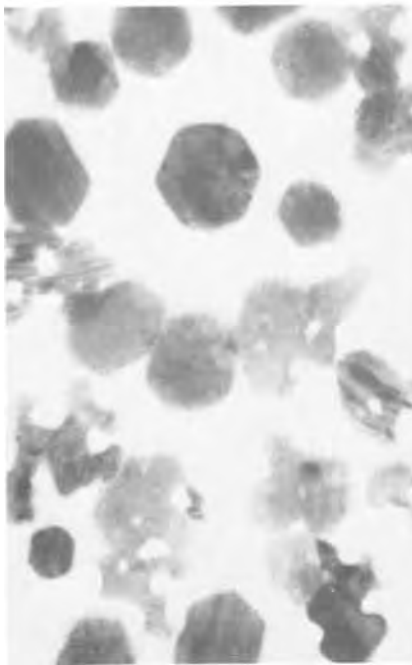
Fig. 4. Electron diffraction patterns corresponding to the films shown in Fig. 3

Further, assuming in Fig. 2 fcc symmetry, one can infer a lattice constant for the nickel of 3.554Å. While this number can be considered somewhat too large (ordinary nickel has a lattice constant of 3.517Å), it might be indicative of a "strained fcc lattice" (4).

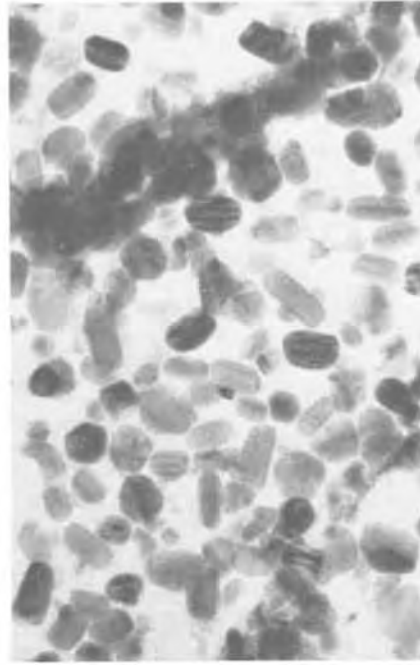
The influence of the change of pH in the metalizing solution for mixed nickel and cobalt is shown in Fig. 3 and 4. Here too the decrease in P content seems to

result in larger average sizes of the crystallites. The crystallographic symmetry of these can be attributed to a fcc structure. It must indeed be remembered that this is known to be one of the simplest systems formed by cobalt, and nickel can form a complete series of solid solutions with fcc cobalt.

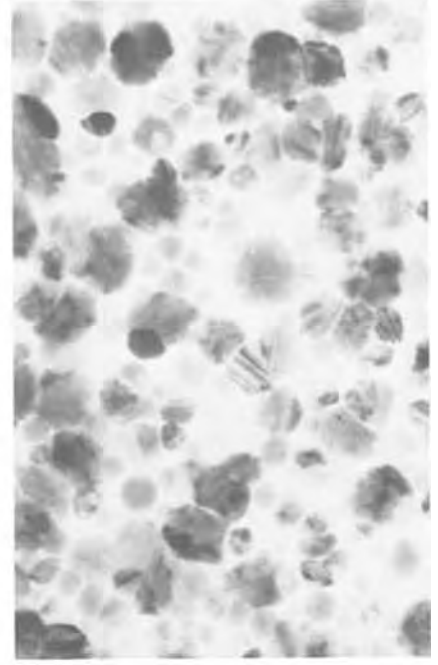
Of more complexity is the series of micrographs and patterns presented in Fig. 5 and 6. Here it is likely



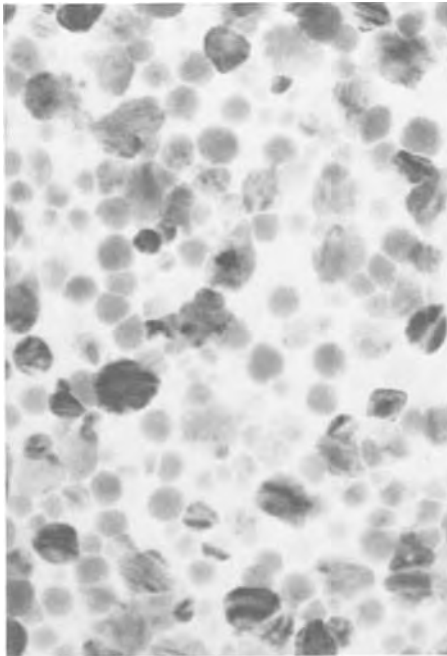
(a)I pH = 7, [hypophosphite] = 40 g/liter, deposition time 1 min



(a)II pH = 7, [hypophosphite] = 5 g/liter, deposition time 1 min



(b) pH = 10, [hypophosphite] = 40 g/liter, deposition time 5 min



(c) pH = 12, [hypophosphite] = 40 g/liter, deposition time 5 min

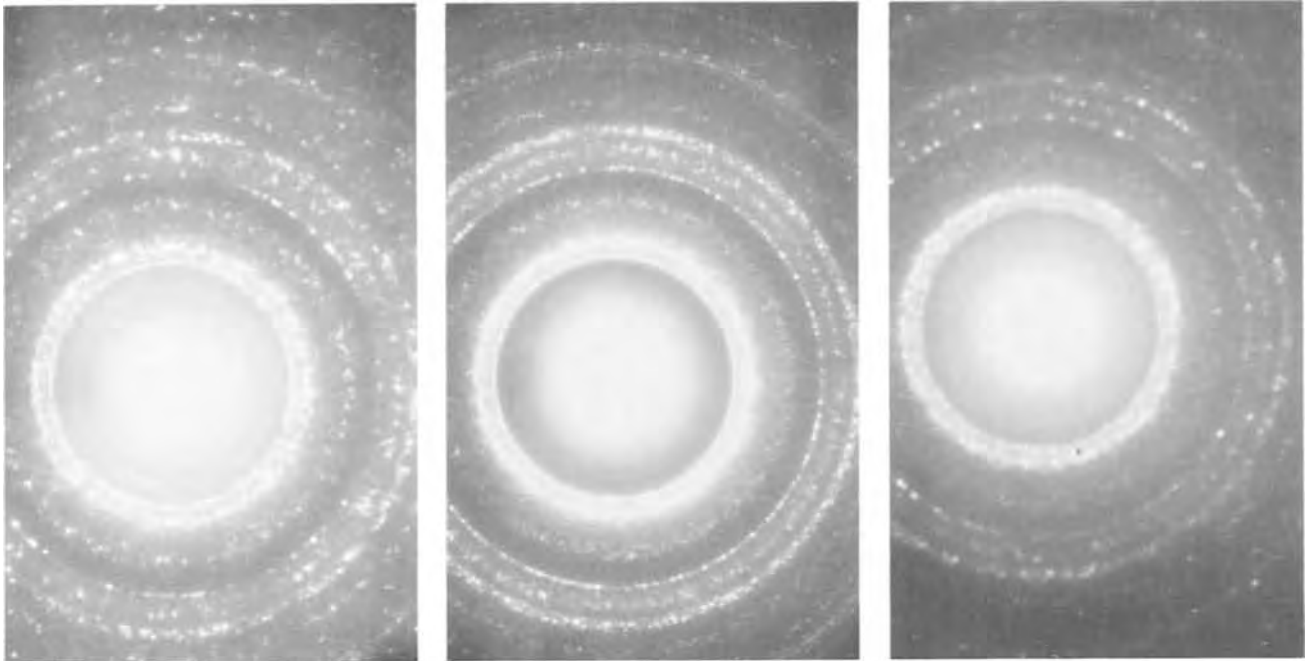
Fig. 5. Transmission electron micrographs of electrolessly deposited cobalt from different metalizing solutions.

1000Å

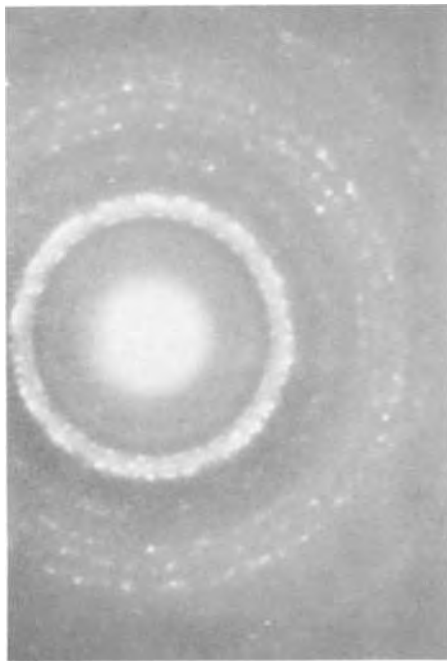
that for low pH but high phosphorus content, the crystal symmetry of Co-P films is predominantly hexagonal [see shapes of "islands" in Fig. 5(a)I]. Decreasing the phosphorus content [see Fig. 5(a)II] or increasing the pH changes the general appearance of islands. Comparison of Fig. 2(e) with the patterns in Fig. 6 reveals a significant difference. In principle it should be possible to distinguish between fcc and hcp on the basis of the strength of the [200] ring, but it is difficult to give an unambiguous assignment to

the rings in Fig. 6. Not much can be inferred quantitatively in this case (at least at present) from the diffraction patterns. Our assumption, however, is that to begin with the Co films constitute a mixture of fcc and hcp phases. Increasing the pH or decreasing phosphorus content tips the ratio more toward the fcc phase.

Frieze, Sard, and Weil (5) have studied the morphology of thin Co-P films in some detail. The film thickness range covered by their experiments is 500-20,000Å



(a) pH = 7, [hypophosphite] = 40 g/liter, deposition time 1 min (a) pH = 7, [hypophosphite] = 5 g/liter, deposition time 1 min (b) pH = 10, [hypophosphite] = 40 g/liter, deposition time 5 min



(c) pH = 12, [hypophosphite] = 40 g/liter, deposition time 5 min

Fig. 6. Electron diffraction patterns corresponding to the films shown in Fig. 5.

while we are interested here in much thinner samples. In addition, the resolution of our micrographs is at least ten times better than theirs. Nonetheless, we

also agree about the role of the co-deposited P as a "growth inhibitor," both for cobalt and nickel. As we see from our work the influence of P content will show at much lower thickness than 1000Å, and an alternative explanation for the difference between Fig. 5(a) and 5(c), for instance, might be the change in fiber axis from $\langle 0001 \rangle$ to $\langle 10\bar{1}0 \rangle$. This will, of course, explain also the lack of change in passing from Fig. 6(a) to 6(c). The difficulty in accepting this approach lies in the fact that in very thin films like ours, one would expect the initial deposition on the palladium-activated surface to have its basal plane of the hexagonal lattice predominantly parallel to the substrate. Only thicker samples would be expected to have their fiber axis orientation dependent on the phosphorus content [see Ref. (5)]. This difficulty returns us to the first suggestion of a mixed hcp-fcc phase.

Manuscript submitted June 1, 1972; revised manuscript received Aug. 7, 1972.

Any discussion of this paper will appear in a Discussion Section to be published in the June 1973 JOURNAL.

REFERENCES

1. M. Schlesinger and J. P. Marton, *J. Phys. Chem. Solids*, **29**, 188 (1968).
2. J. P. Marton and M. Schlesinger, *This Journal*, **115**, 16 (1968).
3. S. T. Pai, J. P. Marton, and J. Brown, *J. Appl. Phys.*, **43**, 282 (1972).
4. P. A. Albert, F. Kovac, H. R. Lilienthal, T. R. McGuire, and Y. Nakamura, *ibid.*, **38**, 1258 (1967).
5. A. S. Frieze, R. Sard, and R. Weil, *This Journal*, **115**, 586 (1968).

Zinc Electrode Shape Change in Secondary Cells

James McBreen*

Electrochemistry Department, Research Laboratories, General Motors Corporation, Warren, Michigan 48090

ABSTRACT

Shape change, the reduction in zinc electrode area with cycling, is a limiting factor in the life of most secondary zinc batteries. This investigation was an attempt to elucidate the mechanism of shape change by monitoring the pattern of current and potential distribution over the surface of a zinc electrode during cycling. This was done while keeping all electrode and cell parameters similar to those found in conventional cells. Differences in the secondary current distribution during charge and discharge result in exhaustion of the reducible zinc species at the plate periphery in the early stages of cycling. This generates a concentration cell which corrodes zinc off the plate edge and deposits it in the plate center. Shape change is a result of these concentration cell effects and the transfer of zincate from the plate periphery to the plate center in the early stages of discharge. Many other hitherto unexplained phenomena related to shape change were rationalized on the basis of these findings and mechanism.

Shape change, the reduction of the zinc electrode geometric area with cycling, is the limiting factor in the life of most secondary zinc batteries (1). On cycling the zinc active material is removed from the plate edges and agglomerates toward the plate center. The movement of zinc continues as cycle life progresses and results in a reduction of the capacity and useful life of the cell (2).

In the past, numerous correlations have been made between the shape-change phenomena and the various operating and construction parameters of secondary zinc cells. Both electroosmotic effects, which cause fluctuations in the anolyte level with cycling, and gravitational effects have been ruled out as being major contributors to shape change in tightly packed cells (3, 4). Shape change occurs more slowly in a tightly packed cell than in a loosely fitting cell pack (5-7). The rate at which shape change occurs with cycling is reduced by decreasing the depth of discharge (2), lowering the KOH concentration in the electrolyte (8), and increasing the stoichiometric ratio of the negative to positive active material in a cell (4). The rate of shape change is increased by amalgamation of zinc plates and is directly proportional to the mercury content of the plate. Other factors which increase the rate of shape change are high resistivity membranes, bare spots or cracks in "green" negative plates (3, 4), and nonalignment of positive and negative plates in the cell pack (4).

Developments which mitigate shape change to some extent are the addition of binders such as Teflon (9, 10) or polyvinyl alcohol (4) to the zinc plate, the extension of the negative plate edges beyond the edges of the positive plate (1, 11), the use of contoured zinc negatives which have more zinc oxide at the plate periphery than the plate center (1, 10, 12), or zinc negatives which are thicker at the plate top than the plate bottom (13).

No proven mechanism of shape change has been reported. A mechanism based on gravitational effects has been proposed (14), but this mechanism is not consistent with the fact that sometimes zinc also moves away from the plate bottom (2). It has been suggested that shape change is due to concentration cell effects (3, 4). However, Lander (2) has pointed out that the remote causes of shape change are still uncertain.

This investigation was an attempt to elucidate the mechanism of shape change. The analytical approach in this investigation was to determine the patterns of potential and current distribution over the surface of a zinc electrode during cycling. All negative electrode and cell parameters corresponded as closely as possible

to those found in an actual operating cell. The current distribution on the zinc electrode was determined by monitoring the current to a sectioned cadmium counterelectrode. The basic assumption underlying the experimental approach was that the current flow through a section of the cadmium counterelectrode was a good indication of the flow through the portion of the zinc electrode just opposite the section.

Experimental

Apparatus and method.—The test cell (Fig. 1) comprised a standard zinc electrode, a separator system, a sectioned cadmium counterelectrode, an array of Hg/HgO reference electrodes, and a third electrode for cycling the counterelectrode independently of the zinc electrode. Current distribution was determined by monitoring the current to the various sections of the cadmium electrode.

Zinc electrode.—The zinc electrode was made by evenly distributing and pressing 15g of electrode mix (94.5 w/o (weight per cent) ZnO + 0.5 w/o HgO + 5 w/o binder) onto an expanded silver screen. The final plate dimensions were $11.1 \times 11.1 \times 0.051$ cm. In the assembled cell, the screen was on the side of the electrode remote from the counterelectrode.

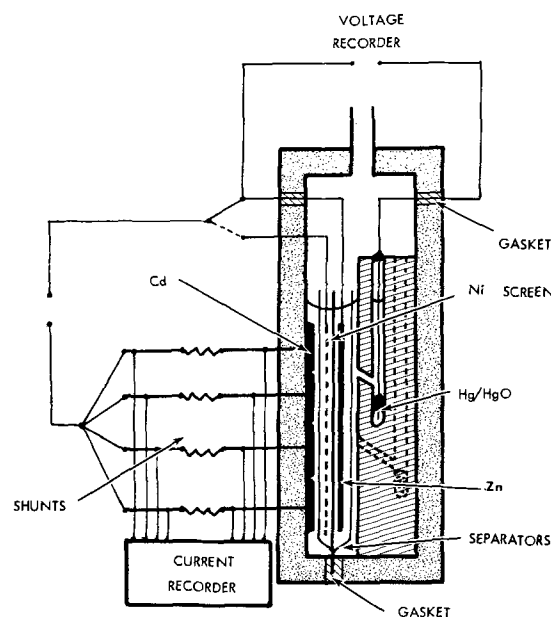
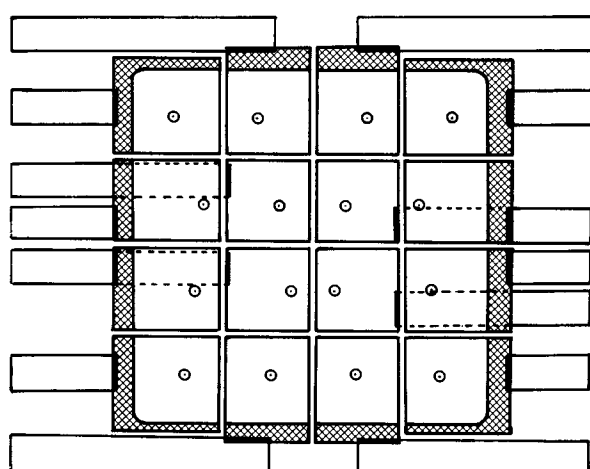


Fig. 1. Test cell and electric circuit

* Electrochemical Society Active Member.
Key words: battery, current distribution, potential distribution, concentration cell.

Counterelectrode.—The cadmium counterelectrode support structure comprised of 16 sections of nickel battery plaque (0.089 cm thick), with coined edges and spot-welded nickel tabs. These sections were arranged on an acrylic plastic sheet as shown in Fig. 2. The spaces between each section were filled with epoxy and the coined edges were masked with epoxy. The finished sectioned electrode was perfectly flat; the uncoined exposed area of each section was 2.54×2.54 cm and the space between each section was 0.12 cm. Cadmium was incorporated in the plaque sections by the standard impregnation method (15). Afterward, the electrode was lightly pressed while still wet and then given four formation cycles against a nickel sheet counterelectrode.

Reference electrodes.—The reference electrode compartments were 0.4 cm diam holes drilled vertically in an acrylic plastic block ($11.4 \times 14.0 \times 1.6$ cm) as shown in Fig. 3. The reference electrode capillaries were 0.1 cm diam holes from the reference compart-



○ = POSITION OF REFERENCE CAPILLARIES

Fig. 2. Arrangement of counterelectrode sections. The relative position of the reference capillaries are also shown. These are on the side of the zinc electrode opposite to the cadmium electrode.

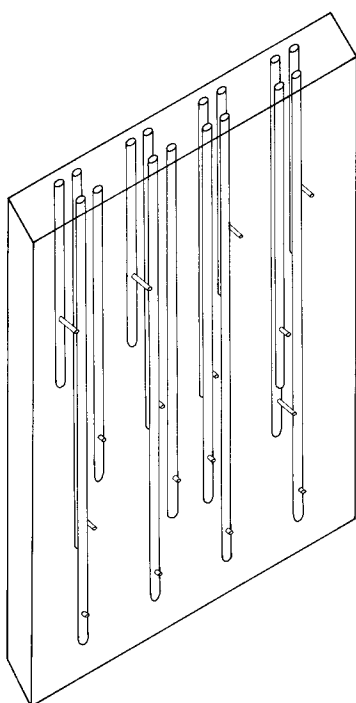


Fig. 3. Reference electrode compartments

ments to one face of the plastic block. These holes were drilled at a 20° angle to the normal of the block face and were packed with cellophane to prevent dewetting. These compartments were used for the fabrication of the array of Hg/HgO electrodes. The relative position of these electrodes with respect to the cell pack is shown in Fig. 1, and the relative position of the capillary exits with respect to the sections of the counterelectrode is shown in Fig. 2.

Third electrode.—The third electrode was an electroformed nickel screen with a 0.25 cm reticulated pattern. The screen thickness was 0.01 cm and the spacing between openings was 0.05 cm. The screen area dimensions were the same as the sectioned cadmium electrode.

Apparatus assembly.—A schematic drawing of the complete cell assembly and circuitry is shown in Fig. 1. The cell separator system for the work reported in this paper was

Cd/1T,F-120/2T,C-25/1T,F-200/Ni screen/1T,F-120/2T,
FSC-76/1T,P-30/Zn/1T,P-30/KOH/HgO/Hg

where 1T = one layer of separator, 2T = two layers of separator, F-120 = 0.012 cm polyamide felt, C-25 = 0.0025 cm unplasticized cellophane, F-200 = 0.020 cm polyamide felt, FSC-76 = 0.0076 cm Fibrous Sausage casing, and P-30 = 0.003 cm acrylic acid grafted polyethylene (RAI, P-2291).

Provisions were made to have the zinc and cadmium electrodes parallel to one another with a spacing of 0.114 cm between the faces of the cadmium and zinc electrodes, thus ensuring a snug fitting cell pack when the cell was filled with electrolyte. The leads from the cadmium counterelectrodes were bolted to 0.050 ohm shunts.

Experimental procedure.—After the cell was wet down with 44 cc of electrolyte (37.5 w/o KOH + 70 mg ZnO/ml), soaked for 72 hr, vacuum treated to remove gas bubbles, the sectioned counterelectrode was deep cycled four times against the nickel screen at a current of 1.0A. The cadmium electrode was then charged to within 100 mV of the zinc deposition potential and the zinc electrode was immediately charged for 4 hr against the cadmium electrode. The counterelectrode was then back-charged at 1.0A against the nickel screen for 2.5 hr and cycling of the zinc electrode against the sectioned electrode was continued on an automatic cycler which had a filtered power supply. During cycling, the current to each section was monitored by measuring the voltage across the shunts on a multipoint recorder that had a zero center scale and a range of -12.5 to $+12.5$ mV full scale. The potential was recorded on a multipoint recorder with a range of 0-2V full scale. Occasionally the potential relaxation at the end of charge and discharge was monitored by a scanning switch in conjunction with a high impedance amplifier and a digital voltmeter.

If the cycling regime consisted of a zinc overcharge, the cadmium electrode was occasionally back-charged against the nickel screen before the cadmium capacity became exhausted. Whenever the nickel screen was used to charge the counterelectrode, the cell was vacuum-treated afterward to remove gas bubbles from the vicinity of the nickel screen. The cadmium electrode sections were monitored from time to time to ensure that they were still charged.

The cycling regime for the run reported in this paper was a 1.0A charge for 105 min followed by a 102-min discharge at the same current. Provisions were made also to terminate the charge if the zinc polarization exceeded 200 mV; thus, the cycling regime of the zinc electrode was similar to that encountered in a cell with an efficient positive electrode such as silver oxide. Other runs were made with as much as 15% overcharge each cycle to simulate the conditions encountered in a nickel-zinc cell (16).

Requirements and choice of the experimental method.—The cell components and configuration were chosen to facilitate application of the findings of this investigation to a practical battery. Cadmium was chosen as the counterelectrode since (a) fabrication of a flat sectioned electrode was easy; (b) gas bubble formation or (c) bridging between sections was unlikely; and (d) complications due to separator oxidation were avoided. The cadmium electrode has the additional advantage of having low polarizability on charge and discharge, and thus does not have an overriding effect on the current distribution in the cell.

The cellulose separators expand on wetting, thus facilitating construction of a snug-fitting cell pack. The layer of grafted polyethylene separator prevented the growth of zinc dendrites to the cadmium electrode. Shorting to the sectioned cadmium electrode would vitiate any current or potential distribution measurement. The other layer of grafted polyethylene between the zinc anode and the reference electrode capillaries prevented the growth of zinc into the capillaries during overcharge. This was a problem in some preliminary cell tests where there was no membrane between the zinc electrode and the reference capillaries.

The positioning of the reference electrodes on the back of the zinc electrode was possible since the electrodes were thin and porous. This juxtaposition of the reference electrodes and the zinc plate did not interfere with the cell current distribution, ensured that all capillary exits were equidistant from the zinc electrode, and facilitated prevention of dendritic growth into the capillaries.

The counterelectrode capacity was not allowed to become discharged for the simple reason that limiting factors at the cadmium electrode would complicate interpretation of the current distribution results. This consideration outweighed any effects the charging screen might have on the current distribution.

The sectioned counterelectrode technique was used since this method gives the most direct measurement and has minimum effect on the current distribution cell. Further sectioning at the electrode edges would be desirable, but it was felt that the effects generated by such sectioning would nullify any increase in resolution that might accrue from this method.

Results

Post-test analysis of cell.—After 120 cycles the cell was taken apart in the charged condition and examined. No visible deterioration of the separators, the cadmium electrode, the charging screen, or the reference electrodes had occurred during cycling. Zinc did not penetrate any of the separator layers. A photograph of the zinc electrode is shown in Fig. 4. The zinc electrode underwent a loss of 45% in geometric area with the zinc agglomerating toward the lower part of the plate. No zinc grew beyond the edges of the current collector screen. In the areas where the zinc agglomerated, the plate thickness increased by as much as a factor of two in some places. The front face (i.e., the face nearest the counterelectrode) of the zinc deposit consisted compacted gray sponge zinc. Underneath this deposit was a cake of uncharged zinc oxide, embedded in the electrode grid. At the edge of the thick zinc deposit, additional zinc was deposited directly on the grid forming a border about 3 mm wide around the zinc oxide cake. Between this border and the zinc oxide cake, small traces of blue zinc material were observed on the back side of the electrode. In the electrode regions beyond the continuous zinc deposit, small scattered deposits of crystalline zinc dendrites were found.

Figure 4 also shows the relative positions of the sixteen counterelectrode sections and the reference electrode capillaries. All of sections No. 1 and 5 were denuded of zinc. Little zinc remained in sections No. 9, 13, and 2. Considerable zinc loss occurred in sections No. 3, 14, 15, and 16. The greatest gain in zinc de-

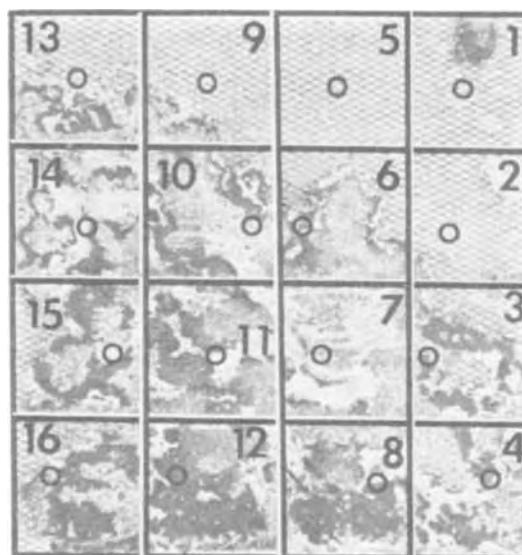


Fig. 4. Photograph of the zinc electrode after 120 cycles; relative positions of the counterelectrode sections and the reference capillaries are also shown. The numbers refer to the portions of the cadmium electrode and the reference capillaries. Sections 1, 5, 9, 13 are along the top of the cell.

posit thickness occurred in sections No. 7, 8, 10, 11, and 12.

Current distribution on the cadmium electrode.—In the formation process, the current to each cadmium electrode section stabilized to a value of 62 ± 4 mA after two formation cycles. The current distribution was equally even on charge and discharge. The over-all electrode capacity was 4.5 A-hr on the fourth formation cycle.

During the preliminary cycling of the cadmium electrode in the cell against the nickel screen, the electrode capacity stabilized at 4.25 A-hr. The section current on charge was 62 ± 5 mA. The heterogeneous deposition of zinc on the nickel screen in the initial stages of discharge caused wide variations in the section current during discharge. This zinc was stripped from the screen in the first few minutes of charge. The cadmium electrode capacity was checked at the end of each run and no significant deterioration of the capacity was found.

Reference electrodes.—After the cell was wet down and vacuum-treated a few times, the reference electrode potentials stabilized at values that varied by no more than 1 mV of one another.

Current and potential distribution on the zinc electrode.—The current and potential distribution for cycles No. 3, 19, 31, 60, 75, 100, and 120 are shown in Fig. 5-11, respectively. Initially, the current distribution between sections was relatively even. However, the current distribution between sections on discharge bore no apparent relationship to the current distribution between the sections when the cadmium electrode was charged with the nickel screen. In the early stages of cycling, there was a greater variation in the current distribution during charge than during discharge. Also, in the early stages of cycling, the current distribution on charge tended to diverge with time whereas the current distribution on discharge tended to converge with time. These trends may be seen in Fig. 12 for sections No. 5, 7, 9, and 10 in cycle No. 2. In the initial stages of cycling, the potential distribution was even on both charge and discharge. However, after about 15 cycles, sections No. 1, 5, 9, and 13 polarized more at the end of charge than any of the

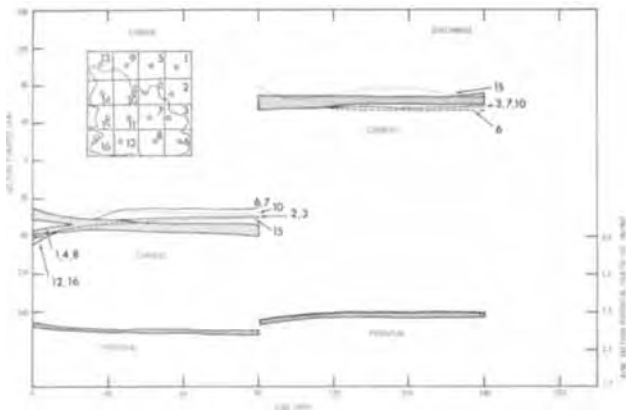


Fig. 5. Current and potential distribution on the zinc electrode, cycle No. 3. Inset in Fig. 5-13 shows the shape change pattern after 120 cycles together with the relative positions of the counterelectrode sections and the reference capillaries. Where there is no distinct convergence or divergence of the current distribution, the data are presented as cross-hatched bands.

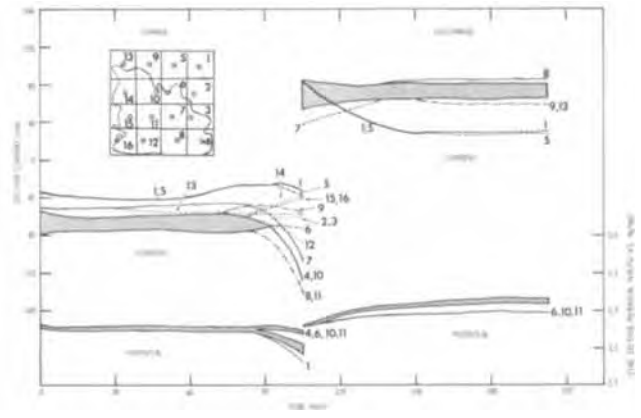


Fig. 8. Current and potential distribution on the zinc electrode, cycle No. 60. Explanation of inset is given in Fig. 5 caption.

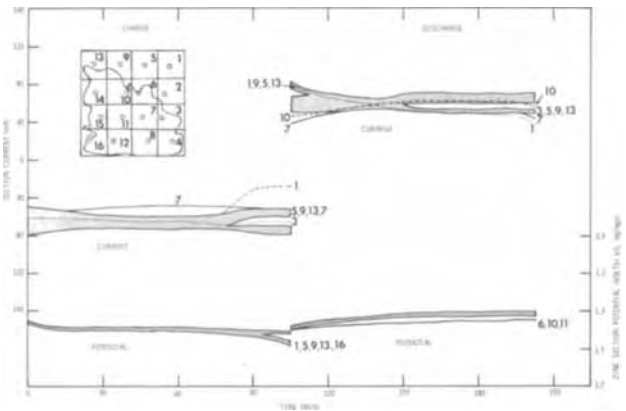


Fig. 6. Current and potential distribution on the zinc electrode, cycle No. 19. Explanation of inset is given in Fig. 5 caption.

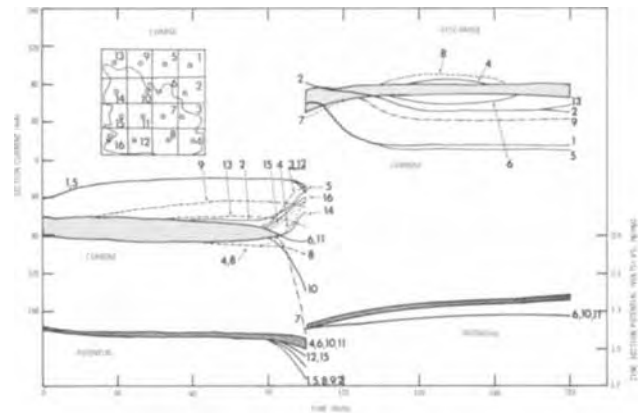


Fig. 9. Current and potential distribution on the zinc electrode, cycle No. 75. Explanation of inset is given in Fig. 5 caption.

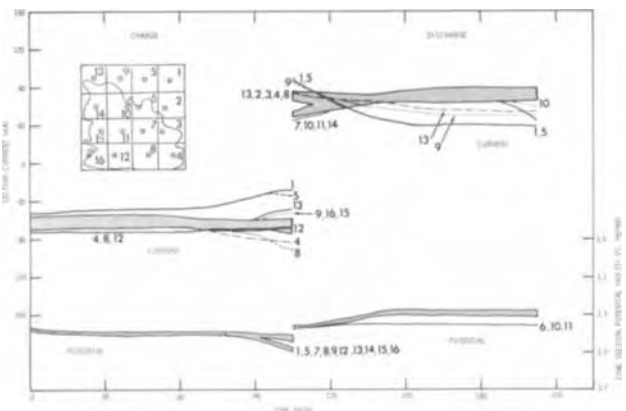


Fig. 7. Current and potential distribution on the zinc electrode, cycle No. 31. Explanation of inset is given in Fig. 5 caption.

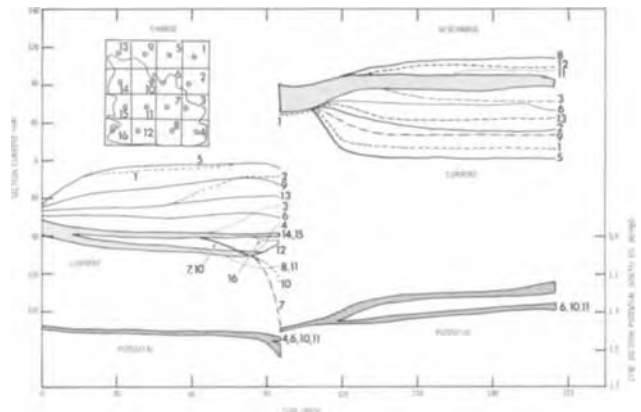


Fig. 10. Current and potential distribution on the zinc electrode, cycle No. 100. Explanation of inset is given in Fig. 5 caption.

other sections. With this polarization, there was a concomitant drop in current to these sections. After about 25 cycles, these same sections also had lower currents in the latter stages of discharge (Fig. 7). This type of trend continued throughout cycling until eventually most of the current was being carried by sections No. 7, 8, 10, 11, and 12 (Fig. 8-11). Toward the end of cycling, the low current areas of the zinc electrode tended to polarize on discharge (Fig. 11). The external IR correction, as determined by a 60-cycle Kordes-Marko interrupter, was negligible (about 2 mV).

In some runs, the cell was cycled in the horizontal position periodically. The various cell orientations pro-

duced no changes in current or potential distribution that could be distinguished from the normal slight variations in these parameters that occurred from cycle to cycle. This was true even when these experiments were repeated with different open-circuit stand times of up to 24 hr in each position before cycling.

Similar potential distribution patterns were observed in two electrode nickel-zinc cells, thus indicating that the results obtained in these experiments were not an artifact of the sectioned electrode. Furthermore, the shape-change patterns in these experiments were similar to those found in nickel-zinc cells with similar separator systems and electrode geometries.

Current interruption.—One salient feature of the current distribution in the latter stages of cycling was

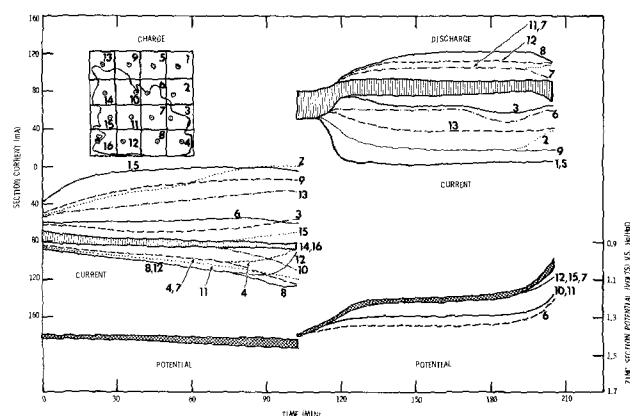


Fig. 11. Current and potential distribution on the zinc electrode, cycle No. 120. Explanation of inset is given in Fig. 5 caption.

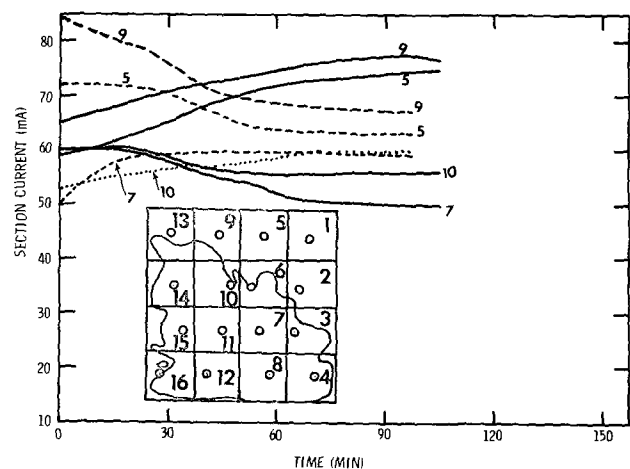


Fig. 12. Current and potential distribution for selected sections, cycle No. 2. Solid lines, charge; broken lines, discharge. Explanation of inset is given in Fig. 5 caption.

that the current distribution was relatively uniform for about the first 7 min of discharge (Fig. 9-11), whereas on charge the current distribution immediately diverged after switching to charge. However, if the current was interrupted after one or two minutes of discharge, and the cell allowed to stand overnight on open circuit, the current distribution on resumption of discharge had a spread similar to that found after half an hour of steady discharge. On the other hand if the current was similarly interrupted after an hour of charge, the current distribution on resumption of charge showed a spread similar to that found at the beginning of charge. Thus, interruption of the current in the initial stages of discharge leads to a divergence in current distribution on switch on, whereas the interruption of the current in the latter stages of charge leads to a convergence of current distribution on switch on.

Potential relaxation.—Figure 13 shows the potential relaxation on the electrode when the current was shut off at the end of charge and discharge during cycle No. 75. Figure 14 shows similar data in another run where the cell was overcharged each cycle. At the end of charge, the potentials initially have a wide spread and eventually, with time, the potentials converge to a common value. At the end of discharge, however, there are little differences in the potential across the surface of the electrode.

Overvoltage on the zinc anode.—Figure 15 shows zinc polarization measurements in a two-electrode nickel-zinc cell with similar anode construction parameters to the zinc electrode used in the current distribution measurements. These data were obtained at the

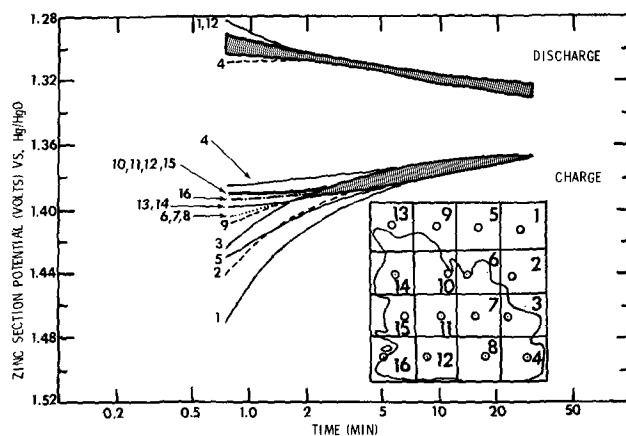


Fig. 13. Potential relaxation on zinc electrode, cycle No. 75. Explanation of inset is given in Fig. 5 caption.

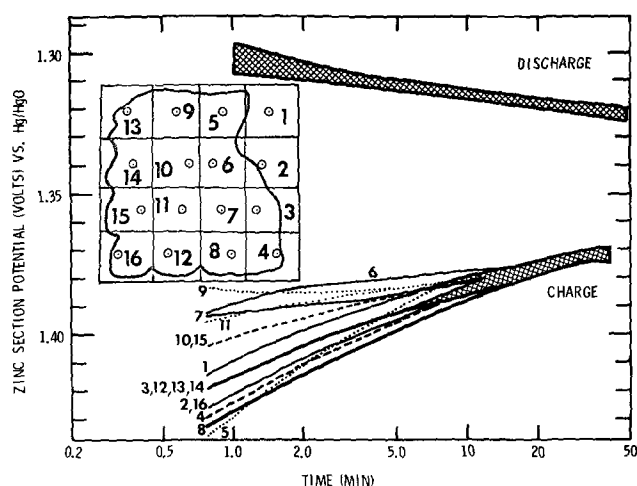


Fig. 14. Potential relaxation on electrode, cycle No. 27. Charge and discharge current, 1.0A. Charge time, 100 min. Discharge time, 87 min. Inset shows final shape change pattern after 70 cycles.

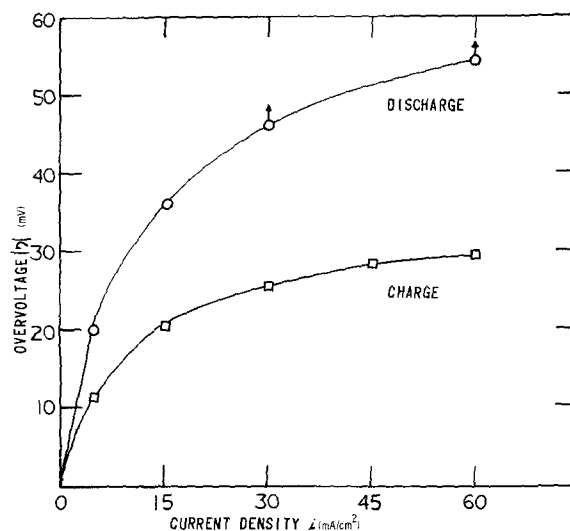


Fig. 15. Polarization curves for zinc electrode on charge and discharge.

same stage of electrode charge. Polarization measurements on charge were reproducible; and at each current density, the polarization reached a plateau value. At the higher current densities, on charge, the polarization went through a maximum before reaching a plateau. This type of behavior is not unknown (17, 18). The plateau values are shown in Fig. 15. On

discharge, the polarization continually increased with time at the higher current densities. The variation of the polarization with current density was greater on discharge than on charge.

Discussion

Significance of potential distribution.—Secondary zinc electrodes usually have a silver grid and are cycled in such a way so as to maintain an excess of metallic zinc in the electrode at all times. Hence, the potential in the metal will be constant throughout the whole area of the electrode, even when current is passed through the cell. If the zincate concentration does not vary over the surface of the electrode, the open-circuit potential, as measured by a reference electrode capillary, will be constant irrespective of where the measurement is made on the surface of the electrode. However, if the concentration of zincate varies from one position to another, a potential difference will exist between these points on the electrode surface. This potential difference will not be the usual Nernstian potential difference. Local differences in zincate activity will result in concentration cells across the surfaces of the electrode. In these concentration cells, the areas with high concentrations of zincate are the cathodes; and the areas with low concentrations of zincate are the anodes. The situation here is a complex example of the thin-film corrosion problem that has been discussed by Waber and his co-workers (19, 21). Accordingly, the measured differences in interfacial potential depend on the relative magnitude of a number of parameters that have the dimensions of length, viz., the separator thickness (t), the radial parameter for the anode area (R_a), the radial parameter for the cathode area (R_c), together with the lengths of the Wagner parameters (22) for the anode and the cathode. The Wagner parameters for the anode and cathode are, respectively, $k_a = \sigma(\partial\eta_a/\partial i)$ and $k_c = \sigma(\partial\eta_c/\partial i)$ where η is the overvoltage and i the current density; σ , in this case, is a complex function of the conductivity of the electrolyte and the separator. The radial parameters R_a and R_c will be the radii of anodic or cathodic areas if they are circular, or the half widths of such areas if they are strips along the edge or middle of the electrode. If R_a and R_c are large in comparison to t , k_a , and k_c , then differences in potential can be measured over the surfaces of the electrode. If one assumes $\sigma = 0.1$ mho cm^{-1} , then both k_a and k_c at low current densities will be 0.6 cm, and at higher current densities, $k_c \approx 0.02$ cm and $k_a \approx 0.06$ cm. Consequently, the only requirement then for locating anodic and cathodic sites on a zinc electrode, by means of a closely placed reference probe, is to have anodic and cathodic sites a few millimeters in diameter and a reference probe that has a capillary diameter of a millimeter or less. The measured interfacial potentials will include anodic and cathodic polarizations together with the ohmic drops in the electrolyte (23). So, even though the electrolyte has a high conductivity, interfacial potential measurements can locate concentration cell anodes and cathodes if they are large enough in area.

When current is passed through the cell, differences in overvoltage can exist over the surface of the electrode either because of differences in the local current density or variations in the zincate concentration at various points on the electrode. Ideally, for these measurements, the reference capillary exits should be at the face of the zinc electrode, that is toward the counterelectrode (24). Since such an arrangement is virtually impossible here, the measured polarization values in these experiments will differ from those found at the plate face. The external IR correction to the measured potential can be isolated by standard interrupter techniques. On interruption of current, however, concentration cell effects can occur, thus rendering absolute measurements impossible.

It is, therefore, evident that potential distribution measurements yield only qualitative data. Such measurements can locate anodic and cathodic sites on an electrode on open circuit (23), detect the position of concentration polarization on charge, and identify local passive areas on discharge.

Significance of the current distribution.—In the later stages of cycling, the current to the areas without zinc (section No. 1 and 5) was essentially zero throughout most of the charge and discharge cycles (Fig. 10 and 11). This strongly indicates that any particular section current was a good quantitative measurement of the current to the zinc electrode area that was in exact register to that counterelectrode section. Since the electrode was amalgamated and no excessive hydrogen evolution was observed, the current distribution on charge is a very direct measurement of the metal deposition distribution.

The predicted current distribution, with no polarization at the electrodes, is the primary current distribution (25); and this is determined by the geometry of the electrodes, the electrolyte, and any other conductive or nonconductive objects in the electrolyte. However, high current density points polarize and some of the current is rerouted to other positions of the electrode, thus yielding the secondary or actual current distribution (25-28). The magnitude of the corrective effect of electrode kinetics on the current distribution is described by the Wagner parameter, $k = \sigma(\partial\eta/\partial i)$. Increasing the value of k results in a more uniform current distribution (22). So, for a given KOH concentration and separator system, the current distribution depends on $\partial\eta/\partial i$, the electrode polarizability (29).

Since the polarizability of the cadmium electrode is low (30), the measured current distribution in the cell was a good indication of the current distribution that is inherent to a zinc electrode operating in a secondary cell with a prismatic construction.

Mechanism for shape change.—In a thin plate prismatic secondary zinc cell, the primary current distribution should be the same for both charge and discharge. However, because the polarization behavior of zinc electrodes is different on charge and discharge (Fig. 15), the secondary current distribution will be different during the anodic and cathodic process. The closest approach to the primary current distribution will be expected the instant the cell is switched to discharge after charging in the early stages of cycling. At the beginning of discharge, in a fresh cell, there will be plenty of active sponge zinc throughout the plate, and the electrode at this stage will have a low polarizability. The increase of this initial low polarizability with time would explain the convergence of the current distribution to more uniform values (Fig. 5, 6, and 12) as the discharge progresses. This increase in polarizability may be due to the formation of the prepassive films that have been described by Powers and Breiter (31, 32) and by Hull *et al.* (33). At the beginning of charge, however, the current distribution will not be as close to the primary current distribution as at the beginning of discharge because high current density points are temporarily highly polarized in the initial stages of charge (17, 18). Further on in the charge, in the initial stages of cycling, the zinc electrode operates under conditions where the substrate area increases continuously and metal deposition occurs in a milieu with an excess of reducible material. Hence, the electrode polarizability is low (Fig. 15); and, thus, the nonuniformity and divergence of the current distribution on charge (Fig. 5 and 12) may be explained.

In a cell with plane parallel electrodes, the primary current distribution will be high at the plate edges since the current lines can pass outside the space between the electrodes (22). In a secondary zinc cell, the edge effect will be greatest at the top and sides of the electrode. Here, the corrective effects of the electrode polarizability on charge and discharge will be greatest. The net effect is that at the beginning of cycling more

zinc is deposited at the edges than is depleted in the subsequent discharge. Because of this, the zinc oxide and zincate supply at the plate edges becomes rapidly depleted in the early stages of cycling; so, after a short period of cycling, some of these positions polarize at the end of charge. This concentration polarization results in a concomitant drop in the current (Fig. 6 and 7) to these positions.

The question arises as to how the depletion of zinc oxide and zincate at the plate edges results eventually in the removal of zinc from these positions (Fig. 4). A plausible explanation is that zinc is removed by a concentration cell which dissolves zinc off the plate edges and deposits it at the center of the plate. The results in Fig. 13 and 14 indicate that, after charging, the edge positions are negative to the center positions of the electrode. The relaxation of these potentials to a common value must occur via a concentration cell rather than by the much slower diffusion process. It is easy to demonstrate that zinc can be plated and depleted by such a process at a reasonable rate by simply shorting one zinc electrode in KOH electrolyte and another electrode in a zincate electrolyte while having both electrolytes in contact with one another. The results of such a test are shown in Fig. 16. Concentration cell effects also explain the divergence in the current distribution after interruption of current at the beginning of discharge and the convergence of the current distribution after current interruption toward the end of charge. In the former case, the concentration cell exhausts the zinc supply at the plate top edges whereas in the latter case, the concentration cell generates a fresh supply of reducible material at these same positions. These concentration cells can occur on termination of charge or may even possibly occur on charge if there is a drop in the over-all electrode polarization during charge.

Very direct evidence of such concentration cell effects was found in one of the early runs in this investigation. The sectioned cadmium electrode was accidentally overcharged, against the nickel screen, to potentials negative to the zinc deposition potential. When the current was interrupted, anodic and cathodic current transients were observed in different sections. Initially, these currents were 30-60 mA, and the cur-

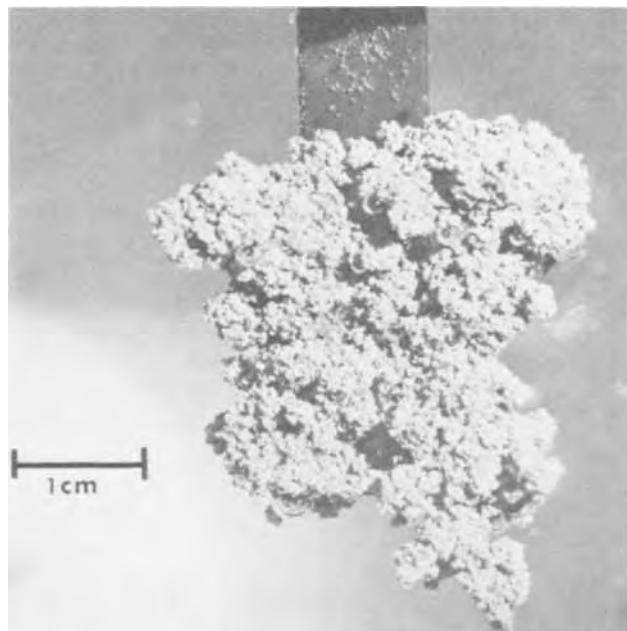


Fig. 16. Zinc concentration cell, 100 hr after shorting. Cell case (12 x 13 x 2.5 cm) was half filled with 37.5 w/o KOH + 70g ZnO/liter, and then filled to the top with 37.5 w/o KOH without mixing. The anode (10 x 5 x 0.050 cm) was electroplated dendritic zinc and the cathode was sheet zinc (2 x 1 cm).

rents decayed to zero in about 5 min after opening the cell circuit. Undoubtedly, these currents were due to zinc concentration cell effects since the sectioned electrode remained at the zinc potential after termination of charge. The currents were much larger than those that could be attributed to pH gradients (34), and the relative positions of the screen and sectioned electrode does not facilitate the formation of pH gradients.

After discharging the electrode, the electrolyte will be supersaturated with zincate (35-38); hence, the small differences in the potentials across the surface of the electrode (Fig. 13 and 14).

With the onset of shape change, the edge positions will start to passivate toward the end of discharge. This passivation will result in a divergence in the current distribution in the latter part of the discharge cycle (Fig. 7-11).

Because the current distribution at the beginning of discharge, in a fresh cell, closely approaches the primary current distribution, the anolyte at the plate periphery will become supersaturated with zincate before the center positions. This will generate a concentration gradient between the edge and center of the electrode and transfer zincate toward the center of the plate. This transfer of zincate toward the plate center together with the erosion of the plate periphery by concentration cells results in shape change.

The sequence of events that has been postulated above to explain the current and potential distribution patterns, as well as the remote and immediate causes of shape change, is consistent with prior visual observations of the onset and progress of shape change. When a secondary zinc cell is cycled, it is observed that after some cycles, some edge position will charge up completely. At the end of charge, this position will consist entirely of zinc whereas other positions will have both gray zinc metal and white zinc oxide. After some more cycling (say, 10 cycles), this area will become bare of zinc; and at the end of charge only a few scattered dendrites will be found here on the grid, thus indicating a position of high polarization on charge (37). Other positions like this will develop, and the electrode will start to lose geometric area rapidly. Then, at the end of a deep discharge, the edges of active material will have a blue tinge. This blue color is due to the passive zinc films that have been described by numerous authors (31-33).

The fact that shape change occurs in cells that are cycled horizontally, and since cell orientation does not affect the current distribution, it is doubtful if gravity has any major effect on shape change. The frequent occurrence of shape change at the plate top is more likely due to the extended current paths that are available in the separator folds and to the fact that conventional cell construction techniques, where cathodes are wrapped in separator "U" folds, tend to raise the top edge of the positive plate above the edge of the zinc electrode. Convection effects can carry zincate to the bottom of a cell with widely spaced electrodes (14), but the possibility of convection in a tightly fitting cell pack is limited.

Consistent interpretation of factors that affect shape change.—Any factor that causes nonuniform current distribution will result in an increase in the rate of shape change. Thus, the bad effects of (a) high resistivity membranes, (b) wrinkling separators, (c) nonalignment of positive and negative plates, and (d) plate defects and bare spots can be readily explained. The decrease in the rate of shape change by the reduction of the KOH concentration from 45 to 30 w/o (8) can be explained on the basis of the improvement in current distribution by the higher conductivity of the electrolyte at lower KOH concentrations. In a secondary zinc-air cell with a third electrode (40), the current distribution will be very poor once shape change starts, since, here, one has a relatively reversible zinc electrode out of alignment with a highly polarizable counterelectrode. Thus, the current distribution will

be quite uniform over the third electrode whereas the edge of the zinc active material, beyond which the third electrode extends, will be a high current density point (41). Hence, shape change should proceed rapidly once it starts.

If the supply of zinc oxide at the plate edges is increased, the number of cycles required to exhaust the zincate supply and thus set up a concentration cell, will be increased. Hence, the onset of shape change will be delayed. Thus, the beneficial effects of increasing the stoichiometric ratio of negative to positive active material, extending the plate edges, and the use of dish-shaped negatives can be readily explained.

Reduction of the zinc plating efficiency will improve the metal distribution on the plate and will mitigate shape change. The beneficial effect of removing mercury from the zinc can thus be rationalized.

The mechanism for shape change also explains why shape change is independent of the grid structure, and why the addition of mechanical barriers, such as fibers, does not mitigate shape change. A possible explanation for the beneficial effect of binders is that they maintain the integrity of the plate during cell construction and prevent the shedding of zinc oxide. The loss of zinc oxide from the grid would generate a site from where shape change could start and proceed by the above mechanism. In electrodes without binders, no shape change occurs at the plate bottom or at the lower part of the plate sides. The shed zinc oxide in the lower part of the cell is a reservoir of zincate that prevents shape change at these positions. Binders reduce the degree of shed and in such electrodes shape change can occur at the plate bottom.

In cells with large electrodes and wrinkling separators, bare spots can occur at random throughout the zinc plate. The mechanism for the occurrence of these spots must be the same as that described above for shape change.

The electrochemical nature of the shape-change phenomena explains why zinc can build up with such enormous pressures at the plate center. In some instances, both the centers of the zinc electrode and the positive electrode become densified and mechanical stresses sufficient to rupture cell cases are generated.

According to this mechanism, cycling is a necessary condition for the occurrence of shape change. This is in agreement with the fact that shape change does not occur on wet stand or when the cell is kept on float.

The current distribution effects which eventually result in concentration cells do not occur until later on in the discharge cycle (Fig. 12). This is in concordance with the fact that shape change occurs more slowly when a cell is cycled at shallow depths of discharge.

Summary

The patterns of current and potential distribution on a cycling zinc electrode have been monitored while keeping the electrode and cell parameters as similar as possible to those found in a conventional secondary zinc cell.

Differences in current distribution throughout cycling have been explained in terms of changes in the secondary current distribution resulting from variations in electrode polarizability. Differences in the secondary current distribution during charge and discharge result in the exhaustion of the reducible zinc species at the plate periphery in the early stages of cycling. The initiation and progress of shape change have been explained on the basis of concentration cells that corrode zinc off the plate edges and deposit metal at the plate center, and current distribution effects at the beginning of discharge. Further variations in the current distribution throughout cycling have been interpreted in terms of local concentration polarization on charge and local areas of passivity on discharge.

Although the electrolyte conductivity was high, the concentration cells could be detected by potential measurements because the anodic and cathodic polarizabil-

ities were low and the electrolyte path in the separator was thin in comparison to the radial dimensions of the anodic and cathodic sites.

The data from this investigation together with the postulated mechanism for shape change were used to rationalize most of the reported phenomena related to zinc shape change in secondary cells.

Acknowledgment

The assistance of Mr. Joseph J. Gondek in carrying out these experiments is gratefully acknowledged.

Manuscript submitted June 7, 1972; revised manuscript received July 31, 1972. This was Paper 19 presented at the Miami Beach Meeting of the Society, Oct. 8-13, 1972.

Any discussion of this paper will appear in a Discussion Section to be published in the June 1973 JOURNAL.

REFERENCES

1. J. J. Murphy, *Chem. Technol.*, **1**, 487 (1971).
2. J. J. Lander, in "Zinc-Silver Oxide Batteries," pp. 457-469, A. Fleischer and J. J. Lander, Editors, John Wiley & Sons, Inc., New York (1971).
3. J. McBreen and G. A. Dalin, "The Mechanism of Zinc Shape Change in Secondary Batteries," Extended Abstracts, The Electrochemical Society, Inc., Battery Division, **11**, 123-124 (1966).
4. G. A. Dalin, Ref. 2, pp. 87-95.
5. T. Z. Palagyi, *This Journal*, **108**, 904 (1961).
6. F. Solomon and G. W. Work, in "Batteries 2," pp. 463-473, D. H. Collins, Editor, Pergamon Press, Oxford (1965).
7. H. K. Farmery and W. A. Smith, in "Batteries," pp. 179-205, D. H. Collins, Editor, The Macmillan Company, New York (1963).
8. G. A. Dalin, M. Sulkes, and Z. Stachurski, *Proc. 18th Ann. Power Sources Conf.*, p. 54, Atlantic City (1964).
9. G. A. Dalin and M. Sulkes, *Proc. 19th Ann. Power Sources Conf.*, p. 69, Atlantic City (1965).
10. J. Goodkin, *Proc. 22nd Ann. Power Sources Conf.*, p. 79, Atlantic City (1968).
11. J. McBreen, U.S. Pat. 3,505,115 (1970).
12. J. Goodkin, U.S. Pat. 3,493,434 (1969).
13. French Pat., 1,601,216 (1970).
14. D. P. Boden, V. J. Spera, and R. B. Wylie, "Potential Distribution over the Surface of Planar Zinc Electrodes During Charge and Discharge at Constant Current," Extended Abstracts, The Electrochemical Society, Inc., Fall Meeting, Detroit (1969).
15. A. Fleischer, *Trans. & J. Electrochem. Soc.*, **94**, 289 (1948).
16. F. P. Kober and A. Clarkey, in "Power Sources 3," pp. 309-326, D. H. Collins, Editor, Oriel Press, Newcastle upon Tyne (1971).
17. S. Arouette, K. F. Blurton, and H. G. Oswin, *This Journal*, **116**, 166 (1969).
18. H. G. Oswin and K. F. Blurton, Ref. 2, pp. 63-85.
19. J. T. Waber, *This Journal*, **102**, 420 (1955).
20. J. T. Waber and B. Fagan, *ibid.*, **103**, 64 (1956).
21. J. T. Waber, *ibid.*, **103**, 567 (1956).
22. C. Wagner, *ibid.*, **98**, 116 (1951).
23. G. W. Akimov, *Corrosion*, **11**, 515t (1955).
24. M. Eisenberg, C. W. Tobias, and C. R. Wilke, *This Journal*, **102**, 415 (1955).
25. H. E. Haring and W. Blum, *Trans. J. Electrochem. Soc.*, **44**, 313 (1923).
26. C. M. Shepherd, *This Journal*, **112**, 252 (1965).
27. R. J. Brodd, *Electrochem. Technol.*, **6**, 289 (1968).
28. T. P. Hoar and J. N. Agar, *Discussion Faraday Soc.*, **1**, 162 (1947).
29. J. O'M. Bockris and A. K. N. Reddy, "Modern Electrochemistry," Vol. 2, p. 894, Plenum Press, New York (1970).
30. P. C. Milner and U. B. Thomas, in "Advances in Electrochemistry and Electrochemical Engineering," pp. 1-86, P. Delahay and C. W. Tobias, Editors, John Wiley & Sons, Inc., New York (1967).
31. R. W. Powers and M. W. Breiter, *This Journal*, **116**, 719 (1969).
32. R. W. Powers, *ibid.*, **116**, 1652 (1969).
33. M. N. Hull, J. E. Ellison, and J. E. Toni, *ibid.*, **117**, 192 (1970).
34. F. G. Will, in "Power Sources," pp. 149-165, D. H. Collins, Editor, Pergamon Press, Oxford (1968).

35. T. P. Dirkse, *This Journal*, **102**, 497 (1955).
 36. V. N. Fierov, *Zh. Fiz. Khim.*, **31**, 49 (1957).
 37. N. A. Hampson, P. E. Shaw, and R. Taylor, *Brit. Corrosion J.*, **4**, 207 (1969).
 38. T. P. Dirkse, Ref. 16, pp. 485-493.
 39. J. W. Diggle, A. R. Despic, and J. O'M. Bockris, *This Journal*, **116**, 1503 (1969).
 40. R. Salcedo Gumucio, U.S. Pat. 3,219,486 (1965).
 41. A. T. Vagramyan and Z. A. Solv'eva, "Technology of Electrodeposition," p. 354, Translation by A. Behr, Robert Draper Ltd., Teddington (1961).

Surface Preparation and Pit Propagation in Stainless Steels

H. S. Isaacs*¹ and G. Kissel

Brookhaven National Laboratory, Upton, New York 11973

ABSTRACT

A scanning reference electrode has been used to measure the number of active pits on 304 stainless steels in ferric chloride solution with time. The probability of a pit deactivating has been discussed in terms of the physical and chemical properties of solid oxide films over the pit which were originally on the steel and undermined by the dissolution process. The properties of these films were varied by different surface preparations.

The pitting of metals has been described as a highly localized form of crevice corrosion (1-3) and this analogy is further emphasized by the presence of a film over pits (1, 2, 4, 5) which restricts the flow of solute and solution in the pit cavity. It has been suggested that the film was the passive oxide layer which remained over the pit after the metal beneath it has been dissolved away during pit growth (4, 5). The presence of the film over the pit was found to play a decisive role during the early stages of the pitting process as any disruption of the film rapidly led to passivation of the pit walls (4). The properties of the passive oxide layer would depend on surface preparation and this investigation set out to determine whether surface preparation in turn influenced the propagation of actively pitting sites.

Experimental

The apparatus used in this study to locate active pitting sites and monitor them during exposure to ferric chloride solution has been described in detail elsewhere (4). Basically the method consists of measuring potential variations in a pitting environment with a fine capillary probe leading from a reference electrode. The tip of the probe scans a plane in solution close to and parallel with the pitting surface. The potential variations in the solution close to the surface arise from the ohmic potential differences which exist between the anodic areas (the pits) and cathodic areas (the passive metal surface) as current flows between them. The variations of potential in the solution are recorded on an X-Y recorder and arranged to show a three-dimensional potential surface with anodic sites as peaks and cathodic sites as troughs. Figure 1 shows examples of the appearance of the X-Y recordings during pitting corrosion of stainless steel in ferric chloride.

Specimens 15 × 30 mm were cut from a single sheet of Type 304 stainless steel, having a composition shown in Table I. The specimens were masked with silicone rubber after surface preparation. Surfaces in an abraded and electropolished condition were tested. The abraded surface was prepared by polishing down to a 600 grade silicon carbide paper. Electropolishing was performed for 10 min in a mixture of 60% phosphoric acid, 20% sulfuric acid, and 20% water at 25°-45°C, at a current density of about 1 A/cm² and 10V

* Electrochemical Society Active Member.

¹ Present address: Metals and Ceramics Division, Oak Ridge National Laboratory, Oak Ridge, Tennessee 37830.
 Key words: scanning reference electrode, pit deactivation, oxide films.

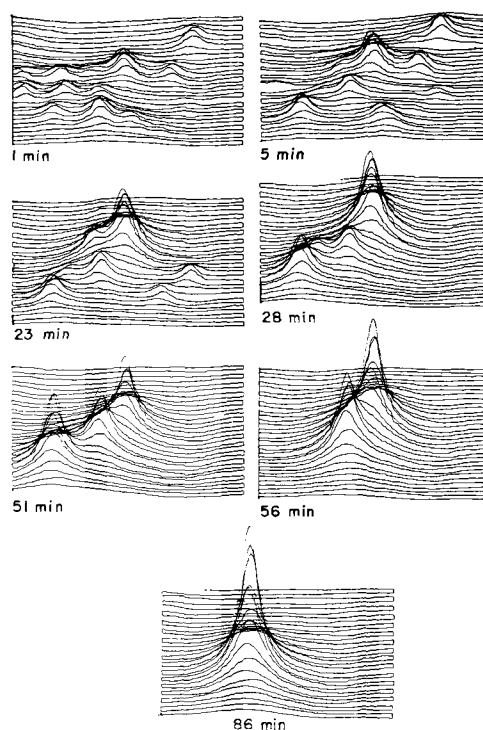


Fig. 1. Potential scans above an electropolished surface initiated at the times shown.

across the cell. The electropolished surfaces were in addition (a) oxidized in air at elevated temperature and (b) cathodically polarized in the polishing solution for 10 min. Specimens were also prepared with one part of the surface having a different preparation from the remaining area. For example, an area of an abraded

Table I. Composition of stainless steel

Cr	17.1%	Mn	0.5*
Ni	8.8%	Si	0.5*
C	0.07%	Mo	0.2*
		Cu	0.07*
		Ti	0.02*

* Spectrographic analysis.

surface was masked and the surrounding area electropolished. The mask was then removed, the specimen degreased, and prepared for testing in the usual manner by applying silicone rubber to the electropolished area leaving both an abraded and electropolished surface exposed.

The ferric chloride solution used for all the tests consisted of 0.4M FeCl_3 with approximately 0.03M HCl giving a pH of 0.9. The tests were conducted at $25^\circ \pm 1^\circ\text{C}$ with the solution unstirred and exposed to air.

Results

Recordings of the potential variations over the electropolished steel surface are shown in Fig. 1. The first scan, initiated 1 min after contact between the specimen and the chloride solution, showed 14 peaks indicating an equal number of active pits on the surface. The second scan initiated 5 min after contact showed that 10 pits were active. Subsequent scans showed that the number of peaks or active pitting sites decreased until after about 86 min only one active pit was present. Figure 2 gives a plot of the number of active pits as a function of time for the results shown in Fig. 1 and for a second test with an "as-electropolished" surface. The latter results are included to show the variations occurring between tests as replicate tests were conducted for all surface preparations. Figure 2 also includes results for different surface treatments of electropolished specimens. Specimens cathodically polarized showed that any pits on the exposed metal surface rapidly deactivated as no active pits could be seen on scanning for 1 min or less after contact between metal and the chloride solution. However, about 10 pits/cm² were present on the exposed surface after removing the specimen from the solution, indicating that pitting did take place and what may be termed crevice corrosion developed extremely rapidly at the specimen-insulation interface. These crevices were initiated by pits which "fanned" out under the protective insulation. The broken line in Fig. 2 for the cathodically polarized specimen is only approximate, giving the minimum rate of pit decay deduced from the observations that 10 pits were observed after exposure and no active pits were present during the first scan which took 3 min.

Air oxidation for 24 hr above 100°C increased the number of active pits and decreased the rate at which

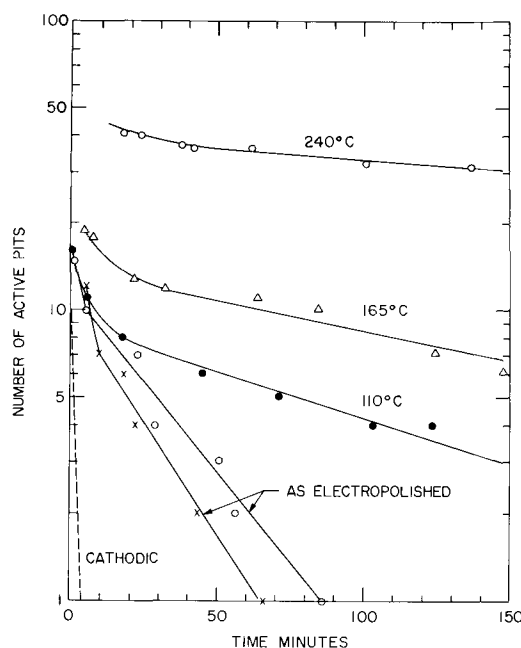


Fig. 2. Influence of surface treatment on the variation of active pits with time for electropolished surfaces. Specimens were oxidized for 24 hr at the temperatures shown. The "cathodic" curve for a cathodically treated surface is an approximation.

these pits deactivated as shown in Fig. 2. These effects became more pronounced as the temperature of oxidation was increased to 240°C. Recordings of scans for a specimen oxidized at 240°C is shown in Fig. 3. When the density of active peaks was high (>30 pits/cm²) difficulty in counting small peaks was encountered. Amplification of the potential variations did not help as this gave overlapping of the larger peaks to an extent that their number could not be counted. The procedure that was adopted involved a low amplification so that the larger peaks could easily be counted, but necessitated the assumption that peaks which developed after a period of time resulted from pits which were initiated when the specimen was immersed in the ferric chloride, but grew slowly. The corrosion potentials of the specimens were also recorded (4) and when high densities of pits were present the potential dropped rapidly during the first 20 min of exposure to less than 0.1V relative to the saturated calomel electrode (i.e., less than 0.15V relative to hydrogen). This value is below that for the critical pitting potential of Type 304 stainless steel in 1.2N chloride solutions (6), and pits would therefore not be expected to initiate during the test.

The effect of higher oxidation temperatures for short times were also studied. These results are shown in Fig. 4 for specimens heated at 250°, 300°, and 375°C for 2 hr. The shorter oxidation period gave essentially the same behavior as may be seen on comparison of the 2-hr oxidation at 250°C with the results of heating at 240°C for 24 hr. The rate of decay of active pits on specimens heated at 375°C was significantly different from those oxidized at lower temperatures. This specimen also showed a first-order straw interference color that disappeared during exposure to ferric chloride, suggesting that the oxide had dissolved.

The results for abraded stainless steel surfaces were similar to those for the cathodically polarized electropolished surface, as the pits which formed on the exposed surface deactivated within a few minutes and crevice corrosion developed. Oxidation of abraded surfaces at 240°C also increased the life of pits but

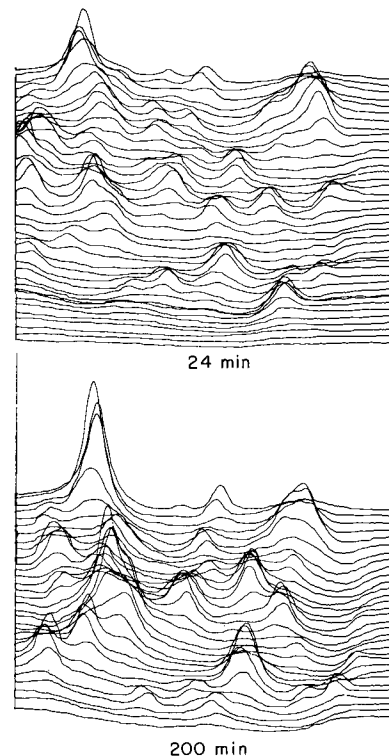


Fig. 3. Potential scans above an electropolished surface oxidized for 24 hr at 240°C initiated at the times shown.

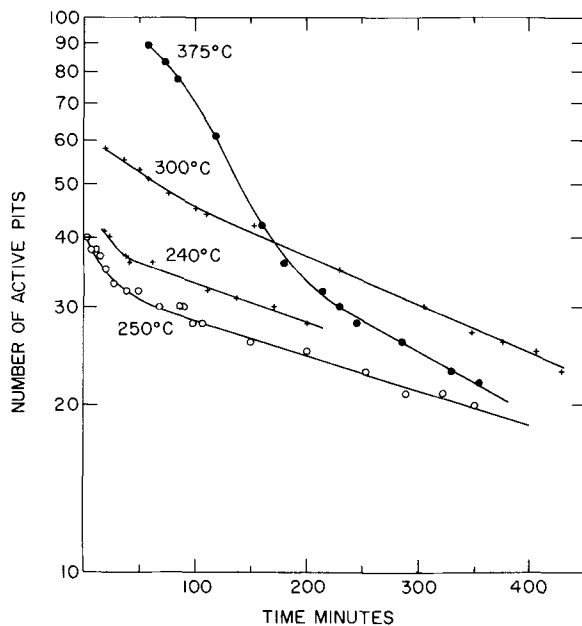


Fig. 4. Influence of oxidation temperature on the variation of active pits with time. ○, +, ●, oxidized for 2 hr at temperatures shown; + oxidized at 240°C for 24 hr.

even these pits deactivated within a relatively short period.

The behavior of active pits on a surface with areas having different preparations was simply an extension of the above results. For example, when the surface had one area which was electropolished and a second area that was abraded active pits propagated only on the electropolished area. The abraded area showed no active pits but was distinctly more cathodic than the unpitted electropolished area. This was clearly indicated by a trough on the X-Y recordings which corresponded to the abraded surface. In another test with a cathodically treated electropolished area and a second as-electropolished area, active pits were again present only on the latter area. In this case, the unpitted area did not show the marked cathodic behavior. An air oxidized electropolished area also showed a higher density of pits than an as-electropolished area on which all the pits decayed after about 40 min.

Discussion

The results in Fig. 2 and 4 clearly show that both the number of active pits and the rate at which they decrease with time depends markedly on surface treatment of the steel. If the probability of pits deactivating remained constant for a given surface preparation, the curves would be linear. This appears to be the case for the majority of the results at longer times after some initial curvature. The linear portions of the curve which are the more important in assessing corrosion resistance from a practical point of view, may be related to a half-life of active pits. The half-life is equal to the time taken for half of a given number of active pits to passivate. Table II gives the half-lives for each of the surface preparations investigated. The smaller the half-life, the greater will be the probability of an active pit on the exposed surface deactivating and the greater will be the resistance to pitting corrosion. From Table II it is, therefore, concluded that the abraded surfaces and the cathodically polarized electropolished surfaces are the more pit-resistant surface preparations. Similar conclusions have been reached by other investigators using different techniques (6, 7).

The variations in pit life result from changes brought about during pitting by the different surface preparations. These changes were not the result of electrochemical kinetics. The electrochemical properties of

Table II. Variation of pit half-life with surface preparation

Surface treatment	Pit half-life, min
Electropolished and cathodically polarized	<1
As electropolished	22
Electropolished and oxidized at 110°C for 24 hr	90
Electropolished and oxidized at 165°C for 24 hr	150
Electropolished and oxidized at 240°C for 24 hr	430
Electropolished and oxidized at 250°C for 2 hr	480
Electropolished and oxidized at 300°C for 2 hr	340
Electropolished and oxidized at 375°C for 2 hr	270
Abraded with 600 grade SiC	<1
Abraded and oxidized at 250°C for 8 hr	5

* Maximum variation of 20%.

the metal surface within the pit would not, per se, be influenced by surface preparation, specifically, when the surface treatment did not involve heating the steel and probably when the heating was conducted for only a few hours at temperatures below 400°C. Tests with specimens prepared with one part of the surface having a different preparation from the remaining area, showed that the pit life depended on the surface treatment of the particular area. The lives of these pits were similar to those in Table II and were independent of the treatment of the remaining area. These observations also indicate that neither the cathodic reduction kinetics nor variations in the corrosion potential (which would be expected to influence pitting or interactions of small pits), played any major part in the life span of active pits in ferric chloride. The influence of surface preparation, however, would be expected to influence the properties of the passive oxide layer.

It has been shown that the perpetuation of small active pits depended on the presence of a solid film over the pit. When these films were purposefully disrupted during the early stages of growth, the pitting action ceased (1, 4). The presence of the film, therefore, played a decisive role in the perpetuation of pitting probably by restricting the diffusion of the high chloride concentration from the pit cavity. The importance of a physical barrier preventing diffusion of chloride away from the pit may be seen on considering the factors which influence the concentration in the active pit. Changes in chloride concentration result from the differences in fluxes of chloride to and away from the pit, carried by the current (8) and diffusion, respectively.

If a pit is small and open to the bulk solution, the concentration gradient down which chloride diffuses away from the pit will be large and the rate of chloride loss will be high. The diffusion gradients would decrease as the pit radius increased, i.e., the rate of concentration change would be inversely related to the radius. Assuming that the current density at the pit walls is constant the flow of current and hence the flow of chloride to the pit will be proportional to the square of the radius. The difference between these rates, as a function of pit radius, indicates that when the pit is small and open, loss of chloride will predominate and the pit would passivate. However, if the radius is greater than some critical value, an open pit would then remain active. In agreement with this model, earlier investigations did show two stages in the propagation of pitting. The second stage was reached after a pit had grown on electropolished surfaces for over an hour and did not deactivate on removing the film (4).

On the basis of this approach, during the early stages of pit growth (when the pit is small), the integrity of the film over the pit plays an important role in determining whether a pit will remain active or passivate, e.g., weak films which are easily disrupted or perforated give a rapid rate at which pits passivate. The results in Fig. 2 and 4 may then be interpreted in terms of the properties of the film on the steel. However, owing to the meager amount of in-

formation available relating to the chemical and physical properties of thin oxides ($<500\text{\AA}$) it has not, in general, been possible to predict the relationship between surface treatment and the behavior of pitting once it has initiated. A large number of factors play a role in the complex behavior of the oxide (9) prior to and after it has been separated from the metal by the pitting process.

The integrity of the film depends on the stress acting on it. Stresses will arise from both internal and external forces. The external forces that result from convection currents in the solution and possibly pressure buildup within the pit may be considered to remain approximately constant and independent of surface preparation.

The influence of the external forces on the breakdown of the film over pits depends on the film thickness as the resulting stresses would be inversely proportional to the thickness. Changes in the intrinsic mechanical properties of the oxide (e.g., plasticity and fracture stress) with thickness do take place but if these were not marked, the thinner film would be more susceptible to breakdown and the half-lives would be shorter. This is, in general, borne out experimentally as shown in Fig. 2. The thinnest films on the cathodically polarized surface gave the shortest half-life (<1 min). The film thickness on the as-electropolished surface would be intermediate between the cathodically polarized surface and that formed by air oxidation above 100°C , and the thickness would be expected to increase with increased oxidation temperatures. The half-life of the active pits does vary in accord (Table II) and for the specimen oxidized at 240°C it was 430 min. These results show that the probability of pits deactivating can be varied by over two orders of magnitude by changes in the thickness of the oxide. Rhodin (10) has also shown that the pitting of Type 304 stainless steel in 10% ferric chloride (0.67M FeCl_3) depended on the oxide thickness. His results give a linear dependence between the estimated oxide thickness and weight loss. However, with films formed by oxidation, there is a change in the characteristics of the film when grown above 300°C .

The composition of the oxide formed on stainless steel varies with surface preparation, as shown by Rhodin (9), and these variations could also lead to changes in the physical and chemical properties of the oxide. For example, oxides grown in oxygen at 100°C had substantially higher chromium concentrations (37.2%) than oxides grown in an oxidizing aqueous solution ($5\% \text{HNO}_3 + 0.5\% \text{K}_2\text{Cr}_2\text{O}_7$ at 60°C) which contained 20% chromium. These changes would be expected to influence the point defect concentrations in the oxide which in turn would alter the plasticity of the oxide (12) and the pitting characteristics, as has been clearly demonstrated by Bianchi *et al.* (13) for annealed oxide films. Variations in composition may also lead to changes in the dissolution rate of the film. It was clear that the oxide formed after oxidation at 375°C did dissolve on exposure to ferric chloride as the interference color disappeared. In this test the pit behavior was also markedly different (Fig. 4) and no definite slope was observed for up to 200 min. These observations suggest that above about 250°C chemical changes take place in the oxide film which render it more soluble and increase the probability of pits deactivating. This effect reverses the trend of increased pit stability with increased oxide thickness as observed up to 250°C .

During the first few minutes of exposure of the steel to the ferric chloride solution the results in Fig. 2 and 4 indicate that the number of active pits increased with increased oxide thickness. This observation contrasts with that of Bianchi *et al.* (13) whose results for oxidized surfaces showed a maximum density of pits after exposure at 300°C . Nevertheless, in view of the different behavior of active pits on the surface oxidized at 375°C (Fig. 4) from those at lower temperatures,

the different solutions used for pitting the steels and the method of measuring the presence of pitting, the two sets of results are not in conflict. Both illustrate marked changes in the characteristics of the oxide when oxidized above 300°C .

Internal forces within the film will depend on processes during its formation. The ratio of the volume of oxide formed from a given volume of metal (the Pilling-Bedworth ratio) would be greater than unity and there is the possibility that high compressive stresses could develop. However, the development of the stress depends on the diffusing species in the oxide and as these are predominantly cationic (11), low or no compressive stresses will be present in the film on the metal (12). Compressive stresses in the oxide, even if present, would lead to the oxide blistering when undermined by pitting and would be less likely to result in rupture of the film during pitting than tensile forces, unless the film showed a sufficient degree of plasticity to relieve the tensile stress. Abrading the surface of the steel would be expected to introduce both defects and stresses in the oxide grown on the surface (9). The results in Table II do show that the active pits on the abraded surfaces even after oxidation at 250°C have very small half-lives and probably reflect both the presence of internal stresses and disruption of the metal surface.

The results obtained at times less than 50 min show that the number of active pits increased as the rate of their decays decreased. This suggests that the number of initiated pits on contacting the steel and the ferric chloride solution may not differ markedly with surface treatment. If this was the case then the influence of the properties of the oxide on the steel plays the major part in determining the number and growth of pits rather than factors involved in pit initiation. Hence, the scanning technique, as do other techniques which depend on current flow from a pit of greater than 10^{-10}A (corresponding to approximately a 100\AA pit), gives information only about the presence of an active pit and conjecture relating to its initiation.

Summary

1. The propagation of active pits is highly dependent on the surface preparation of stainless steel specimens which reflects the properties of the oxide film on the surface.
2. The half-lives of active pits increase with increased thickness of the oxide when grown thermally below 300°C . At and above this temperature significant dissolution of the oxide occurs reflecting changes in the chemical properties of the oxide, and reducing the life of active pits.
3. The number of active pits is more readily related to the properties of the film than to factors that relate to their initiation.

Acknowledgments

The authors wish to thank Dr. L. Newman for his helpful discussions. This work was performed under the auspices of the United States Atomic Energy Commission and supported in part by the United States Army Reactor Engineering Group.

Manuscript submitted May 4, 1972; revised manuscript received July 28, 1972.

Any discussion of this paper will appear in a Discussion Section to be published in the June 1973 JOURNAL.

REFERENCES

1. I. L. Rosenfeld and I. S. Danilov, Proc. Third Int. Conf. on Metallic Corrosion, Moscow, 1966, p. 139.
2. I. L. Rosenfeld and I. S. Danilov, *Z. Phys. Chem.*, **226** (1964).
3. B. F. Brown, *Corrosion*, **26**, 249 (1970).
4. H. S. Isaacs, Int. Conf. on Localized Corrosion, Williamsburg, Virginia, December 1971.
5. J. Yahalom, Int. Conf. on Localized Corrosion, Williamsburg, Virginia, December 1971.

6. M. A. Streicher, *This Journal*, **103**, 375 (1956).
 7. J. M. Kolotyrkin, *Corrosion*, **19**, 261 (1963).
 8. H. P. Leckie and H. H. Uhlig, *This Journal*, **113**, 262 (1966).
 9. U. R. Evans, *Electrochim. Acta*, **16**, 1825 (1971).
 10. T. N. Rhodin, *Corrosion*, **12**, 465 (1956).
 11. O. Kubaschewski and B. E. Hopkins, "Oxidation of Metals and Alloys," Butterworth (1962).
 12. D. H. Bradhurst and J. S. Ll. Leach, *Trans. Brit. Ceram. Soc.*, **62**, 793.
 13. A. Bianchi, A. Cerquetti, F. Mazza, and S. Torchio, Int. Conf. on Localized Corrosion, Williamsburg, Virginia, December 1971.

Passivation of Iron in Sulfuric Acid Medium

Israël Epelboin,* Claude Gabrielli, Michel Keddad, Jean-Claude Lestrade, and Hisasi Takenouti

Groupe de Recherche du C.N.R.S. "Physique des Liquides et Electrochimie," associé à l'Université Paris VI, Paris 5e, France

ABSTRACT

A "Z-shaped" current voltage curve is shown to be controllable with a new device which is equivalent to a voltage source in series with a negative resistance, both being adjustable. The latter was built with an operational amplifier. Using this original regulating device, the steady-state anodic polarization curve of an iron rotating disk in molar sulfuric acid was studied as a function of the rotation speed. The Z-shaped curve thus obtained exhibits a continuous and reversible transition between active and passive states. This particular shape of the polarization curve explains the steep transitions observed with a potentiostatic regulation. In the passive to active state transition the dissolution of the disk is localized to a ring part of the surface, the dimensions of which were followed as a function of the total current and of the rotation speed. The explanation of this quite heterogeneous distribution of current density can be found in the coupling between the convective-diffusive mass transfer and a very steep variation of current density vs. potential.

The anodic behavior of iron in molar sulfuric acid solution, when controlled by a potentiostat, is characterized by a current-voltage curve which exhibits two steep transitions between active and passive state. When the potential is increased toward more anodic values, a sudden drop of current takes place at a passivation potential, V_P . When decreasing the potential, from values more anodic than V_P , a jump of current takes place at an activation potential, V_A , less anodic than V_P . The activation potential has been considered to be identical with the Flade potential (1), as defined by the potential decay method. This idea seems to us more valid than the alternative one which identifies V_P with the Flade potential, because the high current densities in the active state, at potential V_P , lead to considerable overvoltages which originate from ohmic drop and concentration gradients. Moreover, the presence of crystalline $FeSO_4 \cdot 7H_2O$ layers on the electrode surface (2) may induce oscillations in the system.

According to some authors, ohmic drop (3) and/or mass transfer (4) might induce such steep transition as mentioned above, between active and passive state, as well as oscillations of the electrochemical system, which could be explained by a breaking down of control. The observed potentiostatic behavior would thus not be a fundamental property of the iron-sulfuric acid solution interface. In order to verify this assumption, we devised an electronic control apparatus different from the potentiostat.

Polarization Control

Principle.—Let I be the current flowing through an electrochemical cell from a counterelectrode E_2 to a working electrode E_1 (Fig. 1a). The latter may be connected to ground either directly (position 1) or through a resistor R (position 2). If I is a positive current, E_1 is an anode, in the opposite case it is a cathode. If U is the voltage between E_2 and ground, and if the cell is fed by a voltage source E in series

with a resistance ρ , then, whatever the behavior of the cell may be, we can write

$$U = E - \rho I \tag{1}$$

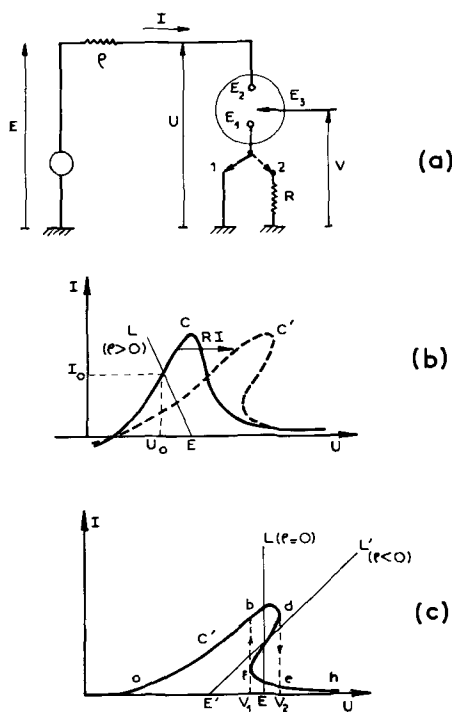


Fig. 1 (a). Electrochemical cell fed by a voltage source E in series with a resistance ρ . E_1 , working electrode; E_2 , counterelectrode; E_3 , reference electrode. E_1 can be connected to ground either directly at 1, or through a resistor R at 2. (b). Current-voltage curve referring to (a) with working electrode grounded (curve C) or connected to ground through R (curve C'). L is the load line corresponding to $U = E - \rho I$, $\rho > 0$. (c) Curve C' of (b) with L , load line with $\rho = 0$ and L' , load line with $\rho < 0$.

* Electrochemical Society Active Member.
 Key words: anodic dissolution, convective-diffusion, disk electrode, discontinuous current distribution, regulation.

The related "load line" L, in the *U-I* plane, is drawn on Fig. 1b. Its slope is $-1/\rho$. On the other hand, the electrochemical cell, with the working electrode connected to ground may be characterized by a curve such as C in the *U-I* plane. If L crosses C in one point (U_0, I_0), this point is an equilibrium one for the system consisting in the cell and the polarization device. In many circumstances, it is possible, with a proper choice of ρ , to determine C only by varying E . The electrochemical cell is then said to be controllable by the polarization device. The current I being a steady one, the voltage V between the working- and counter-electrode can be measured independently by means of a reference electrode, E_3 , so that one gets the usual plot of current-voltage curves in the *V-I* plane.

In the particular case when one value of I corresponds to a value of U , the resistance ρ can be chosen as zero (L parallel to the I axis). But this requirement is not always met, as it can be seen on Fig. 1b where the curve C' corresponds to the same cell as before, but with a resistor R between working electrode and ground. This situation may also arise from an ohmic drop between working- and counterelectrode. A load line parallel to the I axis ($\rho = 0$) crosses C' in three points if $V_1 < E < V_2$ (Fig. 1c). We shall call "Z-shaped" this kind of curve. With this regulation device, the part a-b-d of C' is obtained at increasing voltage. If U is further increased, I drops from d to e, then e-h is obtained. At decreasing voltage, starting from h, h-e-f is obtained, then I jumps from f to b. An analogous situation is met when using a potentiostat, if the current-voltage curve in the *V-I* plane is Z-shaped. Whenever the load line is tangent to the curve in a point such as d or f, this point is unstable (5) and a steep transition of current takes place from the corresponding value of the current to another one. We shall recall this remark later, when discussing the transitions which are observed with an anode of iron in sulfuric acid solution.

Coming back to the control device of Fig. 1, it is easy to see that an electrochemical system, with a curve such as C', can be controlled if the load line L' has a positive slope (Fig. 1c), i.e., if ρ has a negative value. This can be achieved by using a negative impedance converter (NIC), a two port device which has the property that the impedance seen at its output is the negative of the impedance connected across its input.

Polarization control using a NIC.—A NIC can be defined in terms of the two port variables (E', I'), (U, I) shown in Fig. 2, by the equations

$$\begin{aligned} U' &= U \\ I' &= -KI \quad K > 0 \end{aligned} \quad [2]$$

If a voltage source E , in series with a resistance ρ , is connected across the input

$$U' = E - \rho I'$$

Using Eq. [2], this equation is written

$$U = E + K\rho I \quad [3]$$

In the *U-I* plane, the corresponding load line has a positive slope $1/K\rho$. In other words, the control device

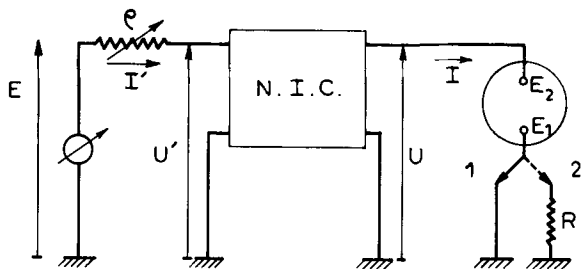


Fig. 2. Negative impedance converter. Sign conventions for currents and voltages.

acts as a voltage source E in series with a negative resistance $-K\rho$.

The NIC, the properties of which have been known for a long time (6), may be realized by using a differential-input operational amplifier as the active element (7), as shown on Fig. 3 which gives the whole set-up used to record current voltage curves in the *V-I* plane. With the usual simplifying assumptions used when dealing with operational amplifiers, the constant K equals R_2/R_1 (full details are given in the Appendix). The values of ρ and E can be adjusted in order to get any load line with positive slope in the *U-I* plane, and the current-voltage curve in the *V-I* plane is obtained by varying either E , or ρ , or both, as necessary. As no current flows into the negative input point of the amplifier, the current flowing through the cell is the same as the current flowing through R_2 . It is measured with the help of a differential amplifier D.

Test of the polarization control device.—The test has been carried out with an austenitic stainless steel disk electrode, rotated at 2000 rpm in 2N H₂SO₄. The composition of the alloy is 16% Cr, 14% Ni, 4.2% Si. The experiment covers the transpassive region. The same curve 1 (Fig. 4) has been obtained, using a potentiostat (8) or the present polarization control device with $\rho = 0$. This result holds with a grounded working electrode. A 50-ohm resistor is then inserted between

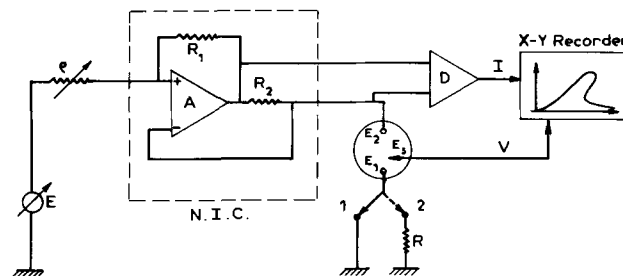


Fig. 3. Experimental set-up. E , adjustable voltage source ($-5V \leq E \leq 5V$); ρ , adjustable resistor ($0 \leq \rho \leq 10$ kohms). The operational amplifier is Analog Devices, 406 Model, with $A \geq 95$ db; $R_1 = 100$ ohms; $R_2 = 1$ ohm. The frequency compensating circuits are not shown. D is a differential amplifier.

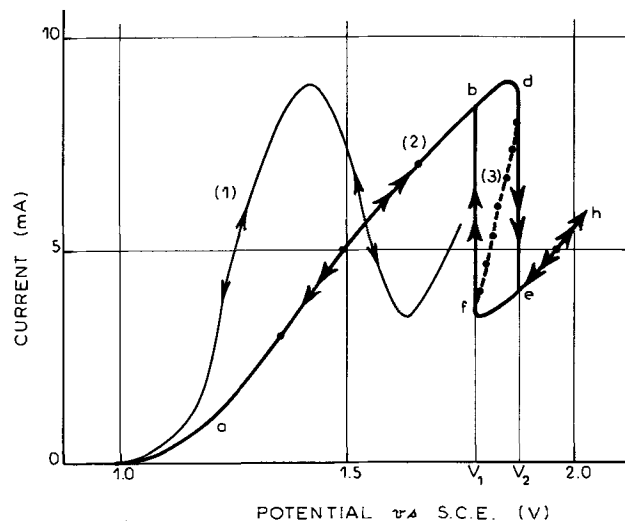


Fig. 4. Test of the NIC control device, carried out with a stainless steel rotating disk electrode (diameter 4 mm). Curve 1 is current voltage curve of the working electrode connected to ground, drawn either with a potentiostat or the NIC control device with $\rho = 0$. Curve 2 is current voltage curve of the working electrode connected to ground through 50 ohms (the voltage is taken between reference electrode and ground). Same polarization device as in curve 1. Curve 3 is current voltage curve of the same system as curve 2, drawn with the NIC control device with $\rho \neq 0$.

this electrode and ground. With a potentiostat, as well as with the present control device with $\rho = 0$, curve 2 is obtained. It exhibits two steep transitions d-e and f-b, and the current is not the same at increasing (a-b-d-e-h) or decreasing (h-e-f-b-a) voltage, as shown by the arrows on Fig. 4. With the polarization control device using a NIC, and a value of ρ different from zero, a continuous curve 3 (a-b-d-f-e-h) is obtained. The dashed part d-f cannot be drawn with a potentiostat, while the remaining parts coincide with the corresponding potentiostatic drawing. This curve does not depend on the value of E and ρ used to draw it. It is perfectly reproducible and reversible. Moreover it coincides with the theoretical curve which can be deduced from curve 1 by adding the ohmic drop corresponding to the resistance $R = 50$ ohms. The same curve is also obtained when the current I is not measured in the way shown in Fig. 3 (i.e., from the voltage across R_2) but from the voltage across a resistance in series with the counterelectrode. With this last procedure, the experimental data is free from any possible artifact coming from the polarization control device, as long as each point of the curve is an equilibrium point, since the measured current is the very current which flows through the interface.

Results

The rotating electrode, which may be disk- or square-shaped, is the cross section of an iron rod (Johnson-Matthey), embedded in an insulating acrylic resin cylinder of circular cross section. The molar electrolyte solution is prepared from Merck Suprapur sulfuric acid, and water purified with ion-exchange resins. Oxygen is removed from the solution by argon bubbling (Air Liquide, "U" quality). The temperature of electrolyte is 25°C controlled within $\pm 0.1^\circ\text{C}$.

Current voltage curves.—Figure 5 shows the steady-state behavior of a disk electrode (5 mm in diameter) rotated at 750 rpm. The curve in Fig. 5(a) refers to potentiostatic conditions, the curve in Fig. 5(b) to polarization control with the device using a NIC. The voltage V is measured between the working electrode and a reference electrode (SCE). With a potentiostat,

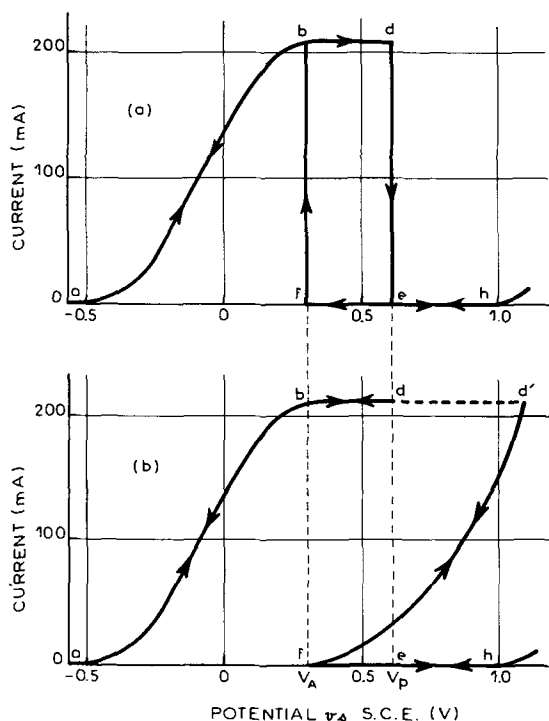


Fig. 5. Current-voltage curves of a disk electrode (diameter 5 mm) rotated at 750 rpm: (a) using a potentiostat, (b) using the device of Fig. 3.

the curve is described through the points a-b-d-e-h at increasing potential, h-e-f-b-a at decreasing potential. When the rate of potential sweep is too fast, a maximum of current is observed in the vicinity of point b (2, 9), but it disappears under steady-state conditions. The steep transitions which take place at V_A and V_P do not occur when the NIC device is used (curve b). The dashed part d-d' of the line corresponds to the average value of a fluctuating current which cannot be controlled. The magnitude of these fluctuations is not negligible, they are rather slow, but have no well-defined frequency. They are not to be mistaken for the oscillations which are known to occur with certain potentiometric polarization conditions (3, 4). The a-b-d and h-e-f part of the curves (a) and (b) are identical with both techniques, but, when using a NIC, any point can be reached at either increasing or decreasing potential. The continuous transition d'-f between active and passive state is also reversible. However in the vicinity of point f, at currents lower than a few milliamperes (not visible on the scale of the drawing), it is difficult to ascertain the reversibility of the curve. We shall ignore this point because all the results to be presented here have been obtained at much higher currents. Anyhow, the shape of curve (b) in the vicinity of f explains the jump of current f-b observed with a potentiostat, as discussed above (see Fig. 1c). The transition d-e (curve a) is probably induced by the coming of the fluctuation observed in d-d' (curve b).

Experiments have been carried out at various rotation speed Ω (Fig. 6). In regions such as b-d (see Fig. 5), the current is limited by diffusion. It increases as $\Omega^{1/2}$, in agreement with Levich's theory (10), extended in this laboratory to concentrated solutions (11).

Localized dissolution of the electrode.—Figure 7 shows photographs of a rotating disk electrode after it has been polarized in the transition region between passive and active state [part of d'-f of curve (b), Fig. 5], with a schematic drawing of the corresponding sections. The general case (12) corresponds to the dissolution of a ring-shaped part of the surface (Fig. 7c). The depth of field of a conventional microscope is small enough for the depth of attack to be determined within $\pm 1 \mu\text{m}$. The edges of the ring are sharp, and its diameters are determined easily with a micrometer. The remaining part of the electrode is not attacked as it can be seen by referring to the insulated part of the disk. An actual profile is given in Fig. 8. It has been tested independently by direct observation after the electrode has been cut along its axis.

The inner and outer diameters of the ring, d_i and d_e , vary with current and rotation speed (Fig. 9). As limiting cases, d_i reduces to zero (Fig. 7b), or d_e becomes identical with the diameter of the disk (Fig. 7a). At a given rotation speed, dissolution takes place

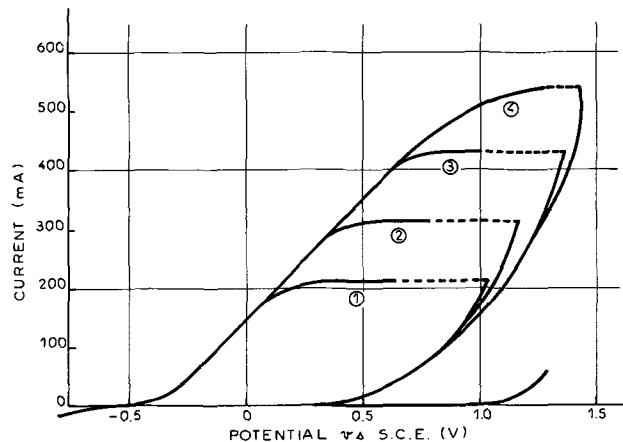


Fig. 6. Current-voltage curve of a disk electrode (diameter 5 mm), at rotation speeds: curve 1, 750 rpm; curve 2, 1600 rpm; curve 3, 3000 rpm; curve 4, 4500 rpm.

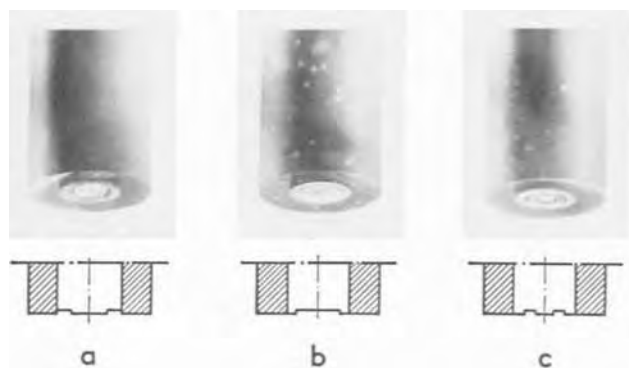


Fig. 7. Localized dissolution of a disk electrode. (a) Rotation speed: 750 rpm; $I = 60$ mA; $V = 740$ mV/SCE. (b) Rotation speed: 4500 rpm; $I = 60$ mA; $V = 740$ mV/SCE. (c) Rotation speed: 3000 rpm; $I = 250$ mA; $V = 1190$ mV/SCE. Under each photograph, schematic section of the electrode.

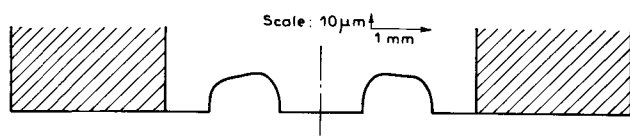


Fig. 8. Actual profile, determined from measurements with a microscope, corresponding to Fig. 7c.

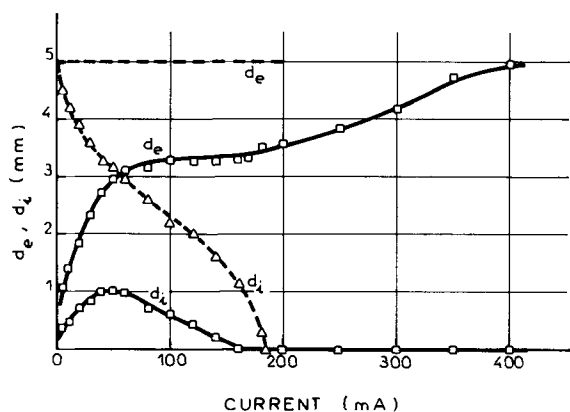


Fig. 9. Inner and outer diameter of the ring-shaped dissolved part of a disk electrode, vs. current, at various rotation speeds: \square solid line 4500 rpm, \triangle broken line 750 rpm.

on an increasing area when current increases, until the whole disk is attacked.

Experiments have also been carried out with rotating square-shaped electrodes. From the hydrodynamical point of view, the rotating body behaves in the same way as in the previous experiments since the electrode is embedded in an insulating coating of circular cross section, but the boundary conditions are different. A localized dissolution is again observed. The attacked part may have many different shapes, depending on rotation speed and current. The limiting cases are given in Fig. 10. At low speed, the undissolved part is a square, the sides of which are parallel to the sides of the electrode (Fig. 10a). At high rotation speed, the attacked region is a circular ring (Fig. 10b). Its center coincides with the center of rotation of the system even if the latter is not the center of the square.

In the transition region between passive and active state, the total current is used to dissolve metal with valency 2, as it has been verified by a spectrophotometric titration of Fe²⁺, with o-phenantroline as an indicator. It proves that no electrochemical reaction of appreciable rate takes place on the part of the

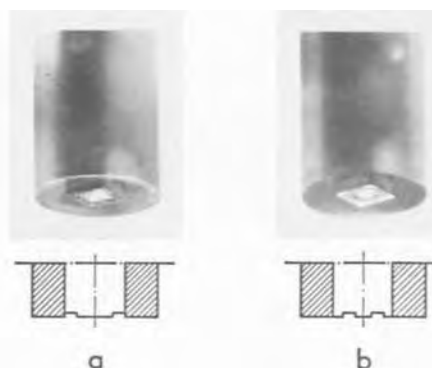


Fig. 10. Localized dissolution of a square shaped electrode. (a) $\Omega = 750$ rpm; $I = 20$ mA; $V = 500$ mV/SCE. (b) $\Omega = 3000$ rpm; $I = 60$ mA; $V = 740$ mV/SCE. Under each photograph, schematic section of the electrode.

electrode which is not attacked. Then it is possible to derive the average dissolution current density from the current and the area of the attacked surface (Fig. 11).

Discussion

As shown by using a new polarization control device, a continuous and reversible transition does exist between the active and passive state of iron in 2N sulfuric acid solutions. The steep transitions which can be observed when using a potentiostat are not related to merely electrochemical processes, as they are generally thought to be (13). They result from the fact that a potentiostatic regulation is not appropriate when dealing with Z-shaped polarization curves.

The decrease of current from a limiting value to zero (d' to f in Fig. 5) is due, not only to a decrease of the active area, but also to a decrease of current density (Fig. 11). As far as we know, this is the first example of an electrochemical system for which several over-all reaction rates can exist for a given potential. To be sure that it is a fundamental property of the iron-sulfuric acid interface, it is necessary to estimate the ohmic drop, which, if large enough, is able to transform a bell-shaped curve into a Z-shaped curve [(8) and Fig. 1b]. The ohmic term is not proportional to the current, since the active area is not constant.

The ohmic drop has been measured with the interrupter technique at the point d' (Fig. 5b) where the whole area of the electrode is active. After correction, this point is more cathodic than the point f if the rotation speed is higher than 1600 rpm. But it is more

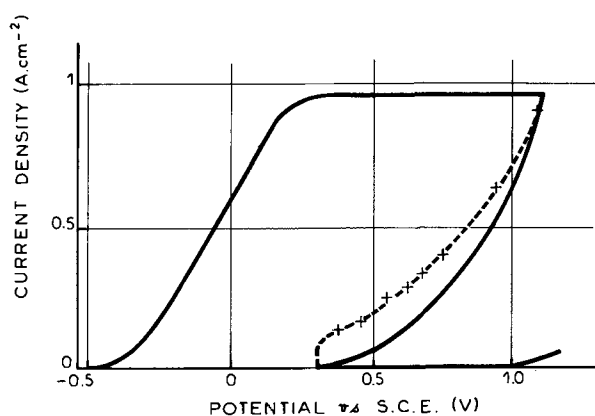


Fig. 11. Full line: experimental current density, i.e., total measured current, divided by the total area of the disk. Dashed line: average current density for the attacked surface, i.e., total measured current, divided by the area of the attacked part of the electrode.

anodic at lower rotation speeds. Then the ohmic drop cannot completely explain the shape of the polarization curve. Mass transfer has also to be taken into account, in particular for the point d'. It also plays a part in the localized dissolution of the electrode, as shown by the above experiments, since the shape and the size of the attacked region depend not only on the shape of the electrode, but also on the rotation speed. Coupling between mass transfer by convective diffusion, ohmic drop in the electrolyte, and charge transfer have been studied by Newman (14) from a theoretical point of view in the case of a rotating disk electrode. According to the author, who assumes an exponential relationship to exist between the charge transfer reaction rate and the potential, a maximum of current can take place at a distance from the center of the disk. It results in a lack of uniformity in the dissolution of the electrode. This is not in quantitative agreement with the present case. However, if the charge transfer reaction rate is not assumed to vary according to an exponential law, but rather steeply in a narrow range of voltage, the main features of Newman's model could explain the localized dissolution of the electrode: a continuous distribution of potential along the radius of the disk would result in discontinuous variations of current density. Further experimental and theoretical work is in progress to support this interpretation.

APPENDIX

Equations of the Negative Impedance Converter

Figure A-1 shows the NIC realized with a differential input operational amplifier. The latter is characterized by a gain A , an input impedance Z_i , and an output impedance Z_o . The three quantities refer to open-loop conditions. Since a voltage $U' - U$ is applied across the amplifier input, its output (between B_2 and ground) acts as a voltage source $A(U' - U)$ in series with Z_o . The circuit of Fig. A-1 is then equivalent to the circuit of Fig. A-2. Kirchoff's laws, applied to U, U', I, I' , and the auxiliary current I_2 , lead to

$$\begin{aligned} U' &= R_1(I' + I_2) + Z_o(I' - I) + A(U' - U) \\ A(U' - U) &= Z_o(I - I') + R_2(I + I_2) + U \\ 0 &= Z_i I_2 + (I_2 + I') R_1 + (I_2 + I) R_2 \end{aligned}$$

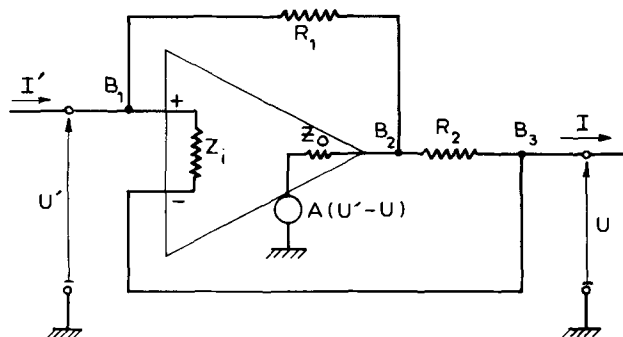


Fig. A-1. Schematic drawing of the NIC. A , open loop gain; Z_o , open loop output impedance; Z_i , open loop input impedance.

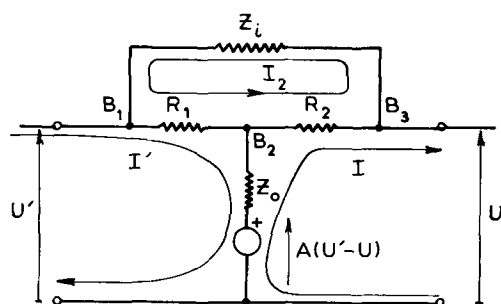


Fig. A-2. Electrical network corresponding to Fig. A-1 showing the currents used to write down Kirchoff's law.

Eliminating I_2 between these equations leads to the NIC equations

$$\begin{aligned} (A - 1)U' + \left[\frac{R_1}{Z_t} (R_2 + Z_i) + Z_o \right] I' &= AU + \left(\frac{R_1 R_2}{Z_t} + Z_o \right) I \\ AU' + \left(\frac{R_1 R_2}{Z_t} + Z_o \right) I' &= (A + 1)U + \left[\frac{R_2}{Z_t} (R_1 + Z_i) + Z_o \right] I \end{aligned}$$

where $Z_t = R_1 + R_2 + Z_i$.

Solved for U' and I' , they are written

$$\begin{aligned} U' &= \frac{U \left[1 - \frac{1}{A} \left(1 - \frac{R_2}{Z_i} - \frac{Z_o Z_t}{R_1 Z_i} \right) \right] - \frac{1}{A} \left(1 + \frac{Z_o}{R_1} + \frac{Z_o}{R_2} \right) R_2 I}{1 + \frac{1}{A} \left(\frac{R_2}{Z_i} + \frac{Z_o Z_t}{R_1 Z_i} \right)} \\ I' &= \frac{-\frac{R_2}{R_1} I \left[1 - \frac{1}{A} \left(1 + \frac{R_1}{Z_i} + \frac{Z_o Z_t}{R_2 Z_i} \right) \right] + \frac{1}{A} \frac{Z_t}{Z_i} \frac{U}{R_1}}{1 + \frac{1}{A} \left(\frac{R_2}{Z_i} + \frac{Z_o Z_t}{R_1 Z_i} \right)} \end{aligned}$$

The equation for the load line in the U - I plane is then written

$$\begin{aligned} E \left[1 + \frac{1}{A} \left(\frac{R_2}{Z_i} + \frac{Z_o Z_t}{R_1 Z_i} \right) \right] &= U \left[1 - \frac{1}{A} \left(1 - \frac{R_2}{Z_i} - \frac{Z_o Z_t}{R_1 Z_i} - \frac{Z_t}{Z_i} \frac{1}{R_1} \right) \right] \\ - I \left[\frac{\rho R_2}{R_1} + \frac{1}{A} R_2 \left(1 + \frac{Z_o}{R_1} + \frac{Z_o}{R_2} \right) - \frac{R_2}{R_1} \left(1 + \frac{R_1}{Z_i} + \frac{Z_o Z_t}{R_2 Z_i} \right) \right] & \end{aligned}$$

As Z_o is very small and Z_i very large, R_1 and R_2 can be chosen so that the following approximations hold

$$R_1 + R_2 \ll Z_i \quad R_1 \gg Z_o \quad R_2 \gg Z_o$$

They lead to

$$\begin{aligned} U &= \frac{E}{1 - \frac{1}{A} \left(1 - \frac{\rho}{R_1} \right)} + I \frac{\rho R_2}{R_1} \left[1 + \frac{1}{A} \frac{R_1}{\rho} \left(1 - \frac{\rho}{R_1} \right) \right] \end{aligned}$$

The open loop gain A can be chosen large enough for these equations to be written, in accordance to Eq. [2] and [3]

$$U' = U; \quad I' = -\frac{R_2}{R_1} I; \quad U = E + I \rho \frac{R_2}{R_1}$$

Acknowledgment

This paper is part of the thesis to be submitted by one of the authors (C. G.) to the Paris VI University.

Manuscript submitted March 1, 1972; revised manuscript received July 10, 1972.

Any discussion of this paper will appear in a Discussion Section to be published in the June 1973 JOURNAL.

REFERENCES

1. U. F. Franck and R. Fitzhugh, *Z. Elektrochem.*, **65**, 156 (1961).
2. M. Froment, M. Keddou, and Ph. Morel, *C. R. Acad. Sci. Paris.*, **253**, 2529 (1961).
3. J. Osterwald, *Z. Elektrochem.*, **66**, 401 (1962).
4. H. Degn, *Trans. Faraday Soc.*, **64**, 1348 (1968).

5. E. S. Kuh and I. N. Hajj, *Proc. IEEE*, **59**, 340 (1971).
6. A. I. Larky, *IRE Trans. on Circuit Theory*, **CT4**, No. 3, 124 (1957).
7. "Handbook of Operational Amplifier—Active RC Networks," p. 45, Burr-Brown Research Corp. (1966).
8. I. Epelboin, C. Gabrielli, and J. C. Lestrade, *Rev. Gén. d'Elect.*, **79**, No. 8, 669 (1970).
9. C. Gabrielli, M. Keddam, and J. C. Lestrade, *C. R. Acad. Sci. Paris*, **271C**, 1428 (1970).
10. V. G. Levich, "Physicochemical Hydrodynamics," Prentice Hall (1962).
11. M. Dagueuet and D. Schuhmann, *C. R. Acad. Sci. Paris*, **260**, 2811 (1965).
12. C. Gabrielli, M. Keddam, J. C. Lestrade, and H. Takenouti, *ibid.*, **274C**, 123 (1972).
13. K. J. Vetter, "Electrochemical Kinetics," Academic Press, New York (1967).
14. J. Newman, *This Journal*, **113**, 1235 (1966).

The Polarization Behavior of Fe-Ni-Cr Alloys in Concentrated Sodium Hydroxide Solutions in the Temperature Range 25° to 150°C

A. K. Agrawal, K. G. Sheth, K. Poteet, and R. W. Staehle*

Department of Metallurgical Engineering, The Ohio State University, Columbus, Ohio 43210

ABSTRACT

Results are reported for the potentiodynamic polarization at 600 mV/hr of Fe, Ni, Cr, and seven Fe-Ni-Cr alloys in concentrated NaOH solutions in the temperature range 25°C to the boiling point. Iron and nickel, as well as the Fe-Ni-Cr alloys, showed an active-passive transition which correlates very well with the predictions of the Pourbaix diagram both with respect to M/HMO₂⁻ dissolution and oxide formations. Chromium on the other hand exhibited a transpassive Tafel behavior with an inflection corresponding to the CrO₃⁻/CrO₄⁻ equilibrium. The HER and OER follow generally predicted behavior. The corrosion rates increased with an increase in the temperature and NaOH concentration. In the sodium hydroxide environment nickel is the most corrosion resistant and desirable component in the Fe-Ni-Cr alloys, whereas Cr is generally deleterious.

The purpose of this study was to survey the polarization behavior of Fe-Ni-Cr alloys in caustic solutions in the temperature range 25° to the boiling point and in NaOH concentrations from 1 to 19.5N (saturated). Anodic and cathodic scans were conducted all at the same scan rate, 600 mV/hr.

Compared to the numerous polarization studies in acid solutions, only a few studies have been conducted in alkaline solutions: Fe (1-8), Cr (9-11), Ni (12-14), and Fe-Ni-Cr (15-17). The behavior of Ni in alkaline solutions is also given in some detail by Hoare (18). In summary, the previous work of this alloy system in caustic environments has not been extensive. The work reported here is the first broad survey. This study was conducted potentiodynamically to rapidly obtain the broadest view of the problem. Certainly, future studies must examine regions of special interest more intensively.

Experimental

Three high-purity metals Fe, Ni, and Cr, and seven of their alloys were investigated in this study. Sources of metals and alloy preparations are described elsewhere (19). The caustic solutions were prepared by using double-distilled water and carbonate-free saturated NaOH solution. High-purity nitrogen was used for deaerating the solution in the cell. The instruments used were Wenking potentiostat Model 68TS3, Keithley electrometer Model 602, Erwin Halstrup motorpotentiometer Model MP165, and Esterline Angus recorder Model S-601-S or Hewlett Packard x-y recorder Model 7001A.

The specimens were cylindrical with a 0.32 cm diam. The exposed surface area was 1.0 cm². One end of the specimen was threaded as shown in Fig. 1A. A stain-

less steel rod which was fitted into a Teflon tubing was threaded at one end and was then screwed into the specimen. Before mounting, the specimen was abraded with emery paper ranging from 200- to 600-grit finish, washed with distilled water, and dried with acetone. This treatment of the specimens gave fairly reproducible results.

A schematic arrangement of the equipment is shown in Fig. 1B. The cell was made of Teflon and heated by heating tapes wrapped around its outer surface. Nitrogen was bubbled continuously through the solution in the cell. The counterelectrode was a circular Pt gauze. A Luggin probe was made from a Teflon U-tube with a nylon wick running inside it. One end of the probe was positioned near the specimen in the cell and the opposite end was connected, via a NaOH bridge, to a saturated calomel reference electrode in saturated KCl at room temperature. All the potential measurements were made against this reference electrode

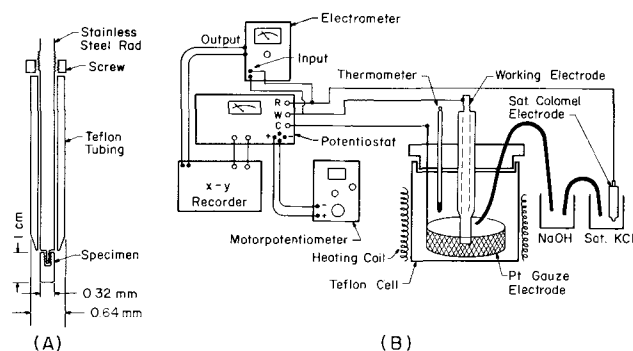


Fig. 1. Schematic diagram of the experimental arrangement used for polarization studies.

* Electrochemical Society Active Member.
Key words: corrosion, Fe-Ni-Cr alloys, sodium hydroxide, electrode kinetics, polarization.

and subsequently converted, by adding 242 mV, to the standard hydrogen electrode scale for reporting.

After the cell was assembled and proper connections were made, the open-circuit potential was measured. In most cases it took approximately 30 min to obtain the steady-state value. The potential was scanned at 600 mV/hr either in the noble direction for the anodic curve, or in the active direction for the cathodic curve. [This scan rate was arbitrarily chosen after a preliminary survey at various scan rates showed no significant changes in the over-all pattern of the polarization curves, although the current density did vary. A similar observation is reported for 18-8 stainless steel in 1N H_2SO_4 by Green *et al.* (20).] Only one polarization curve (anodic or cathodic) was obtained at a time. For the other curve, the specimen was reabraded and the cell reassembled with a fresh caustic solution.

Results

The anodic and the cathodic polarization curves of Fe-Ni-Cr alloys in NaOH solutions are shown in Fig. 2-8. Figures 2-4 show the effect of increasing temperature on the polarization behavior while Fig. 5-8 show effects of changing the NaOH concentration and the alloy composition.

The corrosion potential, E_c , of the specimens as functions of temperature and caustic concentration is shown in Fig. 9 and 10, respectively. The corrosion potential of the specimens became more negative (active) with an increase in temperature or caustic concentration. The E_c of Fe, Ni, and Cr in 10N NaOH changed from -900, -180, and -150 at 25°C to -950, -720, and -270 mV (SHE) at 118°C, respectively. Similarly, the change in E_c with an increase in caustic

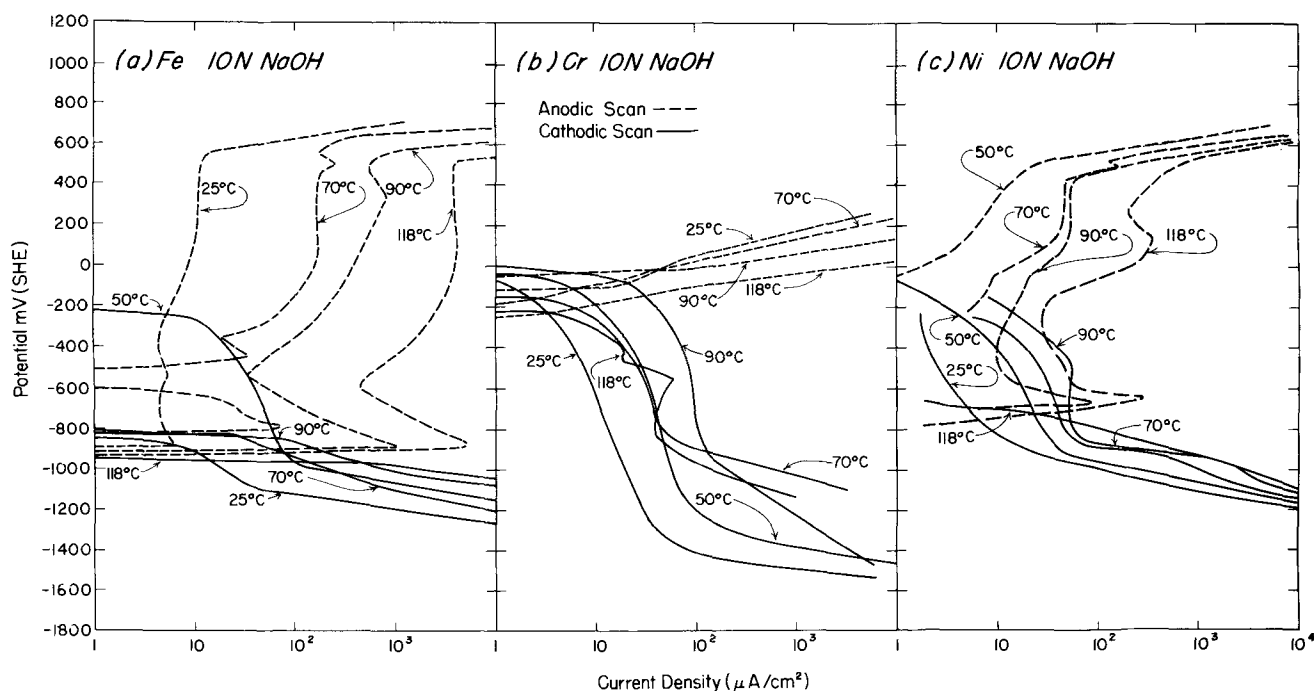


Fig. 2. Polarization behavior of Fe, Cr, and Ni in 10N NaOH in the temperature range 25°-118°C.

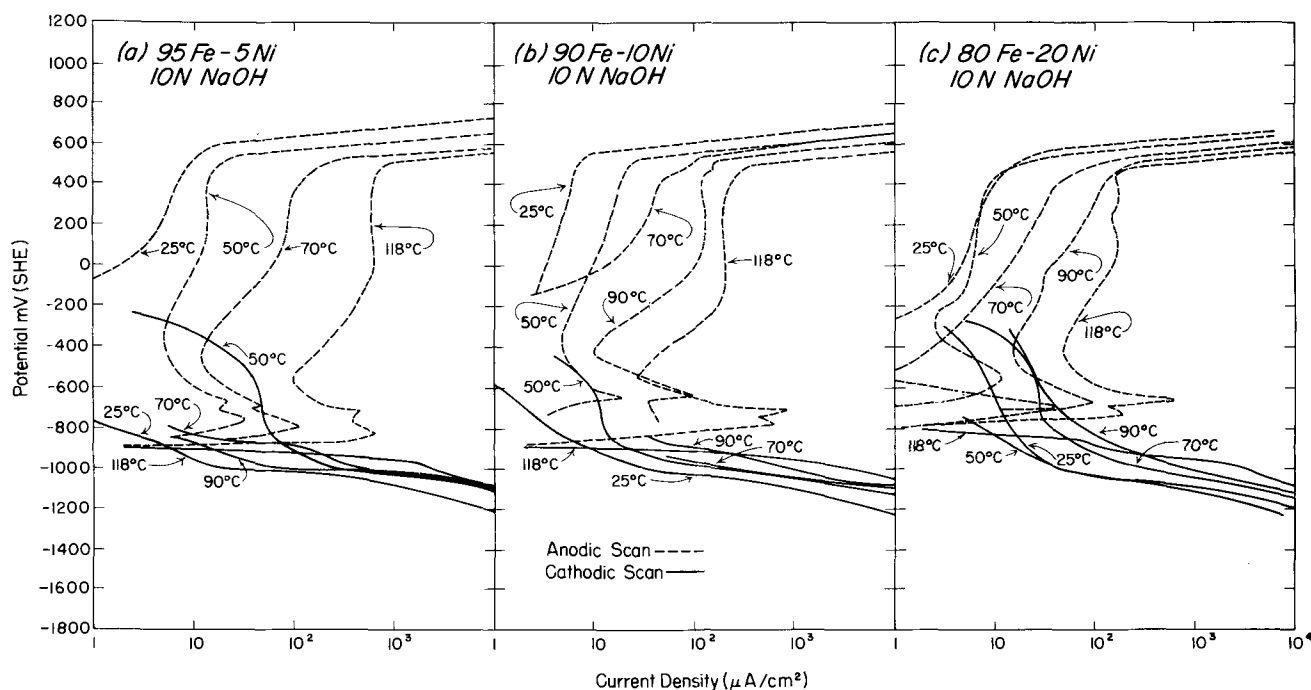


Fig. 3. Polarization behavior of the Fe-Ni binaries in 10N NaOH in the temperature range 25°-118°C.

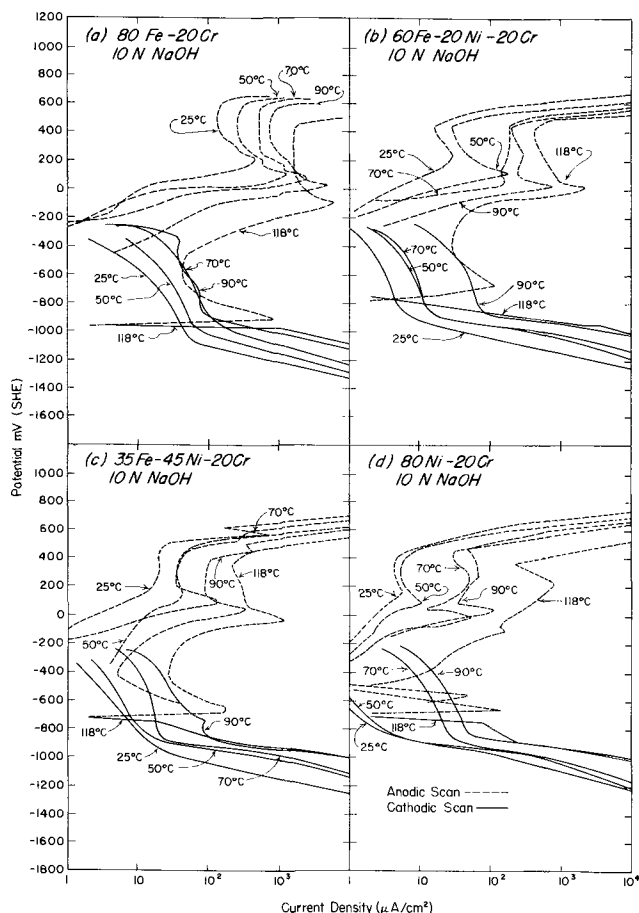


Fig. 4. Polarization behavior of the Fe-Ni-Cr alloys in 10N NaOH in the temperature range 25°-118°C.

concentration from 1 to 10N NaOH at 70°C for Fe, Ni, and Cr was from -220, -40, and 100 to -830, -180, and -190 mV (SHE), respectively. The E_c of alloys, in general, lies intermediately between those of their pure components. The addition of Ni and/or Cr shifted the corrosion potential of Fe alloys to more noble values.

The anodic polarization curves of Fe and Ni in caustic solutions showed conventional active-passive behavior, Fig. 2, 5, and 7. However, the anodic scan of Fe in both 1 and 5N NaOH at 70°C showed only the passive and transpassive part of the polarization curve, Fig. 5. This occurred because the corrosion potential in these cases was in the passive region. The critical peak of Fe in 10N NaOH between 25° and 118°C lies within 40 mV of its corresponding corrosion potential. The current density in the post-passive region in certain instances is higher than that at the critical peak; e.g., in Fig. 7a an anodic hump, which is 750 mV above (noble) the critical peak, has one order of magnitude higher current density than at the critical peak. Jones *et al.* (7) have reported similar observations with mild steel polarization in 1 and 5N NaOH at 300°C.

The critical anodic peak in the polarization curves of Ni does not appear below 90°C in solutions of concentration less than 10N NaOH, Fig. 2 and 5. Nickel, like Fe, shows a hump in the post-passive region; with an increase in temperature or caustic concentration, the value of current density at the hump approximately equals that at its critical peak, see Fig. 2c and 7a.

Chromium in caustic solutions did not exhibit an active-passive behavior, Fig. 2, 6, and 8. The anodic scan produced a Tafel-like increase of the current density from its corrosion potential to the end of the scan 450 mV (SHE). A change in the slope of $\log i$ vs. E plot occurred, depending on the caustic concentration and temperature, at 50-100 mV from its corrosion potential.

The effects of increases in the NaOH concentration and in temperature on the passive current density of pure metals at a fixed potential are summarized in Fig. 11 and 12. An approximately linear dependence of $\log i$ vs. $1/T$ is clearly seen for Fe and Ni which corresponds to an apparent energy of activation of 6.1 kcal. $\log i$ is also directly proportional to the log of NaOH concentration. The slope of $\log i$ vs. $\log N$ is one for Fe and Ni but ~ 2 for Cr. In identical environments the current density of Cr is a decade or more higher than that of Fe which in turn is approximately a decade higher than that of Ni.

The anodic current density of alloys is intermediate between those of their pure components. The anodic kinetics in the passive region in 10N NaOH at 70°C for 95Fe-5Ni is $\sim 1/2$ decade less, and that for 80Fe-

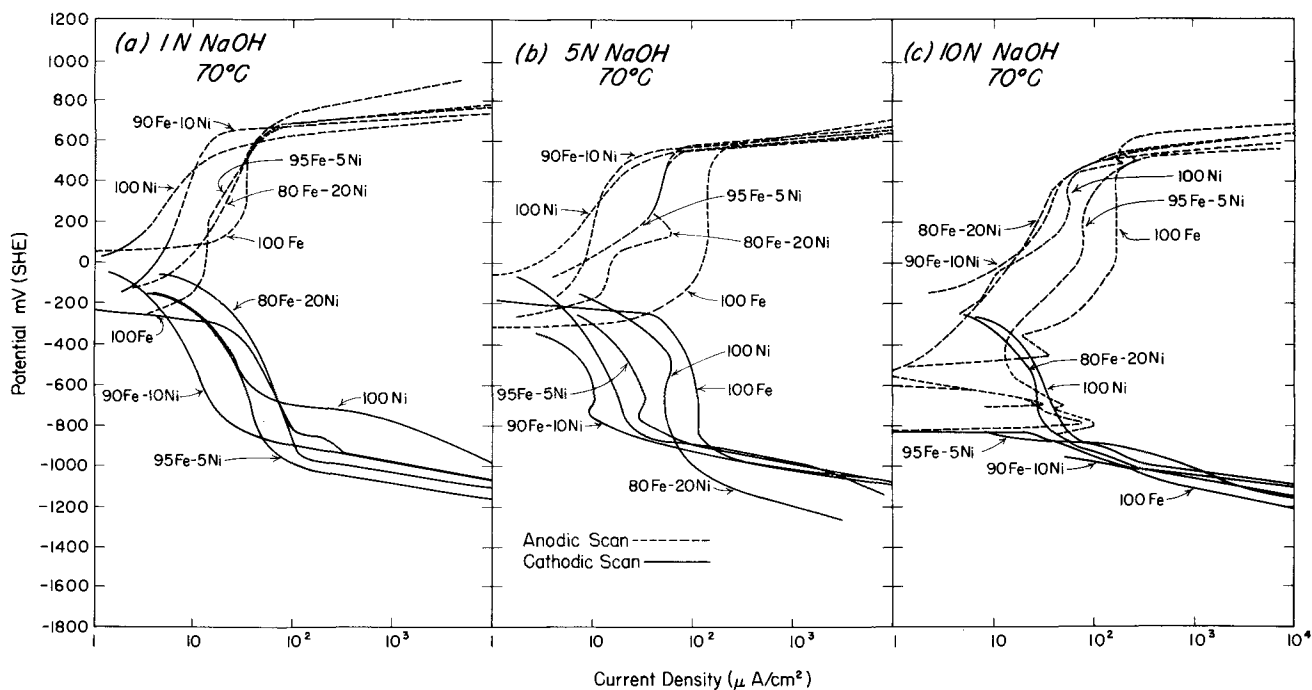


Fig. 5. Polarization behavior of Fe, Ni, and the Fe-Ni binaries in 1, 5, and 10N NaOH at 70°C.

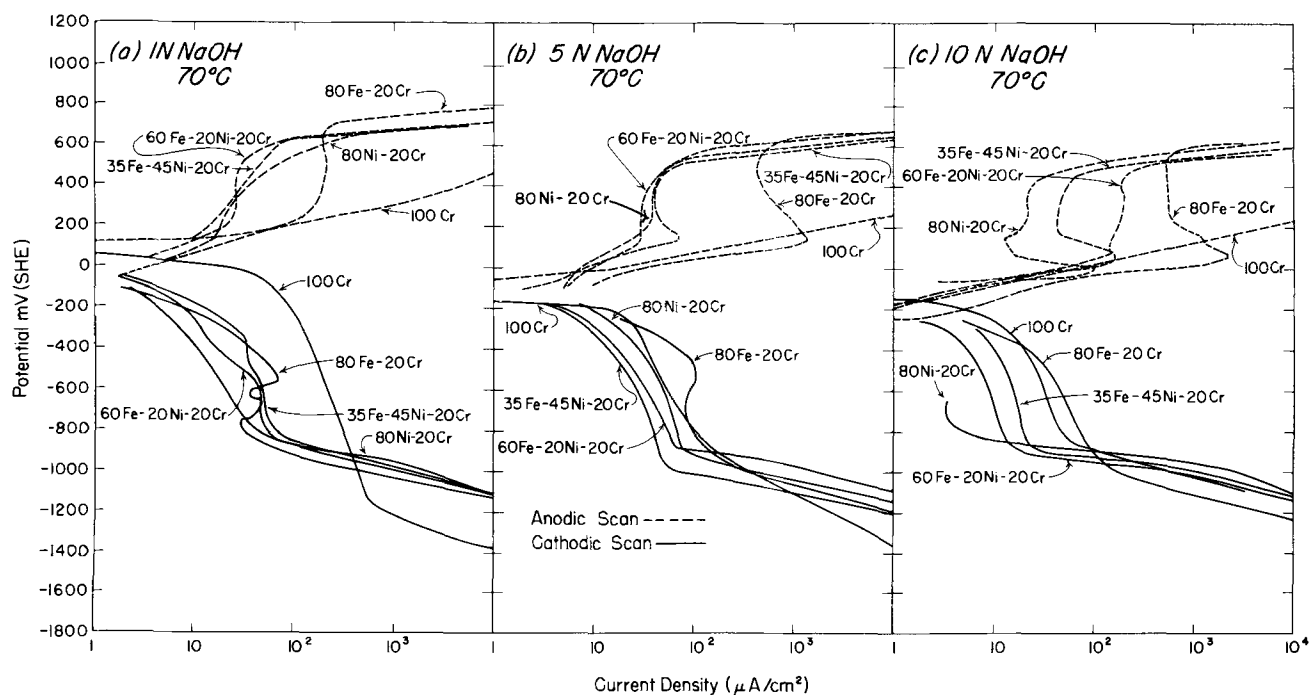


Fig. 6. Polarization behavior of Cr and the Fe-Ni-Cr alloys in 1, 5, and 10N NaOH at 70°C.

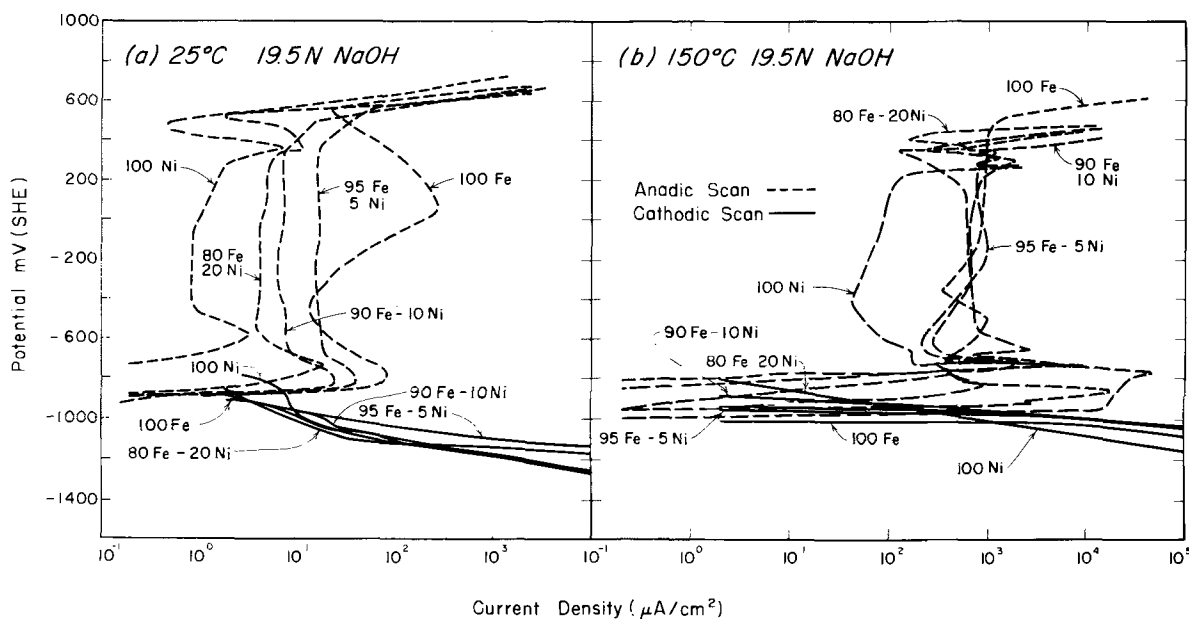


Fig. 7. Polarization behavior of Fe, Ni, and the Fe-Ni binaries in 19.5N NaOH at 25°-150°C.

20Ni is ~ 1 decade less than that of Fe. At elevated temperature in concentrated caustic the results are not as significant; e.g., in 19.5N NaOH at 25°C Fe-Ni binaries show the above-mentioned trend but at 150°C the current densities in the passive region are approximately the same as that of Fe, Fig. 7.

The anodic polarization curves of Cr alloys in concentrated solutions (≥ 10 N NaOH) or at high temperatures ($> 70^\circ\text{C}$) show two distinct anodic peaks below the oxygen evolution potential, Fig. 4 and 8. At lower temperatures ($\leq 70^\circ\text{C}$) in 1-10N NaOH, since the corrosion potential of Cr alloys lies closer to that of Cr, the anodic polarization curves exhibit only the second peak region. A comparison of the polarization curves of Cr alloys with those of pure metals Fe, Ni, and Cr indicates that the current density in the first active-passive region is controlled by Fe-Ni dissolution and formation of their oxides. The second peak in alloys is due to Cr. The current density at the second anodic peak matches closely with the corresponding current

density of pure Cr. The current density at the second anodic peak, depending on the caustic concentration and temperature, is $\sim 1/2$ to 2 decades higher than that at the first active peak.

The oxygen evolution region of the anodic polarization curves of Fe, Ni, and all their alloys exhibit Tafel behavior, Fig. 2-8. The average value of the OER Tafel slope in caustic solutions used in this study between temperatures of 25° and 150°C is 45 ± 10 mV for the majority of the specimens. This value is in full agreement with that reported in the literature (18). In a few exceptional cases, the observed Tafel slope is quite high, e.g., 90 mV for Fe in 1N NaOH at 70°C, and also for 80Ni-20Cr in 10N NaOH at 118°C.

The OER potential is slightly lowered with an increase in the caustic concentration or temperature. The OER potential for Ni, depending on the concentration and temperature, is 50-100 mV less noble than for Fe, and that for all their alloys is intermediate between the two. The effects of the NaOH concentration and

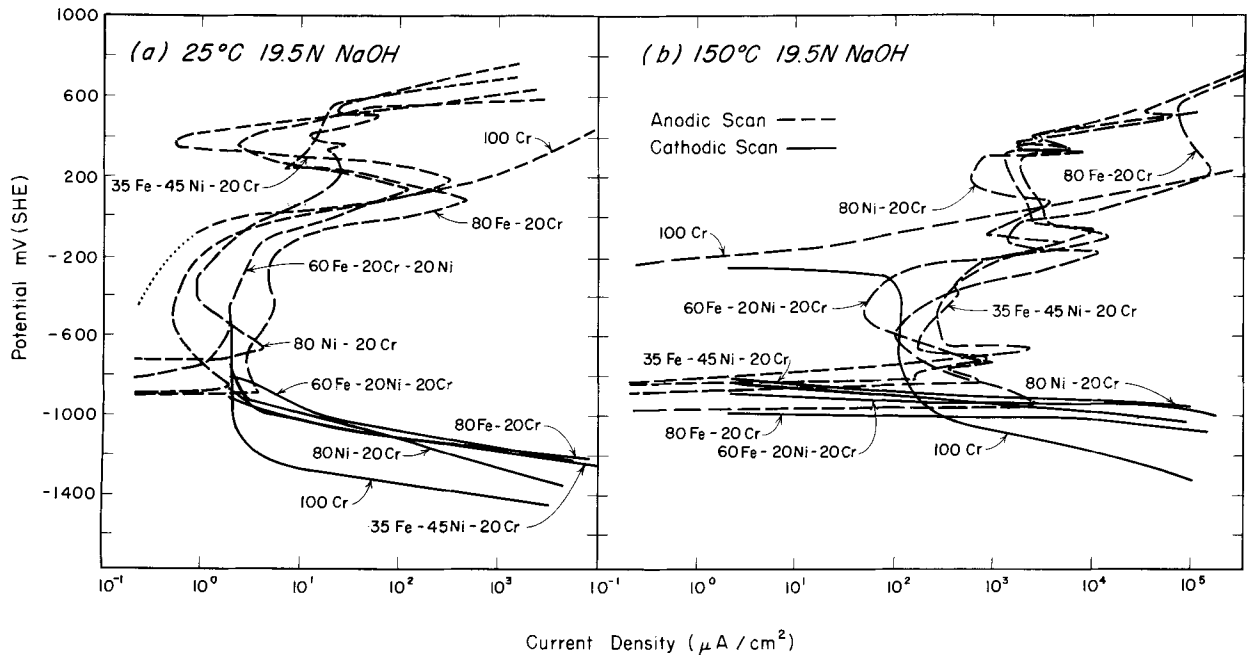


Fig. 8. Polarization behavior of Cr and the Fe-Ni-Cr alloys in 19.5N NaOH at 25°-150°C.

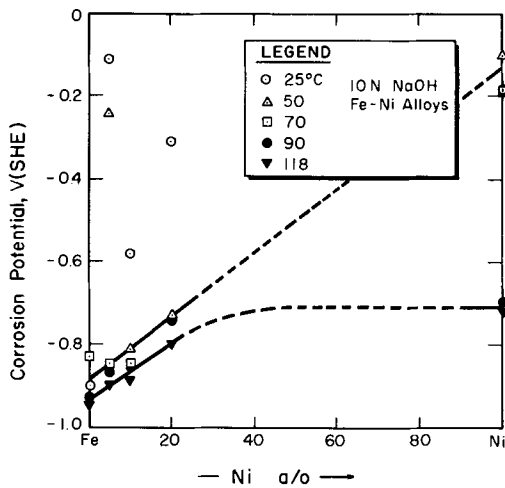


Fig. 9. Corrosion potential of the Fe-Ni alloys in 10N NaOH in the temperature range 25°-118°C.

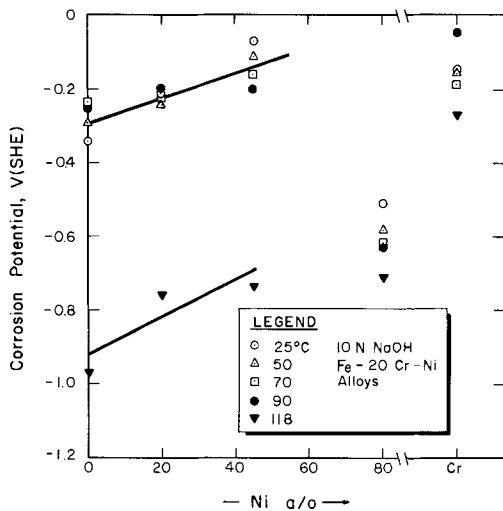


Fig. 10. Corrosion potential of Cr and the Fe-Ni-20Cr alloys in 10N NaOH in the temperature range 25°-118°C.

the temperature on OER kinetics over Fe and Ni is summarized in Fig. 13 and 14, respectively. The OER rates increased directly in proportion to the NaOH concentration with a reaction order of two. The apparent energy of activation for the OER on Fe and Ni is approximately 25.6 and 14.5 kcal, respectively, in 10N NaOH.

The cathodic polarization curves of specimens in Fig. 2-8 all show similar behavior. There are two distinct regions in each curve. During the cathodic scan the surface oxide and oxyanion reduction occur at high potential. As the potential decreases the hydrogen evolution reaction (HER) occurs and exhibits Tafel-type behavior. The oxide and the oxyanion reduction in caustic solutions $\leq 10N$ NaOH at temperatures 25°-118°C appears complete, in all cases except Cr, when

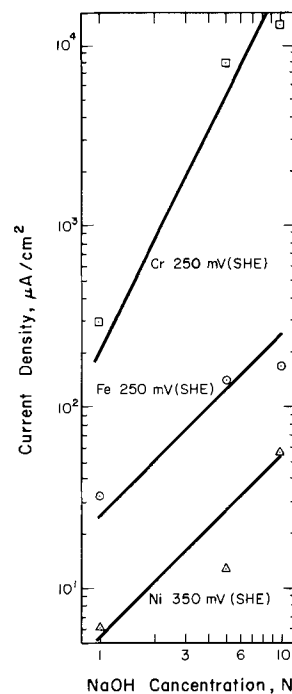


Fig. 11. Current density of Fe, Ni, and Cr at 70°C in the passive or transpassive region as a function of NaOH concentration.

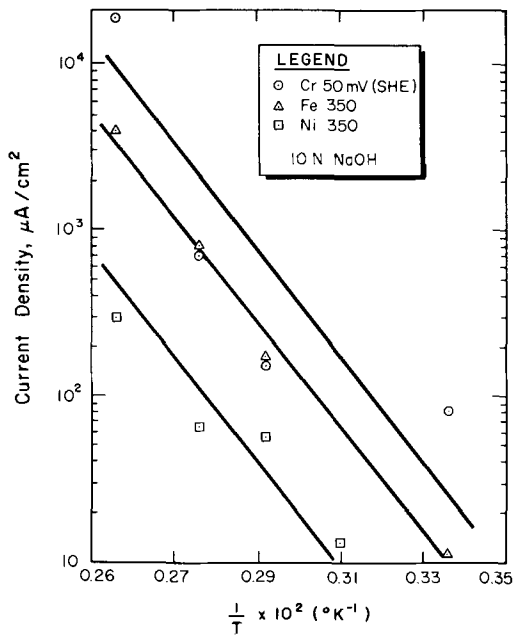


Fig. 12. Arrhenius plot for Fe, Ni, and Cr in 10N NaOH

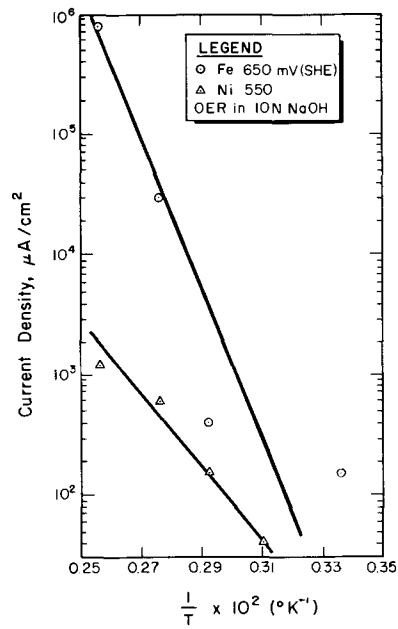


Fig. 14. Arrhenius plot for OER on Fe and Ni in 10N NaOH

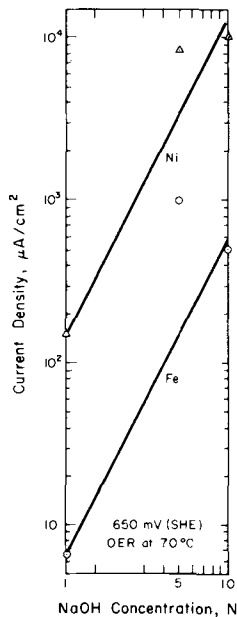


Fig. 13. OER current density on Fe and Ni at 70°C as a function of NaOH concentration.

the cathodic current density reaches $\sim 100 \mu\text{A}/\text{cm}^2$ at $-950 \pm 50 \text{ mV}$ (SHE). The current density and the potential in 19.5N NaOH at 25°C are, except for Cr, $\sim 50 \mu\text{A}/\text{cm}^2$ and $-1050 \pm 50 \text{ mV}$ (SHE). The cathodic scan in 19.5N NaOH at 150°C was done over a very limited potential range because of experimental difficulties; therefore, the above region is not identifiable in the polarization curves.

In the case of Cr, the oxide and oxyanion reduction in 5 and 10N NaOH at various temperatures appears complete at $\sim 100 \mu\text{A}/\text{cm}^2$ as shown in Fig. 2 and 6. The corresponding potential values vary considerably, e.g., in 10N NaOH the approximate values at 25° and 90° are -1450 and -900 mV (SHE), respectively. The potential and the current density in 1N NaOH at 70°C are -1150 mV (SHE) and $\sim 500 \mu\text{A}/\text{cm}^2$, while in 19.5N NaOH the respective values at 25°C are -1250 mV (SHE) with $10 \mu\text{A}/\text{cm}^2$, and at 150°C -110 mV (SHE) with $\sim 400 \mu\text{A}/\text{cm}^2$.

The value of the Tafel slope for HER on Fe-Ni-Cr alloys as a function of temperature and caustic concen-

tration is listed in Tables I and II. There is no specific effect of temperature or caustic concentration on the HER Tafel slope. The slopes on Fe and Ni are approximately 75 and 100 mV, respectively. The slope for Cr varies irregularly with temperature and caustic concentration from 75 to 325 mV.

Figures 15 and 16 show the effects of NaOH concentration and temperature on the HER kinetics. The rate of the HER on Fe and Ni decreased with an increase in the caustic concentration except for Cr where the opposite effect was observed. The apparent energy of activation for all three metals is approximately 11 kcal in 10N NaOH.

Discussion

For convenience in relating the features of the polarization curves with the thermodynamic boundary con-

Table I. Tafel slopes for HER on Fe-Ni-Cr alloys in 1 to 19.5N NaOH solutions

Alloy	Tafel slope, mV NaOH concentration				19.5N
	1N	5N	10N	19.5N	
	Temperature, °C				
	70	70	70	25	150
Fe	80	70	75	80	70
95Fe-5Ni	80	85	75	50	55
90Fe-10Ni	90	75	60	90	50
80Fe-20Ni	90	125	90	35	20
Ni	100	100	90	80	50
80Fe-20Cr	110	135	125	60	—
60Fe-20Ni-20Cr	115	90	75	80	—
35Fe-45Ni-20Cr	125	110	125	75	—
80Ni-20Cr	100	100	100	125	—
Cr	175	250	120	100	—

Table II. Tafel slopes for HER on Fe-Ni-Cr alloys in 10N NaOH in the temperature range 25°-118°C

Alloy	Tafel slope, mV Temperature, °C				
	25	50	70	90	118
Fe	75	85	75	75	75
95Fe-5Ni	100	75	75	75	—
90Fe-10Ni	125	80	65	110	—
80Fe-20Ni	130	100	90	125	—
Ni	100	100	100	100	125
80Fe-20Cr	110	120	125	110	110
60Fe-20Ni-20Cr	125	135	110	80	75
35Fe-45Ni-20Cr	125	125	125	75	50
80Ni-20Cr	130	130	100	80	60
Cr	70	75	120	325	150

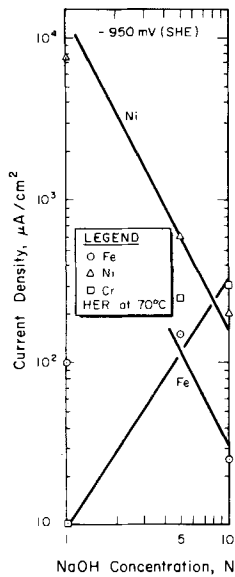


Fig. 15. HER current density on Fe, Ni, and Cr at 70°C as a function of NaOH concentration.

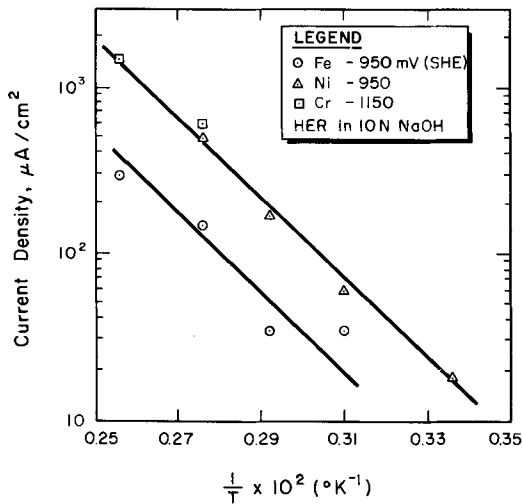


Fig. 16. Arrhenius plot for HER on Fe, Ni, and Cr in 10N NaOH

ditions we show on the polarization curves of the pure components the location of the relevant equilibria in Fig. 17. Where a soluble species is involved we take its concentration as $10^{-6}M$ and the pH is taken as 14. The equilibrium data for Fe and Cr was taken from the Pourbaix Atlas (21) and that for Ni at $100^\circ C$ was taken from Cowan and Staehle (22).

With respect to correlating the potentiodynamic determination with the Pourbaix diagram the OER and HER occur in potential ranges where they are expected.

For iron the anodic peak occurs in the region just above the $Fe/HFeO_2^-$ equilibrium as expected. The passivity observed at higher potentials is possibly due to the formation of Fe_3O_4 and then Fe_2O_3 . The curves for pure iron show also a sharp depression at -550 mV. The current dropped below $1 \mu A$ in one case (curve shown as discontinuous because of the scale limitation), Fig. 2a. This is probably due to the partial anodic and cathodic current densities being of the same order of magnitude, although the HER potential is more negative at -825 mV. It would seem then that the initially formed Fe_3O_4 is very protective but the subsequent Fe_2O_3 is less so.

For pure nickel, like iron, the anodic peak occurs in the region defined by the $Ni/HNiO_2^-$ equilibrium. Despite the broad range of stability of $HNiO_2^-$, a protective film forms above the anodic peak and extends for several hundred millivolts. At approximately the potential where Ni_3O_4 is stable the film becomes less protective.

In the case of pure Cr while the Cr/CrO_3^{---} equilibrium occurs at about -1400 mV the anodic region for chromium is not observed until -200 mV. This may simply result from a submerged anodic region rendered inaccessible by the additivity of partial currents. These partial currents appear to result primarily from the reduction of Cr_2O_3 previously present on the surface. An inflection in anodic kinetics is observed in Fig. 2 where the product changes from CrO_3^{---} to CrO_4^{--} . The inflection occurred at -50 mV compared to the predicted -190 mV from the Pourbaix diagram. Second, for alloys containing Cr, see Fig. 4, the film loses its integrity where CrO_4^{--} becomes stable although at a slightly higher potential a new but less stable film forms. In the 80Ni-20Cr alloys in Fig. 4d it is possible to observe peaks at 0 and 220 mV. The

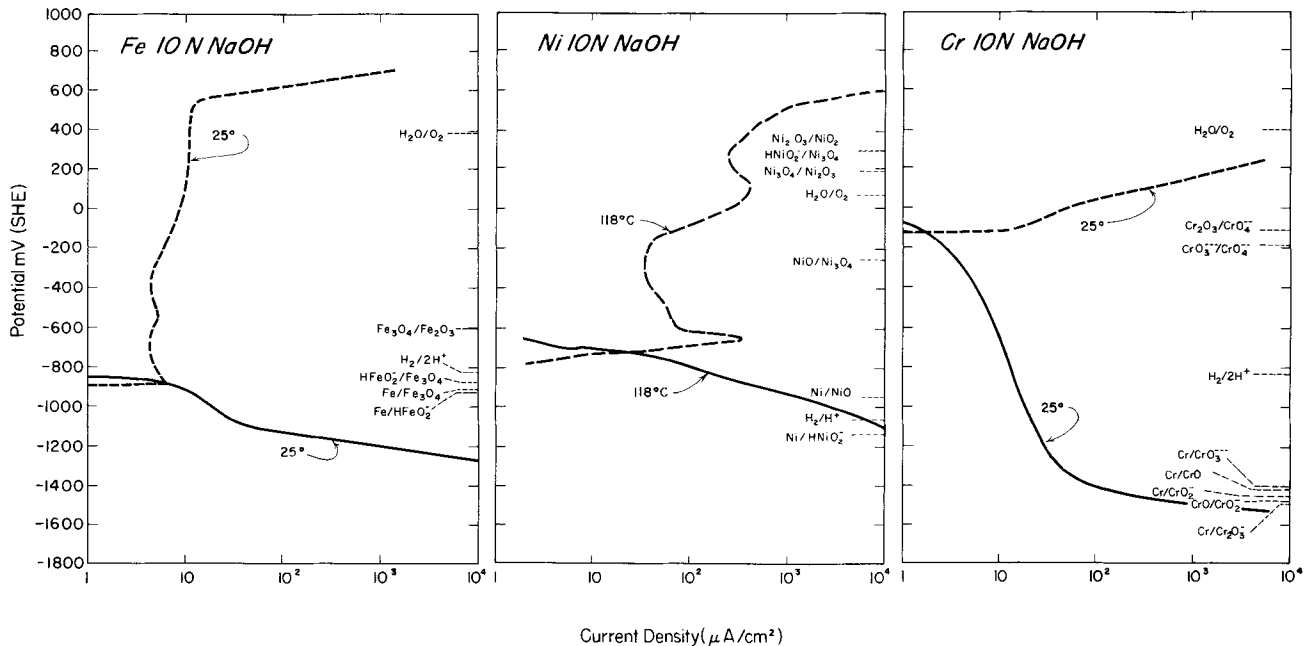


Fig. 17. Polarization behavior of Fe, Ni, and Cr in 10N NaOH and the thermodynamic equilibrium of various species in pH 14 solution

lower peak is due to CrO_4^{--} formation and the higher peak is due to the formation of Ni_3O_4 .

The significant features of the curves for the alloys clearly depend on the characteristic features of the pure components. One has only to compare the pure Fe and Ni curves with that for Fe-Ni alloys in Fig. 2 and 3.

It is interesting that an "anomalous" passivity is observed in the caustic solution as in the acidic solution which is more extensively described in the literature. In particular for Ni while the soluble oxyanion HNiO_2^- is the most stable species the specimen exhibits excellent passivity.

Since the purpose of this study was a broad survey no detailed mechanistic arguments are advanced. The kinetic parameters obtained are not sufficient for mechanistic interpretation of the results. A careful analysis of the partial currents, obtained by chemical analysis of the electrolyte for dissolved components, both in the active and the passive regions, would be required to supplement the present study. Such a study is underway in our laboratory.

With respect to using these alloys in caustic service, the already well-known desirability of nickel is vindicated. In particular see Fig. 5 and 6. In Fig. 5 the pure nickel is at least one order of magnitude more corrosion resistant than the pure iron. In Fig. 6 the 80Ni-20Cr alloy is over an order of magnitude better than the 80Fe-20Cr binary. Polarization in 1-10N concentrations of caustic solutions show generally similar patterns. However, in the saturated solution (19.5N) all alloys exhibit approximately the same features below -250 mV while above this value the superior behavior of the Ni-Cr is again evident.

Conclusions

1. The dominant effects of the alloy composition for Fe-Ni-Cr in caustic solutions at the boiling point and below are the following: (a) The presence of nickel in iron or chromium alloys produces significant improvement in corrosion resistance. (b) Adding chromium to nickel or iron is generally deleterious.

2. Increasing the temperature from room temperature to the boiling point increased the reaction rate by 1-3 orders of magnitude.

3. Increasing the NaOH concentration from 1 to 10N at constant temperature increased the reaction rate about one order of magnitude.

4. Fe-Ni-Cr alloys in the caustic solution exhibit an active-passive behavior. Pure chromium exhibits only the transpassive behavior.

5. Significant features of the polarization curves correlate very well with predictions of the Pourbaix diagram both with respect to M/HMO_2^- dissolution and oxide formations.

6. HER and OER reactions follow generally predicted behavior.

7. The corrosion potential shifts to negative values with an increase in temperature and caustic concentration.

Acknowledgments

It is a pleasure to acknowledge the United States Atomic Energy Commission who supported these studies under Contract AT (11-1)-2018. Some support was also provided by the College of Engineering and the Graduate School of the Ohio State University.

Manuscript submitted Feb. 29, 1972; revised manuscript received Aug. 5, 1972.

Any discussion of this paper will appear in a Discussion Section to be published in the June 1973 JOURNAL.

REFERENCES

1. I. A. Ammar and S. A. Awad, *J. Phys. Chem.*, **60**, 871 (1956).
2. T. Hurlen, *Electrochim. Acta*, **8**, 609 (1963).
3. M. J. Humpheries and R. N. Parkins, *Corrosion Sci.*, **7**, 747 (1967).
4. M. Nagayama and M. Cohen, *This Journal*, **109**, 781 (1962); **110**, 670 (1963).
5. J. Thomas and T. Nurse, *Brit. Corrosion J.*, **2**, 13 (1967).
6. C. H. Shepherd and S. Schuldiner, *This Journal*, **115**, 1124 (1968).
7. R. L. Jones, L. W. Strattan, and E. D. Osgood, *Corrosion*, **26**, 399 (1970).
8. S. Asakura and Ken Nobe, *This Journal*, **118**, 536 (1971).
9. I. M. Issa, I. A. Ammar, and H. Khalifa, *J. Phys. Chem.*, **59**, 492 (1955).
10. F. F. Faizullin and V. K. Levina, *Zashch. Metal.*, **2**, 623 (1966).
11. R. D. Armstrong and M. Henderson, *J. Electroanal. Chem.*, **32**, 1 (1971).
12. J. L. Weininger and M. W. Breiter, *This Journal*, **110**, 484 (1963); **111**, 708 (1964).
13. A. I. Tsinman, *Zhur. Fiz. Khim.*, **37**, 1343 (1963).
14. B. E. Conway, M. A. Sattar, and D. Gilroy, *Electrochim. Acta*, **14**, 677 (1969).
15. I. P. Dezidereva and R. M. Sageeva, *Anodnaya Zash. Metal.*, 483 (1964); from *C. A.*, **62**, 3663C (1965).
16. M. S. Nigman Khodzhaeva and P. Z. Fisher, *Dokl. Akad. Nauk, USSR*, **19**, 47 (1962); **20**, 26 (1963); from *C. A.*, **57**, 16317C (1962); **60**, 8898d (1964).
17. R. N. O'Brien and P. Seto, *This Journal*, **117**, 32 (1970).
18. J. P. Hoare, "The Electrochemistry of Oxygen," Interscience Publishers, New York (1968).
19. R. W. Staehle *et al.*, *Corrosion*, **26**, 451 (1970).
20. N. D. Greene and R. B. Leonard, *Electrochim. Acta*, **9**, 45 (1964).
21. M. Pourbaix, "Atlas of Electrochemical Equilibria in Aqueous Solutions," Pergamon Press, New York (1966).
22. R. L. Cowan and R. W. Staehle, *This Journal*, **118**, 557 (1971).

Electrolytically Formed Polyimide Films and Coatings

I. Electrodeposition from Colloidal Dispersions

D. Colin Phillips

Westinghouse Research Laboratories, Pittsburgh, Pennsylvania 15235

ABSTRACT

A process was developed for the electrophoretic deposition of polyamic acids onto metal electrodes and subsequent conversion to the corresponding polyimide. Polyamic acids were electrodeposited from colloidal dispersions of amine salts of the corresponding acids contained in a mixed organic solvent system. The tough, adherent, pin-hole free coatings have excellent mechanical, physical, and thermal properties. Correlations of coating thickness with current density, bath composition, and electrodeposition time are discussed and a mechanism for polymer electrodeposition is postulated.

Most electrophoretic deposition studies (1) have been involved with aqueous systems. For industrial scale-up of the process, these systems present obvious advantages, such as lack of dangerous fumes, minimized fire hazard, and inexpensive bath media. However, aqueous depositions are adversely affected by gas evolution (from water electrolysis) at the electrodes. Often, in such systems, gas bubbles prevent good film formation at the electrode by rupturing and dislodging the deposit. Electrophoretic deposition is also possible from nonaqueous solvents (2) and, in this instance, the solution conductivity is governed by laws different from those valid in aqueous solutions. In nonaqueous solvent systems, solution conductance is often very low, but may be compensated by applying high voltages at low currents without incurring solvent electrolysis or high heating effects.

The process of organic electrodeposition is thought to be highly complex (3). During electrocoating, several mechanisms are believed to occur to varying degrees. These are generally thought to be electrophoresis, electrocoagulation, electro-osmosis, and electrode reactions (4).

Electrophoresis involves the movement of charged particles or ions, dispersed or dissolved in a liquid medium, toward an electrode under the influence of an electric field. Whereas simple ions have only one to four units of charge, colloidal particles carry a large number of unit charges on their surfaces. Each of these particles is thought to be surrounded by a cloud of counterions. The charge of these particles gives rise to the electrokinetic potential or the zeta potential, which is defined as a measure of the electrokinetic charge that surrounds suspended particulate matter. Because of this charge, there is a mutual repulsion of these particles and this is why these dispersions are stable. The charges on the colloidal particles are probably due to a combination of adsorbed ions from the solution, from adsorbed surfactant groups, and from the particle itself having ionized groups at the liquid-particle interface. The mobility is affected by the viscosity of the medium and the size, shape, and concentration of particles, pH and concentration of electrolyte.

Electrocoagulation is the coalescence of charged moving particles in the vicinity of the electrode. The densification is a highly complex reaction. There is not complete agreement as to the actual process which occurs at this point in the electrodeposition when the particle loses its charge and coagulates. The resin particle has several adsorbed ions distributed on its surface. These negatively charged ions surrounding the resin particle will attract positively charged ions, and thereby create a secondary region encompassing the resin particle. This effect is known as the cloud layer

or double layer. Each particle finds itself in an atmosphere of ions of opposite sign, with a concentration gradient depending essentially on the charge of the particle and on the composition of the dispersing medium. The double layer is thought to be diffuse, with the outer layer possessing an electric density falling off according to an exponential law. The repelling effect exerted when two charged particles approach each other exists only if the liquid medium possesses some degree of ionizing action. Electrophoresis involves a tangential motion of one phase of the double layer with respect to the other, and it occurs only if the two phases carry free charges of opposite sign.

Electro-osmosis is the movement of the liquid phase under the influence of the electric field and is often referred to as the reverse mechanism of electrophoresis. The medium in which the resin particles are dispersed moves in the opposite direction, that is, away from the film forming on the electrode. This seems to be caused by the counterions of the deposited particles which move away from the film.

Numerous organic and inorganic electrochemical reactions occur at or around the electrodes (4). The importance of the significant role played by the electrodeposited metal has been indicated by Fink (5) and Tawn *et al.* (6). A more comprehensive study of the electrode reactions occurring during electrodeposition has been made by Smith and May (7, 8) and substantiated by Mercouris *et al.* (4).

Prior to this work, polypyromellitimide (polyimide) films have been produced by solution casting, followed by a heat cure. One major problem with producing polyimide films by the solution casting technique is that only relatively thin films can be produced in a one coat process. Heavier coating or film thickness must be made as a multicoat system, with each coat being dried (solvent removal) and cured before applying the subsequent coat. Also, polyimide coverage of irregular-shaped objects has proven to be impossible by solution casting. Most, if not all, of the above-mentioned problems are eliminated or become quite insignificant if the polypyromellitic (polyamic) acid precursor is electrodeposited directly onto the substrate. Solution viscosity becomes irrelevant; solvent problems are greatly minimized; much heavier single coat thicknesses are achievable; and the resulting corner and edge coverage is more than adequate.

In the present work, commercially available polyamic acids have been successfully electrodeposited from colloidal dispersions of amine salts of the corresponding acids in mixed organic solvent systems.

Experimental

Materials.—Commercially available polyamic acid solutions, such as, Pyre-M.L. wire enamel (E.I. du Pont de Nemours Company), Dynimel (3M Company), and

Key words: electrodeposition, polyimides, polyamic acids, electrocoating, coatings.

AI-8 wire enamel (Westinghouse Electric) were used as received. The solvents (Fisher Scientific Company), acetone (containing 0.5% water), dimethylsulfoxide (containing 0.2% water), dimethylacetamide (containing 0.2% water), N-methyl-2-pyrrolidone (containing 0.5% water), and the bases (Aldrich Chemical Company), trimethylamine, triethylamine, N,N-dimethylbenzylamine, 1-methylimidazole, were used without further purification.

Apparatus.—Briefly, the apparatus consists of a 1000 ml glass reaction vessel with cover. From the cover, two stainless steel rods are suspended. These are sealed into two glass tubes by means of Teflon insert rings. Normally, two aluminum or copper electrodes were suspended from the lower ends of the steel rods, each electrode having a surface area of approximately 44 in.². The size of electrode or metallic composition could be varied, depending on the parameter being investigated. Approximately 600 ml of colloidal dispersion was placed in the vessel and connection to a d-c power supply (Kepco, Model SM160-4) was made through the two stainless steel bars.

Procedure.—Formation of a colloidal dispersion, suitable for electrodeposition, initially involves dissolving the commercially available polyamic acid in a solvent, such as dimethylsulfoxide. An amine is added to this solution to produce the organic salt of the free carboxyl groups, present in the polyamic acid. The solutions is heated to approximately 40°C and maintained at this temperature for 15 min. Finally, the resulting solution is added to a nonsolvent, such as acetone, during which time the acetone is stirred vigorously. This results in the production of a colloidal suspension of the salt, contained in a mixed organic solvent system, comprised of acetone and dimethylsulfoxide.

Suitable commercially available polyamic acids are Pyre-M.L. wire enamel, Dynimel, and AI-8 resins. Organic bases, such as trimethylamine, triethylamine, N,N-dimethylbenzylamine, and 1-methylimidazole were used for salt formation. Alternative solvents for the resins were dimethylacetamide and N-methyl-2-pyrrolidone and higher boiling ketones could be substituted for acetone. Nonsolvents which electrolyzed during the passage of current were not suitable, since most of these produced gaseous products which prevented good film formation at the electrode.

After electrodeposition, the polyamic acid films and coatings, which were produced at the anode, were heat cured to ~300°C in a convection oven over a period of 30 min. This led to the formation of smooth, uniform, pin-hole free polyimide coatings over the entire anode surface.

Results and Discussion

Parameters investigated.—The relatively large number of parameters involved in this type of system present many difficulties. In general, only the parameters involved in the optimization of electrodeposition were investigated. These were solution composition, electrodeposition time, electrode material, and current density.

Correlations of final, cured coating thickness with base, dimethylsulfoxide, and acetone bath content have been made. No apparent interaction occurred between the amine component and the acetone/dimethylsulfoxide solution. The variation of coating thickness with triethylamine:Pyre-M.L. ratios is shown in Fig. 1. In these experiments all variables, other than the one under investigation, were kept constant. The current density was varied for each concentration and the final coating thicknesses were determined by means of a Permascope film thickness measuring device. Aluminum electrodes having a total surface area of 44 in.² with a 1-in. separation were used. It can be seen that each current density curve flattens when the triethylamine:Pyre-M.L. ratio is approximately 0.2:1. Hence, in this instance, optimum coating properties are

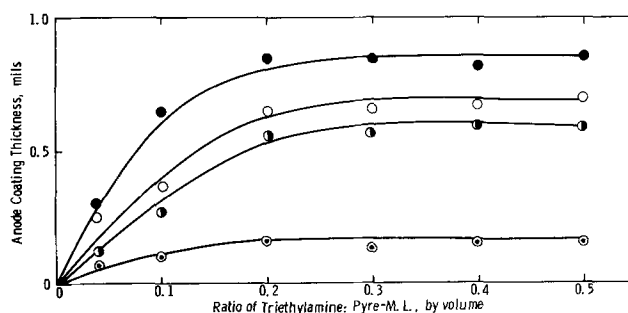


Fig. 1. Variation of coating thickness with triethylamine: Pyre-M.L. ratios. ● Current density 4.6 mA/in.², ○ current density 3.4 mA/in.², ● current density 2.3 mA/in.², ○ current density 1.1 mA/in.². Electrodeposition time 20 sec. Total aluminum electrode area 44 in.². Electrode separation 1 in.

achieved when the polyamic acid concentration is five times that of the base. In dispersions having polyamic acid/amine ratios of greater than 5:1, film thickness is variable because complete salt formation between all the available carboxyl groups, along the polymer chain, has not occurred. Dispersions having polyamic acid/amine ratios of ≤ 5 gave, essentially, the same coating properties. At these values, all the available carboxyl groups, along the polymer chain, have reacted to give the salt. Hence, film thickness is invariant when the amine is in excess of that needed for salt formation.

Figure 2 shows the variation of coating thickness with acetone:dimethylsulfoxide ratios. Constant electrodeposition times of 20 sec were employed for each set of current densities. In this case, optimum coating thicknesses were achieved when the acetone to dimethylsulfoxide ratio is five to one. Whereas the organic salt is soluble in dimethylsulfoxide it is not soluble in acetone. In solutions having acetone/dimethylsulfoxide ratios < 5 , some of the organic salt was soluble in the solvent system. As the solution strengthened in dimethylsulfoxide content, this reduced the concentration of colloidal particles within the over-all dispersion. Hence, less particles are available for electrodeposition and coating thickness is reduced as the amount of acetone decreases in the acetone/dimethylsulfoxide ratio. The salt is not soluble in solutions having acetone/dimethylsulfoxide ratios ≥ 5 and at these values the coating thickness is invariant with acetone concentration.

Utilizing the results found in Fig. 1 and 2, the bath composition giving rise to optimum coating properties was considered to be: 50 ml Pyre-M.L., 10 ml triethylamine, 200 ml dimethylsulfoxide, and 1000 ml acetone.

An additional series of experiments was done to determine the effect which deposition time and current

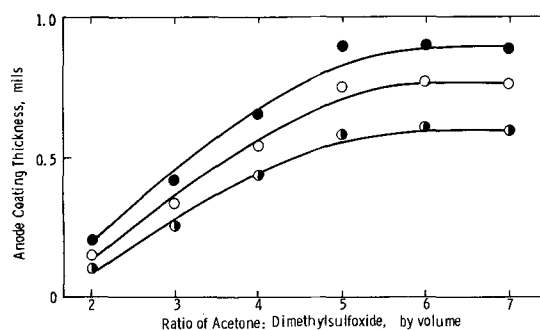


Fig. 2. Variation of coating thickness with acetone:dimethylsulfoxide ratios. ● Current density 3.4 mA/in.², ○ current density 2.3 mA/in.², ● current density 1.1 mA/in.². Electrodeposition time 20 sec. Total aluminum electrode area 44 in.². Electrode separation 1 in.

density had on the final coating thicknesses. The results are shown in Fig. 3, which depicts the variation of coating thickness with the former parameters. Again, identical bath composition, electrode area, and separation were used. Thicker coatings were obtained at longer deposition times and a linear relationship existed between applied current density and final coating thickness. Wet (uncured) coatings of >10 mils could be obtained when the current density was applied for a sufficiently long period of time. Similar results were discovered in a series of experiments in which the effect of applied voltage was studied. Figure 4 shows the effect of applied voltage and electrodeposition time. Again, when other variables were kept constant, a linear relationship existed between anode coating thickness and applied voltage over a time interval range of 20-60 sec.

The decay of current density with electrodeposition time at constant applied voltage was observed in another series of experiments. Some observations were made using a copper anode and cathode, whereas others were made with an aluminum anode and cathode. For similar current densities, very similar coating thicknesses were obtained on both aluminum and copper anodes. Figure 5 shows different current density fall-off curves for each electrode pair. An identical electrodeposition set-up was used in each instance,

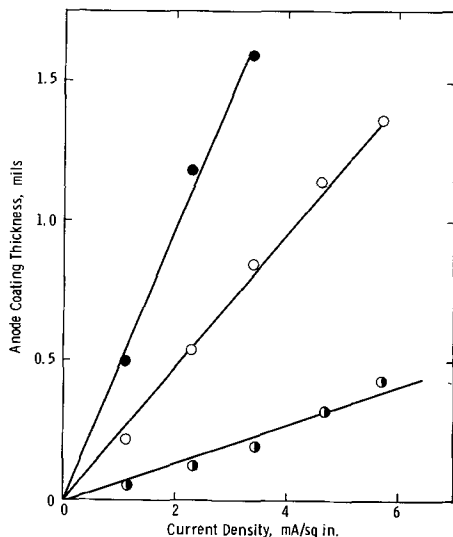


Fig. 3. Variation of coating thickness with current density and electrodeposition time. ● Bath time 70 sec, ○ bath time 40 sec, ⊙ bath time 10 sec. Total aluminum electrode area 44 in.² Electrode separation 1.25 in. Bath composition: 50 ml Pyre-M.L., 10 ml 1-methylimidazole, 200 ml DMSO, 1000 ml acetone.

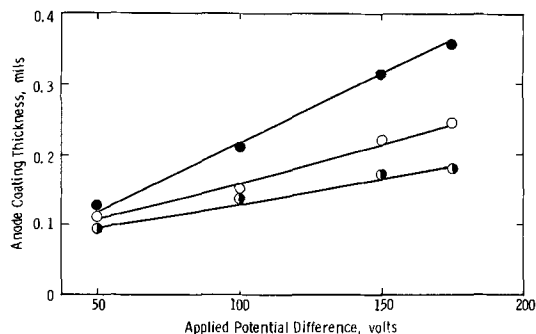


Fig. 4. Variation of coating thickness with applied voltage and electrodeposition time. ● Bath time 60 sec, ○ bath time 40 sec, ⊙ bath time 20 sec. Total aluminum electrode area 40 in.² Electrode separation 1.5 in. Bath composition: 200 ml Pyre-M.L., 300 ml dimethylacetamide, 40 ml 1-methylimidazole, 75 ml methyl isobutyl ketone.

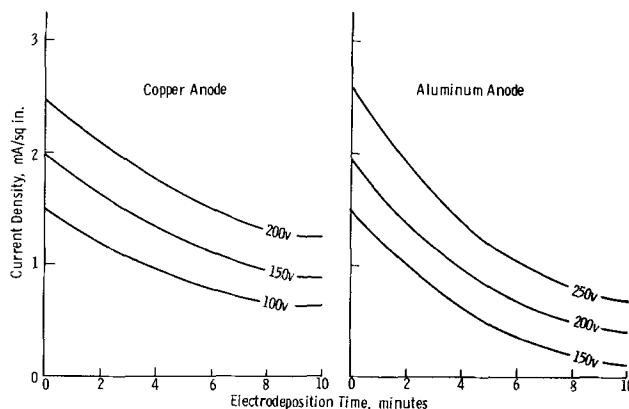


Fig. 5. Constant voltage, current-time plots for colloidal solutions using copper and aluminum anodes. Electrode separation 2 in. Bath composition: 200 ml Pyre-M.L., 40 ml 1-methylimidazole, 300 ml DMSO, 3200 ml acetone.

only the electrode material was varied. The current density fall-off was found to be much more rapid when an aluminum anode and cathode were used. Lower peak current densities were found on aluminum than on copper. This is consistent with the possibility of an oxide layer being present on the aluminum.

Finally, a comparison of the electrocoating capabilities of various commercially available polyamic acids was made. The solutions had identical bath compositions, electrode area, and separation. The electrodeposition time, in each instance, was kept constant at 20 sec and the results are given in Fig. 6. The variation of anode coating thickness with applied current density is shown. Surprisingly, the electrocoating capability is almost identical for Pyre-M.L., Dynimel, and AI-8 resin. This seems to suggest that the basic composition of each of these polyamic acids is very similar. All give rise to approximately a 1 mil coating thickness after applying a current density of 5 mA/in.² for an electrodeposition time of 20 sec. It would appear that the slight differences which were observed were due to the small variations in the solid contents of the original polyamic acid resins.

Under conventional electrodeposition times, increased bath temperature was not observable. Only when the bath was run continuously for more than 3 hr was an appreciable rise in temperature noticed. Bath pH was always in the 8-9 region and for short

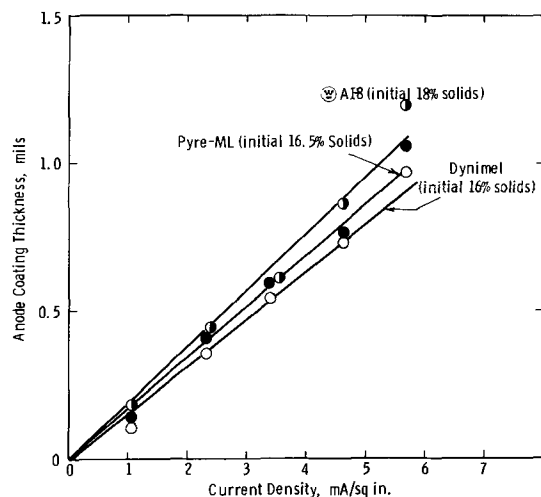


Fig. 6. Variation of coating thickness with current density. Electrodeposition time 20 sec, aluminum electrode separation 1.25 in. Bath composition: 50 ml resin, 10 ml 1-methylimidazole, 200 ml dimethylsulfoxide, 1000 ml acetone.

electrolysis times (i.e., 15 min and under), there was no necessity to stir the solution, as no precipitation or agglomeration of the resin was observed.

Analysis of coatings.—Infrared and emission spectra analyses were made on the "wet" (uncured) and final coatings in order to better understand the electrodeposition process mechanism. The conversion of the free polyamic acid to the polyimide can be followed spectroscopically by the disappearance of the —NH band at 3.1μ (3230 cm^{-1}) and the appearance of imide bands at 5.64μ (1770 cm^{-1}) and 13.9μ (722 cm^{-1}). The appearance of these same bands can be seen in the spectra in Fig. 7, which show the conversion of polyimide from wet electrodeposited polyamic acid films.

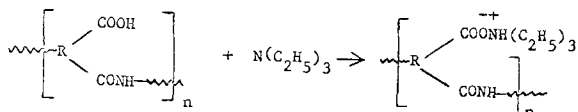
A comparison was also made between the infrared spectra of a polyamic acid cast from dimethylsulfoxide solution and the same acid electrodeposited from colloidal dispersion. The spectra are essentially identical. The corresponding spectra of the cured polyimide were also the same. Hence, no amine component (used in salt formation) is present in the wet electrodeposited film. The identical nature of the spectra is substantiated by the fact that the electrical and mechanical properties of polyimides cast from solution and electrodeposited are very similar.

Emission spectra analyses of cured coatings, which had been carefully stripped from aluminum and copper substrates, were determined. Aluminum content of the coatings was <10 ppm, whereas copper content varied from 0.1 to 2.9% depending on electrolysis time, bath concentration, etc. By comparison with the emf series in aqueous solutions, such behavior is expected. The latter range for copper compares with iron content figures of 0.13–0.27% and 0.01–2.0% found in electrophoretically deposited resin coatings by May (8) and Mercuris (4), respectively. Mercuris was concerned with polyacrylic acid deposition and May with epoxy deposition, both from aqueous media. The iron content in these coatings has not yet been successfully explained. Explanations, for the existence of iron, vary from stable iron oxides (9) to organometallic salts (4, 10) of the form $[(\text{Colloid-R})\text{COO}]_2\text{Fe}$.

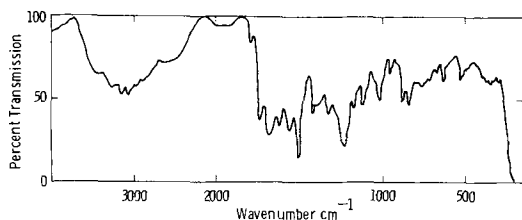
A copper compound, similar to the above organo-iron salt, does not appear to be a feasible suggestion to explain the copper contents of the electrodeposited polyamic acid films, since such a compound would have been detected by infrared analysis, which showed normal polyamic acid films. At this time, the formation of stable inorganic copper salts cannot be ignored, but further work appears necessary to elucidate the true role of copper in this system.

Mechanism.—From analysis studies and the various parameters investigated, the following over-all mechanism for electrodeposition is postulated.

Polymer salt formation



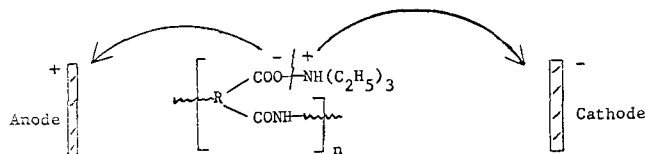
The polyamic acid is depicted by a polymer chain con-



a. Infrared spectrum of uncured Pyre-M.L. film (electrodeposited from colloidal solution).

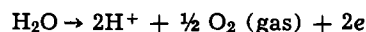
taining carboxyl and amide groups. Addition of a base, such as triethylamine, produces the triethylammonium salt of the free carboxyl group.

Ionization and migration

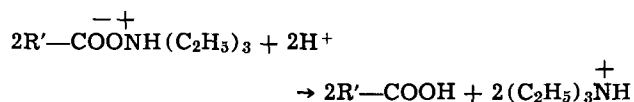


Under the influence of the electric field, it is envisaged that the salt ionizes to produce the triethylammonium ion and the carboxyl ion of the polymer, which subsequently migrate to cathode and anode, respectively.

Anode and cathode reactions.—At the anode, trace amounts of water (present in acetone dimethylsulfoxide, etc.) are thought to be involved in the electrodeposition

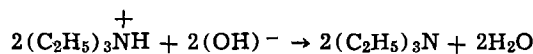
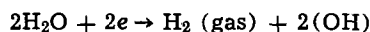


followed by hydrolysis of the salt at the anode surface

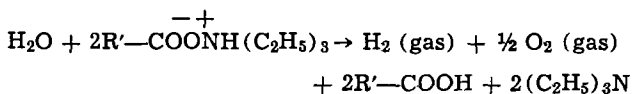


where the remainder of the polymer chain is written as R'.

At the cathode, the following reactions are thought to occur

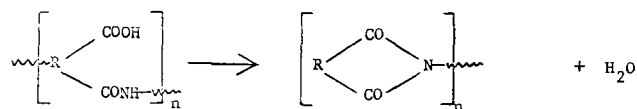


The over-all cell reaction becomes



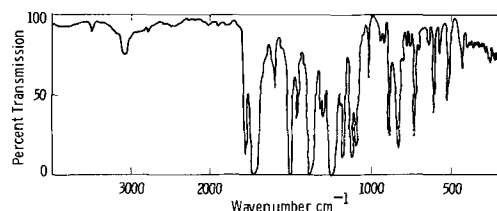
Hence, the formation of the polyamic acid film on the anode would appear to be the consequence of the increased local acidity of the region immediately adjacent to the anode which results from the electrolysis of water.

Heat cure



Subsequent heat cure at 300°C gives rise to the loss of water and produces the characteristic polyimide ring structure.

Coating properties.—It appears that, using the solution formulations previously described, polyamic acids can be successfully electrodeposited on any metallic



b. Infrared spectrum of cured Pyre-M.L. film (electrodeposited from colloidal solution).

Fig. 7. Infrared spectra of uncured and cured electrodeposited films

surface. Adherent polyimide electrocoatings have been produced on such metals as aluminum, copper, nickel, iron, zinc, titanium, lead, chromium, tin, and platinum. Aromatic polyimides are extremely heat-stable organic polymers and maintain their mechanical and physical properties over a wide temperature range ($\sim -60^\circ$ to $+400^\circ\text{C}$). A summary of some of these properties is shown in Table I. Some tests were made on films, which had been carefully stripped from the metallic substrate, whereas others were performed on coatings adherent to the metal.

The electrical properties of the electrodeposited coatings are virtually identical with the same polyimide, which has been cast from solution in the conventional manner. From Table II, it can be seen that the coatings have a high dielectric strength ($\sim 5\text{--}6$ kV/mil), low dissipation factor (~ 0.0007 at 60 Hz), and moderately high dielectric constant ($\sim 3\text{--}3.5$ at 60 Hz).

Table I. Mechanical, physical, and thermal properties of electrodeposited Pyre-M.L.

Property	Typical value at 25°C	Test method
Folding endurance*	>30,000 cycles	ASTM D-2176-63T
Ultimate elongation*	60-70%	ASTM D-882-64T
Impact test†	80 in.-lb (direct and reverse)	Falling ball impact
Abrasion resistance†	>400g	Hoffman scratch test
Adhesion & flexibility†	No cracking or loss of adhesion (1/16 in. bend)	Conical mandrel
Thermal aging†	Expected life >10,000 hr at 250°C	AIEE Method 57
Tensile strength*	24,000	ASTM D-882
Coefficient of friction*	0.42	ASTM D-1505

* Test evaluated on stripped film.

† Test evaluated on substrate (Cu and Al).

Table II. Electrical properties of electrodeposited Pyre-M.L. at 25°C

Property	Typical value	ASTM test method
Dielectric strength at 60 Hz (kv/mil)	5-6	D149
Dissipation factor at 60 Hz	0.0007	D150
Dielectric constant at 60 Hz	3-3.5	D150
Volume resistivity (ohm-cm)	10^{17}	D257
Surface resistivity at 1 kV, 50% RH (ohms)	10^{10}	D257

Insulation resistance is infinite when dry, and $\sim 5 \times 10^5$ megohms after boiling 10 min in water. These properties manifest themselves over a wide temperature range.

Conclusions

The work reported here shows that an electrophoretic technique can be utilized to produce polyamic acid coatings, which subsequently can be heat cured to produce the corresponding polyimide coatings. The technique seems to be applicable to all metallic surfaces and gives rise to defect-free coatings, having strong adherence to the metallic substrate.

The parameters, which were investigated show that reproducible electrodeposition rates can be achieved, under a variety of experimental conditions. By these means, coating thickness can be predicted to a high degree of accuracy.

Thin and thick polyamic acid coatings can be heat processed to effect ring closure without any apparent deterioration of the film properties. The electrical, mechanical, and thermal properties of the electrodeposited polyimide films manifest themselves over a wide temperature range.

Manuscript submitted May 1, 1972; revised manuscript received July 17, 1972. This was Paper 191 presented at the Cleveland Meeting of the Society, Oct. 3-7, 1971.

Any discussion of this paper will appear in a Discussions Section to be published in the June 1973 JOURNAL.

REFERENCES

- M. Bier, "Electrophoresis," Academic Press Inc. (1959).
- M. Hayek, *J. Phys. Colloid Chem.*, **55**, 1527 (1951).
- J. R. Berry, *Paint Technol.*, **27**, (12), 13 (1963); **28**, (1), 24 (1964); **29**, (3), 53 (1964).
- S. Mercouris and W. F. Graydon, *This Journal*, **117**, 717 (1970).
- C. G. Fink and M. Feinleib, *Trans. & J. Electrochem. Soc.*, **94**, 309 (1948).
- A. R. H. Tawn and J. R. Berry, *J. Oil Colour Chemists' Assoc.*, **48**, 790 (1965).
- G. Smith and C. A. May, *Am. Chem. Soc., Div. of Org. Coatings & Plastic Chem.*, **28**, No. 1, 480, San Francisco, April 1968.
- C. A. May and G. Smith, *J. Paint Technol.*, **40**, No. 526, 494 (1968).
- M. R. Sullivan, *ibid.*, **38**, No. 499, 424 (1966).
- J. P. Giboz and J. Hahaye, *ibid.*, **42**, No. 545, 371 (1970).

The Inhibition of the Dendritic Electrocrystallization of Zinc from Doped Alkaline Zincate Solutions

John W. Diggle^{*.1} and A. Damjanovic²

The Electrochemistry Laboratory, The University of Pennsylvania, Philadelphia, Pennsylvania 19104

ABSTRACT

The effect on zinc dendrite initiation and propagation in 10% KOH of the inhibitors lead, quaternary alkyl ammonium salts, Emulphogene BC-420, Triton X-15 and X-100 is examined. All these are found to affect zinc morphology to varying degrees, lead and quaternary salts being the most effective dendrite inhibitors. The role and type of adsorption, either specific or nonspecific, is discussed and related to the effectiveness of inhibition.

Much interest has been shown recently (1-3) in the use of polyethoxylated aliphatic and phenyl hydroxyl compounds as inhibitors in electrochemical power sys-

* Electrochemical Society Active Member.

¹ Present address: Research School of Chemistry, Institute of Advanced Studies, Australian National University, Canberra, A.C.T. 2600, Australia.

² Present address: Physical Chemistry Branch, Xerox Corporation Research Center, Rochester, New York 14603.

Key words: inhibition, dendrites, zinc, electrocrystallization.

tems with rechargeable zinc electrodes to prevent the occurrence of zinc densification, and so-called shape change, and hence extend useful cell cycle life (4). Such inhibitors include the compounds with trade names, Emulphogene, Triton, and Igepal, in which ethylene oxide is combined with an aliphatic grouping (Emulphogene), or a substituted aromatic grouping (Triton and Igepal) in various proportions ranging

from about 10 to 70% ethylene oxide content. Adsorption of such compounds on zinc was reported (5) to affect zinc morphology in the potential range in which a zinc electrode is recharged. Emulphogene members are shown to be especially effective in retarding zinc densification and related zinc capacity losses (1, 6).

It is the aim of this work to examine the effect of Emulphogenes, Tritons, and some other compounds on another problem of the solid zinc electrode, that of the initiation and propagation of zinc dendrites. For this purpose, the effect of the following three classes of compounds was examined:

1. The $\text{Pb}(\text{OH})_6^{2-}$ ions in alkaline solutions. Lead was chosen since it has been shown to affect zinc morphology (7) and reduce the corrosion rate of zinc (8). The addition of metal cations has long been known to affect zinc morphology (9, 10) but little has been offered in the way of explanation apart from the obvious codeposition.

2. A series of the quaternary alkyl ammonium cations ranging from methyl to pentyl. These cations are reported to remain adsorbed even at low negative potentials far below the assumed potential of zero charge (11, 12) and they are thought to be preferentially adsorbed on dendrites (13).

3. The polar molecules (2) Emulphogene BC-420, Triton X-15, and Triton X-100. These compounds were chosen to elucidate the effect of their molecular structure on zinc deposition and inhibition of dendrite growth. Such an effect is expected on the basis of the studies of Blomgren, Bockris, and Jesch (14), and Meibhur (15) according to which aromatic compounds are adsorbed more strongly than aliphatic ones. Emulphogene BC-420 has the given formula tri-decyl- $\text{O} \cdot (\text{CH}_3\text{CH}_2\text{O})_{n-1} \cdot \text{CH}_3\text{CH}_2\text{OH}$, Triton X-15 is $\text{C}_8\text{H}_{17} \cdot \text{C}_6\text{H}_4 \cdot \text{O} \cdot \text{CH}_2\text{CH}_2\text{OH}$, and Triton X-100 $\text{C}_8\text{H}_{17} \cdot \text{C}_6\text{H}_4 \cdot \text{O} \cdot (\text{CH}_3\text{CH}_2\text{O})_9 \cdot \text{CH}_3\text{CH}_2\text{OH}$. Any structural effect can be ascertained by (a) comparing Emulphogene BC-420 (with estimated $n = 1$) with Triton X-15 ($n = 1$), this will ascertain the influence of the aromatic or aliphatic fragment at approximately constant ethylene oxide content; and (b) comparing Triton X-15 with Triton X-100 ($n = 10$), this will ascertain the influence of the ethylene oxide content which is 18 and 70%, respectively.

Experimental

Solution preparation.—The solution used throughout this work was a 10% w/v potassium hydroxide containing 0.1M ZnO. No special purification of the solution was made, since it has been shown that extended purification produces no significant effect on the experimental results (16).

The inhibitor was added to the zincate solution in the as-received condition. The quaternary alkyl ammonium salts were supplied by Eastman Organic Chemicals, and lead, as Pb_3O_4 , was of the Baker analyzed purity. The Emulphogene and Triton compounds were kindly presented by the General Aniline and Film Corporation, and Rohm and Haas, respectively. Addition of the Pb_3O_4 , Triton X-100, and quaternary salts to the alkaline zincate solution did not present any difficulties. However, some difficulties were experienced with the addition of Emulphogene BC-420 and Triton X-15 due to the low solubilities of these compounds in the alkaline zincate solutions. The solution preparation for these two compounds was as follows: to the required amount of Emulphogene and conductivity water a sufficient amount of acetone was added to render the Emulphogene soluble. This solution was then added to a concentrated alkaline zincate solution, followed by dilution with conductivity water to near the required zincate-KOH concentration. Occasionally, it was necessary to add more acetone to solubilize the

Emulphogene.³ The final solution was opaque, thus making difficult the microscopic *in-situ* observation of the propagation rate of dendrites. Therefore, measurements with the Emulphogene and Triton are somewhat more approximate than was previously the case with other additives or in pure zincate solutions (17). The effect of lead was studied in the concentration range 10^{-3} to 10^{-6} M, of quaternary salts in the range 1M to 10^{-5} M, depending upon the individual member, and of the Emulphogene⁴ and Triton in the range 1.5×10^{-4} (this being, under present conditions, saturated for BC-420) to 1.5×10^{-5} M, and 1.8×10^{-4} to 1.8×10^{-5} M, respectively.

Electrode preparation.—Preparation of the zinc electrodes was the same as reported previously (17).

Procedure.—Potentiostatic control (Wenking potentiostat) was used throughout this work. The cell for deposition was similar in design to that used in a previous work (17). The volume of the present cell (70 cm³) was, however, smaller than in the previous cell (500 cm³). The illumination for microscopic observation was provided via two 1/8 in. diam fiber light pipes inserted into glass guide tubes which projected through the cell walls to within 1 cm of the opposite sides of the electrode. Fiber light pipe illumination was supplied through a quartz iodine bulb housed in an illuminator source (Ealing Corporation).

Experimental procedures were identical to those outlined in a previous work (17). Cathodic polarization curves, when determined, were obtained with freshly prepared electrodes which, after the polarization experiments, were not used any further. All potentials reported here are with respect to the zinc electrodes in the same solution.

The effect of inhibitors on dendrite propagation was determined in "solution exchange" experiments. In this procedure, dendrites were initiated in zincate solution without an inhibitor and the ensuing propagation was allowed to continue for some time, then the length of several dendrites was measured (17). The zincate solution was then withdrawn and quickly (30 sec) replaced by the zincate solution containing an inhibitor and the same dendrites were then observed in the microscope to ascertain if, and to what extent, the inhibitor affected their growth and rate of propagation. The potentiostat was in the off position during the exchange of the solution and 2 min following the exchange. This was done because some irregular behavior in the total current-time was observed for a short period (about 1 min) following the exchange.⁵

Results

Effect of Lead Ions on Dendritic Growth

Initiation time.—Figure 1 illustrates the effect of lead ion concentration on the total current density-time behavior.⁶ The effect is negligible at 10^{-6} M, and completely effective at 10^{-4} M lead. At the latter concentration the *i-t* relationship is indicative (16) of compact zinc deposition. At 10^{-5} M, the behavior is indicative neither of dendritic nor of compact growth, but reflects the observed disk-like morphology (Fig. 2) where the real surface is apparently increasing faster than in the case of dendritic growth.

Table I summarizes the influence of lead concentration on the initiation of dendrites and the morphology of zinc deposits at various overpotentials. At the over-

³ Concentration of acetone was usually 200 cm³/1000 cm³ of the final solution. This concentration of acetone in pure zincate electrolyte, i.e., in the absence of Emulphogene or Triton, was found to have no significant effect on either the initiation time or the dendrite propagation rate. In this respect, acetone is as ineffective as benzene (16), probably due to negligible adsorption at potentials far negative with respect to the zero charge potential of zinc.

⁴ In the case of Emulphogene BC-420 1.5×10^{-4} M, was equivalent to 7.4 × 10⁻³% w/v.

⁵ The essential effects of the inhibitor were unaffected by similar exchange procedures.

⁶ In all material that follows reference to a total C.D. implies the total current flowing divided by the initial cathode area 3×10^{-2} cm². Thus as the surface area of the cathode changes during deposition, so the total C.D. reflects such changes.

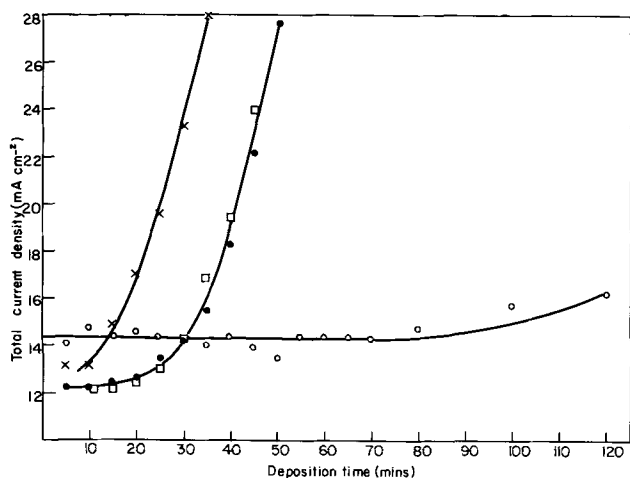


Fig. 1. Total current density-time behavior for the deposition of zinc from pure and lead-doped alkaline zincate solution 10% KOH + 0.1M ZnO, $\eta = -100$ mV, $T = 35^\circ\text{C}$. ● No lead, ○ 10⁻⁴M Pb, x 10⁻⁵M Pb, □ 10⁻⁶M Pb.

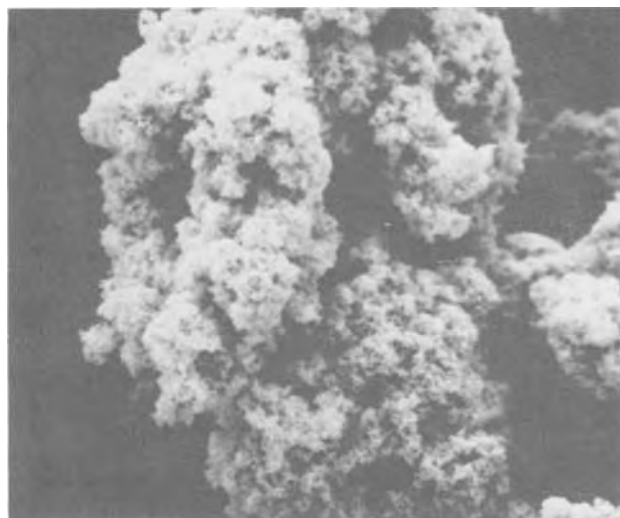


Fig. 3. Sponge-type morphology typical of that formed below dendrite initiation overpotentials. 10% KOH + 0.1M ZnO. $T = 35^\circ\text{C}$. Magnification X300.



Fig. 2. Disk-type zinc morphology produced under the following conditions: 10% KOH, 0.1M ZnO, 10⁻⁵M Pb, $\eta = -100$ mV, $T = 35^\circ\text{C}$. Magnification X22.

potential of -100 mV, the morphology changes from dendritic through a disk type of deposit (Fig. 2), to a spongy (Fig. 3), and finally to a compact zinc deposit as the concentration of lead ions increases from 10⁻⁶ to 10⁻⁴M. When the lead ion concentration was increased further to 10⁻³M, lead dendrites, instead of zinc dendrites, appeared to have formed. The lead dendrites are distinguished from zinc dendrites by the angle that the side branches subtend to the main dendrite axis, this being 90° for lead and 120° for zinc (18). From the same table it is evident that the effectiveness of lead

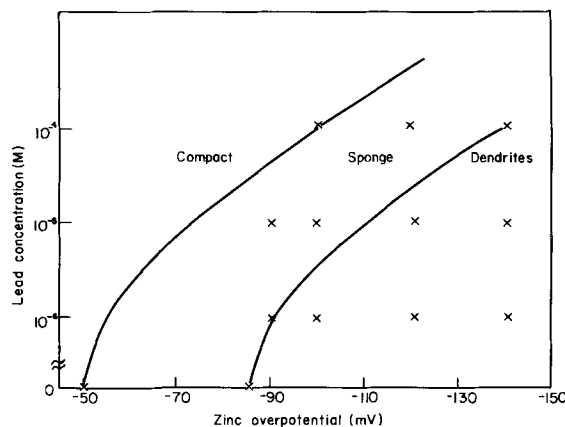


Fig. 4. Zinc morphology profiles with respect to overpotential and dopant lead concentration. Basic electrolyte 10% KOH + 0.1M ZnO. $T = 35^\circ\text{C}$.

ions in preventing the formation of dendrites decreases as the zinc deposition overpotential becomes more negative. Thus, at the concentration of lead of 10⁻⁵M, no dendrites are formed at overpotentials of -90 or -100 mV, but they do form at -120 or -140 mV. The higher the concentration of lead ions, the more negative is the potential (higher overpotential) at which dendrites will appear (Fig. 4).

Propagation of dendrites.—Table I summarizes also the effect of the presence of lead ions in the zincate solution on the rate of propagation of dendrites found in solution exchange experiments. The trend observed parallels that found for the initiation of dendrites, i.e., when the zincate solution with no lead ions is replaced

Table I. Influence of lead concentration on the initiation and propagation of zinc dendrites. Basic electrolyte throughout: 0.10 molar zincate in 10% w/v potassium hydroxide. Temperature 30°C

Lead concentration (molar)	Zinc overpotential (mV)	Effective in preventing initiation	Initiation		Propagation (solution exchange)	
			Morphology observed	Effective in stopping propagation	Morphology produced after solution exchange	
10 ⁻⁴	-100	Yes	Compact	Yes	Compact	
	-140	Yes	Sponge	Yes	Sponge	
10 ⁻⁵	-90	Yes	Compact & Sponge	Yes	Sponge	
	-100	Yes	Disks	Yes	Disks	
	-120	No	Dendrites	No	—	
	-140	No	Dendrites	No	—	
10 ⁻⁶	-90	Partially	Dendrites & sponge	Very slightly effective	—	
	-100	No	Dendrites	No	—	

by the solution containing lead ions in the concentration of $10^{-6}M$, the dendrites which had initially grown in pure zincate solution continued to grow, whereas when the solution was replaced by the one containing $10^{-4}M$ lead ions dendrites stop propagating. Figure 5 shows the total current density at overpotential of -100 mV before and after solution exchange with $10^{-4}M$ lead ion solution. The data on the exchange of pure zincate solution with $10^{-6}M$ lead ion solution are also shown. It is evident that the lead ion concentration of $10^{-6}M$ does not retard dendrite propagation to any extent (the $i-t$ behavior being identical to that obtained in the zincate solution without lead) whereas in the presence of lead ions in the concentration of $10^{-4}M$ any further dendrite growth is completely prevented, as observed in the microscope. Consequently, as already formed dendrites stop propagating and new dendrites are not nucleated, any further rapid increase in total current ceases. Double exchange of solution, i.e., zincate solution with no lead, followed by the solution with $10^{-4}M$ lead ion and then followed again by zincate solution, shows the $i-t$ behavior as in Fig. 6. Upon subsequent removal of the solution containing

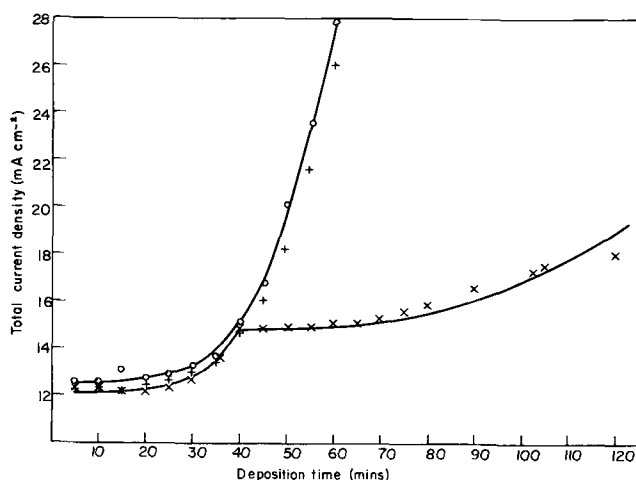


Fig. 5. Total current density-time behavior observed during solution exchange experiments. ○ represents the behavior of pure 10% KOH + 0.1M ZnO, $\eta = -100$ mV, $T = 27^\circ C$; x exchange solution containing $10^{-4}M$ Pb and + exchange solution containing $10^{-6}M$ Pb. Solutions exchanged after 40 min.

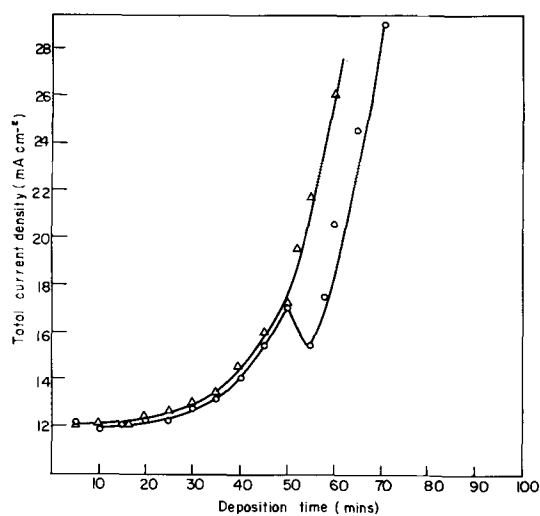


Fig. 6. Total current density-time behavior observed during double solution exchange with $10^{-4}M$ Pb doped alkaline zincate. Δ Pure system 10% KOH + 0.1M ZnO. $\eta = -100$ mV. $T = 27^\circ C$. ○ Double solution exchange with first exchange after 50 min, second exchange after 55 min.



Fig. 7. Photomicrographs illustrating the dendrite tip geometry before (top) and after (bottom) solution exchange with $10^{-4}M$ Pb doped 10% KOH before and after solution exchange with $10^{-4}M$ Pb doped 10% KOH + 0.1M ZnO, $\eta = -100$ mV. $T = 35^\circ C$.

lead ions, dendrites recommence to propagate at a rate close to the original rate as judged from the similar slopes of the $i-t$ curve at points of the same currents, and microscopic observations.

Figure 7 shows the dendrite tip before and after solution exchange with $10^{-4}M$ lead ion solution.⁷ After the exchange, the tip appears to have lost the radius of curvature which was considered to be essential for the fast rate of dendrite propagation (17).

Effect of Quaternary Ammonium Salts on Dendritic Growth

Initiation time.—Figure 8 illustrates the effect of the addition of tetrabutyl ammonium bromide on the $i-t$ behavior as a function of concentration of tetrabutyl ammonium bromide in the range 10^{-5} – $10^{-2}M$.⁸ The effectiveness in suppressing the dendritic growth and producing a compact zinc deposit, as indicated by the $i-t$ behavior (cf. Fig. 8) and confirmed by microscopic observations, increases as the concentration of tetrabutyl ammonium bromide increases. In the solutions with more than $10^{-3}M$ of the salt, the total current at the overpotential of -100 mV is nearly invariant with time and is less than that obtained in

⁷ These photomicrographs were obtained in two separate experiments.

⁸ Concentrations in this range of KBr have been ascertained as having no influence on either the initiation or propagation of zinc dendrites.

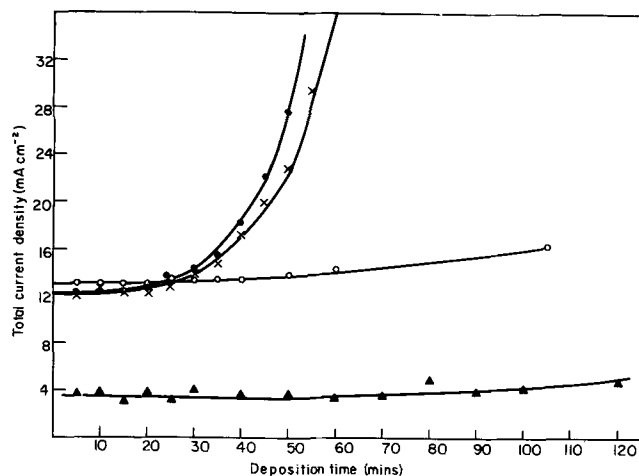


Fig. 8. Total current density-time behavior observed for zinc deposition from ● pure alkaline zincate solution 10% KOH + 0.1M ZnO, $\eta = -100$ mV, $T = 30^\circ\text{C}$. x Doped with 10^{-4}M $(\text{C}_4\text{H}_9)_4\text{N}\cdot\text{Br}$, O 10^{-3}M $(\text{C}_4\text{H}_9)_4\text{N}\cdot\text{Br}$, ▲ 10^{-2}M $(\text{C}_4\text{H}_9)_4\text{N}\cdot\text{Br}$.

the undoped system or in those corresponding to 10^{-3} and 10^{-4}M of the salt.

The polarization curves reported here in Fig. 9, 11, 14, and 15 were obtained using a steady-state potentiostatic technique allowing minimum time at each potential for current stabilization. In all experiments reported graphically in Fig. 9, 11, 14, and 15, the polarization curves could be constructed within 5 min. In such a time, according to Diggle and Lovrecek (19), cathode surface area changes should have been minimal and thus the real area relevant to Fig. 9, 11, 14, and 15 can be considered equal to the original cathode area $3 \times 10^{-2}\text{cm}^2$.

A corresponding trend to that depicted in Fig. 8, namely the decrease in the current at -100 mV overpotential, is evident from the polarization curves for zinc deposition in the presence of tetrabutyl ammonium bromide (Fig. 9). There is a negligible effect of 10^{-4}M tetrabutyl ammonium bromide on the $\log i-\eta$ behavior when the latter is compared with that of the uninhibited systems. With 10^{-3}M , however, a nearly linear

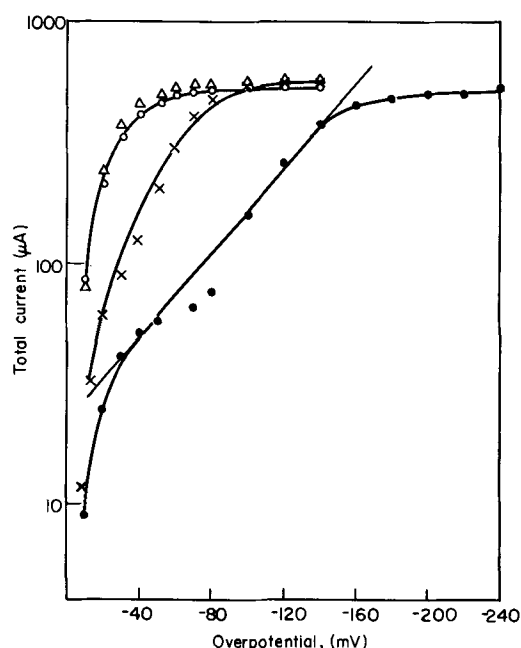


Fig. 9. Polarization curve for the deposition of zinc from pure and doped 10% KOH + 0.1M ZnO. $T = 30^\circ\text{C}$. O Pure system, Δ 10^{-4}M $(\text{C}_4\text{H}_9)_4\text{N}\cdot\text{Br}$, x 10^{-3}M $(\text{C}_4\text{H}_9)_4\text{N}\cdot\text{Br}$, ● 10^{-2}M $(\text{C}_4\text{H}_9)_4\text{N}\cdot\text{Br}$.

Table II. Influence of quaternary ammonium cations on the initiation of zinc dendrites from an electrolyte of 0.1 molar zincate, 10% KOH at 30°C and -100 mV

Quaternary salt	Minimum molar concentration for complete effectiveness in preventing zinc dendrites*
$(\text{CH}_3)_4\text{NOH}$	1
$(\text{C}_2\text{H}_5)_4\text{NBr}$	10^{-1}
$(\text{C}_3\text{H}_7)_4\text{NBr}$	10^{-2}
$(\text{C}_4\text{H}_9)_4\text{NBr}$	10^{-3}
$(\text{C}_5\text{H}_{11})_4\text{NI}$	10^{-4}

* At the quoted concentration, and above, the morphology of the zinc electrodeposit was always compact, except for tetramethyl where the zinc deposit was of a spongy nature.

region of $\eta-\log i$ is observed at overpotential less than -80 mV; at overpotentials greater than -100 mV, the limiting current density is observed; in 10^{-2}M inhibited solutions, Tafel relationship is evident with the slope close to 0.11V in the region of $\eta > 100$ mV. It is apparent, from Fig. 9, that the deposition of zinc at the overpotential of -100 mV becomes more activation controlled as the concentration of tetrabutyl ammonium bromide increases.

No dendrite initiation was observed at $\eta = -100$ mV for tetrabutyl concentrations greater than or equal to 10^{-3}M . In Table II the concentrations are given of tetrabutyl ammonium bromide, along with other quaternary salts, which are required to suppress dendrite initiation at overpotential of -100 mV; a definite dependence on the structure of the tetra-alkyl group is evident. The effectiveness, at the same concentration, in eliminating dendrites increases from tetramethyl to tetrapentyl. The minimum concentration required to suppress the dendrites initiation decreases by about one order of magnitude on passing from one member to the next in the range of compounds examined. At the minimum concentration of each member, except tetramethyl, compact zinc is deposited. In the presence of tetramethyl, a spongy type of deposit is formed.

Propagation rate.—For any quaternary salt, except tetramethyl, there is a minimum concentration at which, in solution-exchange experiments, dendrites stop growing (cf. Table II). Figure 10 shows the $i-t$ behavior for solution exchange with 10^{-3}M tetrabutyl ammonium bromide (cf. Fig. 5, 10^{-4}M lead). As in the lead inhibited system, changes in the dendrite tip

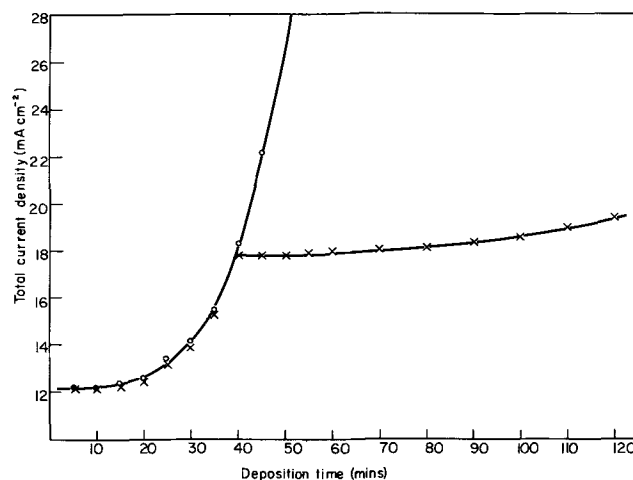


Fig. 10. Total current density-time behavior observed during solution exchange experiments. O represents the behavior of pure 10% KOH + 0.1M ZnO, $\eta = -100$ mV, $T = 30^\circ\text{C}$. x Exchange solution containing 10^{-3}M $(\text{C}_4\text{H}_9)_4\text{NBr}$. Solutions exchange after 40 min.

radius of curvature are observed on the addition of inhibitor.

Effect of Polyethoxylated Hydroxyl-Compounds on Dendrite Growth

Emulphogene BC-420.—Figure 11 illustrates the η -log i polarization curves in zincate solution to which Emulphogene BC-420 was added to concentrations of 7.4 and $3.7 \times 10^{-5}M$ for both increasing and decreasing overpotential. As the overpotential was made increasingly negative, starting from -50 mV, there is a gradual increase in current until an overpotential is reached at which a large increase in the current occurs. This latter overpotential is -110 mV and -240 mV for $3.7 \times 10^{-5}M$ and $7.4 \times 10^{-5}M$ solutions, respectively. For the $7.4 \times 10^{-5}M$ doped solutions at these high potentials, substantial hydrogen evolution was noted. When the overpotential became more positive, a different η -log i relationship was observed and a strong hysteresis in η -log i was evident (cf. Fig. 11).

At overpotentials of -50 mV, or less negative, the current at a given overpotential becomes unstable and decreases with time, as indicated in Fig. 11 by the descending arrows. Figure 12 shows the total current on an electrode which was initially held at an overpotential more negative than that at which sudden increase in current is observed and then brought to -50 mV. The decrease in the current is the more rapid the more concentrated the inhibitor; the slope di/dt increases approximately 2.3 times for a two-fold increase in the Emulphogene concentration. Steady-state current density is established in about 500 and 1000 sec for 7.4 and $3.7 \times 10^{-5}M$ solutions, respectively, in unstirred solutions. In stirred solution the steady state is established faster.

The above phenomenon is indicative of slow adsorption-fast desorption of the Emulphogene, in conformity with the findings of Payne, Tachikawa, and Bard (2) at similar concentrations.

Initiation Process in the Presence of Emulphogene BC-420

In systems containing Emulphogene, at an overpotential of -100 mV, two different total current-time relationships are found depending on whether the

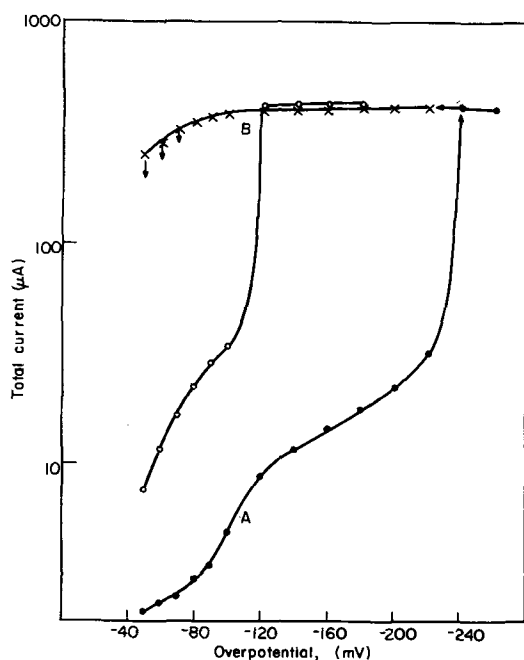


Fig. 11. Polarization curves for the deposition of zinc from 10% KOH + 0.1M ZnO, $T = 33^{\circ}C$ containing \circ $3.7 \times 10^{-5}M$ and \bullet $7.4 \times 10^{-5}M$ Emulphogene BC-420. The points \circ and \bullet were determined with potentials moving cathodic, and the points x , illustrating the hysteresis, were determined with potentials moving anodic.

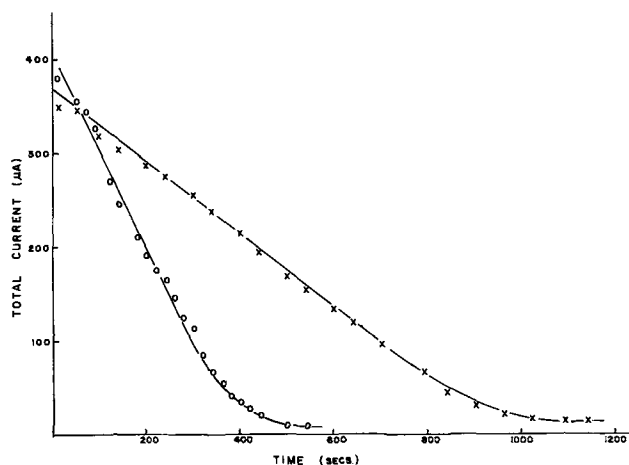


Fig. 12. Total current-time behavior representing Emulphogene BC-420 readsorption at $\eta = -50$ mV following desorption at high potentials 10% KOH + 0.1M ZnO. $T = 33^{\circ}C$ doped with x $3.7 \times 10^{-5}M$ and \circ $7.4 \times 10^{-5}M$ Emulphogene BC-420.

initiation was attempted before or after the apparent desorption of the Emulphogene. The initiation did not occur within 180 min when the electrode was maintained at the potential corresponding to point A in Fig. 11 (compared to normal initiation times in identical uninhibited systems of 10 min), whereas initiation proceeded normally when the electrode was initially kept at the potential corresponding to point B in the same figure. Two i - t dependences were found only when the Emulphogene concentration was higher than $1.5 \times 10^{-5}M$. Below this concentration, the cathodic polarization curve and the initiation times were found essentially to duplicate those in the uninhibited system.

Comparison of photographs obtained in the inhibited system (containing $1.5 \times 10^{-5}M$ Emulphogene BC-420) with those from the uninhibited system, at the same deposition time, shows that an apparent higher initiation rate exists for the inhibited system (Fig. 13). It was observed that although dendrites do initiate in the inhibited system, and propagate in the main axis direction at a rate close to that observed in the uninhibited system, they do so only for a short period. This period of "free" growth appeared to depend on the Emulphogene concentration, being the shorter the higher the concentration. At the cessation of propagation, side branching and tip splitting occur (cf. Fig. 13). This phenomenon of tip splitting to produce side branches has been observed by the present authors occasionally in the uninhibited system and is well documented in other dendritic systems (20-22).

Triton X-15.—The polarization curve for zinc deposition in the presence of $1.5 \times 10^{-4}M$ Triton X-15 is shown in Fig. 14. Again, as in the case of the Emulphogene, as the potential is made more cathodic the current increases at first gradually and then, at a given potential, a larger increase in current occurs. Initiation and growth of zinc dendrites at $\eta = -100$ mV proceeds as in the uninhibited system. Readsorption of Triton X-15 following 5 min desorption at -80 mV is considerably faster than for Emulphogene BC-420, being essentially complete in seconds rather than in minutes (cf. Fig. 11). At the concentration of $1.5 \times 10^{-4}M$ (the highest used for Emulphogene BC-420), Triton X-15 is less effective in preventing dendrites than Emulphogene BC-420.

Triton X-100.—Figure 15 shows the cathodic polarization curves for the deposition on zinc in the presence of 1.8×10^{-4} , 1.4×10^{-4} , and $8.8 \times 10^{-5}M$ Triton X-100. A rapid increase in current occurs at overpotentials in the range -270 to -290 mV, which is somewhat smaller than the value reported by

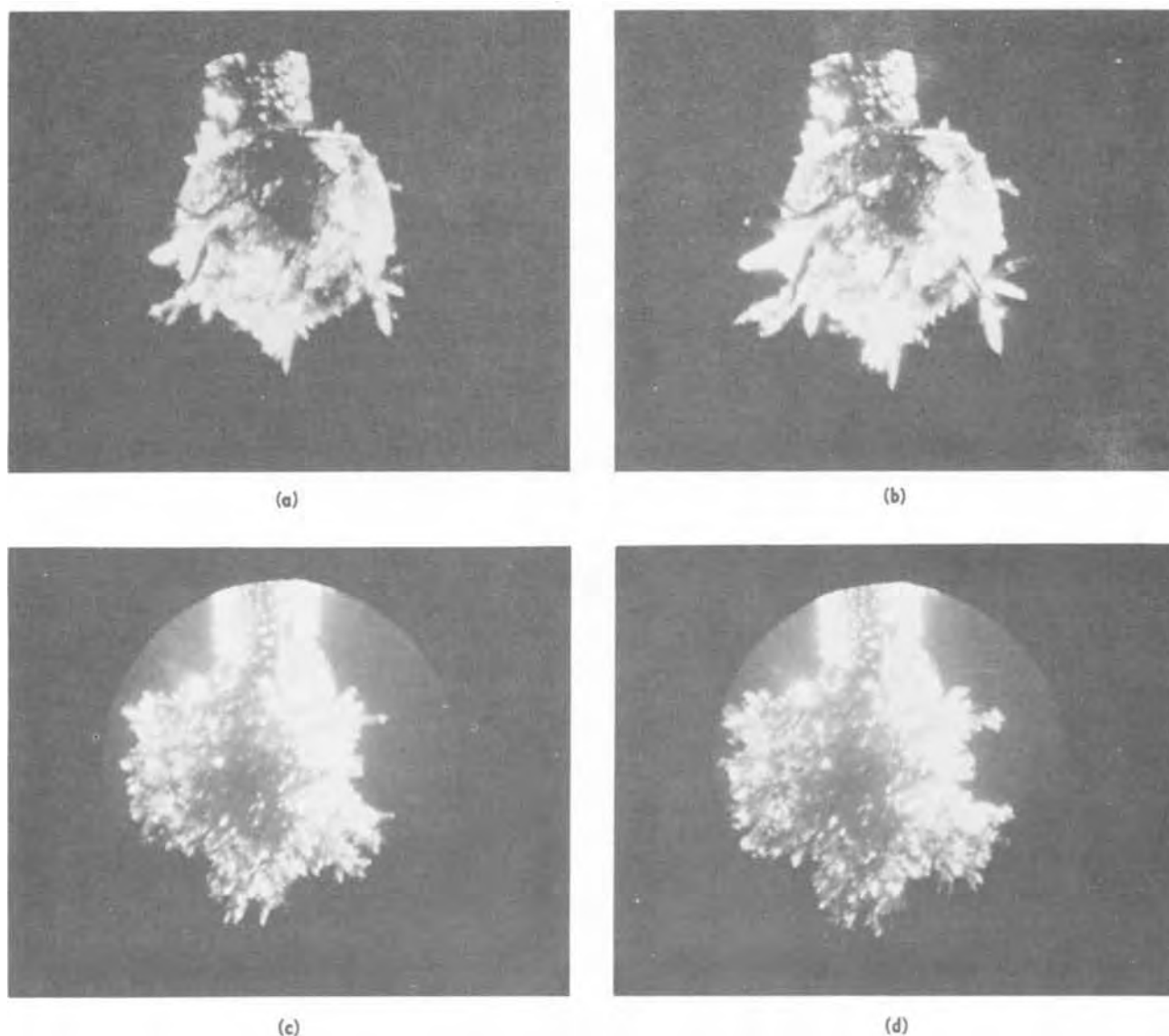


Fig. 13. Typical zinc morphology for the deposition of zinc from pure 10% KOH + 0.1M ZnO, $\eta = -100$ mV, $T = 30^\circ\text{C}$ after 35 (a) and 40 (b) min and from Emulphogene BC-420 doped solution ($1.5 \times 10^{-5}\text{M}$) also after 35 (c) and 40 (d) min Magnification in all cases X22.

Stachurski (5). Some evidence exists as to a concentration dependence of this potential, but this is not so marked as for Emulphogene BC-420 (Fig. 11). Hysteresis in the η -log i relationship was observed on reducing the cathodic potential, but it is considerably less than that observed for the zincate system doped with Emulphogene. Inhibitor readsorption is more rapid for Triton X-100 than for Emulphogene BC-420, but not as rapid as for Triton X-15.

Discussion

In any investigation of inhibition the action of an inhibitor by two basic processes must be considered, (a) inhibition by pure blocking action and (b) inhibition arising from a change in electrode kinetic parameters, e.g., specific adsorption of ions could cause a change in the diffuse layer P.D. and thus produce either an increased or decreased P.D. across the reaction plane, i.e. the Helmholtz double layer. This latter effect has been reported (23) as being unable to account fully for some electrode reactions in the presence of specific adsorption. In the presence of specific adsorption a displacement of the discharge reaction plane position, being outward from the metal for retarded cathodic reactions (23), and a change in the activity coefficient for the activated complex (24) have been proposed as refinements to process (b).

In the following discussion an attempt will be made to discuss the applicability of these possible inhibition mechanisms.

Inhibition due to lead-bearing species.—Lead ions are well known in their influence on the morphology of crystallizing solids (25, 26), blockage by codeposition usually being invoked as an explanation. Figure 4 shows a summary of the influence of lead as a zinc morphology modifier, the degree of modification being dependent both on the lead concentration and the electrode potential. This potential dependence suggests that the inhibiting species is, at least, partially charged as an ion or adion.

A change in morphology from dendritic to compact zinc at $\eta = -100$ mV by the addition of 10^{-4} molar lead has been observed (cf. Fig. 4), i.e., the initiation overpotential for zinc dendrites is now > -100 mV. According to previous theory (17), a lowering of i_0 leads to an increase in the numerical value of the critical overpotential η_{crit} required for dendrite initiation. Thus, if the addition of lead lowered the i_0 for zinc deposition, then compact zinc, rather than dendrites, might be expected at -100 mV. Furthermore, with any one lead concentration, increasing the cathodic overpotential should eventually produce dendrites (as Fig. 4 shows). An alternative explana-

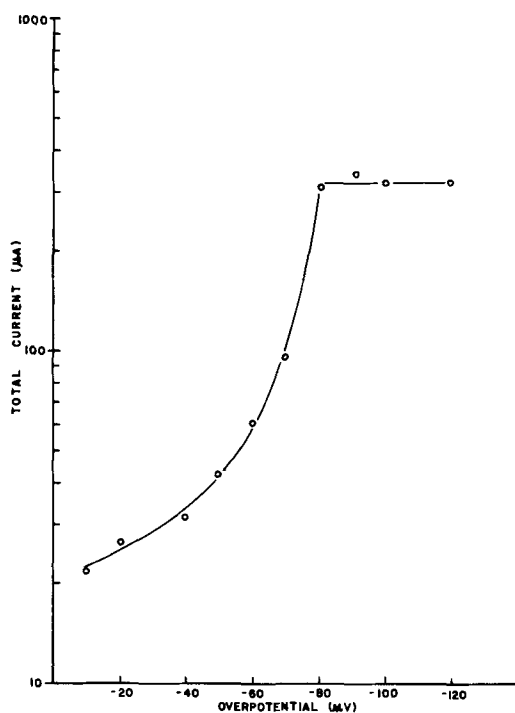


Fig. 14. Polarization curve for 10% KOH + 0.1M ZnO doped with 1.5×10^{-4} M, Triton X-15, $T = 25^\circ\text{C}$.

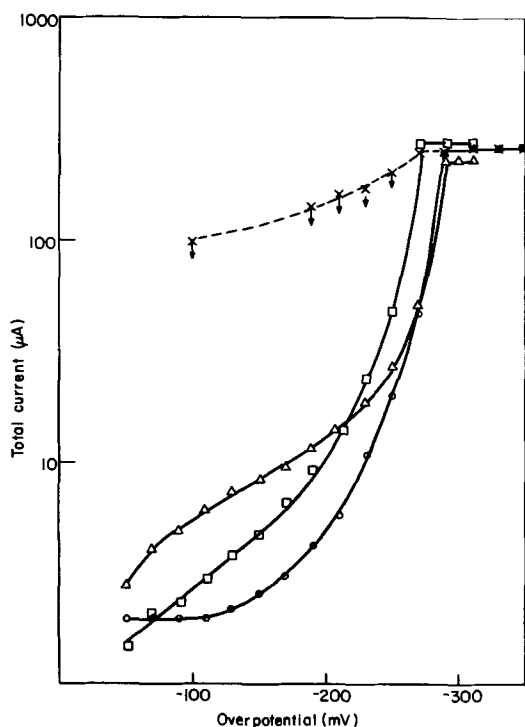


Fig. 15. Polarization curves for Triton X-100 doped 10% KOH + 0.1M ZnO. $T = 25^\circ\text{C}$. \square 8.8×10^{-5} M, \triangle 1.4×10^{-4} M, \circ 1.8×10^{-4} M. A typical polarization hysteresis is indicated by the points x being, in this case, for the concentration 1.8×10^{-4} M. The hysteresis (marked by the downward arrows) observed here is much more short-lived than that in Fig. 11.

tion could be that although the applied overpotential remains constant, the essential driving force for the discharge of a zinc ion, i.e., the electrostatic field, decreases. This could occur when an adsorbed lead species displaces the zinc ion discharge plane outward due to its large ionic size (see later discussion).

Inhibition due to tetra-alkyl ammonium salts.—From Fig. 9 it can be seen that the character of the

E -log i plot changes from diffusion to activation control at $\eta = -100$ mV as the concentration of tetrabutyl ammonium bromide increases. The potential at which the polarization curve, in the presence of tetrabutyl, merges with the uninhibited curve becomes more cathodic as the tetrabutyl concentration increases. This is in agreement with the results of Chuang-Hshin and Iofa (27) who further reported a "desorption potential" for 10^{-3} M tetrabutyl ammonium chloride in 1M KCl of -1.6 V (NHE), i.e., approximately -1.0 V relative to zpc. In the present work, a value for this "desorption potential" is found to be approximately -1.3 V (NHE) for 10^{-3} M tetrabutyl doped zincate solution.

Inhibition mechanism.—Specific adsorption of tetra-alkyl cations is well known (28) and has been shown to produce both accelerating and retarding influences on the discharge of ions (29). From Gierst (29) and other workers (30-32) it may be concluded that the discharge of cations will be retarded by tetra-alkyl cation adsorption due to process (b) outlined earlier, and further retarded due to the blockage process (a) of the electrode surface. However in the present experiments where the KOH electrolyte concentration is 2M, inhibition processes based on changes in diffuse layer P.D. are considered unlikely.

Since specific adsorption of both lead ions and tetra-alkyl cations appear to be involved, a process other than simple electrode surface blockage may be involved. This may take the form of an increasingly outward displacement of the discharge plane as discussed by Elliott (23) and Fawcett (33). If the inhibition were due to simple blockage then the results shown in Fig. 9 are surprising, since electrode blockage would lead to a decrease in current (as observed) without the apparent change from diffusion to activation control as the tetra-alkyl ion concentration increases. Thus, the tentative conclusion is that the dendrite inhibition observed here on addition of tetra-alkyl ammonium salts (and perhaps lead) is that specific adsorption leads to a lowering of the electrostatic field promoting zinc ion discharge arising from an outward movement of the discharge plane. This conclusion is in no way invalidated by the recent work of Bockris, Nagy, and Damjanovic (34) who have concluded that the discharging species is a hydroxy-zinc anion. Only in the case of simple inhibition by process (b) could one say that adsorbed cations inhibit the discharge of a zinc cationic species. The knowledge that a retarding effect is observed for tetra-alkyls, in the case of anionic discharge, itself indicates something other than process (b), process (a) being over-ruled on previous evidence.

Inhibition due to polyethoxylated hydroxy compounds.—Facts are: (i) dendrite initiation, in the presence of Emulphogene, was found to occur following the process of inhibitor desorption, (ii) in the presence of inhibitor adsorption on the zinc substrate [adsorption occurring under diffusion control due to the low inhibitor concentration (2)] no initiation is observed, (iii) the propagation of dendrites in the presence of inhibitor above a certain concentration, proceeds only for a short time before cessation.

The occurrence of initiation, after inhibitor desorption, could be due to the fact that the initiation time is less than the time required for complete inhibitor adsorption, e.g., compare adsorption time for 7.4×10^{-5} M Emulphogene (Fig. 12) with the initiation period for the system, in the absence of Emulphogene, of 10 min (17). Since the dendrites, when initiated, possess a low radius of curvature (10^{-4} - 10^{-5} cm) compared to $\delta_0 = 10^{-2}$ cm the diffusive flux of inhibitor to the tip is greatly enhanced. Thus, propagation proceeds unimpeded for only a short time until complete adsorption of the inhibitor reduces further charge transfer, and hence, growth, to a low level. The time

of unimpeded or "free" growth should decrease as the inhibitor concentration increases, as observed. The higher frequency of dendrite initiation in Emulphogene doped zincate solutions, compared to that in the uninhibited system, is possibly due to the higher linear diffusive flux of zincate which will flow to the substrate surface in the absence of a larger number of spherical diffusive flux points, i.e., propagating dendrites. In the uninhibited systems the presence of these spherical diffusive flux points, i.e., continually propagating dendrites, the linear diffusive flux of zincate ions to the substrate could be considerably reduced and thereby reducing the dendrite initiation rate.

The conclusion that Emulphogene BC-420 is more effective as a morphology modifier than Triton X-15 is somewhat surprising since aromatic compounds are reported to be more strongly adsorbed, and hence, should influence morphology more, than aliphatic compounds (14). This conclusion, however, assumes that the hydrocarbon end lies adjacent to the metal surface. For Emulphogene compounds, Payne, Tachikawa, and Bard (2) have suggested, and have evidence to show, that the negatively charged ethylene oxide grouping lies adjacent to the metal surface, i.e., they have shown that the electrocapillary maximum moves cathodic as the Emulphogene concentration increases. In contrast, Meibhur (15) has reported that the electrocapillary maximum moves anodic for polyethoxylated naphthyl hydroxyl compounds, from which it may be concluded that in the aromatic compounds there is a positive charge adjacent to the metal.

It is suggested that in the case of Emulphogene the molecule is oriented with negatively charged ethylene oxide groups adjacent to the metal,⁹ whereas in Triton, although ethylene oxide groups are still adjacent to the metal, they are positively charged due to the electron withdrawing power of the aromatic ring. This situation is analogous to that of methanol and phenol (35) when one considers only static inductive effects



This would perhaps suggest that the orientation of these polyethoxylated hydroxyl compounds is controlled more by steric than by polarity considerations. The faster re-adsorption of Triton X-15 would appear to confirm the suggestion that Triton is adsorbed with a positive grouping adjacent to the metal (hence there is a migration term, as well as a diffusion term, assisting re-adsorption) whereas Emulphogene has a negative grouping adjacent to the metal (hence re-adsorption occurs only when diffusion supplies sufficient adsorbate). Decreasing the charge density of the positively charged ethylene oxide grouping in Triton may be expected to (a) increase the time required for adsorption, and (b) move the electrocapillary maximum more cathodic, resulting in a shift of the desorption potential in the cathodic direction. Results reported for Triton X-100 suggest that both (a) and (b) are observed.

Polarization curves (Fig. 11) in the presence of Emulphogene show that, providing the Emulphogene remains adsorbed, only a small current flows (region A); in this condition morphology is affected. Desorption of the Emulphogene at high cathodic overpotentials is accompanied by the appearance of the morphology observed in the absence of Emulphogene, and the occurrence of substantial H₂ evolution.

One reason for the large difference in the desorption potentials between Emulphogene BC-420 (Fig. 11) and Triton X-15 (Fig. 14) may be due to the fact that the zinc zpc, in the presence of Emulphogene, is much

⁹ This conclusion differs from that of Meibhur (15) who concluded from surface excess measurements, assuming $\theta = 1$, that the hydrocarbon and either a part, or all, of the ethylene oxide chain lie parallel to the metal surface. This conclusion depends on the validity of the assumption that full coverage of the metal surface is unity.

more cathodic than the zinc zpc in the presence of Triton. Another consideration must be that the cathodic desorption of a molecule with a positive end adjacent to the metal may be more difficult than the desorption of a molecule with a negative end adjacent to the metal.

Since a dependence of the shift of the zpc of a metal on the adsorbed inhibitor concentration is known (14), and has been observed for Emulphogene (2), the desorption potential will be expected to move cathodic for Emulphogene and anodic for Triton as the added inhibitor concentration increases providing all other factors are constant. Figure 11 shows this to be valid for Emulphogene BC-420.

From the work with Triton X-15 and X-100 it would seem that the higher the value of n , the more cathodic the desorption potential. This is in agreement with a decreasing charge density on the positively charged ethylene oxide chain, and a subsequent cathodic shift in the zinc zpc, as the value of n increases.

Triton X-100 shows some small concentration dependence (Fig. 15) of the desorption potential. It does, however, appear to be in the opposite direction to that expected from the above argument.

Triton X-15 is found to be ineffective as a morphology modifier since it is desorbed at $\eta = -80$ mV (Fig. 14). Triton X-100, which possesses higher ethylene oxide content, is much more effective than X-15 and as equally effective as Emulphogene BC-420.

In contrast to the tetra-alkyl inhibitors, polarization curves in the presence of polyethoxylated compounds do not exhibit any marked Tafel region, but do exhibit a marked desorption potential. Therefore, it is suggested that the influence, as inhibitors, of polyethoxylated compounds is due to a blockage, or other related effect, and is unrelated to specific adsorption. Adsorption of polyethoxylated inhibitor compounds on zinc effectively reduces the area available for deposition and consequently the total current, under potentiostatic control, decreases. Thus in conclusion, the polyethoxylated compounds do lead to some small improvement in the recharging processes of the zinc electrode, but are inferior to both lead and tetra-alkyls.

Conclusions

1. The addition of 10^{-4} M lead to alkaline zincate solutions was found to effectively suppress zinc dendrite initiation and propagation. Lead concentrations 10^{-4} M were partially effective or completely ineffective. At lead concentrations greater than 10^{-4} M, lead dendrites were formed preferentially.
2. The potential dependence of the lead inhibition process suggests that the inhibiting species is, at least, partially charged.
3. The influence on zinc morphology of the tetra-alkyl salts was found to be directly analogous to that of lead. Specific adsorption is tentatively proposed as an explanation.
4. Emulphogene BC-420 and Tritons X-15 and X-100 were found to be inferior as dendritic inhibitors to both lead and the tetra-alkyls. All three polyethoxylated compounds exhibited desorption potentials which were a function of the inhibitor concentration.
5. The desorption potentials observed for Emulphogene BC-420 were cathodic with respect to those for Triton X-15. This was suggested as being due to the zinc zpc, in the presence of Emulphogene, being cathodic with respect to the zinc zpc in the presence of Triton X-15. Since the shift in the zpc is dependent on the inhibitor concentration, the desorption potential may also be expected to exhibit an inhibitor concentration dependence.
6. Cathodic shift in zpc for Emulphogene, and the anodic shift for Triton is suggested to be due to the ethylene oxide grouping, adjacent to the zinc surface, possessing a negative charge in the case of Emulphogene and a positive charge in the case of the Tritons.

7. The inhibition of zinc dendrite morphology by lead and tetra-alkyl ammonium salt additions is tentatively suggested as being due to an outward shift in the discharge plane, following specific adsorption, and the consequent lowering of the electrostatic field facilitating discharge.

8. The influence on zinc morphology of the Emulphogene and Triton inhibitors was suggested as being largely a blocking action, and effective in preventing dendrite initiation only when adsorbed. Desorption of the Emulphogene, at high cathodic potentials, results in substantial H₂ evolution.

Acknowledgments

Financial assistance from the National Aeronautics and Space Administration (Contract No. NsG-325) is gratefully acknowledged. The authors are indebted to Professor J.O'M. Bockris for his interest and encouragement throughout the course of this work. Finally the authors are indebted to the referees of this paper for their comments.

Manuscript submitted Oct 4, 1971; revised manuscript received July 21, 1972. This was Paper 18 presented at the Detroit Meeting of the Society, Oct. 5-9, 1969.

Any discussion of this paper will appear in a Discussion Section to be published in the June 1973 JOURNAL.

REFERENCES

- J. A. Keralla and J. J. Lander, *Electrochem. Technol.*, **6**, 202 (1968).
- D. A. Payne, H. Tachikawa, and A. J. Bard, Final Report, Contract No. AF 33 (615)-3487, October 1968.
- T. P. Dirkse and R. Shoemaker, *This Journal*, **115**, 784 (1968).
- T. P. Dirkse, *This Journal*, **115**, 1169 (1968).
- Z. Stachurski, Final Report, Contract No. NAS 5-3873, Yardley Electric Corp., New York (1965).
- J. J. Lander, J. A. Keralla, and R. S. Bogner, Tech. Report AFAPL-TR-66-79, Delco-Remy, August 1966.
- F. Mansfeld and S. Gilman, *This Journal*, **117**, 588 (1970).
- J. E. Oxley and J. R. Humphrey, Final Report, Contract NAS 7-671, Atomics International, October 1968.
- N. T. Kudryavtsev, *Tr. Konf. Korrozii Metal.*, **2**, 173 (1943).
- N. T. Kudryavtsev and A. G. Atanasyants, *Tr. Mosk. Khim. Tekhnol. Inst.*, **22**, 143 (1956); *C. A.*, **52**, 926e.
- A. N. Frumkin in, "Advances in Electrochemistry and Electrochemical Engineering," Vol. 1, P. Delahay and C. Tobias, Editors, Interscience, New York (1961).
- D. Cipris and B. Lovrecek, *J. Electroanal. Chem.*, **11**, 44 (1966).
- P. Bauer, "Batteries for Space Power Systems," Office of Technology Utilization, NASA, p. 156 (1968).
- E. Blomgren, J. O'M. Bockris, and C. Jesch, *J. Phys. Chem.*, **65**, 2000 (1961).
- S. Meibhur, *Electrochim. Acta*, **14**, 169 (1969).
- J. W. Diggle and A. Damjanovic, *This Journal*, **117**, 65 (1970).
- J. W. Diggle, A. R. Despic, and J. O'M. Bockris, *ibid.*, **116**, 1503 (1969).
- G. Wranglen, *Electrochim. Acta*, **2**, 130 (1960).
- J. W. Diggle and B. Lovrecek, *J. Electroanal. Chem.*, **24**, 119 (1970).
- L. R. Morris and W. C. Winegard, *J. Cryst. Growth*, **1**, 245 (1967).
- G. R. Kotler and W. A. Tiller, *ibid.*, **2**, 287 (1968).
- M. Kahlweit, *ibid.*, **7**, 74 (1970).
- D. Elliott, *J. Electroanal. Chem.*, **22**, 301 (1969).
- R. Parsons, *ibid.*, **21**, 35 (1969).
- T. Shichiri and N. Kato, *J. Cryst. Growth*, **3**, 384 (1968).
- M. Bienfait, R. Boistelle, and R. Kern, *Colloq. Int. Centre Nat. Rech. Sci.*, **152**, 577 (1965).
- Tsa Chuang-Hsin and Z. A. Iofa, *Dokl. Akad. Nauk SSSR*, **131**, 137 (1960).
- M. A. V. Devanathan and M. J. Fernando, *Trans. Faraday Soc.*, **58**, 368 (1962).
- L. Gierst, J. Tondeur, and E. Nicolas, *J. Electroanal. Chem.*, **10**, 397 (1965).
- J. Kuta and I. Smoler, *Coll. Czech. Chem. Comm.*, **32**, 2691 (1967).
- A. Aramata and P. Delahay, *J. Phys. Chem.*, **68**, 880 (1964).
- V. K. Venkatesan, B. B. Damaskin, and N. V. Nikolaeva-Fedorovich, *J. Electroanal. Chem.*, **25**, 85 (1970).
- W. R. Fawcett, *ibid.*, **22**, 19 (1969).
- J. O'M. Bockris, Z. Nagy, and A. Damjanovic, *This Journal*, **119**, 285 (1972).
- I. L. Finar, "Organic Chemistry," Chaps. VI and XXVI, Longmans, Green and Company, London (1957).

Electrochemical Oxidation of Uric Acid and Xanthine at the Pyrolytic Graphite Electrode

Mechanistic Interpretation of Electrochemistry

Glenn Dryhurst

Department of Chemistry, University of Oklahoma, Norman, Oklahoma 73069

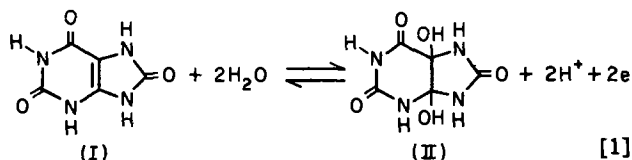
ABSTRACT

The quantitative course of electrochemical oxidation of uric acid and xanthine at the pyrolytic graphite electrode has been examined between pH 1-7, the most commonly encountered pH range in biological systems. Basically, uric acid is oxidized in a primary $2e-2H^+$ oxidation of the $C_4=C_5$ bond to give a readily reducible and highly reactive bis-imine. The bis-imine can be detected as a cathodic peak by fast sweep cyclic voltammetry. Complete hydration of the bis-imine gives rise to uric acid-4,5-diol that breaks down to alloxan and urea at pH 1, allantoin and a small amount of urea at pH 7, and at intermediate pH values mixtures of alloxan, allantoin, urea, and occasionally traces of parabanic acid are formed. Xanthine undergoes a $4e-4H^+$ oxidation that proceeds by two $2e-2H^+$ stages. The first involves oxidation of the $-C_8=N_9-$ bond to give uric acid which, being more easily oxidized than xanthine, is immediately further oxidized ($2e-2H^+$) to the uric acid bis-imine. This then hydrates and fragments in essentially the same way as described for uric acid, the same products being observed. Mechanisms are developed which explain the observed electrochemistry and over-all formation of products from this reaction. The nature and yields of products formed electrochemically and the effect of pH on the reaction parallels the biological (enzymatic) oxidation of these compounds.

Over the past five to six years several reports have appeared concerned with the electrochemical oxidation of naturally occurring biologically important purines (1-11). All of these reports, however, are primarily concerned with qualitative identification and quantitative measurement of the products of the reactions and with detection of possible intermediates using fast sweep cyclic voltammetry. Detailed electrochemical and related chemical mechanisms have not been developed.

The first modern report of the electrochemical oxidation of a purine is that of Struck and Elving (1) who indicated that uric acid is oxidized at a wax-impregnated spectroscopic graphite electrode in 1M HOAc in a process that involves about $2.2e$ per mole of uric acid oxidized. The products formed were CO_2 (0.25 mole), allantoin or an allantoin precursor (0.25 mole), urea (0.75 mole), parabanic acid (0.3 mole), and alloxan (0.3 mole) per mole of uric acid oxidized. On the basis of these products a scheme was proposed whereby uric acid was oxidized in a primary $2e$ process to a short-lived dicarbonium ion, with the positive charge localized on the C_4 and C_5 carbon atoms, which was unstable and underwent hydrolysis to allantoin or its precursor, alloxan and urea and further secondary oxidation to parabanic acid and urea. There are however several objections to this scheme. First, the peak for oxidation of uric acid at both spectroscopic and pyrolytic graphite electrodes is strongly pH dependent (1, 5) and hence protons must be involved in the electrode reaction. The earlier scheme does not indicate the involvement of protons in the primary electrochemical step. Second, the dicarbonium ion formed in the primary electrode reaction was claimed to be further oxidized to parabanic acid at potentials where uric acid is oxidized. The probability of a doubly positively charged species readily losing the two further electrons required to give parabanic acid is obviously remote. In addition, oxidation of the dicarbonium ion intermediate to parabanic acid, theoretically a $2e$ process, and formation of 0.3 mole of parabanic acid on complete oxidation of uric acid should result in a

total transfer of $2.6e$ per mole of uric acid not $2.2e$ as claimed (1). Thus, serious questions are raised as to the actual amount of parabanic acid formed and/or electrons transferred on electrochemical oxidation of uric acid, and to the actual nature of the primary product formed. Dryhurst (4) subsequently claimed that in order to account for the pH dependence of the oxidation peak of uric acid (I, Eq. [1]) at the PGE that the primary product of the oxidation was a uric acid-4,5-diol (II, Eq. [1]).



Fast sweep cyclic voltammetry of uric acid also reveals that the primary electrode product is very readily reducible, and that it is very unstable so that at slow scan rates (*i.e.*, $< 300 \text{ mV}\cdot\text{sec}^{-1}$) the reducible intermediate cannot be detected by cyclic voltammetry (4). It was proposed that the uric acid-4,5-diol (II, Eq. [1]) was the unstable highly reducible primary product (4), and that it very rapidly decomposed to the observed products proposed by Struck and Elving (1), one of which was parabanic acid. The latter was thought to be the cause of a second cathodic peak observed on cyclic voltammetry of uric acid at the PGE. However, the major objection to this scheme is that the uric acid-4,5-diol would not be expected to be very readily reducible, there being no electrochemically reducible sites in the molecule. Similar 4,5-diol products have been proposed to be formed upon electrochemical oxidation of adenine (2), guanine (5), xanthine (7), methylated xanthines (7-9) as well as uric acid (4, 7, 10). Clearly, neither of the primary products (dicarbonium ion or uric acid-4,5-diol) proposed for oxidation of these compounds fits the observed experimental data.

Complete product analysis and characterization in 1M HOAc has been carried out for all the purines mentioned above using pyrolytic graphite as the electrode material with the exception of uric acid, where

Key words: 2,6,8-trihydroxypurine, 2,8-dihydroxypurine, purine-2,6,8-triol, purine,2,6-diol, bioelectrochemistry.

spectroscopic graphite was used, and xanthine which has not previously been examined in detail. In view of the uncertainty regarding the n -value and yield of parabanic acid formed on oxidation of uric acid, the difference in electrode material used for macroscale oxidation (1) and cyclic voltammetry (4,8) of uric acid, and the lack of quantitative data on xanthine, and the obviously incorrect assignment of the structures of the primary electrochemical product of these and other purines, a complete reinvestigation of the uric acid-xanthine systems at the PGE has been carried out. On the basis of the data reported here a different and plausible primary electrode product is proposed and detailed follow-up chemical and electrochemical mechanisms are proposed. In order better to compare the mechanisms and products of electro-oxidation of uric acid and xanthine to known biological oxidations the electrochemical oxidation of these two compounds was studied over a fairly wide pH range.

Experimental

Apparatus employed for d-c voltammetry, cyclic voltammetry, coulometry, and controlled potential electrolysis has been described in detail elsewhere (2, 4, 5, 7-10). The pyrolytic graphite used in this study was obtained from the Super-Temp Company (Santa Fe Springs, California). The fabrication of the micro PGE for voltammetry and massive electrodes for controlled potential electrolysis have been outlined in earlier reports (2, 12). Analytical methods for the detection and determination of parabanic acid, allantoin, urea, and alloxan have also been detailed previously (1, 5, 7-10). All potentials are referred to the SCE at 25°C.

Results and Discussion

Voltammetry.—Uric acid and xanthine both give rise to a single pH-dependent voltammetric oxidation peak at the PGE in aqueous solution. For uric acid the peak potential (E_p) is described by the equation $E_p = 0.755 - 0.069 \text{ pH}$ between pH 0-12 (Fig. 1A). For xanthine $E_p = 1.034 - 0.056 \text{ pH}$ over the same pH range (Fig. 1A). These equations are based on voltammograms obtained at a scan rate of $5 \text{ mV}\cdot\text{sec}^{-1}$ and under such conditions indicate that the peak of xanthine occurs 300-400 mV more positive than the peak of uric acid. The observed peak currents for uric acid and xanthine are largest at low pH and decrease more or less continuously with increasing pH (Fig. 1B). The reason for the very large peak current values at low pH is no doubt related to the very strong adsorption of these compounds. This is evidenced by the very sharp spike-like appearance of the peaks for both compounds, by increases in the peak current function with increasing voltage scan rate, and depressions of the base current in alternating current voltammetry; the latter two studies have been reported elsewhere (13). Assuming a value for the diffusion coefficient of uric acid and xanthine of $10^{-6} \text{ cm}^2\cdot\text{sec}^{-1}$ and n values of 2 and 4, respectively, (*vide infra*) the theoretical reversible peak current for uric acid under the conditions outlined in Fig. 1 is $1.11 \mu\text{A}$ and for xanthine $3.5 \mu\text{A}$. These values are considerably smaller than the experimentally observed peak currents which may indicate that both uric acid and xanthine are appreciably adsorbed even at pH 12. The effect of pH on the extent of adsorption of these compounds and hence the magnitude of the peak current is no doubt related to their very low solubility at low pH and increasing solubility at higher pH.

By use of fast-sweep cyclic voltammetry, it is shown that oxidation of uric acid (peak I_a, Fig. 2A) gives rise to a very reactive yet very easily reducible product (peak I_c, Fig. 2A). The latter peak cannot be observed unless the scan rate exceeds about $300 \text{ mV}\cdot\text{sec}^{-1}$ (4, 7). A further cathodic peak at more negative potential (peak II_c, Fig. 2A) is also observed.

The involvement of uric acid in the electrochemical oxidation of xanthine is clearly established by fast-

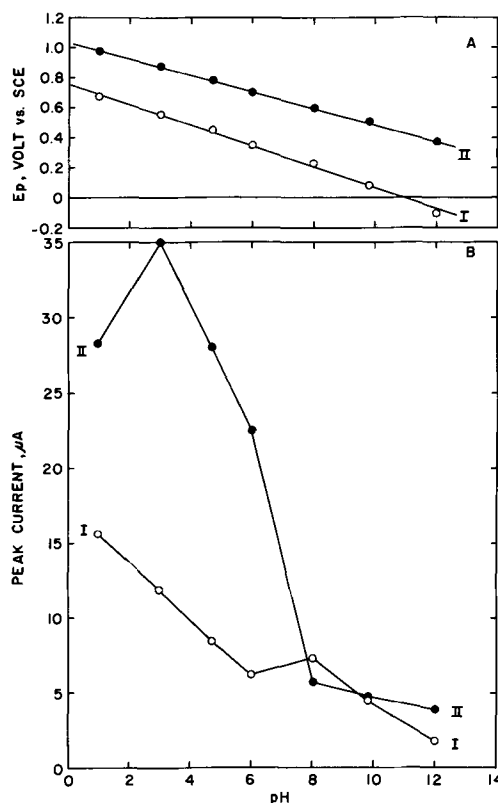


Fig. 1. (A) Variation of peak potential with pH for electro-oxidation uric acid (I) and xanthine (II) at the PGE. (B) Variation of peak current with pH for uric acid (I) and xanthine (II). Data taken at a uric acid concentration of 0.164 mM and xanthine 0.183 mM. Scan rate $5 \text{ mV}\cdot\text{sec}^{-1}$.

sweep cyclic voltammetry. After having scanned the primary oxidation peak of xanthine (designated peak II_a, Fig. 2B) a very readily reducible product can be detected (peak I_c, Fig. 2B) and a second product reduced with greater difficulty (peak II_c, Fig. 2B). The peak potentials for cathodic peaks I_c and II_c of xanthine (Fig. 2B) are the same as for peaks I_c and II_c of uric acid (Fig. 2A). On the second positive-going sweep xanthine exhibits a second and new anodic peak (peak I_a, Fig. 2B). This peak occurs at almost the same peak potential as peak I_a of uric acid. As further confirmation of the fact that peaks I_a, I_c, and II_c observed on cyclic voltammetry of xanthine are identical to the corresponding uric acid peaks a cyclic voltammogram of a mixture of the two compounds was taken (Fig. 2C). The very small differences in peak potentials observed in peak I_a (the uric acid oxidation peak) shown in Fig. 2A, B, and C are caused by differences in concentration of uric acid which must be smaller in the situation extant in Fig. 2B than in Fig. 2A or 2C (*vide infra*). This is so because the peak potential for peak I_a of uric acid (and indeed peak II_a of xanthine) is strongly concentration- and scan-rate dependent. Thus, for a 0.2 mM solution of uric acid in acetate buffer pH 4.7, E_p for peak I_a is 0.45V at $0.005 \text{ V}\cdot\text{sec}^{-1}$ and 0.65V at $5.0 \text{ V}\cdot\text{sec}^{-1}$. In the same medium but 0.01 mM in uric acid, $E_p = 0.50\text{V}$ at $5.0 \text{ V}\cdot\text{sec}^{-1}$. These shifts of peak potential are due to adsorption effects and to some extent to uncompensated ohmic drop in the instrumentation employed (14). As further evidence that peaks I_c, II_c, and II_a of xanthine are identical to those of uric acid the value of the peak potentials for these peaks of both compounds were measured as a function of pH and scan rate (Fig. 3). Clearly, the pH dependence of all peaks can be described by a single straight line indicating that the species giving rise to each peak from uric acid and xanthine are identical. This information confirms that oxidation of xanthine

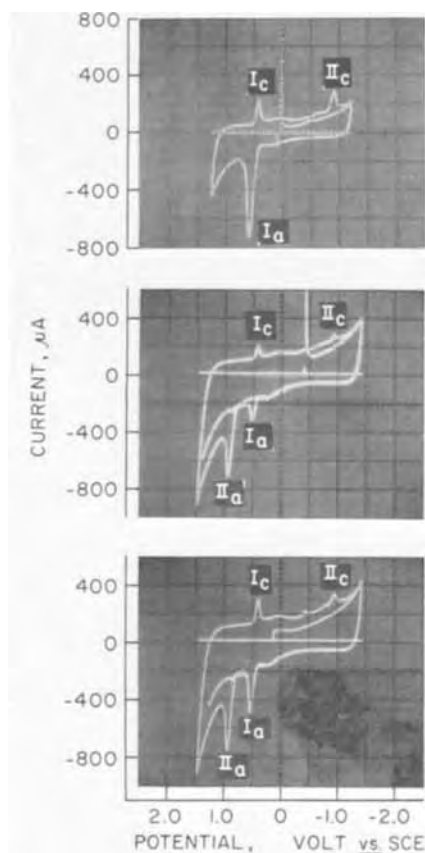


Fig. 2. Cyclic voltammograms at a clean PGE in acetate buffer pH 4.7. (A) 0.075 mM uric acid; scan pattern: 0.00 \rightarrow -1.20 V \rightarrow 1.30V \rightarrow -1.20V \rightarrow 0.00V. Scan rate 5.0 V-sec⁻¹. (B) 0.03 mM xanthine; scan pattern -0.40V \rightarrow -1.40V \rightarrow 1.50V \rightarrow -1.40V \rightarrow 1.50V. Scan rate 5.0 V-sec⁻¹. (C) 0.03 mM uric acid plus 0.03 mM xanthine; scan pattern: 0.00V \rightarrow -1.40V \rightarrow 1.50V \rightarrow -1.40V \rightarrow 0.00V. Scan rate 5.0 V-sec⁻¹.

gives rise to the same readily reducible product obtained on oxidation of uric acid (peak I_c), the reduction product of which is uric acid which can be detected by cyclic voltammetry as peak I_a. Peak II_c is also due to the same product as evidenced by the agreement between the peak potentials of the peak observed from both uric acid and xanthine.

Coulometry and mass electrolysis.—Coulometry of uric acid and xanthine was carried out at various pH values between pH 1-7, the most commonly encountered pH range in biological systems. Typical coulometric data is presented in Table I which clearly indicates that at all pH values examined the *n* value for uric acid is 2 and for xanthine is 4.

Table I. Coulometric *n*-values for the controlled potential electrolysis of uric acid and xanthine at the PGE

pH	Buffer system	Millimoles ^a electrolyzed	Applied potential, V vs. SCE	<i>n</i> -Value		
					Uric acid	Xanthine
1.0	Chloride	0.253	0.80	2.08		
2.3	1M acetic acid	0.169	0.70	1.95		
4.7	Acetate	0.203	0.55	2.30		
7.0	McIlvaine	0.220	0.40	2.01		
1.0	Chloride	0.272	1.05	3.75		
2.3	1M acetic acid	0.181	1.10	3.90		
4.7	Acetate	0.215	0.85	3.85		
7.0	McIlvaine	0.108	0.80	3.93		

^a All electrolyses were continued until all uric acid or xanthine was oxidized.

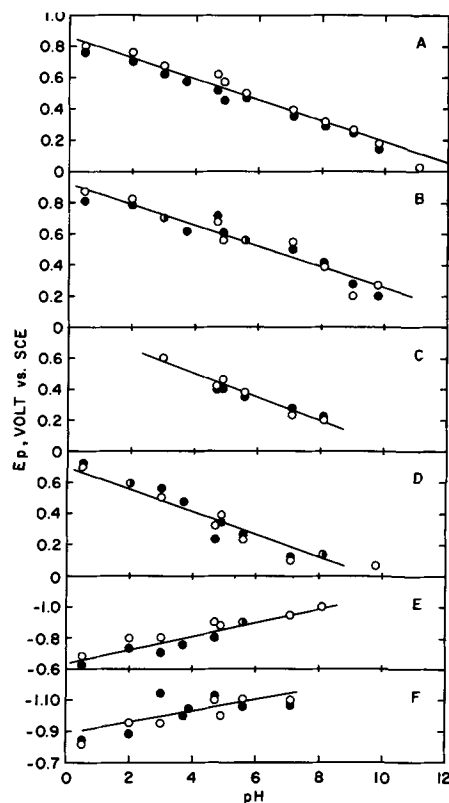


Fig. 3. Comparison of peak potentials for peaks I_a, I_c, and II_c of uric acid and xanthine as a function of scan rate and pH. (A) Peak I_a; scan rate 5 V-sec⁻¹. (B) Peak I_a; scan rate 50 V-sec⁻¹. (C) Peak I_c; scan rate 5 V-sec⁻¹. (D) Peak I_c; scan rate 50 V-sec⁻¹. (E) Peak II_c; scan rate 5 V-sec⁻¹. (F) Peak II_c; scan rate 50 V-sec⁻¹. Open circles uric acid, solid circles xanthine. When two data points were identical a half-shaded circle is used. Uric acid and xanthine concentrations ca. 0.03 mM.

After complete electro-oxidation of solutions of uric acid or xanthine in various background media between pH 1-7 qualitative and quantitative analyses of the electrolysis products were carried out. The various analytical data are presented in Table II. The notable difference between these data and those reported earlier by Struck and Elving (1) at pH 2.3 (1M HOAc) is that alloxan and urea are by far the major products. Much less allantoin is formed and only minute traces of parabanic acid.

It is also clear that at low pH the only products of oxidation of both uric acid and xanthine are alloxan and urea. With increasing pH the amount of alloxan decreases while the yield of allantoin correspondingly

Table II. Quantitative analytical data on products of electrochemical oxidation of uric acid and xanthine at the PGE

pH	Buffer system	Product, moles/mole of uric acid or xanthine electro-oxidized ^a			
		Alloxan	Urea	Allantoin	Parabanic acid
Uric acid					
1.0	Chloride	1.0	1.0	ND ^b	ND
2.3	1M HOAc	0.8	0.8	0.2	ca. 0.03
4.7	Acetate	0.37	0.37	0.63	ND
7.0	McIlvaine	ND	0.18	0.82	ND
Xanthine					
1.0	Chloride	1.0	1.0	ND	ND
2.3	1M HOAc	0.8	0.8	0.2	ca. 0.06
4.7	Acetate	0.49	0.4	0.64	ND
7.0	McIlvaine	ND	0.29	0.71	ND

^a Generally, between 0.15-0.30 mmoles of uric acid or xanthine in 150 ml of buffer were oxidized.

^b Not detected.

increases. At pH 7 the major product is allantoin with smaller amounts of urea and alloxanic acid (not analyzed quantitatively but detected by thin layer chromatography). The change in major product from alloxan at low pH to allantoin in weakly acid and neutral solution is most interesting because it parallels the effect of pH on the products observed on oxidation of uric acid in the presence of peroxidase enzymes (15, 16). Parabanic acid could only be detected in exceedingly small amounts in the products of electro-oxidation of uric acid and xanthine in 1M HOAc pH 2.3.

It should also be noted that the relative yields of products obtained at any pH were somewhat variable from one electrolysis to another, the values quoted in Table II are simply typical values. It can also be seen that on occasion the sum of total products does not total 100% of the initial uric acid or xanthine oxidized. The product yields however can be regarded as equivalent to a complete material balance in view of the analytical accuracy achieved by this worker.

Mechanisms

In summary, the electrochemical and analytical data reported here reveal that uric acid is oxidized in a $2e$, pH-dependent process at the PGE. A very unstable, very reducible product is formed (peak I_c , Fig. 2). The species giving rise to peak II_c cannot be due to reduction of parabanic acid to 5-hydroxyhydantoin (17) as proposed earlier (4, 5, 7) because there is insufficient parabanic acid formed to account for the relatively large peak observed by cyclic voltammetry.

Cyclic voltammetry and analytical data clearly reveal that xanthine is initially oxidized to uric acid which is then further oxidized to the same products obtained with uric acid as the starting material.

As noted earlier, the product giving rise to peak I_c cannot be uric acid-4,5-diol as proposed earlier (4, 5, 7-9). However a diol is formed at some stage in the reactions following electron-transfer as evidenced by the fact that in the presence of methanol, oxidation of uric acid appears to give a 4,5-dimethoxy derivative (10).

In view of these facts, a mechanism is proposed where uric acid (I, Fig. 4) is initially electrochemically oxidized in a $2e-2H^+$ process to give the species designated II (Fig. 4) which will be referred to in subsequent discussion as a bis-imine. The bis-imine formed from uric acid could exist in two tautomeric forms (II_a , II_b , Fig. 4). Such a system of conjugated double bonds would be expected to be very readily electrochemically reducible, indeed molecules having somewhat similar bis-imine structures such as riboflavin (18-23), quinoxalines (24), and bis-quinazolines (25) are rather readily reduced electrochemically. Aldimines and ketimines are also very easily electrochemically reduced (26-28). The expected ease of reduction of structures II_a and/or II_b along with their expected facile hydration across the imine-N=C-double bonds to give a 4,5-diol accounts nicely for part of the observed cyclic voltammetry of uric acid. Thus, provided the sweep rate is fast enough, II_a or II_b formed as the primary products of oxidation of uric acid can be detected as a very reducible species (peak I_c , Fig. 2). At slow scan rates II_a or II_b cannot be detected because they are hydrated too rapidly to uric acid-4,5-diol or other species (*vide infra*). Cathodic peak II_c is observed at slower scan rates than is peak I_c (10) and occurs at potentials very close to those expected for reduction of parabanic acid. However, at completion of an exhaustive electrolysis of uric acid only a very small quantity of parabanic acid is detected (and that only in 1M HOAc solution), quite insufficient to account for the relative peak current observed for peak II_c . Accordingly it is proposed, without any direct supporting evidence, that the bis-imine formed on oxidation of uric acid hydrates in two stages, the first fast, the second slower. Addition of the elements of one molecule of

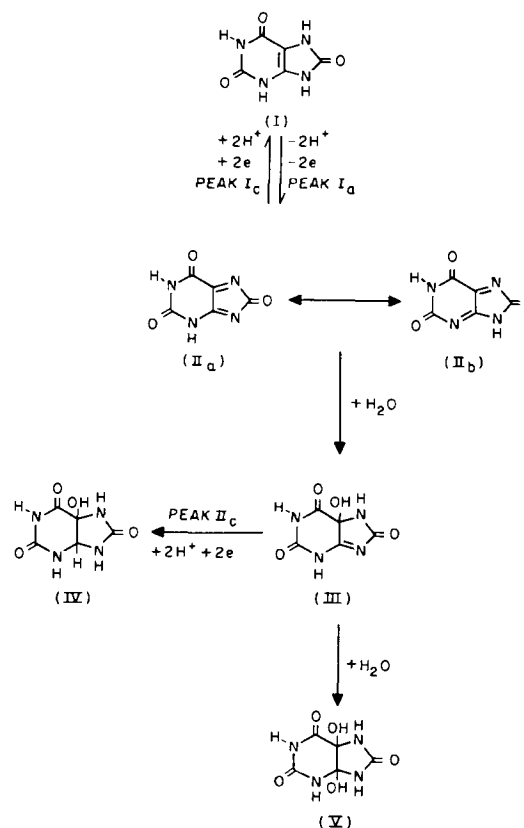
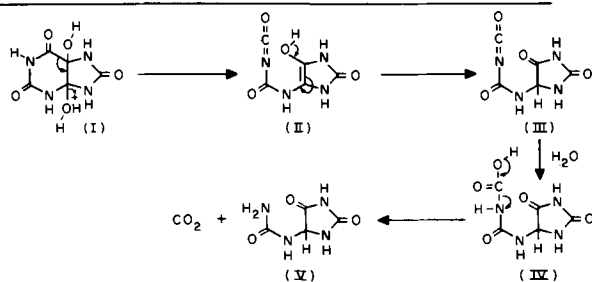


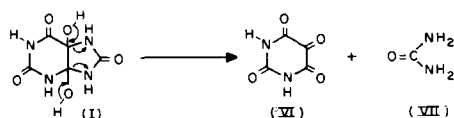
Fig. 4. Primary electrochemical oxidation, and reactions of cyclic voltammetric peaks observed for uric acid.

water gives rise to III (Fig. 4). It may be this compound that gives rise to peak II_c of uric acid being due to reduction of III possibly to IV (Fig. 4). Addition of a second molecule of water to III would give rise to the formation of uric acid-4,5-diol (V, Fig. 4). This diol is a typical intermediate of an imine-like hydrolysis and would be expected to readily fragment to the observed products. A plausible mechanism for formation of allantoin from uric acid-4,5-diol involves cleavage of the C_5-C_8 bond of the diol (I, Fig. 5) giving an imidazole isocyanate (II, Fig. 5). A hydrogen shift reaction must occur in compound II to give III which on hydrolysis would readily form CO_2 and allantoin (V, Fig. 5). A simple fragmentation of the 4,5-diol to alloxan (VI, Fig. 5) and urea (VII, Fig. 5) can also be written. Although only very minor amounts of parabanic acid are formed on electrochemical oxidation of uric acid at the PGE in 1M HOAc, large amounts are claimed to be formed at spectroscopic graphite electrodes in the same medium (1). Formation of parabanic acid necessarily involves some secondary electrochemical oxidation. A mechanism is proposed in Fig. 5 where uric acid-4,5-diol undergoes a ring opening reaction to give the structures $VIII_a$ or $VIII_b$. In acid solution $VIII_a$ should readily cleave across the original C_5-C_8 bond to give an isocyanate (IX) and 2-oxy-4,5-dihydroxyimidazole (X). Alternatively the compound $VIII_b$ could undergo a ring closure to give XI, which in turn should cleave to X and IX. Simple hydrolysis of the isocyanate IX would give urea and CO_2 . 2-Oxy-4,5-dihydroxyimidazole (X, Fig. 5) is an enediol. Enediols are normally very readily oxidizable to α -diketones even by such weak oxidizing agents as cupric ion and, on occasion, oxygen (29). Accordingly it is proposed that the parabanic acid (XIV, Fig. 5) which sometimes appears during the electro-oxidation of uric acid is formed as a result of electrochemical oxidation of the enediol (X) in a $2e-2H^+$ process. The very pronounced difference between the amount of parabanic acid formed on electro-oxidation of uric acid at spec-

SECONDARY REARRANGEMENT and HYDROLYSIS to ALLANTOIN.



SECONDARY REARRANGEMENT to ALLOXAN.



SECONDARY REARRANGEMENT and OXIDATION to PARABANIC ACID.

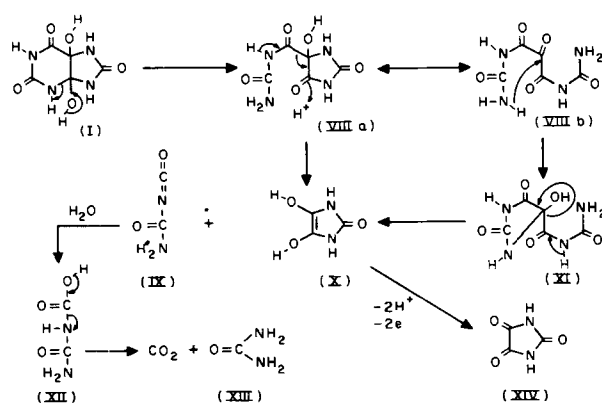


Fig. 5. Proposed tentative mechanisms for decomposition of uric acid-4,5-diol to allantoin (V), alloxan (VI), urea (VII), parabanic acid (XIV), and CO_2 .

troscopic graphite (1) and pyrolytic graphite can only be rationalized by invoking some specific electrode effects related to the nature of the electrode materials.

The mechanism of electrochemical oxidation of xanthine (I, Fig. 6) clearly proceeds by an initial $2e-2\text{H}^+$ oxidation of the $\text{C}_8=\text{N}_9$ (or $\text{N}_7=\text{C}_8$) bond to give uric acid (II, Fig. 6). Since uric acid is more readily oxidized than xanthine (Fig. 1A) it is immediately oxidized in a further $2e-2\text{H}^+$ process to the uric acid bis-imine (III_a , III_b , Fig. 6). Thus, the single initial voltammetric peak of xanthine (peak II_a , Fig. 2B) corresponds to the $4e-4\text{H}^+$ oxidation to the bis-imine (III_a , III_b , Fig. 6). Cathodic peak I_c observed cyclic voltammetrically is due to reduction of the bis-imine back to uric acid (III_a , or $\text{III}_b \rightarrow \text{II}$, Fig. 6). Partial hydration of the bis-imine gives IV which is possibly the species giving rise to cathodic peak II_c resulting perhaps in compound V. Complete hydration of the bis-imine gives uric acid-4,5-diol which decomposes by exactly the same route as shown in Fig. 5. The anodic peak (peak II_a) observed on the second positive-going sweep of xanthine is simply reoxidation of uric acid, formed in the peak I_c process, back to the bis-imine.

It should perhaps be noted here that there is insufficient evidence at this time to definitively explain the effect of pH on the yield products. It is likely however that the various decomposition reactions of uric acid-4,5-diol are acid or base catalyzed hence changing the yields and nature of products with pH. The mechanisms actually proposed for the decomposition of the

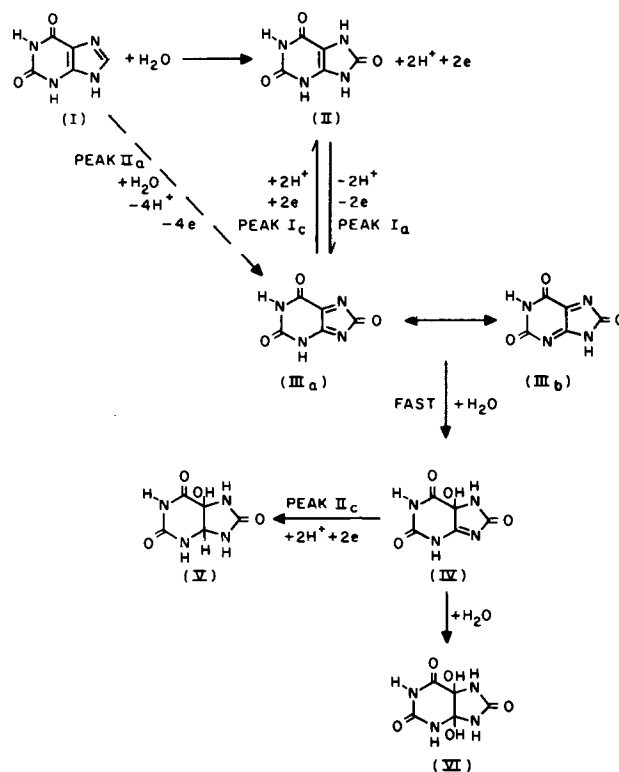


Fig. 6. Primary electrochemical oxidation and reactions of cyclic voltammetric peaks observed for xanthine.

uric acid-4,5-diol (Fig. 5) should accordingly be regarded as tentative since actually several equally plausible mechanisms could be written. However, the basic mechanism presented here can be used to satisfactorily account for the electrochemistry and products formed on electro-oxidation of other purines (11).

Conclusions

At the single pH (1M HOAc, pH 2.3) where the electro-oxidation of uric acid has been examined at both the PGE and spectroscopic graphite electrodes (1M HOAc, pH 2.3) the products obtained are qualitatively similar but quantitatively quite different. More extensive product analyses over pH 1-7 reveals that at the PGE the major products in solutions between about pH 1-3 are alloxan and urea. With increasing pH the yield of alloxan and urea decreases and allantoin becomes the major product.

Product analysis, cyclic and linear sweep voltammetry allow a detailed mechanism for the primary electro-oxidation and follow-up chemical and electrochemical processes to be written. Combination of data obtained from linear and cyclic sweep voltammetry with controlled potential electrolysis and product analysis data to develop a mechanism is always based on the assumption that the electrochemical and related mechanisms are identical. There is no way in which one can confirm this assumption. Nevertheless the data obtained in this study are all consistent with a common mechanism. Although oxidation of uric acid and reduction of its primary $2e-2\text{H}^+$ product, a bis-imine, form an almost reversible couple as evidenced by cyclic voltammetry (Fig. 1), meaningful interpretation of the kinetics of the electron-transfer process and the rates of chemical follow-up reactions is not possible. This is so because uric acid is very strongly adsorbed at the PGE (13) which results in shifts of the anodic and cathodic peak potentials with concentration. In addition, there are clearly on occasion three parallel follow-up reactions which are very complex and are

not amenable to study by, for example, cyclic voltammetric methods.

The products and their yields obtained on electrochemical oxidation of uric acid almost exactly parallel those reported for the enzymatic oxidation of uric acid, particularly with the peroxidase enzymes (15, 16). Accordingly it is proposed that the mechanisms developed here for the electrochemical and related chemical reactions of uric acid can be used to describe the biological oxidation of this compound.

The mechanism of oxidation of xanthine, once the initial $2e-2H^+$ oxidation to uric acid has occurred, almost exactly parallels the mechanism for the latter compound.

The mechanism of oxidation of other naturally occurring biologically important purines can also be nicely explained by advocating that the primary electro-oxidations proceed through sequential $2e-2H^+$ oxidations of available unsubstituted ring $-C=N-$ bonds leading ultimately to oxidation of the $C_4=C_5$ bond to give a bis-imine or on occasion a bis-iminium ion (e.g., in the case of 3,7-dimethylxanthine, methylation at N_3 and N_7 results in formation of a cationic bis-iminium ion intermediate). Hydration to a 4,5-diol then occurs followed by its decomposition to the various products. Details of these mechanisms and their relationship to biological oxidations of these purines will appear elsewhere (11).

Acknowledgments

The author would like to thank the National Science Foundation, Research Corporation and the Faculty Research Committee of the University of Oklahoma for support of the work described.

Manuscript submitted March 15, 1972; revised manuscript received Aug. 7, 1972.

Any discussion of this paper will appear in a Discussion Section to be published in the June 1972 JOURNAL.

REFERENCES

1. W. A. Struck and P. J. Elving, *Biochemistry*, **4**, 1343 (1965).
2. G. Dryhurst and P. J. Elving, *This Journal*, **115**, 1014 (1968).
3. G. Dryhurst, *ibid.*, **116**, 1097 (1969).
4. G. Dryhurst, *ibid.*, **116**, 1411 (1969).
5. G. Dryhurst and G. F. Pace, *ibid.*, **117**, 1259 (1970).
6. G. Dryhurst, *ibid.*, **117**, 1113 (1970).
7. B. H. Hansen and G. Dryhurst, *J. Electroanal. Chem.*, **30**, 417 (1971).
8. B. H. Hansen and G. Dryhurst, *ibid.*, **30**, 407 (1971).
9. B. H. Hansen and G. Dryhurst, *ibid.*, **32**, 405 (1971).
10. G. Dryhurst, *This Journal*, **118**, 699 (1971).
11. G. Dryhurst, *Topics in Current Chemistry*, In press.
12. G. Dryhurst, *Anal. Chim. Acta*, **57**, 137 (1971).
13. G. Dryhurst and P. K. De, *ibid.*, **58**, 183 (1972).
14. G. Dryhurst, M. Rosen, and P. J. Elving, *ibid.*, **42**, 143 (1968).
15. K. G. Paul and Y. Avi-Dor, *Acta Chem. Scand.*, **8**, 637 (1954).
16. E. S. Canellakis, A. L. Tuttle, and P. P. Cohen, *J. Biol. Chem.*, **213**, 397 (1955).
17. G. Dryhurst, B. H. Hansen, and E. B. Harkins, *J. Electroanal. Chem.*, **27**, 375 (1970).
18. R. Brdička and E. Knoblock, *Z. Elektrochem.*, **47**, 721 (1941).
19. R. Brdička, *Coll. Czech. Chem. Commun.*, **12**, 522 (1947).
20. Y. Asahi, *J. Pharm. Soc. Japan*, **76**, 378 (1956).
21. J. R. Merkel and W. J. Hickerson, *Biochim. Biophys. Acta*, **14**, 303 (1954).
22. R. C. Kaye and H. I. Stonehill, *J. Chem. Soc.*, **1952**, 3244.
23. J. J. Lingane and O. L. Davis, *J. Biol. Chem.*, **137**, 567 (1941).
24. J. Pinson and J. Armand, *Coll. Czech. Chem. Commun.*, **36**, 585 (1971).
25. S. Kwee and H. Lund, *Acta Chem. Scand.*, **25**, 1813 (1971).
26. P. Zuman, *Chem. Listy*, **46**, 688 (1952).
27. P. L. Pickard and S. H. Jenkins, *J. Am. Chem. Soc.*, **75**, 5899 (1953).
28. L. Holleck and B. Kastening, *Z. Electrochem.*, **60**, 127 (1956).
29. L. F. Fieser and M. Fieser, "Reagents for Organic Synthesis," pp. 159-160, John Wiley & Sons, Inc., New York (1967).

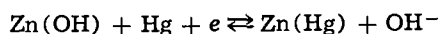
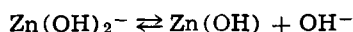
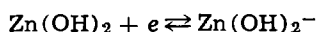
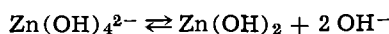
The Mechanism of the Zinc(II)-Zinc Amalgam Electrode Reaction in Alkaline Media As Studied by Chronocoulometric and Voltammetric Techniques

DeWitt A. Payne¹ and Allen J. Bard*

Department of Chemistry, The University of Texas at Austin, Austin, Texas 78712

ABSTRACT

The reduction of zinc(II) and the oxidation of zinc amalgam was studied in 0.18-4.0M KOH solutions. The primary electrochemical technique employed was potential step chronocoulometry with data acquisition on a small digital computer. The kinetic parameters were obtained by fitting the experimental charge-time curves to the complete theoretical equation for a stepwise electron transfer mechanism. The system was also studied by d-c and a-c polarography and linear scan voltammetry. The results of this study were compared to those of previous workers and shown to be consistent with a mechanism based on stepwise electron transfer



One of the most significant features of the study of electrochemical kinetics during the last 20 years has been the evolution of theoretical and experimental procedures which are useful in uncovering the different stages in the complex series of processes which comprise an electrode reaction. An investigation of the kinetics of an electrochemical reaction would ideally lead to the elucidation of the nature of the various steps and a determination of their rate constants, the identification of the intermediates and products, and the determination of the adsorption isotherm for all adsorbed species. Usually, because of experimental and theoretical limitations, only part of the information is accessible for a given system. Although characterization of intermediates is of prime importance, direct observation of these may not be possible if their concentrations are too low or their lifetimes are too short. However, analysis of the current-potential relationship obtained by several nonsteady-state methods can yield further information on complex mechanisms and faster processes.

Of particular interest in this work is the study of electrode processes involving more than one electron transfer step (1). Vetter (2-4), Hurd (5), and Mohilner (6) have calculated the steady-state polarization curves for a set of two or more consecutive single electron transfer steps. Some reactions for which consecutive electron transfer mechanisms have been proposed on the basis of steady state-measurements are Tl(III)/Tl(I) (7) and quinone/hydroquinone (8). The theory of consecutive electron transfer mechanisms for electrochemical techniques involving potential steps, current steps, and a-c polarography has also been given (9-15).

The establishment of the mechanisms of an electrode reaction often requires acquiring large amounts of accurate experimental data and fitting this data to complicated theoretical equations. Digital data acquisition systems (16-21), especially those based on general

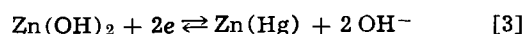
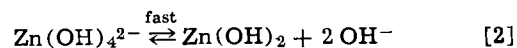
purpose programmable digital computers (20, 21), have been very useful, particularly for experimental times in the sub-second region, in obtaining this data. The data obtained by these methods can be fitted to the equations in their complete form, without the necessity of approximations or linearizations sometimes required to make the analysis of data tractable. We report here a study of the zinc(II)-zinc amalgam system using several electrochemical methods and digital data acquisition techniques.

A number of studies of the alkaline zinc electrode reaction have been made. A significant part of this effort has come from the space program's search for high energy-density primary and secondary batteries and the important role of silver/zinc and zinc/air primary batteries in this connection. Although studies of the alkaline zinc electrode reaction often are concerned with reactions at the pure metal electrode, it is common practice in batteries to amalgamate the zinc plates. Hence, we deemed a study of the alkaline zinc(I)-zinc amalgam electrode reaction justified. Moreover, the reaction at the amalgam electrode is easier to understand than the reaction at the pure metal electrode, which may be complicated by the crystallization process and more difficult surface preparation.

A number of workers (22-31) have studied the alkaline zinc(II)-zinc amalgam electrode reaction with somewhat different results. Gerischer (22, 23) determined reaction orders of hydroxide, zinc, and zincate by measuring the change of the charge transfer resistance with concentration and expressed the exchange current, i_0 , as

$$i_0 = 2FAk^0[\text{Zn(OH)}_4^{2-}]^{0.5}[\text{Zn(Hg)}]^{0.5}[\text{OH}^-]^{0.0} \quad [1]$$

This result led to the reaction mechanism in Eq. [2] and [3]



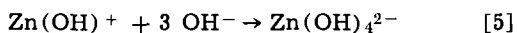
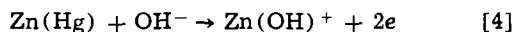
Farr and Hampson (24) duplicated Gerischer's results in ultrapure solutions by faradaic impedance measurements. Matsuda and Ayabe (25) studied the reduction

* Electrochemical Society Active Member.

¹ Present address: Tennessee Eastman Company, Kingsport, Tennessee 37660.

Key words: potential step chronocoulometry, electrode reaction kinetics, polarography, digital data acquisition, consecutive electron transfer reactions.

process by d-c polarography and found that the mechanism was the same as that of Gerischer, but that α was 0.42 Behr *et al.* (26) and Morinaga (27) also obtained results which were consistent with the above mechanism. Stromberg and co-workers (28-31) obtained results which were similar to those of Matsuda and Ayabe (25) for the reduction process but found that the oxidation process did not fit the mechanism proposed from the study of the reduction reaction. They proposed that the reduction and the oxidation involved two different, totally irreversible reactions, each involving a single two-electron transfer step. Their mechanism for the oxidation reaction was



with $\alpha_R = 0.39$ (for [3]) and $1 - \alpha_O = 0.23$ (for [4]).

The measurements of Gerischer, Morinaga, and Farr and Hampson showed that there was essentially no dependence of the exchange current on hydroxide concentration, while the mechanism of Popova and Stromberg (31) would predict a fairly large variation of exchange current with hydroxide concentration. The mechanism we propose, based on the results shown below, involves consecutive one-electron transfer steps.

Experimental

Chemicals.—Stock solutions of 4.0M KOH and 4.0M KF were prepared from "Baker Analyzed" Reagent grade KOH and KF obtained from the J. T. Baker Chemical Company. The KOH solution was standardized by titrating a known amount of reagent grade potassium biphthalate using phenolphthalein as an end-point indicator. A stock solution of 0.05M zinc (II) was made by dissolving "Baker Analyzed" ZnO in 50 ml of stock KOH solution. The Zn(II) solution was standardized by titrating with EDTA buffered to pH 10. Purification of experimental solutions with acid washed activated charcoal (Barker's method) was tried, but the results were the same with or without this step, so this procedure was not used regularly. Solutions were prepared by pipeting a known amount of KOH stock solution into a volumetric flask and then diluting with the stock KF solution, so that all solutions were at the same ionic strength. Zinc amalgam was prepared from 99.9% zinc wire and purified mercury. The zinc wire was amalgamated by dipping in mercuric chloride solution for a few seconds before it was placed in the mercury to aid in more rapid dissolution of the zinc. The amalgam was stored under vacuum and removed from the storage vessel under a blanket of prepurified helium. Under these conditions, the concentration of zinc in the amalgam would remain stable for more than a week.

All experiments were carried out under a blanket of nitrogen. Commercial water-pumped nitrogen was purified by first bubbling it through distilled water, then through a solution of vanadous chloride standing over saturated zinc amalgam, then passing over copper strands heated to at least 350°C, and finally through distilled water again. The copper strands had previously been exposed to oxygen at high temperature and then been reduced by passage of hydrogen gas at high temperature in order to assure an active surface. The water used in all experiments and in preparation of solutions was deionized water that had been further purified by distillation from alkaline potassium permanganate in a Barnstead water still; its conductivity was less than 10^{-7} (ohm-cm) $^{-1}$. Potassium hydroxide, potassium fluoride dihydrate, and zinc oxide were reagent grade chemicals and were used without further purification. Commercial mercury was washed in 5% HNO₃ with air bubbling for several days, then splashed at least twice through a 5% HNO₃ scrubbing tower. After drying, the mercury was distilled twice under vacuum.

Apparatus.—A single compartment electrolytic cell manufactured by Metrohm Ltd. (Model EA664) and obtained from Brinkmann Instruments was used for all experiments. The working electrode was either a hanging mercury drop electrode (h.m.d.e.) or a dropping mercury electrode (d.m.e.). The auxiliary or counterelectrode was a piece of platinum wire immersed directly in the solution. The reference electrode was a saturated calomel electrode (SCE) which was separated from the solution by a Luggin-Haber capillary. The tip of the capillary was placed as close as possible to the working electrode to minimize uncompensated resistance. The hanging mercury drop electrode was manufactured by Metrohm Ltd. (Model E-410). A fresh drop of 0.032 cm² theoretical area was used for each run. The capillary tip had to be cut off at intervals since the strong alkali solution attacked the glass, and eventually the tip would not hold a drop of the proper size. Electrical contact to the drop was made by inserting a platinum wire into the reservoir through the pumping nipple.

The d.m.e. was constructed from a length of Sargent 6-12 second capillary. The mercury flow rate of the d.m.e. was measured before each experiment since the capillary did not last long before the tip had to be cut off, changing the flow rate.

Potential step chronocoulometry was performed with an instrument previously described (32) constructed from Philbrick solid-state operational amplifiers. A fraction of the voltage generated by the current follower could be fed back to the potentiostat for resistance compensation; the stabilization scheme of Brown *et al.* (33) was used. A-C and d-c polarography were performed using a Princeton Applied Research Corporation, Princeton, New Jersey, Model 170 electrochemical instrument. Data from potential step experiments were taken using a PDP-12A computer system (Digital Equipment Corporation, Maynard, Massachusetts). Data for potential sweep experiments at sweep rates below 300 mV/sec were recorded on a Moseley 2D-2 X-Y recorder. For sweep rates above 300 mV/sec, a Tektronix Model 564 storage oscilloscope was used with Type 2A3 (Y axis) and Type 2A63 (X-axis) plug-ins. Permanent records of oscilloscope data were made with a Polaroid camera mounted on the oscilloscope using 3000 speed film.

Initial and final potentials for potential step experiments and initial potentials for potential sweep experiments were measured with a United Systems Corporation Model 204 voltmeter to an accuracy of ± 1 mV. Two of the relays in the relay register of the PDP-12 computer were used to control the potentiostat and integrator. Timing of data acquisition was controlled by internal computer cycle counting; the time scale was calibrated by acquiring data from a function generator (Wavetek Model 114).

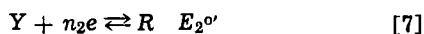
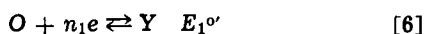
Data were taken at the same potentials and the same time scales with and without zinc present. Different time scales were used at different potentials so that the charge measured with zinc was significantly larger than that without zinc, but at short enough times that sufficient kinetic information was still present. The quantity $nFAD^{1/2}C/\pi^{1/2}$, which is the slope of a Q vs. $t^{1/2}$ plot when the potential is stepped far enough so that the reaction rate is controlled by mass transfer, was evaluated for the reduction of zinc(II) by stepping from -1.0 to -1.7 V and for the oxidation of zinc amalgam by stepping from -1.7 to -1.0 V and least squares analysis on the $Q - t^{1/2}$ data. Three or four steps were averaged for each potential using a fresh drop each time.

The data acquisition system was checked by recording a current-time curve with a simple RC dummy cell ($R = 5$ kohm, $C = 1$ μ f) for the potential stepped from 0 to $+0.400$ V. The accuracy of measurement was 1.2% or better. Further details about the apparatus, procedures, and calibrations are available (34).

Theory

The best method of proving that a charge transfer reaction consists of more than one electron transfer step is to demonstrate the existence of the intermediate products by some unambiguous technique (1).

Consider the case



At equilibrium, from the Nernst equations for [6] and [7]

$$\frac{C_Y^{n_1+n_2}}{C_R^{n_1}C_O^{n_2}} = K = \exp \left\{ \frac{n_1n_2F}{RT} (E_{1o'} - E_{2o'}) \right\} \quad [8]$$

Hence, for a given total concentration of O and R, C^* , the maximum amount of Y is present when $C_R = C_O$. If $E_{1o'}$ is much greater than $E_{2o'}$, then solutions containing essentially only Y can be made. If $E_{1o'} = E_{2o'}$, then $K = 1$ and for $n_1 = n_2 = 1$, the maximum C_Y is given by $C_O = C_Y = C_R$. As the quantity $E_{1o'} - E_{2o'}$ becomes more negative, the maximum amount of Y that can be present decreases rapidly. For example, for $n_1 = n_2 = 1$, and $C_O = C_R = C^*$, if $E_{1o'} - E_{2o'} = -0.2V$, then $C_Y \approx 0.03 C^*$, while if $E_{1o'} - E_{2o'} = -0.4V$, $C_Y \approx (4 \times 10^{-4}) C^*$.

However, depending upon the values of the rate constants for steps [6] and [7], the existence of stepwise electron transfer and transient formation of an intermediate, Y, can be deduced from electrochemical measurements [see Ref. (1) and general treatment of Albery and Hitchman (35)].

Potential step chronocoulometry (33, 34) was chosen as the principal electrochemical investigative procedure in this research, because integration of the current signal removes most of the high-frequency noise from this signal. Moreover, the integrated signal always starts from zero and can always be adjusted to stay on a given scale, while in chronoamperometry initial double-layer charging current may be several orders of magnitude larger than the faradaic current so that to obtain sufficient precision in the region of interest, the signal must be allowed to overdrive the amplifiers of the measuring instrument. Chronocoulometry can also be used to obtain information about the double layer (36, 37). Although the theoretical equations for stepwise electron transfers in chronocoulometry have not been presented previously, they can be obtained quite easily by integration of the appropriate equations of chronoamperometry.

Potentiostatic current-time behavior for systems involving a quasi-reversible two-step charge transfer was first derived by Hung and Smith (10) for the analytical solution for this case in a-c polarography. The partial differential equations and boundary conditions used by these authors in obtaining the following results are given in the Appendix. For the reaction given in Eq. [6] and [7] and following the notation of Hung and Smith (10), let

$$\psi_1(t) = \frac{i_1(t)}{n_1FAC^*D_0^{1/2}} \quad [9]$$

$$\beta_i = 1 - \alpha_i \quad (i = 1, 2) \quad [10]$$

$$D_1 = D_0^{\beta_1} D_Y^{\alpha_1} \quad D_2 = D_Y^{\beta_2} D_R^{\alpha_2} \quad [11]$$

$$f_1 = f_0^{\beta_1} f_Y^{\alpha_1} \quad f_2 = f_Y^{\beta_2} f_R^{\alpha_2} \quad [12]$$

$$E_{r_{1/2,1}} = E_{1o'} - \frac{RT}{n_1F} \ln \left(\frac{f_Y}{f_0} \right) \left(\frac{D_O}{D_Y} \right)^{1/2} \quad [13]$$

$$E_{r_{1/2,2}} = E_{2o'} - \frac{RT}{n_2F} \ln \left(\frac{f_R}{f_Y} \right) \left(\frac{D_Y}{D_R} \right)^{1/2} \quad [14]$$

$$j_i = \frac{n_iF}{RT} (E - E_{r_{1/2,i}}) \quad (i = 1, 2) \quad [15]$$

These authors showed that the current during a step to potential E is given by Eq. [16].

$$i(t) = FAC^*D_0^{1/2} [n_1\psi_1(t) + n_2\psi_2(t)] \quad [16]$$

where

$$\psi_1(t) = \frac{\lambda_1}{(1 + e^{j_1})(\chi_+ + \chi_-)} [(\chi_- - \lambda_2) \exp(\chi_-^2 t) \operatorname{erfc}(\chi_- t^{1/2}) - (\chi_+ - \lambda_2) \exp(\chi_+^2 t) \operatorname{erfc}(\chi_+ t^{1/2})] \quad [17]$$

$$\psi_2(t) = \frac{\lambda_1\lambda_2}{(1 + e^{j_1})(1 + e^{j_2})(\chi_- - \chi_+)} [\exp(\chi_+^2 t) \operatorname{erfc}(\chi_+ t^{1/2}) - \exp(\chi_-^2 t) \operatorname{erfc}(\chi_- t^{1/2})] \quad [18]$$

$$\chi_{\pm} = \frac{\lambda_1 + \lambda_2 \pm [(\lambda_1 + \lambda_2)^2 - 4K]^{1/2}}{2} \quad [19]$$

$$K = \lambda_1\lambda_2 \left[\frac{e^{j_2} + e^{-j_1} + e^{(j_2 - j_1)}}{(1 + e^{j_2})(1 + e^{j_1})} \right] \quad [20]$$

$$\lambda_i = \frac{k_0^{\alpha_i} f_1}{D_i^{1/2}} (e^{-\alpha_i j_1} + e^{\beta_i j_1}) \quad (i = 1, 2) \quad [21]$$

Since we are interested here only in the case where $E_{1o'} \ll E_{2o'}$, and because $E \approx E_{r_{1/2}} = (E_{r_{1/2,1}} + E_{r_{1/2,2}})/2$, some simplifications can be made in these equations, yielding

$$\psi_1(t) = \frac{\lambda_1}{(1 + e^{j_1})(\lambda_1 + \lambda_2)} [\lambda_2 \exp(\chi_-^2 t) \operatorname{erfc}(\chi_- t^{1/2}) + \lambda_1 \exp(\chi_+^2 t) \operatorname{erfc}(\chi_+ t^{1/2})] \quad [22]$$

$$\psi_2(t) = \frac{\lambda_1\lambda_2}{(1 + e^{j_1})(\lambda_1 + \lambda_2)} [\exp(\chi_-^2 t) \operatorname{erfc}(\chi_- t^{1/2}) - \exp(\chi_+^2 t) \operatorname{erfc}(\chi_+ t^{1/2})] \quad [23]$$

The expression for $Q(t)$ is obtained by integrating the above equations to obtain Eq. [24] and [25]

$$\int \psi_1(t) dt = \frac{\lambda_1}{(1 + e^{j_1})(\lambda_1 + \lambda_2)} \left[\frac{\lambda_2}{\chi_-^2} \left(\exp(\chi_-^2 t) \operatorname{erfc}(\chi_- t^{1/2}) + \frac{2\chi_- t^{1/2}}{\pi^{1/2}} - 1 \right) + \frac{\lambda_1}{\chi_+^2} \left(\exp(\chi_+^2 t) \operatorname{erfc}(\chi_+ t^{1/2}) + \frac{2\chi_+ t^{1/2}}{\pi^{1/2}} - 1 \right) \right] \quad [24]$$

$$\int \psi_2(t) dt = \frac{\lambda_1\lambda_2}{(1 + e^{j_1})(\lambda_1 + \lambda_2)} \left[\frac{1}{\chi_-^2} \left(\exp(\chi_-^2 t) \operatorname{erfc}(\chi_- t^{1/2}) + \frac{2\chi_- t^{1/2}}{\pi^{1/2}} - 1 \right) - \frac{1}{\chi_+^2} \left(\exp(\chi_+^2 t) \operatorname{erfc}(\chi_+ t^{1/2}) + \frac{2\chi_+ t^{1/2}}{\pi^{1/2}} - 1 \right) \right] \quad [25]$$

Since χ_+ is much greater than χ_- , the term in the above equations in χ_+ can be neglected compared to the term in χ_- . Under these conditions, then

$$\int \psi_1(t) dt = \int \psi_2(t) dt \quad [26]$$

and, defining Z_c as in Eq. [27]

$$Z_c = \frac{(n_1 + n_2)FAD_0^{1/2}C^*o\lambda_1\lambda_2}{(1 + e^{j_1})(\lambda_1 + \lambda_2)} \quad [27]$$

then

$$Q(t) = \frac{Z_c}{\chi_-^2} \left(\exp(\chi_-^2 t) \operatorname{erfc}(\chi_- t^{1/2}) + \frac{2\chi_- t^{1/2}}{\pi^{1/2}} - 1 \right) \quad [28]$$

For the case where R is initially present but not O and the potential is stepped in the positive direction, the expression for $Q(t)$ is the same as that in [28] except that Z_c is replaced by Z_a

$$Z_a = \frac{(n_1 + n_2)FAD_R^{1/2}C^*R\lambda_1\lambda_2}{(1 + e^{-j_2})(\lambda_1 + \lambda_2)} \quad [29]$$

Thus, for a two-step electron transfer reaction, the equation for $Q(t)$ is identical in form to the expression for $Q(t)$ for single-step charge transfer, Eq. [30] (36, 37)

$$Q(t) = \frac{K}{\lambda^2} \left(\exp(\lambda^2 t) \operatorname{erfc}(\lambda t^{1/2}) + \frac{2\lambda t^{1/2}}{\pi^{1/2}} - 1 \right) \quad [30]$$

$$\lambda = \frac{k^0}{D^{1/2}} (e^{-\alpha j} + e^{\beta j}) \quad [31]$$

$$j = \frac{nF}{RT} (E - E^0) \quad [32]$$

$$K = nFAk^0(C^0_0 e^{-\alpha j} - C^0_R e^{\beta j}) \quad [33]$$

To use Eq. [28] or [29] to determine kinetic parameters and reaction mechanisms, one steps from a potential where no appreciable current flows to one where a measurable cathodic or anodic current is obtained and measures the Q vs. t behavior. From this data K and λ are determined. These values are determined at a number of potentials and then the logarithm of K and λ are plotted vs. the potential. For a single-step charge transfer case, the plot of $\ln K$ vs. E is a straight line with a slope equal to $-\alpha nF/RT$. The plot of $\ln \lambda$ vs. E is a curve which has a minimum near E^0 and asymptotically approaches straight lines for E greater than and less than E^0 . The slope of the asymptote for E less than E^0 is $-\alpha nF/RT$, while for E greater than E^0 , it is $\beta nF/RT$.

In the case of a two-step charge transfer reaction, Z and χ_- can be determined from Q vs. t (or i vs. t) data in the same manner as K and λ in a one-step reaction. However, the behavior of the plots of $\ln Z$ and $\ln \chi_-$ vs. E can be more complex than in the one-step case. It is this difference in behavior that can sometimes allow one to demonstrate the existence of a two-step mechanism. The behavior of $\ln \chi_-$ vs. E and $\ln Z$ vs. E can be illustrated by some examples:

(i) If k^0_1 and k^0_2 are very large, then the over-all rate of the reaction may be so fast that the reaction appears to be Nernstian. In this case, it is not possible to calculate χ_- and Z and the reaction is indistinguishable from a one-step multi-electron transfer reaction (10).

(ii) For $k^0_1 \gg k^0_2$, when $(RT/F) \ln(k^0_2/k^0_1) < E < E^{r_{1/2,2}}$, then $\partial \ln Z_c/\partial E = -(1 + \alpha_2)F/RT$ [see Fig. 1 ($Z_{c,1}$)] and $\ln \chi_-$ has a minimum near $E = 0$ (where $E^{r_{1/2,1}}$ is taken as $-0.2V$, and $E^{r_{1/2,2}}$ is $+0.2V$). When $(RT/F) \ln(k^0_2/k^0_1) < E < 0$, then $\partial \ln(\chi_-)/\partial E = -(1 + \alpha_2)F/RT$ [Fig. 1 ($\chi_{-,2}$)]. When $0 < E < E^{r_{1/2,2}}$, $\partial \ln(\chi_-)/\partial E = (1 - \alpha)F/RT$ [Fig. 1 ($\chi_{-,1}$)] and $\partial \ln Z_a/\partial E = \beta_2 F/RT$ [Fig. 1 ($Z_{a,1}$)]. When $E^{r_{1/2,1}} < E < (RT/F) \ln(k^0_2/k^0_1)$, then $\partial \ln Z_c/\partial E = -\alpha_1 F/RT$ [Fig. 1 ($Z_{c,2}$)], $\partial \ln Z/\partial E = (2 - \alpha_1)F/RT$ [Fig. 1 ($Z_{a,2}$)] and $\partial \ln(\chi_-)/\partial E = -\alpha_1 F/RT$ [Fig. 1 ($\chi_{-,3}$)].

(iii) For $k^0_2 \gg k^0_1$, the results are the mirror image of those for case (ii) above.

(iv) The results for $k^0_2 = k^0_1$ are shown in Fig. 2. Therefore, to determine whether a reaction is single step or multi-step, not only must the over-all reaction be slow enough to be measurable, but also the rate must be slow enough to be measurable in the vicinity of

$$E' = \frac{E^{r_{1/2,1}} + E^{r_{1/2,2}}}{2} + \frac{RT}{F} \ln \frac{k^0_2}{k^0_1} \quad [34]$$

Otherwise, the reaction is indistinguishable from a single-step reaction. For example, for $k^0_2 \gg k^0_1$, if the most positive potential at which measurements of Z and χ_- can be made is less than E' in 38, then $\partial \ln Z_a/$

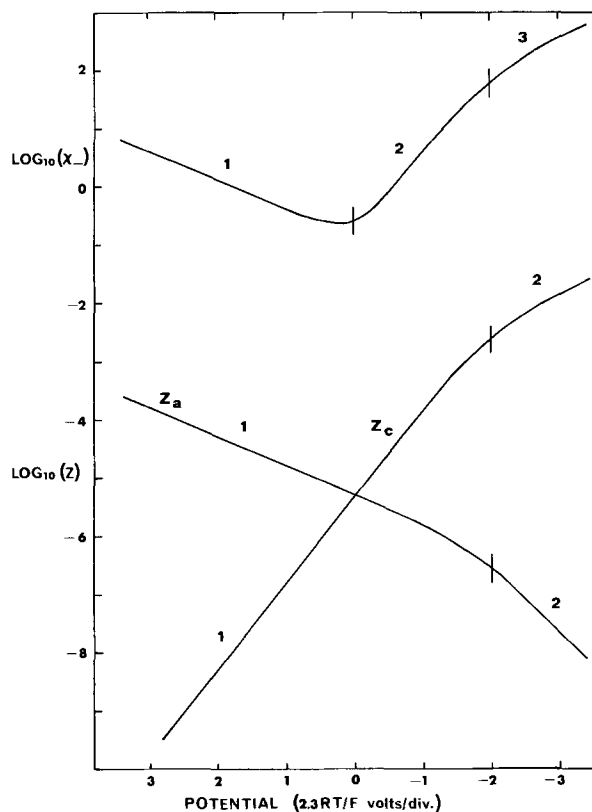


Fig. 1. Log χ_- and log Z vs. E for case (ii). $\alpha_1 = \alpha_2 = 0.5$, $E^{r_{1/2,1}} = -0.2V$, $E^{r_{1/2,2}} = +0.2V$, $k^0_1 = 2.0$, $k^0_2 = 0.02$, $n_1 = n_2 = 1$, $D_1^{1/2} = D_2^{1/2} = 0.00316$, $f_1 = f_2 = 1.0$, $C_0 = C_R = 2.03 \times 10^{-6}$ moles/cm³, $A = 0.032$ cm².

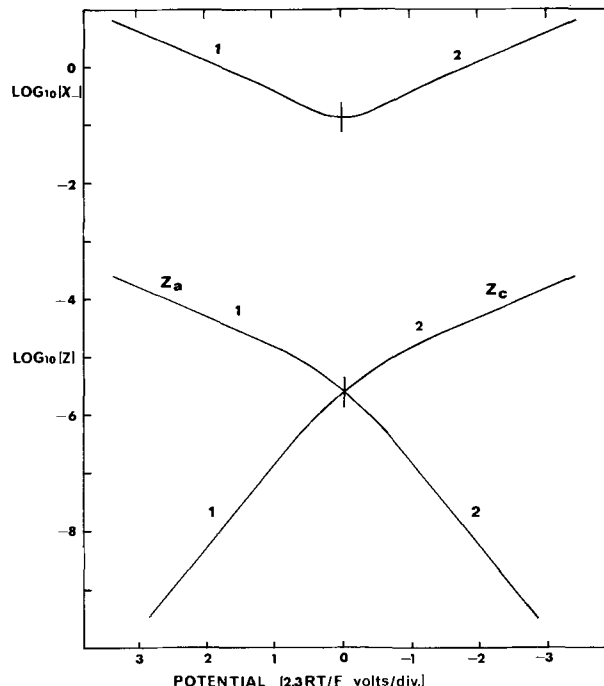


Fig. 2. Log χ_- and log Z vs. E from case (iv). The conditions are the same as in Fig. 1 except $k^0_1 = 0.02$.

$\partial \ln Z/\partial E = (2 - \alpha_1)F/RT$ and $\partial \ln Z_c/\partial E = -\alpha_1 F/RT$. Under these conditions $\partial \ln Z_a/\partial E - \partial \ln Z_c/\partial E = 2F/RT$ and the results cannot be distinguished from a single-step reaction with the same over-all rate and $\alpha = \alpha_1/2$. The behavior of $\ln(\chi_-)$ is similarly indistinguishable.

In order to assign values to both α_1 and α_2 , both cathodic and anodic plots of $\ln Z$ and $\ln \chi_-$ vs. E must have linear segments whose slope is less than $n_1 F/RT$.

Then α_1 can be obtained from the slope of the cathodic plot and α_2 can be obtained from the slope of the anodic plot. $(E_{r_{1/2,1}} + E_{r_{1/2,2}})/2$ can be determined from the potential where $Z_a = Z_c$

$$E_{Z_a=Z_c} = \frac{n_1 E_{r_{1/2,1}} + n_2 E_{r_{1/2,2}}}{n_1 + n_2} + \frac{RT}{(n_1 + n_2)F} \ln \frac{C^*_O}{C^*_R} \quad [35]$$

Even here k°_1} , k°_2} , $E_{r_{1/2,1}}$, and $E_{r_{1/2,2}}$ cannot be assigned absolute values, since the value of $E_{r_{1/2,2}} - E_{r_{1/2,1}}$ is not known. We can, however, measure k_1' and k_2' at $(E_{r_{1/2,1}} + E_{r_{1/2,2}})/2$.

For $n_1 = n_2 = 1$

$$k_1' = \frac{k^{\circ_1}}{\exp \left[\frac{-\alpha_1 F}{RT} \left(\frac{E_{r_{1/2,2}} - E_{r_{1/2,1}}}{2} \right) \right]} \quad [36]$$

$$k_2' = \frac{k^{\circ_2}}{\exp \left[\frac{(1 - \alpha_2) F}{RT} \left(\frac{E_{r_{1/2,2}} - E_{r_{1/2,1}}}{2} \right) \right]} \quad [37]$$

If we could measure the concentration of Y at equilibrium, we could then determine the value of $E_{r_{1/2,2}} - E_{r_{1/2,1}}$. For purposes of calculation it is sufficient to select a value of $E_2 - E_1$ greater than 0.2V and use that to calculate k°_1} and k°_2} from the observed k_1' and k_2' . Using the values determined above for α_1 , α_2 , $E_{r_{1/2,1}}$, $E_{r_{1/2,2}}$, n_1 , n_2 , k°_1} , and k°_2} , one can calculate Z and χ over the whole potential range and see if these values give a good fit in the nonlinear portions of the $\ln Z$ and $\ln \chi$ vs. E plots. If the fit is good, one can say with confidence that the charge transfer is multi-step.

Clearly, potential step techniques are particularly useful for distinguishing between single-step and multi-step electron transfer. Hurd (5) has stated that unequivocal proof of a two-step consecutive electron transfer mechanism can only be obtained from steady-state polarization curves if the exchange currents of the two steps differ by a factor of 100 or more while still being less than the mass transfer limited current. Hence, if rate constants are about equal, concentration ratios would have to be very large in order to achieve the necessary exchange currents. Large concentration ratios usually mean large concentrations, high currents, and problems from solution resistance. Potential step techniques allow examination of the current-potential behavior over a wider range of potentials and larger rates than is possible with steady-state techniques since the effects of mass transfer can be accounted for by proper application of potential step theory.

Results

Potential step chronocoulometry.—Kinetic parameters are usually determined by linearization of Eq. [30] by taking Q values only at times where $\lambda t^{1/2} > 5$, so that $\exp(\lambda^2 t) \operatorname{erfc}(\lambda t^{1/2})$ is negligible compared to the other terms in this equation (36). A similar procedure is often followed in chronoamperometric experiments (38, 39) where current values at times corresponding to $\lambda t^{1/2} < 0.1$ are used. The difficulty of using these approximations in practice has been discussed [see, for example (40, 41)] and is based on the necessity of knowing the value of λ , the parameter to be determined by the experiment, before the valid approximation zone is established. Moreover, the zone of the approximation may be located where perturbations caused by double layer charging or convection are important. However, the best use of the data is made by fitting the experimental results to the complete theoretical Eq. [30] using a high speed digital computer, and this procedure was followed here. Because digital data acquisition was employed, the data were in a particularly convenient form for further processing on the computer. The procedure fol-

lowed consisted of guessing initial values of K and λ and calculating values of Q for each t using [30], Q_{calc} . These values are compared to the experimental ones, Q_{exp} , and the total variance, which is the sum of $(Q_{\text{exp}} - Q_{\text{calc}})^2$, determined. The values of K and λ are changed until the variance has been minimized. Details of this procedure and the method for calculating $\exp(y^2) \operatorname{erfc}(y)$ are discussed elsewhere (34). Preliminary chronocoulometric measurements showed that neither reactant (zincate) or product (zinc in mercury) were adsorbed, so that the number of coulombs required to charge the double layer capacitance, Q_{dl} , was determined on a test solution lacking zinc(II) with a pure mercury electrode; Q_{exp} was then taken as $Q_{\text{meas}} - Q_{\text{dl}}$, where Q_{meas} is the measured charge. This procedure assumes that Q_{dl} is not affected significantly by the presence of the small amounts of zinc in solution or mercury.

The $\log \lambda$ and $\log K$ values at various potentials and various hydroxide concentrations determined by this procedure are given in Table I. These values were plotted vs. E and αn and βn were determined from the slopes of the linear parts of the cathodic and anodic branches of the plots at constant hydroxide concentration. The dependence on hydroxide ion concentration was determined from plots of $\log K$ at constant potential vs. $\log [\text{OH}^-]$. The results are given in Table II. The diffusion coefficients of zinc(II) and Zn(Hg) were determined by measuring K/λ when $|E - E_{r_{1/2}}|$ was large. For the reduction process, this gives the value of $nFAC^*_O D_O^{1/2}$, while for the oxidation $nFAC^*_R D_R^{1/2}$. The effective surface area of the Kemula type Metrohm h.m.d.e. has been shown to be about 90% of the geometrical area (42) yielding a value for our electrode of 0.0291 cm². With this value for A , $C^*_O = 2.03 \times 10^{-6}$ moles/cm³ and $K_c/\lambda = 2.82 \times 10^{-5}$, we obtain a $D_O^{1/2} = 2.47 \times 10^{-3}$ cm/sec^{1/2}. Similarly, with $K_a/\lambda = 2.66 \times 10^{-5}$ and $D_R^{1/2} = 3.98 \times 10^{-3}$ cm/sec^{1/2} (43), the concentration of zinc in the amalgam, C^*_R , was found to be 1.19 mM. The potentials for the intersection of K_a and K_c and the concentrations of Zn(II) Zn(Hg), and OH^- can be used to calculate $E_{r_{1/2}}$ for the over-all reaction. A plot of $E_{r_{1/2}}$ vs. $\log [\text{OH}^-]$ had a slope of -0.118V and an intercept of -1.445V vs. SCE.

D-C polarography.—The zinc(II)/zinc amalgam system in alkaline media exhibits a quasi-reversible polarographic reduction wave. The treatment of the data follows the treatment of Meites and Israel (44) and is similar to that of Matsuda and Ayabe (25). From the Ilkovic equation and the values $m = 1.07$ mg/sec, $t = 1.0$ sec, $i_d = 7.64 \mu\text{A}$ and $C^*_O = 2.03$ mM, we find a value of $D_O^{1/2} = 2.53 \times 10^{-3}$ cm/sec^{1/2}, in good agreement with the value obtained from the potential step experiment. To determine kinetic data, a plot of $\log[i/(i_d - i)]$ vs. E according to the equation for a totally irreversible reaction (44)

$$E = E^{\circ} + \frac{0.059}{\alpha n} \log \frac{1.349k^{\circ} t^{1/2}}{D_O^{1/2}} - \frac{0.0542}{\alpha n} \log \frac{i}{i_d - i} \quad [38]$$

was made for values of E sufficiently negative as to make the reverse reaction slow enough to be negligible. Results are given in Table II.

A-C polarography.—Measurement of kinetic parameters by a-c polarography involved phase-sensitive detection of the current, so that the phase angle of the current as well as its magnitude was measured. From this data the cotangent of the phase angle, θ , was determined and used to calculate λ at different values of E (45)

$$\cot(\theta) = I_{00}/I_{900} = 1 + (2\omega)^{1/2}/\lambda \quad [39]$$

The kinetic parameters can be obtained from a plot of $\log \lambda$ vs. E or directly from a plot of $\cot(\theta)$ vs. E by measuring the potential and magnitude of the maximum value of $\cot(\theta)$ (45)

Table I. Potential step chronocoulometry. Results

(a) Reduction reaction; Steps from -1.00V vs. SCE to E; solution contained 2.03 mM zinc(II) and KOH; electrode was Hg drop				
[OH ⁻]	E (V vs. SCE)	Log λ	Log K	Stand. dev. × 10 ⁶
0.18	-1.36	-0.5675	-5.4399	6.74
	-1.38	-0.3189	-5.0049	9.12
	-1.40	+0.0055	-4.6406	11.20
	-1.42	0.3193	-4.3096	25.20
	-1.44	0.7663	-3.9789	25.60
	-1.46	0.7729	-3.8012	5.14
	-1.48	1.0177	-3.5614	2.46
	-1.50	1.2498	-3.3153	15.40
	-1.52	1.4933	-3.1080	13.50
	-1.40	-0.6829	-5.3471	12.70
	-1.42	-0.4776	-5.0082	38.00
	-1.44	-0.1598	-4.6555	17.10
	-1.46	+0.1881	-4.3466	7.64
	-1.48	0.4876	-4.0607	6.94
	-1.50	0.8026	-3.7670	7.84
-1.52	1.0215	-3.5505	14.40	
-1.54	1.2627	-3.3110	3.05	
-1.56	1.4239	-3.1461	2.65	
0.34	-1.43	-0.5593	-5.8622	6.30
	-1.45	-0.6991	-5.4614	9.96
	-1.47	-0.4673	-5.0589	12.20
	-1.49	-0.1595	-4.7091	10.90
	-1.51	+0.1403	-4.3978	6.51
	-1.53	0.4478	-4.1129	9.58
	-1.55	0.7000	-3.8504	10.00
	-1.57	0.9316	-3.6158	2.88
	-1.59	1.1671	-3.3903	2.05
	-1.61	1.3156	-3.2317	2.02
	-1.46	-0.5434	-5.8832	8.95
	-1.48	-0.6788	-5.4323	9.77
	-1.50	-0.4698	-5.0280	16.30
	-1.52	-0.1748	-4.7138	16.20
	-1.54	+0.0987	-4.4254	13.40
-1.56	0.3821	-4.1427	11.50	
-1.58	0.6573	-3.8857	19.80	
-1.60	0.9402	-3.6369	14.50	
-1.62	1.0412	-3.4839	7.25	
-1.64	1.2536	-3.3069	7.29	

(b) Oxidation reaction: Steps from -1.700V vs. SCE to E, solution contained no zinc(II) and KOH, electrode was zinc amalgam with a [Zn] = 1.2 mM

[OH ⁻] (M)	E (V vs. SCE)	Log λ	Log K	Stand. dev. × 10 ⁶
0.18	-1.38	-0.2117	-5.8534	4.97
	-1.36	-0.3641	-5.4843	10.20
	-1.32	-0.4563	-5.1238	6.47
	-1.28	-0.1335	-4.7542	6.79
	-1.24	+0.1061	-4.4880	4.80
	-1.20	0.3460	-4.2348	3.65
	-1.16	0.6573	-3.9680	16.30
	-1.12	0.7993	-3.7641	2.42
	-1.08	1.0502	-3.5123	10.40
	-1.04	1.5222	-3.0975	36.40
	-1.42	-0.8242	-6.0244	10.60
	-1.40	-0.8504	-5.6479	15.60
	-1.36	-0.8181	-5.1592	27.90
	-1.32	-0.1515	-4.7376	58.30
	-1.28	-0.0120	-4.4963	10.30
-1.24	+0.3497	-4.2217	3.85	
-1.20	0.6166	-3.9595	3.45	
-1.16	0.8588	-3.7272	3.88	
-1.12	0.9097	-3.6416	8.35	
-1.08	1.2846	-3.2853	2.79	
-1.47	-0.3670	-5.8545	2.77	
-1.45	-0.5167	-5.5910	4.45	
-1.41	-0.3864	-5.0590	4.33	
-1.37	-0.0143	-4.6425	12.60	
-1.33	+0.2119	-4.3768	5.53	
-1.29	0.4428	-4.1431	4.30	
-1.25	0.6871	-3.8975	2.67	
-1.21	0.8744	-3.7023	3.59	
-1.17	1.0797	-3.4987	16.00	
-1.13	1.3458	-3.2434	2.64	

$$[E]_{\max} = E_{r_{1/2}} + \frac{RT}{nF} \ln(\alpha/\beta) \quad [40]$$

$$[\cot(\theta)]_{\max} = 1 + \frac{(2\omega D)^{1/2}}{k^{\circ}[(\alpha/\beta)^{-\alpha} + (\alpha/\beta)^{\beta}]} \quad [41]$$

The results are shown in Table II.

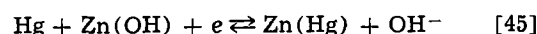
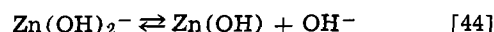
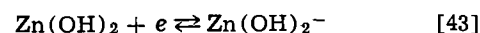
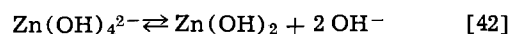
Table II. Summary of experimental results by different techniques

	αn	βn	$k^{\circ}_c/D_0^{1/2}$	$k^{\circ}_a/D_R^{1/2}$	$E_{r_{1/2}}$ (V vs. SCE)	$D_0^{1/2}$ (cm ² /sec ^{1/2})	$\frac{\partial \log K_c}{\partial \log [\text{OH}^-]}$	$\frac{\partial \log K_a}{\partial \log [\text{OH}^-]}$
Potential step	0.82	0.34	0.17	0.30	-1.445	2.47×10^{-8}	-1.85	+0.83
D-C polarography	0.82	—	0.33	—	-1.445	2.53×10^{-8}	—	—
A-C polarography	0.83	—	0.18	—	—	—	—	—
Linear potential sweep voltammetry								
(a) (E_p vs. $\log v$)	0.78	0.33	0.40	0.34	—	—	—	—
(b) ($E_p - E_{p/2}$)	1.00	0.46	—	—	—	—	—	—

Potential sweep voltammetry.—Kinetic parameters can be obtained from linear potential sweep voltammetry at a stationary electrode by observing the variation of E_p or of $E_p - E_{p/2}$ with scan rate, v (46). Kinetic parameters for the cathode reaction were obtained from experiments in a 1.0M KOH solution containing 2.03 mM zinc(II) at a mercury electrode while those for the anodic reaction used a zinc amalgam electrode, [Zn] = 1.2 mM and 1.0M KOH (34). Kinetic parameters obtained from these measurements are shown in Table II.

Discussion

The results obtained by the different electrochemical methods in Table II are in fair agreement with each other. These results show that the electrode reaction of zinc in alkaline media is not a simple quasi-reversible two-electron transfer. First, the quantity $\alpha n + \beta n$ is much less than two, when α and β are calculated from the appropriate slopes measures well away from $E_{r_{1/2}}$. Second, the $\log K$ vs. E plots show definite curvature in the region near $E_{r_{1/2}}$. This curvature cannot be due to double-layer effects, since the rate of change of potential at the outer Helmholtz plane with electrode potential is nearly constant in the region of interest, which is far negative of the potential of zero charge, and the solution has a high ionic strength. Nor can it be explained by uncompensated resistance, since the region of maximum curvature is in the region where K was less than 100 μA , and the uncompensated resistance was less than 10 ohms, i.e., where the curvature was most pronounced, contributions from IR effects were at a minimum. These features correspond quite closely to a consecutive electron transfer mechanism, however, and the following mechanism appears to fit the experimental data quite well



Comparison of this model to the experimental results is simplified by using a modification of the notation of Hung and Smith (10), with O representing $\text{Zn}(\text{OH})_2$; YO, $\text{Zn}(\text{OH})_2^-$; YR, $\text{Zn}(\text{OH})$; and R, $\text{Zn}(\text{Hg})$. With $f_0 = [\text{OH}^-]^2$, $f_{YO} = 1.0$, $f_{YR} = [\text{OH}^-]^{-1}$, and $f_R = [\text{OH}^-]$, the following equations hold for $E_{r_{1/2,1}}$ and $E_{r_{1/2,2}}$

$$E_{r_{1/2,1}} = E_1^{o'} + \frac{RT}{2F} \ln \frac{D_0}{D_{YO}} + \frac{RT}{F} \ln \frac{f_0}{f_{YO}} \quad [46]$$

$$E_{r_{1/2,1}} = E_1^{o'} + \frac{RT}{2F} \ln \frac{D_0}{D_{YO}} - \frac{RT}{F} \ln [\text{OH}^-]^2 \quad [47]$$

$$E_{r_{1/2,2}} = E_2^{o'} + \frac{RT}{2F} \ln \frac{D_{YR}}{D_R} - \frac{RT}{F} \ln [\text{OH}^-]^2 \quad [48]$$

At constant $E - E_{r_{1/2}}$, the hydroxide dependence of λ_1 is proportional to f_1 and λ_2 to f_2 , where f_1 and f_2 are given by Eq. [49] and [50]

$$f_1 = f_0^{\beta} f_{YO}^{\alpha} = [\text{OH}^-]^{-0.36} \quad [49]$$

$$f_2 = [\text{OH}^-]^{-0.32} \quad [50]$$

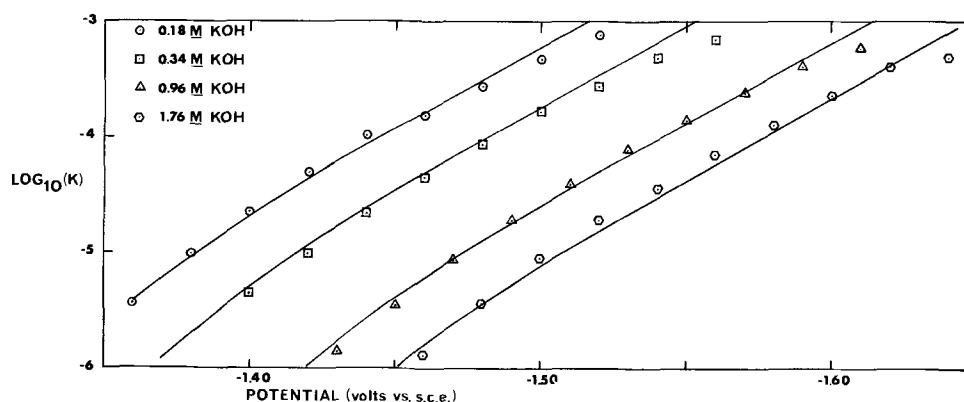


Fig. 3. $\log K_c$ vs. E for reduction reaction. Comparison of experimental data from potential-step chronocoulometry ($[Zn(OH)_4^{2-}] = 2.03 \text{ mM}$) with values calculated from consecutive-electron transfer theory.

This means that for any given value of $E - E_{r_{1/2}}$, the hydroxide dependence will be small. In particular, when λ_1 is nearly equal to λ_2 , and the hydroxide concentration is about $1.0M$, the hydroxide dependence of $\log K$ and $\log \lambda$ will be zero. Since the region where λ_1 is equal to λ_2 is also the region of curvature of the $\log K$ vs. E plot, the apparent α measured in this region will be between the values for the high and low slope linear regions; for the $Zn(II)/Zn(Hg)$ reaction αn would be equal to about 1.0 in this region.

The measured values of the hydroxide dependence of $\log K$ at constant potential yield the following values for f_1 and f_2 : $f_1 = [OH^-]^{-0.21}$ and $f_2 = [OH^-]^{+0.15}$. To obtain a quantitative comparison between model and results, we take $\alpha_1 = 0.82$, $\alpha_2 = 0.66$, $k_1 = 0.228$, $k_2 = 0.0209$, and use these parameters to calculate values for $\log K$ and $\log \lambda$ from consecutive electron transfer theory

$$E_{r_{1/2,1}} = -1.645 - \frac{RT}{F} \ln[OH^-]^2 \quad [51]$$

$$E_{r_{1/2,2}} = -1.245 - \frac{RT}{F} \ln[OH^-]^2 \quad [52]$$

We find that the potential step data fits the theoretical curves quite well (Fig. 3-6). In particular, in the plot of $\log K_a$ vs. E where the curvature is most pronounced, the fit is excellent.

These same parameters can also be used to calculate a-c and d-c polarograms using Hung and Smith's equations (10). In calculating polarograms, the Matsuda function (47) was used instead of $\exp(\lambda^2 t) \text{erfc}(\lambda t^{1/2})$, because a d.m.e. is used for polarography and planar diffusion no longer occurs. The fit between the theoretical a-c polarographic data ($\cot \theta$ vs. E) and d-c polarographic data [$\log(i/i_d - i)$ vs. E] and the experimental results are shown in Fig. 7 and 8. The agreement between theory and experiment for a-c polarography is not too good, but Delmastro and Smith (48) pointed out that amalgam formation reactions

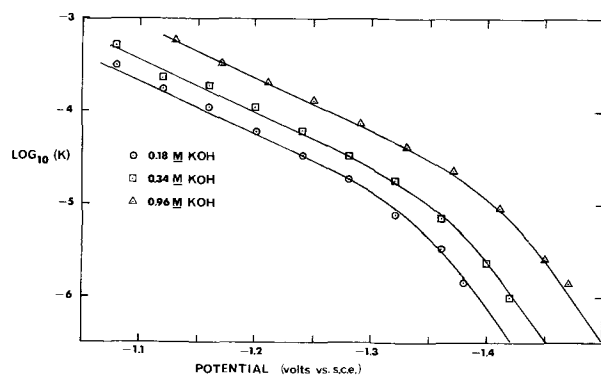


Fig. 4. $\log K_a$ vs. E for oxidation reaction. Comparison of data from potential-step chronocoulometry ($[Zn(Hg)] = 1.2 \text{ mM}$) with theoretical calculations.

may show large distortions of the current because of spherical diffusion inside the drop. Since the theoretical curves in these figures were calculated with parameters from the potential step experiment, the agreement must be considered satisfactory.

It is of interest to compare our results with those of previous studies (Table III). Gerischer (22, 23) and later Farr and Hampson (24) determined the exchange current i_0 by measuring the charge transfer resistance ($R_T = RT/nFi_0$) at the equilibrium potential of a solution and thus determining the variation of i_0 with reactant concentration. From i_0 , one can determine α and k^0 from the relation

$$i_0 = nFAk^0C_0^{1-\alpha}C_R^\alpha \quad [53]$$

The exchange current can also be determined from consecutive electron transfer theory, either from the equation derived by Vetter (2-4) or from the treatment of Hung and Smith (10)

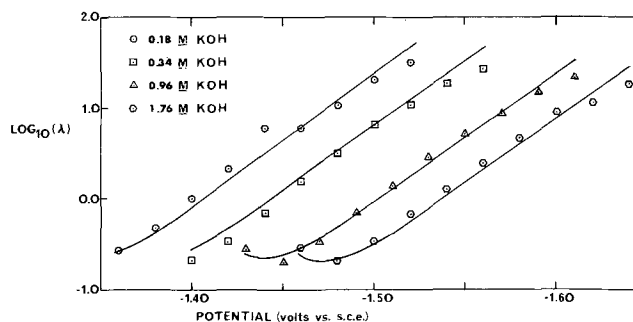


Fig. 5. $\log \lambda$ vs. E for reduction reaction. Comparison of data from potential-step chronocoulometry with theoretical calculations.

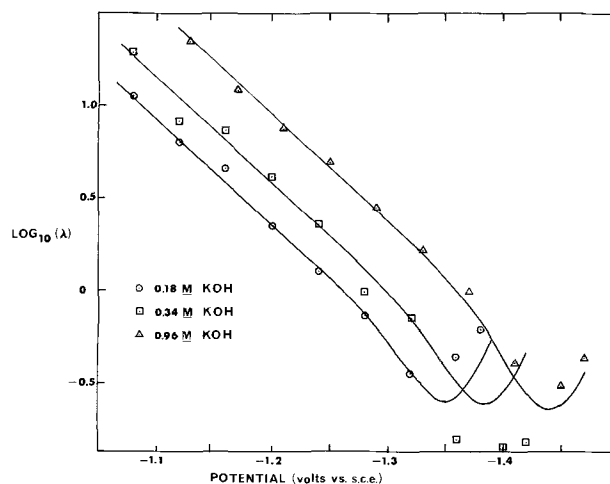


Fig. 6. $\log \lambda$ vs. E for oxidation reaction. Comparison of data from potential step chronocoulometry with theoretical calculations.

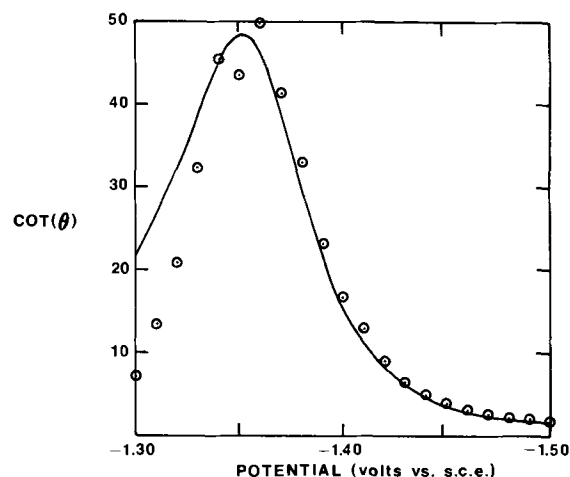


Fig. 7. Comparison of $\text{Cot}(\theta)$ vs. E data from a-c polarographic measurements with theoretical calculations. The solution contained $[\text{Zn}(\text{OH})_4^{2-}] = 2.03 \text{ mM}$ and $[\text{OH}^-] = 0.18 \text{ M}$. The d.m.e. was mercury with a drop time of 1 sec. $\omega = 11.0 \text{ Hz}$.

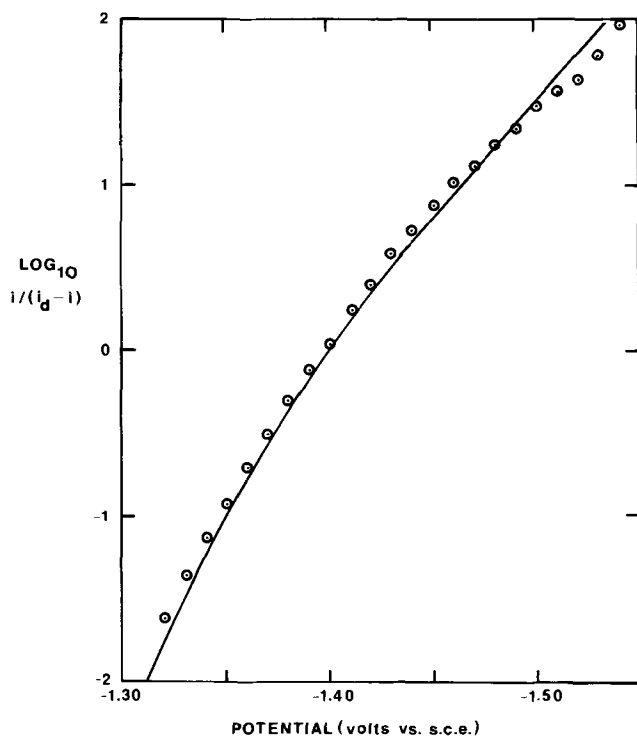


Fig. 8. Comparison of $\log i/(i_d - i)$ vs. E data from d-c polarography with theoretical calculations. Conditions same as in Fig. 7.

$$i_0 = 2FAC^*D_0^{1/2} \frac{\lambda_1\lambda_2}{(1 + e^{j_1})(\lambda_1 + \lambda_2)}$$

$$= 2FAC^*R_D^{1/2} \frac{\lambda_1\lambda_2}{(1 + e^{-j_2})(\lambda_1 + \lambda_2)} \quad [54]$$

Using the kinetic parameters obtained from potential step measurements to calculate i_0 and R_T and comparing these results with the data in Fig. 2 of Farr and

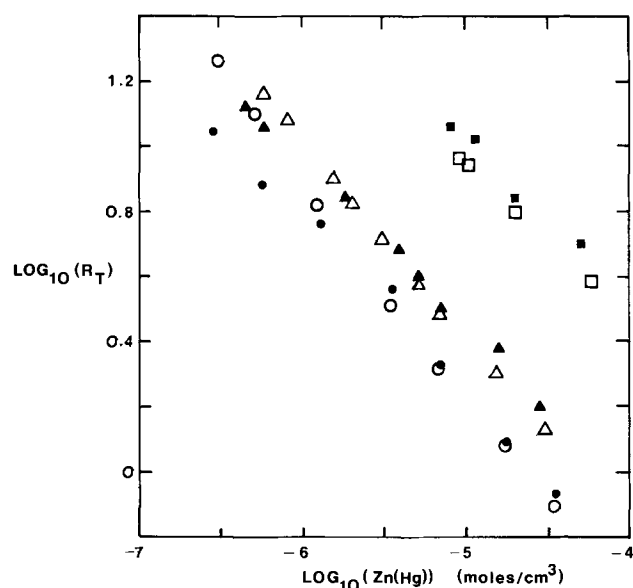


Fig. 9. $\log R_T$ vs. $\log [\text{Zn}(\text{Hg})]$ for different concentrations of $\text{Zn}(\text{OH})_4^{2-}$. Comparison of theoretical calculations with experimental data from Farr and Hampson (24). Squares, $[\text{Zn}(\text{OH})_4^{2-}] = 5.05 \times 10^{-6} \text{ moles/cm}^3$; triangles, $[\text{Zn}(\text{OH})_4^{2-}] = 6.8 \times 10^{-5} \text{ moles/cm}^3$; circles, $[\text{Zn}(\text{OH})_4^{2-}] = 1.834 \times 10^{-4} \text{ moles/cm}^3$. Open symbols are data from this work, solid symbols are from Farr and Hampson.

Hampson (24), we calculate an R_T which is larger than their values by a factor of 3.5. This difference may be attributed to differences in the conditions of measurement in the two studies; for example, the ionic strength of Farr and Hampson's solutions was 3.0M, while in the present work, it was 4.0M. They used NaOH and NaClO_4 while KOH and KF were used in the present work, and the solutions used by Farr and Hampson were purified by circulation over activated charcoal for at least 28 days. However, when the R_T values calculated from potential step data are divided by 3.5, the values at different Zn(Hg) and OH^- concentrations agree fairly well with those of Farr and Hampson (Fig. 9).

Matsuda and Ayabe (25) studied the reduction process by d-c polarography. Using the treatment for quasi-reversible polarographic waves they obtained the results shown in Table III, which agree very well with ours for the reduction process.

Stromberg and Popova (29-31) studied both the oxidation and reduction reactions by d-c polarography with a dropping zinc amalgam electrode used to study the oxidation reaction. Their results do not agree very well with the results of the present work for the oxidation reaction, although the agreement is fairly good for the reduction reaction (Table III). However, their results still lead to the conclusion that one hydroxide is involved in the oxidation reaction rate limiting step, since the oxidation rate shows a dependence on the first power of the hydroxide concentration. This observation led Stromberg and Popova to conclude that the oxidation reaction was a two-electron reaction which occurred by a completely different path than that of the reduction reaction (Eq. [4] and [5]). However, if they were correct, then a plot of $\log K$ vs. E for any one

Table III. Comparison of our results to previous studies

	αn	βn	$\log k_c$	$\log k_a$	$E^{*1/2}$	$\frac{\partial \log K_c}{\partial \log [\text{OH}^-]}$	$\frac{\partial \log K_a}{\partial \log [\text{OH}^-]}$
Present work	0.82	0.34	-3.37	-2.92	-1.445	-1.85	+0.83
Farr and Hampson (24)	1.00	1.00	-3.00	—	—	—	—
Matsuda and Ayabe (25)	0.84	—	-3.3	—	-1.444	-1.82	—
Popova and Stromberg (31)	0.78	0.46	-3.43	-3.70	-1.434	-2.3	+1.4

hydroxide concentration should be linear over the whole potential range (except for curvature due to double layer effects and distortion due to uncompensated resistance); this is not the case. Moreover, this mechanism does not predict the negligible variation of the exchange current with hydroxide concentration at equilibrium which several other researchers have reported (22-24, 26, 27). The consecutive electron transfer mechanism explains all the observed features.

Recently Despic and co-workers (49) demonstrated that the Cd(II)/Cd(Hg) system in H₂SO₄ solutions, long thought to represent a mechanism involving a simple two-electron charge transfer step, probably occurs by a two-step single electron exchange mechanism. The findings here on the Zn(II)/Zn(Hg) system parallel these results and suggest that other electrode reaction mechanisms previously thought to involve multiple electron transfer steps bear reinvestigation.

Acknowledgment

The support of the National Science Foundation (NSF GP 6688X) and Delco-Remy Corporation (under AF 33(615)-3487) is gratefully acknowledged. The PDP-12A computer was acquired under a grant from the National Science Foundation (GP 10360).

Manuscript submitted April 21, 1972; revised manuscript received June 1, 1972.

Any discussion of this paper will appear in a Discussion Section to be published in the June 1973 JOURNAL.

LIST OF SYMBOLS

A	electrode area
C [*] _j	bulk concentration of jth species
D _j	diffusion coefficient of jth species
f _j	activity coefficient of jth species
E ^o _i	formal redox potential of ith step (i = 1, 2)
E ^r _{1/2,i}	reversible half-wave potentials of ith steps
n _i	number of electrons transferred in ith charge transfer step
α _i	charge transfer coefficient for ith steps
β _i	= 1 - α _i
k ₀	standard heterogeneous rate constants for ith step
F	Faraday's constant
R	ideal gas constant
T	absolute temperature
t	time
j, ψ, χ, λ, K	derived parameters, see Eq. [15]-[21]
Z _a , Z _c	derived parameter, see Eq. [27] and [29]
Q(t)	charge
i(t)	current

APPENDIX

The equations and boundary conditions for the solution of the current-time behavior for a quasi-reversible two-step charge transfer are as follows (10)

$$\frac{\partial C_o}{\partial t} = D_o \frac{\partial^2 C_o}{\partial x^2} \quad [1A]$$

$$\frac{\partial C_Y}{\partial t} = D_Y \frac{\partial^2 C_Y}{\partial x^2} \quad [2A]$$

$$\frac{\partial C_R}{\partial t} = D_R \frac{\partial^2 C_R}{\partial x^2} \quad [3A]$$

For t = 0, any x

$$C_o = C^*_o \quad [4A]$$

$$C_R = C_Y = 0 \quad [5A]$$

For t > 0, x → ∞

$$C_o \rightarrow C^*_o \quad [6A]$$

$$C_R \rightarrow C_Y \rightarrow 0 \quad [7A]$$

For t > 0, x = 0

$$D_o \frac{\partial C_o}{\partial x} = \frac{i_1(t)}{n_1 F A} \quad [8A]$$

$$D_Y \frac{\partial C_Y}{\partial x} = \frac{i_2(t)}{n_2 F A} - \frac{i_1(t)}{n_1 F A} \quad [9A]$$

$$D_R \frac{\partial C_R}{\partial x} = -\frac{i_2(t)}{n_2 F A} \quad [10A]$$

$$\frac{i_1(t)}{n_1 F A k_{s,1}} = C_{ox=0} \exp \left\{ \frac{-\alpha_1 n_1 F}{RT} [E(t) - E_1^o] \right\} - C_{Yx=0} \exp \left\{ \frac{(1 - \alpha_1) n_1 F}{RT} [E(t) - E_1^o] \right\} \quad [11A]$$

$$\frac{i_2(t)}{n_2 F A k_{s,2}} = C_{Yx=0} \exp \left\{ \frac{-\alpha_2 n_2 F}{RT} [E(t) - E_2^o] \right\} - C_{Rx=0} \exp \left\{ \frac{(1 - \alpha_2) n_2 F}{RT} [E(t) - E_2^o] \right\} \quad [12A]$$

REFERENCES

1. A. Bewick and H. R. Thirsk, in "Modern Aspects of Electrochemistry," Vol. 5, p. 291ff, J. O'M. Bockris and B. E. Conway, Editors, Butterworths, Washington (1969).
2. K. J. Vetter, *Z. Naturforsch.*, **7a**, 328 (1952).
3. K. J. Vetter, *ibid.*, **8a**, 823 (1953).
4. K. J. Vetter, "Electrochemical Kinetics," p. 149ff, Academic Press, New York (1967).
5. R. M. Hurd, *This Journal*, **109**, 327 (1962).
6. D. M. Mohilner, *J. Phys. Chem.*, **68**, 623 (1964).
7. K. J. Vetter and G. Thiemke, *Z. Elektrochem.*, **64**, 805 (1960).
8. K. J. Vetter, *ibid.*, **56**, 797 (1952).
9. J. M. Hale, *J. Electroanal. Chem.*, **8**, 181 (1964).
10. H. L. Hung and D. E. Smith, *ibid.*, **11**, 237 and 425 (1966).
11. J. Plonski, *This Journal*, **116**, 1688 (1969).
12. T. Berzins and P. Delahay, *J. Am. Chem. Soc.*, **75**, 5716 (1953).
13. M. Smutek, *Coll. Czech. Chem. Comm.*, **18**, 171 (1953).
14. J. Cizek and K. Holub, *ibid.*, **31**, 689 (1966).
15. J. G. Mason, *J. Electroanal. Chem.*, **11**, 462 (1966).
16. E. R. Brown, D. E. Smith, and D. D. DeFord, *Anal. Chem.*, **38**, 1130 (1966).
17. G. Lauer and R. A. Osteryoung, *ibid.*, **38**, 1137 (1966).
18. G. L. Booman, *ibid.*, **38**, 1144 (1966).
19. M. W. Breiter, *This Journal*, **112**, 845 (1965).
20. G. Lauer, R. Abel, and F. C. Anson, *Anal. Chem.*, **39**, 765 (1967).
21. G. Lauer and R. A. Osteryoung, *ibid.*, **40**, 30A (1968).
22. H. Gerischer, *Z. Physik. Chem. (Leipzig)*, **202**, 302 (1953).
23. H. Gerischer, *Anal. Chem.*, **31**, 33 (1959).
24. J. P. G. Farr and N. A. Hampson, *J. Electroanal. Chem.*, **18**, 407 (1968).
25. H. Matsuda and Y. Ayabe, *Z. Elektrochem.*, **63**, 1164 (1959).
26. B. Behr, J. Dojlido, and J. Malyszko, *Roczniki Chem.*, **36**, 725 (1962).
27. K. Morinaga, *J. Chem. Soc. Japan*, **79**, 204 (1958).
28. A. G. Stromberg and L. F. Trushina, *Elektrokhimiya*, **2**, 1363 (1966).
29. A. G. Stromberg and L. N. Popova, *Isv. Tomsk Politekh. Inst.*, **167**, 91 (1967).
30. A. G. Stromberg and L. N. Popova, *Elektrokhimiya*, **4**, 39 (1968).
31. A. G. Stromberg and L. N. Popova, *ibid.*, **4**, 1147 (1968).
32. F. C. Anson and D. A. Payne, *J. Electroanal. Chem.*, **13**, 35 (1967).
33. E. R. Brown, D. E. Smith, and G. L. Booman, *Anal. Chem.*, **40**, 1141 (1968).
34. D. A. Payne, Ph.D. dissertation, The University of Texas at Austin (1970).
35. J. Albery and M. Hitchman, "Ring-Disc Electrodes," pp. 38-41, Oxford University Press (1971).
36. J. H. Christie, G. Lauer, and R. A. Osteryoung, *J. Electroanal. Chem.*, **7**, 60 (1964).
37. J. H. Christie, G. Lauer, R. A. Osteryoung, and F. C. Anson, *Anal. Chem.*, **35**, 1979 (1963).
38. H. Gerischer and W. Vielstich, *Z. Physik. Chem. (Frankfurt)*, **3**, 16 (1955).

39. H. Gerischer and W. Vielstich, *ibid.*, **4**, 10 (1955).
 40. K. B. Oldham and R. A. Osteryoung, *J. Electroanal. Chem.*, **11**, 397 (1966).
 41. J. Osteryoung and R. A. Osteryoung, *Electrochim. Acta*, **16**, 525 (1971).
 42. Katsumi Kanzaki Niki, Ph.D. dissertation, pp. 16 and 80, The University of Texas at Austin (1966).
 43. A. G. Stromberg and E. A. Zakharova, *Elektrokhimiya*, **1**, 1036 (1965).
 44. L. Meites and Y. Israel, *J. Am. Chem. Soc.*, **83**, 4903 (1961).
 45. D. E. Smith in "Electroanalytical Chemistry," Vol. 1, p. 26ff, A. J. Bard, Editor, Marcel Dekker, New York (1966).
 46. R. S. Nicholson and I. Shain, *Anal. Chem.*, **36**, 766 (1964).
 47. H. Matsuda, *Z. Elektrochem.*, **59**, 494 (1955).
 48. J. R. Delmastro and D. E. Smith, *Anal. Chem.*, **38**, 169 (1966).
 49. A. R. Despic', D. R. Jovanovic', and S. P. Bingulac, *Electrochim. Acta*, **15**, 459 (1970).

The Kinetics of the p-Toluquinhydrone Electrode

F. Kornfeil*

*Electronics Technology and Devices Laboratory,
 United States Army Electronics Command, Fort Monmouth, New Jersey 07703*

ABSTRACT

The reaction mechanism of the redox system p-toluquinone/toluhydroquinone (toluquinhydrone electrode) on smooth platinum was elucidated with the aid of the electrochemical reaction order method. It was found that in the pH range 0.1-3.2 the reaction proceeds according to the scheme $Q + H^+ \rightleftharpoons HQ^+$, $HQ^+ + e^- \rightleftharpoons HQ$, $HQ + H^+ \rightleftharpoons H_2Q^+$, $H_2Q^+ + e^- \rightleftharpoons H_2Q$. This mechanism is identical with the HeHe sequence determined by Vetter for the benzoquinone electrode. The relatively fast rate of the charge-transfer steps, however, necessitated measurements of the electrode polarization in the nonsteady state. A method is described to determine the individual exchange current densities in moderately fast consecutive charge-transfer reactions.

The reaction mechanism of the redox couple p-benzoquinone/hydroquinone (quinhydrone electrode) was first elucidated by Vetter (1) who interpreted the steady-state overpotential on smooth platinum with the aid of the electrochemical reaction order method. He showed that, in the over-all electrode reaction $H_2Q \rightleftharpoons Q + 2H^+ + 2e^-$, the electrons are exchanged in two different charge-transfer steps. Hale and Parsons (2), using the Koutecky method on dropping mercury, and Eggins and Chambers (3), employing cyclic voltammetry on polished platinum electrodes, arrived at essentially similar conclusions in more recent studies of the reduction of benzoquinone and other p-quinones. The consecutive charge-transfer mechanism is, however, challenged by Loshkarev and Tomilov who account for their experimental results obtained on Pt (4, 5) and other metals (6) by postulating that both electrons are transferred simultaneously in a single charge-transfer step.

The present paper describes an investigation of the kinetics of the redox system methyl-p-benzoquinone/methyl-hydroquinone (toluquinhydrone electrode). The aim of this study has been (i) to clarify the situation with respect to the reaction mechanism and (ii) to ascertain what effect, if any, the addition of the CH_3 -group to the benzene ring may have on the kinetic parameters of the quinhydrone electrode reaction.

Experimental Procedure

All measurements of the overpotential were made at the same constant temperature ($25^\circ \pm 0.5^\circ C$) in solutions of equal ionic strength $\frac{1}{2}\sum c_i n_i^2 = 1.0$. The excess of supporting electrolyte accomplished, as usual, the suppression of the ζ -potential to negligible values, minimal transference numbers t_j , and the virtual constancy of the activity coefficients of all reacting species S_j , thereby making the substitution of c_j for a_j possible.

Electrolyte solutions.—Both the toluquinone and the toluhydroquinone used were obtained from Eastman

Kodak "practical grade" reagents. The toluquinone was purified by sublimation under atmospheric pressure and the sublimate collected as canary-yellow needles (mp $68.0^\circ C$). The toluhydroquinone, however, required repeated recrystallization from benzene and had to be subsequently twice sublimed in vacuo before snow-white crystals could be obtained (mp $126.5^\circ C$). All other reagents used in the electrolyte solutions were of C.P. quality and were used without further purification. Triply distilled water served as the solvent. The toluquinone and toluhydroquinone concentrations varied from 10^{-2} to 10^{-4} molar.

Because of the known vulnerability of aqueous solutions of toluquinhydrone to photodecomposition (7) the toluquinone and toluhydroquinone were dissolved in the electrolyte immediately before the start of each experiment. No decomposition could be detected within a 6-hr period, provided that the solutions were kept free of dissolved oxygen. Purified argon was, therefore, bubbled through the electrolyte at the start of each series and also, intermittently, between individual measurements within a series of determinations of the overpotential. This procedure insured sufficient stability during the 2-3 hr normally required for establishing the anodic and cathodic current density-potential relation at a given concentration.

Reference electrodes.—The values of all electrode potentials ϵ are referred to the SHE and were measured against a Ag/AgCl/KCl(1M) electrode ($\epsilon_0 = +0.2387$ V). Highly stable reference electrodes were prepared by the electrolytic formation of AgCl on thermally reduced spheres ($r \sim 0.2$ cm) of Ag_2O (8) attached to small Pt spirals. The scatter of potential differences among these electrodes never exceeded 0.05 mV.

Electrolysis cell.—A Pyrex cell as shown in Fig. 1 was used in all the polarization measurements described in this paper. The working electrode, a smooth Pt wire ($r \sim 0.25$ mm), was sealed into a glass tube leaving 2.55 cm exposed to the electrolyte solution, and was located along the axis of a cylindrical Pt counter-electrode through which a small hole had been drilled to accommodate the Haber-Luggin capillary of the

* Electrochemical Society Active Member.
 Key words: toluquinhydrone electrode, reaction mechanism, exchange current densities, electrochemical reaction order.

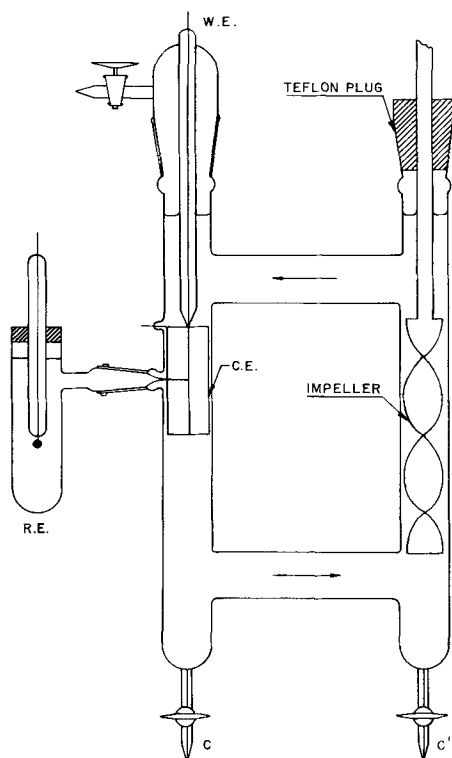


Fig. 1. Electrolysis cell. W.E., working electrode; C.E., counter-electrode; R.E., reference electrode; C, C', argon inlets.

reference electrode. A machined Teflon plug served as the bearing of a Lucite impeller which, driven by a synchronous motor, circulated the electrolyte solution through the cell in the direction indicated by the arrows in order to realize conditions of controlled mass transport during the steady-state electrolysis. The speed of flow (25 cm/sec) was the same as the one reported by Vetter (1) in his work on the benzoquinhydrone electrode and was chosen to facilitate the direct comparison of the test results.

The electrolyte could be drained from the apparatus through stopcocks C and C' which also served as the inlets for the argon. Keeping the working electrode immersed in chromosulfuric acid when not in use and thorough rinsing with distilled water before each series of polarization measurements were the only other precautions necessary to attain a reproducibility of about ± 5 mV over the major portion of the current potential curves.

Electrical.—In the measurements of the steady-state overpotential under forced convection the polarizing current $i \times A$ (i = current density in amperes/square centimeters, A = apparent surface area of the working electrode in square centimeters) was controlled¹ by switching in various portions of a high-ohmic network of induction-free resistors connected to a d-c power source² of about 400V. The resistance network was designed so that successive switch positions resulted in logarithmic increases of the polarizing current. The potential difference between the working and reference electrodes was measured using the Poggendorff compensation method.³

The same circuit was also used in the galvanostatic pulse measurements except that in this case the potentiometer circuit was replaced by a cathode-ray oscilloscope⁴ connected to a mercury wetted relay⁵ in the triggering circuit. This relay was a new type of high contact resistance ($> 5 \times 10^7$ ohm) and capable of

rapid ($< 10^{-9}$ sec), chatter-free closing of the contact. The same milliammeter served to preset the circuit for each desired current density, the electrolysis cell having been temporarily replaced by a suitable resistor.

The electrolyte solution was kept at rest during pulse polarization but was circulated between recordings of the potential-time traces in order to expedite the re-establishment of the equilibrium potential ϵ_0 . Extrapolation of the potential transients for $t \rightarrow 0$ and correction for the iR -drop between the working electrode and the tip of the Haber-Luggin capillary were carried out according to the method of Gerischer (9).

Results and Discussion

General.—Throughout this discussion i and η will be reckoned positive for the anodic and negative for the cathodic branches of the polarization curves.

The over-all redox electrode reaction can be written as a net oxidation process in the generalized form



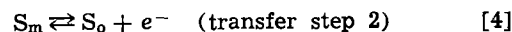
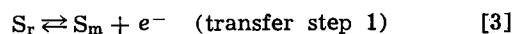
with the equilibrium potential given by

$$\epsilon_0 = E_0 + RT/nF \sum \nu_j \ln a_j \quad [2]$$

where ν_j is the stoichiometric coefficient of the species S_j ($\nu_j < 0$ for a reduced, $\nu_j > 0$ for an oxidized species), E_0 is the standard electrode potential and the remaining symbols have their usual significance. In the case of the toluquinone electrode ($E_0 = 0.623$ V, $n = 2$) the ν_j 's have, therefore, the following values: $\nu_{H_2Q} = -1$, $\nu_Q = +1$, $\nu_{H^+} = +2$.

For the sake of brevity the following indices will be used for ν_j , S_j , and later for the electrochemical reaction order z_j : toluquinone (Q) = 1, toluhydroquinone (H_2Q) = 2, hydrogen ion (H^+) = 3.

The theoretical relationship between the transfer overpotential of a redox electrode and the current density in the stationary state was first derived by Vetter (10, 11) for an electrode reaction of the type $S_r \rightleftharpoons S_o + 2e^-$ proceeding via two consecutive charge transfer steps under the formation of an intermediate S_m



each charge transfer step having its own characteristic transfer coefficient (α_1 , α_2) and exchange current density ($i_{o,1}$, $i_{o,2}$). Moreover, each species appearing in Eq. [3] and [4] may itself be involved in sufficiently fast chemical reactions.

Under these conditions the i - η relationship is, in its most perspicuous form

$$i = 2i_{o,1} \exp\left(\frac{\alpha_1 F}{RT} \eta\right) \times \frac{1 - \exp\left(-\frac{2F}{RT} \eta\right)}{1 + (i_{o,1}/i_{o,2}) \exp\left(-\frac{1 + \alpha_2 - \alpha_1}{RT} F \eta\right)} \quad [5]$$

$$i = -2i_{o,2} \exp\left(-\frac{1 - \alpha_2}{RT} F \eta\right) \times \frac{1 - \exp\left(\frac{2F}{RT} F \eta\right)}{1 + (i_{o,2}/i_{o,1}) \exp\left(\frac{1 + \alpha_2 - \alpha_1}{RT} F \eta\right)} \quad [5a]$$

Equations [5] and [5a] are identical. However, the consequences of large overpotentials (Tafel lines) and high values of the ratios of the exchange current densities in the intermediate range of η (pseudo-Tafel lines) can be seen more clearly when Eq. [5] is used for anodic ($\eta > 0$) and Eq. [5a] for cathodic ($\eta < 0$) polarizations. The complete theoretical polarization

¹ Measured with Greibach milliammeter Model 700.

² Fluke, Model 407 D.

³ Leeds & Northrup potentiometer Type K-3.

⁴ Tektronix Type 561 A, time-base plug-in Type 3B3, differential amplifier Type 3A3, with input resistance modified to 10 megohm, camera system C-12.

⁵ Bell Laboratories, under United States Government contract.

curves have been systematically examined more recently by Hurd (12) who also investigated the general case of n consecutive transfer steps with numerical solutions supplied for $n = 3$.

In the experimental determination of the i - η relationship the concentrations of toluquinone (c_1) and toluhydroquinone (c_2) were varied in the following electrolyte solutions: 1M HCl (pH = 0.1), 0.01M HCl + 0.99M KCl (pH = 2.14), and 0.03M CH₃COOH + 1M KCl (pH = 3.15).

Steady-state polarization.—Figure 2 shows a typical polarization curve obtained at $c_1 = c_2 = 10^{-2}$ molar in 1M HCl. In all steady-state measurements the irregular (~1 Hz) fluctuations of the electrode potential due to the variations in the mean thickness of the diffusion layer in turbulent flow, characteristic of a diffusion current, were observed when the current density approached the limiting value i_L . The limiting anodic current density was found to be proportional to the toluhydroquinone concentration

$$(i_L)_a = 0.8 c_2 \quad (\text{A/cm}^2) \quad [6]$$

and the limiting cathodic current density proportional to the toluquinone concentration according to

$$(i_L)_c = 0.9 c_1 \quad (\text{A/cm}^2) \quad [7]$$

The values of these proportionality constants are somewhat lower than those determined by Vetter (1) under identical conditions, as would be expected from the larger size of the methyl-substituted molecules. It follows (13) from the above that the overpotential associated with the limiting currents is pure diffusion overpotential η_d with no measurable reaction overpotential η_r present.

It can also be seen from Fig. 2 that the contribution of the charge-transfer overpotential to the total overpotential is not nearly large enough for Tafel lines to be drawn with a sufficient degree of accuracy. In addition, the rather steep anodic slope of the polarization curve suggests strongly the possibility of mistaking a pseudo-Tafel line for a true Tafel line. It was for these reasons that the contribution of η_d was eliminated by employing the nonsteady-state method (pulse polarization).

Pulse Polarization.—The appearance of the factor 2 immediately following the equality signs in Eq. [5] and [5a] is due to the fact that, by definition of the stationary state, both charge-transfer reactions proceed at the same rate ($i_1 = i_2 = 0.5i$), otherwise there would occur a net accumulation or depletion of S_m . This condition does, of course, not necessarily prevail at any time before the system has reached the stationary state. It is, therefore, necessary to introduce a "current distribution coefficient" γ in the derivation of the corresponding equation reflecting the condition of

the nonsteady-state. The factor γ is then defined as that fraction of the total current density giving rise to the first charge-transfer reaction (Eq. [3]): $\gamma \equiv i_1/i$, $1 - \gamma \equiv i_2/i$. Following the arguments (10) used in the derivation of Eq. [5] and [5a] one obtains

$$i = i_{o,1}/\gamma \exp\left(\frac{\alpha_1 F}{RT} \eta\right) \times \frac{1 - \exp\left(-\frac{2F}{RT} \eta\right)}{1 + \frac{(1-\gamma)i_{o,1}}{\gamma i_{o,2}} \exp\left(-\frac{1 + \alpha_2 - \alpha_1}{RT} F\eta\right)} \quad [6]$$

$$i = -i_{o,2}/(1-\gamma) \exp\left(-\frac{1-\alpha_2}{RT} F\eta\right) \times \frac{1 - \exp\left(\frac{2F}{RT} \eta\right)}{1 + \frac{\gamma i_{o,2}}{(1-\gamma)i_{o,1}} \exp\left(\frac{1 + \alpha_2 - \alpha_1}{RT} F\eta\right)} \quad [6a]$$

of which the steady-state equations are the special case for $\gamma = 0.5$.

At sufficiently large overpotentials Eq. [6] and [6a] simplify to

$$i = i_{o,1}/\gamma \exp\left(\frac{\alpha_1 F}{RT} \eta\right) \quad \text{and} \quad i = -i_{o,2}/(1-\gamma) \exp\left(-\frac{1-\alpha_2}{RT} F\eta\right) \quad [7]$$

In a plot of $\log i$ vs. η one ought therefore obtain Tafel lines with intercepts $I_a = i_{o,1}/\gamma$ and $I_c = i_{o,2}/(1-\gamma)$ and anodic and cathodic slopes determined by the values of α_1 and $(1-\alpha_2)$, respectively, provided that γ remains reasonably constant over the range of overpotentials under consideration. That this is indeed the case can be seen in Fig. 3-5 which were taken by varying the concentration of only one species at a time, keeping all other concentrations constant. A comparison of corresponding pairs of polarization curves demonstrates that the anodic and cathodic Tafel lines have different intercepts. From the slopes of the Tafel lines the transfer coefficients were calculated as $\alpha_1 = 0.40$ and $\alpha_2 = 0.55$, independently of the concentration. Both criteria for the occurrence of consecutive charge-transfer reactions ($I_a \neq I_c$, $\alpha_1 \neq \alpha_2$) are therefore fulfilled.

Figure 4 also shows the appearance of a pseudo-Tafel line in the intermediate range of the anodic overpotential before the true Tafel region is reached at still larger overpotentials. This phenomenon occurs when the concentrations are chosen so that $I_a \gg I_c$ (10, 12). Under this condition, and at sufficiently large overpotentials ($\exp 2F\eta/RT \gg 1$) Eq. [6a] assumes

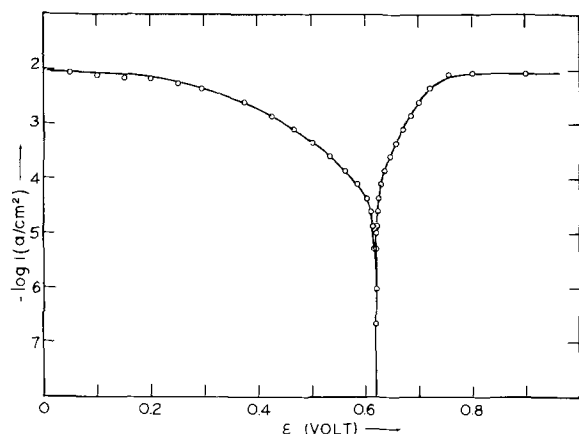


Fig. 2. Steady-state polarization curves for $c_1 = c_2 = 10^{-2}$ M, pH = 0.01.

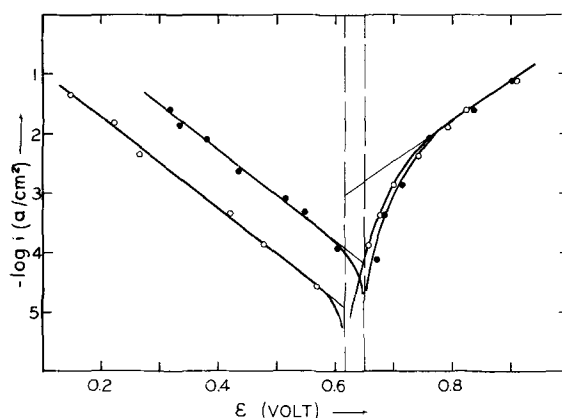


Fig. 3. Pulse polarization curves, $c_2 = 10^{-3}$ M, pH = 0.01. ● $c_1 = 10^{-2}$ M, ○ $c_1 = 10^{-3}$ M.

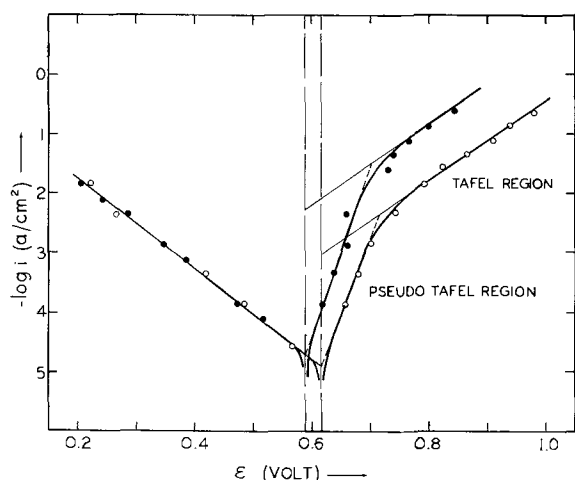


Fig. 4. Pulse polarization curves, c_2 variable; $c_1 = 10^{-3}M$, $pH = 0.10$. ● $c_2 = 10^{-2}M$, ○ $c_2 = 10^{-3}M$.

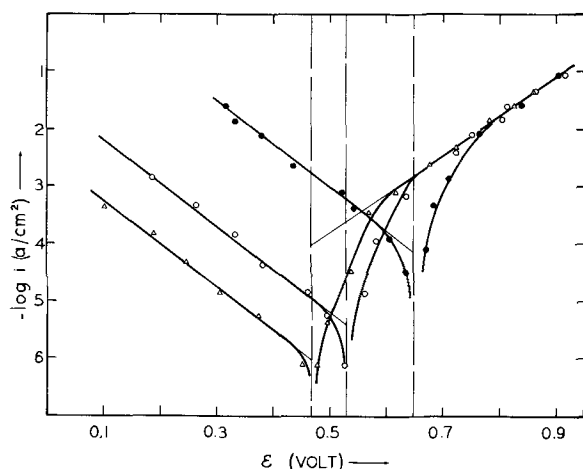


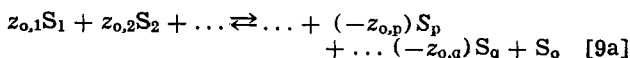
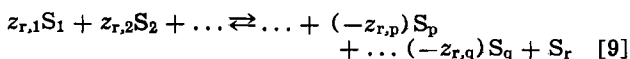
Fig. 5. Pulse polarization curves, c_3 variable; $c_1 = 10^{-2}M$, $c_2 = 10^{-3}M$. ● $pH = 0.01$, ○ $pH = 2.14$, △ $pH = 3.14$.

the pseudo-Tafel form

$$i = i_{o,2}/(1 - \gamma) \exp\left(\frac{1 + \alpha_2}{RT} F\eta\right) \quad [8]$$

with an apparent anodic transfer coefficient $\alpha_a = (1 + \alpha_2)$ whose magnitude $1 < \alpha_a < 2$ simulates the existence of a transferred particle of charge $2e^-$. If one further considers that the intercept $i_{o,2}/(1 - \gamma)$ is identical with the cathodic intercept I_c then it is easily appreciated that in a steady-state experiment under the same conditions, where the anodic limiting current density is approximately 1 mA, the true Tafel line could never be observed. One would then be forced to conclude that the two electrons are indeed transferred in a single step. It seems most likely that these difficulties led Loshkarev *et al.* (4-6) to postulate a single-step mechanism. Such a mechanism is, in any event, difficult to accept unless one is prepared to assume the existence of a dimer electron.

Electrochemical reaction orders, reaction mechanism.—It is well known that the electrochemical reaction order method provides a convenient and powerful means of identifying the stoichiometry of the species S_r and S_o participating directly in the charge-transfer reactions (14), provided that these substances are virtually in thermodynamic equilibrium with other species S_j (*i.e.*, $\eta_r \rightarrow 0$)



In the presence of a large excess of supporting electrolyte the expressions for c_r and c_o follow from the law of mass action as

$$c_r = K_r \Pi c_j z_{r,j} \quad [10]$$

$$c_o = K_o \Pi c_j z_{o,j} \quad [10a]$$

Substitution of Eq. [10] in the expression for the exchange current density of transfer step 1 results in

$$i_{o,1} = k_1 c_r \exp\left(\frac{\alpha_1 F}{RT} \epsilon_o\right) = K_1 \Pi c_j z_{r,j} \exp\left(\frac{\alpha_1 F}{RT} \epsilon_o\right) \quad [11]$$

and, analogously, using Eq. [10a] for transfer step 2

$$i_{o,2} = k_2 c_o \exp\left(-\frac{1 - \alpha_2}{RT} F\epsilon_o\right) = K_2 \Pi c_j z_{o,j} \exp\left(-\frac{1 - \alpha_2}{RT} F\epsilon_o\right) \quad [11a]$$

where the rate and equilibrium constants have been taken together to form the new constants K_1 and K_2 . The stoichiometric coefficients of the equilibria [9] and [9a] reappear now as the anodic and cathodic electrochemical reaction orders $z_{r,j}$ and $z_{o,j}$, respectively, whose knowledge allows the computation of the stoichiometric formulas of S_r and S_o according to the equations

$$S_r = \Sigma z_{r,j} S_j \text{ and } S_o = \Sigma z_{o,j} S_j \quad [12]$$

which follow at once from Eq. [9] and [9a].

Introducing the Tafel line intercepts $I_a = i_{o,1}/\gamma$ and $I_c = i_{o,2}/(1 - \gamma)$ and taking logarithms, Eq. [11] and [11a] become

$$\ln I_a = -\ln \gamma + \Sigma z_{r,j} \ln c_j + \frac{\alpha_1 F}{RT} \epsilon_o + \ln K_1 \quad [13]$$

$$\ln I_c = -\ln(1 - \gamma) + \Sigma z_{o,j} \ln c_j - \frac{1 - \alpha_2}{RT} F\epsilon_o + \ln K_2 \quad [13a]$$

The electrochemical reaction orders can now be calculated by partial differentiation of $\ln I_a$ and $\ln I_c$ with respect to the equilibrium potential ϵ_o , varying the concentration c_k of the species S_k at a time, keeping all other concentrations constant

$$2.303 \left(\frac{\partial \log I_a}{\partial \epsilon_o}\right)_{c_{j \neq k}} = \frac{F}{RT} \left(\alpha_1 + 2 \frac{z_{r,k}}{\nu_k}\right) \quad [14]$$

$$2.303 \left(\frac{\partial \log I_c}{\partial \epsilon_o}\right)_{c_{j \neq k}} = \frac{F}{RT} \left(\alpha_2 + 2 \frac{z_{o,k}}{\nu_k} - 1\right) \quad [14a]$$

where Eq. [2] has been used to obtain $\partial \log c_k / \partial \epsilon_o$.

In the present case a plot of $\log I_{a,c}$ vs. ϵ_o is preferable to the more frequently used $\partial \log i / \partial \log c_k$ because the actual concentration of S_j may not accurately be known owing to the holoquinone/meriquinone equilibria (15) present in the electrolyte solutions. The meriquinone is believed to be the source of the intermediate to sustain the second charge-transfer reaction at $t = 0$ in the nonsteady-state experiments.

In Fig. 6 and 7 the dependence of the anodic and cathodic intercepts is shown as a function of the equilibrium potential ϵ_o , using the variable c_k as the parameter. With the aid of Eq. [14] and [14a] the $z_{r,j}$'s are calculated from $\partial \log I_a / \partial \epsilon_o$ and the $z_{o,j}$'s from $\partial \log I_c / \partial \epsilon_o$ as

$$z_{r,1} = 0, \quad z_{r,2} = +1, \quad z_{r,3} = 0 \\ z_{o,1} = +1, \quad z_{o,2} = 0, \quad z_{o,3} = +1 \quad [15]$$

Substituting these values in Eq. [12] it follows immediately that $S_r = H_2Q$, the toluhydroquinone molecule

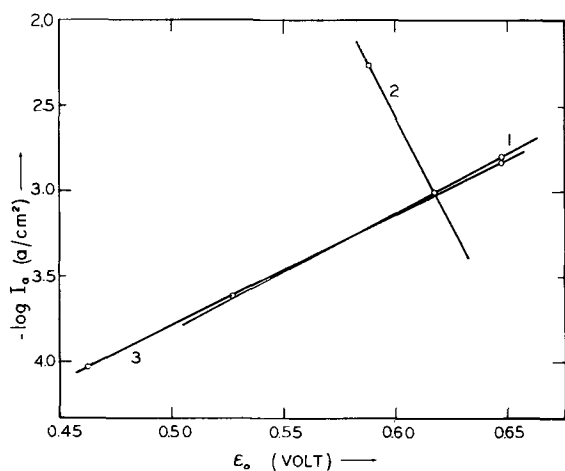


Fig. 6. Determination of the anodic electrochemical reaction orders. Curve 1, $x_{r,1}$; curve 2, $x_{r,2}$; curve 3, $x_{r,3}$.

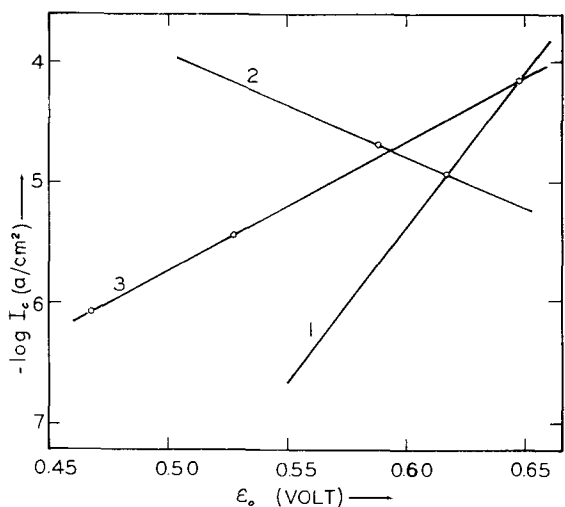
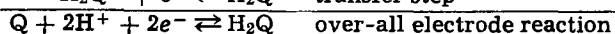
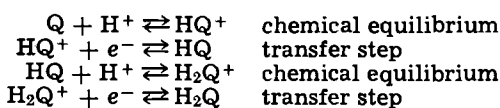


Fig. 7. Determination of the cathodic electrochemical reaction orders. Curve 1, $x_{o,1}$; curve 2, $x_{o,2}$; curve 3, $x_{o,3}$.

itself, while $S_o = HQ^+$, the protonated toluquinone. Since the charge exchanged in each transfer step is obviously e^- , it is clear that the over-all electrode reaction proceeds according to the scheme



Thus, the mechanism of the toluquinhydrone electrode is the same as the HeHe mechanism of the benzoquinhydrone electrode as determined by Vetter (1).

Determination of the individual exchange current densities.—Although the elucidation of the electrode mechanism has been shown not to depend on the knowledge of the individual exchange current densities $i_{o,1}$ and $i_{o,2}$, it would still be desirable to ascertain their values in order to be able to see the influence of the substituent on the rates of the charge-transfer reactions.

When the transfer steps are too fast the Tafel lines become obscured by the early development of limiting current densities in steady-state measurements. On the other hand, inspection of Eq. [6] and [6a] demonstrates that, using the current pulse method alone, the three unknowns $i_{o,1}$, $i_{o,2}$, and γ cannot be separated because they invariably occur in the same combination $i_{o,1}/\gamma$ and $i_{o,2}/(1 - \gamma)$, i.e., the Tafel line intercepts. It is, however, possible to measure γ , and hence the exchange current densities, by combining the results

of the pulse experiments with measurements of the steady-state overpotential in the vicinity ($-10 < \eta < +10$ mV) of the equilibrium potential in the following way: the pulse measurements yield directly the values of the intercepts $I_a = i_{o,1}/\gamma$ and $I_c = i_{o,2}/(1 - \gamma)$. Now, differentiation of Eq. [5] or [5a] with respect to η for $\eta \rightarrow 0$ gives the expression for the charge-transfer resistance R_t (13)

$$R_t = \left(\frac{\partial \eta}{\partial i} \right)_{\eta \rightarrow 0} = \frac{RT}{4F} \left(\frac{1}{i_{o,1}} + \frac{1}{i_{o,2}} \right) \quad [16]$$

independently of the values of the transfer coefficients (10). One can, therefore, calculate γ by combining the expressions for the intercepts I_a and I_c with the slope R_t at the origin of the i - η curve. This leads at once to the equation

$$\gamma = -A/2 \pm \left(\frac{A^2}{4} - \frac{1}{I_a B} \right)^{1/2} \quad [17]$$

with $A = \frac{1}{I_c B} - \frac{1}{I_a B} - 1$, and $B = \frac{4F}{RT} R_t$.

The results of measurements taken near the equilibrium potential are presented in Fig. 8 and 9. In Fig. 8 the experimental conditions were $c_1 = 10^{-3}$, $c_2 = 10^{-2}$, pH = 0.10 for which the intercepts had been determined as $\log I_a = -2.26$ and $\log I_c = -4.68$ (cf. Fig. 4). Using Eq. [17] with $R_t = 0.6$ mV/ μ A, γ is calculated as $\gamma_1 = 0.47$ and $\gamma_2 = 0.005$. For the experiment performed with $c_1 = 10^{-2}$, $c_2 = 10^{-3}$, pH = 3.14 (Fig. 9) the corresponding intercepts are

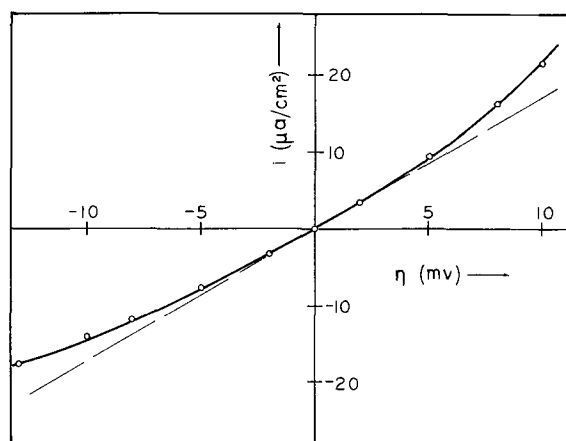


Fig. 8. Determination of the charge-transfer resistance R_t at the equilibrium potential. Experimental conditions: $c_1 = 10^{-3}M$, $c_2 = 10^{-2}M$, pH = 0.10.

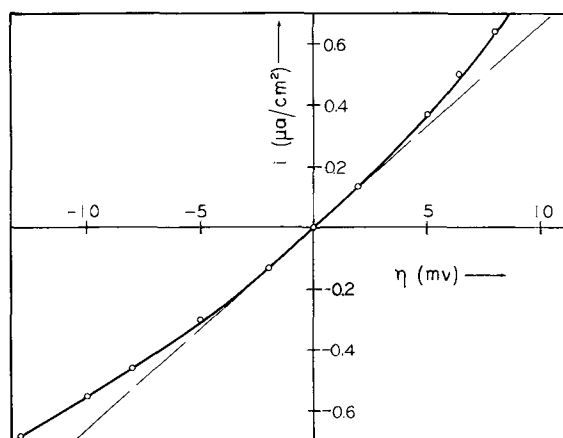


Fig. 9. Determination of the charge-transfer resistance R_t at the equilibrium potential. Experimental conditions: $c_1 = 10^{-2}M$, $c_2 = 10^{-3}M$, pH = 3.14.

$\log I_a = -4.03$, $\log I_c = -6.05$ (cf. Fig. 5), and $R_t = 15 \text{ mV}/\mu\text{A}$, resulting in $\gamma_1 = 0.52$ and $\gamma_2 = 0.007$.

Although it is much more probable that $\gamma \sim 0.5$ is the correct value the ambiguity arising from Eq. [17] having two roots can be removed by employing Eq. [16] with the values of the Tafel line intercepts and charge-transfer resistances obtained in two different sets of experiments. In this case

$$R_t = \frac{RT}{4F} \left(\frac{1}{I_a \gamma} + \frac{1}{I_c(1-\gamma)} \right),$$

$$R_t' = \frac{RT}{4F} \left(\frac{1}{I_a' \gamma} + \frac{1}{I_c'(1-\gamma)} \right) \quad [18]$$

$$\text{and} \quad \gamma = \frac{I_c - KI_c'}{K(I_a' - I_c') - (I_a - I_c)} \quad [19]$$

where $K = R_t I_a I_c / R_t' I_a' I_c'$.

Making use of the same experimental data as in the calculations above one finds $\gamma = 0.5$. Apart from the need of two separate sets of polarization data it is preferable to use Eq. [17] because the error in the calculation of γ using Eq. [19] can become quite appreciable due to the presence, in both numerator and denominator, of ΔI 's. It should also be pointed out that the close agreement between the values of γ obtained with the two methods is, therefore, somewhat misleading and is attributable to the choice of suitable pairs of polarization curves. Equation [19] can, however, serve a useful purpose in deciding between the roots of Eq. [17]. The fact that γ is found to be so close to 0.5 demonstrates that on the time scale of the Gerischer extrapolation the current distribution of the steady state is rapidly reached and that the stationary concentration of S_m can differ only slightly from its thermodynamic equilibrium concentration.

Having thus ascertained the numerical value of γ it is now an easy matter to make a direct comparison between the exchange current densities of the toluquinhydrone and benzoquinhydrone electrodes. Taking Vetter's results and the data presented in this paper it is seen that, at corresponding concentrations, the

exchange current densities of the toluquinhydrone electrode are invariably higher, at some concentrations by as much as a factor of about 300. It seems therefore that the toluquinhydrone electrode should function as the superior indicator and reference electrodes from the point of view of its greater reversibility. This advantage will, however, in most practical cases be negated by the easy photodecomposition of its electrolyte solution.

Acknowledgments

The author wishes to express his gratitude to C. F. Cook for his help in setting up the triggering circuit for the oscilloscopic measurements, and to W. F. Nye for his continued interest and encouragement.

Manuscript received May 9, 1972. This was Paper 248 presented at the New York Meeting of the Society, May 7-9, 1969.

Any discussion of this paper will appear in a Discussion Section to be published in the June 1973 JOURNAL.

REFERENCES

1. K. J. Vetter, *Z. Elektrochem.*, **56**, 797 (1952).
2. J. H. Hale and R. Parsons, *Trans. Faraday Soc.*, **59**, 1429 (1963).
3. B. R. Egdins and J. Q. Chambers, *This Journal*, **117**, 186 (1970).
4. M. Loshkarev and B. I. Tomilov, *Zhur. Fiz. Khim.*, **34**, 1753 (1960).
5. M. Loshkarev and B. I. Tomilov, *ibid.*, **36**, 132 (1962).
6. M. Loshkarev and B. I. Tomilov, *ibid.*, **36**, 1902 (1962).
7. E. A. Cooper and S. D. Nicholas, *J. Soc. Chem. Ind. (London)*, **46**, 59T (1927).
8. D. J. G. Ives and G. J. Janz, "Reference Electrodes," p. 209, Academic Press (1961).
9. H. Gerischer, *Z. Elektrochem.*, **59**, 604 (1955).
10. K. J. Vetter, *Z. Naturforsch.*, **7a**, 328 (1952).
11. K. J. Vetter, *ibid.*, **8a**, 823 (1953).
12. R. M. Hurd, *This Journal*, **109**, 327 (1962).
13. H. Gerischer and K. J. Vetter, *Z. Phys. Chem.*, **197**, 92 (1951).
14. e. g., K. J. Vetter, *ibid.*, **194**, 284 (1950).
15. C. Wagner and K. Gruenwald, *Z. Elektrochem.*, **46**, 265 (1940).

The Electrochemistry of the Liquid Crystal N-(p-Methoxybenzylidene)-p-n-butylaniline (MBBA)

The Role of Electrode Reactions in Dynamic Scattering

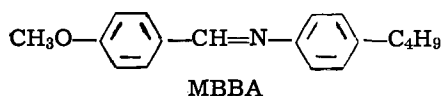
Ann Lomax, Ryo Hirasawa, and Allen J. Bard*

Department of Chemistry, The University of Texas at Austin, Austin, Texas 78712

ABSTRACT

The electrochemical reduction and oxidation of MBBA were studied by cyclic voltammetry and by controlled potential coulometry. The reduction in DMF leads to the formation of the radical anion which decomposes with a half-life of about 4 sec, apparently by both ec and ece pathways. The oxidation product was unstable on the time scale of this study. The possible importance of electrode reactions in interpreting the dynamic scattering phenomenon in nematic liquid crystals is suggested.

The liquid crystal (LC) Schiff base N-(p-methoxybenzylidene)-p-n-butylaniline (MBBA) has been of much recent interest because it undergoes "dynamic

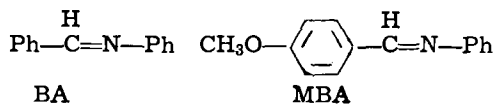


* Electrochemical Society Active Member.
Key words: electro-organic chemistry, cyclic voltammetry, coulometry, electron spin resonance, Schiff base.

scattering" (DS) when subjected to d-c or a-c electrical fields; this electrooptic effect forms the basis of LC display devices. Dynamic scattering has been shown to occur when the LC, sandwiched between two closely spaced (e.g., 10-100 μm) electrodes above a certain threshold voltage, begins to undergo first laminar and then turbulent flow (1). The mechanism of this phenomenon has been the subject of a number of recent studies (2-8) and is apparently different for d-c and low frequency a-c excitations, where the electrodes

must contact the LC phase, and for high frequency a-c excitations, where the electrodes may be insulated or "blocked" from the LC. The d-c low frequency mechanism is based on the "injection of electrons" into the low conductivity LC leading to space charges; transfer of momentum from the resulting moving ions under the influence of the field to the aligned LC molecules results in cellular hydrodynamic flow (1-3). In an alternate model the space charges in the nematic LC originate in the anisotropic conductivity of the LC (4-6). These models generally ignore the electrochemical processes occurring at the electrode-LC interface and the nature of the ionic species formed in the process. Because these processes can affect the threshold voltage for the onset of dynamic scattering and have important ramifications in the occurrence of secondary chemical reactions which may limit the life of the LC device, we have undertaken a study of the electrochemical behavior of LC materials.

Most of the electrochemical studies of MBBA described here were performed using the aprotic solvents N,N-dimethylformamide (DMF) or acetonitrile (ACN) as reaction media; a few preliminary studies in neat MBBA were also attempted, however. Previous electrochemical studies on the reduction of the related molecule, N-benzylideneaniline (BA) (9-12) and the oxidation of N-(p-methoxybenzylidene)aniline (MBA) (13) have been described.



Experimental

The MBBA was special, high-purity material obtained from Texas Instruments. The supporting electrolyte materials, tetra-n-butylammonium perchlorate (TBAP) and iodide (TBAI), were polarographic grade (Southwestern Analytical Chemicals) and were dried in a vacuum oven before use. Purification of the solvents DMF and ACN followed previous practice (14, 15).

All electrochemical data were obtained with a Princeton Applied Research Corporation (PAR) Model 170 electrochemical system. Solution preparation on a vacuum line and freeze-pump-thaw techniques were as previously described (14, 15). The cell for voltammetric studies contained either a platinum disk or a hanging mercury drop working electrode, a platinum auxiliary electrode in a separate chamber, and an aqueous saturated calomel electrode (SCE) connected to the test solution by an agar bridge with its tip positioned near the working electrode. The coulometric studies were done in the same cell with a platinum gauze working electrode. Electron spin resonance (ESR) spectra were obtained on a Varian V-4502 spectrometer and electrolytic cell accessory. The solutions were degassed by the freeze-pump-thaw method and transferred to a reservoir above the ESR electrolytic cell. The cell was flushed with nitrogen and fresh solution from the reservoir was employed for each experiment.

Results

Electrochemical reduction.—The reduction of MBBA at a platinum electrode was studied by both cyclic voltammetry and controlled potential coulometry to obtain information about the electrochemical behavior of the system on both a short and a long time scale. A typical cyclic voltammogram for the reduction in DMF is shown in Fig. 1. The first reduction wave occurs at -2.06V vs. SCE and is nearly reversible at scan rates above 5 V/sec . The second reduction wave occurs at -2.60V and shows no reversal current even at high scan rate. The reduction potential of the first wave is more negative than that of BA (-1.83V) (9) as expected for the introduction of an electron-donating group into the molecule, and is close to that for MBA (-2.15V) (10) in DMF solutions.

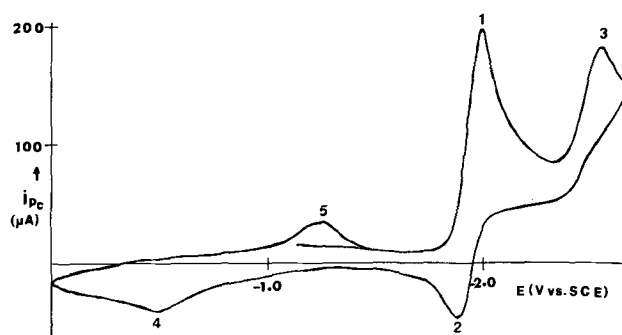


Fig. 1. Cyclic voltammogram at a Pt disk electrode of 6.65 mM MBBA in DMF, 0.1M TBAP . The scan rate was 2 V/sec .

Figure 1 shows, in addition to the two major reduction waves of MBBA (1, 3) and the oxidation of MBBA^- (2), two waves of lesser height. An anodic wave (at -0.54V) (4) appears to a slight extent after scanning through only the first wave, and to a greater degree if the scan is continued beyond the second main reduction wave. The small cathodic wave (at -1.38V) (5) appears only after having scanned through wave 4. Neither the nature nor the source of these waves was investigated. The anodic wave 4 was found to be the only wave remaining after exhaustive electrolysis of the solution at a potential on the plateau of the first wave. The behavior of the diagnostic criteria, i_{pa}/i_{pc} and $i_{pc}/v^{1/2}$, for the first reduction wave is shown as a function of scan rate, v , in Fig. 2 (i_{pc} and i_{pa} are the cathodic and anodic (reversal) peak currents, respectively). The peak height and peak potential separation, as well as the coulometric and ESR results below, show that the first reduction wave leads to the production of the radical anion in a one-electron reaction. The upper curve (Fig. 2a) illustrates the extent of reaction of the radical anion; the reaction is nearly complete at slow scan rates, while at fast scan rates it has scarcely begun. The qualitative shape of curve 2a is characteristic of both the ec and ece mechanisms, where an ec mech-

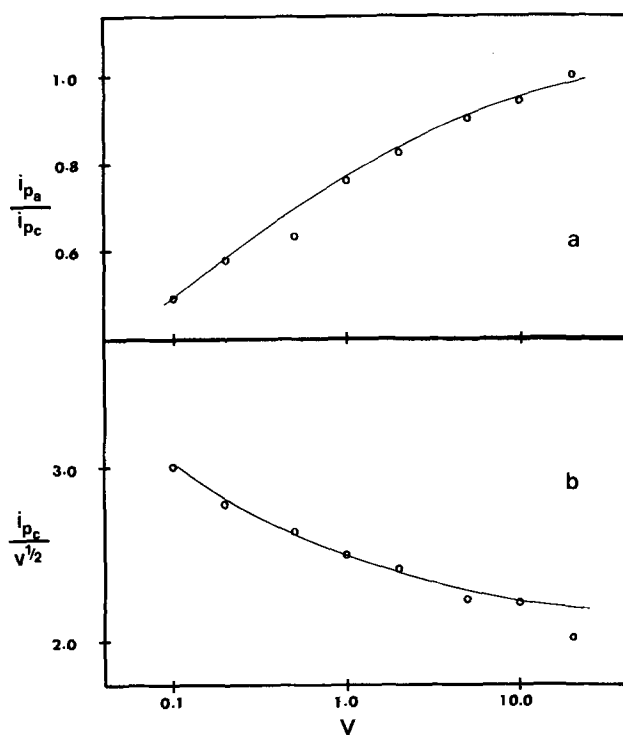


Fig. 2. (a) The peak current ratio, and (b) the normalized cathodic peak current vs. scan rate for the reduction at a hanging mercury drop electrode of 1.66 mM MBBA in DMF, 0.01M TBAP . v is V/sec , $i_{pc}/v^{1/2}$ in $\mu\text{A sec}^{1/2}/\text{v}^{1/2}$.

anism involves reaction of the electrogenerated product to a nonelectroactive species, while an ece mechanism implies that the product of the chemical reaction is reduced at potentials where MBBA is reduced. The data in Fig. 2b are useful in distinguishing between the two. In the ec case, the maximum change is about 10% while for the ece case, in which the product of the reaction is more easily reduced than the starting material, a maximum change of 50% can be observed (16, 17). The change of about 33% observed in the reduction of MBBA indicates a significant degree of ece behavior. The effect of v on the peak potential (Table I) is to shift the peak to more negative values at faster scan rates, as would be expected for an irreversible chemical reaction following electron transfer.

Exhaustive controlled potential coulometric reduction on the plateau of the first reduction wave gave an apparent number of faradays per mole of MBBA, n_{app} , of 1.2 to 1.9.

In ACN only the first reduction wave of MBBA was observed. Its peak potential was more negative ($-2.15V$) than in DMF ($-2.06V$); no reversal current was detected, even at scan rates of 20 V/sec.

Electrochemical oxidation.—The oxidation of MBBA in ACN occurs in two steps; a typical cyclic voltammogram is shown in Fig. 3. Waves 1 (1.45V) and 2 (2.0V) correspond to the oxidation of MBBA, while wave 3 is present in the solvent-supporting electrolyte medium before the addition of the depolarizer. Similar two-step oxidations have been reported for other Schiff bases (13). A small wave at 0.8V is also evident and is presumably caused by an impurity in the MBBA.

Though the occurrence of the second wave at a potential where the residual current is large makes its analysis difficult, a study of the peak characteristics of the first wave indicated that both the peak potential and the normalized peak current were dependent on the scan rate; the behavior is shown in Fig. 4, with the poor reproducibility of the current and potential measurements probably resulting from electrode filming. Neither wave yielded a detectable reversal current at scan rates up to 20 V/sec.

An n_{app} value determined by controlled potential coulometry at the first wave ranged from 0.88 to 1.2 electrons/molecule; the major electroactive product of the oxidation was reducible at $-0.8V$.

Attempts to investigate the electrochemical behavior of neat MBBA using TBAP or octadecyldimethylbenzylammonium bromide as supporting electrolytes in a small three-electrode cell were thwarted by the low solubility of the salts in MBBA and the concomitant low conductivity. The solution of MBBA with 15 volume per cent (v/o) DMF and TBAP had background limits of $-1.8V$ corresponding to the reduction of MBBA, and $+0.8V$, probably the oxidation of the impurity noted in the oxidation of MBBA; there was no significant electrochemical process detected between the two limits.

Electron spin resonance results.—*Intra muros* electrolysis of a 1.5 mM MBBA solution in 0.1M TBAP-DMF at a constant current of 0.2 mA resulted in the ESR spectrum shown in Fig. 5. Attempts to simulate the spectrum and extract coupling constants have thus far been unsuccessful. Alkali metal reduction in MTHF did not produce a radical sufficiently stable to be detected.

Table I. Peak potentials for reduction waves of MBBA^(a)

v , V/sec	V vs. SCE $-E_{pc}$ (1)	V vs. SCE $-E_{pc}$ (2)
0.2	2.04	2.54
2.0	2.06	2.60
20.0	2.08	2.66

^(a) The solution was 0.1M TBAP in DMF, 6.65 mM MBBA; the electrode, a Pt disk.

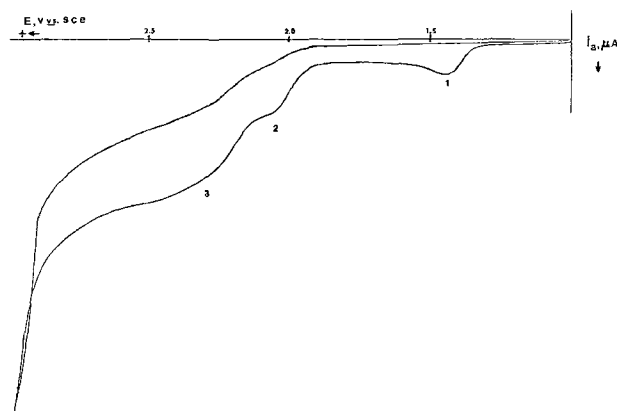


Fig. 3. Cyclic voltammogram at a Pt disk electrode of 2.24 mM MBBA in ACN, 0.1M TBAP. The scan rate was 0.2 V/sec.

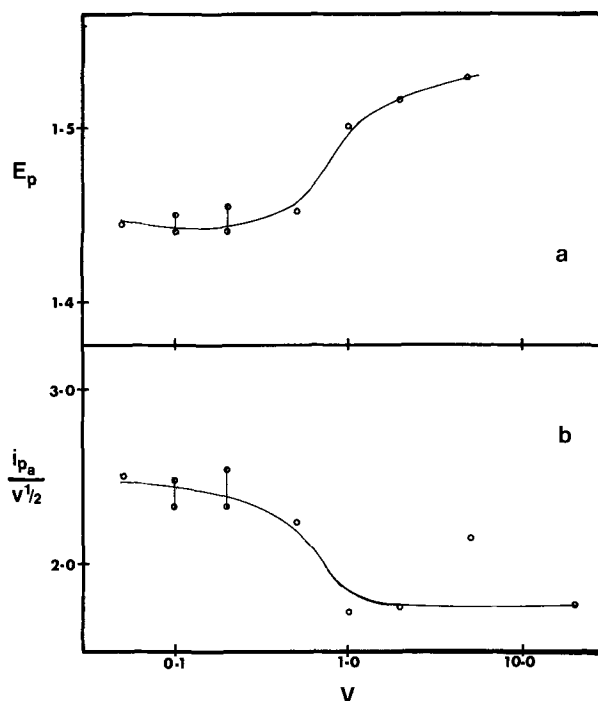


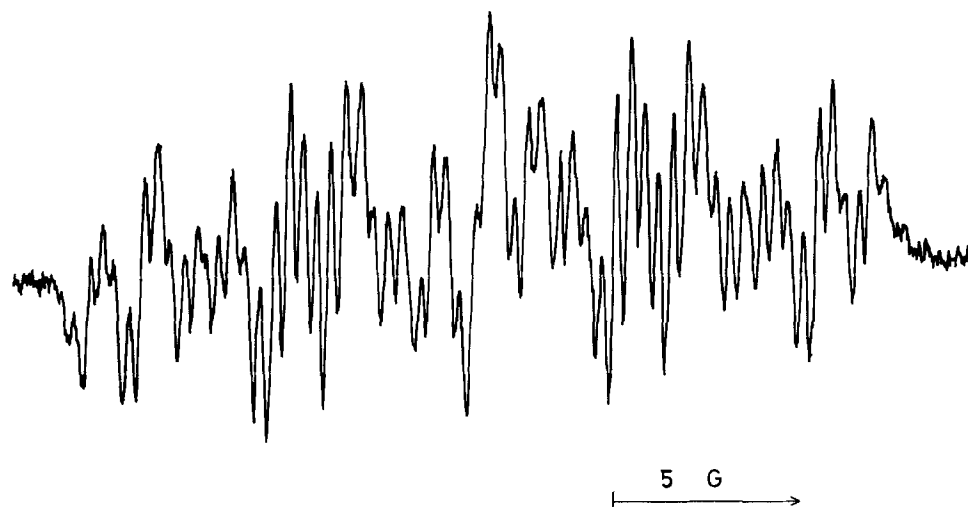
Fig. 4. (a) The peak potential, and (b) the normalized anodic peak current vs. scan rate for the oxidation at a Pt disk electrode of 2.24 mM MBBA in ACN, 0.1M TBAP. v is in V/sec, E_p in V vs. sce; $i_{pa}/v^{1/2}$ in $\mu A \text{ sec}^{1/2}/V^{1/2}$.

A few experiments were performed in the SEESR cell (18) to determine the stability of the radical anion and the potentials where it is formed. For a constant-current pulse where the potential remained on the first voltammetric wave, the ESR signal showed a linear increase during the pulse, and a slow decay when the current was off. Constant-current steps where the potential reached those of the second wave showed a decrease of ESR signal at these potentials.

Discussion

The electrochemical and ESR results for the reduction provide evidence for initial formation of the anion radical of MBBA with a half-life in DMF of approximately 4 sec. The evidence suggests that the radical anion reacts in following ece and ec reactions. Similar behavior has been reported for the reduction of BA (9-12), where both protonation (in the ece pathway) leading to conversion of the $-HC=N-$ structure to $-CH_2-NH-$, and dimerization (in the ec pathway) occur. Andrieux and Saveant (9) and Kononenko *et al.* (11) concluded that both pathways were important and occurred simultaneously. Note that by labeling the protonation reaction as ece we only imply a reac-

Fig. 5. The ESR spectrum of the MBBA radical anion in DMF, 0.1M TBAI.



tion pathway leading to ultimate consumption of two electrons per molecule and do not reject other possible paths (e.g., disproportionation followed by protonation of the dianion) which may yield similar voltammetric and coulometric behavior.

The oxidation of MBBA in ACN parallels a previous study (13) and suggests that the oxidation product (perhaps the cation radical) is very unstable within the voltammetric time scale of these experiments.

Although these experiments were conducted in dilute solutions of MBBA in DMF and ACN rather than in pure MBBA, the results should have some relevance to dynamic scattering studies in MBBA. The measured potentials for reduction and oxidation here are probably somewhat smaller than those for the same processes in MBBA, since the polar solvents DMF and ACN probably solvate the MBBA ions more strongly than MBBA itself. Moreover, the fast reaction following the oxidation electron transfer reaction in ACN shifts the E_{pa} to values less positive than its reversible value. As a first approximation, however, we can take the "decomposition voltage" of MBBA as at least $E_{pa}(\text{ACN}) - E_{pc}(\text{DMF})$, or about 3.5V. The threshold voltage of dynamic scattering must be above this value and include the IR-drop through the MBBA liquid layer at currents (or ion flows) sufficient to induce turbulence. Although previous explanations of DS were given in terms of charge injection and Schottky emission of carriers (1), the current-voltage behavior was independent of the work functions of the metal used for the electrodes. Descriptions in terms of electrogeneration of radical ions and a cell current-voltage characteristic determined by the electrode kinetic equations (which bear a close resemblance to the Schottky emission equation) (19) and resistive drop in the liquid bear consideration. In a recent investigation (20), it was found that trace amounts of water are necessary in an anisylidene-p-aminophenylacetate (APAPA) LC device to promote conduction and DS; this was explained by a model in which water molecules assist the APAPA molecule in accepting an electron from the cathode. A more probable explanation in terms of our study is that ions from water (or hydrolysis products of APAPA) increase the conductivity of the LC material and improve the nature of the electrochemical cell. Doping of the LC with small amounts of different salts should serve the same purpose and decrease the possibility of attack of water molecules on the radical ions. Decomposition of the radical ions, particularly the radical cation, into products which decrease the purity and disrupt the alignment of the molecules in the nematic LC may also be of importance in limiting the life of LC display devices. Finally, although migration of the ions is probably the major mode of conduction through the liquid medium, direct electronic conduction by means of rapid electron exchange between radical ion and parent molecule is also a possibility,

especially in a solvent composed of pure parent molecules where the parent concentration is very high (21, 22). This conduction mode may be of less importance in this LC system, however, where the alignment of the molecules and structural considerations (i.e., the presence of the nonconjugated n-butyl group) decrease the rate of the intermolecular electron transfer reaction.

Acknowledgments

The support of this research by the National Science Foundation (GP-31414X) and the Robert A. Welch Foundation is gratefully acknowledged. We are indebted to Drs. Isaac Trachtenberg, Linda Creagh, and Allen R. Kmetz of Texas Instruments for helpful discussions concerning this research and for pure samples of MBBA.

Manuscript submitted June 12, 1972.

Any discussion of this paper will appear in a Discussion Section to be published in the June 1973 JOURNAL.

REFERENCES

- G. H. Heilmeyer, L. A. Zanoni, and L. A. Barton, *Proc. IEEE*, **56**, 1162 (1968).
- B. J. Lechner, F. J. Marlowe, E. O. Nester, and J. Tufts, *ibid.*, **59**, 1566 (1971).
- N. Felici, *Rev. Gen. Elec.*, **78**, 717 (1969).
- W. Helfrich, *J. Chem. Phys.*, **51**, 4092 (1969).
- P. A. Penz, *Mol. Cryst.*, **15**, 141 (1971).
- E. W. Aslaksen, *ibid.*, **15**, 121 (1971).
- H. Gruler and G. Meier, *ibid.*, **12**, 289 (1971).
- W. H. deJen and C. J. Gerritsma, *J. Chem. Phys.*, **56**, 4752 (1972).
- C. P. Andrieux and J. M. Saveant, *J. Electroanal. Chem.*, **33**, 453 (1971).
- P. Martinet, J. Simonet, and J. Tendil, *Compt. Rend. Acad. Sci. Paris*, **268**, 303 (1969).
- L. V. Kononenko, V. D. Bezuglyi, and V. N. Dmitrieva, *J. Gen. Chem. USSR*, **38**, 2087 (1968).
- J. M. W. Scott and W. H. Jura, *Can. J. Chem.*, **45**, 2375 (1967).
- P. Martinet, J. Simonet, and J. Tendil, *Compt. Rend. Acad. Sci. Paris*, **268**, 2329 (1969).
- L. R. Faulkner and A. J. Bard, *J. Am. Chem. Soc.*, **90**, 6284 (1968).
- L. S. Marcoux, A. Lomax, and A. J. Bard, *ibid.*, **92**, 243 (1970).
- R. S. Nicholson and I. Shain, *Anal. Chem.*, **36**, 706 (1964); *ibid.*, **37**, 178 (1965).
- M. Mastragostino, L. Nadjo, and J. M. Saveant, *Electrochim. Acta*, **13**, 721 (1968).
- I. B. Goldberg and A. J. Bard, *J. Phys. Chem.*, **75**, 3281 (1971).
- J. O'M. Bockris and A. K. N. Reddy, "Modern Electrochemistry," pp. 32, 942, Plenum Press, New York (1970).
- G. H. Heilmeyer, L. A. Zanoni, and L. A. Barton, *IEEE Trans. Electron Devices*, **ED-17**, 22 (1970).
- I. Ruff, *Electrochim. Acta*, **15**, 1059 (1970).
- H. Dahms, *J. Phys. Chem.*, **72**, 362 (1968).

Transient Mass Transfer at the Rotating Disk Electrode

Leonard Nanis*

Chemical Engineering, University of Pennsylvania, Philadelphia, Pennsylvania 19104

and Irving Klein

Carothers Research Laboratory, Experimental Station, E. I. du Pont de Nemours, Wilmington, Delaware 19800

ABSTRACT

Transient mass transfer at the rotating disk has been investigated theoretically and experimentally for cathodic reduction of ferricyanide in the redox system ferricyanide-ferrocyanide with potassium hydroxide supporting electrolyte. It has been shown that overpotential-time predictions for the rotating disk are fitted very well for decay (current interruption) but poorly for build-up following switching on of constant current. As an explanation for this behavior, attention is directed to the inadequacy of the assumption that a radially independent concentration profile exists at the disk surface just at the start of galvanostatic current passage.

Of great importance in the design of electrodes for practical electrolytic processes is knowledge of the current distribution. Predictive methods based on concepts of "throwing power" have been devised for several geometries and types of electrode reaction. These developments are all related to the steady state, *i.e.*, constant current density and overpotential. The question of current distribution during nonsteady electrode processes appears to be hitherto untouched theoretically. Transient electrode processes such as double layer charging, slow kinetic and diffusion steps are of course associated with electrode system impedance. Relatively little attention has been directed to the problem of current distribution during transient electrode response. However, it is essential to know the redistribution of current over an electrode surface during the unsteady portion of the electrode behavior in practical systems such as periodic reverse plating and pulsed battery charging sequences.

The method chosen for investigating the possible existence of nonuniform transient current distribution was the time varying behavior of overpotential for a cathodic redox reaction on a rotating disk electrode. This is of advantage since no change in the roughness of the surface occurs and because the hydrodynamics controlling convection transport are well known. The ferrocyanide-ferricyanide-potassium hydroxide system was selected since the exchange current density is known (1) to be sufficiently large so as to ensure purely diffusion-controlled kinetics and also because transport parameter data are well known (2). The study was based on comparison of overpotential relaxation following current steps of simple on or off switching. To this end, the decay problem was solved to provide a match for the well-studied build-up transient. Both build-up and decay were determined experimentally for comparison with theory.

Theoretical

Because of disk symmetry, the time-dependent convective diffusion equation based on the axial and radial directional coordinates (*cf.* Eq. [1]) theoretically describes mass transfer in the concentration boundary layer adjacent to a rotating disk

$$\frac{\partial C}{\partial t} + V_r \frac{\partial C}{\partial r} + V_z \frac{\partial C}{\partial z} = D \left[\frac{\partial^2 C}{\partial z^2} + \frac{\partial^2 C}{\partial r^2} + \frac{1}{r} \frac{\partial C}{\partial r} \right] \quad [1]$$

Previous theoretical developments (3, 9-11) for nonsteady mass transfer during galvanostatic overpotential build-up have all been based on the assumption that the disk acts as a uniformly accessible surface throughout the transient interval. On the basis of this assumption, all derivatives of the concentration with respect to the radial coordinate can be set equal to zero, resulting in the following simplified version of Eq. [1], *i.e.*

$$\frac{\partial C}{\partial t} + V_z \frac{\partial C}{\partial z} = D \frac{\partial^2 C}{\partial z^2} \quad [2]$$

It should be noted that Levich first introduced the concept of uniform accessibility in terms of a zero concentration of depleted species all along the disk at the maximum rate of steady-state mass transfer. This radially independent boundary condition facilitated the calculation of the steady-state concentration profile developed in the boundary layer (Eq. [2] with time derivative equal to zero). Thus, the concept of uniform accessibility during nonsteady mass transfer (implying a concentration which varies with time but not with radial position) is merely a convenient assumption used to simplify the mathematics.

If uniform accessibility is assumed for nonsteady mass transfer, the following dimensionless variables may be introduced

$$\psi = \frac{C - C_b}{C_{o,0} - C_b}, \quad \tau = \frac{Dt}{\delta_c^2}, \quad \xi = \frac{z}{\delta_c} \quad [3]$$

where δ_c is the steady-state concentration boundary layer thickness arbitrarily defined as the point at which 99% of the bulk conditions are achieved, C_b is the time independent bulk concentration, and $C_{o,0}$ is the concentration at the electrode surface at time zero. A model for V_z has been based on well-known rotating disk hydrodynamics (12) which approximates a parabolic axial velocity distribution in the concentration boundary layer corresponding to laminar flow in a solution of large Schmidt number. Thus

$$V_z = -0.51\omega^{3/2}\nu^{-1/2}Z^2 \quad [4]$$

Following the approach developed by Levich (13), δ_c is described as

$$\delta_c = 2.54D^{1/3}\nu^{1/6}\omega^{-1/2} \quad [5]$$

Substituting Eq. [3], [4], and [5] into Eq. [2] yield the dimensionless result

$$\frac{\partial \psi}{\partial \tau} - 8.361\xi^2 \frac{\partial \psi}{\partial \xi} - \frac{\partial^2 \psi}{\partial \xi^2} = 0 \quad [6]$$

* Electrochemical Society Active Member.
Key words: rotation disk, transient overpotential, mass transfer, current distribution, galvanostatic.

In order to theoretically predict mass transfer behavior occurring during overpotential build-up, Eq. [6] was numerically solved in conjunction with boundary conditions specifying a constant mass flux at $\xi = 0$ (Eq. [7]) and a constant bulk concentration at $\xi = 1$ (Eq. [8]) and in conjunction with an initial condition specifying a uniform concentration, C_b , throughout the boundary layer (Eq. [9]).

$$\frac{\partial \psi(0, \tau)}{\partial \xi} = 1.572 \quad [7]$$

$$\psi(1, \tau) = 0 \quad [8]$$

$$\psi(\xi, 0) = 0 \quad [9]$$

Mass transfer occurring during overpotential decay was theoretically solved using Eq. [6] together with boundary conditions specifying a zero flux at $\xi = 0$ (Eq. [10]) and a constant bulk concentration at $\xi = 1$ (Eq. [8]). The initial condition was obtained following the method of Levich (13), the concentration distribution in the boundary layer being expressed in terms of an incomplete gamma function (Eq. [11]).

$$\frac{\partial \psi(0, \tau)}{\partial \xi} = 0 \quad [10]$$

$$\psi(\xi, 0) = 1 - 1.572 \int_0^\xi e^{-2.759g^3} dg \quad [11]$$

where g represents a dummy variable of integration.

Build-up: Previous Solutions

The theory of unsteady-state processes on the rotating disk electrode has already received considerable attention. Levich (3) presented a solution to the non-steady convective diffusion equation (cf. Eq. [2]) in his treatment of transient mass transfer during galvanostatic overpotential build-up. His first order approximation for the concentration gradient in the convective term (based on a solution for diffusion-controlled mass transfer) however, severely restricts the time interval, i.e., $\tau < 0.15$, over which reasonable correlation between theory and experiment may be expected. Subsequently, theoretical problems related to nonstationary disk processes were solved using the hydrodynamics of the system only to specify a constant concentration boundary condition at $Z = \delta_c$, while neglecting the convective mass transfer term (4,8). Filinovskii (9) solved Eq. [2] using Laplace transforms and an appropriate change of variables to-

large number of terms are necessary in order to describe the concentration behavior.

Build-up and Decay: Present Solutions

Numerical solutions of Eq. [6], [7], [8], and [9] (build-up) and [6], [8], [10], and [11] (decay) were obtained using a machine computed relaxation technique modified as suggested by Allen (14) to allow for solution of parabolic partial differential equations. The grid spacing and the error criterion were systematically reduced until less than a 1% variation in successively calculated values for $\psi(0, \tau)$ was obtained. A square grid spacing of 0.02 and an error criterion of 0.001 produced the desired convergence and the computed values for $\psi(0, \tau)$ during build-up and decay are shown in Table I. The electrode-electrolyte interface concentration $\psi(0, \tau)$ has been compared with Hale's numerically computed results. Of all the build-up solutions available in the literature, Hale's values for $\psi(0, \tau)$ are the most comprehensive. Good agreement, i.e., within 3%, is shown compared with the present results throughout the transient interval, $\tau < 0.8$. It should be noted that the present treatment provides a spatial bound (Eq. [8]) not present in the Hale treatment based on the Crank-Nicholson finite difference procedure applied to Eq. [6], [7], and [9]. The agreement of $\psi(0, \tau)$ build-up obtained by the present relaxation technique provides a degree of certainty that a correct solution has been obtained using this technique for the new, yet mathematically analogous, problem of nonsteady mass transfer during overpotential decay (cf. Eq. [2], [8], [10], and [11]).

Relation of Concentration and Overpotential

Time-concentration behavior is only implicitly related to the directly measured overvoltage transient, so that the Nernst equation has been used to link the functional behavior of the predicted overpotential to the concentration at the electrode-electrolyte interface. Using concentrations in place of activities for a redox reaction at 25°C, $n = 1$, the Nernst equation gives for a net cathodic reaction overvoltage

$$\eta_c = 0.059 \log \frac{(C_{OX})_{0,\tau} (C_{RED})_b}{(C_{OX})_b (C_{RED})_{0,\tau}} \quad [12]$$

where OX and RED refer to the oxidized and reduced species, respectively. Substituting in Eq. [12] for $(C_j)_{0,\tau}$ in terms of $(\psi_j)_{0,\tau}$ (cf. Eq. [3]) and relating the galvanostatic current density to the steady-state concentration at the electrode surface yields

$$(\eta_c)_\tau = 0.059 \log \left[\frac{1 - (\psi_{OX})_{0,\tau} (J/J_{OX,lim})}{1 + (\psi_{RED})_{0,\tau} (J/J_{OX,lim}) (D_{OX}/D_{RED})^{2/3} (C_{OX})_b (C_{RED})_b^{-1}} \right] \quad [13]$$

gether with approximations to permit inversion. The approximations were based on consideration of a narrow region within the concentration boundary layer, immediately adjacent to the disk surface. Within this region a term proportional to the fourth power of the distance was omitted which reduced the problem to the canonical equation for Airy functions. As a result, Filinovskii's analytical solution does not correctly describe the mass transfer behavior occurring at relatively long dimensionless times, i.e., $\tau > 0.4$ of the transient interval. Hale (10) has used a Crank-Nicholson finite difference technique to numerically solve for the concentration distributions occurring during galvanostatic overpotential build-ups. His solution can be used to describe mass transfer behavior occurring throughout the transient interval.

Recently, Krylov (11) has developed an analytical technique for determining a complete solution to the problem in terms of a series of parabolic cylinder functions. The major drawback of his technique is that it becomes exceedingly cumbersome at long times since a

Equation [13] permits computation of concentration overvoltage, for both build-up and decay in terms of

Table I. Transient concentration

τ	Decay, $\psi(0, \tau)$	Build-up, $\psi(0, \tau)$	Build-up [Hale (10)] τ	$\psi(0, \tau)$
0	1.000	0.000	0	0.000
0.04	0.663	0.367	0.041	0.352
0.08	0.510	0.515	0.081	0.492
0.12	0.402	0.617	0.122	0.593
0.16	0.322	0.643	0.163	0.671
0.20	0.261	0.753	—	—
0.24	0.213	0.801	0.244	0.783
0.28	0.174	0.834	0.284	0.824
0.32	0.142	0.870	0.325	0.857
0.36	0.118	0.894	—	—
0.40	0.098	0.914	—	—
0.44	0.082	0.930	0.446	0.923
0.48	0.070	0.943	0.487	0.937
0.52	0.060	0.954	—	—
0.56	0.052	0.962	—	—
0.60	0.046	0.968	—	—
0.64	0.041	0.973	—	—
0.68	0.037	0.977	—	—
0.72	0.035	0.980	—	—
0.76	0.033	0.982	—	—
0.80	0.030	0.984	—	—

the theoretical time dependent dimensionless concentrations, $(\psi)_{0,\tau}$ (cf. Table I), the fraction of the limiting current passing through the system during the electrochemical reaction, J/J_{lim} , and the diffusion coefficients, D , and the bulk concentrations, C_b , of the redox species. The limiting current, J_{lim} , is related (Fick's first law) to the maximum mass flux at the electrode as

$$J_{\text{lim}} = -nFD \left. \frac{\partial C}{\partial Z} \right|_{\text{max}} = nFD \frac{C_b}{\delta_c} \quad [14]$$

Experimental

The disk consisted of a cylindrical nickel plug (0.5 in. \times 0.625 in. diam) imbedded in a 1.25 in. diam Teflon cylinder. The nickel disk was polished smooth using standard metallographic equipment so that projections greater than 1μ were eliminated. The Teflon cylinder was attached to a glass epoxy shaft which was rotated by a rubber belt driven by a variable speed Bodine $\frac{1}{8}$ hp d-c motor (Model NSH-54RL). A Minarik Electric Company control unit (Model SH 63W) was used to regulate the motor speed. Disk speeds were preferably selected by a series of gear trains enabling the motor to operate near its maximum speed rating, thereby eliminating major speed fluctuations. Disk speed fluctuations were usually less than 1% of set value.

The rotating disk was made the cathodic working electrode. An anodic counterelectrode consisting of a circular piece of nickel foil placed atop an adjustable Teflon platform served to complete the electrochemical cell. Its area was more than twenty times that of the disk, so that concentration overpotentials of the anode were small when compared with those occurring at the disk. Potential for an electrochemical reaction at the disk surface was provided by low voltage power supply (battery eliminator).

The electrolyte was equimolar (5×10^{-6} gmole/cm³) $\text{K}_3\text{Fe}(\text{CN})_6$ and $\text{K}_4\text{Fe}(\text{CN})_6$ in excess KOH (2×10^{-3} gmole/cm³). The supporting KOH electrolyte rendered negligible the contribution of migration to the over-all mass transport of the reacting species, and minimized the resistive (ohmic) potential drop in the cell. The potential of the working electrode was continuously measured with respect to a saturated calomel reference electrode connected to the electrolyte by means of a KCl salt bridge. The location of the bridge was found to have no influence on the measured potentials for the currents used, i.e., there was a negligible resistive potential included in the overpotential measurement. The disk-reference potential was monitored by a high impedance electrometer (Keithley 610B) whose output signal was fed into a Tektronix (Model 555) oscilloscope. A permanent record of the transient voltage was obtained with a Model C-12 Tektronix camera using Polaroid film (Type 47). Time-dependent cathodic build-up and decays were obtained for fractional current densities (J/J_{lim}) ranging from 0.225 and 0.995. The rotational Reynolds number was varied between 130 and 8500 so as to produce corresponding relaxation times of about 50-0.5 sec.

Results

Typical data for transient decays are shown in Fig. 1 and for build-ups in Fig. 2 where the solid lines represent theoretical prediction based on Eq. [13]. In a typical sequence at each rotational speed, the current fraction, J/J_{lim} , was chosen by adjusting the current until a desired steady-state overpotential, $(\eta_c)_{\infty}$, was obtained, based on Eq. [13] for $(\psi_{\text{OX}})_{0,\infty} = (\psi_{\text{RED}})_{0,\infty} = 1$. Data of Arvia (2) were used for the ratio of diffusion currents of the redox species.

The experimental overpotentials have been conveniently replotted as discrete points vs. log dimensionless time based on D_{OX} according to Eq. [3]. The correlation of the experimental data with theory as shown in Fig. 1 and 2 is typical of a general trend indicating that

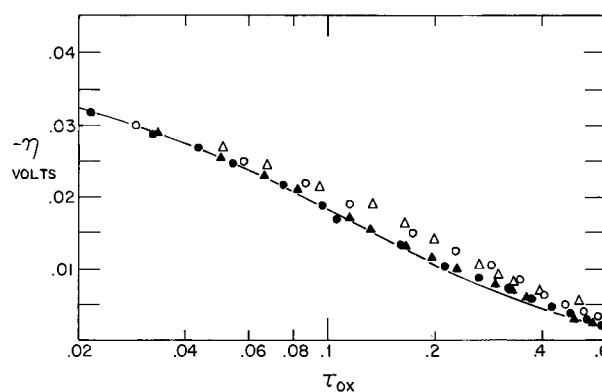


Fig. 1. Transient decay of overpotential; initial value 0.047V for $J = 0.715 J_{\text{lim}}$. Solution: 2M KOH, 0.005M $\text{K}_4\text{Fe}(\text{CN})_6$, 0.005M $\text{K}_3\text{Fe}(\text{CN})_6$. Symbols: ▲ 2.6 rad/sec, Re = 132; ● 8.4 rad/sec, Re = 429; △ 26 rad/sec, Re = 1320; ○ 45 rad/sec, Re = 2290.

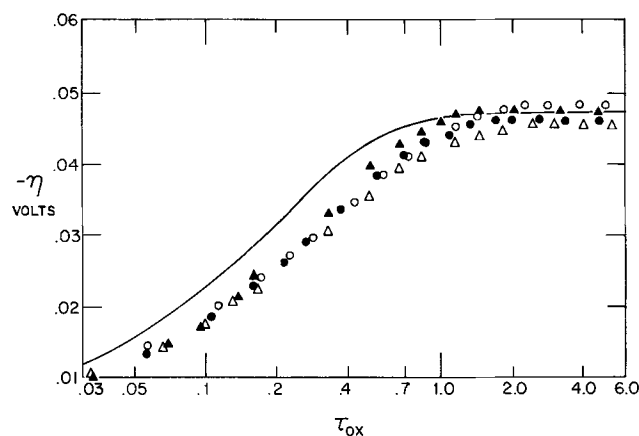


Fig. 2. Transient build-up of overpotential for $J = 0.715 J_{\text{lim}}$. Solution: 2M KOH, 0.005M $\text{K}_4\text{Fe}(\text{CN})_6$, 0.005M $\text{K}_3\text{Fe}(\text{CN})_6$. Symbols: ▲ 2.6 rad/sec, Re = 132; ● 8.4 rad/sec, Re = 429; △ 26 rad/sec, Re = 1320; ○ 45 rad/sec, Re = 2290.

transient overpotential decay data for a given solution, speed of rotation, and current density fraction exhibits better agreement with theory than overpotential build-ups obtained under the same conditions.

Discussion

The poor fit of the build-up data obtained for experimental hydrodynamic conditions essentially identical to those present during decay suggests that previous treatments have oversimplified the model necessary to describe overpotential build-ups. Since the present treatment also includes the assumption of constant concentration at the electrode-electrolyte interface, i.e., $\psi(0,\tau)$ independent of radial position, the discrepancy can be related to the theoretical interpretation of the boundary condition at the disk surface during the build-up period.

In order to utilize a one-dimensional model to describe mass transfer, a uniformly accessible surface has been assumed. In fact, however, at the start of the transient, the overpotential build-up has not had time to develop; therefore a nonuniform, i.e., primary, current distribution must be present at the electrode surface. When there is no overpotential on the electrode, the potential distribution in the electrolyte of course still satisfies the Laplace equation

$$\nabla^2\phi = 0 \quad [15]$$

The solution of Eq. [15] for disk geometry is well known (15) with the current density distribution given as

$$J/J_{\text{AVG}} = 0.5/\sqrt{1 - (r/a)^2} \quad [16]$$

The boundary condition at $\xi = 0$ is, therefore, more complicated than initially considered, and must be a function of the radial coordinate and time, *i.e.*, $\partial C/\partial Z = f(r,t)$. Using a general representation of Fick's first law, *cf.* Eq. [14], to relate this mass flux at the disk surface to the current density, together with the relation describing the primary current distribution initially present at the disk during build-up yields

$$\left. \frac{\partial C}{\partial Z} \right|_{z=0} = -0.5 J_{AVG}/nFD\sqrt{1 - (r/a)^2} \quad [17]$$

However, as steady-state conditions are approached ($\tau = \infty$), a uniform current distribution can be assumed for near limiting current densities, so that

$$\left. \frac{\partial C}{\partial Z} \right|_{z=0} = -J_{AVG}/nFD \quad [18]$$

A mathematical solution based on this time-varying boundary condition is difficult to obtain. However, the solution may be bounded for $\tau = 0$ and $\tau = \infty$. At long times, one may expect the development of a significant amount of overpotential at near limiting current densities so that a uniformly accessible surface is closely approximated (16) and Eq. [18] is an appropriate bounding condition. Indeed, it may be seen (*cf.* Fig. 2) that at $J/J_{lim} = 0.715$, a bounding constraint based on a uniformly accessible surface is a good approximation at long times, since the potential attains the value predicted from steady-state, radially independent considerations.

At short times, however, there is marked deviation from a theoretical model based on uniform accessibility and a bounding condition represented by Eq. [17] is appropriate.

For the inclusion of a radially dependent boundary condition, the two-dimensional Eq. [1] is an appropriate statement of the nonsteady convective diffusion equation. As a first approximation, mass transfer due to radial convection may be considered to be greater than mass transfer due to radial diffusion, so that Eq. [1] reduces to

$$\frac{\partial C}{\partial t} = D \frac{\partial^2 C}{\partial Z^2} - V_z \frac{\partial C}{\partial Z} - V_r \frac{\partial C}{\partial r} \quad [19]$$

For a substance depleted at a cathode, *i.e.*, ferri-cyanide, the rate of accumulation in the boundary layer must be negative, and $\partial C/\partial t$ in Eq. [19] is a negative quantity. The contribution of the term $-V_r \partial C/\partial r$ to the total rate of accumulation is always positive for a species undergoing cathodic reduction, because: (a) $\partial C/\partial r < 0$ throughout the boundary layer [current density at an electrode is always greater at the edges (*cf.* Eq. [15] for $\tau = 0$) than at the center forcing the concentration to be less at the edges], and (b) $V_r > 0$ throughout the boundary layer. Therefore, the surface concentration calculated on the basis of Eq. [19] must be greater (at any given time) than the surface concentration calculated when neglecting the radial term (*cf.* Eq. [2]), causing a slower attainment of steady-state conditions. Similarly, if a substance is built up at a cathode, *i.e.*, ferrocyanide, its rate of accumulation in the boundary layer is positive, $\partial C/\partial t$ is positive, and the contribution of the term $-V_r \partial C/\partial r$ is negative. The surface concentration calculated on the basis of Eq. [19] is less (at any given time) than the surface concentration calculated when neglecting the radial term, also contributing to slower attainment of steady-state conditions.

The good agreement of the decay data with a theory (*cf.* Fig. 1) which omits radial terms suggests that a uniformly accessible surface, *i.e.*, radial independence of surface concentration, does exist throughout the overpotential decay interval. This is to be expected since a significantly large amount of overvoltage is initially present during decay when $J/J_{lim} = 0.715$

essentially producing a radially independent surface concentration at $\tau = 0$. The subsequent decay behavior is not controlled by electrochemical reaction so that a radially independent concentration behavior continues to exist.

A quantitative basis for estimating the relative uniformity of current distribution at steady state may be simply obtained from the familiar throwing-power parameter. The relation of this dimensionless group to the ratio between interface and ohmic resistance has been discussed by Nanis and Kesselman (17). Uniform current density distribution is generally obtained when the dimensionless group in Eq. [20] is numerically greater than unity. Equation [13] may be used to obtain an estimate for $\partial\eta/\partial J$ at steady state by setting $\psi = 1$. Simplification is possible by considering $D_{OX} = D_{RED}$ and $C_{OX} = C_{RED}$. Thus, a criterion for uniform current density at 25°C is a large value of the quantity

$$\frac{\kappa}{a} \left| \frac{\partial\eta}{\partial J} \right| = 0.0513 \frac{\kappa}{aJ_L} \frac{1}{(1 - J/J_L)(1 + J/J_L)} \quad [20]$$

In general, Eq. [20] indicates that uniformity is enhanced by reducing disk size and increasing electrolyte conductivity. In addition, uniformity is seen to be promoted with small values of J_L . In turn, Eq. [14] and [5] may be used to indicate that the greatest control for diminishing the limiting current density is afforded by proportional decrease in the concentration and decrease in the square root of the rotational speed. The J/J_L factor in Eq. [20] strongly influences current uniformity. As J/J_L approaches unity, the denominator factor $(1 - J/J_L)$ goes to zero, causing a large increase in the throwing power parameter. For the conditions shown in Fig. 2, $Re = 2290$ (430 rpm) represents the least favorable current distribution situation, according to the above discussion. Using the limiting current density, 1.4 mA cm^{-2} , together with $\kappa = 0.375 \text{ ohm}^{-1} \text{ cm}^{-1}$, $a = 0.794 \text{ cm}$ and $J/J_L = 0.715$, Eq. [20] is equal to 35, thus assuring uniformity of current in the steady state. At very small current densities (J/J_L approaching zero), Eq. [20] becomes numerically equal to 17, more than satisfying the criterion for uniformity for $Re = 2290$. As discussed above, present results for slower speeds must therefore also be associated with steady-state uniformity of current. In equivalent terms, the boundary layer thickness is uniform at steady state in the present study.

In order to relate the poor fit of build-up data to theory in terms of the good fit for decay, it is helpful to consider the time behavior of this mass transport boundary layer. Initially, the depletion layer does not yet exist and commences growth with the initiation of current. According to the primary current distribution given in Eq. [16], a stable boundary layer thickness should be reached first at the edge of the disk, followed by radial spreading inward to the center. This behavior is not taken into account in the mathematical statement of Eq. [2] since radial terms have been omitted. Since, as indicated above, the steady-state boundary layer thickness was independent of radial position, *i.e.*, uniform current density prevailed, the assumption of radially independent initial condition (Eq. [11]) for decay was valid. Likewise, the radial terms are reasonably omitted from Eq. [1] applied to decay. It should be noted that the boundary condition given in Eq. [8] describes a model meant to approximate the actual behavior of the concentration profile at the outer edge of the boundary layer. During actual decay following current interruption, the thickness of the concentration depletion layer may increase but certainly will not become smaller, since this would correspond to increased stirring. Thus, the present solution (Table I) for the decay of concentration overpotential with time corresponds to a limiting bound of fastest possible decay. Finally, since transient current distribution is a most generally applicable concept, re-

newed attention should be directed to related technical implications in cyclic plating and pulse battery charging (macro and porous electrode size scales) as well as to the rotating disk electrode.

Summary

Experimental mass transport controlled overpotential decay data exhibit better correlation with a theory based on uniform accessibility at the rotating disk electrode than do overpotential build-up data. The discrepancy of the build-up data may be associated with nonuniform current distribution (nonuniform accessibility) present at the disk during the initial stages of build-up.

SYMBOLS

a	disk radius, cm
b	subscript, refers to a bulk condition
C	concentration, gmole/cm ³
D	diffusion coefficient, cm ² /sec
F	Faraday constant, coulombs/gmole (96,500)
J	current density, A/cm ²
n	number of electrons transferred per gram atom of reaction
OX	subscript, refers to oxidized species
r	radial direction, cm
RED	subscript, refers to reduced species
t	time, sec
V	velocity, cm/sec
Z	axial direction, cm
δ_c	concentration boundary layer, cm
η_c	concentration overpotential, volts
θ	angular position, radians
ν	kinematic viscosity, cm ² /sec
ξ	dimensionless distance
τ	dimensionless time
ϕ	Ohm's law type of potential drop in the electrolyte, volts
ψ	dimensionless concentration
ω	angular velocity, radians/sec
κ	electrolyte conductivity, ohm ⁻¹ cm ⁻¹

Acknowledgments

This work is based in part on a thesis submitted by one of the authors (I. K.) to the School of Chemical

Engineering, University of Pennsylvania in partial fulfillment of the requirements for the degree Doctor of Philosophy.

This work was performed for the Jet Propulsion Laboratory, California Institute of Technology, sponsored by the National Aeronautics and Space Administration under Contract NAS7-100.

Manuscript submitted Aug. 10, 1970; revised manuscript received June 20, 1972.

Any discussion of this paper will appear in a Discussion Section to be published in the June 1973 JOURNAL.

REFERENCES

1. C. R. Wilke, C. W. Tobias, and M. Eisenberg, *This Journal*, **101**, 306 (1954).
2. A. J. Arvia, S. L. Marchiano, and J. Podesta, *Electrochim. Acta*, **12**, 259 (1967).
3. V. G. Levich, *Acta Physicochim.*, **19**, 133 (1944).
4. R. P. Buck and E. H. Keller, *Anal. Chem.*, **35**, 400 (1963).
5. S. V. Gorbachev, *Zh. Fiz. Khim.*, **30**, 1487 (1956).
6. L. P. Kholpanov, *ibid.*, **36**, 1077 (1962).
7. G. Yu. Siver, *ibid.*, **33**, 2586 (1959).
8. G. Yu. Siver, *ibid.*, **34**, 577 (1960).
9. V. Yu. Filinovskii, *Dokl. Phys. Chem.*, **156**, 1412 (1964).
10. J. M. Hale, *J. Electroanal. Chem.*, **6**, 187 (1963).
11. V. S. Krylov, 20th C.I.T.C.E., Strasbourg, Sept. 1969, Sec. 1, Paper 35.
12. W. G. Cochran, *Proc. Cambridge Phil. Soc.*, **30**, 365 (1934).
13. V. G. Levich, *Zh. Fiz. Khim.*, **18**, 335 (1944).
14. D. N. de G. Allen, "Relaxation Methods," McGraw-Hill Book Co., New York (1954).
15. H. Weber, *Crelle Journal for Mathematics*, **75**, (1873) (also found in "A Treatise on Bessel Functions and Their Applications to Physics," 2nd edition, p. 142, A. Gray, G. B. Mathews, and T. M. MacRobert, Editors, MacMillan and Co., Ltd., London (1952)).
16. J. Newman, *This Journal*, **113**, 1236 (1966).
17. L. Nanis and W. Kesselman, *ibid.*, **118**, 1967 (1971).

Transient Behavior During Reactant Depletion in Porous Electrodes

Richard Alkire* and Barry Place**

Department of Chemical Engineering, University of Illinois, Urbana, Illinois 61801

ABSTRACT

Transient behavior of porous electrodes during reactant depletion is modeled by a one-dimensional pseudo steady-state calculation based on transport equations. Numerical results are presented for both constant current and constant potential electrolysis.

Withdrawal of energy from a battery is a batch process in which the chemical energy initially available as reactant species is converted into electrical energy upon discharge by electrochemical reaction. Porous electrodes are used in batteries in order to achieve a high reaction rate per unit volume. Since most reactants and/or products are usually incorporated in the solid electrode phase, the conduct of electrolysis will lead to changes in the composition and configuration of the electrode material itself. Although extensive fundamental studies have been conducted on porous

electrode systems of invariant structure (1, 2), rather few analyses have treated transient behavior during discharge of the electrode phase (3-5).

The following study provides an analysis of transient behavior during discharge owing to depletion of a limited quantity of solid reactant from favorable reaction regions within the porous electrode structure. The study represents a step toward the analysis of practical systems which are usually complex. In many electrochemical systems, the local reaction rate is highest on certain portions of the porous electrode surface. During operation, reactive material in these regions would be consumed and subsequent reaction would take place elsewhere within the porous electrode.

* Electrochemical Society Active Member.

** Electrochemical Society Student Associate.

Key words: porous electrode, transient behavior, mathematical model, reactant depletion.

Eventually reactants even in the inaccessible regions would be discharged by reaction. Determination both of the electrode regions which are most accessible and of the rate at which active material becomes depleted depends on the current distribution throughout the porous electrode.

The reactant depletion process involves a straightforward type of composition change in the solid phase in which a local region is either reactive or not depending on the quantity of reactant that is locally available. In actual battery systems, more complicated phenomena take place such as crystallization or precipitation of insoluble product salts on the reacting surface which can lead to gradual insulation of the surface and obstruction of the pore cross-section (6-8). The investigation of the somewhat pristine model which follows will provide a basic approach which may be extended toward the more complex systems once sufficient kinetic data become available.

Model Formulation

The theoretical model is based on consideration of a slab of porous electrode material of high conductivity, of uniform specific surface area, a , and of thickness, l . The porous electrode is contacted on one side ($y = 0$) by a metallic plate, and on the other ($y = l$) by the electrolytic solution which also fills the void volume within the electrode. The pores are sufficiently small that the potential and solute concentrations vary along the pores in essentially one dimension alone. There is no convection of electrolyte within the pores.

Prior to discharge, a limited quantity of solid reactant is uniformly dispersed throughout the interior surface of the porous electrode. During discharge, the distribution of solid reactant within the electrode is changed owing to electrolysis and is determined from Faraday's law

$$q(y,t) = q_0 - \int_0^t j(y,t) dt \quad [1]$$

(The notation is provided at the end of the text.) The current distribution, $j(y,t)$ varies in time during the discharge process and is to be calculated by application of transport laws to the movement of solute species within the porous electrode.

Under many practical circumstances, concentration gradients will become established during electrolysis. As reactive species become depleted, however, the concentration distributions within the porous electrode will vary. In order to take into account the effect of concentration variations during discharge, an approximate method of analysis has been chosen which avoids excessive investment in computation time. It is assumed that the concentration profiles adjust themselves rapidly to small changes in the reactivity distribution within the electrode. That is, a pseudo steady-state condition is said to prevail under which the concentration distributions change during depletion; but at any given moment the concentration distributions are at the steady state which corresponds to the reactivity conditions prevailing at that moment. During the initial moments of discharge, concentration gradients will achieve a steady state before depletion sets in if

$$\frac{alq_0i^*}{n^2F^2c_r^2D_r} > 1$$

The model may now be formulated from the one-dimensional pseudo steady-state conservation equation for each solute species

$$D_i \frac{d^2c_i}{dy^2} + \frac{z_i D_i F}{RT} \frac{d}{dy} \left(c_i \frac{d\phi}{dy} \right) = \frac{\nu_i \sigma a}{nF} j \quad [2]$$

The homogeneous species source term is related to the rate of the electrochemical reaction

$$\sum_i \nu_i M_i z_i = ne^- \quad [3]$$

through the reaction rate expression. The example calculations presented here are intended for comparison with experimental data on a system for which the Butler-Volmer form applies. Upon discharge, the solid reactant begets a soluble ion (species 3) so that the cathodic partial reaction is concentration dependent.

$$j = i_0 \left\{ e^{-\frac{\alpha n F}{RT} (\phi - \phi_e)} - \frac{c_3}{c_3^0} e^{-\frac{(\alpha - 1) n F}{RT} (\phi - \phi_e)} \right\} \quad [4]$$

In addition, electrical neutrality is assumed to prevail throughout the pore region

$$\sum_i z_i c_i = 0 \quad [5]$$

Two sets of boundary conditions have been chosen for study: galvanostatic discharge and potentiostatic discharge. In both cases, the boundary conditions at the metal backing plate ($y = 0$) are the same since no current passes through the rear plane

$$\frac{d\phi}{dy} = \frac{dc_i}{dy} = 0 \quad [6]$$

At the boundary which faces the electrolyte solution, the solute concentrations are equal to their values in the bulk of the electrolyte

$$c_i(l,t) = c_i^0 \quad [7]$$

Under potentiostatic discharge, the potential in the solution at the pore entrance is maintained at a constant value

$$\phi(l,t) = \phi^0 \quad [8]$$

Under galvanostatic discharge, however, the flux of product ions (species 3) released during discharge is constant

$$D_3 \frac{dc_3}{dy} + \frac{z_3 D_3 F c_3}{RT} \frac{d\phi}{dy} = \frac{i_0}{z_3 F} \quad [9]$$

In order to render the mathematical model more compact, the variables may be written in dimensionless form

$$\begin{aligned} Y &= \frac{y}{l} & C_i &= \frac{c_i}{c_r} \\ \Phi &= \frac{F}{RT} (\phi - \phi_e) & J &= \frac{al^2 j}{nF c_r D_r} \\ Q &= \frac{q}{q_0} & \tau &= \frac{nF c_r D_r t}{al^2 q_0} \end{aligned}$$

The equations become

$$\frac{d^2 C_i}{dY^2} + z_i \frac{d}{dY} \left(C_i \frac{d\Phi}{dY} \right) = \frac{\sigma \nu_i l^2}{\pi_i} \left\{ e^{-\alpha n \Phi} - \frac{C_i}{\gamma_i} e^{-(\alpha - 1) n \Phi} \right\} \quad [10]$$

$$\sum_i z_i C_i = 0 \quad [11]$$

$$Q = 1 - \int_0^\tau J d\tau \quad [12]$$

For constant potential discharge the boundary conditions are

$$\begin{aligned} \frac{dC_i}{dY} = \frac{d\Phi}{dY} &= 0 \text{ at } Y = 0 \\ C_i &= C_i^0 \text{ at } Y = 1 \\ \Phi &= \Phi^0 \text{ at } Y = 1 \end{aligned} \quad [13]$$

For constant current discharge the boundary conditions are

$$\begin{aligned} \frac{dC_i}{dY} = \frac{d\phi}{dY} = 0 \text{ at } Y = 0 \\ C_i = C_i^0 \text{ at } Y = 1 \quad [14] \\ \frac{dC_3}{dY} + z_3 C_3 \frac{d\phi}{dY} = -\frac{n\beta}{z_3 \pi_3} \text{ at } Y = 1 \end{aligned}$$

The dimensionless parameters which arise in the foregoing development are

$$\begin{aligned} \xi &= \frac{i_0 a l^2}{n F c_r D_r} \\ \gamma_i &= \frac{c_i^0}{c_r} \\ \beta &= \frac{i^* l^2}{n F c_r D_r} \\ \pi_i &= \frac{D_i}{D_r} \end{aligned}$$

Method of Calculation

The calculation of transient behavior during discharge was carried out in a stepwise manner. At each time step, the electroneutrality and conservation equations, [10] and [11] were solved by using finite difference techniques. The electrode region was divided into segments of equal size and linearized forms of Eq. [10] and [11] were written for each segment; the coupled tridiagonal matrices thus obtained were inverted by a computer-implemented method (9). Calculation of discharge behavior was started by solving the electroneutrality and conservation equations, as described above, to obtain the steady-state current distribution under the condition of uniform reactivity throughout the electrode. The steady-state distribution was assumed to prevail throughout the first moments of electrolysis until sufficient charge passed to deplete reactants from the electrode segment where the reaction rate was highest. A new current distribution was then determined for which the electrode was reactive throughout except for the one exhausted segment. With the revised current distribution, the time necessary for depletion of the second electrode segment was determined. In a like manner, the time needed for depletion of each successive portion of the electrode was computed with use of the prevailing steady-state current distribution.

The numerical results presented below were found not to change appreciably below electrode segments of width 0.005. Calculations were conducted on an IBM 360 computer with FORTRAN IV programming compiled in FORTRAN G language.

Results and Discussion

The calculations reported below are intended for comparison with data from experiments on copper-coated porous stainless steel electrodes. Upon dissolution in acid sulfate electrolyte, the copper will dissolve to form the soluble cupric ion; local depletion of copper will be followed by passivation of the stainless steel substrate. The physical properties of the acid copper sulfate system, given in Table I, have therefore been chosen in order to conduct calculations.

Prior to any depletion whatsoever, the steady-state current distribution for a given current or potential

depends on the value of the dimensionless parameter ξ as indicated in the lower portion of Fig. 1. For large values of ξ , the electrode reaction is relatively reversible and takes place mainly near the electrolyte side of the porous electrode. For sluggish reactions in thin electrodes (small ξ), charge transfer overpotential near the pore entrance region forces current to penetrate into the porous electrode so that for a given applied potential the reaction is more uniformly distributed at the expense of a lower total current. The concentration distributions within the porous electrode are also affected by the value of ξ as indicated in the upper portion of Fig. 1. For large values of ξ , the current is large so that significant concentration differences arise between the bulk and the "pore" solutions in order to transport reaction products out of the pores. For small values of ξ , smaller concentration differences are encountered. For a given applied potential, the concentration gradient at the pore entrance increases with ξ since the total current increases.

Constant Potential Discharge

Transient behavior during battery depletion depends on whether discharge proceeds under conditions of constant potential or of constant current. The constant potential conditions, specified by the boundary conditions of Eq. [13]), are reported first. All calculations are reported for a dimensionless depletion potential of $\phi^0 = -1.0$. Figure 2 indicates how the total current varies during discharge for various values of ξ . It may be seen that the time required for depletion of the first segment of the electrode depends on the uniformity of the current distribution, that is, on ξ . For large values of ξ , the current is large but drops off rapidly since the forward portions of the electrode are rapidly depleted owing to the highly nonuniform current distribution. For small values of ξ , a much lower current is withdrawn from the device owing to charge-transfer overpotential, but the current distribution is more uniform with the result that a uniform current may be withdrawn for longer periods of time.

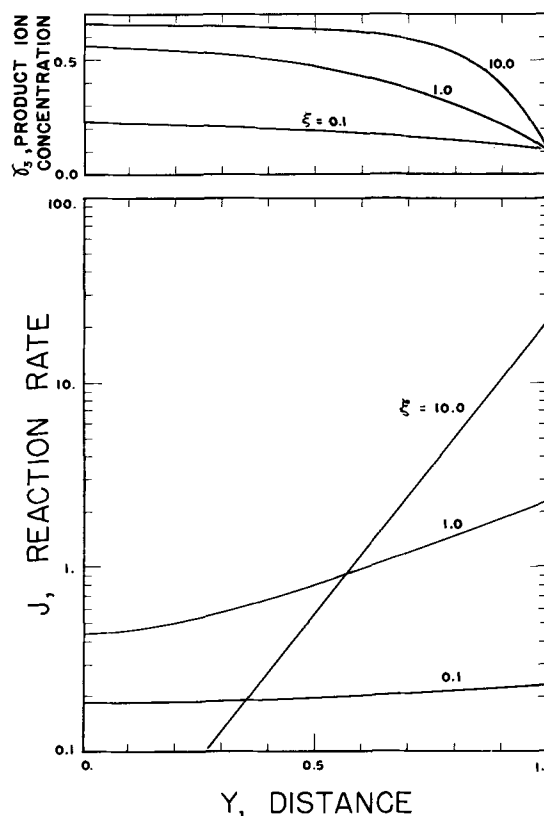


Fig. 1. Steady-state current and concentration distributions in porous electrode prior to reactant depletion for $\phi^0 = -1.0$.

Table I. Physical properties of the acid copper sulfate system chosen for calculations

Species	z_i	γ_i	π_i	ν_i
H ⁺	+1	2.00	9.312	0
SO ₄ ²⁻	-2	1.10	1.065	0
Cu ²⁺	+2	0.10	0.7188	-1

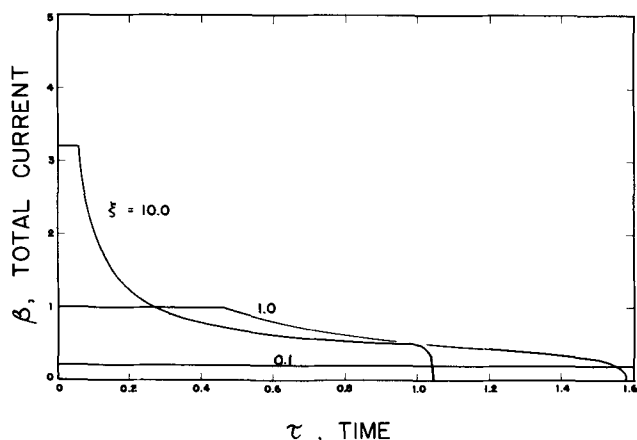


Fig. 2. Current variation during depletion in porous copper electrode for a constant applied potential of $\Phi^0 = -1.0$.

Figure 3 provides the coulombic state of charge distribution during constant potential depletion for $\xi = 1.0$. At the onset of electrolysis, the coulombic distribution (of copper) is uniform throughout the porous electrode. For the example shown here, the reactant nearest the electrolyte side of the porous electrode becomes completely consumed at a dimensionless time of $\tau = 0.432$. Subsequent consumption proceeds in the interior regions; the variation of total current during the depletion process has already been presented in Fig. 2.

During the depletion process depicted by Fig. 3, the current and concentration distributions vary as shown in Fig. 4. From the upper portion it is seen that concentration gradients become established but that they decrease during the course of depletion; the mass transfer driving force decreases as the current drops off during depletion. The lower portion of Fig. 4 shows the current distributions within the electrode at various times during depletion. The dashed line in the lower portion gives the local reaction rate at the "leading edge" of the reaction zone, J_f , as it recedes within the electrode during depletion. It may be seen that J_f is initially large and that it decreases during initial stages of depletion. The dashed line in the upper portion of Fig. 4 gives the cupric ion concentration at the leading edge of the reaction zone as depletion sets in; it is seen that during initial moments of depletion the concentration at the leading edge increases in order to provide a greater diffusion driving force for removal of product ions. When depletion first sets in, a portion of the applied (constant) potential is consumed by concentration overpotential so that the potential available for reaction decreases. However, the concentration overpotential cannot increase indefinitely, since the total quantity of product species retained within the pores is decreasing during depletion. Eventually, the

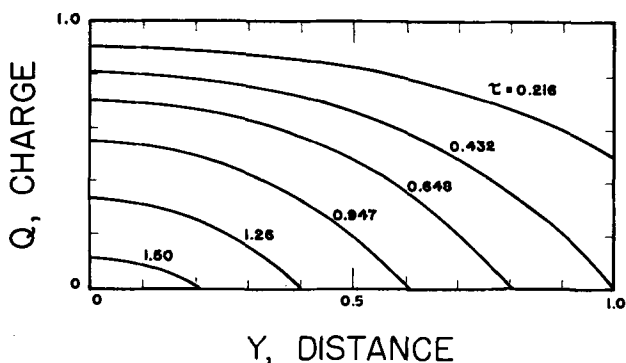


Fig. 3. Coulombic state of charge distribution during anodic depletion of copper from a porous electrode at constant potential, $\Phi^0 = -1.0$ and $\xi = 1$.

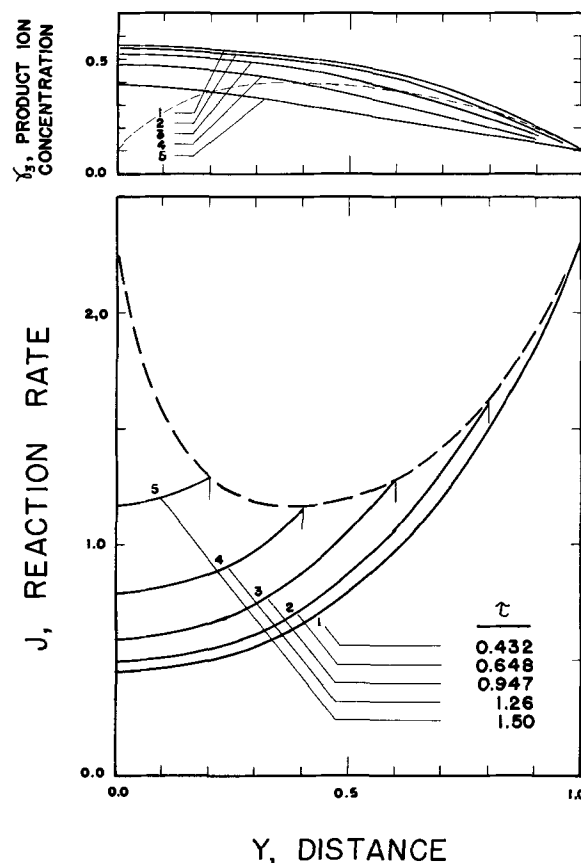


Fig. 4. Current and concentration distributions during potentiostatic anodic depletion of copper from a porous electrode, $\Phi^0 = -1.0$ and $\xi = 1$.

concentration at the leading edge of the reaction zone attains a maximum value and subsequently decreases. Similarly, the potential at the leading edge attains a minimum value and subsequently increases. Thus J_f attains a minimum value during depletion. During the initial moments of depletion, the decrease in current is due primarily to the appearance of a diffusion resistance associated with the unreactive zone of the electrode. During latter stages of depletion, the decrease in current is due to the reduced surface area available for electrolysis in the active region which remains. The current distribution becomes more uniform during depletion because the electrode can produce more product species than the depleted (diffusion) zone can disperse.

Constant Current Discharge

When current is applied to the electrode at a constant rate, the electrode overpotential will increase during depletion with the result that the useful cell voltage decreases. The constant current calculations reported below for the acidified copper sulfate system were carried out for $\beta = 1$. Figure 5 illustrates the variation of potential at the electrolyte side of the porous electrode during depletion. For small values of ξ , the beginning charge-transfer overpotential is large and the useful cell potential is small, but the current distribution is uniform so that the potential plateau is long. During constant current operation, the solute concentration increases within the electrode since an ever larger driving force is needed for removal of product species through the discharged zone.

The current distributions during constant current depletion are shown at various stages of discharge in Fig. 6. Since

$$\beta = \int_0^1 J dY = \text{constant}$$

the area under each distribution curve is the same.

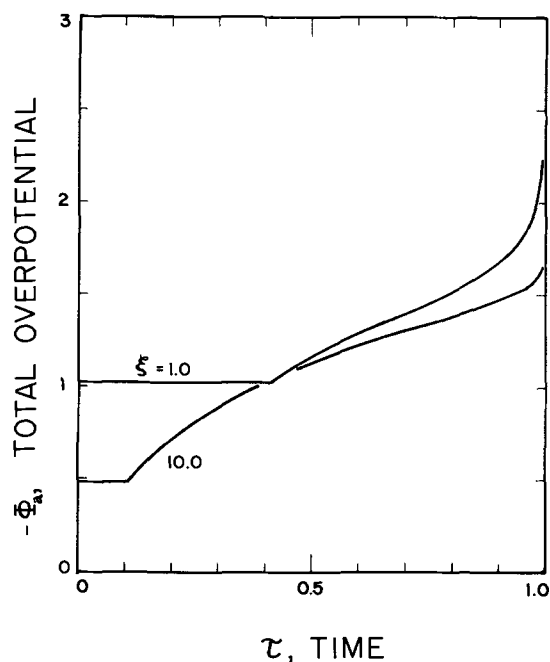


Fig. 5. Overpotential variation during constant current anodic depletion of copper from a porous electrode at $\beta = 1$.

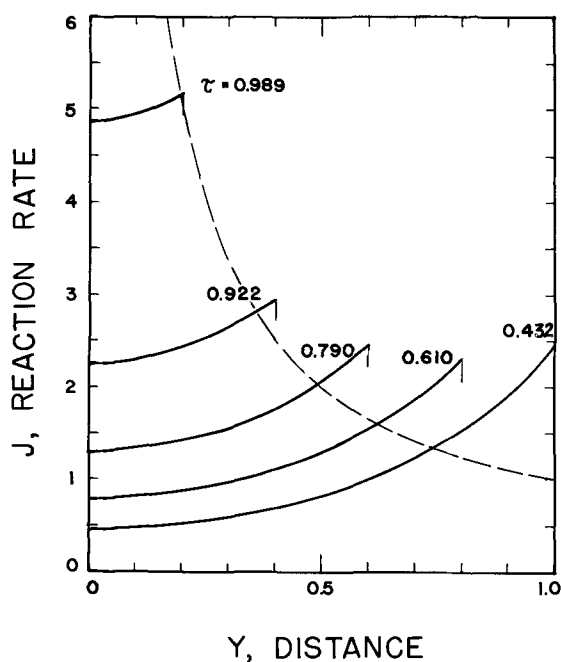


Fig. 6. Current and concentration distributions during anodic depletion of copper from a porous electrode at constant current, $\beta = 1$ and $\xi = 1$.

The dashed line corresponds to the reaction rate at the leading edge which would be observed if the current distribution were uniform throughout depletion. It may be seen that the current distribution over the active zone becomes always more uniform as depletion proceeds.

Concluding Remarks

The calculations presented here, although limited in scope, demonstrate that a simple conceptual model can serve as a basis for approaching transient phenomena in porous electrode systems. The results are capable of verification by somewhat simple experiments which avoid the complicated phenomena which occur in most secondary battery systems. An especially interesting interplay occurs during constant potential

depletion in which the reactivity of the leading edge of the reactive zone passes through a minimum.

The model examined above has some features in common with the treatment of Dunning *et al.* (5), which ascribes transient behavior to mass transfer limitations between crystallites of sparingly soluble reactants. In contradistinction, the present model centers attention on variation of surface reactivity during operation.

The analysis of more complex systems can be accomplished by a straightforward extension of the foregoing pristine model. The pseudo steady-state assumption, although economical, is not necessary and could be discarded in favor of more rigorous unsteady-state calculation methods. Chemical interaction between solute species within the porous electrode may be accounted for easily by superposition of equilibrium-constant constraints on the equation network. Multiple electrode reactions, such as occur during gassing, could be incorporated into the present model without additional complication. Different forms of reaction rate expressions could also be employed were they available; in particular, a rate expression which reflected gradual insulation and blocking of the surface during discharge could be used for examining the role of insoluble products and/or reactant species upon behavior during cycling of secondary battery systems.

Acknowledgment

This work received financial support from the National Science Foundation through Research Initiation Grant GK-5589 and through the NSF Traineeship Program. The programming assistance of Mr. Donald W. Godard is gratefully acknowledged.

Manuscript submitted March 6, 1972; revised manuscript received July 10, 1972.

Any discussion of this paper will appear in a Discussion Section to be published in the June 1973 JOURNAL.

SYMBOLS

a	specific surface area, cm^2/cm^3 void
c_i	concentration of species i , $\text{g-mole}/\text{cm}^3$
C_i	concentration of species i , c_i/c_r , dimensionless
c_r	reference concentration, $\text{g-mole}/\text{cm}^3$
D_i	diffusion coefficient of species, i , cm^2/sec
D_r	reference diffusion coefficient, cm^2/sec
F	Faraday's constant, $96,500$ coulomb/g-eq
i_0	exchange current density at bulk concentration, A/cm^2
i^*	current density in the solution at $y = l$, A/cm^2
j	local reaction rate along electrode surface, A/cm^2
J	local reaction rate, ajl^2/nFc_rD_r , dimensionless
l	thickness of electrode, cm
M_i	chemical symbol for species i
n	number of electrons taking part in electrode reaction, $\text{g-eq}/\text{g-mole}$
q	quantity of reactant available locally within electrode, $\text{coulomb}/\text{cm}^2$ of electrode surface
q_0	quantity of reactant initially available, $\text{coulomb}/\text{cm}^2$
Q	quantity of reactant available, q/q_0 , dimensionless
R	gas constant, 8.31 joules/g-mole $^\circ\text{K}$
t	time, sec
T	temperature, $^\circ\text{K}$
y	spatial variable along porous electrode, cm
Y	spatial variable, y/l , dimensionless
z_i	charge number of species i

Greek Characters

α	transfer coefficient in reaction rate equation
β	current density in the solution at $Y = 1$, i^*/nFc_rD_r , dimensionless
γ_i	bulk concentration of species i , c_i/c_r , dimensionless
ν_i	stoichiometric coefficient of over-all reaction for species i
ξ	ratio of diffusion resistance to charge transfer resistance, i_0al^2/nFc_rD_r , dimensionless
π_i	diffusion coefficient of species i , D_i/D_r , dimensionless

σ reactivity coefficient for reactant (1 if reactive, 0 if depleted)
 τ time, $nF_c D r t / a l^2 q_0$, dimensionless
 ϕ potential in the solution, V
 ϕ_e potential in the solution at equilibrium, V
 Φ potential in the solution, $F(\phi - \phi_e)/RT$, dimensionless
 Φ^0 applied potential, $F(\phi^0 - \phi_e)/RT$, dimensionless

2. L. Austin and E. Gagnon, *Am. Inst. Chem. Engrs. J.* **17**, 1057 (1971).
3. A. Winsel, *Z. Elektrochem.*, **66**, 287 (1962).
4. R. Alkire, E. Grens, and C. Tobias, *This Journal*, **116**, 1328 (1969).
5. J. Dunning, D. Bennion, and J. Newman, *ibid.*, **118**, 1251 (1971).
6. P. Bro and H. Y. Kang, *ibid.*, **118**, 519 (1971).
7. E. Gagnon and L. Austin, *ibid.*, **118**, 497 (1971).
8. D. Simonsson, Session 4:1, Kem-Tek 2 Congress, Copenhagen, Denmark, Nov. 2-4, 1971.
9. J. Newman, *Ind. Eng. Chem. Fundamentals*, **7**, 514 (1968).

REFERENCES

1. R. de Levie, *Advan. Electrochem. Electrochem. Eng.*, **6**, 329 (1967).

Technical Note



Synergistic Effects of Anions in the Corrosion of Aluminum Alloys

A. A. Adams,* K. E. Eagle, and R. T. Foley*

Department of Chemistry, The American University, Washington, D. C. 20016

In a preliminary note (1) it was reported that in specific electrolyte mixtures, *i.e.*, specific concentrations and specific NaCl-NaNO₃ ratios, the corrosion of aluminum alloys Type 7075 and 2024 was increased by an order of magnitude over that in NaCl solutions of the same concentration. This was unexpected as it was known that NaNO₃ inhibits the corrosion of aluminum alloys and, although it was recognized that a lower critical amount was required to achieve passivation (2), no accelerating effect had been reported. We have studied this phenomenon in more detail with chloride-nitrate mixtures of other cations. We have also conducted supporting experiments with the objective of throwing light on the mechanism by which these electrolyte mixtures accelerate the corrosion of aluminum alloys.

Experimental

The experimental procedure was similar to that reported previously (1). Three aluminum alloys, Types 1199-H14, 2024-T3, and 7075-T6, in sheet form were used. The specimens were prepared by standard methods and, following corrosion, were stripped of corrosion products, also by standard procedures. Corrosion products and corroded surfaces were examined by x-ray diffraction and x-ray fluorescence techniques. Metallographic cross sections of selected specimens were examined microscopically. The pH's of the solutions in which the samples were corroded were measured before and after sample exposure. Because it was very pertinent to follow the fate of the NO₃⁻ ion during the course of the reaction the solutions were qualitatively analyzed for nitrite ion and ammonia, reduction products of nitrate. The benzidine test (3) was used for nitrite detection and the p-nitrobenzene diazonium test (4) for ammonia.

Results and Discussion

Some selected but representative data obtained with alloy Type 2024 are given in Table I. Some general observations can be made with respect to data not

shown. The first has to do with the dependence on alloy composition. There was no evidence of accelerated corrosion of alloy 1199 with any electrolyte mixture. The behavior of alloys Type 2024 and 7075 were similar semiquantitatively. The second observation has to do with solutions containing NO₃⁻ without Cl⁻. The corrosion was low in every case so these figures are not tabulated here.

The results in Table I for the sodium-salt mixtures, wherein corrosion is enhanced by a factor of 8-9, is consistent with previously reported results and those obtained with alloy Type 7075 in which case there is a tenfold increase in corrosion in a 0.01N NaCl-0.007N NaNO₃ solution compared to that in a 0.01N NaCl solution. In the earlier work mixtures of potassium and lithium salts in this same concentration range were examined but no synergistic mixture was disclosed. However, when the concentration range was extended and other ratios were studied it was found that there existed for these two systems a specific mixture in which corrosion was accelerated. These mixtures are shown in Table I; the same mixture applies to alloy Type 7075. For the potassium-salt solutions a mixture

Table I. Immersion tests with alloy 2024 in potassium, lithium, and sodium solutions

Solution	Duration (days)	Wt. loss (average) mg/cm ²
0.1N KCl	13	0.83
0.1N KCl/0.005N KNO ₃	13	11.94
0.1N KCl/0.01N KNO ₃	13	10.49
0.1N KCl/0.01N KNO ₃	13	0.64
0.1N KCl/0.05N KNO ₃	13	1.14
0.1N LiCl	18	0.22
0.1N LiCl/0.005N LiNO ₃	18	0.55
0.1N LiCl/0.01N LiNO ₃	18	1.03
0.1N LiCl/0.02N LiNO ₃	18	0.48
0.1N LiCl/0.05N LiNO ₃	18	0.23
0.1N LiCl/0.1N LiNO ₃	18	0.13
0.01N NaCl	14	1.03
0.01N NaCl/0.003N NaNO ₃	14	3.72
0.01N NaCl/0.005N NaNO ₃	14	7.98
0.01N NaCl/0.007N NaNO ₃	14	8.72
0.01N NaCl/0.01N NaNO ₃	14	8.44
0.01N NaCl/0.05N NaNO ₃	14	0.13

* Electrochemical Society Active Member.

Key words: aluminum alloy 7075, aluminum alloy 2024, accelerated corrosion, pitting, complexions.

of 0.1N KCl and 0.005N KNO₃ yields a fourteenfold increase in rate while for the lithium-salt solutions a mixture of 0.1N LiCl and 0.01N LiNO₃ gives about a fivefold increase in rate. It is possible that there are other synergistic mixtures, but it is apparent that for each of the alkali metals there is at least one specific mixture which accelerates corrosion, usually by an order of magnitude. With the sodium-salt system the concentration as well as the ratio appear to be specific. There was no accelerated corrosion when the same ratio was used at other concentrations. Furthermore, when electrolyte mixtures outside the alkali metal group were investigated, it was observed that synergistic mixtures with Al⁺⁺⁺, Be⁺⁺, and NH₄⁺ also exist. In certain ammonium-salt solutions corrosion reaches a catastrophic stage during 1-2 week exposures. Specifically, in mixtures of 1.0N NH₄Cl-0.5N NH₄NO₃ and 1.0N NH₄Cl-0.2N NH₄NO₃, the corrosion rate is enhanced by a factor of 100 and 600, respectively, over a 14 day period.

The corrosion in the alkali-salt solutions starts with many small pits scattered over the surface. The attack spreads rapidly, covering the entire surface and producing a thick layer of corrosion product. In the ammonium-salt solutions the attack appears to be concentrated at fewer, deeper pits which leads to the complete penetration of a 0.8 mm strip in 14 days. Where attack commences at an edge, the strip is exfoliated in several days (Fig. 1).

The kinetics of the reaction of alloy Type 2024 in 0.01N NaCl-0.005N NaNO₃ and 0.1N KCl-0.005N KNO₃



Fig. 1. Cross section of aluminum alloy Type 2024-T3 coupon corroded in 1.0N NH₄Cl-0.2N NH₄NO₃ solution. Magnification, 52X. Duration of test, 14 days. Dark bands are fissures in the metal. Located within fissures are white and blue colored precipitates.

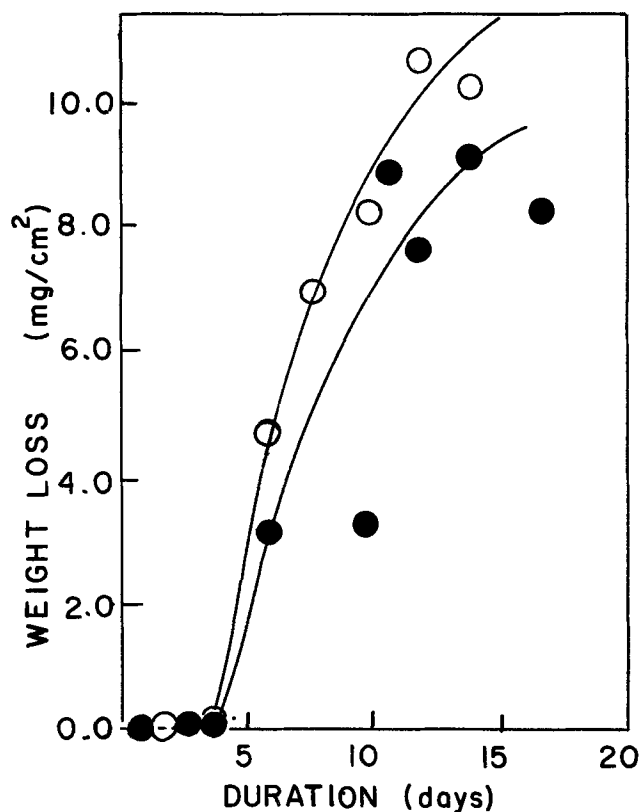


Fig. 2. Reaction of aluminum alloy Type 2024-T3 with synergistic mixtures. ○ = corrosion in 0.01N NaCl-0.005N NaNO₃ solution; ● = corrosion in 0.1N KCl-0.005N KNO₃ solution.

is shown in Fig. 2. The incubation period is characteristic of sodium and potassium salt solutions but not for ammonium in which corrosion commences during the first day.

In addition to the corrosion data there are other observations that are useful in developing a mechanism to explain how these synergistic solutions accelerate corrosion.

The test for nitrite ion was negative in the K⁺, Na⁺, and NH₄⁺ synergistic mixtures before immersion of the coupons. After one day the test was positive and persisted for the duration of the experiment.

The test for ammonia in the K⁺ and Na⁺ synergistic solutions was negative at the start and remained negative during the incubation period (Fig. 2). The test became positive coincident with the increase in reaction rate.

The pH's of the solutions of the alkali-metal salts rose during the reaction proportional to the weight loss. For the synergistic mixture the rise was about 5 pH units, e.g., from 5.73 to 10.78. For the ammonium solutions the increase was less, usually about 2 units, e.g., from 5.18 to 7.52, never exceeding 8.

X-ray diffraction examination indicated that the main corrosion product from NaCl solutions and from NaCl-NaNO₃ synergistic mixtures was the same, γ -Al₂O₃ · 3H₂O.

X-ray fluorescence measurements on samples corroded in synergistic solutions and stripped in the chromic-phosphoric acid stripping solution showed a depletion of alloying element, Cu or Zn, on the metal surface. Specimens corroded in a similar fashion but with the main corrosion layers scraped from the surface indicated an enrichment of the alloying element at the surface. In the case of alloy Type 2024 this consisted of what appeared to be a layer of Cu stratified between the metal and the corrosion scale.

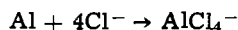
It is obvious from the foregoing that a number of reactions are taking place simultaneously, and the cor-

rosion reaction must be a multistep process. However, the following sequence of steps may be postulated.

The first step, preceding any electrochemical or chemical step, is the adsorption of Cl^- , NO_3^- , H_2O , and O_2 at the oxide-solution interface. This process and the effect of specific anions on the properties of the oxide film related to subsequent transport processes has been described by Pryor (5). Following adsorption, reactions take place affecting either the anodic or cathodic process.

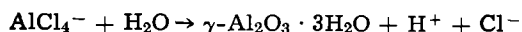
Anodic Reactions

(i) Initiation of pitting by Cl^- .



The evidence for this step has been given by Bogar and Foley (6) and takes place with all three alloys.

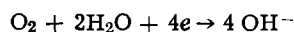
(ii) Hydrolysis of aluminum chloride complex.



The main product is the hydrated oxide observed here by x-ray diffraction. At points of local acidity protons can be reduced to H_2 .

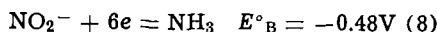
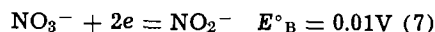
Cathodic Reactions

(iii) Reduction of O_2 .



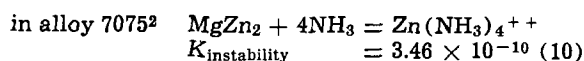
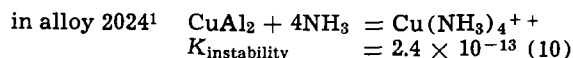
During active corrosion the pH of the solution will rise as indicated above.

(iv) Reduction of NO_3^- , when available, simultaneous with (iii).



Nitrite is produced at the start of the reaction. Ammonia is produced after the incubation period.

(v) Chemical reactions between NH_3 and intermetallic compounds (9).

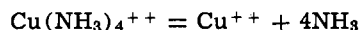


¹ Nominal Cu content = 4.4%.

² Nominal composition = 5.6% Zn, 2.5% Mg, 1.6% Cu.

Both complexes are very soluble and will accelerate the attack.

(vi) Dissociation of soluble complexes in sites of high alkalinity.



This leads to deposition of either Cu° or CuO as a red layer at metal-oxide interface as indicated by x-ray fluorescence. Alloy Type 1199 is immune to this type of accelerated attack because it contains neither Cu nor Zn as alloying elements.

The existence of specific concentrations and anion ratios in solutions with different cations is difficult to explain. However, it appears reasonable that the cations of different polarizability will be adsorbed in the electric double layer to different degrees and influence the composition of the oxide-solution interface. This in turn would influence the relative adsorption of Cl^- , NO_3^- , H_2O , or O_2 .

Acknowledgment

This research was supported by the Advanced Research Projects Agency of the Department of Defense, ARPA Order No. 878, under Contract No. N00014-68-A-0245.

Manuscript submitted Nov. 22, 1971; revised manuscript received July 10, 1972.

Any discussion of this paper will appear in a Discussion Section to be published in the June 1973 JOURNAL.

REFERENCES

1. A. M. McKissick, Jr., A. A. Adams, and R. T. Foley, *This Journal*, **117**, 1459 (1970).
2. L. H. Callendar, *Engineering*, **120**, 340 (1925).
3. F. Feigl, "Spot Tests in Inorganic Analysis," p. 332, Elsevier Publishing Co., Amsterdam (1958).
4. F. Feigl, "Spot Tests in Inorganic Analysis," p. 236, Elsevier Publishing Co., Amsterdam (1958).
5. M. J. Pryor, *Z. Elektrochem.*, **62**, 782 (1958).
6. F. D. Bogar and R. T. Foley, *This Journal*, **119**, 462 (1972).
7. W. M. Latimer, "Oxidation Potentials," p. 94, Prentice-Hall, Inc., Englewood Cliffs, N. J. (1952).
8. W. M. Latimer, "Oxidation Potentials," p. 104, Prentice Hall, Inc., Englewood Cliffs, N. J. (1952).
9. H. P. Godard, "The Corrosion of Light Metals," p. 21, John Wiley & Sons, Inc., New York (1967).
10. K. B. Yatsimirskii and V. P. Vasil'ev, "Instability Constants of Complex Compounds," p. 100, D. Van Nostrand Co., Princeton, N. J. (1966).

DISCUSSION SECTION



This Discussion Section includes discussion of papers appearing in the *Journal of the Electrochemical Society*, Vol. 118, No. 7, 9, 11, and 12; July, September, November, and December 1971; Vol. 119, No. 1 and 4; January and April 1972.

Hydrogen Embrittlement and Hydrogen Traps

J.O'M. Bockris and P.K. Subramanian (pp. 1114-1119, Vol. 118, No. 7)

G. Dubpernell:¹ It is good to see the consideration given to the possible spreading of microcracks in the metal. This theory was suggested by Ferguson and Dubpernell a long time ago,² in an investigation of the behavior of platinum and palladium membranes.

¹ M&T Chemicals Inc., 1700 East Nine Mile Road, Ferndale, Michigan 48220.

² A. L. Ferguson and G. Dubpernell, *Trans. Electrochem. Soc.*, **64**, 221 (1933).

A number of questions or comments occurred during reading the paper under discussion. Why were the membranes annealed for 3 hr at 600°C prior to the experiment? What results are obtained if this treatment is omitted?

The deposition of a thin layer of palladium on the back of the Armco iron membranes seems unnecessary and unimportant in this instance. Iron would show little anodic dissolution in 0.1N NaOH. Was the rate of dissolution checked? It would seem better to use platinum for this purpose if anything is needed, as palladium has a greater tendency to anodic dissolution. What was the visual appearance of the 1.13 cm² area of the back of the membranes after the experiments? Was any corrosion evident compared to the unexposed

parts of the membranes, since the back is subjected to anodic treatment?

One would expect these experiments to be made at room temperature. Why was a temperature of 50° and 60°C used, and in one case 70°C?

On page 1116 of the paper by Bockris and Subramanyan there is a discussion of "H damage." Hydrogen is sometimes referred to as H₂. Is the H in "H damage" merely H₂, and could the expression just as well be "H₂ damage," or is a different form of hydrogen intended to be indicated by the plain "H"?

This writer feels that the results of these experiments are due to the porosity of the membranes, and not to hydrogen diffusion at all. Gross porosity of the membranes could readily be checked by the method which has been suggested² of reversing the polarity of the charging current on the front of the membrane and seeing if there is an immediate change in the polarity of the back of the membrane. This method depends upon the presence of thin threads of solution through the capillaries in the metal of the membrane, from front to back.

If the capillaries in the metal of the membrane are small enough and few enough, it is conceivable that the threads of solution in them might make a poor and irregular connection from the front to the back of the membrane which could easily be broken as by hydrogen bubbles, and easily be re-established when the current was shut off as during the decay tests shown in Fig. 3 and 4 in the paper under discussion. Such re-establishment of solution connections would permit any residual cathode polarization on the front of the membrane to affect the potential on the back, and this would be an explanation of the effects noted in Fig. 3 and 4.

The closely-connected report of Beck, Bockris, Genshaw, and Subramanyan³ is also of considerable interest. The solubility of hydrogen in nickel is given as almost 1000 times the solubility in iron, and yet the permeability of iron-nickel alloys falls to about one thousandth of that of iron at about 40% or more of nickel. This contradiction does not seem adequately explained.

An excellent correlation is noted between the permeability of the membranes and their corrosion resistance, the membranes with 40% or more of nickel having about 1000 times the corrosion resistance of iron. The authors suggest that the higher permeability of iron may be due to the formation of pits caused by corrosion and the spreading of cracks to the surface. Is not this tantamount to saying that iron membranes may become more porous than 40% nickel membranes due to corrosion, and that the permeability of iron membranes in which hydrogen is less soluble, is due to porosity?

The writer again wishes to bring into question the validity of the method proposed by Devanathan, Stachurski, and Beck⁴ for determining the permeability of metal membranes to hydrogen.

Adsorption of Thiourea and its Derivatives at the In-Hg/Electrolyte Interface.

R. Narayan and N. Hackerman (pp. 1426-1430, Vol. 118, No. 9)

A. N. Frumkin and N. B. Grigoryev:⁵ Starting from 1928⁶ the adsorption of thiourea at the metal/electrolyte solution interface has attracted the attention of electrochemists as an example of a reversible adsorption process resulting from a chemisorptive interaction

³ W. Beck, J. O'M. Bockris, M. A. Genshaw, and P. K. Subramanyan, *Metallurgical Transactions*, **2**, 883 (1971).

⁴ M. A. V. Devanathan, Z. Stachurski, and W. Beck, *This Journal*, **110**, 886 (1963).

⁵ Institute of Electrochemistry, Academy of Sciences of the U.S.S.R., Moscow.

⁶ A. Frumkin, *Ergeb. Exakt. Naturw.*, **7**, 235 (1928); *Coll. Symp. Ann.*, **7**, 89 (1930).

of the functional group and the metal surface. This problem is also treated in the interesting paper under discussion of Narayan and Hackerman, who considered the case of thiourea adsorption on indium amalgams.⁷ The aim of this note is to fill up some gaps in their paper.

Adsorption of thiourea leads to a shift of pzc towards negative potentials, which is due to the orientation of the C-S bond with the negatively charged sulfur atom to the metal surface. This conclusion, first obtained from electrocapillary curves,⁶ was confirmed by the determination of pzc from the minimum on the C,E curves in diluted electrolyte solutions.⁹ Analysis of these curves showed that unlike the desorption maxima of many aliphatic and aromatic compounds, the desorption maximum for solutions with thiourea additions is due to the strong shift of pzc in the negative direction, rather than to the effect of thiourea on the double layer capacity. The adsorption of thiourea on a dropping gallium¹⁰ and on a lead electrode was investigated.^{11,12} The adsorption potential shifts on gallium are greater, and on lead smaller, than on mercury. Experimental data on thiourea adsorption on mercury⁹ and gallium¹¹ were used for verification of the theory of the discrete double layer at the metal/solution interface in the presence of specific adsorption of dipole molecules and adsorption of solvent molecules.¹³ The Esin-Markov coefficient, calculated with the use of reasonable values of the double layer parameters, agreed well with the experimental values and, in conformity with the theory, decreased when passing from mercury to gallium.

It was shown¹⁴ that the influence of thiourea adsorption on the kinetics of electrochemical processes on mercury and on thallium amalgams can be well accounted for by taking into consideration the ψ -effect. Meurée and Gierst¹⁴ described for the first time the interesting phenomenon, which is also considered in the paper under discussion, *viz.*, the appearance of sharp peaks on the C,E curves during simultaneous adsorption of thiourea and halogen ions. Such sharp peaks point to a drastic change of the surface charge in a narrow potential range and to the presence of attractive interactions between adsorbed particles at more positive potentials. Narayan and Hackerman, in the paper under discussion, suppose that in this case at anodic potentials thiourea molecules turn towards the amalgam surface with their positive nitrogen end. We think that, considering that urea shows practically no surface activity at the mercury/solution interface,⁶ this concept is unlikely. However, this problem cannot be cleared up without a more thorough examination of the characteristics of the adsorption layer of thiourea in the presence of halogen ions. The C,E curves with such peaks were obtained at our laboratory during thiourea adsorption on mercury in the presence of I⁻, but we decided not to publish them until they could be investigated in more detail.

⁷ The choice of indium amalgams as adsorbent is perhaps not optimum owing to the change in the surface layer composition with changing potential. In the quantitative interpretation of this dependence there are some discrepancies between Butler's results, which are used by Narayan and Hackerman, and those obtained by Frumkin *et al.* We shall not dwell on this problem here since recently it was thoroughly dealt with.

⁸ A. Frumkin, N. Polianovskaya, I. Bagotskaya, and N. Grigoryev, *J. Electroanal. Chem.*, **33**, 319 (1971).

⁹ A. Morozov, N. Grigoryev, and I. Bagotskaya, *Elektrokhimiya*, **3**, 585 (1967).

¹⁰ On a stationary gallium electrode¹¹ in the presence of thiourea, the capacity was found to depend on the a-c frequency and on the age of the electrode/solution interface, which points to a slow chemical interaction of gallium with thiourea (with a dropping gallium electrode such phenomena are not observed). In this connection it would perhaps be useful to carry out measurements with a dropping In-Hg electrode.

¹¹ I. Bagotskaya, S. Fateev, N. Grigoryev, and N. Bardina, *Elektrokhimiya*, **6**, 369 (1970); N. Grigoryev, S. Fateev, and I. Bagotskaya, *ibid.*, **7**, 223 (1971).

¹² N. Grigoryev and D. Machavariani, *ibid.*, **6**, 89 (1970).

¹³ N. Grigoryev and V. Krylov, *ibid.*, **4**, 763 (1968); V. Krylov and N. Grigoryev, *ibid.*, **7**, 511 (1971).

¹⁴ N. Meurée and L. Gierst, *Collection Czech. Chem. Commun.*, **36**, 389 (1971); Extended Abstracts 21st CITCE Meeting Praha (1970).

Finally we should like to mention that there are rather numerous data in literature^{15,16} on the effect of thiourea and its derivatives as corrosion inhibitors, mentioned in the paper under discussion.

R. Narayan and N. Hackerman: We thank the authors of the above discussion for bringing to our attention the extensive Russian literature on the subject. However, our paper was presented at the 1967 October meeting of The Electrochemical Society held in Chicago, and triangular correspondence across 10,000 miles delayed the publication. So, in effect, the paper was written prior to the appearance of the recent references noted by Frumkin and Grigoryev. Therefore, the recent references were not included.

There are at least two points of major difference between the results of Butler^{17,18} and that of the Russian school:¹⁹ (i) variation of the negative surface excess of indium with the potential calculated from electrocapillary measurements and (ii) the presence of the hump in the capacitance curves. Our measurements show the second observation and the results are in general agreement with those of Butler.

The sharp peaks in the capacitance curves in the presence of thiourea and chloride ions could be observed only with the amalgam electrodes of 20 mole per cent In or more. The negative surface excess of indium also shows a maximum at this concentration^{17,18} and hence this result was emphasized. However, the suggestion by Frumkin and Grigoryev regarding possibility of compound formation was also included.

The literature²⁰ available shows that thiourea invariably enhances the double-layer capacitance for the Hg, Pb, and Ga electrodes. Our results show that with In-Hg electrodes there is a region of potentials in which the capacitance is depressed by the presence of thiourea. A transition hump is also obtained with amalgams of higher indium concentrations. This hump apparently becomes a peak in the presence of chloride ions. The mechanism for the peak formation is not clear. As Frumkin and Grigoryev point out strong attractive interactions come into play. Our suggestion was that the adsorbed anions reduce the mutual repulsions between adsorbed thiourea species and that the positive end of the dipole may be oriented towards the amalgam. This suggestion is based on the fact that interfacial composition of indium increases with positive polarization. The absence of surface activity of urea at the Hg solution interface probably indicates the absence of Hg-N interaction. Would this also mean the absence of In-N interaction?

An important fact which we did not consider was that thiourea is present to a large extent as the protonated species in acid solutions. The proton is attached to the sulfur atom. We have evidence of this based on studies with Fe and Hg electrodes in solutions of varying pH containing thiourea and N-substituted thioureas.²¹ What would be the nature of the metal-thiourea interaction under these conditions? It is also worthwhile carrying out investigations with a dropping amalgam electrode.

We described perhaps for the first time the appearance of peaks in the C-E curves during simultaneous adsorption of thiourea and chloride ions, when presenting the paper in Chicago. Gierst and co-worker

observed such peaks in the presence of bromide ions. Frumkin and Grigoryev claim such observations in the presence of iodide ions. Recent studies in the Indian Institute of Technology, Madras, by tensammetry showed that such peaks, rather small and sharp, can be obtained in the presence of chloride ion also using a d.m.e. The minimum chloride ion concentration corresponds to 0.25M KCl or 0.2M HCl. Further work is in progress.

The reference in our paper regarding data on corrosion inhibition was only an illustration of work which emphasizes the cumulative effects of anion and thiourea derivatives on the process of corrosion.

The Electrochemical Behavior of Technetium and Iron Containing Technetium.

G.H. Cartledge (pp. 1752-1758, Vol. 118, No. 11)

S. Trasatti:²² In the paper under discussion, the author reports the value of about 9×10^{-5} A cm⁻² for the exchange current of the electrolytic hydrogen evolution reaction on Tc. To my knowledge, this is the first measurement of this kind reported for Tc, a metal for which data regarding surface properties are indeed almost nonexistent. As an example, in the most recent review by Hayward²³ on chemisorption from the gas phase, Tc is tabulated always in brackets because of lack of any data for characterization. At first sight, it would therefore appear impossible to ascertain the reliability of the $i_{0,H}$ value reported by Cartledge, without repeating experimental measurements. However, I will here attempt to undertake this task by making use of a number of correlations I have recently developed²⁴⁻²⁷ between electrochemical properties and work function of metals. Conversely, this attempt, if positive, will constitute in turn a valuable test of the reliability of such correlations originally devised to predict unknown properties of metals or metallic materials.

The ground datum from which this analysis will start is the value of Pauling's electronegativity,²⁸ (x_M). Recent considerations²⁶ show that Pauling's values are generally dependable also in the case of less common metals. Correlation exists between x_M and the work function ϕ which in the case of transition metals is expressed by the equation²⁶

$$x_M = 0.50\phi - 0.55 \quad [1]$$

Using for Tc $x_M = 1.9$, we obtain $\phi = 4.9$ eV. Now, this value can in turn be used in the correlation between $i_{0,H}$ and ϕ which, for transition metals, is given²⁷ by

$$\log i_{0,H} = 6.7\phi - 36.6 \quad [2]$$

Thus, from Eq. [2] the value of 1.6×10^{-4} A cm⁻² is derived for $i_{0,H}$ of Tc. In view of the factors which may affect exchange current measurements and the fact that the value of x_M given by Pauling is approximate to the first figure^{26,28} the agreement between observed and calculated values of $i_{0,H}$ for Tc can be considered as very satisfactory. It may be noted that coincidence of the two values is obtained with a x_M value of 1.88. Once established that the $i_{0,H}$ obtained by Cartledge is basically correct, it is more reasonable to refine the value of x_M from the experimental value of $i_{0,H}$ than the reverse, as the experimental uncertainty of electrochemical measurements is intrinsically lower than that pertaining to x_M values as claimed by Pauling.²⁸

²² Laboratory of Electrochemistry, the University, Milan, Italy.

²³ D. O. Hayward, in "Chemisorption and Reactions on Metallic Films," Vol. 1, J. R. Anderson, Editor, Academic Press (1971).

²⁴ S. Trasatti, *Chim. Ind. (Milan)*, 53, 599 (1971).

²⁵ S. Trasatti, *J. Electroanal. Chem.*, 33, 351 (1971).

²⁶ S. Trasatti, *J. C. S. Faraday I*, 68, 229 (1972).

²⁷ S. Trasatti, *J. Electroanal. Chem.*, Submitted for publication.

²⁸ L. Pauling, "The Nature of the Chemical Bond," University Press, Ithaca (1960).

¹⁵ Z. Jofa, 2-ème Sympos. Europ. sur les Inhibit. de Corros., Ferrara, 1966, p. 93; Z. Jofa and G. Tomashova, *Zh. Fiz. Khim.*, 34, 1036 (1960); Z. Jofa, *Zashchita Metal.*, 6, 491 (1970).

¹⁶ L. Cavallaro, L. Felloni, G. Trabaneli, and F. Pulidori, *Electrochim. Acta*, 8, 521 (1963); L. Cavallaro, L. Felloni, G. Trabaneli, and F. Pulidori, *ibid.*, 9, 485 (1964); L. Cavallaro, L. Felloni, G. Trabaneli, and F. Zucchi, 2-ème Sympos. Europ. sur les Inhibit. de Corros., Ferrara, 1966, p. 417.

¹⁷ J. N. Butler, M. L. Meehan, and A. C. Makrides, *J. Electroanal. Chem.*, 9, 237 (1965).

¹⁸ J. N. Butler, *J. Phys. Chem.*, 69, 3817 (1965).

¹⁹ E. V. Yakovleva and N. V. Nikolaeva Fedorovich, *Soviet Electrochem.*, 6, 29 (1971).

²⁰ *Ftn.* 8, 9, 11, 12, 13 (English translation).

²¹ R. Narayan and K. Chandrasekara Pillai, *Trans. of SAEST, India* (April-June), In press.

While a disagreement between observed and calculated values of $i_{0,H}$ for Tc would not reveal in principle which value is to be considered as incorrect (however, reliability of the correlation is already supported by the fact that it has been derived from data for more than 30 metals), the resulting agreement between the two values should be regarded in my opinion, as a reciprocal check of the reliability of both the experimental result and the derivation of the correlations.

I would also like to consider along the same lines some more aspects of that part of Cartledge's paper which deals with the Tc/H₂ system. The very high rapidity of hydrogen ionization observed by the author should indicate a nonactivated hydrogen adsorption on Tc, which, together with a Tafel slope for the cathodic reaction of about 40 mV would suggest, along the lines of Thomas' analysis,²⁹ a fast proton discharge followed by a rate determining ion + atom reaction. This mechanism is conceivable in the light of the correlations mentioned above. In fact, from Parsons' analysis³⁰ it is known that the relationship between $i_{0,H}$ and the strength of the M-H surface bond should pass through a maximum. This has been verified^{27,31} and transition metals as a result located in the descending branch of the resulting volcano-shaped curve. Cartledge's value of $i_{0,H}$ places Tc between Pt, Pd, Rh, Ir, for which the combination is the rate-determining step, and those metals for which the ion + atom reaction is rate determining, about in the same position of Re which in fact belongs to the same group and behaves similarly. It should be of interest to note that Ru and Os³² present about the same $i_{0,H}$ as that of Tc and the reaction is governed by the ion + atom mechanism.

A value of 64 kcal mol⁻¹ for the strength of the Tc-H surface bond in solution during hydrogen evolution at $\eta \rightarrow 0$ can be derived from the volcano curve. According to arguments given by Krishtalik³¹ this value should be capable of being ascertained from experimental data. Such a check would definitely prove the reliability and usefulness of correlations proposed elsewhere.²⁵⁻²⁷ It should be added that the value of 64 kcal mol⁻¹ for $E(M-H)$ and the experimental value of $i_{0,H}$ for Tc are compatible with a rather high equilibrium coverage with atomic hydrogen, so that the combination reaction should possess a rate comparable to that of the ion + atom reaction.

I would like to emphasize here the fact that, albeit Mn belongs to group VIIA like Re and Tc and therefore all of them possess 7 electrons in the valency band, the behavior of Mn is quite peculiar. Practically, Cartledge's results demonstrate that Mn is the sole transition metal (more likely, the sole metal) which does not take the expected place in correlations. This would suggest a quite particular structure (or property) of 3d band in respect of other outer d bands.

G. H. Cartledge: Professor Trasatti has developed correlations among several properties of metals which are also related to their behavior as cathodes for the evolution of hydrogen. He observes that the exchange current density which I reported for the technetium cathode is in close agreement with the calculation he makes on the basis of his equations and the estimated electronegativity value of Pauling. For his calculation, Trasatti used the $j_{0,H}$ value given for a cathode of technetium plated over gold, whereas for massive technetium or technetium rather heavily plated over platinum the value is 10⁻³ A cm². His Eq. [2] is not very sensitive to differences in $j_{0,H}$, but use of the

better value gives $\phi = 5.02$ and, by Eq. [1], $x_M = 1.96$. It is gratifying to note the consistency of the results.

Trasatti points out, also, the close similarity of the electrochemical behavior of technetium to that of platinum. This was apparent, not only in the ready response of the technetium electrode to hydrogen, as shown in my paper, but also by reference to the correlation between the heat of adsorption of atomic hydrogen on a metal and the overvoltage for liberation of hydrogen at a fixed current density, as given by Bonhoeffer in 1923. This also indicated a ΔH_{ads} of ca. 64 kcal mole⁻¹, in agreement with Trasatti's comments.

Professor Trasatti concludes, further, that my data indicate the probable mechanism of the discharge of hydrogen on technetium. It is to be noted, however, that the diagnostic properties of the plated electrodes were rather sensitive both to the nature of the substrate and to the presence of slowly reducible surface films. In addition, earlier work³³ suggested strongly that the behavior of technetium electrodes may be affected by their radioactivity, though circumstances did not permit further investigation of this point. Because of these uncertainties, I chose not to discuss the mechanism of the discharge of hydrogen, though I agree that the data, so far as they go, are in accord with the Heyrovsky mechanism, as Trasatti suggests. Such a conclusion is consistent also with the observation (cf. p. 1754 of the paper under discussion) that the cathodic current density at a given overvoltage is temporarily decreased when the degree of coverage by adsorbed hydrogen is reduced.

I am grateful to Professor Trasatti for his interesting discussion.

A Secondary, Nonaqueous Solvent Battery

J. S. Dunning, W. H. Tiedemann, L. Hsueh, and
D. N. Bennion (pp. 1886-1890, Vol. 118, No. 12)

J. Besenhard and H. P. Fritz:³⁴ The authors describe a secondary, nonaqueous battery, consisting of a lithium negative and a graphite compound positive electrode, LiClO₄/dimethyl sulfite being the electrolyte; they suggest the formation of lamellar graphite compounds, e.g., C_nClO₄, in the aprotic system. n is estimated to be 89 and in contrast to the results in acids,³⁵ no color change, no stage formation, and unlimited, irreversible expansion of graphite on oxidation is reported.

We, however, found a fair accord with the behavior of graphite oxidized in conc. acids, particularly with respect to stoichiometry and ionic structure.³⁶

Formation of stages.—On oxidation in aprotic solvents the potential of a graphite electrode slowly rises to a constant value. Galvanostatic oxidation of graphite foils (~0.2 mm thick) in 1M solutions of LiClO₄ or KPF₆ in propylene carbonate (PC) with low-current densities (30-50 μ A · cm⁻² geometrical surface) yields a constant final value of about 2.2V vs. SCE after a current passage corresponding to the stoichiometry C₂₄X; with higher current densities this constant potential is attained before the graphite has reacted completely. Further stages $n > 24$ can be detected, however, they cannot be assigned unambiguously due to their "unsharpness." On further oxidation no stages $n < 24$ were as yet observed; the products formed, however, are reversibly reducible, so that in suitable solvents a markedly higher maximum charge storage capacity is obtained than that calculated on the basis of C₂₄X, in analogy to the

²⁹ J. G. N. Thomas, *Trans. Faraday Soc.*, 57, 1603 (1961).

³⁰ R. Parsons, *ibid.*, 54, 1053 (1958).

³¹ L. I. Krishtalik, in "Adv. Electrochem. Electrochem. Eng.," Vol. 7, Interscience (1970).

³² A. T. Kuhn and P. M. Wright, *J. Electroanal. Chem.*, 27, 319 (1970).

³³ G. H. Cartledge, *This Journal*, 118, 231 (1971).

³⁴ Anorg.-Chem. Laboratorium der Technischen Universität München, 8 München 2, Arcisstrasse 21, Germany.

³⁵ M. J. Bottomley, G. S. Parry, A. R. Ubbelohde, and D. A. Young, *J. Chem. Soc.*, 1963, 5674 (1963).

³⁶ J. Besenhard and H. P. Fritz, *Z. Naturforsch.*, 26b, 1225 (1971).

While a disagreement between observed and calculated values of $i_{0,H}$ for Tc would not reveal in principle which value is to be considered as incorrect (however, reliability of the correlation is already supported by the fact that it has been derived from data for more than 30 metals), the resulting agreement between the two values should be regarded in my opinion, as a reciprocal check of the reliability of both the experimental result and the derivation of the correlations.

I would also like to consider along the same lines some more aspects of that part of Cartledge's paper which deals with the Tc/H₂ system. The very high rapidity of hydrogen ionization observed by the author should indicate a nonactivated hydrogen adsorption on Tc, which, together with a Tafel slope for the cathodic reaction of about 40 mV would suggest, along the lines of Thomas' analysis,²⁹ a fast proton discharge followed by a rate determining ion + atom reaction. This mechanism is conceivable in the light of the correlations mentioned above. In fact, from Parsons' analysis³⁰ it is known that the relationship between $i_{0,H}$ and the strength of the M-H surface bond should pass through a maximum. This has been verified^{27,31} and transition metals as a result located in the descending branch of the resulting volcano-shaped curve. Cartledge's value of $i_{0,H}$ places Tc between Pt, Pd, Rh, Ir, for which the combination is the rate-determining step, and those metals for which the ion + atom reaction is rate determining, about in the same position of Re which in fact belongs to the same group and behaves similarly. It should be of interest to note that Ru and Os³² present about the same $i_{0,H}$ as that of Tc and the reaction is governed by the ion + atom mechanism.

A value of 64 kcal mol⁻¹ for the strength of the Tc-H surface bond in solution during hydrogen evolution at $\eta \rightarrow 0$ can be derived from the volcano curve. According to arguments given by Krishtalik³¹ this value should be capable of being ascertained from experimental data. Such a check would definitely prove the reliability and usefulness of correlations proposed elsewhere.²⁵⁻²⁷ It should be added that the value of 64 kcal mol⁻¹ for $E(M-H)$ and the experimental value of $i_{0,H}$ for Tc are compatible with a rather high equilibrium coverage with atomic hydrogen, so that the combination reaction should possess a rate comparable to that of the ion + atom reaction.

I would like to emphasize here the fact that, albeit Mn belongs to group VIIA like Re and Tc and therefore all of them possess 7 electrons in the valency band, the behavior of Mn is quite peculiar. Practically, Cartledge's results demonstrate that Mn is the sole transition metal (more likely, the sole metal) which does not take the expected place in correlations. This would suggest a quite particular structure (or property) of 3d band in respect of other outer d bands.

G. H. Cartledge: Professor Trasatti has developed correlations among several properties of metals which are also related to their behavior as cathodes for the evolution of hydrogen. He observes that the exchange current density which I reported for the technetium cathode is in close agreement with the calculation he makes on the basis of his equations and the estimated electronegativity value of Pauling. For his calculation, Trasatti used the $j_{0,H}$ value given for a cathode of technetium plated over gold, whereas for massive technetium or technetium rather heavily plated over platinum the value is 10⁻³ A cm². His Eq. [2] is not very sensitive to differences in $j_{0,H}$, but use of the

better value gives $\phi = 5.02$ and, by Eq. [1], $x_M = 1.96$. It is gratifying to note the consistency of the results.

Trasatti points out, also, the close similarity of the electrochemical behavior of technetium to that of platinum. This was apparent, not only in the ready response of the technetium electrode to hydrogen, as shown in my paper, but also by reference to the correlation between the heat of adsorption of atomic hydrogen on a metal and the overvoltage for liberation of hydrogen at a fixed current density, as given by Bonhoeffer in 1923. This also indicated a ΔH_{ads} of ca. 64 kcal mole⁻¹, in agreement with Trasatti's comments.

Professor Trasatti concludes, further, that my data indicate the probable mechanism of the discharge of hydrogen on technetium. It is to be noted, however, that the diagnostic properties of the plated electrodes were rather sensitive both to the nature of the substrate and to the presence of slowly reducible surface films. In addition, earlier work³³ suggested strongly that the behavior of technetium electrodes may be affected by their radioactivity, though circumstances did not permit further investigation of this point. Because of these uncertainties, I chose not to discuss the mechanism of the discharge of hydrogen, though I agree that the data, so far as they go, are in accord with the Heyrovsky mechanism, as Trasatti suggests. Such a conclusion is consistent also with the observation (cf. p. 1754 of the paper under discussion) that the cathodic current density at a given overvoltage is temporarily decreased when the degree of coverage by adsorbed hydrogen is reduced.

I am grateful to Professor Trasatti for his interesting discussion.

A Secondary, Nonaqueous Solvent Battery

J. S. Dunning, W. H. Tiedemann, L. Hsueh, and
D. N. Bennion (pp. 1886-1890, Vol. 118, No. 12)

J. Besenhard and H. P. Fritz:³⁴ The authors describe a secondary, nonaqueous battery, consisting of a lithium negative and a graphite compound positive electrode, LiClO₄/dimethyl sulfite being the electrolyte; they suggest the formation of lamellar graphite compounds, e.g., C_nClO₄, in the aprotic system. n is estimated to be 89 and in contrast to the results in acids,³⁵ no color change, no stage formation, and unlimited, irreversible expansion of graphite on oxidation is reported.

We, however, found a fair accord with the behavior of graphite oxidized in conc. acids, particularly with respect to stoichiometry and ionic structure.³⁶

Formation of stages.—On oxidation in aprotic solvents the potential of a graphite electrode slowly rises to a constant value. Galvanostatic oxidation of graphite foils (~0.2 mm thick) in 1M solutions of LiClO₄ or KPF₆ in propylene carbonate (PC) with low-current densities (30-50 μ A · cm⁻² geometrical surface) yields a constant final value of about 2.2V vs. SCE after a current passage corresponding to the stoichiometry C₂₄X; with higher current densities this constant potential is attained before the graphite has reacted completely. Further stages $n > 24$ can be detected, however, they cannot be assigned unambiguously due to their "unsharpness." On further oxidation no stages $n < 24$ were as yet observed; the products formed, however, are reversibly reducible, so that in suitable solvents a markedly higher maximum charge storage capacity is obtained than that calculated on the basis of C₂₄X, in analogy to the

²⁹ J. G. N. Thomas, *Trans. Faraday Soc.*, 57, 1603 (1961).

³⁰ R. Parsons, *ibid.*, 54, 1053 (1958).

³¹ L. I. Krishtalik, in "Adv. Electrochem. Electrochem. Eng.," Vol. 7, Interscience (1970).

³² A. T. Kuhn and P. M. Wright, *J. Electroanal. Chem.*, 27, 319 (1970).

³³ G. H. Cartledge, *This Journal*, 118, 231 (1971).

³⁴ Anorg.-Chem. Laboratorium der Technischen Universität München, 8 München 2, Arcisstrasse 21, Germany.

³⁵ M. J. Bottomley, G. S. Parry, A. R. Ubbelohde, and D. A. Young, *J. Chem. Soc.*, 1963, 5674 (1963).

³⁶ J. Besenhard and H. P. Fritz, *Z. Naturforsch.*, 26b, 1225 (1971).

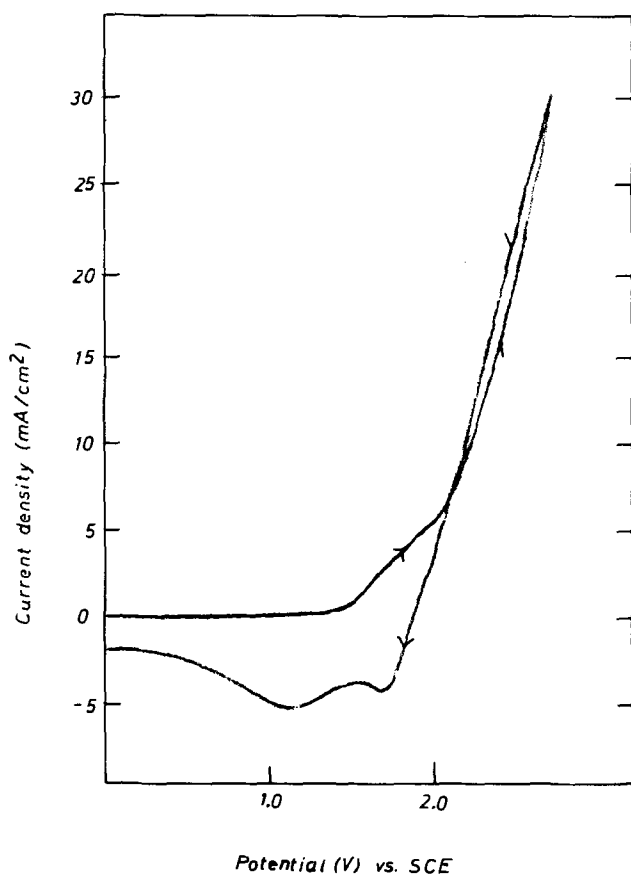
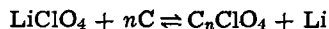


Fig. 1. Cyclic voltammogram at a graphite electrode (foil, 0.2 mm) in $\text{LiClO}_4/\text{dimethyl sulfite}$ (1M). Scan rate 300 mV/min; first cycle.

situation in conc. H_2SO_4 . We found the reaction following the oxidative formation of $\text{C}_{24}\text{HSO}_4 \cdot 2\text{H}_2\text{SO}_4$ (the so-called "build-up of an oxygen overvoltage"³⁵) to be reversible and leading to charge storage capacity five times higher than for the C_{24} -stage.

The steps in the oxidation current and several close-lying reduction peaks can be easily detected by cyclic voltammograms; especially on cycling with increasing amplitude in many organic electrolyte solutions, among them $\text{LiClO}_4/\text{dimethyl sulfite}$, several consecutive reduction peaks were observed.

Existence of electrolytic lamellar compounds.—The postulate of ionic graphite compounds in aprotic solvents was proved by conductivity measurements; on cycling a "Li/graphite" cell in 0.1N LiClO_4/PC the conductivity of the electrolyte solution changed to about 60% of the theoretical value expected for the reaction



For the discharged cell the electrolyte conductivity decreased after cyclization only slightly. During these measurements the size of the graphite electrode was such, that only compounds with $n > 24$ were formed, which was checked by measuring the potential *vs.* a reference electrode.

Maximum coulombic capacity.—Trying to find a maximum oxidation stage of graphite in LiClO_4/PC we as yet had no success in establishing a definite upper limit. With increasing charge input the coulombic efficiency decreases (see Fig. 2), since mainly solvent is decomposed; however, a charge output of more than 1000 coulomb g^{-1} was obtained with a current density of about 1 mA cm^{-2} and a cutoff potential of 3.5V *vs.* Li/Li^+ (1M). The discharge characteristics of these oxidation products are rather flat over a wide range; however, the break downward

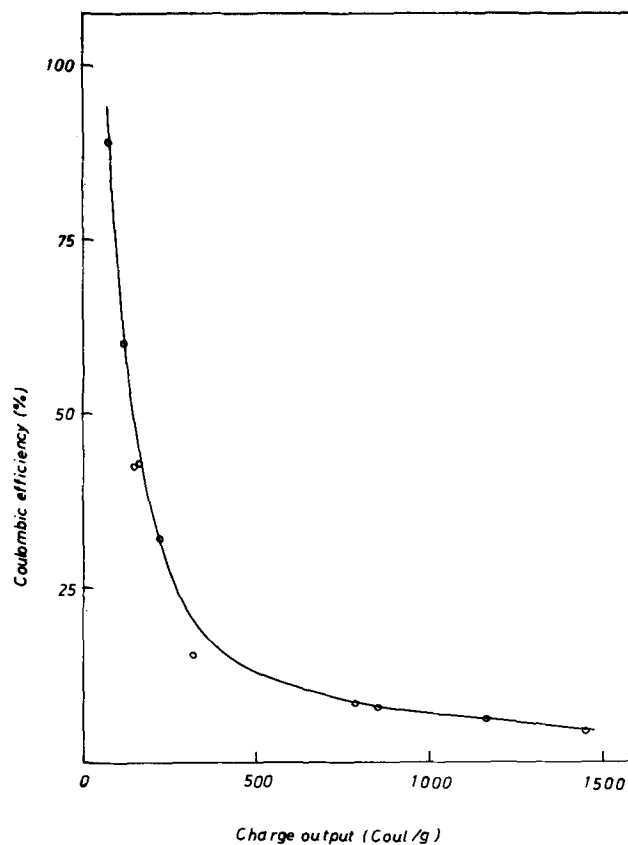


Fig. 2. Coulombic efficiency (charge output/charge input) of graphite foil in LiClO_4/PC (1M); first cycle. Current density (discharge) $\approx 1 \text{ mA/cm}^2$; cutoff potential 3.5V *vs.* Li/Li^+ (1M).

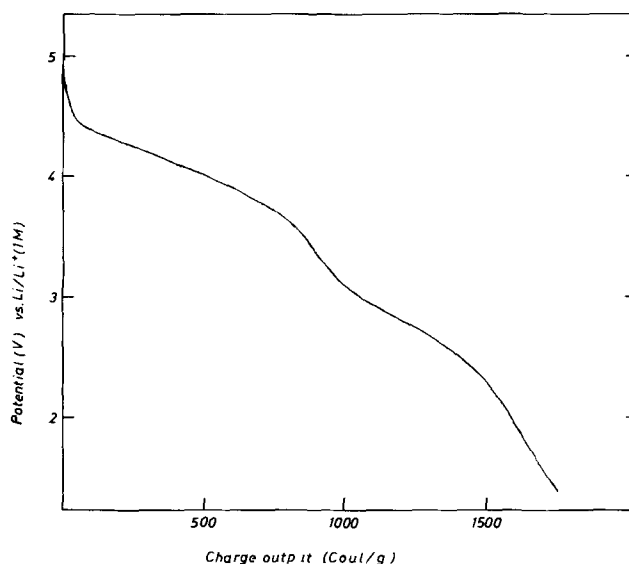


Fig. 3. Typical galvanostatic discharge curve for a graphite electrode (foil sandwiched between porous glass) in LiClO_4/PC (1M). Current density 1 mA/cm^2 ; previous charge input 10,150 coulomb g^{-1} at 2 mA/cm^2 ; first cycle.

in the curve is getting less sharp with increasing charge input (Fig. 3).

In many other organic solvents we were able to obtain charge outputs of $\gg 335 \text{ coulomb g}^{-1}$ ($\hat{=}$ C_{24}X). The reported very low maximum coulombic capacity of graphite in $\text{LiClO}_4/\text{dimethyl sulfite}$ was also observed during our study, although with extreme charge input we obtained a higher charge output than 90 coulomb g^{-1} . Since $\text{LiClO}_4/\text{dimethyl sulfite}$

shows a markedly lower oxidation stability at platinum electrodes, the ease of oxidation of dimethyl sulfite possibly causes the low-charge storage capacity. The grave loss of cell capacity on wet stand is certainly due to solvent oxidation; graphite electrodes vacuum-dried immediately after anodic oxidation could be stored remarkably well.

Cycling tests.—When cycling a half cell in LiClO_4/PC (charge current 2 mA cm^{-2} , discharge current 1 mA cm^{-2} , charge input $167.5 \text{ coulomb g}^{-1}$) we observed after 13 cycles no essential changes in the charge as well as the discharge curves, if the discharge was complete, *i.e.*, until starting reduction of PC at graphite.³⁷ Under these conditions a charge efficiency of about 90% is obtained. With higher cutoff potentials the graphite electrode is discharged only incompletely; increasing coulombic efficiencies during the first cycles are due to this fact.

Expansion of graphite.—The expansion of graphite is strongly dependent on external pressure and therefore caused not only chemically, but mainly mechanically; the solvent also influences the degree of expansion. In order to be able to work quantitatively with high charge input, our investigations were done with graphite foils sandwiched under pressure between porous glass plates.

J. S. Dunning, W. H. Tiedemann, L. Hsueh, and D. N. Bennion: The result of Besenhard and Fritz appear to confirm the results we found. The closer agreement which they observed between their results and the behavior of lamellar compounds of graphite formed in pure acids might be attributed to two causes. (i) We used dimethyl sulfite as a solvent rather than propylene carbonate in most of our experiments. Apparently propylene carbonate is somewhat more stable under these strong oxidizing conditions than dimethyl sulfite. (ii) We used polycrystalline graphite rather than large, well-defined pyrolytic graphite in most of our experiments. Thus, the blue might not have been easily seen and the stages averaged out. In spite of the discrepancies noted, it has been our general opinion that lamellar compounds of graphite, similar to those formed by oxidation in strong acids, are formed by oxidation in selected aprotic, electrolyte solutions. It is gratifying to see that the results of Besenhard and Fritz tend to confirm that opinion. However, the low-current efficiencies observed in some of their tests will require further investigation. It might be noted that we did observe some long cathodic current plateaus at between 2 and 2.5V *vs.* lithium. However, we were concerned that such plateaus might be due to previously formed solvent decomposition products or other impurities.

Mass Transfer to a Rotating Sphere at High Schmidt Numbers

J. Newman (pp. 69-71, Vol. 119, No. 1)

D. T. Chin:³⁸ In the paper under discussion, Newman used the Lighthill transformation to calculate the rate of mass transfer to a rotating sphere at high Schmidt numbers. He made use of Manohar's numerical results³⁹ of the meridional velocity gradient at the surface, $(\partial V_\theta/\partial r)_{r=r_0}$, as the shear stress in the transformation, and integrated the resulting equation numerically to give a correction to Chin's θ -expression theory⁴⁰ for the rate of mass transfer at large θ .

Manohar's results for the tangential velocity gradient, $(\partial V_\phi/\partial r)_{r=r_0}$, can also be used for such calcula-

tions provided that the Chilton-Colburn analogy⁴¹

$$\text{Sh}_x = \text{Re}_x \text{Sc}^{1/3} (f_x/2) \quad [1]$$

is used for the analysis. Here Sc is the Schmidt number; Sh_x , Re_x , and f_x are the local Sherwood number, the local Reynolds number, and the local friction coefficient, respectively, based upon the surface distance, x , from the leading edge of the boundary layer flow.

Although the Chilton-Colburn relation is empirical in nature, it is a simpler method. It has been found to give a reasonably accurate estimate of the rate of heat and mass transfer for flow over a flat plate⁴² and for channel flows.⁴³ In the case of a rotating-disk electrode, the use of Eq. [1] leads to the following relation for mass transfer at high Schmidt numbers⁴⁴

$$\text{Sh} = 0.616 \text{Re}^{1/2} \text{Sc}^{1/3} \quad [2]$$

This equation agrees to within 1% with Levich's exact solution,⁴⁵ which predicts a $0.620 \text{Re}^{1/2} \text{Sc}^{1/3}$ dependence for the Sherwood number.

For flow induced by a rotating sphere, the leading edge of the boundary layer occurs at the pole of rotation, and x should be taken as $r_0\theta$. Thus, using $r_0\omega\sin\theta$ as a characteristic velocity for every local point on the sphere surface, Sh_x , Re_x , and f_x can be calculated from the following relations

$$\text{Sh}_x = \frac{kr_0\theta}{D} \quad [3]$$

$$\text{Re}_x = \frac{r_0^2\omega\theta\sin\theta}{\nu} \quad [4]$$

$$f_x \approx - \frac{\mu \left(\frac{\partial V_\phi}{\partial r} \right)_{r=r_0}}{\frac{1}{2} \rho r_0^2 \omega^2 \sin^2\theta} \quad [5]$$

Substituting Eq. [3]-[5] into Eq. [1], and making use of the dimensionless tangential velocity and the dimensionless radial coordinates defined as $G = V_\phi/r_0\omega$ and $\eta = (r - r_0) (\omega/\nu)^{1/2}$, respectively, we have

$$\text{Sh}_{\text{loc}} = \left(\frac{kr_0}{D} \right) = - \text{Re}^{1/2} \text{Sc}^{1/3} \frac{(\partial G/\partial \eta)_{\eta=0}}{\sin\theta} \quad [6]$$

Here, Re is the Reynolds number, $r_0^2\omega/\nu$, based on the sphere radius.

The tangential shear stress distribution, $(\partial G/\partial \eta)_{\eta=0}$, has been obtained numerically by Manohar.³⁹ A curve fitting of his results indicates that $(\partial G/\partial \eta)_{\eta=0}$ can be expressed as

$$- \left(\frac{\partial G}{\partial \eta} \right)_{\eta=0} = 0.61592\theta - 0.18946\theta^3 - 0.05819\sin^3\theta \quad [7]$$

Substituting the above relation into Eq. [6], we immediately arrive at a correlation for the local rate of mass transfer to the sphere surface

$$\text{Sh}_{\text{loc}} = \text{Re}^{1/2} \text{Sc}^{1/3} \frac{0.61592\theta - 0.18946\theta^3 - 0.05819\sin^3\theta}{\sin\theta} \quad [8]$$

Equation [8] is plotted in Fig. 1 as the thick curve for $\text{Sh}_{\text{loc}}/\text{Re}^{1/2} \text{Sc}^{1/3}$ *vs.* θ . For comparison, Newman's results in the paper under discussion based on the meridional shear stress distribution are given as the thin curve. The dashed curve is calculated from Chin's

⁴¹ T. H. Chilton and A. P. Colburn, *Ind. Eng. Chem.*, **26**, 1183 (1934).

⁴² H. Schlichting, "Boundary Layer Theory," McGraw-Hill Book Co., New York (1960).

⁴³ D. S. Hubbard and E. N. Lightfoot, *Ind. Eng. Chem. Fundamentals*, **5**, 370 (1966).

⁴⁴ L. A. Dorfman, *Soviet Phys., "Doklady"*, **3**, 248 (1958).

⁴⁵ V. G. Levich, "Physicochemical Hydrodynamics," Prentice-Hall, Englewood Cliffs, N. J. (1962).

³⁷ A. N. Dey and B. P. Sullivan, *This Journal*, **117**, 222 (1970).

³⁸ Electrochemistry Department, Research Laboratories, General Motors Corporation, Warren, Michigan 48090.

³⁹ R. Manohar, *Z. Angew. Math. Phys.*, **18**, 320 (1967).

⁴⁰ D. T. Chin, *This Journal*, **118**, 1434 (1971).

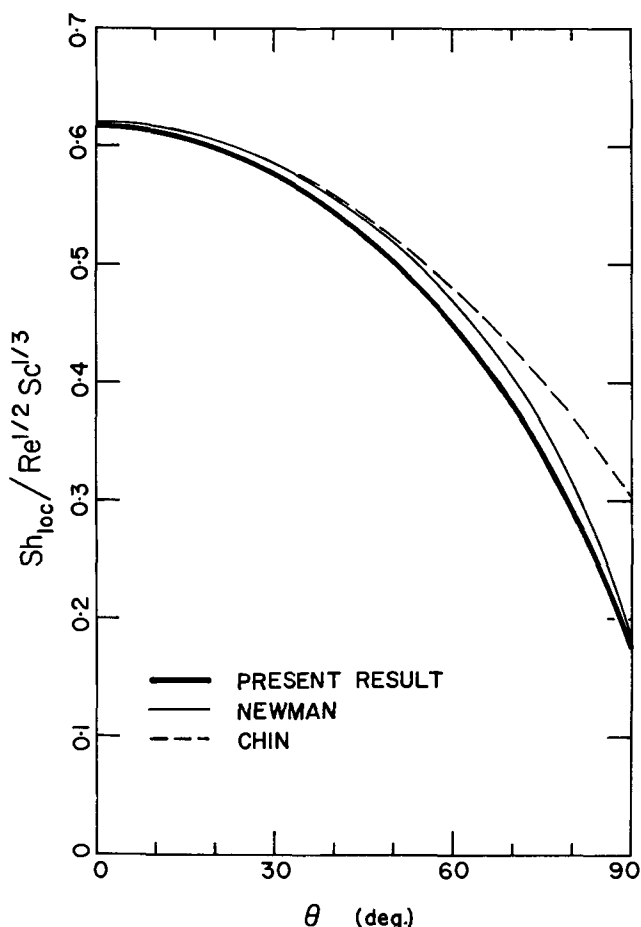


Fig. 1. Local mass transfer rate on the surface of a rotating sphere. The thick curve is the result of the present analysis as calculated from Eq. [8]. Newman's results based on the meridional shear stress distribution are given as the thin curve. The dashed curve represents Chin's θ -expansion theory for small θ .

θ -expansion solution⁴⁰ for small values of θ . It is seen that in spite of being empirical in nature, the present results obtained with the Chilton-Colburn analogy are in good agreement with the two previous theories based on more rigorous mathematical treatment. Whereas Chin's θ -expansion solution considerably overestimates the rate of transfer at large θ , the present results give a good approximation for the rate of transfer in the equatorial region. The maximum deviation of Eq. [8] from Newman's curve, which occurs approximately at $\theta = 80^\circ$, is less than 9%. At the pole of rotation ($\theta = 0^\circ$) and at the equator ($\theta = 90^\circ$), the accuracy of the present results is better than 99%.

Equation [8] can be integrated to give the average rate of mass transfer to the spherical surface

$$\text{Sh} = \frac{\text{Re}^{1/2} \text{Sc}^{1/3}}{1 - \cos\theta} \{0.30796\theta^2 - 0.047365\theta^4 + 0.019397(\sin^2\theta + 2)\cos\theta - 0.03879\} \quad [9]$$

For a sphere or a hemisphere whose entire surface is subject to mass transfer, Eq. [9] gives a $0.433 \text{Re}^{1/2} \text{Sc}^{1/3}$ dependence for the average Sherwood number; this correlation is only 4% smaller than Newman's results which predict a value of 0.451 for the numerical coefficient.

In conclusion, we have used the Chilton-Colburn analogy to discuss laminar mass transfer on a rotating spherical electrode. It is shown that in spite of its empirical nature, the Chilton-Colburn relation is a simple and powerful tool to give a good approximation of the rate of ionic transfer on a complicated electrode geometry (such as the rotating sphere), where the exact

solution is difficult to obtain. The procedures illustrated in this work can also be used for other rotating surfaces, such as a cone or an ellipsoid.

LIST OF SYMBOLS

D	diffusivity of diffusing species, cm ² /sec
f_x	local friction coefficient based upon the surface distance, x , from the leading edge of the flow boundary layer, dimensionless
G	dimensionless azimuthal (or tangential) velocity defined as $V_\phi/\tau_0\omega$
k	local mass transfer coefficient, cm/sec
K	average mass transfer coefficient, cm/sec
r	radial coordinate, cm
r_0	radius of spherical electrode, cm
Re	Reynolds number defined as $r_0^2\omega/\nu$, dimensionless
Re_x	local Reynolds number based upon the surface distance, x , from the leading edge of the flow boundary layer, dimensionless
Sc	Schmidt number defined as ν/D , dimensionless
Sh	average Sherwood number defined as Kr_0/D , dimensionless
Sh_{loc}	local Sherwood number defined as kr_0/D , dimensionless
Sh_x	local Sherwood number based upon the surface distance, x , from the leading edge of the boundary layer, dimensionless
V_θ	meridional velocity component, cm/sec
V_ϕ	azimuthal (or tangential) velocity component, cm/sec
x	surface distance from the leading edge of the boundary layer, cm
η	dimensionless radial distance defined as $(r - r_0)(\omega/\nu)^{1/2}$
θ	latitude coordinate, rad
ν	kinematic viscosity, cm ² /sec
ρ	density of electrolyte, g/cm ³
ϕ	azimuthal coordinate, rad
ω	angular velocity, rad/sec

Electrolytic Determination of Porosity in Gold Electroplates

R. J. Morrissey (pp. 446-450, Vol. 119, No. 4)

F. Mansfeld:⁴⁶ In the paper discussed here and elsewhere⁴⁷ Morrissey uses an expression derived by Stern⁴⁸ for an electrochemical determination of porosity in gold electroplates. Several corrections are necessary for Eq. [1] in Morrissey's paper. The exact (and complete) expression for the galvanic current I_g flowing between two dissimilar metals is⁴⁹

$$\log I_g = \frac{\phi^C - \phi^A}{\beta_a + \beta_c} + \frac{\beta_c}{\beta_a + \beta_c} \log A^C i_{\text{Ccorr}} + \frac{\beta_a}{\beta_a + \beta_c} \log A^A i_{\text{Acorr}} \quad [1]$$

where ϕ^C and ϕ^A are the corrosion potentials and i_{Ccorr} and i_{Acorr} are the corrosion C.D. (not exchange C.D. for the anodic and cathodic processes) of anode and cathode before galvanic coupling. A^C and A^A are the respective areas of the two dissimilar metals (not area fractions). Under Morrissey's assumption⁴⁷ Eq. [1] can be simplified to

$$I_g = C_1 (A^A)^{\frac{\beta_a}{\beta_a + \beta_c}} \quad [2]$$

The form of Eq. [2] (and Eq. [4]) in this paper⁴⁷ seems to result from a typographical error.

It will be noted that ϕ^C and ϕ^A are the corrosion potentials of the uncoupled metals. No information can therefore be obtained for the potential ϕ_g of coupled metals. This relationship has been shown by Stern⁴⁸ and later by Mansfeld⁴⁹, to be

⁴⁶ North American Rockwell Science Center, Thousand Oaks, California 91360.

⁴⁷ R. J. Morrissey, *This Journal*, 117, 742 (1970).

⁴⁸ M. Stern, *Corrosion*, 14, 329t (1958).

⁴⁹ F. Mansfeld, *ibid.*, 27, 436 (1971).

$$\phi_g = k + \frac{\beta_c \beta_a}{\beta_a + \beta_c} \log \frac{A^C}{A^A} \quad [3]$$

If the area fraction of the anode $A_A = \frac{A^A}{A^C + A^A}$ is used instead of the area ratio A^C/A^A , Eq. [3] can be written as

$$\phi_g = k + \frac{\beta_c \beta_a}{\beta_a + \beta_c} \log \frac{1 - A_A}{A_A} \quad [3a]$$

Since the area fraction of Cu is very small ($A_A \ll 1$) under the conditions of Morrissey's experiments, Eq. [3a] can also be written in the form

$$\phi_g = k - \frac{\beta_c \beta_a}{\beta_a + \beta_c} \log A_A \quad [3b]$$

which predicts that the potential of gold plated Cu becomes more negative as the area fraction of Cu increases.

The derivation by Stern assumes that only an oxidation process occurs on the anode and only a reduction process occurs on the cathode. It is further assumed that the reactions are completely under charge transfer control. It is unlikely that the latter assumption is true for a Cu-Au couple in aerated 0.1N KCl or 0.1N NH_4Cl . In these solutions the cathodic reaction is more likely controlled by diffusion of oxygen. In this case the potential of the galvanic couple was shown by Mansfeld⁴⁹ to be related to the area ratio A^C/A^A by

$$\phi_g = \phi^A + \beta_a \log \left(\frac{A^C}{A^A} + 1 \right) \quad [4]$$

Upon introduction of the area fraction of the anode (Cu) $A_A = \frac{A^A}{A^A + A^C}$, Eq. [4] can be written as

$$\phi_g = \phi^A - \beta_a \log A_A \quad [5]$$

A plot of the potential of a Cu-Au couple *vs.* area fraction of Cu should therefore result in a straight line with a slope of $-\beta_a$. The plots by Morrissey have slopes of -34 to -36 mV (Fig. 2, 3⁴⁷), while a Tafel slope $\beta_a = 51$ mV is reported for Cu. Luborsky *et al.*⁵⁰ on the other hand, show plots of $\log A^C/A^A = A_C/A_A$ *vs.* galvanic potential ϕ_g of Cu-Au couples in 1M NH_4Cl which result in a straight line with a slope of 58 mV. The results of Luborsky also suggest that the cathodic reaction is under diffusion control since the potential of the couple becomes independent of the area ratio for $A^{\text{Cu}}/A^{\text{Au}} > 0.05$. This behavior is predicted by Eq. [4] which shows that for $A^C/A^A \ll 1$

$$\phi_g \approx \phi^A = \text{constant}$$

An interpretation of the results of Fig. 3 in the paper under discussion cannot be given since the author does not state clearly how he calculated the "gross area C.D." in the expression $\Delta J/\Delta V$ (mho \cdot cm²). Under the assumption that charge transfer control occurs, which is doubtful as pointed out above, Eq. [1] and Eq. [3] can be combined to give a correlation between the galvanic potential ϕ_g and the galvanic current I_g

$$\phi_g = \phi^A - \beta_a \log i_{\text{Acorr}}^A + \beta_a \log I_g \quad [6]$$

A correlation can also be given between ϕ_g and the galvanic current density $i_g^A = I_g/A^A$ with respect to the area of the anode (Cu)

$$\phi_g = \phi^A - \beta_a \log i_{\text{Acorr}}^A + \beta_a \log i_g^A \quad [7]$$

From Eq. [6] and Eq. [1] it follows

$$\frac{\partial \phi_g}{\partial \log I_g} = \beta_a - \beta_a \frac{\partial \log A^A}{\partial \log I_g} = -\beta_c \quad [8]$$

while from Eq. [7], one derives

$$\frac{\partial \phi_g}{\partial \log i_g^A} = +\beta_a \quad [9]$$

Since both I_g and i_g are proportional to the polarization admittance, one would expect that a logarithmic plot of $\Delta J/\Delta V \approx i_g^A$ *vs.* ϕ_g results in a straight line with a slope of $+\beta_a$, while a similar plot of $\Delta I/\Delta V \approx I_g$ should lead to a slope of $-\beta_c$. If the current density in Fig. 3 were based on the exposed area of Cu, then one would expect a slope of $+51$ mV according to Morrissey's data. Instead a line with a slope of -73 mV is reported.

All derivations above do not take account of potential (*IR*) drops in the pores, which could significantly affect current-potential relationships. It could also affect linear polarization measurements. The results of Fig. 2 which indicate a linear relationship between current and potential over a potential range of more than 50 mV are rather surprising in light of recent considerations⁵³ and might very well be significantly influenced by *IR* drops in the pores.

A further treatment of the dependence of galvanic current and galvanic potential on porosity of a metallic coating can be found in the paper by Oldham and Mansfeld.⁵¹

Morrissey also mentions leakage current measurements for determination of porosity in electrodeposits. A similar technique has recently been described by Mansfeld and Parry.⁵² Using a potential sweep technique a quantitative electrochemical test for porosity in permalloy plated memory wire was described. In this test, which should also be of value for Au plated Cu, a potential sweep is applied to the metal couple immersed in 3.5% NaCl in a potential region where the dissolution rate of the cathode (Au, Permalloy) is very low, while that of the anode (Cu) is high. From integration of the resulting current peak, the area of Cu exposed through pinholes can be determined after suitable calibration.

R. J. Morrissey: As has been pointed out in the foregoing discussion, the mathematics appearing in the paper under discussion and also in our previous reference⁴⁷ are based on expressions originally given by Stern.⁴⁸ These expressions were derived under the assumptions that only oxidation was proceeding at the anode and only reduction at the cathode, and that the over-all process was under activation control. Mansfeld⁴⁹ has recently derived a series of general expressions describing the variation of the corrosion potential and the corrosion current with the respective anodic and cathodic areas. For the case of activation control, the results of the Stern and Mansfeld treatments are consistent, and Mansfeld's Eq. [3b] above is identical to Eq. [2] in Morrissey.⁴⁷

Mansfeld expresses the opinion that for gold-copper couples in 0.1M NH_4Cl or 0.1M KCl, the cathode reaction is probably controlled by the diffusion of oxygen. He then derives expression [5], showing that for this case, a plot of corrosion potential *vs.* the logarithm of the anode area fraction should yield a slope equal to β_a , rather than to $(\beta_a \beta_c / \beta_a + \beta_c)$, which would be the case under activation control. He then cites data from Luborsky *et al.*,⁵⁰ purportedly in support of this hypothesis.

In our own previous work,⁴⁷ plots of corrosion potential *vs.* the logarithm of the anode area fraction yielded slopes of 34-36 mV, which was felt to be in excellent agreement with the value of $(\beta_a \beta_c / \beta_a + \beta_c)$, and thus indicative of activation-controlled kinetics. Luborsky *et al.* plot corrosion potential *vs.* the

⁵¹ K. B. Oldham and F. Mansfeld, Submitted to *J. Appl. Electrochem.*

⁵² F. Mansfeld and E. P. Parry, *Corrosion*, 26, 542 (1970).

⁵³ K. B. Oldham and F. Mansfeld, *ibid.*, 27, 434 (1971).

⁵⁰ F. E. Luborsky, M. W. Breiter, and B. J. Drummond, *This Journal*, 119, 92 (1972).

logarithm of the ratio of the anodic and cathodic area fractions (not of the areas, as implied by Mansfeld). At small values of the anode area fraction, this reduces to a plot of corrosion potential vs. the logarithm of the anode area fraction alone; and in 0.1M NH_4Cl Luborsky *et al.* obtain a slope of approximately 32 mV, which is in close agreement with our own data. In 1.0M NH_4Cl , these authors obtain a slope of greater than 50 mV. This value approximates that of β_A , implying that in this latter electrolyte the cathode reaction is diffusion-controlled. This is quite reasonable, in view of the reduced oxygen solubility in more concentrated electrolytes. It is also significant that the data of Luborsky *et al.* show that the curve for 1.0M NH_4Cl begins to depart from linearity at smaller values of the anode area fraction than does that for 0.1M NH_4Cl . One can thus make a strong case for diffusion control of the cathode reaction for gold-copper couples in 1.0M NH_4Cl . It seems equally clear, however, that at small values of the anode area fraction, the kinetics in 0.1M NH_4Cl are activation-controlled.

Mansfeld questions the significance of plotting values of $(\Delta J/\Delta V)$ in Fig. 3 of the paper under discussion, and derives Eq. [8], which shows that in the case of activation control, a plot of corrosion potential vs. the logarithm of the galvanic current (or, by extension, of $\Delta I/\Delta V$) should yield a slope of $-\beta_C$. He also expresses surprise at the linearity of the polarization curves obtained, citing a previous publication by Oldham and himself⁵¹ which states that polarization curves should ordinarily show curvature in the vicinity of the corrosion potential in order for the Stern-Geary relationship to apply. He then suggests that the apparent linearity might be indicative of ohmic control by the IR drops in the pore channels.

The values of $(\Delta J/\Delta V)$ obtained in this work were arrived at by dividing the experimentally determined values of $(\Delta I/\Delta V)$ by the total geometric areas of the various specimens. These were 2.5 cm² for the gold-plated copper specimens and 10.8 cm² for the solid gold specimens. Figure 3 was presented in the form shown because, plotted in this form, the data points for the solid gold specimens fall nicely along the line extrapolated from the data points for the various gold-plated specimens, whereas in a plot of corrosion potential vs. the logarithm of $(\Delta I/\Delta V)$ they fall well off the line. Such a plot is shown in Fig. 3a. The slope of this plot is -90 mV, which is in excellent agreement with the value of 93.5 mV obtained for β_C and in accordance with Mansfeld's Eq. [8]. It had been shown in the paper under discussion that, also in the case of activation control, a plot of the logarithm of $(\Delta I/\Delta V)$ vs. the logarithm of the anode area fraction should yield a slope equal to $(\beta_A/\beta_A + \beta_C)$. Figure 4 of the paper under discussion is such a plot, and the slope obtained is in close agreement with the predicted value.

As to the linearity of the polarization curves obtained, I can only cite the wealth of instances in the literature of polarization data which are linear or, as noted by Jones,⁵⁴ at least approximately so within the discrimination capabilities of available instrumentation, even over extended ranges of potential.⁵⁵ It remains the opinion of this writer that since the

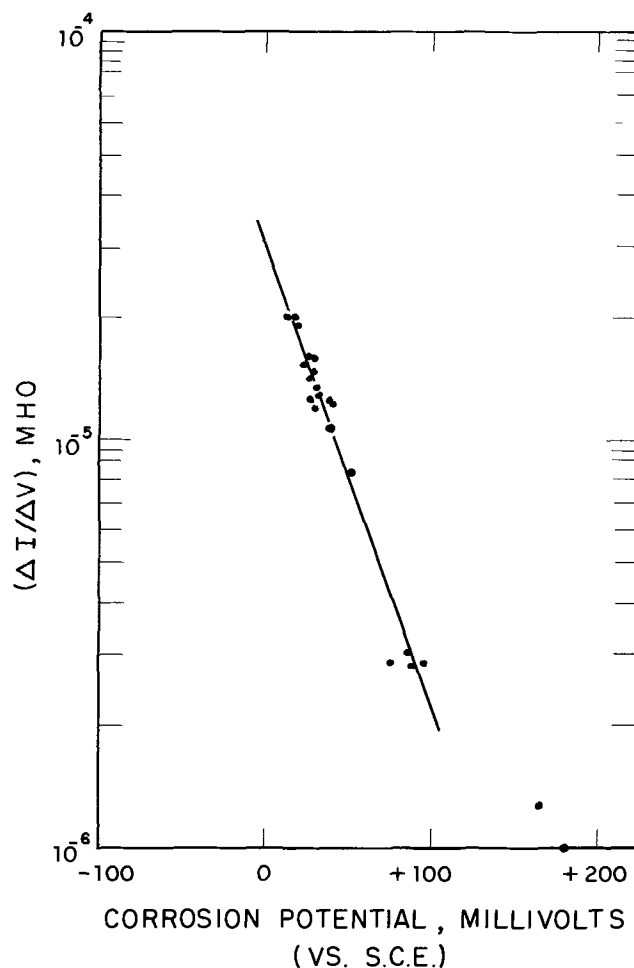


Fig. 3a. Comparison of corrosion potential and polarization admittance values.

Stern-Geary expression represents an approximation, ordinarily applicable over only a relatively limited range of potential, any attempt to ascribe physical significance to what amounts to the derivative of such a function should be approached with caution.

The question of ohmic control by electrolyte in the pore channels has been raised previously,⁴⁷ and is the basis of Clarke and Britton's original treatment⁵⁶ of linear polarization data obtained on specimens coated with porous electroplates. As has been reiterated in these comments, all of the evidence available for gold-copper couples in 0.1M NH_4Cl electrolyte is indicative of activation-controlled kinetics at small overpotentials and for small values of the anode area fraction. A direct test of the effects of concentration and resistance polarization on the corrosion potentials of gold-plated copper specimens in 0.1M NH_4Cl has been described.⁴⁷ The results, shown in Table II in that paper, indicated that such effects were negligible for copper specimens plated with gold deposits of 50, 100, 200, and 400 μm . (1.27, 2.54, 5.08, and 10.16 μm) thickness.

⁵⁴ D. A. Jones, *Corrosion*, 28, 180 (1972).

⁵⁵ S. Barnartt, *Corrosion Sci.*, 9, 145 (1969).

⁵⁶ M. Clarke and S. C. Britton, *Trans. Inst. Metal Finishing*, 36, 58 (1958).



High-Resolution Negative Photoresist

R. M. Walters and R. Brecher

Bayside Research Center, GTE Laboratories Incorporated, Bayside, New York 11360

ABSTRACT

A negative-working high-resolution photoresist system is described. The preparation of the polymer and sensitizer components of the photoresist is outlined. The importance of the molecular weight distribution of the polymer on the properties of the photoresists is discussed. Consideration of this, and other, parameters has led to a resist formulation capable of functioning in film thicknesses of 2000-3000Å, showing an acceptably low pinhole density and having a resolution capability of 400 lines/mm.

Negative-working photoresists are materials of fundamental importance in the fabrication of semiconductor devices by means of photolithographic procedures. In recent years there has been a trend toward microimage device geometries, and the fabrication of these devices calls for etching in silicon dioxide linewidths in the range 1-5 μm . The advent of large scale integrated circuit devices has also occurred in recent years, and these two factors have placed increasingly severe demands on the available photoresist technology.

Kodak Thin Film Resist (KTFR) has received much attention in this field and Clark and Turner (1) have investigated the high-resolution capabilities of this resist. However when used in film thicknesses of 5000Å or less, which are necessary to achieve a resolution of ≥ 400 lines/mm, the tendency of this resist to pinhole can present problems (1, 2).

In view of the need for a photoresist with the capability of giving 1 μm lines on 1 μm spaces (a resolution of 500 lines/mm) using appropriately thin resist films with acceptably low pinhole densities (*i.e.*, ≤ 30 pinholes/in.²), the negative resist system described by Kornfeld (3) was investigated. This resist consists of an ultraviolet-sensitive diazido compound which is used as the photo-initiator (or sensitizer) for the cross-linking of an unsaturated alkyd resin. This system is attractive since the polymer and sensitizer components of the resist are prepared initially as separate species and can then be combined over a wide range of ratios in photoresist formulations. This system was considered to offer a greater probability of giving a resist with the required resolution capabilities than attempts to modify chemically any of the commercially available negative resists.

Experimental

The sensitizer is 4,4' diazido benzophenone-p-carboxyphenylhydrazine; a pale yellow crystalline solid, designated (ABH). This compound is prepared, in a three step synthesis, from 4,4' diamino diphenylmethane. Initially the amino groups are converted to azide groups via diazonium salt intermediates. Oxidation of the central methylene group to carbonyl is then accomplished with chromium (VI) to give 4,4' diazido-

benzophenone. Reaction of this species with p-carboxy phenylhydrazine gives ABH. The over-all yield of ABH is 40%. The ultraviolet absorption spectrum shows a maximum at 360 nm, and ABH shows good photoreponse to a high-pressure mercury arc.

The polymer component of the resist is the commercial alkyd Rezyl 387-5 obtainable from Koppers Company. A fractional precipitation method was used to obtain polymer samples with different molecular weight distribution (4). The standard fractionating procedure was to dissolve 100g of raw alkyd in 2.28 moles of trichloroethylene followed by the addition of 10 moles isopropanol. This solution was stirred at a constant rate and water (*i.e.*, the nonsolvent) was added at a constant rate of 10 g/min until the required amount of water had been added. The bottom resin phase which separates is drawn off and the solid polymer precipitated with petroleum ether. After several washings with petroleum ether the polymer is dissolved in methylethylketone (MEK) and then reprecipitated with petroleum ether. The polymer is again washed with petroleum ether and again dissolved in MEK. Vacuum distillation of this solution served to distill off all the petroleum ether. The polymer solids content of the solution was estimated gravimetrically and then suitably dilute polymer stock solutions were prepared by adding the required solvents. Molecular size distribution data were obtained using a Waters Model 200 gel permeation chromatograph. Photoresist solutions were prepared on a weight/weight basis, by dissolving ABH in a quantity of polymer stock solution.

Resist films were applied to the wafers by spinning. Film thickness was measured with a Talysurf Profilometer. This method proved to be quick and convenient and acceptably accurate (5) for resist thicknesses down to 2000Å. The Talysurf data correlated well with a series of resist film thicknesses measured by an interferometric method (6). The Talysurf method was also used to gain information on the surface quality, *i.e.*, the flatness of the resist films after having first established the flatness of the wafer substrates.

The silicon dioxide films of the various thicknesses used were grown on the silicon wafers as follows: 10,000Å SiO₂ films were grown by using a 1¼-hr steam oxidation at 1200°C followed by a 5-min dry oxidation at the same temperature. The 4000Å SiO₂ films were grown using a 4-hr dry oxidation at 1200°C.

Key words: photolithography, micro-imaging, resist-composition.

The pinhole densities were measured in the following way. A blank measurement was made on the original SiO_2 layers, after which the wafers were prepared and coated with resist and then given the same exposure as was used for imaging in the resist. The mask used in the exposure was a 5.0×5.0 cm glass blank, with no opaque areas on it, so that the entire resist film area was exposed. The exposed wafer was put through the development and post bake cycle followed by an etch in buffered hydrofluoric acid. The etching time was that known to be required for the particular silicon dioxide thickness being used. The etched and stripped wafers were examined by scanning the wafer at 200X magnification and counting the number of circular pinholes, of $1 \mu\text{m}$ diameter or greater, occurring randomly in the silicon dioxide layer. Clusters of pinholes around obvious oxide defects were not included nor were pinholes occurring at the very periphery of the wafer.

The two masks of main interest used were obtained from Qualitron Corporation and were 5×5 cm chrome on glass. The repeat unit patterns of these two masks are shown in Fig. 1 and 2. In Fig. 1 the narrowest set of L shaped lines are $2.5 \mu\text{m}$ lines on $2.5 \mu\text{m}$ spaces. The interdigitated finger pattern of lines are also $2.5 \mu\text{m}$ lines on $2.5 \mu\text{m}$ spaces. In Fig. 2 the numbers on the mask refer to microinches and the narrowest line geometries on this mask ($50 \mu\text{in.}$) are $1.25 \mu\text{m}$ lines on $1.25 \mu\text{m}$ spaces. The photolithographic work was done in a class 100 clean room.

A typical photoresist process cycle would be as follows.

1. Substrates are cleaned with a cycle of various organic solvents. Before coating a 5-min bake at 1200°C is given.

2. Spin coat on Headway spinner, 4000 rpm for 30 sec typically. The resists were filtered at point of use by dispensing the resist onto the wafer from a glass syringe fitted with a Millipore $1 \mu\text{m}$ "Duralon" filter.

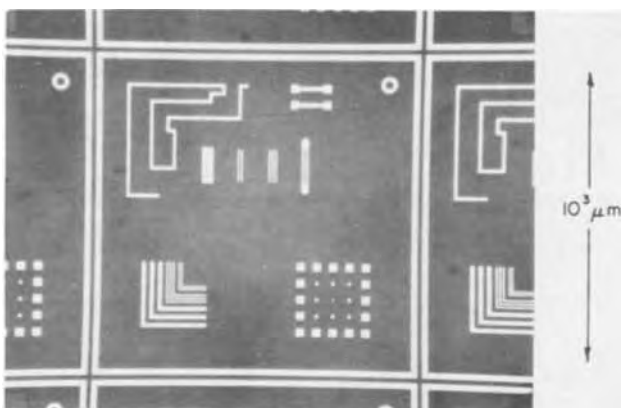


Fig. 1. Unit pattern of Qualitron mask

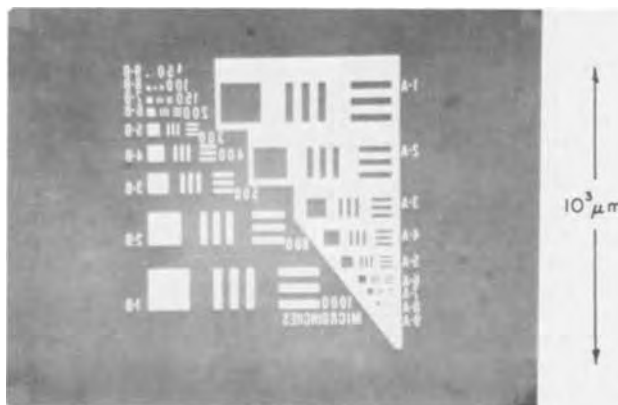


Fig. 2. Unit pattern of Qualitron mask

The wafer surface was flooded with resist immediately prior to spinning.

3. Air dry for at least 10 min. The use of a prebake is not necessary and is in fact deleterious to the behavior of the resist in the development and etching steps.

4. Expose. A Kulicke and Soffa Model 6822 alignment tool was used.

5. Dip development in xylene for 2 min followed by a 20 sec isopropanol rinse. Spray development and rinsing can be used with equal effect.

6. Postbake for 10 min at 250°C .

7. Etch.

8. Strip off photoresist film with J-100 (Indust-Ri-Chem Laboratory) 15 min at 140°C followed by a similar treatment with fresh J-100.

Results and Discussion

The occurrence of pinholes in the silicon dioxide layer during the various photolithographic steps, in the manufacture of integrated circuits, is one of the major factors governing the yield of the devices (7). In general, pinholes of greater than $1 \mu\text{m}$ diameter present the most serious problems. The occurrence of pinholes etched into the oxide arise from pinholes in the resist film which occur during the photomasking process from a variety of distinct causes. Pinholes in the resist film can occur as the resist is being applied onto the wafer; the presence of silicon spikes through the oxide, particulate matter on the oxide surface during spinning, and the inherent film-forming qualities of the resist (at the particular resist thickness being used) are important factors at this point of the process. Immediately before, and during, the exposure step the presence of opaque particulate matter on the resist surface, or on either surface of the mask, will tend to interfere with the insolubilization of the resist and result in the formation of pinholes in the resist and subsequently in the oxide.

The above factors will always operate to some degree but can be minimized by close control of the processing procedures. A further source of pinholes, which is more difficult to control, lies in the nature of the chemistry of negative working photoresists. The commercial negative resists used in microcircuitry, and the system under discussion, all appear to be based on the crosslinking of polymer molecules initiated by a light-sensitive sensitizer species which furnishes free radicals upon irradiation with uv light (8). The exposure of such a film is thus a process whereby the normally soluble polymer molecules are crosslinked and become insoluble, by virtue of the increase in molecular weight which has occurred. Thus in those areas of the resist film where the photocrosslinking does not occur to a sufficient extent to withstand the solvent action of the developer, a pinhole is likely to result. This effect is the major source of pinholes in high-resolution work since achieving adequate crosslinking in the necessary thin resist films becomes increasingly more difficult (1). The pinhole data presented later were derived from experiments where every effort was taken to exclude pinholes from other sources and the pinhole density data obtained are, in the main, a measure of the ability of the resist to crosslink effectively and so withstand the processing conditions.

The resolution capabilities of the resist has been measured in terms of the image structure etched into the silicon dioxide layer. A pattern of lines on spaces, of any particular width, was used since it is generally more difficult to achieve such an etched pattern rather than a single line of the same dimension. The resolution attainable is dependent, among other parameters, on both the thickness of the photoresist layer and the thickness of the silicon dioxide film to be etched through. Both of these films must be as thin as possible to achieve maximum resolution. The silicon dioxide

must be of sufficient thickness to constitute an effective diffusion mask and 4000Å of silicon dioxide was used since this fulfills the diffusion mask criteria and yet still allows the etching of line patterns of 500 lines/mm, i.e., 1 μm lines on 1 μm spaces. The resist film must be as thin as possible commensurate with good adhesion, etch resistance, imaging properties, and pinhole behavior.

Molecular weight distribution.—The molecular weight distribution of the polymer component of the photoresist is one of the major factors governing such properties of the resist as adhesion, etch resistance, image line quality, the tendency to pinhole, and also the ease of handling of the resist. Experiments were therefore carried out to investigate the effect of varying the molecular weight distribution of the Rezyl alkyd on the resist properties. Fractions of the Rezyl 387-5 of different molecular weight distribution were obtained using the fractional precipitation method described previously. In the various fractionations different amounts of water were added to the reaction mixture, at a constant rate of 10 g/min, to isolate fractions with different molecular weight distributions. Stock solutions were prepared from each quantity of polymer using a 1:1 (wt:wt) mixture of MEK and cyclohexanone as the solvent system. The fractions were characterized quantitatively with respect to their molecular weight distributions by the gel permeation chromatograph (GPC) method (9). The instrument was calibrated with a series of polystyrene standards (Waters Associates). The raw data from the GPC are in terms of molecular size, or polymer chain length, and from these data apparent number average chain lengths, \bar{A}_N , and weight average chain lengths, \bar{A}_W , can be calculated and expressed as angstrom unit values. The data are presented in this way since the molecular weight of the polymer per angstrom unit of chain length, (i.e., the Q factor) is not known with any precision.

Table I shows the \bar{A}_N and \bar{A}_W values obtained by the GPC characterization of six samples of fractionated Rezyl. The different fractions were obtained by adding different numbers of moles of water to the standard fractionation mixture.

The \bar{A}_N values are probably more reliable than the \bar{A}_W values due to the marked sensitivity of \bar{A}_W to errors in the estimation of the highest molecular weight species in the samples. Figure 3 shows the \bar{A}_N values plotted as a function of the number of moles of water used in the fractionation. These values fall on a smooth curve which becomes asymptotic to the measured value of 210 for the number average chain length of the raw Rezyl alkyd.

In view of the necessity of working with as thin a resist film as possible, it became of interest to determine how the polymer solids content and the spinning speed influenced the thickness of the resist film obtained. Figure 4 shows the resist film thickness obtained on our apparatus using 20, 15, and 10% polymer solids in 1:1 MEK/cyclohexanone as solvent, with spinning speeds in the range 4000 to 9000 rpm. The solutions were prepared using polymer fractionation 4 in Table I. The curves show that the polymer solids content of

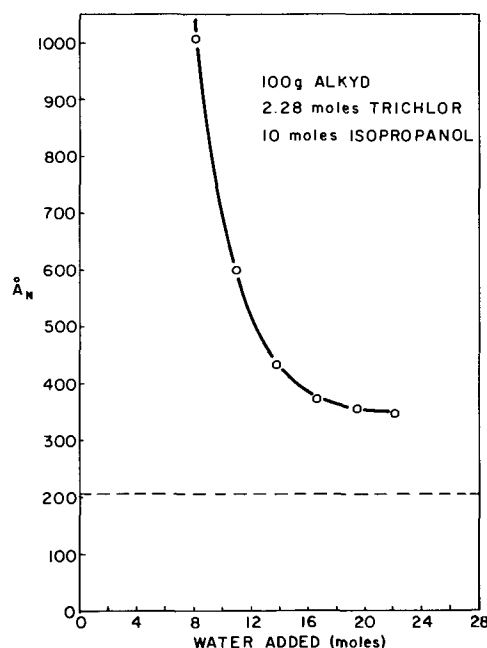


Fig. 3. Number average chain length vs. moles of water added

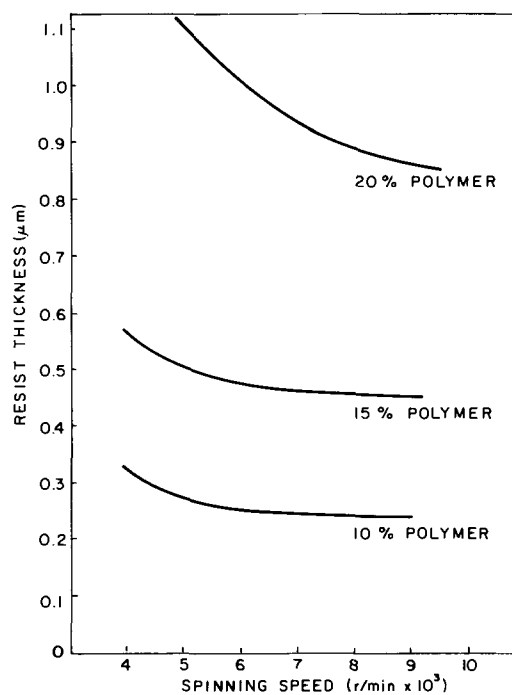


Fig. 4. Resist film thickness vs. spinning speed

the resist is the most important parameter to be varied to achieve film thicknesses of <3000Å and that the final spinning speed is less important as a parameter since the curves for the 15 and 10% solutions are essentially parallel to the abscissa above a spinning speed of 5000 rpm. Therefore adjusting the polymer solids content of the resist solution was the method used to vary the resist film thickness.

Accordingly a series of ten photoresist solutions was prepared from each of the six polymer fractions with the polymer concentration going in 1% increments over the range 1-10% polymer. A constant ratio of polymer solids to sensitizer was maintained; the sensitizer concentration being 8% of the amount of polymer present. It was found that below 5% polymer, for all the fractions, the resist films pinholed badly in all cases during development; varying the sensitizer concentration could not correct this condition. For the polymer fractions of

Table I. \bar{A}_N and \bar{A}_W values obtained by GPC characterization

Fraction No.	Moles water added to reaction mixture	\bar{A}_N	\bar{A}_W	Polydispersity ratio, \bar{A}_W/\bar{A}_N
1	22.2	322	8,670	26.9
2	19.5	354	7,650	21.3
3	16.7	370	9,540	25.7
4	13.9	433	10,010	18.2
5	11.1	599	11,720	19.5
6	8.3	1,012	15,420	15.2

$\bar{A}_N > 550$ the resist solutions became increasingly difficult to filter down to the $1 \mu\text{m}$ level as the polymer concentration increased above 5%. Also the resist images became increasingly difficult to develop out and the line quality of the images consequently deteriorated. For the polymer fractions of $\bar{A}_N < 400$, the trends observed were reduced adhesion of the resist during etching and an increasing tendency for the resist to pinhole during the development step. This tendency to pinhole could not be corrected for resists up to 10% polymer and 8% sensitizer.

Thus, the optimum region for photoresist behavior, for the fractionation procedure described, was judged to be where \bar{A}_N is between 400 and 500 with \bar{A}_W in the region of 10,000.

High-resolution capabilities of the resist.—The high-resolution capabilities of photoresist solutions prepared with polymer from fractionation 4, in Table I, were evaluated. The chrome mask whose repeat unit is shown in Fig. 1 was used. Figure 5 shows sets of L-shaped lines of 5.0 and $2.5 \mu\text{m}$ width etched in 4000\AA of SiO_2 . Figure 6 shows the interdigitated pattern of $2.5 \mu\text{m}$ lines again etched in 4000\AA of SiO_2 . These patterns were obtained with virtually 100% yield over the wafer. The photoresist solution used was 10% in polymer solids with a sensitizer concentration 8% of the polymer solids. This solution had a viscosity of 3.7 cp and yielded 2800\AA films when spun on at 4000 rpm. Exposure time was 2 sec, otherwise the processing was as described previously. Attention was then turned to the chrome mask whose repeat unit is shown in Fig. 2 since this mask contains patterns of lines on spaces down to $1.25 \mu\text{m}$. It was found that the narrowest line patterns that could be etched satisfactorily into 4000\AA of silicon dioxide, with 100% yield over the wafer, were the $100 \mu\text{in.}$ lines or $2.5 \mu\text{m}$ lines on $2.5 \mu\text{m}$ spaces. Figure 7 shows such patterns. Although the patterns of $1.25 \mu\text{m}$ lines were present in the developed photoresist layer, these images had not been etched into the oxide and they occurred only irreproducibly over the wafer.

The problem in etching out these lines was found to be due to incomplete development of the resist from the $1.25 \mu\text{m}$ line areas which caused a subsequent interference with the etching step. Careful microscopic

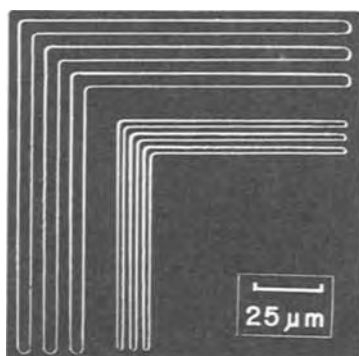


Fig. 5. Dark-field light micrograph of 2.5 and $5.0 \mu\text{m}$ lines etched in 4000\AA of SiO_2 .



Fig. 6. Dark-field light micrograph of interdigitated $2.5 \mu\text{m}$ lines etched in 4000\AA of SiO_2 .

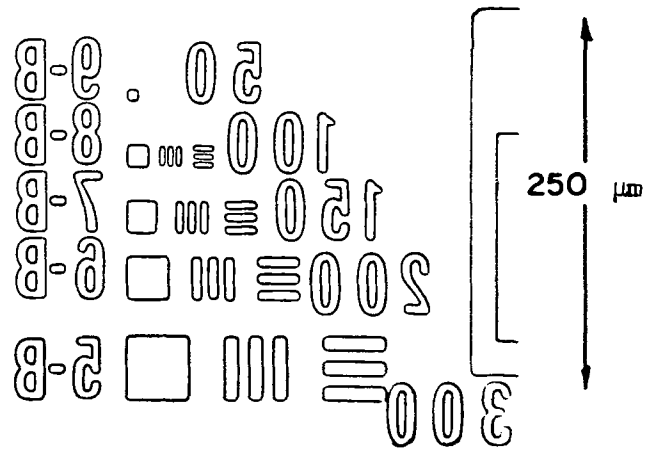


Fig. 7. Resolution test pattern etched in 4000\AA of SiO_2

examination indicated the presence of a very thin layer of resist, remaining after development, in the $1.25 \mu\text{m}$ line areas, whereas the unexposed resist was completely removed down to the oxide, from the $2.5 \mu\text{m}$, and larger, image areas. The presence of resist in the $1.25 \mu\text{m}$ lines is presumably due to partial crosslinking of the resist by scattered light to a sufficient extent to prevent clean development.

Various approaches were taken to circumvent this problem; these included increasing the developing time, extending the etching time, using lower sensitizer concentrations, and the use of more powerful developing solvents. In addition, the polymer solids content of the resist was lowered to allow the use of films approximately 2000\AA thick. Although these approaches often resulted in a higher proportion of the $1.25 \mu\text{m}$ lines being etched out, there was often either an increase in pinhole density, to an unacceptable level, or a deterioration of the image quality. None of the approaches, then, constituted a satisfactory solution to the problem.

The resists prepared from fractionations 5 and 6 in Table I had shown quite strikingly that the ease of development of unexposed photoresist areas is strongly dependent on the molecular weight distribution of the polymer. The highest molecular weight species were more difficultly soluble in the developer. Also the effects of scattered light over the wafer surface during the exposure step, will be most pronounced with high molecular weight polymer molecules since relatively few chemical crosslinks are needed to give a species which shows much reduced solubility in the developer. Thus, it was reasoned that the removal of the highest molecular weight components of the polymer might enable a photoresist to be prepared which would develop cleanly from unexposed $1.25 \mu\text{m}$ line areas, due to the reduced effects of scattered light.

Table II shows the results obtained in three fractionations of the raw Rezyl where a first addition of water was used to separate out the highest molecular weight polymer. This was separated off and discarded. A second addition of water caused a further quantity of polymer to separate out. This was isolated and processed by the usual procedure. The total amount of water used in these three fractionations was 13.9 moles in each case.

Table II. Results of three fractionations of raw Rezyl

Fractionation No.	Moles water added in first addition	Moles water added in second addition	\bar{A}_N	\bar{A}_W	Polydispersity ratio
7	5.00	8.90	430	8,063	18.7
8	5.56	8.34	392	4,999	12.0
9	6.12	7.78	361	3,089	8.5

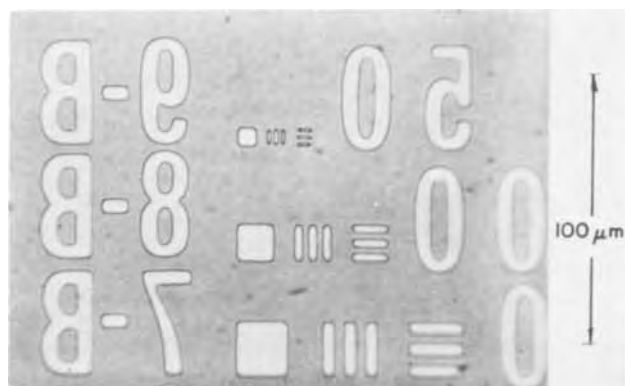


Fig. 8. Resolution test pattern etched in 4000Å of SiO₂

It is apparent from the \bar{A}_W values shown that this modified fractionation procedure has effectively removed the higher molecular weight polymer species to a degree depending on the amount of water used in the first addition.

Photoresist solutions were prepared from these three fractions and examined. The trend toward easier development of the 1.25 μm lines as the \bar{A}_N and \bar{A}_W values decrease was immediately evident. Fractionations 7 and 8 gave less than 100% yields of the 1.25 μm lines, but no development problems were experienced with the resists prepared from Fractionation 9, and 100% yields of the 1.25 μm lines on space patterns were consistently obtained with the normal xylene development. Figure 8 shows the 1.25 μm lines etched through 4000Å of silicon dioxide. The lines on spaces are clearly resolved and correspond to a resolution capability of 400 lines/mm. The processing conditions were as described previously and the 1.25 μm lines were obtained using photoresist solutions containing 10 and 8% polymer solids, respectively, with a sensitizer concentration of 8% of the polymer solids in both cases. The solvent system was the usual 1:1 MEK/cyclohexanone. The resist film thicknesses obtained at 4000 rpm spinning speed were 3000 and 2200Å from the 10 and 8% polymer solutions, respectively. The other important features of the resist such as acid resistance, adhesion, and image quality were judged to be comparable to when polymer of $\bar{A}_N = 430$ and $\bar{A}_W = 10,000$ was used.

Pinhole data comparison with KTFR.—The pinhole data accumulated for the two Rezyl fractions of main interest are shown in Table III together with comparative data for KTFR. The pinhole data are also presented as a function of the percentage of polymer solids, and hence film thickness, of the resist. The KTFR was centrifuged initially and then all the photoresist systems were filtered to the same 1 μm level.

The photoresists of various types prepared from the Rezyl polymer, and described in Table III, are thus capable of functioning in films in the thickness range of 2000 to 3000Å with an acceptably low pinhole density of 30 pinholes/in.². At a film thickness of 3000Å, KTFR shows an unacceptably high pinhole density, and it is only when a KTFR thickness of 10,000Å is used

that the pinhole density becomes approximately equal to the pinhole densities exhibited by the resists described.

It will be noted, however, that no pinhole data are presented for any Rezyl photoresist solutions of less than 8% polymer solids. For all the Rezyl fractions no useful photoresist of less than 5% polymer could be prepared since all developed a large number of pinholes in the development step. Initial pinhole measurements made on photoresist films obtained from 6% polymer photoresist solutions prepared using both Rezyl fractionations 4 and 9 gave acceptably low pinhole densities in films $\sim 1400\text{Å}$ thick. The use of these resists on a day-to-day basis, however, showed that the successful functioning of these resists depended markedly on rigorous control of the processing conditions; otherwise the resists pinholed badly. It was observed for instance that on days when the humidity in the laboratory was toward the high end of the allowed limits, the resist tended to behave in a nonreproducible manner (10). This nonreproducibility negated the routine use of 6% polymer resists. A polymer solids content of at least 8% produced a completely reproducible behavior, within the errors of evaluation, on a day to day basis. The somewhat thicker resist film allowed for the necessary latitude in the processing conditions.

The use of photoresists on phosphorus-doped silicon dioxide surfaces often presents adhesion problems (11). Accordingly a series of silicon wafers were steam oxidized at 1200°C to give a 10,000Å film of silicon dioxide followed by a 7-min doping with phosphorus oxychloride at 1050°C. Patterns of various geometries (down to 10 μm) were etched into the doped oxide using a photoresist prepared from Rezyl fractionation 4 in Table I. The line quality was judged to be not quite as good as obtained with undoped oxide and so the usual techniques, taken with KTFR, etc., to prevent loss of adhesion on phosphorus-doped surfaces, such as a steam leach or the deposition of a thin film of pyrolytic oxide, are probably also appropriate for the Rezyl-based photoresists to insure good adhesion.

Photoresist stability.—The stability of the photoresists with respect to time, i.e., the shelf life, is of great practical importance. The stability of the individual chemical components of the resist is of almost equal importance to the stability of sensitized photoresist solutions. The ABH sensitizer, in the solid crystalline state, is stable when stored under appropriate conditions, i.e., protected from light and in a cool place ($\approx 20^\circ\text{C}$). Solid sensitizer stored for eighteen months showed no signs of decomposition as evidenced by the appearance of the crystals, infrared spectra, and the behavior of photoresists prepared from it.

Photoresist solutions prepared from polymer having $\bar{A}_N = 433$ and $\bar{A}_W = 10,015$ were used on a day-to-day basis for six months with reproducible resist properties; beyond this period, some deterioration in line quality was observed. The use of butylated hydroxy toluene (an anti-oxidant) (12) is currently under investigation as a stabilizing additive. The data accumulated so far indicate that this compound is an effective stabilizer, for polymer stock solutions and sensitized photoresist solutions, with no adverse effects otherwise on the performance of the resist.

Conclusions

The foregoing discussion has covered various photoresist parameters with emphasis on the molecular weight distribution of the polymer. Variation of this latter parameter has allowed the formulation of a photoresist capable of functioning in films in the thickness range of 2000-3000Å, which allows 1.25 μm lines to be etched through an appropriate thickness, i.e., 4000Å of silicon dioxide, and which yields an acceptably low pinhole density. The resolution capability demonstrated is therefore 400 lines/mm. Although

Table III. Pinhole data for two Rezyl fractions and KTFR

Photoresist	\bar{A}_N	\bar{A}_W	Polymer solids in the resist (%)	Viscosity (cp)	Film thickness (Å)	Pinhole density (pinholes/in. ²)
Rezyl fraction No. 4	433	10,015	10	3.7	2,800	10
			8	2.7	1,800	20
Rezyl fraction No. 9	361	3,089	10	1.6	3,000	20
			8	1.4	2,200	30
KTFR	—	—	7	—	3,000	$\approx 1,000$
			12	—	10,000	30

masks with lines-on-spaces patterns smaller than 1.25 μm were not readily available, single 1 μm lines were obtained and the resist formulation described probably possesses a resolution capability of 500 lines/mm.

Acknowledgments

The authors gratefully acknowledge the contributions of Dr. P. Cukor and Mr. E. Lanning for the gel permeation chromatography and spectroscopic measurements. They also thank Dr. W. Salmre and Dr. A. Baczewski for helpful discussions of this work.

Manuscript submitted Feb. 14, 1972; revised manuscript received May 30, 1972.

Any discussion of this paper will appear in a Discussion Section to be published in the June 1973 JOURNAL.

REFERENCES

1. K. G. Clark and R. G. Turner, *Solid State Technol.*, **12**, 25 (1969).

2. R. W. Hodgson, *Electronics Packaging and Production*, **10**, 114 (1970).
3. W. Kornfeld, AFAL-TR-68-45 (1968).
4. M. Cantow, "Polymer Fractionation," Chap. B.1, Academic Press (1967).
5. J. Dey, M. Lundgren, and S. Harrell, "Kodak Photoresist Seminar Proceedings," Vol. II, p. 4 (1968).
6. L. E. Martinson, "Proceedings of the Kodak Seminar on Microminiaturization," p. 49 (1965).
7. M. V. Sullivan, See Ref. (6), p. 30.
8. R. O. Lussow, *J. Vacuum Sci. Technol.*, **6**, 18 (1969).
9. J. F. Johnson and R. S. Porter, "Analytical Gel Permeation Chromatography," Interscience (1968).
10. W. S. Bryan, See Ref. (6), p. 33.
11. K. Ravindran and G. Chandran, *Indian J. Technol.*, **6**, 125 (1968).
12. G. Scott, "Atmospheric Oxidation and Antioxidants," Elsevier (1965).

The Interaction of Photoresists with Metals and Oxides during RF Sputter-Etching

J. L. Vossen* and E. B. Davidson¹

RCA Corporation, David Sarnoff Research Center, Princeton, New Jersey 08540

ABSTRACT

When photoresists are used as masks for rf sputter-etching of various materials, interactions between the material being etched and the photoresist occur as a result of backscattering of some of the ejected material. We have studied these interactions in a variety of ways. Most of the interactions are similar to the interactions of the materials with carbon, and the intrinsic sputter-etch rate of photoresists is the same as that of carbon. When metals and photoresists are etched simultaneously, both materials are eroded at the same rate because backscattering converts the surface to a uniform mixture of all materials present. The etch rate of the composite surface increases over the intrinsic etch rate of the photoresist if metal carbide intermetallics can form. When only solid solutions can form, the composite etch rate decreases with decreasing solubility of carbon in the metal. When oxides are backscattered onto photoresists, the etch rate of the composite surface varies in a way which we cannot explain, and the photoresist is etched preferentially because of oxide decomposition followed by "chemical sputtering." The ability of a photoresist to mask oxides varies from one photoresist material to another. It is not possible to correlate the performance of a sputter-etch resist to its structure at this time, but it is clear that different materials behave differently in every respect.

Radio frequency (rf) sputter-etching has been used extensively to clean substrate surfaces prior to film deposition (1) and to delineate patterns in film surfaces using sacrificial photoresist masks (2-8). The latter application is the subject of this paper. Specifically, we shall describe the techniques required to prepare photoresist layers for sputter-etching and certain observed interactions between photoresists and other materials during sputter-etching.

In rf sputter-etching, the photoresist mask and the material being etched are both eroded. The maximum etch depth is limited by the thickness and quality of the photoresist mask (2, 3, 5, 7). The definition of etched patterns is limited only by the definition of the photoresist mask and there is no undercutting (2-8). Therefore, nearly all the limitations of rf sputter-etching are related to the photoresist.

Preparation of Photoresist for Sputter-Etching

Commercially available photoresist materials are intended primarily for chemical etch masking, not for

masking energetic ions. One might well inquire as to how the resist layer should be prepared for sputter-etching as compared to chemical etching.

It has long been recognized that reactive gases can cause "chemical sputtering" of certain materials (9). Chemical sputtering refers to the formation of a volatile compound at the target surface under the influence of reactive gas ion bombardment. If a photoresist is bombarded by oxidizing gas ions, the photoresist is much more rapidly eroded than it would be by inert gas ion bombardment (physical sputtering) (3, 10). Indeed, this process is often used to strip photoresist materials after etching processes (11-13). Clearly this implies that reactive gases should be excluded from the sputtering system during rf sputter-etching. To accomplish complete solvent removal from the photoresist layer and to avoid oxidation of the layer, we have found that the post-development heat-treatment of the photoresist layer is critical. Figure 1 shows the apparatus used. The substrates are heated on a hot-plate while the photoresisted surface is convectively cooled in a gas jet. The photoresist is thus heated from the bottom of the film, allowing all solvent to escape before the top surface of the film becomes too dense.

* Electrochemical Society Active Member.

¹ Present address: Singer Corporation, Little Falls, New Jersey 07424.

Key words: etching, films, polymers, ion bombardment.

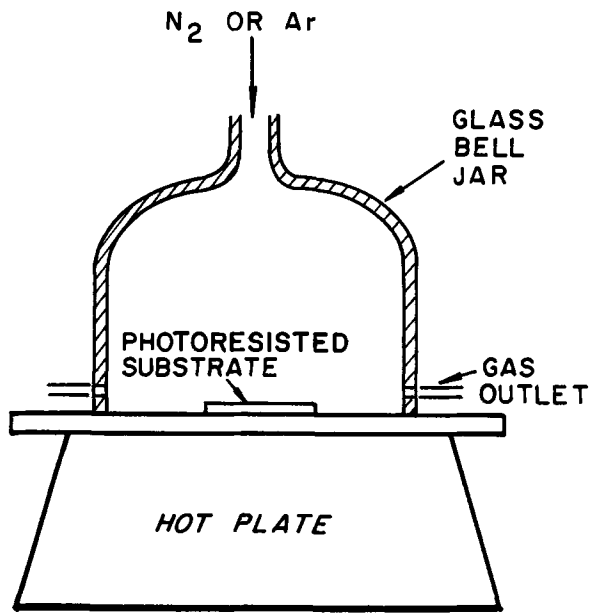


Fig. 1. Apparatus for baking photoresist films

We have observed that oven-baked photoresists tend to develop large holes under mild ion bombardment, whereas hot-plate-baked photoresist layers can withstand higher bombarding voltages. Presumably, the holes are a result of exploding pockets of trapped solvent.

The atmosphere used during the heat-treatment should be inert. Figure 2 illustrates the maximum sputter-etch depth into a photoresist patterned SiO₂ surface which was obtained for fixed initial photoresist thickness and fixed sputtering conditions. The detrimental effect of heating in oxidizing atmospheres is evident. The data plotted in Fig. 2 are for an experimental photoresist that will be described later. The temperatures at which the maxima occur vary from one photoresist to another. These temperatures are given in Table I. The time of the heat-treatment for the data given in Fig. 2 and Table I was 20 min. There was little difference observed if the time was extended.

Reproducibility of the Sputter-Etch System

Assuming that the photoresist layers are prepared in optimum fashion, it was necessary to check the re-

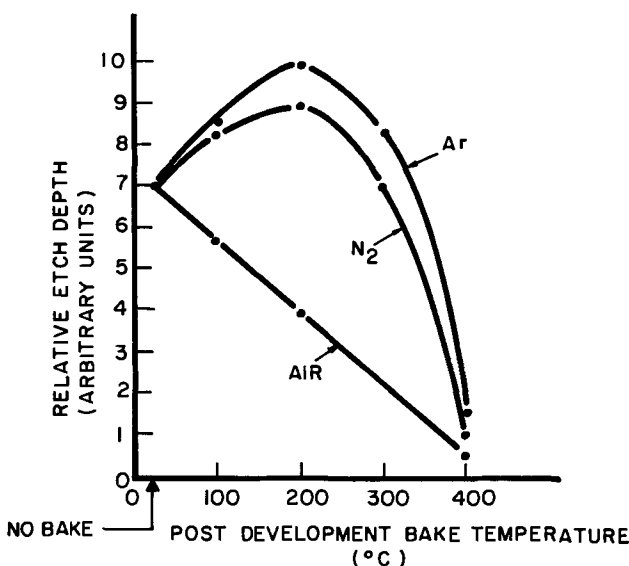


Fig. 2. The effect of post-development photoresist bake temperature and atmosphere on the maximum sputter-etch depth into SiO₂.

Table I. Optimum post-development bake temperature for various photoresist materials in N₂

Material	Temperature (°C)
Shipley AZ-111 and 1350	100
Shipley 1350H	125
Kodak KPR®, KTFR®, and KMER®	150
RCA Experimental	200

producibility of the rf-sputtering system, as nonreproducibility would invalidate results requiring run-to-run repeatability. The system used has been described previously (5).

Six 3 cm diameter silicon wafers were photoresisted with the experimental resist. The photoresist pattern consisted of 1 mm lines and 1 mm spaces. The wafers were sputter-etched one at a time on backing plate smaller than the wafer diameter under the following conditions:

Residual pumpdown pressure	1 × 10 ⁻⁶ Torr
Argon pressure	15 mTorr
Average target potential	-700V
Peak-to-peak rf voltage	2700V
Magnetic flux density	50 gauss
Etch time	20 min

This target configuration was purposely chosen to yield a nonuniform etch profile across the silicon wafer since this provides the most severe test for reproducibility in the sputtering system. After sputter-etching, the etch depth was measured at every step across the wafer using multiple beam interferometry. The results are plotted in Fig. 3. The total spread in measured depths from wafer to wafer is about 10%, which is within the accuracy of the thickness measuring technique. It was concluded that the system and the photoresist preparation techniques used were reproducible.

Limiting Bombarding Voltages and Etch Rates for Various Photoresists

As we shall show later, the presence of other materials on target surfaces has a profound influence on the etch rate of photoresists. To eliminate this variable, all data reported in this section refer to the rf sputter-etching of 1.7 μm thick optical filters which consist of many alternate layers of ZnS and ThF₄. The same photoresist pattern was applied to the films, but the

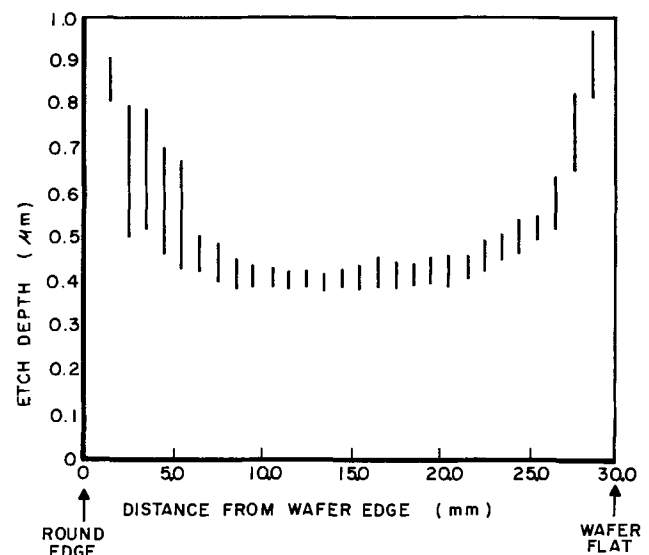


Fig. 3. Range of sputter-etch depths into Si measured at regular intervals across the Si surface for six different Si wafers. The photoresist films used to mask the Si were deposited at different times.

Table II. Maximum bombarding voltages for various photoresists

Material	Voltage (V)
Shipley AZ-111 and 1350	600
Shipley 1350H	700
Kodak KPR® and KTR®	900
Kodak KMER®	1,000
RCA Experimental	1,400

photoresist materials were varied. Each photoresist was bombarded at successively higher voltages until a threshold for large crack and/or hole formation was observed. These threshold voltages are given in Table II. These are the average d-c target sheath potentials and should be taken as being relative to each other rather than absolute, since different materials being etched, different discharge conditions, or different backing plates can change the absolute values. The advantage of higher bombarding potentials is a higher etch rate as shown in Fig. 4.

All further experiments were conducted at bombarding potentials substantially lower than the thresholds given in Table II.

Interaction of Metals with Photoresists

It has been noted in the past (5) that "the" sputter-etch rate of a photoresist has little meaning. When a film is patterned with photoresist and sputter-etched, both the film and the resist are sputtered. Whenever a surface is ion-bombarded in a glow discharge, some of the sputtered material is reflected back to the target surface (14). Recently, the amount and spatial distribution of the back-scattered material has been measured (1, 14). The spatial distributions determined were surprisingly uniform over fairly large areas (up to 5 cm²). As a result of this phenomenon, some resist material is back-scattered onto the film surface and *vice versa* until a new and uniform surface composition comprising film and photoresist material or fragments of photoresist material is present everywhere on the surface being etched. When metals are sputter-etched with photoresist patterns, the composite surface formed by backscattering results in a uniform etch rate for all species on the surface. That is, there is no preferential removal of photoresist or metal regardless of the metal used. This implies that the photoresist thickness needed to mask for a given etch depth into a metal surface is only slightly greater than the etch depth (to account for nonuniformities in photoresist thickness). For example, in Fig. 3, the photoresist thickness averaged 10,000Å, and the wafers were sputter-etched until the photoresist was almost completely removed near the wafer edges. The etch depth near the wafer edge averages about 9000Å, which is very close to the original photoresist thick-

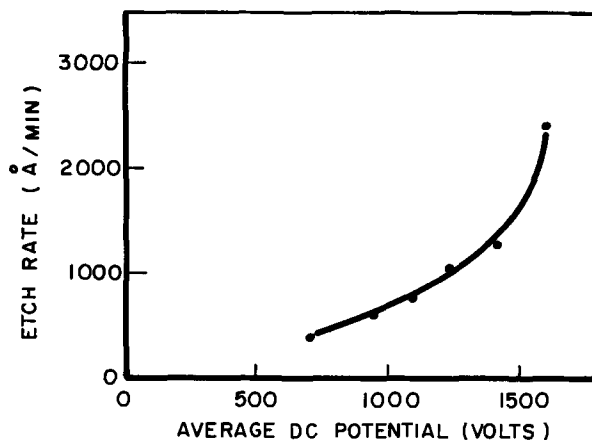


Fig. 4. RF sputter-etch rate of ZnS-ThF₄ optical filters vs. target sheath potential.

ness. Similar observations have been made for a variety of metal-photoresist combinations.

These interactions affect the over-all sputter-etch rate of the composite surface. In an attempt to determine the magnitude of these interactions, Si wafers were completely coated with the experimental photoresist, flood exposed, and baked in N₂ at 200°C for 20 min. The wafers were all spin-coated with approximately the same thickness of photoresist, but the actual thickness was measured using spectrophotometric techniques (15), and all data were normalized for thickness variation. The wafers were sputter-etched while resting on 7.5 cm diameter target backing plates of various metals. The backing plates were pre-sputtered for at least 2 hr in Ar before the sputter-etching runs. The sputtering conditions used to etch the photoresist are:

Residual pumpout pressure	1 × 10 ⁻⁶ Torr
Argon pressure	5 mTorr
Target sheath potential	-700V
Peak-to-peak rf voltage	2800V
Axial magnetic flux density	50 gauss

The wafers were sputtered until all the photoresist was removed. The time to removal and the measured resist thickness were used to calculate the effective etch rate. The data thus obtained for metal backing plates are plotted in Fig. 5 as a function of the sputtering yield of the metal backing plate. Two features of the curve are evident. The relationship displays a maximum etch rate for the Pt-photoresist combination and the Cu-photoresist combination is anomalously low. This behavior is suggestive of specific, but different, chemical interactions between the backscattered materials.

Since the major constituent element of photoresist is carbon, it was expected that the interactions were between the metals and carbon. Several experiments supported the expectation.

First, a glass target backing plate was completely covered with a thick layer of photoresist, flood exposed and baked. A photoresisted silicon wafer was then sputter-etched using this "photoresist backing plate." The etch rate of the photoresist in this configuration was the same as the etch rate of the photoresist resting on a C backing plate within the limits of

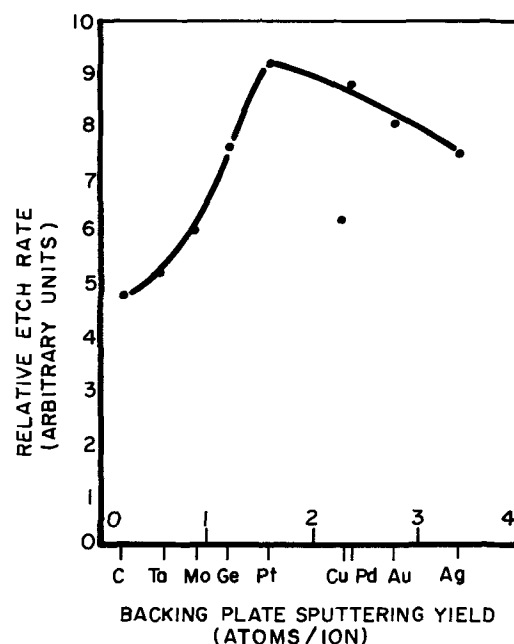


Fig. 5. Relative sputter-etch rate of experimental photoresist films vs. the sputtering yield of the metal backing plate upon which the sample was resting. Each point represents an average of 3 runs.

experimental error. Hence, the intrinsic etch rate of the photoresist is the same as that of carbon.

Next, carbon films were rf sputtered from a vitreous carbon target onto silicon wafers. These carbon films were then rf sputter-etched while resting on backing plates of the same metals used in the earlier experiments. Figure 6 shows the resulting etch rates and compares the carbon and photoresist etch rates. The shapes of the curves are qualitatively the same and the anomalously low Cu point is evident.

All of the metals having sputtering yields lower than that of Pt form inter-metallic carbides (16, 17), while the metals having sputtering yields equal to or higher than Pt form solid solutions of varying degrees of solubility with C (18). If carbide formation in the photoresist is the operable mechanism for the increased etch rates observed, then one must assume that the carbides are formed uniformly over the photoresist surface. This further implies that the sputtering rate of the metal carbides and the metal-photoresist composites are the same. If the entire surface being sputtered is for all practical purposes metal carbide, then the ratio of the sputtering yield of the carbides to that of carbon should be the same as the ratio of the etch rates of the metal-photoresist combinations to the intrinsic etch rate of the photoresist. We have measured the effective sputtering yield of TaC and Mo₂C, by the method of comparing the rf sputter-deposition rate of these materials with metals of known sputtering yield in a system with fixed geometry and using fixed sputtering conditions (19, 20). In this technique, metals of known sputtering yield and the unknown materials are deposited and their thicknesses measured, yielding sputtering rates (*R*). The "effective yield" or the relative sputtering rate (*S*) is then given by the simple proportion

$$S_x = S_{Me} (R_x / R_{Me})$$

where the subscripts *x* and *Me* refer to the unknown and the metal standard respectively. The metals used as standards were Ta and Mo. As has been pointed out by Maissel (20), this method of measuring yields is subject to various uncertainties (different secondary electron yields, re-emission coefficients, etc.). Therefore, it is advisable to use more than one standard to average out these effects. In this case, the ratios of

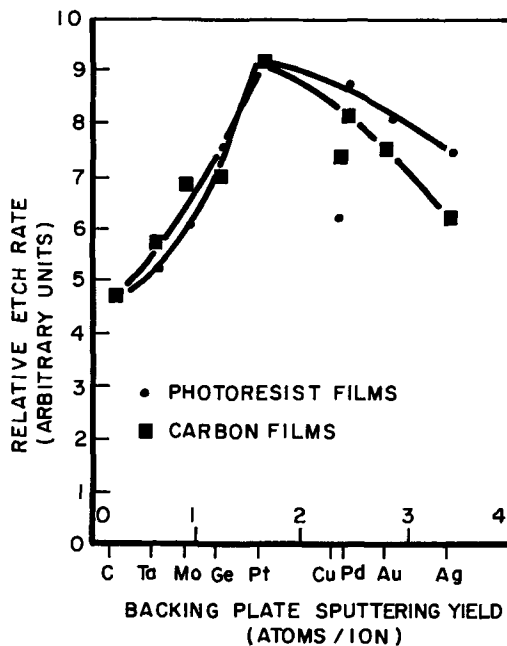


Fig. 6. Relative sputter-etch rate of carbon films vs. the sputtering yield of the metal backing plate upon which the sample was resting. The data for photoresist films are also shown for comparison. Each point represents an average of 3 runs.

Table III. Effect of intermetallic carbide formation on rf sputter-etch rate

Metal or carbide	Sputtering yield (19) (atoms/ion)	Effective sputtering yield (atoms/ion)	(Yield of metal or carbide) / Yield of carbon
C	0.12	—	1.00
Ta	0.57	—	4.75
TaC	—	0.13	1.08
Mo	0.80	—	6.67
Mo ₂ C	—	0.15	1.25

the measured deposition rate to the known sputtering yield of Ta and Mo differed by less than 10%. The results are tabulated in Table III. The sputtering yields given are for 600 eV Ar⁺ bombardment at normal incidence on polycrystalline targets (21). The ratio of the sputter-etch rates for the photoresist on Ta and Mo backing plates to the intrinsic etch rate of the photoresist are 1.10 and 1.25, respectively (Fig. 5). The agreement with the carbide data in Table III is quite close, implying that carbides are formed in the photoresist such that the effective etch rate is increased.

For metals that form solid solutions with carbon, a decrease in etch rate with increasing sputtering yield is observed. The apparently anomalous Cu points fit reasonably well in a plot of etch rate vs. solid solubility of C in metals (Fig. 7).

The general tendency toward lower etch rates for these metal-photoresist or metal carbon combinations may be explained qualitatively based on the backscattering data presented for metals on Si earlier (1). The amount of material backscattered generally decreases with increasing sputtering yield, thus leaving more low yield photoresist exposed to the ion bombardment. For the limiting case of an infinite sputtering yield, no backscattering would occur and there would be no interactions with the photoresist. Hence, the etch rate of the surface would revert to the intrinsic (low) etch rate of the photoresist.

Similar results to those given in Fig. 5 and 6 have been obtained for other photoresists. Figure 8 illustrates the etch rate of a photoresist similar to Kodak KTRF® as a function of the sputtering yield of the backing plate metal. Here, the variation is distinctly resolved into two separate modes of interaction, the formation of intermetallic carbides or solid solutions of the metals and carbon.

Interaction of Inorganic Oxides with Photoresist

To determine the effects of sputter-etching photoresists in the presence of inorganic oxides, experiments similar to those with metals were conducted using 16 hot-pressed oxide backing plates. Before each run the backing plates were pre-sputtered in pure O₂ for at least 3 hr to ensure that a stoichiometric,

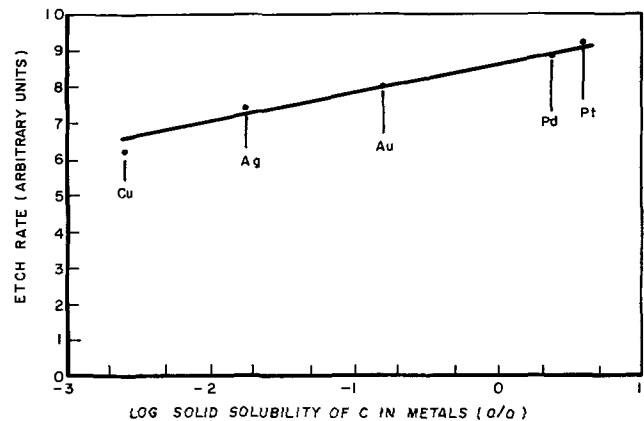


Fig. 7. Relative sputter-etch rate of experimental photoresist films vs. the solid solubility of C in the metals shown at the melting points of the metals. [Solubility data from Ref. (18)]

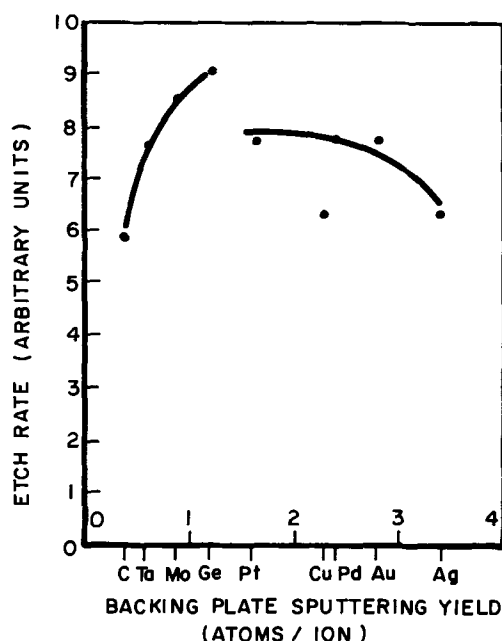


Fig. 8. Relative sputter-etch rate of photoresist films similar to Kodak KTFR® vs. the sputtering yield of the metal backing plate upon which the sample was resting. Each point represents an average of 3 runs.

clean surface was present. The photoresist films were prepared in the same manner as before.

Since there are no data available on the "sputtering yield" of oxides, it was necessary to measure the "yields" for each of the oxides used in the study. This was done by the method of deposition rate comparison as described earlier. Caution should be exercised in using these yield data (Table IV). Many of these materials are known to reduce, chemically, under the influence of Ar ion bombardment (5). Therefore, the surface composition changes continually during ion bombardment. Furthermore, the meaning of "yield" for compounds is not clear since one has no way to determine the nature of the ejected species (atoms, molecules, clusters). Therefore, we shall refer to the "relative deposition rate" of the oxides. These relative deposition rates are normalized to the sputtering rate of metals having known sputtering yields. The metals used as standards were Si, Pt, Cr, and Au. The ratios of the measured deposition rates to the known sputtering yields of these metals differed by less than 10%. The average of these ratios was used to normalize the oxide deposition rates to the sputtering yield of the metals.

The variation of photoresist etch rate with the relative deposition rate of oxides is shown in Fig. 9. The

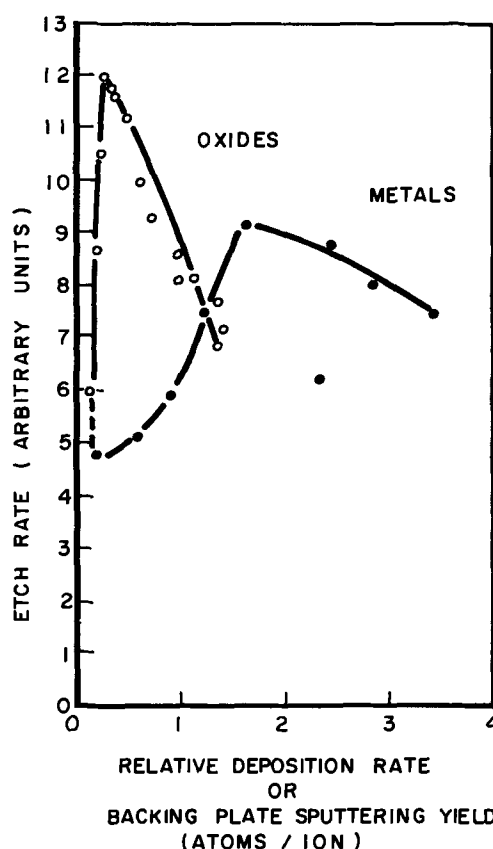


Fig. 9. Relative sputter-etch rate of experimental photoresist films vs. the relative deposition rate of the hot-pressed oxide backing plate upon which the sample was resting. The data for metal backing plates are also shown for comparison. Each point represents an average of 3 runs.

etch rate for the metal backing plates is replotted in the same figure for reference. We have no satisfactory explanation for the shape of the oxide curve. It does not relate to any thermodynamic or thermochemical property of the oxide backing plate, nor to the possibility of chemical reduction followed by either carbide or solid solution formation by backing plate cations with C in the photoresist. All that can be said with certainty is that the etch rates for oxide backing plates are generally higher than those for metals. This leads to the possibility that oxygen is being released from the backing plates into the discharge, thus superimposing chemical sputter-etching on physical sputtering. Because chemical sputtering, resulting from partial chemical reduction of oxides, may cause preferential etching of photoresists when compounds are etched, it is necessary to determine the ratio of photoresist thickness to etch depth required for oxides.

Table IV. Relative deposition rate of inorganic oxides (Normalized to the sputtering yield of metals)

Oxide	Relative deposition rate ($\frac{\text{Å/min}}{\text{Å/min}}$)
Ta ₂ O ₅	0.15
Al ₂ O ₃	0.18
Cr ₂ O ₃	0.18
Nb ₂ O ₅	0.24
ZrO ₂	0.32
MgO	0.36
La ₂ O ₃	0.37
V ₂ O ₅	0.47
In ₂ O ₃	0.57
Fe ₂ O ₃	0.71
SnO ₂	0.96
TiO ₂	0.96
ZnO	1.18
Bi ₂ O ₃	1.32
SiO ₂	1.34
Sb ₂ O ₃	1.37

"Protection Factor" for SiO₂

N-type (111) silicon wafers with 10,000Å of steam oxide were whirl-coated with photoresist and exposed through a mask so that one-half of the wafer was protected by photoresist after development. The wafer was placed on a SiO₂ backing plate in the sputtering system and half of it was shielded by a second oxidized silicon wafer (Fig. 10).

The oxide was sputter-etched for 20 min under the following conditions:

Residual pumpdown pressure	1 × 10 ⁻⁶ Torr
Argon sputtering pressure	5 mTorr
Target sheath potential	-700V
Axial magnetic flux density	25 gauss

The wafer was then removed, a thin layer of chromium was evaporated onto it, and the resulting sur-

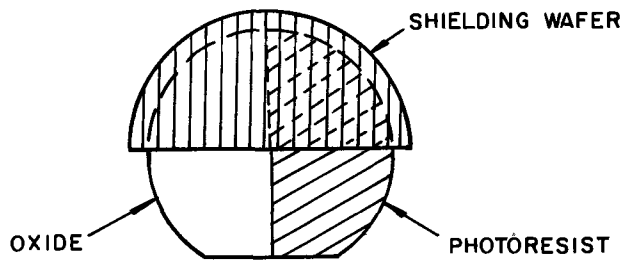


Fig. 10. Sample configuration for sputter-etching of photoresist on SiO_2 for determination of oxide etch rate and protection factor.

face was examined with a Bendix Proficorder®. The arrangement permitted determination of (i) the original oxide thickness, (ii) the amount of photoresist removed, and (iii) the amount of oxide removed (Fig. 11a). The resist was then characterized for the rate of removal of oxide in $\text{\AA}/\text{min}$ and for the protection it afforded in terms of the ratio of photoresist sputtered to oxide sputtered. A good sputter-etch resist is characterized by a large value for the rate (of oxide removal) and a small value for the protection factor (P.F.).

The sputtering conditions were chosen so that the photoresist was not completely removed after 20 min of sputtering. Occasionally a run did result in complete removal of the photoresist resulting in the condition pictured in Fig. 11b. In this case the effective time of sputtering must be calculated since during a portion of the 20 min period oxide was being sputtered off at an equal rate from both sides of d resulting in no change in height. In these cases, the rate ($\text{\AA}/\text{min}$) is calculated as

$$\text{Rate } (\text{\AA}/\text{min}) = \frac{d}{20 - \left[\frac{c + d}{90} \right]}$$

where the value 90 $\text{\AA}/\text{min}$ is the intrinsic sputter-etch rate of SiO_2 . The P.F. value in this case is a/d .

In either case, an internal check on the measurements is available since $(a + c)$ should equal $(b + d)$. Table V lists the rate of oxide removal and the protection factor for the materials evaluated. Individual step heights are not given, however, the per cent deviation of the individual sums $(a + c)$ and $(b + d)$ from the average $[(a + c) + (b + d)]/2$ is listed for each material.

A variety of materials were examined including commercially available photoresists and other materials which could be formulated into photoresists.

This latter group, which includes the RCA experimental resist, was made up of drying oil alkyd resins

Table V. Rate of oxide removal and protection factor (P.F.) of commercial and experimental photoresists

	% Deviation of $a + c$ and $b + d$ from their average	Rate of oxide removal ($\text{\AA}/\text{min}$)	P.F.
KTR® ^(a,b)	2.6	45	6.0
KMER® ^(b)	1.2	45	5.3
AZ 1350 ^(c)	1.5	30	8.2
AZ 1350H ^(c)	0.1	45	3.8
AZ 111 ^(c)	2.2	45	4.8
Waycote ^(d)	0.5	53	5.4
RCA ^(e)	0.7	53	5.7
RCA ^(e)	4.8	68	4.7
p-isophthalate	8.1	45	4.3
p-o-phthalate	1.4	45	5.3
Rezyl 337-5 ^(f)	2.6	40	8.0
Rezyl 873-1 ^(f)	4.2	30	12.3
Rezyl 412-1-50 ^(f)	3.3	8.2	7.0
Rezyl 1102-5 ^(f)	2.3	45	6.0
Amberlac 80x ^(g)	0	45	7.0
Amberlac 292x ^(g)	5.8	53	5.1
Beckosol 11-147 ^(h)	1.1	72	8.5
Beckosol 12-101 ^(h)	5.7	50	7.6
Alkydol 12-704 ^(h)	2.9	45	8.0
13-031 ^(h)	2.7	38	7.2
13-040 ^(h)	2.6	50	5.0
13-046 ^(h)	1.0	45	7.0
13-077 ^(h)	1.2	41	7.2

(a) All commercial photoresists were baked at their recommended temperatures under N_2 for 10 min; experimental resists were baked under N_2 at 185° for 10 min unless stated otherwise.

(b) Eastman Kodak Chemical Company.

(c) Shipley Company.

(d) Hunt Chemical Company.

(e) Unbaked.

(f) Koppers Chemical Company.

(g) Rohm and Haas.

(h) Reichhold Chemical Company.

of the class reported by Walters and Mocsary-Weisz (22).

Species Sputtered from Photoresists

Spark source mass spectroscopy was employed in an attempt to determine the nature of the species sputtered from photoresists. Films were deposited from a photoresist-covered sputtering target, yielding information on the manner in which the photoresist is removed from the target. This film was compared with a photoresist film that had not been ion bombarded and with an rf sputtered C film.

The photoresist layer that was not bombarded showed a preponderance of high molecular weight species. The sputter deposited photoresist film shows hydrocarbons to the extent of the mass scale (280), but species above C_4 , C_5 , C_6 are very weak, indicating that the polymer has been thoroughly fragmented by the ion bombardment. The films deposited from the vitreous carbon target showed mainly C clusters, with traces of hydrocarbons.

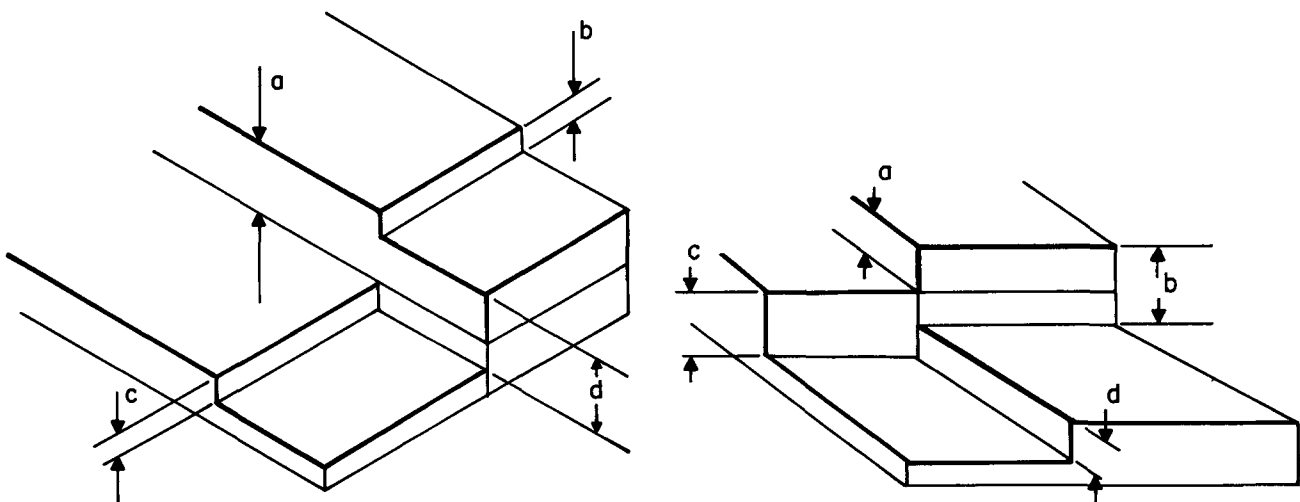


Fig. 11. Substrate configuration after sputter-etching (a, left) with photoresist remaining, (b, right) with photoresist entirely removed

Summary and Conclusions

The main conclusions that may be drawn from this work are as follows:

1. The pretreatment of the photoresist before sputter-etching clearly affects its performance. Baking in an inert atmosphere improves the performance relative to no-baking up to a point; then the performance declines. The performance of the resist when baked in air is always poorer than if no-bake were employed.
2. When prepared under optimum conditions, there is a limit to the maximum bombarding voltage that the photoresist can withstand. This maximum varies from one material to another.
3. The mass spectra of sputtered photoresist differs from that of unspattered photoresist and carbon. The unspattered photoresist shows the presence of masses to the limit of the instrument ($M=280$) with a preponderance of high-mass species. Films deposited from a "photoresist target" showed masses to the extent of the mass scale, but species above C_6 were very weak. The films of rf sputtered carbon showed mainly C clusters with traces of hydrocarbons.
4. The intrinsic sputter-etch rate of photoresists is very close to that of C.
5. When metals and photoresists are sputter-etched simultaneously, the entire target surface is eroded at the same rate, presumably because backscattering converts the surface to a mixture of the materials present.
6. Metal-carbon combinations sputter-etch in a way that is very similar to metal photoresist combinations.
7. The interaction of backscattered metals with carbon or photoresist depends upon whether an intermetallic carbide or a solid solution with carbon is formed. When carbides are formed, the etch rate of the composite surface is increased over the intrinsic etch rate of the photoresist by an amount approximately proportional to the ratio of carbide to carbon sputtering yields. When solid solutions are formed, the etch rate decreases with decreasing solubility of carbon in the metal.
8. When oxides are backscattered onto photoresist, the etch rate of the composite surface varies from one oxide to another in a way which we cannot explain.
9. In the photoresist-oxide case, photoresist is etched preferentially, probably because of oxide decomposition followed by chemical sputtering. The ability of a photoresist to mask oxides varies from one photoresist material to another.
10. It is impossible to correlate the performance of a sputter-etch resist to its structure at this time. It

is clear, however, that different materials behave differently in every respect.

Acknowledgments

L. DiMarco prepared most of the photoresist films used in this study. J. J. O'Neill and E. S. Poliniak conducted many of the sputtering runs. The mass spectrometric analyses were done by W. L. Harrington.

Manuscript submitted March 29, 1972; revised manuscript received July 14, 1972.

Any discussion of this paper will appear in Discussion Section to be published in the June 1973 JOURNAL.

REFERENCES

1. J. L. Vossen, *J. Vacuum Sci. Technol.*, **8**, S12 (1970).
2. P. D. Davidse, Extended Abstracts, p. 51, 13th National Vacuum Symposium, American Vacuum Society, San Francisco (1966).
3. R. T. C. Tsui, Proc. Second Symp. on the Dep. of Thin Films by Sputtering, p. 53, Univ. of Rochester (1967).
4. R. Glang and P. M. Schaible, *Thin Solid Films*, **1**, 309 (1968).
5. J. L. Vossen and J. J. O'Neill, Jr., *RCA Rev.*, **29**, 149 (1968).
6. R. Heil, S. Hurwitt, and W. Huss, *Solid State Technol.*, **11**, 42 (1968).
7. P. D. Davidse, *This Journal*, **116**, 100 (1969).
8. S. Hurwitt, *Ind. Res.*, **12**, 60 (1970).
9. A. Guntherschulze, *Z. Phys.*, **36**, 563 (1926).
10. G. K. Wehner, *Advan. Electron. Electron Phys.*, **7**, 239 (1955).
11. S. M. Irving, Proc. Kodak Photoresist Seminar, Vol. II, p. 26 (1968).
12. R. L. Bersin, *Solid State Technol.*, **13**, 39 (1970).
13. S. M. Irving, *ibid.*, **14**, 51 (1971).
14. J. L. Vossen, J. J. O'Neill, Jr., K. M. Finlayson, and L. J. Royer, *RCA Rev.*, **31**, 293 (1971).
15. L. A. Murray, N. Goldsmith, and E. L. Jordan, *Electrochem. Technol.*, **4**, 508 (1966).
16. M. Hansen, "Constitution of Binary Alloys," 2nd ed., pp. 353, 370, 374, 380, McGraw-Hill Book Co., New York (1958).
17. J. Drowart, G. deMaria, J. H. Boerboom, and M. G. Inghram, *J. Chem. Phys.*, **30**, 308 (1959).
18. M. Hansen, "Constitution of Binary Alloys," 2nd ed., pp. 11, 189, 353, 366, 377, McGraw-Hill Book Co., New York (1958).
19. L. I. Maissel, in "Physics of Thin Films," Vol. 3, p. 78, G. Hass and R. E. Thun, Editors, Academic Press, New York (1966).
20. L. I. Maissel, in "Handbook of Thin Film Technology," p. 4-41, L. I. Maissel and R. Glang, Editors McGraw-Hill Book Co., New York (1970).
21. N. Laegreid and G. K. Wehner, *J. Appl. Phys.*, **32**, 365 (1961).
22. R. M. Walters and E. Mocsary-Weisz, Abs. 186, p. 458, Electrochem. Soc. Extended Abstracts, Fall Meeting, Atlantic City, Oct. 4-8, 1970.

Nuclear Study of the Fluorine Contamination of Tantalum by Various Polishing Procedures and of Its Behavior during Subsequent Anodic Oxidation

B. Maurel, D. Dieumegard,¹ and G. Amsel*

Groupe de Physique des Solides de l'École Normale Supérieure, Tour 23; 11 quai St. Bernard, Paris 5e, France

ABSTRACT

The fixation of fluorine in the film left on tantalum by chemical polishing in a $\text{H}_2\text{SO}_4\text{-HNO}_3\text{-HF}$ mixture was studied using microanalysis by the nuclear reactions $\text{F}^{19}(\text{p},\alpha)\text{O}^{16}$ and $\text{O}^{16}(\text{d},\text{p})\text{O}^{17}$. Typically 2×10^{15} atoms/cm² of fluorine is found in films containing 20×10^{15} atoms/cm² of oxygen. Leaching in boiling water decreases the amount of fluorine by about 50%. On the other hand, the dissolution of these films in a NH_4F saturated 40% HF solution reduces the fluorine contamination to less than 1.5×10^{14} atoms/cm². Hence this double chemical treatment appears to be an effective procedure to obtain low fluorine contaminations on polished tantalum. Leached samples were anodically oxidized in a 5% ammonium citrate aqueous solution up to 90V at 1 mA/cm². It was found both by dissolution techniques and by the observation of the 872 keV narrow resonance of the $\text{F}^{19}(\text{p},\alpha\gamma)\text{O}^{16}$ reaction, that, after oxide growth, the fluorine remains near the metal-oxide interface. The oxide growth laws for the various surface preparation procedures described were investigated. The presence of F^{19} on the surface of tantalum seems to have little influence on the growth laws; the small changes induced are discussed in detail.

It is well known that a metal is subject to contamination by various elements during the process of surface treatment by chemical, electrochemical, or mechanical polishing procedures. The present paper is devoted to an investigation of the contamination with fluorine of the surface of tantalum samples subjected to various treatments in fluorine-containing baths. Attention was paid to the localization, as a function of depth, of fluorine atoms after anodic oxidation of the specimens. The oxide growth laws on various tantalum surfaces were also investigated. The results will be discussed mainly with reference to the work of Young (1) and to several papers (2-4) from this laboratory, the present work being a continuation of the latter. Anodic oxidation leads in most electrolytes, except those with high fluorine content (5), to the formation of nonporous, amorphous, highly insulating films. Young (1) has shown that the thin layer of tantalum oxide which remains after chemical polishing has properties different from those of anodic tantalum oxide; he has explained this fact by a possible introduction of fluorine impurities due to the polishing treatment. However, to the best of our knowledge, no direct evidence, either quantitative or qualitative, has yet been obtained for the existence of such traces of residual fluorine. In the present paper, we made use of a recently developed method for determining the absolute quantities of fluorine and oxygen on the surface of tantalum: that of microanalysis by direct observation of nuclear reactions.

Analytical Techniques

The method of microanalysis used for the measurement of fluorine traces and of oxygen (O^{16}) contents of oxide layers consists in the direct observation of charged particles coming from the nuclear reactions $\text{F}^{19}(\text{p},\alpha)\text{O}^{16}$ and $\text{O}^{16}(\text{d},\text{p})\text{O}^{17}$. One millimeter diameter proton or deuteron beams were produced by the 2 MeV Van de Graaff accelerator of the École Normale Supérieure of Paris. A detailed description of this method has been reported in Ref. (6-9), Ref. (6) being

devoted to the general technical details of the method, Ref. (7) mainly to O^{16} , and Ref. (8) and (9) to F^{19} . It will be recalled here that the counting rates reach the order of 100 counts for a duration of measurement of 15 min (i.e., 10% statistical accuracy) for layers of thickness

$$\begin{aligned} 1.5 \times 10^{13} \text{ O}^{16} \text{ atoms/cm}^2 & (\sim 4 \times 10^{-4} \mu\text{g/cm}^2) \\ 10^{14} \text{ F}^{19} \text{ atoms/cm}^2 & (\sim 3 \times 10^{-3} \mu\text{g/cm}^2) \end{aligned}$$

under the experimental conditions used (intensity of the beam 1 μA ; detection of charged particles by three identical 3 cm² silicon-surface barrier detectors, at an angle of 150° with respect to the direction of the beam, subtending a total solid angle of detection of 0.36 steradian). These figures relate to bombarding energies near the plateaus of the cross-section curves at 900 keV for O^{16} and 1270 keV for F^{19} [using the broad resonance of $\text{F}^{19}(\text{p},\alpha)\text{O}^{16}$ at 1348 keV, the above-counting may be reached in the same conditions for 2×10^{13} atoms/cm² F^{19} ; this procedure, somewhat more critical, was not necessary in the present experiments]. Since the standard error varies as the square root of the counts, it is clear that accuracy improves rapidly for oxygen or fluorine contents exceeding the above-orders of magnitude. For instance, the oxygen contents dealt with in the present investigation, which were of the order of 10^{16} atoms/cm², were determined within 1 min with a statistical precision of the order of 1%.

The absolute oxygen standard was provided by a film of anodic oxide grown on tantalum under well-defined conditions. (3). It has been shown in the latter paper that precise coulometric measurements permit in this case the absolute determination of the number of O^{16} atoms per cm² with an accuracy of about 3%. The absolute fluorine standard was a vacuum deposited film of CaF_2 on a tantalum backing, known with an accuracy of about 7% (8, 9).

Quantitative Results on the Contamination Phenomena

Unannealed, rolled tantalum specimens (from Kawecki-Berylco Ind.) (rated bulk purity 99.95%) were used in this investigation, with a thickness of 0.2 mm. Before use, they were carefully degreased in acetone (3, 4). Investigations of specimens which had not been subjected to any treatment except for de-

* Electrochemical Society Active Member.

¹ Present address: Laboratoire Central Thomson-CSF, Corbeville, 91—Orsay, France.

Key words: tantalum, polishing, fluorine, contamination, anodic oxidation, nuclear reactions.

greasing showed a surface contamination with fluorine varying from 1.4×10^{14} to 3×10^{14} F^{19} atoms/cm². As measurements of F^{19} on high-purity silicon yield zero counts, for measurement times equal to those used for tantalum (5 min), it appears improbable that the presence of the measured quantities of fluorine on tantalum specimens of high purity is caused by contamination in the vacuum of the nuclear reaction detection chamber. This contamination of the raw-rolled tantalum surface remains as yet unexplained. Measurements of O^{16} did not allow us to find a correlation between the observed quantities of O^{16} and F^{19} . The results are shown in Fig. 1 where the number of F^{19} atoms is plotted vs. that of O^{16} atoms contained within the surface layer of natural oxide (the two measurements refer to the same beam impact point of the specimen). It is seen that the quantities of oxygen vary between 3×10^{16} and 8×10^{16} atoms/cm², which corresponds to natural oxide layers of the order of 50-150Å [considering this oxide to be Ta_2O_5 , the equivalence is 5.45×10^{14} atoms/cm² of oxygen for 1Å, assuming a density of 8.0 as in Ref. (4)].

The residual fluorine contamination was investigated on tantalum specimens 11 by 20 mm polished chemically for 15 sec in a mixture of 5 parts of H_2SO_4 (95%), 2 parts of HNO_3 (53%), and 2 parts of HF (40%), as in Ref. (2-4), a classical mixture similar to that used previously by Young [Ref. (1), p 46]. After washing with triply-distilled water at room temperature for 10 min, the specimen surfaces showed an appreciable fluorine content, which was rather variable. It may be noted that measurements at various points of the same sample yield a similar spread of the results as that obtained for different samples. These results (Fig. 1) show that the contamination amounts on the average to 23×10^{14} F^{19} atoms/cm². Figure 1 also shows that the F^{19} content is statistically independent of the thickness of the oxide layer, i.e., its oxygen content. The thickness of this natural oxide layer is of the order of 20-45Å. Washing the specimens in boiling triply-distilled water for 5 min eliminates a large fraction of the fluorine (about 50%), which partly confirms the statements of Young [(1), p 67]. Prolonged washing with boiling water (1 hr) does not lead to any

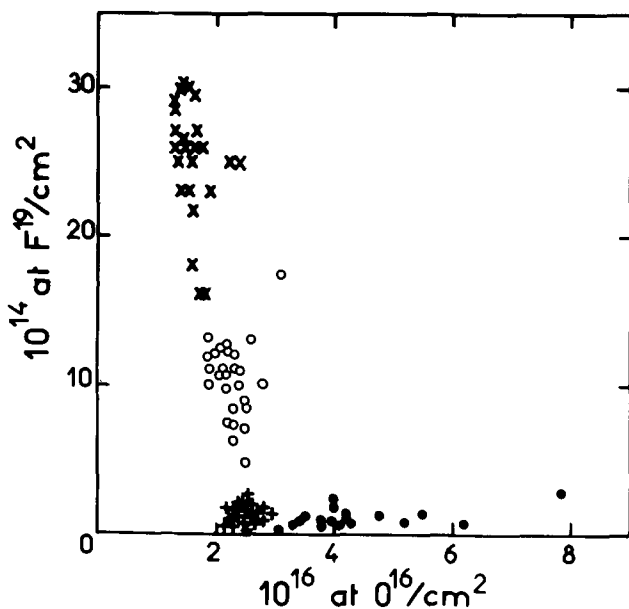


Fig. 1. Correlogram of the F^{19} and O^{16} contents found on the surface of Ta specimens. (●), raw tantalum; (×), polished and washed with cold water; (○), polished and washed with boiling water; (+), polished, treated in the NH_4F -HF bath and washed with boiling water.

noticeable further decrease in the fluorine content, which is hence on the average near 10^{15} F^{19} atoms/cm².

The influence of the relative proportions of the constituents of the polishing bath on the extent of fluorine contamination after boiling in water was next investigated in particular as a function of the HF proportion. No noticeable change in contamination was observed, in both the alteration of the polishing bath by an excess or the defect of HF by as much as $\pm 50\%$.

If one assumes that the 10^{15} F^{19} atoms/cm² are contained in a pure uniform compound of composition TaF_5 (density 4.7), taking a roughness factor for the polished tantalum near unity (10), the corresponding thickness is near 2Å. Hence, the two extreme possibilities are that the fluorine is contained either in a pure submonomolecular fluoride layer, or dispersed throughout the residual oxide layer of thickness near 40Å, i.e., containing about 5 fluorine atoms per 100 oxygen atoms.

In order to attempt to reduce the fluorine contamination of the polished tantalum specimens, they were immersed for 5 min in a bath of NH_4F -HF (about 300g NH_4F per liter of 40% HF) which is generally used for dissolving the oxide. The use of such a solution was suggested by Pringle (Private communication, 1966) and the technique was applied in our laboratory (2-4). Recently Pringle published this method (11), where he also describes a double treatment similar to that investigated here for its effects on F^{19} contamination. This operation was performed at 27.5°C, as usual for oxide dissolution. The samples were then washed for 5 min with boiling triply-distilled water. As seen from Fig. 1, the fluorine content drops to an average value of 1.5×10^{14} atoms/cm². The best results were obtained with a solution saturated with NH_4F . Figure 2 shows the spectra recorded during the measurements of the fluorine content by means of the $F^{19}(p,\alpha)O^{16}$ reaction

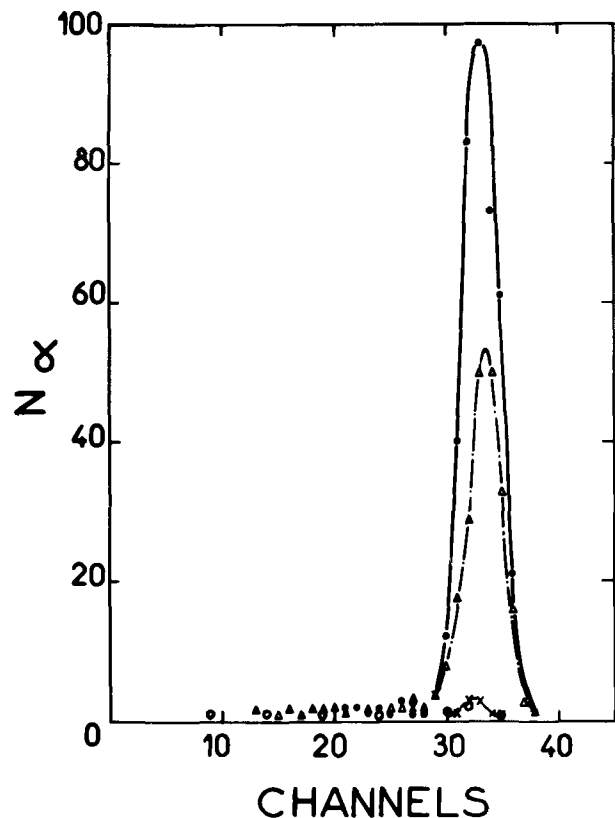


Fig. 2. α particle energy spectra from the reaction $F^{19}(p,\alpha)O^{16}$ recorded for Ta specimens subjected to various treatments. (○), raw tantalum; (●), polished and washed with cold water; (Δ), polished and washed with boiling water; (×), polished, treated in the NH_4F -HF bath, and washed with boiling water.

on the same tantalum specimen subjected, after polishing, to the various successive treatments described above. It clearly appears that this double treatment provides a method for effectively minimizing the fluorine content of the surface of polished tantalum. Moreover, it is seen from Fig. 1 that the thickness of the spontaneous oxide which results from this double treatment is the same as that encountered after washing in boiling triply-distilled water only.

From these results it may be inferred that the mechanism of polishing leads to the formation of an oxide heavily contaminated with fluorine, which then undergoes gradual dissolution. The fluorine atoms seem to be located within the spontaneous oxide layer (or in a region close to the metal) which remains on the material after stopping the polishing process. The NH_4F saturated bath dissolves this film while introducing much less fluorine contamination. The spontaneous reoxidation of the sample leads to an oxide layer of similar thickness as before.

Location of Fluorine after Anodic Oxidation of Polished Tantalum

When the polished tantalum samples are subjected to anodic oxidation, the fluorine atoms located on the specimen surface or within the spontaneous residual tantalum oxide undergo a transport phenomenon under the effect of the electric field. After anodic oxidation, the fluorine atoms may be located at the metal-oxide interface, near the oxide surface or may be distributed throughout the bulk of the oxide. Tantalum samples polished as above and washed for 5 min in boiling triply-distilled water were anodically oxidized in an aqueous solution according to a procedure similar to that used in Ref. (2-4), i.e., a pH 6 buffer solution of high purity (Merck) ammonium citrate (5% by weight) in triply-distilled water of resistivity 0.5 megohm-cm. The oxidations were carried out at a temperature of 26.5°C at a constant current of 1 mA/cm², up to a final potential of 90V between anode and platinum cathode.

The location of fluorine in this oxide layer was first studied by successive dissolution of anodic oxide layers in the above used $\text{NH}_4\text{-HF}$ bath; the remaining number of O^{16} and F^{19} atoms per cm² was recorded as a function of the time of dissolution. The results are shown in Fig. 3. They correspond to a series of initially iden-

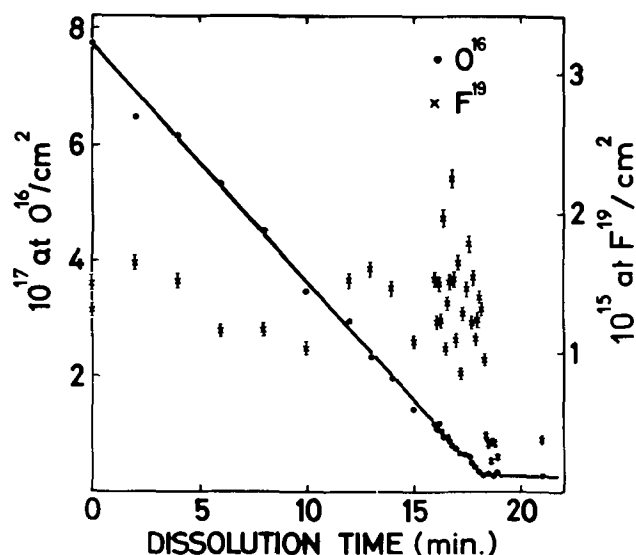


Fig. 3. F^{19} and O^{16} contents found on the surface of polished Ta specimens first subjected to anodic oxidation up to 90V and immersed for various times in the dissolution bath: (●), O^{16} ; (×), F^{19} . Statistical error is indicated for F^{19} ; it is negligible for O^{16} .

tically prepared samples. The initial oxide layer contained 7.8×10^{17} atoms of oxygen per cm² (i.e., equivalent to 1410Å). From the linear decrease with time of the oxygen content of the remaining film one can calculate the dissolution rate under our experimental conditions, i.e., 4.1×10^{16} atoms/cm² (or 75Å) per minute. The oxygen content becomes stationary for dissolution times above about 18 min; this level of stabilization corresponds to the spontaneous formation of a thin oxide layer about 40Å thick. The fluorine measurements show that the concentration remains stationary during the dissolution (around 1.4×10^{15} fluorine atoms/cm²); when the oxide is completely dissolved, one observes a sharp drop in the fluorine content (factor 4). This means that the fluorine which remains after polishing is found in a region close to the metal-oxide interface. A complete dissolution of the oxide allows one to eliminate most of the fluorine, while the residual contamination is probably due to the dissolution bath itself. Complementary experiments showed that the total amount of F^{19} before and after anodic oxidation is, on the average, the same. Hence the F^{19} content is conserved during anodic oxidation.

In order to further confirm the location of the fluorine atoms in the oxide near the oxide-metal interface, we resorted to a second technique in which the ambiguity of the first method (i.e., that the dissolution bath itself contained fluorine) was avoided. The localization was achieved here by the observation of a narrow resonance in the $\text{F}^{19}(\text{p},\gamma)\text{O}^{16}$ reaction, according to a method described in Ref. (6), (8), and (9). The 4.2 keV wide resonance at 872 keV was used, the γ rays being detected with a 3 in. by 3 in. NaI(Tl) scintillation detector. Such a measurement is based on the principle that if the fluorine is detected on the surface, the resonance occurs at the energy E_0 which is the actual energy of the resonance. However, if the fluorine is found at a certain depth, the incident protons must lose an energy ΔE before reaching the fluorine atoms; consequently, the resonance occurs at an energy $E_0 + \Delta E$. Knowing the stopping power of the matrix material to incoming particles (9), one is able to calculate the depth of penetration. The resulting excitation curves are shown in Fig. 4. Curve (a) shows the resonance at 872 keV observed by automatic energy scanning (6) (768 eV/channel) on a tantalum sample chemically polished and then washed for 5 min with boiling triply-distilled water. Total content measurements using the $\text{F}^{19}(\text{p},\alpha)\text{O}^{16}$ reaction showed that 5×10^{14} F^{19} atoms/cm² were on the surface of this specimen. Curve (a) was taken as the reference excitation curve. Curve (b) shows the same resonance observed in identical conditions for the same sample, but further subjected to anodic oxidation up to 90V, as above. This curve is shifted by about $\Delta E = 11$ keV and is somewhat broader than the reference curve (a). The shape of curve (b) may be fully interpreted by assuming that the fluorine atoms remain, after anodic oxidation, in a thin layer near the oxide-metal interface, thus confirming the results obtained by the dissolution method. Full theoretical calculations of the shape of curve (b) according to this assumption are published in Ref. (9). The broadening of curve (b) is well explained by the energy straggling of the incident protons in the F^{19} free anodic oxide. The combination of the results of Fig. 3 and 4 allows us to conclude that the F^{19} is contained, after further anodic oxidation by the order of 1400Å, in a film less than 50Å, near the oxide-metal interface.

Anodic Oxide Growth Laws for Various Surface Treatments of Tantalum

The investigation by Siejka *et al.* (4) of the oxide growth laws on tantalum, as a function of the applied voltage V_{ox} at various current densities, was achieved with samples polished and washed in boiling water, as above. The question arose whether the presence of

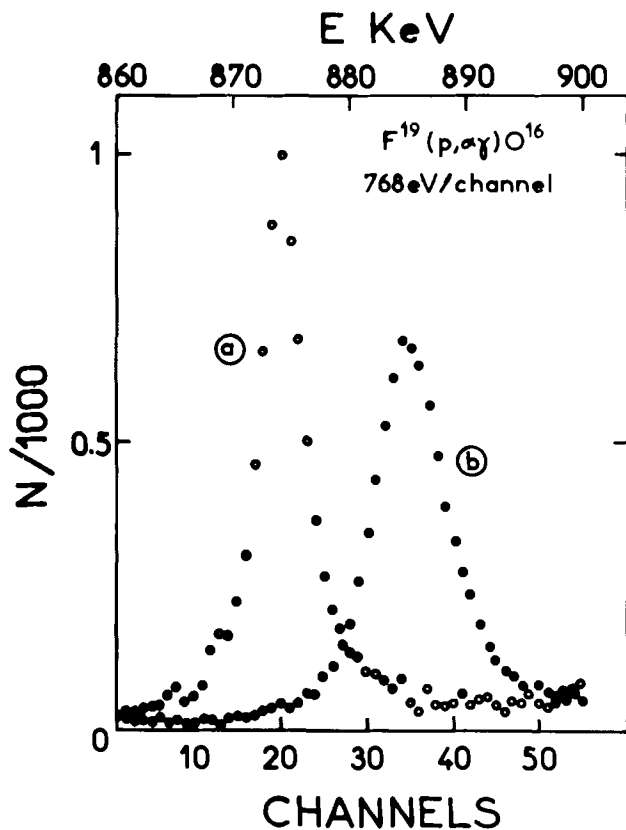


Fig. 4. Excitation curve for γ rays near the 872 keV resonance of the $F^{19}(p, \alpha)\gamma O^{16}$ reaction: (a) Ta specimen polished and washed with boiling water, (b) same specimen, anodically oxidized up to 90V.

F^{19} on the surface of these samples, as evidenced in what precedes, has a noticeable influence on these growth laws. In the experimental conditions of Ref. (4) used here, these laws $N_O = f(V_{ox})$ are straight lines relating V_{ox} , N_O , and $V_{ox}(O)$, N_O being the number of oxygen atoms per cm^2 , and $V_{ox}(O)$ the extrapolated value of V_{ox} for $N_O = 0$. This basic relation and its implications, in particular the meaning of $V_{ox}(O)$, are fully discussed in Ref. (4), to which we refer here systematically. The study of the influence of the various surface preparation techniques described here on the values of $V_{ox}(O)$ and of the slope dN_O/dV_{ox} was undertaken.

All samples were cut in the form of rectangles of 2.2 cm^2 by using a special cutting tool (3,4) in order to ensure an effective reproducibility of their areas. Electrical contact with the specimens was achieved by a special tantalum clamp (12), as in Ref. (4). Anodic oxidation was performed as described above, except for greater care in the measurement of the applied potentials, using a calomel reference electrode, as in Ref. (4). In the following, the potentials are expressed in the hydrogen scale.

Figure 5 shows the results; it appears that, at a given potential, the quantity of oxygen in films grown on polished Ta is the same, for samples washed in either cold or boiling water. Moreover, the oxygen content, at a given potential, of films grown on specimens subjected to the double chemical treatment described above systematically exceeds that found on specimens which were only polished. The latter effect results, on the one hand, in a shift of $V_{ox}(O)$ towards negative potentials by about 0.5V, on the other hand, in an increased slope of the curve $N_O = f(V_{ox})$. It should be noted that this slope is even greater for raw tantalum, while $V_{ox}(O)$ is further shifted in this case towards negative potentials by about 0.3V. Figure

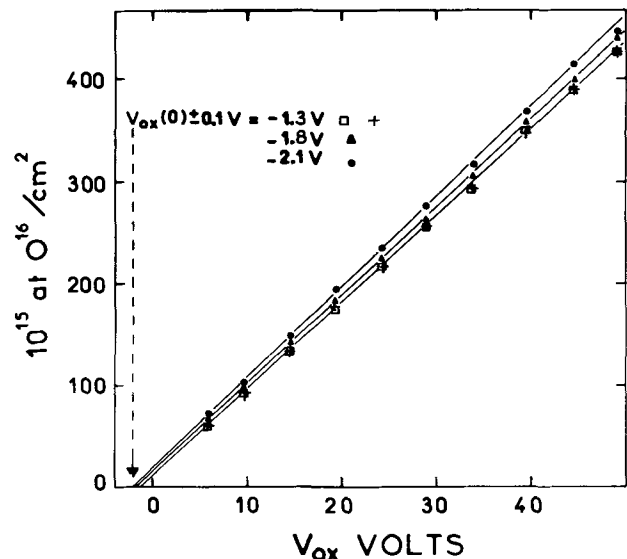


Fig. 5. Growth laws $N_O = f(V_{ox})$ of anodic oxide on Ta. (●), Unpolished; (+), polished, washed with cold water; (□), polished, washed with boiling water; (▲), polished, treated in the NH_4F -HF bath, and washed with boiling water.

6 shows in more detail the data from Fig. 5, represented so as to emphasize the slopes of the growth laws. The corresponding values for raw, doubly-treated and only polished Ta are respectively (in 10^{15} atoms/ cm^2 V): 8.9, 8.6, 8.5, with errors illustrated by Fig. 6. The average slope represented being nearly constant, so is the local slope dN_O/dV_{ox} .

It appears that the influence of F^{19} on the oxide growth laws is only slight. The small observed differences will be discussed in the next section. Moreover the presence of fluorine on the surface of Ta seems to have little effect on the breakdown voltage for anodic oxidation in the above used solution, this voltage being around 200V.

Discussion

Tantalum seems to behave with respect to fluorine in sharp contrast to silicon, which was studied by Croset and Dieumegard (13). These authors found, using the same analytical techniques as in this paper, that the fluorine contamination of silicon after etching in HF and washing in cold water is below 10^{13} atoms/ cm^2 , i.e., about a hundred times less than here. More-

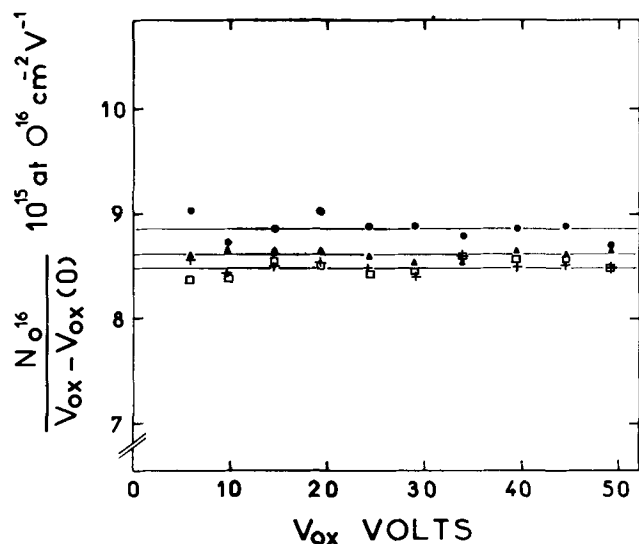


Fig. 6. $N_O/(V_{ox} - V_{ox}(O))$ as a function of V_{ox} for anodic oxides on Ta submitted to various treatments (same symbols as in Fig. 5).

over, the presence of 1.5×10^{14} fluorine atoms per cm^2 in anodic oxide films on silicon (formed in diethylene glycol) leads to a breakdown voltage smaller by at least a factor of 3 than without fluorine contamination of the oxide, whereas the effect of even higher contaminations on the breakdown voltage seems to be small if any for tantalum. Möller and Starfelt (14) [using a $F^{19}(p,\alpha\gamma)O^{16}$ broad resonance with a quoted sensitivity of $0.01 \mu\text{g}/\text{cm}^2$] observed, on the other hand, comparable fluorine contaminations of Zircaloy for various polishing procedures. Barrandon (15) [using the $F^{19}(p,\alpha)O^{16}$ reaction] found very high fluorine contaminations, of the order of 10^{16} atoms/ cm^2 , of zirconium polished chemically in a HF-HNO₃ bath, the washing procedure being not specified. No other direct measurement of low level fluorine contaminations of metals or semiconductors seems to have appeared in the literature.

The fact that the fluorine left by chemical polishing on the surface of tantalum remains near the oxide-metal interface after anodic oxidation is in good agreement with the observations of Pawel *et al.* (16). These authors demonstrated, using an ion microprobe, that fluorine introduced in the oxide film in the course of anodic oxidation in a fluorine containing aqueous bath has a tendency to migrate towards the oxide-metal interface and to accumulate there. Although the way in which fluorine is introduced here in the film is different, the analogy between the two observations is strong; further experiments are in progress to establish whether fluorine originating in chemical polishing or incorporated during anodic oxidation in fluorine containing solutions behave in a completely similar way from the point of view of atomic transport.

The value found for $V_{\text{ox}}(\text{O})$ for chemically polished tantalum at $1 \text{ mA}/\text{cm}^2$, -1.3V , is in good agreement with that of Siejka *et al.* (4), i.e., $-1.15 \pm 0.06\text{V}$, taking into account our estimated error, $\pm 0.1\text{V}$. The identity of the curves $N_{\text{O}} = f(V_{\text{ox}})$ for samples washed in cold or boiling water is on the other hand in contrast to the results of Young [Ref. (1), p. 66] who reports capacity measurements and who observes a shift towards negative potentials of the curve $1/C = f(V_{\text{ox}})$ for samples not leached in boiling water. This might be due to the presence on the surface of a fluorine containing, oxygen-poor compound, which is practically soluble in hot water only, and which, while causing a negligible potential drop at a current density of $1 \text{ mA}/\text{cm}^2$ still contributes to the total capacitance of the film as measured in the frequency region of 1 kHz . The increased adhesion of the oxide films after leaching in boiling water, reported by Young [Ref. (1), p. 68] is clearly not associated with a complete elimination of fluorine. It might be due to a diffusion effect which would change the distribution and (or) chemical state of fluorine in the spontaneous oxide layer. The above-mentioned experiments in progress might shed light on this point.

The behavior of $N_{\text{O}} = f(V_{\text{ox}})$ for raw tantalum observed here is similar to that observed by Siejka *et al.* (4). The higher slope of $N_{\text{O}} = f(V_{\text{ox}})$ and the shift of $V_{\text{ox}}(\text{O})$ for the samples subjected to the double chemical treatment, as compared to those only polished, might be explained by the observation of Halbritter (17), who used the NH₄F-HF bath described here to treat niobium surfaces. This author observed higher residual skin effect rf-losses in superconducting niobium cavities treated in this way and attributed this effect to grain boundary etching of the metal. In fact, this bath does not seem to attack the metal but might do so preferentially at defects like grain boundaries inducing rather narrow and deep microfissure type corrosion figures. This would increase by the order of 1% the roughness factor and increase from 8.5 to 8.6 $dN_{\text{O}}/dV_{\text{ox}}$ (4). This might also explain the shift of $V_{\text{ox}}(\text{O})$ by -0.5V , by the effect of filling the narrowest microfissures by oxide at the early stage of the oxida-

tion; this would appear as an increase of the oxygen coverage by a constant ΔN_{O} , which by shifting $N_{\text{O}} = f(V_{\text{ox}})$ upwards results in a shift of $V_{\text{ox}}(\text{O})$ towards negative potentials (4) ($\Delta N_{\text{O}} \sim 4 \times 10^{15}$ at.oxygen/ cm^2 being equivalent to -0.5V). Scanning microscope measurements might confirm this interpretation. It may be concluded that the presence of 10^{15} at.fluorine/ cm^2 near the metal-oxide interface has negligible influence on the oxide growth laws and that the observation of Siejka *et al.* (4) are correct. In particular, the fact that for tantalum $V_{\text{ox}}(\text{O})$ is very near to the thermodynamic equilibrium potential for the formation of tantalum oxide is confirmed, the observed shifts of $V_{\text{ox}}(\text{O})$ for some surface treatment procedures being probably artifacts.

Work is in progress to improve the double chemical treatment above so as to obtain in a simple fashion fluorine free and still satisfactorily flat tantalum surfaces. The electrochemical polishing procedure described by Diepers *et al.* (18), which seems to give such surfaces for niobium, will be investigated for fluorine contamination. Extension of the present work to niobium is considered with potential applications to the preparation of the surface of niobium superconducting rf-cavities as studied, among others, by Kneisel *et al.* (19).

Acknowledgments

The authors would like to thank Dr. J. Siejka for his continuous interest in this work and for enlightening discussions. They are indebted to Dr. J. Halbritter for the private communication of the results quoted. The contribution of Dr. J. P. Nadai to the interpretation of the excitation curves in Fig. 4 was most appreciated. Mrs. E. d'Artemare and E. Girard provided valuable assistance for the handling of problems related to the automatic energy scanning of the beam and to the electronic set up.

This work was supported by the Centre National de la Recherche Scientifique (RCP No. 157), the DRME, and the DGRST.

Manuscript submitted May 22, 1972; revised manuscript received July 24, 1972. This was Paper 88 presented at the Cleveland, Ohio, Meeting of the Society, Oct. 3-7, 1971.

Any discussion of this paper will appear in a Discussion Section to be published in the June 1973 JOURNAL.

REFERENCES

1. L. Young, "Anodic Oxide Films," Academic Press, New York (1961).
2. C. Cherki, Thesis, Paris (1969).
3. G. Amsel, C. Cherki, G. Feuillade, and J. P. Nadai, *J. Phys. Chem. Solids*, **30**, 2117 (1969).
4. J. Siejka, J. P. Nadai and G. Amsel, *This Journal*, **118**, 727 (1971).
5. A. Guntherschulze and H. Betz, "Electrolytkondensatoren," (Krayn) Berlin (1937).
6. G. Amsel, J. P. Nadai, E. D'Artemare, D. David, E. Girard, and J. Moulin, *Nucl. Instr. Methods*, **92**, 481 (1971).
7. G. Amsel and D. Samuel, *Anal. Chem.*, **39**, 1689 (1967).
8. D. Dieumegard, Thesis 3e cycle; Orsay (1971).
9. G. Amsel, B. Maurel and D. Dieumegard, "Microanalysis of F^{19} , Li^6 and Li^7 by means of nuclear reactions," To be published.
10. L. Young, *Proc. Roy. Soc.*, **A244**, 41 (1958).
11. J. P. S. Pringle, *This Journal*, **119**, 482 (1972).
12. M. Croset, *Rev. Sci. Instr.*, **37**, 123 (1966).
13. M. Croset and D. Dieumegard; Abs. 87, p. 224, Electrochem. Soc. Extended Abstracts, Fall Meeting, Cleveland, Ohio, Oct. 3-7, 1971.
14. E. Möller and N. Starfelt, *Nucl. Instr. Methods*, **50**, 225 (1967).
15. J. N. Barrandon, PhD Thesis, Paris (1970).
16. R. E. Pawel, J. P. Pemsler, and C. A. Evans, Jr., *This Journal*, **119**, 24 (1972).
17. J. Halbritter, Private communication.
18. H. Diepers, O. Schmidt, H. Martens, and F. S. Sun, *Phys. Letters*, **37A**, 439 (1971).
19. P. Kneisel, O. Stoltz, and J. Halbritter, *IEEE Trans. Nucl. Sci.*, **NS-18**, 158 (1971).

Luminescent Properties of Thiogallate Phosphors

II. Ce^{3+} -Activated Phosphors for Flying Spot Scanner Applications

T. E. Peters*

GTE Laboratories Incorporated, Waltham, Massachusetts 02154

ABSTRACT

The cathodoluminescence emission and decay properties of $MGa_2S_4:Ce,Na$ ($M^{2+} = Ca, Sr, Ba$) phosphors were investigated to determine their suitability for use in flying spot cathode ray tubes. The thiogallate phosphors exhibit radiant efficiencies as high as 7.0% and their fluorescence decays to 1% of initial brightness in 1.3-1.55 μ sec. Strontium thiogallate phosphors with decay times as short as 0.6 μ sec were obtained by compositional modifications. Maintenance measurements indicate that $SrGa_2S_4:Ce, Na$ is more stable in CRT applications than $Ca_2Al_2SiO_7:Ce$.

A previous publication (1) presented crystallographic data for thiogallate compounds of the general formula MGa_2S_4 (where $M = Ca^{2+}, Sr^{2+}, Ba^{2+}, Pb^{2+}, Eu^{2+}, [Na^+, La^{3+}]$ and $[Na^+, Ce^{3+}]$) and described some of the luminescence properties of the unactivated and the Ce^{3+} or Eu^{2+} activated alkaline earth compounds. In this report the cathodoluminescence emission and decay characteristics of the Ce^{3+} -activated phosphors are described, particularly as they relate to the use of these materials in flying spot cathode ray tubes.

The fluorescence decay times of Ce^{3+} -phosphors are always very short ($\sim 0.1 \mu$ sec) because allowed $^2D \rightarrow ^2F$ electric dipole transitions are involved in the emission process. Short decay phosphors that fluoresce in the visible region of the spectrum are of particular interest for use in certain types of flying spot scanner tubes that are employed as playback transducers for color television (2). As reported previously (1) the Ce^{3+} -activated alkaline earth thiogallates fluoresce in the blue spectral region and consequently an investigation of their cathodoluminescence emission and decay properties was conducted to determine their suitability for use in this type of device.

Experimental

Phosphor preparation.—The starting materials employed in the preparation of the Ce^{3+} -phosphors were high purity alkaline earth carbonates, Ga_2O_3 (99.99%) and CeO_2 (99.9%). All reagents were subsequently converted to their respective sulfides by reaction at 900°-1200°C in a stream of H_2S gas.

It was found desirable to provide valence compensation for the Ce^{3+} ion when it substitutes for the divalent alkaline earth in the thiogallate lattice. Initially, monovalent sodium was introduced in the form of NaCl to provide compensation according to the general formula $M_{1-2x}Ce_xNa_xGa_2S_4$. In later experiments it was found that the use of 0.035 moles Na_2SO_4 /mole MGa_2S_4 in excess of that required for electro-neutrality resulted in improved activator incorporation and valence compensation.

Stoichiometric quantities of the various sulfides, together with NaCl or Na_2SO_4 , were thoroughly mixed by grinding in a glass mortar and the resulting blend was subjected to a solid-state reaction at 900°-950°C for 2 hr in H_2S . The phosphor cake was then mortared (NaCl compensation) or washed (Na_2SO_4 compensation) and sieved prior to evaluation.

Measurements.—Standard analytical techniques were employed to monitor the purity and stoichiometry of the sulfide reagents and finished phosphors. X-ray powder diffraction was used to ascertain formation of the thiogallate compounds.

Emission and excitation spectra are given in terms of relative energy and relative energy efficiency. Absolu-

te radiant efficiencies under cathode ray excitation (η_{cr}) were determined in a manner analogous to that described by Brill and Klassens (3).

Relative efficiency values (η_{cr} Rel.) were obtained by comparing the integrated area under the spectral energy distribution curves to that of selected thiogallate and NBS-1021 phosphors of known absolute efficiency.

Blue brightness levels were measured under conditions simulating those found in a color video playback system employing flying spot scanners (2). Phosphor-coated conducting glass slides were placed in a demountable CRT and excited with a 25 kV-100 μ A electron beam which was scanned at the normal TV rate over a $2\frac{1}{4} \times 3$ in. raster. The emission was detected by a Gamma photometer equipped with a Wratten No. 47B filter.

Cathodoluminescence decay times were measured by pulsing a 20 kV electron beam of a 5 in. cathode ray tube at a rate of 60 Hz with a pulse duration of 100 nsec. The fluorescence was detected by a photomultiplier tube and displayed on an oscilloscope.

Phosphor maintenance studies were also conducted on the sealed 5 in. CRT's using excitation conditions identical to those employed for the blue brightness measurements.

Thermoluminescence curves were obtained by cooling the phosphor to liquid nitrogen temperatures in an evacuated quartz chamber, irradiating with a 3650Å lamp and then increasing the temperature at $\sim 8^\circ C/min$, while monitoring the emission with a photomultiplier tube.

Results and Discussion

The cathodoluminescence properties of NaCl ($Na/Ce = 1$) compensated $M^{2+}Ga_2S_4:Ce,Na$ phosphors are compared to those of $Ca_2Al_2SiO_7:Ce$, a commercial flying spot scanner material (Table I). The radiant efficiencies of the calcium and strontium thiogallates are greater than that of the barium analog and are comparable to that of the $Ca_2Al_2SiO_7:Ce$. It is to be emphasized that the η_{cr} values given in Table I were obtained on samples whose syntheses were not optimized and are intended only to illustrate the relative performance of analogous alkaline earth compositions. Later in the text it will be pointed out that the η_{cr}

Table I. Cathodoluminescence properties of $MGa_2S_4:Ce,Na$ phosphors

Phosphor*	λ_{max} , nm	$\eta_{cr}^{(a)}$, %	Decay τ , μ sec	β , μ sec
$CaGa_2S_4:Ce,Na$	468	4.5	0.08	1.50
$SrGa_2S_4:Ce,Na$	455	5.0	0.08	1.55
$BaGa_2S_4:Ce,Na$	455	2.9	0.07	1.30
$Ca_2Al_2SiO_7:Ce$	405	4.5 ^(b)	0.05	0.52

* 4% $Ce,NaCl$ compensation, $Na/Ce = 1$.

^(a) Radiant efficiency 20 kV.

^(b) Value from Ref. (4).

* Electrochemical Society Active Member.
Key words: fast decay, short persistence.

of $\text{SrGa}_2\text{S}_4:\text{Ce,Na}$ can be improved substantially by modifications in the preparation method.

Two decay times, τ and β , are given in the last two columns of Table I. The fluorescent lifetime τ , is the time required for the fluorescence to decrease from its initial value I_0 to I_0/e . This assumes that the decay curve is represented by an exponential decay $I \propto e^{-at}$ (where $a = \tau^{-1}$). In many cases, however, the decay curves of Ce^{3+} -phosphors exhibit a nonexponential tail. A more meaningful decay value, particularly for the application in question, is one which includes the nonexponential part of the curve, i.e., the time required for the fluorescence to decrease to 1% I_0 . This value is designated as β in Table I and in the subsequent text. Although the β values in Table I show the thiogallates to have significantly longer decay times than the aluminosilicate, this characteristic alone does not preclude their use in flying spot scanner tubes. The decay times are of a magnitude which would permit electronic compensation to obtain acceptable performance (2). Thus the Ce^{3+} -activated alkaline earth thiogallates are potentially useful flying spot scanner materials.

The τ values in Table I indicate that the exponential portions of the decay curves are similar for the aluminosilicate and thiogallate phosphors. Larger differences in the decay rates of the phosphors occur in the nonexponential part of the curve. This is evident from the divergence of the β values and can be clearly seen in the representative decay curves given in Fig. 1. Figure 1 also indicates that the decay of $\text{Ca}_2\text{Al}_2\text{SiO}_7:\text{Ce}$ is not entirely exponential. Brill *et al.* (4) have shown that $\text{Ca}_2\text{Al}_2\text{SiO}_7:\text{Ce}$ and many other Ce^{3+} -activated phosphors exhibit long decay components that deviate significantly from the exponential law. They suggested that the afterglow might be due to the storage of excitation energy in traps provided by defects or impurities. In order to test this hypothesis as it relates to the thiogallate phosphors, thermo-

luminescence measurements were performed on $\text{Ca}_2\text{Al}_2\text{SiO}_7:\text{Ce}$ and several $\text{SrGa}_2\text{S}_4:\text{Ce,Na}$ phosphors and the results are presented in Fig. 2. In the figure the relative heights of the thermoluminescence peaks do not constitute a meaningful measure of the concentration of trapping species because the surface area and quantity of phosphor varied from sample to sample. However, the curves do yield qualitative information as to trap depth and distribution. In accord with the hypothesis the thermoluminescence curve for the aluminosilicate phosphor indicates a broad distribution of deep lying traps centered around 80°C . The curves for the thiogallate phosphors, on the other hand, exhibit only one thermoluminescence peak centered at -140°C . This indicates that only shallow traps are present that should not be populated at room temperature. Thus a simple trapping process does not seem to explain the nonexponential behavior of the decay of Ce^{3+} fluorescence in SrGa_2S_4 .

The decay of the Ce^{3+} fluorescence in the $\text{SrGa}_2\text{S}_4:\text{Ce,Na}$ phosphor can be shortened by (i) concentration quenching, (ii) improved valence compensation, (iii) energy transfer to Nd^{3+} , and (iv) transition metal quenching. This is shown in Fig. 3 where the decay to 1% I_0 (β) is presented as a function of $[\text{Ce}^{3+}]$ for $\text{SrGa}_2\text{S}_4:\text{Ce,Na}$, $\text{SrGa}_2\text{S}_4:\text{Ce,Nd,Na}$, and $\text{SrGa}_2\text{S}_4:\text{Ce,Na,Co}$. In all of the phosphors examined a reduction in the decay was effected by increasing the $[\text{Ce}^{3+}]$ beyond 2 atomic per cent (a/o) which is optimum for brightness; the reduction in decay attributed to concentration quenching is also accompanied by a decrease in emission intensity and a slight shift in λ_{max} to lower energy.

The effect of improved valence compensation on the Ce^{3+} decay is indicated by a comparison of (a) and (b) in Fig. 3. These data are for two series of $\text{SrGa}_2\text{S}_4:\text{Ce,Na}$ phosphors prepared with NaCl ($\text{Na/Ce} = 1$) and Na_2SO_4 ($\text{Na/Ce} = 1 + 0.07/\text{Ce}$) respectively, as the source of the monovalent compensating ion. It can be seen that substantially smaller β values result when an excess of the compensating ion is included in the phosphor formulation. Similar reductions in β have been observed when other sodium compounds have been employed in the synthesis provided there is an excess of Na^+ over that required for electroneutrality. Sodium sulfate is preferred, however, because it also serves as a mineralizer which improves the uniformity and crystallinity of the phosphor.

The effect of Nd^{3+} coactivation on the decay of Ce^{3+} fluorescence in $\text{SrGa}_2\text{S}_4:\text{Ce,Nd,Na}$ is given by (c) in Fig. 3. The observed shortening of the decay time is attributed to $\text{Ce}^{3+} \rightarrow \text{Nd}^{3+}$ energy transfer. Energy transfer between these ions has been reported by Gandy *et al.* (5) in a Ce,Nd coactivated silicate glass.

Evidence for the $\text{Ce}^{3+} \rightarrow \text{Nd}^{3+}$ energy transfer in $\text{SrGa}_2\text{S}_4:\text{Ce,Nd,Na}$ is given in the excitation spectra shown in Fig. 4(a-c). Comparison of the excitation spectra for Nd^{3+} emission at 900 nm shows that there

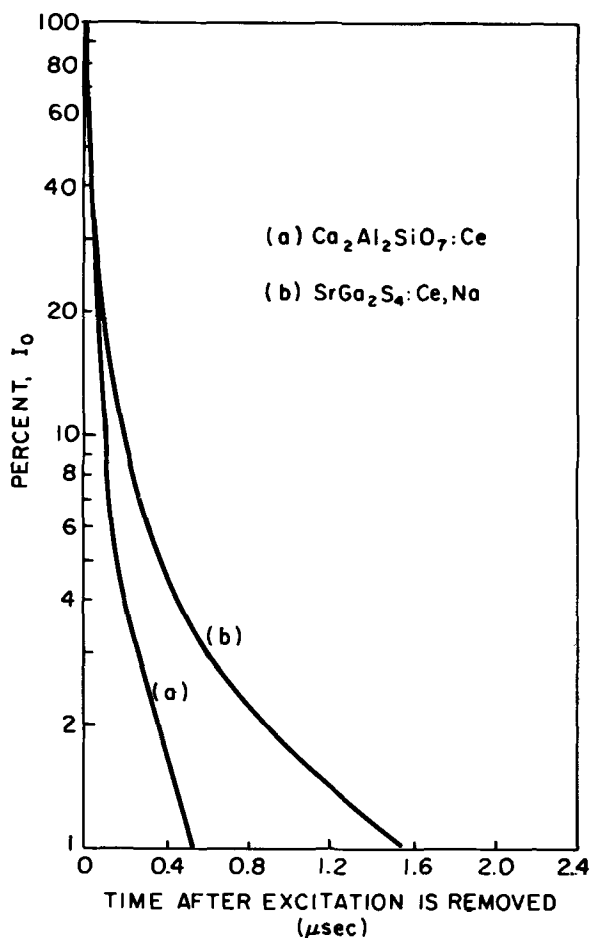


Fig. 1. Decay of fluorescence of Ce^{3+} phosphors

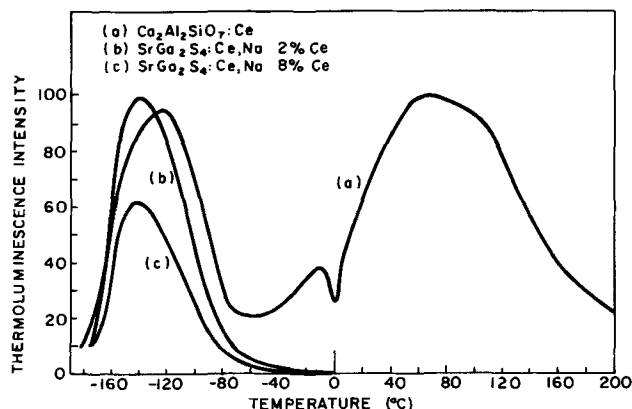


Fig. 2. Thermoluminescence of Ce^{3+} phosphors

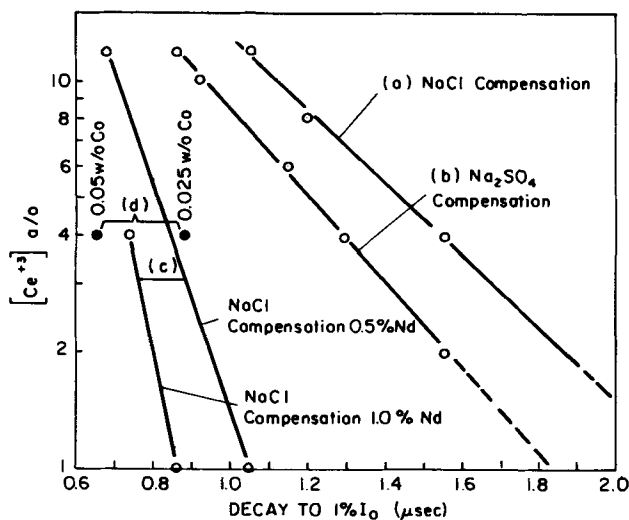


Fig. 3. Decay time β vs. $[Ce^{3+}]$ for $SrGa_2S_4:Ce,Na$ phosphors

is a strong absorption band at 410 nm in the coactivated phosphor (Fig. 4a) which is absent in the material activated only by Nd^{3+} (Fig. 4b). That this band is due to Ce^{3+} absorption can be seen in the excitation spectra for the 460 nm Ce^{3+} emission of $SrGa_2S_4:Ce,Na$ (Fig. 4c). Thus excitation into the Ce^{3+} band at 410 nm produces Nd^{3+} emission at 900 nm confirming $Ce^{3+} \rightarrow Nd^{3+}$ transfer in the $SrGa_2S_4:Ce,Na$ phosphor.

Figure 3(d) depicts the β values for sodium sulfate compensated $SrGa_2S_4:Ce,Na$ (4 a/o) phosphors containing 0.025 and 0.05 w/o cobalt. A comparison of these values with that of the cobalt free 4 a/o Ce^{3+} phosphor shows that extremely small concentrations of cobalt can reduce the decay time of $SrGa_2S_4:Ce,Na$ by approximately 50-70%. Similar reductions in decay resulted when phosphors were prepared with 0.01-0.1 w/o of iron or nickel.

It is believed that the principal effect of the transition metal ion is to increase the probability of radiationless transitions to the ground state. In support of this contention it is noted that the decay curves of

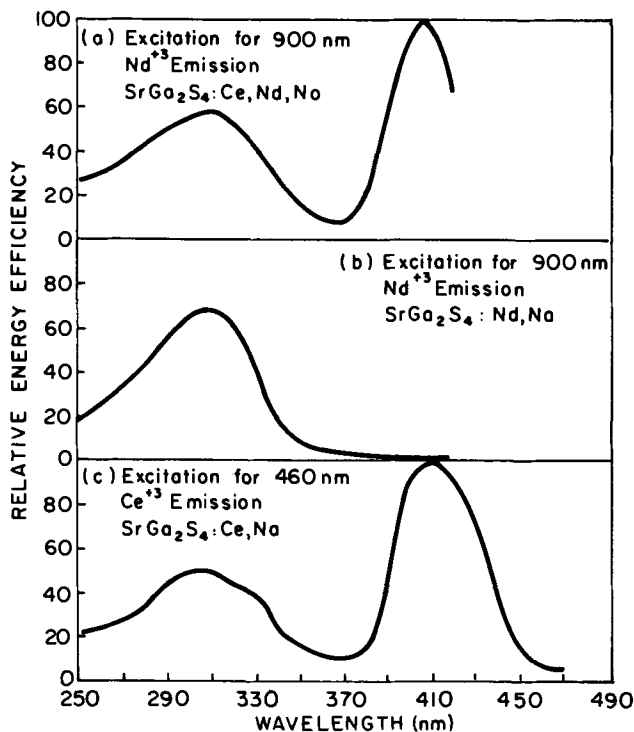


Fig. 4. $Ce^{3+} \rightarrow Nd^{3+}$ energy transfer in $SrGa_2S_4:Ce,Na,Nd$

the cobalt quenched phosphors exhibit a nonexponential tail similar to that of the unquenched $SrGa_2S_4:Ce,Na$ and that the increase in decay rate manifested itself in both the exponential and nonexponential parts of the curve. Furthermore, the intensity of the Ce^{3+} fluorescence, for phosphors containing up to 0.1 w/o Co, was found to decrease in proportion to the increase in decay rate.

Of the four methods found effective in reducing the decay of $SrGa_2S_4:Ce,Na$ only improved valence compensation results in an increase rather than a decrease in cathodoluminescence efficiency. For example, a $SrGa_2S_4:Ce,Na$ (4 a/o Ce) phosphor prepared with excess Na_2SO_4 exhibits an η_{cr} Rel. of 6.5% as compared to 5.0% for a similar phosphor (see Table I) compensated with NaCl ($Na/Ce = 1$).

In a color flying spot scanner system both the efficiency and spectral energy distribution of the phosphor must be considered because it is the response of the systems' photodetectors that constitute the TV signal in video playbacks. Relative brightness measurements were made under conditions simulating the blue detector response in a color flying spot scanner system and the results are given in Table II.

In Table II the blue brightness of several of the phosphors described in Fig. 3 are compared to that of a sodium sulfate compensated $SrGa_2S_4:Ce,Na$ (η_{cr} Rel. = 7.0%). Similar data is reported for a $Ca_2Al_2SiO_7:Ce$ phosphor that is employed as the blue screen component in a commercial color flying spot scanner tube. The best brightness levels were recorded for the $SrGa_2S_4:Ce,Na$ phosphors activated with 2-4 a/o Ce^{3+} . These materials yield a blue detector response which is 1.5-2.0 times that of the $Ca_2Al_2SiO_7:Ce$. The remaining thiogallates in the table provide examples of the brightness levels available from phosphors that employ concentration quenching, transition metal quenching, or energy transfer to improve their decay properties. In general these materials exhibit somewhat lower brightness levels than the $Ca_2Al_2SiO_7:Ce$.

Trivalent cerium-activated phosphors are frequently found to be unstable in cathode ray tube operation. For example, losses in efficiency have been reported for $Ca_2Al_2SiO_7:Ce$ (6), $Ca_2MgSi_2O_7:Ce$ (7), and $(Y,Gd,La)PO_4:Ce$ (8) and we have observed similar losses for the recently described $Y_2SiO_5:Ce$ (9). The $SrGa_2S_4:Ce,Na$ phosphor is remarkably stable in this respect as illustrated by the maintenance data given in Fig. 5. In this figure the initial intensity of each of the phosphors has been normalized to 100%. The thiogallate phosphor loses only 10% of its initial intensity in 10 hr, while the aluminosilicate phosphor, shown here for comparison, suffers an intensity loss of 50% in the same time period.

Phosphor stability is an important consideration in the manufacture of a flying spot scanner tube because drastic changes in brightness frequently make it necessary to age the tube until a relatively stable level of emission intensity is achieved. Use of the $SrGa_2S_4:Ce,Na$ phosphor could eliminate or curtail this costly process. Furthermore, the thiogallate phos-

Table II. Relative blue brightness of $SrGa_2S_4:Ce,Na^*$

Mechanism used to increase decay rate	a/o Ce	a/o Nd	w/o Transition metal	Relative blue brightness
Concentration quenching	2.0	—	—	100
	4.0	—	—	75
	12.0	—	—	40
Transition metal quenching	4.0	—	0.025 Co	46.5
	4.0	—	0.05 Co	19.5
	4.0	—	0.1 Co	15.0
	4.0	—	0.1 Ni	14.0
	4.0	—	0.1 Fe	11.7
Energy transfer	12.0	0.5	—	10.0
	—	—	$Ca_2Al_2SiO_7:Ce$	50.0

* Na_2SO_4 Compensation, $Na/Ce = 1 + 0.07/Ce$.

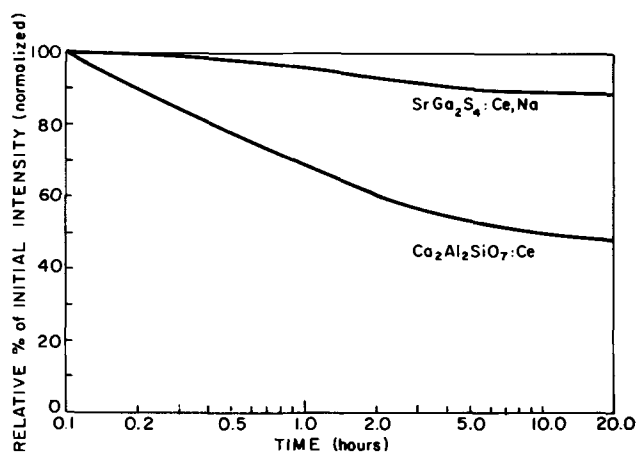


Fig. 5. Maintenance of efficiency of Ce^{3+} phosphors

phors exhibit an even greater brightness advantage when compared to an aged $Ca_2Al_2SiO_7:Ce$. Considering the data in Table II it is apparent that some of this brightness advantage could easily be traded for a somewhat faster decay by employing transition metal or concentration quenching.

Summary

The cathodoluminescence emission and decay properties of $M^{2+}Ga_2S_4:Ce,Na$ ($M^{2+} = Ca, Sr, Ba$) phosphors have been investigated to determine their suitability for use in a version of the flying spot scanner tube that is employed as a playback transducer for color television. Relative efficiencies (η_{cr} Rel.) as high as 7.0% have been recorded for optimum $SrGa_2S_4:Ce,Na$ compositions. The fluorescence of the $M^{2+}Ga_2S_4:Ce,Na$ phosphors decays to 1% of initial intensity (β) in 1.3-1.55 μ sec. The decay of Ce^{3+} fluorescence in $SrGa_2S_4$ can be shortened by (i) improved valence compensation, (ii) concentration quenching, (iii) energy transfer to Nd^{3+} , and (iv) transition metal quenching. Fluor-

escence decay times (β) as short as 0.6 μ sec have been achieved by application of one or more of these mechanisms. Measurements conducted under conditions simulating the blue detector response in a color flying spot scanner system indicate that the brightness of several $SrGa_2S_4:Ce,Na$ compositions exceeds that of the blue screen component, $Ca_2Al_2SiO_7:Ce$, employed in a commercial color flying spot scanner tube. Phosphor maintenance measurements also show the $SrGa_2S_4:Ce,Na$ to be much more stable than the aluminosilicate in CRT operation.

Acknowledgments

The author wishes to express his appreciation to R. Amster who initiated work on $Ce^{3+} \rightarrow Nd^{3+}$ energy transfer, to T. Sisneros for brightness measurements, and to J. Ragusin for technical assistance. Thanks are also due to K. Spiegel of GTE Sylvania's Electronic Tube Division who provided much of the decay data and to F. Palilla and S. Natansohn for manuscript review.

Manuscript submitted May 19, 1972; revised manuscript received July 24, 1972.

Any discussion of this paper will appear in a Discussion Section to be published in the June 1973 JOURNAL.

REFERENCES

1. T. E. Peters and J. A. Baglio, *This Journal*, **119**, 230 (1972).
2. C. B. Neal and H. E. Smithgall, *IEEE Trans.*, **BTR-16**, 56 (1970).
3. A. Bril and H. A. Klasens, *Philips Res. Rept.*, **7**, 401 (1952).
4. A. Bril, G. Blasse, and J. A. de Poorter, *This Journal*, **117**, 346 (1970).
5. H. W. Gandy, R. J. Ginther, and J. F. Weller, *Physics Letters*, **11**, 213 (1964).
6. A. Bril, J. de Gier, and H. A. Klasens, *Philips Tech. Rev.*, **15**, 233 (1954).
7. A. Pfahnl, *Bell System Tech. J.*, **42**, 181 (1963).
8. R. C. Ropp, *This Journal*, **115**, 531 (1968).
9. A. H. Gomes de Mesquita and A. Bril, *ibid.*, **116**, 871 (1969).

Formation of Ultrathin Oxide Films on Silicon

Francis P. Fehlner*

Corning Glass Works, Research and Development Laboratories, Corning, New York 14830

ABSTRACT

Thin silicon dioxide films on silicon have been grown by thermal oxidation in dry oxygen at 400°C. The kinetics of the process and the effect of both impurities and ultraviolet irradiation have been examined and compared with models of the oxidation process.

Silicon dioxide films, in the range of 5-50Å thick, are useful in the fabrication of silicon tunneling devices. Examples of such devices include the memory field effect transistor (1), and the tunneling-mode transistor (2). In both cases, one needs a uniform, high-quality film which is essentially transparent to electrons under the influence of a high electric field.

Prior work (3) has shown that the thermal oxidation of silicon at one atmosphere occurs very slowly when compared with that of metals. As a result, temperatures in the range of 600°C have been utilized (4) to obtain oxide thicknesses in the range 15-60Å. Higher temperatures have also been used in conjunction with a reduced partial pressure of oxygen (5, 6) or with an oxide of nitrogen (7, 8).

Thin oxide films have been observed to grow on silicon at temperatures lower than those noted above. At room temperature, approximately one and one-half monolayers of oxide grow in 2000 min at 40 Torr oxygen (9). In air, a thicker film is formed (10). Boiling, deionized water containing dissolved oxygen forms films approximately 13Å thick (11). Nitric acid has also been found useful in forming 10-20Å thick oxide films on silicon (12).

No reports on the rate of oxidation in the temperature range 100°-600°C have been found in the literature. Since it appears to be the range in which 15-30Å films can be conveniently grown in oxygen, an investigation of the growth rate of silicon dioxide on silicon at 400°C in one atmosphere of dry oxygen has been carried out. The results are reported below as a function of impurity content and ultraviolet irradiation.

* Electrochemical Society Active Member.

Key words: oxidation, silicon surfaces, silicon dioxide, low-temperature oxidation, MNOS devices, tunnel transistors.

Experimental Procedure

MOS-quality silicon wafers [6-9 ohm-cm, n-type, (111)], as supplied by Monsanto Corporation, were cleaned as follows. Approximately 1μ of oxide was grown by wet oxidation at 1050°C in an MOS-quality tube furnace. The wafers were stored in this form until needed. The oxide was eventually stripped in a solution of four parts deionized (DI) water to one part 48% hydrofluoric acid (electronic grade) until clean as determined by ellipsometer measurements. The final rinse was for 15 min in DI water, after which the ellipsometer showed a $4.9 \pm 0.5\text{\AA}$ film remaining on the silicon surface.

A saturated iodine-anhydrous methanol solution (13) was substituted for the water rinse in some cases, in an attempt to remove the residual fluorine which is known to adhere to silicon wafers cleaned in HF (14). The iodine, in turn, was removed by a 25 min bake at 550°C in dry argon.

After an experiment had been completed, the wafers were reclaimed by a one minute dip in 1:4 HF/ H_2O and a 15 min rinse in DI water.

Oxidation was carried out in one of two reactors. Both utilized rf-heated, silicon carbide coated, graphite susceptors. They differed in the construction of the surrounding quartz tube.

The first reactor, shown in Fig. 1A, consisted of a quartz tube closed at the ends with steel plates and silicone rubber gaskets. The adhesive (Dow Corning 732RTV) used to attach the rubber to the steel later proved to be a source of acetic acid (HAc), so a second system was constructed. This is shown in Fig. 1B. The closures on this quartz tube were quartz end caps.

The thermocouple which controlled the susceptor temperature was Chromel-Alumel encased in a stainless-steel sheath.

Gas was supplied via stainless steel tubing as shown in Fig. 1C. Matheson ultrahigh purity argon and oxygen were used. A 2 liter water bubbler held at room temperature was used to humidify the gas for some experiments.

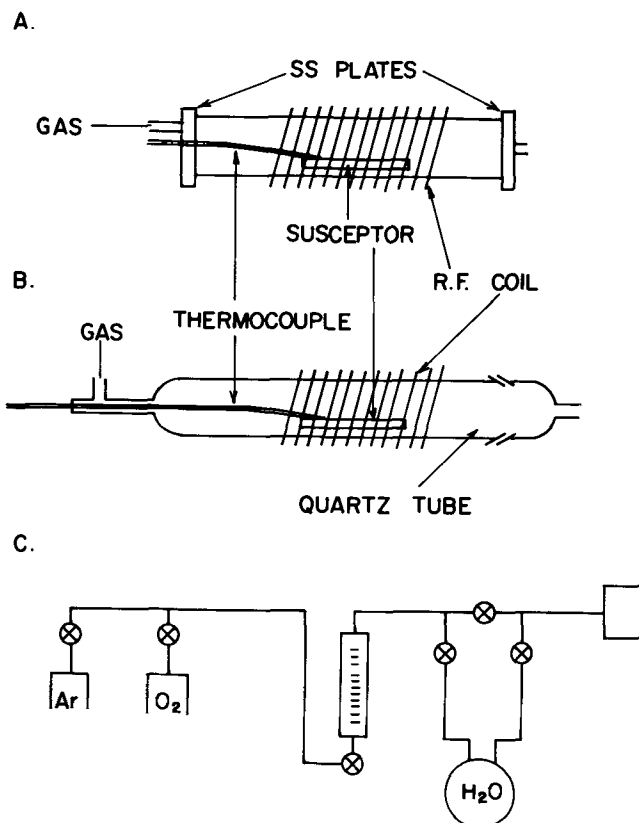


Fig. 1. Apparatus used for oxide growth at 400°C . A, Initial setup; B, final setup; C, gas inlet assembly.

Film thicknesses were measured with an ellipsometer, a Rudolph Model 43603-200E, using $546\text{ m}\mu$ radiation and 70° angle of incidence. Polarizer-analyzer readings were reduced using a time-shared computer program written by J. Conrigan. The measurements were reproducible to $\pm 1\text{\AA}$.

The silicon substrate optical constants were taken to be $4.05-0.027i$ (15). The refractive index of bulk SiO_2 , 1.46, was rounded off to 1.5 on the assumption that the silicon-rich interface layer would have a higher refractive index than bulk silica. However, it proved difficult to check this assumption, since the oxide thickness determined from the ellipsometer data was insensitive to small changes in refractive index.

Results

The study of silicon oxidation at 400°C proceeded only after the question of clean, reproducible starting conditions had been settled. The first apparatus used, shown in Fig. 1A, turned out to be contaminated with acetic acid vapors emanating from the silicone rubber cement used to attach the gaskets to the metal end plates. Although deemed unfortunate at the time, this event later proved useful in showing that silicon oxidation can be an impurity-controlled process, as concluded by Revesz and Evans (16).

The presence of acetic acid was detected by a change in the rate of oxidation after continued use of the apparatus. The initial results are shown in Fig. 2 by X's and squares. An induction period of 60 min was followed by a logarithmic growth rate. Irradiation of the silicon using a medium-pressure mercury arc (Illumination Industries Inc. 202) resulted in an accelerated rate of film growth, perhaps due to acetic acid photolysis and the incorporation of hydrocarbons in the oxide film. Acetic acid is known to yield methyl radicals during photolysis (17).

An increase in water vapor content caused an increase in the photolytic effect. This behavior can be explained by the fact that moisture leads to faster curing of the silicone rubber cement, with concomitant faster release of acetic acid.

After a time, the initial results could not be reproduced, due to depletion of the source of contamination. The induction period lengthened to 100 min and the rate of logarithmic oxidation decreased. Little or no effect due to water vapor or irradiation could be found. This result is shown by the circles in Fig. 2.

The sudden change in behavior was difficult to explain, until every variable in the system had been checked. Water vapor, cleaning procedures, and gas purity were all discounted as causes. The initial results could be reproduced only when the gaskets were reglued. The presence of fresh acetic acid vapor from the silicone cement was the only addition to the system which gave the original results.

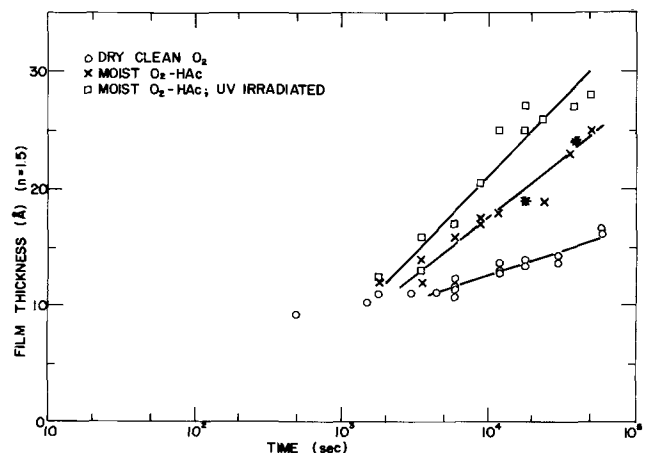


Fig. 2. Oxidation of silicon at 400°C

The problem, once found, was eliminated by constructing a new system as shown in Fig. 1B. Quartz end caps eliminated the problem of silicone rubber. All other parts of the system remained the same.

Excellent results were obtained at 400°C, as shown in Fig. 3. No point on the graph is more than 1Å off the line. The use of (100) n-type or (111) p-type wafers gave the same results at 1200 sec as (111) n-type silicon. Even the displacement of the original fluoride layer by an iodine-dip-and-bake gave no change in oxidation rate, as also found by van der Meulen (5).

It should be noted though, that even the oxide film grown under the more carefully controlled conditions contained impurities. Preliminary results of Auger spectroscopy showed that ~0.01 monolayers of fluorine and a trace of copper were present in the oxide films studied in the present work. Presumably, hydrogen and carbon were also present.

Discussion

Revesz and Evans (16) conclude that the oxidation of silicon is an impurity-controlled process. Their work is confirmed by the results of the present study. The greater the degree of contamination, as shown in Fig. 2, the greater the rate of film growth. Dry, clean oxygen gave a growth rate at 400°C of 4.2 Å/decade. The addition of a small amount of moisture and acetic acid raised the rate to 6.8Å/decade. The combination of moist acetic acid and ultraviolet radiation gave a rate of 13.1 Å/decade.

The results of the reaction of silicon with oxygen under clean dry conditions at 400°C are compared in Fig. 3 with the results of Goodman and Breece (4) at 600°C and Archer and Gobeli (9) at 25°C. Goodman and Breece originally interpreted their work in terms of a linear process, but it will be shown below that a logarithmic plot fits just as well for dry oxidation.

Cabrera and Mott (18) give an expression for estimating the upper temperature limit for application of the inverse logarithmic growth law. For aluminum, they found an upper temperature limit of approximately 300°C. For silicon, the limit is higher.

A graph of current density vs. applied field for anodized silicon (19) was compared with the theoretical expression of Cabrera and Mott [p. 180 of Ref. (18)]. An upper temperature limit for inverse logarithmic growth of approximately 500°C was calculated using only data at the highest fields (where anodization was occurring) and an oxidation efficiency of 1%. An ionic jump distance of 2.8Å was also calculated. As a result of these findings, an attempt to present the results of Goodman and Breece in inverse logarithmic form seemed justified.

However, direct logarithmic kinetics also had to be considered. Since silicon dioxide is an excellent network former in glassy systems, the work of Fehlner and Mott (20) would predict growth by anion transport

at constant field, leading to direct logarithmic kinetics

$$x = C + D \log (t + t_0) \quad [1]$$

where $C = \frac{(qaF/2) - W}{\mu} + \frac{2.3 kT}{\mu} \log \frac{(\mu N \Omega \nu)}{kT}$, $D = \frac{2.3 kT}{\mu}$, $x =$ oxide thickness, $t =$ time, $T =$ tempera-

ture, $N =$ the number of anions in position to move across the oxide, $\Omega =$ volume of oxide per ion, $\nu =$ frequency of vibration, $W =$ barrier to ion motion, $q =$ charge on the ion, $a =$ jump distance of the ion, $F =$ field across the oxide (V/x), $\mu, k, t_0 =$ constants.

The data from Fig. 3 have been plotted according to Eq. [1] and are shown in Fig. 4. The value of t_0 corresponding to the initial oxide thickness was estimated to be 1200 sec. Although reasonable straight-line plots resulted and an increase in μ with T was found, it proved impossible to calculate a positive value of $W - qaF/2$ in Eq. [1] from the data in Fig. 4. As pointed out by Fehlner and Mott, straight-line plots are insufficient to prove the validity of any particular rate law. One must be able to calculate physical parameters which have reasonable values.

Since the direct logarithmic expression was not completely applicable, an inverse logarithmic plot was tried. This is shown in Fig. 5 for the expression

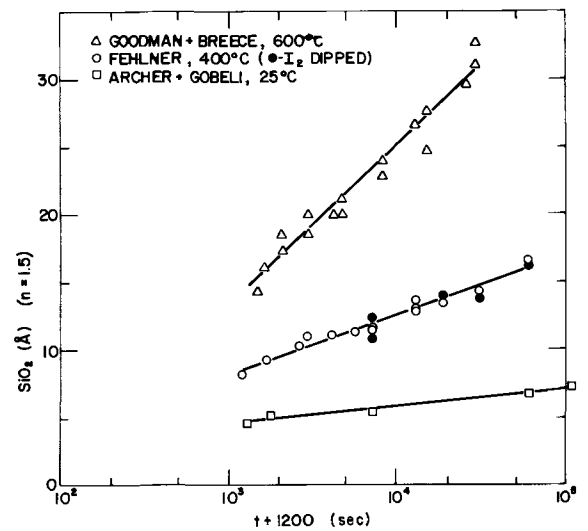


Fig. 4. Figure 3 replotted according to direct logarithmic kinetics, taking into consideration the presence of an initial film.

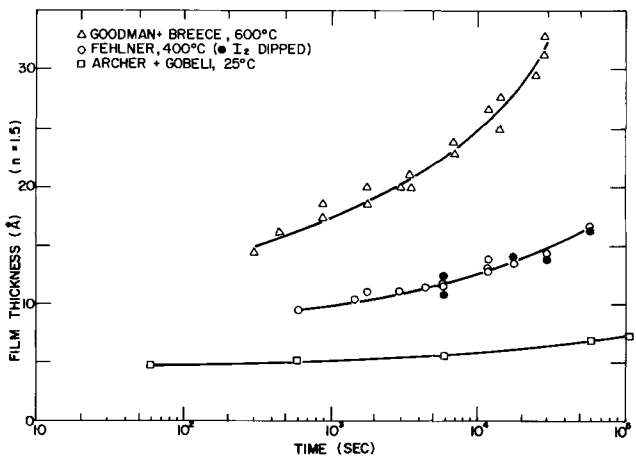


Fig. 3. Dry oxidation of silicon

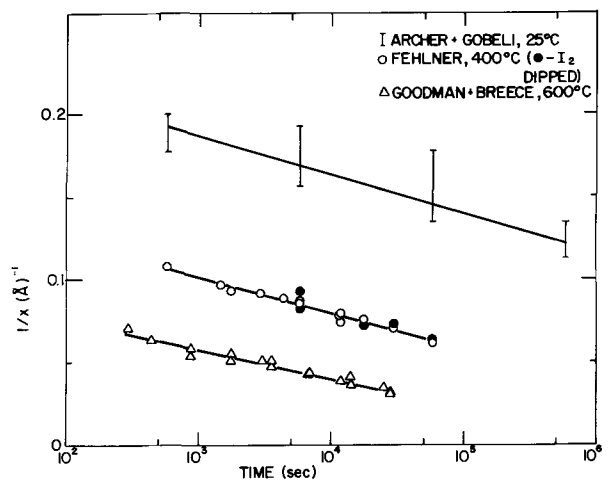


Fig. 5. Data for the dry oxidation of silicon plotted according to the inverse logarithmic law.

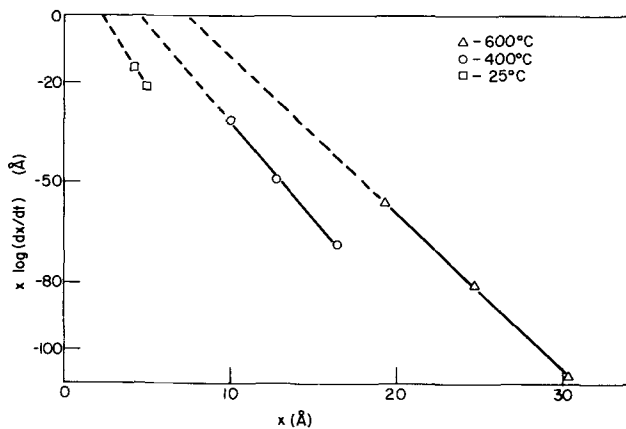


Fig. 6. Rate data for the low-temperature oxidation of silicon tested against the inverse logarithmic law.

$$\frac{1}{x} = A - B \log t \quad [2]$$

$$\text{where } A = \frac{4.6W}{qaV} + \frac{4.6kT}{qaV} \log \left(\frac{x}{N\Omega v} \right)$$

$$\text{and } B = \frac{4.6kT}{qaV}$$

as derived by Hauffe (21).

Again, reasonable straight-line plots resulted, similar to those found by Ligenza (22) for the low-temperature oxidation of germanium. Following Ligenza, a plot of $x \log(dx/dt)$ vs. x (see Fig. 6) was used to find a value of V assuming $q = 4e$ and $a = 5\text{Å}$. This value was checked by determining V directly from Eq. [2] and the data in Fig. 5. The results are shown in Table I. The values calculated from Fig. 5 are considered to be more accurate, since the determination of dx/dt was done graphically. The room-temperature values are only approximate due to scatter in the data of Archer and Gobeli. The values of V so determined agree with work function changes found for a similar system, oxygen on germanium (23).

Again following Ligenza, an attempt to determine the activation energy W was made from a plot of the slopes in Fig. 6 vs. $1/T$. The three points which were available did not fall on a straight line. This would agree with the results found by Ligenza for germanium, which implies that the activation energy is temperature dependent. However, it should be noted in Eq. [2] that W is also a function of x and V . As such, it is not a simple matter to graphically find the temperature dependence of W .

Since it was possible to calculate reasonable values of V from the data presented in inverse logarithmic form, it appears that the Cabrera-Mott mechanism is applicable. It is probable then that the oxidation of silicon at low temperatures proceeds mainly by cation migration under conditions of constant voltage (20).

At high temperatures, anions are the mobile species (24, 25) during silicon oxidation, but during anodization at low temperatures, anions and/or cations can be mobile (26). The determining factor appears to be the field applied across the oxide. At low fields, Schmidt

and Ashner (26) have shown that hydroxyl ions move from the oxide surface into the oxide. Conversely, at high fields, cations move from the silicon interface through the oxide. A less striking example of the same type of behavior is found with aluminum (27) in which a greater fraction of cations move as the field is increased. Brook *et al.* (28) have discussed a similar phenomenon, observed during the anodization of zirconium and aluminum. They propose that the relative rates of movement of two differently charged ions in a growing oxide invert as a function of applied field.

The same reasoning may explain the behavior of silicon during low-temperature oxidation. At low temperatures, charge separation induces a large field across the oxide such that cation migration would be favored. At higher temperatures, the effect of the field is lessened when compared with thermal effects, so that anion movement can predominate. It must not be overlooked though, that as with aluminum, both anions and cations may be mobile and only the ratio of the two changes as a function of temperature and applied field. Even so, theories which treat only one mobile species would still be valid in the extremes.

The absence of any noticeable effect of ultraviolet irradiation on the oxidation rate of silicon under dry, clean conditions may also be related to the thesis that oxidation is an impurity-controlled process. However, Cabrera (29) reported that the rate of aluminum oxidation in air at room temperature is doubled under the influence of ultraviolet irradiation. Oren and Ghandhi (30) have also shown that ultraviolet light can affect the oxidation of silicon at high temperatures. Apparently, both sets of experiments were done under clean, dry conditions. No explanation for the discrepancy between these results and the present work is yet available.

Conclusions

The kinetics of the oxidation of silicon at relatively low temperatures have been analyzed according to the models of anion and cation movement. The best agreement has been found with the cation model, which implies that both cations and anions can be mobile in silicon dioxide depending on the temperature and applied field. The present work cannot resolve this question completely, especially in view of the effect of impurities. It will be necessary to perform marker experiments similar to those of Davis *et al.* (27) and Siejka *et al.* (31) before the complete mechanism of oxide growth on silicon can be resolved.

Acknowledgments

The aid of J. Conrigan and O. W. Kendall in carrying out this project is greatly appreciated.

The experimental portion of this work was carried out at the Signetics Corporation, Sunnyvale, California.

Manuscript submitted May 8, 1972; revised manuscript received Aug. 10, 1972.

Any discussion of this paper will appear in a Discussion Section to be published in the June 1973 JOURNAL.

REFERENCES

1. E. C. Ross, A. M. Goodman, and M. T. Duffy, *RCA Rev.*, **31**, 467 (1970).
2. J. T. Wallmark and J. H. Scott, Jr., *ibid.*, **30**, 335 (1969).
3. A. S. Grove, "Physics and Technology of Semiconductor Devices," pp. 22-34, John Wiley and Sons, New York (1967).
4. A. M. Goodman and J. M. Breece, *This Journal*, **117**, 982 (1970).
5. Y. J. van der Meulen, *ibid.*, **119**, 530 (1972).
6. D. Frohman-Bentchkowsky, *Proc. IEEE*, **58**, 1207 (1970).
7. F. A. Sewell, Jr., H. A. R. Wegener, and E. T. Lewis, *Appl. Phys. Letters*, **14**, 45 (1969).
8. J. A. Aboaf, *This Journal*, **118**, 1370 (1971).
9. R. J. Archer and G. W. Gobeli, *J. Phys. Chem. Solids*, **26**, 343 (1965).
10. F. Lukes, *Surface Sci.*, **30**, 91 (1972).

Table I. Calculated values of voltage across thin oxide films on silicon

Oxidation temperature, °C	Voltage across oxide	
	Calculated from the slope of Fig. 5 (18)	Calculated from the differential plot (22)
25	0.2	0.11
400	0.25	0.35
600	0.33	0.60

11. W. Przyborski, J. Roed, J. Lippert, and L. Sarholt-Kristensen, *Radiation Effects*, **1**, 33 (1969).
12. R. E. Oakley and G. A. Godber, *Thin Solid Films*, **9**, 287 (1972).
13. R. Lieberman and D. L. Klein, *This Journal*, **113**, 956 (1966).
14. G. B. Larrabee, K. G. Heinen, and S. A. Harrell, *ibid.*, **114**, 867 (1967).
15. A. N. Saxena, *J. Opt. Soc. Am.*, **55**, 1061 (1965).
16. A. G. Revesz and R. J. Evans, *IEEE Trans.*, **ED-14**, 789 (1967).
17. P. Ausloos and E. W. R. Steacie, *Can. J. Chem.*, **33**, 1530 (1955).
18. N. Cabrera and N. F. Mott, *Rept. Progr. Phys.*, **12**, 163 (1948-49).
19. A. G. Revesz, *Phys. Status Solidi*, **24**, 115 (1967).
20. F. P. Fehlner and N. F. Mott, *Oxidation of Metals*, **2**, 59 (1970).
21. K. Hauffe, "Oxidation of Metals," pp. 127-128, Plenum Press, New York, (1965).
22. J. R. Ligenza, *J. Phys. Chem.*, **64**, 1017 (1960).
23. N. V. Mileshkina and R. Z. Bakhtizin, *Surface Sci.*, **29**, 644 (1972).
24. W. A. Pliskin and R. P. Gnall, *This Journal*, **111**, 872 (1964).
25. P. Jorgensen, *J. Chem. Phys.*, **37**, 874 (1962).
26. P. F. Schmidt and J. D. Ashner, *This Journal*, **118**, 325 (1971).
27. J. A. Davies, B. Domeij, J. P. S. Pringle, and F. Brown, *ibid.*, **112**, 675 (1965).
28. P. A. Brook, V. R. Howes, J. S. L. Leach, and A. Y. Nehru, Paper 94 presented at Electrochem. Soc. Meeting, Atlantic City, N. J., Oct. 4-8, 1970.
29. N. Cabrera, *Rev. Met.*, **45**, 86 (1948); *Phil. Mag.*, **40**, 175 (1949).
30. R. Oren and S. K. Ghandhi, *J. Appl. Phys.*, **42**, 752 (1971).
31. J. Siejka, J. P. Nadai, and G. Amsel, *This Journal*, **118**, 727 (1971).

Heteroepitaxial Thermal Gradient Solution Growth of GaN

R. A. Logan and C. D. Thurmond*

Bell Telephone Laboratories, Incorporated, Murray Hill, New Jersey 07974

ABSTRACT

The growth of single-crystal epitaxial layers of GaN onto (0001) oriented sapphire substrates from the liquid phase is shown to require three conditions: (i) the partial pressure of NH_3 in the H_2 ambient, P_{NH_3} , greater than the equilibrium pressure, (ii) the growth melt positioned in a thermal gradient to transport the dissolved GaN to the growth interface, and (iii) the control of nucleation by the addition of Bi to the growth melt. Studies of growth at temperatures from 850° to 1050°C show that the layer thickness, t , is approximately linear in time and varies with growth temperature and atom fraction of Ga, x_{Ga} , in the growth melt. When $t \gtrsim 30\mu$, internal cracks in the $[1\bar{1}0]$ basal plane hexagonal directions develop at the layer-substrate interface and for $t \gtrsim 75\mu$ they propagate to the surface and are thermally etched. A description is given of the interaction of liquid Ga with NH_3 as a function of T and P_{NH_3} . The low solubility of GaN in Ga (3×10^{-5} mole fraction at 1150°C) prevents useful growth by slow cooling of the melt. The inability to change the electron concentration, n , with Zn doping and the decrease of n with x_{Ga} in the growth melt support but do not unambiguously confirm the model that the native donor is a nitrogen vacancy.

The bandgap of GaN is both wide (~ 3.4 eV at 300K) and direct (1), so that GaN is potentially an extremely useful electroluminescent material. Single-crystal growth has been achieved by several vapor deposition techniques: by reacting the volatile Ga species GaCl with NH_3 to form epitaxial layers on sapphire (2), by heating GaN in an atmosphere of NH_3 to form GaN needles possibly by virtue of the volatile oxide Ga_2O (3), by thermally decomposing a volatile gallium bromide ammonia complex (4), or by reacting Ga with N generated from N_2 by gaseous discharge (5) or rf fields (6). The failure to obtain p-type crystals to date may imply a limited solubility of the common acceptors in the face of a highly soluble unidentified donor impurity or of compensation of the acceptors by a native donor defect as is observed in the II-VI semiconductors (7).

GaN can be formed by reacting NH_3 with Ga when the partial pressure of NH_3 in H_2 , P_{NH_3} , is greater than the equilibrium pressure, P^* . At 1000°C, $P^* = 1 \times 10^{-3}$ atm and has a shallow temperature dependence (8) (0.53 eV). Growth of GaN has been obtained by reacting NH_3 with Ga (9) or with Ga compounds (10) that dissociated at the growth temperatures, to form small crystals of GaN with dimensions of a few microns. The extension of this growth process to the epi-

taxial growth of GaN on sapphire substrates has been limited by the extensive nucleation of small crystallites on the substrates, so that, in general, only dense, unconnected, small crystals are typically obtained.

It has been found that two modifications are required for epitaxial growth. By addition of Bi to the growth solution, nucleation is inhibited and by imposition of a thermal gradient across the growth melt, dissolved nitrogen is transported to regions of lower temperature where growth occurs. While there is no detailed understanding of the effect of Bi upon the nucleation, a similar effect was observed (11) in the solution growth of GaP where the addition of Bi to the growth melt both increased the crystal size and reduced the number of crystals obtained in a given growth procedure. The low solubility of GaN in the liquid phase does not permit useful amounts of crystals to grow by slow cooling. The thermal gradient produces a concentration gradient of dissolved GaN and thereby a transport mechanism.

In this paper, a description is given of the growth procedures used to grow reproducibly epitaxial layers of GaN on sapphire substrates from the liquid phase. In addition, a description is given of the interaction of liquid Ga with NH_3 at high temperatures as a function of P_{NH_3} . Two features of this interaction, which are encountered under some growth conditions, are described and explained: (i) the flow of Ga out of

* Electrochemical Society Active Member.

Key words: gallium, bismuth, ammonia, zinc, electrons.

the growth boat and (ii) the spattering or propelling of Ga droplets out of the growth crucible onto the furnace wall directly over the crucible.

Experiments performed in attempts to clarify the source of the high-electron concentration in the crystals are described. The inability to change the electron concentration, n , with Zn doping and the decrease in n with reduced atom fraction of Ga in the growth melt support the suggestion that the native donor is a nitrogen vacancy.

Apparatus and Procedures

Epitaxial layers of GaN were grown onto single crystal sapphire substrates from Ga (or Ga diluted with Bi) solutions heated under a partial pressure of NH_3 in H_2 . The growth occurred in a horizontal furnace system in which the spontaneous dissociation of NH_3 was negligible and the NH_3 pressure could be monitored and remained constant during growth. The basic design of the furnace system has been described because of its previous usage to grow (12) epitaxial layers of N-doped GaP and to determine (8) the equilibrium pressure of N_2 over GaN. The principal features of the furnace are: (i) a low level of oxygen (and water vapor) in the ambient which was achieved by the use of stainless steel, Pyrex, and Teflon tubing connecting the gas sources to the main furnace tubing and contributed to the prevention of spontaneous dissociation of NH_3 in the heated furnace ($850^\circ\text{C} < T < 1150^\circ\text{C}$); and (ii) an easily replaceable quartz liner inside the main quartz furnace tube so that each growth occurred under reproducible conditions. The exit gas from the furnace could be titrated with a dilute solution of HCl of known volume and normality, containing methyl red indicator. By observation of the titration time, the NH_3 pressure could be monitored closely. The gas flow rate was generally 140 cc/min.

Spontaneous dissociation of NH_3 in the heated-empty furnace was caused by contaminants in the furnace (devitrified quartz or an inadvertent leak in the gas flow system) and was easily detected by the observation of a variation of P_{NH_3} with furnace temperature. When such dissociation was detected it could easily be eliminated. Devitrified quartz was replaced with new quartz, cleaned in de-ionized H_2O and alcohol prior to use. No bake out was necessary.

The epitaxial layers were grown in pyrolytic graphite boats, of dimensions 7.8 cm \times 1.3 cm \times 1.3 cm. These boats did not cause NH_3 decomposition and the weight loss during growth was negligible (< 1 mg for heatings at 850°C - 1150°C for 20 hr). Quartz and boron nitride boats were also used but the former were more difficult to clean between runs due to wetting by the melts and the latter are relatively expensive.

The single-crystal, Czochralski-grown sapphire substrates were optically polished, oriented slices, 250 μ thick. While several substrate orientations were investigated, the best growth was achieved with the (0001) orientation. Prior to use, the sapphire substrates were cleaned in hot aqua regia and rinsed in de-ionized water and alcohol. In some instances, the sapphire substrate was first covered with a vapor-deposited layer of GaN, a few microns thick, provided by M. Ilegems (13).

The growth solution consisted of 10-20g of 6-9's purity Ga or Ga-Bi alloys. Because of the wetting action of the Ga in the presence of NH_3 (to be described in the following section) the substrates, each of area ~ 1 cm 2 , were placed on top of the melt for atom fractions of Bi, x_{Bi} , in the melt < 0.5 . At higher values of x_{Bi} , where wetting was less, improved large area layer growth was obtained by placing the substrates just below the surface of the melt. This was accomplished by loading the growth boat with about 75% of the small particles of Bi and Ga, placing the substrates into the boat and covering them with

the remaining Bi-Ga mixture. After the growth run, the substrates were generally covered with a thin layer of melt, with GaN growth on both sides of the substrate, but with much thicker growth on the upper side.

The crystal-growth cycle consisted of inserting the loaded boat into the cold furnace, flushing the furnace for 1 hr, and then heating at the growth temperature for typically 20 hr. Approximately 30 min were required to reach the growth temperature and after the growth another 30 min to lower the furnace temperature to $\sim 600^\circ\text{C}$ when the boat was removed. The substrates and melt were then soaked in both HNO_3 and aqua regia. In addition to recovering the substrates with their epitaxial layers in this digestion, approximately 250 mg of small crystals of GaN, which grew away from the substrates, was also obtained.

It was observed that the layer growth was dramatically improved in area coverage when growth occurred in a temperature gradient rather than in the flat zone of the furnace. The crystal growth described here was obtained with about 1/2 of the length of the boat extended into the uniform temperature zone of the furnace and a carbon rod heat sink attached to the downstream colder end of the boat and extending about 10 cm to the end of the furnace. The carbon heat sink was 1.7 \times 1.2 cm in cross section and had a 1.5 cm long cutout that closely fitted around one end of the growth boat. The temperature of growth reported in this work corresponds to that read by a Pt-Pt, 10% Rh thermocouple contained in a quartz protection tube inserted into the growth melt.

Zinc as a dopant was added to the growth melt by vapor transport from an independently heated upstream source. Since similar procedures were used to grow epitaxial layers of Zn-doped GaP from Ga solutions in a 30 min growth cycle (12) the Zn concentration in the melt is expected to be at a steady-state value during most of the 20 hr growth cycle. Less volatile impurities such as Ge, were added directly to the melt. Carbon doping was achieved by adding methane to the gas ambient.

Results and Discussion

NH_3 -Ga(l) reaction.—When the NH_3 pressure is less than the equilibrium pressure, P^* , Ga may be heated without visible reaction; the Ga remains shiny and clean. Since there is no evidence for volatile nitride species (14), any weight loss beyond that expected from the vapor pressure of Ga would be due to oxides contaminating the gas phase and reacting with Ga to form Ga_2O . Heating 40g of Ga at 1150°C for 16 hr, with $P_{\text{NH}_3} = 4.7 \times 10^{-4}$ atm ($< P^*$), and a gas flow of 280 cc/min resulted in a weight loss of 0.135g. This weight loss is about a factor of 2 higher than expected from the vapor pressure of Ga. The additional weight loss can be used to estimate the partial pressure of H_2O in the carrier gas by assuming that the water reacts with Ga to equilibrium producing Ga_2O . A partial pressure of 5×10^{-5} atm would be required to account for the additional weight loss of the Ga. We do not believe that this rather high pressure of H_2O is present in the carrier gas entering the furnace. We believe the reaction of H_2 with SiO_2 in the furnace is the probable source of the contamination. The equilibrium pressures of H_2O and SiO from the H_2 - SiO_2 reaction at 1150°C gives about 2×10^{-5} atm of each as calculated from available thermodynamic information (15). The excess weight loss of our sample can be accounted for within 50% by this reaction.

Digestion of the Ga in HNO_3 and filtration of the residue through filters of 0.8 μ porosity yielded residuals of ~ 1 mg. In three determinations the amount of residual varied approximately linearly with $P_{\text{NH}_3} < P^*$. If one assumes that the nitrogen dissolved in the Ga formed GaN during the cooling of the melt, then the extrapolation of the three experimental points to

$P_{\text{NH}_3} = P^*$ (1.5×10^{-3} atm) (8) gives a solubility of 3×10^{-5} mole fraction of GaN in Ga at 1150°C.

As the NH_3 pressure is increased beyond P^* , visible reaction with the Ga occurs for heating at temperatures in the range 1000°–1150°C. A striking feature of this reaction is the flow of the Ga melt. With $P_{\text{NH}_3} \sim 2P^*$, the melt flows up the inside walls of the boat but is contained inside the boat for heating times as long as 20 hr and will overflow in longer heating times (e.g., 60 hr). The rate of Ga flow increases with P_{NH_3} and at $P_{\text{NH}_3} = 10 P^*$, most of the melt will flow out of the boat in about 1 hr, and collect predominantly upstream. In all of the above cases, the Ga reacts with NH_3 to form small crystals of GaN. The crystal color and dimensions vary with P_{NH_3} , with black crystals of dimensions 75–500 μ at low pressures and smaller, gray crystals 20–100 μ in dimensions formed at higher pressures.

A qualitative explanation for the flow of Ga will now be offered, together with observations that test and support this explanation. It is proposed that Ga evaporates and reacts with NH_3 to form a film of GaN on the surfaces adjacent to the melt. The Ga wets and spreads over the GaN vapor deposited film until the Ga supply is either exhausted or completely reacted. With a large Ga supply at 1025°C and $P_{\text{NH}_3} = 0.03$ atm, the Ga has been observed to flow upstream about 20 cm, where it stopped at a region where the local temperature was $\sim 850^\circ\text{C}$, while there was negligible flow downstream.

The following two observations support this explanation. A drop of Ga was placed on a large area vapor deposited GaN crystal and heated in H_2 on a strip heater and watched. At room temperature no wetting was observed but as the temperature was increased to $\sim 800^\circ\text{C}$, the Ga wetted the surface as a thin film. Upon cooling to room temperature, the Ga drew back into a droplet. In the second experiment, a quartz boat 2 cm \times 2.5 cm \times 0.7 cm deep containing 3g of Ga was heated for 1 hr at 1025°C with $P_{\text{NH}_3} = 0.02$ atm. The Ga flowed so that all walls of the boat, both inside and out, were wetted, as well as the quartz furnace liner in the vicinity of the boat. Weight loss of the boat indicated that about 50% of the Ga had left the boat. The Ga contained small crystals of GaN, and was covered with a gray GaN film. Three more grams of Ga were added to the boat and reheated using a new quartz furnace liner and a hydrogen ambient. Again 2.2g of Ga flowed over the sides of the boat, confirming that the presence of the GaN was essential to the Ga flow.

At lower temperatures ($T < 950^\circ\text{C}$) no apparent reaction occurs when Ga is heated in a uniform temperature zone of the furnace, even with P_{NH_3} as high as 0.2 atm. This is due to the formation of a thin crust of GaN over the melt which blocks further reaction. If the melt is agitated by mechanical vibration or placed in a temperature gradient (using the carbon heat sink described above), the reaction characteristics are similar to those described above for heating at higher temperatures.

The growth of GaN epitaxial layers on sapphire substrates was studied under conditions where the melt was contained in the growth crucible and this was generally achieved with $P_{\text{NH}_3} \sim 2P^*$. A phenomenon, termed spattering, was usually observed. This was characterized by the formation of droplets of Ga or crystallites of GaN directly over the boat on the quartz furnace liner. The amount of spattered Ga and GaN was generally far greater than that vapor transported to the downstream cold end of the furnace, as discussed above. The spattering is attributed to dissociation of GaN, releasing N_2 filled bubbles in the melt, which form at the surface or rise to the surface and burst, causing drops of melt to be propelled out of the boat. N_2 pressures greater than 1 atm can be formed

by dissociation of GaN to Ga and N_2 since the equilibrium N_2 pressure is ~ 100 atm at 1025°C (8). If the spattering occurred during the early part of the growth cycle, the Ga drops would react with NH_3 to form GaN. The spattering phenomenon was reproduced by heating GaN crystallites under Ga in a He ambient with a heating cycle used in layer growth (20 hr at 1025°C). Ga drops were formed over the growth crucible on the quartz furnace liner as observed during growth.

Epitaxial layer growth.—Growth from Ga melts produced GaN crystals predominantly on the top sides of the sapphire substrates. Numerous, well-faceted crystallites were formed along with occasional small areas (1–3 mm in dimension) of epitaxial growth. There usually were evident regions of thermal etching or local dissociation after growth in the small areas of epitaxial layer growth. The small crystallites also grew off of the substrate, predominantly on the walls of the boat and were recovered after digestion of the growth melt. Crystallites, 120 μ thick on the top surface and a few microns thick on the bottom side were obtained after growth for 16 hr at 1000°C (with $P_{\text{NH}_3} = 2 \times 10^{-3}$ atm). Growth thickness was roughly proportional to the growth time. After 64 hr at 1000°C, (with $P_{\text{NH}_3} = 1.3 \times 10^{-3}$ atm), the top surface crystallites were $\sim 300\mu$ thick while the bottom side contained a continuous epitaxial layer 6 μ thick. The dissociation rate

of GaN to Ga + N_2 at temperature $< 1050^\circ\text{C}$ is small compared to the growth rate (16).

While there was a possibility that the addition of Bi to the growth melt might increase the solubility of N (and hence the growth rate), the dominant effect was the suppression of spurious nucleation so that growth occurred predominantly on the sapphire substrate. With melts containing 10–90 atomic per cent (a/o) Bi, the epitaxial growth extended over large areas of the sapphire substrate, typically from 50 to 100% of the total area. In those areas where layer growth was incomplete, the surface was covered with closely spaced crystallites. The effect of the Bi is apparently to suppress nucleation so that the initially nucleated crystallites grow laterally, as well as in thickness, to give complete coverage. The nucleation could be further assisted by using substrates containing a thin vapor deposited film of GaN. Using vapor deposited films (13), a few microns thick, generally with featureless surfaces, solution growth produced clear layers with faceted surfaces, grown reproducibly over the entire substrate area. While the double layer growth procedure was quite successful, it was not routinely used since single layer growth was also quite reproducible in supplying large area epitaxial layers.

The single-crystal epitaxial layers grow in the [0001] direction, the same orientation as the substrates generally used. However, the layer growth orientation was unchanged with (1120) oriented substrates, a phenomena previously observed in GaN vapor growth by Wickenden *et al.* (2).

The epitaxial layer surfaces were sharply faceted and representative surfaces are shown in Fig. 1a and 2a. The surface structure ranged from flat-topped hexagonal platelets (Fig. 1a) to surface patterns containing the three [110] basal plane hexagonal directions of the sides of the hexagonal platelets (Fig. 2a). The small black regions in Fig. 1a are small crystals that grew above the layer, and were randomly oriented. They were found on many layers.

As the atom fraction of Bi, x_{Bi} , in the growth melt increased, a proportionate increase in P_{NH_3} was required to achieve growth. With GaN in equilibrium with the melt, the NH_3 pressure will increase as a result of a decrease in Ga activity with Bi addition. Using data where good layer growth occurred in growth times of ~ 20 hr at 1000°C (Fig. 1a and 2a being typical of the surfaces of such layers), the NH_3

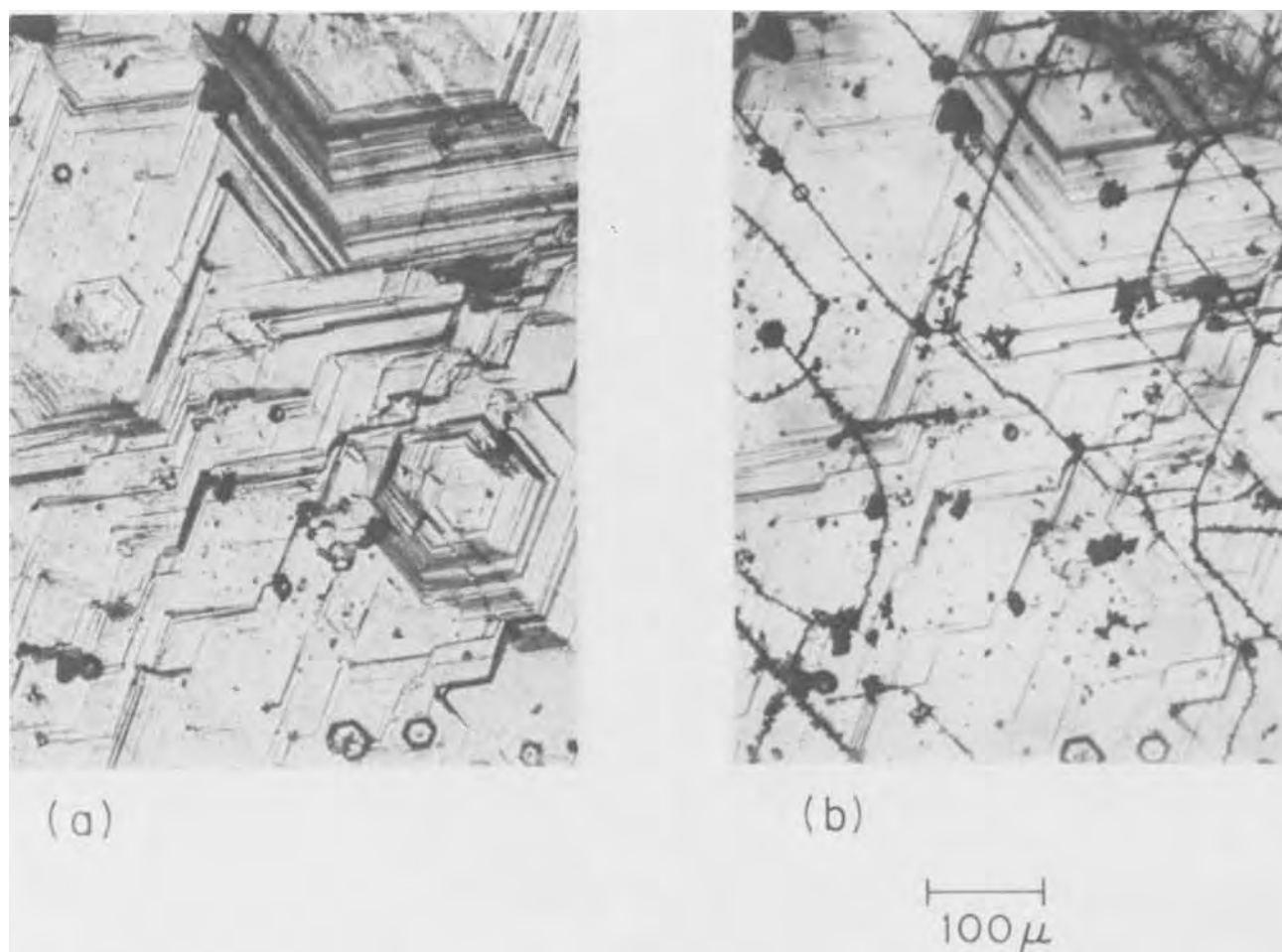
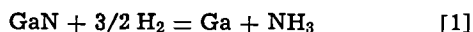


Fig. 1. (a) The surface of a (0001) GaN epitaxial layer containing hexagonal facets with $[1\bar{1}0]$ edges, viewed with incident illumination. The layer was grown at 1000°C in 24 hr with $x_{\text{Ga}} = 0.13$ and $P_{\text{NH}_3} = 0.02$ atm on a (0001) sapphire substrate containing a predeposited GaN layer and is 40μ thick. (b) The same area, below the surface of the layer viewed with transmitted light revealing subsurface cracks at the layer-substrate interface. The cracks lie predominantly in the $[1\bar{1}0]$ directions of the edges of the surface hexagonal facets.

input pressure is plotted in Fig. 3 against the atom fraction of Ga, $x_{\text{Ga}} = 1 - x_{\text{Bi}}$ in the growth melt. The variation in x_{Ga} , due to Bi evaporation during the growth, is indicated. The layer thickness, t , grown directly onto the (0001) sapphire substrates is also plotted against x_{Ga} . If it is assumed that Ga and Bi form an ideal liquid solution, and that GaN is only slightly soluble in it, the dependence of the NH_3 pressure on the Ga atom fraction can be obtained from the reaction



with the equilibrium constant, K , given by

$$x_{\text{Ga}} P_{\text{NH}_3} = K \quad [2]$$

The equilibrium constant of the above reaction contains the observed inverse linear relationship between P_{NH_3} and x_{Ga} . The fact that the layer thickness decreased with decreasing Ga atom fraction indicates that the N atom fraction decreases as Bi is added to the melt, as would be expected if the solubility of GaN is less in Bi than in Ga.

Figure 1b shows the same region of the layer of Fig. 1a but viewed with transmitted light. The series of lines which generally follow the $[1\bar{1}0]$ directions of the hexagonal surface structure are cracks which appear to originate at the interface of the layer and the substrate. It is noted that the cracks do not propagate to the surface of this 40μ thick layer, or to the back of the substrate. For thicker layers ($\sim 100\mu$ thick)

grown with higher x_{Ga} in an otherwise similar growth cycle, many of the cracks propagate to the surface and cause the thermal etching (or dissociation) shown in Fig. 1b. From observation of the surface structure, it is evident that the thermally dissociated regions were formed near the end of the layer growth. Surface dissociation effects were generally not observed in layers $< 75\mu$ thick nor were subsurface cracks observed in layers $< 30\mu$ thick.

Chemical doping.—The small GaN crystals that nucleated and grew away from the substrate were routinely recovered from the growth melt after digestion in aqua regia. Spectroscopic analysis of undoped crystallites gave impurity concentrations at the level of 10 parts per million or less. Hall measurements on the undoped layers yielded electron concentrations $\sim 3 \times 10^{19} \text{ cm}^{-3}$, approximately 2 orders of magnitude larger than the detected impurity levels.

Atomic absorption analysis of the small crystals obtained with Zn doping showed that the Zn concentration was primarily determined by the growth temperature provided the Zn was distilled into the gas stream from a source boat at $T > 600^{\circ}\text{C}$. For growth with $x_{\text{Ga}} = 0.1$, $P_{\text{NH}_3} = 0.02$ atm, Fig. 4 shows a plot of Zn concentration against growth temperature with the Zn source temperature indicated at each experimental point. Also shown are the electron concentrations determined by Hall measurements obtained using epitaxial layers grown under similar conditions. While the

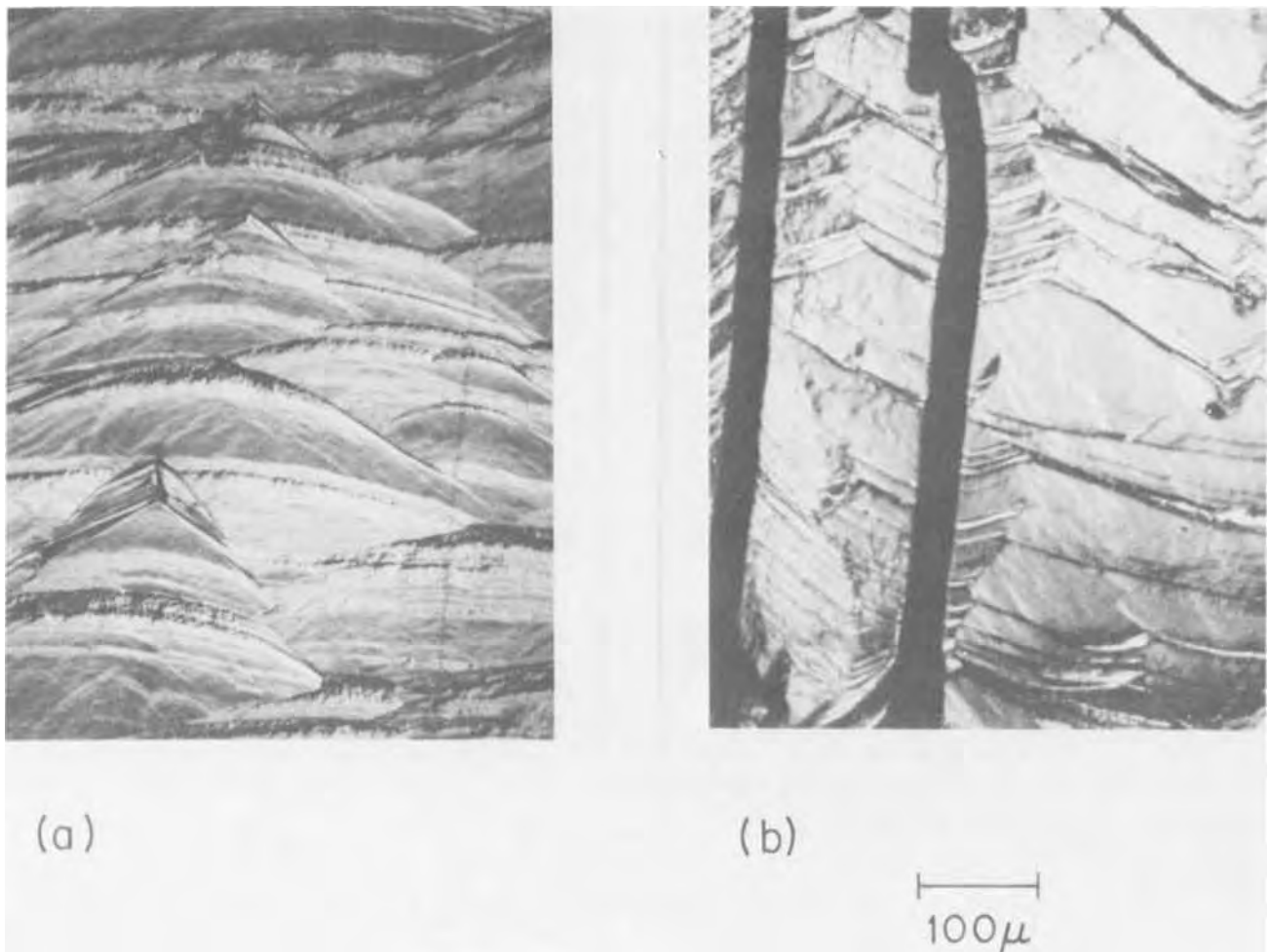


Fig. 2. (a) The surface of a (0001) epitaxial GaN layer grown on a (0001)-oriented sapphire substrate in 20 hr at 1000°C with $x_{\text{Ga}} = 0.88$ and $P_{\text{NH}_3} = 0.006$ atm and is 100 μ thick. The three [110] directions are evident in the surface facets. (b) Another region of the surface where grooves have developed in the surface during the latter part of the growth by thermal dissociation of cracks that propagated to the surface.

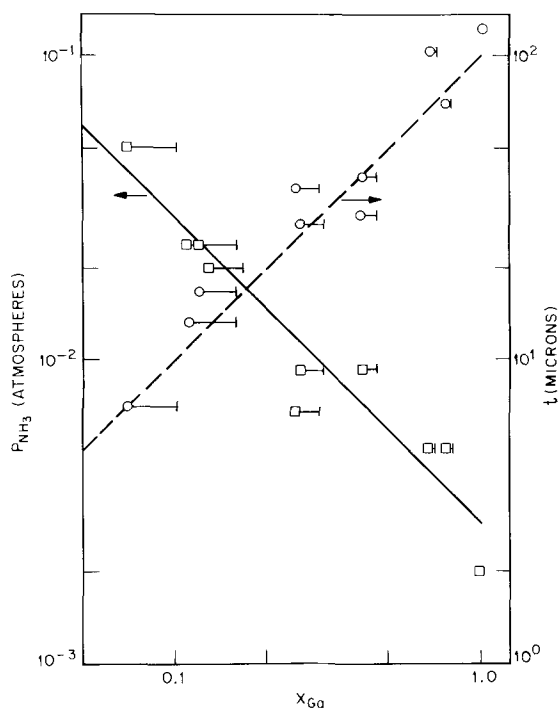


Fig. 3. The NH_3 input pressure and the epitaxial layer thickness as a function of x_{Ga} in the growth melt for 20 hr growth at 1000°C.

Zn concentration ranged up to $3.5 \times 10^{20} \text{ cm}^{-3}$, the electron concentrations did not vary significantly from $\sim 3 \times 10^{19} \text{ cm}^{-3}$. The indicated variation in the latter concentrations are due to the local variations in the layer thickness, which ranged from average values of 4-17 μ depending on the growth T , and by examination of the edge of the layers, the thickness fluctuated $\pm 2\mu$ about average values. The trends expected in Fig. 4 are approximately seen. At constant growth temperature the Zn concentration should increase with Zn pressure and therefore with Zn boat temperature; at constant Zn pressure and therefore Zn boat temperature, the Zn concentration is expected to decrease with increasing growth temperature since the heat of solution of Zn should be positive. The electron concentrations are nearly constant at about the value found when no Zn is added suggesting that most of the zinc has precipitated.

Precipitates were generally observed in the Zn-doped layers, and a representative sample is shown in Fig. 5. The layer was grown at 850°C with $x_{\text{Ga}} = 0.1$, $P_{\text{NH}_3} = 0.02$ atm, and $t \sim 5\mu$. Figure 5a, viewed with incident illumination, shows the hexagonal platelet structure often observed whereas Fig. 5b shows the same area viewed with transmitted light with precipitates in the form of fine lines and inclusions. The lines appear similar to decorated dislocations which have been observed and identified in other semiconductors (17). It is noted that the lines, which are generally not observed in undoped layers, lie in the [110] directions of the edges of

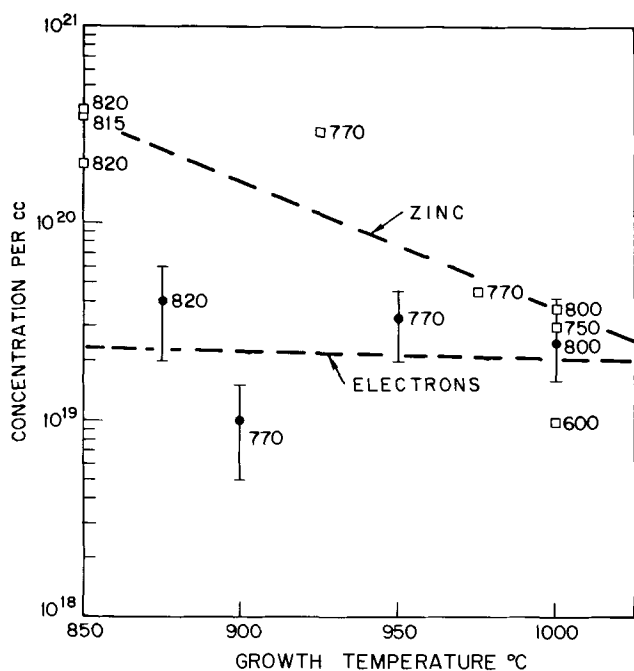


Fig. 4. The concentration of Zn (\square —from atomic absorption analysis) and of electrons (\bullet —from Hall effect measurement) plotted against the growth temperature with the Zn-source boat temperature indicated at each experimental point. The dashed lines indicate the general trend of the variation of the zinc and electron concentrations with the growth parameters, as discussed in the text. The layers were grown in 20 hr with $x_{\text{Ga}} = 0.01$ and $P_{\text{NH}_3} = 0.02$ atm and are 4–17 μ thick. The error bars on the Hall results are due to the estimated variation in the layer thickness.

the hexagonal surface structure similar to the cracks observed in thick layers. Hall measurements indicated that while the electron concentration was unaffected by the Zn doping, the room temperature Hall mobility decreased, however, from ~ 75 cm²/V-sec in undoped layers to ~ 4 cm²/V-sec in the Zn-doped layers. The evidence of precipitation accounts for the ability to dope with high Zn concentrations without observing the electrical behavior expected for the substitutional Zn acceptors.

Atomic absorption analysis of crystals grown from Ga-Bi solutions at 1000°C give a limit on Bi at $\sim 10^{19}$ cm⁻³. After the digestion of these crystals from the growth melt in aqua regia, the white precipitate bismuth oxychloride forms when the crystals are rinsed in water. While the analyzed crystals were recleaned in aqua regia, the presence of the precipitate qualifies the results of this analysis. The photoluminescent spectra of undoped crystals grown from Ga-Bi solutions were indistinguishable from those grown from Ga solution. Carbon doping was achieved by adding methane gas to the growth ambient. The growth properties were unaffected by the presence of methane, but decomposition of the methane (with black carbon deposits) was observed when the fraction of methane in the ambient exceeded 20%. Decomposition is expected when the CH₄ pressure in H₂ is greater than about 1% (15). While the addition of these impurities did not cause changes in the electron concentration, as compared to undoped layers grown under similar conditions, luminescence studies indicated characteristic spectral features that will be discussed elsewhere (18).

Dependence of n upon x_{Ga} .—It has been suggested (2) that nitrogen vacancies are the source of the electron carriers in GaN. In principle, the suggestion can be tested by annealing GaN under various pressures of NH₃ in H₂. If electrons come from the ionization of a nitrogen vacancy, the relationship between the elec-

tron concentration and the ammonia pressure can be calculated



The equilibrium relationship follows

$$\frac{P_{\text{NH}_3}}{P_{\text{H}_2}^{3/2}} [\text{V}_\text{N}^+][e^-] = K \quad [4]$$

and since the electron and vacancy concentrations are equal

$$[e^-] = K^{1/2} P_{\text{H}_2}^{3/4} P_{\text{NH}_3}^{-1/2} \quad [5]$$

That is, for $P_{\text{NH}_3} \ll P_{\text{H}_2}$, $[e^-] \propto P_{\text{NH}_3}^{-1/2}$.

Experiments by Montgomery (19) have shown that no resistivity changes occur in GaN epitaxial crystals annealed at 900°C under NH₃ pressures up to $\frac{1}{2}$ atm. It was suggested that no changes were observed because diffusion processes were too slow.

We have been able to grow GaN crystals from melts containing Bi. As a result it has been possible to grow crystals under various NH₃ pressures simply by varying the Bi atom fraction in the melt. The fact that Bi in GaN is an isoelectronic center keeps it from being an electrically active center. It has been shown (Eq. [2]) that P_{NH_3} is inversely proportional to the Ga atom fraction. Consequently the electron concentration and the Ga atom fraction are related by the expression

$$n = [e^-] \propto x_{\text{Ga}}^{1/2}$$

While n may be determined by Hall measurements, growth thickness variation discussed above, place a large experimental uncertainty on n in thin layers ($t < 10 \mu$). Reflectivity measurements by Barker and Ilegems (20) are found to be independent of t (provided $t \geq 5 \mu$) and the spectral position of the reflectivity minimum is a function of n that can be established independently by Hall measurements. The experimental precision of this method, applied to GaN layers, has not been assessed and the effect upon the reflectivity measurement of surface treatment (polished, as-grown, etc.) and sample uniformity is currently being investigated (20). Reflectivity measurements on our as-grown epitaxial layers have been used to complement the Hall measurements.

Using a group of layers grown at 1000°C in 20 hr with various values of x_{Ga} in the growth melt (and with P_{NH_3} correspondingly adjusted as in obtaining the data of Fig. 3) n obtained from reflectivity and Hall effect data is plotted against x_{Ga} in Fig. 6. The pairs of experimental points at the same value of x_{Ga} were measured by both procedures and scaled to match at $x_{\text{Ga}} = 1$. Due to evaporation of relatively small amounts of Bi during the layer growth, the plotted values of x_{Ga} are average values. Since it is believed that the experimental uncertainty in n , in all cases, exceeds that of x_{Ga} , the latter variation has not been indicated (but is identical to that in the data of Fig. 3).

Due to the large experimental uncertainty in the measured n , the results support but do not unambiguously confirm the dependence $n \propto x_{\text{Ga}}^{1/2}$. It is noted that results from three doped layers are plotted in Fig. 6. The Zn-doped sample contained 6.2×10^{18} Zn/cm³ and the two carbon-doped layers were grown under a partial pressure of methane (with 8% CH₄, $n = 4.5 \times 10^{19}$ cm⁻³ and with 25.6% CH₄, $n = 3.0 \times 10^{19}$ cm⁻³). To within the experimental scatter of the data, the values of n are indistinguishable from those in undoped layers.

If one assumes that vapor growth of GaN occurs under near equilibrium conditions, then from the dependence in n upon $P_{\text{H}_2}^{3/4} P_{\text{NH}_3}^{-1/2}$ in Eq. [5], one would expect a decrease in n by 10^3 from the value of 3×10^{19} cm⁻³ observed here. While values of n approach this value occasionally in vapor grown layers (13, 21), n is generally comparable to the high values observed here.

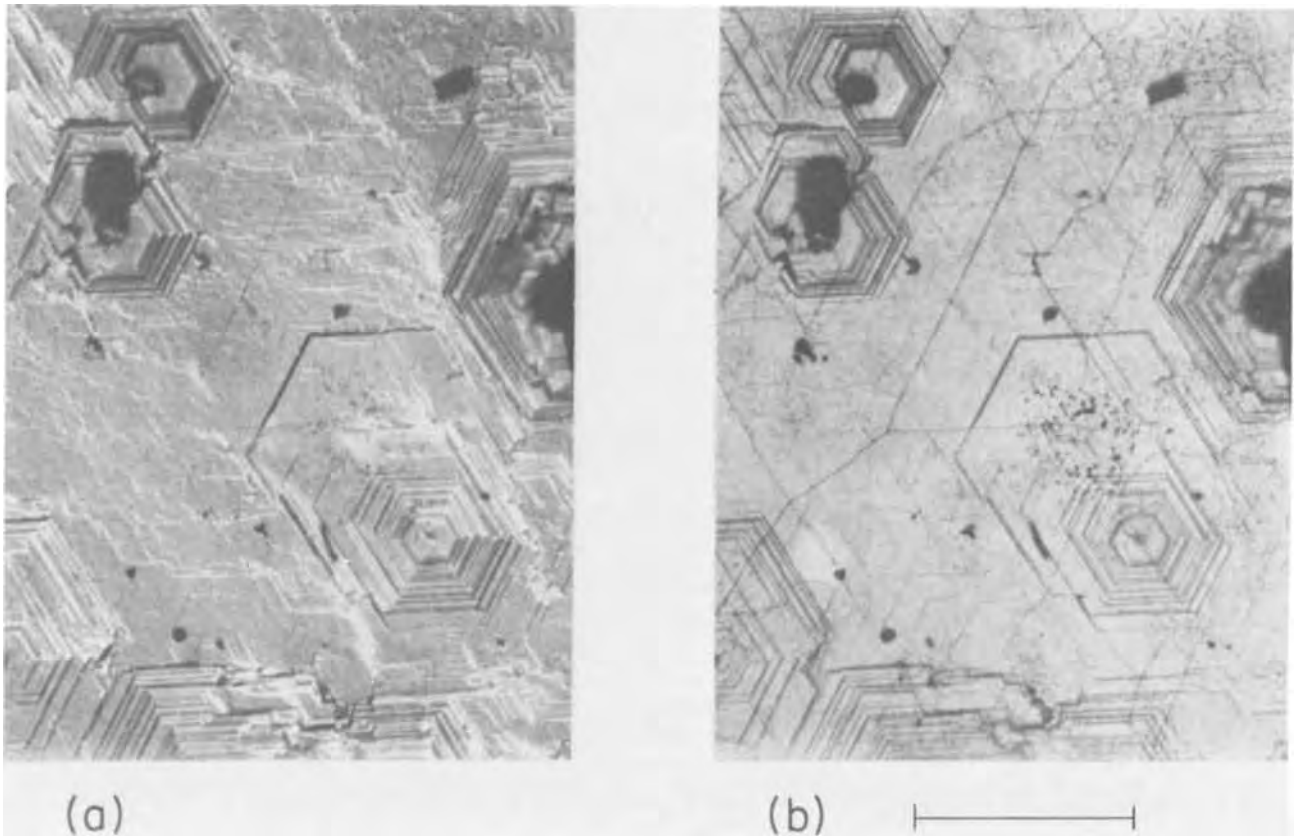


Fig. 5. (a) The surface of a (0001) epitaxial GaN layer grown on a (0001) sapphire substrate, viewed with incident illumination. The layer was grown in 20 hr at 850°C with $x_{\text{Ga}} = 0.1$ and $P_{\text{NH}_3} = 0.02$ atm with the Zn boat temperature at 815°C. The layer is $\sim 5\mu$ thick and from atomic absorption analysis, contains $\text{Zn} = 3.5 \times 10^{20} \text{ cm}^{-3}$. (b) The same area of the layer, viewed below the surface with transmitted light showing precipitates in the form of both lines and inclusions.

Temperature dependence of growth.—Most of the layers obtained in these studies were obtained at a growth temperature of 1000°C. The layer-growth characteristics did not change appreciably over the tem-

perature range 875°-1050°C. For the 20 hr growth cycle used, Bi evaporation became appreciable at 1050°C ($\sim 40\%$ of the original melt) and at higher temperatures severe dissociation of the GaN to Ga and N_2 is anticipated (16).

The layer thickness was observed to vary with growth temperature, and $\log t$ is plotted against $10^4/T$ K in Fig. 7 for a series of layers grown for 20 hr with $x_{\text{Ga}} = 0.12$ and 0.40. The variation in t is indicated. The increased t obtained at a fixed temperature with increased x_{Ga} is consistent with the data of Fig. 3. The slope of the lines drawn through the data is 1.5 eV and if the growth rate is primarily dependent upon the N concentration, this value may tentatively be ascribed to the heat of solution of GaN in Ga-Bi alloys and in Ga.

Reflectivity measurements on three samples grown at 900°, 1000°, and 1050°C, with $x_{\text{Ga}} = 0.4$ showed n between 2.5×10^{19} and $1.5 \times 10^{20} \text{ cm}^{-3}$, uncorrelated with T and evidencing the same unexpected scatter obtained in the data of Fig. 6.

Summary and Discussion

Because of the low solubility of GaN in Ga (mole fraction approximately 3×10^{-5} at 1150°C) it has not been possible to grow GaN with useful crystal dimensions from the liquid phase by cooling of saturated melts. However, in a thermal gradient, with $P_{\text{NH}_3} > P^*$, the equilibrium pressure, epitaxial layers of GaN may be reproducibly grown onto oriented sapphire substrates from the liquid phase if the nucleation is controlled by addition of Bi to the growth melt.

The heating of Ga in an NH_3 ambient, with $P_{\text{NH}_3} > 2P^*$ at high temperature ($T > 950^\circ\text{C}$) forms a vapor deposited film of GaN adjacent to the melt which is wetted by the melt and causes the melt to flow out of

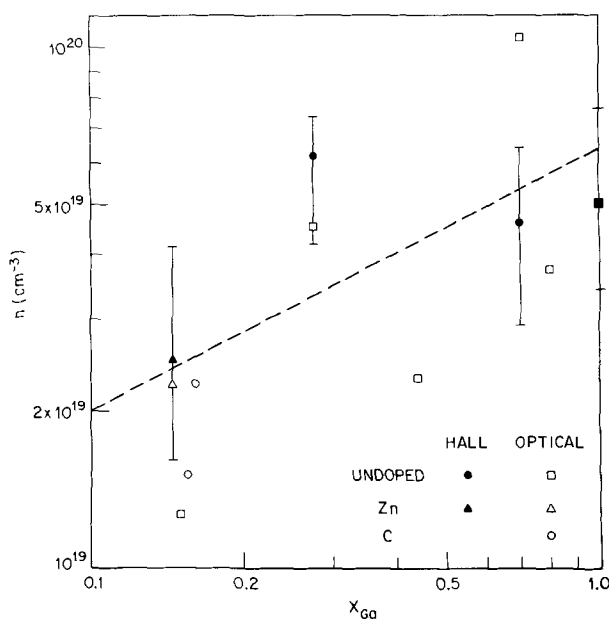


Fig. 6. Carrier concentration determined by Hall effect and reflectivity measurements vs. x_{Ga} in epitaxial layers grown in 20 hr at 1000°C. The dashed line indicates the expected dependence of $n \propto x_{\text{Ga}}^{1/2}$.

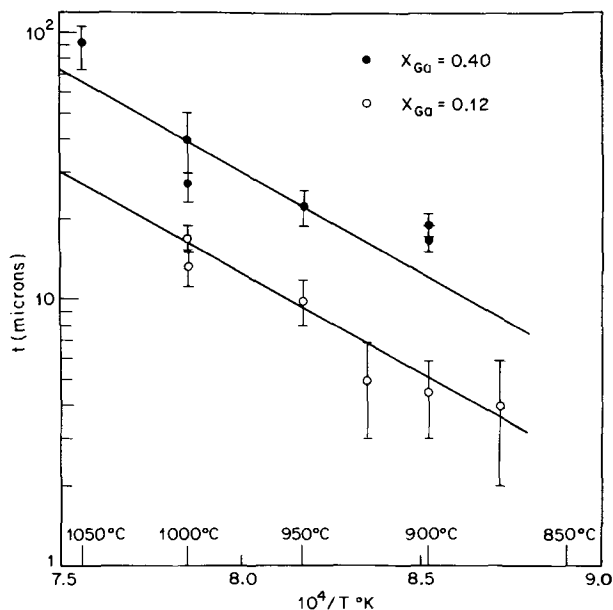


Fig. 7. The layer thickness vs. growth temperature for two sets of layers grown for 20 hr with $x_{\text{Ga}} = 0.12$ and 0.40 with corresponding $P_{\text{NH}_3} = 0.02$ and 0.009 atm respectively.

the growth boat. At low levels of $P_{\text{NH}_3} \sim 2P^*$, this effect is sufficiently reduced so that the melt is contained during growth (20 hr at temperatures in the range 850°C - 1050°C). At $T < 950^\circ\text{C}$, a crust of GaN inhibits the reaction of Ga with the NH_3 ambient even up to very high NH_3 pressures. By mechanical vibration or by placing the melt in a temperature gradient the GaN crust is disturbed and the reaction characteristics are similar to those at higher T . A second interesting reaction observed during growth was termed spattering. This was characterized by the formation of droplets of Ga directly over the boat and shown to be due to dissociation of GaN to Ga and N_2 in the melt, with the bubbles of N_2 rising to the surface and bursting, propelling Ga droplets out of the boat. While the competing process of GaN dissociation to $\text{Ga} + \text{N}_2$ can only be suppressed at very high N_2 pressures [$P_{\text{N}_2} > 10^2$ atm at 1000°C (8)], this dissociation rate is small compared to the growth rate for growth temperature $\lesssim 1050^\circ\text{C}$ (16).

The suppression of spontaneous nucleation of crystal growth by Bi is not understood but the phenomena appears similar to that encountered in the solution growth of GaP (11). The variation of growth thickness with growth time, temperature, and x_{Ga} are consistent with experience for solution growth. The growth mechanism appears to depend on the transport by diffusion of dissolved N, from the melt-ambient interface through a thin film of melt to the substrate, in a region of slightly lower temperature. We conclude that the single-crystal GaN layers are grown by heteroepitaxial solution growth in a thermal gradient.

It has been noted that even though sapphire and GaN possess different crystal lattices, in the c -axis or (0001) orientation of the epitaxial layer and substrate, the $[1\bar{1}0]$ basal plane hexagons are mismatched in dimensions by 13% (5). Evidence of strain at the epitaxial layer-substrate interface is given by the appearance of internal cracks in the $[1\bar{1}0]$ basal plane directions, when the layer thickness exceeds $\sim 30\mu$. In thicker layers ($t \lesssim 75\mu$), the cracks propagate through the layer and are thermally etched by dissociation during the latter part of the growth cycle.

Addition of Zn impurities at concentrations as high as $3 \times 10^{20} \text{ cm}^{-3}$ did not appreciably change the electron concentration of $\sim 3 \times 10^{19} \text{ cm}^{-3}$ measured in un-

doped crystals. Zn precipitates were visually observed in most Zn-doped layers. While similar negative results with Zn doping were observed in vapor grown layers by Ilegems (18,21), high-resistivity, Zn-doped GaN ($\rho > 10^9 \text{ ohm-cm}$) has been grown by Maruska and Tietjen (2) also using vapor-growth procedures, but with H_2 carrier gas instead of He and a 200°C lower growth temperature of 825°C . Since there is presently no information available about the Zn concentration and physical characteristics of the high-resistivity layers, it is not possible to give a detailed comparison with the present growth. The decrease in n with decreased x_{Ga} in the growth melt supports, but does not unambiguously confirm, the model that the crystals contain a native donor defect, a nitrogen vacancy, because of the large experimental uncertainty in the determination of n . The inability to reproducibly change n with Zn doping and the variations in n obtained with differing growth procedures indicate that n is dominantly influenced by growth details that are currently not understood. There is no evidence yet that GaN can be doped to low resistivity, p -type.

Acknowledgments

The Hall-effect measurements were performed by H. C. Montgomery and the optical reflectivity results were obtained by A. S. Barker and M. Ilegems. We also thank M. Ilegems for helpful comments and for providing the sapphire substrates containing GaN vapor deposited epitaxial layers. The atomic absorption and spectrographic analysis were obtained by J. P. Wright. We acknowledge the assistance of H. G. White in performing many of these experiments.

Manuscript submitted May 8, 1972; revised manuscript received July 27, 1972.

Any discussion of this paper will appear in a Discussion Section to be published in the June 1973 JOURNAL.

REFERENCES

1. J. I. Pankove, H. P. Maruska, and J. E. Berkeyheiser, *Appl. Phys. Letters*, **17**, 197 (1970); R. Dingle, D. D. Sell, S. E. Stokowski, and M. Ilegems, *Phys. Rev.*, **B4**, 1211 (1971).
2. H. P. Maruska and J. J. Tietjen, *Appl. Phys. Letters*, **15**, 327 (1969); D. K. Wickenden, K. R. Faulkner, R. W. Brander, and B. J. Isherwood, *J. Crystal Growth*, **9**, 158 (1971); H. M. Manassevit, F. M. Erdmann, and W. I. Simpson, *This Journal*, **118**, 1864 (1971); M. Ilegems, *J. Crystal Growth*, **13**, 14, 360 (1971).
3. R. B. Zetterstrom, *J. Materials Sci.*, **5**, 1102 (1970).
4. T. L. Chu, *This Journal*, **118**, 1200 (1971).
5. B. B. Kosicki and D. Kahng, *J. Vacuum Sci. Technol.*, **6**, 593 (1969).
6. H. J. Hovel and J. J. Cuomo, *Appl. Phys. Letters*, **20**, 71 (1972).
7. See C. H. Henry, K. Nassau, and J. W. Shiever, *Phys. Rev.*, **B4**, 2453 (1971) and references cited therein.
8. C. D. Thurmond and R. A. Logan, *This Journal*, **119**, 622 (1972).
9. W. C. Johnson, J. B. Parsons, and M. C. Crew, *J. Phys. Chem.*, **36**, 2651 (1932); H. G. Grimmeiss and H. Koelmans, *Z. Naturforsch.*, **14a**, 264 (1959).
10. M. R. Lorenz and B. B. Binkowski, *This Journal*, **109**, 24 (1962); J. Isherwood and D. K. Wickenden, *J. Materials Sci.*, **5**, 869 (1970).
11. F. A. Trumbore, M. Gershenson, and D. G. Thomas, *Appl. Phys. Letters*, **9**, 4 (1966).
12. R. A. Logan, H. G. White, and W. Wiegmann, *Solid-State Electron.*, **14**, 55 (1971).
13. M. Ilegems, *J. Crystal Growth*, **13**, 14, 360 (1971).
14. Z. A. Munir and A. W. Searcy, *J. Chem. Phys.*, **42**, 4223 (1965); R. C. Schoonmaker, A. Buhl, and J. Lemley, *J. Phys. Chem.*, **69**, 3455 (1965).
15. D. R. Stull, Project Director, Dow Chemical Co., Midland, Michigan, *JANAF Thermochemical Tables* (1967).

16. C. D. Thurmond and R. A. Logan, To be published.
 17. W. C. Dash, *J. Appl. Phys.*, **27**, 1193 (1956); M. Ger-shenzon and R. M. Mikulyak, *J. Appl. Phys.*, **35**, 2132 (1964).
 18. M. Ilegems, R. Dingle, and R. A. Logan, *Bull. Am. Phys. Soc.*, **17**, 233 (1972), *J. Appl. Phys.*, **43**, 3797 (1972).
 19. H. C. Montgomery, Private communication.
 20. A. S. Barker and M. Ilegems, Private communication.
 21. M. Ilegems and H. C. Montgomery, To be published.

Solid-State Ionics-Mixed Ionic and Electronic Conduction in $\text{Ag}_2\text{Se-Ag}_3\text{PO}_4$ Solid Solutions

Takehiko Takahashi* and Osamu Yamamoto

Department of Applied Chemistry, Faculty of Engineering, Nagoya University, Nagoya, Japan

ABSTRACT

New solid solutions, the conduction in which is partly ionic and partly electronic, have been prepared in the $\text{Ag}_2\text{Se-Ag}_3\text{PO}_4$ system. Solutions containing 5-10 mole per cent (m/o) Ag_3PO_4 have the $\alpha\text{-Ag}_2\text{Se}$ structure and high ionic conductivity at room temperature. For example, $(\text{Ag}_2\text{Se})_{0.925}(\text{Ag}_3\text{PO}_4)_{0.075}$ has an ionic conductivity of $0.13 \text{ (ohm-cm)}^{-1}$ at 25°C . The electronic conductivity and Hall coefficient have been measured as a function of the cation-to-anion ratio. The excess electron concentration varies linearly with the change in the cation-to-anion ratio. The solid solution containing 7.5 m/o Ag_3PO_4 which has been equilibrated with metallic silver has an excess electron concentration of $4.3 \times 10^{19} \text{ cm}^{-3}$ at 18°C . Coulometric titration, carried out with the galvanic cell $\text{Ag/RbAg}_4\text{I}_5/\text{specimen/Pt}$, gives the ratio of the effective mass to the free electron mass. At constant temperature, the effective mass increases with increasing electron concentration.

We may distinguish three types of solid conductors, namely, pure electronic, pure ionic, and mixed (partly electronic and partly ionic). Pure electronic conductors such as metals and semiconductors are well known. Silver halides are typical pure ionic conductors, which generally have extremely low conductivities at room temperature. In recent years, however, some ionic conductors such as Ag_3SI (1, 2) and RbAg_4I_5 (3, 4) with high conductivities, comparable with those of aqueous electrolytes, have been reported. Silver chalcogenides and copper chalcogenides are mixed conductors. Solids having both high ionic and high electronic conductivity have not been reported, except for high temperature modifications such as $\alpha\text{-Ag}_2\text{S}$ ($>175^\circ\text{C}$), $\alpha\text{-Ag}_2\text{Se}$ ($>133^\circ\text{C}$), $\alpha\text{-Ag}_2\text{Te}$ ($>143^\circ\text{C}$), $\text{Na}_{0.4}\text{WO}_3$ (5), and $\text{Na}_2\text{O} \cdot 5(\text{Fe}_{0.95}\text{Ti}_{0.05}\text{AlO}_3)$ (6).

Ionic conduction in solids is of interest both because of its effect on their electrical properties and because of its role in their application to electrochemical elements (7-9). The purpose of this study has been to discover mixed conductors with high ionic and electronic conductivity at or near room temperature. The ionic conductivities of the mixed conductors known so far are summarized in Table I. This table shows that the high temperature (α -phase) modifications have extremely high ionic conductivity and the low temperature (β -phase) modifications very low. Crystal structure analysis (14-16) indicates that all the α -phases have the same type of structure, in which cations apparently move freely through a large number of sites. Therefore, if a compound exists which has this structure at room temperature, it should have high ionic conductivity at room temperature. In order to search for such compounds, we have undertaken studies on various systems of silver compounds. It has been found that some solid solutions obtained by thermal reaction in the $\text{Ag}_2\text{Se-Ag}_3\text{PO}_4$ system have a structure like $\alpha\text{-Ag}_2\text{Se}$ and as expected have extremely high ionic conductivities at room temperature. This paper reports

the results of x-ray diffraction, differential thermal analysis, electrical conductivity, and coulometric titration investigations on this system.

Experimental Procedure

Preparation of samples.—Silver selenide was prepared from the elements. Stoichiometric quantities of silver powder (99.999% purity) and selenium powder (99.999% purity) were weighed, thoroughly ground together, sealed under vacuum in a Pyrex tube, and heated at 350°C for 48 hr. Silver phosphate was prepared by mixing aqueous solutions of silver nitrate (reagent grade) and sodium hydrogen phosphate (reagent grade). The precipitate was washed by decantation, filtered, dried *in vacuo* over phosphorous pentoxide, and then heated in flowing nitrogen gas at 100°C .

To react Ag_2Se and Ag_3PO_4 , weighed quantities of these materials were thoroughly ground together, and the mixture was heated at various temperatures between $400^\circ \pm 5^\circ\text{C}$ and $800^\circ \pm 5^\circ\text{C}$ for 17 hr in a sealed-evacuated silica tube. The dependence of the nature of the reaction products on the reaction temperature was studied. It was found in the preliminary experiments that the melting points of the solid solutions were 830°C for 5 mole per cent (m/o), Ag_3PO_4 , 750°C for 10 m/o Ag_3PO_4 , and 650°C for 15 m/o Ag_3PO_4 . The solid electrolyte, RbAg_4I_5 , was prepared by Owens' procedure (3) for combining AgI with RbI .

X-ray diffraction investigation.—X-ray diffraction patterns for powdered samples were obtained with a

Table I. Ionic conductivity of mixed conductors

Compound	Temperature ($^\circ\text{C}$)	Conductivity (ohm-cm^{-1})	Reference
Cu_2S	400	2×10^{-1}	(10)
$\alpha\text{-Ag}_2\text{Se}$	150	2.7	(11)
$\alpha\text{-Ag}_2\text{Te}$	160	7×10^{-1}	(11)
$\beta\text{-Ag}_2\text{S}$	150	3.8×10^{-4}	(12)
	150	1.6×10^{-2}	(11)
$\beta\text{-Ag}_2\text{Se}$	105	$0.3\text{-}7 \times 10^{-4}$	(13)
$\beta\text{-Ag}_2\text{Te}$	97	$4\text{-}5 \times 10^{-4}$	(13)

* Electrochemical Society Active Member.

Key words: $\alpha\text{-Ag}_2\text{Se}$, ionic conductivity, electronic conductivity, coulometric titration.

Gigerflex D-3P diffractometer (Rigaku Denki Company, Ltd.) using $\text{CuK}\alpha$ radiation. The scanning speeds were $1^\circ/\text{min}$ for structure analysis and $1/4^\circ/\text{min}$ for lattice constant determinations.

Differential thermal analysis.—Differential thermal analysis was used to determine the phase transition temperature as a function of Ag_3PO_4 content. Each sample (about 1g) was sealed in a Vycor tube under vacuum, preheated to 800°C , cooled gradually to room temperature, and kept at room temperature for several days before the experiment. It was then heated and cooled at an automatically controlled rate of $3.5^\circ\text{C}/\text{min}$ while the temperature difference between the sample and an $\alpha\text{-Al}_2\text{O}_3$ standard was measured with a Chromel-Alumel thermocouple.

Ionic conductivity measurements.—The ionic conductivity was measured by the method described in a previous paper (13). The configuration is shown in Fig. 1. Since the ionic conductivity of the material studied was relatively high, a cylindrical sample 2-3 mm in diameter and 12-13 mm long was used, and $\text{Ag}/\text{RbAg}_4\text{I}_5$ probes were used for potential difference measurements. With this arrangement the effects of electrode polarization were negligible. When it was desired to change the cation-to-anion ratio in the sample, current was passed between the lower silver electrode and the platinum electrode wound around the sample.

Electronic conductivity and Hall coefficient measurements.—The material was rolled under a pressure of about $2000 \text{ kg}/\text{cm}^2$ to form a slab 1-2 mm thick and a six-arm bridge-type sample was cut out. The length-to-width ratio was 3.2. The cell assembly used to measure the electronic conductivity and Hall coefficient is shown in Fig. 2. The sample was placed between two silver ion transfer electrodes, $\text{Ag}/\text{RbAg}_4\text{I}_5$, which were used to change the cation-to-anion ratio of the sample by passing direct current between electrodes 3 and 7 or 8 in Fig. 2.

Measurements of the Hall coefficient and resistance were made by standard d-c methods. A constant sample current of about 100 mA was supplied between electrodes 1 and 5 in Fig. 2. The Hall voltage was measured between 3 and 6. The adopted voltage was the arithmetic mean of the four values obtained by reversing directions of both the magnetic field and sample current in order to cancel errors due to, for example, the thermoelectric effect and probe misalignment. Fields of 1900 and 3750G were used. The resistance was calculated from the voltage drop between 2 and 4. The electronic conductivity is equal to the electrical conductivity measured by the arrangement shown in Fig. 2 because the contribution to the sample current due to ionic conductivity is negligible in this case.

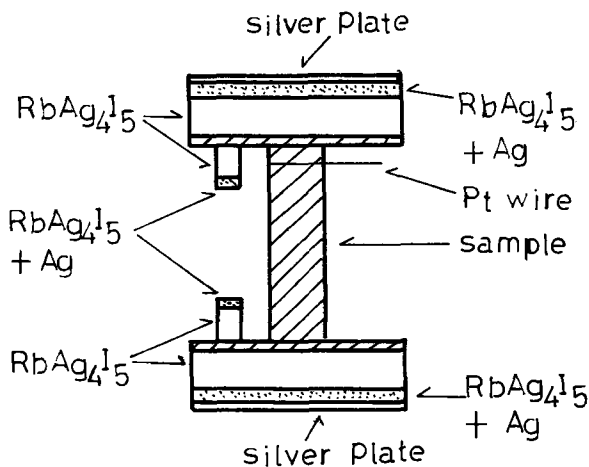


Fig. 1. Arrangement for ionic conductivity measurements

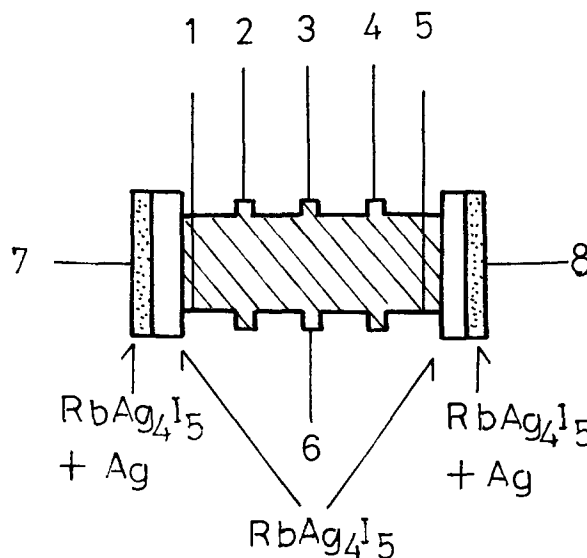
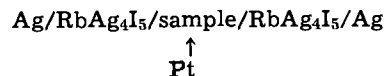


Fig. 2. Arrangement for Hall coefficient and electronic conductivity measurements. Numbers 1-8 represent platinum electrodes.

Coulometric titrations.—The activity of silver in the sample was determined as a function of the cation-to-anion ratio by means of coulometric titrations using the cell



which is analogous to that for silver sulfide (17). The solid electrolyte RbAg_4I_5 is essentially a silver ion conductor and a well-defined amount of silver may be removed from the sample by passing a current across the cell. The sample was a pressed plate, 0.2-0.5 mm thick, contacted on the edge by a platinum wire. At each temperature the potential difference between the platinum and the silver electrode was first maintained at about 100 mV for several hours, after which the coulometric titration was carried out. A constant current of 50-100 μA was passed between the platinum and the left hand silver electrode, and the cell voltage was measured using the platinum and the right hand silver electrode.

Experimental Results and Discussion

Crystal structure of $\text{Ag}_2\text{Se}-\text{Ag}_3\text{PO}_4$ solid solutions.—Mixtures of Ag_2Se and Ag_3PO_4 in various proportions were heated at a number of temperatures for 17 hr and furnace-cooled to room temperature. The x-ray diffraction patterns indicated that the reaction products containing 5 to 10 m/o Ag_3PO_4 prepared above 400°C were single-phase solid solutions with a body-centered cubic structure like that of $\alpha\text{-Ag}_2\text{Se}$. There was a difference in relative intensities of x-ray lines between $\alpha\text{-Ag}_2\text{Se}$ and the solid solutions. For $\alpha\text{-Ag}_2\text{Se}$ the intensities of the (200) and (211) lines were the same, but for the solid solutions the intensity of the (200) line was the strongest. The detailed crystal structure of the solid solutions could not be determined because no single crystals have been obtained. Samples in the composition range of 5 to 10 m/o Ag_3PO_4 which had been kept at room temperature for 6 months or more showed the same x-ray diffraction pattern as those which had been cooled abruptly from 800°C to room temperature. This result indicated that the $\alpha\text{-Ag}_2\text{Se}$ structure was stable at ambient temperature.

Samples containing 4 m/o Ag_3PO_4 or less gave two-phase patterns corresponding to the $\beta\text{-Ag}_2\text{Se}$ and $\alpha\text{-Ag}_2\text{Se}$ structures. In the range 15-40 m/o Ag_3PO_4 , the samples prepared above 500°C gave only broad lines at $2\theta = 34^\circ$. Above 40 m/o Ag_3PO_4 , both the broad lines and lines due to Ag_3PO_4 were observed.

In order to determine the range over which the α - Ag_2Se phase exists at room temperature, the variation of lattice constant of this phase with over-all sample composition was measured. The results, as shown in Fig. 3, indicate that the upper limit for the α - Ag_2Se phase is 12 m/o Ag_3PO_4 . The lower limit could not be established from these data because the diffraction lines for this phase were broad below 3 m/o Ag_3PO_4 .

The $\beta \rightarrow \alpha$ transition in Ag_2Se , which occurs at 133°C (15), is an endothermic process. The transition temperature as a function of composition in the $\text{Ag}_2\text{Se}-\text{Ag}_3\text{PO}_4$ system was determined by differential thermal analysis performed while the samples were heated from room temperature. The results are shown in Fig. 4. The transition temperature is lowered by the addition of Ag_3PO_4 and no thermal arrest was observed for samples containing more than 3 m/o Ag_3PO_4 . This result confirms 4 m/o Ag_3PO_4 as the lower limit of the composition range over which the α - Ag_2Se phase is stable at room temperature.

The melting point in the $\text{Ag}_2\text{Se}-\text{Ag}_3\text{PO}_4$ system decreased as the Ag_3PO_4 content was increased from 0 to 50 m/o. The melting point was about 400°C for 50 m/o Ag_3PO_4 . The phase diagram for the entire $\text{Ag}_2\text{Se}-$

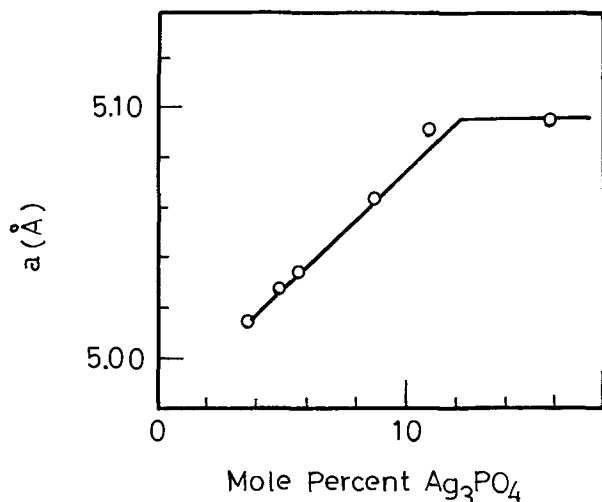


Fig. 3. Lattice constant, a , at 25°C as a function of over-all composition for solid solutions with the α - Ag_2Se structure in the $\text{Ag}_2\text{Se}-\text{Ag}_3\text{PO}_4$ system.

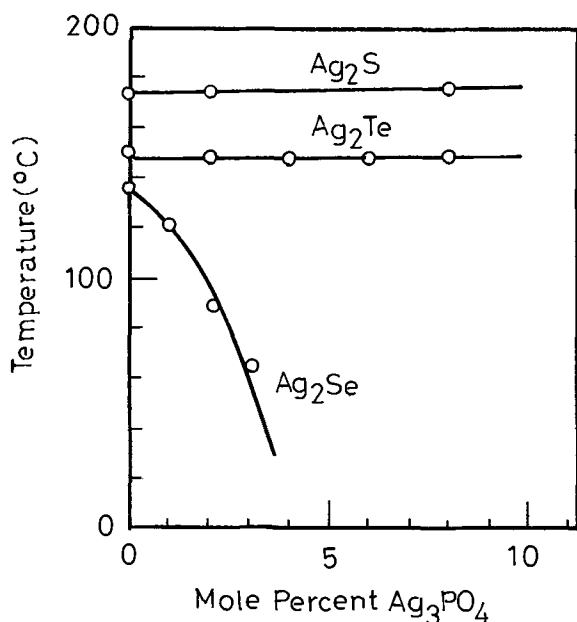


Fig. 4. $\beta \rightleftharpoons \alpha$ transition temperature as a function of composition for the Ag_2X ($\text{X} = \text{S}, \text{Se}, \text{Te}$)- Ag_3PO_4 systems.

Ag_3PO_4 system is too complex to be determined by thermal analysis alone.

Both Ag_2S and Ag_2Te exhibit $\beta \rightarrow \alpha$ transitions with increasing temperature. Their α phases have structures similar to that of α - Ag_2Se and show high ionic conductivity. In order to compare the $\text{Ag}_2\text{S}-\text{Ag}_3\text{PO}_4$ and $\text{Ag}_2\text{Te}-\text{Ag}_3\text{PO}_4$ systems with the $\text{Ag}_2\text{Se}-\text{Ag}_3\text{PO}_4$ system, their $\beta \rightarrow \alpha$ transition temperatures were measured as a function of Ag_3PO_4 content. The results are shown in Fig. 4. In both cases, the transition temperature is independent of composition, indicating that solid solutions are not formed. This was confirmed by the x-ray diffraction patterns of the thermal reaction products in these systems, which showed only two-phase mixtures of Ag_3PO_4 and Ag_2S or Ag_3PO_4 and Ag_2Te at room temperature.

Ionic conductivity.—The ionic conductivity was measured by means of the cell shown in Fig. 1. The relation between the current passed between the two silver plates and the voltage measured between the two $\text{Ag}/\text{RbAg}_4\text{I}_5$ probes obeyed Ohm's law, and the ionic conductivity was calculated from the slope of the current-voltage curve and the dimensions of the sample. The variation in ionic conductivity at 30°C with Ag_3PO_4 content is shown in Fig. 5 for samples prepared at 800°C, cooled to room temperature, and equilibrated with pure silver by connecting the platinum and silver electrodes for about 10 hr at 30°C before making the conductivity measurements. Samples containing 5-10 m/o Ag_3PO_4 show very high ionic conductivity, about $0.1 (\text{ohm}\cdot\text{cm})^{-1}$ at 30°C. This value is comparable with that of RbAg_4I_5 , $0.28 (\text{ohm}\cdot\text{cm})^{-1}$ at 25°C. In Fig. 6, the ionic conductivity of $(\text{Ag}_2\text{Se})_{0.925}(\text{Ag}_3\text{PO}_4)_{0.075}$ equilibrated with silver at each measurement temperature is plotted as a function of temperature. The energy of activation computed from the graph is $4.0 \text{ kcal mol}^{-1}$. The high ionic conductivity and low energy of activation are consistent with the α - Ag_2Se structure assigned to the composition on the basis of x-ray diffraction analysis and differential thermal analysis.

The α -phase solid solutions exhibit deviations from stoichiometry, and their ionic conductivity changes with the cation-to-anion ratio, as observed for β - Ag_2Se and β - Ag_2Te (13). However the stoichiometric composition of the α -phase solid solutions cannot be determined by means of the theory of Wagner and Schottky

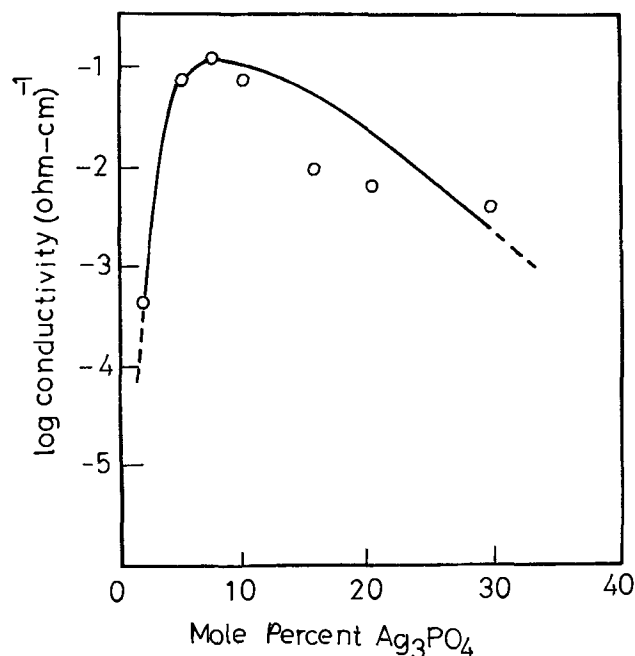


Fig. 5. Ionic conductivity at 30°C as a function of composition for $\text{Ag}_2\text{Se}-\text{Ag}_3\text{PO}_4$ samples equilibrated with pure silver at 30°C.

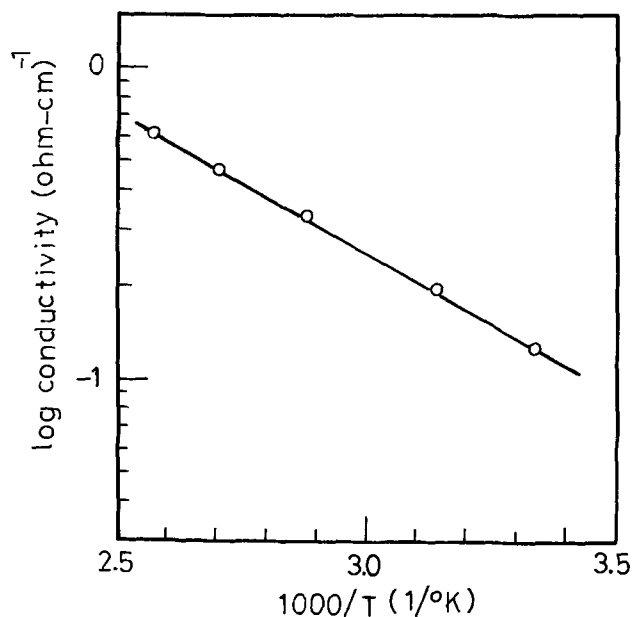


Fig. 6. Ionic conductivity as a function of temperature for $(\text{Ag}_2\text{Se})_{0.925}(\text{Ag}_3\text{PO}_4)_{0.075}$ equilibrated with pure silver at each measurement temperature.

(18), which was used for $\beta\text{-Ag}_2\text{Se}$ and $\beta\text{-Ag}_2\text{Te}$ (13), because the α -phases contain high concentrations of both mobile ions and electrons. In this case, therefore, the composition equilibrated with pure silver was chosen as reference state.

The ionic conductivity (σ_i) of a sample containing 7.5 m/o Ag_3PO_4 was measured at 110°C as a function of the amount of silver (r) removed from the sample after it had been equilibrated with pure silver at 110°C . The reduction in silver content, which was produced by passing current between the platinum electrode and the lower silver electrode, was calculated from

$$r = \frac{q}{xF} \quad [1]$$

where q is the number of coulombs passed, x the number of moles of anion in the sample, and F the Faraday constant. The relative conductivity, $\sigma_i/\bar{\sigma}_i$, where $\bar{\sigma}_i$ is the ionic conductivity of the sample equilibrated with pure silver, is plotted as a function of r in Fig. 7. The change in σ_i with r is small, and the experimental error in $\sigma_i/\bar{\sigma}_i$ is about ± 0.001 .

Silver ions in a solid like $\alpha\text{-Ag}_2\text{Se}$ may be free to move through a large number of sites within the crystal. In that case

$$\sigma_i = en_i\mu_i \quad [2]$$

where n_i is the concentration of silver ion, μ_i the ion mobility, and e the electronic charge. If it is assumed that all the silver is ionized, the relation between n_i and r may be expressed by

$$n_i = \bar{n}_i - r(N_o/V_m) \quad [3]$$

where \bar{n}_i is the concentration of silver ion for the sample equilibrated with pure silver, V_m the molar volume of the material, and N_o Avogadro's number. From Eq. [2] and [3], if μ_i is independent of n_i , we have

$$\frac{\sigma_i}{\bar{\sigma}_i} = 1 - \frac{rN_o/V_m}{\bar{n}_i} \quad [4]$$

According to this equation, the value of \bar{n}_i may be determined from the slope of the $\sigma_i/\bar{\sigma}_i$ vs. r curve. From the slope of the curve in Fig. 7, one obtains $3.5 \times 10^{21} \text{ cm}^{-3}$ for \bar{n}_i . The ionic mobility calculated from $\bar{\sigma}_i$ and \bar{n}_i is about $5 \times 10^{-3} \text{ cm}^2/\text{V}\cdot\text{sec}$. The total

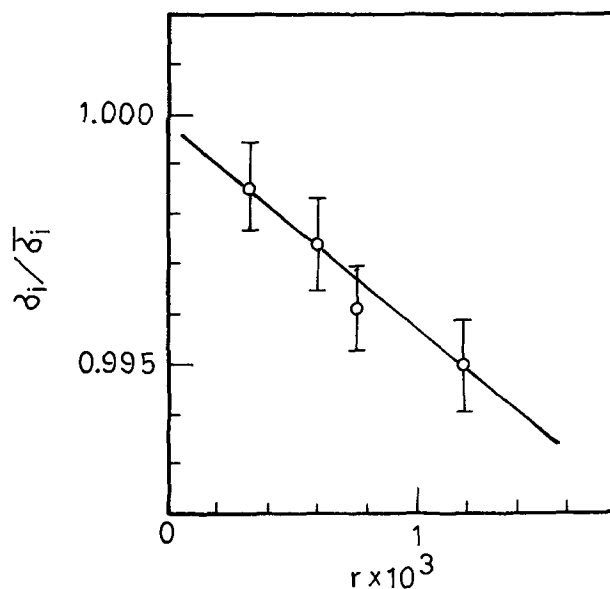


Fig. 7. Relative ionic conductivity, $\sigma_i/\bar{\sigma}_i$, of $(\text{Ag}_2\text{Se})_{0.925}(\text{Ag}_3\text{PO}_4)_{0.075}$ at 110°C as a function of the deviation, r , from the composition equilibrated with pure silver at 110°C .

concentration of silver ion calculated from V_m ($\approx 40 \text{ cm}^3$) is $3.1 \times 10^{22} \text{ cm}^{-3}$ in $(\text{Ag}_2\text{Se})_{0.925}(\text{Ag}_3\text{PO}_4)_{0.075}$, which is about ten times larger than the experimental value of n_i . A possible explanation of this difference is that the transport of ions in solids with an $\alpha\text{-Ag}_2\text{Se}$ type structure differs from transport in liquids, due to interactions between the mobile ions and the other ions.

The concentration of mobile silver ions in the $\alpha\text{-Ag}_2\text{Se}$ solid solution cannot be compared with that in $\alpha\text{-Ag}_2\text{Se}$, because the latter has not been reported. It may be concluded, however, from the experimental results that the concentration of mobile silver ion in the solid solution is extremely high compared with that in $\beta\text{-Ag}_2\text{Se}$, which is only $3.5 \times 10^{17} \text{ cm}^{-3}$ at 105°C (13).

Hall coefficient and electronic conductivity.—The Hall coefficient and electronic conductivity of the $\text{Ag}_2\text{Se}\text{-Ag}_3\text{PO}_4$ solid solutions have also been measured as functions of r . The Hall coefficient R was negative over the whole range of r . The excess electron concentration, n_e , was calculated by using the one-carrier equation

$$n_e = \frac{1}{eR} \quad [5]$$

The excess electron concentrations in $(\text{Ag}_2\text{Se})_{0.925}(\text{Ag}_3\text{PO}_4)_{0.075}$ are shown in Fig. 8 as a function of r . The concentrations are fairly large and comparable to those in $\alpha\text{-Ag}_2\text{Se}$, which were found by Miyatani *et al.* (19) to be in the range from 0.6×10^{19} to $6 \times 10^{19} \text{ cm}^{-3}$ at 150°C . In the range in which the hole concentrations in $(\text{Ag}_2\text{Se})_{0.925}(\text{Ag}_3\text{O}_4)_{0.075}$ are negligible compared to those of excess electrons, the relation between n_e and r is given by

$$n_e = \bar{n}_e - r(N_o/V_m) \quad [6]$$

where \bar{n}_e is the excess electron concentration when the sample is equilibrated with pure silver. According to this equation the slope of the n_e vs. r curve is N_o/V_m . The experimental slope in Fig. 8 is $1.3 \times 10^{19} \text{ cm}^{-3}$ at each temperature investigated, in good agreement with the calculated value of $1.5 \times 10^{19} \text{ cm}^{-3}$ for N_o/V_m .

The dependence of electronic conductivity on r for $(\text{Ag}_2\text{Se})_{0.925}(\text{Ag}_3\text{PO}_4)_{0.075}$ is shown in Fig. 9. The Hall mobility calculated from $\mu_e = \sigma_e/en_e$ is shown in Fig. 10. It depends fairly strongly on r , that is, on the excess electron concentration.

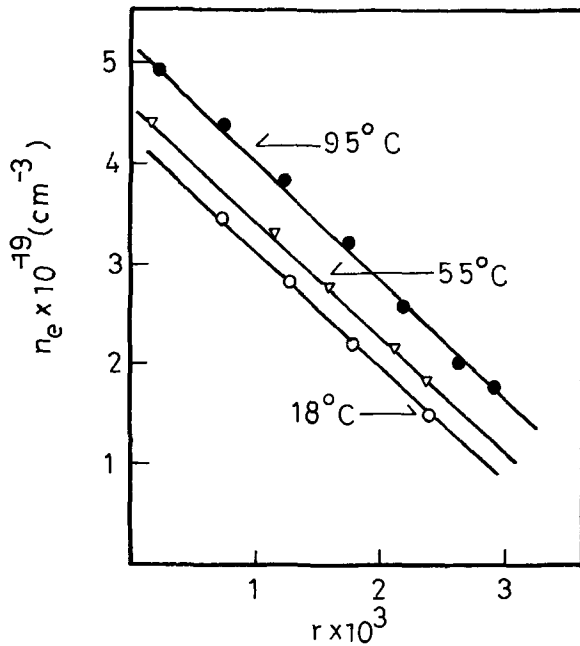


Fig. 8. Electron concentration, n_e , in $(\text{Ag}_2\text{Se})_{0.925}(\text{Ag}_3\text{PO}_4)_{0.075}$ as a function of the deviation, r , from the composition equilibrated with pure silver at each measurement temperature.

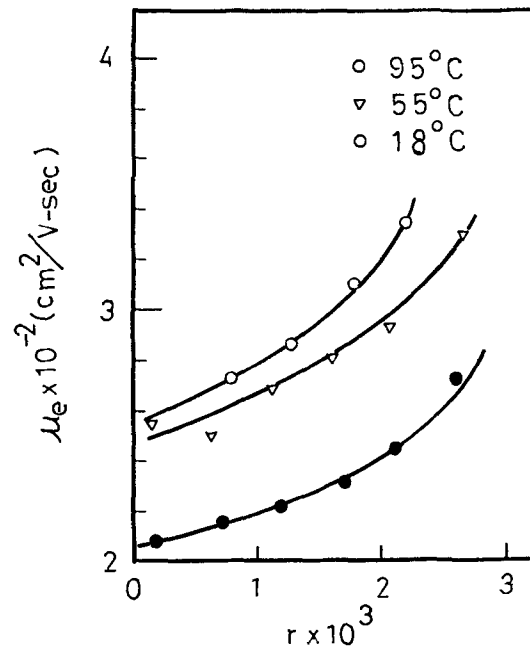


Fig. 10. Hall mobility, μ_e , in $(\text{Ag}_2\text{Se})_{0.925}(\text{Ag}_3\text{PO}_4)_{0.075}$ as a function of the deviation, r , from the composition equilibrated with pure silver at each measurement temperature.

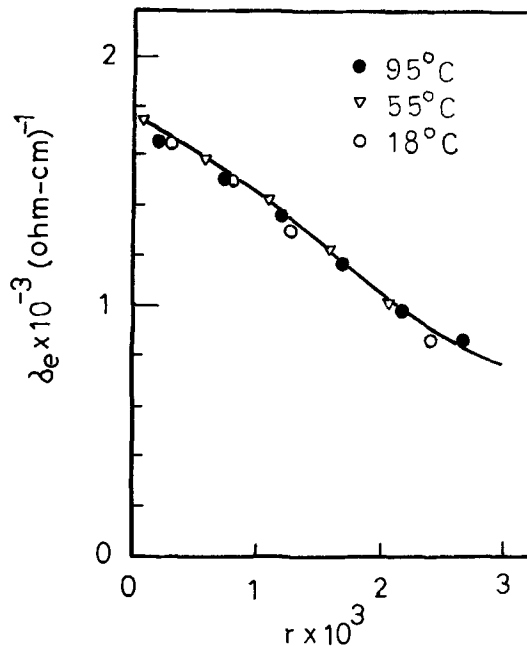


Fig. 9. Electronic conductivity, σ_e , in $(\text{Ag}_2\text{Se})_{0.925}(\text{Ag}_3\text{PO}_4)_{0.075}$ as a function of the deviation, r , from the composition equilibrated with pure silver at each measurement temperature.

Coulometric titration.—The potential difference (E) between the platinum electrode and one of the silver electrodes was measured while a constant current of 50–100 μA was being passed between the platinum electrode and the other silver electrode. Reproducible results were obtained up to a potential of 160 mV for both addition and removal of silver. Above 160 mV, a slow decay of the open-circuit potential was observed, possibly because of a slow decomposition of the $\text{Ag}_2\text{Se}-\text{Ag}_3\text{PO}_4$ solid solution to $\beta\text{-Ag}_2\text{Se}$ and Ag_3PO_4 . Typical results for E as a function of r , obtained at 95°C for the sample containing 7.5 m/o Ag_3PO_4 , are shown in Fig. 11. The curves obtained in the temperature range from room temperature to 100°C for samples containing 5 to 10 m/o Ag_3PO_4 are similar to the one shown in Fig. 11.

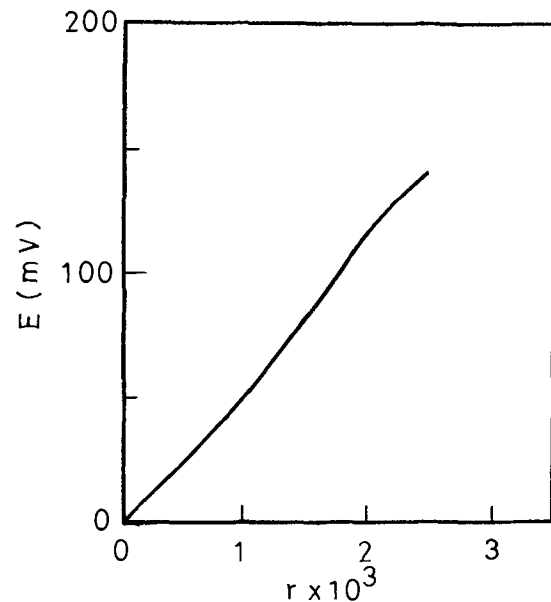


Fig. 11. Coulometric titration curve for $(\text{Ag}_2\text{Se})_{0.925}(\text{Ag}_3\text{PO}_4)_{0.075}$ at 95°C .

For excess electron concentrations (n_e) as high as those in the present samples, n_e is given by Fermi statistics as

$$n_e = \frac{\pi(8m^*kT)^{3/2}}{2h^3} F(\mu_e/RT) \quad [7]$$

where m^* is the effective mass of an excess electron, k the Boltzmann constant, h Planck's constant, μ_e the chemical potential of the electrons, and $F(\mu_e/RT)$ the Fermi-Dirac function. By combining Eq. [6] and [7], and differentiating the resulting equation with respect to μ_e , we obtain

$$-\frac{N_o}{V_m} \frac{dr}{d\mu_e} = \frac{\pi(8m^*kT)^{3/2}}{2h^3RT} F'(\mu_e/RT) \quad [8]$$

Dividing Eq. [8] by Eq. [7] gives

Table II. Properties of Ag₂Se-Ag₃PO₄ solid solutions equilibrated with pure silver

Ag ₃ PO ₄ (m/o)	Temp (°C)	σ_i (ohm-cm) ⁻¹	σ_e (ohm-cm) ⁻¹	n_e (cm ⁻³)	$\frac{\mu_e}{V\text{-sec}}$ (cm ² /V-sec)	m_e^*/m_0
7.5	18	0.10	1.8×10^3	4.3×10^{19}	2.6×10^2	0.21
	55	0.25	1.8×10^3	4.5×10^{19}	2.5×10^2	0.21
	75	0.33	1.7×10^3	4.8×10^{19}	2.2×10^2	0.21
	95	0.44	1.7×10^3	5.1×10^{19}	2.1×10^2	0.21
10	15	0.060	1.5×10^3	3.6×10^{19}	2.6×10^2	0.26
	55	0.17	1.5×10^3	3.7×10^{19}	2.5×10^2	0.24
	75	0.27	1.5×10^3	3.8×10^{19}	2.5×10^2	0.24
	95	0.40	1.6×10^3	3.9×10^{19}	2.5×10^2	0.23
0 (α -Ag ₂ Se)	150	2.7 ^(a)	4×10^{19} ^(b)	6×10^{19} ^(b)	4×10^2 ^(b)	0.16 ^(b)

(a) Ref (11).

(b) Ref (19).

$$-\frac{N_0}{V_m} \cdot \frac{dr}{d\mu_e} = \frac{n_e}{RT} \frac{F'(\mu_e/RT)}{F(\mu_e/RT)} \quad [9]$$

The chemical potential of silver, μ_{Ag} , is related to the electromotive force, E , by

$$\mu_{Ag} - \mu_{Ag}^0 = -EF \quad [10]$$

where μ_{Ag}^0 is the chemical potential of silver in its pure state and F the Faraday constant. Denoting the chemical potential of silver ion by μ_{Ag^+} , we have

$$\mu_{Ag^+} + \mu_e = \mu_{Ag} \quad [11]$$

In view of the high degree of disorder of silver ions in the sample, the chemical potential of silver ions is essentially independent of small variations in the cation-to-anion ratio. Hence, it follows from Eq. [10] and [11] that

$$d\mu_e = d\mu_{Ag} = -d(EF) \quad [12]$$

From Eq. [12], Eq. [9] is rewritten as

$$\frac{dr}{dE} = n_e(F/RT) (V_m/N_0) \frac{F'(\mu_e/RT)}{F(\mu_e/RT)} \quad [13]$$

By using the values of dr/dE and n_e obtained respectively by coulometric titration and Hall coefficient measurements together with tabulated values of F and F' (20), $F(\mu_e/RT)$ can be evaluated for each value

of n_e , and m_e^* is then found by using Eq. [7]. The values of m_e^*/m_0 obtained in this way for (Ag₂Se)_{0.925}(Ag₃PO₄)_{0.075} at 75° and 95°C are shown as a function of r in Fig. 12. These results are comparable with the values of m_e^*/m_0 (0.1-0.15) for α -Ag₂Se measured by Miyatani *et al.* (19).

Summary

The properties of Ag₂Se-Ag₃PO₄ solid solutions with the α -Ag₂Se structure are summarized in Table II, together with the corresponding values for α -Ag₂Se. This table shows that the characteristic quantities for these solid solutions are comparable with those for α -Ag₂Se.

The solid solutions with α -Ag₂Se structure are mixed conductors which have both high ionic and high electronic conductivity at room temperature. These mixed conductors are suitable electrode materials for the electrochemical analog memory element proposed by the present authors (13), because the silver ion diffuses sufficiently fast to maintain a homogeneous activity in the solid phase.

Manuscript submitted Jan. 3, 1972; revised manuscript received July 6, 1972.

Any discussion of this paper will appear in a Discussion Section to be published in the June 1973 JOURNAL.

REFERENCES

1. B. Reuter and K. Hardel, *Naturwissenschaften*, **48**, 161 (1961).
2. T. Takahashi and O. Yamamoto, *Electrochim. Acta*, **11**, 779 (1966).
3. B. B. Owens and G. R. Argue, *Science*, **157**, 308 (1967).
4. J. N. Bradley and P. D. Greene, *Trans. Faraday Soc.*, **63**, 424 (1967).
5. M. S. Whittingham and R. A. Huggins, *J. Chem. Phys.*, **54**, 414 (1971).
6. K. O. Hever, *This Journal*, **115**, 830 (1968).
7. L. Heyne, *Electrochim. Acta*, **15**, 1251 (1970).
8. M. N. Hull, *Energy Conversion*, **10**, 215 (1970).
9. B. B. Owens, *Advan. Electrochem. Electrochem. Eng.*, **8**, 1 (1971).
10. E. Hirahara, *J. Phys. Soc. Japan*, **6**, 422 (1951).
11. N. Valverde, *Z. Physik. Chem.*, **70**, 128 (1970).
12. K. Weiss, *Z. Naturforsch.*, **24a**, 148 (1969).
13. T. Takahashi and O. Yamamoto, *This Journal*, **118**, 1051 (1971).
14. S. Hoshino, *J. Phys. Soc. Japan*, **12**, 315 (1957).
15. A. Boettcher, G. Haase, and H. Treupek, *Z. Angew. Phys.*, **7**, 478 (1955).
16. P. Rahlfs, *Z. Phys. Chem.*, **B31**, 157 (1936).
17. C. Wagner, *J. Chem. Phys.*, **21**, 1891 (1953).
18. C. Wagner and W. Schottky, *Z. Physik. Chem.*, **B11**, 163 (1931).
19. S. Miyatani, Y. Toyota, T. Yanagihara, and K. Iida, *J. Phys. Soc. Japan*, **23**, 35 (1967).
20. J. McDougall and E. C. Stoner, *Phil. Trans. Roy. Soc. (London)*, **A237**, 67 (1938).

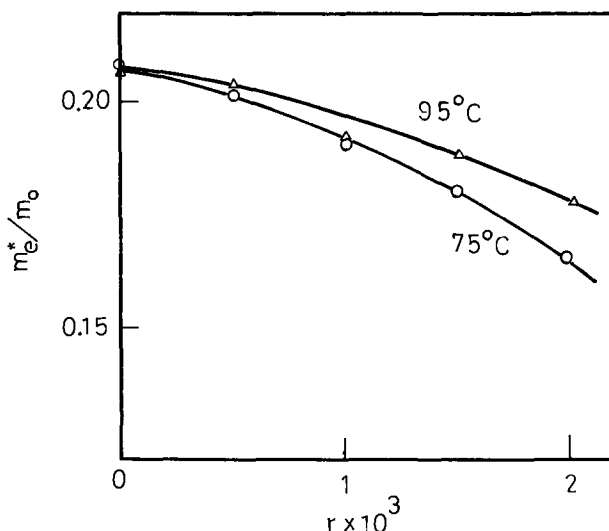


Fig. 12. Ratio of the effective mass, m_e^* , to the free electron mass, m_0 , in (Ag₂Se)_{0.925}(Ag₃PO₄)_{0.075} as a function of the deviation, r , from the composition equilibrated with pure silver at 75° and 95°C.

A Thorough Thermodynamic Evaluation of the Silicon-Hydrogen-Chlorine System

L. P. Hunt and E. Sirtl

Dow Corning Corporation, Solid State Research and Development, Hemlock, Michigan 48626

ABSTRACT

A sensitive computational method allowed the determination of $\Delta H_f^{\circ}_{298}(\text{SiHCl}_3, \text{g}) = -116.9 \pm 0.7$ kcal/mol based on various previously reported experimental investigations. For the first time the gaseous compounds SiCl_3 and Si_2Cl_6 were included in a thermodynamic evaluation of the Si-H-Cl system. Diagrams relating Cl/H (0.01-10) to Si/Cl over the temperature range of 400°-1700°K indicate the equilibrium state of the system with respect to the corresponding increase or decrease of silicon in the gaseous phase.

Many papers have appeared in the literature which have used thermodynamically calculated equilibrium states to aid in explaining experimental data from the synthesis, hydrogenation, pyrolysis, and reduction of various chlorosilanes. Some of these publications contain individual solutions for thermodynamically describing the Si-H-Cl system. More detailed analyses have been made by Lever (1), Niederkorn and Wohl (2), and Harper and Lewis (3). Since the various thermodynamic analyses lead to widely varying results, a recent article (4) critically evaluated the thermodynamic data used in the equilibrium calculations and presented results based on the suggested values. This article also provides a detailed survey of pertinent thermodynamic literature.

The current work thoroughly examines the standard enthalpy of formation of trichlorosilane since prior calculations had indicated that the calculated equilibrium molar ratio of $\text{SiCl}_4/\text{SiHCl}_3$ was highly sensitive to the SiHCl_3 enthalpy used, relative to a fixed enthalpy value of SiCl_4 . The purpose of this paper, based on the revised SiHCl_3 enthalpy and the evaluation of other pertinent thermodynamic data, is to graphically present the equilibrium Si-H-Cl system in a form that depends only upon the initial and final states of the system. We have selected, similar to Lever (1), the temperature variation of the Si/Cl ratio as a function of the Cl/H ratio.

Computational Techniques

Modified versions of a computer program, similar to that described by Cruise (5), were used for all equilibrium calculations. The generalized program minimizes the free energy of a system through an iterative technique in which the concentration of specified species is varied in a controlled manner. A condensed phase species is automatically excluded from the computational process when its concentration reached a preset lower limit. Any number of probable species may be included in the program since input is in the form of a matrix representing the elemental distribution among the species.

The only restraint on the initial estimate of species concentrations is that the species concentrations represent the ratios of the atoms contained in the reactants. The final equilibrium state of a system is independent of the original distribution of the atoms among the species as long as the initial atomic ratios are the same. For example, one reaches the same equilibrium mixture from either 1 mole of SiH_2Cl_2 or from $\frac{1}{2}$ mole each of SiH_4 and SiCl_4 . Therefore, the Cl/H ratio is used to uniquely define the gas-phase composition of the Si-H-Cl system since it represents an infinite num-

ber of conditions made possible by using different proportions of starting materials.

Since the once selected Cl/H ratio has to remain constant for a reaction in this system, the Si/Cl ratio is used to represent the changing composition of the gas phase due to silicon either entering or leaving it via the condensed phase of elemental silicon.

In addition to using the temperature and total pressure of the system as input to the computer program, the physical state of each species must be noted along with its basic thermodynamic values. It is the deviations in these values, the standard enthalpy of formation, $\Delta H_f^{\circ}_{298}$, standard entropy, S°_{298} , and the temperature function of the heat capacity equation, $C^{\circ}_p(T)$, that cause different results to be obtained for the final computed equilibrium state of a system.

Thermodynamic Data

Discussed below are chemical species for which the thermodynamic data have been revised since our previous publication (4), or species that have been added to more thoroughly complete this analysis of the Si-H-Cl system. Data for the species $\text{Cl}(\text{g})$, $\text{Cl}_2(\text{g})$, and $\text{Si}(\text{g})$ are considered well enough characterized to be taken directly from the literature (see Table I).

Standard Enthalpy of Formation

Trichlorosilane.—Scrutinization of $\Delta H_f^{\circ}_{298}(\text{SiHCl}_3, \text{g})$ is necessary since the only two experimental determinations in the literature differ by 13 kcal/mol. Reuther (6) stated that his value of -112 kcal/mol probably was too positive due to partial reaction of elemental chlorine, liberated by the combustion process, with the calorimeter. On the other hand, the enthalpy of -125 kcal/mol, determined by Wolf (7) and corrected for the revised SiO_2 enthalpy, seemed incompatible with experimental data close to equilibrium conditions (8). Similar to the case of several determinations of the standard enthalpy of SiCl_4 , as discussed by Schäfer and Heine (9), the supposed experimental error in Wolf's data may likewise be due to incomplete hydrolysis, and would therefore lead to a negative deviation from the most probable SiHCl_3 enthalpy. Although past estimates (8) of the enthalpy of formation of SiHCl_3 appeared to yield satisfactory results when comparing calculated and experimental data (4, 8), the value of -116 kcal/mol had no direct experimental basis, since it had been obtained by linear interpolation between the enthalpies of $\text{SiH}_4(\text{g})$ and $\text{SiCl}_4(\text{g})$.

During the course of our studies, it became obvious that the enthalpy of formation of trichlorosilane could be determined from already existing experimental data. This is possible because the equilibrium molar ratio $n_{\text{SiCl}_4}/n_{\text{SiHCl}_3}$ is very sensitive (Fig. 1) to the

Key words: silicon, thermochemical equilibrium, transport, enthalpy, vapor deposition.

Table I. Thermochemical data

Species	$\Delta H_f^{\circ 298}$ (kcal/mol)	Ref.	$S^{\circ 298}$ (e.u.)	Ref.	$C^{\circ}_p = A + \frac{BT}{10^3} + \frac{CT^2}{10^5}$ (eu)			Ref.
					A	$B \times 10^3$	$C \times 10^{-5}$	
Cl ₂ (g)	0.0	(a)	53.29	(25)	8.85	0.16	-0.68	(21)
Cl(g)	29.1	(25)	39.46	(25)	5.53	-0.16	-0.23	(21)
HCl(g)	-22.0	(23)	44.65	(23)	6.27	1.24	0.30	(21)
H ₂ (g)	0.0	(a)	31.21	(23)	6.52	0.78	0.12	(23)
Si(g)	107.7	(17)	40.12	(17)	4.82	0.18	0.42	(23)
Si(s)	0.0	(a)	4.50	(17)	5.70	0.70	-1.04	(21)
SiH ₄ (g)	7.3	(20)	48.87	(27)	15.38	4.88	-6.35	(17)(e)
SiH ₂ Cl(g)	-34.0	(8)	59.85	(27)	14.13	7.65	-3.82	(17)(e)
SiH ₂ Cl ₂ (g)	-75.0	(8)	68.47	(27)	20.34	2.58	-5.86	(17)(e)
SiHCl ₃ (g)	-116.9	(b)	74.85	(27)	22.79	1.43	-4.76	(17)(e)
SiCl ₄ (g)	-156.7	(9)	79.01	(27)	25.39	0.23	-3.51	(17)(e)
SiCl ₃ (g)	-78.0	(b)	74.42	(17)(e)	19.60	0.14	-2.44	(20)(e)
SiCl ₂ (g)	-38.2	(13)	67.4	(20)	13.62	0.22	-1.26	(20)(e)
SiCl(g)	45.7	(17)	56.82	(17)	8.89	0.12	-0.34	(17)(e)
Si ₂ Cl ₆ (g)	-236.0	(b)	101.0	(b)	42.15	1.03	-8.46	(17)(e)

(a) Zero by definition.

(b) This paper.

(c) The coefficients were obtained from a regression analysis on the data cited.

(d) Regression analysis on data for Cl₂Co(g).(e) The data of PCl₅(g) was used.Table II. Calculated values of $\Delta H_f^{\circ 298}$ (SiHCl₃,g) for various experimental SiCl₄/SiHCl₃ ratios at $P_T = 1.0$ atm unless otherwise noted

Reference	Feed mixture (Si present)	Cl/H	Temp (°K)	Asymptote correction	$\frac{n_{SiCl_4}}{n_{SiHCl_3}}$	$\Delta H_f^{\circ 298}$ (kcal/mol)
(10)	SiCl ₄ /H ₂	0.23	1200	No	1.6	-117.4
(10)	SiHCl ₃ /H ₂	0.14	1200	No	1.3	-117.6
(28)	H ₂ /HCl	0.048	948	No	0.48	-118.5
		0.048	1073	No	1.5	-116.5
		0.20	948	No	1.5	-117.4
		0.20	1073	No	3.3	-115.9
(11)	SiHCl ₃ /H ₂	0.21	1243	No	3.0	-116.0
		0.25	1243	No	4.3	-115.2
(29)	SiCl ₄ /H ₂	0.30	1023	No	2.8	-116.4
				Yes	2.0	-117.1
(30)	SiHCl ₃ /N ₂	3.0 ($P_T = 0.25$)	948	No	5.4	-117.5
				Yes	11.0	-116.2
				Yes	8.3	-116.4
(31)	SiCl ₄ /H ₂	1.0	773	No	2.3	-117.5

standard enthalpy of formation of SiHCl₃, assuming the enthalpy of SiCl₄ as fixed, and because a less complex chemical equilibria exists at lower temperatures. Below about 1250°K, a negligibly small partial pressure of SiCl₂ exists such that the gas phase essentially contains only the molecules SiCl₄, SiHCl₃, HCl, and H₂.¹ Therefore, the only uncertain enthalpy is that of

¹ The variation of the interpolated standard enthalpy for SiH₂Cl₂(g) by ± 2 kcal/mol showed no major influence on the calculated partial pressures of the above-mentioned species.

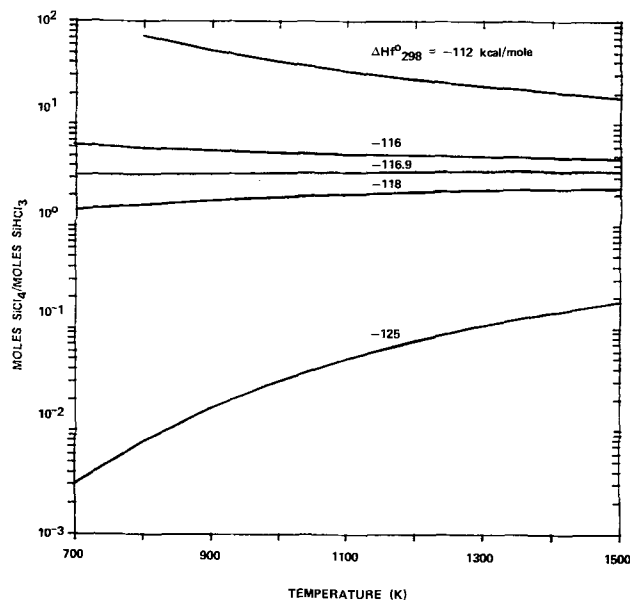


Fig. 1. Temperature variation of the equilibrium SiCl₄/SiHCl₃ ratio for various values of $\Delta H_f^{\circ 298}$ (SiHCl₃,g) at Cl/H = 1.0, 1 atm total pressure, and $\Delta H_f^{\circ 298}$ (SiCl₄,g) = -156.7 kcal/mol.

SiHCl₃ since the work by Schäfer and Heine (9) has given high reliability to $\Delta H_f^{\circ 298}$ (SiCl₄).

Ashen *et al.* (10) pursued the same problem in a similar way, based on their data obtained from the thermal decomposition of SiHCl₃ and SiCl₄ in presence of hydrogen. However, they accepted the SiHCl₃ value (uncorrected) as the point of reference and varied the SiCl₄ value until agreement was found with their kinetic data.

There are several experimental studies available which allow comparison of the different SiCl₄/SiHCl₃ ratios close to or extrapolated toward infinite residence time. These data, and others, compiled in Table II, show our calculated values of $\Delta H_f^{\circ 298}$ (SiHCl₃,g) from reactions involving the decomposition of SiCl₄ or SiHCl₃, the hydrogenation of SiCl₄, and the formation of chlorosilanes by hydrochlorination of silicon. The most probable enthalpy value of -116.9 ± 0.7 kcal/mol deviates only slightly from the value -116 obtained from the linear relationship within the sequence SiH₄ → SiCl₄ proposed earlier (8). The data given by Hata *et al.* (11) must be weighted lightly due to their experimental difficulty of trapping the product gases.

Due to the large concentration of gaseous silicon dichloride in a high-temperature reaction zone the analysis of exhaust gases in any known silicon deposition reactor system must lead to erroneous thermodynamic conclusions. The major reason for this is the recombination of the dichloride with hydrogen chloride to form trichlorosilane in the downstream area. Depending on the quenching rate, polymer subchlorides of very low volatility also may be formed additionally influencing the results and the meaning of any gas analysis.

Silicon subchlorides.—A thorough study of the Si-SiCl₄ system up to 1575°K by Schäfer and Nickl (12), and supported by more recent studies (13, 14), indi-

cates that SiCl_4 and SiCl_2 are the only gases present to within less than the 2% experimental error in the measured partial pressures. Nevertheless, for theoretical as well as practical reasons, we wanted to complete our thermodynamic analysis of the Si-H-Cl system by also including the gaseous compounds SiCl , SiCl_3 , and Si_2Cl_6 . Although SiCl_3 has not been regarded as an equilibrium species by authors (1, 2) who have considered SiCl , recent EPR measurements (15) have shown the relative concentrations of species in the Si-Cl system to be $\text{SiCl}_2 > \text{SiCl}_3 > \text{SiCl}$ at temperatures greater than 600°K. Equilibrium calculations in our subsequent paper (16) are found to agree with these experimental observations in the lower temperature area.

The standard enthalpy value for $\text{SiCl}(g)$ was taken from the JANAF Tables (17). The appreciable uncertainty ($+45.7 \pm 15$ kcal/mol) is the result of two different spectroscopic evaluations. However, calculations at 1500°K using even the lowest value ($+30.7$) show that the amount of SiCl is $< 8 \times 10^{-2}\%$ in the Si-Cl system.

A small change has been made in the enthalpy of $\text{SiCl}_2(g)$ based on the work by Schäfer *et al.* (13).

There is no literature concerning the standard enthalpy of formation of $\text{SiCl}_3(g)$. Unfortunately, a simple linear interpolation, as it was applied successfully to the sequence of "saturated" compounds in the series $\text{SiH}_4 \rightarrow \text{SiCl}_4$, is no longer meaningful in the case of $\text{Si}(g) \rightarrow \text{SiCl}_4(g)$. The energy states of the unbonded valence electrons are different in each case, as are the bonding angles of the ligands. It can be assumed that the compounds having an unpaired electron deviate from incremental linearity in an endothermal sense (more positive enthalpy of formation). This is demonstrated by the diagram shown in Fig. 2. The standard enthalpy of silicon trichloride was obtained from a computational analysis of the Si-Cl system where, based on studies by Schäfer and Nickl (12), the partial pressure of $\text{SiCl}_3(g)$ was not allowed to exceed 0.3%. This gave a minimum enthalpy value of -78 kcal/mol which supported our hypothesis.

A basic estimate leads to the chosen value of $\Delta H_f^{\circ 298}(\text{Si}_2\text{Cl}_6, g)$. When one mole of $\text{Si}_2\text{Cl}_6(g)$ is synthesized from 2 moles $\text{SiCl}_3(g)$, the heat of reaction consists of the sum of the heat of formation of a silicon-silicon bond plus a "rearrangement energy," ΔH_R , of the SiCl_3 molecules characterized by the spatial deviation of the Si-Cl bond orbitals from their tet-

rahedral arrangement in SiCl_4 . Since the term $\Delta H(\text{SiCl}_3, g) + \Delta H_R$, by definition, is nothing else but the hypothetical value of an "ideal" SiCl_3 molecule obtained by linear interpolation (Fig. 2), the standard enthalpy of gaseous Si_2Cl_6 can be calculated directly as follows

$$\begin{aligned} \Delta H_f^{\circ 298}(\text{Si}_2\text{Cl}_6, g) &= 2[\Delta H(\text{SiCl}_3, g) + \Delta H_R] + \Delta H_{\text{Si-Si}} \\ &= 2(-91) + (-54) \\ &= -236 \text{ kcal/mol.} \end{aligned}$$

According to Pauling (18), $\Delta H_{\text{Si-Si}}$ is the negative value of one-half of the atomic sublimation energy $\Delta H^{\circ 298}(\text{subl})$ of silicon. The limit of accuracy is estimated to be less than ± 2 kcal/mol.

The catalytic thermal decomposition of Si_2Cl_6 has been reported (19) to be complete at temperatures between 350° and 400°C according to the reaction



This is in agreement with our calculations and, thus, supports the validity of the proposed enthalpy of formation of hexachlorodisilane.

Standard Entropy

The entropy of $\text{SiCl}_3(g)$ taken from recently tabulated data (20) is nearly 2 kcal/mol higher than that of $\text{AlCl}_3(g)$ or $\text{PCl}_3(g)$. Since the entropy values of both $\text{AlCl}_3(g)$ and $\text{PCl}_3(g)$ are well established, we accepted the entropy of $\text{SiCl}_3(g)$ to be equal to that of $\text{PCl}_3(g)$.

No entropy data appears in the literature in the case of $\text{Si}_2\text{Cl}_6(g)$. The only compound related to Si_2Cl_6 is C_2Cl_6 (Al_2Cl_6 has a different molecular structure). Fortunately, entropy data for hexachloroethane are tabulated (17). Thus, comparisons within a homologous group can be used to make fairly accurate estimates. It is our experience that, within a homologous series of reactions, the difference in reaction entropies between the first and the second element in a group of the Periodic System generally amounts to 1 or 2 eu. Using the reaction $\text{M}_2\text{Cl}_6(g) \rightarrow 2\text{MCl}_3(g)$, a value of 101 ± 1 eu (cal/deg mol) was calculated for $S^{\circ 298}(\text{Si}_2\text{Cl}_6, g)$.

Molar Heat Capacity, $C_p(T)$

The heat capacity data for $\text{HCl}(g)$ and $\text{Si}(s)$ reported (4) earlier have been replaced by more accurate values.

The coefficients of the terms in the heat capacity equation were determined in many cases by regression analysis of the original data cited over a temperature range of 298°-2000°K. The maximum deviation of the calculated from the original data is $< 2\%$ for the compounds predominate under normal conditions. A single form of the heat capacity equation was chosen because of convenience and of its more general use in compilations (21-23).

Results and Discussion

Computations over the Cl/H range of 0.01-10 and over temperature and total pressure spans of 300°-1700°K and 0.1-1.0 atm were carried out with the data compiled in Table I. The thermodynamic analysis indicates that the following species can be ignored at equilibrium due to their low partial pressures while maintaining $\geq 99\%$ accuracy: SiH_4 , SiCl , SiCl_3 , Si_2Cl_6 , Cl , Cl_2 , and $\text{Si}(g)$. A comparative discussion of the experimental and calculated behavior of individual species is given in a subsequent article (16).

The Si-H-Cl equilibrium system is well illustrated by Fig. 3 and 4 which show the variation of the final silicon content of the gas phase (Si/Cl ratio) with the initial chlorosilane concentration (and, therefore, Cl/H ratio) at various temperatures. There are three Si/Cl values in this system that are approached asymptotically in the diagrams; 0, 0.25, and 0.50. Total conversion to elemental silicon (Si/Cl = 0) is the ultimate case to be reached at very low Cl/H ratios and increasing tem-

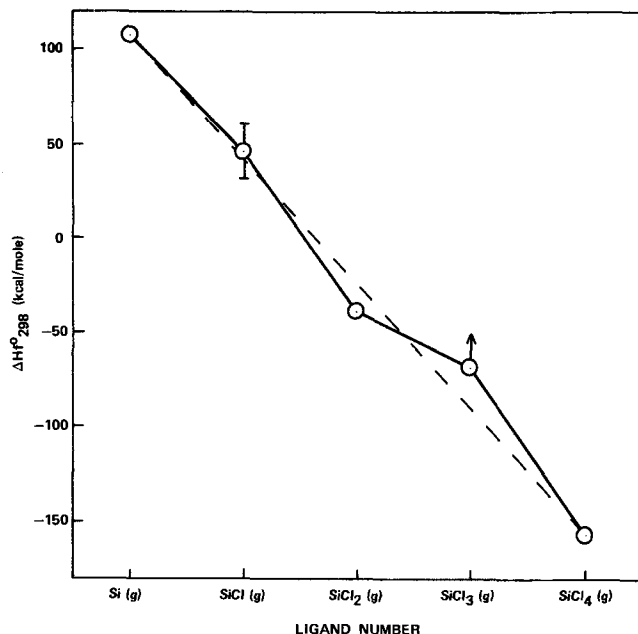


Fig. 2. Enthalpy relationship for the series $\text{Si}(g) \rightarrow \text{SiCl}_4(g)$

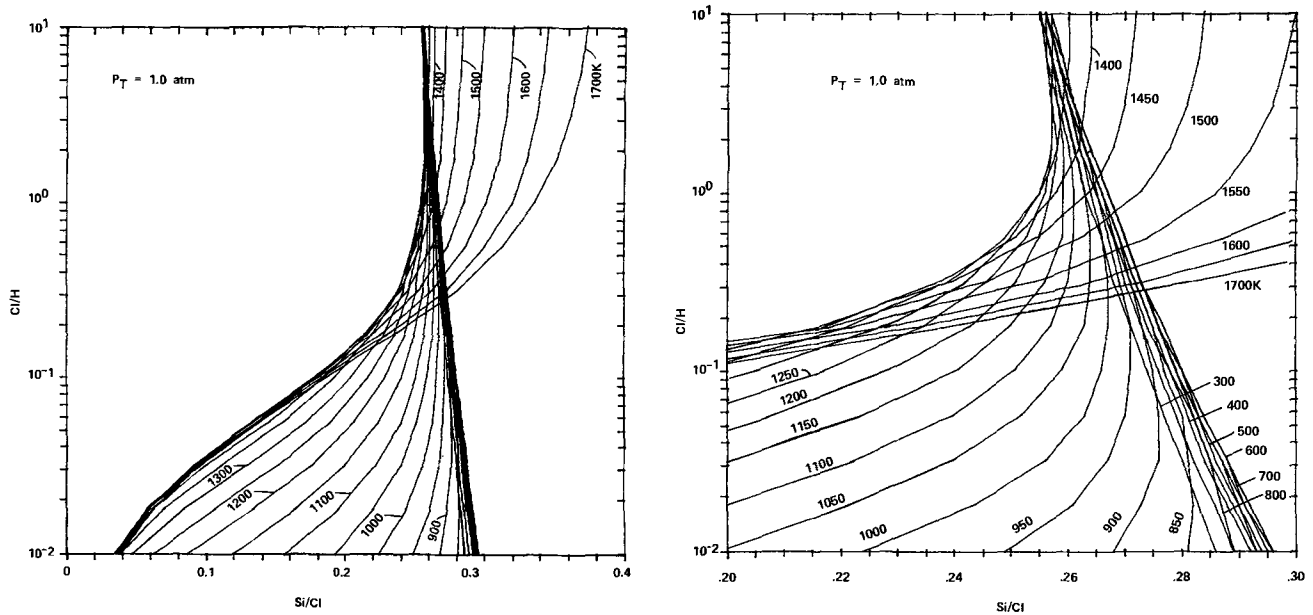


Fig. 3. (a, left) The silicon content of the gas phase as a function of the Cl/H ratio at 1 atm total pressure for 50 degree temperature increments. (b, right) An enlargement of a portion of (a).

peratures. Silicon tetrachloride ($\text{Si/Cl} = 0.25$) is the major compound of significance at high Cl/H values and at temperatures up to approximately 1300°K . At lower temperatures and decreasing Cl/H ratios, the silicon content of the gas phase is changed due to the relative importance of trichlorosilane ($\text{Si/Cl} = 0.33$) with respect to silicon tetrachloride. Both high temperatures and increasing Cl/H ratios strongly favor the formation of silicon dichloride ($\text{Si/Cl} = 0.50$), the most stable of the gaseous subchlorides below the melting point of silicon.

Figures 3 and 4 are particularly useful in determining the maximum yield of silicon from chlorosilane decomposition, or the direction and magnitude of silicon transport reactions. Negative yields, preferably obtained with HCl , HCl-H_2 , or SiCl_4/H_2 mixtures indicate the dissolution (etching) of silicon.

In the first case, the theoretical silicon yield (η) can be easily calculated from the equation $\eta =$

$(V - V')/V$, where V is the Si/Cl ratio of the starting mixture and V' is the ratio at equilibrium. The transport direction of silicon in a temperature gradient for a given Cl/H ratio, can be determined from the equilibrium Si/Cl ratios (V_1', V_2') existing at two silicon subsystems. Transport will occur by diffusion in the direction of the lower Si/Cl ratio. The transport driving force can be formulated according to $\Delta P_{\text{Si}} = V_1' - V_2'$. In the case of $T_1 > T_2$ a positive value of ΔP_{Si} corresponds to a silicon transport to higher temperatures. For a quantitative treatment of a diffusion-limited transport process, equations given in Schäfer's book (24) may be used.

The application of the different diagrams to a number of practical cases will be demonstrated in a subsequent paper (16).

Acknowledgment

The authors wish to thank D. H. Sawyer for his experimental studies of transport reactions.

Manuscript submitted April 13, 1972; revised manuscript received July 29, 1972.

Any discussion of this paper will appear in a Discussion Section to be published in the June 1973 JOURNAL.

REFERENCES

1. R. F. Lever, *IBM J. Res. Develop.*, **8**, 460 (1964).
2. I. Niederkorn and A. Wohl, *Rev. Roumaine Chem.*, **11**, 85 (1966).
3. M. J. Harper and T. J. Lewis, United Kingdom Ministry of Aviation Report ERDE 6/M/66 [Great Britain Explosives Research and Development Establishment, Waltham, England] (1966). CFSTI Document AD 641 310.
4. L. P. Hunt and E. Sirtl, in "Chemical Vapor Deposition, Second International Conference," J. M. Blocher, Jr. and J. C. Withers, Editors, The Electrochemical Society, Softbound Symposium Series, New York (1970).
5. D. R. Cruise, *J. Phys. Chem.*, **68**, 3794 (1964).
6. H. Reuther, *Chem. Tech.*, **2**, 331 (1950).
7. E. Wolf, *Z. Anorg. Allgem. Chem.*, **313**, 229 (1961).
8. H. Seiter and E. Sirtl, *Z. Naturforsch.*, **21a**, 1956 (1966).
9. H. Schäfer and H. Heine, *Z. Anorg. Allgem. Chem.*, **332**, 25 (1964).
10. D. J. Ashen, G. C. Bromberger, and T. J. Lewis, *J. Appl. Chem.*, **18**, 348 (1968).
11. K. Hata, S. Yasuda, S. Yamada, S. Nakamura, and M. Akiyama, *Tokai Denkyoku Giho*, **21**, 14 (1961).

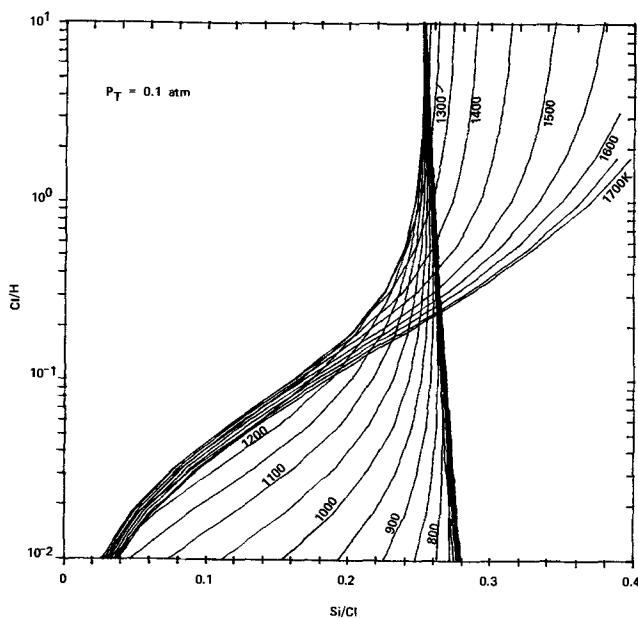


Fig. 4. The silicon content of the gas phase as a function of the Cl/H ratio at 0.1 atm total pressure for 50 degree temperature increments.

12. H. Schäfer and J. Nickl, *Z. Anorg. Allgem. Chem.*, **274**, 250 (1953).
13. H. Schäfer, H. Bruderreck, and B. Morcher, *ibid.*, **352**, 122 (1967).
14. R. Teichmann and E. Wolf, *ibid.*, **347**, 145 (1966).
15. H. A. Meshcheryakov, *Zh. Fiz. Khim.*, **45**, 848 (1971).
16. E. Sirtl, L. P. Hunt, and D. H. Sawyer, Submitted to *This Journal*.
17. D. R. Stull, Editor JANAF Thermochemical Tables [Dow Chemical Co., Midland, Mich.] (1965-1968). CFSTI Documents PB 168 370, -1, -2, -3.
18. L. Pauling, "The Nature of the Chemical Bond," Cornell University Press, Ithaca, New York (1960).
19. W. W. Kohlschutter and H. Mattner, *Z. Anorg. Allgem. Chem.*, **282**, 169 (1955).
20. D. R. Stull and H. Prophet, Editors JANAF Thermochemical Tables, 2nd ed., Nat. Bur. Stand. *NSRDS-NBS 37* (1971).
21. K. K. Kelley, Contributions to the Data on Theoretical Metallurgy. XIII. High-Temperature Heat-Content, Heat-Capacity, and Entropy Data for the Elements and Inorganic Compounds, *Bur. Mines Bull.*, **584** (1960).
22. C. E. Wicks and F. E. Block, Thermodynamic Properties of 65 Elements—Their Oxides, Halides, Carbides, and Nitrides, *Bur. Mines Bull.* **605** (1963).
23. O. Kubaschewski, E. L. Evans, and C. B. Alcock, "Metallurgical Thermochemistry," Pergamon Press, New York (1967).
24. H. Schäfer, "Chemical Transport Reactions," Academic Press, New York (1964).
25. D. D. Wagman, W. H. Evans, V. B. Parker, I. Halow, S. M. Bailey, and R. H. Schumm, Selected Values of Chemical Thermodynamic Properties. *Nat. Bur. Std. Tech. Note*, **207-3** (1968).
26. S. R. Gunn and L. G. Green, *J. Phys. Chem.*, **65**, 779 (1961).
27. S. Mikawa, *Nippon Kagaku Zasshi*, **81**, 1512 (1960).
28. C. Fischer and E. Wolf, *Z. Anorg. Allgem. Chem.*, **333**, 46 (1964).
29. T. Paetkau, Private communication (1967).
30. K. Setinek and J. A. Chernyshev, *Chem. Prumysl*, **12**, 419 (1962).
31. G. H. Wagner and C. E. Erickson, U.S. Pat. 2,595,620 (1952).

Light Scattering from Photoresist Films

F. P. Laming¹ and R. E. Straile

Bell Telephone Laboratories, Murray Hill, New Jersey 07974

ABSTRACT

Nonfluorescent light scattering at 6328Å from films of Kodak Metal Etch Resist and Kodak Thin Film Resist has been measured over an angular range of 1°-75° from the incident direction. A correlation is made between these measurements and resolution loss due to scattering which can occur when the resists are used for photolithography. It is found that such resolution loss can occur if certain limits on thickness or exposure are exceeded.

When high resolution is not an essential requirement there are few unsolved problems in the technology of pattern generation for thin-film circuits. However, when it is required to generate a pattern in which components are separated by distances of the order of only one micron, not only do problems become acute but the origins of many difficulties are as yet undetermined. Although a number of factors contributing to resolution loss can be postulated, they cannot be placed in order of precedence until they have been quantitatively evaluated. The results reported here will allow the relative importance of light scattering to be assessed when other contributing factors (such as edge diffraction, reflection, etc.) have been similarly determined.

Light scattered by a resist film consists of three distinct factors: (i) inelastic scattering, such as fluorescence, (ii) elastic scattering of absorbed light or resonance fluorescence, and (iii) elastic but nonabsorbed scattering, such as that considered by Mie or Rayleigh. In this report we are concerned only with type (iii).

Nonfluorescent scattered light from thin-film materials can originate either at interfacial boundaries or within the film material. The relative contribution from the two sources depends on the nature of the film material and the refractive index differences at the interfaces. In most studies of thin films, interfacial effects are eliminated as far as possible since information on the structure of film material is obtained primarily from the bulk-film scattering (1). In the present work it is the total nonfluorescent light scattering which is of interest. Our measurements, therefore, include the

contribution of boundary scattering as a significant factor.

Figure 1 shows the interaction between a photoresist film and an incident perfectly collimated beam of light of intensity I . For simplicity, only scattering originating at the film surface is illustrated, but similar diagrams could have been drawn at any depth within the film material. The scattered light intensity will, of course, be greatest when the scattering angle θ is small, diminishing to a minimum at $\theta = 90^\circ$. Back-scattering will not be considered. If the scattered intensity at a given angle θ is sufficient to expose the photo-

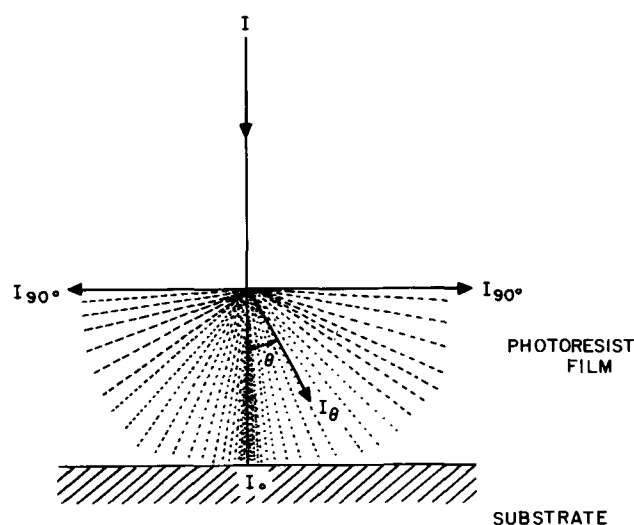


Fig. 1. Scattering of light from a photoresist film

¹ Present address: International Business Machines Corporation, East Fishkill Facility, Hopewell Junction, New York 12533.

Key words: light, scattering, photoresist, Rayleigh.

resist, then loss in resolution will occur. Our present purpose was to determine at what angle θ such resolution loss first begins to occur under the conditions of normal photolithographic practice.

Experimental

Kodak Metal Etch Resist (KMER) was chosen as the material of primary interest since it is known to give poor resolution (2) and is the least purified resist supplied by Kodak. It should, therefore, present more of a scattering problem than any other resist. Kodak Thin Film Resist (KTFR) was also studied.

The resists were deposited as films on glass microscope slides by spinning, without purification by filtration. Thickness measurements were made using a Tallysurf Model 4. Each film was baked at 100°C for 30 min prior to use.

A diagram of the scattering apparatus is presented in Fig. 2. The design is similar to that described by Lundberg *et al.* (3) for measuring light scattering from molecular solutions.

The output of a 25 mW He/Ne laser was interrupted at a rate of 400 Hz by a PAR* Model BZ-1 light chopper, positioned inside the laser cavity to eliminate edge diffraction from the chopper blades. The primary beam was deflected so as to pass at normal incidence through the sample under investigation, which was mounted on a fixed stage above a rotatory table. The beam met the sample at a point precisely above the center of the table. Scattered light was observed with the primary photomultiplier fixed to a rigid arm attached to the center of the table. The arm was motor-driven at a rate of 6° per min.

The apparatus was used as described for measurements down to 15°, and with some care down to 10°. Below 10°, however, a slight modification was necessary because the extension tube attached to the primary photomultiplier began to contact the main laser beam. For low-angle measurements, therefore, the long extension tube was replaced by a short tube with a 1/8 in. circular aperture. This "pin-hole" arrangement enabled measurements to be extended to 1°, though the wider acceptance angle of such an arrangement resulted in some loss of accuracy. The motor drive for the detector arm was not used in this mode of operation. Accuracy of the data decreased with decreasing angle and was approximately $\pm 5\%$ above 15°, $\pm 10\%$ down to 3°, and $\pm 20\%$ at 1°.

In order to eliminate minor fluctuations due to small daily changes in experimental conditions all scattering measurements were made with respect to a fixed standard; a 3 mm thick sample of Mylar² was found to be appropriate. Scattering from this sample at 45° was observed after each determination of resist scattering, and the ratio between the latter and the former taken as a measure of absolute scattering intensity. The ratio

* A commercial polyester resin.

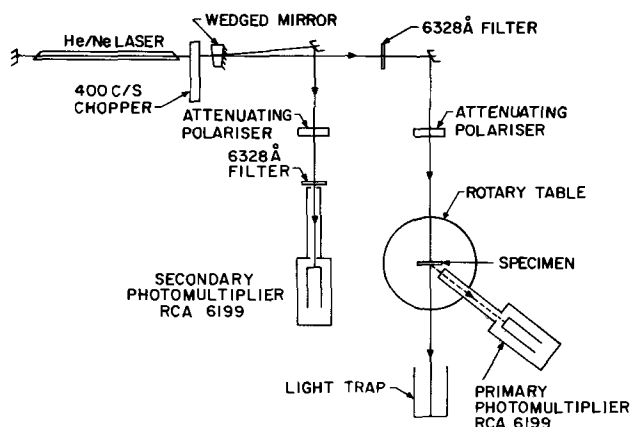


Fig. 2. Light scattering apparatus

obtained in this way also includes a contribution from the microscope-slide substrate. This contribution arises mainly from one surface of the glass slide (neglecting scattering within the bulk of the glass) since the other glass face presents an almost index-matched surface to the resist. The required resist scattering is, therefore, given by the expression

$$I_R = \frac{I_{OBS} - \frac{I_{SUB}}{2}}{I_{MYL}}$$

where I_R = scattering measurement required; I_{OBS} = observed scattering intensity at angle θ ; I_{SUB} = observed scattering from substrate alone at angle θ ; I_{MYL} = observed scattering from Mylar standard at 45°.

Table I lists values of I_R obtained for two sets of KMER films down to 15°. Although no specific attempt was made to vary film thickness, one set of slides was 4.37 μ thick and the other 4.20 μ . The precision of these measurements was sufficient to show clearly the difference in scattering between the two thicknesses; the difference, ΔI_R , must arise from the bulk film material. Values of ΔI_R are also quoted in Table I. Each figure quoted is an average value taken from a minimum of 12 separate measurements on six specimens of each sample.

Below 15° a further correction to the above expression is required because in this region the main laser beam begins to contact the primary photomultiplier housing resulting in an increasingly significant contribution to the measured intensity from unwanted reflections. A measure of this contribution, I_i , was obtained by scanning down to 1° in the absence of either microscope slide or sample. The revised equation is then

$$I_R = \frac{I_{OBS} - \left(\frac{I_{SUB}}{2} + I_i \right)}{I_{MYL}}$$

Because measurements in this region were not so precise, changes in scattering due to small variations in film thickness were not apparent. Table II lists the results obtained for KMER and KTFR films together with substrate measurements over the range 15° to 1°. The difference between KMER and KTFR can best be seen in Fig. 3. Both sets of data were taken from films approximately 4 μ thick. It is apparent that the intensity of scattered light from films of KMER exceeds that from KTFR by approximately 40 times.

In order to convert I_R values to absolute units (as percentages of incident intensity), the intensity of the

Table I. Scattering intensities $I_R \times 10^3$ for various scattering angles θ

	10°*	15°	30°	45°	60°	70°
KMER thickness 4.37 μ	520	112	16.5	6.36	2.68	0.91
KMER thickness 4.20 μ	500	89.9	14.2	5.57	2.35	0.86
ΔI_R thickness 0.17 μ	20	22.1	2.3	0.79	0.33	0.05

* Figures in this column are the least accurate.

Table II. Scattering intensities I_R for $\theta \leq 15^\circ$

	1°	3°	5°	10°	15°
KMER	40	6.8	2.4	0.56	0.18
KTFR	1.0*	0.18	0.059	0.014	0.006
Glass	0.5*	0.056	0.029	0.012	0.006

* Estimate.

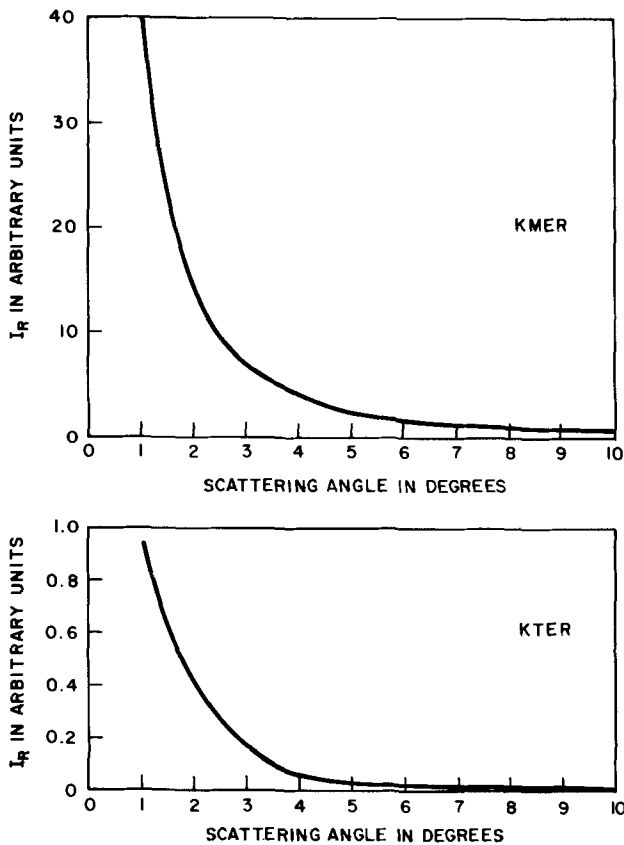


Fig. 3. Light scattering below 10° from films of KMER and KTFR.

incident beam relative to the Mylar standard was measured by scanning through 0°. To do this the incident intensity was reduced with a neutral density filter of transmittance 0.1%. Figure 4 illustrates the scattering profile of the incident beam as observed through (A)

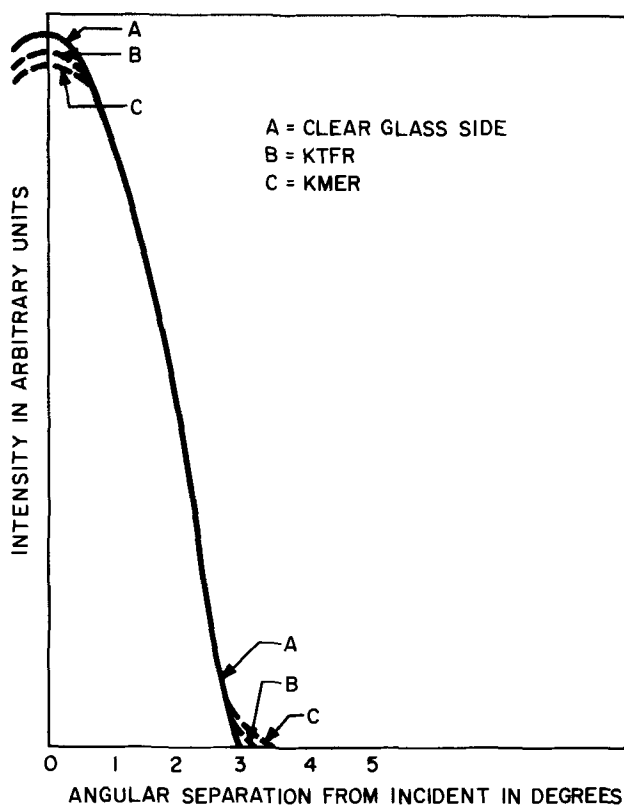


Fig. 4. Incident beam profiles close to 0°

a plane glass slide, (B) a slide coated with KTFR, and (C) a slide coated with KMER. Measured values of I incident at 0° are 7900, 7600, and 7500 for A, B, and C, respectively. The observed difference between these values is largely due to the absorption of the films at 6328Å which in each case is approximately 5%. Clearly, the total scattered intensity over a solid angle of 4π steradians is an insignificant contribution to the loss in forward intensity.

The observed I_R value of 6.8 (see Table II) for a KMER slide at 3° is therefore equivalent to 0.086% of the incident intensity, while that of 0.16 for KTFR at the same angle is equivalent to 0.002% of incident.

Exposure of photoresist materials to light results in structural changes in the resist material which alter its solubility in the developing solvent. For negative resists, such as KTFR and KMER, unexposed areas are thus preferentially removed from the substrate during development. Since the development process is differential there can be some areas where the solubility has been decreased only sufficiently for partial removal to occur. Normal photolithographic procedure attempts to eliminate the effect of partially exposed areas by fairly severe washing techniques, taking advantage of the lower adhesion of the film in these areas. A characteristic curve applicable to this practical approach is represented by the solid line of Fig. 5. This curve is analogous to a photographic H&D curve. Below point A adhesion of the resist to the surface breaks down and the material can be completely removed by the developing agent.

We have extended this characteristic curve for KMER by using a less vigorous development technique so as to retain even the less adherent film. Each slide was exposed to an illumination of 1800 lumens/ft² from a 100W Black Light Eastern high pressure mercury lamp. Exposure times varied between 5-60 sec. After exposure, each slide was developed using KMER developer as follows. The exposed slide was immersed photoresist upwards in a shallow Petri dish containing rapidly stirred solvent. During the final 10 sec of the 3 min wash the upper surface of the slide was subjected to a jet of solvent applied with a syringe. The slide was then removed and dried in a stream of warm air. A measure of the amount of photoresist retained on the glass slide was obtained by measuring the absorption of the retained film at 400 mμ with a Beckman DU2 spectrometer.

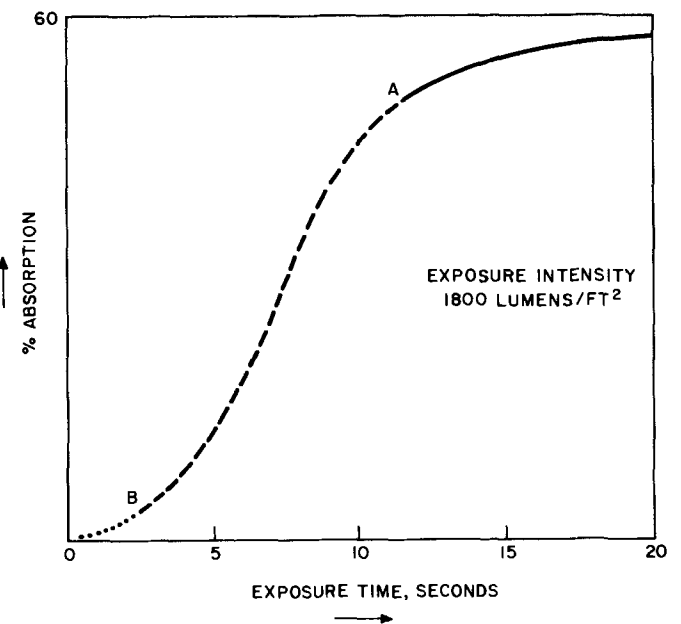


Fig. 5. Characteristic curve of KMER

The resulting characteristic curve is shown as the solid and dashed lines of Fig. 5 down to point B. At B, resist adhesion broke down even under the mild conditions described above. The dotted curve is an extrapolation.

Results and Discussion

The prime purpose of this work was to determine whether the intensity of nonfluorescent light scattered from a photoresist material is a significant factor in determining the resolution of the photolithographic process. The highest scattering value determined from the above measurements was for the KMER film at 1° , and amounted to only 0.51% of the incident intensity. It must be remembered, however, that this figure was determined using light of wavelength 6328Å. Normally, these resists are exposed to a high pressure mercury lamp with a peak emission at about 3600Å. A correction for this discrepancy can be made if the scattering follows Rayleigh theory, when the intensity of scattering will vary inversely as the fourth power of the wavelength. A scattered intensity of 0.51% at 6328Å is therefore equivalent to a scattered intensity of 4.9% at 3600Å, and it is this which would be encountered in practice. Whether this will result in a significant resolution loss depends on the intensity of light used in the exposure step.

Typically, exposure times of 60 sec are used for films of KTFR and KMER 1500Å thick at an intensity of 4500 lumens/ft². Assuming a linear relationship between exposure intensity and exposure time, this is equivalent to an exposure time of 150 sec with our intensity of 1800 lumens/ft². Four and nine-tenths per cent of the typical exposure used in practice would, therefore, be equivalent to an exposure time of approximately 7.5 sec under our conditions. This corresponds to a point between A and B on our sensitivity curve and would therefore result in resolution loss if a mild development procedure were used. But no effect would be observed using the more vigorous conventional development technique.

It is now possible to calculate the amount of overexposure necessary to produce a known resolution loss due to scattering. From Fig. 6 it can be seen that a perfectly collimated beam of light will be broadened by an amount $2x = 2t \cdot \tan \phi$ after passing through a

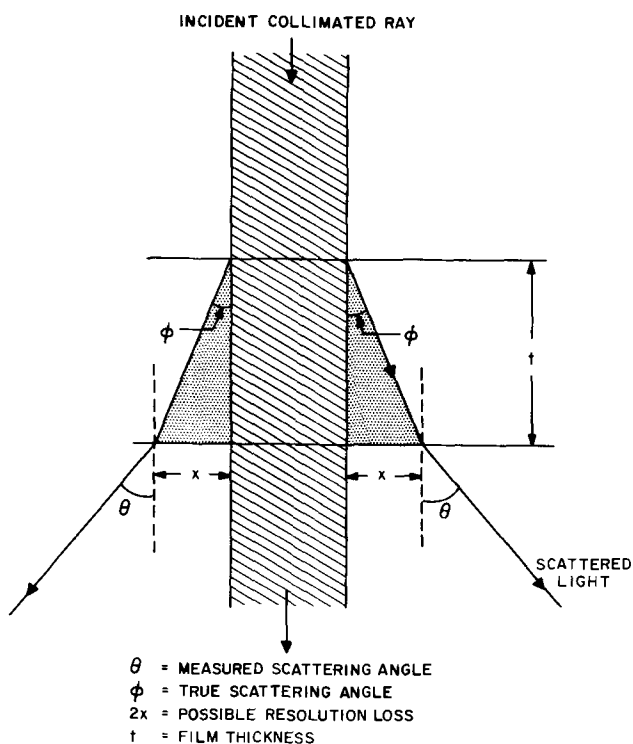


Fig. 6. Resolution loss

resist layer of thickness t (actually this assumes that the total measured scattered intensity arises at the initial resist-air interface; the calculated resolution loss is therefore an over-estimate). The true scattering angle ϕ is related to the measured angle by Snell's Law (for a good index match between resist and glass slide). Measured values of $\theta = 15^\circ, 10^\circ, 5^\circ, 3^\circ,$ and 1° are therefore equivalent to ϕ values of $9^\circ 56', 5^\circ 39', 3^\circ 20', 2^\circ 0',$ and $0^\circ 40'$ respectively.

It can thus be seen that if the scattering intensity at, say, $\theta = 10^\circ$ is sufficient to produce adherence in the photoresist, then a 1μ line will be broadened to a 1.23μ line for a resist layer 1μ thick, and to a 1.03μ line for a resist layer only 1500Å thick. For this to occur the intensity at $\theta = 10$ must be equivalent to an exposure of 12 sec at 1800 lumens/ft² (see Fig. 5). Since the scattered intensity at this angle is only 0.067% of the incident intensity exposure to an illumination of 4500 lumens/ft² would have to be continued for 6.5×10^3 sec for the resolution loss to be real. Such gross overexposure is not likely to occur in practice. Figure 7 illustrates values which have been calculated in this way for KMER and KTFR films 4μ thick. For thinner resist films the resolution loss would be less than that shown because (i) there is a linear relationship between line broadening and film thickness, and (ii) the intensity of scattered light will decrease with film thickness.

It should be remembered that the scattering measurements reported here do not include any contribution from resonance fluorescence. Since a 1μ film of resist will absorb approximately 50% of the incident 3600Å light, this fluorescence may be an appreciable factor, although much of this energy will no doubt be dissipated thermally. Reflectivity of the substrate has also been ignored for the present, but it should be borne in mind that this may increase scattering resolution loss slightly because of multiple reflections. The effect may not be severe, however, because of the high resist extinction coefficient.

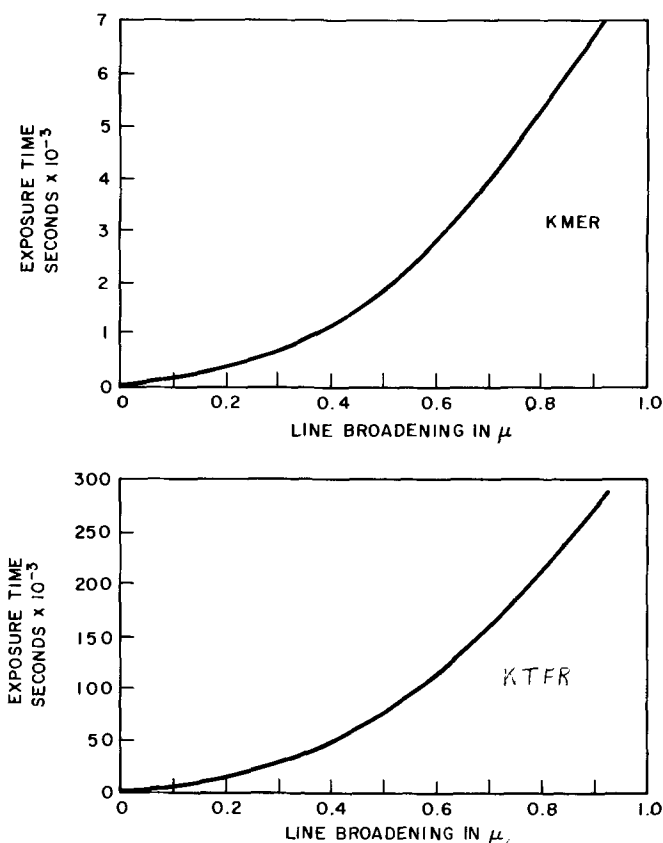


Fig. 7. Degradation as a function of exposure time at an exposure intensity of 4500 lu/ft².

Conclusion

Nonfluorescent light scattering from films of Kodak Metal Etch Resist (KMER) has been measured over an angular range of 1°-75° and from films of Kodak Thin Film Resist (KTFR) over an angular range of 1°-15°. Scattering from KMER is approximately 40 times that from KTFR.

The intensity measurements reported here are used to determine to what extent nonfluorescent light scattering from resists will contribute towards image degradation in high-resolution photolithography. It is concluded that such scattering will not contribute to resolution loss providing the exposure employed does not exceed certain limits which are specified.

Manuscript received June 16, 1972. This was Paper 319RNP presented at the Boston Meeting of the Society, May 5-9, 1968.

Any discussion of this paper will appear in a Discussion Section to be published in the June 1973 JOURNAL.

REFERENCES

1. R. S. Stein and J. J. Keane, *J. Polymer Sci.*, **17**, 21 (1955).
2. L. E. Martinson, Second Kodak Seminar on Micro-miniaturization, April 4-5, 1966.
3. J. L. Lundberg, E. J. Mooney, and K. R. Gardner, *Science*, **145**, 1308 (1969); *Rev. Sci. Instr.*, **33**, 1256 (1962).

Silicon Epitaxial Growth by Rotating Disk Method

Katsuro Sugawara*

Semiconductor and Integrated Circuits Division, Hitachi, Ltd., Kodaira, Tokyo, Japan

ABSTRACT

By a rotating disk method which had quantitatively been treated in fluid motion, silicon epitaxial deposition using the SiCl₄-H₂ system was effected at various susceptor rotation speeds and various pressures. Calculation of the growth rate was initially made with a one-dimensional model of an infinite diameter disk without considering natural convection caused by local heating. This was followed by a numerical solution of Navier-Stokes equations, continuity equation, and equation of energy of cylindrical coordinates, using a three-dimensional model and taking natural convection into consideration. With the three-dimensional model including natural convection, a quantitative description can be given of the influence of susceptor rotation speed and pressure on the growth rate at a temperature higher than 1150°C.

The SiCl₄-H₂ system is most widely used for silicon epitaxial growth. As pointed out by Bylander (1), epitaxial growth is mass-transfer controlled in the higher temperature region, with about 1150°C as the dividing line; while in the lower temperature region, chemical reaction on the substrate surface is the rate-determining step. For a better quality of crystallinity required for semiconductor devices, the reaction is desirably performed in the higher temperature region. Consequently, the growth is closely connected with the concentration of supplied gas, its flow pattern, and the flow-rate control. For this reason, the gas-flow pattern was observed in a horizontal reactor in relation to the pressure, flow rate, and natural convection, using TiO₂ fumes as a tracer (2-3). Then the relation of gas-flow pattern to the epitaxial deposition rate distribution was investigated. This was followed by consideration of a boundary layer of certain thickness on the susceptor, which was determined by the gas-flow rate and pressure. Then a diffusion equation that took into account the diffusion and natural convection of the reactant gases was solved and a comparison with the experimental value was attempted (4). However, since the thickness of the boundary layer was substituted by the value estimated from the experiment, it lacked accuracy. Eversteyn *et al.* (5) similarly treated SiH₄ epitaxial growth, and found an agreement between boundary layer thickness from gas-flow pattern observation and that derived from their model.

Thus, attention was given to the rotating disk method, by which fluid velocity distribution and thickness of the boundary layer could be quantitatively obtained due to its axial symmetry, and the deposition rate was acquired by changing the rotation speed of

the susceptor and the gas pressure. Then calculations were made with the one-dimensional model of an infinite diameter disk without considering natural convection. This was followed by a numerical solution of the Navier-Stokes equations, the equation of continuity, and the equation of energy of cylindrical coordinates, taking natural convection into consideration. In the following pages, theoretical considerations, the experimental method, and the results are presented, and a comparative examination of the experiment and calculations is sought.

Theory

As shown in Fig. 1, a susceptor acts as a rotating disk and silicon epitaxial deposition is effected on its surface.

Velocity and temperature distribution.—In cylindrical coordinates, the Navier-Stokes and continuity equations take these forms (6)

$$V_r \frac{\partial V_r}{\partial r} - \frac{V_\phi^2}{r} + V_y \frac{\partial V_r}{\partial y} = -\frac{1}{\rho} \frac{\partial p}{\partial r} + \nu \left(\frac{\partial^2 V_r}{\partial r^2} + \frac{1}{r} \frac{\partial V_r}{\partial r} - \frac{V_r}{r^2} + \frac{\partial^2 V_r}{\partial y^2} \right) \quad [1]$$

$$V_r \frac{\partial V_\phi}{\partial r} + \frac{V_r V_\phi}{r} + V_y \frac{\partial V_\phi}{\partial y} = \nu \left(\frac{\partial^2 V_\phi}{\partial r^2} + \frac{1}{r} \frac{\partial V_\phi}{\partial r} - \frac{V_\phi}{r^2} + \frac{\partial^2 V_\phi}{\partial y^2} \right) \quad [2]$$

$$V_r \frac{\partial V_y}{\partial r} + V_y \frac{\partial V_y}{\partial y} = -\frac{1}{\rho} \frac{\partial p}{\partial y} + \nu \left(\frac{\partial^2 V_y}{\partial r^2} + \frac{1}{r} \frac{\partial V_y}{\partial r} + \frac{\partial^2 V_y}{\partial y^2} \right) - fg\beta\Delta T \quad [3]$$

* Electrochemical Society Active Member.

Key words: epitaxy by SiCl₄-H₂ system, Navier-Stokes equation, convective diffusion equation, natural convection, numerical calculation.

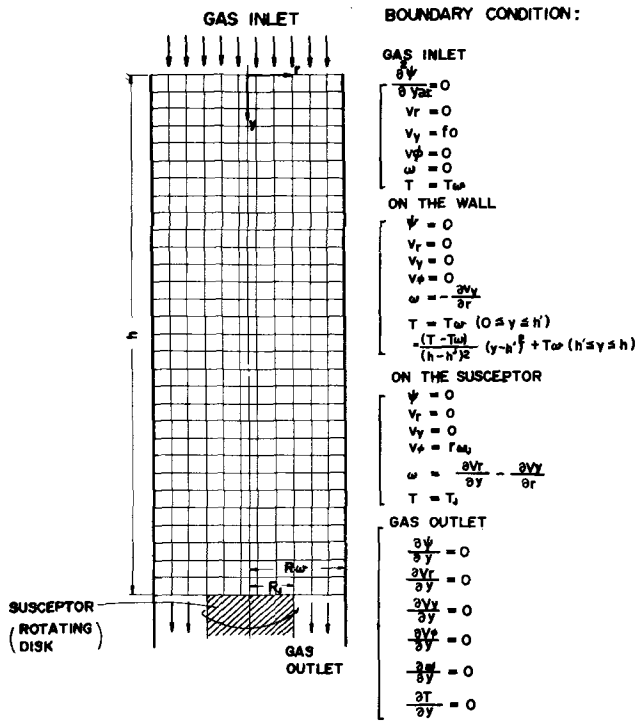


Fig. 1. Model system in the analysis of silicon epitaxial deposition by the rotating disk method and its boundary conditions.

$$\frac{\partial V_r}{\partial r} + \frac{V_r}{r} + \frac{\partial V_y}{\partial y} = 0 \quad [4]$$

where V_r , V_ϕ , and V_y are the radial, tangential, and axial velocity components respectively and f is a correction factor of the natural convection.

To eliminate the terms of the pressure in [1] and [3], $\partial/\partial y$ [1] - $\partial/\partial r$ [3] is calculated as

$$\begin{aligned} & \frac{\partial}{\partial y} \left(V_r \frac{\partial V_r}{\partial r} - \frac{V_\phi^2}{r} + V_y \frac{\partial V_r}{\partial y} \right) \\ & - \frac{\partial}{\partial r} \left(V_r \frac{\partial V_y}{\partial r} + V_y \frac{\partial V_y}{\partial y} \right) \\ & = \nu \frac{\partial}{\partial y} \left(\frac{\partial^2 V_r}{\partial r^2} + \frac{1}{r} \frac{\partial V_r}{\partial r} - \frac{V_r}{r^2} + \frac{\partial^2 V_r}{\partial y^2} \right) \\ & - \nu \frac{\partial}{\partial r} \left(\frac{\partial^2 V_y}{\partial r^2} + \frac{1}{r} \frac{\partial V_y}{\partial r} + \frac{\partial^2 V_y}{\partial y^2} \right) \quad [5] \end{aligned}$$

$$\begin{aligned} \text{Left side} &= V_r \frac{\partial}{\partial r} \left(\frac{\partial V_r}{\partial y} - \frac{\partial V_y}{\partial r} \right) \\ &+ \frac{\partial V_r}{\partial r} \left(\frac{\partial V_r}{\partial y} - \frac{\partial V_y}{\partial r} \right) + \frac{\partial V_y}{\partial y} \left(\frac{\partial V_r}{\partial y} - \frac{\partial V_y}{\partial r} \right) \\ &- V_y \frac{\partial}{\partial y} \left(\frac{\partial V_y}{\partial r} - \frac{\partial V_r}{\partial y} \right) = V_r \frac{\partial \omega}{\partial r} + \frac{\partial V_r}{\partial r} \omega \\ &+ \frac{\partial V_y}{\partial y} \omega + V_y \frac{\partial \omega}{\partial y} - \frac{\partial}{\partial y} \left(\frac{V_\phi^2}{r} \right) \quad [6] \end{aligned}$$

$$\begin{aligned} \text{Right side} &= \nu \left\{ \frac{\partial^2}{\partial r^2} \left(\frac{\partial V_r}{\partial y} - \frac{\partial V_y}{\partial r} \right) \right. \\ &+ \frac{\partial^2}{\partial y^2} \left(\frac{\partial V_r}{\partial y} - \frac{\partial V_y}{\partial r} \right) + \frac{1}{r^2} \left(\frac{\partial V_y}{\partial r} - \frac{\partial V_r}{\partial y} \right) \\ &+ \left. \frac{1}{r} \frac{\partial}{\partial r} \left(\frac{\partial V_r}{\partial y} - \frac{\partial V_y}{\partial r} \right) \right\} + fg\beta \frac{\partial \Delta T}{\partial r} \\ &= \nu \left(\frac{\partial^2 \omega}{\partial r^2} + \frac{\partial^2 \omega}{\partial y^2} - \frac{\omega}{r^2} + \frac{1}{r} \frac{\partial \omega}{\partial r} \right) + fg\beta \frac{\partial \Delta T}{\partial r} \quad [7] \end{aligned}$$

Then, the Navier-Stokes equations can be given in the forms of

$$\begin{aligned} V_r \frac{\partial \omega}{\partial r} - \frac{V_r \omega}{r} + V_y \frac{\partial \omega}{\partial y} - 2 \frac{V_\phi}{r} \frac{\partial V_\phi}{\partial y} \\ = \nu \left(\frac{\partial^2 \omega}{\partial r^2} + \frac{\partial^2 \omega}{\partial y^2} - \frac{\omega}{r^2} + \frac{1}{r} \frac{\partial \omega}{\partial r} \right) + fg\beta \frac{\partial \Delta T}{\partial r} \quad [8] \end{aligned}$$

$$\begin{aligned} V_r \frac{\partial V_\phi}{\partial r} + \frac{V_\phi V_r}{r} + V_y \frac{\partial V_\phi}{\partial y} \\ = \nu \left(\frac{\partial^2 V_\phi}{\partial r^2} + \frac{1}{r} \frac{\partial V_\phi}{\partial r} - \frac{V_\phi}{r^2} + \frac{\partial^2 V_\phi}{\partial y^2} \right) \quad [2] \end{aligned}$$

where ω , a term relating to the rotation, is defined as

$$\omega = \frac{\partial V_r}{\partial y} - \frac{\partial V_y}{\partial r} = -\frac{1}{r} \frac{\partial^2 \psi}{\partial y^2} + \frac{1}{r^2} \frac{\partial \psi}{\partial r} - \frac{1}{r} \frac{\partial^2 \psi}{\partial r^2} \quad [9]$$

A stream function ψ is introduced in such a way that the equation of continuity is automatically satisfied. In cylindrical coordinates, the velocity components can be expressed as derivatives of ψ (7)

$$V_y = -\frac{1}{r} \frac{\partial \psi}{\partial r} \quad [10]$$

$$V_r = \frac{1}{r} \frac{\partial \psi}{\partial y} \quad [11]$$

The equation of energy in terms of the gaseous transport properties is given as [12], taking axial symmetry and small viscosity coefficient into account

$$\begin{aligned} \rho C_p \left(V_r \frac{\partial T}{\partial r} + V_y \frac{\partial T}{\partial y} \right) \\ = k \left\{ \frac{1}{r} \frac{\partial}{\partial r} \left(r \frac{\partial T}{\partial r} \right) + \frac{\partial^2 T}{\partial y^2} \right\} \quad [12] \end{aligned}$$

where C_p and k are the specific heat at constant pressure and the thermal conductivity of hydrogen respectively.

The boundary conditions are determined as follows, referring to the calculation of temperature distribution of the Czochralski pulling crystal (8) in solving the six partial differential equations [2], [8], [9], [10], [11], and [12]:

$$\begin{aligned} \text{at the gas inlet } (y = 0, -R_w \leq r \leq R_w) \\ \left. \begin{aligned} \omega &= 0 & V_\phi &= 0 \\ V_r &= 0 & T &= T_w \\ V_y &= f_0 & \frac{\partial^2 \psi}{\partial y \partial r} &= 0 \end{aligned} \right\} \quad [13] \end{aligned}$$

$$\begin{aligned} \text{on the wall } (0 \leq y \leq h, r = \pm R_w) \\ \left. \begin{aligned} \omega &= -\frac{\partial V_y}{\partial r} & T &= T_w \quad (0 \leq y \leq h') \\ & & T &= \frac{(y-h)^2}{(h-h')^2} (T_{w0} - T_w) + T_w \\ V_r &= 0 & & \\ V_y &= 0 & & \\ V_\phi &= 0 & \psi &= \psi_0 = 0 \end{aligned} \right\} \quad (h' \leq y \leq h) \quad [14] \end{aligned}$$

$$\begin{aligned} \text{on the susceptor } (y = h, -R_s \leq r \leq R_s) \\ \left. \begin{aligned} \omega &= \frac{\partial V_r}{\partial y} - \frac{\partial V_y}{\partial r} & V_\phi &= r\omega_s \\ V_r &= 0 & T &= T_s \\ V_y &= 0 & \psi &= \psi_0 = 0 \end{aligned} \right\} \quad [15] \end{aligned}$$

at the gas outlet

$$(y = h, R_J \leq r \leq R_W, -R_W \leq r \leq -R_J)$$

$$\left. \begin{array}{l} \frac{\partial \omega}{\partial y} = 0 \quad \frac{\partial V_\phi}{\partial y} = 0 \\ \frac{\partial y}{\partial V_r} = 0 \quad \frac{\partial y}{\partial T} = 0 \\ \frac{\partial y}{\partial V_y} = 0 \quad \frac{\partial y}{\partial \psi} = 0 \end{array} \right\} \quad [16]$$

Concentration distribution.—Following the calculation of the velocity and temperature distribution, the concentration distribution of SiCl₄ can be obtained by using the following convective diffusion equation in cylindrical coordinates

$$V_r \frac{\partial C}{\partial r} + V_y \frac{\partial C}{\partial y} = D_1 \left(\frac{\partial^2 C}{\partial y^2} + \frac{\partial^2 C}{\partial r^2} + \frac{1}{r} \frac{\partial C}{\partial r} \right) \quad [17]$$

The boundary conditions are:

$$\left. \begin{array}{l} \text{at the gas inlet } C = C_o \text{ (Const)} \\ \text{on the wall } \frac{\partial C}{\partial r} = 0 \\ \text{on the susceptor } C = a - x^1 \\ \text{at the gas outlet } \frac{\partial C}{\partial y} = 0 \end{array} \right\} \quad [18]$$

Growth rate.—Deposition rate of silicon is

$$G(r) = -\frac{m}{M\rho_1} F \text{ (cm/sec)} \quad [19]$$

where

$$F = -D_2 \left(\frac{\partial C(r)}{\partial y} \right)_{y=h} \text{ (g/sec} \cdot \text{cm}^2) \quad [20]$$

m = atomic weight of Si, *M* = molecular weight of SiCl₄, *ρ*₁ = density of Si, *D*₂ = diffusion constant at the substrate temperature, shown in Appendix II. Symbols and numerical values used in this calculation are summarized in a List of Symbols at the end of this paper.

These partial differential equations were rewritten in calculus of finite differences, and both the *y* and *r* directions were divided into meshes at every 1 cm interval—*y* direction and *r* direction: 31 × 12. Following the flow chart given in Fig. 2, the stream function *ψ*, flow velocities *V_r*, *V_y*, and *V_φ*, temperature *T*, and *ω* connected with rotation were calculated successively, and while judging the convergence by the values of *V_r* and *V_y*, numerical calculations were effected. The computer used was the HITAC 8500 and 20 repetitions required about 90 sec.

In order to speed up convergence

$$V_r = \frac{0.181 r \omega_J}{h \left(1 - \frac{1}{m} \right)} y \quad \left(0 \leq y \leq h \left(1 - \frac{1}{m} \right) \right) \quad [21]$$

where *m* is number of divisions made of *h*, 0.181 is the maximum value of *F* in Eq [24a] of the infinite rotating disk method (6), *V_r* = 0 at *y* = 0, satisfying the boundary condition of Eq. [13], *V_y* = *f*₀, *V_φ* = $\frac{r\omega_J}{h} y$

were given and the first calculation was made. In Fig. 1, calculations commenced from the upper, left-hand corner. Also, gas velocity components *V_r*, *V_y*, and *V_φ*, density *ρ*, and kinematic viscosity coefficient *ν* were corrected by considering temperature dependence of high temperature H₂ as an ideal gas.

¹a-x is calculated from the equilibrium constant of the reaction between SiCl₄ and H₂, as shown in Appendix I.

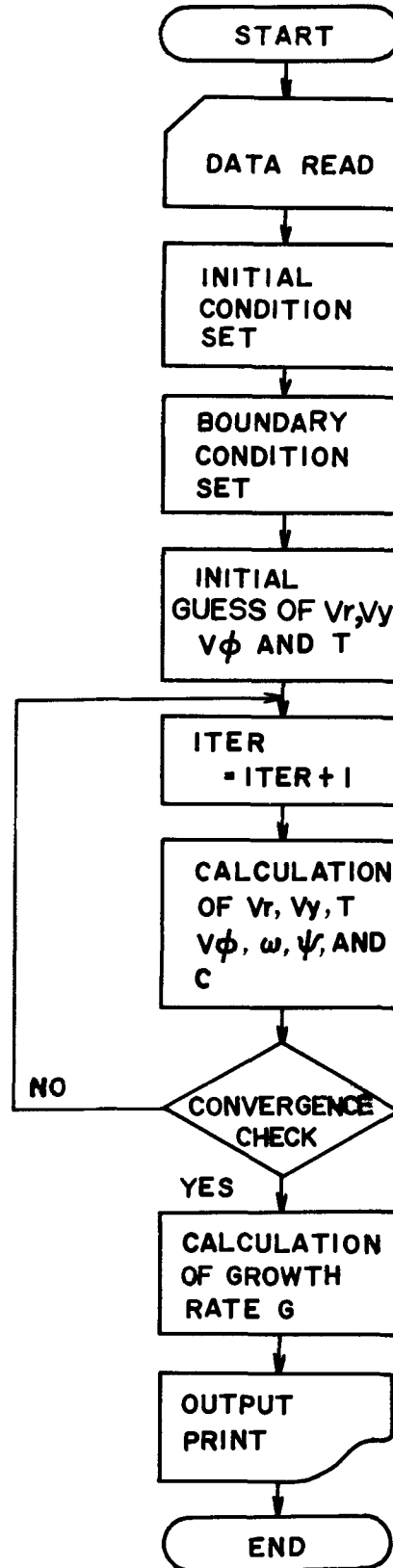


Fig. 2. Flow chart at the numerical calculation of silicon epitaxial deposition by the rotating disk method.

Experimental

As shown in Fig. 3, a quartz tube with an I.D. of 110 mm was used as a reactor for silicon epitaxial deposition. The susceptor was heated in the reactor by using a 400 kHz rf generator. The susceptor was rotated with a variable speed changer at a speed for rotation, 0-300 rpm, combined with a 1:5 pulley. The reactant gas

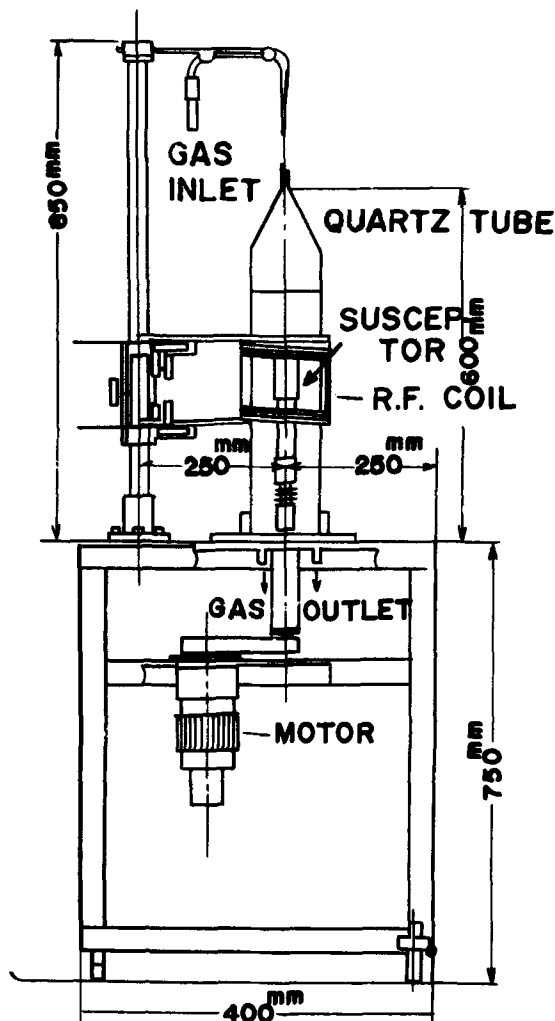


Fig. 3. Schematic diagram for the reactor of silicon epitaxial growth by the rotating disk method.

flowed from the upper part of the reactor. When desired, pressure was reduced to the regulation level by a rotary pump. A liquid nitrogen trap was provided between the reactor and the pump for absorbing unreacted SiCl_4 gas. Figure 4 is a photograph of the reactor; the layout of the reactor system by the rotating disk method appears in Fig. 5.

Silicon substrates used for the experiment were Czochralski-grown, Sb-doped, and (111)-oriented crystals with resistivity of 6×10^{-3} – 2×10^{-2} ohm-cm; these were sliced, lapped, and chemically/mechanically polished. Their thickness was 250μ . A susceptor 50 mm in diameter was used, made of high-purity graphite and having a 300μ coating of SiC. The lower part was scooped out for achieving uniform temperature distribution in the radial direction of the susceptor during rf heating. A slight protrusion was made on the upper part to prevent scattering of the wafer by the centrifugal force generated during rotation.

A cleaned substrate wafer was placed on the susceptor which had been rotated in advance to suppress eccentricity. Then the quartz tube was fixed, 40 liters/min of H_2 was inserted, and rf heating was effected. After reaching the set temperature for the epitaxial reaction, a 5 min interval was taken before feeding SiCl_4 together with H_2 . Reading the wafer temperature with an optical pyrometer, emissivity was corrected according to Allen's data (9) and the real temperature was obtained. The mole fraction of SiCl_4 and H_2 had

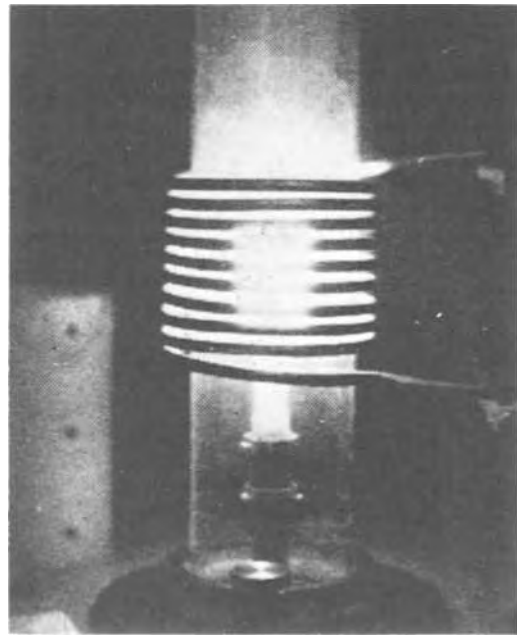


Fig. 4. Reactor of the epitaxial growth by the rotating disk method.

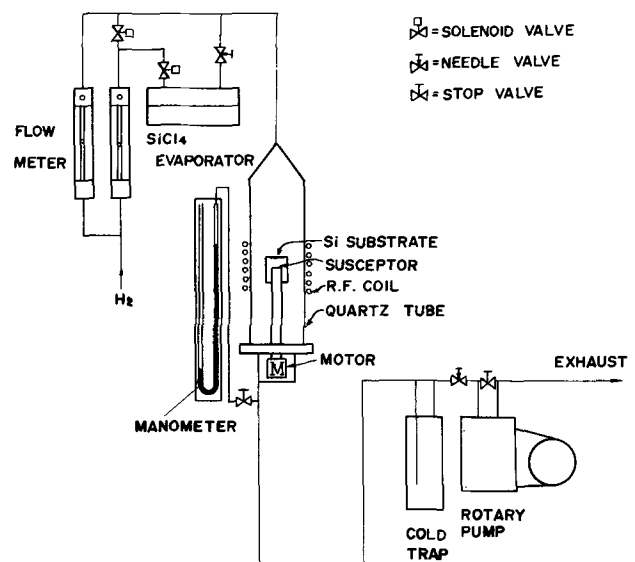


Fig. 5. Layout of the silicon epitaxial reactor system by the rotating disk method.

been obtained in advance by the method given below.² After 10–15 min reaction, power was cut off and the wafer was taken out when it was cooled.

Thickness of the epitaxial layer was measured by the infrared interference method (10–12). The infrared spectrophotometer used was the Hitachi EPI-G2 with a wavelength range of 2.5–25 μ .

Results

Temperature dependence of epitaxial growth rate.—The relation of growth rates to temperature at SiCl_4/H_2 mole fractions of 0.005, 0.01, and 0.02 at 760 Torr is given in Fig. 6, while the result of pressure change at the mole fraction of 0.005 appears in Fig. 7.

In the figures, hyphenated lines represent calculated values of the one-dimensional model in the case of a

² The SiCl_4/H_2 mole fraction was measured with a Perkin Elmer's atomic absorption spectrophotometer (Model 303). The SiCl_4 - H_2 mixture is bubbled through a 4% water solution of NaOH. The atomic absorption measuring wavelength was 2516 Å and analysis was made in N_2O and C_2H_2 gases. The calibration curve was derived from a standard sample of Si fused in alkali.

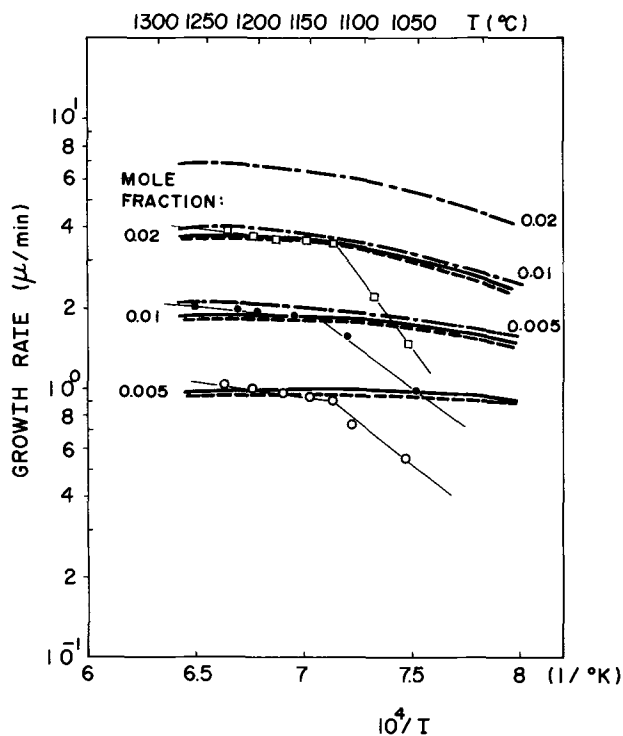


Fig. 6. Temperature dependence of silicon epitaxial growth rate for various SiCl_4/H_2 mole fractions. - - - - Calculated curve in the case of a rotating disk with an infinite diameter. - · - - Calculated curve in the case of a rotating disk with a finite diameter without considering the influence of natural convection. ——— Calculated curve in the case of a rotating disk with a finite diameter taking natural convection into account. — Experimental value. Pressure, 760 Torr; speed of susceptor rotation, 120 rpm.

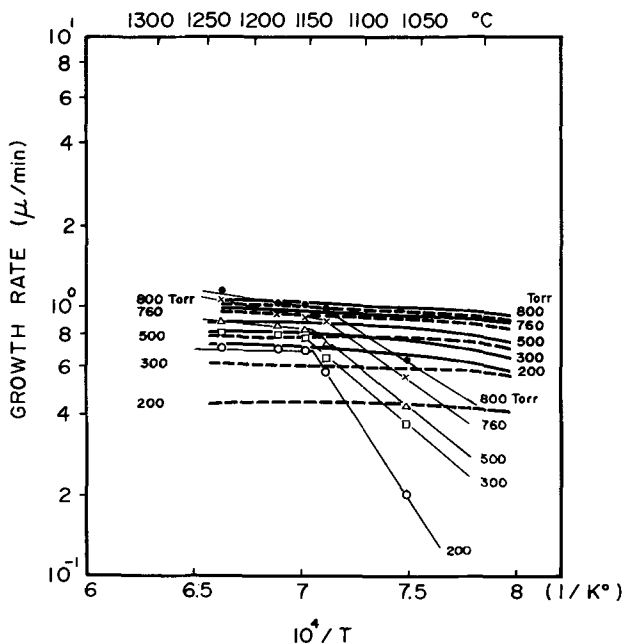


Fig. 7. Temperature dependence of silicon epitaxial growth rate under various pressures. SiCl_4/H_2 mole fraction, 0.005; speed of susceptor rotation, 120 rpm.

disk of infinite diameter; for details of calculations refer to Appendix III. The chain lines represent the case of a finite diameter disk without considering natural convection, and the thick, solid lines represent calculated values with natural convection considered as calculated under the method cited in the theory. As the equilibrium constant of Eq. [28] diminishes in the

lower temperature range, the calculation displays a diminishing growth rate when the temperature drops below 1000°C ; while in the higher temperature region above this, the equilibrium constant and the growth rate are approximately constant.

In the experiments the temperature, where the rate-determining step of the reaction was shifted from surface reaction at the substrate to diffusion in the gaseous phase was higher than the calculated value; it was approximately 1150°C . The difference in the lower temperature region between theory and experiment was caused by neglecting the surface reaction because only mass transfer of the reactant species in the gaseous phase and the chemical equilibrium of the reaction at the substrate surface were considered in the calculating process. Calculation of activation energies was sought from Arrhenius plots in Fig. 6 and 7. In the diffusion-limited, higher temperature range, they were about 1-3 kcal/mol; while in the reaction-limited, lower temperature range, the average value is 20-30 kcal/mol.

The actual growth rate at a higher temperature and 760 Torr, in the one-dimensional model, represents an approximate matching of the calculated and actually measured values. However, as pressure was reduced, the actually measured value became larger than that calculated. The calculated value of a three-dimensional model of the finite diameter disk approximately coincided with the experimental value.

Pressure dependence of epitaxial growth rate.—Figure 8 represents experimental results at 1200°C and mole fractions of 0.005, 0.01, and 0.02 rendered into a dual logarithm graph; Fig. 9 gives the growth rates when the susceptor rotation was changed under the mole fraction of 0.005. At 120 rpm and normal pressure, the growth rate of the one-dimensional model approximately coincides with the calculated value. The pressure (P) dependence is not proportional to $P^{1/2}$ as was calculated, but it is approximately propor-

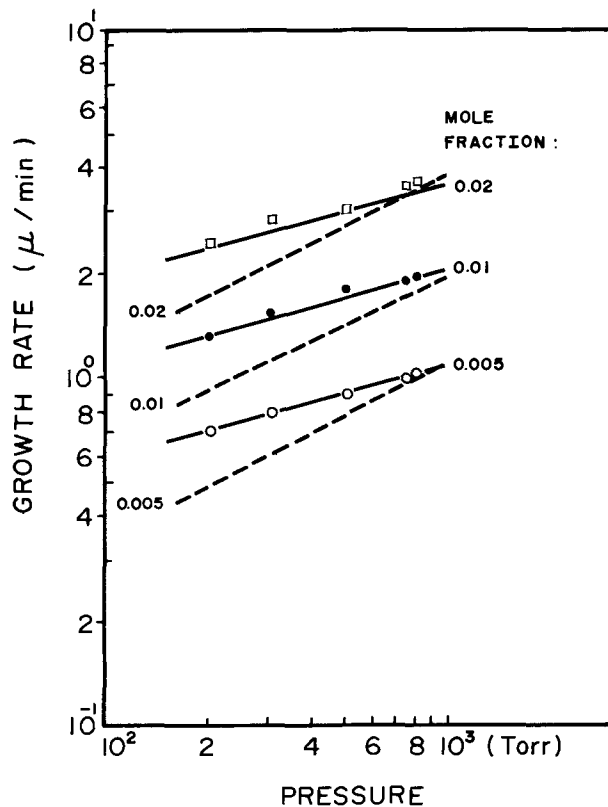


Fig. 8. Pressure dependence of silicon epitaxial growth rate at various SiCl_4/H_2 mole fractions. Growth temperature, 1200°C ; speed of susceptor rotation, 120 rpm.

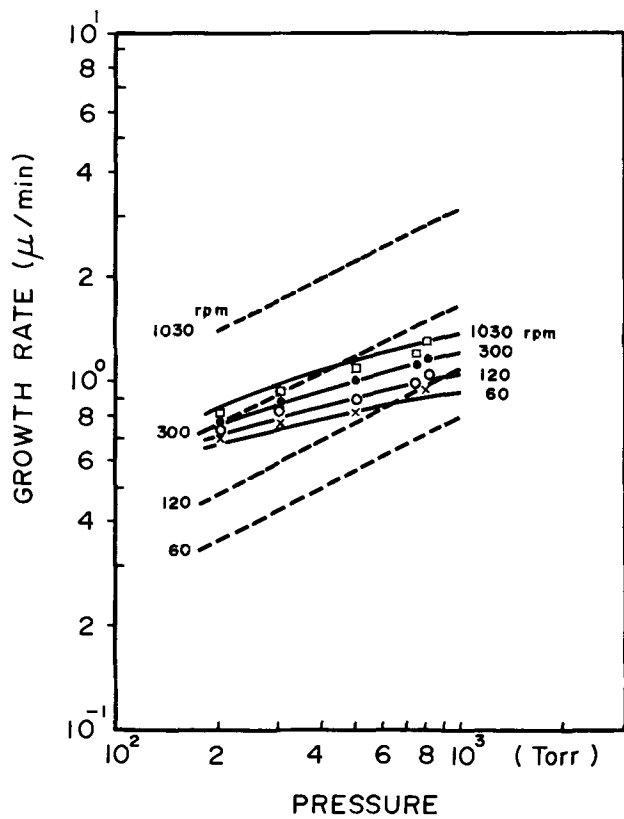


Fig. 9. Pressure dependence of silicon epitaxial growth rate at various speeds of susceptor rotation. Growth temperature, 1200°C; SiCl₄/H₂ mole fraction, 0.005.

tional to $P^{1/5}$ to $P^{1/3}$ dependent on rotation speed which is not to be expected from the theory belonging to the oversimplified model.

Under pressure changes, the three-dimensional model produced results close to the actually measured values.

Susceptor rotation dependence of epitaxial growth rate.—The results of investigation by varying the rotation between 60 and 1030 rpm and the mole fraction at the epitaxial temperature of 1200°C are given in Fig. 10. Figure 11 gives the experimental results obtained by varying the pressure at the mole fraction of 0.005.

With the one-dimensional model, the differences in rotation speed dependence are large between the measured and calculated values; but with the three-dimensional model of finite diameter disk, these values match well.

Discussion

Difference of diameter in a rotating disk system.—The motion of the fluid in relation to the infinite diameter rotating disk was first clarified by von Karman (13) and subsequently by Cochran (14). Assuming that the disk diameter was large enough to ignore the effect of disk edges, solutions to the Navier-Stokes and continuity equations were obtained as below, and the results were as given in Fig. 12. Incidentally, $y = 0$ on the axis of abscissa of this figure is on the disk, corresponding to the $h = 30$ cm point in this numerical calculation.

$$V_r = r\omega F(\xi) \tag{24a}$$

$$V_\phi = r\omega G(\xi) \tag{24b}$$

$$V_y = \sqrt{\nu\omega} H(\xi) \tag{24c}$$

$$\xi = \sqrt{\frac{\omega}{\nu}} y \tag{24d}$$

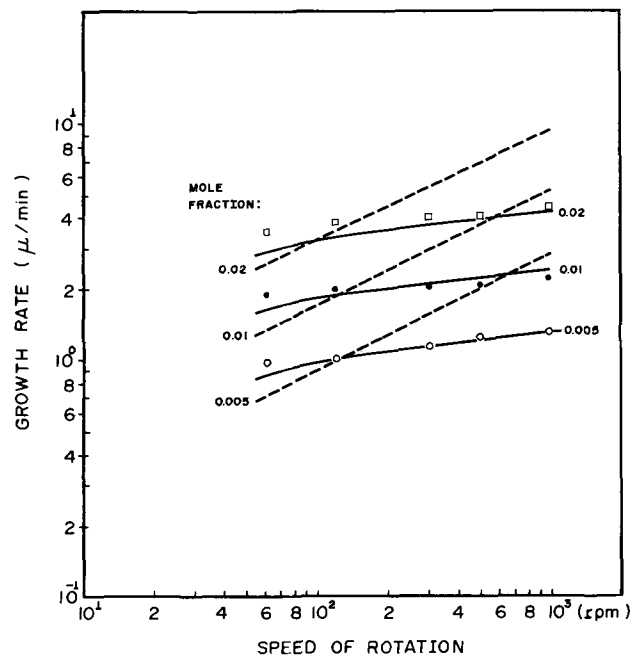


Fig. 10. Growth rate as a function of susceptor rotation speed at various SiCl₄/H₂ mole fractions. Growth temperature, 1200°C; pressure, 760 Torr.

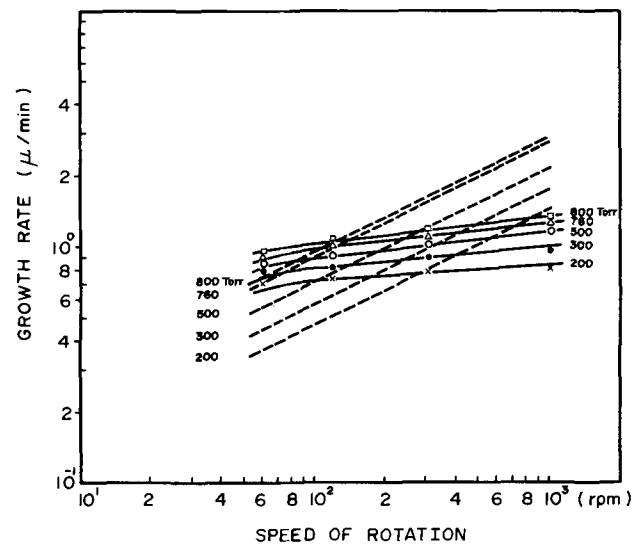


Fig. 11. Growth rate as a function of susceptor rotation speed under various pressures. Growth temperature, 1200°C; SiCl₄/H₂ mole fraction, 0.005.

Meanwhile, numerical solutions obtained by the method of calculus of finite differences are diagrammatically indicated in the order of V_r , V_y , V_ϕ , T , and C in Fig. 13(a)-(e) with and without natural convection. In the figures, the hyphenated lines represent the case where the effect of natural convection was not considered, while the solid lines represent the case where natural convection was taken into account. For reference, the calculated value of the infinite diameter disk mentioned above—calculated for 800°C in Fig. 12—has been included in the chain lines.

The difference between finite and infinite diameter was as follows: (i) In the case of finite diameter, flow velocities V_r , V_y , and V_ϕ were larger by about one digit. (ii) In the case of V_r , with finite diameter, diminution occurred from the maximum value, although in some places, the flow direction was reversed, possibly due to effect of the disk edge. (iii) In the case of the finite disk, V_y increased for a time by the effect of ro-

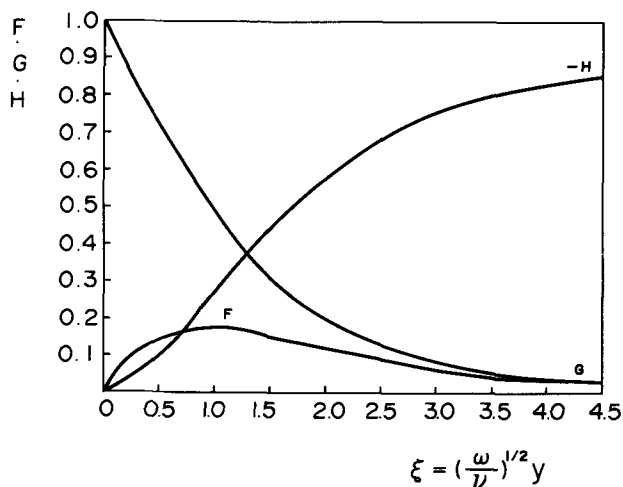


Fig. 12. Values of the functions F , G , and H in the rotating disk system of one-dimensional model calculated for 800°C .

$$V_r = r \omega F(\xi)$$

$$V_\phi = r \omega G(\xi)$$

$$V_y = \sqrt{\nu} \omega H(\xi)$$

tating disk, and after reaching the maximum value, it diminished, approaching the flow velocity at the gas inlet. (iv) With V_ϕ , after the rate was determined by the susceptor rotation speed on the disk, a monotonous decrease occurred. As shown above, the edge effect appeared conspicuously when the disk was finite revealing a broad difference from the former analysis of infinite diameter disk.

Influence of natural convection.—Figure 13(a)-(e) gives the flow velocities, temperature, and concentration distributions for the presence or absence of natural convection. From this figure, the following conclusions may be drawn: (i) The flow velocities, V_r and, V_y , directly above the susceptor decreased when convection was considered. (ii) Changes in flow velocity distributions appeared as changes occurred in the concentration distribution, resulting in differences in the growth rates.

Figure 14 gives the calculated growth rate, when natural convection is represented as a temperature difference of $\Delta T = 200^{\circ}\text{C}$ and the correction factor f is changed. The growth rate is the calculated value of $y = 0.5$ cm. Since diminution which occurred along with an increase of f from 2.05 μ/min in the case of $f = 0$, and 1.15 μ/min at $f = 0.025$ became approximately equal to the experimental value, the correction factor was used to undertake numerical calculations at the pressure of 760 Torr.

A variation of correction factor f along with pressure change is conceivable. Here natural convection is proportional to Gr , the Grashof number; but since it is through kinematic viscosity $\nu \propto 1/\rho$ that the relation arises with pressure, a correction factor of 0.025 at normal pressure having the linear function of pressure was assumed as shown in Fig. 15, and calculations were made for cases of pressure variation.

Pressure dependence of epitaxial growth rate.—As of this date, Bradshaw's paper (16) is the only study made of epitaxial growth rate in relation to pressure. He stated that the growth rate was proportional to half the square of pressure. This conclusion was arrived at from the fact that the thickness L of the boundary layer from the leading edge was

$$L \propto \rho^{-1/2} = \left(\frac{\bar{M}P}{RT} \right)^{-1/2} \quad [25]$$

where \bar{M} indicated the mean molecular weight in the boundary layer. The growth rate became

$$G \propto \frac{1}{L} \propto P^{1/2} \quad [26]$$

His experiment was conducted with a vertical reactor provided with a special nozzle. The result was proportional to $P^{0.44}$.

With the one-dimensional model under the rotating disk method also, $D^{1/3}\nu^{-1/6}$ —actually $D^{1/3}\rho^{1/6}$ —in the equation for the boundary layer δ was related to pressure, and the calculated value was proportional to $P^{1/2}$. This is identical with that which Bradshaw obtained, though the procedure for calculation is different.

With the three-dimensional model, although a definite implication of meaning is difficult, concentration C and diffusion coefficient D respectively are proportional and inversely proportional to the pressure. The flow velocities are obtained by complicated calculations, and as in the case of V_y shown in Fig. 16, they increase together with the pressure but are not necessarily proportional to it. As over-all results, therefore, calculations from the concentration distribution given in Fig. 16(a) and (b) produce the results shown in Fig. 8 and 9. As the disk is finite, the effects of the edge and natural convection double up, rendering the experimental and calculated value closer to each other.

Susceptor rotation dependence of epitaxial growth rate.—Olander experimented with epitaxial growth under the rotating disk method, using $\text{Ge} - \text{I}_2$, which proved easier in treating the system thermodynamically and which grew at low temperature (17). Applying the gas from below and holding the Ge substrate face down, which differed from this experiment, he experimented with reaction temperatures up to 450°C . He showed that the effect of rotation was proportional to $\omega^{1/2}$ theoretically anticipated at 450°C and 900 rpm, but that below this value the dependence of the experimental value diminished. He concluded that failure to follow the trend of calculated values under 900 rpm arose from the influence of natural convection.

In the silicon epitaxial growth, using SiCl_4 , the effect of natural convection is more easily exerted due to temperatures as high as 1200°C . Also, because of problems arising from the shape and rotating mechanism of the susceptor, the above tendency is conceivably magnified compared with the case of $\text{Ge} - \text{I}_2$, since it is not possible to raise the rotation above 1000 rpm. The effect of the periphery of the susceptor is also added.

With the three-dimensional model, the effect of susceptor edge and natural convection is exerted because of the susceptor rotation, and V_y and C distributions become as shown in Fig. 17(a) and (b), thus ultimately explaining the experimental result.

Conclusions

Taking note of the rotating disk method, which allows a quantitative treatment of fluid motion, the solid and gaseous phase boundary layer of an infinite diameter disk was calculated and the growth rate was sought through calculations of a one-dimensional model. However, matching of the actually measured values of pressure dependence and susceptor rotation dependence of the growth rate was unsatisfactory. Therefore, Navier-Stokes equations of the cylindrical coordinates, taking natural convection into account, were numerically solved under the calculus of finite differences—for a three-dimensional model—and the results were compared with the actually measured value.

1. The calculated, both one- and three-dimensional model, and actually measured values of epitaxial growth rate matched in the order tendency at normal pressure and at temperatures higher than 1150°C . Below this temperature, the experimental value was inexplorable.

2. With the one-dimensional model, pressure (P) dependence of the epitaxial growth rate was propor-

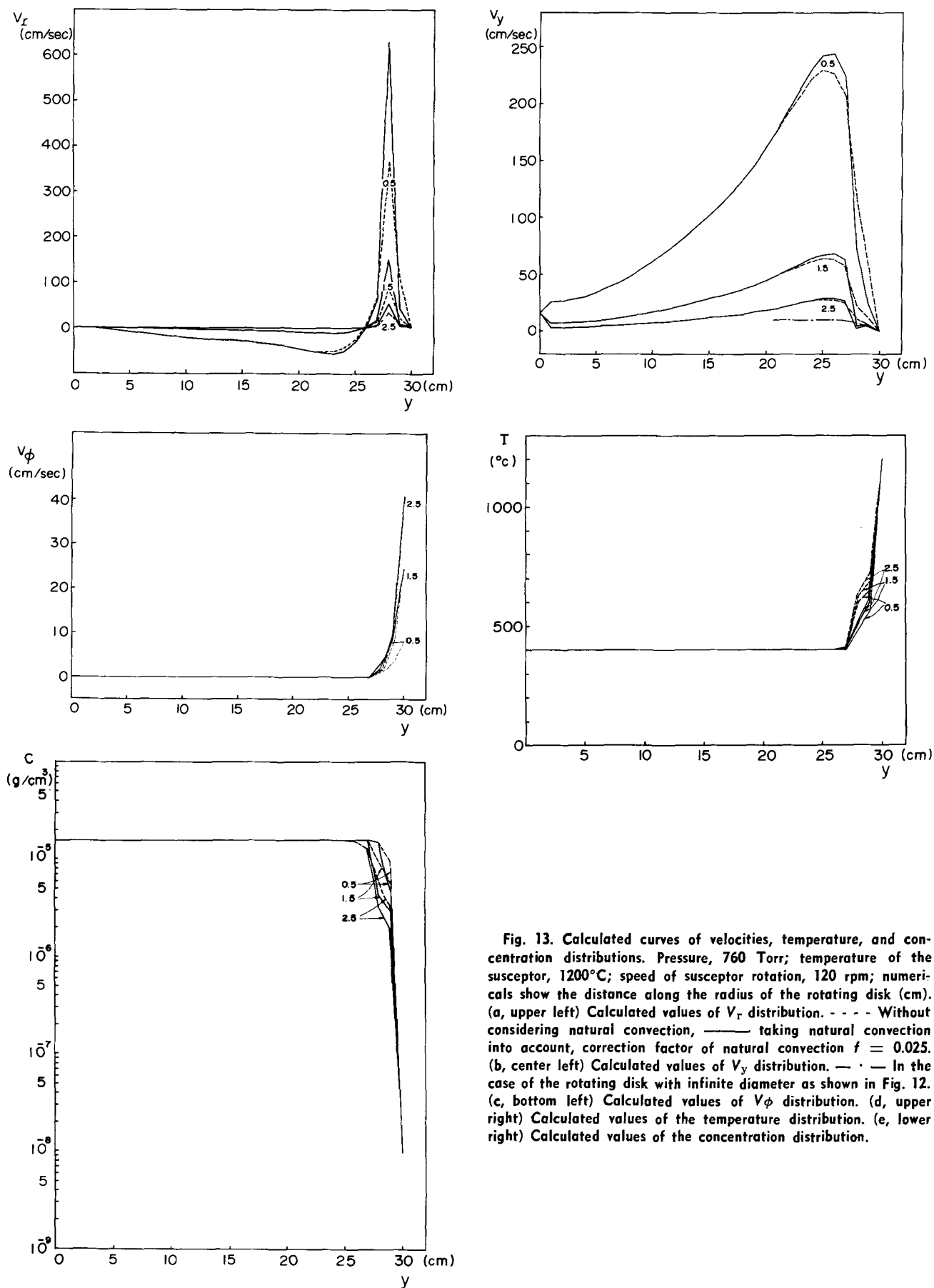


Fig. 13. Calculated curves of velocities, temperature, and concentration distributions. Pressure, 760 Torr; temperature of the susceptor, 1200°C; speed of susceptor rotation, 120 rpm; numericals show the distance along the radius of the rotating disk (cm). (a, upper left) Calculated values of V_r distribution. - - - Without considering natural convection, — taking natural convection into account, correction factor of natural convection $f = 0.025$. (b, center left) Calculated values of V_y distribution. — · — In the case of the rotating disk with infinite diameter as shown in Fig. 12. (c, bottom left) Calculated values of V_ϕ distribution. (d, upper right) Calculated values of the temperature distribution. (e, lower right) Calculated values of the concentration distribution.

tional to $P^{1/2}$ in the calculated value, but in the experimental value, it was proportional to $P^{1/5} - P^{1/3}$.

3. Susceptor rotation speed (ω) dependence of the growth rate was the calculated result of the one-dimensional model, which was proportional to $\omega^{1/2}$, but

the experimental value was proportional to $\omega^{1/20} - \omega^{1/10}$.

4. The difference between experimental and calculated values of pressure and rotation speed dependence of the growth rate conceivably arose from diminish-

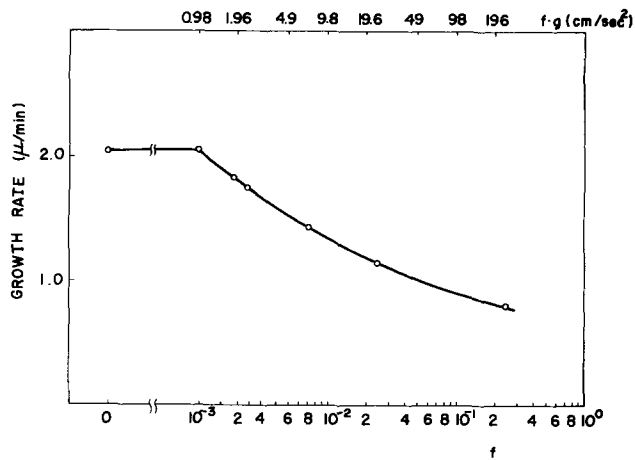


Fig. 14. Growth rate as a function of the natural convection correction factor, calculated in the case of $\Delta T = 200^\circ\text{C}$.

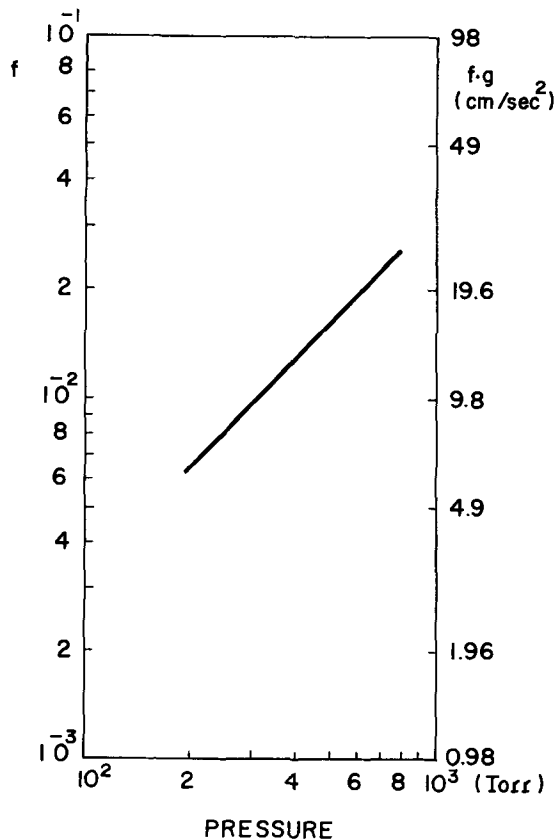


Fig. 15. Assumed correction factor of natural convection vs. pressure.

ing of the boundary layer calculated under the rotating disk method, due to the effect of a finite diameter disk and natural convection. In other words, because of the finite rotating disk diameter, the pressure and susceptor rotation dependence of the growth rate became smaller than in the case of the one-dimensional model. Also, because of the effect of natural convection, the flow velocities on the susceptor diminished, thus diminishing the growth rate and coinciding with the actual measured value.

Acknowledgments

To Prof. H. Inokuchi of Tokyo University for his critical review of and his sincere advice on this manuscript, and to Dr. N. Kobayashi of Toyama University for his helpful suggestion to set boundary conditions of the partial differential equations, I express my sincere gratitude. Appreciation is also due to the continued support of this work by Dr. S. Tauchi and Mr. S. Ni-

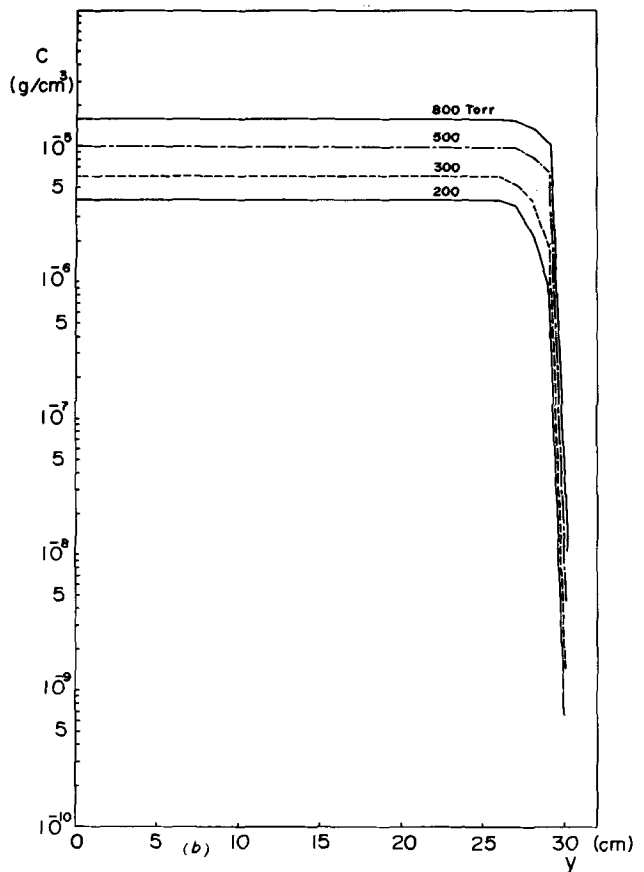
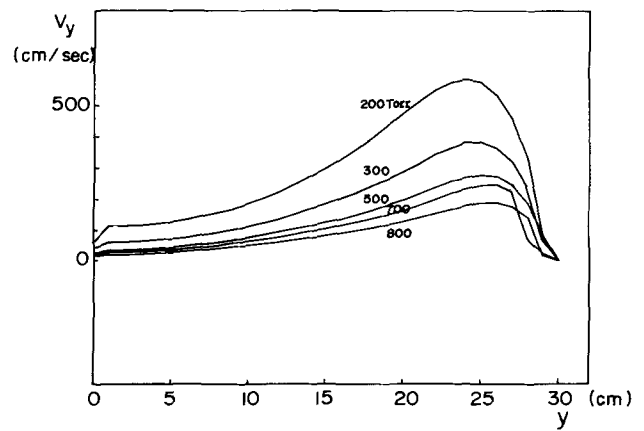


Fig. 16. Calculated values of the velocity and concentration distributions, considering the influence of the natural convection. Temperature of the substrate, 1200°C ; speed of the susceptor rotation, 120 rpm; position: $r = 0.5$ cm. (a, upper) V_y distribution, (b, lower) concentration distribution.

shida, the helpful discussions with Mr. R. Takahashi, and the assistance in computer programming and numerical calculations rendered by Mr. Y. Ishikawa and Mr. H. Tochikubo.

Manuscript submitted Feb. 15, 1972; revised manuscript received June 23, 1972.

Any discussion of this paper will appear in a Discussion Section to be published in the June 1973 JOURNAL.

APPENDIX I

**Concentration of SiCl_4 at the Surface of the Susceptor—
Calculated Values from the Equilibrium Constant of $\text{SiCl}_4\text{-H}_2$
Reaction**

The equilibrium constant of Eq. [27] is given by the following equation

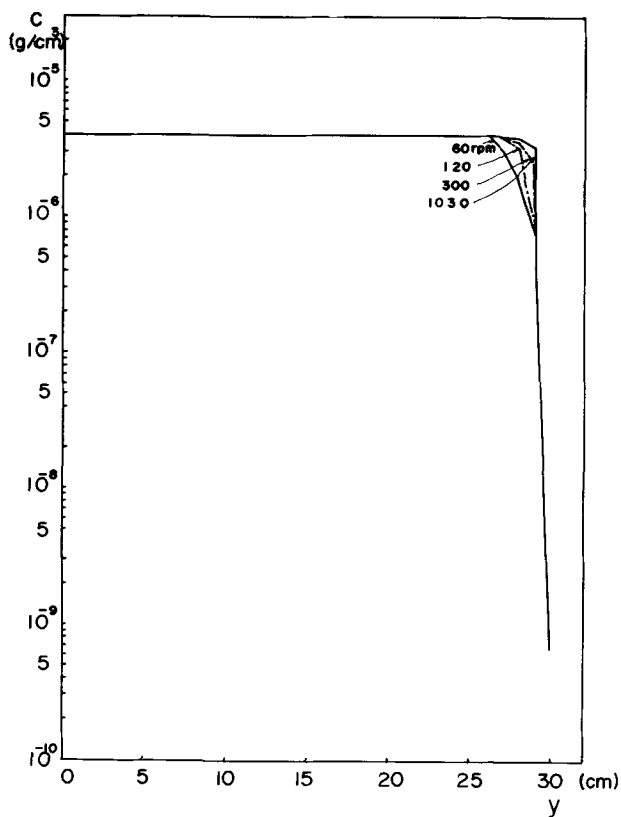
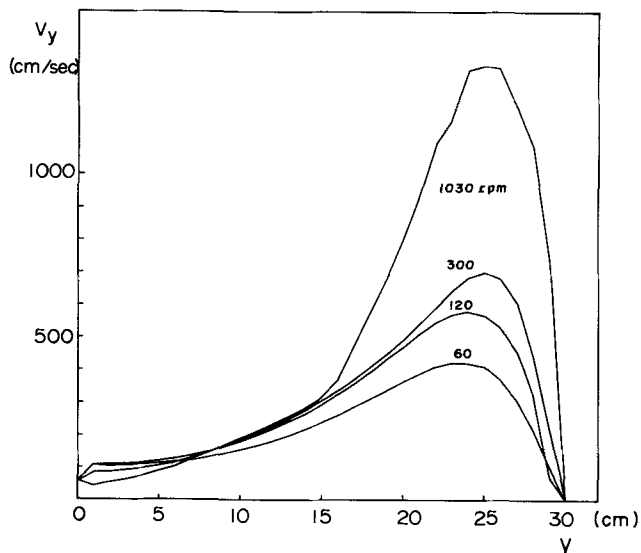
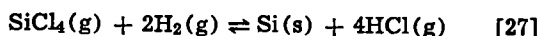


Fig. 17. Calculated values of the velocity and concentration distributions, considering the influence of the natural convection. Pressure, 760 Torr; temperature of the substrate, 1200°C; position, $r = 0.5$ cm. (a, upper) V_y distribution, (b, lower) concentration distribution.



$$K_p = \frac{P_{\text{HCl}}^4}{P_{\text{SiCl}_4} \cdot P_{\text{H}_2}^2} = \frac{(4x)^4}{(a-x)(1-2x)^2} \cdot \frac{P}{N} \quad [28]$$

where P_{HCl} = partial pressure of HCl, a = mole number of input SiCl_4 , x = mole number of reacted SiCl_4 , N = mole number of all gases, P = total pressure. The concentration of SiCl_4 at the surface of the susceptor was calculated and tabulated in Table I. The equilibrium constant K_p of SiCl_4 - H_2 reaction in Eq. [28] was calculated by using the free energy in "JANAF Thermochemical Data" (18).

APPENDIX II

Diffusion Constants in the Gaseous Phase

Fujita's diffusion equation (19-20) and Wilke's formula (21-22) were used to evaluate the diffusion constants in the binary system and in the multicomponent system of gaseous phase respectively. Fujita's formula

$$D_{\text{SiCl}_4\text{-HCl}} = \frac{0.00070T^{1.833}}{\left[\left(\frac{T_c}{P_c} \right)_{\text{SiCl}_4}^{1/3} + \left(\frac{T_c}{P_c} \right)_{\text{HCl}}^{1/3} \right]^3 \sqrt{\frac{1}{M_{\text{SiCl}_4}} + \frac{1}{M_{\text{HCl}}}}} \quad [29]$$

Wilke's formula

$$D_A = \frac{1 - y_A}{\frac{y_B}{D_{AB}} + \frac{y_C}{D_{AC}} + \frac{y_D}{D_{AD}} + \dots} \quad [30]$$

where T_c = critical temperature (°K), P_c = critical pressure (atm), M = molecular weight, D_{AB} = diffusion constant of a component A in B gas, y_A = mole fraction of a component A in the mixed gas. Values thus obtained are plotted in Fig. 18.

APPENDIX III

Deposition Rate Calculation of Epitaxial Growth by Rotating Disk Method Using One-Dimensional Model

In computing, the following assumptions were made: (i) On the susceptor there is a boundary layer produced by the rotating disk with an infinite diameter. (ii) Temperature of the boundary layer is the same as that of Si substrate. (iii) Epitaxial reaction occurs only at the susceptor. (iv) Only the reaction

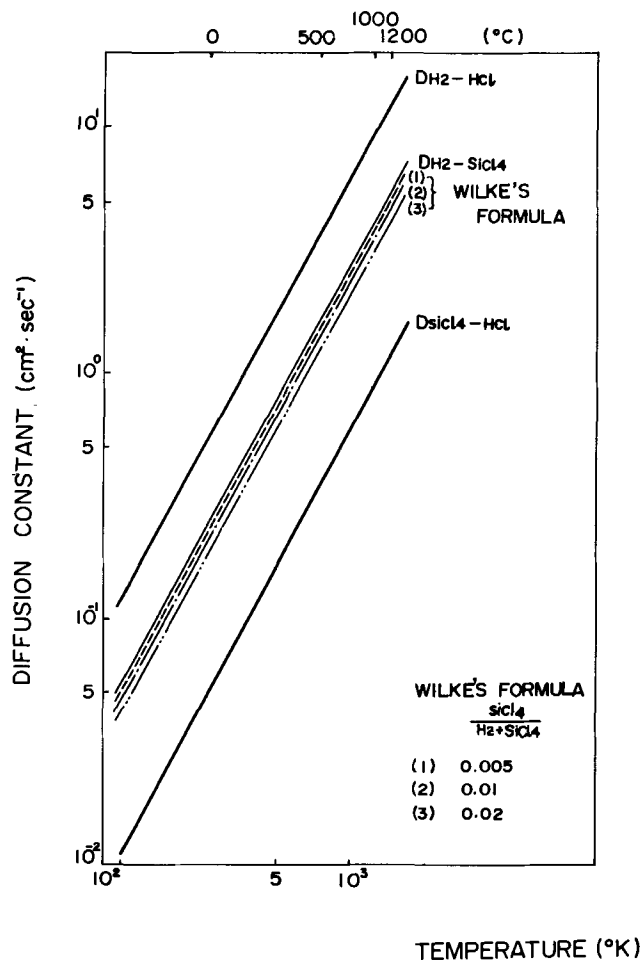
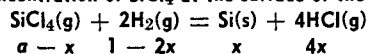
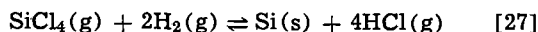


Fig. 18. Diffusion constants in the reaction gases

Table I. Concentration of SiCl₄ at the surface of the rotating disk

α	Torr °K	100	200	300	500	760	800
5.0×10^{-3}	1000	2.6×10^{-3}	2.9×10^{-3}	3.1×10^{-3}	3.3×10^{-3}	3.5×10^{-3}	3.5×10^{-3}
	1300	2.5×10^{-3}	4.8×10^{-3}	7.1×10^{-3}	1.2×10^{-2}	1.7×10^{-2}	1.7×10^{-2}
	1500	9.0×10^{-7}	1.8×10^{-6}	2.6×10^{-6}	4.4×10^{-6}	6.7×10^{-6}	7.0×10^{-6}
1.0×10^{-2}	1000	7.0×10^{-3}	7.4×10^{-3}	7.6×10^{-3}	7.9×10^{-3}	8.1×10^{-3}	8.1×10^{-3}
	1300	3.5×10^{-4}	6.3×10^{-4}	8.5×10^{-4}	1.2×10^{-3}	1.6×10^{-3}	1.6×10^{-3}
	1500	1.4×10^{-5}	2.8×10^{-5}	4.2×10^{-5}	6.9×10^{-5}	1.0×10^{-4}	1.1×10^{-4}
2.0×10^{-2}	1000	1.6×10^{-2}	1.7×10^{-2}	1.7×10^{-2}	1.7×10^{-2}	1.8×10^{-2}	1.8×10^{-2}
	1300	3.2×10^{-3}	4.6×10^{-3}	5.5×10^{-3}	6.6×10^{-3}	7.5×10^{-3}	7.6×10^{-3}
	1500	2.2×10^{-4}	4.3×10^{-4}	6.2×10^{-4}	9.6×10^{-4}	1.3×10^{-3}	1.4×10^{-3}



occurs at the susceptor as Lever (23) and Bradshaw (16) have calculated due to a very low concentration of SiCl₄. (v) Hydrogen is stagnant. SiCl₄ and HCl move in the boundary layer by molecular diffusion. (vi) Consideration of natural convection is not given.

Thickness of boundary layer.—The thickness of the boundary layer is expressed by the following equation, when the rotating disk with an infinite diameter is used (6)

$$\delta = 1.60D^{1/3}\nu^{1/6}\omega^{-1/2} \quad [31]$$

where δ is thickness of the boundary layer.

Mass transfer coefficient.—When H₂ is stagnant in three component system H₂-SiCl₄-HCl, mass transfer coefficient takes the form of

$$k_g = \frac{D_{\text{SiCl}_4\text{-HCl}}}{\delta RT} P \quad [32]$$

where k_g = mass transfer coefficient (mole/cm²sec) and $D_{\text{SiCl}_4\text{-HCl}}$ = diffusion constant which is for ternary nonequimolar counterdiffusion with one component H₂ stagnant (24).

Diffusion potential.—In the ternary system with one component stagnant, diffusion potential is given by

$$\Delta y = \frac{1}{1-x} \ln \left[\frac{\left(\frac{1}{D_{\text{SiCl}_4\text{-HCl}}} - \frac{1}{D_{\text{HCl-H}_2}} \right) y_{\text{SiCl}_4} + \left(\frac{1}{D_{\text{SiCl}_4\text{-HCl}}} - \frac{1}{D_{\text{SiCl}_4\text{-H}_2}} \right) \frac{y_{\text{HCl}}}{x} + \left(\frac{1}{D_{\text{SiCl}_4\text{-H}_2}} - \frac{1}{D_{\text{HCl-H}_2}} \right) \frac{1}{x-1}}{\left(\frac{1}{D_{\text{SiCl}_4\text{-HCl}}} - \frac{1}{D_{\text{HCl-H}_2}} \right) y_{\text{SiCl}_4} + \left(\frac{1}{D_{\text{SiCl}_4\text{-HCl}}} - \frac{1}{D_{\text{SiCl}_4\text{-H}_2}} \right) \frac{y_{\text{HCl}}}{x} + \left(\frac{1}{D_{\text{SiCl}_4\text{-H}_2}} - \frac{1}{D_{\text{HCl-H}_2}} \right) \frac{1}{x-1}} \right] \quad [33]$$

where $D_{A,B}$ = molecular diffusion constant of A and B component (cm²/sec), y_{A1} = mole fraction of A component at the surface of the susceptor, y_A = mole fraction of A component in the gaseous phase, $y_{\text{HCl}} = 0$ for HCl, x = ratio of mole number out of the surface to that towards the surface; in this case $x = 4$, because of the stagnant hydrogen. The value of y_{A1} was computed by using Eq. [28].

Growth rate of Si.—Growth rate is expressed under the above-mentioned assumptions

$$G = \frac{M_{\text{Si}}}{\rho_1} k_g \cdot \Delta y \quad [34]$$

LIST OF SYMBOLS

Symbols	Numerical Values— 760 Torr
$a-x$	concentration of SiCl ₄ on the susceptor
C_0	concentration of SiCl ₄ at the gas inlet
	9.43×10^{-9} g/cm ³ at 1200°C
	1.54×10^{-5} g/cm ³ at 400°C

C_p	specific heat at constant pressure of hydrogen	3.61 cal/g °C at 800°C
D_1	diffusion constant at the average temperature of the reaction gas	2.88 cm ² /sec at 800°C
D_2	diffusion constant at the substrate temperature	5.15 cm ² /sec at 1200°C
f	correction factor of natural convection	0-0.025
f_0	gas velocity at the gas inlet	15.75 cm/sec at 400°C
G	growth rate	cm/sec
g	gravitational acceleration	980 cm/sec ²
h	length of reactor tube	30 cm
k	thermal conductivity of hydrogen	1.01×10^{-3} cal/cm sec °K at 800°C
M	molecular weight of SiCl ₄	170
m	atomic weight of Si	28
R_s	radius of the susceptor	2.5 cm
R_w	radius of the reaction tube	5.5 cm
T_s	temperature of the susceptor	1200°C
T_w	temperature of the wall	400°C
β	expansion coefficient of gas	1/273
ν	kinematic viscosity	8.95 cm ² /sec at 800°C
ρ	density of hydrogen	2.27×10^{-5} g/cm ³ at 800°C
ρ_1	density of Si	2.33 g/cm ³
ω_s	speed of rotation of the susceptor	12.56 rad. (120 rpm)

REFERENCES

- E. G. Bylander, *This Journal*, **109**, 1171 (1962).
- R. Takahashi, K. Sugawara, Y. Nakazawa, and Y. Koga, in "Chemical Vapor Deposition," John M. Blocher, Jr. and James C. Withers, Editors, p. 695, The Electrochemical Society Softbound Symposium Series, New York (1970).
- R. Takahashi, Y. Koga, and K. Sugawara, *This Journal*, **119**, 1406 (1972).
- K. Sugawara, R. Takahashi, H. Tochikubo, and Y. Koga, in "Chemical Vapor Deposition," John M. Blocher, Jr. and James C. Withers, Editors, p. 713, The Electrochemical Society Softbound Symposium Series, New York (1970).
- F. G. Eversteyn, P. J. W. Severin, C. H. J. v d. Brekel, and H. L. Peek, *This Journal*, **117**, 925 (1970).
- V. G. Levich, "Physicochemical Hydrodynamics," p. 65, Prentice-Hall, Inc., Englewood Cliffs, N. J. (1962).
- R. B. Bird, W. E. Stewart, and E. N. Lightfoot, "Transport Phenomena," pp. 130, 316, John Wiley & Sons, Inc., New York (1960).
- N. Kobayashi and T. Arizumi, *Japan. J. Appl. Phys.*, **9**, 361 (1970).
- F. G. Allen, *ibid.*, **28**, 1910 (1957).
- M. P. Albert and J. F. Combs, *This Journal*, **109**, 709 (1963).
- P. A. Schumann, Jr., R. P. Phillips, and P. J. Olsheski, *ibid.*, **113**, 368 (1966).
- K. Sato, Y. Ishikawa, and K. Sugawara, *Solid-State Electron.*, **9**, 771 (1966).
- T. von Karman, *Z. Angew. Math. Mech.*, **1**, 244 (1921).
- W. Cochran, *Proc. Cambridge Phil. Soc.*, **30**, 365 (1934).
- H. Schlichting, "Boundary Layer Theory," p. 87, McGraw-Hill Book Co., New York (1960).

16. S. E. Bradshaw, *Intern J. Electronics*, **23**, 381 (1968).
17. D. R. Olander, *I. EC. Fundamentals*, **6**, 178 (1967).
18. D. R. Stull, "JANAF Thermochemical Tables," Clearinghouse, Washington, D. C. (1965).
19. H. Fujita, *Kagaku Kikai*, **15**, 234 (1951).
20. K. Sato, "Bussei-Josu Suizanho," p. 131, Maruzen, Tokyo (1958) (In Japanese).
21. C. R. Wilke, *Chem. Eng. Progr.*, **46**, 95 (1950).
22. R. C. Reid and T. K. Sherwood, "The Properties of Gases and Liquids," p. 520, McGraw-Hill Book Co., New York (1958).
23. R. F. Lever, *IBM J. Res. Develop.*, **8**, 460 (1964).
24. C. F. Powell *et al.*, "Vapor Deposition," p. 111, John Wiley & Sons, Inc., New York (1966).

Thermal Oxidation of Silicon and Iron-Coated Silicon in the Temperature Range 692°-1003°C

Rong Yau Wang and Owen F. Devereux*

Department of Metallurgy and Institute of Materials Science, University of Connecticut, Storrs, Connecticut 06268

ABSTRACT

Polycrystalline silicon wafers, both clean and with a thin coating of metallic iron, have been oxidized in steam and in moist air ($P_{H_2O} = 24$ mm) in the temperature range 692°-1003°C. Data were analyzed in terms of a linear-parabolic rate equation. For clean silicon oxidized in steam, the parabolic rate constant displays an activation energy for the process of 26.9 kcal/mole below 903°C, and 16 kcal/mole above this temperature. The iron coating was assumed to oxidize and diffuse homogeneously in the oxide film within a relatively short period of oxidation; no evidence to the contrary could be found. In steam, the effect of iron was to extend the "high temperature" Arrhenius behavior to lower temperatures. In moist air, a single Arrhenius line corresponding to the "low temperature" behavior of clean silicon was seen. The activation energies of the "high temperature" and "low temperature" regions of silicon oxidation correspond to those reported for wet and dry oxidation, respectively. An interpretation of these phenomena in terms of a short range order transition in the vicinity of 900°C is postulated.

In their critical survey of their own and previous work, Deal and Grove (1) established that thermal oxidation of silicon in dry or wet oxygen could be described by the relation

$$x^2 + Ax = B(t + \tau) \quad [1]$$

where x is film thickness, t is oxidation time, and τ is a factor to correct for the presence of an oxide film at $t=0$, or for an early stage of oxidation not described by this relation. Thus, early oxidation is linear in time, with a rate constant B/A , while later oxidation is diffusion-controlled, with a parabolic constant, B .

In their studies, Deal and Grove found an activation energy for parabolic oxidation of 16.3 kcal/mole under wet conditions and 28.5 kcal/mole under dry conditions, while the linear oxidation had an activation energy of 46 kcal/mole in either case. The values of the activation energy for B were found to be in accord with those for diffusion of the oxidizing species, hydroxyl ion (2), and superoxide ion (3), respectively. The parabolic constant, B , was found to be proportional to the partial pressure of the oxidant. The time constant, τ , was found to be zero under wet conditions, and to correspond to a positive oxide thickness under dry conditions, reflecting a dependence of the shape of the diffuse charge distribution in the oxide on the ionic content. Many of these observations were confirmed in a very careful study by Pliskin (4).

The mechanism of oxidation is less well established. This question is discussed at some length by Nakayama and Collins (5), who cite market studies indicating that the oxidant is the diffusing species. Jorgensen (6) studied the effect of an external field on oxidation, concluding that the diffusing species was ionic. However, Raleigh (7) demonstrated that these results were also consistent with an electrolytic reaction involving diffusion of a neutral species. The flow of another

charged species in the film, required in the case of ionic diffusion to maintain a zero net charge flux, is discussed by Collins and Nakayama (8), but there are no definitive data dealing with this aspect of the mechanism.

More recently Revesz and Evans (9) have described the very significant effect of sodium (~1%) incorporated in the oxide film during oxidation. In brief, they postulated an interstitialcy mechanism for oxygen diffusion in the oxide in a dry oxygen environment, with both molecular and ionic transport occurring. The presence of sodium in the amorphous silica structure increases the density of broken Si-O-Si bridges, increasing the pre-exponential portion of the diffusion coefficient, but hinders the motion of oxygen, thus increasing the activation energy. They held oxidation by water to be very complex, with silanol (Si-OH), interstitial H_2 , and interstitial H_2O possible as defects. An increase in the pressure of water vapor leads both to an increase in the pre-exponential constant and a decrease in the activation energy due to an increased density of broken Si-O-Si bridges. Inclusion of sodium in the structure increases the degree to which OH⁻ can be incorporated, but also hinders the movement of this species, thus increasing the activation energy.

In a recent paper Devereux, Wang, and Chien (10) reported on the oxidation of silicon through films containing significant quantities of sodium oxide (10-20%). They found that oxidation was cubic in its early stage, but became parabolic at longer times. Both cubic and parabolic constants exhibited an activation energy of 40.8 kcal/mole in wet air ($P_{H_2O} = 24$ mm). These data were found to be consistent with two proposed models. In one, transport rate (diffusion coefficient) decreased in proportion to the increase in viscosity (decrease in broken Si-O-Si bridges) occasioned by addition of silica to a phase containing a fixed quantity of sodium oxide. The alternative proposal was similar, but considered two phases, with the high sodium phase

* Electrochemical Society Active Member.

Key words: oxidation, silicon, impurity, hot corrosion.

Table I. Amount of Fe applied to Si wafers, equivalent weight gain if oxidized to Fe₂O₃, and time required for such oxidation at observed rate

Environment	Temperature (°C)	Wt. Fe (mg/cm ²)	Wt. gain (mg/cm ²)	Elapsed time req'd (hr)
Wet air	692	0.03031	0.01302	19
	798	0.01480	0.00646	0.6
	903	0.01256	0.00539	0.2
	1003	0.01482	0.00636	<0.2
Steam	692	0.01559	0.00669	2.0
	798	0.00811	0.00348	0.3
	903	0.01248	0.00536	<0.1
	1003	0.01547	0.00664	<0.1

decreasing in proportion to the extent of oxidation. As this phase would conduct the major part of the mass transport, this would lead to cubic kinetics. Although in either case the proposed dilution of the sodium content was continuous, the cubic kinetic behavior did not proceed indefinitely, in accord with the autocatalytic mechanism described by Charles (11) wherein a relatively small amount of sodium ion in glass produces a disproportionate amount of hydroxyl ion.

In the work reported herein, the authors have contaminated the growing film on oxidizing silicon with the oxide of a more refractory metal, iron, in order to establish a comparison to the effect of the low melting, highly soluble sodium oxide described above. In view of the large radii of both ferrous and ferric ions (0.83 and 0.67Å, respectively) compared to that of Si⁴⁺ (0.39Å) it was not expected that iron would substitute for silicon in the tetrahedral oxygen structure, but would enter interstitially, as does Na⁺ (0.98Å), contributing its oxygens to neighboring SiO₄⁻⁴ tetrahedra, thus breaking Si-O-Si bridges (12). However, although iron would contribute more oxygen per cation than would sodium, the degree of ionization is much less, and less breaking of the structure would be expected than in the case of the sodium-contaminated film.

Experimental

Specimen preparation and experimental technique were essentially that described previously save in the method of introduction of the contaminating impurity (10). Silicon wafers were prepared from a 1 in. diameter polycrystalline ingot of nine 9's purity.¹ After slicing and lapping the wafers were degreased in hot trichloroethylene followed by hot nitric acid and rinsed in deionized water. The wafers were then polished in a solution of 60 parts nitric acid, 20 parts acetic acid, and 8 parts hydrofluoric acid. After polishing the wafers were rinsed in deionized water and stored under methanol. Final thickness was approximately 200μ. Clean, control specimens were oxidized as prepared; iron-contaminated specimens were coated on both sides with a vacuum-deposited layer of metallic iron (99.95%) prior to oxidation. Amounts of iron applied are shown in Table I.

Specimens were oxidized in both steam (1 atm) and wet air (P_{H₂O} = 24 mm). Oxidation was conducted in a refractory tube with a flowing environment, using a resistance furnace with current proportioning control that maintained temperature at the specimen within 1°C. Oxidation rate was determined by periodically removing the specimens and weighing them. For this purpose a Cahn RG electrobalance with a Varian G-1000 recorder as null indicator was used, yielding a typical weighing accuracy of 10⁻⁶g. This technique was used previously (10) and was found to be more accurate than a continuous recording of the specimen weight. The effect of the thermal cycles on removing and reinserting the specimens was evaluated by comparison to specimens left in the furnace for extended periods of oxidation; the mean deviation between continuous and discontinuous terminal weight gain was

¹ Analysis stated by supplier, Alfa Inorganics, Beverly, Massachusetts. Spectroscopic analysis indicated B: 0.0002 ppm, P: 0.0005 ppm, O: 0.000000 ppm. Resistivity given as ρ > 1800 ohm cm.

2.25% of the mean weight gain and the RMS value was 11.3%. There was no pattern to the sign or magnitude of the deviation, which was thus neglected in this treatment. Use of a direct weight measurement was preferred over an optical film thickness determination because of the complex nature of the binary oxide film.

Results

Kinetic data.—Weight gain data for clean silicon specimens in steam in the temperature range 692°-1003°C are shown in Fig. 1; data are presented as Δw vs. t^{1/2} for convenience and clarity. Oxide film thickness, assuming an oxygen density of 1.0 g/cm³ in the film, is also indicated. Data for iron-coated silicon in moist air are shown in Fig. 2, and data for iron-coated silicon in steam are shown in Fig. 3.

Since the graphical representation used in Fig. 1, 2, 3 will be a straight line corresponding to the diffusion-limited region of oxidation only if the earlier linear and other nonparabolic weight gain is negligible, the appearance of linearity or lack of it in these figures is not proof of parabolic behavior. These data were analyzed by a least squares technique corresponding to Eq. [1]. Although there was no reason, *a priori*, to assume that oxidation of iron-coated silicon would follow the linear-parabolic relation, use of Eq. [1] did provide a means for correcting for early nonparabolic behavior in determining the kinetic constants for the parabolic region. An independent evaluation of the parabolic constants was made graphically from simple Δw² vs. t plots. On these plots all experiments save the iron-coated silicon in wet air at 692°C, with the slowest rate observed in the study, did exhibit at least a terminal parabolic region. Parabolic constants from both of these evaluations are compared in Table II. Arrhenius plots of these constants, using the graphical evaluation, are shown in Fig. 4. Preliminary experiments with clean silicon in moist air, not reported here, showed a reproducibility of the parabolic constant of 2%.

Pre-exponential constants and activation energies determined from this figure, together with values from the literature for comparison, are given in Table III. The parabolic constants for clean silicon oxidation show a behavior not previously reported. In the temperature range 692°-903°C a clearly linear de-

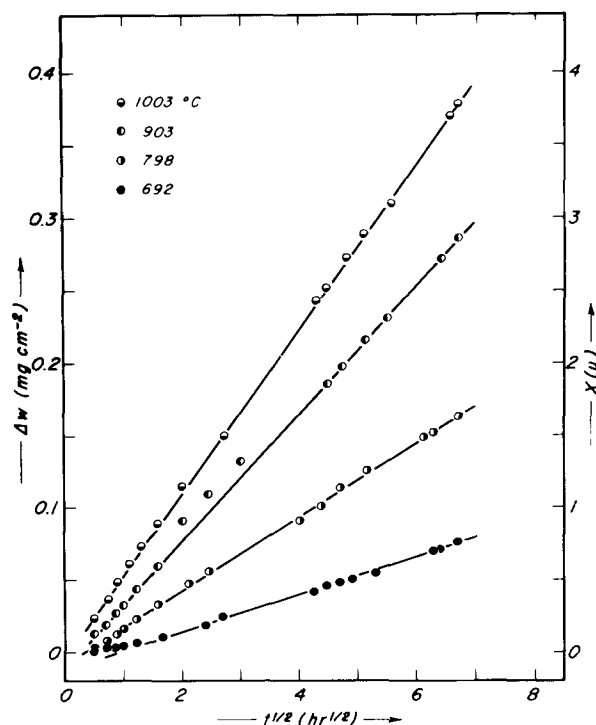


Fig. 1. Weight gain due to oxidation of clean silicon in steam

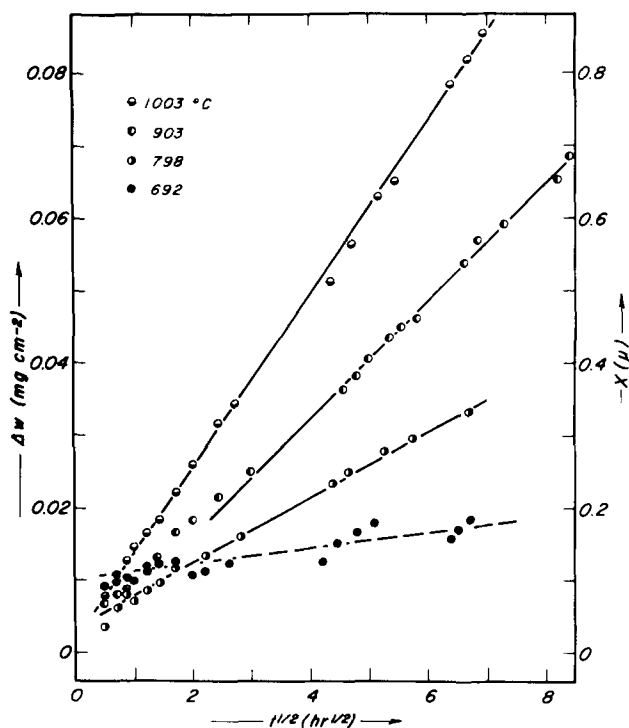


Fig. 2. Weight gain due to oxidation of iron-coated silicon in moist air.

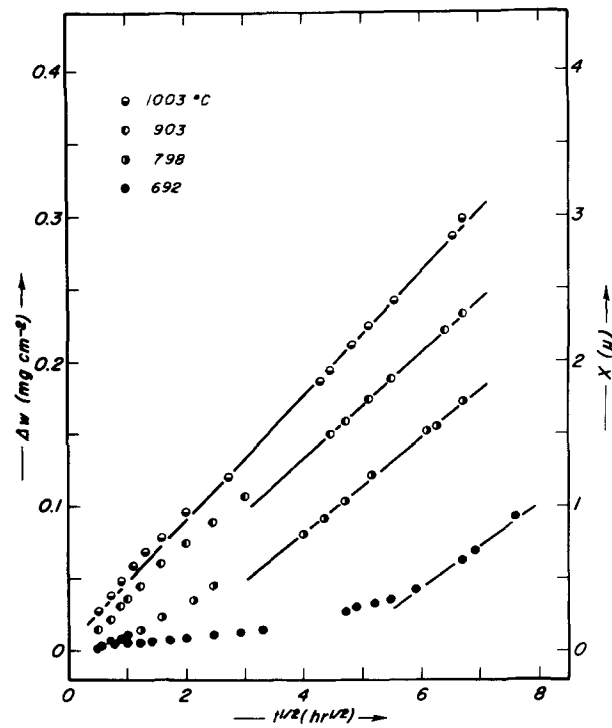


Fig. 3. Weight gain due to oxidation of iron-coated silicon in steam.

pendence is seen in steam ($P_{\text{H}_2\text{O}} = 1 \text{ atm}$), but with an activation energy characteristic of that seen in dry, or nearly dry, oxygen, 26.9 kcal/mole. (See results of Deal and Grove, Nakayama and Collins, and Revesz and Evans cited in Table III.) The slope changes above that temperature; as shown in the figure an exact correspondence to the results of Pliskin (4) and of Deal and Grove (1) is seen. The plot for iron-coated silicon oxidized in steam shows a behavior similar to the high-temperature region of the clean silicon plot; however, it is not clear whether the high-temperature

behavior is followed over the whole range of data, or a break, as for clean silicon, exists. The pre-exponential constant is not significantly different from that for clean silicon at high temperature. The behavior of iron-coated silicon in wet air, however, parallels the low-temperature clean silicon behavior, with a slope corresponding to 26.9 kcal/mole. Approximately a first order dependence on water vapor pressure is seen.

Microscopy.—Optical examination of the oxidized specimens was made directly and in tapered section.

Table II. Parabolic oxidation rate constant determined statistically from Eq. [1], and graphically

System	Temperature	Statistical		Graphical	
		$B \text{ (mg}^2 \text{ hr}^{-1} \text{ cm}^{-4} \times 10^6)$	$B \text{ (cm}^2 \text{ sec}^{-1})$	$B \text{ (mg}^2 \text{ hr}^{-1} \text{ cm}^{-4} \times 10^6)$	$B \text{ (cm}^2 \text{ sec}^{-1})$
Si in steam	692	16.69	4.64×10^{-14}	15.1	4.20×10^{-14}
	798	70.70	1.97×10^{-13}	60.7	1.69×10^{-14}
	903	195.6	5.34×10^{-13}	186	5.17×10^{-13}
	1003	321.8	8.95×10^{-10}	292	8.12×10^{-13}
Fe-Si in wet air	692	0.2015	5.60×10^{-16}	—	—
	692	0.3762	1.046×10^{-15}	—	—
	798	2.2827	6.35×10^{-15}	2.0	5.56×10^{-15}
	903	6.0745	1.69×10^{-14}	5.13	1.43×10^{-14}
	1003	14.10	3.92×10^{-14}	14.6	4.06×10^{-14}
Fe-Si in steam	692	14.44	4.01×10^{-14}	22.6	6.28×10^{-14}
	798	88.28	2.46×10^{-13}	73.3	2.04×10^{-13}
	903	116.1	3.23×10^{-13}	117	3.25×10^{-13}
	1003	177.7	4.94×10^{-13}	200	5.56×10^{-13}

Table III. Kinetic constants

Authors	System	Environment	Temp. range (°C)	$k_0 \text{ (cm}^2 \text{ sec}^{-1})^*$	$\Delta H_k \text{ (kcal/mole)}^*$
This study	Si	H ₂ O (760 Torr)	692-903	5.2×10^{-8}	26.9
This study	Si	H ₂ O (760 Torr)	903-1003	4.7×10^{-10}	16
This study	Fe-coated Si	{ H ₂ O (24 Torr) air (736 Torr) }	798-1003	1.6×10^{-9}	26.9
This study	Fe-coated Si	H ₂ O (760 Torr)	692-1003	3.2×10^{-10}	16
Deal & Grove (1)	Si	O ₂ (760 Torr)	700-1200	3.7×10^{-9}	28.5
Revesz & Evans (9)	Si	O ₂ (760 Torr)	900-1300	1.2×10^{-9}	27.6
Nakayama & Collins (5)	Si	H ₂ O (4.6 Torr)	850-1217	1.1×10^{-10}	25.1
Deal & Grove (1)	Si	{ O ₂ (415 Torr) H ₂ O (345 Torr) }	920-1200	5.6×10^{-10}	16.6
Pliskin (4)	Si	H ₂ O (760 Torr)	917-1202	5.6×10^{-10}	16.3
Revesz & Evans (9)	Si	H ₂ O (760 Torr)	920-1200	4.3×10^{-12}	12.45
Revesz & Evans (9)	Si (~1% Na ₂ O)	H ₂ O (760 Torr)	920-1200	4.4×10^{-4}	52.8
Devereux, Wang, Chien (10)	Si (trace Na ₂ O)	{ H ₂ O (24 Torr) air (736 Torr) }	702-1052	3.2×10^{-7}	39.6
Devereux, Wang, Chien (10)	Si (~10% Na ₂ O)	{ H ₂ O (24 Torr) air (736 Torr) }	702-1052	1.9×10^{-7}	40.8

* $B = k_0 \exp(-\Delta H_k/RT)$.

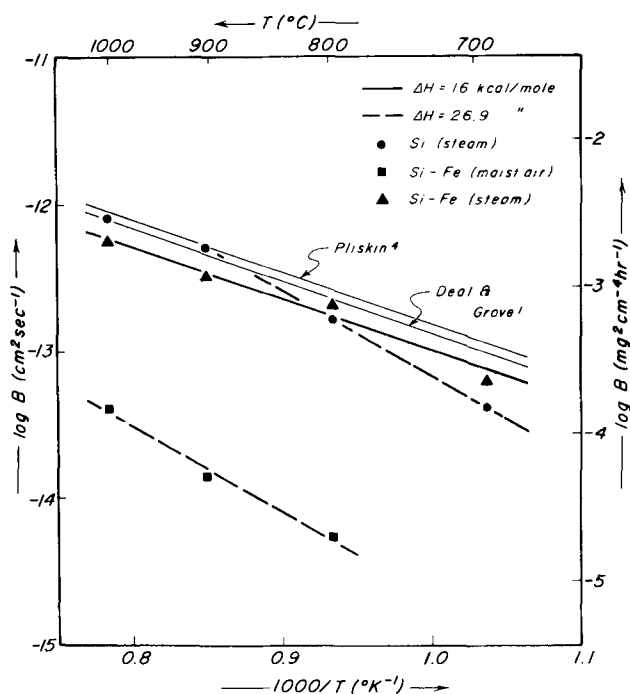


Fig. 4. Arrhenius plot of parabolic rate constants for clean silicon in steam, and for iron-coated silicon, in moist air and in steam. Extrapolated data of Pliskin (4) and Deal and Grove (1) shown for silicon in steam.

Typical observations are shown in Fig. 5, representing the final surface of the iron-coated silicon specimens oxidized in wet air at (a) 692°C, (b) 798°C, and

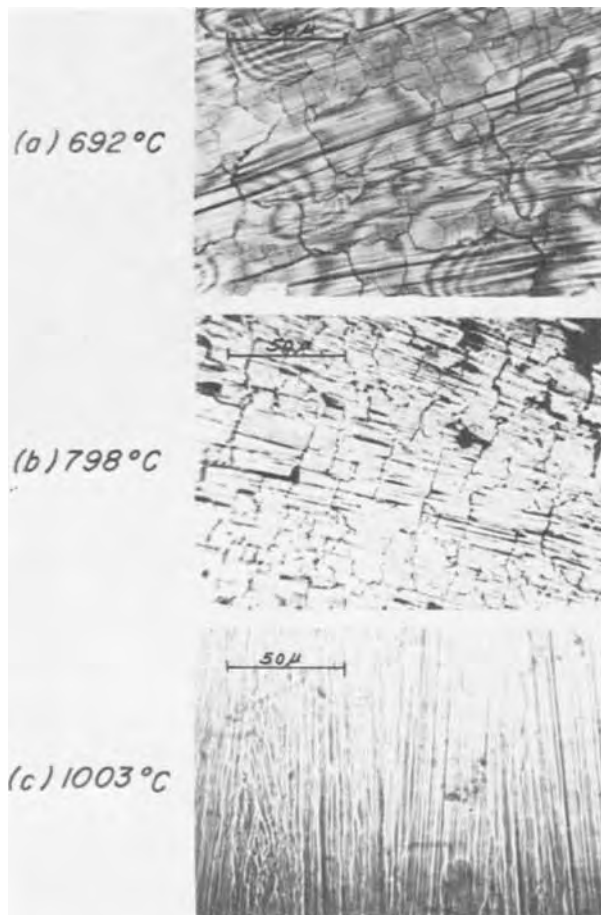


Fig. 5. Microstructure of the film on iron-coated silicon oxidized in moist air at (a) 692°C, (b) 798°C, and (c) 1003°C.

(c) 1003°C. A similar sequence of characteristics was seen for the iron-coated silicon oxidized in steam and, surprisingly, for clean silicon oxidized in steam. The lower temperature specimens display a random crack or grain boundary pattern, an effect which progressively disappears with increase in oxidizing temperature, being only suggested at 1003°C. Similar patterns were seen on examination of the tapered sections. These sections provided the additional information of a marked decrease in roughness at the silicon/oxide interface with increasing temperatures, demonstrating the increasing significance of diffusion control. Scanning electron microscopy of a clean, unoxidized specimen revealed a slight "orange peel" effect due to preparation; this was of a smaller order of magnitude than the pattern shown in Fig. 5 and gradually disappeared with increasing oxidizing time.

While these specimens were removed from the furnace at regular intervals for weighing in order to establish the oxidation rate, it is apparent, due to concurrence with weight gain data for specimens removed only after a terminal period of oxidation, that the observed pattern is not one of thermal-shock-produced cracks in either the metal or the oxide film. Alternatively, if the possibility of thermally produced cracks is admitted, then the conclusion must be reached that such cracking had no effect on oxidation rate.

X-ray diffraction.—X-ray diffraction analyses of the oxidized specimens were made, in which the wafer was employed essentially as a powder sample. Other than a weak diffraction peak from the oxidized iron-coated silicon specimens corresponding to a lattice spacing of 4.1068 Å, no diffraction lines other than those from silicon were seen.

Discussion

The technique used to contaminate the silica film with iron oxide offered a controllable, clean means of putting a quantity of iron on the surface, but has a disadvantage in that the distribution and oxidation state of the iron in the oxide film are not known and that the concentration of iron in the film, and possibly the distribution, is a function of the thickness of the oxide film. It has been assumed by the authors that the iron in each case save one was fully oxidized very early in the experiment. Justification is given in Table I, wherein on assuming oxidation to Fe_2O_3 , it is shown that the weight gain necessary for complete oxidation is attained in a relatively short time. The exception, the experiment performed in wet air at 692°C, was the one with the slowest oxidation rate and the only experiment failing to show a clear parabolic region. Supporting this assumption is the failure to observe a discrete iron or iron oxide phase by x-ray diffraction. A qualitative analysis made of the iron-coated sample oxidized at 798°C in steam by x-ray fluorescence in a scanning electron microscope at 20 kV revealed a Fe/Si count ratio of 0.04, fortuitously approximately the weight ratio of Fe to Si in the oxidized film if all iron applied were retained in the film and uniformly distributed. No iron was seen in an uncoated, oxidized sample.

A surprising aspect of Fig. 4 is the demonstration of a low-temperature oxidation behavior of clean silicon in steam that differs from the well-established behavior at higher temperature. Although the onset of purely parabolic behavior occurs in the vicinity of 1000°C, as opposed to the linear parabolic behavior seen at lower temperatures, the authors are confident that their analysis of the data, in view of the concurrence of both graphical and statistical methods, have yielded true parabolic constants as shown. The data in the range 692°-903°C show a very clear Arrhenius behavior that is quite distinct from that in the interval 903°-1003°C which, although defined only by two points, is in excellent agreement with the work of Deal and Grove (1) and of Pliskin (4). The authors have not seen previous mention of such an effect, but, on the other hand, the silicon/steam oxida-

tion system does not seem to have been studied previously in this temperature interval (Table III). An attempt was made, using a digital nonlinear regression program, to fit all of the oxidation data reported herein for a given system to a single relation, with both linear and parabolic constants expressed in terms of an activation energy and a pre-exponential constant, Eq. [2]

$$t = \frac{1}{a_0} \exp(\Delta H_a/RT) + \frac{1}{k_0} \exp(\Delta H_k/RT) \quad [2]$$

It was not possible, however, to make a satisfactory correlation, further substantiating the change in slope depicted in Fig. 4.

Thermal oxide films on silicon are normally regarded as amorphous, in accord with the observation that devitrification of silica in this temperature range is exceedingly slow and with the absence of any evidence of crystallinity. While it has been reported that water does not alter the relative phase stability in silica significantly at other than very high pressure (13), water does dissolve in silica in appreciable quantity and more recent work has suggested that this might lead to an altered stability diagram (14, 15). Such water would enter the silica structure by replacement of bridging oxygen atoms by nonbridging hydroxyl groups, thus greatly increasing structural mobility. It might be reasoned that such a structure would possess short range order characteristics more nearly akin to those of the thermodynamically stable crystal. Supporting this argument, the temperature at which a change in kinetic behavior is seen is very nearly that of the quartz/tridymite transition, 867°C (15). As the transition to cristobalite occurs at 1470°C, a comparable effect due to this transition would not have been seen in the previously reported work. The resemblance of the "low-temperature" behavior of silicon oxidation in steam to that in dry oxygen is in accord with the relative openness of the tridymite structure in comparison to that of quartz, the densities being 2.30 and 2.655 g/cm³, respectively (16). That is, in the absence of definitive data, it may be anticipated that the solubility of water in the low temperature structure is less than in the high temperature structure, giving corresponding greater importance to the "dry" transport mechanism during low-temperature oxidation.

The introduction of iron into a silica film oxidizing in steam does not appear to alter its behavior significantly. Despite obvious concentration variation during film growth, parabolic behavior is still seen for long-term oxidation. The kinetic parameters are not significantly different from those for clean silicon except that the high temperature behavior may, in steam, extend over the entire temperature range of the experiments. This might be interpreted as an effect of the solute on a short range structure transition as postulated above, thus stabilizing the more open structure at lower temperatures. In moist air, again a similarity between clean and iron-coated silicon is shown with, however, the "low temperature" or "dry oxygen" activation energy being displayed for the iron-coated case.

Conclusions

Clean silicon appears to exhibit different kinetic behavior during oxidation in steam below 900°C from that observed at higher temperatures. It is suggested that this might be due to a change in short-range structure corresponding to the quartz/tridymite transition. The quartz structure is less open than the higher temperature tridymite, suggesting a reduced solubility for water at lower temperatures, in accord with the observation that the activation energy for the parabolic constant at low temperatures in steam is characteristic of that seen during "dry" oxidation.

The effect of iron in the oxide film in steam oxidation is to extend the range of high-temperature behavior; in terms of above model, this would resemble a solute-lowered transition temperature. In moist air in which clean silicon already approaches the behavior seen in dry oxygen, iron-coated silicon exhibits a behavior characteristic of "dry" oxidation.

The authors have no other evidence to suggest the occurrence of a short range order transition in amorphous silica and, thus, at this point are merely suggesting such a transition as a model to explain the behavior reported.

Acknowledgment

The generous support of the National Science Foundation through Grant No. GK 20017, and of the University of Connecticut Research Foundation is gratefully acknowledged. The computations were performed through use of the facilities of the University of Connecticut Computer Center.

Manuscript submitted Feb. 9, 1972; revised manuscript received July 26, 1972.

Any discussion of this paper will appear in a Discussion Section to be published in the June 1973 JOURNAL.

REFERENCES

1. B. E. Deal and A. S. Grove, *J. Appl. Phys.*, **36**, 3770 (1965).
2. A. J. Moulson and J. P. Roberts, *Trans. Faraday Soc.*, **57**, 1208 (1961).
3. F. J. Norton, *Nature*, **171**, 701 (1961).
4. W. A. Pliskin, *IBM J. Res. Develop.*, **10**, 198 (1966).
5. T. A. Nakayama and F. C. Collins, *This Journal*, **113**, 706 (1967).
6. P. J. Jorgensen, *J. Chem. Phys.*, **37**, 874 (1962).
7. D. O. Raleigh, *This Journal*, **113**, 782 (1966).
8. F. C. Collins and T. Nakayama, *ibid.*, **114**, 167 (1967).
9. A. G. Revesz and R. J. Evans, *J. Phys. Chem. Solids*, **30**, 551 (1969).
10. O. F. Devereux, R. Y. Wang, and K. H. Chien, *This Journal*, **118**, 1147 (1971).
11. R. J. Charles, *J. Appl. Phys.*, **29**, 1549 (1958).
12. R. C. Evans, "Crystal Chemistry," Cambridge University Press (1952).
13. O. F. Tuttle and J. L. England, *Bull. Geol. Soc. Am.*, **66**, 150 (1955); "Phase Diagrams for Ceramists II," E. M. Levin and H. F. McMurdie Editors, Am. Ceram. Soc., Columbus (1959).
14. S. B. Holmquist, *Z. Krist.*, **111**, 71 (1958); *J. Am. Ceram. Soc.*, **44**, 82 (1961).
15. A. Muan and E. F. Osborn, "Phase Equilibria Among Oxides in Steelmaking," p. 19, Addison-Wesley, Reading (1965).
16. A. F. Wells, "Structural Inorganic Chemistry," 2nd ed., p. 568, Oxford University Press (1950).

The Etch Rate and Deterioration of Magnesium Aluminum Spinel in Hydrogen

J. M. Green*

IBM Thomas J. Watson Research Center, Yorktown Heights, New York 10598

ABSTRACT

Magnesium aluminum spinel is commonly used as a substrate for the heteroepitaxial chemical vapor deposition of silicon. Hydrogen is usually used as a carrier gas, and a high-temperature pretreatment in hydrogen is typically performed on the substrate with the idea that abrasion polishing damage will either be annealed or removed. In this paper the rate of material removal in hydrogen of stoichiometric spinel is presented as a function of crystallographic orientation, time, and temperature. For example, at 1000°C the rate is ~ 1 Å/min; at 1300°C, ~ 100 Å/min. However, it was found that such a hydrogen ambient promotes crazing of the substrate surface, thus degrading its suitability for heteroepitaxy. This phenomenon was studied, and it is suggested that the cause is due to a preferential out-diffusion of magnesium from the surface, which induces a strain large enough to result in brittle fracture. It has been shown that the crazing is obviated by the use of helium as a carrier gas.

The heteroepitaxial deposition of silicon on insulating substrates has been under investigation by several workers. Good reviews together with bibliographies are given in references (1-3). Sapphire was the first material to be used successfully (4); however, magnesium aluminum spinel has been thought to have some advantages over other materials where consideration is given to compatibility with silicon with respect to crystal class, lattice parameter, temperature coefficient of expansion, and tendency to incorporate constituents into the silicon film.

The silicon heteroepitaxy technologies for both sapphire and spinel have been extensively studied. Nonetheless, preparation of the substrate surface remains a critical consideration for improvement of the epitaxial film quality. At present the wafers are usually abrasion (mechanically) polished. This process induces considerable damage into the wafer surface, which must be removed. Several wet etches have been proposed for both sapphire and spinel (1, 2, 5-8), but a gaseous etch *in situ* would be advantageous. In this regard, oxide reduction by hydrogen clearly suggests itself: it does not contribute baneful reaction products; and it is the usual carrier gas used in the chemical vapor deposition of silicon, and, therefore, convenient to use. The etch rate of sapphire in hydrogen was studied by Zeveke *et al.* (7); the etch rate of spinel is reported in this paper.

Hydrogen is commonly used to prepare sapphire wafers for epitaxial deposition of silicon, and there has been no report of deleterious effects due to this procedure. However, a pernicious phenomenon is attendant to the polishing of spinel by this method: the wafers tend to craze (or crack) by brittle fracture. This is also discussed below.

Etch Rate Determination

The material removal rate of the spinel was determined by gravimetry using a Mettler Micro Gram-Atic Balance. The etch rate was calculated using a value of 3.58 for specific gravity (3, 6). The heat-treatments were effected in a relatively standard horizontal epitaxial reaction chamber (60 cm long by 5 cm in diameter) which was fabricated from fused silica. The wafers were supported by an uncoated graphite susceptor which was heated by rf induction. The hydrogen was purified in an Englehard Industries Palladium Diffusion Unit, and it flowed through the chamber with a gas stream velocity of ~ 10 cm/sec. The temperature was measured using a Pyrometer Instrument Com-

pany Micro Optical Pyrometer which had been calibrated for this particular series of experiments at the melting points of germanium, copper, and silicon. The starting substrates were fabricated from Czochralski grown, single-crystal, stoichiometric, magnesium aluminum spinel by the Crystal Products Division of Union Carbide. They measured 1 in. in diameter and 20 mils in thickness. The face being investigated was, in each case, abrasion polished to a specification of 1μ in. absolute; the reverse face, 1μ in. C.L.A. (center line average). There was no noticeable evidence of reaction between the wafer's reverse side and either the hydrogen or the carbon susceptor.

The etch rate data were collected for wafer orientations of (111), (110), and (100), at each of four temperatures which lie within the usual silicon deposition range (1000°-1400°C), and for two to five intervals of time at each temperature. As an example the data for 1320°C are given in Fig. 1. Here the intervals were 9, 10, 10, 10, and 26 min, and the average rate for each interval was plotted at the mid-interval time. All the data are summarized in the Arrhenius plot of Fig. 2. Here the etch rates were averaged at

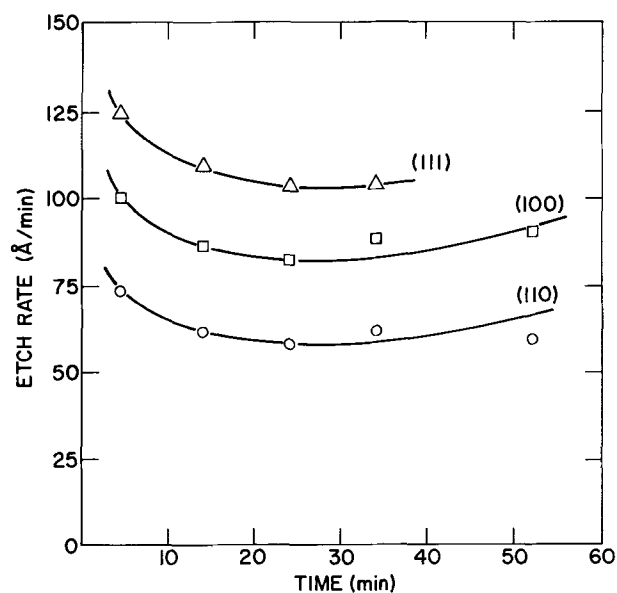


Fig. 1. The etch rate of magnesium aluminum spinel in hydrogen at 1320°C as a function of duration of heat-treatment.

* Electrochemical Society Active Member.
Key words: substrates, polishing, spinel, etch rate.

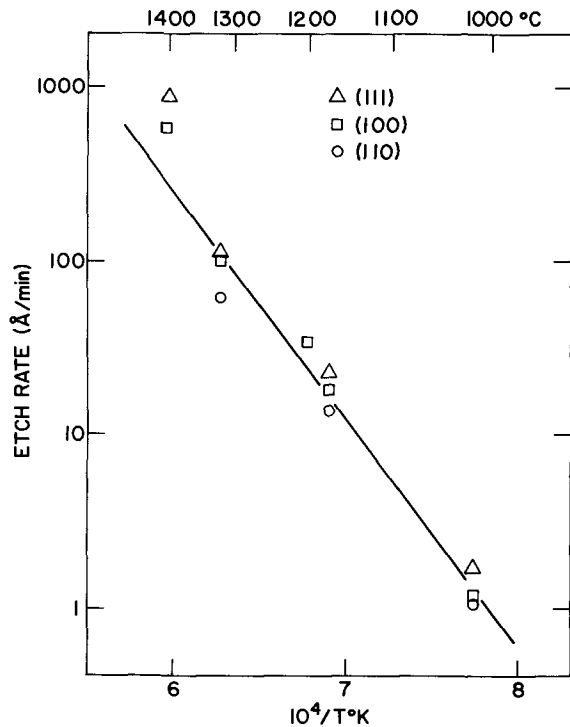


Fig. 2. The etch rate of magnesium aluminum spinel in hydrogen as a function of temperature.

each temperature for each orientation. The associated activation energy for the curve as shown is ~ 3 eV.

The submicroscopic character of the surface of a (100) wafer after moderate hydrogen etching (10 min at 1250°C) can be seen in the replica electron micrographs of Fig. 3. The rectanguloid etch figures are depressions (Fig. 3b); the largest are $\sim 170\text{\AA}$ deep and $\sim 600\text{\AA}$ across. Note further that deep spike-like wells are formed during hydrogen heat-treatment (Fig. 3a). These wells have been seen to extend to a depth of more than $3\ \mu\text{m}$. The typical density of occurrence as exhibited in Fig. 3a is of the order of 10^8 per cm^2 . The diameter of the latex spheres is 5000\AA . Note that the

surface before hydrogen etching would appear featureless by comparison.

Deterioration

A phenomenon which accompanies the hydrogen etching of spinel substrates is the cracking or crazing of the surface of the wafer. The crazing is evident when observed in the optical microscope at 100X. And it can be seen to initiate at the sample periphery after it has been heated in hydrogen at $>1000^\circ\text{C}$ for a period as short as 5 min. A severe example is shown in the photographs of Fig. 4. A magnification of the cracks is seen in Fig. 5. Typically they are 1 mil deep; this depends of course on the extent of the heat-treatment, but the cracks do not extend through the thickness of the wafer. They initiate principally from the periphery of the wafer, and align themselves in low-index crystallographic directions. Occasionally a small surface section of the crazed wafer will break off and quit the wafer bulk; this leaves a depression of the order of 1 mil deep. Also a small elongated section may break off at one end and appear as if it were a curled shaving like those that might be left by a wood plane. None of the above evidence of deterioration has been seen after lengthy heat-treatments in a nitrogen or a helium ambient.

Two possible causes of the crazing were briefly investigated and discounted because of negative results:

1. Thermal shock during rapid heating or cooling. Wafers which were heated briefly to $\sim 1500^\circ\text{C}$ and cooled to room temperature for a few cycles in hydrogen or for >30 cycles in nitrogen ambient did not experience crazing.

2. Relief of asymmetric stress. The two faces of the wafers as received have been polished to different finishes, and hence have different induced strain due to the abrasion-polish damage. However, wafers with some 3 mils etched from each face in hot phosphoric acid and then exposed to hydrogen exhibited similar crazing to that of untreated wafers.

However, the following tentative mechanism does account for the crazing: magnesium is preferentially depleted at the wafer surface. This results in a composition gradient. And in as much as the lattice parameter is a function of the composition (9), a lattice parameter gradient is created, thereby inducing a strain large enough to produce brittle fracture of the

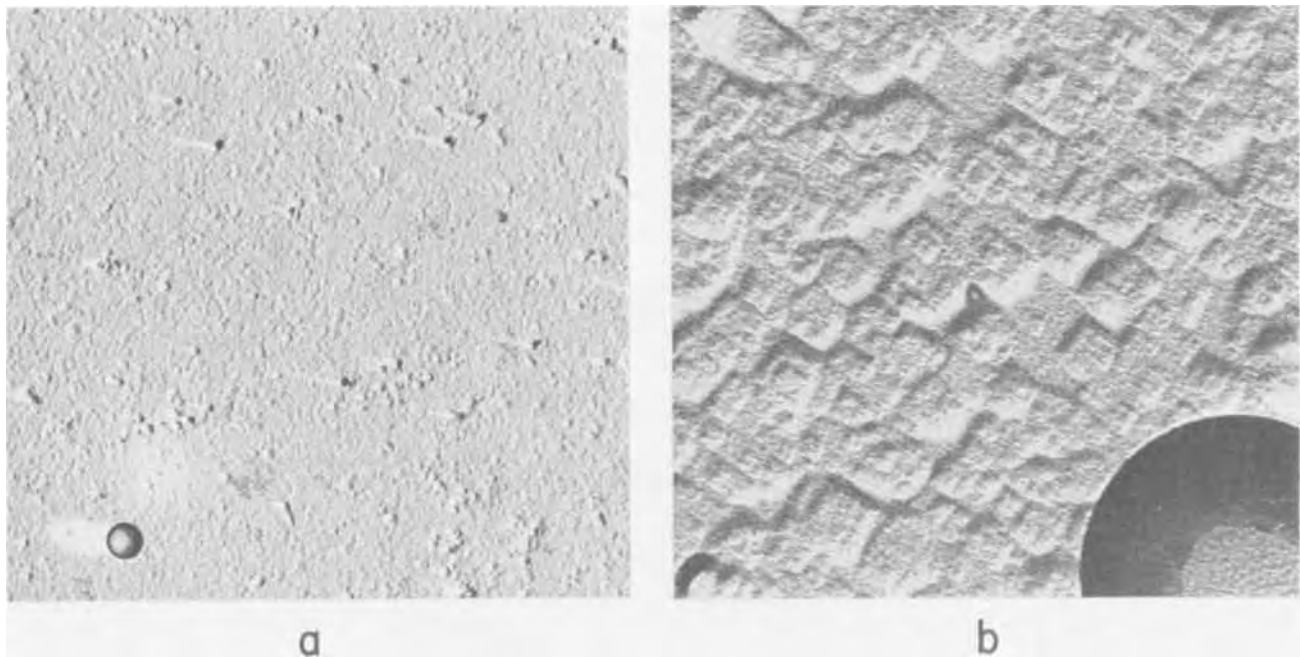


Fig. 3. Replica electron micrographs of a (100) spinel surface after heat-treatment in hydrogen at 1250°C for 10 min. The diameter of the latex spheres is 5000\AA .

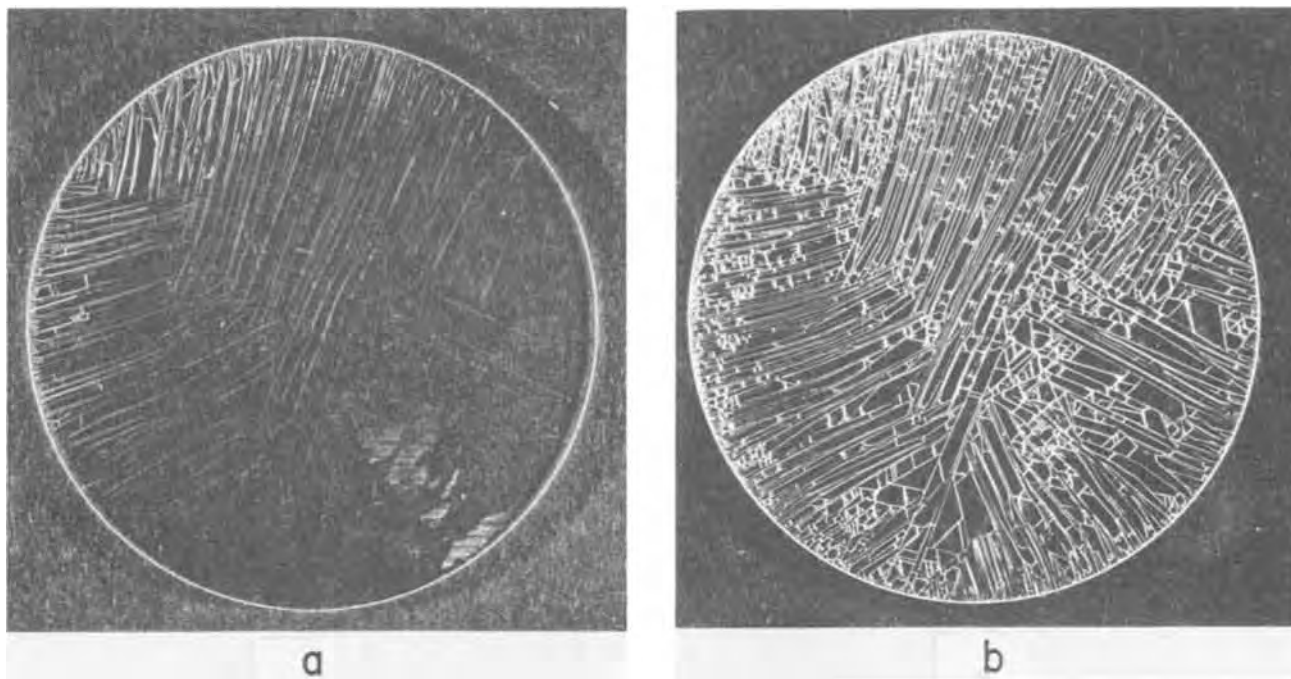


Fig. 4. Photomicrograph of a crazed (111) spinel wafer after heat-treatment in hydrogen at 1350°C (a) for 20 min and (b) for an additional 20 min. The wafer is 1 in. in diameter.

crystal at its surface. To investigate this hypothesis three experiments were performed:

1. Electron microprobe analyses were made on three wafers to determine the chemical composition (i) on the surface of an "as received" wafer, (ii) after extensive heat-treatment in nitrogen (16 hr at 1300°C), (iii) after heat-treatment in hydrogen on the surface of a wafer "shaving," and (iv) underneath the same shaving. The results, which are presented in Table Ia, show a composition gradient normal to the surface. Note that the theoretical weight fractions for a perfectly stoichiometric spinel are 17.1% magnesium and 37.9% aluminum.

2. Another electron microprobe analysis was performed on a single wafer after each of various treatments: (i) on the "as received" wafer, (ii) after the wafer had been heat-treated in hydrogen at a normal processing temperature (1200°C) and period (1 hr), (iii) after an additional 2 hr heat-treatment in hydro-

gen, (iv) after a subsequent etch in a mixture of sulfuric and phosphoric acids (3:1) (8) at 265°C for 60 min, which removed ~ 1 mil from each face. The results are presented in Table Ib and again show a composition gradient. At each step of the analysis, the wafer was scanned with the microprobe in an attempt to detect inclusions or precipitates, however, no evidence of such inhomogeneity was found. The accuracy of these analyses is better than $\pm 5\%$ of the amount of the element detected (i.e., $\pm 3/4\%$ for Mg and $\pm 2\%$ for Al). Pure stoichiometric MgO and Al_2O_3 were used as standards.

3. The relative etch rates in hydrogen of wafers of magnesia (MgO), spinel ($MgO \cdot Al_2O_3$), and sapphire (Al_2O_3) were determined at 1200°C. This was accomplished using the same gravimetric method used for spinel which was discussed above. The magnesia and spinel wafers were heat-treated for 2 hr; the sapphire, for 11.8 hr. The data are presented in Table II.

Discussion

The data seem to support the preferential-depletion-of-magnesium hypotheses. After 3 hr of hydrogen heat-treatment, the spinel wafers do indeed have a composition gradient within a mil or two of the surface.

Table I. The magnesium and aluminum concentrations as determined by electron microprobe analysis of spinel wafers after various treatments

(a)			
Sample	Treatment	w/o Mg	w/o Al
D5 (111)	As received	17.2	39.4
D2 (111)	After 16 hr in N_2 at 1300°C	16.7	40.5
D3 (111)	After 40 min in H_2 at 1300°C	15.3	41.7
	On shaving	16.8	40.2
	Under shaving		
(b)			
Sample	Treatment	w/o Mg	w/o Al
L2 (100)	As received	17.8	39.0
L2 (100)	After 1 hr in H_2 at 1200°C	17.1	39.0
L2 (100)	After an additional 2 hr in H_2 at 1200°C	15.9	42.4
L2 (100)	After subsequent acid etch to remove ~ 1 mil.	16.9	41.8

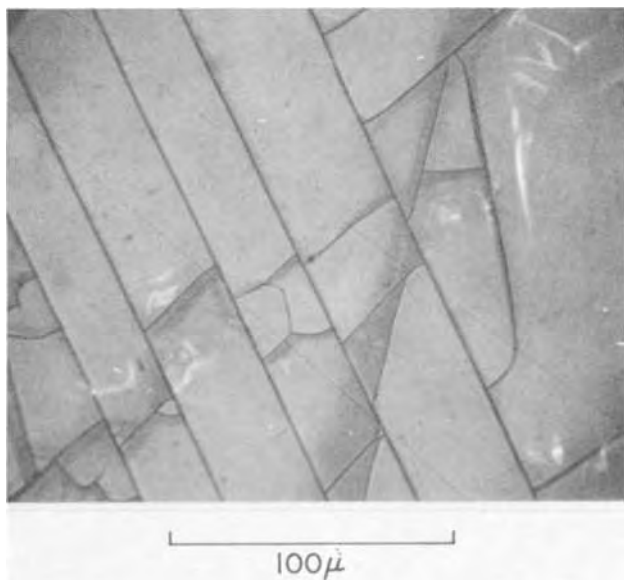


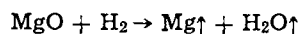
Fig. 5. An interference contrast photomicrograph of the wafer shown in Fig. 4b.

Table II. The etch rates of magnesia, spinel, and sapphire in Å/min

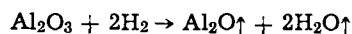
[Note that the sapphire etch rate given here is more than an order of magnitude lower than that given by Ref. (7).]

In H ₂ at 1200°C			In N ₂ at 1300°C	
MgO (100) 278	MgO·Al ₂ O ₃ (100) 35	Al ₂ O ₃ 60° off c-axis 1.5	MgO·Al ₂ O ₃ (100) 3.9	(111) 2.7

The lattice parameter differential at the surface as calculated from the compositions given in Table I and the data of Wang *et al.* (9) indicate that a tensile strain as high as 0.3% could have been achieved. This level of strain in all probability is in excess of that needed to cause brittle fracture. This is especially true, since the abrasion polishing of the wafers induces considerable surface damage (10, 11), which serves as Griffith cracks and lowers the brittle-fracture strength of the material. In this regard it should be noted that wafers which have been more gently abrasion polished show less tendency to craze. It has also been shown that near 1200°C the rate of the hydrogen reduction of magnesia is more than two orders of magnitude higher than that of sapphire (cf. Table II). It is therefore suggested that the etching of spinel can be considered as essentially two separate reactions



and



In addition to Al₂O, Al₂O₃ may decompose to other suboxides or to the metal. This is discussed by Readey and Kuczynski (12). The above aluminum equation is representative of the rate-controlling step, reduction reaction of Al₂O₃. And it is assumed that this reaction is much slower than that for the reduction of magnesium. Note that in equilibrium all these reactions are thermodynamically unfavorable. However, in an open-tube system such as is used for the present work, the reaction products are rapidly swept away, and, therefore, the reaction is likely far from equilibrium.

Now hydrogen is known to diffuse rapidly through various materials (13-16), hence it can be expected to diffuse with high mobility through the spinel wafer. It is therefore reasonable to believe that the magnesium ions are preferentially reduced to the neutral metal, leached from the wafer by out-diffusion, and evaporated from the surface. This process is consistent with the very high vapor pressure of magnesium as compared to that of aluminum and its oxides (12, 17). A similar leaching process was observed by Komarek *et al.* while they were studying the reactions of carbon with magnesia, spinel, alumina, and other oxides (18).

The decreasing etch rate with time shown in Fig. 1 corresponds to the establishing of a steady-state diffusion of magnesium; the rate decreases because of the depletion of magnesium. This rate decrease could be augmented by the concomitant removal of the damaged layer which is left after abrasion polishing and may exhibit an increased etch rate. The increase in rate beginning at ~20 min can be attributed to an increase in the surface area due to crack formation. The data of Table I also shows that even for nitrogen heat-treatments there is a slight tendency for the magnesium to leach out.

The spike wells of Fig. 3a could be due to preferential etching along dislocation lines. If this is the case then the dislocation density would be a surprising 10⁸ per cm². This is in contrast to values of 10³-10⁵

per cm² determined in conjunction with hot, liquid etches (5-7).

Summary

The etch rate of magnesium aluminum spinel in hydrogen has been established for purposes of substrate preparation. However, as a general practice hydrogen should be used with caution as an ambient for processes which use spinel as a substrate. Its use either as a pretreatment etch or as a carrier gas for silicon heteroepitaxy is liable to cause surface deterioration through crazing.

Recently helium was reported to have been used as a carrier gas for silicon iso-epitaxy (19). We have seen that spinel wafers processed in such a fashion do not craze. Also the use of essentially hydrogen-free reaction gases should have the beneficial side effect of lowering the autodoping by minimizing the liberation of metal atoms by oxide reduction.

Acknowledgments

The author gratefully acknowledges the many contributions of his colleagues, especially those of J. M. Eldridge, J. D. Kuptsis, J. W. Matthews, and T. O. Sedgwick.

Manuscript submitted Dec. 18, 1970; revised manuscript received June 26, 1972.

Any discussion of this paper will appear in a Discussion Section to be published in the June 1973 JOURNAL.

REFERENCES

1. J. T. Milek, "Epitaxial Silicon and Gallium Arsenide Thin Films on Insulating Ceramic Substrates—A State of the Art Report," Air Force Contract F 33615-68-C-1225. Hughes Aircraft Co., Culver City, Calif., 1968.
2. J. D. Filby and S. Nielsen, *Brit. J. Appl. Phys.*, **18**, 1357 (1967).
3. G. W. Cullen, *J. Crystal Growth*, **9**, 107 (1971).
4. H. M. Manasevit and W. I. Simpson, *J. Appl. Phys.*, **35**, 1349 (1964).
5. J. E. A. Mauritz and M. L. Hammond, Paper 221RNP presented at Electrochem. Soc. Meeting, Detroit, Michigan, Oct. 5-9, 1969.
6. R. Aeschlimann, F. Gassmann, and T. P. Woodman, *Mater. Res. Bull.*, **5**, 167 (1970).
7. T. A. Zeveke, L. M. Kornev, and V. A. Tolomasov, *Soviet Phys. Cryst.*, **13**, 493 (1968).
8. A. Reisman, M. Berkenblit, S. Chan, and J. Cuomo, *This Journal*, **118**, 1653 (1971).
9. C. C. Wang *et al.*, "Single-Crystal Spinel for Electronic Application," Technical Report for Air Force Contract AFML-TR-68-320 October 1968, p. 26.
10. T. M. Buck and R. L. Meek, "Proceedings of the Symposium on Silicon Device Processing," National Bureau of Standards, Gaithersburg, Md., June 1970.
11. B. G. Koephe and R. J. Stokes, *J. Met. Sci.*, **5**, 240 (1970).
12. D. W. Readey and G. C. Kuczynski, *J. Am. Ceram. Soc.*, **49**, 26 (1966).
13. R. Muller and Hs. H. Gunthard, *J. Chem. Phys.*, **44**, 365 (1966).
14. A. Van Wieringen and N. Warmoltz, *Physica*, **22**, 849 (1956).
15. R. W. Lee, *J. Chem. Phys.*, **38**, 448 (1963).
16. D. G. Thomas and J. J. Lander, *ibid.*, **25**, 1136 (1956).
17. *American Institute of Physics Handbook*, D. E. Gray, *et al.*, Editors, pp. 4-218, McGraw-Hill Book Co., New York (1963).
18. K. L. Komarek, A. Coucoulas, and N. Linger, *This Journal*, **110**, 783 (1963).
19. D. Richman and R. H. Ariett, *ibid.*, **116**, 872 (1969).

A Novel Method for Fabrication of Ultrafine Metal Lines by Electron Beams

T. O. Sedgwick,* A. N. Broers, and B. J. Agule

IBM Thomas J. Watson Research Center, Yorktown Heights, New York 10598

The minimum width of metal lines fabricated by means of electron-beam resist technology has steadily decreased during the last five years. The most important reduction in line width was achieved by the development of a high-resolution electron resist, polymethylmethacrylate. With this resist metal lines down to 1000Å in width can be routinely fabricated using the following procedure developed by Hatzakis (1, 2): apply electron resist, expose, develop, evaporate metal, and finally strip excess metal and unexposed resist.

The limiting factor now in obtaining still narrower metal lines is due to the lateral exposure (Fig. 1a) of the resist from electrons scattered in the substrate (dashed line area). Since most of these electrons from a 15 kV beam are scattered within a depth of about

* Electrochemical Society Active Member.
Key words: silicon nitride, resolution, substrate preferential etching.

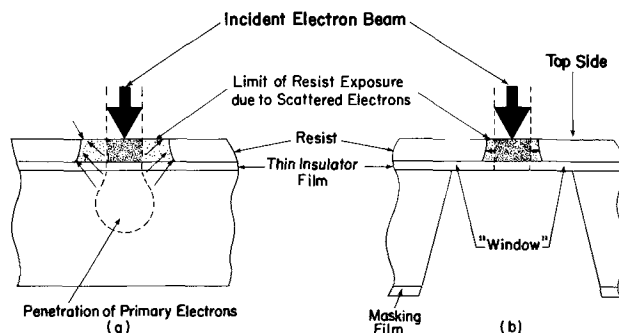


Fig. 1. Schematic diagram of (a) lateral electron resist exposure using a conventional substrate, and (b) reduced lateral resist exposure using a thin-film "window" substrate.

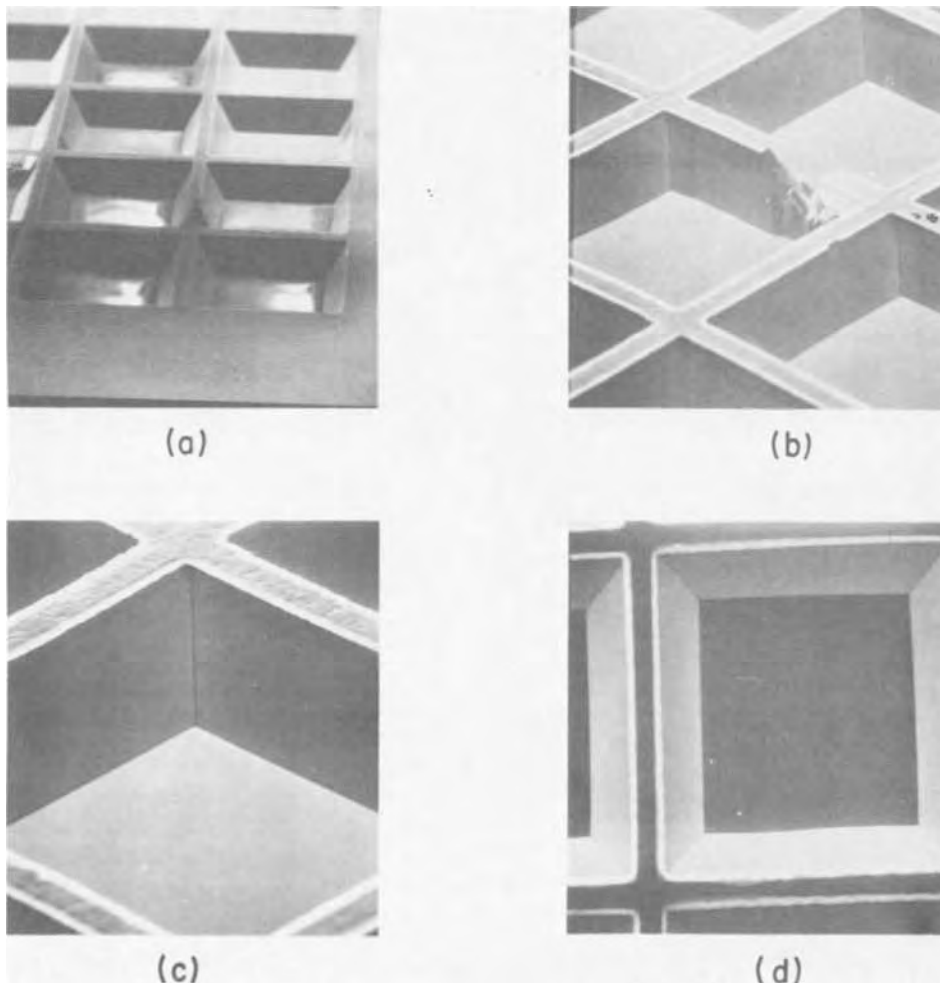


Fig. 2. SEM photographs of etched Si window structure. Masking film opening (top of photo) is 27 mils on a side (a), (b), (c) angle view, (d) top view; (b), (c), (d) metalized before photographing.

2μ in the substrate, presumably the lateral resist exposure could be greatly reduced by removing most of the substrate in the region to be electron-beam exposed. This note describes experiments which show that if the usual thick (compared to 2μ) substrate is replaced by a very thin substrate, e.g., a 1500\AA thick insulating film, as in Fig. 1b, the degree of lateral resist exposure is significantly reduced.

The "window-like" structure of Fig. 1b was fabricated by selective etching of a Si wafer (1 in. diameter, 5-10 mils thick, n-type 2-3 ohm-cm, $\langle 100 \rangle$) as follows. The polished (top) side of the wafer was coated with a thin insulator film of vapor deposited 300-1500 \AA Si_3N_4 (3) or sputtered or thermal SiO_2 . The lapped (bottom) side was coated with 1500 \AA Si_3N_4 for use as a masking film. A pattern of square openings was developed in the masking film with sides oriented along the $\langle 110 \rangle$ directions in the wafer. The Si wafers were etched using aqueous 33.5 weight per cent (w/o) NaOH at 90°C (4) or ethylene diamine 31.5 w/o, pyrocatechol 3.7 w/o, water 61.2 w/o at 110°C (5) to remove the Si under the "window." The NaOH did not etch the Si_3N_4 films noticeably during removal of the Si. However the NaOH etched SiO_2 films so fast that SiO_2 was not useful as the masking film. The ethylenediamine-pyrocatechol solution etched both the SiO_2 and the Si_3N_4 films at about 100 $\text{\AA}/\text{hr}$. The Si etchants were highly preferential and exposed near perfect reflecting $\langle 110 \rangle$ planes as walls of the holes. The size of the openings in the masking films was calculated to give a window size at the bottom of the hole varying from about 4 mils square up to 36 mils square. An opening 14 mils on a side would etch down through a 5 mils thick wafer to produce a window about 4 mils on a side.

Figure 2 is a series of scanning electron micrographs (SEM) of a pattern of etched window structures all shown from the bottom or masking film side of the Si wafer. (View Fig. 1b from the bottom.) The wafer is 8-10 mils thick and the masking pattern is 27 mils wide. The exceptional smoothness of the exposed $\langle 110 \rangle$ Si planes which constitute the sides of the holes is apparent. The edges of the crossed pattern of masking film appear white in the photos because they are no longer supported by Si which was undercut during the etching. Several defects are apparent in Fig. 2a and 2b showing Si walls that have been etched away probably due to defects in the masking film. The insulator windows (hole bottoms) are very flat as seen in Fig. 2b, 2c, and 2d which were metalized to prevent charging while taking the SEM photos. Figure 2a was not metalized and shows an apparent, but not real, irregular bottom surface due to charging while taking the SEM photo.

The SiO_2 windows were fragile and easily broken if larger than 10 mils on a side. The sputtered SiO_2 films gave slightly dimpled or stretched windows, while the thermal SiO_2 gave clearly wrinkled windows, both of which made it difficult to spin on thin uniform electron resist layers for metal line fabrication. On the other hand, the Si_3N_4 windows were extremely flat and relatively strong. Windows as large as 36 mils on a side and only 1500 \AA thick were made. The windows used for the electron-beam resist exposure and metal line fabrication described below were only 4 mils on a side and 1500 \AA thick and most windows were not broken during normal handling procedures. It was even possible to make Si_3N_4 windows about 4 mils on a side down to a thickness of 300 \AA . In order to test the notion that a thin substrate would enable ultra-fine line fabrication due to reduced electron back-scattering, the following experiment was performed: several 1500 \AA thick Si_3N_4 window structures were coated with polymethylmethacrylate resist and exposed with a 100 \AA diameter electron beam (25 kV) at a line-charge density of 1.2×10^{-10} coulombs/cm.

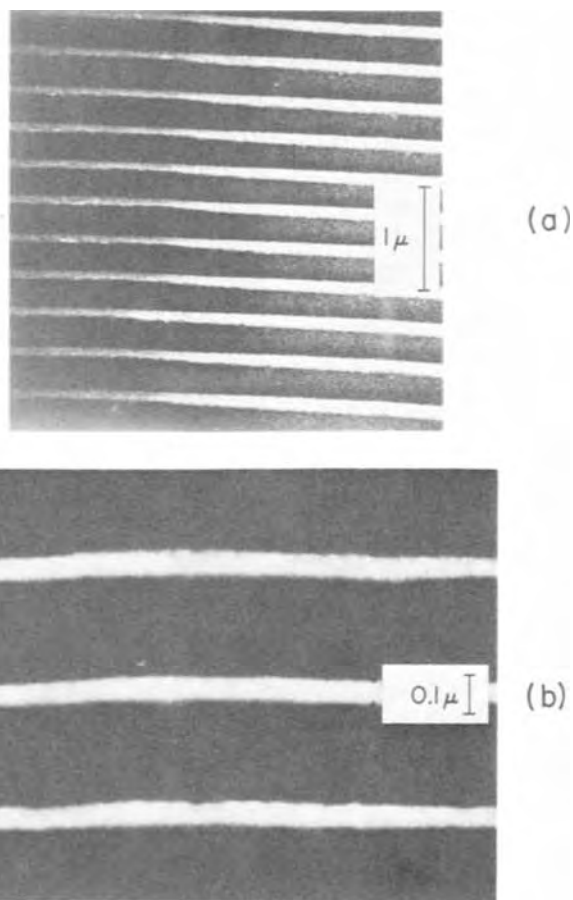


Fig. 3. (a) Metal line pattern fabricated over Si wafer (light, right portion) and over 4 mils Si_3N_4 window (dark, left portion); (b) higher magnification view of metal lines over window.

The beam current was $1.5 \times 10^{-10}\text{A}$. Aluminum metal lines (ca. 600 \AA thick) were fabricated both over the bulk (light portion of Fig. 3a) and over the window (dark portion of Fig. 3a). The fact that the SEM image is darker over the window is direct evidence that fewer electrons are scattered back out of the thin window-like substrate. From Fig. 3a it can be seen that the width of the metal lines is about 1000 \AA over the Si (light portion) and only 600 \AA over the Si_3N_4 window (dark portion). The smaller line width over the window (shown more clearly in Fig. 3b) is apparently due to the reduced intensity of scattered electrons which cause lateral exposure of the resist. The reduction in line width described here was repeated in several experiments. A systematic study of metal-line width as a function of substrate "window" thickness has not yet been undertaken. It should be noted, however, that the metal-line width is reduced gradually, as would be expected, as the lines pass from right to left in Fig. 3a over the edge of the Si substrate which is tapered due to the etching process (see Fig. 1b) and onto the "window" proper.

Acknowledgment

The authors wish to thank C. Bremer for the SEM photos in Fig. 2. They would also like to acknowledge helpful discussions with O. C. Wells, and M. Hatzakis.

Manuscript submitted June 15, 1972; revised manuscript received Aug. 7, 1972.

Any discussion of this paper will appear in a Discussion Section to be published in the June 1973 JOURNAL.

REFERENCES

1. I. Haller, M. Hatzakis, and R. Srinivasan, *IBM J. Res. Develop.*, **12**, 251 (1968).

2. M. Hatzakis, *This Journal*, **116**, 1033 (1969); and A. N. Broers and M. Hatzakis, in *Microscopie Electronique, Proc. 7th Intern. Electron Microscopy Conf. Grenoble (1970)*, Vol. 1, p. 249.
3. J. A. Aboaf, *This Journal*, **116**, 1736 (1969).
4. W. C. Rosvold, W. H. Legat, R. L. Holden, *IEEE Trans. Electron Devices*, **ED-15**, 640 (1968).
5. R. M. Finne and D. L. Hein, *This Journal*, **114**, 965 (1967).

The Rate of the Reaction of Nickel with Gaseous Phosphorus and the Profiles of the Scales Formed

Yoshinori Sasaki and Shiro Ueda

Department of Synthetic Chemistry, Faculty of Engineering, Chiba University, Yayoi-cho, Chiba, Japan

Many studies on nickel phosphides have been reported previously. Recently the catalytic activity of nickel phosphides has been of interest, e.g., the reduction of nitrobenzene (1), the polymerization of α -olefins (2), and the hydrogenation of acetylene hydrocarbons (3).

In an earlier paper (4), the kinetics and mechanism of an attack of phosphorus vapor on nickel sheets were studied by gravimetric means. However, only a few morphological observations were made. The present paper deals with the profiles of the scales produced, together with the kinetics on an increase of the thickness of the phosphide layer.

The specimens phosphidized in a preceding research (4) were used in this study. They were embedded in a polyester resin, and then their cross sections were mirror-polished with a very fine powder of Cr_2O_3 .

Thicknesses of these phosphide layers were determined by microscopic observation, and plotted against a square root of the elapsed time. Figure 1 shows that the reactions have a tendency to follow a parabolic

Key words: phosphidation of Ni, scale morphology.

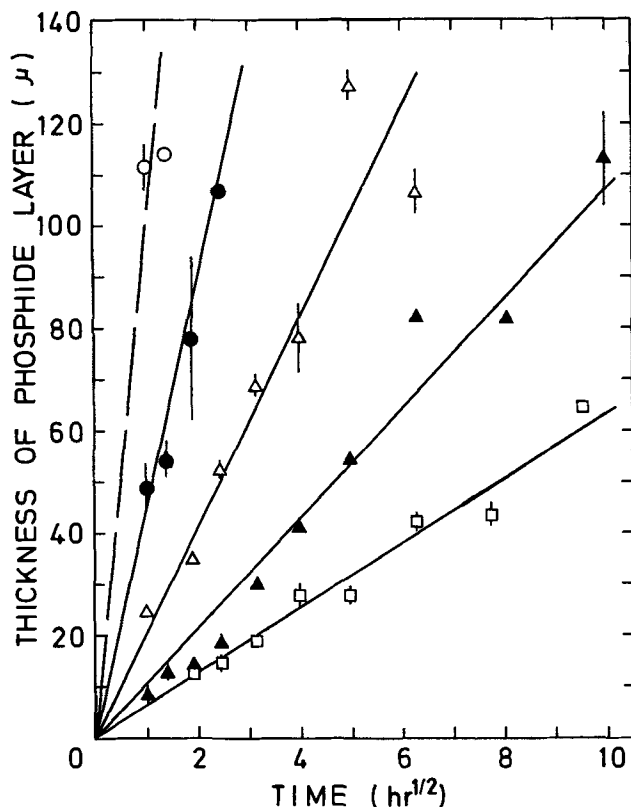


Fig. 1. Parabolic phosphidation of nickel in 2 atm phosphorus: \circ 600°, \bullet 550°, \triangle 500°, \blacktriangle 450°, \square 400°C.

behavior. The scatter in the data may result from the difference in porosity of the layers. Even on the same phosphidized specimen, the thickness is not necessarily the same for the position chosen. All the phosphide phases obtained are very stable at room temperature.

The parabolic-rate constants obtained at the 2 atm-reactions were as follows: $39 \pm 10 \mu^2/\text{hr}$, 400°C; $114 \pm 27 \mu^2/\text{hr}$, 450°C; $455 \pm 108 \mu^2/\text{hr}$, 500°C; $2000 \pm 400 \mu^2/\text{hr}$, 550°C; $10,400 \pm 4,000 \mu^2/\text{hr}$, 600°C. Their Arrhenius plot yielded the activation energies of 26 ± 5 kcal/mole (400°-500°C) and 42 ± 9 kcal/mole (500°-600°C).

The x-ray patterns showed that the Ni_2P compound is certainly formed under all the conditions. The x-ray peaks of NiP_2 were surely observed at 400° and 450°C, but not at 500°C and above. The peaks of Ni_3P_5 were very low, but were recognized in the early stages through 400°-600°C, and, especially at 400° and 450°C, were comparatively higher (4).

Faceted phosphide grains developed over large parts of the surface are shown in Fig. 2, which reveals the crystals to grow stepwise. Its x-ray diffraction peaks (4) were identified as belonging to those of Ni_2P , showing the epitaxial growth of a (111) plane ($2\theta_{\text{CuK}\alpha} = 40.8$) and (300) + (002) planes ($2\theta_{\text{CuK}\alpha} = 54.2$). Faceted grains were not formed except at 500°C in 1 Torr phosphorus for 3-11 hr.

Phosphide whiskers were frequently observed on reactions in 2 atm phosphorus at 450°, 500°, 550°, and 600°C, and in 1 and 4 Torr at 500°C, but not at 400°C.

The growth of platelets was a common phenomenon at 500°C in 1-1520 Torr phosphorus, but was not observed except for these conditions. It is not clear, why such phenomenon took place at 500°C alone. It is not evident by x-ray-spectrography whether the different phase has been formed.

Typical platelets and whiskers, which developed at 500°C, are shown in Fig. 3: a platelet having corners

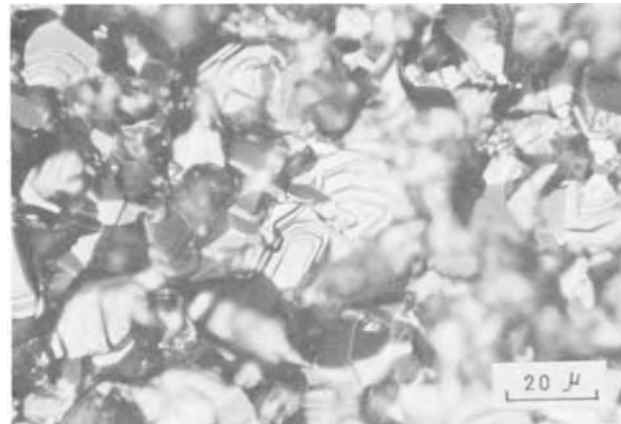


Fig. 2. Faceted phosphide grains formed at 500°C for 11 hr in 1 Torr phosphorus.

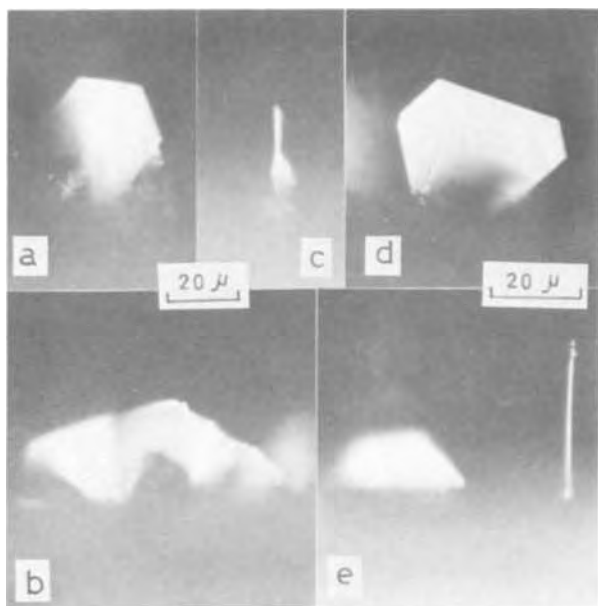


Fig. 3. The nickel-phosphide platelets and the whiskers grown on surfaces of specimens phosphidized at 500°C at (a) 4 Torr for 1 hr, (b) 4 Torr for 8 hr, and (c), (d), and (e) 1 Torr for 8 hr.

of an angle of 120° (Fig. 3a); a platelet possessing several creases (Fig. 3b); a whisker growing on the top of a platelet (Fig. 3c); a stepwise growing platelet (Fig. 3d); and the coexistence of a platelet and a whisker (Fig. 3e). The last three platelets (Fig. 3c, d, e) have grown at different parts of the same specimen.

Cross sections of phosphide-tarnishing layers formed at 400°C (Fig. 4) indicate the formation of thick, continuous phosphide films which appear to be in very close contact with the underlying metal. Long lines of fine pores are visible. In particular, it is of interest

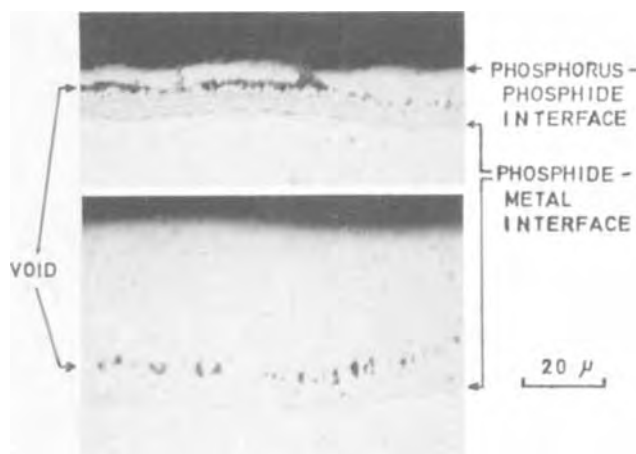


Fig. 4. Cross sections of specimens phosphidized at 400°C in 2 atm phosphorus for 3.5 hr (top) and for 60 hr (bottom).

that the position of voids from the unchanged nickel was not altered significantly throughout the reaction time at 400°C. The formation of voids might be due to the collapse of cation vacancies. Although the cross sections of a series of specimens phosphidized at 400°C were etched with conc nitric acid at room temperature, this treatment did not cause an appearance of a new phase.

Figure 5b shows some phase boundaries on the etching-treatment appearing in the same way, namely, showing an existence of two or three phases. After reaction for 65 hr (Fig. 5c), there is a double line of large elongated voids, parallel to the phosphide/metal interface. This double line was more plainly viewed at lower magnification in a microscope.

In the 500°C reaction, the inner layer (Fig. 6a) corresponds to Ni₂P, and the outer to higher phosphides. The same etching showed that the phases near the

Fig. 5. Transverse sections of specimens phosphidized at 450°C in 2 atm phosphorus for (a) 40 hr, (b) 40 hr, etched with conc HNO₃, and (c) 65 hr.

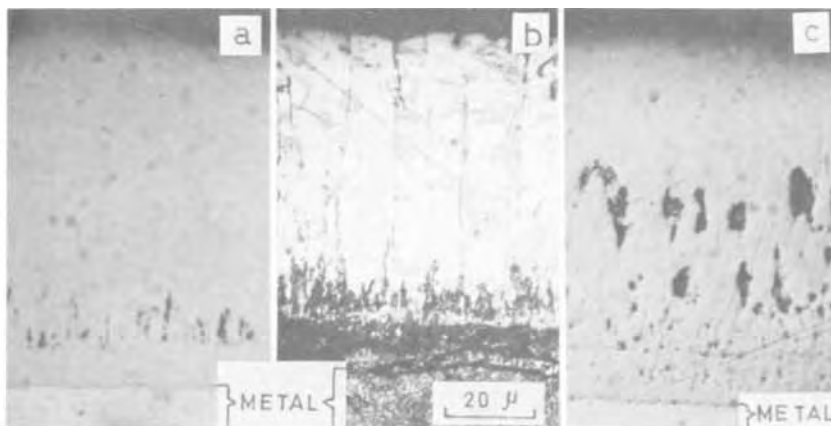
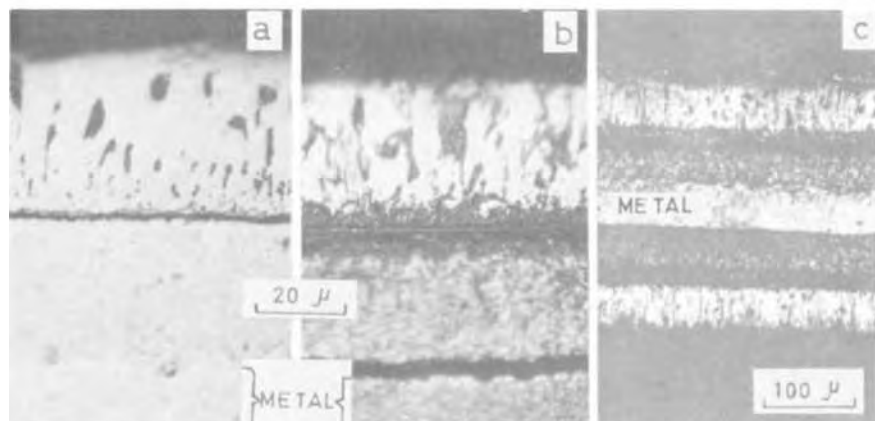


Fig. 6. Transverse sections of specimens phosphidized at 500°C in 2 atm phosphorus for (a) 16 hr, (b) 16 hr, and (c) 40 hr; (b) and (c) etched with conc HNO₃.



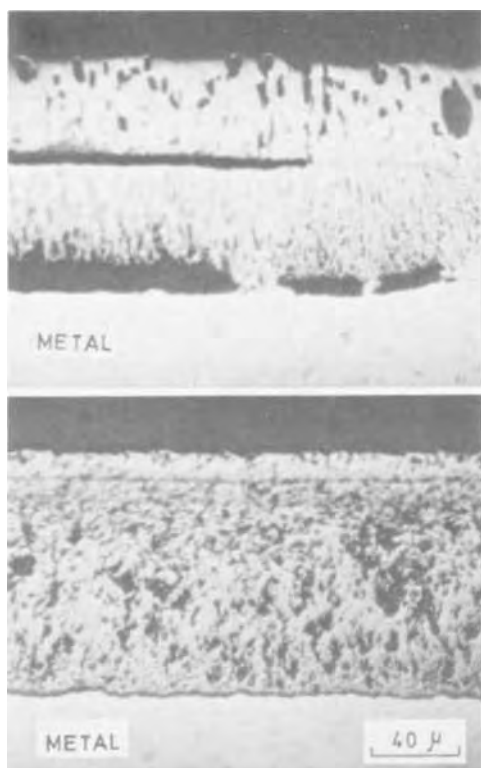


Fig. 7. Transverse sections of specimens phosphidized in 2 atm phosphorus. Upper micrograph, phosphidized at 550°C for 6 hr; lower micrograph, at 600°C for 1 hr.

solid-solid interfaces are corroded much more quickly than bulk phases (Fig. 6b), and that at least three

layers exist (Fig. 6c), being consistent with the phosphorus distribution curve obtained by an electron microprobe (4). The transverse sections in the case of lower phosphorus pressures, namely, 1, 4, and 20 Torr at 500°C, were almost similar to those in 2 atm phosphorus at the same temperature.

In the case of the 550°C reaction too (Fig. 7), the outer layer is obviously porous and the inner is comparatively dense. The dark portions near the solid-solid interfaces are a groove which appeared during polishing, probably because of brittle layers. When the layers of Fig. 7 were etched by conc nitric acid, the aspects similar to Fig. 6c were observed.

When the nickel sheets were phosphidized to completion at 500°, 550°, and 600°C, numerous large voids were observed at the centers of their transverse sections.

The phosphidation rates which were determined by the measurement of the change of both the weight and the thickness were parabolic, and the factor governing the reaction appears to be diffusion processes complicated with the generation of a large number of voids and with the growth of various crystals.

Manuscript submitted May 11, 1972; revised manuscript received Aug. 1, 1972.

Any discussion of this paper will appear in a Discussion Section to be published in the June 1973 JOURNAL.

REFERENCES

1. N. P. Sweeny, C. S. Rohrer, and O. W. Brown, *J. Am. Chem. Soc.*, **80**, 799 (1958).
2. A. P. Stuart, U.S. Pat. 2,996,493; C.A., **56**, 2578d (1962).
3. G. Schiller, German Pat. 1,137,003; C.A., **58**, 3259a (1963).
4. Y. Sasaki, A. Kato, and S. Ueda, *This Journal*, **118**, 101 (1971).

Nondestructive Photovoltaic Technique for the Measurement of Resistivity Gradients in Circular Semiconductor Wafers

D. L. Blackburn and H. A. Schafft

Institute for Applied Technology, National Bureau of Standards, Washington, D. C. 20234

and L. J. Swartzendruber

Institute for Materials Research, National Bureau of Standards, Washington, D. C. 20234

Resistivity gradients in a semiconductor wafer can adversely affect the characteristics, yield, and reliability of devices fabricated from such a wafer. It is therefore of critical importance to be able to identify and cull out wafers with unacceptably large resistivity gradients. The method (1) commonly used to measure resistivity variations in semiconductor wafers involves six four-probe resistivity measurements: two at the wafer center, and four, 3.2 mm from the edge, 90° apart. Several problems are encountered with this method. Swartzendruber (2) has discussed a basic limitation in the application of the four-probe method to the measurement of resistivity variations due to the relatively large sampling region of the probes. Recently, Vieweg-Gutberlet and Schönhofer (3) have examined this limitation in greater detail and have recommended that to obtain more exact information about the radial resistivity profile along a diameter of a wafer, two-probe measurements should be made on a bar cut along that diameter of the wafer. Another

problem is that the off-center correction factor (4) is very sensitive to the location of the probe near the wafer edge. As a result, small uncertainties in the probe placement produce large errors in the apparent resistivity. Another drawback to the standard method is the lack of information about the resistivity variations between the center and the measurement points near the edge of the wafer. Perhaps the most critical difficulty with the four-probe technique results from the placement of the probes on the wafer surface. The damage caused by the probes may of itself be detrimental to the reliability and yield of devices fabricated in the region of the damage.

A practical alternative to the four-probe technique for making resistivity gradient measurements along the diameter of a circular semiconductor wafer is described in this paper. This technique, which is based upon the bulk photovoltaic effect of Tauc (5), requires no contact with the flat surface of the wafer and permits a continuous measurement of the resistivity gradient along the wafer diameter to be made. Oroshnik and Many (6, 7) and Baev and Valyashko

Key words: germanium, inhomogeneities, measurement method, photovoltaic effect, resistivity, semiconductors, silicon.

(8, 9) have described photovoltaic techniques for measuring resistivity variations in bar-shaped germanium specimens and in rectangular germanium wafers. Munakata (10) has described an electron voltaic effect which might also be applied to the measurement of resistivity gradients in semiconductors. Oroshnik and Many (11) have also described a photovoltaic technique for making qualitative resistivity gradient measurements on circular silicon and germanium wafers, but no practical application of the photovoltaic effect to the quantitative measurement of resistivity gradients of circular semiconductor wafers has been attempted.

In this paper, a mathematical expression is derived which relates the resistivity gradient along a wafer diameter to the photovoltage measured at the diameter ends on the rim of the wafer. A measurement technique is described which allows one to determine the radial resistivity profile along a wafer diameter using the derived mathematical relation. Resistivity profiles as determined by the photovoltaic technique are compared with four-probe resistivity profiles made on the same wafer diameter and with two-probe resistivity profiles made on bars cut along that wafer diameter.

Theory

Tauc (5) has derived the underlying physical law of the photovoltaic phenomenon and has discussed its physical aspects. The bulk photovoltaic effect is a physical phenomenon which occurs when electron-hole pairs are photogenerated in a region of an impurity-density gradient. In the region of an impurity-density gradient, or equivalently a resistivity gradient, an internal electric field exists in the semiconductor. This is much like the situation at a p-n junction, only one is concerned here with a much smaller impurity-density gradient and thus a much smaller electric field. When excess electron-hole pairs are generated in this region, they are separated by the internal electric field. The steady-state distribution of the separated carriers is such that the magnitude of the net internal field is reduced. It is the reduction in magnitude of the net internal field which results in the photovoltage which can be measured at contacts made to the specimen. It is possible to relate this measured photovoltage to the resistivity gradient in the region where the excess electron-hole pairs are distributed.

The theory of Tauc (5) is basically a one-dimensional theory, valid for a narrow semiconductor bar. In the measurements which have been performed on bar shaped specimens (6-9), a narrow line of light illuminates the entire width of the bar and the photovoltage is measured at the ends of the bar. The photovoltage which is measured is proportional to the number of excess electron-hole pairs generated as well as the local resistivity gradient. Thus a determination of the number of excess carrier pairs generated is also needed in order to calculate the resistivity gradient. This can be accomplished by measuring the photoinduced change in specimen resistance, ΔR , as measured at the same contacts as the photovoltage, if one knows the relation between ΔR and the photoinduced change in resistivity, $\Delta\rho$, in the region of the excess carrier concentration. The change in resistivity is related to the change in carrier density by the equation

$$\Delta\rho = \rho^2|q|(\mu_n\Delta n + \mu_p\Delta p) \quad [1]$$

where Δn is the excess electron density and Δp the excess hole density. The relation between ΔR and $\Delta\rho$ for the case of a narrow semiconductor bar is trivial, but the development of the relation for the case of a circular wafer is somewhat more involved. An outline of this development appears later in this section. Numerous, not fully controllable, factors such as surface reflectivity and effective carrier lifetime, affect the number of excess carriers generated. Since these may, and probably will, vary as a function of position on the specimen, it has been recognized (6) that it is

important to measure ΔR as a function of position along the specimen.

The extension of the photovoltaic technique to the measurement of resistivity gradients along the diameter of circular wafers required that expressions be developed which describe how the circular geometry affects both the measured photovoltage, V , and ΔR . The assumptions made in the derivation are: (i) the excess carrier concentration is essentially uniform with depth in a cross section beneath the area illuminated by the light; (ii) the excess carrier concentration is always zero at a measurement contact; (iii) the excess carrier concentration is always much less than the equilibrium carrier concentration; (iv) the resistivity gradient is only radial (that is, along a diameter); (v) the light is always several light spot diameters removed from a measurement contact. Except for (iv) and (v), these assumptions are the same as for the case of bar-shaped specimens. Condition (iv) is required so that excess carrier pairs are not separated in a direction perpendicular to the measurement diameter. Such carrier pairs contribute to the measured ΔR but contribute only second order effects to V . Condition (v) is required because of the breakdown of geometrical correction factors as the light spot nears the edge of the wafer. Contrary to the case for bars, a current shunting the illuminated region exists in the wafer when the photovoltage is generated. The specimen geometry appropriate for deriving the expressions describing the effect of the circular geometry on V and ΔR is illustrated in Fig. 1. The wafer is illuminated by a circular spot of light located at a point on the X (measurement) axis.

To obtain the desired expressions, the artifact of replacing the charge separation in the region of the light spot by a potential dipole $\langle U\epsilon \rangle$, is used, where U is the voltage and ϵ the distance between the positive and negative poles. To facilitate the derivation of the relation between $\langle U\epsilon \rangle$ and the potential difference at the contacts at the wafer rim, a current dipole is placed inside the potential dipole such that the proper potential dipole is obtained. The relation, obtained by the method of conformal transformation, is

$$V = \frac{2\langle U\epsilon \rangle}{b} \frac{1}{1 - (x/b)^2} \quad [2]$$

where b is the wafer radius and x is the light spot position with respect to the wafer center. To obtain

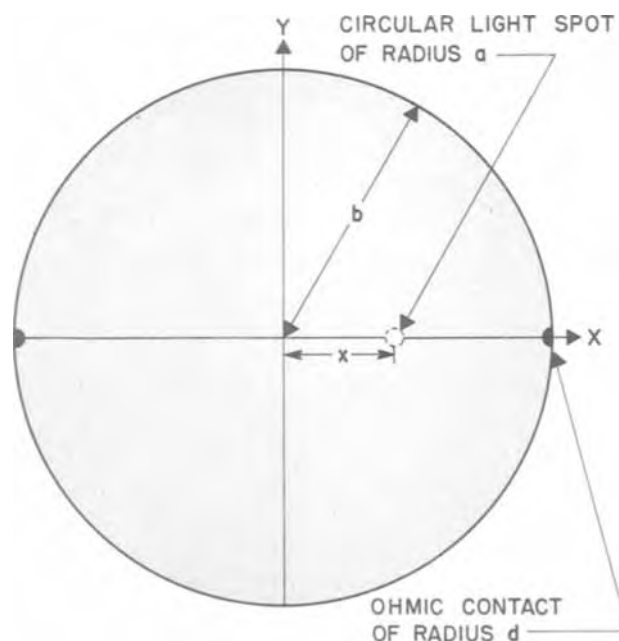


Fig. 1. The specimen geometry for which Eq. [9] applies

the appropriate dipole strength, the expression given by Tauc (5) for the photovoltage measured at the ends of a narrow bar when illuminated by a narrow line of light is used

$$U = \frac{2kT}{q} \frac{1}{(1 + \mu_M/\mu_m)} \frac{d\rho}{dx} L_o \Delta\sigma \quad [3]$$

where L_o is the length of the illuminated segment. For $\Delta\sigma \ll \sigma_o$, this can be written

$$U = - \frac{2kT}{q} \frac{1}{(1 + \mu_M/\mu_m)} \frac{1}{\rho} \frac{d\rho}{dx} \frac{\Delta\rho}{\rho} L_o \quad [4]$$

where ρ is the resistivity at the region illuminated. To simplify the measurement, ρ is replaced by $\bar{\rho}$, the average specimen resistivity, in this expression. Using Eq. [4] and appropriately averaging over a circle of radius a , the average voltage dipole strength for a circular spot of radius a becomes

$$\langle U_e \rangle = - \frac{4kT}{3q} \frac{1}{(1 + \mu_M/\mu_m)} \frac{1}{\bar{\rho}} \frac{d\rho}{dx} \frac{\Delta\rho}{\rho} a^2 \quad [5]$$

Included is a factor of $1/2$ to account for the potential drop within the illuminated region which is a result of the current generated by the shunting of the separated charge by the surrounding material. The factor of $1/2$ is an approximation based upon the fact that, for a circular spot on an infinite sheet, the resistance of the spot as measured at points at the ends of a diameter of the spot assuming the remainder of the infinite sheet removed, is equal to the resistance of the infinite sheet as measured at the same two points with the spot removed.

For contacts as shown in Fig. 1, the resistance of the wafer is

$$R_o = \frac{2\bar{\rho}}{\pi t} \ln \left(\frac{2 - d/b}{d/b} \right) \quad [6]$$

where d is the radius of the contact, $\bar{\rho}$ is the average specimen resistivity, t is the thickness of the wafer, and the contacts are assumed to be ohmic. The perturbation in R_o caused by a spot of radius a and resistivity $\rho + \Delta\rho$ can be calculated if it is assumed that $a \ll b$ and $d \ll b$. The contacts are replaced by current sources of values $+2I$ and $-2I$ and it is assumed the spot lies on an infinite sheet. This yields a problem which can be solved analytically by conformal transformation to yield

$$\frac{\Delta R}{R_o} = \frac{\Delta\rho}{\bar{\rho}} \frac{(a/b)^2}{\ln \left[\frac{2 - (d/b)}{d/b} \right]} [1 - (x/b)^2]^2 \quad [7]$$

To eliminate the need to know d , Eq. [6] and [7] can be combined to give

$$\Delta\rho a^2 = \Delta R b^2 \frac{\pi t}{2} \left[1 - \left(\frac{x}{b} \right)^2 \right]^2 \quad [8]$$

Equations [2], [5], and [8] can be combined to give the relationship of the resistivity gradient at the light spot to V and ΔR .

$$\frac{d\rho}{dx} = - \frac{3q}{4\pi kT} \left(\frac{1 + \mu_M}{\mu_m} \right) \frac{1}{\bar{\rho}^2} \frac{V(x)}{bt \Delta R(x)} \quad [9]$$

Apparatus

The electrical circuit used to make measurements of the photovoltage and photoinduced change in specimen resistance is shown in Fig. 2. The lock-in amplifier was used because the magnitudes of the photovoltaic signals were generally $1 \mu V$ or less. The rate at which the light is chopped must be adjusted so that the on-time of the light is long enough to achieve a steady-state excess carrier distribution. The X-Y recorder produces continuous plots of the photovoltage or

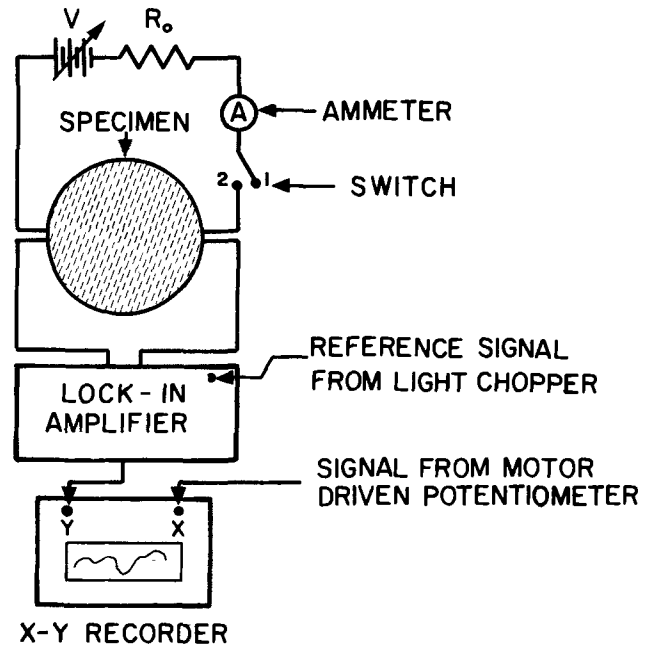


Fig. 2. Schematic of electrical circuitry used to measure the photovoltage and photoinduced change in specimen resistance. With the switch in position 1, the photovoltage can be measured; in position 2, the photoinduced change in specimen resistance can be measured.

photoconductivity as a function of position along the wafer diameter.

The light source was a tungsten filament lamp. The light was concentrated on a circular aperture of variable diameter which was focused by a lens-mirror system onto the wafer surface to form the light spot.

The specimen holder used in this study is shown in Fig. 3. There are four sets of double knife-edge contact elements. The four contact elements permit the measurement of the average wafer resistivity, $\bar{\rho}$, by the van der Pauw technique (12, 13). It is this value

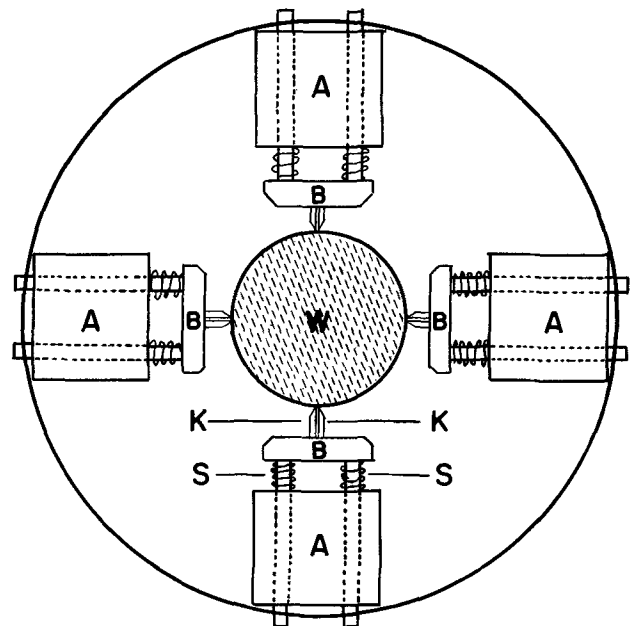


Fig. 3. Schematic illustration of specimen holder, where W is the wafer and K the knife edge. The springs, S, allow a variable knife-edge contact pressure to be applied. The knife-edge holders, B, are insulated from the knife edges. A is a moveable carriage to accommodate various wafer sizes and to allow knife-edge pressure adjustments.

of average specimen resistivity which is used in the evaluation of Eq. [9]. When the photovoltage or photo-induced change in specimen resistance is being measured, only the two contact elements at the ends of the measurement diameter are in contact with the wafer; the other two are retracted. When the photovoltage is measured, only one knife-edge at each contact element is used. When the change in specimen resistance is measured, both knife-edges at the contact element are used, one to carry the current, the other to measure the small, photoinduced change in potential across the specimen. This eliminates the problems associated with trying to measure a small change in potential with a nonohmic, current-carrying contact.

Results and Discussion

Both n- and p-type silicon and germanium wafers were measured in this study. The average resistivities ranged from about 1 ohm-cm to over 5000 ohm-cm. Most of the measurements were made on wafer surfaces lapped with 5 μm alumina abrasive. Preliminary measurements indicate that photovoltaic measurements made on chemically-mechanically polished surfaces differ little from measurements made on lapped surfaces.

To use Eq. [9] to determine the resistivity at points along the measurement diameter, an integration is required. In practice, values for $V(x)$ and $\Delta R(x)$ are determined for small segments of equal but arbitrary length for the entire diameter and a summation is performed. An absolute determination of $\rho(x)$ is not obtained, but the value obtained differs from $\rho(x)$ by the constant of integration, ρ_0 , the value of the resistivity at the point on the diameter where the summation begins. The photovoltaic profiles in the figures have been adjusted to give a best fit to the two-probe or four-probe profiles, since, for this study, it was important to establish how well the photovoltaic technique was able to determine resistivity variations. Since one also measures $\bar{\rho}$, the average specimen resistivity, a good indication of the range of absolute resistivity values is obtained.

A comparison of a photovoltaic and four-probe resistivity profile made along a diameter of a 1 ohm-cm, n-type silicon wafer is shown in Fig. 4.

It has been found that, in general, the agreement between the photovoltaic profiles and the four-probe and two-probe profiles has been very good in the central region but deteriorates somewhat beyond approximately one-half the radius. The deterioration in agreement can partially be explained by the presence of nonohmic measurement contacts. Since the metal

knife-edges are simply making a pressure contact with the wafer rim, the contact is not ohmic. Carriers which are photogenerated and which can diffuse to the metal-semiconductor contact without recombining, in violation of assumption (ii), generate a barrier photovoltage which is superposed on the bulk photovoltage. This does not appear to affect the photovoltaic measurement until the light probe is within a few carrier diffusion lengths of the contact if the wafer rim has been abraded or if the wafer has been cut from a centerless ground crystal.

An indication of the effect of varying the ohmic quality of a measurement contact can be seen in Fig. 5. The apparent increase in resistivity as measured by the photovoltaic method on an as-grown rim, as one approaches the edge of the wafer, results from diffusion of carriers to this highly nonohmic contact. When the rim is abraded, the contact becomes more ohmic and the photovoltaic and four-probe profile are in much better agreement. The nonohmic nature of the contacts was determined by measuring the specimen resistance between the contacts and comparing the magnitude for current in both directions between the contacts. A large difference in measured resistance for the two directions of current with the as-grown rim indicated that one of the contacts was much less ohmic than the other. This is also indicated by the asymmetry of the photovoltaic profile for the as-grown case in Fig. 5.

Three different resistivity profiles for the same wafer diameter are shown in Fig. 6. A four-probe profile and a photovoltaic profile were made on the circular wafer and a two-probe profile was made on a bar cut from the measurement diameter of the wafer. As mentioned previously, it has been recommended that to obtain more exact information about the resistivity gradient of a semiconductor wafer, particularly when steep gradients are present, a two-probe resistivity profile should be made in place of a four-probe profile (3). Note the agreement of the photovoltaic profile with the two-probe profile at the wafer center compared to the agreement between the four-probe and two-probe profiles at the center. It is not uncommon for the four-probe measurement to underestimate the depth of the valley in the resistivity profile at the wafer center when a steep gradient is present, as in Fig. 6. This is due primarily to the large area over which the four-probe measurement averages the resistivity. It is obvious that in this particular instance the resolution of the photovoltaic technique is superior to that of the four-probe technique.

Another difficulty encountered with making four-probe measurements is the sensitivity of the measure-

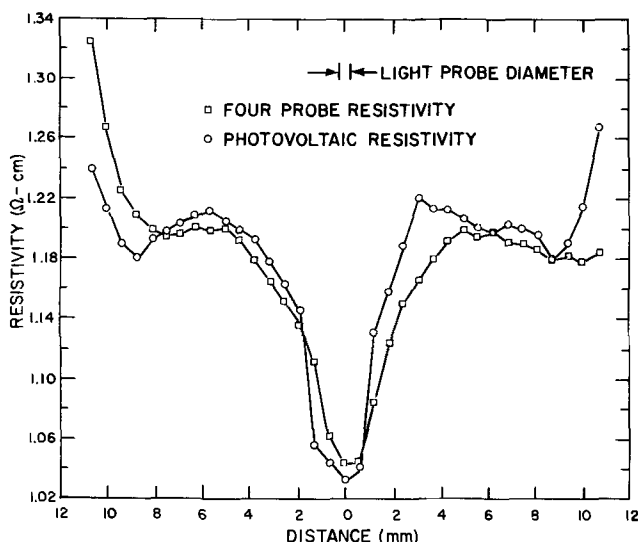


Fig. 4. Photovoltaic and four-probe resistivity profiles made along the diameter of an n-type silicon wafer.

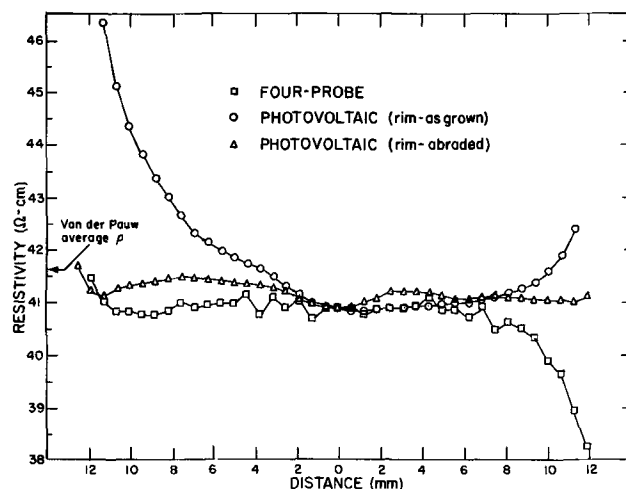


Fig. 5. Photovoltaic and four-probe resistivity profiles made along the diameter of a p-type silicon wafer. The effect of the nonohmic nature of the measurement contact on the photovoltaic profile is shown.

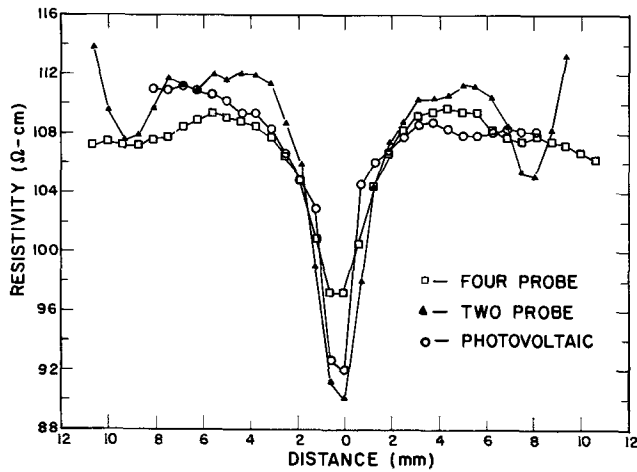


Fig. 6. Photovoltaic, four-probe, and two-probe resistivity profiles made along the same diameter of an n-type silicon wafer. The photovoltaic and four-probe profiles were made on the circular wafer while the two-probe profile was made on a bar cut from along the measurement diameter.

ment near the wafer edge to the placement of the probes. A small error in probe placement may result in a large error in the measured resistivity. This effect can be seen in Fig. 7 where the original four-probe profile was made with an error in the placement of the probes of approximately 0.3 mm. The photovoltaic measurement is relatively insensitive to slight errors in the location of the moving light spot. An error of 0.3 mm in light spot location would be barely detectable for the profile seen in Fig. 7.

In order to obtain an indication of the reproducibility of the photovoltaic technique, four independent photovoltaic resistivity profiles were made along the diameter of an n-type 65 ohm-cm silicon wafer. The results of these measurements can be seen in Fig. 8. The maximum difference at any point between any of the four profiles is less than 2% of the average specimen resistivity. Since the wafer had a large nonradial resistivity gradient along the chosen measurement diameter, and since the apparent resistivity profile of the wafer varied considerably as the measurement diameter was changed slightly, the reproducibility is considered to be indicative of that which could be obtained under less than ideal conditions.

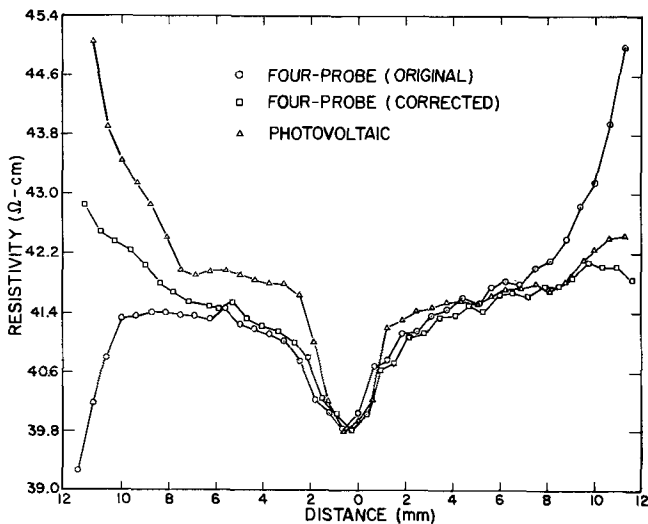


Fig. 7. Photovoltaic and four-probe resistivity profiles made along the diameter of a p-type silicon wafer. The effect on the four-probe resistivity measurement of a slight misplacement of the probes near a wafer edge is shown.

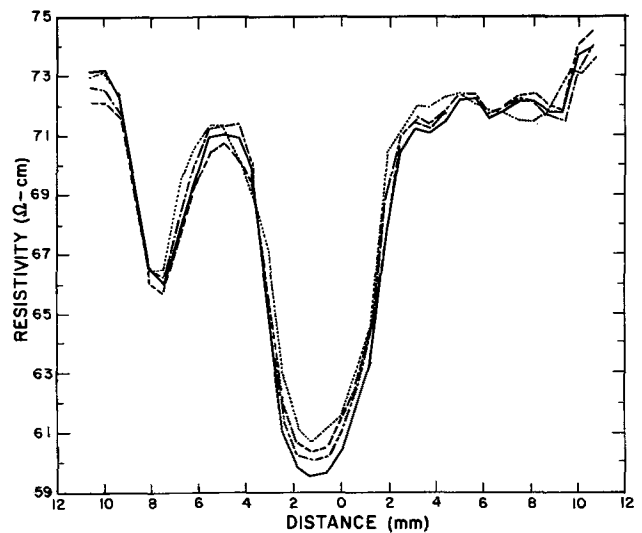


Fig. 8. Four independent photovoltaic resistivity profiles made along the same diameter of an n-type silicon wafer.

Since the magnitude of the photovoltage is proportional to the resistivity gradient, generally the higher the material resistivity the larger the photovoltage. For example, the magnitude of a 1% gradient in 10 ohm-cm material is 10 times the magnitude of a 1% gradient in 1 ohm-cm material. It is this fact which has not made it possible with the apparatus and technique described to measure resistivity gradients in material of resistivity less than 1 ohm-cm. Experiments indicate that the resistivity gradients of specimens with resistivities of less than 0.1 ohm-cm may be measured using the same measurement technique with a 25 mW He-Ne laser in place of the tungsten filament light source.

Conclusion

The theoretical and experimental basis has been provided for a quantitative, nondestructive measurement of the resistivity variations along the diameter of a circular semiconductor wafer. The measurement technique requires little or no special specimen preparation and requires contact only with the rim of the wafer.

It has been shown that resistivity variations in the central portion of a wafer as determined by the photovoltaic technique generally agree very well with those determined by the two-probe technique and with those determined by the four-probe technique when steep resistivity gradients are not present. When steep gradients exist in the central portion, it has been found that the photovoltaic resistivity profiles agree better with the two-probe profiles than the four-probe profiles do, indicating that the spatial resolution of the photovoltaic technique in these instances is superior to that of the four-probe technique. The ability of the photovoltaic technique for making resistivity gradient measurements within a few carrier diffusion lengths of a contact is limited by the nonohmic nature of the measurement contacts used.

The relative insensitivity of the photovoltaic measurement to light-spot location is contrasted with the extreme sensitivity of the four-probe technique near the edge of a wafer to the placement of the probes. The photovoltaic measurement has been found to be repeatable to within a few per cent of the average specimen resistivity, even under less than ideal conditions.

Acknowledgments

The authors thank Mr. M. Cosman for the preparation of the specimens, Mr. A. W. Stallings and Mr. G. P. Spurlock for construction of much of the apparatus, Dr. W. M. Bullis for his many helpful suggestions, and Mr. J. C. French and Dr. A. H. Sher for reviewing the manuscript.

This work was conducted as part of the Joint Program on Methods of Measurement for Semiconductor Materials, Process Control, and Devices at the National Bureau of Standards. Portions of this work were supported by the Defense Nuclear Agency and the National Bureau of Standards.

Manuscript received April 13, 1972.

Any discussion of this paper will appear in a Discussion Section to be published in the June 1973 JOURNAL.

LIST OF SYMBOLS

V	voltage measured at wafer rim, V
U	voltage at potential dipole, V
ϵ	dipole separation, cm
R_0	wafer resistance as measured at diameter ends, ohm
ΔR	photoinduced change in specimen resistance as measured at diameter ends, ohm
b	wafer radius, cm
x	light spot position along the wafer diameter with respect to wafer center, cm
d	measurement contact radius, cm
t	wafer thickness, cm
k	Boltzmann's constant, erg/°K
T	absolute temperature, °K
q	majority carrier charge, C
μ_M	majority carrier mobility, cm ² /V · sec
μ_m	minority carrier mobility, cm ² /V · sec
$d\rho/dx$	average resistivity gradient at illuminated region, ohm
ρ	unilluminated specimen resistivity at region of illumination, ohm-cm
$\bar{\rho}$	average specimen resistivity, ohm-cm
$\Delta\sigma$	change in conductivity of illuminated region, 1/ohm-cm

σ_0	unilluminated conductivity, 1/ohm-cm
μ_n	electron mobility
μ_p	hole mobility

REFERENCES

1. Methods of Test for Bulk Semiconductor Radial Resistivity Variation (ASTM Designation F81-70) in "Annual Book of ASTM Standards," Part 8. American Society for Testing and Materials, Philadelphia (1971).
2. L. J. Swartzendruber, *Solid-State Electron.*, **7**, 413 (1964).
3. F. Vieweg-Gutberlet and F. X. Schönhofer, *Arch. Tech. Messen*, No. 369, 237 (October, 1966) and No. 370, 259 (November, 1966).
4. L. J. Swartzendruber, Natl. Bur. Std. Tech. Note 199, (April, 1964).
5. J. Tauc, *Czech. J. Phys.*, **5**, 178 (1955).
6. J. Oroshnik and A. Many, *Solid-State Electron.*, **1**, 46 (1960).
7. J. Oroshnik and A. Many, *This Journal*, **106**, 360 (1959).
8. I. A. Baev and E. G. Valyashko, *Soviet Phys.-Solid State*, **6**, 1357 (1964).
9. I. A. Baev and E. G. Valyashko, *ibid.*, **7**, 2093 (1966).
10. C. Munakata, *Microelectronics and Reliability*, **6**, 27 (1967).
11. A. Many and J. Oroshnik, Testing of Semiconductors, U.S. Pat. No. 3,034,056 (1962).
12. L. J. Van der Pauw, *Philips Res. Rept.*, **13**, 1 (1958).
13. Standard Method for Measuring Hall Mobility in Extrinsic Semiconductor Single Crystals (ASTM Designation: F76-68) in "Annual Book of ASTM Standards," Part 8. American Society for Testing and Materials, Philadelphia (1971).

An Improved Polishing Technique for GaAs

V. L. Rideout

IBM Thomas J. Watson Research Center, Yorktown Heights, New York 10598

Certain electronic device applications that involve single-crystal GaAs are critically dependent on the substrate condition, *i.e.*, surface finish and flatness. In particular, the surface flatness of GaAs wafers is important in the fabrication of: (i) ultrathin epitaxial-layer devices such as semiconductor superlattices (1) or multilayered acoustic transducers; (ii) surface-wave acoustic devices using electron-beam exposure; and (iii) microwave-integrated circuits, metal-semiconductor field-effect transistors, and other device structures that involve photolithographic processing.

Since its development by Reisman and Rohr (2, 3), the NaOCl chemical-polishing technique has become a popular technique in the semiconductor industry for obtaining smooth mirror-finish surfaces on GaAs. Recently, another chemical polishing technique using H₂O₂ and NH₄OH has been developed by Dymant and Rozgonyi (4). All of these researchers, however, employed the same mechanical means to distribute the chemical etchant over the wafer surfaces, and we find that this can introduce certain undesirable effects.

The procedure employed until now is that the wafers to be polished are affixed to a disk which is allowed to rotate freely about a fixed point near the edge of a polishing plate which is covered by a polishing cloth. The rotation of the wafer-disk assembly is caused by the friction between the wafers and the liquid layer between the wafers and the polishing cloth (3). During rotation the etchant distributes itself over the wafer surfaces. Pressure on the wafers is provided by the weight of the wafer-disk assembly alone. In using this procedure we observed that the wafer-disk assembly

often rotated nonuniformly which invariably resulted in poor quality surfaces. Initially the etchant was applied periodically at 1 min intervals. During this interval the liquid is dispersed by the polishing action and hence the coefficient of friction varies during the time period. Thus we assumed that conversion to a more uniform feed rate would solve the problem; however, nonuniform rotation still often occurred, particularly when square-shaped or large-area samples were used. Increasing the weight of the disk led to more uniform rotation, but then edge rounding was greatly enhanced. To circumvent the problem we used an electric motor to drive the wafer-disk assembly at a constant rotational speed in the natural direction of free rotation. Subsequently it was found that if the wafer-disk assembly was motor driven at a speed slightly higher than the natural speed of rotation due to friction alone, then edge rounding of the polished wafers was significantly decreased, and surface flatness enhanced.

Experimental conditions for a typical polishing operation are as follows. The samples are affixed to a 4 in. diameter ¼ in. thick glass disk (weight, 140g) with wax, and lapped using 6 μ garnet powder in a water slurry. About 3-4 mils of material are removed. After careful rinsing and washing with a mild soap solution to remove particles, the disk is placed on a 12 in. diameter polishing plate. The center of the disk is positioned 3 in. from the center of the plate. Motor speed of the plate is 60 rpm while that of the disk is 30 rpm (the free rotational speed of the disk is about 20 rpm). The disk motor is constrained by a stop that prevents any downward force from being applied to

Key words: GaAs, chemical polishing, surface flatness, NaOCl.

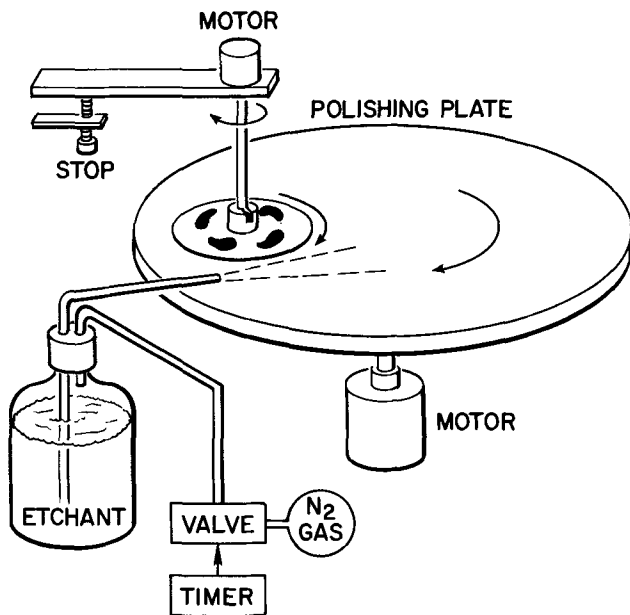


Fig. 1. Chemical polishing apparatus

the disk (see Fig. 1). The Politex PS Supreme polishing cloth (Geoscience Instruments Corporation) was found to be superior to the Pellon PAN-W for our applications. The etchant solution is 20:1 H₂O:NaOCl (Fisher reagent grade) and is replenished every hour. The feed rate is 4 ml of solution every 30 sec and the total polishing time is approximately 3 hr during which time about 1 mil of material is removed.

Both Cr-doped (semi-insulating) and Te-doped ($4 \times 10^{17} \text{ cm}^{-3}$ n-type) single-crystal $\langle 100 \rangle$, $\langle 111 \rangle$ A, and $\langle 111 \rangle$ B GaAs surfaces have been successfully polished with our apparatus. Measurements with a Talysurf instrument showed a surface flatness of better than $\pm 500 \text{ \AA}$ over 250 mils of surface. Dymant and Rozgonyi (4) achieved flatnesses of approximately 10,000 Å over a linear dimension of 1 cm, however, they made no attempts to optimize the over-all flatness of their wafers. To explain the improved surface flatness with our technique we propose that since the NaOCl polishing process is primarily chemical rather than mechanical, the primary purpose of mechanical motion is to distribute the etchant as uniformly as possible over the wafer surface. Thus mechanically driving the wafer-disk assembly in its natural direction of free rotation, but at a speed somewhat higher than its natural speed of free rotation, results in a more even exposure of the wafer surfaces to the etchant, and hence achieves flatter surfaces.

Manuscript received July 6, 1972.

Any discussion of this paper will appear in a Discussion Section to be published in the June 1973 JOURNAL.

REFERENCES

1. L. Esaki and R. Tsu, *IBM J. Res. Develop.*, **14**, 61 (1970).
2. A. Reisman and R. Rohr, *This Journal*, **111**, 1425 (1964).
3. A. Reisman and R. Rohr, U.S. Pat. No. 3,342,652 (1967).
4. J. C. Dymant and G. A. Rozgonyi, *This Journal*, **118**, 1346 (1971).

The Variation of the Solid Composition During the LPE Growth of Ga_{1-x}Al_xAs

W. G. Rado and R. L. Crawley

Ford Motor Company, Scientific Research Staff, Dearborn, Michigan 48121

The phase diagram of the Ga-Al-As ternary system has been calculated and explored experimentally by Ilegems and Pearson (1) and Panish and Sumski (2). Recently additional experimental data were presented by Alferov *et al.* (3) and by Rado, Johnson, and Crawley (4) on the variation of the AlAs concentration in LPE-grown Ga_{1-x}Al_xAs with the Al concentration in the Ga-rich growth solution, as a function of growth temperature. Although these data were in moderately good agreement with the calculated isotherms, deviations as high as 30% in the solid composition were found for solution compositions in the 0.003-0.006 atom fraction Al range for growth temperatures between 800° and 950°C. The purpose of this note is to present experimental data on the variation of the solid Ga_{1-x}Al_xAs composition with temperature during LPE growth runs.

The LPE growth apparatus and the technique for determining the relationship between layer thickness and instantaneous growth temperature have been described previously (5). Briefly, after the initial contact between a Ga-Al-As solution and a GaAs substrate was established, at each of two lower temperatures the solution was pushed off $\frac{1}{4}$ of the substrate, terminating growth on that part, so that a three-step growth profile was obtained. The temperature interval between successive pushes ranged from 20°-70°C.

Key words: solution growth, ternary systems, phase diagrams, III-IV alloys, LED.

Each grown layer was analyzed by slicing the wafer parallel to the push direction, lapping, polishing, and finally staining with 8 K₃Fe(CN)₆: 12 KOH: 100 H₂O by weight to reveal the substrate-layer interface. The thicknesses of the growth steps were measured from photomicrographs and by using the "push" temperatures a correlation between thickness and temperature was established.

The alloy composition was determined by electron-microprobe analysis. Measurements were made along the direction of growth in 2-20 μm steps. The error in these measurements was estimated to be $\pm 2\%$. The variation of the solid Ga_{1-x}Al_xAs composition with the grown layer thickness was converted to a variation with temperature by using the correlation between thickness and temperature established for the same layer earlier. The data for 8 runs are shown in Fig. 1. For comparison, curves calculated by Ilegems and Pearson (1) are also included. The growth parameters of the individual runs are given in Table I.

The values of the initial AlAs concentration in the LPE-grown solid next to the GaAs substrate, given in Table I, are in good agreement with previous experimental observations (4) except for run 4, which has a value slightly higher than expected.

The experimentally determined variations of the solid composition with instantaneous growth temperature plotted in Fig. 1 are in very good agreement with the corresponding calculations of Ilegems and Pear-

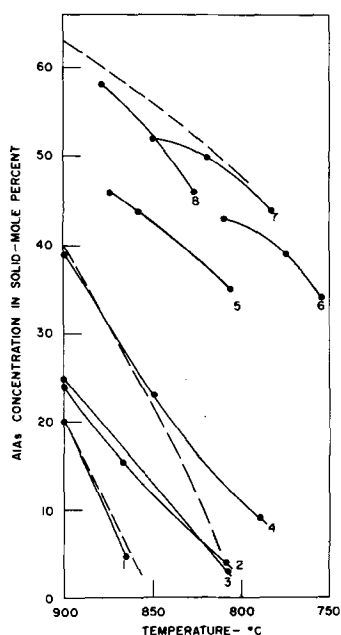


Fig. 1. The measured temperature variation of the solid $\text{Ga}_{1-x}\text{Al}_x\text{As}$ composition during growth from a Ga-Al-As solution (solid lines). The numbers correspond to the run numbers in Table I. The dashed lines are curves calculated by Ilegems and Pearson (1).

son (1). Therefore, although the solid-liquid equilibrium concentrations calculated by Ilegems and Pearson (1) for specific temperatures deviate somewhat from experimental observations (3, 4), once an initial composition of the solid is determined, the variation of the solid's composition with temperature during a growth run can be predicted reliably by using the calculations of Ilegems and Pearson (1).

Calculation of the Solubility and Solid-Gas Distribution Coefficient of N in GaP

G. B. Stringfellow

Hewlett-Packard Company, Palo Alto, California 94304

Several investigators have found that the presence of N in GaP increases the efficiency of green electroluminescent diodes (1-4). Logan *et al.* (4) found that N could be incorporated into GaP during liquid-phase epitaxial (LPE) growth at 1000°-1100°C by using a mixture of NH_3 and H_2 at atmospheric pressure as the N source. The following is a list of phenomena observed by Logan *et al.* (4), Lorimer and Dawson (5), and Thurmond and Logan (6): (i) The N concentration in GaP increased linearly with NH_3 partial pressure (P_{NH_3}) up to a concentration¹ of $\sim 2.5 \times 10^{18} \text{ cm}^{-3}$ at $P_{\text{NH}_3} = 10^{-3} \text{ atm}$; (ii) The efficiency of LED's fabricated in this material increased monotonically with P_{NH_3} below 10^{-3} atm ; (iii) With $P_{\text{NH}_3} > 10^{-3} \text{ atm}$ the crystal growth became disturbed and the efficiency of LED's began to decrease with increasing NH_3 partial pressure; (iv) Lorimer and Dawson found that at 1000°C increasing P_{NH_3} above 10^{-3} atm produced no increase in the N content of the GaP and caused GaN precipitation in the liquid.

Key words: GaP-GaN system, thermodynamics, phase diagrams, solution theory, solidus calculation.

¹The N concentrations reported by Logan *et al.* (4) were obtained from measured optical absorption coefficients by using a proportionality constant which Lightowers (7) found to be too high by a factor of four. Therefore, their reported concentrations have been divided by four before being used in this paper.

Table I. Initial composition for growth of $\text{Ga}_{1-x}\text{Al}_x\text{As}$

Run No.	$T_{\text{saturation}}$ (°C)	Atom per cent As (in solution)	Atom per cent Al (in solution)	Initial mole per cent AlAs (in solid)
1	909	4.90	0.25	20.0
2	900	4.46	0.29	23.9
3	889	4.44	0.29	24.8
4	892	3.51	0.45	39.0
5	873	2.61	0.50	45.8
6	812	1.32	0.34	42.6
7	847	1.51	0.55	51.3
8	880	2.23	0.91	57.8

Acknowledgment

We would like to thank J. Tabock of the Technical Services and Administration Department for the microprobe analyses.

Manuscript submitted April 7, 1972; revised manuscript received July 13, 1972.

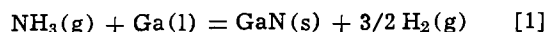
Any discussion of this paper will appear in a Discussion Section to be published in the June 1973 JOURNAL.

REFERENCES

1. M. Ilegems and G. L. Pearson, "1968 Symposium on GaAs," pp. 3-10, Institute of Physics and the Physical Society, London (1969).
2. M. B. Panish and S. Sumski, *J. Phys. Chem. Solids*, **30**, 129 (1969).
3. Zh. I. Alferov, V. M. Andreyev, S. G. Konnikov, V. G. Nikitin, and D. N. Tretyakov, Proc. Internat. Conf. on Heterojunctions I, p. 93 Academy of Sciences, Budapest, 1971.
4. W. G. Rado, W. J. Johnson, and R. L. Crawley, *This Journal*, **119**, 652 (1972).
5. W. G. Rado, W. J. Johnson, and R. L. Crawley, *J. Appl. Phys.*, **43**, 2763 (1972).

From this information it is clear that the solid solubility of N in GaP and the solid-gas distribution coefficient, defined as the ratio of the GaN content in GaP to P_{NH_3} , are important parameters in determining the crystal-growth conditions for GaP:N to be used for the fabrication of green LED's. The purpose of the present paper is to calculate the temperature dependence of these parameters by using the Phillips-Van Vechten model (8, 9) for the solid-pseudobinary alloy $\text{GaP}_{1-x}\text{N}_x$.

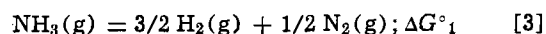
The reaction for incorporation of N during LPE growth of GaP may be written



The standard Gibbs free energy of reaction is given by

$$\Delta G^\circ = -RT \ln \left[\frac{a_{\text{GaN}}(\text{s}) (a_{\text{H}_2}(\text{g}))^{3/2}}{a_{\text{NH}_3}(\text{g}) a_{\text{Ga}}(\text{l})} \right] \quad [2]$$

where $a_i^{(j)}$ is the activity of component i in phase j. ΔG° may be obtained by considering the reaction to be the sum of two reactions



and



Both $\Delta G^{\circ}_1(10)$ and $\Delta G^{\circ}_2(6)$ have been determined as functions of temperature and thus $\Delta G^{\circ} = \Delta G^{\circ}_1 + \Delta G^{\circ}_2$ can be evaluated.

Two approximations can be made to simplify the calculation: (i) At temperatures below 1100°C $X_{Ga}^{(1)} \sim 1$, thus $a_{Ga}^1 \sim 1$; (ii) For the conditions of interest $P_{NH_3} \ll P_{H_2}$, giving $a_{H_2} \approx 1$ and $a_{NH_3} \approx P_{NH_3}$.

The only other parameter needed to calculate the solid-gas distribution coefficient from Eq. [2] is $a_{GaN}^{(s)}$ which is equal to $x\gamma_{GaN}$, where x is the mole fraction of GaN and γ_{GaN} is the activity coefficient of GaN in the solid. The activity coefficient may be written

$$\gamma_{GaN} = \exp(\bar{G}_{GaN}^{xs}/RT) \quad [5]$$

where \bar{G}_{GaN}^{xs} is the partial molar excess free energy of GaN in GaP. The excess free energy of the solid solution is

$$G^{xs} = \Delta H^M - T\Delta S^{M,xs} \quad [6]$$

where ΔH^M is the enthalpy of mixing and $\Delta S^{M,xs}$ is the excess entropy of mixing. For the GaP-GaN system where the solubility limit of GaN in GaP is small, indicating a very large positive ΔH^M , $\Delta H^M \gg T\Delta S^{M,xs}$ and

$$\begin{aligned} \bar{G}_{GaN}^{xs} &\equiv \left. \frac{\partial (N_o \Delta H^M)}{\partial N_{GaN}} \right|_{N_{GaN} = 0} \\ &= \left. \frac{d\Delta H^M}{dx} \right|_{x=0} \end{aligned} \quad [7]$$

which is the partial molar enthalpy of mixing at infinite dilution, denoted \bar{H}^*_{GaN} . N_o in Eq. [7] is the total moles of GaP and GaN. From Eq. [5] and [7], $a_{GaN}^{(s)} = x \exp(\bar{H}^*_{GaN}/RT)$.

Substituting the values of ΔG° and the 4 activities into Eq. [2] gives the following expression for the solid-gas distribution coefficient

$$x/P_{NH_3} = \exp[-(\Delta G^{\circ}_1 + \Delta G^{\circ}_2 + \bar{H}^*_{GaN})/RT] \quad [8]$$

The procedure for the calculation of \bar{H}^*_{GaN} is a modification of a method developed in detail previously (11). It consists of using the Phillips-Van Vechten model (8, 9) to calculate ΔH°_f , the standard enthalpy of formation of the alloy, as a function of alloy composition. This is used to determine the dependence of ΔH on x , from which \bar{H}^*_{GaN} may be obtained.

The Phillips-Van Vechten expression for the enthalpy of formation of the pure compounds and their pseudobinary alloys is

$$\Delta H^{\circ}_f = \Delta H_o a_o^{-3} f_1 P \quad [9]$$

where ΔH_o is a scaling parameter equal to $1.24 \times 10^4 \text{ \AA}^3\text{-kcal/mole}$, and a_o and f_1 are the lattice parameter and fraction of ionic character, both of which are taken as linear in composition. P is the dehybridization factor, which is related to the direct valence to-conduction-bandgaps E_o , E_1 , and E_2 by the expression

$$P = 1 - [0.432 E_2 / (E_o + E_1)]^2 \quad [10]$$

For the $GaP_{1-x}N_x$ alloys the variation of each energy gap with composition is assumed to be parabolic

$$E_j = E_{GaP,j} (1-x) + E_{GaN,j} x - c_j x(1-x) \quad [11]$$

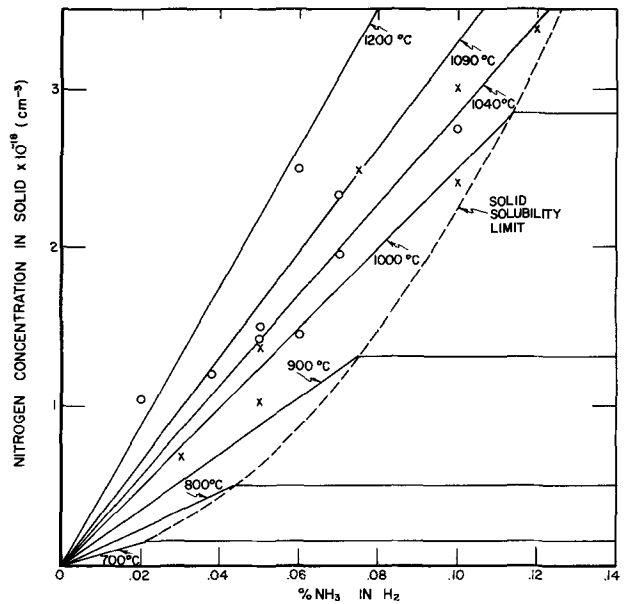


Fig. 1. Nitrogen concentration in GaP vs. P_{NH_3} at various temperatures. The experimental points are based on the data of Logan *et al.* (4) at 1090°C (○) and 1040°C (×). The solid lines were calculated as described in the text.

with $j = 0, 1, 2$. The values of E_o , E_1 , and E_2 have been measured for GaP (12, 8). GaN has the wurtzite lattice, but the bandgaps as well as a_o can be calculated for a hypothetical zincblende GaN as explained in (8, 13). The bowing parameter, c_j , may also be calculated as described in (13). It is the sum of two components

$$c_j = c_{1,j} + c_e \quad [12]$$

where $c_{1,j}$ is the intrinsic component due to the non-linear dependence of E_j on crystal potential, which is linear in x , and c_e is the extrinsic component due to the electronegativity difference between N and P (13)

$$c_e = (C_{NP})^2 = [1.5e Z(1/r_N - 1/r_P)e^{-k_s R}]^2 \quad [13]$$

Due to the large difference in the radii of N and P, $c_e = 21.9 \text{ eV}$.

The compositional dependence of ΔH^M can now be calculated by using the relation

$$\Delta H^M = (1-x)\Delta H^{\circ}_f, GaP + x\Delta H^{\circ}_f, GaN - \Delta H^{\circ}_f \quad [14]$$

where $\Delta H^{\circ}_f, GaP$, $\Delta H^{\circ}_f, GaN$, and ΔH°_f for the alloy are calculated using Eq. [9-11] and the parameters listed in Table I.² From the calculated ΔH^M vs. x , \bar{H}^*_{GaN} was determined from Eq. [7] to be 23 kcal/mole.

The concentration of N in GaP vs. P_{NH_3} at various temperatures can now be calculated with no adjustable parameters by using Eq. [8]. The results, which are plotted as solid lines in Fig. 1, are in excellent agreement with experimental points at 1090° and 1040°C based on the data of Logan *et al.* (4). It should

² The value of $\Delta H^{\circ}_f, GaN$ calculated using the Phillips-Van Vechten model is 52 kcal/mole. This is much higher than the experimental value of 26.4 kcal/mole (6) because of the strong N-N triple bond in the gas phase, which tends to make the GaN less stable relative to Ga liquid plus N_2 gas. Since we are concerned only with bonding in the solid, this discrepancy has no effect on our calculation.

Table I. Parameters used in the calculation of \bar{H}^*_{GaN}

Compound	f_1	a_o (Å)	E_o (eV)	E_1 (eV)	E_2 (eV)	$c_{1,0}$ (eV)	$c_{1,1}$ (eV)	$c_{1,2}$ (eV)
GaP	0.330	5.45	2.77	3.73	5.27			
GaN	0.500	4.49	2.95 ^(a)	6.16 ^(a)	10.38 ^(a)			
GaN-GaP						-1.6	-0.6	0.7

^(a) Calculated by the procedure described in Ref. (8) using D_{av} . As discussed in footnote 2 of this paper, D_{av} gives better agreement with experiment than the refined value of D . Thus the values do not agree with those quoted in Table VII of Ref. (18).

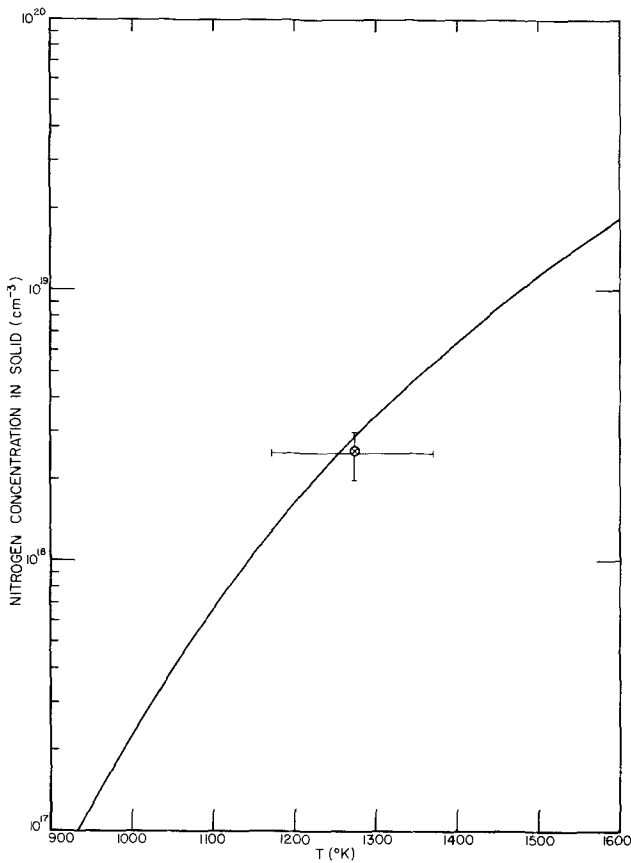


Fig. 2. Solid solubility of N in GaP vs. T . The solid line was calculated as described in the text. The data are taken from Logan *et al.* (4) (\leftarrow) and Lorimer and Dawson (5, 6) (\otimes).

be mentioned that a comparison of their results with our calculated results assumes their NH_3 pressures to be equilibrium pressures, which would be the case if the NH_3 did not decompose. Thurmond and Logan (6) report negligible decomposition if the NH_3 contacts only clean fused SiO_2 and graphite while it is at high temperatures. However, they found that devitrified SiO_2 furnace tubes catalyzed the decomposition of NH_3 . In that case the NH_3 pressure required to produce a given N concentration in the solid would be larger.

Also included in Fig. 1 is the solubility limit of N in GaP, which makes the N concentration independent of P_{NH_3} above a given pressure at each temperature. At the solubility limit, N-saturated GaP is in equilibrium with P-saturated GaN. The solubility limit was calculated by equating the chemical potential of GaN

in the two solid phases

$$\mu_{\text{GaN}}^{(\text{I})} = \mu_{\text{GaN}}^{(\text{II})} \quad [15]$$

where the superscripts I and II represent the GaP- and GaN-rich solid phases respectively. Since the standard state is the same for both phases and $\mu = \mu_0 + RT \ln a$

$$x\gamma_{\text{GaN}} = a_{\text{GaN}}^{(\text{II})} \cong 1 \quad [16]$$

assuming that the GaN-rich phase is nearly pure GaN. Thus the temperature dependence of the solid solubility of GaN in GaP may be written

$$x = \exp(-\bar{H}_{\text{GaN}}^*/RT) \quad [17]$$

Figure 2 is a plot of calculated N solubility vs. T . It includes estimates of the solid solubility at 1000°C, based on the data of Logan *et al.* (4) and Lorimer and Dawson (5, 6), which are in excellent agreement with the calculated curve.

The results of the calculations are useful for determining the conditions under which N can be incorporated into GaP crystals during LPE growth. In the experiments of Logan *et al.*, the efficiency of light emitting diodes increased with increasing N concentration up to the solubility limit. Since the calculations indicate that the solubility of N increases significantly with increasing temperature, they suggest that diodes with higher efficiencies might be obtained by LPE growth at temperatures above 1100°C.

Manuscript submitted March 3, 1972 revised manuscript received June 19, 1972.

Any discussion of this paper will appear in a Discussion Section to be published in the June 1973 JOURNAL.

REFERENCES

1. P. J. Dean, M. Gershenson, and G. Kaminsky, *J. Appl. Phys.*, **38**, 5332 (1967).
2. R. A. Logan, H. G. White, and W. Wiegmann, *Appl. Phys. Letters*, **13**, 139 (1968).
3. D. G. Thomas, *Brit. J. Appl. Phys. (J. Phys. D)*, **2**, 637 (1969).
4. R. A. Logan, H. G. White, and W. Wiegmann, *Solid-State Electron.*, **14**, 55 (1971).
5. O. G. Lorimer and L. R. Dawson, *This Journal*, **118**, 292C (1971).
6. C. D. Thurmond and R. A. Logan, *ibid.*, **119**, 622 (1972).
7. E. C. Lightowers, *J. Electron. Mat.*, **1**, 39 (1972).
8. J. A. Van Vechten, *Phys. Rev.*, **187**, 1007 (1969).
9. J. C. Phillips and J. A. Van Vechten, *ibid.*, **B2**, 2147 (1970).
10. K. K. Kelley, Bulletin 605, Bureau of Mines (1963).
11. G. B. Stringfellow, *J. Phys. Chem. Solids*, **33**, 665 (1972).
12. M. Cardona, K. L. Shaklee, and F. H. Pollak, *Phys. Rev.*, **154**, 696 (1967).
13. J. A. Van Vechten and T. K. Bergstresser, *ibid.*, **B1**, 3351 (1970).

Preparation of X-Ray Sensitive Monoclinic $\text{BaYb}_2\text{F}_8:\text{Er}$ Upconversion Phosphor

Lyuji Ozawa*

Zenith Radio Corporation, Chicago, Illinois 60639

It has been recently reported (1) that the upconversion efficiency for infrared to green light of monoclinic $\text{BaYb}_2\text{F}_8:\text{Er}$ markedly changes upon x-ray irradiation and that no x-ray sensitivity is found with other efficient upconversion phosphors. A screen of $\text{BaYb}_2\text{F}_8:\text{Er}$ has a possibility of being used as the screen of an inversion viewer of negative film and as the screen for nondestructive inspection by x-ray.

This brief communication describes the preparation of this x-ray sensitive monoclinic $\text{BaYb}_2\text{F}_8:\text{Er}$ upconversion phosphor. It was found that the x-ray sensitivity only occurred when the monoclinic $\text{BaYb}_2\text{F}_8:\text{Er}$ was prepared with BaCl_2 flux (which was coprecipitated with BaF_2 from BaCl_2 solution).

The phase diagram of the Ba-Yb fluorides is given by Zhigarnovskii and Ippolitov (2) who characterized monoclinic BaYb_2F_8 . The samples prepared were examined by x-ray diffraction analysis to make sure the crystal forms. Our experimental results, however, indicated that the firing of the proper mixture of BaF_2 and YbF_3 at 950°C in nitrogen atmosphere always resulted in a mixture of crystals, predominantly of cubic phase. The same results (mainly cubic crystals) were obtained even after firing was repeated several times with hard grinding between the refirings. However, an addition of 20-30 weight per cent (w/o) BaCl_2 to the BaF_2 resulted in monoclinic BaYb_2F_8 crystal.

Alternatively, the BaF_2 , which was precipitated from BaCl_2 solution with an addition of HF solution, usually contained about 30 w/o BaCl_2 by chemical determination. This coprecipitated BaF_2 and BaCl_2 mixture was preferable in making the x-ray sensitive monoclinic $\text{BaYb}_2\text{F}_8:\text{Er}$ upconversion phosphor.

The most efficient and x-ray sensitive upconversion phosphor was obtained as follows: the mixture of BaF_2 precipitated from BaCl_2 solution and of $(\text{Yb},\text{Er})\text{F}_3$, mixing ratio one-to-one, was fired at 950°C for 2 hr in an oxygen-free nitrogen atmosphere. The fired sample was washed with deionized water to remove the excess BaCl_2 . The sample was dried at 105°C and then the x-ray sensitive monoclinic $\text{BaYb}_2\text{F}_8:\text{Er}$ upconversion phosphor was obtained. Chemical determination indicated that the amount of chlorine in the $\text{BaYb}_2\text{F}_8:\text{Er}$ washed was less than 1 w/o. The upconversion efficiency of monoclinic phosphor obtained was comparable to that of cubic $\text{Ba}(\text{Y},\text{Yb},\text{Er})\text{F}_5$ phosphor which had been reported as ten times more efficient than the

* Electrochemical Society Active Member.

Key words: upconversion phosphor, x-ray sensitive, $\text{BaYb}_2\text{F}_8:\text{Er}$.

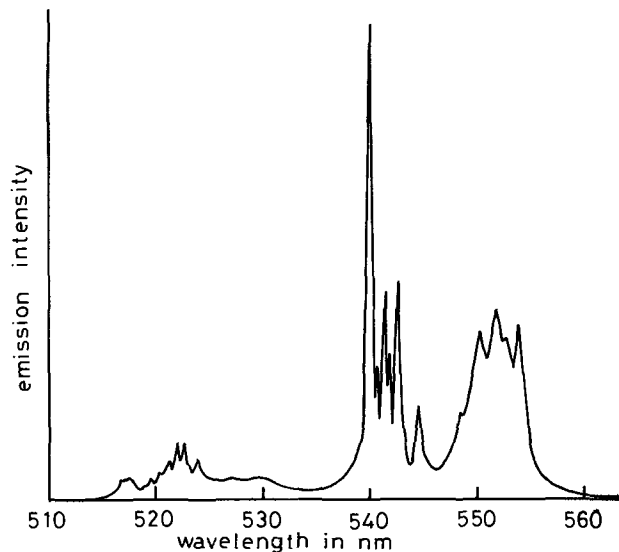


Fig. 1. Luminescent spectrum in green color region of monoclinic $\text{BaYb}_2\text{F}_8:\text{Er}$ phosphor under infrared excitation.

monoclinic phosphor (3). Monoclinic $\text{BaYb}_2\text{F}_8:\text{Er}$ upconversion phosphor was also prepared with other chloride fluxes (such as NH_4Cl), but the phosphor was not sensitive to x-ray irradiation and did not have high efficiency.

The luminescent spectrum in the green color region of monoclinic $\text{BaYb}_2\text{F}_8:\text{Er}$ phosphor under the infrared excitation is shown in Fig. 1. All of the luminescent lines indicated in the figure were identified as transitions from $^4\text{S}_{3/2}$ to $^4\text{I}_{15/2}$.

Manuscript submitted June 16, 1972; revised manuscript received Aug. 4, 1972.

Any discussion of this paper will appear in Discussion Section to be published in the June 1973 JOURNAL.

REFERENCES

1. G. Ban and H. N. Hersh, 1971 Technical Conference on Recent Advances in Electronic Materials, The Metallurgical Society of AIME, 1971, To be published.
2. B. M. Zhigarnovskii and E. G. Ippolitov, *Neorgan. Mater.*, **6**, 1182 (1970).
3. M. Tomkus and S. Natansohn, Paper 53 presented at Electrochem. Soc. Meeting, Washington, D. C., May 9-13, 1971.

DISCUSSION SECTION



This Discussion Section includes discussion of papers appearing in the *Journal of the Electrochemical Society*, Vol. 118, No. 10; October 1971; and Vol. 119, No. 1; January 1972.

Preparation of Beta-Rhombohedral Boron Whiskers

I. Ahmad and W. J. Heffernan (pp. 1670-1675, Vol. 118, No. 10)

K. Ploog:¹ The purpose of this note is to indicate, that it is impossible to prepare whiskers of tetragonal boron, $B_{48}B_2$, in a pure form, because this cited boron modification investigated by Hoard *et al.*² is not a true polymorph of pure elementary boron.

In our investigations we found³ that the II-tetragonal boron, B_{192} , ($a = 10.12\text{\AA}$, $c = 14.14\text{\AA}$, $d = 2.36$ g/ml, space group: $P4_122$, structure as yet unknown) is the only boron modification formed by the reduction of BBr_3 and BCl_3 with hydrogen at 950° - 1400°C on an inert substrate. On the other hand we have now developed a new method to produce the tetragonal lattice of $B_{48}B_2$ in a reproducible manner by preparing a tetragonal boron carbide of composition $B_{48}B_2C_2$ and a tetragonal boron nitride of composition $B_{48}B_2N_2$.⁴ In these tetragonal B-C and B-N phases (space group: $P4_2/nm$) the unstable lattice $B_{48}B_2$ is stabilized by C- resp. N-atoms, which occupy holes in the tetragonal icosahedral framework.

The authors report that especially on graphite leads whiskers of tetragonal boron, $B_{48}B_2$, are formed. I suggest that the formation of this boron "modification" in the reported experiments is induced in the following way: the deposited boron picks up some carbon from the substrate and reacts on the surface, resulting in the nucleation and growth of whiskers, which actually are tetragonal boron carbide and not pure tetragonal boron. A decision between $B_{48}B_2$ and $B_{48}B_2C_2$ only by x-ray diffraction methods is difficult, but it is easily accomplished by determining the density of the material and by analyzing the carbon content.

Activity Coefficients for a Regular Multicomponent Solution

A. S. Jordan (pp. 123-124, Vol. 119, No. 1)

K. Yoshida⁵ and **E. W. Dewing**:⁶ Jordan has given the activity coefficient for a regular multicomponent solution in the form

$$RT \ln \gamma_i = \sum_{\substack{j=1 \\ i \neq j}}^m \alpha_{ij} x_j^2 + \sum_{\substack{k=1 \\ k < j, i \neq k, i \neq j}}^m \sum_{j=1}^m x_k x_j (\alpha_{ij} + \alpha_{ik} - \alpha_{kj}) \quad [1]$$

(his Eq. [8]). This is inconvenient since the coefficients α_{ij} and α_{ik} in the second summation also appear as α_{ij} in the first. Part of the second sum can be replaced by

$$\sum_{\substack{k=1 \\ k < j, i \neq k, i \neq j}}^m \sum_{j=1}^m x_k x_j (\alpha_{ij} + \alpha_{ik}) = \sum_{\substack{j=1 \\ i \neq j}}^m x_j \alpha_{ij} \sum_{\substack{k=1 \\ k \neq j, k \neq i}}^m x_k \quad [2]$$

¹ K. Ploog, Mineralogisches Institut der Universität, Abt. f. Kristallstrukturlehre und Neutronenbeugung, D 53 Bonn, Poppelsdorfer Schloss (BRD).

² J. L. Hoard, R. E. Hughes, and D. E. Sands, *J. Am. Chem. Soc.*, **80**, 4507 (1958).

³ E. Amberger and K. Ploog, *J. Less-Common Metals*, **23**, 21 (1971).

⁴ K. Ploog, H. Schmidt, E. Amberger, K. H. Kossobutzki, and G. Will, *ibid.*, **29**, 161 (1972).

⁵ Nippon Light Metal Research Laboratory Ltd., Kambara, Shizuoka, Japan.

⁶ Alcan Research Laboratory, Arvida, Que., Canada.

since

$$\sum_{\substack{k=1 \\ k < j, i \neq k, i \neq j}}^m \sum_{j=1}^m x_k x_j \alpha_{ik} = \sum_{\substack{k=1 \\ k > j, i \neq k, i \neq j}}^m \sum_{j=1}^m x_j x_k \alpha_{ij} \quad [3]$$

by interchanging j and k .

Combining Eq. [2] with [1] yields

$$RT \ln \gamma_i = \sum_{\substack{j=1 \\ i \neq j}}^m \alpha_{ij} x_j (1 - x_j) - \sum_{\substack{k=1 \\ k < j, i \neq k, i \neq j}}^m \sum_{j=1}^m \alpha_{kj} x_k x_j \quad [4]$$

since

$$\sum_{\substack{k=1 \\ k \neq j, i \neq k}}^m x_k + x_j = 1 - x_i \quad [5]$$

Each coefficient now only appears once. For $m = 4$ and $i = 1$, for example

$$RT \ln \gamma_1 = \alpha_{12} x_2 (1 - x_1) + \alpha_{13} x_3 (1 - x_1) + \alpha_{14} x_4 (1 - x_1) - \alpha_{23} x_2 x_3 - \alpha_{24} x_2 x_4 - \alpha_{34} x_3 x_4 \quad [6]$$

and it can readily be verified by inspection of Jordan's Eq. [9] that the two are identical.

Equation [6] is inherently suitable for finding the coefficients α by linear regression analysis, whereas Jordan's equation is not. Furthermore, if experimental values are available for the activity coefficients of several components they can all be treated simultaneously in the same analysis.

A. S. Jordan: Yoshida and Dewing present the derivation of an alternative form to Eq. [8] (their Eq. [1]) of my paper concerned with the activity coefficients for a regular multicomponent solution. A careful reading of the paper under discussion reveals that the final result of Yoshida and Dewing (their Eq. [4]) was implicitly stated in the original work. To show this, I quote the following section from the paper

$$RT \ln \gamma_i = \sum_{\substack{j=1 \\ i \neq j}}^m \alpha_{ij} x_j - \frac{1}{2} \sum_{k=1}^m \sum_{\substack{j=1 \\ k \neq j}}^m \alpha_{kj} x_k x_j \quad [6]$$

By separating the quadratic terms present in Eq. [6], a more convenient expression for $\ln \gamma_i$ can be derived. Let us exclude the terms from the double sum in Eq. [6] for which $k = i$ and $j = i$ and absorb the resulting single sum

$$-\frac{1}{2} \sum_{\substack{j=1 \\ i \neq j}}^m \alpha_{ij} x_i x_j - \frac{1}{2} \sum_{\substack{k=1 \\ i \neq k}}^m \alpha_{ki} x_k x_i = - \sum_{\substack{j=1 \\ i \neq j}}^m \alpha_{ij} x_i x_j$$

in the single sum in Eq. [6].

For the sake of brevity, this indicated substitution leading to my Eq. [7] was not explicitly given in the printed text, but the operation yields

$$RT \ln \gamma_i = \sum_{\substack{j=1 \\ i \neq j}}^m \alpha_{ij} x_j (1 - x_i) - \frac{1}{2} \sum_{k=1}^m \sum_{\substack{j=1 \\ k \neq j, i \neq k, i \neq j}}^m \alpha_{kj} x_k x_j \quad [6.5]$$

which is identical with Eq. [4] of Yoshida and Dewing apart from a notational difference (1/2 of the double sum and $k \neq j$ being equivalent to the whole sum and $k < j$). It should also be noted that the derivation of

Yoshida and Dewing's Eq. [4] from my Eq. [8] is a reversal of my procedure to obtain Eq. [8] from Eq. [6.5].

My aim in presenting Eq. [8] instead of Eq. [6, 5] as the final result is to some extent a matter of esthetic preference. Certainly, the quadratic (in composition) representation explicit in Eq. [8] is very much in accord with the previously published forms of activity coefficients for regular binary and ternary solutions.

Moreover, a rapid straightforward generation of activity coefficients for a regular solution of any number of components can be realized from my Eq. [8].

However, I agree with Yoshida and Dewing that grouping terms with the same α_{ij} 's is the practical way to treat problems by linear regression analysis. Nevertheless, to obtain for a quaternary solution their Eq. [6] from my Eq. [9] which is given in a quadratic form requires only elementary algebraic manipulations.